Talanta 80 (2009) 1–7

Contents lists available at ScienceDirect

Talanta

journal homepage: www.elsevier.com/locate/talanta

Review

Optimization by the simplex method of the separation of phenolic acids by high-performance liquid chromatography in wastewater olive and sugar beet vinasse

S. Bostyn*, B. Cagnon, H. Fauduet

Laboratoire de Génie des Procédés pour l'Environnement, l'Energie et la Santé (GP2ES-EA21), Institut Universitaire de Technologie, Université d'Orléans, Rue d'Issoudun, BP 16729, 45067 Orléans Cedex 2, France

ARTICLE INFO

Article history:
Received 25 September 2008
Received in revised form 10 June 2009
Accepted 15 June 2009
Available online 24 June 2009

Keywords:
Optimization
Phenolic acids
Simplex
Chromatographic Response Function
Wastewater olive oil (WWOO)
Sugar beet vinasse

ABSTRACT

Optimization of a high-performance liquid chromatography separation has been developed for nine polyphenols by application of the simplex method. The nine polyphenols selected were mainly phenolic acids that can be present in wastewater and they can be removed by adsorption on activated carbon and resins. After the organic solvent (MeOH) had been chosen, a linear gradient in three stages and the furnace temperature were retained as parameters of optimization. The optimal conditions were determined by the super modified simplex and, in order to measure them a Chromatographic Response Function (CRF) was chosen. With the optimal conditions, the time of analysis was decreased from 69 to 40 min. The validation of the method was made on wastewater olive oil (WWOO) and sugar beet vinasse.

© 2009 Elsevier B.V. All rights reserved.

Contents

1. Introduction 1
2. Experimental 2
   2.1. Reagents and standards 2
   2.2. Liquid–liquid extraction 3
   2.3. Saponification 3
   2.4. Apparatus 3
   2.5. Simplex method 3
3. Results and discussion 3
   3.1. Control variables selected and initial simplex 3
   3.2. Chromatographic Response Function 4
   3.3. Optimization of chromatographic conditions 4
   3.4. Calibration 5
   3.5. Application to natural samples 6
4. Conclusion 7
   References 7

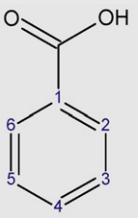
1. Introduction

Polyphenols are valuable natural compounds on account of their antioxidant properties and bactericidal effects, and they contribute to the flavour, colour, astringency and bitterness of beverages like wine, beer, fruit juice. These compounds can be divided into different fractions according to either polarity or molecular weight. The polar fraction is constituted by phenolic acids like 4-hydroxybenzoic acid and hydroxycinnamic acid. These phenolic acid compounds are present in wastewater coming from agro industrial activities related to the manufacturing of olive oil, vinasse, wine, spirits, etc. [1–3]. It is known that phenolic compounds are

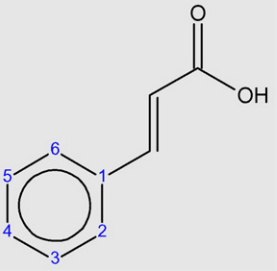
* Corresponding author. Tel.: +33 2 38494437; fax: +33 2 38494425.
E-mail address: stephane.bostyn@univ-orleans.fr (S. Bostyn).

0039-9140/$ – see front matter © 2009 Elsevier B.V. All rights reserved.
doi:10.1016/j.talanta.2009.06.040

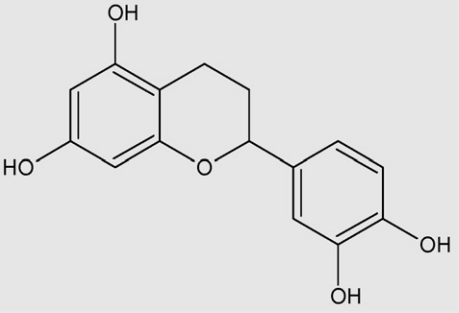
Table 1
Chemical structures of the polyphenols studied.



Benzoic acids: 4-hydroxybenzoic acid, gallic acid (3,4,5-trihydroxybenzoic acid), anisic acid (4-methoxybenzoic acid), syringic acid (4-hydroxy 3,5-methoxybenzoic acid)



Cinnamic acids: p-coumaric acid (4-hydroxycinnamic acid), caffeic acid (3,4-dihydroxycinnamic acid), ferulic acid (3-methoxy 4-hydroxycinnamic acid), synapic acid (3,5-methoxy 4-hydroxycinnaminic acid)



Catechins: (+)-catechin

major contributors to the toxicity and antibacterial activity of olive mill wastewater [4]. Consequently for a safe dispersal of the latter, a suitable treatment is recommended to remove those compounds. The most frequently used method is activated carbon adsorption [5,6]. With in the aim to optimizing such an operation, it is therefore necessary to analyse these compounds in a mixture.

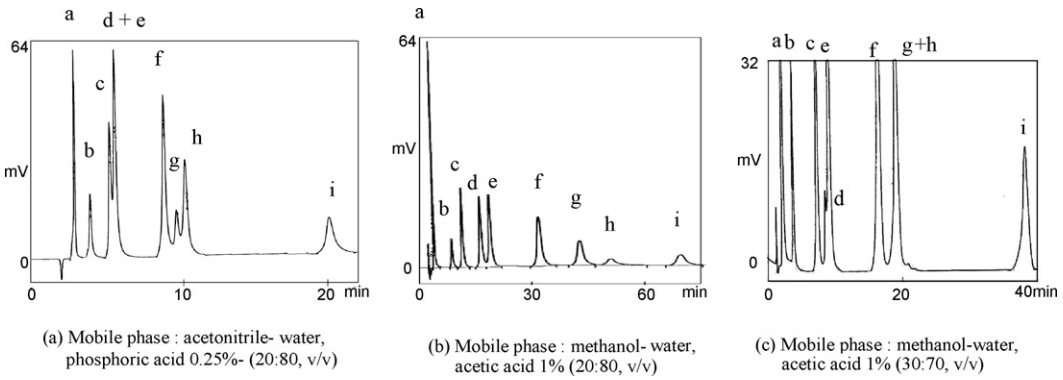
They are usually identified by high pressure liquid chromatography with an ultraviolet detection. In the literature, the analytical column used is generally a C_{18} [1,7], and the detection is commonly made by UV at 280 nm [8] or with a wavelength program [9] by photodiode array detection [1,10] and/or by fluorescence detection [7]. Generally, the column is at room temperature but some analyses can be run at 40 °C. The flow of the mobile phase is around 1 mL min^{-1} and the elution condition uses a gradient condition with two mobile phases. In each case, these phases are acidified by the addition of phosphoric acid, sulfuric acid or acetic acid with an average concentration of 1% in water. In the paper of Tsao and Yang [8], pH conditions were optimized with acetic acid solution and sodium acetate with a final pH at 2.55. Several types of mobile phases were used but the organic solvent is usually methanol or acetonitrile used with or without water. Thus, the aim of the work reported in this paper was to optimize the separation of phenolic acid mixtures by HPLC to envisage the study of the co-adsorption on such an adsorbent material as activated carbon. To this purpose six common phenolic acids were selected: 4-hydroxybenzoic acid, gallic acid, p-coumaric acid, caffeic acid, ferulic acid, synapic acid and two other less usual compounds: anisic and syringic acids (Table 1). Thanks to their functional groups, the two last may be useful for interpreting the interactions between molecule and adsorbent. In addition, catechin was also chosen in order to have a molecule with a more important molar volume.

To carry out this optimization, a simplex method was used. Simplex methods are evolutionary operation techniques in which a series of experiments is set up in such a way that the reaction conditions for a given experiment are dictated by the results of the preceding experiments in the series [11,12]. To set up this method, the Chromatographic Response Function (CRF) was defined in order to quantify the improvement of the analytical system. Moreover, the parameters retained for optimization were: column temperature and three parameters for defining the linear gradient in three stages. These three parameters are: (i) the value of the initial percentage of organic solvent, (ii) the time that corresponds to the first stage or to the isocratic mode and (iii) the value of the gradient slope. Besides, the organic solvent selected was methanol and the upper percentage of methanol during the gradient was set at 30%. The aim of the optimization was to obtain a 45 min analysis time around and a resolution superior or equal to two between the different compounds. The optimized method was applied on natural residues: wastewater olive oil (WWOO) and sugar beet vinasse.

2. Experimental

2.1. Reagents and standards

The caffeic acid and syringic acid were purchased from Sigma (St. Quentin Fallavier, France), the anisic acid and 4-hydroxybenzoic



(a) Mobile phase : acetonitrile- water, phosphoric acid 0.25%- (20:80, v/v)

(b) Mobile phase : methanol- water, acetic acid 1% (20:80, v/v)

(c) Mobile phase : methanol-water, acetic acid 1% (30:70, v/v)

Fig. 1. Selection of organic solvent in isocratic mode—flow rate at 1 mL min^{-1} and column temperature = 25 °C. HPLC–UV chromatogram for a nine polyphenolic mixture standard solution (10 mg L^{-1}). Peaks: (a) gallic acid, (b) catechin, (c) 4-hydroxybenzoic acid, (d) caffeic acid, (e) syringic acid, (f) p-coumaric acid, (g) ferulic acid, (h) synapic acid and (i) anisic acid.

acid from Aldrich (St. Quentin Fallavier, France), the gallic acid synapic acid and (+)-catechin hydrate from Fluka (Buchs, Switzerland) and the p-coumaric acid and ferulic acid from Extrasynthèse (Genay, France). The solvents for liquid chromatography, i.e. methanol, acetonitrile and acetic acid, were purchased from Carlo Erba (Rueil–Malmaison, France). The individual standards were dissolved in water to obtain a stock solution of 100 mg L^{-1} for each compound. These solutions were stored in the dark in the fridge at 4 °C for 1 week to take account of their degradations especially those of the 4-hydroxybenzoic and gallic acids. The individual standard solutions injected to determine the individual retention time were prepared by dilution from the stock solutions. The standard mixture solution was prepared with 0.150 mg of each compound into 100 mL volumetric flask with water and was used for adequate dilution with water.

The vinasse sample was sugar beet vinasse obtained from the ethanol production of a sugar refinery (La Vermandoise, Toury, France) and stored in 1000 mL glass dark containers at 4 °C. WWOO was obtained from a continuous three-phases process (le Moulin à huile Jullien, Saint Saturnin les Apt, France) and stored at −20 °C in 2000 mL low density polypropylene containers. The samples were diluted with water to 50% (w/w) and 8 g were used for the liquid–liquid extraction.

2.2. Liquid–liquid extraction

Due to the natural matrices of WWOO and vinasse, a liquid–liquid extraction was used to facilitate the analyses. For extraction, previously several solvents were tried [13]: ethyl acetate, diethyl ether, trichloromethane. For determining the percent of recovery, the extraction was made with 10 mL of standard mixture adjusted to pH 4 with 10% HCl solution in weight and with the studied solvent (3 × 20 mL). The time of agitation was 15 min for each stage. The organic phase was evaporated off on a Rotavapor. The residue was dissolved in 3 mL of methanol, filtered (0.45 μm, Bioblock France) and analysed by HPLC. The aqueous phase was analysed by HPLC.

2.3. Saponification

To the aim to liberate free ferulic acid from vinasse, a saponification was realized. 100 g of vinasse were added to 400 mL of 4 M NaOH solution at 80 °C for 5 h. A sample of 15 mL was removed and the pH was adjusted at 4 by the addition of an aqueous solution of HCl (10% in weight). Finally, 8 g of this adjusted solution were used for the liquid–liquid extraction.

2.4. Apparatus

The HPLC analyses were carried out using a Varian pump (model Prostar), a TSP® membrane degazer, a Varian autosampler injector (model 400 Prostar), a CROCO-CIL thermostated oven, a Thermo Separation Products multiwave UV detector (model spectra-system UV 2000) and two Shimadzu integrators (model C-R5A). The analytical column (250 mm × 4.6 mm i.d.) used was a LichroCART 250-4 HPLC-Cartridge with a LiChrospher100 RP-18 (5 μm) equipped with a guard column from Merck (Darmstadt, Germany). For HPLC analysis, an aliquot (10 μL) was injected into the column. Wavelengths of λ = 280 nm and λ = 320 nm were used for the absorbance detector. The wavelength of 320 nm is specific to the cinnamic acids.

During the optimization, the elution conditions varied with each experiment but the nature of the mobile phase remained constant and was constituted with acid water (1% acetic acid) and methanol. The flow rate of the solvent was kept at 1 mL min^{-1}.

2.5. Simplex method

The simplex method is an evolutive method that removes the worst experiment from an initial simplex by a new one in the opposite direction. The process goes on until the optimum conditions are reached. The advantage of this kind of evaluative system is to enable the evolution of the simplex with knowledge gained from experiments, especially when data on the system to be optimized are scarce. The design of experiments, in contrast, requires previous knowledge of the system in order to obtain the optimal response within the experimental domain.

3. Results and discussion

3.1. Control variables selected and initial simplex

The literature analysis showed that a gradient was used in all cases to increase the concentration of the organic solvent (methanol or acetonitrile). Therefore, some preliminary experiments were made with each organic solvent in order to determine the elution strength. The experiments conditions, their results and corresponding chromatograms are reported in Fig. 1. This figure shows that acetonitrile is more eluent than methanol. The retention time of the last compound (anisic acid) was equal to 20.2 min with acetonitrile but the resolution needed to be improve to obtain a better separation of compounds (Fig. 1a). For the same methanol concentration, the anisic retention time was equal to 69.3 min (Fig. 1b) but all the resolutions were superior to 1.5. Increasing the methanol percentage to 30% allowed to decrease the anisic retention time to 37.8 min (Fig. 1c) but no separation was observed between the caffeic and

Table 2
Initial simplex in reduced coordinates and in real coordinates.

Experiment number	Reduced coordinate matrix				Real coordinate matrix			
	$X_{i,1}$	$X_{i,2}$	$X_{i,3}$	$X_{i,4}$	MeOH (%)	t_i (min)	Slope (% min^{-1})	T (°C)
0	0	0	0	0	15	18.0	0.68	25
1	1	0	0	0	18	18.0	0.68	25
2	0.5	0.866	0	0	17	21.1	0.68	25
3	0.5	0.289	0.791	0	17	19.0	0.79	25
4	0.5	0.289	0.158	0.775	17	19.0	0.71	29

syringic acids first nor between the ferulic and synapic acids. In view of these results, methanol was selected as the organic solvent and a gradient had to be implemented. To achieve this gradient, several control variables were selected: the initial value of the organic solvent (noted A), the time of the isocratic mode t_i (noted B), and the gradient slope (noted C). Besides, the gradient was stopped when the percentage of organic solvent reached 30% which permitted to have sufficient eluent strength and to decrease the time of equilibration before each following injection. In fact, 6 min were required to return to the initial conditions and 5 min of equilibration were necessary before the next injection. Finally, the last control variable selected for the optimization was the column temperature (noted D).

For these four variables, the reference values had to be defined. In the case of variable A (% MeOH), the reference value taken was 15%. The time of the isocratic mode was selected at 18 min (variable B) because, as Fig. 1b shows, a first group with five polyphenols exhibits resolutions up to 1.5. The last compound of this group is syringic acid with a retention time equal to 18.7 min. Then p-coumaric acid was eluted with a retention time equal to 31.8 min. Therefore, an interval of 13 min exists between the compounds and needs to be reduced by the action of a gradient. The reference value of the gradient slope was equal to 0.68% min^{-1} (C) and finally a 25 °C column temperature was selected. Then the first experiment (number 0 in Table 2) was made with 15% of MeOH during 18 min and then a gradient of 0.68% min^{-1} was performed up to 30% of MeOH with a column temperature at 25 °C and a flow rate at 1 mL min^{-1}. The other experiments of the initial simplex had to be built according to the type of method chosen. In our case, Czech's method [14] chosen whose matrix is represented in Table 2. If a new control variable is added, this method allows keeping the experiments already completed for building the initial simplex.

The value of the real coordinate of each parameter for each experiment was obtained by the following relation:

$$x_{i,j} = x_{0,j} + X_{i,j} \times \Delta_{xj} \quad (1)$$

where i corresponds to the simplex points from 0 to k, j corresponds to the variable from 1 to k, $x_{0,j}$ is the real coordinate for the variable j at the center of the domain studied, $X_{i,j}$ corresponds to the reduced coordinate for the variable j at the point i, and Δ_{xj} corresponds to the step size for the variable j. Moreover, the step size (Δ_{xj}) of each variable was chosen with 20% of variation related to the value at the center of each control variable. The step sizes and the values of the domain center are reported in Table 3 for each variable. For the evolution of the simplex, the modified simplex method was used [15,16]. This method is also called variable-size simplex method and allows expanding or contracting the simplex size by adjusting the step size during the progress of the improvement. The calculation of the coordinate of the new point was based on the following equation:

$$X_{r,j} = X_{g,j} + \alpha(X_{g,j} - X_{w,j}) \quad (2)$$

where $X_{r,j}$ is the reduced coordinate of the new point for the variable j, $X_{g,j}$ is the centroid of the remaining face/hyperface (i.e. the average levels for the remaining trials), $X_{w,j}$ is the rejected trial and α is a coefficient either of expansion or contraction. Therefore, this method allows not to be "too precise" in the choice of the initial step sizes that are sometimes difficult to define due to the lack of experiments in the beginning of the study.

Table 3
The control variables values at the center of the domain and their step sizes.

Control variable	Value of the domain center	Step size	Unit
$x_{0,1}$ (MeOH)	15	3	%
$x_{0,2}$ (t_i)	18	3.6	min
$x_{0,3}$ (gradient slope)	0.68	0.136	% min^{-1}
$x_{0,4}$ (temperature)	25	5	°C

3.2. Chromatographic Response Function

Moreover for measuring the quality of the separation, a response had to be chosen. We opted for the Chromatographic Response Function (CRF) [17–19]. The CRF is described with the following equation:

$$\mathrm{CRF} = \sum_{i=1}^{p-1} R_i + aP + b(t_M - t_L) \quad (3)$$

where R_i is the resolution between adjacent peak pairs, P is the number of peaks detected, t_M is the target retention time in minutes, t_L is the retention time for the last peak, and a and b are two arbitrary weighting factors. In our case, a is equal to 1 and b to 0.5. The term $(t_M - t_L)$ is negative if t_L is superior to t_M, which allows to decrease the CRF when the conditions are not favourable. Moreover under the initial conditions, the study started with a retention time for the last compound superior to the target retention time. Before starting, the optimal values of CRF had to be defined for determining the stopping point of the simplex evolution. Thus in this case, the detection of each of the nine polyphenols on the chromatogram had to be achieved with a resolution superior or equal to 2 for their quantifications and with an analysis time at most equal to 45 min. Therefore, the optimum response could be calculated with (i) $\sum_{i=1}^{p-1} R_i = (9-1) \times 2$, (ii) $P = 9$ and (iii) $0.5 \times (t_M - t_L) = 0$, so its value was 25. Besides, if the values of R_i were superior to 2 then the value 2 was attributed to R_i when inferior they kept the calculated value.

3.3. Optimization of chromatographic conditions

The parameters and results of each experiment have been reported in Table 4. This table shows the value of $\sum_{i=1}^{p-1} R_i$, maximum retention time (t_L), CRF and number of simplex with the best point (b) and the worst point (w). In the case of the initial simplex (1) experiments, the best point corresponds to experiment 4 and the worst to experiment 0. The CRF value of experiment 4 is already near the value of optimum CRF (24.49 instead of 25).

Experiment 5 is a reflection of experiment 0 with $\alpha = 1$. This point is the best of simplex 2. So to continue in this direction, an expansion coefficient was calculated using the rules of the super modified

Table 4
Relation between the Chromatographic Response Function (CRF) and the experiment number during simplex optimization (*w* corresponds to the worst point of the simplex and *b* to the best point of the simplex).

Experiment number	MeOH (%)	t_i (min)	Gradient (% min^{-1})[a]	Temperature (°C)	Time of gradient (min)	$\sum_i R_i$	t_L (min)	CRF	Number simplex					
									1	2	3	4	5	6
0	15	18.00	0.68	25	22.1	15.2	56.70	18.34	5 (w)					
1	18	18.00	0.68	25	17.6	16.0	50.70	22.08	2	3	4	5 (w)		
2	17	21.12	0.68	25	19.9	16.0	54.50	20.23	4	5 (w)				
3	17	19.04	0.79	25	17.1	16.0	52.57	21.21	3	4	5 (w)			
4	17	19.04	0.71	29	19.1	16.0	46.02	24.49	1 (b)	2	3	4	5 (w)	
5	19	20.60	0.75	27	15.0	16.0	44.02	25.42		1 (b)	2	3	4	5 (w)
6	18	17.22	0.78	28	14.8	16.0	43.87	25.56			1 (b)	2	3	4
7	19	18.39	0.67	29	16.0	16.0	42.27	26.36				1 (b)	2	3
8	18	19.63	0.78	32	14.9	16.0	40.80	27.10					1 (b)	2
9	21	19.00	0.78	29	11.6	15.3	31.16	28.51						1 (b)

[a] MeOH ending 30%.

simplex (SMS) that consists in resolving the following polynomial equation to obtain the optimum value:

$$Y = A\alpha^2 + B\alpha + C \quad (4)$$

with the points: *W* represented by the point 0, where $\alpha = 0$ and $Y = 18.34$; *G* centroid of the simplex 1, where $\alpha = 1$ and $Y = 22.00$; *R* represented by the point 5, where $\alpha = 2$ and $Y = 25.42$.

The value of the expansion coefficient was calculated and its value is 15.75. This expansion value is too high and so it was decided to progress with the normal rule of simplex with $\alpha = 1$.

Fig. 2 shows the evolutions of CRF, sum of resolutions and t_L in function of the experiment number. In the case of CRF, the optimum CRF value was reached for experiment 5 after only six experiments. However, it was decided to continue the evolution with a view to decreasing the value of t_L. For experiment 9, the sum of resolutions decreases under 16, this is due to a resolution inferior to 2 between firstly the caffeic and syringic acids, and secondly the ferulic and synapic acids. Therefore, the conditions of experiment 8 were retained as the optimum conditions for the analysis of the nine polyphenols as they gave a maximum retention time of 41 min. Fig. 3 shows a chromatogram obtained under these conditions and points out the good separation of the polyphenols.

Moreover, the results in Table 4 permit to analyse experiments for which only one or two parameters were modified. For example, a comparison can be made between experiments 0 and 1 where only the MeOH percentage changed. Experiment 0 had a weaker eluent strength, which increased the retention times and induced a peak widening showing a resolution inferior to experiment 1. In the same way, the influence of the gradient strength can be observed by the comparison of experiments 2 and 3. Experiment 3 reveals a normal increase in CRF due to a stronger gradient (faster starting time and stronger slope).

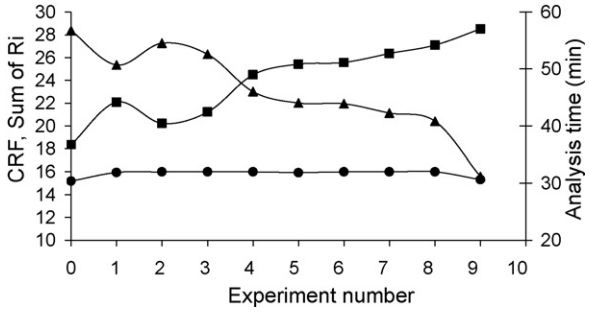


Fig. 2. Evolution of the Chromatographic Response Function (CRF) (■), retention time for the last peak (▲) and total resolution (●) as a function of the experiment number during simplex optimization.

For experiments 3 and 4, if CRF was only based on eluent strength, its value should be higher with experiment 3 (higher content in MeOH) than in experiment 4. In fact, the contrary was observed because it is assumed that the influence of temperature is greater than that of the eluent strength.

3.4. Calibration

With the view to quantify the content of phenolic compounds, the calibration graphs were expressed as chromatographic peak areas of standards corresponding to concentrations ranging from 5 to 30 mg L^{-1}. The linearity of the HPLC method was therefore checked by injecting five mixtures of standard solutions containing 5, 10, 15, 20, 30 mg L^{-1} of each polyphenol and each mixture was analysed five times. The linear range, coefficient of determination (R^2) and the limit of detection (LOD) for each compound

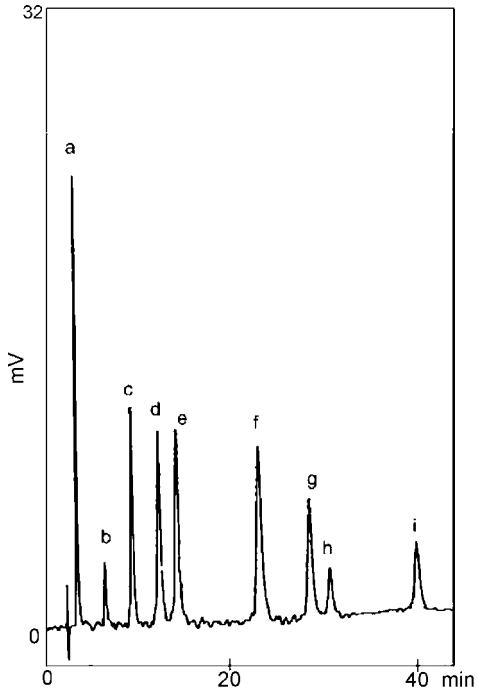


Fig. 3. Chromatogram obtained in optimal conditions: detection at 280 nm, flow rate 1 mL min^{-1}, three stages of linear gradient: started 18% of A during 19.63 min, from 19.63 to 30% in 14.9 min, and finally isocratic mode with 30% of A until the last compound was eluted (total running time of 41 min). Peaks: (a) gallic acid, (b) catechin, (c) 4-hydroxybenzoic acid, (d) caffeic acid, (e) syringic acid, (f) p-coumaric acid, (g) ferulic acid, (h) synapic acid and (i) anisic acid.

Table 5
Calibration range, correlation coefficients of the regression line, limit of detection for the polyphenols studied.

Polyphenol	Linear range (mg L^{-1})	R^2	LOD (3 S/N) (mg L^{-1})	R.S.D. (area, $n=5$)
Gallic acid	5–30	0.9998	0.1	3.00
Catechin	5–30	0.9995	1.4	2.94
4-Hydroxybenzoic acid	5–30	0.9999	0.5	2.00
Caffeic acid	5–30	0.9998	0.6	2.80
Syringic acid	5–30	0.9999	0.6	3.07
p-Coumaric acid	5–30	0.9996	0.3	2.68
Ferulic acid	5–30	0.9993	0.5	2.49
Synapic acid	5–30	0.9997	0.6	3.58
Anisic acid	5–30	0.9997	0.6	2.75

are listed in Table 5. All the R^2 were superior to 0.999. The LOD was defined as the concentration at which the signal to noise ratio (S/N) was equal or superior to three. Table 5 shows that each LOD was inferior to the minimum value of the standard concentration.

3.5. Application to natural samples

To quantify the phenolic carboxylic acids, a liquid–liquid extraction was applied and developed on a standard mixture solution of 150 ppm. To obtain the optimal recovery at pH 4, several solvents were chosen: ethyl acetate, diethyl ether, trichloromethane. With ethyl acetate, the totality of polyphenols was recovered and verified by the analysis of aqueous phase, which contains no polyphenols. Trichloromethane, a less polar solvent, induced a degradation of ferulic and synapic acids and a rate of recovery inferior to 6% for gallic, 4-hydroxybenzoic, caffeic acids and catechin. This result is consistent with the retention times of the last three polyphenols that reveal themselves as the most polar polyphenols. With diethyl ether, the rate of recovery is around 80% for gallic acid and catechin and 100% for the others. Therefore, it could be worth using trichloromethane in order to separate these polyphenols. A study at pH 10 (adjusted by NaOH) was carried out but degradation of catechin, gallic and cafeic acids were observed. Therefore, the conditions retained for the extraction are ethyl acetate at pH 4.

Fig. 4 represents the chromatogram obtained for WWOO at 280 and 320 nm. The flow rate was slightly decreased to 0.92 instead of 1 in order to compensate for the matrix effect. From the chromatogram at 280 nm, several compounds were expected to be found such as 4-hydroxybenzoic acid (tr = 11.9 min) and cinnamic acids like caffeic acid (tr = 17.1 min) or p-coumaric acid (tr = 31.0 min) and ferulic acid (tr = 36.2 min). At 320 nm, the wavelength is specific to cinnamic acids and gallic acid absorbs less. Therefore, from the comparison of the results for the two wavelengths, only caffeic, coumaric and ferulic acids were retained. Their quantifications are respectively 6 ± 2, 10 ± 2 ppm, and less than 5 ppm. These results show no p-hydroxybenzoic, syringic, gallic, sinapic acids in contradiction with the results of Zafra et al. [13]. But the concentration value depends on the process and transport conditions especially for these compounds that undergo degradation. These weak concentrations in real samples do not enable a recovery process of polyphenols with a view to valorising these compounds.

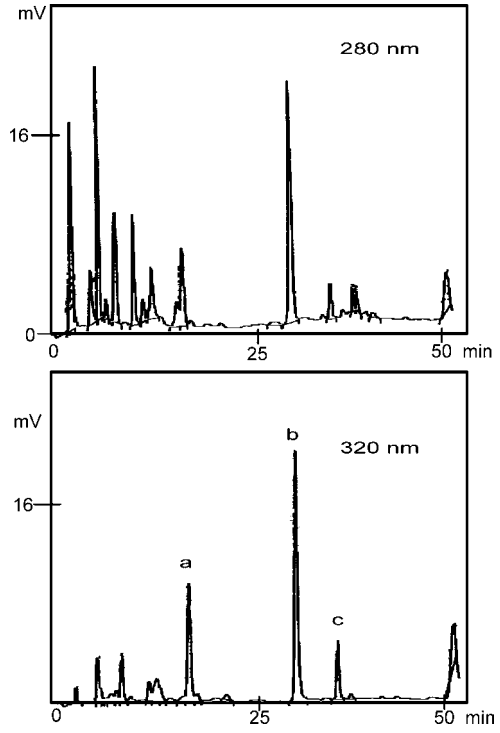


Fig. 4. Chromatogram of wastewater olive oil sample at 280 nm and at 320 nm: (a) caffeic acid, (b) p-coumaric acid, (c) ferulic acid.

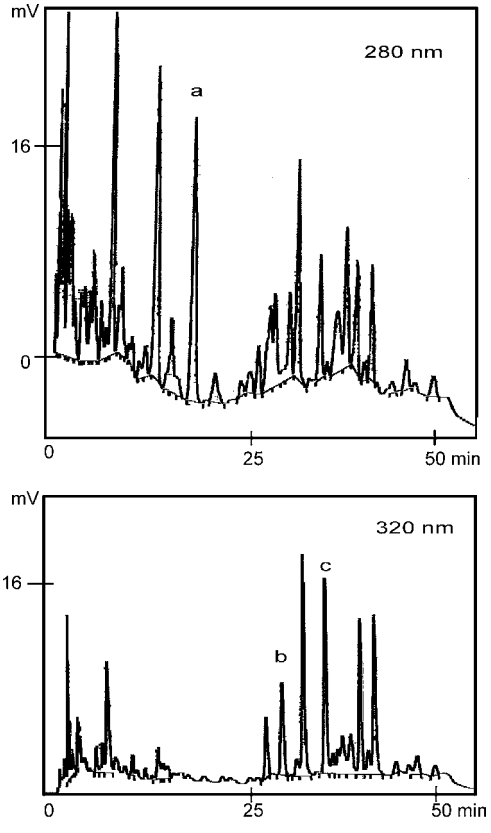


Fig. 5. Chromatogram of sugar beet vinasse at 280 nm (i) and at 320 nm (ii). (a) Syringic acid, (b) p-coumaric acid, (c) ferulic acid.

This method was also applied on sugar beet vinasse which is the last residue in the production of bioethanol. Fig. 5 represents the chromatogram at the two wavelengths obtained by adding 6 mL of MeOH into the organic residue. The latter, when compared with WWOO chromatogram, shows that more compounds are present in the organic phase. At 280 nm, the chromatogram eventually shows the presence of p-hydroxybenzoic, syringic, coumaric, ferulic and synapic acids. Only syringic acid (tr = 19.5 min) was well separated and its concentration was 56 ± 8 ppm. The chromatogram at 320 nm was used to determine 4 ± 2 ppm of coumaric acid and 12 ± 3 ppm of ferulic acid. Synapic acid was rejected because, at 320 nm, its area was inferior to the one obtained at 280 nm. p-Hydroxybenzoic was not quantified because of the bad resolution at 280 nm.

Ferulic acid could be under ferulates form as ferulate dehydrodimers [20]. Therefore a saponification was carried out with the aim to increase the quantity of free ferulic acid. This reaction lasted 5 h under the conditions described previously. It yielded a ferulic acid concentration of 71 ± 9 ppm. The result takes into account the degradation of ferulic acid during the reaction. The ratio of degradation was determined by applying the same process of saponification on a solution of ferulic acid (150 ppm).

4. Conclusion

The optimization of separation conditions was achieved using the simplex method on a mixture of nine common polyphenols. The maximum retention time targeted (45 min) was reached in only six experiments. The number of experiments obviously depends on the choice of: (i) the center of domain, (ii) the step size of factors variation and the objective.

Moreover, the method was applied on two natural samples: WWOO and vinasse in order to quantify the polyphenols selected. For WWOO, only caffeic, coumaric and ferulic were detected. For the vinasse, a saponification was carried out so as to increase the concentration of free ferulic acid. The result of saponification shows that the concentration of ferulic acid effectively increases from 12 ± 8 to 71 ± 8 ppm. The syringic acid concentration was 56 ± 8 ppm. In both cases, the quantities do not enable a recovery process to be developed with a view to valorising these compounds.

The results obtained with this method can be used to envisage the study of co-adsorption on adsorbent materials or on resin of these common polar phenolic compounds.

References

[1] M. Litridou, J. Linssen, H. Schols, M. Bergmans, M. Posthumus, M. Tsimidou, D. Boskou, J. Sci. Food Agric. 74 (1997) 169.
[2] J.F. García-Araya, F.J. Beltrán, P. Álvarez, F.J. Masa, Adsorption 9 (2003) 107.
[3] M.A. Martin Santos, J.L. Bonilla Venceslada, A. Martin Martin, I. Garcia Garcia, J. Chem. Technol. Biotechnol. 80 (2005) 433.
[4] I. Fki, N. Allouche, S. Sayadi, Food Chem. 93 (2005) 197.
[5] P. Galiatsatou, M. Metaxas, D. Arapoglou, V. Kasselouri-Rigopoulou, Waste Manage. 22 (2002) 803.
[6] V. Caqueret, S. Bostyn, B. Cagnon, H. Fauduet, Bioresour. Technol. 99 (2008) 5514.
[7] M.A. Rodríguez-Delgado, G. González-Hernández, J.E. Conde-González, J.P. Pérez Trujillo, Food Chem. 78 (2002) 523.
[8] R. Tsao, R. Yang, J. Chromatogr. A 1018 (2003) 29.
[9] A. Alonso-García, B. Cancho-Grande, J. Simal Gándara, J. Chromatogr. A 1054 (2004) 175.
[10] G. Shui, L.P. Leong, J. Chromatogr. A 977 (2002) 89.
[11] V. Caqueret, S. Bostyn, C. Porte, H. Fauduet, Chem. Eng. J. 145 (2008) 203.
[12] B. Purachat, S. Liawruangrath, P. Sooksamiti, S. Rattanaphani, D. Buddhasukh, Anal. Sci. 17 (2001) 443.
[13] A. Zafra, M.J.B. Juárez, R. Blanc, A. Navalón, J.L. González, Vílchez, Talanta 70 (2006) 213.
[14] F.P. Czech, J. Assoc. Offic. Anal. Chem. 56 (1973) 1489.
[15] C. Porte, Méthodes directes d'optimisation, Techniques de l'Ingénieur P228 (2002) 1.
[16] M.W. Routh, P.A. Swartz, M.B. Denton, Anal. Chem. 49 (1977) 1422.
[17] M.W. Watson, P.W. Carr, Anal. Chem. 51 (1979) 1835.
[18] S.M. Sultan, A.H. El-Mubarak, Talanta 43 (1996) 569.
[19] R. Karnka, M. Rayanakorn, S. Watanesk, Y. Vaneesorn, Anal. Sci. 6 (2002) 661.
[20] A. Oosterveld, J.H. Grabber, G. Beldman, J. Ralph, A.G.J. Voragen, Carbohydr. Res. 300 (1997) 179.

Talanta 80 (2009) 8–18

Contents lists available at ScienceDirect

Talanta

journal homepage: www.elsevier.com/locate/talanta

Review

Integration of electrochemistry in micro-total analysis systems for biochemical assays: Recent developments

Xiaoli Xu, Song Zhang, Hui Chen, Jilie Kong*

Department of Chemistry & Institutes of Biomedical Sciences, Fudan University, Handan Rd. 220#, Shanghai 200433, PR China

ARTICLE INFO

Article history:
Received 10 March 2009
Received in revised form 14 June 2009
Accepted 15 June 2009
Available online 24 June 2009

Keywords:
Micro-total analysis systems
Electrochemistry
Microelectrodes
Integration
Biochemical assays

ABSTRACT

Micro-total analysis systems (μTAS) integrate different analytical operations like sample preparation, separation and detection into a single microfabricated device. With the outstanding advantages of low cost, satisfactory analytical efficiency and flexibility in design, highly integrated and miniaturized devices from the concept of μTAS have gained widespread applications, especially in biochemical assays. Electrochemistry is shown to be quite compatible with microanalytical systems for biochemical assays, because of its attractive merits such as simplicity, rapidity, high sensitivity, reduced power consumption, and sample/reagent economy. This review presents recent developments in the integration of electrochemistry in microdevices for biochemical assays. Ingenious microelectrode design and fabrication methods, and versatility of electrochemical techniques are involved. Practical applications of such integrated microsystem in biochemical assays are focused on in situ analysis, point-of-care testing and portable devices. Electrochemical techniques are apparently suited to microsystems, since easy microfabrication of electrochemical elements and a high degree of integration with multi-analytical functions can be achieved at low cost. Such integrated microsystems will play an increasingly important role for analysis of small volume biochemical samples. Work is in progress toward new microdevice design and applications.
© 2009 Elsevier B.V. All rights reserved.

Contents

1. Introduction 8
2. Design and fabrication of microelectrodes 9
   2.1. Thin-film microelectrode fabrication technologies 9
   2.2. Thick-film microelectrode fabrication methods 10
3. Versatility of electrochemical techniques in microsystems 11
   3.1. Electrochemical detection methodology 11
   3.2. Electrical manipulation of fluids and biomaterials 12
   3.3. Electrochemical sensing for biochemical assays 14
4. Practical applications 15
5. Conclusions 16
   Acknowledgements 16
   References 16

1. Introduction

Since the proposal of the concept of micro-total analysis systems (μTAS) in 1989 [1], a great deal of research has been devoted to the miniaturization of biochemical analysis systems, and many types of microdevices with integration of multi-analytical functions have been developed [2]. Due to the unique advantages of microsize, low cost, ease of fabrication, flexibility in design and fast detection, miniaturized devices from this concept have continued to be a highly hot topic and gain maturity in the latest several years. These miniaturized devices have been applied in a variety of areas including immunoassays, biosensors, clinical diagnostics, environmental monitoring, biochemistry, proteomics and cell biology [3,4]. Used in biochemical assays, microdevices have been reported frequently to control the transportation, immobilization, and manipulation of biological molecules and cells, and to separate, mix, and dilute chemical reagents [5–8]. However, developing more rapid, reliable,

* Corresponding author. Tel.: +86 21 6564 2405; fax: +86 21 6564 1740.
E-mail address: jlkong@fudan.edu.cn (J. Kong).

0039-9140/$ – see front matter © 2009 Elsevier B.V. All rights reserved.
doi:10.1016/j.talanta.2009.06.039

cheap, specific and sensitive methods for biochemical assays, is still the focus of a great deal of research, especially for applications outside the laboratory environment.

Integration of electrochemistry in μTAS is a convenient way to realize multi-analytical functions in a single miniaturized device. Electrochemical techniques have merits of simplicity, rapidity, high sensitivity and specificity, reduced power requirements, ease of microfabrication and good compatibility with biological samples [9–12]. These characteristics make electrochemistry uniquely suitable for integration in miniaturized devices. When coupled with electrochemical techniques, microanalytical devices generally employ conducting elements as electrodes in electrochemical detection [13–15], as electrodes to manipulate liquids or biological materials in electrophoresis microchips [16,17], or as base layers for electrochemical sensing and hybridization sites [18,19]. As a result, it renders microelectrodes a key component to realize the versatility of electrochemical techniques in microanalytical devices. A variety of methods including sputtering [20], evaporation [21], lift-off lithography [22,23], and thick-film techniques [24,25], have been exploited to microfabricate different conducting elements, such as planar (2D) and three-dimensional (3D) microelectrodes, which have been widely used to investigate chemical and biological processes [26,27].

This review presents the recent development of integration of electrochemical elements in μTAS for biochemical assays. After this short introduction, ingenious microelectrode design and the fabrication methods are explored in the following part. Then, the versatility of electrochemical techniques for identifying of biochemical processes is also elaborated. Finally, the potential applications such as in situ analysis, point-of-care testing and portable analyzers for complex sample matrices, are introduced. Notably, in order to overcome drawbacks of conventional analytical procedures, which commonly involve the collection of a sample at one location and then a delay while the sample is sent to the lab and processed, we expect that this review can provide significant hints for researchers to develop new microdevices with integration of electrochemistry, which are able to be used for efficient real sample analysis. Moreover, diverse design and fabrication methods of microelectrodes are now available to conduct electrochemistry conveniently in microsystems, which paves the way well to realize practical applications in complex biosamples.

2. Design and fabrication of microelectrodes

As well known, micro-electro-mechanical system (MEMS) plays a very much important role in fabricating various miniaturized analytical devices in modern analytical chemistry. For the high sensitivity derived from the precisely controlled pattern, MEMS-processed microelectrodes have been employed in electrochemical biosensors, electronic tongues or electronic noses, and detectors of capillary electrophoresis [28–32]. Attention should be firstly paid to the diverse electrode configurations and the involved microfabrication technologies, since microelectrodes serve as an indispensable component on many microanalytical devices integrated with electrochemical elements. Thin-film and thick-film electrode fabrication technologies will be introduced as follows.

2.1. Thin-film microelectrode fabrication technologies

As thin-film microelectronic fabrication technologies, sputtering and evaporation are both commonly used. A thin (typical thickness between 50 and 250 nm) metal film is deposited in vacuum onto the substrate in such cases. In order to deposit metals at designate positions, a shadow mask is always needed which projects a geometrical pattern onto the substrate. This method has a resolution of the order of a few tens of micrometres. As for more precise electrodes, lithography and lift-off process can be employed, which involves photoresist and a further development step [18,22,33,34].

Gold and platinum are often used for thin film metallization. Microelectrodes made in this fashion can be integrated conveniently both in channel and at the end channel of microfluidic chips, and various electrode configurations can be realized with minimized analyte dilution and improved sensitivity for in situ or real-time analysis of biosamples, compared with conventional end-channel detection electrodes made of solid metal wires (Pt, Au and Cu). Kurita et al. [35] developed a microfluidic device encompassing a gold film working electrode modified with lactate oxidase and ospoly(vinylpyridine) mediator containing horseradish peroxide in the microchannel, and achieved quantitative and reproducible measurements of the lactate concentration in blood samples. Compact gold microelectrode array systems, displaying high throughput, enhanced sensing performance, significantly simplified operation procedures, and reduced fabrication costs, have also been reported for in situ monitoring of dopamine release from chip-grown MN9D cells and PC12 Cells [36–38]. Akiyama et al. [39] successfully integrated Pt/Ti thin film electrodes into a Pyrex glass microchip through a newly developed vacuum hot press system, which exhibited improved chip production rate. Castano-Alvarez et al. [40] described a combination of an in-channel thin-film detector and an end-channel detector employing films and metal wires (a 300 μm diameter platinum wire or 250 μm diameter gold wire) performing amperometry on CE-microchips.

Alternatively, different from those foregoing microelectrode designs, simpler microelectrode configurations with very good stability and low mass limits of detection, have been developed by Henry and Garcia's groups [41–47]. In their work, solid metal microwires (Pt, Au and Cu) with a diameter of 25 μm were integrated on microchips as working electrodes, and aligned in the patterned electrode channel perpendicular to the separation channel. Such design allowed isolation of the detector from the separation current through the end column configuration with an electrode channel, and provided excellent chip-to-chip reproducibility of the working electrode location. In addition, an increase in electrode area in contact with solution (relative to planar electrodes) was also achieved as a result of the cylindrical shape of the electrode without an increase in electrode width. Besides single microwire electrode detectors, a microchip CE device fabricated with eight individually addressable, series gold microwire working electrodes, has also been reported recently, showing improved detection selectivity and resolution for analyses of small biological molecules, and its applicability was demonstrated by analyzing a human urine sample [48].

Thin-film fabrication methodologies are capable of constructing variable microelectrode patterns on miniaturized devices, notably. Among the diverse designs is called interdigitated array electrode (IDA). The IDA consists of quite a few electrode pairs, and in each electrode pair the "fingers" of the two microelectrodes are interdigitated in close proximity to provide enhanced sensitivity by redox-cycling. Fig. 1 shows the layout and microscopic photo of the IDA microelectrodes developed by our group [49]. The IDA microelectrodes were fabricated by spluttering thin film of Au/Ti via standard photolithography and lift-off processes. With IDA as electrochemical detectors, screening of the three liver fibrosis markers in human serum could be achieved at ng mL^{-1} concentration level. Other IDA designs for biosensors or for detection of bacteria have also been reported [29,50,51]. A point that should be mentioned is the adhesion of the metal film on the substrate. It can be strengthened either by an adhesion promoter, typically a second metal, or by a pretreatment of the substrate, e.g. by oxidization in O_2 ambient.

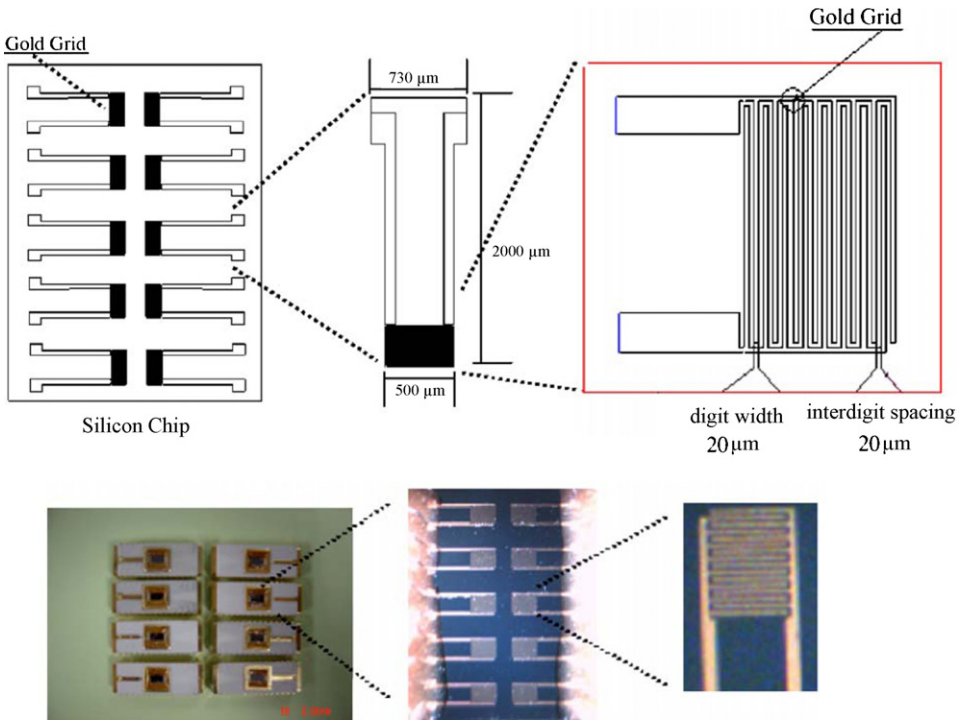


Fig. 1. Layout and photo of microelectrodes array on the silicon chips. The parameters of IDA microelectrodes array were as follows: digit width 20 μm; interdigit spacing 20 μm; number of digits 8 × 2; electrode area 3.2×10^{-3} cm^2 [49].

Apart using a lithography technique, some improved thin-film microelectrode fabrication methods are also available, such as plasma chemical vapor deposition (PCVD) and micromolding. Kadowaki et al. [52] reported that PCVD technique could deposit uniform platinum film inside a microchannel by using the precursor $Pt(C_5H_7O_2)_2$ and controlling the voltage and frequency. Thin-film gold and copper microelectrodes could also be constructed by electroless deposition and micromolding in capillary technique [53]. Such fabrication method was compatible with ordinary chemistry laboratories, and the integrated system created by this method was found to be robust for electrochemical detection of glucose, dopamine, and catechol, and was also suitable for other various applications.

2.2. Thick-film microelectrode fabrication methods

Compared with the somewhat complex fabrication technologies for thin-film microelectrodes, the fabrication methods for thick-film microelectrodes are shown to be simpler, as they obviate the need of clean room facilities and costly apparatus for vacuum deposition [54–59]. And the methods generally have a worse resolution, relative to the shadow-mask process for thin-film microelectrodes, and normally create electrodes with the thickness of some tens of micrometres. Common thick-film microelectrodes employing carbon and metal materials, can be found in the form of screen-printed electrodes (SPEs), electrodes created by airbrushing and micromolding and so on, nanoelectrode ensemble (NEE), and 3-D nano-/microelectrodes. Characteristics of these microelectrodes will be specified as below.

The development of analytical methods that respond to the growing need of performing rapid in situ analysis, shows low-cost and disposable SPEs an alternative to the conventional electrodes. Fabrication of SPEs simply uses a mesh with a geometrical pattern for the three integrated electrodes. Conducting ink made of carbon or Ag/AgCl is initially printed at designate places on a polymer support. Then, the insulating ink is printed to cover the non-working and non-conducting region of the SPEs, and give a definite shape to the working electrode. Batch production of the SPEs can be easily realized, and different configurations of the SPEs have been developed for biochemical testing [60–63].

Microelectrodes fabricated by airbrushing, another effective technique for thick-film design, have been reported lately by Walker et al. [64]. Airbrushing, a technique primarily used for commercial arts, enabled conductive inks to be patterned onto a microfluidic device through a film. The benefits of fabricating electrodes by airbrushing included a simpler process, lower cost, and less skill requirements. This technique was especially useful in circumstances where a commercial screen-printing machine was inaccessible. Additionally, outstanding work from Martin's group successfully incorporated thick-film carbon ink microelectrodes on microchips through a micromolding technique for various biological investigations [65–73]. Other thick-film designs can also be found employing carbon materials in forms of paste [74,75], glassy [76], fiber [77–80], pyrolyzed photoresist film [81], nanotubes and diamond [82].

The ordered NEE with regular pore sizes and spacing, has attracted enormous interest lately due to its excellent electrochemical characteristics, including ultra-fast electron-transfer reactions, high signal-to-noise ratios, and enhanced sensitivity. Various preparation methods for NEE microelectrodes have been proposed [83–85]. The most commonly used method involves a template synthesis process, in which metal ions, such as gold, platinum, copper and nickel, are electrochemically reduced and grown within the cylindrical and monodispersed pores of a nanoporous membrane. Among these metals, gold is mostly selected, and is used to fabricate gold nanoelectrode ensemble (GNEE) for electrochemical applications. Integrating thin GNEE films with a chip-based capillary electrophoresis system was shown feasible for in-column urea/urease reaction and electrochemical detection [86]. The direct hot-press bonding of the PC-based GNEE film onto a planar electrode provided a good electrical contact for the electrochemical detection, and the embedded GNEE electrode exhibited good detec-

tion linearity and reproducibility when detecting NH_4^+. This study proposed a new detection scheme for biosample analysis.

One more amazing design of the thick-film methods is the 3D nano-/microelectrode arrays developed by template synthesis [6,26,87]. These 3D electrodes exhibit enhanced sensitivity, faster response and lower detection limits compared with planar microelectrodes aforementioned, which render them suitable for integration with microdevices for the analysis of complex biosamples. Yun et al. [31] reported the electrochemical impedance measurement of prostate cancer cells using carbon nanotube array electrodes in a microfluidic channel. ESEM images of aligned MWCNT patterned arrays were shown in Fig. 2. The nanoarrays up to 8 mm tall were synthesized in the shape of towers, and were finally embedded into a PDMS channel as electrodes after electrodeposition of Au particles. Simple fabrication processes, including water-assisted chemical vapor deposition (CVD), a printed circuit board technique and electrodeposition, were helpful to future mass production of other cell-based biosensors. To study complex network morphologies and tissue slices containing substantial 3D neuronal structures, Rajaraman et al. [88] reported two novel non-lithographic approaches to fabricate 3D MEAs with embedded microfluidic ports for nutrient perfusion, the one concerning double-side exposure technology to create high aspect ratio structures in SU-8 was shown in Fig. 3. The ingenious fabrication method produced hollow towers, by which a coupled 3D electrical and microfluidic functionality was achieved. The 3D MEAs demonstrated the ability to pick up action potentials from a neuronal culture, and could potentially provide more information about the actual nature of the 3D networks inside the human body.

In this part, we introduced thin-film and thick-film microelectrode fabrication technologies, along with some excellent examples with unique electrode configurations. It can be envisioned that more and more electrode designs will emerge on microanalytical devices, and provide more detailed information for complex biosamples through versatile electrochemical techniques.

3. Versatility of electrochemical techniques in microsystems

Diverse microelectrode design and fabrication methods are the premise to perform the multi-functions of electrochemical techniques in microanalytical devices. The predominance of performing electrochemistry on a small scale includes high sensitivity, simple sample treatment, low-power requirement, inexpensive instrument, easy operation procedure and so forth. Electrochemistry offers significant promise for designing self-contained and totally disposable microdevices to analyze biochemical samples such as amino acids, peptides, DNA, cells and microorganisms. According to different study objectives in combining electrochemical principles in microsystems, the electrochemical detection methodology, electrical manipulation of fluids and biomaterials, and electrochemical sensing for biochemical assays were discussed in detail as below.

3.1. Electrochemical detection methodology

Electrochemical detection (ECD) methods have attracted considerable interest recently due to their compatibility in μTAS, as integration becomes one of the characteristics in modern analytical chemistry [89–93]. Laser-induced fluorescence (LIF), the most widely used detection technique in CE-microchips, is only applicable for fluorescent samples, and generally involves the use of large-scale and expensive optical systems. It always suffers a loss of sensitivity from miniaturization. In contrast, the label-free ECD method, with merits of improved sensitivity and tunable selectivity, is obviously fit for miniaturization in the microchip format.

Electrochemical techniques can be broadly divided into three categories including voltammetry, conductivity, and potentiometry [94,95]. As the most widely used detection method, voltammetry, especially the simplest technique amperometry, exhibits a remarkable performance improvement when electrode sizes are reduced into a low micrometer range. Microscale voltammetric analysis integrating voltammetric procedures with on-chip chemical reactions has been frequently reported [96–99]. When operating chemical reactions on a microscale, the surface area to volume ratio can be much higher, making mass transfer more efficient and chemical interactions much faster as the diffusion distances are shorter. For adaptation of voltammetric techniques to microfluidic chip, it should be taken into consideration that the effect of relevant experimental parameters, particularly the high voltage used for driving the electroosmotic flow, upon the background current, potential window, and size or potential of the voltammetric signal [100–104].

Conductivity detection is a universal tool monitoring conductance differences between two electrodes, and has been increasingly employed for small volume detection of charged biomolecules with tunable sensitivity [105]. Conductivity detection can be realized either by a direct contact of the electrolyte and the electrodes [106], or by a contactless fashion relying on capacitive coupling of an ac electrical field to a solution with external electrodes [107,108]. The contactless detection mode offers several distinct advantages, such as the elimination of surface fouling or bubble formation, a simplified construction and alignment of the detector, and effective isolation from high separation voltages [109,110].

Potentiometry is an ECD technique based upon the potential that arises upon a membrane between two solutions with different ionic activities. Integrated potentiometric detectors in microsystems, are generally exploited for investigation of ions [111–113]. On a microfluidic chip platform, potentiometry is applied much less compared with voltammetry and conductivity. Most probably, since microfluidic chips usually contain an inherent separation step, it is needless to discriminate one analyte from other components of the sample by ion selective electrodes [114]. Work is in progress combining potentiometry with microdevices.

There have been a lot of contributions to the advances in coupling electrochemical detection with microchips using different approaches and electrode materials, from the groups of Lunte [61,94], Henry [115–119], Martin [72,73], and Garcia [120–124]. Besides the unique designs of incorporating solid metal microwires and micromolded thick-film carbon ink microelectrodes on microchips as working electrodes, one more extraordinary design was dual-electrode amperometric detection, which is frequently employed for the selective monitoring of complex biological samples [70,74,78,81,125]. In this detection mode, the dual electrodes were serially configured, electroactive species that underwent reversible redox reactions would be detected at both electrodes, whereas electroactive species that did not have reversible redox couples could only be detected at one of the two electrodes. Additionally, the relative response at the two electrodes, along with migration time, could also be used to verify peak identity. Therefore, greater enhancement of selectivity and sensitivity could be achieved for the analysis of complex samples.

Finally, in order to make up for the shortage of single electrochemical detection method, increase throughput and provide more detailed information about the analytes, some multiple detection strategies have been combined on microchips [126,127]. Quite a few reports proposed dual detection schemes for microchips. Lapos et al. [128] presented two orthogonal detection schemes (amperometric and fluorescence detection) in a microfabricated electrophoresis chip, which allowed analysis of a wider spectrum of compounds per separation, led to higher throughput and provided a better understanding of detector alignment. Dual

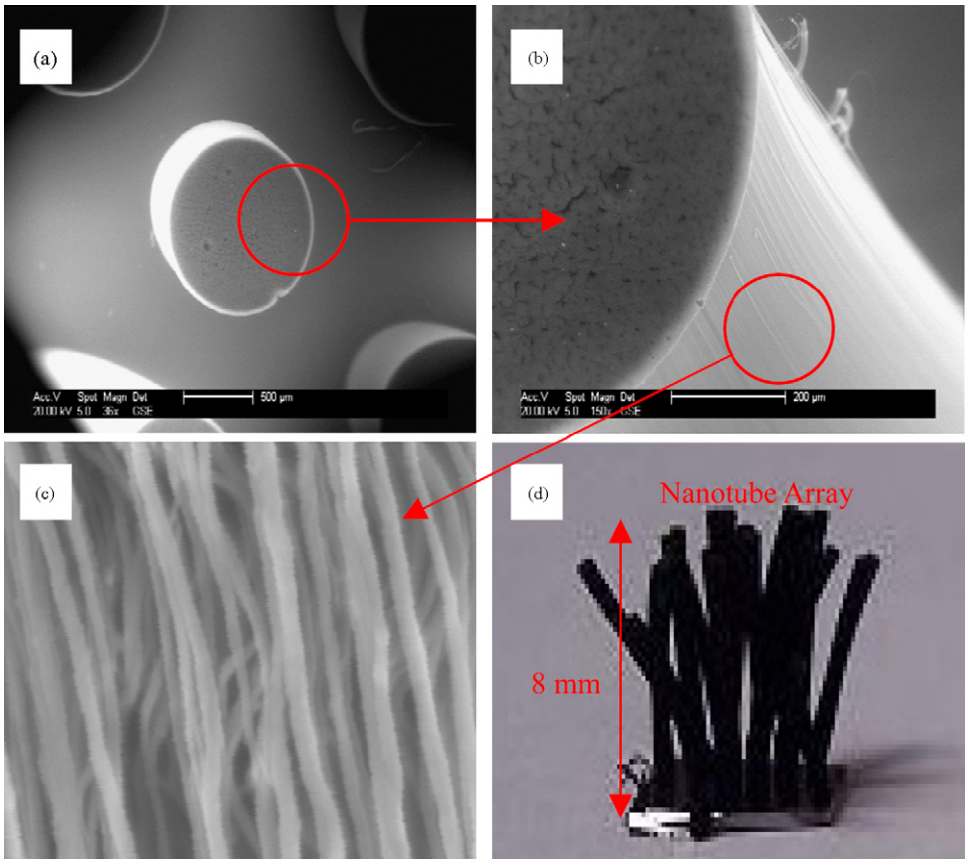


Fig. 2. ESEM images of aligned multi-wall carbon nanotube patterned arrays: (a) one bundle of nanotubes called a tower; (b) top view of a nanotube tower; (c) high resolution side view of a nanotube tower; (d) picture of an 8 mm tall MWCNT patterned array on the Si wafer [31].

fluorescence/contactless conductivity detection and simultaneous electrochemical and electrochemiluminescence detection for microchip have also been reported [129,130].

In brief summary, ECD methodology provides an arsenal of techniques, which are compatible with microfabrication, and tunable for various analytical requirements. Besides, electrochemical principles also exhibit characteristics of simplicity, rapidity, high sensitivity and specificity and so forth. These satisfactory features get ECD methods widely incorporated in μTAS.

3.2. Electrical manipulation of fluids and biomaterials

Besides electrochemical analyses, microelectrodes integrated in the miniaturized devices especially microfluidic chips, have been widely employed to conduct electrical manipulation of fluids and biochemical analytes such as DNA, proteins, cells, microorganisms, nanoparticles, and possibly single molecules in aqueous solutions [131–134]. Microelectrodes have blossomed into one of the most strongly desired elements on microdevices, and a variety of processes, including electroosmosis, dielectrophoresis (DEP) and electroporation, etc., become possible with them in a microchannel. Some significant examples for the manipulation via microelectrodes are discussed as follows.

Fluid control involving mass transport and direction through microchannels, is of crucial importance for the development of multifunctional microchips. Electroosmotic pump (EOP) based on electroosmotic flow (EOF) is the most widely used approach to drive fluids in microfluidic chips because of the simplicity of the design and fabrication methods. Using EOPs, precise flow control can be achieved by a simple current or voltage-control circuit with integrated driving microelectrodes [17,135]. To acquire a high pressure and produce enough flow in the microchannel, there have appeared quite a few designs of EOF pumps with different configurations of driving electrodes [136,137]. Borowsky et al. [138,139] presented the first demonstration of a packed bed microchannel for enhanced microchip EOF pumping, and attained the highest pressure (25 atm) on a microchip platform then. To apply the high voltage, positive and ground electrodes were directly placed in the reservoirs located upstream of the packed bed and at a sidearm channel that branched from the weir, respectively. A new high-pressure EOF pump was presented by Wang et al., utilizing silica monoliths directly bonding with the capillary wall with high charge density and high porosity [140]. While Nie et al. [141] developed a PMMA chip containing a total of nine parallel EOF pump systems, allowing the use of single, double or triple monolithic columns to produce increased flow as required. Additionally, on-chip electrochemical pumping system has also been developed for microfluidic transport, integrated with electrolysis microelectrodes, which were created by evaporation and deposition of either platinum or gold [142–144]. Those foregoing examples concerning the usage of integrated driving electrodes with appropriate designs for fluid flow control, could provide sufficient pressure and flow for determining various analytes, and could be easily combined in μTAS as a promising and indispensable fluid-driving unit.

DEP has been demonstrated to be quite effective and selective in concentrating, manipulating, and separating cells and bacteria with different sizes simultaneously [145]. All DEP microdevices involve integrating microelectrodes (Ti/Au or Cr/Au) to provide an ac electric field for DEP force generation. Cell positioning by DEP is probably the most broadly applied method among all chip-based cell separation technologies. As demonstrated in Fig. 4, Pan et al. [146] present a novel automatic positioning and sensing

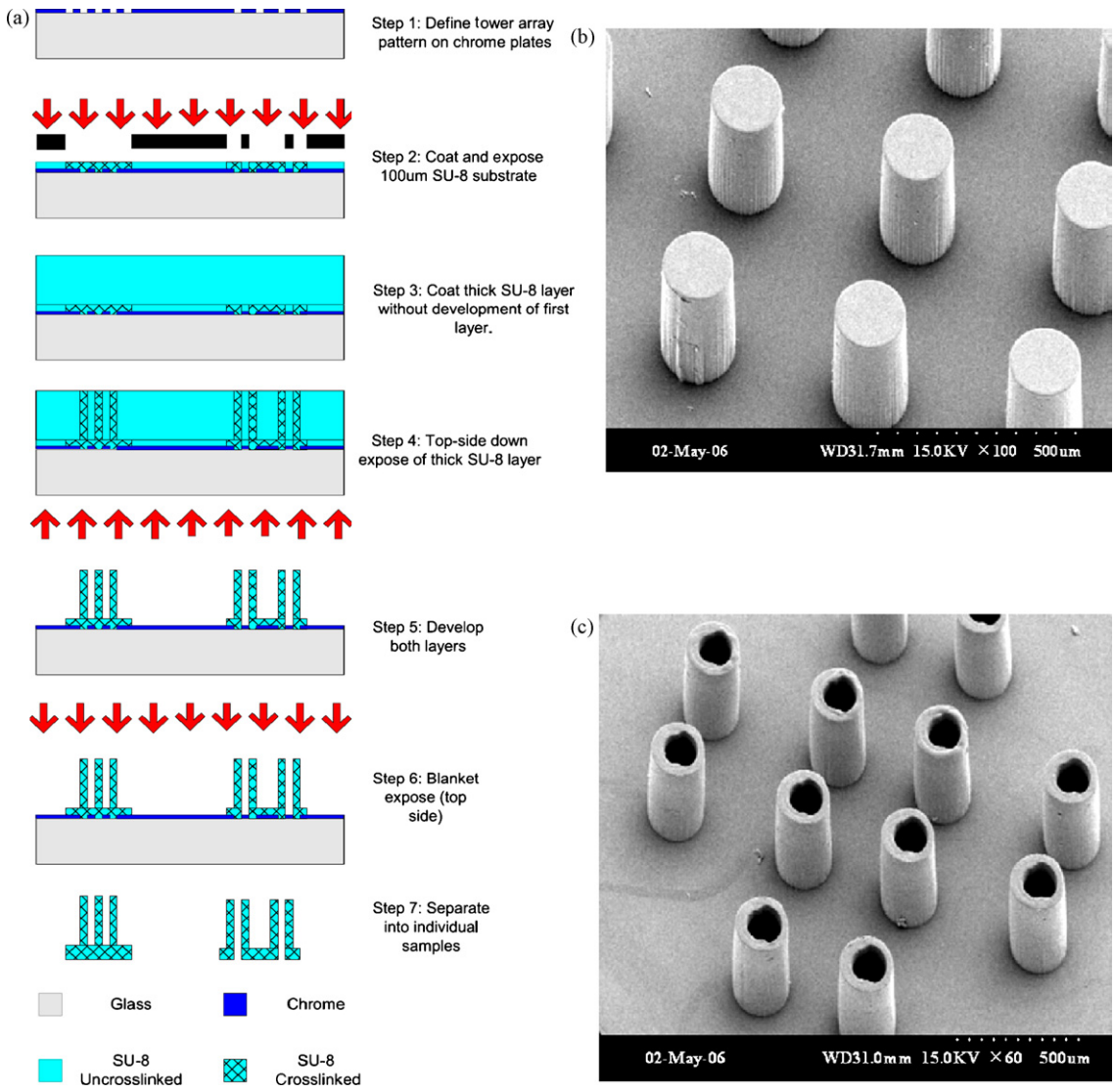


Fig. 3. Fabrication process flow for solid (a, left side) and hollow (a, right side) tower arrays, and SEM images of them (b and c) [88].

microelectrode array (APSMEA). Desired number of neurons was simultaneously positioned onto the microelectrodes automatically and scathelessly, and thus the measurement of the electrophysiological activities of neuronal populations was facilitated after functional synaptic connections formed between neurons. Alternatively, a new flow sandwich-type immunosensing method based on negative DEP was developed in microfluidic devices with 3D microelectrodes fabricated on two substrates [147]. Microparticles trapped in the caged area were used as solid supports for immunoassay. A microdevice with interdigitated electrodes was employed for dielectrophoretic separation and manipulation of viable and heat-treated cells of Listeria by using differences in dielectric properties of the cells [148]. A fixed microelectrode device was designed by Zou et al. [149] for manipulation, position and stimulation of osteoblasts using MEMS technology, on which the viability of osteoblasts under DEP was investigated. Although DEP often suffers from low survival rate of biological cells in electrical field and complicated instrumentation, with the development of microfabrication method and appearance of newly available electrode geometries, DEP manipulation in microfluidics for cell-based assay will have more applications in μTAS [150,151].

One more notable instance that has to be addressed is the usage of microelectrodes in the case of electroporation, an efficient technique for selective biochemical manipulation of contents of cells. Electroporation introduces foreign materials into cells by applying electric field impulses to create multiple transient pores in the cell membrane through a dielectric breakdown of the cell membrane. Since Lundqvist et al. first proposed single cell electroporation using carbon fiber microelectrodes in 1998 [152], significant enhancement of the electroporation system has been made by integrating diverse types of electrodes on microdevices. Huang and Rubinsky developed an electroporation microchip capable of performing controlled electroporation in single ND-1 cells [153], and they further improved the chip by employing microfluidic channels in a flow-through manner to precisely handle ND-1 cells, and achieved high effectiveness in genetic manipulation of the cells [154]. Khine et al. presented an effective polymeric electroporation chip that could selectively immobilize and locally electroporate single HeLa cells using low applied voltage [155]. The electrodes could be placed at a distance from the cell, eliminating the need to incorporate electrodes on chip and the potential of adverse products from electrode reactions. Moreover, Ag/AgCl electrodes and a patch clamp amplifier were used for accurate current traces of the electroporation process. Additionally, Ishibashi et al. [156] employed a porous membrane-based culture substrate for localized in situ electroporation of adherent Hela cells using planar electrodes. Excellent work

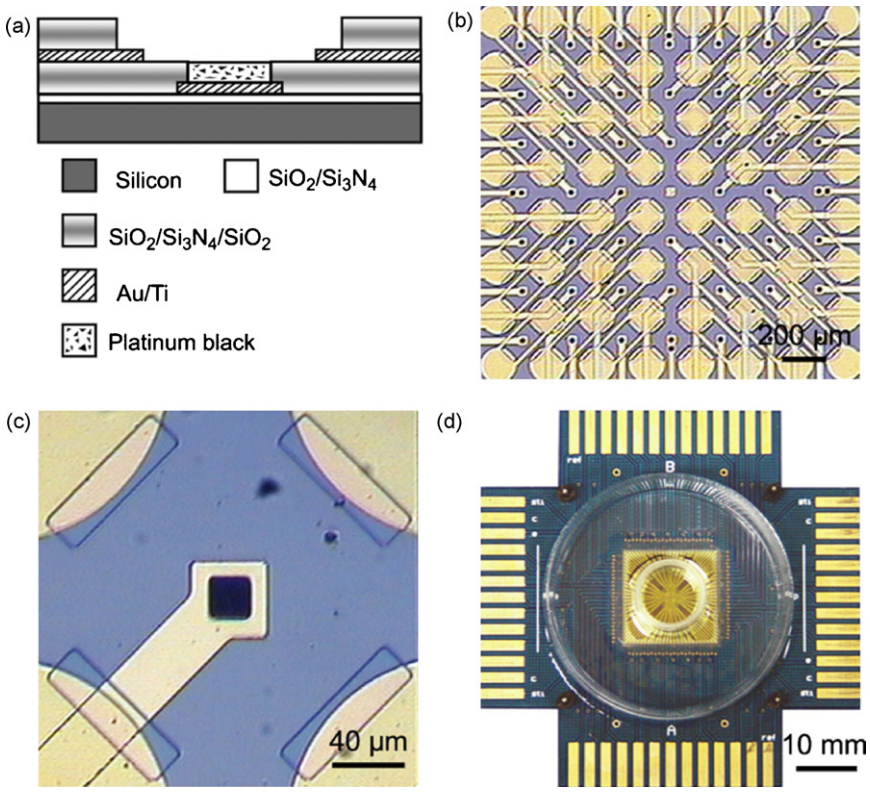


Fig. 4. Fabrication and encapsulation of APSMEAs. (a) Cross-sectional view of an APSMEA (not to scale). (b) Layout of the APSMEA with 49 groups of DEP electrodes arranged in a 7 × 7 square grid, at each center of which is the recording electrode (plated with platinum black). (c) Functional unit of the APSMEA with a recording electrode surrounded by four DEP electrodes. (d) A photo of an assembled APSMEA with a cell culture chamber [146].

from Lin's group has also been reported using interdigitated Au microelectrodes on the electroporation microchips for manipulation of DNA plasmids and NIH-3 T3 cell lines [157–159]. Further miniaturization of the technique would be feasible, by using nanotip electrodes that could be inserted into a cell for exclusive electroporation of organellar structures with minimal impairment of cellular physiology.

Some other unique examples, involving the usage of microelectrodes to apply electric fields for manipulation of biomaterials within the microsystem, have also been reported. Hediger et al. [160,161] realized a compact microsystem with compact integration of measurement electrodes, micro-fluidic channels and feed-throughs for epithelial cell culture and characterization. Control of the epithelial cell layer growth and transepithelial resistance and voltage measurements of the cell monolayer were demonstrated. Mu et al. [162] described a smart microfluidic chip capable of electrically controlled adsorption/release of avidin and streptavidin with a three-electrode system. The gold working electrode was fabricated via a sputtering process, and was subsequently modified with loosely packed SAMs of thiols with terminal carboxylic or amino groups. Upon application of an external electric potential to the gold substrate, conformation of the anchored mercapto chains transformed reversibly between "bent" and "straight" states, and led to a hydrophobic or hydrophilic channel surface capable of interacting with differently charged proteins. The microchips prepared in this way also exhibited the potential of separating low-concentration avidin from the avidin/streptavidin mixture, and provided a novel alternative for preconcentrating low-abundance protein in the research of proteomics.

As seen in this section, the integrated microelectrodes on microdevices act as an important and efficient role in manipulation of biosamples, more electrode designs and new application will be explored continuously in future.

3.3. Electrochemical sensing for biochemical assays

A great variety of electrochemical biosensors fabricated on microdevices have been well documented and reviewed [19,163–165]. Electrochemical biosensing investigates a specific biological event (e.g. antibody–antigen binding) using a combination of biological receptor substances (antibody, enzyme, DNA, nucleic acid, etc.) and electrochemical methods of signal transduction. Biosensors based on amperometric, potentiometric, impedimetric and capacitive transducers can be easily found [166–168], among which amperometric biosensors are mostly employed.

With integration of easily available microelectrodes, Farrell et al. [169] performed bead-based sandwich immunoassays for mouse IgG with femtomolar detection limits. Enzymes are the most prominent labels in electrochemical immunosensor development. Microchip platforms have proven themselves as highly desirable vehicles for conducting various electrochemical immunoassay protocols. Electrochemical enzyme immunoassays, combining antigen–antibody reactions with amperometric detection of the product of the enzymatic reaction, have evolved dramatically [170]. A sensitive enzyme-linked immunosorbent assay system was constructed by encapsulating anti-IgG within the network of Al_2O_3 sol–gel in the microfluidic channels, and this design led to higher sensitivity with the detection limit of 1 pg mL^{-1} by end-column electrochemical detection [171].

A potentiometric biosensor generally consists of a permselective outer layer and a bioactive material, usually an enzyme. The enzyme-catalysed reaction generates or consumes a species, which is detected by an ion selective electrode. A new type of pH biosensor containing two platinum microelectrodes was developed for biological applications, and the microelectrode coated with an electrosynthesized polymer acted as the pH sensitive electrode

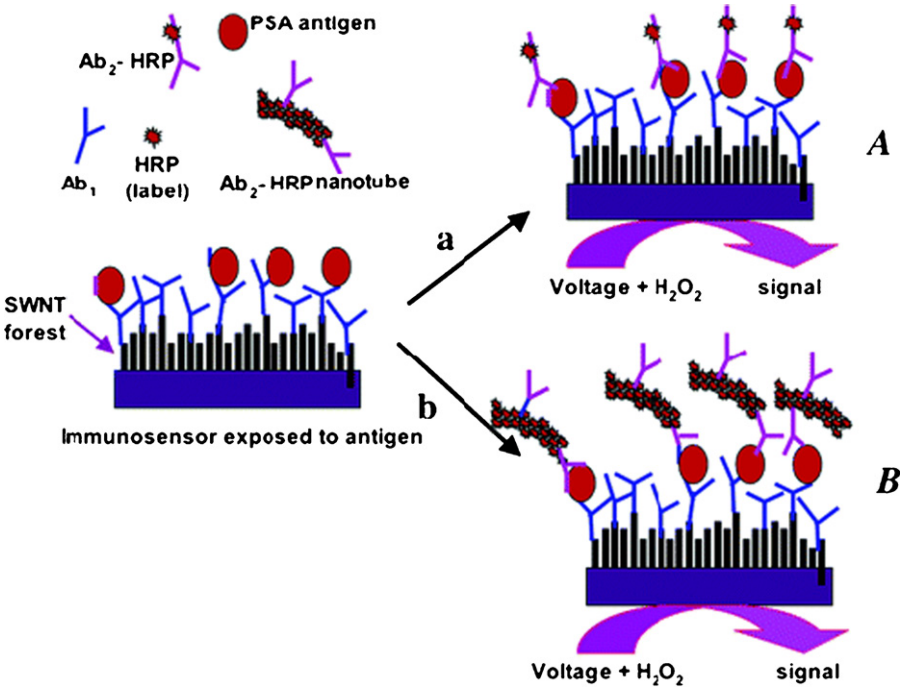


Fig. 5. A scheme for illustration of detection principles of the SWNT immunosensors [180].

[172]. Functional cellular assays were conducted on multiparametric silicon sensor chips with cellular microphysiological patterns, impedimetric electrode structures were employed to monitor cell morphological alterations [173]. A capacitive immunosensor based on ultrathin Al_2O_3 sol–gel films with embedded antibody for direct detection of hIgG antigen and the liver fibrosis markers of hyaluronan and laminin antigens, was realized on arrayed microelectrodes [174].

Recently, electrochemical nanobiosensors have attracted significant attention using nanoscale materials as electrodes or as biomolecular tracers [175], and have been applied in areas of disease diagnostics and detection of infectious organisms and biothreat agents [176,177]. With the growth of nanotechnology new opportunities are provided for biosensors construction and for developing novel electrochemical bioassays. It has been demonstrated that carbon nanotube (CNT) can enhance the electrochemical reactivity of important biomolecules, promote the electron-transfer reactions of proteins, accumulate important biomolecules and alleviate surface fouling effects [178,179]. The features of high surface area, fast heterogenous electron transfer and long-range electron transfer, render CNT extremely attractive to fabricate highly sensitive nanoscale biosensors. CNT-based electrochemical transducers offer substantial improvements in the performance of amperometric enzyme electrodes, immunosensors and nucleic-acid sensing devices. Aligned CNT "forests" lined as molecular wires allow efficient electron transfer between the underlying electrode and the redox centers of proteins. Yu et al. [180] exploited CNT amplification strategies for highly sensitive immunodetection of cancer biomarkers. Electrochemical immunosensors for detection of PSA in serum and tissue lysates, using single-wall carbon nanotube (SWNT) forest platforms, was combined with multi-label secondary antibody–nanotube bioconjugates. Detection principles of the SWNT immunosensor were illustrated in Fig. 5. Greatly amplified sensitivity was attained at high HRP/Ab_2 ratio and accurate detection of PSA was implemented in real samples. To take advantages of the striking characteristics of these unique nanomaterials in such electrochemical sensing applications, the CNT needs to be properly functionalized and immobilized. Several reviews regarding electrochemical biosensors based on nanomaterials have mentioned the important roles of nanoparticles [176,181,182]. Many kinds of nanoparticles, such as metal, oxide and semiconductor nanoparticles have been employed for constructing electrochemical biosensors. The significant functions provided by nanoparticles include immobilization of biomolecules, catalysis of electrochemical reactions, enhancement of electron transfer between electrode surfaces and proteins, labeling of biomolecules and even acting as reactant. Novel designs and fabrication methods of electrochemical biosensors are expected.

The versatility of electrochemical techniques is elaborated there above. Since electrochemistry is ideally compatible with the concept of μTAS, practical applications for real sample assays can be potentially realized by designing highly integrated microdevices.

4. Practical applications

Miniaturization, integration and intelligentization are phenomenal features of modern analytical chemistry, where MEMS plays an important role in fabricating various miniaturized analytical devices. Enormous efforts toward integration of various multifunctional components have led to remarkable developments and expansion of miniaturized instrumentation for biochemical assays of amino acids, nucleic acids, DNA, proteins, cell and tissue, and so forth [183–185]. Electrochemical techniques are highly amenable to small portable devices especially used outside the laboratory environment for clinical diagnoses, environmental monitoring, food analysis, etc. Potentially vigorous practical applications include: clinical instrumentation for point-of-care testing of tumors, genetic disorders and pathogenic bacteria and viruses; methods for glucose monitoring and the subsequent release of insulin; forensics applications including DNA analysis at crime scenes; and environmental monitoring applications such as on-site testing of pollutants or explosives [186,187]. As seen in Fig. 6, a self-contained disposable biochip device that consisted of microfluidic mixers, valves, pumps, channels, chambers, heaters, and DNA microarray sensors

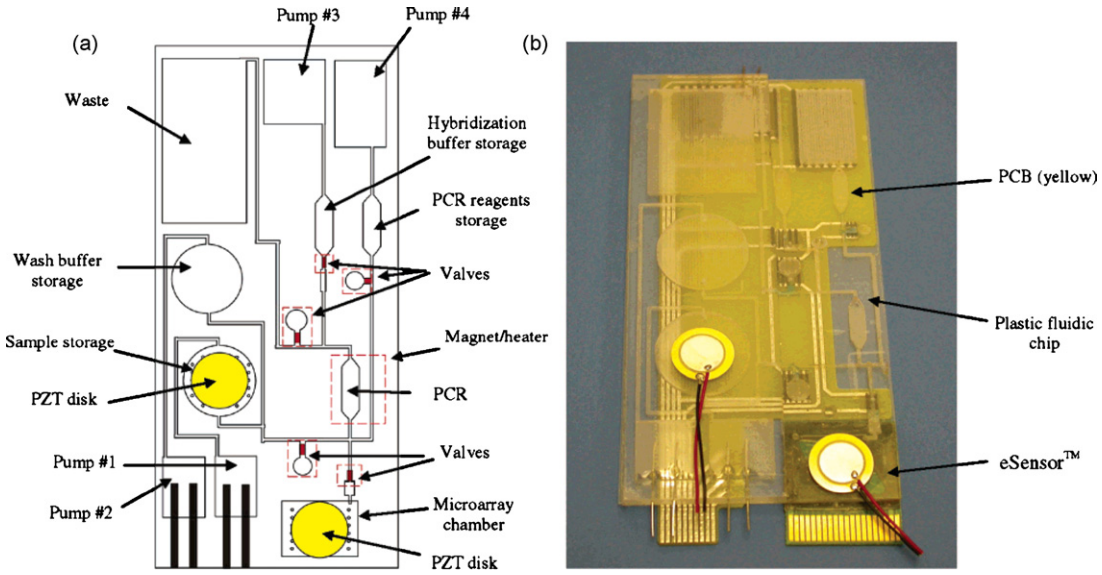


Fig. 6. (a) Schematic of the plastic fluidic chip. Pumps 1–3 are electrochemical pumps, and pump 4 is a thermopneumatic pump. (b) Photograph of the integrated device that consists of a plastic fluidic chip, a printed circuit board (PCB), and a Motorola eSensor microarray chip [188].

was developed to perform DNA analysis in *Escherichia coli*/rabbit blood samples [188]. Pathogenic bacteria detection was tested with approximately milliliters of whole blood samples, and single-nucleotide polymorphism analysis was demonstrated directly from diluted blood. What is more, both low- and high-abundance DNA detections from blood samples were also conducted using the devices. Dill et al. [167] presented the usage of individually addressable microelectrodes on the microarrays with over 1000 electrodes per square centimeter. The results of the redox enzyme amplified electrochemical detection for human α1 acid glycoprotein, ricin, M13 phage, fluorescein, etc. indicated that, this method is one of the most sensitive available, with limits of detection in the attomole range. A novel, simple and label-free multianalyte immunoassay system was described by integrating arrayed gold microelectrodes on a silicon chip for investigation of three liver fibrosis markers, hyaluronic acid, collagen type IV and lamin [189]. The measurement of real serum samples via this method was well consistent with commercial radio immunoassays, which is expected to be applied in clinical diagnosis or environment surveillance.

With the development of fabrication technologies for versatile microdevices, microanalytical processors portable for clinically or environmentally important analytes will be obtained, and accurate measurements with no requirements of experienced technicians can be imagined in the near future [144,190].

5. Conclusions

This review introduces interesting microanalytical devices integrated with electrochemical techniques for biochemical assays. We firstly introduced the microelectrode fabrication technologies and the different microelectrode design with a variety of configurations. Then, the versatility of electrochemical techniques was elaborated, including ECD, electrical manipulation of fluids and biomaterials, and electrochemical biosensing. Finally, potentially practical application of such integrated microdevices was explored. Coupling the versatility of electrochemical techniques with the rich information content of μTAS opens an array of future opportunities. Such highly integrated microdevices hold great promise for mass production of single-use μTAS. After rapid developments in microfabrication technology and their analytical applications, hand-held or portable instruments can be imagined.

Acknowledgements

This work was supported by Shanghai Leading Academic Discipline Project (Project Number: B109 and 08XD14009), the NSFC (20675018, 90606014, 20892022 and 20525519), SH908-HD1, Huoyindong Foundation (no. 94009), CSTC 2007BB5260 and Fudan University.

References

[1] D.R. Reyes, D. Iossifidis, P.A. Auroux, A. Manz, Anal. Chem. 74 (2002) 2623.
[2] T. Vilkner, D. Janasek, A. Manz, Anal. Chem. 76 (2004) 3373.
[3] P.S. Dittrich, K. Tachikawa, A. Manz, Anal. Chem. 78 (2006) 3887.
[4] J. West, M. Becker, S. Tombrink, A. Manz, Anal. Chem. 80 (2008) 4403.
[5] P. Leonard, S. Hearty, J. Brennan, L. Dunne, J. Quinn, T. Chakraborty, R. O'Kennedy, Enzyme Microb. Technol. 32 (2003) 3.
[6] J.E. Koehne, H. Chen, A.M. Cassell, Q. Yi, J. Han, M. Meyyappan, J. Li, Clin. Chem. 50 (2004) 1886.
[7] Y. Tanaka, K. Sato, T. Shimizu, M. Yamato, T. Okano, T. Kitamori, Biosens. Bioelectron. 23 (2007) 449.
[8] C.Q. Yi, C.W. Li, S.L. Ji, M.S. Yang, Anal. Chim. Acta 560 (2006) 1.
[9] J. Wang, M. Pumera, M.P. Chatrathi, A. Escarpa, R. Konrad, A. Griebel, W. Dorner, H. Lowe, Electrophoresis 23 (2002) 596.
[10] C.M. Chen, G.L. Chang, C.H. Lin, J. Chromatogr. A 1194 (2008) 231.
[11] A. Ishida, M. Natsume, T. Kamidate, J. Chromatogr. A 1213 (2008) 209.
[12] R.P. Liang, P.F. Hu, G.H. Gan, J.D. Qiu, Talanta 77 (2009) 1647.
[13] J. Wang, Talanta 56 (2002) 223.
[14] K. Uchiyama, H. Nakajima, T. Hobo, Anal. Bioanal. Chem. 379 (2004) 375.
[15] J. Wang, Electroanalysis 17 (2005) 1133.
[16] N.A. Lacher, K.E. Garrison, R.S. Martin, S.M. Lunte, Electrophoresis 22 (2001) 2526.
[17] H. Yu, F.Y. He, Y. Lu, Y.L. Hu, H.Y. Zhong, X.H. Xia, Talanta 75 (2008) 43.
[18] H. Becker, C. Gartner, Anal. Bioanal. Chem. 390 (2008) 89.
[19] J.J. Gooding, Electroanalysis 14 (2002) 1149.
[20] R.P. Baldwin, T.J. Roussel, M.M. Crain, V. Bathlagunda, D.J. Jackson, J. Gullapalli, J.A. Conklin, R. Pai, J.F. Naber, K.M. Walsh, R.S. Keynton, Anal. Chem. 74 (2002) 3690.
[21] G.S. Virdi, R.K. Chutani, P.K. Rao, S. Kumar, Sens. Actuators B 128 (2008) 422.
[22] B. Grass, A. Neyer, M. Johnck, D. Siepe, F. Eisenbeiss, G. Weber, R. Hergenroder, Sens. Actuators B 72 (2001) 249.
[23] Y.F. Gao, X.H. Chen, S. Gupta, K.D. Gillis, S. Gangopadhyay, Biomed. Microdevices 10 (2008) 623.
[24] D.M. Tsai, K.W. Lin, J.M. Zen, H.Y. Chen, R.H. Hong, Electrophoresis 26 (2005) 3007.
[25] D. Huska, J. Hubalek, V. Adam, R. Kizek, Electrophoresis 29 (2008) 4964.
[26] T. Yasukawa, A. Glidle, M. Nomura, J.M. Cooper, J. Microelectromech. Syst. 14 (2005) 839.
[27] W.K.T. Coltro, J.A.F. da Silva, E. Carrilho, Electrophoresis 29 (2008) 2260.
[28] M.H. Shi, J.J. Xu, S. Zhang, B.H. Liu, J.L. Kong, Talanta 68 (2006) 1089.
[29] L.J. Yang, Y.B. Li, G.F. Erf, Anal. Chem. 76 (2004) 1107.
[30] E. Jeoung, T.H. Galow, J. Schotter, M. Bal, A. Ursache, M.T. Tuominen, C.M. Stafford, T.P. Russell, V.M. Rotello, Langmuir 17 (2001) 6396.

[31] Y.H. Yun, Z.G. Dong, V.N. Shanov, M.J. Schulz, Nanotechnology 18 (2007).
[32] R. Wilke, S. Buttgenbach, Biosens. Bioelectron. 19 (2003) 149.
[33] S. Rajaraman, H. Noh, P.J. Hesketh, D.S. Gottfried, Sens. Actuators B 114 (2006) 392.
[34] Y.H. Jang, S.Y. Oh, J.K. Park, Enzyme Microb. Technol. 39 (2006) 1122.
[35] R. Kurita, N. Yabumoto, O. Niwa, Biosens. Bioelectron. 21 (2006) 1649.
[36] H.F. Cui, J.S. Ye, Y. Chen, S.C. Chong, X. Liu, T.M. Lim, F.S. Sheu, Sens. Actuators B 115 (2006) 634.
[37] H.F. Cui, J.S. Ye, Y. Chen, S.C. Chong, F.S. Sheu, Anal. Chem. 78 (2006) 6347.
[38] Y. Chen, C. Guo, L. Lim, S. Cheong, Q. Zhang, K. Tang, J. Reboud, Anal. Chem. 80 (2008) 1133.
[39] Y. Akiyama, K. Morishima, A. Kogi, Y. Kikutani, M. Tokeshi, T. Kitamori, Electrophoresis 28 (2007) 994.
[40] M. Castano-Alvarez, M.T. Fernandez-Abedul, A. Costa-Garcia, J. Chromatogr. A 1109 (2006) 291.
[41] Y. Liu, J.A. Vickers, C.S. Henry, Anal. Chem. 76 (2004) 1513.
[42] J.A. Vickers, C.S. Henry, Electrophoresis 26 (2005) 4641.
[43] J.A. Vickers, B.M. Dressen, M.C. Weston, K. Boonsong, O. Chailapakul, D.M. Cropek, C.S. Henry, Electrophoresis 28 (2007) 1123.
[44] Y.S. Ding, C.D. Garcia, Analyst 131 (2006) 208.
[45] Y.S. Ding, A. Ayon, C.D. Garcia, Anal. Chim. Acta 584 (2007) 244.
[46] C.D. Garcia, C.S. Henry, Anal. Chem. 75 (2003) 4778.
[47] C.D. Garcia, B.M. Dressen, A. Henderson, C.S. Henry, Electrophoresis 26 (2005) 703.
[48] R.E. Holcomb, J.R. Kraly, C.S. Henry, Analyst 134 (2009) 486.
[49] M.H. Shi, Y.Y. Peng, J. Zhou, B.H. Liu, Y.P. Huang, J.L. Kong, Biosens. Bioelectron. 21 (2006) 2210.
[50] C. Spegel, A. Heiskanen, J. Acklid, A. Wolff, R. Taboryski, J. Emneus, T. Ruzgas, Electroanalysis 19 (2007) 263.
[51] W. Laureyn, D. Nelis, P. Van Gerwen, K. Baert, L. Hermans, R. Magnee, J.J. Pireaux, G. Maes, Sens. Actuators B 68 (2000) 360.
[52] M. Kadowaki, H. Yoshizawa, S. Mori, M. Suzuki, Thin Solid Films 506 (2006) 123.
[53] J.L. Yan, Y. Du, J.F. Liu, W.D. Cao, S.H. Sun, W.H. Zhou, X.R. Yang, E.K. Wang, Anal. Chem. 75 (2003) 5406.
[54] M. Johirul, A. Shiddiky, R.E. Kim, Y.B. Shim, Electrophoresis 26 (2005) 3043.
[55] M.J.A. Shiddiky, D.S. Park, Y.B. Shim, Electrophoresis 26 (2005) 4656.
[56] J. Wang, A. Muck, M.P. Chatrathi, G. Chen, N. Mittal, S.D. Spillman, S. Obeidat, Lab. Chip 5 (2005) 226.
[57] O.D. Renedo, M.A. Alonso-Lomillo, M.J.A. Martinez, Talanta 73 (2007) 202.
[58] J.C. Ball, D.L. Scott, J.K. Lumpp, S. Daunert, J. Wang, L.G. Bachas, Anal. Chem. 72 (2000) 497.
[59] J. Wang, M.P. Chatrathi, G.E. Collins, Anal. Chim. Acta 585 (2007) 11.
[60] J. Wang, M. Pumera, M.P. Chatrathia, A. Rodriguez, S. Spillman, R.S. Martin, S.M. Lunte, Electroanalysis 14 (2002) 1251.
[61] W.R. Vandaveer, S.A. Pasas, R.S. Martin, S.M. Lunte, Electrophoresis 23 (2002) 3667.
[62] J. Wang, G. Chen, M. Pumera, Electroanalysis 15 (2003) 862.
[63] J. Wang, G. Chen, M.P. Chatrathi, M. Wang, R. Rinehart, A. Muck, Electroanalysis 20 (2008) 2416.
[64] C.E. Walker, Z. Xia, Z.S. Foster, B.J. Lutz, Z.H. Fan, Electroanalysis 20 (2008) 663.
[65] D.M. Spence, N.J. Torrence, M.L. Kovarik, R.S. Martin, Analyst 129 (2004) 995.
[66] M.L. Kovarik, N.J. Torrence, D.M. Spence, R.S. Martin, Analyst 129 (2004) 400.
[67] M.L. Kovarik, M.W. Li, R.S. Martin, Electrophoresis 26 (2005) 202.
[68] M.W. Li, D.M. Spence, R.S. Martin, Electroanalysis 17 (2005) 1171.
[69] C.D. Kuhnline, M.G. Gangel, M.K. Hulvey, R.S. Martin, Analyst 131 (2006) 202.
[70] L.C. Mecker, R.S. Martin, Electrophoresis 27 (2006) 5032.
[71] M.K. Hulvey, L.I. Genes, D.M. Spence, R.S. Martin, Analyst 132 (2007) 1246.
[72] L.C. Mecker, R.S. Martin, Anal. Chem. 80 (2008) 9257.
[73] M. Hulvey, R. Martin, Anal. Bioanal. Chem. 393 (2009) 599.
[74] R.S. Martin, A.J. Gawron, B.A. Fogarty, F.B. Regan, E. Dempsey, S.M. Lunte, Analyst 126 (2001) 277.
[75] W. Siangproh, O. Chailapakul, R. Laocharoensuk, J. Wang, Talanta 67 (2005) 903.
[76] T.K. Lim, H. Ohta, T. Matsunaga, Anal. Chem. 75 (2003) 3316.
[77] A.J. Gawron, S.M. Lunte, Electrophoresis 21 (2000) 3205.
[78] A.J. Gawron, R.S. Martin, S.M. Lunte, Electrophoresis 22 (2001) 242.
[79] M.J. Rose, S.M. Lunte, R.G. Carlson, J.F. Stobaugh, J. Pharm. Biomed. Anal. 30 (2003) 1851.
[80] X.A. Li, D.M. Zhou, J.J. Xu, H.Y. Chen, Talanta 75 (2008) 157.
[81] D.J. Fischer, W.R. Vandaveer, R.J. Grigsby, S.M. Lunte, Electroanalysis 17 (2005) 1153.
[82] G. Chen, Talanta 74 (2007) 326.
[83] P. Ugo, L.M. Moretto, S. Bellomi, V.P. Menon, C.R. Martin, Anal. Chem. 68 (1996) 4160.
[84] W.L. Cheng, S.J. Dong, E.K. Wang, Anal. Chem. 74 (2002) 3599.
[85] R. Gasparac, B.J. Taft, M.A. Lapierre-Devlin, A.D. Lazareck, J.M. Xu, S.O. Kelley, J. Am. Chem. Soc. 126 (2004) 12270.
[86] K.T. Liao, C.M. Chen, H.J. Huang, C.H. Lin, J. Chromatogr. A 1165 (2007) 213.
[87] K. Krishnamoorthy, C.G. Zoski, Anal. Chem. 77 (2005) 5068.
[88] S. Rajaraman, S.O. Choi, R.H. Shafer, J.D. Ross, J. Vukasinovic, Y. Choi, S.P. DeWeerth, A. Glezer, M.G. Allen, J. Micromech. Microeng. 17 (2007) 163.
[89] J. Wang, M.P. Chatrathi, B.M. Tian, Anal. Chem. 73 (2001) 1296.
[90] H.Y. Bi, X.X. Weng, H.Y. Qu, J.L. Kong, P.Y. Yang, B.H. Liu, J. Proteome Res. 4 (2005) 2154.
[91] I. Fritsch, Z.P. Aguilar, Anal. Bioanal. Chem. 387 (2007) 159.
[92] Y. Zeng, H. Chen, D.W. Pang, Z.L. Wang, J.K. Cheng, Anal. Chem. 74 (2002) 2441.
[93] D.F. Pozo-Ayuso, M. Castano-Alvarez, A. Fernandez-la-Villa, M. Garcia-Granda, M.T. Fernandez-Abedul, A. Costa-Garcia, J. Rodriguez-Garcia, J. Chromatogr. A 1180 (2008) 193.
[94] W.R. Vandaveer, S.A. Pasas-Farmer, D.J. Fischer, C.N. Frankenfeld, S.M. Lunte, Electrophoresis 25 (2004) 3528.
[95] F.M. Matysik, Microchim. Acta 160 (2008) 1.
[96] J. Wang, B.M. Tian, E. Sahlin, Anal. Chem. 71 (1999) 3901.
[97] Z.M. Liu, O. Niwa, R. Kurita, T. Horiuchi, J. Chromatogr. A 891 (2000) 149.
[98] J. Wang, R. Polsky, B.M. Tian, M.P. Chatrathi, Anal. Chem. 72 (2000) 5285.
[99] M.H. Shi, Y.Y. Peng, S.N. Yu, B.H. Liu, J.L. Kong, Electrophoresis 28 (2007) 1587.
[100] D.C. Chen, F.L. Hsu, D.Z. Zhan, C.H. Chen, Anal. Chem. 73 (2001) 758.
[101] R.S. Martin, K.L. Ratzlaff, B.H. Huynh, S.M. Lunte, Anal. Chem. 74 (2002) 1136.
[102] C.P. Chen, J.H. Hahn, Anal. Chem. 79 (2007) 7182.
[103] S.A. Pasas, N.A. Lacher, M.I. Davies, S.M. Lunte, Electrophoresis 23 (2002) 759.
[104] N.A. Lacher, S.M. Lunte, R.S. Martin, Anal. Chem. 76 (2004) 2482.
[105] P. Kuban, P.C. Hauser, Electroanalysis 16 (2004) 2009.
[106] S.D. Noblitt, C.S. Henry, Anal. Chem. 80 (2008) 7624.
[107] M. Galloway, S.A. Soper, Electrophoresis 23 (2002) 3760.
[108] J. Wang, G. Chen, A. Muck, Talanta 78 (2009) 207.
[109] M. Pumera, J. Wang, F. Opekar, I. Jelinek, J. Feldman, H. Lowe, S. Hardt, Anal. Chem. 74 (2002) 1968.
[110] J. Chen, Y. Lin, G. Chen, Electrophoresis 28 (2007) 2897.
[111] R. Tantra, A. Manz, Anal. Chem. 72 (2000) 2875.
[112] R.D. Johnson, V.G. Gaualas, S. Daunert, L.G. Bachas, Anal. Chim. Acta 613 (2008) 20.
[113] S.S.M. Hassan, H.E.M. Sayour, S.S. Al-Mehrezi, Anal. Chim. Acta 581 (2007) 13.
[114] M. Pumera, A. Merkoci, S. Alegret, Trac-Trends Anal. Chem. 25 (2006) 219.
[115] J.C. Fanguy, C.S. Henry, Electrophoresis 23 (2002) 767.
[116] J.C. Fanguy, C.S. Henry, Analyst 127 (2002) 1021.
[117] R.W. Hompesch, C.D. Garcia, D.J. Weiss, J.M. Vivanco, C.S. Henry, Analyst 130 (2005) 694.
[118] C.D. Garcia, C.S. Henry, Electroanalysis 17 (2005) 1125.
[119] J.A. Vickers, M.M. Caulum, C.S. Henry, Anal. Chem. 78 (2006) 7446.
[120] C. Berg, D.C. Valdez, P. Bergeron, M.F. Mora, C.D. Garcia, A. Ayon, Electrophoresis 29 (2008) 4914.
[121] Y.S. Ding, C.D. Garcia, Electroanalysis 18 (2006) 2202.
[122] Y.S. Ding, C.D. Garcia, Electrophoresis 27 (2006) 5119.
[123] Y.S. Ding, M.F. Mora, C.D. Garcia, Anal. Chim. Acta 561 (2006) 126.
[124] Y.S. Ding, M.F. Mora, G.N. Merrill, C.D. Garcia, Analyst 132 (2007) 997.
[125] R.S. Martin, A.J. Gawron, S.M. Lunte, C.S. Henry, Anal. Chem. 72 (2000) 3196.
[126] J. Wang, M. Pumera, Anal. Chem. 74 (2002) 5919.
[127] M. Novotny, F. Opekar, I. Jelinek, K. Stulik, Anal. Chim. Acta 525 (2004) 17.
[128] J.A. Lapos, D.P. Manica, A.G. Ewing, Anal. Chem. 74 (2002) 3348.
[129] H.B. Qiu, X.B. Yin, J.L. Yan, X.C. Zhao, X.R. Yang, E.K. Wang, Electrophoresis 26 (2005) 687.
[130] C. Liu, Y.Y. Mo, Z.G. Chen, X. Li, O.L. Li, X. Zhou, Anal. Chim. Acta 621 (2008) 171.
[131] M. Durr, J. Kentsch, T. Muller, T. Schnelle, M. Stelzle, Electrophoresis 24 (2003) 722.
[132] S. Gawad, K. Cheung, U. Seger, A. Bertsch, P. Renaud, Lab. Chip 4 (2004) 241.
[133] J.T.Y. Lin, J.T.W. Yeow, Biomed. Microdevices 9 (2007) 823.
[134] H.F. Arata, M. Kumemura, N. Sakaki, H. Fujita, Anal. Bioanal. Chem. 391 (2008) 2385.
[135] Y.C. Chan, M. Carles, N.J. Sucher, M. Wong, Y. Zohar, J. Micromech. Microeng. 13 (2003) 914.
[136] G. Chen, J.J. Guo, X.J. Xu, Microchim. Acta 159 (2007) 191.
[137] F. Zhou, W. Wang, W.Y. Wu, J.R. Zhang, J.J. Zhu, J. Chromatogr. A 1194 (2008) 221.
[138] J. Borowsky, Q. Lu, G.E. Collins, Sens. Actuators B 131 (2008) 333.
[139] J.F. Borowsky, B.C. Giordano, Q. Lu, A. Terray, G.E. Collins, Anal. Chem. 80 (2008) 8287.
[140] P. Wang, Z.L. Chen, H.C. Chang, Sens. Actuators B 113 (2006) 500.
[141] F.Q. Nie, M. Macka, L. Barron, D. Connolly, N. Kent, B. Paull, Analyst 132 (2007) 417.
[142] J. Xie, Y.N. Miao, J. Shih, Q. He, J. Liu, Y.C. Tai, T.D. Lee, Anal. Chem. 76 (2004) 3756.
[143] J. Xie, Y.N. Miao, J. Shih, Y.C. Tai, T.D. Lee, Anal. Chem. 77 (2005) 6947.
[144] F. Sassa, K. Morimoto, W. Satoh, H. Suzuki, Electrophoresis 29 (2008) 1787.
[145] P. Sabounchi, A.M. Morales, P. Ponce, L.P. Lee, B.A. Simmons, R.V. Davalos, Biomed. Microdevices 10 (2008) 661.
[146] L.B. Pan, G.X. Xiang, L.H. Huang, Z.Y. Yu, J. Cheng, W.L. Xing, Y.X. Zhou, J. Neurosci. Methods 170 (2008) 123.
[147] T. Yasukawa, M. Suzuki, T. Sekiya, H. Shiku, T. Matsue, Biosens. Bioelectron. 22 (2007) 2730.
[148] H.B. Li, R. Bashir, Sens. Actuators B 86 (2002) 215.
[149] H. Zou, S. Mellon, R.R.A. Syms, K.E. Tanner, Biomed. Microdevices 8 (2006) 353.
[150] J. Park, B. Kim, S.K. Choi, S. Hong, S.H. Lee, K.I. Lee, Lab. Chip 5 (2005) 1264.
[151] C.H. Tai, S.K. Hsiung, C.Y. Chen, M.L. Tsai, G.B. Lee, Biomed. Microdevices 9 (2007) 533.
[152] J.A. Lundqvist, F. Sahlin, M.A.I. Aberg, A. Stromberg, P.S. Eriksson, O. Orwar, Proc. Natl. Acad. Sci. U.S.A. 95 (1998) 10356.
[153] Y. Huang, B. Rubinsky, Sens. Actuators A-Phys. 89 (2001) 242.
[154] Y. Huang, B. Rubinsky, Sens. Actuators A-Phys. 104 (2003) 205.
[155] M. Khine, A. Lau, C. Ionescu-Zanetti, J. Seo, L.P. Lee, Lab. Chip 5 (2005) 38.

[156] T. Ishibashi, K. Takoh, H. Kaji, T. Abe, M. Nishizawa, Sens. Actuators B 128 (2007) 5.
[157] C.P. Jen, W.M. Wu, M. Li, Y.C. Lin, J. Microelectromech. Syst. 13 (2004) 947.
[158] Y.C. Lin, M. Li, C.C. Wu, Lab. Chip 4 (2004) 104.
[159] S.C. Yang, K.S. Huang, H.Y. Chen, Y.C. Lin, Sens. Actuators B 132 (2008) 551.
[160] S. Hediger, J. Fontannaz, A. Sayah, W. Hunziker, M.A.M. Gijs, Sens. Actuators B 63 (2000) 63.
[161] S. Hediger, A. Sayah, J.D. Horisberger, M.A.M. Gijs, Biosens. Bioelectron. 16 (2001) 689.
[162] L. Mu, Y. Liu, S.Y. Cai, J.L. Kong, J. Chem.-Eur. 13 (2007) 5113.
[163] A. Warsinke, Adv. Biochem. Eng./Biotechnol. 109 (2008) 155.
[164] M. Diaz-Gonzalez, M.B. Gonzalez-Garcia, A. Costa-Garcia, Electroanalysis 17 (2005) 1901.
[165] C.N. LaFratta, D.R. Walt, Chem. Rev. 108 (2008) 614.
[166] F. Ricci, G. Volpe, L. Micheli, G. Palleschi, Anal. Chim. Acta 605 (2007) 111.
[167] K. Dill, D.D. Montgomery, A.L. Ghindilis, K.R. Schwarzkopf, S.R. Ragsdale, A.V. Oleinikov, Biosens. Bioelectron. 20 (2004) 736.
[168] Y.J. Ko, J.H. Maeng, Y. Ahn, S.Y. Hwang, N.G. Cho, S.H. Lee, Electrophoresis 29 (2008) 3466.
[169] S. Farrell, N.J. Ronkainen-Matsuno, H.B. Halsall, W.R. Heineman, Anal. Bioanal. Chem. 379 (2004) 358.
[170] A. Bange, H.B. Halsall, W.R. Heineman, Biosens. Bioelectron. 20 (2005) 2488.
[171] H.X. Wang, S. Meng, K. Guo, Y. Liu, P.Y. Yang, W. Zhong, B.H. Liu, Electrochem. Commun. 10 (2008) 447.
[172] O. Segut, B. Lakard, G. Herlem, J.Y. Rauch, J.C. Jeannot, L. Robert, B. Fahys, Anal. Chim. Acta 597 (2007) 313.
[173] M. Brischwein, E.R. Motrescu, E. Cabala, A.M. Otto, H. Grothe, B. Wolf, Lab. Chip 3 (2003) 234.
[174] D.C. Jiang, J. Tang, B.H. Liu, P.Y. Yang, J.L. Kong, Anal. Chem. 75 (2003) 4578.
[175] J. Gamby, J.P. Abid, B. Tribollet, H.H. Girault, Small 4 (2008) 802.
[176] M. Pumera, S. Sanchez, I. Ichinose, J. Tang, Sens. Actuators B 123 (2007) 1195.
[177] B.V. Chikkaveeraiah, H.Y. Liu, V. Mani, F. Papadimitrakopoulos, J.F. Rusling, Electrochem. Commun. 11 (2009) 819.
[178] J. Wang, Electroanalysis 17 (2005) 7.
[179] P.A. He, Y. Xu, Y.Z. Fang, Microchim. Acta 152 (2006) 175.
[180] X. Yu, B. Munge, V. Patel, G. Jensen, A. Bhirde, J.D. Gong, S.N. Kim, J. Gillespie, J.S. Gutkind, F. Papadimitrakopoulos, J.F. Rusling, J. Am. Chem. Soc. 128 (2006) 11199.
[181] X.L. Luo, A. Morrin, A.J. Killard, M.R. Smyth, Electroanalysis 18 (2006) 319.
[182] J. Wang, Small 1 (2005) 1036.
[183] G.M. Whitesides, Nature 442 (2006) 368.
[184] T.H. Fang, N. Ramalingam, X.D. Dong, T.S. Ngin, X.T. Zeng, A.T.L. Kuan, E.Y.P. Huat, H.Q. Gong, Biosens. Bioelectron. 24 (2009) 2131.
[185] S.S.W. Yeung, T.M.H. Lee, I.M. Hsing, Anal. Chem. 80 (2008) 363.
[186] P. Yager, T. Edwards, E. Fu, K. Helton, K. Nelson, M.R. Tam, B.H. Weigl, Nature 442 (2006) 412.
[187] M. Seidel, R. Niessner, Anal. Bioanal. Chem. 391 (2008) 1521.
[188] R.H. Liu, J.N. Yang, R. Lenigk, J. Bonanno, P. Grodzinski, Anal. Chem. 76 (2004) 1824.
[189] M.H. Shi, Y.Y. Peng, J. Zhou, B.H. Liu, Y.P. Huang, J.L. Kong, Biosens. Bioelectron. 22 (2007) 2841.
[190] T. Revermann, S. Gotz, J. Kunnemeyer, U. Karst, Analyst 133 (2008) 167.

Talanta 80 (2009) 19–23

Contents lists available at ScienceDirect

Talanta

journal homepage: www.elsevier.com/locate/talanta

Spectrofluorimetric method for measuring the activity of the enzyme α-L-fucosidase using the ion associate of 2-chloro-4-nitro phenol–rhodamine-B

M.S. El-Shahawi[a,*], A.M. Othman[b], M.E. El-Houseini[c], B. Nashed[d], M.S. Elsofy[d]

[a] Department of Chemistry, Faculty of Science, King Abduaziz University, P.O. Box 80203, Jeddah 21589, Saudi Arabia
[b] Genetic Engineering and Biotechnology Institute, Menofia University, Menofia, Egypt
[c] National Cancer Institute, Cairo University, Egypt
[d] Modern University for Technology & Information, Egypt

ARTICLE INFO

Article history:
Received 10 February 2009
Received in revised form 11 April 2009
Accepted 13 April 2009
Available online 11 June 2009

Keywords:
α-L-Fucosidase enzyme
Rhodamine-B
2-Chloro-4-nitrophenol
Associate

ABSTRACT

A low cost and accurate method for the detection and analytical determination of the activity of the enzyme α-L-fucosidase (AFU) was developed. The method was based upon measuring the fluorescence intensity of the complex ion associate of the ion associate of rhodamine-B and the compound 2-chloro-4-nitrophenol (RB^+ CNP^-) at 580 nm in phosphate buffer (pH 5) against the reagent blank. The influence of the different parameters, e.g. pH, incubation time, temperature, 2-chloro-4-nitrophenol concentration, foreign ions and surfactants that control the fluorescence intensity of the produced ion associate was critically investigated. The correlation between the fluorescence activity of the enzyme AFU by the developed procedures and the standard method was positive and highly significant in patients and controls ($r^2 = 0.99$, $p < 0.001$). The developed method is simple and proceeds without practical artifacts compared to the standard method.

© 2009 Published by Elsevier B.V.

1. Introduction

Liver cirrhosis is a pre-cancer condition that in many cases can develop into Hepatocellular carcinoma (HCC). Therefore, cirrhotic patients with cirrhosis are usually screened for HCC during their follow-up procedure [1–6]. Tumor markers represent good potential screening tools for the early diagnosis of tumors [7–10]. The primary tumor marker for HCC is a single polypeptide chain glycoprotein namely α-fetoprotein (AFP) [11,12]. The sensitivity and specificity of the AFP as a common tumor marker to detect HCC in all patient samples are insufficient [13,14]. Moreover, it is not secreted in all cases of HCC and may be normal in 40% of patients with early HCC [10,15].

The enzyme α-L-Fucosidase (AFU) can hydrolyze methyl α-L-fucoside and fucosidic linkages of fucoidan and blood-group substances [16]. The AFU enzyme compose of two-enzyme components namely: i, fucosidase which acts on 4-nitrophenyl α-L-fucoside as well as fucosidic linkages of porcine sub-maxillary mucin at optimal activity at pH 2 and ii, the fucoidanase showed highest activity around pH 5 and acts on the synthetic substrate not on the mucin [17]. The enzyme fucoidanase showed hydrolytic activity towards fucoidan, and not towards 4-nitro phenyl α-L-fucoside and blood group of livers of related species [18]. Clinical studies have demonstrated that, the activity of AFU enzyme represent an excellent test for diagnosis of HCC [19,20]. The AFU enzyme was used for the diagnosis of fucosidosis recognized in born disorder of metabolism and increases the sensitivity of detection to 95.5% in patients with HCC [21,22].

Different spectrometric methods have been reported for the determination of the activity of the enzyme AFU in serum [23–25]. These methods are limited by their long incubation time (30–60 min) for the sample and reagent blanks. Moreover, the poor affinity of the enzyme AFU towards the substrate 4-NPF as a colorimetric reagent at pH 4.8, added another disadvantage to these methods. However, the method of Jun and Hua [23] involving the synthesis of 2-chloro-4-nitrophenyl-α-L-fucopyranoside (CNPF) as a substrate has a rapid hydrolytic rate than 4-NPF method [23,24]. The activity of AFU was also determined by spectrofluorescence methods [26,27], affinity chromatography [17], column chromatography packed with Bacillus cereus [28] and disc gel electrophoresis technique [17,29]. Most of these methods are unselective, require careful experimental conditions, considerably time consuming and not compatible to detect the activity of AFU at the early stage of diseases. Thus, the present manuscript is focused on the use of the fluorescent ion associate of 2-chloro-4-nitro phenol–rhodamine-B (RB^+ CNP^-) for measuring the activity of the AFU enzyme and overcoming the difficulties caused by the previous methods [23–27]. The developed procedures will be able to control the quality of

* Corresponding author. Permanent address: Department of Chemistry, Faculty of Sciences at Damiatta, Mansoura University, Mansoura, Egypt. Tel.: +966 2 6952000; fax: +966 2 6952292.
E-mail address: mohammad_el_shahawi@yahoo.co.uk (M.S. El-Shahawi).

0039-9140/$ – see front matter © 2009 Published by Elsevier B.V.
doi:10.1016/j.talanta.2009.04.070

the final marketed product in both qualitative and quantitative approaches to assure the identity of the disease. The method will be useful in medical applications to detect the different diseases at the very early stage of diseases.

2. Experimental

2.1. Apparatus

A Shimadzu RF5301 PC spectrofluorometer (290–750 nm) was used for recording the excitation; emission spectra and measuring the fluorescence intensity of the reagents and the produced complex ion associate. A two matched cuvettes (1.0 cm) and an Orion pH meter VWR scientific model (8000) were used for measuring the fluorescence intensity of the ion associate $RB^+ CN^-$ and other fluorescent species and pH measurements, respectively.

2.2. Reagents and materials and methods

Analytical reagent grade (A.R.) reagents and chemicals (99.9% purity) were used without further purification. Ascorbic acid, bilirubin, hemoglobin, glucose and uric acid, albumin, total protein, total cholesterol and triglyceride were purchased from Fluka (Fluka, AG, Buchs, Switzerland). The substrate 2-chloro-4-nitrophenyl-α-L-fucopyranoside (CNPF) and the enzyme α-L-fucosidase (AFU, EC 3.2.1.51) were laboratory reagent grade from Sigma–Aldrich, Poole, UK. The control enzyme was prepared in bovine serum base and provided in lyophilized powder. The enzyme AFU was also obtained from bovine kidney and the reagents 2-chloro-4-nitro phenol (CNP) and rhodamine-B (RB) were purchased from Sigma Co. Phosphate buffers of various pH (pH 2.5–7) were prepared from phosphoric acid and/or sodium phosphate.

2.3. Preparation of the complex ion associate $RB^+ CNP^-$

In measuring flask (100.0 mL), an accurate volume (10 mL) of the reagent 2-chloro-4-nitrophenol (5×10^{-4} mol L^{-1}) was allowed to react with 20.0 mL of rhodamine-B (5×10^{-4} mol L^{-1}). The solution was then completed to the mark with phosphate buffer of pH 5.0 and the excitation and emission spectra of the reagents 2-chloro-4-nitrophenol and rhodamine-B and the produced complex ion associate ($RB^+ CNP^-$) were then recorded.

2.4. Analytical application

An appropriate amount (450 μL) of the reagent 2-chloro-4-nitro-phenol fucopy-ranoside was immediately mixed with 50 μL of plasma/serum samples of HCC patients (26 persons) and healthy control (7 persons)) in incubator at 37 °C for 6 min. To the resultant solutions an accurate volume (300 μL) of rhodamine-B (5×10^{-4} mol L^{-1}) was added and swirled to mix the contents. Each solution was placed in an incubator at 37 °C for 5 min. The volume was completed to 3.0 mL with phosphate buffer of pH 5 and the emission intensity at 580 nm was then measured against the reagent blank. The main characteristics of the patients (male/female) and control groups are given in Table 1.

3. Result and discussion

3.1. Excitation and emission spectra

Previous studies [26] have shown that, the enzyme AFU reacts with the substrate 2-chloro-4-nitrophenol or 4-nitrophenol at pH 4–5 producing yellow colored product. This reaction has been used for measuring the activity of the enzyme AFU via the absorbance of the produced yellow colored species at pH 5.0 and 37 °C [24]. However, this, method suffered from the interference caused by the yellow color of the serum of patients and of the reagent 2-chloro-4-nitrophenol (or 4-nitro phenol). Another disadvantage was also noticed in many cases of patients of HCC that have high bilirubin [22,23]. Such methods suffered from the lake of sensitivity and accuracy due to the significant interference of the yellow color of the serum. Thus, attempts were made to overcome these disadvantages by testing the interaction of the compound 4-nitro phenol or 2-chloro-4-nitro phenol with rhodamine-B dye in aqueous medium.

In phosphate buffer (pH 5), preliminary investigations showed that, on mixing the reagent CNP with the ion pairing reagent RB and shaking, a green colored complex ion associate was developed and is most likely proceeds according to the following equation:

$$\text{2-Chloro-4-nitrophenol} + \text{Rhodamine-B} \rightleftharpoons [\text{Rhodamine-B}]^+ \text{ [2-Chloro-4-NP]-Ion associate} \quad (1)$$

After equilibrium, the excitation and emission spectra of the produced complex ion associate of rhodamine-2-chloro-4-nitrophenol or rhodamine-4-nitro phenol ($RB^+ CNP^-$) in the aqueous phase at pH 5 were recorded. The excitation and emission spectra (Fig. 1) of the complex associate $RB^+ CNP^-$ showed the characteristic excitation wavelength at 455 nm and the characteristic emission wavelength at 580 nm. The fluorescence intensity of the rhodamine-B in the emission spectrum at 580 nm decreased on adding CNP confirming the associate formation. On the other hand, rhodamine-B showed well defined emission spectrum (Fig. 2) close to the emission spectrum of the complex ion associate $RB^+ CNP^-$ (Fig. 1) while, compound 2-chloro-4-nitrophenol or 4-nitro phenol showed only excitation spectrum and no emission spectrum at 580 nm. Thus, in the subsequent work, the activity of the enzyme AFU was determined through measuring the fluorescence intensity of the ion associate $RB^+ CNP^-$ at 580 nm against a reagent blank at the optimum experimental conditions.

3.2. Analytical parameters

The influence of the hydrogen ion concentration on the fluorescence intensity of the complex ion associate $RB^+ CNP^-$ was investigated. The emission spectrum of the solution of 2-chloro-4-NP (5×10^{-5} mol L^{-1}) in the presence of rhodamine-B (5×10^{-5} mol L^{-1}) in a wide range of pH 2–8 employing dilute HCl and/or dilute sodium hydroxide was measured. The results shown in Fig. 3 revealed maximum change in the emission intensity in the pH range pH 2.5–6.0. At pH less than pH 2.5, the emission intensity of the produced complex associate $RB^+ CNP^-$ at 580 nm

Table 1
Main characteristics of the patients and control groups.

Status	Number of patients	Males/females		Age (year)	
		No.	%	Median	Range
HCC	20	15/5	75/25	51	24–75
Cirrhosis of chronic hepatitis C and B	4	2/2	50/50	48	37–69
Other neoplasms (gallbladder cancer, colon cancer and others)	2	2/0	100/0	42	28–56
Healthy adults	7	4/3	60/45	36	19–58

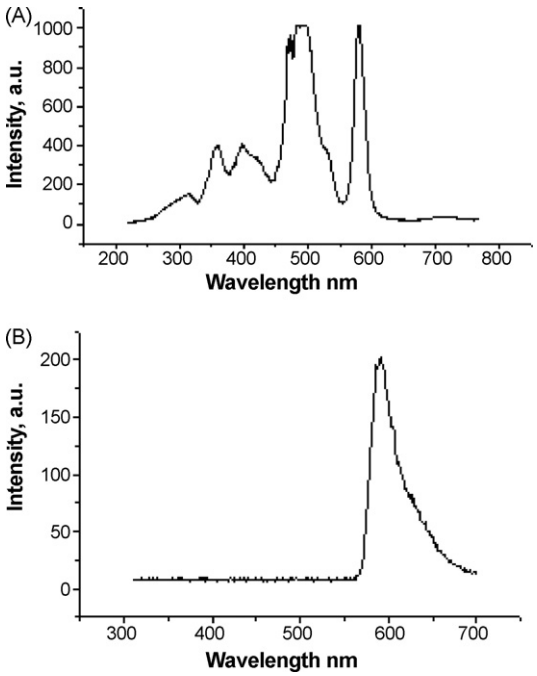


Fig. 1. The excitation (A) and emission (B) spectra of the complex ion associate 2-chloro-4-nitrophenol–rhodamine-B (2.5×10^{-5} mol L^{-1}) in phosphate buffer pH 4–5 at 37 °C.

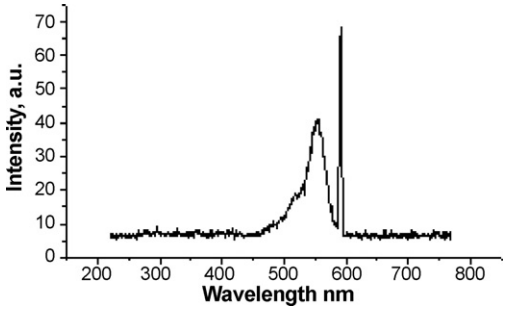


Fig. 2. The emission spectrum of rhodamine-B (5×10^{-5} mol L^{-1}) in phosphate buffer of pH 4–5 at 37 °C.

gradually decreased which is most likely attributed to the instability of the formed ion associate. At pH higher than pH 6.2, the emission intensity at 580 nm was also decreased gradually. Therefore, in the next work, phosphate buffer of pH 5 was selected for recording the enzyme AFU activity through measuring the fluorescence intensity of RB^+ CNP^- against reagent blank.

The effect of reaction time on the formation of the complex ion associate RB^+ CNP^- was critically investigated by mixing the reagent CNP (1.0 mL of 5×10^{-4} mol L^{-1}) with RB (1.0 mL of 5×10^{-4} mol L^{-1}) in phosphate buffer of pH 5 in measuring flask (10 mL). The solutions were completed to the mark with phosphate buffer of pH 5.0 and were left for various time intervals (1.0–30 min) solutions. The fluorescence intensity of the emission spectra of the solutions was then measured at 580 nm. The results revealed that, the fluorescence intensity reached maximum value at 5 min reaction time and slightly decreased at longer time higher than 30 min. Thus, a reaction time of 5–10 min was selected in the subsequent work.

The influence of temperature (15.0–70.0 °C) on the reaction of the reagent CNP and rhodamine-B was investigated in phosphate buffer of pH 5 and 5 min reaction time on a water bath. The fluorescence intensity of the emission spectra of the solutions was recorded at 580 nm versus reagent blank. The results showed that, the maximum intensity change was obtained at 35–40 °C and decreased gradually at higher temperature. This behavior may be attributed to the dissociation of the complex ion associate RB^+ CNP^-.

The influence of sodium dodecyl sulfonate (SDS), cetylpyridinium chloride (CPC) and the non-ionic surfactant Triton X100 on the fluorescence intensity of the produced associate RB^+ CNP^- at 580 nm was critically studied. In this experiment, an aliquot solution of phosphate buffer (pH 5) containing 2-chloro-4-nitrophenol (1.0 mL, 5×10^{-4} mol L^{-1}), rhodamine B (1.0 mL, 5×10^{-4} mol L^{-1}) and the required surfactant (1.0 mL, 0.1% w/v) was allowed to react for 5 min at 40 °C in an incubator. The fluorescence intensity of the produced associate at 580 nm was then measured and compared with that recorded without addition of surfactant. No significant changes on the fluorescence intensity of the associate RB^+ CNP^- were noticed with and without surfactant.

3.3. Interference study

The influence of some interfering species on the selectivity of the developed spectrofluorimetric method was investigated individually. Thus, the developed procedure was applied in the presence of various species commonly associated with the enzyme, e.g. NaCl, KCl (1×10^{-3} mol L^{-1}), albumin (0.5 g), urea (0.005 g L^{-1}), uric acid (0.008 g L^{-1}), total protein (0.001 g L^{-1}) and glucose (0.01 g L^{-1}) in phosphate buffer of pH 5.0 at 5 min contact time at 40 °C. The tolerable limit was defined as the concentration of the added species causing a deviation less than ±3.0% of the fluorescence intensity at the optimum conditions on the fluorescence intensity and emission spectrum of the ion associate RB^+ CNP^- (5×10^{-4} mol L^{-1}). The results revealed no significant change on the fluorescence intensity of RB^+ CNP^- in the presence of the

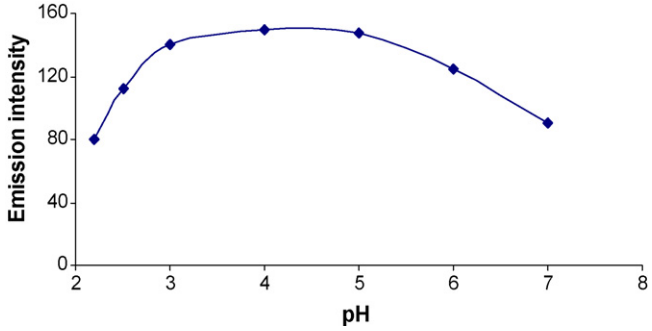


Fig. 3. Effect of pH on the fluorescence intensity on the formation of the complex ion associate 2-chloro-4-nitrophenol–rhodamine-B (2.5×10^{-5} mol L^{-1}) employing phosphate buffer at 37 °C.

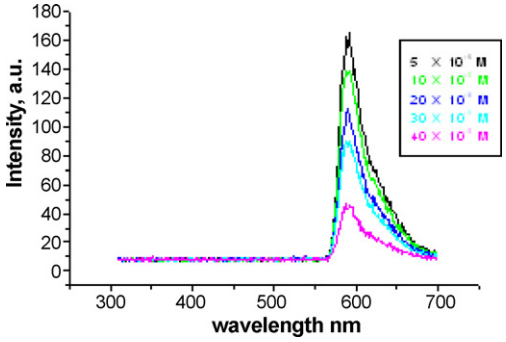


Fig. 4. Emission spectra of various concentrations (5×10^{-6}–40.0×10^{-6} mol L^{-1}) of 2-chloro-4-nitrophenol in the presence of rhodamine-B (2 mL, 5×10^{-4} mol L^{-1}) in 50-μmol L^{-1} phosphate buffer of pH 4–5 at 37 °C.

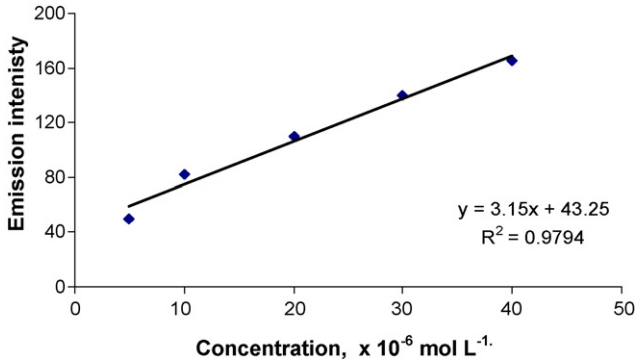


Fig. 5. Calibration plot for different concentrations of CNP in aqueous phosphate buffer of pH 4–5 versus emission intensity at 580 nm at 37 °C in the presence of rhodamine-B.

tested interfering ions indicating the selectivity of the developed method.

3.4. Dynamic range of the calibration graph and limit of detection

The validation of the proposed spectrofluorimetric procedure for measuring the AFU activity was examined via evaluation of the linear range of the plot of the fluorescence intensity measured versus various concentrations of 2-chloro-4-nitrophenol; lower limit of detection (LOD); limit of quantification (LOQ), repeatability, and specificity. The calibration plot of 2-chloro-4-nitrophenol in phosphate buffer (pH 5.0) was constructed by reacting 2-chloro-4-NP solution at various concentrations (5×10^{-6}–40.0×10^{-6} mol L^{-1}) with rhodamine-B (2.0 mL, 5.0×10^{-5} mol L^{-1}) and shaking for 5 min in an incubator at 37 °C. The emission spectra of the produced associate (RB^+ CNP^-) at various concentration of CNP are shown in Fig. 4. The plot of CNP concentration (5×10^{-6}–40.0×10^{-6} mol L^{-1}) versus the fluorescence intensity (at 580 nm) was linear (Fig. 5) with good correlation coefficient ($r^2 = 0.979$) and leveled off at concentration higher than 40.0×10^{-6} mol L^{-1} of CNP. This trend is most likely attributed to the shift of the equilibrium (equation (1)) to the left and the quantity of CNP species available to form complex ion associate with $[RB^+]_{(aq)}$ decreased which minimizes the associate formation [30] may account for the observed effect. A large excess of the reagent slightly decreased the fluorescence intensity possibly owing to the increased acidity of the aqueous phase which minimizes the associate formation [30].

The regression equation of the linear plot (Fig. 5) was: $Y = 3.15\,C$ (μM) + 43.25 with a correlation coefficient $r^2 = 0.979$, where Y = emission intensity and C represents the concentration of CNP in μM. According to IUPAC [31], the value of the LOD calculated using the formula LOD = $3S_{y/x}/b$ where $S_{y/x}$ is the standard deviation of y-residual and b is the slope of the calibration plot was found equal 1.01×10^{-7} mol L^{-1}. The value of LOQ where LOQ = $10S_{y/x}/b$ under the established conditions for lead (II) was found equal 3.4×10^{-9} mol L^{-1} and a relative standard deviation (RSD) for CNP at concentration of 5×10^{-6} was 2.5% ($n = 3$). Such limits could be improved to lower values by increasing the incubation times at the optimum experimental condition. The values of LOD and LQD confirmed the sensitivity of the proposed procedure compared to the reported methods [23–26]. This precision is suitable for the routine analysis of AFU activity for different patients. Moreover, the repeatability of AFU activity based on five replicate measurements for 5×10^{-6} mol L^{-1} of the reagent CNP calculated from the calibration curve was 97.47 ± 3.7% indicating good precision of the proposed method.

It was observed that there is no interference from other additives, e.g. interference from trace metal ions in particular Na, K which are commonly present in combination with the AFU enzyme in the serum of HCC patients. No significant difference could be detected upon comparing the emission intensity of the CNP component alone or in the presence of a high content (1:5) CNP: Na or K ions, respectively. Thus, the developed method is characterized by good specificity.

3.5. Analytical applications

The validation of the proposed spectrofluorimetric method was tested by measuring the activity of the enzyme AFU) for 33 serum samples of male and female patients (26) and healthy (7) in various ages (Table 1). The results obtained are summarized in Table 2. Good agreement between the values obtained by the developed procedure and the standard method [23]. The average value of the AFU enzyme activity obtained by the standard method [23] (29.28 ± 2.75 U/L) for the healthy samples (7) was found close to the value achieved by the developed method (31.14 ± 3.21 U/L) with an acceptable standard error (3.55–3.90). Also, good correlation between the values of the activity of serum AFU enzyme in some selected control samples measured by the standard and the developed spectrofluorometric methods ($r^2 = 0.883$, $p = 0.002$) is shown in Fig. 6. The F-and t-tests at 95% confidence levels did not exceed the theoretical ones and no significant differences between the developed and the standard [22] methods were observed confirming the accuracy of the developed procedure. In the HCC patient samples (20), the mean value of the AFU activity achieved by the standard method [23] (119.55 ± 74.80 U/L) was found also in good agreement with that obtained by the proposed method (123.5 ± 77.8 U/L) with a standard error in the range 13.99–14.08. On the other hand, an excellent correlation between the average values of the activity of the serum AFU enzyme in selected HCC patients

Table 2
Analytical results of the standard (A) and the developed spectrofluorimetric (B) methods for the healthy and patients' samples.[a]

Enzyme activity (U/L)	No	Subject	Methods		
			Standard error (SE)	Mean ± SD	Range
3.55	29.28 ± 2.75	16–41	7	Healthy	Standard method (A)
3.9	31.14 ± 3.21	15–46			Developed spectrofluorimetric method (B)
13.99	119.55 ± 74.80	54–249	20	HCC	Standard method (A)
14.08	123.5 ± 77.8	58–255			Developed spectrofluorimetric method (B)
2.81	29.95 ± 1.68	25–37.8	4	Cirrhosis of Chronic hepatitis C and B	Standard method (A)
2.61	29.25 ± 1.53	24–36.5			Developed pectrofluorimetric method (B)
2.69	29.16 ± 4.67	24–33.1	2	Other Neoplasms (gallbladder cancer, colon cancer and others)	Standard method (A)
1.85	28.33 ± 3.21	26–32			Developed spectrofluorimetric method (B)

[a] Average of three measurements ± standard deviation.

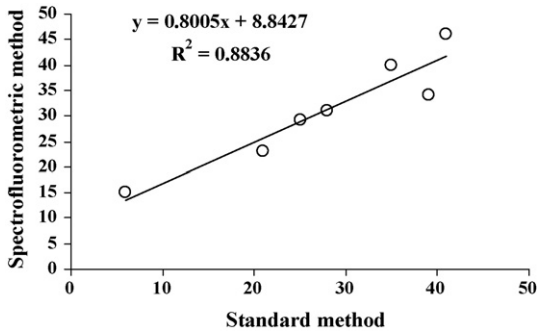


Fig. 6. Correlation between the values of the activity of serum AFU enzyme in some selected control samples as measured by the standard and the developed spectrofluorometric (pH 4–5) methods ($r^2 = 0.883$, $p = 0.002$).

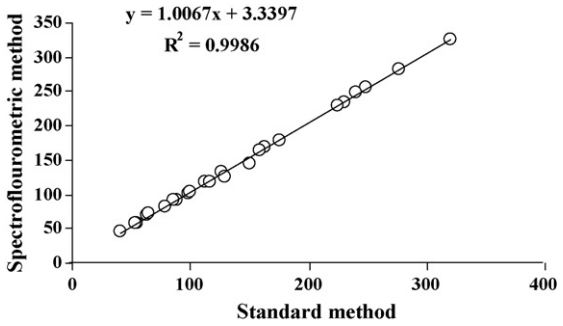


Fig. 7. Correlation between the values of the activity of serum AFU enzyme activity in some selected HCC patients measured by the standard and the developed spectrofluorometric (pH 4–5) methods ($r^2 = 0.99$, $p = 0.001$).

measured by the standard and the developed spectrofluorometric methods ($r^2 = 0.99$, $p = 0.001$) is also shown in Fig. 7 confirming the accuracy of the developed procedure. The correlation is positive and highly significant in patients and controls ($r^2 \approx 0.99$, $p < 0.001$) indicating that the proposed method has more/or less the same accuracy of measurements of AFU activity without its practical artifacts.

Moreover, for Cirrhosis of chronic hepatitis C and B samples (4), the average value obtained by the standard method [24] (29.95 ± 1.68 U/L) was found also quite close to the mean value (29.25 ± 1.53 U/L) obtained by the developed method with a standard error in the range 2.61–2.81 confirming the accuracy of the proposed procedure. In the case of neoplasm's (gallbladder cancer, colon cancer and others) samples (2) the average values obtained by the standard method and the proposed method were found equal 29.16 ± 4.67 and 28.33 ± 3.21 U/L, respectively with a standard error in the range of 1.85–2.69. The *F*-and *t*-tests at 95% confidence levels did not exceed the theoretical ones and no significant differences were observed between the developed and the standard [23] methods confirming the accuracy of the developed procedure.

4. Conclusions

The proposed method is sensitive enough, simple, reliable, fairly rapid and low cost procedure for measuring the activity of the enzyme AFU. This advantage encourages the application of the proposed method in routine quality control of measuring the activity of AFU in human serum. The method able to minimize the limitations, e.g. the interference caused by the yellow color of the serum of patients and the yellow color of 2-chloro-4-nitrophenol (or 4-nitro phenol) related to the sensitivity and selectivity for AFU activity in patients of Cirrhosis of chronic hepatitis C and B, other neoplasm's, e.g. gallbladder cancer, colon cancer and healthy adults compared to the other reported methods [21–24]. The disadvantage noticed for patients of HCC having high value of bilirubin makes the reported methods [15–18] are not compatible with the detection limit of the proposed method. This behavior is not likely attributed to the suppression effect of the interaction of CNP reagent and rhodamine-B under the optimal experimental conditions. Thus, the work is still continuing for studying the effect of various concentrations of bilirubin, memory effect, and competitive complex agents present in the investigated samples.

References

[1] M.G. Giardina, M. Matarazzo, R. Morante, Cancer 83 (1998) 2468.
[2] K. Okuda, E. Tabor, Liver Cancer, Churchill Livingstone, New York, 1997, p. 13.
[3] Y. Kubo, K. Okua, H. Musha, T. Nakashima, Gastroenterology 74 (1978) 578.
[4] M. Zoli, D. Magalotti, G. Bianchi, C. Gueli, G. Marchesini, E. Pisi, Cancer 78 (1996) 977.
[5] B. Cobucci-Ponzano, A. Trincone, A. Giordano, M. Rossi, M. Moracci, J. Biol. Chem. 278 (2003) 14622.
[6] L. Aheng-wen, C. Chao-Sheng, C. Shih-Shen, T.M. Kowk-Kong, L. Chun-Hung, C. Cheng-Wen, T.Y. Chuan, I. Yaw-Kuen, Biochemistry 48 (2009) 10.
[7] W.M. El Shemey, O.S. Desouky, M.S. Mohammed, Phys. Med. Biol. 48 (2003) N 239.
[8] C.A. Burtis, E.R. Ashwood, Tietz Fundamentals of Clinical Chemistry, 5th edn, W.B. Saunders, PA, Philadelphia, 2001.
[9] H.J. Shu, T. Saito, H. Watanabe, Biochem. Biophys. Res. Commun. 293 (2002) 150.
[10] T. Nakatsura, Y. Yoshitake, S. Senju, Biochem. Biophys. Res. Commun. 306 (2003) 16.
[11] A. Marenghini, M. Cottone, E. Sciarrino, M.P. Marceno, F. La Seta, G. Fusco, Dig. Dis. Sci. 33 (1988) 47.
[12] H. Oka, A. Tamori, T. Kuroki, K. Kobayashi, S. Yammamoto, Hepatology 19 (1994) 61.
[13] A.K. Sanki, B.J. Voss, S.J. Sucheck, D.R. Ronning, Anal. Biochem. 385 (1) (2009) 120.
[14] Y. Osaki, T. Kimura, A. Arimoto, H. Oka, O. Yamazaki, T. Manabe, H. Chung, M. Kudo, T. Matsunaga, J. Hepatol. 49 (2008) 223.
[15] M.E. El-Houseini, M. El-Sherbiny, M.E. Awad, J Egypt. Nat. Cancer Inst. 4 (2001) 277.
[16] F. Van Hoof, H.G. Hers, Eur. J. Biochem. 7 (1968) 34.
[17] S. Blumbeig, J. Hildesheim, J. Yariv, K.J. Wilson, Biochim. Biophys. Acta 264 (1972) 171.
[18] G.A. Lewy, A. McAUan, Biochem. J. 80 (1961) 433.
[19] F. Van Hoof, H.G. Hers, Lancet 1 (1968) 1198.
[20] S.W. Johnson, J.A. Alhadeff, Biochem. Physiol. 99B (1991) 479.
[21] Y. Deugnier, Hepatology (1984) 4889.
[22] P. Durand, C. Borrone, C. Della, J. Pediatr. 75 (1969) 665.
[23] K. Zietke, S. Okada, J.S. O'Brien, J. Lab. Clin. Med. 79 (1972) 1649.
[24] J. Troost, M.C. Van der Heijden, G.E. Staal, Clin. Chim. Acta 73 (1976) 329.
[25] W. Ju-Jun, C. En-Hua, Clin. Chim. Acta 347 (2004) 103.
[26] S. Wood, Clin. Chim. Acta 58 (1975) 251.
[27] M. Cuer, A. Barnier, P. de La Salmoniere, G. Durand, N. Seta, Clin. Chem. 46 (2000) 560.
[28] Z.U. Miura, K. Okamoto, H. Yanase, J. Biosci. Bioeng. 99 (2005) 629.
[29] M.W. Ho, J. O'Brien, F R. Natl. Acad. Sci. USA 68 (1971) 2810.
[30] S. Yamaguchi, K. Uesugi, Analyst 109 (1984) 1393.
[31] J.C. Miller, J.N. Miller, Statistics for Analytical Chemistry, 4th edn, Ellis-Howood, New York, 1994, p.115.

Talanta 80 (2009) 24–30

Contents lists available at ScienceDirect

Talanta

journal homepage: www.elsevier.com/locate/talanta

Fabrication of SU-8 based microchip electrophoresis with integrated electrochemical detection for neurotransmitters

Mario Castaño-Álvarez[a], M. Teresa Fernández-Abedul[a], Agustín Costa-García[a,*], María Agirregabiria[b], Luis J. Fernández[b], Jesús Miguel Ruano-López[b], Borja Barredo-Presa[c,1]

[a] Departamento de Química Física y Analítica, Universidad de Oviedo, Asturias, Spain
[b] MEMS/MST Department, IKERLAN-IK4 S. Coop., Mondragón, Spain
[c] Microliquid-Experts in Microfluidics, Avenida Uribarri 19-1, Mondragón, Spain

ARTICLE INFO

Article history:
Received 15 January 2009
Received in revised form 18 May 2009
Accepted 26 May 2009
Available online 25 June 2009

Keywords:
Microchip electrophoresis
Photoresist EPON SU-8
Electrochemical detection
End-channel detector
Platinum thin-film
Neurotransmitters

ABSTRACT

A new SU-8 based microchip capillary electrophoresis (MCE) device has been developed for the first time with integrated electrochemical detection. Embedded electrophoretic microchannels have been fabricated with a multilayer technology based on bonding and releasing steps of stacked SU-8 films. This technology has allowed the monolithic integration in the device of the electrochemical detection system based on platinum electrodes. The fabrication of the chips presented in this work is totally compatible with reel-to-reel techniques, which guarantee a low cost and high reliability production. The influence of relevant experimental variables, such as the separation voltage and detection potential, has been studied on the SU-8 microchip with an attractive analytical performance. Thus, the effective electrical isolation of the end-channel amperometric detector has been also demonstrated. The good performance of the SU-8 device has been proven for separation and detection of the neurotransmitters, dopamine (DA) and epinephrine (EP). High efficiency (30,000–80,000 N/m), excellent precision, good detection limit (450 nM) and resolution (0.90–1.30) has been achieved on the SU-8 microchip. These SU-8 devices have shown a better performance than commercial Topas (thermoplastic olefin polymer of amorphous structure) microchips. The low cost and versatile SU-8 microchip with integrated platinum film electrochemical detector holds great promise for high-volume production of disposable microfluidic analytical devices.
© 2009 Elsevier B.V. All rights reserved.

1. Introduction

Microfabricated fluidic devices have gained a great interest, especially since capillary electrophoresis (CE) microchips were proposed by Manz et al. [1,2]. These miniaturized systems are characterized by high-speed, high-throughput, small sample and reagent requirements as well as integration and compactness.

Although microfluidic devices were initially fabricated using glass substrates, in the last years, polymer materials such as poly(methylmethacrylate) (PMMA) [3,4], poly(dimethylsiloxane) (PDMS) [5], polycarbonate (PC) [6], polyester [7], poly(ethylenterephthalate) (PET) [8] and cyclic olefin copolymers (COC) [9] have been also employed owing to their mechanical and chemical properties, low cost, ease of fabrication and higher flexibility. Recently, the photoresist EPON SU-8 (hereinafter referred to as SU-8) has been used to fabricate devices for biochemical sample preparation and detection [10,11]. SU-8 is a negative tone epoxy photopatternable resist, mechanically reliable, optically transparent, chemically resistant and hydrophilic. Thus, it has been successfully employed to fabricate microfluidic systems [12–14], movable micromechanical components [15] and optical waveguides [16]. A simple process based on bonding and releasing steps of stacked SU-8 films has been developed to fabricate an electrophoretic device, which has been applied to sodium dodecyl sulfate-capillary gel electrophoresis of proteins with optical detection [17]. Electrochemical detection has not been used before in combination with SU-8 microchips.

Among the detectors used for microchip capillary electrophoresis (MCE), electrochemical detection (ED) has proven to be very effective due to characteristics such as inherent miniaturization, sensitivity, low cost, portability and compatibility with microfabrication technology. Amperometric detection, since the first reported in 1998 by Wolley et al. [18], has been the most widely employed electrochemical technique for MCE. In this detection mode, an appropriate design of the detection cell is required for ensuring electrical isolation from the high separation voltage. Various approaches have been developed with this aim including in-channel, end-channel and off-channel configurations [19].

* Corresponding author. Fax: +34 9 85103125.
E-mail addresses: costa@fq.uniovi.es, costa@sauron.quimica.uniovi.es (A. Costa-García), uliquid@uliquid.com (B. Barredo-Presa).
[1] Fax: +34 9 43712223.

0039-9140/$ – see front matter © 2009 Elsevier B.V. All rights reserved.
doi:10.1016/j.talanta.2009.05.049

In- and off-channel detection modes are based on the placement of the working electrode directly within the separation channel without [20,21] or with an electric field decoupler [22,23] respectively. In these approaches, the electrodes have been normally integrated on the chip by means of films of different materials such as platinum [24,25], palladium [22,26,27], gold [21,26] and indium tin oxide (ITO) [28]. Metal layers of titanium, platinum and palladium that were the basis of thirteen electrodes (including three for detection, six for decoupling and four as high-voltage electrodes) have been integrated in a PDMS/glass microchip [5]. Apart from films, carbon fibre electrodes were also employed [29].

The end-channel configuration has been the most commonly used amperometric detection mode, where the working electrode is placed close (10–50 μm) to the outlet of the separation channel. Replaceable disk [9,30–35] or thick-film [34–37] working electrodes can be aligned off-chip using XYZ micromanipulators, guide tubes or other special cell designs. However, in this approach non-total integration of the electrochemical detector on the chip is obtained. The distance electrode–microchannel end [38] and the effect of the separation potential [39] influences the results. On the other hand, the electrodes can also be permanently integrated on-chip by means of thin-films made of platinum [18,40], gold [41–43], copper [42] or carbon [44,45] placed close to the channel exit. Inclusion of electrodes directly on the chip surface takes full advantage of the microfabrication approach. Thus, Baldwin et al. [40,46] have integrated all electrophoresis and electrochemical platinum electrodes on a glass microchip using traditional microfabrication techniques, including photolithographic patterning, wet chemical etching, direct current sputtering and thermal wafer bonding. Wilke and Büttgenbach [47] have also developed a glass microdevice with fully integrated six gold electrodes for electrophoresis and amperometric detection.

Catecholamine family of neurotransmitters: dopamine, epinephrine, norepinephrine, and catechol have been the analytes most frequently studied by MCE-ED. The reasons for this are related both to the important physiological role of these compounds in the transmission of nerve impulses and to the fact that they exhibit nearly ideal electrochemical properties for detection purposes. Thus, microchips of different materials and several electrodes have been successfully employed to separate and detect these analytes [5,18,19,22,30,32,38,46,48–55]. Detection limits cited with these devices have typically been in the nM to μM range.

In this work, a microchip electrophoresis has been fabricated for the first time on SU-8 resist with an integrated electrochemical detector based on platinum film electrodes [56]. The new microfabricated SU-8 chips have been used for separation and detection of the neurotransmitters, dopamine (DA) and epinephrine (EP). Several factors influencing the performance of the SU-8 MCE-ED have been examined. Thus, the buffer composition, separation voltage and detection potential have been evaluated.

2. Experimental

2.1. Reagents

A 125 μm thick polyimide film called Kapton from Teinser (Spain) and a 4 in. Pyrex wafers (750 μm thick) were used as substrates. Positive photoresist S1818 from Shipley was employed for lift-off and as an adhesive layer between Kapton and Pyrex. Two types of SU-8 photoresists are used for microchannel fabrication: SU-8-50 and SU-8-5 ordered from Microresist (Germany). The developer is propyleneglycol-monoether-acetate (PGMEA, Microresist). Isopropanol (IPA) from Aldrich is employed to rinse the samples.

Dopamine (DA), epinephrine (EP), tris(hydroxymethyl)aminomethane (Tris), 2-(*N*-morpholino)-ethanesulfonic acid (MES), L-histidine (His), sodium dodecyl sulfate (SDS), t-octylphenoxypolyethoxyethanol (Triton X-100), sodium hydroxide and boric acid (99.5%) were purchased from Sigma–Aldrich (St. Louis, USA). Sulphuric (95–97%) and perchloric acids (70%) were obtained from Merck (Germany).

Dopamine and epinephrine solutions were prepared daily in the running buffer. All solutions were filtered through nylon syringe filters (Cameo 30N, 0.1 μm, 30 mm) obtained from Osmonics (Minnetonka, USA).

Water was purified employing a Milli-Q plus 185 equip from Millipore (Bedford, USA). All other reagents were of analytical reagent grade.

2.2. Microchip fabrication

The electrophoretic devices have been fabricated at a wafer level using the process described in a previous work [10]. It is based on the bonding of two photopatterned SU-8 layers on two different substrates: (i) the bottom one, which is a pyrex wafer where Ti/Pt electrodes have been previously patterned, contains the SU-8 layer which defines the microfluidic channels of the chip, and (ii) the top one, which is a Kapton film bonded to a Pyrex wafer, includes the SU-8 layer which will be used as cover, closing the whole chip and leaving open the inlets and outlets. The photomasks were generated using a layout software Clewin and were printed on a plastic film photomask by a photoplotter of 64,000 dpi (J.D. Photo-Tools Ltd., UK). Both wafers are put into contact and bonded together by the use of temperature and pressure. Once both SU-8 layers are bonded, the poor adhesion between the Kapton and the SU-8 allows the releasing of the top substrate, and the chip fabrication is finished, simplifying dramatically the external connection. The following sections will describe the fabrication process in more detail.

2.2.1. Fabrication of the bottom substrate

The fabrication process starts with the electrode definition by an S1818 photolithographic step. Then, 15 nm of titanium and 150 nm of platinum are sputtered and lift-off is carried out in an acetone ultrasonic bath. After that, a photolithography of a 5 μm thick SU-8-5 layer is performed in order to improve photoresist to pyrex adhesion. In order to process this layer, is first spun at 2500 rpm and soft-baked at 95 °C for 5 min. Next, the photoresist is polymerised with an exposure of 160 mJ/cm^2 and a 5-min post-bake at 95 °C. Finally, the SU-8-5 is developed in a PGMEA developer bath for 2 min and hard baked at 170 °C for 20 min.

Once the SU-8-5 is highly polymerised to improve the adhesion, a 20 μm thick SU-8-50 layer is photopatterned to fabricate the microchannel cavities and electrode apertures. Briefly, the recipe to obtain this layer is: (i) dynamic spin coating at 5000 rpm; (ii) soft-baking at 90 °C for 8 min using ramps up and down of 7 °C/min temperature ramps to avoid microcracking; (iii) UV exposure of 140 mJ/cm^2; (iv) post-baking at 90 °C for 4 min with progressive temperature ramps; and finally (v) developing in a PGMEA bath and rinsing in IPA.

2.2.2. Fabrication of the top substrate

Firstly, a 125 μm thick Kapton film is bonded to a Pyrex wafer using the photoresist S1818 as an adhesive layer. This photoresist is spun on the Pyrex wafer at 4000 rpm for 30 s. Immediately, both substrates are put into contact under a vacuum of 0.1 Pa in a substrate bonder, pressed together at 25 kPa and heated to 100 °C for 20 min. Thus, a top Kapton–Pyrex substrate, rigid enough to perform photolithography is obtained. Finally, a 20 μm thick SU-8-50 layer is photopatterned to achieve the microchannel covers and electrode apertures using the same recipe as in the previous section.

2.2.3. Bonding

Once the SU-8-50 is photopatterned on both substrates, a bonding recipe is carried out [12]. Both wafers are brought into contact using a substrate bonder at 0.1 Pa, pressed together with 300 kPa and heated to 100 °C for 20 min, which is above the glass transition temperature of the partially polymerised SU-8. When processing parameters are correctly optimized, no changes in the different SU-8 layer dimensions can be observed due to the bonding step [10]. This causes the two polymer layers to become irreversibly bonded together. Due to the transparency of the Kapton film on Pyrex, alignment is straightforward regardless of the bottom wafer.

2.2.4. Kapton releasing

After the bonding step, the top Kapton–Pyrex wafer is detached from the SU-8 stack and bottom substrate. For that purpose, the bonded wafers are immersed in an acetone ultrasonic bath for 10 min. Subsequently, the top Pyrex wafer and the Kapton film are separated by the insertion of a razor blade. Finally, the Kapton film is easily peeled off from the SU-8 stack. Since all the layers are photopatterned before the bonding step, the Kapton releasing left the microchannel inputs/outputs and electrode apertures in contact with the outside world, radically simplifying the packaging.

Fig. 1 shows a schematic diagram of the fabrication process of the device. As a result of the fabrication process, SU-8 based two channel (50 μm wide and 20 μm deep each, Fig. 2b) electrophoresis devices on top of a pyrex wafer with integrated electrodes for electrochemical detection were obtained. SU-8 microchips are fabricated in batches, the size of the batch being 8 microchips.

2.3. Microchip design

The final design of the SU-8 microchip with integrated electrochemical detector is shown in Fig. 2. The device (38 mm × 13 mm) is formed by a 35 mm long separation channel and a 10 mm long injection channel. The injection channel is situated 5 mm from the beginning of the separation channel. The channels had 50 μm wide and 20 μm high. Holes of 2 mm diameter that act as reservoirs were situated at the end of the channels.

A commercial Topas (thermoplastic olefin polymer of amorphous structure) microchip was also used to compare with the fabricated SU-8 microchip. Topas microchips were purchased from Microfluidic-ChipShop (Jena, Germany) and these consisted of a plate (58.5 mm × 13.5 mm) of 2 mm thickness with a 54 mm long separation channel and 9 mm long injection channel. The two channels crossed each other halfway between the sample and sample waste reservoirs and 4.5 mm from the separation channel buffer reservoir. The channels were 20 μm depth with 32 μm width at the bottom and 60 μm width at the top. A cover plate of similar dimensions but 200 μm-thick is adhered for closing the channel at the top. Holes of 2 mm diameter that act as reservoirs were situated on the 2-mm-thick plate at the end of the channels.

Micropipette tips were cut for obtaining 0.5 cm long pieces with a diameter of 0.3 cm at the top. They were adhered concentrically

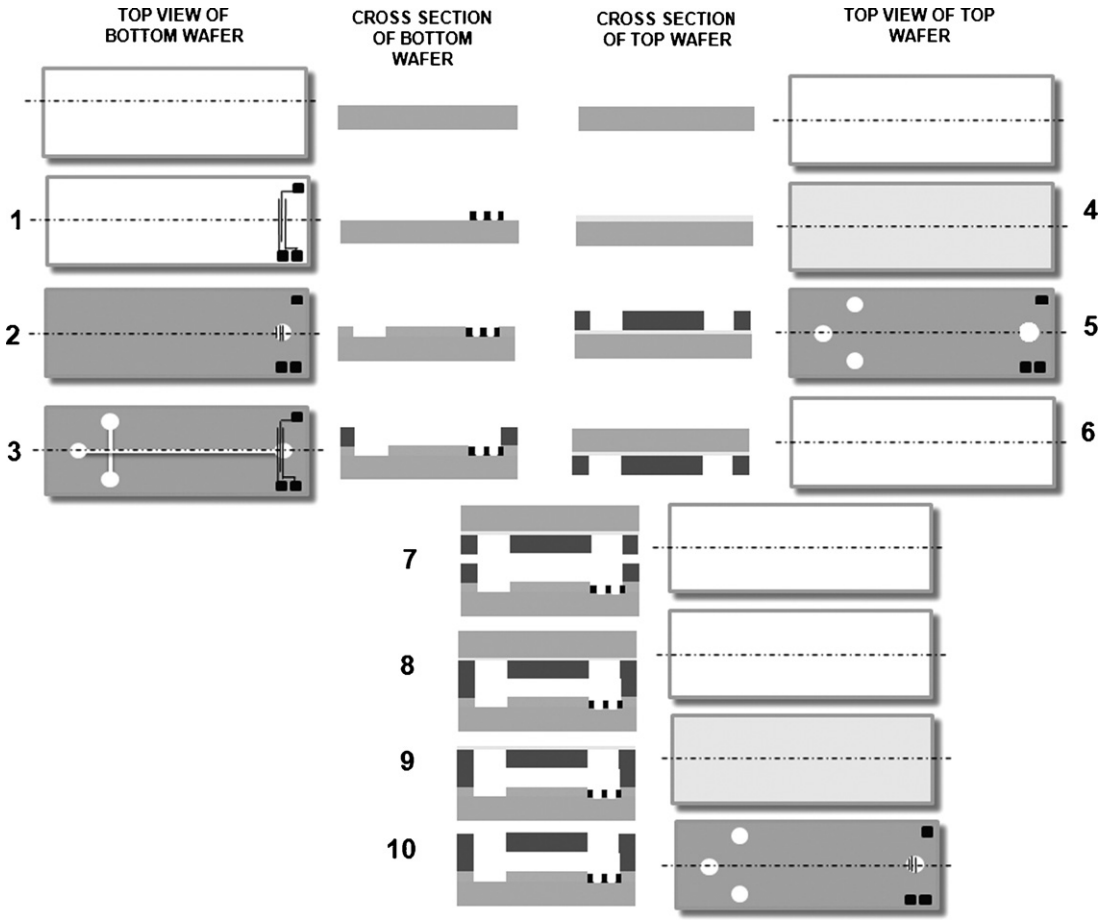


Fig. 1. A schematic diagram of the fabrication process of the device. The numbers in the figure correspond to the different steps carried out in the fabrication process: (1) fabrication of Ti/Pt electrodes by sputtering and lift-off; (2) photolithography of a 5 μm thick SU-8-5 seed layer to improve SU-8-to-glass adhesion; (3) photolithography of a 20 μm thick SU-8-50 layer to fabricate microchannel cavities; (4) bonding of a pyrex wafer and a Kapton film; (5) photolithography of a 20 μm thick SU-8-50 layer to fabricate microchannel covers; (6) turn over the top substrate to be able to align it with the bottom substrate; (7) align both substrates; (8) bonding of the two substrates; (9) pyrex wafer releasing and finally; (10) Kapton releasing.

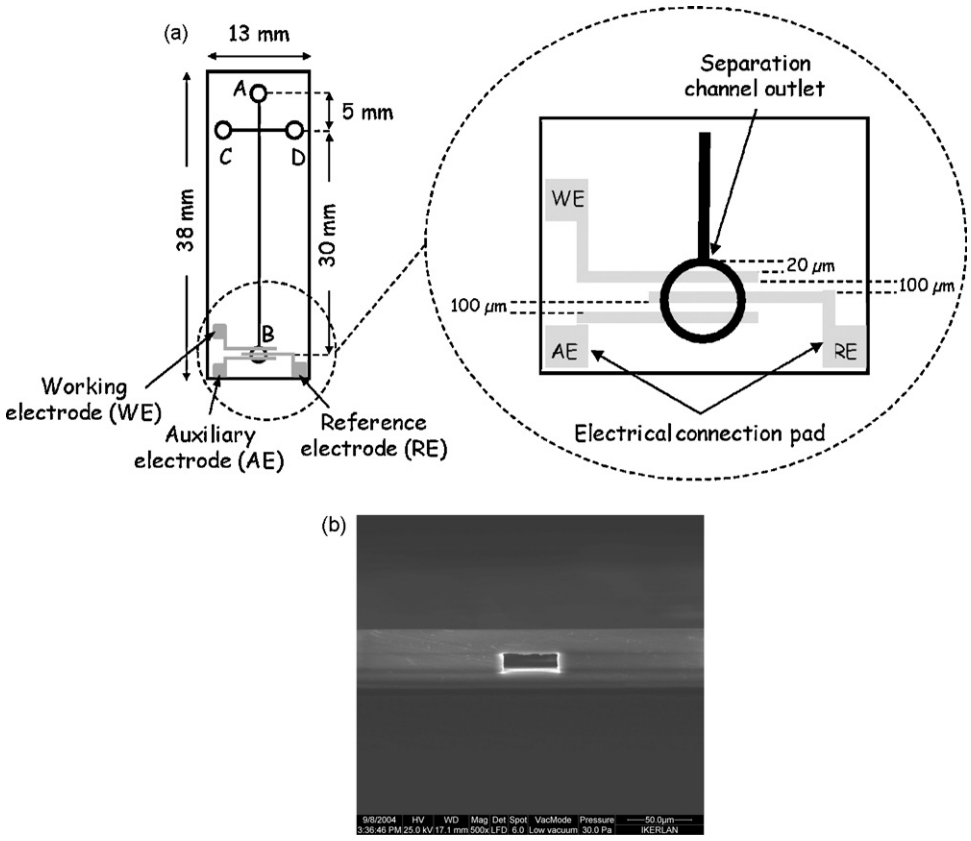


Fig. 2. (a) Scheme of the design and dimensions of the SU-8 microchip with integrated amperometric detector (running buffer (A), detection (B), sample (C) and sample waste (D) reservoirs). (b) SEM picture of the cross-sectional view of a microchannel. The dark rectangle in the center represents the microchannel cross-section.

to the chip holes (Topas and SU-8 microchips) with Araldit (Vantico AG, Basel, Switzerland) forming reservoirs of approximately 50 μL volume. A methacrylate holder (18 cm × 13 cm × 2 cm) was fabricated for accommodating the chips. Once inserted the chip on the holder, a small rectangular piece (5 cm × 1 cm × 0.8 cm) was fixed with screws with the aim of securing the chip.

2.4. Electrochemical detector

The electrochemical detector in the SU-8 microchip was integrated at the end of the separation channel as can be seen in Fig. 2a. The detector is based on three 100 μm wide Ti/Pt electrodes fabricated by sputtering and lift-off as was stated above. The working electrode was placed at a distance of 20 μm from the end of the separation channel. The other two electrodes (reference and auxiliary electrodes) were separated by a distance of 100 μm one from each other. The distance between working and reference electrodes is also 100 μm. A copper cable was fixed to platinum films with a conducting silver epoxy resin (CW2400, RS Components, UK) for electrical connection.

In the Topas microchip, the detector was situated in the waste reservoir with a three-electrode configuration as previously reported [57]. An external Ag/AgCl reference electrode and a 0.3 mm diameter platinum wire (Goodfellow, UK) auxiliary electrode were used. A 100 μm diameter gold wire (Alfa Aesar, Germany) was employed as working electrode with an end-channel configuration. The working electrode was manually aligned through a guide channel practiced on the microchip with the help of a cutter.

Amperometric detection was performed with an Autolab PGSTAT 10 (ECO Chemie, Netherlands) potentiostat interfaced to a Pentium Celeron, 333 MHz, 64MB RAM computer system and controlled by Autolab GPES software version 4.9 for Windows 98.

2.5. Electrophoresis procedure

Capillary zone electrophoresis separations were carried out in uncoated channels using two high-voltage power supplies (HVPS, MJ series) with a maximum voltage of +5000 V from Glassman High Voltage (High Bridge, NJ 08829-0317, USA). They were interfaced to a Pentium Celeron, 333 MHz, 64MB RAM computer system and monitored by a DT300 Series Board, DT Measure Foundry 4.0.6 software for Windows 98. High-voltage electrodes consisting of 0.3 mm diameter, 1 cm long platinum wires (Goodfellow, UK) were manually inserted into each of the reservoirs, except for reservoir B where the detection is located. They are connected by means of crocodile clips to the HVPS.

Prior to electrophoresis, SU-8 microchips were only rinsed with the running buffer. The microchannels were filled with the running buffer solution using a simple vacuum system. The microchip was fixed in its holder and a Faraday cage was used for housing it in order to minimize electrical interferences. The detection potential is applied for baseline stabilization, and afterwards reservoir C was filled with the sample solution and injections were performed by applying the desired voltage to the sample reservoir (C) with the detection reservoir (B) grounded. Separation was performed by applying the corresponding voltage to the running buffer reservoir (A) with the detection reservoir (B) grounded. Then the electropherogram was recorded. All experiments were performed at room temperature. Microchips are stored filled with water at room temperature and kept from the light.

Safety considerations: High-voltage power supplies should be handled with extreme care to avoid electrical shock.

3. Results and discussion

The simple procedure of microfabrication on SU-8 resist allows getting different designs of microchips (single- or dual-channel configurations). Meanwhile the geometry of glass and Topas microchannels is semicircular and trapezoidal respectively, a rectangular section is achieved in this case (see Fig. 2b). Moreover, integration of the electrodes for detection during the same process is possible. Thus, the detector design can be easily modified in order to develop end-channel or off-channel (including 1 or 2 decouplers with different dimensions) approaches. Although it is possible, the SU-8 microchips with integrated amperometric detection have been initially characterized using an only separation channel in combination with the platinum end-channel detector. Dual-channel SU-8 microchips, with a parallel channel that allows simultaneous measurements of the same or different analytes, will be checked in the future.

Several parameters such as composition of the running buffer, separation voltage and detection potential affect to the behaviour of the microchannels and detection system. Thus, the electrochemical response of the integrated platinum film electrodes on the SU-8 microchip was studied using dopamine (DA) and epinephrine (EP) as model analytes. Firstly, TB buffer (50 mM Tris–Boric acid pH = 7.0) was employed for determining the optimal detection potential of the dopamine. SU-8 presents the highest electro-osmotic mobility at pH ≥ 7 (in the order of that found for glass), suggesting equal charge densities on both surfaces [58]. Thus, the hydrodynamic voltammogram (HDV) was recorded (data not shown) between 0.0 and +0.7 V using a separation voltage of +1000 V and an injection voltage of +250 V applied during 5 s. Hydrodynamic curve reached a plateau at +0.5 V. Therefore, +0.6 V was employed as detection potential.

The effect of the separation voltage on the analytical signal (100 μM DA) was studied using an injection voltage of +250 V applied for 5 s, a detection potential of +0.6 V and TB as running buffer. When the separation voltage is varied from +250 to +1250 V, the peak current was increased from 4.4 to 9.2 nA due to the migration speed of analyte zone in the channel is enhanced and a smaller sample dispersion is produced. As expected, by enhancing the separation voltage, the migration time and the half-peak width dramatically decreased, from 166.5 to 35.7 s and from 23.7 to 4.4 s, respectively. However, the increasing interference of the high voltage (on the detection potential producing noise generation) leads to decreased efficiency, thus, a maximum theoretical plate number (N) of 21,000 m^{-1} was obtained using +500 V as separation voltage.

Electropherograms for dopamine, epinephrine and a mixture of both are shown in Fig. 3. Although the migration time of the dopamine and epinephrine was slightly different, it was not enough to separate the two analytes and only one peak was recorded for the mixture.

In order to obtain a better separation of dopamine and epinephrine, pH was lowered and a MES-His buffer was employed. 25 mM MES-His pH = 5.7 was employed as new running buffer. Since both, the analytes charge and the wall charge changes with pH, this is very important in obtaining an adequate resolution [59]. The pH of MES solution was adjusted with histidine to avoid an excessive current in the microchannel when the separation voltage was applied.

With the change of buffer composition and pH, the selection of the optimal detection potential relies newly on the construction of hydrodynamic voltammograms (HDVs). The HDVs were made using a sample mixture of DA and EP 100 μM each, a separation voltage of +750 V and an injection voltage of +250 V applied for 5 s. As is shown in Fig. 4 the curves reached a plateau at +1.1 V, thus, a detection potential of +1.2 V was employed. Compared to pH 7, the detection potential has been increased. Since protons are involved in the electrochemical reaction, the change in pH makes more difficult, in this case, the oxidation process. Therefore, a higher potential has to be employed.

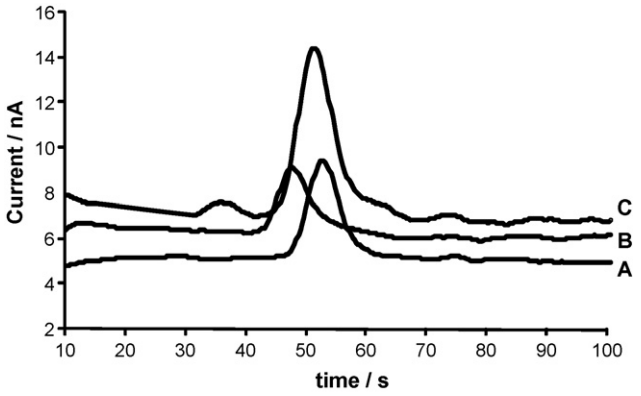


Fig. 3. Electropherograms for (A) 100 μM EP, (B) 100 μM DA and (C) a mixture of 100 μM DA-EP using an SU-8 microchip with integrated platinum film detector. *Conditions*: running buffer: 50 mM TB pH = 7.0, V_{sep} = +750 V; V_{inj} = +250 V for 5 s; E_d = +0.6 V (*vs.* Pt).

The influence of the separation voltage on a mixture of DA and EP was studied using an injection voltage of +250 V applied for 5 s, a detection potential of +1.2 V and 25 mM MES-His pH = 5.7 as running buffer. Fig. 5 displays the electropherograms for the separation of DA and EP using separation voltages between +500 and +1500 V. As expected, the migration time decreased from 161.9 and 205.1 to 51.9 and 65.7 s as well as the half-peak width from 11.7 and 16.1 to 4.0 and 5.9 s for DA and EP, respectively. A higher separation voltage supposed enhancing the peak current from 3.1 to 7.3 nA and 3.0 to 6.8 nA for DA and EP, respectively; due to smaller dispersion of the analytes in the channels. The higher theoretical plate number (39,000 ± 1000 and 30,000 ± 1000 m^{-1} for DA and EP, respectively, $n = 3$) was obtained using a voltage of +750 V. When the voltage was increased up to +750 V the plate number ($N = 5.54(t_m/w_{1/2})^2$) and the resolution ($Rs = 2(t_2 - t_1)/(w_1 + w_2)$) was gradually reduced as can be seen in Fig. 5 (inset). The influence of increasing the electric field can be also noted in a higher initial baseline slope of electropherograms (Fig. 5). However, this did not suppose an increase in the background noise level (1.5 pA), which means, the detector was effectively isolated from the high separation voltage. In this config-

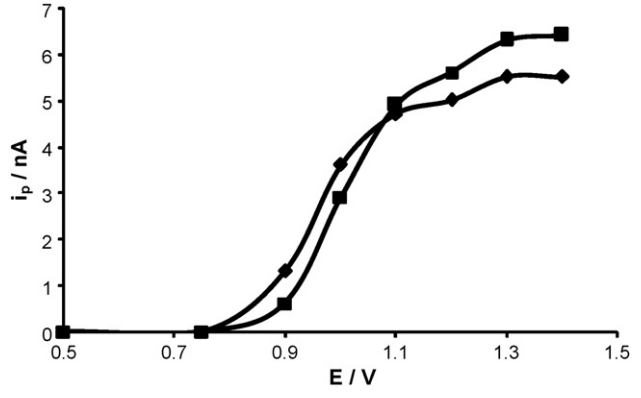


Fig. 4. Hydrodynamic voltammograms for (♦) 100 μM DA and (■) 100 μM EP on the SU-8 microchip with integrated platinum film detector. *Conditions*: running buffer: 25 mM MES-His pH = 5.7, V_{sep} = +750 V; V_{inj} = +250 V for 5 s.

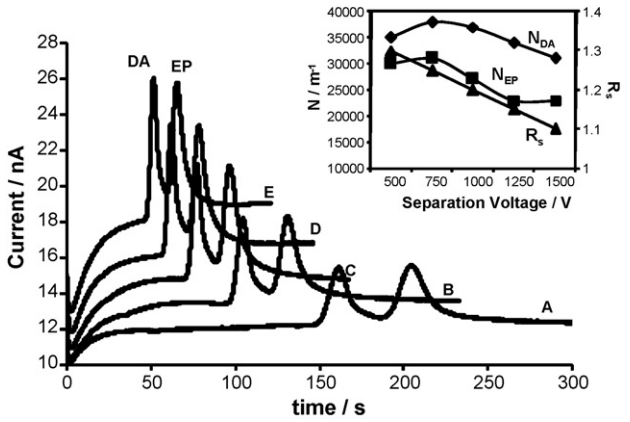


Fig. 5. Influence of the separation voltage on the detection of 100 μM DA and EP on the SU-8 microchip. *Separation voltages*: +500 (A), +750 (B), +1000 (C), +1250 (D) and +1500 V (E). Also shown (inset) the effect of separation voltage upon the resolution (▲) and the theoretical plate number for (♦) DA and (■) EP. *Conditions*: running buffer: 25 mM MES-His pH = 5.7; V_{inj} = +250 V for 5 s, E_d = +1.2 V (*vs*. Pt).

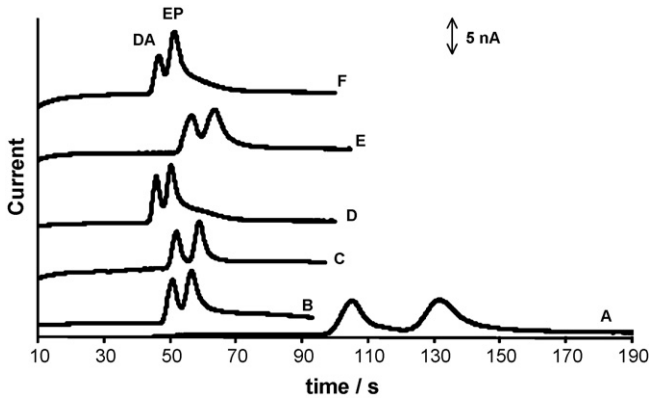


Fig. 6. Electropherograms for mixtures of 100 μM DA and EP in successive days; (A) day 1, (B) day 2, (C) day 3; with different pretreatments; (D) $HClO_4$ 0.1 M, (E) NaOH 0.1 M and (F) using 25 mM MES-His 0.1% Triton X-100 pH = 5.7 as running buffer on the SU-8 microchip. Conditions as in Fig. 5.

uration, the working electrode is outside the channel, and then, the separation voltage has a minimal influence on the baseline noise level because most of the voltage is dropped across the channel.

The precision of analytical signals on the SU-8 microchip with integrated platinum detector was evaluated from a series of repetitive injections of a sample mixture containing 100 μM DA and EP. The relative standard deviation (RSD) of peak current for ten successive signals was 1.8% ($i_{p(average)}$ = 6.4 nA) and 1.2% ($i_{p(average)}$ = 6.8 nA) for DA and EP respectively. RSD of migration time was 2.1% ($t_{m(average)}$ = 105.4 s) and 2.0% ($t_{m(average)}$ = 134.6 s) for DA and EP, respectively. No cleaning of the microchannel or the amperometric detector was necessary between measurements.

The end-channel Pt detector integrated on the SU-8 microchip displayed well-defined concentration dependence for DA and EP. Thus, a good linear relationship over a range of 0.5–200 μM with correlation coefficients (n = 8) of 0.9994 and 0.998 was obtained for DA and EP, respectively. The calibration plots showed sensitivities of 65 and 73 pA μM^{-1} for DA and EP, respectively. A detection limit of 450 nM was estimated for DA and EP considering a signal-to-noise ratio (S/N) of 3. This limit of detection (LOD) was found to be at the nM level, which is in the same order or lower than previous reports for microchips with electrochemical detection at carbon fiber [32,50,53,55], carbon-ink [48,54], CNT-modified gold [52], gold-coated platinum [30], pyrolyzed photoresist carbon [45], platinum [18] and palladium [22] films, where the LOD range was between 0.1 and 5 μM.

The reproducibility (day-to-day) of the analytical signals in the SU-8 microchip was also studied on successive days. Thus, the signals corresponding to the sample mixture containing 100 μM DA and EP in 25 mM MES-His pH = 5.7 were recorded in three successive days. Fig. 6A–C depicts electropherograms for the sample mixture of DA and EP in different days. After the first day (Fig. 6A), when the chip was emptied and newly filled a drastic change in the analytical signals was observed (Fig. 6B). Thus, the migration time decreased from 104.8 and 131.5 to 50.6 and 56.3 s for DA and EP, respectively. The peak current was slightly increased and the theoretical plate number was also enhanced from 39,000 ± 1000 and 30,000 ± 600 to 75,000 ± 2000 and 65,000 ± 1500 m^{-1} for DA and EP, respectively. However, a resolution of 1.1 ± 0.1, lower than the first day (1.55 ± 0.03), was obtained. In the third day (Fig. 6C), the migration time, the peak current and resolution (1.2 ± 0.1) was maintained and only a small increase in the plate numbers (79,000 ± 2500 and 70,000 ± 2500 m^{-1} for DA and EP, respectively) was achieved. Since microchip material is a photoresist, its structure could be modified in the successive days by chemical and light effects changing the different separation parameters. In the case of SU-8 microchips, no preconditioning with NaOH is made. This treatment is very common for other materials but epoxy groups would be open and a different surface is then presented. However, since SU-8 may change with time, studies are in progress in order to understand this behaviour and NaOH pretreatments are among those considered.

In order to get a better resolution of DA and EP, different pretreatments of SU-8 microchannels were evaluated. Firstly, the channels were washed with $HClO_4$ 0.1 M for 30 min. After this cleaning (Fig. 6D), the migration time decreased meanwhile the peak current and the plate number (92,000 ± 3000 and 72,000 ± 2000 for DA and EP respectively) were slightly increased. When the washing was made with an alkaline solution (NaOH 0.1 M, Fig. 6E), the migration time was newly increased and the peak current and the plate number (47,000 ± 4000 and 42,000 ± 4000 for DA and EP respectively) decreased drastically. Then, the channels were cleaned with other acid solution (H_2SO_4 0.1 M, data not shown), so the migration time decreased but the peak current and the plate number did not improve.

A small modification of the buffer was also made in order to enhance the analytical signals, thus, 0.1% Triton X-100 was added to MES based buffer. As is shown in Fig. 6F, the efficiency (64,000 ± 4000 and 49,000 ± 2000 N/m for DA and EP, respectively) of separation was slightly increased, however, this continued being worse than it was after perchloric acid pretreatment.

A singular fact happened when 25 mM MES-His pH = 5.7 with 0.1% SDS was employed as running buffer. In this case, the separation of DA and EP was initially improved with an increase of the resolution (data not shown), but suddenly, after various injections the resolution began to decrease until only one peak was recorded. Although the microchannels were cleaned with different solutions ($HClO_4$, NaOH and H_2SO_4), the microchip did not recover the efficiency and only one signal continued being recorded. Therefore, the SDS modified the channel surface in such a way it lost the capacity for performing separations and it was not possible to regenerate the surface again. In this study, SDS is employed in a concentration below the critical micellar concentration (8 mM). Then, the hydrophobic part of SDS can be adsorbed to the microchannel walls modifying the surface. In this way, in the first injections the channel is starting to be modified and resolution improves but modification seems to change with time and the final effect is a notable decrease of resolution.

The behaviour of the new SU-8 microchip with integrated electrochemical detection was finally compared with a commer-

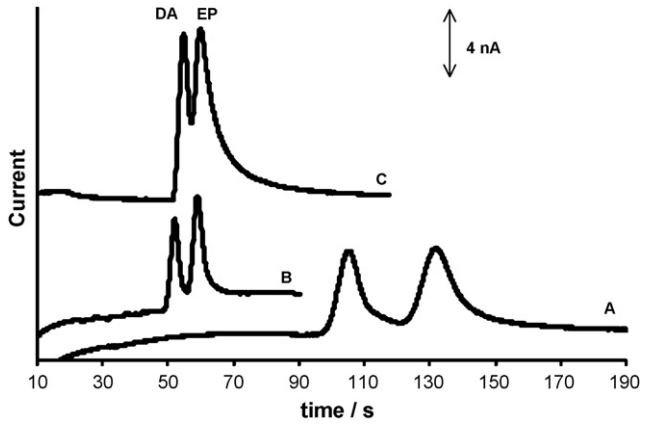


Fig. 7. Electropherograms for mixtures of 100 μM DA and EP using a SU-8 microchip with integrated platinum film detector in successive days; (A) day 1, (B) day 2; and using a Topas-microchip with an end-channel gold wire detector (C). *Conditions*: SU-8 microchip as in Fig. 5; Topas-microchip: running buffer: 25 mM MES-His pH = 5.7, V_{sep} = +2000 V; V_{inj} = +1500 V for 5 s, E_d = +1.2 V (*vs.* Ag/AgCl).

cial microchip. A Topas-microchip with an end-channel gold wire detector [57] was employed in this comparison. Fig. 7 displays the electropherograms for a mixture of DA and EP with the different microchips. The theoretical plate number (19,700 and 11,000 N/m for DA and EP respectively) and the resolution (0.5) in the Topas-microchip (Fig. 7C) were worse than SU-8 microchip, even in the three successive days (38,000 and 31,000 for DA and EP, Fig. 7A, and 73,000 and 71,000 m^{-1} for DA and EP, Fig. 7B). The SU-8 microchip with integrated amperometric detector has shown an excellent efficiency for DA and EP separation, which is in concordance with previous reports in different microchips made of glass [18,30,32,52,55], PDMS [54], PDMS/glass [22,45] or modified-PDMS [50,51,53], where the theoretical plate number range was between 10,000 and 150,000 N/m.

4. Conclusions

A new SU-8 microdevice has been fabricated for the first time with an integrated amperometric detector. After optimization of conditions, an adequate separation of DA and EP was achieved. Linearity between 0.5 and 200 μM with detection limits of 450 nM were found for both compounds. Intra-day precision results very adequate with values for RSD below 2% for ten measurements. Day-to-day precision suggests that these are single-day devices since after the first day, migration time and resolution decreases. Acid and basic solutions produce only slight changes. Treatment with SDS solution prejudices the separation of the analytes. Work is in progress in order to check new designs including multichannel configurations.

Acknowledgements

This work has been supported by the FICYT under project IB05-151C2 and the Basque Government, under the ETORTEK program. Mario Castaño-Álvarez thanks FICYT-Principado de Asturias for the award of a PhD grant.

References

[1] A. Manz, N. Graber, H.M. Widmer, Sens. Actuators B 1 (1990) 244.
[2] A. Manz, D. Harrison, E. Verpoorte, J. Fettinger, A. Paulus, H. Ludi, H. Widmer, J. Chromatogr. 593 (1992) 253.
[3] A. Muck Jr., J. Wang, M. Jacobs, G. Chen, M.P. Chatrathi, V. Jurka, Z. Výborný, S.D. Spillman, G. Sridharan, M.J. Schöning, Anal. Chem. 76 (2004) 2290.
[4] G. Xu, J. Wang, Y. Chen, L. Zhang, D. Wang, G. Chen, Lab Chip 6 (2006) 145.
[5] M.J. Schöning, M. Jacobs, A. Muck, D.-T. Knobbe, J. Wang, M.P. Chatrathi, S. Spillmann, Sens. Actuators B 108 (2005) 688.
[6] Y. Liu, D. Ganser, A. Schneider, R. Liu, P. Grodzinski, N. Kroutchinina, Anal. Chem. 73 (2001) 4196.
[7] W.K.T. Coltro, J.A.F. da Silva, H.D.T. da Silva, E.M. Richter, R. Burlan, L. Angnes, C.L. do Lago, L.H. Mazo, E. Carrillo, Electrophoresis 25 (2004) 3832.
[8] X. Bai, C. Roussel, H. Jensen, H.H. Girault, Electrophoresis 25 (2004) 931.
[9] M. Castaño-Álvarez, M.T. Fernández-Abedul, A. Costa-García, Electrophoresis 26 (2005) 3160.
[10] M. Agirregabiria, F.J. Blanco, J. Berganzo, M.T. Arroyo, A. Fullaondo, K. Mayora, J.M. Ruano-López, Lab Chip 5 (2005) 545.
[11] J. El-Ali, I.R. Perch-Nielsen, C.R. Poulsen, D.D. Bang, P. Telleman, A. Wolff, Sens. Actuators A 110 (2004) 3–10.
[12] F.J. Blanco, M. Agirregabiria, J. García, J. Berganzo, M. Tijero, M.T. Arroyo, J.M. Ruano, I. Aramburu, K. Mayora, J. Micromech. Microeng. 14 (2004) 1047.
[13] S. Tuomikoski, S. Franssila, Sens. Actuators A 120 (2005) 408.
[14] T. Sikanen, S. Tuomikoski, R.A. Ketola, R. Kostieninen, S. Franssila, T. Kotiaho, Lab Chip 5 (2005) 888.
[15] C. Luo, A. Govindaraju, J. Garra, T. Schneider, R. White, J. Currie, M. Paranjape, Sens. Actuators A 114 (2004) 123.
[16] J.M. Ruano-López, M. Agirregabiria, M. Arroyo, J. Berganzo, F.J. Blanco, P. de la Fuente, K. Castaño, K. Mayora, Proc. of 8th Int. Conf. Miniaturized Chem. Biochem. Anal. Syst., vol. 2, 2004, p. 34.
[17] M. Agirregabiria, F.J. Blanco, J. Berganzo, A. Fullaondo, A.M. Subyaga, K. Mayora, J.M. Ruano-López, Electrophoresis 27 (2006) 3627.
[18] A.T. Woolley, K. Lao, A.N. Glazer, R.A. Mathies, Anal. Chem. 70 (1998) 684.
[19] W.R. Vandaveer IV, S.A. Pasas-Farmer, D.J. Fischer, C.N. Frankenfeld, S.M. Lunte, Electrophoresis 25 (2004) 3528.
[20] R.S. Martin, K.L. Ratzlaff, B.H. Huyng, S.M. Lunte, Anal. Chem. 74 (2002) 1136.
[21] M. Castaño-Álvarez, M.T. Fernández-Abedul, A. Costa-García, Anal. Bioanal. Chem. 382 (2005) 303.
[22] N.A. Lacher, S.M. Lunte, R.S. Martin, Anal. Chem. 76 (2004) 2482.
[23] J. Vickers, C.S. Henry, Electrophoresis 26 (2005) 4641.
[24] Y. Du, J. Yan, W. Zhou, X. Yang, E. Wang, Electrophoresis 25 (2004) 3853.
[25] C.-C. Wu, R.-G. Wu, J.-G. Huang, Y.-C. Lin, H.-C. Chang, Anal. Chem. 75 (2003) 947.
[26] C.-C.J. Lai, C.-h. Chena, F.-H. Ko, J. Chromatogr. A 1023 (2004) 143.
[27] D.-C. Chen, F.-L. Hsu, D.-Z. Zhan, C.-H. Chen, Anal. Chem. 73 (2001) 758.
[28] J.-H. Kim, C.J. Kang, D. Jeon, Y.-S. Kim, Microelectron. Eng. 78–79 (2005) 563.
[29] J.-J. Xu, N. Bao, X.-H. Xia, Y. Pen, H.-Y. Chen, Anal. Chem. 76 (2004) 6902.
[30] M.A. Schwarz, B. Galliker, K. Fluri, T. Kappes, P.C. Hauser, Analyst 126 (2001) 147.
[31] Y. Liu, J.A. Vickers, C.S. Henry, Anal. Chem. 76 (2004) 1513.
[32] Y. Zeng, H. Chen, D.-W. Pang, Z.-L. Wang, J.-K. Cheng, Anal. Chem. 74 (2002) 2441.
[33] Y. Wang, H. Chen, J. Chromatogr. A 1080 (2005) 192.
[34] M. Castaño-Álvarez, M.T. Fernández-Abedul, A. Costa-García, J. Chromatogr. A 1109 (2005) 291.
[35] M. Castaño-Álvarez, M.T. Fernández-Abedul, A. Costa-García, Instrum. Sci. Technol. 34 (2006) 697.
[36] J. Wang, B. Tian, E. Sahlin, Anal. Chem. 71 (1999) 5436.
[37] J. Wang, S. Mannino, C. Camera, M.P. Chatrathi, M. Scampicchio, J. Zima, J. Chromatogr. A 1091 (2005) 177.
[38] K. Wang, X.-W. Xia, J. Chromatogr. A 1110 (2006) 222.
[39] K. Wang, F.-Y. He, A.-L. Liu, J.-J. Xu, H.-Y. Chen, X.-H. Xia, Langmuir 22 (2006) 7052.
[40] R.S. Keyton, T.J. Roussel Jr., M.M. Crain, D.J. Jackson, D.B. Franco, J.F. Naber, K.M. Walsh, R.P. Baldwin, Anal. Chim. Acta 507 (2004) 95.
[41] A.A. Dawoud, T. Kawaguchi, Y. Markushin, M.D. Porter, R. Jankowiak, Sens. Actuators B 120 (2006) 42.
[42] J.L. Yan, Y. Du, J.F. Liu, W.D. Cao, X.H. Sun, W.H. Zhou, X.R. Yang, E.K. Wang, Anal. Chem. 75 (2003) 5406.
[43] P. Ertl, C.A. Emrich, P. Singhal, R.A. Mathies, Anal. Chem. 76 (2004) 3749.
[44] N.E. Hebert, S.A. Brazill, Lab Chip 3 (2003) 241.
[45] N.E. Hebert, B. Snyder, R.L. McCreery, W.G. Kuhr, S.A. Brazill, Anal. Chem. 75 (2003) 4265.
[46] R.P. Baldwin, T.J. Roussel Jr., M.M. Crain, V. Bathlagunda, D.J. Jackson, J. Gullapalli, J.A. Conklin, R. Pai, J.F. Naber, K.M. Walsh, R.S. Keynton, Anal. Chem. 74 (2002) 3690.
[47] R. Wilke, S. Büttgenbach, Biosens. Bioelectron. 19 (2003) 149.
[48] Y. Ding, A. Ayon, C.D. García, Anal. Chim. Acta 584 (2007) 244.
[49] G. Chen, J. Li, S. Qu, D. Chen, P. Yang, J. Chromatogr. A 1094 (2005) 138.
[50] A.-J. Wang, J.-J. Xu, H.-Y. Chen, J. Chromatogr. A 1107 (2006) 257.
[51] W. Wang, L. Zhao, J.-R. Zhang, X.-M. Wang, J.-J. Zhua, H.-Y. Chen, J. Chromatogr. A 1136 (2006) 111.
[52] M. Vlcková, M.A. Schwarz, J. Chromatogr. A 1142 (2007) 214.
[53] A.-J. Wang, J.-J. Xu, Q. Zhang, H.-Y. Chen, Talanta 69 (2006) 210.
[54] J. Wang, M. Pumera, M.P. Chatrathi, A. Rodriguez, S. Spillman, R.S. Martin, S.M. Lunte, Electroanalysis 14 (2002) 1251.
[55] Y. Wu, J.-M. Lin, R. Su, F. Qu, Z. Cai, Talanta 64 (2004) 338.
[56] A. Costa-García, M.T. Fernández-Abedul, M. Castaño-Álvarez, A. Fernández-la-Villa, D.F. Pozo-Ayuso, Spanish Patent Application No. P200802006, 2008.
[57] M. Castaño-Álvarez, M.T. Fernández-Abedul, A. Costa-García, Electrophoresis 28 (2007) 4679.
[58] T. Sikanen, S. Tuomikoski, R.A. Ketola, R. Kostiainen, S. Franssila, T. Kotiaho, Lab Chip 5 (2005) 888.
[59] H. Yu, F.-Y. He, Y. Lu, Y.-L. Hu, H.-Y. Zhong, X.-H. Xia, Talanta 2008 (2008) 43.

Talanta 80 (2009) 31–38

Contents lists available at ScienceDirect

Talanta

journal homepage: www.elsevier.com/locate/talanta

Voltammetric studies of sumatriptan on the surface of pyrolytic graphite electrode modified with multi-walled carbon nanotubes decorated with silver nanoparticles

Masoumeh Ghalkhani [a], Saeed Shahrokhian [a,b,*], Fatemeh Ghorbani-Bidkorbeh [a]

[a] Department of Chemistry, Sharif University of Technology, Tehran 11155-9516, Iran
[b] Institute for Nanoscience and Technology, Sharif University of Technology, Tehran, Iran

ARTICLE INFO

Article history:
Received 28 April 2009
Received in revised form 7 June 2009
Accepted 8 June 2009
Available online 16 June 2009

Keywords:
Sumatriptan
Decorated multi-walled carbon nanotube
Silver nanoparticle
Modified electrode
Voltammetry

ABSTRACT

Multi-walled carbon nanotube decorated with silver nanoparticles (AgNPs-MWCNT) is used as an effective strategy for modification of the surface of pyrolytic graphite electrode (PGE). This modification procedure improved colloidal dispersion of the decorated MWCNTs in water, affording uniform and stable thin films for altering the surface properties of the working electrode. Robust electrode for sensing applications is obtained in a simple solvent evaporation process. The electrochemical behavior of sumatriptan (Sum) at the bare PGE and AgNPs-MWCNT modified PGE is investigated. The results indicate that the AgNPs-MWCNT modified PGE significantly enhanced the oxidation peak current of Sum. A remarkable enhancement in microscopic area of the electrode together with strong adsorption of Sum on the surface of the modified electrode resulted in a considerable increase in the peak current of Sum. Experimental parameters, such as scan rate, pH, accumulation conditions and amount of the modifier used on the PGE surface are optimized by monitoring the CV responses toward Sum. It is found that a maximum current response can be obtained at pH 7.4 after accumulation at open circuit for 150 s. Further experiments demonstrated that the oxidative peak currents increased linearly with Sum concentration in the range of 8.0×10^{-8}–1.0×10^{-4} mol L^{-1} with a detection limit of 4.0×10^{-8} mol L^{-1}. The modified electrode showed high sensitivity, selectivity, long-term stability and remarkable voltammetric reproducibility in response to Sum. These excellent properties make the prepared sensor suitable for the analysis in pharmaceutical and clinical preparations. The modified electrode was successfully applied for the accurate determination of trace amounts of Sum in pharmaceutical preparations.

© 2009 Elsevier B.V. All rights reserved.

1. Introduction

Sumatriptan (Sum), a triptan drug including a sulfonamide group, is used in human medicine for the treatment of acute migraine episodes (vascular headaches) [1,2]. Often, serotonin levels in the brain become extremely low before the onset of a migraine. Sum is administered to aid in leveling the serotonin levels in the brain. Sum is also shown to decrease the activity of the trigeminal nerve, which probably accounts for Sum's efficacy in treating cluster headaches. This type of headache is extremely painful and debilitating [3]. Large doses of Sum (200 mg day^{-1}) can cause sulfhemoglobinemia, a rare condition in which the blood changes from red to greenish-black, due to the integration of sulfur into the hemoglobin molecule. If Sum is discontinued, the condition reverses within a few weeks. Various techniques have been reported for the analytical determination of Sum in plasma and pharmaceutical formulations in the literature including: spectrophotometry [4,5], high performance thin layer chromatography (HPTLC) [5], capillary electrophoresis [6,7], high performance liquid chromatography (HPLC) with electrochemical detection [8,9], HPLC with fluorescence detection [10], HPLC with ultraviolet (UV) detection [11,12], liquid chromatography–mass spectroscopy (LC–MS) [13], liquid chromatography–electron spray ionization mass spectrometry (LC–ESI-MS) [14], liquid chromatography–mass spectrometry/mass spectrometry (LC–MS/MS) [15–18] and also, electroanalytical chemistry [19]. However, these methods suffer from some disadvantages such as high costs, long analysis times and requirement for complex and tedious sample pretreatment, and in some cases, low sensitivity and selectivity that makes them unsuitable for a routine analysis. It is essential to look for a new method with high sensitivity, simplicity and efficiency for the detection of this drug. Electrochemical techniques using modified electrodes

* Corresponding author at: Department of Chemistry, Sharif University of Technology, Tehran 11155-9516, Iran. Tel.: +98 21 66005718; fax: +98 21 66002983.
E-mail address: shahrokhian@sharif.edu (S. Shahrokhian).

0039-9140/$ – see front matter © 2009 Elsevier B.V. All rights reserved.
doi:10.1016/j.talanta.2009.06.019

can be considered for the determination of Sum as a strong alternative to the mentioned methods.

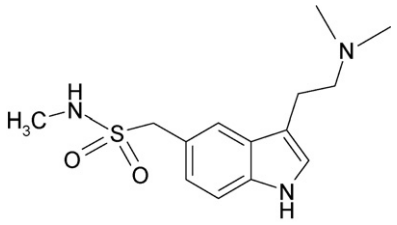
Although Sum is an electroactive compound which can be oxidized electrochemically, only one work can be found in the literature describing the electrochemical analysis of this compound by means of differential pulse voltammetry using a glassy carbon electrode [19]. The electrochemical reaction of Sum at the bare electrode involves slow electron transfer kinetics that can be catalyzed by attaching a suitable electron transfer mediator to the surface. The electrode surface modification can facilitate charge transfer between the analyte and the electrode, thereby enhancing the sensitivity and selectivity of the analysis. To our knowledge, there are no antecedents found in the literature on using modified electrodes for determination of Sum. Modification of carbon electrodes is particularly easy and can be achieved either through physical adsorption of the modifier onto the carbon surface, or by covalent attachment of the modifier [20].

Since the discovery of multi-walled carbon nanotubes (MWCNTs) by Iijima [21], this material has attracted enormous interest because of its unique structural, mechanical and electronic properties. Some of these properties include high chemical and thermal stability, high elasticity, high tensile strength, and in some instances, metallic conductivity [22]. The modification of electrode substrates with MWCNT for use in analytical sensing is well documented to result in low detection limits, increased sensitivities, reduced overpotentials, and resistance to surface fouling.

The insolubility of CNTs in most solvents, however, limits their application in designing CNTs-based biosensing devices. The best solvents reported for effecting CNT dispersions are *N*,*N*-dimethylformamide and *N*-methylpyrrolidone [23]. Further, several strategies relied on dispersion in polyelectrolytes [24], Nafion [25,26] and surfactants [27,28] have been proposed for immobilization of CNT on electrochemical transducers. Unfortunately, the dispersions aggregate on a time scale of days.

Recent activity has focused on the development of nanoscaled particles applied in analytical chemistry for its special physicochemical characteristics [29,30]. Nanoparticle modified electrodes present unusual advantages in electroanalysis such as catalysis, enhancement of mass transport and high effective surface area [31,32]. In this region metal nanoparticles have attracted much more attention in electroanalysis because of their unusual physical and chemical properties. An interesting class of carbon nanotube derivatives results from deposition of metallic or semiconducting nanoclusters on the tubular surfaces [33–35]. Furthermore, uniform dispersion of metallic nanoparticles decorated on CNT surfaces can yield ideal nanocatalysts for application in chemically modified electrodes.

In the present work, we synthesized composite MWCNTs decorated with silver nanoparticles by a simple chemical plating method. Characterization of the morphology and nanoparticles distribution on the surface of the decorated MWCNT was performed by transmission electron microscopy (TEM). The excellent dispersibility of the resulting MWCNT decorated with silver nanoparticles in water leads to formation of a stable colloidal dispersion, which is capable to form a completely uniform and stable thin film on the surface of PGE. The prepared modified electrode was successfully applied for voltammetric determination of Sum in pharmaceutical samples. A good linear relationship was realized between the anodic peak currents and Sum concentrations in the range of 6.0×10^{-8}–1.0×10^{-4} mol L^{-1} with the detection limit of 4.0×10^{-8} mol L^{-1} and good reproducibility.



Scheme 1. Structure of sumatriptan.

2. Experimental

2.1. Chemicals and reagents

Sum, in the form of sumatriptan succinate (1:1) (>99.0% purity), was purchased from Natco India (Scheme 1). Multi-walled carbon nanotubes synthesized by catalytic chemical vapor deposition (CVD) method (purity more than 95%) with o.d. of 10–20 nm, i.d. of 5–10 nm and tube length of 0.5–200 nm was obtained from Nanostructured & Amorphous Materials (Houston, TX, USA). All other chemicals were of analytical reagent grade from Merck. All aqueous solutions were prepared with doubly distilled deionized water. Stock solutions of Sum were freshly prepared as required in appropriate buffer solution. In these experiments, a stock Britton–Robinson (BR) buffer solution was prepared which was 0.04 mol L^{-1} in each of glacial acetic acid, orthophosphoric acid and boric acid. Buffer solutions of varying pH were then prepared by the addition of 0.2 mol L^{-1} sodium hydroxide. Voltammetric experiments were carried out in the buffered solutions of Sum, deoxygenated by purging with pure nitrogen (99.999% from Roham Gas Company). Nitrogen gas was also maintained over the surface of the test solutions during the experiments. Tablets of Sum were purchased from Hakim Pharmaceutical Co. (Tehran, Iran).

2.2. Apparatus

Voltammetric experiments were performed using a Metrohm potentiostat/galvanostat model 797VA. A conventional three-electrode system was used with a basal plane pyrolytic graphite working electrode (BPPGE, unmodified or modified, $d = 3$ mm), a saturated Ag/AgCl reference electrode and a Pt wire counter electrode. A BPPGE, or an EPPGE (4.9 mm diameter, Le Carbone, Ltd., Sussex, U.K.) was used as the working electrodes. A digital pH/mV/Ion meter (CyberScan model 2500) was used for the preparation of the buffer solutions.

Electrochemical impedance spectroscopy (EIS) measurements were performed with a Potentiostat/Galvanostat/Frequency response analyzer (FRA) EG&G model 273A between 1 Hz and 1 kHz using a 5 mV rms sinusoidal modulation in 0.1 mol L^{-1} KCl solution of pH 7.0 containing 1 mmol L^{-1} of $K_4Fe(CN)_6$ and 1 mmol L^{-1} $K_3Fe(CN)_6$ (1:1) mixture, and at the $E_{1/2}$ of the $[Fe(CN)_6]^{3-/4-}$ (0.13 V vs. Ag/AgCl). All experiments were performed at 25 ± 1 °C. Solutions were deaerated by bubbling nitrogen prior to the experiments and the electrochemical cell was kept under a nitrogen atmosphere throughout the experiments.

2.3. Preparation of nanosilver decorated multi-walled carbon nanotube

The MWCNTs were purified in boiling concentrated nitric acid for 2 h, followed by rinsing with deionized water and drying at 383 K under dry N_2 atmosphere. Open-end MWCNTs with hydrophilic surface were thus obtained [36]. AgNPs-MWCNT was prepared by the reported procedure in literature [37]. In the first step, 1.0 g purified and functionalized MWCNTs was mixed with 50 mL mixture solution of 38% formaldehyde, absolute ethyl alcohol and double distilled water (volumetric ratio 3:10:10). In the second step, 50 mL

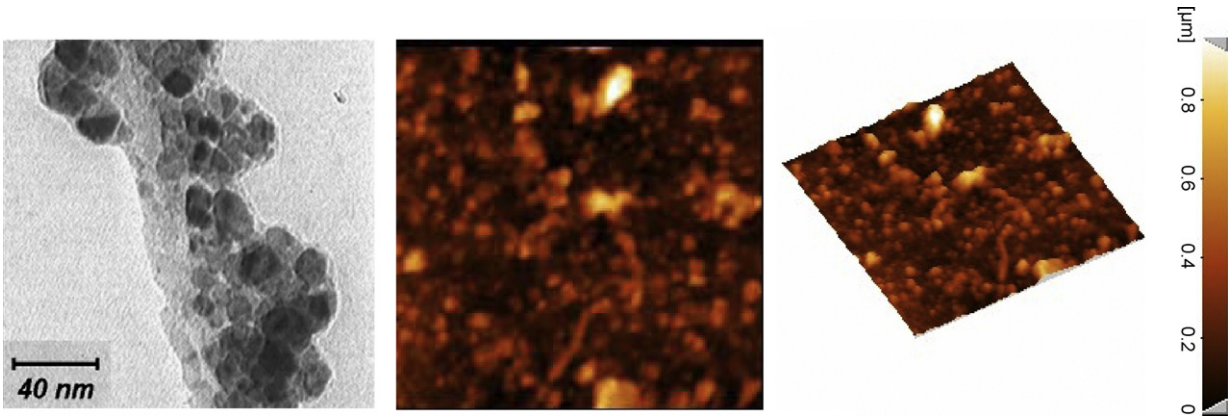


Fig. 1. Left: TEM image of MWCNTs decorated with silver nanoparticles. Right: AFM images of the surface of PGE decorated by the film of AgNPs-MWCNT.

mixture solution of 35 g L^{-1} silver nitrate ($AgNO_3$) solution and 25% ammonia solution (volumetric ratio 1:2) were dropped one by one into the mixture of MWCNT–formaldehyde–alcohol–water solution. The pH value of strongly stirred reacted solution was kept about 8–9. After completing the reaction, the product was centrifuged and washed by doubly distilled water several times then dried in vacuum oven at 60 °C.

2.4. Preparation of modified PGE

Before modification, the PGE was polished with 0.05 μm alumina slurry on a polishing cloth, rinsed thoroughly with doubly distilled water, and then sonicated in ethanol and doubly distilled water for 5 min, sequentially. The modifier suspension was prepared by dispersing 2 mg of the AgNPs-MWCNT in 2.0 ml of doubly distilled water under sonication for 30 min, giving a black dispersion that is quite stable for 4–5 months. The AgNPs-MWCNT modified PGE was prepared by casting 5 μL of the mentioned black suspension on the PG electrode surface using a micropipette and left to dry at room temperature. Before the voltammetric measurements, the modified electrode was cycled between 0 and 1 V (scan rate 100 mV s^{-1}) in 0.04 mol L^{-1} Britton–Robinson buffer solution pH 7.4 for several times until acquiring the reproducible responses. The surface morphology and the thickness of the film modifier on the surface of PGE were characterized by AFM experiments. AFM images were recorded in the contact mode in air with a MultiMode Nanoscope IV Microscope (Digital Instruments) at a scan rate of 0.50 Hz.

3. Results and discussion

3.1. Surface morphology of AgNPs-MWCNT/PG modified electrode

The surface morphology and distribution of Ag nanoparticles on the MWNT support surfaces was explored using TEM images. Fig. 1 shows the well dispersed/deposited Ag nanoparticles on the surface of MWCNTs. From the TEM images, the size of Ag nanoparticles decorated on MWCNTs was estimated to be 5–20 nm.

3.2. Electrochemical behavior of Sum at AgNPs-MWCNT/PGE

The electrochemical response of AgNPs-MWNT/PG electrode in purged N_2 Britton–Robinson buffer solution (0.04 mol L^{-1}, pH 7) is presented in Fig. 2A. A pair of redox peak was observed on the surface of AgNPs-MWCNT modified PGE at 0.26 and −0.23 V. It can be suggested that the observed redox peak is corresponding to the redox behavior of the Ag nanoparticles on the surface of the modified electrode, which proves that MWCNTs were decorated with AgNPs.

The electrochemical impedance spectroscopy (EIS) was employed to investigate the impedance changes of the electrode surface in the modified process. Fig. 2B shows the Nyquist

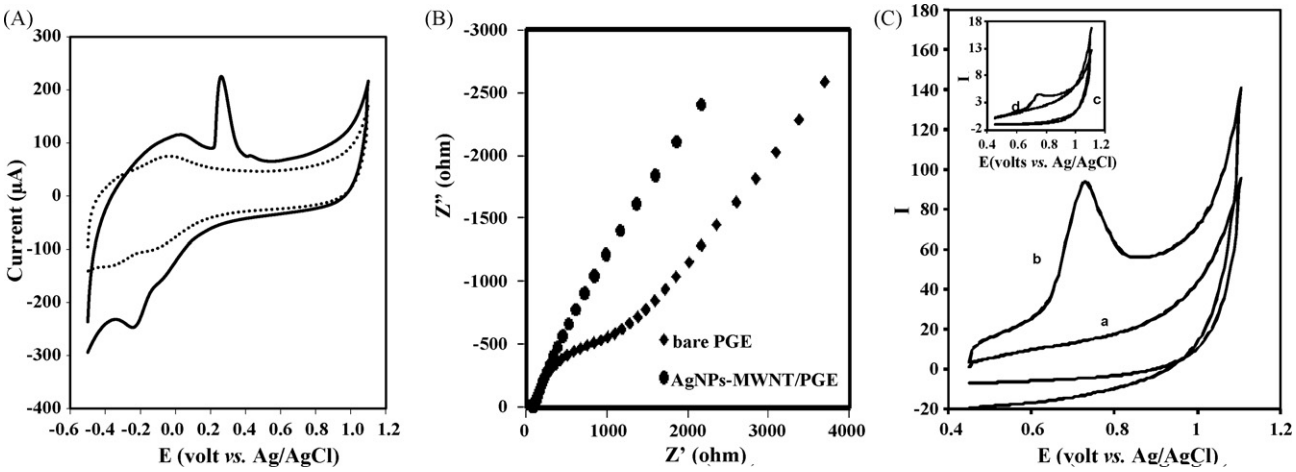


Fig. 2. (A) CVs of MWCNT/PGE (dashed) and AgNPs-MWCNT/PGE (solid) in 0.04 mol L^{-1} BR buffer solution (pH 7.4), (B) Nyquist diagram (Z″ vs. Z′) for the EIS measurements in 1 mmol L^{-1} $K_3Fe(CN)_6/K_4Fe(CN)_6$ in 0.1 mol L^{-1} KCl at the $E_{1/2}$ = 0.13 V for the bare PGE (■) and AgNPs-MWCNT/PGE (●) and (C) CVs of AgNPs-MWCNT/PGE in 0.04 mol L^{-1} BR buffer solution (pH 7.4) containing various concentrations of Sum: (a) 0.0 μmol L^{-1} and (b) 10 μmol L^{-1}; scan rate 100 mV s^{-1}. Inset shows CVs of bare PG electrode with: (c) 0.0 μmol L^{-1} and (d) 10 μmol L^{-1} Sum.

plots of $K_3Fe(CN)_6/K_4Fe(CN)_6$ at the bare PGE and the AgNPs-MWNT/PGE. High frequency zone is ascribed to the ohmic process within porous structure and the low frequency zone to the kinetic impedance of electrochemical reaction. As can be seen, a semicircle with a very large diameter is observed at the bare PGE. However, the diameter of the semicircle is significantly reduced at AgNPs-MWNT/PGE, suggesting that the surface of modified electrode exhibits lower electron transfer resistance and greatly increases the electron transfer rate.

The high electroactive surface area and excellent electronic conductivity of the decorated MWCNT make this material an attractive candidate for use as an active electrode modifier [38]. Fig. 2C shows voltammetric behavior of 10 μmol L^{-1} Sum at AgNPs-MWCNT/PGE and the bare PGE, recorded in the 0.04 mol L^{-1} BR buffer solution (pH 7.4) following 150 s accumulation at open circuit at the scan rate of 100 mV s^{-1}. Obviously, Sum's response at bare PGE is rather poor and only a weak oxidation peak is observed at 0.75 V (curve a). However, the current obtained at the AgNPs-MWCNT/PGE (curve b) is significantly larger (about 33 times) than that obtained at the bare PGE, probably reflecting the larger surface area of the modified electrode. Furthermore as shown in Fig. 2C, the ratio of faradic peak current for oxidation of Sum to background current on the AgNPs-MWCNT/PGE is much more than the bare PGE confirming that the adsorption is much stronger on the modified electrode. By considering the slight shift in the peak potential, with respect to the unmodified electrode, the observed enhancement in voltammetric response at the AgNPs-MWCNT/PGE is attributed to the increased electrode surface area and the strong adsorption of analyte on the surface of the modified electrode as a consequence of the AgNPs-MWCNT coating. Additionally, owing to the large surface area of MWCNTs, the higher background current of the modified electrode than that of the bare PGE is observed but the baseline remains flat. During these experiments, no cathodic peak is resulted for Sum during the reverse scan, suggesting a totally irreversible behavior for the electrode process.

The microscopic areas of the modified and the bare PGE were obtained by CV method and using $K_3Fe(CN)_6$ as a probe at different potential scan rates [39]. A pair of well-defined peaks was observed at about 0.2 V with peak separation of 0.077 V on the AgNPs-MWCNTs/PGE. For a reversible process, the following Randles–Sevcik formula has being used:

$$i_{pa} = 2.69 \times 10^5 n^{3/2} A C_0 D_R{}^{1/2} \nu^{1/2} \quad (1)$$

where, i_{pa} refers to the anodic peak current, n the electron transfer number, A the electroactive surface area of the electrode (cm^2), D_R the diffusion coefficient, C_0 the concentration of $K_3Fe(CN)_6$ and ν is the scan rate. From the slope of the i_{pa} vs. $\nu^{1/2}$ relation, the microscopic areas can be calculated. For 1 mmol L^{-1} $K_3Fe(CN)_6$ in the 0.1 mol L^{-1} KCl electrolyte, $n = 1$, $D_R = 7.6 \times 10^{-6}$ cm^2 s^{-1}, the electrode surface area of the AgNPs-MWCNT/PGE was 0.17 cm^2 and for bare PGE was 0.06 cm^2, indicating that the microscopic area of the AgNPs-MWCNT/PGE increased significantly and was about 2.8 times larger than the microscopic area of the bare PGE.

3.3. Optimization of the amount of the modifier

As above-mentioned, by introducing AgNPs-MWCNT on the surface of the PGE, a considerable enhancement is resulted in the electrochemical behaviors of Sum. It is obvious that the response of the modified electrode toward Sum can be affected by the amount of AgNPs-MWCNT on the electrode surface. This can be controlled by using the same volume (5 μL) of the suspensions with the different concentrations of AgNPs-MWCNT, casted on the surface of PGE. The experiments showed that, the oxidation peak current for 0.1 mmol L^{-1} Sum increased quickly by increasing the concentration of AgNPs-MWCNT suspension deposited on the surface of PGE up to 1 mg mL^{-1} (Fig. 3A). Further increase, caused a gradual decrease in the anodic peak current of Sum with increase in background current. As a result, 5 μL of 1 mg mL^{-1} AgNPs-MWCNT suspension was selected as optimum volume for preparation of the modified electrode.

3.4. Effect of accumulation potential and time

The considerable enhancement in the electro-oxidation peak current of Sum on the surface of the modified electrode is in part attributed to the strong adsorptive ability of the AgNPs-MWCNT film on PGE. It is important to fix the accumulation potential and time when adsorption studies are undertaken. Both the conditions could affect the amount of adsorption of Sum at the modified electrode. Therefore, the effect of accumulation potential and time on the peak current in the solution with 50 μmol L^{-1} of Sum was studied by CV. The oxidation peak current of 50 μmol L^{-1} Sum was compared after 150 s accumulation at different potentials. The results showed that oxidation peak current remained almost constant as accumulation potential was changed from −0.5

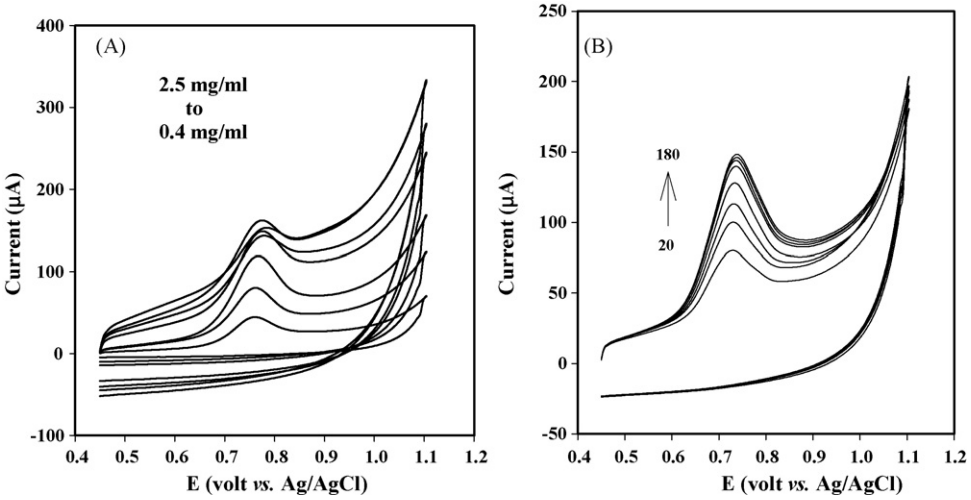


Fig. 3. (A) CVs of 50 μmol L^{-1} of Sum on the surface of the PGE decorated with 5 μL of suspension containing various amounts of AgNPs-MWCNT and (B) effect of accumulation time (min) on the CV of 50 μmol L^{-1} of Sum on the surface of the AgNPs-MWCNT/PGE. Supporting electrolyte was 0.04 mol L^{-1} BR buffer solution of pH 7.4 and sweep rate was 100 mV s^{-1}.

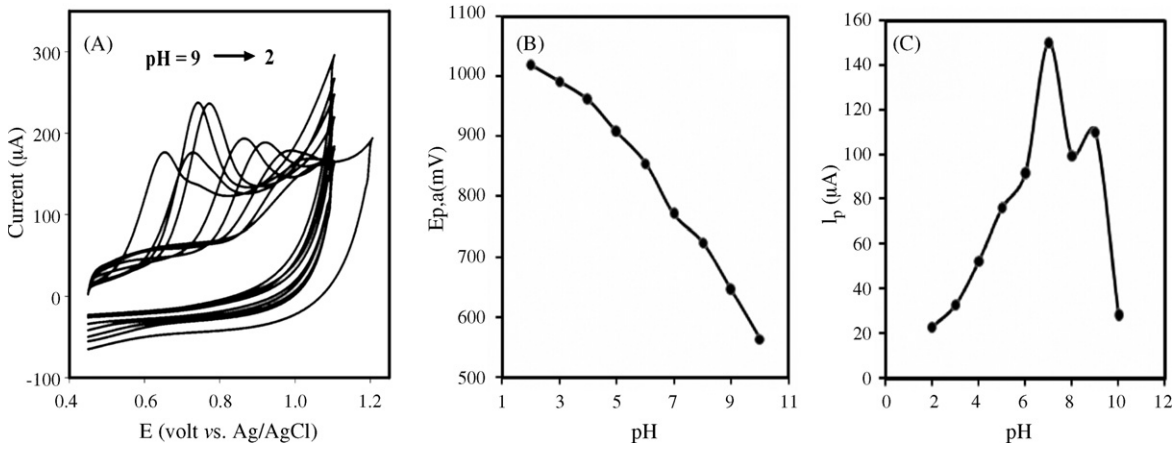


Fig. 4. (A) CVs of 50 μmol L^{-1} Sum at the AgNPs-MWCNT/PGE in various pHs (from 2 to 9: 2, 3, 4, 5.0, 5, 6.0, 7, 7.4, 8.0, 9.0) of buffer solution, dependence of (B) the oxidation peak potential (E_{pa}) and (C) the oxidation peak current (i_{pa}) with pH solution; scan rate 100 mV s^{-1}.

to 0.5 V, revealing that the accumulation potential has no influence on the oxidation peak current of Sum (Fig. 3B). Moreover, compared with an open circuit, accumulation potential had no obvious effect. Hence, the accumulation of Sum was carried out under open circuit. By increasing the accumulation time, the peak current significantly increased. The results indicated that, as the adsorptive equilibrium was reached (longer accumulation times), the amount of the adsorbed analyte (and therefore, the resulted peak currents) is increased. The oxidation peak current increased quickly within 100 s and then showed a very slow increase from 100 to 180 s. Further increasing the accumulation time would cause the peak currents to level off, so the accumulation time was set at 150 s.

3.5. Influence of pH

To optimize the experimental conditions for the determination of Sum, the effects of the composition of the buffer systems (such as phosphate, Britton–Robinson or acetate buffer) were examined. The results showed that the highest oxidation peak current for Sum can be obtained in Britton–Robinson buffer. Then, the influence of pH on the electrochemical behavior of Sum was investigated at different pH values in the range of 2.0–10.0 using 0.04 mol L^{-1} Britton–Robinson buffer as supporting electrolyte. Fig. 4A shows the CVs of 50 μmol L^{-1} Sum on the surface of the modified electrode over the discussed pH range at the potential scan rate of 100 mV s^{-1}. It was found that the peak potential shifted negatively with increasing pH (suggesting participation of H^+ in the oxidation process) and a good linear relationship was observed between the E_p and pH values (in the range of 3–9, Fig. 4B) with the following equation:

$$E_{pa}(\text{mV}) = -62.13\,\text{pH} + 1206 \quad (R^2 = 0.9870) \tag{2}$$

A value of about −62.21 mV per pH unit clearly indicates that equal numbers of electrons and protons are involved in the electro-oxidation of Sum on the surface of the modified electrode. On the other hand, the anodic peak current showed to be increased by the pH from 2 to 7.4. However, further increase in the pH of the buffer solution would make the peak height decrease slowly (Fig. 4C). Therefore, Britton–Robinson buffer with pH 7.4 was used as supporting electrolyte in all voltammetric determinations.

3.6. Effect of potential scan rate

Useful information involving electrochemical mechanism usually can be gained from the investigation of CVs in the different potential sweep rates. Therefore, the CV investigations for 50 μmol L^{-1} Sum were performed on the surface of the AgNPs-MWCNT/PGE in buffered solution of pH 7.4 at different potential sweep rates. Fig. 5A illustrates the influence of scan rate on the cyclic voltammograms of Sum in the range of 25–450 mV s^{-1}. A slope of 0.707 was revealed for the linear relation between the log(i_{pa}) and the log(ν) (Fig. 5B) indicating a mixed adsorption–diffusion

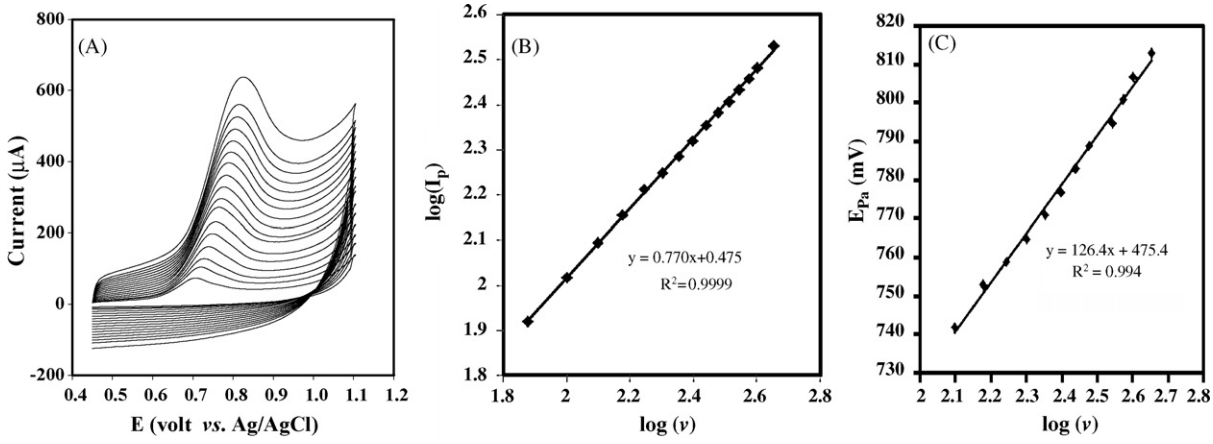


Fig. 5. (A) CVs of 50 μmol L^{-1} Sum at the AgNPs-MWCNT/PGE at different scan rates in 0.04 mol L^{-1} BR buffer solution (pH 7.4), (B) the plot of log(i_{pa}) vs. log(ν), and (C) variation of peak potential (E_{pa}) with log(ν).

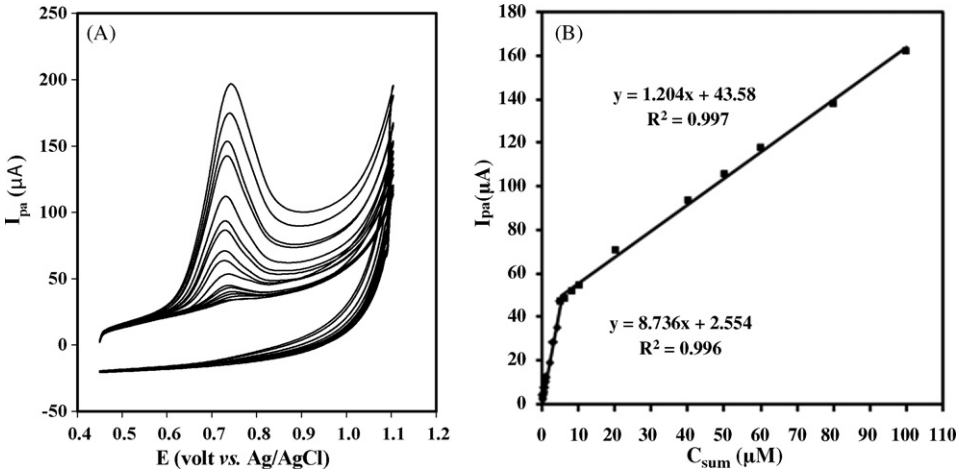


Fig. 6. (A) CVs for various concentrations of Sum in the range of (down to up), 0.08–80 μmol L^{-1} in 0.04 mol L^{-1} BR buffer solution (pH 7.4) and (B) corresponding linear calibration curve of peak current vs. Sum concentration; scan rate 100 mV s^{-1}.

controlled process on the surface of the modified electrode. The regression equation for this relationship is:

$$\log(i_{pa}) = 0.770 \log(\nu) + 0.475 \quad (R^2 = 0.9990;\ i_{pa}:\ \mu A,\ \nu:\ mV\,s^{-1}) \tag{3}$$

The relationship between the oxidation peak potential and scan rate is shown in Fig. 5C. It can be seen that the oxidation peak potential shifts positively with increasing scan rate. There is a linear relationship between E_p and the logarithm of the scan rate, Eq. (4). Such a behavior reveals the irreversible nature of the electrochemical process for Sum. Furthermore, only an oxidation peak was observed even at low scan rates, suggesting that the electrode reaction of Sum under these conditions were totally irreversible:

$$E_p = 126.4 \log \nu + 475.4 \quad (R^2 = 0.9940;\ E_p:\ mV,\ \nu:\ mV\,s^{-1}) \tag{4}$$

This behavior is in conformity with the equation for irreversible electrochemical processes [40]:

$$E_p = \left(\frac{1}{2}\right) b \log \nu + a \quad \left(b = \frac{2.303RT}{(1-\alpha)n_a F}\right) \tag{5}$$

where, α is the transfer coefficient, n_a the number of electrons involved in the rate-determining step of the electrode process, F the Faraday constant, R the gas constant and T is the absolute temperature.

The Tafel plot and its corresponding slope were used for elucidating the mechanism of the electrode process. The polarization curves (log I/E plots) for the electro-oxidation of Sum on the surface of the modified electrode were obtained at various potential sweep rates. The slopes of Tafel plots show $(1-\alpha)n_a$ values between 0.42 and 0.36 for potential sweep rates in the range of 50–250 mV s^{-1}. By considering $n_a = 1$, the value of α was calculated to be in the range of 0.58–0.64, which indicates that the activation free energy curve is not symmetrical in such an irreversible oxidation process.

3.7. Voltammetric determinations, reproducibility evaluations

The relationship between the oxidation peak current and the concentration of Sum was examined by CV on the surface of AgNPs-MWCNT/PGE, and the results are shown in Fig. 6A. Under the previous mentioned optimum conditions, the oxidation peak currents were proportional to Sum concentrations over two intervals in the range of 8.0×10^{-8}–5.0×10^{-6} and 5.0×10^{-6}–1.0×10^{-4} mol L^{-1} in 0.04 mol L^{-1} Britton–Robinson buffer solution (pH 7.4) (Fig. 6B). The linear regression equation for first region was:

$$i_{pa}(\mu A) = 8.736\, C(\mu mol\,L^{-1}) + 2.554 \quad (R^2 = 0.9960) \tag{6}$$

and for second region was:

$$i_{pa}(\mu A) = 1.204\, C(\mu mol\,L^{-1}) + 43.58 \quad (R^2 = 0.9970) \tag{7}$$

The break in the calibration curve of Sum probably reflects the formation of a sub-monolayer in the first range of calibration and the formation of a monolayer in the second range. Using the first range of this calibration plot, the detection limit ($S/N = 3$) of 40 nmol L^{-1} is obtained for Sum. This indicates that the system is quite sensitive in comparison with that reported [19]. After each determination, the modified electrode was refreshed by successive cyclic voltammetric sweeps between 0.0 and 1.0 V in a buffer solution about three cycles.

3.8. Repeatability, stability and reproducibility of the modified electrode

The repeatability of the modified electrode was investigated by repetitive recording at a fixed Sum concentration of 1×10^{-5} mol L^{-1}. The RSD for the peak currents in CVs based on six replicates was 2.9%, indicating excellent repeatability of the response of the modified electrode. Also, on using the AgNPs-MWCNT/PGE daily and storing under ambient conditions over a period of 3 weeks, the electrode retained 96.4% of its initial peak current response for a Sum concentration of 1.0×10^{-5} mol L^{-1}, which shows long-term stability of the film modifier on the surface of PGE. As well the fabrication reproducibility was evaluated by preparing five modified electrodes independently. The RSD for the peak current determinations with five prepared electrodes on 5.0×10^{-5} mol L^{-1} Sum was calculated to be 3.8% (for averages of five determinations on each electrode). The results indicate that the modified electrode has an excellent repeatability and reproducibility in both preparation procedure and voltammetric determinations with good long-term stability.

3.9. Determinations in sumatriptan succinate tablets

To assess the applicability of the proposed method, the AgNPs-MWCNT/PGE was used to determination of the content of Sum in "sumatriptan" tablets as a real pharmaceutical sample by applying CV method. Four tablets containing labeled amounts of 50 mg Sum were accurately weighted and ground to a fine powder. The amount

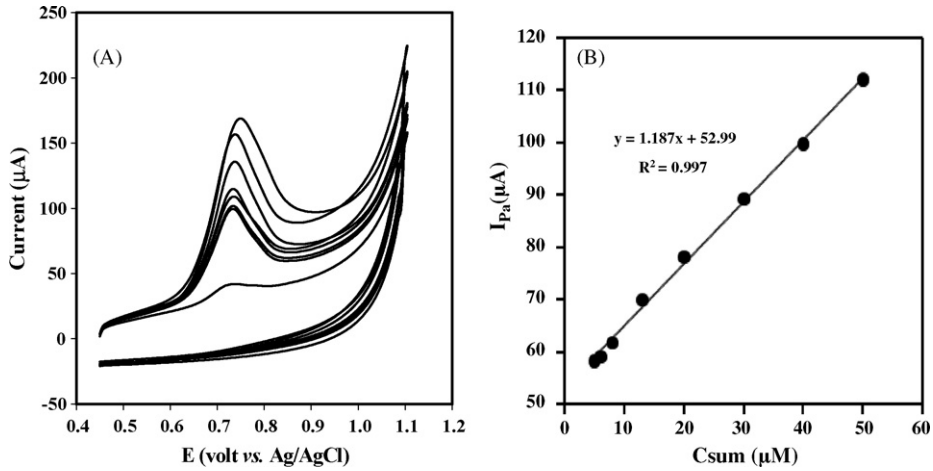


Fig. 7. (A) CVs for the addition of different amount of Sum (from down to up: 5, 6, 8, 13, 20, 30, 40, 50 μmol L^{-1}) in the real sample solution Sum diluted with 0.04 mol L^{-1} BR buffer solution (pH 7.4) at the AgNPs-MWCNT/PGE; scan rate 100 mV s^{-1} and (B) the plot of peak current vs. added concentration of Sum.

Table 1
Results of the recovery analysis of Sum spiked in tablet samples.

No	Spiked (μM)	Expected (μM)	Found[a] (μM)	Recovery (%)
1	0	5	4.93	–
2	0.5	5.5	5.30	96.44
3	1	6	6.06	101.02
4	5	10	10.15	101.50
5	10	15	15.78	105.13
6	50	55	54.89	99.80

[a] Average of four replicate measurements (rounded).

equal to 10 mg of the powdered sample was dissolved in 100 ml of 0.04 mol L^{-1} Britton–Robinson buffer solution of pH 7.4 to get a nominal concentration of 3.39×10^{-4} mol L^{-1}. Then a nominal concentration of 1×10^{-5} mol L^{-1} was achieved with further diluting with the same buffer solution. A 2.0 ml portion of the resulted solution was transferred to a 25 ml volumetric flask and spiked with the standard Sum solution in the range of 5×10^{-6}–5×10^{-5} mol L^{-1}. The CVs for various spiked solutions of Sum are shown in Fig. 7A. The linear dynamic range and the slopes of the calibration curves of the standard addition method were utilized to the evaluation of the recovery of the presented procedure. The equation for the resulting standard addition-calibration plot of peak current vs. concentration of Sum added was:

$$i_{pa}(\mu A) = 1.187C_{Sum}(\mu mol\,L^{-1}) + 52.99 \quad (R^2 = 0.9970) \qquad (8)$$

Although the accuracy was calculated on the recovery of known amounts of the standard Sum solution spiked in tablet solution. Spiked samples were prepared at five levels. The results are demonstrated in Table 1, and the recoveries were in the range from 96.44% to 105.13%. Using this standard addition method, the Sum content was obtained to be 49.30 mg with a RSD of 4.3% ($n = 4$) per tablet, which is very close to the labeled amount 50.0 mg.

4. Conclusions

In this work, it was demonstrated that modification of PGE with MWCNTs decorated with silver nanoparticles is a new and effective method for obtaining highly sensitive electrodes for electrochemical measurements. The procedure enables preparation of highly stable and reproducible uniform modifier films, which leads to a considerable enhancement in repeatability and reproducibility in the voltammetric measurements. A remarkable enhancement in microscopic area of the electrode together with effective accumulation of Sum on the surface of the modified electrode resulted in a considerable increase of the peak current of Sum. High sensitivity and improved detection limit of the AgNPs-MWCNT/PGE are promising for the determination of trace amounts of SUM in pharmaceutical and clinical preparations.

Acknowledgement

The authors gratefully acknowledge the support of this work by the Research Council and the Center of Excellence for Nanostructures of the Sharif University of Technology, Tehran, Iran.

References

[1] P. Schoeffter, D. Hoyer, Arch. Pharmacol. 340 (1989) 135.
[2] W. Paulus, K. Butzel, H. Plendl, A. Straube, Lancet 335 (1990) 51.
[3] R. Heald, P. Maskell, B. Hill, Longmore, Br. J. Clin. Pharmacol. 47 (2008) 75.
[4] A.B. Avadhanulu, J.S. Srinivas, Y. Anjaneyulu, Indian Drugs 33 (1996) 334.
[5] D.N. Tipre, P.R. Vavia, Indian Drugs 36 (1999) 501.
[6] K.D. Altria, S.D. Filbey, J. Liq. Chromatogr. 16 (1993) 2281.
[7] K.D. Altria, S.D. Filbey, Anal. Proc. 30 (1993) 363.
[8] M. Dunne, P. Andrew, J. Pharm. Biomed. Anal. 14 (1996) 721.
[9] F. Franklin, J. Odontiadis, E.M. Clement, J. Chromatogr. Biomed. Anal. 681 (1996) 416.
[10] Z. Ge, E. Tessier, L. Neirinck, Z. Zhu, J. Chromatogr. B 806 (2004) 299.
[11] A. Femenía-Font, V. Merino, V. Rodilla, A. López-Castellano, J. Pharm. Biomed. Anal. 37 (2005) 621.
[12] V.A. Shirsat, S.Y. Gabhe, S.G. Deshpande, Indian Drugs 35 (1998) 404.
[13] J. Oxford, M.S. Lant, J. Chromatogr. Biomed. Anal. 496 (1989) 137.
[14] B.D. Dulery, M.A. Petty, J. Schoun, M. David, N.D. Huebert, J. Pharm. Biomed. Anal. 15 (1997) 1009.
[15] A. Tan, P. Hang, J. Couture, S. Hussain, F. Vallée, J. Chromatogr. B 856 (2007) 9.
[16] K. Vishwanathan, M.G. Bartlett, J.T. Stewart, Rapid Commun. Mass Spectrom. 14 (2000) 168.
[17] K.N. Cheng, M.J. Redrup, A. Barrow, P.N. Williams, J. Pharm. Biomed. Anal. 17 (1998) 399.
[18] D.A. McLoughlin, T.V. Olah, J.D. Ellis, J.D. Gilbert, R.A. Halpin, J. Chromatogr. A 726 (1996) 115.
[19] K. Sagar, J.M.F. Alvarez, C. Hua, M.R. Smyth, R. Munden, J. Pharm. Biomed. Anal. 10 (1992) 17.
[20] C.E. Banks, T.J. Davies, G.G. Wildgoose, R.G. Compton, Chem. Commun. 7 (2005) 829.
[21] S. Iijima, Nature 354 (1991) 56.
[22] P.M. Ajayan, Chem. Rev. 99 (1999) 1787.
[23] P.J. Boul, J. Liu, E.T. Mickelson, C.B. Huffman, L.M. Ericson, I.W. Chiang, K.A. Smith, D.T. Colbert, R.H. Hauge, J.L. Margrave, R.E. Smalley, Chem. Phys. Lett. 310 (1999) 367.
[24] M.C. Rodríguez, J. Sandoval, L. Galicia, S. Gutiérrez, G.A. Rivas, Sens. Actuators B 134 (2008) 559.
[25] G. Rivas, S. Miscoria, J. Desbrieres, G. Barrera, Talanta 71 (2007) 270.
[26] S. Shahrokhian, H.R. Zare–Mehrjardi, Electrochim. Acta 52 (2007) 6310.
[27] K. Wu, Y. Sun, S. Hu, Sens. Actuators B 96 (2003) 658.
[28] J. Zhang, L. Gao, Mater. Lett. 61 (2007) 3571.
[29] C.Y. Wang, X.Y. Hu, Talanta 67 (2005) 625.
[30] W.J. Jin, F.J.M. Costa, P. Rosario, et al., Anal. Chim. Acta 522 (2004) 1.
[31] N.S. Lawrence, J. Wang, Electrochem. Commun. 8 (2006) 71.

[32] K. Zhao, H. Song, S. Zhung, L. Dai, P. He, Y. Fang, Electrochem. Commun. 9 (2007) 65.
[33] A.V. Ellis, K. Vijayamohanan, R. Goswami, N. Chakrapani, L.S. Ramanathan, P.M. Ajayan, G. Ramanath, Nano Lett. 3 (2003) 279.
[34] X. Lin, Y. Li, Biosens. Bioelectron. 22 (2006) 253.
[35] Y.C. Tsai, Y.H. Hong, J. Solid State Electrochem. 12 (2008) 1293.
[36] J. Wang, M. Musameh, Anal. Chem. 75 (2003) 2075.
[37] H.P. Wu, X.J. Wu, M.Y. Ge, G.Q. Zhang, Y.W. Wang, J. Jiang, Compos. Sci. Technol. 67 (2007) 1182.
[38] M. Zhang, K. Gong, H. Zhang, L. Mao, Biosens. Bioelectron. 20 (2005) 1270.
[39] Q. Xu, S.F. Wang, Microchim. Acta 151 (2005) 47.
[40] Z. Zhang, E. Wang, Electrochemical Principles and Methods, Science Press, Beijing, 2000, p. 242.

Talanta 80 (2009) 39–47

Contents lists available at ScienceDirect

Talanta

journal homepage: www.elsevier.com/locate/talanta

Fire impact on forest soils evaluated using near-infrared spectroscopy and multivariate calibration

A. Vergnoux[a,b,*], N. Dupuy[c], M. Guiliano[a], M. Vennetier[d], F. Théraulaz[b], P. Doumenq[a]

[a] Université Paul Cézanne Aix-Marseille 3, ISM2, UMR 6263, équipe AD²EM, chimie analytique et environnement, Europole de l'Arbois, Bâtiment Villemin BP 80, 13545 Aix-en-Provence Cedex 4, France
[b] Université de Provence Aix-Marseille 1, Laboratoire Chimie Provence, UMR 6264, 3 pl. Victor Hugo – Case 29, 13331 Marseille Cedex 3, France
[c] Université Paul Cézanne Aix-Marseille 3, ISM2, UMR 6263, équipe AD²EM, systèmes chimiques complexes, Faculté Saint Jérôme – Case 451, 13396 Marseille Cedex, France
[d] Cemagref Aix en Provence, Mediterranean Ecosystems and Risks Research Unit, 3275 Route de Cézanne, CS 40061, 13182 Aix en Provence Cedex 5, France

ARTICLE INFO

Article history:
Received 25 November 2008
Received in revised form 6 June 2009
Accepted 9 June 2009
Available online 17 June 2009

Keywords:
Fire
Soil
Fire recurrence index
NIR spectroscopy
PCA
PLS

ABSTRACT

The assessment of physico-chemical properties in forest soils affected by fires was evaluated using near infrared reflectance (NIR) spectroscopy coupled with chemometric methods. In order to describe the soil properties, measurements were taken of the total organic carbon on solid phase, the total nitrogen content, the organic carbon and the specific absorbences at 254 and 280 nm of humic substances, organic carbon in humic and fulvic acids, concentrations of NH_4^+, Ca^{2+}, Mg^{2+}, K^+ and phosphorus in addition to NIR spectra. Then, a fire recurrence index was defined and calculated according to the different fires extents affecting soils. This calculation includes the occurrence of fires as well as the time elapsed since the last fire. This study shows that NIR spectroscopy could be considered as a tool for soil monitoring, particularly for the quantitative prediction of the total organic carbon, total nitrogen content, organic carbon in humic substances, concentrations of phosphorus, Mg^{2+}, Ca^{2+} and NH_4^+ and humic substances $UVSA_{254}$. Further validation in this field is necessary however, to try and make successful predictions of K^+, organic carbon in humic and fulvic acids and the humic substances $UVSA_{280}$. Moreover, NIR coupled with PLS can also be useful to predict the fire recurrence index in order to determine the spatial variability. Also this method can be used to map more or less burned areas and possibly to apply adequate rehabilitation techniques, like soil litter reconstitution with organic enrichments (industrial composts) or reforestation. Finally, the proposed recurrence index can be considered representative of the state of the soils.
© 2009 Elsevier B.V. All rights reserved.

1. Introduction

The Mediterranean region is seriously affected by forest fires. Each year more than 50,000 fires burn an estimated average of 600,000–800,000 ha. This area represents 1.3–1.7% of the total Mediterranean forests [1]. The studied Mediterranean ecosystem is situated in the Maures Mountains, in the south-east of France, near Sainte Maxime and Saint Tropez. Every year, forest fires cause a lot of damage in this area. Indeed, many physical, chemical, mineralogical and biological soil properties can be affected by forest fires [2]. The extent and duration of the effects of fire depend on the severity of the fire. They are controlled by several environmental factors that affect the combustion process, such as quantity, nature and moisture of live and dead fuel, air temperature and humidity, wind speed and topography of the site [2]. As a remark, it is quite impossible to obtain this data "*a posteriori*". The status of Mediterranean ecosystems may be balanced with the fire, up to a certain point depending on the frequency of the fires. A high frequency may lead to a significant degradation of the environment and to a reduction of ecological and remediation potentialities. The study of burned soils is necessary to estimate the degradation of soils and to apply adequate rehabilitation techniques like organic enrichment or reforestation. However, it would be very interesting to study the spatial variability of soils affected by fires and to map more or less affected areas taking into account fire frequencies. For such a study in a large area, it is necessary to connect observed changes with an estimation of fire frequencies. Fire-frequency, commonly used for describing or assessing fire regimes, is a rather complex concept which can be based on several descriptors, taking into account time or space, or both time and space [3]. The number of fires at a given point in a given time unit, is the simplest time-based definition for fire-frequency [4]. In such a case, fire interval can be calculated as the average time between two fires, generally many years in forest environments. However fire frequency can also be assessed with the distribution of intervals between two fires, or the average age of forest whose age distribution fits a mathematical distribution, for example negative exponential or Weibull [5]. In this work, a fire recurrence index was built, tested and calculated in order to display

* Corresponding author. Tel.: +33 491106380; fax: +33 491106377.
E-mail address: aurore_vergnoux@hotmail.com (A. Vergnoux).

0039-9140/$ – see front matter © 2009 Elsevier B.V. All rights reserved.
doi:10.1016/j.talanta.2009.06.028

numerical values representative of the different fire conditions that affect the different soils.

Physico-chemical analyses can also be planned in order to manage the forest, such as organic carbon content, nitrogen content, nutrients and humic substances. However, these techniques are time consuming, expensive and sample destructive. Moreover, a single parameter is insufficient to give an accurate evaluation of the soil alteration. That is why several parameters need to be taken into consideration. So, reliable, inexpensive methods have to be developed for soil analyses.

Near infrared reflectance (NIR) spectroscopy is a fast, simple and non-destructive analytical method, with no chemical reagent needed and it is also cost effective. NIR spectroscopy is an alternative method replacing usual physico-chemical analysis. Moreover, the sample preparation is very easy and "*in situ*" technology application is available. Such advantages lead to an emerging awareness of near infrared spectroscopy as a tool for environmental and biological analyses. NIR spectra contain a wide variety of information due to the absorption of NIR radiation by organic matter, particularly the overtone and combination bands of C—H, N—H, S—H, O—H and O═C bonds. As a consequence of overlapping bands, it is impossible to directly interpret a spectrum by correlating the intensity or the peak areas with concentrations. That is why NIR spectroscopy should be coupled with statistical methods. Previous works [6–15] have shown the usefulness of NIR spectroscopy for soil analyses in the prediction of some physico-chemical properties, like moisture, organic carbon content, nitrogen content, cation exchange capacity and nutrients (Mg^{2+}, Ca^{2+}, K^+, NH_4^+, etc.). In addition, a recent study [16] shows the successful use of burned soils to predict maximum temperature of fires. So, NIR spectroscopy could be a valuable tool for soil characterization and management.

In this work, we have monitored the changes in various physico-chemical characteristics of forest soils affected by different fire recurrences. The measured parameters, in addition to NIR spectra, were total organic carbon, total nitrogen content, aromaticity and organic carbon in humic substances, organic carbon in humic and fulvic acid fractions, NH_4^+, Mg^{2+}, Ca^{2+} and K^+ contents.

The aim of this study was to build a numeric model for the prediction of these parameters on the basis of chemometric analyses of NIR spectra of soils samples. A prediction was made of the proposed recurrence index as well as the number of fires and the duration of time since the last fire. The main advantage was to centralize all analyses in one device which can be used "*in situ*" by low skill level operators. The evaluation of the impact of different fire events on forest soils using near-infrared spectroscopy and multivariate calibration was explored. The aim of the evaluation of fire perturbations was to select the most sustainable management practices.

2. Experimental

2.1. Sampling

The studied area is a Mediterranean ecosystem situated in the Maures Mountains, in the south-east of France (Fig. 1). The annual average rainfall is about 800–1200 mm. The monthly temperature in the area fluctuates from 12 °C in December and January to 30 °C in August; annual average temperature is 20 °C. Regarding vegetation, non-disturbed forest soils presents a tree stratum of *Quercus ilex* L., *Quercus suber* L., *Pinus pinaster Aiton* subsp. *pinaster*. Soils recently affected by fires show a total elimination of the vegetation cover

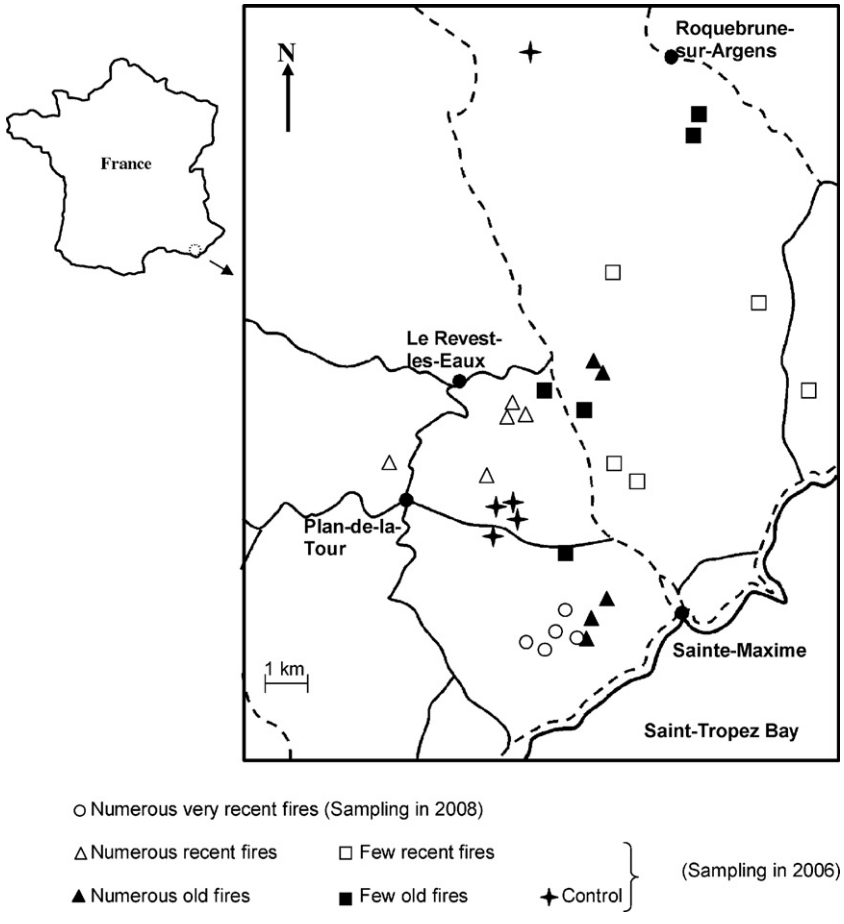


Fig. 1. Location of the sampling sites in the south-east of France.

Table 1
Number and dates of the fires affecting the different studied sites.

Condition	Number of fires	Dates of forest fire events	Fire recurrence index, RI
Control (C)	Unburned until 1950	0.13	
	Unburned until 1950	0.13	
	Unburned until 1950	0.13	
	Unburned until 1950	0.13	
	Unburned until 1950	0.13	
Few, old (FO)	2	1990/1964	0.33
	2	1982/1959	0.29
	2	1990/1962	0.33
	1	1990	0.25
	1	1982	0.20
Numerous, old (NO)	4	1990/1985/1978/1964	0.60
	4	1990/1985/1978/1964	0.60
	4	1990/1985/1978/1964	0.60
	4	1990/1982/1978/1962	0.59
	4	1990/1982/1978/1962	0.59
Few, recent (FR)	2	2003/1962	0.62
	2	2003/1982	0.65
	2	2003/1982	0.65
	2	2003/1970	0.62
	2	2003/1962	0.62
Numerous, recent (NR)	4	2003/1990/1982/1959	0.82
	4	2003/1990/1982/1959	0.82
	4	2003/1990/1982/1959	0.82
	3	2003/1990/1962	0.73
	3	2003/1990/1970	0.74
Numerous, very recent (NVR)	5	2007/1990/1985/1978/1964	1.22
	5	2007/1985/1978/1970/1964	1.19
	4	2007/1985/1970/1964	1.12
	4	2007/1985/1970/1964	1.12
	4	2007/1985/1978/1964	1.13

with a reconstitution of the vegetal cover more or less advanced, mainly occupied by herbaceous, fast growing species, *Erica arborea* L., *Cistus monspeliensis* L., *Q. suber* L. This latter species is also present in these sites due to its high capacity of regeneration after fires.

In our studied area, the fire regime in recent years is correctly known through fire history maps including all medium and larger fires since 1950. These maps were used to select the plots. However, due to the broad spatial distribution of these plots, several fire regimes could be found for the same number of fires, with different fire dates. The chosen sites involve areas unburned for 50 years and areas affected by different fire regimes. So, soil samples were collected at 30 different sampling sites (Fig. 1 and Table 1) in order to represent 6 different fire conditions (NVR: numerous very recent fires, NR: numerous and recent fires, NO: numerous and old fires, FR: few and recent fires, FO: few and old fires, C: control sites, unburned since 1950), with 5 different sites for each condition. These sites are relatively preserved from human impact and have been chosen amongst others for this reason. Moreover, they present similar aspect, exposition, slope, altitude and ecological characteristics. So, in this work the "fire factor" was the sole studied influencing factor.

First, the soils NR, NO, FR, FO and C were sampled in May 2006 for two layers (A: 0–5 cm and B: −5 to 15 cm). Then, according to the first results, a second sampling was done in May 2008, only for the A layers of NVR soils.

To take soil heterogeneity into consideration as much as possible, sampling was carried out on five positions at each site, resulting in 5 replicates per layer and per site. Then, equal volumes of the five replicates were mixed, homogenized and sieved (2 mm), to obtain one composite sample per site and per layer. The soil samples were then stored in glass bottles at −18 °C before analysis. Each sample was divided into two equal parts: one for physico-chemical analyses, and another for near infrared spectroscopy.

2.2. Fire recurrence index

To take into account the resilient dynamics of studied parameters, fitting fire-frequency to these parameters required a fire-frequency index (FRI). This had to be designed to include not only the number of fires, but also their dates and the time interval between fires.

So, a fire recurrence index was defined and calculated for all soils in order to assess the number and the date of fires according to Eq. (1).

$$\mathrm{RI} = \sqrt{\sum_{i=1}^{n} \frac{i}{S - F_i}} \quad (1)$$

where S is the sampling year, n the total number of fires, i the number of the fire from more recent to older fires (1 for the most recent, 2 for the second most recent, etc.) F_i the years of the fire i.

This equation takes into account the date of the fires by the difference between the year of sampling and the year of fires in the denominator. The more recent the fire, the greater the result of the division. Then, the number of fires appears by the number of divisions, with a multiplying factor to accentuate the fact that many fires have a bigger impact on the soils. Finally, a square root of the sum is applied to reduce the variability of the values displayed for very recent fires.

2.3. Physico-chemical analyses

Humic substances (HS), humic acids (HA) and fulvic acids (FA) amounts were obtained after alkali extraction (pH 13.0 for 20 h) and precipitation of humic-like fraction (pH 1.0) by addition of 6 mol l^{-1} HCl. Then, FA were cleaned-up with a column packed with XAD-8 resin. This method was adapted from [17].

HS, HA and FA in solution were analyzed using a high temperature combustion carbon analyzer (Shimadzu TOC analyzer 5050A, Shimadzu) in order to determine organic carbon concentrations (OC). Before analysis, all fractions were acidified to pH 2.0 with HCl to eliminate residual inorganic carbon and then N_2 bubbled during 10 min to remove dissolved CO_2.

Total organic carbon (TOC) contents of soils were quantified with the same analyzer coupled with a solid module. Organic carbon concentrations were expressed in $g\,kg^{-1}$ of dried soil.

UV absorbance spectra were recorded at room temperature for HS. Acquisition was performed using 1 cm quartz cell with an UV–vis spectrometer (UV-light, Secomam, France). Data was processed using LabPowerJ™ software package (Secomam, France). Spectra were recorded with a resolution of 1 nm between 200 and 400 nm. UV specific absorbances (UVSA) were calculated at 254 and 280 nm according to the Eq. (2) [18,19].

$$\mathrm{UVSA}_{254} = \frac{\text{Absorbance 254 nm}}{\mathrm{OC(mg/l)}} \times 100 \quad (2)$$

The $UVSA_{254}$ and $UVSA_{280}$ represent the humic substance aromaticity.

The total nitrogen content ($g\,kg^{-1}$) was obtained with a combustion method NF ISO 13878. Ammonium plus ammonia nitrogen were extracted from soils in a KCl solution [20,21]. Ammonium content in the extract was determined by continuous flow colorimetry [22,23], and expressed in $mg\,kg^{-1}$.

Phosphorus contents, expressed in $g\,100\,g^{-1}$, were determined according to the Joret Hebert method [24,25] which is a standard method (AFNOR NF X 31-161).

Exchangeable potassium, magnesium and calcium contents ($g\,kg^{-1}$) were obtained by the standard method AFNOR NF X 31-108 which uses exchangeable cation extraction by ammonium acetate [26–28].

For the physico-chemical parameters, the standard error of every method (SEM) was calculated according to Eq. (3).

$$\mathrm{SEM} = \sqrt{\frac{\sum_{i=1}^{N_1}(X_i - \overline{X_1})^2 + \sum_{j=1}^{N_2}(X_j - \overline{X}_2)^2 + \sum_{k=1}^{N_3}(X_k - \overline{X_3})^2 + \cdots}{N_1 + N_2 + N_3 + \cdots + N_t}} \quad (3)$$

where i, j, k, ... are different samples analyzed with the same method; N_1, N_2, N_3, ... are the number of replicates for each sample; X are the measured values; $\overline{X}$ is the mean of the different X; N_t is the total number of samples.

We assumed that the random error sources are the same for all measurements, because the different samples have similar composition and have been analyzed with the same analytical method.

For each analytical method, the relative error of the method (REM) was also calculated according to Eq. (4).

$$\mathrm{REM} = \frac{\mathrm{SEM}}{\bar{Y}} \times 100 \quad (4)$$

where $\bar{Y}$ is the mean of the values measured by the corresponding analytical method.

2.4. Near infrared spectroscopy

Soils were dried and ground before spectroscopic analyses. Aliquots of around 50 g of soil samples were placed in a specific round glass-sampling cup.

Fourier transformation near infrared (FT-NIR) spectra were recorded in reflectance with an integration sphere using a Nicolet Antaris spectrometer interfaced to a computer. Spectra were computed at $8\,cm^{-1}$ resolution from 4500 to 10,000 cm^{-1} using Thermo Nicolet 2.1 software. Co-addition of 64 scans symmetrical interferograms was performed for each spectrum, resulting in 1557-absorbance point's spectra.

Three spectra per sample were collected at ambient temperature (total of 165 spectra). For each sample, the subset of 3 spectra was then reduced to 1 by working out an average. Lastly, for each sample measurement, the background correction was obtained using a clean empty glass cup before each sample scan. These latter spectra were then used for PCA and PLS (55 spectra). Spectral pretreatment and multivariate calibration were performed with Unscrambler (version 9.0 from CAMO, Norway).

2.5. Principal component analysis

Principal component analysis (PCA) is a method for extraction of the systematic variations in one data set [29]. This method can be used for visualizing information in large data sets as well as for interpretation [30]. In this work, PCA was employed to verify the feasibility of classifying soils according to the fire event that affects them. This tool can show if physico-chemical and spectral results are differentiated by the different kinds of fire events. So, two different PCA were achieved with the A layer of all the studied sites: one with the spectral data and another one with physico-chemical parameters. The second one also allowed us to understand the impact of fires on the physico-chemical properties of the soils. For the PCA with spectral data, multiplicative scatter correction (MSC) of the original spectra was used [31].

2.6. Partial least square regression

Partial least square (PLS) regression is a powerful multicomponent analysis. PLS [32–34] allows a sophisticated statistical approach using the full spectral region rather than unique and isolated analytical absorption bands.

In our case, we are only looking for physico-chemical modifications, i.e. total organic carbon, total nitrogen content, ammoniacal nitrogen, humic substances, humic and fulvic acids, using the same data processing.

The evaluation of the calibration performance was estimated by computing both the standard error of calibration (SEC) after comparing the real modification with the computed one for each component and the standard error of prediction (SEP) for the estimation of the prediction performance during the step of validation of the calibration equation. Additionally, we used the relative error of prediction (REP) that shows the predictive ability of the model.

With regards to calibration and prediction of the models; after rather inconclusive tests with different parts of spectra, the whole spectra were chosen to be used for calculation.

Firstly, the physico-chemical parameters of the soils were modeled by PLS1 with all samples both A and B layers. PLS1 is a version of the PLS method in which only one Y-variable is modeled. Models were constructed using full cross validation to define the factor number (FN). A set of 44 samples was then used for the calibration to establish the model. The validation set composed of 11 samples. One soil of each kind of fire event and each layer was randomly selected to constitute this validation set in order to evaluate the ability of the multivariate calibration method for prediction. The PLS1 regression was achieved with different spectroscopic pretreatments of the spectra: no data processing, MSC, standard normal variate (SNV), normalization, first derivative and smoothing [35]. In each case, we chose the pretreatment leading to the best correlation between spectra and physico-chemical data.

Then, in the same way as for physico-chemical data, three other variables were modeled by PLS1 with the multiplicative scatter corrected spectra only for the A layer. These variables are: number of fires (NF), time elapsed since the last fire (TE) and the fire

recurrence index. MSC was chosen because it displayed the best correlation between spectra and these three variables. The calibration and validation sets were constituted of 24 and 6 samples respectively.

3. Results and discussion

3.1. Fire recurrence index

To take into account the resilient dynamics of studied parameters, fitting fire-frequency to these parameters required a fire-frequency index. This had to be designed to measure not only the number of fires but also their dates, the time in between and the last fire, and the time interval between fires. An area-based index was not required as plots were considered as points in the landscape.

So, on the basis of the sampling year S, the total number of fires (n) and the date of the fires (F_i), the fire recurrence index was designed (i) to increase with the number of fires and (ii) to decrease in a negative exponential way with the time since the last fire. It was designed to fit in with what was observed with the dynamics of most of the parameters and, more generally (iii) to give more importance to recent fires than to old fires. FRI was computed with the Eq. (1) (see Section 2).

Fig. 2 shows the graphical results of RI calculated values by the simulation of different fire conditions with a sampling date in 2008. The abscissa axis represents the date of the last fire, which is the only variable in the FRI equation. For calculation with several fires, the other dates of fire are held fixed (captions in Fig. 2). FRI values were calculated in this way from 1 to 4 fires, moving the date of the last fire and changing intervals between fires.

The FRI values show that a hierarchy between the different fire recurrences exists according to both fire number and dates of the fires. Moreover, comparing results for the 2 conditions with 4 fires, the FRI values are greater when the fires are grouped around the same time than when they are becoming less frequent. So, the index takes into account the notion of a greater impact caused by frequent fires.

Table 1 shows the calculated FRI for all sites. The controls, unburned since 1950, present a FRI of 0.13. The highest value obviously corresponds to the more impacted site and reaches 1.22. It represents 5 fires about every 15 years since 1964, the last one being in 2007. The other values consequently range from 0.13 to 1.22, reaching about 0.25, 0.60, 0.65 and 0.78 for FO, NO, FR and NR respectively. So, the FRI values of the studied sites are arranged according to a "theoretical fire impact".

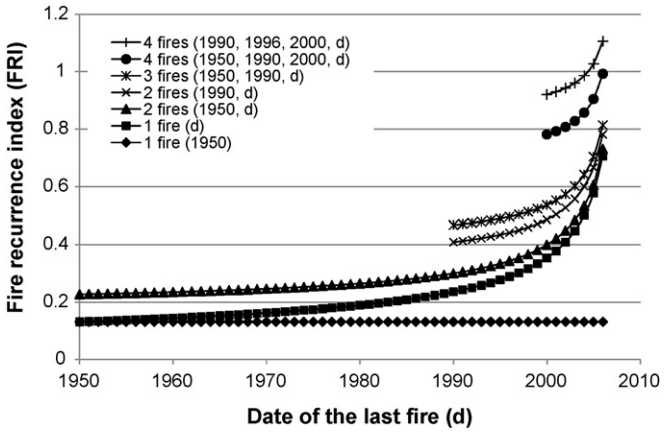


Fig. 2. FRI calculated values by the simulation of different fire conditions. Sampling date is 2008.

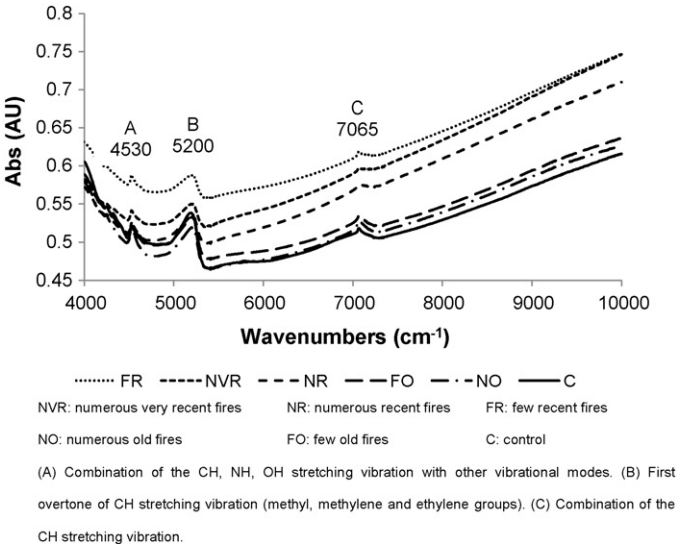


Fig. 3. Representative spectra from the soils affected by different recurrences of fires. Each presented spectra is the average of 3 raw spectra.

3.2. Spectral data

Fig. 3 shows representative spectra of the different soils affected by the different fire conditions. All spectra are very close and look like those of a previous study of Mediterranean soils [14]. According to previous works [7,11,13,14,36], all NIR spectra showed 3 large absorption bands due to harmonic and/or combination vibrations at: (i) 4530 cm^{-1}, combination of the CH, NH, OH stretching vibration with other; (ii) 5200 cm^{-1}, first overtone of CH stretching vibration (methyl, methylene and ethylene groups); (iii) 7065 cm^{-1}, combination of the CH stretching vibration.

We notice that soil spectra are arranged in order along the absorbance axis, from old to recent fires. The latter condition leads globally to a significant increase of the baseline of absorbance spectra [16], particularly in the spectral domain from 5500 to 10,000 cm^{-1}. Consequently, the spectra of soils recently burned are at the top of Fig. 3 whereas the spectra of control and formerly burned soils are at the bottom.

The interpretation of individual spectra nevertheless remains difficult. So, all additional information needs to be and will be "extracted" and highlighted by statistical treatments as principal component analysis and partial least square regression as described in the following section.

3.3. Principal component analysis of the spectral data

Fig. 4 shows the principal component analysis for NIR spectra after MSC correction of control and soils affected by the different fire conditions for the A layer. About 99% of the total spectral variance was explained after computing the first principal component on corrected spectra.

The samples are represented by bars positioned from left to right, according to the fire recurrence. The bargraph shows 2 differentiated zones. The first one gathers spectra of soils affected by recent fires, showing negative scores. The second one corresponds to spectra from controls and soils affected by old fires, showing positive scores except for 2 samples.

The examination of the first loading plot (Fig. 5) showed a similarity with sample spectra, they have the same 3 absorption bands at 4530, 5200 and 7065 cm^{-1}. However, these bands present higher intensity in the first loading plot. Spectra with positive scores (Fig. 4, control and soils affected by old fires) are correlated to the positive

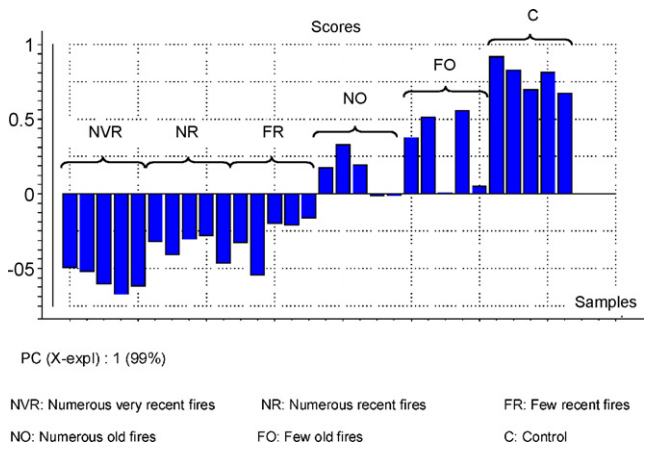


Fig. 4. Principal component analysis for multiplicative scatter corrected spectra of the layer A of soils.

part of the first loading plot, i.e. A and B bands, which are relative to the organic matter content. Spectra with negative scores (Fig. 4, soils affected by recent fires) are correlated to the negative part of the first loading plot, i.e. C band and the baseline shift, which could represent inorganic matter. So, recent fires and old fires can respectively be allocated to spectra with a large baseline deviation and spectra with intense A and B bands due to high organic matter amounts (Fig. 3).

These baseline drifts were previously shown by Zornoza et al. [14], for soils with different land-uses. We also found such drifts in industrial compost NIR spectra in a previous work [37]. Generally, baseline drifts in IR are due to light scattering because of samples granulometry (as a result of soil grinding) and/or sample composition (organic and/or inorganic).

It clearly appears that it is possible to assess the spatial heterogeneity of a burned area in this way. So, PCA can be a useful, rapid and inexpensive method for monitoring forest soils and planning adapted remediation strategies.

Soils affected by old fires are differentiated from control sites (Fig. 4). Sixteen years after the last fire, the burned soils do not return to the control state. Moreover, Fig. 4 shows that the variability between old fires is greater than the variability between recent fires. Recent fires clearly homogenize the soils. After that, the reconstruction is more or less efficient, conducting to contrasted results as shown by NO and FO fires. It suggests variability in "remediation rates" at the site level. Nevertheless, after sufficient period of time (e.g. controls), the samples seem more homogeneous. Finally, it is quite difficult to differentiate numerous fires from few fires or recent or old fires. The preponderant factor that differentiates soils appears to be the time elapsed since the last fire. The difficulty to differentiate few from numerous fires can be explained by

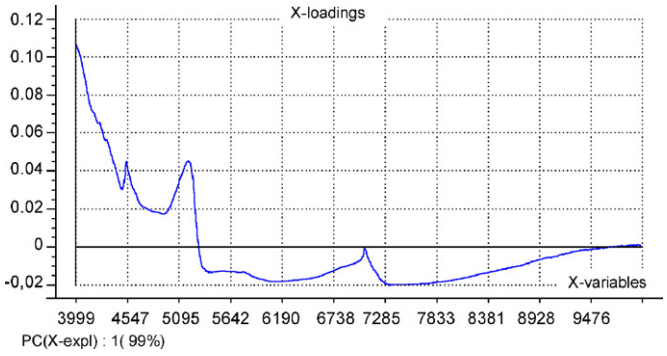


Fig. 5. First loading plot (99% of the variance).

Table 2
Variability of soil physico-chemical parameters.

Parameter	n^g	Mean	Minimum	Maximum
TOC[a]	55	30.6	14.2	81,0
Total N[b]	50	1.57	0.63	4.31
Phos[c]	50	0.10	0.06	0.15
Mg^{+d}	50	0.23	0.10	0.49
Ca^{2+d}	50	1.51	0.59	3.59
NH_4^{+d}	50	7.12	2.29	33.50
OC HS[e]	55	9.50	3.56	19.90
OC HA[e]	55	2.30	0.53	6.10
OC FA[e]	55	2.50	0.92	5.40
$UVSA_{254}$ HS[f]	55	3.17	2.06	4.56
$UVSA_{280}$ HS[f]	55	2.73	1.68	3.93

[a] Total organic carbon ($g\,kg^{-1}$).
[b] Total nitrogen ($g\,kg^{-1}$).
[c] Phosphorus ($g\,100\,g^{-1}$).
[d] Contents ($g\,kg^{-1}$).
[e] Organic carbon in humic substances, humic acids and fulvic acids ($mg\,g^{-1}$).
[f] Specific absorbance at 254 and 280 nm of humic substances.
[g] Sample number.

the intensity of the fires that affected the soils [16,38]. The intensity of fires consists of the maximum temperature reached, and the duration of fire. These latter parameters cannot be taken in account here, but remain important for the evaluation of the fire impact. Few, intense fires could lead to a greater impact than less intense, numerous fires.

3.4. Principal component analysis of the physico-chemical parameters

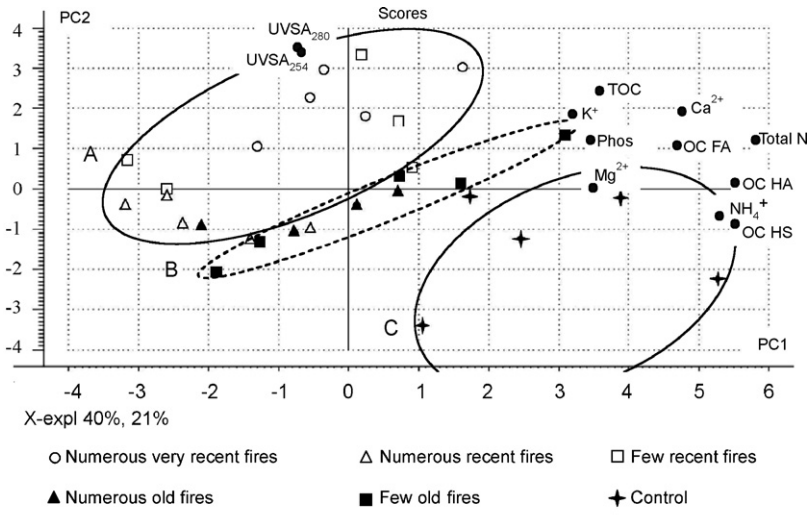
Table 2 highlighted for each considered parameter, the mean, the standard deviation and the range for all studied soils and depths. The displayed variability and range are important due to the different recurrence conditions and depths computed.

Fig. 6 shows the positions of the samples (and variables) along the two PC. Contrary to the previous spectral PCA, it is impossible to distinguish the different kinds of fire recurrences with only one axis. However, we note the separation of the A layer of recently, and very recently burned soils from formerly burned soils and from controls. This shows three different clusters respectively, A, B and C. They are distributed from the bottom right to the top left of the graph.

The position of the variables in the set of axis shows their relative contribution to the PC's construction. 61% of the total variance was explained by two components. The first PC, explaining 40% of the compositional data, is positively correlated to total nitrogen, organic carbon of humic substances and humic acids and with NH_4^+. In the same way, the second PC, explaining 21% of the compositional data, is positively correlated to the $UVSA_{254}$ and $UVSA_{280}$.

The proximity of the A cluster with the variable $UVSA_{254}$ and $UVSA_{280}$ indicates high specific absorbance values at 254 and 280 nm for soils affected by NVR, NR and FR fires included in this cluster. Moreover, the position and separation of the three clusters can be explained by the $UVSA_{254}$ and $UVSA_{280}$ representing the HS aromaticity. The soils, both very recently and recently burned show a greater HS aromaticity than the formerly burned soils. These present in their turn, a greater HS aromaticity than the controls. This trend was described in previous works, showing that in burned soils, new aromatic structures are issued from the alteration of carbohydrates [39–42], lipids and peptides [43,44].

The soils affected by NVR can be differentiated from those affected by NR by the organic carbon content, nitrogen and some nutrients. The soils affected by NVR present greater organic carbon contents, nitrogen and nutrients. After a moderate wildfire, an increase of carbon in soil is usually observed, suggesting a substantial incorporation of forest necromass [45]. Increases in soil organic



$UVSA_{254}$ and $UVSA_{280}$: HS specific absorbance at 245 and 280nm respectively;

Phos: phosphorus; Total N: total nitrogen; TOC: total organic carbon; OC HS, OC HA and OC FA: organic carbon in humic substances, humic acids and fulvic acids respectively;

(A) cluster with soils affected by very recent and recent fires; (B) cluster with soils affected by old fires; (C) cluster with control soils.

PC1 and PC2 respectively for principal component 1 and 2.

Fig. 6. Two dimensional plot of the layer A of soils using physico-chemical parameters.

matter content are also reported, due to an increased deposition of dry leaves and more or less charred plant materials in fires that affect the tree canopy [46].

Fig. 6 shows lower TOC contents for NR soils. This is probably due to an alteration of changes in soil physico-chemical properties [47,48]. Furthermore, the well known soil erodibility accentuates the loss of the soil organic matter by leaching of topsoil layers [49–51].

The FR soils are scattered, probably because of the intensity of fires once again.

For NO and FO conditions, the soils are not discriminated according to the number of fires, but are grouped in the cluster B (Fig. 6). The observed differences could again be attributed to the intensity of fires and above all, to their different reconstitution level since the last fire.

Moreover, the control soils present the greater concentrations of organic carbon contents, nitrogen and nutrients. According to previous works, the fires have a quantitative impact on the nutrients and a quantitative and qualitative impact on the organic matter [2].

4. Predictions by NIRS

4.1. Physico-chemical parameter predictions

In this part, we try to predict physico-chemical parameters with multivariate calibration models, using the NIR spectra, by partial least squares regression. The calibration set comprises of 44 samples.

The evaluation of the results was done with standard error of calibration (SEC), R^2 of calibration, standard error of prediction (SEP), R^2 of prediction, relative error of prediction (REP) and a number of factors from the PLS model (FN). The more FN are used, the greater is the noise in the model. Table 3 shows the best results obtained for physico-chemical parameters predictions with various spectral treatments.

The majority of the physico-chemical parameters are better calibrated and predicted with SNV pre-treatments. Results show that all physico-chemical parameters are very well correlated to NIR spectra, with R^2 for calibration mainly over 0.90. The exceptions are NH_4^+, HS $UVSA_{254}$ and $UVSA_{280}$ and the OC of FA which exhibit slightly lower R^2 for calibration, 0.84, 0.89, 0.77 and 0.62 respectively. Nevertheless, for all physico-chemical parameters, the observed SEC values are relatively low.

PLS models were validated by an independent prediction set of 11 samples. According to a previous work [52], $0.66 < R^2$ prediction < 0.8 indicates a rough quantitative prediction, $0.81 < R^2$ prediction < 0.9 a good prediction and R^2 prediction > 0.9 an excellent prediction. In our study, all R^2 for the prediction are greater than 0.9, except for HS $UVSA_{254}$ $UVSA_{280}$. These results allow us to expect excellent predictions. It is possible to verify this with the observation of REP values. The predictions seem very good for 5 parameters (TOC, total nitrogen, phosphorus, Mg^+ and OC in HS), with corresponding REP about 10%. The prediction of the OC in HS is particularly interesting because the REP is very close to REM (Table 3) and the usual analytical method is very time-consuming. For other parameters: Ca^{2+}, NH_4^+ and the HS $UVSA_{254}$, the predictions are not as good, with REP ranging from 15 to 20%. Concerning OC in HA and FA and the HS $UVSA_{280}$, the corresponding REP are too significant to consider an acceptable prediction. Nevertheless, the differences between REP and REM, of about 10%, are not so great for the OC in HA and FA, as the usual analytical methods present REM to be quite important. Table 3 does not show results for K^+, because, as for previous works [13,53], no correlation was found between results and NIR spectra. One explanation could be the non-direct relationship between K^+ and NIR absorption bands.

Finally, according to previous works [6,7,10,11,13–15,36,54–57], these results show the ability of NIR to predict some physico-chemical parameters of soils.

As a partial conclusion, this study shows that PLS regression models using NIR spectra are a valuable tool to assess wildfires effect on impacted soils.

Table 3
Best results obtained for predictions of physico-chemical parameters with various spectral treatments and with PLS1 regression method.

Parameter	Concentration range	REM[g] (%)	Pre-treatments	R^2 calibration	SEC[j]	R^2 prediction	SEP[k]	REP[l] (%)	FN[m]
TOC[a]	14.2–80.1	2.8	Smoothing derivative	0.90	3.39	0.97	3.05	9.9	7
Total N[b]	0.63–4.31	4.7	Smoothing derivative	0.95	0.075	0.97	0.17	10.8	6
Phos[c]	0.06–0.15	4.1	–	0.92	0.0078	0.93	0.0083	8.3	14
Mg^{2+}[d]	0.10–0.49	3.3	SNV[h]	0.93	0.034	0.99	0.026	11.3	6
Ca^{2+}[d]	0.63–3.59	4.5	–	0.93	0.11	0.91	0.25	16.6	10
NH_4^+[d]	2.3–17.2	7.1	MSC[i]	0.84	1.09	0.93	1.15	16,1	8
OC HS[e]	3.56–19.83	7.0	Smoothing derivative	0.96	0.37	0.96	1.16	12.1	9
OC HA[e]	0.53–6.11	14.3	SNV[h]	0.90	0.56	0.90	0.59	25.3	8
OC FA[e]	0.92–5.38	12.1	SNV[h]	0.89	0.56	0.90	0.62	25.1	6
$UVSA_{254}$ HS[f]	2.06–4.55	6.8	SNV[h]	0.77	0.48	0.76	0.49	15.5	3
$UVSA_{280}$ HS[f]	1.72–3.93	7.0	SNV[h]	0.62	0.40	0.60	0.57	20.8	11

[a] Total organic carbon (mg g^{-1}).
[b] Total nitrogen (g kg^{-1}).
[c] Phosphorus (g.100 g^{-1}).
[d] Contents (g kg^{-1}).
[e] Organic carbon in humic substances, humic acids and fulvic acids (mg g^{-1}).
[f] Specific absorbance at 254 and 280 nm of humic substances.
[g] Relative error of the method.
[h] Standard normal variate.
[i] Full multiplicative scatter correction.
[j] Standard error of calibration.
[k] Standard error of prediction.
[l] Relative error of prediction.
[m] Factor number.

4.2. Other parameter predictions

In this part, the prediction of three other variables was realized by PLS1 regression of the multiplicative scatter corrected NIR spectra for A layer of all soils. These variables are: number of fires (NF), time elapsed since the last fire (TE) and the recurrence index described above. The calibration set comprises of 24 samples. The number of samples is less than for the physico-chemical parameters because these parameters are only evaluated for A layer. As a remark, A layer was chosen because it is obviously the most impacted by wildfires.

Table 4 shows the best results obtained for calibrations and predictions. TE and RI are very well correlated to corrected NIR spectra. Their R^2 of calibration values are over 0.90 and they present low SEC. As regards NF, results are not as good, with R^2 of calibration and SEC about 0.85 and 0.37, respectively.

As for physico-chemical parameters, PLS models were also validated by an independent prediction set of 6 samples. Despite good prediction R^2, the predictions are not so good for NF and TE according to REP values over 20%. With regards to FRI, the prediction results are very good, with a R^2 of prediction about 0.98 and a REP about 10.2%. So, the soil matter evolution level does not depend on NF or TE separately, but depends on a relation between them, corresponding to the integrating parameter FRI (Table 1). The good correlation and prediction of FRI show that it is a major controlling parameter in our study. The intensity of fires could be a part of the error sources of prediction, as well as the biomass (qualitative and quantitative) presents in the studied sites. Moreover, a recent work [58] showed that the presence of ash could be an interfering factor in the estimation of the maximum temperature reached in burned soils using near-infrared spectroscopy. Another hypothesis could be the interference due to the presence of ash in the estimation of parameters studied in this work, even if it is impossible to estimate it. Nevertheless, this work shows the interest of the fire FRI. PLS regression models are successful in predicting these parameters as the fire recurrence modify NIR spectra of soils.

Table 4
Results for predictions of the number of fire (NF), the time elapsed since the last fire (TE) and the fire recurrence index (FRI) for multiplicative scatter corrected spectra of the layer A of the soils and with PLS1 regression method.

Parameter	Range	R^2 calibration	SEC[a]	R^2 prediction	SEP[b]	REP[c] (%)	FN[d]
NF	0–5	0.85	0.37	0.90	0.62	27.7	6
TE	1–56	0.93	1.21	0.98	3.52	20.1	4
FRI	0.13–1.22	0.90	0.061	0.98	0.060	10.2	5

[a] Standard error of calibration.
[b] Standard error of prediction.
[c] Relative error of prediction.
[d] Factor number.

5. Conclusions

NIR spectroscopy has a number of advantages. It is a rapid, non-destructive and green (because no chemical reagent is needed and no waste is produced) method that does not require sample pre-treatment. Despite the impossibility to directly interpret a NIR spectrum by correlating the intensity or the surface of peaks with concentrations, NIR spectroscopy coupled with chemometric methods confirms its usefulness for monitoring the forest soils affected by fires.

It clearly appears that the evaluation of the fire recurrence of unknown samples is possible with PCA and particularly the evaluation of the time elapsed since the last fire.

This study shows that NIR spectroscopy coupled with PLS is a valuable tool for soil monitoring, particularly for the prediction of the total organic carbon, total nitrogen, organic carbon and $UVSA_{254}$ of humic substances, phosphorus, Mg^+, Ca^{2+} and NH_4^+. However, further investigation should to be carried out in this field to try to make successful predictions of K^+, organic carbon in humic and fulvic acids and HS $UVSA_{280}$.

Furthermore, the proposed recurrence index can be predicted easily. NIR spectroscopy appears to be a very valuable tool to evaluate the fire effects on soils, to study the spatial variability, to map more or less burned areas and to apply adequate rehabilitation techniques, like reforestation or organic enrichment. A larger number of studied samples could lead to more robust models for a better prediction, but this study is a very promising first approach.

Acknowledgements

Financial support was provided by Region PACA, the IRISE project (http://irise.mediasfrance.org/) funded by the European Union, Forest Focus Regulation (No. 2152/2003) and the French Ministry of Agriculture and Fisheries. The authors wish to thank the IRISE staff for considerable work concerning *in situ* experiment and sampling, in particular Max Bresson for equipment support and active sampling.

References

[1] M.A. Olivella, T.G. Ribalta, A.R. de Febrer, J.M. Mollet, F.X.C. de las Heras, Sci. Total Environ. 355 (2006) 1.
[2] G. Certini, Oecologia 143 (2005) 1.
[3] C. Li, Ecol. Model. 154 (2002) 103.
[4] D.F. Merrill, M.E. Alexander, Glossary of Forest Fire Management Terms, National Research Council of Canada, Canadian Committee on Forest Fire Management, Ottawa, Ontario, 1987 (Publication NRCC No. 26516).
[5] J.K. Agee, Fire Ecology of Pacific Northwest Forests, Island Press, Washington, DC, 1993.
[6] E. Ben-Dor, A. Banin, Soil Sci. Soc. Am. J. 59 (1995) 364.
[7] C. Chang, D.A. Laird, M.J. Mausbach, C.R. Hurburgh, Soil Sci. Soc. Am. J. 65 (2001) 480.
[8] B.W. Dunn, H.G. Beecher, G.D. Batten, S. Ciavarella, Aust. J. Exp. Agric. 42 (2002) 607.
[9] D.F. Malley, L. Yesmin, R.G. Eilers, Soil Sci. Soc. Am. J. 66 (2002) 1677.
[10] K.D. Shepherd, M.G. Walsh, Soil Sci. Soc. Am. J. 66 (2002) 988.
[11] D. Cozzolino, A. Moron, J. Agric. Sci. 140 (2003) 65.
[12] M. Chodak, P. Khanna, B. Horvarth, F. Beese, J. Near Infrared Spec. 12 (2004) 315.
[13] Y. He, M. Huang, A. Garcia, A. Hernandez, H. Song, Comput. Electron. Agric. 58 (2007) 144.
[14] R. Zornoza, C. Guerrero, J. Mataix-Solera, K.M. Scow, V. Arcenegui, J. Mataix-Beneyto, Soil Biol. Biochem. 40 (2008) 1923.
[15] O. Galtier, N. Dupuy, Y. Le Dréau, D. Ollivier, C. Pinatel, J. Kister, J. Artaud, Anal. Chim. Acta 595 (2007) 136.
[16] C. Guerrero, J. Mataix-Solera, V. Arcenegui, J. Mataix-Beneyto, I. Gómez, Soil Sci. Soc. Am. J. 71 (2007) 1029.
[17] M. Schnitzer, Organic matter characterization, in B.L. Page, R.H. Miller, D.R. Keeney (Ed.), Methods of Soil Analysis, Part 2, Chemical and Microbiological Properties, second ed., Agronomy Monograph No. 9, Madison, 1982, pp. 581–594.
[18] S. Traina, J. Novak, N. Smeck, J. Environ. Qual. 19 (1990) 151.
[19] R. Chen, J.L. Bada, Mar. Chem. 45 (1994) 31.
[20] P. Viaux, Sci. du Sol. 1 (1981) 73.
[21] T. Sterckeman, H. Ciesielski, Principaux facteurs influant sur la détermination de l'azote minéral des sols, in: Frontières (Ed.), L'azote et le soufre des sols—Troisièmes journées de l'analyse de terre, Blois, Gif sur Yvette, 1991, pp. 101–121.
[22] M.D. Krom, The Analyst 105 (1980) 305.
[23] P.L. Searle, The Analyst 109 (1984) 549.
[24] G. Joret, J. Hebert, Ann. Agron. 2 (1955) 233.
[25] L. Duval, Chim. Anal. 45 (1963) 237.
[26] D. Knudsen, G.A. Peterson, P. Pratt, Lithium, Sodium and Potassium, Methods of Soil Analysis, vol. 2, American Society of Agronomy and Soil Science Society of America Journal, Madison, 1982, pp. 225–246.
[27] G.W. Thomas, Agronomie 9 (1982) 154.
[28] H. Ciesielski, T. Sterckeman, Agronomie 17 (1997) 9.
[29] N. Kettaneh, A. Berglund, S. Wold, Comput. Stat. Data Anal. 48 (2005) 69.
[30] S. Millar, P. Robert, M.F. Devaux, R.C.E. Guy, P. Maris, Appl. Spectrosc. 50 (1996) 1134.
[31] J.M. Andrès, M.T. Bona, Anal. Chim. Acta 535 (2005) 123.
[32] M. Fuller, P.R. Griffiths, Anal. Chem. 50 (1988) 1906.
[33] D.M. Haaland, E.V. Thomas, Anal. Chem. 60 (1988) 1193.
[34] Y.L. Liang, O.M. Kvalheim, Chemometr. Intell. Lab. 32 (1996) 1.
[35] A. Savitzky, M.J.E. Golay, Anal. Chem. 36 (1964) 1627.
[36] P.H. Fidencio, R.J. Poppi, J.C. Andrade, H. Cantarella, Commun. Soil Sci. Plan. 33 (2002) 1607.
[37] A. Vergnoux, M. Guiliano, Y. Le Dréau, J. Kister, N. Dupuy, P. Doumenq, Sci. Total Environ. 407 (2009) 2390.
[38] E. Chuvieco, D. Riaño, F.M. Danson, P. Martin, J. Geophys. Res. 111 (2006) 4.
[39] L.W. Dennis, G.E. Maciel, P.G. Hatcher, B.R.T. Simoneit, Geochim. Cosmochim. Acta 46 (1982) 901.
[40] G. Almendros, J. Dorado, F.J. Gonzalez-Vila, F. Martin, J. Anal. Appl. Pyrol. 40 (1997) 599.
[41] J.A. Baldock, R.J. Smernik, Org. Geochem. 33 (2002) 1093.
[42] F.J. Gonzalez-Vila, P. Tinoco, G. Almendros, F. Martin, J. Agric. Food Chem. 49 (2001) 1128.
[43] H. Knicker, G. Almendros, F.J. Gonzalez-Vila, F. Martin, H.D. Lüdemann, Soil Biol. Biochem. 28 (1996) 1053.
[44] G. Almendros, H. Knicker, F.J. Gonzalez-Vila, Org. Geochem. 34 (2003) 1559.
[45] G.H. Rashid, Plant Soil 103 (1987) 89.
[46] C. Chandler, P. Cheney, P. Thomas, L. Trabaud, D. Williams, Forest Fire Behavior and Effects, Fire in Forestry, vol. I, Wiley, New York, 1983.
[47] L.F. DeBano, J. Hydrol. 231 (2000) 195.
[48] R.A. Shakesby, S.H. Doerr, Earth-Sci. Rev. 74 (2006) 269.
[49] F. Diaz-Fierros, B.E. Rueda, R. Pérez Moreira, Catena 14 (1987) 189.
[50] D.H. McNabb, F.J. Swanson, Effects of fire on soil erosion, in: J.D. Walstad, S.R. Radosevich, D.V. Sandberg (Eds.), Natural and Prescribed Fire in Pacific Northwest Forests, Oregon State University Press, Corvallis, OR, 1990, pp. 159–176.
[51] V. Andreu, J.L. Rubio, J. Forteza, R. Cerni, Int. J. Wildland Fire 6 (1996) 53.
[52] W. Saeys, A.M. Mouazen, H. Ramon, Biosyst. Eng. 91 (2005) 393.
[53] I. Kamrunnahar, B. Singh, A. McBratney, Aust. J. Soil Res. 41 (2003) 1101.
[54] G. Fystro, Plant Soil 246 (2002) 139.
[55] B. Ludwig, P.K. Khanna, J. Bauhus, P. Hopmans, Forest Ecol. Manag. 171 (2002) 121.
[56] K. Islam, B. Stingh, A. McBratney, Aust. J. Soil Res. 41 (2003) 1101.
[57] P.D. Martin, D.F. Malley, G. Manning, L. Fuller, Can. J. Soil Sci. 82 (2002) 413.
[58] V. Arcenegui, C. Guerrero, J. Mataix Solera, J. Mataix Beneyto, R. Zornoza, J. Morales, A.M. Mayoral, Catena (2008), doi:10.1016/j.catena.2007.11.00.

Talanta 80 (2009) 48–53

Contents lists available at ScienceDirect

Talanta

journal homepage: www.elsevier.com/locate/talanta

A methodology based on NIR-microscopy for the detection of animal protein by-products

Dolores Pérez-Marín[a,*], Tom Fearn[b], José Emilio Guerrero[a], Ana Garrido-Varo[a]

[a] Department of Animal Production, E.T.S.I.A.M., Universidad de Córdoba, 14071 Cordoba, Spain
[b] Department of Statistical Science, University College London, UK

ARTICLE INFO

Article history:
Received 3 February 2009
Received in revised form 3 June 2009
Accepted 9 June 2009
Available online 17 June 2009

Keywords:
NIR-microscopy
Animal protein by-products detection
Compound feeds
SIMCA
KNN

ABSTRACT

This study develops a methodology based on NIR-microscopy analysis and chemometric tools for the detection of animal protein by-products in mixtures, such as compound feeds and mixtures of ingredients, using a library of animal meal by-products only. The proposed methodology is a two-step strategy which worked better than the SIMCA approach it was compared with. In the first step, animal particles are identified using one of two methods, a global or a local distance measure. In the second, *K*-nearest-neighbours (KNN) is used to discriminate between terrestrial and fish particles. The models were developed using a training set comprising 11,727 spectra of pure terrestrial meals and 5843 of fish meals. KNN using second derivative spectra and five neighbours correctly classifies 98.5% of these samples under cross-validation. The procedure was validated using two external datasets, one made up of mixtures of species (fish and bovine), and a second of commercial compound feeds. The results obtained confirm that the procedure is able to reliably detect the presence of animal meals, although further work would be needed to develop it into an accurate quantitative method.

© 2009 Elsevier B.V. All rights reserved.

1. Introduction

The ban on the use of animal protein by-products in compound feeds [1] is one of the measures adopted by the European Union to stop the spread of BSE and to prevent its re-occurrence. From October 2003, the European Union (EU) adopted Regulation (EC) No. 1774/2002 governing animal by-products (ABPs), which seeks to address the possible risks inherent in recycling potential infectivity due to the absence of barriers within species, and to exclude the cannibalism that may be induced by intra-species recycling [2]. This ban (avoiding cannibalism) will only be lifted if reliable analytical methods are available that ensure both the identification of species in animal by-products and the detection of animal by-products in compound feeds.

A recent review includes a revision about the methods of detection of animal proteins in feeding stuffs [3], concluded that near infrared microscopy (NIRm) is one of the methods with wider scope for this purpose, together with near infrared imaging, PCR (Polymerase Chain Reaction) and immunology. In the framework of an EU research project titled "Strategies and methods to detect and quantify mammalian tissues in feedingstuffs" (STRATFEED, G6RD-2000-CT-00414) [4], NIRm was one of the methods studied and tuned for the detection of animal proteins, obtaining promising results in this field. NIR-microscopy allows the measurement of spectra of single particles in a sample, in contrast to standard NIR technology, now also called macro-NIR, in which each spectrum collected belongs to a whole sample. Microscopic sample analysis may be necessary for the evaluation of small areas of specific interest [5].

The main advantages of NIR-microscopy, compared with the reference method according to the European Legislation, i.e. optical microscopy, or with other methods such as PCR, are that it is non-destructive, can be automated and that it does not require highly qualified and experienced analysts [6]. On the other hand, the main limitation of this technique arises from its not being a universal method, i.e. that it only allows inference for samples similar to those used in training when the application was developed, so that the construction of a spectral library that captures the variability in the application area being studied is one of the key aspects when working with this technology.

Previous works have shown the potential of this technology for the detection of animal meals, using both sedimented and raw fractions and a variety of chemometric approaches including ANN, PLS, and support vector machines [6–10]. Nevertheless, all these works have been based on the building of spectral libraries containing not only animal particles, but also vegetal particles, in order to train the model in the identification of animal and other particles presented in the compound feeds. This fact makes more difficult the building of the database for the model development, because it is necessary

* Corresponding author at: Ctra Madrid-Cádiz km 396, Campus Rabanales, Ed. Producción Animal, Spain. Tel.: +34 957 212221; fax: +34 957 218436.
E-mail address: dcperez@uco.es (D. Pérez-Marín).

0039-9140/$ – see front matter © 2009 Elsevier B.V. All rights reserved.
doi:10.1016/j.talanta.2009.06.026

not only to collect a library of animal meals with large variability, but also to analyse many particles of many different vegetable products to cover the variability in these products, multiplying further the number of possibilities and the analysis time.

The goal of this work was to develop and optimize a methodology, based on NIR-microscopy and chemometric tools and using a library of animal meal by-products only, for the detection/quantification of animal protein by-products in mixtures such as compound feeds and mixtures of ingredients.

2. Materials and methods

2.1. Training set

The first and main step is the building of an adequate database for the development of the prediction model. This database will be based on the analysis of pure samples of animal protein by-products, i.e. collecting spectra of animal meals of each species of interest. Some of the samples were provided by Spanish rendering plants, while others were provided by European partners in the framework of different research projects. It must be highlighted that some of these samples were authenticated by PCR and some others were provided by dedicated plants, avoiding the cross-contamination of them.

The database used in this work comprises spectra of particles belonging to bovine (4657 spectra from 8 samples), ovine (2560 spectra from 4 samples), porcine (2382 spectra from 40 samples), avian (2128 spectra from 41 samples) and fish (5843 spectra from 65 samples) meals. In building the training set, it is important to include as much variability as possible. Thus it was decided to analyse as many different samples as could be obtained, taking a modest number of spectra per sample. However for some types of animal meals, especially bovine ones, their availability was limited and larger numbers of spectra per sample were collected to compensate. Since the training is based on individual spectra, and since there is considerable variability both within and between samples, the lack of balance is not important.

2.2. External validation sets

Two different sample sets were used for the validation of the models performed. The origins of these sets were totally different to the calibration samples. Validation set 1 comprised 20 experimental mixtures of fish meal adulterated with bovine meal, in inclusion percentages of 2.5–16%. Several meals were used to make these samples; none of them was represented in the training database. Validation set 2 was made up of 20 commercial compound feeds. Among them, there are five samples free of animal meals, six that only had fish meal and nine that had animal meals different from fish meals in their composition.

2.3. Analysis of the samples

The raw fraction of the sample, i.e. without sedimentation, previously milled with a 1 mm screen, was analysed. According to the methodology proposed in the SAFEED-PAP Project (FOOD-CT-2006-036221), the samples were mixed and about 100 mg was taken four times. Then, everything was put in a sieve of 250 μm and agitated for 2 min. The particles >250 μm were then taken from the sieve and placed on a spectralon plate. The particles must be disposed in a thin layer for the analysis. For the training set, between 30 and 600 particles were analysed per sample. For the validation sets, the number of particles analysed was around 200 for each sample in validation set 1 (fish meals adulterated with bovine meal) and around 600 for samples in validation set 2 (commercial compound feeds) which are much more heterogeneous.

The spectra were collected in an Auto Image Microscope connected to a Fourier Transform Near-Infrared Spectrometer (FT-NIR; PerkinElmer, Waltham, MA, USA). Using the pointer of the microscope, the light beam was focused on each particle located on the spectralon plate and the NIR spectrum (1112–2500 nm) was collected. A resolution of 4 cm^{-1}, a gain of 4, and a number of co-added scans of 10 were used. The spectra were obtained from the ratio between the raw spectra and the background consisting of the measurement of the spectralon plate. The software Autoimage v.3.2.1 from PerkinElmer was used to collect and store the spectra. The Convert Abs NM software from PerkinElmer was used to convert the tabulation of the spectra from wavenumber (cm^{-1}) to wavelength (nm) at 4 nm intervals.

2.4. Chemometric data processing

The data processing was carried out using MATLAB software version 7.0 (The Mathworks Inc., Natick, MA, USA).

The spectral range was reduced at the outset to 1500–2280 nm, in order to discard regions with high noise levels. Moreover, the main water region (1824–1976 nm) was removed, because the technological processes associated with this kind of product can cause different levels of moisture in them, and the goal of this range cutting is to avoid basing the classification on different moisture levels instead of on the main features of each animal species. Some further restrictions of the range, for example using only the region from 2040 to 2180 nm, were investigated during the development of the algorithm.

Several pre-treatment options were investigated. Smoothed $\log(1/R)$ spectra, and first and second derivatives, all computed using a Savitzky-Golay filter [11] with a window size of 15 data points and a polynomial order of 2, were tested. Each was tried without scatter correction and with scatter correction using the Standard Normal Variate (SNV) method [12], applied after the Savitzky-Golay treatment.

The aim was to develop a method for the detection of animal protein by-products in mixtures analysed by NIRm, with the ability to distinguish between terrestrial and fish meals. Two classification algorithms were investigated, SIMCA and *K*-nearest-neighbours (KNN).

The SIMCA method [11,13] constructs a principal component model for each different group of interest. As it is used here an unknown sample is compared with each group in turn by computing two distances: the Euclidean distance from the spectrum to its projection into the model for that group (distance from the model) and the Mahalanobis distance from the projected spectrum to the group mean (distance within the model), and comparing these distances with thresholds derived from the training data. If both distances are less than the threshold, the unknown is a possible member of that group. After all the comparisons have been made, the unknown sample may be identified as a possible member of none, one, or more than one of the groups. Tuning the method involves choosing a number of principal components and a pair of thresholds for each model. To calibrate the thresholds, they were expressed as percentiles of the empirical distribution of the distances for the training data. Thus a threshold of 0.95 means that the distance computed for the unknown sample must lie within the range of the smallest 95% of the corresponding distances for the training samples for the group under consideration.

The KNN method [11] classifies an unknown according to the group memberships of the *K* most similar spectra in the training database. As applied here, similarity is measured by Euclidean distance between spectra, and the classification is made by a simple majority vote of the *K* nearest spectra, with ties broken using the sums of the relevant distances. Tuning most obviously involves choosing a value for *K*, in the range 1–20 here, but also comparing

Table 1
KNN(5) classification results by cross-validation on the training set.

	Classified as terrestrial	Classified as fish
Terrestrial (n = 11,727)	11,586 (98.8%)	141 (1.2%)
Fish (n = 5843)	118 (2.0%)	5725 (98.0%)

Table 2
SIMCA classification results by cross-validation on the training set.

	Classified as terrestrial	Classified as fish	Not classified
Terrestrial (n = 11,727)	9415 (80.3%)	179 (1.5%)	2133 (18.2%)
Fish (n = 5843)	17 (0.3%)	4708 (81.8%)	1118 (19.1%)

the effect of different spectral ranges and pre-treatments, to which the method may be quite sensitive.

The overall strategy needs to work with samples that include ingredients not represented in the training database. This is not a logical problem for SIMCA, where the philosophy is the positive identification of group membership, and the option of not classifying a spectrum is available. To use KNN in this situation it was extended to a two-step procedure as follows:

Step 1 attempts to identify animal particles. This uses either a single group SIMCA, with the group defined by the whole of the database, or an extension to the KNN procedure, in which unknown spectra with at least K spectra from the database within a predetermined radius are identified as being of animal origin. Both of these approaches use distance from the training database to identify animal particles. The key difference is that SIMCA uses a global measure, depending on a model for the whole database and measuring to the centre of the model, while the alternative approach is local and more flexible, looking only at the part of the database nearest to the unknown spectrum.
Step 2 uses KNN to classify those particles identified as animal meals as either terrestrial or fish.

Given that there are four non-fish groups in the database (as described in Section 2.1), one could either treat the problem as one with five groups, combining the classifications to non-fish at the end, or combine the four non-fish groups at the outset to make it a two-group problem. Both options were investigated.

The main tuning was carried out using cross-validation on the training database, leaving out the whole of one sample (as opposed to one spectrum) at time so that other particles from the same sample did not contribute to the classification of a particle. The success of the model obtained was evaluated using the percentage of correctly classified particles (ratio of correctly classified particles to total particles). The tuning of step 1 is described in Section 3.2.

3. Results and discussion

3.1. Model development and results on the training database

The training database comprising a total of 11,727 spectra of terrestrial meals (including avian, porcine, bovine and ovine samples) and 5843 spectra of fish meals was first used to develop a detection model that allows discrimination between terrestrial and fish meal particles. Both KNN and SIMCA were investigated.

The best pre-treatment option was second derivative. Results with and without subsequent scatter correction using SNV were comparable. It seems preferable to include SNV because this will make the method more robust to minor changes in instrumentation, etc. [14], and so the results presented below all use second derivative followed by SNV. Some limited experimentation with reduced spectral ranges did not lead to better results, nor did compressing the spectra to principal components before computing the distances to the neighbours in KNN.

The selected number of neighbours for KNN with this pre-treatment was K = 5. Table 1 shows the classification results obtained by cross-validation on the training database. Overall, 98.5% of the particles were correctly classified. These results were achieved by treating the problem as one of five groups, and then combining the resulting classifications for the four terrestrial groups. The alternative strategy of combing the groups and then classifying also produces 98.5% correct classifications, but now with slightly more fish particles erroneously classified as terrestrial (134) and slightly fewer terrestrial particles classified as fish (123). This is what one would expect: KNN is affected in an obvious way by the numbers representing each group in the database. The results are not particularly sensitive to the choice of K, though K = 5 gave the best results on cross-validation.

Tuning SIMCA by cross-validation on the database resulted in the selection of a two-group model, i.e. pooling the 4 non-fish groups and making 2 principal component models only, with 10 components in each model, and thresholds of 0.99 and 0.90 for the distances to and within the model respectively. The results are given in Table 2. There are fewer total errors than for KNN, but the price is a failure to classify 18.5% of the spectra. Of these, 11.8% fail to be assigned to either group, 6.7% are judged to be possible members of both.

Similar classifications rates have been obtained by other authors. Thus, Piraux and Dardenne [7] working with raw samples and ANN to discriminate between what the authors called allowed particles (vegetal and fish) and forbidden particles (terrestrial animal meals) obtained an overall hit rate of 99.36%, while in the STRATFEED project [4], PLS was used to discriminate into several groups step by step successively (vegetal *vs* animal, terrestrial animal *vs* fish, poultry *vs* bovine and pig), resulting that 94.3% of the animal particles were correctly classified, being by classes the 95.5% of the analysed particles classified as terrestrial and the 90% as fish. De la Haba et al. [9] working with samples after sedimentation and support vector machine algorithm for the discrimination between fish and meat and bone meal obtained percentages of correctly classified samples of 95%.

3.2. The tuning of step 1

Before applying the KNN methodology to external validation sets, it needs to be extended to distinguish between particles of animal meal, similar to those in the database, and particles that are not recognised.

The SIMCA procedure for this was based on a single group principal component model using all the database samples. The number of components was chosen as 10. This is somewhat arbitrary, and is based on the (possibly irrelevant) fact that this number of components worked best for the fish/non-fish classification within the database. It would of course be possible to tune this choice using the validation samples, but then it becomes more difficult to interpret the validation results. The thresholds were both set at 0.99, a choice that if applied to the database would exclude 300 spectra, not quite 2% because some points fail on both criteria.

The KNN procedure with K = 5 was extended by applying an upper threshold to the distance from the unknown spectrum to its fifth nearest neighbour in the database. Only particles satisfying this criterion, and therefore having at least five near neighbours in the database are identified as animal. The threshold was chosen as 2 by inspecting the histogram of distances generated by the cross-validation reported in Section 3.1. Approximately 2% of these cross-validated distances are greater than 2. Some of the spectra in this tail may be outliers, the majority probably just happen to lie on the edges of the database. However these 2% (349 spectra) were

Table 3
Predicted values for samples of fish meal adulterated with bovine animal meals using KNN at steps 1 and 2.

Sample	Total number of particles	Detection of animal particles				Classification of animal particles				Reference data (%)	
		Animal		Non-animal		Fish	Terr.	%F[a]	%T[a]	Fish	Terr.
		Number	%	Number	%						
M1	171	168	98.2	3	1.8	162	6	94.7	3.5	98.0	2.0
M2	214	200	93.5	14	6.5	193	7	90.2	3.3	97.5	2.5
M3	193	180	93.3	13	6.7	170	10	88.1	5.2	97.0	3.0
M4	206	201	97.6	5	2.4	190	11	92.2	5.3	96.8	3.3
M5	158	152	96.2	6	3.8	143	9	90.5	5.7	96.5	3.5
M6	187	182	97.3	5	2.7	160	22	85.6	11.8	87.8	12.3
M7	205	198	96.6	7	3.4	182	16	88.8	7.8	87.5	12.5
M8	170	164	96.5	6	3.5	129	35	75.9	20.6	87.3	12.8
M9	170	165	97.1	5	2.9	145	20	85.3	11.8	87.0	13.0
M10	172	153	89.0	19	11.0	141	12	82.0	7.0	86.8	13.3
M11	185	167	90.3	18	9.7	133	34	71.9	18.4	86.5	13.5
M12	166	160	96.4	6	3.6	136	24	81.9	14.5	86.0	14.0
M13	158	153	96.8	5	3.2	133	20	84.2	12.7	85.8	14.3
M14	160	157	98.1	3	1.9	148	9	92.5	5.6	85.5	14.5
M15	195	193	99.0	2	1.0	178	15	91.3	7.7	85.3	14.8
M16	195	193	99.0	2	1.0	168	25	86.2	12.8	85.0	15.0
M17	168	163	97.0	5	3.0	136	27	81.0	16.1	84.8	15.3
M18	194	187	96.4	7	3.6	164	23	84.5	11.9	84.5	15.5
M19	184	174	94.6	10	5.4	158	16	85.9	8.7	84.3	15.8
M20	197	183	92.9	14	7.1	153	30	77.7	15.2	84.0	16.0

[a] As percentage of total number of particles in column 2.

removed from the database before analysing the validation sets, to reduce the chance of false positives.

3.3. External validation

The procedure was validated using two external sample sets. The first was made up of mixtures of two species, fish and bovine. The ability to discriminate between these is essential if the use of fish meal is to be allowed in all ruminant feeds. The second set comprises 20 varied commercial compound feeds. In each case, the results for one of the three combinations studied, KNN at steps 1 and 2, are presented in detail, and then the results for the other two options, SIMCA at step 1 with KNN at step 2 or a single SIMCA, are discussed more briefly.

3.3.1. Fish meal samples adulterated with bovine meal

The validation results for KNN + KNN applied to the fish meal samples adulterated with bovine meal are shown in Table 3. This shows for each sample analysed the total number of particles analysed, the numbers and percentages of particles classified as animal or non-animal at step 1, the numbers and percentages of particles classified as fish or terrestrial in step 2, and in the last two columns the actual composition of the sample. For all the percentages quoted for the classification the divisor is the total number of particles in column 2.

The results in Table 3 show that the screening in step 1 rejects a total of 155 particles out of the 3648 analysed, 4.2%. It is not surprising that this is a little greater than the corresponding 2% for the training database: these are external samples. The percentage of

Table 4
Predicted values for compound feeds using KNN at steps 1 and 2.

Sample	Total number of particles	Detection of animal particles				Classification of animal particles				Reference data (%)	
		Animal		Non-Animal		Fish	Terr.	%F[a]	%T[a]	Fish	Terr.
		Number	%	Number	%						
CF1	644	0	0.0	644	100.0	0	0	0	0	0.0	0.0
CF2	574	0	0.0	574	100.0	0	0	0	0	0.0	0.0
CF3	619	0	0.0	619	100.0	0	0	0	0	0.0	0.0
CF4	580	0	0.0	580	100.0	0	0	0	0	0.0	0.0
CF5	636	0	0.0	636	100.0	0	0	0	0	0.0	0.0
CF6	577	5	0.9	572	99.1	5	0	0.9	0	3.0	0.0
CF7	601	5	0.8	596	99.2	5	0	0.8	0	2.5	0.0
CF8	590	10	1.7	580	98.3	10	0	1.7	0	2.5	0.0
CF9	595	11	1.8	584	98.2	11	0	1.8	0	2.5	0.0
CF10	628	11	1.8	617	98.2	11	0	1.8	0	3.0	0.0
CF11	586	2	0.3	584	99.7	2	0	0.3	0	2.5	0.0
CF12	567	13	2.3	554	97.7	6	7	1.1	1.2	0.0	14.6
CF13	583	16	2.7	567	97.3	10	6	1.7	1.0	0.0	14.5
CF14	590	21	3.6	569	96.4	15	6	2.5	1.0	0.0	14.3
CF15	595	19	3.2	576	96.8	10	9	1.7	1.5	0.0	14.3
CF16	581	37	6.4	544	93.6	22	15	3.8	2.6	0.0	29.4
CF17	623	43	6.9	580	93.1	29	14	4.7	2.2	0.0	28.1
CF18	621	53	8.5	568	91.5	49	4	7.9	0.6	0.0	27.8
CF19	635	35	5.5	600	94.5	21	14	3.3	2.2	0.0	29.0
CF20	562	39	6.9	523	93.1	29	10	5.2	1.8	0.0	27.4

[a] As percentage of total number of particles in column 2.

particles classified as terrestrial in step 2 shows broad agreement with the true sample composition, though with some considerable variations. The potential of the method for quantification will be discussed in Section 3.4. From Table 3, it does seem to be satisfactory for the detection of bovine meal in these samples.

Replacing step 1 by a single group SIMCA has little effect on the results. The number of particles rejected at step 1 falls from 155 (4.2%) to 142 (3.9%), while the total number of terrestrial particles found by KNN in step 2 changes from 371 to 369. Thus there is nothing to choose between the use of KNN and SIMCA at step 1.

Using a two-group SIMCA for the whole exercise gives less satisfactory results. Overall 563 (15.4%) of the spectra are not classified to either group, while a further 371 (10.2%) are declared to be possible members of either the fish or terrestrial groups. The classified spectra are split 2601 (71.3% of the total) to fish, 113 (3.1% of the total) to terrestrial. The number of identified terrestrial particles in samples M1–M5 are 1, 1, 2, 1 and 0, respectively, so that the method fails to detect the contamination in sample M5.

3.3.2. Commercial compound feeds

The validation results for KNN + KNN applied to the commercial compound feeds are shown in Table 4, whose structure is the same as that of Table 3.

For samples CF1–CF5 the results are perfect. These samples have no animal meal, and none is detected. For samples CF6–CF11 the results are good. These samples contain fish meal in relatively low proportions. This is detected each time, and there are no false positives for terrestrial meal. However the proportions of fish detected are systematically low, by a factor of about 2. For samples CF12–CF20 the results are rather less impressive. These samples all contain substantial proportions of terrestrial animal meal. Particles of animal meal are always detected, but in much smaller numbers than they should be by a factor of roughly 4. Further, more than half of the identified animal particles are wrongly classified as fish.

As was observed with the other validation set, changing the first step to a single group SIMCA has little effect on the results, with all the zeros in Table 4 being maintained, and other numbers of particles changing by one or two.

Using a two-group SIMCA gives qualitatively similar results, but with a tendency to detect even fewer animal particles than KNN. For samples CF1–CF5 all the particles are correctly classified as belonging to neither group. For samples CF6–CF11 a total of 38 particles (1.1% of the total) are classified as fish, with 2 further particles possibly belonging to either of the animal meal groups. For comparison, KNN finds 44 fish particles. For samples CF12–CF20 SIMCA classifies 121 particles (2.2% of the total) as fish, 27 (0.5%) as terrestrial and 70 (1.3%) as consistent with either, compared with the 191 (3.6%) fish and 85 (1.6%) terrestrial found by KNN.

The underestimation of the quantitative prediction of animal meals was observed also in the results reported by De la Roza et al. [10] for a validation set of commercial compound feeds. Four possible reasons are:

1. A bias may be caused by the preparation of the sample previous to the analysis. A sieve is used and only particles bigger than 250 μm are analysed. Animal meals tend to be finely milled compared to some of the other ingredients present, and thus a higher proportion of these particles may pass through the sieve.
2. Because of the technological process that the compound feeds have undergone, including high pressures and temperatures, and being formed into pellets, the particles that are analysed may not be pure ingredients in most cases. If the spectra of particles correspond to a conglomerate of different ingredients, that will make difficult their identification as animal particles by a model based on pure ingredients.

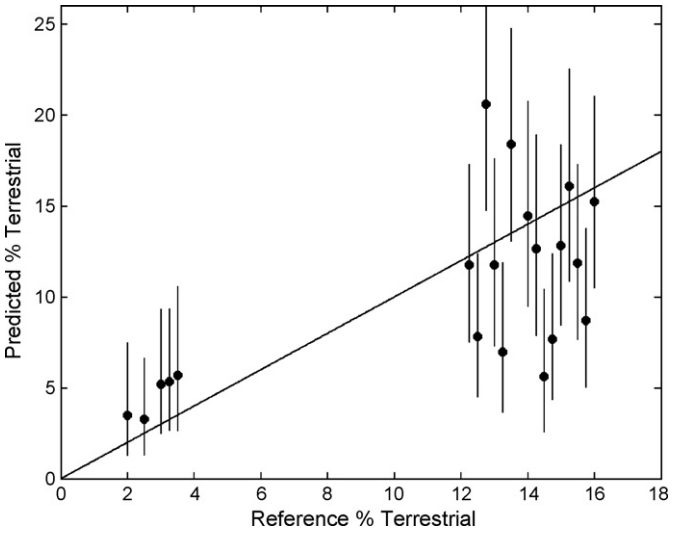


Fig. 1. Predicted *vs* reference percentages of terrestrial meal in the mixture samples M1–M20, with 95% binomial confidence intervals for sampling variability.

3. The training library, though it includes many spectra, only has a limited number of samples. Expanding the variability in the library would be expected to increase its ability to recognise animal particles.

3.4. Potential for quantification

The validation results with the mixtures of fish and bovine meals, though not those with the compound feeds, are good enough to make it worth discussing the potential of the method for quantification. Fig. 1 plots predictions *versus* reference percentages of terrestrial meal in the 20 mixtures. The predicted percentages are calculated simply as ratios of numbers of particles, whereas the reference data are percentages by weight. Since the sizes and densities of the particles vary by ingredient this might be expected to cause some discrepancies, but no attempt has been made, so far, to apply any corrections.

Also shown for each plotted point is a 95% confidence interval for the true percentage given the observed one, assuming binomial variability in the numbers of terrestrial particles that will be present in samples of the sizes analysed (approximately 200). It is clear from the plot that there are other sources of random variability affecting the results, because there is much more variability between the points in the 12–16% range than the intervals would suggest there should be. The plot also suggests that there is a downwards bias in this group of results, and probably an upwards bias in the group at 3%. The broad agreement between predicted and reference is encouraging, but further work will be necessary before the method can be regarded as anything better than semi-quantitative. Particular problems are the potential for bias in the sieving stage, biases due to particle size distributions and densities when a weight fraction is estimated by a number fraction, and the fact that the database, though it contains a large number of spectra, does not yet include all that many distinct samples.

4. Conclusions

Of the methods investigated the use of a two-stage methodology performed better than a simple SIMCA. The combination KNN + KNN was a little better than SIMCA + KNN, though the difference was not large. The method was able to detect though not quantify animal meals in compound feeds, despite having been trained only on pure animal meals. It was also able to produce

semi-quantitative results for mixtures of fish and terrestrial meals. A number of challenges remain for the development of a fully quantitative method.

Acknowledgements

This work was carried out within the frame of the European Project SAFEED-PAP (FOOD-CT-2006-036221), belonging to the 6th FP. The authors are grateful to Mrs. Mª Carmen Fernández for technical assistance.

References

[1] European Commission, Off. J. Eur. Comm. L306 (2000) 32.
[2] European Commission, Off. J. Eur. Comm. L339 (2003) 78.
[3] O. Fumière, P. Veys, A. Boix, C. von Holst, V. Baeten, G. Berben, Biotechnol. Agron. Soc. Environ. 13 (S) (2009) 59–70.
[4] European Commission, Stratfeed (European Project G6RD-2000-CT-00414) Strategies and methods to detect and quantify mammalian tissues in feedingstuffs, Belgium, 2005.
[5] A.E. Dowrey, G.M. Story, C. Marcott, in: R. Bhargava, I.W. Levin (Eds.), Spectrochemical Analysis Using Infrared Multichannel Detectors, Blackwell Publishing, Oxford, UK, 2005, pp. 175–188.
[6] V. Baeten, A. Michotte-Renier, G. Sinnaeve, A. Garrido-Varo, P. Dardenne, in: A.M.C. Davies, A. Garrido-Varo (Eds.), Near Infrared Spectroscopy: Proceedings of the 11th International Conference, NIR Publications, Chichester, UK, 2004, pp. 663–666.
[7] F. Piraux, P. Dardenne, in: A.M.C. Davies, R. Giangiacomo (Eds.), Near Infrared Spectroscopy: Proceedings of the 9th International Conference, NIR Publications, Chichester, UK, 2000, pp. 535–541.
[8] V. Baeten, C. Von Holst, A. Garrido, J. Vancutsem, A. Michotte Renier, P. Dardenne, Anal. Bioanal. Chem. 382 (2005) 149–157.
[9] M.J. De la Haba, J.A. Fernández-Pierna, O. Fumiere, A. Garrido-Varo, J.E. Guerrero, D.C. Pérez-Marín, P. Dardenne, V. Baeten, J. Near Infrared Spectrosc. 15 (2007) 81–88.
[10] B. De la Roza-Delgado, A. Soldado, A. Martínez-Fernández, F. Vicente, A. Garrido-Varo, D. Pérez-Marín, M.J. De la Haba, J.E. Guerrero-Ginel, Food Chem. 105 (2007) 1164–1170.
[11] T. Næs, T. Isaksson, T. Fearn, T. Davies, A User-friendly Guide to Multivariate Calibration and Classification, NIR Publications, Chichester, UK, 2002.
[12] R.J. Barnes, M.S. Dhanoa, S.J. Lister, Appl. Spectrosc. 43 (1989) 772–777.
[13] S. Wold, Pattern Recogn. 8 (1976) 127–139.
[14] T. Fearn, J. Near Infrared Spectrosc. 9 (2001) 229–244.

Talanta 80 (2009) 54–60

Contents lists available at ScienceDirect

Talanta

journal homepage: www.elsevier.com/locate/talanta

Spectral library validation to identify ingredients of compound feedingstuffs by near infrared reflectance microscopy

V. Fernández-Ibáñez[a], T. Fearn[b], A. Soldado[a], B. de la Roza-Delgado[a,*]

[a] Department of Animal Nutrition, Grasslands and Forages, Regional Institute for Research and Agro-Food Development, SERIDA, PO Box 13, 33300 Villaviciosa, Spain
[b] Department of Statistical Science, University College London, Gower Street, London WC1E 6BT, UK

ARTICLE INFO

Article history:
Received 6 March 2009
Received in revised form 1 June 2009
Accepted 9 June 2009
Available online 17 June 2009

Keywords:
Near infrared (NIR) microscopy
Spectral library
Ingredients
Compound feedingstuffs
Mixtures

ABSTRACT

To guarantee feed quality and safety the development and improvement of analytical methods for feed authentication and detection of contaminants is fundamental. Near infrared reflectance microscopy (NIRM) has been investigated as an alternative method to contribute to control systems for feed materials. The major task is the need to build NIRM reference spectral libraries that must represent the variability in feed ingredients. The aim of the present work was to evaluate the performance of a NIRM reference spectral library on animal feed, with external samples of animal feed ingredients and possible contaminants such as processed animal proteins, and in particular to assess its ability to identify ingredients in mixtures. Three external sample sets were used: (A) artificial mixtures, (B) synthetic mixtures and (C) synthetic binary mixtures. The prediction and repeatability results for set A, in which the spectra are from pure ingredients, were very good for both animal and vegetable ingredients and confirm that the spectral library is very good at identifying spectra from pure ingredients. For sets B and C, in which the spectra were measured on mixtures, the prediction results were very disappointing compared with the artificial samples. This means that a strategy that tries to match the spectra taken from a mixture with those of pure ingredients is unlikely to meet with much success. It is possible that an interpolation between pure ingredients for suitably chosen spectral ranges may provide a way to extend this system to mixtures, including mixtures of several ingredients.

© 2009 Elsevier B.V. All rights reserved.

1. Introduction

Optimal nutrition implies that animal feeds must be considered not only in terms of production efficiency but also in the light of their ability to promote health and protect against disease [1]. The health of the animal is fundamental for determining the quality, safety and wholesomeness of foods of animal origin for human consumption [2]. These new nutritional concepts require the development and dissemination of improved and more readily available analytical methods for feed authentication and detection of contaminants, to support various aspects of feed quality and safety and contribute to the improvement of existing control systems across the world.

The official analytical method to obtain qualitative and quantitative information about the ingredients in mixtures and compound feedstuffs is classical microscopy. Optical microscopy is at the moment the only official method in the European Union for detection of constituents of animal origin in feeds [3].

A number of other methods, such as polymerase chain reaction, immunoassay, and macro near infrared spectroscopy have been investigated for the analysis of ingredients in feed samples, including the detection of banned processed animal proteins [4–6]. The method studied here, near infrared reflectance microscopy (NIRM), allows the collection of hundreds or thousands of spectra from a feed sample and has been proposed as a new analytical approach for identifying ingredients in animal feeds [7,8] and detecting and quantifying undesirable substances such as meat and bone meal (MBM) in feedstuffs [9–12].

A major task in implementing this methodology is the need to build NIRM reference spectral libraries comprising thousands of spectra taken from samples from reliable sources in order to represent the natural variability in animal, vegetable and mineral feed ingredients. Once the library is built, spectra collected from animal feeds may be compared with the spectra in the library to identify the ingredients included in the feeds. As the number of possible ingredients becomes large, not only does it increase the effort involved in constructing the library and the computational effort involved in comparing an unknown with all the spectra in the library, but it becomes more difficult to discriminate between the ingredients. For example Gendrin et al. [13] reported that it becomes more difficult to find discriminating wavelengths when large numbers of ingredients are involved.

The optimization of conditions for sample presentation and spectral measurement and treatment, and the building of an NIRM

* Corresponding author.
E-mail address: broza@serida.org (B. de la Roza-Delgado).

0039-9140/$ – see front matter © 2009 Elsevier B.V. All rights reserved.
doi:10.1016/j.talanta.2009.06.025

Table 1
Ingredients, samples and total number of NIRM spectra included in the spectral library. Percentage ingredient contents for sample set A (artificial mixtures) and set B (synthetic mixtures).

Ingredients of library	ns	nsp	Sample 1		Sample 2		Sample 3		Sample 4		Sample 5		Sample 6	
			A	B	A	B	A	B	A	B	A	B	A	B
Lucerne dehydrated	24	5109												
Maize silage	23	4836												
Fababean silage	2	450												
Grass silage	13	2713												
Grass hay	2	421												
Cereal straw	27	5644												
Beet pulp	14	3039											0.9	1.0
Cotton seed	7	1016												
DDGS barley	1	202												
Soybean meal	15	3330	50.0	50.0	40.2	40.0	32.5	32.3	25.2	25.0	25.2	25.0	25.2	25.0
Sunflower seed	7	1578												
Oats	4	847												
Wheat	15	3210							9.8	10.0	9.8	10.0	9.8	10.0
Barley	21	4449			19.7	20.0	32.5	32.3	35.0	35.0	35.0	35.0	34.6	35.0
Rye	5	1146												
Maize	21	4826	50.0	50.0	40.2	40.0	32.5	32.3	25.2	25.0	25.2	25.0	25.2	25.0
Bran	2	419												
Corn flakes	1	210												
Peas	2	427												
Palm seed	1	218												
Wheat middlings	1	210												
Mineral correctors	6	1222									1.7	2.0	2.1	2.0
By-pass fat	3	630												
Citrus pulp	3	663												
Milk powder	1	234												
Whey powder	1	210												
Blood meal	1	235												
Meat and bone meal	4	937					2.6	3.0	4.7	5.0	3.0	3.0	2.1	2.0
Haemoglobin	1	234												
Animal plasma	1	234												

ns: number of samples; nsp: number of spectra.

reference library have been reported previously [7,14]. An internal cross-validation of the use of the *K*-nearest neighbours algorithm [15] to classify spectra by comparison with the library showed some confusion between similar vegetal ingredients but good discrimination between ingredients of animal and vegetal origin [7].

The aim of present work was to evaluate the performance of this NIRM reference spectral library on animal feed, challenging it with external samples of animal feed ingredients and possible contaminants such as processed animal proteins, and in particular to assess its ability to identify ingredients in mixtures.

2. Materials and methods

2.1. Samples

The samples used to construct the spectral library, and the samples used for validation, were all provided by industrial sources in the north of Spain. They are samples of pure ingredients representing the natural variability encountered in the production process. The types and numbers of samples in each set are described in Sections 2.2 and 2.3.

Prior to analysis all samples were ground to a particle size of 1 mm. The ground sample was spread on a sample holder as a continuous film for spectroscopic measurement. This procedure has been described elsewhere in detail [7,14].

2.2. Spectral library

The construction of the spectral library has been described in a previous work [7]. The library includes a total of 48 456 spectra measured on 227 samples representing 30 different ingredients corresponding to the detailed list in Table 1. It includes the most common feed ingredients of different origins, the first 26 in the list, together with the most important banned ingredients, the last four in the list.

2.3. Mixtures

To assess the ability of the NIRM reference spectral library to identify ingredients in mixtures three sample sets were used. In all cases the samples, though sourced in the same way as the library samples, were external to the library.

Sample set A, which will be called "artificial mixtures" was made not by measuring spectra on mixtures, but by measuring samples of pure ingredients and constructing the artificial mixtures by combining appropriate numbers of spectra randomly selected from those measured on the pure ingredients. This set contains six samples, with the percentage ingredient contents shown in Table 1.

Sample set B, which will be called "synthetic mixtures" was produced by physically mixing pure samples in the laboratory and measuring spectra on the mixtures. This set, also shown in Table 1, contains six samples with similar percentage ingredient contents to those of sample set A.

Sample set C, which will be called "synthetic binary mixtures" was produced in the same way as sample set B. Each of the three samples in the set is a 50/50 mixture of meat and bone meal with one other ingredient. This other ingredient is barley in sample 1, maize in sample 2, and soya meal in sample 3. Spectra were measured not only on the three mixtures, but also on the four pure ingredients used to construct them. Sample set C was constructed in an attempt to understand why the system does not work well when the spectra are measured on mixtures, especially for the identification of animal by-products.

Table 2
Percentage ingredient contents and predictions for sample set A, artificial mixtures.

Artificial sample number	Ingredient	True composition (%)	Results	
			Average estimated composition (%)	SD
1	Maize	50.0	46.6	0.9
	Soybean	50.0	49.7	0.3
	Other	0.0	3.7	1.1
2	Maize	40.2	39.3	0.6
	Soybean	40.2	39.6	0.2
	Barley	19.7	20.0	0.5
	Other	0.0	1.1	0.5
3	Maize	32.5	31.6	1.2
	Soybean	32.5	32.0	0.4
	Barley	32.5	32.4	1.2
	Meat and bone meal	2.6	2.6	0.0
	Other	0.0	1.4	0.6
4	Maize	25.2	25.3	1.6
	Soybean	25.2	24.8	0.3
	Barley	35.0	35.5	1.5
	Wheat	9.8	7.3	0.6
	Meat and bone meal	4.7	4.7	0.0
	Other	0.0	2.4	0.5
5	Maize	25.2	25.6	1.2
	Soybean	25.2	23.6	1.1
	Barley	35.0	35.3	1.4
	Wheat	9.8	7.4	0.7
	Mineral correctors	1.7	1.6	0.2
	Meat and bone meal	3.0	3.0	0.0
	Other	0.0	3.6	1.3
6	Maize	25.2	25.5	1.6
	Soybean	25.2	23.2	1.1
	Barley	34.6	35.4	2.0
	Wheat	9.8	6.9	0.9
	Mineral correctors	2.1	2.0	0.2
	Beet pulp	0.9	0.9	0.3
	Meat and bone meal	2.1	2.1	0.0
	Other	0.0	4.0	1.4

2.4. Sample analysis and treatment of the NIRM spectra

Spectra were measured using an Auto Image Microscope connected to a Perkin-Elmer Spectrum One Fourier transform near infrared (FT-NIR) spectrometer in reflectance mode (1112–2500 nm), employing a resolution of 8 cm^{-1}. Spectra were obtained from the ratio between raw spectra and the background as measurement of the spectralon plate and the spectral information was stored as $\log(1/R)$. This instrument is equipped with an InGaAs detector.

For each sample presented to the instrument, approximately 230 spectra (the number varies because of occasional bad spectra), each the average of 70 scans, were measured using fields of view of size 50 $\mu m \times 50\ \mu m$ arranged in a 13×18 grid over an area selected near the center of the sample. After referencing to a Spectralon standard and conversion to $\log(1/R)$ at 4 nm intervals, the spectra were transformed to first derivative using a Savitzky-Golay filter (The PLS Toolbox, version 3.5, Eigenvector Research, Manson, WA) with a window of 15 data points, and cut to a range of 1500–2448 nm. In the first derivative spectra of many of the ingredients there is a large peak centered on approximately 1900 nm. This peak is strongly influenced by the water band seen in the near infrared at around 1940 nm [16]. To reduce the influence of water content on the classification, the range from 1824 to 1976 nm was removed.

For mixture samples in the sets B and C 10 subsamples of each were measured as described above, to obtain information on the variability of the results. For the artificial samples in set A, 10 replicates were constructed by repeated random sampling of spectra from those measured on the pure samples, keeping the numbers of spectra from each ingredient fixed.

2.5. Data analysis

All three sets of mixture samples were analysed by comparing each spectrum in turn with all the spectra in the library, using a *K*-nearest neighbours (KNN) rule with $K = 10$ to classify the spectrum [7]. This simple algorithm finds the 10 spectra in the library that are closest to the unknown, and classifies according to the identity of these neighbours.

Each of the synthetic binary mixtures in set C was subjected to the following additional analysis. The first derivative spectra over the range 1500–2448 nm, without the removal of any peak, underwent an additional pre-treatment by SNV [17]. The combined set of spectra for the two pure ingredients and the mixture were subjected to a principal component analysis (PCA) and reduced to 20 scores. The scores for the two pure ingredients were then input to a linear discriminant analysis (LDA) and thus reduced to a single number for each spectrum, its score on the canonical variate from the LDA. Using the loadings, the canonical variate scores were calculated for the spectra from the mixture samples.

For the main computations the spectral data were exported in ASCII format from the Perkin-Elmer Spectrum v. 5.0113 software into Matlab v7.4 (The Mathworks, Inc., Natick, MA, USA), and the analyses carried out with programs specially written by one of the authors (T.F.). Coding the KNN algorithm directly is a simple task. The principal component analysis applied to sample set C employed Matlab's singular value decomposition.

To evaluate the results, the composition of each replicate was estimated using the proportions of individual spectra classified to each ingredient. Spectra classified to an ingredient not present in the mixture concerned were counted as 'other' for presentation in

Table 3
Repeatability of predictions for one artificial mixture.

Ingredient	True composition (%)	Estimated composition for each replicate (%)										SD	Coef. Var.
		1	2	3	4	5	6	7	8	9	10		
Maize	25.2	22.7	24.4	27.4	26.1	26.5	24.4	26.1	24.8	24.8	27.8	1.6	6.1
Soybean	25.2	21.8	23.9	22.7	23.5	24.4	23.9	24.4	23.9	21.8	21.8	1.1	4.7
Barley	34.6	39.3	37.6	34.6	34.6	32.9	36.3	34.6	35.0	35.9	32.9	2.0	5.6
Wheat	9.8	5.6	5.6	6.0	7.3	7.3	7.3	8.1	7.3	6.8	7.7	0.9	12.7
Mineral correctors	2.1	2.1	2.1	1.7	2.1	2.1	2.1	2.1	1.7	1.7	1.7	0.2	10.6
Beet pulp	0.9	0.9	0.4	1.3	0.9	1.3	0.9	1.3	0.9	0.9	0.9	0.3	28.4
Meat and bone meal	2.1	2.1	2.1	2.1	2.1	2.1	2.1	2.1	2.1	2.1	2.1	0.0	0.0

Table 4
Percentage ingredient contents and predictions for sample set B, synthetic mixtures.

Synthetic sample number	Ingredient	True composition (%)	Results	
			Average estimated composition (%)	SD
1	Maize	50.0	25.8	7.2
	Soybean	50.0	40.6	9.1
	Other	0.0	33.6	5.7
2	Maize	40.0	30.7	4.3
	Soybean	40.0	16.5	3.8
	Barley	20.0	25.4	4.7
	Other	0.0	27.4	6.3
3	Maize	32.3	33.3	6.4
	Soybean	32.3	13.3	3.4
	Barley	32.3	19.9	3.1
	Meat and bone meal	3.0	0.0	0.0
	Other	0.0	33.5	6.7
4	Maize	25.0	35.9	6.7
	Soybean	25.0	7.7	2.9
	Barley	35.0	31.8	4.6
	Wheat	10.0	0.1	0.2
	Meat and bone meal	5.0	0.0	0.0
	Other	0.0	24.6	4.9
5	Maize	25.0	36.4	7.7
	Soybean	25.0	6.0	2.6
	Barley	35.0	27.2	9.7
	Wheat	10.0	0.0	0.0
	Mineral correctors	2.0	0.5	0.9
	Meat and bone meal	3.0	0.0	0.0
	Other	0.0	29.9	9.6
6	Maize	25.0	37.0	5.9
	Soybean	25.0	4.8	2.1
	Barley	35.0	36.4	6.7
	Wheat	10.0	0.1	0.2
	Mineral correctors	2.0	0.4	0.4
	Beet pulp	1.0	1.6	1.1
	Meat and bone meal	2.0	0.0	0.0
	Other	0.0	19.7	5.0

Table 5
Percentage ingredient contents and predictions for sample set C, synthetic binary mixtures.

Synthetic sample number	Ingredient	True composition (%)	Results	
			Average estimated composition (%)	SD
1	Barley	50.0	4.4	2.2
	Meat and bone meal	50.0	0.0	0.0
	Other	0.0	95.6	11.4
2	Maize	50.0	67.6	4.8
	Meat and bone meal	50.0	0.3	0.4
	Other	0.0	32.0	5.9
3	Soybean meal	50.0	76.9	4.0
	Meat and bone meal	50.0	21.0	3.9
	Other	0.0	2.1	1.3

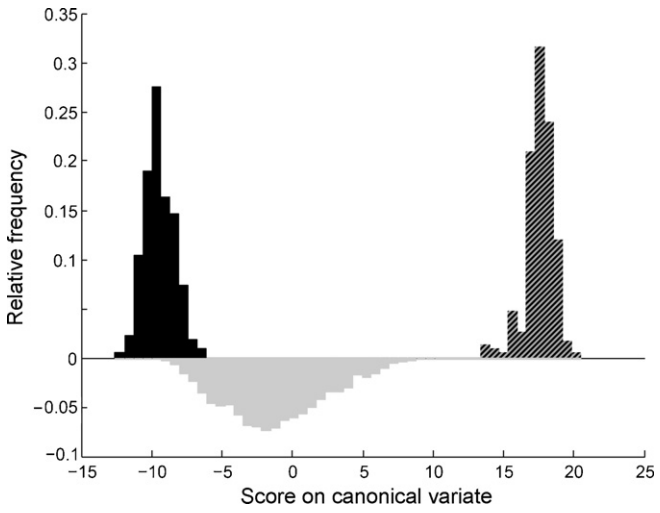


Fig. 1. Synthetic binary mixture of barley and MBM. Distributions of canonical scores of the spectra from the two pure ingredients (above the zero line, barley on the left, MBM on the right) and the spectra from the 50–50 mixture (below the line).

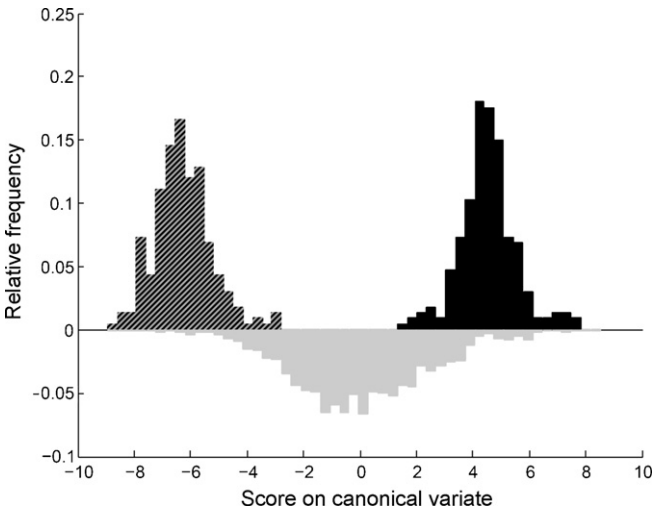


Fig. 2. Synthetic binary mixture of soya meal and MBM. Distributions of canonical scores of the spectra from the two pure ingredients (above the zero line, MBM on the left, soya on the right) and the spectra from the 50–50 mixture (below the line).

the tables of results. The mean and standard deviation over the 10 replicates were calculated for each ingredient and for the category 'other'.

3. Results and discussion

3.1. Sample set A, artificial mixtures

Table 2 shows the true composition and the prediction results for the six artificial mixtures. The spectra of the animal ingredient, MBM, were always correctly classified, and there were no false positives. Even the cereal ingredients were generally correctly identified, despite the fact that there is some overlap between these ingredients in the library [7]. In Table 2, the classification 'other' corresponds to ingredients not present in the sample but included in the estimated composition. These were mainly confusions with other cereals. The standard deviations over the 10 replicates ranged from 0 to 2%. Table 3 shows an example of this repeatability in detail for the sixth artificial mixture. For the minor ingredients the fact that the result is a count of spectra is evident. There are exactly two beet pulp spectra in each mixture, and the number found varies from one to three, hence the large coefficient of variation for this ingredient.

These samples are not a very stringent test of the system, being collections of spectra of pure ingredients rather than spectra measured on mixtures of ingredients. However their use confirms that the library is able to classify accurately such spectra, and enables an assessment of accuracy that is free of sampling variability. When a real mixture is measured, there is considerable uncertainty about the composition of the portion of the sample actually examined, especially for ingredients present in only small proportions in the bulk sample.

3.2. Sample set B, synthetic mixtures

The composition and prediction results for sample set B, the synthetic mixtures are displayed in Table 4. The results are very disappointing when compared with those for the artificial samples in Table 2. There are major confusions among the cereal ingredients, for example the wheat in samples 4–6 was almost undetected. The

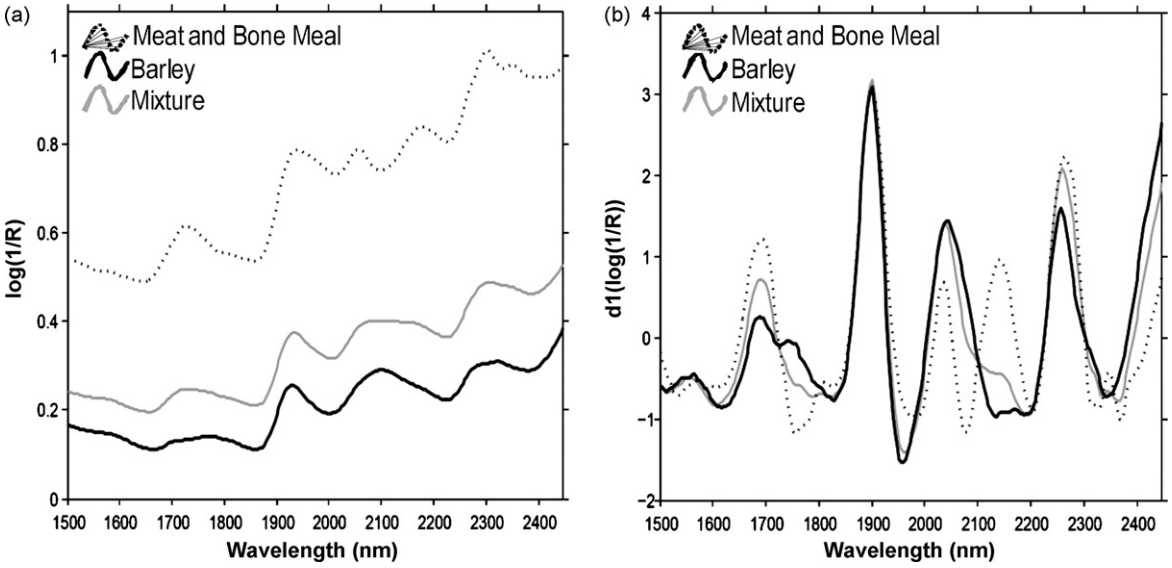


Fig. 3. Mean spectra for barley, MBM, and their mixture: (a) raw log(1/*R*) and (b) snv-treated first derivative.

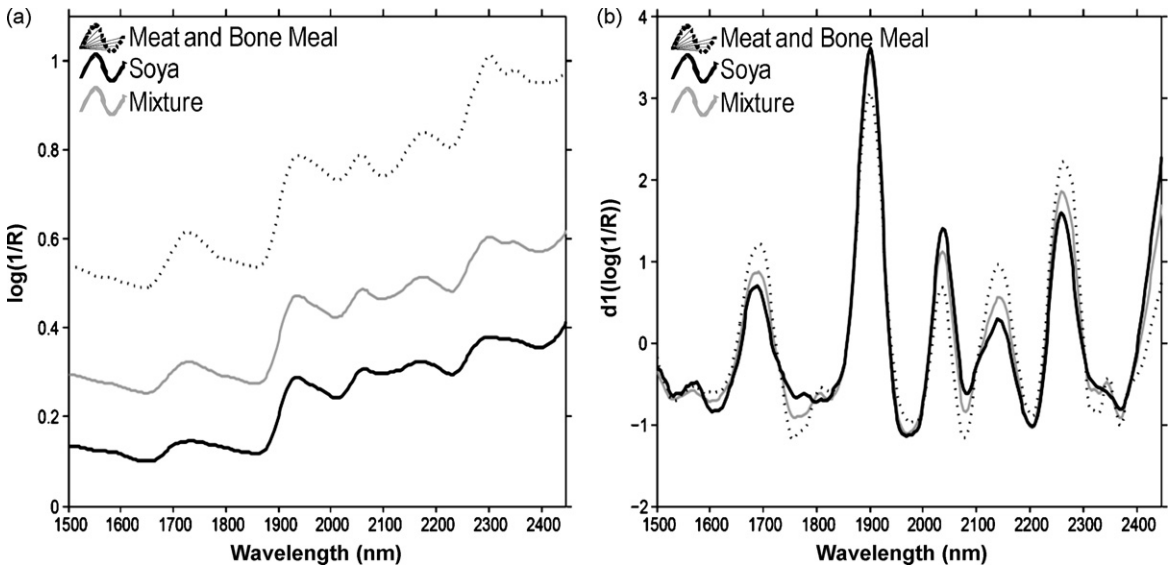


Fig. 4. Mean spectra for soya, MBM, and their mixture: (a) raw log(1/*R*) and (b) snv-treated first derivative.

main contributors to the 'other' category were oats and bran, in all the samples, and barley in sample 1. None of the four banned animal ingredients appeared in this category. Nevertheless, these confusions between cereal grains are not particularly important. In fact, the mandatory labelling for feed materials according to Article 16 (1) of Proposal for regulation of the European Parliament (2008/005 COD) says that the label shall include the name of the feed material corresponding to the respective category. Cereal grains are the category that includes oats, wheat and barley. Worse, though, is the failure to detect the MBM in any of samples 3–6, even though it is present at 5% in sample 4.

3.3. Sample set C, synthetic binary mixtures

The results for the three binary mixtures of sample set C are shown in Table 5. They are no better than those for sample set B, with the MBM being misclassified completely in sample 1, and almost completely in sample 2. Only in sample 3, a mixture of soya and MBM, does comparison with the library detect the correct two ingredients, and even in this case the estimated proportions are incorrect. The main contributors to the 'other' category are maize, soya and DDGS barley in sample 1; and soya in sample 2.

Some understanding of the spectral behaviour of the mixtures can be obtained by comparing the spectra from the mixtures with the spectra of the pure ingredients they contain. Figs. 1–4 show such a comparison for samples 1 and 3, the barley–MBM and soya–MBM mixtures. The case of sample 2, the maize–MBM mixture is very similar to that of sample 1, and will not be discussed in detail.

Figs. 1 and 2 show scores on the canonical variates for binary discrimination in the case of samples 1 and 3 respectively. The canonical variate is the direction in spectral space that best discriminates between the two ingredients. These scores are shown as relative frequency histograms for each of the three sets of spectra. The histogram for the mixture points downwards merely so that it can be distinguished from the other two where it overlaps.

The most important conclusion that can be drawn from these two figures is that in the mixture, despite the very small sample area that an individual spectrum represents, most if not all of the individual spectra are spectra of mixtures, of varying proportions. Some spectra may resemble those of the pure ingredients, and thus be correctly classified, but the majority will not, and their correct classification using the KNN rule will be a matter of chance. This explains the poor results obtained when classifying the real mixtures.

In neither case is the system quite linear, though it is much closer to being so for the soya–MBM mixture than for the barley–MBM mixture. In Fig. 1, the scores from the mixture have a distribution much closer to those of the barley than those of the MBM, despite the equal proportions in the mixture. In Fig. 2, although the separation between the two ingredients is much less, the mixture is much more symmetrically placed between them, with a slight bias in the direction of the soya, on the right of the figure. This fits with the failure to identify any MBM in sample 1 and with the too-high proportion of soya predicted for sample 3.

The source of the nonlinearity is in the spectra. Figs. 3 and 4 show the mean raw and SNV-treated first derivative spectra for the pure ingredients and the mixture in each of the two cases. In both panels of Fig. 3 it can be seen that the mean spectrum from the mixture, although between those of the two pure ingredients, is generally closer to that of the barley. This is especially true in the region around 2000–2200 nm. In Fig. 4, the mean mixture spectrum is roughly mid-way between the other two for most of the

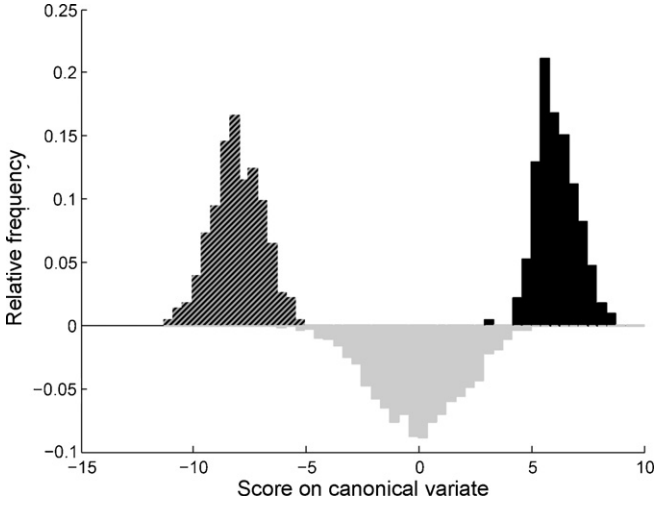


Fig. 5. Synthetic binary mixture of barley and MBM. Distributions of canonical scores of the spectra from the two pure ingredients (above the zero line, barley on the left, MBM on the right) and the spectra from the 50–50 mixture (below the line), with the spectral range restricted to 1600–1800 nm.

spectral range, especially for the derivative spectra. The positions of the mean mixture spectra explain the behaviour seen in Figs. 1 and 2, and suggest a way of making the barley–MBM system more linear. Fig. 5 is the result of carrying out the same analysis that gave rise to Fig. 1, but restricting the spectral range to 1600–1800 nm. In this region the mean mixture spectrum in Fig. 3 does resemble an average of the pure ingredient spectra, and as expected the scores for the mixture spectra have a much more symmetric and centrally situated distribution in Fig. 5.

Given the problems that arise when mixtures are measured with the methodology used here, it would be tempting to conclude that only the measurement of individual particles offers a way forward. However the sample presentation and measurement procedures used in this work offer advantages of simplicity and speed, and the results with the binary mixtures of set C are encouraging enough to suggest that further work to develop chemometric strategies to deal with the problem is a worthwhile prospect.

4. Conclusions

The artificial samples of set A confirm that the spectral library is very good at identifying spectra taken from pure ingredients. However, these excellent results were not repeated for sets B and C, in which the spectra were measured on mixtures. The explanation for this is clear from the investigation of sample set C. Even though the sample area from which the spectra are taken was small, the samples are so well mixed that few if any of the resulting spectra correspond to pure ingredients. This means that a strategy that tries to match the spectra taken from the mixture with those of pure ingredients is unlikely to meet with much success. The evidence from sample set C is that interpolation between pure ingredients is possible, and that the choice of spectral ranges is likely to be important in achieving this. Much work remains to be done to extend this system to mixtures of larger numbers of ingredients, and hence solve the general problem.

Acknowledgements

This research work was developed during a stay of the first author in the Department of Statistical Science of University College London with Prof. Tom Fearn, with a grant INIA (National Institute of Agro-food Research). This work was supported by the Spanish projects RTA2005-00212-C02-00 and RTA2008-00113-C02-01 from the INIA. The authors are grateful to INIA by a pre-doctoral fellowship of Mª del Valle Fernández Ibáñez and post-doctoral financial support of Dr. Ana Soldado. Thanks are also given to Alfonso Carballal and Nutrition Laboratory staff for their technical assistance.

References

[1] M.A. Granero, Feed for Health (COST Action FAO802): Joint Meeting WG1+2+3+4 and Second Management Committee Meeting, Milan (2009) 21.
[2] L. Pinotti, COST Action FAO802: Feed for Health. European Union (2008).
[3] European Commission, Off. J. Eur. Commun. L 339 (2003) 78–84.
[4] L.W.D. van Raamsdonk, C. von Holst, V. Baeten, G. Berben, A. Boix, J. de Jong, Anim. Feed Sci. Technol. 133 (2007) 73–83.
[5] D. Pérez-Marín, A. Garrido-Varo, J.E. Guerrero-Ginel, A. Gómez-Cabrera, Anim. Feed Sci. Technol. 116 (2004) 333–349.
[6] D. Pérez-Marín, A. Garrido-Varo, J.E. Guerrero, Appl. Spectrosc. 60 (2006) 1432–1437.
[7] V. Fernández-Ibáñez, T. Fearn, A. Soldado, B. de la Roza-Delgado, Food Chem., submitted for publication.
[8] M.J. De la Haba, J.A. Fernández-Pierna, O. Fumière, A. Garrido-Varo, J.E. Guerrero, D.C. Pérez-Marín, P. Dardenne, V. Baeten, J. Near Infrared Spectrosc. 15 (2007) 81–88.
[9] B. de la Roza-Delgado, A. Soldado, S. Madroño, A. Martinez-Fernández, F. Vicente, A. Garrido-Varo, D. Pérez-Marín, J.E. Guerrero-Ginel, in: G.R. Burling-Claridge, S.E. Holroyd, R.M.W. Summer (Eds.), Near Infrared Spectroscopy: Proceedings of the 12th International Conference, NIR Publications, Chichester, UK, 2006, pp.140–145.
[10] B. de la Roza-Delgado, A. Soldado, A. Martinez-Fernández, F. Vicente, A. Garrido-Varo, D. Pérez-Marín, M.J. de la Haba, J.E. Guerrero-Ginel, Food Chem. 105 (2007) 1164–1170.
[11] V. Baeten, C. von Holst, A. Garrido, J. Vancutsem, A.M. Renier, P. Dardenne, Anal. Bioanal. Chem. 382 (2005) 149–157.
[12] C. von Holst, V. Baeten, A. Boix, B. Slowikowski, J.A. Fernández-Pierna, S. Tirendi, P. Dardenne, Anal. Bioanal. Chem. 392 (2008) 313–317.
[13] C. Gendrin, Y. Roggo, C. Collet, J. Near Infrared Spectrosc. 16 (2008) 151–157.
[14] V. Fernández-Ibáñez, A. Soldado, F. Vicente, A. Martínez-Fernández, B. de la Roza-Delgado, J. Near Infrared Spectrosc. 16 (2008) 43–48.
[15] T. Naes, T. Isaksson, T. Fearn, T. Davies, Multivariate Calibration and Classification, NIR Publications, Chichester, UK, 2002, pp. 221–259.
[16] B.G. Osborne, T. Fearn, P.H. Hindle, Practical NIR Spectroscopy with Applications in Food and Beverage Analysis, Longman, Harlow, UK, 1993, p. 31.
[17] R.J. Barnes, M.S. Dhanoa, S.J. Lister, Appl. Spectrosc. 43 (1989) 772–777.

Talanta 80 (2009) 61–70

Contents lists available at ScienceDirect

Talanta

journal homepage: www.elsevier.com/locate/talanta

A multi-analytical study of degradation of lignin in archaeological waterlogged wood

Maria P. Colombini[a], Jeannette J. Lucejko[a,*], Francesca Modugno[a], Marco Orlandi[b], Eeva-Liisa Tolppa[b], Luca Zoia[b]

[a] Department of Chemistry and Industrial Chemistry, University of Pisa, Via Risorgimento 35, I-50126 Pisa, Italy
[b] Department of Environmental and Earth Sciences, University of Milano-Bicocca, Piazza della Scienza 1, I-20126 Milano, Italy

ARTICLE INFO

Article history:
Received 20 March 2009
Received in revised form 4 June 2009
Accepted 9 June 2009
Available online 17 June 2009

Keywords:
Archaeological waterlogged wood
Lignin
Py(silylation)-GC/MS
NMR spectroscopy
GPC analysis

ABSTRACT

Historical or archaeological wooden objects are generally better conserved in wet environments than in other contexts. Nevertheless, anaerobic erosion bacteria can slowly degrade waterlogged wood, causing a loss of cellulose and hemicellulose and leading to the formation of water-filled cavities. During this process, lignin can also be altered. The result is a porous and fragile structure, poor in polysaccharides and mainly composed of residual lignin, which can easily collapse during drying and needs specific consolidation treatments. For this reason, the chemical characterization of archaeological lignin is of primary importance in the diagnosis and conservation of waterlogged wood artifacts. Current knowledge of the lignin degradation processes in historical and archaeological wood is extremely inadequate. In this study lignin extracted from archaeological waterlogged wood was examined using both Py-GC/MS, NMR spectroscopy and GPC analysis. The samples were collected from the Site of the Ancient Ships of San Rossore (Pisa, Italy), where since 1998 31 shipwrecks, dating from 2nd century BC to 5th century AD, have been discovered. The results, integrated by GPC analysis, highlight the depolymerization of lignin with cleavage of ether bonds, leading to an higher amount of free phenol units in the lignin from archaeological waterlogged wood, compared to sound lignin from reference wood of the same species.

© 2009 Elsevier B.V. All rights reserved.

1. Introduction

Wooden objects from past civilizations are very rare, because they can be easily degraded by fungi, bacteria and insects. They are therefore considered to be extremely valuable and require careful attention, conservation and study. It is particularly important to improve our understanding of the processes and the chemical changes that affect archaeological wooden artifacts during ageing and degradation, in order to develop efficient conservation treatments.

Archaeological wooden artifacts can survive better in environments where microbial and fungal activity is limited, as is the case of underwater shipwrecks. Waterlogged wood has unique features that require special consideration in terms of conservation and preservation. In aquatic environments anaerobic bacteria are primarily responsible for the depletion of wood carbohydrates, leaving a porous and unstable residual structure mainly consisting of lignin [1,2]. If these kinds of objects are allowed to dry without proper consolidation, e.g. by impregnation or bulking with polymeric materials, the wood may shrink, fragment and collapse into pieces [3]. Lignin can also degrade or become transformed to a limited extent, and very little is known about the chemical decay of lignin, although it is believed to be limited compared to the degradation undergone by cellulose and hemicellulose [4].

The type of deterioration, and how these processes impact the wood are important issues in terms of the study and appropriate preservation of waterlogged wooden objects and cultural properties. If there are variations in the composition of lignin these may influence the interactions between the wood and the impregnant/consolidant materials used to fill the cavities when the object is brought to ambient conditions and exhibited.

The optimal conservation treatment for waterlogged wood artifacts is far from being definitively assessed, and depends on many factors that vary from case to case. The choice of conservation is made even more difficult by the cost, the long period of time required and the technical problems arising when large objects such as shipwrecks need to be conserved [5]. Moreover, the long-term stability of impregnated waterlogged wood artifacts is still a matter of discussion and research, also given the recently highlighted degradation phenomena observed in world-famous

* Corresponding author. Tel.: +39 050 2219252; fax: +39 050 2219260.
E-mail addresses: perla@dcci.unipi.it (M.P. Colombini), j.lucejko@ns.dcci.unipi.it, jlucejko@gmail.com (J.J. Lucejko), frances@dcci.unipi.it (F. Modugno), marco.orlandi@unimib.it (M. Orlandi), eeva-liisa.tolppa@unimib.it (E.-L. Tolppa), luca.zoia@unimib.it (L. Zoia).

0039-9140/$ – see front matter © 2009 Elsevier B.V. All rights reserved.
doi:10.1016/j.talanta.2009.06.024

shipwrecks such as the Vasa in Stockholm, which was treated with polyethyleneglycol [6].

In this study we investigated the chemical alteration of lignin in wood samples from the archaeological site of the Ancient Ships of San Rossore (Pisa, Italy), where over the last 10 years 31 Roman shipwrecks dating between 2nd century BC to 5th century AD have been discovered [7].

Lignin is a complex three-dimensional macromolecule, made up of various different monomeric units, basically derived from coniferyl alcohol in softwoods, and from both coniferyl alcohol and sinapyl alcohol in hardwoods, bound through different bonds [8,9]. In view of the difficulties in its characterization, the adopted analytical approach integrated pyrolysis-gas chromatography/mass spectrometry (Py-GC/MS) with a set of nuclear magnetic resonance spectroscopic techniques, namely: bidimensional heteronuclear single quantum coherence (2D-HSQC,) quantitative carbon nuclear magnetic resonance (^{13}C NMR), and phosphorous nuclear magnetic resonance (^{31}P NMR).

The study was supported by Zeisel analysis to quantify lignin methoxyl groups, and gel permeation chromatography (GPC) to determine the molecular weight distribution of lignin.

The purpose was not only to gain information on lignin decay patterns in waterlogged archaeological wood, and to contribute to the complex issue concerning the study and conservation of degraded wood artifacts, but also to compare the results obtained with the adopted techniques, and to evaluate the potential of an integrated analytical approach to gain information on the chemical structure of the lignin polymer.

In terms of the specific problem of studying lignin decay processes in a highly degraded waterlogged wood, containing a very low amount of holocellulose (10–20% or less), a comparison of the analyses of sound reference wood and degraded waterlogged wood can be limited by the fact that the presence or absence of polysaccharides can influence or interfere with the analysis of lignin. For these reasons, in this study we characterized lignin extracted from archaeological wood, and compared it with lignin extracted from sound wood of the same species in the same extraction conditions. Extraction was performed in mild conditions in order to avoid further degradation. In this experimental set-up, sound reference lignin and archaeological lignin, treated in the same way in terms of the extraction, can be analyzed in the same conditions and in particular in the absence of polysaccharides.

The use of pyrolysis techniques in combination with mass spectrometry has proved to be of particular interest in the study of lignocellulosic macromolecules. In particular, Py-GC/MS provides useful information on the chemical structure of lignin [10–13]. In Py-GC/MS the macromolecules are depolymerized by heat, and the fragments produced are identified by mass spectrometry, after gas chromatographic separation. In the case of lignin, it is assumed that pyrolysis products represent, to a greater or lesser degree, the structural units that make up the macromolecule. Polymer subunits undergo thermal degradation under pyrolysis, consequently the information obtained is strictly dependent on the adopted instrumental conditions: primarily the selected pyrolysis temperature and asset of the pyrolyser; secondly, the parameters of the transfer line/interface between the pyrolyser and the GC, where secondary reactions occur. A low temperature will not produce sufficient fragmentation of the stronger bonds in the macromolecules, while on the other hand a high pyrolysis temperature will produce extensive fragmentation of the sample, yielding less informative low molecular weight fragments, and producing secondary reactions. A possible method to increase the volatility of pyrolysis products for GC/MS analysis, thus improving the analytical response, accelerating their transfer to the GC column and limiting the possibility of thermal degradation, is to perform *in situ* thermally assisted derivatization of the pyrolysis products. In the literature, the application of *in situ* derivatization methods in the pyrolysis of wood appears to be limited: results obtained with methylating [10,13,14] and silylating [15,16] reagents are described, while the majority of published applications do not use derivatization.

Py-GC/MS has been applied in the study of cellulose and lignin, to investigate decay processes in degraded wood [17–22] and also in a few cases in the specific study of historical or archaeological wood samples [23–26]. The literature data show that highlighting chemical alterations in the residual lignin structure of waterlogged wood is not straightforward. A comparison of Py-GC/MS profiles of degraded wood with those obtained from sound wood of the same species enables differences in the variations of the relative amounts (in terms of chromatographic peak areas) of minor pyrolysis products of lignin [22] to be observed. A comparison of pyrolysis profiles with those in the literature is of limited use because of the variability of pyrolysis products depending on the instrumental conditions used.

High-resolution nuclear magnetic resonance (NMR) spectroscopy has been one of the most important analytical techniques for 40 years, nevertheless until recently its impact on archaeology has been minimal for two reasons well described by Lambert et al. [27] and concerning the sensibility, sensitivity and resolution of this technique. Recent developments have dramatically changed this situation and now this technique is also used with good results in the field of cultural heritage. In particular, the possibility to determine and quantify functional groups and intermonomeric bonds in lignin by NMR has been demonstrated. In addition the high-resolution nuclear magnetic resonance of ^{13}C, developed in the field of geochemistry to characterize fungal degraded wood [28] and to evaluate lignin in organic matter [29] and sediments [30], was used to characterize archaeological wood samples from the 11th century excavation site at the Lake Paladru at Charavines, France [31]. The main result was the preservation of the most abundant intermonomeric bond in lignin structure, the so-called β-O-4. The solid state ^{13}C NMR is not sensitive enough to characterize and quantify the other important intermonomeric bonds present in lignin structure, and with this technique is not possible to observe and quantify the important functional groups such as carboxylic and alcoholic moieties. In order to avoid this problem new NMR analytical tools have been adopted, such qualitative and quantitative 2D-HSQC, quantitative ^{13}C NMR and ^{31}P NMR analysis [32,33] and especially qualitative and quantitative 2D-HSQC, which is nowadays the best tool for analyzing lignin [34,35], giving a complete picture of the chemical features of lignin.

2. Materials and methods

2.1. Reagents

The derivatization reagent for Py-GC/MS analysis was 1,1,1,3,3,3-hexamethyldisilazane (HDMS, 99.9%, Sigma–Aldrich Inc., USA). All solvents, including deuterated methyl sulfoxide-d_6 (DMSO, 99.9% Sigma–Aldrich Inc., USA) were of analytical grade and used without any further purification.

2.2. Samples

Archaeological waterlogged wood samples from bollards recovered from the excavations at the site of the Ancient Ships of Pisa (Tuscany, Italy) were made available by the Archaeological Superintendence of Tuscany (Florence), within the framework of a project for the development and evaluation of conservation treatments for waterlogged wood archaeological artifacts [36]. The wood *taxa* were: *Fagus sylvatica* (G, beech), *Ulmus* cfr. *minor* (D, elm), *Pinus pinaster* (F, pine), the same wood used to build the shipwrecks

Table 1
Value of lignin content (Klason lignin) and holocellulose content (w/w, %), previously reported by Giachi et al. [36] for the archaeological and sound wood examined in this study.

	Pine		Elm		Beech	
	Sound	Arch.	Sound	Arch.	Sound	Arch.
Klason lignin (w/w) %	25.0 ± 1.0	68.0 ± 1.0	27.0 ± 1.0	75.1 ± 0.5	24.0 ± 1.0	77.5 ± 1.0
Holocellulose (w/w) %	58.0 ± 1.0	19.3 ± 1.0	55.0 ± 1.0	6.4 ± 0.6	74.0 ± 1.0	9.2 ± 1.0

recovered at the site. The archaeological artifacts from the site are dated from a period between the 2nd century BC and the 4th century AD. Seasoned wood samples of the same species used as references were provided by IVALSA CNR (Florence). These wood samples were previously characterized [37] according to classical methods for the determination of lignin (Kalson lignin) [38], holocellulose [39], and extractives [36] and some of the results, highlighting the extensive loss of polysaccharides, are reported in Table 1.

2.3. Lignin preparation

The lignin was extracted from archaeological and reference wood using a modification of the milled wood method developed by Björkman [40] and modified by Holmbom and Stenius [41]. Wood fragments (10 g) were freeze-dried, then ground in a mortar. The wood powder was extracted in Soxhlet with ca. 250 ml of acetone–water (9:1) for 48 h and then dried at 50 °C to a constant weight. The dry wood powder was milled in a laboratory ball mill for 48 h at 75 rpm. The powder (9.5 g) was sonicated in dioxane–water (9:1) for 2 h and the dioxane–water-solution was distilled under reduced pressure until almost dry. Iced acetic acid (80 ml) was added to the powder suspension and the wood suspension was kept, under magnetic stirring, at 50 °C for 2 h. The suspension was then filtered and washed with 50 ml of iced acetic acid. Subsequently, 50 ml of distilled water was added to the filtrate and kept at a temperature of 4 °C over night in order to obtain a precipitate. The precipitate was isolated by centrifugation and washed with distilled water. The lignin was then lyophilized in order to dry it. The amount of lignin obtained was about 500 mg. Approximately 60 mg of the extracted lignin was acetylated with acetic anhydride for NMR analysis: pyridine 1:1 (v/v).

2.4. Zeisel analysis

Zeisel analyses were performed using a GC-FID as reported by Girardin and Metche [42], in order to quantify the methoxyl groups in lignin. The Zeisel method is based on the following reaction:

$$\text{L-OCH}_3 + \text{HI} \rightarrow \text{L-OH} + \text{CH}_3\text{I} \quad (140\text{–}150\,^\circ\text{C})$$

2.5. Py-HMDS/GC/MS

Py-GC/MS (pyrolysis-gas chromatography/mass spectrometry) was performed in a 5150 CDS Pyroprobe 5000 Series with a coil filament connected to a 6890 Agilent gas chromatograph (USA) coupled to a 5973 Agilent mass selective detector operating in electron impact mode (EI) at 70 eV. On the basis of a careful comparison of the literature, pyrolysis temperatures between 450 and 600 °C were tested and 500 °C was chosen. Pyrolysis was carried out for 20 μs using a platinum coil probe and quartz sample tubes. We adopted hexamethyldisilazane (HMDS) as *in situ* derivatizing agent for hydroxyl and acidic moieties. Constant amounts (40–60 μg) of lignin and hexamethyldisilazane (5 μl) solution (70% in acetone) were inserted in the centre of the pyrolysis quartz tube and placed in the pyrolysis coil filament. Chromatographic separation was performed on an HP-5MS fused silica capillary column (stationary phase 5% diphenyl–95% dimethyl-polysiloxane, 30 m × 0.25 mm i.d., Hewlett Packard, USA) with a de-activated silica pre-column (2 m × 0.32 mm i.d., J. and W. Scientific, Agilent Technologies, USA). Chromatographic conditions were as follows: an initial temperature of 31 °C, 8 min isothermal, 10 °C min^{-1} up to 240 °C, 3 min isothermal, 20 °C min^{-1} up to 300 °C, 30 min isothermal. Carrier gas: He (purity 99.995%), constant flow 1.0 ml min^{-1}. Each sample was analyzed in four replicates. Quantification was based on peak areas (total integral of identified compounds equals 100).

2.6. 2D-HSQC and ^{13}C NMR

2D-HSQC and ^{13}C NMR spectra were run in DMSO on acetylated samples, to avoid fractionation of the material before NMR analysis and to increase both solubility and chemical shift dispersion of the side chain units [43]. Thus, before NMR analyses, the extracted lignin (0.1 g) was acetylated with acetic anhydride/pyridine 1:1 (v/v) (2 ml), then 60 mg of acetylated lignin were dissolved in 0.75 ml DMSO-d_6. The inverse detected ^1H–^{13}C correlation (2D-HSQC–NMR) spectra were recorded on a Bruker (USA) 500 MHz instrument at 308 K. The spectral width was set at 5 kHz in F2 and 25 kHz in F1. A total of 128 transients in 256 time increments were collected. The polarization transfer delay was set at the assumed coupling of 140 Hz and a relaxation delay of 2 s was used. Spectra were processed using $\Pi/2$ shifted squared sinebell functions in both dimensions before Fourier transform. The assignment of predominant signals in 2D-HSQC–NMR spectra was based on the chemical shift data of lignin model compounds and milled wood lignin (MWL), as reported in the literature [32,44–46].

The 1D-^{13}C spectra were recorded at 333 K using a Varian Mercury 400 MHz instrument. Chemical shifts were referred to the solvent signal at 39.5 μg g^{-1}. To obtain quantitative ^{13}C NMR spectra, a relaxation delay of 10 s (45° pulse angle) was used between the scans [47]. A line broadening of 2–5 Hz was applied to FIDs before the Fourier transform. For each spectrum, about 16,000 scans were typically accumulated.

2.7. ^{31}P NMR

In order to characterize and quantify all the different functional groups with labile –OH, nuclear magnetic resonance analysis of phosphorus (^{31}P NMR) of lignins extracted from woods was performed, as reported in the literature [33]. Accurately weighed lignin samples (40 mg) were dissolved in a solvent mixture composed of pyridine and deuterated chloroform 1.6:1 (v/v 0.5 ml). Then 100 μl of 2-chloro-4,4,5,5-tetramethyl-1,3,2-dioxaphospholane were added, together with a solutions of N-hydroxynaphthalimide as an internal standard and tris(acetylacetonate)chromium(III), [$Cr(acac)_3$], as relaxation reagent (100 μl each). The ^{31}P NMR spectra were then recorded at 333 K using a Varian Mercury 400 MHz instrument. The ^{31}P NMR data reported in this paper are averages of three experiments. The maximum standard deviation of the reported data was 2×10^{-2} mmol g^{-1}, while the maximum standard error was 1×10^{-2} mmol g^{-1}.

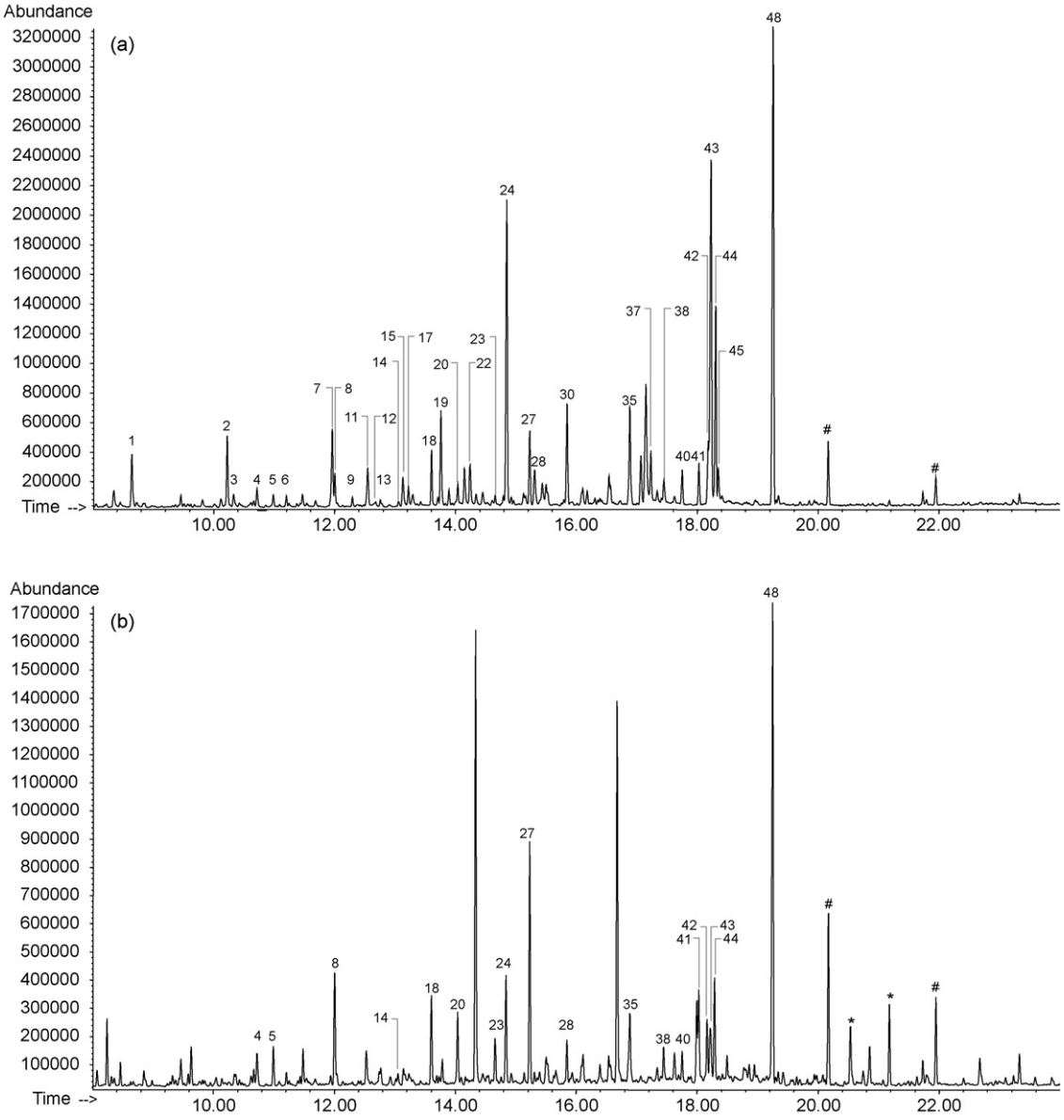


Fig. 1. Py-GC/MS profiles of lignin extracted from (a) sound pine wood (*Pinus pinaster*) and (b) archaeological pine wood from San Rossore site. (*): unidentified impurities deriving from the sediment; (#): fatty acids.

2.8. GPC

The investigation was carried out on acetylated lignin samples, following the methodology developed by Himmel et al. [48]. The analyses were performed using a Waters (USA) 600 E liquid chromatograph connected to an HP 1040 ultraviolet diode array (UV) detector set at 280 nm. The GP-column was an Agilent (USA) PL 3 μm MIXED gel E and the solvent used was tetrahydrofuran. Polystyrene (PS) standards from Polymer Laboratories (USA) were used for the calibration. The PS calibration curve was tested using acetylated dimeric, tetrameric, and hexameric lignin model compounds. The acetylated lignin samples were dissolved in THF (1 mg ml^{-1}) and analyzed at a flow rate of 0.8 ml min^{-1}.

3. Results and discussion

3.1. Py(HMDS)GC/MS

A complex mixture of phenolic products, diagnostic for the different lignin units, is formed in the pyrolysis of lignin and determined by GC/MS. Softwood lignin is characterized by guaiacyl compounds only, while the presence of both guaiacyl and syringyl compounds among pyrolysis products indicates that the lignin is of an angiosperm origin (hardwood).

In the presence of HMDS, alcoholic, phenolic and carboxylic functionalities are transformed into the corresponding trimethylsilyl-ethers and esters, although for some compounds the silylation reaction is not complete during pyrolysis, and leads to the presence of underivatized or partially derivatized compounds. The yield of the silylation is the result of many factors, including the formation rate of the pyrolysis product and its transfer rate to the GC. The partial derivatization of some peaks has the effect of increasing the complexity of the chromatograms, but this drawback is balanced by the possibility of highlighting compounds bringing polar carboxylic moieties, and of differentiating free and bound phenol groups on the basis of their degree of derivatization.

Fig. 1 shows the chromatogram obtained for reference pine lignin and archaeological pine lignin. Table 2 reports peak identification, on the basis of the mass spectral library, of the literature data, and of the interpretation of mass spectra. The most abundant

Table 2
Relative amounts, in terms of % peak area compared to the total area of identified compounds, of pyrolysis products in the GC/MS program of lignin extracted from reference wood and archaeological wood (average of four replicates). G: guaiacyl; S: syringyl; H-hydroxyphenyl.

Peak	Tr	Product	Origin	MW	Pine		Elm		Beech	
					Sound	Arch.	Sound	Arch.	Sound	Arch.
1	8.65	Guaiacol	G	124	1.75	0.05	1.03	–	2.19	–
2	10.21	4-Methylguaiacol	G	138	2.56	0.17	1.42	–	0.35	0.05
3	10.33	Catechol-TMS		182	0.87	0.33	1.11	–	0.79	0.04
4	10.71	Guaiacol-TMS	G	196	1.49	2.57	1.64	1.55	2.15	0.62
5	10.98	Benzoic acid-TMS		194	0.55	1.03	0.56	0.88	0.23	0.23
6	11.46	4-Ethylguaiacol	G	152	0.53	–	0.26	–	0.56	–
7	11.96	4-Vinylguaiacol	G	150	2.10	–	1.49	–	2.71	–
8	12.00	4-Methylguaiacol-TMS	G	210	3.28	8.52	1.95	3.13	0.31	1.10
9	12.30	Catechol-2(TMS)		254	0.41	–	0.94	0.42	0.21	0.05
10	12.45	Syringol	S	154	–	–	0.46	–	3.56	0.29
11	12.55	Eugenol	G	164	1.07	0.33	0.62	–	0.40	–
12	12.67	4-Propylguaiacol	G	166	0.13	–	0.10	–	0.13	–
13	12.75	4-Hydroxybenzaldehyde-TMS		194	0.01	–	0.10	–	–	–
14	13.05	4-Ethylguaiacol-TMS	G	224	0.55	0.73	0.56	0.42	0.24	0.13
15	13.12	Vanillin	G	152	1.78	1.14	1.85	–	–	–
16	13.14	Syringol-TMS	S	226	–	–	0.35	1.45	5.41	2.19
17	13.22	*Z*-isoeugenol	G	164	0.96	–	0.40	–	0.25	–
18	13.61	4-Vinylguaiacol-TMS	G	222	3.92	4.78	3.53	2.63	3.93	1.21
19	13.76	*E*-Isoeugenol	G	164	1.94	1.18	2.40	0.44	1.42	–
20	14.04	Eugenol-TMS	G	236	1.81	3.65	1.80	1.51	0.43	0.71
21	14.20	4-Methylsyringol-TMS	S	240	–	–	0.95	2.05	0.92	3.67
22	14.24	Acetovanillone	G	166	1.43	2.54	1.15	0.10	1.79	0.18
23	14.66	*Z*-Isoeugenol-TMS	G	236	1.03	1.56	0.68	1.06	0.28	0.49
24	14.85	Vanillin-TMS	G	224	9.23	4.05	5.82	5.27	2.50	2.06
25	15.05	4-Ethylsyringol-TMS	S	254	–	–	0.11	0.33	0.32	0.41
26	15.17	4-Vinylsyringol	S	180	–	–	0.71	–	2.79	0.24
27	15.23	*E*-isoeugenol-TMS	G	236	4.52	10.43	3.36	3.17	0.88	1.92
28	15.30	4-Propylguaiacol-TMS	G	238	1.18	0.37	1.95	0.55	0.73	–
29	15.60	4-Vinylsyringol-TMS	S	252	–	–	1.36	1.70	3.85	2.78
30	15.85	Acetovanillone-TMS	G	238	3.17	2.42	2.62	2.28	2.03	0.71
31	15.91	4-Propylsyringol-TMS	S	268	–	–	0.51	1.06	0.72	2.26
32	16.45	4-*Z*-propenylsyringol-TMS	S	266	–	–	0.35	0.67	0.50	1.20
33	16.73	4-Allylsyringol	S	194	–	–	1.23	–	1.80	0.51
34	16.83	Syringaldehyde-TMS	S	254	–	–	2.91	3.56	4.75	7.40
35	16.90	4-*Z*-coniferaldehyde-TMS	G	250	3.32	4.23	3.81	6.93	1.07	2.64
36	17.08	4-*E*-propenylsyiringol-TMS	S	266	–	–	2.57	3.10	2.46	5.13
37	17.19	*Z*-coniferyl alcohol-TMS	G	252	4.17	0.49	1.18	0.09	1.18	0.16
38	17.46	Vanillic acid 2(TMS)	G	312	2.15	3.10	1.02	3.04	0.26	0.98
39	17.55	Acetosyringone-TMS	S	268	–	–	1.27	1.88	1.83	3.28
40	17.75	4-Cumaryl alcohol 2(TMS)	H	294	1.09	1.82	0.78	0.83	1.05	0.52
41	18.03	Vanillylpropanol-2(TMS)	G	326	2.62	4.61	1.51	2.30	0.65	0.52
42	18.18	*Z*-coniferyl alcohol 2(TMS)	G	324	2.01	4.10	2.27	2.47	2.00	2.50
43	18.26	*E*-coniferyl alcohol TMS	G	252	13.71	5.54	10.10	3.19	11.10	2.75
44	18.31	4-*E*-coniferaldehyde-TMS	G	250	6.32	5.80	4.73	4.93	1.66	1.99
45	18.35	4-Cumaric acid-TMS	H	252	0.33	–	1.03	–	1.31	0.14
46	18.50	*Z*-sinapaldehyde-TMS	S	280	–	–	1.05	3.12	0.65	4.59
47	18.86	syringic acid-2(TMS)	S	342	–	–	0.33	1.92	3.39	3.68
48	19.28	*E*-coniferyl alcohol-2(TMS)	G	324	18.04	24.44	15.25	15.76	8.64	9.10
49	19.55	*Z*-sinapyl alcohol 2(TMS)	S	354	–	–	0.74	1.69	1.57	3.71
50	19.93	*E*-sinapaldehyde-TMS	S	280	–	–	1.25	3.42	1.08	7.96
51	20.56	*E*-sinapyl alcohol-TMS	S	282	–	–	2.01	0.74	5.60	4.46
52	20.66	*E*-sinapyl alcohol 2(TMS)	S	354	–	–	2.82	10.36	5.39	15.40
E-coniferyl alcohol: *mono*/*bis*-TMS					0.8	0.2	0.7	0.2	1.3	0.3
E-sinapyl alcohol: *mono*/*bis*-TMS					–	–	0.7	0.1	1.0	0.3

product of the pyrolysis of pine lignin, in the adopted conditions, is *E*-coniferyl alcohol. This alcohol, with a cinnamylic structure, appears in the chromatogram in two forms: the *bis*-TMS form (no. 48, MW 324) where both the alcoholic and the phenolic –OH are transformed into the corresponding silyl-ethers, and the *mono*-silylated form (no. 43, MW 252) where only the alkyl OH function is derivatized. The formation of cinnamylic alcohols as main pyrolysis product of lignin has been reported in the analysis of lignin using filament pyrolysers and in the presence of an *in situ* derivatizing agent [16]. According to the literature on the other hand, it is generally not observed when a furnace pyrolyser is used [26] and also when pyrolysis is performed in the absence of a derivatizing agent [21]. This may be explained with the fact that the trimethylsilyl group has a protective effect, during pyrolysis, towards the defunctionalisation of the primary alcohol function on the propylic side chains of lignin units. This means that, in the conditions adopted in this study, in the presence of HMDS, the pyrolysis conditions are particularly mild and pyrolysis products nearly reflect the structure of lignin monomers, avoiding the shortening and defunctionalisation of the propenyl side chain.

Other abundant pyrolysis compounds of pine lignin include guaiacol, methylguaiacol, isoeugenol, vanillin and acetovanillone.

A comparison between the pyrogram of reference pine lignin with archaeological pine lignin, shows a very good level of lignin preservation in archaeological wood, which gives the same pyrolysis products observed in non-aged lignin. The difference between the two chromatograms is not qualitative (appearance or disappearance of peaks is not observed), but it is rather in the relative

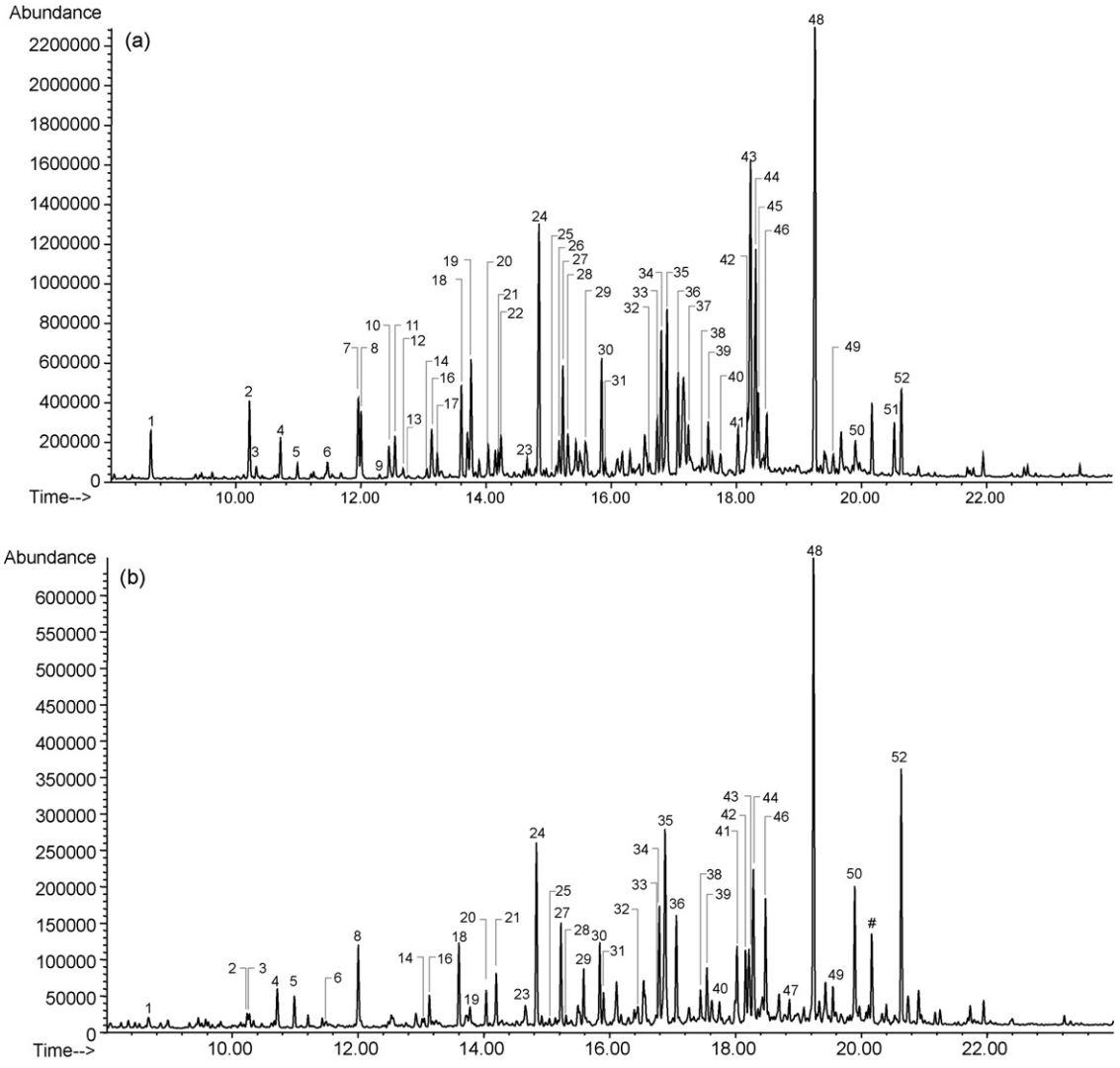


Fig. 2. Py-GC/MS profiles of lignin extracted from (a) sound beech wood (*Fagus sylvatica*) and (b) archaeological beech wood from the San Rossore site.

amounts of pyrolysis products. The evaluation of the pyrograms was therefore based on the calculation of relative peak areas, which can be considered a semi-quantitative information, even if not indicative of absolute amounts. For this reason, particular attention was given to reproducibility, and analyses were performed in four replicates of each kind of lignin. We observed that taking special care in using the same sample amount for each replicated analysis, and in positioning the sample in the centre of the tube with the aid of a capillary, permitted to enhance reproducibility, achieving a relative standard deviation for relative peak areas around 15%. The average results, in term of percentage peak areas with respect to the total area of identified peaks, are reported in Table 2.

The main difference observed in archaeological pine lignin with respect to sound lignin is in the different yield of derivatization of the phenolic function of coniferyl alcohol: in the sound pine lignin pyrogram the ratio between the *mono*-TMS form (where only the alkylic OH function is silylated) and the *bis*-TMS form (where both the alkylic and phenolic OH functions are silylated) is around 0.8, while in the archaeological lignin pyrogram the ratio between the two forms is neatly different: 0.2. Many other pyrolysis product give a higher derivatization yield in the analysis of archaeological lignin, while their underivatized form is abundant in the pyrogram of sound lignin: guaiacol, methylguaiacol, 4-ethylguaiacol, 4-vinylguaiacol, and isoeugenol.

This behavior needs to be put in relation to an increased reactivity of phenolic –OH towards HMDS in the pyrolysis of lignin extracted from archaeological wood, compared to the lignin extracted from sound wood, addressing to the fact that in aged archaeological lignin there is a higher concentration of free phenolic OH, which is more prone to react with HMDS.

This trend is also observed in the analysis of archaeological lignin from beech and elm samples, the results of which are also reported in Table 2. Chromatograms obtained in the analysis of reference and archaeological beech lignins are shown in Fig. 2. In addition to guaiacyl compounds observed in pine lignin, in beech and elm the corresponding syringyl components are present. In particular, in hardwoods, in addition to coniferyl alcohol, cinnamyl alcohol with a syringyl structure is also present: namely sinapyl alcohol. As in the case of pine, hardwood archaeological lignin from beech and elm samples produces pyrolysis products which are similar to those observed in sound lignin from the same species and analyzed in the same conditions, as can be seen from Table 2. This suggests a very good conservation state of lignin. The most interesting difference between reference and archaeological lignin from elm and beech is, as with pine, the derivatization yield of the phenolic groups, especially in terms of cinnamyl alcohols. The ratio between the amounts of *mono*-TMS-coniferyl alcohol and *bis*-TMS-coniferyl alcohol is on average 0.2 for archaeological elm lignin compared to 0.7 in refer-

Table 3
Values of methoxyl group content expressed in mmol g^{-1} for the three archaeological wood samples and three sound wood samples.

	Pine		Elm		Beech	
	Sound	Archaeological	Sound	Archaeological	Sound	Archaeological
O–CH_3 (mmol g^{-1})	3.1 ± 0.2	2.4 ± 0.2	4.1 ± 0.2	3.1 ± 0.2	3.7 ± 0.2	3.4 ± 0.2

ence elm lignin, and 0.3 in archaeological beech lignin compared to 1.3 in reference beech lignin. The corresponding values for sinapyl alcohols had the same trend: they varied from 0.7 for sound lignin to 0.1 for archaeological lignin in elm, and from 1.0 to 0.3 in beech lignin.

It is evident that in the pyrolysis-GC/MS of archaeological lignin from the San Rossore site in the presence of HMDS, phenolic groups on lignin units are silylated with a higher yield compared to the correspondent sound lignin. From the literature, this can be explained by the presence of a higher amount of the free phenol unit in archaeological lignin [16]. In fact, it is known that, due to the high stability of phenol ether bonds with respect to alkyl ether bonds, only free phenol groups on lignin units are derivatized with a high yield with thermally assisted silylation reagents, while phenol groups that are linked in a β-aryl ether bond or a β-5 bond do not react efficiently with the derivatizing agent [15]. This shows that the main difference between archaeological lignin and sound lignin is in that archaeological lignin contains a relatively greater amount of free phenol groups, not involved in intermonomeric bonds, on guaiacyl and syringyl units. A waterlogged environment would thus seem to lead to chemical pathways which themselves lead to the cleavage of phenol ether bonds, with depolymerization and a resulting increase in free phenolic groups. One important consequence is that an increased amount of free phenols creates a more polar and acidic lignin network.

These results were confirmed by the analysis of the same samples using NMR and GPC, illustrated in the following sections.

Another parameter that presents a substantial variation in archaeological elm and beech lignin compared to reference lignin is the content of *E*-sinapaldehyde-TMS, which in the pyrograms is higher in aged lignin, suggesting oxidation processes.

Py-HMDS-GC/MS has permitted also to evidence the presence of enhanced amounts of carboxyl acid functionalities on lignin units, in particular in position α respect to the aromatic ring, in some of the analyzed archaeological samples, with respect to the corresponding sound lignin. This can be seen in Table 2 which reports the amounts of vanillic and syringic acids determined in archaeological and reference lignin.

Due to the polarity of carboxylic benzyl acids and to their low amounts, their increase would not have been observed without using HMDS, which renders them volatile by transforming them into the corresponding TMS-esters.

3.2. Quantification of total methoxyl groups using the Zeisel method

A quantitative evaluation of the methoxyl content in lignin extracted from archaeological waterlogged wood and from sound wood using the Zeisel method [42] gave the values shown in Table 3. A slight demethylation was observed in archaeological lignin. Although demethylation has been shown to be a typical reaction of the enzymes present in brown rot fungi [49], underwater environments do limit the growth of fungi. Py-HMDS-GC/MS did not highlight an increase in catechols or methoxycatechols in aged lignin, compounds that are considered as products of the fungal degradation of lignin.

3.3. NMR analyses

3.3.1. 2D-HSQC

Lignin samples were analyzed by 2D-HSQC spectroscopy to identify the principal intermonomeric units in lignin and to evaluate any significant changes in the lignin structure of archaeological wood compared to lignin in the reference wood sample. The predominant intermonomeric units present in softwood and hardwood lignin (Fig. 3) include: arylglycerol-β-arylether (β-O-4), phenylcoumaran (β-5), pinoresinol (β–β), and dibenzodioxocine (5-5′-O-4). In Fig. 3 the 2D-HSQC of acetylated lignin extracted from pine used as reference is also reported. Fig. 4 reports the expansion of the intermonomeric zone of the 2D-HSQC spectrum of acetylated lignin from archaeological pine.

The results highlight that lignin from all archaeological wood samples are rich in arylglycerol β-O-4 units and at the same time cross-peaks were identified that relate to other principal intermonomeric bonds. These results confirm and reinforce the conclusion of Bardet et al. [31]: in aged waterlogged wood the

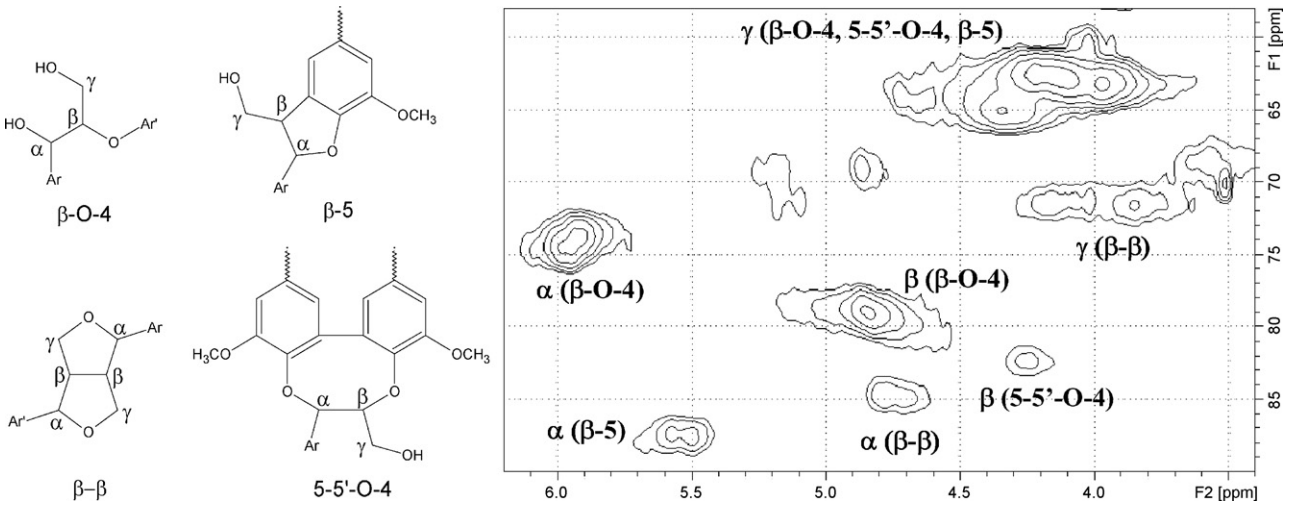


Fig. 3. 2D-HSQC of acetylated lignin sample extracted from sound pine (*Pinus pinaster*) with the interpretation of the predominant intermonomeric bonds. The symbols α, β, γ on HSQC spectra indicate the corresponding atom on the dimeric lignin structure where the H–C cross-peak is observed.

Table 4
The relative amounts of the predominant intermonomeric units are, expressed as "+" marks, where each "+" the three archaeological wood samples and three sound wood samples.

	Pine		Elm		Beech	
	Sound	Archaeological	Sound	Archaeological	Sound	Archaeological
β-O-4	+++++	++++	+++++	++++	+++++	+++
β-5	+++	++	++	+	++	traces
β–β	++	+(+)	++	+(+)	+++	+++
5-5′-O-4	++	n.d.	n.d.	n.d.	n.d.	n.d.

chemical structure of lignin is not heavily modified, and the principal intermonomeric bonds are still present. In the case of lignin extracted from archaeological pine the 5-5′-O-4 unit was not observed.

3.3.2. ^{13}C NMR

In order to better evaluate the changes in the intermonomeric units of lignin extracted from archaeological and sound wood, quantitative ^{13}C NMR analysis was performed by relating the intensity of each characteristic ^{13}C signal (80 ppm for α in β-O-4, 86 ppm for α in β-5, 84 ppm for α in β–β and 80 ppm for β in 5-5′/β-O-4) to that of the methoxyl signal (56 ppm) and multiplied by the average number of methoxyl groups per aromatic ring. The relative amounts of predominant intermonomeric units are reported in Table 4, expressed as a "+" sign, where each "+" means 0.06–0.09 referring 1 the intensity of methoxyl signal. The relative amounts were roughly estimated due to the overlap of the signals.

The results show that in all lignins extracted from archaeological wood there is was a reduction in β-O-4 intermonomeric bonds and a significant reduction in hardwood archaeological lignin (elm and beech) of β-5 intermonomeric bonds. In archaeological pine lignin it is confirmed that the 5-5′-O-4 intermonomeric bond is not detected. We were not able to detect any significant changes in the relative amounts of β–β bonds.

3.3.3. ^{31}P NMR

The lignin extracted from archaeological and sound wood was therefore also analyzed using ^{31}P NMR techniques, following procedures from the literature [33]. With this technique it is possible to distinguish and quantify *p*-hydroxycumaryl, guaiacyl, syringyl and condensed (by a C–C or C–O bond in position 5) free phenolic units, as well as carboxylic acids (Table 5).

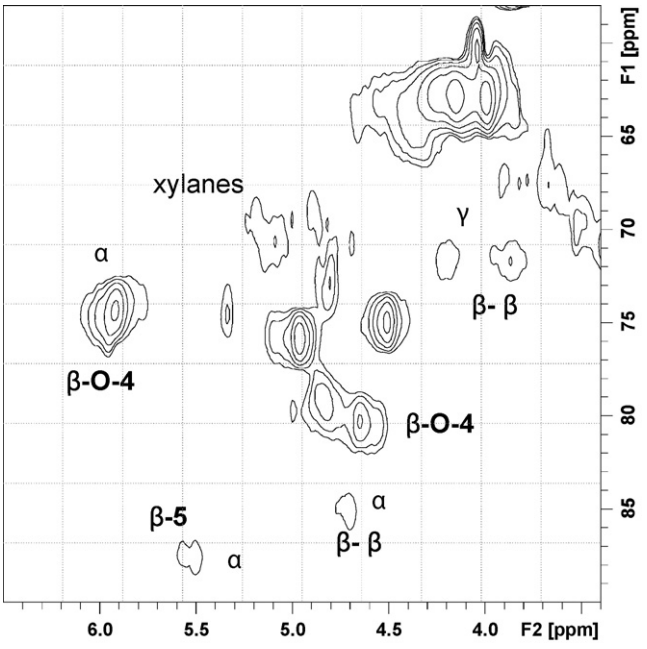


Fig. 4. 2D-HSQC of acetylated lignin sample extracted from archaeological pine.

Table 5
Content values of different free phenols (guaiacyl, syringyl, *p*-hydroxycumaryl, condensed in position 5 and total) and total acidic groups, expressed in mmol g^{-1} of lignin. The maximum standard deviation of the reported data was 2×10^{-2} mmol g^{-1}.

	Pine		Elm		Beech	
	Sound	Arch.	Sound	Arch.	Sound	Arch.
–OH guaiacyl	0.94	1.07	0.90	0.84	0.34	0.35
–OH syringyl	n.d.	n.d.	0.13	0.30	0.30	0.31
–OH *p*-hydroxy cumaryl	0.10	0.24	0.10	0.13	0.10	0.12
Condensed –OH	0.29	0.60	0.23	0.54	0.30	0.33
Total free phenols	1.33	1.91	1.36	1.81	1.04	1.11
Acidic groups	0.24	0.35	0.13	0.40	0.24	0.38

In all cases a significant increase in total free phenolic content and of acidic moieties is observed. These results are in agreement with the data from Py-HDMS-GC/MS, where an increase in free phenol and acidic compounds in three types of archaeological wood was found. The main increase in phenol content was due to condensed phenols (bringing an intermonomeric bond in position 5). The condensed phenols are represented mainly by 5-5′ and 4-O-5 units. The increase in condensed phenols and acidic units is reported in the literature by Crestini and Argyropoulos [50]. This variation can be explained by assuming that the condensed structures are the most stable to oxidation, and by assuming some condensation reactions.

3.3.4. GPC

The effects of ageing on the lignin structure of archaeological waterlogged wood were further elucidated by evaluating the changes in molecular weight distribution in the extracted acetylated lignin, in order to detect a possible increase/decrease in lignin molecular weight.

Estimating the lignin molecular weight distribution (MWD) is complicated: lignins are irregular multiple branched polymers containing various polar functionalities and are insoluble in most

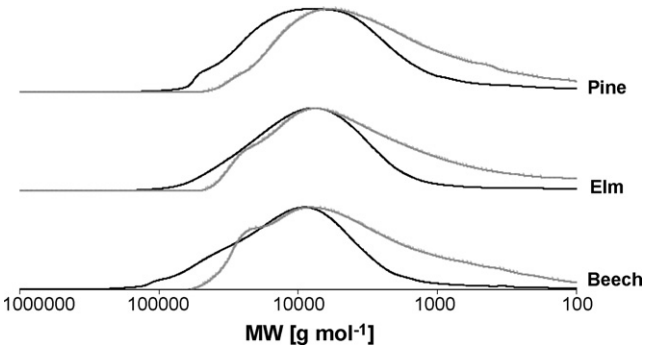


Fig. 5. Gel permeation chromatogram of acetylated lignin from beech, elm and pine. The black line refers to the sound wood samples, the grey line refers to the archaeological wood samples.

common solvents. The acetylation of lignin enhances solubility and allows the use of THF as a solvent, which decreases interactions between lignin chains thus avoiding macromolecular association. Fig. 5 reports the chromatograms obtained by GPC for lignin extracted from sound beech, elm and pine wood (black line) and the corresponding archaeological lignin (grey line). A slight decrease in lignin molecular weight for all the archaeological woods is noted compared to the sound wood. For beech and elm we only observe a loss in high fraction molecular weight, while for pine the decrease in MWD is clearer. In fact it is possible to note a shift in the chromatogram towards the region a lower molecular weight. These results generally demonstrate a partial degradation of lignin in archaeological wood.

4. Conclusions

The chemical structure of lignin in archaeological wood from San Rossore, which after a prolonged period in an aquatic environment have lost most of their original holocellulose content, is still very similar to the chemical structure of sound lignin. This confirms that in anaerobic environments, and in particular in the absence of fungi, the modifications induced in lignin are quite limited.

The use of many complementary techniques based on NMR in conjunction with the results obtained by analytical pyrolysis and GPC enables to highlight minor changes in the polymer structure of lignin. The main difference highlighted by using Py-GC/MS in the presence of HMDS as a silylating reagent of pyrolysis product is the different reactivity towards the derivatizing agent of reference lignin and archaeological lignin. The phenol groups in cinnamyl units of archaeological lignin are derivatized in a much higher yield in the three examined archaeological lignin samples compared to reference lignin. This can be explained by the fact that archaeological lignin has undergone partial depolymerization, with the cleavage of ether intermonomeric bonds and the production of a higher concentration of free phenol groups, which are free to react easily with HMDS. As alcoholic ether bonds are more easily cleaved compared to phenol ether bonds, the cinnamyl alcohols undergo fragmentation and chain shortening, producing the lower molecular weight compounds seen in the chromatogram. The phenolic ether bonds take longer to cleave, and give rise above all to *mono*-TMS cinnamyl alcohols.

The adoption of *in situ* sylilating conditions permits to enhance this specific difference in the reactivity of the two lignins (archaeological and sound), performing the same analysis in the absence of HMDS, on the other hand, does not lead to highlight significant differences between archaeological lignin and reference lignin. The main advantage of Py(HMDS)-GC/MS is that it gives meaningful information in a very short time, avoiding sample manipulation, and with only the need for a minimal amount of sample.

The data provided by Py-GC/MS are confirmed and completed by the detailed NMR investigation, which highlights many aspects of the complex chemical features of lignin including:

- The kinds of intermonomeric bonds, and how some of them are partially cleaved in pine archaeological lignin.
- The amount of methoxy groups and free phenols groups on aromatic rings, and the formation of carboxylic acid functionalities in α position that is also suggested Py-GC/MS profiles.

Moreover, although the GPC of extracted lignin does not give absolute quantitative parameters for assessing the distribution of molecular weight in lignin polymer, due to the absence of appropriate standards, it shows that the partial cleavage of intermonomeric bonds can also be highlighted using a chromatographic approach. This shows shifts, and the formation of shoulders at lower molecular weights in archaeological lignin. This is the first time that the depolymerization of lignin and the cleavage of intermonomeric bonds have been chemically shown as a result of wood degradation in ancient objects.

The most important conclusion from this investigation is that lignin from waterlogged wood samples from the site at San Rossore has been shown to have undergone the cleavage of phenol–ether bonds with the formation of free phenol groups, and oxidation with the formation of carboxyl acid groups. The presence of an increased concentration of carboxylic and free phenol functionalities in the lignin network confers enhanced polarity and cation exchange properties to archaeological wood. This needs to be taken into consideration in terms of its influence on the chemical interaction between waterlogged wood and any consolidating materials that might be used for conservation.

Acknowledgments

The authors wish to thank Dott.ssa G. Giachi (Archaeological Superintendence of Florence, Italy), Prof. I.D. Donato (University of Palermo) and IVALSA (CNR, Florence) for providing samples and for their valuable collaboration. Economic support was provided by the Archaeological Superintendence of Tuscany and by the Italian MIUR funding PRIN Cofin05.

References

[1] P. Hoffmann, M.A. Jones, in: R.M. Rowell, R.J. Barbour (Eds.), Archaeological Wood Properties, Chemistry, and Preservation. Developed from a Symposium Sponsored by the Cellulose Paper and Textile Division at the 196th National Meeting of the American Chemical Society, Los Angeles, California, September 25–30, 1988, American Chemical Society Washington, 1990, pp. 35–65.
[2] R.A. Blanchette, Int. Biodeter. Biodegr. 46 (2000) 189–204.
[3] P. Hoffmann, La Chimica e l'Industria 88 (2006) 96–101.
[4] F.D. Geoffrey, T. Nilsson, A.P. Singh, Can. J. Microbiol. 33 (1987) 943–948.
[5] D.W. Grattan, R.W. Clarke, in: C. Pearson (Ed.), Conservation of Marine Archaeological Objects, Butterworths, London, 1987, pp. 164–206.
[6] M. Sandström, F. Jalilehvand, I. Persson, U. Gelius, P. Frank, I. Hall-Roth, Nature 415 (2002) 893–897.
[7] G. Giachi, F. Bettazzi, S. Chimichi, G. Staccioli, J. Cult. Heritage 4 (2003) 75–83.
[8] J. Ralph, K. Lundquist, G. Brunow, F. Lu, H. Kim, P.F. Schatz, J.M. Marita, R.D. Hatfield, S.A. Ralph, J.H. Christensen, W. Boerjan, Phytochem. Rev. 3 (2004) 29–60.
[9] D. Feldman, Wood—chemistry, ultrastructure, reactions, by D. Fengel and G. Wegener, Walter de Gruyter, Berlin and New York, 1984, 613 pp. Price: 245 DM, J. Polym. Sci.: Polym. Lett. Ed. 23 (1985) 601–602.
[10] F. Martín, J.C. del Río, F.J. González-Vila, T. Verdejo, J. Anal. Appl. Pyrol. 35 (1995) 1–13.
[11] S. Reale, A. Di Tullio, N. Spreti, F. De Angelis, Mass Spectrom. Rev. (2004) 87–126.
[12] M.F. Nonier, N. Vivas, N. Vivas de Gaulejaca, C. Absalon, P. Soulié, E. Fouquet, J. Anal. Appl. Pyrol. 75 (2006) 181–193.
[13] K.-i. Kuroda, A. Izumi, B.B. Mazumder, Y. Ohtani, K. Sameshima, J. Anal. Appl. Pyrol. 64 (2002) 453–463.
[14] D.J. Clifford, D.M. Carson, D.E. McKinney, J.M. Bortiatynski, P.G. Hatcher, Org. Geochem. 23 (1995) 169–175.
[15] T. Hosoya, H. Kawamoto, S. Saka, J. Anal. Appl. Pyrol. 77 (2006) 121–126.
[16] K.-I. Kuroda, J. Anal. Appl. Pyrol. 56 (2000) 79–87.
[17] Á.T. Martínez, M. Speranza, F.J. Ruiz-Dueñas, P. Ferreira, S. Camarero, F. Guillén, M.J. Martínez, A. Gutiérrez, J.C. del Río, Int. Microbiol. 8 (2005) 195–204.
[18] C.H. Vane, Int. Biodeter. Biodegr. 51 (2003) 67–75.
[19] M.C. Terron, M.L. Fidalgo, G.C. Galletti, A.E. Gonzalez, J. Anal. Appl. Pyrol. 33 (1995) 61–75.
[20] V. Vinciguerra, A. Napoli, A. Bistoni, G. Petrucci, R. Sgherzi, J. Anal. Appl. Pyrol. 78 (2007) 228–231.
[21] J.C. del Río, A. Gutiérrez, M.J. Martínez, A.T. Martínez, J. Anal. Appl. Pyrol. 58–59 (2001) 441–452.
[22] H. Yang, Y. Huang, Q. Leng, B.A. Le Page, C.J. Williams, Rev. Palaeobot. Palynol. 134 (2005) 237–256.
[23] C.-M. Popescu, G. Dobele, G. Rossinskaja, T. Dizhbite, C. Vasile, J. Anal. Appl. Pyrol. 79 (2007) 71–77.
[24] P.F. van Bergen, I. Poole, T.M. Ogilvie, C. Caple, R.P. Evershed, Rapid Commun. Mass Spectrom. 14 (2000) 71–79.
[25] V. Richards, N. West, The Use of Pyrolysis Gas chromatography Mass Spectrometry to Study the Extent of Degradation of Waterlogged Wood, Proceedings of the 8th ICOM Group on Wet Organic Archaeological Materials Conference, Stockholm, 2001.
[26] M.P. Colombini, M. Orlandi, F. Modugno, E.-L. Tolppa, M. Sardelli, L. Zoia, C. Crestini, Microchem. J. 85 (2007) 164–173.

[27] J.B. Lambert, C.E. Shawl, J.A. Stearns, Chem. Soc. Rev. 29 (2000) 175–182.
[28] T.R. Filley, P.G. Hatcher, W.C. Shortle, R.T. Praseuth, Org. Geochem. 31 (2000) 181–198.
[29] M.J. Simpson, P.G. Hatcher, Org. Geochem. 35 (2004) 923–935.
[30] C. Saiz-Jimenez, J.J. Boon, J.I. Hedges, J.K.C. Hessels, J.W. De Leeuw, J. Anal. Appl. Pyrol. 11 (1987) 437–450.
[31] M. Bardet, M.F. Foray, Q.-K. Trân, Anal. Chem. 74 (17) (2002) 4386–4390.
[32] C. Canevali, M. Orlandi, L. Zoia, R. Scotti, E.-L. Tolppa, J. Sipila, F. Agnoli, F. Morazzoni, Biomacromolecules 6 (2005) 1592–1601.
[33] A. Granata, D.S. Argyropoulos, J. Agric. Food Chem. 43 (1995) 1538–1544.
[34] J. Ralph, J.M. Marita, S.A. Ralph, R.D. Hatfield, F. Lu, R.M. Ede, J. Peng, S. Quideau, R.F. Helm, J.H. Grabber, H. Kim, G. Jimenez-Monteon, Y. Zhang, H.-J.G. Jung, L.L. Landucci, J.J. MacKay, R.R. Sederoff, C. Chapple, A.M. Boudet, in: D.S. Argyropoulos (Ed.), Advances in Lignocellulosics Characterization, TAPPI Press, Atlanta, 1999, pp. 55–108.
[35] H. Koskela, I. Kilpeläinen, S. Heikkinen, J. Magn. Reson. 174 (2005) 237–244.
[36] G. Giachi, B. Pizzo, I. Santoni, Gradus 3 (2008) 91–103.
[37] G. Giachi, Gradus 3 (2008) 17–24.
[38] T.-F. Yeh, T. Yamada, E. Capanema, H.-M. Chang, V. Chiang, J.F. Kadla, J. Agric. Food Chem. 53 (2005) 3328–3332.
[39] T. Yokoyama, J.F. Kadla, H.M. Chang, J. Agric. Food Chem. 50 (2002) 1040–1044.
[40] A. Björkman, Sven. Papperstidn. 59 (1956) 477–485.
[41] B. Holmbom, P. Stenius, in: P. Stenius (Ed.), Forest Products Chemistry, Fapet Oy, Jyväskylä, 2000, pp. 105–169.
[42] M. Girardin, M. Metche, J. Chromatogr. A 264 (1983) 155–158.
[43] E. Adler, Wood Sci. Technol. 11 (1977) 169–218.
[44] M. Drumond, M. Aoyama, C.L. Chen, D. Robert, J. Wood Chem. Technol. 9 (1989) 421–441.
[45] S.A. Ralph, J. Ralph, L.L. Landucci, NMR database of lignin and cell wall model compounds, 2004.
[46] I. Kilpelaeinen, J. Sipilae, G. Brunow, K. Lundquist, R.M. Ede, J. Agric. Food Chem. 42 (1994) 2790–2794.
[47] L.L. Landucci, Holzforschung 39 (1985) 355–359.
[48] M.E. Himmel, K. Tatsumoto, K.K. Oh, K. Grohmann, D.K. Johnson, H.L. Chum, in: W.G. Glasser, S. Sarkanen (Eds.), Lignin Properties and Materials, American Chemical Society, Washington, 1989, p. 82.
[49] T.R. Filley, G.D. Cody, B. Goodell, J. Jellison, C. Noser, A. Ostrofsky, Org. Geochem. 33 (2002) 111–124.
[50] C. Crestini, D.S. Argyropoulos, in: D.S. Argyropoulos (Ed.), Oxidative Delignification Chemistry: Fundamentals and Catalysis, ACS Books, Washington, 2001, pp. 373–390.

Talanta 80 (2009) 71–83

Contents lists available at ScienceDirect

Talanta

journal homepage: www.elsevier.com/locate/talanta

Advanced combined application of μ-X-ray diffraction/μ-X-ray fluorescence with conventional techniques for the identification of pictorial materials from Baroque Andalusia paintings

L.K. Herrera[a,*], S. Montalbani[b], G. Chiavari[b], M. Cotte[c,d], V.A. Solé[c], J. Bueno[e,f], A. Duran[a], A. Justo[a], J.L. Perez-Rodriguez[a]

[a] Materials Science Institute of Seville, CSIC-Seville University, Avda Americo Vespucio 49, 41092 Seville, Spain
[b] Univ Bologna, CIRSA, Chem Lab, Via S Alberto 163, I-48100 Ravenna, Italy
[c] European Synchrotron Radiation Facility, BP 220, 38043 Grenoble Cedex, France
[d] Centre de Recherche et de Restauration des Musées de France (C2RMF), CNRS UMR 171, Palais du Louvre, Porte des Lions, 14, quai François Mitterrand, 75001 Paris, France
[e] Faculty of Fine Arts, University of Seville, Spain
[f] Pedrela Painting Restorers, Spain

ARTICLE INFO

Article history:
Received 15 October 2008
Received in revised form 5 June 2009
Accepted 9 June 2009
Available online 21 June 2009

Keywords:
Works of art
Pigments
Cultural heritage
XRD
SEM/EDX
FT-IR
PY–GC/MS
Synchrotron radiation
μ-X-ray diffraction/μ-X-ray fluorescence

ABSTRACT

The process of investigating paintings includes the identification of materials to solve technical and historical art questions, to aid in the deduction of the original appearance, and in the establishment of the chemical and physical conditions for adequate restoration and conservation. In particular, we have focused on the identification of several samples taken from six famous canvases painted by Pedro Atanasio Bocanegra, who created a very special collection depicting the life of San Ignacio, which is located in the church of *San Justo y Pastor* of Granada, Spain. The characterization of the inorganic and organic compounds of the textiles, preparation layers, and pictorial layers have been carried out using an XRD diffractometer, SEM observations, EDX spectrometry, FT-IR spectrometry (both in reflection and transmission mode), pyrolysis/gas chromatography/mass spectrometry and synchrotron-based μ-X-ray techniques. In this work, the advantages over conventional X-ray diffraction of using combined synchrotron-based μ-X-ray diffraction and μ-X-ray fluorescence in the identification of multi-layer paintings is demonstrated.

© 2009 Elsevier B.V. All rights reserved.

1. Introduction

Analytical methods are an essential requirement in the cultural heritage field, as they provide the means to understand the objects under investigation. By identifying materials (such as pigments, binders, mixtures, and processes), we can reach back through time and develop a deeper understanding of the craftsmanship and technology used. Analytical methods allow us to contribute to the blooming activity at the interface between art and science. Contributing to the development of diagnostic techniques is necessary for practical applied art conservation. The techniques concerned include: scanning electron microscopy (SEM), energy dispersive X-ray spectrometry (EDX), μ-X-ray analyses (including synchrotron radiation μ-X-ray diffraction (μXRD) and μ-X-ray fluorescence (μXRF)), Fourier transform-infrared spectrometry (FT-IR), and analytical pyrolysis in-line with gas chromatography and mass spectrometry (PY–GC/MS) [1–3]. The analytical methods used in this field of research are identical to those used at the cutting edge of modern materials science. Methods developed for advanced physics and chemistry can be applied to ancient and modern materials, as the problems encountered in the areas of advanced technology and cultural heritage are surprisingly similar. Depending on the information required, one might use a combination of non-invasive techniques; however, one should aim at the maximization of information and the minimization of the sample consumed volume [4,5]. The use of non-invasive techniques is increasing due to the improved development of instruments (e.g. able to determine the elemental and mineral composition of the micrometric multilayers of micro-samples) [6].

Analytical studies of paintings performed at the microscopic and at molecular level are the focus of this paper. Microscopic and molecular studies are carried out on paint samples derived from the painting itself. These samples are unique and in limited supply. Assuming that such samples are representative of an area

* Corresponding author.
E-mail address: lkaren@icmse.csic.es (L.K. Herrera).

0039-9140/$ – see front matter © 2009 Elsevier B.V. All rights reserved.
doi:10.1016/j.talanta.2009.06.032

under study, valuable general information about the painting can be deduced. The information can be maximized by sequential analyses using different complimentary techniques.

Synchrotron radiation has become an increasingly important tool for research in the fields of art, archaeometry, and the conservation of objects of cultural heritage significance. Synchrotron is a source of intense, bright light of variable wavelength; the principal properties of synchrotron radiation are as follows: high flux and brilliance, ability to produce a fast data collection and the possibility to use small sample size, small beam footprint: it enables area mapping at millimeter to micron length-scale. The wavelength tunability and the energy region can be selected to suit the problem at hand [7–10]. Synchrotron techniques are particularly suited to non-destructive or to the micro-characterization of different materials including organic and inorganic materials, either amorphous or crystalline. New developments in synchrotron radiation techniques result in a significant advance to study the samples at micrometer length scale through the combination of different non-destructive techniques. The most employed till now have been synchrotron X-ray fluorescence and diffraction and, to a lesser extent, small angle scattering (on wood, bone and hair) and infrared microscopy. The synchrotron beam can be focused in sub micrometric spots, allowing the examination of very small samples. The list of artwork studied by using SR is made up of a large variety of materials [7,11].

This article is intended to illustrate the chemical description of the organic and inorganic components of the stratigraphy sequence using, in parallel, the recent applications of microanalytical methods using synchrotron radiation and the information supplied by laboratory techniques. This is exemplified by the identification of pigments and binders in six famous canvases painted by Bocanegra (XVIth century).

2. Experimental

2.1. Historical context

The first reports of Pedro Atanasio Bocanegra as a painter are from 1661 [12]. He included in his paintings many elements of his master, Alonso Cano.

According to Gomez Moreno [12], the Bocanegra paintings of the *San Justo y Pastor* of the church that represents the passages of the *S. Ignacio of Loyola life* (1491–1540) were carried out in two steps. In the first, Bocanegra painted three canvases: "*San Ignacio herido a las puertas de Pamplona*", "*La Aparición de San Pedro*" and "*San Ignacio azotado por un armenio*". In the second step, he created the other three paintings between 1670 and 1671, where these are considered the most important works of oriental Andalusia painting [13]. These canvas paintings are "*La Visión de la Storta*", "*La Aparición de la Trinidad a San Ignacio*" and "*S. Ignacio enviando a predicar a S. Fco. Javier and S. Fco. de Borja*". In these paintings, the author shows technical advances and a greater intensity of color that is reminiscent of the art of Valdes Leal [14]. The painting details are described in Fig. 1. The six paintings are a complex multi-layered composition of organic and inorganic compounds.

2.2. Sampling

The samples were collected by taking small samples close to areas that were already damaged. Twenty samples were careful extracted from different zones of the paintings using a scalpel. The obtained samples were a representative collection of white, red, and blue colors.

Sample preparation is often a tricky point for the study of micrometric fragments of paintings [15]. It may be difficult to carry out all the experiments of a unique sample; conversely, when the quantity of painting fragment is enough, different sample preparations may be followed to fit the technical requirements of each analytical technique. Three types of sample preparation were performed.

Conventional cross-section. The samples were prepared as cylinder moulds and were embedded in epoxy resin as follows: The paint piece was placed on top of the hardened block and carefully covered with resin, and then cast and left to cure for 24 h at room temperature. Next, the sample was cut to expose a face showing the cross-section of the paint layer. Finally, the surface was carefully polished on a rotating disc covered with abrasive SiC paper which spanned a grain size from 800 to 1200 mesh, and then finished with a cloth [16,17]. This method is useful for observation with an optical microscope, SEM/EDX, or FT-IR spectrometer that requires a more careful preparation in terms of surface polish.

Thin transversal cuts. Samples were embedded in a resin (Leica Historesin) to prepare thin sections with a microtome. Several thicknesses were tested, and 20–30 μm was chosen as the most appropriate thickness [18] for SR μXRF/μXRD analyses.

Raw fragments of the samples. Small fragments of the samples were ground to a powder for examination by conventional XRD and for PY–GC/MS [18,19].

Single fibres (a few micrometers in diameter) were carefully extracted from the canvas for textile identification by XRD.

2.3. Analytical techniques: instruments and methods

Observations of the cross-sections were performed by *optical microscopy* using a stereo microscope (Nikon HOPITHOT) with objectives of 20×, 50×, 100×, 200× and equipped for microphotography using a digital camera (Nikon COOLPIX 4500), which was also used to identify the stratigraphy sequences of the different paint cross-sections. The inorganic pigments have been characterized as cross-sections on a Jeol model JSM 5400 *SEM*. Analyses of elemental compositions of the different painting layers were obtained using *EDX* on a Link ISIS X-ray energy dispersive spectrometer equipped with an ultra-thin beryllium window, using an accelerating voltage of 20 keV. The cross-sections were coated with gold film before the SEM/EDX investigations. X-rays analyzed with an energy dispersive detector (EDX) result in a characterization of different chemical elements in the paint cross-section.

The crystalline phases were characterized by *X-ray diffraction* (*XRD*), using a Siemens diffractometer, model Kristalloflex D-5000 using Cu $K\alpha_1$ radiation (40 kV, 30 mA), a diffracted-beam graphite monochromator and a scintillation counter. Measurements were carried out on powders of the sample in the range of $3 < 2\theta < 65^\circ$ with steps of 0.05° and a 2 s counting time. Subsequently, the EVA data bank of standard X-ray powder diffraction patterns was used for phase identification. For textile identification by XRD, the fibres were introduced into a 0.3 mm glass capillary and these were then used to collect X-ray diffraction patterns in transmission mode on a Siemens D5000 dual diffractometer, equipped with a Ge monochromator in the incident beam and Cu $K\alpha_1$ radiation.

Fourier transformed-infrared spectrometry (*FT-IR*) is relevant for the identification of organic compounds, but the surface of the cross-section must be totally planar in order to obtain good reflections [20]. Unfortunately, when organic compounds are mixed with large amounts of inorganic matter, such as in an argillaceous earth layer or lead white, the peaks representative of the inorganic composition predominate in the FT-IR spectrum. The organic constituents are often not visualized with FT-IR, as their reflectance and relative concentrations are low [18], and the signal is reduced in a heterogeneous layer due to scattering of the infrared light within the cross-section. The Kramer–Krönig transformation is applied to the specular reflectance spectrum to transform it into an absorbance-like spectrum, which is more workable and easier to interpret. The *FT-IR spectra* were registered on a Nicolet



Fig. 1. Bocanegra paintings. (a) "San Ignacio herido en las puertas de Pamplona", (b) "Aparición de San Pedro a San Ignacio para curarle", (c) "San Ignacio azotado por un armenio a su vuelta del Monte de los Olivos, consolado por Cristo", (d) "San Ignacio envía a predicar a San Francisco Javier a las Indias y a San Francisco de Borja a Occidente", (e) "Visión de La Storta, camino de Roma, en que se aparece la Trinidad a San Ignacio", and (f) "Aparición de la Trinidad a San Ignacio".

510 spectrometer equipped with a nitrogen-cooled MCT detector and an Olympus optical microscope. The spectra were collected in reflectance mode, in the 4000–700 cm^{-1} range, with a resolution of 4 cm^{-1}. The final format of the data was in absorbance, where the background was collected through a gold film substrate. For each spectrum, at least 100 scans were accumulated. Peak positions were determined using the Nicolet Omnic software (based on a polynomial least squares method). The advantage of infrared spectroscopy is to simultaneously obtain information on both organic and mineral compounds of the painting layers.

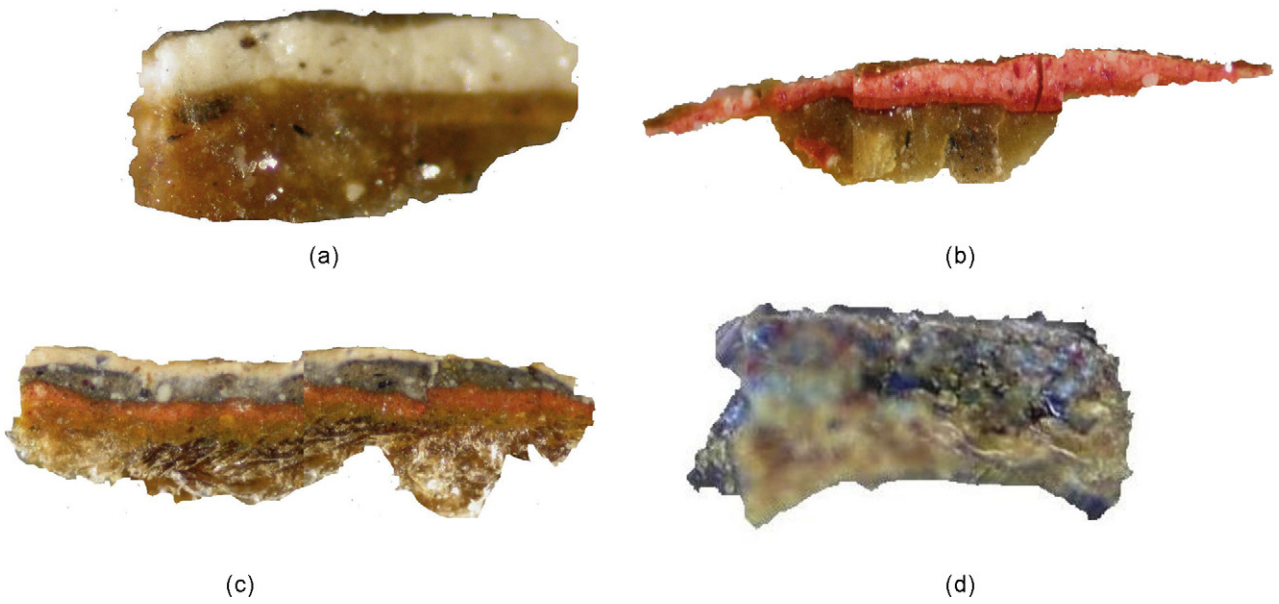


Fig. 2. Images of the conventional cross-section of paint samples (100×) (a) originating from Trinidad's dress in the "Visión de La Storta", (b) originating from San Ignacio's dress in the "Aparición de San Pedro a San Ignacio para curarle", (c) originating from San Ignacio's dress in the "San Ignacio azotado por un Armenio", and (d) originating from the dress in the San Ignacio Herido en las Puertas de Pamplona.

2.3.1. Synchrotron-based μ-X-ray diffraction and μ-X-ray fluorescence techniques

μ-X-ray diffraction and μ-X-ray fluorescence were performed at the ID18F beamline, at the ESRF. This beamline is a high-energy multi-technique X-ray microscope. The double-crystal monochromator, equipped with both Si[1 1 1] and Si[3 1 1] crystals, offers a wide energy range (6–70 keV) for optimal excitation conditions of a broad range of elements [21]. In this experiment, the excita-

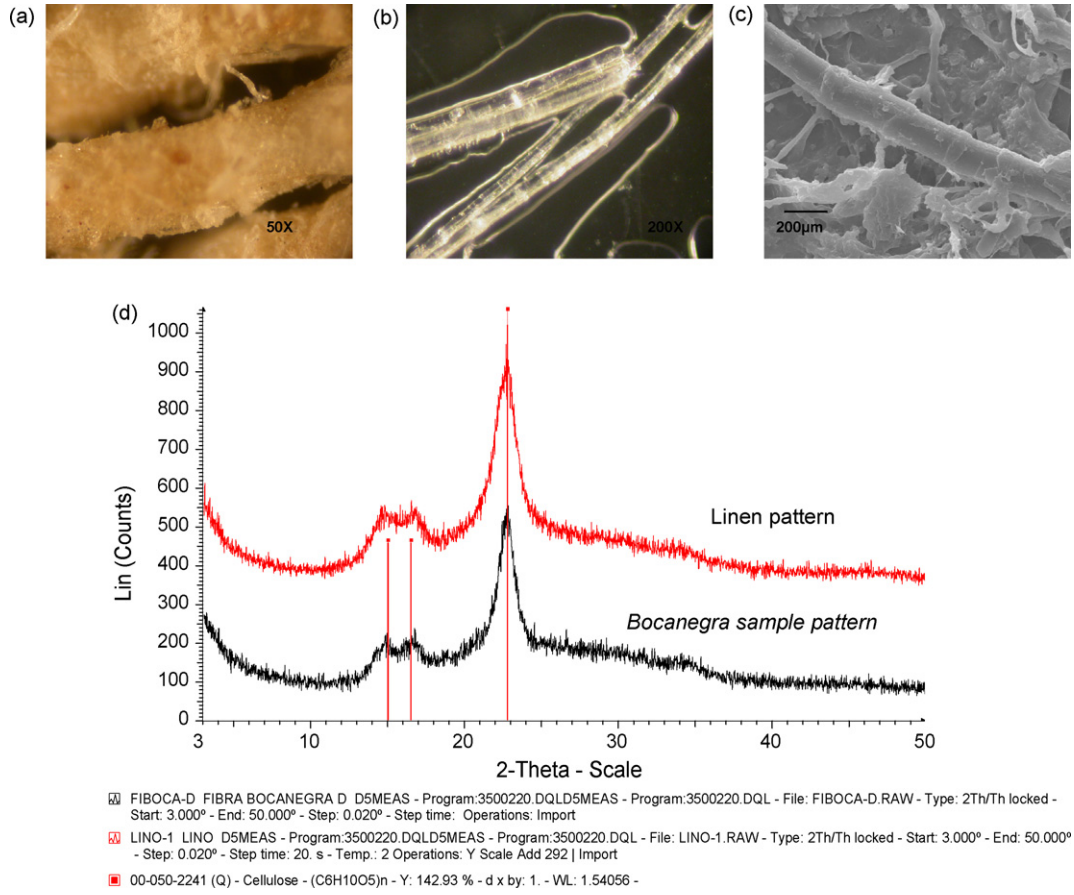


Fig. 3. Optical micrographs (a) without any clearing treatment, (b) the organic compounds were removed by water with continuous heating for 24 h, (c) SEM image of the fibres of Bocanegra paintings, and (d) X-ray diffractogram of the fibres. Linen pattern and Bocanegra fibre pattern.

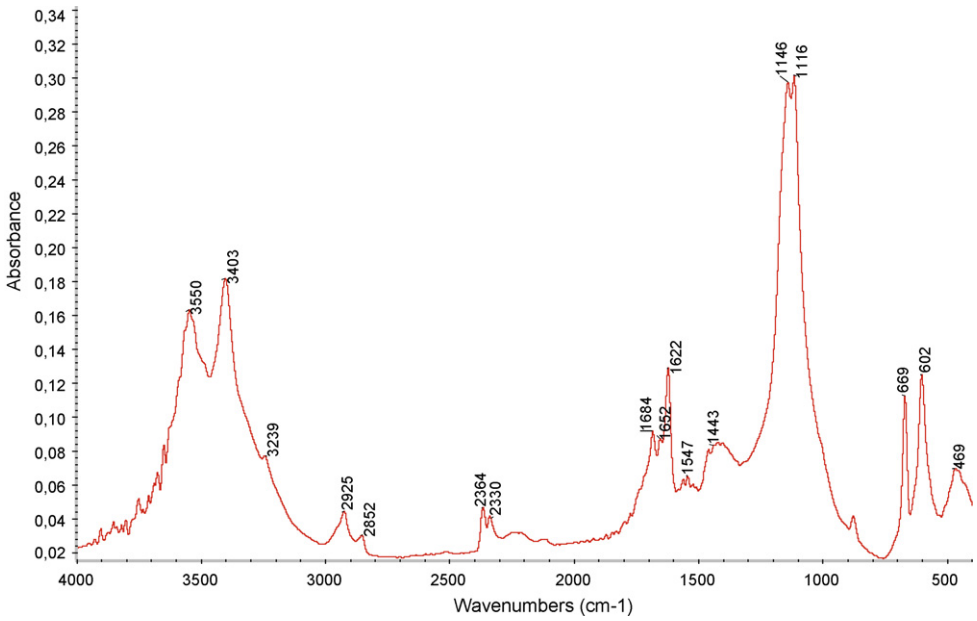


Fig. 4. FT-IR spectra corresponding to the preparation layer of the Bocanegra painting sample.

tion energy was fixed at 28 keV, corresponding to a wavelength of 0.44281 Å. The acquisition time was 20 s per pattern and the beam was focussed down to 15 μm (horizontal) × 1 μm (vertical). A two-dimensional CCD based X-ray detector (refined detector distance 134.1967 mm) was used to collect X-ray diffraction patterns in transmission mode. The X-ray fluorescence spectra were simultaneously detected with a Si(Li) detector. For these measurements, thin transversal cuts were mounted vertically, between two foils of ultralene, and the whole set was raster-scanned horizontally and vertically to obtain two-dimensional images. Thin transversal cuts were oriented horizontally such that the best resolution of the beam (1 μm, vertical) was aligned with the axis of maximum sample heterogeneity, whereas the average in the horizontal direction (15 μm) was obtained over the rather homogeneous colored layer. Three vertical line scans were acquired in each painting cross-section. X-ray fluorescence spectra were treated with PyMCA code [22] and used to identify the elemental composition of the different layers of the samples. In this program, a Levenberg–Marquardt algorithm is implemented to fit the spectra with constraints on the fitting parameters. A complete emission line series is fitted by taking into account theoretical line emission energies and theoretical energy ratios corrected by the experimental conditions (detector characteristics, detection geometry, matrix composition, excitation energy, etc.). A more detailed description of this code is given in [22]. The fitting configuration used to fit the average spectrum of a map is applied to each pixel of the 2D map to calculate the different elemental maps through a batch treatment. For each 2D X-ray diffraction pattern, the Debye–Scherrer diffraction rings were unwrapped and integrated versus the azimuthal angle to produce a 1D diffraction pattern using the ESRF package Fit2D [23]. The set of data thus generated has a format similar to fluorescence data, with a 1D diffraction pattern for each pixel.

Analytical pyrolysis was performed in the Chemical Department of Bologna University. Analytical pyrolysis, on-line with GC and mass spectrometry (PY–GC/MS), was used to generate a qualitative characterization of the organic components in a complex mixture such as the painting layers [24]. PY–GC/MS was carried out at 600 °C for 10 s at the maximum heating rate using a CDS pyroprobe-heated filament pyrolyzer (CDS, Oxford, USA) directly connected to the injection port of a Varian 3400 gas chromatograph coupled to a Saturn II ion-trap mass spectrometer (Varian Analytical Instruments, Walnut Creek, USA). A Supelco SPB-5 capillary column (30 m, 0.32 mm i.d., 0.25 μm film thickness) was used with a temperature programmed from 50° (held for 10 min) to 300 °C at 5 °C/min step intervals, with helium as the carrier gas. The temperature of the split/splitless injector and the PY–GC/MS interface were kept at 250 °C. Mass spectra were recorded at 1 scan/s under electron impact at 70 eV in the mass range of 45–650 *m/z*. Structural assignment of the pyrolytical fragments was based on matching with the NIST mass spectra library. To improve the gas chromatographic behaviour of polar pyrolytic fragments, such as carboxylic or dicarboxylic acids, 10 μl of tetramethylammonium hydroxide solution (TMAH 25% (w/w) in water) was added to the solid sample (few micrograms) before the pyrolysis. The study of the pyrogram, a gas chromatogram of the fragments of the volatile compounds of the sample, gives an indication about the organic chemical nature of the paint layer samples.

Table 1
Analyses of the preparation layer of the six samples of the six paintings.

Painting	Sample	EDX	Phase identification (XRD)	Phase identification (SR μXRD)
1	3	C, O, Mg, Al, S, Si, K, Ca, Fe		
2	6	C, O, Mg, Al, Si, S, K,Ca, Fe	Gypsum	Calcite
3	8	C, O, Mg, Al, Si, S, K, Ca, Fe	Anhydrite	Quartz
4	1	C, O, Mg, Al, Si, S, K, Ca,Fe		Goethite
5	11	C, O, Mg, Al, Si, S, K, Ca, Fe		Gypsum
6	4	C, O, Mg, Al, Si, S, K,Ca, Fe		

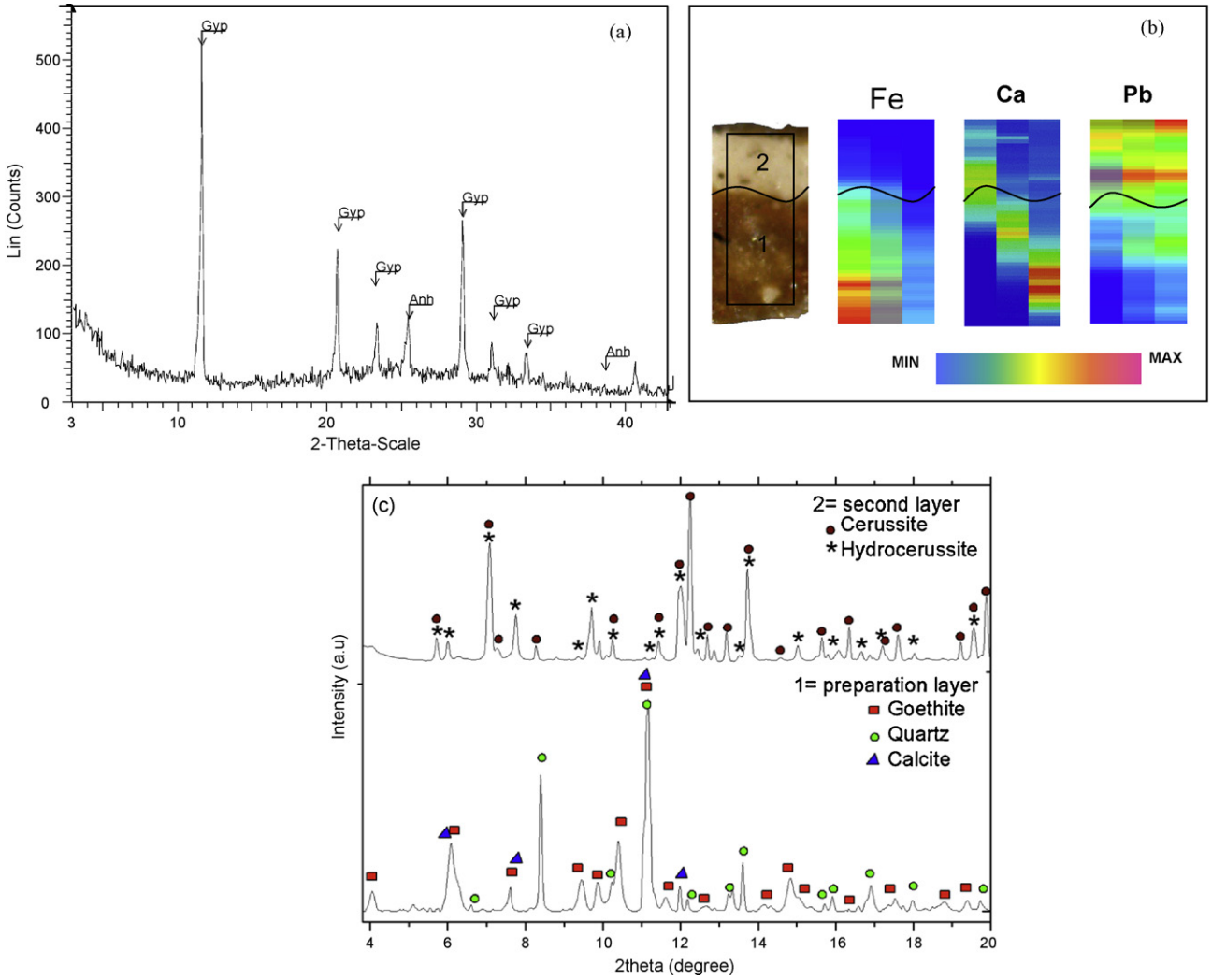


Fig. 5. (a) The XRD pattern of the powder total sample whose peaks can be attributed the presence of gypsum (Gyp), calcite (Cal) and anhydrite (Anh). (b) μXRF elemental mapping of the first layer: calcium and iron; elemental mapping of second layer: lead. (c) SR μXRD of the first layer: goethite, calcite and quartz. SR μXRD of the second layer: cerussite and hydrocerussite.

3. Results and discussion

Fig. 2 depicts the light-optical micrograph of the different samples taken from (a) "*San Ignacio azotado por un armenio*", (b) "*La Visión de la Storta*", (c) "*La Aparición de San Pedro*" and (d) "*San Ignacio Herido en las Puertas de Pamplona*" and the information gained concerns mainly the sequence and the thickness of the paint layers and the distribution of the pigments.

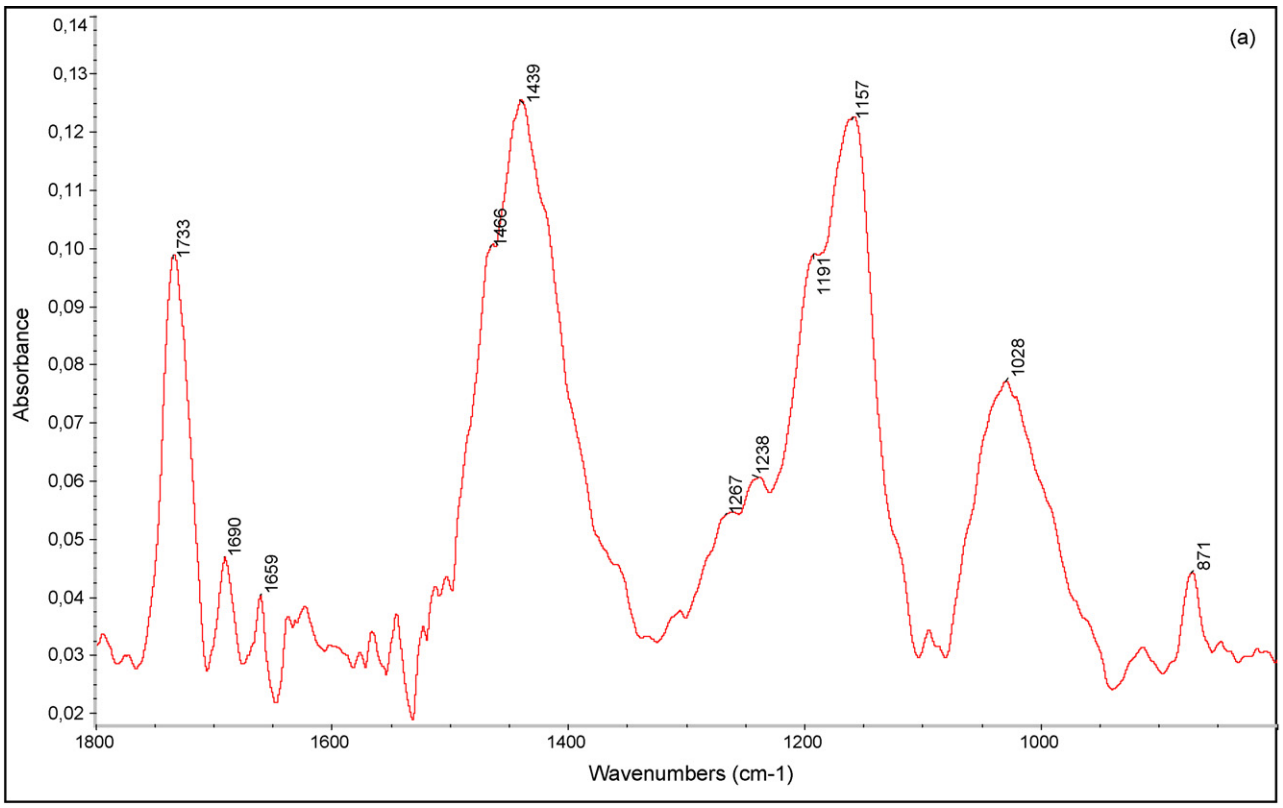
3.1. Textile identification

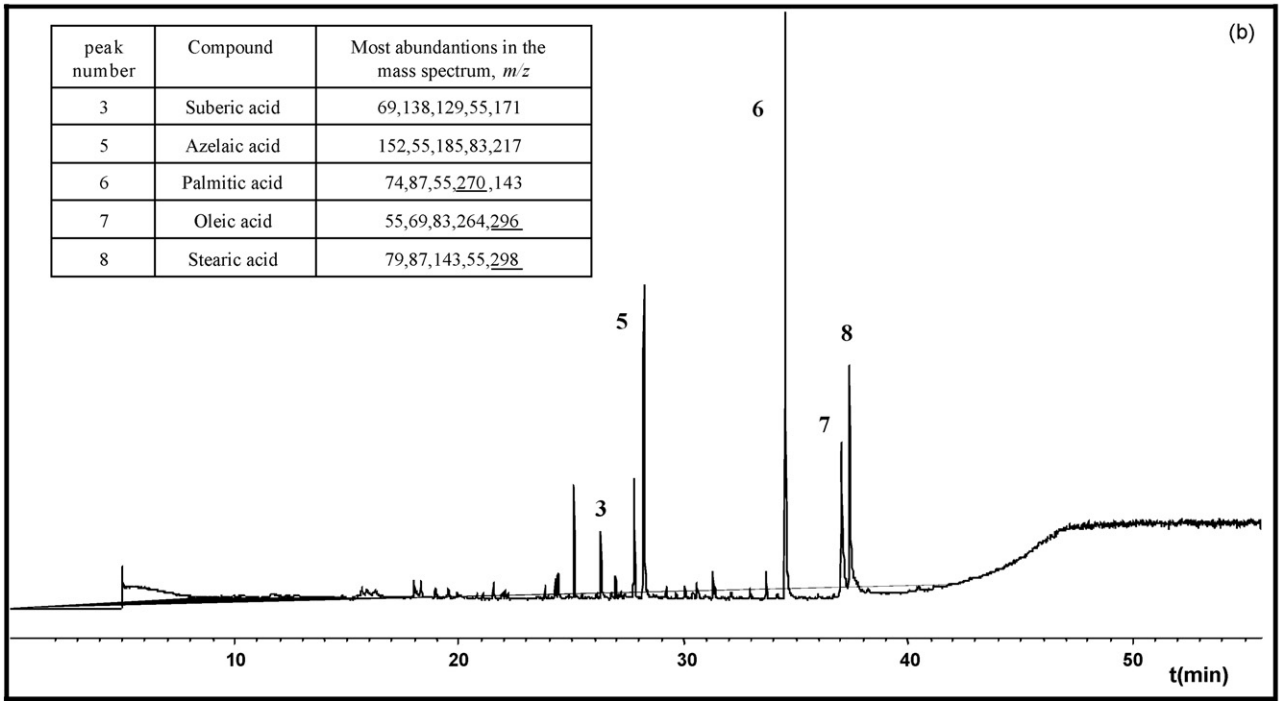
The morphological studies of fibres were realized using optical and scanning electron microscopy. SEM images of single fibres from textile fragments are shown in Fig. 3a and b. The fibre has a diameter of 16.8–16.9 μm, which, together with its morphology, is a very typical for linen (Fig. 3c) [25]. The XRD diffractograms of the fibre obtained from the painting and linen fibre used as a standard are included in Fig. 3d. The XRD pattern of the fibre sample recorded for 2θ in the range of 3–50° revealed pronounced Bragg peaks at 2θ values of around 15.2–16.6° and 22.8°, indicating the presence of a cellulose crystalline phase. The linen used in these canvases contains a greater proportion of lignified material that has survived the retting process. This factor imparts strength and color, but makes the linen more prone to deterioration. Factors that contribute to the deterioration of canvas can be summarized as follows: light, external pollution, and, to a lesser extent, the volatile acids trapped within a frame enclosure.

These results show that Bocanegra used a traditional canvas support that normally consisted of stretched linen fabric, onto which was brushed an aqueous glue, which will be discussed later. Studies of paper and linen show that the oxidation products of cellulose are carboxylic acids, which can catalyse and promote the hydrolysis of cellulose [26]. However, the fibres studied in this work have not suffered from high alteration as indicated by the presence of crystalline phases of cellulose in the XRD patterns.

Table 2
Analyses of the third white layer of the six samples of the six paintings.

Painting	Sample	EDX	Pigment identification by SR μXRD
1	3	C, O, Pb, S, Ca	Lead white (cerussite, hydrocerussite), calcium carbonate
2	6	C, O, Pb, Ca, Fe, Si	
3	8	C, O, Pb, Ca	
4	1	C, O, Pb, Ca, Si, K, Fe	
5	11	C, O, Pb, Ca	
6	4	C, O, Pb, Ca	





peak number	Compound	Most abundantions in the mass spectrum, *m/z*
3	Suberic acid	69,138,129,55,171
5	Azelaic acid	152,55,185,83,217
6	Palmitic acid	74,87,55,270,143
7	Oleic acid	55,69,83,264,296
8	Stearic acid	79,87,143,55,298

Fig. 6. (a) FT-IR spectra corresponding to: top pictorial layer, that shows the presence of bands of silicates (1028 cm^{-1}), carbonates (1439 and 1466 cm^{-1}), and drying oils (1733 and 1157 cm^{-1}). (b) Reconstructed ion chromatogram obtained from pyrolysis/methylation of Bocanegra painting sample. Numbers on top of peak refer to table (mass spectra characteristics of compounds evolved from pyrolysis methylation and structural attribution to peak numbers).

3.2. Identification of preparation layers

The preparation layer of all 20 samples is composed of gypsum, argillaceous earth, iron oxides and animal glue mixed in different proportions. Gypsum was confirmed by FT-IR spectroscopy (Fig. 4) showing, respectively, the stretching and bending absorptions of SO_4^{-2} groups at 1146–1116 cm^{-1}, the water of hydration (ν O–H at 3403 and 3547 cm^{-1}, and the δ O–H at 1684 and 1622 cm^{-1}) and animal glue was suspected by the protein bands (3239 cm^{-1}-stretching ν N–H, 1652 cm^{-1}-stretching ν C=O amide I and 1547 cm^{-1} bending δ N–H amide II). Moreover, not all elements can be detected with EDX, because the detection threshold is relatively high and the X-

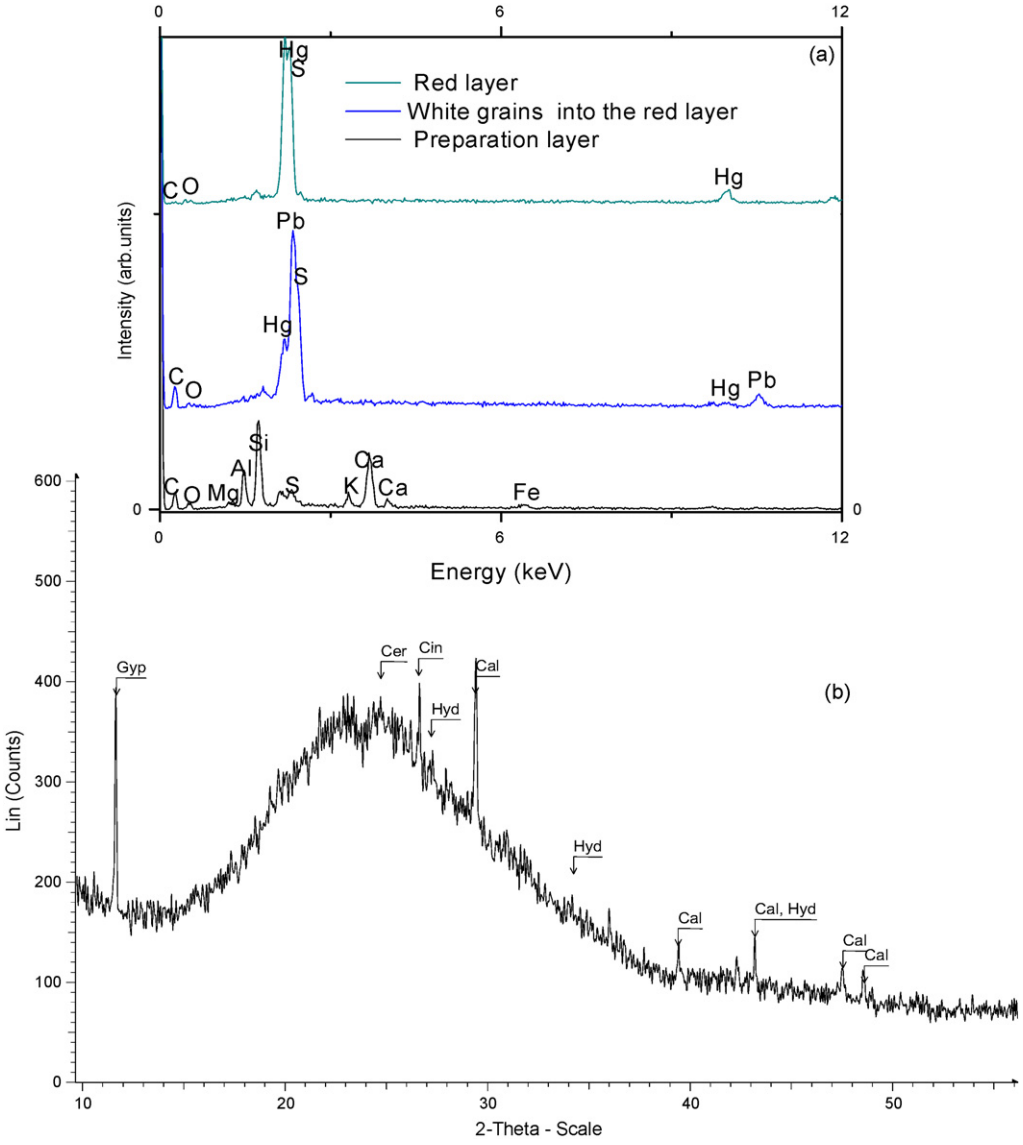


Fig. 7. (a) EDX spectra of the different three layers of the cross-section originating from red San Ignacio's dress and (b) the X-ray diffraction pattern of powder total sample obtained with under incidence angle 1° (θ), whose peaks can be attributed the presence of gypsum (Gyp), cerussite (Cer), hydrocerussite (Hyd), calcite (Cal) and cinnabar (Cin).

ray energies of several elements overlap. In general, light elements in low concentrations are hard to detect with EDX. EDX is not a suitable technique for the detection of trace elements in pigments because their concentration is often below the detection limit (the detection limit is approximately 0.1 wt% for pure materials) [27]. In Table 1, EDX analyses confirm the presence of C, O, Mg, Al, S, Si, K, Ca, and Fe. However, this technique is not sufficient to characterize the different phases.

The separation of different layers is very complicated. For this reason, the samples (including all the layers) were ground for XRD characterization. The XRD study is carried out in powder form using the conventional Bragg–Brentano method with a focusing geometry (θ–2θ coupled) that requires a very small quantity of sample. The XRD pattern of the preparation layer (Fig. 5a) confirmed the presence of calcium sulphate in two phases (mainly gypsum ($CaSO_4{\cdot}2H_2O$) and anhydrite ($CaSO_4$)).

The XRD and FT-IR techniques confirm that the preparation layers were carried out with some pieces of textile mixture with animal glue associated to the support followed by the preparation of a lean character (animal glue and gypsum) layer. In some of the preparation layers, Bocanegra employs calcite and animal glue. In addition, a superficial colored layer in which iron compounds contribute to the yellow to ochre-reddish tone variation is present. However, in these samples, the iron compounds were only detected by EDX analyses and not by conventional XRD because this instrument may not be sensitive enough to detect minor phases of the cross-section. The iron phases are present in a low proportion in the preparation layer. In addition, the powder reflections are very small in comparison with the other minerals present in the mixture. These facts are responsible for the difficult characterization of the iron compounds by conventional X-ray diffraction. Experiments on thin cross-sections with combined SR μXRF/μXRD were performed. Fluorescence and diffraction data sets were simultaneously handled with PyMCA. This set-up shows high potential by concomitantly analysing element distribution (μXRF) and structure information (μXRD) in the cross-sections.

The elemental mapping distribution of iron in the preparation layer is shown in Fig. 5b. Over the same region, the diffraction pattern is calculated (Fig. 5c) and shows the goethite phase mixture with calcite and quartz in the preparation layer. These results

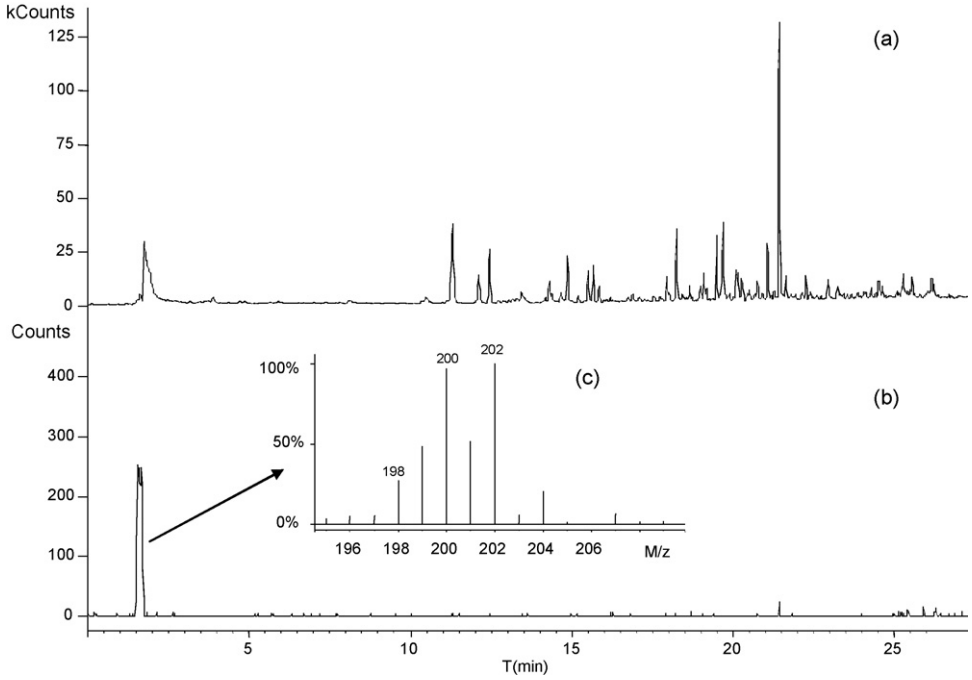


Fig. 8. (a) Reconstructed ion chromatogram, (b) single ion monitoring for m/z (198 + 200 + 202) obtained from direct pyrolysis of the Bocanegra painting sample, and (c) mass spectrum of Hg atoms.

confirm that Bocanegra used goethite in the mixture of support preparation like other famous Baroque painters such as Zurbaran and Murillo [28], and indicates that Bocanegra used a dark background due to the influence of the Tenebrism style.

3.3. Identification of pictorial layers

Above the preparation layers, different colored layers were detected in the paintings such as red, blue, ochre, and white.

3.3.1. White pigment

The EXD analyses (Table 2) show that the white layers are constituted of C, Pb and O. The μXRF map shows the elemental distribution of lead (Fig. 5b). In the white layer, mainly lead and calcium can be distinguished, with lead being the major constituent. In the lead region, μXRD confirms the presence of lead white (Fig. 5c) and shows the mineralogical phases hydrocerussite, $Pb_3(CO_3)_2(OH)_2$ and cerussite, Pb_3CO_3. The presence of the organic binding media was revealed through FT-IR spectrometry (Fig. 6a) carried out on the cross-section. The bands at 1738, 1162 and 1114 cm^{-1} could be attributed, respectively, to the C=O stretching and C–O–C stretching of the drying oils. PY–GC/MS confirms the presence of siccative oils, which gave a chromatogram (Fig. 6b) with high concentrations of palmitic, oleic, stearic and dicarboxylic acids (azelaic and suberic acids). These data show that the different pictorial layers were painted using drying oil as a ligand.

3.3.2. Red pigment

SEM/EDX and XRD give an approximation of the composition of the red pictorial layers in the different paint cross-sections. According to optical microscopy (Fig. 7a) observations, the red pigments in the pictorial layers are distributed as random aggregates of very thin particles. The EDX elemental analyses of these thin particles (Fig. 7b) identify Hg and S. The XRD diffraction pattern of the powder sample confirmed the presence of cinnabar (Fig. 7c). Pyrolysis shows the use of a siccative oil as ligand and, at the same time, the presence of Hg; in Fig. 8 the reconstructed ion chromatogram (a) and single ion monitoring for m/z (198 + 200 + 202) are reported (Fig. 8b); the mass spectrum in Fig. 8c presents the isotopic pattern of mercury that probably results from cinnabar. As reported in a previous paper [19] HgS, at high temperature and in helium atmo-

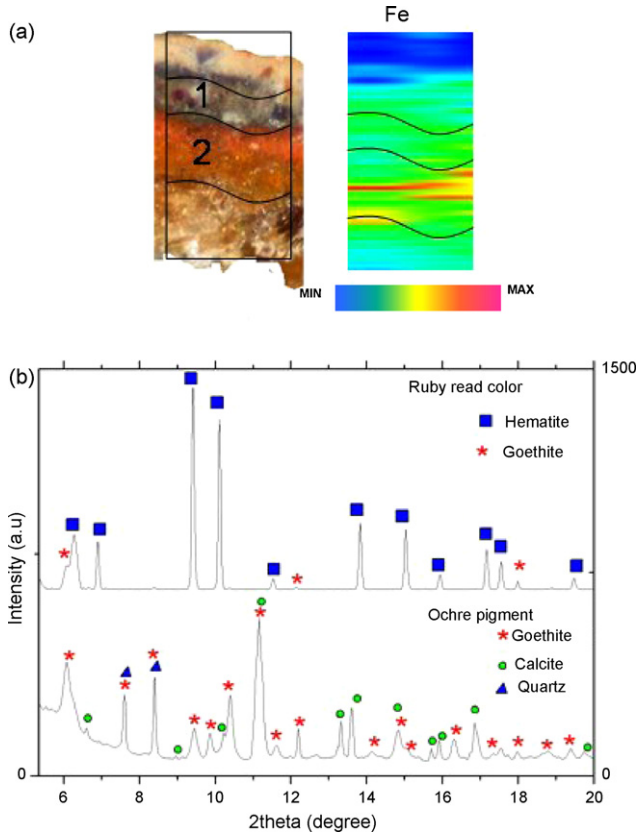


Fig. 9. (a) μXRF elemental mapping of red particles in the layer: iron elemental mapping of the preparation layer: iron. (b) SR μXRD of red particles: phases of mainly hematite with a low contribution of goethite. SR μXRD of red preparation layer: phases of goethite, calcite and quartz.

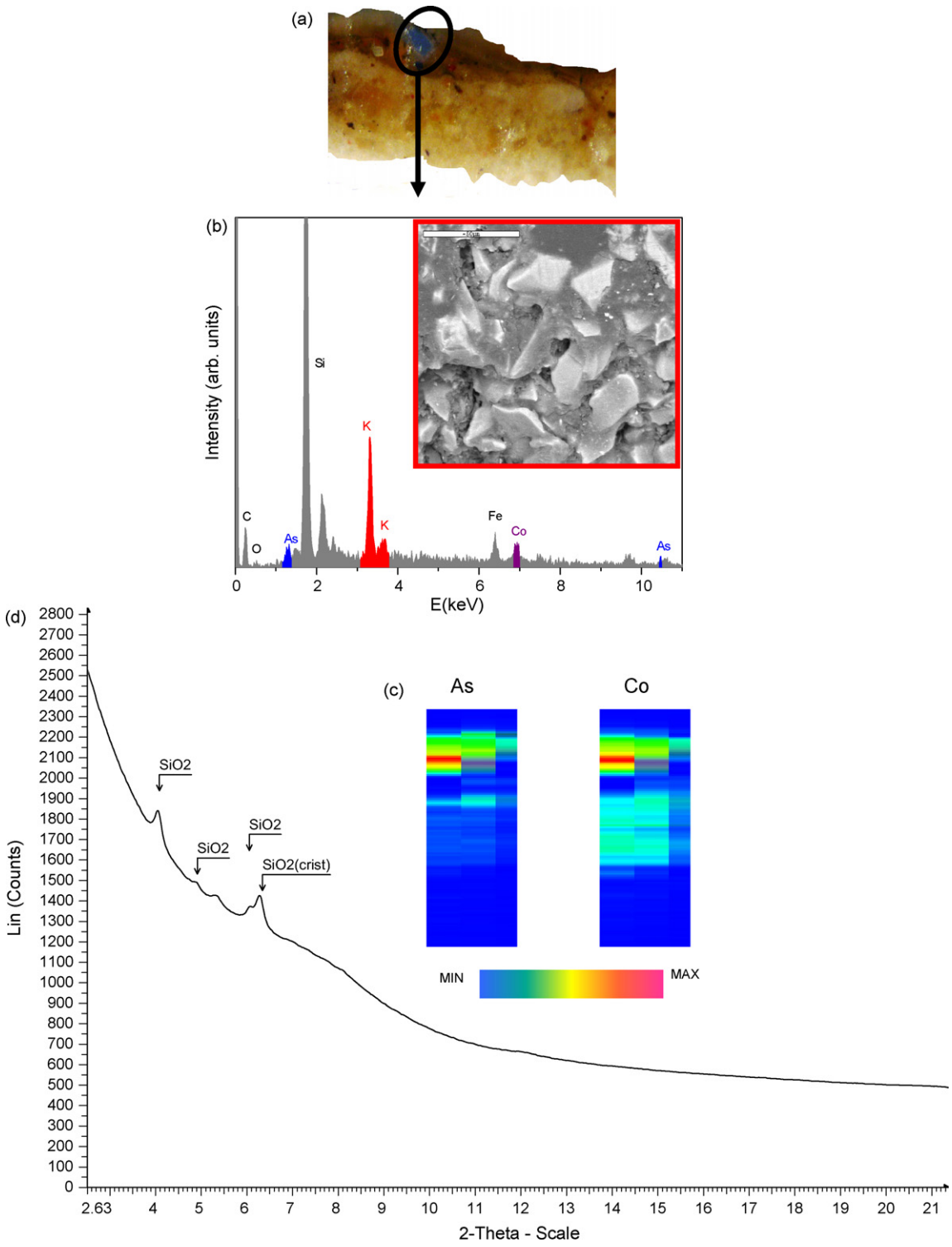


Fig. 10. (a) Paint cross-section originating from ground. The cross-section shows the blue particles in the upper layer; the color of the pigment has faded, causing yellowing of the oil medium. (b) SEM/EDX analyses show the presence of Co, As, and K in the blue particles. (c) μXRF elemental mapping of the blue particles: arsenic and cobalt. (d) SR μXRD of the amorphous phases.

sphere, is degraded into atomic mercury which is volatile and can be detected by GC–MS. The most important source of mercury is normally brilliant red, which has been used through our history as a pigment for paints. Cinnabar and vermilion are names assigned to a single chemical composition of different origin. The first is a natural compound while the second refers to the synthetic pigment. In both cases, there were no differences in structure and composition. In the Bocanegra samples, it was difficult to distinguish between cinnabar and vermilion. In Spain, the cinnabar mines in Almaden were already known from the Roman times, and the use of vermilion (artificial mercuric sulphide) was described by the Arabs in the 8th-century. In China, vermilion has been used since antiquity [29].

Using μXRF/μXRD, it was possible to distinguish between the composition of the iron phase present in the red layers of both the pictorial layer and the preparation layer. The ruby red color, similar to vermilion [30] of the pictorial layer, is constituted of hematite

in a higher proportion of goethite. The presence of only iron oxides suggests an artificial pigment. The mixture of goethite in a higher proportion together with silicates in the preparation layer suggests natural pigments with the calcite and quartz that Bocanegra used in the preparation layer. Bocanegra used different ochre pigments that contained varying amounts of octahedral iron oxides, namely hematite (αFe_2O_3) or/and goethite ($\alpha FeOOH$), mixed with quartz and calcium. When hematite is the main iron oxide, a red color is observed, whereas the ochre is yellow when the goethite dominates. These colors are due to the ion Fe^{3+} contained in both oxides, and more precisely to the charge transfer between Fe^{3+} and its ligands, O_2- or OH^- [31]. In Fig. 9a, the scheme of the stratigraphy is superimposed with the iron mapping and diffraction patterns (Fig. 9b) calculated in the same areas.

3.3.3. Blue pigments

The use of cobalt as a blue pigment in the Iberian Peninsula was reported in the 13th [32] and 14th centuries [33]. In Fig. 10a, the cross-section is shown and it is possible to observe the blue particles in the dark brown layer. In Fig. 10b, the blue particles were examined using SEM/EDX, which showed the presence of potassium, calcium, iron, cobalt, silicon and arsenic in low proportions. The thin cross-section was analyzed using μXRF/μXRD to confirm that this blue pigment was associated with a blue colored potassium glass (smalt). The scheme of the distribution is superimposed with the arsenic and cobalt mappings (Fig. 10c), and the diffraction patterns were calculated in the same areas. The XRD pattern shows an amorphous phase with a small contribution of silicon oxide that is associated with a vitreous material (glass), as shown in Fig. 10d. The presence of arsenic in the blue pigment is reported from the 16th century [34]. The uses of the benefit of the brightness of synchrotron radiation in combination with both techniques (μXRD/μXRF) confirm that this blue pigment was prepared from cobalt-rich minerals, such as cobaltite and smaltite to form cobalt oxide (Zaffer) [35]. Added as cobalt oxide during the manufacturing, with much of the arsenic being volatilized [34]. When this cobalt blue glass pigment degrades [36], it not only loses its color, but also causes yellowing of the oil so that the paintings become brownish-yellow. When smalt containing oil paint deteriorates, the alkaline component of the glass, which in the case of smalt is potassium, is lost from the pigment particles and migrates into the binding medium. There it has the potential to cause concurrent alteration and degradation of the oil, with possible processes including reactions with carboxylic acids in the oil to form potassium fatty acid soaps, or with anion sources in the environment to form species such as carbonates and sulphates [37]. Bocanegra used this blue pigment that consists of a potassium silicate glass containing cobalt oxide and a low quantity of arsenic, which is still present in the cobalt matrix.

XRD has been proven to be a valuable tool for the clear identification of copper inorganic pigments. However, with conventional XRD, it is rather difficult to acquire all of the information from these samples due to the thinness of the color layers, which are in the range of several tens of microns. Furthermore, the contributions of the small quantities of the copper pigments to the total sample are very low. Due to the small grains present in blue sample, it was difficult to identify the pigments that appeared mixed within a single layer.

To solve the difficulties involving the characterization of small quantity of pigments, experiments using μXRF/μXRD on the thin cross-sections of this sample were conducted to illustrate the potential of the combination of these techniques. Fluorescence and diffraction data sets were simultaneously handled with PyMCA. There is clear redundancy in analyzing the parallel elemental and structure information provided by XRF and XRD. The average

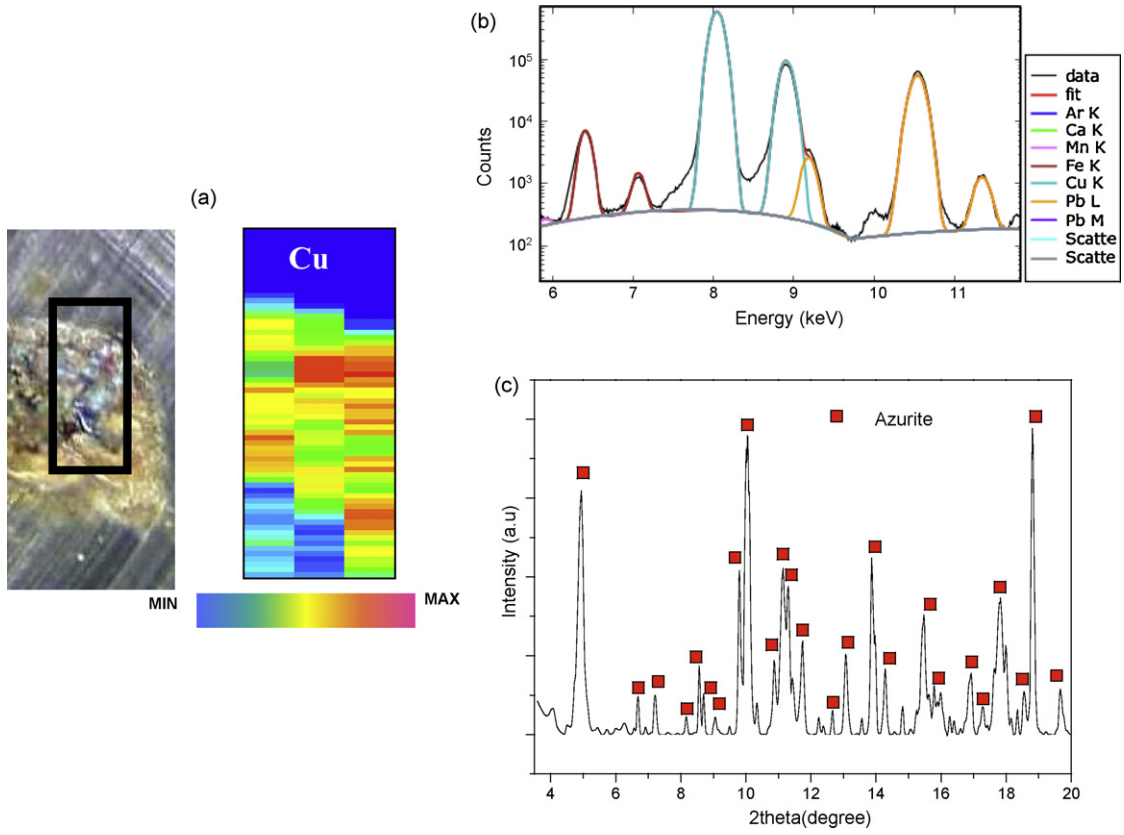


Fig. 11. (a) Thin cross-section micrographs and elemental map of Cu obtained in the pictorial layer, of sample from the dress in the San Ignacio Herido en las Puertas de Pamplona, (b) SR μXRF spectrum, and (c) SR μXRD pattern of blue grains.

diffraction patterns were calculated over the same identified areas (see Fig. 11a). In Fig. 11b, an μXRF spectrum shows the K lines for Cu, the thin cross-section is superimposed on some of the elemental mapping (Cu). The use of this technique allowed for the determination that the blue grains had an azurite pattern (Fig. 11c). Azurite is a natural blue pigment that is derived from the mineral azurite, a basic copper carbonate. Bocanegra used it in the mixture of blue and red pigments. Using μXRF/μXRD, it was possible to obtain only the contribution of azurite without any interference of the other pigments. μXRD enables a precise identification of the crystalline phase of azurite.

3.4. Organic binding medium

Analytical pyrolysis shows that all of the samples of the six paintings have, as an organic ligand, siccative oils. This gives them a high content of dicarboxylic acids, particularly azelaic acid. These acids are considered, in high concentrations, markers of this type of material. Additionally, the egg used in tempera painting has glycerides with long chain aliphatic acids, but due the scarce content of polyunsaturated acids, reactions with oxygen and the polymerisation reaction of the siccative process is practically absent, and only a low concentration of azelaic acid is observed. Chromatographic peaks indicative of proteins are absent but their presence is not excluded because the pyrolytical degradation of proteinaceous materials generally gives insignificant fragments. Only in the presence of a high concentration of protein it is possible to identify markers such as diketopiperazines, as reported in [38].

4. Conclusions

The analysis carried out in Bocanegra paintings of the San Ignacio of Loyola life using different physical–chemical techniques and analytical methodology, and evaluating the relationships between them, gave useful information about the employed materials and painting techniques in the cultural heritage field.

Scanning electron microscopy, especially in combination with energy dispersive X-ray microanalysis, has been an indispensable tool and contributed extensively to the identification of the elements that constituted the different inorganic pigments of the conventional cross-sections of the paintings studied in this work. However the phases present can not be detected, and is not a suitable technique for the detection of trace elements in pigments because their concentration is often below the detection limit. FT-IR supplied information on the organic components that the painter used in the preparation layers. The advantages of PY–GC/MS as a tool for the rapid screening of the organic composition of art objects is apparent from the results of this study; it permitted the identification of siccative oils like those used in the organic medium in these paintings. This technique is capable of providing information on the presence of inorganic compounds such as HgS.

Synchrotron-based μXRD and μXRF are particularly suited to the non-destructive study and micro-characterization of the different materials present in multi-layered paintings. This study demonstrated that synchrotron radiation micro-imaging techniques have yielded the ability to analyze pictorial layers, including grains, at the micrometer scale. μXRD is very useful for the identification of phases that are present in low proportion in multi-layer paintings with different inorganic pigments such as cerussite and hydrocerussite, and those with low powder reflection like azurite, cobalt blue, hematite, and goethite. The conventional XRD is not sensitive enough to detect these pigments in the multi-layer paintings; only cinnabar that has a high powder reflection was identified by this technique.

The non-destructive conventional technique of XRD has been applied in the study of ancient textile fibres of Bocanegra paintings. Using a glass capillary, it was possible to use only one fibre of the material. The presence of crystalline parts of the cellulose possibly means that the fibres are only partially degraded.

Acknowledgements

This work was supported by the European Commission, Marie Curie Action MEST-CT2004-513915, MAT2004-04498 and MAT2005-04838. The authors are very grateful to ESRF (ID 21 and ID 18F) for their assistance during our experiments (experiment EC-101). The authors thank the restoration team (PREDELA SL, Conservación y Restauración de Obras de Arte). A part of this study has been funded by the Andalusian Government (Proyecto Andalucía Barroca 2007).

References

[1] E. Ciliberto, G. Spoto (Eds.), Modern Analytical Methods in Art and Archaeology, Wiley–Interscience, New York, USA, 2000, p. 763.
[2] D.C. Creagh, D.A. Bradley (Eds.), Radiation in Art and Archaeometry, Elsevier Science, Amsterdam, The Netherlands, 2000, p. 297.
[3] M. Cotte, J. Susini, A. Solé, Y. Taniguchi, J. Chillida, E. Checroun, P. Walter, J. Anal. At. Spectrom. 23 (2008) 820.
[4] J. Cassar, C. Degrigny, in: A. Adriaens, C. Degrigny, J. Cassar (Eds.), Benefits of Non-destructive Analytical Techniques for Conservation, Office for the Official Publications of the European Union, Luxembourg, 2005, pp. 9–12.
[5] K. Keune, Binding Medium, Pigments and Metal Soaps Characterized and Localized in Paint Cross Sections, Dissertation, Molart Report, Archetype, London, 2005.
[6] E. Dooryhee, Ph. Colomban, Phase Transit. 81 (2–3) (2008) 139.
[7] L. Bertrand, D. Vantelon, E. Pantos, Appl. Phys. A 83 (2006) 225.
[8] E. Pantos, in: M. Uda, G. Demortier, I. Nakai (Eds.), X-rays for Archaeology, Springer, London, 2005, pp. 199–208.
[9] M. Uda, G. Demortier, I. Nakai, X-rays for Archaeology, Springer-Verlag, Netherlands, 2005, p. 459.
[10] D.C. Creagh, Radiat. Phys. Chem. 74 (2005) 426.
[11] L.K. Herrera, Physico-Chemical Research of Cultural Heritage Materials Using Microanalytical Methods, PhD Thesis, Seville University and Material Science Institute, Seville, Spain, 2009, ISBN 846920906-X.
[12] A. Von Haartman, Metodología y técnicas en la restauración de obras pictóricas del Siglo de Oro español de la catedral de Almería, Universidad de Granada, 1992, p. 85.
[13] E. Orozco Diaz, Pedro Atanasio Bocanegra, Boletín Facultad de Letras, Granada, 1937, p. 24.
[14] F. García Gutierrez, Boletín de las Artes 9 (1991) 49.
[15] M. Cotte, E. Checroun, V. Mazel, V.A. Solé, P. Richardin, Y. Taniguchi, P. Walter, J. Susini, e-PRESERVATIONScience (2009) 1–9.
[16] N. Khandekar, Rev. Conserv. 4 (2003) 52.
[17] A. Duran, L.K. Herrera, Mª.D. Robador, J.L. Perez-Rodriguez, Color Res. Appl. 32 (6) (2007) 489.
[18] L.K. Herrera, M. Cotte, M.C. Jimenez de Haro, A. Duran, A. Justo, J.L. Perez Rodriguez, Appl. Clay Sci. 42 (1–2) (2009) 57.
[19] G. Chiavari, S. Prati, Chromatographia 58 (2003) 543.
[20] J. Boon, S. Asahina, Microsc. Microanal. 12 (2) (2006) 1322.
[21] A. Somogyi, M. Drakopoulos, L. Vincze, B. Vekemans, C. Camerani, K. Janssens, A. Snigirev, F. Adams, X-ray Spectrom. 30 (2001) 242.
[22] V.A. Solé, E. Papillon, M. Cotte, P.H. Walter, J. Susini, Spectrochim. Acta Part B 62 (1) (2007) 63.
[23] A.P. Hammersley, C. Riekel, Synchrotron Radiat. News 2 (1989) 24.
[24] G. Chiavari, S. Prati, G. Lanterna, C. Lalli, A. Cagnini, Microchim. Acta 159 (3–4) (2007) 357.
[25] A. Satta, R. Hagege, M. Sotton, Bull. Sci. ITF 15 (1986) 3.
[26] G.F. Davidson, T.P. Nevell, J. Textile Inst. 47 (1956) 439.
[27] J.I. Goldstein, D.E. Newbury, D.C. Joy, C.E. Lyman, P. Echlin, E. Lifshin, L.C. Sawyer, J.R. Michael, Scanning Electron Microscopy and X-ray Microanalysis, 3rd ed., Kluwer Academic/Plenum Publishers, New York, 2003, p. 40.
[28] A. Duran, Metodología de Estudio y Análisis de diferentes tipos de obras pertenecientes a la Escuela Sevillana de los siglos XVII y XVIII, PhD Thesis, Universidad de Sevilla, 2006, 480 pp.
[29] R.J. Gettens, R.L. Feller, W.T. Chase, in: A. Roy (Ed.), A Handbook of their History and Characteristics, vol. 2, National Gallery of Art, Washington and Oxford University Press, Oxford, 1993, pp. 159–182.
[30] R.J. Gettens, G.L. Stout, Painting Materials: A Short Encyclopaedia, Dover Publications, New York, 1966, pp. 157–159.
[31] M. Elias, C. Chartier, G. Prévot, H. Garay, C. Vignaud, Mater. Sci. Eng. B 127 (2006) 70.
[32] C. Roldaĭn, J. Coll, J. Ferrero, J. Cult. Herit. 7 (2) (2006) 134.

[33] J. Pérez-Arantegui, M. Resano, E. García-Ruiz, F. Vanhaecke, C. Roldán, J. Ferrero, J. Coll, Talanta 74 (5) (2008) 1271.
[34] G. Pappalardo, E. Costa, C. Marchetta, L. Pappalardo, F.P. Romano, A. Zucchiatti, P. Prati, P.A. Mandò, A. Migliori, L. Palombo, M.G. Vaccari, J. Cult. Herit. 5 (2004) 183.
[35] B. Mühlethaler, J. Thissen, in: A. Roy (Ed.), Artists' Pigments: A Handbook of their History and Characteristics, vol. 2, National Gallery of Art, Washington, DC, 1993, pp. 113–130.
[36] M. Spring, C. Higgitt, D. Saunders, Natl. Gallery Tech. Bull. 26 (2005) 56.
[37] M. Spring, N. Penny, R. White, M. Wyld, Natl. Gallery Tech. Bull. 22 (2001) 54.
[38] G. Chiavari, N. Gandini, P. Russo, D. Fabbri, Chromatographia 47 (1988) 420.

Talanta 80 (2009) 84–91

Contents lists available at ScienceDirect

Talanta

journal homepage: www.elsevier.com/locate/talanta

Metabolism profile of scutellarin in urine following oral administration to rats by ultra performance liquid chromatography coupled to time-of-flight mass spectrometry

Qingfei Liu[a,*], Yun Shi[b], Yong Wang[c], Juan Lu[a], Wenjuan Cong[c], Guoan Luo[a], Yiming Wang[a]

[a] School of Medicine, Tsinghua University, Beijing 100084, China
[b] The 1st hospital, Guangzhou University of Traditional Chinese Medicine, Guangzhou 510405, China
[c] School of Pharmacy, East China University of Science and Technology, Shanghai 200237, China

ARTICLE INFO

Article history:
Received 1 February 2009
Received in revised form 8 June 2009
Accepted 10 June 2009
Available online 18 June 2009

Keywords:
UPLC/TOF MS
Scutellarin
Metabolism profile
Rat
Urine

ABSTRACT

Scutellarin, a flavone glucuronide of 5,6,4′-trihydroxyflavone-7-O-glucoronide, is the main active component of the traditional Chinese botanic drug *Erigeron breviscapus* (*Vant.*) *Hand.-Mazz*. In this study, a method based on ultra performance liquid chromatography coupled with a time-of-flight mass spectrometer (UPLC/TOF MS) was established and validated to profile the metabolites of scutellarin in Sprague-Dawley rat urine following oral administration of single dose of scutellarin at 80.8 mg/kg. The column utilized was an Acquity BEH C18 (150 mm × 2.1 mm, 1.7 μm). The mobile phase was 0.2% formic acid and acetonitrile with gradient condition. Two standard curves of scutellarin were obtained for the concentration range of 1.065–10.65 μg/mL and 10.65–63.92 μg/mL, respectively. By automating the data processing of the software Masslynx developed by Waters Ltd., 17 metabolites of scutellarin were found and determined in rat urine, with the corresponding reactions *in vivo* such as isomerism, reduction, methylation, glucuronide conjugation, hydroxylation, hydroxylation and methylation, *etc*., most of which were discovered for the first time. For most metabolites, the time (T_p) of peak excretion was 8–12 h. Calculated as scutellarin, the cumulative urine excretion rate of the metabolites was 1.93%.
© 2009 Elsevier B.V. All rights reserved.

1. Introduction

Scutellarin, a flavone glucuronide of 5,6,4′-trihydroxyflavone-7-O-glucoronide (Fig. 1), is the main active component of the traditional Chinese botanic drug *Erigeron breviscapus* (*Vant.*) *Hand.-Mazz*. Recent pharmacological research showed that scutellarin favored of myocardial protection by expanding blood microvessels, improving blood microcirculation, activating K^+ channels and blocking Ca^{2+} channels [1]. It could also attenuate hydrogen peroxide (H_2O_2)-induced nitrogen monoxide (NO), cytotoxicity, intracellular accumulation of reactive oxygen species (ROS) and Ca^{2+}, lipid peroxidation, and loss of mitochondrial membrane potential (MMP) and DNA [2,3]. Furthermore, it was exciting that scutellarin could inhibit HIV-1 reverse transcriptase activity, HIV-1 particle attachment and cell fusion, all of which are essential activities for viral transmission and replication [4].

With the increasing importance of scutellarin in human health, it is important to research its absorption, distribution, metabolism, and excretion (ADME). As for the determination of scutellarin and its metabolites in biological samples, such as plasma, bile, urine and other tissues, high performance liquid chromatography coupled with ultraviolet or mass spectrometry (HPLC/UV, HPLC/MS) was often used. However, HPLC/UV methods can only be used to determine the parent drug or the metabolites with standards, limiting its usage [5–9]. HPLC/MS provides more information on molecular formulae and fragments for identification and quantification [10]. Taking scutellarin for example, using HPLC/MS/MS four metabolites could be found in human urine: scutellarin, two isomers of scutellarin, and methylated scutellarin. Isoscutellarin and the parent drug could also be found in plasma. With the aid of nuclear magnetic resonance spectroscopy (NMR), isoscutellarin could be identified as 5,7,4′-trihydroxyflavone-6-O-glucoronide [11]. Besides, HPLC/MS and HPLC/NMR could also help to find five metabolites in rat plasma and bile after oral administration of scutellarin: two compounds of scutellarin conjugated with two sulfate groups, scutellarein, 6-methyl-scutellarin, and 6-methyl scutellarein [12].

However, it has been known that the *in vivo* biochemical transformation of the drug is complicated and various reactions probably occur such as oxidation, reduction, methylation, glucuronide conjugation, sulfation, *etc*. Many metabolites, which are biomarkers of interest, will often be of low abundance, and ionization

* Corresponding author at: B104, Medical Building, School of Medicine, Tsinghua University, Beijing 100084, China. Tel.: +86 10 62797450; fax: +86 10 62772263.
E-mail address: liuqf@mail.tsinghua.edu.cn (Q. Liu).

0039-9140/$ – see front matter © 2009 Elsevier B.V. All rights reserved.
doi:10.1016/j.talanta.2009.06.031

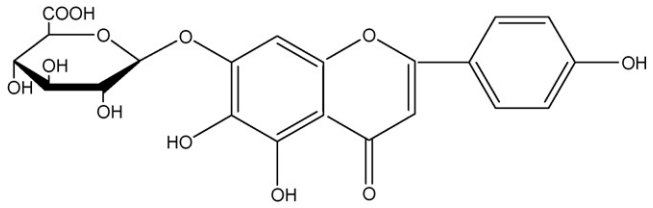


Fig. 1. Chemical structure of scutellarin.

suppression from high abundance endogenous metabolites may prevent their detection [13]. Comprehensive detection and quantitation of metabolites from a biological sample constitute the major challenges of current metabolomics research.

Compared to HPLC, ultra performance liquid chromatography (UPLC) is a recently developed technology. It can provide a higher peak capacity, greater resolution, increased sensitivity, and higher speed of analysis. For example, 11 familiar components in biodiesel, 15 flavonoids in *Epimedium*, and 11 saponins in *Panax notoginseng* could be detected in only 5 min, 12 min, and 12 min, respectively [14–16]. Since 2006, UPLC/MS has been widely used in environmental monitoring [17,18], food contamination detection [19,20], botanic and biological sample analysis [21–25], *etc*. The advantages of UPLC/MS are unique and obvious.

Therefore, the objective of this paper is to establish and validate a simple, selective, and specific UPLC/MS method in the multiple reaction monitoring (MRM) mode for the identification and quantification of scutellarin and its metabolites in urine following an oral single dose to rats, which can provide more comprehensive insights and guidance for the elucidation of side effect mechanism and safety monitoring as well as for rational formulation design in drug delivery system.

2. Experimental

2.1. Chemicals

Scutellarin was purchased from the Kunming Institute of Botany, Chinese Academy Sciences (Yunnan, China). A scutellarin standard (99.5% purity) was purchased from the National Institute for the Control of Pharmaceutical and Biological Products (Beijing, China). Acetonitrile was of HPLC grade (Fisher, USA). HPLC grade water was obtained using a water purification system (Milli-Q Reagent Water System, MA, USA). All other chemicals were of analytical reagent grade. All mobile phases were filtered through 0.22 μm micropore filters (Jinteng Ltd., Tianjin, China) prior to use.

2.2. Instrumentation and chromatographic conditions

The UPLC/MS system "LCT Premier^{TM} XE" comprised a Waters UPLC system connected in-line with a time-of-flight mass spectrometer (TOF MS) (Waters Ltd. USA). The column utilized was an Acquity BEH C18 (100 mm × 2.1 mm, 1.7 μm) maintained at 50 °C. Mobile phases were A (0.2% formic acid) and B (acetonitrile). LC gradient condition of B was as follows: 0–5 min: 5 → 50%; 5–7 min: 50 → 95%; 7–8 min: 95 → 95%; 8–10 min: 95 → 5%; 10–15 min: 5 → 5%. The flow rate was set at 0.5 mL/min. Samples were maintained at 4 °C throughout.

2.3. Mass spectrometry

Analytes were quantified using TOF MS in negative-ion mode. Source parameters included capillary voltage of 2.2 kV, cone voltage of 35 V, source temperature of 120 °C, desolvation temperature of 350 °C, cone gas flow of 10 L/h, desolvation gas flow of 700 L/h. Product ions were monitored in W^- extended mode. In the full scan mode, the mass spectrometer was operated over a range of m/z 50–1000. Injection volumes for samples and standards were 4 μL with an auto-injector.

2.4. Animals

Six Sprague-Dawley (SD) rats (3 male and 3 female), weighing 225.4 ± 11.1 g, were purchased from Beijing Weitong Lihua Biotechnology Co., Ltd. (Beijing, China). The animals were housed and cared for under a constant temperature at (22 ± 1 °C) and humidity (50 ± 10%). Food was withheld prohibited for one day before the experiment while water was provided freely.

2.5. Drug administration and urine sample preparation

Scutellarin was dispersed in deionized water at 20.20 mg/mL by sonication for 10 min (KQB-100, Kunshan Supersonic Instrument Co., Kunshan, China) to obtain a homogeneous suspension. It has been clear that scutellarin is absorbed in the gastrointestinal (GI) tract by passive diffusion. With its low water solubility, it cannot be easily absorbed through enterocytes. Moreover, scutellarin can be hydrolyzed into scutellarein and glucuronate by gastric acid, intestinal flora, and enzymes of liver and intestine. These reasons explain the low absorption of scutellarin into blood [26] and low absolute bioavailability of scutellarin oral preparations (0.4 ± 0.19%, in Beagle dogs) [27]. Furthermore, the amount excreted into urine is often limited which complicate its determination. Therefore, the dosage of scutellarin to rats was set high at 80.8 mg/kg body weight. After administration, food was withheld for 48 h for all rats while water was provided freely. The whole urine of each rat was collected at 0–4 h, 4–8 h, 8–12 h, 12–16 h, 16–20 h, 20–24 h, 24–32 h, 32–40 h, and 40–48 h. A blank urine sample was collected before administration.

Each urine sample was centrifuged at 4500 rpm for 10 min at 4 °C (TGL 16C, Medical centrifuge Co., Beijing, China). Hundred microlitres of the upper layer was mixed with 100 μL methanol using vortex-mixing for 1 min and then centrifuged at 12,000 rpm for 15 min at 4 °C. The upper layer was transferred to another tube and mixed with 600 μL water. The mixture was centrifuged at 10,000 rpm for 10 min at 4 °C. The supernatant was injected into the UPLC system for analysis. The same sample handling process was used for the recovery and precision determinations in urine.

2.6. Identification of the metabolites

Urine samples were analysed by TOF MS. Using the MS data and Masslynx software installed on the instrument, the molecular formulae of scutellarin and its metabolites were identified. The potential biochemical transformations between the metabolites and the parent compound could also be provided by the Masslynx software.

2.7. Standard solution, calibration curves, and quality control (QC) samples

A standard stock solution (639.2 μg/mL) was prepared by dissolving 15.98 mg scutellarin in 25 mL methanol. A series of standard working solutions with concentration range of 1.065–63.92 μg/mL for scutellarin were obtained by further dilution of the standard stock solution with methanol. All solutions were stored at 4 °C. A series of 0.2 mL standard working solutions were evaporated to dryness at 40 °C under a gentle stream of nitrogen. The residues were reconstituted in 0.2 mL of blank urine to prepare the two calibration standards at the low concentration range of 1.065, 2.130, 4.260, 6.390, 8.520, and 10.65 μg/mL

and high concentration range of 10.65, 21.31, 31.96, 42.61, 53.27, and 63.92 μg/mL, respectively. Linearity was demonstrated by statistical analysis of a linear regression model: $y = ax + b$ (where x represents the concentration of scutellarin and y represents the peak area of scutellarin).

Quality control (QC) samples were prepared in the same way as calibration standards with blank plasma, and concentrations were 1.065, 10.65, and 63.92 μg/mL, respectively. The QC samples were stored at −80 °C until analysis.

2.8. Method validation

2.8.1. Recovery

Three 0.2 mL standard working solutions, with concentrations of 1.065, 10.65, and 63.92 μg/mL, were evaporated to dryness and redissolved with each in 0.2 mL of blank urine. The recoveries were calculated by comparing the peak areas of the urine samples to those of the standard working samples.

2.8.2. LOD and LOQ

The limits of quantification (LOQ) and detection (LOD) were defined as scutellarin responses which yielded a signal to noise ratio, without smoothing, of greater than 10 and 3, respectively.

2.8.3. Intra- and Inter-day precision

The intra- and inter-day precisions (%, RSD) of the method were assessed by analyses of scutellarin in QC samples of low, middle, and high concentrations (1.065, 10.65, and 63.92 μg/mL) on the same day and on three consecutive days, respectively.

2.8.4. Stability

One of the urine samples for precision determination was examined for stability at 4 °C after 0 h, 4 h, 8 h, and 12 h. The amount of scutellarin in the urine samples was determined using a freshly prepared calibration curve.

2.9. Pharmacokinetic study

The concentrations of the parent drug and the isomers of scutellarin were calculated according to the equations of linear regression of scutellarin. The concentrations of the other metabolites were calculated by the method of semi-quantification with the equations of scutellarin $y = ax + b$, x as molar concentration (μmol/mL) [28–31]. Based on the molecular weight (MW), the concentration (C, μmol/mL), and excreted urine volume (V, mL), the amounts (μg) of the metabolites (M) were calculated ($M = C \times \mathrm{MW} \times V$). Furthermore, all data on the amount of scutellarin and the metabolites were normalized to the same body weight of 250 g ($M_{250g} = M/W \times 250$, where W was the real body weight). Pharmacokinetic parameters were calculated by the method of urine excretion using DAS (ver. 2.0) pharmacokinetic software [32] provided by the Chinese Pharmacology Association.

3. Results and discussion

3.1. Identification of scutellarin and its metabolites

The main criteria for the search for metabolites were strong induction in test samples and the absence in blank control ones. The base peak intensity (BPI) chromatograms of two urine samples collected in 0–4 h and 4–8 h, respectively, are shown in Fig. 2, compared to the blank urine. The extracted ionic currents (EIC) and MS of the urine samples were studied (Fig. 3). It could be found that in BPI chromatograms, interference and ionization suppression induced by high abundance endogenous metabolites could strongly prevent the detection of these metabolites. However, with

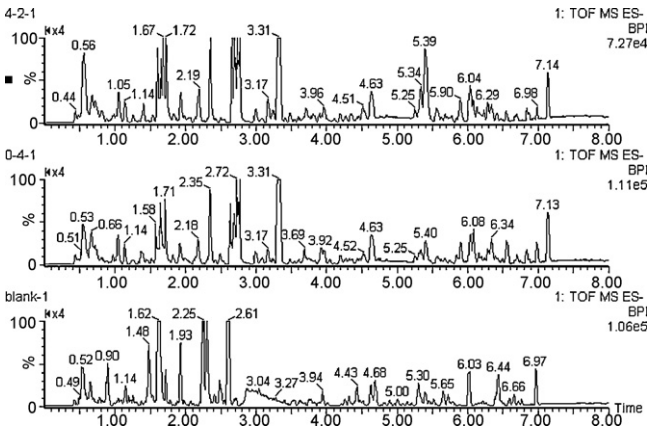


Fig. 2. The TOF MS base peak intensity (BPI) chromatograms of the metabolites of scutellarin in urine after oral single dose of scutellarin to rats.

the high selectivity of EIC, the metabolites of scutellarin showed high specificity.

By automating the data processing, Masslynx enabled rapid metabolite identification. From the information of molecular formulae of the metabolites provide by Masslynx, 17 distinct metabolites were found in rat urine, as shown in Table 1. It could also be demonstrated that some biochemical transformations occurred for scutellarin after oral administration, such as reduction, methylation, glucuronide conjugation, hydroxylation, hydroxylation + methylation, *etc*.

It was very interesting that the retention time of the scutellarin standard was 2.83 min with m/z 461.07 $(M-1)^-$. However, a compound with m/z 461.07, identical to scutellarin, was found with a retention time of 3.95 min, implicating that it was not scutellarin. It had been reported that scutellarein, with m/z of 287 $(M+1)^+$ could easily be found in rat plasma after oral administration and there are two possible pathways of metabolism. In the first pathway, scutellarin is absorbed into the blood and metabolized to scutellarein by a glucuronate enzyme. In the second pathway, scutellarin is first biotransformed into scutellarein in the gastrointestinal (GI) tract and scutellarein is then absorbed into the blood [12]. Therefore, it could easily be concluded that scutellarin is metabolized into scutellarein in the GI tract, liver or blood and scutellarein is reconjugated with glucuronate and then excreted into the urine. From the chemical structure of scutellarein, each of 5, 6, 7, and 4′ positions is a possible site for conjugation with glucuronate. The compound scutellarein conjugated with glucuronate at position 6 was identified in human plasma and named isoscutellarin [11]. Therefore, the metabolite with m/z 461.07 eluting at 3.95 min in this study could also be named isoscutellarin which is scutellarein conjugated with glucuronate at positions 5, 6, or 4′.

As for the compound with m/z 477.09, there were two main peaks in the chromatogram with retention time of 5.63 min and 5.72 min, respectively, indicating that they are isomers with molecular formula $C_{21}H_{18}O_{13}$. Each one is scutellarin with a hydroxyl group at a different site.

The glucuronide conjugate of scutellarin was also found as $C_{27}H_{26}O_{18}$ with m/z 637.10. A similar compound had been reported in mouse blood, liver, and intestine [33].

The compound $C_{21}H_{18}O_{11}$ with m/z 445.05, lacking a molecular O compared with the parent scutellarin, might be baicalin (5,6-bihydroxyflavone-7-O-glucuronide) or its isomer.

The molecular formulae of 17 metabolites are shown in Table 1. The potential biochemical transformations that occurred *in vivo* are also provided, such as reduction, hydrolysis, hydroxylation, hydroxylation and methylation, reduction and hydroxylation, decarboxylation and glucuronidation, *etc*. For three metabolites,

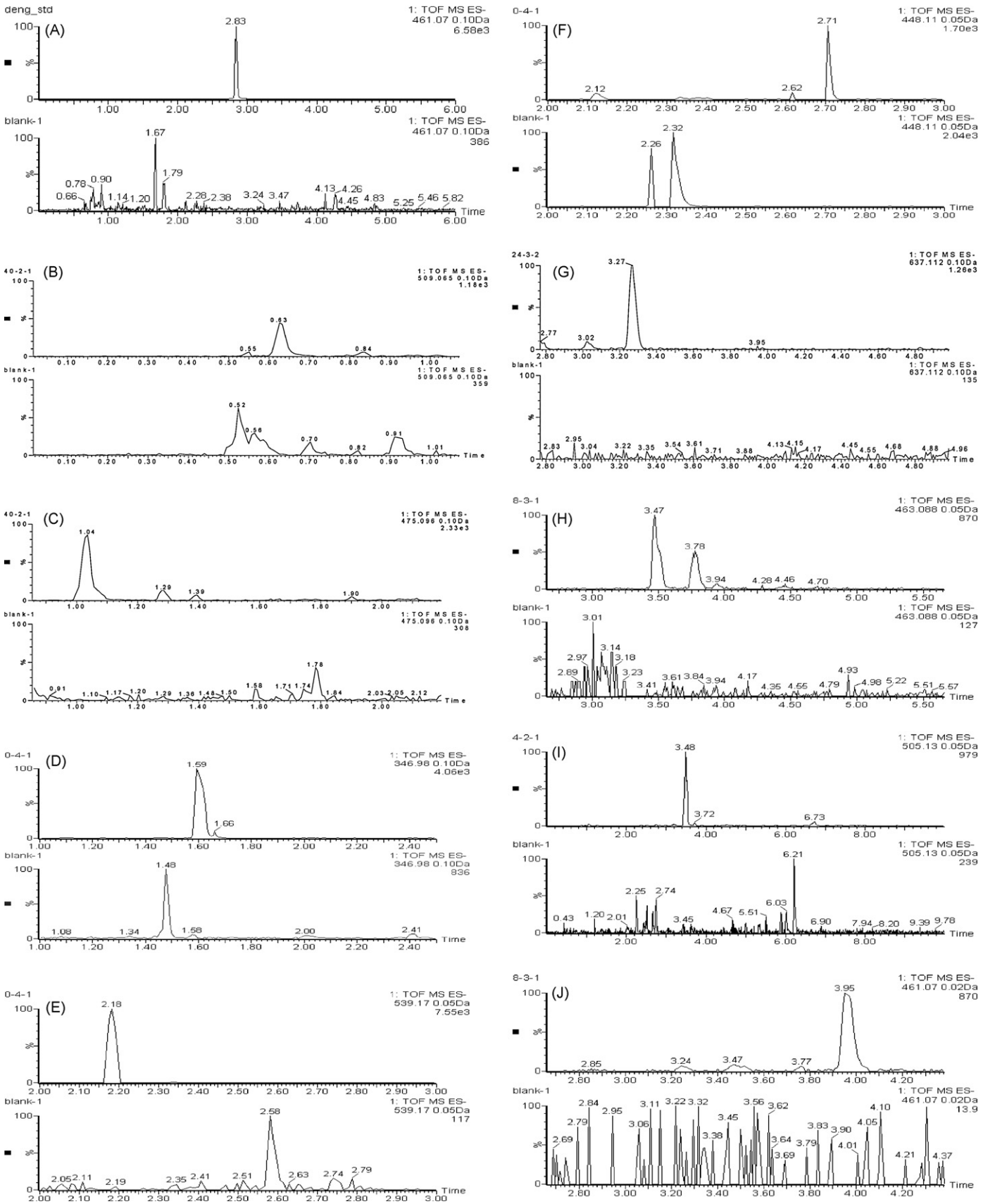


Fig. 3. EIC and MS of the metabolites of scutellarin in urine after oral single dose of scutellarin to rats. (A) Scutellarin standard with *m*/*z* 461.07, (B) *m*/*z* 509.06, (C) *m*/*z* 475.10, (D) *m*/*z* 346.98, (E) *m*/*z* 539.17, (F) *m*/*z* 448.11, (G) *m*/*z* 637.10, (H) *m*/*z* 463.08, (I) *m*/*z* 505.13, (J) Isoscutellarin with *m*/*z* 461.07, (K) *m*/*z* 443.09, (L) *m*/*z* 445.05, (M) *m*/*z* 609.12, (N) *m*/*z* 477.09, (O) *m*/*z* 447.06, (P) *m*/*z* 491.06, (Q) *m*/*z* 479.11.

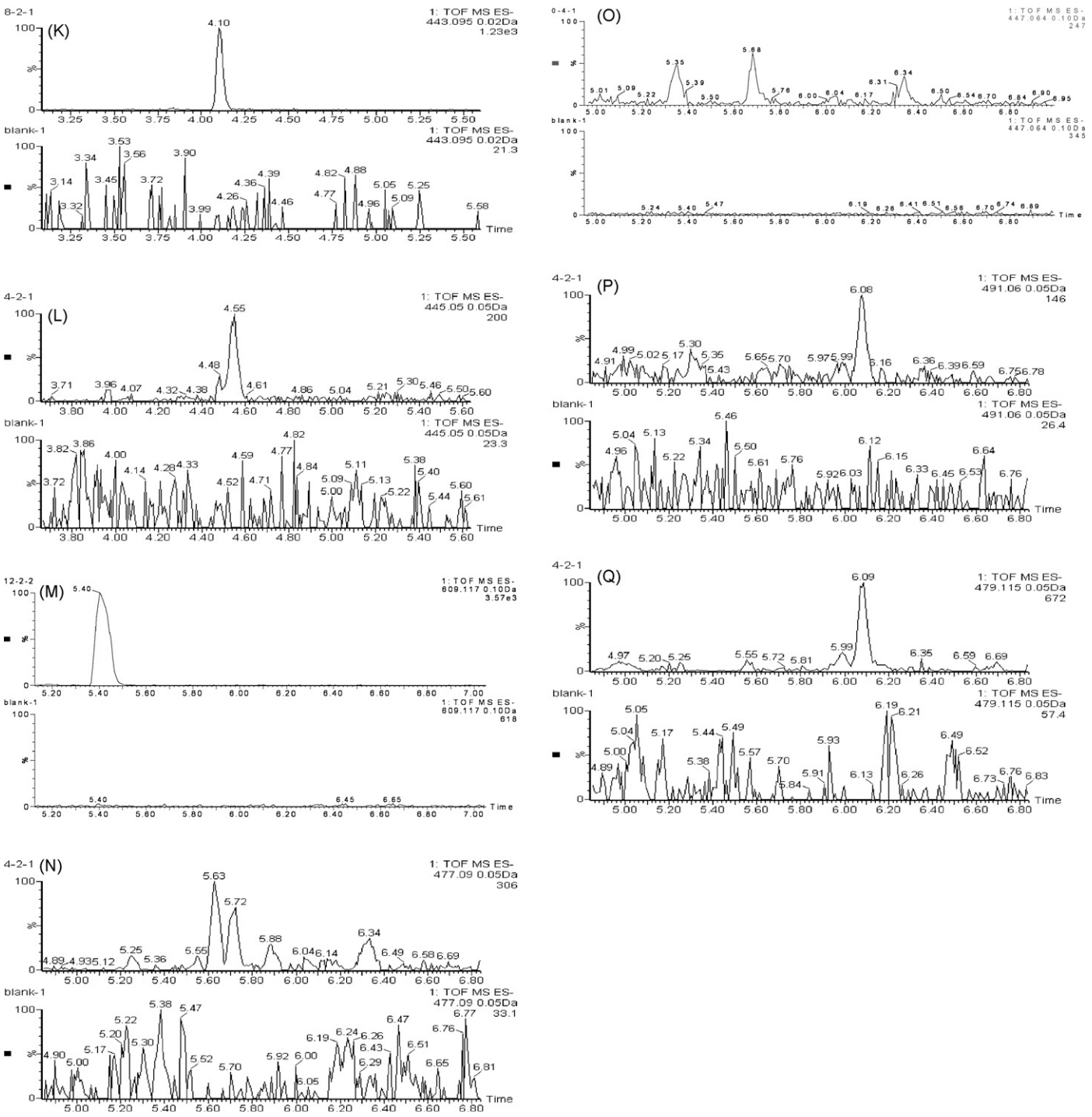


Fig. 3. (*Continued*).

the transformations are still unknown and need to be studied further.

For TOF MS, the most outstanding advantage is that it can provide accurate molecular formulae for the compounds, although its disadvantage is also obvious in that it cannot produce fragments as MS/MS or MS(n) just like Ion Trap MS, which is very helpful for structural identification. However, for metabolite studies, so many unknown compounds may be produced and most are even new and without reference standards. Therefore, using TOF MS to identify the molecular formulae of the metabolites is very important. Based on the known molecular formulae, further study will be much easier.

3.2. Metabolism profile in urine

Only a few metabolites of scutellarin were reported after administration to humans [11], Wistar rats [12], and Kunming mice [33]. From the present study, 17 metabolites could easily be found and determined, most of which were discovered for the first time. According to the biochemical transformations of

Table 1
Metabolites of scutellarin in rat urine after oral single dose of scutellarin.

Peak number	Rt (min)	Reaction	Molecular formula	$[M-H]^-$	Chemical structure
1	0.63	Unknown	$C_{21}H_{18}O_{15}$	509.06	Unknown
2	1.01	Methylation	$C_{22}H_{20}O_{12}$	475.10	M + CH_3
3	1.62	Hydrolysis + sulfate	$C_{15}H_8O_8S$	346.98	Aglycone – H_2O + SO_3
4	2.19	Unknown	$C_{22}H_{20}O_{14}S$	539.17	Unknown
5	2.69	Unknown	$C_{20}H_{19}O_{11}N$	448.11	Unknown
6	3.27	Glucuronide conjugation	$C_{27}H_{26}O_{18}$	637.10	M + glucuronate – H_2O
7	3.47	Reduction	$C_{21}H_{20}O_{12}$	463.08	M – 2H
8	3.49	Reduction + acetylation	$C_{23}H_{22}O_{13}$	505.13	M – 2H + $COCH_3$
9	3.96	Isoscutellarin	$C_{21}H_{18}O_{12}$	461.07	Iso-M
10	4.11	Hydrolysis	$C_{21}H_{16}O_{11}$	443.09	M – H_2O
11	4.55	Loss of O	$C_{21}H_{18}O_{11}$	445.05	M – OH (baicalin or its isomer)
12	5.39	Decarboxylation + Glucuronidation	$C_{26}H_{26}O_{17}$	609.12	M + glucuronate – COOH
13	5.63	Hydroxylation	$C_{21}H_{18}O_{13}$	477.09	M + OH
14	5.72				
15	5.68	Demethylation	$C_{20}H_{16}O_{12}$	447.06	M – CH_3
16	6.08	Hydroxylation + methylation	$C_{22}H_{20}O_{13}$	491.06	M + OH + CH_3
17	6.09	Reduction + hydroxylation	$C_{21}H_{20}O_{13}$	479.11	M – 2H + OH

the metabolites provided by Masslynx, the potential metabolism profile of scutellarin in SD rat urine following oral administration could be described as shown in Fig. 4.

For the compounds $C_{22}H_{20}O_{13}$ and $C_{21}H_{20}O_{13}$, there might be two pathways. For $C_{22}H_{20}O_{13}$, the first pathway is methylation of scutellarin to $C_{22}H_{20}O_{12}$, which is then hydroxylated to be $C_{22}H_{20}O_{13}$. In the second one scutellarin is first hydroxylated to $C_{21}H_{18}O_{13}$ and then methylated to $C_{22}H_{20}O_{13}$. For $C_{21}H_{20}O_{13}$, the first pathway is hydroxylation of scutellarin to $C_{21}H_{18}O_{13}$, followed by reduction to $C_{21}H_{20}O_{13}$. In the other pathway scutellarin is reduced to $C_{21}H_{20}O_{12}$ and then hydroxylated to $C_{21}H_{20}O_{13}$.

For the compound $C_{21}H_{18}O_{13}$, two isomers exist which are products of hydroxylated scutellarin. For the compound $C_{23}H_{22}O_{13}$, the metabolism mechanism might be that scutellarin is reduced to $C_{21}H_{20}O_{12}$ and then acetylated to $C_{23}H_{22}O_{13}$.

There are also two metabolites of scutellarin with glucuronation occurring at two different sites. One is $C_{27}H_{26}O_{18}$, where scutellarin is glucuronated and a molecular H_2O was lost. The other one is $C_{26}H_{26}O_{17}$, where scutellarin is glucuronated and decarboxylated.

3.3. Method validation

Two regression equations of the standard curves for scutellarin were obtained: $y = 2220.5x + 2.2247$ (correlation coefficient $r = 0.9944$) for the concentration range of 0.0023–0.023 μmol/mL (1.065–10.65 μg/mL) and $y = 1830.6x + 5.2046$ ($r = 0.9981$) for

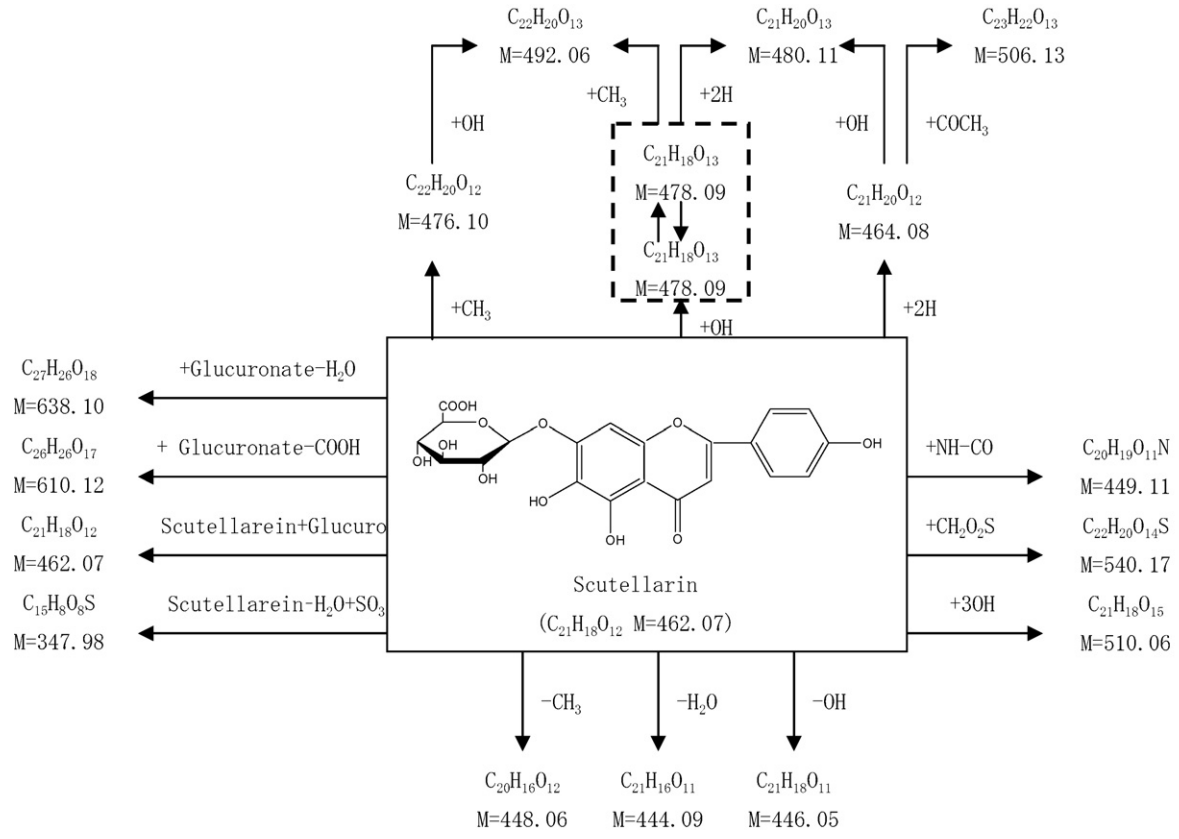


Fig. 4. Metabolism profile of scutellarin in urine after oral single dose of scutellarin to rats (80.8 mg/kg, $n = 6$).

Table 2
Recoveries and precisions of QC levels of scutellarin ($n = 3$).

Spiked concentration (μg/mL)	Recovery (%)	Intra-day precision (RSD%)	Inter-day precision (RSD%)
1.065	96.51 ± 2.11	11.16	13.22
10.65	99.33 ± 1.27	5.43	7.39
63.92	99.24 ± 0.88	3.18	4.91

0.023–0.138 μmol/mL (10.65–63.92 μg/mL). They showed good linear relationships between y and x. LOQ for scutellarin was 1.065 μg/mL, which actually was the lowest concentration of the standard curves. And the LOD was 0.365 μg/mL.

The recoveries, intra-day precisions, inter-day precisions of low, middle, and high QC levels of scutellarin (1.065, 10.65, and 63.92 μg/mL) are shown in Table 2. Using the content of scutellarin as index, the determined urine sample was stable at 4 °C for at least 8 h with RSD of 6.22%.

3.4. Urine pharmacokinetics

For the metabolites, it is best if their chemical structures can be confirmed by comparison with synthesized reference compounds [34]. However, the reference standards were hard to get and some compounds are even new. Considering that most metabolites have the same or a similar parent nucleus, using the parent drug to semi-quantitate is a useful tool. The excreted amount time profiles of the main metabolites of scutellarin are shown in Fig. 5. For most metabolites, the time (T_p) of peak excretion was 8–12 h. Only for the compounds with MW of 347.98, 540.17, and 448.06, T_p was 4–8 h. The main pharmacokinetic parameters of the metabolites are shown in Table 3. It is clear that the compounds with MW of 449.11, 638.10, 540.17, 610.02, 347.98, and 506.13 are the main metabolites. Calculated as scutellarin, the cumulative amount of metabolites excreted into urine was 389.26 μg and the cumulative urine excretion rate was 1.93% compared with the oral dosage of 20.2 mg per rat with a body weight of 250 g (i.e. 80.8 mg/kg).

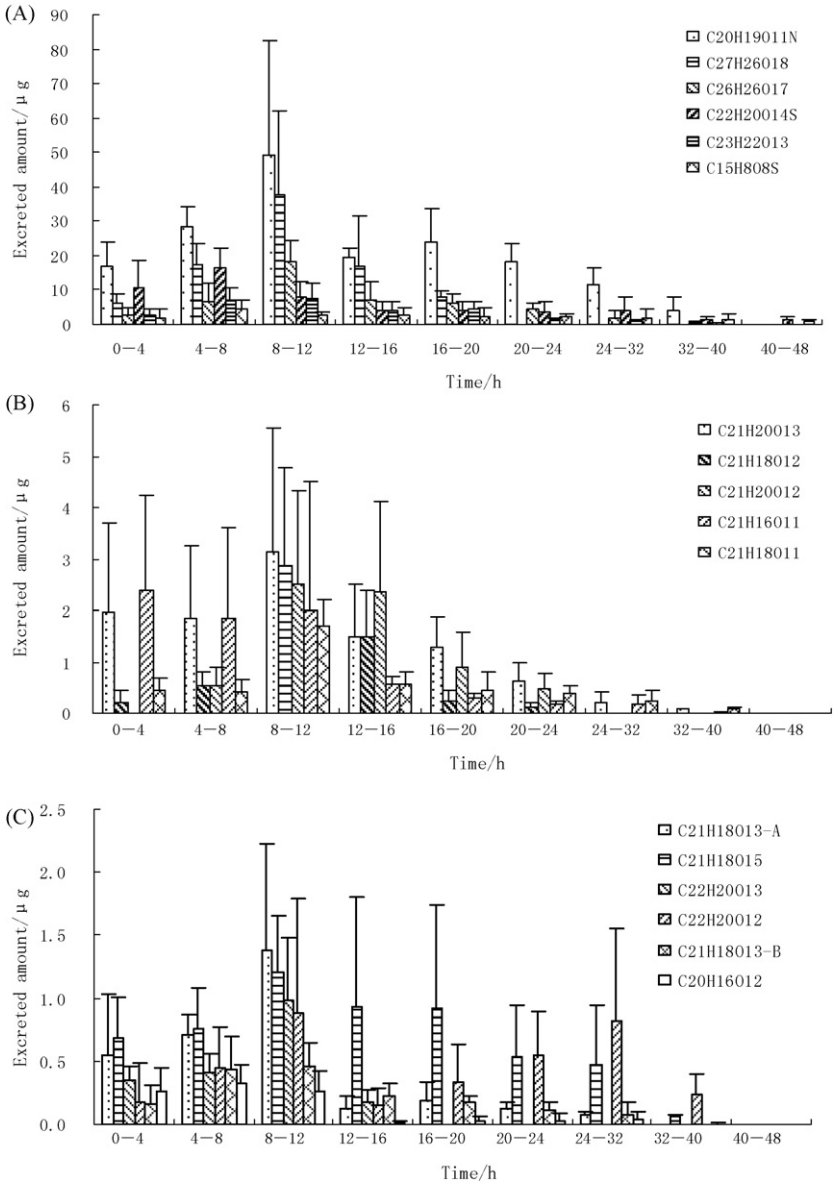


Fig. 5. Excreted amount of the metabolites of scutellarin in urine after oral single dose of scutellarin to rats (80.8 mg/kg, $n = 6$). (A) Compounds of $C_{20}H_{19}O_{11}N$, $C_{27}H_{26}O_{18}$, $C_{26}H_{26}O_{17}$, $C_{22}H_{20}O_{14}S$, $C_{23}H_{22}O_{13}$, and $C_{15}H_8O_8S$, (B) Compounds of $C_{21}H_{20}O_{13}$, $C_{21}H_{18}O_{12}$, $C_{21}H_{20}O_{12}$, $C_{21}H_{16}O_{11}$, and $C_{21}H_{18}O_{11}$, (C) Compounds of $C_{21}H_{18}O_{13}$-A ($t_r = 5.63$ min in UPLC), $C_{21}H_{18}O_{15}$, $C_{22}H_{20}O_{13}$, $C_{22}H_{20}O_{12}$, $C_{21}H_{18}O_{13}$-B ($t_r = 5.72$ min in UPLC), and $C_{20}H_{16}O_{12}$.

Table 3
Main pharmacokinetical parameters of the metabolites of scutellarin in rat urine after oral single dose of scutellarin with 80.8 mg/kg ($n = 6$, calculated as body weight of 250 g).

Number	Compound (M.W.)	$t_{1/2}$ (h)	K_e (h^{-1})	Cumulative urine excretion amount (μg)	Cumulative urine excretion amount calculated as scutellarin (μg)	Cumulative urine excretion rate calculated as scutellarin (%)
1	510.06	8.255 ± 2.253	0.089 ± 0.023	5.57 ± 2.07	5.05 ± 1.88	0.0250 ± 0.0093
2	476.10	61.768 ± 55.984	0.025 ± 0.025	3.63 ± 1.00	3.52 ± 0.97	0.0174 ± 0.0048
3	347.98	16.676 ± 11.383	0.056 ± 0.029	19.50 ± 12.16	26.02 ± 16.23	0.129 ± 0.0803
4	540.17	12.243 ± 4.098	0.065 ± 0.033	49.37 ± 34.50	42.40 ± 29.63	0.210 ± 0.147
5	449.11	18.541 ± 9.034	0.042 ± 0.012	160.26 ± 24.35	165.62 ± 25.16	0.820 ± 0.125
6	638.10	6.796 ± 3.790	0.120 ± 0.040	82.06 ± 28.45	59.64 ± 20.68	0.295 ± 0.102
7	464.08	4.667 ± 0.233	0.149 ± 0.008	4.48 ± 4.02	4.48 ± 4.03	0.0222 ± 0.0199
8	506.13	9.017 ± 9.030	0.114 ± 0.046	19.30 ± 16.80	17.69 ± 15.40	0.0876 ± 0.0762
9	462.07	8.543 ± 2.724	0.091 ± 0.040	4.89 ± 1.93	4.89 ± 1.93	0.0242 ± 0.0096
10	444.09	4.905 ± 0.503	0.143 ± 0.017	5.43 ± 6.32	5.67 ± 6.61	0.0281 ± 0.0327
11	446.05	7.172 ± 1.176	0.099 ± 0.021	3.41 ± 2.20	3.55 ± 2.29	0.0176 ± 0.0113
12	610.02	13.57 ± 10.822	0.072 ± 0.037	47.49 ± 19.69	35.97 ± 14.91	0.178 ± 0.0738
13	478.09 (5.63 min)	4.667 ± 0.418	0.150 ± 0.014	2.70 ± 1.32	2.62 ± 1.28	0.0130 ± 0.00634
14	478.09 (5.72 min)	4.514 ± 0.461	0.155 ± 0.014	1.10 ± 0.83	1.07 ± 0.81	0.00528 ± 0.0040
15	448.06	7.853 ± 0.973	0.09 ± 0.012	0.94 ± 0.19	0.97 ± 0.20	0.00480 ± 0.001
16	492.06	3.590 ± 0.908	0.171 ± 0.098	1.91 ± 0.40	1.80 ± 0.38	0.00894 ± 0.0019
17	480.11	5.526 ± 0.460	0.126 ± 0.012	10.08 ± 5.38	9.70 ± 5.18	0.129 ± 0.0257
	Sum	–	–	422.12	389.26	1.93

4. Conclusion

The metabolism profile of scutellarin in urine was studied following oral administration of a single dose of scutellarin to SD rats. Using UPLC/TOF MS, 17 metabolites of scutellarin were found and determined in rat urine, including isoscutellarin, methylated scutellarin, reduced scutellarin, scutellarin conjugated with glucuronate, *etc*., most of which were discovered for the first time. The main advantages of UPLC/MS were that the separation time was much shorter and the resolving power was significantly improved. Therefore, the method could be used to assay trace metabolites and to identify the reactions generating these metabolites especially with the aid of software such as Masslynx. This could provide more comprehensive insights and guidance for elucidation of side effect mechanism and safety monitoring as well as for rational formulation design in drug delivery system.

Acknowledgement

The project was supported by the National Natural Science Fund (No. 30500666) and the Tsinghua Yuyuan Medical Fund (No. 20240000548).

References

[1] X.L. Li, Y.Q. Li, W.M. Yan, H.Y. Li, H. Xu, X.X. Zheng, D.W. Guo, L. Tang, Planta Med. 70 (2004) 1–6.
[2] H. Hong, G.Q. Liu, Life Sci. 74 (2004) 2959–2973.
[3] H. Liu, X.L. Yang, R. Tang, J. Liu, H.B. Xu, Pharm. Res. 51 (2005) 205–210.
[4] G.H. Zhang, Q. Wang, J.J. Chen, X.M. Zhang, S.C. Tam, Y.T. Zheng, Biochem. Biophys. Res. Commun. 334 (2005) 812–816.
[5] X.H. Hao, G. Cheng, J. Sun, M.J. Zou, J. Yu, S. Zhang, F.D. Cui, J. Pharm. Biomed. Anal. 38 (2005) 360–363.
[6] D.F. Zhong, B.H. Yang, X.Y. Chen, K. Li, J.H. Xu, J. Chromatogr. B 796 (2003) 439–444.
[7] F. Xiong, H. Wang, J. Cheng, J.B. Zhu, J. Chromatogr. B 835 (2006) 114–118.
[8] J.M. Huang, N. Li, Y.Q. Yu, W.Y. Weng, X.B. Huang, J. Pharm. Biomed. Anal. 40 (2006) 465–471.
[9] F. Cao, J.X. Guo, Q.N. Ping, Z.G. Liao, Eur. J. Pharm. Sci. 29 (2006) 385–393.
[10] Y.L. Shen, F. Feng, J. Chromatogr. B 830 (2006) 1–5.
[11] X.Y. Chen, L. Cui, X.T. Duan, B. Ma, D.F. Zhong, Drug Metab. Dispos. 34 (2006) 1345–1352.
[12] J.L. Zhang, Q.M. Che, S.Z. Li, T.H. Zhou, J. Asian Nat. Prod. Res. 5 (2003) 249–256.
[13] E.J. Want, C.A. Smith, C.A. Qin, K.C. VanHorne, G. Siuzdak, Metabolomics 2 (2006) 145–154.
[14] Y.Z. Li, G.R. Bao, H. Wang, Chin. J. Chromatogr. 26 (2008) 494–498.
[15] X.J. Chen, H. Ji, Q.W. Zhang, P.F. Tu, Y.T. Wang, B.L. Guo, S.P.A. Li, J. Pharm. Biomed. Anal. 46 (2008) 226–232.
[16] J. Guan, C.M. Lai, S.P. Li, J. Pharm. Biomed. Anal. 44 (2007) 996–1000.
[17] J. Wang, X.L. Pang, F. Ge, Z.Y. Ma, Toxicon 49 (2007) 1120–1128.
[18] H. Chang, S.M. Wu, J.Y. Hua, M. Asami, S. Kunikane, J. Chromatogr. A 1195 (2008) 44–51.
[19] Z.X. Cai, Y. Zhang, H.F. Pan, X.W. Tie, Y.P. Ren, J. Chromatogr. A 1200 (2008) 144–155.
[20] R.R. González, A.G. Frenich, J.L.M. Vidal, Talanta 76 (2008) 211–225.
[21] B. Avula, Y.H. Wang, R.S. Pawar, Y.T.J. Shukla, T.J. Smillie, I.A. Khan, J. Pharm. Biomed. Anal. 48 (2008) 722–731.
[22] G.X. Xie, Y. Ni, M.M. Su, Y.Y. Zhang, A.H. Zhao, X.F. Gao, Z. Liu, P.G. Xiao, W. Jia, Metabolomics 4 (2008) 248–260.
[23] M. Dan, M.M. Su, X.F. Gao, T. Zhao, A.H. Zhao, G.X. Xie, Y.P. Qiu, M.M. Zhou, Z. Liu, W. Jia, Phytochemistry 69 (2008) 2237–2244.
[24] J. Tang, R.H. Zhu, R.K. Zhao, G. Cheng, W.X. Peng, J. Pharm. Biomed. Anal. 47 (2008) 923–928.
[25] P.M.W. Lam, T.H. Marczylo, M.E. Talatini, M. Finney, V. Nallendran, A.H. Taylor, J.C. Konje, Anal. Biochem. 380 (2008) 195–201.
[26] W.Z. Ju, J.H. Chu, R.X. Tan, N.N. Xiong, Chin. J. Clin. Pharm. Ther. 11 (2006) 292–295.
[27] Q.H. Ge, Z. Zhou, X.J. Zhi, L.L. Ma, Chin. J. Pharm. 34 (2003) 618–632.
[28] J.I. García Alonso, M.G. Camblor, M.M. Bayón, J.M. MarchanteGayon, A. Sanz-Medel, J. Mass Spectrom. 32 (1997) 556–564.
[29] M.M. Bayón, J.I. García Alonso, A. Sanz-Medel, J. Anal. At. Spectrom. 13 (1998) 277–282.
[30] M.M. Bayón, J.I. García Alonso, A. Sanz-Medel, J. Anal. At. Spectrom. 13 (1998) 1027–1032.
[31] H.D. Chen, E. Dabek-Zlotorzynska, P.E. Rasmussen, N. Hassan, M. Lanouette, Talanta 74 (2008) 1547–1555.
[32] J. He, T. Bernd, C. Zang, B.K. Zhang, R.H. Zhu, F. Wang, F.L. Su, J. Song, J. Tang, W.X. Peng, Eur. J. Clin. Pharmacol. 63 (2007) 663–668.
[33] C.G. Ding, Q.H. Ge, Chin. J. Pharm. 37 (2006) 26–31.
[34] G. Horváth, M. Pátfalusi, S. Mészáros, L. Vereczkey, J. Chromatogr. 578 (1992) 91–101.

Talanta 80 (2009) 92–97

Contents lists available at ScienceDirect

Talanta

journal homepage: www.elsevier.com/locate/talanta

A ratiometric fluorescent probe for fluoride ion employing the excited-state intramolecular proton transfer

Xiao-Feng Yang*, Haiping Qi, Liping Wang, Zhuan Su, Gang Wang

Key Laboratory of Synthetic and Natural Functional Molecule Chemistry of Ministry of Education, Institute of Analytical Science, Department of Chemistry, Northwest University, North Taibai Road 229#, Xi'an 710069, Shaanxi, China

ARTICLE INFO

Article history:
Received 1 April 2009
Received in revised form 6 June 2009
Accepted 10 June 2009
Available online 18 June 2009

Keywords:
Fluoride ion
Fluorescent probe
2-(2′-Hydroxyphenyl)benzimidazole
Ratiometric
Excited-state intramolecular proton transfer

ABSTRACT

A ratiometric fluorescent probe **1** for fluoride ion was developed based on modulation of the excited-state intramolecular proton transfer (ESIPT) process of 2-(2′-hydroxyphenyl)benzimidazole (HPBI) through the hydroxyl group protection/deprotection reaction. The probe **1** was readily prepared by the reaction of HPBI with *tert*-butyldimethylsilyl chloride (TBS-Cl) and shows only fluorescence emission maximum at 360 nm. Upon treatment with fluoride in aqueous DMF solution, the TBS protective group of probe **1** was removed readily and ESIPT of the probe was switched on, which resulted in a decrease of the emission band at 360 nm and an increase of a new fluorescence peak around 454 nm. The fluorescent intensity ratio at 454 and 360 nm (I_{454}/I_{360}) increases linearly with fluoride ion concentration in the range 0.3–8.0 μmol L^{-1} and the detection limit is 0.19 μmol L^{-1}. The proposed probe shows excellent selectivity toward fluoride ion over other common anions. The method has been successfully applied to the fluoride determination in toothpaste and tap water samples.

© 2009 Elsevier B.V. All rights reserved.

1. Introduction

The development of fluorescent sensors and probes for anions has received considerable attention due to their important roles in chemical and biological process [1–3]. Fluoride ion is of particular interest because of its role in preventing from dental cares and in treatment of osteoporosis [4]. However, a high intake of fluoride ion can lead to fluorosis [5], which corresponds to a fluoride 'disease'. Therefore, the design of reliable sensing method for fluoride ion is needed for environment and human health care. Unfortunately, most fluoride probes developed so far are operative at only the detection signal [6–11], factors such as instrumental efficiency, environmental conditions, and the probe concentration can interfere with the signal output.

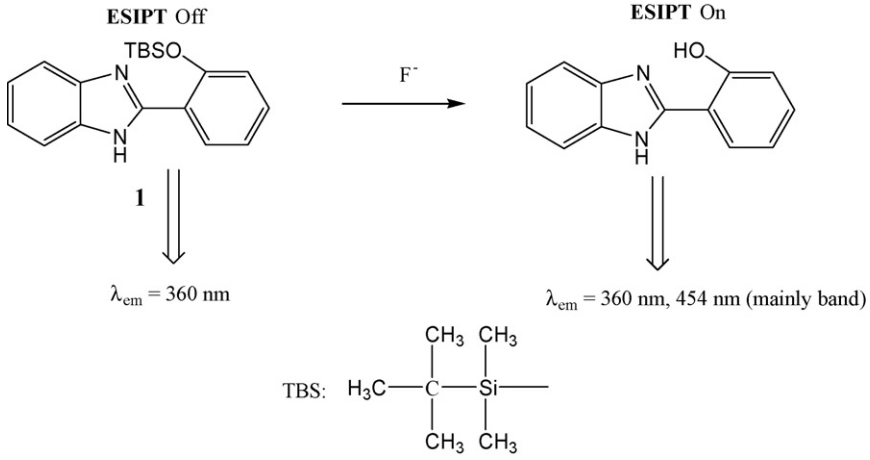
Ratiometric fluorescent probes allow the measurement of emission intensities at two different wavelengths, which can overcome the drawbacks of intensity-based measurements due to a built-in correction for environmental effects (i.e. cancelling artifacts due to probe concentration variations) and increase the selectivity, sensitivity and dynamic ranges of the method [12–14]. However, up to now, only a few ratiometric fluorescent probes for fluoride ion [15–17] have been reported and they suffered some drawbacks such as low sensitivity [17] or non-aqueous solvent media requirement [16]. Therefore, there is a strong desire to develop new ratiometric fluorescent probes for fluoride with new mechanism.

It is well-known that 2-(2′-hydroxyphenyl)benzimidazole (HPBI) can undergo an excited-state intramolecular proton transfer (ESIPT) from the acidic (hydroxyl proton) to the basic site (aromatic nitrogen) when photoexcitation changes their charge density distribution [18–21]. In the ground state, the most stable form of HPBI is usually the enol form (**E**). However, in the first excited singlet state, in which the hydroxyl group is much more acidic and the nitrogen much more basic than in the ground state, the most stable structure is usually the keto tautomer (**K**). As a result, excitation of the enol form of HPBI tends to be followed by transformation to the keto form in the excited state via ESIPT reaction. This photo-induced tautomerization process is usually ultrafast because the transferring proton is already next to the proton acceptor at the moment of excitation. Accordingly, HPBI can emit two emission bands upon photoexcitation. The emission near 360 nm is the E* form, and the emission near 454 nm is the K* form. As the regulation of ESIPT can effectively shift the emission wavelength, we envisioned that this signal transduction mechanism could be employed to probe design.

Herein, a ratiometric fluorescent probe **1** for fluoride ion was developed. The probe **1** was prepared by the reaction of HPBI with *tert*-butyldimethylsilyl chloride (TBS-Cl). Once its hydroxyl group was protected by TBS group, the ESIPT process of HPBI was switched off and probe **1** shows only fluorescence emission maximum at 360 nm (the E* form). Because of the high affinity of fluoride for silicon, silyl ethers are easily cleaved by fluoride. Upon introducing fluoride in DMF/water (80:20, v/v), the TBS group of probe **1** was

* Corresponding author. Tel.: +86 29 88302604; fax: +86 29 88303798.
E-mail address: xfyang@nwu.edu.cn (X.-F. Yang).

0039-9140/$ – see front matter © 2009 Elsevier B.V. All rights reserved.
doi:10.1016/j.talanta.2009.06.030



Scheme 1. Design concept of ratiometric fluorescent probe **1** for fluoride.

removed readily through a fluoride-induced Si–O bond cleavage and the ESIPT process of the probe was switched on. Accordingly, it was observed that the fluorescence emission at 360 nm shows "turn-off", while the fluorescence emission at 454 nm shows "turn-on" (Scheme 1). The fluorescent intensity ratio of I_{454}/I_{360} (where I_{454} and I_{360} represents the fluorescence emission signal at 454 and 360 nm, respectively) increases linearly with fluoride concentration in the range 0.3–8.0 μmol L^{-1} and the detection limit is 0.19 μmol L^{-1}. The proposed probe shows excellent selectivity toward fluoride over other common anions, and the proposed probe has been successfully applied to the fluoride determination in toothpaste and tap water samples.

2. Experimental

2.1. Apparatus

The fluorescence spectra and relative fluorescence intensity were measured with a Sanco CRT-970 spectrofluorimeter (Shanghai, China) with a 10 mm quartz cuvette. The excitation and emission wavelength bandpasses were both set at 10 nm. The absorption spectra were measured with a Shimadzu UV-1700 spectrophometer (Tokyo, Japan). The pH was measured with a Model pHs-3B meter (Shanghai, China). Infrared spectra were taken in KBr pellets on a Bruker Tensor 27 FTIR spectrometer. Mass spectra were obtained with AXIMA-CFR plus MALDI-TOF Mass Spectrophotometer. ^{1}H NMR spectra were recorded on an INOVA-400 spectrometer (Varian Unity), using tetramethylsilane (TMS) as internal standard.

2.2. Reagents

A stock solution of 0.01 mol L^{-1} fluoride was prepared by dissolving 42.0 mg of sodium fluoride in 100 mL water. Standard test solutions were prepared by appropriate dilution of the stock solution. The solution of **1** (0.5 mmol L^{-1}) was prepared by dissolving 16.2 mg of the probe in 100 mL ethyl acetate, and this solution was stored in the refrigerator at 4 °C. A 0.2 mol L^{-1} Na_2HPO_4–NaH_2PO_4 buffer solution (pH 7.0) was employed. The sources of reagents were as follows: sodium fluoride was obtained from Beijing Chemical Reagent factory; *tert*-butyldimethylsilyl chloride was obtained from Shanghai Heqi Chemical Reagent Co.; 2-phenylbenzimidazole (PBI) was obtained from Alfa Aesar; o-phenylenediamine and salicylaldehyde were obtained from Xi'an Chemical Reagent Co.

All the reagents were of analytical-reagent grade, and doubly distilled water was used throughout.

2.3. Synthesis of probe *1*

HPBI was synthesized according to the method reported by Tavman for the synthesis of 2-(5-methyl-1H-benzimidazol-2-yl)-4-bromo/nitro-phenols [22]. The probe **1** was prepared by a modification of published method [11,24] using a simple one-step reaction of HPBI with *tert*-butyldimethylsilyl chloride (TBS-Cl) by using imidazole as catalyst and THF as solvent. Briefly, HPBI (0.30 g, 1.43 mmol) was combined with imidazole (0.2769 g, 4.07 mmol) in 7 mL anhydrous THF and stirred. To the above solution TBS-Cl was added (0.3441 g, 2.28 mmol). The reaction mixture was stirred at room temperature overnight. Then, the reaction mixture was poured into saturated brine (~50 mL) and extracted with ethyl acetate. The combined organic extracts were washed with saturated brine, dried over anhydrous Na_2SO_4 and the solvent evaporated to dryness, giving 0.34 g of orange solid. This solid was subjected to silica gel (200–300 mesh) chromatography eluted with acetone/petroleum ether (1:4, v/v) to afford the desired product (0.25 g, 55% yield) as off-white solid. TLC R_f 0.46 (1:4, acetone/petroleum ether). IR (KBr, cm^{-1}), 2929, 2857, 1602, 1489, 1471, 1457, 1389, 1256, 1159, 1109, 917, 838, 826, 782, 759 (Fig. S1). MS (MALDI-TOF): calculated for MH^+, 325.50; found 325.47 (Fig. S2). ^{1}H NMR (400 MHz, $CDCl_3$): δ 8.02 (d, 1H, J = 7.6 Hz), 7.72 (d, 1H, J = 7.6 Hz), 7.54 (d, 1H, J = 7.2 Hz), 7.44 (m, 2H), 7.25–7.13 (m, 2H), 6.82–6.95 (m, 1H), 1.07 (s, 9H), 0.28 (s, 6H).

2.4. General procedure

The fluorogenic reaction was performed in a 10-mL volumetric tube. Typically, to a test tube containing 4.0 mL of DMF and 24 μL of 0.5 mmol L^{-1} of **1**, different concentrations of fluoride was added and the reaction mixture was diluted to 5.0 mL with water. The reaction solution was kept at room temperature (25 °C) for 40 min, then 1.0 mL of 0.2 mol L^{-1} Na_2HPO_4–NaH_2PO_4 buffer solution (pH 7.0) was added and the solution was diluted to 10 mL with water. The fluorescence ratio of I_{454}/I_{360} was measured with the excitation and emission wavelengths at 310 and 454/360 nm, respectively.

3. Results and discussion

3.1. Design of probe *1*

It was reported that HPBI displays dual fluorescence emission due to ESIPT [19–21]. To identify the above results, the absorption and fluorescence spectra of HPBI were measured and compared with that of PBI (the structure is shown Fig. 1). As can be seen from

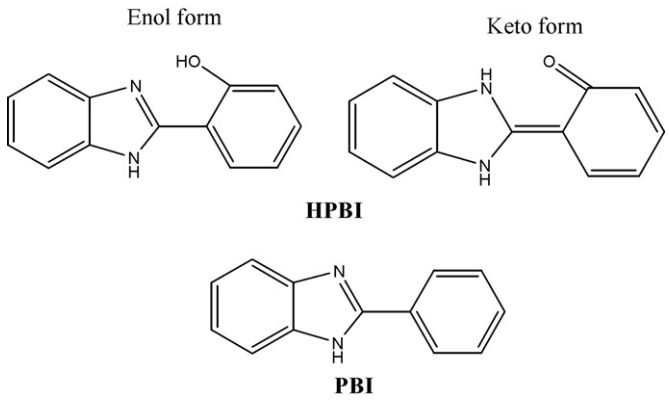


Fig. 1. Chemical structures of PBI, enol and keto form of HPBI.

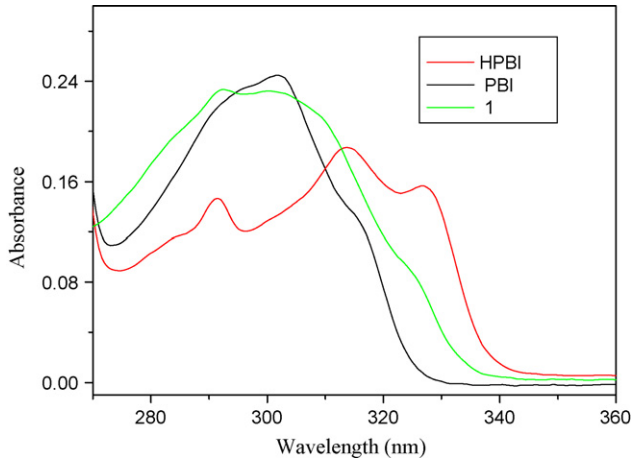


Fig. 2. Absorption spectra of 10 μmol L^{-1} HPBI, PBI and **1** in 20% (v/v) methanol–water solution buffered at pH 7.0.

Fig. 2, the absorption spectrum of HPBI shows absorption at 291, 315 and 324 nm, while for PBI, only a broad absorption band centered at 308 nm is observed. Furthermore, the fluorescence spectra of HPBI and PBI were recorded under identical conditions (Fig. 3). It can be observed that HPBI shows two emission bands centered at 360 and 454 nm, respectively. As for PBI, ESIPT cannot occur because of lacking hydroxyl group on its structure, thus only a single fluorescence emission band at 360 nm being observed. The above results

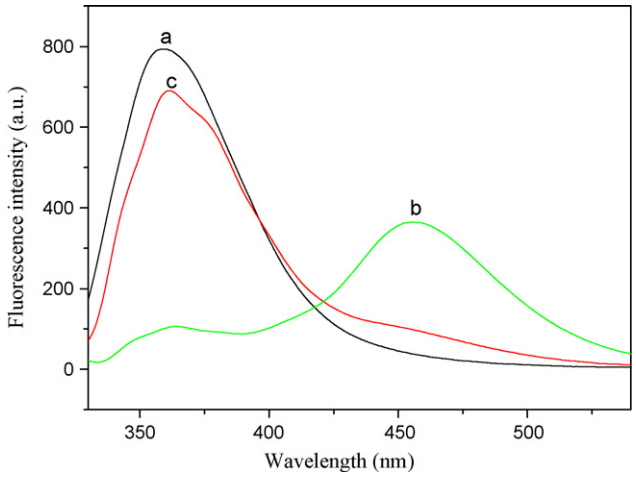


Fig. 3. Fluorescent spectra of 1.0 μmol L^{-1} PBI (a), HPBI (b) and **1** (c) in 40% (v/v) DMF–water solution buffered at pH 7.0 (λ_{ex} = 310 nm).

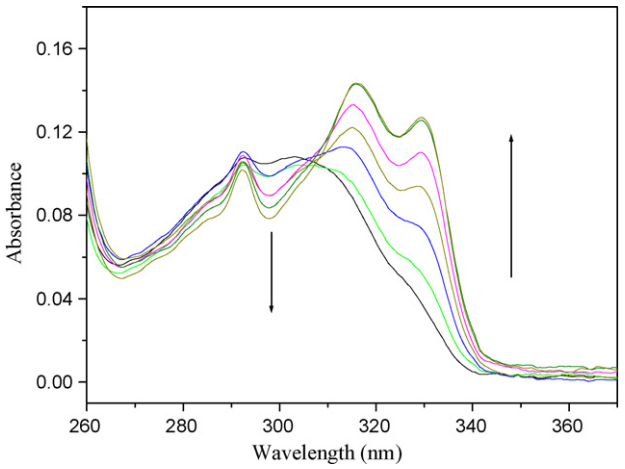


Fig. 4. Absorption spectra of **1** (5.0 μmol L^{-1}) after incubation with increasing concentrations of fluoride ion [0, 2, 4, 6, 8, 10 and 20 μmol L^{-1}, respectively] in DMF–water solution buffered at pH 7.0. Other reaction conditions are the same as those described in Section 2.4.

indicate that hydroxyl group on HPBI plays a key role for its emission characteristics. Encouraged by these results, we anticipated that ESIPT process of HPBI would be switched off if the hydroxyl group of HPBI was modified, and its spectral characteristics should behave like that of PBI. As expected, when the hydroxyl radical of HPBI was protected by TBS group (yielding the probe **1**), its absorption and fluorescence spectra are very similar to that of PBI at the same conditions (shown in Figs. 2 and 3). In the presence of hydroxyl group, ESIPT can take place and the K* emission at 454 nm is the major emission band. However, when the hydroxyl group is in a state of protection, only the E* emission at 360 nm can be recorded. Therefore, modulation of the features of the functional hydroxyl group of HPBI can manipulate ESIPT to afford a large wavelength shift in the spectra of the probe with and without the addition of analyte.

On the other hand, it is well known that *tert*-butyldimethylsilyl ether has been extensively utilized as protecting group in organic synthesis for hydroxy functionality [23–28]. The resulting silyl ethers can be easily converted to their parent compounds by fluoride ion [27]. Such mechanism has been exploited in the design of fluoride-sensing systems [8,10,11,29,30] but no ratiometric fluorescent probes for fluoride were reported. Based on these considerations, probe **1** was designed as a ratiometric fluorescent probe for fluoride based on modulation of ESIPT process via protection/deprotection of the functional hydroxyl group.

3.2. Spectral characteristics

Fig. 4 depicts the spectrophotometric changes of probe **1** upon mixing with fluoride ion in aqueous DMF solution. With an increasing amount of fluoride ion, the absorption band at 293 nm decreased, while the new band at 315 and 324 nm increased gradually. The final spectrum is in agreement with the characteristic absorption of HPBI, indicating that HPBI is formed in the present deprotection reaction. Furthermore, the probe **1** was mixed with different concentrations of fluoride, and the changes of fluorescence spectra are shown in Fig. 5. In the absence of fluoride, probe **1** exhibited one typical fluorescence peak at 360 nm. However, upon addition of an increasing concentration of fluoride, the emission band of probe **1** at 360 nm gradually decreased with the concomitant growth of a new emission band at 454 nm due to the restoration of ESIPT process.

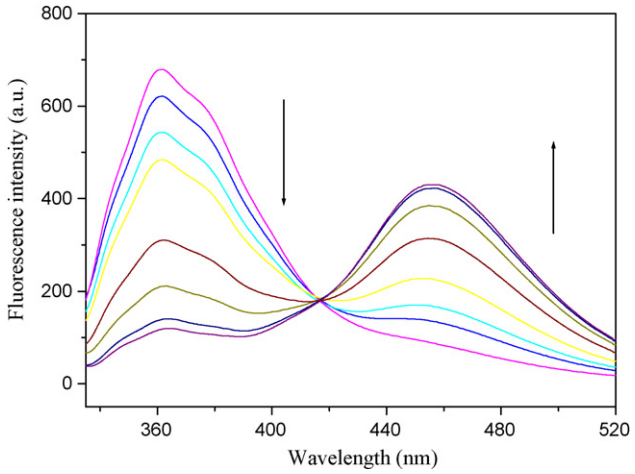


Fig. 5. Fluorescent emission spectra (λ_{ex} = 310 nm) of **1** (1.2 μmol L^{-1}) after incubation with increasing concentrations of fluoride ion [0, 0.3, 0.5, 1, 2, 4, 6 and 8 μmol L^{-1}, respectively] in DMF–water solution buffered at pH 7.0. Other conditions are the same as those described in Section 2.4.

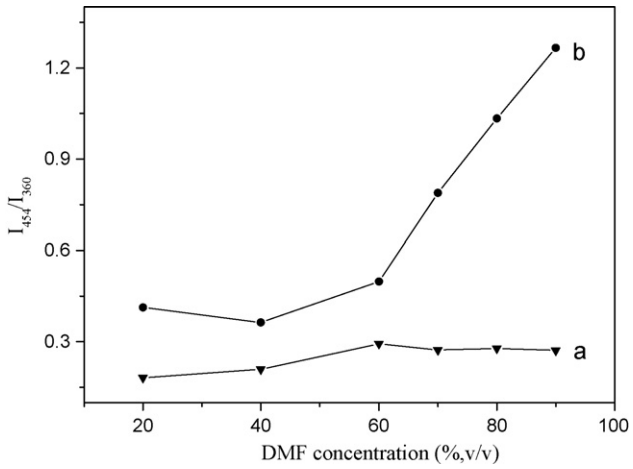


Fig. 6. Effect of DMF concentration on I_{454}/I_{360} of **1** (1.2 μmol L^{-1}) in the absence (a) and presence (b) of fluoride ion (2.0 μmol L^{-1}) in DMF–water solution buffered at pH 7.0. Other conditions are the same as those described in Section 2.4.

3.3. Effect of the reaction media and detection pH

It was reported that the removal of silyl protecting group by fluoride ion was favorable in aprotic medium [27]. However, non-aqueous reaction media was unfavorable for real sample assays. In the present study, we tuned the reaction conditions to the water/organic cosolvent mixtures and different organic solvents were tested under identical conditions. It can be seen from Table 1 that organic solvent has great effects on the deprotection reaction. When the deprotection reaction was performed in DMF–water solution, a high I_{454}/I_{360} was obtained, indicating that the cleavage of silyl ether by fluoride ion was more efficient in DMF–water solution.

Further, the effect of DMF concentration on I_{454}/I_{360} value of the reaction system was studied, and the results are shown in Fig. 6. It can be seen that I_{454}/I_{360} value remains almost unchanged when DMF concentration is in the range 0–60%, and increases dramatically when the concentration of DMF is above 60%. To facilitate the real sample analysis, 80% DMF–water solution was selected as the reaction media in the following experiment.

The detection pH of the reaction solution was investigated in the range 4.0–12.0, and it was found that probe **1** was unstable in high or low pH media and would cause a high background signal (Fig. S3). On other hand, the fluorescence ratio signal of HPBI remained stable in the pH range 4.0–10.0 (Fig. S4). Therefore, pH 7.0 phosphate buffer solution was selected as the detection media in the following study.

Table 1
Effect of solvent on the deprotection of **1** by fluoride ion.

Solvent[a]	I_{454}/I_{360}[b]	I_{454}/I_{360}[c]
Methanol	0.09	0.11
Ethanol	0.07	0.11
Acetone	0.25	0.38
DMF	0.13	0.92
Acetonitrile	0.09	0.22
THF	0.08	0.16

[a] Solvent concentration: solvent/water, 4:1 (v/v). Probe **1**: 1.2 μmol L^{-1}. Other conditions are the same as those described in Section 2.4.

[b] The emission ratio of probe **1** in the absence of fluoride.

[c] The emission ratio of probe **1** in the presence of fluoride (2.0 μmol L^{-1}).

3.4. Effect of reaction time

The effect of the reaction time on I_{454}/I_{360} of the system was studied and the results are shown in Fig. 7. It can be seen that I_{454}/I_{360} increased gradually with increasing the reaction time, and the complete cleavage of TBS group from the probe required several hours under the selected reaction conditions. Though the sensitivity of the present method could be increased with increasing the incubation time, a 40-min reaction time was selected as a compromise of sensitivity and analytical frequency.

3.5. Effect of probe concentration and reaction temperature

The effect of probe concentration on I_{454}/I_{360} of the system was studied and the results are shown in Fig. S5. It can be observed that I_{454}/I_{360} decreased with increasing the concentration of probe **1**. As a compromise of high sensitivity and wide linear range, the concentration of probe **1** was selected at 1.2 μmol L^{-1}.

The effect of reaction temperature on the fluoride-induced cleavage of TBS group from probe **1** was investigated in the range 20–60 °C (Fig. S6). The results showed that both background and fluorescence ratio signal increased with increasing temperature, but the signal-to-noise ratio (S/N) remained stable in the range

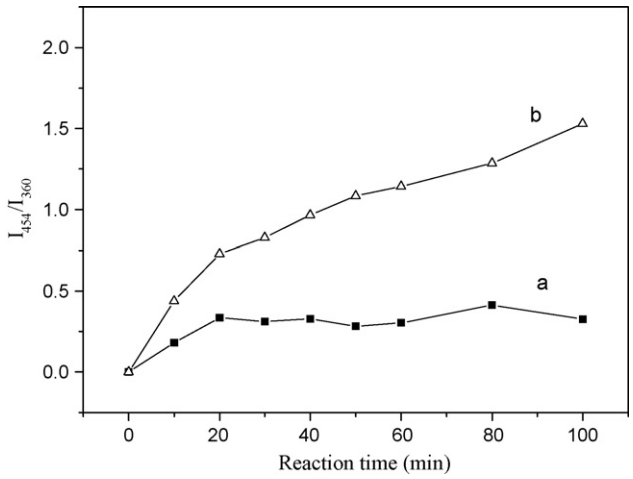


Fig. 7. Reaction-time profile of **1** (1.2 μmol L^{-1}) in the absence (a) and presence (b) of fluoride ion (2.0 μmol L^{-1}). The I_{454}/I_{360} changes were continuously monitored at time intervals. Other conditions are the same as those described in Section 2.4.

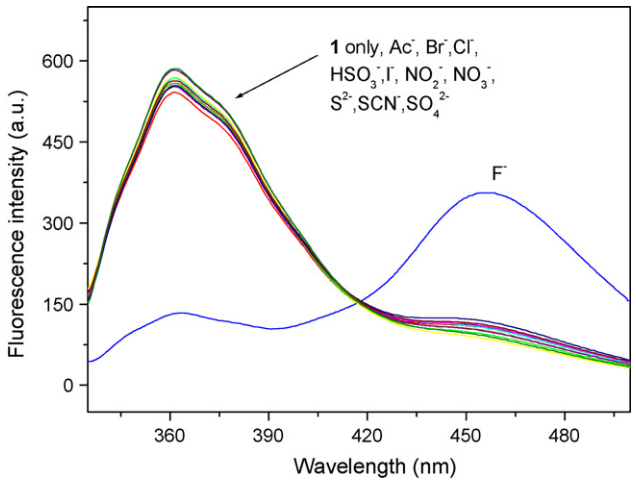


Fig. 8. Fluorescent emission changes (λ_{ex} = 310 nm) of **1** (1.2 μmol L^{-1}) upon addition of various anions (4.0 μmol L^{-1}) in DMF–water solution buffered at pH 7.0. Other conditions are the same as those described in Section 2.4.

20–50 °C, and thereafter decreased. Therefore, the reaction temperature was selected at 25 °C (room temperature) in the subsequent experiments.

3.6. Selectivity study

Changes in the fluorescence spectra of probe **1** caused by other anions, such as Cl^-, Br^-, I^-, NO_3^-, NO_2^-, S^{2-}, HSO_3^-, SO_4^{2-}, SCN^-, Ac^- were also investigated. After the addition 1.0 equiv. of each of these anions for 40 min, the fluorescence spectra of solution **1** were measured and shown in Fig. 8. It can be observed that only fluoride gave dramatic changes in fluorescence spectra, while other anions did not cause obvious changes under identical conditions. This result implies that the selectivity of **1** to fluoride over other anions is remarkably high.

To further investigate the effective applications of the probe, the effect of coexisting ions on fluoride determination were also studied by analyzing a standard solution of fluoride ion (2.0 μmol L^{-1}) to which increasing amounts of interfering species were added, using an error <5% as the criterion. The results are shown in Table 2. It can be seen that most of ions have little interference with the determination of fluoride. The high selectivity of the present probe toward fluoride over other anions can be explained by the specificity with which fluoride reacts with silicon atom. Moreover, though some heavy ions such as I^- can lead to the fluorescence quenching of the present system, the ratiometric response of probe **1** remains unchanged under these conditions, which is valuable for measuring fluoride ion in complex solutions.

3.7. Analytical characteristics of *1* for fluoride ion

Under the selected experimental conditions, I_{454}/I_{360} was plotted as a function of the fluoride concentration, and a typical calibration graph was obtained. The I_{454}/I_{360} value is linear with fluoride concentration (C) in the range 0.3–8.0 μmol L^{-1} with a correlation coefficient of r = 0.9974 (n = 7). The linear regression equation was determined to be $I_{454}/I_{360} = 0.451 \times 10^6 C$ [mol L^{-1}] + 0.095 (n = 7, r = 0.9974). According to IUPAC, the detection limit was determined from three times the standard deviation of the blank signal (3σ) as 0.19 μmol L^{-1}. The relative standard deviation (n = 7) was 4.1% for 2.0 μmol L^{-1} of fluoride ion.

Table 2
Tolerance limits of some foreign ions on the determination of fluoride ion.

Foreign ions	Molar ratio to fluoride ion[a]
Br^-, I^-, SO_4^{2-}, NO_3^-, SCN^-, Cl^-, Ba^{2+}, HSO_3^-, S^{2-}, NO_2^-, Mn^{2+}, Co^{2+}	100
Ac^-	50
Ni^{2+}, Hg^{2+}	10
Mg^{2+}, Pb^{2+}	1

[a] Fluoride concentration: 2.0 μmol L^{-1}.

Table 3
Results of determination fluoride ion in toothpaste and tap water[a].

Sample	Proposed method	ISE method
Toothpaste 1	1.19 ± 0.035 mg g^{-1}	1.16 ± 0.040 mg g^{-1}
Toothpaste 2	1.68 ± 0.025 mg g^{-1}	1.59 ± 0.052 mg g^{-1}
Tap water 1	11.06 ± 0.16 μmol mL^{-1}	11.41 ± 0.29 μmol mL^{-1}
Tap water 2	12.89 ± 0.21 μmol mL^{-1}	12.71 ± 0.19 μmol mL^{-1}

[a] Average of three measurements (±S.D.).

3.8. Sample analysis

To investigate the feasibility of probe **1** for analysis fluoride in real samples, fluoride content in toothpaste was examined. An accurately weighed amount of the commercial toothpaste sample (~1.0 g) was dispersed in 30.0 mL of double-distilled water, and stirred for 3 h at 70 °C in a polypropylene vessel with a magnetic stirrer [29]. The resulting solution was cooled to room temperature and then filtered to eliminate solids in suspension. The insoluble part was washed several times with water, and the resulting solution was diluted to 100 mL with water. This solution was diluted appropriately with water and was analyzed by the proposed method and fluoride ISE standard method [31], respectively. Moreover, the proposed probe was applied to the determination of fluoride in tap water samples by appropriate dilution with water. The results are listed in Table 3. It can be seen that the fluoride content determined using the proposed method is close to the values determined by the fluoride ISE standard method.

4. Conclusions

In summary, we have developed a ratiometric fluorescent probe for fluoride ion which operates by modulation of the ESIPT of the probe through protection/deprotection of the functional hydroxyl group. The probe **1** features a ratiometric fluorescent response to fluoride with a marked emission wavelength shift and displays high selectivity for fluoride over other anions. The method is proved to be simple, sensitive and can be broadly applicable to detection of fluoride ion in an aqueous environment. Moreover, the successful fabrication of the proposed probe provides a suitable platform to design ratiometric fluorescent probes by controlling its ESIPT process through molecular recognition reaction.

Acknowledgements

This work was supported by The Science & Technology Department of the Shaanxi Province of China (SJ08B05) and NWU Graduate Experimental Research Funds (08YSY08).

Appendix A. Supplementary data

Supplementary data associated with this article can be found, in the online version, at doi:10.1016/j.talanta.2009.06.030.

References

[1] P.D. Beer, P.A. Gale, Angew. Chem. Int. Ed. 40 (2001) 486.
[2] C. Caltagirone, P.A. Gale, Chem. Soc. Rev. 38 (2009) 520.
[3] R. Martínez-Máñez, F. Sancenón, Chem. Rev. 103 (2003) 4419.

[4] K.L. Kirk, Biochemistry of the Halogens and Inorganic Halides, Plenum Press, New York, 1991, p. 58.
[5] A. Wiseman, Handbook of Experimental Pharmacology XX/2, vol. 2, Springer-Verlag, Berlin, 1970, p. 48.
[6] E.J. Cho, J.W. Moon, S.W. Ko, J.Y. Lee, S.K. Kim, J. Yoon, K.C. Nam, J. Am, Chem. Soc. 125 (2003) 12376.
[7] S.K. Kim, J.H. Bok, R.A. Bartsch, J.Y. Lee, J.S. Kim, Org. Lett. 7 (2005) 4839.
[8] S.Y. Kim, J.I. Hong, Org. Lett. 9 (2007) 3109.
[9] Z.Q. Liu, M. Shi, F.Y. Li, Q. Fang, Z.H. Chen, T. Yi, C.H. Huang, Org. Lett. 7 (2005) 5481.
[10] C.Q. Zhu, J.L. Chen, H. Zheng, Y.Q. Wu, J.G. Xu, Anal. Chim. Acta 539 (2005) 311.
[11] X.F. Yang, S.J. Ye, Q. Bai, X.Q. Wang, J. Fluoresc. 17 (2007) 81.
[12] M.S. Tremblay, M. Halim, D. Sames, J. Am. Chem. Soc. 129 (2007) 7570.
[13] X. Zhang, Y. Xiao, X. Qian, Angew. Chem. Int. Ed. 47 (2008) 8025.
[14] W. Lin, L. Long, L. Yuan, Z. Cao, B. Chen, W. Tan, Org. Lett. 10 (2008) 5577.
[15] N. DiCesare, J.R. Lakowicz, Anal. Biochem. 301 (2002) 111.
[16] S. Kumar, V. Luxami, A. Kumar, Org. Lett. 10 (2008) 5549.
[17] R. Badugu, J.R. Lakowicz, C.D. Geddes, Sens. Actuator B 104 (2005) 103.
[18] M. Mosquera, M.C.R. Rodríguez, F. Rodríguez-Prieto, J. Phys. Chem. A 101 (1997) 2766.
[19] M. Mosquera, J.C. Penedo, M.C. Ríos Rodríguez, F. Rodríguez-Prieto, J. Phys. Chem. 100 (1996) 5398.
[20] F.R. Prieto, M.C.R. Rodríguez, M.M. González, M.A.R. FemPndez, J. Phys. Chem. 98 (1994) 8666.
[21] F. Rodríguez-Prieto, J.C. Penedo, M. Mosquera, J. Chem. Soc. Faraday Trans. 94 (1998) 2775.
[22] A. Tavman, Spectrochim. Acta A 63 (2006) 343.
[23] S.C. Burdette, C.J. Frederickson, W. Bu, S.J. Lippard, J. Am. Chem. Soc. 125 (2003) 1778.
[24] R.C. Ronald, J.M. Lansinger, T.S. Lillie, C.J. Wheeler, J. Org. Chem. 47 (1982) 2541.
[25] A.J. Liu, K. Dillon, R.M. Campbell, D.C. Cox, D.M. Huryn, Tetrahedron Lett. 37 (1996) 3785.
[26] E.J. Corey, B.B. Snider, J. Am. Chem. Soc. 94 (1972) 2549.
[27] E.J. Corey, A. Venkateswarlu, J. Am. Chem. Soc. 94 (1972) 6190.
[28] Y. Urano, M. Kamiya, K. Kanda, T. Ueno, K. Hirose, T. Nagano, J. Am. Chem. Soc. 127 (2005) 4888.
[29] A.B. Descalzo, D. Jiménez, J.E. Haskouri, D. Beltrán, P. Amorós, M.D. Marcos, R. Martínez-Máñez, J. Soto, Chem. Commun. (2002) 562.
[30] T.H. Kim, T.M. Swager, Angew. Chem. Int. Ed. 42 (2003) 4803.
[31] M.S. Frant, J.W. Ross Jr., Science 154 (1966) 1553.

Talanta 80 (2009) 98–103

Contents lists available at ScienceDirect

Talanta

journal homepage: www.elsevier.com/locate/talanta

Preparation and characterization of an immunoaffinity chromatography column for the selective extraction of trace contraceptive drug levonorgestrel from water samples

Yuwei Qiao[a], Hong Yang[b], Bin Wang[a], Juan Song[a], Anping Deng[a,*]

[a] Key Laboratory of Green Chemistry & Technology, Ministry of Education of China, College of Chemistry, Sichuan University, Wangjiang Road 29, Chengdu, 610064, China
[b] West China School of Pharmacy, Sichuan University, Renmin South Road 17, Chengdu, 610041, China

ARTICLE INFO

Article history:
Received 23 April 2009
Received in revised form 8 June 2009
Accepted 10 June 2009
Available online 18 June 2009

Keywords:
Immunoaffinity chromatography column
Levonorgestrel
Progestogens
Water sample
HPLC

ABSTRACT

The preparation and characterization of an immunoaffinity chromatography (IAC) column for the specific extraction and enrichment of trace contraceptive drug levonorgestrel (LNG) from water samples were described. The IAC column was constructed by covalently coupling specific polyclonal antibody against LNG to CNBr-activated Sepharose 4B and packed into a common solid phase extraction (SPE) cartridge. The extraction conditions including loading, washing and eluting solutions, as well as the effect of flow rate on the extraction were carefully optimized. Pure water, 5% of methanol and 50% of methanol were respectively selected as loading, washing and eluting solutions, while the flow rates in the loading, washing and eluting steps were selected to be 1.0, 2.0 and 0.5 mL min^{-1}, respectively. Under optimal conditions, the IAC column was characterized in terms of maximum capacity, extraction recovery and stability. It was found that, for IAC column packed with 0.2 g of solid support immobilized with antibody, the maximum capacity for LNG was about 260 ng. The extraction recoveries of the column for LNG at three different spiked concentrations were within 95.3–106.9%. After more than 35 times repeated usage, there was not significant loss of specific recognition. Using high performance liquid chromatography (HPLC) as an analytical tool, trace amount of LNG in the range of ng L^{-1} was found in river water and wastewater samples after 600-fold enrichment, demonstrated the feasibility of the prepared IAC column for LNG extraction.
© 2009 Elsevier B.V. All rights reserved.

1. Introduction

Levonorgestrel (LNG, Fig. 1) is a synthetic progestin used as a progestin-only emergency contraceptive, and when administered at lower doses either alone or in combination with an estrogen, as an oral contraceptive [1]. LNG was considered to be safe with highly effective contraceptive for humans and has been widely used in the world. However, it has been reported that LNG has deleterious reproductive effects including the turbulence of catamenia, increasing rate of galactophore cancer, etc. [2,3]. LNG and other steroids were normally excreted from the human body, entering the receiving water through sewage effluent. Long time existence of such drugs at trace concentration in aquatic system may disrupt endocrines of aquatic animals. LNG and other steroids are stable in environment, so they may be cumulated in human bodies through food-chain and cause a potentially adverse effect on humans. On the other hand, as the content of steroids in real wastewater samples was extremely low (in the range of ng L^{-1}) [4,5] and the interference from other compounds on the determination of LNG was unavoidable. With the increasing concern of the adverse effect of LNG and other steroids on aquatic animals and human being, effective and specific extraction of LNG or other steroids from water samples prior to analysis is urgently demanded.

Natural and synthetic steroids in water matrix are usually determined by instrumental analysis such as gas chromatography –mass spectrometry (GC–MS) [6], GC–MS/MS [7], liquid chromatography–diode array detector (LC–DAD) [4], LC–DAD–MS [5,8], LC–MS/MS [9] and LC–MS/MS with electrospray ionization (ESI) [10] or with atmospheric pressure chemical ionization (APCI) [11]. In most cases, these chromatographic methods could detect trace levels of target analytes when an extensive pre-treatment step such as solid phase extraction (SPE) was coupled with. However, current SPE is based on physicochemical retention on functionalized surface which captures not only the target analyte but also other matrix components [12,13]. The drawbacks of routine SPE techniques are their low selectivity toward the particular target analyte. New efficient cleanup techniques employing the sorbents with the high selectivity for analyte are indispensable.

Immunoaffinity chromatography (IAC) is a separation method that takes advantage of the specific and reversible interaction

* Corresponding author. Tel.: +86 28 85471302; fax: +86 28 85412907.
E-mail address: denganping6119@yahoo.com.cn (A. Deng).

0039-9140/$ – see front matter © 2009 Elsevier B.V. All rights reserved.
doi:10.1016/j.talanta.2009.06.029

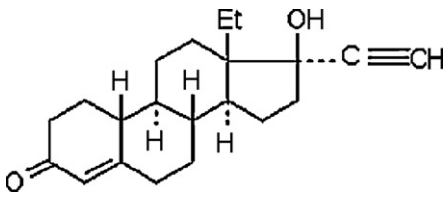


Fig. 1. Molecular structure of LNG.

between antibody and antigen [14,15]. Antibodies produced against a target analyte (antigen) are immobilized on a solid support. The immobilized antibodies will specifically retain the antigen from a solution passed through the support. Bound antigen can then be eluted and the support regenerated for reuse. IAC offers unique and powerful techniques, which enables selective extraction and enrichment of individual compounds or classes of compounds in one step. Additionally, IAC uses little or no organic solvents and columns may be reused and easily automated. IAC techniques have been widely used in clinical, biological, food and environmental areas for the extraction and enrichment of enzymes, peptides, hormones, receptors, viruses, drugs, mycotoxins, pesticides, organic contaminants in different matrices prior to analysis by on-line and off-line HPLC, gas chromatography (GC), capillary electrophoresis, or enzyme-linked immunosorbent assay (ELISA) [16–26].

In our previous study, we properly modified the LNG molecule and produced polyclonal antibody (pAb) against LNG. Then, coupled with SPE, we successfully developed a sensitive and specific ELISA for the detection of LNG in wastewater samples [27]. To overcome the non-specific absorption of SPE column, taking advantage of the specific binding of the antibody against target analyte (LNG), the aim of this work is to develop and characterize an IAC column for the effective extraction and enrichment of trace LNG from water samples prior to the analysis by HPLC. The purified pAb was covalently coupled to CNBr-activated Sepharose 4B particles and packed into a SPE column. The extraction conditions of the IAC column for LNG from water samples were optimized and the IAC column was characterized in terms of maximum capacity, extraction recovery and stability. Then IAC column was applied for the extraction and enrichment of trace LNG in real water samples. To our knowledge, it is the first report for the extraction of LNG in water samples with IAC column.

2. Experimental

2.1. Chemicals, buffers and solutions

Levonorgestrel (LNG), casein, bovine serum albumin (BSA), chicken egg ovalbumin (OVA), goat anti-rabbit IgG labeled with peroxidase (GaRIgG-POD) were purchased from Sigma (St. Louis, MO, USA). Dimethyl formamide (DMF), dimethyl sulfoxide (DMSO) and 3,3,5,5-tetramethylbenzidine (TMB) were purchased from Ameresco (Solon, Ohio, USA). CNBr-activated Sepharose 4B was purchased from Pharmacia Biotech (Uppsala, Sweden). Acetonitrile and methanol (HPLC grade) were obtained from Fluka (Buchs, Switzerland). The other reagents are all analytical grade.

Buffers and solutions: (1) coating buffer: 0.05 mol L^{-1} carbonate buffer, pH 9.8; (2) assay buffer: 0.01 mol L^{-1} phosphate-buffered saline (PBS), pH 7.4; (3) washing buffer (PBST): PBS with 0.1% (v/v) of Tween-20; (4) blocking buffer: 1% of casein in PBS; (5) acetate buffer: 100 mmol L^{-1} sodium acetate acid buffer, pH 5.7; (6) substrate solution (TMB + H_2O_2): 200 μL of 10 mg mL^{-1} TMB dissolved in DMF, 20 μL of 5% H_2O_2 and 1 mL of acetate buffer were added to 20 ml of pure water; (7) stop solution: sulfuric acid (5%); (8) LNG standard solution: the stock solution was prepared by dissolving LNG with methanol to a concentration of 1 mg mL^{-1} and stored at 4 °C. LNG standard solutions at concentrations of 0, 0.1, 0.3, 1, 3, 10, 30, 100 ng mL^{-1} was prepared by diluting the stock solution with pure water.

2.2. Instruments

Microtiter plate reader (Sunrise Remote/Touch Screen) and plate washer (M12/2R, Tecan) were bought from Tecan. Com. (Columbus plus, Austria). Ultraviolet visible spectrophotometer (UV-2300) was purchased from Techcom Com (Shanghai, China). Microtiter plate shaker (KJ-201C, Oscillator) was from Kangjian Medical Apparatus Co., Ltd. (Jiangsu China). Microtiter plates were from Haimen Plastic Co., Ltd. (Jiangsu, China). Deionized-RO water machine (DZG-303A) was purchased from AK Company (a conjunctive company between Chengdu and Taiwan, Chengdu, China).

2.3. Production and purification of polyclonal antibodies

The polyclonal antibody against LNG was produced according to the procedure described in our previous study [27]. The carbonyl group at position 3 on LNG molecule was reduced to hydroxyl group, which was then linked to ethyl bromoacetate. After hydrolysis, the LNG derivative with carboxylic group at the end of a spacer arm was obtained and covalently coupled to carrier protein. The LNG-BSA conjugate was used as immunogen for antibody production. The obtained antiserum was purified using a saturated ammonium sulfate method. The purification processes were as follows. To 2 mL of antiserum diluted with the same volume of saline, 4 mL of saturated $(NH_4)_2SO_4$ solution (pH adjusted to 7.4) was added dropwise under gently magnetic stirring at 4 °C. The obtained turbid solution was transferred to a centrifuge tube and allowed to stand for more than 1 h or overnight. Then the solution was centrifuged at 13,000 rpm for 10 min at 4 °C. The supernatant was discarded and the precipitates were dissolved in 2 mL of saline. To this solution, 1 mL of saturated $(NH_4)_2SO_4$ solution was added under magnetic stirring and allowed to stand for 1 h. Then the solution was centrifuged at 13,000 rpm for 10 min at 4 °C and the supernatant was discarded. The precipitates were dissolved in 1 mL of saline and dialyzed against 0.01 mol L^{-1} PBS. The immunoglobulin (IgG) concentration in the obtained solution was measured with a 1 cm cell using a UV 2300 spectrophotometer and calculated based on the UV absorption difference between 280 and 260 nm. The formula used for the calculation was: $C_{protein}$ (mg mL^{-1}) = $1.45A_{280\,nm} - 0.74A_{260\,nm}$ [28].

2.4. Preparation of IAC column

The IAC column was prepared by covalently coupling polyclonal antibodies against LNG to CNBr-activated Sepharose 4B and packed into a common SPE cartridge.

The covalent immobilization of Ab on solid support was performed according to the manufacturer's instructions and related literature [28,29]. Briefly, 0.2 g freeze–dried powder of CNBr-activated Sepharose 4B was weighed into a clean beaker with 20 mL of 1 mmol L^{-1} HCl to remove the protecting suspended groups. The suspension was transferred to a sintered glass filter and the gel was washed with 200 mL of 1 mmol L^{-1} HCl in three to four fractions. The outlet of the filter was sealed, then 1.5 mL coupling buffer (0.1 mol L^{-1} $NaHCO_3$ containing 0.5 mol L^{-1} NaCl, pH 8.3) was added to the gel. The obtained gel solution was pipetted into a conical flask containing 1.0 mL (~9.0 mg) purified antibody and the reaction proceeded in the incubator shaker at room temperature for 3 h.

The resultant immunosorbent was transferred to a common SPE cartridge with frits placed on both top and bottom. The effluent was collected and measured with UV spectrophotometer. The column was washed with the coupling buffer until the UV absorbance of

Table 1
The extraction recovery of the IAC column for LNG.

Spiked concentration (ng mL^{-1})	Volume added (mL)	LNG measured (ng)	Recovery (%)	RSD (%) (n = 3)
0.01	500	4.76	95.3	7.3
0.1	100	10.69	106.9	2.1
1.0	100	103.1	103.1	9.2

the effluent at 280 nm was zero. The excess active groups on the immunosorbent were capped with the blocking buffer (0.1 mol L^{-1} Tris–HCl buffer, pH 8.0). To ensure complete blocking, the outlet of the column was sealed and the gel was immersed in two column volumes of the blocking buffer and allowed to stand for 2 h. Then the column was washed extensively with of 0.1 mol L^{-1} acetate buffer containing 0.5 mol L^{-1} NaCl (pH 4.0), and 0.1 mol L^{-1} Tris–HCl buffer containing 0.5 mol L^{-1} NaCl (pH 8.0). Finally, the column was washed with 0.01 mol L^{-1} PBS (pH 7.4) and stored in 0.01 mol L^{-1} PBS containing 0.02% NaN_3 at 4 °C until use. For comparison, a blank column without antibody immobilization was prepared as the same way described above.

2.5. Optimization of extraction conditions for IAC column

To obtain high extraction efficiency, the extraction conditions such as loading, washing and eluting solutions, as well as the effect of flow rate on the extraction should be carefully optimized. In this study, to find the optimal extraction conditions, three loading solutions (10% acetone, pure water, 0.01 mol L^{-1} PBS) at flow rate of 0.5, 1.0, 2.0 and 4.0 mL min^{-1}, two washing solutions (pure water, 5% methanol) at flow rate of 1.0, 1.5 and 2.0 mL min^{-1} and four eluting solutions containing 20%, 30%, 40% and 50% of methanol/water (v/v, %) at flow rate of 0.5, 1.0 and 2.0 mL min^{-1} were examined. 1 mL of LNG standard solution prepared in either 10% acetone, pure water or 0.01 mol L^{-1} PBS at the concentration of 100 ng mL^{-1} (total LNG: 100 ng) was loaded onto the IAC column. Then 3 mL of washing solution (pure water or 5% methanol) was applied to the column to remove the unspecific binding. Finally, 2 mL of eluting solution was loaded onto the column to elute the target analyte specifically bound on the column. All fractions in the loading, washing and eluting steps are collected (0.5 mL/tube) and evaporated to dryness by low-pressured rotation evaporator at 45 °C. The residues were dissolved in 0.5 mL pure water and detected by ELISA.

2.6. Maximum capacity of IAC column

The LNG-binding capacity (e.g. the maximum amount of LNG to be retained by immobilized antibodies in IAC column) was determined by continuously loading LNG standard solution onto the IAC column so that excess amount of LNG would saturate all accessible sites of the IAC. Under optimal extraction conditions, 9 mL of LNG standard solution at concentration of 50 ng mL^{-1} (total LNG: 450 ng) was loaded on the column. All fractions in the loading, washing and eluting steps were collected and evaporated to dryness by low-pressured rotation evaporator at 45 °C. The residues were dissolved in 0.5 mL pure water and detected by ELISA.

2.7. Procedures of ELISA

During the processes of optimizing extraction conditions and testing maximum capacity of IAC column, many fractions from the column should be collected and detected. As high throughput and low testing cost, the previously developed ELISA was employed for the detection of LNG in the fractions. The ELISA procedures were as follows. 200 μL/well of coating antigen dissolved in carbonate buffer, pH 9.8 was added to a microtiter plate (96 wells). The plate was incubated overnight at 4 °C and then washed with PBST using an automatic plate washer. Some binding sites not occupied by the coating antigen were blocked by the blocking buffer (280 μL/well) for 1 h at room temperature. After the plate was washed as before, standard solutions or samples (100 μL/well) and diluted antiserum (100 μL/well) were added and incubated for 1 h at room temperature. After washing plate, GaRIgG-POD was added (200 μL/well) and the plate was incubated for 1 h at room temperature. Washing plate again, the substrate solution (200 μL/well) was added and then the plate was shaken for about 15 min for the color development. Sulfuric acid (5%, 80 μL/well) was added to stop the enzyme reaction and the absorbance was measured at 450 nm with ELISA reader. The calibration curve in the form of absorbance ~log C was plotted automatically by the corresponding software embedded in ELISA reader. The concentrations of LNG in samples could be calculated from the standard curve run in the same plate.

2.8. Extraction recovery of IAC column

Under optimal extraction conditions, the recovery of the IAC column was measured by loading three different concentrations of LNG standard solution: 0.01, 0.1 and 1 ng mL^{-1}. Each concentration was loaded onto the column with the volume of 500, 100 and 100 mL (total LNG: 5.0, 10 and 100 ng, respectively, Table 1). The eluting solution in the eluting step was collected and evaporated to dryness by low-pressured rotation evaporator at 45 °C. The residues were dissolved in 0.5 mL mobile phase and analyzed by HPLC. The same recovery testing was performed three times

2.9. Extraction of LNG from real water samples by IAC column

Three types of water samples were collected and extracted by IAC column. Tap water, river water and wastewater (one influent and one effluent) were respectively collected from this lab, Funan River (Chengdu, China) and Wastewater Treatment Plant (Chengdu, China). River and wastewater samples were filtrated with a 0.45 μm nylon membrane filter, then the pH value of the samples was adjusted to 7.0 using 0.1 mol L^{-1} of NaOH.

300 mL of above water samples without LNG spiking was loaded to the IAC column. After loading, the column was washed with 3.0 mL methanol/water (5/95), then the LNG retained on the column was eluted with 2.0 mL of 50% of methanol/water (v/v, %). The eluting solution from eluting step was collected and evaporated to dryness by low-pressured rotation evaporator at 45 °C. The residues were dissolved in 0.5 mL of mobile phase to obtain 600-fold enrichment and analyzed by HPLC.

2.10. HPLC method

HPLC was considered a more accurate analytical method for the detection of small organic compounds, so in this study, the LNG concentration in eluting solutions in Sections 2.8 and 2.9 were measured by HPLC. A HPLC system from Alltech Associates, Inc. (Deerfield, IL, USA) with a C18 column (250 mm × 4.6 mm, 5.0 μm particle size) and the HPLC work station software used for the instrument control and data analysis was employed for detection of LNG. 20 μL sample loop was used and the detection was realized with a UV–vis 201 detector integrated into the HPLC. The mobile phase was acetonitrile/water (54:46, v/v) and the flow rate was at

1.0 mL min^{-1}. The UV detection wave length was set at 242 nm and the standard curve for LNG was constructed in the concentrations of 0, 5, 10, 50, 100, 500, 1000 ng mL^{-1}. The linear equation was found to be $y = 71.86x + 141.64$ ($R^2 = 0.999$, $n = 7$) with the detection limit of 2.5 ng mL^{-1}.

3. Results and discussions

3.1. Antibody property and purification

The property of antibody is the key parameter for the preparation of the IAC column. A high specific antibody was utilized, whose property was described in reference [28]. There are many methods for antibody purification. In this study, the saturated $(NH_4)_2SO_4$ precipitate method was employed for antibody purification due to its simplicity and avoiding loss of antibody activity. By measuring absorbance at 280 and 260 nm, the concentration of purified antibody was calculated to be 9.0 mg mL^{-1}.

3.2. Preparation of IAC column

The solid support is also a critical parameter for the preparation of IAC column. Generally, an immunoaffinity support should be mechanically and chemically stable, porous, inert, easily activated to allow antibody attachment, and possess good flow properties. Commonly used support materials include silica, agarose, cellulose, and synthetic polymers. In this study, CNBr-activated Sepharose 4B was used as a solid support because the activated functional ligands on the surface make the particles to be easy for antibody immobilization. In addition, Sepharose 4B with the properties of good chemical stability, low back pressure resistance and poor non-specific interactions is also considered to be ideal particles used in off-line applications.

The IAC column was constructed by packing the antibody immobilized Sepharose 4B into a common SPE cartridge. The effluent was collected and measured with UV spectrophotometer. The antibody bound on the column was calculated by subtracting the antibody in the effluent from initial antibody. The coupling efficiency of LNG antibody on solid support was estimated according to the ratio of Ab coupled to solid support/initial Ab. In this study, three IAC columns were prepared and the coupling efficiencies were found to be 90.0%, 91.4% and to 91.9%, e.g. about 8.1 mg of antibody was covalently coupled to 0.2 g Sepharose 4B gel packed into one IAC column.

3.3. Optimization of extraction conditions for IAC

The extraction conditions should be optimized so that in the loading step, all target analyte can be specifically bound on the column, while in the washing step, the possibly non-specifical adsorption should be removed completely, and moreover, in the eluting step, all the bound analyte should be eluted and the Ab activity should be remained as much as possible. In this study, when total 100 ng of LNG was loaded onto the IAC column, three loading solutions (10% acetone, pure water, 0.01 mol L^{-1} PBS), two washing solutions (pure water, 5% methanol) and four eluting solutions (20%, 30%, 40% and 50% of methanol/pure water, v/v) were examined. It was found that when 10% acetone was used as loading solution at flow rate of 1.0 mL min^{-1}, only about 80% of LNG was bound on the column; while when pure water or 0.01 mol L^{-1} PBS was used as loading solution at 1.0 mL min^{-1}, almost all analyte was specifically bound on the column. As the IAC column was expected to be used for the extraction of LNG from water sample, therefore, pure water was selected as loading solution. At pure water as a loading solution, it was found that, at flow rate of 0.5, 1.0, 2.0 and 4.0 mL min^{-1}, 98.5%, 97.5%, 88.2% and 80.4% of analyte was specifically bound on the column, respectively. As the amount of analyte bound on the column at 0.5 and 1.0 mL min^{-1} was very close and near 100%, to reduce the loading time, the rate of 1.0 mL min^{-1} was selected for loading sample. In washing step, it was observed that either with pure water or 5% methanol to wash the column, there was no LNG in the effluent fractions, e.g. no LNG was removed from the column, but 5% methanol had the higher capability to remove non-specific binding, so 5% methanol was chosen as washing solution. At 5% methanol as a washing solution, it was found that, at flow rate of 1.0, 1.5 and 2.0 mL min^{-1}, there was no LNG removed from the column. To reduce washing time, 2.0 mL min^{-1} was chosen for washing sample. In most off-line IAC procedures, eluting the analyte bound on the column was achieved with a high percentage of an organic solvent mixed with water [26,27]. As shown in Fig. 2, with the increase of methanol concentration from 20% to 50%, the LNG content found in eluting solution at flow rate of 0.5 mL min^{-1} were increased too, from 39 to 90 ng. High concentration of methanol in eluting solution might enhance the extraction efficiency, but also would be more harmful to the antibody, decreasing the stability of the column. Therefore, 50% of methanol/water (v/v) was used as eluting solution. It was also found that, when

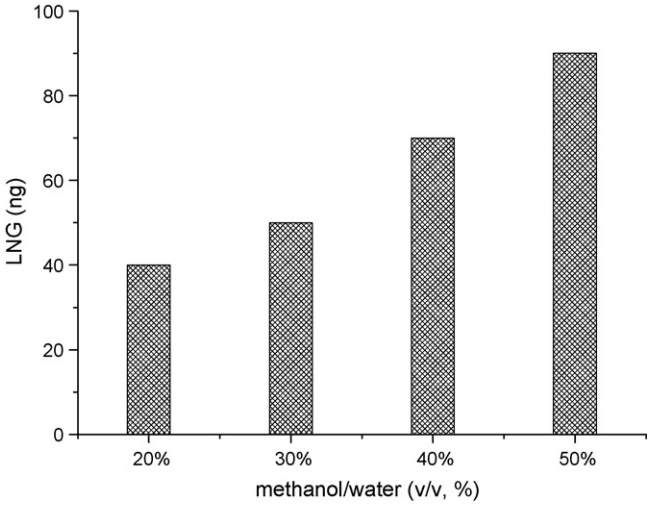


Fig. 2. LNG content found in the fractions of eluting step when 20%, 30%, 40% and 50% of methanol/water (v/v, %) were used as eluting solutions. 100 ng of LNG was loaded onto the IAC column.

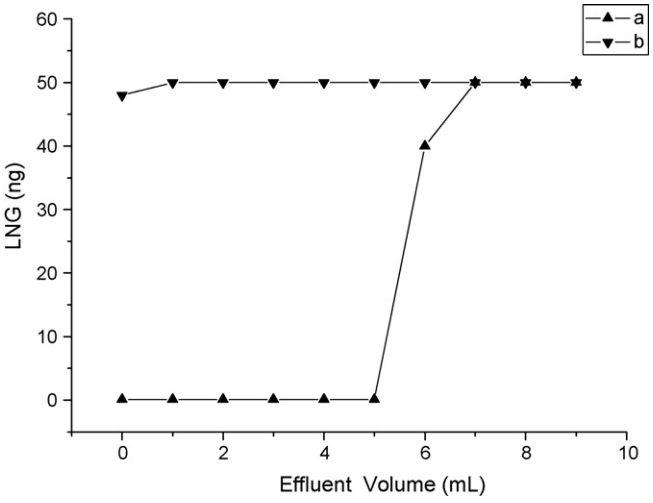


Fig. 3. Elution profiles for the continuous loading 9 mL of LNG standard solution at concentration of 50 ng mL^{-1} onto IAC column (a) and blank column (b).

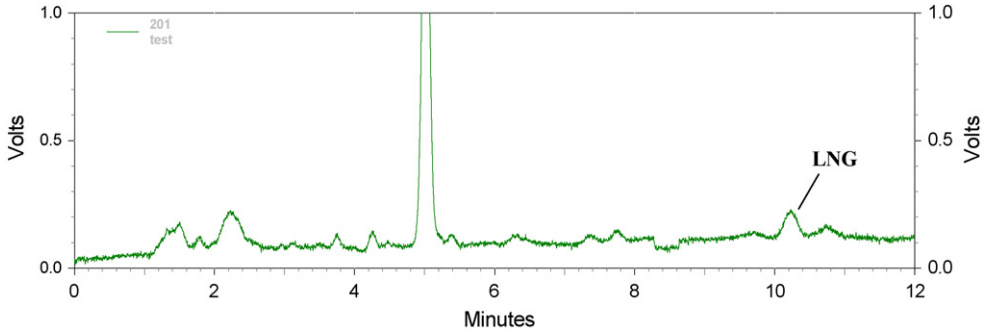


Fig. 4. HPLC chromatogram of LNG after a 600-fold enrichment by IAC column from river water sample. The LNG peak represents the concentration of 0.0075 ng mL^{-1} × 600 = 4.5 ng mL^{-1}.

2 mL 50% of methanol/water (v/v) was used as eluting solution at flow rate of 0.5, 1.0, 2.0 mL min^{-1}, 92.5%, 81.3% and 70.6% of analyte bound on the column was respective removed, therefore, so 0.5 mL min^{-1} was chosen for eluting sample.

3.4. Maximum capacity of IAC column

Under optimal extraction conditions, e.g. pure water, 5% of methanol and 50% of methanol were respectively selected as loading, washing and eluting solutions; the flow rates in the loading, washing and eluting steps were selected to be 1 mL min^{-1}, 2.0 mL min^{-1} and 0.5 mL min^{-1}, respectively, the IAC column was characterized in terms of maximum capacity, extraction recovery and reusability.

The maximum LNG-binding capacity of the IAC was measured by breakthrough volume test. 9 mL of LNG standard solution at concentration of 50 ng mL^{-1} was loaded on the column. The results of continuous samples loading on the IAC and blank columns were illustrated in Fig. 3. It was seen that the all LNG loaded on blank column went through the column immediately without any specific binding; while for IAC column, after loading 5 mL, there was still no LNG found in the effluents, showing its ability to recognize and retain the LNG. During loading 6 mL of LNG standard, 40 ng of LNG was observed in the effluent. Therefore, the maximum LNG-binding capacity of the IAC column packed with 0.2 g CNBr-activated Sepharose 4B was estimated to be: 5 × 50 + 10 = 260 ng. In another word, the maximum capacity of CNBr-activated Sepharose 4B was about 1.5 μg LNG/g of the solid support.

3.5. Extraction recovery of IAC column

500 mL of LNG standard solutions at concentrations of 0.01 ng mL^{-1}, 100 mL at 0.1 ng mL^{-1} and 100 mL at 1 ng mL^{-1} were respectively loaded on IAC column. The LNG content in the fraction of eluting step was detected and compared with that of total loading. As shown in Table 1, the LNG recoveries from the IAC column were found to be 95.3%, 106.9% and 103.1% with the relative standard deviation of 7.3%, 2.1% and 9.2%, respectively, indicating high extraction efficiency of the column.

3.6. Stability of IAC column

The antibodies against small molecular compounds are normally difficult to obtain and are very expensive. Therefore, the prepared IAC columns are expected to be used for many times. Actually most antibodies are tolerant to some extent of organic solvent without significant loss of activity and the IAC column can be easily regenerated with PBS solution.

The IAC column with the maximum capacity of 260 ng LNG was tested for its stability. It was observed that within 20 repeated usages, there was no any decrease of maximum capacity. After 35 times usage, about 80% of the maximum capacity was still remained, indicating high stability of the IAC column.

The regeneration and storage of the IAC column should be mentioned. After each extraction, the IAC column should be washed alternatively with no less than three column volumes of 0.1 mol L^{-1} pH 4.5 acetate buffer containing 0.5 mol L^{-1} NaCl and 0.1 mol L^{-1} Tris–HCl buffer, pH 8.5, containing 0.5 mol L^{-1} NaCl for three cycles. Finally, the column was washed with 0.01 mol L^{-1} PBS. For short-term (2–3 days) storage, the IAC column was simply kept in 0.01 molL^{-1} PBS at 4 °C; while for relatively long-term storage (over a week), it was kept in 0.01 mol L^{-1} PBS containing 0.02% NaN_3 at 4 °C. The IAC column was stable for at least 3 months without significant loss of binding activity.

3.7. Extraction of LNG from real water samples by IAC column

After filtrating and pH adjustment, 300 mL of collected water samples without LNG spiking was extracted with IAC column. The residues dissolved in 0.5 mL mobile phase with 600-fold enrichment were detected by HPLC. It was found that there was no detectable LNG in tap water, however, very small amount of LNG was found in other water samples. The trace concentrations of LNG found in original Funan river water, influent and effluent were 0.0075, 0.0743 and 0.0081 ng mL^{-1}, respectively. A HPLC chromatogram of LNG in Funan river water sample after 600-fold enrichment was illustrated in Fig. 4. Obviously, a small absorption peak of LNG with the retention time at 10.2 min was appeared, demonstrating the capability of the IAC to enrich the trace analyte and to clean the sample. It was also noticed that the LNG concentration in effluent was about 9-fold lower than that in influent, demonstrating that most of LNG was eliminated during the processes at wastewater treatment.

4. Conclusions

By covalently coupling the highly specific anti-LNG antibody on CNBr-activated Sepharose 4B and packing the immunosorbents into a SPE cartridge, the IAC column for selective extraction and enrichment of trace contraceptive drug LNG was firstly prepared and applied to real water samples prior to analysis by HPLC. The extraction conditions in the processes of loading, washing and eluting were optimized and the IAC column was characterized in terms of maximum capacity, extraction recovery and reusability. The recoveries values of LNG at three different spiked concentrations were within 95.3–106.9%, and after 35 times usage, about 80% of the maximum capacity was still remained. Trace amount of LNG in the range of ng L^{-1} was found in river water and wastewater samples after 600-fold enrichment, demonstrating the feasibility of the prepared IAC column for LNG extraction.

Acknowledgement

The authors thank the National Natural Science Foundation of China (NSFC) for financial support of this study (contact no. 20675054).

References

[1] A.R. Fakhari, A.R. Khorrami, M. Shamsipur, Anal. Chim. Acta 572 (2006) 237–242.
[2] S.L. Camp, D.S. Wilkerson, T.R. Raine, Contraception 68 (2003) 309.
[3] T. Backman, Drug Saf. 27 (2004) 1185.
[4] M.J. López de Alda, D. Barceló, J. Chromatogr. A 911 (2001) 203–210.
[5] M.J. López de Alda, D. Barceló, J. Chromatogr. A 892 (2000) 391–406.
[6] H.M. Kuch, K. Ballschmiter, Fresenius J. Anal. Chem. 366 (2000) 392–395.
[7] C.H. Huang, D.L. Sedlak, Environ. Toxicol. Chem. 20 (2001) 133–139.
[8] M.J. López de Alda, D. Barceló, J. Chromatogr. A 938 (2001) 145–153.
[9] C.W. Cui, S.L. Ji, H.Y. Ren, Environ. Monit. Assess. 121 (2006) 409–419.
[10] C. Baronti, R. Curini, R.G. D'Ascenzo, A.D. Corcia, A. Gentili, R. Samperi, Environ. Sci. Technol. 34 (2000) 5059–5066.
[11] P. Adler, T. Steger-Hartmann, W. Kalbfus, Acta Hydrochim. Hydrobiol. 29 (2001) 227–241.
[12] C. Baggiani, P. Baravalle, G. Giraudi, C. Tozzi, J. Chromatog. A 1141 (2008) 158.
[13] Q. Zhu, P. Degelmann, R. Niessner, D. Knopp, Environ. Sci. Technol. 36 (2002) 5411.
[14] M.C. Hennion, V. Pichon, J. Chromatogr. A 1000 (2003) 29–52.
[15] V.I. Muronetz, T. Korpelab, J. Chromatogr. B 790 (2003) 53–66.
[16] C. Li, Z.H. Wang, X.Y. Cao, R.C. Beier, S.X. Zhang, S.Y. Ding, X.W. Li, J.Z. Shen, J. Chromatogr. A 1209 (2008) 1–9.
[17] O. Heudi, T. Kilinc, P. Fontannaz, E. Marley, J. Chromatogr. A 1101 (2006) 63–68.
[18] K. Schoringhumer, M. Cichna-Markl, J. Chromatogr. B 850 (2007) 361–369.
[19] D. Tardieu, A. Auby, C. Bluteau, J.D. Bailly, P. Guerre, J. Chromatogr. B 870 (2008) 140–144.
[20] L. Li, J.B. Wang, S.A. Zhou, M.P. Zhao, Anal. Chim. Acta 620 (2008) 1–7.
[21] J.C. Chuang, J.M. Van Emon, R. Jones, J. Durnford, R.A. Lordo, Anal. Chim. Acta 583 (2007) 32–39.
[22] M.L. Sanchez-Martinez, M.P. Aguilar-Caballos, S.A. Eremin, A. Gomez-Hens, Anal. Bioanal. Chem. 386 (2006) 1489–1495.
[23] H.X. Chen, Q.P. Deng, L.W. Zhang, X.X. Zhang, Talanta 78 (2009) 464–470.
[24] A.E. Prince, T.S. Fan, B.A. Skoczenski, R.J. Bushway, Anal. Chim. Acta 444 (2001) 37–49.
[25] F.G. Sanchez, A.N. Diaz, R.G. Herrera, L.P. San Jose, Talanta 71 (2007) 1411–1416.
[26] H. Mhadhbi, S. Ben-Rejeb, C. Cléroux, A. Martel, P. Delahaut, Talanta 70 (2006) 225–235.
[27] C. Pu, Y.F. Wu, H. Yang, A.P. Deng, Anal. Chim. Acta 628 (2008) 73–79.
[28] M.P. Zhao, Y. Liu, Y.Z. Li, X.X. Zhang, W.B. Chan, J. Chromatogr. B 783 (2003) 401–410.
[29] J.B. Mi, S. Wang, X.J. Ding, Z.Q. Guo, M.P. Zhao, W.B. Chang, J. Chromatogr. B 843 (2006) 125–130.

Talanta 80 (2009) 104–108

Contents lists available at ScienceDirect

Talanta

journal homepage: www.elsevier.com/locate/talanta

Determination of aromatic compounds in eluates of pyrolysis solid residues using HS-GC–MS and DLLME–GC–MS

Maria S. Bernardo[a,*], M. Gonçalves[a], N. Lapa[a], R. Barbosa[a], B. Mendes[a], F. Pinto[b], Ibrahim Gulyurtlu[a,b]

[a] Ubia, Faculdade de Ciências e Tecnologia, Universidade Nova de Lisboa, 2829-516 Caparica, Portugal
[b] INETI-DEECA, Estrada do Paço do Lumiar 22, 1649-038 Lisboa, Portugal

ARTICLE INFO

Article history:
Received 12 November 2008
Received in revised form 9 June 2009
Accepted 12 June 2009
Available online 21 June 2009

Keywords:
Headspace
Solid phase microextraction
Eluates
Volatile aromatic hydrocarbons
Pyrolysis residues

ABSTRACT

A method for the determination of 15 aromatic hydrocarbons in eluates from solid residues produced during the co-pyrolysis of plastics and pine biomass was developed. In a first step, several sampling techniques (headspace solid phase microextraction (HS-SPME), static headspace sampling (HS), and dispersive liquid–liquid microextraction (DLLME) were compared in order to evaluate their sensitivity towards these analytes. HS-SPME and HS sampling had the better performance, but DLLME was itself as a technique able to extract volatiles with a significant enrichment factor.

HS sampling coupled with GC–MS was chosen for method validation for the analytes tested. Calibration curves were constructed for each analyte with correlation coefficients higher than 0.999. The limits of detection were in the range of 0.66–37.85 ng/L. The precision of the HS method was evaluated and good repeatability was achieved with relative standard deviations of 4.8–13.2%. The recoveries of the analytes were evaluated by analysing fortified real eluate samples and were in the range of 60.6–113.9%.

The validated method was applied in real eluate samples. Benzene, toluene, ethylbenzene and xylenes (BTEX) were the compounds in higher concentrations.

The DLLME technique coupled with GC–MS was used to investigate the presence of less volatile contaminants in eluate samples. This analysis revealed the presence of significant amounts of alkyl phenols and other aromatic compounds with appreciable water solubility.

© 2009 Elsevier B.V. All rights reserved.

1. Introduction

The evaluation of the toxicity of industrial residues is a fundamental task to define the disposal methods more adequate to each particular waste. To assess the environmental impact of the landfill disposal of solid residues, leaching tests are made in order to define the mobility of organic and inorganic contaminants present in their matrices. The eluates are complex mixtures that can contain volatile and/or water soluble organic compounds whose toxicity and mobility might be environmentally relevant [1–11].

One of the industrial processes that produce wastes with an important organic content is pyrolysis. In this process, the wastes are subjected to thermal degradation in the absence of oxygen, producing a hydrocarbon mixture (vapour and liquid fractions) and a carbonaceous residue (the solid fraction). The vapour and liquid fractions have an economical value since they can be used as fuel or as feedstock in chemistry industries. The solid fraction is not normally reused and is, therefore, disposed off in landfills. However, this carbonaceous residue is saturated with the components of the liquid fraction. Therefore, it must be treated in order to reduce its organic load before it can be disposed off.

In a previous work [12] it was studied the qualitative profile of volatile organic compounds present in eluates from solid residues produced in the co-pyrolysis of plastics and biomass using static headspace sampling (HS) and gas chromatography coupled with mass spectrometry (GC–MS). Benzene, toluene, ethylbenzene and xylenes (BTEX) were detected at high levels and several other aromatic compounds as well as phenol derivatives, among others, were also detected. Although BTEX are the only volatile organic compounds whose determination in eluates from industrial wastes is required by the European legislation [13] for establishing a classification for this kind of wastes (hazardous, non-hazardous or inert), the presence of a relatively high number of other organic compounds can greatly increase the toxicity of the eluates [5,11,12].

In this work an analytical method, using HS-GC–MS, for the quantitative determination of 15 volatile aromatic compounds in eluates from solid residues produced during the co-pyrolysis of plastics and biomass, was validated. These 15 aromatic compounds are the main volatile contaminants in this kind of eluates produced from the non-treated pyrolysis residues [12].

The more common sampling methods for volatile organic compounds (VOCs) in aqueous samples are HS sampling with

* Corresponding author. Tel.: +351 21 2948543; fax: +351 21 2948543.
E-mail address: maria.b@fct.unl.pt (M.S. Bernardo).

0039-9140/$ – see front matter © 2009 Elsevier B.V. All rights reserved.
doi:10.1016/j.talanta.2009.06.037

a gastight syringe or solid phase microextraction (SPME) [1,6,14–17].

A comparative study of static headspace (HS), headspace solid-phase microextraction (HS-SPME) and dispersive liquid–liquid microextraction (DLLME) as sampling techniques for the 15 volatile aromatic compounds was made in order to evaluate the sensitivity of each of these techniques towards this group of aromatic hydrocarbons. Other organic contaminants present in these eluates were studied using the DLLME technique and a tentative identification of the less volatile organic contaminants was made.

Recently, the DLLME technique has been used in the determination of a great variety of analytes, such as: polycyclic aromatic hydrocarbons (PAHs) [18], chlorophenols [19], triazine herbicides [20], PCBs [21], phthalate esters [22], chlorobenzenes [23], volatile phenols [24] and even BTEX [18], among others. The advantages of this technique are its simplicity and low volume consumption making it an attractive choice to perform screening of organic compounds in environmental liquid samples.

2. Experimental

2.1. Pyrolysis and leaching

A mixture of pine biomass and plastics (mixture of polypropylene, polyethylene, and polystyrene) was submitted to pyrolysis, and part of the solid residue produced was subjected to extraction with dichloromethane (DCM) as already described elsewhere [12,25–27]. The extracted residue (residue A) and the raw residue (residue B) were submitted to the leaching test ISO/TS 21268-2 [28]. The leachant solution used was a calcium chloride solution with a concentration of 0.001 mol/L (according to the standard). Two types of eluates were obtained: eluates from residue A (eluate 1) and eluates from residue B (eluate 2). The eluates were maintained at a temperature of 4 ± 1 °C until analysis.

2.2. Sampling and extraction procedures

The static HS was performed using the following optimized experimental conditions: equilibration time, 30 min; extraction temperature, 60 °C; vial volume, 50 ml; sample solution volume, 25 ml; injection volume, 0.5 ml.

The HS-SPME was performed using two types of fibers, namely, the PDMS (Polydimethylsiloxane) 100 μm fiber and the Car–PDMS (Carboxen–Polydimethylsiloxane) 85 μm fiber. The experimental conditions for the HS-SPME experiments were: vial volume, 50 ml; sample volume, 25 ml; equilibration time, 30 min; extraction temperature, room temperature; extraction time, 5 min; desorption time, 3 min; desorption temperature: PDMS, 200 °C and Car–PDMS, 250 °C.

The experimental conditions for the DLLME technique were: sample volume, 5 ml; extraction solvent volume, 50 μL of carbon tetrachloride (CCl_4); disperser solvent volume, 0.5 ml of acetone; centrifugation, 5 min at 4000 rpm; injection volume, 1 μL.

2.3. GC–MS analysis

The chromatographic analysis conditions for the static HS experiments were performed using a Focus gas chromatograph equipped with a split–splitless injector, a TR-V1 capillary column (30 m × 0.25 mm I.D. × 1.4 μm film) and a Polaris Q mass spectrometer detector. The carrier gas was helium at 1.5 ml/min; samples were injected at 60 °C in the splitless mode with a splitless time of 1 min and a split flow of 50 ml/min; the interface and ion source were kept at 220 °C; the oven temperature program was as follows: 32 °C (hold 5 min), up to 100 °C (5 °C/min), up to 250 °C (10 °C/min) and finally up to 280 °C (50 °C/min, hold 1 min). The MS system was operated in the full scan mode with a mass range from m/z 50 to 200.

For the HS-SPME experiments the equipment and GC–MS conditions were the same except for the injection temperature (250 °C for the Car–PDMS fiber and 200 °C for the PDMS fiber).

The GC–MS analysis of the DLLME extracts was performed in the same equipment but with a DB5 column (30 m × 0.32 mm × 1 μm); the injector was kept at 220 °C; the carrier gas flow was 1 ml/min and the injection volume was 1 μL. The oven temperature program was 35 °C (hold 3 min) and heating ramp up to 300 °C (5 °C/min). The MS detector was operating with the full scan mode covering a mass range from m/z 50 to 650. All the other chromatographic parameters were the same as in the previous experiments.

2.4. Reagents and chemicals

Pure dichloromethane (99.9% purity, supplied by Fischer Scientific), methanol (99.8% grade, supplied by Fluka), acetone (99.8% purity, supplied by Labscan) and carbon tetrachloride (99.8% purity, supplied by Pronalab) were used.

The aromatic standards were purchased from: Panreac (benzene and toluene, 99.5%), Fluka (ethylbenzene, >99%), Acros Organics (*m*/*p*/*o*-xylenes, 99%), Aldrich (cumene, 98%; propylbenzene, 98%; 4-ethyltoluene, 90%; *tert*-butylbenzene, 99%; 1,2,4-trimethylbenzene, 98%; 1-methylpropylbenzene, 99%; butylbenzene, 99%; 1,4-diethylbenzene, 96% and 1,2,4,5-tetramethylbenzene, 98%).

A stock standard solution with a concentration of 1 mg/L of each 15 analytes in methanol was prepared. A standard solution of 500 ng/L was prepared by dilution of the stock standard solution in the leachant solution ($CaCl_2$ 0.001 mol/L) and used to evaluate the limits of detection of the three techniques tested. The HS method was selected for complete validation. For this method, calibration curves were constructed for each analyte using standard solutions with concentrations in the range of 100–2000 ng/L.

3. Results and discussion

3.1. Determination of the 15 aromatic volatiles using different extraction techniques

In the first part of this work, the efficiency of different techniques (static HS, HS-SPME and DLLME) for sampling volatile aromatic compounds was tested using a standard aqueous solution of benzene, toluene, ethylbenzene, xylenes, cumene, propylbenzene, 4-ethyltoluene, *tert*-butylbenzene, 1,2,4-trimethylbenzene, 1-methylpropylbenzene, butylbenzene, 1,4-diethylbenzene and 1,2,4,5-tetramethylbenzene, with a concentration of 500 ng/L and making the analytical separation by GC–MS.

The limits of detection for each analyte were estimated using the signal-to-noise ratio of 3 ($LOD_{S/N}$) from the corresponding chromatographic peaks (Table 1). Although it is known that the limits of detection evaluated from the signal-to-noise ratio are in general overestimated, this measure can be used as a basis for comparison of different techniques before making a more detailed study of each one [29]. Most of the analytes tested (except benzene and toluene) were detected in the pg/L range using static HS or HS-SPME (with PDMS or Carboxen). The lowest $LOD_{S/N}$, in the range of 10–290 pg/L, was obtained using HS-SPME with a 100 μm PDMS fiber. Benzene and toluene had higher $LOD_{S/N}$ than the other analytes (16.5 and 1.3 ng/L, respectively, with PDMS fiber) reflecting their higher volatility and therefore their smaller partition into the SPME fiber. Using HS-SPME with the Carboxen–PDMS fiber or using static HS we were able to obtain lower $LOD_{S/N}$ for benzene and toluene (0.72–6.76 ng/L).

Table 1
Comparison of the limits of detection ($LOD_{S/N}$), in ng/L, of the three techniques proposed for the determination of 15 volatile aromatic compounds.

Analyte	PDMS 100 μm	Carboxen–PDMS 85 μm	HS-GC–MS	DLLME–GC–MS
Benzene	16.5	6.76	3.57	n.d.
Toluene	1.30	0.83	0.72	8.82
Ethylbenzene	0.29	0.32	0.32	24.6
m/*p*-Xylene	0.13	0.11	0.15	10.4
o-Xylene	0.23	0.27	0.27	19.6
Cumene	0.06	0.13	0.13	8.25
Propylbenzene	0.04	0.08	0.12	16.0
4-ethyltoluene	0.03	0.08	0.12	14.0
Tert-butylbenzene	0.02	0.09	0.10	6.45[a]
1,2,4-Trimethylbenzene	0.03	0.09	0.13	
1-Methylpropylbenzene	0.02	0.06	0.10	14.2
Butylbenzene/1,4-diethylbenzene	0.01	0.05	0.08	6.47
1,2,4,5-Tetramethylbenzene	0.02	0.07	0.11	1.02

n.d., not detected.
[a] co-elution.

With the DLLME technique, higher $LOD_{S/N}$ were obtained as it would be expected since it is not a technique specific for volatiles. However, the sensitivity of this technique with volatiles, in the range of ng/L, is remarkable and can be improved with an optimization study.

In conclusion, all of the techniques tested seemed to be adequate for the detection and quantification of these 15 aromatic hydrocarbons in the eluates from industrial residues at levels that are considerably lower than the limits proposed in legislation for the hydrocarbons of the BTEX group (100 μg/L) [13].

The static HS was chosen for method validation because it is a solvent-free technique and considerably less expensive than SPME. Moreover, the HS-SPME showed some fiber memory effects that require frequent conditioning of the SPME fiber.

3.2. Validation of the HS-GC–MS method for the determination of volatile aromatic compounds in eluates

The chromatographic conditions were optimized in order to obtain baseline separation for most analytes. The exceptions are the pairs butylbenzene/1,4-diethylbenzene and *m*/*p*-xylene that completely co-elute in all conditions tested and were, therefore, quantified together. The calibration curves were constructed in the range of 100–2000 ng/L, with five concentration levels. The calibration standard solutions were prepared by spiking the leachant solution with appropriated amounts of the methanolic standard solution (1 mg/L) of the 15 volatile aromatics. Duplicates were made at each concentration level. Table 2 shows the calibration equations and the correlation coefficients for each analyte. All analytes presented correlation coefficients above 0.999. The limits of detection (LOD) and of quantification (LOQ) for each aromatic hydrocarbon (Table 2) were calculated according to the criteria $33 \times (S_{y/x}/m)$ and $10 \times (S_{y/x}/m)$, respectively, where $S_{y/x}$ is the standard error of the calibration curve and m is the slope for each calibration curve. The LOQs were in the range of 2.2–126.2 ng/L, which are far bellow the maximum admissible values for leachates of industrial wastes (100 μg/L for the compounds of the BTEX group) [13], and even bellow the maximum admissible values for some of these analytes in drinking water (1 μg/L for benzene) [30]. The LODs evaluated from the calibration curves are in the range of 0.66–37.85 ng/L.

The repeatability of this proposed HS-GC–MS method was evaluated by analysing five replicates of the leachant solution spiked with the analyte mixture at two different concentration levels (Table 3). The relative standard deviations (R.S.D.) were between 4.8% and 13.2%. The accuracy of the method was evaluated using the recoveries of real eluate samples spiked with the methanolic standard solution at a concentration of 500 ng/L (Table 3). The average recovery for all analytes was 100.8% for both leachates tested, and varied in a range from 96.4% to 113.9%. Benzene was an exception with recoveries of 60.6% and 66.9%, due to the poor chromatographic focusing of the corresponding peak.

3.2.1. Analysis of eluates

The validated HS-GC–MS method was used to determine the concentrations of the 15 volatile aromatic compounds in both eluates (Table 4). Duplicate analyses were performed for each determination. When the concentration of the analytes exceeded the linearity range, the samples were diluted to an appropriate concentration using the leachant solution.

None of the 15 volatile compounds were detected in eluate 1 obtained from residue A that was previously extracted with dichloromethane which means that this extraction step was effi-

Table 2
Analytical performance of the HS-GC–MS method for the determination of 15 volatile aromatic compounds in eluates.

Analyte	Linearity range (ng/L)	Regression equation	Correlation coefficient, R^2	LOD (ng/L)	LOQ (ng/L)
Benzene	250–2000	$Y = 13{,}628x + 143{,}130$	>0.9999	12.86	42.88
Toluene	250–1000	$Y = 19{,}141x + 1E+06$	0.9995	37.85	126.16
Ethylbenzene	100–1000	$Y = 19{,}629x - 987{,}555$	0.9998	25.99	86.62
m/*p*-Xylene	100–1000	$Y = 38{,}350x - 2E+06$	>0.9999	7.98	26.61
o-Xylene	100–1000	$Y = 16{,}896x - 917{,}978$	>0.9999	0.66	2.20
Cumene	100–1000	$Y = 25{,}475x - 1E+06$	0.9997	27.23	90.77
Propylbenzene	100–1000	$Y = 24{,}416x - 1E+06$	0.9998	22.8	76.1
4-Ethyltoluene	100–1000	$Y = 21{,}254x - 1E+06$	>0.9999	4.8	16.0
Tert-butylbenzene	100–1000	$Y = 28{,}338x - 2E+06$	0.9998	19.9	66.3
1,2,4-Trimethylbenzene	100–1000	$Y = 18{,}132x - 1E+06$	0.9999	13.5	44.9
1-Methylpropylbenzene	100–1000	$Y = 24{,}668x - 2E+06$	>0.9999	1.84	6.12
Butylbenzene/1,4-diethylbenzene	100–1000	$Y = 48{,}782x - 4E+06$	0.9999	17.50	58.34
1,2,4,5-Tetramethylbenzene	100–1000	$Y = 16{,}393x - 2E+06$	0.9997	24.97	83.24

LOD, limit of detection; LOQ, limit of quantification.

Table 3
HS-GC–MS analytical method validation.

Analyte	Precision (R.S.D.%) $n=5$		Recoveries (%) ± S.D. $n=2$	
	500 ng/L	1000 ng/L	Eluate 1	Eluate 2
Benzene	11.4	4.8	61 ± 3	67 ± 2
Toluene	9.0	9.2	101 ± 8	103 ± 9
Ethylbenzene	10.2	8.5	99 ± 8	101 ± 7
m/*p*-Xylene	9.8	8.9	104 ± 6	105 ± 5
o-Xylene	11.8	12.1	101 ± 4	104 ± 2
Cumene	13.0	11.2	100 ± 7	103 ± 2
Propylbenzene	10.7	10.1	101 ± 9	103 ± 7
4-Ethyltoluene	13.1	11.7	106 ± 5	109 ± 3
Tert-butylbenzene	11.0	10.2	100 ± 2	100 ± 2
1,2,4-Trimethylbenzene	13.2	10.9	108 ± 2	107 ± 2
1-Methylpropylbenzene	12.2	11.9	108 ± 4	114 ± 2
Butylbenzene/1,4-diethylbenzene	9.7	9.8	108 ± 6	109 ± 2
1,2,4,5-Tetramethylbenzene	11.4	9.3	96 ± 4	103 ± 3

R.S.D., relative standard deviation; S.D., standard deviation.

Table 4
Concentrations of the 15 target organic compounds in both eluates determined by HS-GC–MS.

Analyte	Concentrations (μg/L) mean ± S.D. ($n=2$)	
	Eluate 1	Eluate 2
Benzene	<0.013	3.8 ± 0.3
Toluene	<0.038	511 ± 9
Ethylbenzene	<0.026	277 ± 2
m/*p*-Xylene	<0.008	1.8 ± 0.4
o-Xylene	<0.0007	49 ± 2
Cumene	<0.027	9 ± 3
Propylbenzene	<0.023	1.6 ± 0.5
4-Ethyltoluene	<0.005	1.0 ± 0.3
Tert-butylbenzene	<0.02	0.08 ± 0.03
1,2,4-Trimethylbenzene	<0.014	0.7 ± 0.3
1-Methylpropylbenzene	<0.0018	0.3 ± 0.1
Butylbenzene/1,4-diethylbenzene	<0.018	0.2 ± 0.1
1,2,4,5-Tetramethylbenzene	<0.025	0.14 ± 0.02

S.D., standard deviation.

cient in removing the majority of the volatile organic fraction from the pyrolysis residue.

Eluate 2 showed a high contamination with toluene, ethylbenzene, *o*-xylene and cumene (Fig. 1), in concentrations from 9 to 511 μg/L, as shown in Table 4, with predominance of toluene. This is consistent with the fact that toluene and ethylbenzene are also the compounds detected in higher amounts, in the liquid fractions obtained in the pyrolysis process [25,26]. Other volatile benzene derivatives appear in eluate 2 in concentrations from 0.08 to 1.59 μg/L. Although these concentrations can be considered low when considered individually their sum gives a value of 3.96 μg/L. Besides the benzene derivatives studied, several other minor peaks corresponding to phenolics, polycyclic aromatic hydrocarbons (PAHs) and other aromatics were also detected [12]. These less volatile contaminants tend to remain in the water phase because they are heavier or more polar than the compounds monitored in the HS-GC–MS method.

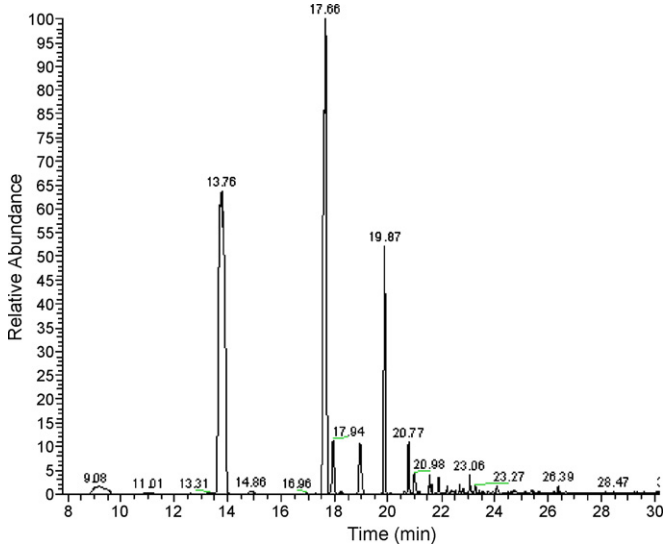


Fig. 1. HS-GC–MS chromatogram of eluate 2. Major peaks: RT = 9.08, benzene; RT = 13.76, toluene; RT = 17.66, ethylbenzene; RT = 17.94, *m*/*p*-xylenes, RT = 18.96, *o*-xylene; RT = 19.87, cumene; RT = 20.77, propylbenzene, RT = 20.98, 4-ethyltoluene.

Table 5
List of the organic compounds identified in eluate 2 using DLLME–GC–MS.

Name	R.T. (min)	Relative peak area (%)
		Eluate 2
Toluene[a]	9.00	5.69
Ethylbenzene[a]	12.61	8.64
m/*p*-Xylene[a]	12.90	0.45
o-Xylene[a]	13.83	0.71
Cumene[a]	15.01	1.43
Phenol[b]	16.81	0.75
o-Methylphenol[a]	19.36	4.49
m/*p*-Methylphenol[a]	20.01	4.83
Hexachloroethane[b]	20.37	0.94
2,3,4-Trimethylcyclopent-2-ene-1-one[b]	20.69	1.21
2,6-Dimethylphenol[a]	21.21	3.00
Ethylphenol (isomer)[b]	22.06	2.42
2,4/2,5-Dimethylphenol[a]	22.42	8.96
2,3-Dimethylphenol[a]	23.00	5.92
3,5-Dimethylphenol[a]	23.36	2.24
1-(ethyl)-2-methoxybenzene[b]	23.66	0.95
3,4-Dimethylphenol[b]	23.79	2.04
2,4,6-Trimethylphenol[a]	24.26	1.70
3-(1-methylethyl)phenol[b]	24.83	2.01
Ethylmethylphenol (isomer)[b]	24.94	1.16
Ethylmethylphenol (isomer)[b]	25.15	3.86
Ethylmethylphenol (isomer)[b]	25.29	1.58
2-Ethyl-4-methylphenol[b]	25.73	3.79
2,3,6-Trimethylphenol[a]	26.05	1.51
2,3,5-Trimethylphenol[a]	26.18	2.01
2,4,5/2,3,4-Trimethylphenol[b]	27.10	1.02
Methyl-(methylethyl)phenol (isomer)[b]	27.58	0.74
2/4-(1-methylpropyl)phenol[b]	27.74	0.89
3,5-Diethylphenol[b]	27.86	0.49
4-Phenylbutyronitrile[b]	28.10	4.72

R.T., Retention time.
[a] Compound identified by co-injection of standards.
[b] Compound tentatively identified by comparison with the spectra of NIST and Wiley libraries and by comparison between isomer molecular structures.

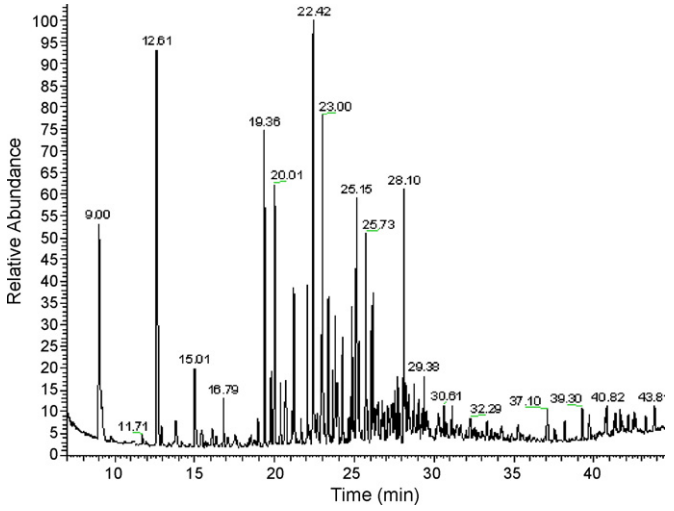


Fig. 2. DLLME–GC–MS chromatogram of eluate 2.

3.3. DLLME–GC–MS analysis

The identification of less volatile compounds present in the eluates was performed using DLLME and GC–MS (Table 5). The DLLME extract from eluate 1 showed no detectable chromatographic peaks indicating that the dichloromethane extraction was also effective in removing non-volatile contaminants from the pyrolysis residues as previously observed for the volatile ones. The DLLME extract from eluate 2 showed a strong contamination with alkyl phenols that were tentatively identified by GC–MS. These phenolic compounds result from the pine biomass pyrolysis [31]. The identity of 15 alkyl phenol contaminants was confirmed by co-injection of authentic standards. Fig. 2 shows the DLLME chromatogram of eluate 2.

4. Conclusions

The HS-GC–MS method developed allowed the determination of the 15 selected volatile aromatic hydrocarbons at levels adequate to the monitorization of these analytes in water samples (either surface and groundwaters for human consumption or leachates from industrial residues).

In the case of more contaminated water samples, this method has the advantage of being specific for volatile compounds, therefore eliminating polar or heavier matrix interferences. It is also a robust method when compared with HS-SPME because is not affected by fiber performance that can be highly variable in the case of complex samples with large organic loads.

The DLLME method used is a fast and simple procedure to screen the presence of organic compounds in water samples. The only drawback of the DLLME method is the use of a chlorinated solvent but since the solvent consumption is in the microliter range it produces very small amounts of residues.

Eluates from untreated pyrolysis residues are heavily contaminated with aromatic volatiles. BTEX concentration measured in eluate 2 is 843 μg/L when the corresponding limit value is of 600 μg/L [13] and heavier alkyl benzenes are present at a concentration of 13 μg/L. Eluates from residues extracted with dichloromethane showed a BTEX concentration of less than 0.09 μg/L, far bellow the legislation limit value [13] and concentrations of heavier alkyl benzenes lower than 0.13 μg/L. Comparison of the chromatographic profile of extracts obtained from leachates of treated and untreated pyrolysis residues shows that phenolic compounds are also removed by the extraction with dichloromethane. The decontamination of the residues with dichloromethane is, therefore, an efficient method to reduce their organic content.

The toxicity of the eluates depends on the total amount of organic contaminants as well as on the specific toxicity of each contaminant. Both the extracts analysed with HS-GC–MS or with DLLME–GC–MS revealed the presence of a large number of minor aromatic contaminants that can influence the toxicity of the eluate due to their individual toxicity properties, to the occurrence of synergistic effects or simply because of their overall concentration.

References

[1] K. Vaajasaari, M. Kulovaara, A. Joutti, E. Schultz, K. Soljamo, J. Hazard. Mater. A 106 (2004) 71–79.
[2] E. Schultz, K. Vaajasaari, A. Joutti, J. Ahtiainen, Environ. Res. B 52 (2002) 248–255.
[3] M. Isidori, M. Lavorgna, A. Nardelli, A. Parrella, Chemosphere 52 (2003) 85–94.
[4] C.S. Chen, J. Zoltek Jr., Chemosphere 31 (1995) 3455–3464.
[5] A. Baun, A. Ledin, L.A. Reitzel, P.L. Bjerg, T.H. Christensen, Water Res. 38 (2004) 3845–3858.
[6] J.C. Flórez Menéndez, M.L. Fernández Sánchez, E. Fernández Martinez, J.E. Sánchez Uria, A. Sanz-Medel, Talanta 63 (2004) 809–814.
[7] W. Brack, H. Franck, Chemosphere 34 (1997) 849–854.
[8] A. Bispo, M.J. Jourdain, M. Jauzein, Org. Geochem. 30 (1999) 947–952.
[9] E. Korenková, E. Matisová, J. Slobodník, Waste Manage. 26 (2006) 1005–1016.
[10] A. Yasuhara, H. Shiraishi, M. Nishikawa, T. Yamamoto, T. Uehiro, O. Nagasugi, T. Okumura, K. Kenmotsu, H. Fukui, M. Nagase, Y. Kawagoshi, Waste Manage. Res. 17 (1999) 186–197.
[11] X. Domene, J.M. Alcañiz, P. Andrés, Environ. Pollut. 151 (2008) 549–558.
[12] M.S. Bernardo, N. Lapa, R. Barbosa, M. Gonçalves, B. Mendes, F. Pinto, J. Hazard. Mater. 166 (2009) 309–317.
[13] 2003/33/EC: Council Decision of 19 December 2002 establishing criteria and procedures for the acceptance of waste at landfills pursuant to Article 16 of and Annex II to Directive 1999/31/EC.
[14] T.C. Schmidt, S.B. Haderlein, R. Pfister, R. Forster, Water Res. 38 (2004) 1520–1529.
[15] J.C. Floréz Menéndez, M.L. Fernández Sánchez, S. Uría, E. Fernández Martinez, A. Sanz-Medel, Anal. Chim. Acta 415 (2000) 9–20.
[16] I. Arambarri, M. Lasa, R. Garcia, E. Millán, J. Chromatogr. A 1033 (2004) 193–2003.
[17] M. Llompart, K. Li, M. Fingas, J. Chromatogr. A 824 (1998) 53–61.
[18] M. Rezaee, Y. Assadi, M.M. Hosseini, E. Aghaee, F. Ahmadia, S. Berijani, J. Chromatogr. A 1116 (2006) 1–9.
[19] N. Fattahi, Y. Assadi, M.R.M. Hosseini, E.Z. Jahromi, J. Chromatogr. A 1157 (2007) 23–29.
[20] D. Nagaraju, S. Huang, J. Chromatogr. A 1161 (2007) 89–97.
[21] F. rezaei, A. Bidari, A. Pajand, M.R.M. Hosseini, Y. Assadi, J. Hazard. Mater. 158 (2008) 621–627.
[22] H. Farahani, P. Norouzi, R. Dinarvand, M.R. Ganjali, J. Chromatogr. A 1172 (2007) 105–112.
[23] R.R. Kozani, Y. Assadi, F. Shemirani, M.R.M. Hosseini, M.R. Jamali, Talanta 72 (2007) 387–393.
[24] L. Fariña, E. Boido, F. Carrau, E. Dellacassa, J. Chromatogr. A 1157 (2007) 46–50.
[25] F. Paradela, "Study of the pyrolysis of plastics and biomass residues mixtures", Master thesis, Faculty of Sciences and Technology—New University of Lisbon, 2007.
[26] F. Paradela, F. Pinto, I. Gulyurtlu, I. Cabrita, N. Lapa, Clean Technol. Environ. Policy, doi: 10.1007/s10098-008-0176-1.
[27] P.A. Costa, F.J. Pinto, A.M. Ramos, I.K. Gulyurtlu, I.A. Cabrita, M.S. Bernardo, Energy Fuels 21 (2007) 2489–2498.
[28] ISO/TS 21268, Soil quality—leaching procedure for subsequent chemical and ecotoxicological testing of soil and soil materials.
[29] M.S. Altaki, F.J. Santos, M.T. Galceran, Talanta 78 (2009) 1315–1320.
[30] 98/83/EC: Council directive of 3 November 1998 on the quality of water intended for human consumption.
[31] A. Aho, N. Kumar, K. Eränen, T. Salmi, M. Hupa, D.Y. Murzin, Fuel 87 (2008) 2493–2501.

Talanta 80 (2009) 109–116

Contents lists available at ScienceDirect

Talanta

journal homepage: www.elsevier.com/locate/talanta

Ultrasound-assisted emulsification of cosmetic samples prior to elemental analysis by different atomic spectrometric techniques

I. Lavilla, N. Cabaleiro, M. Costas, I. de la Calle, C. Bendicho*

Departamento de Química Analítica y Alimentaria, Área de Química Analítica, Facultad de Química, Universidad de Vigo, As Lagoas-Marcosende s/n, 36310 Vigo, Spain

ARTICLE INFO

Article history:
Received 13 March 2009
Received in revised form 8 June 2009
Accepted 12 June 2009
Available online 21 June 2009

Keywords:
Ultrasound-assisted emulsification
Cosmetics
Trace elements
Atomic spectrometry techniques (plasma, flame, cold vapour)

ABSTRACT

In this work, ultrasound-assisted emulsification with a probe system is proposed as a rapid and simple sample treatment for atomic spectrometric determinations (Electrothermal Atomic Absorption Spectrometry, Inductively Coupled Plasma Optical Emission Spectrometry, Flame Atomic Absorption Spectrometry and Cold Vapour Atomic Absorption Spectrometry) of trace elements (As, Cd, Cr, Cu, Hg, Mg, Mn, Ni, Sr and Zn) in cosmetic samples such as shampoos, gel (hair gel), crèmes (body milk, hair conditioner) and oil (body oil). The type of dispersion medium, the sample mass-to-dispersion medium volume ratio, as well as the parameters related to the ultrasound-assisted emulsification (sonication amplitude and treatment time) were exhaustively studied. Only 1 min of ultrasonic shaking and a dispersion medium containing 0.5% (w/v) of SDS + 3% (v/v) of HNO_3 or HCl allows obtaining a stable emulsion at least for 3 months. Thermal programs, nebulization of emulsions, speed of pumps and concentration of reagents used in cold vapour generation were optimized. Calibration using aqueous standards was feasible in all cases. Calibration by the standard addition method and recovery studies was also applied for validation. Microwave-assisted digestion and Inductively Coupled Plasma Mass Spectrometry were used for comparison purposes. Relative standard deviations from analysis of five independent emulsions were less than 9% in all cases.

© 2009 Elsevier B.V. All rights reserved.

1. Introduction

At present, cosmetics represent an important industry worldwide, but especially in Europe. These products are subjected to restrictive regulations, such as the European Directive 76/768/EEC [1], in order to ensure their safety and usefulness [2,3]. Legislations include information requirements about: (i) substances banned (these must not be found in the finished product); (ii) substances restricted; (iii) substances subjected to positive listing (used in controlled concentration). Among these, some metals and metalloids are included, namely, Cd, Pb and Sb (prohibited all their compounds); Co, Cr and Ni (most of their compounds are prohibited); Se (only as disulphur, up to 1% w/w) or Zn (up to 1% w/w) [1]. Therefore, sensitive and selective determinations of different metals in cosmetics are necessary for the control of these products.

Matrix of cosmetics is not simple; it usually contains a high number of ingredients and often requires time-consuming and tedious sample treatments [4]. Official analytical methods have been recommended in different legislations. Most of these methods use digestion or calcination as sample treatment and atomic spectrometry as determination technique [5,6].

It is advisable to improve cosmetic quality control using different recent developments of sample treatment but the number of papers focusing on this subject is scarce. Sample treatments, which involve the use of concentrate acids (i.e. HNO_3, $HClO_4$, H_2SO_4 or HF) and high temperatures and pressures, similar to those recommended by the official methods, are applied [7–14]. Sometimes, even with these strong treatments, complete solubilization of a sample is not feasible. Substances such as metallic oxides and pigments form a residue that must be removed by means of filtration or centrifugation, or submitted to a fusion treatment [10,12,15].

Sample emulsification procedures have been proposed as an interesting strategy for sample solubilization when liposoluble matrices are analyzed by Atomic Spectrometry [16–23]. This allows a direct and rapid analysis of samples, avoiding the use of strong acids and large volumes of organic solvents. The use of emulsification as sample treatment for metal determination in cosmetics can minimize the above problems. Nevertheless, this strategy has been scarcely used. Vondruska [24] determined Cd by Electrothermal Atomic Absorption Spectrometry (ETAAS) in cosmetic oil forming a water emulsion. Salvador et al. [12] determined Zn and Fe by Flame Atomic Absorption Spectrometry (FAAS) in sunscreen, forming a sample emulsion by shaking with a non-ionic tensioactive and isobutyl ketone.

* Corresponding author. Tel.: +34 986 812281; fax: +34 986 812556.
E-mail address: bendicho@uvigo.es (C. Bendicho).

0039-9140/$ – see front matter © 2009 Elsevier B.V. All rights reserved.
doi:10.1016/j.talanta.2009.06.036

In general, mechanical or manual agitation is used for emulsion formation, and in addition, agitation is required to maintain its stability during analysis [23]. The use of ultrasound for shaking allows obtaining a stable and homogeneous emulsion more quickly in comparison with mechanical processes [25]. Ultrasound-assisted emulsification is considered an interesting approach for accelerating the formation of emulsions in analytical chemistry, as well as for the determination of organic compounds and metals [26]. Two processes occurs in ultrasonic emulsification: (a) interfacial instability of the oil–water interface and (b) transient cavitation bubbles that generate micro streaming, high-pressure shock wave and high local temperature during their collapse. These phenomena accelerate the mass-transfer process between two immiscible phases by generating smaller droplet size of the dispersed phase [27,28]. However, some drawbacks related to the possible surfactant degradation can appear during ultrasonic emulsification [29]. Then, detailed studies of the process must be performed when this approach is followed.

In this work, we propose a simple and fast methodology based on ultrasound-assisted emulsification with a probe as a minimalist sample treatment for the determination of metals and metalloids in different cosmetics. This sample preparation was assessed in combination with different analytical techniques: Electrothermal Atomic Absorption Spectrometry, Inductively Coupled Plasma Optical Emission Spectrometry (ICP-OES), Flame Atomic Absorption Spectrometry and Cold Vapour Atomic Absorption Spectrometry (CV-AAS). Different variables related to ultrasonic emulsification were studied: surfactants, sonication time, sonication amplitude, sample mass and dispersive phase volume. Microwave-assisted digestion and ICP-MS (Inductively Coupled Plasma Mass Spectrometry) were used as a comparative methodology.

2. Experimental

2.1. Instrumentation

A Unicam atomic absorption spectrometer Model Solaar 939 (Cambridge, UK) equipped with a Unicam GF-90 graphite furnace and a Unicam FS-90 autosampler was used for Cd, Cr and Ni determination. A multielement hollow cathode lamp of Cr/Ni/Cu/Mn (Thermo Scientific, Cambridge, UK) and a hollow cathode lamp of Cd (Unicam) were used as radiation sources. Pyrolytically coated graphite tubes with platform were employed for Cd and without platform for Cr and Ni.

ICP-OES measurements were performed using an Optima 4300 DV inductively coupled plasma optical emission spectrometer (PerkinElmer, Überlingen, Germany) equipped with an AS-90 autosampler, a concentric glass nebulizer (Meinhard Type K), a cyclonic spray chamber and nickel interface sampler and skimmer cones. Axial and radial viewings were used. ICP-OES measurement conditions for As, Cd, Cr, Cu, Mg, Mn, Ni, Sr and Zn were optimized to achieve maximum signal-to-noise ratio.

A Unicam atomic absorption spectrophotometer Model Solaar 969 (Cambridge, UK) equipped with 10 cm burner head was used for Mg and Zn determination. Hollow cathode lamps Thermo Electron (Cambridge, UK) and Heraeus (Cambridge, UK) were used as radiation sources for Mg and Zn, respectively.

A PerkinElmer (Überlingen, Germany) Model 4110 ZL atomic absorption spectrometer equipped with a quartz cell atomizer and a flow injection system FIAS-400 (PerkinElmer) was used for Hg determination. The hollow cathode lamp PerkinElmer Lumina was employed as radiation source for Hg. The quartz cell was maintained at room temperature during operation.

ICP-MS measurements were performed using a Thermo Elemental X7 Series ICP-MS equipped with an ASX-520 autosampler (CETAC, Omaha, USA), a glass expansion concentric nebulizer, a spray chamber of quartz impact bead with a Peltier system, a quartz vessel torch and nickel interface cones. The isotopes ^{111}Cd, ^{65}Cu, ^{24}Mg, ^{55}Mn, ^{60}Ni, ^{88}Sr and ^{66}Zn were measured using standard mode with guard electrode (plasma screen) and isotopes ^{75}As and ^{52}Cr were measured using cell collision technology (CCT).

The operating conditions for ETAAS, ICP-OES, FAAS, CV-AAS and ICP-MS are summarised in Table 1. Thermal programs for Cd, Cr

Table 1
Operating conditions.

ETAAS	Unicam AAS Model Solaar 939				
Element	Cd	Cr	Ni		
Detection wavelengths (nm)	228.8	357.9	232.0		
Lamp current (mA)	8	10	15		
Spectral bandpass (nm)	0.5	0.2	0.5		
Sample volume (μL)	10	20	20		
Chemical modifier (μL)	10	–	–		
Data processing	Area				
Thermal program:					
Stage	1	2	3	4	5
Temperature (Cd)	90	150	800	1500	2800
(Cr)			1300	2400	
(Ni)			1500	2200	
Ramp (°C s^{-1})	5	10	50	0	
Hold time (s)	10	30	20	3	3

ICP-OES	Perkin Elmer Optima 4300 DV
Elements	As, Cr, Cu, Mg, Mn, Ni, Sr, Zn
Radiofrequency power (W)	1500
Sample flow rate (mL min^{-1})	2
Argon flow rates (L min^{-1})	Plasma, 15.0; auxiliary, 0.2; nebulizer, 0.4
Stabilization time (s)	15
Replicate time (s)	5

FAAS	Unicam AAS Model Solaar 969	
Element	Mg	Zn
Detection wavelengths (nm)	285.2	213.9
Lamp current (mA)	6	10
Spectral bandpass (nm)	0.5	0.5
Burner height (mm)	7	7
Air/acetylene flow rate (L min^{-1})	1	1.2
Analysis time (s)	4	4

CV-AAS	PerkinElmer AAS Model 4110 ZL
Element	Hg
Detection wavelengths (nm)	253.7
Lamp current (mA)	6
Spectral bandpass (nm)	0.7
Integration time (s)	25
Cell temperature (°C)	100
Sample volume (μL)	500
Data processing	Peak height
FIAS program:	
Step	Prefill / Fill Injection
Time (s)	15 / 10 15
Pump 1 (rpm)	100 / 1000
Pump 2 (rpm)	120 / 120120
Valve	Fill / Fill Inject

ICP-MS	Thermo Elemental X7 Series
Elements	As, Cd, Cr, Cu, Mg, Mn, Ni, Sr, Zn
Forward power (W)	1300
Sample flow rate (L min^{-1})	0.6
Argon flow rates (L min^{-1})	Plasma, 13.0, auxiliary, 0.7, nebulizer, 0.85
Scanning mode	Peak hop
Points per peak	1
Dwell time (ms)	10
Sweeps per peak	50
Replicates	3
Collision cell technology (CCT)	
CCT gas	8% H_2 and He
Flow cell gas (mL min^{-1})	6

and Ni were carefully optimized with the emulsified samples. Optimum conditions for emulsion nebulization in FAAS and ICP-OES were used. Speed of pumps in the flow injection system and concentrations of $NaBH_4$ and HCl were also appropriately optimized.

A 100 W 20 KHz Sonic and Materials (Danbury, CT, USA) high intensity ultrasonic processor, model VC 50-1, equipped with titanium microtip of 3 and 6 mm of diameter was used for ultrasound-assisted emulsification. A Multiwave 3000 Oven system (Anton Paar, Graz, Austria) equipped with a sample rotor of 8 vessels was used for microwave-assisted digestion of samples. A UVIKON XS UV/VIS spectrophotometer (Domont, France) equipped with quartz cells was used to acquire the spectrum of the emulsions. A Cannon-Fenske Serie 150 viscosimeter (Afora, Barcelona, Spain) was used for viscosity measurements.

2.2. Reagents and samples

High-purity deionised water was obtained from a PETLAB ultrapure water production system (Peter Taboada, Vigo, Spain). Multielement standard stock solution of 10 mg L^{-1} for Cd, Cr, Cu, Mg, Mn, Ni and Sr and 100 mg L^{-1} for As and Zn (ICP Multi Element Standard Certipur® VI Merck, Darmstadt, Germany) were used for calibration purposes in ICP-OES and ICP-MS. Internal standardization was carried out with ^{89}Y (0.5 μg L^{-1}) and ^{115}In (5 μg L^{-1}) prepared from a single element standard stock solution of 1000 mg L^{-1} (Merck). Single element standard stock solutions containing 1000 mg L^{-1} were prepared dissolving the pure metal or the appropriate salts: magnesium chips (Aldrich, Steinheim, Germany), nickel metal (Aldrich), zinc fine powder (Prolabo, Fontenay-sous-Bois, France), cadmium nitrate (Panreac, Barcelona, Spain), potasium chromate (Prolabo), mercury chloride (Prolabo).

Surfactants used for preparing ultrasound-assisted emulsifications were: sodium dodecyl sulphate (SDS, Fluka, Steinheim, Germany), hexadecyl trimethylammonium bromide (CTAB, Sigma–Aldrich, Milwaukee, USA), Tween 80 (Sigma–Aldrich) and triton X-100 (Merck). Concentrated HNO_3 (Suprapur, Merck), H_2O_2 33% (w/v) (Panreac) and HF 40% (v/v) (Merck) were used for microwave-assisted digestion procedures. Palladium nitrate (Fluka) was used as chemical modifier for Cd determination by ETAAS. Concentrated HCl of analytical grade quality (Prolabo), NaOH (Prolabo), $NaBH_4$ (Merck) and the Antifoam A (Fluka) were used for CV-AAS measurements.

Four hairs care products (conditioner, antidandruff shampoo, intensive antidandruff shampoo and hair gel) and two bath/shower preparations (body milk and body oil) were analyzed. In general, these products are emulsions and hence, a re-emulsification is necessary prior to analysis. These samples content a large number of components, such as tensioactives, fragrance agents, stabilizer agents, antimicrobial preservatives and water. Moreover, shampoos, hair gel and body milk contained a SiO_2-based compound (i.e. dimethicone). Elements like Zn (present in the anti-dandruff shampoo as pyrithione or carbonate) and Mg (present in the antidandruff shampoo as sulphate or carbonate) are active principles in shampoos. Levels of these elements were not mentioned in the commercial labels.

Glassware and plasticware used throughout the work were washed with 10% (v/v) nitric acid followed by repeated rinsing with ultrapure water.

2.3. Procedures for ultrasound-assisted emulsification

Different emulsification procedures were proposed in order to adapt this approach to some monoelemental and multielemental atomic spectrometry techniques: ETAAS, ICP-OES, FAAS and CV-AAS.

For the determinations by ETAAS (Cd, Cr and Ni): a portion of 15 mg of cosmetic sample was weighed into an autosampler cup and 1 mL of acid solution with surfactant (0.5% w/v SDS and 3%, v/v HNO_3 solution) was added as dispersing medium. Then, the mixture was sonicated for 1 min at 20% amplitude by means of the 3 mm probe.

For the determinations by ICP-OES (As, Cd, Cr, Cu, Mg, Mn, Ni, Sr and Zn) and FAAS (Mg and Zn): a portion of cosmetic sampled in the range 0.05–0.2 g was weighed into a 50 mL polyethylene tube, and then 15 mL of dispersing solution was added. This mixture was sonicated for 1 min at 20% amplitude by means of the 6 mm probe.

For the determination of Hg by CV-AAS, the emulsification procedure was similar to that employed in ICP-OES and FAAS, but HCl was used instead of HNO_3 in the composition of the dispersion medium. Also, addition of 200 μL of antifoam after sonication was needed in order to avoid foam formation in the gas–liquid separator.

Blanks were treated in the same way. In all cases the emulsion obtained was directly introduced in the analytical instrument.

2.4. Procedure for microwave-assisted digestion

Different digestion procedures were studied for the cosmetic samples containing a SiO_2-based compound, such as shampoos, hair gel and body milk. When digestions were carried out using only HNO_3 (4 mL of concentrated nitric acid), it was necessary to filtrate in order to remove the silicate residues [8,11]. The addition of HF was also tried for the digestion of these samples (a mixture of 3 mL of HNO_3 and 0.5 mL of HF was used and then, the resulting solution was heated in a sand bath nearly to dryness). The mixture of H_2O_2 and HNO_3 was also tried (4 mL of HNO_3 and 2 mL of H_2O_2). No significant differences were observed when the different procedures were statistically compared.

Microwave-assisted digestion of the cosmetics was carried out for comparison purposes. The selected procedure was as follows: about 0.2 g of sample was weighed into the PFA vessel, and then, 4 mL of concentrated HNO_3 and 2 mL of ultrapure water were added. The digestion vessels were closed and heated in a microwave oven using a preselected program: first stage of 5 min at 900 W, second stage of 2 min at 0 W and a third stage of 20 min at 900 W. After cooling, digests were quantitatively transferred into a 50-mL volumetric flask and made up to volume with ultrapure water. Blanks were treated in the same way. A dilution 1:5 was made for As, Cu, Sr and Zn measurements by ICP-MS in order to avoid matrix effects. Determinations by ICP-MS were based on a calibration graph obtained from standard aqueous solutions. Recovery studies were carried out for validation purposes.

3. Results and discussion

The type of surfactant and its concentration, the acid and its concentration, the quantity of sample in relation to the volume of dispersion medium, as well as the parameters related to the ultrasound-assisted emulsification (amplitude and sonication time) were exhaustively investigated. Preliminary experiments were carried out in order to visually check the stability of emulsions and then to establish suitable conditions in which stable emulsions were formed. In this work, an oil-in-water emulsion (o/w) is formed because the aqueous medium forms the continuous phase.

3.1. Study of the dispersion medium

Different surfactants were considered in this work: Triton X-100 (non-ionic), Tween 80 (non-ionic), SDS (anionic) and CTAB (cationic). These surfactants were selected due to their high solubility in water. All them have a HLB (hydrophilic lipophilic balance) higher than 10 (dimensionless scale) and can form (o/w) emulsions.

In general, surfactants with high HLB, as SDS (40), display high solubility in water and generally act as good solubilizing agents, detergents and stabilizers for (o/w) emulsions. The lower HLB of the others surfactants studied (15 for Tween 80, 13.5 for Triton X-100, and 10 for CTAB) can predict their lowest performance in (o/w) emulsification. These surfactants have been successfully used by other workers for samples such as gasoline, crude oil or edible oil [16,22,30,31].

Surfactants play a basic role in the formation and stability of emulsions (electrostatic and/or steric repulsion between emulsion droplets mainly depend on the surfactant), but an increasing viscosity can occur. On the other hand, the cavitation pressure threshold in a liquid increases on increasing viscosity. Less viscous emulsions allow achieving cavitation more easily [32]. In order to prevent potential problems in the emulsification procedure and, especially, during the sample introduction step in the different analytical instruments, viscosity of emulsions was tested. Emulsions with different surfactant concentration were prepared: CTAB (between 0.1% and 1% w/v), Tween 80 (between 0.005% and 0.5% w/v), SDS (between 0.05% and 1% w/v) and Triton X-100 (between 0.001% and 0.5% w/v). Small quantities of surfactant were tried in order to obtain suitable blanks for trace metal determinations. The blanks obtained with the different surfactants were suitable in all cases. When ultrasound energy is used, less surfactant could be necessary, and it would represent an important advantage of ultrasound-assisted emulsification procedures.

The minimum concentration of surfactant that forms a visually stable emulsion was established and then, kinematic viscosity of stable emulsions was measured. Table 2 shows the results obtained. As can be seen, emulsions formed with CTAB showed high viscosity, which was troublesome in some measurements, so this surfactant was rejected. Emulsions formed with Triton X-100 showed low stability and the breakup of the emulsion occurred at 30 min for concentrations up to 0.01% (w/v). The emulsions formed with Tween 80 showed good stability but their turbidity increased with time. SDS showed very good stability and no turbidity for concentrations up to 0.05% (w/v).

Stability and turbidity studies were made by ETAAS (Ni was determined in hair conditioner emulsions prepared with different surfactants) (Fig. 1) and by spectrophotometry (absorption spectra of the formed emulsions were obtained). The results were in good agreement with those obtained visually. SDS was selected for preparing emulsions on the basis of its good stability and lack of turbidity. A SDS concentration of 0.05% (w/v) was necessary to reach stable emulsions. Then, a concentration in the range 0.1–0.5% (w/v) of SDS was used for this purpose. Stability studies were also carried out for the rest of elements.

Nitric acid is usually added to the dispersion medium because it helps improving the stability of the analyte in emulsions of samples such as biodiesel [23]. HNO_3 can also convert organic species, metallic solid particles and oxide species of the analytes into their inorganic forms. In addition, it has been demonstrated that the use of emulsions (gasoline and kerosene) acidified with HNO_3 enables direct correlation between the signal of the analyte in the samples and the signal of it in aqueous inorganic standards [33]. When

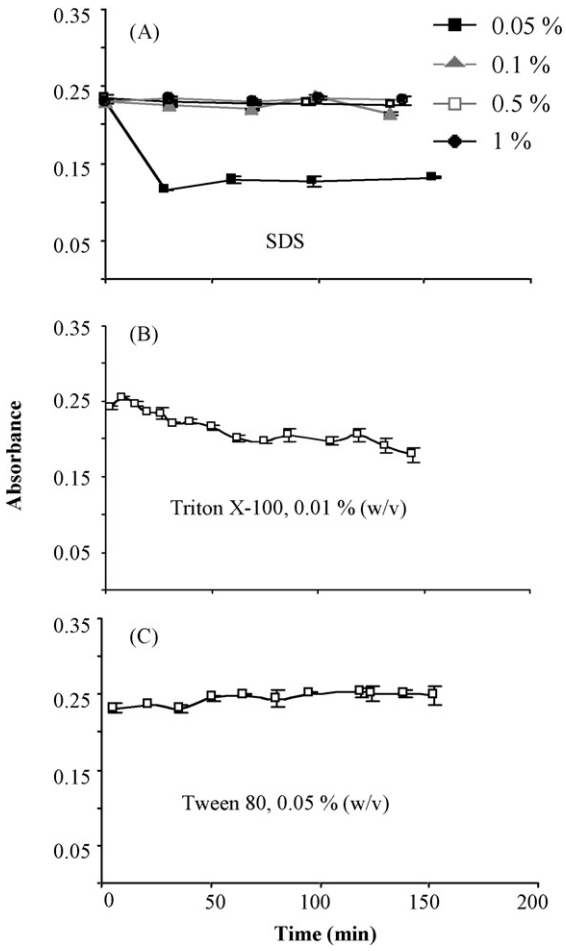


Fig. 1. Variation of absorbance *vs.* time for 20 μg L^{-1} of Ni in emulsions of hair conditioner (0.015 g of sample in 1 mL of dispersion medium) prepared with different surfactants (A) ■, SDS 0.05%; ▲, 0.1%; □, 0.5%; ♦, 1% (w/v); (B) Triton X-100, 0.01% (w/v) and (C) Tween 80, 0.05% (w/v).

only SDS was added to the water phase in our experiments, persistent foam and slight turbidity were observed in the formed emulsion. Therefore, acid concentration was studied in the range 0.5–4% (v/v). Foam formation was observed for acid concentrations lower than 1% (v/v), a nitric acid concentration of 3% (v/v) being selected. The use of hydrochloric acid was also considered in the application of the CV-AAS technique, although no differences were observed.

3.2. Oil/water ratio

The use of a maximum amount of sample in the emulsion is desirable in order to increase the analytical sensitivity, but it also increases the viscosity, thereby reducing the cavitation and the nebulization efficiency. Then, the sample mass was varied between

Table 2
Kinematic viscosity of emulsions.

Surfactant	Visually non-stable emulsions (up to % w/v)	Assayed range		Concentration (% w/v)	K. viscosity[a] (cSk)
		Concentration (% w/v)	K. viscosity (cSk)		
SDS	0.05	0.1–1	0.989–1.082	0.50	1.007
Tween 80	0.01	0.02–0.5	1.120–1.176	0.05	1.160
Triton X100	0.005	0.01–0.5	1.138–1.176	0.01	1.145
CTAB	0.5	1	43.5	–	–

[a] K. Viscosity is kinematic viscosity. The kinematic viscosity for deionized water is 0.999 cSk.

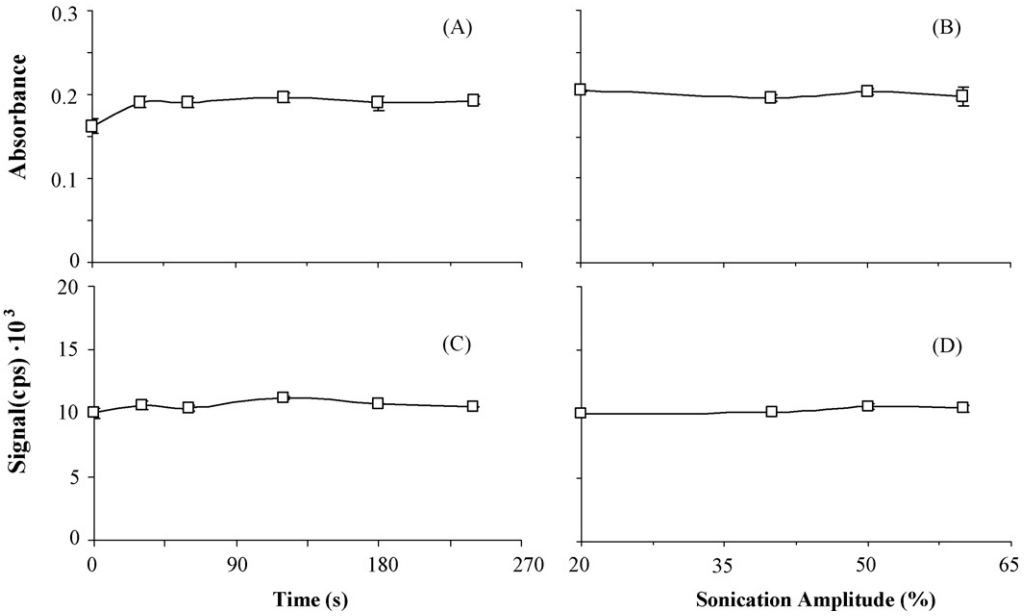


Fig. 2. Optimization of the sonication time (min) and amplitude (%) in emulsions formed with hair conditioner. (A) Absorbance of Ni obtained by ETAAS *vs.* ultrasound time; (B) absorbance of Ni *vs.* sonication amplitude; (C) emission signal of Mg by ICP-OES *vs.* sonication time and (D) emission signal of Mg *vs.* ultrasound amplitude. Experimental conditions for (A) and (B) were: 0.015 g of sample in 1 mL of dispersion medium (0.5% w/v of SDS and 3% v/v nitric acid). Experimental conditions for (C) and (D) were: 0.2 g of sample in 15 mL of dispersion medium.

0.05 and 0.2 g for 15 mL of dispersion medium and the viscosity was measured. Viscosities were found in the range 1.008–1.119 cSk. Larger sample masses caused an important increase in viscosity and besides persistent foams. Then, under these conditions, a (o/w) ratio of about 0.015 g mL^{-1} was established for the different analytical techniques including ETAAS, where 1 mL of dispersion medium was used.

3.3. Sonication parameters

Besides the surfactant concentration and the (o/w) ratio, main parameters influencing the emulsification process included power or amplitude and sonication time. In general, it is considered that an increase in the irradiation time and power causes a decrease in droplet size and an increase in the stability of the emulsion [34]. Then, sonication time and sonication amplitude were optimized for the emulsions formed with 1 or 15 mL of dispersion medium. Different techniques and samples were used for this purpose. In all cases, the results showed that 1 min is enough to form a stable and homogeneous emulsion (Fig. 2). Higher sonication amplitude had no effect on the emulsion formation so it was maintained at 20% level.

In comparison with the probe system, when an ultrasound bath was used in this work, a time of 15 min was necessary in order to obtain a transparent emulsion. When mechanical stirring was used, a turbid emulsion was obtained after 30 min. Similar times have been required by other authors with ultrasonic baths [22,35–38] and with mechanical stirring [30].

Sonication probe systems bring about some benefits for ultrasound-assisted emulsification, such as faster formation of stable emulsions and lower surfactant concentration, since cavitation is easily reached with these systems.

3.4. Studies of stability

Emulsions of the different cosmetic samples, prepared as pointed out above, were visually stable at least for 3 months. For longer times, phase separation takes place.

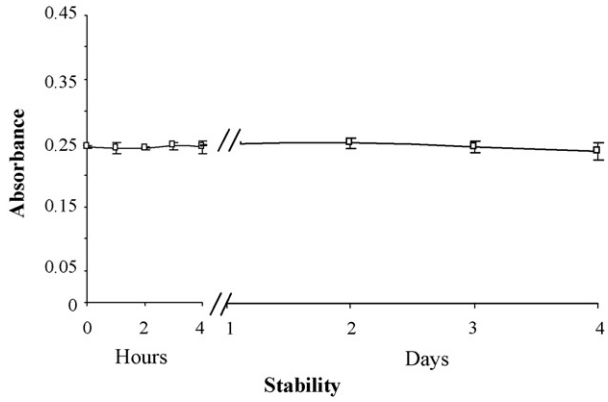


Fig. 3. Stability study of an emulsion prepared with the antidandruff shampoo (0.2 g of sample in 15 mL of dispersion medium). Zn absorbance measured by FAAS during four consecutive days.

The stability of emulsions was investigated for a period of several days. As can be seen in Fig. 3, the analytical signal of Zn in the antidandruff shampoo emulsion indicates a very good stability. Then, no immediate determinations need to be carried out.

3.5. Calibration studies

Chemical interferences caused by matrix components when emulsions are directly introduced into the analytical instruments, makes it necessary the development of different strategies for calibration. Aqueous standards have been adequate in the determination of several metals in oil-water emulsions [19,39]. de Souza et al. [18] used aqueous standards containing surfactant. Standard additions have been used with inorganic standards [38] and metal-organic standards [22]. Emulsions prepared with a single organic solvent using aqueous or organometallic stock solutions have also been used [40]. Different emulsions prepared by using purified samples and adding the metal as inorganic or as organic form have also been employed by several authors for calibration purposes [16,17,20,22,23,35].

In our work, potential matrix effects were studied by comparison of slopes obtained for aqueous standards and standard addition calibration methods. Calibration curves were built from three measurement replicates and, in all cases, regression coefficients were higher than 0.995. The slopes obtained and the linear ranges used are shown in Table 3. The comparison of slopes is presented in terms of percentage of change in slope (aqueous standard/standard addition). In all cases these percentages of change were less than 5%. These results indicate that there are not significant matrix effects and hence, calibration with aqueous standard can be carried out in all cases.

3.6. Validation of the proposed methodology

Validation of the ultrasound-assisted emulsification procedure in order to demonstrate its applicability to cosmetic samples was performed. This included detection and quantification limits, linearity, precision and accuracy.

Instrumental limits of detection (LOD) and quantification (LOQ) were determined following the 3σ and 10σ criteria, respectively. Procedural LOD and LOQ values in cosmetic samples were determined considering the instrumental LOD and LOQ values and the sample treatment (0.015 g of sample in 1 mL of solution for ETAAS and 0.2 g of sample in 15 mL of solution for ICP-OES, FAAS and CV-AAS). These limits are shown in Table 4.

Precision of the method, expressed as relative standard deviation (RSD), was evaluated in terms of repeatability. RSDs from five independent emulsions are shown in Table 4. Emulsions of cosmetic samples provided good precision. In all cases, repeatability from three replicates of the same emulsion was lower than 3% for all elements.

Accuracy was tested by means of recovery studies because certified reference materials for determining trace elements in cosmetics were not available. These studies were carried out in triplicate upon addition of known amounts of the element under study prior to sonication. As can be seen in Table 4, quantitative results were obtained in all cases.

Although mercury is used in cosmetics as a preservative in the form of phenylmercury salts and thiomersal, in this work, only inorganic mercury was determined. When ultrasound irradiation is performed in aqueous media, a series of radicals that are formed at the gas-phase interface of the cavitation bubble and to a lesser extent in the bulk solution, can reduce Hg(II) to Hg(0). However, when the medium contains HCl, this reaction does not take place [41]. Then, nitric acid was replaced by hydrochloric acid in the dispersion medium. Recovery studies confirm the maintenance of Hg(II) in the emulsion and further generation of Hg(0) from Hg(II) upon reduction with $NaBH_4$.

3.7. Analytical results for analyzed samples

Hair care products and bath/shower preparations were analyzed following the established procedure of ultrasound-assisted emulsification and different atomic spectrometric techniques (ETAAS, ICP-OES, FAAS and CV-AAS). External calibration with aqueous standards was used throughout. As a comparative methodology, samples were analyzed following microwave-assisted digestion and ICP-MS. Analytical results from three sample preparations for both ultrasound-assisted emulsification and microwave-assisted digestion procedures and three replicates of each one are shown in Table 5. After application of a t-test, no significant differences were generally observed between the results obtained by ultrasound-assisted emulsification and those obtained following microwave-assisted digestion.

In general, elements considered toxic such as Cd or Hg display concentrations below the LODs in the cosmetics under study.

Table 3
Slopes of the calibration lines obtained with external calibration (aqueous standards) and standard addition method for the analysis of different cosmetics.

Element	Technique	Range ($\mu g L^{-1}$)	Slope aqueous stand[a]	Matrix									
				Conditioner		Antidandruff shampoo		Intensive antidandruff shampoo		Hair gel		Body milk	
				Slope st.ad.[b]	Change %	Slope st.ad.[b]	Change %	Slope st.ad.[b]	Change %	Slope st.ad.[b]	Change %	Slope st.ad.[b]	Change %
As[c]	ICP-OES	10–100	10.2203	10.3741	−1.5	10.4393	−2.1	10.3196	−1.0	10.0303	+1.9	9.8919	+3.3
Cd[c]	ETAAS	1–10	0.1083	0.1061	+2.1	–	–	–	–	–	–	–	–
Cr[c]	ETAAS	1–50	0.0161	0.0160	+1.0	–	–	–	–	–	–	–	–
	ICP-OES	10–100	73.7289	73.9930	−0.3	74.4422	−0.9	74.9242	−1.6	73.6395	+0.1	73.0435	+0.9
Cu[c]	ICP-OES	10–100	59.8394	60.0202	−0.3	59.5530	+0.5	59.7747	+0.1	61.5325	−2.7	60.7756	−1.5
Hg[c]	CV-AAS	1–40	0.0085	0.0088	−3.4	–	–	–	–	–	–	–	–
Mg[d]	ICP-OES	100–1000	0.4049	0.4159	−2.6	0.4069	−0.5	0.4064	−0.4	0.4059	−0.2	0.3936	+2.9
	FAAS	100–500	0.6442	0.6240	+3.2	0.6440	0.0	0.6642	0.0	0.6236	+3.3	0.6338	+3.4
Mn[d]	ICP-OES	10–100	0.3563	0.3425	+4.0	0.3594	−0.9	0.3545	+0.5	0.3465	+2.8	0.3463	+2.9
Ni[c]	ETAAS	1–50	0.0084	0.0084	0.0	–	–	–	–	–	–	–	–
	ICP-OES	10–100	19.1195	18.4681	+3.5	18.9148	+1.1	19.2630	−0.7	18.4496	+3.6	18.3887	+4.0
Sr[d]	ICP-OES	10–100	7.2152	7.2241	−0.1	7.1768	+0.5	7.2809	−0.9	7.2708	−0.8	7.2832	−0.9
Zn[d]	ICP-OES	100–1000	0.5590	0.5445	+2.7	0.5374	+4.0	0.5839	−4.3	0.5628	−0.7	0.5620	−0.5
	FAAS	1–100	0.2776	0.2733	+1.6	0.2806	+1.1	0.2758	+0.6	0.2741	+1.3	0.2725	+1.9

–Not determined.
[a] Slope obtained for aqueous standards.
[b] Slopes obtained for standard addition.
[c] Slopes expressed in $\mu g L^{-1}$.
[d] Slopes expressed in $mg L^{-1}$.

Table 4
Validation of the emulsification method.

Element	Technique	LOD ($\mu g\,g^{-1}$)	LOQ ($\mu g\,g^{-1}$)	RSD (%)	Recoveries (%)				
					Conditioner	Antidandruff shampoo	Intensive antidandruff shampoo	Hair gel	Body milk
As	ICP-OES	0.03	0.11	1.7–8.7	102 ± 3	104 ± 2	107 ± 2	100 ± 4	96 ± 0.3
Cd	ETAAS	0.95[a]	3.2[a]	1.2–5.6	95 ± 3	96 ± 2	97 ± 2	102 ± 2	100 ± 2
Cr	ETAAS	6.2[a]	21[a]	0.6–8.3	109 ± 3	98 ± 2	99 ± 1	97 ± 2	100 ± 2
	ICP-OES	0.07	0.23	1.0–8.7	99 ± 5	101 ± 1	99 ± 2	99 ± 2	97 ± 3
Cu	ICP-OES	0.13	0.44	1.5–7.5	94 ± 5	90 ± 3	99 ± 2	95 ± 4	94 ± 2
Hg	CV-AAS	5.5[a]	18[a]	0.4–4.7	102 ± 2	99 ± 3	96 ± 3	96 ± 2	98 ± 1
Mg	ICP-OES	0.02	0.06	1.3–8.6	91 ± 2	91 ± 3	97 ± 3	107 ± 2	92 ± 2
	FAAS	0.20	0.67	0.8–9.3	96 ± 1	98 ± 1	96 ± 2	95 ± 1	95 ± 2
Mn	ICP-OES	0.02	0.09	2.0–9.1	97 ± 2	102 ± 2	101 ± 1	97 ± 3	96 ± 4
Ni	ETAAS	11[a]	35[a]	0.8–9.2	103 ± 3	102 ± 2	96 ± 3	93 ± 3	98 ± 2
	ICP-OES	28[a]	95[a]	1.7–8.3	94 ± 4	92 ± 4	91 ± 3	101 ± 3	95 ± 2
Sr	ICP-OES	3.7[a]	11[a]	0.6–9.1	91 ± 1	93 ± 3	94 ± 3	90 ± 3	90 ± 2
Zn	ICP-OES	0.12	0.39	0.8–5.0	102 ± 4	94 ± 3	108 ± 2	101 ± 2	102 ± 2
	FAAS	0.47	1.6	0.3–5.3	97 ± 1	101 ± 1	98 ± 1	97 ± 1	97 ± 2

[a] LODs expressed in $ng\,g^{-1}$.

Table 5
Concentrations ($ng\,g^{-1}$) in different cosmetic samples.

Element	Technique	Samples					
		Conditioner	Antidandruff shampoo	Intensive antidandruff shampoo	Hair gel	Body milk	Body oil
As	ICP-OES	<LOD	90 ± 6 (0.005)[b]	234 ± 20 (1.091)[b]	<LOD	<LOD	<LOD
	ICP-MS	<LOD	87 ± 4	252 ± 19	<LOD	14 ± 2	<LOD
Cd	ETAAS	<LOD	<LOD	<LOD	<LOD	<LOD	<LOD
	ICP-MS	<LOD	<LOD	<LOD	<LOD	<LOD	<LOD
Cr	ETAAS	66 ± 4 (2.947)[b]	418 ± 11	159 ± 13 (1.318)[b]	46 ± 4 (1.619)[b]	93 ± 9 (1.011)[b]	57 ± 6 (2.305)[b]
	ICP-OES	<LOD	373 ± 23 (0.877)[b]	186 ± 16	<LOD	<LOD	<LOD
	ICP-MS	58 ± 4	389 ± 21 (2.065)[b]	170 ± 14 (0.909)[b]	42 ± 4	88 ± 8	69 ± 7
Cu	ICP-OES	<LOD	<LOD	269 ± 20 (1.349)[b]	<LOD	<LOD	<LOD
	ICP-MS	<LOD	84 ± 6	292 ± 21	44 ± 1	151 ± 13	<LOD
Hg	CV-AAS	<LOD	<LOD	<LOD	<LOD	<LOD	<LOD
Mg	ICP-OES	5.4 ± 0.1[a] (1.254)[b]	464 ± 16[a] (2.121)[b]	6.8 ± 0.6[a] (5.068)[b]	38 ± 2[a] (0.229)[b]	26 ± 2[a] (0.651)[b]	<LOD
	FAAS	5.8 ± 0.1[a] (2.493)[b]	454 ± 13[a] (1.395)[b]	9.5 ± 0.7[a] (0.364)[b]	37 ± 1[a] (0.845)[b]	24 ± 0[a] (2.748)[b]	691 ± 64 (0.567)[b]
	ICP-MS	5.5 ± 0.1[a]	439 ± 14[a]	9.7 ± 0.8[a]	38 ± 2[a]	27 ± 1[a]	720 ± 60
Mn	ICP-OES	<LOD	221 ± 20 (1.833)[b]	<LOD	<LOD	<LOD	<LOD
	ICP-MS	<LOD	197 ± 11	2.4 ± 0.1	1.9 ± 0.1	6.7 ± 0.4	<LOD
Ni	ETAAS	<LOD	13 ± 1[a] (1.008)[b]	5.4 ± 0.5[a] (2.295)[b]	<LOD	<LOD	<LOD
	ICP-OES	<LOD	10 ± 1[a] (2.168)[b]	4.8 ± 0.4[a] (0.207)[b]	<LOD	<LOD	<LOD
	ICP-MS	12 ± 1	12 ± 1[a]	4.8 ± 0.3[a]	<LOD	25 ± 1	10 ± 1
Sr	ICP-OES	25 ± 1 (2.177)[b]	149 ± 10 (3.783)[b]	352 ± 32 (1.159)[b]	38 ± 4 (1.241)[b]	299 ± 26 (0.971)[b]	<LOD
	ICP-MS	28 ± 1	109 ± 10	381 ± 30	42 ± 3	321 ± 31	<LOD
Zn	ICP-OES	<LOD	12872 ± 53[a] (4.306)[b]	2.0 ± 0.1[a] (2.306)[b]	<LOD	<LOD	<LOD
	FAAS	<LOD	12755 ± 40[a] (1.688)[b]	1.9 ± 0.1[a] (0.097)[b]	<LOD	<LOD	<LOD
	ICP-MS	<LOD	12694 ± 47[a]	1.8 ± 0.1[a]	<LOD	<LOD	<LOD

[a] Concentrations are expressed in $\mu g\,g^{-1}$.

[b] t_{exp} values are shown between parenthesis. t_{crit} is 2.776 ($N = 3$, $p < 0.05$).

LODs for ICP-MS were: 0.01 $\mu g\,g^{-1}$ for As, 2.0 $ng\,g^{-1}$ for Cd, 0.04 $\mu g\,g^{-1}$ for Cr, 0.01 $\mu g\,g^{-1}$ for Cu, 5.0 $ng\,g^{-1}$ for Mg, 1.8 $ng\,g^{-1}$ for Mn, 9.3 $ng\,g^{-1}$ for Ni, 10. $ng\,g^{-1}$ for Sr and 0.04 $\mu g\,g^{-1}$ for Zn.

Only shampoos have a detectable content of As (87 $ng\,g^{-1}$ in antidandruff and 271 $ng\,g^{-1}$ in intensive antidandruff shampoos). Cr was detected at low levels (between 38 and 429 $ng\,g^{-1}$). In the case of Ni, for which most of their compounds are prohibited, levels found were between the LOD and 14 $\mu g\,g^{-1}$. Cu concentration ranged between the LOD and 313 $ng\,g^{-1}$. Mg displays a large variability depending of the cosmetic sample. The antidandruff shampoo, where Mg is one of the active principles, contains around 480 $\mu g\,g^{-1}$. Mn concentration was between LOD and 241 $ng\,g^{-1}$. Sr concentration ranged between undetectable concentrations and 412 $ng\,g^{-1}$, with the maximum level in the intensive antidandruff shampoo. For Zn, only detectable concentrations were observed in the shampoos, with the maximum content in the antidandruff shampoo (about 13 $mg\,g^{-1}$), in which is used as an active principle.

Overall, element concentrations are below the sensitizing limit proposed for consumer products and therefore, in agreement with the European legal regulations [1].

4. Conclusions

The developed procedure based on ultrasound-assisted emulsification with a probe ultrasonic processor provides an accurate and precise methodology for preparation of cosmetic samples prior to elemental analysis by ETAAS, ICP-OES, FAAS and CV-AAS. It can

be considered as an advantageous alternative in respect to digestion procedures due to its simplicity (minimal operations involved), rapidity and low consumption of reagents. These characteristics make this sample preparation suitable for routine analysis in the cosmetic industry.

An emulsion with very high stability is obtained. High intensity sonication for emulsion preparation facilitates the use of a surfactant (SDS) at low concentration. Addition of acid to the dispersion medium is necessary in order to remove foaming when cosmetics containing detergents such as shampoos are analyzed. A significant reduction in treatment time used for emulsion formation is achieved with probe sonication as compared to bath sonication.

Oil/water emulsions have similar viscosities in comparison with aqueous solutions and hence, no problems were found with nebulization systems in FAAS and ICP-OES instruments, with the flow injection system used in CV generation or with the autosampler used in ETAAS determinations. Also, matrix effects were not present when emulsions are used. Conventional calibration with aqueous standards can be made in all cases.

Acknowledgements

Financial support from the Spanish Education and Science Ministry (project CTQ2006-04111/BQU) is gratefully acknowledged.

N.C. and I.C. thank the Galicia Government (Xunta de Galicia) for a grant.

References

[1] European Directive 76/768/EEC, Council Directive 76/768/EEC of 27 July 1976 on the approximation of the laws of the Member States relating to cosmetic products.
[2] L. Gagliardi, S. Dorato, in: A. Salvador, A. Chisvert (Eds.), Analysis of Cosmetic Products, Elsevier, 2007, pp. 3–28.
[3] L. Gagliardi, D. De Orsi, S. Dorato, in: A. Salvador, A. Chisvert (Eds.), Analysis of Cosmetic Products, Elsevier, 2007, pp. 45–71.
[4] A. Salvador, J.G. March, M.T. Vidal, A. Chisvert, A. Balaguer, in: A. Salvador, A. Chisvert (Eds.), Analysis of Cosmetic Products, Elsevier, 2007, pp. 72–82.
[5] European Directive 83/514/EEC, Third Commission Directive 83/514/EEC of September 1983 on the approximation of the laws of the Member States relating to methods of analysis necessary for checking the composition of cosmetic products.
[6] European Directive 93/73/EEC, Fifth Commission Directive 93/73/EEC of 9 September 1993 on the methods of analysis necessary for checking the composition of cosmetic products.
[7] Z.A.A. Khammas, M.H. Farhan, Talanta 36 (1989) 1027.
[8] K.D. Besecker, C.B. Rhoades, B.T. Jones, K.W. Barnes, Atom. Spectrosc. 19 (1998) 48.
[9] Z. De-Qiang, N. Zhe-Ming, S. Han-Wen., Spectrochim. Acta Part B 53 (1998) 1049.
[10] E.L. Sainio, R. Jolanki, E. Hakala, Contact Dermatitis 42 (2000) 5.
[11] A. Salvador, M.C. Pascual-Marti, E. Aragó, A. Chisvert, J.G. March, Talanta 51 (2000) 1171.
[12] A. Salvador, M.C. Pascual-Martí, J.R. Adell, A. Requeni, J.G. March, J. Pharm. Biomed. Anal. 22 (2000) 301.
[13] A. Lopez-Molinero, R. Gimenez, P. Otal, A. Callizo, P. Chamorro, J.R. Castillo, J. Anal. At. Spectrom. 17 (2002) 352.
[14] B. Bocca, G. Forte, F. Petrucci, A. Cristaudo, J. Pharm. Biomed. Anal. 44 (2007) 1197.
[15] A. Kawauchi, M. Ishida, I. Saitoh, Spectrosc. Lett. 29 (1996) 345.
[16] B. Du, Q. Wei, S. Wang, W. Yu, Talanta 44 (1997) 1803.
[17] R.C. de Campos, H.R. dos Santos, P. Gringberg, Spectrochim. Acta Part B 57 (2002) 15.
[18] R.M. de Souza, C.L.P. Da Silveira, R.Q. Aucelio, Anal. Sci. 20 (2004) 351.
[19] J.L. Burguera, M. Burguera, R.L. Anton, J.L. Salager, M.A. Arandia, C. Rondon, P. Carrero, Y. Petit de Peña, R. Brunetto, M. Gallignani, Talanta 68 (2005) 179.
[20] I.C.F. Damin, M.G.R. Vale, M.M. Silva, B. Welz, F.G. Lepri, W.N.L. dos Santos, S.L.C. Ferreira, J. Anal. At. Spectrom. 20 (2005) 1332.
[21] G.P. Brandao, R.C. de Campos, A.S. Luna, Spectrochim. Acta Part B 60 (2005) 625.
[22] D.S.S. dos Santos, A.P. Teixeira, J.T.P. Barbosa, S.L.C. Ferreira, M.G.A. Korn, L.S.G. Teixeira, Spectrochim. Acta Part B 62 (2007) 1072.
[23] A. de Jesús, M.M. Silva, M.G.R. Vale, Talanta 74 (2008) 1378.
[24] M. Vondruska, Chem. Listy 89 (1995) 383.
[25] B. Abismaïl, J.P. Canselier, A.M. Wilhelm, H. Delmas, C. Gourdon, Ultrason. Sonochem. 6 (1999) 75.
[26] M.D. Luque de Castro, F. Priego-Capote, Talanta 72 (2007) 321.
[27] M.K. Li, H.S. Fogler, J. Fluid Mech. 88 (1978) 513.
[28] A. Cucheval, R.C.Y. Chow, Ultrason. Sonochem. 15 (2008) 916.
[29] A.E. Alegria, Y. Lion, T. Kondo, P. Riesz, J. Phys. Chem. 93 (1989) 4908.
[30] M. Murillo, Z. Benzo, E. Marcano, C. Gomez, A. Garaboto, C. Martin, J. Anal. At. Spectrom. 14 (1999) 815.
[31] T.D. SaintïPierre, L.F. Dias, D. Pozebon, R.Q. Aucelio, A.J. Curtius, B. Welz, Spectrochim. Acta Part B 57 (2002) 1991.
[32] J.P. Lorimer, T.J. Mason, Chem. Soc. Rev. 16 (1987) 239.
[33] R.M. de Souza, B.M. Mathias, I.S. Scarminio, C.L.P. da Silveira, R.Q. Aucelio, Microchim. Acta 153 (2006) 219.
[34] S.G. Gaikwad, A.B. Pandit, Ultrason. Sonochem. 15 (2008) 554.
[35] J.R. Castillo, M.S. Jiménez, L. Ebbon, J. Anal. At. Spectrom. 14 (1999) 1515.
[36] T. Wang, X. Jia, J. Wu, J. Pharm. Biomed. Anal. 33 (2003) 639.
[37] D.S.S. dos Santos, A.P. Teixeira, M.G.A. Korn, L.S.G. Teixeira, Spectrochim. Acta Part B 61 (2006) 592.
[38] Y.T. Chang, S.J. Jiang, J. Anal. At. Spectrom. 23 (2008) 140.
[39] M.S. Jiménez, R. Velarte, J.R. Castillo, J. Anal. At. Spectrom. 18 (2003) 1154.
[40] M.N.M. Reyes, R.C. Campos, Spectrochim. Acta Part B 60 (2005) 615.
[41] S. Gil, I. Lavilla, C. Bendicho, Anal. Chem. 78 (2006) 6260.

Talanta 80 (2009) 117–126

Contents lists available at ScienceDirect

Talanta

journal homepage: www.elsevier.com/locate/talanta

Simultaneous multiresponse optimization of an HPLC method to separate seven cephalosporins in plasma and amniotic fluid: Application to validation and quantification of cefepime, cefixime and cefoperazone

Emirhan Nemutlu[a,*], Sedef Kır[a], Doruk Katlan[b], M. Sinan Beksaç[b]

[a] Hacettepe University, Faculty of Pharmacy, Department of Analytical Chemistry, Sıhhiye, Ankara, Turkey
[b] Hacettepe University, Faculty of Medicine, Department of Obstetrics and Gynecology, Sıhhiye, Ankara, Turkey

ARTICLE INFO

Article history:
Received 30 March 2009
Received in revised form 8 June 2009
Accepted 12 June 2009
Available online 21 June 2009

Keywords:
Cephalosporin
Experimental design
Solid-phase extraction
Validation
Maternal and fetal plasma
Amniotic fluid

ABSTRACT

An HPLC method for the separation of seven cephalosporins [Cefepime (CEP), ceftazidime (CTA), ceftizaxime (CTI), ceftriaxone (CTR), cefotaxime (COT), cefixime (CIX) and cefoperazone (COP)] in human plasma and amniotic fluid has been developed. Optimization of the chromatographic method was performed in three steps: a series of initial experiments followed by two sets of experiments based on different experimental designs. The initial experiments were performed to decide the basic analytical requirements of the method. Then screening experiment fractional factorial design was used in order to decrease the number of parameters by eliminating parameters which having insignificant effect on responses. The parameters having significant effect were further optimized through a full factorial design. Having studied two responses (retention times and resolutions), a desirability function that assess the responses together, was used to find experimental conditions where the system generated desirable results. The desirable results were obtained with XTerra C18 (250 mm × 4.6 mm, 5 μm i.d.) column, 40 mM phosphate buffer, pH 3.2, 18% MeOH, 0.85 mL min^{-1} flow rate and 32 °C column temperature. Gradient elution with MeOH was applied. A simple and efficient solid-phase extraction was applied for the preparation of plasma and amniotic fluid samples. The validation parameters of the method were evaluated in accordance with ICH guideline. The method validated was applied to the analysis of CEP and COP in maternal venous, fetal venous and fetal arterial plasma, and to the analysis of CIX in maternal venous plasma and amniotic fluid.

© 2009 Elsevier B.V. All rights reserved.

1. Introduction

Cephalosporins are structurally and pharmacologically related to the penicillins. Like the penicillins, cephalosporins have a beta-lactam ring structure that interferes with the synthesis of the bacterial cell wall. They are used for the treatment of infections caused by Gram (+) and Gram (−) bacteria. They are among the safest and the most effective broad-spectrum bactericidal antimicrobial agents and therefore, they are the most frequently prescribed class of antibiotics [1,2].

It is well accepted that changes in body compartments and alterations in cardiac output and renal function occur during pregnancy along with subsequent subtherapeutic maternal serum levels for several antibiotics. For many drugs, absorption is decreased and elimination increased, thus tending to reduce plasma concentrations [3]. Therefore, the concentration of drugs in pregnancy must be determined in order to be monitored if therapeutic dosage is to be achieved or over-dosage prevented. Moreover, the determination of drugs in amniotic fluid is an important piece of information as an indicator of placental penetration [4].

The analysis of cephalosporins in biological materials from human origin [5–12] and in food-producing animals [10,13] foods [10,14], waters [11,15] and pharmaceuticals [16–18] was performed with liquid chromatographic [5–11,13–15], capillary electrophoretic [10,18], spectroscopic [10,14,16–18] and electrochemical methods [7,10,12]. None of them, however, was analyzed the seven cephalosporins simultaneously. In addition, to the authors knowledge, no other article has previously been written regarding the analysis of CEP, CTA, CTI, COT, CIX and COP in amniotic fluid by HPLC.

The method of changing one variable at a time to investigate the outcome of an experiment most likely dates back to the beginnings of systematic scientific research. The idea was fairly simple. In order to simplify control and interpretation of the results, only one of the factors was chosen for variation while the rest keep at constant values. However, the influence of several factors also needed to be investigated during optimization. Thus the conventional step-by-step optimization procedure was too tedious due to the number of

* Corresponding author. Fax: +90 312 311 47 77.
E-mail address: enemutlu@hacettepe.edu.tr (E. Nemutlu).

0039-9140/$ – see front matter © 2009 Elsevier B.V. All rights reserved.
doi:10.1016/j.talanta.2009.06.034

variables involved, and did not take into account possible interactions between factors. With this in mind, the experimental design selects the best location of experimental points in the predictor space and collects these points in a design matrix [19,20].

In this study, chemometric approaches were employed to systematically optimize the relevant operating parameters. The optimization of the method was performed in three steps i) initial experiments to decide basic requirements of the method ii) screening to select important parameter(s) and iii) response surfacing to find the optimum point. During the optimization steps, resolution and retention time responses were screened in order to maximize the resolutions and minimize the analysis time of the developed method.

In the study, fourteen responses (retention time of the seven cephalosporins and seven resolutions between the adjacent peaks) were screened. To evaluate all these responses at the same time, a multicriteria decision-making approach (the desirability function) was used to find the best compromise between the responses [21–23].

Sample preparation from plasma and amniotic fluid was performed with the solid-phase extraction (SPE) method in order to make use of its benefits, i.e. it consumes less solvent, provides more complete extraction of the analyte, and especially, provokes more efficient separation of interfering substances from analytes [24,25].

In this paper, an HPLC method with UV detection was presented for seven cephalosporins given in Fig. 1. The cephalosporins selected in the present study were those that were currently on the market in Turkey for the treatment of humans. The cephalosporins were determined from two matrices (plasma and amniotic fluid). Specifically, the aim was to develop a general method that allowed the determination of each agent without the need for the development of separate and distinct methods. Validation studies were performed with respect to system suitability, stability, linearity, LOD, LOQ, precision, accuracy, selectivity and robustness. Finally, the method was applied to the analysis of CEP and COP in maternal venous and fetal arterial and venous plasma obtained during delivery and CIX in maternal venous plasma and amniotic fluid, obtained from pregnant women between the 16th and 20th gestational weeks during amniocentesis.

2. Experimental

2.1. Reagents

Cefixime (CIX), Cefepime (CEP), Ceftazidime (CTA), Ceftizoxime (CTI), Ceftriaxone (CTR), Cefotaxime (COT) and Cefoperazon (COP) were kindly supplied from Eczacıbaşı Drug Inc. (Turkey).

All reagents were of analytical grade. Acetonitrile, methanol (MeOH) and potassium dihydrogenphosphate were purchased from Merck (Darmstadt, Germany). Milli-Q water was used for the preparation of buffer and other aqueous solutions.

The SPE cartridges used in the study were Strata X (30 mg/1 mL; Phenomenex; California, USA), Oasis HLB (60 mg/3 mL; Waters, Massachusetts, USA), Chromapack C_{18} and C_8 (100 mg/1 mL; Macherey-Nagel, Düren, Germany) and Isolute ENV$^+$ (200 mg/3 mL; Biotage, Uppsala, Sweden).

2.2. Instrumentation

Chromatographic separation of the cephalosporins was performed on a XTerra C_{18} column (250 × 4.6 mm, 5 μm i.d.; Massachusetts, USA) protected with a Phenomenex C_{18} guard column (4 × 3.0 mm i.d.; California, USA).

The HPLC equipment comprised of a solvent delivery system (Shimadzu 10 AT_{VP}, Tokyo, Japan), an auto sampler (Shimadzu SIL 10 AD_{VP} Tokyo, Japan), a column oven (Shimadzu CTO 10 AS_{VP}, Tokyo, Japan) and a photodiode array detector (Shimadzu M 10$_{VP}$, Tokyo, Japan). A ChromQuest software (Shimadzu Technologies) was used for data acquisition and evaluation.

A Mettler Toledo MA 235 pH meter connected with a Mettler Toledo Inlab 413 pH electrode were used to measure the pH of the aqueous mobile phase.

Microsoft Excel 2007 (California, USA) and SPSS 16 (Illinois, USA) was used to calculate matrices and *p* values of the regression coefficients.

2.3. Standards and stock solutions

A stock solution of the CIX (1000 μg mL^{-1}) was prepared in MeOH while the other stock solutions of the cephalosporins (1000 μg mL^{-1}) were in water. All of the stock solutions were stored at +4 °C. Working solutions, containing all cephalosporins, used to spike plasma, amniotic fluid and water were prepared at 10.00, 1.00 and 0.10 μg mL^{-1} concentrations from stock solutions by diluting with water.

2.4. Buffer solutions

An aliquot of 2.7 mL concentrated phosphoric acid for 40 mM phosphate buffer (pH 3.2) and 3.3 mL concentrated phosphoric acid for 50 mM phosphate buffer (pH 2) were transferred into two separate 500 mL volumetric flasks and then diluted to the mark with distilled water and the desired pH was adjusted by the addition of 5 M NaOH.

2.5. Sample collection

Maternal venous, fetal venous and fetal arterial blood were taken during delivery (cesarean section). Single dose antibiotic administration (COP and CEP) was started one hour before delivery intravenously and completed in 30 min. Blood samples were taken from the maternal left hand venous and the umbilical cord of the placenta, discarding material, to obtain fetal veneous and arterial blood samples during delivery. Blood samples were centrifugated at 4500 rpm for 10 min to obtain plasma.

Amniotic fluid was taken from pregnant women between the 16th and 20th gestational weeks to investigate the karyotype of the fetus. To prevent development of an infection, a single dose of antibiotic (CIX) was given orally. After two hours, amniotic fluid and maternal venous blood were taken and venous plasma was obtained from blood by centrifugation at 4500 rpm for 10 min.

Plasma and amniotic fluid samples were stored at −20 °C protected from light until analysis.

The Local Ethical Committee of the Faculty of Medicine at the Hacettepe University, approved this study (LUT 05/112) and the informed written consent was obtained from all patients accepted to the study.

2.6. Sample preparation

An aliquot of 0.5 mL plasma (excepting COP administrated maternal plasma samples; 0.25 mL plasma) or amniotic fluid was transferred into 1.5 mL of an eppendorf tube. Subsequently, 50 μL stock solution of the internal standard (CTI) (100 μg mL^{-1}) was added. After gently mixing, the sample was prepared as explained in the section entitled SPE.

2.7. SPE

A polymeric sorbent (Strata X) was activated with 2 mL of MeOH, 1 mL of water and 1 mL of 50 mM phosphate buffer (pH 2). Samples were diluted to 1.5 mL with 50 mM phosphate buffer (pH 2) and then the samples were loaded without any delay. After pass-

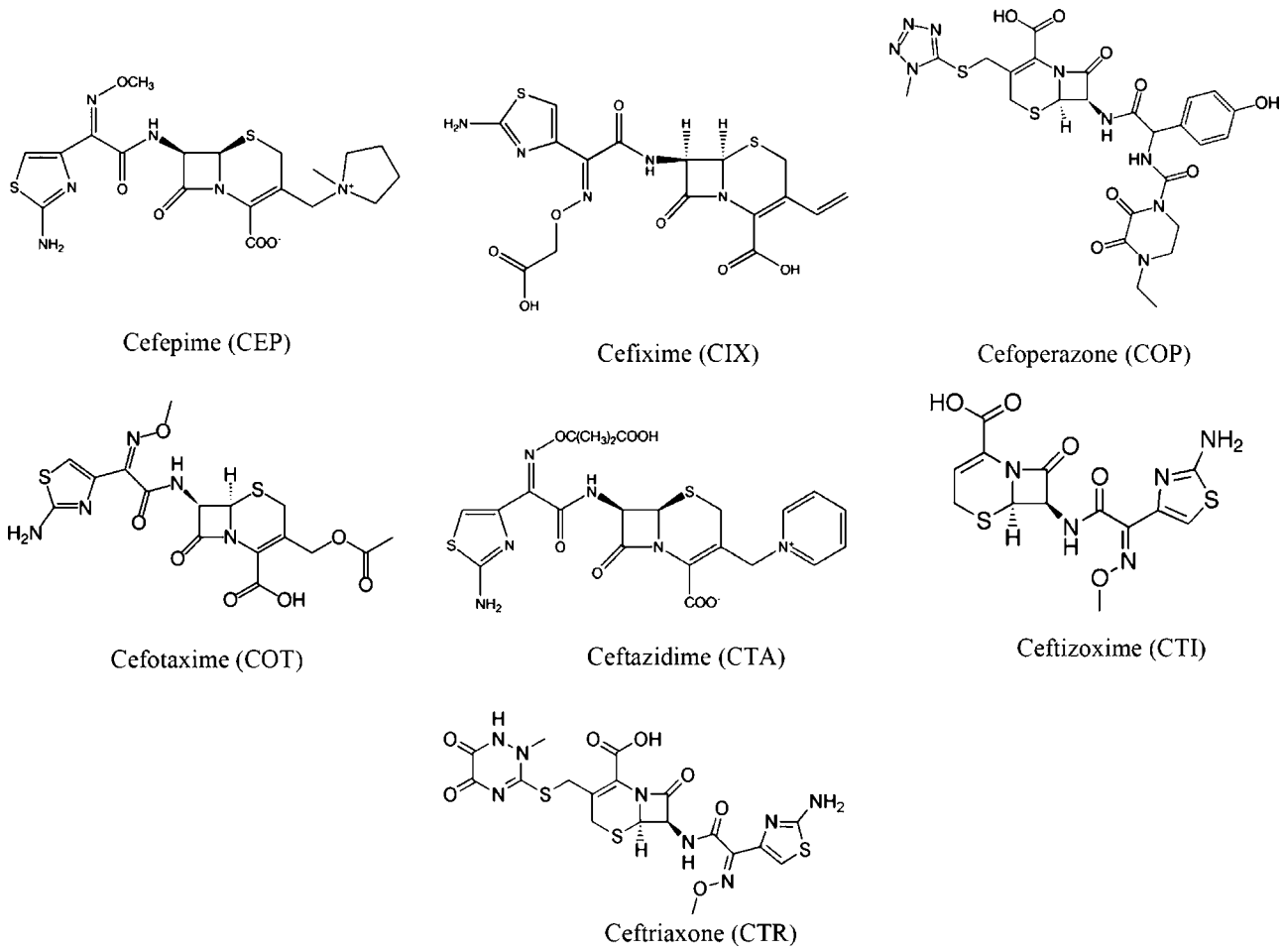


Fig. 1. Chemical structure of the cephalosporins.

ing all the sample through the cartridge, the cartridge was washed with 2 mL of 50 mM phosphate buffer (pH 2) and dried with passing air for two minutes. Elution was done with 2 mL of MeOH and the eluate was evaporated to the dryness at 45 °C under a stream of nitrogen. The residue was reconstituted with 200 μL of MeOH:water (20:80, v/v) mixture and then injected into the HPLC system.

2.8. Chromatographic conditions

The mobile phase was a mixture of 40 mM phosphate buffer (pH 3.2) and MeOH. The mixing of the mobile phase was done during the analysis with the help of a quaternary gradient pump. Gradient elution was applied with the mobile phase as follows: from 0 to 5 min the mobile phase contained 18% MeOH; from 5 to 15 min the percentage of MeOH linearly increased to 45%; from 15 to 16 min the MeOH percentage increased to 55% and maintained at this percentage until 21 min; finally the percentage of MeOH decreased to 18% from 21 to 22 min. The flow rate was 0.85 mL min^{-1}, the injection volume was 20 μL and the column temperature was 32 °C.

2.9. Validation

Validation parameters (system suitability, stability, linearity, sensitivity, accuracy, precision, selectivity, and robustness) of the proposed method were evaluated according to ICH guideline [26].

3. Results and discussion

3.1. Optimization of separation

Optimization of the chromatographic method was performed in three steps: a series of initial experiments followed by two sets of experiments based on different experimental designs. The experimental designs were carried out to obtain maximum resolution in short analysis time.

3.1.1. Initial experiments

The initial experiments were performed to decide the basic analytical requirements of the method, such as the type of column (C_{18} and C_8), buffer, pH range, organic modifier in the mobile phase, ion-pairing reagent, flow rate, and column temperature. A standard solution containing 10 μg mL^{-1} of each of cephalosporins was used during the initial experiments.

The performance of three analytical columns (Zorbax Eclipse XDB-C_8 150 mm × 4.6 mm, 5 μm i.d.; Zorbax Eclipse XDB-C_{18} 150 mm × 4.6 mm, 5 μm i.d. and XTerra C_{18} 250 mm × 4.6 mm, 5 μm i.d.) was checked by running different mobile phases. The better peak asymmetries and resolutions were obtained with XTerra C_{18}. Therefore this was selected as the analytical column.

Phosphate and citrate buffer were tested on the separation of cephalosporins. The better resolutions and peak shapes were obtained with phosphate buffer. Therefore the phosphate buffer was selected as the buffer in the mobile phase. To investigate

Table 1
Experimental conditions according to the fractional factorial design and total desirability function calculated from the responses.

Exp. No.	Run Order	MeOH	pH	Phosphate conc.	Flow rate	Temp.	D_{tR}	D_{Rs}	D_{All}
1	4	−1	−1	−1	1	1	0.2	1.0	0.5
2	1	1	−1	−1	−1	−1	0.3	1.0	0.6
3	10	−1	1	−1	−1	1	0.4	0.3	0.3
4	8	1	1	−1	1	−1	0.9	0.2	0.4
5	11	−1	−1	1	1	−1	0.2	1.0	0.5
6	6	1	−1	1	−1	1	0.4	1.0	0.8
7	7	−1	1	1	−1	−1	0.4	0.9	0.7
8	3	1	1	1	1	1	0.8	0.3	0.5
9	2	0	0	0	0	0	0.7	0.7	0.7
10	9	0	0	0	0	0	0.7	0.7	0.7
11	5	0	0	0	0	0	0.7	0.7	0.7

D_{tr}: Desirability of retention times, D_{Rs}: Desirability of resolutions, and D_{All}: Desirability of resolutions + retention times.

the effect of buffer concentration (ionic strength) within a range, 20–40 mM was selected.

The pH range of the buffer and the column temperature were determined according to column user's instruction in order to get long column life. According to the column user's instruction, the best column life was achieved with the operation at ≤40 °C and pH 2.5–6.0. Therefore these recommendations were accepted for the further optimization procedure of screening.

The effects of an organic modifier in the mobile phase were investigated by using different percentages of MeOH, acetonitrile or MeOH–acetonitrile mixture. Better resolutions and peak asymmetries were obtained with MeOH resulting in MeOH being selected as the organic modifier in the mobile phase.

The effects of different ion-pairing reagents (tetramethylammonium bromide, triethylamine and tetramethylammonium hydroxide) on separation were investigated. Contrary to expectations, it was noted that the peak shapes of cephalosporins were not effected significantly by the ion-pairing reagents. Moreover the baseline noise increased during the gradient elution done with MeOH. Therefore an ion-pairing reagent was not used.

Finally, 0.7–1.0 mL min^{-1} flow rate range was selected to investigate flow rate effects on the retention times and resolutions of cephalosporins.

3.1.2. Screening based on a fractional factorial design

If the number of variables is high, a complete response surface would be a complicated multidimensional structure requiring much more experimental research in order to be fully determined [20]. Thus a screening phase was applied to select significant parameters on separation.

A two level fractional factorial design consisting 11 experiments ($2^{5-2}+n$) (Table 1), was applied, where $n=3$ was the number of replicates of the central point in order to test the model linearity and to obtain an estimate of experimental variance. This fractional factorial design permitted evaluation of whether parameters have a significant influence on the selected response or not. The experiments were performed in a random order to prevent systemic errors. The parameters considered in the fractional factorial design were the MeOH percentage, the pH and concentration of the phosphate buffer, the temperature of the column, and the flow rate. The experimental ranges of the variables were selected on the basis of initial experiments (Table 2). The defined responses of the variables were the resolution between adjacent peaks and retention times.

Evaluation of the parameters was done according to their regression coefficient, but the evaluation of each parameters individually was very difficult because the number of responses (retention times and resolutions) was relatively high and they had two different scales. In order to overcome these difficulties, all of these results were evaluated at the same time with a total desirability function. This function was based on the transformation of the measured properties to a dimensionless desirability scale for each criterion, so that values of several properties, obtained from different scales of measurements, may be combined [21–23,27]. The scale of the desirability function ranges between $d=0$ for a completely undesired response to $d=1$ for a fully desired response, above which further improvements would have no importance. In the second step the overall quality D was calculated combining the desirability values obtained for the different criteria by means of the geometric mean:

$$D = (d_1^{w_1} \times d_2^{w_2} \ldots d_n^{w_n})^{1/(w_1+w_2 \ldots w_n)}$$

where d_i was the individual desirability function of each response obtained from the transformation of the individual response of each experiment, w_i was the weight of the response and n the number of responses.

The retention times and resolutions acquired from experiments were transformed to a desirability scale to get maximum resolution and minimum retention time (Table 1). The scale of the desirability function ranged between $d=0.1$ and 1 in this study. The total desirability function for many experiments was calculated as zero and this caused the occurrence of invalid models, when the range between $d=0$ and 1 was applied. Therefore the scale of the desirability function ranging between $d=0.1$ and 1 was used. The weight for retention times of cephalosporins was the same ($w=1$) while the weight for resolutions was different. The weight of the resolutions between some cephalosporins was given the value of 1 because the resolutions between them were bigger than 2 in all experimental conditions. For the others, the weight for resolution was two (Table 1). According to these values the desirability of retention times (D_{tr}), desirability of resolutions (D_{Rs}), and desirability of resolutions + retention times (D_{All}) were calculated (Table 1).

The regression coefficients calculated from the total desirability function is shown in Fig. 2. As can be seen in Fig. 2, phosphate buffer concentration for D_{Rs}, and pH, flow rate and temperature for D_{All} had a negative effect while the others had a positive effect on D_{tR}. Nevertheless pH, MeOH% and phosphate buffer concentration had significant effect on three total desirability functions, pH and MeOH% were selected for further optimization. Phosphate buffer concentration was not selected for examination because of its positive effect on three total desirability functions. It was, therefore, fixed to its maximum value (40 mM). The flow rate

Table 2
Selected variables and their levels in the fractional factorial design.

Variable	Level		
	−1	0	+1
MeOH (%)	8	14	20
pH	2.5	4.25	6
Phosphate buffer concentration (mM)	20	30	40
Temperature (°C)	25	32.5	40
Flow rate (mL min^{-1})	0.7	0.85	1

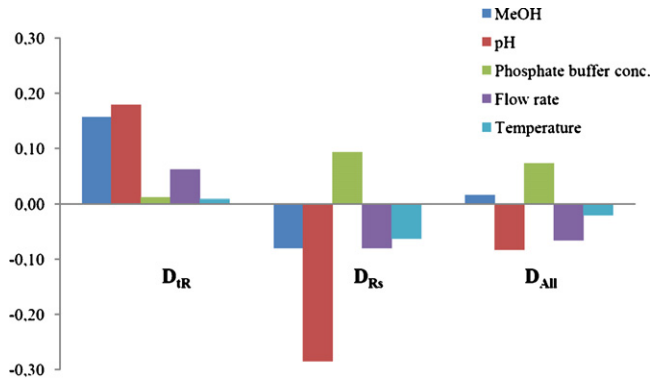


Fig. 2. Regression coefficients of the variables for D_{tR} (desirability scale of retention times), D_{Rs} (desirability scale of resolutions) and D_{All} (desirability scale of resolutions + retention times).

and temperature were fixed to their central levels, which were 0.85 mL min^{-1} and 32 °C, respectively, to minimize analysis time and maximize resolution.

3.1.3. Response surfacing based on 3^k full factorial design

Response surface mapping was an effective way to find the optimum condition. In this case, the 3^k full factorial design was employed to draw response surface graphs to determine the optimal conditions and to investigate parabolic interactions between parameters (pH and MeOH%). This design permitted the response surface to be modeled by fitting a second-order polynomial with the number of experiments equal to $3^k + n$, where k is the number of variables and n the number of center runs. In this study, $k = 2$ and n was set to 3, which composed a total of 12 experiments to be executed (Table 3). The design fitted with a full quadratic model is given below:

$$y = b_0 + b_1x_1 + b_2x_2 + b_{12}x_1x_2 + b_{11}x_1^2 + b_{22}x_2^2$$

where y represents the experimental response, x the independently evaluated factors (in coded variables), b_0 the intercept and b_n the parametric coefficients of the model obtained by multiple regression. Experiments were performed according to the design listed in Table 3 and responses measured are given in the same table.

The regression coefficients calculated from full factorial design are given in the equations below. For the models fitted, ANOVA tests were applied to calculate F-values, and significant probabilities of the models. The ANOVA tests showed that the models appeared to be adequate, with no significant lack of fit ($p < 0.05$), and with a satisfactory coefficient of correlation (r). Thus the models could be used to navigate the design space.

$$D_{Rs} = 0.474 + 0.245x_1 + 0.118x_2 - 0.003x_1x_2 + 0.049x_1^2 - 0.031x_2^2 \quad (r = 0.9791)$$

$$D_{tR} = 0.932 - 0.103x_1 - 0.262x_2 - 0.088x_1x_2 + 0.049x_1^2 - 0.296x_2^2 \quad (r = 0.9712)$$

$$D_{All} = 0.722 + 0.062x_1 - 0.100x_2 - 0.108x_1x_2 + 0.030x_1^2 - 0.205x_2^2 \quad (r = 0.9488)$$

The response surface graphs were drawn as a function of pH and MeOH (Fig. 3). These response surface graphs allowed the determination of an optimal zone, where a good-quality separation could be established.

Optimum conditions were chosen by total desirability as near as 1.00. The highest desirability (around 0.85) was achieved at pH 3.2 and 20% MeOH. However, at 20% MeOH there was an interference with CEP. Therefore, MeOH% was decreased to 18% to eliminate interference. The final optimum conditions for chromatographic separation were 40 mM phosphate buffer, pH 3.2, 18% MeOH, 0.85 mL min^{-1} flow rate and 32 °C column temperature. At these conditions, the seventh cephalosporin, COP, was not eluted in 50 min. Therefore, different gradient elutions were tried in order to obtain short analysis time. The short analysis time obtained with as explained in the section entitled chromatographic conditions. At these conditions, the separation of seven cephalosporins was completed within 25 min (Fig. 4).

Table 3
Experimental conditions according to the full factorial design and total desirability function calculated from the responses.

Exp. No.	Run Order	MeOH	pH	D_{tR}	D_{Rs}	D_{All}
1	2	−1	−1	0.17	1.00	0.53
2	4	0	−1	0.26	0.82	0.54
3	11	1	−1	0.64	0.97	0.84
4	7	−1	0	0.24	1.00	0.60
5	3	0	0	0.48	0.99	0.77
6	9	1	0	0.78	0.79	0.78
7	8	−1	1	0.36	0.66	0.53
8	1	0	1	0.60	0.28	0.37
9	6	1	1	0.82	0.28	0.41
10	10	0	0	0.49	0.92	0.72
11	5	0	0	0.54	0.93	0.79
12	12	0	0	0.41	1.00	0.73

D_{Rs}: Desirability of resolutions, D_{tR}: Desirability of retention times, and D_{All}: Desirability of resolutions and retention times.

3.2. Optimization of SPE

Sample preparation from plasma and amniotic fluid was performed with SPE method to utilize the benefits mentioned earlier.

In the previously published literature, a lot of sorbents and different conditions, washing and elution steps in SPE were used to gain high recovery from food, biological tissues and waters [8,10,24,25,28]. In this study, the optimization of SPE was performed in three steps. The experiments in the first step, endeavored to discover the most suitable sorbent(s). For this purpose, six different commercial SPE cartridges (M&N, Strata X, ENV+, Oasis HLB, Oasis MAX, Chromabond C_{18} and Chromabond C_8) were tried in order to get high recovery without interference. In the initial experiments, the sorbents were conditioned with 2 mL of MeOH and 2 mL of water, respectively. Then the 0.5 mL sample was diluted with 1 mL water and loaded to sorbents. Washing of the sorbents was carried out with 2 mL of water and then eluted with 2 mL of MeOH. The eluate was evaporated to the dryness at 45 °C under a stream of nitrogen. The residue was reconstituted with 200 μL of MeOH:water (20:80, v/v) mixture and then injected into the HPLC system. To decide which sorbent was useful for sample preparation, the endogen peak numbers which may cause interference and absolute recovery were evaluated. Although the least endogen peaks were obtained with ENV+, the other sorbents were also evaluated for absolute recovery (Table 4). The highest recovery was obtained with Oasis HLB (62%). However, it was not high enough. Therefore Oasis HLB and Strata X, which have higher recovery than others, were selected to improve recoveries of cephalosporins. Secondly the effect of buffer solution on the recoveries was investigated. During the optimization of chromatographic conditions, it was realized that at low pH, the retention times of cephalosporins on the C_{18} column increased. Therefore, pH 3 phosphate buffer was tried in order to increase recoveries. When the conditioning and washing steps of the sorbents and dilution of the samples were completed with the phosphate buffer, the mean recovery of the cephalosporins was increased. The highest mean recovery

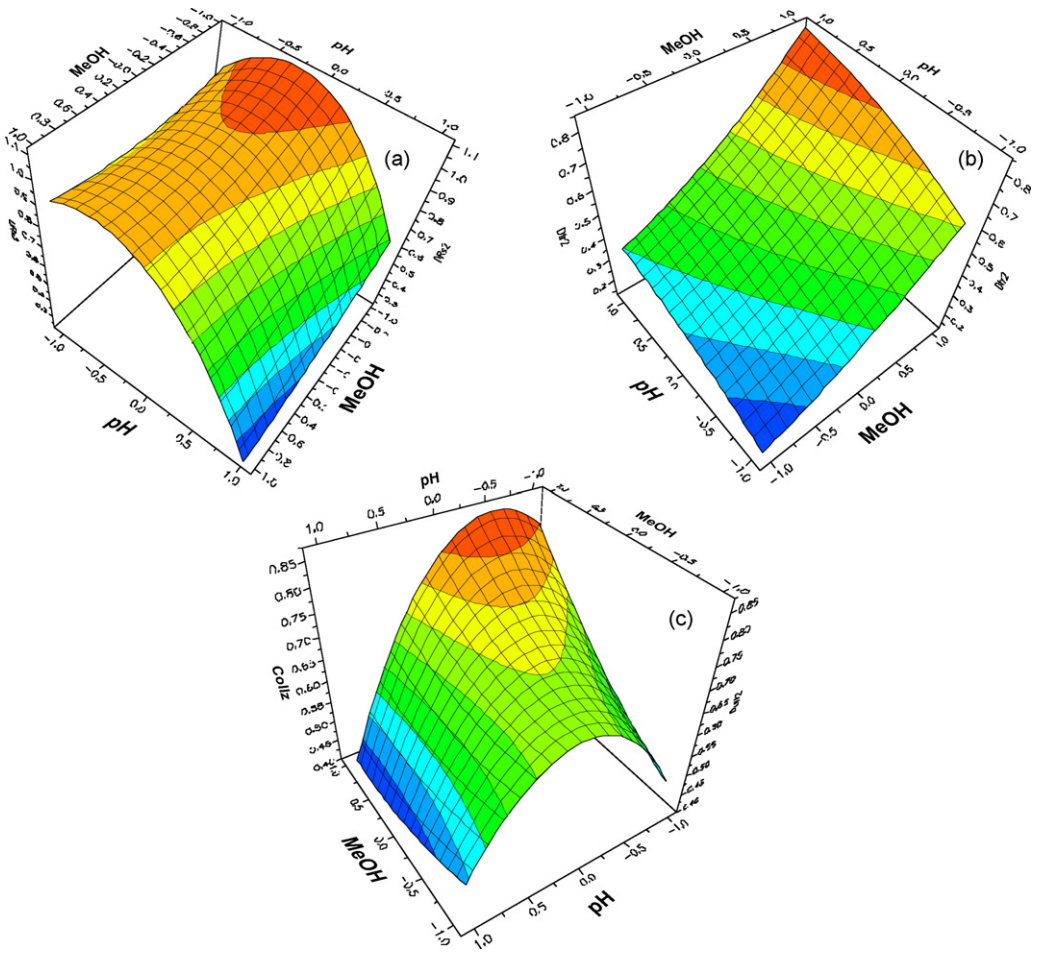


Fig. 3. Response surface graph functions of MeOH% and pH, a) D_{Rs}, b) D_{tR} and c) D_{All}.

was obtained with Strata X but the recovery was still not high enough for CIX and CTR. In the last step the effect of pH was investigated, Strata X was selected to improve recovery of CIX and CTR by changing pH of the buffer (pH 2 and 3). High mean recovery was obtained with 50 mM phosphate buffer solution at pH 2. Thus this buffer was selected for sample preparation in SPE.

Cephalosporins were less stable in solutions, in comparison to other drugs. The stability of the cephalosporins in solutions depends on temperature, pH, etc. [8,10,28]. Therefore samples were diluted with phosphate buffer just before sample loading to prevent degradation.

3.3. Validation

The validation studies were applied for CIX, COP and CEP, for which placental passage rates were unknown. CTI was selected as an IS in order to compensate for errors from extraction process. CIX and CTI were monitored at 285 nm while COP and CEP at 260 nm. The assay was validated with respect to system suitability, stability, LOD, LOQ, linearity, precision, accuracy, selectivity and robustness.

3.3.1. System suitability

The system suitability was assessed by ten replicate analyses of the CEP, CIX, COP and IS at a concentration of 10.0 μg mL^{-1}.

Table 4
The absolute recoveries of cephalosporins obtained from different sorbents and conditions.

Cephalosporins	Steps									
	First						Second		Third	
	C_8 [1]	C_{18} [1]	ENV+[1]	M&N[1]	Oasis HLB[1]	Strata X[1]	Oasis HLB[2]	Strata X[2]	Strata X[3]	Strata X[4]
CEP	19.4	8.1	0.0	0.0	94.1	81.8	83.0	83.5	92.5	93.8
CTA	54.9	57.1	0.0	29.2	42.3	31.6	87.8	90.3	96.4	47.8
CTI	22.7	36.2	39.9	0.0	80.6	46.7	97.7	98.9	98.6	81.6
CIX	0.6	8.7	17.8	0.0	15.2	8.5	5.5	52.5	90.6	46.8
COT	81.5	89.2	39.1	17.6	90.6	48.7	98.5	95.5	99.1	87.0
CTR	12.8	16.7	2.6	0.0	18.6	10.9	3.5	25.9	66.4	12.7
COP	96.7	97.9	32.4	79.2	97.2	87.9	96.7	101.9	102.0	87.8

[1] Conditioning: 2 mL MeOH and 2 mL water; Sample: 0.5 mL sample + 1 mL water (containing 10 μg mL^{-1} cephaloporins); Washing: 2 mL water; Elution: 2 mL MeOH.
[2] Conditioning: 2 mL MeOH, 1 mL water and 1 mL 50 mM (pH 3) phosphate buffer; Sample: 0.5 mL sample + 1 mL 50 mM (pH 3) phosphate buffer (containing 10 μg mL^{-1} cephaloporins); Washing: 2 mL 50 mM (pH 3) phosphate buffer; Elution: 2 mL MeOH.
[3] and [4]: The conditions are the same as in [2] except for the pH of the 50 mM phosphate buffer. The pH of the 50 mM phosphate buffer of [3] and [4] are 2.0 and 2.5, respectively.

Table 5
System suitability parameters for CEP, CIX and COP.

	CEP	CTI (IS)	CIX	COP
Retention time (min)[a]	5.3 (0.2%)	10.6 (0.7%)	14.0 (0.2%)	23.7 (0.2%)
Capacity factor[b]	2.5	6.1	8.4	14.8
Resolution[c]	–	8.3	3.6	14.0
Theoretical plate numbers	8304	10488	10630	40903
Peak asymmetry (%10)	1.1	1.0	1.1	1.2

[a] The values given in blankets were RSD % of retention times ($n = 10$).
[b] Dead retention time was found with the injection of urasil at the same conditions: $t_0 = 1.5$ min.
[c] Values are resolution between adjacent peaks.

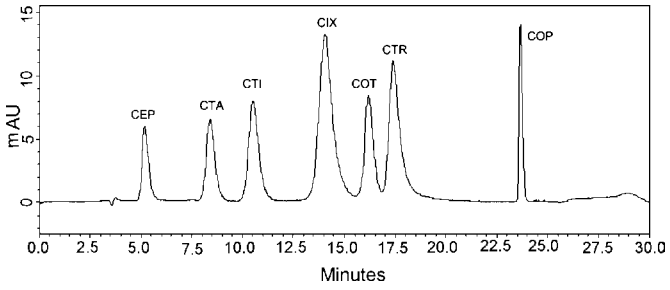


Fig. 4. Chromatogram of cephalosporins (gradient elution with MeOH) (40 mM phosphate buffer, pH 3.2, 18% MeOH, 0.85 mL min^{-1} flow rate and 32 °C column temperature).

Their retention times, capacity factors, resolutions, theoretical plate numbers and peak asymmetries were within acceptable criterion (Table 5).

3.3.2. Stability

The stabilities of CEP, CIX and COP (at 10.00 μg mL^{-1}) were evaluated according to a freeze–thaw cycle, short term (+4 °C in refrigerator), long term (−20 °C in deepfreeze) and autosampler stability.

A sample spiked and a freshly prepared one were compared to determine whether the analyte concentration had changed by more than 10% [29].

In the freeze–thaw cycle test, plasma and amniotic fluid samples spiked with CEP, CIX and COP were stored at −20 °C. Samples were taken out of the deepfreeze and equilibrated to room temperature and analyzed in duplicate. This process was repeated three times and results were compared with the control sample which was freshly prepared (without freezing). According to results the changing of the analyte concentration (from 90.6 to 100.3%) was within the limits. Therefore they were stable at least three freeze–thaw cycles in plasma and amniotic fluid.

The short term (+4 °C in refrigerator) stabilities of CEP, CIX and COP were evaluated in plasma and amniotic fluid. Plasma and amniotic fluid samples spiked with CEP, CIX and COP were refrigerated. The samples were periodically taken out of the refrigerator (2, 6, 12, and 24 h) and equilibrated to room temperature and analyzed in duplicate. The results were compared with a freshly prepared one to determine refrigerator stability. The analyte concentration of CEP in plasma and amniotic fluid decreased 25% at the end of 24 h, while CIX and COP was decreased in the range of 14–18%. This results showed the necessity to perform the analysis of CEP from plasma within 2 h and from amniotic fluid within 6 h, CIX from plasma within 12 h and from amniotic fluid within 6 h and COP from plasma and amniotic fluid within 12 h.

Long-term (−20 °C in deep freeze) stability studies of the CEP, CIX and COP were assessed after storage of spiked plasma and amniotic fluid samples in the deepfreeze at −20 °C for 2 months. CEP, CIX and COP were found stable at least 2 months in both biological materials.

Autosampler stabilities of CEP, CIX and COP in the reconstituted plasma and amniotic fluid extracts were evaluated for 24 h. Eluates were analyzed at 0, 6, 12, and 24 h and CEP, CIX and COP were found stable at least 24 h in autosampler.

3.3.3. The limit of detection (LOD) and quantitation (LOQ)

The LOD and LOQ of CEP, CIX and COP were estimated on the basis of the results for three replicates of plasma and amniotic fluid spiked at different levels, considering a signal-to-noise ratio of 3 and 10, respectively. The LOD values of CEP, CIX and COP were found to be 25, 10 and 15 ng mL^{-1}, respectively. Those for LOQ were 80, 35 and 50 ng mL^{-1}, respectively.

3.3.4. Linearity

The calibration curve consisted of eight concentration levels of spiked standards samples (LOQ, 0.5, 1, 5, 10, 20, 30, and 50 μg mL^{-1}) to distilled water, plasma and amniotic fluid. Each level was pre-

Table 6
Data for the calibration graph of CEP, CIX and COP spiked in water, plasma and amniotic fluid.

	Slope	Intercept	r	p[a]
Water				
CEP	2.8582 (2.6481–3.0676)	0.2464 (−0.2413–0.7341)	0.9986	0.2334
CIX	4.0253 (3.9071–4.1436)	0.1195 (−0.1559–0.3949)	0.9998	0.2946
COP	0.1960 (1.8384–2.0813)	0.1887 (−0.0938–0.4712)	0.9990	0.1372
Plasma				
CEP	3.1625 (2.8621–3.4614)	0.4221 (−0.2750–1.1193)	0.9977	0.1680
CIX	3.9850 (3.7982–4.1714)	0.0305 (−0.4036–0.4645)	0.9994	0.8550
COP	1.8507 (1.7120–1.9870)	0.2588 (−0.0618–0.5794)	0.9985	0.0885
Amniotic fluid				
CEP	2.9788 (2.6249–3.3324)	0.4515 (−0.3769–1.2757)	0.9963	0.2029
CIX	4.0699 (3.5953–4.5435)	0.8200 (−0.2836–1.9236)	0.9965	0.1081
COP	1.9501 (1.7862–2.1132)	0.2308 (−0.1501–0.6116)	0.9982	0.1678

The interval range of calibration curves were LOQ—50 μg mL^{-1}; y = Slope × C + Intercept (y = area cephalosporin/internal standard; C = concentration cephalosporin/internal standard).
[a] p value of intercept.

Table 7
Data of precision, accuracy and recovery.

	CEP	CIX	COP
Precision			
Intra-day ($n=6$)[a]	3.6–7.8	4.2–5.9	1.6–4.8
Inter-day ($n=6$)[a]	5.2–8.0	6.8–9.8	0.8–7.8
Accuracy			
Intra-day ($n=6$)[b]	2.0–2.5	0.0–4.0	2.3–6.0
Inter-day ($n=6$)[b]	0.0–2.2	1.2–3.0	0.8–2.4
Recovery[c] %			
Plasma			
Absolute	94.7 ± 0.8 (2.3%)	94.2 ± 1.6 (4.5%)	95.4 ± 1.5 (4.1%)
Relative	98.8 ± 1.3 (3.6%)	98.1 ± 1.5 (4.0%)	99.1 ± 2.3 (5.8%)
Amniotic fluid			
Absolute	96.4 ± 0.9 (2.2%)	98.3 ± 1.4 (3.5%)	95.5 ± 1.3 (3.6%)
Relative	98.5 ± 0.9 (2.4%)	99.2 ± 1.0 (2.9%)	99.8 ± 2.1 (5.8%)

[a] and [b] The intra- and inter-day data showed are the minimum and maximum RSD % and Bias % values, respectively. The corresponding samples were prepared at 0.50, 5.00 and 30.00 μg mL^{-1}.
[c] Numbers in brackets were RSD.

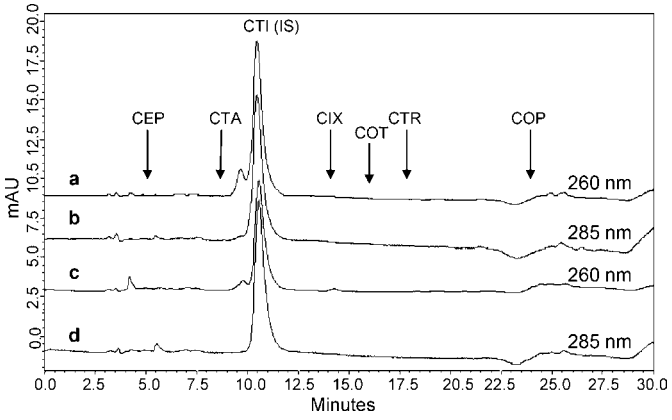


Fig. 5. Chromatogram of blank plasma (a and b), and blank amniotic fluid (c and d) spiked with 10.00 μg mL^{-1} IS (CTI) (40 mM phosphate buffer, pH 3.2, 18% MeOH, 0.85 mL min^{-1} flow rate and 32 °C column temperature, gradient elution with MeOH).

pared in duplicate. The results were calculated as a ratio of the peak area of the respective cephalosporin and the IS vs. cephalosporin/IS concentration ratio. The linear calibration curve between the ratio of the peak area and the concentration of the target cephalosporin was established by linear regression. The calibration curves for all compounds present determination coefficients were higher than 0.992, as can be seen in Table 6.

3.3.5. Precision

The assay was investigated with respect to injection repeatability and intermediate precision. The injection repeatability of the system was evaluated by ten consecutive injections. The RSD values of retention times were <1% (Table 5). This result indicates that the system had a good injection repeatability.

To assess intra-day precision, six spiked samples at three concentration levels (0.50, 5.00 and 30.00 μg mL^{-1}) were prepared and analyzed twice. For inter-day precision, three different daily renewals of the intra-day precision were carried out. The RSD values of intra- and inter-day studies varied from 0.8 to 9.80% showed that the intermediate precision of the method was satisfactory (Table 7).

3.3.6. Accuracy

The accuracy of a method is expressed as the closeness of agreement between the found value and reference value. It is determined by calculating the percentage relative error between the measured mean concentrations and added concentrations (Bias %). Intra-day and inter-day accuracies (Bias %) were <6.0 which shows good accuracy (Table 7).

The accuracy of the proposed method was also tested by recovery experiments. Recovery experiments were performed at six concentrations (0.5, 1, 5, 10, 20, and 50 μg mL^{-1}) by duplicate analysis. Spiked plasma, amniotic fluid and water samples were treated as described in the procedure for sample preparation. The recovery of CEP, CIX and COP were evaluated as relative and absolute recovery. The relative recoveries of the analytes were measured by comparison of the peak area ratios obtained from extraction of spiked plasma and amniotic fluid samples with those obtained from extraction of equivalent amounts of analyte in spiked water. Absolute recoveries were determined by comparison of the peak area ratios of analytes obtained from spiked plasma and amniotic fluids samples with those obtained from equivalent standard solutions spiked after the extraction procedure that were considered to be showing 100% recovery. High relative and absolute recovery for CEP, CIX and COP were obtained from both matrices (Table 7).

The recovery values were higher than 94% and in all cases comparable results were obtained among absolute and relative recovery (Table 7). The slopes of the calibration curves obtained from different spiked samples were close (Table 6). All of these results indicate that water spiked standards can be used as the calibration curve.

3.3.7. Selectivity

The selectivity of an analytical method allows to quantification of the cephalosporins in the presence of components that may be expected to be present as impurities, degradedness or matrix components. The selectivity of the method was evaluated by analyzing blank amniotic fluid and plasma obtained from different pregnant women. In the evaluation of the selectivity, cephalosporins were

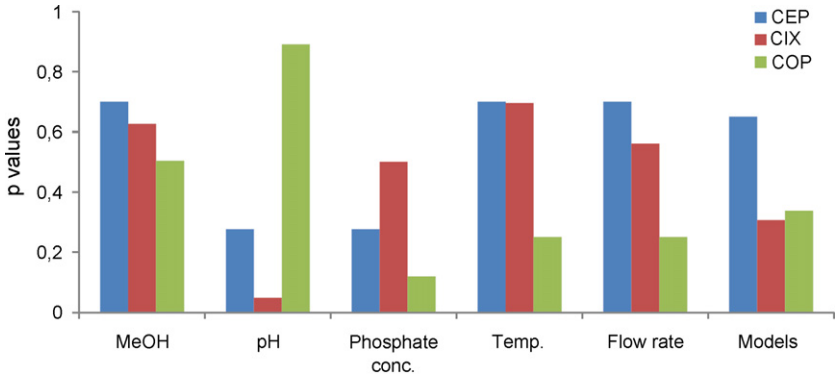


Fig. 6. *p* values calculated from robustness studies of CEP, CIX and COP.

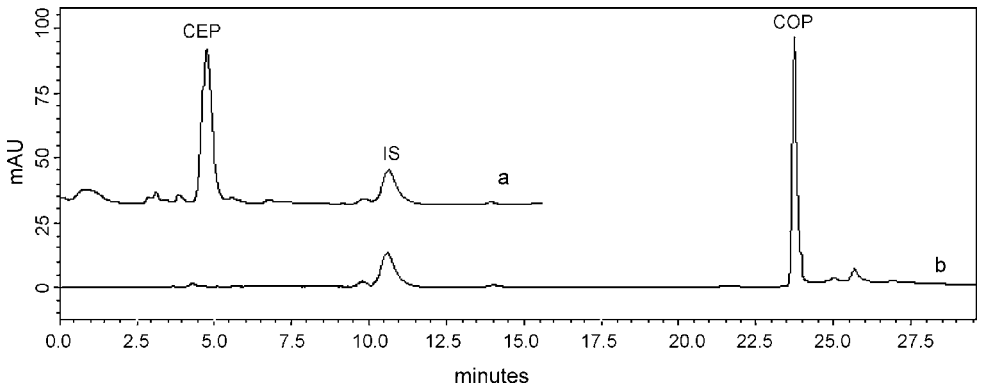


Fig. 7. Chromatogram of a) plasma obtained from pregnant woman administrated CEP and b) plasma obtained from pregnant woman administrated COP (40 mM phosphate buffer, pH 3.2, 18% MeOH, 0.85 mL min^{-1} flow rate and 32 °C column temperature, gradient elution with MeOH) (IS: 10 μg mL^{-1}).

well resolved from baseline and separated from each other and there was no matrix effect from plasma or amniotic fluid (Fig. 5) at the same time of cephalosporins. The peak purity index of CEP, CIX and COP belonging to their analysis in plasma, amniotic fluid and water were found to be higher than 0.9951. In addition, the slopes of the CEP, CIX and COP obtained from different matrix were not different from each other and confidence intervals were overlapping. All of these results showed that the method presented in this study was specific.

3.3.8. Robustness

In robustness testing of an analytical method, the aim is to explore how sensitive the responses are to small changes in the factor settings. The robustness of the method was tested using experimental design in order to study the simultaneous variation of the factors. An eleven-run fractional factorial design, three experiments within the optimized conditions, were chosen to evaluate whether a change in factor value produced a statistically significant variation in the observed responses. In the study the ranges examined were small deviations from the method settings with regard to MeOH % (16–20), buffer pH (3.0–3.4), phosphate buffer concentration (38–42 mM), column temperature (30–34 °C) and flow rate (0.8–0.9 mL min^{-1}). To evaluate the robustness of the method, ANOVA test was applied and p values of regression coefficient and regression equation were calculated. The p values were ≥0.05 which indicates that small changes didn't significantly effects on the peak area ratio (Fig. 6). Thus, the method could be considered robust.

3.3.9. Analysis of COP, CEP and CIX

The method was applied to the analysis of plasma and amniotic fluid samples obtained from pregnant women. CEP (n = 6) or COP (n = 6) was administered intravenously during delivery (Fig. 7) while CIX (n = 6) were administrated orally before amniocenteses (Fig. 8) to prevent any infection. The results of the analysis are given in Tables 8 and 9. All concentrations were higher than the lower determination and quantitation levels of the CEP, CIX and COP.

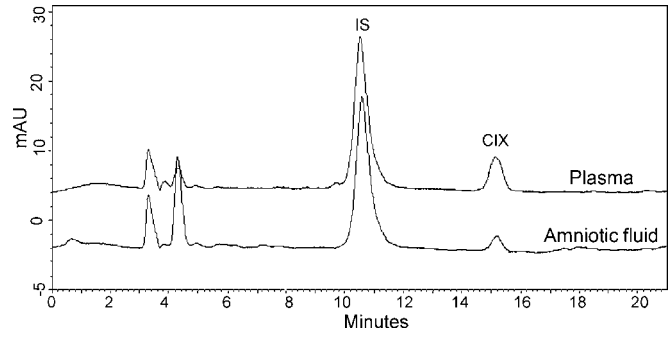


Fig. 8. Chromatogram of plasma and amniotic fluid obtained from pregnant woman administrated CIX (40 mM phosphate buffer, pH 3.2, 18% MeOH, 0.85 mL min^{-1} flow rate and 32 °C column temperature, gradient elution with MeOH) (IS: 10 μg mL^{-1}).

Table 8
The amounts of CEP and COP in maternal and fetal plasma samples.

	Plasma (Maternal venous) (μg mL^{-1})	Plasma (Fetal arterial) (μg mL^{-1})	Plasma (Fetal venous) (μg mL^{-1})
CEP			
1	37.2	6.2	8.8
2	39.1	4.7	6.2
3	42.0	5.5	7.6
4	37.4	10.0	10.2
5	41.9	7.1	7.6
6	46.0	3.5	7.9
COP			
1	85.3	5.3	6.1
2	63.8	3.7	5.4
3	60.1	6.3	6.7
4	49.7	7.8	9.4
5	59.2	11.5	15.1
6	77.6	2.8	5.2

Table 9
The amounts of CIX in maternal plasma and amniotic fluid samples.

Pregnant woman	Plasma (Maternal venous) (μg mL^{-1})	Amniotic fluid (μg mL^{-1})
1	3.7	1.4
2	3.2	1.3
3	2.5	0.4
4	1.3	0.7
5	1.3	0.8
6	3.7	0.5

4. Conclusion

An HPLC method was developed to separate seven cephalosporins in human plasma and amniotic fluid and applied to quantify CEP and COP in plasma and CIX in plasma and amniotic fluid. Experimental designs have been utilized during the development of the method to minimize retention times and maximize resolutions. A total desirability function has been used to evaluate more than one response at a time (retention times and resolutions) and the optimum conditions were found by plotting response surface graphs. An efficient SPE method was developed for extraction and the clean-up process. Detailed validation studies were performed to evaluate the validity of the methods according to ICH guideline and the method was found to be sensitive, linear,

accurate, precise, specific and robust. Finally, the method was applied to the analysis of CEP and COP in maternal and fetal plasma and CIX in maternal plasma and amniotic fluid obtained from pregnant women.

References

[1] P.M. Shah, Int. J. Antimicrob. Agents 19 (2002) 163–164.
[2] J.D. Williams, K.G. Naber, A. Bryskier, N. Hoiby, I.M. Gould, P. Periti, H. Giamarellou, B. Rouveix, Int. J. Antimicrob. Agents 17 (2001) 443–450.
[3] M. Dawes, P. Chowienczyk, Baillière's Best Pract. Res. Clin. Obstet. Gynaecol. 15 (2001) 819–826.
[4] H. Giamarellou, E. Kolokythas, G. Petrikkos, J. Gazis, D. Aravantinos, P. Sfikakis, Am. J. Med. 87 (1989) 49S–51S.
[5] F. Jehl, P. Birckel, H. Monteil, J. Chromatogr. B 413 (1987) 109–119.
[6] R.D. Toothaker, D.S. Wright, L.A. Pachla, Antimicrob. Agents Chemother. 31 (1987) 1157–1163.
[7] H. Fabre, M.D. Blanchin, W.T. Kok, Analyst 113 (1988) 651–655.
[8] A. Marzo, L. Dal Bo, J. Chromatogr. A 812 (1998) 17–34.
[9] F. Péhourcq, C. Jarry, J. Chromatogr. A 812 (1998) 159–178.
[10] S.R. El-Shaboury, G.A. Saleh, F.A. Mohamed, A.H. Rageh, J. Pharm. Biomed. Anal. 45 (2007) 1–19.
[11] M.D. Glaria, G.G. Moscciati, R.G. Ramos, M.M. Riquelme, J. Sep. Sci. 26 (2003) 939–942.
[12] S. Altinoz, A. Temizer, S. Beksac, Analyst 115 (1990) 873–874.
[13] E.K. Yun, A.J. Prince, J.E. McMillin, L.E. Welch, J. Chromatogr. B 712 (1998) 145–152.
[14] W.M.A. Niessen, J. Chromatogr. A 812 (1998) 53–75.
[15] E. Benito-Peña, A. Partal-Rodera, M. León-González, M. Moreno-Bondi, Anal. Chim. Acta 556 (2006) 415–422.
[16] I. Al-Momani, J. Pharm. Biomed. Anal. 25 (2001) 751–757.
[17] H. Salem, H. Askal, J. Pharm. Biomed. Anal. 29 (2002) 347–354.
[18] C. Coleraine, N. Ireland, Electrophoresis 26 (2005) 1334–1357.
[19] V.M. Morris, C. Hargreaves, K. Overall, P.J. Marriott, J.G. Hughes, J. Chromatogr. A 766 (1997) 245–254.
[20] R.G. Brereton, Chemometrics Data Analysis for the Laboratory and Chemical Plant, John Wiley, Wiltshire, 2004.
[21] R. Gotti, S. Furlanetto, V. Andrisano, V. Cavrini, S. Pinzauti, J. Chromatogr. A 875 (2000) 411–422.
[22] M. Medenica, B. Jancic, D. Ivanovic, A. Malenovic, J. Chromatogr. A 1031 (2004) 243–248.
[23] F. Safa, M.R. Hadjmohammadi, J. Chromatogr. A 1078 (2005) 42–50.
[24] S. Bompadre, L. Ferrante, L. Leone, J. Chromatogr. A 812 (1998) 191–196.
[25] C. Molins-Legua, P. Campins-Falcó, Anal. Chim. Acta 546 (2005) 206–220.
[26] ICH Tripartite Guideline, Validation of Analytical Procedures: Text and Methodology Q2(R1) (2005) 1–13.
[27] F. Safa, M.R. Hadjmohammadi, Anal. Chim. Acta 540 (2005) 121–126.
[28] L. Sokolova, A. Chernyaev, Pharm. Chem. J. 36 (2002) 263–269.
[29] R. Causon, J. Chromatogr. B 689 (1997) 175–180.

Talanta 80 (2009) 127–132

Contents lists available at ScienceDirect

Talanta

journal homepage: www.elsevier.com/locate/talanta

Determination and interference studies of bismuth by tungsten trap hydride generation atomic absorption spectrometry☆

İbrahim Kula[a,b,*], Yasin Arslan[b,e], Sezgin Bakırdere[b], Serap Titretir[c], Erdal Kendüzler[d], O. Yavuz Ataman[b]

[a] Department of Chemistry, Muğla University, 48000 Muğla, Turkey
[b] Department of Chemistry, Middle East Technical University, 06531 Ankara, Turkey
[c] Department of Chemistry, İnönü University, 44280 Malatya, Turkey
[d] Department of Primary Education, Faculty of Education, Ahi Evran University, 40100 Kırşehir, Turkey
[e] Department of Chemistry, Atatürk University, 25240 Erzurum, Turkey

ARTICLE INFO

Article history:
Received 17 December 2008
Received in revised form 9 June 2009
Accepted 12 June 2009
Available online 6 August 2009

Keywords:
Interference
Bismuth
Tungsten trap
Hydride generation atomic absorption spectrometry (HGAAS)

ABSTRACT

The determination of bismuth requires sufficiently sensitive procedures for detection at the $\mu g\,L^{-1}$ level or lower. W-coil was used for on-line trapping of volatile bismuth species using HGAAS (hydride generation atomic absorption spectrometry); atom trapping using a W-coil consists of three steps. Initially BiH_3 gas is formed by hydride generation procedure. The analyte species in vapor form are transported through the W-coil trap held at 289 °C where trapping takes place. Following the preconcentration step, the W-coil is heated to 1348 °C; analyte species are released and transported to flame-heated quartz atom cell where the atomic signal is formed. In our study, interferences have been investigated in detail during Bi determination by hydride generation, both with and without trap in the same HGAAS system. Interferent/analyte (mass/mass) ratio was kept at 1, 10 and 100. Experiments were designed for carrier solutions having 1.0 M HNO_3. Interferents such as Fe, Mn, Zn, Ni, Cu, As, Se, Cd, Pb, Au, Na, Mg, Ca, chloride, sulfate and phosphate were examined. The calibration plot for an 8.0 mL sampling volume was linear between 0.10 $\mu g\,L^{-1}$ and 10.0 $\mu g\,L^{-1}$ of Bi. The detection limit (3 s/m) was 25 $ng\,L^{-1}$. The enhancement factor for the characteristic concentration (C_o) was found to be 21 when compared with the regular system without trap, by using peak height values. The validation of the procedure was performed by the analysis of the certified water reference material and the result was found to be in good agreement with the certified values at the 95% confidence level.

© 2009 Elsevier B.V. All rights reserved.

1. Introduction

It is known that bismuth (Bi) has been used for different medical purposes. For instance, some of its compounds have been added to pharmaceutical samples for the treatment of gastritis and peptic ulcer [1]. It was also reported that though Bi is not essential element for human being, nearly 5–20 μg of this element is taken with food in general population [2]. Indeed, due to its potential for inducing metallothionein expression, this element has some effect on reducing tissue toxicity after cisplatin cancer therapy [3].

For the determination of Bi in different matrices, many analytical techniques have been applied. For example, atomic absorption spectrometry (AAS), electro thermal atomic absorption spectrometry (ETAAS), inductively coupled plasma optical emission spectrometry (ICP-OES) and inductively coupled plasma mass spectrometry (ICP-MS) in different matrices [4–6]. Even though AAS has been presented in many analytical laboratories, sensitivity of this technique is not enough for the trace level. Thus, ETAAS has been largely used for trace levels. However, elimination of matrix causing interferences to improve the lifetime of graphite tubes is the requirement [4]. Although ICP-MS has very low detection limits, this instrument is not commonly used for Bi determination due to its high cost. Hydride generation atomic absorption spectrometry (HGAAS) is undoubtedly one of the most sensitive and convenient analytical techniques for the determination of bismuth because of its appropriate sensitivity. Therefore, this technique is ideally suited for the trace and ultratrace analysis of Bi. In addition, in the literature, the detection limits for Bi have varied from one technique to other. For instance, the detection limit was found as 0.02 $ng\,mL^{-1}$ determination of Bi in tap water and biological samples such as urine and hair by ETAAS after preconcentration by the

☆ A part of this paper was presented at the Colloquium Spectroscopicum Internationale XXXV, held in Xiamen, China, 23–27 September 2007.

* Corresponding author at: Department of Chemistry, Muğla University, 48000 Muğla, Turkey. Fax: +90 252 223 86 56.
E-mail address: ikula@mu.edu.tr (İ. Kula).

0039-9140/$ – see front matter © 2009 Elsevier B.V. All rights reserved.
doi:10.1016/j.talanta.2009.06.084

cloud point extraction technique [7]. By using ICPOES system with a continuous-flow hydride generation technique (HG-ICP) detection limit was found to be 0.7 ng mL^{-1} [8]. Although it is expected that ICP-MS has very low detection limit, this value was found to be 9.7 ng mL^{-1} for Bi in serum and urine by direct injection nebulization inductively coupled plasma mass spectrometry [9].

In order to improve sensitivity in Bi determination, different sorts of traps have been applied. W-coil was used for on-line trapping of volatile bismuth species using HGAAS; a limit of detection of 2.7 ng L^{-1} was obtained [10]. Quartz was also used as an atom trap with a detection limit of 3.9 ng L^{-1} [11].

In the analytical chemistry, elimination of any possible interferences during measurement step is very crucial in order to obtain accurate results. Although Dedina and Tsalev have explained the basic mechanism of interferences, number of studies in this field is not high [12]. Recently, interference effects of some elements were studied for hydride generation system [13,14]. According to Dedina and Tsalev, interferences can be categorized not only as spectral and non-spectral interferences but also as liquid phase and gas phase interferences occurring during either in transportation or in the atomizer. It is expected that most of the liquid phase interferences can be eliminated using W-coil trap HGAAS system due to elimination of these type interferences prior to atom cell. In the literature, there have been so many studies related with the effects of different kinds of interferences on Bi determination using hydride generation technique.

The objective of the present study was not only to find and develop a sensitive method but also decide whether the tungsten trap has any advantages for the elimination of different interferences on Bi signal or not. Interferences have been investigated in detail during Bi determination by hydride generation in both with and without W-coil trap in the same HGAAS system.

2. Experimental

2.1. Instrumentation

An ATI Unicam 929 atomic absorption spectrometer equipped with a deuterium background correction system was used. A Philips data coded hollow cathode lamp was operated at 12.0 mA; the analytical line at 223.1 nm was used in the measurements with 0.5 nm as the spectral bandwidth. Quartz T-tube atomizer (QTA) heated by a stoichiometric air/acetylene flame was used as atomizer. QTA consisted of a horizontal arm with dimensions of 140 mm in length, 15 mm in od and 12.8 mm in id; inlet arm was 90 mm in length, 7 mm in od and 4.5 mm in id. Another smaller quartz tube was inserted and fixed in the inlet arm with dimensions of 4.0 mm in od and 2.0 mm in id; it extended between the open end of the inlet arm and a point that was 5.0 mm away from the W-coil; analyte vapor was transported through this inner tube. Hydride generation for both conventional and trap systems was carried out in continuous-flow (CF) mode using a Gilson Minipuls 3 (Villers le Bell, France) 4-channel peristaltic pump. Tygon peristaltic pump tubing of 0.8 mm id (Ismatec, Germany) was used for pumping the analyte and reductant solutions that are mixed in a 3-way PTFE connector (Cole Parmer Instrument Co., USA). For the separation of Bi hydride from the liquid phase, a laboratory-made cylindrical gas–liquid separator (GLS) was employed. Tygon tubing of length of 4.0 cm and 6.0 mm id (Masterflex, Cole Parmer Instrument Co.) was used between the GLS and the inlet arm of the silica T-tube atomizer. The composition of the gas mixture was the same for both conventional HGAAS and collection stage on W-coil trap. A mixture of H_2 and Ar was used in both conventional HGAAS and W-coil trap studies. The flow rates of these gases were measured by two separate flow meters (Cole Parmer Instrument Co., USA). The W-coil used for trapping was obtained from a 15 V, 150 W projector bulb (Halogen Photo optic Lamp Xenophot, Osram, Germany) and placed in the inlet arm of a silica T-tube, 5.0 cm away from the connection point to the horizontal arm. The experimental set-up for hydride generation and trap was reported previously [15] except for the fact that the way W-coil was inserted into the inlet arm. In this study, a laboratory-made quartz female joint was attached to the inlet arm. The W-coil with its socket base was fixed inside the male portion of the glass joint; in order to assure immobilization of the set-up, ordinary silicone type glue was used. This configuration allows a very rapid and convenient change of W-coil trap when needed. The W-coil was positioned so that its longer axis was perpendicular to the gas flow that is reaching to it through the smaller quartz tube in the inlet arm. The coil temperature was manually controlled by a variable potential power supply (Variac) and a 750 W transformer connected to mains electricity (220 V ac) through a power switch. The input voltage of the variable potential power supply was 220 V. The temperature measurements were carried out with a Ni–Cr thermocouple.

2.2. Reagents

All reagents used throughout the study were at least analytical reagent grade. The standard solutions of Bi were prepared by making necessary dilutions from 1000 mg L^{-1} Bi (Aldrich) of stock standard solution. In order to obtain the optimum acidification of reagents, appropriate amount of analytical grade 65% (w/w) HNO_3 (Merck) was used. Reductant solutions were prepared daily from the powder sodium tetrahydroborate (III) (Merck, min. Purity 98%). For the stabilization of the $NaBH_4$ solution, NaOH (Carlo Erba, Milano, Italy) was used. Dilutions were made using 18 MΩ cm deionised water obtained from a Milli-Q water purification system (Millipore, Bedford, MA, USA).

2.3. Procedure

The experiments were carried out in continuous-flow (CF) mode in both the conventional HGAAS and the W-coil trap-HGAAS studies. The HNO_3 and $NaBH_4$ concentrations were optimized in conventional HGAAS studies by using a 20.0 ng mL^{-1} of Bi solution containing 1.0 mol L^{-1} HNO_3. Blank was 1.0 mol L^{-1} HNO_3 solution. The reductant and analyte solutions were pumped at the flow rates of 8.0 mL min^{-1} which were optimised by both reductant and analyte solutions. The optimizations were made in several cycles until the results obtained did not differ from the last optimized value. During any optimization as the value of the parameter in question was varied, all the other parameters were in their optimized values. The generated Bi hydride was separated from the liquid phase by the GLS and was transferred to QTA through a Tygon tubing using a carrier gas mixture composed of H_2 and Ar at flow rates of 37.5 mL min^{-1} and 75 mL min^{-1}, respectively.

In trap experiments, initially the carrier gas mixture was sent through the system. Then, the trap was brought to its optimum collection temperature and the pumps were activated to start the flow of carrier and reductant solutions. The transferred bismuth hydride was trapped on the W-coil atom trap placed in the inlet arm of quartz T-tube explained in Section 2.1. At the end of the collection period, the power to heat the trap was discontinued and the pumps were deactivated. Under optimum gas flow, the trap temperature was brought to the optimum value for revolatilization and the residence time of the 0.1 ng L^{-1} for Bi on the light path is very short and transient signal is obtained in less than 1.0 s shown in Fig. 1.

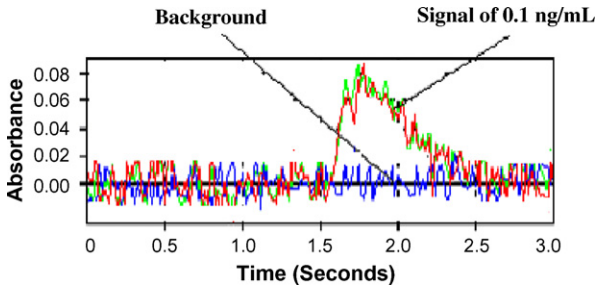


Fig. 1. The analytical signal obtained by the W-trap HGAAS method for 0.1 ng mL^{-1} Bi.

3. Results

3.1. W-coil system

For the Bi determination, resistively heated W-coil was used as a trap medium in this study. Each coil can be used for at least 100 firings under optimum parameters. H_2 flow in the system directly affects the firing amount. If W-coil trap is not changed, sensitivity of system is around 25% decreased because of oxidation of W-coil. If the flow rate of the H_2 is lower than 37.5 mL min^{-1} in collection and revolatilization step, the lifetime of W-coil becomes shorter. The presence of H_2 gas is necessary for both affecting a more efficient revolatilization and protecting the W-coil against oxidation. The coil should be heated as fast as possible at the revolatilization stage to obtain relatively sharp signals. For this purpose, a power switch was connected in front of the variable potential power supply and then the switch was turned on to assure the highest heating rate. Although the chemical nature of the revolatilized analyte species is not known, heating of quartz T-tube atomizer was necessary.

3.2. Optimization of system

The optimization of the experimental parameters was carried out using both CF-HGAAS and W-coil trap HGAAS. In the optimization studies, one parameter was varied while the others were kept constant. Optimization cycles were repeated until stable and repeatable signal was obtained. Optimizations of reaction and stripping coil lengths, concentrations of carrier and reductant solutions were common in both CF-HGAAS and W-coil trap HGAAS systems. The optimum HNO_3 and $NaBH_4$ concentrations were determined in no-trap studies in CF mode by using 20.0 ng mL^{-1} Bi as a standard solution.

3.2.1. Optimization of lengths of reaction and stripping coils

Reaction coil consists of the tubing between the merging point of sample and reductant solutions and the point where Ar and H_2 are introduced as the purge gases; as the continuation of the flow system, stripping coil is the tubing between the Ar/H_2 introduction point and the GLS. In the optimization study, length of reaction coil was varied between 5 cm and 30 cm while length of stripping coil was changed between 2 cm and 30 cm. The optimum lengths for reaction coil and stripping coils were found to be 10 cm and 4 cm, respectively. The analyte signal decreased with the values both lower and higher than the optimum values.

3.2.2. Optimization of concentration of reductant solution

For the production of Bi hydride species, $NaBH_4$ was used as a reductant solution. The effect of $NaBH_4$ concentration on BiH_3 production was investigated by using continuous flow. In order to find the optimum $NaBH_4$ concentration in the reductant solution, concentration was varied between 0.1% and 1.2% (w/v); 0.5% (w/v) $NaBH_4$ was found as the optimum reductant solution using the changes in the peak height of the analytical signal with respect to reductant concentration for no-trap studies. In this optimization, it was observed that the signal increased up to a concentration of 0.5% (w/v) and decreased for higher values. The decrease can be explained by the dilution effect, since more H_2 was generated at higher concentrations of reductant.

In addition, NaOH was used for the stabilization of $NaBH_4$. Concentration of NaOH was varied between 0.1% and 0.5% (w/v). Concentration of NaOH was optimized in no-trap studies and then checked also in W-trap HGAAS system. It was found that concentration of NaOH has a significant effect on the analytical signal of bismuth. The highest signal for bismuth was obtained using the reductant solution containing 0.2% (w/v) of NaOH while the other parameters were kept at their optimum found values.

3.2.3. Optimization of concentration of carrier solution

In this study, HNO_3 was used as carrier solution. In order to find the optimum HNO_3 concentration, HNO_3 concentration in the analyte solution was varied between 0.5 mol L^{-1} and 3.0 mol L^{-1}. The optimum value for HNO_3 was found as 1.0 mol L^{-1}, somewhat in the middle of the plateau. Higher and lower values resulted in a gradual decrease in the peak height of the analytical signal. When the concentration of HNO_3 in either solution exceeds 1.0 mol L^{-1}, decreases in signals were investigated. The effect of sample acidity was also checked in W-coil trap HGAAS system and found to be as same as in no-trap system.

3.2.4. Optimization of flow rates and composition of gases in the collection and revolatilization stages

In the hydride generation system, different carrier gases introduced before the stripping coil are used to separate the volatile species from the liquid phase and furthermore transport these species from GLS to externally heated quartz T-tube atomizer. In this study, a mixture of Ar and H_2 was applied not only in the collection but also in the revolatilization steps. In general, the flow rate of H_2 was kept constant at an optimized value where the oxidation of the W-coil trap was minimized or eliminated. Here, H_2 was used not only to prevent oxidation of the W-coil by creating a reducing environment around the W-coil but also to improve the revolatilization efficiency of Bi species from the W-coil trap. If flow rate of H_2 higher than optimized value, excess H_2 causes temparature decrease around the coil that affects sensitivity.

In the optimum collection and revolatilization steps, Ar flow rates were determined in CF mode in both without and with trap studies. Ar and H_2 flow rate were kept constant at 75 mL min^{-1} and 37.5 mL min^{-1} for both steps; and found that lower H_2 flow rates caused oxidation of the W-coil, which resulted in relatively higher background absorption.

The flow rate of Ar was varied between 50 mL min^{-1} and 400 mL min^{-1} during the optimization. The optimum value was found to be 75 mL min^{-1}; signal decreased for lower and higher values. Also the flow rate of H_2 was varied between 10 mL min^{-1} and 150 mL min^{-1} during the optimization. The optimum value was found to be 37.5 mL min^{-1}; signal decreased for lower and higher values.

3.2.5. Optimization of flow rates of carrier and reductant solution

The efficiency of the production of Bi hydride species is directly related with the flow rates of carrier and reductant solutions. In this study, the flow rate of HNO_3 that was used as the carrier solution was varied between 1.0 mL min^{-1} and 10.0 mL min^{-1} and the optimum value was found to be 8.0 mL min^{-1}. The signal increased as the flow rate was increased until the value of 8.0 mL min^{-1} is reached and stayed constant afterwards. The flow rate of $NaBH_4$ solution was varied between 1.0 mL min^{-1} and 10.0 mL min^{-1}; the optimum result was found as 8.0 mL min^{-1}. For the higher and

lower flow rates of $NaBH_4$, the peak height of Bi signal sharply decreased.

Optimization of concentrations and flow rates for HNO_3 and reductant solutions were carried out by keeping all parameters constant while only the test parameter was varied.

In this study, also the suction rate of the waste rate optimization was carried. The suction rate of the waste affected the Bi signal. If the suction rate of the waste was increased, Bi signal was decreased. In this study, suction rate of the waste was selected as 6 mL min^{-1}. As an example, if suction rate of the waste is selected 15 mL min^{-1} instead of 6 mL min^{-1}, signal intensity is decreased around 28%. Therefore, the waste rate must be minumum. If the suction rate is very low, waste could have gone to the atomizer. To the best of our knowledge, waste rate optimization is the first study in the literature.

3.2.6. Optimization of collection and revolatilization trap temperatures

In order to obtain a high trapping efficiency, W-coil atom trap temperature should be carefully optimized. In this study, collection trap temperature was varied from 100 °C to 540 °C. The trapping efficiency of W-coil increases sharply as the temperature increases up to approximately 289 °C. Increasing the trapping temperature resulted in a decrease in the analytical signal due to the partial release of the trapped Bi species and lowered trapping efficiency. Hence, 289 °C was found as the optimum trap temperature for efficient preconcentration of Bi species on W-coil trap. Revolatilization trap temperature was varied from 750 °C to 1500 °C while the collection temperature was kept constant at its optimized value. The optimum temperature for revolatilization was 1348 °C at which the highest signal was obtained. There is no need for waiting to cool the W-coil atom trap after revolatilization step or heat for the activation of W-coil before each collection cycle because the trap cools down very rapidly in only few seconds due to the continued gas flow. In order to protect the W-coil trap, hydrogen flow should be on throughout the experiment.

3.3. Analytical figures of merit

3.3.1. Calibration plots and linearity

Calibration plots with and without using W-coil trap were constructed. The linear portion of calibration without trap included Bi concentrations of 2.0–100 ng mL^{-1} using peak height values. In this linear range, linearity equation was found as $y = 0.0105x + 0.0263$ and correlation coefficient (R^2) was found as 0.9977; y is absorbance value for CF mode and x is concentration in ng mL^{-1}. In the W-coil trap studies, linear range included Bi concentrations of 0.1–10.0 ng mL^{-1}; best line equation was found to be $y = 0.2603x + 0.0376$ and correlation coefficient (R^2) was found as 0.9997; y is absorbance for peak height measurement and x is concentration in ng mL^{-1}. When the slope of calibration curve in trap studies is divided to that of the without trap studies, preconcentration factor was found to be 24.8.

3.3.2. LOD, LOQ and C_o

Three and ten times the standard deviation of blank values were used in the LOD and LOQ calculations, respectively. In W-coil trap studies, 1.0 min collection period was applied for the LOD and LOQ calculations. LOD values in W-coil trap and no-trap study are 25 ng L^{-1} and 470 ng L^{-1}, respectively. The enhancement factor in the limit of detection found to be 19 when compared to conventional CF-HGAAS. In calculations of characteristic concentration, C_o, for W-coil trap and no-trap studies, 15.9 ng L^{-1} of Bi and 336 ng L^{-1} Bi were used, respectively. Peak height values were used in all calculations. Analytical figures of merit mentioned above are shown in Table 1. Using C_o values, an enhancement factor of 21 is found for the present conditions.

Table 1
Analytical figure of merit and enhancement factors for Bi calculated by using peak height of analytical signal without trap and with trap medium.

	With trap	Without trap
LOD (ng L^{-1})	25	470
C_o (ng L^{-1})	15.9	336
% RSD	5.2	9.21

The accuracy of the method was tested using the certified reference material (CRM) Trace metals in Drrinking Water (Cat. No. CRM-TMDW Lot # 818921) supplied by High Puritiy Standarts (Charleston, SC, USA) and containing 10 ng mL^{-1} Bi. Analysis of CRM was carried out by diluting 1.0 mL of the CRM to 100 mL with 1.0 mol L^{-1} HCl, resulting in a solution of 0.100 ng mL^{-1} Bi. The result ($n = 3$ for each analysis) was 10.2 ± 1.3 ng mL^{-1} Bi and the result is in good agreement with the certified value.

3.4. Interference studies

Two classes of interferences are observed in AAS that is spectral and non-spectral. Spectral interferences are owing to radiation absorbed by species rather than free atoms of the analyte. Non-spectral interferences are due to influence of sample constituents on the analyte signal. Owing to the separation of analyte from the matrix, spectral interferences in hydride generation AAS are much less serious than for liquid sampling AAS. Line interferences do not occur at all; nonselective background absorption can be observed when a significant amount of species transported to the atomizer from a hydride generator. This may typically happen in the presence of an excess of other hydride forming elements in sample matrix or in the case of hydride generation from non-aqueous media [12].

Recently, interference effects of some elements were studied for hydride generation system. In our study, interferences have been investigated in detail during Bi determination by hydride generation, both with and without trap in the same HGAAS system. It is known that since W-coil trap system is capable of having better sensitivity and diluted interferents are less effective. Interferent/analyte (mass/mass) ratio was kept at 1, 10 and 100. Experiments were designed for carrier solutions having 1.0 M HNO_3. Interferents such as Fe, Mn, Zn, Ni, Cu, As, Se, Cd, Pb, Au, Na, Mg, Ca, chloride, sulfate and phosphate were examined in this study.

In the preliminary of the intereference studies, a concentration level was used to be the same for both systems that are with and without trap, thus 20 ng mL^{-1} was chosen for analyte concentrations. And also in trap studies, collection time was selected as 6 s to reach same absorbance value with no-trap studies. Interferant/analyte (mass/mass) ratio was kept as 1, 10 and 100, respectively. Experiments were designed for carrier solutions having 1.0 M HNO_3. In this circumstance, Mn and Cu which are called as transition elements, As, Cd and Pb which are called as hydride forming elements and Au show severe interferences in both cases. Besides this study, Bi concentration was changed as 0.4 ng mL^{-1} and collection time was selected as 300 s in order to keep total amount of Bi constant with 20 ng mL^{-1} Bi where collection time was selected as 6 s in trap studies. When this solution was used, interference effects of Mn, Cu, As, Cd, Pb and Au were obviously decreased by using W-coil trap study as shown in Figs. 3, 5 and 7, respectively. This shows that if the analyte solution is diluted, interference effects of these elements on Bi signal are decreased.

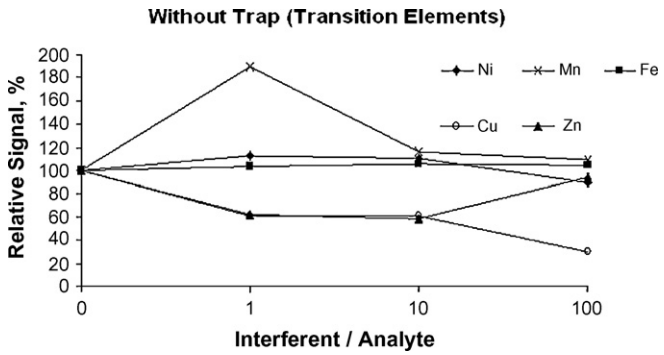


Fig. 2. Relative signal of Bi in different transition metals medium by without trap studies.

4. Discussion

Optimization of the systems was carried out by keeping all parameters constant while only the test parameter was varied. The analyte signal decreased with the values both lower and higher than the optimum values.

The analytical signal obtained by W-coil trap HGAAS under optimum conditions was very sharp. The residence time of the 0.1 ng mL^{-1} for Bi on the light path is very short and transient signal is obtained 0.1 ng mL^{-1} for Bi in less than 1.0 s shown in Fig. 1. The shape and base width of the analytical signal depend on the heating rate of the coil and also the carrier gas flow rates. If higher collection temperatures were used, the quartz around W-coil trap reaches to temperatures at which volatile Bi species are partially trapped on this surface. At the releasing stage, these trapped species revolatilized gradually as quartz surrounding the W-coil trap is being heated relatively slow compared to the W-coil trap. Under these conditions, a tailing is observed in the analytical signal. In addition, since there is a temperature gradient between the trap and the atomizer due to the heating effect of flame, some of the volatile Bi species are trapped on the inner surface of quartz inlet arm between trap and the atomizer. Regardless of the collection temperature, if a higher releasing temperature, which is sufficient for revolatilization of Bi species trapped on quartz surface, the analytical signal tails due to gradually revolatilization of Bi species from quartz surface between trap and the atomizer. Deviations from the optimized collection and release cycles may cause degraded repeatability due to undesired trapping and releasing effects. Under optimum conditions, where optimum collection and revolatilization temperatures were not exceeded, only a single sharp peak created by volatile Bi trapped on W-coil trap is achieved. The precision of the measurements based on the peak height of the analytical signal has an RSD of 5.2%, which is obtained by replicate measurements of reagent blanks for a collection volume of 8.0 mL corresponding to 1.0 min collection.

Effects of some transition elements on Bi determination using both without trap and W-coil trap studies can be seen in Figs. 2 and 3, respectively. As seen, Mn and Cu show severe interference in without trap experiment. It is well known that Cu is an interferent in HGAAS determination of Bi. During the determination of Bi in geological reference samples, the Cu/Bi mass ratio was only 3 and no interference was observed. Elsewhere, a signal reduction of 77% and 100% signal reductions was reported for Cu/Bi mass ratio values of 20 and 200, respectively [10]. Trap system has lower interference effect in cases Fe and Zn. In these interference studies, the concentration of the Bi analyte was selected as 20.0 ng mL^{-1} in without trap experiments and in with trap experiment Bi concentration was selected as 0.4 ng mL^{-1}, collection time was 300 s. When 0.4 ng mL^{-1} was used, interference effects of Mn, Fe, Cu, Zn and Ni were obviously decreased using W-trap studies as seen in

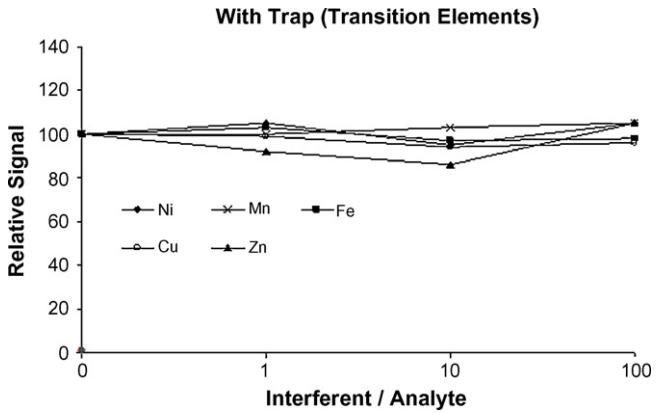


Fig. 3. Relative signal of Bi in different transition metals medium by trap studies (Bi concentration: 0.4 ng mL^{-1} and collection time: 300 s).

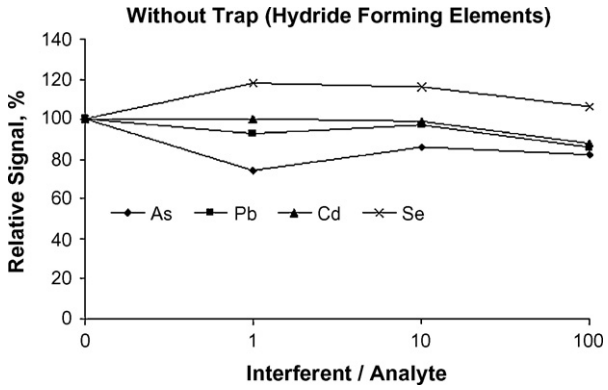


Fig. 4. Relative signal of Bi in hydride forming elements medium by without trap studies.

Fig. 3. This shows that if the analyte solution is diluted, interference effect of the elements on Bi signal is decreased.

Effects of some hydride forming elements on Bi determination using both without trap and W-coil trap studies shown in Figs. 4 and 5, respectively. Hydride forming elements may be in gas phase interferents and liquid phase interferents. In the liquid phase interferences, due to compound and matrix interferences, signal may be decreased. If these types of interferences occurred, using trap, these effects could not be eliminated because interfering effects of liquid phase interferents are finished before the trap medium. So, trap is not a way to minimize effects of liquid phase interferents. On the other hand, when 0.4 ng mL^{-1} Bi concentration

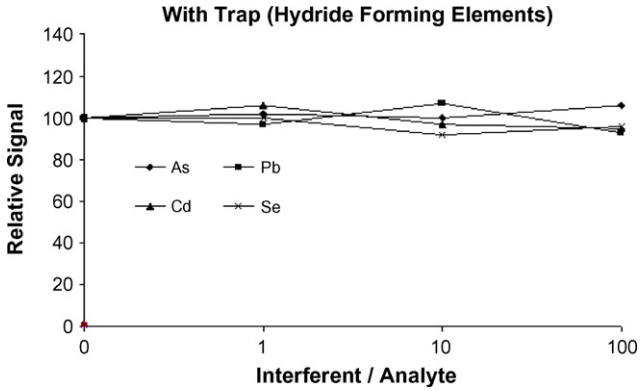


Fig. 5. Relative signal of Bi in hydride forming elements medium by trap studies (Bi concentration: 0.4 ng mL^{-1} and collection time: 300 s).

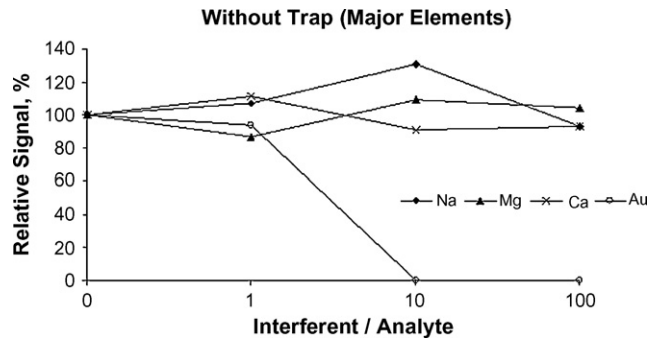


Fig. 6. Relative signal of Bi in major elements medium by without trap studies.

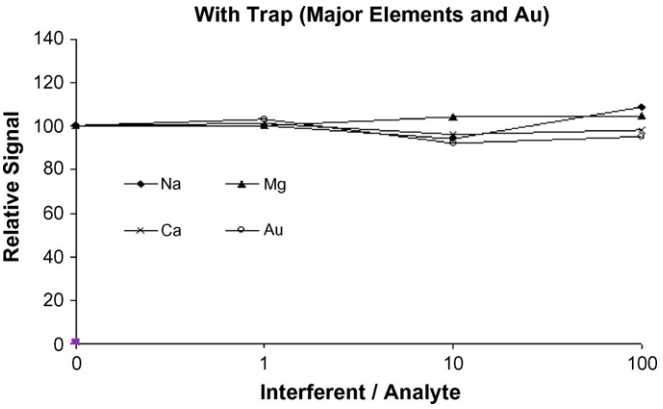


Fig. 7. Relative signal of Bi in major elements medium by trap studies (Bi concentration: 0.4 ng mL^{-1} and collection time: 300 s).

was used, interference effect of As was reduced owing to dilution effect as shown in Fig. 5.

Figs. 6 and 7 show the effect of major elements on Bi determination using both without trap and W-coil trap studies. It can be seen from Fig. 6, Au shows very high interferent effect on Bi signal especially interferent/analyte concentration is 10 and 100 in without trap study. On the other hand, when the Bi concentration was changed from 20 ng mL^{-1} to 0.4 ng mL^{-1} in trap study, interference effect of the Au on Bi signal was reduced using W-coil trap due to dilution effect as shown in Fig. 7.

And also, the interference effect of the some anions on the Bi signal in both without trap and W-coil trap were studied. By using W-coil trap, intereference effect of the PO_4^{3-}, SO_4^{2-} and Cl^- was reduced. Therefore interference effect of these anions is in gas phase.

Besides, for the decreasing of the interference effect of the some elements on the Bi signal, analyte concentration was diluted but total amount of the analyte was not changed. By doing this, interference effect of the elements on the Bi signal was decreased very well. This shows that trap has two advantages regarding interferences: dilution + trap itself.

5. Conclusion

A simple flame AAS instrument, a peristaltic pump and a simple flow system are needed to obtain sensitivity at ng L^{-1} Bi concentration level. All experimental parameters that influence the collection/volatilization efficiency were optimized in order to have the best sensitivity in W-coil trap HGAAS system.

Interferences have been investigated in detail during Bi determination by hydride generation in both with and without W-coil trap in the same HGAAS system. Experiments were designed for carrier solutions having 1.0 M HNO_3. Interferents such as Fe(III), Mn(II), Zn(II), Ni(II), Cu(II), As(III), Se(IV), Cd(II), Pb(II), Au(III), Na(I), Mg(II), Ca(II), chloride, sulfate and phosphate were examined in this study. In the case of W-coil trap, interference effects from chloride, sulfate and phosphate ions are significantly reduced as compared with the no-trap system. Cd, Pb and Mg have effects within ±10% in without trap study. On the other hand, when W-coil trap is used, the interference effect of these analyte is decreased. Mn, Zn, Se, As, Na and Cu show severe interference effect on Bi signal in without trap study. Trap system has lower interference effect in cases of these elements. Another important point is that in no-trap study, Au shows severe interference effect on Bi signal especially interferent/analyte concentration is 10 and 100. When the W-coil trap is used, the interference effect of Au was decreased severely. In this study, also optimization of waste suction rate was carried. The calibration plot for an 8.0 mL sampling volume was linear between 0.10 μg L^{-1} and 10.0 μg L^{-1} Bi. The detection limit (3 s) was 25 ng L^{-1}. The enhancement factor for the characteristic concentration (C_o) was found to be 21 when compared with the regular sytem without trap, by using peak height values.

Acknowledgement

İ. Kula is grateful for the post-doc scholarship of Mugla University SKV (Sıtkı Koçman Foundation).

References

[1] S. Cadore, A.P. dos Anjos, N. Baccan, Analyst 123 (1998) 1717–1719.
[2] T. Murata, J. Environ. Sci. Health A 41 (2006) 161–172.
[3] Larsen, M. Stoltenberg, C. Sondergaard, M. Bruhn, G. Danscher, Basic Clin. Pharmacol. 97 (2005) 188–196.
[4] A.S. Ribeiro, M.A.Z. Arruda, S. Cadore, Spectrochim. Acta Part B 57 (2002) 2113–2120.
[5] O. Acar, A. Rehber Türker, Fresen. J. Anal. Chem. 360 (1998) 645–649.
[6] P. Schramel, I. Wendler, J. Angerer, Int. Arch. Occup. Environ. Health 69 (1997) 219–223.
[7] F. Shemirani, M. Baghdadi, M. Ramezani, M.R. Jamali, Anal. Chim. Acta 534 (2005) 163–169.
[8] A. Marrow, G. Wiltshire, A. Hursthouse, Atom. Spectrosc. 18 (1997) 23–28.
[9] H.Y. Li, B.M. Keohane, H.Z. Sun, P.J. Sadler, J. Anal. Atom. Spectrom. 12 (1997) 1111–1114.
[10] O. Cankur, N. Ertas, O.Y. Ataman, J. Anal. Atom. Spectrom. 17 (2002) 603–609.
[11] J. Kratzer, J. Dedina, J. Anal. Atom. Spectrom. 21 (2006) 208–210.
[12] J. Dedina, D.L. Tsalev, Hydride Generation Atomic Absorption Spectrometry, John Wiley and Sons Ltd., Chichester, 1995.
[13] W. Chuachuad, J.F. Tyson, J. Anal. Atom. Spectrom. 20 (2005) 273–281.
[14] W. Chuachuad, J.F. Tyson, J. Anal. Atom. Spectrom. 20 (2005) 282–288.
[15] O. Cankur, O.Y. Ataman, J. Anal. Atom. Spectrom. 22 (2007) 791–799.

Talanta 80 (2009) 133–138

Contents lists available at ScienceDirect

Talanta

journal homepage: www.elsevier.com/locate/talanta

Molecularly imprinted solid-phase extraction for the selective determination of bromhexine in human serum and urine with high performance liquid chromatography

Mehran Javanbakht[a,*], Mohammad Hadi Namjumanesh[a], Behrouz Akbari-adergani[b]

[a] Department of Chemistry, Amirkabir University of Technology, Tehran, Iran
[b] Food & Drug Laboratory Research Center, Food & Drug Department, Ministry of Health and Medical Education, Tehran, Iran

ARTICLE INFO

Article history:
Received 19 April 2009
Received in revised form 11 June 2009
Accepted 15 June 2009
Available online 21 June 2009

Keywords:
Molecularly imprinted polymer
Solid-phase extraction
Bromhexine
Human serum
Urine

ABSTRACT

In this work, a novel method is described for the determination of bromhexine in biological fluids using molecularly imprinted solid-phase extraction as the sample cleanup technique combined with high performance liquid chromatography (HPLC). The water-compatible molecularly imprinted polymers (MIPs) were prepared using methacrylic acid as functional monomer, ethylene glycol dimethacrylate as cross-linker, chloroform as porogen and bromhexine as the template molecule. The novel imprinted polymer was used as a solid-phase extraction sorbent for the extraction of bromhexine from human serum and urine. Various parameters affecting the extraction efficiency of the polymer have been evaluated. The optimal conditions for molecularly imprinted solid-phase extraction (MISPE) consisted of conditioning 1 mL methanol and 1 mL of deionized water at neutral pH, loading of 5 mL of the water sample (25 $\mu g\,L^{-1}$) at pH 6.0, washing using 2 mL acetonitrile/acetone (1/4, v/v) and elution with 3× 1 mL methanol/acetic acid (10/1, v/v). The MIP selectivity was evaluated by checking several substances with similar molecular structures to that of bromhexine. Results from the HPLC analyses showed that the calibration curve of bromhexine using MIP from human serum and urine is linear in the ranges of 0.5–100 and 1.5–100 $\mu g\,L^{-1}$ with good precisions (3.3% and 2.8% for 5.0 $\mu g\,L^{-1}$), respectively. The recoveries for serum and urine samples were higher than 92%.

© 2009 Elsevier B.V. All rights reserved.

1. Introduction

Bromhexine (Fig. 1), N-cyclohexyl-N-methyl-(2-amino-3,5-dibromobenzyl)-amine, was proved to be antitussive and mucolytic because of promotion of bronchial secretion and splitting of polysaccharide fiber. Bromhexine, is a mucolytic agent used in the treatment of respiratory disorders associated with viscid or excessive mucus [1]. It undergoes oxidation and conjugation hepatic biotransformation, and the drug and its metabolites are excreted in urine and feces [2]. The drug has been quantified using different methods such as UV–vis spectrophotometry [3–5], voltammetry [6], thin layer chromatography (TLC) [7], high performance liquid chromatography (HPLC) [8,9], inductively coupled plasma mass spectrometry [10], capillary zone elecrophoresis [11], capillary isotachophoresis [12], electrokinetic chromatography [13], gas liquid chromatography [14], chemiluminecence [15] and flow injection analysis with ion-selective electrode [16]. Most of them are, however, difficult and/or time-consuming, requiring a derivatisation step or a specific solvent extraction. HPLC technique has been extensively applied to the determination of bromhexine in pharmaceutical or biological samples but it combined with a liquid–liquid extraction (LLE) step [17–19] that hindered the degree of automation. However, none of the available methods was ideal, and an improved method for selective extraction and determination of bromhexine was necessary.

Sample preparation is essential for the analysis of compounds in real samples. Due to unsatisfactory selectivity, the traditional sorbents usually cannot separate analytes efficiently in complex biological or environmental samples. Solid-phase extraction (SPE) is the most popular of cleanup techniques due to factors such as convenience, cost, time saving and simplicity. Compared to LLE, SPE can reduce the time required, especially for automated methods, can handle small samples, and consumes small amount of solvent [20]. As a result, SPE is the most accepted sample pretreatment method today [21]. A relatively new development in the area of SPE is the use of molecularly imprinted polymers (MIPs) for the sample clean up [22–25]. MIPs are synthetic polymers possessing specific cavities designed for a target molecule. MIPs are synthesized by polymerization of different components. In the most common preparation process, monomers form a complex with a template

* Corresponding author. Tel.: +98 21 64543295; fax: +98 21 64543296.
E-mail address: mehranjavanbakht@gmail.com (M. Javanbakht).

0039-9140/$ – see front matter © 2009 Elsevier B.V. All rights reserved.
doi:10.1016/j.talanta.2009.06.033

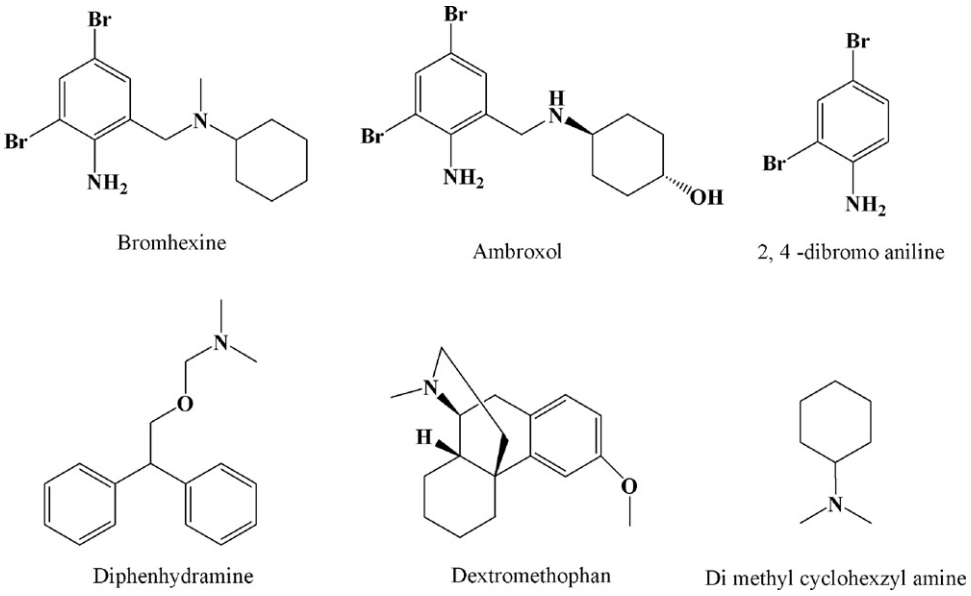


Fig. 1. Chemical structure of investigated organic compounds and drugs.

through covalent or non-covalent interactions and are then joined by using a cross-linking agent. After removing of the template by chemical reaction or extraction, binding sites are exposed which are complementary to the template in size, shape, and position of the functional groups, and consequently allow its selective uptake. MIPs are often referred to as 'artificial antibodies'. Unlike antibodies, MIPs are stable to extremes of pH, organic solvents and temperature which allows for more flexibility in the analytical methods [22,26]. The use of MIPs for SPE can involve various modes, including conventional SPE where the MIP is packed into columns or cartridges [27,28] and batch mode SPE where the MIP is incubated with the sample [29]. Another major advantage of MIP-based SPE, related to the high selectivity of the sorbent, is the achievement of an efficient sample clean up.

Recently, we applied MIPs as new sensing material in potentiometric detection of hydroxyzine [30], cetirizine [31] and SPE of verapamil [32]. In this article we present a novel method for the performance evaluation of bromhexine based MIPs as selective SPE sorbents for efficient sample clean up and followed determination of bromhexine from complex matrices by high performance liquid chromatography. This scheme as molecularly imprinted solid-phase extraction (MISPE) allows the sensitive, simple and inexpensive extraction and determination of the analyte in human serum and urine samples.

2. Experimental

2.1. Chemicals and reagents

Methacrylic acid (MAA) from Merck (Darmstadt, Germany) was distilled in vacuum prior to use in order to remove the stabilizers. Ethylene glycol dimethacrylate (EGDMA), 2,2′-azobis isobutyronitrile (AIBN), 2,4-dibromo-aniline and dimethyl-cyclohexyl-amine from Sigma–Aldrich (Steinheim, Germany) were of reagent grade and were used without any further purification. All solvents used in chromatography analyses were HPLC grade and supplied by Merck. Bromhexine HCl, ambroxol HCl, dextromethorphan HBr and diphenhydramine HCl were obtained from the ministry of health and medical education (Tehran, Iran). Bromhexine USP reference standard was used for preparing stock and standard solutions. The bromhexine stock solutions (1000 $\mu g\,L^{-1}$) were prepared monthly and stored at 4 °C. Intermediate standard solution of 10 $\mu g\,L^{-1}$ was prepared weekly by dilution of stock solutions with water. Working standard solutions of different concentrations were prepared daily by diluting the intermediate standard solution with mobile phase solution.

2.2. Apparatus

The HPLC system consisted of a Waters 515 pump, a 486 Waters UV/vis detector, a model 7725i Rehodyne injector with a 25 μL sample loop and a micro-Bondapak C18 column of 4.6 mm × 150 mm HPLC column. HPLC data were acquired and processed using a PC and Millennium 2010 Chromatogram Manager software (Version 2.1 Waters). pH of solutions were adjusted using a model 630 digital Metrohm pH meter equipped with a combined glass-calomel electrode. FT-IR spectra (4000–400 cm^{-1}) in KBr were recorded on a Bruker VERTEX 70 spectrometer.

2.3. Procedures

2.3.1. MIP and NIP preparation with bulk polymerization

For the preparation of the bromhexine imprinted polymer, the template (94 mg, 0.25 mmol) was dissolved in chloroform in a 25-mL thickwalled glass tube. The functional monomer (MAA) (0.129 mL, 1.5 mmol), the cross-linking monomer (EGDMA) (2.6 mL, 14 mmol), and the initiator (AIBN) (24 mg, 0.164 mmol) were then added to the above solution. The mixture was uniformly dispersed by sonication for 40 min to remove oxygen. Then the solution was placed in a water bath at 60 °C. The reaction was allowed to proceed for 16 h. The hard polymers, P(MAA-co-EGDMA), that were obtained were crushed. After the polymerization procedure and drying, the polymer particles were washed with methanol and acetic acid (10:1, v/v, of 98% methanol and pure acetic acid) for three times and with distillated water for two times. The complete removal of template was followed by HPLC-UV, after three times washing spectra of bromhexine were not seen. In order to verify that retention of template was due to molecular recognition and not to non-specific binding, a control, non-imprinted polymer (NIP) was prepared as the same procedure, including washing, but with the omission of the target molecule, bromhexine. The size of the particles used after crushing and sieved was between 30 and 45 μm.

2.3.2. MISPE conditions

MIP and NIP columns were prepared by packing 150 mg of the polymer into 2 mL empty cartridge. The cartridge was conditioned sequentially with 1 mL of methanol and 1 mL of deionized water. Extraction experiments involved loading the column with 5 mL of water solution containing 25 $\mu g\,L^{-1}$ bromhexine (pH 6.0, 20 $mmol\,L^{-1}$ citrate buffer) at a flow rate of 1 $mL\,min^{-1}$. After loading, column was washed with 2 mL of acetonitrile/acetone (1/4, v/v) and a full vacuum was applied through the cartridge for 2 min to remove residual solvent. Finally, the elution was performed by passing 3× 1 mL of methanol–acetic acid (10:1, v/v). All fractions were evaporated to dryness at 20 °C under a stream of nitrogen and finally recovered in 1 mL of mobile phase. Then, 20 μL of each sample was injected onto the analytical column of HPLC.

2.3.3. Chromatographic conditions

The HPLC was carried out at room temperature. A degassed mixture of acetonitrile:phosphate buffer (0.01 $mol\,L^{-1}$, pH 3.0) (30:70) at a flow rate of 1.0 $mL\,min^{-1}$ was selected as a mobile phase [6]. All of the analyses were carried out at an operation wavelength of 245 nm and the results were recorded by Millennium chromatography software.

2.3.4. Rebinding experiments

Batch adsorption experiments were used to evaluate the binding affinity of the imprinted polymer as reported before [33,34]. The general procedure for extraction of bromhexine by the MIP was as follows: the polymer beads were suspended in aqueous solutions and the pH was adjusted at 6. Then 25 mg of polymer particles were added in 5-mL flask containing bromhexine solutions of various concentrations (5–100 $\mu g\,L^{-1}$). The mixtures were thermo-stated at 25 °C for 1 h under continuous stirring at 200 rpm and then were filtrated on a paper filter (flow rate = 100 $mL\,min^{-1}$ by applied vacuum). The free concentration of bromhexine after the adsorption was recorded by HPLC-UV at 245 nm. Three replicate extractions and measurements were performed for each aqueous solution. The adsorbed bromhexine was desorbed from the MIP by treatment with 2 mL of methanol and acetic acid (10:1, v/v, of 98% methanol and pure acetic acid). The amount of bound analyte to the polymer was calculated by subtracting the nonbounded amount, from the initial bromhexine concentration in the mixture. The binding experiments were carried out by triplicate. In order to know that the bromhexine is retained by specific interactions and not the non-specific ones, the same procedure was followed for NIP particles.

2.3.5. Extraction procedure for human serum and urine samples

Drug free human serum was obtained from the Iranian blood transfusion service (Tehran, Iran) and stored at −20 °C until use after gentle thawing. Urine was also collected from healthy volunteers (males, around 30-year old). Stock standard solutions of bromhexine were prepared in water. Standard solutions were prepared by adding appropriate volumes of bromhexine solution to a 10 mL volumetric flask and the solution was diluted to the mark with biological fluids and vortexed for 3 min. 2 mL of the serum and urine samples spiked by bromhexine were diluted with 2 mL buffer pH 6.0 and were centrifuged for 20 min at 8000 rpm and then filtered through a cellulose acetate filter (0.20 μm pore size, Advantec MFS Inc. CA, USA). The filtrate were collected in glass containers and stored at −20 °C until analysis was performed. 2 mL of the filtered supernatant was collected to be directly percolated through the MIP or the NIP.

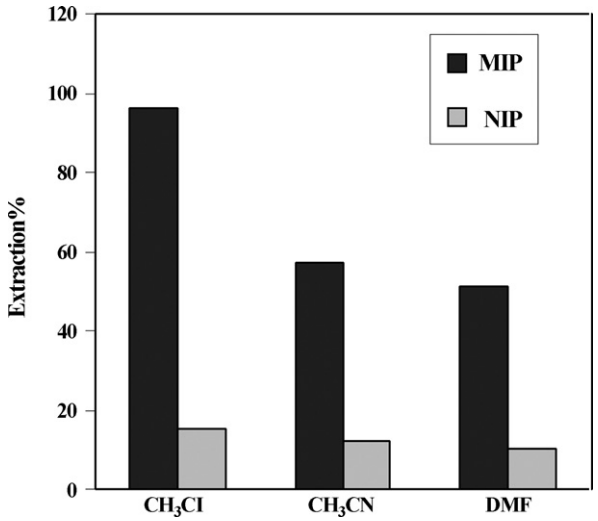


Fig. 2. Recoveries obtained using the MIP and NIP polymers synthesized in different organic solvents. Batch experiments with 25 mg or polymer particles; sample volume, 5 mL; pH, 6.0; bromhexine concentrations, 25 $\mu g\,L^{-1}$.

3. Results and discussion

3.1. Characterization

In the IR spectra, as a result of the hydrogen binding with the –COOH group of MAA, the O–H stretching and the bending vibrations at 3473 and 1394 cm^{-1} in the leached MIP materials were shifted to 3457 and 1388 cm^{-1} in the corresponding unleached MIP, respectively. Furthermore, there were two other distinct differences between the IR spectra of the leached and unleached MIPs. In the leached polymer, there were one broad band around 2704 cm^{-1} and one sharp band around 2956 cm^{-1}. The first was shifted to 2636 cm^{-1} and another appeared around 2987 cm^{-1}. Other absorption peaks match both those of MIP, as well as NIP: 1731 cm^{-1} (stretching vibration of C=O bonds on carbonyl groups); 1636 cm^{-1} (stretching vibration of residual vinylic C=C bonds) and vibrations at 1259, 1157, 954, 875, 817 and 757 cm^{-1}.

3.2. Optimal MIP formulation and progenic solvent

There are several variables, such as amount of monomer or nature of cross-linker and solvent that affects the final characteristics of the obtained materials in terms of capacity, affinity and selectivity for the target analyte. Thus, by achieving an optimum combination of cross-linker and functional monomer non-specific binding should be able to be minimized. Primary experiments revealed that the imprinted polymers prepared in chloroform show better molecular recognition ability than acetonitrile (AN) and dimethyl formamide (DMF) in aqueous environment (Fig. 2). Thus, in chloroform, different formulations for the obtainment of MIPs with improved molecular recognition capabilities have been used. Generally, proper molar ratios of functional monomer to template are very important to enhance specific affinity of polymers and number of MIPs recognition sites. High ratios of functional monomer to template result in high non-specific affinity, while low ratios produce fewer complexation due to insufficient functional groups [35]. Four molar ratios of the monomer MAA to the template of 2:1, 4:1, 6:1 and 8:1 were used in the experiments. The optimum ratio of functional monomer to template for the specific rebinding of bromhexine was 6:1 (Table 1), which had the best specific affinity and the highest recovery of 96%, while that of the corresponding NIPs was low at 15%. The specific adsorption recovery of bromhexine at 6:1 was 81%, while those at 2:1, 4:1 and 8:1

Table 1
Compositions and comparisons of the extraction of polymers.

MIP	MAA (mmol)	Bromhexine (mmol)	EGDMA (mmol)	AIBN (mmol)	Extraction (%) (mean ± SD)[a]
MIP1	2.0	1.0	64	0.347	41 (±1.9)
MIP2	4.0	1.0	64	0.347	51 (±2.2)
MIP3	6.0	1.0	64	0.347	96 (±4.1)
MIP4	8.0	1.0	64	0.347	41 (±2.0)
NIP1	2.0	0	64	0.347	26 (±1.7)
NIP2	4.0	0	64	0.347	32 (±2.1)
NIP3	6.0	0	64	0.347	15 (±1.1)
NIP4	8.0	0	64	0.347	24 (±1.8)

[a] Average of three determinations.

were 15%, 19% and 17%, respectively. Therefore, a typical 1:6:64 template:monomer:cross-linker molar ratio was used for further studies.

3.3. Effect of pH, choice of loading, washing and eluent solution

It has been demonstrated that efficient imprint rebinding is possible in aqueous buffer solutions, showing high binding affinity and selectivity as a result of hydrophobic interactions. The effect of pH on the rebinding efficiency of bromhexine was investigated by varying the solution pH from 2.0 to 9.0 Several batch experiments were performed by equilibrating 25 mg of the imprinted and non-imprinted particles with 5 mL of solutions containing 25 $\mu g\,L^{-1}$ of bromhexine under the desired range of pH. It was observed that bromhexine underwent complete rebinding/elution at pH 6.0. The lower responses observed at lower and higher pHs may be attributed to the protonation of the amine group of bromhexine and deprotonation of carboxyl groups of the polymer, respectively.

Generally, the polymers have binding ability with both specific and non-specific interactions. The specific interactions may originate mainly from the imprinting procedure, which creates selective recognition sites for the template. The non-specific interactions were assessed by measuring the binding of the non-imprinted polymer. At first, cartridges were conditioned with 1 mL of methanol followed by 1 mL of deionized water at neutral pH. Water samples were then loaded onto the cartridges at a flow rate of 1 mL min^{-1} and the wash procedure was assessed for obtaining maximum recovery of the analytes using a variety mixtures including: acetonitrile, acetone, tetrahydrofuran, dimethyl formamide, acetonitrile–acetone, dichloromethane–acetone, acetonitrile–methanol and dichloromethane–methanol. In order to investigate the usefulness of the washing step, 5 mL of 25 $\mu g\,L^{-1}$ bromhexine aqueous solution was loaded on the MIP and NIP cartridges separately, followed by the desorption with the washing solvent. The results were showed that washing with 2 mL of acetone, tetrahydrofuran and dichloromethane had no obviously effect on the retention of bromhexine on both MIP and NIP cartridges. In contrast, polar organic solvents, such as methanol, dimethyl formamide and acetonitrile had noticeably effect on the retention of bromhexine on both MIP and NIP cartridges. With the mixture of acetonitrile/acetone (1/4, v/v), the recovery of bromhexine in NIP cartridge was decreased to 8%, while the recovery of bromhexine by the MIP cartridges was not reduced (94.0%). For the recovery of strongly bound bromhexine, the polymer were eluted with 3× 1 mL of methanol/acetic acid (10/1, v/v). As a result, recovery after the whole SPE process avoids contaminating HPLC column. Meanwhile, increasing of the sample volume up to 100 mL, just had a light effect on the extraction of bromhexine.

The reproducibility and repeatability of the method were evaluated from run-to-run MISPE experiments (5 $\mu g\,L^{-1}$ standard solution, $n = 5$) and day-to-day experiments (five successive days) and RSDs of 5.8% and 2.5% for the extraction amounts of bromhexine were obtained, respectively.

3.4. Adsorption capacity

The capacity of the sorbent is an important factor that determines how much sorbent is required to remove a specific amount of drug from the solution quantitatively. In the measurement of the adsorption capacity of MIP and NIP absorbents, the absorbents (10 mg) were added into 5 mL bromhexine solutions at concentrations of 1.0–500 mg L^{-1}, and the suspensions were mechanically shaken for 1 h at room temperature, followed by centrifugally removing of the absorbents. The remained bromhexine in the supernatant was measured by HPLC, and the isothermal adsorptions are plotted in Fig. 3. According to these results, the maximum amount of bromhexine that can be absorbed by MIP was found to be 90 mg g^{-1} (240 $\mu mol\,g^{-1}$) at pH 6.0. Such behavior is coherent with previous data with MIP capacities ranged from 40 to 200 μmol per gram [36,37]. For higher bromhexine amounts, a slight increase of retained bromhexine was observed on MIP capacity curve.

3.5. Study of MIP selectivity

Dextromethorphan and diphenhydramine as antitussive (cough suppressant) drugs, ambroxol as an active metabolite of bromhexine, 2,4-dibromo-aniline and dimethyl-cyclohexyl-amine as structural analogues of bromhexine were selected to investigate the selectivity of the MIP. Their molecular structures are shown in Fig. 1. Solutions of all compounds were prepared individually with the concentration of 50 $\mu g\,L^{-1}$. Extraction solvent was methanol/acetic acid (10/1, v/v). The extraction yields of the selected compounds with the MIP and NIP are shown in Fig. 4. Obviously, the extraction yields of analogues with the MIP were much higher than that of the NIP. It was indicated that the bromhexine based-MIP possessed better affinity to the structural analogues of template molecule.

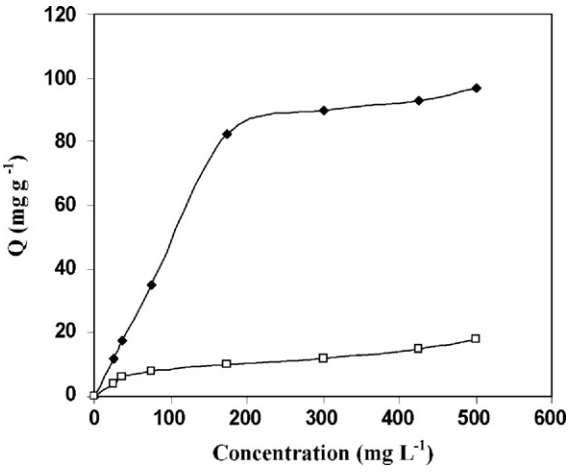


Fig. 3. Curve of capacity obtained after the loading of 5 mL aqueous solution spiked with increasing amounts of bromhexine onto the MIP particles.

Table 2
Assay of bromhexine in human serum and urine by means of the described MISPE procedure.

Sample	Spiked value (ng/mL)	Proposed SPE-HPLC procedure (recovery% ± SD)[a]	
		MIP	NIP
Human serum	5.0	93 ± 3.3	23 ± 2.0
	10	96 ± 3.1	20 ± 2.1
	25	92 ± 2.8	22 ± 2.5
Human urine	5.0	97 ± 2.8	19 ± 2.0
	10	95 ± 3.0	18 ± 1.8
	25	93 ± 2.7	18 ± 1.9

[a] Average of three determinations.

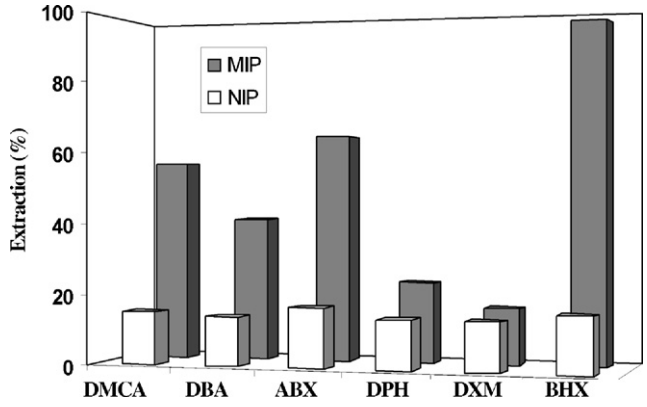


Fig. 4. Extractions of bromhexine (BHX), dextromethorphan (DXM), diphenhydramine (DPH), ambroxol (ABX), 2,4-dibromo-aniline (DBA) and dimethyl-cyclohexyl-amine (DMCA) with MIP and NIP at 50 μg L^{-1} level. Batch experiments at 25 °C and 200 rpm; sample volume, 5 mL; pH, 6.0.

This affinity is mainly caused by the hydrogen bonding interaction between amino groups possessed by all analogues and carboxylic groups in the MIP. However, for the MIPs, the extractions of dextromethorphan, diphenhydramine, ambroxol, 2,4-dibromo-aniline, dimethyl-cyclohexyl-amine and bromhexine according to adsorption experiments (without using washing step) were 16, 23, 65, 41, 57, and 97 percent, respectively. A possible reason for the difference was that the extractions of analogues were relative to their structural similarity with the template molecule of MIP. Ambroxol, having identical structural analogues, could be extracted 65%. For the NIPs, the extractions of less than 18% were obtained for all compounds because of the non-specific adsorption.

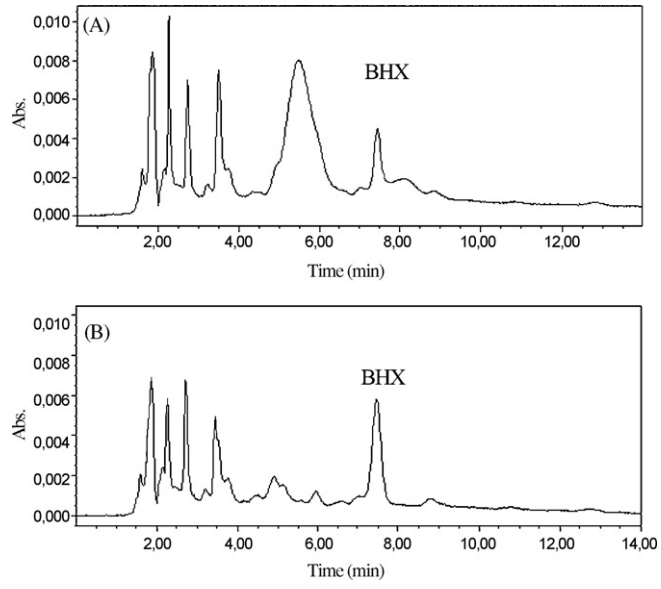


Fig. 5. HPLC chromatograms obtained after percolation of 2 mL human serum spiked with 10.0 μg L^{-1} of bromhexine with a cleanup step comprising the (A) NIP and (B) MIP monitored at 245 nm; conditions: column ACE 5 μm, C18 4.6 mm × 250 mm at +40 °C, eluent acetonitrile:phosphate buffer (0.01 mol L^{-1}, pH 3.0) 30:70 at flow rate of 1.0 mL min^{-1}.

3.6. Bromhexine assay in human serum and urine samples

To demonstrate the potential of MIP for the selective clean up of analyte, the MIP was applied to the purification of spiked bromhexine in human serum and urine. Aqueous media was employed for the loading solution and the wash procedure was assessed for obtaining maximum recovery of the analytes using acetonitrile–acetone (1:3). It was seen that acetonitrile–acetone

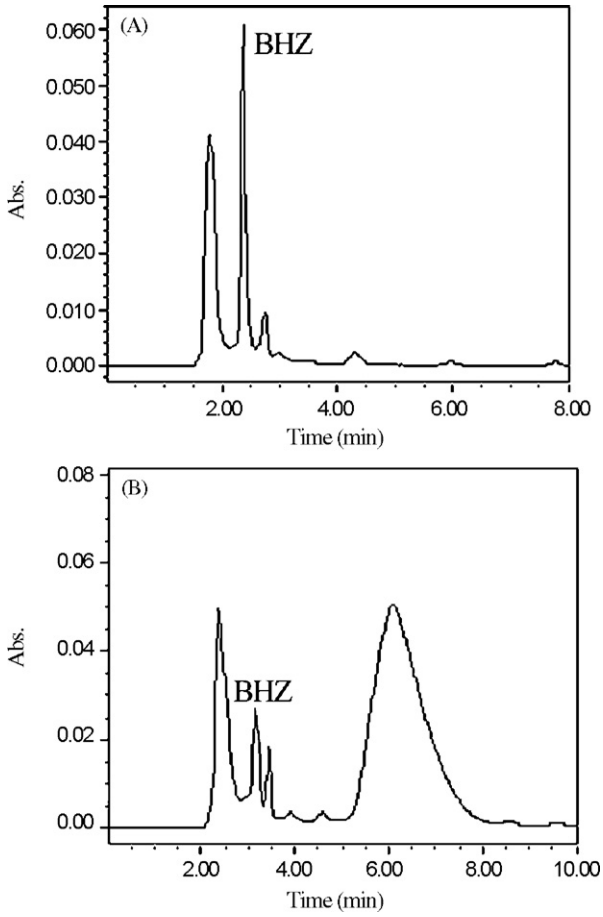


Fig. 6. HPLC chromatograms obtained after clean up a 50.0 μg L^{-1} solution of bromhexine (BHX) in urine samples with the (A) MIP and (B) NIP monitored at 245 nm; conditions: column ACE 5 μm, C18 4.6 mm × 250 mm at +40 °C, eluent acetonitrile:phosphate buffer (0.01 mol L^{-1}, pH 3.0) 25:75 at flow rate of 1.1 mL min^{-1}.

(1:3) mixture can elute interferences and avoid contaminating HPLC column. The chromatograms obtained for serum and urine samples were compared in Figs. 5 and 6. This efficient method allowed cleaner extracts to be obtained and interfering peaks arising from the complex biological matrices to be suppressed. Results from the HPLC analyses showed that the calibration curve of bromhexine for serum and urine samples are linear in the ranges 0.5–100 $\mu g\,L^{-1}$ and 1.5–100 $\mu g\,L^{-1}$ with good precision (3.3% for and 2.8% for 5.0 $\mu g\,L^{-1}$) and recoveries (between 92–96% and 93–97%), respectively (Table 2). Typical chromatograms presented in Figs. 5 and 6 reveal that the MIP can be used for clean up and when MIP sorbent was used, a board peak in chromatogram was omitted. The limit of detection (LOD) and limit of quantification (LOQ) for bromhexine in serum samples were 0.1 and 0.4 $\mu g\,L^{-1}$ respectively. These limits for bromhexine in urine samples were 0.3 and 1.0 $\mu g\,L^{-1}$ respectively.

4. Conclusions

In this paper for the first time, a novel bromhexine MIP was prepared by bulk polymerization. The bromhexine MIP showed higher molecular recognition than NIP on chromatographic evaluation. A SPE-HPLC method based on MIP has been developed for the extraction of bromhexine from aqueous solutions. Furthermore, the MIP particles as new sorbents in SPE were successfully investigated for the clean up of human serum and urine samples with an optimized procedure. This efficient method allowed cleaner extracts to be obtained and interfering peaks arising from the complicated biologic samples to be suppressed. The method was applied to the trace bromhexine determination at three levels, and the recoveries for the spiked human serum and urine samples were higher than 92% in the 5–25 $\mu g\,L^{-1}$. It could be concluded that the technique has great potential in developing selective extraction method for other compounds.

Acknowledgement

Financial support provided by the Amirkabir University of Technology (Tehran, Iran) is acknowledged.

References

[1] L. Parvez, M. Vaidya, A. Sakhardande, S. Subburaj, T.G. Rajagopalan, Pulm. Pharmacol. Ther. 9 (1996) 299.
[2] Z. Kopitar, R. Jauch, R. Hankwitz, H. Pelzer, Eur. J. Pharmacol. 21 (1973) 6.
[3] T. Perez-Ruiz, C. Martinez-Lozano, A. Sanz, S. Mondejar, J. Pharmaceut. Biomed. Anal. 13 (1995) 1101.
[4] A.C.B. Dias, J.L.M. Santos, J.L.F.C. Lima, E.A.G. Zagatto, Anal. Chim. Acta 499 (2003) 107.
[5] V. Tantishaiyakul, C. Poeaknapo, P. Sribun, K. Sirisuppanon, J. Pharmaceut. Biomed. Anal. 17 (1998) 237.
[6] M. Turchan, P. Jara-Ulloa, S. Bollo, L.J. Nunez-Vergara, J.A. Squella, A. Alvarez-Lueje, Talanta 73 (2007) 913.
[7] E. Sumarlik, G. Indrayanto, J. Liq. Chromatogr. R. T. 27 (2004) 2047.
[8] G. Bazylak, L.J. Nagels, J. Liq. Chromatogr. R. T. 32 (2003) 887.
[9] S.K. Lee, S.H. Choi, H.S. Kwak, Y.S. Kang, K.R. Chae, Eur. J. Pharm. Sci. 23 (2004) S39.
[10] B.P. Jensen, B. Gammelgaard, S.H. Hansen, J.V. Andersen, J. Anal. At. Spectrom. 20 (2005) 204.
[11] T. Pereze-Ruiz, C. Martineze-Lozano, A. Sanz, E. Bravo, J. Chromatogr. B 692 (1997) 199.
[12] M. Pospisilova, M. Polasek, V. Jokl, J. Pharm. Biomed. Anal. 24 (2001) 421.
[13] H. Okamoto, T. Nakajima, Y. Ito, T. Aketo, K. Shimada, S. Yamato, J. Pharm. Biomed. Anal 37 (2005) 517.
[14] A.P. De Leenheer, L.M.R. Vandecasteele-Thienpont, J. Chromatogr. 175 (1979) 301.
[15] Q. Jiang, F. Nie, J. Lu, Luminescence 23 (2008) 32.
[16] N.T. Abdel-Ghani, Y.M. Issa, H.M. Ahmed, Sci. Pharm. 74 (2006) 121.
[17] J.L. Kumar, W.C. Mann, A. Rozanski, J. Chromatogr. 249 (1982) 373.
[18] M. Johansson, S. Lenngren, J. Chromatogr. 432 (1988) 243.
[19] E. Bechgaard, A. Nielsen, J. Chromatogr. 228 (1982) 392.
[20] C.W. Huck, G.K. Bonn, J Chromatogr. A 885 (2000) 51.
[21] M.-C. Hennion, J. Chromatogr. A 856 (1999) 3.
[22] B. Sellergren (Ed.), Molecularly Imprinted Polymers: Man-Made Mimics of Antibodies and their Applications in Analytical Chemistry (Techniques and Instrumentation in Analytical Chemistry), vol. 23, Elsevier, Amsterdam, 2001.
[23] E. Caro, R. Marce, P. Cormack, D. Sherrington, F. Borrul, Anal. Chim. Acta 562 (2006) 145.
[24] S.G. Hu, L. Li, X.W. He, Prog. Chem. 17 (2005) 531.
[25] N. Masque, R.M. Marce, F. Borrull, Trends Anal. Chem. 20 (2001) 477.
[26] C. He, Y. Long, J. Pan, K. Li, F. Liu, J. Biochem. Biophys. Methods 70 (2007) 133.
[27] M. Walshe, J. Howarth, M.T. Kelly, R. O'Kennedy, M.R. Smyth, J. Pharm. Biomed. Anal. 16 (1997) 319.
[28] A. Zander, P. Findlay, T. Renner, B. Sellergren, A. Swietlow, Anal. Chem. 70 (1998) 3304.
[29] L.I. Andersson, A. Paprica, T. Arvidsson, Chromatographia 46 (1997) 57.
[30] M. Javanbakht, S. Eynollahi Fard, A. Mohammadi, M. Abdouss, M.R. Ganjali, P. Norouzi, L. Safaraliee, Anal. Chim. Acta 65 (2008) 612.
[31] M. Javanbakht, S. Eynollahi Fard, M. Abdouss, A. Mohammadi, M.R. Ganjali, P. Norouzi, L. Safaraliee, Electroanalysis 20 (2008) 2023.
[32] M. Javanbakht, N. Shaabani, A. Mohammadi, M. Abdouss, M.R. Ganjali, P. Norouzi, Curr. Pharm. Anal., in press.
[33] Y. Zhai, Y. Liu, X. Changa, S. Chena, X. Huanga, Anal. Chim. Acta 593 (2007) 123.
[34] R. Panahi, E. Vasheghani-Farahani, S.A. Shojaosadati, Biochem. Eng. J. 35 (2007) 352.
[35] M. Komiyama, T. Takeuchi, T. Mukawa, H. Asanuma, Molecular Imprinting: From Fundamentals to Applications, John Wiley & Sons, 2003.
[36] M. Zi-Hui, L. Qi, Anal. Chim. Acta 435 (2001) 121.
[37] C. Cacho, E. Turiel, A. Matrin-Esteban, C. Perez-Conde, C. Camara, J. Chromatogr. B 802 (2004) 347.

Talanta 80 (2009) 139–142

Contents lists available at ScienceDirect

Talanta

journal homepage: www.elsevier.com/locate/talanta

Determination of bismuth in solid samples by hydride generation atomic fluorescence spectrometry with a dielectric barrier discharge atomizer

Zhi Xing, Juan Wang, Sichun Zhang, Xinrong Zhang*

Key Laboratory for Atomic and Molecular Nanosciences of the Education Ministry, Department of Chemistry, Tsinghua University, Beijing 100084, PR China

ARTICLE INFO

Article history:
Received 30 March 2009
Received in revised form 11 June 2009
Accepted 15 June 2009
Available online 24 June 2009

Keywords:
Dielectric barrier discharge
Atomizer
Hydride generation
Atomic fluorescence spectrometry

ABSTRACT

An atmospheric pressure dielectric barrier discharge (DBD) atomizer was investigated for bismuth (Bi) determination with hydride generation (HG) atomic fluorescence spectrometry (AFS). The characteristics of the atomizer and the effects of experimental parameters, including observation height, discharge power, flow rate of discharge gas and AFS carrier gas were optimized. The linear range of present method for Bi determination is 0.5–300.0 $\mu g\,L^{-1}$ with a detection limit of 0.07 $\mu g\,L^{-1}$ (3σ). The method was validated by the analysis of reference materials (GBW08517 and GSB-14) and the results agreed well with the reference values. The established method was applied to the determination of Bi in ore, soil and ash samples.

© 2009 Elsevier B.V. All rights reserved.

1. Introduction

Although bismuth (Bi) is a relatively rare element in earth, large quantities of bismuth are produced annually in different areas, such as semiconductors, cosmetic products (e.g. pigments in eye shadow, lipsticks and hair dyes), medicines (such as for treatment of syphilis, peptic ulcers and dermatological disorders), alloys, by-product of copper and tin refining, metallurgical additives, and preparation and recycling of uranium in nuclear fuels [1]. There are many methods available for the determination of Bi at trace level, such as molecular spectrometry [2], inductively coupled plasma mass spectrometry (ICP-MS) [3], X-ray fluorescence spectrometry [4], nuclear techniques [5] and electrochemical techniques [6]. Especially, hydride generation (HG) coupled to atomic fluorescence spectrometry (AFS) [7,8] offers a useful tool for ultra-trace determination of hydride-generable elements including Bi [9,10]. Both excellent sensitivity and low cost make this method grow tremendously in recent years [11–14]. Normally, AFS was equipped with hydrogen–air and hydrogen–oxygen–argon combustion flame quartz furnace atomizer. For the sake of the high temperature and unenclosed nature of flame quartz furnace atomizer, it is difficult to make AFS become a miniaturized instrument for on-site, real time monitoring.

Recently, numerous studies have focused on the development of miniaturized instruments for the determination of trace elements [15,16]. Small atomization/ionization sources, based on inductively coupled plasma (ICP) [17,18], microwave-induced plasma (MIP) [19], laser-induced plasma [20], glow discharge (GD) [21], and the dielectric barrier discharge (DBD) [22], have been developed for this purpose. The advantages of small size, simplicity, low gas temperature, atmospheric operation and excellent dissociation capability made DBD plasma become an attractive technique when it is coupled with atomic absorption spectrometry (AAS) [23], atomic fluorescence spectrometry (AFS) [24], optical emission spectrometry (OES) [25], and mass spectrometry (MS) [26]. DBD is a suitable technique to develop an effective low-temperature atomizer for miniaturized AFS, since the DBD atomizer do not need a H_2 flame to atomize the hydride [24]. In previous studies, DBD used as atomizer coupled with AFS showed features of low operation temperature (between 44 and 70 °C, depending on the operation conditions), low power consumption and operation at atmospheric pressure, small size, simplicity of fabrication, and prevention of the contamination from the electrodes. This not only facilitates the treatment of the residue poisonous hydride, but also greatly reduces the gas consumption. However, previous work based on DBD microatomizer/microplasma [23–25,27] is focused on the determination of mercury and arsenic. It is still unknown that this new atomizer is capable of dissociating other hydride-forming elements, such as Bi. Therefore, it is still needed to further expand the applicable scope of the new atomization method.

In this work, a microplasma DBD atomizer combined with HG-AFS for the determination of Bi in solid environment samples has been proposed. After validation by the analysis of reference materials, the method has been applied to the quantitative analysis of Bi in ore, soil and ash samples. The results presented in this paper

* Corresponding author. Tel.: +86 10 62776888; fax: +86 10 62782485.
E-mail address: xrzhang@mail.tsinghua.edu.cn (X. Zhang).

0039-9140/$ – see front matter © 2009 Elsevier B.V. All rights reserved.
doi:10.1016/j.talanta.2009.06.038

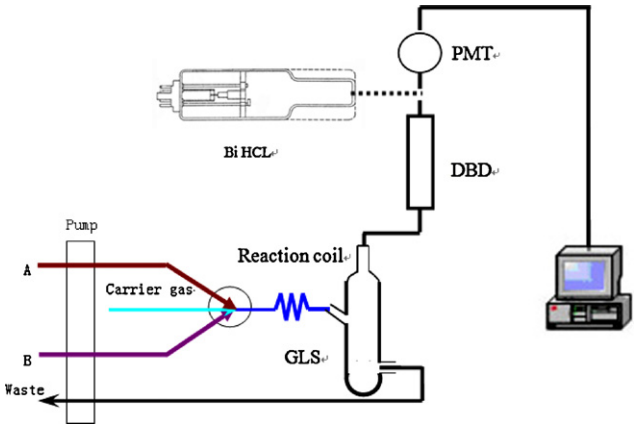


Fig. 1. The schematic diagram of the experiment setup of DBD–HG–AFS system. (A) Acidified sample or carrier solution and (B) KBH_4 solution.

show that the method is highly sensitive for the detection of Bi in real samples.

2. Experimental

2.1. Instrumentation

The AFS-3000 HG-AFS (KCHG Co. Ltd., China) fitted with a programmable intermittent reactor was employed in this study. The experimental set-up includes a sample introduction unit, a DBD chamber, a high-performance hollow cathode lamp (HCLs, Beijin Haiguang Co. Ltd., China) and a photomultiplier tube (Fig. 1). DBD power supplies were purchased from Coronalab (Coronalab Co. Ltd., China).

The gaseous hydrides were produced by mixing acidified samples and KBH_4 in 0.5% NaOH through a two-channel peristaltic pump into a Y conjunction. The hydrides were separated by a gas–liquid separator (GLS) and transported to DBD atomizer by Ar gas. The plasma atomization cell was positioned between the Bi hollow cathode lamp (HCL) and the detector (Photomultiplier Tube, PMT). The radiation from the Bi HCL was focused with a lens onto outlet of the atomization cell. The gaseous hydrides were decomposed by the plasma and the formed atoms were excited by radiation beam of Bi HCL at the outlet of DBD chamber. The fluorescence was collected at an angle of 90 °C with respect to the excitation beam. The operation conditions of the AFS were listed in Table 1 and the working program of the intermittent reactor was given in Table 2.

For the comparison of analytical results, a Thermo X II ICP-MS (Thermo Fisher Scientific, Bremen, Germany) was used for the determination of Bi in certified reference materials (CRMs) and real samples. A standard glass concentric nebulizer and a standard glass conical impact bead spray chamber were employed with a sample introduction rate of about 0.5 mL min^{-1}. The radio frequency power was set to 1200 W, and the coolant gas flow, nebulizer gas flow and auxiliary gas flow were set to 14, 0.84 and 0.7 L min^{-1} respectively.

Table 1
The parameters of AFS and DBD atomizer.

Parameters	Setting value
Lamp primary current	60 mA
Lamp boost current	30 mA
Negative high voltage of PMT	300 V
Flow rate of carrier gas	0.6 L min^{-1}
Discharge power	18.6 W
Flow rate of shield gas	5.3 L min^{-1}
KBH_4 concentration (m/v)	2%

Table 2
Program of the intermittent flow reactor.

	Step	Pump rate (rpm)	Time (*s*)	Function
1	Sample KBH_4 solution	120 100	10	Sample tube in sample solution
2	Sample KBH_4 solution	0 0	6	Sample tube in 5%HCl solution
3	5%HCl solution KBH_4 solution	120 120	16	Readout
4	5%HCl solution KBH_4 solution	0 0	6	Return to step 1

2.2. Reagents and samples

Bi standard solutions were prepared just before use by the dilution of the Bi stock solution (National Research Center for Certified Reference Material, China). The KBH_4 solution was prepared by dissolving KBH_4 (Beijing Chemicals Co., China) in a 0.5% (m/v) NaOH (Beijing Chemicals Co., China). Argon (99.99%) (Praxair Inc., Beijing, China) was used as the carried gas and shield gas. All the reagents in the present work were of analytical grade. Water was purified with a water purification system (Membrapure, Astacus, Germany).

2.3. Samples and sample pretreatment

To validate the accuracy of the developed method, the certified reference materials were obtained from the National Research Center for Certified Reference Material of China: Lamiaria Japonica Aresch GBW08517 (certified value 3.3 ± 0.4 mg kg^{-1}), and Laver GSB-14 (certified value 3.1 ± 0.4 mg kg^{-1}). Soil, ore and coal ash samples were also used for the validation of the method. Samples were decomposed using microwave-assisted digestion. Briefly, 0.5 g of the sample was added to Teflon vessels containing 9 mL HNO_3, 3 mL HCl and 1 mL HF. The Teflon vessels were closed tightly and put into the microwave oven for digestion. The heating program was 120 °C for 8 min and 180 °C for 8 min. After cooling to ambient temperature, the digests were then quantitatively transferred into Teflon crucibles and heated to almost dry on the electric hot plate at 160 °C. The residues were diluted with pure water and adjusted to the final composition containing 5% (v/v) HCl.

3. Results and discussion

The operation parameters of DBD–HG–AFS were optimized with respect to the DBD shield flow rate, observation height, discharge power, and flow rate of carrier gas. For the optimization studies, the peak area read mode was used and three replicate injections were made for each experimental condition.

3.1. Optimization of shield gas flow rate and observation height

The two key factors, which have effect on the fluorescence signal synchronously, were the shield gas flow rate and observation height of the DBD–HG–AFS. Intermittent flow injection was used in the optimization with standard solutions of 100 μg L^{-1} Bi. A single Ar stream was used as discharge shield gas owing to the lower fluorescence quenching and lower cost [8]. Fig. 2 shows the effects of observation height (4.5–10.5 mm) on the fluorescence signal intensity at different flow rate of shield gas (160–480 L h^{-1}). The maximum signal intensity was obtained with the shield gas flow rate of 320 L h^{-1} and the observation height of 7.5 mm. The lower flow rates than 320 L h^{-1} may cause the decrease of free atom population caused by oxygen contamination, while higher flow rates can lead to the dilution of the bismuth atoms in the Ar/H_2 flame.

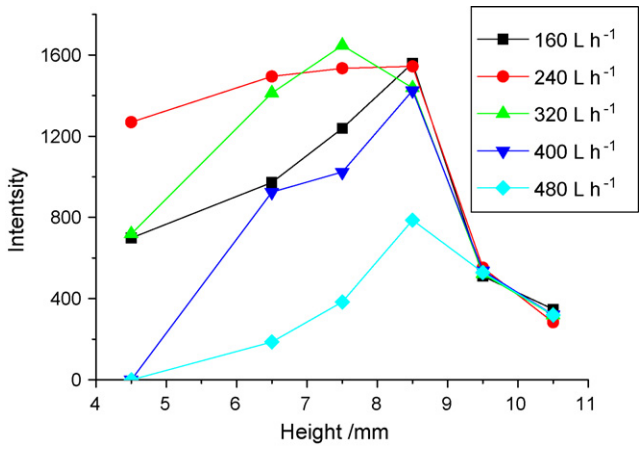


Fig. 2. The effect of observation height and flow rate of shield gas on the fluorescence signal intensities.

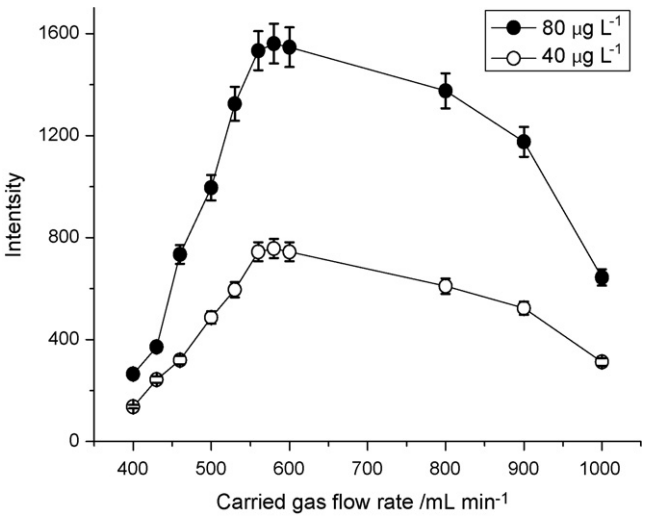


Fig. 3. Effect of the flow rate of carried gas on the fluorescence signal intensity.

[9] The signal intensity was sensitive to observation height, and the optimum observation height was found to be 7.5 mm probably due to the fine alignment of fluorescence light path.

3.2. Optimization of carried gas flow rate

The effect of carried gas flow rate (40–1000 mL min^{-1}) was optimized with standard solutions of 40 and 80 μg L^{-1} (Fig. 3). It was shown that increasing carried gas flow rate from 400 to 600 mL min^{-1} lead to the increase of signal intensity. After that, the signal decreased gradually. The maximum signal was obtained at 600 mL min^{-1} for both concentrations.

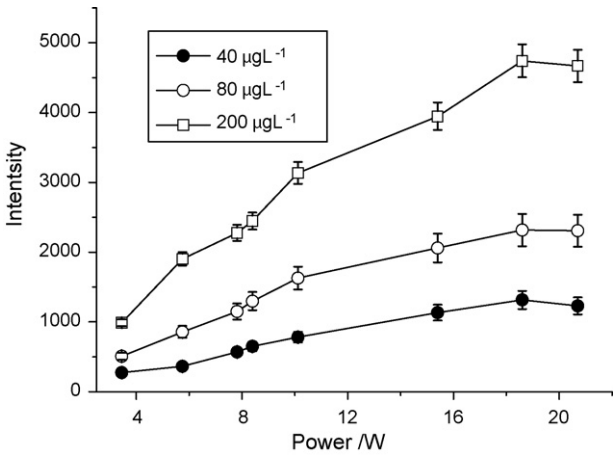


Fig. 4. Investigation of discharge power on the fluorescence signal.

3.3. Optimization of discharge power

A higher discharge power gives stronger signal intensity of Bi. The effects of discharge power (2–22 W) on the fluorescence signal of 40, 80 and 200 μg L^{-1} of Bi were shown in Fig. 4. The maximum fluorescence signal was observed at the power of 19 W. The plasma became unstable with observable flicker when the power is above 22 W.

3.4. Analytical performance

Using the peak area as quantitative parameter, the calibration curve of Bi concentration was linear over the range of 0.5–300 μg L^{-1}. The relative standard deviation for 10 and 50 μg L^{-1} Bi standard solution were 2.0% and 2.2% ($n = 11$) respectively. The limit of detection was 0.07 μg L^{-1}, calculated by the concentration of analyte producing a signal equal to three times the standard deviation of the blank (3σ).

3.5. Validation and sample analysis

To demonstrate the analytical accuracy of the present procedure, the use of HG–DBD–AFS for Bi determination was validated by the analysis of reference materials (Lamiaria Japonica Aresch GBW08517, and Laver GSB-14). The results were shown in Table 3 and the determined results are in agreement with the certified values, indicating the effectiveness of the established method.

The method was applied for the determination of Bi in soil, ore and coal ash samples. The results were given in Table 3. For comparison, results obtained by using ICP-MS were also given in Table 3. The results showed good agreement with the values of ICP-MS. The samples were also spiked with a standard Bi solution and recovery factors were found to be from 95.2 to 106.

Table 3
Analytical results of Bi in CRMs and real samples*.

Sample	Certified (mg kg^{-1})	ICP-MS (mg kg^{-1})	HG-AFS (mg kg^{-1})	Recovery (%)
GBW08517 (Lamiaria Japonica Aresch)	3.3 ± 0.4	2.97 ± 0.01	2.93 ± 0.06	106.3
GSB-14 (Laver)	3.1 ± 0.4	2.85 ± 0.02	2.85 ± 0.07	105.4
Ore	–	0.493 ± 0.007	0.490 ± 0.008	98.6
Soil	–	0.221 ± 0.004	0.21 6 ± 0.002	95.2
Coal ash	–	0.728 ± 0.003	0.71 5 ± 0.012	96.7

* Means ± s, $n = 3$.

Acknowledgements

We gratefully acknowledged the financial support from the Innovation Method Fund of China (No. 2008IM040600) and the NSFC (Nos. 20535020 and 20775041).

References

[1] A. Das, R. Chakraborty, M. Cervera, M. Guardia, Trends Anal. Chem. 25 (2006) 599.
[2] Z. Zhu, Fenxi Huaxue 23 (1995) 1467.
[3] J. Pavlickova, J. Zbiral, E. Cizmarova, V. Kuban, Anal. Bioanal. Chem. 376 (2003) 118.
[4] R. Schramm, GIT-Labor-Fachz 46 (2002) 444.
[5] J. Labrecque, L. Melo, P. Cordoves, F. Urbani, J. Radioanal. Nucl. Chem. 261 (2004) 343.
[6] M. Taher, E. Rzazeipour, D. Afzali, Talanta 63 (2004) 797.
[7] C. West, Anal. Chem. 46 (1974) 797.
[8] J. Winefordner, R. Elser, Anal. Chem. 43 (1971) 24A.
[9] R. Liu, P. Wu, K. Xu, Y. Lv, X. Hou, Spectrochim. Acta Part B 63 (2008) 704.
[10] O. Muñiz-Naveiro, R. Domĩınguez-Gonzaĩlez, A. Bermejo-Barrera, P. Bermejo-Barrera, J.A. Cocho, J.M. Fraga, Talanta 71 (2007) 1587.
[11] K. Thompson, G. Reynolds, Analyst 96 (1971) 771.
[12] K. Thompson, R. Goldden, Analyst 100 (1975) 544.
[13] M.N.M. Reyes, M.L. Cervera, R.C. Campos, M. Guardia, Talanta 75 (2008) 811.
[14] L.O. Leal, R. Forteza, V. Cerd'a, Talanta 69 (2006) 500.
[15] J. Franzke, M. Miclea, Appl. Spectrosc. 60 (2006) 80A.
[16] V. Karanassios, Spectrochim. Acta Part B 59 (2004) 909.
[17] A. Montaser, V.A. Fassel, Anal. Chem. 48 (1976) 1490.
[18] S.Y. Zhand, Z.B. Gong, B.L. Hung, Spectrosc. Spectral. Anal. 26 (2006) 331.
[19] Y. oki, E. Tashiro, M. Maeda, C. Honda, Y. Hasegawa, H. Futami, J. Izumi, K. Matsuda, Anal. Chem. 65 (1993) 2096.
[20] K. Niemax, A. Zybin, D. Eger, Anal. Chem. 73 (2001) 134A.
[21] N.G. Orellana-Velado, R. Pereiro, A. Sanz-Medel, J. Anal. Atom Spectrom. 13 (1998) 905.
[22] B. Eliasson, U. Kogelschatz, IEEE Trans. Plasma Sci. 19 (1991) 1063.
[23] Z. Zhu, S. Zhang, Y. Lv, X. Zhang, Anal. Chem. 78 (2006) 865.
[24] Z. Zhu, J. Liu, S. Zhang, X. Na, X. Zhang, Anal. Chim. Acta 607 (2008) 136.
[25] Y. Yu, Z. Du, M. Chen, J. Wang, Angew. Chem. Int. Ed. 47 (2008) 7909.
[26] N. Na, M. Zhao, S. Zhang, C. Yang, X. Zhang, J. Am. Soc. Mass Spectrom. 18 (2007) 1895.
[27] Z. Zhu, G.C.-Y. Chan, S.J. Ray, X. Zhang, G.M. Hieftje, Anal. Chem. 80 (2008) 8623.

Talanta 80 (2009) 143–150

Contents lists available at ScienceDirect

Talanta

journal homepage: www.elsevier.com/locate/talanta

Rapid determination of actinides in urine by inductively coupled plasma mass spectrometry and alpha spectrometry: A hybrid approach

Sherrod L. Maxwell III[a,*], Vernon D. Jones[b]

[a] Savannah River Nuclear Solutions, LLC, Building 735-B, Aiken, SC 29808, USA
[b] Savannah River Nuclear Solutions, LLC, Building 772-F, Aiken, SC 29808, USA

ARTICLE INFO

Article history:
Received 20 May 2009
Received in revised form 15 June 2009
Accepted 16 June 2009
Available online 24 June 2009

Keywords:
ICP-MS
Inductively coupled plasma mass spectrometry
Actinides
Alpha spectrometry
Rapid
Separations
Extraction chromatography

ABSTRACT

A new rapid separation method that allows separation and preconcentration of actinides in urine samples was developed for the measurement of longer lived actinides by inductively coupled plasma mass spectrometry (ICP-MS) and short-lived actinides by alpha spectrometry; a hybrid approach. This method uses stacked extraction chromatography cartridges and vacuum box technology to facilitate rapid separations. Preconcentration, if required, is performed using a streamlined calcium phosphate precipitation. Similar technology has been applied to separate actinides prior to measurement by alpha spectrometry, but this new method has been developed with elution reagents now compatible with ICP-MS as well. Purified solutions are split between ICP-MS and alpha spectrometry so that long- and short-lived actinide isotopes can be measured successfully. The method allows for simultaneous extraction of 24 samples (including QC samples) in less than 3 h. Simultaneous sample preparation can offer significant time savings over sequential sample preparation. For example, sequential sample preparation of 24 samples taking just 15 min each requires 6 h to complete. The simplicity and speed of this new method makes it attractive for radiological emergency response. If preconcentration is applied, the method is applicable to larger sample aliquots for occupational exposures as well. The chemical recoveries are typically greater than 90%, in contrast to other reported methods using flow injection separation techniques for urine samples where plutonium yields were 70–80%. This method allows measurement of both long-lived and short-lived actinide isotopes. ^{239}Pu, ^{242}Pu, ^{237}Np, ^{243}Am, ^{234}U, ^{235}U and ^{238}U were measured by ICP-MS, while ^{236}Pu, ^{238}Pu, ^{239}Pu, ^{241}Am, ^{243}Am and ^{244}Cm were measured by alpha spectrometry. The method can also be adapted so that the separation of uranium isotopes for assay is not required, if uranium assay by direct dilution of the urine sample is preferred instead. Multiple vacuum box locations may be set-up to supply several ICP-MS units with purified sample fractions such that a high sample throughput may be achieved, while still allowing for rapid measurement of short-lived actinides by alpha spectrometry.

© 2009 Elsevier B.V. All rights reserved.

1. Introduction

The use of nuclear power and the risks associated with nuclear proliferation have led to growing public concern about potential contamination of radioactive materials on the environment and on the health of individuals. Actinides are considered extremely hazardous radionuclides due to their chemical toxicity and high dose contribution for many of the isotopes. Even small quantities of actinides can cause can cause serious health hazards. The measurement of actinides in urine is not only important for occupational health monitoring but also in response to a radiological emergency event, such as the nuclear accident at Chernobyl or detonation of a radiological dispersal device (RDD) by terrorists. There is an increasing need to develop faster analytical methods with high sample throughput for emergency response, including emergency urine samples [1]. Rapid methods using extraction chromatography and alpha spectrometry have been reported by this laboratory for both emergency water and urine samples [2–4]. Inductively coupled plasma mass spectrometry (ICP-MS) is a versatile technique for elemental and isotopic analysis. The measurement time for sequential assay by ICP-MS is typically shorter than alpha spectrometry, although the alpha spectrometry measurements may be performed simultaneously with large numbers of detectors. ICP-MS is particularly effective for longer lived actinide isotopes, where alpha spectrometry works very well for short-lived actinide isotopes. Alpha spectrometry cannot differentiate well between alpha isotopes with overlapping alpha energies. Although alpha spectrometry can measure total ^{239}Pu + ^{240}Pu, for example, it cannot differentiate between ^{239}Pu and ^{240}Pu isotopes. In contrast, ^{239}Pu and ^{240}Pu are easily differentiated by ICP-MS. Actinide determination by ICP-MS, however, can be hampered by isobaric, polyatomic interferences and signal suppression [5]. Both mea-

* Corresponding author. Tel.: +1 803 952 7473; fax: +1 803 952 7881.
E-mail address: sherrod.maxwell@srs.gov (S.L. Maxwell III).

0039-9140/$ – see front matter © 2009 Elsevier B.V. All rights reserved.
doi:10.1016/j.talanta.2009.06.041

surement techniques may require separation of interferences to determine actinide isotopes accurately, depending on the sample matrix and the detection limit required. A variety of online and offline separation techniques have been reported in recent reviews for ICP-MS applications, covering a wide range of matrices (soil, sediment, water, biological and urine samples) [6]. This paper will focus more specifically on recent developments and progress with regard to assay of actinides in urine samples, but progress in rapid actinide separation techniques for urine have application to environmental and biological matrices as well.

A large number of flow injection techniques coupled with ICP-MS instrumentation have been reported for urine. Hang et al. using TRU Resin to separate actinides, but this work lacked the selectivity needed to measure actinides at ultra trace levels in urine, due to overlapping of actinide peaks [7]. Pappas et al. reported a rapid method for emergency response for Pu in 1 ml urine samples without digestion or coprecipitation before chemical separation. TEVA resin was used along with a desolvating introduction system to minimize the impact of $^{238}U^{1}H^{+}$ and other interferences at $m/z = 239$. The plutonium was eluted from TEVA Resin with 1 ml 1.4 M HF, after rinsing TEVA Resin with 0.8 M HNO_3. The reduction in uranium interference was significant, and the accuracy of Pu-239 in spiked urine samples was very good, but Pu-242 yield results were not reported. [8]. Epov et al. reported an automated preconcentration system using TRU Resin, but indicated that the separation of uranium from plutonium was not complete. In addition, the Pu yields using TRU Resin were variable and at times less than 50%, without yield correction using ^{175}Lu tracer. After correction using ^{175}Lu tracer, which was also retained on TRU Resin, the Pu recoveries were typically greater than 90%. Urine sample matrix effects were reduced with sample digestion, but this increased sample analysis time from 1 to 4 h for 5 samples [9]. Lariviere et al. reported an automated flow injection system using TEVA Resin with chemical yields averaging 83% for 10 ml urine sample aliquots, but when a co-precipitation step was added for larger sample aliquots, the chemical yield for Pu dropped to approximately 70% [5]. This system was very rapid and effective, but this work was limited to plutonium separation only. Zoriy, who used a similar calcium phosphate protocol for occupational health samples, also reported chemical yields of about 70% for plutonium in urine using TEVA Resin [10].

Varga et al. used alpha spectrometry to determine the relatively short-lived isotopes ^{241}Am and ^{238}Pu and inductively coupled plasma sector field mass spectrometry (ICP-SFMS) for ^{239}Pu, ^{240}Pu and ^{241}Am in small soil samples [11]. UTEVA and TRU Resins were used to separate Am and Pu fractions. The Pu strip solution (0.1 M ammonium bioxalate) and the Am strip solution (9 M HCl + 4 M HCl) from TRU Resin were evaporated to dryness multiple times and wet-ashed with concentrated HNO_3 and H_2O_2 to prior to analysis by ICP-SFMS and alpha spectrometry, increasing the sample preparation time.

Ayranov et al. reported a method which employed TOPO (tri-n-octylphosphine oxide) in cyclohexane liquid–liquid extraction combined with subsequent TRU Resin and TEVA Resin separations [12]. The initial separation using TOPO extraction was reported to be somewhat time-consuming, but more effective for removal of U and Th interferences than using the TRU Resin/TEVA Resin alone. The chemical yields for Pu and Am using this method were good. The Pu recoveries were greater than 90% by high resolution inductively coupled mass spectrometry (HR-ICP-MS), but 79.7% by alpha spectrometry. The Am recoveries were 87% by HR-ICP-MS, but 79% by alpha spectrometry. Pu was stripped from TEVA Resin using 0.02 M HNO_3–0.02 M HF, referencing a 1997 paper from this SRS laboratory [13].

TEVA Resin has been used in the Savannah River Site (SRS) Environmental Bioassay Laboratory for many years, with excellent recovery of Pu. The key to achieving quantitative elution for trace level Pu from TEVA Resin is the use of a reductant during the elution step to reduce Pu(IV) to unretained Pu(III) [1,14]. Our experience has been that TEVA Resin eluant strip solutions such as 0.02 M HNO_3–0.02 M HF work well for higher level Pu samples (nuclear process level samples), but not very well for low level Pu (environmental and bioassay samples). Low level Pu is not stripped effectively from TEVA Resin without the presence of a reductant in the eluant solution. With a reductant present, the stripping of Pu from TEVA Resin is quantitative.

Recently, the SRS lab participated in the NIST NRIP emergency response exercise and reported actinide results for emergency urine samples in 3–4 h. This rapid method employed calcium phosphate precipitation, stacked TEVA Resin and TRU Resin cartridges and alpha spectrometry with very rapid flow rates [3]. This work has shown that alpha spectrometry methods, using vacuum boxes and stacked cartridge technology, can be performed very rapidly. The goal of this work was to adapt this rapid separation technology for ICP-MS measurements of actinides in urine samples.

A new method has been developed in the Savannah River Site (SRS) Environmental Bioassay Laboratory to allow a flexible, hybrid approach for urine samples: the separation of longer lived actinide isotopes for measurement by ICP-MS and short-lived actinide isotopes by alpha spectrometry.

The rapid separation method uses stacked TEVA and TRU Resin cartridges, followed by DGA Resin to allow additional purification of Am/Cm isotopes and the use of a more desirable eluant for ICP-MS applications. If uranium separation is not required for measurement (direct dilution for U isotopes is used instead), TRU Resin is not required, and a stacked TEVA Resin plus DGA Resin column may be used. ^{239}Pu, ^{242}Pu, ^{237}Np, ^{243}Am, ^{234}U, ^{235}U and ^{238}U were measured by ICP-MS, while ^{236}Pu, ^{238}Pu, ^{239}Pu, ^{241}Am, ^{243}Am, and ^{244}Cm were measured by alpha spectrometry. The same column chemistry may be used with small or large urine aliquots. Direct urine aliquots (20 ml or less) may be analyzed with acidification, while large volume sample aliquots may be analyzed when a calcium phosphate preconcentration step is applied. The calcium phosphate precipitation has been streamlined such that it only adds about an hour to the sample preparation time. The goal of this work was to provide a rapid separation chemistry compatible with both alpha spectrometry and ICP-MS to offer maximum flexibility so that both short-lived and long-lived actinide isotopes can be measured using a complementary, hybrid approach.

2. Experimental

2.1. Reagents

The resins employed in this work are TEVA Resin® (Aliquat™336), TRU-Resin® (tri-n-butylphosphate (TBP) and N,N-diisobutylcarbamoylmethylphosphine oxide (CMPO)), and DGA Resin® (N,N,N′,N′ tetraoctyldiglycolamide), available from Eichrom Technologies, Inc., (Lisle, IL, USA). Nitric, hydrochloric and hydrofluoric acids were prepared from reagent-grade acids (Fisher Scientific, Inc., Pittsburgh, PA, USA). All water was obtained from a Milli-Q2™ water purification system. All other materials were ACS reagent grade and were used as received. Radiochemical isotopes ^{239}Pu, ^{242}Pu, ^{237}Np, ^{243}Am, ^{234}U, ^{235}U, ^{238}U ^{236}Pu, ^{238}Pu, ^{241}Am and ^{244}Cm were obtained from Analytics, Inc. (Atlanta, GA, USA) and diluted to the appropriate levels. The synthetic urine composition is shown in Table 1.

2.2. Procedures

2.2.1. Column preparation

TEVA, TRU, and DGA-Resin columns were obtained as cartridges containing 2 ml of each resin from Eichrom Technologies, Inc. (Lisle,

Table 1
Composition of the synthetic urine material.

	Reagent	CAS #	% Weight
$H_2C_2O_4{\cdot}2H_2O$	Oxalic acid	6153-56-6	0.002
Pepsin	Pepsin	9001-75-6	0.003
$CH_3CHOHCO_2H$	Lactic acid (liquid)	50-21-5	0.009
$MgSO_4{\cdot}7H_2O$	Magnesium sulfate	10034-99-8	0.044
$C_5H_{11}O_5CHO$	Glucose(dextrose)	50-99-7	0.046
Citric acid	Citric acid	77-92-9	0.051
$CaCl_2{\cdot}2H_2O$	Calcium chloride	10035-04-8	0.060
$C_9H_9NO_3$, 98%	Hippuric acid	495-69-2	0.060
$Na_2SiO_3{\cdot}9H_2O$	Sodium silicate	13517-24-3	0.007
NH_4Cl, 99%	Ammonium chloride	12125-02-9	0.101
$C_4H_9N_3O_2{\cdot}H_2O$	Creatine	6020-87-7	0.104
NaCl	Sodium chloride	7647-14-5	0.220
$NaH_2PO_4{\cdot}H_2O$	Sodium dihydrogen phosphate	10049-21-5	0.259
KCl	Potassium chloride	7447-40-7	0.325
Na_2SO_4	Sodium sulfate	7757-82-6	0.409
CH_4N_2O, 98%	Urea	57-13-6	1.517
HNO_3	Conc. nitric acid (50 ml)	7697-37-2	6.701
H_2O	Water		90.084

IL, USA). Small particle size (50–100 μm) resin was employed, along with a vacuum extraction system (Eichrom Technologies). Flow rates of 1–2 ml min^{-1} were typically used for this work.

2.2.2. Sample preparation

Two different approaches were used. A small volume urine aliquot (5 ml) was acidified to ~3 M HNO_3 and processed through the column chemistry. For large urine aliquots (100 ml), calcium phosphate co-precipitation was applied.

2.2.3. Sample preparation-No Co-precipitation

A 5 ml urine sample was aliquoted into a 50 ml plastic tube. Tracers were added and 1.5 ml 15.7 M HNO_3 was added to adjust the acidity of each sample to ~3 M HNO_3. The samples were swirled to mix each solution. Valence adjustment of the samples was performed by adding 0.25 ml 1.5 M sulfamic acid and 0.5 ml 1.5 M ascorbic acid with a 3-min wait step to reduce plutonium to Pu^{3+}. When ^{237}Np separation was desired, 0.05 ml 5 mg/ml Fe as ferric nitrate was also added to facilitate ^{237}Np reduction to Np^{4+}. The ferric ions are reduced to ferrous ions by the ascorbic acid, which reduces Np effectively to Np^{4+}. After the reduction step, 1 ml 3.5 M sodium nitrite was added to oxidize plutonium to Pu^{4+}. This column load solution was now ready for column separation as described below.

2.2.4. Sample co-precipitation

After the 100 ml urine sample aliquots were dispensed, 1 ml 1.25 M calcium nitrate (50 mg Ca) and 3 ml 3.2 M ammonium hydrogen phosphate were added to each sample. For samples, the sample dispensing and the above reagent additions were performed in 225 ml (urine) centrifuge tubes to save time. The pH was adjusted to ~pH 9.5 with concentrated ammonium hydroxide using a dark pink phenolphthalein endpoint. For darker urine samples, pH paper or a pH meter may be used. The samples were centrifuged at 3500 rpm for ~7 min. After discarding the supernatant, the precipitate was rinsed once with ~15–20 ml of water and centrifuged again at 3500 rpm for ~5 min. The precipitate was dissolved in 8 ml 6 M HNO_3 and 8 ml 2 M $Al(NO_3)_3$ directly in the centrifuge tubes. The final load solution contained 16 ml 3 M HNO_3 and 1 M $Al(NO_3)_3$. The aluminum nitrate was previously scrubbed to remove trace uranium by passing approximately 250 ml 2 M aluminum nitrate through a large column (Environmental Express, Mount Pleasant, SC, USA) containing ~7 ml of UTEVA Resin® (Eichrom Technologies) at ~10 ml/min. The column was prepared from a water slurry of the UTEVA resin. For the 100 ml samples, valence adjustment was performed by adding 0.5 ml 1.5 M sulfamic acid and 1.25 ml 1.5 M ascorbic acid with a 3-min wait step to reduce plutonium to Pu^{3+}. When ^{237}Np separation was desired, 0.4 ml of 5 mg/ml Fe as ferric nitrate was also added to facilitate ^{237}Np reduction to Np^{4+}. To oxidize plutonium to Pu^{4+}, 2 ml 3.5 M sodium nitrite was added to each sample solution. This column load solution was now ready for column separation.

2.2.5. Column separation

The following column separation was performed on small volume or large volume urine sample aliquots (Fig. 1). TEVA and TRU Resin cartridges were stacked on the vacuum box from top to bottom, in that order. Fifty-milliliter centrifuge tubes were used to collect rinse or final purified fractions.

After the valence adjustment, the sample solution was loaded onto the stacked column at approximately ~1 drop/s. After the sample was loaded, a tube rinse of ~ 5 ml 3 M HNO_3 was transferred to the stacked column and allowed to pass through the resin at ~1–2 drop/s. Years of experience in this laboratory has shown there are no channeling or performance issues with small particle resin cartridges going dry. A rinse of 5 ml 3 M HNO_3 was added directly to the stacked column at ~2 drop/s. The TRU Resin cartridges were removed and the TEVA cartridges were kept on the vacuum box. The TEVA cartridge was rinsed with 10 ml 3 M HNO_3 at ~2 drop/s to remove sample matrix components. To elute thorium from TEVA Resin, 15 ml 9 M hydrochloric acid was added at ~1–2 drop/s and discarded. An additional 10 ml 3 M HNO_3 rinse was added after the 9 M HCl rinse to minimize extractant bleedoff during the plutonium elution step and to reduce ICP-MS signal suppression, which may occur with a change in solution viscosity.

The plutonium was stripped from TEVA Resin with 14 ml 0.25 M hydrochloric acid–0.005 M hydrofluoric acid–0.0001 M titanium(III) chloride. The volume was adjusted after elution to exactly 15 ml with the same solution. Typically in this laboratory, when a tracer is used, no volume adjustment is made and 15 ml would be added directly to the column. Since no tracer was used to perform chemical yield adjustment for the ICP-MS measurements, the eluant volume was added in this way with a final volume adjustment to 15 ml after elution. The purified solutions were analyzed by alpha spectrometry and ICP-MS. Five milliliters of each plutonium/neptunium eluant solution was transferred to a separate 50 ml tube and 50 μg of cerium as cerium nitrate were added to the tubes, along with 1 ml concentrated hydrofluoric acid (49%). A 0.5 ml volume of 30 wt% hydrogen peroxide was added after the plutonium was eluted to oxidize any residual uranium to U^{6+} as a precaution. After waiting 15 min, the solutions were filtered onto 0.1 μm 25 mm polypropylene filters (Resolve® filter-Eichrom Technologies) and counted by alpha spectrometry. The remaining solution was transferred to the ICP-MS for Pu and Np measurement.

The TRU cartridges were placed on a separate vacuum box and processed at the same time as the TEVA Resin cartridges to save time. DGA Resin cartridges were placed below each TRU Resin cartridge. Americium/curium was eluted from TRU Resin onto DGA Resin with 15 ml 4 M HCl at ~1–2 drop/s. The TRU Resin cartridges were removed and the DGA Resin was rinsed with 3 ml 1 M HNO_3, then 5 ml of 0.1 M HNO_3 at ~1 drop/s to remove any residual uranium. Am and Cm were eluted using 9.5 ml of 0.25 M HCl at ~1 drop/s. The volume was adjusted after elution to exactly 10 ml with the same solution for reasons described previously. Two milliliters of each solution was transferred to a separate 50 ml tube containing ~10 ml of 0.25 M HCL and 50 μg of cerium as cerium nitrate were added to the tubes, along with 1 ml of concentrated hydrofluoric acid (49%), and filtered after about 15 min to prepare alpha spectrometry mounts. The remaining solution was transferred to the ICP-MS for Am measurement.

Uranium was stripped from TRU Resin using 14 ml 0.01 M ammonium bioxalate at ~1–2 drop/s. The volume was adjusted after elution to exactly 15 ml with the same solution. If uranium sep-

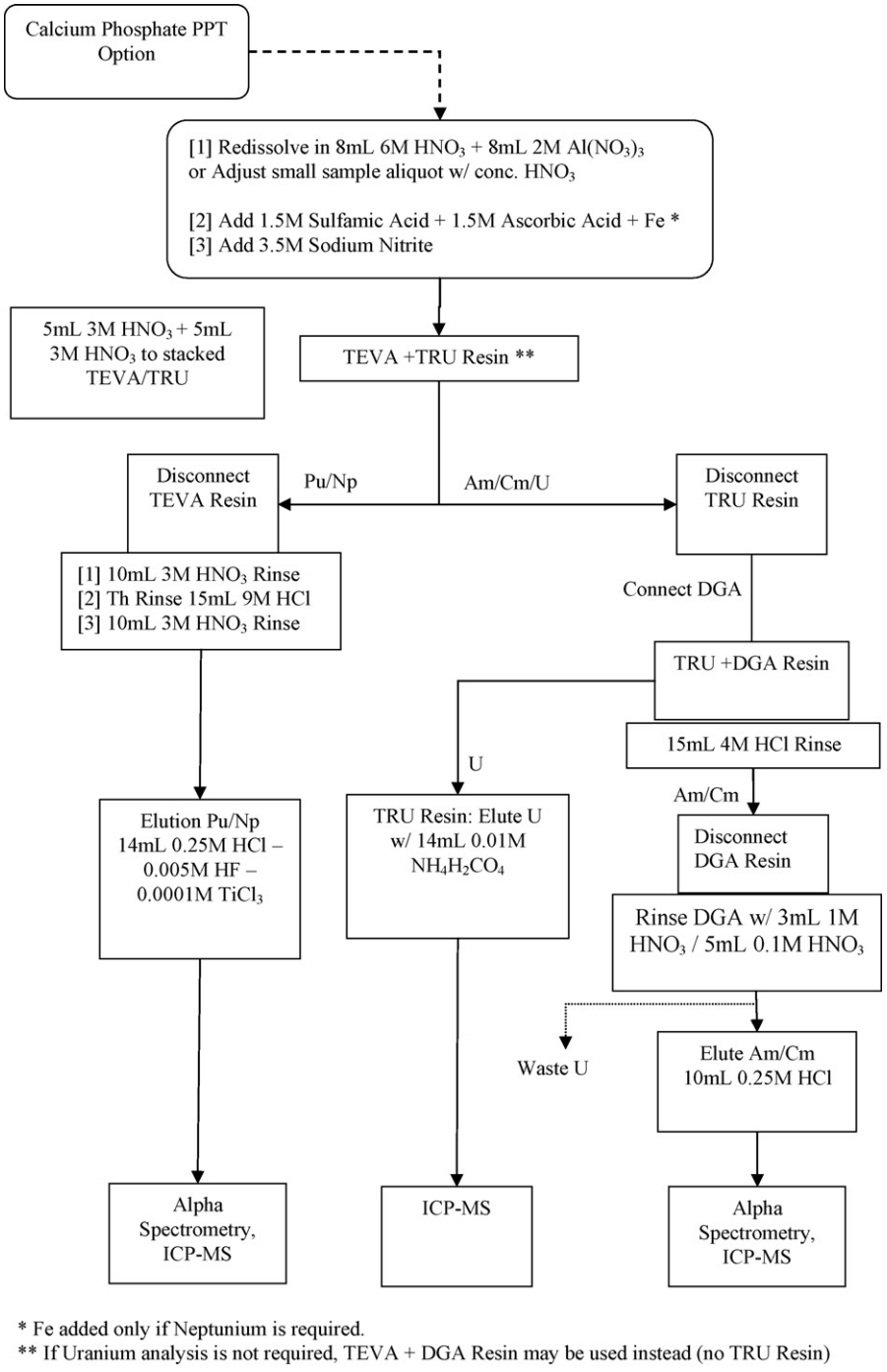


Fig. 1. Flow chart of rapid column extraction method for urine.

aration and measurement is not required, TRU Resin is not needed, and TEVA and DGA Resins can be stacked in tandem without TRU Resin. An increased rinse volume of DGA Resin (15 ml 0.1 M HNO_3 vs 5 ml HNO_3) can be used to remove uranium if TRU Resin is not in place to collect U. It would be possible to strip Am/Cm directly from TRU Resin without DGA Resin but this would require a strong acid such as 4 M HCl, which would typically have to be diluted or evaporated and wet-ashed prior to analysis using ICP-MS. DGA allows Am/Cm elution with 0.25 M HCl, which is more compatible with ICP-MS, and can provide additional uranium removal if needed.

Actinide filters were counted by alpha spectrometry for approximately 16 h, but shorter count times (<1 h) can also be performed for emergency response samples using higher level tracers [2], depending on the detection limit needed.

2.3. Apparatus

Plutonium, americium, and uranium measurements were performed by alpha-particle pulse-height measurements using Passivated Implanted Planar Silicon (PIPS) detectors. Polycarbonate vacuum boxes with 24 positions and a rack to hold 50 ml plastic tubes were used. Two boxes were connected to a single vacuum source by using a T-connector and individual valves on the tubing to each box.

An Agilent Quadrupole ICP-MS was used to perform the ICP-MS measurements. The instrument operating conditions are shown in Table 2.

The ICP-MS methodology is described in "Standard Practice for Alternate Actinide Calibration for Inductively Coupled Plasma-Mass

Table 2
Operating conditions for Agilent 7500 ICP-MS.

Plasma conditions	
RF power	1300 W
RF matching	1.7 V
Torch depth	6 mm
Plasma gas	15 l/min
Carrier gas	1 l/min
Sample pump	0.1 rps
Ion lenses	
Extract 1	−195 V
Extract 2	−100 V
Einzel 1, 3	−100 V
Einzel 2	18 V
Omega bias	−33 V
Omega (+)	11 V
Omega (−)	8 V
QP focus	12 V
Plate bias	−36 V
Q-pole	
AMU gain	122
AMU offset	124
Axis gain	0.999
Axis offset	0.04
QP bias	0 V
Detector	
Discriminator	8.7 V
Analog HV	1820 V
Pulse HV	1230 V
Typical tune	
Counts	>100,000 cps Tl-205 at 10 μg/l
RSD%	<5%
Oxide 156/140	<1%
Background	<10 cps at Tl-205
Resolution	0.65–0.80 amu at 10% peak height
Data acquisition	
Integration	0.33 s/pt., 3 pt/amu, 0.99 s/amu
Replicates	6

Spectrometry" [15]. The calibration is mass bias adjusted using thorium-232 (^{232}Th) and uranium-238 (^{238}U) standards. At each standard concentration, the slope of the line defined by ^{232}Th and ^{238}U is used to derive linear calibration curves for each mass of interest (232–244 amu) using interference equations. The mass bias corrected calibration curves, although generated from interference equations, are specific to the instrument operating parameters and tuning in effect at the time of data acquisition. One of the benefits of this standard practice is the ability to calibrate for the analysis of highly radioactive actinides using calibration standards at much lower specific activities.

3. Results and discussion

The rapid separation of actinides was performed on ten 100 ml urine samples. Samples 1–5 were blank human urine, while samples 6–10 were synthetic urine samples. Known amounts of actinide isotopes were added to each sample. Calcium phosphate precipitation, as described above, was applied to all 10 samples. Samples were analyzed for short-lived isotopes by alpha spectrometry and longer lived actinide isotopes were analyzed by ICP-MS. ^{239}Pu and ^{243}Am isotopes were measured by both ICP-MS and alpha spectrometry techniques. The results for the determination of Am–Cm isotopes by alpha spectrometry are shown in Table 3. The average tracer recovery for ^{243}Am was 105% (±2.5% RSD), with an average measured value for ^{243}Am of 72.0 mBq (−2.65% bias) and an average measured value for ^{244}Cm of 65.4 mBq (+2.14% bias). The ^{241}Am and ^{244}Cm results were corrected for the ^{243}Am tracer recoveries in each sample. The Am/Cm recoveries were excellent, with high chemical yield and very little bias for ^{241}Am and ^{244}Cm.

Table 3
Am and Cm isotope results by alpha spectrometry.

	^{243}Am % Recovery	^{241}Am mBq	^{244}Cm mBq
1	104.1	73.3	62.5
2	102.9	65.5	71.0
3	108.2	72.2	61.8
4	102.2	72.5	72.2
5	105.6	72.5	66.2
6	108.6	68.5	59.6
7	108.3	79.9	64.0
8	103.3	77.0	65.5
9	101.9	70.3	59.2
10	105.2	68.8	71.8
Avg.	105.03	72.0	65.4
% RSD	2.5	5.8	7.5
	Reference	74.0	64.0
	% Difference	−2.65	2.14

Table 4
Pu isotope results by alpha spectrometry.

	^{236}Pu % Recovery	^{238}Pu mBq	^{239}Pu mBq
1	96.7	70.3	939.8
2	110.5	61.4	769.6
3	91.0	77.3	917.6
4	115.3	67.0	762.2
5	99.1	79.2	880.6
6	98.0	74.7	895.4
7	81.7	91.0	950.9
8	98.9	72.5	817.7
9	108.9	64.4	717.8
10	89.8	79.2	888.0
Avg.	99.0	73.7	854.0
% RSD	10.4	11.7	9.5
	Reference	72.9	832.5
	% Difference	1.12	2.58

The results for the Pu isotopes by alpha spectrometry are shown in Table 4. The average tracer recovery for ^{236}Pu was 99.0% (±10% RSD). The average result for ^{238}Pu was 73.7 mBq (1.12% bias) and the average result for ^{239}Pu was 854 mBq (2.58% bias). The MDA using alpha spectrometry, which is dependent on sample volume used and count time, can be adjusted as needed for emergency or routine samples [3].

The Pu and Np isotope results by ICP-MS are shown in Table 5. The average ^{239}Pu result at the ICP-MS was 0.0252 ng/ml (4.02% bias) and the average ^{242}Pu result was 0.1366 ng/ml (−0.01% bias). The Pu results by ICP-MS were not corrected for tracer, but instead were corrected for a negative bias at the ICP-MS observed on a Pu standard in the same matrix that did not undergo column separation. This bias was only seen on this particular analysis run and does not seem to be caused by the eluant matrix, which has been used previously with no negative bias. Tracer correction using ^{242}Pu would have also corrected for the bias observed for this analysis run. The average result for ^{237}Np was 0.1829 ng/ml (0.24% bias), indicating excellent recovery of ^{237}Np as well. Six additional 100 ml urine samples were analyzed for Pu isotopes by ICP to verify that the Pu eluant matrix does not cause a significant negative bias at the ICP-MS. Table 6 shows the Pu results by ICP-MS from this test. The average ^{239}Pu result was 0.0447 ng/ml (−7.71% bias) and the average ^{242}Pu result was 0.1278 ng/ml (−6.42%), indicating the Pu eluant matrix does not cause any significant bias at the ICP-MS and confirming that the method provides a high chemical yield for plutonium. Tracer correction using ^{242}Pu could have been applied, if desired, and an even smaller negative bias would have resulted.

Table 5
Pu and Np isotope results by ICP-MS.

	^{237}Np ng/ml	^{239}Pu ng/ml	^{242}Pu ng/ml
1	0.1790	0.0233	0.1511
2	0.1649	0.0211	0.1357
3	0.1666	0.0226	0.1319
4	0.1684	0.0189	0.1434
5	0.1821	0.0253	0.1431
6	0.1915	0.0241	0.1325
7	0.1910	0.0246	0.1268
8	0.1990	0.0294	0.1376
9	0.1903	0.0374	0.1293
10	0.1968	0.0251	0.1344
Avg.	0.1829	0.0252	0.1366
% RSD	6.62	19.31	5.15
Reference	0.1825	0.0242	0.1366
% Difference	0.24	4.02	−0.01

Pu results corrected by result of direct Pu standard vs. calibration. Concentration (ng/ml) in final solution at ICP-MS.

Table 6
Pu isotope results by ICP-MS.

	^{239}Pu ng/ml	^{242}Pu ng/ml
1	0.0440	0.1260
2	0.0440	0.1270
3	0.0450	0.1260
4	0.0450	0.1280
5	0.0440	0.1280
6	0.0460	0.1320
Avg.	0.0447	0.1278
% RSD	1.67	1.59
Reference	0.0484	0.1366
% Difference	−7.71	−6.42

No correction made for direct Pu standard vs. calibration. Concentration (ng/ml) in final solution at ICP-MS.

Fig. 2 shows the ^{209}Bi internal standard measurements for the same set of six urine samples analyzed for Pu isotopes by ICP-MS. There is a slight reduction in ^{209}Bi internal standard signal for the urine samples in the Pu sample eluant matrix (avg. = 1.24E6 cps) compared to the 1% nitric acid blanks (avg. = 134E6 cps) analyzed along with the samples. This is only a 7.5% reduction in internal standard signal, well within the normal range of instrument drift, demonstrating minimal potential impact on signal reduction using the Pu eluant matrix (0.25 M HCL–0.005 M HF–0.0001 M $TiCl_3$) without dilution. The decontamination factor (DF) from uranium is very good using TEVA Resin, with sufficient rinsing with 3 M HNO_3 to remove U. The amount of U-238 found in most of the Pu fractions was not detectable by ICP-MS. The DF for uranium was estimated at >1000, which is typical for a single column extraction chromatography separation.

Table 7 shows Am-243 isotope results by ICP-MS. The Am-241 and Cm-244 levels were too low to determine, but the Am-243 measurements were very good. The average ^{243}Am result at the ICP-MS was 0.0244 ng/ml (−2.44% bias). No chemical yield correction was applied. This test demonstrates that Am can be measured by ICP-MS using this method, including ^{241}Am if the ICP-MS used had sufficient sensitivity. The decontamination factor from uranium is excellent because the Am and Cm is moved from TRU Resin to DGA Resin, with a additional rinsing prior to elution of Am and Cm. The average amount of U-238 found in the Am fraction was 0.0013% (DF = ~75,000). The Am/Cm eluant strip solution for DGA, 0.25 M HCl, was analyzed directly by ICP-MS without evaporation or wet-ashing. As noted earlier, if U measurement is not required, a stacked column using TEVA Resin + DGA Resin may be used instead. The only change in protocol is increased rinsing of DGA with 0.1 M HNO_3 to ensure adequate uranium removal from DGA.

The results for ^{238}U by ICP-MS are shown in Table 8. The first five results from human urine sample show an average result for ^{238}U of 3.556 ng/ml at the ICP-MS (6.79% bias), while the synthetic urine sample showed a significant positive bias. It was found that the synthetic urine had ^{238}U content in the blank solution of

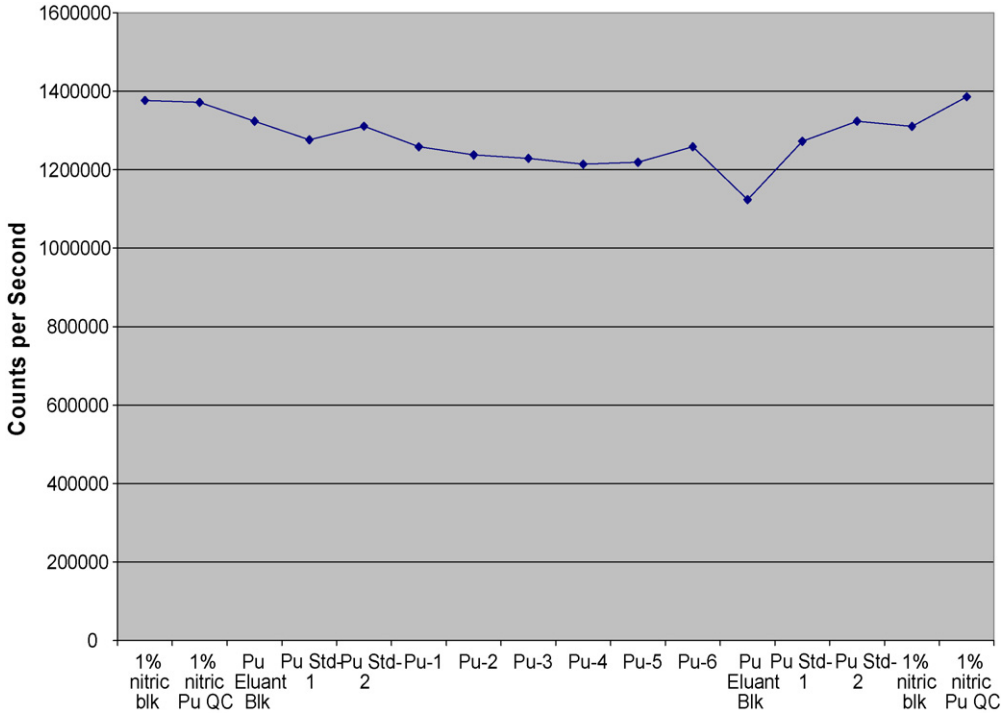


Fig. 2. ^{209}Bi internal standard response for Pu samples by ICP-MS.

Table 7
Am isotope results by ICP-MS.

	^{243}Am ng/ml
1	0.0238
2	0.0240
3	0.0253
4	0.0249
5	0.0252
6	0.0239
7	0.0245
8	0.0250
9	0.0223
10	0.0250
Avg.	0.0244
% RSD	3.58
Reference	0.025
% Difference	−2.44

Concentration (ng/ml) in final solution at ICP-MS.

Table 8
^{238}U results on urine samples by ICP-MS.

Human urine			
	^{238}U ng/ml		
1	3.671		
2	3.554		
3	3.605		
4	3.546		
5	3.406		
Average	3.556		
% RSD	2.75		
Reference	3.33		
% Difference	6.79		
Synthetic urine			
	^{238}U ng/ml	Blank ng/ml	[a]Net ^{238}U ng/ml
6	5.355	1.79	3.565
7	5.475	1.79	3.685
8	5.511	1.79	3.721
9	5.782	1.79	3.992
10	5.554	1.79	3.764
Average	5.535		3.745
% RSD	2.83		4.18
Reference	3.33		3.33
% Difference	66.22		12.46

Concentration (ng/ml) in final solution at ICP-MS.
[a] U-238 corrected for U-238 content in blank synthetic urine.

1.79 ng ^{238}U/ml. After the sample results were corrected for this uranium content in the unspiked synthetic urine the result was reduced from 5.54 to 3.74, only a 12.5% positive bias.

Table 9 shows uranium isotope results from the analysis of an emergency urine sample received from the National Institute of Standards and Technology (NIST). Five ml replicate sample aliquots were analyzed without calcium phosphate preconcentration. The average result for ^{234}U was 0.0036 ng/ml (13.28% bias). This result is very good, considering the shorter half life of ^{234}U and the low level of ^{234}U present. The average result for ^{235}U was 0.4296 ng/ml (−0.44%) and the average ^{238}U measured value was 60.99 (2.71% bias). The other shorter lived actinide isotopes (^{238}Pu, ^{241}Am) in the NIST emergency exercise samples were too low to measure by ICP-MS with the 5 ml aliquots analyzed. This illustrates the value of rapid calcium phosphate precipitation preconcentration step to improve detection limits. Other shorter lived actinide isotopes

Table 9
U isotopes results on NIST emergency urine samples by ICP-MS.

	^{234}U ng/ml	^{235}U ng/ml	^{238}U ng/ml
1	0.0036	0.4593	63.32
2	0.0040	0.4576	63.45
3	0.0033	0.4440	61.76
4	0.0036	0.4191	58.02
5	0.0038	0.4460	60.82
6	0.0035	0.4093	56.73
7	0.0029	0.3877	54.38
8	0.0043	0.4136	56.22
Avg.	0.0036	0.4296	59.34
% RSD	11.77	6.02	5.83
Reference	0.0032	0.4315	60.99
% Difference	13.28	−0.44	−2.71

Concentration (ng/ml) in final solution at ICP-MS.

Table 10
LLD and LLQ ICP-MS results using 100 ml sample aliquots.

	^{237}Np ng/ml	^{238}U ng/ml	^{239}Pu ng/ml	^{242}Pu ng/ml	^{243}Am ng/ml
Overall method LLD	5.4E-03	6.7E-02	1.3E-03	2.4E-03	2.6E-04
Overall method LLQ	1.8E-02	2.2E-01	4.3E-03	7.9E-03	8.6E-04

Table 11
LLD and LLQ ICP-MS results using 5 ml sample aliquots.

	^{234}U ng/ml	^{235}U ng/ml	^{238}U ng/ml
Overall method LLD	3.8E-03	2.3E-01	3.1E+01
Overall method LLQ	1.3E-02	7.8E-01	1.0E+02

(^{238}Pu, ^{241}Am) present in the NRIP urine samples were too low to determine using ICP-MS using a 5 ml sample aliquot.

Table 10 shows method LLD and LLQ values for the different isotopes by ICP-MS using a 100 ml sample aliquot. The LLD and LLQ results were calculated using the equations as prescribed by Taylor [17]. These method LLD and LLQ results include a preconcentration factor of 6.67 for all the isotopes except the ^{243}Am results, which include a preconcentration factor of 10. The LLD and LLQ results can be lowered by increasing the sample aliquots as needed. Table 11 shows method LLD and LLQ values for the uranium isotopes by ICP-MS using a 5 ml direct sample aliquot. These method LLD and LLQ results include a dilution factor of 1/3 when a 5 ml aliquot is taken, increasing the LLD and LLQ. The LLD and LLQ results can be lowered by increasing the sample aliquots as needed. The ^{238}U LLD and LLQ values are likely higher due to slight ^{238}U contamination, which may have added variability to the ^{238}U measurements.

The MDA (Minimum Detectable Activity) for the actinide isotopes by alpha spectrometry were calculated according to equations prescribed by Currie [16]:

$$\mathrm{MDA} = \frac{3 + 4.65\sqrt{B}}{\mathrm{CT} \times R \times V \times \mathrm{EFF} \times 0.060}$$

where B = total background counts, =BKG (rate) × BKG count time; CT = sample count time (min); R = chemical recovery; V = sample volume (l); EFF = detector efficiency; 0.060 = conversion from dpm to mBq

In low-level counting, where a zero background count is quite common, the constant 3 is used to prevent an excessively high false positive rate.

The MDA for the alpha spectrometry results can be adjusted as needed, depending on the sample aliquot and count time. Pappas has established the ^{239}Pu action level as 4.8 mBq l^{-1} based on a single dose exposure of 500 mSv [5]. For a 100 ml sample aliquot,

the MDA for a 2 h count time is 16.3 mBq l^{-1}. For a 400 ml sample aliquot and 2 h count time the MDA is 4.07 mBq l^{-1}. For a 100 ml sample aliquot, the MDA for a 22 h count time is 1.5 mBq l^{-1}. For a 400 ml sample aliquot and 22 h count time the MDA is 0.37 mBq l^{-1}. Depending on the MDA required, the sample aliquot and count time may be adjusted accordingly.

The rapid column separation is compatible with ICP-MS or alpha spectrometry and can be used with or without calcium phosphate preconcentration. The chemical yields were very good and the accuracy and precision of the measurements on the actinide isotopes spiked into the urine samples standards were excellent. The trace level titanium chloride (0.0001 M) used in the plutonium stripping solution effectively reduces Pu to Pu^{3+} for effective elution of Pu from TEVA Resin without adversely affecting the ICP-MS assay. The 0.25 M HCl and 0.01 M ammonium bioxalate eluting reagents are also very compatible with ICP-MS.

The vacuum box column separation system is a low budget alternative to flow injection separation techniques. This stacked cartridge approach provides rapid flow rates and effective removal of spectral and other sample matrix interferences for a large number of samples prepared simultaneously. The separation method is flexible and can be adapted to fit specific analytical needs. For example, if uranium separation is not required, TRU Resin is not required in the separation method. Direct urine aliquots up to ~20 ml may be analyzed with acidification, while calcium phosphate coprecipitation may be applied to very large urine aliquots as needed. Multiple vacuum box locations can be used to prepare a large number of samples in an emergency that can be analyzed by alpha spectrometry and/or ICP-MS. Tracer corrections were not applied to the ICP-MS results to highlight the high chemical yields and minimal sample matrix impacts observed, but tracer corrections may be easily applied as needed.

4. Conclusions

A new rapid separation method that allows separation and preconcentration of actinides in emergency or routine urine samples was developed for the determination of longer lived actinides by inductively coupled plasma mass spectrometry (ICP-MS) and short-lived actinides by alpha spectrometry, a hybrid approach. This method uses stacked extraction chromatography cartridges and vacuum box technology to facilitate rapid separations. The method can be used with small acidified urine aliquots or using a streamlined calcium phosphate co-precipitation to preconcentrate actinides in larger sample aliquots. Similar technology has been applied to separate actinides prior to measurement by alpha spectrometry, but this new method has been developed with elution reagents now compatible with ICP-MS as well. The ASTM standard practice for alternate actinide ICP-MS calibration is a good analytical fit with the separation methods described. A single mass bias corrected calibration based on ^{232}Th and ^{238}U enables rapid ICP-MS determination of a suite of actinide isotopes. Purified solutions are split between ICP-MS and alpha spectrometry so that long and short-lived actinide isotopes can be measured successfully. The method is rapid, flexible, offers high chemical recoveries, excellent removal of interferences and can be used to provide high sample throughput in a radiological emergency.

Acknowledgments

This work was performed under the auspices of the Department of Energy, DOE Contract No. DE-AC09-96SR18500. The authors wish to acknowledge Rebecca Chavous for her assistance with this work.

References

[1] D.L. Stricklin, et al., J. Radioanal. Nucl. Chem. 251 (1) (2002) 69.
[2] S. Maxwell, et al., J. Radioanal. Nucl. Chem. 275 (3) (2008) 497.
[3] S. Maxwell, et al., J. Radioanal. Nucl. Chem. 279 (1) (2009) 105.
[4] S. Maxwell, et al., J. Radioanal. Nucl. Chem. 279 (3) (2009) 901.
[5] D. Larivere, et al., J. Anal. At. Spectrom. 23 (2008) 352.
[6] C.S. Kim, et al., J. Anal. At. Spectrom. 22 (2007) 827.
[7] W. Hang, et al., J. Anal. At. Spectrom. 19 (2004) 966.
[8] R.S. Pappas, et al., J. Anal. At. Spectrom. 19 (2004) 762.
[9] V. Epov, et al., J. Anal. At. Spectrom. 20 (2005) 424.
[10] M. Zoriy, et al., Int. J. Mass Spectrom. 232 (2004) 217.
[11] Z. Varga, et al., Radiochim. Acta 95 (2007) 81.
[12] M. Aryanov, et al., Radiochim. Acta 93 (2005) 249.
[13] S. Maxwell, et al., Radioact. Radiochem. 8 (2000) 28.
[14] S. Maxwell, et al., Radioact. Radiochem. 8 (1997) 36.
[15] V. Jones, American Society for Testing and Materials (ASTM), vol. 12.01, C1590-04, 2004.
[16] L.A. Currie, Anal. Chem. 40 (1968) 586.
[17] J.K. Taylor, Quality Assurance of Chemical Measurements, Chapter 9—Principles of Measurement, Section—Limit of Detection and Limit of Quantitation, Lewis Publishers, 1987.

Talanta 80 (2009) 151–157

Contents lists available at ScienceDirect

Talanta

journal homepage: www.elsevier.com/locate/talanta

Utility of certain σ- and π-acceptors for the spectrophotometric determination of ganciclovir in pharmaceutical formulations

Ayman A. Gouda*

Chemistry Department, Faculty of Science, Zagazig University, Zagazig 44519, Egypt

ARTICLE INFO

Article history:
Received 28 March 2009
Received in revised form 17 June 2009
Accepted 17 June 2009
Available online 25 June 2009

Keywords:
Ganciclovir
Charge–transfer complexes
Spectrophotometry
Pharmaceutical analysis

ABSTRACT

Studies were carried out, for the first time, to investigate the charge–transfer reactions of ganciclovir as n-electron donor with the σ-acceptor iodine and various π-acceptors: 7,7,8,8-tetracyanoquinodimethane; tetracyanoethylene; 2,3-dichloro-5,6-dicyano-1,4-benzoquinone; *p*-chloranilic acid; 2,3,5,6-tetrabromo-1,4-benzoquinone; 2,3,5,6-tetrachloro-1,4-benzoquinone and 2,4,7-trinitro-9-fluorenone. The formation of the colored charge–transfer complexes was utilized in the development of simple, rapid and accurate spectrophotometric methods for the analysis of ganciclovir in pure form as well as in its pharmaceutical formulation (capsules). Different variables affecting the reactions were studied and optimized. Under the optimum reaction conditions, linear relationships with good correlation coefficients (0.9993–0.9998) were found between the absorbance and the concentration of ganciclovir in the range of 2.0–240 μg mL^{-1}. For more accurate analysis, Ringbom optimum concentration range was found to be between 5.0 and 225 μg mL^{-1}. The limits of detection ranged from 0.36 to 2.45 μg mL^{-1} and the limits of quantification ranged from 1.20 to 8.17 μg mL^{-1}. A Job's plot of the absorbance versus the molar ratio of ganciclovir to each of acceptors under consideration indicated (1:1) ratio. The proposed methods were applied successfully for simultaneous determination of ganciclovir in capsules with good accuracy and precision and without interferences from common additives. The recovery percentages ranged from 99.45 ± 0.73% to 100.35 ± 1.40%. The results were compared favourably with the reported method.

© 2009 Elsevier B.V. All rights reserved.

1. Introduction

Ganciclovir (GCV), (2-amino-9-{[(1,3-dihydroxypropan-2-yl)-oxy]methyl}-6,9-dihydro-3*H*-purin-6-one) is an antiviral medication used to treat or prevent cytomegalovirus (CMV) infections, a virus that affects the eyes of immunosuppressed patients. Ganciclovir (GCV), is nucleoside analogue with antiviral activity for prophylaxis and treatment against herpes simplex virus or CMV [1]. The structures of this antiviral drug (GCV) is shown in Scheme 1.

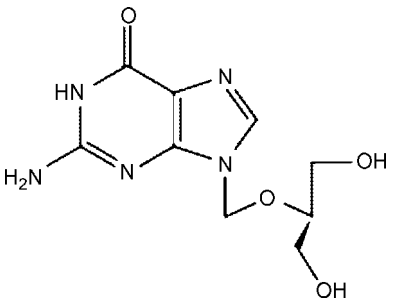
The quantitation of GCV in biological samples poses an important challenge because this drug is structurally similar to endogenous substances. Hence, this complicates analysis and requires using a highly selective analytical method. Some analytical methods have been reported for determination of GCV including voltammetry [2], chemiluminescence [3], capillary electrophoresis [4], high-performance liquid chromatography (HPLC) [5–17]. Visible spectrophotometry, because of simplicity and cost effectiveness, sensitivity and selectivity, fair accuracy, precision and available in most quality control laboratories, has remained competitive in an area of chromatographic techniques for pharmaceutical analysis. Furthermore, they do not need costly instrumentation required for published HPLC methods.

The molecular interactions between electron donors and acceptors are generally associated with the formation of intensely colored charge–transfer complexes, which absorb radiation in the visible region [18]. A variety of electron donating compounds have been reported to yield charge-transfer complexes with various acceptors. The rapid formation of these complexes leads to their utility in the development of simple and convenient spectrophotometric methods for these compounds [19–39].

Ganciclovir is a good n-electron donor and will form charge–transfer complexes with σ-acceptor like iodine and π-acceptors such as 7,7,8,8-tetracyanoquinodimethane (TCNQ); tetracyanoethylene (TCNE); 2,3-dichloro-5,6-dicyano-1,4-benzoquinone (DDQ); *p*-chloranilic acid (*p*CA); 2,3,5,6-tetrabromo-1,4-benzoquinone (BL), 2,3,5,6-tetrachloro-1,4-benzoquinone (CL) and 2,4,7-trinitro-9-fluorenone (TNF) are known to yield charge–transfer complexes and radical anions. The charge– transfer reaction has not yet been reported for GCV; therefore the aim of the present study was directed to investigate simple, direct, sensitive and precise spectrophotometric methods for simultaneous determination of GCV via complexation with σ- and π-acceptors in pure form and its dosage forms (capsules).

* Fax: +20 55 230 8213.
E-mail address: aymanchimca@yahoo.com.

0039-9140/$ – see front matter © 2009 Elsevier B.V. All rights reserved.
doi:10.1016/j.talanta.2009.06.042



Scheme 1. Structural formula of ganciclovir.

2. Experimental

2.1. Apparatus

All absorption spectra were made using Kontron 930 (UV–visible) spectrophotometer (German) with a scanning speed of 200 nm min^{-1} and a bandwidth of 2.0 nm, equipped with 10 mm matched quartz cells.

2.2. Materials and reagents

Pure grade ganciclovir (GCV) and its pharmaceutical formulations were obtained from Roche Pharm. Inc. (New Zealand) and were used as working standard.

7,7,8,8-tetracyanoquinodimethane (TCNQ), Aldrich Chem. Co., Milwaukee, USA, and tetracyanoethylene (TCNE), Nacalai Tesque, Kyoto, Japan, 1.0 mg mL^{-1} were prepared in acetonitrile, the solutions were stable for at least one week at 4 °C. Chloranilic acid (*p*CA) and chloranil (CL), Fluka, Switzerland, 2.0 mg mL^{-1} in acetonitrile, were prepared fresh daily.

2,3-Dichloro-5,6-dicyano-p-benzoquinone (DDQ), Merck-Schuchardt, Munich, Germany and p-bromanil (BL), Hopkin and William, Essex, England, 2.0 and 5.0 mg mL^{-1} in methanol, the solutions were prepared fresh daily.

Iodine resublimed, Riedel De-Haen, Germany and 2,4,7-trinitro-9-fluorenon (TNF), Fluka, Switzerland, 5.0 and 2.0 mg mL^{-1} in 1,2-dichloroethane were prepared, the solutions were stable for at least one week at 4 °C. All reagents and solvents used were of analytical-reagent grade. In the same manner, stock solution of 2×10^{-3} M of acceptor was also prepared.

2.3. Pharmaceutical formulations

The commercial capsules used in the present investigation were Cymevene capsules (Roche Pharm. Inc., New Zealand), labeled to contain 250 mg GCV per capsule.

2.4. Preparation of stock standard solution

Standard stock solution of GCV (1.0 mg mL^{-1}) was prepared by accurately weighting and dissolving 100 mg of GCV in 2.0 mL methanol in a 100 mL calibrated flask and completed to volume with the same solvent (for DDQ and BL), with 1,2-dichloroethane (for iodine and TNF), and with acetonitrile (for the other acceptors, TCNQ, TCNE, *p*CA an CL). These stock solutions were diluted with the respective solvents to obtain suitable concentrations that lie in the linear range of each particular assay method, in the same manner, stock solution of 2×10^{-3} M of drug was also prepared. The solutions were stable for at least one week at 4 °C.

2.5. General analytical procedure

Into 10-mL calibrated flasks were placed 0.1–2.4 mL aliquot volumes of 1000 μg mL^{-1} of GCV in methanol for DDQ and BL, in 1,2-dichloroethane for iodine and TNF and in acetonitrile for TCNE, *p*CA and CL and placed 0.1–2.5 mL aliquot volumes of 200 μg mL^{-1} of GCV in acetonitrile for TCNQ. One milliliter of the acceptor reagent solutions was added. The reaction mixture was allowed to stand for 5.0, 10 and 15 min at (60 ± 2 °C) in case of (TCNE and DDQ), (TCNQ, *p*CA and CL) and (BL and TNF), respectively. The reaction in case of iodine was achieved instantaneously. The volume was made up 10 mL with methanol (for DDQ and BL), 1,2-dichloroethane (for iodine and TNF) and with acetonitrile (for the other acceptors, TCNQ, TCNE, *p*CA an CL). The absorbance of the resulting solutions was measured at the wavelengths of maximum absorption 365, 840, 415, 465, 530, 460, 550, and 413 nm for iodine, TCNQ, TCNE, DDQ, *p*CA, BL, CL, and TNF, respectively against reagent blank prepared in the same manner.

2.6. Procedure for capsules

Ten capsules of the drug were weighed and a quantity of the content capsules equivalent to 100 mg was transferred into a 50-mL calibrated flask, dissolved in 2.0 mL methanol, swirled and sonicated for 5 min, completed to volume with the corresponding solvent (as in stock solutions), shaken well for 10 min, and filtered. The first portion of the filtrate was rejected, and a measured volume of the filtrate was diluted quantitatively with a suitable solvent to yield suitable concentrations lie in the linear range of each particular assay method; then the procedure was followed as above.

2.7. Determination of molar ratio of reactants in complex

Job's method of continuous variation [40] was employed, a 2.0×10^{-3} M standard solution of drug and reagents were used. A series of solutions was prepared in which the total volume of GCV and reagent was constant (2.0 mL). The drug and reagents were mixed in various complementary proportions (0:10, 1:9, . . ., 9:1, 10:0, inclusive) and then diluted in a 10-mL calibrated flask with

Table 1
Optimum reaction conditions for the charge–transfer reaction of GCV with various acceptors.

Acceptor	Reagent concentration (mg mL^{-1})	Solvent	Time (min)	Temp, °C	λ_{max}, nm
Iodine (1.7)[a]	5.0	1,2-Dichloroethane	At once	25 ± 2	365
TCNQ (1.7)	1.0	Acetonitrile	10	60 ± 2	840
TCNE (2.2)	1.0	Acetonitrile	5	60 ± 2	415
DDQ (1.9)	2.0	Methanol	5	60 ± 2	465
pCA	2.0	Acetonitrile	10	60 ± 2	530
Bromanil (1.37)	5.0	Methanol	15	60 ± 2	460
Chloranil (1.37)	2.0	Acetonitrile	10	60 ± 2	550
TNF (1.1)	2.0	1,2-Dichloroethane	15	60 ± 2	413

[a] Figures in parenthesis are the electron affinities of the acceptors; from Ref. [18].

the optimum solvent. The reactions were allowed to proceed for the optimum reaction time (Table 1) and the absorbance of the resulting solutions was measured at the corresponding wavelengths of maximum absorbance (λ_{max}) against a reagent blank under the same conditions.

2.8. Association constant

Serial volumes of 1.0–5.0 mL of 2.0×10^{-3} M GCV solution (in 1.0 mL steps) in the optimum solvent were transferred in 10-mL calibrated flasks. To each flask, 1.0 mL of acceptor solution (2.0×10^{-3} M) was added and continued as directed under general procedure.

3. Results and discussion

3.1. Spectral characteristics of the reaction

3.1.1. Reaction with σ-acceptor (iodine)

The color of iodine in 1,2-dichloroethane is violet showing absorption maximum (λ_{max}) at 520 nm. This color was immediately changed into lemon yellow, and the absorption spectrum of GCV-iodine reaction product showed absorption peaks at 290 and 365 nm (Fig. 1). This change in color, and the appearance of these two peaks were attributed to the formation of charge–transfer complex between the GCV and iodine, having an ionized structure $DI^+ \ldots I_3^-$, taking into account that the absorption spectrum of I_3^- in 1,2-dichloroethane showed the two absorption maxima at 290 and 365 nm. This complex should originate from an early intermediated outer complex $D \ldots I_2$, according to the following scheme:

$$D + I_2 \rightleftharpoons \underset{\text{Outer complex}}{D\text{-}I^+ I^-} \rightleftharpoons \underset{\text{inner complex}}{[D\text{-}I^+]} + I^- \rightleftharpoons \underset{\text{tri-iodide ion pair}}{I_3^-}$$

Further confirmation for the charge–transfer nature of the reaction, GCV was extracted from the complex by shaking with aqueous mineral acids. The color of iodine in 1,2-dichloroethane layer was restored to violet, confirming the charge–transfer nature of the reaction. Measurements were carried out at 365 nm due to the interference from the native UV absorption of GCV at 290 nm.

3.1.2. Reaction with π-acceptors

The interaction of GCV with selective polyhaloquinone and polycyanoquinone π-acceptors in non-polar solvents such as dichloroethane was found to produce colored charge–transfer complexes with low molar absorptivity values [41]. In polar solvents such as methanol or acetonitrile, complete electron transfer from the GCV (D), as an electron donor, to the acceptor moiety (A) takes place with the formation of intensely colored radical ions with high molar absorptivity values, according to the following scheme:

$$D^{\bullet} + A \rightleftharpoons \underset{\text{DA complex}}{\left[D^{\bullet\bullet} \rightarrow A\right]} \overset{\text{Polar solvent}}{\rightleftharpoons} D^{\bullet+} + \underset{\text{radical anion}}{A^{\bullet-}}$$

The dissociation of the (D–A) complex was promoted by the high ionizing power of the polar solvent and the resulting peaks in the absorption spectra of GCV-acceptor reaction mixtures were similar to the maxima of the radical anions of the acceptors obtained by the iodide reduction method [41].

The interaction of GCV with π-acceptors at optimum temperature gave colored chromogens showing different absorption maxima at 840, 415, 465, 530, 460, 550, and 413 nm for TCNQ, TCNE, DDQ, *p*CA, BL, CL and TNF, respectively (Figs. 2–5).

The resulting maxima of the investigated drug with DDQ, TNF, *p*CA, BL and CL are similar to that of the radical anion of these acceptors obtained by the reduction method and coincide with the values reported in previous work [42,43].

The predominent chromogen with TCNQ in acetonitrile is the bluish-green colored radical anion, which exhibits strong absorption maxima at 840, 825, 762, and 742 nm. These bands may be attributed to the formation of the radical anion $TCNQ^{\bullet-}$, which was probably formed by the dissociation of an original donor–acceptor

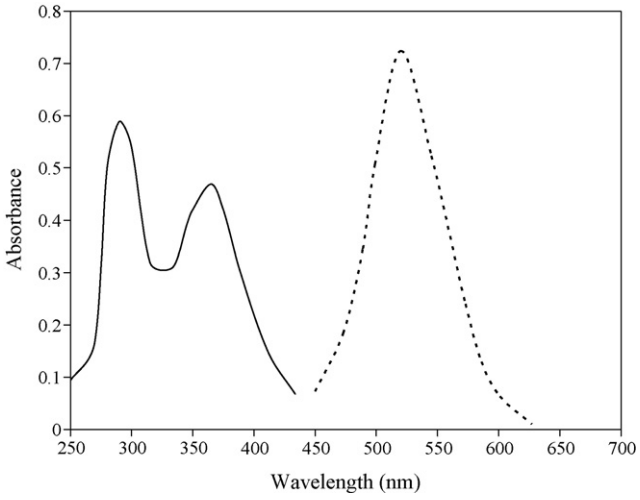


Fig. 1. Absorption spectra of iodine (. . .)and the reaction product of 100 μg mL^{-1} GCV with iodine (—) in 1,2-dichloroerthane.

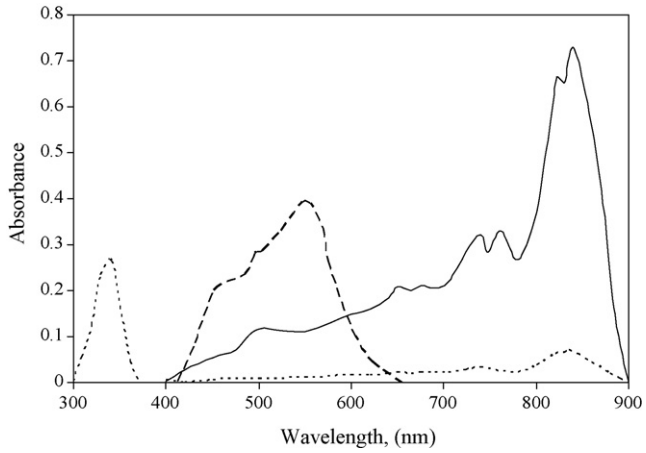


Fig. 2. Absorption spectra of TCNQ and CL (. . .) and the reaction product of 25 and 50 μg mL^{-1} GCV with TCNQ (—) and CL (- - - -), respectively in acetonitrile.

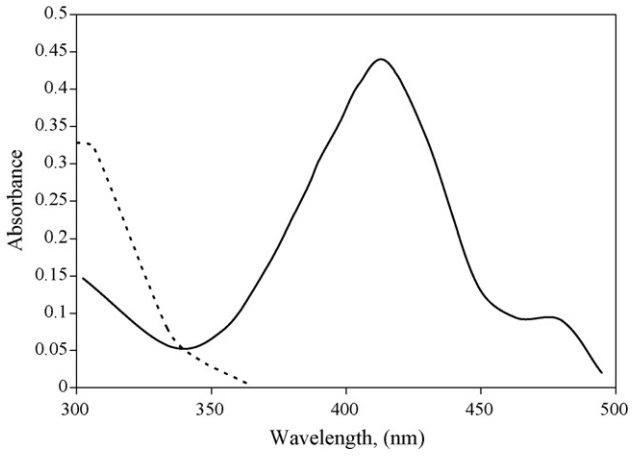


Fig. 3. Absorption spectra of TCNE (. . .) and the reaction product of 100 μg mL^{-1} GCV with TCNE (—) in acetonitrile.

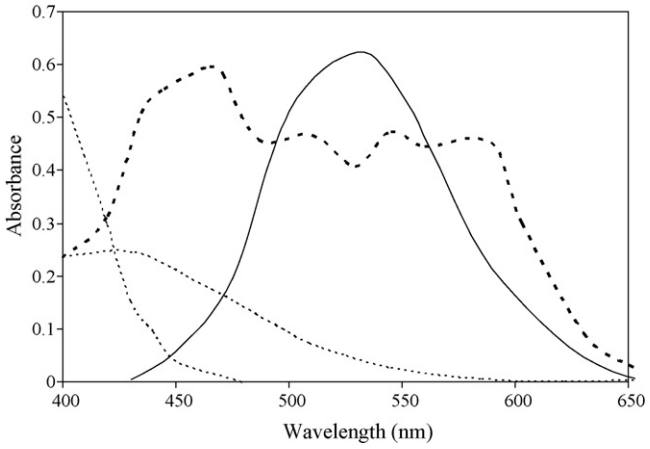


Fig. 4. Absorption spectra of DDQ and *p*CA (. . .) and the reaction product of 100 and 75 μg mL^{-1} GCV with DDQ (—) in methanol and *p*CA (- - - -) in acetonitrile, respectively.

(D–A) complex with GCV. The dissociation of the complex was promoted by the high ionizing power of acetonitrile. Further support of this assignment was provided by the absorption maxima with those of TCNQ radical anion produced by the iodide reduction method [43] (Fig. 2).

For GCV and TCNE, the characteristically shaped absorption band of TCNE radical anion with reported maximum in acetonitrile at 432 nm was not formed. Instead a doublet at 394 and 415 nm in acetonitrile was formed which corresponds to the 1,1,2,3,30-pentacyanopropenide (PCNP) anion. From the quantitative point of view, PCNP anion is preferable to TCNE anion on grounds of its higher molar absorptivity [41] (Fig. 3).

Chloranilic acid (*p*CA) exists in three ionic forms, the neutral yellow–orange H_2A at very low pH, the dark purple HA^- which is stable at pH 3 and a colorless A^{2-}, which is stable at high pH; these transformations are illustrated in the following scheme:

$$H_2A \rightleftharpoons H^+ + HA^- (\text{violet})$$

$$HA^- \rightleftharpoons H^+ + A^{2-} (\text{colorless})$$

Since the interaction of GCV with *p*CA in acetonitrile gave a violet product, it might be concluded that HA^- was the form of pCA involved in the reaction described herein (Fig. 4).

The relative sensitivity of the eight acceptors employed in the present analytical work may be attributed to their difference in electron affinities (Table 1), as well as the conditions employed in the reaction (reagent concentration, reaction time, and solvent).

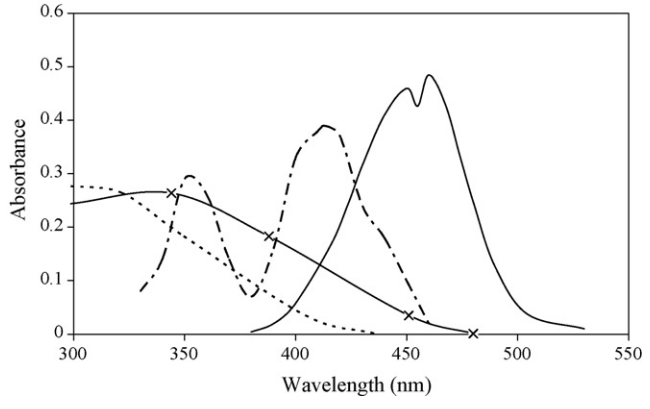


Fig. 5. Absorption spectra of BL (. . .) and TNF (-×-×-) and the reaction product of 100 μg mL^{-1} GCV with BL (—) in methanol and TNF (- - - -) in 1,2-dichloroerthane.

The weak and small molar absorptivity values in cases of TCNE, BL, CL and TNF may be explained on the basis of insufficient ionization of these relatively weak π-acceptors that possess lower electron affinities, than TCNQ, *p*CA and DDQ, exhibiting higher molar absorptivities.

3.2. Optimization of reaction conditions

3.2.1. Effect of reagent concentration

The results for variation of reagent concentration, indicated that 1.0 mL of either 5.0 mg mL^{-1} iodine and BL, 1.0 mg mL^{-1} TCNQ and TCNE and 2.0 mg mL^{-1} DDQ, pCA, CL and TNF are suitable. The higher concentrations of the reagents may, on the other hand, be useful for rapidly reaching equilibrium and complete color development, the results are given in Table 1. This minimizes the time required to attain the maximum absorbance at the corresponding wavelength of the charge–transfer complex.

3.2.2. Effect of solvent

Although charge–transfer complexes are probably formed in many solvents, the high cut-off points of some solvents obscured the scanning of the shorter wavelengths and therefore clear-cut spectroscopic evidence for charge–transfer formation could not be ascertained. Also the low solubility of the GCV in some other solvents restricted their use.

1,2-Dichloroethane was found to be an ideal solvent in case of iodine and TNF (Table 1), because it is favourable for the formation of tri-iodide ion pair (inner complex). With iodine, GCV showed a major charge–transfer band at 365 nm. Methylene chloride, chloroform and carbon tetrachloride produced lower absorption readings. Polar solvents were found to be unsuitable as their blanks with iodine and TNF gave higher readings.

The formation of TCNQ radical was possible in methanol; however, the response between absorbance and concentration was not linear. Furthermore, the molar absorptivity of the obtained chromogen was relatively low compared with that in acetonitrile. The latter was considered as an ideal solvent because it offered excellent solvating power for TCNQ reagent and gave high absorbance.

For TCNE, *p*CA, CL complex formation, acetonitrile afforded maximum sensitivity when compared with all other solvents (benzene, chloroform, ethylene chloride and methanol). This is because it possesses the highest dielectric constant of all solvents examined [44], a property which is known to promote the dissociation of the original charge–transfer complexes to the radical ions. Methylene chloride is a possible candidate, although it suffers from low boiling point which could result in fluctuations of concentration during handling and manipulation. Benzene and chloroform were unsuitable owing to the limited solubility of the reagents [45,46]. The results obtained with *p*CA, as a representative example, are given in Table 2.

Table 2
Effect of solvents on the position and intensity of absorption of the reaction of GCV (100 μg mL^{-1}) with *p*CA (2.0 mg mL^{-1}).

Solvent	Dielectric constant [a]	λ_{max} (nm)	Absorbance
Acetonitrile	37.5	530	0.632
Methanol	32.7	527	0.531
Ethanol	24.6	525	0.450
Acetone	20.7	525	0.432
Propan-1-ol	20.3	525	0.416
Butan-1-ol	17.5	525	0.347
Diethylether	4.3	530	0.321
Benzene	2.3	535	0.345
Carbon tetrachloride	2.2	520	0.322
Toluene	2.4	535	0.307
1,4-Dioxane	2.2	520	0.281

Full-size table.

[a] Ref. [50].

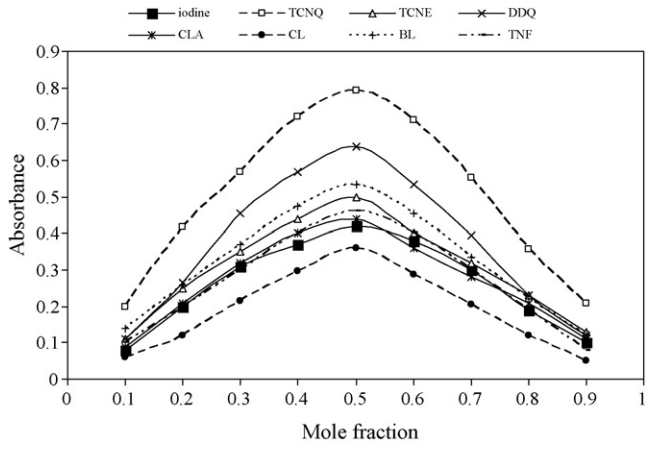


Fig. 6. Continuous variation graph for the reaction of GCV with iodine, TCNQ, DDQ, TCNE, *p*CA, CL, BL and TNF.

On the other hand, methanol affords maximum sensitivity and full color development with DDQ and BL. In addition, it is a good solvent for the reagent. Of the other solvents examined, acetonitrile, dichloromethane and 1,2-dichloroethane are possible substitutes.

3.2.3. Effect of reaction time

Complete color development, was attained instantaneously using iodine, whereas for TCNQ, TCNE, DDQ, *p*CA, CL, BL and TNF, complete color development was attained after 60, 40, 50, 50, 60, 90 and 75 min, respectively. To consume the time required for complete color development heating in a water bath at $60 \pm 2\,^{\circ}C$ for 5.0, 10 and 15 min in case of (TCNE and DDQ), (TCNQ, *p*CA and CL) and (BL and TNF), respectively. The color remained stable for 2.0, 1.5, 2.0, 3.0, 2.5, 2.0 and 1.0 h using TCNQ, TCNE, DDQ, *p*CA, CL, BL and TNF, respectively, except in case of iodine whereas the color decreased dramatically resulting in high imprecision of the readings.

3.3. Molar ratio of the reaction

Job's continuous variation graph [40] for the reaction between GCV and different reagents (Fig. 6) shows that the interaction occurs on an equimolar basis via the formation of a charge–transfer complex (1:1). The colored reaction product can be represented, taking TCNQ as an example, by Scheme 2. A more detailed examination was made for GCV complexes with the studied acceptors. The absorbance of the complex was used to calculate the association constant using the Benesi–Hildebrand equation [47].

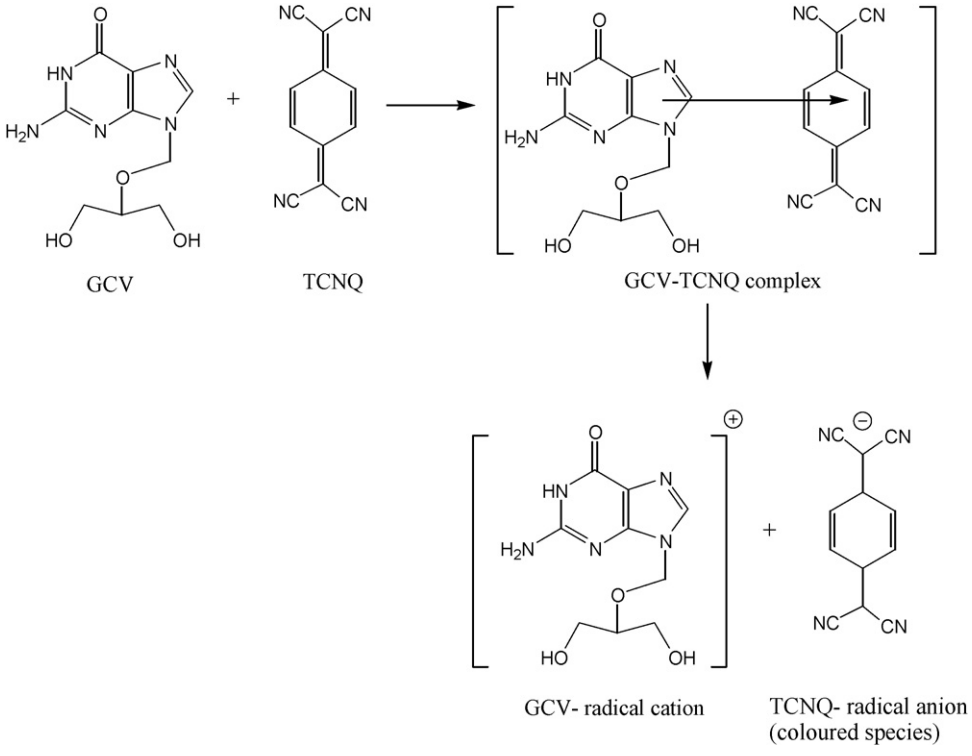
$$\frac{[A_0]}{A^{AD}} = \frac{1}{\varepsilon_\lambda^{AD}} + \frac{1}{K_c^{AD}\varepsilon_\lambda^{AD}} \times \frac{1}{[D_0]}$$

where $[A_0]$ and $[D_0]$ are the total concentrations of the interacting species, A_λ^{AD} and ε_λ^{AD} are the absorbance and molar absorptivity of the complex at their λ_{max}, and K_c^{AD} is the association constant of the complex. On plotting the values of $[A_0]/A_\lambda^{AD}$ versus $1/[D_0]$, a line was obtained with slope equals $(\varepsilon_\lambda^{AD} \cdot K_c^{AD})^{-1}$ and intercept of this line with the ordinate is $(\varepsilon_\lambda^{AD})^{-1}$. The calculated association constants are recorded in Table 3, whereas the molar absorptivities were comparable with those obtained from regression line equation of Beer's law. The low values obtained for the association constants are common in these complexes due to the dissociation of the original donor–acceptor complex to the radical anion.

3.4. Development and validation of the analytical methods

3.4.1. Calibration curves, linearity and sensitivity

Under the specified optimum reaction conditions, the calibration curves for GCV with the different analytical reagents employed in the present work were constructed. The regression equations for the results were derived using the least-squares method. In all cases, Beer's law plots ($n = 6$) were linear with very small intercepts and good correlation coefficients in the general concentration range of 2.0–240 $\mu g\,mL^{-1}$ (Table 3). For comparison, the HPLC reported



Scheme 2. Suggested structure of GCV-TCNQ charge–transfer complex.

Table 3
Quantitative parameters for the charge–transfer reaction of GCV with various acceptors.

Parameters	Iodine	TCNQ	TCNE	DDQ	*p*CA	CL	BL	TNF
Beer's law limits ($\mu g\,mL^{-1}$)	10–160	2.0–50	20–200	10–240	20-180	20–240	20-160	15-150
Ringboom limits ($\mu g\,mL^{-1}$)	20–150	5.0–45	30–185	20–225	35–170	30–225	25–150	25–140
Molar absorptivity ε, $\times 10^3$($L\,mol^{-1}\,cm^{-1}$)	1.051	6.345	0.582	1.26	0.70	0.435	0.661	0.550
Sandell's sensitivity ($\mu g\,cm^{-2}$)	0.243	0.040	0.439	0.203	0.365	0.587	0.386	0.464
Association constant log *K*	3.70	3.90	3.85	4.05	3.80	3.75	3.85	3.65
Regression equation[a]								
Slope (*b*)	0.0038	0.0166	0.0022	0.0041	0.0028	0.0011	0.0023	0.002
Intercept (*a*)	0.0096	0.0567	0.005	0.0264	−0.0037	0.0017	0.016	0.0126
Correlation coefficient (*r*)	0.9994	0.9996	0.9994	0.9998	0.9994	0.9996	0.9993	0.9993
Detection limits LOD ($\mu g\,mL^{-1}$)	1.10	0.36	1.90	1.25	1.65	2.45	1.80	1.45
Quantification limits LOQ ($\mu g\,mL^{-1}$)	3.67	1.20	6.33	4.17	5.50	8.17	6.0	4.83
RSD%	0.98	0.85	1.15	1.34	1.12	1.41	1.20	1.10
RE%	1.03	0.894	1.21	1.41	1.18	1.48	1.26	1.15

LOD, limit of detection; LOQ, limit of quantification; ε, molar absorptivity coefficient.
[a] $A = a + bC$, where A is the absorbance, a is the intercept, b is the slope and C is the concentration of drug in $\mu g\,mL^{-1}$.

Table 4
Statistical analysis of the results obtained for assay of authentic GCV drug using the proposed methods compared with the reported HPLC method [9].

Parameter	Reported	Iodine	TCNQ	TCNE	DDQ	pCA	BL	CL	TNF
Mean recovery, %[a]	100.43	99.45	100.20	99.85	100.05	100.35	99.80	99.76	99.90
±Standard deviation	0.78	0.73	1.15	0.84	1.07	1.40	1.34	0.97	1.08
Number of experiments	6	6	6	6	6	6	6	6	6
Variance	0.61	0.50	1.32	0.71	1.14	1.96	1.80	0.94	1.17
t-test[b]		1.26	0.37	1.13	0.64	0.39	0.91	1.20	0.89
F-ratio[b]		1.22	2.16	1.16	1.87	3.21	2.95	1.54	1.92

[a] Average values of six determinations were used for the reported and the proposed methods, respectively.
[b] Theoretical values for *t* and *F* at 95% confidence limit are 2.57 and 5.05, respectively.

method [9] was applied. Statistical analysis of the results obtained (Table 4), indicated that the proposed procedures were accurate and precise.

The limits of detection (LOD) and limits of quantitation (LOQ) were determined [48] using the formula:

$$\text{LOD or LOQ} = \kappa \text{S.D.}\frac{a}{b},$$

where $\kappa = 3$ for LOD and 10 for LOQ, S.D.*a* is the standard deviation of the intercept, and *b* is the slope. Based on the basis of six replicate measurements, the limits of detection were 0.36–2.45 $\mu g\,mL^{-1}$ and the limits of quantification were 1.2–8.17 $\mu g\,mL^{-1}$. Both LOD and LOQ values confirmed the sensitivity of the proposed methods.

3.4.2. Precision

The precisions of the assays (within-assay and between-assays) were determined at the GCV concentrations cited in Table 5. The within-assay precision was assessed by analyzing six replicates of each sample as a batch in a single assay run, and the between-assays precision was assessed by analyzing the same sample, as triplicate, in two separate assay runs. The relative standard deviations (R.S.D.) were less than 2% (Table 5). This level of precision of the proposed methods was adequate for the quality control analysis of GCV.

Table 5
Precision of the proposed methods for analysis of GCV ($n = 6$).

Method ($\mu g\,mL^{-1}$)	GCV	Within-assays		Between-assays	
		Mean ($\mu g\,mL^{-1} \pm$ S.D.)	R.S.D.	Mean ($\mu g\,mL^{-1} \pm$ S.D.)	R.S.D.
Iodine	100	98.75 ± 1.24	1.26	99.30 ± 0.63	0.63
TCNQ	25	24.78 ± 0.26	1.05	25.10 ± 0.19	0.76
TCNE	100	100.73 ± 0.43	0.43	99.35 ± 0.26	0.26
DDQ	100	99.51 ± 0.23	0.23	99.50 ± 0.56	0.56
*p*CA	90	88.90 ± 0.31	0.35	90.05 ± 0.72	0.80
BL	80	80.17 ± 0.57	0.71	89.90 ± 1.15	1.28
CL	100	100.50 ± 0.64	0.64	99.25 ± 1.10	1.11
TNF	150	148.48 ± 1.70	1.14	151.10 ± 1.25	0.83

S.D.; Standard deviations. R.S.D.; Relative standard deviations.

3.4.3. Specificity and interference

The proposed spectrophotometric methods have the advantages that the measurements in all of these methods are performed in the visible region, away from the UV-absorbing interfering substances that might be co-extracted from GCV containing dosage forms. Regarding the interference of the excipients and additives usually presented in pharmaceutical formulation (croscarmellose sodium, magnesium stearate, povidone, gelatin, titanium dioxide and yellow iron oxide), the energy of the charge–transfer (ECT) depends on the ionization potential (IP) of the donor and the electron affinity of the acceptor (EA), hence the λ_{max} values of the other π-donors mostly differ from that of the investigated compounds if they are able to form CT complexes. Preliminary experiments showed that all additives and excipients did not form CT complexes with the studied acceptors indicating the high selectivity of the proposed methods and applicability to use for routine determination in pure and in dosage forms.

3.4.4. Ruggedness and robustness

The ruggedness of the proposed methods was assessed by applying the procedures using two different instruments in two different laboratories at different elapsed time. Results obtained from lab-to-lab and day-to-day variations were found to be reproducible as R.S.D did not exceed 2%. Robustness of the procedures was assessed by evaluating the influence of small variation of experimental variables: concentrations of acceptor reagent, and reaction time, on the analytical performance of the method. In these experiments, one experimental parameter was changed while the other parameters were kept unchanged, and the recovery percentage was calculated each time. The small variations in any of the variables did not significantly affect the results; recovery percentages were 98.48–101.50 ± 0.78–1.84%. This provided an indication for the reliability of the proposed methods during routine work.

Table 6
Determination of GCV in Cymevene® capsules (250 mg GCV/capsule) by the proposed and reported HPLC method [9].

Parameter	Reported	Iodine	TCNQ	TCNE	DDQ	*p*CA	BL	CL	TNF
Mean recovery, %[a]	99.47	100.41	100.07	99.59	99.92	100.18	99.54	100.32	99.85
±Standard deviation	0.66	0.86	0.94	1.10	0.69	0.88	1.20	0.78	1.09
Number of experiments	6	6	6	6	6	6	6	6	6
Variance	0.44	0.74	0.88	1.21	0.48	0.77	1.44	0.61	1.19
t-test[b]		1.93	1.17	0.21	1.05	1.44	0.11	1.86	0.67
F-ratio[b]		1.68	2.0	2.75	1.09	1.75	3.27	1.39	2.70

Full-size table.

[a] Average values of six determinations were used for the reported and the proposed methods, respectively.

[b] Theoretical values for *t* and *F* at 95% confidence limit are 2.57 and 5.05, respectively.

3.5. Application of the method to the analysis of capsules

The obtained satisfactory validation results made the proposed procedures suitable for the routine quality control analysis of GCV and its pharmaceutical formulations (Cymevene® capsules). The results obtained by the proposed methods were statistically compared with those obtained by the reported method [9]. The obtained mean values of the labeled amounts ranged from 99.54 ± 1.20% to 100.41 ± 0.86% (Table 6). In the *t*- and F-tests, no significant differences were found between the calculated and theoretical values of both the proposed and the reported methods at 95% confidence level [49]. This indicated similar precision and accuracy in the analysis of GCV in its formulations. It is evident from these results that all the proposed methods are applicable to the analysis of GCV in its capsules with comparable analytical performance. However, the critical recommendations of some of these methods might be based on the experimental conditions (e.g. reaction time), and the ultimate sensitivity that determines the amount of specimen required for analysis. For example, the methods involving TCNE and DDQ are recommended whenever rapid analysis is required; this is because they have very short reaction time. The method involving TCNQ is recommended, as high sensitivity is required on the expense of the analysis time.

3.6. Conclusions

The charge–transfer complexation reaction of GCV as electron donor and some electron acceptors has been investigated. The obtained colored complexes were utilized in the development of eight simple, accurate and sensitive with good precision and accuracy spectrophotometric methods for the analysis of GCV in pure form as well as in dosage forms. With these methods, one can do the analysis at low cost without losing accuracy. The proposed methods can be used as alternative methods to the reported ones for the routine determination of Cymevene® capsules. This encourages their successful use in routine analysis of these drugs in quality control laboratories and they involve very simple procedures.

Acknowledgment

The author is grateful to *Dr. Alaa S. Amin* (Department of Chemistry, Faculty of Science, Benha University) for helping him.

References

[1] T. Schacker, H.L. Hu, D.M. Koelle, J. Zeh, R. Saltzman, R. Boon, M. Shaughnessy, G. Barnum, L. Corey, Ann. Int. Med. 128 (1998) 21.
[2] B. Uslu, B. Doğan, S.A. Özkan, Anal. Chim. Acta 537 (2005) 307.
[3] M. Abudukeremu, W. Nannan, T. Yuhai, M. Tu'erhong, J. Xi'an Jiaotong Univ. (Med. Sci.) 28 (2007) 710.
[4] S. Saleh, G. Hempel, Electrophoresis 27 (2006) 2439.
[5] T. Page, C. Sherwood, J.D. Connor, T. Tarnowski, J. Chromatogr. B Biomed. Appl. 675 (1996) 342.
[6] A. Asberg, C.N. Hansen, L. Reubsaet, J. Pharm. Biomed. Anal. 43 (2007) 1039.
[7] F. Chu, C.H. Kiang, M.L. Sung, B. Huang, R.L. Reeve, T. Tarnowski, J. Pharm. Biomed. Anal. 21 (1999) 657.
[8] M.A. Campanero, B. Sadaba, E. Garcia-Quetglas, J.R. Azanza, J. Chromatogr. B Biomed. Sci. Appl. 706 (1998) 311.
[9] M. Merodio, M.A. Campanero, T. Mirshahi, M. Mirshahi, J.M. Irache, J. Chromatogr. A 870 (2000) 159.
[10] R. Boulieu, N. Bleyzac, S. Ferry, J. Chromatogr. 567 (1991) 481.
[11] R. Boulieu, N. Bleyzac, S. Ferry, J. Chromatogr. 571 (1991) 331.
[12] M. Tsuchie, S. Hara, M. Kimura, M. Fujii, N. Ono, M. Kai, Anal. Sci. 17 (2001) 811.
[13] N. Perrottet, A. Beguin, P. Meylan, M. Pascual, O. Manuel, T. Buclin, J. Biollaz, L.A. Decosterd, J. Chromatogr. B Analyt. Technol. Biomed. Life Sci. 852 (2007) 420.
[14] C.M. McMullin, B. Kirk, J. Sunderland, L.O. White, D.S. Reeves, A.P. MacGowan, J. Antimicrob. Chemother. 38 (1996) 739.
[15] D. Teshima, K. Otsubo, T. Yoshida, Y. Itoh, R. Oishi, Biomed. Chromatogr. 17 (2003) 500.
[16] Y.-j. Dao, Z. Jiao, M.-k. Zhong, J. Chromatogr. B Anal. Tech. Biomed. Sci. 867 (2008) 270.
[17] H.R. Xu, X.N. Li, W.L. Chen, G.Y. Liu, N.N. Chu, C. Yu, J. Chromatogr. B Anal. Technol. Biomed. Life Sci. 848 (2007) 329.
[18] R. Foster, Organic Charge–Transfer Complexes, 51, Academic Press, London, 1969, p. 387.
[19] C.N.R. Rao, S.N. Bhat, P.C. Dwivedi, in: E.G. Brame (Ed.), Applied Spectroscopy Review, vol. 5, Dekker, NewYork, 1972, p. 1.
[20] A.S. Amin, G.O. EL-Sayed, Y.M. Issa, Analyst 120 (1995) 1189.
[21] S.M. AL-Ghannam, A.M. El-Brashy, L.A. AL-Hussein, J. AOAC Int. 82 (1999) 239.
[22] M.M. Ayad, A.A. Shalaby, H.E. Abdellatef, H.M. Elsaid, J. Pharm. Biomed. Anal. 18 (1999) 975.
[23] Z.F. Deng, Z.L. Zhu, T.M. Yao, T.H. Li, Liha Jianyan, Huaxue Fence 35 (1999) 8.
[24] H. Wu, L.M. Du, Spect. Chim. Acta A 67 (2007) 976.
[25] G.G. Mohamed, F.A.F. Nour El-Dien, N.A. Mohamed, Spect. Chim. Acta A 68 (2007) 1244.
[26] M.E. El-Zaria, Spect. Chim. Acta A 69 (2008) 216.
[27] Z. Aydogmus, Spect. Chim. Acta A 70 (2008) 69.
[28] E. Khaled, Talanta 75 (2008) 1167.
[29] F.M. Abdel-Gawad, Y.M. Issa, H.M. Fahmy, H.M. Hussein, Mikrochim. Acta 130 (1998) 35.
[30] H.E. Abdellatef, J. Pharm. Biomed. Anal. 17 (1998) 1267.
[31] A.F.M. Albendazole-Wolily, M.A. Korany, A. El-Gindy, M.F. Bedair, J. Pharm. Biomed. Anal. 17 (1998) 435.
[32] G.A. Salah, Talanta 45 (1998) 111.
[33] S.R. EL-Shabouri, K.M. Emara, P.Y. Khashaba, A.M. Mohamed, Anal. Lett. 31 (1998) 1367.
[34] A.S. Amin, A.M. El-Beshbeshy, Mikrochim. Acta 137 (2001) 63.
[35] A.S. Amin, I.S. Ahmed, Mikrochim. Acta 137 (2001) 35.
[36] A.A. Gouda, R. EL-Sheikh, A.S. Amin, Chem. Pharm. Bull. 56 (2008) 34.
[37] Y.M. Issa, F.M. Abou-Attia, F.M. Abdel-Gawad, S.M. Abdel-Hamid, Anal. Lett. 35 (2002) 451.
[38] I.A. Darwish, I.H. Refaat, J. AOAC Int. 89 (2006) 326.
[39] I.A. Darwish, Anal. Chem. Acta 549 (2005) 212.
[40] P. Job, Ann. Chem. 16 (1936) 97.
[41] A. Taha, G. Rücker, Arch. Pharm. (Weinheim) 310 (1977) 485.
[42] L.R. Melby, in: S. Patai (Ed.), The Chemistry of the Cyano Group, Interscience Publisher/John Wiley & Sons, New York, 1970, p. 656.
[43] A. Yamagishi, Bull. Soc. Jpn. 48 (1975) 2440.
[44] S. Budavari, M.J. O'Neil, A. Smith, P.E. Heckelman, The Merck Index- an encyclopaedia of chemicals, drugs and biologicals, 11th ed., Merck, New Jersey, USA, 1990.
[45] T.L. Antonovsky, A.Á.S. Gukovskaja, G. Netrasova, J. Biochim. Biophys. Acta 331 (1973) 9.
[46] P.M. Qureshi, R.K. Varshey, S.I.M. Kampoonuri, Spectrochim. Acta 45 (1989) 963.
[47] H.A. Benesi, J. Hildebrand, J. Am. Chem. Soc. 71 (1949) 2703.
[48] Compendium of Analytical Nomenclature IUPAC, in: H.M.N.H. Irving, H. Freiser, T.S. West (Eds.), Definitive Rules, Pergamon Press, Oxford, 1981.
[49] J.C. Miller, J.N. Miller, Statistics in Analytical Chemistry, third ed., Ellis Horwood, Chichester, 1993.
[50] G.H. Jeffery, J. Bassett, J. Mendham, R.C. Dennery, Vogel's Textbook of Practical Organic Chemistry, fifth ed., Longman Group UK Ltd., England, 1989, pp. 1442–1444.

Talanta 80 (2009) 158–162

Contents lists available at ScienceDirect

Talanta

journal homepage: www.elsevier.com/locate/talanta

Separation and preconcentration of trace amounts of aluminum ions in surface water samples using different analytical techniques

Sumaira Khan [1], Tasneem G. Kazi*, Jameel A. Baig [1], Nida F. Kolachi [1], Hassan I. Afridi [1], Abdul Q. Shah [1], Ghulam A. Kandhro [1], Sham Kumar [1]

Center of Excellence in Analytical Chemistry, University of Sindh, Jamshoro 76080, Pakistan

ARTICLE INFO

Article history:
Received 24 April 2009
Received in revised form 16 June 2009
Accepted 17 June 2009
Available online 3 July 2009

Keywords:
Aluminum
Water sample
8-Hydroxyquinoline
Triton X-114
Cloud point extraction

ABSTRACT

A separation/preconcentration of aluminum (III) (Al^{3+}) has been developed to overcome the problem of high matrix species, which may interfere with the determination of trace quantity of Al^{3+} in natural water samples. The separation of Al^{3+} in water samples was carried out from interfering cations by complexing them with 2-methyle 8-hyroxyquinoline (quinaldine) on activated silica. Whereas the separated trace amounts of Al^{3+} was preconcentrated by cloud point extraction (CPE), as prior step to its determination by spectrofluorimetry (SPF) and flame atomic absorption spectrometry (FAAS). The Al^{3+} react with 8-hydroxyquinoline (oxine) and then entrapped in non-ionic surfactant Triton X-114. The main factors affecting CPE efficiency, such as pH of sample solution, concentration of oxine and Triton X-114, equilibration temperature and time period for shaking were investigated in detail. The validity of separation/preconcentration of Al^{3+} was checked by certified reference material of water (SRM-1643e). After optimization of the complexation and extraction conditions, a preconcentration factor of 20 was obtained for Al^{3+} in 10 mL of natural water samples. The relative standard deviation for 6 replicates containing 100 $\mu g\,L^{-1}$ of Al^{3+} was 5.41 and 4.53% for SPF and FAAS, respectively. The proposed method has been applied for determination of trace amount of Al^{3+} in natural water samples with satisfactory results.

© 2009 Elsevier B.V. All rights reserved.

1. Introduction

Aluminum (Al^{3+}) is a non-essential, toxic metal to which humans are frequently exposed. Normally it is very insoluble and in most neutral natural waters its concentration is very low. In recent years, however, a large amount of Al^{3+} has been released into the environment through water acidification, waste discharge, and soils extract from acidic rain. The maximum permissible content of Al^{3+} in drinking water is only 200 $\mu g\,L^{-1}$ [1]. Nowadays, much interest has been raised by the toxicity and biological effect of Al^{3+} [2]. Some studies suggested that Al^{3+} may be accumulated in the brain via different routes (drinking waters, food, and medicines) and interfere with the normal activities of nervous system [3,4]. This metal ion has been considered as a possible cause of renal osteodystrophy, Parkinson and Alzheimer disease [4]. The determination of very low levels of Al^{3+} has become increasingly very important in environmental and clinical chemistry since its negative role in the human life [5]. Therefore, there is a strong need for Al^{3+} monitoring in natural water resources [6].

There are a variety of analytical techniques such as, atomic absorption spectrometry [7], inductively coupled plasma-atomic emission spectrometry (ICP-AES) and spectrofluorimetry are used for the determination of Al^{3+} in environmental samples [8,9]. However, all of the techniques are required enrichment methods for the determination of trace amounts of Al^{3+} [10].

Due to presence of interfering cations such as iron (Fe^{3+}), chromium (Cr^{3+}), copper (Cu^{2+}), lead (Pb^{2+}) and zinc (Zn^{2+}) in environmental samples or the presence of Al^{3+} below the detection limit, becomes difficult for accurate determination of Al^{3+} by spectroscopic techniques [11]. So, the separation and preconcentration steps for Al^{3+} contents are still necessary to applying simple and less expensive techniques such as spectrofluorometry (SPF) and flame atomic absorption spectrometry (FAAS) [12,13]. The widely used techniques for the separation and preconcentration of Al include liquid–liquid extraction [14], ion exchange [15], solid-phase extraction (SPE) [16] and cloud point extraction (CPE) [17]. Separation and preconcentration based on SPE and CPE are important alternatives and have a lot of practical applications in the field of surface chemistry [16,18]. The SPE and CPE are offered the most frequently used extraction methodologies, which are simple, cheap, most

* Corresponding author. Tel.: +92 022 2771379; fax: +92 022 2771560.
E-mail addresses: skhanzai@gmail.com (S. Khan), tgkazi@yahoo.com (T.G. Kazi), jab_mughal@yahoo.com (J.A. Baig), nidafatima6@gmail.com (N.F. Kolachi), hassanimranafridi@yahoo.com (H.I. Afridi), aqshah07@yahoo.com (A.Q. Shah), gakandhro@yahoo.com (G.A. Kandhro), wadhwashamkumar@yahoo.com (S. Kumar).
[1] Tel.: +92 022 2771379; fax: +92 022 2771560.

0039-9140/$ – see front matter © 2009 Elsevier B.V. All rights reserved.
doi:10.1016/j.talanta.2009.06.055

efficient and less toxic than other extraction methods [19]. Recently, the SPE technique has become increasingly popular, by using a suitable complexing reagent which initiates the separation or elimination of interference [20]. The CPE is based on the preconcentration of metal ions after the formation of sparingly water-soluble complexes in the surfactant-rich phase prior to the determination by different spectrophotometric techniques [21,22]. The CPE coupled with spectrophotometry for the determination of Al^{3+} has also been reported [23]. In addition, the cloud point strategies can enlarge the FAAS applications, because depending on preconcentration factors obtained, its sensitivity can significantly be increases, thus making the method more advantageous when compared with those bases on direct determination using electrothermal atomic absorption spectrometry and ICP-AES techniques [24].

The complexing reagent 8-hydroxyquinoline (oxine) has been acknowledged as one of the most sensitive organic ligands used for the determination of Al^{3+} [25,26]. It forms a highly fluorescent complex, without showing any intrinsic fluorescence itself. In the extraction of Al^{3+} by complexing with oxine, the interference of Fe^{3+}, Cu^{2+}, Cr^{3+}, Zn^{2+} and other metals ions, which are made complex with oxine, can be eliminated partly by using a masking agent, but it is inconvenient in operation and not very sensitive because of the use of organic reagent [16].

The aim of present work was to develop and establish a separation/preconcentration of trace quantity of Al^{3+} in surface water (river, canal and lake) samples. For separation of Al^{3+} from other interfering cations, 2-methyl 8-hydroxyquinoline (quinaldine) was used which is selective for complexation with different metal ions adsorbed on activated silica, while for enrichment of separated Al^{3+}, a CPE was used to react with oxine and resulted complex entrapped by Triton X-114 prior to its determination by SPF technique, and for comparative purpose FAAS with nitrous oxide-acetylene flame. Several experimental variables affecting the method sensitivity and stability were investigated in detail. The proposed method has been applied for determination of trace amount of Al^{3+} in surface water samples of different origin with acceptable results.

2. Experimental

2.1. Instrumentation

A centrifuge of WIROWKA Laboratoryjna type WE-1, nr-6933 (speed range 0–6000 rpm, timer 0–60 min, 220/50 Hz, Mechanika Phecyzyjna, Poland) used for centrifugation. The pH was measured by pH meter (720-pH meter, Metrohm) and global positioning system (iFinder GPS, Lowrance, Mexico) was used for sampling locations [27]. Fluorescence measurement of Al–oxine was made on a Shimadzu RF-510 (Kyoto, Japan) spectrofluorophotometer equipped with a 150 W Xenon lamp and using 1.00 cm quartz cells. Instrument excitation and emission slits were adjusted to 10 nm. The concentration of Al^{3+} in extracts was also determined by a double beam PerkinElmer model A Analyst 700 atomic absorption spectrometer (Norwalk, CT, USA) equipped with deuterium background correction. An aluminum hollow-cathode lamp was used as radiation source at wave length (nm) 309.3, slit width (nm) 1.3, and lamp current (10 mA). The Al^{3+} was measured under optimized operating conditions by FAAS with fuel (acetylene 0.45 kg cm^{-1}) and oxidant (nitrous oxide as oxidant = 1.6 kg cm^{-2}) at burner height (12.5 mm).

2.2. Reagents

Ultrapure water obtained form ELGA labwater system (Bucks, UK), was used throughout the work. The non-ionic surfactant Triton X-114 was obtained from Sigma (St. Louis, MO, USA) and was used without further purification. Stock standard solution of Al^{3+} at a concentration of 1000 μg L^{-1} was obtained from the Fluka Kamica (Bush, Switzerland). Working standard solutions were obtained by appropriate dilution of the stock standard solutions before analysis. Concentrated nitric acid, hydrochloric acid were analytical reagent grade from Merck (Darmstadt, Germany) and were checked for possible trace Al^{3+} contamination by preparing blanks for each procedure. The 8-hydroxy quinoline and 2-methyl 8-hydroxyquinoline were obtained from (Merck), both reagents were prepared by dissolving appropriate amount of these reagents in 10 mL ethanol (Merck) and diluting to 100 mL with 0.01 M acetic aid and were kept in refrigerator (4 °C) for one week. The 0.01 mol L^{-1} acetate buffer was used to control the pH of the solutions. The pH of the samples was adjusted to the desired pH (3–8) by the addition of 0.1 mol L^{-1} HCl or NaOH solution in acetate buffer. For the accuracy of methodology, certified reference material of water SRM-1643e (National Institute of Standards and Technology (NIST), Giathersburg, MD, USA) was used.

For analysis of trace quantity of Al^{3+}, contamination is a serious problem. Hence, the utmost care was taken in preparing standards and samples, and the working area around the instruments was kept as clean as possible, especially for the determination of Al^{3+} by SPF technique. The glass and plastic wares were soaked in 10% nitric acid overnight and rinsed many times with deionized water prior to use to avoid contamination.

2.3. Sampling

The surface water samples of different origin (river, canal and lake) were collected on alternate month in 2008 from 210 sampling sites of Jamshoro, Sindh (southern part of Pakistan) with the help of Global positioning system (GPS). The understudy district positioned between 25°19′–26°42′N and 67°12′–68°02′E. The sampling network was designed to cover a wide range of determinates of whole district. From each sampling site, a fresh surface water samples from canal (CS), river (RS), and lake (LS) were collected from main stream of five to six different sampling points at a depth of 20–30 cm. The collection of surface water samples was performed by using Van Dorn plastic bottles (1.5 L capacity) and was kept in well stoppered polyethylene plastic bottles previously soaked in 10% nitric acid for 24 h and rinsed with ultra pure water. All water samples were filtered through a 0.45 μm pore size membrane filter to remove suspended particulate matter and were stored at 4 °C.

2.4. Solid-phase extraction

For separation of Al^{3+} from different interfering cationic species present in matrices of water samples, a glass column with an inner diameter of 20 mm and a length of 25 cm was filled up to a height of about 20 cm with activated silica gel at 100 °C. Prior to use, the column was preconditioned with buffer solution (acetate buffer pH 6.2), and passed 10 mL of 0.1 mol L^{-1} quinaldine solution prepared in ethyl alcohol-acetic acid at pH 6.2. A 25 mL of replicate six sample of SRM and real water samples were passed through this column to separate Al^{3+} from other interfering cations at the flow rate of 0.5–5.0 mL min^{-1}. The treated SRM and real water samples were then divided into two sub-samples of 10 mL each. After several separation experiments (n = 20), the column was rinsed with 10% ethanol in 0.1 mol L^{-1} HNO_3 and deionized water then used for further experiments.

2.5. Cloud point extraction

For Al^{3+} preconcentration, aliquots of 10 mL of standard solutions containing Al^{3+} (in the range of 10–200 μg L^{-1}), replicate six samples of SRM, surface water samples, treated with quinaldine to

remove interfering species were simultaneously preconcentrated by CPE. The same sub-samples of SRM and water without removing interfering cations were taken in graduated centrifuge tubes and subjected to preconcentration for comparison purposes.

In 10 mL of each standard SRM, and real samples, added 0.2–0.8 mL of oxine solution (6.90×10^{-3} mol L^{-1}), 2 mL of Triton X-114 (0.05–0.2%, v/v) and 2 mL of different buffers to adjust a pH range of 4–8. The tubes were placed in an ultrasonic bath at 30–70 °C for 10–30 min. After different time intervals, the separation of the two phases was achieved and then centrifuged for 5 min at 3500 rpm ($1852 \times g$). The contents of tubes were cooled in an ice-bath, the surfactant-rich phase became viscous and the supernatant aqueous phase was decanted.

To decrease the viscosity of one of the duplicate extracts, added 0.5 mL of ethanol–water mixture (1:1) and fluorescence intensity of obtained Al^{3+} chelate in the micellar phase was measured by SPF at $\lambda_{excitation}$ 375 ± 3 nm and $\lambda_{emission}$ at 510 ± 3 nm against a corresponding reagent blank. While simultaneously, the viscosity of surfactant-rich phase of other sub-sample was decreased by adding acidic-ethyl alcohol (0.1 mol L^{-1} HNO_3) and introduced into flame by conventional aspiration. A blank submitted to the same procedure was measured parallel to the calibration solutions of standards, SRM and real samples.

3. Results and discussion

To overcome the problem of high matrices concentration, which is thought to interfere with the determination of low levels of Al^{3+} in environmental samples. The Al^{3+} was separated from interfering species in real water sample by adsorbing on quinaldine modified silica, then separated Al^{3+} was react with oxine in a micellar medium and form a hydrophobic complex (Al–oxine), which is subsequently trapped in the non-ionic surfactant and separated from the aqueous phase. The oxine is strong chelators for Al^{3+} and gives rise to fluorescent complex [20,5]. To check the accuracy of the SPE and CPE, the results obtained by spectrofluorimetry were compared with those obtained by FAAS.

3.1. Optimization of SPE

As reported earlier that Al^{3+} was not reacted with quinaldine due to stearic hindrance of the methyl group at the 2-position of aromatic ring [28]. The quinaldine adsorbed on activated silica used as absorbent for SPE of interfering species (Fe^{3+}, Cr^{3+}, Cu^{2+}, Pb^{2+} and Zn^{2+}), which can quantitatively eliminate the interfering cations at pH 5.5 with high adsorption capacity. The separation of Al^{3+} from interfering ions is necessary for determination of its trace quantity, particularly to measure the fluorescence intensity of Al–oxine complex using SPF technique.

3.1.1. Effect of pH on sorption

The influence of pH on the retention of interfering elements was determined. The pH ranges of (4–8) of standards solution of interfering ions, SRM and real water samples were adjusted by buffer solution with either 0.1 mol L^{-1} nitric acid or sodium hydroxide. These solutions were then passed through the column at 0.5–5.0 mL min^{-1}. It was found that the maximum retention of interfering ions were achieved at pH 5.0–6.0 and begins to decrease when the solution is over pH 6.5. Therefore, the pH 5.5 was used for separation of Al^{3+} ions from interfering cations.

3.1.2. Effect of flow rate on sorption

The retention of interfering ions on the quinaldine modified silica was studied at different flow rates. The separation of Al was >95% at optimum flow rate of the sample solution up to 2 mL min^{-1}. However, at a flow rate above 5 mL min^{-1}, there was a decrease in the sorption percentage of interfering ions, because ligand formation between interfering ions and quinaldine is slow at room temperature. The retention of interfering ions was confirmed by FAAS (not reported) and for further work a 1.0 mL min^{-1} flow rate was selected. The SPE is a highly selective and sensitive method for simple and quick elimination of interfering of matrixes elements, to determined fluorescence intensity of Al–oxine chelate.

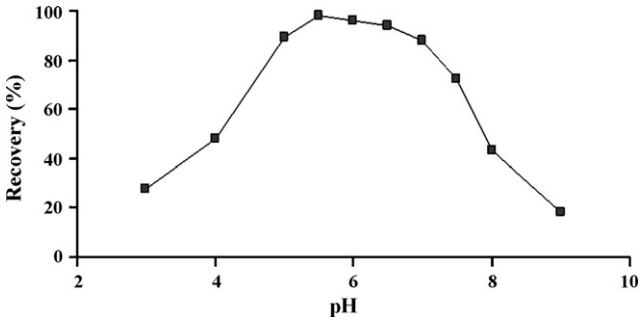


Fig. 1. Effect of pH on the spectrofluorimetric responses: 100 μg L^{-1} Al, 6.85×10^{-5} mol L^{-1} 8-HQ, 0.1% (w/v) Triton X-114, temp. 40 °C, stirring time 20 min.

3.2. Optimization of CPE

3.2.1. pH effects

The pH plays a distinctive role on metal-chelate formation and subsequent extraction, this factor is proved to be a main parameter for CPE method. The replicate six standard, SRM and real sample solution of Al^{3+} (100 μg L^{-1}) were adjusted to the pH range of (pH 3–8), each desired pH value was obtained by the addition of 0.1 mol L^{-1} HNO_3 and/or 0.1 mol L^{-1} NaOH solution in the presence of acetate buffer solution. Fig. 1 shows the effect of pH on the extraction recovery of Al-oxinate which were calculated on the basis of certified value of Al in SRM and in the surfactant-rich solution after CPE using SPF. As can be seen that quantitative extraction (>96%) was obtained for Al^{3+} in the pH range of 5–7 and starts to decrease after pH 7.0. Hence, a pH of 6.5 was chosen for optimum CPE of Al^{3+}. Based on the obtained results, there may be no need for adjusting the pH in the case of understudy water samples, because their pH values fall near to the required range (6.8–7.5), while it was also observed that after pH 7, abrupt decline in % recovery.

3.2.2. Effect of oxine concentration

The % recovery of Al^{3+} as a function of the concentration of the chelating agent, oxine is shown in Fig. 2, where 10 mL of standard, SRM and real sample solution containing Al^{3+} in the presence of 0.1% (w/v) Triton X-114 and added appropriate buffer solution to kept pH 6.5 and concentrations of oxine solutions in the range of $(1.37–10.9) \times 10^{-5}$ (0.1–0.8 mL from 1.37×10^{-3} mol L^{-1}

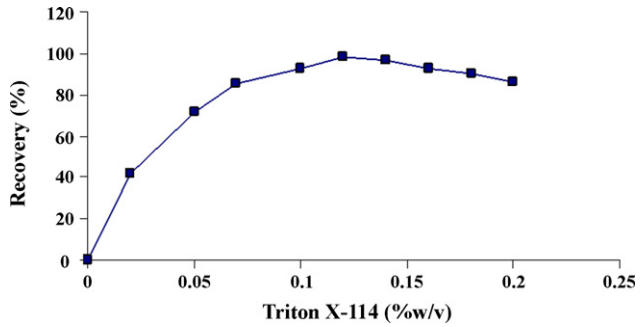


Fig. 2. Effect of oxine concentration on the %recovery: 100 μg L^{-1} Al, 0.1% (w/v) Triton X-114, pH 6.5, temp. 40 °C, stirring time 20 min.

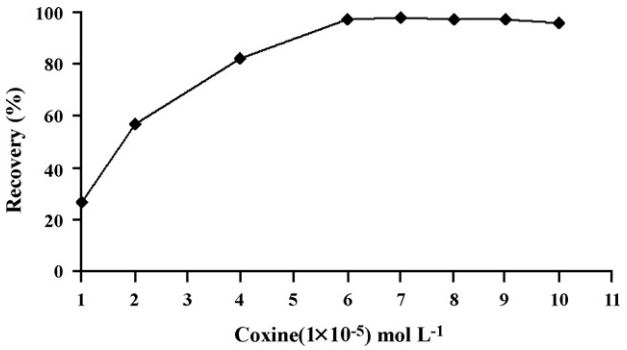


Fig. 3. Effect of Triton X-114 on the %recovery: 100 μg L^{-1} Al, 6.85 × 10^{-5} mol L^{-1} 8-HQ, pH 6.5, temp. 40 °C, stirring time 20 min.

oxine solution) were subjected to cloud point preconcentration. The extraction efficiency of Al^{3+} increases up to 6.85 × 10^{-5} mol L^{-1} of oxine, then reaching a plateau, indicated that this amount of oxine is sufficient for total complexation and the extraction. The concentrations above this value have no significant effect on the efficiency of CPE. The stoichiometry of the Al–oxine ternary complex, as reported in literature is 1:3 ratios [29].

3.2.3. Effect of Triton X-114 concentration

In present work Triton X-114 was chosen because of its higher extraction efficiency and lower cloud point temperature as compared with other reported surfactants [30]. The low cloud point temperature avoids back extraction during centrifugation. Fig. 3 shows the variation in extraction efficiency of Al–oxine complex within the concentration range of 0.05–0.2% (w/v) of Triton X-114, while other factors were at optimum levels. The 60–70% recovery was observed at 0.05% of Triton X-114, while the extraction efficiency reaches a maximum in the concentration range of 0.1–0.15%. A concentration of 0.1% (w/v) of Triton X-114 was chosen as the optimum surfactant concentration in order to achieve the highest possible extraction recovery of Al^{3+} from standards, SRM and real samples. Whereas at lower than 0.1% of Triton X-114, the extraction efficiency of complexes is low probably because of the inadequacy of the assemblies to entrap the hydrophobic complex quantitatively, on the contrary at higher concentrations, the signals decrease because of the increment in the volumes and the viscosity of the surfactant phase (ethanol–water for SPF and ethanol–nitric acid for FAAS) to reducing the viscosity of the surfactant.

3.2.4. Effect of temperature and time

A sufficiently long reaction time was allowed for the Al–oxine complex formation to precede up to 300 min at room temperature. The effects of equilibration temperature and time on the analytical signal were studied in the range of 30–60 °C in ultrasonic bath for 10–60 min, respectively. In the present study low temperature was required for optimum extraction efficiency of Al^{3+}. It was observed that the optimum % recovery of Al^{3+} was achieved at equilibration temperature of >50 °C and a time of 20 min. At higher temperature the fluorescent intensity of Al–oxine complex was lowered, may effects the viscosity of medium and the number of collisions of molecules of the fluorophore with solvent molecules. So, 40 °C was chosen for further experiments. We preferred to stop the reaction at 60 min, as a longer reaction time did not increase fluorescence intensity and % recovery of Al^{3+}.

3.3. Interferences

The interferences studied were those relating to the preconcentration step, i.e. cations may react with oxine or species that may react with Al^{3+} and decrease the extraction efficiency and also interference in determination of fluorescence intensity using SPF. The interference from these ions can be eliminated by SPE using quinaldine that form chelate with these ions except Al^{3+}. To perform this study, 10 mL solution containing 100 μg L^{-1} of Al^{3+} and interfering ions in different interferent to analyte ratios were subjected to the complete procedure. The determination of Al^{3+} in the presence of Zn (50 μg L^{-1}) produce positive error and broad band in emission spectrum was observed, while Fe^{3+}, Cr^{3+}, Pb^{2+} and Cu^{2+} (1000, 20, 20 and 100 μg L^{-1}), respectively, can interfere with the determination of Al^{3+}, to produce negative effects (Table 1). Our results are not consistent with other study to determine simultaneously Al^{3+} and Zn^{2+} using oxine as chelating reagent [17].

3.4. Validity and applicability

The calibration graph using the preconcentration system for Al^{3+} was linear with a correlation coefficient of 0.9997 at 10–200 μg L^{-1}. The surfactant-rich phase was diluted with 0.5 mL of water–ethanol and the fluorescence intensity of the chelate was measured. In all cases, linear relationships between the fluorescence measured and the concentration of the Al in the standards, SRM and real water were attained. Simultaneous same sub samples diluted with acidic alcohol were subjecting to FAAS for comparison purposes.

The reproducibility was calculated as % relative standard deviation for 6 replicates containing 100 μg L^{-1} of Al^{3+}, obtained 5.41 and 4.53% for SPF and FAAS, respectively. The limit of detection (LOD) calculated (0.5 μg L^{-1}) as three times the standard deviation of the blank signals.

The obtained LOD was sufficiently low as compared to reported work [5] and to be valuable for detecting Al^{3+} in different types of surface water samples. Quantitatively accurate results were obtained by adopting matrix-matched calibration of certified standards and certified reference material of water, thus avoiding the use of more time-consuming and laborious standard additions into each sample.

The Student's *t*-test showed that the results obtained by SPF and FAAS were not significantly different at 95% confidence level (Table 1). After optimization, the preconcentration factor (CF) of 20 was achieved. The CF obtained in this work was comparable with those obtained in other CPE methods used for extraction and preconcentration of Al^{3+} [20]. It is obvious that this CF and LOD can be improved by using larger volume of initial solution or small-volume cells and diluting the surfactant-rich phase by small amounts of ethanol. The method was successfully applied to the determination of Al^{3+} in different natural water samples.

The obtained results showed variations among the concentration of Al^{3+} in surface water samples of three origins (Table 2). The concentration of Al^{3+} in RS, CS and LS water samples was

Table 1
Validation of CPE of Al^{3+} in certified sample of water SRM 1643e using spectrofluorimetry (SPF) and flame atomic absorption spectrometry (FAAS) (μg L^{-1}).

Element (Al^{3+})	Certified value of SRM 1643e (water)	SPF $\bar{x} \mp ts/\sqrt{n}$	FAAS $\bar{x} \mp ts/\sqrt{n}$	Paired *t* test[a] $t_{Experiment}$
CPE	141.8 ± 8.6	139 ± 7.5 (98.0%)	140 ± 6.4 (98.7%)	0.78
Without CPE		137 (96.6%)	138 (97.3%)	

Value in parenthesis = % recovery.

[a] $t_{certical}$ = 2.28 at 95% confidence limit (*n* = 6) (5.41) (4.53).

Table 2
Ranges of pH and Al^{3+} concentration in the surface and ground water samples of district Jamshoro, Sindh, and Pakistan.

Parameter	Unit	WHO values	Canal water			River water			Lake water		
			$n = 120$			$n = 30$			$n = 30$		
			Min	Max	Mean	Min	Max	Mean	Min	Max	Mean
pH	–	6.5–8.5	7.1	7.6	7.27	7.0	7.5	7.2	7.10	8.20	7.4
Al^{3+}	$\mu g\,L^{-1}$	200	90	150	80	10	150	90	750	1340	1000

observed in the ranges of 10.0–150, 90–150 and 750–1340 $\mu g\,L^{-1}$, respectively. The concentration of Al^{3+} in three studied origins was obtained in increasing order: RS < CS < LS. It was observed that concentration of Al^{3+} in RS and CS water samples are within WHO permissible level for drinking water [1], while in LS water samples high content of Al^{3+} was found. This can be attributed to reduction in precipitation, surface wastage runoff with rain water into understudy Lake and increasing rate of evaporation during summer [31]. All this provides evidence that anthropogenic and geological environment play a key role in the distribution of Al^{3+} in understudy water bodies. Number of epidemiological studies showed an association between Al in drinking water and Alzheimer's disease, an important form of senile dementia in man [29,32].

4. Conclusions

The separation and preconcentration methodologies for the determination of trace quantities of Al^{3+} in water samples, offers a simple, sensitive, inexpensive and non-polluting alternative to other separation/preconcentration techniques using toxic organic solvents. To the best of our knowledge, modified silica with 2-methyl 8-hydroxyquinoline as a solid-phase extractor is first time used by us to separate interference elements from environmental sample matrixes, to determine the fluorescence intensity of Al–oxine complex. The Al^{3+} is not reacting with quinaldine due to stearic hindrance effect of methyl group. The proposed CPE method gives low LOD, good RSD, less time-consuming, achievement of high enrichment factors and solvent-free extraction of trace quantity of Al^{3+} in natural water matrixes. The surfactant-rich phase can be easily diluted with ethyl alcohol–water and ethyl alcohol–0.1 mol L^{-1} HNO_3 systems prior to its determination by SPF and FAAS. Due to versatility, it can be applied to the monitoring of trace quantity of Al^{3+} in various samples of environmental, toxicological and clinical analysis.

References

[1] WHO, Aluminium, World Health Organization, International Programme on Chemical Safety, Geneva, 1997 (Environmental Health Criteria 194).
[2] M. Venturini-Soriano, G. Berthon, J. Inorg. Biochem. 71 (1998) 135.
[3] G.L. Klein, Curr. Opin. Pharmacol. 5 (2005) 637.
[4] M. Soylak, U. Sahin, A. Ulgen, L. Elci, M. Dogan, Anal. Sci. 13 (1997) 287.
[5] M. Buratti, C. Valla, O. Pellegrino, F.M. Rubino, A. Colombi, Anal. Biochem. 353 (2006) 63.
[6] J. Tria, E.C.V. Butler, P.R. Haddad, A.R. Bowie, Anal. Chim. Acta 588 (2007) 153.
[7] L. Zhu, K. Li, S. Zhou, Q. Hu, G. Yang, Z. Huang, J. Chen, Asian J. Chem. 20 (2008) 4433.
[8] B. Bocca, A. Alimonti, F. Petrucci, N. Violante, G. Sancesario, G. Forte, O. Senofonte, Spectrochim. Acta B 59 (2004) 559.
[9] A. Sanz-Medel, A.B. Soldado Cabezuelo, R. Milacic, T. Bantan Polak, Coordin. Chem. Rev. 228 (2002) 373.
[10] I. Narin, M. Tuzen, M. Soylak, Talanta 63 (2004) 411.
[11] E.K. Paleologos, C.D. Stalikas, S.M. Tzouwara-Karayanni, M.I. Karayannis, Anal. Chim. Acta 436 (2001) 49.
[12] E.K. Paleologos, C.D. Stalikas, M.I. Karayannis, Analyst 126 (2001) 389.
[13] E.K. Paleologos, C.D. Stalikas, S.M. Tzouwara-Karayanni, G.A. Pilidis, M.I. Karayannis, J. Anal. At. Spectrom. 15 (2000) 287.
[14] J. Komarek, R. Cervenka, T. Ruzicka, V. Kuban, J. Pharm. Biomed. Anal. 45 (2007) 504.
[15] S.B. Erdemoglu, K. Pyrzyniska, S. Gucer, Anal. Chim. Acta 411 (2000) 81.
[16] M.B. Luo, S.P. Bi, J. Inorg. Biochem. 97 (2003) 173.
[17] A.B. Tabrizi, Food Chem. 100 (2007) 1698.
[18] S. Rubio, D. Perez-Bendito, Trends Anal. Chem. 22 (2003) 470.
[19] C.D. Stalikas, Trends Anal. Chem. 21 (2002) 343.
[20] P. Vanloot, J.L. Boudenne, L. Vassalo, M. Sergent, B. Coulomb, Talanta 73 (2007) 237.
[21] J.L. Manzoori, A.B. Tabrizi, Anal. Chim. Acta 470 (2002) 215.
[22] M. Tuzen, M. Soylak, J. Hazard. Mater. 154 (2008) 519.
[23] L. Sombra, M.O. Luconi, M.F. Silva, R.A. Olsina, L. Fernandez, Analyst 126 (2001) 1172.
[24] M. Bahram, T. Madrakian, E. Bozorgzadeh, A. Afkhami, Talanta 72 (2007) 408.
[25] F. Papadimitrakopoulos, X. Zhang, K.A. Higginson, J. IEEE 4 (1998) 49.
[26] A. Alonso, M.J. Almendral, M.J. Porras, Y. Curto, C. García de María, Anal. Chim. Acta 447 (2001) 211.
[27] J.A. Baig, T.G. Kazi, M.B. Arain, H.I. Afridi, G.A. Kandhro, R.A. Sarfraz, M.K. Jamal, A.Q. Shah, J. Hazard. Mater. 166 (2009) 662.
[28] A. Asrar, T.G. Kazi, G.H. Kazi, J. Phys. Chem. 4 (1985) 21.
[29] A. Ohashi, A. Tsuguchi, H. Imura, K. Ohashi, Anal. Sci. 20 (2004) 1091.
[30] D.R.C. McLachlan, C. Bergeron, J.E. Smith, D. Boomer, S.L. Rifat, Neurology 46 (1996) 401.
[31] M.B. Arain, T.G. Kazi, M.K. Jamali, N. Jalbani, H.I. Afridi, A. Shah, Chemosphere 70 (2007) 1845.
[32] V. Rondeau, D. Commenges, H.G. Jacqmin, J.F. Dartigues, Am. J. Epidemiol. 1521 (2000) 59.

Talanta 80 (2009) 163–167

Contents lists available at ScienceDirect

Talanta

journal homepage: www.elsevier.com/locate/talanta

Voltammetric determination of sericin based on its interaction with carmine

Ming-Ming Ma [a,b,*], Jun-Feng Song [b]

[a] College of Environment & Chemical Engineering, Xi'an Polytechnic University, Xi'an 710048, PR China
[b] Institute of Analytical Science, Northwest University, Xi' an 710069, PR China

ARTICLE INFO

Article history:
Received 8 October 2008
Received in revised form 19 June 2009
Accepted 22 June 2009
Available online 1 July 2009

Keywords:
Sericin
Carmine
Interaction
Voltammetry

ABSTRACT

A simple yet sensitive method is developed for the determination of sericin using voltammetry based on the interaction between sericin and carmine for the first time. In the absence of sericin, carmine has a pair of well-defined redox peaks in a pH 1.81 Britton–Robinson buffer solution. Although no new redox peaks appear upon the addition of sericin into a carmine solution, the peak currents of the old peaks reduce while the peak potentials shift positively. This observation is attributed to the decrease in the diffusion coefficient and electrode reaction rate constant of carmine in the presence of sericin. A binding mechanism is proposed and discussed, and the binding constant and binding ratio are calculated as 2.32×10^6 L mol^{-1} and 1:1, respectively. Furthermore, the decrease in the peak currents is found proportional to the sericin concentration in the range of 32.0–800.0 μg mL^{-1} with a detection limit of 13.52 μg mL^{-1}. The method is further applied to the determination of sericin in degumming wastewater with satisfied average recoveries from 96.7 to 103.3%. The results are in good agreement with those obtained by the conventional Coomassie brilliant blue G-250 spectrophotometric method.

Crown Copyright © 2009 Published by Elsevier B.V. All rights reserved.

1. Introduction

Sericin (SE) is a family of water-soluble globular proteins found in silkworms. It constitutes 20–30% of cocoons and executes the function of gluing the silk fibers together and imparting strength to them [1–3]. SE has exhibited excellent moisture absorption and release properties [1,4]. It also has many desired biological properties, e.g. antibacterial activity [5], UV resistance [6], tyrosinase activity inhibition and antioxidation [7], which make SE extensively applicable in many fields, including food, cosmetics, pharmaceutical products, textile and biomaterials [8,9].

Although SE is considered a valuable natural protein source [10] widely used in above mentioned applications, so far, little work has been performed for its quantitative determination. SE is generally either extracted directly from cocoons or recovered from degumming wastewaters [11]. Therefore, a practical analytical method with simple procedures for monitoring SE is highly desired.

Several methods based on dye-binding for protein determination, such as spectrophotometry [12,13], fluorimetry [14,15], light scattering technique [16–18] and electrochemical methods, have been reported in the past [19–22]. Compared with spectroscopic methods, electro-analysis is especially suitable for studying binding reactions between dyes and proteins because the required amount of samples on the electrode/solution interface is minimal. The electro-analysis is also simple and practical yet with good selectivity, high sensitivity, low cost, rapid response and wide dynamic ranges. Thus, the electrochemical methods have attracted more and more attention in recent years.

Carmine (CA) is a monoazo dye which has been well-known to food and textile industries for a long time. Recently, it is also more and more widely applied in the electrochemistry. For example, a modified glass carbon electrode (GCE) prepared by the electro-polymerizing CA has shown great electro-catalytic properties [23–25]. However, to the best of our knowledge, there is still no report on its binding protein. In the current paper, electrochemical studies in the interactions between CA and SE at a carbon paste electrode are reported for the first time. In the presence of SE, the peak currents of CA are found to decrease with the positively moving potential. The concentration of SE is revealed linear with the decrease of the oxidative peak currents of CA. Hence, a sensitive method based on these observations can be developed for the determination of SE.

2. Experimental

2.1. Reagents

Standard SE (purity > 99%) was purchased from Zhejiang Silk Institute, China. Fresh silkworms were obtained from Hangzhou Jin Li Silk Limited Company, China. An SE standard solution (1.00 g L^{-1})

* Corresponding author. Fax: +86 029 82330169.
E-mail address: mmm0002007@yahoo.com.cn (M.-M. Ma).

0039-9140/$ – see front matter. Crown Copyright © 2009 Published by Elsevier B.V. All rights reserved.
doi:10.1016/j.talanta.2009.06.045

was prepared by dissolving SE in twice-distilled water and stored at 4 °C before use. CA (analytical pure) was purchased from Beijing Hongxing Chemical Plant, and its solution (9.91×10^{-4} mol L^{-1}) was prepared and used as a stock solution. Working solutions were thus prepared by diluting the stock solution to certain concentrations prior to use.

Graphite powders (spectral pure) were purchased from Tianjing Fendeng Reagent Corporation, China, while di-methyl silicone oil (chromatographic pure) was from Chengdu Kelong Reagent Corporation, China. All other chemicals were of analytical-reagent grade or better. Twice-distilled water was used throughout the experiments.

2.2. Apparatus

All voltammetric experiments were performed by a CHI 660A electrochemical workstation (Shanghai Chenghua, China) with a three-electrode configuration: a homemade carbon paste working electrode (CPE), a saturated calomel reference electrode (SCE) and a platinum wire auxiliary electrode. UV–Vis absorption spectra were recorded on a model UV-2450 PC UV–Vis spectrophotometer (Shimadzu, Japan). pH values of all solutions were measured with a RHSJ-4A pH meter (Shanghai Ridao, China), which was first calibrated with three common standard pH buffer solutions at 25 °C. These standard pH buffer solutions were potassium hydrogen phthalate (pH 4.01), potassium phosphate monobasic–sodium phosphate dibasic (pH 6.86) and sodium tetraborate (pH 9.18).

2.3. General procedure

To a 10 mL volumetric flask, a CA solution (2.0 mL, 9.91×10^{-4} mol L^{-1}), a Britton–Robinson buffer (2.0 mL, 0.04 mol L^{-1}, pH 1.81), and appropriate amounts of the standard SE solution or a degumming wastewater sample were added consecutively. The mixture was further diluted to 10 mL with twice-distilled water and then mixed homogeneously at room temperature. After 40 min, it was transferred into a voltammetric cell. The oxidative peak current (i_{pa}) was recorded in the potential range of 0.40–1.00 V (*vs.* SCE) by square wave voltammetry with the following parameter settings: frequency 20 Hz, pulse amplitude 80 mV, and scan increment 4.0 mV.

Under the same conditions, the mixture without the addition of SE was used as the blank solution and the voltammetric peak current ($i_{pa,0}$) was also recorded. The differences between these two peak currents ($\Delta i = i_{pa,0} - i_{pa}$) were calculated and used to indicate the changes in the electrochemical responses in the reaction systems.

The degumming wastewater samples were prepared as follows: The cocoon silk of silkworms was first degummed with 5.0 g L^{-1} Na_2CO_3 solution at 90 °C. The degumming wastewater was then collected, and its pH was adjusted to neutral with 0.1 mol L^{-1} HCl before it was used in analysis.

The spent CPE was renewed after each measurement. The preparation and renewal of the CPE were similar to reference reported [26] except that the ratio of the graphite powder and di-methyl silicone oil in the CPE was 7:3 (m/m). All the potentials reported in this work were referred to the SCE, and all the experiments were carried out at room temperature (25 ± 2 °C) unless described otherwise.

3. Results and discussion

3.1. Spectra and voltammetry characteristics

Fig. 1 showed the UV–Vis absorption spectra of CA in both the absence (CA system) and presence of SE (CA–SE system). With the

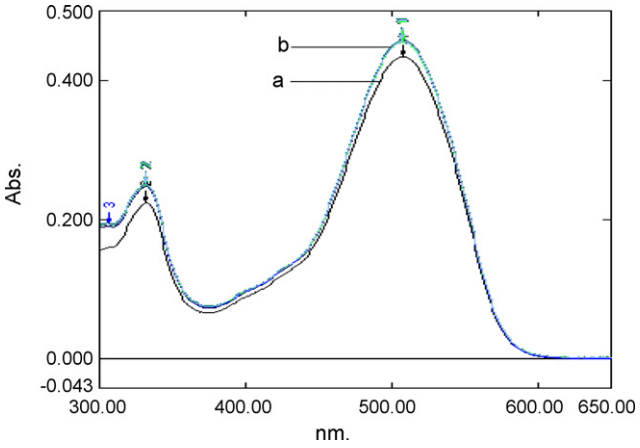


Fig. 1. UV–Vis absorption spectra of CA in the absence (a) and presence of SE (b) in the pH 1.81 Britton–Robinson buffer solution. C_{CA}: 2.00×10^{-5} mol L^{-1}; C_{SE}: 80.0 μg mL^{-1}; Reaction time: 20 min.

pH 1.81 Britton–Robinson buffer solution and in the scanning range of 300–650 nm, CA showed a maximum absorption peak at 508 nm (curve a). When SE was mixed with CA, the absorbance of CA at 508 nm increased without any shift in the maximum absorption wavelength (curve b), which suggested a binding reaction between CA and SE took place and a new complex was formed.

Cyclic voltammograms of the CA and CA–SE systems were recorded under certain conditions, and the results were shown in Fig. 2. In the potential range of 0.30–1.20 V and with the potential scan rate of 0.10 V s^{-1}, a pair of well-defined oxidative and reductive peaks at 0.71 and 0.60 V (both *vs.* SCE) with peak currents 20.79 and 18.57 μA, respectively, was observed in the CA system (curve a); but no voltammetric response was recorded in the SE system (curve b). For the CA–SE system (curve c), no new redox peaks appeared in the same scan potential range. However, the peak currents of the old oxidative and reductive peaks decreased to 12.70 and 12.20 μA, and their peak potentials shifted positively to 0.77 and 0.64 V, respectively. These results suggested that there were interactions existing between CA and SE.

On the other hand, like other proteins, the dissociation of SE in an aqueous solution can be expressed as follows [27]:

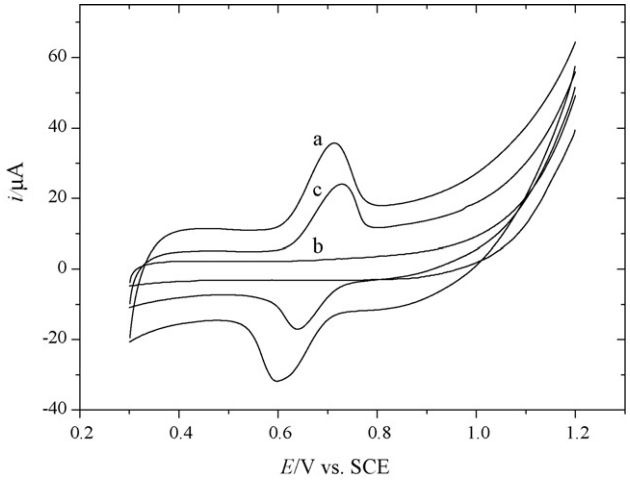


Fig. 2. Cyclic voltammograms of CA (a), SE (b) and CA – SE (c) in the pH 1.81 Britton–Robinson buffer solution. C_{CA}: 1.98×10^{-4} mol L^{-1}; C_{SE}: 200.0 μg mL^{-1}; Scan rate: 0.10 V s^{-1}.

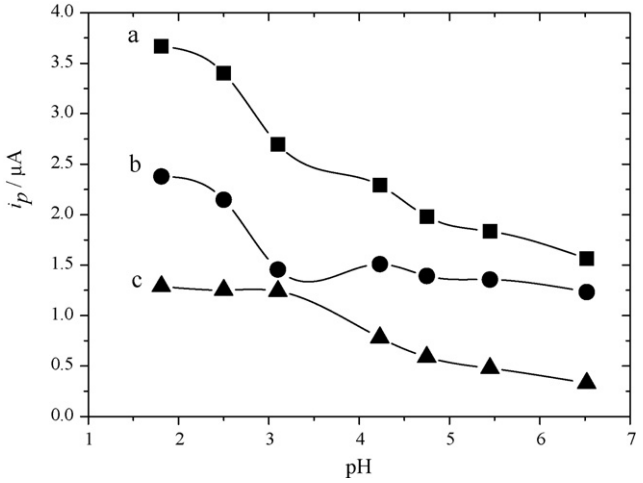
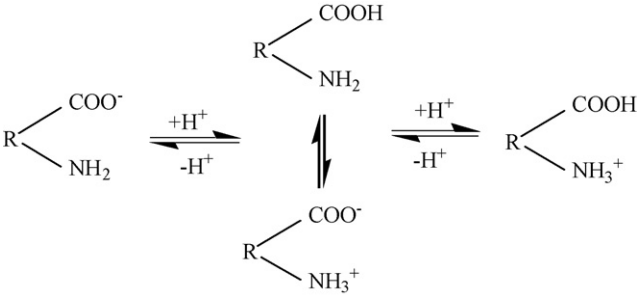
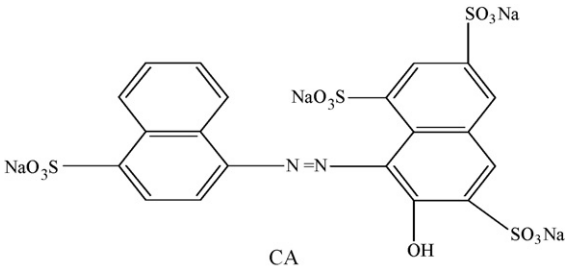


Fig. 3. Influence of pH over oxidative peak currents of the CA in the absence (a) and presence of SE (b). C_{CA}: 1.98×10^{-5} mol L^{-1}; C_{SE}: 200.0 μg mL^{-1}; Curve (c): the plot of Δi *vs.* pH.



Moreover, the isoelectric point (pI) of SE is in the range of 3.8–4.5. Thus, in the pH 1.81 Britton–Robinson buffer solutions, SE was positively charged, while CA was negatively charged because of the deprontonated of sulfonic groups. According to Refs. [21,22], the binding of proteins with small molecules can result from either ionic, van der Waals and hydrogen bonding, electrostatic binding, or hydrophobic interactions. Therefore, it was possible that the electrostatic attraction played a key role in the interactions of CA with SE here.



3.2. Analytical application

3.2.1. Optimization of reaction conditions and SWV parameters

The oxidative peak of CA was used as the study signal because it was much more sensitive than the reductive one. Different supporting electrolytes, such as H_2SO_4, HAc–NaAc and Britton–Robinson buffers, were investigated, and the response in the Britton–Robinson buffer was the strongest. The influence of pH over the peak currents of CA in both the absence and presence of SE was studied in the pH range of 1.81–6.52, and the results were shown in Fig. 3. As shown, the difference of the peak currents reached a maximum at pH 1.81. So the pH 1.81 Britton–Robinson buffer was selected as the supporting electrolyte in all measurements. In addition, in the final 10 mL solution, the 0.04 mol L^{-1} Britton–Robinson buffer (pH 1.81) performed well with the volume of 1.5–3.5 mL, thus the 2.0 mL volume of the buffer solution was chosen for the reactions.

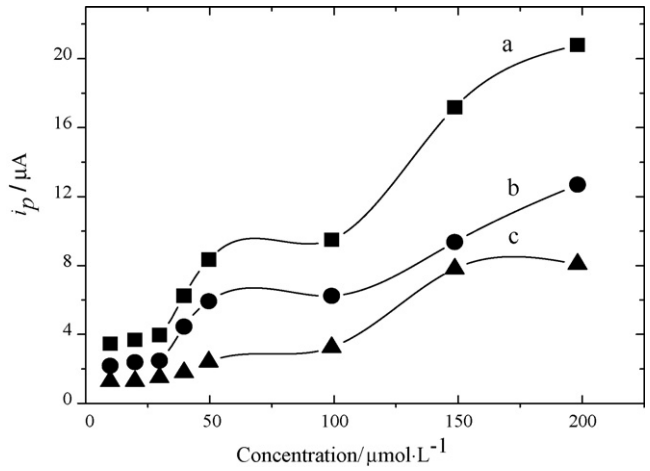


Fig. 4. Effects of CA concentrations on oxidative peak currents of the CA (a), CA – SE systems (b), and Δi (c) in the pH 1.81 Britton–Robinson buffer solution. C_{SE}: 200.0 μg mL^{-1}.

Different addition orders of CA, SE and Britton–Robinson buffer solutions were also studied. The best addition sequence was found to be CA, the Britton–Robinson buffer and then SE in terms of stability and intensity of the voltammetric response, which suggested that mixing CA with the Britton–Robinson buffer solution as the first step provided a proper acidic condition for the dissociation of CA and SE and the combination of CA with SE by the electrostatic binding mode.

The temperature influence over the reaction systems was investigated at 15 °C, room temperature (25 ± 2 °C), and 40, 60 and 90 °C. No obvious differences were observed among these temperatures. So room temperature was used throughout the experiments because of its simplicity. After CA and SE were mixed, the difference in the peak currents reached a maximum when the reaction underwent for 40 min at room temperature, and then the difference remained almost a constant for at least 2 h. Therefore, the reaction time of 40 min was used in later measurements.

The influence of the CA concentration was studied subsequently. As illustrated in Fig. 4, curve a was the plot of $i_{pa,0}$ *vs.* the CA concentration; curve b represented the change of i_{pa} at various concentrations of CA in the presence of 200.0 μg mL^{-1} SE, and curve c was the differences between curves a and b, which revealed the correlation between Δi and the concentration of CA. With the increase of the CA concentration from 9.91×10^{-6} to 9.91×10^{-5} mol L^{-1}, the Δi raised gradually; when the final CA concentration was in the range of 1.49×10^{-4} to 1.98×10^{-4} mol L^{-1}, the Δi reached a maximum and remained basically unchanged thereafter. Therefore, 1.49×10^{-4} mol L^{-1} CA was used in later assays.

Square wave voltammetry (SWV) was proposed because it was much more sensitive than cyclic voltammetry. The SWV parameters were optimized for the CA–SE system (1.49×10^{-4} mol L^{-1} CA + 200.0 μg mL^{-1} SE) in the pH 1.81 Britton–Robinson buffer. At scan increment of 4 mV and pulse amplitude of 25 mV, the oxidative peak currents increased with the rise of the frequency and reached the maximum at 20 Hz; when the frequency was above 20 Hz, the peak currents started to decrease gradually. The optimum pulse amplitude was examined at the 20 Hz frequency and 4 mV scan increment. Although the peak currents increased with the increase of the pulse amplitude from 15 to 100 mV, a much better-defined

Table 1
Results for the determination of SE in degumming wastewater ($n = 6$).

Samples	Degumming time (min)	Number of times for degumming	SWV -method			CBBG-250-method			$t_{calculated}$ [b]
			C_{SE} ($\mu g\,mL^{-1}$)	SD[a]	Average recovery (%)	C_{SE} ($\mu g\,mL^{-1}$)	SD[a]	Average recovery (%)	
1	15	2	208.94	5.22	98.6	206.89	3.93	100.3	0.77
2	35	1	530.21	20.76	96.7	526.03	14.20	104.2	1.71
3	45	1	688.36	28.22	103.3	680.21	21.09	98.9	0.55

[a] Standard deviation.
[b] The value of calculated *t*-test.

and sharper peak was obtained at 80 mV. Thus, the pulse amplitude of 80 mV was chosen for the assays.

3.2.2. Calibration curve and detection limit

Under the above selected optimum conditions, the peak current difference Δi was linear with the SE concentration in the range between 32.0 and 800.0 $\mu g\,mL^{-1}$ with a linear regression equation as follows: $\Delta i = 16.77 + 0.05C_{SE}$ ($\mu g\,mL^{-1}$) ($R = 0.999$ and $n = 5$). The detection limit was 13.52 $\mu g\,mL^{-1}$ ($3\sigma/s$, where σ is the standard deviation of the intercept, and s is the slope of the calibration curve). The reproducibility of the proposed method was tested with a 200.0 $\mu g\,mL^{-1}$ SE solution. The relative standard deviation of Δi was calculated at 3.22% for seven parallel measurements. Therefore, the method was sensitive and reproducible.

3.2.3. Effect of coexisting species

The effect of coexisting substances, such as metal ions and amino acids, over the measurement in the 200.0 $\mu g\,mL^{-1}$ SE solution was studied. The tolerance limit of the interference was determined when the maximum concentration gave a relative error <±5%. No interference was found with 800-fold Na^{2+}, Cl^-, 200-fold Zn^{2+}, Mn^{2+}, 50-fold Cu^{2+}, 30-fold Al^{3+}, 35-fold tyrosine monomer, 40-fold tryptophan monomer, and 100-fold other 16 kinds of amino acid monomers, such as glycine, alanine, valine, leucine, isoleucine, phenylalanine, serine, threonine, cystine, aspartic acid, glutamic acid, methionine, arginine, lysine, histidine and proline. Thus, the proposed method was effective for the determination of SE.

3.2.4. Sample determination

The proposed method was further applied to monitor SE in the degumming wastewater. The obtained results were compared with those measured using the Coomassie brilliant blue G-250 spectrophotometric method. Student's *t*-test was also used to evaluate the two methods. As shown in Table 1, the average recovery of SE for the two methods was from 96.7 to 103.3% and 98.9 to 104.2%, respectively. Additionally, all calculated values of t for the three samples were less than 2.23 (the critical value of t_{10}, $P = 95\%$), indicating the difference between the two methods was insignificant at a 95% confidence level. Therefore, the two methods used for the determination of SE in degumming wastewater were in good agreement and comparable.

3.3. Evaluation of electrochemical parameters of two systems

The electrochemical parameters of CA in both the absence and presence of SE were calculated and compared. Firstly, with potential-controlled coulometry, the numbers of electron transfer in the CA and CA–SE systems were estimated at 2.02 and 1.95, respectively. Such results indicated that ~2 electrons were transferred in the electrode reaction for each of these two systems. Secondly, the effect of the scan rate was studied. As shown in Fig. 5, their redox peak currents were both linear with the square root of the scan rate in the range of 0.10–0.45 $V\,s^{-1}$, suggesting that their electrode processes were both diffusion-controlled. Also, the diffusion coefficient can be estimated with

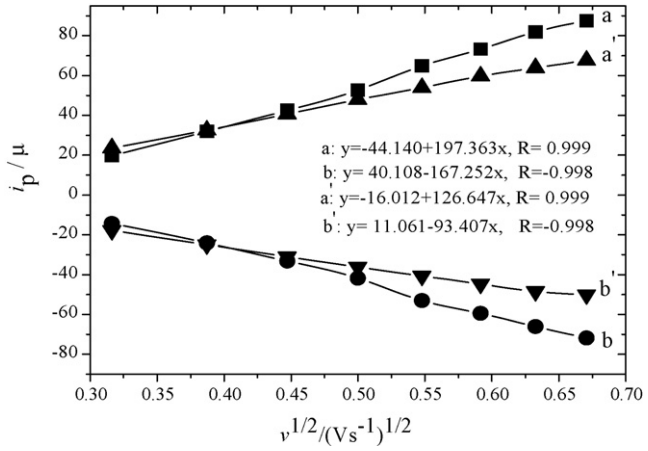


Fig. 5. Plots of i_p vs. $v^{1/2}$ of 1.49×10^{-4} mol L^{-1} CA in the pH 1.81 Britton–Robinson buffer solution in the absence (a and b) and presence of 200.0 $\mu g\,mL^{-1}$ SE (a′ and b′).

Table 2
Rate constant k_s and diffusion coefficient D of the CA and CA–SE systems.

System	k_s (s^{-1})	D ($cm^2\,s^{-1}$)	
		Oxidative process	Reductive process
CA	0.45	4.32×10^{-4}	6.01×10^{-4}
CA–SE	0.35	1.45×10^{-4}	2.67×10^{-4}

the Randles–Sevick equation [28]: $i_p = 2.69 \times 10^5 n^{3/2} S C^0 v^{1/2} D^{1/2}$. Assuming $S = 0.071\ cm^2$, based on the slope of i_p *vs.* $v^{1/2}$, the diffusion coefficients D were calculated and disclosed in Table 2.

The plots of peak potentials E_p *vs.* ln v for the CA and CA–SE systems were shown in Fig. 6. All of them revealed well-defined straight line fittings. Based on the Laviron's theory [29], the electron transfer coefficients α were determined by examining the potential

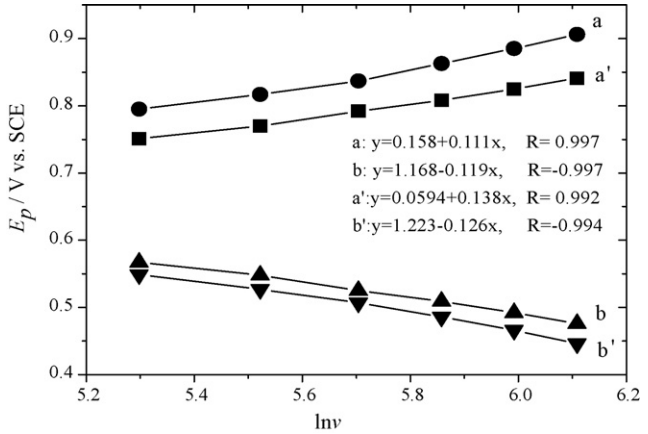


Fig. 6. Plots of E_p vs. ln v for the CA (a and b) and CA–SE systems (a′ and b′). Other conditions the same as Fig. 5.

variations with the logarithm of the scan rate. From the slopes of them, α was calculated at 0.48 and 0.52 for the CA and CA–SE systems, respectively. Moreover, the electrode reaction rate constant k_s could also be determined according to the following equation:

$$\log k_s = \alpha \log(1-\alpha) + (1-\alpha)\log\alpha - \log\left(\frac{RT}{nF\nu}\right) - \frac{\alpha(1-\alpha)nF\Delta E_p}{2.3RT}$$

where ΔE_p is the peak-to-peak potential separation of the oxidative and reductive peak potentials, and other symbols have normal meanings. The calculated values of k_s for CA in both the absence and presence of SE were also listed in Table 2.

Finally, the correlation between the formal potential $E^{0\prime}$ and the solution pH value (from pH 1.81 to 6.52) was studied by cyclic voltammetry. The formal potential $E^{0\prime}$ ($E^{0\prime} = (E_{pa} + E_{pc})/2$) of them both shifted negatively with the increasing pH. The linear regression equations could be expressed as follows: $(E^{0\prime}{}_{\text{CA system}}\ (\text{V}) = 0.753 - 0.033\,\text{pH}$ ($R = 0.999$, $n = 7$) and $(E^{0\prime}{}_{\text{CA–SE system}}\ (\text{V}) = 0.751 - 0.023\,\text{pH}$ ($R = 0.992$, $n = 7$), which indicated one proton was involved in the electrode reaction for each of these two electrochemical systems.

It was clear that the two systems were both two-electron and one-proton electrode processes. However, the diffusion coefficients and rate constants of the electrode reactions of CA in the absence and presence of SE showed significant differences. Compared with the CA system, the diffusion coefficient and rate constant of the electrode reaction of CA–SE system both decreased, which leaded to the peak current of CA reducing and the peak potential moving positively.

3.4. Measurement of stoichiometry of CA–SE complex

It is assumed that CA and SE produce a single complex of SE–*m*CA. Since the new complex SE–*m*CA was formed between electro-inactive SE and electro-active CA, the apparent binding constant β and the binding ratio m of SE with CA could be measured on the basis of peak current differences of CA in the absence and presence of SE when CA was in excess [30]. The equilibrium forming SE–*m*CA was listed below:

$$\text{SE} + m\text{CA} \leftrightarrow \text{SE} - m\text{CA}$$

The equilibrium constant was expressed as follows:

$$\beta = \frac{[\text{SE–CA}]}{[\text{SE}][\text{CA}]^m}$$

And the following equations were then derived:

$$\Delta i = k[\text{SE}–m\text{CA}], \quad [\text{SE}] + [\text{SE}–m\text{CA}] = C_{\text{SE}}, \quad \Delta i_{\max} = kC_{\text{SE}}$$

Therefore, $\Delta i_{\max} - \Delta i = k(C_{\text{SE}} - [\text{SE}–m\text{CA}]) = k[\text{SE}]$; where $\Delta i = i_{pa,0} - i_{pa}$, $i_{pa,0}$ and i_{pa} were oxidative peak currents of the CA and CA–SE systems, respectively; $\Delta i_{\max}$ was the oxidative peak current when the concentration of CA was extremely higher than that of SE. C_{SE}, [SE–*m*CA], and [SE] were corresponding to the total, SE bound, and free concentration of SE in the solution, respectively. The above equations could lead to the following equation: $(1/\Delta i) = (1/\Delta i_{\max}) + (1/\beta\Delta i_{\max}[\text{CA}]^m)$. By keeping the SE concentration at 200.0 μg mL^{-1} and varying the concentration of CA, a linear correlation of $1/\Delta i$ with $1/[\text{CA}]^m$ was obtained as follows: $(1/\Delta i) = 0.452 + (1.945 \times 10^{-7}/[\text{CA}])$ ($R = 0.994$, $n = 5$). From the intercept and slope, the binding constant $\beta = 2.32 \times 10^6$ L mol^{-1} and the binding ratio $m = 1$ were calculated.

4. Conclusion

In this paper, detailed studies were carried out on the interaction of CA with SE by the electrochemical methods. The studies showed that a 1:1 complex was formed between CA and SE, and the main binding mode was through the electrostatic attraction. The diffusion coefficient (D) and electrode reaction rate constant (k_s) of CA–SE system were both less than those of free CA, which resulted in a decrease in the voltammetric peak current of CA with the peak potential shifting positively. The binding of SE with CA was applied to the quantitative detection of SE. The results confirmed the proposed method as being a suitable alternative for the analysis of SE in degumming wastewater. Moreover, this method had great potential as a sensitive and simple detection technique with the advantages of wide linear range, low detection limit and good selectivity.

Acknowledgements

We thank the National Natural Science Foundation of China (Grant No. 20475043), the scientific research project from the Ministry of Education of Shaanxi Province (Grant No. 07JK254), and the scientific research project from Xi'an Polytechnic University (Grant No. 06XG017) for their financial supports.

References

[1] T. Wei, M.Z. Li, R.J. Xie, Macromol. Mater. Eng. 290 (2005) 188.
[2] Y. Takasu, H. Yamada, K. Tsubouchi, Biosci. Biotechnol. Biochem. 66 (2002) 2715.
[3] R. Dash, S. Mukherjee, S.C. Kundu, Int. J. Biol. Macromol. 38 (2006) 255.
[4] P. Vaithanomsat, V. Kipreechavanich, Sep. Purif. Technol. 59 (2008) 129.
[5] T. Masakazu, T. Kazuhisa, Y. Hideyuki, T. Hiroshi, N. Shigeru, Biotechnol. Lett. 25 (2003) 1805.
[6] Z. Siqin, Y. Noriyuki, S. Masahiro, W. Hiromitsu, K. Norihisa, J. Photochem. Photobiol. B: Biol. 71 (2003) 11.
[7] N. Kato, S. Sato, A. Yamanaka, H. Yamada, N. Fuwa, M. Nomura, Biosci. Biotechnol. Biochem. 62 (1998) 145.
[8] Y.Q. Zhang, Biotechnol. Adv. 20 (2002) 91.
[9] J.H. Wu, Z. Wang, S.Y. Xu, Process Biochem. 43 (2008) 480.
[10] J.H. Wu, Z. Wang, S.Y. Xu, Food Chem. 103 (2007) 1255.
[11] A. Anghileri, R. Lantto, K. Kruus, C. Arosio, G. Freddi, J. Biotechnol. 127 (2007) 508.
[12] H.W. Gao, J. Jiang, L.Q. Yu, Analyst 126 (2001) 528.
[13] Z.X. Guo, Y.M. Hao, X. Cong, H.X. Shen, Anal. Chim. Acta 403 (2000) 225.
[14] W.W. You, R.P. Hanglang, D.K. Ryan, R.P. Haugland, Anal. Biochem. 244 (1997) 277.
[15] C.Q. Ma, K.A. Li, S.Y. Tong, Anal. Chim. Acta 333 (1996) 83.
[16] C.Q. Ma, K.A. Li, S.Y. Tong, Anal. Chim. Acta 338 (1997) 255.
[17] Q.E. Cao, Z.T. Ding, R.B. Fang, X. Zhao, Analyst 126 (2001) 1444.
[18] M.L. Zhang, G.P. Sheng, H.Q. Yu, Water Res. 42 (2008) 3464.
[19] M.F. Cerda, E. Mendez, G. Obal, C. Kremer, J.S. Gancheff, A.M.C. Luna, J. Inorg. Biochem. 98 (2004) 238.
[20] W. Sun, K. Jiao, X.L. Wang, L.D. Lu, Electroanalysis 17 (2005) 162.
[21] W. Sun, K. Jiao, X.L. Wang, L.D. Lu, J. Electroanal. Chem. 578 (2005) 37.
[22] W. Sun, J.Y. Han, K. Jiao, L.D. Lu, Bioelectrochemistry 68 (2006) 60.
[23] X.Y. Liu, C.Y. Li, S.S. Hu, Micro. Acta 154 (2006) 275.
[24] C.Y. Li, J. Appl. Polym. Sci. 103 (2007) 3271.
[25] C.H. Wang, F. Wang, C.Y. Li, X.L. Xu, T. Li, C.F. Wang, Dyes Pigments 75 (2007) 213.
[26] M.M. Ma, J.F. Song, Chin. J. Chem. 26 (2008) 2081.
[27] H.D. Belitz, W. Grosch, P. Schieberle, Food Chemistry, 4th ed., Springer, Berlin, Heidelberg, 2009, p. 8.
[28] A.J. Bard, L.R. Faulkner, Electrochemical Methods: Fundamentals and Applications, New York, 1960, p. 213.
[29] E. Laviron, J. Electroanal. Chem. 101 (1979) 19.
[30] N.Q. Li, J. Min, Chin. J. Anal. Chem. 17 (1989) 346.

Talanta 80 (2009) 168–172

Contents lists available at ScienceDirect

Talanta

journal homepage: www.elsevier.com/locate/talanta

Flame atomic absorption spectrometry for the determination of trace amount of rhodium after separation and preconcentration onto modified multiwalled carbon nanotubes as a new solid sorbent

S. Ghaseminezhad [a,*], D. Afzali [b], M.A. Taher [a]

[a] Chemistry Department, Shahid Bahonar University of Kerman, Kerman, Iran
[b] Environment Department, Research Institute of Environmental Sciences, International Center for Science, High Technology & Environmental Sciences, Kerman, Iran

ARTICLE INFO

Article history:
Received 25 March 2009
Received in revised form 21 June 2009
Accepted 22 June 2009
Available online 1 July 2009

Keywords:
Carbon nanotubes
Solid phase extraction
Rhodium determination
Sorbent
Preconcentration

ABSTRACT

The present article reports on the application of modified multiwalled carbon nanotubes (MMWCNTs) as a new, easily prepared and stable solid sorbent for the preconcentration of trace rhodium ion in aqueous solution. Rhodium ions were complexed with 1-(2-pyridylazo)-2-naphthol (PAN) in the pH range of 3.2–4.7 and then the formed Rh-PAN complex was adsorbed on the oxidized MWCNTs. The adsorbed complex was eluted from MWCNTs sorbent with 5.0 mL of N,N-dimethylformamide (DMF). The rhodium in eluted solution was determined by flame atomic absorption spectrometry (FAAS). Linear range for the determination of rhodium was maintained between 0.16 ng mL^{-1} and 25.0 μg mL^{-1} in initial solution. Relative standard deviation for the 10 replicated determination of 4.0 μg mL^{-1} of rhodium was ±0.97%. Detection limit was 0.010 ng mL^{-1} in initial solution ($3S_{bl}$, $n = 10$) and preconcentration factor was 120. Sensitivity for 1% absorbance of rhodium (III) was 0.112 μg mL^{-1}. The sorption capacity of oxidized MWCNTs for Rh (III) was 6.6 mg g^{-1}. The effects of the experimental parameters, including the sample pH, flow rates of sample and eluent solution, eluent type, breakthrough volume and interference ions were studied for the preconcentration of Rh^{3+}. The proposed method was successfully applied to the extraction and determination of rhodium in different samples.

© 2009 Elsevier B.V. All rights reserved.

1. Introduction

Carbon nanotubes (CNTs) are an allotrope of carbon. A carbon nanotube is a one atom thick sheet of graphite rolled up into a seamless cylinder with diameter of the order of a nanometer. It caused in an essentially one-dimensional nanostructure where the length-to-diameter ratio exceeds 1000. Such cylindrical carbon molecules have novel properties that make them potentially useful in a wide variety of applications in nanotechnology, electronics, optics and other fields of materials science. They exhibit extraordinary strength and unique electrical properties, and are efficient conductors of heat [1]. Carbon nanotubes name is derived from their size, since the diameter of a nanotube is on the order of a few nanometers, while they can be up to several millimeters in length. There are two main types of carbon nanotubes: single walled carbon nanotubes (SWCNTs) and multiwalled carbon nanotubes (MWNTs) depending on the carbon atom layers in the wall of the nanotubes [2]. Since carbon nanotubes were first prepared in 1991 [3], they have become attractive materials for their novel structure characteristics [4]. CNTs have high surface area, mechanical strength, thermal and chemical stability. Due to their unique characteristic and strong adsorption ability [5], they have been successfully used to remove many kinds of pollutants such as dioxin from air [6], lead [7], cadmium [8], zinc [9], fluoride [10], 1,2-dichlorobenzene [11] and trihalomethanes [12] from different matrices.

Rhodium is present at about 0.001 μg mL^{-1} in the crust of the earth. Rhodium metal is known for its stability in corrosive environments, physical beauty and unique physical and chemical properties. The determination of rhodium has been studied by different techniques such as atomic absorption spectrometry [13], spectrophotometric methods [14], ICP-OES and ICP-MS [15] in catalysts, geological, environmental and alloy samples. The direct determination of rhodium ions in complex matrices is limited due to their usually low concentrations and matrix interferences. In trace analysis, therefore, a preconcentration and separation are necessary to improve sensitivity and selectivity of determination. Ideally, an analytical separation method should be rapid, simple, and inexpensive, give quantitative recovery of analytes without loss or degradation; should yield a solution of analyte that is sufficiently concentrated to permit the final measurement to be made without the need for concentration, and generate little or no laboratory waste that has to be disposed [16].

* Corresponding author. Tel.: +98 341 3222033; fax: +98 341 3222033.
E-mail address: sima.ghaseminezhad@gmail.com (S. Ghaseminezhad).

0039-9140/$ – see front matter © 2009 Elsevier B.V. All rights reserved.
doi:10.1016/j.talanta.2009.06.049

Several procedures have been proposed and applied for the separation and determination of rhodium by atomic spectrometry based on the nature of samples, the content of analytes and the measurement techniques [17,18].

For many decades the most common method for performing analytical separation on complex environmental was liquid extraction. Unfortunately, liquid–liquid extractions frequently fail to meet several of the ideal criteria listed in the previous paragraph. The use of solid phase extraction is an attractive way to avoid many difficulties associated with liquid extraction. Various sorbents such as thiol cotton [19], silanized glass beads [20], silica gel [21], Amberlite XAD-4resin [22], cellulose [23], green tea leaves [24] and polythioether foams [25] were used in solid phase extraction. To the best of our knowledge, however, there were no references to the application of MWCNTs for the preconcentration of trace amounts of Rh^{3+}. The goal of this work is the application of MWCNTs as a new sorbent for the preconcentration of trace amounts of Rh^{3+}.

2. Experimental

2.1. Apparatus

A Varian Model SpectrAA 220 atomic absorption spectrometer was used for the measuring of Rh^{3+} in an air–acetylene flame. The operating conditions were as follows: wavelength, 343.5 nm; lamp current, 5.0 mA and slit width, 0.5 nm. The acetylene flow and the air flow were 1.5 and 3.5 L min^{-1}, respectively. The pH measurement was carried out using a Metrohm pH meter (model 713) with a combined pH glass electrode calibrated against two standard buffer solutions at pH 4.0 and 7.0. A funnel-tipped glass tube (80 mm × 10 mm) was used as a column for preconcentration. All glassware and columns were washed with a mixture of concentrated hydrochloric acid and concentrated nitric acid (1:1) before application.

2.2. Reagents and materials

High purity reagents from Sigma (St. Louis, MO, USA) and Merck (Darmstadt, Germany) were used for the preparation of all standard and sample solutions. Stock solutions were prepared daily from Rh^{3+} standard solution 1000.0 mg L^{-1} (Merck, Germany) by serial dilution water. A 0.025% solution of 1-(2-pyridylazo)-2-naphtol (Merck, Germany) was prepared by dissolving an appropriate amount in ethanol. Platinum–iridium alloy purchased from Fine Wire Company (CA, USA). Buffer solutions were prepared from 0.5 mol L^{-1} acetic acid and 0.5 mol L^{-1} sodium acetate for pH 3–6, from 0.1 mol L^{-1} potassium dihydrogen phosphate and 0.1 mol L^{-1} disodium hydrogen phosphate for pH 6–8 and from 0.5 mol L^{-1} ammonia and 0.5 mol L^{-1} ammonium acetate for pH 8–10. MWCNTs with an average outer diameter of 3–20 nm, length of 1–10 μm, number of walls 3–15 and surface area of 350 m^2 g^{-1} were obtained from Plasma Chem. GmbH (Berlin, Germany).

2.3. Preparation of oxidized MWCNTs

Raw MWCNTs were heated at 300 °C for 40 min to remove amorphous carbon. Prior to use, MWCNTs were oxidized with concentrated HNO_3 according to the literature, in order to create binding sites onto the surface of MWCNTs [26]. The treatment was carried out by dispersing 25 mL of concentrated HNO_3 to 1.0 g of MWCNTs, and then refluxing for 6 h at 100 °C. Afterward, the oxidized MWCNTs were washed with distilled water until removing any excess of nitric acid (neutral pH of solution) [27].

2.4. Preparation of column

20 mg of oxidized MWCNTs was slurred in water, and then poured into a funnel-tipped glass tube plugged with a small piece of glass wool at the ends. A glass column packed with 0.02 g of oxidized MWCNTs sorbent (height of packing being about 10 mm) was used as the operational column. The column could be used repeatedly for 50 times after washing with distilled water.

2.5. General procedure

Initially, distilled water was passed through the column for column conditioning. An aliquot of rhodium solution and 5.0 mL of 0.025% PAN reagent was placed in a 100 mL beaker and the mixture was diluted to 30 mL with distilled water. The pH was adjusted to 3.7 with acetate buffer and the solution was heated for 60 min at 90 °C to form Rh-PAN complex [28]. Then, the obtained Rh-PAN complex was passed through the column at a flow rate of 2 mL min^{-1}. Finally, the adsorbed Rh-PAN complex was eluted from sorbent with 5.0 mL of DMF. The eluted solution was aspirated directly into the flame of atomic absorption spectrometry and compared with a blank that was prepared in the same manner without the addition of Rh^{3+}.

3. Results and discussion

Preliminary experiments showed that although, oxidized MWCNTs have a low tendency for the retention of adsorption Rh^{3+} (less than 50%), they are not selective for the separation of rhodium ions. Therefore, the oxidized MWCNTs do not judge a suitable sorbent for the separation of rhodium ions. A recent work [29] indicates that MWCNTs can be adsorbed on organic materials. So, we decided to form complex between Rh^{3+} and PAN ligands. Then, the formed Rh-PAN complex was adsorbed onto oxidized MWCNTs. The results showed that the recovery of rhodium ions by using oxidized MWCNTs is higher than 97%. Moreover, oxidized MWCNTs are selective for the separation of Rh-PAN complex. In order to obtain highly sensitive, accurate, and reproducible results, analytical parameters including pH, type and volume of eluent solution, breakthrough volume and flow rates of sample and eluent were optimized for the preconcentration of Rh^{3+}.

3.1. Effect of the sample pH

As pH is one of the important analytical factors in the solid phase extraction of metal ions [30], the influences of pH of the aqueous

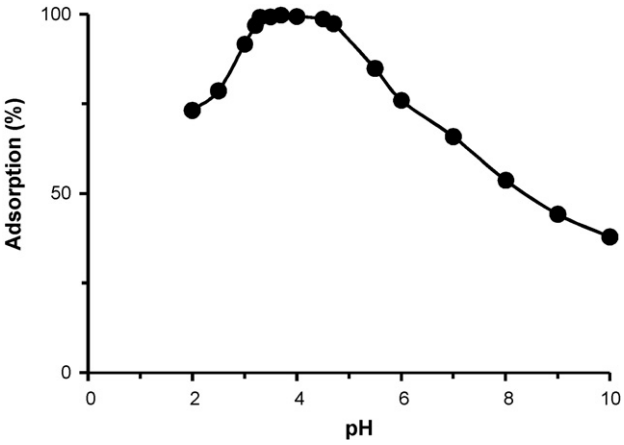


Fig. 1. The effect of sample solution pH on the percent sorption of Rh^{3+}. Conditions: Rh, 20.0 μg; sample flow rate, 2 mL min^{-1}; eluent solution, 5.0 mL DMF with a flow rate 1 mL min^{-1}. Instrumental settings: wavelength, 343.5 nm; lamp current, 5.0 mA; slit width, 0.5 nm; acetylene flow, 1.5 L min^{-1}; air (as oxidant) flow, 3.5 L min^{-1}.

Table 1
Obtained recoveries in choosing the eluent type.

Eluent (5.0 mL)	Recovery (%)
THF	5.2
Ethanol 96%	10.19
Acetone	12.9
1-Propanol	13.42
DMSO	40.15
1-Butanol	41.46
DMF	98.9

Conditions and instrumental settings were same as Fig. 1, except eluent solution.

Table 2
Effect of interferences.

Interference	Tolerance limit (mg)
NO_3^-	35
Cl^-	35
CH_3COO^-	30
Al^{3+}	20
K^+	20
Na^+	20
Ca^{2+}	20
Mg^{2+}	5
Thiourea	5
Mn^{2+}	2
Pb^{2+}	2
Hg^{2+}	1
Co^{2+}	0.6
Zn^{2+}	0.5
Cd^{2+}	0.5
Pd^{2+}	0.4
Fe^{3+}	0.3
Ag^+	0.3
Cu^{2+}	0.3
Au^{3+}	0.2
Ni^{2+}	0.2

Conditions and instrumental settings were same as Fig. 1.

solution on the recovery of rhodium ions on oxidized MWCNTs were investigated. The percent sorption of rhodium ion on the sorbent surface as a function of sample pH is shown in Fig. 1. As can be seen, the sorption percent of Rh(III) depends on the pH of the sample solution. The optimum pH range was around 3.2–4.7. In subsequent studies, the pH was maintained at approximately 3.7 with acetate buffer.

3.2. Sorption capacity

In order to evaluate the sorption capacity of oxidized MWCNTs for rhodium ion, a batch method was used. Accordingly, 40 mL of solution containing 0.6 mg of rhodium and 32 mg of PAN reagent at pH 3.7 was prepared. This solution was heated for 60 min at 90 °C, and then was added to it 20 mg oxidized MWCNTs. After shaking for 30 min, the mixture was filtered. The maximum capacity of the sorbent was 6.6 mg of Rh^{3+} per gram of sorbent. The oxidized MWCNTs sorbent were subjected to several loadings with the sample solution and subsequent elution. It was found that the adsorption properties of the adsorbent remained constant after 50 cycles of sorption and desorption.

Table 4
Determination of rhodium in the real and spiked samples.

Sample	Spiked (ng mL^{-1})	Found (ng mL^{-1})[a]	Recovery (%)
Tap water (Kerman)	0.0	N.D.[b]	–
	5.0	4.82 ± 0.11	96.40
	20.0	19.21 ± 0.34	96.06
Well water (Kerman)	0.0	N.D.	–
	5.0	5.07 ± 0.12	101.54
	20.0	20.92 ± 0.47	104.63
River water (Shoor, Shahdad)	0.0	N.D	–
	5.0	4.98 ± 0.09	99.60
	20.0	19.74 ± 0.52	98.70
Sea water (Persian Golf)	0.0	B.L.R.[c]	
	5.0	5.09 ± .08	101.80
	20.0	20.17 ± 0.43	100.85
Wastewater (Copper factory)	0.0	B.L.R.	–
	5.0	5.13 ± 0.15	102.61
	20.0	20.17 ± 0.34	100.85

Conditions and instrumental settings were same as Fig. 1.
[a] Mean ± standard deviation (n = 4).
[b] N.D.: not detected.
[c] B.L.R.: below of linear range.

Table 5
Determination of rhodium in a platinum–iridium alloy.

Composition (%)	Certified value (%)	Found[a] (%)	Recovery (%)
Pt, 55; Ir, 28; Cu, 3.0; Fe, 3.5; Pd, 3.5	Rh, 7.0	6.94 ± 0.16	99.14

[a] Mean ± standard deviation (n = 4).

3.3. Effect of flow rate of sample

Flow rate of the sample solution is a measure of the contact time between the sample solution and the sorbent. The results showed that the flow rate variation in the range of 0.2–2.5 mL min^{-1} did not have a significant effect on the sorption of the rhodium. It was found that the adsorption of Rh-PAN complex on oxidized MWCNTs is relatively rapid. In order to achieve good precision, a flow rate of 2 mL min^{-1} was therefore chosen for further studies.

3.4. Effect of eluent flow rate

The effect of eluent flow rate on desorption of Rh-PAN complex from the sorbent surface was studied in the range of 0.2–2.5 mL min^{-1}. Flow rate of 1 mL min^{-1} was chosen in subsequent work.

3.5. Selection of eluent

Desorption of the adsorbed material on the solid phases is an important step for the solid phase extraction studies [30]. A series of solvents such as, DMF, dimethyl sulfoxide (DMSO), tetrahydrofuran (THF), 1-butanol, 1-propanol, ethanol and acetone, were used in order to find the best eluent. The results showed that the best recovery was achieved when DMF was used as eluent. It was found that 5.0 mL of this solvent was sufficient to elute the complex from oxidized MWCNTs. The results are shown in Table 1.

Table 3
Analysis of rhodium ion in synthetic samples.

Composition of synthetic sample (μg)	Found (μg)[a]	Recovery (%)
Pb^{2+}, 500; Pd^{2+}, 300; Co^{2+}, Mn^{2+}, 200; Au^{3+}, Ag^+, 150; Ni^{2+}, Cu^{2+}, Fe^{3+}, Hg^{2+}, Zn^{2+}, Cd^+, 100; Rh^{3+}, 20.0;	19.67 ± 0.46	98.37
Na^+, K^+, 1000; Pb^{2+}, Mn^{2+}, Ca^{2+}, Mg^{2+}, 200; Rh^{3+}, 20.0	19.83 ± 0.34	99.16

Conditions and instrumental settings were same as Fig. 1.
[a] Mean ±standard deviation (n = 4).

Table 6
Comparison of the present method with other methods for preconcentration and determination of rhodium.

Determination technique	Preconcentration method	Sorbent	Enrichment factor	Detection limit ($ng\,mL^{-1}$)	R.S.D. (%)	Linear range ($ng\,mL^{-1}$)	Ref.
DPP[a]	SPE[b]	Microcrystalline naphthalene	–	60	0.79	250–7,500	[31]
Spectrophotometry	SPE	Microcrystalline naphthalene	–	20	1.2	40–7,500	[32]
FIA-FAAS	SPE	Cross-linked polystyrene sorbent	–	3	–	–	[33]
ETAAS	IEM[c]	Dowex 1×8-200	20	0.3	1.8	0.9–50	[34]
LI-TLS[d]	CPE[e]	–	450	0.06	–	0.5–50	[35]
FAAS	CPE	–	50	0.052	–	0.16–1.5	[36]
Spectrophotometry	SLS[f]	–	40	14.4	–	30–2,500	[37]
FAAS	SPE	MWCNTs	120	0.01	0.97	0.16–25,000	This work

[a] DPP: differential pulse polarography.
[b] SPE: solid phase extraction.
[c] IEM: ion exchange microcolumn.
[d] LI-TLS: laser induced-thermal lens spectrometry.
[e] CPE: cloud point extraction.
[f] SLS: solid liquid separation.

3.6. Breakthrough volume

When solutions containing 20.0 μg of rhodium in 350, 400, 450, 500, 550 and 600 mL of water were passed through the columns, the Rh(III) was quantitatively retained in all cases. We concluded that the breakthrough volume of the method under optimum conditions should be greater than 600 mL. Consequently, by considering the final elution volume of 5.0 mL of DMF, and a breakthrough volume of 600 mL, a preconcentration factor of 120 was easily achievable.

3.7. Interferences

The interferences of coexisting ions in binary mixtures of Rh (III) with foreign ions were studied on the percent recovery of rhodium ($4.0\,\mu g\,mL^{-1}$). After introducing the binary solution into a column, the adsorbed rhodium ion was eluted by DMF solvent. The content of rhodium ions in effluents was determined using FAAS, and the recoveries were calculated. The results, summarized in Table 2, clearly indicate that most of the tested ions do not interfere with the determination of rhodium. The tolerance limit was set as the amount of foreign ions required to cause a ±4% error.

3.8. Analytical figure of merit

Analytical figure of merit was evaluated for the determination of rhodium according to the recommended procedure. Under optimum conditions, the calibration curve was linear from $0.16\,ng\,mL^{-1}$ to $25.0\,\mu g\,mL^{-1}$ in initial solution or 0.02 to $25.0\,\mu g\,mL^{-1}$ in final solution with a correlation coefficient (R^2) of 0.999 and the equation of the calibration curve was $A = 0.034C + 0.006$, where A is the absorbance value of the eluent and C is the concentration of Rh (III) ($\mu g\,mL^{-1}$) after preconcentration in the eluent. The recommended procedure was repeated 10 times to find the relative standard deviation in the determination of $4.0\,\mu g\,mL^{-1}$ of Rh (III) ion, whose RSD was found to be ±0.97% in final solution. The obtained limit of detection $0.010\,ng\,mL^{-1}$ was based on three times the standard deviation of the blank solution measurements ($n = 10$) in original solution. The sensitivity for 1% absorbance was $0.112\,\mu g\,mL^{-1}$.

3.9. Determination of rhodium in synthetic samples

Since no standard samples were available for testing the validity of the developed method for analysis of real samples, the method was applied to synthetic mixtures. Accordingly, various synthetic mixtures simulating different cations were prepared. Aliquots of the synthetic mixture were taken; pH was adjusted to ~3.7 with acetate buffer of pH 3.7 and then the general procedure applied. The results are given in Table 3.

3.10. Analysis of water samples

In order to test the applicability and reliability of the proposed method, tap water, well water, river water, sea water and waste water samples were analyzed. For this purpose, 100.0 mL of each sample was preconcentrated in accordance to the proposed method. The results are shown in Table 4. In all cases the spiked recoveries confirmed the reliability of the proposed method. Also, we applied standard addition method for the determination of rhodium ion in spiked real samples mentioned in Table 4. The results showed that good recoveries of 96.06–104.63% were achieved for analyzed samples.

3.11. Analysis of a platinum–iridium alloy

In order to test the applicability of the proposed method for the analysis of real samples, one platinum–iridium alloy was analyzed. To 5.0 mg of the alloy with known composition, 7 mL of aqua regia was added and the solution was evaporated. Five milliliters of concentrated hydrochloric acid was added to it and the solution was warmed, transferred to a 100 mL volumetric flask, and made up to the mark with distilled water. An aliquot of this solution was taken and rhodium was determined by the general procedure. Four determinations were made, and the result is given in Table 5.

4. Conclusion

The present study demonstrates the use of oxidized MWCNTs as a new sorbent in the preconcentration of rhodium ion in different matrices. The preparation of oxidized MWCNTs is simple and of low cost. These sorbents are simple and of low cost, which can be used several times without a marked loss in sorption capacity. The developed method is simple, rapid, precise, accurate and reliable offering a higher preconcentration factor and lower detection limit for rhodium ion than the other sorbents. Table 6 compares the proposed method with those reported previously for the determination of rhodium after preconcentration procedure. It shows that the proposed method has a low detection limit compared with previous studies [31–37] and it allows the determination of $ng\,mL^{-1}$ levels of rhodium. The method is economical due to the possibility of multiple uses of the sorbent.

References

[1] M. Meyyappan, Carbon Nanotubes Science and Applications, CRC Press, Florida, USA, 2005.
[2] S. Iijima, T. Ichihashi, Nature 363 (1993) 603.
[3] C.D. Stalikas, Trends Anal. Chem. 21 (2002) 343.
[4] M. Miro, W. Frenzel, Trends Anal. Chem. 23 (2004) 624.

[5] C. Saridara, R. Brukh, Z. Iqbal, S. Mitra, Anal. Chem. 77 (2005) 1183.
[6] Q.R. Long, R.T. Yang, J. Am. Chem. Soc. 123 (2001) 2058.
[7] Y.H. Li, Y.Q. Zhu, Y.M. Zhao, Diamond. Relat. Mater. 15 (2006) 90.
[8] Y.H. Li, S. Wang, Z. Luan, J. Ding, C. Xu, D. Wu, Carbon 41 (2003) 1057.
[9] C.X. Lu, H.S. Chiu, Chem. Eng. Sci. 61 (2006) 1138.
[10] Y.H. Li, S. Wang, J. Wei, X. Zhang, Mater. Res. Bull. 38 (2003) 469.
[11] X. Peng, Y.H. Li, Z. Luan, Z. Di, H. Wang, Chem. Phys. Lett. 376 (2003) 154.
[12] C. Lu, Y.L. Chung, K.F. Chang, Water Res. 39 (2005) 1183.
[13] C.B. Ojeda, F.S. Rojas, Talanta 68 (2006) 1407.
[14] C.B. Ojeda, F.S. Rojas, Talanta 67 (2005) 1.
[15] C.B. Ojeda, F.S. Rojas, Talanta 71 (2007) 1.
[16] M.A. Mostafa, M.A. Kabil, Indian J. Chem. 24 (1985) 260.
[17] M.A. Kabil, M.A. Mostafa, Rev. Roum. Chim. 30 (1985) 631.
[18] J.S. Fritz, Analytical Solid-Phase Extraction, John Wiley and Sons, Inc., New York, 1999.
[19] Y.M. Quig, L.G. Quin, Talanta 30 (1983) 265.
[20] S. Taguchi, T. Yal, Y. Shimada, K. Goto, Talanta 30 (1983) 169.
[21] M. Kubota, K. Matseemoto, K. Terada, Anal. Sci. 3 (1987) 45.
[22] Y. Sakai, N. Mori, Talanta 33 (1986) 161.
[23] P. Burba, P.G. Willmer, Talanta 30 (1983) 381.
[24] M. Kimura, H. Yamashita, J. Komada, Bunseki Kagaku 35 (1986) 400.
[25] A.S. Khan, A. Chow, Talanta 33 (1986) 182.
[26] J. Xu, Y. Wang, Y. Xian, L. Jin, K. Tanaka, Talanta 60 (2003) 1123.
[27] L.Y. Hui, D. Jun, L. Zechao, Z. Yuefeng, X. Cailu, W. Dehai, W. Binging, Carbon 41 (2003) 2787.
[28] J.R. Stokley, W.D. Jacobs, Anal. Chem. 35 (1963) 149.
[29] Q. Zhou, W. Wang, J. Xia, Anal. Chim. Acta 559 (2006) 200.
[30] Z. Mester, R. Sturgeon, Sample Preparation for Trace Element Analysis, Elsevier, Amsterdam, Netherlands, 2003.
[31] R.K. Dubey, A. Bhalotra, M.K. Gupta, B.K. Puri, Microchem. J. 58 (1998) 117.
[32] M.A. Taher, Anal. Chim. Acta 382 (1999) 339.
[33] I.A. Kovalev, L.V. Bogacheva, G.I. Tsysin, A.A. Formanovsky, Y.A. Zolotov, Talanta 52 (2000) 39.
[34] F.S. Rojas, C.B. Ojada, J.M.C. Pavon, Talanta 64 (2004) 230.
[35] N. Shokoufi, F. Shemirani, Talanta 73 (2007) 662.
[36] K. Suvardhan, K.S. Kumar, D. Rekha, P. Subrahmanyam, K. Kiran, B. Jayaraj, S. Ramanaiah, K. Janardhanam, P. Chiranjeevi, Microchim. Acta 157 (2007) 237.
[37] J.P. Pancras, B.K. Puri, Anal. Sci. 15 (1999) 575.

Talanta 80 (2009) 173–178

Contents lists available at ScienceDirect

Talanta

journal homepage: www.elsevier.com/locate/talanta

A novel cloud point extraction approach using cationic surfactant for the separation and pre-concentration of chromium species in natural water prior to ICP-DRC-MS determination

Noorbasha N. Meeravali [a], Shiuh-Jen Jiang [b,*]

[a] National Centre for Compositional Characterization of Materials, Hyderabad 500062, India
[b] Department of Chemistry, National Sun Yat-sen University, Kaohsiung 80424, Taiwan

ARTICLE INFO

Article history:
Received 1 May 2009
Received in revised form 22 June 2009
Accepted 22 June 2009
Available online 1 July 2009

Keywords:
Cloud point extraction
Aliquat-336
Triton X-114
Chromium speciation
ICP-DRC-MS

ABSTRACT

A novel cloud point phase separation of cationic surfactant, Aliquat-336 and capabilities of its reactive solubilizing sites for selective extraction of chromium species at ultra trace levels was examined in natural water. The phase separation behavior of Aliquat-336 is studied with various additives. The nonionic surfactant, Triton X-114 was found to induce the cloud point phase separation of Aliquat-336. The separation of anionic Cr(VI) was enabled by the formation of ion associate with quaternary ammonium head group of Aliquat-336 at pH 2, and the recovery of Cr(VI) and Cr(III) were 101.4 ± 1.4% and 2.2 ± 0.4%, respectively at 0.5–1 ng mL^{-1}, Total Cr was pre-concentrated as Cr-APDC species using the hydrophobic tail group at pH 6.5. The Cr(III) concentration was obtained by subtracting Cr(VI) from total Cr. The recovery of total Cr was 99.5 ± 1.2%. Parameters affecting extraction were assessed. The procedure was applied to NIST 1643c and NIST 1643d waters, and the sum of individual species obtained was compared with the certified chromium values. The method was also applied to various natural waters with limits of detection and pre-concentration factor of 0.010 and 0.025 ng mL^{-1}; 10 and 10, respectively, for Cr(VI) and Cr(III)-APDC using ICP-MS operated in DRC mode.

© 2009 Elsevier B.V. All rights reserved.

1. Introduction

Since its introduction in the early 1980s nonionic surfactant based phase separation (cloud point extraction, CPE) has proved to be the most efficient and environmental friendly procedure for the separation and pre-concentration of a various metal-chelates and organic compounds [1–4]. Phase separation is easily achieved by altering the solution properties such as temperature or additives. Furthermore, a common concept of hydrophobic interaction of nonionic micelles is used to account for the success of all these CPE procedures. However, nonionic surfactants have some major drawbacks such as lower extraction efficiencies and instability of the thermally labile water soluble organic and inorganic species [5,6]. One of the main reasons for these drawbacks is due to the lack of electrostatic interacting sites in the extracting nonionic micelles. Hence, there is a continuous quest to overcome these limitations.

Ionic surfactant based phase separation (coacervate extraction, CE) is being used for the extraction of partially water soluble organic compounds through their interaction with charged hydrophilic head groups, which partially alleviate the above problem [7–11]. In these cases, the phase separation is induced by the addition of dehydrating agents such as high electrolytes and acids. Unfortunately, these agents partially neutralize the useful reactive charge of the hydrophilic head groups [7,11], which diminish the extraction efficiencies and elevates the procedural blank in case of inorganic ionic species. These difficulties are further exacerbated due to the troublesome surfactant-rich phase separation process [6,12]. There is a dearth of information about the phase separation of number of ionic surfactants. Thus, CE is exploited scarcely, for the extraction of hydrophilic inorganic ionic species, despite having reactive charged head groups.

For clear phase separation, balancing the hydrophobic to hydrophilic interaction is very important in micelle solutions [13]. The phase separations of all the reported CPE and CE procedures have used the same concept of reducing the hydrophilic character of micelles by the addition of dehydrating agents. On the other hand, the concept of increasing the hydrophobic character of micelles has not received much attention. The success of this new concept in ionic surfactants is more useful to develop efficient procedures for the extraction of hydrophilic ionic species along with organic compounds. Fewer research groups are involved in this topic and have studied only changes in the physical properties of ionic surfactants by addition of hydrophobic counter ions [14]. Until now, no analytical procedure has been reported by using this concept

* Corresponding author. Fax: +886 7 5253908.
E-mail address: sjjiang@faculty.nsysu.edu.tw (S.-J. Jiang).

0039-9140/$ – see front matter © 2009 Elsevier B.V. All rights reserved.
doi:10.1016/j.talanta.2009.06.051

of hydrophobic species induced phase separation of ionic surfactant. Therefore, we have put efforts in this direction and studied the phase separation behavior of cationic surfactant with various additives. Cationic cloud point phase separation has been achieved for the first time using the novel concept of increasing the hydrophobic character of micelles with nonionic surfactant. This process provides the uncompromised cationic active sites in the cationic surfactant based CPE, which overcomes the limitations related to high salts in CE and drawbacks in nonionic surfactant based CPE processes. It is envisioned that the micelle aggregates formed must have significantly high hydrophobic interacting sites along with unaltered active cationic head group sites, which react more selectively with anionic and organic species, avoiding the requirement to add other chelating agents for extraction of hydrophilic anionic species.

For demonstrating the analytical applicability of this novel concept, we have selected the chromium speciation in natural waters, as these species show opposite toxicity and reactivity [15]. Furthermore, Cr(VI) is classified as a Class A carcinogen that dissolves more in water and spreads easily to all natural water bodies [16]. Hence, there is a demand to develop a simple extraction procedure for the ultra trace speciation analysis of chromium in natural water. The nonionic surfactant based CPE has been applied for the speciation analysis of chromium in water only by using chelating agents [17,18].

Determination of chromium species at ultra trace levels in organic and chloride rich matrices is still a difficult task even after using more versatile quadrupole ICP-MS [19]. A major concern in ICP-MS analysis is caused by severe spectral interferences on major isotopes, which hamper the accuracy of the results. For alleviating these interferences dynamic reaction cell (DRC) facility of ICP-MS with ammonia as the reaction gas has been used effectively [20].

This paper describes, a novel nonionic surfactant induced cationic cloud point extraction procedure and explores its capabilities to ultra trace speciation analysis of chromium from natural water using ICP-DRC-MS. Aqueous solution of cationic surfactant (Alquat-336) separates into two phases, same as in CPE, in presence of Triton X-114. Surfactant-rich phase settle at the bottom of solution, which entraps selectively the highly water soluble anionic hydrophilic ($HCrO_4^-$) and hydrophobic (Cr-APDC) species from bulk aqueous phase, which confirm our assumption. To confirm the accuracy of our assumption, the developed procedure is verified by analyzing two certified reference materials such as NIST 1643c and 1643d Trace Elements in Water and also been applied to real natural water samples collected locally.

2. Experimental

2.1. Instrumentation

An ELAN 6100 DRC II ICP-MS (Perkin-Elmer SCIEX, Concord, Ontario, Canada) was used. Using ammonia as a reaction gas, the DRC conditions were optimized for obtaining the best signal to noise ratio at two isotopes of chromium [19]. The optimized operating conditions are given in Table 1.

Table 1
Optimized operating conditions of ICP-DRC-MS.

ICP-MS instrument	PE-SCIEX ELAN 6100 DRC II
Plasma conditions	
Rf power	1150 W
Plasma gas flow	15 L min^{-1}
Auxiliary gas flow	1.1 L min^{-1}
Nebulizer gas flow	0.9 L min^{-1}
Sample up take rate	0.7 mL min^{-1}
Mass spectrometer setting	
Resolution	0.7 amu at 10% peak maximum
Analytical masses	^{52}Cr and ^{53}Cr
Internal standard	^{103}Rh
Dwell time	50 ms
Sweeps per reading	20
Readings per replicate	1
Replicates	3
Auto lens	On
Scanning mode	Peak hopping
Reaction gas	NH_3
Reaction gas flow rate	0.6 mL min^{-1}
Rejection parameter, *q*	0.6
Rejection parameter, *a*	0.0

2.2. Reagents standards and samples

Ultrapure water (18.2 MΩ cm) was obtained from a Millipore (Bedford, MA, USA) system. $K_2Cr_2O_7$ from Merck (Darmstadt, Germany) and Cr(III), nonionic (Triton X-114) and cationic (Aliquat-336) surfactants and ammonium pyrrolidinedithiocarbamate (APDC) were procured from Aldrich (Steinheim, Germany). Methanol and hydrochloric acid (Suprapur, Merck, Darmstadt, Germany) were used for dissolving the surfactant-rich phase. The pH of water samples was adjusted by using HCl and acetate buffer solutions. Rhodium internal standard was purchased from SPEX, USA. The interferences studies were performed by using varying amounts of single elemental stock standard solutions of 1 mg mL^{-1} Ca, Mg, Cd, Cu, Sn, F and Pb (Fisher, Fair Lawn, NJ, USA), Ni, Pd, Pt, NaCl, KCl, $NaNO_3$, NaH_2PO_4 and Na_2SO_4 (Merck, Darmstadt, Germany) and humic acid (Sigma–Aldrich, Steinheim, Germany). Certified reference materials 1643c and 1643d trace elements in waters were obtained from NIST. Natural water samples such as tap, lake, under ground and municipal drinking water were collected locally, and filtered through a 0.45 μm membrane filter and used immediately.

2.3. Procedures

2.3.1. Determination of the phase separation behavior and CPT of Aliquat-336

The phase separation behavior of Aliquat-336 was studied after adding various amounts of additives such as Triton X-114, HCl and NaCl. The phase separation behavior was observed as a function of Aliquat-336 and additive concentrations at room temperature (RT), which is 25 °C, after 24 h. The cloud point temperature (CPT) of various solutions, obtained by varying the HCl and Aliquat-336 concentrations in presence of 1% (m/v) Triton X-114, was measured as the temperature at which the turbidity appeared in the solution.

2.3.2. CPE procedure

2.3.2.1. Extraction of hydrophilic Cr(VI). An aliquot of 15 mL water sample was taken in a tube and maintained the pH 2 using HCl. To this solution, 0.3 mL of 10% (m/v) Aliquat-336 and 1.5 mL of 10% (m/v) Triton X-114 were added. The solution was left to stand for 2 h at RT, which lead to phase separation. The head group of the cationic surfactant behaves like a chelating agent and react with anionic species of Cr(VI) and pre-concentrated into surfactant-rich phase, which avoids the addition of external chelating agent. The surfactant-rich phase formed was easily separated by removing the bulk aqueous phase by using micropipette and used for determination of Cr(VI).

2.3.2.2. Extraction of hydrophobic Cr-APDC. For the determination of total Cr, fresh aliquot of water sample was taken into a tube and maintained the pH 6.5 using acetate buffer. To this solution,

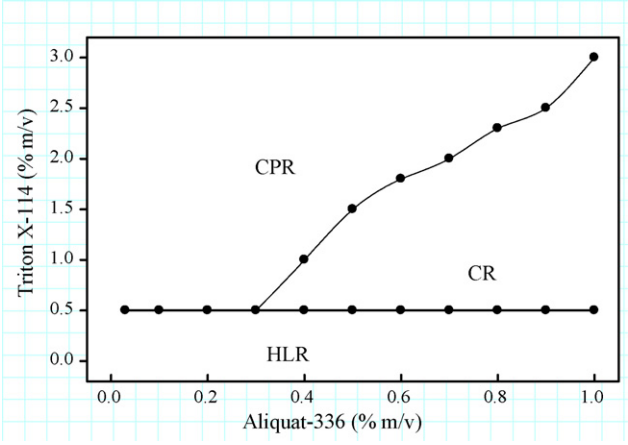


Fig. 1. Phase behavior of Aliquat-336 with Triton X-114 in presence of 1% (v/v) HCl at room temperature.

0.45 mL of 10% (m/v) APDC was added and mixed well for 2 min. Mixture of Aliquat-336 and Triton X-114 was added and the above procedure was followed. The APDC reacts with both chromium [Cr(III) and Cr(VI)] species, and the Cr-APDC hydrophobic species pre-concentrated into the surfactant-rich phase was used for the determination of total Cr [17,18]. The viscosity of 0.4 mL surfactant-rich phase was reduced by dissolving in 1.5 mL of 0.2% HCl, and analyzed for Cr(VI) and total Cr. Procedural blanks were also prepared in the similar manner.

3. Results and discussion

3.1. Effect of additives on the phase separation behavior and CPT of Aliquat-336

The phase separation behavior of ionic surfactant can be varied by the addition of certain dehydrating additives [9]. Therefore, the phase separation behavior of Aliquat-336 was studied with various additives, such as Triton X-114, HCl and NaCl, at room temperature. Fig. 1 shows the phase behavior of Aliquat-336 with Triton X-114 taken in 1% (v/v) HCl when their concentrations were varied independently in the range 0.03–1% (m/v) and 0.1–3% (m/v) respectively. As shown in Fig. 1, three different regions were observed with a clear phase boundary. They were formed by nonionic surfactant induced cloud point region (CPR) and cationic surfactant dominated coacervate region (CR) and a homogeneous liquid region (HLR). The breadth of each region depends up on the concentrations of Aliquat-336 and Triton X-114. Clear HLR was observed at all studied concentrations of Aliquat-336, when Triton X-114 concentration was below 0.5%. Above 0.5%, there was a clear phase boundary between CPR and CR when concentration of Aliquat-336 was more than 0.3%. Both CPR and CR regions contain mixed micelles nonionic being predominant in CPR and vice versa. At higher concentrations of HCl (>10%) and NaCl (>4%) coacervate region was found to be predominant.

Cloud point temperature of surfactants depends on the balance between hydrophilic and hydrophobic interactions of the system, which changes with additives [13]. Hence, the variation of CPT of Aliquat-336 was studied by varying the Aliquat-336 concentration in the range of 0–0.4% (m/v) with HCl in the range of 1–30% (v/v) at 1% Triton X-114. The results showed that at 0% Aliquat-336, the CPT was increased with HCl concentration. However, when Aliquat-336 was added the CPT was constant up to a concentration of 0.005% and then decreased to <10 °C beyond 0.2% Aliquat-336 at all studied concentrations of HCl.

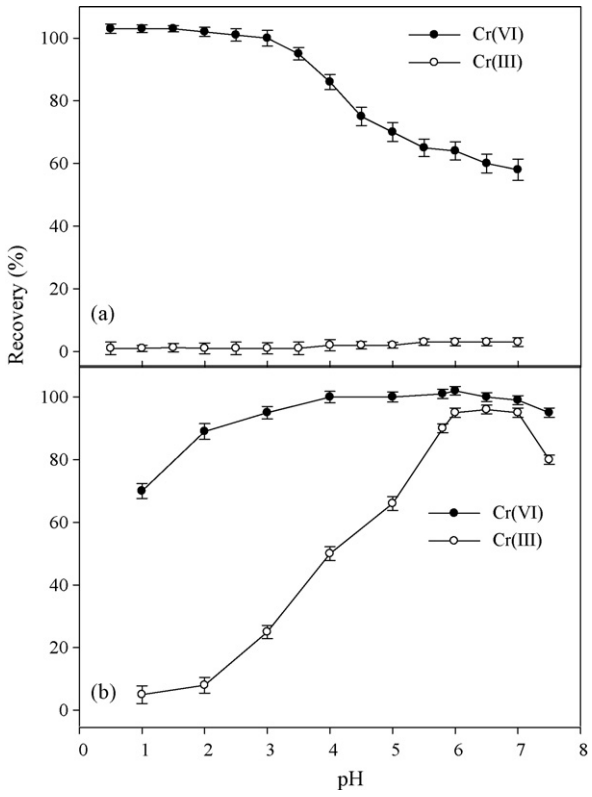


Fig. 2. Effect of pH on the analytical recovery of Cr(III) and Cr(VI) using room temperature cloud point extraction in presence of 0.2% (m/v) Aliquat-336 and 1% (m/v) Triton X-114. (a) Without APDC; (b) with 0.3% (m/v) APDC. The error bars indicate the relative standard deviation (%) at each measurements ($n = 4$).

3.2. Optimization of cationic cloud point extraction parameters

The parameters affecting the extraction of hydrophilic anionic species of Cr(VI) such as $HCrO_4^-$ and hydrophobic Cr-APDC species by the reactive solubilizing sites of Aliquat-336 were studied individually using 0.5 ng mL^{-1} each Cr(VI) and Cr(III) spiked tap water.

Chromium exists in various forms and the relative concentration of each species depends up on the total chromium concentration and pH of the aqueous solution. Hence, the effect of pH on the recovery of Cr(III) and Cr(VI) was studied in the pH range 1–7.5, in presence of 0.2% (m/v) Aliquat-336 and 1% (m/v) Triton X-114, with and without APDC, and the results are shown in Fig. 2(a) and (b). The results indicate that without APDC in Fig. 2(a), 100–103% recovery of Cr(VI) was achieved in the pH range 0.5–3, and then decreased to 60% by further increase in the pH of the solution to 7.5. Whereas, only 2–3% recovery of Cr(III) was observed at the whole studied pH range. Thus, pH 2 was used for selective separation and pre-concentration of Cr(VI) in presence of Cr(III), without using any external chelating agent. In presence of APDC in Fig. 2(b), 100–102% and 94–96% recoveries of Cr(VI) and Cr(III) were achieved in the pH range 5.5–7. Therefore, a pH 6.5 was selected for simultaneous extraction of Cr(III) and Cr(VI), which gives the total chromium concentration. As the reactivity of Cr(VI) with APDC is very fast, the optimization studies were carried out using Cr(III) standard alone.

In order to develop a successful nonionic surfactant induced cationic CPE procedure, optimization of concentrations of cationic and nonionic surfactant required is a must. Fig. 3(a) shows the effect of Aliquat-336 concentration on percentage recovery of Cr(VI) as $HCrO_4^-$ and Cr(III)-APDC, by keeping the Triton X-114 concentration at 1% m/v. The results showed that without Aliquat-336, at RT, no phase separation was observed because the CPT of the solution was 31 °C. Clear phase separation was observed at 0.01% Aliquat-

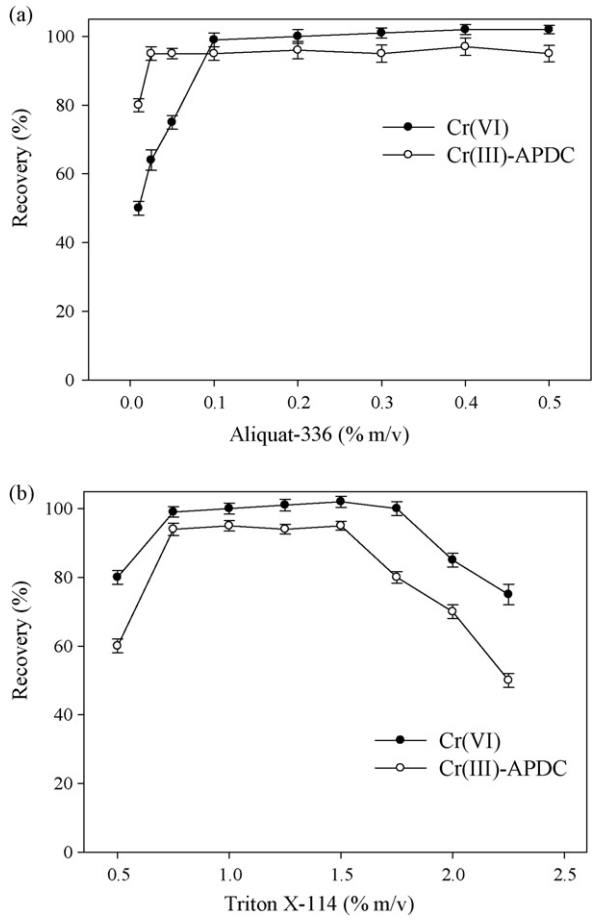


Fig. 3. Effect of Aliquat-336 (a) and Triton X-114 (b) concentration on the recovery (%) of Cr(VI) and Cr(III)-APDC using room temperature cloud point extraction in presence of (a) pH 2 for Cr(VI) and pH 6.6 for Cr(III), 0.3% (m/v) APDC and 1% (m/v) Triton X-114; (b) pH 2 for Cr(VI) and pH 6.6 for Cr(III), 0.3% (m/v) APDC and 0.2% (m/v) Aliquat-336. The error bars indicate the relative standard deviation (%) at each measurements ($n = 4$).

336 addition at RT. This is mainly because of the increase in the hydrophobic nature of the formed mixed micelles that reduces the CPT to 10 °C. Under this condition, the recovery of Cr(VI) and Cr(III)-APDC species were 50 and 80%, respectively. These recoveries were increased gradually to 65 and 95%, respectively by the addition of 0.025% Aliquat-336. Further increase in the concentration of Aliquat-336 to 0.1%, increase the recovery of Cr(VI) and reached a plateau, without any adverse effect in the recovery of Cr(III)-APDC. The low recoveries of Cr(VI) and Cr(III)-APDC at 0.01% Aliquat-336 may be due to non-availability of sufficient hydrophilic and hydrophobic solubilizing sites. Therefore, a concentration of 0.2% Aliquat-336 was selected for quantitative extraction of both the species. Fig. 3(b) shows the effect of Triton X-114 on the percentage recovery of Cr(VI) as $HCrO_4^-$ and Cr(III)-APDC species in the range 0–2.25%, by keeping the Aliquat-336 concentration at 0.2% at RT. The results showed that no phase separation was observed in the range of 0–0.5% Triton X-114. The recoveries increased with increase in the Triton X-114 concentration up to 0.75%, and then reached a plateau up to 1.5%. Further increase caused reduction of the recoveries of both the species. Therefore, a concentration of 1% Triton X-114 was selected. The concentration of APDC required was also studied in the range of 0.1–0.6% (m/v) and 0.3% was found to be optimum for the extraction of both Cr(VI) and Cr(III) species.

The optimization of incubation temperature is necessary, especially, for complete complexation and extraction of water soluble $HCrO_4^-$ and hydrophobic Cr-APDC species into various solubilizing micelles aggregates. For the formation of cloud point phase separation, the selected incubation temperature must be higher than the cloud point temperature of the clouding solution. The clouding temperature of the solution under optimized conditions was 5 °C. Therefore, the effect of incubation temperature was studied in the range 20–90 °C for efficient extraction using incubation time of 120 min. The results showed that the recoveries of Cr(VI) and Cr(III)-APDC were 102 and 96%, respectively at 25 °C. These recoveries were constant up to 40 °C for both the species, and further increase in the incubation temperature to 90 °C, caused decrease in the recovery of Cr(VI) without any adverse effect in the recovery of Cr-APDC. The constant recovery of Cr(III)-APDC over the studied temperature range indicates that the interaction of hydrophobic species (Cr-APDC) with the hydrophobic solubilizing sites of the micelles aggregates is efficient. The reduction in the recovery of Cr(VI) at higher temperatures (>40 °C) may be due to change in the hydrated sphere and ionic environment of extracted species and hydrophilic solubilizing sites compared to the species extracted at room temperature. Therefore, room temperature incubation temperature was selected for both the species.

Sufficient incubation time is required for completing the formation of extractable ion associated and chelating species and their effective interaction and quantitative transfer into the solubilizing sites. Therefore, the effect of incubation time was investigated over a time period from 30 to 240 min at RT. The experiments showed that the phase separation was achieved with in 30 min with 60 and 70% recoveries, respectively for Cr(VI) and Cr-APDC, which were increased to 100 and 97% at 100 min time. Further increase in the incubation time up to 240 min did not change the recoveries. Therefore, 120 min incubation time was selected.

At the optimum conditions the pre-concentration factors, i.e., the ratio of the analyte concentration in the final surfactant-rich phase to that of the initial aqueous phase was evaluated. The final dilution of surfactant-rich phase was performed by compromising the pre-concentration factor in order to make solution suitable to pass through conventional pneumatic nebulizer. Therefore, the 0.4 mL surfactant-rich phase was diluted to 1.5 mL using 0.2% (v/v) HCl. A pre-concentration factor of 10 was achieved for both the species. The dissolved surfactant-rich phase was homogeneous and

Table 2
Recoveries of Cr(III), Cr(VI) and total chromium from spiked tap water samples at different concentration ratios ($n = 4$)[a].

Spiking ratio (ng mL^{-1}) Cr(III):Cr(VI)	Found (ng mL^{-1})			Recovery (%)		
	Cr(III)	Cr(VI)	Total Cr	Cr(III)	Cr(VI)	Total Cr
0.5:0	0.483 ± 0.01	ND[b]	0.483 ± 0.01	96.6 ± 2.0	ND[b]	96.6 ± 2.0
0:0.5	ND[b]	0.507 ± 0.007	0.507 ± 0.007	ND[b]	101.4 ± 1.4	101.4 ± 1.4
0.5:0.5	0.475 ± 0.01	0.498 ± 0.006	1.004 ± 0.014	95.0 ± 2.0	99.6 ± 1.2	100.4 ± 1.4
0.5:1.0	0.482 ± 0.009	1.022 ± 0.008	1.493 ± 0.015	96.4 ± 1.8	102.2 ± 0.8	99.5 ± 1.0
1.0:1.0	0.973 ± 0.014	1.015 ± 0.009	1.996 ± 0.008	97.3 ± 1.4	101.5 ± 0.9	99.8 ± 0.8

[a] Values are mean of four measurements ± standard deviation.
[b] Not detected.

Table 3
Comparison of the proposed cationic CPE procedure with some of the reported CPE procedure for the speciation analysis of chromium.

Species	Chelating agent	Surfactant system	Solubilizing sites	Incubation temp. (°C)	LOD (ng mL^{-1})	Ref.
Cr(VI)	APDC	Triton X-114	Hydrophobic	40	0.6	[18]
Total Cr				80		
Cr(III)	HQ[a]	Triton X-114	Hydrophobic	85	1.4	[17]
Cr(VI)	APDC			40	0.65	
Cr(III)	AA[b]	Triton X-100	Hydrophobic	80	0.32	[23]
Cr(III)	TTA[c]	Triton X-114	Hydrophobic	60	0.22	[24]
Cr(VI)	Br-PF[d]	Triton X-100	Hydrophobic	85	0.01	[22]
Cr(III)	No	Triton X-114 and SDS	Hydrophilic	RT	0.005	[21]
Cr(VI)	No	Aliquat-336 and Triton X-114	Hydrophilic and Hydrophobic	RT	0.01	Present procedure
Total Cr	APDC				0.025	

[a] Hydroxyquinoline.
[b] Acetyle acetone.
[c] Thenoyl triflouro acetone.
[d] Dibromo phenyl fluorone.

provided stable signal for Cr(VI) and Cr(III)-APDC extracted species for more than 2 weeks.

3.3. Analytical recovery

The recovery studies of Cr(VI), Cr(III) and total Cr were performed separately after spiking tap water samples with Cr(III) and Cr(VI) species individually in the range of 0.5–1 ng mL^{-1} and at different ratios. The recoveries obtained are given in Table 2. Cr(III) values were obtained by subtracting the Cr(VI) values from total chromium. As shown in Table 2, the recoveries were in between 95 and 102% for all types of waters studied. Therefore, this procedure was used for determination of individual chromium species in natural water samples. The relative standard deviations were in between 0.8 and 2%.

3.4. Interferences

In order to evaluate the performance of this procedure, the highest tolerability of various common interfering ions were studied. Interferences may occur mainly due to competition of other existing anionic species in the water samples that may form ion associated complexes with the cationic hydrophilic solubilizing sites and also from the natural organic matter in the form of humic acid, which forms strong complexes with the hydrophobic solubilizing sites of the aggregates. Therefore, the tolerable limits of various foreign ions were studied in tap water, spiked with 1 ng mL^{-1} each of Cr(VI) and Cr(III) independently, by keeping the relative error between ±5%. It was found that 2 and 1 g L^{-1} of Na^+ and K^+; 500 mg L^{-1} of Mg^{2+}; 50 mg L^{-1} of Ca^{2+}; 100 mg L^{-1} of Ni^{2+}; 50 mg L^{-1} of Cu^{2+}; Cd^{2+} and Pb^{2+}; 1 mg L^{-1} of Pd^{2+}; 0.2 mg L^{-1} of Pt^{4+} and Sn^{4+} cations and 3 g L^{-1} of Cl^-; 0.5 g L^{-1} of SO_4^{2-}; 3 g L^{-1} of NO_3^-; 1 mg L^{-1} of F^- and PO_4^{2-} anions showed no interference. In addition to the above, no interference was observed from humic acid up to 6 mg L^{-1}. These results demonstrated the selectivity of the procedure, and which can be applied to the analysis of real water samples.

3.5. Analytical figures of merit

Under the optimized experimental conditions, the calibration curves were obtained by pre-concentrating the tap water samples successively spiked with five standards of Cr(VI) and Cr(III) with APDC in the range of 0.2–10 and 0.3–5 ng mL^{-1}, respectively. The correlation coefficient was 0.9998 and 0.9956 for Cr(VI) and Cr(III) with APDC, respectively. Quantifications have been performed by using aqueous standards prepared in 0.2% HCl. The relative standard deviation (% RSD) of Cr(VI) and Cr(III)-APDC were in between 0.6 and 3% at 1 ng mL^{-1}. The limits of detection calculated based on three times the standard deviations of the ten measurements of procedural blanks of Cr(VI) and Cr(III)-APDC were 0.010 and 0.025 ng mL^{-1}, respectively. A comparison of the proposed cationic CPE procedure with the previously reported CPE procedures for the speciation analysis of chromium is given in Table 3, which indicates that the present procedure shows the comparable or better LOD with the reported procedure. The other advantages are i) The analytical capabilities of the both (hydrophilic and hydrophobic) solubilizing sites of the Aliquat-336/Triton X-114 mixed micelles have been proved by selective extraction of Cr(VI) and Cr-APDC species separately. ii) The cationic head group of the mixed micelle act as an internal chelating as well as extracting agent for the extraction of $HCrO_4^-$ species and avoids the addition of external chelating agents. iii) Temperature independent extraction of Cr-APDC species shows the high reactivity of the hydrophobic solubilizing sites of mixed micelles. iv) The room temperature phase separation and stability of the extracted chromium species in surfactant-rich phase are useful to handle the samples at sampling sites and transporting

Table 4
The determined values of Cr(III), Cr(VI) and total Cr in certified and real natural water samples using the procedure described in this work.

Type of matrix	Measured value (ng mL^{-1})			Certified value (ng mL^{-1})
	Cr(VI)[a]	Cr(III)[b]	Total Cr[a]	
NIST 1643c water	1.45 ± 0.16	17.21 ± 0.17	18.66 ± 0.19	19.0 ± 0.6
NIST 1643d water	1.96 ± 0.21	16.29 ± 0.14	18.25 ± 0.16	18.53 ± 0.2
Water samples				
Tap[c]	85 ± 9	231 ± 5	316 ± 6	–
Lake[c]	55 ± 6	300 ± 10	355 ± 12	–
Under ground[c]	189 ± 12	239 ± 6	428 ± 9	–
Municipal[c]	65 ± 7	93 ± 6	158 ± 8	–

[a] Mean of six determinations ± standard deviation.
[b] Values are obtained by subtracting the Cr(VI) values from total Cr.
[c] Values are in pg mL^{-1}.

the small volume of surfactant-rich phase containing Cr species to environmental laboratories.

3.6. Validation of the method and analysis of real samples

The accuracy of the proposed procedure was verified by analyzing certified reference materials such as NIST 1643c and 1643d water. This procedure was also applied to the determination of Cr(VI) and Cr(III) species in real samples analyzed directly without any sample pretreatment. The results are given in Table 4. The results showed that there is good agreement between the measured chromium and the certified values indicating the accuracy of the procedure. Both the isotopes of the chromium showed the same results indicating the interference free measurements. The values of Cr(VI) in tap, lake, under ground and municipal water samples were 85, 55, 189 and 65 pg mL^{-1}, respectively. The precision of the results were between 0.2–0.6 and 0.5–1.1% for total chromium and Cr(VI), respectively.

4. Conclusions

We have presented a new concept of increasing the hydrophobic nature of cationic micelles with nonionic surfactant for inducing the cloud point phase separation. Its analytical applicability has been demonstrated by extraction of both hydrophilic anionic and hydrophobic species of chromium. The limits of detection of Cr achieved are comparable or superior to reported procedures. Additionally, the room temperature phase separation and stability of the extracted species in surfactant-rich phase are useful to handle the collected samples at sampling sites and transporting the small volume SRP to environmental laboratories. Therefore, these features make the procedure more attractive to handle the thermally labile analytes easily.

Acknowledgment

We are grateful to the National Science Council (NSC) of the Republic of China for providing the PDF grant to Dr. N.N. Meeravali under the Contract NSC 97-2811-M 110-018.

References

[1] H. Watanabe, H. Tanaka, Talanta 25 (1978) 585.
[2] C.D. Stalikas, Trends Anal. Chem. 21 (2002) 343.
[3] E.K. Paleologos, D.L. Giokas, M.I. Karayannis, Trends Anal. Chem. 24 (2005) 426.
[4] N.N. Meeravali, S.J. Jiang, J. Anal. At. Spectrom. 23 (2008) 854.
[5] R.P. Frankewich, W.L. Hinze, Anal. Chem. 66 (1994) 944.
[6] S. Rubio, D.P. Bendito, Trends Anal. Chem. 22 (2003) 470.
[7] I. Casero, D. Sicilia, S. Rubio, D.P. Bendito, Anal. Chem. 71 (1999) 4519.
[8] F.J. Ruiz, S. Rubio, D.P. Bendito, J. Chromatogr. A 1030 (2004) 109.
[9] F.J. Ruiz, S. Rubio, D.P. Bendito, Anal. Chem. 78 (2006) 7229.
[10] X. Jin, M. Zhu, E.D. Conte, Anal. Chem. 71 (1999) 514.
[11] B.K.W. Man, M.H.W. Lam, P.K.S. Lam, R.S.S. Wu, G. Shaw, Environ. Sci. Technol. 36 (2002) 3985.
[12] G.Z. Tsogas, D.L. Giokas, E.K. Paleologos, A.G. Vlessidis, N.P. Evmiridis, Anal. Chim. Acta 537 (2005) 239.
[13] W.N. Maclay, J. Colloid Sci. 11 (1956) 272.
[14] R.A. Rahem, Adv. Colloid Interface Sci. 141 (2008) 24.
[15] V. Gómez, M.P. Callao, Trends Anal. Chem. 25 (2006) 1006.
[16] http://www.atsdr.cdc.gov/cercla/07list.html, Agency for Toxic Substances and Disease Registry (ATSDR), CERCLA Priority list of Hazardous Substances, US Department of Health and Human Services, Public Health Services, 2007.
[17] E.K. Paleologos, C.D. Stalikas, S.M.T. Karayanni, G.A. Pilidis, M.I. Karayannis, J. Anal. At. Spectrom. 15 (2000) 287.
[18] E.K. Paleologos, C.D. Stalikas, M.I. Karayannis, Analyst 126 (2001) 389.
[19] Y.L. Chang, S.J. Jiang, J. Anal. At. Spectrom. 16 (2001) 1434.
[20] C.Y. Kuo, S.J. Jiang, A.C. Sahayam, J. Anal. At. Spectrom. 22 (2007) 636.
[21] E.K. Paleologos, A.G. Vlessidis, M.I. Karayannis, N.P. Evmiridis, Anal. Chim. Acta 477 (2003) 223.
[22] X. Zhu, H. Bin, Z. Jaing, M. Li, Water Res. 39 (2005) 589.
[23] Z. Sun, P. Liang, Microchim. Acta 162 (2008) 121.
[24] Y. Li, H. Bin, Z. Jaing, Y. Wu, Anal. Lett. 39 (2006) 809.

Talanta 80 (2009) 179–183

Contents lists available at ScienceDirect

Talanta

journal homepage: www.elsevier.com/locate/talanta

Novel enzyme-linked immunosorbent assay for determination of fluvastatin in plasma at picogram level

Ibrahim A. Darwish*, Abdul-Rahman M. Al-Obaid, Hamoud A. Al-Malaq

Department of Pharmaceutical Chemistry, College of Pharmacy, King Saud University, P.O. Box 2457, Riyadh 11451, Saudi Arabia

ARTICLE INFO

Article history:
Received 27 May 2009
Received in revised form 20 June 2009
Accepted 22 June 2009
Available online 1 July 2009

Keywords:
Atherosclerosis
HMG-CoA reductase inhibitors
Fluvastatin
ELISA

ABSTRACT

For the first time, an enzyme-linked immunosorbent assay (ELISA) has been developed and validated for the determination of fluvastatin (FLV) in plasma samples at picogram level. The assay employed a polyclonal antibody that specifically recognizes FLV with high affinity, and FLV conjugate of bovine serum albumin (FLV–BSA) immobilized onto microplate wells as a solid-phase. The assay involved a competitive binding reaction between FLV, in plasma sample, and the immobilized FLV–BSA for the binding sites on a limited amount of the anti-FLV antibody. The bound anti-FLV antibody was quantified with horseradish peroxidase-labeled second anti-rabbit IgG antibody (HRP-IgG) and 3,3′,5,5′-tetramethylbenzidine (TMB) as a substrate for the peroxidase enzyme. The concentration of FLV in the sample was quantified by its ability to inhibit the binding of the anti-FLV antibody to the immobilized FLV–BSA and subsequently the color intensity in the assay wells. The conditions for the proposed ELISA were investigated and the optimum conditions were employed in the determination of FLV in plasma samples. The assay limit of detection was 10 pg mL^{-1} and the effective working range at relative standard deviations (RSD) of ≤5% was 20–1000 pg mL^{-1}. Analytical recovery of FLV from spiked plasma was 97.1–102.7 ± 2.85–6.25%. The precision of the assay was satisfactory; RSD was 2.46–5.37 and 3.19–6.64% for the intra- and inter-assay precision, respectively. The analytical procedure is convenient, and one can analyze ~200 samples per working day, facilitating the processing of large-number batch of samples. The proposed ELISA has a great value in routine analysis of FLV for its therapeutic monitoring and pharmacokinetic studies.

© 2009 Elsevier B.V. All rights reserved.

1. Introduction

Atherosclerosis of the coronary and peripheral vasculature is the principal cardiovascular disease that causes morbidity and mortality worldwide [1]. Elevated plasma levels of the total cholesterol (hypercholesterolemia) are predictive for the premature coronary heart disease [2]. Lowering the cholesterol levels can arrest or reverse atherosclerosis in all vascular beds and can significantly decrease the morbidity and mortality associated with the atherosclerosis [3]. The most efficient and frequently prescribed drugs for the treatment of hypercholesterolaemia are the 3-hydroxy-3-methylglutaryl-coenzyme A (HMG-CoA) reductase inhibitors [4]. These agents specifically inhibit HMG-CoA reductase, the enzyme that catalyzes the conversion of HMG-CoA to mevolanate, which is the early rate-limiting step in the biosynthesis of cholesterol in the body [5].

Fluvastatin [*R**,*S**-(*E*)]-(±)-7-[3-(4-fluorophenyl)-1-(1-methylethyl)-1H-indol-2-yl]-3,5-dihydroxy-6-heptenoic acid, is a totally synthetic highly potent HMG-CoA reductase inhibitor. As well, FLV reduces the level of low-density lipoprotein (LDL) in plasma, and it is well tolerated by the patients [6]. FLV has a short elimination half-life, and is highly bound to plasma proteins. Furthermore, the bioavailability and pharmacodynamics of FLV are not affected by food. Because of the hydrophilicity of FLV, it does not cross the blood–brain barrier, thus it has no central nervous system side effects (e.g. insomnia) [7]. These qualities made FLV one of the most prescribed drugs for the treatment of hypercholesterolemia.

Because of the therapeutic importance and clinical success of FLV, several methods have been developed for its quantitative determination in plasma samples. These methods include HPLC [8–13], gas chromatography [14], and capillary electrophoresis [15]. These methods involved tedious steps for the pre-treatment of the samples, pre-derivatization with critical derivatizing reagents, and use of expensive detectors (e.g. tandem mass spectrometry) that are not available in most laboratories [13]. For these reasons, the development of new alternative analytical technology for determination of FLV in plasma with adequate sensitivity, improved simplicity, and lower cost was seriously needed.

Immunoassays have been widely used in pharmaceutical and clinical analysis because of their inherent specificity, applicability for a wide range of analytes, high-throughput, and low cost [16]. ELISA is the most versatile format of the immunoassays. ELISA is

* Corresponding author. Tel.: +966 14677348; fax: +966 14676220.
E-mail address: idarwish@ksu.edu.sa (I.A. Darwish).

0039-9140/$ – see front matter © 2009 Elsevier B.V. All rights reserved.
doi:10.1016/j.talanta.2009.06.052

remarkably quick, easily performed, and also offers great sensitivity when appropriate enzyme labels are used. As well, ELISA, as it uses analyte-specific antibodies, does not require pre-treatment for the samples and it is well suited for the screening of large-number of samples.

The present study describes, for the first time, the development and validation of a highly sensitive ELISA for determination of FLV at concentrations as low as 20 pg mL^{-1} in plasma samples.

2. Experimental

2.1. Instruments

FLX808 microplate reader (Bio-Tek Instruments Inc., USA). FLX50 microplate washer (Bio-Tek Instruments Inc., USA). EM-36N microtube shaker (Taitec, Japan). Biofuge Pico centrifuge (Heraeus Instruments, Germany). Incubator (Mini/18, Genlab Ltd., UK). Water purification system (Milli-Q Labo, Millipore Ltd., Bedford, USA).

2.2. Materials

Fluvastatin was obtained from Biocon India Ltd., India. HRP-IgG, BSA, 2,4,6-trinitrobenzene sulfonic acid, 1-ethyl-3-(3-dimethylaminopropyl) carbodiimide hydrochloride (EDC), and tween-20 were purchased from Sigma Chemical Co. (St. Louis. MO, USA). TMB peroxidase substrate was obtained from Kirkegaard-Perry Laboratories (Gaithersburg, MD, USA). ELISA high-binding microwell plates were a product of Corning/Costar, Inc. (Cambridge, MA, USA). Centricon-30 filter (Amicon, Inc., Beverly, MA, USA). BCA reagent for protein assay was obtained from Pierce Biotechnology Inc. (Rockford, IL, USA). All water was purified by filtration through a water purification system.

2.3. Procedures

2.3.1. Preparation of anti-FLV antibody and FLV–BSA conjugate

Anti-FLV polyclonal antibody was induced by immunization of an eight weeks old female New Zealand white rabbits with FLV conjugated with keyhole limpt hemocyanin protein (FLV-KLH). The procedures for preparation of FLV-KLH, immunization, purification, and characterization of the antibody have been submitted for publication elsewhere. The coating conjugate (FLV–BSA) was prepared by linking FLV (via its carboxylic group) with BSA protein (via its amino group) by EDC reagent (Fig. 1). EDC (150 mg) was added to FLV solution (10 mL, 5 mg mL^{-1}) in 1.25×10^{-2} mol L^{-1} phosphate buffer (PB) of pH 5, and the pH was maintained at pH 5–5.5 using 0.01 mol L^{-1} HCl for 5 min. Five mL of BSA solution (5 mg mL^{-1}, in 5×10^{-2} mol L^{-1} PB of pH 7.2) was added, and the pH of the reaction mixture was rapidly adjusted to 6.4 and maintained constant for 90 min. The reaction was left to proceed overnight in dark at 4 °C. The uncojugated FLV residues were removed from the FLV–BSA conjugate by buffer exchange using a Centricon-30 filter. Protein content of the conjugate was determined by BCA reagent kit and the extent of substitution of free amino groups on the BSA was determined by estimation of free amino groups on equal amounts of unreacted BSA and on BSA subjected to the conjugation by the procedure described by Habeeb [17]. The extent of conjugation = $(A_{FLV-BSA}/A_{BSA}) \times 100$; where $A_{FLV-BSA}$ and A_{BSA} were the absorbances obtained from the reaction of 2,4,6-trinitrobenzene sulfonic acid with FLV–BSA and BSA, respectively. The extent of conjugation was found to be 24.8% of the total amino group residues.

2.3.2. Determination of the optimum concentrations of antibody and coating conjugate

The optimum FLV–BSA concentration required for coating onto the microwell plates and the best working concentration of the anti-FLV antibody were determined by checkerboard titration employing the procedures described by Darwish et al. [18]. Different concentrations (0.1–5 μg mL^{-1}) of FLV–BSA in 50 μL of PBS were coated onto the microwell plates in triplicate rows by incubation for 2 h at 37 °C with gentle agitation by microtube shaker. After incubation, the plates were washed with PBS containing 0.05% Tween-20 (PBS-T) using microplate washer. The wells were blocked with 200 μL of 3% BSA in PBS by incubation at 37 °C for 1 h. Fifty microliters of different concentrations (0.5–4 μg mL^{-1}) of anti-FLV antibody solution (in PBS) was added in columns across the microwell plates. After incubation for 1.5 h at 37 °C, the plates were washed with PBS-T, and 50 μL of HRP-IgG (1/5000 in PBS) was added to each well. After similar incubation and washing step, 50 μL of TMB substrate solution was added and the reaction was allowed to proceed for 10 min at 37 °C for color development. The absorbance of each well was measured at 630 nm by the microplate reader. Concentrations of FLV–BSA conjugate and anti-FLV antibody that yielded absorbance units of 1–1.5 were considered as reference binding conditions for further testing.

2.3.3. ELISA procedures and data analysis

Plasma samples were centrifuged at 3500 rpm at 4 °C for 10 min and the supernatants were collected, and spiked with FLV. Aliquots (50 μL) of the spiked samples were diluted five-fold with PBS. The diluted samples were mixed with equal volumes of anti-FLV antibody (4 μg mL^{-1}). Aliquot (50 μL) of the mixture was added to each well of the microwell plate that had been previously coated with FLV–BSA (1 μg mL^{-1}) and blocked with BSA (3%, w/v). After incubation for 1.5 h at 37 °C, the plates were washed with PBS-T, and 50 μL of HRP-IgG (1/5000 in PBS) was added to each well. After incubation

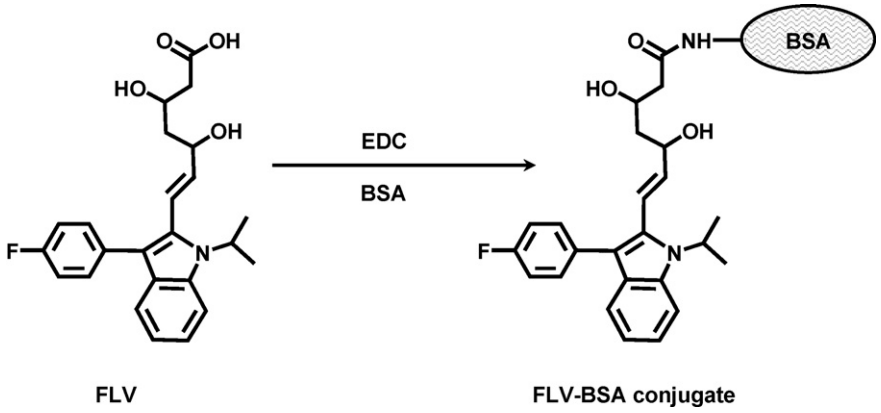


Fig. 1. Preparation of FLV–BSA conjugate.

for 1.5 h, the plates were washed with PBS-T and the amount of the bound HRP-IgG was quantified using TMB as described above. The data were acquisitioned by KC Junior software (Bio-Tek Instruments Inc., USA), and transformed to a four-parameter curve fitting using Slide Write software, version 5.011 (Advanced Graphics Software, Inc., USA). Values for IC_{50} were those that gave the best fit to the following equation: $A = A_0 - \{(A_0 - A_1)[FLV]/(IC_{50} + [FLV])\}$

Where A is the signal at a definite known concentration of FLV, A_0 is the signal in the absence of FLV, A_1 is the signal at the saturating concentration of FLV, and IC_{50} is the FLV concentration that produces a 50% inhibition of the signal. The concentrations of FLV in the samples were then obtained by interpolation on the standard curve.

3. Results and discussion

This study describes the development of a highly sensitive ELISA for determination of FLV in plasma samples; Fig. 2 describes the features of this ELISA. In this assay, microwell plates were coated with FLV–BSA conjugate. A polyclonal antibody that recognizes FLV with high affinity and specificity was mixed with FLV sample, and the mixture was incubated with FLV–BSA immobilized onto the microwells. During this incubation, FLV competed with FLV–BSA for binding to the available limited binding sites on the anti-FLV antibody. After removal of the unbound reagents, the amount of anti-FLV antibody bound to the microwells was determined using HRP-IgG and TMB as a chromogenic substrate. The concentration of FLV in the sample was quantified by its ability to inhibit the binding of anti-FLV antibody to the immobilized FLV–BSA, and the color development was inversely proportional to the concentration of FLV in the original sample solution.

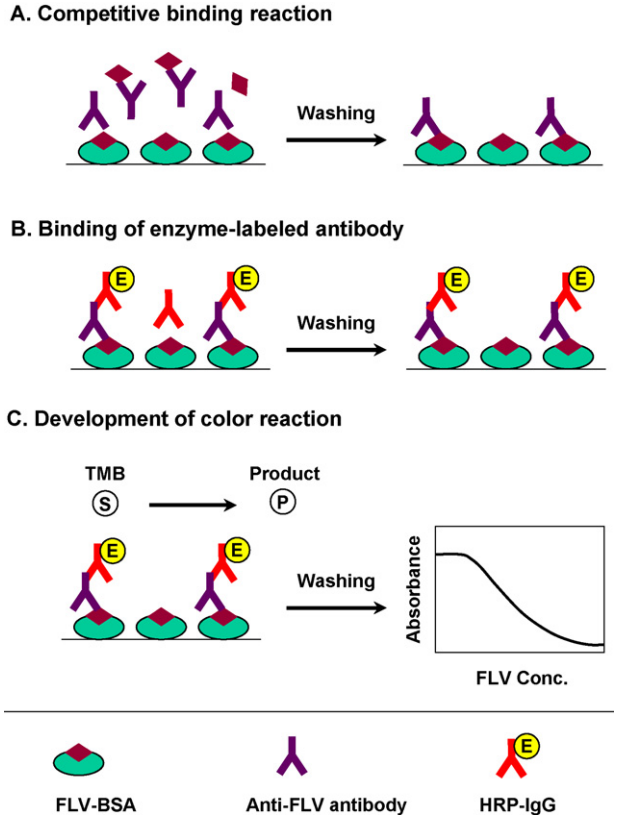


Fig. 2. Schematic diagram of the competitive ELISA for FLV. (A) Sample containing FLV is premixed with anti-FLV antibody. The mixture solution containing the FLV and its specific antibody is dispensed into microwell plates that have been coated with FLV–BSA conjugate. The soluble FLV competes with the immobilized FLV–BSA conjugates for the anti-FLV antibody binding sites. (B) After a wash step to remove any antibody bound to the soluble FLV, HRP-IgG is added. A second wash step removes unbound secondary antibody. (C) The signal is generated by the addition of TMB as a colorimetric substrate, and the measured color intensity are correlated with the FLV concentrations for generating the calibration curve for determination of FLV.

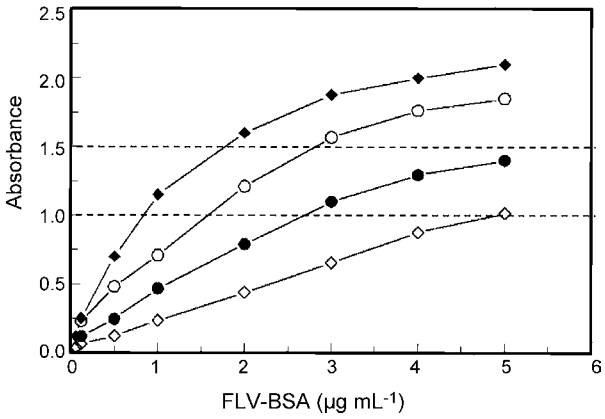


Fig. 3. Checkerboard titrations for FLV–BSA versus anti-FLV antibody. Varying concentrations (0.01–4 μg mL^{-1}) of FLV–BSA conjugate were coated onto the microwell plates. Varying concentrations of anti-FLV antibody were allowed to bind to the immobilized FLV–BSA. These concentrations were 0.5 (◊), 1 (●), 2 (○), and 4 (♦) μg mL^{-1}. Signals were generated as described in the Section 2. Absorbance values were plotted as a function of FLV–BSA concentrations.

3.1. Optimization of assay variables

3.1.1. Choice of conjugate and antibody concentrations

To determine the optimum concentration of FLV–BSA required for immobilization onto the microwell plates and the concentration of anti-FLV antibody for an effective competitive binding reaction, checkerboard titration of FLV–BSA versus anti-FLV antibody was carried out. The conjugate and antibody concentrations that gave absorbance units of 1–1.5 (in the direct ELISA), and lowest IC_{50} (in the competitive ELISA) were considered as reference optimum binding conditions. These conditions were attained at varying concentrations of FLV–BSA conjugate and anti-FLV antibody (Fig. 3). In order to select the most appropriate concentrations that give the most sensitive assay, competitive ELISA was carried out using FLV as a competitor. The most sensitive assay (lowest IC_{50}) was achieved when the concentrations of FLV–BSA conjugate and anti-FLV antibody were 1 and 4 μg mL^{-1}, respectively (Table 1). Therefore, these concentrations were used in all the further investigations.

3.1.2. Binding of FLV–BSA to microplate wells

Optimum binding of the FLV–BSA conjugate to the microwells was attained when the incubation time was 2 h at 37 °C, and more than 6 h at room temperature (25 ± 5 °C) (Fig. 4). For more convenience in the screening of clinical specimens, it was important to check the lifespan of the FLV–BSA after its immobilization onto the microwell plates. Plates were coated with the FLV–BSA and stored at 4 and −20 °C for varying periods of time, and then the plates were analyzed for the amount of immunoreactive conjugate remained on

Table 1
IC_{50} values that have been obtained at varying concentrations of coating FLV–BSA conjugate and anti-FLV antibody.

FLV–BSA (μg mL^{-1})	Anti-FLV antibody (μg mL^{-1})	IC_{50}[a] (pg mL^{-1})
1	4	100
2	2	400
3	1	1000
4	1	2000
5	0.5	5000

[a] Values are mean of 3 determinations.

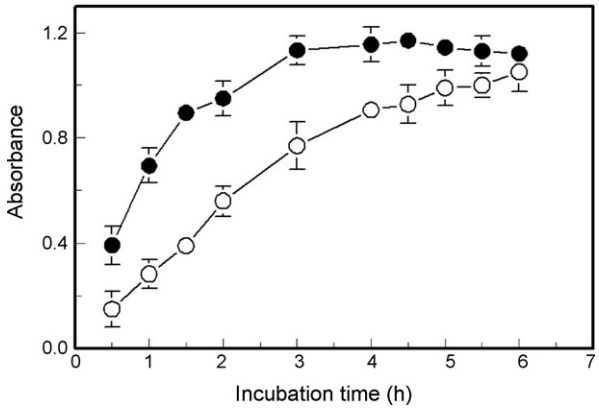


Fig. 4. Effect of temperature and incubation time on the immobilization of FLV–BSA onto the microwells. Incubations were carried out at 37 °C (●), and room temperature (25 ± 5° C) (○).

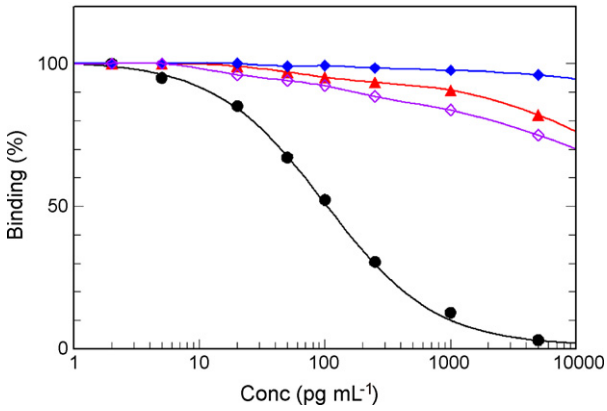


Fig. 6. Competitive binding assay for FLV (●), atorvastatin (◊), pitavastatin (▲), and rosuvastatin (♦).

the microwells. The results indicated that the plates could be stored for at least 4 and 6 weeks at 4 and −20 °C, respectively. This gives an advantage that the use of pre-coated and blocked plates could reduce 3 h from the total assay time.

3.2. Validation of the assay

3.2.1. Calibration curve and detection limit

The calibration curve for determination of FLV by the proposed ELISA is shown in Fig. 5. This curve was generated using FLV concentrations in the range of 2–5000 pg mL^{-1}, prepared in PBS. The data showed good correlation coefficient (r = 0.9985) on the four-parameter curve fit. The limit of detection of the proposed ELISA, defined as the lowest FLV concentration significantly different from zero concentration at 95% confidence limit (mean of zero ± 4.65 SD) was determined [19]. Based on the basis of 8 replicate measurements, the limit of detection was found to be 10 pg mL^{-1}. This high sensitivity enables the determination of low concentrations of FLV in plasma without any sample pre-concentration procedure as the reported FLV plasma level were 53–370 and 200–440 ng mL^{-1} after 20 and 40 mg-daily dosing, respectively [20]. It is worth noting that none of the previously reported HPLC [8–13], gas chromatography [14], and capillary electrophoretic [15] methods could achieve the high sensitivity of the proposed ELISA (pg level) as all the reported limits of detection of these methods were in ng levels. As well, the selective determination of FLV by most of the reported methods was not possible without prior selective liquid–liquid or solid-phase extraction for the drug followed by its careful separation from endogenital sample component. However, the proposed ELISA as it relied on a selective antibody, was able to selectively determine FLV without such extraction and separation procedures.

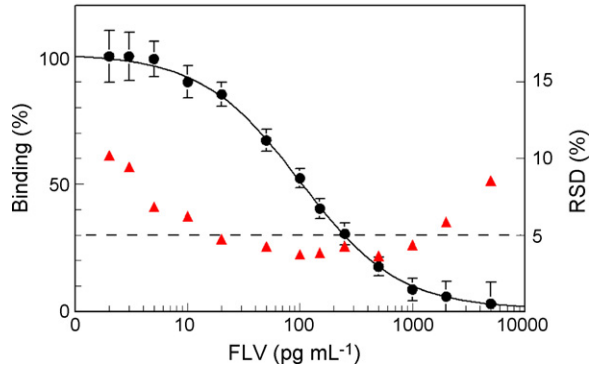


Fig. 5. Calibration curve (●) and precision profile (▲) of the proposed ELISA for FLV. Varying concentrations of standard FLV were mixed with anti-FLV antibody (2 μg mL^{-1}). The reaction mixtures were further manipulated as described in the Section 2. The values plotted are mean ± SD of three determinations.

3.2.2. Precision profile

The assay precision profile obtained from the results of calibration standard samples, assayed in triplicate, is shown in Fig. 6. From this profile, the working range of the assay at RSD values of less than 5% was derived. This range was found to be 20–1000 pg mL^{-1}. The RSD at the detection limit of the assay (10 pg mL^{-1}) was found to be 6.21%. The intra- and inter-assay precisions were tested at three varying levels of FLV. The intra-assay precision was assessed by analyzing eight replicates of each sample in a single run and the inter-assay precision was assessed by analyzing the same samples, as duplicates, in four separate runs. According to the recommendations of immunoassay validation [21], the assay gave satisfactory results; the RSD was 2.46–5.37 and 3.19–6.64% for the intra- and inter-assay precision, respectively (Table 2).

In general, the precision in competitive immunoassays depends mainly upon the uniformity in the quantity of the coated reagent from well to well in a microwell plate. Any interference in this uniformity could arise from the experimental protocol and other manipulations; change in the temperature of incubation and dispensing the reagents. The good precision observed in the proposed ELISA was attributed to the facts that all the incubation steps of the assay were carried out at the same temperature.

3.2.3. Assay specificity

Although, the assay utilized an antibody specific to FLV, it was necessary to investigate this specificity under the specified experimental assay conditions. The specificity of the present method was determined by carrying out the competitive assay using various HMG-Co A reductase inhibitors (atorvastatin, pravastatin, lovastatin, simvastatin, rosuvastatin, and pitavastatin), and various drugs that are administered in combined therapy with FLV (ezetimibe [22], gemfibrozil [23], aspirin [24], gemcitabine [25], cholestyramine [26] and estradiol [27]) as competitors at concen-

Table 2
Precision of the proposed ELISA for determination of FLV.

FLV (pg mL^{-1})	Intra-assay		Inter-assay	
	Mean ± SD[a] (pg mL^{-1})	RSD (%)	Mean ± SD (pg mL^{-1})	RSD (%)
20	20.5 ± 1.1	5.37	21.1 ± 1.4	6.64
100	101.5 ± 2.5	2.46	100.4 ± 3.2	3.19
500	489.4 ± 15.8	3.23	98.56 ± 20.5	4.16

[a] Values are mean of 8 determinations ± SD.

Table 3
Analytical recovery of FLV spiked into three different batches of plasma samples.

Spiked FLV (pg mL^{-1})	Recovery[a] (% ± RSD)		
	Batch A	Batch B	Batch C
25	102.0 ± 4.25	97.1 ± 5.12	100.2 ± 6.25
50	100.4 ± 4.21	99.6 ± 5.45	101.2 ± 5.12
100	100.5 ± 2.85	102.1 ± 3.48	97.8 ± 3.55
200	99.1 ± 4.12	100.5 ± 5.02	98.2 ± 3.24
400	102.7 ± 4.05	98.5 ± 3.52	100.1 ± 4.58

[a] Values are mean of three determinations.

trations considerably higher than that may be present in patient plasma. The cross reactivity was calculated using the formula: IC_{50} (competitor)/IC_{50} (FLV) × 100. It was found that the values of IC_{50} for all the competitors used were higher than the maximum FLV concentration used in the assay (5000 pg mL^{-1}). The data that have been generated for atorvastatin, pitavastatin, and rosuvastain are given in Fig. 6. The other competitors gave binding profile very similar to that of rosuvastatin. These data proved that none of these competitors showed any cross reactivity with FLV in the assay indicating the high specificity of the proposed ELISA for determination of FLV.

3.2.4. Accuracy and application of the proposed ELISA

The accuracy of the proposed ELISA and its applicability was assessed by the recovery study. Samples were prepared by spiking varying concentrations (25–400 pg mL^{-1}) of FLV into three different batches of drug-free plasma. The spiked samples were analyzed for their contents of FLV, as described in the Section 2. The analytical recovery was calculated as the ratio of the found FLV concentration to that of the spiked concentration, and the ratio was expressed as percentage. The analytical recovery values were 97.1–102.7% with RSD 2.85–6.25% (Table 3). These recovery values, according to the guidelines for immunoassay validation [21], indicated the accuracy of the proposed method for determination of FLV in plasma samples, and absence of endogenous interfering substances in the plasma samples.

4. Conclusions

The present study described, for the first time, the development and validation of a highly sensitive ELISA for the determination of FLV in plasma at picogram level. The entire protocol of the present assay is very easy to perform in a 96-well plate and permits an operator to analyze a batch of 200 samples, in triplicate, per day when the plates have been previously coated with FLV–BSA and blocked with BSA. This facilitates the processing of large-number of samples. Since the assay produces a colored read-out, only a colorimetric plate reader is required. Unlike HPLC, the marked specificity of the proposed ELISA eliminates the need for pre-treatment of plasma samples by affinity chromatography or other sophisticated equipment. For these reasons, the proposed ELISA is expected to contribute to the therapeutic monitoring and pharmacokinetic studies of FLV.

Acknowledgments

The authors thank King Abdulaziz City for Science and Technology, and the Research Center at College of Pharmacy, King Saud University for the funding the work.

References

[1] World Health Organization, World Health Report, Report of the Director-General, Geneva, WHO, 2004.
[2] P.J. Barter, Atherosclerosis 1 (2000) 21.
[3] R.P. Byington, J.W. Jukema, J.T. Salonen, B. Pit, A.V. Bruschke, H. Hoen, C.D. Furberg, G.B. Mancini, Circulation 92 (1995) 2419.
[4] D.W. Kaufman, J.P. Kelly, L. Rosenberg, T.E. Anderson, A.A. Mitchell, J. Am. Med. Assoc. 287 (2002) 337.
[5] J.H. Block, J.M. Beale, Organic Medicinal and Pharmaceutical Chemistry, 11th ed., Lippincott Williams & Wilkins, New York, 2004, pp. 662–663.
[6] A. Yamamoto, K. Hoshi, K. Ichihara, Eur. J. Pharmacol. 361 (1998) 143.
[7] W.R. Garneti, Am. J. Cardiol. 78 (1996) 20.
[8] S. Ertürk, A. Onal, C.S. Müge, J. Chromatogr. B 793 (2003) 193.
[9] S. Al-Rawithi, R.F. Hussein, A. Alzahranif, Ther. Drug Monitor. 25 (2003) 88.
[10] R. Nirogi, K. Mudigonda, V. Kandikere, J. Pharm. Biomed. Anal. 44 (2007) 379.
[11] S.Y. Um, S.H. Jung, S.J. Jung, J.I. Kim, S.Y. Chung, H.J. Lee, S.B. Han, S.O. Choi, J. Pharm. Biomed. Anal. 41 (2006) 1458.
[12] D.P. Giuliano, C.E. Barbosa, G.T. Magalhaes, M.M. Paula, L.V. Lucia, J. Chromatogr. B 832 (2006) 256.
[13] R.V.S. Nirogi, V.N. Kandikere, W. Shrivastava, K. Mudigonda, Rapid Commun. Mass Spectrom. 20 (2006) 1225.
[14] H.J. Leis, W. Windischhofer, Rapid Commun. Mass Spectrom. 19 (2005) 128.
[15] T.Q. Trung, P.T. Dung, N.N. Hoan, D.J. Kim, J.H. Lee, K.H. Kim, Arch. Pharm. Res. 31 (2008) 1066.
[16] I.A. Darwish, Int. J. Biomed. Sci. 2 (2006) 217.
[17] A.F. Habeeb, Anal. Biochem. 14 (1966) 328.
[18] I.A. Darwish, A.M. Mahmoud, T. Aboul-Fadl, A.A. Al-Majed, Y. Nasr, Khalil, Anal. Chim. Acta 632 (2009) 266.
[19] D.J. Anderson, Clin. Chem. 35 (1989) 2152.
[20] Y. Shitara, Y. Sugiyama, Pharmacol. Ther. 112 (2006) 71.
[21] J.W.A. Findlay, W.C. Smith, J.W. Lee, G.D. Nordblom, I. Das, B.S. DeSilva, M.N. Khan, R.R. Bowsher, J. Pharm. Biomed. Anal. 21 (2000) 1249.
[22] E.A. Stein, C.M. Ballantyne, E. Windler, P.A. Sirnes, A. Sussekov, Z. Yigit, C. Seper, C.R. Gimpelewicz, Am. J. Cardiol. 15 (2008) 490.
[23] J.D. Spence, C.E. Munoz, L. Hendricks, L. Latchinian, H.E. Khouri, Am. J. Cardiol. 76 (1995) 80A.
[24] A. Ijaz, H.N. Bhatti, S. Rasheed, B. Sadaf, R. Nawaz, Pak. J. Biol. Sci. 6 (2003) 1404.
[25] D.R. Budman, A. Calabro, Oncology 70 (2006) 147.
[26] E. Hagen, H. Istad, L. Ose, E. Bodd, H.M. Eriksen, V. Selvig, J.M. Bard, J.C. Fruchart, M. Borge, M.C. Wolf, Eur. J. Clin. Pharmacol. 46 (1994) 445.
[27] A.O. Mueck, H. Seeger, F.U. Deuringer, D. Wallwiener, Menopause 8 (2001) 216.

Talanta 80 (2009) 184–188

Contents lists available at ScienceDirect

Talanta

journal homepage: www.elsevier.com/locate/talanta

Determination of lead in the presence of morin-5′-sulfonic acid and sodium dodecyl sulfate by adsorptive stripping voltammetry

Verónica Arancibia*, Edgar Nagles, Shasmmin Cornejo

Facultad de Química, Pontificia Universidad Católica de Chile, Santiago 7820436, Chile

ARTICLE INFO

Article history:
Received 4 February 2009
Received in revised form 22 June 2009
Accepted 23 June 2009
Available online 1 July 2009

Keywords:
Lead(II)
Adsorptive stripping voltammetry
Sodium dodecyl sulfate

ABSTRACT

A simple and sensitive electroanalytical method is developed for the determination of lead by adsorptive stripping voltammetry (AdSV) in the presence of morin-5′-sulfonic acid (MSA) and sodium dodecyl sulfate (SDS). The Pb-MSA complex accumulates on the surface of a hanging mercury drop electrode (HMDE) and peak current is measured by square wave voltammetry (SWV). The complex is reduced at −0.48 V and peak current increases when low concentrations of SDS are added to the sample solution. The experimental variables pH, MSA concentration (C_{MSA}); accumulation time (t_{acc}); accumulation potential (E_{acc}), and SDS concentration (C_{SDS}), as well as potential interferences, are investigated. Under the optimized conditions (pH 3.2; C_{MSA}: 0.5 μmol L^{-1}; t_{acc}: 60 s; E_{acc}: −0.35 V, and C_{SDS}: 20 μmol L^{-1}), peak current is proportional to the concentration of Pb(II) over the 0.1–32.0 μg L^{-1} range, with a detection limit of 0.04 μg L^{-1}. The relative standard deviation for a solution containing 5.0 μg L^{-1} of Pb(II) solution was 1.5% for seven successive assays. The method was validated by determining Pb(II) in synthetic sea water (ASTM D665) spiked with ICP multi-element standard solution and in certified reference water (GBW08607). Finally, the method was successfully applied to the determination of Pb(II) in tap water and sea water after UV digestion.

© 2009 Elsevier B.V. All rights reserved.

1. Introduction

Lead is a ubiquitous environmental pollutant with no known biological functions that has strong chemical toxicity at low concentrations. It can occur as a result of industrialization in the production of pigments, anticorrosion coatings, lead smelters, alloys, and batteries, causing significant disturbances in air, dust, soil, water, sediments, food, etc. The World Health Organization (WHO) and the U.S. Environmental Protection Agency (EPA) have set maximum levels of 50 and 10 μg L^{-1} of Pb in seawater and drinking water, respectively [1,2].

Anodic stripping voltammetry (ASV) has long been recognized as a powerful technique for trace metals owing to its sensitivity, relatively inexpensive instrumentation, and ability for multi-element determination. The mercury film electrode (MFE) and the hanging mercury drop electrode (HMDE) have been traditionally used for ASV because of the advantageous analytical properties of mercury in the negative potential range, however in the last years a large number of electrodes have been used. de Carvalho et al. [3] made a comparative study of the determination of Pb and other metal ions in highly saline samples using mercury film electrode (MFE) and bismuth film electrode (BiFE), achieving limits of detection (LODs) of 0.060 and 0.10 μg L^{-1}, respectively. The following have also been used: thin mercury film electrode (TMFE) [4]; bismuth-modified carbon nanotube electrode [5] (LOD: 1.3 μg L^{-1}); mercury film deposited on a wax-impregnated carbon paste electrode [6] (LOD: 1.12 ng L^{-1}); bismuth powder-modified carbon paste electrode [7] (LOD: 0.9 μg L^{-1}); bismuth-modified zeolite-doped carbon paste electrode [8] (LOD: 0.10 μg L^{-1}); disposable pencil-lead graphite as substrate for BiFE [9] (LOD: 0.4 μg L^{-1}); multiwall carbon nanotubes dispersed in Nafion solution in combination with bismuth [10] (LOD: 25 ng L^{-1}); titanium carbide [11] (LOD: 0.4 μg L^{-1}); silver ring [12] (LOD: 41 ng L^{-1}) and lately screen-printed electrodes [13] (LOD: 1.8 μg L^{-1}).

Because of the sensitivity enhancement obtained with adsorption stripping voltammetry, several complexing agents have been studied for the adsorptive collection of complexes with Pb on HMDE, among them 2-acetylpyridine salicyloylhydrazone [14] (LOD: 35 ng L^{-1}); calcein blue [15] (LOD: 8 ng L^{-1}); o-cresolphthaleine [16] (LOD: 40 ng L^{-1}); 8-hydroxyquinole [17,18] (LODs: 0.931 μg L^{-1} and 4 ng L^{-1}, respectively); xylenol orange [19,20] (LODs: 6 ng L^{-1} and 0.98 μg L^{-1}, respectively); morin [21] (LOD: 0.08 μg L^{-1}). Catechol, 4-methylcatechol, 4-t-butylcatechol, and resorcinol [22] have also been used as complexing agent to determine Pb and other metal ions.

One possible way of enhancing the adsorptive process and the sensitivity of the method is the use of surfactants, whose beneficial effects are unpredictable, as they tend to interfere by

* Corresponding author.
E-mail address: darancim@uc.cl (V. Arancibia).

0039-9140/$ – see front matter © 2009 Elsevier B.V. All rights reserved.
doi:10.1016/j.talanta.2009.06.046

competitive adsorption. However, addition of the anionic surfactant sodium dodecylbenzene sulfonate (SDBS) has been found to greatly improve the adsorption of palladium-dimethylglyoxime complex [23], and the cationic surfactant cetyltrimethylammonium bromide (CTAB) has increased at least 40-fold the sensitivity of the determination of progesterone and cobalt in the presence of nioxime with a mercury electrode [24,25]. The effect of surfactants has been studied in the determination of organic compounds such as pharmaceuticals, hormones, biomolecules, proteins, pesticides, etc. [26–32]. The presence of surfactants can shift the complexation pH to a more acidic region, and it has been reported that they increase molar absorptivities [33], fluorescence properties [34], the solubility of ligands and complexes in organic solvents [35], they can change the kinetics of the electron-transfer reaction and affect the reversibility of the systems, etc. [36,37]. Cationic or anionic surfactants can be adsorbed easily onto the mercury electrode by hydrophobic and electrostatic attraction. Neutral metal complexes in the solution can be attracted by the positively charged surfactant to form stable compounds and be transported consequently to the electrode surface in the accumulation step.

The interaction of the flavonoids morin and quercetin with anionic (SDS) and cationic (CTAB) surfactants has been studied by Liu and Guo using electronic absorption, fluorescence emission spectra, ATR-FTIR spectra, cyclic voltammetry, and ab initio quantum calculations [38,39]. They reported that when the concentration of morin is about 4×10^{-5} mol L^{-1} it exists mainly as a monomer, but when the concentration is about 1×10^{-4} mol L^{-1} morin undergoes H-aggregation forming a dimer. In the presence of CTAB, depending on concentration it forms premicelles, spherical micelles, and rodlike micelles in the aqueous solution. These micelles shift the wavelength and intensity of the absorption maximum.

We now report the effect of SDS on the sensitivity of the determination of lead in the presence of morin-5′-sulfonic acid. The sulfonic group, which does not participate directly in the metal–ligand bond, can be adequate for this study because it contributes a negative charge which strengthens the bond with the surfactant and then with the electrode. The procedure is based on the reduction of the complex after accumulation on the surface of a hanging mercury drop electrode (HMDE). SDS was added to synthetic and real samples. Morin-5′-sulfonic acid is also adequate for the determination of cadmium, but the optimum conditions are different from those for lead.

2. Experimental

2.1. Reagents

Water used for washing and for preparing solutions was 18.2 MΩ cm deionized water from a Millipore system. All the chemicals (nitric acid, hydrochloric acid, peroxide, boric acid, acetic acid, etc.) were analytical grade from Merck (Darmstadt, Germany). Standard stock solutions with 1.0 or 0.1 mg L^{-1} of Pb(II) and Cd(II) were prepared from standard Pb(II) and Cd(II) 1000 mg L^{-1} solutions (Merck). Morin-5′-sulfonic acid (MSA) was synthesized as reported by Kopacz [40] and was prepared in water or methanol for lead and cadmium analysis, respectively. Sodium dodecyl sulfate (SDS, Sigma) and cetylpyridinium bromide (CPB, Aldrich) were prepared by dissolving the reagent in water. Synthetic sea water (ASTM D665, Aldrich) contaminated with ICP multi-element standard solution IV (23 elements in dilute nitric acid. Merck); and certified reference natural water (GBW08607) containing K^+ 2.2; Na^+ 23, Ca^{2+} and Mg^{2+} 11 mg L^{-1} in 0.5 mol L^{-1} HNO_3 with certified values of Cd 0.100; Cr 0.500; Cu 1.00; Ni 0.500; Pb 1.00 and Zn 5.00 μg g^{-1} were used for validation measurements. Britton-Robinson buffer [41] was prepared by mixing equal volumes of 0.4 mol L^{-1} orthophosphoric acid, acetic acid, and boric acid, adjusting to the required pH with 0.2 mol L^{-1} NaOH solution, and diluting 10 times with water.

2.2. Instrumentation

Square wave adsorptive stripping voltammetry (SWAdSV) was carried out on an MDE 150 polarographic stand (Radiometer Analytical, Lyon, France). The MDE 150 was controlled with TraceMaster 5 PC software. The three-electrode classical cell consisted of an HMDE, an auxiliary platinum electrode, and an Ag/AgCl/KCl 3 mol L^{-1} reference electrode, a mechanical mini stirrer, and a capillary to supply an inert gas. The solutions were de-aerated using high-purity argon. An Orion 430 pH meter was used for pH measurements. UV-irradiation of water samples was carried out in quartz tubes in a 705 UV-digester with a high-pressure mercury lamp (Metrohm).

2.3. Sample preparation

Nine seawater samples from the sea surface were collected in early spring (September 20, 2008) from three points of the Quintero beach, which is close to several industries and belongs to a highly populated and tourist area (South Pacific coast, Chile). The samples were collected in high-density polyethylene bottles which had been acid-washed and rinsed with Milli-Q water. Prior to filling with sample, the bottles were conditioned three times with the same water. The collected seawater samples were filtered through a polycarbonate 0.45 μm membrane filter, acidified with HNO_3 to pH close to 2, and stored frozen until analysis. Domestic tap water samples were collected in our laboratory. Before the analysis all the samples were digested for 90 min at 90 °C in the presence of H_2O_2 (10.0-mL of sample with 100 μL of 30% H_2O_2) to decompose organic substances. To make sure of the reliability of the method the samples were analyzed by ICP-AES.

2.4. Voltamperometric procedure

Voltammetric measurements were made using the following procedure: 10.0-mL of deionized water, 100-μL of Britton-Robinson buffer (0.04 mol L^{-1}), 100–400 μL of morin-5′-sulfonic acid solution (0.04 mmol L^{-1}), and aliquots of Pb(II) or Cd(II) solution (0.1 or 1.0 mg L^{-1}) were pipetted into the voltammetric cell. The measurements were made in the presence and absence of surfactants. The solution was purged with argon (saturated with water vapor) for 5 min. Then, after eliminating five drops, a new mercury drop was extruded to initiate the preconcentration step for a given t_{acc} and E_{acc} at a stirring speed of 400 rpm. After an equilibration time of 10 s, the adsorptive voltammogram was recorded, while the potential was scanned from −0.35 to −1.20 V using square wave modulation with 0.01 V step amplitude, 0.05 V pulse amplitude, and a frequency of 25 Hz. The calibration curves were drawn and linear regression and detection limits were calculated. All data were obtained at room temperature (≈25 °C).

For the voltammetric analysis of real samples, a 10.0-mL aliquot of UV-digested seawater (or tap water) was pipetted in the cell, 100 μL of Britton Robinson pH 3.2 buffer, and aliquots of ligand solution were added, and the determination was carried out using the standard addition method. Each voltammogram was repeated three times.

3. Results and discussion

Morin-5′-sulfonic acid ($pK_1 = 4.7$; $pK_2 = 7.8$; $pK_3 = 9.8$; $pK_4 = 10.7$) has good aqueous solubility and forms complexes

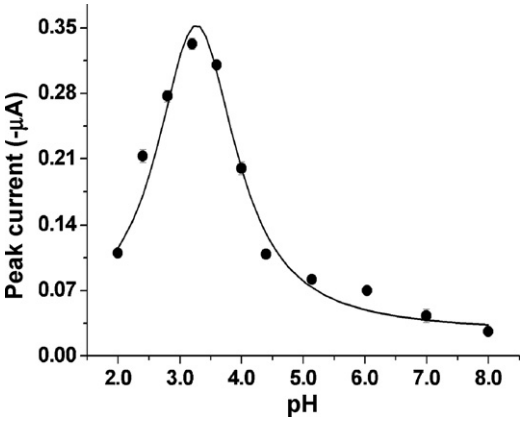


Fig. 1. Influence of pH on the peak current of the Pb-MSA complex. Conditions: Pb(II), 4.9 μg L^{-1}; C_{MSA}: 0.5 μmol L^{-1}; t_{acc}: 60 s; E_{acc}: −0.35 V; step amplitude: 10 mV, pulse amplitude: 50 mV, and frequency: 25 Hz.

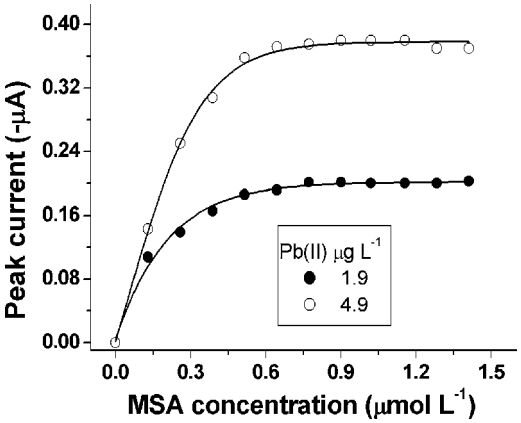


Fig. 2. Influence of C_{MSA} concentration on the peak current of the Pb-MSA complex. Conditions: Pb(II), 1.9 and 4.9 μg L^{-1}; pH 3.2; t_{acc}: 60 s; E_{acc}: −0.35 V. Other conditions as in Fig. 1.

with lead (PbH_4L) and cadmium ($Cd(H_3L)_2$) that are poorly soluble in water (10^{-4} to 10^{-5} mol dm^{-3}, 20 °C). In the complexes the metal is chelated by three C–OH and four C=O, and the sulfonic group contributes a negative charge [40,42].

Preliminary experiments were carried out to determine the effect of SDS and CPB on the absorbance and electrochemical reactions of free morin-5′-sulfonic acid at pH 4.0 and 6.0. The results showed the same trends found by Liu and Wou [38,39] with morin and quercetin. SDS and CPB shift the absorption peaks (λ, ε) and electrochemical oxidation (E_{peak}, i_{peak}, glassy carbon electrode) of morin-5′-sulfonic acid. In order to find the optimum conditions with the highest sensitivity for the determination of Pb(II) with HMDE, the influence of various parameters such as pH, C_{MSA}, t_{acc}, E_{acc}, and C_{SDS} on peak current was studied.

3.1. Effect of operational parameters

3.1.1. Effect of pH variation

The effect of the solution's pH on peak current of the Pb-MSA complex was studied in the 2.0–8.0 range. In order to keep the composition of the buffer constant when studying the effect of pH, Britton Robinson (BR) buffers were used (Fig. 1). C_{Pb} and C_{MSA} were 4.9 μg L^{-1} and 0.5 μmol L^{-1}, respectively (E_{acc}: −0.35 V, t_{acc}: 60 s). It is clear that the peak current of the Pb-MSA complex is maximum at pH 3.2 and decreases rapidly at pH values between 4.0 and 8.0. At pH 8.0 the signal is very broad. On the other hand, peak potential was −0.47 V at pH 2.0 and −0.56 V at pH 6.0. The charge of the Pb-MSA complex at higher pH values changes and it is probably not adsorbed onto the electrode (pK_1 MSA 4.7). A pH value of 3.2 was chosen for the whole study. A study as a function of buffer concentration was carried out adding aliquots of 0.04 mol L^{-1} of BR buffer, getting the highest peak current of the Pb-MSA complex when 100 μL was added.

3.1.2. Effect of morin-5′-sulfonic acid concentration (C_{MSA})

MSA concentration had a considerable effect on the method's linear range and sensitivity. The effect of C_{MSA} was studied for Pb(II) at the levels of 1.9 and 4.9 μg L^{-1}, while other standard measuring conditions remained constant (pH: 3.2; t_{acc}: 60 s, E_{acc}: −0.35 V). C_{MSA} was changed from 0.0 to 1.4 μmol L^{-1}. The results show that peak current increases with increasing MSA concentration up to 0.5 μmol L^{-1} (Fig. 2). At higher C_{MSA} the peak current tended to level off. Therefore, an optimum C_{MSA} of 0.5 μmol L^{-1} was chosen for further optimization study with synthetic solutions. However, when the spiked or real water samples contained several metal ions a ligand concentration of 1.2–1.5 μmol L^{-1} was added to ensure complete complex formation.

3.1.3. Effect of accumulation time (t_{acc})

Accumulation time is one of the important parameters that have a pronounced effect on sensitivity in stripping procedures. Accumulation time was examined in the 0–300 s range, while other standard measuring conditions remained constant (Pb(II), 4.9 μg L^{-1}; C_{MSA}, 0.5 μmol L^{-1}; pH: 3.2; E_{acc}: −0.35 V). Peak current increases with increasing accumulation prior to the potential scan, indicating that the Pb-MSA complex is readily adsorbed on the HMDE. Peak current increased linearly with increasing accumulation time up to 300 s and no saturation of the electrode surface was observed. However, for longer accumulation times (above 180 s) a small shoulder at −0.62 V is seen in the adsorptive voltammograms. On that basis, and considering the speed of the measurement, a t_{acc} of 60 s was used for further studies.

3.1.4. Effect of accumulation potential (E_{acc}) in the absence and presence of sodium dodecyl sulfate (C_{SDS})

The effect of E_{acc} was studied for Pb(II) at the levels of 1.9 and 4.9 μg L^{-1}, while other standard measuring conditions remained constant (pH: 3.2; C_{MSA}: 0.5 μmol L^{-1}; t_{acc}: 60 s). E_{acc} varied from 0.00 to −0.40 V. Fig. 3 shows the results obtained with Pb(II) 1.9 μg L^{-1}. These measurements were carried out in the absence

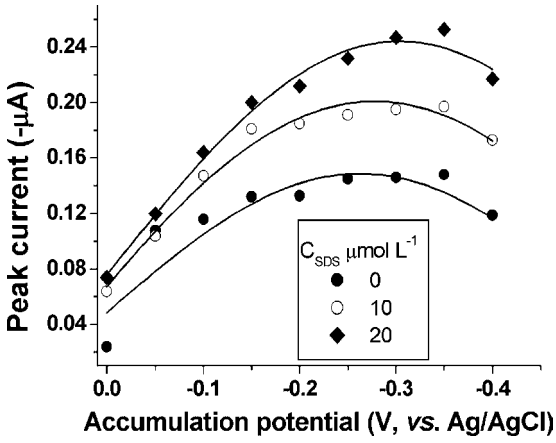


Fig. 3. Influence of E_{acc} on the peak current of the Pb-MSA complex in the absence and presence of SDS. Conditions: Pb(II), 1.9 μg L^{-1}; C_{SDS}: 10 and 20 μmol L^{-1}; pH 3.2; C_{MSA}: 0.50 μmol L^{-1}; t_{acc}: 60 s. Other conditions as in Fig. 1.

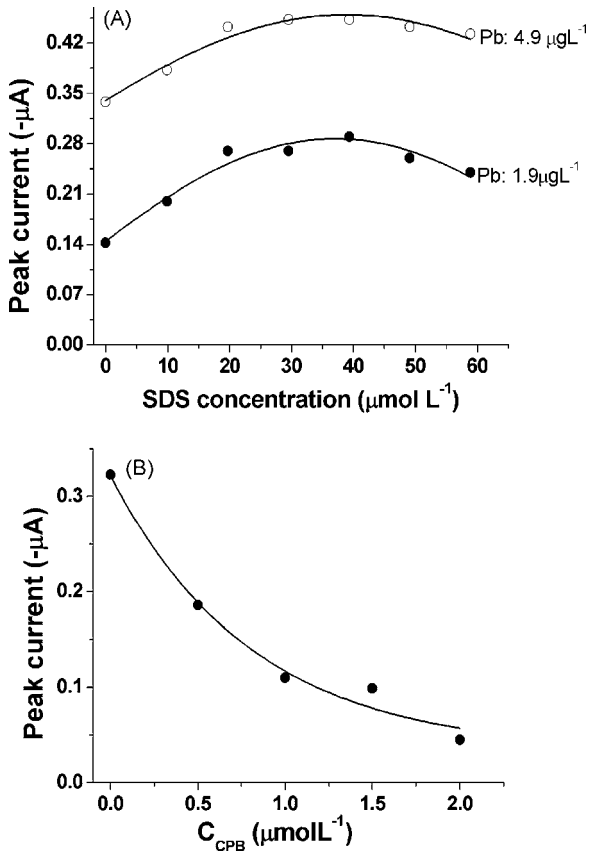


Fig. 4. Influence of C_{SDS} and C_{CPB} on the peak current of the Pb-MSA complex. Conditions: (a) Pb(II), 1.9 μg L^{-1}, (b) Pb(II), 4.9 μg L^{-1}. pH 3.2; C_{MSA}: 0.50 μmol L^{-1}; E_{acc}: −0.35 V; t_{acc}: 60 s. Other conditions as in Fig. 1.

and in the presence of SDS 10 and 20 μmol L^{-1}. As shown in Fig. 3, in the presence or absence of SDS, peak current increased with changing potential from 0.00 to −0.35 V. However, it decreased slightly when the potential was changed to −0.40 V. An accumulation potential of −0.35 V gives the best sensitivity and was chosen for the study. More negative potential values cause electrolysis of Pb(II). In the presence of small amounts of a surfactant such as SDS the peak current of the Pb-MSA complex increases, the possible mechanism of this enhancement effect involves the formation of negatively charged micelles of SDS with the lead complex and the positive charge of mercury electrode to potentials about −0.40 V.

3.1.5. *Effect of sodium dodecyl sulfate (SDS) and cetylpyridinium bromide (CPB) concentration*

The influence of C_{SDS} was studied for Pb(II) at the levels of 1.9 and 4.9 μg L^{-1}, while other standard measuring conditions remained constant (pH: 3.2; C_{MSA}: 0.5 μmol L^{-1}, t_{acc}: 60 s, E_{acc}: −0.35 V). The SDS concentration range examined was 0–60 μmol L^{-1}. The influence of C_{SDS} on the peak current of the Pb-MSA complex is presented in Fig. 4a, which shows that the peak current suddenly increases as SDS concentration increases from 0 to 10 μmol L^{-1} and then reaches a maximum at 20 μmol L^{-1}. At SDS concentrations of 50–60 μmol L^{-1} peak current decreased slowly. At pH 3.2 the Pb-MSA complex is positively charged ($[Pb(H_4L)^+]$) [40]. SDS and the negatively charged Pb complex-SDS micelles may be adsorbed on the surface of the mercury electrode by electrostatic attraction. SDS concentration had no influence on peak potential. The effect of the presence of CPB was examined in the 0.0–2.0 μmol L^{-1} range. The results are shown in Fig. 4b, where it is seen that, in contrast with the effect of SDS, in the presence of small amounts of cationic surfactant the peak current of the Pb-MSA complex decreases rapidly as C_{CPB} increases. At a C_{CPB} of 2.0 μmol L^{-1} peak current is only 14% of the initial value when C_{CPB} is 0.

3.2. *Effect of instrumental variables (frequency, step potential, and amplitude)*

A linear increase of the peak current of the complex was seen when the size of the mercury drop varied from 0.25 to 1.25 mm^2, and 0.75 mm^2 was adopted as optimum, with larger sizes not convenient because mercury drops fall more frequently. The peak current of the Pb-MSA complex increased when the frequency increased from 25 to 50 Hz. However, at frequencies of 50 Hz there was a deterioration of the peak shape and the backgroundand and 25 Hz was adopted as optimum. Peak current increased linearly with step potential variations from 1 to 10 mV and pulse amplitude from 5 to 50 mV. 10 and 50 mV were adopted as optimum for step potential and pulse amplitude, respectively.

3.3. *Analytical parameters*

The calibration graph for the determination of lead was obtained under the optimized conditions. pH 3.2 (100 μL of 0.04 mol L^{-1} BR buffer); C_{MSA}: 0.5 μmol L^{-1}; t_{ads}: 60 s; E_{ads}: −350 V. If C_{MSA} is 0.50 μmol L^{-1}, adsorptive curves of Pb(II) at concentrations from 0.1 to 10.0 μg L^{-1} produce a linear calibration plot (r = 0.9996), but if C_{MSA} is 1.50 μmol L^{-1} the plot is linear until 32.0 μmol L^{-1}. The precision expressed as the relative standard deviation (R.S.D.) was 1.5% for seven successive measurements of the same sample containing 5.0 μg L^{-1} of Pb(II). The limit of detection (LOD) was calculated according to the IUPAC upper limit approach (ULA) [43] and was 0.062 μg L^{-1} in the absence and 0.043 μg L^{-1} in the presence of 20 μmol L^{-1} of SDS.

In the voltammetric determination of Pb(II) the main interference may be caused by the presence of Cd(II) because of its reduction potential close to that of Pb. Fig. 5 shows adsorptive voltammograms of Pb(II) and Cd(II) in the presence of MSA, with cadmium concentrations twice those of lead, and yet the currents are smaller. The method is not sensitive for the determination of lead and cadmium simultaneously. Higher peak currents for Cd-MSA were obtained at pH 4.0 and the optimum C_{MSA} was 2.5 μmol L^{-1}. For cadmium similar peak currents were obtained applying adsorptive potentials between 0.00 and −0.50 V (t_{acc}: 60 s).

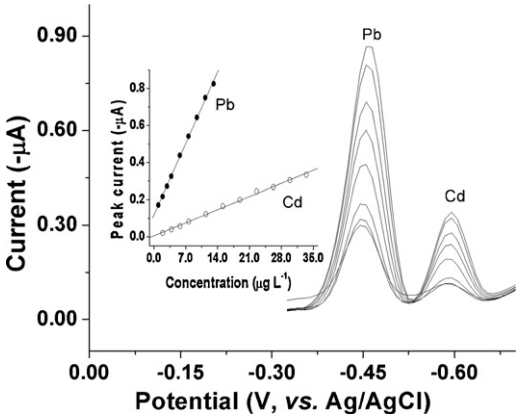


Fig. 5. Adsorptive voltammograms (top) and corresponding calibration plot (bottom) of Pb(II) and Cd(II) standard solutions. Conditions: pH 3.2; C_{MSA}: 1.50 μmol L^{-1}; E_{acc}: −0.35 V; t_{acc}: 60 s. Other conditions as in Fig. 1.

Table 1
Determination of lead in water samples[a,b].

Sample	Pb(II) found ($\mu g\,L^{-1}$)	S.D.
Tap water	4.9	0.5
Sea water[c]	1.4	0.1
Sea water[d]	6.9	0.2
Sea water[e]	1.3	0.0

[a] All the samples were analyzed by ICP-AES and the level of Pb was low 10 $\mu g\,L^{-1}$.
[b] Three replicate analyses were performed for each sample.
[c] Borders of the beach.
[d] Near the dock.
[e] 12 m towards the interior of the sea.

3.4. Interference studies and validation of the method

An aliquot of synthetic sea water (ASTM D665) was contaminated with an ICP multi-element standard solution containing metal ions such as Ag, Al, Cd, Co, Cr, Cu, Fe, Ga, Ni, Zn, Pb and others in equal concentration (5.0 $\mu g\,L^{-1}$), and aliquots of MSA were added until the Pb-MSA current peak reached a maximum before the analysis of Pb was carried out using the standard addition method. The results obtained for Pb(II) were $5.1 \pm 0.3\ \mu g\,L^{-1}$ (pH 3.2; C_{MSA}: 1.50 $\mu mol\,L^{-1}$, t_{acc}: 60 s; E_{acc}: −0.35 V). The usefulness of the present method was also evaluated by determining Pb(II) in certified reference water (20 μL. GBW08607) containing Cd 0.100; Cr 0.500; Cu 1.00; Ni 0.500; Pb 1.00, and Zn 5.00 $\mu g\,g^{-1}$. Three replicate analyses were performed for each sample. The value obtained was $1.08 \pm 0.10\ \mu g\,g^{-1}$. These measurements were made in the presence and absence of SDS (20 $\mu mol\,L^{-1}$), giving higher values and slopes in the presence of the anionic surfactant.

3.5. Analysis of real samples

The proposed method was applied to the detection of lead in sea water and domestic tap water previously digested with UV radiation in the presence of H_2O_2 solution. The samples were obtained from three points of the Quintero beach: the edge of the beach, near the dock, and 12 m away from the edge. These analyses (10-mL samples) were carried out in the presence of SDS 20 $\mu mol\,L^{-1}$ (pH 3.2; C_{MSA}: 1.20 $\mu mol\,L^{-1}$; t_{acc}: 60 s; E_{acc}: −0.35 V). To check the reliability of the method the samples were analyzed by ICP-AES, however the results obtained with this technique were below 10 $\mu g\,L^{-1}$, which is the detection limit of this procedure. Table 1 shows the results. The highest value was $6.9 \pm 0.2\ \mu g\,L^{-1}$ of Pb (sea water). The Pacific ocean where the samples were collected is close to several industries and belongs to a highly populated and tourist area, however the levels are below the limit proposed by the EPA [1].

4. Conclusions

This work reports the trace determination of Pb(II) in the presence of morin-5′-sulfonic acid and the effect of SDS on the peak current of the corresponding Pb-MSA complex. The presence of SDS always increases the peak current of the complex and the slope of the i_{peak} vs. Pb concentration plot, but the exact i_{peak} ratio in the presence and absence of SDS is dependent on the analyte's concentration.

Acknowledgement

Financial support by FONDECYT under project 1080524 is gratefully acknowledged.

References

[1] E. Süren, S. Yilmaz, M. Türkoglu, S. Kaya, Environ. Monit. Assess. 125 (2007) 91.
[2] Current drinking water standards, 2002, EPA. Office of water, http://www.epa.gov/safewater/mcl.html.
[3] L.M. de Carvalho, P.C. do Nascimento, A. Koschinsky, M. Bau, R.F. Stefanello, C. Spengler, D. Bohrer, C. Jost, Electroanalysis 19 (2007) 1719.
[4] A. Annibaldi, C. Truzzi, S. Illuminati, G. Scarponi, Mar. Chem. 113 (2009) 238.
[5] G.H. Hwang, W.K. Han, J.S. Park, S.G. Kang, Talanta 76 (2008) 301.
[6] B.S. Sherigara, Y. Shivaraj, R.J. Mascarenhas, A.K. Satpati, Electrochim. Acta 52 (2007) 3137.
[7] S.B. Hocevar, I. Svancara, K. Vytras, B. Ogorevc, Electrochim. Acta 51 (2005) 706.
[8] L. Cao, J. Jia, Z. Wang, Electrochim. Acta 53 (2008) 2177.
[9] D. Demetriades, A. Economou, A. Voulgaropoulos, Anal. Chim. Acta 519 (2004) 167.
[10] H. Xu, L. Zeng, S. Xing, Y. Xian, G. Shi, L. Jin, Electroanalysis 20 (2008) 2655.
[11] B. Bas, R. Piech, E. Niewiara, M. Ziemnicka, L. Stobierski, W.W. Kubiak, Electroanalysis 20 (2008) 1655.
[12] B. Baś, M. Jakubowska, Anal. Acta Chim. 615 (2008) 39.
[13] R. Güell, G. Aragay, C. Fontàs, E. Anticó, A. Merkoci, Anal. Chim. Acta 627 (2008) 219.
[14] E. Espada-Bellido, M.D. Galindo-Riaño, M. García-Vargas, J. Hazard. Mater. 166 (2009) 1326.
[15] K. Yokoi, A. Yamaguchi, M. Mizumachi, T. Koide, Anal. Chim. Acta 316 (1995) 363.
[16] J. Wang, J. Lu, C. Yarnitzky, Anal. Chim. Acta 280 (1993) 61.
[17] E. Suren, S. Yilmaz, M. Turkoglu, S. Kaya, Environ. Monit. Assess. 125 (2007) 91.
[18] C. Collado-Sanchez, J. Perez-Peña, M.D. Gelado-Caballero, J.A. Herrera-Melian, J.J. Hernandez-Brito, Anal. Chim. Acta 320 (1996) 19.
[19] Q. Wu, G.E. Batley, Anal. Chim. Acta 309 (1995) 95.
[20] A.A. Ensafi, T. Khayamian, A. Benvidi, E. Mirmomtaz, Anal. Chim. Acta 561 (2006) 225.
[21] E. Shams, A. Babaei, M. Soltaninezhad, Anal. Chim. Acta 501 (2004) 119.
[22] J. Limson, T. Nyokong, Anal. Chim. Acta 344 (1997) 87.
[23] Z. Zhao, Z.Q. Gao, Electroanalysis 1 (1989) 371.
[24] S. Hu, Y. Yan, Z. Zhao, Anal. Chim. Acta 248 (1991) 103.
[25] M. Korolczuk, A. Moroziewicz, M. Grabarczyk, K. Paluszek, Talanta 65 (2005) 1003.
[26] X. Cao, L. Luo, Y. Ding, X. Zou, R. Bian, Sens. Actuators B-Chem. 129 (2008) 941.
[27] C. Li, Bioelectrochemistry 70 (2007) 263.
[28] X. He, L. Zhu, Electrochem. Commun. 8 (2006) 615.
[29] I. Svancara, P. Foret, K. Vytras, Talanta 64 (2004) 844.
[30] B. Zeng, F. Zhao, Fresen. J. Anal. Chem. 369 (2001) 433.
[31] N.F. Atta, S.A. Darwish, S.E. Khalil, A. Galal, Talanta 72 (2007) 1438.
[32] J. Carvalho, B.M. Lenzi, T. Alfonso, J.L. Raposo, N.R. Poppi, V. Souza, J. Microchem. 85 (2007) 301.
[33] V.M. Ivanov, A.M. Mamedov, J. Anal. Chem. 61 (2006) 1040.
[34] F. Wang, W. Huang, Y. Wang, J. Lumin. 128 (2008) 110.
[35] J. Liu, W. Wang, G. Li, Talanta 53 (2001) 1149.
[36] J. Wang, B. Zeng, C. Fang, X. Zhou, J. Electroanal. Chem. 484 (2000) 88.
[37] M. Shinshi, T. Sugihara, T. Osakai, M. Goto, Langmuir 22 (2006) 5937.
[38] W. Liu, R. Guo, J. Colloid Interface Sci. 290 (2005) 564.
[39] W. Liu, R. Guo, J. Colloid Interface Sci. 302 (2006) 625.
[40] M. Kopacz, J. Anal. Chem. 58 (2003) 225.
[41] J. Heyrovsky, Practical Polarography and Introduction for Chemistry Students, Academic Press, London, 1968.
[42] A. Kuniar, M. Kopacz, D. Nowak, J. Coord. Chem. 61 (2008) 1005.
[43] J. Mocak, A.M. Bond, S. Mitchell, G. Scollary, Pure Appl. Chem. 69 (1997) 297.

Talanta 80 (2009) 189–194

Contents lists available at ScienceDirect

Talanta

journal homepage: www.elsevier.com/locate/talanta

Nanoporous membrane-based cell chip for the study of anti-cancer drug effect of retinoic acid with impedance spectroscopy

Jinjiang Yu, Zongbin Liu, Mo Yang*, Arthur Mak

Biomedical Sensor and Nanotechnology Laboratory, Department of Health Technology and Informatics, The Hong Kong Polytechnic University, Hung Hom, Kowloon, Hong Kong, PR China

ARTICLE INFO

Article history:
Received 23 February 2009
Received in revised form 19 June 2009
Accepted 23 June 2009
Available online 1 July 2009

Keywords:
Nanoporous alumina membrane
Poly(ethylene glycol) (PEG)
Impedance spectroscopy
KYSE30 cancer cells

ABSTRACT

This paper presents a novel microchip with nanoporous anodic alumina membrane for the study of anti-cancer drug effect of retinoic acid (RA) on human esophageal squamous epithelial KYSE30 cancer cells *in vitro* with impedance spectroscopy. The impedance experiments with 0.01 M retinoic acid (RA) were explored for the study of anti-cancer drug effects on KYSE30 cancer cells. The impedance was monitored in the time domain at 0.1 Hz. After addition of 0.01 M RA to the cell chip, the impedance magnitude decreased with time from the value with confluent cell layer and returned to the initial base line after around 12 h. The fluorescence experiments testified that this impedance decrease was due to the cell morphology change induced by RA.

© 2009 Elsevier B.V. All rights reserved.

1. Introduction

In drug-curable cancers, apoptosis is a prominent mechanism associated with the induction of cancer remission [1]. Thus, a drug that activates apoptosis might achieve significant efficacy in treatment of cancer. Since apoptosis was formerly defined on morphological grounds, identification of apoptotic cells should be morphology-based [2]. The majority of existing techniques to monitor apoptosis *in vitro* is based on fluorescence probes designed to specifically label relevant molecules in apoptotic cells which can then be detected either by fluorescence microscopy or by flow cytometry [3,4]. However, there are several limitations for the conventional techniques, which are labor-intensive, time-consuming, invasive and not in real time. Electric cell-substrate impedance sensing (ECIS) has been used to monitor the morphology, viability, and environmental change for the adherent cells [5–8]. Recently, it has increased interest in using ECIS for *in vitro* cell apoptosis monitoring [9]. Arndt et al. [10] used endothelial cells as the sensory elements to study the cycloheximide induced apoptosis. Aspirin-treated human colon cancer HT-29 cell shape was also monitored during apoptosis [11]. However, this method has some restrictions. As the size of electrodes decreases, the electrode impedance caused by the electrode polarization is increased at the low frequency range. If the impedance related with adherent cells is much smaller than this high electrode impedance, it is hard to extract the portion of adherent cells from total measured impedance spectrum. It is necessary to develop a new morphology-sensitive electrochemical system with high sensitivity in low frequency range.

Generally, the measured signals of impedance spectroscopy provide the interfacial dielectric information of liquid/surface layer based on the charge transfer rate and surface electrochemical reaction. Due to the nanoscale dimension, the nanostructured substrates have enhanced charge transfer rate and increased surface reaction/affinity area compared with flat substrates. With the capabilities of integrating electrochemical impedance spectroscopy with nanometrology, nanostructured substrates have been widely used for biosensing. High aspect ratio nano-ordered materials are particularly intriguing for the dramatic increasing of surface area, surface chemical reaction rate and intensification of the electron transfer (i.e. biosensor output signal) through the solid–liquid interface. Nanoporous anodic alumina membrane is of particular interest due to its excellent biocompatibility as well as the established fabrication process [12–14]. Precise control of pore diameter and length can also be achieved [15,16]. Due to these fairly well-defined nanopores, nanoporous alumina membrane has found wide applications in areas such as DNA biological and chemical separations [17], micro-flow regulation [18,19], and lipid membrane-based biosensors [20]. However, the usage of nanoporous alumina membrane for cell-based sensing with impedance spectroscopy has not been explored. The biocompatibility for cell culture and non-conductive frame with pores make nanoporous alumina membrane a suitable electrochemical platform for cell study.

Fig. 1 shows the sensing mechanism of this cell chip. After seeding, cells adhere closely to the nanoporous alumina membrane.

* Corresponding author. Tel.: +852 2766 2946; fax: +852 2334 2429.
E-mail address: htmems@polyu.edu.hk (M. Yang).

0039-9140/$ – see front matter © 2009 Elsevier B.V. All rights reserved.
doi:10.1016/j.talanta.2009.06.047

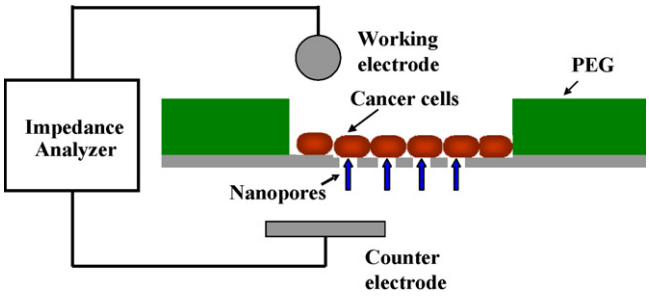


Fig. 1. Schematic diagram for impedance sensing using nanoporous membrane with PEG hydrogel microwell.

When the nanopores are covered by the adherent cells, the electrolyte current is blocked which can be monitored by the impedance spectrum. When the electric fields are applied in the cell culture medium through the nanopores on the insulated membrane, ionic current are generated through the nanoholes but no electric double layers are generated. The non-conductive alumina membrane avoids the electrode polarization effects during the impedance monitoring compared with the traditional metal-based electrode impedance sensor.

In this work, a novel nanostructured cell chip with impedance spectroscopy has been developed. The impedance experiments testified that the new morphology-sensitive electrochemical micro-system with nanoporous membranes could detect the impedance change induced by a limited number of cancer cells covering on the nanopore membranes in the low frequency domain. The effect of anti-cancer drug retinoic acid (RA) on cell adherence and morphology change was also monitored by impedance spectroscopy.

2. Materials and methods

2.1. Nanoporous alumina membrane fabrication

In this experiment, nanoporous alumina membrane was made from pure aluminum foil (99.9% purity, Alfa Aesar) by the standard two-step anodization process. The first anodization process was taken in 0.25 M oxalic acid and the aluminum was used as anode while copper (Cu) sheet was used as cathode. The oxidation layer was characterized by numerous defects, originally caused by defects in the aluminum surface. Owing to the decreasing current with the increase of the thickness of the barrier layer, the formation of pores was initiated at defect positions. Then, alumina and hydroxide at the pore walls were preferentially dissolved by the acidic electrolyte which consists of 4 wt% chromic acid and 8 wt% phosphoric acid in the etching step. The second anodization step was then repeated in 0.25 M oxalic acid. Finally, the amorphous barrier layer of alumina was etched away using a solution of 8 wt% phosphoric acid and 0.1 M $CuCl_2$.

2.2. Functionalizaiton of nanoporous alumina membrane

With the goal of improving hydrogel adhesion on nanoporous alumina membrane, the substrate was silanized with 3-(trimethoxysilyl)propyl methacrylate (TPM) (Aldrich). Briefly, the chip with alumina membranes was boiled in 30% hydrogen peroxide for 30 min to clean the surface. This step introduced OH groups on the surface which facilitated subsequent modification by silane. After treating with hydrogen peroxide, washing in boiling deionized water was followed for 15 min. The chip was then air-dried. For the silanization, the chip was immersed into a 5% (v/v) solution of 3-(trimethoxysilyl)propyl methacrylate (TPM) in anhydrous toluene at 50 °C for 2 h. Then the membranes were washed by toluene, followed by methanol and deionized water. The membranes were further air-dried and stored in nitrogen.

2.3. Fabrication of PEG hydrogel microwell on nanoporous alumina membrane

Poly(ethylene glycol) (PEG) hydrogel micropatterns were generated from the precursor solution of PEG-DA (MW 700, Aldrich) with 1% (w/v) photoinitiator DMPA using photolithography method. The precursor solution was first injected into a pre-fabricated SU-8 chamber with the height of 20 μm on the silane-treated nanoporous alumina surface. A glass slide was then used to cover the chamber and a photomask with the desired pattern was put into proximity of the gel precursor. Photoreactions were performed by exposure to 365 nm UV light (30 mW/cm^2) for 90 s using a UV spot curing system (EXFO, S1000 Omnicure, Canada). The UV exposed PEG region was solidified and the desired micropatterns were achieved by washing away the unreacted precursor solution with DI water.

2.4. Cell culture

The chamber, fabricated of Teflon, consists of two compartments A and B separated by the desired nanoporous alumina membrane. The upper chamber is open for cell culture purpose. Human esophageal squamous epithelial cancer cell line KYSE30 was obtained from American Type of Culture Collection (ATCC). The cells were maintained routinely in Dulbecco's modified eagle medium (DMEM) with 4500 mg/L glucose (Invitrogen) as basic medium supplemented with 5% fetal bovine serum (FBS, Invitrogen) together with penicillin and streptomycin (Invitrogen). They were cultured on a 35 mm diameter tissue culture dish (Nunc GmbH & Co. KG, Germany) in a humidified incubator at 37 °C with 5% CO_2/95% air. The culture medium was exchanged three times a week and routine subculturing of confluent cell layers was performed using standard trypsinization (0.05% (w/v)/1.5 mM EDTA) techniques. The cells were then seeded on the hydrogel patterned nanoporous alumina membrane treated with fibronectin and cultured for 1 day. Phalloidin-TRITC (Sigma–Aldrich) was used to stain actin filaments of the cells. The sample was finally viewed using a fluorescence microscope (Nikon, ECLIPSE 80i).

2.5. Impedance measurement

An Ag/AgCl counter electrode was placed in the lower chamber and a Pt wire was immersed into upper chamber as the working electrode. Impedance data was obtained from an electrochemical analyzer VersaSTAT3 (METEK) with the software V3-Studio (Princeton Applied Research). The impedance measurements were performed in the cell culture medium. To validate the applicability of this device, impedance spectrum with addition of retinoic acid (RA) (Sigma–Aldrich Co., USA) was monitored.

3. Results

3.1. Patterning of cells in the hydrogen microwell on nanoporous alumina membrane

Protein/cell repelling hydrogel layer with 500 μm microwell was fabricated on the functionalized nanoporous alumina membrane with the nanopore size of 75 nm (Fig. 2a). The microwell was surrounded by PEG hydrogel layer and the height of microwell was approximately 15 μm (Fig. 2b). Based on the SEM images (Fig. 2c), the fabrication process did not change the pore structure of the membrane and the "open" pores are observed.

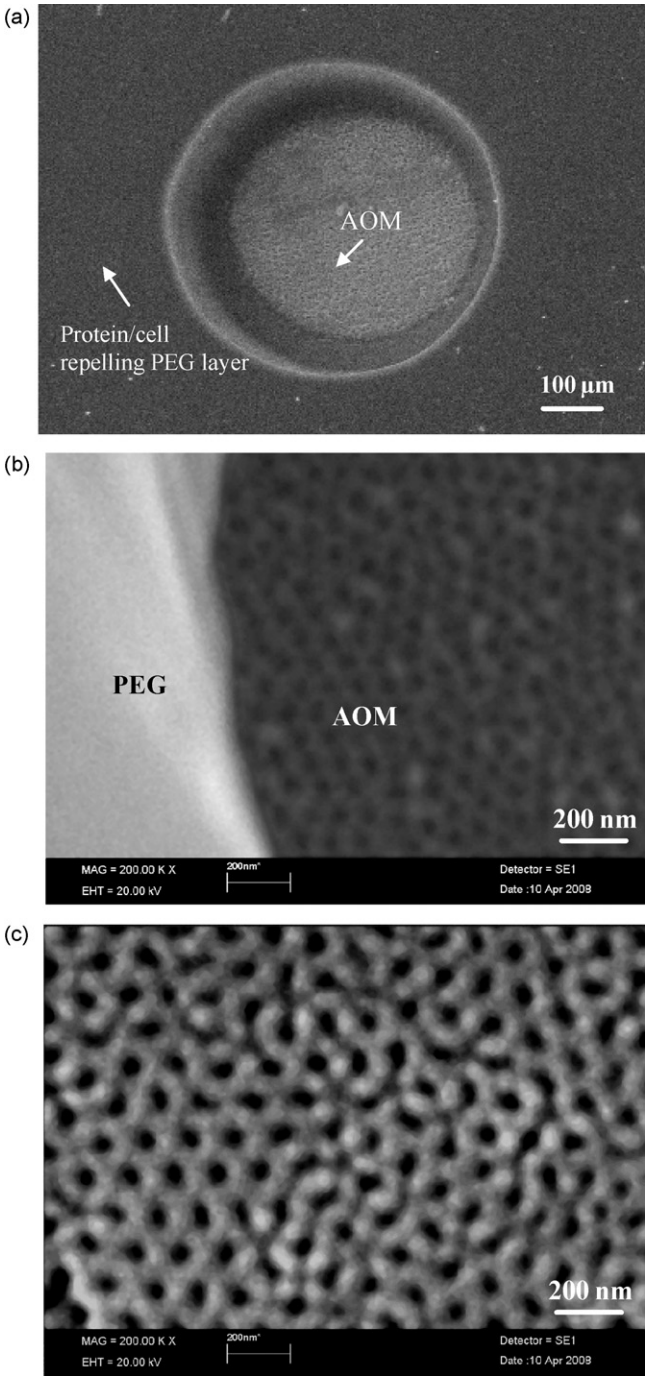


Fig. 2. Scanning electron microscopy image of (a) PEG layer with a microwell on the modified nanoporous membrane; (b) boundary of PEG/alumina membrane microwell; (c) open nanopores were observed on the nanoporous membrane within the fabricated microwell.

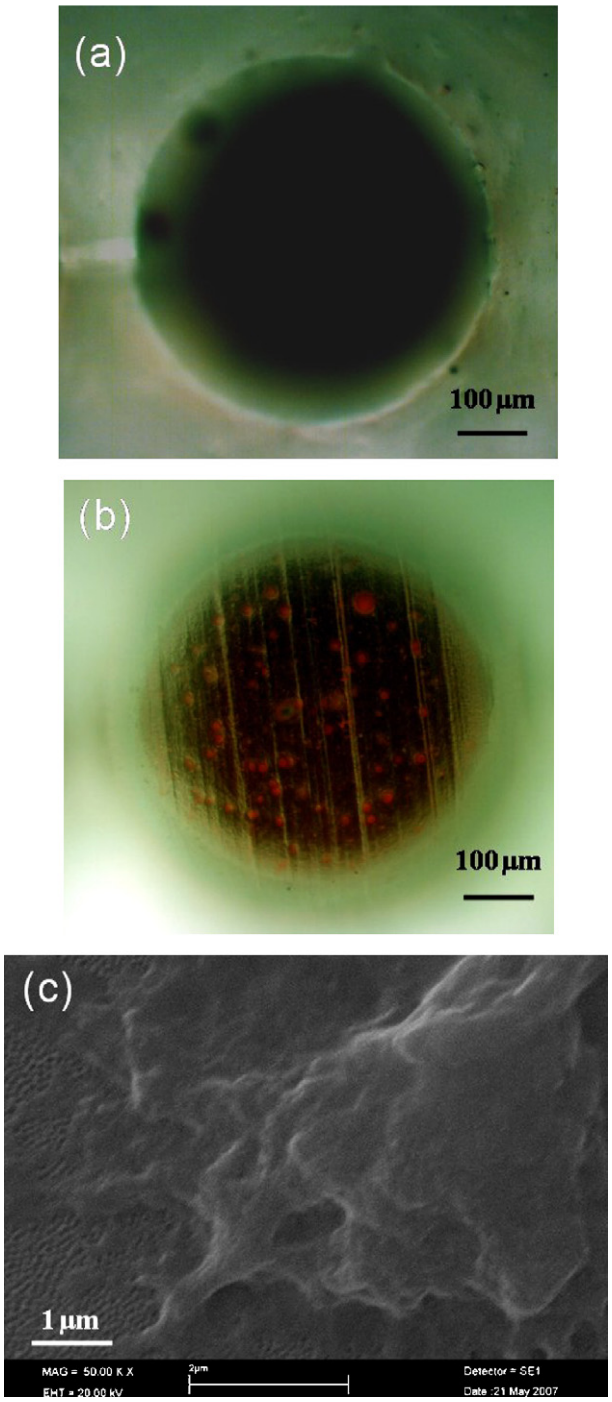


Fig. 3. Fluorescence images (a) before and (b) after cancer cells seeding; (c) SEM image of an adherent KYSE30 cancer cell on the surface of nanoporous alumina membrane.

The PEG hydrogel micropattern on the silane modified nanoporous alumina surface created controlled spatial distribution of hydrophobic and hydrophilic regions, which interacted differently with cells. The PEG patterned substrates were incubated with KYSE30 cancer cells for 1 day. After incubation, the chip with adhered cells was removed from cell culture media followed by briefly washing. The patterned cells were then stained and observed using fluorescence microscopy. The microwell surfaces were examined using fluorescent microscopy before and after the cells seeding (Fig. 3a and b). The results showed that fluorescence labeled cells were captured within the microwell after the experiments. The difference of cell adhesion between PEG and modified nanoporous alumina membrane surface enabled the spatial control of cells. The modified nanoporous alumina membrane was more capable of cell adhesion than PEG surface. Fig. 3c shows a SEM image of a KYSE30 cell on the nanoporous alumina membrane. It can be noted that part of the membrane was blocked by the adherent cell.

3.2. Impedance characterization without cells

The impedance spectrum of PEG coated nanoporous membrane with the microwell, immersed in culture medium DMEM is

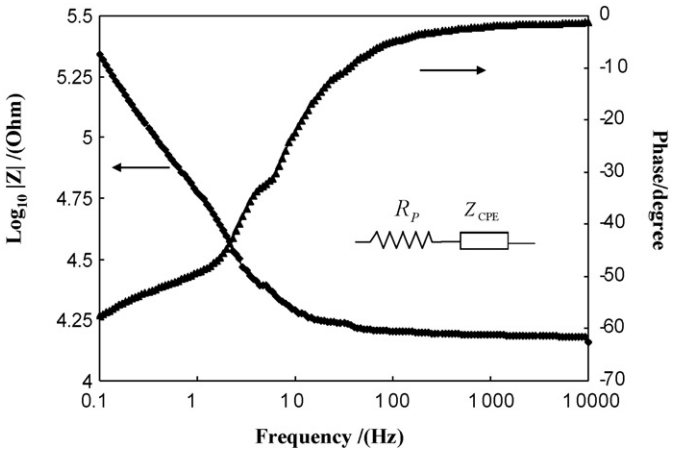


Fig. 4. Impedance spectrum of device without cells in the cell culture medium. Inset is the equivalent circuit.

shown in Fig. 4. The effective sensing area of nanoporous alumina membrane is around 0.002 cm^2 with the diameter of 250 μm. The impedance module $|Z|$ showed a plateau region from 10^4 to 10^1 Hz and increased linearly from 10^1 to 10^{-1} Hz. The linear increase of $|Z|$ indicated the generation of surface/electrolyte double layer. Compared with reported literature data of gold microelectrodes for cell impedance sensing with larger area [21], where the electrode polarization started around 10^5 Hz, this fluidic-pore system with non-conductive membrane layer could obviously decrease the electrode polarization effects. Impedance spectra for bare nanoporous membrane and PEG modified membranes with the same area in culture medium DMEM were measured to determine whether surface modification process influenced the charge transport properties of the membranes. No obvious difference of the impedance spectra could be observed between the bare and modified membranes. This can be explained by the following reasons: (1) the hydrophilic PEG molecules do not cause much change for the water permeability of the membranes; (2) most ions in the DMEM cell culture medium such as Na^+, K^+, Ca^{2+} have stokes radius less than 1 nm, which are much smaller than the nanopore size of 75 nm. The slight decrease of effective nanopore size by PEG molecule adsorption will not have much effect on the ion transport property of the membranes.

The impedance spectrum of this system without cells can be represented by an equivalent circuit with two parameters R_P and Z_{CPE} shown in Fig. 4. R_P is the resistance related to the electrical current flow through the nanopores of nonconductive alumina layer; Z_{CPE} is the constant phase element (CPE) which represents the interfacial double layer effects of the pore surfaces. Here, the constant phase element Z_{CPE} is represented by [8,22]:

$$Z_{CPE} = \frac{1}{(j\omega A)^{\alpha}} \quad (1)$$

where A is analogous to capacitance, ω is the frequency expressed in rad/s, and $0 \le \alpha \le 1$. When $\alpha = 1$, Z_{CPE} becomes a capacitance, and when $\alpha = 0$, Z_{CPE} becomes a resistance. The impedance spectrum with nanoporous membrane was interpreted using this equivalent circuit model, where $R_P = 574.1 \pm 7.5\ \Omega$, $A = 12.4 \pm 0.8\ \mu F$, and $\alpha = 0.868 \pm 0.009$.

3.3. Impedance spectrum of cancer cell grown on nanoporous membrane

Measured impedance spectra with different days of cell cultivation were shown in Fig. 5. When KYSE30 cancer cells were cultured on the nanoporous alumina membrane, the impedance spectra were measured in the low frequency of 10^{-1} Hz to 1 kHz

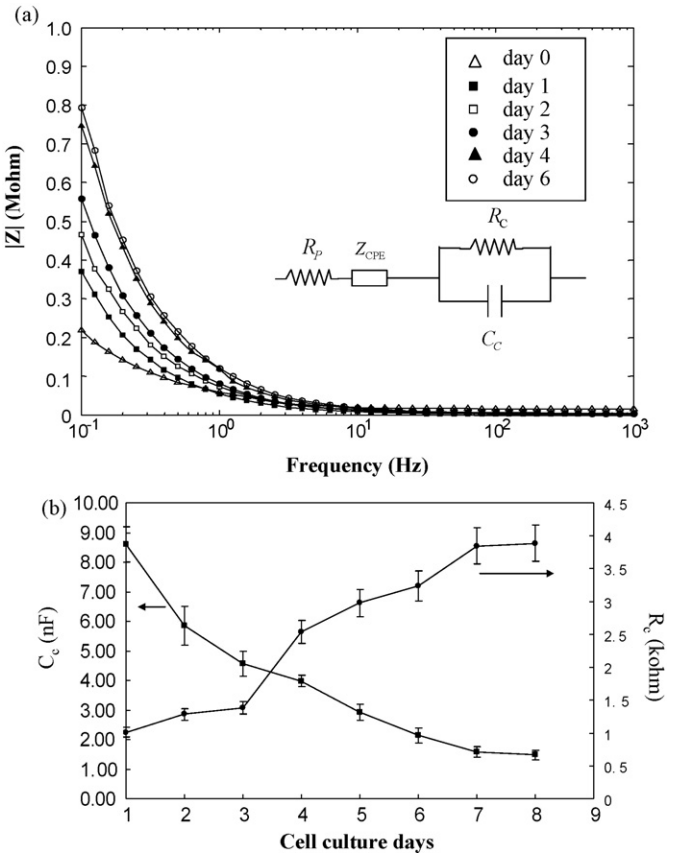


Fig. 5. (a) Measured impedance magnitude of cell growth for different cultivation days; (b) circuit model parameters R_C and C_C variation versus cell cultivation days.

from day 0 to day 6. The impedance magnitude increased with days and became stable after 6 days, as can be seen from Fig. 5a. The average impedance amplitude of day 0 was $218.8 \pm 8.4\ k\Omega$ at 0.1 Hz. When cancer cells achieved confluence on the nanoporous membrane after 6 days of cultivation, the average impedance amplitude was increased to $793.5 \pm 14.3\ k\Omega$ at 0.1 Hz. No big difference of impedance amplitude could be observed when the frequency was above 10 Hz.

To correlate the variation of impedance to KYSE30 cells behavior, the impedance spectra were fitted with the equivalent circuit

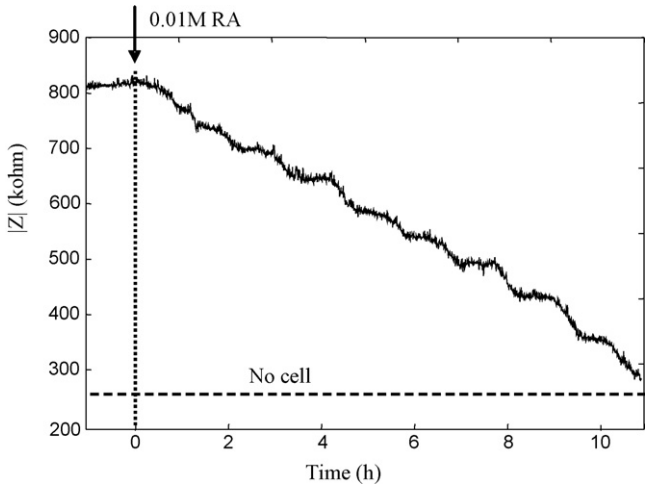


Fig. 6. Impedance amplitude change with time under the effect of retinoic acid (0.01 M) at 0.1 Hz.

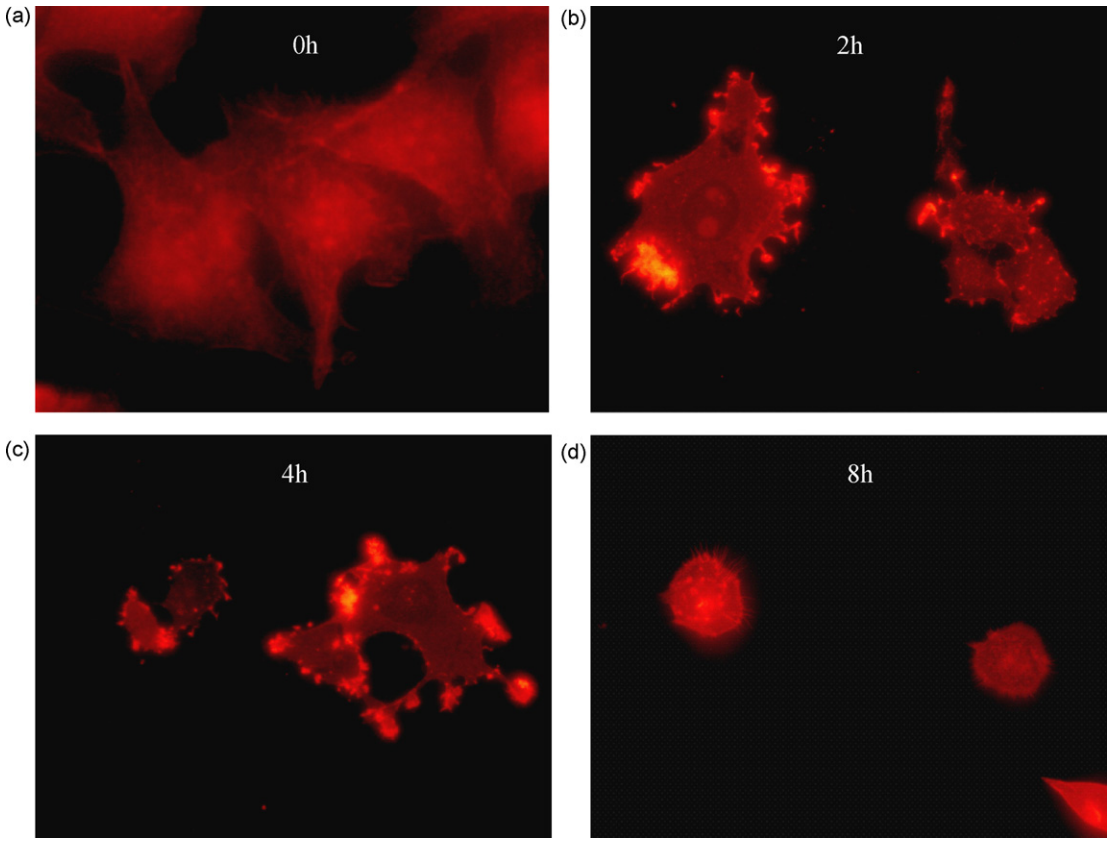


Fig. 7. Fluorescence images of KYSE30 cancer cells cultured on the nanoporous membranes for the treatment of retinoic acid (0.01 M). (a) $t = 0$ h; (b) $t = 2$ h; (c) $t = 4$ h; (d) $t = 8$ h.

shown in the inset of Fig. 5a. Here R_C and C_C are resistance and capacitance related to the cell layer covered on the pores. R_P and Z_{CPE} are the electrolyte resistance and constant phase element, respectively. Values of $R_P = 485.3 \pm 11.6\ \Omega$, $A = 4.48 \pm 0.11\ \mu$F, and $\alpha = 0.802 \pm 0.006$ remain constant in the equivalent circuit while values of R_C and C_C components vary as a function of cultivation days as shown in Fig. 5b. The average values and error bar were indicated in the diagram. As shown in Fig. 5b, the cell layer resistance R_C changes from 1.01 to 3.88 kΩ and the capacitance C_C decreases from 8.59 to 1.49 nF. The change of R_C and C_C may be related to the increase of blocked nanopore area by cell spreading or cell proliferation and the gap decrease between cells and the nanopores during the cell culture process.

3.4. Retinoic acid impedance monitoring

Retinoic acid (RA) is an immunomodulator and both a preventive and chemotherapeutic anti-cancer agent, and its derivatives have been already used to treat many cancer and tumor types [23,24]. The anti-cancer effects of retinoic acid are in part due to their ability to inhibit proliferation of cancer cells. RA inhibits cancer cell-substrate adhesion and motility and also induces morphological and functional terminal differentiation of a cell line.

In this experiment, the cell chip was initially inoculated with a cell density of 3.2×10^5/ml. After 6 days culture, the impedance amplitude was stable around a constant value of 800 kΩ. Then, retinoic acid (RA) with 0.01 M concentration was added for the anti-cancer drug experiment. The impedance was monitored at 0.1 Hz. After addition of 0.01 M RA to the cell chip, the impedance magnitude decreased with time and returned to the initial base line without cells after 12 h (Fig. 6).

The cellular morphology changes due to the RA addition were also studied. To visualize stress fibers of the cytoskeletal structure, the cells were fixed and labeled. Then the stained cells were visualized using fluorescence microscope. Before the experiments, the cells were cultured 1 day for the good attachment and spreading on the membranes. Fig. 7 shows the change of cell morphology after exposure to 0.01 M RA. In the absence of RA, typical cell spreading and cytoskeletal organization were observed shown in Fig. 7a, where $t = 0$ h. RA treatment reduced the abundance of large fibers and started to shrink from the edges after 2 h (Fig. 7b). After 4 h, an obvious morphology change could be observed in Fig. 7c with a much smaller covering area compared with initial morphology. The KYSE30 cells on the nanoporous membrane rounded up completely after 8 h (Fig. 7d). This experiment testified that the impedance amplitude decrease was really due to the cell morphology change after the treatment of RA.

4. Conclusion

In this work, a novel poly(ethylene glycol) (PEG) hydrogel-based microchip with patterned nanoporous alumina membrane was presented for nanopore based impedance sensing in the low frequency domain. The PEG hydrogel layer with the microwell was fabricated on the silane modified nanoporous alumina surface with controlled spatial distribution of hydrophobic and hydrophilic regions. The KYSE30 cancer cells were patterned within the microwell. Impedance experiments with single microwell were explored. This new morphology-sensitive electrochemical micro-system was testified by detecting the impedance change for both cell growth and drug induced change in the low frequency domain.

Acknowledgements

This work was supported by the Hong Kong Research Council General Research Grant (B-Q07N) and Internal Research Grant of the Hong Kong Polytechnic University (A-PH75).

References

[1] D. Hanahan, R.A. Winberg, Cell 100 (2000) 57.
[2] W.R. Sellers, D.E. Fisher, J. Clin. Invest. 104 (1999) 1655.
[3] M. Rodriguez, J. Schaper, J. Mol. Cell. Cardiol. 38 (2005) 15.
[4] G. Häcker, Cell Tissue Res. 301 (2000) 5.
[5] I. Giaever, C.R. Keese, Proc. Natl. Acad. Sci. 88 (1991) 7896.
[6] I. Giaever, C.R. Keese, Nature 366 (1993) 591.
[7] R. Ehret, W. Baumann, M. Brischwein, A. Schwinde, K. Stegbauer, B. Wolf, Biosens. Bioelectron. 12 (1997) 29.
[8] M. Yang, C.L. Chee, R.L. Liao, X. Zhang, Biosens. Bioelectron. 22 (2007) 1688.
[9] Q.J. Liu, J.J. Yu, L.D. Xiao, J.C.O. Tang, Y. Zhang, P. Wang, M. Yang, Biosens. Bioelectron. 24 (5) (2009) 1305.
[10] S. Arndt, J. Seebach, K. Psathaki, H.J. Galla, J. Wegener, Biosens. Bioelectron. 19 (2004) 583.
[11] H.Y. Yin, Y.X. Zhou, Anal. Lett. 40 (2007) 85.
[12] S. Tajima, Adv. Corros. Sci. Technol. 1 (1970) 229.
[13] K. Itaya, S. Sugawara, K. Arai, S. Saito, J. Chem. Eng. Jpn. 17 (1984) 514.
[14] Y. Xu, G.E. Thompson, G.C. Wood, Trans. Inst. Met. Finish. 63 (1985) 3.
[15] K.C. Popat, P. Mor, C.A. Grimes, T.A. Desai, Langmuir 20 (2004) 8035.
[16] F. Matsumoto, M. Kamiyama, K. Nishio, H. Masuda, Jpn. Appl. Phys. 44 (2005) 355.
[17] I. Vlassiouk, A. Krasnoslobodtsev, S. Smirnov, M. Germann, Langmuir 20 (2004) 9913.
[18] D.J. Odom, L.A. Baker, C.R.J. Martin, J. Phys. Chem. B 109 (2005) 20887.
[19] W. Chen, J.H. Yuan, X.H. Xia, Anal. Chem. 77 (2005) 8102.
[20] E. Reimhulta, K. Kumara, Trends Biotechnol. 26 (2008) 82.
[21] X. Huang, D. Nguyen, D.W. Greve, M.M. Domach, IEEE Sens. J. 4 (2004) 576.
[22] J.R. MacDonald, Impedance Spectroscopy, Emphasing Solid Materials, John Wiley and Son, New York, 1987.
[23] D.L. Crowe, R. Kim, R.A.S. Chandraratna, Mol. Cancer Res. 1 (2003) 532.
[24] A. Ertesvag, N. Engedal, S. Naderi, H.K. Blomhoff, J. Immunol. 169 (2002) 5555.

Talanta 80 (2009) 195–201

Contents lists available at ScienceDirect

Talanta

journal homepage: www.elsevier.com/locate/talanta

Functionalized gold nanoparticles as additive to form polymer/metal composite matrix for improved DNA sequencing by capillary electrophoresis

Dan Zhou, Liping Yang, Runmiao Yang, Weihua Song, Shuhua Peng, Yanmei Wang*

Department of Polymer Science and Engineering, CAS Key Laboratory of Soft Matter Chemistry, University of Science and Technology of China, Hefei 230026, China

ARTICLE INFO

Article history:
Received 17 March 2009
Received in revised form 20 June 2009
Accepted 23 June 2009
Available online 1 July 2009

Keywords:
Capillary electrophoresis
Composite sieving matrix
DNA sequencing
Functionalized gold nanoparticle
Quasi-interpenetrating network

ABSTRACT

A new matrix additive, poly (*N*,*N*-dimethylacrylamide)-functionalized gold nanoparticle (GNP-PDMA), was prepared by "grafting-to" approach, and then incorporated into quasi-interpenetrating network (quasi-IPN) composed of linear polyacrylamide (LPA, 3.3 MDa) and PDMA to form novel polymer/metal composite sieving matrix (quasi-IPN/GNP-PDMA) for DNA sequencing by capillary electrophoresis. Without complete optimization, quasi-IPN/GNP-PDMA yielded a readlength of 801 bases at 98% accuracy in about 64 min by using the ABI 310 Genetic Analyzer at 50 °C and 150 V/cm. Compared with previous quasi-IPN/GNPs, quasi-IPN/GNP-PDMA can further improve DNA sequencing performances. This is because the presence of GNP-PDMA can improve the compatibility of GNPs with the whole sequencing system, enhance the entanglement degree of networks, and increase the GNP concentration in system, which consequently lead to higher restriction and stability, higher apparent molecular weight (MW), and smaller pore size of the total sieving networks. Furthermore, the composite matrix was also compared with quasi-IPN containing higher-MW LPA and commercial POP-6. The results indicate that the composite matrix is a promising one for DNA sequencing to achieve full automation due to the separation provided with high resolution, speediness, excellent reproducibility, and easy loading in the presence of GNP-PDMA.

© 2009 Elsevier B.V. All rights reserved.

1. Introduction

The separation medium has played an important role in high-performance capillary electrophoresis (CE) for DNA separations. Although a lot of polymers have been developed and tested as sieving matrices for CE, searching for an ideal matrix simultaneously possessing low viscosity, high-sieving ability and self-coating ability is still an important issue for high-throughput DNA analysis [1]. Recently, a noncross-linking quasi-interpenetrating network (quasi-IPN) consisting of linear polyacrylamide (LPA) with very high molecular weight (MW, up to 9.9 MDa) and poly (*N*,*N*-dimethylacrylamide) (PDMA) was prepared as a high-performance single-stranded DNA (ssDNA) sequencing medium, which combined the high sieving ability of high-MW LPA and the dynamic coating ability of PDMA [2]. However, the viscosity of the matrix containing LPA (9.9 MDa) is high and the preparation of long-chain LPA is not so easy. Inspired by previous papers [1,3–6] in which various nanoparticle additives were incorporated into polymer solutions to increase double-stranded DNA (dsDNA) separation performances, gold nanoparticles (GNPs) were selected as an additive and added into quasi-IPN consisting of LPA with low MW (3.3 MDa) and PDMA to form polymer/metal composite matrix (quasi-IPN/GNPs) in order to compensate for the loss of the ssDNA sequencing properties using low-MW LPA [7,8]. The interactions between GNPs and polymer chains and the formation of physical cross-linking points may help to stabilize the sieving network, so that the performances of quasi-IPN/GNPs were better than those of quasi-IPN without GNPs.

At high concentration of salt in buffer solution, however, GNPs tended to aggregate especially when GNP concentration in matrices increased [7,8] and the compatibility of GNPs with the sequencing system was not so good. To overcome this kind of difficulty, it is necessary to design the coating of GNPs to make them more compatible with the polymer matrix, and it is speculated that GNPs whose polymer coat is chemically the same as the matrix would be more thermodynamically favorable to their incorporation [9]. "Grafting-to" approach has mainly been developed for the synthesis of metal (or metal oxide)/polymer hybrid structures, in which preformed end-functionalized polymers with controllable MW were directly immobilized to the surface of substrates by coupling reactions, chemical bonding, electrostatic interactions, or spin coating. In the case of GNPs, dithioester groups on polymers prepared by reversible addition-fragmentation chain transfer (RAFT) polymerization (an exceptionally versatile controlled/"living" free

* Corresponding author. Tel.: +86 551 3607652; fax: +86 551 3601592.
E-mail address: wangyanm@ustc.edu.cn (Y. Wang).

0039-9140/$ – see front matter © 2009 Elsevier B.V. All rights reserved.
doi:10.1016/j.talanta.2009.06.048

radical polymerization technique) can be chemically modified to thiol groups (–SH) for the direct grafting of the polymers onto GNPs through Au–S interactions [10]. Clearly, polymer-protected GNPs possess the functionality and dispersibility derived from the polymer shell. And the modified nanoparticles can be stored for long periods in the dry state and are easily redispersed in aqueous solutions where they give stable solutions, even at high concentration. So we consider polymer-functionalized GNPs may be the potential additive for the separation and sequencing analysis of DNA by CE.

In this work, in order to improve the compatibility of GNPs with the whole sequencing system and further improve the ssDNA sequencing properties using quasi-IPN/GNPs, a novel matrix additive, PDMA-functionalized gold nanoparticle (GNP-PDMA) was prepared by "grafting-to" approach, and then incorporated into quasi-IPN containing LPA (3.3 MDa) and PDMA to form polymer/metal composite sieving matrix (quasi-IPN/GNP-PDMA). PDMA was selected to functionalize GNPs because PDMA is one of components of quasi-IPN and is soluble in water and compatible with biological components and quasi-IPN, furthermore, PDMA could reduce electroosmotic flow (EOF) and the adsorption of DNA on the capillary wall for its dynamic coating ability. The CE results demonstrated that DNA sequencing performances were enhanced by the addition of GNP-PDMA. The effect of GNP-PDMA concentration in matrices on ssDNA sequencing performances was studied in detail in the bare fused-silica capillaries and this novel composite matrix was compared with quasi-IPN/GNPs, quasi-IPN containing higher-MW LPA, and commercial POP-6.

2. Materials and methods

2.1. Materials

$HAuCl_4{\cdot}4H_2O$, trisodium citrate dihydrate, $NaBH_4$, dioxane, tetrahydrofuran (THF), diethyl ether, and other reagents were obtained from Sinopharm Chemical Reagents (Shanghai, China). 2, 2′-Azobis(isobutyronitrile) (AIBN) was purified by recrystallization from ethanol. RAFT chain transfer agent, 2-cyanoprop-2-yl dithiobenzoate (CPDB) was synthesized according to the procedure [11]. *N*,*N*-dimethylacrylamide (DMA) was purchased from Aldrich Chemical Company (Milwaukee, WI, USA) and distilled under reduced pressure before use. The details of other reagents used for the preparation of quasi-IPN and 1× TTE buffer (50 mM Tris/50 mM TAPS/2 mM EDTA in water) or 1× TTE/7 M urea buffer can be seen in the previous works [7,8]. BigDye Terminator kit V3.1 sequencing standard (hsp69) sample and formamide (Hi-Di™) were purchased from Applied Biosystems (Foster City, CA, USA). Prior to sequencing, 100 μL formamide was added to the vial containing the lyophilized sequencing standard DNA. The sample was mixed thoroughly on a vortex mixer and centrifuged at 3000 rpm for 60 s, then denatured by heating for 2 min at 95 °C and quickly chilled on ice until ready to load on the instrument.

2.2. Preparation and characterization of quasi-IPN/GNP-PDMA

Here the synthesis of PDMA with terminal dithioester groups (PDMA-SC(S)Ph) through RAFT polymerization [12,13] is described in brief, as shown in Fig. 1A. In a typical run, DMA monomer (2.0 mL), CPDB chain transfer agent (10.2 mg), and AIBN initiator (1.6 mg) were dissolved in dioxane solvent (4 mL) in a round-bottom tube equipped with a magnetic bar. The mixture was degassed by three freeze-pump-thaw cycles, flame sealed under vacuum, and polymerized in a thermostated oil bath at 80 °C for 24 h. Then the tube was cooled to room temperature rapidly. After the tube was broken, THF was added. The polymer was precipitated by pouring the polymer solution into excess of anhydrous diethyl ether (15 times volume), and the light pink polymerization product was washed with diethyl ether several times to remove residual DMA monomer. The precipitation-washing operation was repeated for three times at least, and the polymer product was finally dried under vacuum.

Au colloids (citrate-capped GNPs) were prepared according to the citrate reduction protocol [14] with slight modifications. In a typical synthesis, 100 mL of 1 mM $HAuCl_4$ solution was added in a 250-mL round-bound flask equipped with a condenser and heated to boil with vigorous stirring. 10 mL of 38.8 mM trisodium citrate solution were rapidly added into this $HAuCl_4$ solution, and the solution changed color from pale-yellow to blue and then to wine-red, indicating the formation of the GNPs. Boiling continued for an additional 10–15 min, then the heating source was removed. The colloids were stirred for another 15 min and cooled to room temperature.

GNP-PDMA was synthesized using the "grafting-to" technique (Fig. 1A), similar to Refs. [15–17]. PDMA with thiol end groups (PDMA-SH) was prepared by reduction of PDMA-SC(S)Ph with $NaBH_4$ in N_2 atmosphere. Into a round-bottom flask equipped with a magnetic stirring bar, PDMA-SC(S)Ph was dissolved in deionized water and 1.0 M $NaBH_4$ aqueous solution was added under vigorous stirring, with a molar ratio of 1/25 for PDMA/$NaBH_4$. The reaction mixture was stirred at room temperature for more than 3 days to ensure that the dithioester terminal groups were completely reduced to yield PDMA-SH. Then a calculated amount of citrate-capped GNPs (at a thiol/gold molar ratio of 1:10) was added dropwise under vigorous stirring. After 3 days of equilibrium at room temperature, the reaction solution was centrifuged at

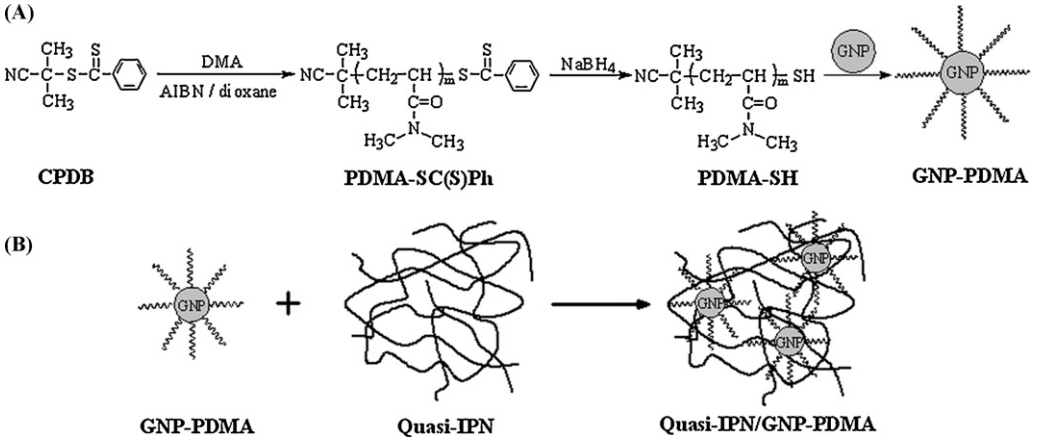


Fig. 1. The schematic representation of reaction routes for (A) GNP-PDMA and (B) quasi-IPN/GNP-PDMA.

12,000 rpm for 1 h at room temperature and the supernatant was removed. This process removed the free polymer chains that were not conjugated to GNPs. The resulting precipitate was redispersed in deionized water followed by centrifugation to wash away residue polymers and this washing procedure was repeated three times to ensure that only covalently bound polymers remained in the colloidal solutions of the stabilized nanoparticles. Finally, pure purple GNP-PDMA was obtained free of polymer contamination.

The synthetic procedures of quasi-IPN have been reported elsewhere [7,8]. Various quasi-IPN/GNP-PDMA composite sieving matrix solutions were prepared by mixing quasi-IPN and GNP-PDMA with 1× TTE/7 M urea buffer to the desired concentrations: the same 2.5% (m/v) of quasi-IPN but different amounts of GNP-PDMA, i.e., quasi-IPN/GNP-PDMA-1, -2, and -3 with the neat GNP concentrations of 0.002, 0.080 and 0.400 mg/mL, respectively. For the sake of comparison, quasi-IPN/GNPs solution (0.002 mg/mL GNPs) was also prepared.

The molecular weight distribution of PDMA-SC(S)Ph ($\overline{M}_w/\overline{M}_n$ = 1.07) was characterized using gel permeation chromatography (GPC) (Waters 1515 using narrow polydispersity polystyrene as calibration standard and *N*,*N*-dimethylformamide as eluent at a flow rate of 1.0 mL/min and 30 °C, USA). The size and shape of GNPs and GNP-PDMA were determined by a Hitachi H-800 Transmission Electron Microscope (Hitachi High-Technologies, Japan). The surface plasmon resonance band of GNPs and GNP-PDMA in water were recorded by a UV-2401PC UV–vis Spectrophotometer (Shimadzu Corp., Japan). ^{1}H NMR and FTIR spectra were recorded by an AVANCE 300 ^{1}H NMR Spectrometer (BRUKER BIOSPIN AG, Switzerland) and a Bruker EQUINOX55 Fourier Transform Infrared Spectrometer (Bruker, Germany), respectively. Thermogravimetric analysis (TGA) data were obtained by a Shimadzu DTG-60H Thermal Analyzer (heating rate of 10 °C/min, nitrogen flow of 30 mL/min, Shimadzu, Japan). Intrinsic viscosities [η] of the samples were measured using an Ubbelohde viscometer in 1× TTE/7 M urea buffer at 30 °C.

2.3. DNA sequencing by CE and data processing

Sequencing (base C, T, A, and G) of standard DNA sample was carried out on an ABI 310 PRISM™ Genetic Analyzer (PerkinElmer, Applied Biosystems Division, USA) with four-color laser-induced fluorescence (LIF) detection. Sequencing conditions: effective/total length of bare fused-silica capillaries (Polymicro Technologies, Phoenix, AZ, USA), 50/61 cm; id/od, 75/365 μm; sequencing electric field strength, 150 V/cm; DNA electrokinetic injection, 41 V/cm for 30 s; anode buffer, 1× TTE; cathode buffer, 1× TTE/7 M urea; sequencing temperature, 50 °C. The four-color raw data were collected and analyzed by ABI PRISM 310 Data Collection Software and ABI PRISM DNA Sequencing Analysis Software, respectively. The raw LIF data were also transformed through the ABI-Browser software and Origin 7.5 software (Microcal, Northampton, MA, USA) was used to extract data from transformed data, which were fitted into Gaussian peaks by using PeakFit™ 4.06 software (SPSS Inc., Chicago, USA). All the peak fittings had $r^2 > 0.99$. In order to quantify the separation performance of a matrix and compare it with other matrices, the resolutions (R) of selected nine pairs of DNA fragments with

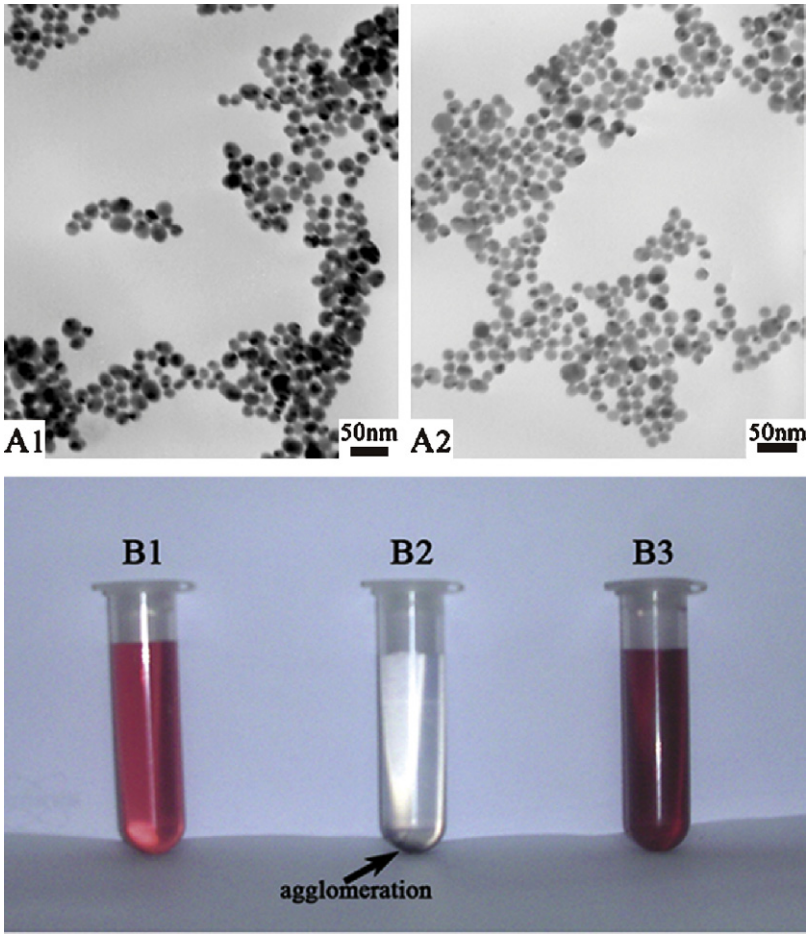


Fig. 2. TEM images of (A1) GNPs (~18 nm) and (A2) GNP-PDMA; photographs of (B1) fresh GNP solution, (B2) GNP solution after two months, and (B3) GNP-PDMA solution after ten months.

base length of 79/80, 98/99, 192/193, 344/345, 412/413, 514/515, 635/638, 828/830, and 924/927 were calculated according to the following equation [18], respectively:

$$R = 2 \times \frac{t_2 - t_1}{[1.699 \times (w_2 + w_1)]} \quad (1)$$

where t and w are migration time and full peak width at half height of selected peaks, respectively, which can be obtained from sequencing electropherogram using PeakFit. There are two parameters (separation selectivity S and separation efficiency N) affecting resolution. R, S, and N have the following relationship:

$$R = \frac{(SN^{1/2})}{4} \quad (2)$$

The selectivity and separation efficiency can be calculated by the following two equations:

$$S = 2 \times \frac{(t_2 - t_1)}{(t_2 + t_1)} \quad (3)$$

$$N = 5.54 \times \left(\frac{t}{w}\right)^2 \quad (4)$$

3. Results and discussion

3.1. Preparation and characterization of quasi-IPN/GNP-PDMA

Approximately spherical GNPs with mean diameter of about 18 nm, prepared through citrate reduction, are observed according to the TEM image (Fig. 2A1). The photograph of red fresh GNP solution is shown in Fig. 2B1. The surface of GNPs was negatively charged with citrate. After mixing of GNPs with PDMA-SH, the polymer can directly covalently bind onto GNP surface through Au–S interactions. The bond strength between Au and S is stronger than that between Au and citrate, so citrates could be exchanged with thiol [10]. After the exchange, GNP-PDMA was easily obtained and the TEM image can be seen in Fig. 2A2. As shown in Fig. 2B2, GNP agglomeration in buffer solution with high salt concentration appeared in the bottom of the tube and the system changed from red to colorless less than two months, whereas GNP-PDMA easily dispersed and no precipitation was observed even after ten months (Fig. 2B3). These phenomena prove that GNP-PDMA synthesized by "grafting-to" method enhanced the dispersivity and stability of GNPs.

UV–vis spectra (Fig. 3) of the citrate-capped GNPs and GNP-PDMA in water reveal that the characteristic maximum absorbance wavelengths were 521 and 526 nm for GNPs and GNP-PDMA, respectively, which indicates the formation of GNPs and shows a slight red-shift after GNPs grafted by PDMA. The position of the surface plasmon resonance band is sensitive to particle size and shape as well as to the optical and electronic properties of the particle surroundings, such as the stabilizing ligand shell, which can further change the optical properties of the GNPs. Thus, the wine-red color of the citrate-coated GNPs solution was changed to purple color and band displays a red-shift after GNPs were modified with PDMA.

PDMA-SC(S)Ph and GNP-PDMA were characterized by ^{1}H NMR using D_2O as the solvent, and the characteristic peaks of PDMA are clearly found: the chemical shifts of methylene and methylidyne protons appear at ~1.6 and ~2.6 ppm, respectively, and the characteristic signals of methyl protons appear at 2.8–3.2 ppm, as shown in Fig. 4. Furthermore, the three weak peaks (7.4–8.0 ppm) represent the aromatic protons of the phenyl groups on PDMA-SC(S)Ph (Fig. 4A) revealing the presence of dithioester end groups, whereas, they disappear after the formation of GNP-PDMA (Fig. 4B), which indicate the complete transformation of dithioester end groups into thiol groups with the addition of $NaBH_4$.

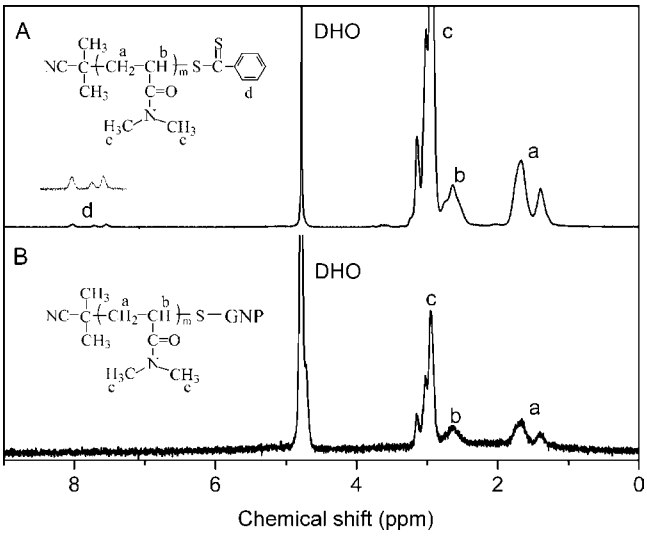


Fig. 4. ^{1}H NMR spectra of (A) PDMA-SC(S)Ph and (B) GNP-PDMA using D_2O as the solvent.

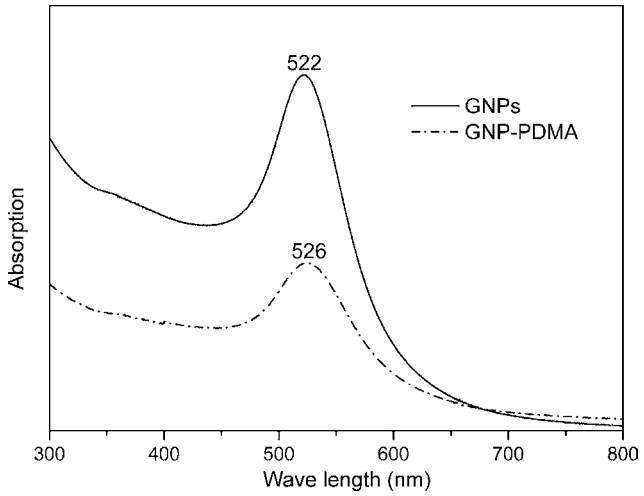


Fig. 3. UV–vis spectra of (A) GNPs and (B) GNP-PDMA in water.

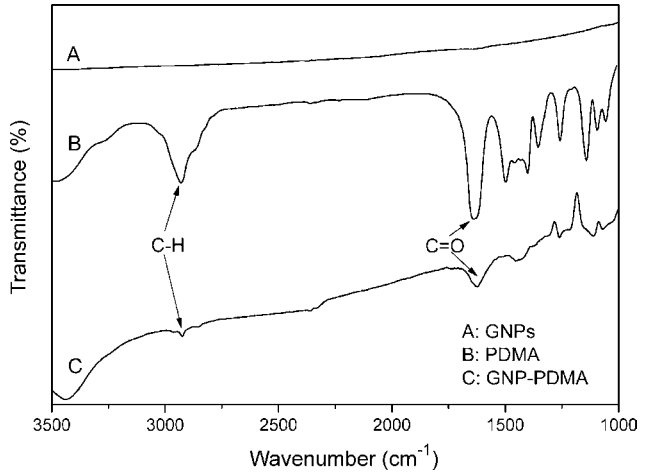


Fig. 5. FTIR spectra of (A) GNPs, (B) PDMA, and (C) GNP-PDMA.

Fig. 5 shows FTIR spectra of GNPs, PDMA, and GNP-PDMA. The characteristic absorption peaks in Fig. 5B, such as C=O (acylamide carbonyl) at 1630 cm^{-1} and C–H at 2926 cm^{-1} demonstrates the successful preparation of PDMA. Different from Fig. 5A (GNPs), Fig. 5C (GNP-PDMA) also reveals these peaks similar to Fig. 5B, which indicates that PDMA chains have been bound successfully to the surface of GNPs.

Because the grafted polymer and metal display distinct thermal stabilities, TGA results can give content of the PDMA grafted on GNPs. GNP sample is steady without significant weight loss below 600 °C, whereas the GNP-PDMA sample displays weight loss of ~20% from TGA data (Fig. 6), and this weight loss results from the thermal degradation of polymer layer on the surface of GNPs. The major decomposition temperature of PDMA grafted on GNPs is higher than that of pure PDMA, indicating that PDMA were covalently linked to GNPs, which is consistent with the previous work [19].

LPA (3.3 MDa) was produced through inverse emulsion polymerization [7,8]. Quasi-IPN was formed by solution polymerization of DMA in LPA aqueous solution [7,8], which is a noncross-linking network with a higher sieving ability [2,20,21] different from traditional cross-linking IPN network. Estimated from the integral peak area ratio in ^{1}H NMR spectra, the molar ratio of acrylamide unit to DMA unit for polymer versions in the resultant quasi-IPN is about 30/1.

The intrinsic viscosities ([η]) of quasi-IPN and composite matrices in 1× TTE/7 M urea buffer were measured in order to study the effect of addition of GNP-PDMA on matrix solution properties. Compared with that of quasi-IPN (0.799 mL/mg), intrinsic viscosities of all quasi-IPN/GNP-PDMA matrices (0.850, 0.877, and 0.888 mL/mg for quasi-IPN/GNP-PDMA-1, -2, and -3, respectively) increased. The overlap concentration ($c^* \approx 1/[\eta]$), is the concentration of polymer in solution at which polymer chains interact with each other in solution, and the c^* values are 1.252, 1.176, 1.140, and 1.126 mg/mL for quasi-IPN, quasi-IPN/GNP-PDMA-1, -2, and -3, respectively. The ratio of polymer concentration to polymer overlap concentration (c/c^*), i.e., the extent of polymer–polymer entanglements, controls the lifetime of the virtual polymer "tube" that the DNA migrates through under the electric field [22]. Consequently, c^* decreased and c/c^* increased after addition of GNP-PDMA, which suggests the enhancement of entanglement extent and the increase in apparent MW and stability of the total sieving networks in the presence of GNP-PDMA. Moreover, the extent of inter-chain entanglements (c/c^*) will be enhanced with the increase in GNP-PDMA concentration.

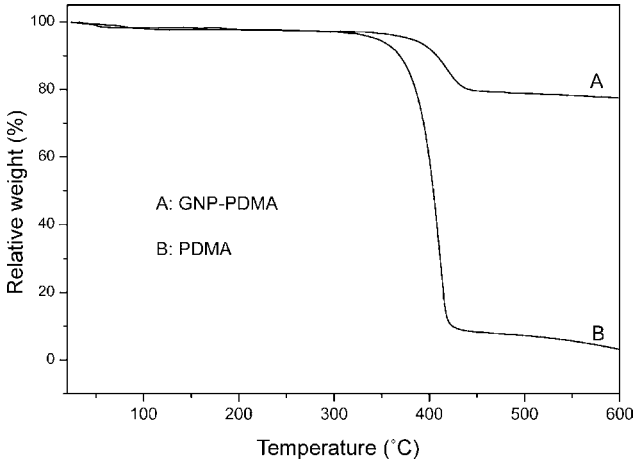


Fig. 6. TGA curves of (A) GNP-PDMA and (B) PDMA.

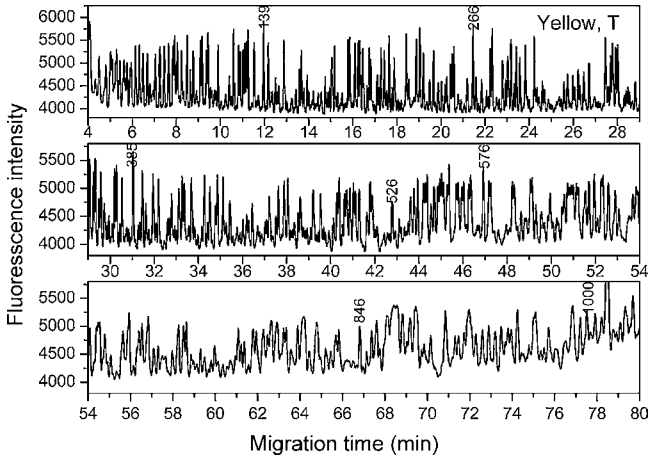


Fig. 7. A part (e.g. yellow-track, base T) of four-color electropherograms of Bigdye Terminator V 3.1 sequencing standard DNA sample by CE using quasi-IPN/GNP-PDMA-2 as sequencing matrix. Sequencing conditions: effective/total length of bare fused-silica capillaries, 50/61 cm; id/od, 75/365 μm; sequencing electric field strength, 150 V/cm; DNA electrokinetic injection, 41 V/cm for 30 s; anode buffer, 1× TTE; cathode buffer, 1× TTE/7 M urea; sequencing temperature, 50 °C; solution concentration, 2.5% (m/v) quasi-IPN + 0.080 mg/mL neat GNP for quasi-IPN/GNP-PDMA-2.

3.2. Effect of GNP-PDMA on DNA sequencing by CE

Fig. 7 shows a part (e.g. yellow-track, base T) of four-color electropherograms of DNA sample using quasi-IPN/GNP-PDMA-2 as sequencing matrix at 50 °C. Resolution comparison of DNA sequencing using quasi-IPN, quasi-IPN/GNPs, quasi-IPN/GNP-PDMA-1, -2, and -3 at 50 °C are shown in Fig. 8, to reveal the relationship between the resolutions and GNPs as well as the GNP-PDMA concentration in the matrices. Obviously, additives (whether GNPs or GNP-PDMA) can improve the sequencing abilities of quasi-IPN. In order to further examine the reasons for better separation performances using quasi-IPN/GNPs or quasi-IPN/GNP-PDMA matrices, two parameters (selectivity and separation efficiency of nine pairs of DNA fragments) affecting the resolution were calculated and plotted against the base number (figures not shown). Selectivity is defined as the mobility difference between two peaks divided by the average mobility. It is observed there was no significant change in selectivity with increasing the concentration of GNPs or GNP-PDMA. On

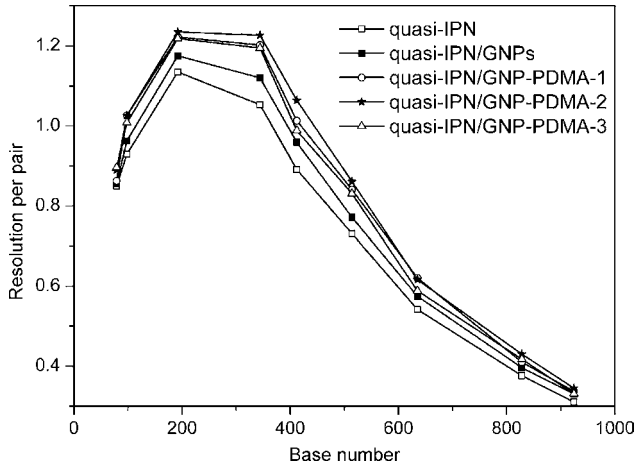


Fig. 8. Resolution vs. base number in sequencing of standard DNA sample by CE using quasi-IPN, quasi-IPN/GNPs, quasi-IPN/GNP-PDMA-1, -2, and -3. Solution concentration: 2.5% (m/v) quasi-IPN + 0, 0.002, 0.002, 0.080 and 0.400 mg/mL neat GNP for quasi-IPN, quasi-IPN/GNPs, quasi-IPN/GNP-PDMA-1, -2, and -3, respectively. Other sequencing conditions and DNA sample are as in Fig. 7.

the other hand, the separation efficiency (theory plate numbers per meter) implies the peak broadening effect since the peak width is involved. At a solution concentration above c^*, the linear polymer chains entangled one another to form a transient network with a certain mesh size (pore size). If the DNA fragment has a size larger than the mesh size, it will adjust itself to migrate through like a snake, as described by the reptation model [23,24]. At the same time, the network would also make an "adjustment" to enlarge the mesh size by changing the positions of the entanglements by a slide of the chains, resulting in a lower sieving ability [25]. However, it is clearly showed that the addition of GNPs or GNP-PDMA into the quasi-IPN networks could improve separation efficiency, which was mainly originated from more stable networks due to the interactions of GNPs or GNP-PDMA with polymer chains, slower polymer chain disentanglement (longer pore lifetime) and more extended chains of the networks [26]. Moreover, it is also noted that high efficiency was partially due to minimized DNA adsorption on the capillary wall in the presence of GNPs or GNP-PDMA that were adsorbed on the wall [27]. Depending on the selectivity and separation efficiency, the resolutions using quasi-IPN/GNPs or quasi-IPN/GNP-PDMA are better than those using quasi-IPN (Fig. 8).

We can find from Fig. 8 that the resolutions of quasi-IPN/GNPs were higher than those of quasi-IPN without GNPs, but the resolutions would decrease with further increase of GNP concentration (data not shown), as described in previous works [7,8]. This is because local aggregation of GNPs in polymer network might occur as the GNP concentration increased. This incompatibility could then result in non-homogeneous polymer–DNA interactions and decrease the efficiency in sequencing, so the GNP concentration in the sequencing system is very limited and the effect of GNPs on sequencing performance is also restricted. But when GNP-PDMA with the same neat GNP concentration (0.002 mg/mL) as GNPs were added in quasi-IPN, the resolutions increased markedly, that is, quasi-IPN/GNP-PDMA-1 showed higher resolutions than not only quasi-IPN but also quasi-IPN/GNPs. In previous works [7,8], the addition of GNPs in matrix could improve ssDNA sequencing performances due to the interactions between GNPs and quasi-IPN polymer chains and the formation of physical cross-linking points. In this work, besides the reasons mentioned above, functionalized GNPs with PDMA chains on the surface possess higher compatibility with quasi-IPN system and higher solubility in water; on the other hand, PDMA chains on the GNPs result in easier and more entanglement between GNP-PDMA themselves or between GNP-PDMA and quasi-IPN system (Fig. 1B). All these factors cause the network with GNP-PDMA more restricted and stable, polymer chain disentanglement slower, and the apparent MW higher, and thus lead to the increase in separation efficiency and resolution for long DNA fragments. In addition, the addition of GNP-PDMA enhances the separation of small DNA molecules due to the network exhibiting smaller pore size than quasi-IPN. Anyway, the improved sequencing of both long and small DNA fragments can be obtained by the addition of GNP-PDMA due to more restricted, stable and smaller nanopore structure.

Furthermore, it should be noted that, different from that of quasi-IPN/GNPs, the resolutions of quasi-IPN/GNP-PDMA continue increase with an increase in GNP concentration up to 0.080 mg/mL (i.e., quasi-IPN/GNP-PDMA-2). It is expected that the matrix network will become more stable because more entanglement points will form as the amount of GNP-PDMA increases. However, the resolutions will not always improve with increased GNP-PDMA concentration, and further increase in concentration even results in decreased resolutions (i.e., quasi-IPN/GNP-PDMA-3). Too high concentration of GNP-PDMA in the solution probably leads to too small pores and too many entanglement points, and local non-homogeneous matrix causes the decrease in sequencing efficiency, which is similar to the GNP system studied previously [7,8].

The presence of GNP-PDMA has little effect on migration time of DNA fragments, for instance, quasi-IPN and quasi-IPN/GNP-PDMA-2 both resulted in 1000 bases being detected in about 78 min. On the one hand, some GNP-PDMA adsorbed on the capillary wall surface, leading to the decrease in EOF and thus the increase in observed DNA mobility; on the other hand, the network with smaller pore size will make DNA molecules migration slower. These two contrary factors affect DNA movement together and result in neglectable change in migration time. However, the readlength at 98% accuracy of quasi-IPN increased from 715 to 801 bases after the addition of GNP-PDMA.

3.3. Comparison with other matrices

Generally, the higher LPA MW, the better the DNA sequencing performance. That is, higher LPA MW helps to obtain higher resolution and longer readlength, but high MW will cause drawbacks such as difficult preparation and high viscosity of LPA. Quasi-IPN containing LPA with higher MW of 6.5 MDa (quasi-IPN-H) were also prepared and used for further comparison. It is shown from Fig. 9 that when both quasi-IPN concentrations are 2.5% (m/v), the resolutions of quasi-IPN/GNP-PDMA-2 with lower LPA MW of 3.3 MDa are even slightly higher than those of quasi-IPN-H without GNP-PDMA, further indicating that the addition of GNP-PDMA in quasi-IPN would form more robust sieving matrix network, increase apparent MW of quasi-IPN, consequently, improve sieving properties based on separation mechanisms. And the readlength at 98% accuracy of quasi-IPN/GNP-PDMA-2 is also slight higher than that of quasi-IPN-H (801 bases vs. 785 bases). So the use of LPA with lower MW (which is easily prepared and not so viscous) in the presence of GNP-PDMA will be more practical and feasible.

Performance Optimized Polymer (POP-6) obtained from Applied Biosystems is a commercial product used widely for ABI 310 Genetic Analyzer, so it was also selected and compared with our matrix. For a proper comparison, sequencing by using POP-6 was conducted under its individual conditions, which were suggested by the suppliers to optimize sequencing performances, for example, sequencing electric field strength was 200 V/cm for POP-6 (while 150 V/cm for our sequencing matrices). As can be seen in Fig. 9, quasi-IPN/GNP-PDMA-2 shows better resolutions than POP-6 with the exception of small DNA fragments (smaller than about 250 bases) owing to higher solution concentration of POP-6 helpful to separate small ones. And the composite matrix pos-

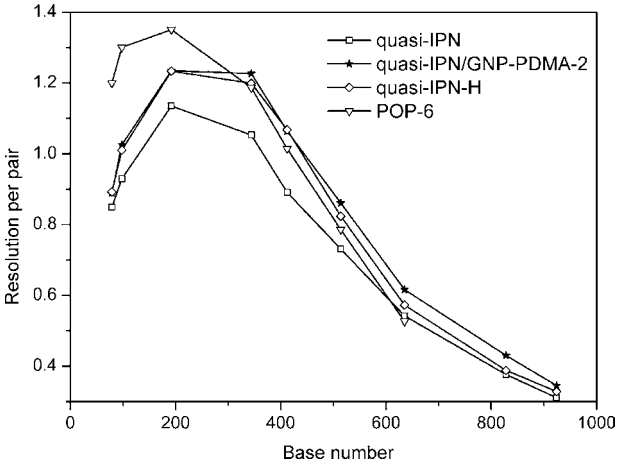


Fig. 9. Resolution vs. base number in sequencing of standard DNA sample by CE using quasi-IPN (2.5%, m/v), quasi-IPN/GNP-PDMA-2 (2.5%, m/v + 0.080 mg/mL), quasi-IPN-H (2.5%, m/v) and commercial POP-6. Sequencing electric field strength, 150 V/cm for our sequencing matrices and 200 V/cm for POP-6. Other sequencing conditions and DNA sample are as in Fig. 7.

sesses longer readlength (801 bases vs. 638 bases at 98% accuracy) and much shorter migration time (50.4 min vs. 107.0 min for base 620, respectively) than POP-6. All the above results demonstrate that quasi-IPN/GNP-PDMA composite matrix is potential for DNA sequencing. It should be noted that separation performance of small DNA fragments strongly depends on the overall concentration of sieving matrix [28,29], and small DNA molecules interact preferentially with these low-MW polymer fibers [30,31]. The concentration of the composite sieving matrix can be increased by addition of very-low-MW (such as ~50 kDa) LPA. As a result, in order to obtain higher-performance separation of both short and long DNA fragments, the mixed quasi-IPN/GNP-PDMA composite matrix containing both very-low-MW and high-MW LPA can be selected for use as a compromise to balance the requirements according to Salas-Solano et al. [32]. On the other hand, for the analysis of some very small templates or exons, the quasi-IPN/GNP-PDMA composite (containing only low-MW LPA) with high solution concentration (such as LPA concentration) and high GNP-PDMA concentration can be used as sieving matrix directly. Moreover, the matrix viscosity is not high because of low-MW LPA.

3.4. Reproducibility

The relative standard deviation (RSD) of the migration time and resolution using quasi-IPN/GNP-PDMA matrices in the same bare fused-silica capillary for the first ten runs shows high reproducibility and are all less than 2.3%.

4. Conclusions

Novel polymer/metal composite sieving matrix for DNA sequencing by CE was formed by incorporating GNP-PDMA additive into quasi-IPN. Without complete optimization (such as base calling software), quasi-IPN/GNP-PDMA-2 yielded a readlength of 801 bases at 98% accuracy in about 64 min by using the ABI 310 Genetic Analyzer at 50 °C and 150 V/cm, showing the composite matrix combines optimal sieving ability with dynamic coating ability and with moderate viscosity. Quasi-IPN/GNP-PDMA can further improve ssDNA sequencing performances because the presence of GNP-PDMA can lead to higher restriction and stability, higher apparent molecular weight, and smaller pore size of the total sieving networks. Furthermore, the comparison studies between the composite matrix with other matrices indicate that it is a promising one for DNA sequencing to achieve full automation (especially for microfluidic systems) due to the separation provided with high resolution, speediness, excellent reproducibility, and easy loading owing to the addition of GNP-PDMA. The raw materials used to prepare the composite matrix are commercial and cheap and the preparation process is easily carried out, so the cost of this matrix is low and it is applicable to high throughput DNA sequencing. Moreover, considering excellent performances of the composite matrix for DNA sequencing, it is expected that quasi-IPN/GNP-PDMA matrix with lower concentration may also be used for other models of ABI Genetic Analyzer, such as fragment analysis, microsatellite and single nucleotide polymorphism (SNP) genotyping analysis.

Other parameters will be optimized in the future to further improve the DNA sequencing performances, and one of our interests is to use functionalized nanoparticles to separate other biomacromolecules by CE.

Acknowledgements

We greatly acknowledge the support of this work by the National Natural Science Foundation of China (Grant No. 50773074), Specialized Research Fund for the Doctoral Program of Higher Education (Grant No. 20070358029), Ministry of Science and Technology of China (Grant No. 2007CB936401), the Foundation for Development of Talent of Anhui Province (Grant No. 2005Z026).

References

[1] M.F. Huang, C.C. Huang, H.T. Chang, Electrophoresis 24 (2003) 2896–2902.
[2] Y.M. Wang, D.H. Liang, Q.C. Ying, B. Chu, Electrophoresis 26 (2005) 126–136.
[3] D.H. Liang, L.G. Song, Z. Chen, B. Chu, Electrophoresis 22 (2001) 1997–2003.
[4] M. Tabuchi, Y. Katsuyama, K. Nogami, H. Nagata, K. Wakuda, M. Fujimoto, Y. Nagasaki, K. Yoshikawa, K. Kataoka, Y. Baba, Lab. Chip 5 (2005) 199–204.
[5] M. Tabuchi, Y. Baba, Anal. Chem. 77 (2005) 7090–7093.
[6] Y. Xu, S.F.Y. Li, Electrophoresis 27 (2006) 4025–4028.
[7] D. Zhou, Y.M. Wang, W.L. Zhang, R.M. Yang, R.H. Shi, Electrophoresis 28 (2007) 1072–1080.
[8] D. Zhou, Y.M. Wang, R.M. Yang, W.L. Zhang, R.H. Shi, Electrophoresis 28 (2007) 2998–3007.
[9] M.K. Corbierre, N.S. Cameron, M. Sutton, S.G.J. Mochrie, L.B. Lurio, A. Ruhm, R.B. Lennox, J. Am. Chem. Soc. 123 (2001) 10411–10412.
[10] D.J. Kim, S.M. Kang, B. Kong, W. Kim, H. Paik, H. Choi, I.S. Choi, Macromol. Chem. Phys. 206 (2005) 1941–1946.
[11] J. Zhu, X.L. Zhu, Z.P. Cheng, J.M. Lu, F. Liu, J. Macromol. Sci. A: Pure Appl. Chem. 40 (2003) 963–975.
[12] P. Relógioa, M. Charreyrea, J.P.S. Farinhab, J.M.G. Martinhob, C. Pichot, Polymer 45 (2004) 8639–8649.
[13] Y. Li, B.S. Lokitz, C.L. McCormick, Macromolecules 39 (2006) 81–89.
[14] K.C. Grabar, R.G. Freeman, M.B. Hommer, M.J. Natan, Anal. Chem. 67 (1995) 735–743.
[15] A.B. Lowe, B.S. Sumerlin, M.S. Donovan, C.L. McCormick, J. Am. Chem. Soc. 124 (2002) 11562–11563.
[16] M.Q. Zhu, L.Q. Wang, G.J. Exarhos, A.D.Q. Li, J. Am. Chem. Soc. 126 (2004) 2656–2657.
[17] S.Z. Luo, J. Xu, Y.F. Zhang, S.Y. Liu, C. Wu, J. Phys. Chem. B 109 (2005) 22159–22166.
[18] J.C. Giddings, Separ. Sci. 4 (1969) 181–189.
[19] H. Kong, C. Gao, D.Y. Yan, J. Am. Chem. Soc. 126 (2004) 412–413.
[20] Y.M. Wang, D.H. Liang, J.C. Hao, D.F. Fang, B. Chu, Electrophoresis 23 (2002) 1460–1466.
[21] L.G. Song, T.B. Liu, D.H. Liang, D.F. Fang, B. Chu, Electrophoresis 22 (2001) 3688–3698.
[22] E.A.S. Doherty, C.W. Kan, A.E. Barron, Electrophoresis 24 (2003) 4170–4180.
[23] T. Duke, J.L. Viovy, Phys. Rev. E 49 (1994) 2408–2416.
[24] A.N. Semenov, T.A.J. Duke, J.L. Viovy, Phys. Rev. E 51 (1995) 1520–1537.
[25] B. Chu, D.H. Liang, J. Chromatogr. A 966 (2002) 1–13.
[26] H. Cottet, P. Gareil, J.L. Viovy, Electrophoresis 19 (1998) 2151–2162.
[27] Y.W. Lin, M.F. Huang, H.T. Chang, Electrophoresis 26 (2005) 320–330.
[28] E. Carrilho, M.C. Ruiz-Martinez, J. Berka, I. Smirnov, W. Goetzinger, A.W. Miller, D. Brady, B.L. Karger, Anal. Chem. 68 (1996) 3305–3313.
[29] A.E. Barron, W.M. Sunada, H.W. Blanch, Electrophoresis 17 (1996) 744–757.
[30] Y. Kim, E. Yeung, J. Chromatogr. A 781 (1997) 315–325.
[31] A.E. Barron, H.W. Blanch, D.S. Soane, Electrophoresis 15 (1994) 597–615.
[32] O. Salas-Solano, E. Carrilho, L. Kotler, A.W. Miller, W. Goetzinger, Z. Sosic, B.L. Karger, Anal. Chem. 70 (1998) 3996–4003.

Talanta 80 (2009) 202–206

Contents lists available at ScienceDirect

Talanta

journal homepage: www.elsevier.com/locate/talanta

A novel nonenzymatic fluorescent sensor for glucose based on silica nanoparticles doped with europium coordination compound

Feng Gao[a,*], Fabao Luo[a], Xiaoxiao Chen[a], Wu Yao[a,b], Jun Yin[a], Zhen Yao[a], Lun Wang[a,*]

[a] Anhui Key Laboratory of Chemo/Biosensing, Anhui Key Laboratory of Functional Molecular Solids, College of Chemistry and Materials Science, Anhui Normal University, Wuhu 241000, PR China
[b] Department of Chemistry, Huangshan College, Huangshan 245021, PR China

ARTICLE INFO

Article history:
Received 4 April 2009
Received in revised form 21 June 2009
Accepted 23 June 2009
Available online 1 July 2009

Keywords:
Aminated luminescent silica nanoparticles
Europium coordination compound
Fluorescence sensor
Glucose

ABSTRACT

Amino-functionalized luminescent silica nanoparticles (LSNPs) doped with the europium(III) mixed complex, $Eu(TTA)_3phen$ with 2-thenoyltrifluoroacetone (TTA) and 1,10-phenanthroline(phen) were synthesized successfully using an revised Stöber method. Scanning electron microscopy (SEM), transmission electron microscopy (TEM), Fourier-transform infrared (FTIR), and fluorescence spectroscopy were performed for characterizing the synthesized nanoparticles. In the presence of glucose, the fluorescence intensity of the amino-functionalized LSNPs was enhanced due to the enhanced fluorescence resonance energy transfer. Based on fluorescence-enhancing effect, a simple and sensitive method for the determination of glucose was proposed. Under the optimized experimental conditions, the enhanced fluorescence intensity ratio ($\Delta F/F_0$) was linear with the concentration of glucose (c) in the range of 0.0–180 $\mu g\,ml^{-1}$ with a detection limit of 0.8 $\mu g\,ml^{-1}$ (S/N = 3). The R.S.D. values were 0.33% and 0.37% at the levels of 22.5 and 100 $\mu g\,ml^{-1}$, respectively. The proposed method was applied to the determination of glucose in synthetic samples with satisfactory results. The proposed method was also performed to the analysis of blood glucose in human serum samples and the results were in good agreement with clinical data provided by the hospital, which indicates that the method presented here is not only simple, sensitive, but also reliable and suitable for practical applications.

© 2009 Elsevier B.V. All rights reserved.

1. Introduction

In recent years, the development of glucose sensors has been received considerable attention, due to the demands of glucose controlling in various food processing, fermentation and biotechnological processes, as well as the continuous glucose self-monitoring for substantially reducing morbidity and mortality among diabetes patients [1–4]. To date, many different approaches to develop glucose sensors have been pursued including different electrochemical methods [1,5–9], Fourier-transform infrared spectroscopy [10], UV–vis spectroscopy [11], localized surface plasmon resonance [12,13], capillary enzyme bioreactor [14] as well as fluorometry [15–21]. Among these approaches, fluorescence-based systems are actively explored and receiving increasing attention encouraged by special advantages of fluoremetry for biological analysis [2,15–21]. For example, the technique is extremely sensitive; fluorescence measurements cause little or no damage to the host systems; measurements can be made by different parameters such as fluorescence intensity, fluorescence decay time, etc.; the structure and distribution of biomolecules can also be probed by the phenomenon of fluorescence (or Förster) resonance energy transfer (FRET).

Among these fluorescence-based glucose sensors, traditional organic fluorophores (*e.g.* organic dyes) are widely used as recognition elements. Recently, fluorescent quantum dots (QDs) have also attracted much attention [17–20]. Interests in fluorescent QDs derive from their broad adsorption, narrow emission, intense brightness, and good photostability relative to conventional organic dyes. However, they do have some drawbacks [22]. QDs are difficult to make; the surface-modification chemistry is still under investigation; the "blinking" behavior (luminescence emission switches "on" and "off" by sudden stochastic jumps under continuous excitation) is a limiting factor for in vivo applications. Compared with the above-mentioned fluorophores, fluorophore-doped silica nanoparticles (NPs) possess several distinguished properties [22–32]. Silica NPs are easy to separate via centrifugation during particles preparation, surface modification, and other solution treatment processes because of the high density of silica; silica NPs are more hydrophilic and biocompatible; silica NPs surface can be modified easily with many biomolecules for added biochemical functionality and extended application. Silica NPs also have intense brightness and anti-photobleaching.

* Corresponding authors. Tel.: +86 553 3869302; fax: +86 553 3869303.
E-mail addresses: fgao@mail.ahnu.edu.cn (F. Gao), wanglun@mail.ahnu.edu.cn (L. Wang).

0039-9140/$ – see front matter © 2009 Elsevier B.V. All rights reserved.
doi:10.1016/j.talanta.2009.06.050

Generally, the dye-doped silica nanoparticles can be synthesized easily via the reverse microemulsion (water-in-oil microemulsion) system, which is a robust and efficient method for the preparation of monodisperse spherical nanoparticles in the nanometer range [23–32]. In our previous research work, we have developed dye-doped silica NPs for pH sensing [33,34] and aminated silica NPs for the determination of γ-globulin [35] and hydrogen peroxide [36]. In the present study, amino-functionalized luminescence silica nanoparticles (aminated LSNPs) doped with the fluorescent europium(III) mixed complex, $Eu(TTA)_3phen$ (TTA: 2-thenoyltrifluoroacetone, phen: 1,10-phenanthroline), in place of conventional fluorescent dyes, were synthesized successfully by using an revised Stöber method. The reason to choose rare earth complex rather than conventional dyes is based on its particular luminescence advantages [37,38]. Rare earth complexes exhibit strong, spiculate, and narrow spectrum; the fluorescence lifetime of rare earth complexes spans six magnitudes from nanosecond to millisecond; rare earth complexes present a multifluorescence characteristic due to special electronic structure of rare earth ions. The aminated LSNPs was demonstrated as an indicator for nonenzyme fluorescence determination of glucose in this paper.

2. Experimental

2.1. Apparatus

Fluorescence spectra were recorded on an F-4500 fluorescence spectrophotometer (Hitachi, Japan). Morphological and size measurement of the silica nanoparticles were performed by an S-4800 field emission scanning electron microscopy (SEM, Hitachi, Japan). The transmission electron microscopy (TEM) image of the LSNPs was acquired on an H-600 transmission electron microscope (Hitachi, Japan). Infrared spectra of the NPs was measured on a Fourier-transform infrared (FT-IR) 8400S spectrophotometer (Shimadzu, Japan). The desired pH buffer solutions were adjusted with a model pHS-3C pH meter (Zhejiang, China).

2.2. Reagents

Europium oxide (Eu_2O_3, purity ≥99.9%) was purchased from Shanghai No. 3 Chemical Reagent Co. (Shanghai, China). 1,10-Phenanthroline (Phen) and polyethylene glycol (PEG, with molecular weight of 2000 Da) were provided by Sinopharm Chemical Reagent Co. (Shanghai, China). 2-Thenoyltrifluoroacetone (TTA) was obtained from Sigma Co. (USA). Tetraethylorthosilicate (TEOS) and (3-aminopropyl)triethoxysilane (APTS) were purchased from Fluka (USA). Glucose was obtained from Shanghai Sangon Co. (shanghai, China). All other reagents were of analytical grade and used as received. Prior to use, 10 mg ml^{-1} of glucose stock solution was kept in fridge at 4 °C to equilibrium the isomers of glucose for 24 h. Triplex distilled water was used throughout the experiments.

Five serum samples were obtained by centrifuging (2000 rpm, 5 min) the fresh blood samples which were taken from three healthy adults and two diabetes patients (provided by Yijishan Hospital, Wuhu, China).

2.3. Analytical procedure for the determination of glucose

Ten milligrams of the as-prepared amino-functionalized LSNPs were dispersed in 10 ml of anhydrous ethanol and 1 mg ml^{-1} colloid solution was obtained. To a 2-ml test-tube, 100 μl of the LSNPs colloid solution and a known concentration of glucose were added, then diluted to the mark with phosphate buffer solution (PBS) and shaken thoroughly in order to mix well. After 20 min, the fluorescence intensity was measured at 618 nm with excitation at 350 nm in a 1-cm quartz cell. The difference of fluorescence intensity is represents as $\Delta F = F - F_0$. Here F_0 and F are the fluorescence intensity of the system without and with glucose, respectively.

For the measurement of human serum samples, 200 μl human serum was added to the test-tube instead of glucose standard solution, other procedures are same as above mentioned.

3. Results and discussion

3.1. Synthesis of the luminescent silica nanoparticles aminated LSNPs

$Eu(TTA)_3phen$ with quite strong red fluorescence were prepared by our previous reported procedure [38]. Briefly, in a 500 ml three-necked round-bottomed flask, 100 ml of water, 200 μl of 0.5 mol l^{-1} of $EuCl_3$ and 100 μl of polyethylene glycol were added into the flask, respectively. Under vigorous stirring, 10 ml of 0.03 mol l^{-1} of TTA aqueous solution was added, then 10 ml of 0.01 mol l^{-1} of 1,10-phenanthroline ethanol solution was added slowly. All the mentioned procedures were carried out in the nitrogen atmosphere. After that, the mixture was kept for 24 h without stirring. Then it was centrifuged and washed with water and ethanol several times to remove any uncoordinated molecules and the straw yellow powder of the metal-organic luminescent coordination compound, $Eu(TTA)_3phen$ was obtained after drying for about 8 h at 60 °C. The preparation of luminescent silica nanoparticles (LSNPs) doped by $Eu(TTA)_3phen$ was described as following: 10 mg of the $Eu(TTA)_3phen$ powder was dissolved in 1 ml of acetone. Then 0.5 ml of the acetone solution was added to a 100 ml mono-necked round-bottomed flask containing 30 ml of ethanol and 18 ml of water under vigorous stirring. Subsequently, 2 ml of ammonium hydroxide (NH_4OH) and 1 ml of TEOS were introduced into the reaction and kept stirring for 6 h. The LSNPs were obtained by centrifuging and washing with water and ethanol. The LSNPs were then dispersed into the mixed solution of anhydrous ethanol (8.0 ml) and triplex water (0.6 ml). Thereafter, 600 μl of NH_4OH and 200 μl of APTS were added and the mixture was stirred overnight. The amino-functionalized LSNPs (aminated-LSNPs) were obtained by centrifuging and washing with water and ethanol for at least three cycles. Ultrasonication was performed while washing the nanoparticles in order to remove any physically adsorbed moleculars from the surface of nanoparticles.

3.2. Characterization of the aminated LSNPs

Fig. 1a shows the scan electron microscopy (SEM) image of the as-prepared aminated-LSNPs. 10 μl of the NPs colloid solution was dropped on a small copper grid. The copper grid was adhered by conductive adhesive on a silicon tray after the colloid solution dried. SEM image was performed on an S-4800 field emission scanning electron microscopy operating at an accelerating voltage of 5 kV. The sample was observed without any metal coating. It can be clearly seen that the as-prepared NPs presented monodisperse nanospheres ($d = 75 \pm 15$ nm). Fig. 1b shows the transmission electron microscopy image of the aminated LSNPs. The sample was prepared similar to the SEM, one drop of the aminated LSNPs colloid solution was dropped on a small copper grid. The size and structure of the LSNPs were observed by using a Hitachi H-600 transmission electron microscope with a tungsten filament at an accelerating voltage of 100 kV. From the SEM and TEM images, we can see that the prepared aminated nanoparticles are monodispersed and uniform in size.

The Fourier-transform infrared (FTIR) spectrum of the aminated LSNPs was shown in Fig. 2. The wave number was set in the range from 400 to 4000 cm^{-1}. As shown in Fig. 2, the most

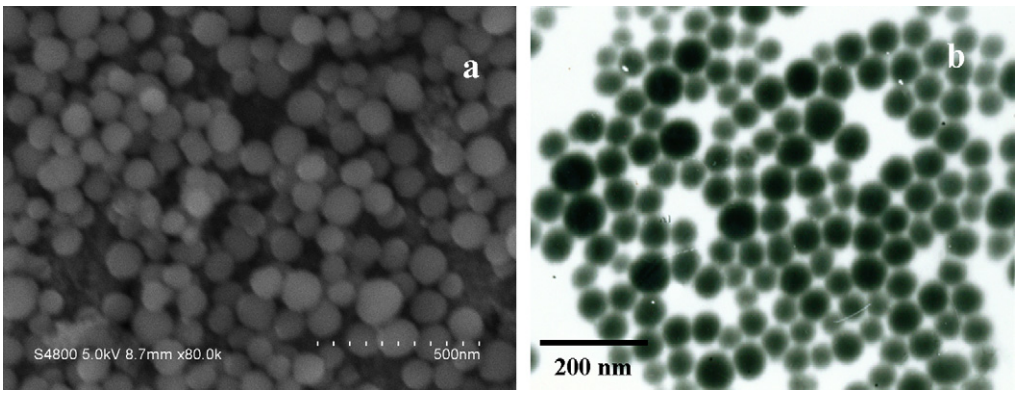


Fig. 1. (a) SEM image with magnitude ×80,000 of the LSNPs and (b) TEM image of the amino-functionalized LSNPs.

notable moiety is the absorption peak at 3448 cm^{-1}, which is assigned to amino groups attached to the surface of LSNPs [35]. This demonstrates that the LSNPs were successfully functionalized by amino groups on its surface. There is a superstrong absorption peak located at 1091 cm^{-1}, which is assigned to the asymmetric stretching vibrations of the Si–O–Si from the silica shells [29,39]. Meanwhile, the C=O group of the ligand TTA exhibits an asymmetry stretching vibration peak at 1637 cm^{-1}, which conforms the rare earth complex was doped in the silica matrix [38]. All of the results indicate that rare earth complexes are doped into the silica nanoparticles and the LSNPs are functionalized by amino groups successfully.

3.3. Fluorescence spectra of the aminated LSNPs in the presence of glucose

As shown in Fig. 3 (curve a), the as-prepared aminated LSNPs show a strong fluorescence peak located at 618 nm under the excitation at λ_{ex} = 350 nm. The red emission at 618 nm is attributed to the transition of $^5D_0 \rightarrow {}^7F_2$ of Eu^{3+} ion [38]. In the presence of different concentration of glucose, the location of fluorescence emission changed little, but the fluorescence intensities were increased with the increasing of glucose concentration as shown in Fig. 3(from curve b to curve j). Based on the enhancement effect of aminated LSNPs in the presence of glucose, a method for determining glucose was proposed.

As we know, in the preparation of europium ion–organic coordination compounds, coordinated water moleculars are often present in their structure as an additional ligand at the ninth coordination site due to the strong coordination ability between water moleculars and europium [38,40,41]. From the experimental findings, we assume the C=O groups from glucoses penetrate into the SiO_2 network and coordinate with europium instead of water molecular. Because water moleculars act as quenchers in the europium compound [41], the fluorescence intensity will be increased after the water molecular are replaced by glucose. Furthermore, the coordination of C=O groups with europium ion cause the structural arrangement of the europium complex, which is favorable to transfer energy from ligands to the europium, resulting in the enhanced energy transfer. In addition, the abundant amino groups on the surface of nanospheres are more favorable for glucose to approach the nanospheres.

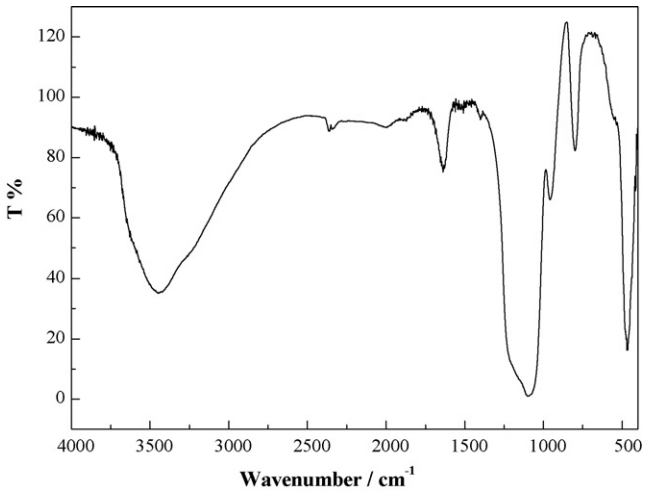


Fig. 2. FTIR spectrum of the amino-functionalized LSNPs.

3.4. Analytical application of aminated LSNPs in glucose sensor

3.4.1. Optimum of experimental conditions

In order to further enhance the performance of the analytical system for glucose sensor, the experimental conditions including pH and duration of the reaction between NPs and glucose were investigated.

The effect of pH on the fluorescence intensity of this system in presence or absence of 35 μg ml^{-1} of glucose was investigated from pH 4.5 to 8.5. The results showed that the maximum differ-

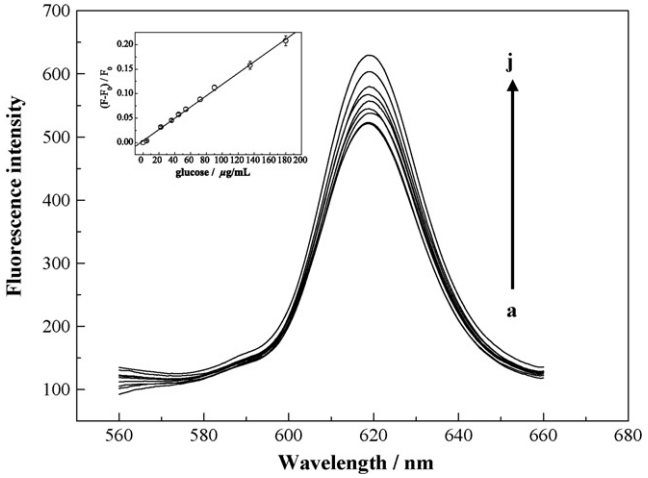


Fig. 3. The fluorescence emission spectra of the amino-functionalized LSNPs with variable concentrations of glucose from bottom to up: 0.0, 4.5, 22.5, 40, 50, 60, 80, 100, 140, 180 μg ml^{-1}, respectively. NPs: 50 μg ml^{-1}, 0.1 M phosphate buffer solution, pH 6.5. Inset: The linear plot of $\Delta F/F_0$ against glucose concentration in the range of 0.0–180 μg ml^{-1}.

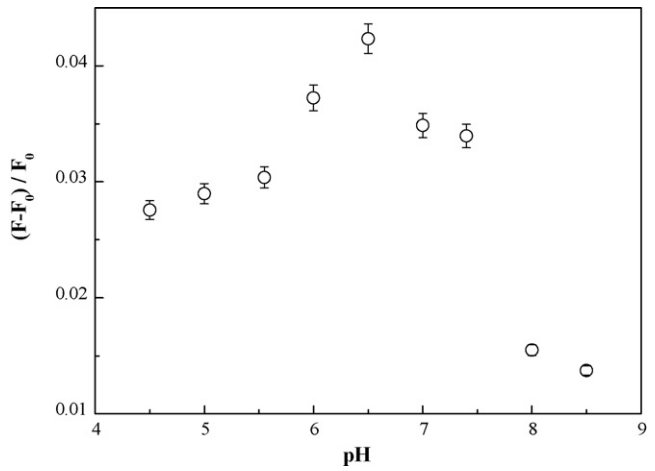


Fig. 4. Effect of pH on the fluorescence intensity in this system in the presence or absence 35 μg ml^{-1} glucose. NPs: 50 μg ml^{-1}, 0.1 M phosphate buffer solution, pH 6.5.

ence of the fluorescence intensity ($\Delta F/F_0$) was obtained at pH 6.5 (as shown in Fig. 4). In all experiments, a pH of 6.5 was, therefore, chosen to run the assay. Different buffers, such as Tris–HCl, Na_2HPO_4–NaH_2PO_4, Briton–Robison, were studied and the results showed a similar changing trend with slightly different effect on the fluorescence intensity. Finally, 0.1 M Na_2HPO_4–NaH_2PO_4 buffer with pH 6.5 was chosen.

The reaction time of the aminated LSNPs and glucose was also investigated. As shown in Fig. 5, in the presence of 100 μg ml^{-1} glucose, the maximum fluorescence intensity of the reaction system was obtained in 20 min and the fluorescence intensity showed little change in an hour at room temperature. In the subsequent studies, duration of 20 min was recommended for the determination of glucose.

3.4.2. Linearity, detection limit, and reproducibility

Under optimized experimental conditions, the changes in fluorescence spectra of aminated LSNPs in the presence of different concentrations of glucose in the range of 0.0–180 μg ml was monitored, as shown in Fig. 3. The plot of $\Delta F/F_0$ against glucose concentration showed linear relationship in the range of 0.0–180 μg ml (shown in inset of Fig. 3). The linear fit was described as $\Delta F/F_0 = 0.0035 + 0.0012c$ (c: μg ml) with a correlation coefficient r^2 of 0.998 ($n = 10$). The detection limit was calculated to be 0.8 μg ml from the statistical analysis (S/N = 3). The precision of the method was evaluated at two glucose concentrations (22.5, 100 μg ml), and the relative standard deviations, R.S.D. ($n = 7$ for each level) were 0.33% and 0.37%, respectively. These results demonstrate that the proposed method is sensitive and reproducible and may be applied to the determination of glucose in real samples.

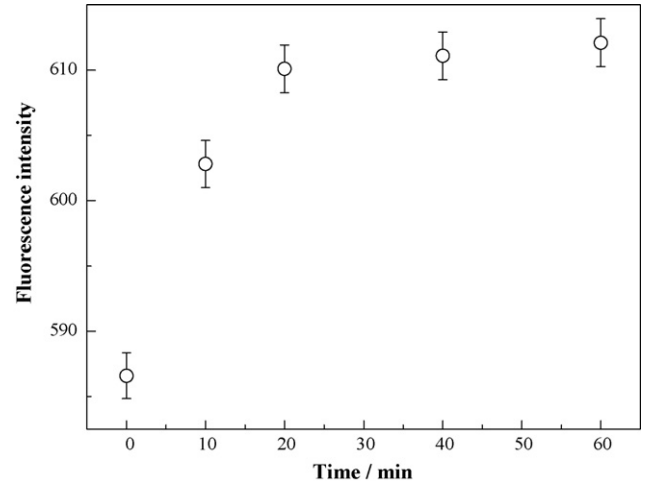


Fig. 5. The fluorescence intensity as a function of the time of reaction between the NPs and glucose in this system. NPs: 50 μg ml^{-1}, glucose: 100 μg ml^{-1}, 0.1 M phosphate buffer solution, pH 6.5.

Table 1
Effects of co-existing substances on the fluorescence intensity[a].

Co-existing substances	Concentration (μg ml^{-1})	Change of the fluorescence intensity (%)
Fructose	100	+1.05
Sucrose	100	−0.09
Ca^{2+}, Cl^-	100	−1.86
Ba^{2+}, Cl^-	100	+1.06
Na^+, Cl^-	100	−0.50
Al^{3+}, Cl^-	50	−3.06
K^+, Cl^-	100	+0.78
Zn^{2+}, Cl^-	100	−0.73
Hg^{2+}, NO_3^-	100	+1.11
Mn^{2+}, Cl^-	100	−0.27
Fe^{3+}, Cl^-	50	+1.59
Cu^{2+}, Cl^-	50	+1.91
L-Cysteine	50	−2.46
L-Tryptophan	50	+0.62
DL-Glutamine	50	−1.88
Hs DNA	10	+2.09
Ascorbic acid	100	+0.48
HSA	10	−0.72
Uric acid	100	+0.04

[a] Glucose: 20 μg ml^{-1}; the amino-functionalized LSNPs: 50 μg ml^{-1}; buffer solution used: 0.1 mol l^{-1} PBS; pH 6.5.

3.4.3. Interference of co-existing foreign substances

To investigate the selectivity of the system for determining glucose, the influence of common foreign substances including sugars, common species present in biological systems was studied (see Table 1). A relative error of ±5% in the change of fluorescence intensity with and without co-existing substance is considered tolerable. It can be seen that the relative errors of the common interferences were within ±5% and exhibited little influence on the determination of glucose, so no special treatment was taken before using in real sample analysis. Among the electrochemical methods for the determination of glucose, ascorbic acid and uric acid present in biological fluids are the most important interferences due to their electrochemical oxidation on electrodes especially nonenzymatic sensors [42]. In this system, ascorbic acid and uric acid show little interference on the determination of glucose, which suggests that the proposed method is suitable for the direct determination of glucose in biological fluids.

3.5. Sample analysis

3.5.1. Determination of glucose in synthetic samples

The concentration of glucose in synthetic samples was determined with the proposed method. The synthetic samples were prepared by mixing some ions, organic substances, and biomolecules with a known concentration of glucose. The determination was performed by the procedure described above and the determination for each sample was reproduced five times. As shown in Table 2, the recovery for each determination is located in the range of 96–104%. The results show that the proposed method is reliable for the determination of glucose in synthetic samples and suitable for application.

Table 2
Results of the determination of glucose in synthetic samples.

Sample no.	Glucose added ($\mu g\,ml^{-1}$)	Co-existing substances ($\mu g\,ml^{-1}$)	Found average ($\mu g\,ml^{-1}$, $n=5$)	Recovery (%)	R.S.D. (%)
1	60	Fructose 100, Al^{3+} 200, L-cystein 100, Cl^- 300, ascorbic acid 50	61.6	99–104	2.9
2	140	Sucrose 300, K^+ 500, HAS 100, NO_3^- 500, DL-glutamine 250	138.5	96–103	3.8

Table 3
Analysis results of the direct determination of glucose in human serum samples.

Sample no.	Data provide by hospital (mM)	This method (mM) ($n=7$)	R.S.D (%)
1	4.78	4.90	−1.77
2	5.79	6.40	7.13
3	6.31	6.37	1.90
4	9.83	9.87	3.6
5	11.78	11.90	−1.77

3.5.2. Determination of glucose in real human serum samples

To further evaluate the applicability of the proposed glucose sensor in biological samples, a comparative study with clinically used glucose analyzer (Hitachi 7170, Japan) in measuring blood glucose of human serum samples was performed. Serum samples were obtained by centrifuging (2000 rpm, 5 min) the fresh blood samples which taken from three healthy adults and two diabetes patients (provided by Yijishan Hospital, Wuhu, China). The serum glucose concentration was determined with the above-mentioned procedures. The detected glucose content in serum samples was derived from the standard curve and the regression equation. The final concentration was converted into molar concentration in mM. The measurement results and the clinical data provided by hospital were summarized in Table 3. As shown in Table 3, the results obtained by proposed method show reasonable agreements with the data provided by the hospital. The results indicate that the proposed method has the potential for practical applications in the determination of blood glucose in real human serum.

4. Conclusions

In summary, amino-functionalized LSNPs doped with the europium complex $Eu(TTA)_3phen$ were synthesized successfully using an revised Stöber method. SEM, TEM, FTIR, and fluorescence were performed for characterization. Due to the enhanced effect of glucose on the fluorescence intensity of amino-functionalized LSNPs, a simple and sensitive fluorescence sensor for glucose was proposed. The results of sample analysis show that the reproducibility and the reliability of the proposed method are satisfactory, indicating that the proposed method has potential applications in the determination of glucose.

Acknowledgements

The authors are grateful for the financial support from the Natural Science Foundation of China (grant no. 20705001), the Key Project of Educational Committee of Anhui Province (grant no. KJ2007A008), the Innovation Group Project of Anhui Normal University and Starting Foundation for PhD of Anhui Normal University.

References

[1] J. Wang, Chem. Rev. 108 (2008) 814.
[2] J.C. Pickup, F. Hussain, N.D. Evans, O.J. Rolinski, D.J.S. Birch, Biosens. Bioelectron. 20 (2005) 2555.
[3] The Diabetes Control and Complications Trial Research Group, New Engl. J. Med. 329 (1993) 977.
[4] The DCCT Research Group, Diabetes 46 (1997) 271.
[5] C. Zhao, C. Shao, M. Li, K. Jiao, Talanta 71 (2007) 1769.
[6] L. Özcan, Y. Sahin, H. Türk, Biosens. Bioelectron. 24 (2008) 512.
[7] X.D. Shangguan, H.F. Zhang, J.B. Zheng, Electrochem. Commun. 10 (2008) 1026.
[8] H.P. Yang, Y.F. Zhu, Anal. Chim. Acta 554 (2005) 92.
[9] C. Li, Y. Liu, L. Li, Z. Du, S. Xu, M. Zhang, X. Yin, T. Wang, Talanta 77 (2008) 455.
[10] F. Severcan, G. Gorgulu, S.T. Gorgulu, T. Guray, Anal. Biochem. 339 (2005) 36.
[11] V. Sanz, S.D. Marcos, J. Galbán, Talanta 78 (2009) 846.
[12] K. Asian, J.R. Lakowicz, C.D. Geddes, Anal. Chem. 77 (2005) 2007.
[13] X.W. Shen, C.Z. Huang, Y.F. Li, Talanta 72 (2007) 1432.
[14] J.A. Ho, L.c. Wu, N.C. Fan, M.S. Lee, H.Y. Kuo, C.S. Yang, Talanta 71 (2007) 391.
[15] J.T. Suri, D.B. Cordes, F.E. Cappuccio, R.A. Wessling, B. Singaram, Angew. Chem. Int. Ed. 42 (2003) 5857.
[16] M. Morikawa, N. Kimizuka, M. Yoshihara, T. Endo, Chem. Eur. J. 8 (2002) 5580.
[17] B. Tang, L.H. Cao, K.H. Xu, L.H. Zhuo, J.C. Ge, Q.L. Li, L.J. Yu, Chem. Eur. J. 14 (2008) 3637.
[18] D.B. Cordes, S. Gamsey, B. Singaram, Angew. Chem. Int. Ed. 45 (2006) 3829.
[19] J.P. Yuan, W.W. Guo, E.K. Wang, Biosens. Bioelectron. 23 (2008) 1567.
[20] C.P. Huang, S.W. Liu, T.M. Chen, Y.W. Li, Sens. Actuators B 130 (2008) 338.
[21] J. Yuan, W. Guo, J. Yin, E. Wang, Talanta 77 (2009) 1858.
[22] L. Wang, K. Wang, S. Santra, X. Zhao, L.R. Hilliard, J.E. Smith, Y. Wu, W. Tan, Anal. Chem. 78 (2006) 646.
[23] S. Santra, P. Zhang, K.M. Wang, R. Tapec, W.H. Tan, Anal. Chem. 73 (2001) 4988.
[24] W.H. Tan, K.M. Wang, X.X. He, X.J. Zhao, T. Drake, L. Wang, R.P. Bagwe, Med. Res. Rev. 24 (2004) 621.
[25] L. Wang, C.Y. Yang, W.H. Tan, Nano Lett. 5 (2005) 37.
[26] L. Wang, W.H. Tan, Nano Lett. 6 (2006) 84.
[27] R.P. Bagwe, C.Y. Yang, L.R. Hilliard, W.H. Tan, Langmuir 20 (2004) 8336.
[28] W. Lian, S.A. Litherland, H. Badrane, W.H. Tan, D.H. Wu, H.V. Baker, P.A. Guling, D.V. Lim, S.G. Jin, Anal. Biochem. 334 (2004) 135.
[29] M. Qhobosheane, S. Santra, P. Zhang, W.H. Tan, Analyst 126 (2001) 1274.
[30] Y.H. Yang, M.Y. Gao, Adv. Mater. 17 (2005) 2354.
[31] X.X. He, J.H. Duan, K.M. Wang, W.H. Tan, X. Lin, C.M. He, J. Nanosci. Nanotechnol. 4 (2004) 585.
[32] S. Santra, H. Yang, D. Dutta, J.T. Stanley, P.H. Holloway, W.H. Tan, B.M. Moudgil, R.A. Mericle, Chem. Commun. (2004) 2810.
[33] F. Gao, L. Wang, L.J. Tang, C.Q. Zhu, Microchim. Acta 152 (2005) 131.
[34] F. Gao, L.J. Tang, L. Dai, L. Wang, Spectrochim. Acta Part A 67 (2008) 517.
[35] F. Gao, F.B. Luo, J. Yin, L. Wang, Luminescence 23 (2008) 392.
[36] F.B. Luo, J. Yin, F. Gao, L. Wang, Microchim. Acta 165 (2009) 23.
[37] F. Gao, F.B. Luo, L.J. Tang, L. Dai, L. Wang, J. Lumin. 128 (2008) 462.
[38] F. Gao, F. B.Luo, X.X. Chen, Y. Wu, J. Yin, Z. Yao, L. Wang, in press, doi:10.1007/s00604-009-0180-0.
[39] Y.L. Qi, M. Chen, S. liang, J. Zhao, W. Yang, Colloids Surf. A Physicochem. Eng. Aspects 302 (2007) 383.
[40] L.R. Matthews, E.T. Knobbe, Chem. Mater. 5 (1993) 1697.
[41] O.S. Wolfbbeis, A. Dürkop, M. Wu, Z. Lin, Angew. Chem. Int. Ed. 41 (2002) 4495.
[42] J. Yuan, K. Wang, X. Xia, Adv. Funct. Mater. 15 (2005) 803.

Talanta 80 (2009) 207–211

Contents lists available at ScienceDirect

Talanta

journal homepage: www.elsevier.com/locate/talanta

Determination of organic and inorganic mercury species in water and sediment samples by HPLC on-line coupled with ICP-MS

José Soares dos Santos[a,*], Miguel de la Guárdia[b], Augustin Pastor[b], Maria Lúcia Pires dos Santos[a]

[a] Departamento de Ciências Naturais, Universidade Estadual do Sudoeste da Bahia, Estrada do Bem Querer km 4, CP 95, Vitória da Conquista, Bahia, Zip 45083-900, Brazil
[b] Department of Analytical Chemistry, University of Valencia, C/ Doctor Moliner 50, 46100, Valencia, Spain

ARTICLE INFO

Article history:
Received 14 April 2009
Received in revised form 22 June 2009
Accepted 23 June 2009
Available online 2 July 2009

Keywords:
Preconcentration and speciation of mercury
Environmental matrices
Inductively coupled plasma mass spectrometry
High-performance liquid chromatography

ABSTRACT

This paper describes a preconcentration method for Hg^{2+} and $MeHg^{+}$ in water samples using sodium diethyldithiocarbamate immobilized in polyurethane foam (PU-NaDDC) and an extraction method for several mercury species in sediment samples, including $MeHg^{+}$, $EtHg^{+}$ and $PhHg^{+}$, which is simple, rapid, and uses a single organic solvent. Separation and measurement were done by high-performance liquid chromatography on-line with inductively coupled plasma mass spectrometry (HPLC/ICP-MS). Initially, the test of recovery was applied using procedures compatible with HPLC. Under the optimum extraction conditions, recoveries of 96.7, 96.3 and 97.3% were obtained for $MeHg^{+}$, $EtHg^{+}$, and $PhHg^{+}$, respectively, from $n = 4$ spiked sediment samples. This study also demonstrates that the combination of solid-phase extraction on PU-NaDDC with HPLC separation and ICP-MS detection is an effective preconcentration procedure for simultaneous measurement of Hg^{2+} and $MeHg^{+}$ at ultra-trace levels in water samples. The application of the proposed procedure to the determination of mercury species in drinking water sample was investigated. The proposed method clearly gave satisfactory average recoveries between 93.7 and 101.5%.

© 2009 Elsevier B.V. All rights reserved.

1. Introduction

Mercury traces are usually determined by cold vapor techniques using atomic spectroscopic detection. However, due to the toxicity differences of the different species of mercury, a speciation analysis is increasingly necessary. Mostly, hyphenated procedures based on systems coupling chromatography separation with atomic spectrometric detection have been proposed [1–3].

For instance gas chromatography (GC) using capillary columns as separation technique has been widely used. However, interferences due to the strong interaction between the polar mercury halides and the column material have been observed [4].

Liquid chromatography (LC) is also proposed for mercury speciation analysis. Among its advantages are the possibility of separating the native mercury species without prior derivatisation and operation at ambient temperature.

For water samples, with extremely low mercury concentrations a preliminary preconcentration step is required [5]. The solid-phase extraction allows the preconcentration from large sample volumes with high yield, as confirmed by some procedures used polyurethane foam with immobilized diethyldithiocarbamate (DDTC) [1,5].

In sediment samples the mercury species are strongly bound to the matrix and have to be released prior to their determination. In total elemental analysis microwave-assisted digestion is a well-accepted technique [6–8]. However, it has rarely been used for organomercury speciation analysis because under the usual conditions (high pressures and temperatures) the compounds are destroyed and all speciation information is lost [9–13].

A popular procedure for selective removal of the organic mercury species from sediment samples is liquid extraction using organic solvents. Most methods consist of an extraction into an organic solvent containing HCl, HBr or HI followed by the subsequent formation of a water-soluble adduct of the organic mercury species with cysteine or thiosulfate. This adduct is then back-extracted to water; the organic mercury species are then liberated by acidification and re-extracted to the organic solvent. However, these procedures are skilful and time consuming, impairing the sample throughput of the whole analytical procedure [14–18].

The aim of the present work was optimization of the quantitative preconcentration of Hg^{2+} and $MeHg^{+}$ in water samples by solid-phase extraction on sodium diethyldithiocarbamate immobilized in polyurethane foam (PU-NaDDC). The extraction of $MeHg^{+}$, $EtHg^{+}$ and $PhHg^{+}$ species from sediment samples was also investi-

* Corresponding author. Tel.: +55 77 3424 9422; fax: +55 77 3424 1059.
E-mail address: zesoares@uesb.br (J.S. dos Santos).

0039-9140/$ – see front matter © 2009 Elsevier B.V. All rights reserved.
doi:10.1016/j.talanta.2009.06.053

gated aiming their posterior separation and determination on-line by HPLC–ICP-MS.

2. Materials and methods

2.1. Apparatus

The chromatographic system used was an HP 1050 model (Hewlett Packard, Waldbronn Germany) equipped with a UV detector (HP 1050 Series, model 79853C) and controlled by HP Chem Station Software (HPLC 2D, reference G2170AA). To perform the Hg speciation, a Nucleosil 100-5 C8 column (5 μm, 10 cm × 4 mm) was used. The mobile phase was composed by 0.06 mol L^{-1} ammonium acetate, 0.005% (v/v) 2-mercaptoethanol, and 3% (v/v) *n*-butanol. In all cases, an eluent flow of 1 mL min^{-1} was employed, and the analytical measurements were performed at 230 nm.

The detector consisted of a PerkinElmer Sciex (ELANTM 5000 ICP-MS spectrometer (Toronto, Canada) equipped with a PerkinElmer Ryton Scott-type spray chamber and cross-flow nebulizer. The optimized instrumental settings are shown in Table 1. The sample solutions were aspirated into the argon plasma via a peristaltic pump, and data were acquired using an IBM PS/2 Model 77 computer.

2.2. Reagents and materials

All reagents used were of the highest purity available and at least of analytical reagent grade. A solution of ammonium acetate (1 mol L^{-1} in *n*-butanol) was used in the sediment extraction procedure, and the ligand sodium diethyldithiocarbamate (NaDDTC) (Fluka, Switzerland) was used as sorbent in the preconcentration procedure.

An Hg^{2+} stock solution (1000 mg L^{-1}) was prepared by dissolving the appropriate amount of $HgCl_2$ (Merck, Darmstadt, Germany) in high purity water (18 MΩ^{-1} specific resistivity) obtained from a MillQ system (Millipore Saint-Quentin Yvelines, France). The $MeHg^+$, $EtHg^+$, and $PhHg^+$ 1000 mg L^{-1} stock solutions were prepared by dissolving their chlorides (Merck, Darmstadt, Germany) in the smallest possible volume of methanol and diluting to volume with nanopure water. High purity ammonium acetate (Scharlau, Spain), 2-mercaptoethanol (Fluka, Switzerland), *n*-butanol (Scharlau, Spain), and chloroform (Normasolv, Spain) were used. High purity argon (C-45 99.995% purity) was supplied by Carburos Metálicos (Barcelona, Spain).

For sieving the sediment samples, a nylon sieve with mesh screen of 0.063 mm (Cole-Parmer Canada Inc., Montreal, Canada) was used.

2.3. Preconcentration of mercury compounds from water samples

Preconcentration of mercury compounds in water samples was performed according to Sonja et al. [1]. Cubical foam pieces 5 mm long were cut from commercially available polyurethane foam. The cleaned and dried foam pieces were soaked in a chloroform solution NaDDTC and then squeezed occasionally until all the solution was retained in the PU cubes. The foam cubes were air dried until the evaporation of the organic solvent.

The NaDDTC-loaded PU foam pieces were transferred to a disposable tube packed with a small wad of cotton wool at its end covered with a filter paper disc. Water samples were passed through the column at a 2 mL min^{-1} flow rate, using a peristaltic pump. After this step the physically immobilized organic chelating ligand, NaDDTC and the analyte–dithiocarbamate complexes formed were completely eluted by *n*-butanol. The performance of the column was stable at least over 15 preconcentration cycles.

Table 1
ICP-MS operating parameters.

Plasma argon flow	9–11 (L min^{-1})
Auxiliary gas	1.4 (L min^{-1})
Nebulizer flow rate	0.8–0.9 (L min^{-1})
Sample flow	1.0 (mL min^{-1})
Forward power	1.10 kW
Sampling cone	Ni, 1.14 mm orifice
Skimmer cone	Ni, 0.89 mm orifice
Total analysis time	600 (s)

2.4. Sediment samples and spiking procedure

The use of certified reference materials (CRMs) is the only viable way to validate current procedures in speciation analysis. Unfortunately, there are only a few CRMs available for limited species and matrices, and those already available may have quite large uncertainties in the certified values [19].

The production of CRMs for organic mercury species has been essentially focused on methylmercury. Thus, there is no standardized method to assess the extraction efficiency of $MeHg^+$, $EtHg^+$, and $PhHg^+$ in sediment samples. However, a recent overview of the certification of total Hg and methylmercury in estuarine sediment recommended the use of standard additions as the best means to establish the efficiency of the method. This is achieved by spiking the material under investigation prior to extraction. However, this method does not guarantee that there is no loss or complete recovery of a given compound from the matrix. It is current practice to apply compensation for these losses by correcting the results with a recovery factor in order to achieve a better approximation to the true value in a material. These correction factors are established after undertaking recovery studies, which are an essential component of the validation of extraction-based techniques [20,21].

The sediment material was collected in Gavião River and Anajé Reservoir, located in the southwest area of the state of Bahia, Brazil. This material was used to prepare the sediment samples to be used in optimization studies. The samples were collected in polyethylene bags and stored at 0 °C. Before the analysis, the sediment samples were dried at 60 °C until a constant mass was reached, as recommended by the EPA [22]. After that, the sediment samples were then ground and sieved through a nylon sieve. The fraction less than 63 μm was spiked with methylmercury, ethylmercury, and phenylmercury according to Vazquez et al. [23]. An amount of 10 g of sediment was mixed with 2 mL of methanol containing a known concentration of $MeHg^+$, $EtHg^+$, and $PhHg^+$, which was slowly added to form a dough that was mechanically stirred for several minutes. The sample was then stored in the dark and allowed to air dry for 1 day. Assuming no losses had taken place during drying or storage, the theoretical concentrations of mercury species were (260.0, 135.7, and 125.2 ng g^{-1} for $MeHg^+$, EtHg, and $PhHg^+$, respectively) on a dry weight basis.

2.5. Extraction of mercury compounds from sediment samples

Spiked samples and sediment samples collected in Gavião River and Anajé Reservoir, located in the southwest area of the state of Bahia, Brazil were extracted as follows: a 1.0 g weight portion was removed from sediment samples that was placed in an extraction container with 10 mL of *n*-butanol containing ammonium acetate (1 mol L^{-1}), and this samples were mechanically stirred for 2 h. After extraction, the sample was filtered through a 0.45 mm filter; the volume was adjusted to 10 mL with *n*-butanol, and it was stored until use at 4 °C.

In order to check the absence of organomercurial in the extraction solution, the sediment samples (P1, P4 and, P9) were selected, because $MeHg^+$, $EtHg^+$ and $PhHg^+$ were not detected in measur-

able quantities in those samples, as shown in Table 5. Each one of the sediment samples was extracted three times with 10 mL of *n*-butanol containing ammonium acetate (1 mol L^{-1}), followed by HPLC/ICP-MS analysis. The chromatogram obtained for those samples was very clean; no interference compounds were present in the extract.

3. Results and discussion

3.1. Performance of the sorbent extraction preconcentration of Hg^{2+} and $MeHg^{+}$ in water samples

In previous work we developed a preconcentration system for the extraction of Hg^{2+} and $MeHg^{+}$ present in water samples. The influence of the pH on the retention of Hg^{2+} and CH_3Hg^{+} on PU-DDTC was studied at different pH varies between 1.0 and 10.0 for the single mercury species solutions. The effect of pH on chelate sorption was different in each case; thus, sorption was maximal at pH 1–7 for Hg^{2+} and 4–7 for CH_3Hg^{+}.

The influence of the flow rate of the samples loaded onto the columns on the retention efficiency of $MeHg^{+}$ and Hg^{+} was investigated in the range of 0.5–3.0 mL min^{-1} using the solutions containing the mercury species at a concentration of 20 ng mL^{-1}. It was established that at a flow rate higher than 2.0 mL min^{-1}, the mercury species uptake lessened successively owing to lower residence time of the sample solution in the column. For that reason, the flow rate of 2.0 mL min^{-1} was considered appropriate for further column operation.

The preconcentration of larger sample volumes at a defined sample flow rate usually results in the enhancement of the enrichment factor expressed as ratio of the volume of the sample loaded onto the column to the volume of an eluent used for the recovery of the analytes retained. For that reason, the influence of sample volume was examined for 200, 300 and 500 mL solutions containing 1.0, 1.5 and 2.5 mg each of the analysed mercury species, respectively. After passage of the test solutions through the columns, the mercury species were recovered using 5 mL of pure *n*-butanol. The resulting 5 mL aliquots of the eluate were measured to determine the concentrations of Hg^{2+} and $MeHg^{+}$ and evaluate the efficiency of the elution procedure.

In order to check the performance of the sorbent extraction preconcentration followed by HPLC–ICP-MS for determination, ten samples of ultrapure water containing Hg^{2+} and $MeHg^{+}$ were passed through the columns. The results showed a good recovery of the two organic species: $92 \pm 2\%$ for Hg^{2+} and $102 \pm 1\%$ for $MeHg^{+}$. Quantitative solid-phase preconcentration of Hg^{2+} and $MeHg^{+}$ on PU-MDC sorbent, was achieved with water samples of up to 500 mL. Hence, considering an elution volume of 5 mL (*n*-butanol) an enrichment factor of 100 was obtained.

3.2. Performance of the solvent extraction of mercury species in sediment samples

The key step of speciation in environmental samples is to extract the target compounds in their original forms without any disturbance. Typically, alkyl mercury species are determined by acid digestion with solvent extraction, followed by several cleanup steps, and then back-extracted into an aqueous phase. However, previous studies have shown that the organomercurials are not stable under very acidic conditions. In this study, three organic solvents (chloroform, methanol, and *n*-butanol) containing ammonium acetate (1 mol L^{-1}) were tested to extract $MeHg^{+}$, $EtHg^{+}$, and $PhHg^{+}$ from spiked sediment samples. The *n*-butanol presented a better recovery of the three organic species. Under the optimum extraction conditions, recoveries of 96.7, 96.3, and 97.3% were obtained for $MeHg^{+}$, $EtHg^{+}$, and $PhHg^{+}$, respectively, from $n = 4$ spiked sediment samples as shown in Table 2.

Table 2
Extraction recoveries in percent of organomercury compounds in four spiked sediment samples.

Ammonium acetate (1 mol L^{-1}) in	$MeHg^{+}$	$EtHg^{+}$	$PhHg^{+}$
Chloroform	89.5 ± 2.1	81.3 ± 2.8	80.5 ± 3.1
Methanol	90.5 ± 2.3	83.2 ± 3.7	77.8 ± 3.8
n-Butanol	96.7 ± 5.7	96.3 ± 7.6	97.3 ± 2.9

3.3. Chromatographic separation of mercury species

Fig. 1a shows the chromatographic separation of a 50 μg L^{-1} mixed standard solution of Hg^{2+}, $MeHg^{+}$, $EtHg^{+}$, and $PhHg^{+}$ by HPLC/ICP-MS detection. The elution sequence is the same as that observed by Dos Santos et al. [24]. The optimized isocratic eluent consists of 3% (v/v) *n*-buthanol and 0.005% (v/v) 2-mercaptoethanol with 0.06 mol L^{-1} ammonium acetate. The eluent flow for the separation was adjusted to 1 mL min^{-1}. During a measuring time of 10.0 min all four peaks appeared well resolved without any other peaks arising from the solvent front or complexing agent. The baseline was stable, and the noise and the drift of the baseline did not increase with increasing concentration of the mobile phase. All the Hg^{2+}, $EtHg^{+}$, $MeHg^{+}$, and $PhHg^{+}$ signals were optimized by varying the carrier gas flow rate and the rf power of the ICP-MS. A mixed standard was injected and the settings for the rf power and carrier gas flow rates on the ICP-MS varied accordingly. The optimum settings were 1100 W and 1.4 L min^{-1}, respectively.

Fig. 1b shows the chromatographic separation of two different mercury species: methylmercury and inorganic mercury with ICP-MS detection. 20 ng mL^{-1} mixed standard solution of inorganic and methylmercury was preconcentrated after complexation by NaDDTC for optimization of the chromatographic conditions. The two species were fully resolved and completely separated in a time of 4 min.

Fig. 1c shows the chromatogram of a sediment sample extracted with *n*-butanol and analysed by HPLC–ICP-MS. In the aforementioned conditions, $MeHg^{+}$, $EtHg^{+}$ and $PhHg^{+}$ were fully resolved and completely separated in a time of 10 min.

3.4. Analytical figures of merit

The analytical performances (accuracy and precision) for the preconcentration procedure of Hg^{2+} and $MeHg^{+}$ in water samples have been checked by added found method. Ultrapure water and mineral water samples were spiked with Hg^{2+} and CH_3Hg^{+} at different ratios and analysed as described. Results obtained are presented in Table 4. The calibration graphs obtained using these conditions were linear with correlation coefficients (r) of 0.9995 and 0.9996 for Hg^{2+} and CH_3Hg^{+}, respectively. The detection limit (LODs), defined as three times the standard deviation of the blank signal ($n = 12$) divided by the slope of each calibration graph, ranged from 4.6 ng L^{-1} for inorganic mercury to 5.2 ng L^{-1} for methylmercury.

The analytical performances for the extraction procedure of $MeHg^{+}$, $EtHg^{+}$ and $PhHg^{+}$ in sediment samples are summarized in Table 3. Precision was evaluated in terms of repeatability (inter-day) and reproducibility (intra-day), and it was determined using the relative standard deviations (RSDs) for five successive injections of spiked extract at 20 μg L^{-1} for each one of the Hg species. Calibration curves for the three mercury compounds were examined under the best experimental conditions between 1.0 and 40.0 μg L^{-1} concentration of each compound. In each case, the peak height was used for quantification. Linear regression curves of the individual

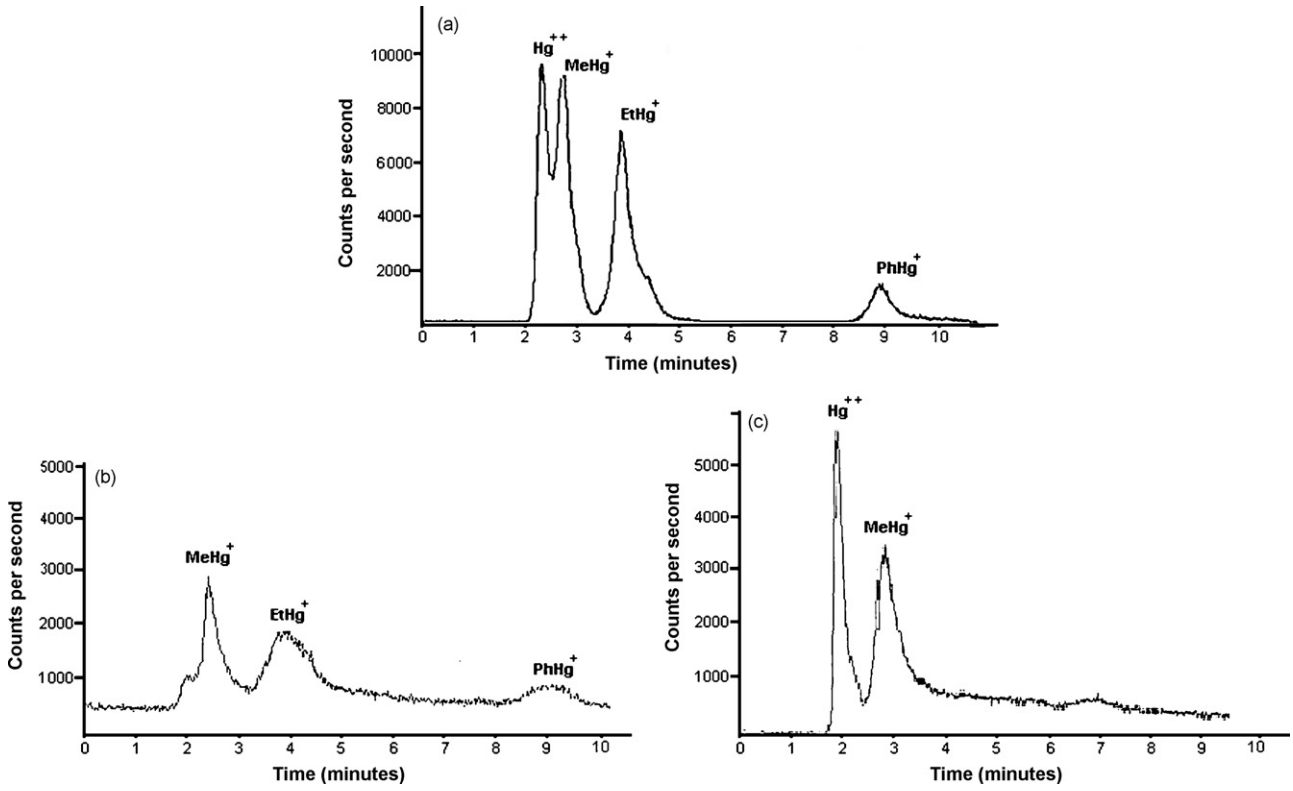


Fig. 1. (a) Chromatogram showing the separation of 50 μg L^{-1} Hg^{2+}, $MeHg^+$, $EtHg^+$ and $PhHg^+$ standards using HPLC/ICP-MS detection. (b) Chromatogram of a sediment sample extracted with *n*-buthanol and analysed by HPLC–ICP-MS. (c) Chromatographic separation of 20 μg L^{-1} Hg^{2+}, $MeHg^+$, ICP-MS detection after preconcentration with NaDDTC immobilized on polyurethane foam. The mobile phase consisting of 3% (v/v) *n*-buthanol and 0.005% (v/v) 2-mercaptoethanol with 0.06 mol L^{-1} ammonium acetate, using the Nucleosil (100 mm × 4 mm) C8 column. (+) Solvent and system peaks.

Table 3
Figure of merit of the extraction procedure method.

Species	LOD (μg L^{-1})	Repeatability (%RSD)	Reproducibility (%RSD)	Correlation
Coefficient				
$MeHg^+$	0.5	2.8	3.0	0.9996
$EtHg^+$	0.8	1.8	2.5	0.9999
$PhHg^+$	1.0	3.0	3.0	0.9994

Table 4
Results for the determination of Hg^{2+} and $MeHg^+$ in drinking water (real sample), ($n = 3$).

Sample	Found ± σ (ng L^{-1})	Added ng L^{-1}	Total found ± σ (ng L^{-1})	Recovery ± σ (%)
Hg^{2+}	30.7 ± 0.6	50	75.6 ± 0.4	93.7 ± 0.3
$MeHg^+$	10.8 ± 0.7	50	61.7 ± 0.5	101.5 ± 0.2

compounds gave correlation coefficients of at least 0.9994. Limits of detection (LODs) were calculated as three times the standard deviation of 12 blank extractions divided by the slope of each calibration graph.

3.5. Analysis of water and sediment samples

The preconcentration procedure was applied to determination of Hg^{2+} and $MeHg^+$ in mineral water samples. The results are summarized in Table 4. The proposed method clearly gave satisfactory average recoveries between 93.7 and 101.5%.

The extraction and determination of $MeHg^+$, $EtHg^+$, and $PhHg^+$ in sediment by HPLC coupled on-line with ICP-MS were applied in river sediment samples. Sediment samples were collected along the Gavião River and Anajé Reservoir (Bahia, Brazil) located in a semi-arid zone (Fig. 2). Table 5 shows the results obtained. Concentration levels of mercury species of a few ng g^{-1} were found for all sam-

Table 5
Determination of Hg species in sediment samples by standard addition HPLC–ICP-MS, concentration values in ng g^{-1}.

Sediment samples	$MeHg^+$	$EtHg^+$	$PhHg^+$
P1	<0.5	<0.8	<1.0
P2	12.1 ± 0.3	<0.8	<1.0
P3	13.7 ± 0.4	<0.8	<1.0
P4	<0.5	<0.8	<1.0
P5	80.1 ± 1.0	13.3 ± 0.3	<1.0
P6	81.5 ± 1.0	31.2 ± 1.0	11.5 ± 0.3
P7	25.2 ± 0.5	12.1 ± 0.4	<1.0
P8	61.2 ± 1.0	25,2 ± 1.0	5.4 ± 0.4
P9	<0.5	<0.8	<1.0

< Detection limit, calculated as three times the standard deviation of the blank divided by the slope of each calibration graph.

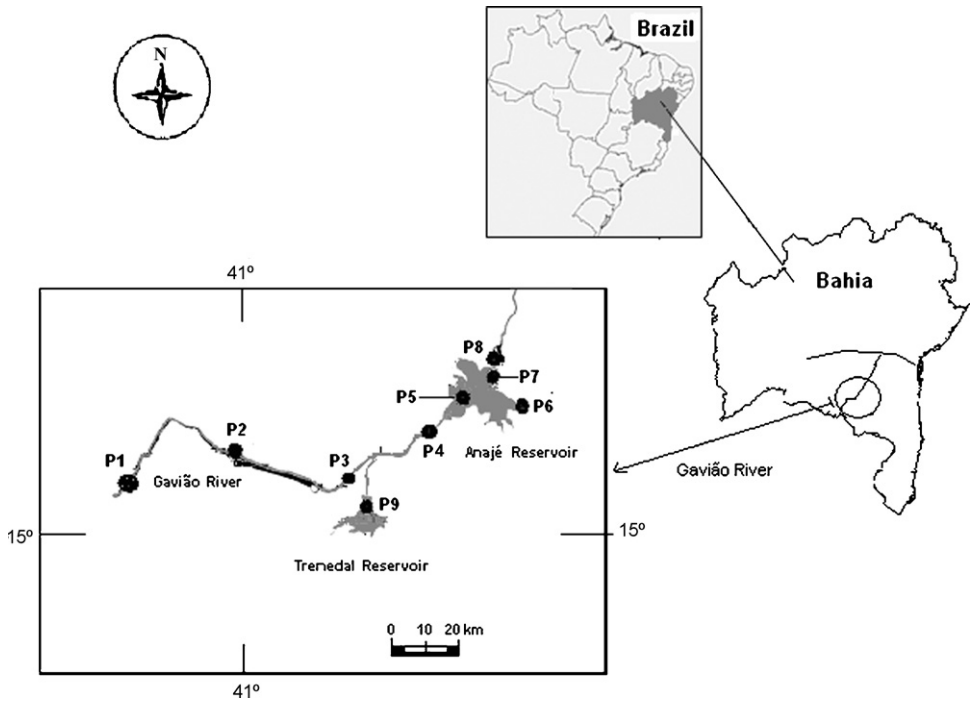


Fig. 2. Map showing the network of sampling sites on Gavião River and Anagé Reservoir.

ples collected along Gavião (P1, P2, P3 and P4). Thus, it is likely that the small variation of mercury species concentrations in the study site is of natural origin. The highest levels of mercury species were detected in sediment samples collected in the Anagé Reservoir (P5, P6, P7 and P8). This can be indicative of pesticides used in crop soil around of the reservoir. Although $EtHg^+$ and $PhHg^+$ are not usually detected in measurable quantities in environmental samples, the concentrations of these two mercury species detected in some sediment samples were consistent with results previously reported in the literature [17,25–27].

4. Conclusions

This study demonstrates that the combination of solid-phase extraction on PU-NaDDC with HPLC separation and ICP-MS detection is an effective preconcentration procedure for simultaneous measurement of Hg^{2+} and $MeHg^+$ at ultra-trace levels in water samples. The application of the proposed procedure to the determination of mercury species in drinking water sample was investigated. The proposed method clearly gave satisfactory average recoveries between 93.7 and 101.5%.

The extraction of mercury species from sediment samples was also investigated. Applying a single organic solvent is a procedure suitable for the simultaneous extraction and determination of methylmercury, ethylmercury, and phenylmercury in sediment by HPLC coupled on-line with ICP-MS. The major advantages in comparison to the extraction procedures currently preferred for mercury speciation are the reduction of the number of sample preparation steps along with a concomitant reduction in the inherent risk of contamination. The reliability of the method was checked by recovery experiments. Recovery values obtained (Table 3) lie in the range of 96.3–97.3%, which demonstrates the applicability of the method to determine alkyl mercury species in sediment samples without any pretreatment.

Acknowledgments

Authors acknowledge the financial support of the projects GV99–115–1-02 and PB98-0947-C02-02 and J.S.S. acknowledge the agency CAPES, for the financial support to do studies in Spain.

References

[1] A. Sonja, V. Lili, K. Elena, Analyst 122 (1997) 243.
[2] C. Kantipuly, S. Katragadda, A. Chow, H. Gesser, Talanta 37 (1990) 491.
[3] T. Braun, Fresenius J. Anal. Chem. 314 (1983) 652.
[4] M. De la Guardia, M.L. Cervera, A.R. Morales, Speciation studies by atomic spectroscopic, in: J. Sneddon (Ed.), Advances in Atomic Spectrocopy, JAI Press, Stamford, 1999.
[5] C.R. Pedro, G.T. Amparo, M.C.P. José, R.C. Enrique, J. Anal. Atom. Spectrom. 13 (1998) 243.
[6] H.M. Kingston, L.B. Jassie, Anal. Chem. 58 (1986) 2534.
[7] C.S.E. Papp, L.B. Fischer, Analyst 112 (1987) 337.
[8] G.M.M. Rahman, H.M. Kingston, Anal. Chem. 76 (2004) 3548.
[9] E.S. Ralph, N.W. Scott, A.M. Brad, W.H.L. Joseph, J. Anal. Atom. Spectrom. 10 (1995) 981.
[10] M. Burguera, J.L. Burguera, O.M. Alarcón, Anal. Chim. Acta 179 (1986) 351.
[11] D.L. Tsalev, M. Sperling, B. Welz, Analyst 117 (1992) 1729.
[12] R.D. Wilken, Fresenius J. Anal. Chem. 342 (1992) 795.
[13] E. Gao, G. Jiang, B. He, Y. Yin, J. Shi, J. Anal. Atom. Spectrom. 23 (2008) 1397.
[14] H. Walter, Analyst 107 (1982) 1457.
[15] H. Maximilian, K. Jurgen, J. Eckard, Fresenius J. Anal. Chem. 366 (2000) 470.
[16] H. Maximilian, H. Holger, D.W. Rolf, Analyst 117 (1992) 669.
[17] X. Gaona, M. Valiente, Anal. Chim. Acta 480 (2003) 219.
[18] J.H. Huang, G. Ilgen, E. Matzner, Anal. Chim. Acta 493 (2003) 23.
[19] L. Martine, B. Willy, Q. Philippe, H. Milena, Trends Anal. Chem. 24 (2005) 383.
[20] J.R. Encinar, P.R. Gonzalez, J.I.G. Alonso, A.S. Medel, Trends Anal. Chem. 22 (2003) 108.
[21] I. Kazumi, K. Takayoshi, N. Tomohiro, Y. Takashi, T. Akiko, O. Kensaku, C. Koichi, Anal. Bioanal. Chem. 391 (2008) 2047.
[22] Environmental Protection Agency (EPA), Methods for Chemical Analysis of Water and Wastes (EPA 600/4-79-020), Environmental Protection Agency (EPA), Cincinnati, 1983.
[23] M.J. Vazquez, A.M. Carro, R.A. Lorenzo, R. Cela, Anal. Chem. 69 (1997) 221.
[24] J.S. Dos Santos, M. De la Guardia, A. Pastor, Talanta 69 (2006) 534.
[25] Y. Cai, R. Jaffé, R. Jones, Environ. Sci. Technol. 31 (1997) 302.
[26] H. Bin, J. Guibin, Fresenius J. Anal Chem. 365 (1999) 615.
[27] J. Muñoz, M. Gallego, M. Valcárcel, J. Chromatogr. A 1055 (2004) 185.

Talanta 80 (2009) 212–217

Contents lists available at ScienceDirect

Talanta

journal homepage: www.elsevier.com/locate/talanta

Simultaneous extraction and preconcentration of uranium and thorium in aqueous samples by new modified mesoporous silica prior to inductively coupled plasma optical emission spectrometry determination

Seyed Reza Yousefi [a], Seyed Javad Ahmadi [b,*], Farzaneh Shemirani [a], Mohammad Reza Jamali [c], Masoud Salavati-Niasari [d]

[a] School of Chemistry, University College of Science, University of Tehran, Tehran, Iran
[b] Jaber Ibne Hayan Research Laboratories, Nuclear Science and Technology Research Institute, Kargar, Tehran, Iran
[c] Department of Chemistry, Payam Noor University, Behshahr, Iran
[d] Department of Chemistry, Faculty of Science, University of Kashan, Kashan, Iran

ARTICLE INFO

Article history:
Received 26 March 2009
Received in revised form 23 June 2009
Accepted 25 June 2009
Available online 3 July 2009

Keywords:
Preconcentration
Determination of uranium and thorium
Mesoporous silica (MCM-41)
Solid phase extraction (SPE)
Inductively coupled plasma optical emission spectrometry (ICP OES)

ABSTRACT

A new synthesized modified mesoporous silica (MCM-41) using 5-nitro-2-furaldehyde (fural) was applied as an effective sorbent for the solid phase extraction of uranium(VI) and thorium(IV) ions from aqueous solution for the measurement by inductively coupled plasma optical emission spectrometry (ICP OES). The influences of some analytical parameters on the quantitative recoveries of the analyte ions were investigated in batch method. Under optimal conditions, the analyte ions were sorbed by the sorbent at pH 5.5 and then eluted with 1.0 mL of 1.0 mol L^{-1} HNO_3. The preconcentration factor was 100 for a 100 mL sample volume. The limits of detection (LOD) obtained for uranium(VI) and thorium(IV) were 0.3 μg L^{-1}. The maximum sorption capacity of the modified MCM-41 was found to be 47 and 49 mg g^{-1} for uranium(VI) and thorium(IV), respectively. The sorbent exhibited good stability, reusability, high adsorption capacity and fast rate of equilibrium for sorption/desorption of uranium and thorium ions. The applicability of the synthesized sorbent was examined using CRM and real water samples.

© 2009 Elsevier B.V. All rights reserved.

1. Introduction

Uranium and thorium are important elements not only in industrial application but also in energy and environmental problems. In view of the extensive usage of uranium and thorium for various industrial purposes and their toxicity, precise determination of these elements in environmental and biological samples is a challenging task [1–3]. Both of the metal ions are known to cause acute toxicological effects in human and their compounds are potential occupational carcinogens [4]. The WHO, Health Canada and Australian drinking water guidelines fixed the maximum uranium concentration in drinking waters to be less than 9, 20 and 20 μg L^{-1}. Uranium is present in seawater, in concentration of approximately 3 μg L^{-1} [1,5].

The low concentration of these ions in the presence of relatively high concentration of divorce ions makes it difficult to determine directly uranium and thorium ions. So, a separation and preconcentration is mandatory prior to their determination by highly versatile techniques such as inductively coupled plasma optical emission spectrometry (ICP OES).

Many separation and preconcentration techniques for metal ions have been developed such as liquid–liquid extraction [6,7] and solid phase extraction (SPE) [8–18]. Among these methods, SPE was used widely in separation and preconcentration systems. Compared with traditional technologies, SPE offers several advantages such as faster, higher enrichment factor, inexpensive and less polluting to the environment [19,20]. In SPE technique, it is important to select a suitable adsorption material, which can not only enrich the analytes, but also eliminate the matrix interference effectively. Several solid phase sorbents such as organic chelating resin [21–25], modified activated carbon [26], modified silica gel [27,28] and polyurethane foam [29–31] have been employed for the separation and preconcentration of uranium(VI) and thorium(IV).

The rapid development of mesoporous materials such as MCM-41 has attracted much attention in various scientific areas including physics, chemistry and material science. The advantages of large surface area, well-defined pore size, excellent mechanical resistance, non-swelling, excellent chemical stability and easy to modify, make the ordered mesoporous materials an ideal supporting material in SPE. They are synthesized with surfactant used as template.

* Corresponding author. Tel.: +98 21 880003793.
E-mail address: sjahmadi@aeoi.org.ir (S.J. Ahmadi).

0039-9140/$ – see front matter © 2009 Elsevier B.V. All rights reserved.
doi:10.1016/j.talanta.2009.06.058

Table 1
The optimized conditions for ICP OES determination of the target ions.

RF generator power (W)	1200
Plasma gas flow rate (L min^{-1})	15
Auxiliary gas flow rate (L min^{-1})	1.3
Nebulizer pressure (kPa)	200
Torch type	Axial
Pump rate (rpm)	15
U wavelength (nm)	385.958
Th wavelength (nm)	339.203

The structure of the wall of the pores consists of a disordered network of siloxane bridges and free silanol groups that could act as reacting site against appropriate organic chemical species. This fact allows MCM-41 material can be functionalized with different organic groups. By functionalizing the surface of mesoporous materials, selectivity of these sorbents for metal ions can be improved. Modified mesoporous materials have been successfully used for the preconcentration and separation of trace metals recently [32–40].

In this work, mesoporous silica, MCM-41 was chemically modified by (3-aminopropyl) triethoxysilane groups and fural as a new solid phase extractant. Solid phase extraction in batch mode using this new synthesized sorbent was applied for simultaneous preconcentration and determination of uranium and thorium by ICP OES in water samples.

2. Experimental

2.1. Instrumentation

A simultaneous inductively coupled plasma optical emission spectrometry (ICP OES, Varian Vista-MPX, Australia) equipped with a charge-coupled device detector (CCD), a peristaltic pump and a cyclonic spray chamber with a concentric nebulizer was used for simultaneous determination of the target elements. The argon gas with 99.999% purity for ICP OES was purchased from Roham Gas Company (Tehran, Iran). The operation conditions and analytical wavelength were summarized in Table 1. A Metrohm digital pH-meter (model 692, Herisau, Switzerland), equipped with a glass-combination electrode was used. Separation of sorbent was assisted using a centrifuge equipped with a swing out rotor (Universal 320R).

2.2. Reagents and solutions

All chemicals used in this work were of analytical grade of Merck (Darmstadt, Germany) or Aldrich (Chemical Co., Milwauke, WI, USA). All aqueous solutions were prepared in double-distilled deionized water. All organic solvents (HPLC grade) were purchased from Aldrich. Stock standard solutions (1000 mg L^{-1}) of uranium(VI) and thorium(IV) were prepared by dissolving the appropriate amounts of uranyl nitrate hexahydrate and thorium nitrate tetrahydrate, respectively, in deionized water containing 1% HNO_3. The pH adjustment was made with nitric acid (for acidic pH values) or sodium hydroxide (for basic pH values) or standard acetic acid/acetate buffer solution (pH 5.5). The glassware used were kept in 10% nitric acid overnight and subsequently washed several times with double-distilled deionized water before using.

2.3. Preparation of MCM-41 and (3-aminopropyl) triethoxysilane modified MCM-41 (APS-MCM-41)

Mesoporous molecular sieve MCM-41 was prepared according to reported method [41]. Modification of the prepared MCM-41 was performed as followed (Scheme 1A): MCM-41 (2 g) was suspended in dry toluene (70 mL) and then 1 g of (3-aminopropyl) triethoxysilane (APS) was added under dry nitrogen atmosphere and the mixture was refluxed for 12 h. The solid was filtered, washed with dichloromethane and ethanol and dried. It was then soxhlet extracted with a mixture of ethanol and dichloromethane (1:1) to remove the silylating reagent residue and was vacuum dried at 343 K. Characterization of APS-MCM-41 was performed using FT-IR spectroscopy and X-ray diffraction.

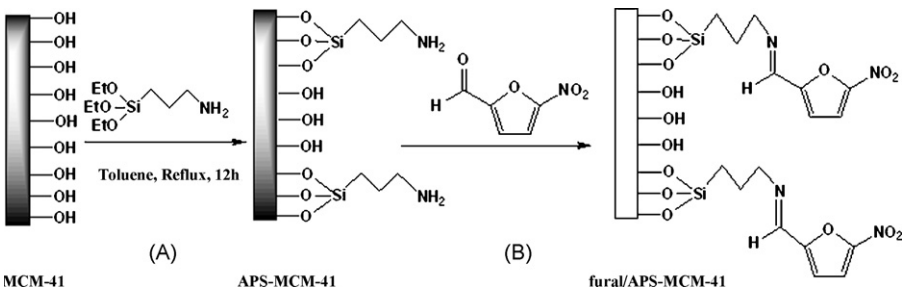
2.4. Preparation of fural/APS-MCM-41

For preparation of 5-nitro-2-furaldehyde (fural) modified MCM-41 (Scheme 1B), APS-MCM-41 (2 g) was suspended in 100 mL of methanol and to this mixture was added excess of 5-nitro-2-furaldehyde (1.35 g, 9.58 mmol) and refluxed for 8 h. The yellow solid was filtered, dried and then soxhlet extracted with ethanol and dried under vacuum at 343 K (Scheme 1). FT-IR spectrum shows that the Schiff-base group was covalently grafted to the silica successfully (characteristic C=N stretching at 1650 cm^{-1}) after the co-condensation process.

The molecular formula of the complexes has been assigned on the basis of the results of their elemental analyses. A preliminary identification of the metal complexes was made on the basis of their IR spectra, which exhibited no bands characteristic of free primary amine, thus supporting the proposed ligand skeleton. The C, H, N analysis results (Found—C: 9.34; H: 0.96; N: 2.79; C/N: 3.35%) showed close similarity to the theoretical values (Anal—C: 53.04; H: 5.01; N: 15.46%). The molecular formula of the ligand has been assigned on the basis of the results of their elemental analyses. A preliminary identification of the ligand was made on the basis of their IR spectra, which exhibited no bands characteristic of free primary amine, thus supporting the proposed skeleton.

2.5. Procedure

Batch method was performed for the extraction and preconcentration of uranium and thorium ions. The general procedure for the extraction of these ions by modified MCM-41 was as follows: an aliquot of 10 mL buffered sample solution (pH 5.5) containing ura-



Scheme 1. (A) Preparation of APS-MCM-41. (B) Preparation of fural/APS-MCM-41.

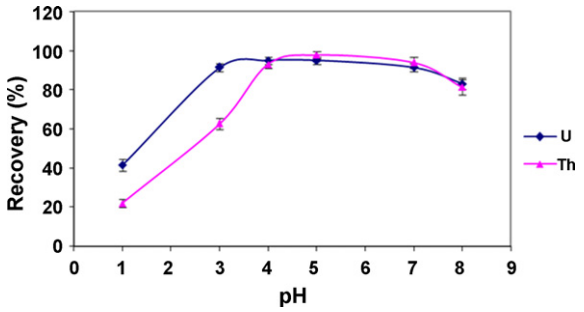


Fig. 1. Effect of pH on the recovery of U(VI) and Th(IV). Amount of metal ions: 1.0 μg, sample volume: 10 mL, amount of sorbent: 20.0 mg, eluent (HNO_3) concentration: 1.0 mol L^{-1}, eluent volume: 1.0 mL.

nium and thorium and 20.0 mg of modified MCM-41 was added to a test tube. The mixture was shaken manually for about 1 min. After that, test tubes were placed in centrifuge and separation of sorbent was achieved by centrifugation for 2 min at 3000 rpm. The aqueous phase was easily decanted by simply inverting the tube. Desorption of target ions was performed by adding 1.0 mL of 1.0 mol L^{-1} HNO_3 solution to sorbent. After shaking manually, the sorbent was separated by centrifugation (2 min at 3000 rpm) and the concentration of uranium and thorium in acidic aqueous phase was determined by ICP OES.

3. Results and discussion

The solid phase extraction of 1.0 μg of uranium and thorium presented in 10 mL of aqueous solution with the modified MCM-41 and non-modified MCM-41 was investigated. The results showed that the modified MCM-41 gave quantitative enrichment while non-modified alone gave a recovery of ~6% and ~9% of uranium and thorium, respectively.

The extraction recovery was defined as the percentage of the total amount of analyte (m), which was extracted into the eluent (acidic aqueous phase):

$$R\% = \left(\frac{m_e}{m_s}\right) \times 100 = \left(\frac{C_e V_e}{C_s V_s}\right) \times 100$$

where V_e, V_s, C_e and C_s are the volume of eluent, volume of sample solution, initial concentration of analyte in aqueous sample and concentration of analyte in eluent, respectively.

3.1. Effect of pH

In order to evaluate the effect of pH on the recovery, the pH was investigated in the range of 1–8 by adding nitric acid or sodium hydroxide solutions. The results of the effects of pH on the recoveries of studied ions were shown in Fig. 1. As can be seen, the pH of maximum recovery for uranium and thorium were found to be 4.0–7.0 and 5.0–7.0, respectively. So, pH 5.5 was chosen as the optimum value for extraction. In all subsequent studies, the pH was adjusted to 5.5 (±0.2) by the addition of acetic acid–acetate buffer solution.

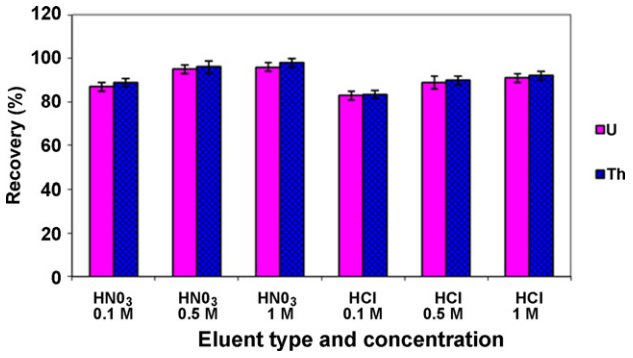


Fig. 2. Effect of eluent type and concentration on the recovery of U(VI) and Th(IV). Amount of metal ions: 1.0 μg, sample volume: 10 mL, pH: 5.5, amount of sorbent: 20.0 mg.

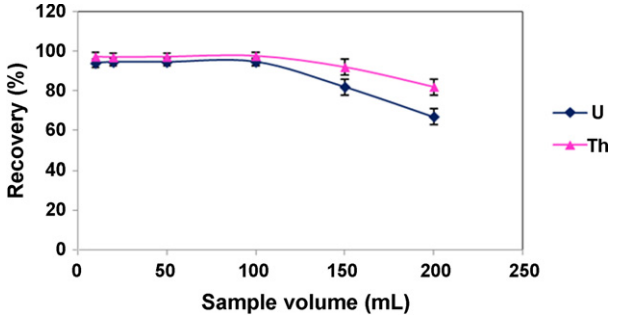


Fig. 3. Effect of sample volume on the recovery of U(VI) and Th(IV). Amount of metal ions: 1.0 μg, pH: 5.5, amount of sorbent: 20.0 mg, eluent (HNO_3) concentration: 1.0 mol L^{-1}, eluent volume: 1.0 mL.

3.2. Choice of eluent: type, concentration and volume

In order to choose a proper eluent, the metal ions were desorbed with different concentrations of nitric acid and hydrochloride acid. The results were shown in Fig. 2. As can be seen, quantitative elution was possible with nitric acid at a concentration of 1.0 mol L^{-1}. So, nitric acid at a concentration of 1.0 mol L^{-1} was selected as eluent for the subsequent experiments.

By using 1.0 mol L^{-1} HNO_3 as eluent, the effect of eluent volume was studied with 1.0–3.0 mL of eluent. The results showed that the recoveries were not influenced noticeably by increasing the eluent volume. So, for obtaining higher preconcentration factor, 1.0 mL of nitric acid (1.0 mol L^{-1}) was selected for the subsequent experiments.

3.3. Effect of sample volume

In order to investigate the effect of sample volume on the sorption of uranium and thorium ions, aliquots of 10, 20, 50, 100, 150 and 200 mL of sample solution containing 1.0 μg of these ions and 20.0 mg of modified MCM-41 were used and the general procedure was applied. It was found that the quantitative recovery of uranium and thorium ions was obtained for sample volume up to 100 mL (Fig. 3).

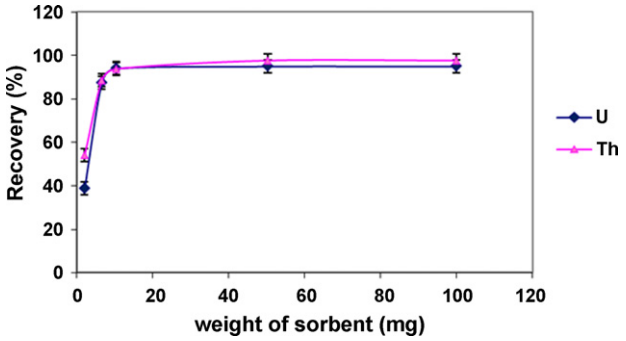


Fig. 4. Effect of sorbent amount on the recovery of U(VI) and Th(IV). Amount of metal ions: 1.0 μg, sample volume: 10 mL, pH: 5.5, eluent (HNO_3) concentration: 1.0 mol L^{-1}, eluent volume: 1.0 mL.

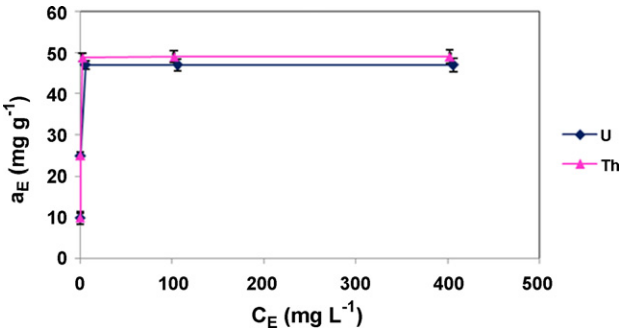


Fig. 5. Adsorption isotherm of U(VI) and Th(IV) ions from aqueous solution on the surface of sorbent at pH 5.5.

Table 2
Analytical characteristics of the method.

Parameters	U(VI)	Th(IV)
Without preconcentration		
Regression equation ($\mu g\,L^{-1}$)	$I = 23.81C + 34.30$	$I = 7.71C + 8.66$
Correlation coefficient (r)	0.9990	0.9991
LOD ($\mu g\,L^{-1}$)[a] ($n = 8$)	22	28
After preconcentration		
Regression equation ($\mu g\,L^{-1}$)	$I = 2301.4C + 62.1$	$I = 725.7C + 25.2$
Correlation coefficient (r)	0.9983	0.9989
Concentration range ($\mu g\,L^{-1}$)	1–1500	1–1500
LOD ($\mu g\,L^{-1}$)[a,b] ($n = 8$)	0.3	0.3
R.S.D. (%) ($n = 8$)[b,c]	2.8	2.6
Recovery (%)	95.0	97.5
Preconcentration factor[b]	100	100

[a] Limit of detection. Calculated as three times the S.D. of the blank signal to slope of calibration curve ratio.
[b] Using sample volume of 100 mL.
[c] Ions concentration: 10 $\mu g\,L^{-1}$.

3.4. Effect of amount of modified MCM-41

The effect of amount of modified MCM-41 on the recovery of uranium(VI) and thorium(IV) ions was examined by varying the amounts of the modified MCM-41 in the range of 2.0–100.0 mg. The results were shown in Fig. 4. As can be seen, the extraction of these ions was quantitative by using 10.0 mg of modified MCM-41. Subsequent extraction experiments were carried out with 20.0 mg of modified MCM-41 in order to achieve high capacity and account for other extractable species.

3.5. Adsorption capacity

For investigation of adsorption capacity of sorbent, aliquots of 10 mL of sample solution with different concentrations of uranium(VI) and thorium(IV) ions were contacted with 20.0 mg of sorbent. The adsorption capacity (a_E, mg g^{-1}) was calculated as

$$a_E = (C_0 - C_E)Vm^{-1}$$

where C_0 and C_E are the initial and equilibrium concentrations (mg L^{-1}) of analyte ions in the solution, respectively. The equilibrium concentration (the remaining uranium(VI) and thorium(IV) in the solution) was determined directly by ICP OES. m is the weight of the sorbent in g and V is the volume of the aqueous solution in L. The mg of uranium(VI) and thorium(IV) sorbed per gram of sorbent, a_E, versus equilibrium concentration as adsorption isotherm is shown in Fig. 5. According to these results, the maximum amount of uranium and thorium ions that can be sorbed by modified MCM-41 was found to be 47 and 49 mg g^{-1}, respectively.

Table 4
Uranium(VI) and thorium(IV) levels of Montana I Soil CRM (NIST-SRM 2710).

	Certified value ($\mu g\,g^{-1}$)	Measured value ($\mu g\,g^{-1}$)[a,b]
U(VI)	25	25.3 ± 2.9
Th(IV)	13	12.6 ± 2.5

[a] Mean of three replicate experiments.
[b] The standard deviation values were calculated at 95% of confidence level.

3.6. Effect of equilibrium time

In order to investigate the effect of shaking time on the extraction recovery, extraction experiments for series of solution containing 1.0 μg U(VI) and Th(IV) were carried out. The results showed that the shaking time from 30 s to 3 min has no effect on the extraction recovery of uranium and thorium. In subsequent experiments, the mixtures have been shaken for at least 30 s.

3.7. The effect of ionic strength and coexisting ions

The effect of ionic strength on the extraction of uranium and thorium was studied in the presence of electrolytes like KNO_3 and NaCl with various concentrations from 0.5% to 5% (w/w), as these salts are the main electrolytes present in nuclear spent fuel waters and environmental samples, respectively [42]. The limit of tolerance defined as the amount of electrolyte ions causing an error of 5% in the recovery of metal ions. Results have shown that there is no interference in the presence of KNO_3 and NaCl up to 5% (w/w).

The effect of commonly occurring ions in water samples has been studied on the recovery of uranium and thorium ions. 10 mL of sample solutions containing 1.0 μg of the target ions and foreign ions in different interference-to-analyte ratios were subjected to the extraction procedure. The obtained results showed that under the conditions specified in the procedure, the major ions in the water samples had no obvious influence on the recovery of the target ions; the alkali and alkaline earth metal ions did not show interferences at the concentration of 10,000 times higher than that

Table 3
Comparison of analytical features of presented method with other SPE methods.

Ion	Sorbent	Detection technique	LOD ($\mu g\,L^{-1}$)	Capacity of sorbent (mg g^{-1})	Ref.
U(VI)–Th(IV)	Modified MCM-41	ICP OES	0.3–0.3	47–49	Present method
U–Th	Actinide-specific extraction resin	ICP-MS	0.015–0.006	–	[11]
U(VI)–Th(IV)	Modified merrifield chloromethylated resin anchored	UV–vis	6.14–4.29	48.7–41.2	[4]
U(VI)–Th(IV)	Modified Duolite XAD761	ICP-MS	0.045–0.063	–	[10]
U(VI)–Th(IV)	Modified Amberlite XAD-2000	UV–vis	10–20	28.8–26.2	[12]
U(VI)	Modified Amberlite XAD-4	UV–vis	2	12.3	[13]
U(VI)	Modified silica gel	UV–vis	4	64.5	[14]
U(VI)	Modified alumina	UV–vis	0.4	3.07	[15]
U(VI)	Modified activated carbon	UV–vis	5	18.35	[19]
U(VI)	Ion imprinted polymer	UV–vis	5	34.05	[18]
Th(IV)	Modified benzophenone	UV–vis	0.5	1.1	[16]
Th(IV)	Ion imprinted polymers	ICP OES	0.51	21.8	[17]

Table 5
Determination of uranium(VI) and thorium(IV) in water samples.

Sample	U(VI)			Th(IV)		
	Added ($\mu g\,L^{-1}$)	Found[a] ($\mu g\,L^{-1}$)	Recovery (%)	Added ($\mu g\,L^{-1}$)	Found[a] ($\mu g\,L^{-1}$)	Recovery (%)
Seawater[b]	–	2.6 (3.6)[c]	–	–	n.d[d]	–
	10.0	11.8 (2.9)	92	10.0	9.4 (2.7)	94
Tashk[e]	–	12.5 (2.8)	–	–	1.3 (4.0)	–
	10.0	21.9 (2.5)	94	10.0	11.0 (2.7)	97
Anarak[f]	–	22.7 (2.4)	–	–	1.3 (3.9)	–
	10.0	32.4 (2.4)	97	10.0	11.4	96

[a] Mean of three replicate experiments.
[b] Caspian seawater, Iran.
[c] Values in the parenthesis are R.S.D.
[d] n.d. = not detected.
[e] Spring water, Bandar Abbas, Iran.
[f] Spring water, Yazd, Iran.

of uranium and thorium concentration, and Cu(II), Ni(II), Cd(II), Pb(II), Zn(II), Co(II), Mn(II), Ce(IV), La(III), Mo(VI), Al(III), Fe(III), Zr(IV), $C_6H_5O_7^{3-}$ (citrate), CN^-, SCN^-, SO_4^{2-}, and CH_3COO^- did not show interference at the concentration 1000 times higher than that of analytes. From the recovery data, it can be seen that the modified MCM-41 shows high selectivity towards the studied analytes when compared to other divorce ions.

3.8. Reusability of modified MCM-41

The modified MCM-41 reusability was examined by shaking 40.0 mg of the sorbent under recommended procedure. After desorption of uranium and thorium ions with 1.0 mol L^{-1} HNO_3, the sorbent was washed with double-distilled water to remove acid. A series of sorption/desorption experiments were performed with the same sorbent and it was found that the modified MCM-41 was able to extract metal ions quantitatively more than 8 cycles.

3.9. Analytical performance

Calibration curves were obtained by preconcentrating 100 mL of sample standard solutions containing 20.0 mg of the sorbent and known amounts of the target ions at optimum conditions of the method. Table 2 shows the analytical characteristics of the method. The preconcentration factor is defined as the ratio of the volumes of the solutions, before and after extraction.

A comparison between the figures of merit of this method with other SPE methods that are used for preconcentration/separation of uranium and thorium were summarized in Table 3. As can be seen, the new synthesized sorbent has high capacity for uranium and thorium. Also, the obtained LODs are better than those obtained by some presented methods and higher than WHO and Health Canada and Australian drinking water guideline levels [5]. Higher LOD levels of the proposed method comparing to the inductively coupled plasma-mass spectrometry (ICP-MS) method are related to the higher sensitivity of the ICP-MS instrument.

3.10. Real sample analysis

The validation of the presented procedure was performed by the analysis of Montana I Soil certified reference material (CRM) (NIST-SRM 2710). 0.2 g of CRM was digested according to Ref. [10] and diluted to 100 mL with double-distilled deionized water. pH of this solution was adjusted to 5.5, then the proposed preconcentration procedure was applied. The certified and observed values for NIST-SRM were given in Table 4. The results found were in good agreement with the certified values of CRM.

In order to demonstrate the applicability of the method, seawater and two different water samples taken from the springs near the uranium mines of Tashk (Bandar Abbas, Iran) and Anarak (Yazd, Iran) were analyzed and the results obtained were summarized in Table 5. Water samples were filtered using a 0.45 μm pore size membrane filter to remove suspended particular solids. Aliquots of 100 mL of each sample were used for extraction of uranium and thorium under optimal conditions of the method. The results of triplicate analysis of each water sample showed that the recovery values were almost quantitative.

4. Conclusion

A new modified mesoporous silica (MCM-41) was synthesized using 5-nitro-2-furaldehyde and applied as an effective sorbent for the solid phase extraction of uranium(VI) and thorium(IV) ions in batch mode. This sorbent exhibited fast adsorption/desorption kinetics and high adsorption capacity. The method has given very low detection limits and good R.S.D. values. Comparative information from some recent studies on solid phase extraction of uranium(VI) and thorium(IV) for the figure of the merits is given in Table 3. The analytical performance of the presented method is comparable with other works. The results of this study clearly showed the potential of this method, which could apply to determination of uranium and thorium in various samples.

Acknowledgements

Support of this investigation by The Research Council of University of Tehran through Grant is gratefully acknowledged.

References

[1] T. Prasada Roa, P. Metilda, J. Mary Gladis, Talanta 68 (2006).
[2] M. Tamada, N. Seko, F. Yoshii, Radiat. Phys. Chem. 71 (2004) 223.
[3] P.G. Barbano, L. Rigali, Anal. Chim. Acta 96 (1978) 199.
[4] V.K. Jain, R.A. Pandya, S.G. Pillai, P.S. Shrivastav, Talanta 70 (2006) 257.
[5] WHO, Guidelines to Drinking Water Quality, Health Criteria and Other Supporting Information, vol. 2, 2nd ed., WHO, Geneva, 1998, p. 283.
[6] V.G. Torgov, M.G. Demidova, A.I. Saprykin, I.V. Nikolaeva, T.V. Us, E.P. Chebykin, J. Anal. Chem. 57 (2002) 303.
[7] O. Fujino, S. Umetani, E. Ueno, K. Shigeta, T. Matsuda, Anal. Chim. Acta 420 (2000) 65.
[8] G. Koulouris, B. Slowikowski, R. Pilvio, T. Bostrom, M. Bichel, Appl. Radiat. Isotopes 53 (2000) 279.
[9] M.E. Khalifa, Sep. Sci. Technol. 33 (1998) 2123.
[10] F. Armagan Aydin, M. Soylak, Talanta 72 (2007) 187.
[11] E.R. Unsworth, J.M. Cook, S.J. Hill, Anal. Chim. Acta 442 (2001) 141.
[12] S. Seyhan, M. Merdivan, N. Demirel, J. Hazard. Mater. 152 (2008) 79.
[13] P. Metilda, K. Sanghamitra, J.M. Gladis, G.R.K. Naidu, T.P. Rao, Talanta 65 (2004) 192.
[14] P.G. Krishna, J.M. Gladis, K.S. Rao, T.P. Rao, G.R.K. Naidu, J. Radioanal. Nucl. Chem. 266 (2005) 251.

[15] F. Shemirani, Sh. Dehghan Abkenar, M.R. Jamali, Bull. Chem. Soc. Jpn. 76 (2003) 545.
[16] C.R. Preetha, J.M. Gladis, T.P. Rao, Talanta 58 (2002) 701.
[17] Q. He, X. Chang, Q. Wu, X. Huang, Z. Hu, Y. Zhai, Anal. Chim. Acta 605 (2007) 192.
[18] P. Metilda, J.M. Gladis, T.P. Rao, Anal. Chim. Acta 512 (2004) 63.
[19] E.M. Thuman, M.S. Mills, Solid Phase Extraction, Principles and Practice, Wiley, New York, 1998.
[20] N.J.K. Simpson (Ed.), Solid Phase Extraction: Principles, Strategies and Applications, Marcel Dekker, New York, 2000.
[21] N. Demirel, M. Merdivan, N. Pirinccioglu, C. Hamanci, Anal. Chim. Acta 485 (2003) 213.
[22] R. Pathak, G.N. Rao, Anal. Chim. Acta 335 (1996) 283.
[23] D. Prabhakaran, M.S. Subramanian, Anal. Bioanal. Chem. 380 (2004) 578.
[24] D. Prabhakaran, M.S. Subramanian, Anal. Lett. 36 (2003) 2277.
[25] R.S. Praveen, P. Metilda, S. Daniel, T.P. Rao, Talanta 67 (2005) 960.
[26] A.M. Starvin, T.P. Rao, Talanta 63 (2004) 225.
[27] F. Barbette, F. Rascalou, H. Chollet, J.L. Babouhot, F. Denat, R. Guilard, Anal. Chim. Acta 502 (2004) 179.
[28] K. Pyrzynska, M. Trojanowicz, Crit. Rev. Anal. Chem. 29 (1999) 313.
[29] S. Katragadda, H.D. Gesser, A. Chow, Talanta 42 (1995) 725.
[30] S. Katragadda, H.D. Gesser, A. Chow, Talanta 44 (1997) 1865.
[31] V.K. Jain, A. Handa, S.S. Sait, P. Shrivastav, Y.K. Agrawal, Anal. Chim. Acta 429 (2001) 237.
[32] M.R. Jamali, Y. Assadi, F. Shemirani, M. Salavati-Niasari, Talanta 71 (2007) 1524.
[33] D. Peĭrez-Quintanilla, I. Hierro, M. Fajardo, I. Sierra, J. Mater. Chem. 16 (2006) 1757.
[34] C.Z. Huang, B. Hu, Z.C. Jiang, Spectrochim. Acta Part B 62 (2007) 454.
[35] M.R. Jamali, Y. Assadi, F. Shemirani, M.R. Milani Hosseini, R. Rahnama Kozani, M. Masteri-Farahani, M. Salavati-Niasari, Anal. Chim. Acta 579 (2006) 68.
[36] B.J.S. Johnson, A. Stein, Inorg. Chem. 40 (2001) 801.
[37] M.R. Ganjali, L. Hajhagha Babaei, A.R. Badiei, K. Saberian Ghodsi, S.M.R. Behbahani, M. Mohammadi Ziarani, M. Salavati-Niasari, Quim. Nova 29 (2006) 440.
[38] M.R. Ganjali, A. Daftari, L. Hajiagha-Babaei, Water, Air Soil Pollut. 173 (2006) 71.
[39] M.R. Ganjali, L. Hajiagha Babaei, L.H. Badaei, G.M. Ziarani, A. Tarlani, Anal. Sci. 20 (2004) 725.
[40] M.R. Ganjali, L. Hajiagha Babaei, P. Norouzi, M.R. Pourjavid, A. Badiei, K. Saberian, M. Ghannadi Maragheh, M. Salavari Niasari, G. Mohammadi Ziarani, Anal. Lett. 38 (2005) 1813.
[41] Q. Cai, W.Y. Lin, F.S. Xiao, W.Q. Pang, X.H. Chen, B.S. Zou, J. Micropor. Mesopor. Mater. 32 (1999) 1.
[42] Ch. Siva Kesava Raju, M.S. Subramanian, J. Hazard. Mater. 145 (2007) 315.

Talanta 80 (2009) 218–223

Contents lists available at ScienceDirect

Talanta

journal homepage: www.elsevier.com/locate/talanta

Monitoring microbial populations of sulfate-reducing bacteria using an impedimetric immunosensor based on agglutination assay

Yi Wan[a,b], Dun Zhang[a,*], Baorong Hou[a]

[a] Key Lab of Corrosion Science, Shandong Province, Institute of Oceanology, Chinese Academy of Sciences, 7 Nanhai Road, Qingdao 266071, China
[b] Graduate School of the Chinese Academy of Sciences, 19 (Jia) Yuquan Road, Beijing 100039, China

ARTICLE INFO

Article history:
Received 3 April 2009
Received in revised form 25 June 2009
Accepted 25 June 2009
Available online 3 July 2009

Keywords:
Microbial population
Sulfate-reducing bacteria
Impedimetric immunosensor
Agglutination assay
Lectin

ABSTRACT

An impedimetric immunosensor was fabricated for rapid and non-labeled detection of sulfate-reducing bacteria, *Desulforibrio caledoiensis* (SRB) by immobilizing lectin-Concanavalin A using an agglutination assay. The immobilization of lectin was conducted using amine coupling on the surface of a gold (Au) electrode assembled with 11-Mercaptoundecanoic acid. Electrochemical impedance spectroscopy (EIS) was used to verify the stepwise assembly of the sensor system. The work conditions of the impedimetric immunosensor, such as pH of the buffer solutions and the incubation time of lectin, were optimized. Faradic impedance spectra for charge transfer for the redox probe $Fe(CN)_6^{3-/4-}$ were measured to determine SRB concentrations. The diameter of the Nyquist diagram that is equal to the charge-transfer resistance (R_{ct}) increased with increasing SRB concentration. A linear relationship between R_{ct} and SRB concentration was obtained in SRB concentration range of 1.8 to 1.8×10^7 cfu/ml. The variation of the SRB population during the growth process was also monitored using the impedimetric immunosensor. This approach has great potential for simple, low-cost, and time-saving monitoring of microbial populations.
© 2009 Elsevier B.V. All rights reserved.

1. Introduction

Sulfate-reducing bacteria (SRB) are anaerobic microorganisms that use sulfate as a terminal electron acceptor, resulting in the production of sulfide [1]. Sulfide is highly corrosive and toxic, thus it can be a serious problem for industries, economies, and ecological systems, such as the offshore oil industry. Therefore, a rapid and easy method for monitoring SRB populations is essential for the control of microbiological-induced corrosion and environmental contamination.

In general, conventional methods for monitoring microbial SRB populations, such as the most probable number (MPN) method, involve a pre-enrichment step or a selective enrichment step followed by a biochemical test, and the sophisticated series of assays required can take up 15 days to complete [2,3]. A variety of protocols have been presented for monitoring microbial SRB populations, including the MPN-improved method [4], the enzyme-linked immunosorbent assay (ELISA) [5], and pertinent molecular techniques such as polymerase chain reaction (PCR) [6] or fluorescence in situ hybridization (FISH) [7]. Although promising, these techniques are still the development phase, and several problems occur when they are used in situ and in real time. For example, because of the longer exponential growth phase of SRB compared to other microorganisms, it may take several days for these bacteria to produce an adequate amount of metabolic product; this makes the MPN-improved method very time-consuming and of little practical use when real-time monitoring is required. Although bovine serum albumin has been used in the ELISA method in an attempt to block non-specific binding sites, it is far from completely effective. In addition, the phylogenetic tree based on nearly complete 16S rRNA sequences reveals a total of 33 members of the phylum and domains of SRB [8].

Various sensitive, reliable, and more rapid methods have been reported for determination and monitoring of microorganisms, including surface plasma resonance (SPR) [9,10], flow cytometry [11], epifluorescence microscopy [12], quartz crystal microbalance (QCM) [13,14], mass spectrometry [15,16], and insulator-based dielectrophoresis [17]. Other methods use gold- or silver-nanoparticles [18,19] or quantum dots [20,21] as detecting mediators, and still others selectively detect cellular compounds such as ATP [22], nucleic acids [23], and whole cells with specific antigens [24,25] or typical structures of the carbohydrate domain [26]. For example, lectin is a structurally diverse protein that can selectively and reversibly integrate with carbohydrate structure domains in the cell membrane of microorganisms, and this process can be recognized by an agglutination test [27]. Agglutination has been used previously as a method for identifying bacteria because the clumping reaction occurs quickly and is easy to produce. Wang [28] and Danielsson [29] reported that a carbohydrate non-labeled

* Corresponding author. Tel.: +86 532 82898960; fax: +86 532 82898960.
E-mail address: zhangdun@ms.qdio.ac.cn (D. Zhang).

0039-9140/$ – see front matter © 2009 Elsevier B.V. All rights reserved.
doi:10.1016/j.talanta.2009.06.057

mass sensor in combination with lectin-bacterial antigen recognition can be used to detect *Escherichia coli* using QCM.

Recently, a very promising protocol that uses electrochemical impedance spectroscopy (EIS) was reported; this method involves immobilizing antibodies that are specific to the target microorganisms on the surface of electrodes to detect minute microorganisms. In fact, EIS assays were developed initially for detection of bacteria based on impedance changes due to the release of ionic metabolites from live cells [30]. Currently, the impedance system equipped with a redox probe is regarded as an effective and efficient method for characterizing changes in the interfacial properties of a modified electrode. Initially, impedance biosensor chips in the presence of $Fe(CN)_6^{3-/4-}$ were fabricated for the detection of *E. coli* O157:H7 using antibody-modified indium tin oxide electrode chips [31]. EIS has been used to study bacteria, but until now it has not been used to monitor the growth process of microbial population.

In this study, we fabricated an impedimetric immunosensor based on the self-assembly technique to detect SRB and to monitor microbial populations. To build this biosensor, we used a self-assembled monolayer (SAM) on a gold (Au) electrode surface. Subsequently, lectin immobilized on the SAM-modified Au electrode was used to selectively recognize elements to specifically bind to SRB.

2. Materials and methods

2.1. Chemicals

11-Mercaptoundercanoic acid (MPA), *N*-hydroxysuccinimide (NHS), 1-ethyl-3[3-dimethylaminopropyl] carbodiimide hydrochloride (EDC), and a freeze-dried lectin: Concanavalin A (ConA) were purchased from Sigma. For the ConA solution, 0.1 mg/ml ConA was dissolved in 10 mM phosphate buffer solution (PBS, pH 7.4) containing 1 mM Ca^{2+} and 1 mM Mn^{2+}. The PBS was prepared from analytical grade K_2HPO_4 and KH_2PO_4 (Sinopharm Chemical Reagent Co., Ltd.), and water purified by an ultrapure water system (Mili-Q, 18.2 MΩ). Potassium ferricyanide $[K_3Fe(CN)_6]$ and potassium ferrocyanide $[K_4Fe(CN)_6]$ were also supplied by Sinopharm Chemical Reagent Co., Ltd., as were the analytical grade $MgSO_4$, NH_4Cl, Na_2SO_4, $CaCl_2$, Na_2HPO_4, NaOH, sodium lactate, and yeast extract used to prepare the modified Postgate's medium. The Postgate's medium was filtered with a 0.2 μm pore size filter.

2.2. Culture of SRB

The seed bacteria were isolated from marine mud collected from the Bohai Sea, China. The pure SRB culture was grown in modified Postgate's medium at 30 °C for 4 days [32]. Before measurements, SRB samples were stored in the refrigerator at 4 °C for slow growth. The culture was serially diluted with physiological saline solution, and viable cell number was determined by the MPN method according to the American Society of Testing materials standard D4412-84.

2.3. Fabrication of impedance biosensor

Before use, an Au electrode (CH Instruments, Inc.) was polished with silicon carbide paper and then alumina powder, cleaned ultrasonically in absolute ethanol, rinsed with Mili-Q water, and dried in a flow of air. The electrode was then electrochemically pretreated by cycling the potential range from −0.2 to 1.6 V in a 0.05 M H_2SO_4 solution at a scan rate of 10 V s^{-1} until a steady cyclic voltammogram was obtained [33].

The MPA-modified Au electrode (MPA/Au electrode) was fabricated by immersing the freshly polished Au electrode into an ethanol solution containing 10 mM MPA solution for 2 h [34]. The electrode then was rinsed with ethanol to remove the physically

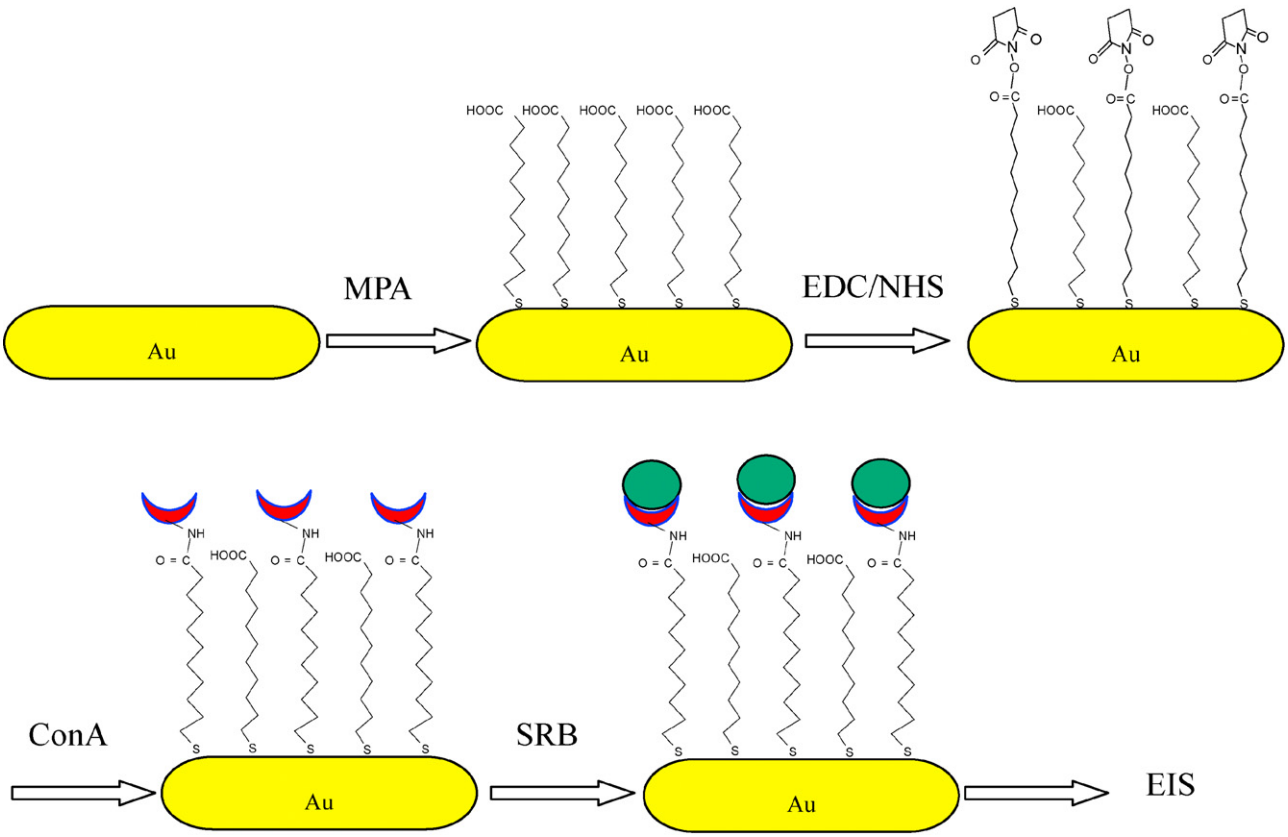


Fig. 1. Scheme showing the binding reactions involved in this study: MPA assembly, EDC/NHS activation, ConA immobilization, and SRB detection.

adsorbed MPA prior to use in the following procedure. As shown in Fig. 1, the ConA/MPA-modified biosensor was prepared by soaking the MPA/Au electrode in an aqueous solution of 40 mM EDC and 10 mM NHS to activate the carboxylic groups onto the surface of the NHS/MPA/Au electrode. Next, ConA was introduced onto the NHS/MPA/Au electrode by dropping 10 μl of 0.1 mg/ml ConA in PBS onto the electrode and allowing it to incubate at 4 °C for at least 2 h in a humidified glass chamber. After the immobilization of ConA, the modified ConA/MPA/Au electrode was rinsed with PBS solution (pH 7.4) to remove the excess non-chemisorbed lectin.

2.4. Electrochemical measurements

All experiments were conducted at room temperature. Electrochemical measurements were made using a CHI760C (CH Instruments, Inc.) conventional three electrode system that included a platinum wire and an Ag/AgCl, 3 M KCl wire as the counter electrode and a reference electrode, respectively. The functionalized Au electrode was used as the working electrode.

EIS was used to characterize the stepwise modification process of the functionalized electrodes. After preparing the multilayer biosensor surface, SRB detection was performed by EIS. The ConA/MPA/Au electrode was immersed in culture containing SRB in a series of concentrations ranging from 1.8 to 1.8×10^7 cfu/ml; incubation time was 2 h. The functionalized work electrode (SRB/ConA/MPA/Au electrode) was then cleaned by PBS, and the Faradic impedance spectra were measured at the open circuit potential.

EIS was conducted in 10 ml PBS in the presence of the redox probe with 5 mM $K_3Fe(CN)_6$ and 5 mM $K_4Fe(CN)_6$ (1:1) at the open circuit potential vs. Ag/AgCl, 3 M KCl and an alternating potential with amplitude of 10 mV at the frequency range from 0.1 Hz to 100 kHz. The experiments were repeated three times. The reproducibility of the impedance responses is represented by the error bar, which was obtained from the standard deviation for the three replicates.

2.5. Monitoring microbial population

The microbial SRB population during the growth process was monitored using the impedimetric immunosensor. The microorganisms were taken out of the incubator to detect impedance shifts on each day from exponential phase to stationary phase (from the 1st to the 6th day). Test samples were incubated at 30 °C for all experiments. The MPN method was used in a control experiment to monitor the variation of the microbial population.

3. Results and discussion

3.1. Measurement principle

EIS has been applied in biosensor studies as a sensitive and reliable tool to measure changes in biological/chemical molecules at electrode interfaces. Faradic impedance spectra often are simulated using the modified Randles circuit (Fig. 2) and used as a model for a reaction controlled by electron transfer and diffusion processes. In the modified Randles circuit, the ohmic resistance of an electrolyte solution between the working electrode and the counter electrode is represented by R_S; C_{dl} is the double layer capacitance; and R_{ct} is the charge-transfer resistance of the $Fe(CN)_6^{3-/4-}$ redox couple. The Warburg impedance (Z_W) with a semi-infinite diffusion mechanism in the measurement system arises from the diffusion resistance of the $Fe(CN)_6^{3-/4-}$ redox probe between the bulk solution and the interface of the modified work electrode. The R_{ct} value can be directly obtained from the Nyquist plots based on the intercept of the semicircle with the real axis, which is the most sensitive and straightforward parameter used to characterize the recognition events that occur on the surface of the work electrode.

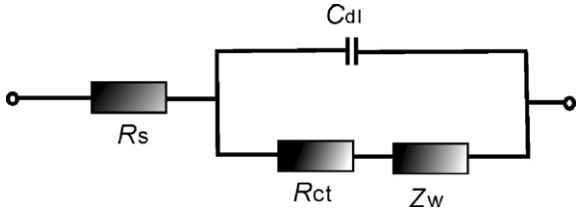


Fig. 2. Equivalent circuit diagram used to fit the experimental impedance spectra.

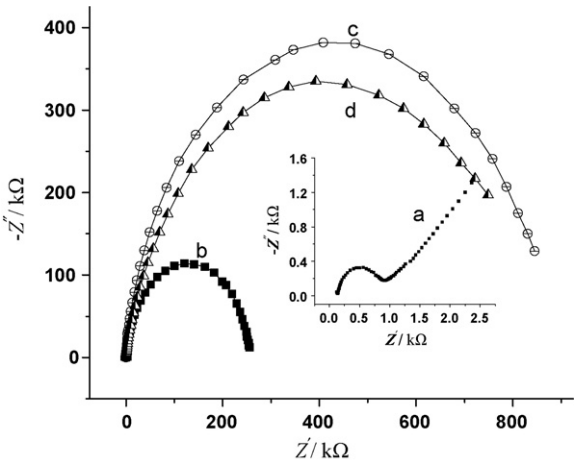


Fig. 3. Nyquist diagram obtained in pH 7.4 PBS containing 5 mM $[Fe(CN)_6]^{3-/4-}$ (1:1 mixture) on bare Au (a), MPA/Au (b), NHS/MPA/Au (c), and ConA/MPA/Au (d) electrodes.

3.2. Biosensor fabrication

Fig. 3 shows the Faradic impedance spectra for the redox of $Fe(CN)_6^{3-/4-}$ measured in the stepwise modification processes of the Au electrode. The diameter of the semicircle represents the magnitude of R_{ct} on the electrode surface. The impedance response on the bare Au electrode reveals a very small domain, implying a low R_{ct} of the redox probe (curve a, 0.778 kΩ). After the electrode was assembled with MPA, the R_{ct} distinctly increased (curve b, 254.7 kΩ) because the SAM retarded the charge-transfer process. Subsequently, NHS/EDC was covalently immobilized on the MPA/Au electrode and a remarkable rise in the R_{ct} was observed (curve c, 834.5 kΩ) because of the spatial hindrance effect of NHS. Additionally, the impedance response on the ConA/MPA/Au electrode (curve d, 633.0 kΩ) was slightly reduced compared to curve c because ConA was combined on the SAM because of the EDC/NHS-mediated amidation/coupling and because the NHS esters completely hydrolyzed within 4–5 h.

3.3. Optimization of the assay conditions

The influence of pH on the response of the impedance biosensor was investigated using 0.1 M PBS containing 5 mM $Fe(CN)_6^{3-/4-}$ to optimize the assay conditions. As seen in Fig. 4, the R_{ct} response increased when pH increased from 6.0 to 7.4 but then decreased at pH > 7.4. We also studied the variation of the R_{ct} response on the bare Au electrode under the same solution conditions (data not shown). The R_{ct} responses on the bare Au electrode barely changed; this finding indicates that changes in pH do not affect the R_{ct} on the bare Au electrode, but they do influence the response of the

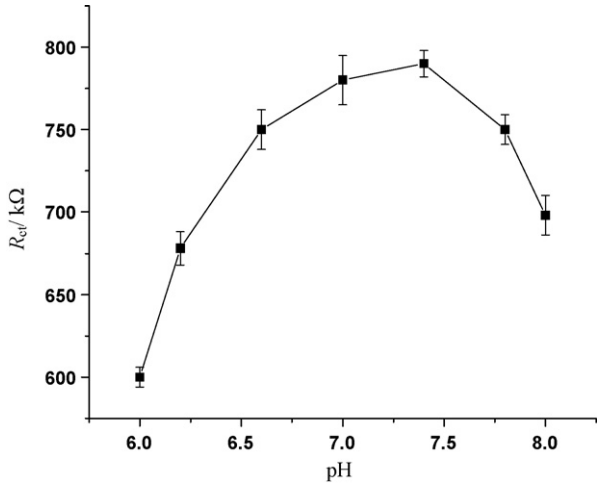


Fig. 4. A plot of R_{ct} response on SRB/ConA/MPA/Au electrodes in PBS with different pH values. Error bars represent one standard deviation of three parallel replicates.

biosensor system for detecting SRB. Therefore, the optimized pH level of 7.4 was used in our study for the detection of SRB.

The incubation time of the MPA-activated electrode in the ConA solution is critically important for the agglutination assay of SRB. Fig. 5 illustrates the dependence of the incubation time and R_{ct} response when a fixed SRB concentration (10^2 cfu/ml) was maintained. As the incubation time increased, the R_{ct} response was rapid and almost linear at first, but then it leveled off until a stable platform (ca. 800 kΩ) was reached after 2 h. Therefore, we used an incubation time of 2 h for the subsequent experiments.

The agglutination assay time between ConA and SRB to take place also play a key role in the detection of SRB. When the agglutination reaction time was less than 1.5 h, the R_{ct} response increased with increasing reaction time. When the reaction time was more than 3 h, the R_{ct} response decreased with increasing reaction time due that the complex of ConA and SRB cell became unstable at room temperature. Therefore, 2 h was selected as the optimal agglutination assay time in this study.

3.4. Specificity of the impedimetric immunosensor

The specificity of biosensor was investigated in relation to other bacteria such as Gram-negative bacteria, *V. anguillarum* as marine

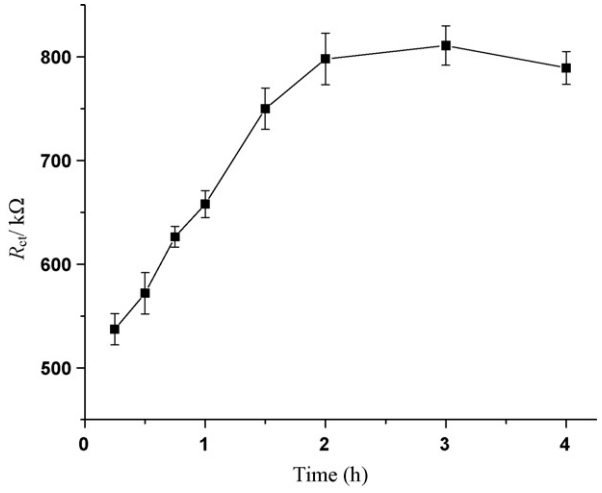


Fig. 5. Effect of the incubation time in ConA solution containing 1 mM Mn^{2+} and 1 mM Ca^{2+} on the R_{ct} response. Error bars represent one standard deviation of three parallel replicates.

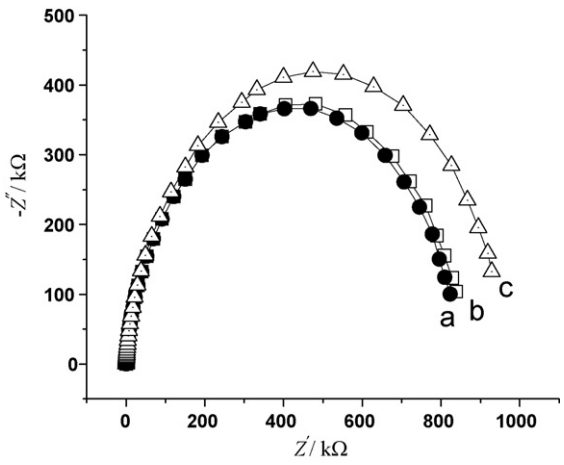


Fig. 6. Impedimetric spectra obtained in pH 7.4 PBS containing 5 mM $[Fe(CN)_6]^{3-/4-}$ (1:1 mixture) on ConA/MPA/Au electrodes before (a) and after their incubation with *V. anguillarum* (b) and SRB (c) culture sample with a fixed concentration of 1.8×10^2 cfu/ml for 2 h.

pathogenic bacteria. Fig. 6 are impedimetric spectra obtained in pH 7.4 PBS containing 5 mM $[Fe(CN)_6]^{3-/4-}$ (1:1 mixture) on ConA/MPA/Au electrodes before (curve a) and after their incubation with *V. anguillarum* (curve b) and SRB (curve c) culture sample with a fixed concentration of 1.8×10^2 cfu/ml for 2 h. It is clearly that the R_{ct} response changes are different between the ConA/MPA/Au electrode incubated with SRB and *V. anguillarum*. The R_{ct} response change for ConA-modified electrode after and before immersing in *V. anguillarum* is 14 kΩ, but the R_{ct} response change for the ConA-modified electrode after and before immersing in SRB increases distinctly to 161 kΩ. Different species bacteria with same concentration induce the different change of R_{ct} value, which lead to the variation of the slope of the R_{ct} value versus bacterial concentration curve. The special slope of the R_{ct} value versus bacterial concentration curve is shown in Fig. 8.

3.5. Detection of SRB

Fig. 7 shows the Faradic impedance spectra obtained on the SRB/ConA/MPA/Au electrodes prepared with different SRB concentrations. The diameter of the Nyquist plots increased regularly with the increase of the SRB concentration, indicating that SRB were adsorbed on the surface of the ConA/MPA/Au electrode to produce

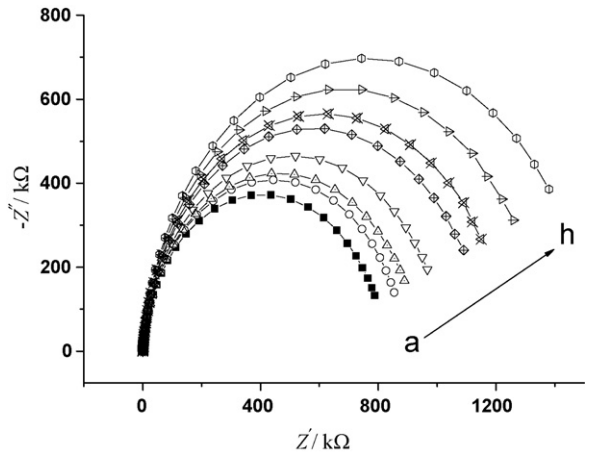


Fig. 7. Faradic impedance spectra obtained on SRB/ConA/MPA/Au electrodes. Curves a–h represent SRB concentrations of 1.8×10^0, 1.8×10^1, 1.8×10^2, 1.8×10^3, 1.8×10^4, 1.8×10^5, 1.8×10^6, and 1.8×10^7 cfu/ml, respectively.

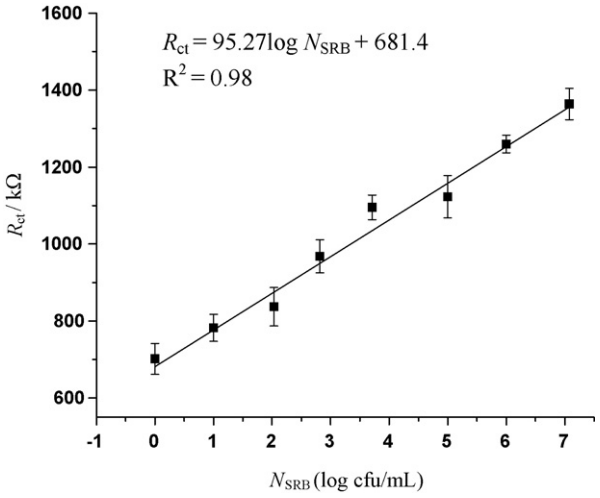


Fig. 8. Concentration of SRB (log cfu/ml) versus the R_{ct} values obtained from Fig. 7. Error bars represent one standard deviation of three parallel replicates.

a packed film that showed electron transfer for the redox probe. Other research groups reported similar results for the detection of *Saccharomyces cerevisiae* by directly binding yeast cells on a gold surface modified with an alkanethiolate SAM [35]. Geng et al. also prepared an electrochemical impedance immunosensor for determination of *E. coli* by immobilizing antibodies on an MPA-modified electrode [36].

Fig. 8 displays the R_{ct} values calculated from Figs. 2 and 7 on SRB/ConA/MPA/Au electrodes prepared with a series of SRB concentrations. A linear relationship between R_{ct} values and the logarithm of the SRB concentrations was obtained for the SRB concentration range of 1.8 to 1.8×10^7 cfu/ml, with a slope of 95.27 and a correlation coefficient of 0.98. These results illustrate that the fabricated Faradic impedance biosensor has a wider detection range compared to the aforementioned immunosensors [35,36]. However, the variation of the slopes obtained using different immobilization methods for detection of bacteria using impedance measurements implies that the different chemical/biological anchors for bacterial cells have very different affinities. For example, the affinity constant of the peanut protein Arah h 1 and its antibody recently was investigated based on a Langmuir adsorption isotherm using an impedance biosensor [37]. The slope of the standard curve for bacteria detection was 16.0 for mercaptopropionic acid directly binding the yeast cells [35] and 1288.9 for the antibody immobilizing *E. coli* [36]. With greater affinity, the slope becomes steeper. In other words, the specific affinity of lectin for the bacterial cells is less than that of its antibody.

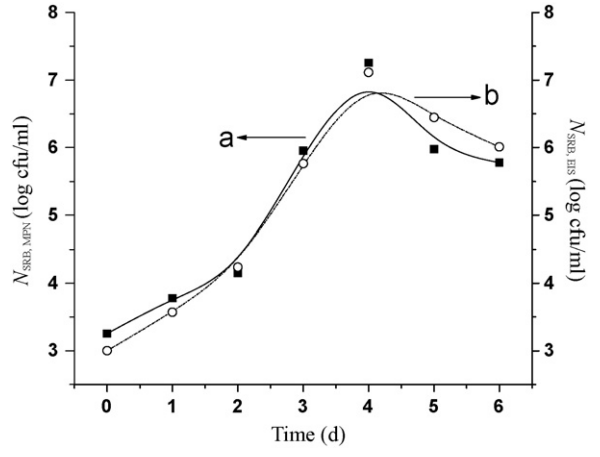


Fig. 9. The variation of the SRB population monitored by the MPN method (a) and by the impedance immunosensor (b).

3.6. Monitoring microbial populations

The impedimetric immunosensor designed in this study was used to monitor the variation in a microbial SRB population that was isolated from marine mud. As shown in Fig. 9(a), the growth curve had two phases: exponential and stationary. In the exponential phase, the microbial population increased rapidly from 2.3×10^3 to 1.3×10^7 cfu/ml in 0–4 days; then it remained constant in the stationary phase. This trend displays a typical bacterial growth process. In addition, the MPN method was used as a control experiment to monitor the growth of the SRB population; the obtained growth curve was similar to that measured with the impedance immunosensor.

4. Conclusion

We have described a simple and reliable method suitable for determination and monitoring of microbial SRB populations; this method uses ConA on a carboxylic-terminated alkanethiolate-modified Au electrode and Faradic impedance measurements. A linear relationship between R_{ct} values and the logarithm of the SRB concentrations was observed in the SRB concentration range of 1.8 to 1.8×10^7 cfu/ml. Our lectin-based impedance biosensor can perform direct, sensitive, and rapid label-less monitoring of the SRB bacterial populations. This technique is a promising alternative to the traditional MPN method for monitoring microbial populations.

Acknowledgements

Y.W. thanks Dr. Zhaolan Mo for the contribution of *Vibrio anguillarum*. This work was supported by the National Natural Science Foundation of China (Grant No. 40876041), Science & Technology Basic Research Program of Qingdao (Grant No. 09-1-3-16-jch), and the National Key Technology R&D Program of China (Grant No. 2007BAB27B01).

References

[1] M.W. Beijerinck, Zentralbl. Bakteriol. Abt. 2 (1895) 49–59.
[2] R.L. Starkey, J. Am. Water Works Ass. 40 (1948) 1291–1298.
[3] Y. ABD-EL-Malek, S.G. Rizk, Nature 182 (1958) 538.
[4] F. Vester, K. Ingvorsen, Appl. Environ. Microbiol. 64 (1998) 1700–1707.
[5] C. Gaylarde, P. Cook, Int. Biodeterior. 26 (1990) 337–345.
[6] K.L. Cook, T.R. Whitehead, C. Spence, M.A. Cotta, Anaerobe 14 (2008) 172–180.
[7] S. Lücker, D. Steger, K.U. Kjeldsen, B.J. MacGregor, M. Wagner, A. Loy, J. Microbiol. Methods 69 (2007) 523–528.
[8] G. Muyzer, A.J.M. Stams, Nat. Rev. Microbiol. 6 (2008) 441–454.
[9] S.D. Mazumdar, M. Hartmann, P. Kämpfer, M. Keusgen, Biosens. Bioelectron. 22 (2007) 2040–2046.
[10] M. Piliarik, L. Párová, J. Homola, Biosens. Bioelectron. 24 (2009) 1399–1404.
[11] O. Karo, A. Wahl, S.B. Nicol, J. Brachert, B. Lambrecht, H.P. Spengler, F. Nauwelaers, M. Schmidt, C.K. Schneider, T.H. Muller, T. Montag, Clin. Chem. Lab. Med. 46 (2008) 947–953.
[12] J.D. Brewster, A.G. Gehring, R.S. Mazenko, L.J. Van Houten, C.J. Crawford, Anal. Chem. 68 (1996) 4153–4159.
[13] Y.S. Fung, Y.Y. Wong, Anal. Chem. 73 (2001) 5302–5309.
[14] H.-C. Han, Y.-R. Chang, W.-L. Hsu, C.-Y. Chen, Biosens. Bioelectron. (2008), doi:10.1016/j.bios.2008.07.033.
[15] K.-C. Ho, P. -J, Y.-S. Tsai, Y.-C. Lin, Chen, Anal. Chem. 76 (2004) 7162–7168.
[16] Y.-S. Lin, P.-J. Tsai, M.-F. Weng, Y.-C. Chen, Anal. Chem. 77 (2005) 1753–1760.
[17] W.B. Betts, Trends Food Sci. Technol. 6 (1995) 51–58.
[18] R.L. Phillips, O.R. Miranda, C.-C. You, V.M. Rotello, U.H.F. Bunz, Angew. Chem. Int. Ed. 47 (2008) 2590–2594.
[19] H. Sun, T.S. Choy, D.R. Zhu, W.C. Yam, Y.S. Fung, Biosens. Bioelectron. 24 (2009) 1405–1410.
[20] X. Xue, J. Pan, H. Xie, J. Wang, S. Zhang, Talanta 77 (2009) 1808–1813.
[21] Y. Liu, R. Brandon, M. Cate, Anal. Chem. 79 (2007) 8796–8802.
[22] Y. Cheng, Y. Liu, J. Huang, K. Li, W. Zhang, Y. Xian, L. Jin, Talanta 77 (2009) 1332–1336.

[23] Y.J. Liu, D.J. Yao, H.Y. Chang, C.M. Liu, C. Chen, Biosens. Bioelectron. 24 (2008) 558–565.
[24] Y.-H. Lin, S.-H. Chen, Y.-C. Chuang, Y.-C. Lu, T.Y. Shen, C.A. Chang, C.-S. Lin, Biosens. Bioelectron. 23 (2008) 1832–1837.
[25] M.H.F. Meyer, M. Stehr, S. Bhuju, H.-J. Krause, M. Hartmann, P. Miethe, M. Singh, M. Keusgen, J. Microbiol. Methods 68 (2007) 218–224.
[26] C.-C. Huang, C.-T. Chen, Y.-C. Shiang, Z.-H. Lin, H.-T. Chang, Anal. Chem. 81 (2009) 875–882.
[27] H. Lis, N. Sharon, Chem. Rev. 98 (1998) 637–674.
[28] Z. Shen, M. Huang, C. Xiao, Y. Zhang, X. Zeng, P.G. Wang, Anal. Chem. 79 (2007) 2312–2319.
[29] G. Safina, M. Van Lier, B. Danielsson, Talanta 77 (2008) 468–472.
[30] J.C. Owicki, J.W. Parce, Biosens. Bioelectron. 7 (1992) 255–272.
[31] C. Ruan, L. Yang, Y. Li, Anal. Chem. 74 (2002) 4814–4820.
[32] F. Kuang, J. Wang, L. Yan, D. Zhang, Electrochim. Acta 52 (2007) 6084–6088.
[33] H. Angerstein-Kozlowska, B.E. Conway, A. Hamelin, L. Stoicoviciu, Electrochim. Acta 31 (1986) 1051–1061.
[34] S.-J. Ding, B.-W. Chang, C.-C. Wu, M.-F. Lai, H.-C. Chang, Anal. Chim. Acta 554 (2005) 43–51.
[35] H. Chen, C.K. Heng, P.D. Puiu, X.D. Zhou, A.C. Lee, T.M. Lim, S.N. Tan, Anal. Chim. Acta 554 (2005) 52–59.
[36] P. Geng, X. Zhang, W. Meng, Q. Wang, W. Zhang, L. Jin, Z. Feng, Z. Wu, Electrochim. Acta 53 (2008) 4663–4668.
[37] Y. Huang, M.C. Bell, I.I. Suni, Anal. Chem. 80 (2008) 9157–9161.

Talanta 80 (2009) 224–230

Contents lists available at ScienceDirect

Talanta

journal homepage: www.elsevier.com/locate/talanta

Direct electrochemistry and electrocatalysis of myoglobin based on silica-coated gold nanorods/room temperature ionic liquid/silica sol–gel composite film

Wen-Lei Zhu, Yang Zhou, Jian-Rong Zhang*

Key Laboratory of Analytical Chemistry for Life Science (Ministry of Education of China), School of Chemistry and Chemical Engineering, Nanjing University, Hankou Road, Nanjing 210093, PR China

ARTICLE INFO

Article history:
Received 4 April 2009
Received in revised form 23 June 2009
Accepted 25 June 2009
Available online 3 July 2009

Keywords:
Silica-coated gold nanorods
Myoglobin
Room temperature ionic liquid
Biosensors

ABSTRACT

A novel biosensor based on the silica-coated gold nanorods (GNRs@SiO_2) and hydrophilic room temperature ionic liquid (RTIL) 1-butyl-3-methylimidazolium tetrafluroborate ([bmim][BF_4]) was fabricated for the determination of hydrogen peroxide (H_2O_2) and nitrite. GNRs@SiO_2 can not only act as a binder to hinder [bmim][BF_4] (RTIL) leaking from the electrode surface, but also provide a favorable microenvironment for direct electrochemistry of myoglobin (Mb). A pair of well-defined and quasi-reversible redox peaks of Mb was obtained at the GNRs@SiO_2–Mb/RTIL–sol–gel composite film modified GCE (GNRs@SiO_2–Mb/RTIL–sol–gel/GCE) through direct electron transfer between Mb and the underlying electrode. This biosensor showed an excellent electrocatalytic activity towards hydrogen peroxide and nitrite. The linear range for the determination of H_2O_2 was from 0.2 to 180 μM with a detection limit of 0.12 μM based on the signal-to-noise ratio of 3. In addition, the biosensor also exhibited high selectivity, good reproducibility, and long-term stability. Therefore, this kind of composite film can provide an ideal matrix for protein immobilization and biosensor fabrication.

© 2009 Elsevier B.V. All rights reserved.

1. Introduction

The direct electron transfer between redox proteins or enzymes and underlying electrodes is of great significance in the construction of third-generation biosensors. Myoglobin (Mb) is a small heme protein found in muscle cells. Mb functions physiologically in the storage of oxygen and in the enhancement of the rate of oxygen diffusion, and has catalytic activity for H_2O_2 similar to horseradish peroxidase (HRP) [1]. It is an ideal model molecule for the electron transfer study of heme proteins and for biosensing and biocatalysis. However, Mb does not easily undergo facile redox reactions at electrode surfaces because of its electroactive centers embedded deeply in the protein structure. Hence, various materials such as surfactants [2], polymers [3] and nanoparticles [4–6] were exploited to modify the electrodes. Their properties of hydrophilicity, nontoxicity, excellent film-forming ability and remarkable biocompatibility offer excellent prospects for direct electrochemistry of redox proteins.

Room temperature ionic liquid (RTIL) entirely comprised of ions at ambient temperature has attracted extensive attention because of its unique chemical and physical properties such as negligible vapor pressure, low toxicity, wide potential windows, relatively high ionic conductivity and good chemical and thermal stabilities [7]. It has been widely used in synthetic chemistry [8], phase transfer catalysis [9], materials science [10] and electrochemistry [11]. Particularly in electrochemistry, the high ionic conductivity and the ability of retaining and enhancing the enzyme activity make RTIL as a kind of interesting material to modify electrodes and construct new biosensors. For example, Li et al. [12] proposed a novel chitosan–RTIL composite and used as an immobilization matrix to entrap proteins. Zhao et al. [13] used a RTIL modified basal plane graphite (BPG) electrode to immobilize hemoglobin (Hb) and investigated its electrocatalytic ability.

Recently, much attention has been paid to modify electrodes with RTIL and nanocomposites for combining their unique advantages. Sun et al. [14] investigated the electrocatalysis of Hb in a Nafion/nano-$CaCO_3$ film on an ionic liquid modified carbon paste electrode, and found that the immobilized Hb kept its native structure and showed good electrochemical behavior. Cai et al. [15] studied the direct electron transfer of heme-containing proteins immobilized in a single-walled carbon nanotube supported room temperature ionic liquid matrix. However, it is still a challenge for the combinations of RTIL with the nanoparticles to fabricate novel biosensors.

Silica-coated gold nanorods (GNRs@SiO_2) are a kind of novel biocompatible nanocomposite, which has been widely used as the immobilization matrix for biosensors [16] and biocatalysis [17]. On the other hand, sol–gel method has been demonstrated to be an alternative way to immobilize proteins or enzymes [18]. In this

* Corresponding author. Tel.: +86 25 83686130; fax: +86 25 83317761.
E-mail address: jrzhang@nju.edu.cn (J.-R. Zhang).

0039-9140/$ – see front matter © 2009 Elsevier B.V. All rights reserved.
doi:10.1016/j.talanta.2009.06.056

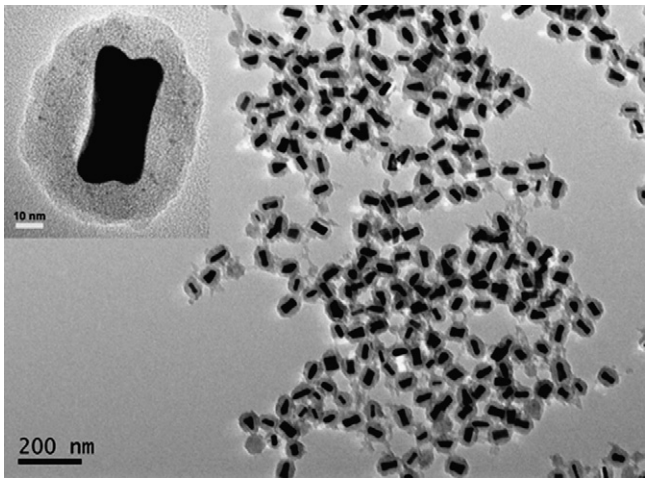


Fig. 1. TEM image of GNRs@SiO_2 composites.

paper, a novel biocomposite film based on GNRs@SiO_2, RTIL and silica sol–gel was prepared and further used to construct an excellent electrochemical biosensor for the determination of H_2O_2 and nitrite. Two chief aspects for the work have been highlighted. First, adding the GNRs@SiO_2 into RTIL–sol–gel can improve adhering ability of the composite film on electrode surface and provided an ideal matrix for protein immobilization and biosensor fabrication. Second, doping RTIL in GNRs@SiO_2/sol–gel can greatly enhance the conductivity of the composite film, and enzyme activity. The method by entrapping enzyme into biocompatible GNRs@SiO_2 and RTIL–sol–gel composite provided an effective means for realizing direct electrochemistry and electrocatalysis of enzymes along with good stability.

2. Experimental

2.1. Chemicals and reagents

Mb (horse heart) and cetyltrimethylammonium bromide (CTAB) were purchased from Sigma. Hydrogen peroxide (H_2O_2, 30%), $HAuCl_4{\cdot}4H_2O$ and tetraethoxysilane (TEOS) were from Shanghai Chemical Reagent Co. (Shanghai, China). Sodium borohydride ($NaBH_4$), sodium nitrite ($NaNO_2$) and ascorbic acid (AA) were obtained from Tianjin Reagent Factory (Tianjin, China). Ionic liquid 1-butyl-3-methylimidazolium tetrafluroborate ([bmim][BF_4]) was purchased from Acros Organics and used as received. All other chemicals were of analytical grade. All aqueous solutions were prepared with doubly distilled water and were deaerated with high purity nitrogen before performing the experiments.

2.2. Apparatus

Electrochemical measurements were performed on a CHI 660a workstation (Shanghai Chenhua, Shanghai, China) with a conventional three-electrode system comprised of a platinum wire as the auxiliary, a saturated calomel electrode as the reference and the modified glass carbon electrode (GCE) as the working electrode. Electrolyte solutions were deoxygenated by bubbling highly pure nitrogen for at least 10 min, and a nitrogen atmosphere was kept over the solution during measurements. Electrochemical impedance spectroscopy (EIS) was performed with an Autolab Electrochemical Analyzer (Eco Chemie, Netherlands) in 10 mM $K_3Fe(CN)_6$/$K_4Fe(CN)_6$ (1:1) mixture with 1.0 M KCl as supporting electrolyte, using an alternating current voltage of 5.0 mV, within the frequency range of 0.1 Hz–100 KHz. Transmission electron micrographs (TEM) were measured on a JEOLJEM 200CX transmission electron microscope, using an accelerating voltage of 200 KV. Scanning electron micrographs (SEM) were obtained with a Hitachi S4800 scanning electron microscope. Fourier transform infrared (FT-IR) spectra were recorded on a Vector 22 FT-IR spectrometer (Bruker). The real surface area (A) of the GC electrode could be obtained by cyclic voltammetry using 1 mM $K_3Fe(CN)_6$ as a probe at different scan rates. A straight line of peak currents (I_{pa}) vs. scan rates ($\upsilon^{1/2}$) could be obtained according to the equation of $I_{pa} = 299(\alpha n_a)^{1/2} A D_R^{1/2} C_o^* \upsilon^{1/2}$ (T = 298.2 K), and the value of A for the bare GC was estimated to be 0.097 cm^2 from the slope of the line.

2.3. Synthesis of GNRs@SiO_2 nanocomposite

GNRs were prepared according to the seed growth method as described in the reference [19]. GNRs@SiO_2 nanocomposite was prepared using an improved Stöber method. Briefly, the as-prepared GNRs were first washed by centrifugation twice at 9000 rpm for 10 min and redispersed in pure water. Then pH of the GNRs dispersion was adjusted to ca. 10 with ammonia (28 wt%), followed by the addition of appropriate amount of TEOS. The reaction was allowed to continue for 24 h at a constant temperature of 37 °C under vortex mixing. After the reaction was over, the GNRs@SiO_2 nanocomposites were collected by centrifugation at 9000 rpm for 10 min and further washed with abundance water.

2.4. Preparation of the GNRs@SiO_2–Mb bioconjugates and RTIL–sol–gel solution

The GNRs@SiO_2–Mb bioconjugates were prepared by adding 20 mg of GNRs@SiO_2 composites into 5 mg mL^{-1} Mb solution under vortex mixing. The resulting solution was further allowed to react for 24 h, followed by centrifugation and washing with water twice. We found that about 630 μg of Mb was immobilized onto 1 mg of GNRs@SiO_2 nanocomposite by calculating the difference in the concentration of the protein before and after adsorption.

A homogeneous RTIL–sol–gel solution was prepared by mixing 600 μL of ethanol, 50 μL of TEOS, 10 μL of 5 mM NaOH, 60 μL of H_2O and 50 μL of [bmim][BF_4] in a small test tube at room temperature. After being sonicated, the RTIL–sol–gel was formed and stored at 4 °C.

2.5. Construction of GNRs@SiO_2–Mb/RTIL–sol–gel/GCE biosensor

Prior to modification, the GCE (3 mm diameter) was first polished with 0.05 μm alumina slurry, then sonicated in nitric acid (1:1), ethanol and redistilled water in turn. The mixture containing 10 μL of biconjugates and 10 μL of RTIL–sol–gel was mixed round for 15 min, and then a 10 μL aliquot of the as-prepared GNRs@SiO_2–Mb/RTIL–sol–gel composite was dropped onto the pretreated GCE. The electrode was left to dry in a silica gel desiccator and stored at 37 °C overnight. As a comparison, the electrodes modified by GNRs@SiO_2/RTIL–sol–gel and GNRs@SiO_2–Mb/sol–gel were also prepared by the similar manner.

3. Results and discussion

3.1. Characterization of GNRs@SiO_2 and GNRs@SiO_2–Mb/RTIL–sol–gel bioconjugates

A method for silica coating GNRs with the Stöber technique was previously reported. However, in the preparation, besides prepared GNRs@SiO_2, some free silica is still observed [17]. In order to obtain a more homogeneous mixing, vortex mixing rather than mechanical

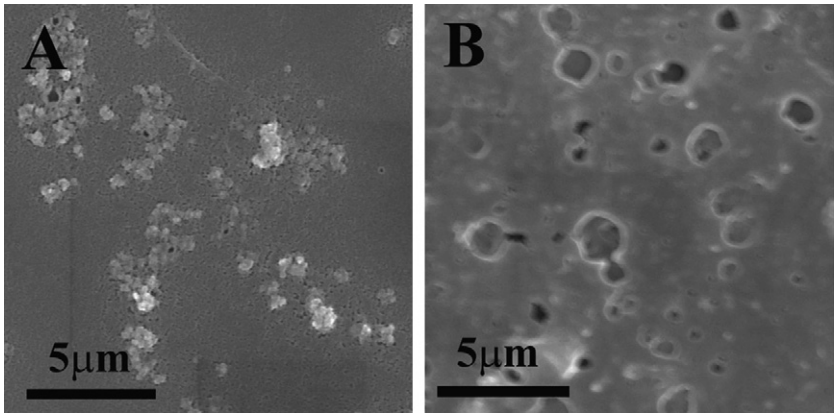


Fig. 2. SEM images of the GNRs@SiO_2–Mb/sol–gel biocomposite film (A) and the GNRs@SiO_2–Mb/RTIL–sol–gel biocomposite film (B).

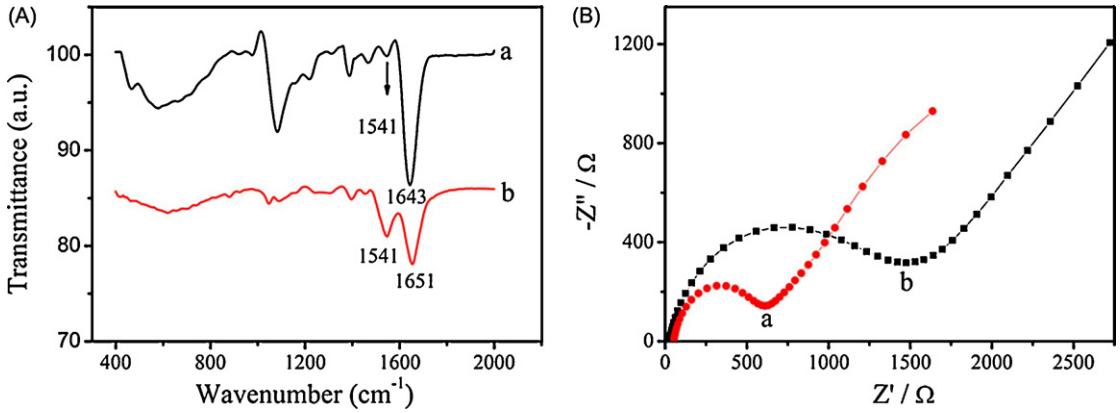


Fig. 3. (A) FT-IR spectra of (a) GNRs@SiO_2–Mb and (b) Mb. (B) EIS for (a) GNRs@SiO_2–Mb/RTIL–sol–gel biocomposite and (b) GNRs@SiO_2–Mb/sol–gel biocomposite modified GCE.

mixing and magnetic stirring was adopted. In addition, the reaction temperature was controlled at 37 °C to avoid the nucleation of free silica in solution. Fig. 1 shows a representative TEM image of the nanocomposite with an average aspect ratios of 2.1 (length: ca. 44 nm, width: ca. 21 nm) for the GNRs cores and a uniform thickness of the silica shell (ca. 18 nm). The homogeneous silica shell not only can control the dipolar interactions between GNRs, but also can enhance the versatility of the particles in biosensing.

SEM images were used to characterize and compare the morphologies of the GNRs@SiO_2–Mb/sol–gel and the GNRs@SiO_2–Mb/RTIL–sol–gel biocomposite film as shown in Fig. 2. It was found that the GNRs@SiO_2–Mb/sol–gel film in Fig. 2A exhibited an isolated and irregularly shaped surface, while the GNRs@SiO_2–Mb/RTIL–sol–gel film in Fig. 2B exhibited a highly porous surface with regularly network-like structure. This porous structure was attributed to the incorporated of RTIL into the composite film. The RTIL–sol–gel matrix provided a non-aggressive Mb enzyme immobilization approach at room temperature, which can improve the enzyme activity, biosensor sensitivity and the response signal.

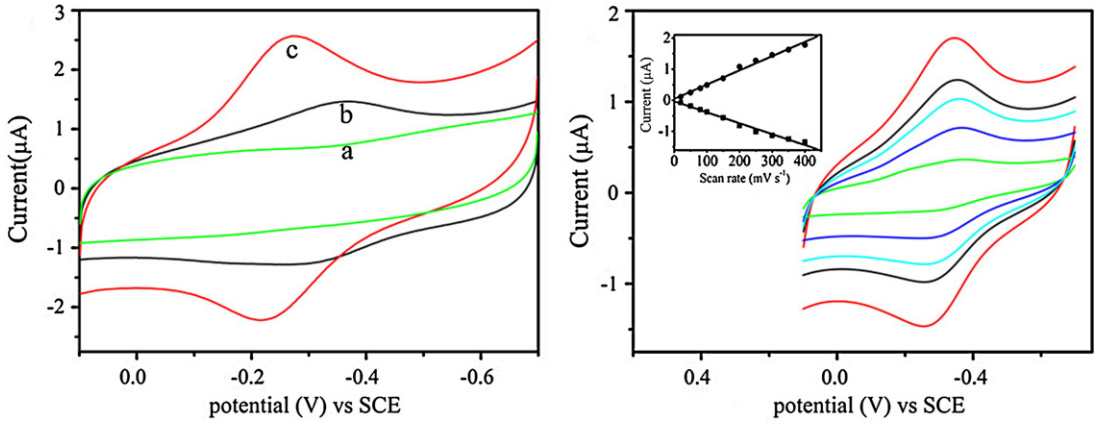


Fig. 4. (A) CVs of (a) GNRs@SiO_2/RTIL–sol–gel, (b) GNRs@SiO_2–Mb/sol–gel and (c) GNRs@SiO_2–Mb/RTIL–sol–gel modified GCE in 0.1 M pH 7.0 PBS at 0.2 V s^{-1}. (B) CVs of GNRs@SiO_2–Mb/RTIL–sol–gel/GCE in 0.1 M PBS solution (pH 7.0) at the scan rates of 0.02, 0.05, 0.08, 0.1 and 0.15 V s^{-1} (from inner to outer). Inset is the plot of cathodic and anodic peak currents vs. scan rate.

FT-IR spectroscopy is sensitive to the secondary structure of the protein. The characteristic amide I and amide II bands of protein provide detailed information on the secondary structure of polypeptide chain [20]. The amide I (1700–1600 cm^{-1}) was ascribed to C=O stretching vibrations of peptide linkages in the protein backbone. The amide II band (1600–1500 cm^{-1}) was attributed to a combination of N–H in plane bending and C–N stretching of the peptide groups. As shown in Fig. 3A, the spectra of amide I (1643 cm^{-1}) and II (1541 cm^{-1}) of Mb in the GNRs@SiO_2–Mb/RTIL–sol–gel biocomposite was nearly the same as those of native Mb. The slight shift of amide I bands from 1651 to 1643 cm^{-1} revealed the interaction between Mb and the GNRs@SiO_2 hybrids. Therefore, Mb retained the essential features of native secondary structure in the porous composite film.

Furthermore, EIS was employed to characterize the electrode surface impedance. Fig. 3B shows the Nyquist plots of EIS for the GNRs@SiO_2–Mb/RTIL–sol–gel and the GNRs@SiO_2–Mb/sol–gel biocomposite modified GCE. Significant differences in the impedance spectroscopy were observed. By mixing the GNRs@SiO_2–Mb/sol–gel with RTIL, the electron transfer resistance (Ret) of the composite film decreased from 1622 to 605 Ω, indicating that the RTIL–sol–gel composite film had good ionic conductivity and obviously improved the diffusion of ferricyanide toward the electrode surface.

3.2. Direct electrochemistry of Mb immobilized in GNRs@SiO_2/RTIL–sol–gel composite film-modified GC electrode

The direct electrochemistry of Mb modified electrode was studied by cyclic voltammetry. As shown in Fig. 4A, the GNRs@SiO_2/RTIL–sol–gel/GCE did not exhibit discernible peaks under the given conditions. However, when the GNRs@SiO_2–Mb/sol–gel/GCE was immersed in PBS, a pair of ill-defined and not symmetric redox peaks (curve b) corresponding to $MbFe^{III}/Fe^{II}$ redox couple was showed in cyclic voltammograms (CVs). This indicated that GNRs@SiO_2 could provide a favorable microenvironment for Mb to retain its natural structure and realize its direct electrochemistry. After the mixing [bmim][BF_4] with composite-sol–gel film, a remarkable enhanced electrochemical response was observed (curve c) with nearly the same value of anodic and cathodic peak current. A stable, well-defined and quasi-reversible redox peaks with the reduction and oxidation peak potentials appeared at −0.271 and −0.217 V at a scan rate of 200 mV s^{-1}, respectively. Compared with curve b, the current responses of Mb in curve c were remarkable increased, demonstrating that the presence of [bmim][BF_4] could greatly enhance the electron transfer process between Mb and the electrode surface. Moreover, it should be noted that the redox peaks of Mb almost disappeared after continuous potential cycling without GNRs@SiO_2 in RTIL–sol–gel film, indicating GNRs@SiO_2 could act as a binder to hinder [bmim][BF_4] leaking from the electrode surface. Thus, both biocompatibility of GNRs@SiO_2 and inherent conductivity of [bmim][BF_4] enable the composite to become an excellent matrix for realizing the direct electrochemistry of Mb.

The effect of scan rate on electrochemistry of the immobilized Mb was shown in Fig. 4B. With an increasing scan rate, the anodic peak potential of Mb shifted to a more positive value and the cathodic peak potential shifted in a negative direction. Furthermore, both the cathodic and anodic peak currents are linearly proportional to the scan rate in the wide range from 20 to 400 mV s^{-1} (inset of Fig. 4B), indicating a surface-controlled quasi-reversible process. The electron transfer rate constant (ks) between Mb and electrode was estimated to be 4.7 s^{-1} according to Laviron method [21]. It is higher than the 3.08 s^{-1} at Mb–TiO_2/MWCNTs/GC electrode [22], 1.0 s^{-1} at Mb/nanoporous ZnO/graphite electrode [23] or 0.34 s^{-1} at Mb/NiO NPs/GC electrode [24]. This faster ks indicates that the GNRs@SiO_2/RTIL–sol–gel composite film is an excellent promoter for the electron transfer between Mb and the electrode. The integration of the reduction peaks at different scan rates gave nearly constant charge values. According to Faraday's law, the average surface concentration of electroactive Mb in GNRs@SiO_2/RTIL–sol–gel/GCE was calculated to be 7.65×10^{-9} mol cm^{-2}. The result was larger than the theoretical monolayer coverage of 1.58×10^{-11} mol cm^{-2} for Mb [25], showing that several layers of Mb entrapped in the composite film participated in the electron transfer process.

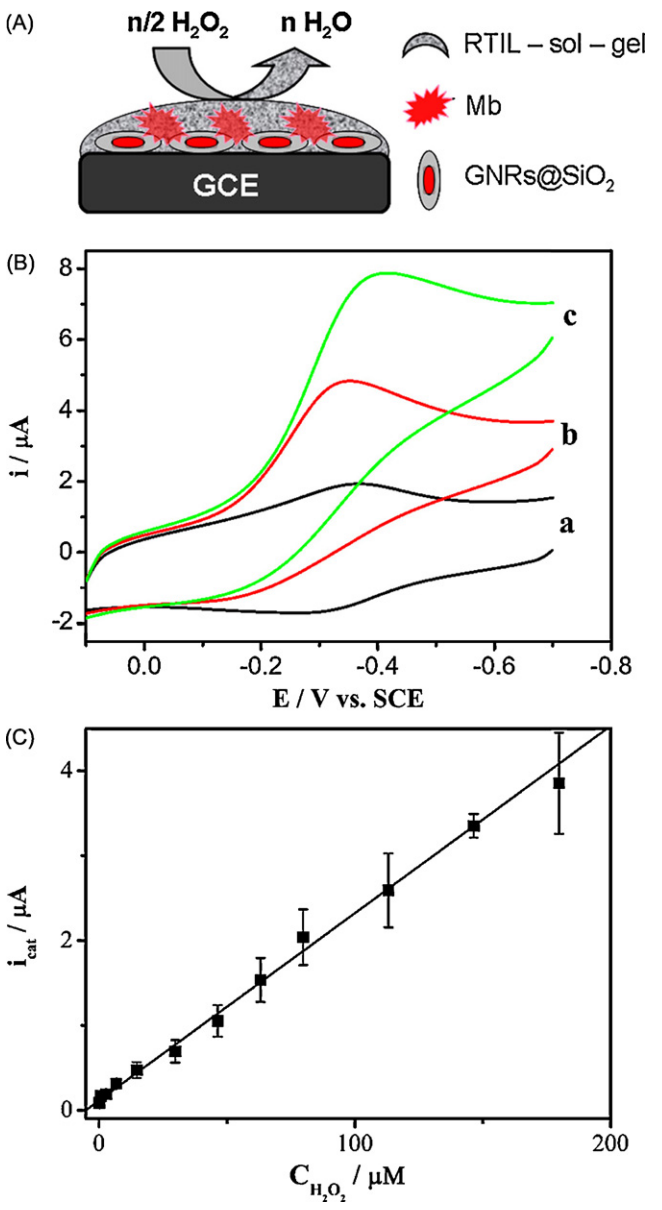


Fig. 5. (A) Schematic of the modification of GCE with GNRs@SiO_2, Mb and RTIL–sol–gel for efficient detection of H_2O_2. (B) CVs of GNRs@SiO_2–Mb/RTIL–sol–gel/GCE in 0.1 M PBS (pH 7.0) containing different concentration of H_2O_2 (a) 0, (b) 113.1 μM, and (c) 346.5 μM. (C) Linear plots of catalytic current (i_{cat}) vs. H_2O_2 concentration.

3.3. Electrocatalysis of GNRs@SiO_2–MbRT/IL–sol–gel/GCE to reduction of H_2O_2

It was reported that enzymes and proteins containing heme groups were able to reduce hydrogen peroxide electrocatalytically [26]. A possible mechanism of H_2O_2 catalyzed by

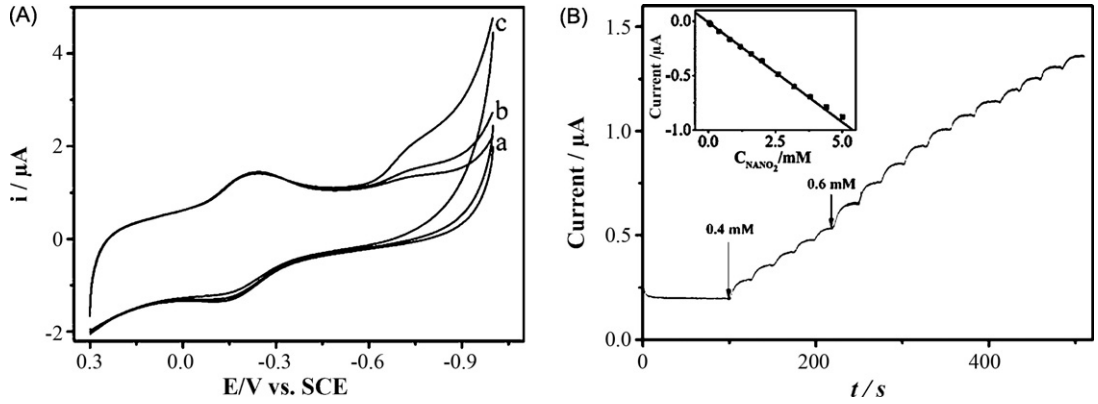


Fig. 6. (A) CVs of GNRs@SiO_2–Mb/RTIL–sol–gel/GCE in 0.1 M pH 5.0 acetate buffer containing different concentration of $NaNO_2$ (a) 0, (b) 100 μM and (c) 400 μM. (B) Typical amperometric current–time response curves of the biosensor upon successive addition of $NaNO_2$ into pH 5.0 acetate buffer solution. Applied potential: −0.7 V. Inset: linear relation between the amperometric response and NO_2^- concentration.

GNRs@SiO_2–Mb/RTIL–sol–gel modified electrode is postulated as shown in Fig. 5A. Fig. 5B shows the cyclic voltammograms of the GNRs@SiO_2–Mb/RTIL–sol–gel/GCE in a 0.1 M pH 7.0 PBS in the absence and presence of H_2O_2 at a scan rate of 200 mV s^{-1}. Upon addition of H_2O_2 to the solution, the reduction peak current increases obviously, while the oxidation peak current decreases with increasing the H_2O_2 concentration, showing a typical electrocatalytic reduction process to H_2O_2. Furthermore, the cathodic peak potentials shifted to negative value slightly with increasing the concentration of H_2O_2. As shown in Fig. 5C, the electrocatalytic peak current (i_{cat}) had good linear relationship with the concentration of H_2O_2 in the range of 0.2–80 μM. The linear regression equation was I (μA) = 0.115 + 0.022c (μM) (R = 0.997, n = 12) with a detection limit of 0.12 μM at 3σ. Thus, the entrapped Mb molecules are of good electrocatalytic activity, and the substrates for enzyme reaction can freely enter the porous RTIL–sol–gel film. The possible mechanism of electrocatalytic reduction of H_2O_2 at Mb-based enzyme electrode has been reported [27], which can be expressed as follows:

$$\mathrm{MbFe} + \mathrm{H_2O_2} \rightarrow \mathrm{CompoundI} + \mathrm{H_2O}$$

$$\mathrm{Compound\,I} + \mathrm{e^-} + \mathrm{H^+} \rightarrow \mathrm{Compound\,II}$$

$$\mathrm{Compound\,II} + \mathrm{e^-} + \mathrm{H^+} \rightarrow \mathrm{MbFe} + \mathrm{H_2O}$$

When the concentration of H_2O_2 was higher than 180 μM, a platform emerged in the catalytic peak current, showing the characteristics of Michaelis–Menten kinetics. The Michaelis–Menten constant (K_m^{app}), which gives an indication of the enzyme–substrate kinetics, is 0.42 mM as calculated from the electrochemical version of the Lineweaver–Burk equation $1/I_{ss} = 1/I_{max} + K_{app}^{m}/I_{max}C$, where I_{ss}, I_{max} and C stand for steady-state current, maximum current and the bulk concentrate of the substrate. This value was smaller than Hb on the sol–gel film modified CPE [28] or HRP on the chitosan/carbon microsphere/GCE [29], implying that Mb in the porous composite film is of a higher affinity to H_2O_2.

3.4. Amperometric response of the biosensor for nitrite

As is well known, nitrite is a carcinogen that widely exists in antiseptic food and polluted water. So the quantitative determination of nitrite concentrations is of rapidly increasing interest. In this study, electrochemical catalytic reduction of nitrite was also observed at the GNRs@SiO_2–Mb/RTIL–sol–gel modified electrode. After the addition of $NaNO_2$ into pH 5.0 acetate buffer solutions, a new reduction peak at about −0.7 V appeared (Fig. 6A), while direct reduction of NO_2^- at GNRs@SiO_2/RTIL–sol–gel/GCE showed a peak potential at about −1.3 V. Thus, the presence of Mb in the film decreased the reduction overpotential of NO_2^- for at least 0.6 V. Furthermore, the reduction current increases with an increase of NO_2^- concentration.

Fig. 6B shows the amperometric response of the biosensor with successive additions of $NaNO_2$ to 0.1 M pH 5.0 acetate buffer solutions at an applied potential of −700 mV. The current is produced from the reduction of NO that came from the disproportionation reaction of nitrite in acidic solution [30]. Upon addition of $NaNO_2$, the biosensor responded rapidly to the substrates and could achieve 90% of the steady-state current within 5 s, indicating a fast amperometric response to NO_2^- reduction. Such a rapid response can be attributed to the fast diffusion of the substrate in the porous and open frameworks of RTIL–sol–gel composite film. The amperometric response showed a linear relation with nitrite concentration from 0.04 mM to 5.0 mM with a correlation coefficient of 0.995 (n = 11) (inset of Fig. 6), which is wider than the previous nitrite sensors. The detection limit was estimated to be 0.02 mM at a signal-to-noise of 3. It is notable that this detection limit is obviously lower than the results obtained at some nitrite biosensors such as Mb–zirconium phosphate nanosheets film modified GCE [31] or Mb/clay–chitosan–gold nanoparticle nanohybrid modified GCE [32], indicating that the fabricated sandwich structured biosensor can potentially be used for monitoring of the concentration of nitrite sensitively. When the concentration of NO_2^- was higher than 5.0 mM, a plateau was observed, showing the characteristics of the Michaelis–Menten kinetics. The Lineweaver–Burk plot showed that Michaelis–Menten constant (K_m^{app}) was about 10.5 mM.

3.5. Reproducibility and stability of hydrogen peroxide biosensor

The reproducibility of the developed biosensor was examined at a H_2O_2 concentration of 1 μM, and the relative

Table 1
Interference experiment with the hydrogen peroxide biosensor.

External matters	Current ratio[a]	R.S.D. (%)
Glucose	0.931 ± 0.041	1.7
Glycin	0.997 ± 0.036	1.5
Ascorbic acid	1.02 ± 0.07	2.8
Citric acid	0.971 ± 0.028	1.6
Enthanol	0.958 ± 0.073	3.0
Acetic acid	1.02 ± 0.12	5.0

[a] Each value (mean of six measurements) was obtained by comparing the current for a mixture of a 20 μM interfering substance and 10 μM H_2O_2 with that for 10 μM H_2O_2 alone.

Table 2
Comparison of the developed H_2O_2 biosensor with other protein–RTIL-based biosensors.

Types of H_2O_2 electrode	Linear range (μM)	Detection limit (μM)	Stability	Reference
GNRs@SiO_2–Mb/RTIL–sol–gel/GCE	0.2–180	0.12	93%/21d	This work
HRP–Chi–BMIM•BF_4/GCE	0.75–135	0.25	95%/30d	[12]
SA/Hb/CILE	1.0–100	1.0	–	[33]
Mb–[EMIM][BF_4]–HA/GCE	2.0–270	0.6	–	[34]
SA/HRP/CILE	1.0–6.0	0.5	90%/21d	[35]

Chi, chitosan; HA, hyaluronic acid; SA, sodium alginate; CILE, carbon ionic liquid electrode.

Table 3
Determination of H_2O_2 concentration in an eyedrop sample with the biosensor and the $KMnO_4$ titration method, respectively.

H_2O_2 found by the biosensor (mM)			Average value (mM)	R.S.D. (%)	H_2O_2 average value found by $KMnO_4$ titration (mM)
0.8546	0.7136	0.8477	0.8220	7.8	0.8450
0.8193	0.8750				

standard deviation (R.S.D.) was 4.2% for six successive assays. To evaluate the electrode-to-electrode reproducibility, six GNRs@SiO_2–Mb/RTIL–sol–gel/GCEs were prepared under the same conditions independently. The R.S.D. of the prepared biosensors was 9.7%. The storage stability of the biosensor was also studied. When not in use, the electrode was suspended at 4 °C in a refrigerator. The response to 10 μM H_2O_2 retains 92.6% of its initial currents after three weeks storage. The good long-term stability could be mainly attributed to the excellent biocompatible microenvironment around the myoglobin provided by the composite film and the three-dimensional network structure of the RTIL–sol–gel film preventing the leaking of the biomacromolecules. Due to the good biocompatibility of GNRs@SiO_2 and inherent conductivity of [bmim][BF_4], the novel composite film could provide an excellent biosensing platform for realizing direct electrochemistry and electrocatalysis of Mb along with good stability. The analytical performance of the GNRs@SiO_2–Mb/RTIL–sol–gel/GCE developed in this study was compared with other protein–RTIL-based biosensors as shown in Table 2. As can be observed, our proposed biosensor exhibited excellent performance in terms of wide linear range, low limit of detection and high stability, which fulfill the requirement of in vivo or on line tracking of H_2O_2 concentration.

3.6. Selectivity and real sample analysis of the H_2O_2 biosensor

Selectivity is also important in practical use of the biosensor. In our experiment, six interfering substances were tested and the results are listed in Table 1. It can be observed that glucose, glycin, ascorbic acid, citric acid, ethanol, and acetic acid did not cause significant interferences to the determination of H_2O_2. The high selectivity of GNRs@SiO_2–Mb/RTIL–sol–gel/GCE verified its applicability of the proposed biosensor for real sample analysis Table 2.

To further assess the possible application of our proposed biosensor for real analytical usefulness, we investigated the concentration of H_2O_2 in commercial eyedrops. As listed in Table 3, using the proposed biosensor, the mean concentration of H_2O_2 in the sample was detected to be 0.822 mM, which was close to the actual concentration determined by the potassium permanganate titration method. This suggests that the developed biosensor is reliable and effective to determine H_2O_2 in industry or medicine sample.

4. Conclusions

In this work, a novel nanocomposite film based on biocompatible GNRs@SiO_2, conductivity [bmim][BF_4] and silica sol–gel was prepared and applied in Mb immobilization and biosensor construction. Due to the excellent biocompatible microenvironment and good conductivity provided by GNRs@SiO_2 and RTIL–sol–gel film, direct electrochemistry of the immobilized Mb was realized. The electrochemical results revealed that the GNRs@SiO_2–Mb/RTIL–sol–gel/GCE showed good bioelectrocatalytic activity in the reduction of both H_2O_2 and NO_2^-. The resulting biosensor exhibited excellent analytical performance in the determination of H_2O_2 and NO_2^-, with wider linear range, lower detection limit, and smaller K_m^{app} value than previously reported materials. The biosensor also showed good precision, reproducibility and storage stability, and acceptable accuracy for real samples determination. Therefore, the GNRs@SiO_2/RTIL–sol–gel hybrid material provides a promising matrix for the fabrication of electrochemical biosensors, and may find wide potential applications in biomedical detection and environmental analysis.

Acknowledgments

We greatly appreciate the support of the Students Innovative Training Programs Foundation from Nanjing University, and the National Natural Science Foundation of China (20821063, J0730422). The authors also thank the kind help from Mr. Jing-Jing Zhang and Ms. Xing-Hua Li, School of Chemistry and Chemical Engineering, Nanjing University.

References

[1] D.P. Hildebrand, H.L. Tang, A.G. Mauk, J. Am. Chem. Soc. 118 (1996) 12909.
[2] J.W. Li, L.H. Liu, F. Xiao, B.Z. Zeng, J. Electroanal. Chem. 613 (2008) 51.
[3] N. Li, J.Z. Xu, H. Yao, J.J. Zhu, J. Phys. Chem. B 110 (2006) 11561.
[4] J.H. Lin, L.J. Zhang, S.S. Zhang, Anal. Biochem. 370 (2007) 180.
[5] L. Zhang, Q. Zhang, X.B. Lu, J.H. Li, Biosens. Bioelectron. 23 (2007) 102.
[6] Q. Zhang, L. Zhang, B. Liu, X.B. Lu, J.H. Li, Biosens. Bioelectron. 23 (2007) 695.
[7] M.C. Buzzeo, C. Hardace, R.G. Compton, Anal. Chem. 76 (2004) 4583.
[8] Y. Liu, M. Wang, Z. Li, H. Liu, P. He, J.H. Li, Langmuir 21 (2005) 1618.
[9] D.B. Zhao, M. Wu, Y. Kou, E.Z. Min, Catal. Today 74 (2002) 157.
[10] P. Wasserscheid, W. Keim, Angew. Chem. Int. Ed. 39 (2000) 3772.
[11] G.C. Zhao, M.Q. Xu, Q. Zhang, Electrochem. Commun. 10 (2008) 1924.
[12] X.B. Lu, Q. Zhang, L. Zhang, J.H. Li, Electrochem. Commun. 8 (2006) 874.
[13] G.C. Zhao, M.Q. Xu, J. Ma, X.W. Wei, Electrochem. Commun. 9 (2007) 920.
[14] W. Sun, R.F. Gao, K. Jiao, J. Phys. Chem. B 111 (2007) 4560.
[15] P. Du, S.N. Liu, P. Wu, C.X. Cai, Electrochim. Acta 52 (2007) 6534.
[16] C.G. Wang, Z.F. Ma, T.T. Wang, Z.M. Su, Adv. Funct. Mater. 16 (2006) 1673.
[17] J.J. Zhang, Y.G. Liu, L.P. Jiang, J.J. Zhu, Electrochem. Commun. 10 (2008) 355.
[18] D. Chen, G. Wang, J.H. Li, J. Phys. Chem. C 111 (2007) 2351.
[19] C.G. Wang, Z.F. Ma, Z.M. Su, Nanotechnology 17 (2006) 1819.
[20] C.H. Fan, H.Y. Wang, S. Sun, D.X. Zhu, F. Wagner, G.X. Li, Anal. Chem. 73 (2001) 2850.
[21] E. Laviron, J. Electroanal. Chem. 101 (1979) 19.
[22] L. Zhang, D.B. Tian, J.J. Zhu, Bioelectrochemistry 74 (2008) 157.
[23] G. Zhao, J.J. Xu, H.Y. Chen, Anal. Biochem. 350 (2006) 145.
[24] A.B. Moghaddam, M.R. Ganjali, R. Dinarvand, S. Ahadi, A.A. Saboury, Biophy. Chem. 134 (2008) 25.
[25] J.C. Kendrew, G. Bodo, H.M. Dintzis, R.G. Parrish, H. Wyckoff, D.C. Phillips, Nature 181 (1958) 622.
[26] F.A. Armstrong, H.A.O. Hill, N.J. Walton, Acc. Chem. Res. 3 (1994) 313.
[27] S.J. Dong, Q.H. Chu, Chin. J. Chem. 11 (1993) 12.
[28] Q.L. Wang, G.X. Lu, B.J. Yang, Biosens. Bioelectron. 19 (2004) 1269.
[29] X. Chen, C.C. Li, T.H. Wang, Talanta 77 (2008) 37.

[30] M.H. Barley, K.J. Takcuchi, T.J. Meyer, J. Am. Chem. Soc. 108 (1986) 5876.
[31] Y.H. Zhang, X. Chen, W.S. Yang, Sens. Actuators B: Chem. 130 (2008) 682.
[32] X.J. Zhao, Z.B. Mai, X.H. Kang, Z. Dai, X.Y. Zou, Electrochim. Acta 53 (2008) 4732.
[33] W. Sun, D.D. Wang, R.F. Gao, K. Jiao, Electrochem. Commun. 9 (2007) 1159.
[34] Y. Zhang, J.B. Zheng, Electrochem. Commun. 10 (2008) 1400.
[35] C.F. Ding, M.L. Zhang, F. Zhao, S.S. Zhang, Anal. Biochem. 378 (2008) 32.

Talanta 80 (2009) 231–235

Contents lists available at ScienceDirect

Talanta

journal homepage: www.elsevier.com/locate/talanta

Simple, rapid, and highly sensitive detection of diphosgene and triphosgene by spectrophotometric methods

Abraham Joy, Emmanuel Anim-Danso, Joachim Kohn*

New Jersey Center for Biomaterials and the Department of Chemistry and Chemical Biology of Rutgers, The State University of New Jersey, 145 Bevier Rd, Piscataway, NJ 08854, United States

ARTICLE INFO

Article history:
Received 24 April 2009
Received in revised form 25 June 2009
Accepted 26 June 2009
Available online 4 July 2009

Keywords:
Triphosgene
Phosgene
Spectrophotometry
Spectrofluorimetry
Test strip
Poly(bisphenol-A carbonate)

ABSTRACT

Methods for the detection and estimation of diphosgene and triphosgene are described. These compounds are widely used phosgene precursors which produce an intensely colored purple pentamethine oxonol dye when reacted with 1,3-dimethylbarbituric acid (DBA) and pyridine (or a pyridine derivative). Two quantitative methods are described, based on either UV absorbance or fluorescence of the oxonol dye. Detection limits are ~4 μmol/L by UV and <0.4 μmol/L by fluorescence. The third method is a test strip for the simple and rapid detection and semi-quantitative estimation of diphosgene and triphosgene, using a filter paper embedded with dimethylbarbituric acid and poly(4-vinylpyridine). Addition of a test solution to the paper causes a color change from white to light blue at low concentrations and to pink at higher concentrations of triphosgene. The test strip is useful for quick on-site detection of triphosgene and diphosgene in reaction mixtures. The test is easy to perform and provides clear signal readouts indicative of the presence of phosgene precursors. The utility of this method was demonstrated by the qualitative determination of residual triphosgene during the production of poly(bisphenol-A carbonate).

© 2009 Elsevier B.V. All rights reserved.

Phosgene and its safer derivatives – diphosgene and triphosgene – are industrially important chemicals used in the manufacture of polyurethanes [1] and polycarbonates [2] and in the synthesis of various active pharmaceutical ingredients [3]. This market sector generates approximately 8 million tons of products and the global demand for phosgene is about 5 million tons per year [4]. Phosgene is very corrosive and has a high acute toxicity if inhaled. The danger of inhalation poisoning is particularly grave, since phosgene can be lethal before its odor is recognizable [5].

Current methods for the detection of phosgene are predominantly electrochemical and spectrophotometric [6,7]. A cellulose tape impregnated with 4-nitrobenzylpyridine and benzylaniline has been developed for monitoring phosgene in air [8]. It has also been shown that 1,2-bis-nucleophiles like 2-aminophenol can be used to detect phosgene by mass spectrometry [9].

Over the past few decades, safer alternatives to phosgene, e.g. diphosgene [10,11] and triphosgene [12,13], have been developed. Diphosgene (trichloromethyl chloroformate), is a liquid and triphosgene (bis-(trichloromethyl) carbonate), a solid, at room temperature, making them much easier to handle than gaseous phosgene. In addition, they are more stable to decomposition. Recently colorimetric methods for the detection of diphosgene vapors were reported [14,15] and a FRET (Förster resonance energy transfer) method was developed for triphosgene [16].

In spite of these advances, there is still a need for a quick and reliable test to detect phosgene precursors *in-situ*. In addition, since triphosgene is increasingly used as a reagent in chemical synthesis, it would be advantageous for the user to have a simple and quick method to detect triphosgene in reaction mixtures. In the current work, we demonstrate efficient detection systems for diphosgene and triphosgene, which have rapid response times and stable reaction products.

Kohn and coworkers developed a spectrophotometric method for the detection of organic cyanates [17] and carbodiimides [18] based on work by König [19] on colored oxonol dyes. They have shown that organic cyanates react with dimethylbarbituric acid in pyridine–H_2O to produce an intensely colored purple oxonol dye. The mechanism of color formation is based on the nucleophilic reaction of pyridine with an activated electrophilic species. This reaction is also used for the detection and determination of HCN [20]. A similar reaction between phosgene precursors and pyridine, and the subsequent reaction of the resulting intermediate with dimethylbarbituric acid is employed here to detect nanomole quantities of diphosgene and triphosgene. In pyridine–H_2O, the oxonol dye can be detected by absorbance or fluorescence, the latter extending detection limits for triphosgene to <0.4 μmol/L (or 0.4 nmoles of analyte in a 1 mL cuvette). Additionally a methodology for the preparation of a test strip is illustrated, which can be

* Corresponding author. Tel.: +1 732 445 0488; fax: +1 732 445 5006.
E-mail address: kohn@rutgers.edu (J. Kohn).

0039-9140/$ – see front matter © 2009 Elsevier B.V. All rights reserved.
doi:10.1016/j.talanta.2009.06.059

used for rapid visual detection and semi-quantitative estimation of triphosgene.

1. Experimental

1.1. Materials

1,3-Dimethylbarbituric acid, 3-cyanopyridine, 4-(4-nitrobenzyl)-pyridine and poly(4-vinylpyridine) were obtained from Sigma Aldrich. 4-Cyanopyridine, 4,4′-bipyridine, 2,2′-bipyridine, cyanuric acid and dimethylaminopyridine and pyridine were obtained from Acros Chemicals.

1.2. Spot test

Silica gel plates (0.5 cm × 5 cm) were dip coated with a solution of 1,3-dimethylbarbituric acid (20 mg/mL) and poly(4-vinylpyridine) (15 mg/mL) in ethanol and air-dried overnight. Selectivity for various triphosgene type reagents was tested by spotting a solution (5 mg/mL) of each test compound on a silica gel plate previously moistened with a mist of water.

1.3. System 1: absorbance method

All absorption measurements were carried out on a Thermo-Fisher Evolution 100 UV–VIS spectrophotometer using 1 cm quartz cuvettes at room temperature.

(i) Reaction of triphosgene with pyridine and 1,3-dimethylbarbituric acid: Triphosgene solutions of various concentrations (0.25–2 mg/mL) were prepared in CH_2Cl_2 and aliquots (5–50 μL) were added to solutions of 1,3-dimethylbarbituric acid (30 mg, 0.19 mmol) in 1 mL of pyridine–H_2O (9:1, v/v). An intense blue colored solution with a red fluorescence developed instantly.

(ii) Reaction of triphosgene with pyridine derivatives and 1,3-dimethylbarbituric acid in methanol–H_2O: Triphosgene solutions of various concentrations (0.25–2 mg/mL) were prepared in CH_2Cl_2 and aliquots (5–50 μL) were added to solutions of 4,4′-bipyridine (30 mg, 0.19 mmol) and 1,3-dimethylbarbituric acid (30 mg, 0.19 mmol) in 1 mL of methanol–H_2O (9:1, v/v). A pink color developed within 10 s, which then changed to an emerald (greenish blue) color within 1 min. The same protocol was used for the other pyridine derivatives. The absorption maximum was dependent upon the pyridine derivative.

1.4. System 2: fluorescence method

Fluorescence spectra were recorded on a Varian Eclipse spectrofluorimeter using a 1 cm quartz cuvette at room temperature. The emission spectrum was collected between 600 and 700 nm. All spectra were recorded at identical PMT voltage and slit widths.

Reaction of triphosgene with 1,3-dimethylbarbituric acid in pyridine–H_2O: Triphosgene solutions of various concentrations (0.025–0.2 mg/mL) were prepared in CH_2Cl_2 and aliquots (5–50 μL) were added to solutions of 1,3-dimethylbarbituric acid (30 mg, 0.19 mmol) in 1 mL of pyridine–H_2O (9:1, v/v). An intense blue colored solution with a red fluorescence developed instantly.

1.5. System 3: test strips

(i) For higher concentrations of triphosgene: 3-cyanopyridine (42 mg), poly(4-vinylpyridine) (14 mg) and 1,3-dimethylbarbituric acid (43 mg) were dissolved in ethanol (2 mL) and coated onto a filter paper (VWR 413) by dripping the solution as evenly as possible over the paper. The filter paper was dried. Prior to the test, the paper was moistened with a mist of water and drops of triphosgene solutions at two different concentrations (0.84 and 6.72 mM) were added onto the paper. Within 1–2 min, the filter paper became pink at the higher concentration of triphosgene and light blue at the lower concentration.

(ii) For lower concentrations of triphosgene: poly(4-vinylpyridine) (30 mg) and 1,3-dimethylbarbituric acid (40 mg) were dissolved in ethanol (2 mL) and coated onto a filter paper (VWR 413) by dripping the solution as evenly as possible over the paper. Drops of triphosgene solutions (0.84 and 6.72 mM) were added onto the paper and both the lower and higher concentrations of triphosgene gave a blue color to the test strip. The blue color was more intense for the higher concentration of triphosgene.

2. Results and discussion

Phosgene precursors react with 1,3-dimethylbarbituric acid (DBA) in pyridine–H_2O (9:1, v/v) to produce an intense blue colored solution (λ_{max} 598 nm) with a red fluorescence. As shown earlier by Kohn et al. [17], for organic cyanates and carbodiimides, the species at 598 nm is the pentamethine oxonol dye that is formed by the reaction with DBA in pyridine–H_2O. From the proposed mechanism, phosgene precursors should react with DBA similarly to the cyanates and carbodiimides to produce the same oxonol dye (Scheme 1). Support for this comes from the similarity of the absorption spectra of the oxonol dye (prepared by Kohn et al.) in pyridine–H_2O (9:1) and that of the reaction between triphosgene and DBA in pyridine–H_2O (9:1) (Fig. 1).

First, the selectivity of the assay was established by comparing the reaction of various phosgene substitutes phosgene on silica gel plates that were dip coated with a solution of 1,3-dimethylbarbituric acid and poly(4-vinylpyridine). Each test solution (5 mg/mL) was spot tested on the silica gel plates using a capillary tube. The solution of triphosgene gave a purple spot that turned to a blue spot in <1 min. Diphosgene also gave a purple/pink spot instantly. 1-Ethyl-3-(3-dimethylaminopropyl) carbodiimide hydrochloride (EDC) and *N*,*N*′-dicyclohexylcarbodiimide (DCC) also gave a purple spot, although the color formation with carbodiimide was much slower (2–3 h). Acetyl chloride, di-t-butyl dicarbonate (Boc_2O) and benzylchloroformate gave a faint yellow color, and all other compounds failed to produce any color (Table 1). This established the potential of the current assay for the rapid and selective detection of diphosgene and triphosgene. We then developed three different analytical methods.

2.1. System 1: absorbance measurements

Two quantitative assays for triphosgene were developed. The first method was based on the reaction between triphosgene and

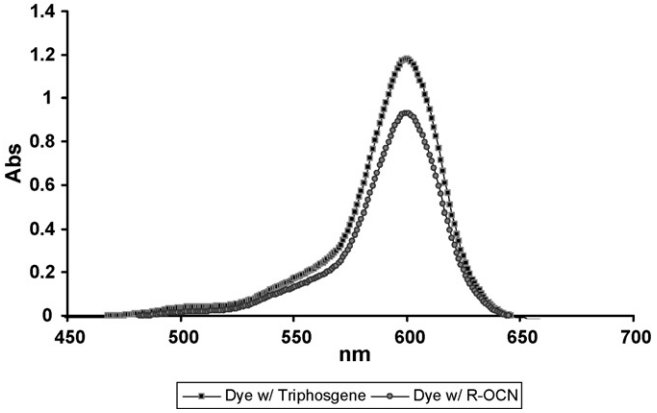


Fig. 1. Comparison of absorption spectra of the dye prepared by the method in Ref. [16] and that of the reaction product of triphosgene and DBA in pyridine–H_2O.

Table 1
Selectivity of the assay.

Test compound	Test result
Triphosgene (TP)	Purple spot turning to blue spot in ~20 s
Diphosgene	Pink spot
DCC	Pink spot; slower response time (2–3 h)
EDC	Pink spot; slower response time (2–3 h)
Acetyl chloride	Faint yellow spot
Benzyl chloroformate	Faint yellow spot
FMOC-Cl	Faint yellow spot
Di-t-butyl dicarbonate (Boc_2O)	Yellow spot
Oxalyl chloride	Colorless
Carbonyldiimidazole (CDI)	Colorless
Disuccinimidyl carbonate (DSC)	Colorless
Trifluoroacetic anhydride	Colorless
PyBOP	Colorless
Choline chloroformate HCl	Colorless

pyridine and the subsequent reaction with 1,3-dimethylbarbituric acid in pyridine–H_2O, which yields an oxonol dye with λ_{max} at 598 nm. Quantitative determination of triphosgene concentration was established by monitoring the absorbance of the oxonol dye at this wavelength. As seen in Fig. 2, the detection limit was about 2 μmol/L, and the dynamic range extends to 80 μmol/L.

In order to extend the dynamic range, we evaluated other pyridine derivatives. In agreement with the proposed mechanism, the λ_{max} of the absorbing species depends upon the pyridine derivative. Noteworthy is the fact that derivatives that contain electron-withdrawing groups give a positive test, (4-cyanopyridine λ_{max} 648 nm; 4-(4-nitrobenzyl)pyridine λ_{max} 624 nm; 3-cyanopyridine λ_{max} 563 nm; 4,4′-bipyridine λ_{max} 618 nm), while those that contain electron-donating groups like dimethylaminopyridine do not produce colored products.

For development of an analytical method we selected 4,4′-bipyridine due to its relatively quick response time (<1 min), high absorbance and stability of the colored product (12–18 h). Immediately after the addition of triphosgene to a solution of 4,4′-bipyridine and DBA in MeOH–H_2O (9:1, v/v), a pink solution forms that turns to an emerald (greenish blue) colored solution within 1 min. As expected from the proposed mechanism, the absorbance maximum of the oxonol dye is red shifted to 618 nm due to a more delocalized structure resulting from 4,4′-bipyridine. The quantitative determination of triphosgene was established by monitoring the absorbance of the oxonol dye at this wavelength. The range of detection of triphosgene is between 4 and 230 μmol/L of triphosgene (Fig. 3). Similar results were obtained when the experiment was done in ethanol–H_2O, isopropanol–H_2O or sec-butanol–H_2O.

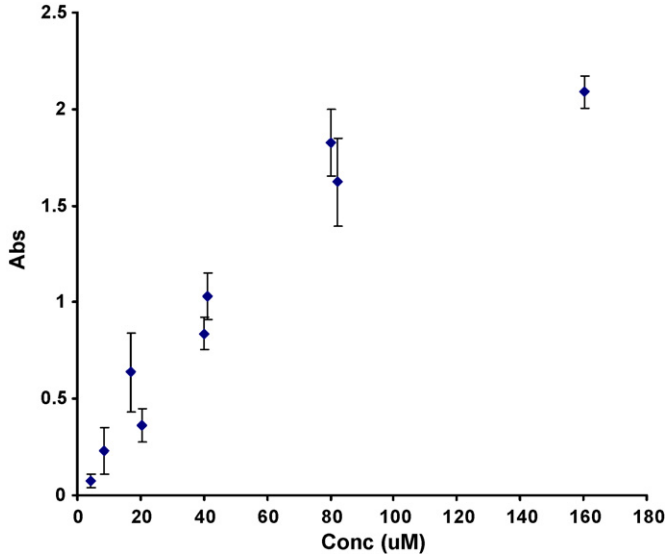


Fig. 2. Dynamic range of detection of triphosgene utilizing the 1,3-dimethylbarbituric acid/pyridine–H_2O method showing breakdown of linearity at 80 μM.

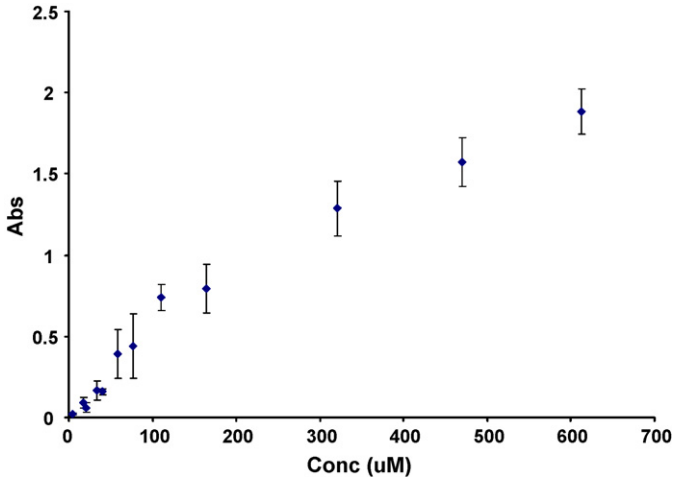


Fig. 3. Dynamic range of detection of triphosgene utilizing the 1,3-dimethylbarbituric acid/4,4′-bipyridine in MeOH–H_2O method showing enhanced linearity over system shown in Fig. 1.

2.2. System 2: fluorescence measurements of the reaction of triphosgene with 1,3-dimethylbarbituric acid in pyridine–H_2O

The high sensitivity of fluorescence based detection methods have resulted in their use for the detection of a wide variety of chemicals [21]. The reaction of triphosgene with 1,3-dimethylbarbituric acid in pyridine–H_2O produces an oxonol dye, which has a very high extinction coefficient and is also highly fluorescent. Hence the possibility of detecting and estimating the amount of triphosgene from the fluorescence of the pentamethine oxonol dye was examined. The fluorescence was recorded between 600 and 700 nm and the λ_{max} of the emission peak is at 624 nm. As seen in Fig. 4, even a concentration of 0.4 μmol/L of triphosgene can be reliably measured and the resulting plot of fluorescence intensity and concentrations has a high correlation. Potentially, an even lower amount of triphosgene can be detected by increasing the amount of DBA in the reaction mixture and/or increasing the sensitivity of the instrument. A recent study [16] has shown that triphosgene can be detected by FRET at concentrations of 5×10^{-5} M. The detection limit of this current spectrofluorimetric method is significantly lower.

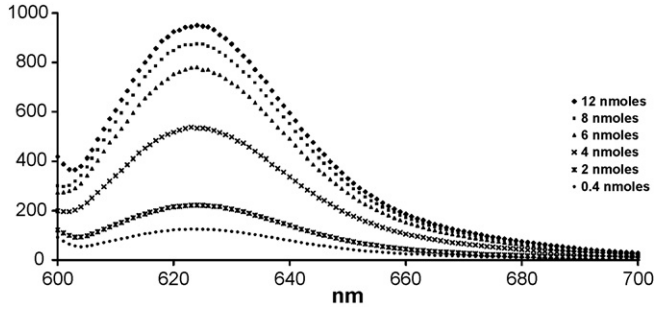
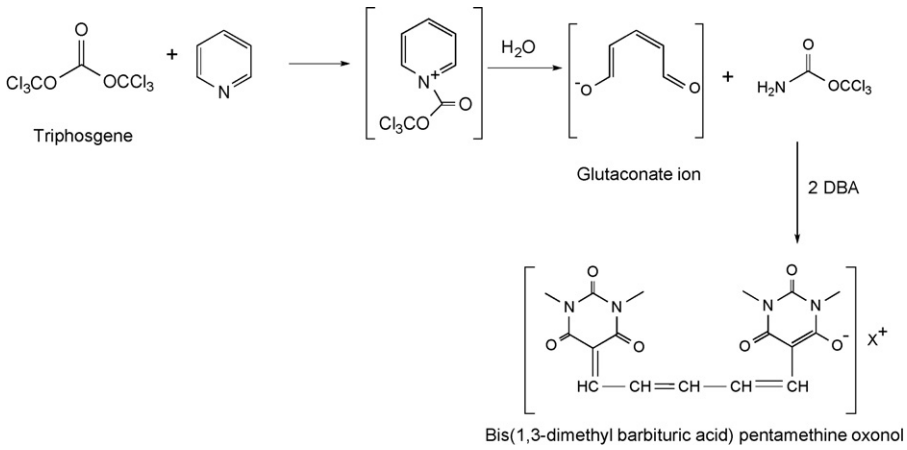


Fig. 4. Fluorescence spectra of pentamethine oxonol dye formed from the reaction of triphosgene, 1,3-dimenthylbarbituric acid (DBA) in pyridine–H_2O (9:1). Shown are spectra taken upon addition of aliquots of a triphosgene solution to a solution of DBA in pyridine–H_2O.



Scheme 1. Mechanism of formation of pentamethine oxonol dye.

2.3. System 3: fabrication of test strips for the detection and estimation of triphosgene

A test strip, similar to pH paper, a glucose test [22] or a pregnancy test [23] is widely used and highly desirable for simple and rapid monitoring. In order to facilitate the adoption of our methodology by end users – for example chemists using triphosgene as a reagent, it would be advantageous to develop a test where the user adds a drop of the reaction mixture to the test strip and determines the presence of a phosgene precursor by the color of the strip. To develop such a test strip, we employed the pyridine derivative – poly(4-vinylpyridine).

A filter paper (VWR 413) was coated with a solution of poly(4-vinylpyridine) (15 mg) and DBA (20 mg) in 1 mL ethanol, which was then dried. Addition of a triphosgene test solution (in CH_2Cl_2) to the strip (pre-moistened with a mist of water) produces a blue color within 1 min. This method was able to clearly indicate the presence of triphosgene since the color change is very discernible from white to light blue (Fig. 5).

DBA / PVP		DBA / PVP / 3CN-Py	
TP conc:		TP conc:	
0.84 mM	6.7 mM	0.84 mM	6.7 mM
1	**2**	**3**	**4**



Fig. 5. Test strips contain PVP and DBA (1, 2) or PVP, 3CN-Py and DBA (3, 4) embedded within a filter paper. The tests show a difference in color with and without 3CN-Py. PVP: poly(4-vinylpyridine); 3CN-Py: 3-cyanopyridine; DBA: dimethylbarbituric acid; TP: triphosgene.

Although this is a powerful 'yes' or 'no' method for the presence of triphosgene, it is not very useful for the semi-quantitative estimation of triphosgene. To generate a more quantitative method, a system that produces different colors for two different concentrations of triphosgene was designed.

Test strips were prepared using a combination of polyvinylpyridine (14 mg) and 3-cyanopyridine (42 mg) along with DBA (43 mg) in 2 mL ethanol. A triphosgene solution at a concentration of 6.7 mM resulted in a pink color on the paper, while a triphosgene concentration of 0.84 mM produced a blue color. Without the 3-cyanopyridine, both the higher and lower concentrations of triphosgene give a blue color although the intensity of the color is less for the lower concentration. These results provide the basis to develop semi-quantitative methods for the determination of the amount of triphosgene. Due to the non-homogeneous nature of our coating process, there is variability in the color generated on various parts of the paper. However this is a simple and promising method for the semi-quantitative detection and estimation of triphosgene. In contrast, the published cellulose tape method for the estimation of phosgene shows only a single color at all concentrations.

This test strip also works for phosgene vapors. The decomposition of a 5% solution of diphosgene in toluene was initiated with triethylamine and a test strip positioned above this solution turns red immediately. However, the test strip decolorizes within a few minutes due to the presence of HCl vapors.

2.4. Utilization of the assay to indicate the end-point of polycarbonate synthesis

Polycarbonates such as poly(bisphenol-A carbonate) and tyrosine derived polycarbonates, are commercially valuable materials that are efficiently synthesized using triphosgene [24,25]. Due to its toxicity, it is crucial that all excess triphosgene be quenched prior to work up and precipitation of the polymer. The utility of the current assay was demonstrated by using it to test for the presence of triphosgene during the polymerization reactions of poly(bisphenol-A carbonate) and tyrosine polycarbonates and to confirm that all the triphosgene was quenched prior to precipitation of the polymer. During the course of the reaction, aliquots of the reaction mixture were taken and added to solutions of 1,3-dimethylbarbituric acid (30 mg) in pyridine–H_2O, and the presence of triphosgene was indicated by the formation of a blue solution. After the reaction was quenched, the same test produced a colorless solution indicating that the triphosgene has been consumed (within the limits of detection of this test).

2.5. Comparison between the current assay and an established method

A published method for the determination of phosgene is to use a mixture of 4-(4-nitrobenzylpyridine) and *N*-phenylbenzylamine, which produces a yellowish-orange color to indicate the presence of phosgene. Although the above protocol is most commonly used for the detection of phosgene or diphosgene in air samples, we compared our assay with this published procedure under the same experimental conditions. In the experiment, aliquots of triphosgene in CH_2Cl_2 were added to either a solution of 1,3-dimethylbarbituric acid in pyridine–water (test method) or to a solution of 4-(4-nitrobenzylpyridine) and *N*-phenylbenzylamine (control method) in methanol. In the test method, the change in color was obvious and readily discernable – from a clear solution to a blue/red solution while in the control method the change in color before (light yellow) and after (yellowish-orange) addition of triphosgene was sutble and more difficult to detect. Hence the assay developed here presents a clearer indication of the presence of phosgene precursors.

3. Conclusion

Due to the increased use of phosgene precursors (notably diphosgene and triphosgene) in industrial and academic laboratories, and their potential toxicity, methods for *in-situ* detection and estimation of these reagents are very useful. The reaction system consisting of pyridine and dimethylbarbituric acid system described here is an efficient method for *in-situ* detection and estimation of diphosgene and triphosgene. The long wavelength absorbance (or fluorescence) of the resulting oxonol dye decreases the possibility of interference from other chemicals in the reaction mixture. In addition, this reaction system is highly sensitive, allowing the detection of phosgene precursors in nanomole quantities of analyte. Three different protocols were developed which makes it feasible for the end user to adopt a method based on the user's needs and available instrumentation.

Acknowledgment

The authors thank Prof. Kenneth Breslauer and Dr. Jens Volker for the use of their spectrofluorimeter, Dr. Linda Anthony for helpful discussions and significant editorial assistance. This work was supported by NIH grant T32 EB005583 (Training Grant), NIH P41 EB001046 (RESBIO; Integrated Resources of Polymeric Materials) and the New Jersey Center for Biomaterials. The content is solely the responsibility of the authors and does not necessarily represent the official views of the NIH or NIBIB.

References

[1] G.B. Kauffman, J. Chem. Edu. 69 (1992) 909.
[2] W.B. Kim, U.A. Joshi, J.S. Lee, Ind. Eng. Chem. Res. 43 (2004) 1897–1914.
[3] A. Kleemann, J. Engel, B. Kutscher, Pharmaceutical Substances: Syntheses, Patents, Applications, Thieme, Stuttgart, 2001.
[4] L. Cotarca, H. Eckert, Phosgenations—A Handbook, Wiley–VCH, Weinheim, Germany, 2004.
[5] U.P. Kodavanti, D.L. Costa, S.N. Giri, B. Starcher, G.E. Hatch, Fundam. Appl. Toxicol. 37 (1997) 54–63.
[6] T.A. Ryan, C. Ryan, E.A. Sedon, K.R. Seddon, Phosgene and Related Carbonyl Halides, Elsevier, Amsterdam, 1996.
[7] S.K. Dangwal, Ind. Health 32 (1994) 41–47.
[8] N. Nakano, A. Yamamoto, Y. Kobayashi, K. Nagashima, Talanta 42 (1995) 641–645.
[9] B. Muir, D.B. Cooper, W.A. Carrick, C.M. Timperley, B.J. Slater, S. Quick, J. Chromatogr. A 1098 (2005) 156–165.
[10] M. Ueda, H. Oikawa, N. Kawaharasaki, Bull. Chem. Soc. Jpn. 56 (1983) 2485.
[11] K. Kurita, Y. Iwakura, Org. Synth. 59 (1980) 195.
[12] H. Eckert, B. Forster, Angew. Chem. Int. Ed. 26 (1987) 894–895.
[13] L. Cotarca, P. Delogu, A. Nardelli, V. Sunjic, Synthesis (1996) 553–576.
[14] V. Pitschmann, Z. Kobliha, E. Halamek, I. Tusarova, J. Serb. Chem. Soc. 72 (2007) 1031–1037.
[15] V. Pitschmann, Z. Kobliha, E. Halamek, I. Tusarova, Chemia Analityczna (Warsaw, Poland) 53 (2008) 47–57.
[16] H.X. Zhang, D.M. Rudkevich, Chem. Commun. (2007) 1238–1239.
[17] J. Kohn, E.C. Albert, M. Wilchek, R. Langer, Anal. Chem. 58 (1986) 3184–3188.
[18] M. Wilchek, T. Miron, J. Kohn, Anal. Biochem. 114 (1981) 419–421.
[19] W. Konig, J. Prakt. Chem. 69 (1904) 105–110.
[20] L.S. Bark, H.G. Higson, Analyst 88 (1963) 751–760.
[21] M. Burnworth, S.J. Rowan, C. Weder, Chem. Eur. J. 13 (2007) 7828–7836.
[22] L.A. Cohn, D.L. McCaw, D.J. Tate, J.C. Johnson, J. Am. Vet. Med. Assoc. 216 (2000) 198–202.
[23] L.A. Bastian, K. Nanda, V. Hasselblad, D.L. Simel, Arch. Fam. Med. 7 (1998) 465–469.
[24] S. Pulapura, J. Kohn, Biopolymers 32 (1992) 411–417.
[25] R. Rojas, N.K. Harris, K. Piotrowska, J. Kohn, J. Polym. Sci. Part A: Polym. Chem. 47 (2009) 49–58.

Talanta 80 (2009) 236–241

Contents lists available at ScienceDirect

Talanta

journal homepage: www.elsevier.com/locate/talanta

Multivariate optimization and validation of an analytical methodology by RP-HPLC for the determination of losartan potassium in capsules

Rudy Bonfilio[a,*], César Ricardo Teixeira Tarley[b,d], Gislaine Ribeiro Pereira[a], Hérida Regina Nunes Salgado[c], Magali Benjamim de Araújo[a]

[a] Departamento de Farmácia, Universidade Federal de Alfenas, Rua Gabriel Monteiro da Silva, 700, 37130-000, Alfenas, MG, Brazil
[b] Departamento de Ciências Exatas, Universidade Federal de Alfenas, Rua Gabriel Monteiro da Silva, 700, CEP 37130-000, Alfenas, MG, Brazil
[c] Departamento de Fármacos e Medicamentos, Faculdade de Ciências Farmacêuticas, UNESP, Universidade Estadual Paulista "Júlio de Mesquita Filho", Rodovia Araraquara-Jaú, km 1, CEP 14801-902, Araraquara, SP, Brazil
[d] Instituto Nacional de Ciência e Tecnologia (INCT) de Bioanalítica, Universidade Estadual de Campinas (Unicamp), Instituto de Química, Departamento de Química Analítica, Cidade Universitária Zeferino Vaz s/n, CEP 13083-970, Campinas, SP, Brazil

ARTICLE INFO

Article history:
Received 16 April 2009
Received in revised form 2 June 2009
Accepted 27 June 2009
Available online 4 July 2009

Keywords:
Doehlert design
Fractional factorial design
Losartan potassium
Reversed-phase chromatography
Validation

ABSTRACT

This paper describes the optimization and validation of an analytical methodology for the determination of losartan potassium in capsules by HPLC using 2^{5-1} fractional factorial and Doehlert designs. This multivariate approach allows a considerable improvement in chromatographic performance using fewer experiments, without additional cost for columns or other equipment. The HPLC method utilized potassium phosphate buffer (pH 6.2; 58 mmol L^{-1})–acetonitrile (65:35, v/v) as the mobile phase, pumped at a flow rate of 1.0 mL min^{-1}. An octylsilane column (100 mm × 4.6 mm i.d., 5 μm) maintained at 35 °C was used as the stationary phase. UV detection was performed at 254 nm. The method was validated according to the ICH guidelines, showing accuracy, precision (intra-day relative standard deviation (R.S.D.) and inter-day R.S.D values <2.0%), selectivity, robustness and linearity (r = 0.9998) over a concentration range from 30 to 70 mg L^{-1} of losartan potassium. The limits of detection and quantification were 0.114 and 0.420 mg L^{-1}, respectively. The validated method may be used to quantify losartan potassium in capsules and to determine the stability of this drug.

© 2009 Elsevier B.V. All rights reserved.

1. Introduction

Losartan potassium, chemically described as 2-butyl-4-chloro-1-[*p*-(*o*-1*H*-tetrazol-5-ylphenyl)benzyl] imidazole-5-methanol monopotassium salt [1], is an angiotensin II receptor (type AT1) antagonist for the treatment of hypertension. Losartan has been demonstrated to be superior to previous peptide receptor antagonists and angiotensin converting enzyme (ACE) inhibitors because of its enhanced specificity, selectivity and tolerability [2,3]. Losartan potassium has a molecular weight of 461, a p*K*a value of 4.9 and an aqueous solubility of 3.3 mg mL^{-1} at pH 7.8 [4].

Several methods have been reported for the analysis of losartan potassium and its degradation products. In biological fluids, the active principle has been determined by high performance liquid chromatography (HPLC) methods [5–8]. For applications in pharmaceutical products, there are methods that make use of HPLC [9–18], high performance thin layer chromatography (HPTLC) [19,20], capillary electrophoresis (CE), capillary electrochromatography (CEC) [21] and spectrophotometry [22–24]. Recently, there have been reports in the literature of the employment of HPLC for bioequivalence studies of tablets containing losartan potassium [25,26]. The HPLC methods described employ different conditions and columns, which result in different performances. The drug substance monograph on losartan potassium provided by the United States Pharmacopoeia [1] recommends an HPLC method on a C-18 (4.0 mm × 25 mm) column with a 0.1% solution of phosphoric acid in water and acetonitrile (60:40, v/v) as the mobile phase, flow rate at 1 mL min^{-1}, column temperature at 35 °C, methanol as diluent and detection at 254 nm.

Despite the variety of analytical methods for losartan potassium in pharmaceutical products or biological fluids, a routine pharmaceutical analysis laboratory may encounter difficulty in applying a described method due to a limited availability of chromatographic columns or equipment. This challenge points to the necessity of analytical method development using conventional materials, reagents and equipment. Moreover, in spite of the utility and benefits of the modern focus of method development in pharmaceutical analysis on enhancing analytical performance, reducing costs for routine analysis is also an important concern.

* Corresponding author. Tel.: +55 35 3299 1350; fax: +55 35 3299 1350.
E-mail addresses: rudybonfilio@yahoo.com.br, rudyfarmacia@hotmail.com (R. Bonfilio).

0039-9140/$ – see front matter © 2009 Elsevier B.V. All rights reserved.
doi:10.1016/j.talanta.2009.06.060

A good tool to be included in method development strategies or in the improvement of analytical performance is the multivariate approach, which without additional costs can yield a reduction in the number of experiments and, consequently, in the analysis time. Furthermore, the multivariate approach allows investigation of the interaction effects between parameters, which is not possible with a univariate approach [27].

Considering the variability of chromatographic conditions used in analysis of losartan potassium and the necessity of cost reductions in routine pharmaceutical analysis, the aim of the present work was to develop and validate a simple and reliable HPLC method for analysis of losartan potassium in capsules, as an alternative to existing methods. A multivariate approach was adopted as an analytical tool to study the influence of different chromatographic conditions and to improve chromatographic performance, using the available resources in our laboratory.

2. Experimental

2.1. Chemical and reagents

All reagents used in the experimental work were of analytical grade. Potassium dihydrogenphosphate (KH_2PO_4), phosphoric acid, sodium hydroxide, hydrochloride acid and HPLC grade acetonitrile were purchased from Vetec® (Rio de Janeiro, Brazil); reverse osmosis water obtained using a reverse osmosis water purifier OS 10 LTH (Gehaka®, São Paulo, Brazil) was used to prepare the mobile phase. Losartan potassium salt of 98.90% purity was supplied by IPCA Laboratories Limited® (Athal, India). Losartan potassium capsules were supplied by three local drug stores, coded as A, B and C. They were described as containing 50 mg losartan potassium (as the anhydrous base of the drug) and the following inactive excipients: magnesium stearate, aerosil, sodium dodecyl sulphate, talc, starch and microcel MC-102 1. The placebo mixture, containing pharmaceutical grade excipients with the same quantitative composition as the pharmaceutical formulations, was also obtained from local drug stores A, B and C.

2.2. Apparatus and chromatographic conditions

Chromatographic separations were carried out using a Shimadzu® HPLC system (Kyoto, Japan) series LC-10A, consisting of a LC AVP pump, a CLASS-VP 5.02 integration system, a DGU-14 A degasser, a 7725i manual injector with a 20 μL loop (Rheodyne®, California, USA), a SPD-10AVP integrated UV detector, a FCV-10ALVP valve, a CTO-10AVP column oven and a SCL-10 AVP controller. The peak purity was determined on a SPD-M 10A VP photodiode-array (PDA) detector. Chromatographic columns and equipment consisted of a LiChroSpher RP-18 (Merck®, Darmstadt, Germany) packed column (100 mm × 4.6 mm i.d., 5 μm particle size) combined with a guard column (10 mm × 4.6 mm i.d.) and a Nucleosil C8 analytical column, 5 μm particle size, 125 mm × 4.6 mm i.d. (Macherey Nagel®, Düren, Germany) with a guard column (20 mm × 4.6 mm i.d., 5 μm); digital pH meter PA 200 (Marconi® S.A., Piracicaba, Brazil); ultrasonic Bath model USC2800A (Unique®, São Paulo, Brazil); analytical balance model 410 (Kern®, Kern, Germany); reverse osmosis water purifier OS 10 LTH (Gehaka®, São Paulo, Brazil); vacuum filtration system (Millipore®, Bedford, USA); and PTFE membrane filters with a pore size of 0.45 μm and diameter of 13.0 mm (Millipore®, Bedford, USA). Peak identify was confirmed by retention time comparison.

The mobile phase was composed of acetonitrile and phosphate buffer. The proportions of these mobile phase components as well as the phosphate buffer pH were changed according to each level of the multivariate optimization. The mobile phases were prepared daily, filtered through a 0.45 μm membrane filter Millipore and degassed using the degasser of the chromatographic system prior to use. The UV detection was carried out at 254 nm wavelength, and the injection volume was 20 μL.

2.3. Preparation of solutions

2.3.1. Stock and working standard solutions of losartan potassium

Stock standard solution of 0.5 mg mL^{-1} of losartan potassium was prepared by accurately weighing approximately 25 mg of losartan potassium (98.90% purity) into a 50 mL volumetric flask and diluting to volume with mobile phase.

Working solutions were prepared immediately before use by suitable dilutions of the corresponding stock solutions to appropriate concentration levels, using mobile phase as the diluent.

2.3.2. Sample capsules solution

Pharmaceutical formulations from three different local drug stores were used and coded as A, B and C. In each case, 20 capsules were weighed and the content of the capsules was removed. The emptied shells were weighed, and the average weight of the contents was obtained by subtracting the weight of the shell from the weight of the full 20 capsule, as recommended by the United States Pharmacopeia [1]. The weight equivalent to 0.5 average dosage unit of each product was transferred into a 50 mL volumetric flask and diluted to volume with mobile phase. The solution was filtered, then diluted immediately before use to appropriate concentration levels, using mobile phase.

2.3.3. Losartan potassium excipient solutions

Excipients solutions (A, B and C) were prepared by transferring a homogeneous mixture of the placebo mixture with the same quantitative composition as the pharmaceutical formulations (A, B and C) into a 50 mL volumetric flask and diluting to volume with mobile phase. This solution was filtered, and 1 mL was transferred to a 10-mL calibrated flask and diluted to the mark with mobile phase.

2.4. Screening design to investigate the chromatographic parameters

The experimental approach adopted in this work was carried out according to the literature [28] in order to investigate which experimental factors are the most important and which factors do not significantly affect the experimental results. Five variables were examined in two levels, lower (−) and upper (+). The factors and their levels were as follows: pH of buffer used in the mobile phase (2.5 and 7.0), proportion of the phosphate buffer in the mobile phase (60% and 70%), column temperature (25 °C and 35 °C), mobile phase flow rate (0.8 and 1.2 mL min^{-1}) and column type (silica C8 and RP-18). A losartan potassium work standard solution at 50 mg L^{-1} concentration was utilized in these experiments (Section 2.3.1).

The analytical response used in this experimental design was based on the theoretical plates/retention time ratio (TP/RT), in order to optimize analytical performance with a reduced analysis time. The number of theoretical plates was calculated according to chromatographic theory, via Eq. (1):

$$\mathrm{TP} = 16\left(\frac{tr}{Wb}\right)^2 \quad (1)$$

where *tr* is retention time of the losartan potassium and *Wb* is width of the peak at its base, obtained by extrapolating the relatively straight sides of the peak to the baseline.

After establishment of answers based on the theoretical plates/retention time ratio, a 2^{5-1} fractional factorial design was chosen with a total of 16 experiments, and each experiment was carried out twice in random order. In Table 1, the combinations of

Table 1
The 2^{5-1} fractional factorial design and the results obtained for the HPLC method for determination of losartan potassium in capsules.

Runs	Buffer proportion (a) −(60%) +(70%)	Column temperature (b) −(25 °C) +(35 °C)	pH of the buffer (c) −(2.5) +(7.0)	Flow (mL min^{-1}) (d) −(0.8) +(1.2)	Column type (e) −(C8) +(C18)	Responses (theoretical plates/retention time) Response 1	Response 2	Response mean values	Variance
1	−	−	−	−	+	1030.41	1041.13	1035.77	57.46
2	+	−	−	−	−	370.05	367.04	368.55	4.53
3	−	+	−	−	−	1062.10	1062.48	1062.29	0.07
4	+	+	−	−	+	491.99	506.51	499.25	105.42
5	−	−	+	−	−	1383.48	1440.35	1411.91	1617.10
6	+	−	+	−	+	544.96	546.49	545.73	1.17
7	−	+	+	−	+	1189.10	1144.31	1166.70	1003.07
8	+	+	+	−	−	1209.44	1201.76	1205.60	29.49
9	−	−	−	+	−	1227.04	1233.30	1230.17	19.59
10	+	−	−	+	+	560.19	555.09	557.64	13.01
11	−	+	−	+	+	1359.02	1386.12	1372.57	367.20
12	+	+	−	+	−	565.95	571.43	568.69	15.02
13	−	−	+	+	+	1295.58	1270.80	1283.19	307.02
14	+	−	+	+	−	1169.95	1321.93	1245.94	11548.96
15	−	+	+	+	−	1802.13	1802.05	1802.09	0.003
16	+	+	+	+	+	792.31	786.04	789.18	19.66

Table 2
Estimated contrast of the factors and estimated error.

Factors and interactions	Estimated contrasts
Phosphate buffer proportion	−573.02
Column temperature	98.43
pH of the buffer	344.43
Mobile phase flow	194.21
Column type	−205.65
Phosphate buffer proportion × column temperature	−12.22
Phosphate buffer proportion × pH of the buffer	103.65
Phosphate buffer proportion × mobile phase flow	−58.63
Phosphate buffer proportion × column type	−43.59
Column temperature × pH of the buffer	20.77
Column temperature × mobile phase flow	−44.54
Column temperature × column type	2.91
pH of the buffer × mobile phase flow	3.40
pH of the buffer × column type	116.47
Mobile phase flow × column type	−5.43
Estimated error	23.03

factors and their levels are shown with the results of each experiment.

The values of responses were used to calculate the mean values of the analytical responses, as well as the variance of each experiment (Table 1). The variance of each experiment was obtained using Eq. (2):

$$s^2 = \frac{1}{n-1}\sum_{i=1}^{n}(x_i - \bar{x})^2, \tag{2}$$

where n is the number of times that the assay was repeated, x_i represents the analytical responses of each assay (theoretical plates/retention time), and $\bar{x}$ represents the mean value of the analytical responses. The analytical responses were also used to calculate the estimated contrast of each factor (Table 2). Estimated contrast, like the effect of each factor, is the average of all the values obtained (in this case, theoretical plates/retention time) when the factors were at the positive level, minus the average of the values corresponding to the lines where there are negative levels. For example, the estimated contrast for phosphate buffer proportion is obtained from: [(1/8)(368.55 + 499.25 + 545.73 + 1205.60 + 557.64 + 568.69 + 1245.94 + 789.18) − [(1/8) (1035.77 + 1062.29 + 1411.91 + 1166.70 + 1230.17 + 1372.57 + 1283.19 + 1802.09] = −573.02. The estimated contrasts of the interaction were calculated similarly to the main estimated contrasts. The levels column (−1 and +1) of the interaction factors is equal to the product of the columns of the main factors, element to element on the same row.

In order to determinate the statistical significance of the factors and their interactions, the standard variance (s_p^2) was calculated via Eq. (3):

$$s_p^2 = \frac{(n_A - 1)s_A^2 + (n_B - 1)s_B^2}{(n_A - 1) + (n_B - 1)} \tag{3}$$

where n is the number of times the assay was repeated and s^2 is the variance obtained in each assay. Moreover, the estimated variance of the contrast was obtained from Eq. (4):

$$V(\text{estimated}) = \frac{s_p^2}{n} + \frac{s_p^2}{n} \tag{4}$$

where s_p^2 is the standard variance and n is the number of assays with low and high levels ($n = 8$). The error of the estimate of the contrast was obtained by extracting the root of the variance. By multiplying the error by the critical $t_{16\text{-}1}$ (2.120) for a confidence interval of 95%, the estimated error was obtained.

2.5. Final optimization by Doehlert design

After establishing the significant factors from the fractional factorial design, the final optimization was further carried out using a Doehlert design, which comprises seven conditions, with the central point carried out in triplicate [27]. The factors and their levels were the pH of buffer used in the mobile phase (2.0; 3.25; 4.5; 5.75 and 7.0) and the proportion of the phosphate buffer in the mobile phase (60%; 65% and 70%). From this design, it was possible to apply the response surface method (RSM) to optimize the factors' levels. All data were processed using the STATISTICAL package software (version 6.0; StatSoft, Inc., Tulsa, OK, USA).

2.6. Chromatographic conditions after optimization

After method optimization, HPLC analyses were carried out using potassium phosphate buffer (pH 6.2; 58 mmol L^{-1}) and acetonitrile (65:35, v/v) as mobile phase, flow rate at 1.0 mL min^{-1} with column temperature of 35 °C, Nucleosil C8 analytical column, UV detection wavelength at 254 nm and 20 μL of injection volume.

2.7. Method validation

Method validation was performed following ICH and FDA specifications [29,30] for selectivity, linearity, accuracy, precision, robustness, detection limit and quantitation limit.

3. Results and discussion

3.1. Method development and optimization

Different methods are described for the analysis of losartan potassium in pharmaceutical products by using different chromatographic conditions. The pharmacopoeia method for analysis of drug substance [1], when applied for the determination of losartan potassium in capsules, yields a smaller number of theoretical plates than expected (less than 2000). This phenomenon was attributed to the differences between the analytical column recommended by USP and the available columns in our laboratory. Therefore, we decided to develop an HPLC analytical method for analysis of losartan potassium capsules, taking into consideration the influence of chromatographic parameters on the method and aiming to improve the chromatographic efficiency, with the available resources, through a multivariate approach.

Since theoretical plate number is indicative of column efficiency, we decided to use this parameter as analytical response. However, as expected, it was observed experimentally that the number of theoretical plates increased with the increase of retention time. Considering that retention time should be short in order to decrease analysis time and mobile phase consumption, the response based on TP/RT ratio was successfully employed as a compromise between the higher required theoretical plates and low run time. This condition is appropriate for application by routine quality control laboratories.

The results of the factorial design are shown in Table 2. When the estimated contrasts of factorial design exceed the estimated error, this effect becomes statistically significant [28]. Furthermore, variables with positive estimated contrasts indicate that an increase of their level provides a significant increase in the analytical response, and negative effects mean that a higher TP/RT ratio is obtained with a decrease in the levels of the variables.

Comparing the results of the estimated contrast with the estimated error (Table 2), it was concluded that all factors were statistically significant. The positive estimated contrasts for temperature, pH of the buffer and mobile phase flow rate indicate that the analytical signal increases significantly with increase of these factors' levels. On the other hand, the estimated contrasts for proportion of the phosphate buffer and column type are negative, which indicates that a higher analytical signal will be achieved by decreasing their levels. As column type is a qualitative factor, we decided to adopt the C8 column for the subsequent studies. Column temperature values above 35 °C were not tested because the use of mobile phase at high pH and high temperatures can damage the silica of the stationary phase. Thus, column temperature was set at 35 °C. The increase in the analytical response observed with the increase of the mobile phase flow rate was attributed to the decrease in retention time and, of course, accompanied by the decrease of the theoretical plates. A very high increase of the mobile phase flow rate is not beneficial, because it can harm the process of diffusion of the losartan potassium between the stationary and mobile phases. Therefore, the mobile phase flow rate was fixed at an intermediate value (1 mL min^{-1}).

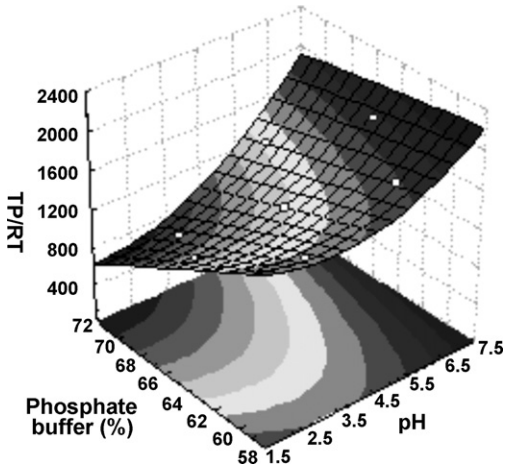


Fig. 1. Response surface of the theoretical plates divided by retention time (TP/RT). The selected working conditions were 65% of 58 mmol L^{-1} phosphate buffer (pH 6.2).

Due to the significant interaction between proportions of the components in the mobile phase and the pH of the buffer used in the mobile phase, a final optimization of these factors was accomplished by Doehlert design (Section 2.5). From this design, the response surface was obtained using the STATISTICAL package software. As verified in Fig. 1, the decrease in proportions of phosphate in the mobile phase when the pH value is low leads to a significant improvement of the analytical signal. On the other hand, when pH is maintained at a high value, for instance pH 7.0, the decrease in proportions of phosphate is only slightly significant. Therefore, using high pH values within the experimental domain, any proportion of phosphate could be employed without significant change in analytical response. In addition, it must be emphasized that such results could never have been observed if a univariate method had been used. So, although high pH values provide the best results, we decided to adopt a phosphate buffer at pH 6.2 in order to preserve the lifetime of the column, while the proportion of phosphate in the buffer at pH 6.2 was fixed at 65%. Smaller ratios of buffer mobile phase content were not used, since it was experimentally observed that this condition can cause a very low retention time.

Therefore, the method developed for the determination of losartan potassium capsules has the following chromatographic parameters: potassium phosphate buffer (pH 6.2; 58 mmol L^{-1})–acetonitrile (65:35, v/v) as mobile phase, flow rate at 1.0 mL min^{-1} with column temperature of 35 °C, C8 analytical column, UV detection wavelength at 254 nm and 20 μL of injection volume.

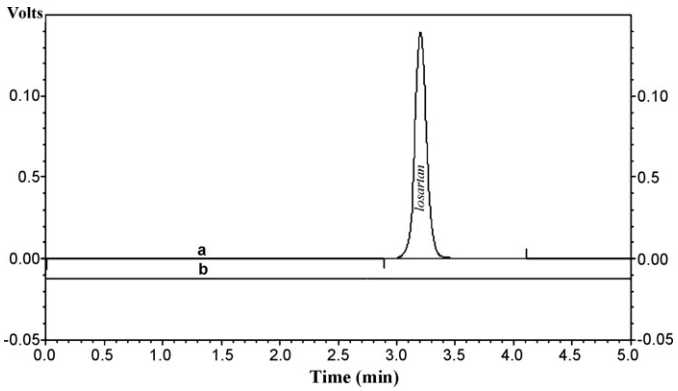


Fig. 2. Chromatogram of losartan potassium capsules (a) and placebo (b).

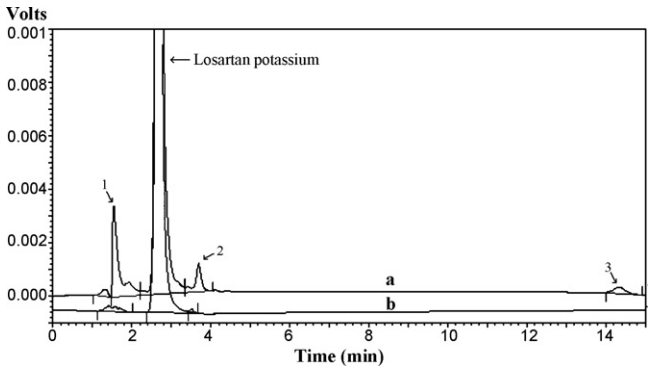


Fig. 3. Chromatogram of losartan potassium reference substance after reflux at 105 °C for 2 h in 1.0 hydrochloric acid (a) and under normal conditions (b).

3.2. Method validation

3.2.1. System suitability testing

System suitability testing was carried out by injecting six replicates of a work standard solution of losartan potassium (Section 2.3.1) containing 50 mg L^{-1} (100% level). According to the FDA [30], the capacity factor (k') must be higher than 2, tailing factor less than 2 and theoretical plate number higher than 2000. These parameters were calculated using CLASS-VP 5.02 software. The observed retention time was 3.19 min; theoretical plates higher than 4900; capacity factor higher than 2.19; and asymmetry of 1.06. All parameters are in accordance with FDA recommendations [30].

3.2.2. Selectivity

Selectivity of the method was evaluated by observing the chromatograms of losartan potassium excipient solutions (Section 2.3.3) and losartan potassium work standard solution at a concentration of 50 mg L^{-1} (Section 2.3.1). The chromatogram depicted in Fig. 2 shows that the excipients have negligible contribution to the losartan potassium peak.

In order to evaluate selectivity of the method for potential degradation products, 25 mg of losartan potassium standard was accurately weighted and diluted in 1.0 mol L^{-1} HCl to a concentration of 50 mg L^{-1}. This solution was heated under reflux at 105 °C for 2 h, then neutralized by adjusting the pH to 7.0 using sodium hydroxide 1 mol l^{-1} solution. The solution was filtered and injected into HPLC. This procedure was performed based on previous reported works [12,17,18], in which degradation products for losartan potassium were observed under the same stress conditions. Other conditions that usually cause degradation were not performed because in those studies no degradation products were obtained under those conditions.

The chromatogram depicted in Fig. 3 shows that after this stress study, additional peaks were observed that were attributed to possible degradation products. They were numbered 1, 2 and 3, based on the order of elution. Through PDA purity study, the losartan potassium peak was found to be pure. The peak purity index was 0.9973. Moreover, the resolutions between losartan and potential degradation products 1, 2 and 3 were 1.70, 1.64 and 14.70, respectively, indicating adequate separation of losartan potassium from each other peak. This separation confirmed the selectivity of the method.

3.2.3. Linearity

Linearity was evaluated by the analysis of working standard solutions of losartan potassium (Section 2.3.1) in five replicates in the final concentrations of 30, 40, 50, 60 and 70 mg L^{-1} of losartan potassium (ranging from 60% to 140% of a 50 mg nominal dose in capsules). The data of peak area versus drug concentration were examined by linear least square regression analysis. The response for the drug was linear in the concentration range between 30 and 70 mg L^{-1}. The calibration equations and determination coefficient obtained were $A = 20321[\text{losartan potassium}] + 2917.2$ and 0.9998, respectively. The relative standard deviations for each point ($n = 5$) were smaller than 2%.

3.2.4. Precision

Precision was evaluated with respect to both repeatability and intermediate precision. Repeatability was evaluated by analyzing six replicates of losartan potassium work standard solutions at a concentration of 50 mg L^{-1} (Section 2.3.1). This procedure was repeated over a short period of time on the same day. Intermediate precision also was evaluated by injection of six independent solutions of losartan potassium at 50 mg L^{-1}, but this procedure was repeated on different days. All samples were prepared and evaluated daily. The observed R.S.D. values for repeatability and intermediate precision were <2%, confirming that the method is sufficiently precise (Table 3).

3.2.5. Accuracy

The accuracy of the losartan potassium capsules method was determined by measuring the reference standard recovery in triplicate at three levels from 80% to 120% of the method concentration (50 mg L^{-1}), added at the beginning of the procedure, according to ICH recommendations. The mean recoveries, expressed in terms of percent recovery of the pharmaceutical dosage forms by the assay and the respective relative standard deviation (R.S.D.), were determined. As shown in Table 4, the mean percentage recoveries of products A, B and C were 98.2, 102.1 and 99.7, respectively, indicating the suitability of the developed method in quantifying the concentration of losartan potassium in pharmaceutical capsules.

Table 3
Results for losartan potassium capsules method precision.

Level	Conditions	Concentration level (mg L^{-1})	Mean of the areas	R.S.D (%)
Repeatability	Series 1	50	1 023 643.83	1.46 ($n = 6$)
	Series 2	50	1 036 100.50	1.21 ($n = 6$)
				1.43 ($n = 12$)
Intermediated precision	Day 1	50	1 043 889.67	0.74 ($n = 6$)
	Day 2	50	1 030 716.67	1.55 ($n = 6$)
				1.33 ($n = 12$)

Table 4
Results for losartan potassium capsules method accuracy.

Sample	Final concentration (mg L^{-1})		R.S.D. (%) ($n = 3$)	Mean recovery (%)
	Added	Found		
A	40	39.3	1.32	98.2
	50	48.7	1.08	
	60	59.4	0.26	
B	40	39.0	1.95	102.1
	50	54.6	1.14	
	60	59.7	0.92	
C	40	42.2	0.10	99.7
	50	51.0	0.95	
	60	54.9	1.86	

Table 5
Assay of losartan potassium in pharmaceutical capsule samples A, B and C.

	Standard	Sample A	Sample B	Sample C
Mean of the areas	948 455.33	913 982.80	928 446.40	944 336.80
R.S.D. (%)	0.39 ($n = 5$)	0.34 ($n = 5$)	0.53 ($n = 5$)	0.48 ($n = 5$)
Losartan (%)	98.90	95.31	96.81	98.47
Losartan (mg)	–	48.19	48.94	49.78

3.2.6. Robustness

The robustness of the method was evaluated by analyzing recovery values data after varying, individually, mobile phase phosphate buffer pH (6.0 and 6.4); organic solvent content (30% and 40%); and column temperature (33 °C and 37 °C). Losartan potassium work standard solutions (Section 2.3.1) at a concentration of 50 mg L^{-1} (100% level) were used in this experiment. According to literature, deliberate variations of HPLC parameters should cause relative errors of less than ±5.0% in analyses of synthetic samples at the 100% level [31]. Recovery values obtained at the 100% level confirmed the robustness of the HPLC assay, since the obtained values were within the acceptance limits (95.0–105.0%) in all cases.

3.2.7. Detection limit and quantitation limit

Detection limit (DL) and quantitation limit (QL) parameters were established based on signal-to-noise (3:1 for DL and 10:1 for QL), according to ICH recommendations [29]. The noise was measured from chromatograms of blank (by injection of the mobile phase) in the same regions as the peaks of the analytes. Using this approach, DL and QL values were found to be 0.114 and 0.420 mg L^{-1}, which demonstrated that the analyses were being performed in a region above the quantitation limit value. Furthermore, these results are in agreement with the literature values of 0.023 and 0.420 mg L^{-1} for the DL and QL, respectively [5].

3.2.8. Analysis of the marketed products

The validated method was applied for determination of losartan potassium in capsule dosage forms. Five samples from each local drug store (A, B and C) were analyzed. The results, expressed as percentage drug related to label claim, are shown in Table 5. The results for the drugs assayed were in good agreement with the label claims.

4. Conclusion

In this study, the application of a multivariate approach using factorial design and the Doehlert matrix was a useful tool for simultaneous study of the five factors that play important roles in chromatographic separation. This strategy produces considerable improvement in HPLC efficiency and, therefore, could be applied in analytical laboratories that are looking to improve chromatographic performance without additional cost for columns or equipment. Another advantage we have noted is the reduction in the total number of simulations necessary to obtain a satisfactory result. The proposed and validated HPLC method was shown to be useful, simple and efficient for determination of losartan potassium in pharmaceutical capsules and could effectively separate the drug from its degradation products. All parameters meet the acceptance criteria for method validation. Therefore, the method is demonstrated to be in compliance with the requirements of quality control.

Acknowledgements

The authors are grateful to the Center of Pharmaceutical Equivalence of the Federal University of Alfenas for financial support and to the Laboratory of Toxicological Analysis of the Federal University of Alfenas for the analyses using the PDA detector. The authors César Ricardo Teixeira Tarley and Hérida Regina Nunes Salgado are grateful to the CNPq for fellowships.

References

[1] The United States Pharmacopoeia, 31st ed., United States Pharmacopoeial Convection, Rockville, MD, 2008, p. 2554.
[2] E.J. Barreiro, C.A.M. Fraga, Química Medicinal: as bases moleculares da ação dos fármacos, Artmed, São Paulo/Porto Alegre, 2001, p. 97.
[3] J.A. Schoenberger, J. Hypertens. 13 (1995) S43–S47.
[4] R.C. Williams, M.S. Alasandro, V.L. Fasone, R.J. Boucher, J.F. Edwards, J. Pharm. Biomed. Anal. 14 (1996) 1539–1546.
[5] C.I. Furtek, M.W. Lo, J. Chromatogr. 573 (1992) 295–301.
[6] L. Kristoffersen, E.L. Øiestad, M.S. Opdal, M. Krogh, E. Lundanes, A.S. Christophersen, J. Chromatogr. B 850 (2007) 147–160.
[7] H. Lee, H.O. Shim, H.S. Lee, Chromatographia 42 (1996) 39–42.
[8] P.K. Yeung, A. Jamieson, G.J. Smith, D. Fice, P.T. Pollak, Int. J. Pharm. 204 (2000) 17–22.
[9] M. Ansari, M. Kazemipour, F. Khosravi, M. Baradaran, Chem. Pharm. Bull. 52 (2004) 1166–1170.
[10] G. Carlucci, G. Palumbo, P. Mazzeo, M.G. Quaglia, J. Pharm. Biomed. Anal. 23 (2000) 185–189.
[11] N. Erk, J. Pharm. Biomed. Anal. 24 (2001) 603–611.
[12] D.L. Hertzog, J.F. McCafferty, X. Fang, R.J. Tyrrell, R.A. Reed, J. Pharm. Biomed. Anal. 30 (2002) 747–760.
[13] M. Lusina, T. Cindri'c, J. Tomai'c, M. Peko, L. Pozai'c, N. Musulin, Int. J. Pharm. 291 (2005) 127–137.
[14] M.A. Obando, J.M. Estela, V. Cerda, Anal. Bioanal. Chem. 391 (2008) 2349–2356.
[15] R. Seburg, J.M. Ballard, T. Hwang, C.M. Sullivan, J. Pharm. Biomed. Anal. 42 (2006) 411–422.
[16] N. Sreekanth, K. Shivshanker, P. Shanmuga Pandian, C. Roosewelt, G. Srinivasa Rao, V. Gunasekaran, Asian J. Chem. 19 (2007) 2850–2856.
[17] Z. Zhao, Q. Wang, E. Tsai, X. Qin, X.D. Ip, J. Pharm. Biomed. Anal. 20 (1999) 129–136.
[18] V.M.P. Maio, C.L. Dias, A.M. Bergold, Acta Farm. Bonaerense 24 (2005) 250–255.
[19] K.E. McCarthy, Q. Wang, E.W. Tsai, R.E. Gilbert, D.P. Ip, M.A. Brooks, J. Pharm. Biomed. Anal. 17 (1998) 671–677.
[20] S.R. Sathe, S.B. Bari, Acta Chromatogr. 19 (2007) 270–278.
[21] M.G. Quaglia, E. Donati, G. Carlucci, P. Mazzeo, S. Fanali, J. Pharm. Biomed. Anal. 29 (2002) 981–987.
[22] O.C. Lastra, I.G. Lemus, H.J. Sánchez, R.F. Pérez, J. Pharm. Biomed. Anal. 33 (2003) 175–180.
[23] R.M. Maggio, P.M. Castellano, T.S. Kaufman, Anal. Bioanal. Chem. 391 (2008) 2949–2955.
[24] A.H. Prabhakar, R. Giridhar, J. Pharm. Biomed. Anal. 27 (2002) 861–866.
[25] Y. Choi, J. Liq, Chromatogr. Rel. Technol. 31 (2008) 2643–2656.
[26] R. Neves, Arzneim. Forsch. 58 (2008) 369–375.
[27] S.L.C. Ferreira, W.N.L. Santos, C.M. Quintella, B.B. Neto, J.M. Bosque-Sendra, Talanta 63 (2004) 1061–1067.
[28] D.C. Montgomery, Design, Analysis of Experiments, Wiley, New York, 2000, pp. 177–185.
[29] International Conference on Harmonization of Technical Requirements for the Registration of Pharmaceutical for Human Use: Validation of Analytical Procedures, Text and Methodology – Q2 (R1), 2005.
[30] FDA. Center for Drug Evaluation and Research (CDER) Validation of Chromatographic Methods, Reviewer Guidance, obtained from web site: http://www.fda.gov/CDER/GUIDANCE/cmc3.pdf.
[31] P.D. Tzanavaras, D.G. Themelis, A. Zotou, J. Stratis, B. Karlberg, J. Pharm. Biomed. Anal. 46 (2008) 670–675.

Talanta 80 (2009) 242–245

Contents lists available at ScienceDirect

Talanta

journal homepage: www.elsevier.com/locate/talanta

Microwave-assisted on-line derivatization for sensitive flow injection fluorometric determination of formaldehyde in some foods

Xiao-Qing Zhao, Zhi-Qi Zhang*

Key Lab of Analytical Chemistry for Life Science of Shaanxi Province, School of Chemistry and Material Science, Shaanxi Normal University, 199 South Chang'an Road, Xi'an, Shaanxi 710062, China

ARTICLE INFO

Article history:
Received 16 February 2009
Received in revised form 25 June 2009
Accepted 28 June 2009
Available online 4 July 2009

Keywords:
Microwave-assisted fluorometry
Flow injection analysis
Formaldehyde
Food analysis

ABSTRACT

A rapid and sensitive flow injection fluorometry has been developed for the determination of formaldehyde based on the microwave on-line accelerating its Hantzsch reaction with cyclohexane-1,3-dione. Under the optimized conditions, the fluorescent intensity is proportional to formaldehyde content in the range from 0.05 ng/mL to 2.000 μg/mL. The detection limit (S/N = 3) is 0.02 ng/mL and the analytical frequency is 28 injections per hour. The relative standard deviations are 2.2% and 3.1% for eleven injections of 0.100 and 0.001 μg/mL of formaldehyde, respectively. With the assistance of microwave irradiation, a best sensitive fluorometry was established for the determination of formaldehyde at a high analytical frequency. This method was successfully applied to food analysis without requiring any sample pretreatment, and the determination results were correlated well with those obtained by the standard method with a sample pretreatment of steam distillation.

© 2009 Elsevier B.V. All rights reserved.

1. Introduction

Formaldehyde is a most widespread carbonyl compound coming from combustion and oxidation of hydrocarbons [1]. The toxicity of formaldehyde to man and animals is well known [2–4], and recently the International Agency for Research on Cancer (IARC) classified it as "carcinogenic to humans" in the Group 1 [5]. An acceptable daily intake (ADI) of 0.2 mg/kg body weight has been set by the US Environmental Protection Agency (EPA) for formaldehyde [6]. Acute toxicity after ingestion of a large amount can cause severe abdominal pain, vomiting, coma, renal injury and possible death. Formaldehyde is found as a contaminant in many foods. The common incriminated food items are beverages like beer and juices, meat, mushroom, bean curd, vermicelli, and hydrated food such as fish, tripe, chicken claws, etc. The formaldehyde content in foods depends on methods of cooking or processing. Sometimes it is added inappropriately in food processing, such as in the process of brewing beer to eliminate unpleasant odour.

In recent years, the determination of formaldehyde has received a great deal of attention. A large number of analytical methods have been reported, such as high-performance liquid chromatography (HPLC) [7,8], biosensors [9], catalytic [10–14] and solid-phase [15,16] photometry, solid-phase microextraction in conjugation with isotope dilution mass spectrometry (ID-MS) [17], GC–MS [18] and capillary zone electrophoresis [19]. The spectrophotometry and fluorometry with Hantzsch reaction are commonly used for the determination of formaldehyde. Cyclohexane-1,3-dione (CHD) [20,21], 2,4-pentandione [22], acetylacetone [23] and Fluoral-P [24] have been used as Hantzsch reaction reagents. Although these methods are sensitive and selective, the derivatization reaction mostly requires high temperature. A spectrofluorometry based on the reaction with acetoacetanilide at room temperature was proposed for the determination of formaldehyde in water [25], and a detection limit of 0.09 ng/mL was reported.

Flow injection analysis (FIA) shows many advantages on rapidity, reproducibility, simplicity and less reagent consumption because it goes along at the nonequilibrium state. Flow injection fluorometry was also reported for the determination of formaldehyde based on Hantzsch reaction. However, the relatively slow derivatization reaction rate limits the development of sensitivity in flow injection system. Though reducing flow rate [20] and extending length of reaction coil [21] could prolong the residence and reaction time, the former would bring bad precision and the latter would increase the dispersion of sample zone. A flow injection fluorometry adopting stopped-flow technique was recently reported and a detection limit of 0.04 ng/mL was reached [26].

As to the determination of formaldehyde in beverages and foodstuffs, a sample pretreatment process, such as steam distillation [11–13,27,28] and extraction [8,18], was necessary for most of the current methods on account of lower detecting sensitivity and the serious effect of sample matrixes. Though a catalytic method was reported for the determination of formaldehyde in beers, it is not suitable for black beers because of the absorption of sample matrix at measuring wavelength [14]. Another method without

* Corresponding author. Tel.: +86 29 85303939; fax: +86 29 85307774.
E-mail address: zqzhang@snnu.edu.cn (Z.-Q. Zhang).

0039-9140/$ – see front matter © 2009 Elsevier B.V. All rights reserved.
doi:10.1016/j.talanta.2009.06.066

sample pretreatment was a flow injection fluorometry with Fluoral-P derivatization reaction used for determination of formaldehyde in alcoholic beverages [24].

Microwave energy has been applied to the field of analytical chemistry, primarily dealing with rapid sample digestion [29–31] and extraction [32,33]. The microwave FIA method not only has the features of FIA but also has the advantage of on-line rapid heating. More importantly, some slow reactions could not proceed in the FIA with conventional heaters because of requiring a long heating time, while microwave radiation on-line assistance makes these reactions suitable for the FIA system [34].

Based on the reaction of formaldehyde with CHD and ammonium to produce a strong fluorescence derivative, the present work combines the selectivity of fluorometry with the effectiveness of microwave-accelerated reaction in a flow injection system to develop a rapid and sensitive method for determination of formaldehyde. Due to the sufficient selectivity and sensitive, proposed method was directly applied to the determination of formaldehyde in black and draft beers, fruit and alcoholic beverages, and extraction solutions of dried food without requiring any sample pretreatment.

2. Materials and experiment

2.1. Apparatus

The manifold of the instrument system established for this work is illustrated in Fig. 1. It consists mainly of a flow-injection analyzer, a microwave oven and a fluorescence detector. An IFIS-C intelligent flow-injection analyzer (Xi'an Ruilian Electronic, China) equipped with two peristaltic pumps and an injection valve was used for sampling and transporting solution. The pumps and valve were controlled by a microprocessor. A 2475 Multi λ Fluorescence detector (Waters Corporation, USA) equipped with a 150 W continuous xenon lamp and a flow cell of 8 μL was used for recording fluorescence spectra and measuring fluorescence intensity. A model XH-100B microwave preparation system (Xianghu Science and Technology Co. Ltd., Beijing, China) was employed for providing microwave irradiation to accelerate the chemical reaction. The power level of the microwave oven could be adjusted from 100 to 800 W. All flow tubes used were 0.9 mm i.d. PTFE. A Model 868 pH meter (Thermo Orion, USA) was used for adjusting solution pH.

2.2. Reagents

All chemicals used in this work were of analytical reagent grade, and water used for the preparation of all solutions was purified with a Milli-Q Labo (Millipore, USA). The formaldehyde standard stock solution (1 mg/mL) was prepared by diluting 2.57 mL of formaldehyde (36%) to 1000 mL with water, and the accurate concentration was standardized with iodimetry. The working standards were daily prepared by accurately diluting the standard stock solution. A buffer solution of acetic acid–ammonium acetate was prepared by dissolving 15 g of ammonium acetate in 500 mL of water and adjusting pH to 5.0 with acetic acid. The CHD solution of 0.150 mg/mL was prepared daily by dissolving 0.0300 g of cyclohexane-1,3-dione (J&K Chemica, USA) in 200 mL of acetic acid–ammonium acetate buffer solution.

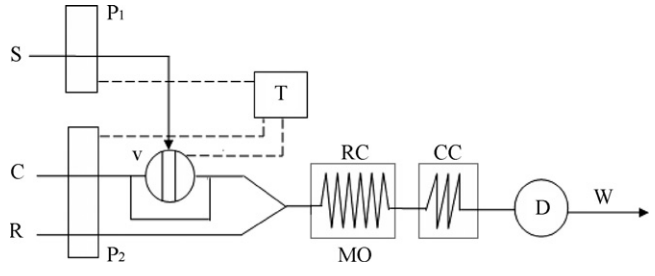


Fig. 1. Schematic diagram of microwave-assistant flow-injection manifold used for determination of formaldehyde. S: sample solution; C: carrier (water); R: reagent solution (0.150 mg/mL CHD in acetic acid–ammonium acetate buffer solution, pH 5.0); P_1, P_2: peristaltic pumps; V: injection valve; T: timer (microprocessor); RC: reaction coil (0.9 mm × 150 cm); CC: cooling coil (0.9 mm × 90 cm, in water bath of 10 °C); MO: microwave oven; D: fluorescence detector; W: waste.

2.3. Flow injection fluorometric procedure

The carrier (water) and the CHD solution are delivered at a flow rate of 0.76 mL/min. The sample of 250 μL is injected into the carrier by means of injection valve V and mixes with the CHD solution. The derivatization reaction of formaldehyde with CHD and ammonium occurs in a reaction coil (150 cm) which was located in the cavity of microwave oven. After derivatization, the mixture stream flows through a cooling coil (90 cm), and then the relative fluorescence intensity of the derivatives is monitored at excitation and emission wavelength of 397 and 465 nm. At the same time, valve V turns to the sampling position and pump 2 runs 35 s for the next sample to be loaded.

2.4. Sample solution preparation

Samples of dried food (mushroom, vermicelli and been curd) were purchased from local market. 5.000 g of portion of each sample was minced and transferred to a 100 mL volumetric flask. Then the flask was filled to 100 mL with water and ultrasoniced for 1 h. After filtrating with micropore membrane, the filtrate was dimensioned to 100 mL with water and the sample solution was obtained. The only further treatment needed is appropriately diluting with water before analysis. Several kinds of drink were randomly collected from different local stores. The test solutions were obtained by direct diluting samples with 20 times water.

For the recovery test, a known amount of formaldehyde standard solution was added into the samples, and then treated as mentioned above.

3. Results and discussion

3.1. Effect of microwave power

The available power in the microwave oven could be calculated using the following equation [29]:

$$\mathrm{Wa} = (Kcm\Delta T)/t$$

where Wa is the available power in the microwave cavity, K the conversion factor, c the heat capacity of water, m the mass of water loading, ΔT the temperature difference between the initial temperature and the final temperature, and t is the heating time. For each segment of the solution in the reaction coil, the K, c and m are identical, considering the reactor length and the flow rate have been fixed, the temperature increase of each segment lies on the irradiation power. The irradiation power was studied from 100 to 600 W (Fig. 2). Though the fluorescence intensity increased with microwave irradiation power enhancing, a great deal of vapour bubbles would be produced due to overmuch temperature enhancing and the repeatability would be poor when irradiation power was higher than 300 W. Therefore, a microwave irradiation power of 300 W was chosen.

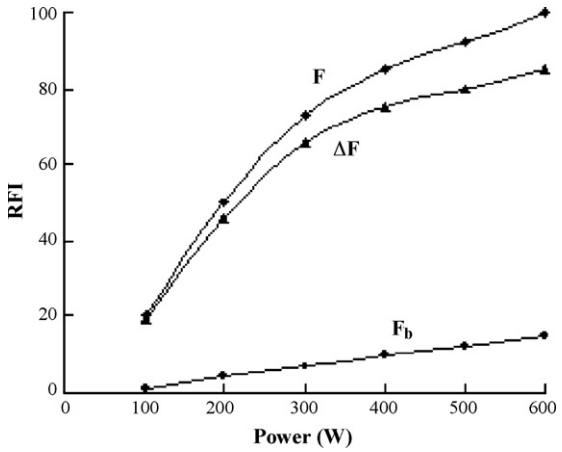


Fig. 2. Effect of microwave irradiation power on the relative fluorescence intensity (RFI). F_b: 0.15 mg/mL CHD; F: 0.100 μg/mL of formaldehyde with 0.15 mg/mL CHD; ΔF: $F - F_b$.

3.2. Effect of chemical variables on the microwave-accelerated derivatization reaction

The effect of the pH was studied in the range 3.5–7. The highest fluorescence intensity was obtained at pH 5.0; further enhancing the pH value drastically decreased the fluorescence intensity because the deprotonation of nitrogen inhibited fluorescence intensity. Hence, the buffer solution of pH 5.0 was chosen to dissolve CHD and prepare CHD solution.

The influence of the CHD concentration was investigated from 0.01 to 0.5 mg/mL (Fig. 3). The fluorescence intensity increased with the concentration increase both for background and formaldehyde. However, the difference of fluorescence intensity between background and formaldehyde (ΔF) retained constant over 0.15 mg/mL of CHD. Therefore, a concentration of 0.150 mg/mL CHD was chosen for the analysis. Compared with previous method [26], a higher CHD concentration was allowed because microwave power accelerated the derivatization reaction rate of formaldehyde and depressed relatively the background.

The effect of concentration of ammonium acetate was studied in the range 1–20% (w/v). It was found that an appropriate peak signal was obtained at an ammonium acetate concentration of 3%. If the concentration was higher, the repeatability would decrease.

3.3. Optimisation of the FI parameters

Under the assistance of microwave power to on-line derivatization, it was necessary to cool the reaction mixture in a cooling bath to obtain a stronger and reproducible fluorescence signal. The FI parameters investigated were the flow rate of sample, carrier and reagent, both lengths of the reaction coil and cooling coil, and the sample volume injected.

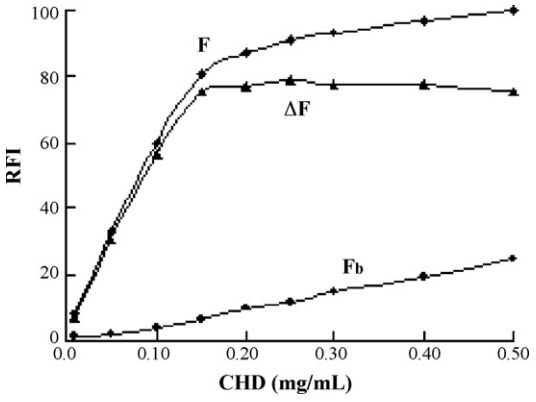


Fig. 3. Effect of CHD concentration on the relative fluorescence intensity (RFI). F_b: background; F: for 0.100 μg/mL of formaldehyde; ΔF: $F - F_b$.

The sensitivity for the determination of formaldehyde obviously depended on the reaction time because of the lower rate of the derivatization reaction. Lower flow rates and a longer reaction coil could give a longer reaction time, but under the assistance of microwave power, too long a reaction time would result in the temperature to be high enough to cause a lot of vapour bubbles. Moreover, too low a flow rate could lead to poor reproducibility and low sample frequency. As a compromise of sensitivity and reproducibility, a flow rate of 0.76 mL/min and a reaction coil of 150 cm were chosen to continue the experiment. The flow rate for sampling was fixed at 2 mL/min to fill the sampling loop with sample solution during the fluorescence measurement (35 s). After heating with microwave, the mixture was cooled in a cooling coil to enhance the fluorescence signal and to reduce the interference of generated bubbles. The cooling coil was immersed in a water bath at 10 °C, and a length of 90 cm was chosen to get an accepted reproducibility without too much dispersion. The fluorescence intensity increased as the injection volume increased across a range of 100–250 μL, and an injection volume of 250 μL was chosen. A period of determination would take 130 s, and the analytical frequency was 28 injections per hour.

3.4. Analytical characteristics

Under the optimized conditions, the calibration graph obtained by plotting fluorescence intensity versus formaldehyde concentration was linear in the range from 0.05 ng/mL to 2.000 μg/mL of formaldehyde, and fitted with the regression equation:

$$\mathrm{RFI} = 738.05 \pm 17.46C + 1.35 \pm 0.04, \quad r = 0.9994$$

where RFI is relative fluorescence intensity, and C is the concentration of formaldehyde in μg/mL. The detection limit calculated from three times the standard deviation of the blank was 0.02 ng/mL. The relative standard derivations for 11 replicate determinations of 0.100 and 0.001 μg/mL of formaldehyde solutions were 2.2% and 3.1%, respectively.

3.5. Interference study

The effect of foreign species concurrently presented in drinks and foods was studied. A similar result with previous work [26] was obtained. It shows that the developed method can be used directly for the determination of formaldehyde in drink and food products.

3.6. Sample analysis

The method has been applied to the determination of formaldehyde in some drink and food products, and was validated with a standard reference method of steam distillation-acetyl acetone spectrophotometry [28].

The determination results of real samples are shown in Table 1 for both proposed method and reference method. The results for recovery tests are also shown in Table 1. It can be seen from Table 1 that the determination results with proposed method are consistent with those obtained with the reference method. The t-test results showed that no significant difference is found between two methods at a confidence level of 95%.

Table 1
Result for the determination of formaldehyde in some drink and food products.[a].

Sample	This method[b]	Rreference method[c]	Recovery		
			Add	Found	Rec (%)
Dried mushroom 1	132.1 ± 32.2	116.5	10.0	141.9	98.0
Dried mushroom 2	256.4 ± 36.2	267.3	10.0	265.6	92.0
Vermicelli	0.047 ± 0.008	0.044	0.100	0.138	91.0
Been curd	0.065 ± 0.011	0.059	0.100	0.159	94.0
Alcoholic beverage	0.093 ± 0.013	0.087	0.100	0.185	92.0
Draft beer	0.172 ± 0.024	0.157	0.200	0.369	98.5
Black beer	0.224 ± 0.042	0.219	0.200	0.405	90.5
Lemon beverage	0.313 ± 0.101	0.302	0.200	0.499	88.0
Apple beverage	0.279 ± 0.053	0.259	0.200	0.484	102.5
Cola beverage	0.532 ± 0.136	0.507	0.200	0.718	93.0

[a] Content express: mg/kg for solid samples and mg/L for liquid samples.
[b] Average ± S.D. (n = 3).
[c] Steam distillation-acetyl acetone spectrophotometry [28].

4. Conclusions

The application of microwave irradiation accelerates considerably the derivatization reaction of formaldehyde with CHD, and allows attaining a higher sensitivity for the determination of formaldehyde in a shorter derivatization reaction time than using the water bath to heat reaction. Therefore, the sensitivity of proposed method is enhanced about one order of magnitude than the references with the same derivatization reagent of CHD [20,21], and a best sensitive FI fluorometry is developed at a high analytical frequency. Owing to the higher sensitive and selective, the procedure excludes the influence of sample matrixes, and allows the direct determination of formaldehyde in several kinds of drink, including black and draft beers; alcoholic, fruit and cola beverages; and some dried food extracts without requiring any sample pretreatment. Compared with stopped-flow method [26], the detection limit descends from 0.04 to 0.02 ng/mL with an increase in analytical frequency from 18 into 28 per hour, and the operating procedure is simpler without preheating the water bath to a controlled higher temperature. The proposed method could be an alternative method for rapid determination of low levels of formaldehyde in drink and food products.

Acknowledgement

The project was supported by National Natural Science Foundation of China (no. 20875060).

References

[1] WHO, Formaldehyde, Environmental Health Criteria, Geneva, Swizerland, 1989.
[2] Agency for Toxic Substances and Disease Registry, Toxicological Profile for Formaldehyde (Draft), Public Health Service, US Department of Health and Human Services, Atlanta, GA, 1997.
[3] R.B. Conolly, J.S. Kimbell, D.B. Janszen, F.J. Miller, Regul. Toxicol. Pharmacol. 35 (2002) 32.
[4] F.A. Malek, K.U. Moritz, J. Fanghanel, J. Ann. Anat. 185 (2003) 277.
[5] International Agency for Research on Cancer, Monograghs on the Evaluation of Carcinogenic Risks to Humans, Formaldehyde, 2-Butoxyethanol and 1-*tert*-Buxy-2-Propanol, IARC, Lyon, France, 2006.
[6] Environmental Protection Agency (US), Integrated Risk Information System on Formaldehyde, National Center for Environmental Assessment, Office of Research and Development, Washington, DC, 1999.
[7] G. Burini, R. Coli, Anal. Chim. Acta 511 (2004) 155.
[8] J.-F. Liu, J.-F. Peng, Y.-G. Chi, G.-B. Jiang, Talanta 65 (2005) 705.
[9] S. Achmanna, M. Hermann, F. Hilbrig, V. Jerome, M. Hammerle, R. Freitag, R. Moos, Talanta 75 (2008) 786.
[10] Z.-Q. Zhang, H.-T. Yan, X.-F. Yue, Microchem. Acta 146 (2004) 259.
[11] T. Pérez-Ruíz, C. Martínez-Lozano, V. Tomás, J. Fenoll, J. Anal. Bioanal. Chem. 375 (2003) 661.
[12] J.-P. Liu, X. Ge, Chin. J. Health Lab. Technol. 115 (2005) 132.
[13] X. Cui, G. Fang, L. Jiang, S. Wang, Anal. Chim. Acta 590 (2007) 253.
[14] X.-F. Yue, Y.-N. Zhang, Z.-Q. Zhang, Food Chem. 102 (2007) 90.
[15] L.S.G. Teixeira, E.S. Leão, A.F. Dantas, H.L.C. Pinheiro, A.C.S. Costa, J.B. de Andrade, Talanta 64 (2004) 711.
[16] A.A. Hill, R.J. Lipert, J.S. Fritz, M.D. Porter, Talanta 77 (2009) 1405.
[17] R.T. Rivero, V. Topiwala, J. Chromatogr. A 1029 (2004) 217.
[18] F. Bianchi, M. Careri, M. Musci, A. Mangia, Food Chem. 100 (2007) 1049.
[19] F.R. Rocha, L.H.G. Coelho, M.L.A. Lopes, L.R.F. Carvalho, J.A.F. da Silva, C.L. do Lago, I.G.R. Gutz, Talanta 76 (2008) 271.
[20] Q. Fan, P.K. Dasgupta, Anal. Chem. 66 (1994) 551.
[21] T. Sakai, H. Nagasawa, H. Nishikawa, Talanta 43 (1996) 859.
[22] K. Motyka, P. Mikuska, Anal. Chim. Acta 518 (2004) 51.
[23] P. Sritharathikhun, M. Oshima, S. Motomizu, Talanta 67 (2005) 1014.
[24] F.S. Oliveira, E.T. Sousa, J.B. de Andrade, Talanta 73 (2007) 561.
[25] Q. Li, M. Oshima, S. Motomizu, Talanta 72 (2007) 1675.
[26] X.-Q. Zhao, Z.-Q. Zhang, Int. J. Food Sci. Technol. 44 (2009) 216.
[27] Z. Li, H. Ma, H. Lu, G. Tao, Talanta 74 (2008) 788.
[28] CNS (The National Standard of China), Method for Analysis of Hygienic Standard of Fermented Wine, GB/T 5009.49, 2003.
[29] H.M. Kingston, L.B. Jassie, Anal. Chem. 58 (1986) 2534.
[30] B. Marin, E.I.B. Chopin, B. Jupinet, D. Gauthier, Talanta 77 (2008) 282.
[31] N. Ratola, S. Lacorte, D. Barcelo, A. Alves, Talanta 77 (2009) 1120.
[32] H. Ulrich, W. Didier, H. Peter, S. Volker, J. Agric. Food Chem. 51 (2003) 1539.
[33] F. Hu, C. Deng, Y. Liu, X. Zhang, Talanta 77 (2009) 1299.
[34] X.-Y. Wu, H. Zhao, X.-G. Chen, Z.-D. Hu, Z.-F. Zhao, Anal. Chim. Acta 374 (1998) 61.

Talanta 80 (2009) 246–249

Contents lists available at ScienceDirect

Talanta

journal homepage: www.elsevier.com/locate/talanta

Fabrication of a novel impedance cell sensor based on the polystyrene/polyaniline/Au nanocomposite

Miaomiao Gu, Jingjing Zhang, Ye Li, Liping Jiang, Jun-Jie Zhu*

Key Lab of Analytical Chemistry for Life Science (MOE), School of Chemistry and Chemical Engineering, Nanjing University, 22 Hankou Road, Nanjing 210093, PR China

ARTICLE INFO

Article history:
Received 3 March 2009
Received in revised form 26 June 2009
Accepted 28 June 2009
Available online 4 July 2009

Keywords:
Gold nanoparticles
PS@PANI
HL-60 cells
Biosensor
Electrochemical impedance spectroscopy

ABSTRACT

Gold nanoparticles (AuNPs) were assembled on the surface of polystyrene (PS) and polyaniline (PANI) core–shell nanocomposite (PS@PANI) for the immobilization of HL-60 leukemia cells to fabricate a cell electrochemical sensor. The immobilized cells exhibited irreversible voltammetric response and increased the electron transfer resistance with a good correlation to the logarithmic value of concentration ranging from 1.6×10^3 to 1.6×10^8 cells mL^{-1} with a limit of detection of 7.3×10^2 cells mL^{-1} at 10σ. This biosensor was simple, low cost and disposable, which implied that the PS@PANI/Au composites can regard as the potential applications for clinical applications.

© 2009 Elsevier B.V. All rights reserved.

1. Introduction

In recent years, there is an increasing demand to use rapid and simple procedures for the detection of cells viability and proliferation. A series of important biochemical and physiological processes in a living cell involve electron generation and transfer. Therefore, the electrochemical and photoelectric techniques have attractive considerable attention for studying efficiently intact living cells [1,2]. For example, the voltammetric responses of the redox centers in living cells usually show irreversible electron transfer processes [3]. This has been used to characterize the viability of cells in homogeneous solution. However, the anodic peak currents in cyclic voltammograms of cells were generally weak. It is important for searching some methods to improve the electrochemical response signal.

With unique chemical and physical properties, gold nanoparticles (AuNPs) are nowadays the subject of a wide field of research [4,5]. Particularly, there is an enormous interest in exploiting gold colloids in biotechnology for biosensing, imaging, and drug delivery [6,7]. Incorporation of AuNPs with polymers or inorganic materials has attracted increasing interest in improving the stability and biocompatibility to enhance the capability of immobilization. Among these materials, polyaniline (PANI) has been proven particularly useful in the development of biosensors, because of its low cost, readily film forming ability, chemical and electrochemical stability [8]. Polystyrene (PS) latex beads are a kind of functional polymer materials, which have many admirable properties such as biocompatibility, nontoxicity, high surface area and chemical inertness. Taking into account the advantages of PS, PANI and AuNPs, the core–shell nanocomposite has been fabricated, and was applied to assemble a glucose biosensor [9]. As far as I know, it was not used for the detection of cells concentration and monitoring the growing states of tumor cells.

Electrochemical impedance spectroscopy (EIS) is usually regarded as an effective way for probing the interfacial properties and has been used to develop the cell sensors [10–12]. Herein, gold nanoparticles were combined with core–shell nanocomposite (PS@PANI) to form a novel 3D architecture conjunction (PS/PANI/Au), which can be further used to immobilize HL-60 leukemia cells to fabricate a cell electrochemical sensor. The biosensor was more effective for the rapid determination of cell concentration ranging from 1.6×10^3 to 1.6×10^8 cells mL^{-1} with a limit of detection of 7.3×10^2 cells mL^{-1} at 10σ. Moreover, the 3D architecture interface can be used for the electrochemical monitoring of the cells adhesion and proliferation, leading a rapid, simple, and more importantly, convenient way to study and monitor the viability of living tumor cell.

2. Experimental

2.1. Materials

Aniline, styrene, ammonium persulfate ($(NH_4)_2S_2O_8$, APS), potassium persulfate ($K_2S_2O_8$, KPS), $HAuC1_4$ and trisodium cit-

* Corresponding author. Tel.: +86 25 83594976; fax: +86 25 83594976.
E-mail address: jjzhu@nju.edu.cn (J.-J. Zhu).

0039-9140/$ – see front matter © 2009 Elsevier B.V. All rights reserved.
doi:10.1016/j.talanta.2009.06.065

rate ($C_6H_5O_7Na_3{\cdot}2H_2O$) were purchased from Shanghai Chemical Reagent Company. Aniline and styrene were distilled under reduced pressure before use. Poly(sodium 4-styrenesulfonate) (PSS, M_w ~70,000) was from Aldrich Chemical Company. Phosphate buffer solution (PBS) (pH 7.4) containing NaCl 137 mM, KCl 2.7 mM, $Na_2HPO_4{\cdot}12H_2O$ 87.2 mM, and KH_2PO_4 14.1 mM was used as electrolyte. All other reagents were of analytical grade and used without further purification.

2.2. The preparation of the core–shell PS/PANI/Au nanocomposite interface

The glass carbon electrode (GCE) was first polished with 1.0, 0.3, and 0.05 μm alumina slurry successively, and then rinsed with doubly distilled water. The PS/PANI/Au nanocomposite was prepared according to the literature [9]. The obtained nanocomposite was then dispread in water to form a 5.0 mg mL^{-1} solution by sonication. Finally, 5 μL of PS/PANI/Au sol was dropped onto the GCE to form a nanocomposite film (PS/PANI/Au/GCE). The modified electrode was stored in air prior to use.

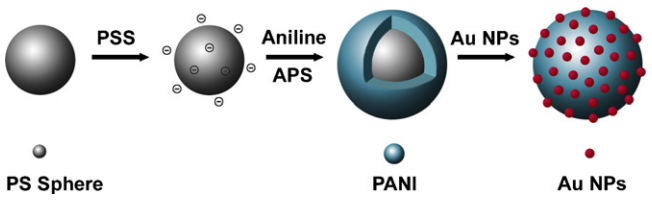
2.3. Cells culture and immobilization

HL-60 cells were cultured in a flask in RPMI 1640 medium (GIBCO) supplemented with 10% fetal calf serum (FCS, Sigma), penicillin (100 μg mL^{-1}), and streptomycin (100 μg mL^{-1}) at 37 °C in a humidified atmosphere containing 5% CO_2. At the growth retardation stage 3 days, the cells reached a number of 1.0×10^7 cell mL^{-1}, which was determined using a Petroff–Hausser counter (USA). They were collected and separated from the medium by centrifugation at 1000 × *g* for 10 min, followed by washing twice with a sterile PBS (pH 7.4) and resuspending in PBS to obtain cell suspension. Finally, 5 μL of the cell suspension was dropped on the PS/PANI/Au modified GCE, and was incubated at 37 °C for 2 h to achieve cell immobilization.

2.4. Apparatus

The morphologies of the PS/PANI/Au nanocomposite were characterized by scanning electron microscopy (SEM, LEO1530VP) and transmission electron microscopy (TEM, JEOLJEM-200CX).

Cyclic voltammetric and amperometric experiments were conducted with a CHI660B workstation (Shanghai Chenhua, Shanghai).



Scheme 1. Schematic illustration of the synthesis of complex PS/PANI/Au.

All experiments were carried out using a conventional three-electrode system in 0.1 M PBS, where nanocomposite-modified GCE was used as working electrode, a platinum wire as auxiliary electrode and a saturated calomel electrode (SCE) as reference electrode. EIS measurements were carried out on a PGSTAT30/FRA2 system (Autolab, Netherlands) using the three-electrode system in solution containing 10 mM $Fe(CN)_6^{3-/4-}$ and 1.0 M KCl. The impedance spectra were recorded within the frequency range of 10^{-2} to 10^6 Hz. The amplitude of the applied sine wave potential in each case was 5 mV. The applied DC potential was about 0.18 V.

3. Results and discussion

3.1. Characterization of the PS/PANI/Au nanocomposite

The formation of the three-component nanocomposite was described in Scheme 1. Briefly, PSS was modified onto the surface of PS beads for the purpose of increasing the negative charges. Then the positive charged aniline monomer was adsorbed onto the PSS modified PS beads. Through in situ polymerization, PS/PANI core–shell structural composite could be obtained. The Au-decorated PS/PANI nanocomposite was finally formed by an electrostatic effect after introducing PS/PANI into the negative charged Au colloid. Fig. 1 shows the typical TEM and SEM images of the PS/PANI/Au nanocomposite. The PS/PANI/Au nanocomposite with an average diameter of 500 nm was uniform in size and morphology. The numerous individual dark nanodots spread along the grey nanospheres in Fig. 1A and the corresponding outside particles in Fig. 1B are AuNPs, which indicates that well-dispersed AuNPs decorate the core–shell structured PS/PANI surface quite uniformly. The nanoparticle-decorated core–shell nanocomposite can be used to fabricate a cell-based biosensor due to the excellent conductivity of PANI and prominent biocompatibility of AuNPs. The biocom-

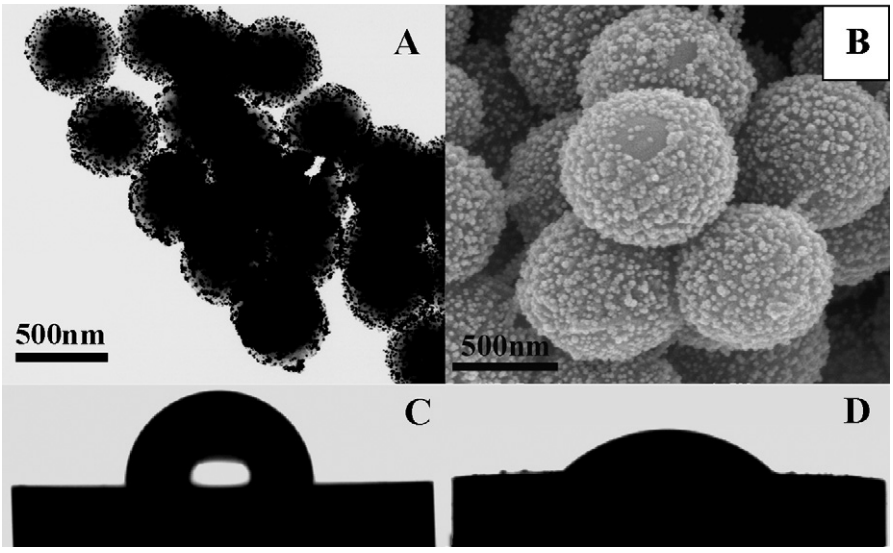


Fig. 1. (A) TEM and (B) SEM images of the PS/PANI/Au nanocomposite. Contact angle of bare electrode (C) and PS/PANI/Au modified electrode (D).

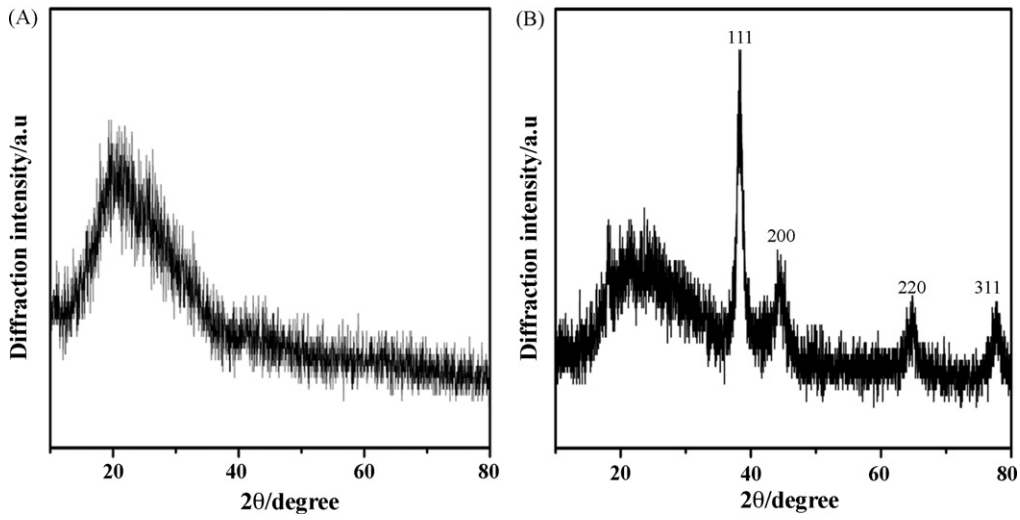


Fig. 2. The XRD patterns of the PS/PANI nanocomposite (A) and the PS/PANI/Au nanocomposite (B).

patibility for loading biomolecules and preserving their bioactivity could be characterized by the hydrophilicity, which could be measured by the contact angle of the substrate. As shown in Fig. 1 (C and D), the contact angle of the bare and PS/PANI/Au modified electrode surface was of 92° (C) and 46° (D) respectively, which indicates the high hydrophilicity of PS/PANI/Au. Thus, the prepared nanocomposite could offer a high hydrophilic surface for promoting cell adhesion and retaining cell activity.

In order to prove Au NPs have been attached on the PS/PANI nanospheres, XRD measurement was carried out. Fig. 2A shows the XRD pattern of the PS/PANI nanospheres, and there was only a broad peak at 22°, which can be assigned to the periodicity parallel to the polymer chains of PANI. While in Fig. 2B, which indicates the XRD pattern of PS/PANI/Au nanocomposite, four additional peaks located at about 38°, 44°, 65°, and 77° are observed besides the broad peak located at 22°. Those peaks can be assigned to the (1 1 1), (2 0 0), (2 2 0), and (3 1 1) lattice planes of fcc-Au.

3.2. Cyclic voltammetric behavior of HL-60 cells on modified electrode

It is well known that many important processes in living cells possess certain electrochemical characteristics. Electron generation and charge transfer exist in all living cells due to the redox reactions and the changes of ionic composition and concentration in life processes [13]. Fig. 3 shows the electrochemical behavior of living cells immobilized on PS/PANI/Au modified electrode. Owning to the larger accessible surface area of the modified electrode, the background current of the PS/PANI/Au modified GCE (Fig. 3b) was greater than that of bare GCE (Fig. 3a). At the modified GCE, the HL-60 tumor cell suspension showed a well-defined irreversible oxidation peak at +0.87 V, while no peak was observed on both bare and PS/PANI/Au (Fig. 3c) modified GCE. The irreversible oxidation peak disappeared in the second scan, and no corresponding reduction peak appeared in the inverse scan, which is the characteristic of an irreversible electrode process. The conversion of guanine in cell cytoplasm to 8-oxo-guanine led to the irreversible electrochemical response of HL-60 tumor cells. In the electrochemical process, the guanine molecules could go through the cell membrane rapidly [14]. Considering the irreversibility of the electrode process of HL-60 cells, the peak current on the first scan was applicable to study tumor cells viability.

3.3. Impedance characteristics of modified electrodes

The electrochemical impedance spectra (EIS) of the modified electrodes were shown in Fig. 4. The electron transfer resistance (R_{et}) was extracted parameters by fitting the EIS data into a suitable equivalent circuit on each independently fabricated electrode. The R_{et} can be used to describe the interface properties of the electrode [15]. At a bare GCE, the redox process of the probe showed a low electron transfer resistance 41.2 Ω (Fig. 3a). When PS/PANI/Au

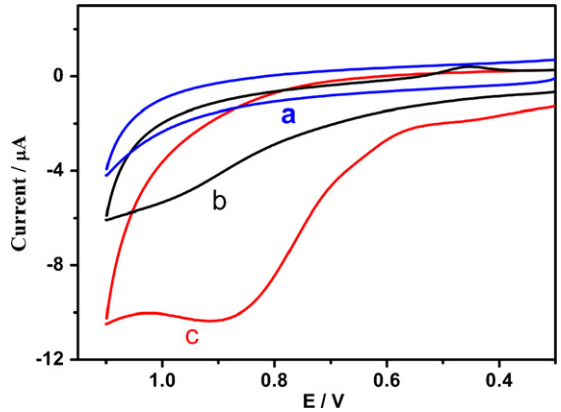


Fig. 3. Cyclic voltammograms of bare GCE (a), PS/PANI/Au/GCE (b), and cells/PS/PANI/Au/GCE (c) in pH 7.4 PBS. Scan rate: 50 mV s^{-1}.

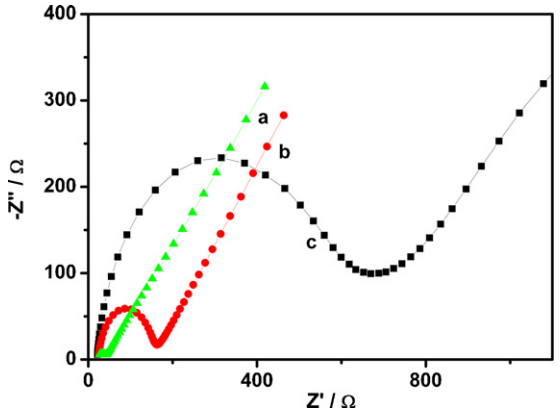


Fig. 4. Nyquist diagrams of electrochemical impedance spectra of bare GCE (a), PS/PANI/Au/GCE (b), and cells/PS/PANI/Au/GCE (c).

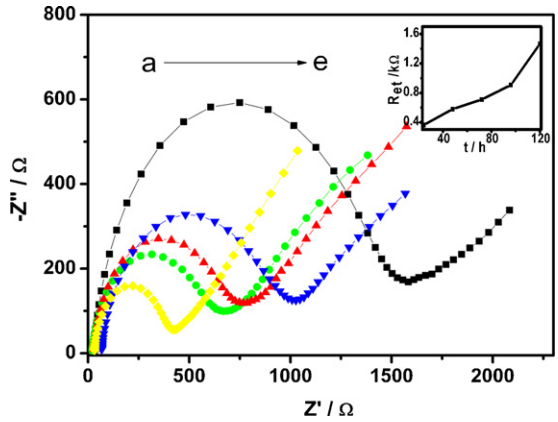


Fig. 5. EIS measurements of HL-60 cells proliferated on PS/PANI/Au/GCE after cell incubation for (a) 24 h, (b) 48 h, (c) 72 h, (d) 96 h and (e) 120 h. Inset: relationship between electron transfer resistance and proliferation time of HL-60 cells on PS/PANI/Au/GCE.

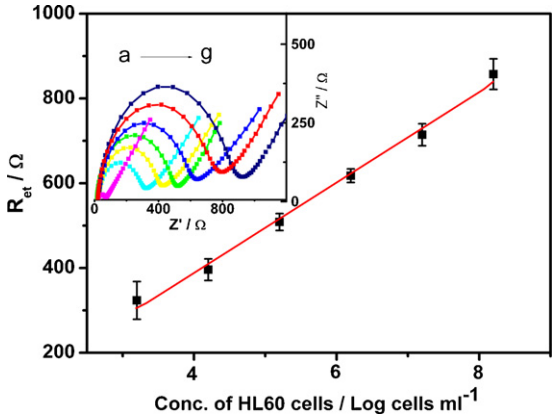


Fig. 6. Linear relationship between electron transfer resistance and logarithm of HL-60 cells concentration. Inset: Nyquist diagrams of PS/PANI/Au modified GCE after immersed in (a) 0 cells mL^{-1}, (b) 1.6×10^3 cells mL^{-1}, (c) 1.6×10^4 cells mL^{-1}, (d) 1.6×10^5 cells mL^{-1}, (e) 1.6×10^6 cells mL^{-1}, (f) 1.6×10^7 cells mL^{-1}, and (g) 1.6×10^8 cells mL^{-1} HL-60 cells suspension.

was assembled on the bare electrode, the semicircle increased dramatically (Fig. 3b). The R_{et} value was about 133.3 Ω, suggesting that the assembly of the nanocomposite layer on the electrode surface inhibited the interfacial electron transfer. When cells were attached to the PS/PANI/Au/GCE, a barrier of the cell membrane would further hinder the redox probe close to the electrode surface and increase the R_{et} value to 601.0 Ω (Fig. 3c). The increasing impedance depended on the surface coverage of the cells, which was proportional to the concentration of the cells used in the adhesion process.

3.4. Monitoring of cell proliferation on electrode surface

EIS measurement was further used to monitor the change of support surface resulting from cell proliferation. Electrochemically monitoring of cell proliferation could be achieved conveniently by placing a set of cells/PS/PANI/Au in culture medium in batch, and measuring at different incubation times. As seen from Fig. 5, with the increasing incubation time, the electron transfer resistance of the redox probe at the produced electrode increased (curves a–e). Obviously resulted from the cell proliferation on the electrode, the increasing amount of cells could lead to a greater barrier for electrochemical process. The inset in Fig. 5 indicates that the R_{et} increased gradually up to the incubation time of 48 h and then tended to a relatively steady value during the incubation time of 48–96 h. After 96 h a sharply increasing resistance was observed, indicating that a majority of HL-60 cells was already dead. This change might be related to the apoptosis of cells, which was congregated on the electrode surface.

3.5. Impedance detection of HL-60 cells

The PS/PANI/Au/GCE could be used for the detection of HL-60 cell concentration. With the increasing concentration of HL-60 cells, the R_{et} value increased, showing increasing diameter of the semicircle on the Nyquist diagram (inset of Fig. 6), implying a higher amount of HL-60 cells immobilized on the electrode. The R_{et} value was proportional to the logarithm of HL-60 cells concentration ranging from 1.6×10^3 to 1.6×10^8 cells mL^{-1} (Fig. 6), with a correlation coefficient of 0.9965. The limit of detection was calculated to be 7.3×10^2 cells mL^{-1} at 10σ, which was comparable with those of several methods developed by other researchers such as the impedance immunosensor for *Escherichia coli* O157:H7 [11] and EIS technique for leukemia K562 cells [16]. Five different biosensors were tested independently for the detection of cells concentration, providing the RSD value of 2.47%.

4. Conclusions

While fabricating a sensitive impedance cell sensor, we took the advantageous features of PANI and gold nanoparticle to construct a nontoxic biocompatible interface for immobilization of tumor cells. Gold nanoparticles with excellent biocompatibility was used to modify leukemia HL-60 cells, which could not only efficiently preserve the activity of tumor cells, but also accelerate the electron transfer between electrode and the immobilized cells. The cell-based impedance sensor showed the wide detection range, low detection limit, good detection precision and simple fabrication process, which could be further developed as a convenient means for the study of cells adhesion, proliferation and apoptosis.

Acknowledgments

The work was supported by the National Natural Science Foundation of China for the Key Program (20635020), Creative Research Group (20821063), and National Basic Research Program of China (2006CB933201).

References

[1] Y.X. Ci, C.Y. Zhang, J. Feng, Bioelectrochem. Bioenerg. 45 (1998) 247.
[2] C. Hao, F. Yan, L. Ding, Y.D. Xue, H.X. Ju, Electrochem. Commun. 9 (2007) 1359.
[3] J. Feng, G.A. Luo, H.Y. Jiang, R.G. Wang, C.C. An, Electroanalysis 12 (2000) 513.
[4] M.C. Daniel, D. Astruc, Chem. Rev. 104 (2004) 293.
[5] H. Vallhov, J. Qin, S.M. Johansson, N. Ahlborg, M.A. Muhammed, A. Scheynius, S. Gabrielsson, Nano Lett. 6 (2006) 1682.
[6] F. He, Q. Shen, H. Jiang, J. Zhou, J. Cheng, D.D. Guo, Q.N. Li, X.M. Wang, D.G. Fu, B.A. Chen, Talanta 77 (2009) 1009.
[7] J.J. Li, L. Zou, D. Hartono, C.N. Ong, B.H. Bay, L.Y. Lanry Yung, Adv. Mater. 20 (2008) 138.
[8] A. Morrin, F. Wilbeer, O. Ngamna, S.E. Moulton, A.J. Killard, G.G. Wallace, M.R. Smyth, Electrochem. Commun. 7 (2005) 317.
[9] Y.G. Liu, X.M. Feng, J.M. Shen, J.J. Zhu, W.H. Hou, J. Phys. Chem. B 112 (2008) 9237.
[10] C.Z. Li, Y. Liu, J.H.T. Luong, Anal. Chem. 77 (2005) 478.
[11] L. Yang, Y. Li, G.F. Erf, Anal. Chem. 76 (2004) 1107.
[12] C. Ruan, L. Yang, Y. Li, Anal. Chem. 74 (2002) 4814.
[13] W. Nonner, B. Eisenberg, J. Mol. Liq. 87 (2000) 149.
[14] M.L. Pedano, G.A. Rivas, Electrochem. Commun. 6 (2004) 10.
[15] S. Hleli, C. Martelet, A. Abdelghani, F. Bessueille, A. Errachid, J. Samitier, H.C.W. Hays, P.A. Millner, N. Burais, N. Jaffrezic Renault, Mater. Sci. Eng. C 26 (2006) 322.
[16] H.L. Hu, H. Jiang, X.M. Wang, B.A. Chen, Electrochem. Commun. 10 (2008) 1121.

Talanta 80 (2009) 250–256

Contents lists available at ScienceDirect

Talanta

journal homepage: www.elsevier.com/locate/talanta

Supported imidazolium ionic liquid phases: A new material for solid-phase extraction

Núria Fontanals[a], Sylwia Ronka[b], Francesc Borrull[a], Andrzej W. Trochimczuk[b], Rosa M. Marcé[a,*]

[a] Departament de Química Analítica i Química Orgànica, Universitat Rovira i Virgili, Campus Sescelades, Marcel·lí Domingo, s/n 43007 Tarragona, Spain
[b] Laboratory of Polymer and Carbon Materials, Faculty of Chemistry, Wrocław University of Technology, Wyspianskiego 27, 50-370 Wrocław, Poland

ARTICLE INFO

Article history:
Received 17 December 2008
Received in revised form 12 June 2009
Accepted 29 June 2009
Available online 4 July 2009

Keywords:
Supported ionic liquid phases
Solid-phase extraction
Anion exchange sorbent
Acidic compounds
Aqueous samples

ABSTRACT

This study reports a material that is based on the concept of ionic liquid analogue: a slightly crosslinked polymer-supported imidazolium trifluoroacetate salt (IL-CF_3COO^-) that favorably combines the properties of ionic liquids (ILs) and the advantages of a solid support.

The ionic liquid-supported material was evaluated for the first time as a solid-phase extraction (SPE) sorbent for selectively and quantitatively extracting pharmaceuticals from aqueous samples.

The novel IL-CF_3COO^- was evaluated under reversed-phase (RP), weak anion exchange (WAX), strong anion exchange (SAX) and strong cation exchange (SCX) SPE procedures, and we found that SAX conditions are the most suitable for investigating the behaviour of the IL-CF_3COO^- material. Under SAX conditions, the IL-CF_3COO^- material was capable of selectively and quantitatively extracting a group of acidic compounds from aqueous samples, while washing basic analytes that were also present in the sample.

The SPE method using IL-CF_3COO^- material was used to analyse 1000 ml of different aqueous samples (ultrapure, tap and river) with complete recovery of the acidic compounds studied. Moreover, the method provided clean chromatogram and high recoveries when percolating complex real samples, such as 1000 ml of river water and 250 ml of effluent wastewater from a sewage treatment plant spiked at low levels with the analytes studied.

© 2009 Elsevier B.V. All rights reserved.

1. Introduction

Ionic liquids (ILs) are inorganic and organic salts with a melting point below 100 °C. The most characteristic features of IL are of negligible volatility and high polarity, comparable to the polarity of lower alcohols [1]. Most organic IL are made up of large cations such as imidazolium, pyridinium, quaternary ammonium and quaternary phosphonium and a suitable anion such as chloride, bromide, trifluoroacetate, trifluoromethane sulfonate, p-toluenosulfonate, etc. By using a proper combination of the cation and anion either hydrophilic ionic liquids or hydrophobic ionic liquids can be obtained. However, even relatively hydrophobic ILs are not totally immiscible with water. The features of high polarity and very low miscibility with water make it possible to use ILs in solvent extraction processes.

In this sense, several examples of IL applications in separation techniques have been reported [2–13]. Thus, ILs are used in many chromatographic applications: as stationary phases in gas chromatography [5–7], as mobile phase additives or stationary phases in liquid chromatography [8,9,14,15], as chemical modifiers in capillary electrophoresis or stationary phases in electrochromatography [16]. Another attractive application is as an extraction solvent, in liquid–liquid extraction for benzene derivatives [2] or for phenol, tyrosol and p-hydroxybenzoic acid [3] or for polyaromatic hydrocarbons in direct-immersion and headspace liquid-phase microextraction [10,11] or in single-drop microextraction [12,13]. The excellent sorptive properties of ionic liquids towards such groups of organic compounds as benzene derivatives [2,12,13], polyaromatic hydrocarbons [10] and alkylphenols [17] prompted some of us to investigate the possibility of polymer-supported imidazolium type ionic liquids [18] and the sorptive properties of such material. We found [18] that the polymer-immobilized imidazolium salts have very good capacity to extract benzene derivatives from aqueous phase. The polymer-supporting of imidazolium salts opens up new possibilities because it solves the problem of the small but measurable solubility of IL, what is an obvious disadvantage in extraction.

Another field of application in which ILs show potential is solid-phase extraction (SPE), the most widely used preconcentration technique largely because of the variety of different materials that can be used as SPE sorbents [19,20]. To date, polymeric

* Corresponding author. Tel.: +34 977 55 81 70; fax: +34 977 55 84 46.
E-mail address: rosamaria.marce@urv.cat (R.M. Marcé).

0039-9140/$ – see front matter © 2009 Elsevier B.V. All rights reserved.
doi:10.1016/j.talanta.2009.06.068

sorbents are regarded as the best SPE materials since they can enhance capacity (i.e. hydrophilic polymers and polymers with high specific surface areas) [21], selectivity (molecularly imprinted polymers—MIPs) [22,23] or both (mixed mode ion-exchange polymers) [24] and, therefore, enlarge the type of sample and the analyte to be extracted. To the best of our knowledge, just two studies [25,26] reported in 2009 the application of immobilized IL onto silica sorbents to isolate tanshinones [25] or enrich polyunsaturated fatty acid methyl esters [26] from complex samples.

In this paper we present a step forward in SPE sorbent technology: we prepared a new material based on the novel concept of ionic liquid-supported phase onto polymer phase, and then pioneered its evaluation as a SPE sorbent to evaluate pharmaceuticals, which are emerging pollutants in the environmental field.

2. Experimental

2.1. Reagents and standards

The reagents used for the supported ionic liquid syntheses were vinylbenzyl chloride (VBC), divinylbenzene (DVB), N-methylimidazole, trifluoroacetic acid and formic acid (HCOOH), all purchased from Sigma–Aldrich (Steinheim, Germany). The VBC (mixture of isomers) was distilled under vacuum before polymerization. DVB (80%) was extracted with 2 M sodium hydroxide (NaOH), washed a few times with water and dried over sodium sulfate. Other reagents were used as received.

The analytes selected to evaluate the sorbents were: salicylic acid, 4-nitrophenol (4-NP) carbamazepine, nalidixic acid, flumequine, naproxen, fenoprofen, diclofenac sodium, ibuprofen and gemfibrozil, all obtained from Aldrich. The structure and pK_a values of all the analytes are shown in Fig. 1.

Standard stock solutions at 1000 mg l^{-1} were prepared for each analyte in methanol (MeOH), except nalidixic acid, which was prepared in 0.1 M NaOH aqueous solution, and flumequine, which was prepared in 50/50 (v/v) MeOH/H_2O at basic pH with NaOH. Working solutions of the mixture of all the compounds were all prepared in 50/50 (v/v) MeOH/H_2O. All the solutions were stored at 4 °C.

Ultrapure reagent water purified by a Milli-Q gradient system (Millipore, Bedford, MA, USA) was used throughout. Acetonitrile (ACN) and MeOH were purchased from SDS (Peypin, France). Other reagents used in the SPE procedures were: phosphoric acid (H_3PO_4) (Merck, Barcelona, Spain), ammonium hydroxide (NH_4OH) (Merck), HCOOH (Probus, Barcelona, Spain), sodium acetate (CH_3COONa) (VWR, Mollet del Vallès, Spain), acetic acid (CH_3COOH) (SDS) and nitrogen of 99.995% purity (Carburos Metálicos, Barcelona, Spain).

2.2. Resin preparation and characterization

The starting polymer was obtained by suspension polymerization of VBC and DVB (2 wt.%) in the presence of 20 wt.% of toluene. The reaction was catalyzed with 0.5 wt.% of benzoyl peroxide and was carried out at 60 °C for 1 h, 70 °C for 1 h, and 85 °C for 2 h and it finished after 5 h at 95 °C. After the polymerization, the material obtained was washed with hot water and acetone, dried and then extracted with toluene in a Soxhlet apparatus.

The VBC/DVB was reacted with the excess of N-methylimidazole. Thus, 15.0 g of dry polymer was placed in the round bottom flask and refluxed with the excess of neat N-methylimidazole for 17 h. After this time the polymer was placed in the column and subjected to a conditioning with: water, 1 M HCl, water, 1 M NaOH, water, 0.1 M CF_3COOH and water at a neutral pH.

The chlorine content in polymers was determined by the Volhard method after the samples (ca. 20 mg) had been burned in

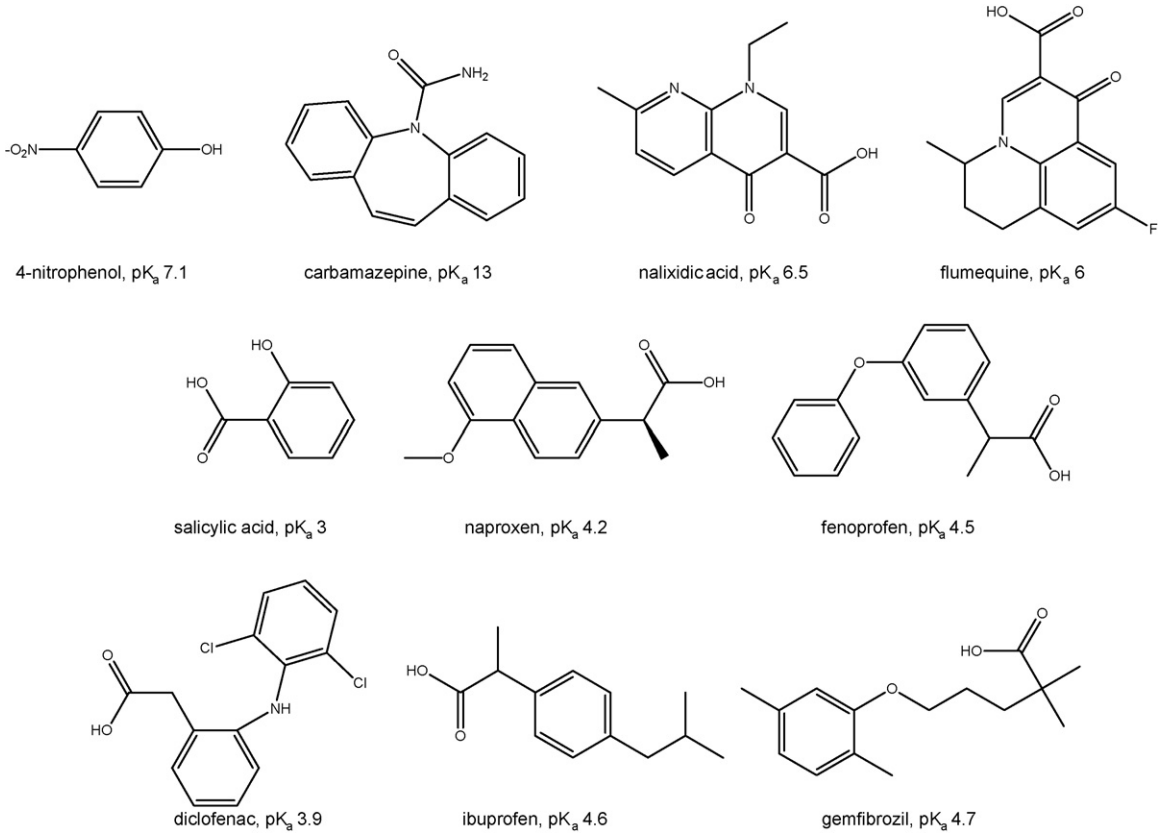


Fig. 1. Structures and pK_a values (calculated using Advanced Chemistry Development (ACD/Labs) Software V8.1) of the studied analytes.

Table 1
SPE conditions for RP, WAX, SAX and SCX evaluation.

	SPE conditions			
	Reversed-phase (RP)	Weak anion exchange (WAX)	Strong anion exchange (SAX)[a]	Strong cation exchange (SCX)
1. Condition	5 ml MeOH + drying at 10 mmHg for 10 min + 5 ml water			
2. Load	5 ml ultrapure water, pH 7	5 ml ultrapure water, pH 7	5 ml ultrapure water, pH 7	5 ml 2% HCOOH in ultrapure water
3. Equilibrate	1 ml water	1 ml 25 mM sodium acetate buffer, pH 5	1 ml 25 mM sodium acetate buffer, pH 7	–
4. Washing	–	1 ml MeOH	1 ml MeOH	1 ml MeOH 1 ml of 2% HCOOH in 20/80 (v/v) MeOH/ACN
5. Elution 1	4 × 5 ml MeOH	5 ml of 2% NH_4OH in 20/80 (v/v) MeOH/ACN	5 ml of 2% HCOOH in 20/80 (v/v) MeOH/ACN	5 ml of 5% NH_4OH in MeOH
6. Elution 2	10 ml of 2% HCOOH in 20/80 (v/v) MeOH/ACN			

[a] The conditions detailed for the SAX procedure are the initial conditions. They vary as they are optimized along the manuscript.

oxygen and the fumes absorbed in 20 ml of H_2O_2 solution. The nitrogen content was determined by the Kjeldahl method.

2.3. Instrumentation

The chromatographic experiments were performed with two LC-10AD$_{VP}$ pumps, a DGU-14A degasser and a CTO-6AS column oven (all from Shimadzu, Tokyo, Japan), an injection valve with a 20 μl loop and a Hewlett-Packard (Avondale, PA, USA) Series 1100 UV spectrophotometric detector. The analytical column was a 250 mm × 4.6 mm i.d. stainless-steel column packed with Kromasil 100 C_{18}, 5 μm (Teknokroma, Sant Cugat del Vallès, Spain).

2.4. Chromatographic conditions

The mobile phase was: ultrapure water adjusted to pH 2.8 with H_3PO_4 and acetonitrile (ACN). The flow-rate was 1 ml min^{-1} and the temperature of the column oven was set at 30 °C. The gradient profile was 40% initially for 8 min, which was increased to 60% ACN in 12 min, and to 100% ACN in 8 min (held for 2 min). The mobile phase was then returned to the initial conditions (40% ACN) in 2 min.

The wavelength used to detect all the compounds was set at 210 nm throughout the analysis.

2.5. Solid-phase extraction procedure

The SPE evaluation was performed in an off-line mode using 500 mg of IL-CF_3COO^- resin packed into 6 ml polypropylene cartridges equipped with two polyethylene frits (Symta, Madrid, Spain). The cartridges were connected to an SPE manifold (Teknokroma), which was connected to a vacuum pump.

The laboratory-synthesized IL-CF_3COO^- resin was compared to the commercially available sorbent Oasis MAX (500 mg) from Waters (Milford, MA, USA).

The SPE protocols used depended on whether the sorbent was being evaluated as reversed-phase (RP), weak anion exchange (WAX), strong anion exchange (SAX), or strong cation exchange (SCX). They are listed in Table 1 and are all adapted from standard SPE procedures [27,28]. After the optimization studies, the sorbent was evaluated under SAX conditions and using the following protocol: sample: ultrapure water at pH 7; equilibration: 1 ml of 25 mM CH_3COONa, pH 5; washing: 20 ml of MeOH; elution: 10 ml of 5% HCOOH in MeOH; regeneration: 5 ml of 5% HCOOH in MeOH.

In real water samples, the optimum protocol was used, but, the two eluates from the washing and the elution steps were reduced to dryness under a stream of nitrogen and the respective residues were redissolved with 0.5 ml 50/50 (v/v) MeOH/H_2O to decrease the analyte concentration levels as close as possible to the low levels found in the environmental water samples.

2.6. Sample collection and preparation

Real water samples (tap water from Tarragona, Ebro river water and effluent waste water from a treatment plant in Tarragona) were acidified and kept in the fridge at 4 °C. Before analysis they were readjusted to pH 7 with NaOH and filtered through 0.45 μm nylon membranes (Osmonics Inc., Minnetonka, MN, USA) to remove the particulate matter before the SPE step.

3. Results and discussion

3.1. Preparation and characterization of the IL-CF_3COO^- material

The polymer-immobilized imidazolium salt was prepared in a one-step simple reaction of VBC–DVB copolymer with N-methylimidazole (Fig. 2). The elemental analysis gave 0.32 mmol of residual Cl per g and 5.47 mmol of N per g of dry material in the form of CF_3COO^-, which corresponds to 2.73 mmol of imidazolium groups per g. These results show that the modification leading to the immobilized imidazolium salt proceeds with very high yield and the resultant material contains almost the maximum possible amount of immobilized salt. After the reaction (Fig. 2), the polymer contains the Cl^- groups but these groups can be easily substituted by an ion-exchanger to the desired ionic form. These forms, chosen for the purpose of this research, were trifluoroacetate and formate. The former is used in ionic liquid chemistry, and the latter was tried because HCOOH is being used in the elution solutions of SPE experiments. The high water content (2.55 and 4.26 g of water per g of polymer for trifluoroacetate and formate, respectively) ensures the good kinetics of solute diffusion within the polymeric beads. Moreover, a copolymer with 2 wt.% of crosslinking agent was used to ensure that the resulting material swelled appropriately and to provide sufficient mechanical strength.

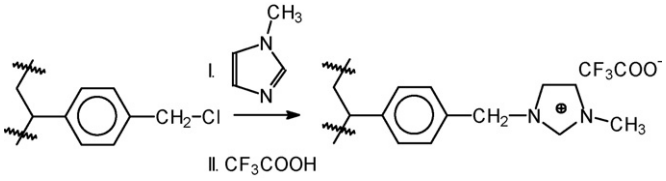


Fig. 2. Scheme of the IL-CF_3COO^- synthesis.

Table 2
% Recovery values of the analytes with the IL sorbent using the different SPE protocols after extracting 5 ml of ultrapure water solution at pH 7 with the analyte mixture.

Solutes	pK_a	% Recovery											
		RP			WAX			SAX			SCX		
		Wash	Elution 1	Elution 2	Wash	Elution 1	Elution 2	Wash	Elution 1	Elution 2	Wash	Elution 1	Elution 2
Carbamazepine	13	5	61	0	89	2	11	69	4	5	15	73	0
4-NP	7.1	12	63	0	33	0	50	45	39	12	9	26	54
Nalidixic acid	6.5	14	43	11	85	6	18	81	27	0	25	54	8
Flumequine	6	10	46	12	88	2	19	87	20	0	15	47	9
Gemfibrozil	4.7	3	90	10	82	2	11	0	96	0	25	36	21
Ibuprofen	4.6	2	38	63	49	1	48	0	98	3	19	45	7
Fenoprofen	4.5	3	13	92	31	2	52	0	93	8	13	37	17
Naproxen	4.2	0	11	85	25	3	44	0	101	13	8	23	28
Diclofenac	3.9	4	11	96	12	2	43	0	102	5	16	19	24
Salicylic acid	3	10	4	5	3	3	12	0	89	0	0	0	18

For the experimental conditions, see text. % Relative standard deviation (RSD) ($n = 3$) were lower than 4% when % recovery >15%.

3.2. Selection of the optimum protocol in SPE

We first tested several SPE procedures in order to determine which retention mechanisms the interaction of IL-CF_3COO^- with the analytes is based on. For this, in order to test a wide range of interactions we selected a group pharmaceuticals considered emerging contaminants of environmental interest (see Fig. 1), and also 4-NP. The studied compounds include polar analytes with different basic–acidic properties, and particularly acidic compounds.

We tested four SPE protocols: reversed-phase (RP), weak anion exchange (WAX), strong anion exchange (SAX) and strong cation exchange (SCX). Table 1 summarizes the conditions in each of the procedures tested. At the end of each SPE procedure, an extra 10 ml of 2% HCOOH in 80/20 (v/v) MeOH/ACN (called elution 2) was passed through the cartridge to ensure that the compounds, mainly the acidic ones, had completely eluted from the sorbent, since the acidic solution ensures the protonation of the analytes – which at loading sample pH (pH 7) might be in their anionic form – and releases them from the sorbent.

Table 2 summarizes the % recovery values provided in each respective protocol, which point out that the SAX protocol is the more efficient, since all the most acidic compounds studied (pK_a < 5) eluted during the elution step with recovery values ranging between 90 and 100% in all instances. The less acidic compounds (pK_a > 5) also eluted (% recoveries from 87 to 69% for all this type of compounds, and 45% for 4-NP) in the washing step. All the analytes, then, completely eluted during the washing and elution steps, and none (or just traces) of the analytes were recovered in elution 2. On the other hand, when the other three protocols were used (i.e. RP, WAX and SCX), the analytes did not elute in either the washing or the elution step, and the extra step (elution 2) was required to completely elute all the analytes from the sorbent.

If the SAX conditions are the most suitable for extracting acidic analytes, this means that the IL-CF_3COO^- resin retains the analytes through ionic interactions with its imidazole groups (which involves SAX interactions). Therefore, we shall now focus on the extraction of the most acidic compounds, but we shall maintain all the initial compounds (i.e. including the basic and less acidic ones) in order to provide as much information as possible about how IL-CF_3COO^- behaves with compounds of different characteristics.

3.3. Optimisation of the SAX protocol

Once SAX had been seen to be the optimal procedure for eluting the analytes studied from IL-CF_3COO^-, our next aim was to tune the conditions. For these experiments, we increased the sample volume to 250 ml in order to study the effect of each parameter at conditions more pertinent to the off-line SPE extraction.

3.3.1. Loading sample conditions

The loading step was fixed at pH 7 in order to ensure the deprotonation of the most acidic compounds (pK_a < 5) and retain them in the resin (which is charged) through ionic interactions.

The ionic strength of the sample was also tested, to do this, we compared the recovery results of two type of samples both adjusted to pH 7 with H_3PO_4: one based on ultrapure water and another based on isotonic saline buffer. The results were better when the sample was prepared merely with ultrapure water adjusted to pH 7, which may be due to the lower ionic strength of this type of sample.

3.3.2. Elution solution

We increased the percentage of the HCOOH (2%, 5% and 10%) in the solution and then we changed the solvent in the solution (20/80 (v/v) MeOH/ACN or pure MeOH) in order to completely elute the most acidic compounds with the minimum volume of solvent. We found that 5% HCOOH solution in either 20/80 (v/v) MeOH/ACN or pure MeOH provided the best results (data not shown). We finally chose 5% HCOOH in MeOH as the elution solution because it is more straightforward to prepare.

To determine the optimum elution volume, we tested volumes from 1 to 15 ml of 5% HCOOH in MeOH, and the minimum volume to ensure the complete elution of all the acidic compounds was 10 ml of this acidic solution.

3.3.3. Washing step

In order to enhance the selectivity of the whole extraction process, another parameter that had to be optimized is the type and volume of solvent in the washing step. We had already used 1 ml of MeOH as washing solvent, but we were interested in increasing the volume to more effectively wash out the interferences, so we tested up to four aliquots of 5 ml of MeOH (total 20 ml of MeOH). With 20 ml of washing solvent, none of the most acidic analytes underwent any loss during the washing step and they were completely recovered in the elution step (data not shown). On the other hand, when 20 ml of MeOH was used as washing solvent, the less acidic compounds partially eluted in the washing step (as expected, since they are just retained by reversed-phase interactions) and completed their elution in the elution step. However, increasing the volume of washing solvent further led to the elution of some acidic compounds, such as gemfibrozil, but other less acidic compounds still did not elute.

We also tested the effect of combining two types of washing solvents – 10 ml of 5% NH_4OH in MeOH followed by 10 ml of MeOH – to check whether the addition of a basic solution helped to completely elute the basic and neutral compounds in the washing step. However, we ruled out this possibility since we could not see any

Table 3
% Recovery values of the analytes with the different sorbents studied (IL and Oasis MAX) after extracting 1000 ml of ultrapure, tap and Ebro river water sample at pH 7 with the analyte mixture spiked at 10 μg l^{-1}.

Solutes	pK_a	% Recovery											
		Ultrapure water				Tap water				Ebro river water			
		IL		Oasis MAX		IL		Oasis MAX		IL		Oasis MAX	
		Wash	Elution	Wash	Elution	Wash	Elution	Wash	Elution	Wash	Elution	Wash	Elution
Carbamazepine	13	16	0	89	0	15	0	101	0	13	0	89	1
4-NP	7.1	30	81	0	97	40	0	0	67	43	57	0	102
Nalidixic acid	6.5	71	25	44	54	7	4	83	23	4	0	97	6
Flumequine	6	75	20	48	47	9	0	62	32	7	0	99	8
Gemfibrozil	4.7	0	100	0	96	0	60	0	83	0	80	0	110
Ibuprofen	4.6	0	98	0	93	0	76	23	56	0	63	0	106
Fenoprofen	4.5	0	102	0	103	0	92	0	105	0	92	0	102
Naproxen	4.2	0	99	0	94	0	74	0	59	0	87	0	97
Diclofenac	3.9	0	98	0	92	0	76	0	57	0	100	0	101
Salicylic acid	3	0	68	0	99	0	76	0	20	2	63	0	100

For the experimental conditions, see text. % Relative standard deviation (RSD) (n = 3) were lower than 4% when % recovery >25%.

improvement, and some of the less acidic compounds continued eluting in the elution step.

3.3.4. Regeneration of the ILs

Another point to consider was the regeneration of the IL after each extraction. We tried to regenerate the cartridge by passing the stoichiometric amount of CF_3COOH, to maintain the IL-CF_3COO^- form, or 5 ml of 5% HCOOH in MeOH (also used in the elution step) to maintain the IL-$HCOO^-$ form, and the results obtained in the following respective SPE experiments were the same. Thus, we predict that the important point is to maintain the IL in the protonated form, but we can use any counter-ion to do so. Moreover, in view of the water content (Section 3.1) of the $HCOO^-$ form in comparison with that of the CF_3COO^- form, we decided to use 5 ml of 5% HCOOH in MeOH as the regeneration solution to maintain the imidazole moiety in its charged form and at the same time to continue working with the more suitable IL-$HCOO^-$ form.

3.3.5. Sample volume

After the different conditions that might affect the extraction had been evaluated, the following optimized conditions were selected for all further experiments: sample: ultrapure water at pH 7; equilibration: 1 ml of 25 mM CH_3COONa, pH 7; washing: 20 ml of MeOH; elution: 10 ml of 5% HCOOH in MeOH; regeneration: 5 ml of 5% HCOOH in MeOH.

Once the SPE protocol had been established, we tested different sample loading volumes (i.e. 250, 500 and 1000 ml) and the recovery results were similar for all the tested volumes. Table 3 lists the recoveries (%) obtained after loading 1000 ml of ultrapure water sample (pH 7) spiked at 10 μg l^{-1} with the analyte mixture through IL material. All the most acidic compounds provided % recoveries ~100%, with the exception of salicylic acid, which polarity let its recoveries to fall to 68%. Previous studies [29,30], where it used conventional SPE sorbents, also reported problems in the extraction of salicylic acid.

As far as the less acidic compounds studied are concerned, 4-NP showed partial elution with the IL-CF_3COO^- during the elution step, which might be because it interacts through the nitro moiety (see the structure of 4-NP in Fig. 1) and the amine moiety in the imidazole ring of IL-CF_3COO^-. On the other hand, carbamazepine is almost lost during the loading step when extracted with IL-CF_3COO^-, because it is retained by the sorbent as a result of the π–π interactions between the aromatic rings in the analyte (see structure in Fig. 1) and the ones in the sorbent structure (Fig. 2). However, the SAX protocol used enhanced ionic interactions with the analytes rather than RP, which are more suitable for extracting this basic compound.

3.3.6. Comparison to conventional sorbent

For purposes of comparison, we also evaluated the SPE performance of Oasis MAX, which is a commercially available polymeric sorbent based on N-vinylpyrrolidone–DVB with a specific surface area of ~800 m^2 g^{-1} and it contains quaternary ammonium moieties, so it behaves like a SAX sorbent.

Table 3 also summarizes the recovery values obtained for Oasis MAX under the same conditions as those listed for IL-CF_3COO^-. From these recoveries, we can see that the performance of the IL-CF_3COO^- sorbent is comparable to that of the Oasis MAX sorbent in the extraction of the studied compounds. With this comparison, we demonstrate that polymer-supported IL (with just a 2% crosslinking degree) performance is as good as other established polymeric SPE sorbents that use macroporous resins with crosslinking degrees up to 80%.

3.4. Application to real samples

To assess the applicability of IL-CF_3COO^- in real water samples, we evaluated tap river and wastewater samples. As with the ultrapure water, we initially percolated 1000 ml of each sample spiked at 10 μg l^{-1} and then followed the rest of the SPE procedure as described above. Table 3 shows that the recoveries for real samples are similar to those in ultrapure water, but, in tap water the recoveries slightly decrease, i.e. 60% for gemfibrozil. This decrease in recovery values in tap water samples might be attributed to the chloride content in this type of sample, which might block the amine moiety and prevent interaction with the target analytes. More interesting are the results with river water, the recoveries of which are close to 100%, except for salicylic acid and ibuprofen (63% in both cases). The decrease in the recovery of these two acidic compounds is not surprising; in fact, salicylic acid recoveries are similar to those obtained in ultrapure water and several studies have shown that ibuprofen has more recovery problems than other compounds with similar acidic and polar characteristics when it is extracted with such neutral polymeric sorbents as Oasis HLB [31–33] and Strata-X [34] or weak anion exchange polymeric sorbent Oasis WAX [27].

For purposes of comparison, we also ran the same experiments using Oasis MAX as the sorbent (see Table 3 for the % recovery values). The results obtained for the most acidic compounds when Oasis MAX was used in tap water samples are slightly lower (about 50–60% compared to 60–70% for IL-CF_3COO^-) and in river water samples they are slightly higher (values about 100% for all the compounds studied while the recoveries of salicylic acid and ibuprofen fall to 63% when IL-CF_3COO^- is used) than those obtained with IL-CF_3COO^-.

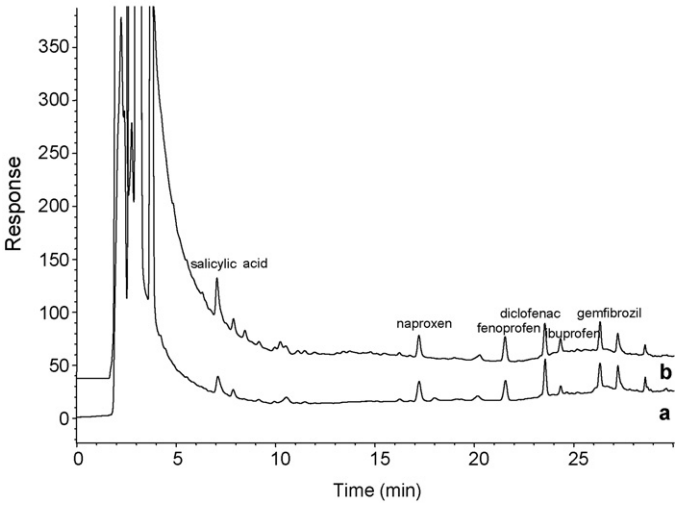


Fig. 3. Chromatograms obtained after off-line trace enrichment of 1000 ml of Ebro river water sample with the addition of a 0.5 $\mu g\,l^{-1}$ level of the analyte mixture followed by the washing step and elution of the most acidic compounds using IL-CF_3COO^- (a) and Oasis MAX (b).

As expected, the less acidic compounds studied followed the same trends as in ultrapure water.

The next experiments in real water samples consisted of decreasing the analyte concentrations at 0.5 $\mu g\,l^{-1}$ so that they reassembled those found in the environment. In order to determine lower concentrations, in this set of experiments the SPE eluate was evaporated to dryness and then reconstituted with 0.5 ml of 50/50 (v/v) H_2O/MeOH solution. With the evaporation step, an additional concentration factor of 20 was achieved. Recovery values were similar to those of the extraction of the Ebro river water sample spiked at higher concentration (i.e. 10 $\mu g\,l^{-1}$). Fig. 3 shows the chromatograms obtained after preconcentrating 1000 ml of Ebro river water on IL-CF_3COO^- (a) and Oasis MAX (b) with the addition of the analyte mixture at 0.5 $\mu g\,l^{-1}$, and performing first the washing step and then the elution. It is worth mentioning that non-spiked sample chromatograms (not shown) were run with each respective sample, and neither any compounds studied nor any important interference were detected. We can also see that the chromatogram profile for IL-CF_3COO^- (Fig. 3a) shows a smaller initial hump than Oasis MAX (Fig. 3b), which might help to quantify the analytes that appear at the initial retention times, such as salicylic acid.

To further show the capacity of ILs material to selectively extract acidic compounds, we used the IL-CF_3COO^- to percolate much more complex aqueous samples, such as effluent water from the waste water treatment plant (WWTP) in Tarragona. Table 4 summarizes the recovery results after 250 ml of effluent WWTP sample at pH 7 were extracted spiked at 5 $\mu g\,l^{-1}$ with the analyte mixture. At this point, we would like to clarify that the sample volume was decreased to 250 ml because the WWTP sample is much more complex than the rest of water samples analyzed. The SPE material IL-CF_3COO^- and Oasis MAX were used for purposes of comparison. The results for IL-CF_3COO^- are satisfactory and comparable to those for Oasis MAX, though slightly lower in the case of ibuprofen and gemfibrozil (~75% for IL-CF_3COO^- compared to ~100% for Oasis MAX) and salicylic acid (~55% for IL-CF_3COO^- compared to ~100% for Oasis MAX). In fact, these compounds have also shown some recovery problems in the other matrices analyzed in this study; and when samples are more complex, the weaker retention of these compounds might be further weakened by the presence of interferences that mask the interaction points of the sorbent, thus preventing proper interaction with the target compounds.

Table 4
% Recovery values of the studied analytes with IL sorbent and Oasis MAX in SPE after percolating 250 ml of effluent WWTP water sample at pH 7 spiked at 5 $\mu g\,l^{-1}$ with the analyte mixture.

Solutes	pK_a	% Recovery			
		IL		OASIS MAX	
		Wash	Elution	Wash	Elution
Carbamazepine	13	43	0	104	0
4-NP	7.1	0	81	0	57
Nalidixic acid	6.5	61	0	79	0
Flumequine	6	2	0	84	0
Gemfibrozil	4.7	0	72	0	97
Ibuprofen	4.6	0	77	0	99
Fenoprofen	4.5	0	93	0	102
Naproxen	4.2	0	101	0	100
Diclofenac	3.9	0	101	0	99
Salicylic acid	3	0	55	0	94

For the experimental conditions, see text. % Relative standard deviation (RSD) ($n = 3$) were lower than 7%.

Fig. 4 shows the chromatograms obtained after preconcentrating 250 ml of effluent WWTP sample on IL-CF_3COO^- (a and b) and Oasis MAX (c and d) with the addition of the analyte mixture at 5 $\mu g\,l^{-1}$ (b and d). The most acidic compounds of the group studied were first washed and then eluted (see chromatograms). Fig. 4 also shows the non-spike sample chromatograms (a and c) for each SPE material evaluated (i.e. IL-CF_3COO^- (a) and Oasis MAX (c)), which display some unknown peaks and two peaks at the same retention time as diclofenac and gemfibrozil; therefore, we took them into account in the quantification of these compounds. The chromatograms in Fig. 4 show that, although the samples are complex, the baseline is flatter and allows the most acidic analytes to be properly quantified at low concentration levels, which might be partially attributed to the effective washing step that can be performed in this type of material. Again, a comparison of the chromatograms reveals a smaller initial hump in the IL-CF_3COO^- (Fig. 4a and b) than in the Oasis MAX (Fig. 4c and d), due to the contribution of the non-specific RP interactions of Oasis MAX material. It should also be pointed out that the chromatograms are clean thanks to the material used in the SPE, and that both the cleanliness and the sensitivity achieved with this type of complex samples could be further enhanced by using a more powerful detection technique, such as mass spectrometry.

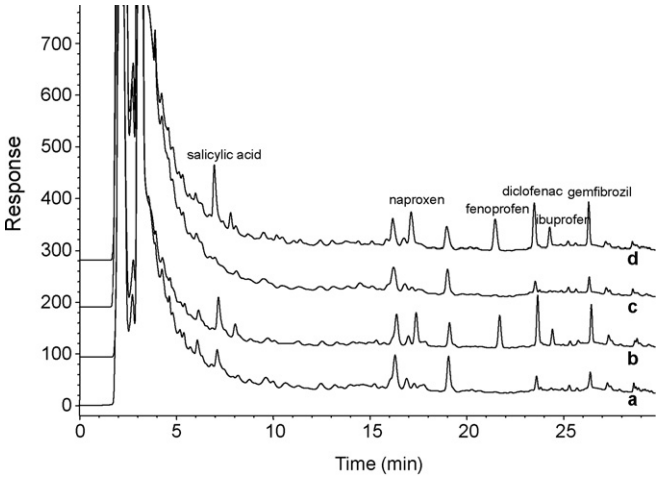


Fig. 4. Chromatograms obtained after off-line trace enrichment of 250 ml of effluent WWTP sample without (a and c) and with (b and d) the addition of a 5 $\mu g\,l^{-1}$ level of the analyte mixture followed by the washing step and elution of the most acidic compounds using IL-CF_3COO^-: without (a) and with (b), and Oasis MAX: without (c) and with (d), the addition of the analyte mixture.

4. Conclusions

This paper describes a pioneering study of the synthesis, evaluation and application of polymer-supported ILs as SPE material, which effectively extracts a group of acidic compounds from complex aqueous samples.

The imidazolium trifluoroacetate was linked to a 2% crosslinked resin in order to combine the advantages of ionic liquid properties and those of a solid material.

We tested the different functional groups of the ionic liquid resin and their capacity to interact with the analytes selected by using various SPE protocols. We found that the SPE performed best when using the SAX interaction that the imidazole group provides with the acidic compounds studied.

We have shown that the IL-CF_3COO^- is a good alternative for extracting acidic analytes at low concentration levels from complex samples (tap, river and effluent WWTP), since it presented clear chromatograms and high recoveries; using ILs as a SPE material is sometimes even a better option than such well-established anionic exchange SPE sorbents as Oasis MAX sorbent.

We have, then, described a novel application of these promising media, which are still in the process of being explored. This study is just the first step towards new applications of these materials in the sorptive extraction field.

Acknowledgements

The authors thank the *Dirección General de Investigación* from Spain for the Project (Ref. CTQ2008-00825/BQU) for financial support. NF also thanks for personal funding through the Juan de la Cierva program from the *Ministerio de Educación y Ciencia* (Spain).

References

[1] A.J. Carmichael, K.R. Seddon, J. Phys. Org. Chem. 13 (2000) 591.
[2] J.G. Huddleston, H.D. Willauer, R.P. Swatloski, A.E. Visser, R.D. Rogers, Chem. Commun. (1998) 1765.
[3] S.T.M. Vidal, J.N. Correia, M.M. Marques, M.R. Ismael, M.T.A. Reis, Sep. Sci. Technol. 39 (2004) 2155.
[4] H. Zhao, S. Xia, P. Ma, J. Chem. Technol. Biotechnol. 80 (2005) 1089.
[5] D.W. Armstrong, L.F. He, Y.S. Liu, Anal. Chem. 71 (2005) 3873.
[6] A. Berthod, L.F. He, D.W. Armstrong, Chromatographia 53 (2001) 63.
[7] Y.-N. Shsieh, R.S. Horng, W.-Y. Ho, P.-C. Huang, C.-Y. Hsu, T.-J. Whang, C.-H. Kuei, Chromatographia 67 (2008) 413.
[8] A. Berthod, M.J. Ruiz-Angel, S. Carda-Broch, J. Chromatogr. A 1184 (2008) 6.
[9] M.P. Marszall, R. Kaliszan, Crit. Rev. Anal. Chem. 37 (2007) 127.
[10] J.F. Liu, G.B. Jiang, Y.G. Chi, Y. Cai, Q. Zhou, J.T. Hu, Anal. Chem. 75 (2003) 5870.
[11] V. Pino, Q.Q. Baltazar, J.L. Anderson, J. Chromatogr. A 1148 (2007) 92.
[12] E. Aguilera-Herrador, R. Lucena, S. Cárdenas, M. Valcárcel, J. Chromatogr. A 1201 (2008) 106.
[13] L. Vidal, E. Psillakis, C.E. Domini, N. Grané, F. Marken, A. Canals, Anal. Chim. Acta 584 (2007) 189.
[14] M.J. Ruiz-Angel, A. Berthod, J. Chromatogr. A 1189 (2008) 476.
[15] G. Le Rouzo, C. Lamouroux, C. Bresson, A. Guichard, P. Moisy, G. Moutiers, J. Chromatogr. A 1164 (2007) 139.
[16] M. López-Pastor, B.M. Simonet, B. Lendl, M. Valcárcel, Electrophoresis 29 (2008) 94.
[17] J.F. Liu, Y.G. Chi, G.B. Jiang, C. Tai, J.F. Peng, J.T. Hu, J. Chromatogr. A 1026 (2004) 143.
[18] A.W. Trochimczuk, S. Ronka, React. Funct. Polym., submitted (2009).
[19] W.W. Buchberger, Anal. Chim. Acta 593 (2007) 129.
[20] S.D. Richardson, Anal. Chem. 78 (2006) 4021.
[21] N. Fontanals, R.M. Marcé, F. Borrull, J. Chromatogr. A 1152 (2007) 14.
[22] E. Caro, R.M. Marcé, F. Borrull, P.A.G. Cormack, D.C. Sherrington, Trends Anal. Chem. 25 (2006) 143.
[23] V. Pichon, J. Chromatogr. A 1152 (2007) 41.
[24] U. Neue, C.R. Mallet, Z. Lu, Y.F. Cheng, J. Mazzeo, in: I.D. Wilson (Ed.), Bioanalytical Separations Handbook of Analytical Separations, Elsevier, Amsterdam, 2003, p. 73.
[25] M. Tian, H. Yan, K.H. Row, J. Chromatogr. B 877 (2009) 738.
[26] M. Li, P.J. Pham, T. Wang, C.U. Pittman Jr., T. Li, Sep. Purif. Technol. 66 (2009) 1.
[27] N. Fontanals, P.A.G. Cormack, D.C. Sherrington, J. Chromatogr. A 1215 (2008) 21.
[28] N. Fontanals, B.C. Trammell, M. Galià, R.M. Marcé, P.C. Iraneta, F. Borrull, U.D. Neue, J. Sep. Sci. 29 (2006) 1622.
[29] J. Bones, K. Thomas, P.N. Nesterenko, B. Paull, Talanta 70 (2006) 1117.
[30] M. Pedrouzo, S. Reverté, F. Borrull, E. Pocurull, R.M. Marcé, J. Sep. Sci. 30 (2007) 297.
[31] Z. Yu, S. Peldszus, P.M. Huck, J. Chromatogr. A 1148 (2007) 65.
[32] J.B. Quintana, T. Reemtsma, Rapid Commun. Mass Spectrom. 18 (2004) 765.
[33] M. Farré, I. Ferrer, A. Ginebreda, M. Figueras, L. Olivella, L. Tirapu, M. Vilanova, D. Barceló, J. Chromatogr. A 938 (2001) 187.
[34] T. Kosjek, E. Heath, A. Krbavcic, Environ. Int. 31 (2005) 679.

Talanta 80 (2009) 257–262

Contents lists available at ScienceDirect

Talanta

journal homepage: www.elsevier.com/locate/talanta

LC–ESI-MS determination of diethylene glycol pollution in sea water samples collected around gas extraction platform plants

A. Cappiello[a,*], G. Famiglini[a], P. Palma[a], V. Termopoli[a], H. Trufelli[a], R. Di Mento[b], M. Mannozzi[b]

[a] Istituto di Scienze Chimiche "F. Bruner", Università di Urbino "Carlo Bo", Piazza Rinascimento 6, 61029 Urbino, Italy
[b] Istituto Superiore per la Protezione e la Ricerca Ambientale-ISPRA,Via di Casalotti 300, 00166, Rome, Italy

ARTICLE INFO

Article history:
Received 8 January 2009
Received in revised form 16 June 2009
Accepted 29 June 2009
Available online 4 July 2009

Keywords:
Diethylene glycol
Offshore gas platforms
Sea water
Glycols benzoylation
LC–ESI-MS

ABSTRACT

Produced formation waters (PFWs) represent the largest aqueous wastes that are normally discharged into the marine environment during the offshore gas production processes. The chemical additive diethylene glycol (DEG) is widely used in the gas production line and therefore can be found in the PFW, becoming of environmental concern. In this study, a new method has been developed for trace determination of DEG in sea water samples collected around offshore gas platforms. The method is based on liquid chromatography coupled to electrospray ionization mass spectrometry (LC–ESI-MS). Prior to analysis, water samples were derivatized using the Schotten–Baumann method for the benzoylation of glycols. The derivatization procedure allowed us to maximize the ESI-MS response of DEG and minimize the influence of interfering compounds. The method was validated and allowed a quantification of DEG in sea water samples with a method LOD of 0.4 ng/mL. The applicability of the procedure was demonstrated by analyzing sea water samples collected around eight gas platforms located in the Adriatic Sea (Italy).

© 2009 Elsevier B.V. All rights reserved.

1. Introduction

Diethylene glycol is a widely used industrial chemical, which is well known for causing acute toxicity phenomena in humans [1–5]. Due to its extensive use this compound primarily enters the environment from manufacturing effluents and emissions, and upon release during its use in commercial products [6–12]. Regarding the marine environment, an important source of contamination from DEG can be found in the gas extraction offshore platforms.

Produced formation waters (PFWs) are the largest aqueous wastes that are normally discharged into the marine environment during the offshore gas production processes. It has been estimated that about 7 million cubic meters of water are produced and discharged daily by offshore platforms [13]. The chemical composition of PFWs is complex and strongly field-dependent. It also depends upon time period over which hydrocarbons have been produced from a particular field [14–16] and the production practice [15]. Offshore platforms extensively use DEG as inhibitor of the gas hydrate formation and as dehydrating additive to eliminate water vapors that normally saturate the extracted gas [16,17]. The dehydrating process is also necessary to avoid the corrosion and clogging of the gas transport lines. Sometime DEG can also be injected as antifreeze additive in wellhead or/and into oilwell. Sorensen et al. [18] describe the generation, handling, and disposal of gas dehydration discharges as well as how those wastes may be introduced into the subsurface environment. Large volumes of produced formation water (PFW), used to maintain gas reservoir pressure and additioned with corrosion inhibitors, demulsifiers, defoamers as DEG, are discharged directly into the marine environment [15,16]. After discharge into the sea, the PFW will be diluted depending on local conditions and biodegradation processes will change their composition [19–21]. Dissolved and particulate components from produced water are found both in the water column and in the marine sediment, and are thus available to the total ecosystem. For this reason, chronic and toxic effects of oil and gas platforms wastes have been monitored by regular surveys of benthic communities around the platforms [22]. Published data regarding the environmental impact of PFW have been addressed to the investigation of released pollutants such as heavy metals and hydrocarbons coming from the water reservoir, antifoams (e.g. fluorosilicone-based products), biocides (e.g. formaldehyde and glutaraldehyde-based compounds), demulsifies (e.g. phenol formaldehyde resin ethoxylates) [16,22–26]. However, exhaustive information regarding biodegradability, fate and toxic effects of wastes associated with DEG are still lacking [19,27]. Recent findings regarding the impact of glycol-based gas dehydration units on ground water demonstrated that glycols could act as a co-solvent for other pollutants (e.g. benzene, toluene, ethylbenzene and xylenes), thus greatly increasing the transport of such contaminants [18]. Failure to consider this co-solvent property of DEG and other glycols may result in underestimation of the risk associated to PFW discharges.

* Corresponding author. Tel.: +39 0722303344; fax: +39 0722303311.
E-mail address: achille.cappiello@uniurb.it (A. Cappiello).

0039-9140/$ – see front matter © 2009 Elsevier B.V. All rights reserved.
doi:10.1016/j.talanta.2009.06.067

Due to its specificity, gas chromatography coupled to mass spectrometry (GC–MS) represents the widely used assay for the determination of glycols [9,10,28,29]. However, the hydrophilic character of DEG makes the trace determination of this compound in water samples a substantial analytical problem. Sample preparation represents the major drawback in the development of methods characterized by acceptable sensitivity. In fact, most of the protocols based on solid phase extraction (SPE) or liquid–liquid extraction (LL) are characterized by low recoveries due to the difficulty of finding adequate adsorbent materials and to the final elution step in an organic solvent [30]. In order to overcome these problems, in one previous work we proposed a new approach for detecting DEG in PFW wastes and seawater samples collected around offshore gas platforms [31]. The experiments were performed exploiting an innovative instrumentation, the Direct–EI interface, totally developed in our laboratory [32–34]. The Direct–EI interface is able to couple a liquid chromatograph with an electron ionization ion source of a mass spectrometer. The Direct–EI capability to acquire EI spectra and operate in SIM mode allowed us to detect DEG in sea water with a method limit of detection (LOD) of 31 ng/L. However, the lack of commercial availability of the interface makes the proposed method not yet universally applicable for a routine monitoring of DEG. For this reason, the aim of this study was to develop an alternative analytical approach for trace determination of DEG in PFW discharges and sea water. The new method is based on the use of a conventional LC–ESI-MS system. ESI represents a powerful technique for the quantitation of polar pollutants in aqueous matrices [23,35]. However the sensitivity of this technique for low molecular weight compound, such as glycols, is reduced due to the matrix effects (ME) and to the formation of adduct ions coming from the mobile phase that increase the background noise signal [36–38]. A derivatization process using benzoyl chloride has been used by Holčapek et al. [30] to minimize this phenomenon. This procedure was successfully applied for trace determination of several glycols in bitumen samples. In this work, the derivatization process has been modified enhancing the quality of the results. The method has been validated considering selectivity, limit of detection (LOD), limit of quantitation (LOQ), linearity, working range, precision and evaluation of ME, and it has been applied to the analysis of sea water samples collected around eight offshore gas platforms located in the Adriatic Sea.

2. Experimental

2.1. Sampling procedure

Samples collection was carried out during summer 2007 by the Research Vessel ASTREA of the High Institute for the Environmental Protection and Research (ISPRA, Rome, Italy). They were all collected around gas platforms situated in the Adriatic Sea. Sampling was conducted at different distances from the PFW diffuser and at different deep. Mercury chloride was added to the samples until saturation to inhibit bacterial activity. Samples were stored in refrigerator at 4 °C in dark glass bottles.

2.2. Reagents and derivatization procedure

Diethylene glycol, pentane, benzoyl chloride, benzyl alcohol were purchased from Sigma–Aldrich (Milan, Italy). Acetonitrile HLPC-grade and sodium hydroxide were obtained from VWR (Milan, Italy). A milliQ water purification system (Millipore, Bedford, MA, USA) was used to obtain reagent grade water. A 10 mg/mL DEG standard solution was prepared in water and stored at 4 °C. This stock solution was diluted appropriately to prepare the working solutions used for the method validation experiments. The internal standard (IS) benzyl alcohol solution was prepared in milliQ water at a concentration of 1 mg/mL.

The Schotten–Baumann method of the benzoylation of glycols in aqueous solution using an excess of the derivatization agent in a strongly alkaline medium was employed to derivatize DEG [39]. The reaction follows this scheme:

$$(1)R(OH_2) + 2C_6H_5COCl + 2NaOH \rightarrow R(OCOC_6H_5)_2 + 2NaCl$$

2.5 mL of a sample or working solution were added with 12.5 μL of the IS solution, 1.75 mL of 30% NaOH, and 50 μL of benzoyl chloride. The mixture was shaken for 2 min and incubated at ambient temperature for 10 min. After that, a liquid–liquid extraction was conducted utilizing 2.5 mL of pentane collected after shaking vigorously. This procedure was repeated twice. Then, the two collected aliquots of about 2.5 mL were mixed and was evaporated to dryness under a gentle stream of nitrogen at ambient temperature. The residue was dissolved in 250 μL of a mixture of acetonitrile:water (50:50), with a net preconcentration factor of 10. Respect to the procedure of Holčapek, the volumes of samples and reagents were modified and benzyl alcohol was used as the internal standard (IS).

2.3. LC–ESI-MS conditions

Chromatographic separations were conducted with a SpectraSystem P2000 binary gradient pump (ThermoFisher Corporation, San Josè, CA) equipped with a Waters Nova-Pack Column (150 mm × 2.1 mm i.d., 5 μm particle size) obtained from Waters (Milford, MA). Instead of an isocratic elution (30), a gradient elution program was used starting from 90% water and 10% acetonitrile to 100% acetonitrile in 8 min. The flow rate was set at 300 μL/min, and the injection volume was of 5 μL. The eluent coming out from the column was introduced on an ion trap mass spectrometer equipped with an ESI source (LCQDuo, ThermoFisher Scientific, San Josè, CA). Derivatized DEG and IS, benzyl alcohol, gave a better response in positive ion mode. Chromatographic separation was necessary to separate DEG from the IS and from the eventually present co-eluted interfering compounds maximizing the selectivity and the specificity of the method and eliminating any possible matrix effects. HPLC-MS analyses were conducted in Selected Ion Monitoring (SIM) on the m/z 235 (sodium adduct ion of the derivatized IS) and 337 (sodium adduct ion of the derivatized DEG). Three microscan of 500 ms were summed to obtain the entire scan. The voltage between the needle and the transfer capillary was set to 4.5 kV. The heated capillary voltage and temperature were kept to 10 V and to 225 °C respectively. To assist the nebulization and desolvation processes, nitrogen was used as sheath gas (60 arbitrary unit) and as auxiliary gas (20 arbitrary unit).

3. Results and discussion

This work is focused on quantification of DEG in marine water samples collected nearby offshore gas extraction platforms. These industrial plants use large quantity of DEG in their application processes and sometimes this chemical is discharged with PFWs creating potential impact on the marine ecosystem. Many authors have studied composition and effects of the PFW wastes [16,24,25] but from our knowledge nobody has applied LC–ESI-MS for the investigation of the chemical composition of the sea water surrounding the platforms. LC–ESI-MS represents the method of choice for the analysis of polar compounds in water matrices. However, as reported in Section 1, this analytical approach has a low sensitivity for glycols. This disadvantage is mainly due to the mobile phase background, which interferes with the signal of these low molecular weight compounds [30]. In addition, when dealing with matrices such as sea water, detection drawbacks can arise for the

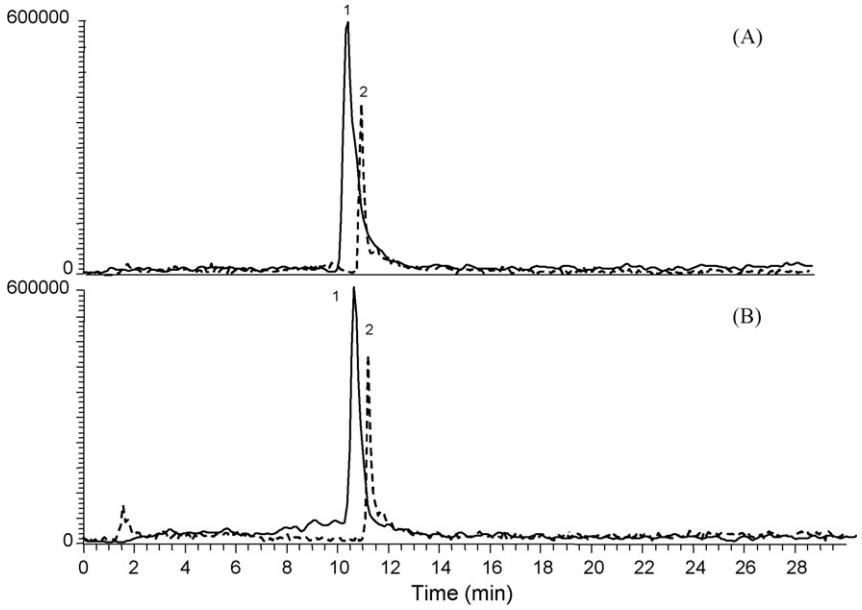


Fig. 1. Chromatograms relative to the separation of two extracts from: (A) a standard mixture in milliQ water containing DEG at a concentration of 0.4 μg/mL; (B) a blank sea water sample spiked with DEG at the same concentration of the standard mixture. Peaks: (1) derivatized DEG; (2) derivatized IS.

contemporary presence of salts which can co-elute with glycols in reversed phase chromatography, thus leading to ion suppression phenomena into the ESI source. In this work we applied a glycol benzoylation procedure as an efficient tool to overcome the above mentioned limitations. Respect to the underivatized DEG, its benzoyl derivative is characterized by a lower polarity and a higher molecular weight. The decreased polarity allows to facilitate the extraction procedure from the aqueous matrix and to improve the chromatographic separation from inorganic salts, preventing ME [36,37].

The optimization of chromatographic and mass spectrometric conditions was performed using a standard solution containing the derivatized DEG and benzyl alcohol at a concentration of 1 μg/mL. As widely reported in the literature [37,39,40], to compensate for possible ME, the target analyte and its IS must have identical or very close retention time. In these conditions, both compounds will be subjected to the same interferences, thus correcting for the degree of ME (Fig. 1). Mass spectrometric conditions were carefully optimized with the aim of achieving the best response for both derivatized compounds.

3.1. Method validation

Method performance was carefully evaluated taking into account *selectivity*, *linearity*, working range, *precision* and *matrix effects evaluation*. Selectivity was defined as the ability of the method to measure an analyte in the presence of interferences that may be expected to be present in the sample matrix [41]. A first step in obtaining the required method *selectivity* was obtained through the derivatization procedure, which was able to modify only the analytes reacting with benzoyl chloride excluding most of the other interfering substances. Subsequently, a pentane liquid–liquid extraction was carried out with the purpose of separating the DEG and IS derivatives from the sea water salts, benzoyl reagent and reaction by-products. The extract was finally analyzed by LC–ESI-MS in SIM mode. As reported in Fig. 2, the spectrum in scan mode of the dibenzoyl DEG is characterized by the presence of the sodium adduct ion at m/z 337. During the chromatographic separation, SIM detection enhances instrumental selectivity for both derivatives of DEG and of the IS ($[M+Na]^+$ at m/z 235). Fig. 1 reports the chromatograms relative to the separation of two extracts from: (A) a standard mixture in milliQ water containing benzyl alcohol and DEG at known concentration; (B) a blank sea water sample spiked with DEG and IS at the same concentration of the standard mixture. As it can be seen, the presence of the selected ion at the same retention time of the standard is a first satisfactory criterion in confirming the presence of DEG in the sea water sample. Moreover, as it will be demonstrated afterwards, the absence of ME represents the last goal in achieving a satisfactory selectivity.

The detection limit of the method was calculated taking into account the recovery of both extraction and derivatization procedures, the initial volume of the sample, the final volume of the extract and the instrumental LOD. Accordingly to the work of Holčapek [30] the percentage of recovery of the liquid–liquid extraction is very high (only less than 0.16% of the derivatives are lost). Different is the case of derivatization, where the recovery is about 40%, showing that the process is not complete. However, the reproducibility of this result and the use of an IS improve quality of quantitative results. In order to evaluate the instrumental LOD and LOQ, diluted working solutions containing DEG were subjected to the derivatization procedure and analyzed as reported in Section 2. The instrumental LOD was expressed as the minimum analyte amount that the instrumentation can detect with a signal-to-noise ratio (S/N) of 3, while the LOQ was defined as the amount that can be detected with a S/N of 10. Considering the derivatization process efficiency of 40% [30], these experiments demonstrated an instrumental LOD and LOQ of 4 and 12 ng/mL respectively (Table 1). Based on the above results, the proposed method has a limit of detection of 0.4 ng/mL.

To calculate the *linearity and working range*, calibration curves were constructed by plotting the peak area ratio of the dibenzoyl DEG to the derivatized IS versus the DEG concentration. The linear regression lines demonstrated a good linearity for 3 orders of magnitude starting from the instrumental LOD (Table 1). These experiments were carried out on column using the same conditions reported in Section 2. A correlation coefficient (R^2) of 0.9990 was achieved in the working range from 4 ng/mL to 4 μg/mL.

Precision was evaluated in terms of intraday and interday repeatability as the relative standard deviation percentage (RSD) of the peak areas of an LL extract containing the derivatized DEG at

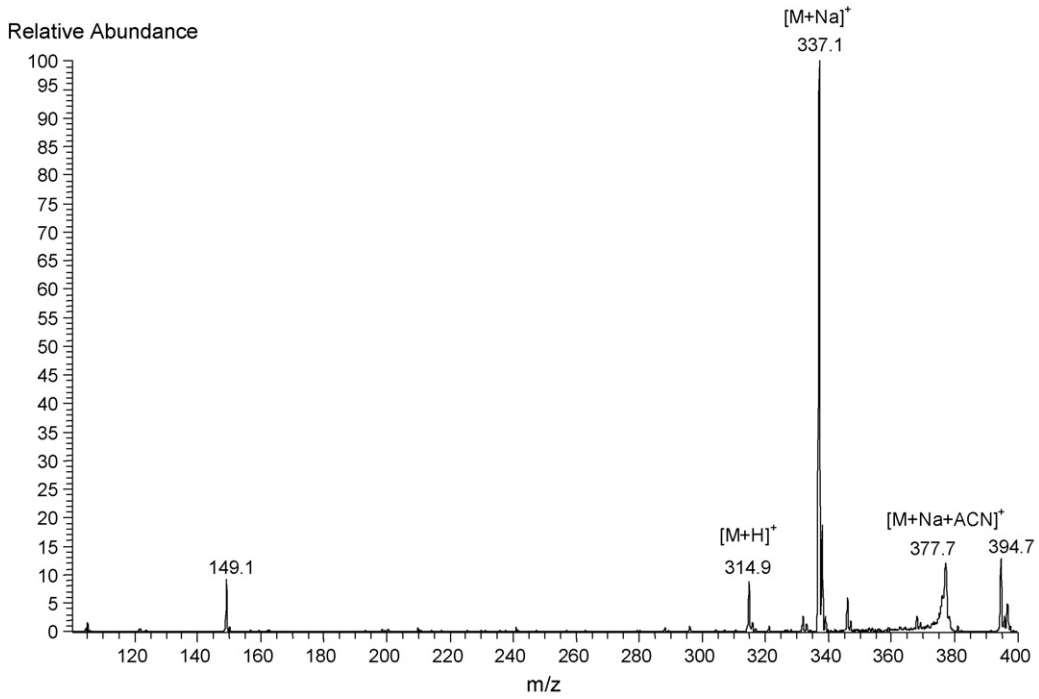


Fig. 2. ESI-MS spectrum obtained in infusion of a 10 μg/mL derivatized DEG solution.

a concentration of 0.1 μg/mL DEG solution. For the determination of the intraday repeatability, five replicates were analyzed in one day. The interday repeatability was evaluated injecting the solution on a working period of five days (three injections/day with a total of 15 replicates). RSD values together with all the other validation parameters are reported in Table 1.

A major limitation in quantitative analysis with LC–ESI-MS is represented by ME in which the matrix co-extracted with the analytes can alter the signal response, causing either suppression or enhancement [36,37]. This phenomenon can heavily affect the performances of the analytical method leading to erroneous quantitation [38–43]. For this reason, a careful evaluation of ME represents an important step in the development and validation of an LC–ESI-MS method. The exact mechanism of ME is still unknown. It is assumed that the co-eluted matrix can influence signal intensity in a possible competition for the available charges and for the access to the droplet surface for gas-phase emission. Due to the high salts concentration, ME represents one of the major drawback when analyzing sea water samples by LC–ESI-MS [44,45]. In order to investigate the capability of our derivatization method to overcome ion suppression phenomena due to the presence of salts, ME was carefully evaluated. In the literature, ME is usually calculated performing a comparison between the signal of an analyte in a pure solution and a matrix-matched standard [46,47]. In the present work, ME effect evaluation was carried out performing two different set of experiments. In the first set, three samples of milliQ water were spiked with DEG at a concentration of 0.4 μg/mL. Each spiked sample was then subjected to the IS addition and derivatization protocol described in Section 2. In the second set of experiments the derivatization procedure was carried out on three different aliquots of blank sea water sample spiked with DEG at a concentration of 0.4 μg/mL, and mercury chloride was added until saturation, as required by the sample collection procedure used for the real samples. The value of the ratio between the signal of the derivatized DEG and of the derivatized IS were then estimated in all the investigated samples. Finally, the ME was calculated in percent as the ratio between B and A multiplied by 100 (A = average peak area of the derivatized DEG/derivatized IS in pure water; B = average peak area of the derivatized DEG/derivatized IS in sea water). A ME value >100% indicates ionization enhancement, while a value <100% indicates ionization suppression. The final results indicate that an average ME of 90% was obtained, thus demonstrating that the proposed protocol exhibits an excellent performance toward the presence of matrix interferences.

3.2. Analysis of seawater samples

The method has been applied to the analysis of 48 seawater samples collected around eight gas platform located in the Adriatic Sea. DEG was extensively used as production chemical during the extraction processes of the investigated platforms. DEG identification in real samples was confirmed by chromatographic retention time and mass spectrometric SIM response. Quantification was based on the calibration curve values with the method of internal standard, that can correct instrumental and procedure fluctuations. The results are reported in Table 2. The variability of DEG concentrations on samples is due to the distance and deepness of the sampling locations respect to the discharge diffuser. Anyway, the values obtained show the presence of DEG at concentration that does not exceed the toxicity threshold for these substances in sea water [19].

Table 1
Validation data.

Instrumental LOD	Instrumental LOQ	Method LOD	Instrumental working range	Linear regression equation	R^2	Intraday repeatability (%RSD, n = 5)	Interday repeatability (%RSD, n = 15)
4 ng/mL	12 ng/mL	0.4 ng/mL	4 ng/mL to 4 μg/mL	$Y = 4.464X + 0.555$	0.9990	12%	26%

Table 2
DEG concentration in the investigated seawater samples.

Sample number	Sampling points		DEG Concentration (mg/L)
	Discharge length (m)	Depth (m)	
A Platform			
1	Under diffusor	0	1.8
2	Under diffusor	−12	n.d
3	25	0	n.d
4	25	−12	n.d
5	50	0	n.d
6	500	0	n.d
B Platform			
1	Under diffusor	0	0.23
2	Under diffusor	−11	n.d
3	25	0	1.3
4	25	−11	0.99
5	50	0	n.d
6	500	0	n.d
C Platform			
1	Under diffusor	0	1.3
2	Under diffusor	−12	n.d
3	25	0	n.d
4	25	−12	n.d
5	50	0	n.d
6	500	0	n.d
D Platform			
1	Under diffusor	0	0.44
2	Under diffusor	−19	n.d
3	25	0	n.d
4	25	−19	4.9
5	50	0	n.d
6	500	0	n.d
E Platform			
1	Under diffusor	0	n.d
2	Under diffusor	−12	n.d
3	25	0	n.d
4	25	−12	1.0
5	50	0	n.d
6	500	0	n.d
F Platform			
1	Under diffusor	0	n.d
2	Under diffusor	−12	n.d
3	25	0	n.d
4	25	−12	0.73
5	50	0	n.d.
6	500	0	n.d.
G Platform			
1	Under diffusor	0	n.d
2	25	0	n.d
3	25	−12	n.d
4	50	0	0.73
5	50	−12	n.d.
6	500	0	n.d.
H Platform			
1	Under diffusor	0	n.d
2	Under diffusor	−15	0.29
3	25	0	n.d
4	25	−15	0.73
5	50	0	n.d
6	500	0	0.93

4. Conclusions

From the results obtained, it can be concluded that the direct benzoylation of DEG followed by LC–ESI-MS can be proposed as a convenient experimental approach for monitoring the levels of this chemical in sea water. Validation parameters such as selectivity, linearity, instrumental LOD and LOQ were relevant to environmental analysis. This method was successfully applied in a real world application regarding the analysis of marine water collected around offshore gas platforms. Because of the relative simplicity and robustness, this method can be proposed as a routine protocol in monitoring programs addressed at the investigation of the glycols environmental impact during gas extraction processes.

References

[1] R.E. Osterberg, N.A. See, Int. J. Toxicol. 22 (2003) 377.
[2] B. Ballantyne, W.M. Snellings, Food Chem. Toxicol. 43 (2005) 1637.
[3] L.A. Ferrari, L. Giannuzzi, Forensic Sci. Int. 153 (2005) 45.
[4] D.B. Barr, J.R. Barr, G. Weerasekera, J. Wamsley, S.R. Kalb, A. Sjodin, J.G. Schier, E.D. Rents, L. Lewis, C. Rubin, L.L. Needham, R.L. Jones, E.J. Sampson, J. Anal. Toxicol. 31 (2007) 295.
[5] J. Kraut, A. Jeffrey, I. Kurtz, Clin. J. Am. Soc. Nephrol. 3 (2008) 208.
[6] A. Raksit, S. Punani, J. Chromatogr. Sci. 35 (1997) 489.
[7] P. Baffi, S. Elneser, M. Baffi, M. De Melin, J. AOAC Int. 83 (2000) 793.
[8] A. Szymansky, B. Wyrwas, M. Szymanowska, Z. Lukaszawsky, Water Res. 35 (2001) 3599.
[9] R.H. Williams, S.M. Shah, J.A. Maggiore, T.B. Erickson, J. Anal. Toxicol. 24 (2000) 621.
[10] S.A. Savchuk, G.M. Kolesov, J. Anal. Chem. 60 (2005) 752.
[11] M. Lopez-Sanchez, A. Dominguez-Vidal, M.J. Ayora-Canada, A. Molina-Diaz, Anal. Chim. Acta 620 (2008) 113.
[12] T. Zhou, H. Zhang, G. Duan, J. Sep. Sci. 30 (2007) 2620.
[13] OGP-International Association of Oil & Gas Producers, Fate and effects of naturally occurring substances in produced water on the marine environment, International Association of Oil & Gas Producers, 2005, p. 364.
[14] J. Wills, J. Ekologicheskaya Vahkta Sakhalina (Sakhalin Environment Watch), (2000) 139.
[15] OSPAR 2004, On harmonized pre-screening scheme for offshore chemicals, Website: http://www.ospar.org.
[16] S.B. Henderson, S.J.W. Grigson, P. Johnson, B.D. Roddie, Mar. Pollut. Bull. 12 (1999) 1141.
[17] D.L. Katz, R.L. Lee, Natural Gas Engineering-Production and Storage, McGraw Hill Publishing Company, New York, 1990, p. 617.
[18] J.A. Sorensen, J.R. Gallagher, S.B. Hawthorne, T.R. Aulich, AAD Document Control, National Energy Technology Laboratory (US Department of Energy); JV TASK3 – Gas Industry Groundwater Research Program – Final Report AAD, 2000.
[19] J. Bianchi, B. Catalano, O. Faraponova, C. Maggi, L. Manfra, M.M. annozzi, L. Mariani, G. Moltedo, F. Onorati, F. Regoli, F. Savorelli, A. Tornambè, C. Virno Lamberti, ICRAM (2006) 167.
[20] EERC—Energy & Environmental Researche Center. Gas industry groundwater research program Final Report US, 2000. http://www.osti.gov.
[21] CEFAS. UK guidelines on interpreting the requirements of the OSPAR harmonised offshore chemical notification format. Centre for Environment, Fisheries & Aquaculture Science, 2001. http://www.cefas.co.uk.
[22] T. Strømgren, S.E. Sørstrøm, L. Schou, I. Kaarstad, I. Aunaas, T. Brakstad, Ø. Johansen, Mar. Environ. Res. 40 (1995) 147.
[23] S.D. Richardson, Anal. Chem. 78 (2006) 4021.
[24] D.A. Holdway, Mar. Pollut. Bull. 44 (2002) 185.
[25] L. Mariani, L. Manfra, C. Maggi, F. Savorelli, R. Di Mento, A.M. Cicero, Fresen. Environ. Bull. 13 (2004) 1427.
[26] K.A. Burns, S. Codi, M. Furnas, D. Heggie, D. Holdaway, B. King, F. Mcallister, Marine Pollut. Bull. 38 (1999) 593.
[27] N. Nyholm, P. Kristensen, Ecotox. Environ. Safe. 23 (1992) 161.
[28] F.T. Peters, L.D. Paul, T. Kraemer, J. Chromatogr. B 754 (2001) 401.
[29] V. Gembus, J. Goulle, C. Lacroix, J. Anal. Toxicol. 26 (2002) 280.
[30] M. Holčapek, H. Virelizier, J. Chamot-Rooke, P. Jandera, C. Moulin, Anal. Chem. 71 (1999) 2288.
[31] A. Cappiello, G. Famiglini, F. Mangani, P. Palma, Mass Spectrom. Rev. 20 (2001) 88.
[32] A. Cappiello, G. Famiglini, F. Mangani, P. Palma, J. Am. Soc. Mass Spectr. 13 (2002) 265.
[33] A. Cappiello, G. Famiglini, P. Palma, Anal. Chem. 75 (2003) 497A.
[34] A. Cappiello, G. Famiglini, P. Palma, E. Pierini, H. Trufelli, C. Maggi, L. Manfra, M. Mannozzi, Chemosphere 69 (2007) 559.
[35] T. Reemtsma, Trends Anal. Chem. 20 (2001) 533.
[36] J.P. Antignac, K. de Wasch, F. Monteau, H. De Brabander, F. Andre, Anal. Chim. Acta 529 (2005) 129.
[37] P.J. Taylor, Clin. Chem. 38 (2005) 328.
[38] W.M.A. Niessen, P. Manini, R. Andreoli, Mass Spectrom. Rev. 25 (2006) 881.
[39] T.M. Annesley, Clin. Chem. 49 (2003) 1041.
[40] L.L. Jessome, D.A. Volmer, LCGC 24 (2006) 498.
[41] EURACHEM Guide, The Fitness for Purpose of Analytical Methods: A Laboratory Guide to Method Validation and Related Topics. Ltd., Teddington, UK, 1998. http://www.eurachem.ul.pt.
[42] P.A. Vollmer, D.C. Harty, N.B. Erickson, A.C. Balhon, R.A. Dean, J. Chromatogr. B 685 (1996) 370.

[43] A. Cappiello, G. Famiglini, P. Palma, E. Pierini, V. Termopoli, H. Trufelli, Anal. Chem. 80 (2008) 9343.
[44] R. King, R. Bonfiglio, C. Fernandez-Metzler, C. Miller-Stein, T. Olah, J. Am. Soc. Mass Spectrom. 11 (2000) 942.
[45] T.L. Constantopoulos, G.S. Jackson, C.G. Enke, J. Am. Soc. Mass Spectrom. 10 (1999) 625.
[46] D. Buhrman, P.I. Price, P.J. Rudewicz, J. Am. Soc. Mass Spectrom. 7 (1996) 1099.
[47] B.K. Matuszewsky, M.L. Constanzer, C.M. Chavez-Eng, Anal. Chem. 75 (2003) 3019.

Talanta 80 (2009) 263–268

Contents lists available at ScienceDirect

Talanta

journal homepage: www.elsevier.com/locate/talanta

Volatile organic compounds sensing properties of tetrakis(alkylthio)-substituted lutetium(III) bisphthalocyanines thin films

Necmettin Kılınç[a], Devrim Atilla[b], Ayşe Gül Gürek[b], Zafer Ziya Öztürk[a,c,*], Vefa Ahsen[b,c]

[a] Gebze Institute of Technology, Faculty of Science, Department of Physics, P.O. Box 141, 41400 Gebze-Kocaeli, Turkey
[b] Gebze Institute of Technology, Faculty of Science, Department of Chemistry, 41400 Gebze-Kocaeli, Turkey
[c] TÜBİTAK-Marmara Research Center, Materials Institute, 41470 Gebze-Kocaeli, Turkey

ARTICLE INFO

Article history:
Received 3 March 2009
Received in revised form 15 June 2009
Accepted 29 June 2009
Available online 4 July 2009

Keywords:
Lanthanide
Lutetium phthalocyanine
Thin films
Conductivity
VOC sensing

ABSTRACT

The effect of volatile organic compounds (VOCs) such as acetone, methanol, ethanol, chloroform, carbon tetrachloride, dichloromethane, and hexane on electrical conductivity of thin films of bis[tetrakis(alkylthio)phthalocyaninato]lutetium(III) double decker complexes $[(C_nH_{2n+1}S)_4Pc]_2Lu(III)$ was investigated. The $[(C_nH_{2n+1}S)_4Pc]_2Lu(III)$ molecules substituted with different alkylthia chains (n = 6, 8, 10, 12, and 16) were coated on interdigital transducers using a jet spray technique. A change (increase or decrease) in the conductivity of the $[(C_nH_{2n+1}S)_4Pc]_2Lu(III)$ films was observed depending on the concentration of the VOCs, which was ranging from 500 to 5000 ppm. The decrease in the conductivity of the sensors for the dissolvent of the compounds (chloroform, carbon tetrachloride, dichloromethane and hexane) could be related to swelling of the films. On the other hand, the increase in the conductivity of the sensors for the other VOCs (acetone, methanol and ethanol) could be resulted from that the VOCs act as electron donors and/or acceptors in the films. A linear relationship between the sensor response and concentration of the VOC vapors is obtained. The sensitivities of the $[(C_nH_{2n+1}S)_4Pc]_2Lu(III)$ films were in the range of 2.10^{-4}–3.10^{-3}%/ppm.

© 2009 Elsevier B.V. All rights reserved.

1. Introduction

During the past decade, metalophthalocyanines (MPcs) have attracted considerable attention in solar cells, photo dynamic therapy, gas sensors, as liquid crystal, and electrochoromic displays because of their remarkable optical, and electrical properties, the conjugated π system, as well as chemical, and thermal stability [1–3].

Several review papers about chemical sensing properties of the MPcs have been published [4–8]. The MPcs may be utilized for different types of chemical sensors, including in particular electronic sensors (such as resistive sensor, field-effect transistors (FET), solid-state ionic, and capacitance sensors), mass-sensitive sensors utilizing a quartz crystal microbalance (QCM) or surface acoustic-wave (SAW) sensors, and optical sensors. It is well known that the sensor response, stability and other sensing characteristics of the MPc films are affected by many factors, such as film morphology, molecular orientation and so on. To achieve optimal sensor performance, requirements for coating properties of the MPc films are good control of thickness, uniformity, viscosity and adhesive strength of the film. Various techniques are used to prepare MPc thin films, such as vacuum deposition, spin-coating and Langmuir–Blodgett technique depending on the structure and solubility of the used MPc molecule.

Most researchers studying the gas sensitivity of MPcs using chemoresistive sensors are focused on oxidizing and reducing gases such as NO_2, O_3, and Cl_2 which have strong electron interactions with the phthalocyanine film [4–9]. However, only a few papers were published on chemoresistive gas sensors for non-oxidizing gases such as volatile organic compounds (VOCs). The main reason is that the exposure of a MPc film to a gas leads to variations in the charge carrier density in the molecular units of the film. These types of organic compounds generally are not so strong electron donors or acceptors, and hence the changes are less intense when compared with those observed with the inorganic gases mentioned above [10].

Among the large family of the phthalocyanines, lanthanide bisphthalocyanines, and especially the lutetium derivatives have been subject of extensive investigations because of their characteristic properties such as intense color, redox activity, and high thermal stability [2,3]. There are special properties of this class of compounds that make them suitable for applications in the field of

* Corresponding author at: Gebze Institute of Technology, Faculty of Science, Department of Physics, P.O. Box 141, 41400 Gebze-Kocaeli, Turkey.
Tel.: +90 2626051306.
E-mail addresses: nkilinc@gyte.edu.tr (N. Kılınç), datilla@gyte.edu.tr (D. Atilla), gurek@gyte.edu.tr (A.G. Gürek), zozturk@gyte.edu.tr (Z.Z. Öztürk), ahsen@gyte.edu.tr (V. Ahsen).

0039-9140/$ – see front matter © 2009 Elsevier B.V. All rights reserved.
doi:10.1016/j.talanta.2009.06.064

molecular electronics such as photovoltaic cells [3], organic light emitting diodes [11,12], and sensor devices for industrial and environmental applications [13]. de Saja and coworkers have been working for several years extensively with lanthanide phthalocyanines which are sandwich type complexes for chemoresistive sensor applications [8,10,14–16]. However, the sensing mechanism between MPc and VOCs is not yet well understood [8].

In this work we have investigated the effect of VOCs on the electrical conductivity of thin films of bis[tetrakis (alkylthio)phthalocyaninato]lutetium(III) double decker complexes $[(C_nH_{2n+1}S)_4Pc]_2Lu(III)$ and have explained VOCs sensing mechanism.

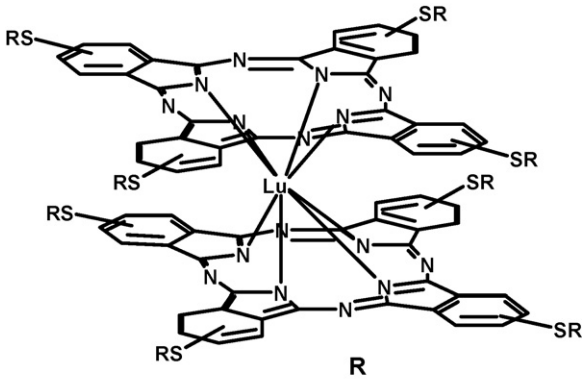
2. Experimental details

The synthesis procedure of bis[tetrakis(alkylthio)phthalocyaninato]lutetium (III) double decker complexes, $[(C_nH_{2n+1}S)_4Pc]_2Lu(III)$ (n = 6, 8, 10, 12, 16), has been extensively described in Ref. [17]. The chemical structure and the sample notation (**1–5**) of the compounds are given in Fig. 1 [17].

The interdigital transducer (IDT) used in the experiment consists of an array of metal electrodes photolithographically patterned on pre-cleaned microscope slides. Before vacuum evaporation, microscope slides were thoroughly cleaned with soap (micro 90), pure acetone and deionized water (18 MΩ) by an ultrasonic cleaner and then coated with ca. 20 nm of chromium followed by 130 nm of gold in a Leybold Univex 450 coater system with a Inficon Deposition Monitor (XTM/2). The film is patterned photolithographically and etched to provide 10 finger pairs of electrodes having a width of 100 μm, spaced 100 μm from the adjacent electrodes. The finger overlap distance was 5 mm. Gold was selected as the electrode material, since it is well-known metal which forms ohmic contacts with the phthalocyanines.

Thin films of the compounds were coated onto the IDTs using a homemade air brush system in an inert ambient from a solution of the compounds in chloroform. The thickness of the films determined by a Surface Profilometer (Veeco, Dektak 6) was approximately 150 nm. The films used on the sensors were annealed at 150 °C in high purity dry nitrogen ambient to get a liquid crystal order of the film before gas sensing measurements.

The sensor devices were mounted in a homemade aluminum test chamber of a volume of 1 l which was connected with MFC controlled high purity N_2 lines. All measurements were done in dark because it is known that with a glass chamber, light can induce the formation of ozone whose presence, even at very low concentration (10 ppb), can increase the density of charge carriers in the radical lutetium bismacrocyclic derivatives, then the measured conductivity [13,18]. A constant bias voltage of 1 V was applied to the devices and the dc current was measured with a Keithley 6517A Electrometer/High Resistance Meter. The dc current (sensor responses) was monitored continuously under N_2 atmosphere to establish the baseline of the device and recorded using an IEEE 488 data acquisition system incorporated to a personal computer. The high purity N_2 stream flowed through the test chamber until the electric current reached a steady value and then the valves of the chamber were closed. A certain amount of volatile organic compound (from 15 to 150 μmol, resulting in concentrations of 500, 1000, 2000, 3000, 4000, 5000 ppm consequently) was injected into the test chamber through a septum with a gas tight micro syringe. The VOCs exposed to the sensors were the dissolvent of the compounds such as chloroform, carbon tetrachloride, dichloromethane, and hexane, and other VOCs such as acetone, methanol, and ethanol.



	R
1	C_6H_{13}
2	C_8H_{17}
3	$C_{10}H_{21}$
4	$C_{12}H_{25}$
5	$C_{16}H_{33}$

Fig. 1. The chemical structures of the lutetium(III) bisphthalocyanines **1–5**.

3. Results and discussion

It is well known that when an analyte gas molecule is adsorbed on the surface of a phthalocyanine film it causes a variation in the physical or chemical properties of the film, such as swelling, capacity or conductivity changes, etc. In order to measure the effect of different VOC vapors on the conductivity of the Pc films, after the baseline current reached a steady state value, the films were exposed to atmospheres containing a certain amount of them (500, 1000, 2000, 3000, 4000, 5000 ppm). Fig. 2a shows the current versus time behavior of compound **1** exposed to 3000 ppm of the dissolvent chloroform, carbon tetrachloride, dichloromethane and hexane at room temperature. After the dissolvent exposure (3000 ppm), the current decreased sharply for a few minutes and then the rate of decrease slowed down and then the current reached a steady value. When the dissolvent vapors are removed with high purity N_2 flow, the recovery shows a rapid increase and then the rate of increase slows down. A drift in the baseline is observed while monitoring the operation of the sensors. This type of behavior has been previously reported [19] for other sensors based on phthalocyanine derivatives, and has been attributed to an incomplete recovery of the original properties of the films. This problem could be overcome by heating the samples in order to facilitate the desorption of the vapors from the sensing layer. It is obviously seen in Fig. 2a that the sensor response is in the order: chloroform > hexane > dichloromethane > carbon tetrachloride.

Fig. 2b shows a typical current versus time of compound **1** exposed to 500–5000 ppm of chloroform at room temperature which is a dissolvent of the compounds (**1–5**). After first exposure (500 ppm), the current decreased sharply for a few minutes and finally the rate of decrease slowed down and then the current reached a steady value. Similar behavior is observed for second and further exposures to chloroform (1000–5000 ppm). When the chloroform vapor is removed with high purity N_2 flow, the recovery shows a rapid increase and then the rate of increase slows down. Similarly, as can be seen in Fig. 3 a decrease in the current is obtained when the dissolvent chloroform is exposed to the other four compounds (**2–5**). After every indicated concentration of chloroform exposed to the sensors, the current decreased sharply for a few minutes and finally the rate of decrease slowed down and then the current reached a steady value. If we pay attention to the current scale in Fig. 2b and Fig. 3, it is clearly seen that the amplitude of the current is depending on the length of alkyl chain. The relationship between conductivity and the length of alkyl chain is previously given in Ref. [17].

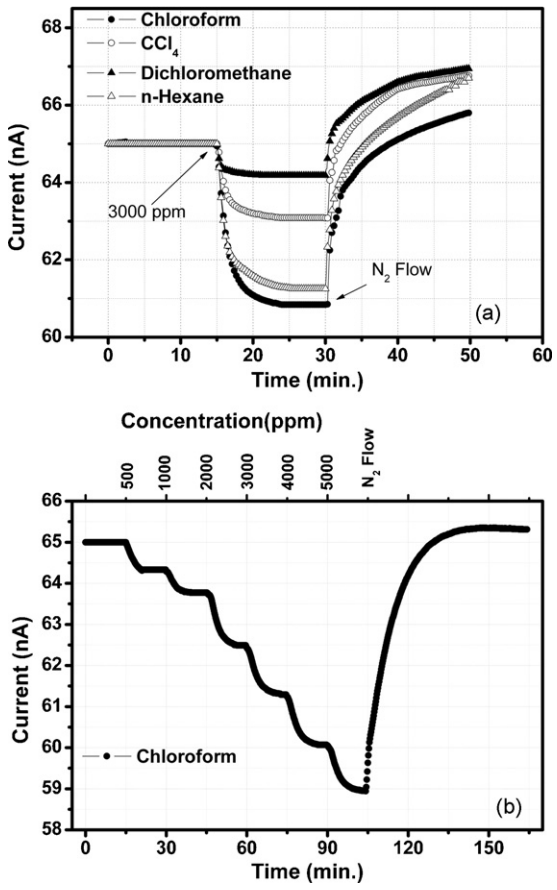


Fig. 2. Current versus time of a film of compound **1** exposed to the 3000 ppm of the dissolvents chloroform, carbon tetrachloride, dichloromethane and hexane at room temperature (a) and current versus time of compound **1** at room temperature as a function of chloroform concentration (b).

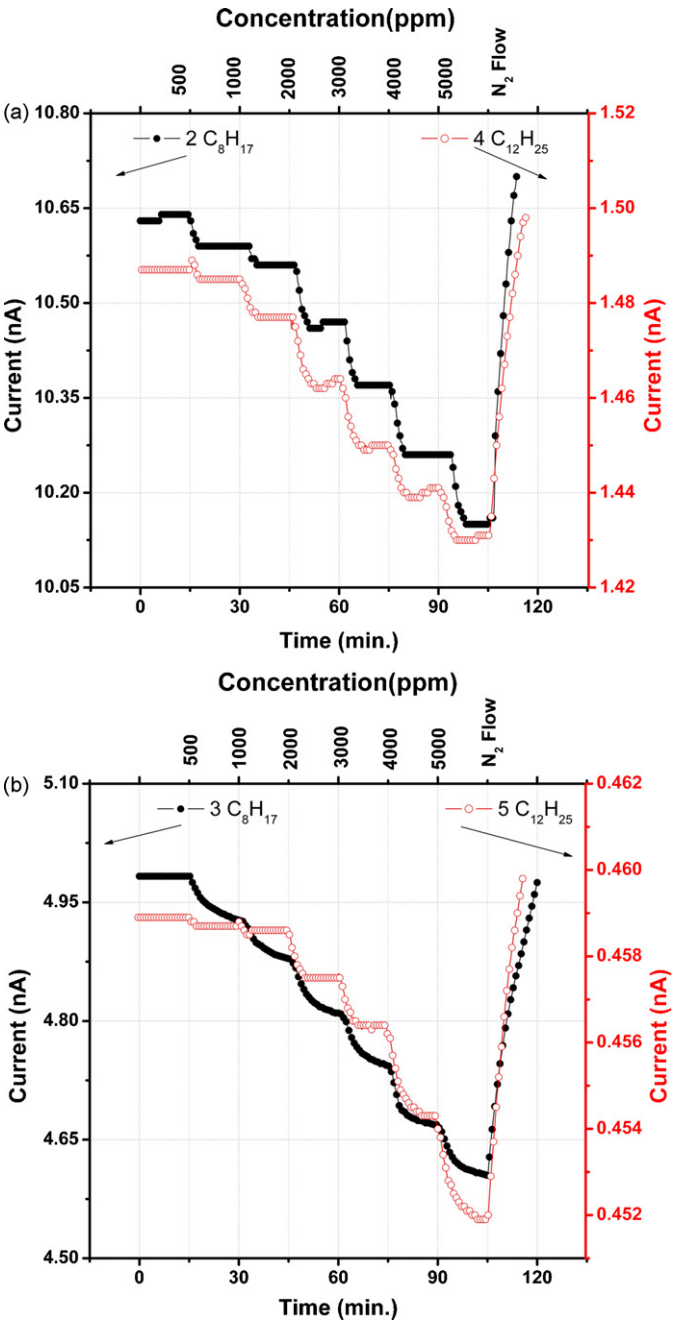


Fig. 3. Current versus time of films of compounds (**2–5**) exposed to 500–5000 ppm of chloroform at room temperature. (a) and (b) represent the response curves of compounds **2**–**4** and **3**–**5**, respectively.

Fig. 4 shows typical current versus time curves of a sensor of compound **1** exposed to 500–5000 ppm of the three different VOCs acetone, methanol and ethanol. After first exposure to the VOCs (500 ppm), the current increased sharply in a few minutes and then the rate of increase slowed down and then the current reached a steady value (saturation). Similar behavior is observed for the second and so on exposures to the VOCs (1000–5000 ppm). When the VOCs are purged with a high purity N_2 flow, the sensor response goes back to the baseline. The recovery curve shows a rapid decrease and then the rate of decrease slows down. A slight drift in the baseline is observed while monitoring the operation of the sensors such as for the dissolvent VOCs of the compounds. If two alcohols are compared, the sensitivity to ethanol is higher than of the methanol. This effect can be explained by looking at the electric dipole polarizabilities of the alcohols; ethanol has a greater polarizability than methanol (5.41×10^{-24} and 3.23×10^{-24} cm^3, respectively). For the other four compounds (**2–5**) similar results are obtained. In generally, the conductivity changes as determined using interdigital transducers may result from changes of the relative dielectric coefficients in the gas phase, in the sensitive layer and/or from the changes of the effective thickness of the sensitive layer (swelling). So, the increase in the current could be naively interpreted bearing in mind that phthalocyanines are p-type semiconductors and that electron donor molecules can oxidize the phthalocyanine molecules.

A different behavior for the dissolvent of the compounds (**1–5**) such as chloroform, carbon tetrachloride, dichloromethane and hexane from the other VOCs has been observed. While the dissolvent is exposed to the sensor the current decreases, but for the other VOCs exposed the current increases. In the literature, de Saja and coworkers have investigated chemoresistor sensors based on Pc_2Lu for VOCs sensing. They obtained a decrease in the conductivity, when the sensors were exposed to the VOCs such as hexanol, hexanal, *n*-butyl acetate, acetic acid [8,10], trimethylamine [14], and olive oil aroma [15]. Miller et al. obtained a similar behavior for cobalt phthalocyanine (CoPc) which was exposed to dimethylmethylphosphonate, methanol, water, and toluene [20]. In our case, the decrease of the conductivity would be the result of the swelling effect caused by the diffusion of dissolvent of the compounds that would lead to a decrease in the mobility of the charge carriers. The investigation of the mesoscopic phase under VOC vapors under polarized microscope showed us, the dissolvent of the compounds disturbed the ordered structure of the films which leads to decrease

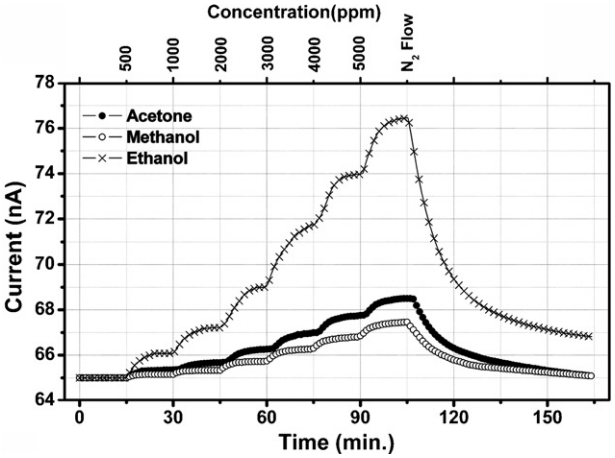


Fig. 4. Current versus time of a film of compound **1** exposed to 500–5000 ppm of three different VOCs at room temperature.

in conductivity, but other VOCs have no effect on the film structure. Fig. 5 shows the polarized microscope photos of the thin film of compound **1** when the compound **1** was exposed to dry air, 10,000 ppm acetone and 10,000 ppm chloroform. There is no structural metamorphosis when the compound **1** was exposed to acetone but it is clearly seen a change in the structure when the compound **1** was exposed to chloroform. Dark lines or dark parts are gold electrode fingers under the thin film as seen in Fig. 5. The mesophase of the compound **1** was disappeared when the compound 1 was exposed to chloroform (Fig. 5c).

On the other hand, Gorbunova et al. have obtained an increase in the conductivity for chemoresistor sensors based on samarium bisphthalocyanine, when the sensors were exposed to VOCs such as hexanol, hexanal, *n*-butyl acetate and acetic acid [16] like our results for acetone, methanol and ethanol. Similarly Bekaroglu and coworkers acquired an increase in the conductivity for chemoresistor sensors based on zinc phthalocyanine (ZnPc) [21,22] and CoPc [21] exposed to VOCs such as chloroform, acetone, carbontetrachloride, methanol, ammonia, and ethanol. Similar results were obtained by Ma et al. for the ZnPcs zinc hexadecafluorophthalocyanine [23], zinc tetraphenylporphyrin, and zinc meso-tetra(2,3,4,5,6-pentafluorophenyl)-porphyrin [24]. Gupta and Misra observed an increase in conductivity for manganese phthalocyanine when trimethylamine was exposed to the sensor [25]. In our results the increase in the conductivity of the sensors for the other VOCs (acetone, methanol and ethanol) could be naively interpreted to electron-donating to the films.

A linear relationship between the sensor response and concentration of VOC gases, which is based on the low concentration region of a Langmuir adsorption model, is observed in the concentration range 500–5000 ppm at room temperature. The sensor response is defined as

$$R = \frac{\Delta I}{I_0} 100 \quad (1)$$

where ΔI is the change in current and I_0 is the reference value of the coated devices exposed to dry nitrogen. Fig. 6a shows the sensor

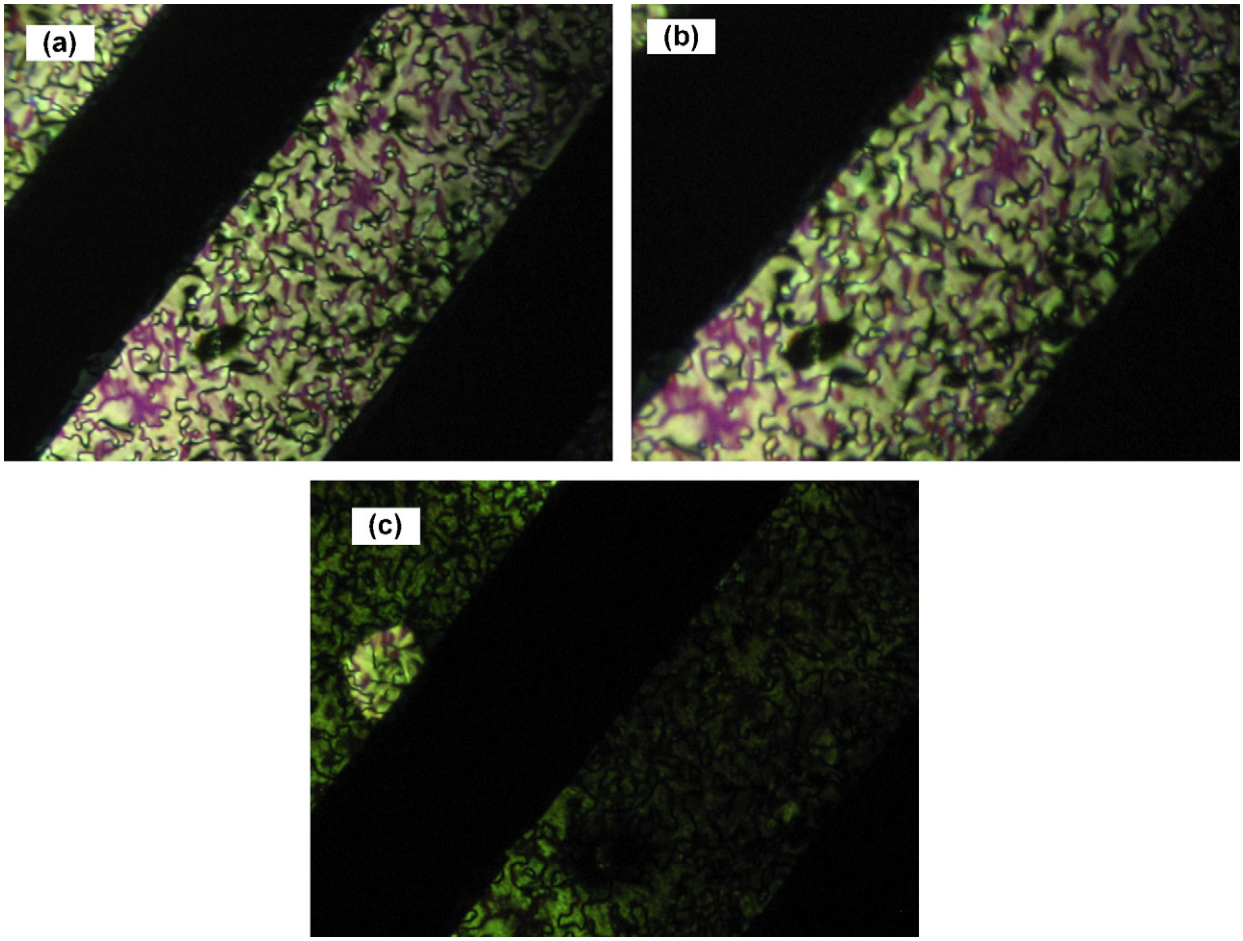


Fig. 5. The polarized microscope photos of the thin film of compound **1** when the compound **1** was exposed to dry air (a), 10,000 ppm acetone (b) and 10,000 ppm chloroform (c). Dark lines are gold electrodes fingers under the thin film.

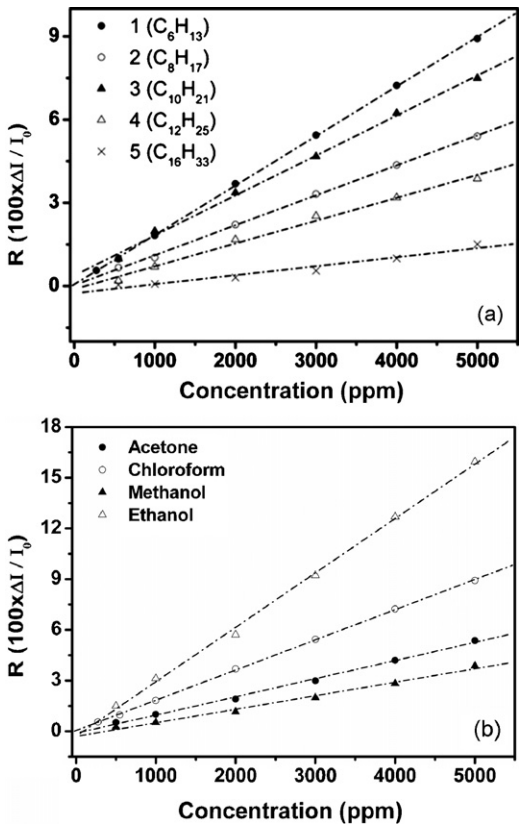


Fig. 6. Sensor response versus concentration of chloroform for all compounds (**1–5**) (a) and for all VOCs for compound **1** (b) at room temperature. The side chain formula of the compounds is represented in the parentheses.

responses versus concentration of chloroform for all compounds (**1–5**) at room temperature. The sensor response decreased with increasing length of the alkyl chain, except for compound **3**. It can be clearly seen from Fig. 6a that the maximum sensor response is observed for compound **1** which has the shortest alkyl chain and the minimum sensor response is observed for compound **5** which has the longest alkyl chain. However, no relationship between sensor response and the length of alkyl chain was observed for the other VOC vapors. Fig. 6b shows the sensor response versus concentration of VOCs for a film of compound **1**. The electric dipole polarizability of chloroform, acetone, ethanol and methanol is 8.23×10^{-24}, 6.33×10^{-24}, 5.41×10^{-24}, and 3.23×10^{-24} cm^3, respectively [26]. There is no relationship between the electric dipole polarizability of VOCs and the sensor response (Fig. 6b), because the sensitivity is not only depending on polarizability but also depends on polarity, acidity, basicity, dispersion, etc. of the VOCs. For the other four compounds (**2–5**) similar results are obtained.

The sensing properties of these films were compared by sensitivity. The sensitivity is defined as

$$S = \frac{\Delta R}{\Delta C} \quad (2)$$

where ΔR is the change in sensor response and ΔC is the change in the concentration of the VOC. Fig. 7 depicts the sensitivity of compounds **1–5** for acetone, chloroform, methanol and ethanol at room temperature. It is clearly seen from Fig. 7 that if alcohols are compared, the sensitivity for the ethanol is higher than of the methanol for all compounds. The sensitivities of the $[(C_nH_{2n+1}S)_4Pc]_2Lu(III)$ films were in the range of 2.10^{-4}–3.10^{-3}%/ppm. Previously, a logarithmic relationship between the dc conductivities of the compounds and the length of the alkyl chains on the periphery of the compounds was observed [17] and self-orientation of

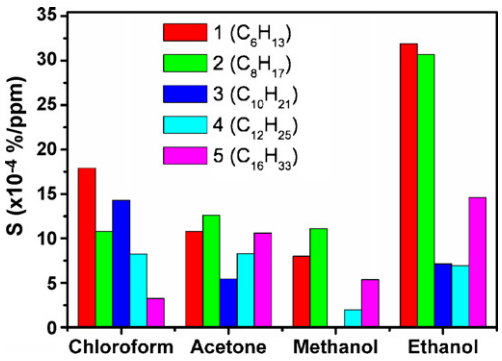


Fig. 7. Sensitivity of compounds **1–5** for VOCs at room temperature. The side chain formula of the compounds is represented in the parentheses.

$[(C_nH_{2n+1}S)_4Pc]_2Lu(III)$ films after heated to liquid crystal phase region caused a decrease in the conductivities of the films [27]. However, we did not obtain such a relationship between the sensitivity and the length of the alkyl chains on the periphery of the compounds except for dissolvent chloroform. Fig. 7 shows that the sensitivities of the $[(C_nH_{2n+1}S)_4Pc]_2Lu(III)$ films are varying. This could be related to different reorganizations of the $[(C_nH_{2n+1}S)_4Pc]_2Lu(III)$ films after heating to 150 °C as the $[(C_nH_{2n+1}S)_4Pc]_2Lu(III)$ compounds have various phase and phase transition temperature up to 150 °C. The phase and phase transition temperature of the all compounds were given in Ref. [17].

4. Conclusions

The use of the tetrakis(alkylthio)-substituted lutetium(III) bisphthalocyanines can contribute greatly to the development of VOC monitoring systems. The behavior of the sensing elements when exposed to VOCs has been analyzed. The sensing units give rise to fast and reproducible signals, without a noticeable loss of their properties. The reproducibility and complete reversibility of the signals further encourage the development of these in-situ detectors for VOCs.

The linear relationship between the sensor response and concentration of VOC vapors allows the quantification of trace amount of VOCs. A different sensing behavior for the dissolvent of the compounds such as chloroform, carbon tetrachloride, dichloromethane and hexane from the other VOCs has been observed depending on the swelling effect caused by the diffusion of dissolvent of the compounds that leads to a decrease of the mobility of the charge carriers. For the other VOCs (acetone, methanol and ethanol), the increase in the conductivity of the sensors can be related to the electro-donating and -accepting properties of the films.

Acknowledgements

This research was supported, in part, by Gebze Institute of Technology under Grant nos. GYTE-BAP 2005-A-02 and GYTE-BAP 2007-A-13. The authors would like to thank Dr. Mika HARBECK for his valuable discussions.

References

[1] J. Simon, J.J. Andre, Molecular Semiconductors, Springer-Verlag, Berlin, 1985.
[2] C.C. Leznoff, A.B.P. Lever (Eds.), Phthalocyanines. Properties and Applications, vols. 1–4, Wiley–VCH, New York, 1989–1996.
[3] J. Simon, P. Bassoul, Design of Molecular Materials: Supramolecular Engineering, John Wiley & Sons, New York, 2000.
[4] R. Zhou, F. Josse, W. Göpel, Z.Z. Öztürk, Ö. Bekaroğlu, Appl. Organomet. Chem. 10 (1996) 557.
[5] L. Valli, Adv. Colloid Interface 116 (1–3) (2005) 13.
[6] M. Bouvet, Anal. Bioanal. Chem. 384 (2) (2006) 366.
[7] J. Janata, M. Josowicz, J. Solid State Electrochem. 13 (1) (2009) 41.

[8] J.A. de Saja, M.L. Rodriguez-Mendez, Adv. Colloid Interface 116 (2005) 1.
[9] N. Kılınç, D. Atilla, S. Öztürk, A.G. Gürek, Z.Z. Öztürk, V. Ahsen, Thin Solid Films 517 (2009) 6206.
[10] M.L. Rodriguez-Mendez, J. Souto, R. de Saja, J. Martinez, J.A. de Saja, Sens. Actuator B-Chem. 58 (1999) 554.
[11] D. Hohnholz, S. Steinbrecher, M. Hanack, J. Mol. Struct. 521 (2000) 231.
[12] G. Guillaud, M. Al Sadoun, M. Maitrot, J. Simon, M. Bouvet, Chem. Phys. Lett. 167 (1990) 503.
[13] M. Bouvet, A. Leroy, J. Simon, F. Tournilhac, G. Guillaud, P. Lessnick, A. Maillard, S. Spirkovitch, M. Debliquy, A. De Haan, A. Declory, Sens. Actuator B-Chem. 72 (2001) 86.
[14] R. de Saja, J. Souto, M.L. Rodriguez-Mendez, J.A. de Saja, Mater. Sci. Eng. C 8/9 (1999) 565.
[15] N. Gutierrez, M.L. Rodriguez-Mendez, J.A. de Saja, Sens. Actuator B-Chem. 77 (2001) 437.
[16] Y. Gorbunova, M.L. Rodriguez-Mendez, I.P. Kalashnikova, L.G. Tomilova, J.A. de Saja, Langmuir 17 (2001) 5004.
[17] D. Atilla, N. Kılınç, F. Yüksel, A.G. Gürek, Z.Z. Öztürk, V. Ahsen, Synth. Met. 159 (2009) 13.
[18] M. Bouvet, G. Guillaud, A. Leroy, A. Maillard, S. Spirkovitch, F.G. Tournilhac, Sens. Actuator B-Chem. 73 (2001) 63.
[19] P. Roisin, J.D. Wright, R.J.M. Nolte, O.E. Sielcken, S.C. Thorpe, J. Mater. Chem. 2 (1992) 131.
[20] K.A. Miller, R.D. Yang, M.J. Hale, J. Park, B. Fruhberger, C.N. Colesniuc, I.K. Schuller, A.C. Kummel, W.C. Trogler, J. Phys. Chem. B 110 (2006) 361.
[21] T. Ceyhan, A. Altındal, M.K. Erbil, Ö. Bekaroğlu, Polyhedron 25 (2006) 737.
[22] M. Özer, A. Altındal, A.R. Özkaya, M. Bulut, Ö. Bekaroğlu, Synth. Met. 155 (2005) 222.
[23] X.F. Ma, H.Z. Chen, M.M. Shi, G. Wu, M. Wang, J. Huang, Thin Solid Films 489 (2005) 257.
[24] X.F. Ma, J.Z. Sun, M. Wang, M. Hu, G. Li, H.Z. Chen, J. Huang, Sens. Actuator B-Chem. 114 (2006) 1035.
[25] S. Gupta, T.N. Misra, Sens. Actuator B-Chem. 41 (1997) 199.
[26] D.R. Lide (Ed.), CRC Handbook of Chemistry and Physics, CRC Press, Boca Raton, FL, Internet Version 2005, http://www.hbcpnetbase.com/.
[27] N. Kılınç, A.Ş. Ahsen, D. Atilla, A.G. Gürek, S.E. San, Z.Z. Öztürk, V. Ahsen, Sens. Lett. 6 (2008) 607.

Talanta 80 (2009) 269–278

Contents lists available at ScienceDirect

Talanta

journal homepage: www.elsevier.com/locate/talanta

Pressurised liquid extraction of flavonoids in onions. Method development and validation

Malene Søltoft[a,b], Jan H. Christensen[b], John Nielsen[b], Pia Knuthsen[a,*]

[a] Department of Food Chemistry, National Food Institute, Technical University of Denmark, Mørkhøj Bygade 19, DK-2860 Søborg, Denmark
[b] Department of Basic Sciences and Environment, Faculty of Life Sciences, University of Copenhagen, Thorvaldsensvej 40, DK-1871 Frederiksberg C, Denmark

ARTICLE INFO

Article history:
Received 6 March 2009
Received in revised form 15 June 2009
Accepted 29 June 2009
Available online 8 July 2009

Keywords:
PLE
Flavonoids
Phenolic acids
Onions
Method optimization and validation

ABSTRACT

A rapid and reliable analytical method for quantification of flavonoids in onions was developed and validated. Five extraction methods were tested on freeze-dried onions and subsequently high performance liquid chromatography (HPLC) with UV detection was used for quantification of seven flavonoids.

The extraction efficiencies were lowest for the conventional water bath extraction compared to pressurized liquid extraction (PLE), ultrasonication, ultrasonic liquid processor, and microwave extraction, which yielded similar efficiencies. The reproducibility was in the same range (RSD: 1–11%) for all tested extraction methods. However, PLE was the preferred extraction method because the method can be highly automated, use only small amounts of solvents, provide the cleanest extracts, and allow the extraction of light and oxygen-sensitive flavonoids to be carried out in an inert atmosphere protected from light.

The method parameters: extraction temperature, sample weight, flush volume and solvent type were optimised, and a clean-up step was integrated in the PLE procedure by in-cell addition of C18-material to the extraction cells, which slightly improved the recovery and reproducibility of the method. The one-step PLE method showed good selectivity, precision (RSDs = 3.1–11%) and recovery of the extractable flavonoids (98–99%). The method also appeared to be a multi-method, i.e. generally applicable to, e.g. phenolic acids in potatoes and carrots.

© 2009 Elsevier B.V. All rights reserved.

1. Introduction

Flavonoids belong to the group of polyphenols and are secondary metabolites [1], which play an important role in the normal growth, development and defence of plants [2]. Polyphenols in general have antioxidant properties and are proposed to have beneficial health effects such as decreasing the risk of heart diseases and protection against cancer [3–5].

Onions are a rich source of flavonoids [6,7], which generally occur widely in the plant kingdom [3], and onions are one of the main sources of polyphenols in daily food intake [8–10]. The content of polyphenols varies in different plant parts [11,12] and between varieties due to genetic factors [13–15], environmental and cultural factors [1], as well as time of harvest, processing and storage [16].

The main flavonoids in onions are quercetin mono- and diglucosides [17,18], which account for up to 80% of the total content of flavonols, but kaempferol [17] and isorhamnetin derivates [18,19] as well as myricetin [2] have also been found (see chemical structures in Fig. 1).

Conventional liquid extraction methods, e.g. water bath or ultrasonication, with aqueous methanol or acetonitrile have been widely used as simple and easy methods for analysis of flavonoids [20,21]. Extraction of flavonoid aglycones has most often been done by acid hydrolysis [2,22,23], but harsh extraction conditions (e.g. acid or heating) should be avoided if intact flavonoid-glycosides are desired [21]. An increased risk of degradation is often seen with conventional extraction methods owing to long extraction times, where samples are exposed to light and oxygen, which facilitate the degradation of flavonoids [24,25].

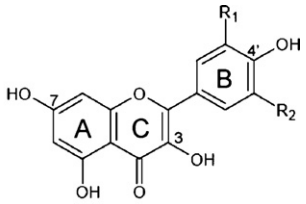
More rapid and automated methods have recently been used, e.g. supercritical fluid extraction (SFE), pressurized liquid extraction (PLE) or microwave-assisted extraction (MAE). They are advantageous compared to conventional methods because they can be carried out in the absence of light and protected from oxygen, cope with the demand for a reduction in organic solvent consumption and improve the extraction time due to the possibility of working at elevated temperatures and/or pressures in inert atmospheres [26].

SFE has been used for extraction of polyphenols in grapes [27]. However, SFE of polyphenols requires a high percentage of organic modifiers, which is a disadvantage as it decreases the method selectivity [25]. PLE is advantageous because high temperatures and pressures can be applied, which accelerate the extraction [25], but its application in food analyses has been limited although it

* Corresponding author. Tel.: +45 35 88 74 32; fax: +45 72 34 74 48.
E-mail address: pknu@food.dtu.dk (P. Knuthsen).

0039-9140/$ – see front matter © 2009 Elsevier B.V. All rights reserved.
doi:10.1016/j.talanta.2009.06.073

	Abbreviation	R_1	R_2
Quercetin [a]	Q	OH	H
Kaempferol [b]	K	H	H
Isorhamnetin [c]	I	OCH_3	H
Myricetin [d]	M	OH	OH



[a] 2-(3,4-dihydroxyphenyl)-3,5,7-trihydroxychromen-4-one
[b] 3,5,7-trihydroxy-2-(4-hydroxyphenyl)chromen-4-one
[c] 3,5,7-trihydroxy-2-(4-hydroxy-3-methoxyphenyl)chromen-4-one
[d] 3,5,7-trihydroxy-2-(3,4,5-trihydroxyphenyl)chromen-4-one.

Fig. 1. Chemical structures of selected flavonols. The full chemical names are listed in the footnotes.

has been used to extract polyphenols from various food products [28,29]. MAE has been used for extraction of polyphenols from food products and plants and has the advantage of being rapid with a low solvent-consumption [32]. Another promising technique is Ultrasonic Liquid Processing (ULP), which has so far not been used for extraction of polyphenols from plants. The principle of ULP is the same as sonication, but shorter extraction times are expected due to a more intense cavitational action and greater disruption of the sample [33].

The objective of our study was to develop a rapid, sensitive and robust analytical method, which sets a new standard for extraction of flavonoids in onions. The recommended method of choice should be based on a comparison of the efficiency, reproducibility and sensitivity of conventional methods (water bath and ultrasonication) with more modern extraction methods (PLE, MAE and ULP). The best extraction method will be optimised with regards to relevant extraction parameters and validated.

2. Materials and methods

2.1. Reagents and chemicals

Methanol (HPLC-grade, Rathburn Chemicals Ltd., Scotland) and Milli-Q water (18 MΩ, Millipore, USA) were used for standards and eluents. Dimethyl sulfoxide (DMSO, >99%) and formic acid (98–100%) were purchased from Merck (Germany). The following standards were purchased: quercetin (Q) and isorhamnetin (I) from Extrasynthése (France), quercetin-3,4′-diglucoside (Q-3,4′-diglu) from Polyphenols (France), quercetin-7,4′-diglucoside (Q-7,4′-diglu) from Apin (United Kingdom), quercetin-4′-glucoside (Q-4′-glu) from Plantech (United Kingdom), and quercetin-3-glucoside (Q-3-glu, purity >90%), chlorogenic acid (ChlAcid, purity >95%) and caffeic acid (CafAcid, purity >99%) from Sigma–Aldrich (Germany).

Individual standard stock solutions were prepared by dissolving the solid compounds in DMSO (100 μg/mL). Working solutions were prepared by 10-times dilutions of the stock solutions with methanol. Stock solutions were stored at −80 °C (<1 year), while the working solutions were prepared shortly before analyses and kept at −20 °C until analyses.

2.2. Samples

The onion sample (*Allium cepa* var. *zittauer*, 40–60 mm, Soeris I/S) used for comparison of extraction methods and PLE method optimisation was organic and purchased in a local supermarket. The onion (*Allium cepa* var. *hytech*), carrot (*Daucus carota* var. *bolero*), potato (*Solanum tuberosum* var. *sava*) and white cabbage (*Brassica oleracea* var. *impala*) samples used for method validation were internal reference samples. Only the bulb of the onion sample was used for analysis comprising the eatable part by removing the top, bottom and outer leaves. The stalk and outer leaves of the white cabbage heads were also removed. The top and bottom of the carrots were discarded and both carrots and potatoes peeled. The samples were freeze-dried at 1×10^{-3} bar for approximately 2 days and afterwards crushed and homogenised in a blender. The samples were stored at −20 °C in a nitrogen atmosphere until analysis. In general, the samples were protected from light and oxygen during the entire sample preparation.

2.3. Extraction methods

Throughout the entire method comparison 60% aqueous methanol was used as extraction solvent because it has previously been used successfully in our conventional water bath method (data not shown).

2.3.1. Ultrasonication

The sample material (0.1 g) was mixed with 5 mL solvent and sonicated at room temperature for 60 min (Branson 5200 Ultrasonic Cleaner, 120 W) following the procedure suggested by Lin and Harnley [34].

2.3.2. Water bath

The sample material (0.5 g) was extracted with 50 mL solvent at 30 °C for 60 min in a shaking-water bath (Julabo SW 23). The extracts were then filtered through a filter paper (Whatman1) and evaporated close to dryness *in vacuo* at 30 °C on a rotary evaporator. The residue was redissolved in 5 mL solvent.

2.3.3. Microwave-assisted extraction

The sample material (0.1 g) was transferred to a glass tube and 5 mL solvent was added. The extraction was carried out in the tubes on a Microwave Synthesizer (Initiator, Biotage, 15 watt) at 60 °C for 2 min.

2.3.4. Ultrasonic liquid processor

The sample material (0.1 g) was transferred to a glass tube and 5 mL solvent was added. The microprobe was immersed into the tube and the extraction was performed at room temperature for 30 s using an ultrasonic liquid processor (Microson XL 2000, Misonix, 10 W).

2.3.5. Pressurised liquid extraction

The extractions were carried out using an ASE-200 (Dionex). The sample material (0.1 g) was mixed with 3 g of glowed and chemically inert Ottawa sand (particle size 20–30 mesh, Fisher Chemicals) and added to 5 mL extraction cells. Two glass fiber filters (90 mm, Advantec) were placed at the bottom and one at the top of the extraction cell, which was filled with Ottawa sand. The extraction parameters were: temperature: 40 °C, pressure: 1500 psi, pre-heating time: 1 min, static extraction time: 5 min, heating: 5 min, static cycles: 2, flush volume: 100% of cell volume, purge time with N_2: 60 s. The extracts were collected in vials and

the volume adjusted to 20 mL with extraction solvent in volumetric flasks.

All extracts were filtered through a 0.20 μm filter (Sartorius Minisart) before chemical analysis.

2.4. Quantification of flavonoids by HPLC–UV

A Waters 2695 Alliance Separation Module was used for the chemical analysis of flavonoids in combination with a Waters 2996 Photodiode Array Detector (PDA) and a Waters 2487 Dual λ Absorbance Detector. Empower 2 was used for instrument control and data acquisition. The chromatographic separation was carried out at a flow rate of 1.0 mL/min at 30 °C with an injection volume of 20 μL (temperature of autosampler: 5 °C). The column was a Phenomenex Prodigy RP-C18 column (4.6 mm × 250 mm, 5 μm). The A-eluent was a mixture of 0.1% formic acid in Milli-Q water (v/v) and methanol (90:10, v/v) and the B-eluent was 100% methanol. The gradient program was as follows: 5% B for 1 min, a linear gradient to 50% B for 34 min, a linear gradient to 100% B for 5 min, isocratic elution for 4 min, followed by a 1-min ramp back to 5% B and re-equilibration for 6 min giving a total run-time of 51 min. The PDA collected data from 190–500 nm (sampling rate: 1.0 spectra/s and resolution: 1.2 nm). The Dual λ Absorbance Detector was used for quantification and set at 254 nm (sampling rate: 1.0/s), which is in the range of the first UV-maximum of flavonoids (240–285 nm) [21]. The flavonoids were quantified relative to quercetin and it is common practise in analyses of bioactive compounds to quantify relative to one or more selected reference compounds [20].

2.5. Identification of flavonoids by HPLC–MS and MS/MS

Structure elucidation of flavonoids in onions was based on accurate mass measurements, isotopic pattern fit of measurement compared to theoretical (i-FIT values, Elemental Composition version 4.0 in MassLynx software version 4.1, Waters, USA) and MS/MS fragmentation patterns. An ultra performance liquid chromatograph (UPLC) interfaced to a quadropole time of flight tandem mass spectrometer (qTOF) was used for exact mass determinations and an HPLC interfaced to a triple quadropole mass spectrometer (HPLC–QqQ) was used to study fragmentation patterns. Afterwards, the identities were confirmed with available and affordable standards by comparison of retention times, UV and MS data.

2.5.1. UPLC–qTOF

The same mobile phases as those used for the HPLC–UV analyses were used for the UPLC (Waters) analyses. The column was a Waters Acquity BEH-C18 column (2.1 mm × 100 mm, 1.7 μm), which was retained at 30 °C. The HPLC gradient was scaled according to the column dimensions and gradient flow rate applied in UPLC in order to obtain a UPLC gradient with the same number of column volumes and linear velocity. The gradient program was as follows (flow rate of 0.2 mL/min): 5% B until 0.4 min, a linear gradient to 50% B until 14.6 min, a linear gradient to 100% B until 15.4 min, isocratic elution until 17.5 min, a 0.4 min ramp back to 5% B and re-equilibration for 2.1 min giving a total run-time of 20 min. A sample volume of 8 μL was injected using the partial loop with needle overfill mode. The qTOF (Waters/Micromass qTOF Ultima Global) used electrospray ionisation in negative ion mode. The operating conditions were: ion source temperature: 120 °C, desolvation gas (N_2): 350 °C, 600 L/h, cone gas: 50 L/h, capillary voltage: 3 kV, scan time: 1.0 scan/s and inter-scan delay time: 0.1 s. MassLynx software version 4.1 was used for instrument control and data acquisition and leucine enkephaline (554.2615 g/mol) was used as lock-spray mass (reference standard). External mass calibration (*m*/*z* 150–1000) was carried out before the analyses using a sodium formate solution containing 10 mM sodium hydroxide in isopropanol/0.2% formic acid (1:1, v/v).

2.5.2. HPLC–QqQ

A Waters 2699 Alliance Separations Module combined with a PDA (Waters 2996) and a QqQ (Waters Micromass Quattro LC) mass spectrometer with an electrospray interface was used for analyses. The same chromatographic conditions as in the quantitative analyses (see section above) were used. The initial scanning for flavonoids in onions included both negative and positive full scan (single MS) mode at different cone voltages (±10, 30, 50 and 70 V; *m*/*z* 100–850). MS/MS analyses were carried out at different collision energies (±10, 30 and 50 V) with a cone voltage of 30 V. The operating conditions were: ion source temperature: 120 °C, desolvation gas (N_2): 300 °C, 580 L/h, nebulizer gas: 90 L/h, capillary voltage: 3 kV, scan time: 1.0 scan/s and inter-scan delay time: 0.10 s. MassLynx software version 4.1 was used for instrument control and data acquisition.

2.6. Optimisation and validation of PLE method

The following PLE parameters were optimised: temperature (40, 75 and 100 °C), sample weight (0.1, 0.3 and 0.5 g), flush volume (100,

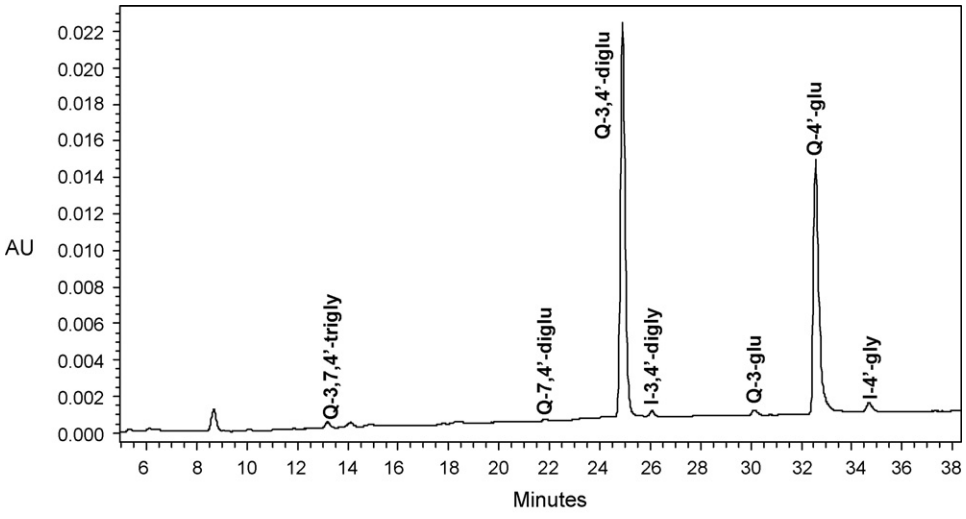


Fig. 2. Chromatogram of an onion extract (HPLC–UV, 254 nm).

Table 1
Flavonoids present in the onion extracts. The MS/MS–MS fragmentation pattern is described in the structure and the low *m*/*z* values are derived from multiple fragmentations.

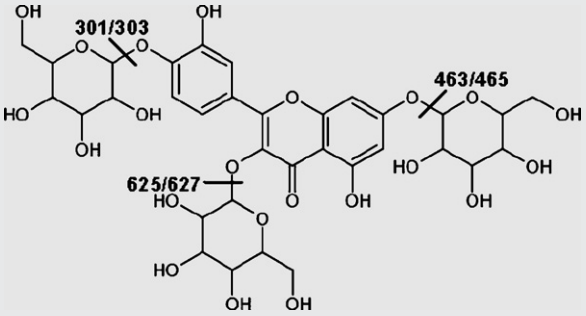
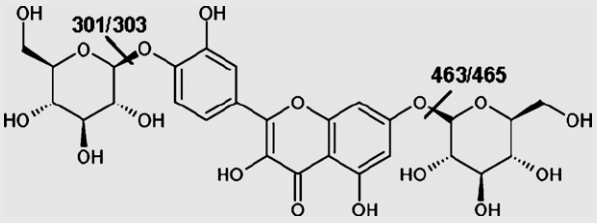
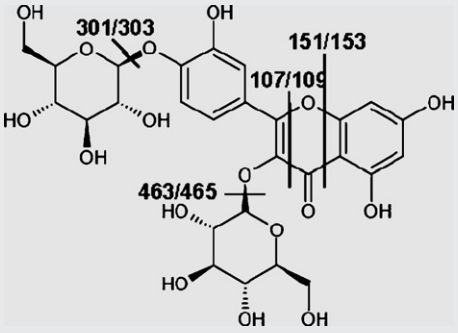
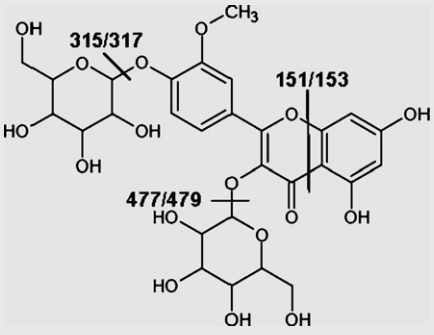
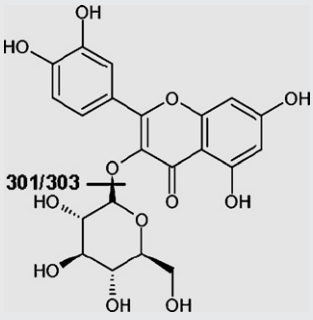
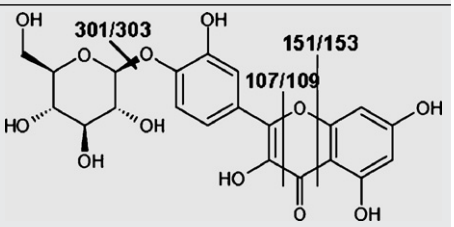
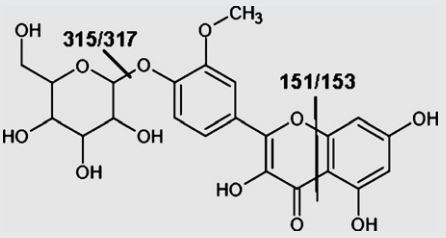
Compound	Measured mass (amu)	Formula	Δm (ppm)	i-FIT[b]	t_R[c] (min)	UV_{max} (nm)	Structure
Q-3,7,4′-trigly	788.27	$C_{33}H_{40}O_{22}$	3.4	0.6	13.2	253 266sh 345	
Q-7,4′-diglu[a]	626.22	$C_{27}H_{30}O_{17}$	−0.5	0.9	21.8	253 270sh 362	
Q-3,4′-diglu[a]	626.22	$C_{27}H_{30}O_{17}$	−0.5	15.5	24.9	255 265 345	
I-3,4′-digly	640.23	$C_{28}H_{32}O_{17}$	−0.1	2.8	26.1	252 266 345	
Q-3-glu[a]	464.17	$C_{21}H_{20}O_{12}$	−5.9	0.8	30.1	256 266sh 355	

Table 1 (*Continued*)

Compound	Measured mass (amu)	Formula	Δ*m* (ppm)	i-FIT[b]	t_R[c] (min)	UV_{max} (nm)	Structure
Q-4′-glu[a]	464.17	$C_{21}H_{20}O_{12}$	−5.9	1.7	32.6	253 267sh 363	
I-4′-gly	478.18	$C_{22}H_{22}O_{12}$	−0.6	13.3	34.7	254 269sh 364	

sh: shoulder.

[a] Identity confirmed with standards.

[b] Isotopic pattern fit of measurement compared to theoretical.

[c] Retention time.

125 and 150%) and solvent type (30, 40, 50, 60, 70, 80 and 90% aqueous methanol). It was also tested whether a clean-up step by in-cell addition of 0.5 g C18-material (Sepra E-C18, 50 μm, Phenomenex, Denmark) to the extraction cells would improve the method selectivity and reproducibility. Each sample was extracted three times during the optimisation experiments.

The PLE method was validated. The selectivity was determined from blank samples containing Ottawa sand and the reproducibility by two replicate analyses in four series. The limit of detection (LOD) and quantification (LOQ) was determined as three and ten times the standard deviation. Diluted reproducibility samples with a concentration close to the expected LOQ were used for determination of LOD and LOQ. The trueness of the method was determined by recovery experiments using the internal onion reference sample because no samples were available without or with a low concentration of the relevant flavonoids. The recovery was determined by extraction of five onion samples with and without addition of flavonoid standards. Linearity, sensitivity and range of measurements were determined for Q-7,4′-diglu, Q-3,4′-diglu, Q-4′-glu, Q-3-glu and Q (10 μg/mL) by varying the injection volumes of the standards, which provided comparable results to serial dilution of standards. We did not use an internal standard in the analysis because it was not possible to find a reference standard, which had similar chemical and physical properties, did not co-elute with the compounds of interest and was not present in the matrix.

3. Results and discussion

3.1. Identification of flavonoids (HPLC–MS and MS/MS)

An HPLC chromatogram confirmed that onions are a rich source of quercetin compounds (Fig. 2). The two most abundant compounds were Q-3,4′-diglu and Q-4′-glu in agreement with previous studies [12,18,35], but Q-3,7,4′-trigly, Q-7,4′-diglu and Q-3-glu were also present. Two isorhamnetin compounds, I-3,4′-digly and I-4′-gly were also identified in the onions. The flavonoid profile was similar to that found in southern Italian red onions [18] and white onions [12]. Neither aglycone quercetin (retention time (t_R): 37.1 min) nor isorhamnetin (t_R: 40.5 min) were detected in the onion extract indicating that hydrolysis of glycosides did not take place during sample preparation and analysis [35].

Two absorption maxima were observed in the UV spectra of the identified flavonoids at 345–363 nm (band I) and 253–256 nm (band II) (Table 1) associated with the absorption owing to the cinnamoyl B-ring and benzoyl A-ring, respectively [18]. The UV spectra were in agreement with previously obtained spectra of similar compounds [18,34] and confirmed the characteristic maxima of flavonols [36].

The glucosidic compounds showed loss of glucosyl moieties (162 amu per glucose moiety) in the mass spectral data leading to the aglycone fragment of quercetin (*m*/*z* 301/303 in ESI−/ESI+) or isorhamnetin (*m*/*z* 315/317) as earlier observed with similar compounds [12,18]. We observed fragments at *m*/*z* 151/153, which are typical for flavonoids and results of a retro-Diels–Alder fragmentation [21,37,38]. The fragments at *m*/*z* 107/109 are also characteristic, especially in negative mode [21].

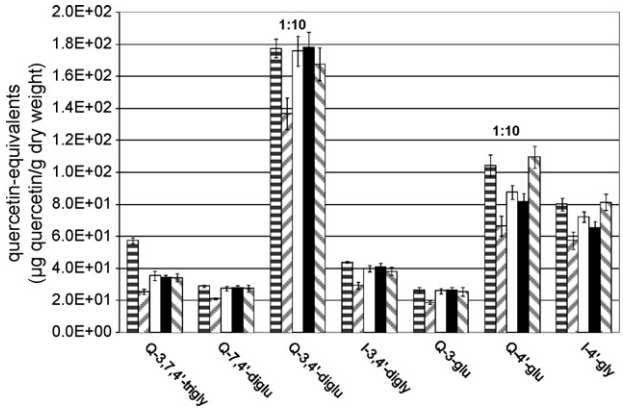


Fig. 3. Efficiency (expressed in quercetin equivalents) of the tested extraction methods. The concentrations of Q-3,4′-diglu and Q-4′-glu have been reduced by a factor of 10 to improve the visualisation of the remaining five less abundant flavonoids. (▤) Ultrasonication, (▨) water bath, (□) microwave-assisted extraction, (■) ultrasonic liquid processor, (▧) pressurised liquid extraction. The error bars describe the standard deviation ($n = 3$).

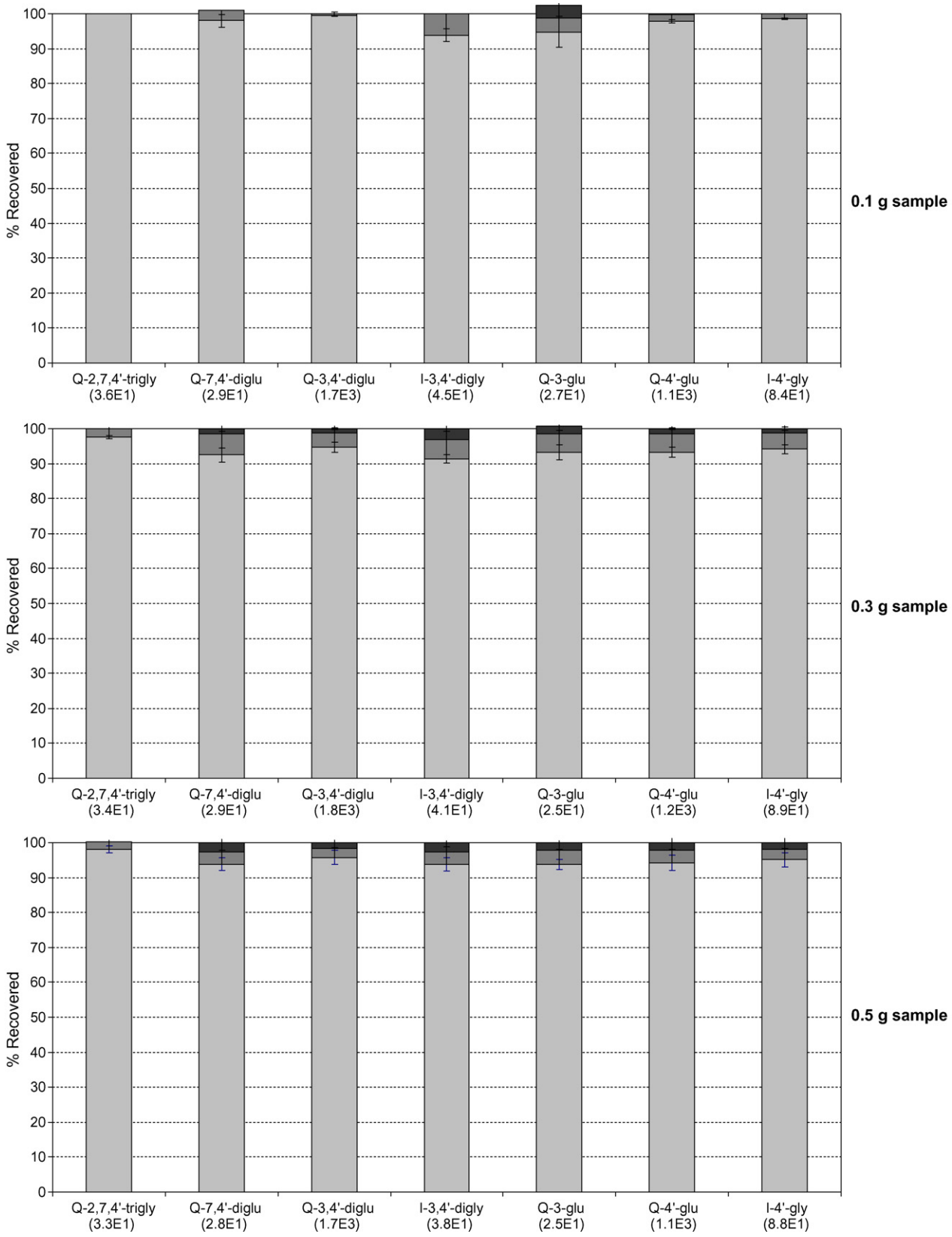


Fig. 4. Effect of sample weight on recovery in the three collected extracts (pressurised liquid extraction). (▒) 1st extract; (▒) 2nd extract and (■) 3rd extract. The total recovery in all three extracts (μg quercetin-equivalents/g dry weight) is shown in parenthesis below each compound. The error bars describe the standard deviation ($n = 3$).

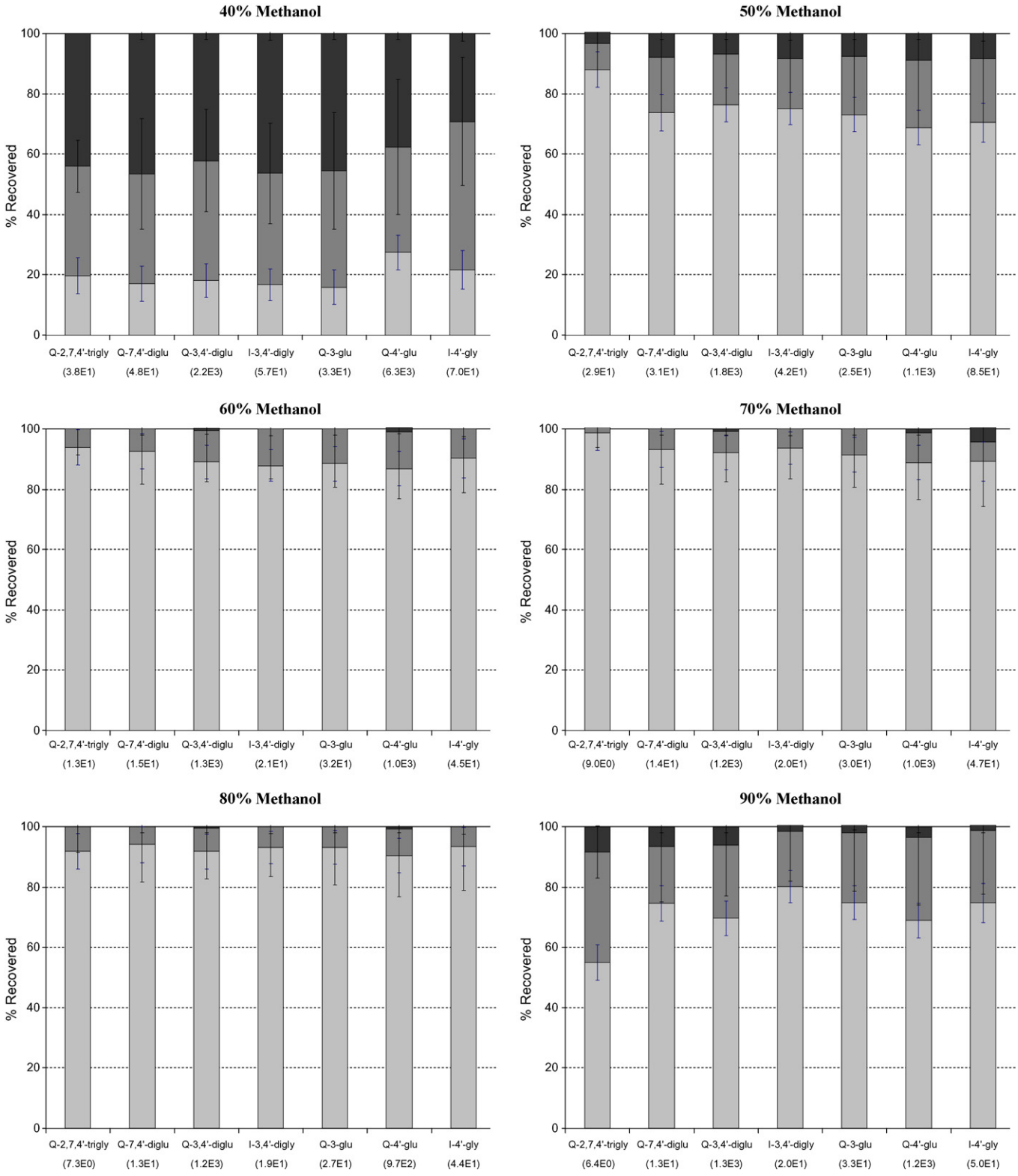


Fig. 5. Effect of solvent type on recovery in the three collected extracts (pressurised liquid extraction). (▒) 1st extract; (▓) 2nd extract; (■) 3rd extract. The total recovery in all three extracts (μg quercetin-equivalents/g dry weight) is shown in parenthesis below each compound. The error bars describe the standard deviation ($n = 3$).

The identified isorhamnetin glycosides might contain glucose as the sugar moiety, but also other sugars like galactose and mannose are possible (loss of 162 amu). However, glucose is the most frequently found sugar moiety in flavonoids [21], but it was not possible to determine the exact identity of the sugars and the linkage positions for the attached sugars. The loss of a methyl radical $[M\pm H\text{-}15]^{\bullet+/-}$ is often seen for methoxylated flavonols such as isorhamnetin [21,39], but was not observed in our experiments. Nevertheless, the identification is supported by previous studies, where both I-3,4′-digly and I-4′-gly have been identified in red [18] and white onions [12], respectively, with similar relative retention time and in other studies of onions [12,15].

3.2. Comparison of extraction methods

The efficiencies of MAE and ULP were comparable and at the same level as ultrasonication and PLE (Fig. 3) despite an expected strong disruption of the tissue structure with MAE and ULP due to the powerful shock waves radiating throughout the sample. Lower extraction efficiency was observed for the water bath extraction method. However, lower and thus better LODs were obtained with the water bath extraction method owing to the required preconcentration step of this method. An increase in sample weight and flush volume in PLE is expected to improve the LODs, which were otherwise the highest among the methods. The reproducibilities of the extraction methods were in a similar range (relative standard deviation (RSD): 1–11%, $n = 3$), which is generally considered acceptable for this type of analyses.

Ultrasonication is a fast and easy method, but difficulties were observed during the filtration of extracts as with MAE and ULP, so an additional sample preparation step (e.g. centrifugation) was needed. In contrast, PLE yielded clean extracts, which could be filtered directly after extraction. We also observed an increase in sample temperature during ultrasonication, which is a disadvantage as heating should be avoided during extraction [21]. High temperatures accelerate the oxidation of flavonoids [25] though no effects on recovery were observed in this study.

Higher efficiencies of MAE in comparison with conventional extraction methods have previously been obtained in extraction studies of anthocyanins from raspberries [30] and isoflavonoids and saponins from Chinese medicinal plants [31]. However, we did not observe such superior efficiencies, maybe because some cell structures were already destroyed during the freeze-drying process, which might also explain the non-superior efficiencies obtained with ULP.

An advantage of PLE is that it is a highly automated extraction process carried out in an inert atmosphere and protected from light. High extraction temperatures in PLE should yield improvements relative to time and solvent usage [40]. Flavonoids are temperature-sensitive [25], but the extraction can be carried out at high temperatures in PLE because it is performed in an inert atmosphere, which decreases the risk of chemical degradation [25]. The efficiencies of PLE were similar or higher than those found for the other tested methods. The solvent consumption (20 mL) was also decreased by its application in comparison with the conventional water bath method (50 mL), whereas the solvent consumption was lower for the other methods (5 mL). Altogether, we recommend PLE as the method of choice for extraction of flavonoids from onions because it shows several advantages and possibilities, e.g. simultaneous extraction and clean-up, which can otherwise be very time-consuming.

3.3. Optimization of PLE method

Extraction temperatures of 40, 75 and 100 °C were tested, but no significant differences in the efficiencies were observed. So, we decided to carry out the extractions at 40 °C in agreement with the temperatures used in previous PLE studies [28,41] and because of the known temperature-sensitivity of polyphenols [25].

Decreases in the LODs were observed as the sample weight increased and the total efficiencies after three extractions at all tested sample weights (0.1, 0.3 and 0.5 g) were comparable. The recoveries in the first extract were always greater than 91%, but increased with sample weight for the second and third extract (Fig. 4). The RSDs were acceptable (0.1–6.2%), but a slight tendency towards lower RSDs with higher sample weights was observed. So, 0.5 g is the recommended sample weight due to the improved LODs as well as acceptable recovery (98–99% of the total extracted with two extraction cycles) and reproducibility. Larger sample weights have been used in previous studies in combination with larger extraction cells [25,29,42], but larger sample weights caused clogging of our system due to the fine freeze-dried powder used.

Neither the total efficiency nor the efficiency in each extract was affected by the flush volumes (viz. 100, 125 and 150%) tested in this study (see Figure S1 in supporting information). A further increase in flush volume would have been interesting; however, the ASE-200 system does not allow flush volumes above 150%. A 100% flush volume is in accordance with flush volumes used by others [43,44] and was preferred because lower extract volumes were obtained at lower flush volumes, which leads to an improvement in the LODs.

The total extraction efficiencies were almost constant using a solvent composition of methanol between 50 and 90%, while slightly higher efficiencies were obtained at lower percentages of methanol. However, the results showed lower RSDs at methanol percentages below 50 as well as above 80% and the largest percentages were recovered in the second and third extracts, while only 1% of the total extracted flavonoids were recovered in the third extract with 60–80% methanol, except I-4′-gly with 70% methanol (Fig. 5). The decreased reproducibility when using solvents with high percentages of water has also previously been observed in another PLE study of polyphenols in apples [42]. An interfering compound was observed in the chromatogram of the second extract with 70–90% methanol (data not shown) and it more or less co-eluted with Q-3,4′-glu. Hence, the optimum solvent type appeared to be 60% methanol, but 65% methanol was afterwards tested. The recommended extraction solvent was 65% methanol owing to the obtained recovery as well as no co-eluting compounds in the HPLC analyses were observed (results not shown).

A clean-up step was included in the extraction by in-cell addition of C18-material, which has often been used as sorbent for solid-phase extraction (SPE) of flavonoids [21]. The total recoveries were improved with 13–35% in the samples added C18-material (data not shown). The RSDs were slightly higher (0–19%) for the majority of compounds in the samples without addition of C18-material, especially the more polar compounds (Table 2). This might be because of reduced interferences and/or increased selectivity. However, the HPLC–UV chromatograms did not reveal any immediate differences with respect to interference or noise. The simultaneous extraction and clean-up is a considerable improvement because the alternative SPE can be very time and solvent consuming and additional sample handling increases the risk of chemical degradation, though it has previously been used for clean-up of onion-extracts [19,22].

Our results show that two extraction cycles were sufficient and the third extract only contained 1–2% of the total extracted flavonoids in the three extracts. The optimum number of extraction cycles is in accordance with previous used extraction cycles (1–4) in PLE studies of polyphenols from plant materials [29,41,42] and so is the recovery, which in other similar PLE studies ranged from 81 to 100% of the total extractable polyphenols [25,41,42].

Table 2
Precision in extractions with and without addition of C18-material to the extraction cells ($n = 3$).

Compound	RSD (%)	
	Addition of C18-material	No addition of C18-material
Q-2,7,4′-triglu	5.8	25
Q-7,4′-digly	4.3	7.7
Q-3,4′-digly	3.8	7.0
I-3,4′-diglu	3.8	9.0
Q-3-gly	9.9	7.3
Q-4′-gly	6.8	6.8
I-4′-glu	9.9	9.7

Table 3
Limit of detection (LOD) and quantification (LOQ) as well as the precision (expressed as the relative standard deviation, RSD) of the analysis of polyphenols in vegetables ($n = 8$).

Compound	Vegetable	LOD (μg q-eq/g dw)	LOQ (μg q-eq/g dw)	Precision (RSD, %)	Concentration (μg q-eq/g dw)
Q-2,7,4′-trigly	Onion	3.0	20	11	4.6×10^1
Q-7,4′-diglu	Onion	1.4	60	10	2.5×10^1
Q-3,4′-diglu	Onion	0.90	20	3.1	2.7×10^3
I-3,4′-digly	Onion	1.5	20	8.6	4.5×10^1
Q-3-glu	Onion	2.0	20	4.9	4.6×10^1
Q-4′-glu	Onion	1.1	20	5.7	2.0×10^3
I-4′-gly	Onion	4.8	20	9.6	9.1×10^1
Chorogenic acid	Potato	0.4	20	1.8	1.2×10^2
Chorogenic acid	Carrot	1.5	20	7.3	1.3×10^2
Caffeic acid	Potato	2.7	20	–[a]	<LOQ

The average concentration of the compounds in the vegetables used for precision measurements can be seen in the last column. The LOD, LOQ and concentrations are expressed in μg quercetin-equivalents/g dry weight (μg q-eq/g dw).

[a] Precision was not determined because the concentration was below LOQ.

3.4. Method validation

The selectivity of the method was studied by extraction of blank samples (Ottawa sand) because onion samples without flavonoids were not available. The selectivity was good as interfering compounds were neither immediately detected in blank samples nor in the alternative analysis by LC–MS with electrospray ionization in negative ionization mode. The linearities of the standard curves of selected flavonoids (Q-7,4′-diglu, Q-3,4-diglu, Q-4′-glu, Q-3-glu and Q) were in the range of 0.5–10 μg/mL (equal to 20–400 μg/g dry weight), except for Q-7,4′-diglu (linearity between 1.5 and 10 μg/mL), and regression coefficients (R^2) were above 0.998. The sensitivity (measured in area/(μg/mL)) ranged from 2.2×10^4 to 7.0×10^4.

LODs ranged from 0.9 to 4.8 μg quercetin-equivalents/g dw (μg q-eq/g dw) and LOQs were equal to the lower limit of the linear range (20 μg q-eq/g dw), except for Q-7,4′-diglu (i.e. LOQ of 60 μg q-eq/g dw) (Table 3). The precisions were in an acceptable range for our purpose (RSD: 3.1–11%, Table 3).

Recovery experiments were used to estimate the trueness of the method, but the experiment was only of relevance for Q-7,4′-diglu and Q-3-glu due to insufficient amounts of pure standards in comparison with the high content of flavonoids in the reference sample. The recovery of Q-7,4′-diglu and Q-3-glu were 127% and 98%, respectively., which we consider acceptable though it is in the higher range for Q-7,4′-diglu. Furthermore, as previously stated the PLE method prior to optimization yielded satisfactory recoveries compared to the other tested extraction methods (Fig. 3) and 98–99% of the extracted flavonoids were recovered within two consecutive extraction cycles.

Our method was also applicable to other matrices and groups of polyphenols, e.g. extraction of phenolic acids from potatoes and carrots. The reproducibility (RSD: 1.3–7.3%, Table 3), linearity (0.5–10 μg/mL equal to 20–400 μg/g dw, $R^2 > 0.998$) and sensitivity ($2.4–4.6 \times 10^4$ area/(μg/mL)) of phenolic acids were in the similar range of flavonoids in onions. The LODs of chlorogenic acid and caffeic acid were between 0.4 and 2.7 μg q-eq/g dw, while LOQs of 20 μg q-eq/g dw were obtained (Table 3). Extraction of white cabbage was also possible, but the compound identification is ongoing.

4. Conclusion

Five extraction methods (water bath extraction, pressurized liquid extraction (PLE), ultrasonication, ultrasonic liquid processor and microwave extraction) were tested and PLE was the preferred extraction method. The PLE method sets a new standard for analyses of flavonoids from onions and showed considerable improvements, especially the simultaneous extraction and clean-up by in-cell addition of a stationary phase (in this case C18-material) improved the extraction efficiency and reproducibility. However, the integration of extraction and clean-up into one combined analytical step can also be advantageous in future development of PLE methods for rapid and reliable extraction and clean-up of bioactive compounds from various food products. The PLE method yielded similar efficiency and reproducibility in comparison with the other modern extraction methods (ULP and MAE), but it is advantageous because it can be highly automated, small amounts of solvents are used, the cleanest extracts are obtained and the extraction of the light and oxygen-sensitive flavonoids is carried out in an inert atmosphere protected from light. The optimised and validated method is rapid, reliable, sensitive and its application can be extended to other food matrices and polyphenols, e.g. phenolic acids in potatoes and carrots.

Acknowledgements

We acknowledge the International Centre for Research in Organic Food Systems (ICROFS, former the Danish Research Centre for Organic Farming and Food Systems (DARCOF)) for financial support through the OrgTrace project (http://www.orgtrace.elr.dk/uk) and the COWI Foundation and Ib Henriksens Foundation for funding of the ASE-200 instrument. We also thank Kasper Kildegaard Sørensen for technical assistance with the microwave-assisted extraction and Lawrence White for thorough proof-reading.

Appendix A. Supplementary data

Supplementary data associated with this article can be found, in the online version, at doi:10.1016/j.talanta.2009.06.073.

References

[1] A.J. Parr, G.P. Bolwell, J. Agric. Food Chem. 80 (2000) 985–1012.
[2] S. Sellappan, C.C. Akoh, J. Agric. Food Chem. 50 (2002) 5338–5342.
[3] F. Shahidi, C.-T. Ho, in: F. Shahidi, C.-T. Ho (Eds.), Phenolic Compounds in Food and Natural Health Products, American Chemical Society, Washington, DC, 2005, pp. 1–8.
[4] P. Kroon, G. Williamson, J. Sci. Food Agric. 85 (2005) 1239–1240.
[5] P.M. Aron, J.A. Kennedy, Mol. Nutr. Food Res. 52 (2008) 79–104.
[6] P.C.H. Hollmann, I.C.W. Arts, J. Sci. Food Agric. 80 (2000) 1081–1093.
[7] K.H. Miean, S. Mohamed, J. Agric. Food Chem. 49 (2001) 3106–3112.
[8] M.V. Galvan-Portillo, M.S. Wolff, L.E. Torres-Sanchez, M. Lopez-Cervantes, L. Lopez-Carrillo, Salud Publica Mex. 49 (2007) 126–131.
[9] P. Brat, S. George, A. Bellamy, L. Du Chaffaut, A. Scalbert, L. Mennen, N. Arnault, M.J. Amiot, J. Nutr. 136 (2006) 2368–2373.
[10] L. Sampson, E. Rimm, P.C.H. Hollman, J.H.M. de Vries, M.B. Katan, J. Am. Diet. Assoc. 102 (2002) 1414–1420.
[11] J.B. Harborne, Plant Phenolics in: J.B. Harborne, P.M. Dey (Eds.), Methods in Plant Biochemistry, vol. 1, Academic Press Limited, London, 1989, pp. 1–28.
[12] S.U. Lee, J.H. Lee, S.H. Choi, J.S. Lee, M. Ohnisi-Kameyama, N. Kozukue, C.E. Levin, M. Friedman, J. Agric. Food Chem. 56 (2008) 8541–8548.
[13] J. Yang, K.J. Meyers, J. van der Heide, R.H. Liu, J. Agric. Food Chem. 52 (2004) 6787–6793.

[14] M. Marotti, R. Piccaglia, J. Food Sci. 67 (2002) 1229–1232.
[15] I.M. Vagen, R. Slimestad, J. Sci. Food Agric. 88 (2008) 404–411.
[16] C. Manach, A. Scalbert, C. Morand, C. Remesy, L. Jimenez, Am. J. Clin. Nutr. 79 (2004) 727–747.
[17] M.J.C. Rhodes, K.R. Price, Food Chem. 57 (1996) 113–117.
[18] P. Bonaccorsi, C. Caristi, C. Gargiulli, U. Leuzzi, J. Agric. Food Chem. 53 (2005) 2733–2740.
[19] Y.-K. Park, C.Y. Lee, J. Agric. Food Chem. 44 (1996) 34–36.
[20] K. Robards, J. Chromatogr. A 1000 (2003) 657–691.
[21] E. de Rijke, P. Out, W.M.A. Niessen, F. Ariese, C. Gooijer, U.A.T. Brinkman, J. Chromatogr. A 1112 (2006) 31–63.
[22] G. Jungbluth, W. Ternes, Nahrung/Food 46 (2002) 349–352.
[23] A.M. Nuutila, K. Kammiovirta, K.-M. Oksman-Caldentey, Food Chem. 76 (2002) 519–525.
[24] A. Liazid, M. Palma, J. Brigui, C.G. Barroso, J. Chromatogr. A 1140 (2007) 29–34.
[25] M. Palma, Z. Piñero, C.G. Barroso, J. Chromatogr. A 921 (2001) 169–174.
[26] D. Sterbova, D. Matejicek, J. Vlcek, V. Kuban, Anal. Chim. Acta 513 (2004) 435–444.
[27] M. Palma, L.T. Taylor, J. Chromatogr. A 849 (1999) 117–124.
[28] R.M. Alonso-Salces, E. Korta, A. Barranco, L.A. Berrueta, B. Gallo, F. Vicente, J. Agric. Food Chem. 49 (2001) 3761–3767.
[29] M. Papagiannopoulos, B. Zimmermann, A. Mellenthin, M. Krappe, G. Maio, R. Galensa, J. Chromatogr. A 958 (2002) 9–16.
[30] F. Chen, Y.Z. Sun, G.H. Zhao, X.J. Liao, X.S. Hu, J.H. Wu, Z.F. Wang, Ultrason. Sonochem. 14 (2007) 767–778.
[31] J.Z. Song, S.F. Mo, Y.K. Yip, C.F. Qiao, Q.B. Han, H.X. Xu, J. Sep. Sci. 30 (2007) 819–824.
[32] A. Nieto, F. Borrull, R.M. Marce, E. Pocurull, Curr. Anal. Chem. 4 (2008) 157–167.
[33] X.L. Microson, Ultrasonic Liquid Processor, Operator's Manual, Misonix, USA, 2000.
[34] L.-Z. Lin, J.M. Harnly, J. Agric. Food Chem. 55 (2007) 1084–1096.
[35] R. Slimestad, T. Fossen, I.M. Vagen, J. Agric. Food Chem. 55 (2007) 10067–10080.
[36] B.A. Bohm, in: B. Ravindranath (Ed.), Chemistry and Biochemistry of Organic Natural Products, Harwood Academic Publishers, 1998, pp. 175–241.
[37] Y.L. Ma, Q.M. Li, H. van den Heuvel, M. Claeys, Rapid Commun. Mass Spectrom. 11 (1997) 1357–1364.
[38] N. Fabre, I. Rustan, E. de Hoffmann, J. Quetin-Leclercq, J. Am. Soc. Mass Spectrom. 12 (2001) 707–715.
[39] U. Justesen, J. Chromatogr. A 902 (2000) 369–379.
[40] B.E. Richter, B.A. Jones, J.L. Ezzell, N.L. Porter, N. Avdalovic, C. Pohl, Anal. Chem. 68 (1996) 1033–1039.
[41] D.L. Luthria, S. Mukhopadhyay, A.L. Kwansa, J. Sci. Food Agric. 86 (2006) 1350–1358.
[42] R.M. Alonso-Salces, E. Korta, A. Barranco, L.A. Berrueta, B. Gallo, F. Vicente, J. Chromatogr. A 933 (2001) 37–43.
[43] B.F. Zimmermann, R. Galensa, Eur. Food Res. Technol. 224 (2007) 385–393.
[44] F.B. Williams, L.C. Sander, S.A. Wise, J. Girard, J. Chromatogr. A 1115 (2006) 93–102.

Talanta 80 (2009) 279–285

Contents lists available at ScienceDirect

Talanta

journal homepage: www.elsevier.com/locate/talanta

Simultaneous analysis of diazepam and its metabolites in rat plasma and brain tissue by HPLC-UV and SPE

Laura Mercolini[a], Roberto Mandrioli[a], Carmelina Iannello[a], Francesco Matrisciano[b], Ferdinando Nicoletti[b,c], Maria Augusta Raggi[a,*]

[a] Faculty of Pharmacy, Department of Pharmaceutical Sciences, Alma Mater Studiorum-University of Bologna, Via Belmeloro 6, I-40126 Bologna, Italy
[b] Department of Human Physiology and Pharmacology, "Sant'Andrea" Hospital, 2nd Medical School, Sapienza University, Via di Grottarossa 1035-1039, 00189 Rome, Italy
[c] I.N.M. Neuromed, Via Atinense 18, 86077 Pozzilli (IS), Italy

ARTICLE INFO

Article history:
Received 21 March 2009
Received in revised form 16 June 2009
Accepted 29 June 2009
Available online 8 July 2009

Keywords:
Diazepam
Metabolites
Rat plasma
Rat brain tissue
Liquid chromatography
Solid-phase extraction

ABSTRACT

Diazepam is frequently used as an adjuvant during antidepressant therapy. Recently, some studies have suggested that the treatment with benzodiazepines could have different efficacy in depressed patients as opposed to non-depressed ones. To clarify the matter, a study is currently underway, regarding the drug metabolism in rats. In order to obtain a more complete and significant set of data, the main diazepam metabolites have also been considered, namely: nordiazepam, temazepam and oxazepam. A feasible and reliable HPLC method has been developed for the simultaneous determination of these compounds in plasma and brain tissue of rats. The method has been applied to "normal" rats and to genetic rat models of depression in order to estimate drug metabolism in different breeds. Analyte separation was achieved on a C8 reversed phase column using an acidic phosphate buffer/acetonitrile mixture as the mobile phase. The detection wavelength was 238 nm. An original sample pre-treatment, based on solid-phase extraction (SPE) was developed in order to eliminate endogenous interference, using only 250 μL of matrix (brain homogenate or plasma) for a complete analysis. The method has been validated with good results in terms of precision, extraction yield, sensitivity, selectivity and accuracy on both matrices and has been successfully applied to samples from some rats subjected to the preliminary study. The obtained data will hopefully contribute to the clarification of possible differences between depressed and non-depressed subjects with respect to benzodiazepine biotransformation.

© 2009 Elsevier B.V. All rights reserved.

1. Introduction

Diazepam (DZP, Fig. 1a) was the second benzodiazepine to be introduced into clinical practice, after chlordiazepoxide, and is still one of the most frequently prescribed drugs of this class. It is widely used for the treatment of anxiety and insomnia, but also for seizures (especially *status epilepticus*), alcohol withdrawal and muscle spasms [1]. In the therapy of major depressive syndromes, DZP is often prescribed as an adjuvant to control anxious symptoms and to treat anxiety associated with the beginning of treatment with second-generation antidepressants [2]. DZP is a core medicine in the World Health Organization's (WHO) "Essential Drugs List", which is a list of minimum medical needs for a basic health care system [3].

Like all 1,4-benzodiazepine drugs, DZP acts by allosterically interacting with neuronal $GABA_A$ receptors, thus facilitating the interaction between the receptor and the neurotransmitter, which in turn leads to a decrease in neuronal activity. For this reason, benzodiazepines are generally considered much safer than the older sedative barbiturates (which are direct GABA agonists), especially in case of overdose. However, side effect such as somnolence, amnesia, dizziness and impaired concentration are commonly reported. Furthermore, DZP and other benzodiazepines induce tolerance during chronic administration and an abstinence syndrome upon discontinuation. Consequently, pure DZP is considered a controlled substance in several Western countries (it is a schedule IV drug according to the convention on psychotropic substances) [4].

DZP is mainly metabolised by cytochrome P450 (CYP) enzymes. Hepatic *N*-demethylation results in the formation of an active metabolite, desmethyldiazepam (also known as nordiazepam, NDZ, Fig. 1b). This metabolite is hydroxylated to form oxazepam (OXZ, Fig. 1c), which is also active and is metabolised to form oxazepam glucuronide. A minor active metabolite is temazepam (TMZ, Fig. 1d), which can be in turn demethylated to oxazepam or glucuronidated [5]. The main active species found in blood are DZP and NDZ [6].

* Corresponding author at: Laboratory of Pharmaco-Toxicological Analysis, Department of Pharmaceutical Sciences, Via Belmeloro 6, I-40126 Bologna, Italy. Tel.: +39 051 2099700; fax: +39 051 2099740.
E-mail address: mariaaugusta.raggi@unibo.it (M.A. Raggi).

0039-9140/$ – see front matter © 2009 Elsevier B.V. All rights reserved.
doi:10.1016/j.talanta.2009.06.074

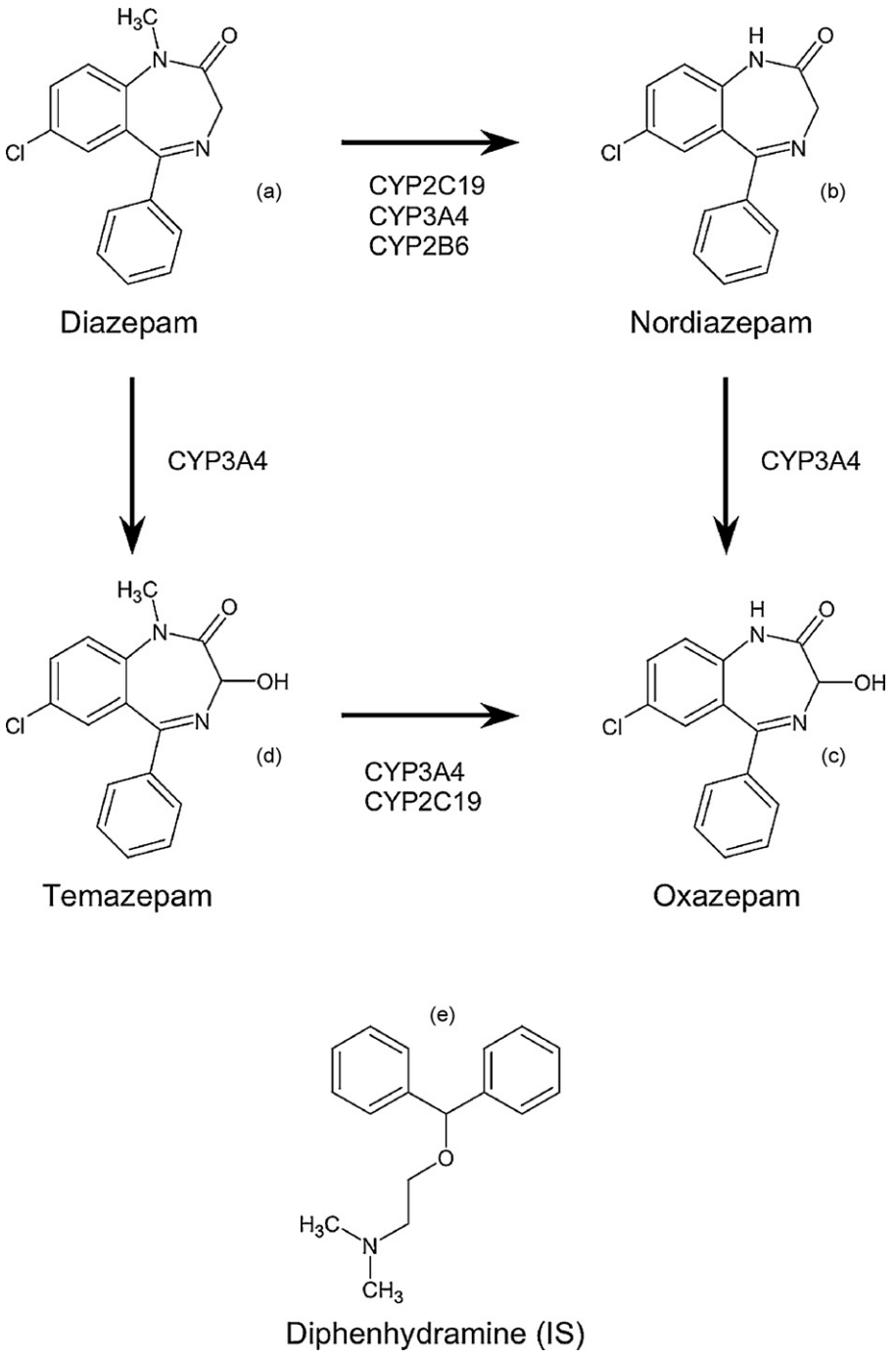


Fig. 1. Main metabolic pathways of DZP with (a–d) the chemical structures of its main metabolites; (e) chemical structure of diphenhydramine (IS).

Since all these metabolites are pharmacologically active and have a long half-life, they can significantly contribute to the pharmacological effect of DZP administration.

Recent studies have found a hyper-responsivity to DZP treatment in some animal models of depression, and in particular in the Flinders sensitive line (FSL) rats. FSL animals are spontaneously showing a behaviour corresponding to the animal model of depression (e.g., immobility in the forced swim test). These two facts combined point out to possible pharmacokinetic or pharmacodynamic differences between depressed and non-depressed subjects with respect to DZP treatment. Thus, an interdisciplinary research has been started, aiming to discover the mechanism(s) underlying the hyper-responsivity to DZP. Here, an original analytical method is presented for the simultaneous determination of DZP and its main phase I metabolites NDZ, OXZ and TMZ. Of course, the determination of the metabolites is necessary to obtain a complete idea of the metabolic state of the subject and thus of the causes leading to different responses. The method has been validated and applied to the quantification of the analytes in plasma and brain tissue of FSL and control (Sprague–Dawley, SD and Flinders resistant line, FRL) rats.

Several methods can be found in the literature regarding the determination of these metabolites in plasma of humans [7–10] or animals [11], by HPLC coupled to mass spectrometric (MS) [7,11] or UV [8–10] detection. One method deals with rat cerebrospinal fluid using HPLC-MS [12]. Other methods only analyse diazepam

and one or two metabolites in human plasma [13–16], in rat plasma and urine [17] or plasma and brain tissue [18] and in dog plasma [19].

As one can see, none of these methods is suitable for the purposes of this study, since none of them simultaneously determines all analytes in both matrices.

2. Experimental

2.1. Chemicals

The analytes DZP, NDZ, OXZ and TMZ were purchased from LGC Standards (Teddington, UK) as methanolic solutions (1 mg mL^{-1}). The internal standard diphenhydramine (IS, Fig. 1e) and bovine serum albumin were purchased from Sigma Chemicals (St. Louis, MO, USA).

Disodium hydrogen phosphate anhydrous (Na_2HPO_4), phosphoric acid, methanol and acetonitrile were analytical grade from Carlo Erba (Milan, Italy).

Ultrapure water (18.2 MΩ cm) from a MilliQ apparatus by Millipore (Milford, Mass., USA) was used.

2.2. Apparatus and chromatographic conditions

The chromatographic system was composed of a Jasco (Tokyo, Japan) PU-980 chromatographic pump and a Jasco UV-975 spectrophotometric detector set at λ = 238 nm.

Separations were obtained on an Agilent (Waldbronn, Germany) Zorbax Eclipse C8 reversed-phase column (150 × 4.6 mm ID, 5 μm) kept at room temperature. The mobile phase was a mixture of acetonitrile (38%, v/v) and a pH 2.5, 30 mM phosphate buffer containing 0.3% triethylamine (62%, v/v). One litre of mobile phase was prepared as follows: 1.25 mL of 85% phosphoric acid and 1.9 mL of triethylamine were added to about 500 mL of water, then the pH of the solution was brought to 2.5 with diluted phosphoric acid. The solution was made up to 620 mL with water and mixed with 380 mL of acetonitrile.

The mobile phase was filtered through a Phenomenex (Torrance, CA, USA) membrane filter (47 mm nylon membrane, 0.2 μm) and degassed by an ultrasonic bath. The flow rate was 1.0 mL min^{-1} and the injections were carried out through a 50 μL loop. Data processing was handled by means of a Varian (Palo Alto, CA, USA) Star Chromatography 4.0 software.

Solid-phase extraction (SPE) was carried out on a Varian VacElut apparatus. A Crison (Barcelona, Spain) Basic 20 pH meter and a Hettich (Tuttlingen, Germany) Universal 32 R centrifuge were used.

2.3. Solutions

Stock solutions of the analytes and the IS were 1 mg mL^{-1} and were stored at −80 °C in actinic glass vials. The stock solution of the IS was prepared by dissolving 2.0 mg of the substance in 2.0 mL of methanol. Standard solutions were prepared daily by diluting the stock solutions with the mobile phase.

2.4. Sample collection

The study was carried out in collaboration with the Department of Human Physiology and Pharmacology, "Sant'Andrea" Hospital of the Sapienza University, Rome, Italy. Flinders sensitive line (FSL, kindly provided by Dr. A.A. Mathè, Department of Psychiatry, Karolinska Institute, Stockholm, Sweden), Flinders resistant line (FRL) and Sprague–Dawley (SD) rats were housed in groups of three under controlled conditions of light (from 07.00 to 19.00 h), temperature (22 ± 2 °C) and humidity (65%) and were allowed free access to standard laboratory diet and tap water. The experimental protocol was approved by a local bioethical committee and the procedures and animal comfort were controlled by the University Veterinary Service. All efforts were made to minimise suffering and the number of animals used was kept to a minimum by experimental design. They were divided into two groups: the "control" rats were not subjected to any pharmacological treatment, while the "treated" rats were subjected to one intraperitoneal diazepam dose (0.3 mg/kg). The rats were weighed, anaesthetised and sacrificed by decapitation. Blood was collected from the carotid arteries in glass tubes containing EDTA as the anticoagulant, then centrifuged at 5000 × *g* for 15 min; the supernatant (plasma) was transferred to polypropylene test tubes and stored at −80 °C until HPLC analysis. The brain was removed and separately weighed (mean weight: 2 g), rinsed with saline and homogenized with 5 mL of methanol. After centrifugation (9000 × *g* for 15 min), aliquots of the supernatant were stored at −80 °C until analysis.

2.5. Sample pre-treatment: SPE procedure

The sample pre-treatment procedure was carried out on plasma by means of solid-phase extraction (SPE) on IST International (Hengoed, UK) Isolute C2 (50 mg, 1 mL) cartridges; for brain tissue, polymeric Strata-X (30 mg, 1 mL) cartridges from Phenomenex were used.

- Plasma: the C2 cartridges were activated and conditioned with 2× 1 mL of methanol and 2× 1 mL of water, respectively. After adding 50 μL of the IS standard solution (2.5 μg mL^{-1}) and 500 μL of water to 250 μL of plasma, the resulting mixture was loaded onto the previously conditioned cartridge. It was then washed with 2× 1 mL of water and 50 μL of methanol and dried applying full vacuum (−30 kPa) for 1 min. Analyte elution was carried out with 1 mL of methanol, applying full vacuum again for 1 min. The eluate was brought to dryness with a rotary evaporator and the residue was re-dissolved in 125 μL of mobile phase.
- Brain tissue: the activation, conditioning and loading steps were identical to those used for plasma (loading was carried out with 250 μL of brain homogenate supernatant). The cartridges were then washed with 2× 1 mL of water, 1 mL of water/methanol (80/20, v/v) mixture and 50 μL of methanol. Elution, drying and re-dissolution were carried out as for plasma.

2.6. Method validation

2.6.1. Linearity

Analyte standard solutions at seven different concentrations were added to 250 μL of blank sample, subjected to the SPE procedure and analysed. The volume of standard solution added was 50 μL and each spiked blank sample was prepared in triplicate. The analyte/IS peak area ratios were plotted against the corresponding concentrations and the calibration curves were set up by means of the least-squares method.

2.6.2. Limit of quantitation and limit of detection

According to international guidelines [20,21], limit of quantitation (LOQ) and limit of detection (LOD) values were determined as the analyte concentrations which give rise to peaks whose height is 10 and 3 times that of the baseline noise, respectively. Decreasing concentrations of samples (standard solutions or spiked blank plasma) were injected and the heights of the resulting analyte peaks were compared to the baseline noise, as calculated by the integration software. The concentrations that produced analyte peaks equal to 10 times the baseline noise were prepared and injected six times in order to evaluate the R.S.D.% of peak areas. These values should be lower than 20%.

2.6.3. Extraction yield (absolute recovery)

Spiked blank samples were prepared and analysed as described under Section 2.6.1, however, three concentrations were prepared and analysed for each analyte, corresponding to the lower limit, middle point and upper limit of the corresponding linearity curve. The analyte peak areas thus obtained were compared to those obtained from standard solutions at the same concentration, and the percentage extraction yield was calculated.

2.6.4. Precision

Spiked blank samples were prepared and analysed as described under Section 2.6.3. The procedure was repeated six times within the same day to obtain repeatability (intraday precision) values and six times over six different days to obtain intermediate (interday) precision values, both expressed as percentage relative standard deviation (R.S.D.%).

2.6.5. Selectivity

Six different blank samples were subjected to the SPE procedure and analysed. The acceptance criterion was: no peak should be detected at the retention times of the analytes or the IS, with an area larger than that of a LOQ peak.

2.6.6. Accuracy

Analyte standard solutions at three different concentrations were added to 250 μL of plasma or brain tissue homogenate (in order to obtain analyte additions corresponding to the lower limit, middle point and a high level of each calibration curve) and the mixture subjected to the SPE procedure. Recovery values were calculated according to the following formula: 100 × ([after spiking] − [before spiking])/[added]. The procedure was repeated three times at each concentration level to obtain standard deviation (S.D.) values.

3. Results and discussion

3.1. Choice of the chromatographic conditions

Our previous work on the simultaneous determination of fifteen benzodiazepines [22] (which did not include TMZ nor NDZ) prompted us to develop a new, narrower method only for DZP and its four metabolites. When the previously published conditions (C8 column, mobile phase composed of pH 3.0 phosphate buffer and 35% acetonitrile) were applied to this different set of analytes, however, NDZ and TMZ were not baseline resolved. Moreover, their peaks showed a moderate degree of tailing. To reduce it, triethylamine was added to the mobile phase. To increase peak resolution, it was decided to exploit the differences in pK_a values between NDZ (pK_a = 3.5) and TMZ (pK_a = 1.9), lowering the pH of the mobile phase to 2.5 to retain the protonation of TMZ while increasing that of NDZ. In this way, the retention of NDZ should become significantly lower, since its protonation disrupts the lipophilic interactions with the C8 sorbent. For this reason, a Zorbax Eclipse column was chosen, since it has increased stability under acidic conditions (down to pH 2.0) with respect to other silica-based columns. These changes allowed the complete separation of all analytes with good efficiency and within reasonable run times, without compromising the stationary phase stability.

Among the different compounds tested as possible ISs, diphenhydramine was chosen for its retention time, similar but not identical to those of the analytes, and its good peak efficiency.

The chromatogram of a standard solution containing OXZ (50.0 ng mL^{-1}), NDZ (50.0 ng mL^{-1}), TMZ (50.0 ng mL^{-1}), DZP (50.0 ng mL^{-1}) and the IS (1.0 μg mL^{-1}), analysed under the chosen chromatographic conditions, is shown in Fig. 2. As one can see, all peaks are baseline resolved and one complete chromatographic run lasts about 12 min.

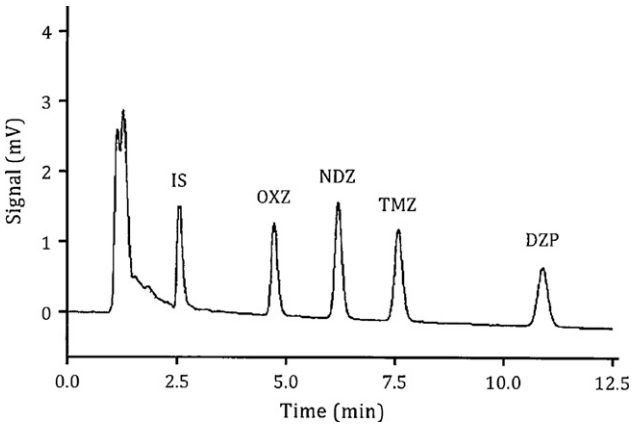


Fig. 2. Chromatogram of a standard solution containing DZP (50 ng mL^{-1}), NDZ (50 ng mL^{-1}), OXZ (50 ng mL^{-1}), TMZ (50 ng mL^{-1}) and the IS (1 μg mL^{-1}).

3.2. Application to standard solutions

Calibration curves were built for all analytes by injecting standard solutions at different concentrations, containing the IS at a constant concentration. The analyte/IS peak area ratios thus obtained were plotted against the corresponding analyte concentrations and the calibration curves set up by means of the least-squares method. Good linearity values ($r^2 > 0.9997$) were found for all analytes in the following concentration ranges: 4.0–250.0 ng mL^{-1} for OXZ, 3.0–250.0 ng mL^{-1} for NDZ, 4.0–250.0 ng mL^{-1} for TMZ and 5.0–250.0 ng mL^{-1} for DZP. LOD values were between 1.0 and 1.7 ng mL^{-1} and LOQ values between 3.0 and 5.0 ng mL^{-1}.

Precision values were also satisfactory, with R.S.D. values always lower than 3.0% for repeatability and lower than 3.3% for intermediate precision.

3.3. Development of the sample pre-treatment procedure

Several different kinds of sorbents were tested for the development of the SPE procedure: C2, C18, cyanopropyl (CN), phenyl (PH) and hydrophilic–lipophilic balance (HLB). Only the C2 sorbent suitably retained all the analytes while giving good purification of the plasma matrix. Of the two cartridge sizes tested (100 and 50 mg, 1 mL), the smaller one granted better extraction yields and an easier elution of the analytes. For this reason, C2 (50 mg, 1 mL) cartridges were chosen for all subsequent assays on rat plasma, using 250 μL of matrix. Unfortunately, the same (or a similar) procedure was not suitable for the extraction of the analytes from brain tissue: severe interference was detected when injecting this matrix, irrespective of the sorbent used. On the other hand, adding a further washing step with a water/methanol mixture caused a sharp drop in extraction yields. Thus, a completely different kind of sorbent was tested for the analysis of brain samples, and namely the Strata-X reversed phase polymer. According to the manufacturer [23], this sorbent is a surface modified styrene divinylbenzene polymer with superior H-bonding and π–π bonding capabilities for enhanced retention of polar and aromatic analytes. Thus, it should be suitable for the extraction and purification of both polar metabolites and less polar parent compounds. Moreover, its multimode retention

mechanisms lend themselves to strong washing with organic solvents without dramatically affecting analyte recovery. The Strata-X sorbent proved to be efficient in adequately retaining the analytes even when an additional washing step (with methanol/water) was added to obtain a good purification from endogenous constituents of the brain matrix. Both matrices were then subjected to a final washing step with a small volume of methanol, which increases matrix clean-up without significantly lowering extraction yields. Elution was carried out with 1 mL of methanol, followed by drying under vacuum and re-dissolving in 125 μL of mobile phase. Thus, the pre-treatment procedure concentrates the analytes two times.

Preliminary assays were carried out on blank samples (both of brain tissue and of plasma) from all three rat strains (FSL, FRL and SD); the purification and extraction results obtained were statistically not significantly different among strains.

The chromatogram of a blank plasma sample spiked with the analytes and the IS and subjected to SPE is shown in Fig. 3a, while the chromatogram of a blank brain sample spiked with the same concentrations of the analytes and the IS is reported in Fig. 3b. As one can see, a good purification of the matrix and neat, symmetrical peaks for all analytes are obtained in both cases.

With regard to stability, a formal, complete study was not carried out, since benzodiazepines are usually considered stable under the mild conditions used in our method. However, all spiked blanks and samples were analyzed more than once, storing them for 1–4 weeks at −20 °C. No significant change in peak areas was observed. Moreover, no significant change was observed when storing samples after SPE (i.e., ready to be injected) for up to 1 h at 4 °C.

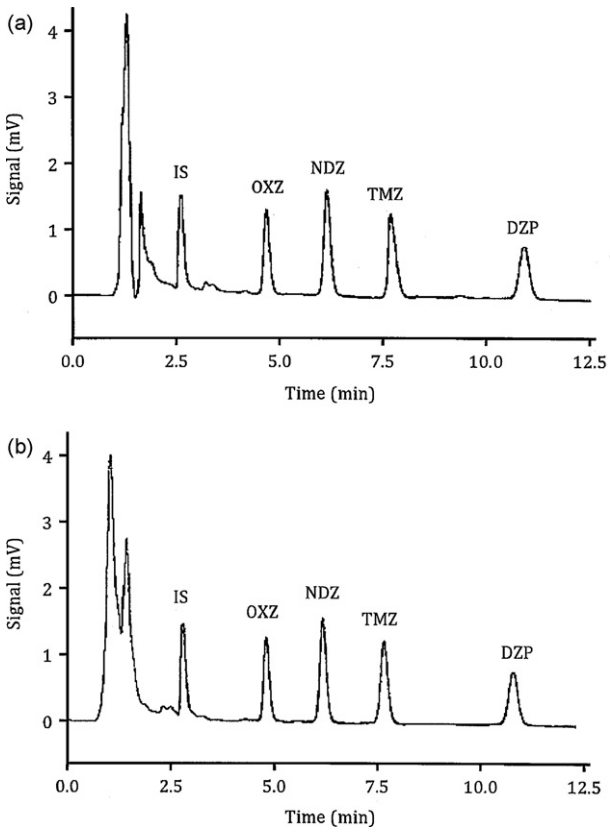


Fig. 3. Chromatograms of: (a) a blank rat plasma sample spiked with DZP (25 ng mL^{-1}), NDZ (25 ng mL^{-1}), OXZ (25 ng mL^{-1}), TMZ (25 ng mL^{-1}) and the IS (0.5 μg mL^{-1}); (b) a blank rat brain sample, spiked with the same concentrations of the analytes and the IS. Concentrations in the injected solutions are twice those reported. Brain concentrations are calculated in the homogenate supernatant.

3.4. Method validation

3.4.1. Method linearity, LOQ and LOD values

Calibration curves were set up on blank plasma and brain tissue by adding to the matrix known amounts of analyte standard solutions at different concentrations (and of IS standard solution at constant concentration) and subjecting the resulting mixture to the SPE procedure.

Calibration curves were set up in the expected concentration ranges. Good linearity values ($r^2 > 0.9992$) were found for all analytes in plasma and brain, with LOQ values ranging from 1.5 to 2.5 ng mL^{-1} (R.S.D. always lower than 20%) and LOD values ranging from 0.5 to 0.8 ng mL^{-1} for both matrices. Complete linearity, LOQ and LOD details are reported in Table 1.

3.4.2. Extraction yield and precision

Extraction yield (absolute recovery) and precision assays were carried out on blank plasma and brain tissue spiked with analyte concentrations corresponding to the lower limits, middle levels and upper limits of the respective calibration curves. The results of these assays are reported in Table 2.

As one can note, mean extraction yields were always higher than 91%. Precision results were also satisfactory: R.S.D. values for repeatability were always lower than 3.3% on plasma and 3.4% on brain tissue; R.S.D. values for intermediate precision were lower than 3.8% on plasma and 3.7% on brain tissue.

3.4.3. Method selectivity

Selectivity was evaluated by injecting into the HPLC six different samples of blank rat plasma and brain tissue after subjecting it to the SPE procedure. In all cases, no significant peak was observed at retention times corresponding to those of the analytes, as can be seen from Fig. 4a and b.

3.5. Analysis of rat plasma and brain samples

Having thus successfully validated the method, it was applied to the analysis of DZP and its metabolites in plasma and brain tissue of FSL, FRL and SD rats treated with DZP 0.3 mg/kg, as well as in plasma and brain tissue of control rats, which received

Table 1
Linearity parameters for DZP and metabolites on spiked blank plasma and brain tissue.

Analyte	LOD[a] (ng/mL)	LOQ[a] (ng/mL)	Linearity concentration range[a] (ng/mL)	Plasma			Brain tissue		
				Linearity equation ($y = a + bx$)		r^2	Linearity equation ($y = a + bx$)		r^2
				a	b		a	b	
OXZ	0.7	2.0	2.0–125	0.0024	0.0007	0.9997	0.0028	0.0008	0.9996
NDZ	0.5	1.5	1.5–125	−0.0017	0.0015	0.9996	0.0033	0.0012	0.9993
TMZ	0.7	2.0	2.0–125	0.0018	0.0014	0.9995	0.0011	0.0013	0.9995
DZP	0.8	2.5	2.5–125	−0.0012	0.0016	0.9996	0.0004	0.0013	0.9996

[a] LOD, LOQ and linearity range values were identical for the two matrices.

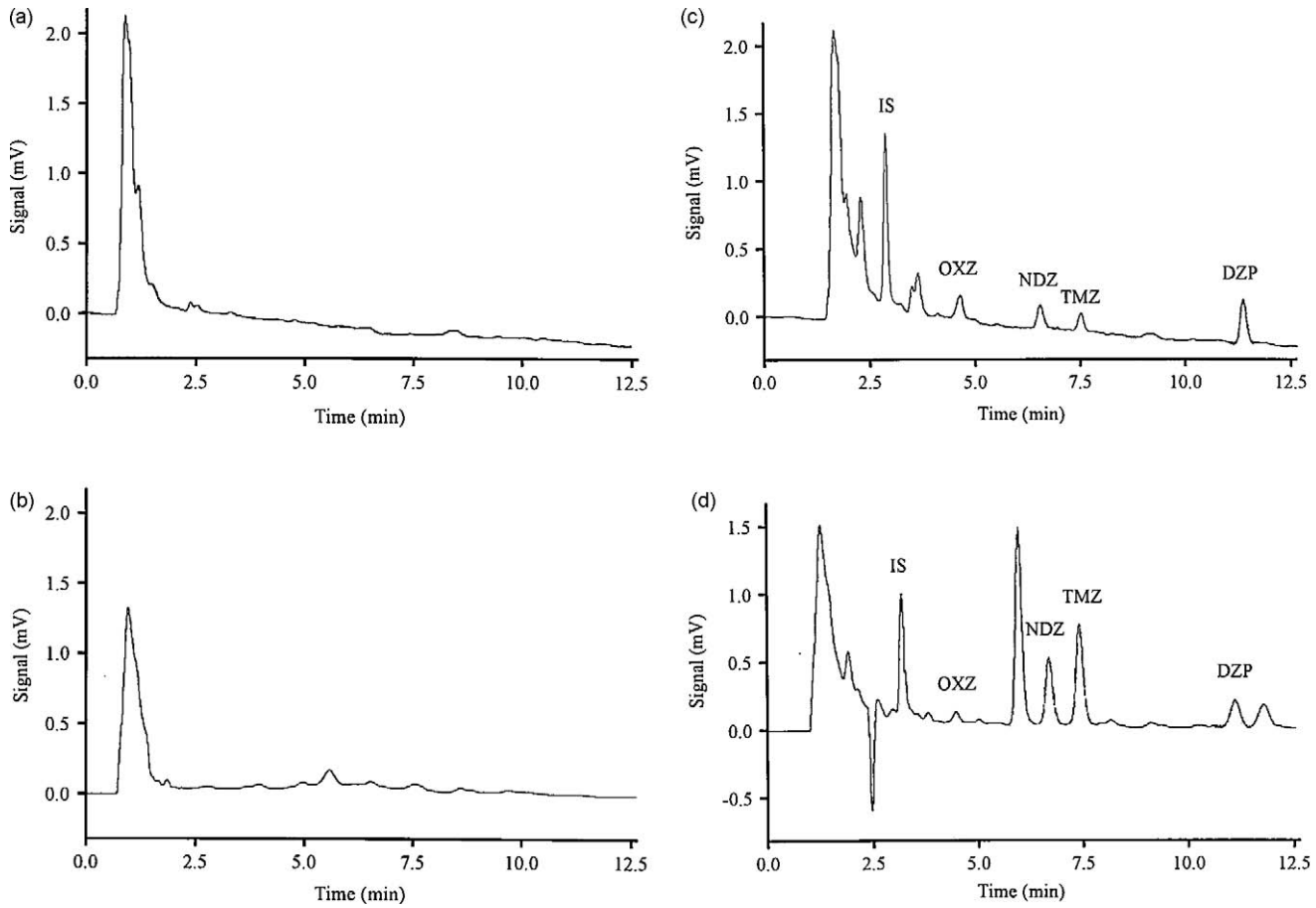


Fig. 4. Chromatograms of (a) a control FSL rat plasma sample; (b) a control FSL rat brain sample; (c) a plasma sample from a FSL rat treated with DZP; (d) a brain sample from a FSL rat treated with DZP.

only saline. A chromatogram of a plasma sample from a FSL rat treated with DZP is reported in Fig. 4c, while a chromatogram of a brain sample is shown in Fig. 4d. As can be seen, the sample pretreatment allows obtaining chromatograms devoid of interference from the biological matrix. The plasma sample shown in Fig. 4c contained the following analyte concentrations: OXZ 4.3 ng mL^{-1}, NDZ 3.4 ng mL^{-1}, TMZ 4.0 ng mL^{-1}, DZP 12.6 ng mL^{-1}; analyte concentrations in the brain sample shown in Fig. 4d were: OZP 3.3 ng g^{-1}, NDZP 12.5 ng g^{-1}, TZP 26.3 ng g^{-1} and DZP 12.6 ng g^{-1}.

3.6. Accuracy

Method accuracy was evaluated by means of recovery studies at three different concentration levels ($n = 3$ for each level), corresponding to the lower limit, the middle point and a high point of the respective calibration curve. Results were satisfactory: mean recovery values were always higher than 90% and standard deviation values were also good, always lower than or equal to 3%. Complete detailed results are reported in Table 3.

Table 2
Extraction yield and precision values for DZP and metabolites on spiked blank plasma and brain tissue.

Analyte	Concentration (ng/mL)	Plasma			Brain tissue		
		Mean extraction yield (%)[a]	Repeatability (R.S.D.%)[a]	Intermediate precision (R.S.D.%)[a]	Mean extraction yield (%)[a]	Repeatability (R.S.D.%)[a]	Intermediate precision (R.S.D.%)[a]
	2.0	96	2.9	3.0	95	2.4	2.8
OXZ	25.0	96	2.6	2.9	96	2.3	2.6
	125.0	99	2.3	2.4	96	2.2	2.5
	1.5	93	2.9	3.2	92	3.0	3.4
NDZ	25.0	97	2.6	2.7	96	2.8	2.8
	125.0	99	2.2	2.5	99	2.3	2.6
	2.0	98	2.7	3.3	94	2.9	3.1
TMZ	25.0	98	2.5	3.0	94	2.8	2.9
	125.0	99	2.1	2.9	97	2.6	2.6
	2.0	97	3.2	3.7	94	3.3	3.6
DZP	25.0	97	3.1	3.3	94	3.1	3.3
	125.0	99	2.9	3.1	96	2.5	3.0
IS	1.0 (μg/mL)	99	2.5	3.5	98	3.1	3.3

[a] $n = 6$.

Table 3
Accuracy assay results.

Analyte	Concentration added (ng/mL)	Recovery (%) ± S.D.[a]	
		Plasma	Brain tissue
OXZ	2.0	91 ± 3	91 ± 3
	15.0	93 ± 2	94 ± 3
	60.0	95 ± 2	96 ± 2
NDZ	1.5	94 ± 3	93 ± 3
	15.0	95 ± 2	95 ± 2
	60.0	92 ± 3	94 ± 3
TMZ	2.0	96 ± 2	96 ± 2
	15.0	96 ± 2	98 ± 2
	60.0	98 ± 2	95 ± 2
DZP	2.5	97 ± 2	97 ± 2
	15.0	95 ± 2	98 ± 2
	60.0	96 ± 2	96 ± 2

[a] $n = 3$.

4. Conclusion

An original HPLC-UV method has been developed for the simultaneous analysis of DZP and its main active metabolites NDZ, OXZ and TMZ in rat plasma and brain tissue. The SPE procedures implemented for the sample pre-treatment allowed obtaining good extraction yields (>91%) and precision values (R.S.D. < 3.8%) for all analytes and in both matrices, as well as a satisfactory purification form endogenous interference. The method has been successfully applied to the analysis of DZP and metabolites in samples from different strains of rats (FSL, FRL and SD), with good accuracy (recovery >90%), sensitivity and selectivity.

Among the numerous methods reported in the literature for the determination of these analytes, none had been developed, validated and applied to these two specific matrices. Furthermore, some of them [7,11,18] require very expensive instrumentation (such as MS/MS detectors), which is not always available in clinical analysis laboratories. Others give less satisfactory precision and extraction yield results, using less feasible and more polluting procedures (such as liquid–liquid extraction) [8], or have lower sensitivity [9]. Thus, the proposed method has significant advantages with respect to those available in the literature.

The method has been applied to the simultaneous determination of DZP and its metabolites in the tissues of rats within a study regarding differences in responsivity to DZP treatment. This will allow obtaining a complete idea of the metabolic state of the laboratory animals, possibly contributing to the clarification of the causes leading to different therapeutic responses.

Acknowledgements

This research was financially supported by MIUR (Ministero dell'Università e della Ricerca, Italy) with PRIN (ex-40%) and RFO (ex-60%) funds.

The authors would like to thank Dr. Domenico Lateana for his technical assistance.

References

[1] S.C. Sweetman (Ed.), Martindale—The Complete Drug Reference, Thirty-fifth ed., Pharmaceutical Press, London, 2007, pp. 674–682.
[2] M. Zienowicz, A. Wisłowska-Stanek, M. Lehner, E. Taracha, P. Maciejak, A. Sobolewska, J. Szyndler, D. Turzynska, J. Walkowiak, A. Płaznik, Pharmacol. Rep. 58 (2006) 115–119.
[3] WHO Model List of Essential Medicines, Fifteenth ed., World Health Organization, Geneva, 2007, Available from http://www.who.int/medicines/publications/08_ENGLISH_indexFINAL_EML15.pdf (last accessed on 10 June 2009).
[4] List of Psychotropic Substances Under International Control, Forty-seventh ed., International Narcotics Control Board, Vienna, 2007, Available from http://www.incb.org/pdf/yellow_lists_all/47th_edition_dec_07_yellow-list_eng.pdf (last accessed on 10 June 2009).
[5] R. Mandrioli, L. Mercolini, M.A. Raggi, Curr. Drug Metab. 9 (2008) 827–844.
[6] R.C. Baselt, R.H. Cravey, Disposition of Toxic Drugs and Chemicals in Man, Fourth ed., Chemical Toxicology Institute, Foster City, 1995.
[7] S.J. Marin, R. Coles, M. Merrell, G.A. McMillin, J. Anal. Toxicol. 32 (2008) 491–498.
[8] M.-R. Rouini, Y.H. Ardakani, K.A. Moghaddam, F. Solatani, Talanta 75 (2008) 671–676.
[9] R.M. Azzam, L.J. Notarianni, H.M. Ali, J. Chromatogr. B 708 (1998) 304–309.
[10] P. Fernandez, I. Hermida, A.M. Bermejo, M. Lopez-Rivadulla, A. Cruz, L. Concheiro, J. Liq. Chromatogr. 14 (1991) 2587–2599.
[11] Z. Liu, J. Short, A. Rose, S. Ren, N. Contel, S. Grossman, S. Unger, J. Pharmaceut. Biomed. 26 (2001) 321–330.
[12] J. Wang, X. Shen, J. Fenyk-Melody, J.V. Pivnichny, X. Tong, Rapid Commun. Mass Spectrom. 17 (2003) 519–525.
[13] E. Figueiredo Freire, L. Miranda, P. Penido Maia, E. Pizzamiglio Bieira, K. Bastos Borges, M.E. Pereira Bastos de Siqueira, Quim. Nova 28 (2005) 773–776.
[14] A. Meinitzer, W. Maerz, H. Mangge, G. Halwachs-Baumann, J. Anal. Toxicol. 30 (2006) 196–201.
[15] F. Xu, Y. Zhang, Y. Lou, J. Chin. Pharm. Sci. 8 (1999) 53–58.
[16] F. Kamali, J. Pharmaceut. Biomed. 11 (1993) 625–627.
[17] A.W. Abu-Qare, M.B. Abou-Donia, J. Chromatogr. B 754 (2001) 503–509.
[18] D.J. Greenblatt, J. David, V.H. Sethy, Psychopharmacology (Berl.) 102 (1990) 373–378.
[19] M.G. Papich, J. Alco, Am. J. Vet. Res. 56 (1995) 1629–1636.
[20] V.P. Shah, K.K. Midha, J.W.A. Findlay, H.M. Hill, J.D. Hulse, I.J. McGilveray, G. Mckay, K.J. Miller, R.N. Patnaik, M.L. Powell, A. Tonelli, C.T. Viswanathan, A. Yacobi, Pharm. Res. 17 (2000) 1551–1557.
[21] The United States Pharmacopeia, Twenty-eighth ed., United States Pharmacopeial Convention, Rockville, 2005, pp. 2748–2751.
[22] L. Mercolini, R. Mandrioli, M. Amore, M.A. Raggi, J. Sep. Sci. 31 (2008) 2619–2626.
[23] Strata-X polymeric sorbents for sample preparation, 2007, Available from http://www.phenomenex.com/WorkArea/showcontent.aspx?id=8397 (last accessed on 10 June 2009).

Talanta 80 (2009) 286–293

Contents lists available at ScienceDirect

Talanta

journal homepage: www.elsevier.com/locate/talanta

Excitation emission and time-resolved fluorescence spectroscopy of selected varnishes used in historical musical instruments

Austin Nevin[a,*], Jean-Philippe Echard[b,c], Mathieu Thoury[d], Daniela Comelli[a], Gianluca Valentini[a], Rinaldo Cubeddu[a]

[a] ULTRAS-CNR-INFM and IFN-CNR, Politecnico di Milano, Dipartimento di Fisica, Piazza Leonardo da Vinci 32, I-20133 Milan, Italy
[b] Laboratoire de Recherche et de Restauration, Musée de la Musique, Cité de la Musique, 221 avenue Jean Jaurès, 75019 Paris, France
[c] Centre de Recherche sur la Conservation des Collections, CNRS UMR 7188, Muséum National d'Histoire Naturelle, 36, rue Geoffroy Saint-Hilaire, 75005 Paris, France
[d] Scientific Research Department, National Gallery of Art, 6th & Constitution, Washington, DC, 20565, USA

ARTICLE INFO

Article history:
Received 26 March 2009
Received in revised form 12 June 2009
Accepted 29 June 2009
Available online 4 July 2009

Keywords:
Varnish
Terpenoid
Fluorescence spectroscopy
Fluorescence lifetime
Musical instrument

ABSTRACT

The analysis of various varnishes from different origins, which are commonly found on historical musical instruments was carried out for the first time with both fluorescence excitation emission spectroscopy and laser-induced time-resolved fluorescence spectroscopy. Samples studied include varnishes prepared using shellac, and selected diterpenoid and triterpenoid resins from plants, and mixtures of these materials. Fluorescence excitation emission spectra have been collected from films of naturally aged varnishes. In parallel, time-resolved fluorescence spectroscopy of varnishes provides means for discriminating between short- (less than 2.0 ns) and long-lived (greater than 7.5 ns) fluorescence emissions in each of these complex materials. Results suggest that complementary use of the two non destructive techniques allows a better understanding of the main fluorophores responsible for the emission in shellac, and further provides means for distinguishing the main classes of other varnishes based on differences in fluorescence lifetime behaviour. Spectrofluorimetric data and time resolved spectra presented here may form the basis for the interpretation of results from future in situ fluorescence examination and time resolved fluorescence imaging of varnished musical instruments.

© 2009 Elsevier B.V. All rights reserved.

1. Introduction

Fluorescence spectroscopy is particularly useful for the examination of works of art and historic musical instruments, as many binding media [1–5], modern pigments [6] and colorants [7] may be luminescent. With the advantage of not requiring any sample and being non-contact, fluorescence spectroscopy can also be coupled with multispectral and time-resolved fluorescence imaging techniques for the analysis of painted surfaces [8–10], thus increasing the utility of fluorescence spectroscopy for the characterisation of materials and works of [11]. In this work, time resolved and fluorescence excitation emission spectroscopy have been employed for the first time for the analysis of selected musical instrument varnishes.

The conservation and assessment of musical instrument varnishes may require the characterisation of their constituent materials. Varnishes represent a sensitive interface between painted or unpainted wooden surfaces and their environment, serving to protect an instrument, as well as to enhance and change the object's appearance. While paintings and musical instruments are significantly different in terms of their use, history and technique, parallels between the materials used for the construction and varnishing of historical string instruments and polychromy are apparent [5]. Paintings are often coated with multiple and thin layers of natural resins (from a variety of animal and plant sources) dispersed in a solvent as a varnish or surface coating, as described in historical treatises on painting and gilding [12], and varnishes are often applied to paintings during conservation or restoration. Recent analysis of Leonardo's *Mona Lisa* has suggested the presence of multiple layers of oxidised and yellowed varnish, which significantly alter the appearance of the masterpiece, but which have been retained for their historical value [13]. On the other hand, an integral part of the construction of stringed instruments (including lutes and violins, among others) is the varnishing and finishing of the wooden surface, which contributes to the appearance (colour and gloss) and to the protection of an instrument, and, hypothetically, to the quality of sound produced [14].

The presence of different varnishes and other conservation materials on musical instruments is easily appreciable due to the variation in fluorescence emissions from the surface of instruments which may increase with age [1]. In fact, due to their composition and degradation, many varnishes are naturally fluorescent or develop fluorescence upon ageing (which may also be accom-

* Corresponding author. Tel.: +39 0223996010; fax: +39 0223996126.
E-mail address: austinnevin@gmail.com (A. Nevin).

0039-9140/$ – see front matter © 2009 Elsevier B.V. All rights reserved.
doi:10.1016/j.talanta.2009.06.063

panied by yellowing). The visual assessment of the fluorescence from musical instruments (as well as paintings) with UV excitation using a Wood lamp (emitting a broad band around 365 nm) is widespread, providing immediate indications to conservators and curators regarding the potential presence of retouching, repainting and surface heterogeneity. For example, it is common to inspect the abrasion or wear on the back of some stringed instruments, where varnish may be consumed due to cumulative use. Indeed, some violin experts claim that they can recognise specific "fluorescing colours" on varnishes of famous violins from Cremona, which include those by Amati and Stradivari.

Although UV-excitation is commonly used in museums for the examination of musical instruments, the spectrofluorimetric analysis of varnishes found on the surfaces of stringed instruments and paintings is relatively limited: laser induced fluorescence (LIF) of varnishes has highlighted significant differences in emissions of common varnishes [2,15] and recently spectrofluorimetry has been proposed for the differentiation between sandarac, mastic and dammar [4]. Because of the complex chemistry and large number of sensitive molecules present in most varnishes it has not been possible to attribute or fully interpret fluorescence spectra.

In most cases, the determination of the chemical composition of varnishes is carried out using sensitive and highly specific chromatographic/spectrometric analysis [16–20], providing indications regarding original composition, mixtures of materials and degradation mechanisms associated with ageing and light exposure; indeed, results from analysis form the basis for the differentiation of many organic materials, including varnishes, and also provide the framework for the rationalisation of results from other complementary spectroscopic techniques, including fluorescence spectroscopy in this work. Alternative and complementary non-destructive techniques, which can provide information about the surface of musical instruments, are particularly advantageous; sampling is not limited by access to fragments, and when it is possible to integrate punctual analysis with imaging, more representative indications regarding the composition surfaces may be obtained. The specificity of most non-invasive techniques can be limited to the elemental level (for example X-ray fluorescence spectrometry) [21] or to the detection of broad classes of molecular materials (using Fourier-transform infrared spectroscopy) [22].

In this work, fluorescence spectroscopy integrated with time-resolved fluorescence analysis is investigated on model samples of vanishes. For a more complete visualisation of the contribution from multiple-fluorophores present in the complex systems found in varnishes, where variations in fluorescence may be small and not related directly to the position of the maximum [4], maps of the fluorescence emissions as a function of excitation wavelength have been generated. Studies of different materials from food have demonstrated the potential of fluorescence excitation emission (EE) spectroscopy, in which a series of emission spectra that have been collected over a range of excitation energies, allowing the discrimination between complex multiple protein [23] and multiple oil-based systems [24]. In addition to EE spectra, the modelling of the nanosecond decay of fluorescence can be particularly helpful for the analysis of complex systems which contain multiple fluorophores, as has been demonstrated for binding media used in paintings [11]. Various portable instruments based on LIF devices have been developed and time-resolved fluorescence spectroscopy and imaging have been used to examine complex inorganic and organic painted surfaces [9] and sculptures [25], with significant advantages for the detection of the presence of superimposed organic materials. However no time-resolved fluorescence spectra of varnishes found on paintings or musical instruments have been published.

Therefore, in this work, both fluorescence EE spectra and time-resolved fluorescence spectra of varnishes are presented for the first time. Films of selected varnishes were prepared according to historical treatises [12,26] by a lacquer conservator at the Musée de la Musique to replicate typical thickness and surface morphology of varnishes found on musical instruments. The aim of this work is to measure fluorescence properties of these materials and to assess the potential of such measurements for material classification, thus providing a useful framework for the interpretation of fluorescence imaging of instruments.

2. Experimental

2.1. Description of samples

The materials analysed in this work were specifically chosen to reflect commonly found varnishes used for historical musical instruments. While most varnishes typically used in violin manufacture [26,27] are obtained from plants, shellac is excreted by the *Kerria lacca* insect and may be red-brown in colour prior to purification. Two different shellac samples have been considered in this work: cherry shellac which has not been extensively purified and which yields a slightly yellow varnish film, and platina shellac, which is bleached and colourless, having been washed and treated prior to use. Other varnishes studied can be broadly grouped into two categories based on their terpenic chemical composition. The triterpenoids considered are elemi and mastic. Diterpenoid varnishes included colophony, Venice turpentine, sandarac, and copal from two sources, Manila (Philippines) and Congo.

For this research samples have been prepared from the restoration materials stored at the laboratory of the Musée de la Musique and purchased more than 10 years ago from local suppliers (Prolabo, HMB and Art & Conservation, Paris). Most of these materials have been previously analysed with GC/MS [14].

Varnish solutions have been prepared by dissolving each of the following resins in ethanol (1:2, w/w), and undissolved residual materials were decanted. Further, mixtures of equal parts of colophony:sandarac, colophony:elemi, elemi:sandarac and colophony:elemi:sandarac were also prepared. Varnishes were painted out in single layers on non-fluorescent quartz slides. The choice of a smooth non-fluorescent substrate for an assessment of fluorescence of varnishes is important for two main reasons. First, only fluorescence from the varnish (and not from the substrate) is assessed. Second, coloured surfaces may selectively reflect photons generated during fluorescence, which may compromise the detection of fluorescence emissions [28].

Varnishes were prepared in 2006 and were analysed with fluorescence devices in 2008. Therefore, while natural and artificial ageing are both recognised as significant factors in the oxidation of varnishes [18], which may influence fluorescence emissions [1,4], for this work only naturally aged reference samples have been considered in an effort to assess if fluorescence spectroscopy can allow the differentiation between naturally aged materials.

2.2. System set-up and data analysis

2.2.1. Fluorescence excitation emission spectroscopy

EE spectra of films of varnishes were acquired using a scanning spectrofluorimeter with excitation provided by a Xenon arc lamp (Fluorolog, Jobin-Yvon/Horiba); a front-face geometry was employed during collection (detection at 23° with respect to the excitation slits) and the detected signal was automatically corrected for excitation and detection efficiency. Spectra matrices were constructed by recording a series of synchronous fluorescence spectra with variable excitation between 300 and 500 nm (resolution of 1 nm), with synchronous fluorescence offsets between 10 and 250 nm in 5 nm steps, and with slits of 1 nm (excitation) and 5 nm (emission). The precision of the measurement is thus ±1 nm for the

excitation monochromator and ±5 nm for the emission wavelength (and hence ±6 nm for Stokes Shift). Matrices were then transformed into EE spectra using Matlab (Mathworks) and have been plotted as contour plots with 20 different levels of intensity from the maximum (white) to 10% of the maximum intensity (black). The maximum peak is defined by the excitation and emission wavelengths at the maximum emission intensity. Peaks are reported in the text as ($\lambda_{excitation}$/nm:$\lambda_{emission}$/nm).

2.2.2. Time-resolved fluorescence spectroscopy

Time-resolved fluorescence spectra were recorded using an Optical Multichannel Analyser working in nanosecond gated mode, as described previously [9] and briefly summarised below.

UV pulsed excitation was provided by a nanosecond N_2 laser with 337 nm excitation; the emitted fluorescence was collected through a monochromator, with sensitivity between 400 and 650 nm and a spectral resolution of 1 nm, coupled to a time-gated multichannel analyser. The time-resolved detector is associated with a temporal gate of 10 ns and a jitter below 0.5 ns.

The kinetics of the emission was analysed by recording a set of fluorescence spectra with increasing delays with respect to the excitation pulse. Following data acquisition, spectral data are automatically corrected for the detection efficiency and are pre-processed with a moving average smoothing filter in order to reduce the level of noise. The fluorescence decay is then analysed at each wavelength by using a procedure based on a non-linear regression least-squares fit.

When using conventional fluorimetric techniques, the presence of a variety of fluorophores in complex fluorescent materials is indicated by the dependency of the fluorescence emission on the excitation wavelength. Moreover, the fluorescence spectra are composed of one or several broad band emissions generated by contributions from numerous fluorophores. In terms of fluorescence decay, a complex fluorescent material commonly shows a multi-exponential decay where the emission from each one of the main emitting species or group of fluorophores can be modelled as a single-exponential decay characterized by a specific lifetime and emission. Hence, the analysis of the decay kinetics of the emission spectrum of a complex material can provide a way for distinguishing amongst its main emitting fluorophores characterized by different lifetimes.

In this work, the analysis of the nanosecond emission decay following excitation at 337 nm was performed considering three different models: a mono-, a bi- and a tri-exponential decay. For all the selected materials, whereas the application of the bi-exponential decay model highly improves the result of the fitting procedure with respect to the mono-exponential model, the use of a tri-exponential decay model does not yield significant information. Therefore, in the following section, only results from the application of a bi-exponential model will be discussed.

Specifically, the application of a bi-exponential fitting procedure assumes that the optical fluorescence fluence $f(t, \lambda)$ which is emitted t seconds after the excitation pulse at the emission wavelength λ can be modelled as:

$$f(t,\lambda) = A_{SHORT}(\lambda)\ \exp\left(\frac{-t}{\tau_{SHORT}(\lambda)}\right) + A_{LONG}(\lambda)\ \exp\left(\frac{-t}{\tau_{LONG}(\lambda)}\right) \quad (1)$$

where $A_{SHORT}(\lambda)$ and $A_{LONG}(\lambda)$ indicate the wavelength-dependent amplitudes of the short-lived and long-lived fluorescent components identified in the emission, and $\tau_{SHORT}(\lambda)$ and $\tau_{LONG}(\lambda)$ are the associated wavelength-dependent lifetimes. Following a suitable non-linear regression least-squares fitting procedure, $A_{SHORT}(\lambda)$, $A_{LONG}(\lambda)$, $\tau_{SHORT}(\lambda)$ and $\tau_{LONG}(\lambda)$ are estimated, and the mean reduced χ^2 value is used for assessing the reliability of the fit. Generally, with this model, while the wavelength-dependent functions $A_{SHORT}(\lambda)$ and $A_{LONG}(\lambda)$ are associated with spectral shapes characterized by distinct spectral features, $\tau_{SHORT}(\lambda)$ and $\tau_{LONG}(\lambda)$ are associated with relatively constant spectral behaviour. In principle, $A_{SHORT}(\lambda)$ and $A_{LONG}(\lambda)$ describe the emission spectrum of the two main emitting groups of fluorophores present in each one of the materials studied.

In the following section, the outcome of the bi-exponential fitting procedure is shown in terms of $A_{SHORT}(\lambda)$ and $A_{LONG}(\lambda)$, which, for an easier comparison, are always shown normalized to their maximum value. The mean lifetime τ_{SHORT} and τ_{LONG} associated with each one of the reconstructed components is further indicated, together with the ratio R between the total intensity of the short-lived and long-lived component, calculated according to the following formula:

$$R = \frac{\int A_{SHORT}(\lambda)\ d\lambda}{\int A_{LONG}(\lambda)\, d\lambda} \quad (2)$$

Hence, in each varnish studied, in addition to picosecond lifetime components that cannot be resolved with the instrumentation employed here, two main emitting groups can be well separated.

3. Results

EE spectra of the materials studied can be classified based on the number of evident peaks in the contour plots, the position of the maximum emission and excitation wavelengths and the general shape of the excitation/emission contours present in the spectra. Spectra below can be divided into three basic groups: those from (1) shellac, (2) triterpenoid and (3) diterpenoid varnishes and are presented in this order in the following subsections. Finally the EE and time-resolved spectra of mixtures of selected varnishes are shown.

3.1. Shellac

Shellac is composed of a resinous fraction and of a solid colorant fraction, containing various laccaic acids. The differences between the distinctly red cherry shellac and the colourless platina shellac are likely due to the extraction of red-coloured laccaic acids during the washing and bleaching process associated with the production of platina shellac. EE spectra of purified (platina) shellac, and red-coloured (cherry) shellac are seen in Fig. 1. Although of similar origin, the different shellac varnishes exhibit significantly different EE spectra. Specifically, while the former is associated with one broad emission centred at (307:487), as well as significant fluorescence at longer excitation wavelengths, the latter has multiple fluorescence bands: a broad fluorescence pattern centred at (307:410) with the addition of intense peaks at (307:554) and (465:635) [2,29]. The last two peaks may be attributed to the fluorescent laccaic acids. The fluorescence of shellac is clearly dependent on its degree of purification.

The analysis of the kinetics of the fluorescence emission decay confirms the differences ascribable to the two materials and further provides indications on the presence of secondary fluorescent compounds in each one of the two different shellacs studied. In detail, in Fig. 2 the fluorescence spectra of the short- and long-lived components of the emission from the two shellacs are shown: emission from the purified platina shellac is characterised by a short-lived component with a major peak at 420 nm and a further broad emission centred around 600 nm, possibly ascribable to residual laccaic acids. In the long-lived component the red-emission almost disappears and instead a broad emission at 440 nm with a shoulder at 520 nm is evident. Cherry shellac is characterised by an intense short-lived component with two peaks at 420 and 600 nm, similarly to those observed in the platina shellac, but in this case the emission ascribed to laccaic acids is predominant. The long-lived

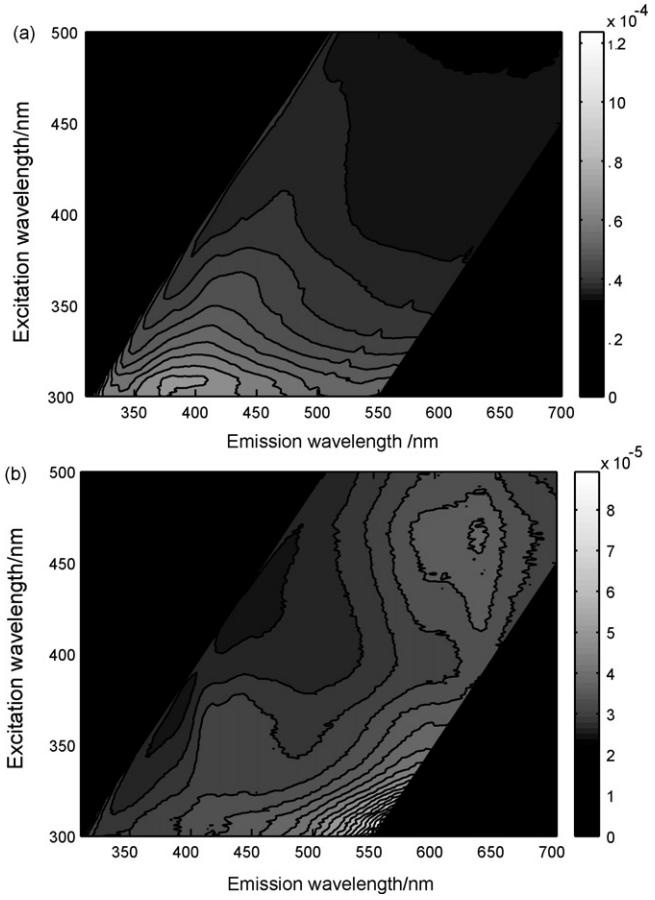


Fig. 1. EE spectra of naturally aged films of varnishes made from (a) shellac (platina), (b) shellac (cherry); intensity is given in counts and 20 contours represent 90% of the fluorescence of materials as a function of excitation.

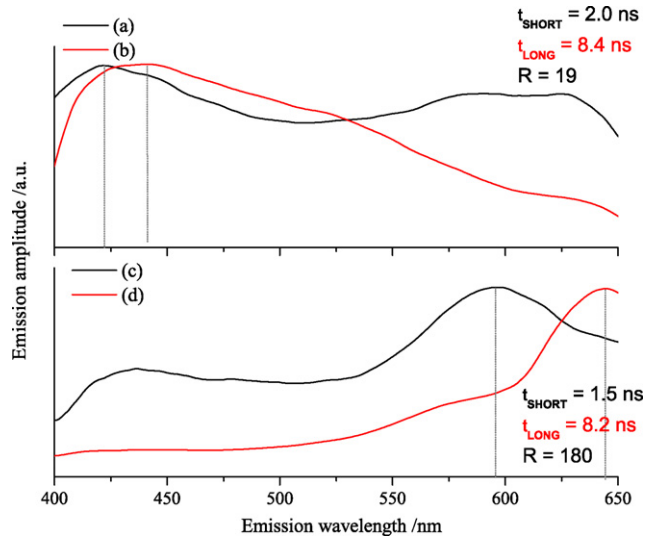


Fig. 2. Fluorescence spectra of the short- and long-lived components of the emission from naturally aged films of shellac following a bi-exponential fit of time-resolved spectral data: (a) short-lived and (b) long-lived component of platina shellac; (c) short-lived and (d) long-lived component of cherry shellac. For an easier comparison fluorescence amplitudes are shown normalized to the maximum value and values of τ_{SHORT}, τ_{LONG} and R are provided. Dashed vertical lines indicate the main peak wavelength of each fluorescent component.

component of the emission of cherry shellac shows further emission in the red with a peak at 630 nm, again possibly ascribable to laccaic acids.

3.2. Triterpenoid varnishes

The EE spectra of two triterpenoid varnishes elemi and mastic (Fig. 3) reflect small difference in their chemical composition, which may be related to the presence of specific terpenic acids [17]. In detail, EE spectra of elemi and mastic have symmetrical fluorescence emission bands and both varnishes are associated with maximum emission at excitation around 310 nm. However the emissions of the two varnishes differ significantly, with Stokes shifts of 85 and 135 nm, respectively, suggesting that the materials are characterised by a different group of fluorophores which may have similar absorption spectra. The EE spectra of mastic and elemi also indicate the presence of significant visible fluorescence at longer excitation wavelengths and the shape of the contours is relatively similar for both materials. While specific fluorophores have not been identified for either varnish, these results are comparable with fluorescence reported by others who suggest emissions in mastic at 440–460 nm [1,4,15]. Moreover, excitation at 365 nm of samples of mastic aged naturally for 50 years has been reported with emission spectra similar to those represented above [1]. It is further of interest that elemi and platina shellac have a common excitation-emission maximum (as can be observed in Table 1), but EE spectra of the two varnishes are completely different.

The analysis of the kinetics of the emission at 337 nm excitation in shown in Fig. 4. Fluorescence emissions from elemi appear

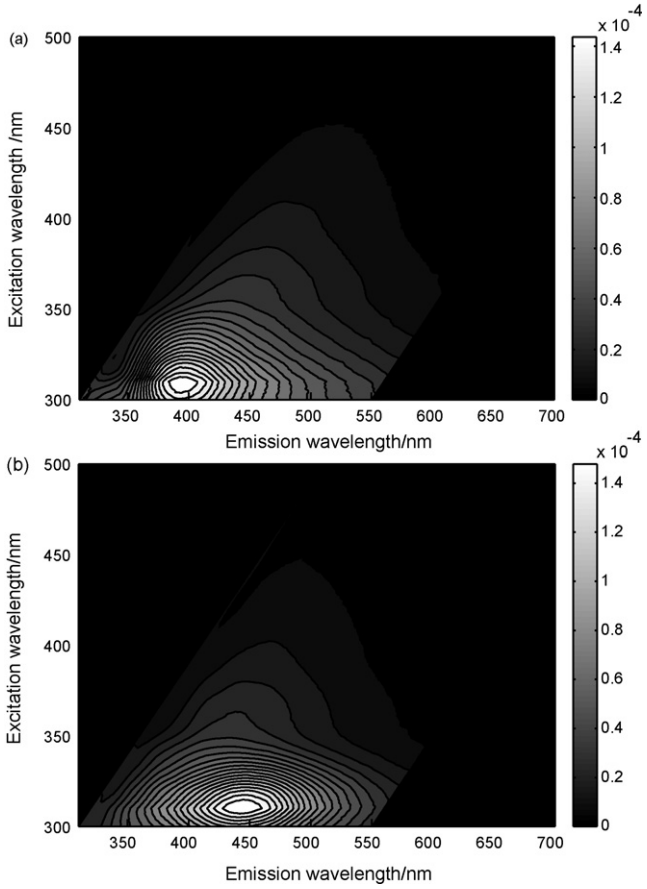


Fig. 3. EE spectra of naturally aged films of varnishes (a) elemi (b), mastic; intensity is given in counts and 20 contours represent 90% of the fluorescence of materials as a function of excitation.

Table 1
Fluorescence properties of samples examined with continuous wave excitation between 300 and 500 nm and with pulsed excitation at 337 nm.

Sample	λ_{ex} max (nm)	λ_{em} max (nm)	Stokes shift (nm)	λ_{em} max (nm) of A_{SHORT} (λ)	λem max (nm) of A_{LONG} (λ)	Mean τ_{SHORT} (ns)	Mean τ_{LONG} (ns)	Mean reduced χ^2 value of the bi-exponential fit	Mean reduced χ^2 value of the mono-exponential fit
Shellac (cherry)	307 307 465	410 554 635	103 247 170	430 600	580 640	2.0	8.4	0.009	0.112
Shellac (platina)	307	387	80	425 600	440 625	1.5	8.2	0.013	0.270
Elemi	310	395	85	410	480	1.9	8.8	0.006	0.125
Mastic	310	445	135	430	460	1.8	8.0	0.009	0.071
Colophony	310	505	195	420	530	1.7	7.7	0.010	0.170
Venice turpentine	305	465	160	410	480	1.8	9.0	0.010	0.133
Sandarac	320	415	95	400	460	2.1	7.5	0.004	0.050
Copal (Manila)	314	389	75	405	465	2.0	7.5	0.004	0.061
Copal (Congo)	316	401	85	430	450	1.8	8.7	0.012	0.212
Colophony:sandarac	313	445	132	415	485	1.9	8.2	0.007	0.079
Colophony:elemi	320	412	92	410	490	1.9	8.2	0.011	0.160
Elemi:sandarac	310	395	85	410	460	2.0	8.4	0.005	0.088
Colophony:elemi:sandarac	310	405	95	420	480	2.0	8.6	0.006	0.071

characterised by an intense short-lived component with a strong and narrow peak at 410 nm, whereas in the long-lived component a broader emission centred at 480 nm is evident. In turn, mastic is characterised by a short-lived component peaked at 430 nm with a shoulder at 410 nm and a long-lived component peaked at 460 nm, which, compared to that of elemi, is much narrower. Nevertheless, despite some detectable differences in their time-resolved spectra, the two materials clearly show common features related to their similar chemical composition. Moreover, differences between the results of time-resolved analysis of triterpenoid-based and shellac-based materials indicate these two classes of varnishes can be distinguished easily.

3.3. Diterpenoid varnishes

The EE spectra of the diterpenoid varnishes analysed (Fig. 5) vary in terms of the position of the emission maximum, with the exception of sandarac and copal. Moreover, in comparison with the emission from triterpenoid varnishes, the distribution of fluorescence is significantly different; specifically, more intense fluorescence is observed at longer excitation wavelengths, providing an immediate means of distinguishing between diterpenoids and triterpenoids analysed.

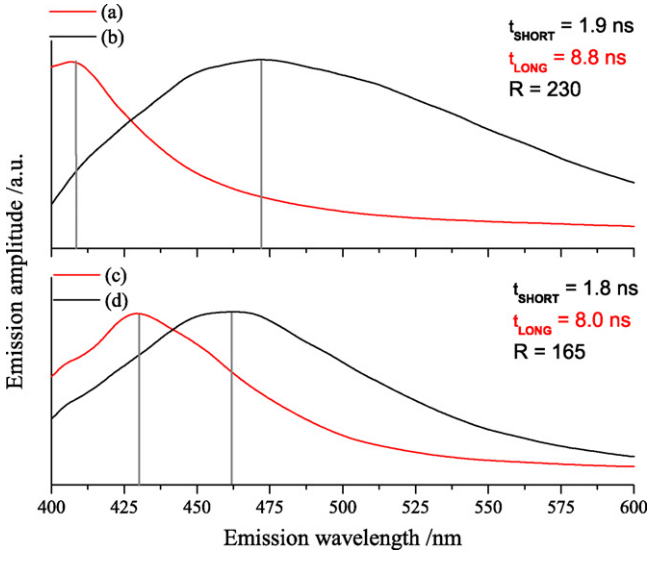


Fig. 4. Fluorescence spectra of the short- and long-lived components of the emission from naturally aged films of varnishes following a bi-exponential fit of time-resolved spectral data: (a) short-lived and (b) long-lived component of elemi; (c) short-lived and (d) long-lived component of mastic. For an easier comparison fluorescence amplitudes are shown normalised to the maximum value and values of τ_{SHORT}, τ_{LONG} and *R* are provided. Dashed vertical lines indicate the main peak wavelength of each fluorescent component.

The most distinctive and complex EE spectrum of the diterpenoid-based varnishes studied in this work is associated with colophony, the solid residue obtained after filtration and distillation of pine turpentine. Indeed, two different groups of fluorophores have been assigned to the bands present: (370:480) and another stronger peak at around (310:505). Multiple groups of fluorophores which are characterised by different bands are likely present in the sample. In contrast, the resin from larch trees, commonly known as Venice turpentine, is associated with a similar maximum emission band but has fewer contributions to fluorescence at longer excitation wavelengths. This phenomenon may be related to variation in extraction and processing of the resins or to variation in the polymerisation of the varnish films [20].

Sandarac and copals (Fig. 5(c and d)) are other diterpenoid conifer resins, and form cross-linked fraction of polycommunic acids upon oxidation, but differ in terms of the age of the collected tree-resins prior to their use as varnishes. Sandarac is harvested directly from the tree while copal is a semi-fossilised resin collected from the ground and the two materials share common chemical markers: agathic acid and related labdane compounds are predominant in copals, and are also present in sandarac [30]. Only subtle differences are observed in the EE spectra of copal and sandarac which are associated with the shape of contours describing fluorescence, and spectra of the two varnishes share a common maximum at approximately (310–20:390–415). Small differences were found in the EE spectra of the two copal-based varnishes (Congo copal not shown); rather than a shift in the position of the fluorescence maximum, fluorescence emissions excited at wavelengths above 400 nm are more apparent in Congo copal (from *Copaifera guibourthiana*) which has a spectrum more similar to sandarac than to that observed in Manila copal (from *Agathis dammar*), likely due to the differences in the source and age between the two semi-fossilised copals. Published spectra of aged sandarac are comparable to those represented in EE spectra [4].

The time-resolved analysis of the emission performed on the five diterpenoid varnishes (Fig. 6) indicates the presence of common features for these materials, ascribable to their similar chemical composition: in particular, it is possible to observe the presence of a common short-lived and intense component peaked between 400 and 420 nm, characterized by a much broader emission with

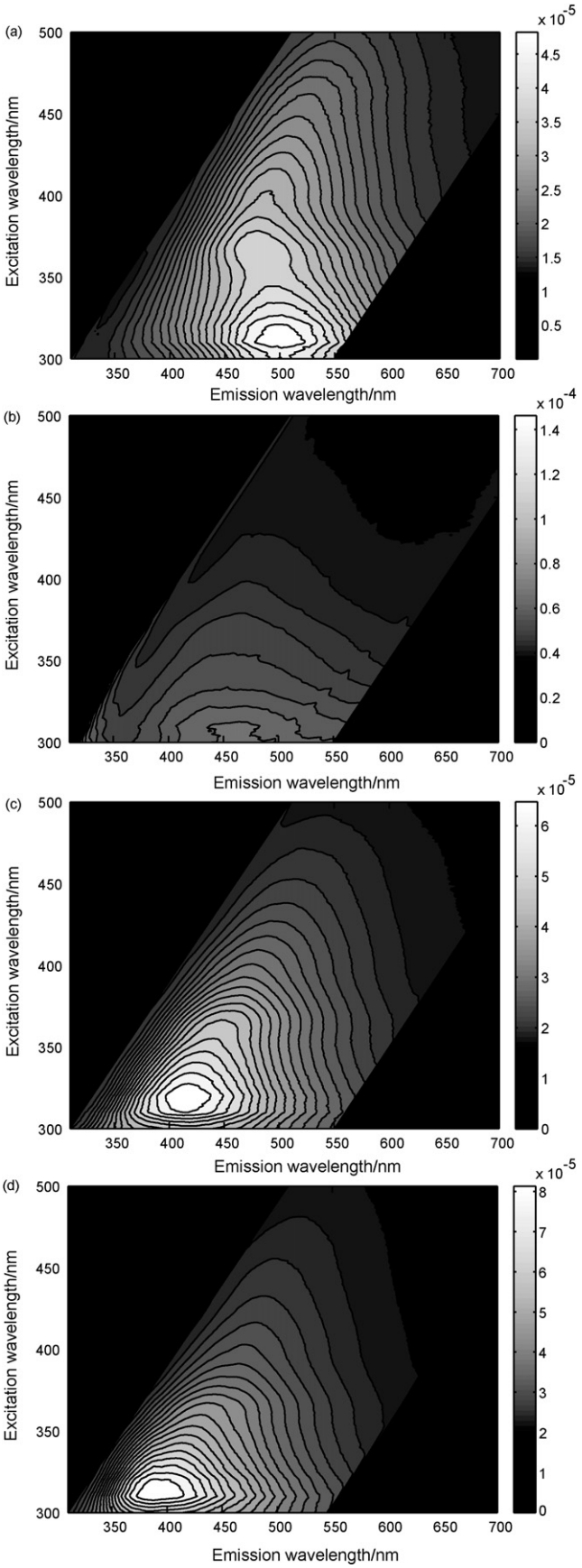


Fig. 5. EE spectra of naturally aged films of varnishes (a) colophony (b) Venice turpentine (c) sandarac (d) Manila copal, where intensity is given in counts and 20 contours represent 90% of the fluorescence of materials as a function of excitation.

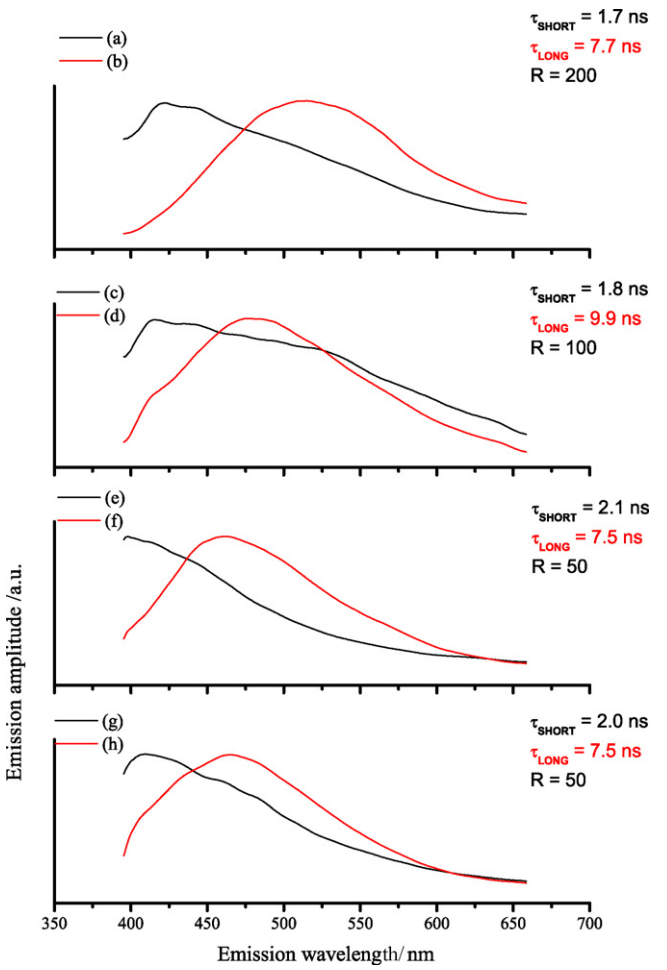


Fig. 6. Fluorescence spectra of the short- and long-lived components of the emission from naturally aged films of varnishes resulting following a bi-exponential fit of time-resolved spectral data: (a) short-lived and (b) long-lived component of colophony; (c) short-lived and (d) long-lived component of Venice turpentine; (e) short-lived and (f) long-lived component of the mixture of sandarac; (g) short-lived and (g) long-lived component of the mixture of Manila copal. For an easier comparison fluorescence amplitudes are shown normalised to the maximum value and values of τ_{SHORT}, τ_{LONG} and R are provided. Dashed vertical lines indicate the main peak wavelength of each fluorescent component.

respect to that observed in the triterpenic varnishes, which extends into the red region of the electromagnetic spectrum in the case of colophony and Venice turpentine and towards the green spectral region in the case of sandarac and Manila and Congo copal. In its turn the long-lived component shows small differences ascribable to the five materials analysed: a broad and symmetric emission peaked at 520 nm for colophony, an emission peaked at 480 nm with a small shoulder at 420 nm for Venice Turpentine and an emission peaked at 460 nm for sandarac (Fig. 6), at 450 nm for Congo copal and at 470 nm for Manila copal.

3.4. Mixtures of different varnishes

Mixtures of varnishes containing colophony, elemi and sandarac yield different EE spectra than those observed in single varnish samples seen in Figs. 3 and 5, however the EE spectra in mixtures (Fig. 7) may retain features from the constituent materials.

In general, the presence of colophony in mixtures contributes to emissions at longer excitation wavelengths (seen in all three mixtures containing colophony). For example in a mixture of colophony:sandarac (Fig. 7a) the maximum emission is observed with similar excitation wavelength as that seen in colophony, but

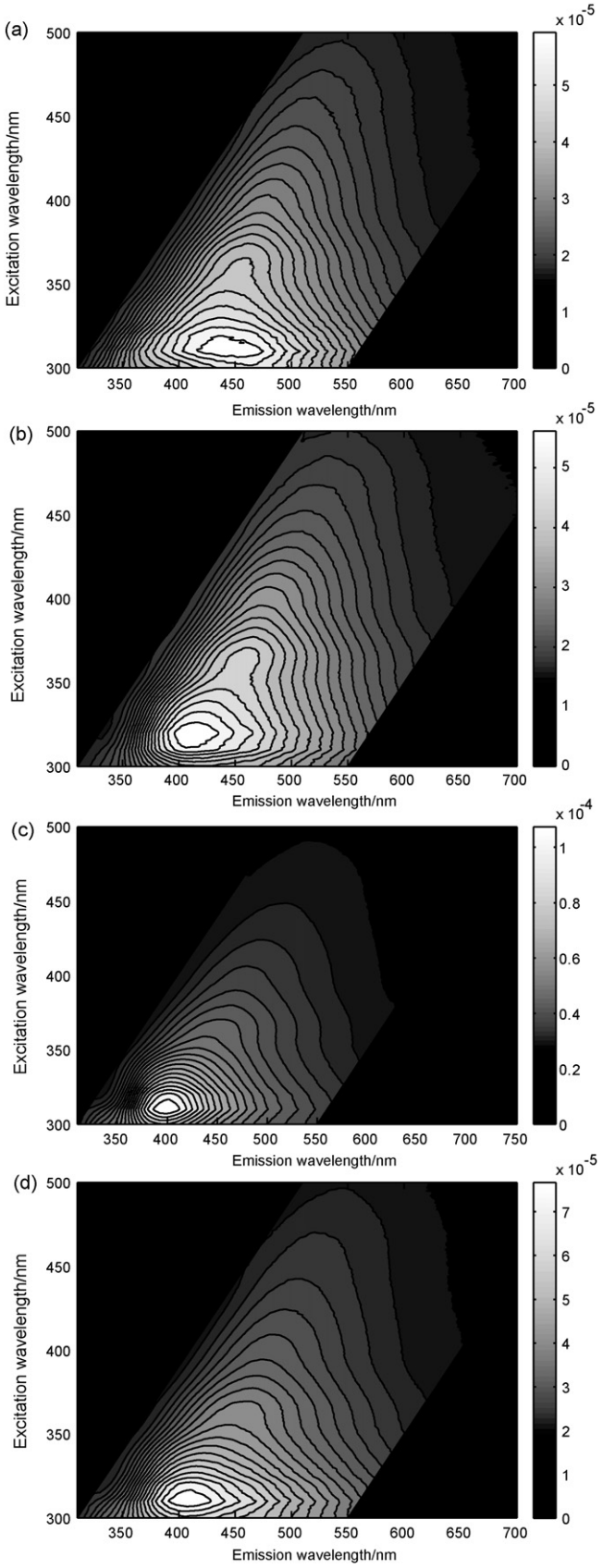


Fig. 7. EE spectra of varnishes made from mixtures of (a) colophony:sandarac, (b) colophony:elemi, (c) elemi:sandarac and (d) colophony:elemi:sandarac.

with a Stokes shift of 90 nm, greater than that seen in sandarac and less than that of colophony. The time-resolved analysis of the emission from the mixtures appears to be quite complicated. In fact, it can happen, as for the case of the mixture of colophony:sandarac, that both the short- and long-lived components of the emission from the mixture are characterised by spectral features which are found between those observed in the pure varnishes forming the mixture, but, in general, it is not possible to easily differentiate fluorescence contributions from mixed varnishes.

In Table 1, the positions of the maximum of the short- and long-lived component of the emission are further summarised.

4. Discussion

While in most cases it is difficult to interpret spectra with reference to specific fluorophores [4], the presence of small but appreciable differences in EE spectra and spectrally resolved fluorescence decays is an indication of the chemical variation among the varnishes analysed, which is ascribed to different sources of materials employed. Importantly, despite the dependence of fluorescence on ageing, spectra of materials reported here are comparable to those published previously by others [1,4,15].

From an initial examination of the maximum excitation and emission wavelengths as shown in Table 1, shellac is easily distinguished from other varnishes. However only small differences in the maximum excitation and emission wavelength are found for diterpenoids and triterpenoids; for example mastic and Venice turpentine have maxima at (305–10:445–65). Mastic, colophony and Venice turpentine seem to present high Stokes shifts ($\geq$135 nm), significantly greater than the other terpenoids. However, in comparison with fluorescence excitation and emission maximum, EE spectra indicate further differences in the emission properties of the varnishes studied, hence corroborating the limitation of considering only maxima in fluorescence spectra. Using a single excitation wavelength, it may still be possible to better distinguish materials with the aid of time-resolved fluorescence spectroscopy.

Since materials analysed are characterized by multiple fluorophores which emit in different spectral bands, bi-exponential modelling of time-resolved data provides a better fit with respect to results obtained with a mono-exponential fit. In detail, in Table 1 the mean reduced χ^2 values for the two exponential models are given, where the mono-exponential fit was carried out by considering only the decay following the first 10 ns after excitation. Indeed, fluorescence lifetime analysis of spectral bands provides a better indication of the presence of emissions from at least two distinct groups of fluorophores in each material: specifically, the emission spectrum of the long-lived component can be used to distinguish colophony from the other terpenic resins, whereas the narrower emission spectrum of the short-lived component of triterpenic varnishes can be used to distinguish them from diterpenoid media.

However, the resolution of mixtures of varnishes using fluorescence spectroscopy indicates that the contribution from one varnish of the mixture is predominant. As a general observation, in many cases time-resolved and EE spectroscopy are not able to separate the fluorescent components of mixed materials, but more refined statistical analyses on spectral and time-resolved data could be carried out to address the resolution of mixtures of multiple varnishes. For example, the combination of colophony:elemi (Fig. 7b) does not yield EE spectra which are easily rationalised, as the position of the maximum shifts and broadens with respect to that of the two varnishes. In turn, the EE spectrum of elemi:sandarac (Fig. 7c) does not differ from that of pure elemi in the position of maximum emission, whereas fluorescence intensity at the maximum is more intense than that of individual varnishes and a change is observed in the shape of the contours. The reason for this phenomenon is

not clear; it is possible that both chemical and physical interactions between the mixed materials occur or that a stratigraphic separation of the components takes place. In this latter case, the use of confocal fluorescence microscopy or other stratigraphic sampling techniques (MALDI) could be investigated.

5. Conclusion

The analysis and identification of varnishes using fluorescence remains a complex problem, which can be addressed, in part, by the integration of excitation emission spectroscopy and complementary time-resolved fluorescence spectroscopy, as shown in this work. Clear differences in EE spectra and short- and long-lived fluorescence emissions are evident and can be employed to better understand the materials responsible of the emission observed in varnishes. Based on the position of emission maximum, as well as the shape of the contours describing fluorescence, it may be possible to classify simple varnishes into groups which correspond to their chemical composition: sesquiterpenoids and polyesters (shellac), triterpenoids and diterpenoids.

The analysis of mixtures has also been carried out, and revealed that in some cases various contributions to the observed fluorescence spectra may be discerned from careful analysis of EE and time-resolved spectra. Further work based on factor analysis (for example PARAFAC), which has been applied to EE spectra of mixtures of fluorophores in food [23], may be used to create a more robust method for the deconvolution of EE spectra of single and multiple varnishes. Such analysis could be strengthened by the precise identification of specific groups of fluorophores present in the complex mixtures of resins employed as varnishes, potentially achievable with chromatographic techniques.

Instrument varnishes may also be mixed with dyes and colorants, as well as pigments (for example cinnabar) [14], which may complicate the interpretation of fluorescence spectra [31]. The presence of underlying varnish and pigmented layers may also compromise the detection of fluorescence; indeed fluorescent or absorbent substrates (wood or painted surfaces) may also modify the observed emission spectrum of materials through scattering and reflectance of emitted photons [28]. Therefore, the role of pigments and colorants in the modification or absorption of fluorescence should be further studied.

Another important factor which has not been directly addressed in this work, but which has been investigated by others [1,4], is the ageing and oxidation of varnishes, which is well-known to produce chemical and physical changes [18], both of which may have significant implications for varnish detection using fluorescence; further work is therefore necessary on a larger set of naturally aged materials which would better reflect materials found on works of art and historical musical instruments.

Finally, within the context of the analysis of both instruments as well as paintings, fluorescence spectroscopy, while unable to provide the specific and definite identification of materials and markers, which is afforded by alternative destructive techniques [15], remains an important tool for analysis. Extensively used in practice by restorers and art historians, fluorescence can indeed provide indications which go beyond the identification of areas of repainting and repairs, and may be used to guide further analytical investigations of musical instruments using selected complementary techniques.

Acknowledgements

Linda Berger is thanked for the preparation of the varnish films. Collaborative work at CUSBO was supported in part by the European Commission through the Research Infrastructures activity of FP6 ("Laserlab-Europe" RII3-CT-2003-506350).

References

[1] E. De la Rie, Stud. Conserv. 27 (1982) 65–69.
[2] T. Miyoshi, Jpn. J. Appl. Phys. 29 (1990) 1727–1728.
[3] A. Nevin, S. Cather, D. Anglos, C. Fotakis, Anal. Chim. Acta 573 (2006) 341–346.
[4] M. Thoury, M. Elias, J.M. Frigerio, C. Barthou, Appl. Spectrosc. 61 (2007) 1275–1282.
[5] B.H. Berrie, De la peinture de chevalet à l'instrument de musique: vernis, liants et couleurs, Cité de la musique, Paris, 2008, pp. 35–41.
[6] D. Anglos, M. Solomidou, I. Zergioti, V. Zafiropulos, T.G. Papazoglou, C. Fotakis, Appl. Spectrosc. 50 (1996) 1331–1334.
[7] C. Miliani, G. Favaro, A. Romani, Spectrochim. Acta A 54 (1998) 581–588.
[8] D. Comelli, G. Valentini, A. Nevin, A. Farina, L. Toniolo, R. Cubeddu, Rev. Sci. Instrum. 79 (2008) 086112–086113.
[9] D. Comelli, C. D'Andrea, G. Valentini, R. Cubeddu, C. Colombo, L. Toniolo, Appl. Opt. 43 (2004) 2175–2183.
[10] D. Lognoli, G. Cecchi, I. Mochi, L. Pantani, V. Raimondi, R. Chiari, T. Johansson, P. Weibring, H. Edner, S. Svanberg, Appl. Phys. B 76 (2003) 457–465.
[11] A. Nevin, D. Comelli, G. Valentini, D. Anglos, A. Burnstock, S. Cather, R. Cubeddu, Anal. Bioanal. Chem. 388 (2007) 1897–1905.
[12] M.P. Merrifield, Original Treatises on the Arts of Painting, Dover Publications, New York, 1967.
[13] M. Elias, P. Cotte, Appl. Opt. 47 (2008) 2146–2154.
[14] J.P. Echard, C. Benoit, J. Peris-Vicente, V. Malecki, J.V. Gimeno-Adelantado, S. Vaiedelich, Anal. Chim. Acta 584 (2007) 172–180.
[15] L. Larson, K. Shin, J. Zink, J. Am. Inst. Conserv. 30 (1991) 89–104.
[16] M.T. Doménech-Carbó, Anal. Chim. Acta 621 (2008) 109–139.
[17] M.P. Colombini, F. Modugno, S. Giannarelli, R. Fuoco, M. Matteini, Microchem. J. 67 (2000) 385–396.
[18] K.J. Van Den Berg, J.J. Boon, I. Pastorova, L.F.M. Spetter, J. Mass Spectrom. 35 (2000) 512–533.
[19] J.P. Echard, L. Bertrand, J. Cult. Herit. 9 (2008) 420–429.
[20] D. Scalarone, M. Lazzari, O. Chiantore, J. Anal. Appl. Pyrol. 64 (2002) 345–361.
[21] J.P. Echard, Spectrochim. Acta B 59 (2004) 1663–1667.
[22] C. Miliani, F. Rosi, I. Borgia, P. Benedetti, B.G. Brunetti, A. Sgamellotti, Appl. Spectrosc. 61 (2007) 293–299.
[23] E. Sikorska, A. Gliszczynska-Swiglo, I. Khmelinskii, M. Sikorski, J. Agric. Food Chem. 53 (2005) 6988–6994.
[24] C.M. Andersen, R. Bro, J. Chemometr. 17 (2003) 200–215.
[25] D. Comelli, G. Valentini, R. Cubeddu, L. Toniolo, Appl. Spectrosc. 59 (2005) 1174–1181.
[26] J. Hammerl, R. Hammerl, Violin Varnishes, Hammerl, Baiersdorf, 1988.
[27] J.S. Mills, R. White, The Organic Chemistry of Museum Objects, Butterworth Heinemann, Oxford, 1994.
[28] M. Elias, C. Magnain, C. Barthou, D. Comelli, A. Nevin, G.Valentini, Proc. SPIE, Vol. 7391, 739104 (2009); doi:10.1117/12.825093.
[29] J.H. Hofenk de Graaff, Colorful Past. Origins, Chemistry and Identification of Natural Dyestuffs, Archetype Publications, London, 2004.
[30] D. Scalarone, M. Lazzari, O. Chiantore, J. Anal. Appl. Pyrol. 68 (2003) 115–136.
[31] C. Clementi, B. Doherty, P.L. Gentili, C. Miliani, A. Romani, B.G. Brunetti, A. Sgamellotti, Appl. Phys. A 92 (2008) 25–33.

Talanta 80 (2009) 294–306

Contents lists available at ScienceDirect

Talanta

journal homepage: www.elsevier.com/locate/talanta

Nanoelectrospray with ion-trap mass spectrometry for the determination of beta-casomorphins in derived milk products

Ana Juan-García*, Guillermina Font, Cristina Juan, Yolanda Picó

Laboratori de Bromatologia i Toxicologia, Facultat de Farmàcia, Universitat de València, Av. Vicent Andrés Estellés s/n, 46100 Burjassot, València, Spain

ARTICLE INFO

Article history:
Received 26 March 2009
Received in revised form 14 June 2009
Accepted 29 June 2009
Available online 4 July 2009

Keywords:
b-CMs
NanoMate
QIT
MS
Nanoelectrospray

ABSTRACT

beta-Casomorphins (b-CMs) are bioactive peptides derived from casein with opioid agonist effects similar to morphine. The use of electrospray (ESI) with quadrupole ion-trap mass spectrometry (QIT-MS) for these compounds in two matrices, cheese and milk, was examined. It was compared to a liquid chromatography (LC) coupled to mass spectrometry (LC–MS), and a "soft" ionisation technique, NanoMate, with selected ion monitoring (SIM), which are unreliable for the determination of trace casomorphins in derived milk products. b-CM mass fragmentation pathways were done for the four most common b-CMs: β-casomorphin (1-5) bovine (b-CM-5), β-casomorphin (1-7) bovine (b-CM-7), [D-Ala2, D-Pro4,Tyr5]-β-casomorphin (1-5) amide (b-CM-10) and β-casomorphin (1-5) amide [D-Ala2,Hyp4,Tyr5] (b-CM-11). The major product ions obtained in QIT-MS were used to construct fragmentation pathways for b-CMs. The different collision energies using automated nanoelectrospray ion source NanoMate and conventional LC in QIT-MS were studied. Calibration data for b-CMs, using spiked milk or cheese samples (10 g or 10 mL), were: NanoMate/MS (25–1000 μg/L), $r^2 = 0.998$; NanoMate/MS^2 (5–1000 μg/L), $r^2 = 0.9992$; NanoMate/MS^3 (2.5–1000 μg/L), $r^2 = 0.9998$. Reproducibility data (% RSD, $N = 5$) for NanoMate/MS^n mode ranged between 2.0 at 500 μg/L and 7.0 at 10 μg/L.

© 2009 Elsevier B.V. All rights reserved.

1. Introduction

Peptides yielded by the digestion of beta-casein have opioid agonist effects similar to morphine. They are named beta-casomorphins (b-CMs) [1]. These bioactive peptides are bound to opioid receptors and exhibit morphine-like effects. They have high content on proline residues which it is related with effects as opioid (casomorphins) antithrombotic, antihypertensive, immunomodulators or mineral carriers [6,5].

Although their effect in adult human is limited to the gastrointestinal tract, as they are not absorbed or are subject to enzymatic degradation in the intestinal wall, in newborns and young infants, the effects presented are more evident, as the widespread hypothesis used to explain autistic symptoms in autism spectrum disorders (ASD) as shown in some studies [2,3]. It has been observed that many children with ASD present gastrointestinal symptoms such as inflammation, diarrhea, gastroesophageal reflux, abdominal pain and increased intestinal permeability [4,5]. It has also been observed that b-CMs induce alteration of the intestinal electrolyte transport, affect the human mucosal immune system, possibly via opioid receptors, and an important function in the digestive process may be served [6]. Investigations have shown that b-CMs significantly inhibited stimulated lamina propria lymphocyte proliferation (LPL) [5,7].

Continued developments in food technology and nutritional scientific interest in food peptides have grown considerably in the last years and in consequence it has given rise to the synthesis or production of potential bioactive peptides. This interest has been increased due to the presence of food component necessaries for organism such as amino acids, nitrogen and nutritional and functional values. In fact in the food industry, peptides derived from whey proteins, sometimes are used as skim milk replacers in ice cream, as fat replacers, as whole eggs replacers, as nondiary dessert products and in enteral, infant and sport nutrition [8,9]. And in consequence, detrimental components are sometimes presented in natural forms in food, but others, some effects on food components could cause effects and provide bioactive peptides because of the development of modern food processing and storage techniques.

Methods used in food processing such as hydrolysis, oxidation, fermentation, pH changes, heat and microbial enzymes can cause structural and chemical changes and synthesis or production of potential bioactive peptides. In the case that it concerns us the biologically active peptides produced from milk proteins are generated in natural way like in fermentation process of milk products. Milk is of great importance in the early years of human life and adult age [6,8], it is one of the basic foods well studied over the years, and its major proportion of nutrient components are proteins, the main source of natural biologically active peptides (b-CMs).

* Corresponding author.
E-mail address: ana.juan@uv.es (A. Juan-García).

0039-9140/$ – see front matter © 2009 Elsevier B.V. All rights reserved.
doi:10.1016/j.talanta.2009.06.062

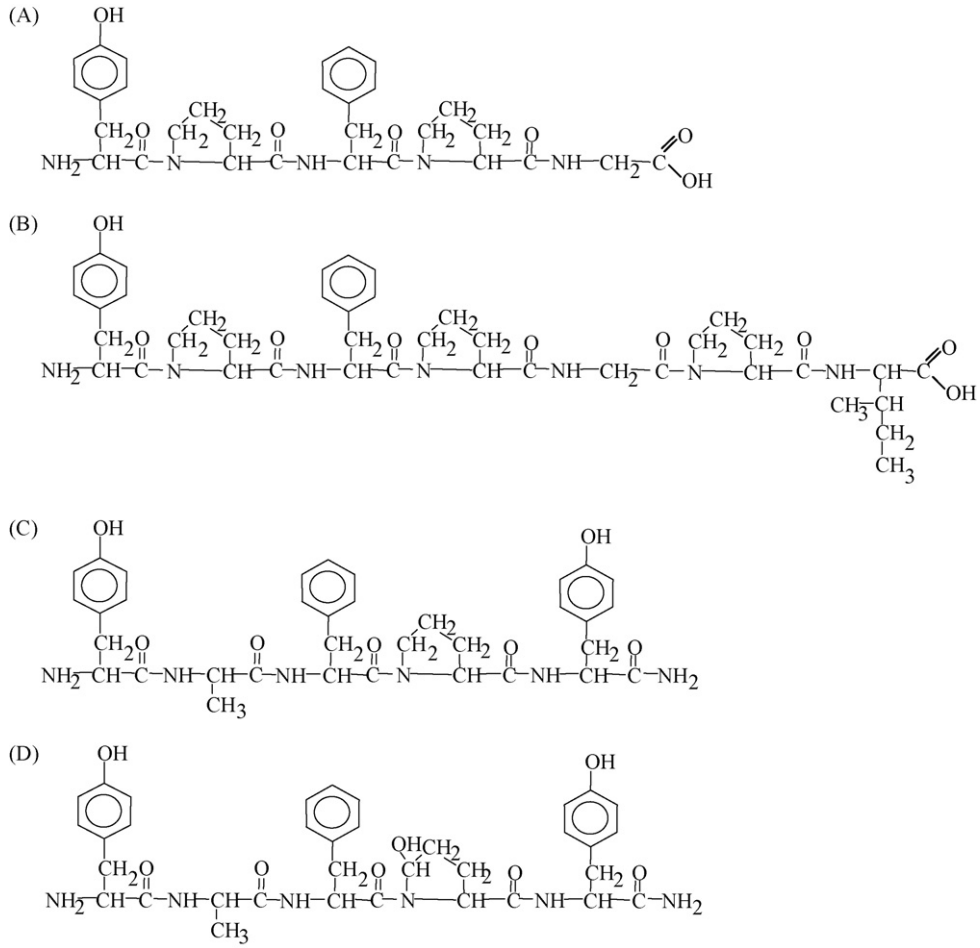


Fig. 1. Structure of the b-CMs studied: (A) β-casomorphin (1-5) bovine (b-CM-5); (B) β-casomorphin (1-7) bovine (b-CM-7); (C) [D-Ala2, D-Pro4,Tyr5]-β-casomorphin (1-5) amide (b-CM-10); and (D) β-casomorphin (1-5) amide [D-Ala2,Hyp4,Tyr5] (b-CM-11).

The beta-CMs have been isolated and identified in different origins of fresh milk: in cow, bovine, ovine, water buffalo and human milk, as well as in dried infant formula [1,10–13] and analytical and preparative separations in food proteins, LC coupled with conventional UV and fluorescence detectors has been the most widely used method. New developments in detection and separation facilities of LC have introduced robust and easy-operating LC–MS instruments capable of providing selective separation on-line with sensitive and selective mass detection.

Knowledge of importance in food derived bioactive peptides and the ionisation provided by analytical tools of the identification with a near complete certainly it has taken us to develop a method based on a quadrupole ion-trap (QIT) MS for identification of different b-CMs (Fig. 1) in milk and cheese samples. These MS instruments are quite specific to allow the identification of unknown analytes with a high degree of confidence, and they have been used for our studies. MS instruments are a powerful tool for the determination of the relative molecular mass of milk proteins as it is shown in some papers [9,14]. It has allowed the sequence of a large number of peptides in a relatively short analysis time and made such analyses by mass spectrometry possible for proteins and peptides with high accuracy [15–18].

Analytical methods for derived milk products using multiple tandem MS with electrospray ionisation (ESI) and nanoESI sources have been developed in this study. The multiple tandem mass spectrometer has been examined for the determination of b-CMs in cheese and milk; a quadrupole ion-trap (QIT) MS permits structural studies on casomorphins since mass fragmentation pathways can be studied using MS^n. An improved detection sensitivity using LC and automated nanoESI (NanoMate), linked to the QIT-MS, applied to determine b-CMs in cheese and milk samples, was reached.

The presented method achieves the identification of different b-CMs (Fig. 1) in milk and cheese samples and it is novel because there is no paper that studies the best conditions for optimal sensitivity and selectivity using the mass analyser QIT-MS to determine b-CMs in milk and cheese, and that establishes the strong points of each instrument that can be profit to more sensitive and selective quantification. It shows best conditions for the most common four b-CMs using LC-QIT/MS, studying the fragmentation pathway of these compounds, and also a comparison between different collision energies used by LC-QIT-MS and NanoMate-QIT-MS. Infusion NanoMate-ESI-MS demonstrates the successful possibility to analyse samples at ng/mL regime.

2. Materials and methods

2.1. Chemicals

β-Casomorphin (1-5) bovine, β-casomorphin (1-7) bovine, [D-Ala2, D-Pro4,Tyr5]-β-casomorphin (1-5) amide and β-casomorphin (1-5) amide [D-Ala2,Hyp4,Tyr5] were obtained from American Peptide Company, Inc. (Sunnyvale, CA, USA) as shown in Fig. 1. Individual standard stock solutions of 1000 mg/mL were prepared in methanol and stored in stained glass-stopper bottles under refriger-

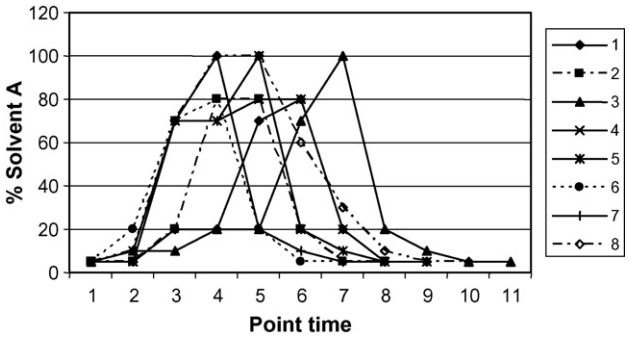


Fig. 2. Diagram of gradient of % solvent A in eight proofs to obtain the best separation of the four b-CMs. Each point time corresponds to a different minute depending on the proof. Time ranged between 50 and 60 min. The definite gradient is not represented, and it is detailed in Section 3.1.

ation at 4 °C. Standard working mixtures at various concentrations were prepared daily by appropriate dilution of aliquots of the stock solutions in methanol. A working standard mixture containing 5 μg/mL of each compound was prepared in methanol to be used as a spiking solution.

All chemicals and solvents used were of analytical grade or HPLC quality. Acetonitrile, water and methanol were purchased from Lab-Scan (Dublin, Ireland). Trifluoroacetic acid (TFA) was obtained from Sigma–Aldrich (Dorset, UK).

2.2. Liquid chromatography

The LC system was a Waters 2690 Alliance (Mildford, MA, USA) that included a thermostated autosampler, operated at 4 °C. The analytical column was a Luna-2 C_{18} (5 μm, 150 mm × 2.00 mm, Phenomenex, Macclesfield, UK) that was maintained at 35 °C. Isocratic chromatography was carried out using water–acetonitrile (70:30) containing 0.05% TFA at a flow rate of 200 μL/min. The injection volume was 5 μL.

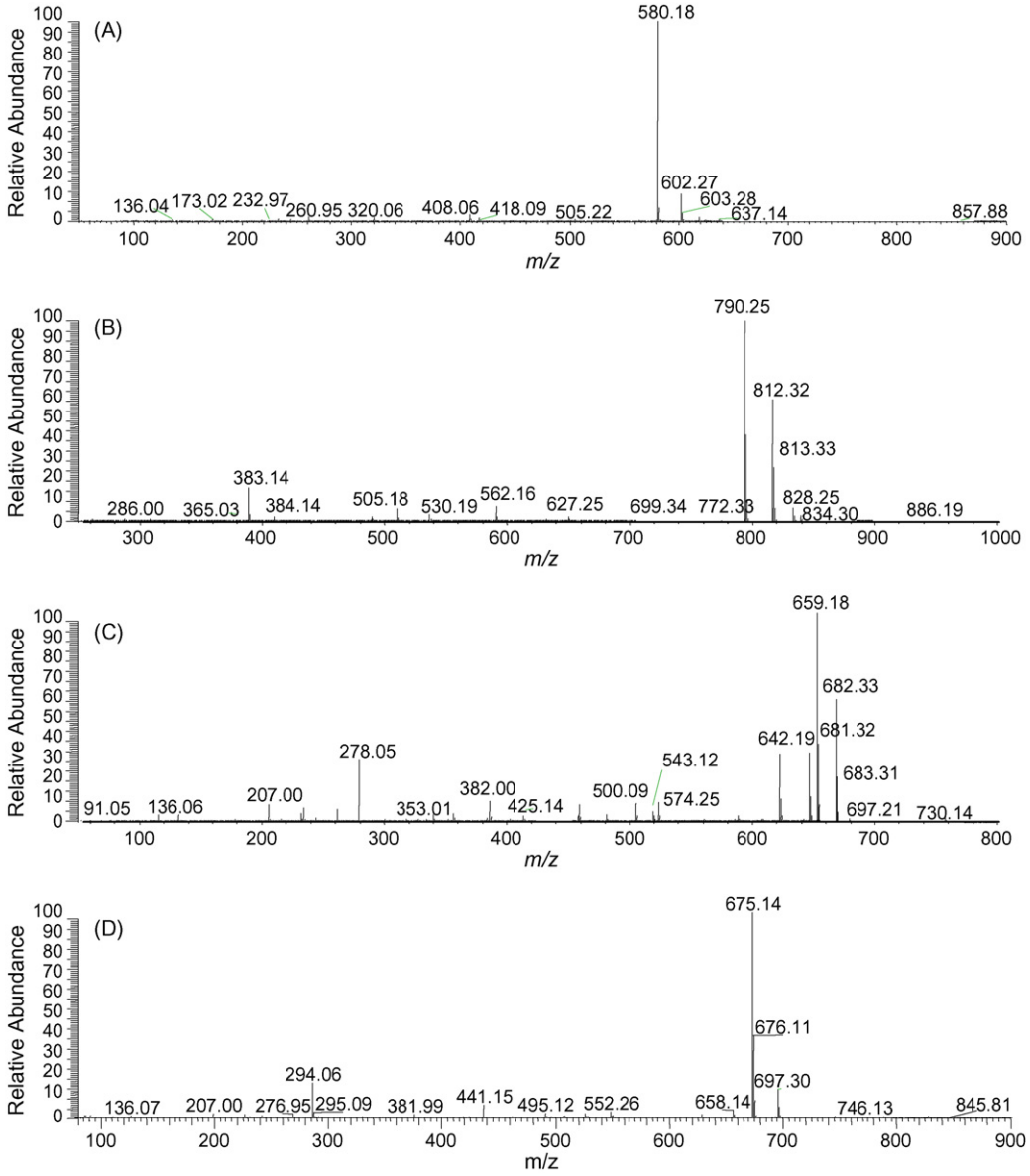


Fig. 3. QIT-full MS of the b-CMs studied by NanoMate: (A) b-CM-5; (B) b-CM-7; (C) b-CM-10; and (D) b-CM-11.

Table 1
Molecular weight, amino acid sequences and formula of the four b-CMs studied.

	Molecular weight	Sequence	Formula
Beta-casomorphin (1-5) bovine	579.7	Tyr-Pro-Phe-Pro-Gly	$C_{30}H_{37}N_5O_7$
Beta-casomorphin (1-7) bovine	789.9	Tyr-Pro-Phe-Pro-Gly-**Pro-Ile**	$C_{41}H_{55}N_7O_9$
Beta-casomorphin (1-5) amide [D-Ala2, D-Pro4,Tyr5]	658.8	Tyr-DAla-Phe-**DPro**-Tyr-NH_2	$C_{35}H_{42}N_6O_7$
Beta-casomorphin (1-5) amide [D-Ala2,Hyp4,Tyr5]	673.8	Tyr-DAla-Phe-**Hyp**-Tyr-NH_2	$C_{35}H_{41}N_6O_8$

Table 2
Ions and relative abundance of b-CMs obtained with NanoMate and LC in ESI mode by QIT-MS (full MS).

Compound	MW	*m/z* (% relative abundance)	
		LC-QIT-MS	NanoMate-QIT-MS
Beta-casomorphin (1-5) bovine	579.7	580 $[M+H]^+$ 100; 213 $[M+2H]^{2+}$ 100; 624 $[M+2Na-H]^+$ 70; 602 $[M+Na]^+$ 85	580 $[M+H]^+$ 100; 602 $[M+Na]^+$ 85
Beta-casomorphin (1-7) bovine	789.9	790 $[M+H]^+$ 100; 834 $[M+2Na-H]^+$ 15; 812 $[M+Na]^+$ 25	790 $[M+H]^+$ 100; 812 $[M+Na]^+$ 80
Beta-casomorphin (1-5) amide [D-Ala2, D-Pro4,Tyr5]	658.8	659 $[M+H]^+$ 25; 681 $[M+Na]^+$ 100; 697 $[M+K]^+$ 10	659 $[M+H]^+$ 100; 681 $[M+Na]^+$ 70; 697 $[M+K]^+$ 10
Beta-casomorphin (1-5) amide [D-Ala2,Hyp4,Tyr5]	673.8	675 $[M+H]^+$ 45; 697 $[M+Na]^+$ 100	675 $[M+H]^+$ 100; 697 $[M+Na]^+$ 20

MW: molecular weight.

2.3. Quadrupole ion-trap mass spectrometer (QIT-MS) conditions

Experiments were carried out using a Finnigan MAT LCQ Classic ion-trap mass spectrometer system (Thermo-Finnigan, San Jose, CA, USA) equipped with electrospray ionisation (ESI) Finnigan Xcalibur™ Rev. BXCALI-97001 software of ThermoQuest Corporation trademark and Data Analysis BioWorks™ ver. 3.1. The coupling of LC to QIT-MS was carried out using the binary pump and through its ESI interface in positive mode using the standard scan at normal resolution.

The sample was introduced from the HPLC into the ion-trap mass spectrometer using an uncoated fused-silica capillary (Metal Services Ltd.) with a length of 18 cm, at room temperature, 100 μm I.D., and 200 μm O.D. The polyamide coating was removed from the end of the capillary (ca. 5 mm) to maintain a stable electrospray. The voltage on the ESI needle was set at 4 kV, producing a spray current of approximately 80 μA. The capillary voltage was set at 10 V and the temperature of the heated capillary was 200 °C. The sheath gas flow rate used was 60 (arbitrary units). The QIT-MS was tuned for b-CMs and the voltages on the lenses were optimised in TunePlus (Excalibur Software) whilst infusing a standard solution (1 μg/mL methanol) at the rate of 3 μL/min. The optimised lens voltages were as follows: tube lens offset (0.0 V); octapole 1 offset (−3.0 V); octapole 2 offset (−7.0 V); inter-octapole lens voltage (0–16.0 V); trap DC offset voltage (−10.0 V). The microscan value was set at 3 ms and the maximum inject time was 50 ms.

Multiple tandem MS spectra, produced by collision-induced dissociation (CID), were obtained using the primary and majority ion provided at the conditions above mentioned. For most of the b-CMs studied compounds the protonated molecule $[M+H]^+$ was obtained.

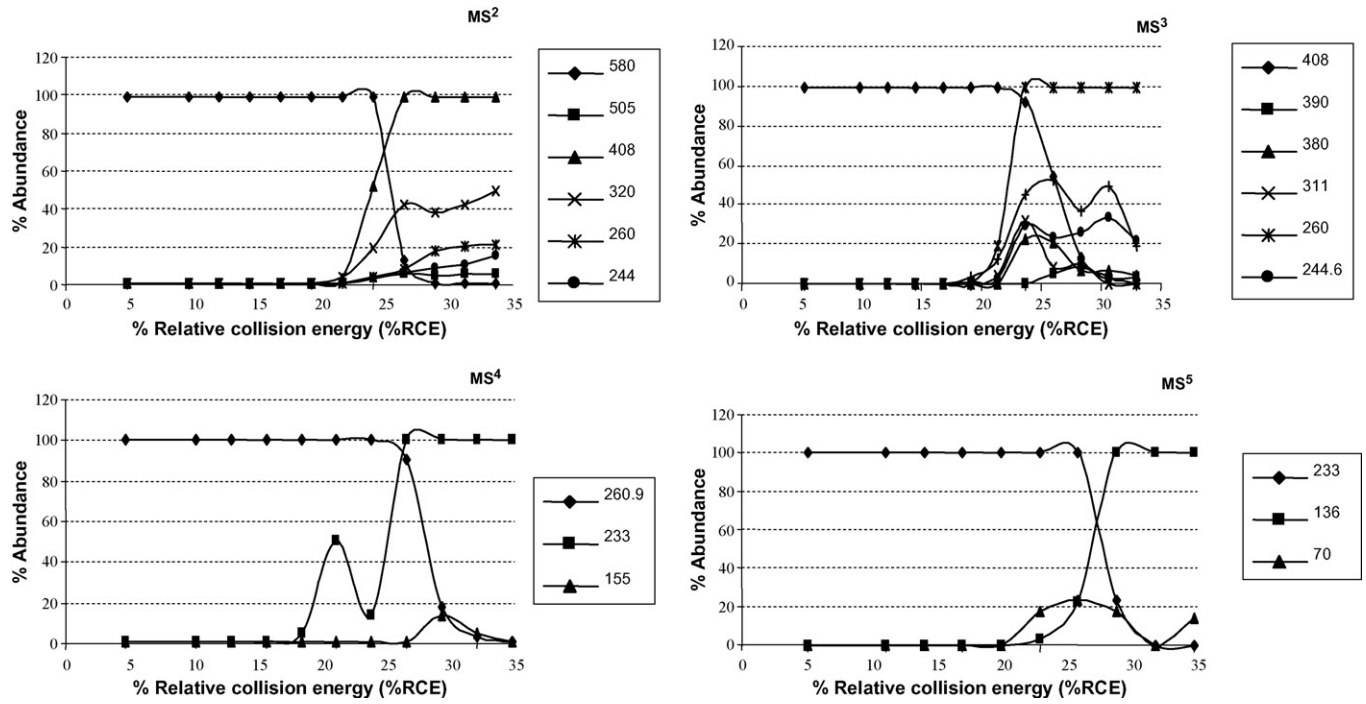


Fig. 4. Abundance of product ions from the reaction of protonated b-CM-5 with helium in the quadrupole ion-trap as a function of relative collision energy (RCE).

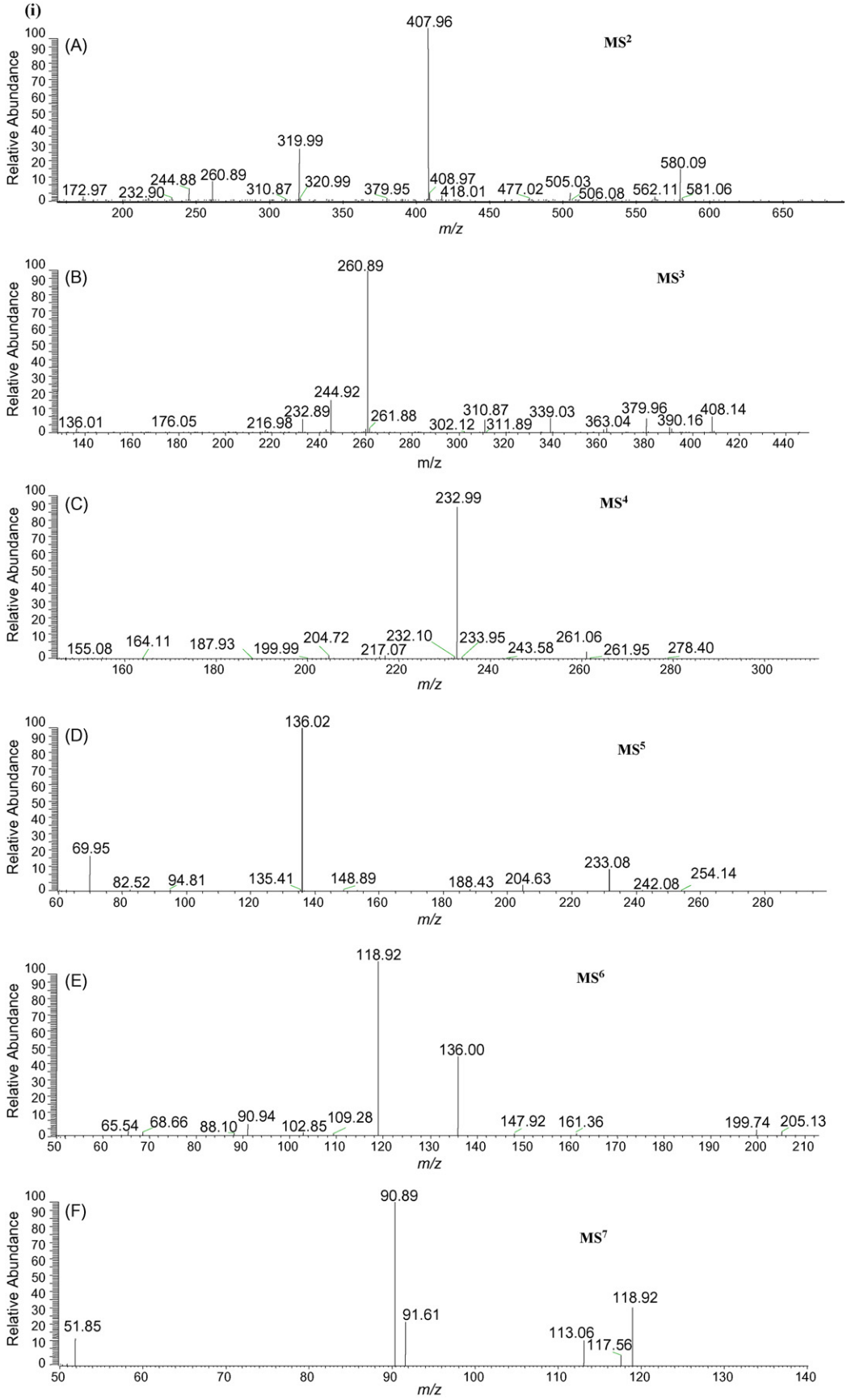


Fig. 5. Positive ion NanoMate-ESI mass spectra of (i) b-CM-5 and (ii) b-CM-11. CID product ion spectra of b-CM-5: (A) MS^2; (B) MS^3; (C) MS^4; (D) MS^5; (E) MS^6; and (F) MS^7, and of (ii) b-CM-11: (A) MS^2; (B) MS^3; (C) MS^4; (D) MS^5; (E) MS^6; (F) MS^7; and (G) MS^8. The selected ions for trapping and fragmentation, together with the optimised RCE, are shown in Table 3.

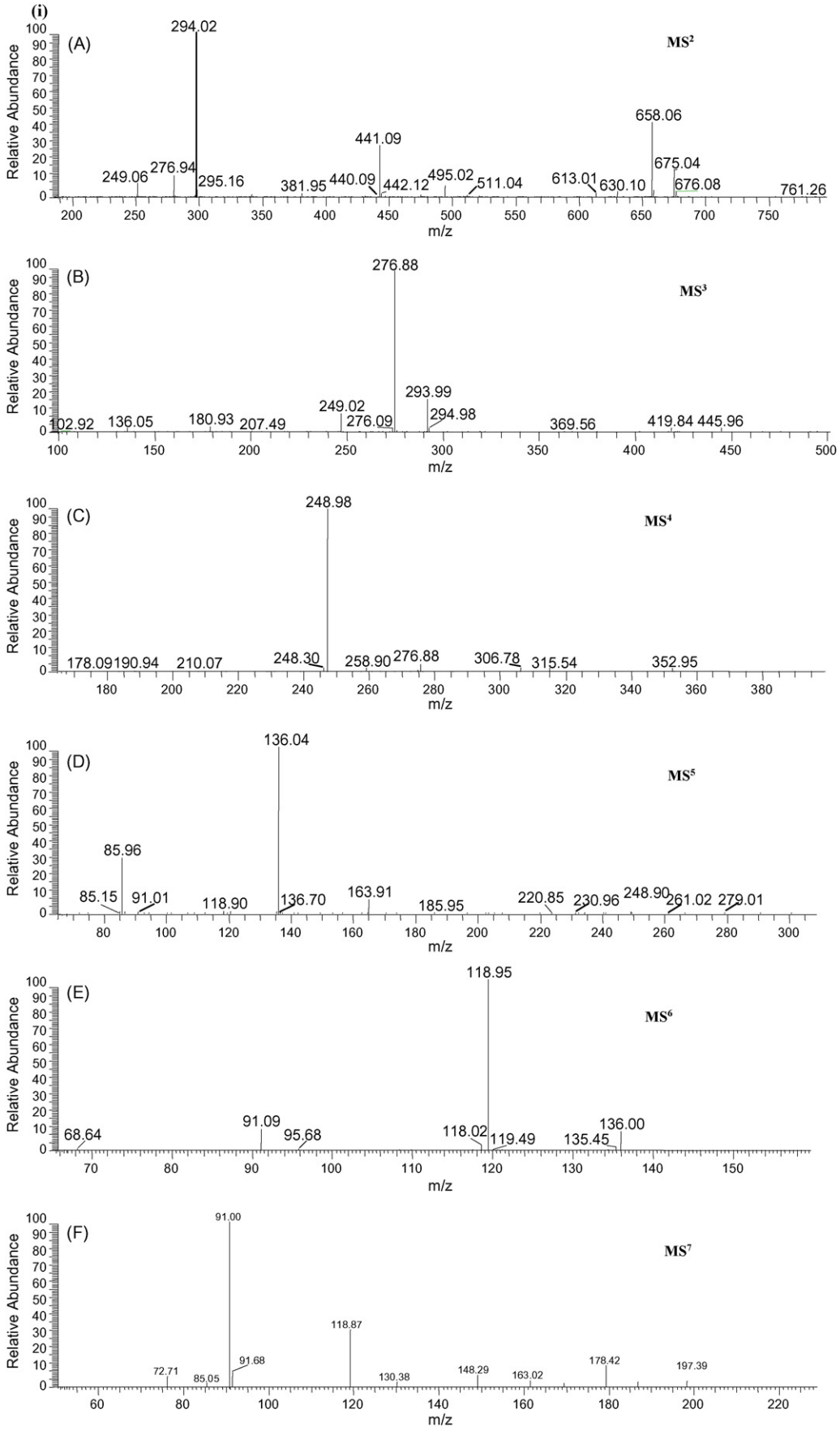


Fig. 5. (*Continued*)

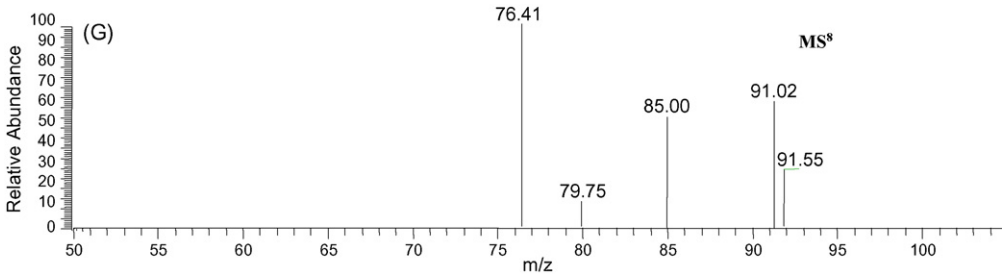


Fig. 5. (*Continued*).

All separations were conducted using 2 mL sample glass vials. The sample volume injected was 10 μL with a syringe draw rate of 0.50 μL/s.

The sheath liquid was water:trifluoroacetic acid 0.05% (A) and acetonitrile:trifluoroacetic acid 0.05 (B) with 70:30 (A:B, v/v), delivered at 200 μL/min. Electrospray ionisation/MS was conducted in the positive ion mode, and the capillary voltage was set at 4.0 kV. Dry nitrogen gas was heated to 250 °C and delivered at a flow rate of 7 L/min. The pressure of nebulizing nitrogen gas was set at 10 psi.

The parameters in the LCQ Classic ion-trap mass spectrometer system were recorded using full-scan event with a mass range *m*/*z* 50–1000 with a scan time of 0.75 s and acquisition data time of 4 min, or selected ion monitoring (SIM) ($[M+H]^+$ molecules at *m*/*z*, 580 for β-casomorphin (1-5) bovine, *m*/*z* 790 for β-casomorphin (1-7) bovine, *m*/*z* 659 for [D-Ala2, D-Pro4,Tyr5]-β-casomorphin (1-5) amide, *m*/*z* 674 for β-casomorphin (1-5) amide [D-Ala2,Hyp4,Tyr5] with a gain of 3, fragmentor voltage of 90 V, and dwell time of 63 ms. CID was performed on the ion of interest by collision with the helium background gas present in the trap for 50 ms. The fragmentation steps for each compound were optimised visualizing the changes in the intensities of fragment ions.

The HPLC and ion-trap MS instruments were connected and synchronized by signal programmed from the Software.

2.4. Chip based nanoelectrospray emitters

Nanoelectrospray infusion analysis was achieved using a NanoMate 100 (Advion BioSciences, Ithaca, NY), an automated chip based nanoelectrospray device using a disposable ESI-Chip with a fully integrated array of 10 × 10 nozzles etched from the surface of a silicon wafer. This system holds a 96-well plate, a rack of 96 disposable conductive pipette tips, and the nanoelectrospray mentioned above. During infusion analysis, the system sequentially picks up a pipette tip, aspirates 1–5 μL of sample from one position of the 96-well plate, and then delivers the sample to the inlet side of the ESI chip. In this study, 5 μL of sample solution was delivered to the back lane of the nanoESI chip. The electrospray process was initiated by applying 1.67 kV and approximately 0.6 psi nitrogen head pressure to the sample in the pipette tip to ensure constant sample flow to the chip. These settings gave an approximate sample flow rate of 150–200 nL/min for samples prepared in methanol. The nanoelectrospray chip was positioned directly in front of the aperture in the curtain plate. Samples were analysed in approximately 60 s

Table 3
Major product ions in the mass spectra of protonated studied b-CMs obtained using (A) a NanoMate-quadrupole ion-trap mass spectrometer and (B) a LC-quadrupole ion-trap mass spectrometer.

b-CM	M	MS^2	MS^3	MS^4	MS^5	MS^6	MS^7	MS^8	MS^9
(A) NanoMate-QIT-MS									
Beta-casomorphin (1-5) bovine	580.1 (27)	408.0 (30)	260.9 (28)	232.9 (27)	136.0 (30)	118.9 (28)	90.9		
Beta-casomorphin (1-7) bovine	790.2 (29)	530.0 (29)	512.1 (27)	393.1 (29)	164.9 (33)	109.1			
			285.9 (25)	154.2 (21)	126.8 (22)	70.0			
		383.1 (27)	229.0 (29)	70.0					
Beta-casomorphin (1-5) amide [D-Ala2, D-Pro4,Tyr5]	659.2 (25)	642.0 (26)	614.2 (26)	597.3 (27)	525.9 (27)	362.9 (24)	335.2 (29)	199.8 (29)	172.2
								238.1 (32)	146.2
								171.2	
Beta-casomorphin (1-5) amide [D-Ala2,Hyp4,Tyr5]	674.7 (25)	294.2 (25)	276.3 (24)	249.0 (32)	136.0 (31)	119.0 (27)	91.0 (24)	76.1	
				249.0 (31)	220.9 (23)	86			
					204.1 (35)	186.1			

b-CM	M	MS^2	MS^3	MS^4	MS^5	MS^6	MS^7	MS^8
(B) LC-QIT-MS								
Beta-casomorphin (1-5) bovine	580.1 (30)	408.0 (38)	260.9 (28)	232.9 (28)	136.0 (33)	118.9		
Beta-casomorphin (1-7) bovine	790.2 (33)	530.0 (33)	383.1 (30)	229.1, 251.2	346.0			
			512.1 (30)	466.1 (20)				
		383.1 (30)	229.0 (33)	70.0				
Beta-casomorphin (1-5) amide [D-Ala2, D-Pro4,Tyr5]	659.2 (33)	642.0 (33)	614.2 (35)	597.3 (30)	525.9 (33)	362.9 (28)	335.2 (30)	183.1
Beta-casomorphin (1-5) amide [D-Ala2,Hyp4,Tyr5]	674.7 (43)	294.2 (30)	276.3					

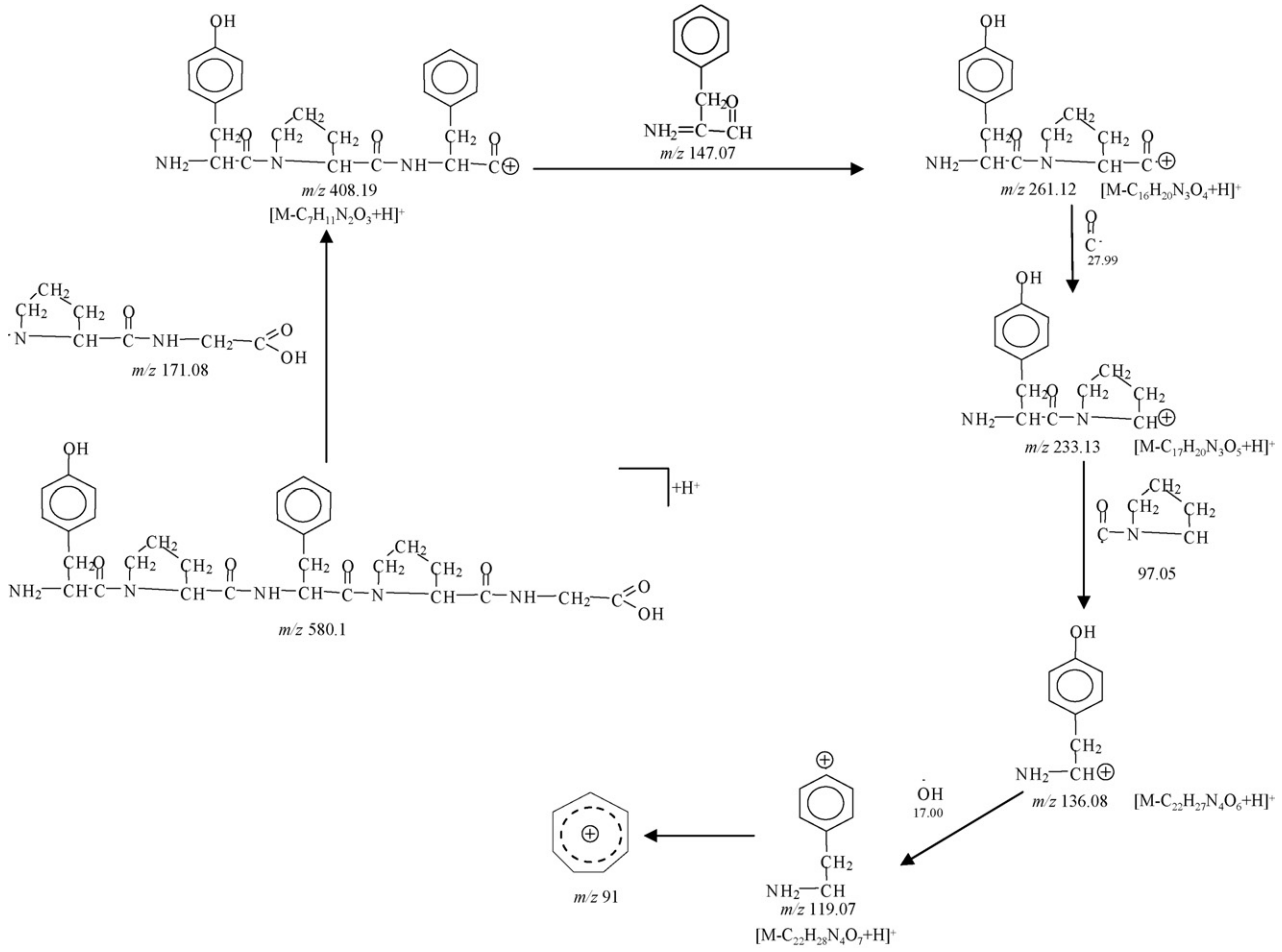


Fig. 6. Proposed CID fragmentation pathway showing the losses and structures of product ions from protonated b-CM-5 as determined by ion-trap MS^n experiments.

intervals using ChipSoft 6.4.2 software (Advion Biosciences), which controlled the automated nanoESI system.

2.5. Sample preparation

20 samples, 10 of milk and 10 of cheese, of different local markets from Cork, Ireland were collected. 12 g of sample was mixed with 12 mL of water:trifluoroacetic acid (TFA) 0.1%. 2 mL was taken and 2 mL of water:TFA 0.1% was added, homogenized and centrifuged at 4024 g for 5 min. The resulting supernatant was collected and 4 mL of methanol was added, mixed and filtered through a Buchner funnel. The extract obtained was passed through SPE C_{18}, X-Strata cartridges at a flow rate of 2 mL/min. These cartridges were previously conditioned with 5 mL of methanol and 5 mL of water. The sample was transferred to the cartridge and b-CMs were eluted using 4 mL of methanol and the solvent was removed at 40 °C, under stream of nitrogen until 1 mL. The sample was filtered prior to analysis.

3. Results and discussions

3.1. Separation of b-CMs

The direct combination of LC with MS reduces the emphasis on chromatographic separations due to the mass selectivity and distinctive fragmentation patterns. There are some previous studies showing satisfactory chromatographic separation of two b-CMs (b-CM-5 and b-CM-11), among the four studied in this work [6]. However poor peak shapes, low or variable retention and high retention time were observed for the above b-CMs analysed in the study.

Some of the b-CMs found in the literature differ only in one unity of the molecular weight, and polarity of them is similar, so it made the separation more difficult. In this study more attention was paid to the b-CMs that were usually studied and well known, as it has been mentioned in Section 1, which are b-CM-5, b-CM-7, b-CM-11 and b-CM-10 and different molecular weights they present.

Prior to the analysis with quadrupole ion-trap the four b-CMs, were injected separately in a conventional LC-UV Shimadzu to optimise its separation. This separation was studied with two different length columns 150 mm × 2.00 mm and 250 mm × 4.60 mm. Different mobile phases were tested to obtain the best separation of b-CMs as shown in Fig. 2.

The four b-CMs studied were successfully separated at a flow of 1 mL/min: starting at 5% of B, increased to 10% in 5 min and maintained for 1 min. B was increased until 20% in 1 min, maintained for 7 min and in 10 min 70% of B was reached. After that, 100% was reached with the high proportion of solvent B in 1 min. The return to the initial conditions was from 100% to 20% in 5 min, in 2 min to 10% and in 2 min more to 5%. The total time employed was 34 min, and the four b-CMs were resolved in 25 min.

3.2. MS spectrum of b-CMs

QIT multi-stage mass spectrometry (MS^n) has previously been applied for the determination of many organic contaminants in different matrices. These studies have now been extended to a wide variety of compounds and degradation products since QIT-MS

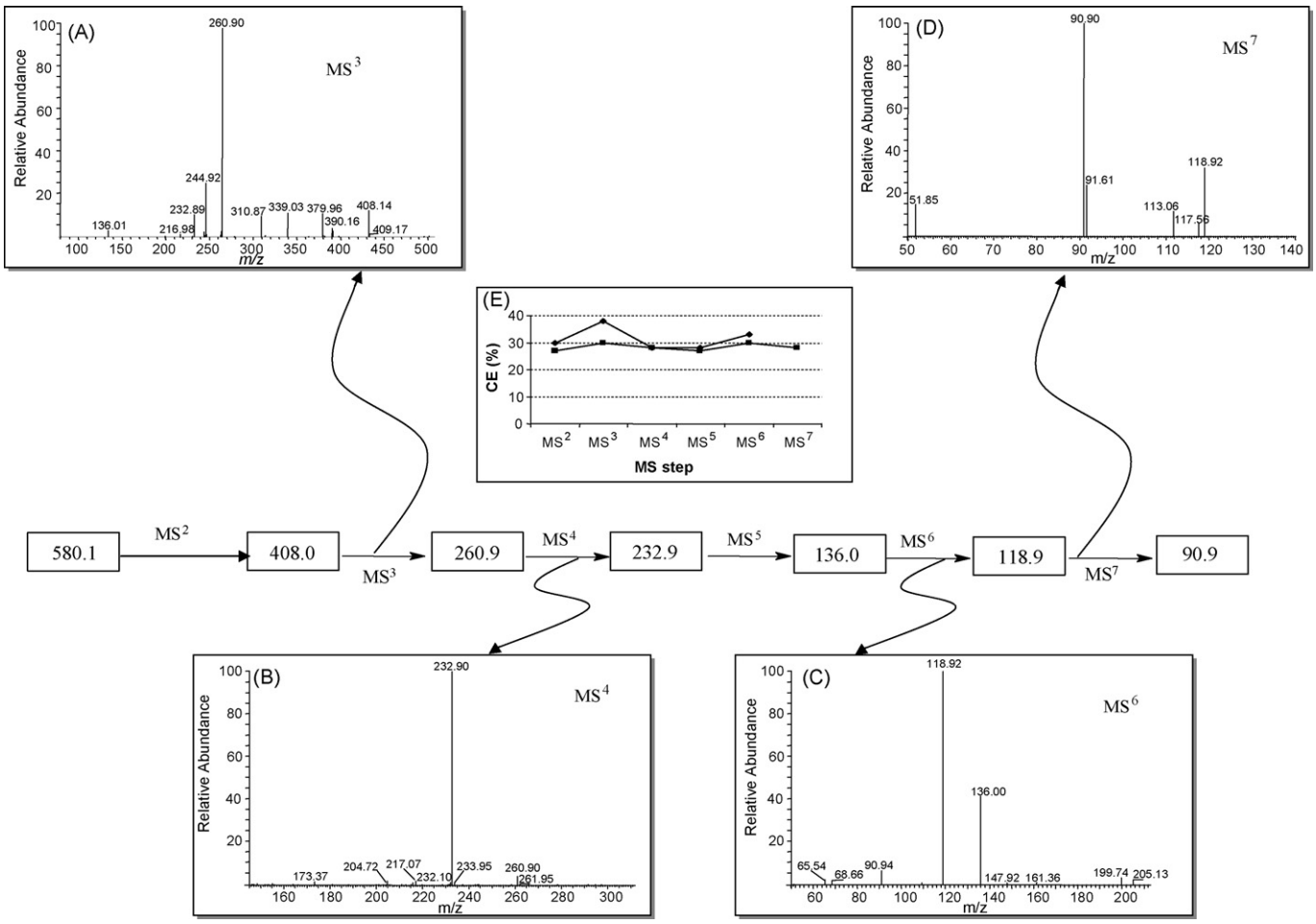


Fig. 7. Fragmentation scheme of b-CM-5: (A) MS^3; (B) MS^4; (C) MS^6; (D) MS^7; (E) collision energy (CE) diagram in LC (♦) and NanoMate (■).

permits the elucidation of fragmentation pathways. The coupled NanoMate-electrospray ionisation (ESI), a valuable source that enables detailed MS studies carried out on very small quantities, is particularly relevant to these studies since only micrograms of most of the b-CMs were extracted.

The b-CMs examined in this work are illustrated in Fig. 1. As it can be appreciated structural variants involve the union of different amino acids, see also Table 1. The ESI mass spectra of b-CMs are relatively simple and it can be observed in Fig. 3 by NanoMate. The molecular-ion species formed in positive mode in the acidic mobile phase are mainly protonated molecules, but some sodium adducts could also be observed. High background signals and potential interferences warranted additional characteristic fragmentation of the analytes. Quantification was done on the most intense ion transition.

The abundance of $[M+H]^+$ is greater than that of $[M+Na]^+$ for most of the b-CMs. In general, the maximum abundances of both $[M+H]^+$ and $[M+Na]^+$ ions were observed when the CID voltage was set around 30 V. The ESI-MS spectra of b-CMs are shown in Fig. 3. At a lower voltage, low ion intensity was measured. When the voltage was higher than 35 V, less $[M+H]^+$ and $[M+Na]^+$ ions, and more fragmented ions were detected. That is the reason to set at 30 V the fragmentor voltage.

3.3. Multiple tandem MS experiments

In the ThermoFinningan LCQ, relative collision energy (RCE) is the energy that is applied to trapped ions in the mass analyser. The RCE value varies in the range 0–100% and corresponds to 0–5 V peak-to-peak of resonance excitation RF voltage. Different scan events were prescribed to run simultaneously in the instrument. The first scan event was full-scan MS to acquire data on ions in the range m/z 50–1500. The optimum RCE value was studied ramping with an initial point of 10% to reveal the major fragmentation pathways and to ascertain the energy required to generate the optimum population of target ions for subsequent MS stages. The predominant product ions, acquired at the optimised RCE value, were selected for MS^3 experiments where the RCE was again ramped to establish the next generation of product ions. The ions selected in the ramped RCE studies are shown in Table 2. The difference between the two MS^2 experiments carried out for each b-CM was the initial ion, because the $[M+H]^+$ ions and sodium adduct $[M+Na]^+$ in all b-CMs, and $[M+2Na-H]^+$ adduct in b-CM-5 and b-CM-7, and potassium adduct in b-CM-10 were studied.

All these experiments were also carried out by using the nano-electrospray NanoMate 100 and as it would be observed further different RCE values were necessary for each MS step and the step number reached it could be observed in the figures presented.

3.4. MS fragmentation studies of b-CMs

The fragmentation of b-CM was examined using TFA as a buffer for positive ion mode operation. In this study, multiple tandem MS (MS^n) was used for the repeated trapping and fragmenting ions. An advantage of the ion-trap MS instruments is the ability to switch between a full-scan MS and MS^n scan of fragments without a signif-

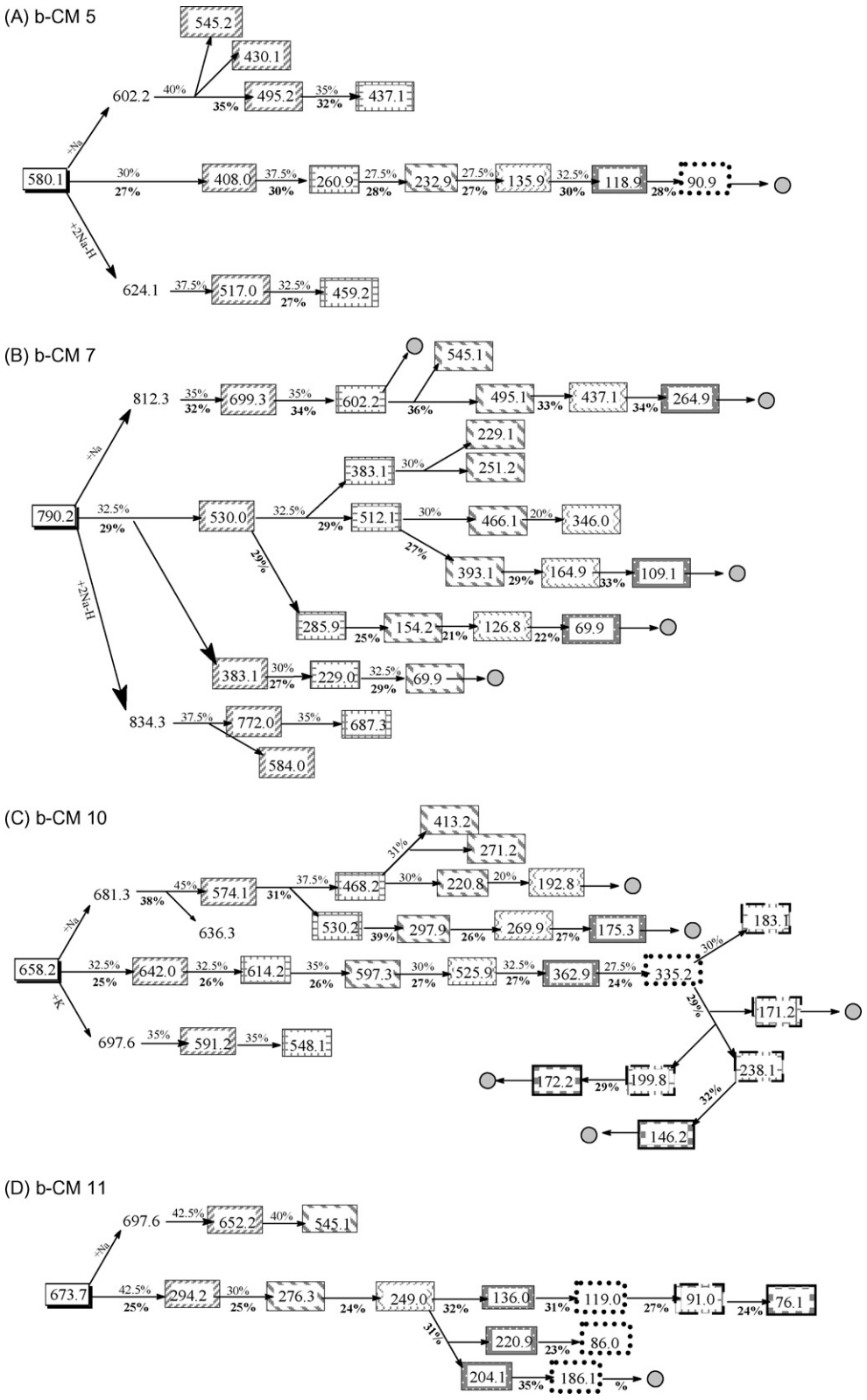


Fig. 8. Scheme of the proposed pathway for the b-CMs studied. Each colour box belongs to one MS step; MS^2 ( ), MS^3 ( ), MS^4 ( ), MS^5 ( ), MS^6 ( ), MS^7 ( ), MS^8 ( ) and MS^9 ( ). It is also indicated the RCE for LC and for NanoMate (in black).

icant loss in sensitivity [19]. Once the precursor ion was selected, explained above and shown in Table 2, the effect of varying the energy of the helium collision processes was determined by plotting the relative abundances of the product ions versus % RCE (Fig. 4) for each b-CM. Fig. 4 shows the product ions plotted for b-CM-5. These data were used to select candidate ions for subsequent MS^n experiments.

For b-CM-5 (Fig. 4), MS^2 gave major fragment ion at m/z 408 $[M-C_7H_{11}N_2O_3+H]^+$ and MS^3 yielded product ions from the m/z 408 fragment ion of b-CM-5 at m/z 261 $[M-C_{16}H_{20}N_3O_4+H]^+$, m/z

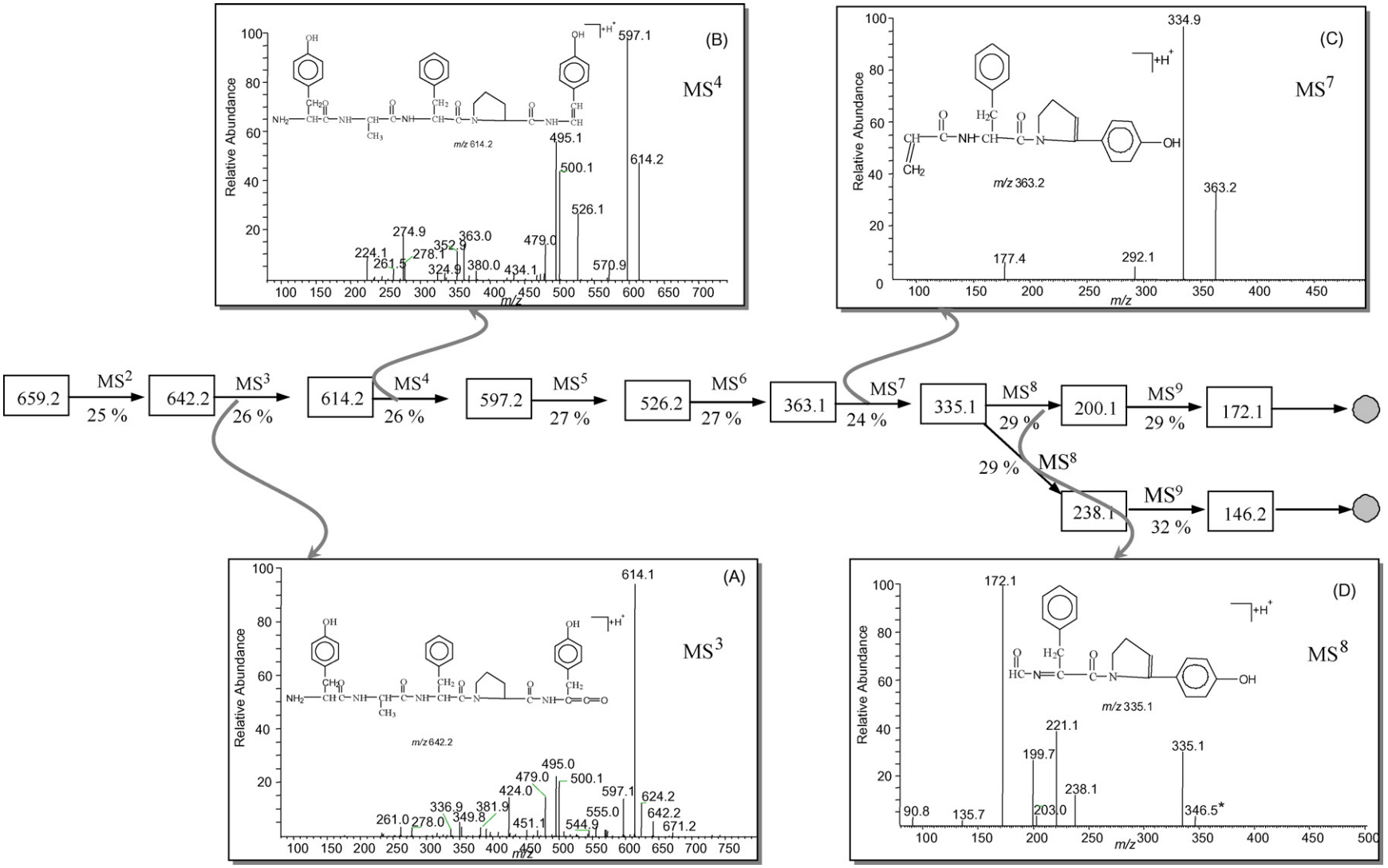


Fig. 9. Fragmentation scheme of b-CM-11: (A) MS^3; (B) MS^4; (C) MS^7; and (D) MS^8. % Relative collision energy when NanoMate was used.

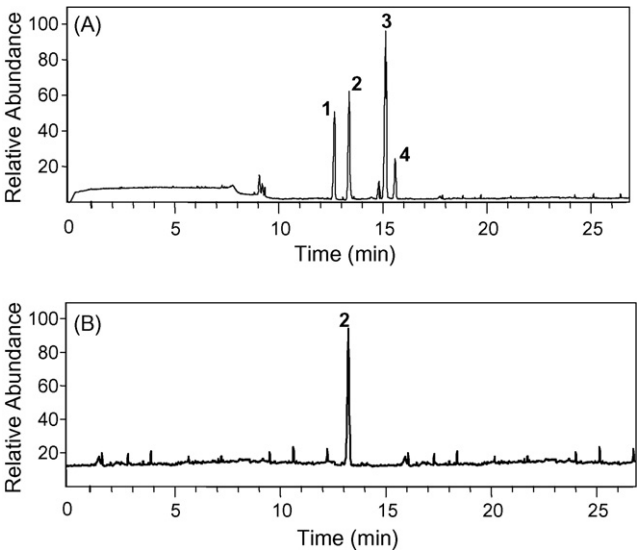


Fig. 10. (A) NanoMate/MS chromatographic separation of standard b-CM-5 (1), b-CM-7 (2), b-CM-11 (3) and b-CM-10 (4) following C_{18} solid phase extraction. (B) NanoMate/MS chromatograms of b-CM-7 identified in a milk sample from local supermarket. Chromatographic conditions: Luna-2 C_{18} (5 μm, 150 mm × 2.00 mm) at 35 °C; mobile phase water:acetonitrile (70:30) containing 0.05% TFA; flow rate 200 μL/min.

233, 244, 176, 136 and 119 (see also Table 3 and Fig. 5). MS^4 experiments, targeting *m/z* 261, gave the product ion *m/z* 233 $[M-C_{17}H_{20}N_3O_5+H]^+$, MS^5 experiments, targeting *m/z* 233, gave the product ion *m/z* 136 $[M-C_{22}H_{27}N_4O_6+H]^+$, MS^6 experiments, targeting *m/z* 136, gave the product ion *m/z* 119 $[M-C_{22}H_{28}N_4O_7+H]^+$ and finally when for MS^7 experiments, targeting *m/z* 119, a majority single ion *m/z* 91 $[C_7H_7]^+$ as can be observed from the spectra shown in Fig. 5(i). A similar fragmentation process was carried out for the other three b-CMs studied.

b-CM-11's mass spectra are also shown in Fig. 5(ii). The ions at *m/z* 136, *m/z* 119 and *m/z* 91 were observed in MS^5, MS^6 and MS^7 spectra for both b-CMs shown in Fig. 6. The fragmentation pathway obtained for b-CM-5 and proposed structures for the major fragment ions observed in the mass spectra are shown in Fig. 6.

3.5. Comparison between LC infusion and NanoMate in QIT fragmentation

The ions formed from the b-CM studied by the initial collision process are shown in Table 2 where it can be seen that both NanoMate and LC gave practically identical initial majority ions for all the b-CMs studied.

The most abundant ion obtained in the spectra of all b-CMs, when NanoMate system was used, was the protonated molecule $[M+H]^+$. However, this phenomenon only happens for b-CM-5 and -7, when LC system was used.

Sodium adducts are important, and needs to be taken into account because relative abundance ranged between 85–20% and 100–25% for NanoMate and LC systems respectively was obtained. The sodium adduct $[M+Na]^+$ was the majoritary ion for b-CM-10 and -11 not been in that way for NanoMate, where no b-CM presented the sodium adduct as majoritary ion. Otherwise some other adducts as potassium $[M+K]^+$ or two molecules of sodium added to the molecule, $[M+2Na-H]^+$ were also observed and they were taken into account for b-CM-5 and -7 analyses.

The potassium adduct was observed although in a low relative abundance, only at 10%, in b-CM-10 when LC system and NanoMate system were used and in consequence a fragmentation study with increasing collision energies was carried out, however this adduct ion did not appear for any of the other b-CMs studied, b-CM-5, -7 and -11 when NanoMate or LC system was used. The $[M+2Na-H]^+$ adduct was formed and observed in relevance only for b-CM-5 and -7 ranged from 70% to 15% of relative abundance as it was mentioned above, when LC system was used, but no $[M+2Na-H]^+$ was observed for any of the b-CM when NanoMate system was used.

Table 3 shows the MS steps achieved for each b-CM and the relative collision energy necessary to obtain the next MS step is shown in brackets. To be focused in b-CM-5 identical fragment ions are presented in all stages with LC and NanoMate system respectively, however with this last system (NanoMate) was possible to achieve one stage higher than with LC, arriving until MS^7. In Fig. 7 a fragmentation scheme of b-CM-5, the collision energy diagram (see also Fig. 8) and the MS spectra obtained are shown. However for b-CM-11, the information of the fragmentation pathway was more different when both system NanoMate and LC were compared. Likewise, only MS^3 was achieved in LC system and MS^8 when NanoMate system was used. In Figs. 9 and 8 the fragmentation scheme is shown.

In b-CM-7 the obtained ions were different between NanoMate and LC systems once MS^3 for the studied ion *m/z* 512 was obtained. For b-CM-10 the fragmentation pathway proposed allows to achieve MS^9 with NanoMate system; however, once MS^7 is achieved with LC system for this b-CM the predominant product ion was different from the same step in NanoMate. For b-CM-7 and -10 the scheme is represented in Fig. 8.

Figs. 7 and 9D also indicate and represent the relative collision energy necessary to reach each MS step. As it could be observed, in general, collision energies are higher by using LC than using NanoMate. This is the first reported study where a comparison between LC and NanoMate collision energies is carried out, the first in which high MS steps could be reached and a comparison between LC and NanoMate MS steps is done and the first reported study of the most common b-CMs to employ QIT and the CID spectra for the four compounds is shown in Fig. 3.

3.6. NanoMate/MS^n

Good linear correlations were obtained for the b-CMs in each MS mode. The selected ions (Table 2) were generated by trapping and fragmenting the product ions from the MS stage, *m/z* 580 (b-CM-5), *m/z* 790 (b-CM-7), *m/z* 659 (b-CM-10) and *m/z* 675 (b-CM-11).

The calibration data for standard b-CM, spiked into milk or cheese (10 g or 10 mL), were: NanoMate/MS (25–1000 μg/L), $r^2 = 0.998$; NanoMate/MS^2 (5–1000 μg/L), $r^2 = 0.9992$; NanoMate/MS^3 (2.5–1000 μg/L), $r^2 = 0.9998$. Good reproducibility data were obtained for b-CM using the NanoMate/MS^3 and the NanoMate/MS^4 modes, with the latter being slightly better. The relative standard deviation (% RSD) values for NanoMate/MS^5 were ≤2.0 at 500 μg/L and ≤7.0 at 10 μg/L ($N = 5$). Although valuable structural data were acquired at the MS^8 or even at MS^9 stages, using the product ions above mentioned for each b-CM for fragmentation, reproducible data were not obtained with spiked cheese and milk samples.

3.7. Analysis of the b-CMs in cheese and milk

To demonstrate the utility of this NanoMate/MS^n analytical protocol for the determination of the b-CMs, in milk and cheese samples, 20 samples were examined using each NanoMate/MS^n method. Fig. 10 shows the NanoMate/MS^3 chromatograms obtained for a milk sample from a local supermarket in Cork, Ireland. b-CM-7 was identified in this milk sample, at 14 μg/L. MS^1 to MS^4 spectra were obtained simultaneously and compared with those obtained from the isolated standard of b-CM-7 to confirm the presence of this bioactive peptide.

4. Concluding remarks

Under the hypothesized that b-CMs are the cause of sudden infant death syndrome, and that bonded to the opioid receptors could exhibits morphine-like effects and many other consequences, most of them unknown, it is necessary to develop sensitive techniques that unequivocal confirm of the presence of b-CMs in milk and cheese samples. The use of the NanoMate nanoelectrospray device enabled fast and easy analysis of b-CMs from milk and cheese sample. The infusion conditions can be adjusted very easily to the analyte in order to obtain optimal fragments for the MS experiments

QIT-ESI-MS has permitted to elucidate the main fragmentation pathways for b-CMs and structures for the major fragment ions that were observed in the mass spectra, as shown for b-CM-5 and b-CM-11.

Acknowledgements

A.J.G. thanks the Ministry of Science and Education for the FPI grant (2004FPI) and the complementary short stay grant in Spain and foreign countries for FPI recipient.

References

[1] K.J. Rutherfurd-Markwick, P.J. Moughan, J. AOAC Int. 88 (2005) 955.
[2] J. Panksepp, Trends Neurosci. 2 (1979) 174.
[3] A.M. Knivsberg, K.L. Reichelt, T. Hoien, M. Nodland, Nutr. Neurosci. 5 (2002) 251.
[4] K. Dettmer, D. Hanna, P. Whetstone, R. Hansen, B.D. Hammock, Anal. Bioanal. Chem. 388 (2007) 1643.
[5] H. Meisel, Int. Dairy J. 8 (1998) 363.
[6] B. Jarmołowska, K. Sidor, M. Iwan, K. Bielikowicz, M. Kaczmarski, E. Kostyra, H. Kostyra, Peptides 28 (2007) 1982.
[7] Y. Elistur, G.D. Luk, Clin. Exp. Immunol. 85 (1991) 493.
[8] S.J. Bell, G.T. Grochoski, A.J. Clarke, Crit. Rev. Food Sci. 46 (2006) 93.
[9] J. Hau, L. Bovetto, J. Chromatogr. A 926 (2001) 105.
[10] M.R. Muehlenkamp, J.J. Warthesen, J. Diary Sci. 79 (1999) 20.
[11] S.S. Haileselassie, B.H. Lee, B.F. Gibbs, J. Diary Sci. 82 (1999) 1612.
[12] S.V. Silva, F.X. Malcata, Int. Dairy J. 15 (2005) 1.
[13] Z. Sun, Z. Zhang, X. Wang, R. Cade, Z. Elmir, M. Fregly, Peptides 24 (2003) 937.
[14] I. Losito, T. Carbonara, M.D. De Bari, M. Gobbetti, F. Palmisano, C.G. Rizzello, G. Zambonin, Rapid Commun. Mass Spectrom. 20 (2006) 447.
[15] J. Léonil, V. Gagnaire, D. Mollé, S. Pezennec, S. Bouhallab, J. Chromatogr. A 881 (2000) 1.
[16] H.F. Alomirah, I. Alli, Y. Konishi, J. Chromatogr. A 893 (2000) 1.
[17] A. Juan-García, G. Font, Y. Picó, Electrophoresis 28 (2007) 4180.
[18] A. Juan-García, G. Font, Y. Picó, Electrophoresis 27 (2006) 2240.
[19] A. Furey, J. Crowley, M. Lehana, K.J. James, Rapid Commun. Mass Spectrom. 17 (2003) 583.

Talanta 80 (2009) 307–312

Contents lists available at ScienceDirect

Talanta

journal homepage: www.elsevier.com/locate/talanta

Enhancement of sensitivity and specificity of the fluoroimmunoassay of Hepatitis B virus surface antigen through "flexible" coupling between quantum dots and antibody

Qinghui Zeng[a,b], Youlin Zhang[a,c], Kai Song[a], Xianggui Kong[a,*], Maurice C.G. Aalders[d], Hong Zhang[c,**]

[a] Key Laboratory of Excited State Processes, Changchun Institute of Optics, Fine Mechanics and Physics, Chinese Academy of Sciences, 16 Eastern South Lake Road, Changchun 130033, China
[b] Graduate School of Chinese Academy of Sciences, Beijing 100039, China
[c] Van't Hoff Institute for Molecular Sciences, University of Amsterdam, Nieuwe Achtergracht 166, 1018 WV Amsterdam, The Netherlands
[d] Department of Biomedical Engineering and Physics, Academic Medical Centre, University of Amsterdam, Meibergdreef 9, 1105 AZ Amsterdam, The Netherlands

ARTICLE INFO

Article history:
Received 30 March 2009
Received in revised form 13 June 2009
Accepted 29 June 2009
Available online 4 July 2009

Keywords:
CdTe/CdS core/shell quantum dots
Protein G
Flexible coupling
Fluorescent immune detection
Specificity

ABSTRACT

Quantum dots (QDs) are widely used in the immune detection. Yet, the sensitivity and specificity of the immune detection are not satisfactory because the binding sites of QDs onto antibody (Ab) are often arbitrary and the influence of the large surface electronic potential energy of QDs on the directly conjugated Ab is nonnegligible. In this work, we provide a "flexible" coupling method, in which protein G (PG) is selected as the flexible bridge between the QDs and the Hepatitis B virus surface antibody (HBsAb), to improve the sensitivity and specificity of the fluoroimmunoassay compared to the directly covalent conjugation. Successful coupling of the HBsAb to our highly luminescent CdTe/CdS core/shell QDs is proven with Gel electrophoresis and atomic force microscopy (AFM). The assay results, based on the microelisa well plate as matrix to immobilize the sandwich structure, show that both sensitivity and specificity can be improved greatly through the flexible coupled QDs–PG–Ab conjugates.

© 2009 Published by Elsevier B.V.

1. Introduction

Quantum dots (QDs) hold immense promise for optoelectronical and biological/biomedical applications due to their unique optical properties, such as size-tunable photoluminescence (PL), high PL quantum yields (QY), narrow emission line width, broad absorption profile, superior photostability, and flexible solution-processing [1–3]. Compared to organic fluorophores, the QDs also have high resistance to chemical degradation and photodegradation [4]. The number of publications on applications of QDs in bio-labeling and bio-detection has increased enormously during the recent years [3,5–12]. Attempt of in vivo applications, e.g., cell-imaging with the glutathione capped CdTe QDs has been reported [7]. In the mean time, focus has been given on in vitro applications based on the toxicity concern of the QDs. Mattoussi's group reported the detection of pathogens by using the conjugates of dihydrolipoic acid capped CdSe/ZnS QDs and the recombinant maltose binding protein [8,9]. Peng et al. improved the sensitivity of pathogens detection to be as low as 5 ng/ml via CdSe/ZnS dendron QDs and a porous membrane immunofilter [10]. In spite of these efforts, the large surface electronic potential energy and the resulting influence of the QDs on the antibody (Ab) are still large, which will ultimately reduce the immunoreactivity and increase the nonspecific binding of the labeled antibody. This disadvantage will be reduced by applying "flexible" coupling where a proper soft bridge is built up providing a single coupled site to the Ab and the single site linkage can minimize the orientation alteration of the Ab, thus maintaining its native immunoreactivity.

The biotin–avidin system (BAS) has been widely applied in the bio-conjugation of QDs and proteins as a "bridge" [4,8]. However, this requires the antibody (or antigen) to be conjugated to biotin molecules, the non-epitaxial conjugation will finally sacrifice the sensitivity and specificity of the bio-detection. It is well known that the Fab fragments of the antibody contain the antigen binding regions. And protein G (PG) is an immunoglobulin-binding protein expressed in group C and G streptococcal bacteria. It is a cell surface protein that has found application in purifying or coupling antibodies because the $\beta 2$ domain of PG can bind strongly with the Fc fragment of the antibody [9]. The fluorescent labels can thus be connected to the antibodies through protein G – a "flexible bridge" – without occupying the Fab domain and influencing the bio-specificity of the Ab. Early in 2002, Mattoussi et al. reported the detection of explosive 2,4,6-trinitrotoluene with conjugates of

* Corresponding author. Tel.: +86 431 86176313.
** Corresponding author. Tel.: +31 20 5256976.
E-mail addresses: xgkong14@ciomp.ac.cn (X. Kong), h.zhang@uva.nl (H. Zhang).

0039-9140/$ – see front matter © 2009 Published by Elsevier B.V.
doi:10.1016/j.talanta.2009.06.061

QDs and a specific antibody using PG as a bridge [13], however, they did not give a systematical discussion and manifestation on the high-specificity of the fluoroimmunoassay. In this work, flexible conjugation is realized by covalently coupling carboxylic highly luminescent aqueous CdTe/CdS core/shell QDs with PG to form a QDs–PG complex which is then bounded to the antibodies. The effect on the specificity and sensitivity of detection based on the sandwich structure is studied with choosing microelisa well plate as the matrix for antibody immobilization. As far as virus is concerned we have chosen Hepatitis B virus (HBV)—known to be one of the leading causes of death worldwide [14]. In our experiments, Hepatitis B surface antigen (HBsAg) are detected with much lower detect limitation and non-specificity when the flexible coupling is realized of the HBsAb with highly luminescent CdTe/CdS QDs.

2. Experimental

2.1. Materials

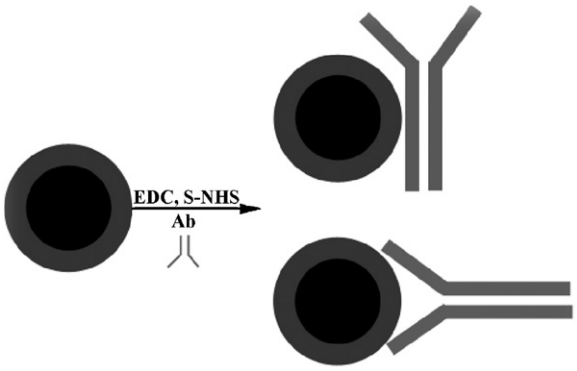
1-Ethyl-3-(3-dimethylaminopropyl) carbodiimide hydrochloride (EDC) (99%), sulfo-N-hydroxysulfosuccunimide (sulfo-NHS) (98.5%), aminopropyltriethoxysilane (APTES) (98%) and glutaraldehyde (Glu) were purchased from Aldrich. Protein G, HBsAb, HBsAg, Bovine serum albumin (BSA) and the microelisa well plate were all subscribed from Beijing DingGuo Biotechnology co. Ltd. All the reagents were used without further purification. Deionized water was purified through Milli-Q water purification system and the resistivity was 18.2 MΩ cm.

2.2. Apparatus

Ultraviolet–visible (UV–vis) absorption and fluorescence spectra were measured at room temperature (RT) by a UV-3101 spectrophotometer and a Hitachi F-4500 fluorescence spectrofluorimeter, respectively. Unless claimed otherwise, the excitation wavelength was set to 350 nm and the excitation and emission splits are 5 nm. The QY of nanocrystal solutions was determined using Rhodamine 6G in ethanol as a standard. The sizes and concentration of CdTe QDs were calculated based on the wavelength of the first excitonic absorption peak [15]. The photo-irradiation experiments were performed under ambient condition and irradiation from a 365 nm ultraviolet lamp at certain time intervals. The samples were prepared by the 1:200 dilution of a stock solution.

2.3. Synthesis of highly luminescent CdTe/CdS core/shell QDs

CdTe/CdS core/shell QDs were prepared according to our previous publication [16]. The CdTe QDs were capped with 2 monolayers (ML) of CdS shell with a 530 nm emission and QY of 40%. The average size of the aqueous core–shell QDs was calculated to be only about 3 nm, which successfully discards the drawback of the large size (12–20 nm) water-soluble QDs after the multilayer coating, e.g., phospholipids [17], silica [2,18], or polymer [19,20], etc. This is because that the small dimension would dramatically improve the biological labeling and detection efficiency.



Scheme 1. Covalent conjugation of CdTe/CdS QDs and HBsAb.

2.4. Conjugation of antibody onto CdTe/CdS QDs

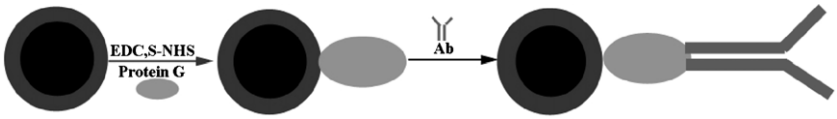
The HBsAb was conjugated to the CdTe/CdS QDs classically by using EDC and sulfo-NHS (S-NHS) as crossing-linking reagent [10]. The schematic route of the conjugation is shown in Scheme 1. Firstly, 0.1 ml of QDs (60 μM) was mixed with 10 μl of EDC and sulfo-NHS in phosphate buffer saline (PBS, pH 7.4) with the molar ratio of 1:100:200. After 30 min of magnetic stirring, 3 nmol HBsAb was added into the reacted bottle and stirred at room temperature for another 2 h. In this way, the amide linkage can be formed through the amino of the Ab and the active carboxyl of QDs. In order to remove the excess small molecules, e.g., EDC and sulfo-NHS, the resulting samples were centrifuged in Microcon Centrifugal Filter Devices (50,000 Nominal Molecule Weight Limit). Afterwards, the product was purified by sephadex-150 filtration column chromatography. The conjugation of Ab and QDs was confirmed by the agarose gel (0.8%) electrophoresis technique.

2.5. Flexible conjugation of antibodies onto CdTe/CdS QDs

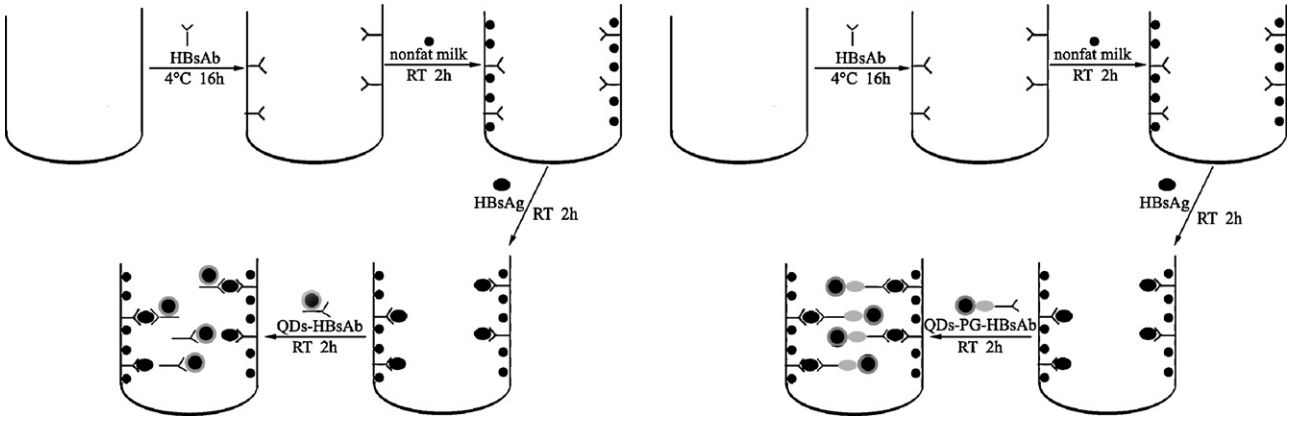
The HBsAb was conjugated with QDs flexibly by using protein G as a bridge. Firstly, the PG was covalently linked with QDs by an EDC-mediated coupling reaction as described above. Then the complex was purified by centrifugation in Microcon Centrifugal Filter Devices (50,000 Nominal Molecule Weight Limit). Afterwards, the HBsAb was added into the QDs–PG PBS solutions with equal molar ratio under stirring for 2 h. Because the $\beta 2$ domain of protein G can bind with the Fc domain of the Ab specially, the Ab can be oriented as shown in Scheme 2. The product was then purified by sephadex-150 filtration column chromatography to separate the by-products and the excessive QDs. The conjugation of Ab and QDs was also confirmed by the agarose gel (0.8%) electrophoresis technique.

2.6. Fluorescent immune detection

As depicted in Scheme 3, firstly, 200 μl designed amount of monoclonal HBsAb was planted into the transparent microelisa well plate and incubated at 4 °C for about 16 h. Then, the solution was discarded away and 200 μl 5% (w/v) nonfat powdered milk in PBS was added into the well to block the plates. After 2 h of blocking time at RT, the nonfat dried milk solutions were also discarded and the wells were rinsed with PBS for 3 times. Afterwards, 200 μl series of



Scheme 2. Flexible coupling of CdTe/CdS QDs and HBsAb by using PG as a bridge.



Scheme 3. Immune microelisa well plate detection route of HBsAg based on the normal (left) and flexible (right) coupling of HBsAb and QDs.

dilutions of HBsAg solutions were dropped into the well for about two hours' specific adsorption reaction and then the solutions were removed again and rinsed with PBS for 3 times. Control well was always included in which no HBsAg was added to capture the Ab adsorbed on the walls of the wells. At last, the designed concentration of QDs labeled HBsAb was added into the well and reacted specifically with HBsAg for 2 h. The solutions were taken out for additional PL measurement to obtain the detection curves.

2.7. AFM measurement

The atomic force microscopy (AFM) (Veeco Instrument, DI-3100) was measured via immobilizing the QDs labeled Ab covalently onto the silicon slice to evaluate the flexible coupling. Tapping mode silicon probe with spring constants of ~180 N/m and resonance frequencies of ~1 kHz was used. Prior to silanization, the silicon slice surface was pre-cleaned by treatment in $HCl:CH_3OH = 1:1$ solution, followed by strong vitriol for 30 min and being boiled for 10 min, then extensive rinsing with deionized water, and were stored in 25% ethanol. Chemically cleaned silicon slice surface was reacted with an acetone solution of APTES for 90 min at RT, followed by rinsing several times with acetone, and dried with nitrogen flowing and baked for 2 h at 120 °C in a vacuum oven. Finally, the APTES-treated silicon slice was immersed in the 10% solution of glutaraldehyde in PBS (pH 7.4) for 2 h, followed by rinsing with PBS (pH 7.4). QDs labeled Ab was immobilized on the APTES-Glu surface by incubation at 4 °C with an aqueous solution overnight. The QDs labeled Ab was covalently immobilized on this surface by an imine linkage between the aldehyde group on surface and primary amine of the Ab. The images were obtained in air after drying the samples in a gentle stream of nitrogen.

3. Results and discussion

The absorption and emission spectra of bare CdTe and CdTe/CdS core/shell QDs are shown in Fig. 1a, the calculated QY of the CdTe QDs increases from 15 to 40% after growing 2 monolayers CdS shell. The photo-irradiation experiments of the diluted samples (0.3 μM) were performed under ambient condition and irradiation from a 365-nm ultraviolet lamp at certain time intervals. It is reported that the PL peak will shift to blue side with time under ultraviolet light irradiation due to photo-oxidation reaction of the diluted samples [21]. In our experiments, a blue-shift of 39.6 nm of the PL spectrum of the CdTe bare core is observed after four hours' photo-irradiation, however, the blue-shift of the CdTe/CdS core/shell QDs is only 2.8 nm under the same conditions (cf Fig. 1b). In fact, these aqueous core/shell QDs are found to be stable and the optical properties of them in a sealed vial remain invariable over one year's storage under ambient condition. Therefore the core/shell QDs are capable to act as the fluorescent marker in the immunoassay.

In order to purify the QDs–Ab complexes and investigate the combination of proteins and CdTe/CdS QDs, the sephadex G-150

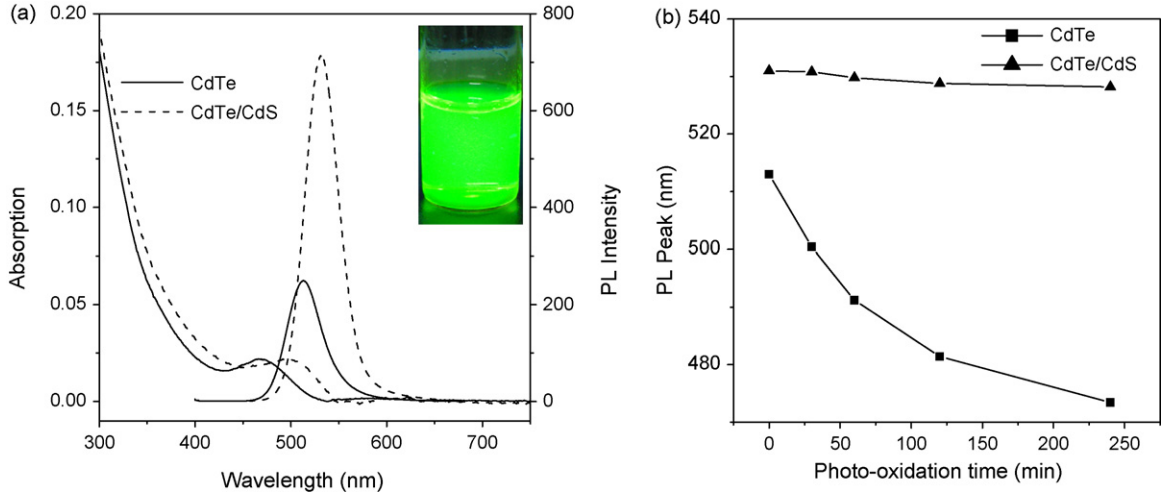


Fig. 1. (a) Absorption and PL spectra of CdTe (solid line) and CdTe/CdS (dashed line) QDs. Inset shows the photo of the CdTe/CdS core/shell QDs under an ultraviolet lamp irradiation. (b) Time-evolution of the blue-shift of the PL peak positions of diluted CdTe and CdTe/CdS samples under the photo-irradiation of a 365-nm ultraviolet lamp.

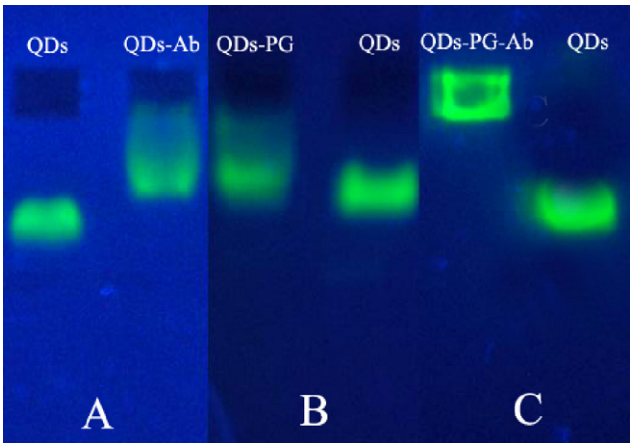


Fig. 2. The digital photos of the QDs-based AGE gel electrophoresis for probing the proteins under the excitation of a 365-nm ultraviolet lamp. (A) Photo shows AGE electrophoresis of the QDs and QDs–Ab. (B) photo shows AGE electrophoresis of the QDs and QDs–PG. (C) photo shows AGE electrophoresis of the QDs and QDs–PG–Ab.

gel filtration column chromatography is employed. After collection of first peaks, QDs–Ab and QDs–PG–Ab are collected and condensed for the next electrophoresis and detection experiment. In general, electrophoretic analysis can be used to confirm the conjugation of biomolecules to QDs [22,23]. The agarose gel electrophoresis (AGE) technique is applied here to further identify the bio-conjugation of QDs and proteins. Because the COOH-QDs carry a high negative charge density, they migrate quickly through the gel matrix under an electric field. The mobility of the proteins in electrophoresis is determined by the mass/charge ratio of proteins. As shown in Fig. 2, the green luminescence bands of QDs and QDs labeled proteins are observed under the excitation of a 365-nm ultraviolet lamp. Because the sizes (equal to the mass/charge ratio) of QDs–Ab, QDs–PG and QDs–PG–Ab bio-conjugates are larger than the QDs, they all migrate more slowly than pure QDs and separate well in 0.8% agarose gels, which strongly suggests the presence of the corresponding conjugates. Considering that PG is a kind of small molecular protein than HBsAb, the electrophoretic mobility of QDs–PG is slightly slower than that of QDs (Fig. 2B) and faster than that of QDs–Ab (Fig. 2A). The fluorescent band of QDs–PG–Ab migrates most slowly (Fig. 2C), which is due to the fact that the highest molecular-weight QDs–PG–Ab complexes have formed.

AFM is a powerful technique for studying biomolecule interactions and it provides topographic images with high resolution [24]. The AFM imaging has previously been used to characterize the size of QDs [25]. In this work, AFM imaging is used to demonstrate the success in flexible conjugation of the QDs to Ab based on the fact that the height of the flexible coupling should be higher compared to that of the normal covalent coupling. In order to keep the proteins stable on the silicon surface, covalent immobilization is a preferred method. APTES surfaces are used to immobilize the proteins covalently, because the amido groups on their surfaces can react with glutaraldehyde, yielding aldehyde groups that could form an imine linkage with the primary amine groups on the surface of the proteins. The size of a protein measured from AFM is directly correlated to its molecule weight [26]. Hence, AFM can be used to study the binding behavior of Ab to QDs. Fig. 3 is the AFM image of QDs–Ab and QDs–PG–Ab bio-conjugates. Because the binding sites of QDs onto Ab are arbitrary, the conformational dimension of QDs–Ab complex must be tanglesome. On the contrary, the conformational dimension of QDs–PG–Ab complex should be uniform. In our image, the QDs–Ab exhibits a heterogeneous and dissymmetrical shape with the AFM height of approximately 6–8 nm, and reversely, the QDs–PG–Ab exhibits a homogeneous and symmetrical shape with the AFM height of approximately 10–12 nm. Considering that the sizes of QDs, Ab and PG are 3, 7 and 3 nm, respectively, the result from AFM match closely with the heights of QDs–Ab and QDs–PG–Ab with only a few nanometers less, and this shortening can be ascribed to the fact that Ab protein molecules on QDs surface can be compressed by the imaging process due to forces applied to the samples [27,28]. In line with this idea, the average AFM heights of QDs–Ab and QDs–PG–Ab are a little smaller than the estimated ones. In any case, the height of QDs–PG–Ab is obviously higher than that of QDs–Ab, which can be used to efficiently testify the flexible coupling between QDs and Ab via PG bridges.

The fluorescent immune detection is based on the sandwich method with bright and robust CdTe/CdS QDs as the indicator. In order to enhance the efficiency of the immunoreaction between Ab and Ag, shorten the detection time, and reduce the detection limit, the flexible coupling based immunoassay is employed with microelisa well plate as the matrix. The microelisa well plate can provide a large surface area for protein immobilization and proper-sized pores in the plate to force the immunoreaction between Ab and Ag in a limited space that is small but sufficiently large for the volume of the sample solution. In order to immobilize the Ab sufficiently, the adsorption time of the Ab on the pores should be enough (not less than 12 h). The detecting signal of the HBsAg is based on measuring the subtraction between the PL intensity of the control value of the QDs–Ab without any Ag injection and the value of the excessive unreacted QDs–Ab on the sandwich immunoplexes of the wells. The schematic bio-detection of HBsAg by using the microelisa well plate is given in Scheme 3, whereas Fig. 4 illustrate the PL spectra of the normal coupling (QDs–Ab) and flexible coupling (QDs–PG–Ab) with different concentrations of the HBsAg. Fig. 4C and D show the experimental results where

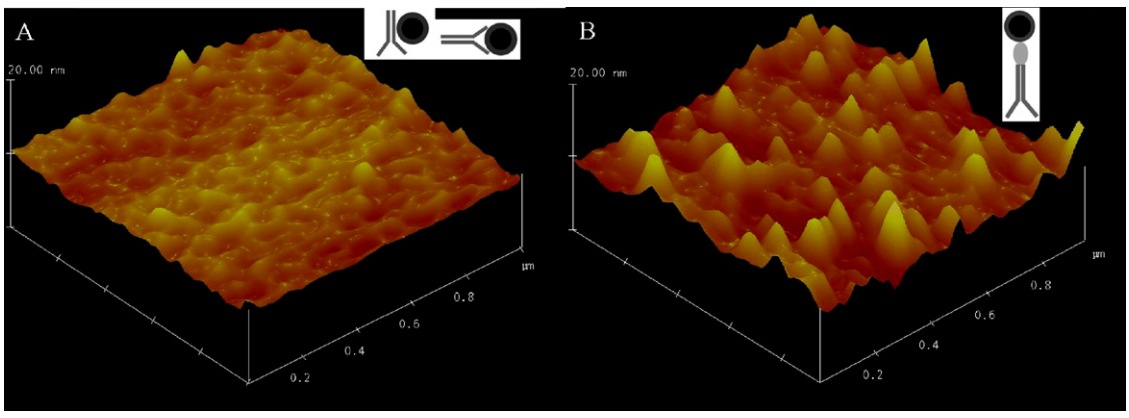


Fig. 3. AFM images of the complexes of QDs–HBsAb (A) and QDs–PG–HBsAb (B).

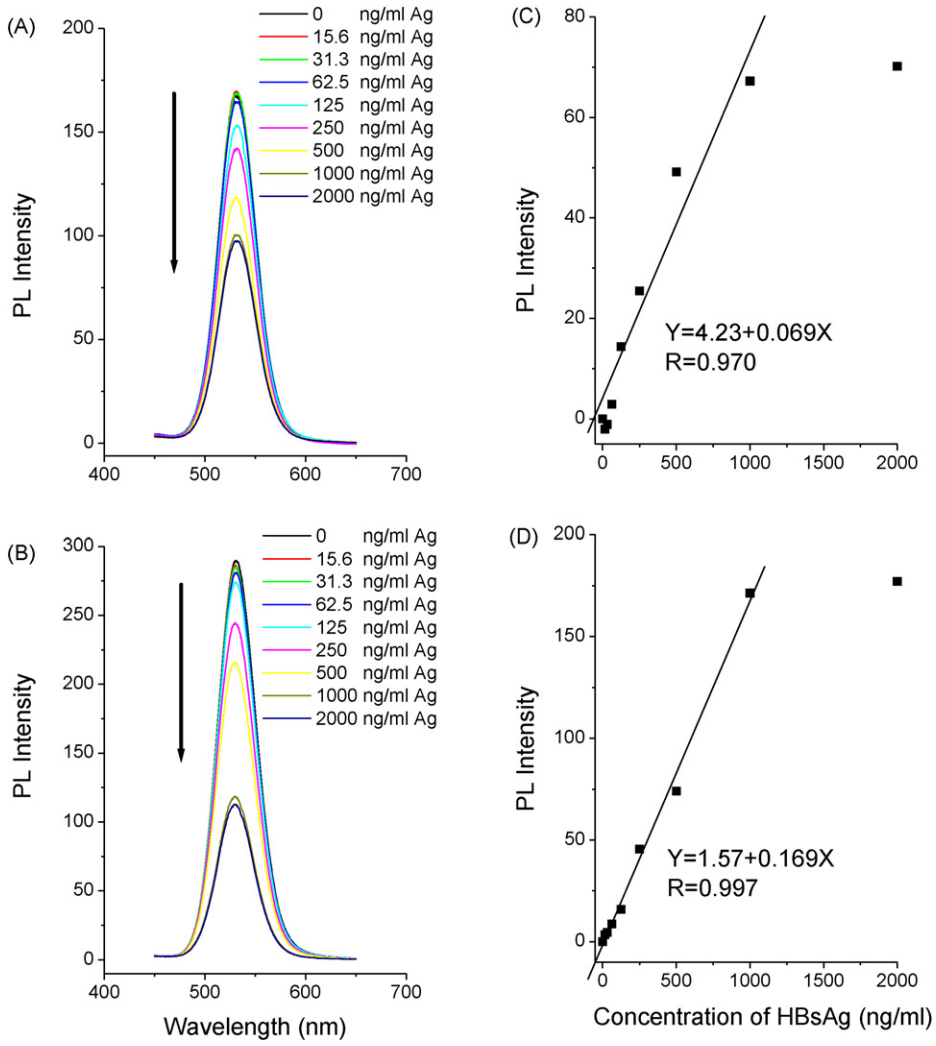


Fig. 4. PL spectra (A and B) and the detection curves (C and D) of the PL intensity vs the concentration of HBsAg. A and C show the results based on the normal coupling product of QDs–Ab, B and D show the results based on the flexible coupling product of QDs–PG–Ab. C and D are the PL intensity difference between control (without antigen) and the sample (with antigen). The fitted linear equations are also shown.

the PL intensity from bound HBsAb conjugate is measured over a range of HBsAg concentration till 2000 ng/ml. It should be noted that the signal increases monotonically with the increase of the concentration of HBsAg until saturation is reached at ~1000 ng/ml. The detection limit can be defined as the lowest concentration of detected sample that give positive value of the PL intensity difference between control (without antigen) and detected sample (with antigen) [4,13]. It can be clearly seen from Fig. 4 that the subtracted PL intensity is still discernable to be positive even when the concentration of HBsAg is as low as 62.5 ng/ml for normal conjugation and 15.6 ng/ml for flexible conjugation, which indicates that the sensitivity of detection is improved due to flexible coupling. The lower detection limit and broad working range in the flexible situation result from high capturing efficiency of QDs with the microelisa well plate. The higher capturing efficiency is due to the flexible coupling of QDs and Ab (as shown in Scheme 2) which enables sufficiently mutual affinity between QDs labeled HBsAb and the HBsAg immobilized onto the pores of the well plates. On the contrary, the normal coupling are commonly accompanied with certain non-efficient conjugation by occupying the specific site or influencing the bioactivity of the Ab (as shown in Scheme 1), which will reduce the ability of the recognition between the QDs labeled Ab and the detected Ag consequently and result in a lower detection sensitivity.

The specificity of an immunoassay system mainly depends on the immunoreactivity of the labeled monoclonal Ab. However, due to the larger surface electronic potential energy of the nanocrystals, the property of the Ab can be easily manipulated by the nature of the fluorescence labels. PG acts as a “flexible bridge” for connecting the QDs with Ab to avoid the non-specific and null combination, and thus to increase the specificity of the immunoassay. As is shown in Fig. 4C, detect signal shows negative value at certain low cencentrations, which is not observed in Fig. 4D. The negative value is mainly a consequence of the non-specific adsorption between QDs–Ab and the blocking molecules immobilized on the wall of the well. To further validate the specificity enhancement based on the flexible coupling, a control experiment was designed by using a 1% BSA PBS solution as the detected sample. The results are given in Fig. 5, in which the PL intensity is normalized to the value of HBsAg detection. When the QDs–Ab is used to monitor the nonspecific binding of the BSA molecules, a low PL intensity can be obtained, which indicates that there is 31.5% non-specific adsorption of BSA molecules during the detection process. Comparably, when the QDs–PG–Ab is used to monitor the nonspecific binding of the BSA molecules, only a small PL signal is observed under the same detection condition, which indicates that only 2.4% non-specificity with BSA exists. Clearly the immunoassay using the QDs–PG–HBsAb conjugate is much

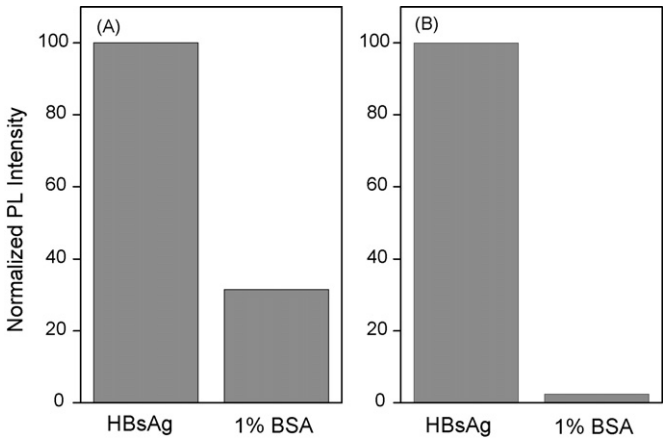


Fig. 5. The normalized PL intensity on the non-specific adsorption experiments of 1% BSA solution using the normal coupled QDs–Ab product (A) and the flexible coupled QDs–PG–Ab product (B).

more specific for HBsAg than that using the QDs–HBsAb conjugate.

4. Conclusions

Highly luminescent aqueous CdTe/CdS core/shell QDs are covalently conjugated with HBsAb and PG by using EDC and S-NHS as cross-linking reagents. The flexible coupling using protein G as a bridge between the QDs and HBsAb is characterized by the gel electrophoresis technique and AFM measurement. The fluoroimmunoassay based on the microlisa strip plates via the conjugates of QDs and HBsAb is applied to detect the HBsAg. The detect limitation can reach about 15.6 ng/ml and 62.5 ng/ml by using the complexes of QDs–PG–Ab and QDs–Ab, respectively. In addition, the immune detection using QDs–PG–Ab conjugate shows higher specificity, accompanied with the higher sensitivity. Therefore, the flexible coupling by using PG as a bridge is feasible and the fluorescent immune detection via microelisa well plate based on the coupling of the highly luminescent aqueous CdTe/CdS QDs and biomolecules is also acceptable and can be applied into the future biological diagnosis.

Acknowledgements

This work was supported by NSFC of China (60771051, 60601015, and 10674132), the National High Technology Development Program (2006AA03Z335), and exchange program between CAS of China and KNAW of the Netherlands.

References

[1] V.L. Colvin, M.C. Schlamp, A.P. Alivisatos, Nature 370 (1994) 354.
[2] M.J. Bruchez, M. Moronne, P. Gin, S. Weiss, A.P. Alivisatos, Science 281 (1998) 2013.
[3] W.C.W. Chan, S. Nie, Science 281 (1998) 2016.
[4] E.R. Goldman, E.D. Balighian, H. Mattoussi, M.K. Kuno, J.M. Mauro, P.T. Tran, G.P. Anderson, J. Am. Chem. Soc. 124 (2002) 6378.
[5] X. Michalet, F.F. Pinaud, L.A. Bentolila, J.M. Tsay, S. Doose, J.J. Li, G. Sundaresan, A.M. Wu, S.S. Gambhir, S. Weiss, Science 307 (2005) 541.
[6] I.L. Medintz, H.T. Uyeda, E.R. Goldman, H. Mattoussi, Nat. Mater. 4 (2005) 435.
[7] Y. Zheng, S. Gao, J.Y. Ying, Adv. Mater. 19 (2007) 376.
[8] B.M. Lingerfelt, H. Mattoussi, E.R. Goldman, M. Mauro, G.P. Anderson, Anal. Chem. 75 (2003) 4043.
[9] E.R. Goldman, A.R. Clapp, G.P. Anderson, H.T. Uyeda, J.M. Mauro, I.L. Medintz, H. Mattoussi, Anal. Chem. 76 (2004) 684.
[10] Y. Liu, R. Brandon, M. Cate, X. Peng, R. Stony, M. Johnson, Anal. Chem. 79 (2007) 8796.
[11] Y. Shan, L. Wang, Y. Shi, H. Zhang, H. Li, H. Liu, B. Yang, T. Li, X. Fang, W. Li, Talanta 75 (2008) 1008.
[12] J. Yuan, W. Guo, J. Yin, E. Wang, Talanta 77 (2009) 1858.
[13] E.R. Goldman, G.P. Anderson, P.T. Tran, H. Mattoussi, P.T. Charles, J.M. Mauro, Anal. Chem. 74 (2002) 841.
[14] A.H. Malik, W.M. Lee, Ann. Intern. Med. 132 (2000) 723.
[15] W.W. Yu, L.H. Qu, W.Z. Guo, X.G. Peng, Chem. Mater. 15 (2003) 2854.
[16] Q. Zeng, X. Kong, Y. Sun, Y. Zhang, L. Tu, J. Zhao, H. Zhang, J. Phys. Chem. C 112 (2008) 8587.
[17] B. Dubertret, P. Skourides, D.J. Norris, V. Noireaux, A.H. Brivanlou, A. Libchaber, Science 298 (2002) 759.
[18] S.T. Selvan, T.T. Tan, J.Y. Ying, Adv. Mater. 17 (2005) 1620.
[19] X. Gao, Y. Cui, R.M. Levenson, L.W.K. Chung, S. Nie, Nat. Biotechnol. 22 (2004) 969.
[20] D.R. Larson, W.R. Zipfel, R.M. Williams, S.W. Clark, M.P. Bruchez, F.W. Wise, W.W. Webb, Science 300 (2003) 1434.
[21] L. Spanhel, M. Haase, H. Weller, A. Henglein, J. Am. Chem. Soc. 109 (1987) 5649.
[22] F. Pinaud, D. King, H.P. Moore, S. Weiss, J. Am. Chem. Soc. 126 (2004) 6115.
[23] T. Pons, H.T. Uyeda, I.L. Medintz, H. Mattoussi, J. Phys. Chem. B 110 (2006) 20308.
[24] Y. Yang, H. Wang, D.A. Erie, Methods 29 (2003) 175.
[25] A. Wolcott, D. Gerion, M. Visconte, J. Sun, A. Schwartzberg, S. Chen, J.Z. Zhang, J. Phys. Chem. B 110 (2006) 5779.
[26] G.C. Ratcliff, D.A. Erie, J. Am. Chem. Soc. 123 (2001) 5632.
[27] J.H. Hoh, C.A. Schoenenberger, J. Cell Sci. 107 (1994) 1105.
[28] H. Wang, I. Tessmer, D.L. Croteau, D.A. Erie, B.V. Houten, Nano Lett. 8 (2008) 1631.

Talanta 80 (2009) 313–320

Contents lists available at ScienceDirect

Talanta

journal homepage: www.elsevier.com/locate/talanta

Integration of microfiltration and anion-exchange nanoparticles-based magnetic separation with MALDI mass spectrometry for bacterial analysis

Shuping Li [a], Zhongxian Guo [a,*], Ying Liu [a], Zhaoguang Yang [a], Hui Kim Hui [b]

[a] Center for Advanced Water Technology, Public Utilities Board, 82 Toh Guan Road East, WaterHub, #C4-03, Singapore 608576, Singapore
[b] Institute of Materials Research and Engineering, Agency for Science, Technology and Research (A*STAR), 3 Research Link, Singapore 117602, Singapore

ARTICLE INFO

Article history:
Received 11 May 2009
Received in revised form 28 June 2009
Accepted 29 June 2009
Available online 7 July 2009

Keywords:
Bacterial analysis
MALDI mass spectrometry
Functionalized nanoparticles
Water analysis
Membrane filtration

ABSTRACT

Matrix-assisted laser desorption ionization mass spectrometry (MALDI-MS) is powerful in characterizing and identifying bacterial isolates. However, sufficient quantities of bacterial cells are required for generating MALDI mass spectra and a procedure to isolate and enrich target bacteria from sample matrix prior to MALDI-MS analysis is often necessary. In this paper, anion-exchange superparamagnetic nanoparticles (NPs), i.e., fluidMAG-DEAE and fluidMAG-Q, were employed to capture *Aeromonas*, *Salmonella*, *Pseudomonas*, *Enterococcus*, *Bacillus*, *Staphylococcus* and *Escherichia coli* from aqueous solutions and fresh water. The magnetically isolated bacteria were then characterized by whole cell MALDI-MS. The capture efficiency was found to be dependent on bacterial species, medium pH, the functional group and concentration of the NPs. The experimental results demonstrated that fluidMAG-DEAE and fluidMAG-Q were broad spectrum probes for bacteria. Furthermore, both dead and live bacteria could be captured by the NPs, and the live bacteria captured remained viable. Membrane filtration prior to the magnetic isolation could increase enrichment factor and eliminate potential matrix interference. A detection limit of 1×10^3 cfu/ml was achieved for the bacteria spiked in tap water and reservoir water, and the analytical time was around 2 h.

© 2009 Elsevier B.V. All rights reserved.

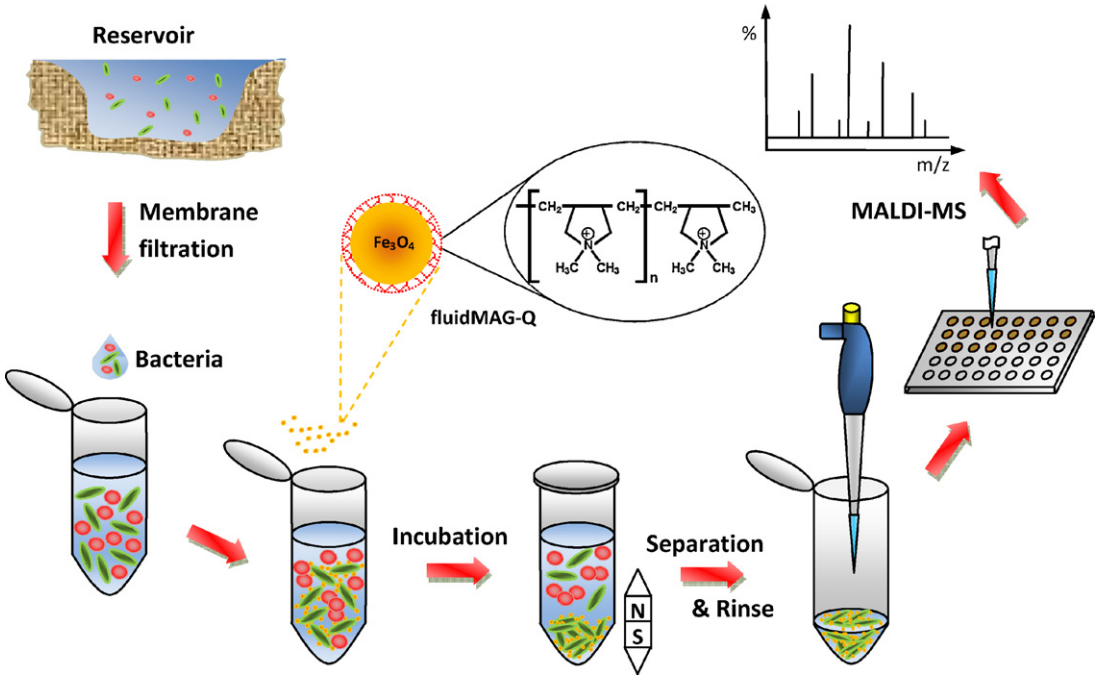
1. Introduction

Pathogenic bacteria are often found in clinical isolates, spoiled food and contaminated water. Some of them are considered as potential bioterrorism agents [1]. Rapid identification of bacteria is important for surveillance, prevention and control of disease outbreaks. MALDI-MS has become a powerful technique for rapid characterization and identification of microorganisms, especially bacteria [2–14]. In whole cell MALDI-MS, characteristic mass spectral fingerprints of bacteria can be employed for bacterial identification [9,14]. The mass spectrum of an isolate can be searched against a well-established mass spectral library of bacterial strains following an appropriate preparation protocol. The comparison will produce the most matching results as well as related evaluation. However, sufficient amount of bacterial cells (typically, $\sim 10^4$ cells per MALDI well) are required to generate MS signals, and a time-consuming culture step is often involved. In contrast, preconcentration of target bacteria from a big sample volume to a small volume provides a much faster alternative to increase the levels of bacterial cells [15]. A combination of enriching/isolating technique and MALDI-MS has been demonstrated as an efficient strategy for accurate identification of target bacteria. For example, immobilized lectins on different substrates [16–18], antibodies coated magnetic beads [19–22], immunoglobulin- [23], vancomycin- [24] or pigeon ovalbumin-conjugated magnetic nanoparticles (NPs) [25] have been used as affinity probes to capture bacteria from food, clinical, biological and environmental samples. Compared with common separation techniques, such NPs-based magnetic separation is rapid and simple. However, specific affinity separation has a limitation in the enrichment of unknown target bacterial species.

Magnetic ion-exchange microparticles and NPs have previously been applied in cell- and drug-targeting experiments, gene transfection studies, and novel DNA extraction [26]. It is interesting to note that anion-exchange particles are potentially non-selective ligands to bacteria since the outer membranes of bacterial cells are generally negatively charged [27]. With such a merit, magnetic separation of bacteria could be carried out [28]. In this paper, we proposed to study the interaction of anion-exchange magnetic NPs, i.e., fluidMAG-DEAE and fluidMAG-Q [29], with several genera of bacteria and the potential to use them to enrich and isolate bacteria. *Escherichia coli*, *Aeromonas*, *Salmonella*, *Pseudomonas*, *Staphylococcus*, *Enterococcus* and *Bacillus* strains were used as target bacteria. Furthermore, we integrated membrane filtration, magnetic isolation and whole cell MALDI-MS for rapid analysis of bacteria in tap water and reservoir water.

* Corresponding author. Tel.: +65 63262925; fax: +65 63262936.
E-mail address: Guo_Zhongxian@pub.gov.sg (Z. Guo).

0039-9140/$ – see front matter © 2009 Elsevier B.V. All rights reserved.
doi:10.1016/j.talanta.2009.06.069



Scheme 1. The process employed for bacterial separation and MALDI-MS characterization.

2. Experimental

2.1. Materials and bacteria

FluidMAG-DEAE and fluidMAG-Q NPs (particle size, 250 nm; particle weight, 50 mg/ml; particle number, 1.1×10^{14} g^{-1}; density, 1.25 g/ml) and MagnetoPURE magnetic separator were purchased from Chemicell (Berlin, Germany). α-Cyano-4-hydroxycinnamic acid (CHCA), 3,5-dimethoxy-4-hydroxycinnamic acid (sinapinic acid, SA, for MALDI-MS), acetonitrile (HPLC grade) and trifluoroacetic acid (TFA, ≥99%, for protein sequencing) were obtained from Sigma (St. Louis, MO, USA). Deionized (DI) water (18.2 MΩ cm) from a Milli-Q Plus pure water system (Millipore, Bedford, MA, USA) was autoclaved before use.

All bacterial strains used in this study were purchased from the National Collection of Type Cultures (NCTC), UK, and the American Type Culture Collection (ATCC), USA. Table S1 of the Supplementary material lists the details of the strains used. Pure strains were cultured on Columbia blood agar (CBA) plates (Oxoid, Basingstoke, UK) for 24 h at 37 °C. Plate counting was used to check concentrations of bacteria in suspensions [30]. Phosphate-buffered saline (PBS) was used to dilute bacterial samples. All microbiological procedures were carried out in a Biosafety Level 2 cabinet (Nuaire, Plymouth, MN, USA).

2.2. MALDI plate preparation for direct bacterial analysis

A few bacterial colonies were harvested from a CBA plate with a sterilized loop and placed in a microcentrifuge tube with 2 ml of DI water. The suspension was vortexed for 1 min and centrifuged at 8000 rpm for 5 min. The pellets were washed twice with DI water and re-suspended in 20 μl of DI water. One microliter of the bacterial suspension was deposited into a well of a MALDI plate (12 wells for a sample), air-dried and overlaid with 1 μl of SA (10 mg/ml in 7:3 acetonitrile–0.1% TFA). The MALDI plate was air-dried again prior to MALDI-MS running.

2.3. Microfiltration and magnetic separation of bacteria

Scheme 1 represents the process of the separation and MALDI-MS analysis of bacteria in water. A portion of tap water or reservoir water sample was first filtered through a cellulose nitrate membrane (0.45-μm pore size, 47-mm diameter) under negative pressure. After filtration, the membrane was transferred into a test tube. It was washed with PBS (1 ml × 2) with gentle vortex for 1 min. The supernatant was transferred to a microcentrifuge tube and incubated with 2.5 μl of fluidMAG-Q or 5.0 μl of fluidMAG-DEAE for 30 min with gentle vortex. The tube was then seated with a MagnetoPURE magnetic separator for a few minutes to separate the NPs-bacteria aggregates from the liquid. The supernatant was removed by pipetting carefully. The isolated NPs-cell aggregates were washed with DI water (200 μl × 3) to remove unbound impurities. Subsequently, the NPs-bacterial cell aggregates were re-suspended in 20 μl of DI water. One microliter of the suspension was deposited into a MALDI well, overlaid with 1 μl of SA solution and air-dried for MALDI-MS analysis.

2.4. Instrumentation

All MALDI mass spectra were obtained at the *m*/*z* range of 1000–20,000 using a Micro MX MALDI time-of-flight mass spectrometer (Waters Micromass, Manchester, UK) equipped with a 337-nm nitrogen laser beam (maximum 350 μJ) and a 96-well MALDI target plate. The system had a mass accuracy (RMS error) of ≤300 ppm (using linear external calibration) and a mass resolution of ≥1000 for cytochrome *c* (MH^+ 12361) in linear positive mode. MALDI-MS analyses of whole cell bacteria were conducted in linear positive mode. The accelerating voltage was set to 12,000 V while the laser radiation, pulse voltage and detector voltage were adjusted to obtain good resolutions and high intensities. The raw data was processed with MassLynx 4.0. A JEM-2100 transmission electron microscope (TEM) (JEOL, Tokyo, Japan) was employed to obtain TEM images of the NPs after trapping the bacteria.

3. Results and discussion

3.1. Optimization of the MALDI-MS analysis conditions

A number of researchers [8,9,11,13] have found that experimental factors can influence mass spectral characteristics, signal intensity and reproducibility of whole cell MALDI-MS to different extents. Hence, optimizing experimental parameters can produce informative and reproducible spectra for specified bacteria. We have developed a protocol for whole cell MALDI-MS characterization of aerobic bacteria [31], including all those involved in current study. SA was found more suitable than ferulic acid, CHCA and 5-chloro-2-mercaptobenzothiazole as the MALDI matrix to produce more peaks at m/z >4000 in bacterial mass spectra.

The amount of NPs and the incubation time of bacterial cells with the NPs were also optimized. The capture efficiency of bacteria increased when the incubation time was increased, but the increase was slight in short period (within 3 h). For a 2-ml aqueous solution containing $\sim 10^7$ cfu/ml bacteria, 2.5 μl of fluidMAG-Q (1.4×10^{10} NPs) or 5.0 μl fluidMAG-DEAE (2.8×10^{10} NPs) was added and an incubation of 30 min was necessary to obtain good MALDI mass spectra. Hence, all the capture experiments were under this condition unless otherwise stated.

3.2. Capture of Escherichia coli using anion-exchange nanoparticles

After fluidMAG-DEAE and fluidMAG-Q were separately incubated with aqueous *E. coli* ATCC 700891 suspension, the isolated cells-NPs aggregates were characterized by whole cell MALDI-MS with SA as the MALDI matrix. Their mass spectra were compared with the spectrum of *E. coli* cells directly suspended in DI water at a much higher concentration (without being treated with NPs). Some ions appeared at m/z 3576, 4538, 4876, 5996, 6862, 7714, 9070, 9752, 10,466, 11,987, 13,496, 15,115 and 18,145 as shown in the spectrum of the pure bacterial suspension (Fig. 1). They were potential biomarkers of this species or strain. The *E. coli* cells treated with fluidMAG-DEAE and fluidMAG-Q had very similar MS profiles to corresponding "intact" cells, although their relative intensities were different.



Fig. 2. TEM image obtained after incubation of *E. coli* ATCC 700891 with fluidMAG-DEAE NPs and magnetic isolation.

When the concentration of *E. coli* suspension was lowered to 4.7×10^6 cfu/ml and 8.3×10^5 cfu/ml, the spectra of captured cells by fluidMAG-DEAE consistently retained the peaks at m/z 3576, 4538, 4876, 5996, 6857, 7714, 9063, 9742, 10,466, 11,988, 13,496, 15,115 and 18,145 (Fig. S1 of the Supplementary material). The same phenomenon was observed for cells captured with fluidMAG-Q from low concentrations of spiked solutions. The results demonstrated that neither the capture process nor the magnetic NPs bound to the cells influenced the MALDI-MS characterization of the bacteria. Fig. 2 shows a TEM image obtained after incubating fluidMAG-DEAE with *E. coli* ATCC 700891 and the subsequent magnetic isolation. A few bacterial cells-NPs conjugates were visible, which proves that the NPs successfully captured the bacteria.

3.3. Capture of various bacteria using fluidMAG-DEAE and fluidMAG-Q

Besides *E. coli* ATCC 700891, other bacteria involved in the capture experiments from aqueous solutions were *Aeromonas hydrophila*, *Aeromonas sobria*, *Pseudomonas aeruginosa*, *Salmonella enterica subsp. arizonae*, *Salmonella enterica subsp. enterica*, *Staphylococcus aureus subsp. aureus*, *Bacillus subtilis*, *Enterococcus faecalis* and *E. coli* ATCC 700609. The comparison of the MALDI mass spectra

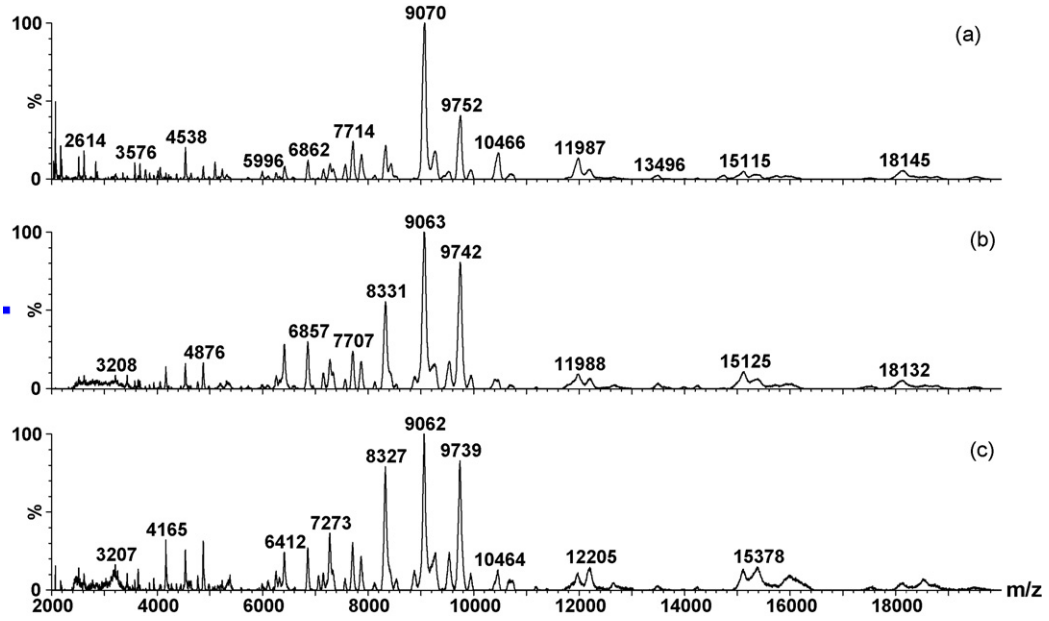


Fig. 1. MALDI spectra of *E. coli* ATCC 700891: (a) pure culture; concentrated from aqueous solution of 4.7×10^7 cfu/ml (b) with fluidMAG-DEAE; and (c) with fluidMAG-Q.

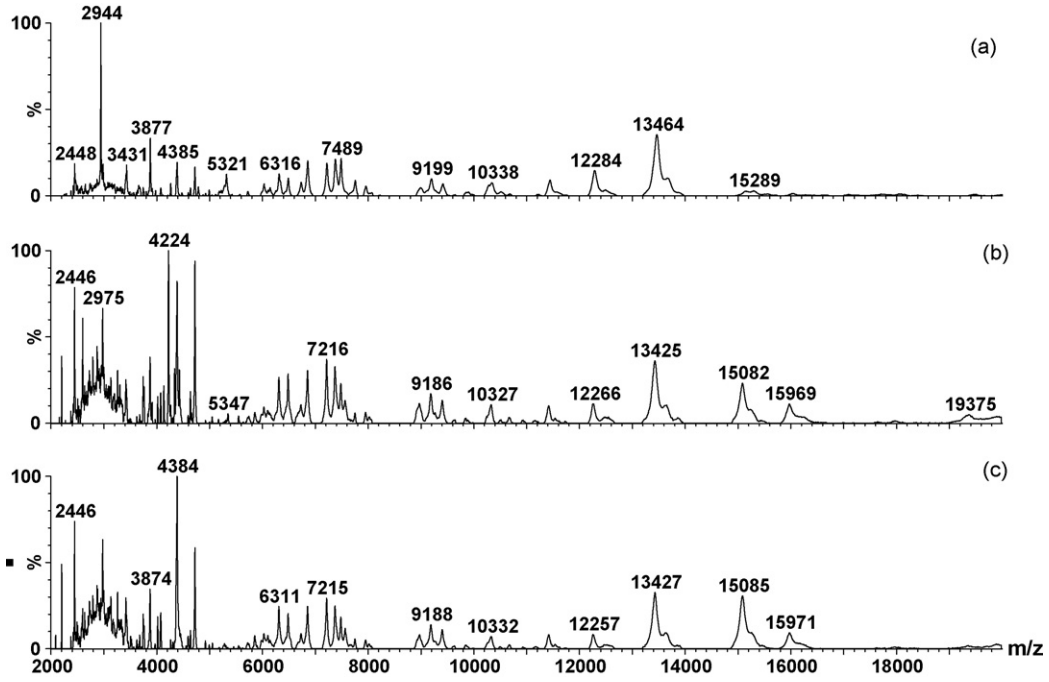


Fig. 3. MALDI mass spectra of *Aeromonas hydrophila* NCTC 8049: (a) pure culture; concentrated from aqueous solution of 8.6×10^7 cfu/ml (b) with fluidMAG-DEAE; and (c) with fluidMAG-Q.

of respective cells with and without the NPs-based magnetic isolation indicated that fluidMAG-DEAE and fluidMAG-Q were capable of recognizing all the bacteria examined and capturing them from aqueous solutions. For example, Fig. 3 shows the MALDI mass spectra of *A. hydrophila* NCTC 8049. Although bacteria with and without NPs treatment yielded ions with different intensity, they were still located at the same *m*/*z* positions (within mass error). Table 1 lists the ions that reproducibly appeared in the MALDI mass spectra of the bacterial strains investigated in this study. Whole cell MALDI-MS clustering analysis is mainly based on the mass spectral peak

Table 1
MALDI mass peaks of bacteria (pure cultures and trapped by the nanoparticles).

Bacteria	Position (*m*/*z*) of peaks	Percentage of signals reproducibly present in the spectra of pure cultures[a]	Percentage of signals reproducibly present in the spectra of isolated cells-NP aggregates[a]
Escherichia coli ATCC 700891	3207, 3576, 4165, 4537, 4876, 5235, 5996, 6412, 6862, 7273, 7711, 8327, 9068, 9744, 10,466, 11,981, 12,205, 13,496, 15,140, 15,378, 18,139	90.5	91.7
Escherichia coli ATCC 700609	3209, 3677, 4369, 4773, 5101, 6261, 6418, 6862, 7339, 7714, 7876, 9541, 10,904, 12,212, 13,481, 15,103, 15,995	91.9	95.6
Aeromonas hydrophila NCTC 8049	3430, 3744, 3874, 4018, 4074, 4224, 4384, 4722, 5321, 6311, 6486, 6854, 7215, 7374, 7565, 8972, 9188, 9401, 10,332, 11,418, 12,257, 13,427, 15,085, 15,971	91.7	90.6
Aeromonas sobria ATCC 11217	3934, 4103, 4976, 6102, 6308, 6484, 6862, 7214, 7369, 7558, 8690, 9184, 9372, 10,334, 10,467, 11,319, 12,189, 13,483, 15,072	94.7	96.7
Pseudomonas aeruginosa NCTC 10662	3162, 3644, 3792, 5740, 6190, 6351, 6981, 7206, 7332, 7582, 8567, 8973, 9303, 10,268, 11,731, 12,356, 13,925, 15,076, 15,974, 17,426, 19,705	95.2	94.6
Pseudomonas aeruginosa NCTC 12924	3178, 3630, 3751, 3794, 4670, 5728, 6191, 6353, 7005, 7209, 7584, 9278, 10,274, 11,679, 12,356, 13,135, 13,972, 15,085, 15,976, 17,267, 19,821	95.4	93.5
Salmonella enterica subsp. arizonae ATCC 13314	3345, 3645, 4356, 4942, 5742, 6084, 6355, 6663, 7059, 7274, 7584, 8011, 8572, 9521, 10,270, 10,977, 12,363, 15,070, 15,929	89.5	91.4
Salmonella enterica subsp. enterica ATCC 14028	3685, 4085, 4312, 4553, 4967, 5220, 6098, 6390, 7276, 7562, 7663, 7871, 8009, 8418, 9405, 10,176, 10,952, 12,211, 13,424, 15,094, 15,979	90.5	90.5
Staphylococcus aureus NCTC 13131	3007, 4300, 4827, 5028, 5523, 6422, 6886, 8139	99.2	98.5
Bacillus subtilis ATCC 6051	3404, 3880, 4316, 4522, 4601, 4828, 5059, 5255, 5430, 5716, 6040, 6506, 7556, 7714, 9886, 10,855, 15,085	97.5	96.3
Enterococcus faecalis ATCC 7080	3430, 3695, 4426, 4714, 5212, 5351, 5450, 5540, 6136, 6220, 6397, 6856, 7326, 7571, 8109, 8874	98.1	97.6

[a] Average percent frequency of the peaks listed observed in 12 replicate spectra.

positions rather than peak intensities [11]. The absence of one or even a few small peaks in the spectra of isolated cells could decrease the confidence or probability of the bacterial identification, but did not hamper the correct alignment of bacterial identity. The obtained spectra may be used for bacterial identification by searching against the mass spectral databases already available. However, it should be pointed out that a MALDI mass spectral database has been set up by following a specified sample preparation protocol and a mass spectral algorithm processing. To obtain correct identification, the mass spectra should be acquired under same conditions. When the mass spectra acquired from the isolated cells were searched against a Microbelynx-based database developed by the Manchester Metropolitan University (MMU) [9], the searching results did not always match to the real. This was because that we used a different sample preparation protocol and a different mass range to acquire the mass spectra and such factors could contribute to the mass spectral variation. The mass range for the mass spectral entries in the MMU database was m/z 1000–10,000, while fluidMAG-Q and fluidMAG-DEAE had some strong peaks at $m/z < 3000$. It is necessary to change the mass range setting of automated searching to avoid potential interference from the peaks of NPs.

Wide mass shifts were observed in the spectra under different occasions. For example, the signal at m/z 9752 in Fig. 1 corresponded to those reported in Fig. S1 at m/z 9742 in panel (a) and at m/z 9739 in panel (b). The spectra were acquired on different days. The MALDI-MS system used in this study had a mass accuracy of ≤300 ppm (using linear external calibration). That means a typical mass shift of $m/z \leq \pm 3$ for a signal at m/z 10,000 may occur. Actually, bigger mass shifts of ≥±5 were possible. During the implementation of this study, the system underwent several repair and maintenance services, which may affect the mass accuracy. Such mass shifts were also observed by other researchers [11]. That was why the ions within m/z ±20 of each other were binned together for peaks at $m/z > 9000$ in the peak list [11]. To avoid big mass shifts, it is recommended to use a bacterial strain [11] or internal standards covering whole m/z range [13] to calibrate the mass spectra of the samples.

The culture tests showed that the live cells going through the magnetic separation with fluidMAG-DEAE and fluidMAG-Q remained viable and cultivable. Dead bacterial cells (colonies after heating) could also be isolated with the NPs and further characterized by MALDI-MS.

3.4. Effect of medium pH

The surface charges of bacteria originate from the ionization of surface molecules and the adsorption of ions from the solution [32]. Bacterial cell walls and membranes contain a variety of proteins, lipids, teichoic acids and lipopolysaccharides. Carboxyl, phosphate and hydroxyl groups, with pK_a values of 4.82 ± 0.14, 6.9 ± 0.5 and 9.4 ± 0.6, respectively [27], exposed on the outer surface of the cell wall will result in the negative charge of bacteria at neutral medium [27,33,34]. Amino groups in the cell membrane molecules are positively charged at low pH values while neutral at high pH values. They are unlikely to contribute significantly to the surface charge of the bacteria at high pH values. Therefore, medium pH has significant influence on the bacterial surface charges and their adherence to different materials [27,33–37]. Here, the effects of pH on the interaction of the two magnetic NPs with *E. coli* ATCC 700891, *S. enterica* ATCC 13314 and *S. aureus* NCTC 13131 were examined over the range of pH 2–12.

The MALDI mass spectra of *E. coli* ATCC 700891 separated with fluidMAG-DEAE from aqueous solutions at pH 4.3 and pH 7.3 were much better than those obtained at pH 2.0, pH 10.0 and pH 12.0 (Fig. S2 of the Supplementary material). At pH 2.0, the bacterial surface became less negatively charged which would reduce the interactions between bacterial cells and the particles. Meanwhile, a part of the superparamagnetic NPs were dissolved in acidic solution. Therefore, fewer particles were left as anion-exchanger to be isolated by an external magnet. At pH 10.0 and pH 12.0, the anion-exchange groups of the NPs could not function well although the bacterial surface seemed more negatively charged. In contrast, at pH 4.3 and pH 7.3, the bacterial surface became more negatively charged and the functional groups of NP were oppositely charged. As a result of stronger electrostatic attractive forces, the capture yield has been improved.

For *S. aureus* NCTC 13131 and *S. enterica* ATCC 13314, the best spectra were obtained at pH 7.0, followed by those obtained at pH 10.0. No spectrum was observed at pH 2.0 and pH 12.0. In summary, the magnetic separation worked well only in a nearly neutral medium. Therefore, DI water and fresh water were not pH-adjusted during the experiments.

3.5. Reproducibility of the MALDI-MS spectra

Reproducibility of MALDI-MS spectra is very important for reliable microbial identification and has been addressed in a number of studies [8–14]. It can be evaluated with the frequency of appearance for ions in the mass spectra when the spectra were collected from replicate MALDI wells (well-to-well) or from same bacteria samples prepared on different days (day-to-day). Ions with at least 10% of the strongest ion intensity observed in the spectra within an m/z difference of ±10 were considered reproducible. In this study, we compared the MALDI mass spectra of magnetically isolated bacteria deposited on 12 MALDI wells in a same batch and on three separate days. Table 2 displays the reproducibility of peaks of *E. coli* ATCC 700891 and *S. enterica* ATCC 13314 from different MALDI wells in a batch and on different days. The results showed that the integrated separation-characterization method was reproducible.

3.6. Capture efficiencies of bacteria

The capture efficiencies of bacteria by the anion-exchange NPs were evaluated by counting the colonies grown on the nutrient broth agar plates from the isolated supernatant and the initial bacterial suspension. In these experiments, fluidMAG-Q (2.5 μl) or fluidMAG-DEAE (5.0 μl) was added to a 2-ml suspension containing ~10^7 cfu/ml of specific bacteria. As Table 3 displays, the capture efficiency was obviously dependent on both the NPs functional groups and the bacterial surface charges. The enrichment factor

Table 2
Reproducibility of the MALDI-MS spectral peaks.

Bacteria	Peak m/z (average ± SD)[a]
Salmonella enterica ATCC 13314	2622 ± 1.0
	3645 ± 1.0
	5742 ± 2.0
	6355 ± 2.2
	7584 ± 3.0
	8572 ± 3.5
	10,270 ± 2.9
	12,363 ± 4.0
	13,920 ± 3.5
	15,070 ± 3.0
Escherichia coli ATCC 700891	4537 ± 1.0
	5235 ± 1.3
	7291 ± 3.8
	7711 ± 2.8
	8437 ± 2.1
	9068 ± 2.8
	9744 ± 2.8
	10,466 ± 3.5
	11,981 ± 2.6
	15,140 ± 4.5

[a] $n = 12$.

Table 3
The efficiency of bacterial capture with fluidMAG-DEAE and fluidMAG-Q (incubation time of 30 min).

Bacteria	Capture efficiency (%)[a]	
	FluidMAG-DEAE (5.0 μl)	FluidMAG-Q (2.5 μl)
Escherichia coli ATCC 700891	21.9 ± 1.8	23.1 ± 0.4
Escherichia coli ATCC 700609	21.6 ± 0.9	24.6 ± 0.7
Staphylococcus aureus NCTC 13131	14.3 ± 0.7	19.2 ± 1.5
Salmonella enterica ATCC 13314	20.3 ± 0.4	25.7 ± 0.3
Aeromonas sobria NCTC 11217	8.0 ± 0.5	10.6 ± 0.8
Aeromonas hydrophila NCTC 8049	9.2 ± 0.6	11.6 ± 0.3
Bacillus subtilis ATCC 6051	24.8 ± 1.3	28.4 ± 0.6
Enterococcus faecalis ATCC 7080	15.4 ± 0.8	18.4 ± 1.1

[a] Expressed as average ± standard deviation ($n = 3$).

is equal to the capture efficiency times the volume change factor (i.e., 100 for magnetic isolation only). For example, it was 23.1 ± 0.4 for *E. coli* with fluidMAG-Q under the conditions examined. Both fluidMAG-Q and fluidMAG-DEAE had higher capture efficiencies for *E. coli*, *S. enterica* and *B. subtilis* than for *S. aureus*, *A. hydrophila* and *A. sobria*. FluidMAG-Q had a higher efficiency for each of the bacterial species than fluidMAG-DEAE, even when the number of particles used to capture bacteria was half of fluidMAG-DEAE's. This efficiency difference can be explained in terms of interaction mechanism between the NPs and bacteria. The binding force between bacteria and the NPs is mainly electrostatic force. FluidMAG-Q has a polymer structure with more positive charges at its surface [37] while fluidMAG-DEAE has a linear structure with only one positive charge at the surface [26].

The capture efficiency was also found to be related with the concentration of the magnetic NPs. Fig. 4 shows a much higher efficiency, even up to 99%, was obtained for *E. coli* ATCC 700891 (3.4×10^7 cfu/ml) with increasing amount of NPs used. During the capture process, there is a dynamic equilibrium between the NPs and bacterial cells [10]. When the concentration of the NPs is higher, more bacterial cells would be bound by the particles. However, high capture efficiency does not ensure good MALDI mass spectra of captured cells. Too many particles may "dilute" the bacterial cells in a MALDI spot, and also affect the interaction among laser radiation, MALDI matrix molecules and bacterial cells.

In view of the enrichment factor, the NPs-based magnetic separation lowered the detection limit of bacteria by 8–28-folds. The detection limit was also related to the MALDI-MS system used. For the equipment we used, it was ~10^5 cfu/ml for all bacteria investigated. To further lower the detection limit, microfiltration using 0.45-μm membrane was introduced into the procedure for analysis of water samples.

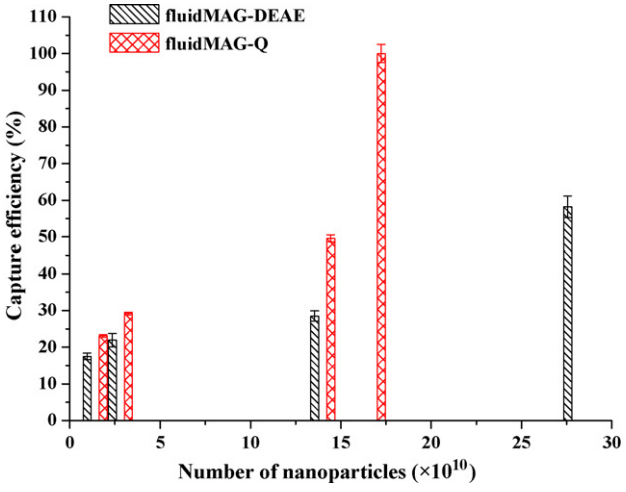


Fig. 4. Relationship between capture efficiency and the amount of the nanoparticles used. The nanoparticles were incubated with 3.4×10^7 cfu/ml of *E. coli* ATCC 700891 for 30 min.

3.7. Separation of the bacterial mixtures

It was worthwhile to check whether fluidMAG-Q and fluidMAG-DEAE preferred certain bacteria to others during the capture. Therefore, six aqueous suspensions were prepared by mixing two bacterial species with similar concentrations in DI water. After the magnetic separation, the mass spectrum for each mixture was found as the mass spectral addition of two spiked species. For example, in the spectra (Fig. S3 of the Supplementary material) of the mixture of *S. aureus* NCTC 13131 (Gram-positive) and *E. coli* ATCC 700891 (Gram-negative), the peaks positioned at $m/z < 4000$ and peaks at $m/z > 7000$ were mainly attributed to *S. aureus* NCTC 13131 and *E. coli* ATCC 700891, respectively. Fig. S4 shows the mass spectra of the mixture of two Gram-negative bacteria, *S. enterica* ATCC 13314 and *E. coli* ATCC 700891. Similarly, the peaks from both species were observed. The results indicated that fluidMAG-DEAE and fluidMAG-Q were non-specific and broad spectrum isolation materials for both Gram-positive and Gram-negative bacteria.

3.8. Analysis of bacteria in spiked waters using the integrated method

Bacterial analysis is important in many areas including food quality, clinical diagnosis and water quality monitoring. In this study, we were more interested in the applicability of MALDI-MS coupled with separation in the identification of bacterial contamination in fresh water. Reservoir water and tap water, i.e., source and finished drinking water, is more meaningful to drinking water supply than other high ion strength water (e.g., wastewater and seawater). Three concerns would arise when fluidMAG-DEAE and fluidMAG-Q NPs were used to directly concentrate bacteria in fresh water and the obtained isolates were subsequently detected by MALDI-MS. Firstly, bacteria in contaminated water were commonly below ~10^4 cfu/ml. That means the pre-concentration step would require a bigger volume (a few liters rather than a few milliliters) for each sample. Secondly, inorganic ions and negatively charged organic compounds in water have potential interferences on the magnetic separation. Thirdly, it is impractical to conduct magnetic separation from a big-volume sample. In order to overcome such issues, water samples were subjected to microfiltration using 0.45-μm cellulose nitrate membrane filter prior to the magnetic separation. To evaluate the applicability of the proposed approach, *E. coli*, *S. enterica*, *A. hydrophila*, *P. aeruginosa*, *S. aureus* and *B. subtilis* were individually spiked into 2 L of tap water or reservoir water to a final concentration in the range of 10^2–10^5 cfu/ml. Table S2 of the Supplementary material lists the main matrix components and contaminants of the water samples. Finally, the bacteria were detected with the detection limit of 1×10^3 cfu/ml. Figs. 5 and 6 display two examples: *B. subtilis* ATCC 6051 spiked in reservoir water and *P. aeruginosa* NCTC 12924 spiked in tap water. The peaks from the captured cells matched well with those from the pure bacteria and no sample matrix peaks were found. An additional example is provided as Fig. S5 of the Supplementary material. Furthermore, the current method was also applied to a tap water sample and a reservoir water sample. In their mass spectra (Fig. S6), no peaks except those for the NPs were observed. This indicated that bacteria in the water samples examined were non-detected, i.e., lower than the detection limit. Compared with the traditional culture method, the current method requires a running time of around 2 h.

The detection limit of bacteria by the proposed method is 1×10^3 cfu/ml, and contaminated water with bacteria concentration higher than the detection limit can be rapidly tested.

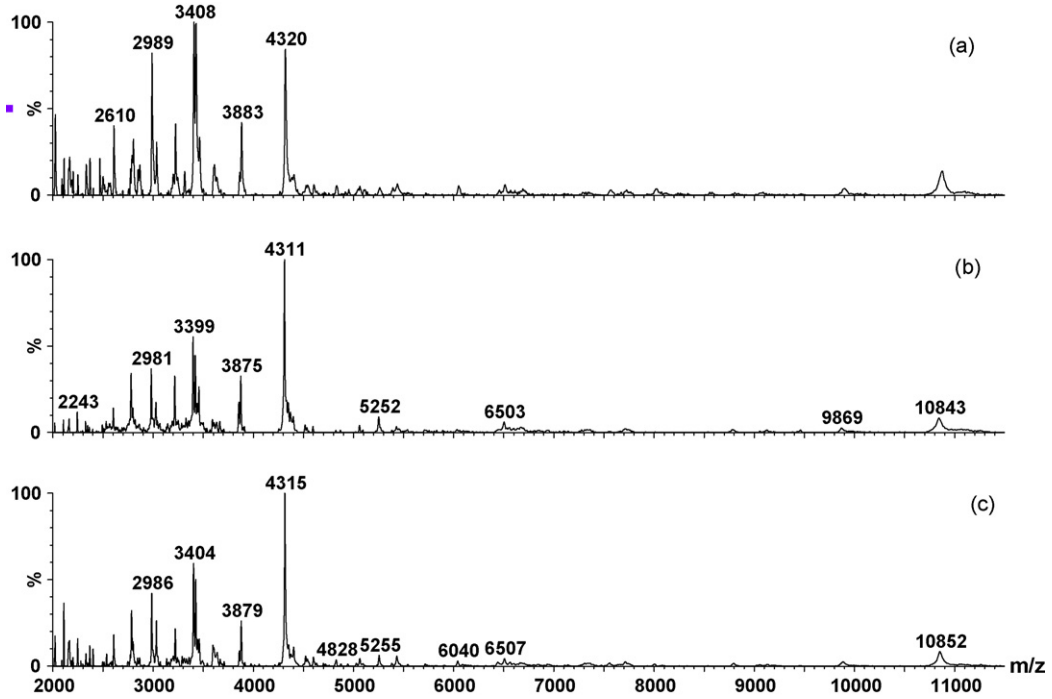


Fig. 5. MALDI mass spectra of *Bacillus subtilis* ATCC 6051: (a) pure culture; (b) membrane filtered and separated with fluidMAG-DEAE from reservoir water spiked at 1×10^3 cfu/ml; and (c) membrane filtered and separated with fluidMAG-Q from reservoir water spiked at 1×10^3 cfu/ml.

Otherwise, the results would be non-detected. In this term, pre-enrichment on a selective culture media can be avoided. When different bacterial species are present in a sample, as discussed above, they are concentrated together and a combined spectrum is produced. By comparing with the blank, it is easy to justify the existence of bacteria. But when searching using an algorithm or software against a mass spectral library of pure bacterial species or strains, the result of bacterial identity may not be correct. In this case, the identification strategy on the basis of specific ions (biomarkers) is more reliable [38,39].

When 5-ml human urine samples were individually spiked with 10^6 cfu/ml of *E. coli* ATCC 700891, *S. enterica* ATCC 13314 and *S. aureus* NCTC 13131 and then processed through magnetic separation (without membrane filtration), the analytical results were not satisfactory. Extra peaks appeared in the mass spectra for spiked urines, compared with pure cultures. Urine is a more complicated

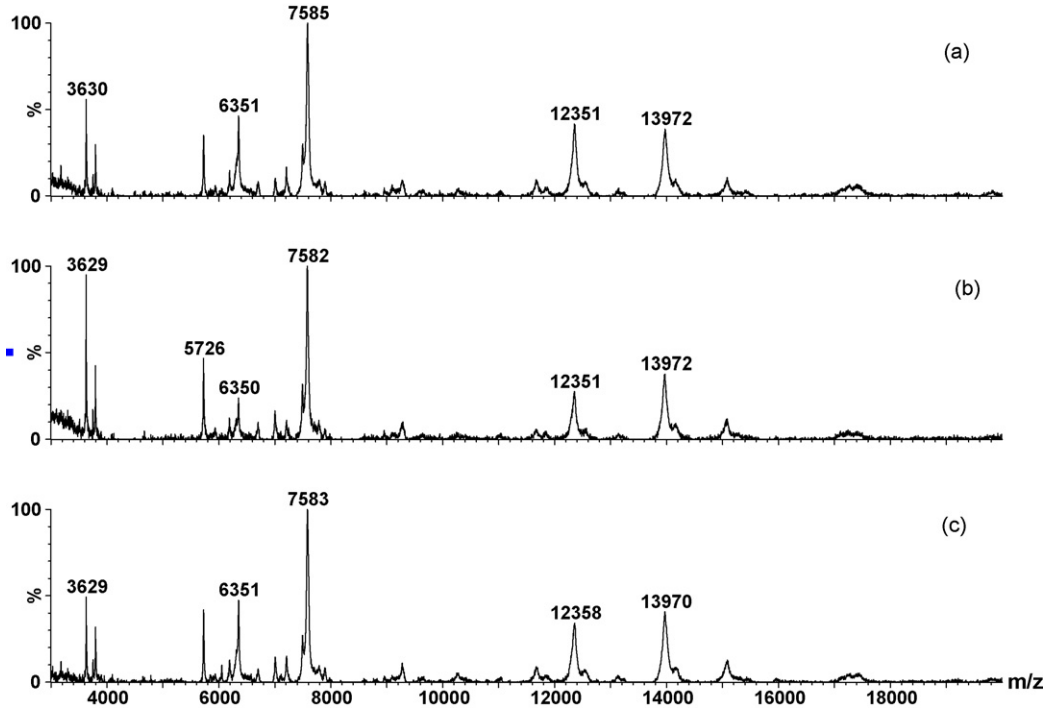


Fig. 6. MALDI mass spectra of *Pseudomonas aeruginosa* NCTC 12924: (a) pure culture; (b) membrane filtered and separated with fluidMAG-DEAE from a tap water spiked at 2×10^3 cfu/ml; and (c) membrane filtered and separated with fluidMAG-Q from a tap water spiked at 2×10^3 cfu/ml.

matrix than fresh water. A number of inorganic ions and negatively charged organic compounds were easily found in urine, and they have potential interferences on the magnetic separation and MALDI-MS spectra. The current method does not apply to urine analysis.

4. Conclusions

This paper addressed a combination of microfiltration, magnetic separation using anion-exchange NPs to concentrate bacteria from aqueous suspensions and fresh water, and the characterization of the isolates by whole cell MALDI-MS. Various bacteria, e.g., *E. coli*, *Salmonella*, *Aeromonas*, *Pseudomonas*, *Staphylococcus*, *Bacillus* and *Enterococcus*, were analyzed in this strategy. Bacterial species, medium pH, concentration and functional group of the NPs were found to influence the capture efficiency. With fluidMAG-DEAE and fluidMAG-Q, bacteria could be enriched and magnetically isolated from simple matrix solutions without affecting their vitality and cultivability. With such an integrated method, bacteria in fresh water could be analyzed in 2 h with a detection limit of 1×10^3 cfu/ml. Rapid and accurate identification of bacterial contamination in water can be expected up to species level by the proposed method when a MALDI library of bacterial strains has been established.

Supplementary materials

Additional tables and figures as noted in the text are given in the Supplementary material.

Acknowledgements

This work is part of a research project funded by the Public Utilities Board, Singapore's national water agency (Project No.: ERH/X6-TECH-WA-QU-MALTOF). We also thank Mr. Wei Ning Yap for producing Scheme 1.

Appendix A. Supplementary data

Supplementary data associated with this article can be found, in the online version, at doi:10.1016/j.talanta.2009.06.069.

References

[1] B. Anderson, H. Friedman, M. Bendinelli, Microorganisms and Bioterrorism, Springer, New York, 2006.
[2] C. Fenselau, P.A. Demirev, Mass Spectrom. Rev. 20 (2001) 157–171.
[3] J.O. Lay Jr., Mass Spectrom. Rev. 20 (2001) 172–194.
[4] K. Cottingham, Anal. Chem. 78 (2006) 18–23.
[5] A. Fox, J. Clin. Microbiol. 44 (2006) 2677–2680.
[6] C.L. Wilkins, J.O. Lay Jr., Identification of Microorganisms by Mass Spectrometry, Wiley-VCH, New Jersey, 2006.
[7] P.A. Demirev, C. Fenselau, Annu. Rev. Anal. Chem. 1 (2008) 71–93.
[8] K.J. Welham, M.A. Domin, D.E. Scannell, E. Cohen, D.S. Ashton, Rapid Commun. Mass Spectrom. 12 (1998) 176–180.
[9] C.J. Keys, D.J. Dare, H. Sutton, G. Wells, M. Lunt, T. McKenna, M. McDowall, H.N. Shah, Infect. Gen. Evol. 4 (2004) 221–242.
[10] J.E. Camara, F.A. Hays, Anal. Bioanal. Chem. 389 (2007) 1633–1638.
[11] M.J. Donohue, J.M. Best, A.W. Smallwood, M. Kostich, M. Rodgers, J.A. Shoemaker, Anal. Chem. 79 (2007) 1939–1946.
[12] P. Chen, Y. Lu, P.B. Harrington, Anal. Chem. 80 (2008) 1474–1481.
[13] N. Valentine, S. Wunschel, D. Wunschel, C. Petersen, K. Wahl, Appl. Environ. Microbiol. 71 (2005) 58–64.
[14] R. Dieckmann, I. Graeber, I. Kaesler, U. Szewzyk, H. von Döhren, Appl. Microbiol. Biotechnol. 67 (2005) 539–548.
[15] K.A. Stevens, L.A. Jaykus, Crit. Rev. Microbiol. 30 (2004) 7–24.
[16] J. Bundy, C. Fenselau, Anal. Chem. 71 (1999) 1460–1463.
[17] J. Bundy, C. Fenselau, Anal. Chem. 73 (2001) 751–757.
[18] C. Afonso, C. Fenselau, Anal. Chem. 75 (2003) 694–697.
[19] A.J. Madonna, F. Basile, E. Furlong, K.J. Voorhees, Rapid Commun. Mass Spectrom. 15 (2001) 1068–1074.
[20] A.J. Madonna, S.V. Cuyk, K.J. Voorhees, Rapid Commun. Mass Spectrom. 17 (2003) 257–263.
[21] M.L. Ochoa, P.B. Harrington, Anal. Chem. 77 (2005) 5258–5267.
[22] J. Jiang, C.E. Parker, J.R. Fuller, T.H. Kawula, C.H. Borchers, Anal. Chim. Acta 605 (2007) 70–79.
[23] K.C. Ho, P.J. Tsai, Y.S. Lin, Y.C. Chen, Anal. Chem. 76 (2004) 7162–7168.
[24] Y.S. Lin, P.J. Tsai, M.F. Weng, Y.C. Chen, Anal. Chem. 77 (2005) 1753–1760.
[25] J.C. Liu, P.J. Tsai, Y.C. Lee, Y.C. Chen, Anal. Chem. 80 (2008) 5425–5432.
[26] C. Bergemann, D. Muller-Schulte, J. Oster, L. Brasard, A.S. Lubbe, J. Magn. Magn. Mater. 194 (1999) 45–52.
[27] J.B. Fein, C.J. Daughney, N. Yee, T.A. Davis, Geochim. Cosmochim. Acta 61 (1997) 3319–3328.
[28] S. Deponte, J. Steingroewer, C. Löser, E. Boschke, T. Bley, Anal. Bioanal. Chem. 379 (2004) 419–426.
[29] http://www.chemicell.com.
[30] J.P. Harley, L.M. Prescott, Laboratory Exercises in Microbiology, 5th ed., McGraw-Hill Science, New York, 1996.
[31] Z. Guo, Y. Liu, S. Li, C.H. Woo, Z. Yang, Proceedings of 60th Pittsburgh Conference on Analytical Chemistry and Applied Spectroscopy, Chicago, IL, USA, March 8–13, 2009, P2700-9.
[32] E. Klodzinska, B. Buszewski, Anal. Chem. 81 (2009) 8–15.
[33] T.J. Beveridge, R.G.E. Murray, J. Bacteriol. 141 (1980) 876–887.
[34] N. Yee, J.B. Fein, C.J. Daughney, Geochim. Cosmochim. Acta 64 (2000) 609–617.
[35] J. Li, L.A. McLandsborough, Int. J. Food Microbiol. 53 (1999) 185–193.
[36] T.J. Kinnari, J. Esteban, N.Z. Martin-de-Hijas, O. Sánchez-Muñoz, S. Sánchez-Salcedo, M. Colilla, M. Vallet-Regí, E. Gomez-Barrena, J. Med. Microbiol. 58 (2009) 132–137.
[37] S. Ulmeanu, H.J. Lee, H.H. Girault, Electrochem. Commun. 3 (2001) 539–543.
[38] P.A. Demirev, Y.P. Ho, V. Ryzhov, C. Fenselau, Anal. Chem. 71 (1999) 2732–2738.
[39] K.H. Jarman, S.T. Cebula, A.J. Saenz, C.E. Petersen, N.B. Valentine, M.T. Kingsley, K.L. Wahl, Anal. Chem. 72 (2000) 1217–1223.

Talanta 80 (2009) 321–328

Contents lists available at ScienceDirect

Talanta

journal homepage: www.elsevier.com/locate/talanta

Classification from microarray data using probabilistic discriminant partial least squares with reject option

Cristina Botella, Joan Ferré*, Ricard Boqué

Department of Analytical Chemistry and Organic Chemistry, Rovira i Virgili University. Marcel·lí Domingo s/n, 43007 Tarragona, Spain

ARTICLE INFO

Article history:
Received 4 February 2009
Received in revised form 18 June 2009
Accepted 30 June 2009
Available online 7 July 2009

Keywords:
DPLS
Microarrays classification
Reject option

ABSTRACT

Microarrays are used to simultaneously determine the expressions of thousands of genes. An important application of microarrays is in the classification of samples into classes of interest (e.g. either healthy cells or tumour cells). Discriminant partial least squares (DPLS) has often been used for this purpose. In this paper, we describe an improvement to DPLS that uses kernel-based probability density functions and the Bayes rule to classify samples whilst keeping the option of not classifying the sample if this cannot be done with sufficient confidence. With this approach, those samples outside the boundaries of the known classes or from the ambiguity region between classes are rejected and only samples with a high probability of being correctly classified are indeed classified. The optimal model is found by simultaneously minimizing the misclassification and rejection costs. The method (*p*-DPLS with reject option) was tested with two datasets. For the human cancers dataset the accuracy (obtained by leave-one-out cross-validation) was improved from 97% to 99% when compared to *p*-DPLS without reject option. For the breast cancer dataset, *p*-DPLS with reject option was able to reject 100% of the test samples that did not belong to any of the modelled classes. These samples would have been misclassified if the reject option had not been considered.

© 2009 Elsevier B.V. All rights reserved.

1. Introduction

Supervised classification is increasingly being applied to microarray gene expression data in order to predict tumour types [1–3], to differentiate between healthy and tumour samples [4–6] and to differentiate between pharmacological mechanisms [7], among other applications. Microarray data are characterized by thousands of variables (genes) and few samples, resulting in high redundancy and a high number of non-informative measurements. There has been a lot of interest in using factor-based multivariate classification methods such as discriminant partial least squares (DPLS) to analyze these data [8,9]. The DPLS uses a few latent variables rather than a lot of measured variables and this brings with it a series of advantages. DPLS takes variable correlations into account, filters noise and leads to classification rules with good predictive performance, especially when DPLS is implemented together with variable selection methods. DPLS has been used to differentiate between samples before and after chemotherapy [10], to determine the different states of a breast cancer tumour [11], to predict the efficacy of a drug by using expression data biomarkers [12], and to predict the quality of DNA-microarray spots [13].

Like other classification rules, DPLS must have two main qualities: it must provide reliable classifications of forthcoming samples and it must minimize the number of misclassifications (i.e. the expected error rate). Both of these are improved if the classifier is allowed to reject doubtful samples instead of always being forced to classify them in one of the modelled classes. By classifying only the most well-defined cases, both the accuracy of the classifier and the reliability of each classification are improved.

In this paper we implement the reject option in the recently developed *p*-DPLS classifier and show how it can be used for microarray data classification. *p*-DPLS is a variant of DPLS, which uses kernel functions to calculate a probability density function (PDF) for each class. This allows a flexible implementation of the Bayes rule for classification, and also provides a measure of the reliability of the classification. Reliability is a primary concern in statistical classification, especially when this classification is used in critical health applications such as cancer diagnosis [14], an issue which has also led to several other studies [15].

In classification, rejection is advantageous when: (a) the new sample does not belong to any of the trained classes, (b) the new sample belongs to one of the classes but is very different from the samples used for training the classifier, or (c) the sample is in the boundary region between classes. Situation (a) occurs when the sample is an outlier. Forcing the classifier to decide among one of the modelled classes will produce a classification error (e.g. a cell does not belong to any of the modelled cell types but it is classified

* Corresponding author.
E-mail address: joan.ferre@urv.cat (J. Ferré).

0039-9140/$ – see front matter © 2009 Elsevier B.V. All rights reserved.
doi:10.1016/j.talanta.2009.06.072

as one of them). Situation (b) typically arises when the sampling of the training samples is incomplete or not representative. Finally, situation (c) may arise, for example, because of the limited discriminative power of the measured variables or because the classification algorithm has limited discriminative power. Although samples in situations (b) and (c) might finally be classified correctly, they might also be classified incorrectly because either they are unique samples or they are ambiguous samples and can belong to either of the classes, respectively.

The reject option aims to overcome situations (a) to (c) by rejecting the sample and not classifying it when the probability of error is too high. This is a safeguard against errors and improves the accuracy of the classifier, which is evaluated as the percentage of samples correctly classified among the number of samples classified [16]. This in turn leads to greater confidence in the samples that are finally classified. The reject option can be fine-tuned in order to avoid rejecting too many samples that would otherwise be classified correctly. Since too high a rejection rate would decrease the usefulness of the classifier, a compromise must be reached between improving the accuracy and reducing the usefulness of the classifier. There has been extensive research into the theoretical aspects of the reject option [14,17–28], most of which relates to Chow's reject option [29], which implemented the reject option for the Bayes rule. Chow's reject option has recently been used to microarray expression data [30].

There are still two limitations to jointly applying the Bayes and Chow rules. First, they are not adequate for the extreme (outlying) samples (situations (a) and (b)) which are typically found at the extremes of the probability density functions (PDFs). These samples must be rejected according to a different criterion. Second, both rules require knowledge of the *a priori* probabilities and the PDFs of the classes [31], which makes applying these rules more difficult. In this paper, the first limitation is overcome by including distance based thresholds, which is equivalent to selecting a confidence interval around each class and rejecting samples outside this interval [17]. The second limitation is overcome by the calculating PDF-like functions in *p*-DPLS [32], which makes an approximate Bayesian classification easier.

2. Methods

2.1. Probabilistic DPLS

The DPLS method applies partial least squares (PLS) regression to binary classification problems, in which the dependent variable y codifies the class of each sample [8,33]. A DPLS model is calculated by regressing $\mathbf{y}$ on $\mathbf{X}$ using the adequate number of factors. For microarray gene expression data, $\mathbf{X}$ is an $n \times p$ matrix of n samples and p gene expressions and $\mathbf{y}$ is a $n \times 1$ vector of ones and zeros, where the integer 0 codifies the sample as belonging to class ω_0 (e.g. "cancer of type I") and the integer 1 codifies the sample as belonging to class ω_1 (e.g. "cancer of type II"). For a sample i, the value predicted by the PLS model is $\hat{y}_i = \mathbf{x}_i{}^{\mathrm{T}}\mathbf{b}$, where the b's are the regression coefficients for the model of A factors and the adequate preprocessing is implicit (e.g. if the b's had been calculated from mean-centred data, then $\mathbf{x}_i$ should be mean-centred, and the predicted $\hat{y}_i$ should be unprocessed accordingly). With the coding of y, the prediction for a sample should be close to 0 if the sample belongs to class ω_0, and it should be close to 1 if the sample belongs to class ω_1. In order to better define the cut-off value between classes, Pérez et al. [32] developed *p*-DPLS, a probabilistic version of the DPLS in which the uncertainty of the predicted value $\hat{y}$ is accounted for in the calculation of the model. This method is described here for completeness. The method starts by calculating a DPLS model of A factors with $\mathbf{X}$ and $\mathbf{y}$. Then, this model is used to predict the training samples and, for each training sample i, a Gaussian function centred at the predicted value $\hat{y}_i$ is calculated as:

$$f_i(\hat{y}) = \frac{1}{\mathrm{SEP}_i\sqrt{2\pi}} \cdot e^{-\frac{1}{2}\left(\frac{(\hat{y}-\hat{y}_i)}{\mathrm{SEP}_i}\right)^2} \tag{1}$$

$$\mathrm{SEP}_i = \mathrm{RMSEC}\sqrt{1+h_i} \tag{2}$$

$$\mathrm{RMSEC} = \sqrt{\frac{\sum_{i=1}^{n}(\hat{y}_i - y_i)^2}{n-A-\delta}} \tag{3}$$

where SEP_i is the standard error of prediction for sample i, h_i is the leverage of the sample, RMSEC is the root mean square error of calibration, y_i is the known class of the training sample i (i.e. value 0 for a sample of class ω_0 and value 1 for a sample of class ω_1) and δ is 1 if the data has been centred and 0 if it has not. Fig. 1 shows the Gaussian functions calculated from the predictions of three training samples of class ω_0 and four samples of class ω_1. Note that the width of the Gaussian kernel for sample i depends on SEP_i, which is particular to that sample, and depends on the relative position of the sample in the multivariate space. Then, for classes ω_0 and ω_1, a PDF is calculated as the average of the individual kernel functions of the training samples of each class:

$$p(\hat{y}|\omega_0) = \frac{1}{n_0}\sum_{i=1}^{n_0} f_i(\hat{y}) \tag{4}$$

$$p(\hat{y}|\omega_1) = \frac{1}{n_1}\sum_{i=1}^{n_1} f_i(\hat{y}) \tag{5}$$

where n_0 and n_1 are the number of samples of class ω_0 and class ω_1 respectively.

2.2. Bayes rule for classification

In *p*-DPLS, the predicted class for sample i is obtained using the Bayes rule. The prediction $\hat{y}_i$ for that sample is used to obtain the *a posteriori* probabilities $P(\omega_0|\hat{y}_i)$ and $P(\omega_1|\hat{y}_i)$. These are the probabilities that the sample belongs either to class ω_0 or to class ω_1, once it is known that the sample's prediction is $\hat{y}_i$. For the two-class classification problem:

$$P(\omega_0|\hat{y}_i) = \frac{p(\hat{y}_i|\omega_0)\cdot P(\omega_0)}{p(\hat{y}_i)} \tag{6a}$$

$$P(\omega_1|\hat{y}_i) = \frac{p(\hat{y}_i|\omega_1)\cdot P(\omega_1)}{p(\hat{y}_i)} \tag{6b}$$

where $p(\hat{y}_i|\omega_0)$ and $p(\hat{y}_i|\omega_1)$ are the *conditional* probabilities evaluated from the PDFs of classes ω_0 and ω_1 and $P(\omega_0)$ and $P(\omega_1)$ are the *a priori* probabilities. Both *a priori* probabilities may be estimated as the proportion of samples of each class in the training set, provided that the set is representative of the overall population. That is, $P(\omega_0) = n_0/n$ and $P(\omega_1) = n_1/n$ where $n = n_0 + n_1$. The denominator of Eqs. (6a) and (6b) is:

$$p(\hat{y}_i) = p(\hat{y}_i|\omega_0)\cdot P(\omega_0) + p(\hat{y}_i|\omega_1)\cdot P(\omega_1) \tag{7}$$

The Bayes rule assigns the sample to the class in which it has the highest *a posteriori* probability [31]. The rule is:

$$\begin{array}{lll} \text{Assign the sample to} & \text{class } \omega_0 & \text{if } P(\omega_0|\hat{y}_i) > P(\omega_1|\hat{y}_i) \\ & \text{class } \omega_1 & \text{if } P(\omega_1|\hat{y}_i) > P(\omega_0|\hat{y}_i) \end{array} \tag{8}$$

Although this rule is optimal in the sense that no other rule can yield a lower error probability, it is not always satisfactory. For example, when the $\hat{y}_i$ is at one of the extremes of the PDF (Fig. 2), both $p(\hat{y}_i|\omega_0)$ and $p(\hat{y}_i|\omega_1)$ are low, and the products $p(\hat{y}_i|\omega_0)\cdot P(\omega_0)$ and $p(\hat{y}_i|\omega_1)\cdot P(\omega_1)$ are also low but the *a posteriori* probability for one

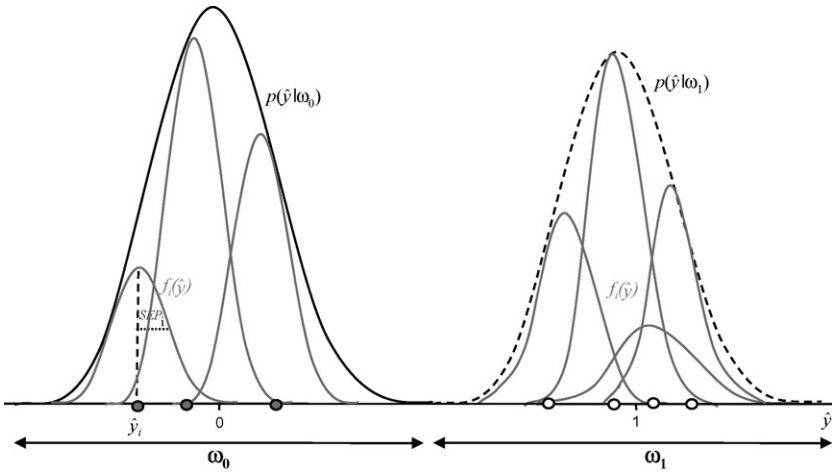


Fig. 1. Simulated PDFs of class ω_0 and class ω_1 obtained from Eqs. (4) and (5). The kernel functions (Eq. (1)) are centred on prediction $\hat{y}_i$ of each training sample. According to the code assigned to the classes, the sample predictions of class ω_0 and class ω_1 should be located around the values 0 and 1 respectively.

of the classes (the ratio in Eqs. (6a) and (6b)) is high. This means that the further the prediction $\hat{y}_i$ is from one class, the more likely it will be allocated to the other class. This is a reasonable result since the classifier only expects to receive samples from the two modelled classes. In most multivariate applications, however, samples from non-modelled classes (outliers) may also be inadvertently submitted to the classifier. The predictions for those samples will most probably be found at the tails of a PDF, and, hence give a misleading high *a posteriori* probability for one of the classes. Consequently, forcing the two-class Bayes rule to classify any input sample may involve a high risk because outliers may be erroneously classified in one of the modelled classes.

Another situation in which the usefulness of the Bayes rule is limited occurs when the predicted value $\hat{y}$ is in the boundary between classes (the ambiguity region). The dot in the centre of Fig. 2A represents a sample whose characteristics are similar for both classes, with the result that the model cannot clearly distinguish whether it belongs to one class or to the other. Again, the sample will be assigned to the class to which, according to the Bayes rule, it has the highest probability of belonging. However, since the probability that the sample belongs to class ω_0 is similar to the probability that it belongs to class ω_1, there is a high risk of misclassification and the reliability of the classification is low.

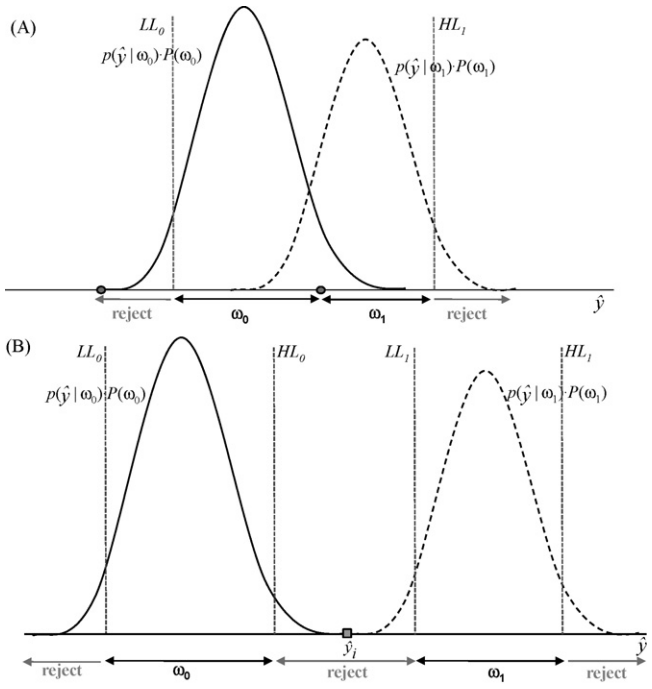


Fig. 2. Possible distributions of class ω_0 and class ω_1 with the distance reject limits: (A) overlapped classes and (B) well separated classes. ● and □ indicate possible predictions of unknown samples for which the Bayes rule gives questionable results. LL_0, HL_0, LL_1 and HL_1 are the limits for rejection based on the distance reject option.

These situations show that the reject option might be an advantageous addition to the decision rule. In this paper, we implement the reject option in *p*-DPLS. Both the classification reliability and accuracy of the *p*-DPLS model are improved by identifying unreliable classifications and rejecting the sample instead of running the risk of misclassifying it.

2.3. Implementation of the reject option in p-DPLS

The reject option in the case of classification ambiguity (i.e. for overlapped PDFs) can be derived by adapting Chow's rule to the PDFs obtained in *p*-DPLS. Chow's rule sets a threshold t so that the sample is rejected if the highest *a posteriori* probability is lower than $1-t$. In other words, the sample is classified only if:

$$\max(P(\omega_0|\hat{y}_i), P(\omega_1|\hat{y}_i)) > (1-t) \tag{9}$$

Thus, only those samples whose classification is reliable enough are indeed classified. The other samples are rejected because they could be misclassified. The threshold that optimizes the trade-off between the error rate and reject rate can be derived from the costs associated with each classification result [29]:

$$t = \frac{\lambda_r - \lambda_c}{\lambda_e - \lambda_c} \tag{10}$$

where λ_e, λ_r, and λ_c, are the costs of incorrect classification, of rejection and of correct classification, respectively. The values that are assigned to these costs make the reject option tuneable. The cost of being wrong is higher than the cost of both rejecting and classifying correctly ($\lambda_e > \lambda_r > \lambda_c$). In fact, it is preferable to reject a sample and gather additional information than to classify the sample incorrectly. It is also generally assumed that classifying correctly has no cost ($\lambda_c = 0$). Note that Eq. (9) is a generalization of the standard Bayes rule. In particular, for the extreme case in which the cost of rejection λ_r equals the cost of misclassification λ_e, the reject threshold is $t = 1$ and Chow's rule is reduced to the standard Bayes rule, in which samples are never rejected. A sample is also not rejected if $t > 1/C$, where C is the number of possible classes ($C = 2$ for a binary classification) [34].

The second reason for using the reject option is to avoid classifying extreme samples that have a large *a posteriori* probability but low values at both PDFs. In order to solve this problem, Dubuisson and Masson [18] added a distance reject criterion to Chow's ambiguity reject option. This idea is implemented here for the *p*-DPLS model by imposing limits on the $\hat{y}$ values, which define the extreme regions in which the samples will be rejected. The limits are chosen so that the sum of the area in the tails of each PDF is five percent of the total area of the distribution (i.e. the distance reject probability equals 0.05 for each class, see Fig. 2) [19]. Since the limits depend on the shape of the distributions of each class, they are particular for each *p*-DPLS model with a given number of factors. In practice, when the PDFs are overlapped we have two operative limits, a High Limit (HL) and a Low Limit (LL) and when the PDFs are separated we have four limits (HL and LL for each class, see Fig. 2).

Assuming the constraints for the distance reject and the ambiguity reject, the Bayes rule with reject option is:

$$\begin{array}{lll} \text{Reject} & \text{if} & \hat{y}_i < \mathrm{LL}_0 \\ & \text{or if} & (\mathrm{HL}_0 < \hat{y}_i < \mathrm{LL}_1) \\ & \text{or if} & \hat{y}_i > \mathrm{HL}_1 \\ & \text{or if} & \max(P(\omega_0|\hat{y}_i), P(\omega_1|\hat{y}_i)) < (1-t) \\ \text{Otherwise} & & \\ \text{classify into } w_0 & \text{if} & P(\omega_0|\hat{y}_i) > P(\omega_1|\,\hat{y}_i) \\ \text{or into } w_1 & \text{if} & P(\omega_1|\hat{y}_i) > P(\omega_0|\hat{y}_i) \end{array} \quad (11)$$

2.4. Evaluation of the classification method performance

The *p*-DPLS models can be calculated for a different number of factors that are needed to explain the relevant information. Thus, every *p*-DPLS model will produce different $\hat{y}$ predictions for the calibration samples and, therefore, for the different PDFs, which, in turn, will influence the performance of the classifier. The performance of a classifier is commonly characterized by its error rate (or the classification rate, which is the percentage of correctly classified samples) when classifying a test set of unseen samples that were not used during the training phase. The actual class of every sample in the test set is compared to the class to which it is assigned by the classifier. In general terms, however, it is not the misclassification (and rejection) rate that we want to minimize, but the misclassification (and rejection) cost [35], since the cost more accurately reflects the objective of the classification rule [36]. The cost is here defined as:

$$\text{Cost} = \lambda_r \cdot N_r + \lambda_e \cdot N_e \quad (12)$$

where N_r is the number of rejected samples and N_e is the number of misclassified samples. The cost of correctly classifying a sample has been set to zero. Here, the minimization of the cost will be used to decide on the optimal number of factors in the *p*-DPLS model.

3. Results and discussion

3.1. Datasets

The proposed classification rule (Eq. (11)) was applied to two datasets, the human cancers dataset [37] and the breast cancer dataset [38]. These datasets have been studied extensively in the literature [39,40] and also used to evaluate the performance of classification models [41–44]. The human cancers dataset consists of 282 microRNA (miRNA, non-coding RNA species) normalized expression profiles for 218 samples, including 46 healthy samples (class ω_0) and 172 tumour samples (class ω_1) from several healthy and tumour tissues (ovary, colon and lung to mention a few). The dataset was divided into a training set and a test set by applying the Kennard–Stone algorithm [45] to the scores of the first 20 Principal Components (PCs), which were obtained from the Principal Component Analysis (PCA) of the raw gene expression matrix. For this dataset, the training set contained 153 samples (116 samples of class ω_1 and 37 samples of class ω_0), and the test set had 65 samples (56 of class ω_1 and 9 of class ω_0). The breast cancer dataset consists of 5361 normalized gene expression ratios. These were used in [38] to prove that a hereditable mutation influences the gene expression profile of breast cancer. Seven samples of the BRCA1 mutation were used as class ω_0, eight samples of BRCA2 mutation were used as class ω_1, and six samples of sporadic mutation were used as test samples.

3.2. Human cancers dataset

Although *p*-DPLS is a full-variable method, it can often be improved by carefully selecting the variables and removing irrelevant miRNA expressions that interfere with the discriminative power of the relevant miRNA [46]. For this dataset, the 100 variables with the highest VIP values (variable importance for the projection) were considered. VIP values were calculated as described in [8,47]. These values quantify how each variable influences the response summed over all components and classes.

For the selected variables, six *p*-DPLS models were calculated with 1–6 factors using mean-centred miRNA expression patterns (we will denote each model as *p*-DPLS$_A$, where A is the number of factors). The *a priori* probabilities for these six models were $P(\omega_0) = 37/153 = 0.24$ and $P(\omega_1) = 116/153 = 0.76$.

The PDF of classes ω_0 and ω_1 were calculated for each *p*-DPLS model (Eqs. (1)–(5)). The test sample was classified by obtaining its $\hat{y}$ prediction and then calculating the *a posteriori* probabilities (Eqs. (6a) and (6b)). Finally, the sample was either rejected or classified in the class with the highest *a posteriori* probability (Eq. (11)). In this dataset, the high and low limits (HL and LL) for $\hat{y}_i$ were defined so as to retain the five percent of the total area of the PDF in the tails of the distributions. The costs were arbitrarily set to $\lambda_c = 0$, $\lambda_r = 0.25$, and $\lambda_e = 1$ because no information was available about the costs of each classification decision. Note that these costs are relative, and indicate that it is preferable to reject four samples than to classify one wrongly. These values are illustrative and should be adjusted for each particular classification problem. With these values, the threshold value for rejection in the ambiguity zone is $t = 0.25$ (Eq. (10)). The models with $A = 1$–6 factors were validated by leave-one-out cross-validation (CV). In this process, sample *i* was left out of the training set, the *p*-DPLS$_A$ model was calculated, and the prediction $\hat{y}_i$ for the left-out sample was obtained (note that the *a priori* probabilities were recalculated to take into account that one sample had been left out). This procedure was repeated for all the samples of the training set and for all the *p*-DPLS models.

Fig. 3 and Table 1 show the cross-validation results obtained for the different *p*-DPLS models when the reject option (Eq. (11)) is considered. Note that predictions for samples in class ω_0 are around 0 and predictions for samples in class ω_1 are around 1, but that the predictions partially overlap in models with less than four factors (underfitted models). As a result of the overlap, many samples are either rejected or wrongly classified and the cost of these models (Table 1) is high. For example, for *p*-DPLS$_2$, 51% of the samples in class ω_0 were rejected by CV and 27% were misclassified. On the other hand, the predictions from the models with four to six factors are grouped tighter together. Consequently, these models have fewer misclassifications, fewer rejections, and lower classification costs.

In terms of classification cost, the optimal model is *p*-DPLS$_5$ since no further improvement is obtained for the model of six factors. The PDFs for this model are presented in Fig. 4A and the *a posteriori* probabilities across the $\hat{y}$ domain are presented in Fig. 4B. The limits were found to be $\mathrm{LL}_0 = -0.43$ and $\mathrm{HL}_1 = 1.42$. Thus, samples with a predicted value $\hat{y}_i < -0.43$ or $\hat{y}_i > 1.42$ would be flagged as

Table 1
Classification of validation samples by leave-one-out cross-validation and test samples for the different p-DPLS models for $t = 0.25$. In brackets, classifications performed without considering the reject option.

Factors	Cost	Cross-validation samples					Test samples				
		Wrongly classified	Rejected	Correctly classified	Wrongly classified	Rejected	Correctly classified	Wrongly classified	Rejected	Correctly classified	Wrongly classified	Rejected	Correctly classified
		Samples of class ω_0			Samples of class ω_1			Samples of class ω_0			Samples of class ω_1		
1	30.3	0 (6)	24	10 (31)	2 (19)	89	25 (97)	0 (2)	6	3 (7)	0 (0)	17	39 (55)
2	15.5	10 (22)	19	8 (15)	0 (0)	3	113 (116)	2 (4)	5	2 (5)	0 (0)	0	56 (56)
3	7.3	4 (9)	13	20 (28)	0 (0)	0	116 (116)	0 (2)	4	5 (7)	0 (0)	0	56 (56)
4	5	2 (4)	8	27 (33)	0 (0)	4	112 (116)	0 (0)	2	7 (9)	0 (0)	0	56 (56)
5	3	1 (4)	4	32 (33)	0 (1)	4	112 (115)	0 (0)	0	9 (9)	0 (0)	0	56 (56)
6	3	1 (5)	7	29 (32)	0 (1)	1	115 (115)	0 (0)	0	9 (9)	0 (0)	0	56 (56)

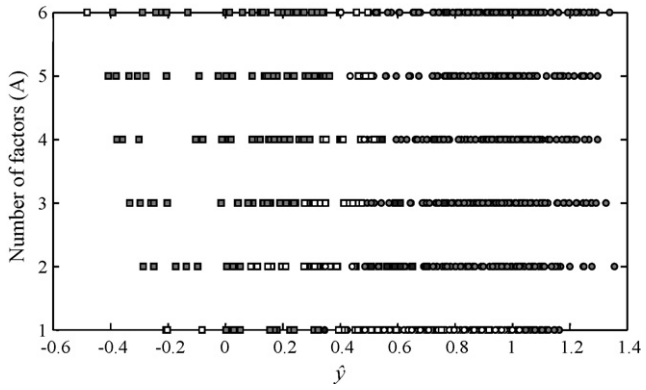


Fig. 3. Prediction of the training samples by CV for the different p-DPLS models with reject option. *Squares*: healthy samples (class ω_0). *Circles*: tumour samples (class ω_1). *Grey*: samples correctly classified. *White*: samples rejected. *Black*: samples wrongly classified.

outliers and rejected. These limits were different for each p-DPLS$_A$ model because the training sample predictions changed. According to the rejection criterion, eight samples (four from class ω_0 and four from class ω_1) were rejected, all of them in the ambiguity region (Table 1). As an example, the dot in Fig. 4 corresponds to the sample T_BRST_2 (tumour sample, class ω_1) during the leave-one-out process. The prediction is $\hat{y}_i = 0.44$ and the calculated *a posteriori* probabilities are $P(\omega_0|\hat{y}_i) = 0.59$ and $P(\omega_1|\hat{y}_i) = 0.41$ (Eqs. (6a) and (6b)). Since both probabilities are similar, the confidence (reliability) that the classification is correct is low because a slight shift in $\hat{y}_i$ due to measurement errors could have changed the assigned class. The application of the classic Bayes rule (Eq. (8)) would assign the sample to the class with the highest *a posteriori* probability, meaning that the sample would be wrongly classified into class ω_0. By allowing the reject option, defined here by Chow's rule (with $t = 0.25$), the sample was rejected and not classified because the highest *a posteriori* probability was below $1 - t$ (i.e. $\max(P(\omega_1|\hat{y}_i), P(\omega_0|\hat{y}_i)) < 0.75$). In this case, the reject option prevented us from classifying a tumour sample as a healthy sample, and the expert would be prompted to make more tests before the final diagnosis. It is interesting to note, as we indicated before, that the reject option's performance depends on the relative costs assigned to the classification results. Thus, by setting different costs, the threshold (and hence the number of samples rejected) will be tuned to meet the experimenter's needs.

For comparison, Table 1 shows in brackets the classification results when the classical Bayes rule is applied. For the model that best minimizes the cost, that is, p-DPLS$_5$, five samples were misclassified if the reject option was not applied, whereas only one sample was misclassified (a healthy sample) when the reject constraints were applied. Thus, this model's classification accuracy (i.e. the ratio of samples well classified and the number of samples classified) was improved from 97% (148/153) to 99% (144/148). Notice, however, that the reject option also rejected some samples that would otherwise be correctly classified: the number of samples well classified decreased from 148 to 144. This reduction in the number of well classified samples is the price to pay for safeguarding against errors, and follows the trend of the suggested costs of classifications, in which rejecting four samples was preferable to misclassifying one.

Different reject thresholds were tested by varying the classification costs (Table 2). When $\lambda_r = 0.10$, $\lambda_e = 1$ and $\lambda_c = 0$, the threshold was $t = 0.10$. As expected, the number of rejected samples increased because the cost of doing so decreased (i.e. we preferred to reject ten samples rather than classify one wrongly). However, the number of misclassified samples did not change, which means that the rule rejected samples that would have been correctly classi-

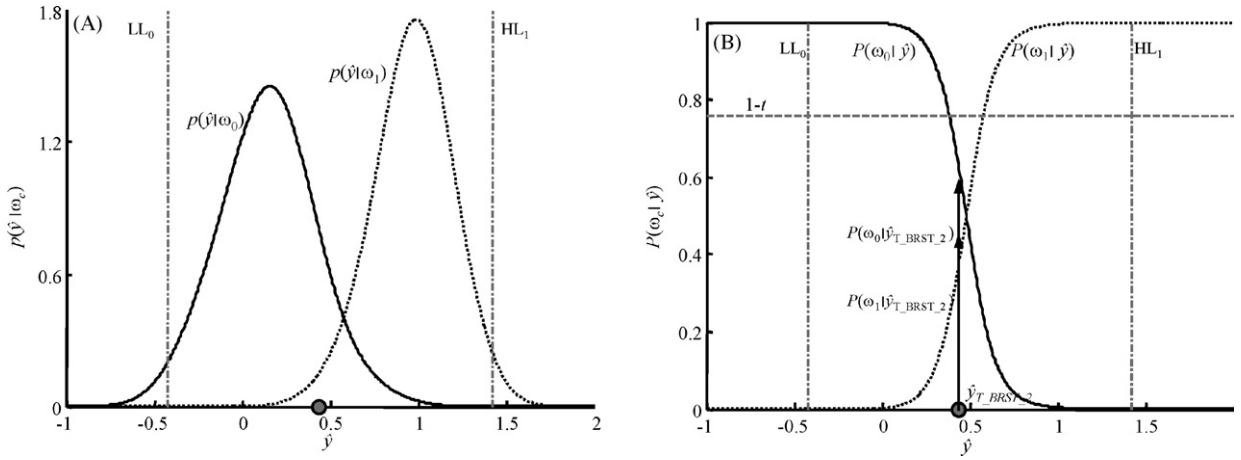


Fig. 4. (A) PDFs for the five factor *p*-DPLS model obtained from the training samples during the LOOCV process when T_BRST_2 is used as the validation sample. (B). *A posteriori* probabilities across the $\hat{y}$ domain (Eq. (6a) and (6b)) derived from the PDFs in (A). The prediction and the *a posteriori* probability for sample T_BRST_2 during the LOOCV process are also shown.

fied with $t = 0.25$. Thus, decreasing t to below 0.25 did not improve the model's classification performance for this dataset. On the other hand, when t was set to 0.35 (i.e. $\lambda_r = 0.35$, $\lambda_e = 1$, $\lambda_c = 0$), the results (not shown) were the same as those obtained for $t = 0.25$. Hence, $t = 0.25$ was considered optimal for this p-DPLS$_5$ model.

The samples of the test set were also classified according to Eq. (11). For the p-DPLS$_5$ model using $t = 0.25$, 100% of the samples were well classified and there were no rejects (Fig. 5 and Table 1). By setting the threshold to $t = 0.10$, two correctly classified healthy samples turned into rejects (Table 2). This was seen in the classification of the training samples above and highlights the need to set an adequate reject threshold in order to obtain an adequate trade-off between the rejects and the misclassifications. This will depend on the needs of the experimenter and the cost constraints in each particular application.

3.3. Breast cancer dataset

This dataset demonstrates the rejection of test samples that are outside the class limits. The same methodology as for the human cancers dataset was used except that the Kennard Stone algorithm was not applied. Instead, the samples of mutations BRCA1 and BRCA2 were used as a training set and the sporadic mutation samples were used as a test set. The aim was to show that the classification rule could reject prediction samples from non-modelled classes. This would prevent the classification error that would otherwise occur if the classifier had to assign the samples to one of the two modelled classes. Detecting this type of outlier is fundamental to the application of any classification rule.

Probabilistic DPLS models were calculated for one to three factors by using $\log_2$ mean-centred gene expression data from BRCA1 (class ω_0) and BRCA2 (class ω_1) mutation samples. This data consisted of the 51 most relevant gene expressions according to [38]. These genes were found to be the most discriminative between the three mutations. The costs of classifying correctly, rejecting and misclassifying were set at $\lambda_c = 0$, $\lambda_r = 0.25$, and $\lambda_e = 1$ respectively. The one factor p-DPLS model (p-DPLS$_1$) was the optimal model with the lowest cost (i.e. cost of 0.5). Models with two and three factors were overfitted, with costs of 2.5 and 3.25 respectively. These higher costs are due to the fact that most of the samples are rejected and, although there are no misclassifications, the classifiers become useless. For example, for the p-DPLS$_2$ model, 10 of the 15 training samples were rejected during LOOCV. Similarly, the p-DPLS$_3$ model rejected 13 of the training samples.

The p-DPLS$_1$ calculated with the 51 gene expressions selected in the bibliography was able to distinguish the samples of class ω_0 from those of class ω_1, thus providing well separated PDFs (Fig. 6). Only the sample *s1252_P2*, of class ω_0, and the sample *s1816_P13*, of class ω_1, were rejected during LOOCV. The predictions of both samples were outside the limits of the classes (i.e. $\hat{y}_{s1252_P2} > HL_0$ and $\hat{y}_{s1816_P13} > HL_1$). Notice that because the PDFs were not overlapped,

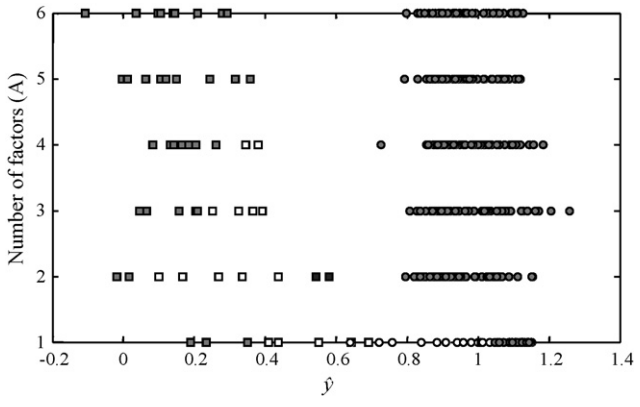


Fig. 5. Classification of test samples for the different *p*-DPLS models with reject option. *Squares*: healthy samples (class ω_0). *Circles*: tumour samples (class ω_1). *White*: correctly classified. *Grey*: rejected. *Black*: wrongly classified.

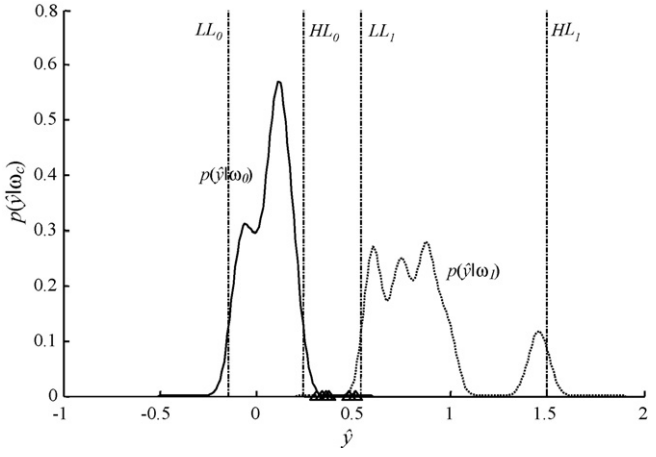


Fig. 6. PDFs for the one factor *p*-DPLS model. Limits on $LL_0 = -0.15$, $HL_0 = 0.24$, $LL_1 = 0.54$ and $HL_1 = 1.50$. *Triangles* represent the test samples classified with p-DPLS$_1$.

Table 2
Classification of validation samples via leave-one-out cross-validation and test samples for the different p-DPLS models for $t = 0.10$.

Factors	Cost	Cross-validation samples						Test samples					
		Wrongly classified	Rejected	Correctly classified	Wrongly classified	Rejected	Correctly classified	Wrongly classified	Rejected	Correctly classified	Wrongly classified	Rejected	Correctly classified
		Samples of class ω_0			Samples of class ω_1			Samples of class ω_0			Samples of class ω_1		
1	16.1	0	36	1	1	115	0	0	9	0	0	56	0
2	6.5	2	31	4	0	14	102	0	9	0	0	0	56
3	5.9	3	23	11	0	6	110	0	7	2	0	0	56
4	3.5	1	17	19	0	8	108	0	3	6	0	0	56
5	3.3	1	14	22	0	9	107	0	2	7	0	0	56
6	2.9	1	13	23	0	4	110	0	2	7	0	0	56

there was no ambiguity region and the limits of the classes were defined by four operative limits. The classification performance of the p-DPLS$_1$ did not change when the reject threshold was varied to $t = 0.35$ and 0.10.

The p-DPLS$_1$ model was used to classify the six test samples of sporadic mutation of breast cancer. This mutation was not modelled in the training step; hence, all these samples should be pointed as outliers and not classified. Classifying these samples in any of the two modelled classes would result in a classification error. Fig. 6 shows the PDFs (Eqs. (4) and (5)) of class ω_0 and class ω_1 for p-DPLS$_1$ together with the predictions for the test samples. According to Eq. (11), all test samples were correctly detected as outliers and rejected since their predictions $\hat{y}$ were between the limits HL$_0$ ($\hat{y} = 0.24$) and LL$_1$($\hat{y} = 0.54$). If the reject constraints had not been applied, the classifier would have assigned the test samples to the class with the highest *a posteriori* probability. In this case, the samples *s1572_P16* and *s1324_P17* would have been incorrectly classified into class ω_1 (i.e. as BRCA2 mutation samples) and the remaining samples (*s1649_P15*, *s1320_P18*, *s1542_P19* and *s1281_P21*) would have been incorrectly classified into class ω_0 (as BRCA1 mutation samples). For these samples, the *a posteriori* probability for one class was near 1. For example, sample *s1572_P16* had $p(\hat{y}_i|\omega_0) = 6 \times 10^{-6}$ and $p(\hat{y}_i|\omega_1) = 2 \times 10^{-3}$ which results in $P(\omega_0|\hat{y}_i) \approx 0$ and $P(\omega_1|\hat{y}_i) \approx 1$. Therefore, if it is believed that the *a posteriori* probability demonstrates the classification's reliability, then the high values of probability obtained for the test samples would suggest that we can trust the classifications, despite the fact that all of them were incorrect. This shows that the classic Bayes rule is unreliable when both conditional probabilities $p(\hat{y}_i|\omega_0)$ and $p(\hat{y}_i|\omega_1)$ are low. Moreover, it should be noted that the predicted values are not as extreme as those expected for outliers. Hence, these are not directly suspicious samples because of their $\hat{y}_i$ values. It was the reject option, which set limits on the classes, which allowed these samples to be detected.

4. Conclusions

Recently, the DPLS method has received much attention in the field of gene expression data analysis. We have applied a new version of DPLS, namely probabilistic DPLS (p-DPLS), to classify biological samples using their microRNA (miRNA) expression patterns and cDNA-microarray data. p-DPLS takes into account the uncertainty of the PLS predictions in the definition of the classification model. In this version, the possibility of rejection has been introduced. p-DPLS with reject option performs better than the original p-DPLS, because only those samples that have the highest probability of being correctly classified are indeed classified, whereas doubtful cases are rejected. The methodology involves evaluating the probability of each classification together with the overall cost of the classifications performed for each model. In addition, the reject option allows us to deal with situations in which the results of the Bayes rule may be questioned. Moreover, the classification rule with reject option can help the experimenter to check that a sample does not belong to any of the classes modelled in the training step and therefore to ensure that it is rejected rather than misclassified. Thus, the reject option enables the classifier to detect outliers, and this in turn provides a new approach for improving outlier detection methods in the near future.

Acknowledgements

The authors thank the Department of Universities, Research and the Information Society of the Catalan Government for providing Cristina Botella's doctoral fellowship, and of the Spanish Ministry of Education and Science (project CTQ2007-66918/BQU). The

authors would like also to acknowledge the useful comments of the referees.

References

[1] A.A. Alizadeh, M.B. Eisen, R.E. Davis, C. Ma, I.S. Lossos, A. Rosenwald, J.C. Boldrick, H. Sabet, T. Tran, X. Yu, J.I. Powell, L. Yang, G.E. Marti, T. Moore, J.H. Jr, L. Lu, D.B. Lewis, R. Tibshirani, G. Sherlock, W.C. Chan, T.C. Greiner, D.D. Weisenburger, J.O. Armitage, R. Warnke, R. Levy, W. Wilson, M.R. Grever, J.C. Byrd, D. Botstein, P.O. Brown, L.M. Staudt, Nature 403 (2000) 503–511.

[2] T.R. Golub, D.K. Slonim, P. Tamayo, C. Huard, M. Gaasenbeek, J.P. Mesirov, H. Coller, M.L. Loh, J.R. Downing, M.A. Caligiuri, C.D. BloomÞeld, E.S. Lander1, Science 285 (1999) 531–537.

[3] L. Li, T.A. Darden, C.R. Weinberg, A.J. Levine, L.G. Pedersen, Combinatorial Chemistry & High Throughput Screening 4 (2001) 727–734.

[4] M.P.S. Brown, Proceedings of the National Academy of Sciences 97 (2000) 262–267.

[5] T.S. Furey, N. Cristianini, N. Duffy, D.W. Bednarski, M. Schummer, D. Haussler, Bioinformatics 16 (2000) 906–914.

[6] D.V. Nguyen, D.M. Rocke, Bioinformatics 18 (2002) 1216–1226.

[7] E.C. Gunther, Proceedings of the National Academy of Sciences 100 (2003) 9608–9613.

[8] A.-L. Boulesteix, K. Strimmer, Briefings in Bioinformatics 8 (2007) 32–44.

[9] D.V. Nguyen, D.M. Rocke, Bioinformatics 18 (2002) 39–50.

[10] M. Pérez-Enciso, M. Tenenhaus, Human Genetics 112 (2003) 581–592.

[11] O. Modlich, H.B. Prisack, M. Munnes, W. Audretsch, H. Bojar, Journal of Translational Medicine 3 (2005).

[12] M.Z. Man, G. Dyson, K. Jonhson, B. Liao, Journal of Biopharmaceutical Statistics 14 (2004) 1065–1084.

[13] M. Bylesjö, D. Eriksson, A. Sjödin, M. Sjöström, S. Jansson, H. Antti, J. Trygg, BMC Bioinformatics 6 (2005) 250.

[14] D.M.J. Tax, R.P.W. Duin, Pattern Recognition Letters 29 (2008) 1565–1570.

[15] B. Knauthe, S. Steffen, M. Barth, L. Niewoehner, M. Otto, Journal of Chemometrics 22 (2008) 252–258.

[16] G. Fumera, F. Roli, G. Giacinto, in: SSPR & SPR (Ed.), Advances in Pattern Recognition, Springer, Berlin, Heidelberg, 2000, pp. 863–871.

[17] P.R.R. Devarakota, B. Mirbach, B. Ottersten, Pattern Recognition Letters 29 (2008) 243–253.

[18] B. Dubuisson, M. Masson, Pattern Recognition 26 (1993) 155–165.

[19] R. Muzzolini, Y.-H. Yang, R. Pierson, Pattern Recognition 31 (1998) 345–369.

[20] B.D. Ripley, in: B.K.a.S. Gielen (Ed.), Neural Networks: Artificial Intelligence and Industrial Applications, Springer, 1995, pp. 183–190.

[21] B.D. Ripley, Pattern Recognition and Neural Networks, Cambridge University Press, Cambridge, United Kingdom, 2000.

[22] F. Tortorella, et al., in: F.J. Ferri (Ed.), Advances in Pattern Recognition: Joint IAPR International Workshops, SSPR 2000 and SPR 2000, Lecture Notes in Computer Science, vol. 1876, Springer-Verlag, Heidelberg, 2000, pp. 611–620.

[23] G. Fumera, I. Pillai, F. Roli, Proceedings of the 12th International Conference on Image Analysis and Processing (ICIAP'03), 2003.

[24] G. Fumera, F. Roli, in: S. Ed (Ed.), Proceedings of 2nd International Workshop on Multiple Classifier Systems (MCS 2001), Lecture Notes in Computer Science, Robinson College, Cambridge, UK, 2001, pp. 329–338.

[25] G. Fumera, F. Roli, G. Giacinto, Pattern Recognition 33 (2000) 165–167.

[26] L.P. Cordella, C.D. Stefano, F. Tortorekka, M. Vento, IEEE Transactions on Neural Networks 6 (1995) 1140–1147.

[27] T. Landgrebe, D. Tax, P. Paclík, R. Duin, Pattern Recognition Letters 27 (2006) 908–917.

[28] T. Landgrebe, D. Tax, P. Paclík, R. Duin, C. Andrew, Fifteenth Annual Symposium of the Pattern Recognition Association of South Africa, 2004, pp. 57–62.

[29] C.K. Chow, IEEE-Transactions on Information Theory 16 (1970) 41–46.

[30] B. Hanczar, E.R. Dougherty, Bioinformatics 24 (2008) 1889–1895.

[31] R.O. Duda, P.E. Hart, D.G. Store, Pattern Classification, 2nd edition, John Wiley & Sons, Inc., New York, 2001.

[32] N.F. Pérez, J. Ferré, R. Boqué, Chemometrics and Intelligent Laboratory Systems 95 (2009) 122–128.

[33] H. Wold, in: K.a.N.L. Johnson (Ed.), Encyclopedia of Statistical Sciences, Wiley, New York, 1985, pp. 581–591.

[34] A. Webb, Statistical Pattern Recognition, 2n edition, Malvern, UK, 2002.

[35] A.P. Bradley, Pattern Recognition 30 (1997) 1145–1159.

[36] M. Li, I.K. Sethi, Pattern Recognition 39 (2006) 1230–1240.

[37] J. Lu, G. Getz, E.A. Miska, E. Alvarez-Saavedra, J. Lamb, D. Peck, A. Sweet-Cordero, B.L. Ebert, R.H. Mak, A.A. Ferrando, J.R. Downing, T. Jacks, H.R. Horvitz, T.R. Golub, Nature Letters 435 (2005).

[38] I. Hedenfalk, D. Duggan, Y. Ghen, M. Radmacher, M. Bittner, R. Simon, P. Meltzer, B. Gusterson, M. Esteller, O.-P. Kallioniemi, B. Wilfond, A. Borg, J. Trent, The New England Journal of Medicine 344 (2001) 539–548.

[39] Y. Zheng, C.K. Kwoh, Data Mining for Biomedical Applications, Proceedings, vol. 3916, 2006, pp. 143–154.

[40] J. Lin, M. Li, Expert Review of Molecular Diagnostics 8 (2008) 263–276.

[41] A.-L. Boulesteix, Statistical Applications in Genetics and Molecular Biology 3 (2004), article 33.

[42] M. Raza, I. Gondal, D. Green, R.L. Coppel, Proceedings of the Third International Conference on Information Technology and Applications (ICITA'05), IEEE, vol. 2, 2005, pp. 475–480.

[43] K.V. Branden, S. Verboven, Computational Biology and Chemistry 33 (2009) 7–13.

[44] N. Pochet, F.D. Smet, J.A.K. Suykens, B.L.R.D. Moor, Bioinformatics 20 (2004) 3185–3195.

[45] R.W. Kennard, L.A. Stone, Technometrics 11 (1969) 137–148.

[46] Y. Lu, J. Han, Information Systems 28 (2003) 243–268.

[47] G. Musumarra, V. Barresi, D.F. Condorelli, C.G.F.a.S. Scire', Journal of Chemometrics 18 (2004) 125–132.

Talanta 80 (2009) 329–337

Contents lists available at ScienceDirect

Talanta

journal homepage: www.elsevier.com/locate/talanta

An interlaboratory study as useful tool for proficiency testing of chemical oxygen demand measurements using solid substrates and liquid samples with high suspended solid content

F. Raposo[a,*], M.A. de la Rubia[a], R. Borja[a], M. Alaiz[a], J. Beltrán[b], C. Cavinato[c], M. Clinckspoor[d], G. Demirer[e], E. Diamadopoulos[f], B. Helmreich[g], P. Jenicek[h], N. Martí[i], R. Méndez[j], J. Noguerol[k], F. Pereira[l], S. Picard[m], M. Torrijos[n]

[a] *Instituto de la Grasa, Consejo Superior de Investigaciones Científicas (CSIC), Avenida Padre García Tejero 4, 41012 Seville, Spain*
[b] *Chemical Engineering Department, Extremadura University (UEx), Avenida de Elvas S/N, 06071 Badajoz, Spain*
[c] *Department of Environmental Science, University CaïFoscari of Venice, Calle Larga Santa Marta, 2137-30123 Venice, Italy*
[d] *Organic Waste System N.V. Dok Noord 4, 9000 Gent, Belgium*
[e] *Department of Environmental Engineering, Middle East Technical University, Inönü Bulvari, 06531Ankara, Turkey*
[f] *Department of Environmental Engineering, Technical University of Crete, 73100 Chania, Greece*
[g] *Institute of Water Quality Control, Technical University of Munich, Am Coulombwall, 85748 Garching, Germany*
[h] *Department of Water Technology and Environmental Engineering, Institute of Chemical Technology Prague, Technická 5, 16628 Prague, Czech Republic*
[i] *Chemical Engineering Department, University of Valencia, Dr. Moliner 50, 46100 Burjassot, Valencia, Spain*
[j] *Department of Chemical Engineering, School of Engineering, University of Santiago de Compostela, Rua Lope Gómez de Marzoa S/N, 15782 Santiago de Compostela, Spain*
[k] *GIRO Technological Centre, Rambla Pompeu Fabra 1, 08100 Mollet del Valles, Barcelona, Spain*
[l] *Institute for Biotechnology and Bioengineering (IBB), Centre of Biological Engineering, University of Minho, Campus de Gualtar, 4710-057 Braga, Portugal*
[m] *Cemagref, Environmental Management and Biological Treatment of Wastes Research Unit, Avenue de Cucilleï 17, 35044 Rennes Cedex, France*
[n] *INRA, UR50, Laboratoire de Biotechnologie de l'Environnement, Avenue des Etangs, F-11100, Narbonne, France*

ARTICLE INFO

Article history:
Received 6 February 2009
Received in revised form 17 June 2009
Accepted 30 June 2009
Available online 7 July 2009

Keywords:
Interlaboratory study
Proficiency testing
Chemical oxygen demand
Anaerobic digestion
Homogeneity test
Solid substrate
Suspended solids

ABSTRACT

In 2008, the first Proficiency Testing Scheme of Chemical Oxygen Demand (*1st COD-PT^{ADG}*) was conducted to assess the results obtained for different research groups whose field work is mainly anaerobic digestion. This study was performed using four samples, two solid samples as raw materials and two solid samples to prepare high concentration suspended solid solutions. Invitations were sent to a large number of laboratories, mainly to anaerobic digestion research groups. Finally, thirty labs from sixteen countries agreed to participate, but for different reasons four participants could not send any data. In total, twenty-six results were reported to the *COD-PT* coordinator.

This study showed the importance of continuous participation in proficiency testing (PT) schemes in order to compare the results obtained. Taking into account the lack of a general standard method and high quality certified reference materials (*CRMs*), the traceability of COD determination is not currently easy to check. In addition, the spread of participants' results obtained was high and pointed to the advisability of using consensus values due to their unreliability. Therefore, the theoretical oxygen demand (ThOD) values were considered as assigned values for all the samples analysed. On the other hand, in this PT the established standard deviation (*ESD*) has been determined by the Horwitz modified function.

Participants of this *1st COD-PT^{ADG}* were asked to give a short report on the analytical method used. Although all the participants used potassium dichromate as their oxidant reagent, their experimental procedures were very different. With the purpose of comparing the results obtained, the different experimental conditions used were classified into five methods, corresponding to two main categories, open and closed reflux. The performance of laboratories was expressed by the *z*-score, whose value is considered satisfactory when *z*-score $\leq \pm 2$. The overall analytical data evaluation showed that 64% of *z*-scores obtained were outside the accepted limits.

© 2009 Elsevier B.V. All rights reserved.

1. Introduction

There are a large number of laboratories that can measure the chemical oxygen demand (COD). COD is an empirical determination

* Corresponding author. Tel.: +34 95 4689654; fax: +34 95 4691262.
E-mail address: fraposo@cica.es (F. Raposo).

0039-9140/$ – see front matter © 2009 Elsevier B.V. All rights reserved.
doi:10.1016/j.talanta.2009.06.071

used worldwide to find out the index of pollution of any aqueous sample, although it is also used to determine the organic content of solid substrates. For COD determinations, a wide range of chemicals has been used as oxidizing agents, including dichromate, permanganate, ceric acid, iodate and persulphate. The dichromate method is preferable to other methods using different oxidants because of its superior oxidizing ability, its applicability to a wide variety of samples and its easy manipulation. In the COD reference method, samples are oxidised by potassium dichromate in an acid sulphuric medium. Silver sulphate and mercury sulphate are added to catalyse the oxidation and to suppress the interference effects of chloride, respectively. The resulting mixture is refluxed for 2 h and the residual dichromate reagent is determined by titration with standardised ferrous ammonium sulphate or spectrophotometrically. The amount of dichromate reduced is expressed as COD in the form of milligrams of oxygen consumed per litre or gram of sample.

Proficiency testing (PT) is an essential element of laboratory quality assurance. The interlaboratory comparison of an external quality control test material allows individual laboratories to compare their analytical results with those from other laboratories whilst providing them with objective standards to perform with.

The performance evaluation of anaerobic digestion processes is based on chemical analysis measurements. Accurate and precise results are essential when monitoring anaerobic reactors because only reliable analytical results can serve as a basis for drawing meaningful conclusions about the situation of the biological process and thus avoid misinterpretation. However, the COD determination of samples typically from anaerobic reactors, as solid substrates and liquid samples with a high concentration of suspended solids, is currently in the following situation:

- no companies organise COD-PT schemes.
- no appropriate certified reference materials are available for this determination.
- no references of COD analytical methods are cited in the literature.
- the frequent use of the APHA-AWWA-WPCF standard methods [1] for COD determination of solid samples and high concentration suspended solids solutions by dilution of the sample, with the consequent inaccuracy in the final results obtained.

No previous interlaboratory studies are reported in the literature about the quality of COD measurements obtained in such types of samples. For this reason, a PT was organised. The aim of this *1st COD-PT* was to take some information from the results obtained for all participants, testing the different analytical methods used and comparing the results reported in order to check their day-to-day analytical performances and improve their quality. The objective of this PT was not the evaluation of participants by a general proficiency ranking. Therefore, the ranking of participants was totally rejected and not reported.

2. Organisation of proficiency testing scheme

This study is the first attempt of a COD worldwide interlaboratory comparison using solid samples and high concentration suspended solids solutions. The scheme was organised by the Spanish National Research Council (CSIC) through the Instituto de la Grasa, specifically by the Water and Wastewater Treatment group. The PT coordinator and collaborators were responsible for designing the scheme, the preparation and validation of test materials, the production and distribution of instructions and test materials to participating laboratories, the collection and statistical analysis of the data obtained from the PT and feedback of the results to the participants.

This PT was carried out according to the International Harmonised Protocol for the PT of Analytical Chemistry Laboratories [2]. The exercise took place from September 2008, when the samples were shipped to the laboratories for analysis, to the beginning of October 2008, when the last reports of the results were received. The deadline for the reporting of results was extended upon the request of eight participants so as not to exclude their results. Although initially, thirty groups from sixteen countries agreed to participate, finally four participants could not send any data: 1 lab never received the samples, 2 labs admitted to being unable to determine the samples and 1 lab gave no explanation. Finally, twenty-six results were reported to the *COD-PT* coordinator. Firstly, the individual lab reports, including the specific results of each participant, and secondly a draft general report with the whole results were sent to participants.

The determination of COD does not require great laboratory skills or highly selective and sensitive analytical techniques and procedures with difficult validation or accreditation by recognized bodies. Therefore, no information was required to participants about their accreditation status for COD parameter according to ISO/IEC 17025 [3], or their participation in previous PTs.

3. Materials and methods

3.1. Materials

3.1.1. Description of samples

All laboratories participating in the PT to assess the COD measurement quality were required to analyse four different samples. The samples were divided into two main groups; solids samples (SS) and high concentration suspended solid samples (HC3S).

Table 1
Characterisation of solid substrates used in the *1st COD-PT*^{ADG}.

	(CRM)	(Qu)	(SuOC)
Particle size (mm)	0.2–1.0	1.4–2.0	<0.355
Moisture (%)	7.0 ± 0.3	10.1 ± 0.1	6.7 ± 0.3
Chemical composition (%dry basis)			
Carbohydrates	N.D.	67.3	20.3
Fat	N.D.	5.0 ± 0.1	0.8 ± 0.1
Protein	N.D.	18.0 ± 0.5	36 ± 1
Fibre	N.D.	7 ± 1	34.4 ± 0.5
Elemental analysis (%dry basis)			
Organic content	60.5 ± 0.2	97.3 ± 0.2	91.5 ± 0.3
C	33.3 ± 0.2	44.9 ± 0.2	45.9 ± 0.1
H	4.6 ± 0.1	6.2 ± 0.2	5.7 ± 0.2
N	4.7 ± 0.2	2.8 ± 0.1	6.6 ± 0.1
S	1.27 ± 0.04	0.009 ± 0.001	0.36 ± 0.04
Theoretical oxygen demand (mg O_2 g^{-1} TS)	988	1210	1239

3.1.1.1. Sample 1 (SS-1) – certified reference material (CRM). This sample is a sewage sludge provided by LGC Promochem as the certified reference material 055-050 (it included the certified values of 19 metals plus COD, Kjeldahl nitrogen and total phosphorus). This CRM was produced and certified by Resource Technology Corporation (USA and UK). The COD certified value was 771 ± 192 mg O_2 g^{-1} total solids (dry-weight basis). This value was rejected as the assigned value due to significant discrepancy with theoretical oxygen demand (ThOD) and disagreements with the data reported by the company organising the material-certification study.

3.1.1.2. Sample 2 (SS-2) – Quinoa (Qu). This substrate is a species of goosefoot (*Chenopodium quinoa*) grown as a crop primarily for its edible oil, but its leaves can also be used as food. Quinoa is also named Andean rice because it originates from the Andean region of South America where it had the greatest nutritional importance in pre-Columbian Andean civilizations. It is a pseudo-cereal rather than a true cereal as it is not a grass.

3.1.1.3. Samples 3 and 4 (HC3S-1 and HC3S-2) – sunflower oil cake (SuOC). SuOC is a by-product made up of what remains after the oil extraction processes of whole sunflower seeds. It is a heterogeneous substrate that can be broken down into three main components: a proteinaceous fraction, a lignocellulosic fraction and a soluble fraction.

Table 2
Homogeneity of solid substrates—summary of statistical parameters obtained.

Sample	Test	Experimental value	Critical value	Result
(*CRM*)	Cochran	0.31833	0.5410	Pass
	Precision of method	0.48336	0.5	Pass
	Homogeneity	0	0.00022	Pass
(*Qu*)	Cochran	0.31703	0.5410	Pass
	Precision of method	0.38969	0.5	Pass
	Homogeneity	0.00009	0.00027	Pass
(*SuOC*)	Cochran	0.33469	0.5410	Pass
	Precision of method	0.27901	0.5	Pass
	Homogeneity	0.00014	0.00021	Pass

3.1.2. Preparation of samples

To ensure that identical samples were analysed for all participating laboratories, the preparation of samples is a fundamental and critical step of the PT scheme.

The commercially available *CRM* was re-bottled and re-labelled without further manipulation, and could be analysed as raw material. The two remaining substrates were sieved prior to subsampling in order to keep only the particles of desired size and, consequently, to avoid the lack of uniformity in the samples tested.

Samples 3 and 4 were two spiked suspensions with different substrate concentration levels of. These samples required in-lab

Table 3
Summary of participants' analytical procedures.

Lab	Method	Digestion reagent		Acid reagent			$HgSO_4$	Water	End-point
		$K_2Cr_2O_7$		H_2SO_4–Ag_2SO_4					
Code		Vol. (mL)	Conc. (N)	Vol. (mL)	Conc.[a] (%)	Conc.[b] (g/L)		Vol. (mL)	
2	(1) OR-LCM	40	0.5	25	98	10	No	0	PT[c]
4	(1) OR-LCM	20	0.25	15	98	0	Yes	10	TT[d]
5	(1) OR-LCM	10	0.25	30	98	10	Yes	20	TT
6	(1) OR-LCM	10	0.25	30	98	15	Yes	0	TT
7[e]	(1) OR-LCM	5	0.24	15	98	10	Yes	10	TT
10	(1) OR-LCM	50–100	0.5	75	98	10	Yes	0	TT
11[e]	(1) OR-LCM	10	0.12	30	98	10	Yes	20	TT
12[f]	(1) OR-LCM	25	0.24	75	98	41	Yes	50	PT
12[e]	(1) OR-LCM	6	0.24	14	98	41	Yes	10	TT
17	(1) OR-LCM	50	0.4	50	98	0	No	0	PT
22[f]	(1) OR-LCM	25	0.25	75	98	10	Yes	50	PT
22[e]	(1) OR-LCM	25	0.25	75	98	10	Yes	0	PT
3[e]	(2) OR-HCM	25	2.0	40	98	0	No	0	PT
7[e]	(2) OR-HCM	25	1.0	30	98	10	Yes	0	TT
11[e]	(2) OR-HCM	20	1.2	30	98	10	Yes	20	TT
13	(2) OR-HCM	20	1.2	30	98	10	Yes	10	TT
14	(2) OR-HCM	20	1.0	40	98	10	Yes	40	PT
18[e]	(2) OR-HCM	15	1.0	45	98	10.7	Yes	20	TT
19	(2) OR-HCM	20	1.2	30	95	10	Yes	15	PT
24	(2) OR-HCM	20	1.2	30	98	10	Yes	10	TT
8	(3) CR-TM	1.5	0.2	3.5	98	10	Yes	2.5	TT
9	(3) CR-TM	1.5	0.24	3.5	98	10	Yes	2.5	TT
1	(4) CR-SM	1.5	0.24	3.5	98	10	Yes	2.5	SP[g]
16	(4) CR-SM	1.5	0.21	3.5	98	10	Yes	2.5	SP
18[e]	(4) CR-SM	1.5	0.21	3.5	98	9.4	Yes	2.5	TT
20	(4) CR-SM	3[h]	0.5	3[h]	98	2.5	Yes	2.0	SP
23	(4) CR-SM	1.5	0.1	3.5	98	10	Yes	2.5	TT
25	(4) CR-SM								SP
3[e]	(5) CR-KM						Yes	0.5	SP
15	(5) CR-KM						Yes	0.5	SP
21	(5) CR-KM						Yes	1.0	SP
26	(5) CR-KM						Yes	0.5	SP

[a] Concentration of H_2SO_4.
[b] Concentration of Ag_2SO_4.
[c] PT (partial titration).
[d] TT (total titration).
[e] Suspension samples (HC3S).
[f] Solid samples (SS).
[g] SP (spectrophotometrically).
[h] Mix of 25 g $K_2Cr_2O_7$, 2.5 g Ag_2SO_4, 0.5 L H_2SO_4 and 0.5 L H_3PO_4 (85%).

suspension immediately before analysis, by adding 200 mL of distilled water to the exact weight of substrate previously packaged, specifically 4 and 10 g of total solids (dry-weight basis), respectively. Additionally, in order to avoid variability in the preparation, all participants were advised to stir the samples (1 h) before analysis and during the sampling procedure.

3.1.3. Characterisation of samples

General characterisations of the different substrates selected for this PT were carried out. The substrates were analysed in triplicate, including moisture, chemical composition, elemental analysis and theoretical oxygen demand. Table 1 presents the results obtained.

3.1.4. Homogeneity of samples

Testing the homogeneity of samples is time-consuming and expensive, but the significance of sample homogeneity is very important for the effectiveness of the PT scheme. Therefore, the samples were tested for sufficient homogeneity by the COD-PT coordinator immediately after packaging the samples, using the standard analytical method developed in this lab and used on a routine basis. To check for sufficient homogeneity the protocol devised by Fearn and Thompson [6] was used. Following the author's approach, three tests were carried out to estimate the corresponding experimental statistical parameters and compared with their theoretical critical values: (i) Cochran's test procedure for duplicate results or the detection of outliers by differences between pairs; (ii) precision of the analytical method used; (iii) homogeneity test or test for acceptable between-sample variance.

For this purpose, the duplicated results for 12 distribution units of solid substrates were randomly selected to analyse the COD and values were statistically evaluated. Results obtained in the statistical analysis of homogeneity data are summarized in Table 2, which shows that substrates selected were homogeneous enough to be used in this PT.

3.2. Methods

3.2.1. Analytical methods

3.2.1.1. Chemical oxygen demand. The participating laboratories were free to choose the analytical method that they consider appropriate to perform the COD analysis, but were advised to analyse samples using their usual techniques. Each participant was required to include detailed information about the methodology used. A summary with all the experimental conditions of the analytical methods used are compiled in Table 3.

All participants of this PT have used the standard procedure that uses potassium dichromate as the oxidizing agent. However, there are some experimental conditions that define specifically the

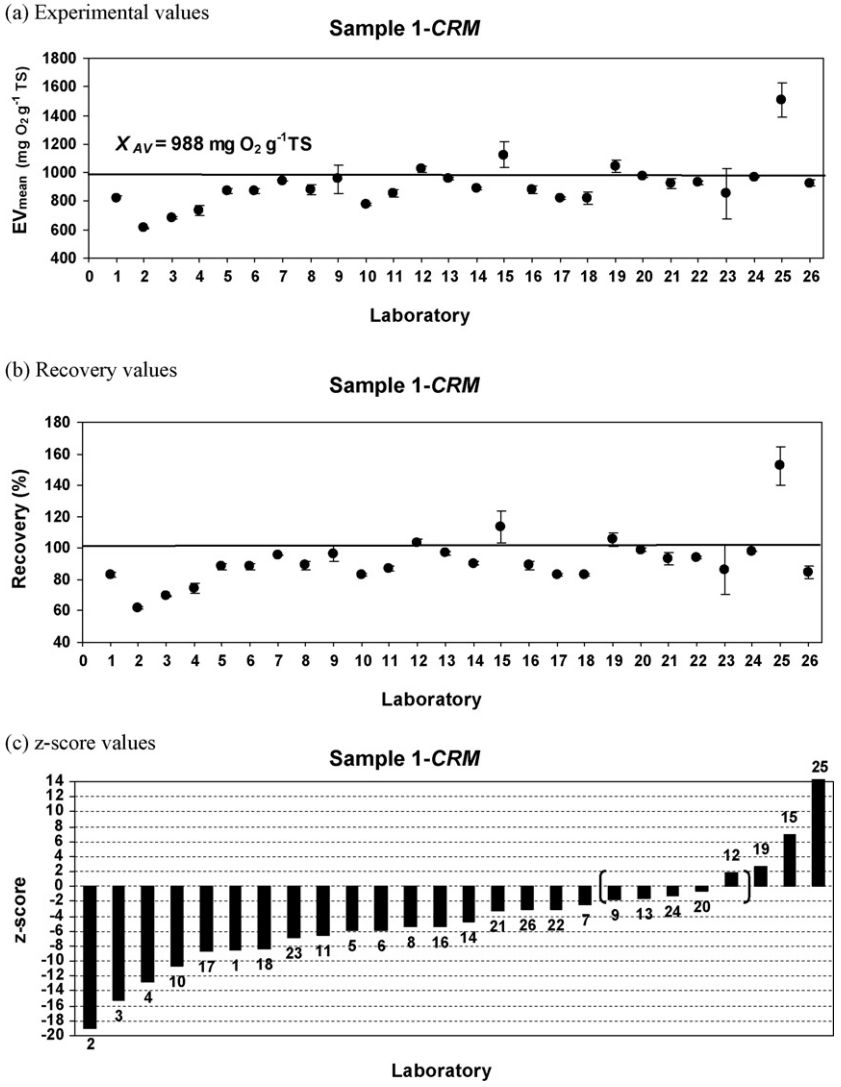


Fig. 1. Participants' results of sample 1 (*CRM*). (a) Experimental values. (b) Recovery values. (c) *z*-Score values.

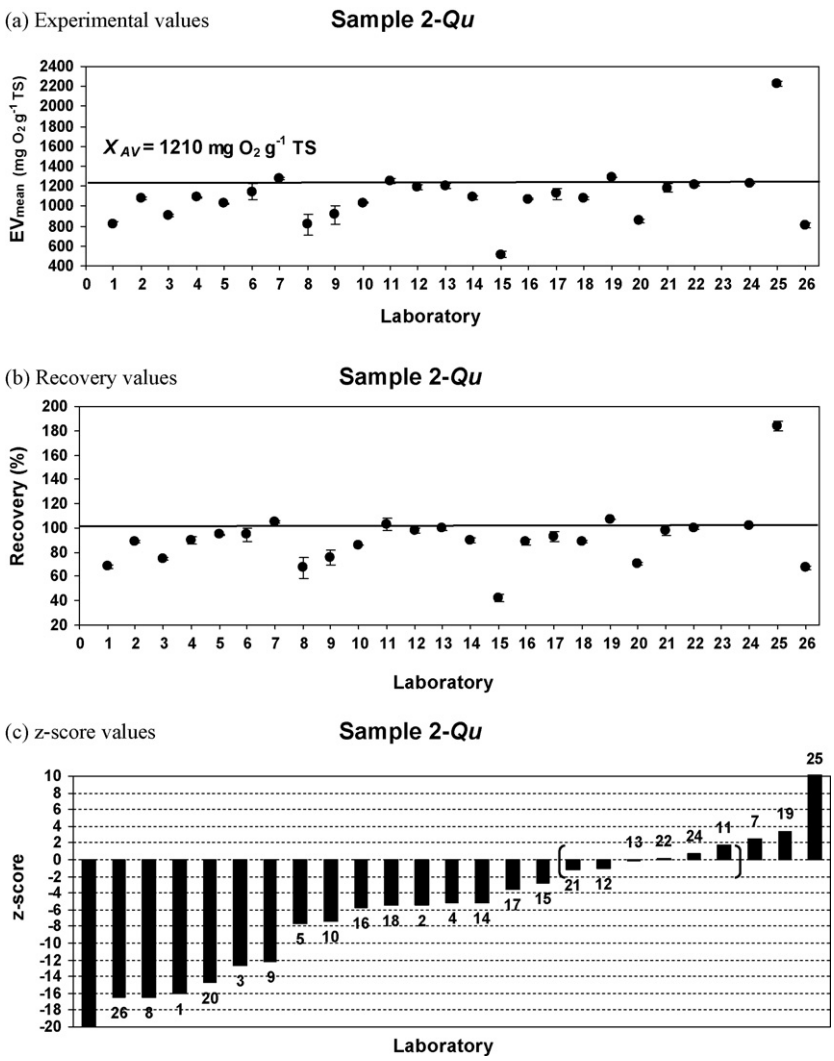


Fig. 2. Participants' results of sample 2 (*Qu*). (a) Experimental values. (b) Recovery values. (c) *z*-Score values.

method used: (i) volume and concentration of oxidant reagent; (ii) volume and concentration of the mixture H_2SO_4–Ag_2SO_4 reagent; (iii) volume of water/sample used; (iv) use of $HgSO_4$; (v) visualisation of end-point redox system by titration (total or partial) or spectrophotometrically; (vi) the reflux system. With the purpose of comparing the results obtained, the thirty-two variants of the standard procedure reported to determine this parameter have been classified, firstly in two main groups and secondly in five methods:

I. Open reflux (*OR*)
(1) *OR-LCM.* Low concentration of $K_2Cr_2O_7$ ($N < 1$)
(2) *OR-HCM.* High Concentration of $K_2Cr_2O_7$ ($N \geq 1$)
II. Closed reflux (*CR*)
(3) *CR-TM.* End-point by titration
(4) *CR-SM.* End-point by spectrophotometric determination
(5) *CR-KM.* Kits

Samples 1 and 2 were analysed in duplicate, whilst samples 3 and 4 in triplicate. The results must be reported on a dry-weight basis. The percentages of each method used were as follows: *OR-LCM* (38%), *OR-HCM* (25%), *CR-TM* (6%), *CR-SM* (19%) and *CR-KM* (12%). An interesting point is that although the *OR-LCM* was the main method used, any of twelve experimental conditions reported were repeated by the participating labs. On the other hand, the eight experimental conditions of *OR-HCM* were very similar, only five of which used different volumes of water added and two were exactly the same (labs 13 and 24). The experimental conditions followed in *CR-TM* and *CR-SM* were also very similar (only lab 20 reported a different method). Finally, two commercial kit brands (Hach and Merck) were used to apply the *CR-KM.*

3.2.1.2. Other parameters. Moisture was obtained by dryness at 105 °C and organic content by calcination at 550 °C [1]. Fat was determined by extraction with hexane using a soxhlet system. Protein and elemental composition was analysed by LECO CHNS-932 elemental analyzer, using sulphametazine as standard substrate. Fibre content was obtained using the method reported by Lee et al. [4]. Carbohydrates content was reported by subtraction of fat, protein and fibre contents. Theoretical oxygen demand was calculated according to ISO 10707 [5].

3.2.2. Data treatment

All results from the participating laboratories were considered. No randomization tests for quantitative results, such as Grubb's or Cochran's tests, were performed for the detection of possible outliers. Robust statistics have been applied to the estimation of average values and standard deviations from data reported.

The performance of each individual participating laboratory was assessed by the internationally accepted *z*-score. A participant's

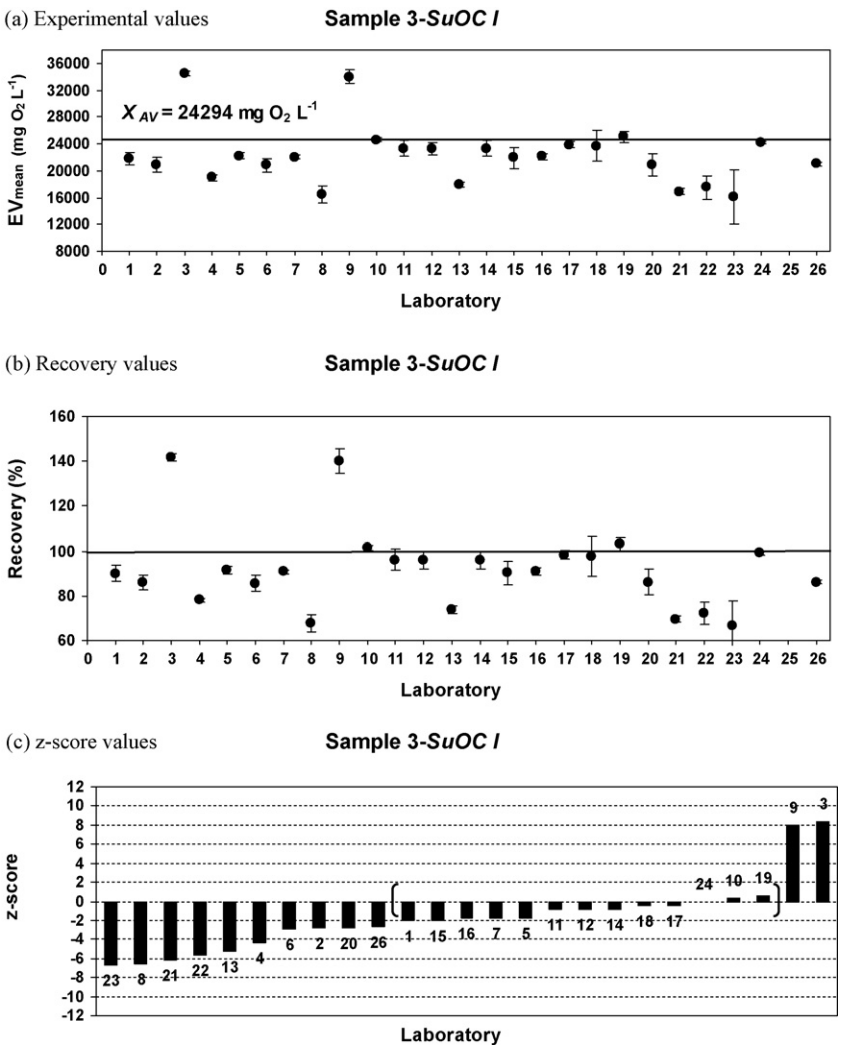


Fig. 3. Participants' results of sample 3 (*SuOC I*). (a) Experimental values. (b) Recovery values. (c) *z*-Score values.

result is converted into a *z*-score according to the following equation:

$$z\text{-score} = \frac{(X_{EV} - X_{AV})}{ESD}$$

where X_{EV} is the laboratory experimental value, X_{AV} is the assigned value (estimation of the true value of the measurand that is used for the purpose of calculating scores), and *ESD* is the fitness for purpose-based "established standard deviation for proficiency assessment", defined as a target value for the acceptable deviation from the assigned value. It means that the *z*-score compares the participant's deviation from the reference value with *ESD*.

The *z*-score values can be used for assessing the acceptability of the results reported according to the following generally accepted limits:

- *z*-score = 0 (rarely happens). Perfect result.
- *z*-score $\leq \pm 2$ (95%). Satisfactory or acceptable result. No action is required.
- $\pm 2 <$ *z*-score $\leq \pm 3$ (5%). Questionable or doubtful result. Preventive action is required.
- *z*-score $> \pm 3$ (unusual). Unsatisfactory or unacceptable result. Corrective action is required.

In this PT, the X_{EV} value was the mean value for each sample, independently of the analytical method used. The X_{AV} and *ESD* values were assigned as follows:

3.2.2.1. Establishing the assigned value (X_{AV}). There are various procedures available for establishing the assigned values. The most common are listed as follows: (i) known values; (ii) certified reference values; (iii) reference values; (iv) consensus values from expert laboratories; (v) consensus values from participating labs.

Taking into account the lack of a general standard method and high quality CRMs, the traceability of the COD determination is not currently easy to check. In addition, the spread of participants' results obtained was high and pointed to the advisability of using consensus values due to their unreliability. Therefore, the assigned values in this PT cannot be obtained for any of the earlier procedures described. With this situation in mind, a useful alternative, previously reported by Raposo et al. [7], was to consider the ThOD values as assigned values. The X_{AV} for samples 1 and 2 were 988 and 1210 mg O_2 g^{-1} TS, respectively. For liquid samples (samples 3 and 4) which were prepared gravimetrically (which required correction for the solid substrate volume occupied), were 24 294 and 59 855 mg O_2 L^{-1}, respectively.

3.2.2.2. Setting the established standard deviation (ESD). This parameter was previously defined as a target value for the acceptable deviation from the assigned value. It is determined in advance by the PT organisation in order to describe their notion of fitness for purpose; it does not depend in any way on the results obtained by the participants.

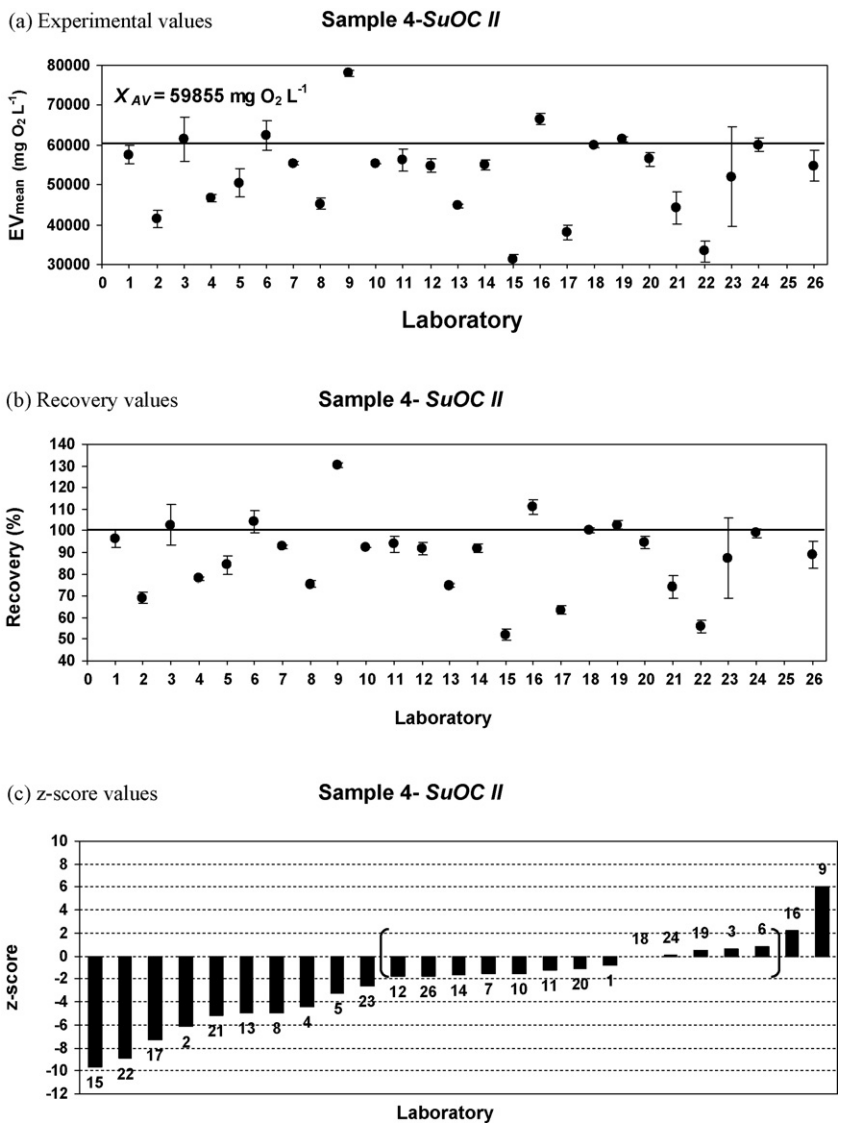


Fig. 4. Participants' results of sample 4 (*SuOC II*). (a) Experimental values. (b) Recovery values. (c) *z*-Score values.

In this PT, the *ESDs* have been determined as suggested by Thomson [8] by the Horwitz modified function, a useful generalisation about the reproducibility standard deviation expected in a collaborative trial. This equation predicts a standard deviation from a given concentration level of analyte, and requires the expression of this amount as a dimensionless mass ratio (e.g. 1 ppm = 10^{-6}, 1% = 10^{-2}).

In this PT, the theoretical *ESDs* for SS and HC3S obtained were 1% and 4%, respectively. In order to avoid a larger number of *z*-scores >± 2, the experimental values used for performance calculation were slightly increased for SS and HC3S up to 2.5% and 5%, respectively.

4. Results and discussion

4.1. Individuals results

Participants' results are summarized in graph form (Figs. 1–4) by a set of three figures for each sample analysed, including experimental values, recoveries and *z*-scores. In general, the repeatability of duplicate or within-laboratory variability expressed by repeatability relative standard deviation (RSD_r) was good. In the present PT, only 1–2 labs reported values of RSDr higher than 10% for each sample analysed.

4.2. Evaluation of results obtained for different analytical methods

To evaluate and compare the participants' results reported for different analytical methods, all the data have been summarized in Table 4. In order to compare the results obtained for samples analysed, firstly the data has been detailed by specific analytical method and secondly grouped in two main categories, open reflux methods (*OR-M*) and closed reflux methods (*CR-M*).

At first sight, it can be seen that averages values are not too bad, but closer inspection of the data using the *z*-scores reveals that most of the results obtained can be considered as unacceptable.

4.2.1. Comparison of averages values

No major differences among the methods used in this PT were observed during the evaluation of average values. Based on the results reported, it can be stated that the individual performance of participants was not good. Compared with assigned values, the mean values obtained were always lower. The underestimation of samples analysed might be related to negative bias in the analytical methods used. Therefore, only few labs reported positive recoveries compared to a general trend of numerous negative recoveries. In addition, some of the positive recoveries were obtained after

Table 4
Summary of participants' results obtained for different analytical methods.

Sample	Analytical method			Average values				*z*-scores					
	Name	N^{er}	%	Mean	SD_R	RSD_R	Recovery	*z*-score ≤±2		±2 < *z*-score ≤±3		*z*-score >±3	
				(mg/g)	(mg/g)	(%)	(%)	N^{er}	(%)	N^{er}	(%)	N^{er}	(%)
SS-1 (*CRM*)	(1) OR-LCM	8	31	830	125	15	84	1	12	0	0	7	88
	(2) OR-HCM	8	31	896	109	12	91	2	25	2	25	4	50
	OR-M	16	62	863	118	14	87	3	19	2	12	11	69
	(3) CR-TM	2	8	918	52	6	93	1	50	0	0	1	50
	(4) CR-SM	5	19	1007	285	28	102	1	20	0	0	4	80
	(5) CR-KM	3	11	991	115	12	99	0	0	0	0	3	100
	CR-M	10	38	985	201	20	99	2	20	0	0	8	80
	Total	26	100	910	163	18	92	5	19	2	8	19	73
SS-2 (*Qu*)	(1) OR-LCM	8	31	1111	68	6	92	1	12	1	12	6	75
	(2) OR-HCM	8	31	1165	132	11	96	4	50	1	12	3	38
	OR-M	16	62	1138	105	9	94	5	31	2	12	9	56
	(3) CR-TM	2	8	865	71	8	71	0	0	0	0	2	100
	(4) CR-SM	5	19	1244	663	53	103	0	0	0	0	5	100
	(5) CR-KM	3	11	837	333	40	69	1	33	0	0	2	67
	CR-M	10	38	1024	487	48	85	1	10	0	0	9	90
	Total	26	100	1097	298	27	91	6	23	2	8	18	69
				(mg/L)	(mg/L)	(%)	(%)	N^{er}	(%)	N^{er}	(%)	N^{er}	(%)
HC3S-1 (*SuOC I*)	(1) OR-LCM	10	39	21754	2238	10	90	6	60	1	10	3	30
	(2) OR-HCM	4	15	22626	3206	14	93	3	75	0	0	1	25
	OR-M	14	54	22003	2451	11	91	9	64	1	7	4	29
	(3) CR-TM	2	8	25224	12412	49	104	0	0	0	0	2	100
	(4) CR-SM	6	23	20956	2851	14	86	3	50	1	17	2	33
	(5) CR-KM	4	15	23563	7575	32	97	1	25	1	25	2	50
	CR-M	12	46	22680	6242	28	93	4	33	2	17	6	50
	Total	26	100	22301	4428	18	92	13	50	3	12	10	38
HC3S-2 (*SuOC II*)	(1) OR-LCM	10	39	49393	9264	19	83	5	50	0	0	5	50
	(2) OR-HCM	4	15	55303	7537	14	92	3	75	0	0	1	25
	OR-M	14	54	51081	8956	18	85	8	57	0	0	6	43
	(3) CR-TM	2	8	61580	23221	38	103	0	0	0	0	2	100
	(4) CR-SM	6	23	58497	5344	9	98	3	50	2	33	1	17
	(5) CR-KM	4	15	47950	13227	28	80	2	50	0	0	2	50
	CR-M	12	46	55223	12346	22	92	5	42	2	17	5	42
	Total	26	100	52903	10553	20	88	13	50	2	8	11	42

processing potential outliers. The general values of recovery were very similar and ranged from 88% to 92%, which is too low. On the other hand, the reproducibility of between-laboratory variability, expressed by reproducibility relative standard deviation (RSD_R), showed an extremely high variation. The precision obtained in 3 out of 4 samples analysed was low and very similar (18–20%), whilst the largest substrate (sample 2) gave a higher total value (27%), achieving up to 53% for *CR-SM*.

Sample 1 (*CRM*): The total average value was 910 ± 163 mg O_2 g^{-1} TS, with an RSD_R of 18% and a recovery of 92%. The accuracy of *OR-M* was lower than *CR-M*, mainly due to the compensatory effect of the data reported by lab 25, which could be considered as clear outlier. The precision of both groups of methods was very similar, being slightly better for *OR-M* (14% versus 20%).Considering only the results of *OR-M*, the accuracy and precision of *OR-HCM* (91–12%) were slightly better than *OR-LCM* (84–15%).

Sample 2 (*Qu*): The total average value was 1097 ± 298 mg O_2 g^{-1} TS, with an RSD_R of 27% and a recovery of 91%. The accuracy of *OR-M* (94%) was higher than *CR-M* (85%). In addition, the precision of *OR-M* (9%) was better than *CR-M* (48%). The results can be attributed to the difficulties found in sampling when a substrate with no powder form was analysed.Considering only the results of *OR-M*, the accuracy (96% versus 92%) was slightly better for *OR-HCM* as was the precision (6% versus 11%) for *OR-LCM*.

Sample 3 (*SuOC I*): The total average value was $22\,301 \pm 4428$ mg O_2 g^{-1} TS, with an RSD_R of 18% and a recovery of 92%. The accuracy of both groups of methods was very similar, although the influence of two potential outliers (labs 3 and 9) in the average values of *CR-M* must be mentioned. The precision was also better in the *OR-M*, nearly three times less than *CR-M* (11% versus 28%). The comparative study of the *OR-M* did not show any significant difference.

Sample 4 (*SuOC II*): The total average value was $52\,903 \pm 10\,553$ mg O_2 g^{-1} TS, with an RSD_R of 20% and a recovery of 88%. The accuracy of *OR-M* was slightly lower than *CR-M* (85% versus 92%), due to low values of *OR-LCM* (83%) compared with *OR-HCM* (92%) and also to the influence of some potential outliers.

4.2.2. Comparison of z-score values

The statistical parameter used to measure the COD performance was the *z*-score. The general trend of data obtained showed a few positive *z*-scores compared to the numerous negative *z*-scores. Moreover, some labs obtained *z*-scores excessively out of range, with values ranging between −30 and +40. The data of this PT show that overall there is a clear difference between the methods, with *CR-M* normally providing worse results than *OR-M*, whilst *OR-HCM* usually provides better results than *OR-LCM*. The cause of these results could be attributed to the amount of sample taken for each analytical method, so it should be ensured that test samples (portion or aliquot) are representative of the laboratory sample. For solid

samples, the amount ranged between 100–200 mg, 30–50 mg and 4–6 mg for *OR-HCM*, *OR-LCM* and *CR-M,* respectively. At the same time, for liquid samples *OR-HCM* uses a volume of 1–10 mL directly whilst *OR-LCM* and *CR-M* use a previous dilution of the sample.

Sample 1 (*CRM*): This sample presented the worst results, with only 5 labs (19%) reporting satisfactory results, 2 labs (8%) questionable results and 19 labs (73%) unsatisfactory results. Nevertheless, no differences between either group of methods were found.
Sample 2 (*Qu*): The results were similar to earlier samples, with 6 labs (23%) reporting satisfactory results, 2 labs (8%) questionable results and 18 labs (69%) unsatisfactory results. This sample showed differences between the groups of method used; the acceptable results of *OR-M* against *CR-M* were 31% and 10%, whilst unacceptable results were 56% and 90%, respectively. The possible influence of substrate size again was reflected in the results obtained.
Sample 3 (*SuOC I*): According to the *z*-score approach, 13 labs (50%) reported acceptable results, 3 labs (12%) doubtful results and 10 labs (38%) unacceptable results. Once again, differences between O*R-M* and C*R-M* were appreciated, with the percentages for acceptable results being 64% as against 33% and unacceptable results being 29% as against 50%.
Sample 4 (*SuOC II*): Considering the *z*-score for this sample, 13 labs (50%) reported satisfactory results, 2 labs (8%) questionable results and 11 labs (42%) unsatisfactory results. The results obtained comparing both groups of methods were not like the earlier sample, although *OR-M* reflected better satisfactory results than *CR-M* (57% against 42%).

To outline the results obtained in this PT the substrates analysed were firstly divided into two main categories, as solid and liquid samples, and finally grouped as total samples:

Solid samples: 11 *z*-scores (21%) were satisfactory, 4 (8%) doubtful and 37 (71%) unacceptable. Only 3 labs (12, 13 and 24), which represents 12% of participants, reported good values for both samples. All of them used *OR-M.* Special attention should be brought to the situation of labs 13 and 24 – they used the same method and reported in agreement with expected values.
Liquid samples: 26 *z*-scores (50%) were satisfactory, 5 (10%) doubtful and 21 (40%) unacceptable. For this type of samples, 9 labs (1, 7, 10, 11, 12, 14, 18, 19 and 24), which represents 35% of participants, reported good values for both samples. The methods used were *OR-LCM* (4 of 9), *OR-HCM* (3 of 9) and *OR-SM* (2 of 9).
Total samples: 37 *z*-scores (36%) were satisfactory, 9 (9%) doubtful and 58 (55%) unacceptable. In summary, the present PT revealed that about two thirds of results reported did not agree with the expected values. Only 2 labs (12 and 24), which represents 8% of participants, reported the four samples adequately.

5. Conclusions

In order to assess the results obtained for the performance of laboratories determining the COD of solid substrates and liquid samples with high suspended solid content, a PT scheme was organised. The interest in this PT was very high taking into consideration the numbers of labs participating. In addition, the results were representative of sixteen countries, reflecting the current situation in the analytical laboratories COD performances, mainly related to anaerobic research groups.

The present study demonstrates the current lack of uniformity in the analytical methods used to determine the COD of solid samples and liquid samples with high concentration of suspended solids. On the other hand, the PT allowed the study of some variables that can influence COD determination, such as the clear influence of substrate size. Furthermore, the study of the suspended solid concentration influence shows that bias was not concentration-dependant, and therefore it was totally rejected as a reason for obtaining unsatisfactory results.

Results from PT performance using the *z*-score indicated that only 36% of the results (from a total of 104 reported results) were satisfactory, with 9% doubtful and 55% unacceptable. This suggests that the majority of participating laboratories obtained inappropriate performances. Specifically, only two out of twenty-six participants reported a full set of acceptable *z*-scores.

Potentials reasons for achieving unsatisfactory results might be:

- Lack of experience with this type of samples.
- Sampling procedures. The analysis should be undertaken on homogeneous sub-samples. It should be ensured that test samples (portions or aliquots) are representative of the laboratory sample.
- Additional calculation errors. Only moisture content could be considered when correcting the results obtained. In fact, one lab stated the fault in moisture content determination as the cause of the unsatisfactory results obtained.
- The application of improper analytical methods. The detailed study of labs performance for the type of samples used in this PT showed that in general C*R-M* provides worse results than *OR-M*, whilst *OR-HCM* usually provides better results than *OR-LCM*. This fact could not be demonstrated without the participating in a PT, because the substrates (potassium hydrogen phthalate, glucose and cellulose) used as standard for COD determination are easily oxidizable compounds. For this reason, the oxidation of these substances is complete even in the absence of a catalyst, achieving recoveries close to 100% [9]. In this way, all the experimental conditions reported by participants obtained excellent standard's recoveries. To sum up, the laboratory internal quality control procedure failed because these standard substrates are poorly matched to the test material analysed.

Finally, the interlaboratory study showed the importance of a PT as an additional way to verify that all aspects of the laboratory measurement system are reliable in order to guarantee the production of analytical data of adequate quality.

Acknowledgements

The participating research groups are acknowledged for their contribution in running this *1st COD-PT^{ADG}* and their interest in its overall objectives. All the individual analysts are acknowledged to contribute with their work in the results obtained.

References

[1] APHA-AWWA-WPCF, Standard Methods for the Examination of Water, Wastewater and Sludge, twentieth ed., APHA-AWWA-WPCF, Washington, DC, 1988.
[2] ISO/IEC 17025, General Requirements for the Competence of Testing and Calibration Laboratories, 2005.
[3] M. Thompson, S.L.R. Ellison, R. Wood, Pure Appl. Chem. 78 (2006) 145.
[4] S.C. Lee, L. Prosky, J.W. De Vries, J. AOAC Int. 75 (1992) 395.
[5] ISO 10707, Evaluation in an AQUEOUS Medium of the "Ultimate" Aerobic Biodegradability of Organic Compounds. Method by Analysis of Biochemical Oxygen Demand (closed bottle test), 1994.
[6] T. Fearn, M. Thompson, Analyst 126 (2001) 1414.
[7] F. Raposo, M.A. de la Rubia, R. Borja, M. Alaiz, Talanta 76 (2008) 448.
[8] M. Thompson, Analyst 125 (2000) 385.
[9] Y.M. Dedkov, O.V. Elizarova, S.Y. Kelina, J. Anal. Chem. 55 (2000) 777.

Talanta 80 (2009) 338–345

Contents lists available at ScienceDirect

Talanta

journal homepage: www.elsevier.com/locate/talanta

Immobilization strategies of *Brucella* particles on optical fibers for use in chemiluminescence immunosensors

Yael Liebes[a], Liron Amir[a,b], Robert S. Marks[a,c,d,*], Menachem Banai[e]

[a] *Department of Biotechnology Engineering, Ben-Gurion University of the Negev, Beer-Sheva 84105, Israel*
[b] *Department of Chemistry, Ben-Gurion University of the Negev, Beer-Sheva 84105, Israel*
[c] *The National Institute of Biotechnology in the Negev, Ben-Gurion University of the Negev, Beer-Sheva 84105, Israel*
[d] *The Ilse Katz Center for Meso and Nanoscale Science and Technology, Ben-Gurion University of the Negev, Beer-Sheva 84105, Israel*
[e] *Department of Bacteriology, Kimron Veterinary Institute, P.O. Box 12, Bet Dagan 50250, Israel*

ARTICLE INFO

Article history:
Received 6 February 2009
Received in revised form 18 June 2009
Accepted 30 June 2009
Available online 7 July 2009

Keywords:
Brucellosis
Chemiluminescence (CL)
Enzyme-linked immuno-sorbent assay (ELISA)
Immunosensor
Optical fiber immunosensor (OFIS)
Silane coupling agent (SCA)

ABSTRACT

Immunosensors are powerful analytical tools in clinical and veterinary diagnostics. This has led us to design a chemiluminescent immunosensor aimed at identifying anti-*Brucella* antibodies using optical fibers as the transducer. In order to develop the optimal transducer, to achieve an optimal chemical modification thereby allowing an optimal covalent binding of the protein receptor, several cleaning strategies and silane coupling agents were investigated. *Brucella* killed organisms were used as a model receptor for quantifying anti-*Brucella* IgG antibodies in a suspension compared to conventional colorimetric and chemiluminescent ELISA. A silane–benzophenone derivative was selected as the best performing silane coupling agent: the optical fiber immunosensor (OFIS) has showed the lowest limit of detection at 0.207 μg/ml, compared to 0.828 μg/ml and 0.414 μg/ml achieved by colorimetric and chemiluminescent ELISAs, respectively. These results, together with the additional advantages of rapidity, lower reagent volumes and moderate operating conditions, have set the grounds for further study in order to adapt this platform for on-site diagnostics of brucellosis disease markers.

© 2009 Elsevier B.V. All rights reserved.

1. Introduction

The selective recognition between an elicited antibody and its specific antigen is the basis of a humoral immune response. Based on this principle, immunosensors have been designed by measuring the analyte binding to its corresponding immobilized biospecific recognition entity on the surface of a transducer and ensuring a signal obtained by this recognition given as a measured value. Immunosensors are being exploited in recent years for clinical diagnosis and environmental monitoring [1–3].

One such technology is based on optical fibers [4] which are ideal transducers governed by Snell's law. Fiber optics have many advantages reviewed before [5], including: (1) high efficiency in the blue region that is ideal for chemiluminescence [6], (2) their silica composite enables macromolecular conjugation via silanization [7], and (3) as an optrode system, they are polyvalent and can be easily adapted to different biorecognition systems, especially for the detection of antibodies [8–12], antigens [13], nucleic acids and toxins [14,15] with high sensitivity and specificity.

However, one of the greatest challenges in the field of immunosensors, and in particular when the transducer is an optical fiber, is the covalent immobilization of the receptor molecule to the solid phase transducer. One of the most common methods used to immobilize molecules on the transducer's surface is achieved by silanization with a silane coupling agent (SCA), [17], a bi-functional silane with the general structure [Y–$(CH_2)_n$–Si–X_3]. Y stands for the tail functional group that will further bind to the protein receptor and X stands for the head hydrolysable group, usually an alkoxy or a chloro, used in the covalent binding of the silane to the glass surface after physisorption, hydrolysis, formation of siloxane bonds and cross linking, or curing, between neighboring alkyl chains [7,16]. Compared to adsorption or entrapment, silanization suffers from fewer problems of leakage and diffuse controlled reaction [18,19]. Further, it allows for robust, covalent, stable and durable attachment of a proteinaceous receptor [20].

In order to compare the different chemical modification methods of the optical fiber and suitability of the modified fibers to serve as a platform for a chemiluminescent optical fiber immunosensor (CL-OFIS), a model analyte anti-*B. melitensis* IgG antibody immunosensor for was used.

Brucellosis was selected as a useful model of interest to many end-users because it is a worldwide bacterial zoonotic disease caused by the genus *Brucella* [21], and is considered to be a

* Corresponding author at: Department of Biotechnology, Ben-Gurion University of the Negev, Beer-Sheva 84105, Israel. Tel.: +972 08 6472857; fax: +972 08 6477182.
E-mail address: rsmarks@bgu.ac.il (R.S. Marks).

0039-9140/$ – see front matter © 2009 Elsevier B.V. All rights reserved.
doi:10.1016/j.talanta.2009.06.070

re-emerging problem in several countries of the Middle East, Africa, the Far East and Central and South America [22–24]. As a highly contagious and costly disease, with putative bioterror potential [25], rapid and accurate diagnosis of brucellosis is important.

The gold test that confirms brucellosis is bacterial isolation of the strain from suspected samples. However, the diagnosis succeeds in only 50–90% of the cases due to the low persistent number of cells in some of the infected materials, the intracellular localization of the organisms in the host and, and sometimes *Brucella* exhibits a slow or fastidious growth [26,27]. Serodiagnosis of IgM and IgG antibodies is a common diagnostic approach and indirect enzyme-linked immuno-sorbent assays (i-ELISA) have become a preferred method that allows mass surveillance of the population without loosing the sensitivity and specificity required for an accurate diagnosis [28–31].

We report the comparison of several types of SCA-modified optical fiber surfaces and the development of a prototype CL-OFIS for the detection of anti-*Brucella* IgG antibodies. The performances of the OFIS, as well as its ability to serve as a future analytical tool, were superior to conventional colorimetric and CL-ELISA using the same immunological rationale.

2. Experimental

2.1. Chemicals and biochemicals

2.1.1. Commercial chemicals

Allylbromide (A29585), potassium carbonate (P1472), sodium sulphate anhydrous (71962), triethylamine (T0886), sodium cyanoborohydride (71435), sodium m-periodate (S1878), sodium phosphate (S9390), potassium phosphate (P0662), potassium chloride (P9333), glycine (241261), chromium (VI) oxide (27081), 4-hydrozybenzophenone (54800), dichloromethylsilane (440248), (3-mercaptopropyl)trimethoxysilane (MPTS) (A1521), (3-aminopropyl)trimethoxysilane (AMPTS) (181778), (3-glycidyloxypropyl)trimethoxysilane (GOPS) (440167), (T0886), 3,3′,5,5′-tetramethylbenzidine (TMB) (T0440), skim milk powder (SM) (70166), 6-maleimidohexanoic acid *N*-hydroxysuccinimide ester (EMCS) (M9794), 30% (v/v) hydrogen peroxide solution (H1009), 50% (v/v) gluteraldehyde solution (G7651), polyoxyethylene-sorbitan monolaurate (Tween® 20) (P7949), dimethyl sulfoxide (DMSO) (41650) and rabbit anti-bovine IgG HRP conjugated (A5295) and all other chemicals were purchased from Sigma.

Luminescence measurements were carried out using the Western Blot Chemiluminescence Reagent kit (Immuno-star-HRP™) from BIO-RAD Laboratories (170-5040).

2.1.2. Synthesis of 4-(3′-dichloromethylsilyl)propyloxybenzophenone (DCBZS)

Silane–benzophenone derivative was synthesized in a two-step process as described before [32]. The first step, synthesis of 4-allyloxybenzophenone, had 65% yield. The second step, synthesis of 4-(3′-dichloromethylsilyl)propyloxybenzophenone (DCBZS), had a 72% yield (see supplemental information section 1 (SI.1)).

2.2. Preparation of the Brucella antigen solution

B. abortus strain B1119 (a strain used in antigen production for serological tests) and *B. melitensis* strain Huddleson (a laboratory strain) were provided by the Israeli National Brucellosis Center, also serving as an OIE Reference Laboratory, Kimron Veterinary Institute, Bet Dagan, Israel. The *Brucella* strains stored as a freeze-dried culture as part of the national collection were reconstituted in water, propagated in tryptic soy agar (TSA) enriched with serum-dextrose (1% and 5% (v/v), respectively), and incubated at 37 °C in atmospheric air containing 5% CO_2 (v/v) till growth to a logarithmic phase [33]. Bacteria were then harvested in saline and the bacterial suspensions at concentration of 10^8 bacteria/ml were heat-killed at 70 °C in 0.5% (v/v) phenol–saline solution.

2.3. Preparation of bovine anti-Brucella IgG serum

A large volume of anti-*B. melitensis* biovar 1 bulk serum was collected from a *B. melitensis* biovar 1 infected cow on August 15, 1990. Serum was frozen at −20 °C until IgG purification. The IgGs were purified from the bulk sera by Dr. Gil Korner, Kamada, Kiryat Weizmann, Rehovot 76327, Israel, using an industrial pipeline, and eluted from the column by 0.3 M glycine solution. The purification grade was determined by HPLC as 99.8% and the protein concentration was determined to be 21.2 mg/ml. The presence of anti-*Brucella* antibodies in the original serum sample and the purified IgG fraction was confirmed by serological tests that were carried out in the National Reference Laboratory for Brucellosis. The original serum was positive by rose bengal test (RBT) and produced 1:640 and 1:320 positive titers by plate-micro-agglutination test (MAT) and complement fixation test (CFT), respectively. The purified fraction produced MAT titers of 1:640 and 1:40 using *B. melitensis* strain Huddleson and *B. abortus* strain 1119 antigens, respectively. The IgG fraction was positive by fluorescence polarization assay using Diachemix Sentry 100 reader and Brucella O-polysaccharide fluorescing tracer.

2.4. Detection of anti-Brucella IgG antibodies by i-ELISA and CL-ELISA

An indirect ELISA (i-ELISA) was performed using the same rationale as described before with some modifications (Fig. 1E) [30,34] and after selecting the optimal reagents and concentrations (data not shown). 100 μl volume of a 1:1 (v/v) mixture of the *B. abortus* and *B. melitensis* antigens, diluted 1:20 (v/v) in phosphate buffer saline (PBS) (80 g l^{-1} NaCl, 5 g l^{-1} Na_2HPO_4 11.2 g l^{-1} KCl and 2 g l^{-1} KH_2PO_4 adjusted to pH 7.2 with NaOH/HCl), was added into each well of a 96-well microtiter plate (MaxiSorp, Nunc). The plate was sealed to avoid evaporation and a coating of *Brucella* cells was allowed to take place overnight at 4 °C. After the incubation, the coating buffer was decanted and the plate was blocked by adding 100 μl/well of blocking solution, 5% (w/v) SM–0.1% (v/v) PBS-Tween (PBST) (pH 7.2). A blocking step was allowed for 1 h at 37 °C in order to reduce the overall background and to increase the sensitivity of the assay. Following blocking, the wells were washed thrice with PBST. Then, 50 μl/well of milk samples that included serum dilutions ranging from 10^{-1} to 10^{-7} or milk as negative control were added in triplicates and the plate was incubated for 1 h at 37 °C. The wells were then washed thrice with PBST and 50 μl/well of the rabbit anti-bovine IgG HRP conjugated antibodies diluted 1:10,000 (v/v) in 1% (w/v) SM–PBST were added and the plate incubated at 37 °C for 1 h. After incubation, the plate was prepared for reading by washing the wells thrice with PBST.

Colorimetric i-ELISA measurements were accomplished by adding a volume of 100 μl of chromagen (TMB) into each well and the plate was incubated at room temperature for 30 min in the dark. Then, 50 μl/well of 2N H_2SO_4 were added and the absorbance at 450 nm was determined with the Labsystems Multiscan RC ELISA reader after 10 s shaking. The data was collected by using the Labsystems Transmit software and the mean and the standard deviation of the triplicates were calculated for each point.

Chemiluminescence i-ELISA measurements were accomplished by adding oxidizing reagent and enhanced luminol reagent solutions into each well in a 1:1 ratio before each measurement. A total

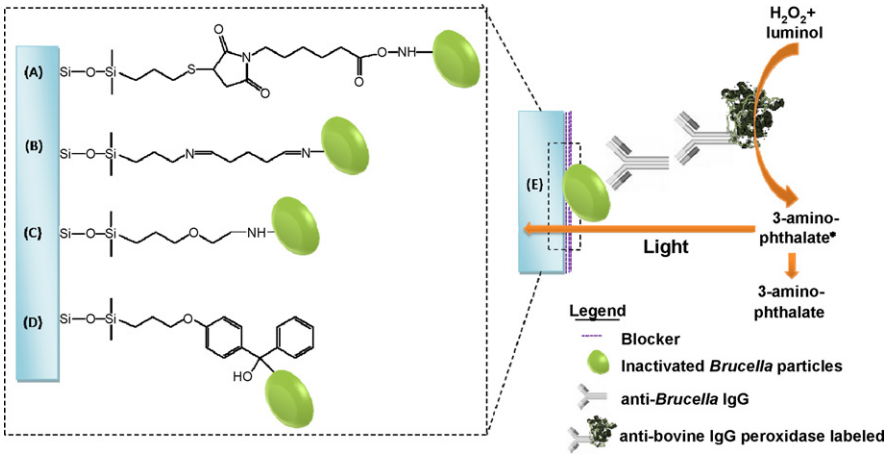


Fig. 1. Different immobilization strategies and immunosensor model. Left panel: the different silanes and cross linkers used for binding of the inactivated *B. melitensis* and *B. abortus* particles: (A) MPTS with EMCS, (B) AMPTS with gluteraldehyde, (C) GOPS after serial chemical reactions, and (D) DCBZS enables photochemical attachment. Right panel (E): the immunosensor served as a model. Scheme not to scale.

of 20 measurements were performed with a gap of 1 s between each reading. The data were collected with the Luminoskan Ascent Software, the mean and the standard deviation of each triplicate were calculated and the signal reported in RLU (relative light units).

2.5. Chemical modification of the optical fiber

2.5.1. Optical fibers

All fibers used were SFS400/440B Superguide G UV-Vis (Fiberguide Industries, Stirling, NJ, USA) with an original numerical aperture (NA) of 0.22. Their core was 400 μm in diameter (refractive index of 1.457 at 633 nm) and surrounded by a 40 μm silica cladding (refractive index of 1.44 at 633 nm), followed by a 150-μm thick silicon buffer and finally a 210-μm thick black Tefzel® jacket. The length of any single fiber used in the experiments was approximately 25 cm. The black Tefzel® jacket and silicon buffer were stripped away mechanically using a fiber stripping tool (Micro-Strip®, from Micro-Electronics Inc., MA, USA), leaving a 1 cm nude optical fiber core tip.

2.5.2. Cleaning procedures

Several cleaning strategies were evaluated ($n = 15$ for each method) using different combinations of acid treatments (Table 1, part A). In order to assure the complete removal of the silica cladding, fibers were soaked in 48% (v/v) hydrofluoric acid for 5 min at room temperature (RT), washed thrice with deionized water, once with absolute ethanol and blow dried with air flow. Removal of major micro-contaminants from the newly exposed fiber was done by either soaking in 5 M chromic acid for 1 h at 90 °C, rinsing five times in deionized water, and blow dried with air flow or sonicating the fibers in 1:1 (v/v) methanol/97% HCl solution for 5 min, soaking in fresh 1:1 (v/v) methanol/97% HCl solution for 45 min at 90 °C and finally blow dried with air flow.

Enhancement of hydroxyl groups exposed on the clean silica surface of the fiber tips was achieved by either soaking in 95% (v/v) sulfuric acid for 45 min at RT; or in piranha solution of 7:3 (v/v) 96% sulfuric acid and 30% hydrogen peroxide for 60 min at 90 °C and then blow dried with air flow.

2.5.3. Silanization procedures

Four SCAs were used for the silanization procedure: MPTS [8,11,12,35], AMPTS [36], GOPS [5,37], and DCBZS [10,13], using different silanization methods ($n = 15$ for each method). The first five methods were liquid phase deposition and included soaking the fibers for 1 h at 90 °C in a solution of 100%, 25%, 3%, 1% or 0.3% (v/v) silane in dry toluene, followed by a quick rinse with deionized water and blow dried with air flow. The sixth method was a vapor phase deposition. Fibers were placed in a pre-saturated silane reactor chamber with 1 ml silane injected to the bottom of the reactor and 1.2 l/min argon flow for 30 min (see SI.2) at ambient pressure and temperature. These methods were all employed for the commercial SCAs. When home-made DCBZS was used as SCA, only dilute liquid phase deposition methods were employed in order to economize the precious amount of silane and because of the much fewer procedures used in previous manuscripts then the commercial SCAs. The fibers were left to stand overnight at RT with gentle shaking in a solution of 3%, 1% or 0.3% (v/v) DCBZS in toluene and 0.5% (v/v) triethylamine as a catalyst and acid scavenger, followed by rinsing with fresh toluene and then with PBS.

Table 1
Comparison of different cleaning and activation methods. Five different methodologies were evaluated by a simple i-ELISA for the detection of anti-*Brucella* IgG antibodies after silanization with 25% AMPTS.

#	(A) Treatment			(B) i-ELISA signals		
	De-cladding[a]	Cleaning[b]	Activation[c]	Positive[d]	Negative[d]	S/N
1	HF	CrO_3	Piranha	34,559 (25.3)	142 (19.4)	242.8
2	HF	MeOH:HCl	Piranha	3,133 (64.6)	109.5 (29.6)	28.6
3	HF	MeOH:HCl	H_2SO_4	34,564 (26.5)	94.4 (16.0)	366.2
4	None	MeOH:HCl	H_2SO_4	46,332 (9.7)	116.0 (19.6)	398.3
5	None	CrO_3	H_2SO_4	35,874 (46.30)	122.9 (15.6)	292.6

[a] De-cladding step was done using 48% HF.
[b] Cleaning step for the removal of micro-contaminants.
[c] Activation step for enhancement of hydroxyl groups.
[d] Number in brackets indicates the coefficient of variance of groups of 10 fibers.

2.6. Detection of anti-Brucella IgG antibodies using the optical fiber immunosensors

2.6.1. Cross linking using the four used silane coupling agents

After silanization, the strategy for cross linking of the capture protein, 1:1 (v/v) *B. abortus* and *B. melitensis* antigens diluted 1:20 (v/v) in PBS, was dependent on the type of silane used and was done similar to previous reports.

MPTS cross linking employed the hetero-bi-functional cross linker, EMCS and was achieved simply by immersing the fibers in 4 mM EMCS in 1:9 DMSO/PBS pH 7.2 (Fig. 1A). The maleimide group of the EMCS reacted strongly with the thiol group of the silane to form a covalent bond [8,11,12,35].

AMPTS cross linking employed gluteraldehyde (Fig. 1B), and was achieved by immersing the fibers in 2.5% gluteraldehyde in PBS pH 7.2. The two aldehyde groups form amide bonds with the AMPTS's amine from one side and with the receptor from the other one [36].

GOPS facilitates direct linking using several steps of chemical reactions (Fig. 1C). In brief, vicinal diols were formed by treating the fibers in 12 mM hydrochloric acid for 60 min and oxidized to aldehyde using 100 mM sodium m-periodate dissolved in 10% (v/v) acetic acid for 60 min at RT. Then the fibers were rinsed with deionized water. Finally, fibers were incubated overnight at 4 °C with the capture protein, un-reacted aldehyde groups were blocked using 1 M glycine for 30 min at RT and the unsaturated amines were stabilized by a Schiff base by dipping the fibers in 0.3 M sodium-cyanoborohydride for 60 min at RT [5,37].

DCBZS also does not require a cross linker and direct linking of the receptor is achieved via photo-immobilization (Fig. 1D). The photo-immobilization is achieved by activation of the benzophenone groups using a 345-nm wavelength light input, with light intensity of 80 mW cm^{-2}, projected for 7 min into the far end of the DCBZS coated fiber soaked in the capture protein solution. This resulted in binding neighboring *Brucella* cells from the surrounding solution to the optical fiber [10,13].

2.6.2. Detection of anti-Brucella IgG antibodies using CL-OFIS

Following the cross linking of the receptor *Brucella* killed cells and its fragments onto the optic-fibers, the following conventional ELISA steps as detailed in Section 2.5 were performed from the blocking step (using AMPTS, MPTS and DCBZS) or from the sera step (using GOPS) with slight modifications: incubation steps were carried out for 30 min at RT using 250 μl per sets of five fibers and double rinsing, each for 5 min, carried out after each treatment.

2.6.3. Signal measurements of the chemiluminescent optical fiber immunoassay

The instrument set-up for the fiber chemiluminescence measurements has previously been described [15,38,39]. A Hamamatsu HC135-01 Photo Multiplier Tube (PMT) Sensor Module was used for chemiluminescence measurements in a light-tight box. The far end of the fiber was held by a fiber holder (FPH-DJ, Newport) and placed into an adjustable single-fiber mount (77837, Oriel). Monitoring the chemiluminescent signal and data handling at real time was performed by using LabView (version 3.1, National Instruments Corporation). During measurement, each fiber optic was placed in a 400-μl sample tube containing the combined oxidizing reagent, and enhanced luminol reagent solutions in a 1:1 (v/v) ratio. The chemiluminescence readings were integrated for 1 s and each measurement was obtained by taking a mean value of photon counts during 15 s. The mean and standard deviation were calculated for each dilution and reported as RLU (Relative Light Units).

2.7. Stability and short term storage conditions

On-site field diagnostics must be as fast as possible. Thus, examination of the ready to use immunosensor (after silanization, cross linking of the receptor and blocking steps) shelf life was done. Following the blocking step, the fibers were soaked in a stabilizing solution of 5% (w/v) trehalose–0.02% (w/v) sodium azide–0.1% (w/v) skim milk in PBS [40] for 4 h at RT, blow dried with air flow and stored at 4 °C, RT and 37 °C for 1, 2, 4, 7, 14 and 30 days.

2.8. Fiber surface characterization techniques

2.8.1. Scanning electron microscopy (SEM)

Scanning electron microscopy (SEM) micrographs were taken by a JEOL JSM-7400F system with 129 eV resolution of detector (Si) and exposure time of 100 s. The specimens were analyzed using energy-dispersive X-ray spectrometry (EDS) microanalysis analytical equipment installed in the scanning electron microscope.

2.8.2. Atomic force microscopy (AFM)

AFM measurements were performed in non-contact mode at ambient conditions using a Nanonics NSOM/AFM 100 system (Jerusalem, Israel) with a flat scanner, which allows two optical microscopes to examine the sample simultaneously, from above and below.

3. Results and discussion

3.1. Cleaning methodology

As SCAs react with exposed hydroxyl groups on the glass surface, the creation of a uniform, reproducible and functional silane layer also depends on glass pre-treatments: elimination of contamination and hydroxylation of the surface [41].

There is no universal protocol for glass cleaning, therefore five combinations of common acid pre-treatments (Table 1, part A) were evaluated. SEM–EDS (SI.3) was used in evaluating surface structures and composites and i-ELISA procedure (Table 1, part B) for evaluating the influence of silanization with 25% AMPTS over the immunosensor. SEM-EDS revealed that the smoothest surface with the minimal non-silanol molecules was achieved using MeOH:HCl for cleaning and H_2SO_4 for hydroxylation. This method was therefore chosen for all of the next experiments, which also included the fact that it gave the highest S/N ratio [42] and the lowest coefficient of variance in the bioassay, as well as being relatively simple, environmentally friendly and safe.

3.2. Comparison of silanization techniques

The effectiveness of various silianization strategies using all of the SCAs was compared using several methods.

First, SEM micrographs (SI.3 and Fig. 3) provided a qualitative measure of the homogeneity of the modified surface. It was seen that each SCA, in each silanization technique, generated a different morphology without directly correlating to SCA type and concentration. Yet, AMPTS and MPTS, in all of the silanization techniques, provided a relatively homogenous yet thick multi-layer surface. The DCBZS provided a relatively homogenous coverage with aggregates fairly equally distributed over the modified surface.

Secondly, AFM (insets, Fig. 3) provided complementary semi-quantitative data. It is not possible to deduce the exact thickness of the silane layer mainly because of the fiber curvature and only the comparison of roughness reflecting homogeneity was achieved. DCBZS modified surface had the lowest roughness values (102, 293

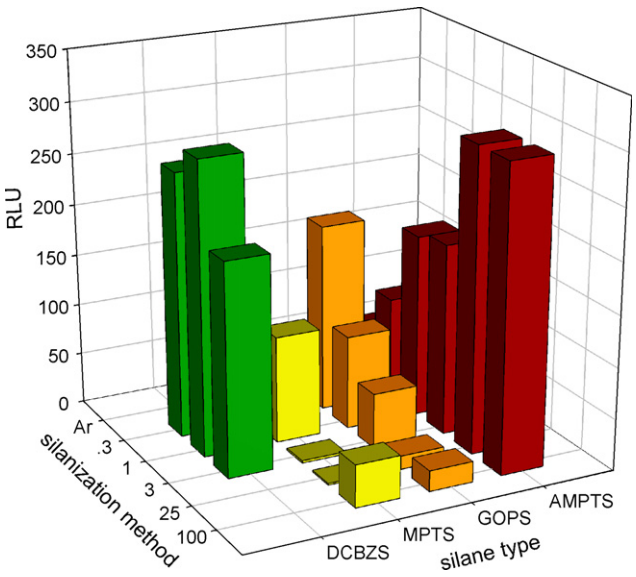


Fig. 2. S/N values in an i-ELISA for detecting anti-*Brucella* IgG antibodies. Several commercially available silane coupling agents and home-made silane coupling agents were tested in different silanization conditions.

and 595 nm for DCBZS, AMPTS and MPTS modified surfaces, respectively), thus demonstrated maximal surface homogeneity.

Thirdly, EDS analysis was executed only on the surfaces modified with SCA which has a unique functional group (–SH of MPTS and –NH of AMPTS (SI.3)). The two representative scans validated the cleaning effectivity per method (no foreign atoms), and that the C:N and C:S ratios were 1:2.2 and 1:3.3 for AMPTS and MPTS surfaces, respectively, which is close to the theoretical value of 1:3 (in case of densely packed SAM formation). The exception from the theoretical value can be explained by incomplete hydrolysis and condensation, thus forming lateral and vertical polymerization in parallel, with excess of methoxy groups [7,16,19,43,44].

Finally, OFIS was used to test the modified surface suitability for an immunosensor (Fig. 2). Significant S/N values were obtained using all the SCA, and the best (about 285) was achieved using between 25–100% AMPTS and 1% DCBZS solutions.

The improvement in the immunosensor performances using DCBZS over the other SCAs can be explained by the efficiency of the cross linking methodology, with high yield for photo-immobilization [32,45], or by the nature of the silane hydrolysable group, with the hydrolysis of the chloro group being more efficient than the methoxy group, thus allowing for a more stable and homogenous coverage [17,43,46].

Only the best three silanization methods, according to those results, were further employed for the calibration curve: 25% AMPTS and 1% DCBZS in liquid phase silanization and Ar phase silanization using MPTS. Although the last was not found best in means of S/N values, it was selected because it is routinely used in our Biosensors Laboratory.

3.3. Immunosensor performances

Three OFIS techniques (having the best silanization as discussed in Section 3.2) and two conventional ELISA techniques were employed. The methods were compared using a model for the detection of anti-*Brucella* IgG antibodies with the same assay principles as for i-ELISA. The respective calibration curves (Fig. 3) were reproducible and demonstrated the essential parameters of any biosensor: dynamic range, sensitivity and lower limit of detection [47].

3.3.1. Calibration curves

The calibration curves describing the general detection of the anti-*Brucella* IgG antibodies were derived using various concentrations of the analyte in milk solutions, ranging in dilutions from 10^{-1} to 10^{-8} of the original concentration, correlating to 2.12 mg/ml to 0.212 ng/ml of the total IgGs per sample, respectively. The calibration curves were calculated by analyzing the data with SigmaPlot 8.2 (Systat) and by applying the sigmoid logistic four parameters model described by Eq. (1), where x and y represent the measured titer of the antigen, respectively:

$$y = \frac{y_0 + a}{(x + x_0)^b} \quad (1)$$

Results are shown in Fig. 3 and the mathematical parameters are reported in Table 2. The applied mathematical model proved to be a good description of the relation between the anti-*Brucella* IgG antibody reported by the signal as shown by the r^2 values.

Influence of non-specific interactions over the colorimetric or chemiluminescent responses was examined using a set of control experiments, each lacking one step of the complete assay. The results (SI.4) showed that the responses obtained in the lack of capture *Brucella* cells, anti-*Brucella* IgG antibodies (the analyte) and secondary labeled antibodies were all relatively negligible, thus the designed immunosensor did not exhibit non-specific binding. High values obtained in the absence of a blocking step reflect the necessity of a blocking step to avoid receptor unsaturated sites of receptors, thus avoiding background noises. High values in the absence of SCA can be explained by the high reactivity of a silane surface towards protein adsorption using van der Walls, polar and ionic interactions. However, those interactions are weaker and less stable and durable compared to covalent attachment of the receptor using SCA [19,20,48]. The signals in the absence of cross linker can be explained by the exclusivity of the cross linker active groups: thiol of MPTS can form disulphide bonds with the receptor, amine of AMPTS can form amide bonds with carboxyl groups in protein, and the benzophenone of the DCBZS can utilize ambient surrounding UV light [32].

3.3.2. Dynamic ranges

The dynamic range is the anti-*Brucella* IgG antibodies titer range where the detection system displays a linear relationship between analyte concentration and measured signal. The dynamic range can be calculated from the previous results by applying a two-parameter linear regression analysis of the data according to Eq. (2):

$$y = y_{01} + d\ \ln(x) \quad (2)$$

Dynamic ranges can be visualized in the upper right corner of each graph in Fig. 3 and the mathematical data are reported in Table 2. The dynamic ranges were with good reliability according to their high r^{2*} values and calculated to be 3.31–0.53 μg/ml, 53–0.42 μg/ml, 212–0.21 μg/ml, 2120–6.65 μg/ml and 106–2.12 μg/ml for colorimetric ELISA, CL-ELISA and MPTS, AMPTS and DCBZS based CL-OFIS methodologies, respectively.

3.3.3. Lower detection limit

The lower detection limit of the immunosensor is defined as the amount (or concentration of the analyte) that gives a response (YDL) significantly different (three standard deviations, STD) from the background analysis obtained from negative control milk (NEG). Therefore, the lower detection limit (LDL) was calculated using Eq. (3) and the sample response considered positive according to Eq. (4):

$$\mathrm{LDL} = 3(\mathrm{STD}) + \mathrm{NEG} \quad (3)$$

$$\mathrm{YDL} > \mathrm{LDL} \quad (4)$$

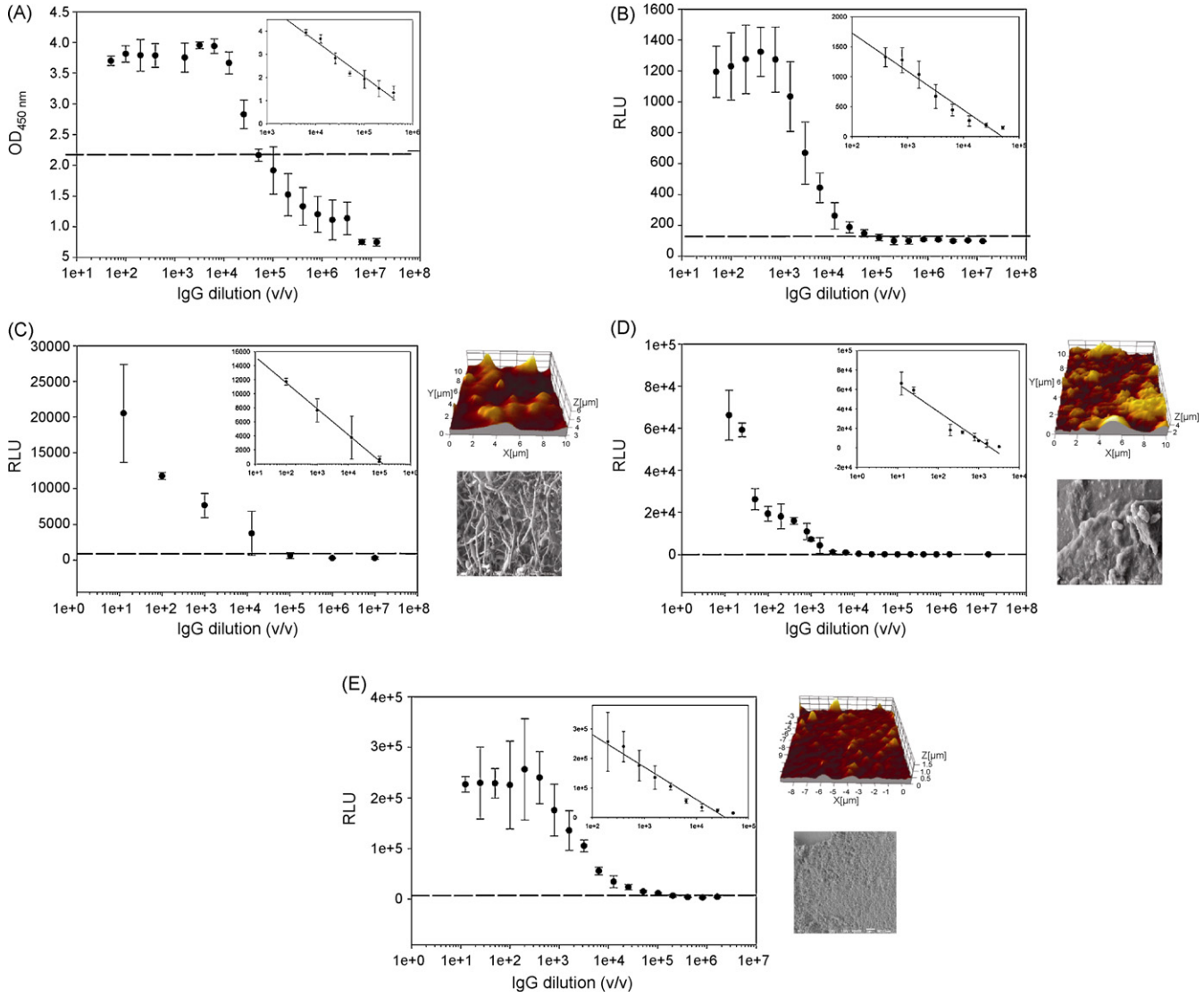


Fig. 3. Calibration curves for detecting anti-*Brucella* IgG antibodies in spiked milk. (A) Colorimetric ELISA. (B) Chemiluminescent ELISA. (C) OFIS using MPTS as silane coupling agent. (D) OFIS using AMPTS as silane coupling agent. (E) OFIS using DCBZS as silane coupling agent. In all of the graphs, linear range is shown in the upper right corner, the lower detection limit is plotted in a dashed line and fitting curve in a dotted line. Insets: AFM and SEM micrographs (top and bottom, respectively) of the optical fiber after modification with the silane coupling agent.

Table 2
Different immunosensors for the detection of anti-*Brucella* IgG antibodies. Summary of all mathematical models and performance description of the methodologies.

Characteristics	Colorimetric ELISA	Chemiluminescent ELISA	OFIS using MPTS	OFIS using AMPTS	OFIS using Si–Bz
Curve mathematical model parameters (Eq. (1))					
a	2.476	948.115	10,399.445	37,093.540	190,223.203
b	1.533	2.224	0.944	1.318	1.684
x_0	62,625.696	4525.673	4708.998	235.128	3129.734
y_0	1.026	119.131	291.321	633.202	9609.924
r^2	0.956	0.881	0.671	0.692	0.879
Linear domains parameters (Eq. (2))					
d	−0.671	−278.275	−18,984.812	−12,470.578	−47,558.486
y_{01}	9.756	2009.959	−1610.143	94,729.801	499,477.653
r^{2*}	0.995	0.984	0.999	0.976	0.984
Performance criteria of methodology					
Linear range	3.31–0.53 μg/ml	53–0.42 μg/ml	212–0.21 μg/ml	2120–6.65 μg/ml	106–2.12 μg/ml
Sensitivity	0.176/ln	0.210/ln	0.078/ln	0.188/ln	0.186/ln
LDL	0.828 μg/ml	0.414 μg/ml	2.120 μg/ml	1.656 μg/ml	0.207 μg/ml
Maximum response	3.810	1323.500	20,520.580	66,142.640	256,278.300

The LDL was calculated for each method and plotted in Fig. 3 as a dotted line. The LDL was 0.828 μg/ml, 0.414 μg/ml, 2.12 μg/ml, 1.656 μg/ml and 0.207 μg/ml, for colorimetric ELISA, CL-ELISA and MPTS, AMPTS and DCBZS based CL-OFIS methodologies, respectively. The OFIS methodology using DCBZS gave two times lower LDL than the CL-ELISA, and four times lower than the colorimetric ELISA. This OFIS methodology is therefore more sensitive and subject to less background noise.

The amount of the immobilized antigen on the solid phase immunoassays has greatly influenced the LDL of the test. This parameter depends on both the binding surface available and the chemistry used to immobilize the biological molecules. Though the binding surface of the microtiter wells is 6.5 times greater than on the OFIS (79 mm^2 and 12 mm^2, respectively), the DCBZS based OFIS showed the best LDL. Major reasons for the improved results are: (1) the proteins are covalently attached to the fiber optic and not only adsorbed on the surface which may increase the stability of the antigen–antibody complex on the optical fiber surface, (2) the CL reaction occurs with high proximity to the transducer surface and enhances light collection efficacy, and (3) the washing method in ELISA technique is manual and passive, and with OFIS the washing steps are more active, the fibers being dipped in the washing solution. This may enhance removal of non-specific binding and decrease noise level.

3.3.4. Sensitivity

The sensitivity is defined as the slope of the linear range, representing the ability of the system to discriminate between two different concentrations *A* and *B* in the solution. It is based on the ratio $(Y_A - Y_B)/(X_A - X_B)$, where *Y* represents the measured signal and *X* represents the concentration. In order to compare the sensitivity of the five different methodologies, each having a different scale, the results were normalized by dividing the signal obtained in the linear range by their respective maximal responses. It was found that all methodologies had similar sensitivity indicating the reliability of the developed OFIS.

3.3.5. Short term shelf life

After preparation, the ready-to-use probes were kept dried at the different temperatures until use. Results (data not shown) revealed that even after a 30-day storage, probes retained similar activity, and the intensities of the signals ranged between 298% and 397%, 109% and 124%, and 85% and 105% from the initial signal for MPTS, AMPTS and DCBZS modified probes, respectively. This stability, confirmed for a minimum of 30 days period that was tested, has shown the reliability of the different techniques, AMPTS and DCBZS modified fibers, at the different storage temperatures. Further work needs to be carried out to establish longer shelf life stability but this was out of the scope of the present study.

4. Conclusions

The chemical modification step is one of the most crucial steps in designing a silanization based immunosensor as it allows the introduction of a new reactive group on the optical fiber in a covalent manner for further immobilization of the bio-receptor. The results have clearly shown that CL-OFIS based on in-house DCBZS modified fibers was superior to other commercial SCAs and conventional colorimetric and CL-ELISA in detecting anti-*Brucella* IgG antibodies at the lowest LDL, therefore making the immunosensor an appropriate tool for detecting and quantifying antibodies at low protein concentrations. Moreover, this immunosensor makes it feasible to work with lower amounts of reagents and as a result, allowing a price reduction of the reagents used and utilizing smaller volumes of sample. Finally, the rapidity of the fiber based procedures compared to the conventional ELISA platform (2 h versus 4 h) and the moderate working operation (RT versus 37 °C) make OFIS preferable in allowing putative real time on-site testing. While only presenting a prototype of the innovative immunosensor, future developments of the OFIS should focus on adjusting the test for mass surveillance.

From the clinical and veterinary point of view, our developed immunosensor identifies anti-*Brucella* antibodies in terms of protein concentration rather than serological activity. Therefore, this work can set the ground for further work that will enable quantifying low amount of anti-*Brucella* antibodies, irrespective of their serological activity, allowing identification of the disease at the earliest possible time following exposure of the host to the organisms.

Acknowledgments

Dr. Gil Korner, Kamada, Israel, is kindly thanked for his work in purifying the anti-*B. melitensis* IgG bovine antibodies used in this research. Luba Burlaka from the Center for Meso, Nanoscale Science and Technology, Department of Chemical engineering (BGU), is thanked for performing SEM-EDS measurements and Inbal Tsarfati and Dr. Levi Gheber, Department of Biotechnology Engineering (BGU) are thanked for performing the AFM measurements. Gina Hughes is thanked for her editorial help and Dr. Michal Shani-Sekler and Dr. Sebastien Herrmann are thanked for their advice and insights. This work was supported by Yeshaya Horowitz Association, project BioPen #84534101 and the Technical Support Working Group project #T-582.

Appendix A. Supplementary data

Supplementary data associated with this article can be found, in the online version, at doi:10.1016/j.talanta.2009.06.070.

References

[1] M.E. Bosch, A.J.R. Sanchez, F.S. Rojas, C.B. Ojeda, Sensors 7 (2007) 797.
[2] S. Herrmann, R.S. Marks, Chemiluminescent optical fiber immunosensor, in: R.S. Marks, D.C. Cullen, I. Karube, C.R. Lowe, H.H. Weetall (Eds.), Handbook of Biosensors and Biochips, John Wiley & Sons Ltd., 2007.
[3] D. Marazuela, M.C. Moreno-Bondi, Analytical and Bioanalytical Chemistry 372 (2002) 664.
[4] M. Mehrvar, C. Bis, J.M. Scharer, M. Moo-Young, J.H. Luong, Analytical Sciences 16 (2000) 677.
[5] R.S. Marks, E. Bassis, A. Bychenko, M.M. Levine, Optical Engineering 36 (1997) 3258.
[6] C. Dodeigne, L. Thunus, R. Leheune, Talanta 51 (2000) 415.
[7] D.K. Aswal, S. Lenfant, D. Guerin, J.V. Yakhmi, D. Vuillaume, Analytica Chimica Acta 568 (2005) 84.
[8] D. Atias, Y. Liebes, V. Chalifa-Caspi, K. Bremand, L. Lobel, R.S. Marks, P. Dussart, Sensors and Actuators: B, Chemical 140 (1) (2009) 206.
[9] T. Konry, A. Novoa, S. Cosnier, R.S. Marks, Analytical Chemistry 75 (2003) 2633.
[10] B. Leshem, G. Sarfati, A. Novoa, I. Breslav, R.S. Marks, Luminescence 19 (2004) 69.
[11] O. Salama, S. Herrmann, A. Tziknovsky, B. Piura, M. Meirovich, I. Trakht, B. Reed, L.I. Lobel, R.S. Marks, Biosensors and Bioelectronics 22 (2007) 1508.
[12] A. Sobarzo, J.T. Paweska, S. Herrmann, T. Amir, R.S. Marks, L. Lobel, Journal of Virological Methods 146 (2007) 327.
[13] Y. Liebes, R.S. Marks, M. Banai, Sensors and Actuators B: Chemical 140 (2) (2009) 568.
[14] K. Hakkila, T. Green, P. Leskinen, A. Ivask, R. Marks, M. Virta, Journal of Applied Toxicology 24 (2004) 333.
[15] B. Polyak, E. Bassis, A. Novodvorets, S. Belkin, R.S. Marks, Sensors and Actuators B (2000) 1.
[16] C.M. Halliwell, A.E.G. Cass, Analytical Chemistry 73 (2001) 2476.
[17] J. Genzer, K. Efimenko, D.A. Fischer, Langmuir 18 (2002) 9307.
[18] W. Kusnezow, J.D. Hoheisel, Journal of Molecular Recognition 16 (2003) 165.
[19] D.G. Pijanowska, E. Remiszewska, J.M. Lysko, J. Jazwinski, W. Torbicz, Sensors and Actuators 91 (2003) 152.
[20] J. Yakovleva, R. Davidsson, A. Lobanova, M. Bengtsson, S. Eremin, T. Laurell, J. Emneus, Analytical Chemistry 74 (2002) 2994.
[21] M.L. Boschiroli, V. Foulongne, D. O'Callaghan, Current Opinion in Microbiology 4 (2001) 58.
[22] S.J. Cutler, A.M. Whatmore, N.J. Commander, Journal of Applied Microbiology 98 (2005) 1270.
[23] J. Godfroid, A. Cloeckaert, J.P. Liautard, S. Kohler, D. Fretin, K. Walraves, B. Garin-Bastuj, J.J. Letesson, Veterinary Research 36 (2005) 313.

[24] G. Pappas, P. Papadimitriou, N. Akritidis, L. Christou, E.V. Tsianos, Lancet Infectious Diseases 6 (2006) 91.
[25] G. Pappas, P. Panagopoulou, L. Christou, N. Akritidis, Cell and Molecular Life Science 63 (2006) 2229.
[26] Z.A. Memish, H.H. Balkhy, Journal of Travelers Medicine 11 (2004) 49.
[27] P. Yagupsky, Journal of Clinical Microbiology 37 (1999) 3437.
[28] P. Chand, B.S. Rajpurohit, A.K. Malhotra, J.S. Poonia, Veterinary Microbiology 108 (2005) 305.
[29] M.J. Corbel, Brucellosis in humans and animals, WHO, 2006.
[30] N.D. Funk, L.B. Tabatabai, P.H. Elzer, S.D. Hagius, B.M. Martin, L.J. Hoffman, Journal of Clinical Microbiology 43 (2005) 721.
[31] C. Romero, M. Pardo, M.J. Grillo, R. Diaz, J.M. Blasco, I. Lopez-Goni, Journal of Clinical Microbiology 33 (1995) 3198.
[32] G.D. Prestwich, G. Dorman, J.T. Elliott, D.M. Marecak, A. Chaudhary, Photochemistry and Photobiology 65 (1997) 222.
[33] G. Rajashekara, D.A. Glover, M. Banai, D. O'Callaghan, G.A. Splitter, Infection and Immunity 74 (2006) 2925.
[34] C. Saegerman, L. De Waele, D. Gilson, J. Godfroid, P. Thiange, P. Michel, B. Limbourg, Veterinary Microbiology 100 (2004) 91.
[35] S. Herrmann, B. Leshem, S. Landes, B. Rager-Zisman, R.S. Marks, Talanta 66 (2005) 6.
[36] S.S. Lateef, S. Boateng, N. Ahluwalia, T.J. Hartman, B. Russell, L. Hanley, Journal of Biomedical Materials Research 72 (2005) 373.
[37] Z.M. Hale, F.P. Payne, R.S. Marks, C.R. Lowe, M.M. Levine, Biosensors and Bioelectronics 11 (1996) 137.
[38] R.S. Marks, A. Novoa, T. Konry, R. Krais, S. Cosnier, Materials Science and Engineering C (2002) 189.
[39] B. Polyak, E. Bassis, A. Novodvorets, S. Belkin, R.S. Marks, Water Science and Technology 42 (2000) 305.
[40] V.K. Nguyen, N. Leclerc, C.M. Wolff, P. Kennel, P. Fonteneau, R. Deyes, J.M. Warter, P. Poindron, Journal of Biotechnology 72 (1999) 115.
[41] E. Metwalli, D. Haines, O. Becker, S. Conzone, C.G. Pantano, Journal of Colloid and Interface Science 298 (2006) 825.
[42] S/N, signal to noise ratio, calculated as a positive value obtained divided by the background level.
[43] A.Y. Fadeev, T.J. McCarthy, Langmuir 16 (2000) 7268.
[44] E. Pavlovic, A.P. Quist, U. Gelius, U. Oscarsson, Journal of Colloid and Interface Science 254 (2002) 200.
[45] A. Petrosova, T. Konry, S. Cosnier, I. Trakht, J. Lutwama, E. Rwaguma, A. Chepurnov, E. Muhlberger, L. Lobel, R.S. Marks, Sensors and Actuators B (2007) 578.
[46] M. Wang, K.M. Liechti, Q. Wang, J.M. White, Langmuir 21 (2005) 1848.
[47] D.R. Thevenot, K. Toth, R.A. Durst, G.S. Wilson, Biosensensors and Bioelectronics 16 (2001) 121.
[48] M.A.V. Vargas, G. Busca, T. Montanari, M.C.H. Delgado, L.J. Alemany, Journal of Material Chemistry 15 (2005) 910.

Talanta 80 (2009) 346–351

Contents lists available at ScienceDirect

Talanta

journal homepage: www.elsevier.com/locate/talanta

Gas chromatography–mass spectrometry method for determination of metoprolol in the patients with hypertension

Bilal Yilmaz [a,*], Sakir Arslan [b], Vedat Akba [c]

[a] Department of Analytical Chemistry, Faculty of Pharmacy, Ataturk University, 25240 Erzurum, Turkey
[b] Department of Cardiology, Faculty of Medicine, Ataturk University, 25240 Erzurum, Turkey
[c] Criminal Police Laboratory, 25060 Erzurum, Turkey

ARTICLE INFO

Article history:
Received 17 February 2009
Received in revised form 23 June 2009
Accepted 30 June 2009
Available online 8 July 2009

Keywords:
Metoprolol
GC–MS
Plasma
Method validation

ABSTRACT

A sensitive and efficient method was developed for determination of metoprolol in human plasma by gas chromatography–mass spectrometry (GC–MS). Metoprolol and atenolol (internal standard, IS) were extracted from human plasma with a mixture of ethylacetate and diethylether at basic pH with liquid–liquid extraction. Calibration curves were linear over the concentration range 15–500 ng/ml. Intra- and inter-day precision values for metoprolol in human plasma were less than 6.4, and accuracy (relative error) was better than 8.8%. The analytical recovery of metoprolol from human plasma averaged 91.20%. The limits of detection (LOD) and quantification (LOQ) of metoprolol were 5.0 and 15 ng/ml, respectively. Also the developed and validated GC–MS method was successfully applied to three patients with hypertension who had been given an oral tablet of 100 mg metoprolol.

© 2009 Elsevier B.V. All rights reserved.

1. Introduction

Metoprolol, 1-(isopropylamino)-3-[p-(2-methoxyethyl)phenoxy]-2-propanol, is a kind of β adrenaline receptor blocker. It is widely used for the treatment of hypertension, angina, myocardial infarction, arrhythmia, hyperthyroidism and other related diseases [1,2].

Several methods have been reported for determination of metoprolol including gas chromatography–mass spectrometry (GC–MS) [3–5], high-performance liquid chromatography (HPLC) [6–10], LC–MS [11–13] and LC–MS–MS [14] in human plasma and other biological fluids.

β-Blockers have similar chemical structures with highly polar functional groups that yield them unsuitable for analysis by GC methods. Recently the use of mass selective detectors with a capillary GC coupled to mass spectrometry as a mode of detection has considerably increased. Suitable derivatization should improve the gas chromatographic properties of the compounds and yield compounds with mass spectra containing high relative intensity and high-mass fragments suitable for selected ion monitoring (SIM) [15].

The present work describes the O-silylation of the hydroxyl group of metoprolol using *N-methyl-N-(trimethylsilyl)trifluoroacetamide* (*MSTFA*) as a silylating reagent. This is followed by determination of metoprolol after a derivatization procedure in human plasma using internal standard methodology by GC–MS. The developed method was validated by using linearity, stability, precision, accuracy and sensitivity parameters according to International Conference on Harmonization (ICH) guidelines [16]. The advantages of present method include simple and single step extraction procedure using inexpensive chemicals and short run time. Also, this method was used to assay the metoprolol in plasma samples obtained from three patients with hypertension who had been given an oral tablet of Problok (100 mg metoprolol).

2. Experimental

2.1. Chemicals and reagents

Metoprolol tartrate was obtained by Sigma–Aldrich (St. Louis, MO, USA). Atenolol as internal standard (IS) was kindly donated from Abdi Ibrahim Pharmaceutical Industry (Istanbul, Turkey). *N-methyl-N-trimethylsilyl-trifluoroacetamide* (*MSTFA*), ethylacetate, diethylether and acetonitrile were purchased from Sigma–Aldrich (St. Louis, MO, USA). Problok tablet (100 mg metoprolol tartrate) was obtained Terra Pharmaceutical Industry (Istanbul, Turkey).

2.2. Apparatus and analytical conditions

Chromatographic analysis was carried out on an Agilent 6890N gas chromatography system equipped with 5973 series mass selective detector, 7673 series autosampler and Agilent chemstation

* Corresponding author. Tel.: +90 0442 2311401; fax: +90 0442 2360962.
E-mail address: bilalylmaz@yahoo.com (B. Yilmaz).

0039-9140/$ – see front matter © 2009 Elsevier B.V. All rights reserved.
doi:10.1016/j.talanta.2009.06.079

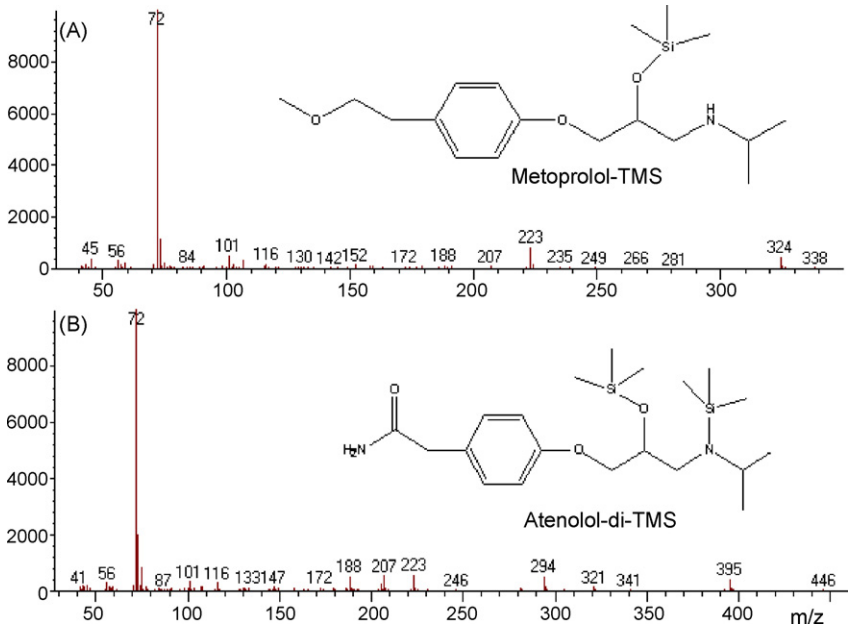


Fig. 1. MS spectra after derivatization of metoprolol (A) and atenolol (IS) (B) with *MSTFA*.

(Agilent Technologies, Palo Alto, CA). HP-5 MS column with 0.25 μm film thickness (30 m × 0.25 mm I.D., USA) was used for separation. Splitless injection was used and the carrier gas was helium at a flow rate of 1.0 ml/min. The injector volume was 1 μl. The MS detector parameters were transfer line temperature 280 °C, solvent delay 3 min and electron energy 70 eV.

2.3. Preparation of stock and working solutions

10 mg metoprolol and IS was weighed, transferred 500 ml volumetric flask, differently. 250 ml acetonitrile was added and the flask was sonicated. The flask was filled to volume with acetonitrile (20 μg/ml). After, 5000 ng/ml standard solution was prepared by diluting with acetonitrile appropriate volumes of 20 μg/ml stock solution and stored at −20 °C under refrigeration. IS working solution was prepared at final concentration of 2500 ng/ml. The working solutions were prepared by diluting the standard stock solution from 15 to 500 ng/ml. Also, quality control (QC) solutions were prepared from stock solution at concentrations of 75, 250 and 450 ng/ml together with 250 ng/ml IS.

2.4. Sample preparation and derivatization procedure

MSTFA is an effective trimethylsilyl (TMS) donor. *MSTFA* reacts to replace labile hydrogens on a wide range of polar compounds with a TMS group and is used to prepare volatile and thermally stable derivatives for GC–MS [17] To increase the performance of the gas chromatographic separation, metoprolol and IS were derivatized using *MSTFA* (Fig. 1). The secondary amine (–NH) and hydroxy (–OH) groups were converted to the corresponding silyl (–N-TMS) and (–O-TMS) groups.

A 0.5-ml aliquot plasma sample was transferred to a 10-ml glass tube. After, a suitable amount of standard metoprolol solutions together with 0.1 ml IS solution (250 ng/ml) and 0.5 ml 1 M sodium hydroxide solution were added. After vortex mixing for 5 s, 3 ml of ethylacetate and diethylether was added (2:1, v/v), the mixture was vortexed for 30 s and then centrifuged at 3000 × *g* for 7 min. The organic layer was transferred into another tube and evaporated to dryness at room temperature under nitrogen gas. The dry residue was dissolved in 100 μl of a mixture of acetonitrile and *MSTFA* (50:50, v/v). The mixture was vigorously shaken and then delayed at room temperature for 10 min. 1 μl sample was injected into the GC–MS system.

3. Results

3.1. Method development

The method development for the assay of metoprolol was based on its chemical properties. The column and acquisition parameters were chosen to be a starting point for the method development. Metoprolol is a polar molecule. Therefore, the capillary column coated with 5% phenyl and 95% dimethylpolysiloxane is a good choice for separation of metoprolol.

The GC/MS parameters used in the method development were based on the boiling point. The injection port and detector temperature was set to 280 °C for GC/MS. Different temperature programs were investigated for method. The end of this investigation, the temperature program of the GC/MS was as follows: initial temperature was 150 °C, held for 1 min, increased to 220 °C at a rate of 20 °C/min held for 1 min, and finally to 300 °C at a rate of 10 °C/min and held for 1 min.

The effects of time and temperature on the reaction were investigated. To confirm the complete derivatization of metoprolol and IS, since only one peak appears on the chromatogram, each compound was derivatized and analyzed separately. After establishing the optimum reaction conditions, the compounds were mixed together and then derivatized in order to perform a simultaneous analysis. To 100 μl of 1000 ng/ml metoprolol and 100 μl of *MSTFA* solution was added and reacted at room temperature, 50 and 75 °C for 5, 10 and 20 min. The resulting samples were quantitated by GC/MS system. The effects of the time and temperature were shown in Fig. 2.

3.2. Validation of the method

The validation was carried out by establishing specificity, linearity, intra- and inter-day precision, accuracy, recovery and sensitivity parameters according to ICH [16] and Center for Drug Evaluation and Research (CDER) guidance for Bio-analytical Method Validation [18].

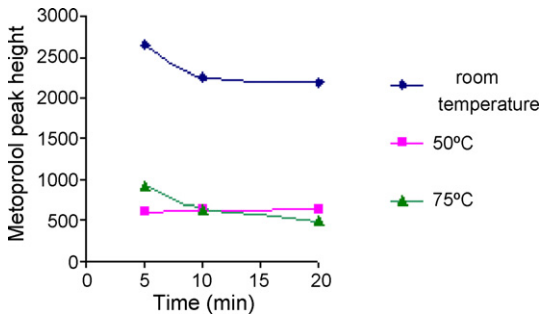


Fig. 2. The effect of reaction time and temperature on derivatization reaction.

3.2.1. Specificity

The specificity criterion tries to demonstrate that the result of the method is not affected by the presence of interferences [19]. The specificity of method was determined by checking the chromatograms obtained from blank plasma samples, and no endogenous interferences were encountered. The fragment ion $[CH_2NHCH(CH_3)_2]^+$ (m/z 72) was used for quantification of metoprolol and IS. The retention time of metoprolol-TMS and IS-di-TMS was approximately 7.8 and 10.6 min in human plasma (Fig. 3).

3.2.2. Linearity

The linearity of an analytical method is its ability within a definite range to obtain results directly proportional to the concentrations (quantities) of an analyte in the sample. The concentrations of the spiked metoprolol in human plasma were 15, 50, 100, 200, 300, 400 and 500 ng/ml with constant concentration of IS (250 ng/ml). The calibration curves were established by plotting the ratio of the peak areas of metoprolol and IS obtained after extraction of the spiked plasma sample. The equation of the calibration curve obtained from seven points was $y = 0.052x + 0.2134$ with a correlation coefficient ($r = 0.998$). The linear regression equation was calculated by the least-squares method using Microsoft Excel® program and summarized in Table 1.

3.2.3. Precision and accuracy

Assay precision was determined by repeatability (intra-day) and intermediate precision (inter-day). Repeatability during the same day and intermediate precision on different days (3 days) were evaluated with six replicates of QC samples. The accuracy of analytic method was assessed as the percentage relative error (% RE). The accuracy and precision of the method were evaluated with QC samples at concentrations of 75, 250 and 450 ng/ml. The intra- and inter-day accuracy and precision results are shown in Table 2. The intra- and inter-day precisions of the QC samples were satisfactory with RSD less than 6.4% and accuracy with RE within ±8.8% (should be less than 15 according to CDER guidance for Bioanalytical Method Validation) [18].

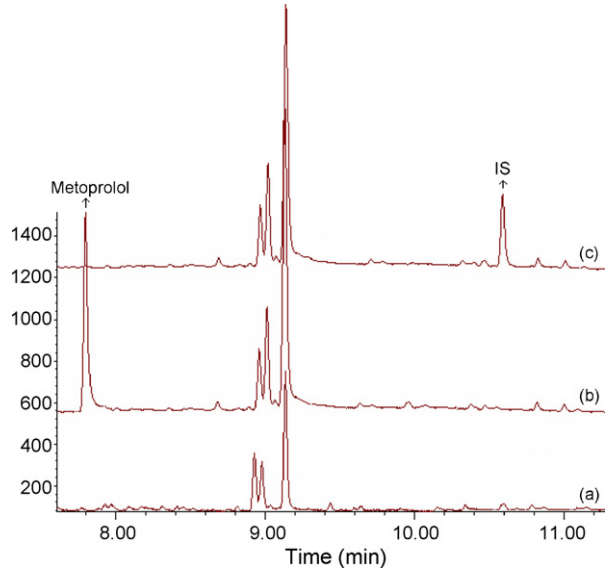


Fig. 3. Typical SIM chromatogram of blank plasma (a), plasma spiked with 100 ng/ml metoprolol (b) and 250 ng/ml atenolol (IS) (c).

Table 1
Linearity of metoprolol in human plasma.

Linearity (ng/ml)	15–500
Regression equation[a]	$y = 0.052x + 0.2134$
Standard deviation of slope	1.62×10^{-3}
Standard deviation of intercept	6.24×10^{-2}
Correlation coefficient	0.998
Standard deviation of correlation coefficient	4.23×10^{-3}
Limit of detection (ng/ml)	5.0
Limit of quantification (ng/ml)	15

[a] Based on three calibration curves, y: peak-area ratio, x: metoprolol concentration (ng/ml).

3.2.4. Sensitivity [limits of detection (LOD) and quantification (LOQ)]

The LOD and LOQ were studied to test the sensitivity of the method. The LOD defined as signal/noise = 3 in method (RSD > 20% for LOD) was found to be 5.0 ng/ml. The LOQ defined as signal/noise = 10 in method (RSD > 10% for LOQ) was found to be 15 ng/ml (Table 1). Both accuracy and precision of these values were well within the proposed criteria (RSD % < 20%).

3.2.5. Recovery

The recovery of an analyte is the extraction efficiency of an analytical process, reported as a percentage of the known amount of an analyte carried through the sample extraction and processing steps of the method [20]. The liquid–liquid extraction was used for the sample preparation in this work. Several solvents (ethylacetate, diethylether, dichloromethane, acetonitrile, butanol and chloroform) were tested for the extraction. Finally, ethylacetate and diethylether mixture (2:1, v/v) proved to be the most efficient in extracting metoprolol from human plasma. After extraction procedure, the dry residue was dissolved in 100 μl of a mixture of acetonitrile and *MSTFA* (50:50, v/v). The mixture was vigorously shaken and then delayed at room temperature for 10 min. Spiked plasma samples were prepared three times at all levels (15, 50, 100, 200, 300, 400 and 500 ng/ml) of the calibration graph of metoprolol. The recovery of metoprolol was determined by comparing the peak areas measured after analysis of spiked plasma samples with those found after direct injection of standard solutions at the same concentration levels. The extraction recoveries of metoprolol from human plasma were between 88.6 and 95.1% as shown in Table 3.

3.2.6. Matrix effect

The matrix effect (ME) was defined as the direct or indirect alteration or interference in response due to the presence of unintended analytes or other interfering substances in the sample [18]. The ME of metoprolol was investigated by comparing amount of metoprolol solutions with processed blank samples reconstituted with metoprolol solutions. The blank plasmas used in this study were from five different batches of healthy human blank plasma. If the ratio <85 or >115%, a matrix effect was implied. The relative matrix effect of metoprolol at three different concentrations (50, 200 and 500 ng/ml) was less than ±10.9% (Table 4). The results showed that

Table 2
Precision and accuracy of metoprolol in human plasma.

Added (ng/ml)	Intra-day			Inter-day		
	Found (mean ± SD[a])	Precision (% RSD[b])	Accuracy[c]	Found (mean ± SD[a])	Precision (% RSD[b])	Accuracy[c]
Plasma pools[d]						
75	81.53 ± 2.767	3.39	8.71	78.56 ± 2.948	3.75	4.75
250	256.7 ± 2.522	0.98	2.68	241.9 ± 15.48	6.39	−3.24
450	458.5 ± 6.869	1.49	1.89	461.8 ± 9.749	2.11	2.62

[a] SD: standard deviation of six replicate determinations; RSD: relative standard deviation.
[b] Average of six replicate determinations.
[c] Accuracy: (% relative error) (found − added)/added × 100.
[d] Plasma volume (0.5 ml).

Table 3
Recovery of metoprolol in human plasma.

Added (ng/ml)	Found (mean ± SD[a])	% Recovery	% RSD[b]
15	13.35 ± 1.125	89.0	8.43
50	45.60 ± 2.941	91.2	6.45
100	93.40 ± 4.931	93.4	5.28
200	184.2 ± 8.049	92.1	4.37
300	266.1 ± 19.85	88.7	7.46
400	380.4 ± 21.79	95.1	5.73
500	443.0 ± 28.39	88.6	6.41

[a] SD: Standard deviation of three replicate determinations; RSD: relative standard deviation.
[b] Average of three replicate determinations.

there was no matrix effect of the analytes observed from the matrix of plasma in this study.

3.2.7. Stability

The stability of metoprolol in human plasma was studied under a variety of storage and handling conditions at low (100 ng/ml) and high (500 ng/ml) concentration levels. The short-term temperature stability was assessed by analyzing three aliquots of each of the low and high concentration samples that were thawed at room temperature and kept at this temperature for 8 h. Freeze–thaw stability (-20 °C in human plasma) was checked through three cycles. Three aliquots at each of the low and high concentrations were stored at -20 °C for 24 h and thawed unassisted at room temperature. When completely thawed, the samples were refrozen for 24 h under the same conditions. The freeze–thaw cycles were repeated three times and then analyzed on the third cycle. The long-term stability was determined by analyzing three aliquots of each of the low and high concentrations stored at −20 °C for 1 week. The accuracy of metoprolol stability was obtained for the short-term temperature, freeze–thaw and long-term 97.8, 96.2 and 95.4%, respectively. The stability results indicated that no significant degradation of metoprolol in human plasma was observed under the tested conditions.

3.3. Application of the method

Prior to the study, the clinical protocol was approved by the Ethics Committee of Faculty of Medicine, Ataturk University (2009/Number 41). All volunteer patients were given written informed consent to participate in the study according to the principles of the Declaration of Helsinki. The patients who submitted the agreements to attend this project were medically examined and three patients with hypertension were selected (34.3 ± 1.154 years; 72.7 ± 1.528 kg; 169.3 ± 2.517 cm) for the pharmacokinetics study of metoprolol. The subjects were required to abstain from taking any other drug for 7 days prior the start of test. They were also demanded not to smoke or drink alcohol or xanthine-containing beverages for 24 h before the beginning of the study until its end. Three patients with hypertension received an oral tablet (Problok 100 mg) containing 100 mg of metoprolol. Then, they were allowed to drink water. The total amount of water drunk during the day was 1500 ml. The volunteers were sitting during lunch. They had normal activity (standing or sitting) during the study, but were never in a supine position during the 12 h after administration. Blood samples were taken into EDTA tubes before and 0.5, 1, 1.5, 2, 3, 4, 6, 8 and 12 h after oral administration. The blood was centrifuged 3000 × *g* for 10 min at ambient temperature, extracted and derivatized with *MSTFA*. Representative chromatograms obtained before and after administration of the drug are shown in Fig. 4. Metoprolol plasma concentrations were shown in three patients with hypertension following oral application of Problok in Fig. 5.

3.4. Pharmacokinetic analysis

The present method was used to determine the plasma concentration of metoprolol. The peak plasma level (C_{max}) is the highest observed concentration and T_{max} is the corresponding time of this concentration. The areas under the plasma concentration–time curves (AUC) were calculated with the linear trapezoidal rule. The $AUC_{0-\infty}$ was calculated by dividing the last measured concentration (C_t) by elimation rate constant (k_{el}) and adding the result to the AUC_{0-t}. The elimination rate constant was calculated by the least-squares regression using the last five time points of each curve. The apparent elimination half-life was the quotient of the natural logarithm of 2 and the elimination rate constant [21].

Analysis of metoprolol concentration in plasma samples from three patients following oral administration of 100 mg of Problok provided the following pharmacokinetic parameters (mean ± SD): C_{max}, 104.3 ± 7.09 ng/ml; area under curve (AUC),

Table 4
Matrix effect evaluation of metoprolol and IS in human plasma (n = 3).

Samples	Concentration level (ng/ml)	A (mean ± SD)	B (mean ± SD)	% Matrix effect
Metoprolol	50	46.3 ± 3.12	51.1 ± 2.87	90.6
	200	184.7 ± 9.47	207.2 ± 8.34	89.1
	500	457.9 ± 13.45	513.1 ± 10.28	89.2
IS	250	228.6 ± 11.53	240.7 ± 9.54	94.9

(A) The amount of metoprolol and IS derivatized in blank plasma sample's reconstituted solution (the final solution of blank plasma after extraction and reconstitution). (B) The amount of metoprolol and IS derivatized with MSTFA.

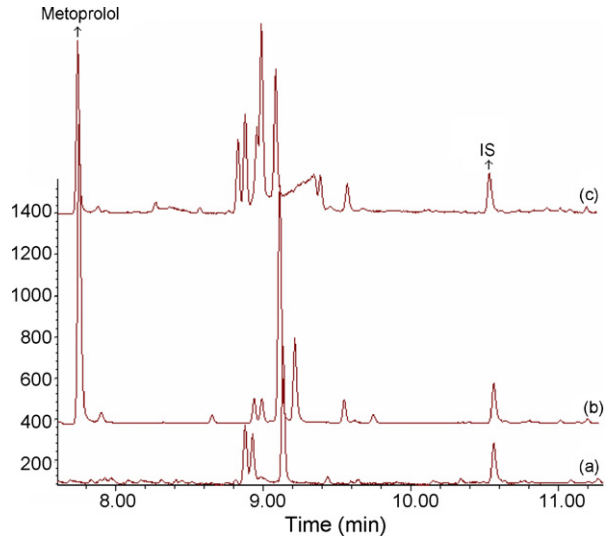


Fig. 4. Typical SIM chromatogram of plasma obtained from a patient at before (a) and after 1.5 h (b), 4 h (c) oral administration of 100 mg metoprolol.

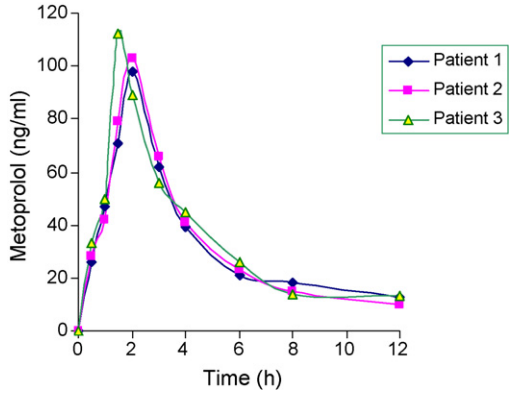


Fig. 5. The plasma concentration–time profiles of metoprolol in patients ($n = 3$) after application of Problok tablet.

$AUC_{0-12\,h}$, 381.4 ± 11.22 h ng/ml; $AUC_{0-\infty}$, 475.4 ± 19.30 h ng/ml; T_{max}, 1.83 ± 0.29 h and elimination half-life, $t_{1/2}$, 4.12 ± 0.16 h.

4. Discussion

Kim et al. [3] have reported GC–MS method after pre-column derivatization with α-methoxy-α-(trifluoromethyl)phenylacetyl chloride as a chiral derivatizing agent for the determination of metoprolol in human urine. Angier et al. [4] have reported the determination of metoprolol with other β-blockers in biological fluids by GC–MS method after pre-column derivatization with pentafluoropropionic anhydride. Gowda et al. [14] have reported LC method with tandem mass detection for the analysis of metoprolol in human plasma. The calibration curve of LC–MS–MS method was linear for metoprolol in the range 5.0–500 ng/ml. Intra- and inter-day precision ranged from 4.82 to 8.42 and from 7.2 to 11.11% for metoprolol, respectively. The maximum recovery of metoprolol was 77.68%. The LOQ and LOD of method were found 5.0 and 1.0 ng/ml, respectively. Detection using LC–MS–MS would be a more sensitive approach but is costly and not yet available for every laboratory.

Albers et al. [6] have reported HPLC method with fluorescence detection for the analysis of metoprolol in human plasma. The calibration curve of the method was linear for metoprolol in the range 2.4–195.2 ng/ml. Precision throughout the whole working range was between 0.6 and 15.5%. Metoprolol recovery was determined at 73.0 ± 20.5, and the LOQ was 2.4 ng/ml.

Today, GC–MS is a powerful technique for highly specific and quantitative measurements of low levels of analytes in biological samples. As compared to HPLC, high-resolution capillary GC has been less frequently used. Because it requires pre-conversion of multifunctional β-blockers into thermally stable volatile derivatives. However, it has inherently high resolving power and high sensitivity with excellent precision and accuracy allowed simultaneous detection of expected and unexpected β-blockers, their metabolites and contaminants. Also, the detection limits were lowered to pg levels by GC combined with MS [22].

The specificity of GC–MS method has been demonstrated by the representative chromatograms for metoprolol in human plasma (Figs. 3 and 4). The recovery of metoprolol was achieved by developed liquid–liquid extraction procedure in human plasma. Metoprolol was extracted from human plasma with a mixture of ethylacetate and diethylether solvents. This solvent mixture gave an excellent recovery. The analytical recovery of metoprolol from human plasma averaged 91.20%. Intra- and inter-day precision values for metoprolol in human plasma were less than 6.4%. Metoprolol was extracted from urine with a solid phase extraction procedure by Chiu et al. [8]. This method is also the most comprehensive method which can extract metoprolol in a single extraction procedure.

In statistical comparison ($p > 0.05$) with other methods in the literature [3,6–8,12,14] the proposed method has indicated high accuracy, precision and recovery.

Metoprolol in plasma, amniotic fluid and capillary blood was analyzed by GC–MS according to Ervik et al. [23]. The minimum determinable concentration at standard deviation of 10% was 1 nmol/l. The present method has the following advantage over the reported method [24]. The LOQ of the reported method was 15.7 ng/ml whereas the present method LOQ was 15 ng/ml. When this method is applied to plasma samples, its sensitivity was found to be adequate for pharmacokinetic studies.

Additionally, this method was applied to three patients with hypertension who had been given an oral tablet of 100 mg metoprolol. The amount of metoprolol was determined between 0 and 12 h in human plasma.

5. Conclusion

In the present work, a simple and sensitive GC–MS method has been developed for the determination of metoprolol in human plasma. Also, the method was completely validated by using sensitivity, stability, specificity, linearity, accuracy and precision parameters for determination of metoprolol in human plasma. Additional advantages of this method include small sample volume (0.5 ml), good extraction recovery from plasma and a readily available internal standard. Also, the extraction and derivatization procedures in this study were simple. Therefore, the proposed method can be used as a therapeutic drug monitoring method in clinic to check the plasma concentration of metoprolol in the patients with hypertension.

Acknowledgements

The authors would like to thank Abdi Ibrahim Pharmaceutical Industry for the atenolol (IS) standard. The authors also wish to thank M. Resul KARADAS for expert advises on the use of English.

References

[1] British Pharmacopoeia Commission, British Pharmacopoeia, 34th ed., Pharmaceutical Press, London, 2005.

[2] The United States Pharmacopeial Convention, USP28-NF23 (2005) 1281.
[3] K.H. Kim, J.H. Lee, M.Y. Ko, K.S. Shin, J.S. Kang, W.C. Mar, J.R. Youm, Chromatographia 55 (2002) 81.
[4] M.K. Angier, R.J. Lewis, A.K. Chaturvedi, D.V. Canfield, J. Anal. Toxicol. 29 (2005) 517.
[5] K. Hartonen, M.L. Riekkola, J. Chromatogr. B 676 (1996) 45.
[6] S. Albers, J. Elshoff, C. Volker, A. Richter, S. Laer, Biomed. Chromatogr. 19 (2005) 202.
[7] A.J. Braza, P. Modamio, C.F. Lastra, E.L. Marino, Biomed. Chromatogr. 16 (2002) 517.
[8] F.C.K. Chiu, L.A. Damani, R.C. Li, B. Tomlinson, J. Chromatogr. B 696 (1997) 69.
[9] V.B. Boralli, E.B. Coelho, P.M. Cerqueira, V.L. Lanchote, J. Chromatogr. B 823 (2005) 195.
[10] D. Schuster, M.W. Modi, D. Lakla, F.M. Gengo, J. Chromatogr. 433 (1988) 318.
[11] R.D. Johnson, R.J. Lewis, Forensic Sci. Int. 156 (2006) 106.
[12] B.P. Jensen, C.F. Sharp, S.J. Gardiner, E.J. Begg, J. Chromatogr. B 865 (2008) 48.
[13] C. Dupuis, J.M. Gaulier, A.L. Pelissier-Alicot, P. Marquet, G. Lachatre, J. Anal. Toxicol. 28 (2004) 674.
[14] K.V. Gowda, U. Mandal, P.S. Selvan, W.D.S. Solomon, A. Ghosh, A.K. Sarkar, S. Agarwal, T.N. Rao, T.K. Pal, J. Chromatogr. B 858 (2007) 13.
[15] J. Lee, D. Lho, M. Kim, K. Kim, Y. Kim, Rapid Commun. Mass Spectrom. 12 (1998) 1150.
[16] Proceedings of the International Conference on Harmonization (ICH), Commission of the European Communities, 1996.
[17] M. Donike, J. Chromatogr. 42 (1969) 103.
[18] Guidance for Industry, Bioanalytical Method Validation, US Department of Health and Human Services, Food and Drug Administration, Center for Drug Evaluation and Research (CDER), Rockville, MD, 2001.
[19] M.J. Saiz-Abajo, J.M. Gonzalez-Saiz, C. Pizarro, Anal. Chim. Acta 528 (2007) 63.
[20] G. Milena, G. Ramirez, O. Velasquez, M. Perez, P. Restrepo, ARS Pharm. 46 (2005) 411.
[21] M. Gibaldi, D. Perrier, Pharmacokinetics, 2nd ed., Marcel Dekker, New York, 1990.
[22] M.J. Paik, J. Lee, K.R. Kim, Anal. Chim. Acta 601 (2007) 230.
[23] M. Ervik, K.J. Hoffman, K. Kyhlberg-Hanssen, Biomed. Mass Spectrom. 8 (1981) 322.
[24] J. Fang, H.A. Semple, J. Song, J. Chromatogr. B 809 (2004) 9.

Talanta 80 (2009) 352–362

Contents lists available at ScienceDirect

Talanta

journal homepage: www.elsevier.com/locate/talanta

Determination of uranium and thorium in complex samples using chromatographic separation, ICP-MS and spectrophotometric detection

Martina Rožmarić[a,*], Astrid Gojmerac Ivšić[b], Željko Grahek[a]

[a] Laboratory for Radioecology, Rudjer Boskovic Institute, Bijenička 54, 10 000 Zagreb, Croatia
[b] Laboratory of Analytical Chemistry, Faculty of Science, University of Zagreb, Horvatovac 102a, 10 000 Zagreb, Croatia

ARTICLE INFO

Article history:
Received 3 March 2009
Received in revised form 18 June 2009
Accepted 30 June 2009
Available online 8 July 2009

Keywords:
Uranium
Thorium
Anion exchange
Mixed solvent
Extraction chromatography
Spectrophotometry

ABSTRACT

The paper describes a research of possible application of UTEVA and TRU resins and anion exchanger AMBERLITE CG-400 in nitrate form for the isolation of uranium and thorium from natural samples. The results of determination of distribution coefficient have shown that uranium and thorium bind on TRU and UTEVA resins from the solutions of nitric and hydrochloric acids, and binding strength increases proportionally to increase the concentration of acids. Uranium and thorium bind rather strongly to TRU resin from the nitric acid in concentration ranging from 0.5 to 5 mol L^{-1}, while large quantities of other ions present in the sample do not influence on the binding strength. Due to the difference in binding strength in HCl and HNO_3 respectively, uranium and thorium can be easily separated from each other on the columns filled with TRU resin. Furthermore, thorium binds to anion exchanger in nitrate form from alcohol solutions of nitric acid very strongly, while uranium does not, so they can be easily separated. Based on these results, we have created the procedures of preconcentration and separation of uranium and thorium from the soil, drinking water and seawater samples by using TRU and UTEVA resins and strong base anion exchangers in nitrate form. In one of the procedures, uranium and thorium bind directly from the samples of drinking water and seawater on the column filled with TRU resin from 0.5 mol L^{-1} HNO_3 in a water sample. After binding, thorium is separated from uranium with 0.5 mol L^{-1} HCl, and uranium is eluted with deionised water. By applying the described procedure, it is possible to achieve the concentration factor of over 1000 for the column filled with 1 g of resin and splashed with 2 L of the sample. Spectrophotometric determination with Arsenazo III, with this concentration factor results in detection limits below 1 μg L^{-1} for uranium and thorium. In the second procedure, uranium and thorium are isolated from the soil samples with TRU resin, while they are separated from each other on the column filled with anion exchanger in alcohol solutions. Anion exchanger combined with alcohol solutions enables isolation of thorium from soil samples and its separation from a wide range of elements, as well as spectrophotometric determination, ICP-MS determination, and other determination techniques.

© 2009 Elsevier B.V. All rights reserved.

1. Introduction

Determination of uranium and thorium in environmental and biological samples has considerable potential as a tool for assessing human exposure. Despite the relatively low specific activity of natural uranium and thorium isotopes, there exists an important health concern because of their chemical toxicity and radio toxicity of their decay products. These elements, present in soil, rocks, water and other samples, can be incorporated into human food chain through various pathways. The simplest way for their intake is through water and beverages consumption. Therefore WHO recommends that U and ^{232}Th in drinking water should not exceed 15 μg L^{-1} and 1 Bq L^{-1} respectively and for daily water consumption of 2 L per day this limit leaves a considerable safety margin [1]. Furthermore, the European directive requires measurement of radionuclides (prescribes ^{3}H and total indicative dose) in drinking water and in Annex define parameters to perform radioactivity monitoring of water. It could be expected in near future that Directive will define reference values for single radionuclides as well as their limits of detection [2]. These recommendations require a regular monitoring of uranium (as isotopes and element), and consequently, forces the analysts to find rapid, inexpensive and sensitive methods for its determination.

Although a series of methods for determination of uranium and thorium in different kinds of samples have been developed, in consideration of the mentioned requests there is no superior method [3–30]. Direct determination of uranium and thorium isotopes is possible on inductively coupled plasma mass spectrometry

* Corresponding author.
E-mail address: rozmar@irb.hr (M. Rožmarić).

0039-9140/$ – see front matter © 2009 Elsevier B.V. All rights reserved.
doi:10.1016/j.talanta.2009.06.078

ICP-MS [13,15,16] in solutions (excluding rather sophisticated and expensive techniques of laser ablation ICP-MS or accelerator mass spectrometry which can be used for determination in solid samples). The lower detection limit depends on a number of factors, the main being the occurrence of interferences caused by the structure and concentration of matrix elements. In conditions of low concentrations of matrix elements, it is possible to achieve very low detection limits. However, it is not possible to achieve the same detection result with concentrated samples without removing the interfering factors. In practice, the most frequently used methods are coupling ion chromatography and ICP-MS [10,12,16,18,29]. Nevertheless, IC-ICP-MS also has limitations due to sample structure (column capacity, acidity). Other determination techniques as fluorimetry [16,23] neutron activation analysis [24,25] and alpha spectrometry [11,26–28] can be used for their determination but these techniques require more or less sample preparation (preconcentration and separation from the sample). An exception to the rule is gamma spectrometric determination, which enables direct determination through their decay products [11,25]. Although a rather elegant determination procedure, it requires time in order to establish radio-chemical equilibrium between decay products.

For determination of low concentrations of uranium and thorium, some of the most appropriate techniques are above mentioned methods. However, spectrophotometry is always an acceptable alternative method, due to its acceptable precision and accuracy, associated with its lower cost compared to the some of mentioned techniques [4,5,8]. The critical point against the use of spectrophotometry for determination of uranium and thorium is generally associated with low sensitivity of the spectrophotometric determinations and impossibility of direct determination without sample preparation. Considering the advantages and disadvantages of the existing techniques the set objective is the development of a robust, simple, and relatively cheap determination method that can be used in any laboratory.

Preconcentration and elimination of interfering elements is characteristic almost for all developed methods, so various separation and preconcentration techniques are often employed prior to detection on available instruments [30]. Preconcentration improves the detection limits, increases the sensitivity by several orders of magnitude and enhances the accuracy of the results. The preconcentration techniques hitherto developed for uranium and thorium are based on physico-chemical and chemical principles. Among many others, ion exchange and extraction chromatography are very popular methods due to their applicability to both preconcentration and separation [30]. Horwitz et al. have developed several types of extraction chromatographic resins that can be used for enrichment and separation of uranium and thorium. So it is well known that uranium tetravalent actinide specific resin UTEVA and transuranium specific resin TRU are very applicable for separation of U and Th from various types of samples [31–35]. Also thorium can be chromatographically separated from number of elements on anion exchange column with alcoholic solution of nitric acid [36–38].

Therefore, the main aim of this work is the development of simple methods for preconcentration and separation of uranium and thorium from water samples that can be easily adapted for separation and preconcentration from various types of samples and that will enable their spectrophotometric determination with satisfactory sensitivity and detection limit. It will be shown that a combination of mixed solvent anion exchange and extraction chromatography can ensure a simple and efficient procedure for uranium and thorium separation and preconcentration from various types of samples. Considering the fact that alpha spectrometric determination in general requires separation of uranium and thorium from the sample as well as ICP-MS in some cases, it will be discussed how to use the developed procedure in these determination procedures.

2. Experimental

Based on the literature data [36–38], obtained results and experience, the procedures for isolation of uranium and thorium from the soil, drinking and seawater samples, and their subsequent determination were created. In the first step, the distribution coefficients of the mentioned elements on extraction chromatographic resins TRU and UTEVA and strong base anion exchanger Amberlite CG-400 in nitrate form were determined. In the second step, the optimal conditions for preconcentration and separation of uranium and thorium from other elements in real samples were established. Finally, uranium and thorium were quantitatively determined by spectrophotometry and parallel with ICP-MS and gamma spectrometry. In the first step, the research was conducted with model systems and then with real systems.

2.1. Determination of distribution coefficients and elution curves

The distribution coefficients of uranium and thorium and their elution curves for the TRU and UTEVA resins from nitric and hydrochloric acids and for anion exchanger Amberlite CG-400 (100–200 mesh) in the nitrate form and alcohol solution of nitric acid were determined. For distribution coefficients determination, 10 mL of solution containing 20–50 mg L^{-1} of uranium, thorium or lead were equilibrated with 0.2 g of the mentioned resins or exchanger for 24 h.

Amberlite CG-400 had to be transferred into nitrate form. The distribution coefficients were calculated according to the equation:

$$K_D = \frac{c_0 - c}{c} \cdot \frac{V}{m}$$

where c_0 is the initial concentration of cations, c: concentration after equilibrating, V: solution volume and m: mass of resin or exchanger.

Columns of 0.9 cm in diameter and 25 cm long were used for determination of elution curves. Columns were filled with (1–3) g of extraction chromatographic resins or anion exchanger. The isolation procedures from model and real samples of natural waters and soil were created based on the obtained data.

2.2. Preconcentration of uranium and thorium from model water samples and real samples

In order to determine the efficiency of isolation from seawater and drinking water samples, model samples were tested first. The preconcentration method on TRU and TEVA resin with simultaneous separation of uranium from thorium on the same resin and on the anion exchanger Amberlite CG-400 was tested. As real samples of tap water (Zagreb), mineral water (Studenac) and seawater from Adriatic sea were used. Sample of seawater was taken near the island Vis.

Model sample solution of seawater with known concentration of thorium and uranium was prepared by dissolving of $Th(NO_3)_4{\cdot}5H_2O$ and of $UO_2(NO_3)_2{\cdot}6H_2O$ in artificial seawater. Artificial seawater was prepared by dissolving of salts of Na, Ca, Mg, K in Mili-Q (Millipore) deionised water (18 MΩ) according to Bowen [39]. Model solution of drinking water with known concentration of thorium and uranium was prepared by dissolving of $Th(NO_3)_4{\cdot}5H_2O$ and of $UO_2(NO_3)_2{\cdot}6H_2O$ in model drinking water. Model sample of drinking water was prepared by dissolving of salts of Na, Ca, Mg, K in Mili-Q deionised water. Concentration of Na, Ca and other cations was equivalent to concentration of these elements in bottled spring and mineral water. Final concentration of acid in model samples was obtained by mixing of concentrated acids and

model sample. For 3 mol L^{-1} HNO_3 1 L of water was mixed with 330 mL of 14 mol L^{-1} HNO_3.

2.2.1. Preconcentration on TRU resin and separation on anion exchange resin

1 L of the prepared solution (0.5 mol L^{-1} HNO_3 in sample) was passed through a column (I.D. = 0.9 cm) filled with TRU resin (1.5 g) at a flow rate of (1–2) mL min^{-1}. Before that, the column had to be prepared for separation by passing 50 mL of 3 mol L^{-1} HNO_3. After passing the sample, 50 mL of 3 mol L^{-1} HNO_3 were passed through the column. Thorium and uranium were stripped together with 50 mL of deionised water and then separated on the anion exchange column. Water fraction was reduced (by evaporation) to 1 mL and then prepared for separation on the anion exchange column filled with Amberlite CG-400 in nitrate form. 1 mL sample was mixed with 5 mL of 0.25 mol L^{-1} HNO_3 in methanol and passed through the column filled with 1 g Amberlite CG-400 at a flow rate of 1 mL min^{-1}. Uranium was eluted with 25 mL of 0.25 mol L^{-1} HNO_3 in methanol, and after that thorium was stripped from the column with 5 mL of deionised water. To perform spectrophotometric determination, the volume of uranium and thorium fractions must be reduced by evaporation exactly to 1 mL. The same procedure is applied for isolation from model drinking water. The concentration of acid in the sample is 0.5 mol L^{-1} (see Section 3).

2.2.2. Preconcentration on UTEVA resin and separation on anion exchange resin

1.33 L of the prepared solution (3 mol L^{-1} HNO_3 in sample) was passed through a column (I.D. = 0.9 cm) filled with UTEVA resin (3 g) at a flow rate of (1–2) mL min^{-1}. Before that, the column had to be prepared for separation by passing of 50 mL of 3 mol L^{-1} HNO_3. After passing the sample, 50 mL of 3 mol L^{-1} HNO_3 were passed through the column. Thorium and uranium were stripped together with 50 mL of deionised water and then separated on the anion exchange column. Water fraction was reduced (by evaporation) to 1 mL and then prepared for separation on the anion exchange column filled with Amberlite CG-400 in nitrate form. 1 mL sample was mixed with 5 mL of 0.25 mol L^{-1} HNO_3 in methanol and passed through the column filled with 1 g Amberlite CG-400 at a flow rate of 1 mL min^{-1}. Uranium was eluted with 25 mL of 0.25 mol L^{-1} HNO_3 in methanol, and after that thorium was stripped from the column with 5 mL of deionised water. To perform spectrophotometric determination, the volume of uranium and thorium fractions must be reduced by evaporation to 1 mL exactly. The same procedure is applied for isolation from model sample of drinking water. The concentration of acid in the sample is 3 mol L^{-1} (see Section 3).

2.2.3. Preconcentration and separation on TRU resin

1 L of the prepared solution (0.5 mol L^{-1} HNO_3 in sample) was passed through a column (I.D. = 0.9 cm) filled with TRU resin (1.5 g) at a flow rate of (1–2) mL min^{-1}. Before that, the column had to be prepared for separation by passing of 50 mL of 3 mol L^{-1} HNO_3. After passing the sample, 50 mL of 3 mol L^{-1} HNO_3 were passed through the column. After that, thorium was eluted with 25 mL of 0.5 mol L^{-1} HCl and uranium was stripped with 25 mL of deionised water. To perform spectrophotometric determination, the volume of uranium and thorium fractions must be reduced to precisely 1 mL by evaporation.

2.2.4. Preconcentration and separation on UTEVA resin

1.33 L of the prepared solution (3 mol L^{-1} HNO_3 in sample) was passed through a column (I.D. = 0.9 cm) filled with UTEVA (3 g) at a flow rate of (1–2) mL min^{-1}. Before that, the column had to be prepared for separation by passing of 50 mL of 3 mol L^{-1} HNO_3. After passing the sample, 50 mL of 3 mol L^{-1} HNO_3 were passed through the column. After that, thorium was eluted with 25 mL of 5 mol L^{-1} HCl and uranium with 25 mL of 0.1 mol L^{-1} HCl.

2.3. Preconcentration and isolation of uranium and thorium from drinking and seawater

Drinking water and seawater samples were prepared by mixing 1 L of the sample and 100 mL conc. HNO_3 (1 mol L^{-1} final concentration of nitric acid). Prior to that, water samples had to be filtered through G4 sinter funnel. After passing the sample, 50 mL of 3 mol L^{-1} HNO_3 were passed through the column. After that, thorium was eluted with 25 mL of 0.5 mol L^{-1} HCl and uranium was stripped with 25 mL of deionised water. To perform spectrophotometric determination, the volume of uranium and thorium fractions must be reduced to 1 mL exactly. This procedure was repeated with 2 L of water. In water and seawater samples uranium was also directly determined by ICP-MS.

2.4. Preconcentration and isolation of uranium and thorium from soil samples

Different soil samples for the analysis was used; NIST SRM 2710 Montana soil, IAEA 312 soil and natural soil taken on the island Vis and on the Adriatic coast (terra rossa and dolomite soil). Natural soil samples were prepared for analysis by drying and sieving through 250 μm sieve.

Soil samples require special ways of treatment in order to be transferred in soluble form suitable for isolation of the matrix elements with extraction chromatographic resins or ion exchangers. Soil samples can be dissolved with concentrated acids and hydrogen peroxide in the following sequence (HCl, HNO_3, HF, $HClO_4$, H_2O_2, HNO_3) by heating or using microwave digestion [20]. If 10 g of sediment or soil are destroyed, it requires acid volumes of 100 mL respectively (except HF, which is added twice á 50 mL) and 10 mL of hydrogen peroxide. After final evaporation, the sample is dissolved in the smallest possible volume of desired concentration of HNO_3 (100 mL) and then transferred into the form suitable for separation. For direct determination of U and Th by ICP-MS aliquot of 1 mL solution of NIST, IAEA and natural soil samples was diluted before analysis.

2.4.1. Preconcentration and separation of uranium and thorium on TRU resin

Prepared solution in 3 mol L^{-1} HNO_3 was passed through a column (I.D. = 0.9 cm) filled with TRU resin (1.5 g) at a flow rate of (1–2) mL min^{-1}. Before that, the column had to be prepared for separation by passing of 50 mL of 3 mol L^{-1} HNO_3. After passing the sample, 50 mL of 3 mol L^{-1} HNO_3 were passed through the column. After that, thorium was eluted with 25 mL of 0.5 mol L^{-1} HCl and uranium was stripped with 25 mL of deionised water. To perform spectrophotometric determination, the volume of uranium and thorium fractions must be reduced to precisely 1 mL by evaporation.

2.4.2. Preconcentration and separation of thorium on anion exchange column

The soil after digestion was dissolved in the minimal quantity of 5 mol L^{-1} HNO_3 and mixed with methanol so that the concentration is 0.25 mol L^{-1} in methanol [37,38]. Alcohol solution was passed through a column (I.D. = 0.9 cm) filled with 1 g Amberlite CG-400 in nitrate form. After passing the sample, 100 mL of 0.25 mol L^{-1} HNO_3 were passed through the column in order to separate macroconstituents. Following that, thorium was eluted with 10 mL of deionised water. Since soil samples often contain lead that binds strongly to anion exchanger and is eluted from column with water.

Lead also makes complex with Arsenazo III and interfere with thorium in spectrophotometric determination. Therefore it must be separated from thorium. In order to achieve that, a water fraction of thorium and lead from the anion exchanger was passed through a column filled with 0.2 g of Sr resin (0.1 mol L^{-1} HNO_3). In such conditions, thorium did not bind to the column, while lead bound strongly. To perform spectrophotometric determination, the volume of thorium must be reduced to precisely 1 mL by evaporation. Thorium was also determined by mass spectrometry. For the thorium analysis aliquot of 0.1 mL of water fraction was taken and diluted in deionised water.

2.5. Spectrophotometric and ICP-MS determination of uranium and thorium

Spectrophotometric determination was based on measuring the absorption of the complex compounds with Arsenazo III or Thorin in the visible part of the spectrum from 400 to 800 nm. Measurements were performed according to blind samples. The samples were prepared in flasks of 10 mL by adding of the specific sample volume and 0.8 mL of 0.05% solution of Arsenazo III or 1.2 mL of 0.1% solution of thorin. The pH values were adjusted by adding conc. 10% NaOH or 5 mol L^{-1} HNO_3 or HCl, and the flasks were refilled with water, methanol, or ethanol.

ICP-MS Element 2 mass spectrometer with conical nebuliser (Thermo) and glass spray chamber (Scott-Thermo) was used for the U and Th determination (RF powers 1200 W, Coolant flow 15.5 L min^{-1}, sample gas flow 1.004 L min^{-1}, Resolution LR = 300, MR = 4000, HR = 10 000, sample uptake 1 mL min^{-1}, acquisition mode E-scan, sample time 5 min). Before analysis, the ICP-MS measuring conditions were optimised using a solution containing In and U at a concentration of 1 μg L^{-1}. Calibration standards for ICP-MS determination were prepared by dilution of 10 mg L^{-1} U and Th Merck standards solution in model drinking water and seawater samples. Model samples (without U and Th) were prepared as described previously.

2.6. γ-Spectrometric determination of ^{232}Th and ^{238}U in soil samples

Prior to gamma spectrometry measurement dried soil samples were placed into counting vessel of known geometry, sealed and stored for at least 6 weeks to allow ingrowths of decay products and to equilibrate with their long lived precursor. After that samples were counted on a gamma spectrometer with HPGe broad detector and 8192 channel analyzer. The system was calibrated and validated by using γ-standards (Czech Metrological Institute) and IAEA reference materials IAEA-306, IAEA-311 and IAEA-314. Counting time was 200 000 s and spectra were analysed by GENIE 2000 software (Canberra). ^{232}Th activities were determined from 911.1 keV peak of its progeny ^{228}Ac(Ra). 186 keV peak of ^{235}U (after subtracting of ^{226}Ra overlapping peak) were used for ^{238}U determination taking into account activity ratio ^{235}U/^{238}U of 0.046. Calculated ^{238}U activity was additionally controlled using 1001 keV line of its progeny ^{234M}Pa as well as ^{235}U activities using 143.7 keV and some other lines [26,40,41].

2.7. Instruments

The instruments used for the detection and quantitative determination of cations were the atomic absorption spectrometer PerkinElmer 3110, Varian Cary 3 UV–VIS spectrophotometer with 1 **cm** quartz cells and HR ICP-MS Element 2 (Thermo Finnegan, Germany). Gamma spectrometry system with HPGe Broad detector was used (Canberra).

Table 1
Distribution coefficients of thorium and uranium for UTEVA resin and solutions of nitric and hydrochloric acid in deionised water and seawater (K_D/mL g^{-1}).

c (acid) (mol L^{-1})	De-ionised water		Seawater	
	K_D(Th)	K_D(U)	K_D(Th)	K_D(U)
HNO_3				
0.5	311	94	86	97
1	488	179	168	115
3	711	629	367	685
5	1180	671	1254	1674
HCl				
0.5	<0.01	<0.01	<0.01	<0.01
1	4	<0.01	0.2	4.8
3	7.4	92	8	120
5	12.7	192	11.7	417

<0.01: metal is not bound

2.8. Chemicals

The EiChrom extraction chromatographic resins TRU, UTEVA and Sr resin and the Fluka Amberlite CG-400 strong anion exchange resin (100–200 mesh) were used. Arsenazo III and thorin were used as ligands for complexation. All other chemicals used in this paper were of analytical or supra pure grade (Merck).

3. Results and discussions

As we have mentioned in Section 1, the main aim of this paper is the development of methods for uranium and thorium preconcentration and separation from complex samples. On the one hand, these methods will enable their spectrophotometric determination, and on the other hand will improve determination performances (removal of matrix influence) for other methods, primarily for ICP-MS. That means that the creation of an effective and simple procedure for direct binding and preconcentration of uranium and thorium with their mutual separation from matrix elements is required. As we have mentioned, Horwitz and co-workers have developed specific resins for simple binding of uranium and thorium. These resins are TRU and UTEVA (macro-elements and series of other elements can be also bound on these resins), and are now most often used for their isolation. The characteristics of these resins are very well described in literature [31–35]. However, in concrete applications additional research for optimal conditions of binding and separation from the series of other elements are required. Therefore, uranium and thorium binding on the mentioned resins from aqueous solutions of different composition has been studied.

3.1. Binding of uranium and thorium on the TRU, UTEVA resins and anion exchanger Amberlite CG-400

Solutions of nitric and hydrochloric acids in deionised and seawater were chosen for the experiment. Seawater was chosen for its complex composition and the fact that it can be used as a model for binding from other sample types containing large quantities of macro-constituents. Furthermore, uranium is possible to determine in natural and seawater sample directly by ICP-MS but such determination of thorium is not possible due to its low concentration [16,28]. On the other hand ICP-MS provides a rapid and sensitive technique for their determination but high levels of sample matrix can produce interference in the plasma which result in a suppression of analyte ionisation or block the nebuliser or torch due to the deposition of dissolved solids coming out of solution [19,24].

Tables 1 and 2 contain the results of determination of distribution coefficients of uranium and thorium for UTEVA and TRU resins

Table 2
Distribution coefficients of thorium and uranium for TRU resin and solutions of nitric and hydrochloric acid in deionised water and seawater (K_D/mL g^{-1}).

c (acid) (mol L^{-1})	De-ionised water		Seawater	
	K_D(Th)	K_D(U)	K_D(Th)	K_D(U)
HNO_3				
0.5	>2000	3438	>2000	417
1	>2000	>5000	>2000	719
3	>2000	>5000	>2000	1232
5	>2000	>5000	>2000	>5000
HCl				
0.5	1.9	105	<0.01	255
1	7.1	325	7.7	450
3	428	>5000	1369	2536
5	>2000	>5000	>2000	2950

>5000 and >2000: very strong binding.
$K_D = \frac{c_0 - LOD}{LOD} \cdot \frac{V}{m}$, where LOD is limit of determination, which is 0.24 mg L^{-1} for uranium and 0.43 mg L^{-1} for thorium.

from the solutions of nitric and hydrochloric acids in deionised water as well as the solutions of nitric and hydrochloric acids in seawater. The results in Table 1 have shown that U and Th bind stronger on the UTEVA resin from the solutions of nitric acid then from solutions of hydrochloric acid. The binding strength of U and Th increases with increasing of concentration of both acids. But it is obvious that binding strength of U and Th depends on presence of matrix ions. So distribution coefficients of Th are higher in deionised water than in seawater for concentration of nitric acid of 0.5–3 mol L^{-1}. On the other hand distribution coefficients of U are similar in both deionised and seawater in the mentioned nitric acid concentration range. But for 5 mol L^{-1} nitric acid K_D of U is three times higher in seawater while Th distribution coefficients is almost same in both solution. For the distribution coefficient of Th in HCl solution there is no difference between deionised water and seawater. Behaviour of U is almost the same except for the 5 mol L^{-1} where K_D of U is three times higher. If these results are compared with Horwitz it can be seen that trend of increasing of binding strength with increasing of acid concentration are the same for both elements in deionised water [31–34]. It should be mentioned that only trend can be compared because of Horwitz gave dependence of capacity factor about concentration of acid. But Horwitz in these articles did not study influence of anions like F^-, Cl^- on the behaviour of U and Th on UTEVA resins or other resins. As seawater contains high concentration of Cl^- ions it can be suppose that differences in K_D of Th and U in seawater and deionised water is result of interaction of Th^{4+} and UO_2^{+} ions with Cl^-, NO_3^- and diamylphosphonate (DAAP) the extractant impregnated on UTEVA resin. DAAP acts as neutral ligand and charge of Th and U can be neutralized by counter ions. Since the major anions are Cl^- and NO_3^- it is possible that Th^{4+} and UO_2^{+} form complexes with these anions. It is well known that nitrate complexes are extracted with UTEVA resin [31–33]. In the case of 5 mol L^{-1} HNO_3 Th nitrate complexes should proceed. As HNO_3 concentration increases NO_3^- concentration also increases and Cl^- concentration decreases due to binding of Cl^- with H^+. This would promote nitrate formation and tend to increase binding strength. In fact it seems that its chloride complex has high Gibbs energy for transfer from aqueous to organic phase and at lower concentration of nitrate ions formation of thorium nitrate was not dominant. This implies that thorium chloride complex is hard to extract with UTEVA resins and presence of chloride ions decrease binding strength. On the other hand U form chloride complexes which can be extracted with DAAP and presence of chloride ions from seawater can additionally stabilized complex formation in resin and increase binding strength [42,43].

Results in Table 2 showed that in the whole range of the tested HNO_3 concentrations, binding of Th and U on TRU resin is very strong for both deionised and seawater sample. It has also been noted that the binding of uranium from seawater samples on TRU resin does not follow the binding trend of thorium. Namely, the results have shown that thorium binds very strongly in the tested range of concentrations and from all acid solutions, while uranium binds less strongly from acid solutions in seawater at lower concentrations of acids. Results in Table 2 also shows that U from the solution of hydrochloric acid binds on TRU resin more strongly, unlike thorium that does not bind, or binds rather weakly from the hydrochloric acid solution of concentration lower than 3 mol L^{-1}. It should be mentioned that U binding strength decreases in seawater solution and difference between binding strength of U and Th on TRU resin from seawater and deionised water can be explained at previous manner but for exact explanation more detailed study is needed. As in previous case our results follows Horwitz results from which can be seen that trend of increasing of binding strength with increasing of acid concentration are the same for both elements [31–34].

Considering that a range of macro-constituents does not bind on UTEVA and TRU resins and that, according to the obtained results, uranium and thorium binding on TRU resin from the solutions of nitric acid is very strong, it can be expected that preconcentration will be successful. Therefore, developing a method of preconcentration and isolation of uranium and thorium from drinking water and seawater will not require a high concentration of acid, since both elements are bound strongly on UTEVA and TRU resin at concentration of 3 and 0.5 mol L^{-1} HNO_3 respectively. Thus, it is possible to perform preconcentration from a great amount of sample, as it will be shown. In order to ensure the conditions for obtaining the accurate results of quantitative determination of uranium and thorium by spectrophotometry, it is necessary to perform 100% isolation and separation of uranium and thorium along with preconcentration.

Uranium and thorium can be isolated from the samples and separated from each other by classical ion exchange on strong base anion exchangers. The procedure requires the usage of concentrated acids and is rather time consuming. However, thorium can be bound on the mentioned exchanger from the alcohol solutions of nitric acid. It should be mentioned that it is possible to selectively bind cations on anion exchanger in nitrate form from alcohol solutions [36–38]. In this case binding is governed by sorption (not ion exchange) of cations on strong base anion exchanger in nitrate form in presence of high portion of alcohol. So Table 3 shows the binding of a range of cations on anion exchanger from the solution of nitric acid in methanol and ethanol. From these results, can be seen that number of elements does not bind on the exchanger at this manner. Furthermore, Tables 4 and 5 show the results of determination of Pb, U and Th distribution coefficients from ethanol and methanol solutions of nitric acid. From these results, we can see that Th binds strongly on anion exchanger, unlike uranium, whose binding is weak. The reason for that is probably in the fact that uranium is in the form of UO_2^{+} ions, while thorium is in Th^{4+} form, so that thorium binding is much stronger due to the difference in ion charges [37,38]. Along with thorium, lead also binds strongly on the anion exchanger. The results have shown that thorium binds more strongly from methanol than from ethanol, and lead behaves in opposite manner. They have also shown that the presence of water decreases binding strength. It is to be expected, since water increases the polarity of the solution. It has to be mentioned that the mechanism of this binding has not been clarified and that some deviations, such as weaker binding of thorium in ethanol solution, cannot be explained by polarity. The presence of water in alcohol mixtures is useful in practical application because of better dissolution of nitrate salts. However, a larger quantity of water prevents binding, so it has to be taken into consideration during the preparation of a real sample solution. If we increase the concentration of acid in alcohol, it also decreases binding strength.

Table 3
Behaviour of elements on column filled with Amberlite CG-400 (NO_3^- form) elution by 0.25 mol L^{-1} HNO_3 in alcohol.

Elements	Methanol	Ethanol
Li, Na, K and Cs	Not retained	Weakly adsorbed
Mg	Not retained	Weakly adsorbed
Ca	Weakly adsorbed	Medium adsorbed
Sr	Medium adsorbed	Strongly adsorbed
Ba	Strongly adsorbed	Strongly adsorbed
Co	Not retained	Not retained
Ni	Not retained	Not retained
Cu	Not retained	Not retained
Ag	Not retained	Not retained
Zn	Not retained	Not retained
Cd	Not retained	Not retained
Al	Not retained	Not retained
Y	Not retained	Not retained
Pb	Strongly adsorbed	Strongly adsorbed
Ti	Not retained	Not retained
Zr	Not retained	Not retained
Hf	Not retained	Not retained
Bi	Strongly adsorbed	Strongly adsorbed
V	Not retained	Not retained
Cr	Not retained	Not retained
Mo	Weakly adsorbed	Weakly adsorbed
Mn	Not retained	Not retained
La	Strongly adsorbed	Strongly adsorbed
Ce	Strongly adsorbed	Strongly adsorbed
Nd	Strongly adsorbed	Strongly adsorbed
Yb	Strongly adsorbed	Strongly adsorbed

3.2. Separation of uranium and thorium on the chromatographic column

The separation of uranium and thorium is necessary in spectrophotometric determination. The previous results have shown that U and Th demonstrate a pronounced difference in the intensity of binding on UTEVA resin from hydrochloric acid solution in concentration higher than 3 mol L^{-1}, as well as in binding on TRU resin from hydrochloric acid solution in concentration range from 0.5 to 3 mol L^{-1}, which can be applied for the procedure of their separation.

Table 4
Distribution coefficients (K_D/mL g^{-1}) of lead, thorium and uranium for Amberlite CG-400 in nitrate form and alcoholic–water solution of 0.25 mol L^{-1} nitric acid.

0.25 mol L^{-1} HNO_3 in	Pb	Th	U
100% CH_3OH	700	4100	19
90% CH_3OH and 10% H_2O	165	1026	4.9
80% CH_3OH and 20% H_2O	81	74	6.5
70% CH_3OH and 30% H_2O	42	4.3	4
60% CH_3OH and 40% H_2O	26	–	2.9
50% CH_3OH and 50% H_2O	3	–	0.9
100% CH_3CH_2OH	2000	514	26
90% CH_3CH_2OH and 10% H_2O	283	138	10
80% CH_3CH_2OH and 20% H_2O	99	47	3.5
70% CH_3CH_2OH and 30% H_2O	55	19	6.2
60% CH_3CH_2OH and 40% H_2O	35	15	7.8
50% CH_3CH_2OH and 50% H_2O	5	6.9	2.2

Table 5
Distribution coefficients (K_D/mL g^{-1}) of lead, thorium and uranium for Amberlite CG-400 in nitrate form and alcoholic solution of nitric acid.

	Pb	Th	U
0.25 mol L^{-1} HNO_3 in CH_3OH	700	4100	19
0.50 mol L^{-1} HNO_3 in CH_3OH	332	798	8.4
0.75 mol L^{-1} HNO_3 in CH_3OH	205	416	2.8
1.00 mol L^{-1} HNO_3 in CH_3OH	144	261	0.9
0.25 mol L^{-1} HNO_3 in CH_3CH_2OH	2000	514	26
0.50 mol L^{-1} HNO_3 in CH_3CH_2OH	934	367	19
0.75 mol L^{-1} HNO_3 in CH_3CH_2OH	571	198	13.3
1.00 mol L^{-1} HNO_3 in CH_3CH_2OH	384	168	12.6

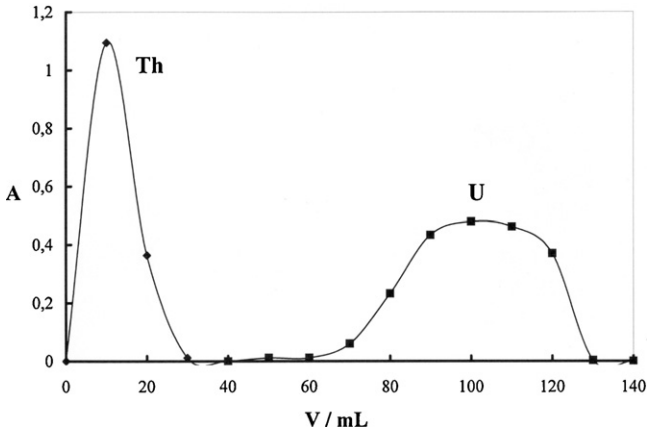


Fig. 1. Separation of uranium from thorium on TRU column (I.D. = 0.9 cm, 10.6 cm bed height, 2 g TRU resin, flow rate 1.7 mL min^{-1}) by elution with 0.5 mol L^{-1} HCl.

Based on the previous results, elution curves are determined. It can be seen from Fig. 1 that uranium can be easily separated from thorium on TRU column by elution with 0.5 mol L^{-1} of hydrochloric acid because, in given conditions, uranium is much more strongly bound than thorium. However, a large quantity of 0.5 mol L^{-1} HCl is needed for elution, which is not acceptable in cases when preconcentration of the sample has been applied. In this case, uranium can be eluted with 0.1 mol L^{-1} of HCl or deionised water in two column volume.

Based on the obtained results for TRU resin, we have developed a procedure of isolation and simultaneous separation of uranium and thorium from natural samples, which is described in detail in the experimental part of the paper. In the previous part, we have also tested binding of these elements on UTEVA resin and determined the elution curves presented in Fig. 2. The separation of uranium from thorium on the column filled with UTEVA resin, in the given conditions for 1 g of resin, cannot be achieved by eluting with hydrochloric acid. However, it is possible to achieve better separation results by increasing the height of resin in the column, which suggests that it could be possible to perform a complete separation—see Fig. 2. Nevertheless, this procedure should be avoided if preconcentration is performed.

A complete separation of uranium from thorium on the given resin can be achieved by eluting with 5 mol L^{-1} of hydrochloric acid due to their significant difference in distribution coefficients. Due

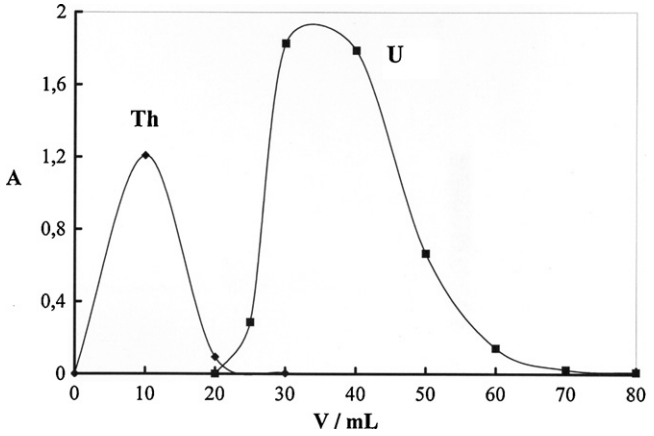


Fig. 2. Separation of uranium from thorium on UTEVA column (I.D. = 0.9 cm, 10.6 cm bed height, 2 g UTEVA resin, flow rate 1.2 mL min^{-1}) by elution with 3 mol L^{-1} HCl.

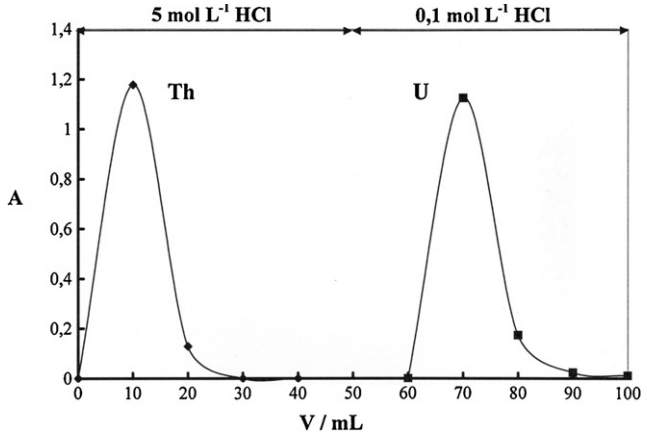


Fig. 3. Separation of uranium from thorium on UTEVA column (I.D. = 0.9 cm, 10.6 cm bed height, 2 g UTEVA resin, flow rate 1.4 mL min^{-1}) by elution with 5 mol L^{-1} HCl and 0.1 mol L^{-1} HCl.

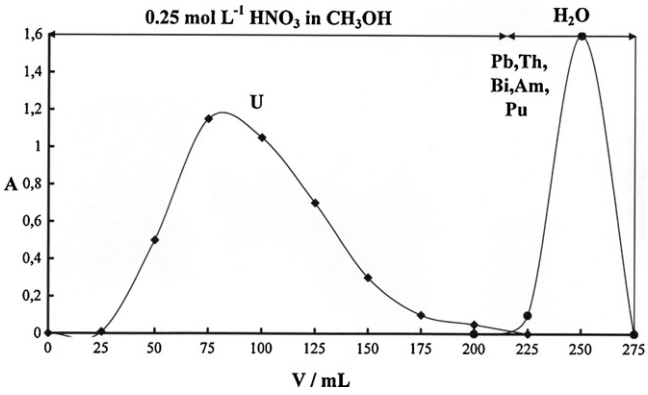


Fig. 4. Separation of uranium and thorium on anion exchange column (I.D. = 0.9 cm, 15 cm bed height, 5 g of Amberlite CG-400 in nitrate form, flow rate 1 mL min^{-1}) by elution with 0.25 mol L^{-1} HNO_3 in methanol.

to its weak binding on the resin, thorium is first eluted from the column with a small eluents volume—Fig. 3.

However, certain elements that can interfere with spectrophotometric determination also bind on TRU and UTEVA resins together with uranium and thorium. Furthermore, extraction chromatographic resins are expensive compared to ion exchangers, and it is possible to remove the extraction medium from the inert carrier during preconcentration and separation. As it has been shown by previous results, uranium and thorium are bound on anion exchanger in nitrate form from alcohol solutions of nitric acid. Thus, it is possible to separate them on the chromatographic column. Since zirconium, which binds on UTEVA resin [43], does not bind on anion exchanger, it can be separated from thorium in the described manner. The elution curves given in Fig. 4 show that it is possible to separate uranium from zirconium, thorium, and lead on the column filled with Amberlite CG-400 (NO_3^- form) [38].

3.3. Spectrophotometric determination of uranium and thorium

The elution of uranium and thorium from chromatographic resins (Amberlite CG-400, TRU and UTEVA) depends on the kind of acid and its concentration, as well as on the type and the mass percent of the used alcohol. Because of this, the influence of the solution composition on the colour development in optimal conditions for complex formation has been investigated. The calibration graphs obtained under optimal conditions for U-Arsenazo III obeyed the Beer's law in the range (0–8.00) mg L^{-1}. The colour reaction has almost the same sensitivity in water solution of hydrochloric or nitric acids. However, it has been found that in the alcohol solutions the absorptivity of U-Arsenazo III decreases, especially when the solution contains methanol. For Th–thorin complex, a linear relationship between absorbance and concentration is obtained between (0 and 12.0) mg L^{-1}. The obtained results in Table 6 show that the absorptivity of Th–thorin method has larger value in nitric than in hydrochloric water solution. In addition, the sensitivity of the method increases in alcohol solution—Table 6. For Th–Arsenazo III complex, a linear relationship between absorbance and concentration is obtained between (0 and 8.0) mg L^{-1}. The obtained results show that the absorptivity of Th–Arsenazo III method has larger value in nitric than in hydrochloric water solution. In addition, the absorptivity increases very little in methanol–nitric acid solution—Table 6. It has to be mentioned that the absorptivity is almost twice as high for Th–Arsenazo III than for Th–thorin complex.

Due to the fact that the binding strength of uranium and thorium onto ion exchanger depends on the water content in alcohol mixture, it is necessary to know how the absorptivity depends on the composition of water–alcohol mixture. We attempted to connect the relation between absorptivity and volume portion of alcohol in solution with simple linear relation. It can be assumed that the absorptivity of the coloured species in water–alcoholic mixture depends on portion of alcohol according the following equation:

$$a = X_A \cdot a_A + X_B \cdot a_B$$

X_A: volume portion of water; a_A: absorptivity in water solution; X_B: volume portion of alcohol; a_B: absorptivity in alcoholic solution.

The calculated value for the absorptivity is compared with the experimental data obtained by measuring the absorbance of the coloured species in solutions containing various portion of alcohol. On one hand, it can be seen from the obtained results that the sensitivity of the uranium–Arsenazo III method decreases with increasing the alcohol portion in the solution. On the other hand, the sensitivity of thorium–thorin method is larger in the alcohol solution. The deviation data calculated according to above mentioned equation from experimental data are in range of maximal 6% for methanol and 10% for ethanol—Table 7. However, in thorium–arsenazo complex, the presumed relation cannot be discussed because the presence of alcohol causes a great deviation from the Beer's law, which can be seen in Fig. 5 .

Since the concentration of uranium and thorium in environmental samples is very low, it is necessary for the spectrophotometric analysis to know the smallest concentration that can be reported with a certain level of confidence. Such a concentration can be cal-

Table 6
Effect of the composition of solution on the absorptivity (a/mg^{-1} L cm^{-1}) of coloured species.

	Uranium–arsenazo III λ_{max} = 652 nm; pH = 2		Thorium–thorin λ_{max} = 545 nm; pH = 1		Thorium–arsenazo III λ_{max} = 662 nm; pH = 2	
	a	R^2	a	R^2	a	R^2
H_2O/HNO_3	0.2318	0.9997	0.0735	0.9999	0.1312	0.9969
H_2O/HCl	0.2400	0.9999	0.0706	0.9999	0.1260	0.9982
CH_3OH/HNO_3	0.1874	0.9998	0.0910	0.9998	0.1358	0.9991
CH_3CH_2OH/HNO_3	0.2139	0.9999	0.0887	1.0000		

Table 7
Effect of the alcohol portion on the absorptivity of uranium–arsenazo III and thorium–thorin complexes.

	a (exp) (mg^{-1} L cm^{-1})	a (teor) (mg^{-1} L cm^{-1})
Uranium–arsenazo III		
0.25 mol L^{-1} HNO_3 in		
100% EtOH	0.1874	0.2174
20% H_2O, 80% EtOH	0.2280	0.2282
40% H_2O, 60% EtOH	0.2315	0.2390
60% H_2O, 40% EtOH	0.2355	0.2499
80% H_2O, 20% EtOH	0.2355	0.2607
100% H_2O	0.2318	0.2715
Thorium–thorin		
0.25 mol L^{-1} HNO_3 in		
100% MeOH	0.0910	0.0888
20% H_2O, 80% MeOH	0.0936	0.0862
40% H_2O, 60% MeOH	0.0918	0.0837
60% H_2O, 40% MeOH	0.0880	0.0812
80% H_2O, 20% MeOH	0.0826	0.0786
100% H_2O	0.0735	0.0761

Table 8
Critical detection limit, detection limit and determintion limit for uranium and thorium with Arsenazo III.

	L_C	L_D	L_Q (mg L^{-1})
Water	$B = 0.004$		
Th ($a = 0.1312$)	$A = 0.009$	$A = 0.02$	$c = 0.43$
U ($a = 0.2318$)	$A = 0.009$	$A = 0.02$	$c = 0.24$
$Th - tho(a = 0.0735)$	$A = 0.009$	$A = 0.02$	$c = 0.77$
Methanol			
Th	$A = 0.009$	$A = 0.02$	
U ($a = 0.1874$)	$A = 0.009$	$A = 0.02$	$c = 0.30$
Ethanol			
Th	$A = 0.009$	$A = 0.02$	
U ($a = 0.2139$)	$A = 0.009$	$A = 0.02$	$c = 0.26$

culated from the Curie statistical treatment [44] of the experimental data—Table 8. The level of detection was obtained from critical level for blank fluctuation ($L_c = 2.33\sigma_b$, $L_d = 4.65\sigma_b$, $L_Q = 14.1\sigma_b$). Limit of determination LOD (C in mg L^{-1}) was estimated from absorptivity coefficient a (assuming negligible error) and quantification level ($L_Q = aC$). L_Q was chosen in order to obtain a precision as small as 10%. Limit of determination in Table 8 is given for spectrophotometric determination. Considering that the absorptivity coefficient for thorium–arsenazo III is almost twice as high as for thorium–thorin, for quantitative determination and detection Arsenazo III form was used.

3.4. Isolation and determination of uranium and thorium in model water samples

It has to be said that uranium in surface seawater exist in the hexavalent oxidation state and anionic uranium carbonato complexes. Acidification of samples results in destabilization of carbonato complexes and formation of uranium (VI)–aqua-complexes. At pH = 1 only UO_2^{2+} is present [16,40,45]. Thorium is presented in water in

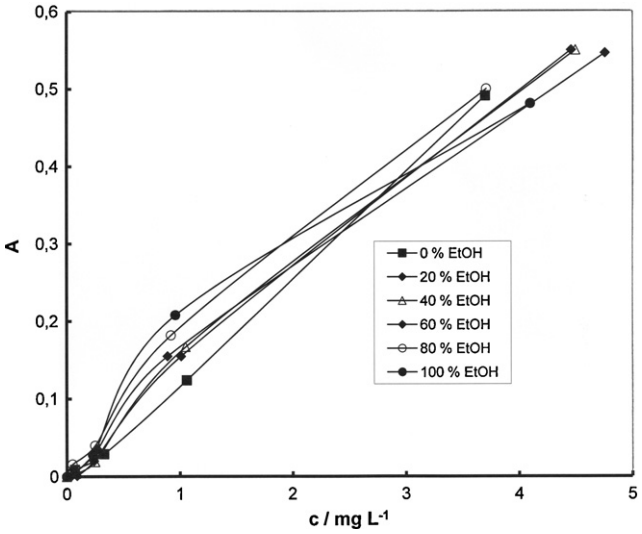


Fig. 5. Dependence of thorium–arsenazo III complex absorptivity on ethanol contents.

quadrivalent state but due to low solubility it will be present in water as suspended particles. Soluble thorium ions in water will hydrolyse at pH above 5 forming $Th(OH)_4$ precipitate or hydroxy complexes. The hydroxy complexes will be adsorbed by particulate matter in water, with the results that most of the thorium is presented in suspended matter or sediment and concentration of soluble thorium in water is very low, but in some cases due to formation of soluble complexes with carbonate and other ligands concentration can increase [28,46].

The procedure of preconcentration and separation of uranium and thorium from water samples is described in the experimental part of the paper. In order to test the proposed methodology, uranium and thorium were first isolated from model samples by concentration on TRU and UTEVA resins from 0.5 and 3 mol L^{-1} HNO_3, and then separated from each other on Amberlite CG-400 (NO_3^-) exchanger with 0.25 mol L^{-1} HNO_3 in methanol. Model samples contained the known concentrations of uranium and thorium. After preconcentration and separation, thorium and uranium were determined by spectrophotometry. Sample volume was 1.33 L for UTEVA resin and 1.04 L for TRU resin, while concentration of uranium and thorium was about 10 μg L^{-1}. At the beginning "high" concentration was used due to easier and accurate spectrophotometric determination. Concentration of U and Th was also determined by ICP-MS in model samples. Table 9 provides the results of uranium and thorium determination before and after completing the procedure. The results have shown that the isolation is quantitative for both resins from both samples (recovery is 90–100%). It has to be said that ICP-MS analysis of uranium and thorium fractions was performed. The thorium has not been found in uranium fraction and vice versa.

The other way of isolating uranium and thorium from model drinking water and seawater samples was by using the TRU resin on

Table 9
The efficiency of uranium and thorium isolation on TRU and UTEVA resins (column diameter Φ = 0.9 cm, mass TRU $m = 1$ g, mass UTEVA $m = 3$ g, flow rate 1 mL min^{-1}).

Samples	Resin	γ_0(U) (μg L^{-1})	γ (U) (mg L^{-1})	R(%)	γ_0(Th) (μg L^{-1})	γ(Th) (mg L^{-1})	R(%
Seawater	TRU	10.6	9.7 ± 0.4[a]	95	10.2	10.4 ± 0.3[a]	102
Seawater	UTEVA	10.6	9.8 ± 0.4	96	10.2	10.4 ± 0.4	102
Water	TRU	10.6	9.4 ± 0.6	92	10.2	10.2 ± 0.3	100
Water	UTEVA	10.6	9.9 ± 0.4	97	10.2	10.6 ± 0.3	103

γ_0: known concentration.
γ: measured concentration after preconcentration.
[a] Mean (procedure was repeated 3 times).

Table 10
The efficiency of uranium and thorium isolation from model seawater and drinking water samples on TRU resin (column diameter Φ = 0.9 cm, resin column height = 10.6 cm, resin mass m = 1.5 g, flow rate 1 mL min^{-1}).

Sample	γ_0 (U) (mg L^{-1})	γ(U) (mg L^{-1})	[a]R_U (%)	γ_0(Th) (mg L^{-1})	γ(Th) (mg L^{-1})	[a]R_{Th} (%)
Seawater	0.200	0.190 ± 0.020	95.0	0.400	0.310 ± 0.050	77.5
Dwater 1[b]	0.040	0.037 ± 0.004	92.5	0.080	0.070 ± 0.008	87.5
Dwater 2	0.040	0.039 ± 0.004	97.5	0.080	0.074 ± 0.009	92.5

γ_0: added (known) concentration.
γ: measured concentration.
[a] Mean (procedure was repeated 3 times).
[b] Model mineral water

which U and Th are bound from 0.5 mol L^{-1} HNO_3 in drinking water or seawater. Thorium was eluted with 0.5 mol L^{-1} of HCl, and uranium with 0.1 mol L^{-1} of HCl or with deionised water. The obtained results in Table 10 have shown that uranium and thorium can be preconcentrated and simultaneously separates on TRU resin in the separation procedure from water samples where they are present in low concentrations. These results show that it is possible to isolate quantitatively uranium and thorium from water samples. But results also suggest that it is possible to acquire thorium losses that can lead to determination error. Losses are probably caused due to low cation and acid concentration in water sample. It must be said that certain losses of extraction medium into mobile phase may be acquired in the course of isolation during the eluting procedure (considering the fact that binding of the extraction medium on the carrier is not of covalent nature, but an absorption), which results in shorter retention on the resin and earlier elution.

The results in Table 10 have also shown that uranium and thorium can be preconcentrated from water samples where they are present in low concentrations. But spectrophotometric determination is limited on the concentration over LOD. As we seen earlier LOD for the U and Th in our case are 0.24 and 0.43 mg L^{-1} respectively. As concentration of U and Th are far below these values, even in case of concentration by 1000 times (volume reducing from 1 L to 1 mL) U and Th could not be determined. Therefore concentration was determined by ICP-MS. U and Th was determined by spectrophotometry only in samples with highest concentration (0.2 μg L^{-1} of U and 0.4 μg L^{-1} of Th) after the separation from 2 L of water and reducing a volume of to 1 mL (2000 times). In this case obtained concentration of U and Th was 0.17 and 0.37 μg L^{-1}.

3.5. Determination of uranium and thorium in real water samples

Based on the previous results, a procedure for isolation and determination of uranium and thorium from seawater and drinking water samples (spring and mineral water) was created. Uranium and thorium were bound from 1.5 mol L^{-1} HNO_3 on TRU resin. 1.5 mol L^{-1} of HNO_3 was chosen based on the previous results of K_D determination and the results obtained from model solutions, as an optimal concentration that, on one hand, enables quantitative isolation, and on the other, decreases the consumption of concentrated acid. Prior to isolation, uranium was determined in drinking water and seawater on ICP-MS before and after processing. Thorium could not be determined directly on the available instrument. The isolation was performed from 2 L of water. Uranium and thorium were separated with 0.5 mol L^{-1} HCl, and then determined by spectrophotometry. U and Th were also determined on ICP-MS. Obtained results can be seen from Table 11. From these results it can be seen that thorium was determined only in seawater by ICP-MS after preconcentration (factor 1000) and separation on the columns. Results also show that concentration of U which can be determined by spectrophotometry after the separation from 2 L sample lie below 1 μg L^{-1}. In addition obtained results correspond with results of other authors (2.1 μg L^{-1} U in seawater and 0.99 μg L^{-1} in mineral water) [40,48].

Table 11
Determination of U and Th after the preconcentration and separation on TRU column.

	ICP-MS		Proposed method	
	γ(U) (μg L^{-1})	γ(Th) (μg L^{-1})	γ(U) (μg L^{-1})	γ(Th) (μg L^{-1})
Seawater	2.3 ± 0.3	–	–	–
Seawater	1.9 ± 0.3*	1.1 ± 0.4**	1.7 ± 0.4*	–
Studenac	1.1 ± 0.1		0.9 ± 0.3*	–
Tap water	1.2 ± 0.1	–	1.1 ± 0.4*	–

* Determined after preconcentration, mean concentration is given as average of results obtained after three determinations (both preconcentration, separation and detection).
** (Conc. factor 2000).

3.6. Determination of uranium and thorium in NIST and IAEA soil sample

For the test of the method for the determination of U and Th in soil sample NIST SRM 2710 and IAEA-312 soils were used. After dissolving of the 10 g soil sample in acids, and filtering through G4 sinter funnel, 100 mL of 3 mol L^{-1} HNO_3 of sample solution was passed through a TRU column, and uranium and thorium were isolated from other elements by eluting with 50 mL of 3 mol L^{-1} HNO_3 and separated from each other with HCl solution as it has been described earlier and determined by spectrophotometry and on ICP-MS. For the direct ICP-MS determination an aliquot of 1 mL of original solution of samples was used. As it well known one of the major problems in determining trace elements by ICP-MS in soil is the matrix effects caused by major constituent elements Ca, Mg, Al and Fe. The matrix effect caused by these elements has been carefully studied by Shinotsuka and Ebihara [24]. As a result, a dilution factor was proposed for the U and Th determination. In our case we have used different dilution factor depending on U and Th concentration in sample and reference sample composition. The obtained results are shown in Table 12. By comparison of obtained results it can be concluded that ICP-MS results match well with oriented value. Results obtained by spectrophotometer determination are satisfactory in relation to oriented results. But it should be mentioned that in case of chemical separation it is visible that all obtained results are below the oriented value. Reason for that can be some loses of U and Th during the separation procedure.

As we have already said, thorium can be isolated rather easily on a column filled with anion exchanger in the procedure described in experimental part of the paper. This procedure was used for isolation of thorium from the soil samples, and determined by spectrophotometry and ICP-MS. The results obtained are also shown in Table 12. Specifically, thorium is strongly bound from alcohol solutions on exchanger Amberlite CG-400 (NO_3^- form) and easily separated from a range of elements, except from lead. However, it is easily separated from lead on the small quantity of Sr resin. Considering the given characteristics, in this procedure, the smallest risk of losses occurs during concentration and isolation.

Table 12
Determination of U and Th in NIST SRM 2710 and IAEA 312 soil samples.

	ICP-MS		Proposed method	
	γ(U) ($\mu g\,g^{-1}$)	γ(Th) ($\mu g\,g^{-1}$)	γ(U) ($\mu g\,g^{-1}$)	γ(Th) ($\mu g\,g^{-1}$)
NIST 2710	(25 $\mu g\,g^{-1}$)*	(13 $\mu g\,g^{-1}$)*		
Direct determination	26.1 ± 3.9	15.2 ± 3.9	–	–
After separation on TRU	23.5 ± 1.8	11.9 ± 2.3	27.5 ± 2.8	14.3 ± 1.4
After precon. on TRU and separation on CG-400	22.1 ± 1.9	12.1 ± 1.3	22.5 ± 2.8	11.3 ± 2.4
After separation on CG-400 and Sr resin		12.2 ± 0.6		11.9 ± 1.1
IAEA-312	(16.5 $\mu g\,g-1$)**	(91.4 $\mu g\,g-1$)**	–	–
Direct determination	15.8 ± 2.9	92.2 ± 4.9	–	–
After separation on TRU	14.0 ± 1.8	87.9 ± 5.3	14.5 ± 3.0	85.3 ± 7.4
After precon. on TRU and separation on CG-400	13.7 ± 2.0	87.1 ± 4.3	13.5 ± 2.8	85.8 ± 5.4
After separation on CG-400 and Sr resin		89.2 ± 3.6		88.1 ± 5.1

Mean concentration and standard deviation are given as average of results obtained after three determinations (both preconcentration, separation and detection).
* Oriented value NIST SRM 2710
** Mean concentration IAEA-312

Table 13
Determination of U and Th in natural soil samples.

	Gamma spectrometry		ICP-MS		Proposed method	
	γ(U) ($\mu g\,g^{-1}$)	γ(Th) ($\mu g\,g^{-1}$)	γ(U) ($\mu g\,g^{-1}$)	γ(Th) ($\mu g\,g^{-1}$)	γ(U) ($\mu g\,g^{-1}$)	γ(Th) ($\mu g\,g^{-1}$)
SoilT	4.8 ± 0.2	14.0 ± 0.2	3.8 ± 0.4	12.5 ± 1.2	4.3 ± 0.5	15.0 ± 2.0
SoilD	1.4 ± 0.1	1.7 ± 0.1	1.0 ± 0.1	1.5 ± 0.2	1.0 ± 0.2	2.0 ± 0.3

Mean concentration and standard deviation are given as average of results obtained after three determinations, SoilT-terra rosa, SoilD-dolomite.

3.7. Determination of uranium and thorium in soils

As in previous case after dissolution in 3 mol L^{-1} HNO_3, and filtering through G4 sinter funnel, the solution was passed through a TRU column, and uranium and thorium were isolated from other elements by eluting with 50 mL of 3 mol L^{-1} HNO_3, separated from each other as it has been described earlier, and determined by spectrophotometry. The same procedure was applied to determination on ICP-MS. Both uranium and thorium were also determined by high-resolution gamma spectrometry as described in experimental part. The obtained results are shown in Table 13. It is shown that deviations for both elements and for all three methods amount to 25%. Similar to the previous case, the results obtained by spectrophotometric determination are, as a rule, lower than those obtained by gamma spectrometric determination. It should be mentioned that results in table are given as mean from three determinations and error is expressed as standard deviation.

In our paper uncertainty for single spectrophotometric determination is not discussed because an overview of the most important uncertainty sources that affect analytical UV–VIS spectrophotometric measurements was described and generic uncertainty budget for absorbance was presented elsewhere [49]. It was demonstrated that the well-known intrinsic sources of uncertainty that originate from the instrument itself (repeatability of spectrophotometer reading, spectrophotometer drift, stray light, etc.) often have significantly lower contributions to the combined uncertainty of the result than the "chemical" sources of uncertainty that originate from the object under study (interference from the constituents of the matrix, decomposition of the photometric complex, etc.).

At the end it can be said that spectrophotometric determination in combination with preconcentration and separation step is time consuming. Nevertheless, the determination is simple and can meet the requirements regarding detection limits prescribed by the authorised institutions, since the obtained detection limits in water samples are lower than 1 $\mu g\,L^{-1}$ for uranium and thorium. In addition, it is a cheaper method if compared to ICP-MS. In case when ICP-MS determination requires removing of the matrix elements for some types of samples, the proposed separation methods can successfully used. Moreover, it is possible to use the TRU isolation method for determination of uranium and thorium by other method (polarography, alpha spectrometry) in different samples [27,28,47]. Also mixed solvent anion exchange method can be used for thorium isolation and its determination.

4. Conclusion

The results of determination of distribution coefficients have shown that uranium and thorium are bound on TRU and UTEVA resins from the solutions of nitric and hydrochloric acids, and that the binding intensity increases parallel with increasing the acids' concentration. Uranium and thorium are bound very strongly on TRU resin from nitric acid in concentration ranges from 0.5 to 5 mol L^{-1}, and large quantities of other ions present in the sample do not influence the binding strength. Due to the difference in binding strength in HCl and HNO_3, uranium and thorium can be easily separated from one another on the columns filled with TRU resin. Furthermore, thorium binds very strongly, while uranium binds rather weakly, on the anion exchanger in nitrate form from alcohol solutions of nitric acid, so they can be separated rather easily. These results render possible the creation of flexible and simple preconcentration and isolation procedures for uranium and thorium from the samples of drinking water, seawater, soil and sediments. In combination with spectrophotometric determination with Arsenazo III at concentration factor 1000, which can be achieved easily, we obtain determination limits below 1 $\mu g\,L^{-1}$. The developed procedures are easy to apply in any laboratory.

References

[1] WHO (2003) Uranium in drinking-water. Background document for preparation of WHO Guidelines for drinking-water quality. Geneva, World Health Organization (WHO/SDE/WSH/03.04/118).
[2] European Commission Directive, 98/83 European Commission Directive, 98/83/EC, related with drinking water quality intended for human consumption, Brussels, Belgium, 3/11/1998.
[3] A.S.F. de Sousaa, E.M.M. Ferreira, R.J. Cassella, Anal. Chim. Acta 620 (2008) 89.
[4] M. Haleem Khan, P. Warwick, N. Evans, Chemosphere 63 (2006) 1165.
[5] S. Sadeghi, D. Mohammadzadeh, Y. Yamini, Anal. Bioanal. Chem. 375 (2003) 698.
[6] T. Madrakian, A. Afkhami, A. Mousavi, Talanta 71 (2007) 610.

[7] C. Galindo, L. Mougin, A. Nourreddine, Appl. Radiat. Isotopes 65 (2007) 9.
[8] P.A. Greene, C.L. Copper, D.E. Berv, J.D. Ramsey, G.E. Collins, Talanta 66 (2005) 961.
[9] A.P. Krinitsyn, O.L. Strikhar, A.V. Terletskaya, T.A. Bogoslovskaya, Radiochemistry 42 (2005) 209.
[10] K. Benkhedda, V. Epov, R. Douglas Evans, Anal. Bioanal. Chem. 381 (2005) 1596.
[11] X. Hou, P. Roos, Anal. Chim. Acta 608 (2008) 105.
[12] J. Zheng, M. Yamada, Talanta 68 (2006) 932.
[13] M. Betti, L.A. de las Heras, G. Tamborini, Appl. Spect. Rev. 41 (2006) 491.
[14] S.L. Ziegler, B.A. Bushaw, Anal. Chem. 80 (2008) 6029.
[15] J. Sabine Becker, Int. J. Mass Spectrosc. 242 (2005) 183.
[16] D.P.S. Rathore, Talanta 77 (2008) 9.
[17] P. Grinberg, S. Willie, R.E. Sturgeon, Anal. Chem. 77 (2005) 2432.
[18] P. Goodall, C. Lythgoe, The Analyst 124 (1999) 263.
[19] E.R. Unsworth, J.M. Cook, S.J. Hill, Anal. Chim. Acta 442 (2001) 141.
[20] M.L.D.P. Godoy, J.M. Godoy, R. Kowsmann, G.M. dos Santos, R.P. da Cruz, J. Environ. Radioact. 88 (2) (2006) 109.
[21] K. Tagami, S. Uchida, Anal. Chim. Acta 592 (2007) 101.
[22] C. Boonpanaid, K. Oguma, Anal. Sci. 21 (2005) 155.
[23] S.A. Kumar, N.S. Shenoy, S. Pandey, S. Sounderjan, G. Venkateswaran, Talanta 77 (2008) 422.
[24] K. Shinotsuka, M. Ebihara, Anal. Chim. Acta 338 (1997) 237.
[25] A.R. Byrne, L. Benedik, Talanta 35 (1988) 161.
[26] Saïdou, F. Bochud, J.P. Laedermann, M.G. Kwato Njok, P. Froidevaux, Appl. Radiat. Isotopes 66 (2008) 215.
[27] L. Benedik, M. Vasile, Y. Spasova, U. Wätjen, Appl. Radiat. Isotopes 67 (2009) 770.
[28] G. Jia, G. Torri, R. Ocone, A. Di Lullo, A. De Angelis, R. Boschetto, Appl. Radiat. Isotopes 66 (2008) 1478.
[29] M. Betti, J. Chromatogr. 789 (1997) 369.
[30] T. Prasada Rao, P. Metilda, J. Mary Gladis, Talanta 68 (4) (2006) 1047.
[31] E.P. Horwitz, M.L. Dietz, R. Chiarzia, H. Diamond, A.M. Essling, D. Graczyk, Anal. Chim. Acta 266 (1992) 25.
[32] E.P. Horwitz, R. Chiarzia, M.L. Dietz, H. Diamond, Anal. Chim. Acta 281 (1993) 361.
[33] W.C. Burnett, D.R. Corbett, M. Schultz, E.P. Horwitz, R. Chiarizia, M. Dietz, A. Thakkar, M. Fern, J. Radioanal. Nucl. Chem. 226 (1–2) (1997) 121.
[34] M.L. Dietz, E.P. Horwitz, L.R. Sajdak, R. Chiarizia, Talanta 54 (2001) 1173.
[35] L.E. Jassin, J. Radioanal. Nucl. Chem. 263 (1) (2005) 93.
[36] J. Korkisch, F. Tera, Anal. Chem. 33 (1961) 1264.
[37] Ž. Grahek, I. Eškinja, K. Košutić, S. Lulić, K. Kvastek, Anal. Chim. Acta 379 (1999) 107.
[38] Ž. Grahek, M. Rožmarić Mačefat, S. Lulić, Anal. Chim. Acta 560 (2006) 84.
[39] IAEA Technical report series 118, Reference methods for marine radioactivity studies, Vienna, 1970, pp. 93.
[40] V. Cuculić, N. Cukrov, D. Barišić, M. Mlakar, J. Environ. Radioact. 85 (2006) 59.
[41] M. Garcia-Talavera, J.P. Laedermann, M. Décombaz, M.J. Daza, B. Quintana, Appl. Radiat. Isotopes 54 (2001) 769.
[42] A. Fujiwara, Y. Kameo, A. Hoshi, T. Haraga, M. Nakashima, J. Chromatogr. 1140 (2007) 163.
[43] T. Yokoyama, A. Makishima, E. Nakamura, Anal. Chem. 71 (1) (1999) 135.
[44] L. Curie, Anal. Chem. 40 (1968) 586.
[45] I. Pashalidis, H. Tsertos, J. Radioanal. Nucl. Chem. 260 (2) (2004) 439.
[46] P.H. Santschi, J.W. Murray, M. Baskaran, C.R. Benitez-Nelson, L.D. Guo, C.-C. Hung, C. Lamborg, S.B. Moran, U. Passow, M. Roy-Barman, Mar. Chem. 100 (2006) 250.
[47] Dj. Dojozan, M.H. Pournaghi-Azar, J. Toutounchi-Asr, Talanta 46 (1998) 123.
[48] Ž. Fiket, V. Roje, N. Mikac, G. Kniewald, Croat. Chem. Acta 80 (2007) 91.
[49] L. Sooväli, E. Rõõm, A. Kütt, I. Kaljurand, I. Leito, Accredit. Qual. Assur. 11 (2006) 246.

Talanta 80 (2009) 363–371

Contents lists available at ScienceDirect

Talanta

journal homepage: www.elsevier.com/locate/talanta

Multi-residue method for trace level determination of pharmaceuticals in solid samples using pressurized liquid extraction followed by liquid chromatography/quadrupole-linear ion trap mass spectrometry

Aleksandra Jelić[a], Mira Petrović[a,b,*], Damià Barceló[a,c]

[a] Department of Environmental Chemistry, IDAEA-CSIC, c/Jordi Girona 18-26, 08034 Barcelona, Spain
[b] Institució Catalana de Recerca i Estudis Avançats (ICREA), Passeig Lluis Companys 23, 80010 Barcelona, Spain
[c] Institut Català de Recerca de l'Aigua (ICRA), c/Pic de Peguera 15, 17003 Girona, Spain

ARTICLE INFO

Article history:
Received 6 April 2009
Received in revised form 26 June 2009
Accepted 30 June 2009
Available online 8 July 2009

Keywords:
Pharmaceuticals
Sewage sludge
Multi-residue method
Pressurized liquid extraction
Liquid chromatography–tandem mass spectrometry

ABSTRACT

A simple and sensitive method for simultaneous analysis of 43 pharmaceutical compounds in sewage sludge and sediment samples was developed and validated. The target compounds were extracted using pressurized liquid extraction (PLE) and then purified and pre-concentrated by solid phase extraction (SPE) using a hydrophilic–lipophilic balanced polymer. PLE extraction was performed on temperature of 100 °C, with methanol/water mixture (1/2, v/v) as extraction solvent. The quantitative analysis was performed by liquid chromatography tandem mass spectrometry using a hybrid triple quadrupole-linear ion trap mass spectrometer (LC–QqLIT-MS). Data acquisition was carried out in selected reaction monitoring (SRM) mode, monitoring two SRM transitions to ensure an accurate identification of target compounds in the samples. Additional identification and confirmation of target compounds were performed using the Information Dependent Acquisition (IDA) function. The method was validated through the estimation of the linearity, sensitivity, repeatability, reproducibility and matrix effects. The internal standard approach was used for quantification because it efficiently corrected matrix effects. Despite the strong matrix interferences, the recoveries were generally higher of 50% in both matrixes and the detection and quantification limits were very low. Beside the very good sensitivity provided by LC–QqLIT-MS, an important characteristic of the method is that all the target compounds can be simultaneously extracted, treated and analysed. Hence, it can be used for routine analysis of pharmaceuticals providing large amount of data. The method was applied for the analysis of pharmaceuticals in river sediment and wastewater sludge from three treatment plants with different treatment properties (i.e. capacity, secondary treatment, quality of influent waters). The analysis showed a widespread occurrence of pharmaceuticals in the sludge matrices.

© 2009 Elsevier B.V. All rights reserved.

1. Introduction

The pharmaceutical products have an important role in the treatment and prevention of disease in both humans and animals. They are designed either to be highly active and interact with receptors in humans and animals or to be toxic for many infectious organisms. Because of the nature they can also have unintended effects on animals and micro-organisms in the environment. Although the effects of the pharmaceuticals are investigated through safety and toxicology studies, the potential environmental impacts of their production and use are less understood and have recently become a topic of research interest [1].

The main point of collection and subsequent release of pharmaceuticals into the environment are wastewater treatment plants (WWTP), where they enter via domestic and hospital sewages or through industrial discharges. The studies of effluent waters and river sediment show that wastewater treatment achieves only partial removal of organic pollutants [2–4]. The analysis of effluent and receiving waters itself is not enough to understand comportment of pharmaceuticals during the whole wastewater treatment. Occurrence and distribution of pharmaceuticals in sewage sludge demands detailed investigations, especially because the digested sludge is disposed to landfills or used as agricultural fertilizer. This is another significant route of these micro-pollutants to the environment [5]. It is very difficult to presume the comportment of pharmaceuticals in wastewater treatment because the pharmaceutical products belonging to the same therapeutic groups do not

* Corresponding author at: Department of Environmental Chemistry, IDAEA-CSIC, c/Jordi Girona 18-26, 08034 Barcelona, Spain. Tel.: +34 934006172; fax: +34 932045904.
E-mail address: mpeqam@cid.csic.es (M. Petrović).

0039-9140/$ – see front matter © 2009 Elsevier B.V. All rights reserved.
doi:10.1016/j.talanta.2009.06.077

show the similar removal. This is caused by the fact that they have different chemical structure and thus they differ in issue. The available data just give very general overview. The existing analytical methods are mostly focused on specific therapeutic classes, paying special attention to the antibiotics due to their potential for antibiotic resistance [6]. But with the quantity and variety of pharmaceuticals and organic pollutants in general, the interactive and synergetic effects in environment are very possible. For this reason, new trends in analytical chemistry are focused on development of methods for simultaneous analysis of many various compounds. The qualitative and quantitative analysis is a good starting point for the further planning of wastewater treatment as well as the establishment of new regulations related to this subject.

Recent development of the advanced instruments and improved analytical methodologies made possible detection of pharmaceuticals in low levels in different environmental matrixes [5,7–11]. Several methodologies have been developed for determination of pharmaceuticals in solid environmental samples. In recent years, the target compounds have usually been extracted by liquid partitioning with ultrasonication (USE) [6,12–15], microwave assisted extraction (MAE) [16] or the more advanced pressurized liquid extraction (PLE). In order to minimize interferences with matrix components and to pre-concentrate target analytes, solid phase extraction (SPE) has been introduced in preparation procedure as a clean-up step. The combination of pressurized liquid extraction (PLE) with solid phase extraction (SPE) as clean-up step becomes mostly employed technique for preparation of solid samples for instrumental analysis. The PLE technique provides good recoveries, saves time and organic solvent, which makes this technique being preferred one for these kind of samples [5,17–21]. Recently, Radjenović et al. [7] used the PLE–SPE combination for the isolation of 31 pharmaceuticals from sludge samples proceeding from the conventional activated sludge treatment and pilot-scale membrane bioreactors. Barron et al. [5] used the same approach for sample preparation for analysis of 27 pharmaceuticals in soil and treated sludge. Also, Nieto et al. [17] and Göbel et al. [22] extracted the target compounds from sludge samples using the PLE–SPE. In all the mentioned methods a hydrophilic–lipophilic balance (HLB) reversed-phase sorbent was used as SPE packaging. This sorbent has been found suitable for multi-residue methods in neutral pH condition, with a proper selection of the eluent (solvent) [23–25].

The majority of current analytical methods for separation and detection of pharmaceuticals uses liquid chromatography–tandem mass spectrometry (LC–MS/MS) because of its versatility, specificity and selectivity [26]. Triple quadrupole (QqQ) [7,12,17,27] and ion trap MS (IT) [5,6,15] have been widely applied in quantitative target analysis. Recently, a hybrid instrument consisting of a quadrupole and a linear ion trap (QqLIT) have been applied for analysis of pharmaceuticals in waters, thus good results related to analysis of pharmaceuticals in sludge could be expected. This instrument allows powerful scan combinations which lead to rapid identification and confirmation of analytes [8,24,28,29].

The objective of the present study was to develop and validate a sensitive multi-residual method for determination of 43 pharmaceuticals in sludge and sediment. The target compounds belong to different therapeutic groups of pharmaceuticals. They are listed in Table 1 classified according to their therapeutic effects. The pharmaceuticals are extracted using PLE and purified by SPE (Oasis® HLB). High performance liquid chromatography (HPLC) coupled to a QqLIT-MS has been applied for separation and determination of the target pharmaceuticals. Quantitation was performed by the internal standard approach. The performance of the method was evaluated through the estimation of the linearity, sensitivity, repeatability, reproducibility and matrix effects.

The developed method offers simple and simultaneous extraction, treatment and analysis of 43 pharmaceutical compounds in sludge and sediment. Comparing to the previously published methods for determination of pharmaceuticals in environmental solid matrices this method exhibits significantly improved sensitivity due to the QqLIT capabilities. Finally, the method was successfully applied for analysis of pharmaceuticals in sludge from three WWTPs which proves that it can be used for routine analysis of pharmaceuticals providing a large amount of data.

2. Experimental part

2.1. Chemicals

All the pharmaceutical standards for target compounds were of high purity grade (>90%). Ibuprofen, neproxen, ketoprofen, diclofenac and gemfibrozil were supplied by Jescuder (Rubí, Spain). Acetaminophen, indometacin, mefenamic acid, phenazone, bezifibrate, mevastatin, fenofibrate, Pravastatin (as sodium salt), carbamazepine, famotidine, ranitidine (as hydrochloride), cimetidine (as hydrochloride), erythromycin (as hydrate), azithromycin (as dehydrate), roxitromycin, clarithromycin, josamycin, tylosin A, sulfamethazine, trimethoprim, chloramphenicol, atenolol, sotalol, metoprolol (as tartrate), timolol, pindolol, nadolol, salbutamol, clenbuterol (as hydrochloride), enalapril (as maleate), glibenclamide, furosemide, hydrochlorothiazide and metronidazole were purchased from Sigma–Aldrich (Steinheim, Germany). Standard atorvastatin (as calcium salt) was provided by LGC Promochem (London, UK), while diazepam, lorazepam and butalbital were from Cerilliant (Texas, USA).

Isotopically labelled compounds, used as internal standards, were sulfathiazole-d_4 from Toronto Research Chemicals, diazepam-d_5 and phenobarbital-d_3 from Cerilliant (Texas, USA), atenolol-d_7, carbamazepine-d_{10}, ibuprofen-d_3, clotrimazole-d_5, enalapril-d_5, hydrochlorothiazide-d_2, glyburide-d_3, albuterol-d_3, cimetidine-d_3, ethyl clofibrate-d_4, antipyrine-d_3, acetaminophen-d_4, diclofenac-d_4 from CDN Isotopes (Quebec, Canada), mecoprop-d_3 from Dr. Ehrenstorfer (Augsburg, Germany) and ^{13}C-erythromycin and ^{13}C-phenacetin from Sigma–Aldrich (Steinheim, Germany).

The solvents, HPLC grade methanol, acetonitrile, water (Lichrosolv) and formic acid 98% were provided by Merck (Darmstadt, Germany). Nitrogen used for drying from Air Liquide (Spain) was of 99.995% purity.

The cartridges used for solid phase extraction were Oasis® HLB (200 mg, 6 ml) from Waters Corporation (Milford, MA, USA). The syringe filters of 0.45 μm pore size were purchased from Pall Corp (USA).

The individual standard solutions as well as isotopically labelled internal standard solutions were prepared on a weight basis in methanol. Furosemide and butalbital were obtained as solutions in acetonitrile, while lorazepam and diazepam were dissolved in methanol, at a concentration of 1 mg/ml. The solutions were stored at −20 °C. Fresh stock solutions of antibiotics were prepared monthly due to their limited stability while stock solutions for the rest of substances was renewed every three months. A mixture of all pharmaceuticals was prepared by appropriate dilution of individual stock solutions in methanol–water (25:75, v/v) and it was renewed before each analytical run. A separate mixture of isotopically labelled internal standards, used for internal standard quantification, was prepared in methanol and further diluted in methanol–water (25:75, v/v) mixture.

2.2. Sample pretreatment

River sediment and sludge samples, provided from three wastewater treatment plants (WWTP), were used for development

Table 1
Target compounds and the corresponding isotopically labelled compounds. SRM transitions and MS/MS parameters for the analysis of the target compounds.

Therapeutic groups	Compounds	CAS number	Internal standards	Precursor ion (m/z)	SRM1	DP-CE-CXP	SRM2	DP-CE-CXP	SRM ratio (SRM1/SRM2)
Analgesics/anti-inflammatories	Ketoprofen	22071-15-4	Mecoprop-d_3	253 $[M-H]^-$	209	40-12-11	197	40-6-9	15.6
	Naproxen	22204-53-1	Ibuprofen-d_3	229 $[M-H]^-$	185	35-10-13	169	35-38-9	2.1
	Ibuprofen	15687-27-1	Ibuprofen-d_3	205 $[M-H]^-$	161	45-10-7	–	–	–
	Indomethacine	53-86-1	Ibuprofen-d_3	356 $[M-H]^-$	312	50-12-3	297	50-24-17	4.7
	Diclofenac	15307-86-5	Diclofenac-d_4	294 $[M-H]^-$	250	40-16-1	214	40-30-15	17.6
	Mefenamic acid	61-68-7	Ibuprofen-d_3	240 $[M-H]^-$	196	45-20-5	180	45-38-35	19.1
	Acetaminophen	103-90-2	Acetaminofen-d_3	150 $[M-H]^-$	107	55-22-7	–	–	–
Phenazone type drugs	Phenazone	60-80-0	Phenazone-d_3	189 $[M+H]^+$	56	76-40-4	147	76-33-4	1.9
Lipid regulators and cholesterol lowering statin drugs	Bezafibrate	41859-67-0	Ethyl clofibrate-d_4	360 $[M-H]^-$	274	70-26-1	154	70-38-5	2.9
	Fenofibrate	49562-28-9	Ethyl clofibrate-d_4	361 $[M+H]^+$	139	76-43-10	–	–	–
	Gemfibrozil	25812-30-0	Ibuprofen-d_3	249 $[M-H]^-$	121	85-20-7	127	85-14-5	21.7
	Mevastatin	73573-88-3	Carbamazepine-d_{10}	391 $[M+H]^+$	185	56-19-16	159	56-39-14	1.6
	Pravastatin	81093-37-0	Carbamazepine-d_{10}	447 $[M+H]^+$	327	81-29-10	–	–	–
	Atorvastatin	134523-00-5	Carbamazepine-d_{10}	559 $[M+H]^+$	440	71-27-20	250	71-63-4	2.0
Psychiatric drugs	Diazepam	439-14-5	Diazepam-d_5	285 $[M+H]^+$	193	91-45-8	154	91-50-15	1.9
	Lorazepam	846-49-1	Diazepam-d_5	323 $[M+H]^+$	174	66-45-18	229	66-45-8	1.2
	Carbamazepine	298-46-4	Carbamazepine-d_{10}	237 $[M+H]^+$	194	76-29-19	–	–	–
Histamine H2 receptor antagonists	Ranitidine	66357-35-5	Cimetidine-d_3	315 $[M+H]^+$	176	56-25-14	130	56-39-6	2.0
	Famotidine	76824-35-6	Cimetidine-d_3	338 $[M+H]^+$	189	56-27-4	259	56-20-8	1.6
	Cimetidine	51481-61-9	Cimetidine-d_3	253 $[M+H]^+$	95	46-30-8	159	46-23-12	1.5
Macrolide antibiotics	Erythromycin	114-07-8	Erythromycin ^{13}C	734 $[M+H]^+$	158	71-41-8	576	71-35-8	3.8
	Roxithromycin	80214-83-1	Erythromycin ^{13}C	838 $[M+H]^+$	158	56-49-14	679	56-31-8	4.2
	Clarithromycin	81103-11-9	Erythromycin ^{13}C	748 $[M+H]^+$	591	61-35-12	158	61-40-12	12.6
	Josamycin	16846-24-5	Erythromycin ^{13}C	828 $[M+H]^+$	174	101-45-14	600	101-37-18	6.6
	Tylosin A	1401-69-0	Erythromycin ^{13}C	916 $[M+H]^+$	174	86-63-14	773	86-41-10	14.2
Sulfonamid antibiotics	Sulfamethazine	57-68-1	Sulfathiazole-d_4	279 $[M+H]^+$	186	71-25-0	124	71-33-10	1.0
Other antibiotics	Trimethoprim	738-70-5	Carbamazepine-d_{10}	291 $[M+H]^+$	230	76-33-0	261	76-31-20	1.2
	Chloramphenicol	56-75-7	Ibuprofen-d_3	323 $[M-H]^-$	152	75-22-13	194	75-18-27	3.5
	Metronidazole	443-48-1	Clotrimazole-d_5	172 $[M+H]^+$	172	61-21-8	82	61-37-6	1.8
ß-blockers	Atenolol	29122-68-7	Atenolol-d_7	267 $[M+H]^+$	145	60-35-8	190	60-35-14	3.6
	Sotalol	3930-20-9	Atenolol-d_7	273 $[M+H]^+$	213	60-25-6	255	60-25-6	1.1
	Metoprolol	37350-58-6	Atenolol-d_7	268 $[M+H]^+$	121	60-35-10	133	60-35-8	1.0
	Timolol	26839-75-8	Atenolol-d_7	317 $[M+H]^+$	261	60-30-20	244	60-30-6	1.2
	Nadolol	42200-33-9	Atenolol-d_7	310 $[M+H]^+$	254	46-30-2	201	46-35-4	1.4
	Pindolol	13523-86-9	Atenolol-d_7	249 $[M+H]^+$	116	60-30-8	98	60-30-14	7.0
ß-agonists	Clenbuterol	37148-27-9	Albuterol-d_3	277 $[M+H]^+$	203	61-23-14	132	61-33-10	2.2
	Salbutamol	18559-94-9	Albuterol-d_3	240 $[M+H]^+$	148	61-25-12	166	61-20-12	1.7
Barbiturates	Butalbital	77-26-9	Phenobarbital-d_5	223 $[M-H]^-$	180	60-16-9	85	60-18-5	3.8
Antihypertensive	Nifuroxazide	965-52-6	Phenacetine ^{13}C	276 $[M+H]^+$	121	81-25-10	65	81-73-4	7.3
	Enalapril	75847-73-3	Enalapril-d_5	377 $[M+H]^+$	234	91-29-12	303	91-35-6	16.8
Diuretic	Hydrochlorothiazide	58-93-5	Hydrochlorthiazide-d_2	296 $[M-H]^-$	78	90-28-17	–	–	–
	Furosemide	54-31-9	Ibuprofen-d_3	329 $[M-H]^-$	205	65-22-19	285	65-32-11	1.2
Antidiabetic	Glibenclamide	10238-21-8	Glibenclamide-d_3	494 $[M+H]^+$	369	81-23-6	169	81-55-12	1.8

and validation of the method. The sludge samples are products of aerobic (WWTP Tudela) and anaerobic digestion (WWTP Arazuri and WWTP Terrassa) of sludge.

The sediment was collected from the middle course of river Ebro (Spain) in 2004. The samples from WWTP Tudela (Sludge I) were collected in October 2007 and July 2008. This plant serves 37,300 inhabitants, with a total capacity of 110,000 equivalent inhabitants. Sludge processing is based on thermophilic aerobic digestion in bacterial beds with approximately 9 days of retention time. The samples from WWTP Arazuri (Pamplona) (Sludge II) were collected in October 2007 and from WWTP Terrassa in April 2007. The WWTP Arazuri serves around 356,000 inhabitants, with a total capacity of 722,000 equivalent inhabitants in 2007. The sludge treatment involves anaerobic digestion with retention time of 19 days. The WWTP Terrassa has a total treatment capacity of 277,000 equivalent inhabitants. The sludge is treated by anaerobic digestion with the solid retention time of approx. 10 days.

All the solid samples were freeze-dried (LioAlfa 6, Telstar) at −40 °C and with 0.044 bar vacuum and stored at −20 °C until the analysis.

2.3. Extraction and clean-up

The samples of sludge and sediment were extracted by PLE using ASE 300 accelerated solvent extractor (Dionex, Sunnyvale, CA) equipped with 11 ml stainless extraction cells. Aliquots of freeze-dried and grinded sludge and sediment (1 g) were mixed in the extraction cells with Hydromatrix. This dispersing agent is used

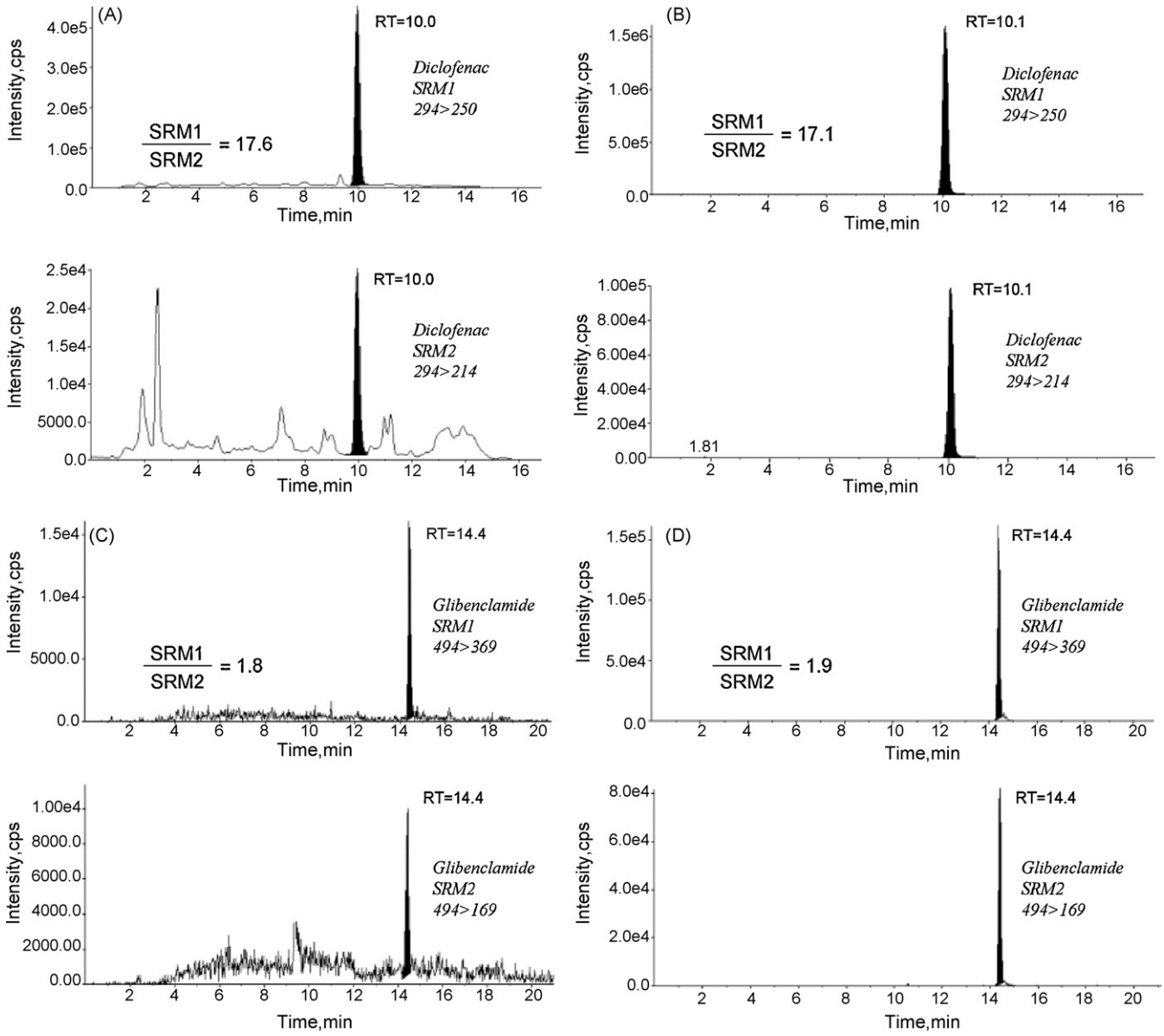


Fig. 1. Chromatograms of the two SRM transitions of diclofenac and glibenclamide in Sludge II (A and C, respectively) and in standard solution (B and D).

to prevent aggregation of sample particles and reduce interstitial volume in the cells [30]. Optimization of extraction parameters included selection of solvent and variation of temperature, time and number of extraction cycles. The extraction method was established with the following parameters: methanol/water, 1/2 (v/v) as extraction solvent, temperature of 100 °C, a preheating period of 5 min, 3 static cycles, each lasting 5 min, total flush volume of 100% of cell with 60 s of nitrogen purge.

The extract obtained in PLE (~22 ml) was diluted in 500 ml of HPLC water (methanol < 5%), and processed by SPE. Oasis HLB cartridges (200 mg, 6 ml) from Waters Corporation (Milford, MA) were used for clean-up. The cartridges were conditioned with 5 ml of methanol followed by 5 ml of HPLC water at neutral pH. Then the dilution of ASE extract was percolated through the cartridges using a Baker vacuum system (J.T. Baker, The Netherlands). Finally, the compounds were eluted with 8 ml of methanol at a 1 ml min^{-1} flow and then the SPE extracts were evaporated under a nitrogen stream and reconstituted with 1 ml of methanol–water mixture (25:75, v/v). Prior to the LC–MS/MS analysis, the samples were passed through 0.45 μm filters and fortified with a standard mixture of the internal standards to the concentration of 20 ng ml^{-1}.

2.4. LC–ESI-(QqLIT)-MS^2 analysis

LC analysis was performed using Symbiosis™ Pico (SP104.002, Spark, Holland), equipped with an autosampler and connected in series with a 4000 QTRAP hybrid triple quadrupole-linear ion trap mass spectrometer equipped with a Turbo Ion Spray source (Applied Biosystems-Sciex, Foster City, CA, USA). Chromatographic separation was achieved with a Purospher Star RP-18 endcapped column (125 mm × 2.0 mm, particle size 5 μm) preceded by a C_{18} guard column (4 × 4, 5 μm), both supplied by Merck (Darmstadt, Germany).

Knowing that an aqueous, purified and pre-concentrated extract of a solid environmental sample is quite similar to a water sample, already established protocol by Gros et al. [8] was used for quantitative analysis of water samples.

The elution gradients were adapted for the LC by Symbiosis™ Pico. For the analysis in negative ionization mode, solvent A was a mixture of acetonitrile–methanol (1:1, v/v) and solvent B was HPLC water. The elution started with 20% of eluent A, increasing to 80% in 15 min, raising to 90% in 2 min and then back to initial conditions within 3 min. The column was re-equilibrated for 10 min before another injection. The analysis in positive ionization mode was performed using acetonitrile as solvent A and HPLC water with 0.1% formic acid as solvent B. The elution started with 5% of eluent A, increasing to 95% in 20 min, raising to 100% in the following 2 min and then back to initial conditions within 5 min. The re-equilibration time was 10 min. The sample injection volume was set at 20 μl and the flow on 0.2 ml/min in both modes.

Data acquisition was performed in selective reaction monitoring (SRM) mode. For each compound two SRM transitions between the precursor ion and two most abundant fragment ions were monitored, as illustrated in Fig. 1. Only one transition was monitored for the isotopically labelled standards since they are normally not present in environmental samples. In total, 70 transitions in positive ionization mode (corresponding to 30 compounds and 12 internal standards) and 29 transitions in negative ionization mode (13 compounds and 7 internal standards) were monitored. In order to obtain additional confirmation, especially for compounds showing poor fragmentation, an Information Dependent Acquisition (IDA) experiment was performed, with SRM as the survey scan and an enhanced product ion scan (EPI), at three different collision energies, as dependent scan. The obtain spectra were compared with library data based on EPI spectra at the three collision energies used. This allows broad accomplishment of the requirements set by the EU regulations (EU Commission Decision 2002/657/EC) [31] related to identification and confirmation of pharmaceuticals in LC–tandem MS analysis.

2.5. Method validation

The performance of the method was evaluated through estimation of the linearity, sensitivity, repeatability, reproducibility and matrix effects of the method.

Quantification, based on peak areas, was performed by internal standard calibration. The internal standards used for quantification of the compounds were following: sulfathiazole-d_4, diazepam-d_5, phenobarbital-d_3, atenolol-d_7, carbamazepine-d_{10}, ibuprofen-d_3, clotrimazole-d_5, enalapril-d_5, hydrochlorothiazide-d_2, glyburide-d_3, albuterol-d_3, cimetidine-d_3, ethyl clofibrate-d_4, antipyrine-d_3, acetaminophen-d_4, diclofenac-d_4, mecoprop-d_3, ^{13}C-erythromycin and ^{13}C-phenacetin. Seven-point calibration curves (0.5–100 ppb) were generated using linear regression analysis. The linearity was qualified by linear correlation coefficient, r^2.

To determine the recoveries, sediment and sludge samples were spiked in triplicate with a standard mixture of analytes in methanol/water, 25/75 (v/v) to 50 ng g^{-1} concentration. The spiked samples were stirred vigorously in order to enable better contact of analytes with the matrix. After 24-h equilibration, these samples together with the correspondent blank samples were extracted and treated by the previously described protocol. The internal standards for correcting matrix effects were added to the final sample extract. The recoveries were determined in triplicate comparing the obtained concentrations, after subtraction of concentrations found in blank samples, with the initial spiking level.

Method detection limits (MDL) and method quantification limits (MQL) were determined as the minimum detectable amount of analyte with a signal-to-noise of 3 and 10, respectively.

Intra-day and inter-day precision were determined from five repeated injections 50 ng g^{-1} standards during the same day (repeatability) and in five successive days (reproducibility). These two parameters were expressed as relative standard deviation of result (RSD, %).

Matrix effect was evaluated. In order to express it as percentage of suppression or enhancement, Eq. (1) was applied. The peak-areas from the analysis of spiked sludge and sediment extracts ($\text{area}_{\text{matrix}}$) reduced by the peak areas corresponding to the native analytes present in the sample ($\text{area}_{\text{blank}}$), were compared with the peak areas from spiked solvent at the same concentration ($\text{area}_{\text{solvent}}$). The spiked concentration was 25 ng g^{-1} for all the solid samples.

$$\text{signal suppression } (\%) = 100 - \left(\frac{(\text{area}_{\text{matrix}} - \text{area}_{\text{blank}}) \times 100}{\text{area}_{\text{solvent}}}\right) \quad (1)$$

The efficiency of internal standard and standard addition calibration were evaluated comparing the relations of calibration curves made in pure solvent with those prepared in matrix extracts.

3. Results and discussion

3.1. PLE conditions

The combination of solvent, temperature, flush volume, number and time of extraction cycles were investigated in order to obtain optimum extraction conditions for analysis of 42 pharmaceutical compounds. This method is one step forward in development of multi-residual analytical methods in our group [7,8]. Thus the starting point for PLE extraction were conditions reported by Radjenović et al. [7], adopted for the extraction of extended list of compounds.

The influence of the parameters was investigated simultaneously. The experiments were organized combining different solvent mixtures with different temperatures in 30 extractions, and then the other parameters were examined (time and number of cycles). Extraction pressure was set to 1500 psi for all PLE experiments, because it is not considered as a critical experimental parameter and it has negligible impact on analytical recovery [30].

Solvent: The solvent must be able to solubilize the target analytes leaving the sample matrix integrate. Since the analysed pharmaceuticals vary in physicochemical properties, the choice of the solvent mixture was limited and it could not match all the compounds in their polarity. The neutral conditions were required. In this study the following extraction solvents tested were: methanol/water (1/1, 1/2, 1/3, 2/1, 3/1, v/v) and acetonitrile/water (1/1, 1/2, 1/3, 2/1, 3/1, v/v). The combination methanol/water, 1/2, (v/v) yielded relatively better recoveries than other ones. For enalapril, metronidazole, bezifibrate and chloramphenicol, higher percent of water (i.e. methanol/water, 1/3, v/v) gave higher recoveries. More methanol (i.e. methanol/water, 1/1, v/v) gave better results for gemfibrozil, sulfamethazine and erythromycin. In the group of experiments with mixtures of acetonitrile and water, the best ratio was 1/2 (v/v) as well, but still it gave lower recoveries than methanol/water combination.

Temperature: This is very important parameter in PLE extraction. Application of higher temperature in PLE decreases the viscosity of solvents, thus allowing its better penetration into the sample matrix. The increase of temperature decreases significantly the dielectric constant of the water so the organic solvents can be used in smaller amount or avoided. But too high temperature can lead to degradation of the compounds or loss in method selectivity due to more efficient extraction of interfering matrix components. In the described experiments, all the combinations of the solvents on three extraction temperatures were tested: 60, 80 and 100 °C. The temperature higher of 100 °C was not tested since thermal

Table 2
Method performance parameters: reproducibility (RSD% for $n=5$), repeatability (RSD% for $n=5$), recoveries (%) and method precision (RSD%), matrix effect (%), method detection (MDL, ng g^{-1}) and quantification limits (MQL, ng g^{-1}) obtained in sludge and sediment samples.

Therapeutic groups	Compounds	Repeat. (RSD%) ($n=5$)	Reprod. (RSD%) ($n=5$)	Sludge				Sediment			
				Recovery,% (RSD,%) ($n=3$)	Matrix effect (%)	MDL (ng g^{-1})	MQL (ng g^{-1})	Recovery, % (RSD, %) ($n=3$)	Matrix effect (%)	MDL (ng g^{-1})	MQL (ng g^{-1})
Analgesics/anti-inflammatories	Ketoprofen	2	2	98.4 (10)	14	0.56	1.86	105 (0.6)	35	0.93	3.11
	Naproxen	5	5	125 (4.6)	41	0.07	0.24	105 (5.2)	48	0.84	2.79
	Ibuprofen	1	2	118 (13)	38	0.10	0.32	129 (1.0)	45	0.12	0.40
	Indomethacine	2	3	107 (7.0)	87	0.22	0.73	81.4 (0.7)	68	0.15	0.49
	Diclofenac	3	2	81.4 (9.1)	79	0.94	3.13	101 (1.2)	54	0.03	0.09
	Mefenamic acid	8	7	69.3 (12)	68	0.07	0.24	95.2 (5.3)	58	0.22	0.74
	Acetaminophen	3	3	40.7 (8.8)	-24	0.07	0.24	60.3 (9.8)	9	0.22	0.74
Phenazone type drugs	Phenazone	6	6	194 (4.1)	76	1.12	3.72	169 (1.8)	73	0.34	1.15
Lipid regulators and cholesterol lowering statin drugs	Bezafibrate	7	13	107 (5.1)	47	0.01	0.05	95.1 (3.8)	56	0.02	0.06
	Fenofibrate	3	11	204 (9.0)	81	1.04	3.46	123 (7.4)	75	0.79	2.62
	Gemfibrozil	4	11	76.1 (13)	82	0.51	1.69	77.7 (4.9)	72	1.24	4.14
	Mevastatin	13	14	94.1 (1.0)	66	8.84	29.4	89.0 (1.5)	85	3.16	10.5
	Pravastatin	12	15	215 (5.4)	78	1.32	4.42	186 (6.9)	57	0.71	2.38
	Atorvastatin	6	5	72.9 (4.5)	97	0.99	3.31	34.6 (3.3)	98	0.72	2.41
Psychiatric drugs	Diazepam	1	4	96.8 (2.5)	93	1.83	6.10	107 (9.3)	77	0.23	0.77
	Lorazepam	2	10	70.2 (13)	79	5.75	19.2	125 (6.3)	71	3.20	10.7
	Carbamazepine	2	8	134 (3.5)	89	0.04	0.13	137 (1.7)	81	0.03	0.09
Histamine H_2 receptor antagonists	Ranitidine	1	9	106 (13)	99	0.03	0.10	126.2 (13)	89	0.02	0.06
	Famotidine	4	14	83.5 (14)	97	0.01	0.05	97.8 (8.1)	73	0.02	0.07
	Cimetidine	7	7	78.3 (14)	80	0.07	0.24	87.4 (7.2)	72	0.01	0.02
Macrolide antibiotics	Erythromycin	6	5	43.2 (1.2)	100	1.17	3.88	68.0 (12)	92	0.01	0.02
	Roxithromycin	5	6	146 (15)	97	6.75	22.5	149 (9.9)	89	0.04	0.13
	Clarithromycin	8	14	38.2 (9.1)	95	3.51	11.7	130 (11)	86	0.10	0.34
	Josamycin	9	8	42.1 (13)	94	0.08	0.27	206 (7.0)	88	0.64	2.12
	Tylosin A	7	5	142 (1.8)	93	0.81	2.69	157 (8.8)	84	0.04	0.14
Sulfonamide antibiotics	Sulfamethazine	6	9	40.3 (14)	74	0.14	0.48	45.7 (8.9)	74	0.32	1.06
Other antibiotics	Trimethoprim	10	11	93.1 (12)	96	0.14	0.47	97.2 (9.6)	83	0.25	0.83
	Chloramphenicol	10	14	76.0 (9.3)	65	0.03	0.09	72.9 (0.3)	45	0.10	0.32
	Metronidazole	9	11	80.5 (15)	62	0.55	1.83	41.7 (3.9)	69	0.38	1.26
ß-blockers	Atenolol	5	4	97.1 (11)	77	0.16	0.54	90.4 (14)	66	0.11	0.36
	Sotalol	3	5	105 (12)	84	0.06	0.20	105 (8.8)	74	0.06	0.20
	Metoprolol	4	8	195 (2.9)	98	0.30	1.00	144 (11)	84	0.21	0.71
	Timolol	9	7	169 (9.0)	98	0.08	0.25	109 (14)	85	0.05	0.17
	Nadolol	6	4	46.1 (8.7)	94	0.06	0.19	66.7 (8.7)	82	0.01	0.03
	Pindolol	4	5	53.0 (7.9)	99	0.42	1.41	77.2 (12)	90	0.03	0.10
ß-agonists	Clenbuterol	5	4	86.4 (14)	88	0.02	0.07	168 (3.3)	97	0.07	0.25
	Salbutamol	0	3	86.0 (4.8)	82	0.08	0.27	84.1 (11)	68	0.02	0.08
Barbiturates	Butalbital	8	7	44.5 (2.1)	69	0.39	1.31	33.2 (1.2)	77	0.05	0.16
Antihypertensives	Nifuroxazide	13	9	65.0 (6.4)	78	0.06	0.20	125 (8.8)	96	0.05	0.17
	Enalapril	6	14	100 (8.8)	96	0.10	0.32	97.7 (5.6)	81	0.01	0.03
Diuretics	Hydrochlorothiazide	9	8	42.3 (12)	73	0.08	0.27	71.0 (13)	65	0.06	0.20
	Furosemide	10	13	106 (3.3)	51	0.19	0.64	77.7 (3.3)	57	0.76	2.52
Antidiabetics	Glibenclamide	6	5	87.8 (11)	89	1.67	5.56	89.1 (9.4)	85	0.29	0.96

degradation can occur at higher temperatures [22]. The recoveries obtained on 60 °C were low for most of analysed compounds. Salbutamol, gemfibrozil, mefenamic acid and diazepam gave better recoveries at temperature of 80 °C. For the compounds that were recovered in small or exaggerated percent is difficult to conclude which temperature suits better (i.e. prevastatine, atorvastatine, macrolides).

Extraction cycles: Optimization of the conditions included the screening of number and duration of static cycles. Each static cycle introduce fresh solvent which is very useful for the samples with complex matrix as sludge, while the longer time of a cycle can allow better diffusion of analytes into the extraction solvent. It is recommended to divide the extraction into more cycles [30]. The extracts of individual cycles of 5 min were collected as well as extracts from 2 and 3 cycles. Through the first and second fraction had almost all the compounds extracted completely, the third cycle was introduced to insure the complete extraction of diclofenac, indometacin, mefenamic acid, gemfibrozil, bezifibrate and lorati-

dine. With the three-cycle extraction, it is presumed that all the spiked and native analytes were removed. Finally, the PLE extraction was performed under the following conditions: 1 g of sample, temperature of 100 °C, as extraction solvent—methanol/water, 1/2 (v/v), a preheating period of 5 min, 3 static cycles, each lasting 5 min, total flush volume was 100% of cell with 60 s of nitrogen purge.

3.2. Method validation

The quantification was based on peak area. The shift of peaks in both transitions was noticed in the matrices comparing to the position in pure solvent. But, the retention times for all the analytes in the matrix varied less than 1%. In Fig. 1 are illustrated the chromatographic peaks of the two SRM transitions of diclofenac and glibenclamide in sludge and standard solution. The parts of the figure marked by A and C stand for the chromatograms of analytes in Sludge II, and B and D for chromatograms of standard solutions of diclofenac and glibenclamide, respectively. As illustrated, the retention times and SRM ratios concord well. Reproducibility and repeatability expressed as relative standard deviation, RSD%, were lower than 13% for intra-day and 15% for inter-day analysis, respectively (Table 2). Seven points calibration curves gave very good fits, $r^2 > 0.99$, over the established concentration range of 0.5–100 ng g^{-1} for all the compounds in all the matrices. The limits of detections in sludge and sediment were lower than 1 ng/g for the most compounds. The method provided lower sensitivity for phenazone, fenofibrate, prevastatine, mevastatine, diazepam, lorazepam, erythromycin, roxitromycin and

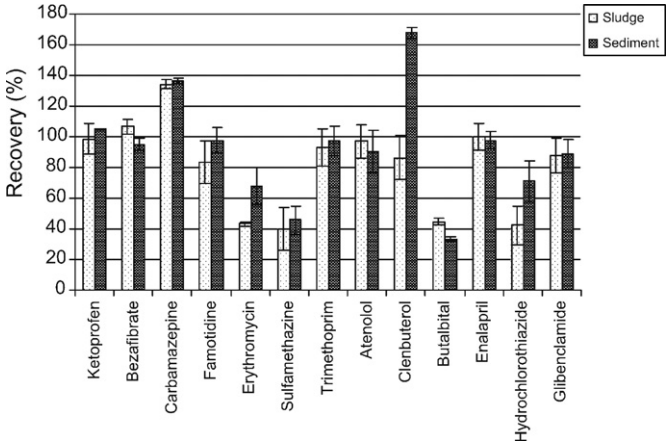


Fig. 2. Recoveries obtained for the representative compounds of each therapeutic group.

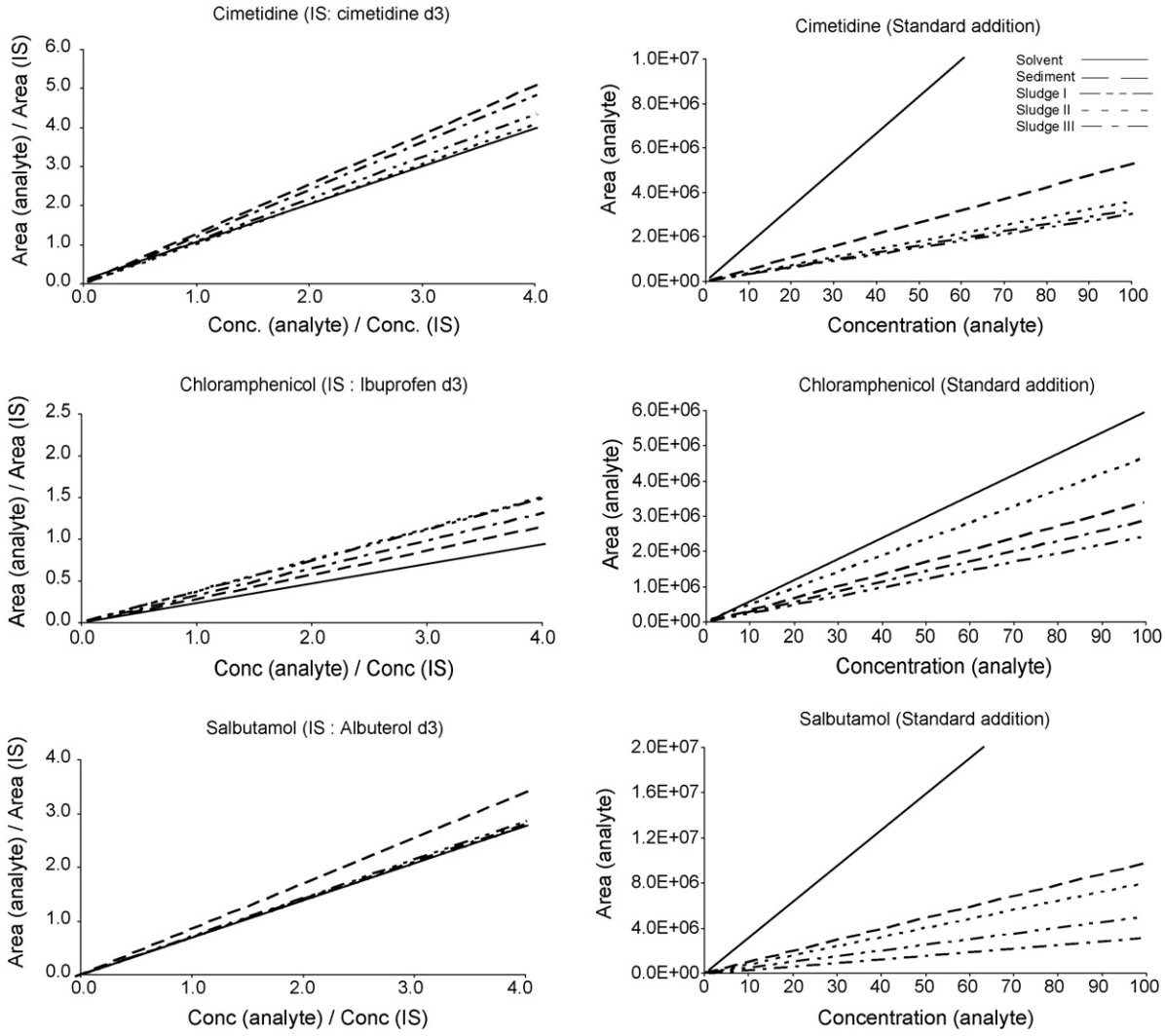


Fig. 3. Internal standard calibration curves (left) and standard addition calibration curves (right) of spiked solvent and extracts of sludge and sediment for cimetidine, salbutamol and chloramphenicol.

clarithromycin in sludge (1.12 < MDL < 6.75) and for mevastatine, gemfibrozil, lorazepam in sediment samples (1.24 < MDL < 3.20). Generally, the sensitivity was lower for sludge than for sediment samples, due to the more complex matrix. The values of MDL and MQL for sludge (Sludge I) and sediment are presented in Table 2. Compared to the method detection limits obtained for pharmaceuticals in solid matrices using some other instruments [5,7,12,13,32], with the LC–QqLIT-MS the improvement in sensitivity is significant.

In Table 2 are listed only the recovery results obtained for Sludge I and sediment, with the corresponding relative standard deviations. The RSD% was less than 15% for all the compounds in both matrices, which is considered as good method precision. The recoveries varied significantly depending on compound and matrix. For the pharmaceuticals in Sludge I only acetaminophen (40.7%), josamycin (42.1%), sulfamethazine (40.3%) and hydrochlorthiazide (42.3%) had recoveries <45%, wherein acetaminophen and hydrochlorthiazide were quantified with their deuterated standards. For the samples of sediment, recoveries were <50% for atorvastatin (34.6%), sulfamethazine (45.7%), metronidazole (41.7%) and butalbital (33.2%). In Fig. 2 are illustrated the results for some representative compounds for each therapeutic group, and the rest of the compounds followed a similar pattern. Some compounds yielded extremely high recoveries (»100%) in both matrices, like prevastatine, phenazone, fenofibrate and metoprolol. Elevated recoveries have already been reported in some studies about pharmaceuticals in sludge [5,7,32]. The properties of matrix itself and the complexity of the interaction with analytes, as well as possible errors in procedure could be the reason for the extreme (high or low) recoveries. Hence, it is difficult to give logical explanation and expect certain values of recoveries. If the accurate results are requested, the recoveries in the investigated matrix must be determined prior to quantification.

Matrix effect: The performance of HPLC–ESI-MS/MS analysis is strongly affected by the ionisable impurities coming from matrix (e.g. natural organic matter, salts, ion-pairing agents, non-target contaminants, etc.) that can interfere with the ionization processes. This may result in a signal suppression or enhancement leading to low sensitivity and inaccurate results. These effects are more extensive when the matrix is more complex as sludge matrix, for example. It is advisable to evaluate matrix effect as a part of validation of the method to ensure the reliability of results obtained. In this study, standard addition and internal standard addition experiments were performed to investigate and minimize matrix effect.

The calibration curves obtained from real sludge and sediment extracts with standard addition were compared with those in pure solvent (methanol/water, 25/75, v/v). All curves were linear over the concentration range of 0.5–100 ng g^{-1} with correlation factors $r^2 > 0.99$. For illustration, Fig. 3 (right) presents calibration curves of cimetidine, chloramphenicol and salbutamol in 4 real matrices (sediment and three samples of sludge) and one in solvent. Significant difference in slopes was observed proving the existence of matrix effects.

Fig. 3 (left) shows the calibration curves of the same compounds acquired by isotopically labeled compounds added into sludge and sediment extracts and in the pure solvent. The curves were linear over the concentration range of 0.5–100 ng g^{-1} with good correlation factors of $r^2 > 0.99$. Despite the fact that the matched isotopically labeled standards were not available for all the target compounds, the calibration curves appear to be overlapped well enough. This means that internal standards compensated the matrix effects considerably; therefore the internal standard addition was used for quantification in this study. Although the selected isotopically labeled standards seem to be appropriate for the target compounds (Fig. 3), cannot be expected that they give very accurate results. More precise results could be achieved using the surrogate standards of the target compounds. It is expected that the surrogate standards compensate for any error that can occur during the sample preparation. But since the surrogate standards were not available for all the analysed compounds and the internal standard quantification gave repeatable results, we decided to use only internal standard approach. The application of only one approach allowed more comparable and reproducible results. The lack of fully compatible surrogate/internal standards is considered as the main limitation of one multi-residual method for pharmaceuticals in environmental samples [33].

Matrix effect was quantified comparing the areas of compounds in spiked matrix samples with the areas obtained in spiked solvent (methanol/water, 25/75, v/v). The effect was expressed by percentage of signal suppression/enhancement and the results are summarized in Table 2. Knowing that the nature of matrix effect is pretty varying, the percentage is just a relative indicator of the degree of suppression and enhancement. The percentage varies from 14 to 100% in sludge and from 9 to 98% for sediment samples. The impact of matrix interferences was different for each compound and except acetoaminophen, all the compounds were subjected to ion suppression. Strong MS signal suppression effects were observed for most of the compounds.

3.3. Application of the method

The developed method was applied for determination of pharmaceuticals in sediment from middle course of river Ebro and in the sewage sludge from WWTPs Tudela, Pamplona and Terrassa. Target pharmaceuticals were not detected in sediment samples. Of

Table 3
Average concentrations of target compounds detected in sludge-samples from WWTP Tudela (Sludge I), Pamplona (Sludge II) and Terrassa (Sludge III).

Compound	Concentration (ng g^{-1}, d.w.)		
	Sludge I	Sludge II	Sludge III
Ketoprofen	BLD[a]	18.9 ± 1.42	21.1 ± 1.3
Naproxen	BLD	5.9 ± 0.7	4.27 ± 0.1
Ibuprofen	43.2 ± 5.5	117 ± 5.9	91.5 ± 3.8
Indomethacine	BLD	2.5 ± 0.3	2.9 ± 0.1
Diclofenac	27.5 ± 0.5	69.1 ± 7.6	74.9 ± 4.1
Mefenamic acid	26.2 ± 3.2	19.3 ± 2.3	14.3 ± 2.2
Acetaminophen	103 ± 9.0	77.8 ± 10.3	42.1 ± 6.4
Phenazone	3.2 ± 0.1	16.0 ± 1.4	BLD
Bezafibrate	2.9 ± 0.2	7.2 ± 0.6	18.7 ± 0.7
Fenofibrate	3.3 ± 0.3	BLD	17.1 ± 3.7
Gemfibrozil	14.3 ± 1.9	33.9 ± 4.61	31.8 ± 3.8
Atorvastatin	42.1 ± 2.8	65.0 ± 3.21	21.4 ± 2.7
Diazepam	3.20 ± 0.1	8.5 ± 0.2	4.6 ± 0.4
Carbamazepine	10.1 ± 0.1	11.0 ± 1.60	12.7 ± 1.4
Ranitidine	0.2 ± 0.02	2.3 ± 0.3	BLD
Famotidine	2.14 ± 0.3	12.4 ± 1.3	14.7 ± 2.3
Cimetidine	0.5 ± 0.06	2.5 ± 0.2	6.1 ± 0.5
Roxithromycin	BLQ	BLQ[b]	BLQ
Clarithromycin	BLD	47.0 ± 2.9	27.0 ± 2.1
Josamycin	BLD	4.8 ± 0.5	47.8 ± 4.8
Sulfamethazine	BLD	BLQ	1.1 ± 0.4
Trimethoprim	BLD	9.2 ± 0.8	11.2 ± 1.2
Chloramphenicol	BLD	1.2 ± 0.3	BLD
Metronidazole	BLD	10.6 ± 0.6	BLD
Atenolol	10.8 ± 1.1	8.8 ± 0.7	3.96 ± 0.4
Sotalol	1.7 ± 0.2	BLD	BLD
Nadolol	0.8 ± 0.1	3.3 ± 0.5	2.70 ± 0.3
Pindolol	13.6 ± 1.1	23.1 ± 1.9	BLD
Clenbuterol	BLD	40.2 ± 2.5	BLD
Salbutamol	BLD	3.8 ± 0.6	BLD
Nifuroxazide	BLD	0.5 ± 0.05	BLD
Hydrochlorothiazide	29.0 ± 3.6	126 ± 8.5	30.5 ± 1.9
Furosemide	10.1 ± 0.3	16.8 ± 1.4	11.7 ± 0.4
Glibenclamide	7.7 ± 0.6	15.8 ± 1.7	42.4 ± 1.5

BLD and BLQ determined for each matrix individually.
[a] BLD—below limits of detection.
[b] BLQ—below limits of quantification.

43 analysed compounds, 34 were detected in sewage sludge samples from WWTPs. The average concentrations ($n = 5$) determined in those samples are summarized in Table 3. The recoveries and limits of detection and quantification were determined for each kind of sludge individually, prior to quantification. The concentrations below the limits of detection and quantification are not presented. In general, the pharmaceuticals were identified in concentrations of 0.1–120 ng/g. Ibuprofen, acetaminophen, diclofenac, atorvastatin and hydrochlorthiazide were detected in the highest concentrations in samples from all 3 WWTP. These compounds were present in average concentrations from 43.2 to 117 ng g^{-1}, 42.1 to 103 ng g^{-1}, 27.5 to 74.9 ng g^{-1}, 21.4 to 65 ng g^{-1} and 29.0 to 126 ng g^{-1}, respectively. Carbamazepine, mefenamic acid, gemfibrozil, furosemide and glibenclamide were frequently detected as well. The presence of these compounds was reported in recent works related to pharmaceuticals in sludge in similar concentrations [7,13,14]. WWTP Pamplona serves more inhabitants and has higher capacity of treatment than the other two, so the samples from this plant are more contaminated by analysed pharmaceutical residues.

4. Conclusion

The study involved development and validation of a method for simultaneous analysis of 43 pharmaceutical compounds in sludge and sediment. Differences in physicochemical properties of the compounds required neutral experimental conditions. The pharmaceuticals were isolated from solid samples using PLE followed by SPE clean-up step, and submitted to the analysis in LC–QqLIT-MS.

The influence of extraction parameters (i.e. solvent composition, temperature, and number and time of extraction cycles) on the extraction and overall recoveries were evaluated. Strong effects of signal suppression and extreme values of recoveries ($\gg$100%) were noticed as result of matrix interferences. The chosen isotopically labelled compounds compensated for the matrix effects well enough; therefore the internal standard approach was used for quantification. Linearity of the method was satisfactory ($r^2 < 0.99$) in the defined concentration range (0.5–100 ng g^{-1}). The instrument exhibited very good sensitivity with the MDLs and MQLs lower than 1 ng g^{-1} for most of the compounds. The instrumental precision was acceptable with RSDs < 15% for intra- and inter-day analysis and <1% for peak position shifts.

The applicability of the method for routine multi-residue analysis was demonstrated through the analysis of sludge samples from three WWTPs. The recoveries were higher of 50% for most of the compounds and the variance of values was observed depending on the origin of the sludge samples. The presence of 35 pharmaceuticals was confirmed, wherein ibuprofen, acetaminophen, diclofenac, atorvastatin and hydrochlorothiazide were detected in the highest concentrations.

Acknowledgements

The work was financially supported by the Spanish Ministry of Education and Science, project CEMAGUA (CGL2007-64551/HID), and project SOSTAQUA (led by Aguas de Barcelona and founded by CDTI in the framework of the Ingenio 2010 Programme under the CENIT call) and Spanish Ministry of the Environment and Rural and Marine Affairs through the project MMAMRM 010/PC08/3-04. A. Jelic gratefully acknowledges the JAE Program (Junta para la Ampliación de Estudios–JAE Predoc), co-financed by CSIC (Consejo Superior de Investigaciones Científicas) and European Social Funds, for a predoctoral grant. Waters (Milford, USA) is gratefully acknowledged for providing the SPE cartridges and Merck (Darmstadt, Germany) for providing the HPLC columns.

References

[1] A.B.A. Boxall, EMBO Rep. 5 (2004) 1110.
[2] A. Nikolaou, S. Meric, D. Fatta, Anal. Bioanal. Chem. 387 (2007) 1225.
[3] J.L. Zhou, Z.L. Zhang, E. Banks, D. Grover, J.Q. Jiang, J. Hazard. Mater. 166 (2009) 655.
[4] T.A. Ternes, TrAC Trends Anal. Chem. 20 (2001) 419.
[5] L. Barron, J. Tobin, B. Paull, J. Environ. Monit. 10 (2008) 353.
[6] R.H. Lindberg, P. Wennberg, M.I. Johansson, M. Tysklind, B.A.V. Andersson, Environ. Sci. Technol. 39 (2005) 3421.
[7] J. Radjenović, A. Jelicĭ, M. Petrović, D. Barcelo, Anal. Bioanal. Chem. 393 (2009) 1685.
[8] M. Gros, M. Petrović, D. Barceló, Anal. Chem. 81 (2009) 898.
[9] B. Kasprzyk-Hordern, R.M. Dinsdale, A.J. Guwy, J. Chromatogr. A 1161 (2007) 132.
[10] D. Fatta, A. Achilleos, A. Nikolaou, S. Meriç, TrAC Trends Anal. Chem. 26 (2007) 515.
[11] M.J. Gómez, M. Petrović, A.R. Fernández-Alba, D. Barceló, J. Chromatogr. A 1114 (2006) 224.
[12] A.L. Spongberg, J.D. Witter, Environ. Sci. Technol. 397 (2008) 148.
[13] W. Chenxi, A.L. Spongberg, J.D. Witter, Chemosphere 73 (2008) 511.
[14] K. Kimura, H. Hara, Y. Watanabe, Environ. Sci. Technol. 41 (2007) 3708.
[15] A.K.W.B. Matthias Ferdig, J. Sep. Sci. 28 (2005) 1448.
[16] S. Morales, P. Canosa, I. Rodríguez, E. Rubí, R. Cela, J. Chromatogr. A 1082 (2005) 128.
[17] A. Nieto, F. Borrull, E. Pocurull, R.M. Marcé, J. Sep. Sci. 30 (2007) 979.
[18] A. Göbel, A. Thomsen, C.S. McArdell, A.C. Alder, W. Giger, N. Theiß, D. Löffler, T.A. Ternes, J. Chromatogr. A 1085 (2005) 179.
[19] M.S. Díaz-Cruz, M.J. López de Alda, D. Barceló, J. Chromatogr. A 1130 (2006) 72.
[20] A.M. Jacobsen, B. Halling-Sørensen, F. Ingerslev, S. Honoré Hansen, J. Chromatogr. A 1038 (2004) 157.
[21] T.A. Ternes, M. Bonerz, N. Herrmann, D. Löffler, E. Keller, B.B. Lacida, A.C. Alder, J. Chromatogr. A 1067 (2005) 213.
[22] A. Göbel, A. Thomsen, C.S. McArdell, A.C. Alder, W. Giger, N. Theiβ, D. Lo□ffler, T.A. Ternes, J. Chromatogr. A 1085 (2005) 179.
[23] K.A. Krogh, E. Björklund, D. Loeffler, G. Fink, B. Halling-Sørensen, T.A. Ternes, J. Chromatogr. A 1211 (2008) 60.
[24] W.W. Buchberger, Anal. Chim. Acta 593 (2007) 129.
[25] R.A. Trenholm, B.J. Vanderford, J.C. Holady, D.J. Rexing, S.A. Snyder, Chemosphere 65 (2006) 1990.
[26] M. Petrović, M.D. Hernando, M.S. Díaz-Cruz, D. Barceló, J. Chromatogr. A 1067 (2005) 1.
[27] R. Rodil, J.B. Quintana, P. López-Mahía, S. Muniategui-Lorenzo, D. Prada-Rodríguez, J. Chromatogr. A 1216 (2009) 2958.
[28] M.J. Martinez Bueno, A. Aguera, M.J. Gomez, M.D. Hernando, J.F. Garcia-Reyes, A.R. Fernandez-Alba, Anal. Chem. 79 (2007) 9372.
[29] G. Hopfgartner, E. Varesio, V. Tschappat, C. Grivet, E. Bourgogne, L.A. Leuthold, J. Mass Spectrom. 39 (2004) 845.
[30] Technical note—DIONEX; http://www.dionex.com/en-us/webdocs/4736_TN208.pdf.
[31] Commission Decision (2002/657/EC) of 12 August 2002 Implementing Council Directive 96/23/EC concerning the performance of analytical methods and the interpretation of results, Official Journal of the European Communities L221, Brussels, Belgium, pp. 8–36.
[32] A. Nieto, F. Borrull, R.M. Marcé, E. Pocurull, J. Chromatogr. A 1174 (2007) 125.
[33] M. Gros, M. Petrović, D. Barceló, Talanta 70 (2006) 678.

Talanta 80 (2009) 372–376

Contents lists available at ScienceDirect

Talanta

journal homepage: www.elsevier.com/locate/talanta

Screen-printed electrografted electrode for trace uranium analysis

Stéphanie Betelu[a,*], Christine Vautrin-Ul[a,*], Jacques Ly[b], Annie Chaussé[a]

[a] Laboratoire Analyse et Modélisation pour la Biologie et l'Environnement (LAMBE), UMR CNRS-CEA 8587, Université d'Evry-Val-d'Essonne, Boulevard François Mitterrand, F-91025 Evry Cedex, France
[b] Laboratoire Mesures et Modélisation de la Migration des Radionucléides (L3MR), CEA, Centre d'Etudes de Saclay, DEN/DANS/DPC/SECR, 91191 Gif-sur-Yvette Cedex, France

ARTICLE INFO

Article history:
Received 11 April 2009
Received in revised form 23 June 2009
Accepted 30 June 2009
Available online 8 July 2009

Keywords:
Screen-printed electrode
Surface functionalization
Diazonium salt
Uranium detection
Environmental analysis

ABSTRACT

This paper reports the interest of the novel 4-carboxyphenyl-grafted screen-printed electrodes (4-CP-SPEs) for sub-nanomolar analysis of uranium in water samples. Electrodes were easily prepared via electrochemically reduction of the corresponding diazonium salt. The stability of the grafted layer has been clearly demonstrated. Uranium detection was then achieved by immersing the grafted electrode into the sample solution, followed by the electrochemical measurement of adsorbed U(VI) by square wave voltammetry.

Adsorption time was investigated so as to find the best compromise between analysis time, repeatability and reproducibility. Limit of detection and quantitation reached 7×10^{-10} and 2×10^{-9} mol L^{-1}, respectively. Moreover, interference study was conducted with Zn(II), Cd(II), Pb(II) and Cu(II); no major interference was established. 4-CP-SPEs were finally applied for uranium determination in estuarine water demonstrating the convenience of these electrodes for environmental analysis.

© 2009 Elsevier B.V. All rights reserved.

1. Introduction

Trace uranium monitoring in aquatic ecosystem is of a great importance because of its chemical and radiologic toxicity [1]. Although uranium can exist in different oxidation states, from +III to +VI, U(VI) is the oxidation state the most prevalent in oxygenated waters [2]. It would thus be useful to be able to determinate the concentration of U(VI) directly in the sample [3].

Even if extensive efforts have been devoted for developing highly sensitive analytical procedures for uranium determination in natural water samples, the development of portable sensing probes for on site analysis is a growing necessity and therefore a serious challenge to any analytical technique in terms of sensitivity, accuracy and repeatability.

Among the strategies investigated, electroanalytical techniques appear as the most appropriate for direct determination of uranium owing to the portable instrumentation character and low power requirement [4]. The use of calixarenes or ion imprinted polymers has proved to be an excellent choice in ion selective electrodes elaboration [5–7]. Although ion selective electrodes showed large selectivity factors, measurements yield detection limits that were not low enough (2×10^{-8} mol L^{-1}); elsewhere uranium natural concentrations may be as low as 2×10^{-9} mol L^{-1} in river water and 10^{-8} mol L^{-1} in sea water [8,9].

Because of its high sensitivity, adsorptive cathodic stripping voltammetry (ACSV) was widely used to determine uranium at sub-nanomolar level. U(VI) complexes with 8-hydroxyquinoline [10], aluminon [11], N,N′-ethylenebis(salicylidenimine) [12], potassium hydrogen phthalate [13], cupferron (nitrosoarylhydroxylamines) [14], 2,6-pyridinedicarboxylic acid [15]... have been successfully used for uranium detection with mercury drop electrodes. A limitation of these electrodes is their unsuitability for on site analysis. New alternative electrode materials, with similar performances, were thus investigated for this purpose: carbon paste electrodes modified with propyl gallate [16], multi-wall carbon nanotubes modified glassy carbon electrodes (GCEs) [17], mercury film silver-based electrodes [18], lead-coated GCEs [19], bismuth-coated carbon fiber electrodes [20] or iridium-based mercury electrodes [21].

Attention was recently being paid to self-assembled monolayers (SAM's) grafted on gold electrodes [6,7]. However, limitations with regard to the stability of the gold-thiolate covalent bound and hence the stability of the resultant SAM's have been demonstrated [22]. Another approach consists in reduction of diazonium salts. Indeed, grafting of aryldiazonium is a versatile method allowing stable grafted organic layers bearing a wide range of functional groups on many conductive surfaces [23–34].

We have recently reported the elaboration of 4-carboxyphenyl-grafted screen-printed electrodes (4-CP-SPEs) for copper analysis [35]. Screen-printed electrodes (SPEs) were easily functionalized via electrochemically reduction of 4-carboxyphenyldiazonium salt. Copper analyses were achieved by direct immersion of the grafted electrode into the sample solution for a specific time, followed by

* Corresponding authors. Tel.: +33 169477709; fax: +33 169477655.
E-mail addresses: stephanie.betelu@univ-evry.fr (S. Betelu), christine.vautrin-ul@univ-evry.fr (C. Vautrin-Ul).

0039-9140/$ – see front matter © 2009 Elsevier B.V. All rights reserved.
doi:10.1016/j.talanta.2009.06.076

the electrochemical reduction of accumulated Cu(II) by square wave voltammetry. Detection limit reached 5×10^{-9} mol L^{-1} and 4-CP-SPEs were successfully used for environmental analysis.

The main purpose of this paper is to show the benefit of 4-CP-SPEs for sub-nanomolar uranium determination. The stability of the grafted layer was considered. Electrode performances and reliability were investigated for the determination of the total concentration of uranium in environmental sample. Adsorption time was studied so as to find the best compromise between analysis time, repeatability and reproducibility. Zn(II), Cd(II), Pb(II) and Cu(II) interference study was also examined. Analyses were then performed in natural water sample.

2. Experimental

2.1. Materials and reagents

Suprapur CH_3COONH_4 (5 mol L^{-1}), H_2SO_4 (0.1 mol L^{-1}) and suprapur standards solutions: $Cd(NO_3)_2$, $Cu(NO_3)_2$, $Pb(NO_3)_2$, $Zn(NO_3)_2$ (1 g L^{-1}) were purchased from JT Baker; certified estuarine water (NRC-CNRCSLEW-3) from Sodipro.

4-carboxyphenyldiazonium tetrafluoroborate (DCOOH) was synthesized as previously described [36]. Working electrodes were 9.6 mm^2 carbon-based SPEs [37]. SPEs were cleaned by sonication in H_2SO_4 for 10 min before grafting [36].

Experiments were performed with an Autolab (low current PGSTAT12, Metrohm) [38]. All the potentials were measured versus the saturated calomel electrode (SCE). A Pt wire was used as counter electrode.

Grafted layer was generated by the reduction of DCOOH in H_2SO_4 (0.1 mol L^{-1}) either by (i) cyclic voltammetry (CV) (1 scan at 0.1 V s^{-1} between +0.8 and −0.8 V/SCE), leading to a grafted pseudo-monolayer [30,38] or (ii) under chronoamperometry (CA) (−0.6 V/SCE during 300 s), leading to grafted multilayer [30,38]. Once grafted electrodes were rinsed, sonicated for 10 min and stored in H_2SO_4.

2.2. Uranium analysis

Experiments were conducted at constant temperature 21.0 ± 0.5 °C in CH_3COONH_4 (5×10^{-2} mol L^{-1}, pH 7). Analyses were achieved by (i) direct adsorption of U(VI) at the grafted layer followed by (ii) electrochemical reduction of adsorbed U(VI) to U(V) [15]. (i) Adsorption was achieved by immersing the grafted electrode into 10 mL of stirred CH_3COONH_4 containing U(VI). (ii) Electrodes were then transferred to the electrochemical cell containing only CH_3COONH_4 in order to perform square wave voltammetry (SWV) measurements (pulse amplitude: 25 mV, step: 4 mV, frequency: 100 Hz). As otherwise stated SWV was performed in deoxygenated solutions. After use, 4-CP-SPEs were regenerated: electrodes were rinsed with milli-Q water and stored in H_2SO_4 in order (i) to ensure desorption of uranium species that would remain complexed at the working surface and (ii) to be sure of getting data free from memory effect. It was found (by ensuring blanks between successive measurements of U(VI)) that a period of 15 min of storage in H_2SO_4 was enough to remove uranium from the electrode.

3. Results and discussion

3.1. SPEs grafting via electrochemical reduction of diazonium salt

3.1.1. Elaboration of grafted-SPEs

Because they can easily be modified to enhance sensitivity and/or selectivity [35,37,39,40], SPEs appeared particularly well suited for being functionalized. Moreover, due to the very low capacitive current [35], SPEs exhibit fine and well define signal leading to low detection limits. Electrochemical reduction of diazonium salt was selected as the most attractive method to functionalize SPEs working surface because it leads to the rapid formation of organic stable layers covalently bound to conductive substrates [25,28–34,36,38]. In this study, SPEs were grafted via electrochemical reduction of 4-carboxyphenyldiazonium salt. Acetate functions, known for their complexation properties towards U(VI) in solution ($\log \beta_1 = 3.03$, 25 °C, 0 mol L^{-1}) ($\log \beta_2 = 5.57$, 25 °C, 0 mol L^{-1}) [41], are assumed to complex U(VI) at the grafted SPEs. The well shaped peak observed at −0.25 V/SCE in Fig. 1 illustrates the electrochemical reduction of 4-carboxyphenyldiazonium salt at SPEs.

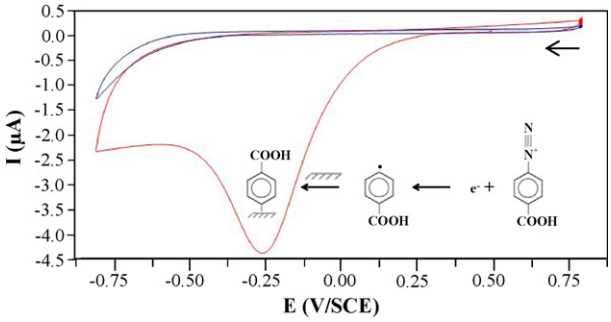


Fig. 1. Blank and reduction of 4-carboxyphenyldiazonium (2×10^{-3} mol L^{-1}) in H_2SO_4 by CV (CV—scan rate: 0.1 V s^{-1} between +0.8 and −0.8 V/SCE).

3.1.2. Stability of SPEs grafted layer

To investigate the stability of the SPEs grafted layer, four SPEs were grafted (the same day) via 4-nitrophenyldiazonium salt chosen for the electrochemical properties of the nitro groups [42–44]. It was previously shown that the oxidation/reduction reaction of the nitro compounds (Ar–NO_2) in acidic solutions should proceed according to the following mechanism [43]:

$$Ar\text{–}NO_2 + 4e^- + 4H^+ \leftrightarrow Ar\text{–}NHOH + H_2O \quad (1)$$

$$Ar\text{–}NHOH + 2e^- + 2H^+ \leftrightarrow Ar\text{–}NH_2 + H_2O \quad (2)$$

$$Ar\text{–}NHOH \leftrightarrow Ar\text{–}NO + 2H^+ + 2e^- \quad (3)$$

Grafted nitro groups can electrochemically be reduced into amine groups (2), via the formation of intermediate hydroxylamine functions (1). Reduction of these functions is not complete so that they can be detected during the reverse oxidation process (3) [44].

In this work, investigation has consisted in comparing the electrochemical signals obtained from freshly grafted SPEs (two electrodes) to those obtained from grafted SPEs (two electrodes) that were stored for 18 days in H_2SO_4. Experiments conducted with nitro-grafted SPEs were achieved by CV in HCl 0.1 mol L^{-1}: each time, 2 cycles were realised, the first one between +0.85 and −0.85 V/SCE, the second one between +0.8 and −0.3 V/SCE. Fig. 2 presents the cyclic voltammograms obtained with (i) freshly grafted SPEs (straight line) and (ii) SPEs that were stored for 18 days in H_2SO_4 (broken line).

The first cycle conducted between +0.85 and −0.85 V/SCE (Fig. 2A) shows an irreversible reduction peak at −0.52 V, unambiguously assigned to the reduction of nitro groups immobilized at the electrode surface in amino and hydroxylamine functions [36]. The oxidation peak located at +0.33 V/SCE is attributed to the oxidation of NHOH. The second cycle (Fig. 2B) conducted between +0.8 and −0.3 V/SCE shows the reversible reduction of NO at the working surface. No significant difference was observed in the shape of the voltammograms, demonstrating the stability of the grafted layer for long time.

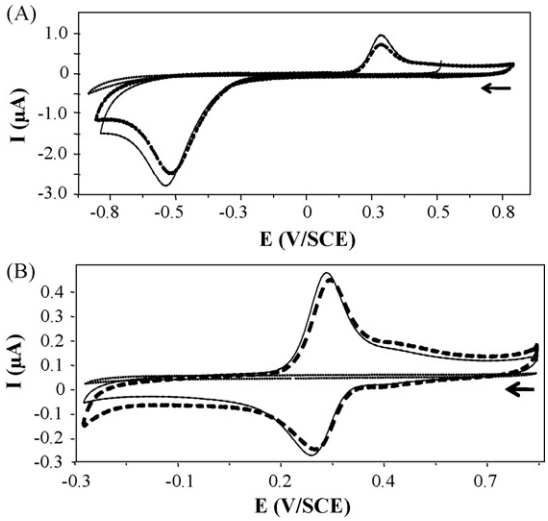


Fig. 2. Cyclic voltammograms obtained at 4-nitrophenyl-grafted SPEs in HCl (0.1 mol L^{-1}) with naked-SPEs (doted line), freshly grafted SPEs (straight line) and grafted SPEs that were stored for 18 days in H_2SO_4 (broken line) (CV—scan rate: 0.1 V s^{-1}). (A) First cycle conducted between +0.85 and −0.85 V/SCE. (B) Second cycle conducted between +0.8 and −0.3 V/SCE.

3.2. U(VI) electrochemical behaviour on SPEs

Uranium stable oxidation state is U(VI) in oxygenated waters. It would obviously be useful to be able to determinate the concentration of U(VI) directly in the sample [3].

The feasibility of qualitative analysis was investigated by studying the analytical signal obtained after the direct electrochemical reduction of uranium in a solution containing U(VI) 10^{-4} mol L^{-1}. U(VI) reduction was examined with both naked-SPEs and 4-CP-SPEs. Voltammograms are presented in Fig. 3. In accordance with Gholivand et al. who studied the U(VI) electrochemical behaviour by CV in acetate media (pH 6.7) [15], the single peak observed at −0.37 V/SCE with naked-SPEs is attributed to the reduction of U(VI) to U(V) (E° = −0.175 V/SCE [13]). With 4-CP-SPEs, the shift of 0.13 V/SCE in the reduction peak towards more negative values is assumed to the presence of the grafted complexing layer. Even if

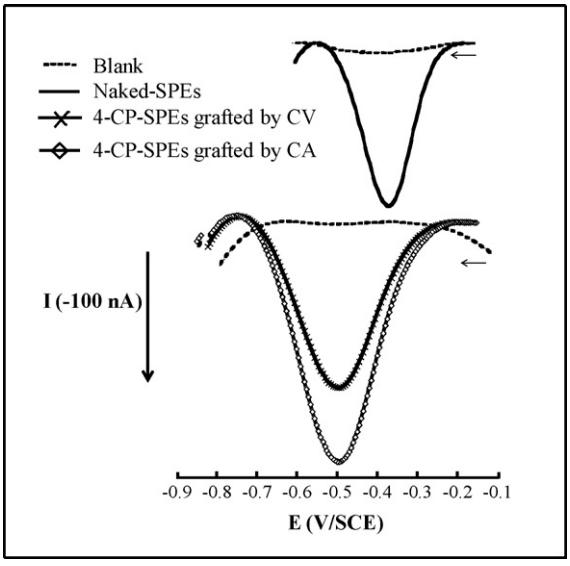


Fig. 3. U(VI) reduction peak obtained with naked-SPEs and 4-CP-SPEs after the direct reduction of U(VI) 10^{-4} mol L^{-1} by SWV in CH_3COONH_4 (SWV—pulse: 25 mV, step: 4 mV, frequency: 25 Hz).

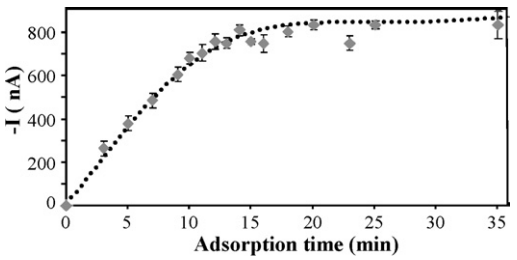


Fig. 4. Influence of adsorption time for U(VI) 3.5×10^{-8} mol L^{-1} (SWV—pulse: 25 mV, step: 4 mV, frequency: 100 Hz).

the thickness of the grafted layer does not influence peak potential, it influences peak current. Indeed, in comparison with naked-SPEs, pseudo-monolayer grafted by CV induces an increase in the peak current of 4%; multilayer grafted by CA induces an increase of 50%, demonstrating the interest of the grafting via CA for U(VI) analysis. In other respect, electrodes grafted by CA were shown to lead to a better reproducibility for Cu(II) analysis [35]. For further studies, all 4-CP-SPEs were grafted by CA.

3.3. Adsorption time

Particular attention was paid to the influence of the adsorption time. Experiments were conducted with U(VI) 3.5×10^{-8} mol L^{-1}. As displayed in Fig. 4, peak current increases linearly with adsorption time up to 10 min; the thermodynamical equilibrium was achieved at 12 min. 15 min was retained as optimal time, best compromise between analysis time, repeatability and reproducibility.

3.4. Interference study

Effects of co-existing ions Cu(II) (E° = 0.1 V/SCE), Cd(II) (E° = −0.65 V/SCE), Pb(II) (E° = −0.37 V/SCE) and Zn(II) (E° = −1 V/SCE), noted M(II), which are of great significance in environmental matrices [3], were examined on the behaviour of U(VI) 10^{-8} mol L^{-1}. M(II) ranged from 3.5×10^{-9} to 10^{-7} mol L^{-1} (Fig. 5). Voltammograms are presented in Fig. 5A. It is worth noting that only the voltammogram obtained in the presence of Cu(II) shows a second peak at −0.1 V/SCE attributed to Cu(II) reduction [35]. Moreover, neither U(VI) peak location (Fig. 5A) nor repeatability (Fig. 5B) were affected by the presence of the investigated interfering. According to the standard errors, neither Zn(II), nor Cd(II), nor Pb(II) seems to affect electrodes sensitivity. No major interferences of these ions are thus expected in the determination of uranium in natural water samples in which these trace-elements ambient concentration is lower than 10^{-7} mol L^{-1}. In the case of copper, peak current remained unchanged as long as the concentration of Cu(II) remained three times higher than that of U(VI). For higher concentrations, Cu(II) induces a decrease of the U(VI) analytical response correlated to an increase of Cu(II) peak current showing the competition between U(VI) and Cu(II) at the working surface. In agreement with the repeatability of the analyses, the standard addition method can thus be performed to quantify uranium in natural samples [13].

3.5. Analytical performances

3.5.1. Limit of detection (LOD) and quantitation (LOQ)

The analytical performances were determined from U(VI) calibration curves, in the range of 8.5×10^{-10} to 10^{-7} mol L^{-1} (Fig. 6A). Experiments were carried out with three 4-CP-SPEs and each data was duplicated. In Fig. 6B, only voltammograms related to the lowest concentrations are presented.

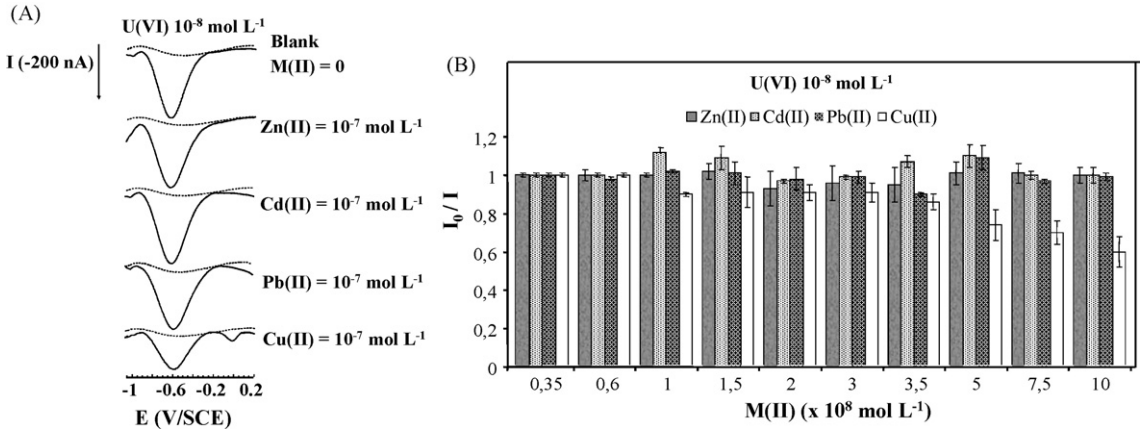


Fig. 5. Influence of Zn(II), Cd(II), Pb(II) and Cu(II), noted M(II), on the analytical response of 4-CP-SPEs. (A) Superposition of U(VI) voltammograms obtained in CH_3COONH_4 in absence and in presence of M(II). (B) U(VI) relative intensity, I/I_0, (where I and I_0 are the U(VI) intensity in presence and in absence of M(II)) versus M(II) concentration (adsorption time: 15 min; SWV—pulse: 25 mV, step: 4 mV, frequency: 100 Hz).

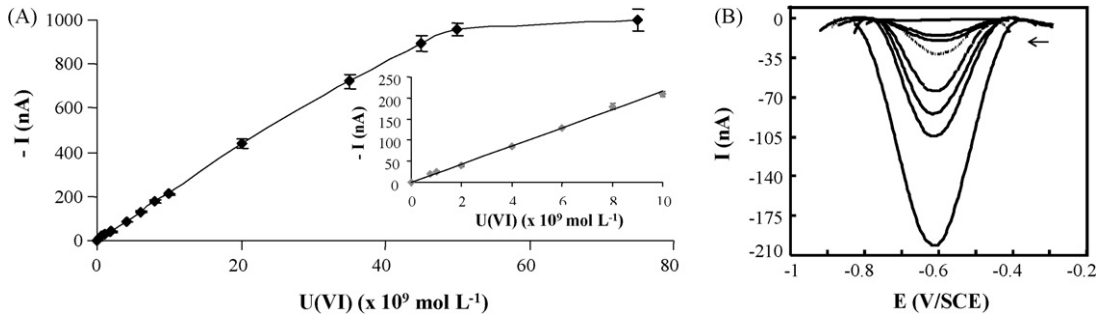


Fig. 6. (A) 4-CP-SPEs U(VI) calibration curve obtained in CH_3COONH_4. (B) SWV voltammograms for U(VI) 0, 8.5×10^{-10}, 10^{-9}, 2×10^{-9}, 4×10^{-9}, 8×10^{-9}, 10^{-8} mol L^{-1} (adsorption time: 15 min; SWV—pulse: 25 mV, step: 4 mV, frequency: 100 Hz).

The calibration plot was found to be linear over the range 8.5×10^{-10} to 5×10^{-8} mol L^{-1}. LOD 7×10^{-10} mol L^{-1}, and LOQ 2×10^{-9} mol L^{-1} were calculated statistically from Norme AFNOR [45]. These performances appeared superior to those obtained with carbon-based electrodes (LOD $\geq 10^{-9}$ mol L^{-1} [16,17]) and reached those obtained with metallic-coated electrodes [18–21] (LOD $\geq 10^{-10}$ mol L^{-1}). In comparison with metallic-coated electrodes (Bi, Pb or Hg-based electrodes), 4-CP-SPEs are non-pollutant. As uranium natural concentrations in water range from 2×10^{-9} to 10^{-8} mol L^{-1} [8,9], electrodes appeared adequate to quantify U(VI) in environmental samples.

3.5.2. Repeatability and reproducibility

Repeatability was verified with repetitive analyses of U(VI) 3.5×10^{-8} mol L^{-1} with single sensor. Well shaped voltammograms were obtained for all experiments; relative standard deviation was 7% after 25 analyses, indicating 4-CP-SPEs can be reusable.

Reproducibility between 4-CP-SPEs was evaluated by performing a series of U(VI) calibration curves with 16 electrodes coming from two different plates on which eight electrodes were printed. Calibration curves were based on two replicates of four concentration levels from 0 to 3.5×10^{-8} mol L^{-1}. Average sensitivity was 21 ± 2 A/(mol L^{-1}). Such performances reach those obtained with usually used SPEs [35,37,39,40], demonstrating the convenience of 4-CP-SPEs.

3.6. Di-oxygen influence

Because removal of O_2 is not suitable for on site analysis, 4-CP-SPEs sensitivity was compared for SWV measurements carried out with or without deoxygenating. Voltammetric responses obtained for U(VI) 3.5×10^{-8} mol L^{-1} in the presence of oxygen showed no loss of sensitivity compared to those obtained in absence of oxygen. In accordance with Brett et al. [46] and Wojciechowski and Balcerzak [47], SWV leads to minimize background oxygen reduction for fast scans. Analyses can thus be performed without deoxygenating during all the procedure, which constitutes a great advantage for on site measurements.

3.7. Natural water sample

4-CP-SPEs performances being proved, experiments were conducted in a certified estuarine water (pH 1.6, salinity 15) which composition was (10^{-9} mol L^{-1}): U(VI) 6.6; Cu 2.4 ± 0.2; Cd 0.42 ± 0.03; Pb 0.040 ± 0.007; Zn 3.05 ± 0.60. The measurement of the total uranium concentration was performed using a conventional approach, sample acidification and UV irradiation [48]. Estuarine water sample was UV digested and adjusted to pH 7 with appropriate amount of CH_3COONH_4 and NaOH. Results $(5.8 \pm 0.2) \times 10^{-9}$ mol L^{-1} were in agreement with those given by ICP-MS comparative analyses $(6.1 \pm 0.2) \times 10^{-9}$ mol L^{-1}, demonstrating the 4-CP-SPEs reliability for U(VI) analysis in natural water samples.

4. Conclusion

These novel and easy to realise 4-carboxyphenyl-grafted screen-printed electrodes (4-CP-SPEs) which have demonstrated their ability for Cu(II) analysis [35], present high performances for U(VI) trace analysis. Electrodes were able to detect and quantify U(VI) as low as 7×10^{-10} and 2×10^{-9} mol L^{-1}. No significant interference of Cd(II), Zn(II) or Pb(II) was established. In the presence of copper, standard addition method can be performed to quantify

U(VI) in natural water samples. It is worth noting that work is in progress to increase electrodes selectivity. The possibility of non-deoxygenating the samples was clearly demonstrated. 4-CP-SPEs were successfully used for trace U(VI) analysis in estuarine water. In comparison with electrodes described in the literature, 4-CP-SPEs appear as the best compromise between reliability, sensibility and environmental compatibility for U(VI) trace analysis in water samples.

Acknowledgments

Authors would like to thank CNRS for his financial support of post-doc and T. Advocat, C. Ferry and A. Juery (DEN/DANS/DPC/SECR) for their collaboration.

References

[1] J.L. Domingo, Reprod. Toxicol. 15 (2001) 603.
[2] S.C. Sheppard, M.I. Sheppard, M.O. Gallerand, B. Sanipelli, J. Environ. Radioact. 79 (2005) 55.
[3] N.A. El-Maali, D.A. El-Hady, Electroanalysis 11 (1999) 201.
[4] J. Wang, Analyst 119 (1994) 763.
[5] P. Metilda, K. Prasad, R. Kala, J.M. Gladis, T. Prasada Rao, G.R.K. Naidu, Anal. Chim. Acta 582 (2007) 147.
[6] A. Becker, H. Tobias, Z. Porat, D. Mandler, J. Electroanal. Chem. 621 (2008) 214.
[7] C.J. Evans, G.P. Nicholson, Sens. Actuator B 105 (2005) 204.
[8] G. Michard, Equilibres chimiques dans les eaux naturelles, Publisud, Paris, 1989.
[9] J. Gaillardet, J. Viers, B. Dupré, Trace elements in river waters, in: J.I. Drever (Ed.), Surface and Ground Water, Weathering, and Soils, vol. 5, in: H.D. Holland, K.K. Turekian (Eds.), Treatise on Geochemistry, Elsevier-Pergamon, Oxford, 2003, pp. 225–272.
[10] C.M.G. van den Berg, M. Nimmo, Anal. Chem. 59 (1987) 924.
[11] K.W. Cha, C.H. Park, S.H. Park, Talanta 52 (2000) 983.
[12] M.B.R. Bastos, J.C. Moreira, P.A.M. Farias, Anal. Chim. Acta 408 (2000) 83.
[13] O.A. Farghaly, M.A. Ghandour, Talanta 49 (1999) 31.
[14] J. Wang, R. Setiadji, Anal. Chim. Acta 264 (1992) 205.
[15] M.B. Gholivand, H. Rashidi Nassab, H. Fazeli, Talanta 65 (2005) 62.
[16] J. Wang, J. Lu, D.D. Larson, K. Olsen, Electroanalysis 7 (1995) 247.
[17] A. Nozad Golikand, M. Asgari, M. Ghannadi Maragheh, E. Lohrasbi, J. Appl. Electrochem. 39 (2009) 65.
[18] R. Piech, B. Baś, W.W. Kubiak, Electroanalysis 19 (2007) 2342.
[19] M. Korolczuk, K. Tyszczuk, M. Grabarczyk, Talanta 72 (2007) 957.
[20] G. Kefala, A. Economou, A. Voulgaropoulos, Electroanalysis 18 (2006) 223.
[21] J. Wang, J. Wang, B. Tian, M. Jiang, Anal. Chem. 69 (1997) 1657.
[22] G. Liu, T. Bocking, J.J. Gooding, J. Electroanal. Chem. 600 (2007) 335.
[23] A. Adenier, N. Barré, E. Cabet-Deliry, A. Chaussé, S. Griveau, F. Mercier, J. Pinson, C. Vautrin-Ul, Surf. Sci. 600 (2006) 4801.
[24] A. Adenier, E. Cabet-Deliry, A. Chaussé, S. Griveau, F. Mercier, J. Pinson, C. Vautrin-Ul, Chem. Mater. 17 (2005) 491.
[25] J. Pinson, F. Podvorica, Chem. Soc. Rev. 34 (2005) 429.
[26] M.C. Bernard, A. Chausse, E. Cabet-Deliry, M.M. Chehimi, J. Pinson, F. Podvorica, C. Vautrin-Ul, Chem. Mater. 15 (2003) 3450.
[27] A. Chaussé, M.M. Chehimi, N. Karsi, J. Pinson, F. Podvorica, C. Vautrin-Ul, Chem. Mater. 14 (2002) 392.
[28] T. Itoh, R.L. McCreery, J. Am. Chem. Soc. 124 (2002) 10894.
[29] A.J. Downard, M.J. Prince, Langmuir 17 (2001) 5581.
[30] J.K. Kariuki, M.T. McDermott, Langmuir 17 (2001) 5947.
[31] A.J. Downard, Electroanalysis 12 (2000) 1085.
[32] A.J. Downard, Langmuir 16 (2000) 9680.
[33] J.K. Kariuki, M.T. McDermott, Langmuir 15 (1999) 6534.
[34] C. Saby, B. Ortiz, G.Y. Champagne, D. Bélanger, Langmuir 13 (1997) 6803.
[35] S. Betelu, C. Vautrin-Ul, A. Chaussé, Electrochem. Commun. 11 (2009) 383.
[36] S. Griveau, D. Mercier, C. Vautrin-Ul, A. Chaussé, Electrochem. Commun. 9 (2007) 2768.
[37] C. Parat, S. Betelu, L. Authier, M. Potin-Gautier, Anal. Chim. Acta 14–19 (2006) 573.
[38] J. Haccoun, C. Vautrin-Ul, A. Chaussé, A. Adenier, Prog. Org. Coatings 63 (2008) 18.
[39] S. Betelu, C. Parat, N. Petrucciani, L. Authier, A. Castetbon, M. Potin-Gautier, Electroanalysis 19 (2007) 399.
[40] C. Parat, L. Authier, S. Betelu, N. Petrucciani, M. Potin-Gautier, Electroanalysis 19 (2007) 403.
[41] E.L. Shock, C.M. Koretsky, Geochim. Cosmochim. Acta 59 (1995) 1497.
[42] M. Delamar, R. Hitmi, J. Pinson, J.M. Saveant, J. Am. Chem. Soc. 114 (1992) 5883.
[43] B. Ortiz, C. Saby, G.Y. Champagne, D. Bélanger, J. Electroanal. Chem. 455 (1998) 75.
[44] M. Pandurangappa, N.S. Lawrence, R.G. Compton, Analyst 127 (2002) 1568.
[45] Norme, AFNOR: XP T90-210, December 1999.
[46] C.M.A. Brett, M.B. Quinaz Garcia, J.L.F.C. Lima, Electroanalysis 8 (1996) 1169.
[47] M. Wojciechowski, J. Balcerzak, Anal. Chem. 62 (1990) 1325.
[48] J. Buffle, M.L. Tercier-Waeber, Trends Anal. Chem. 24 (2005) 172.

Talanta 80 (2009) 377–384

Contents lists available at ScienceDirect

Talanta

journal homepage: www.elsevier.com/locate/talanta

Evaluation of the environmental contamination at an abandoned mining site using multivariate statistical techniques—The Rodalquilar (Southern Spain) mining district

M.G. Bagur[a,*], S. Morales[b], M. López-Chicano[c]

[a] Department of Analytical Chemistry, Faculty of Sciences, Avda. Fuentenueva, University of Granada, E-18071, Granada, Spain
[b] Department of Mineralogy and Petrology and Instituto Andaluz de Ciencias de la Tierra (University of Granada-CSIC), Faculty of Sciences, Avda. Fuentenueva, University of Granada, E-18071, Granada, Spain
[c] Department of Geodynamic, Faculty of Sciences, Avda. Fuentenueva, University of Granada, E-18071, Granada, Spain

ARTICLE INFO

Article history:
Received 22 April 2009
Received in revised form 26 June 2009
Accepted 30 June 2009
Available online 8 July 2009

Keywords:
Environmental contamination
Heavy metals
Water samples
Box–Cox transformation
Pattern recognition methods
Rodalquilar mining district

ABSTRACT

Unsupervised and supervised pattern recognition techniques such as hierarchical cluster analysis, principal component analysis, factor analysis and linear discriminant analysis have been applied to water samples recollected in Rodalquilar mining district (Southern Spain) in order to identify different sources of environmental pollution caused by the abandoned mining industry. The effect of the mining activity on waters was monitored determining the concentration of eleven elements (Mn, Ba, Co, Cu, Zn, As, Cd, Sb, Hg, Au and Pb) by inductively coupled plasma mass spectrometry (ICP-MS). The Box–Cox transformation has been used to transform the data set in normal form in order to minimize the non-normal distribution of the geochemical data. The environmental impact is affected mainly by the mining activity developed in the zone, the acid drainage and finally by the chemical treatment used for the benefit of gold.

© 2009 Elsevier B.V. All rights reserved.

1. Introduction

Metals as gold, lead, zinc, copper, etc. have been exploited from immemorial time. Naturally, these elements appear mainly associated to sulphur as part of sulphides, which constitute a minimal proportion of the host rocks. As consequence, their extraction generates important volume of dumps waste, which in contact with air and rainwater could cause acid drainage. In addition, with the extractive activity of mines exploiting metallic minerals, it is frequent to find mineral processing plants focused to obtain mineral concentrate. These plants could also product tailing impoundments. Then, during different processes involved in the extraction and in mineral processing to obtain metals, several products (rocks, metals, chemical products, polluted/unpolluted water,. . .) can be overturned to environment, being these facts, the presence of waste dump and tailing impoundments, a potential inconvenience for environment. Among other environmental impacts, they can be the source for possible contamination of ground waters (turbidity, changes in pH, increasing of dissolved toxic metals, acid mine drainage, etc.). In addition, acid drainage dissolves sulphide and could liberate other elements present in sulphides as trace elements (Cd, Co, Ni, etc.). These metals could also be dissolved and transported in water. Fortunately, environmental policies are increasingly restrictive and the overturned must be produced in a controlled and supervised way.

In the particular case of Rodalquilar mining district (Almería, Southern Spain), the target of the mine activity was mainly the gold, but other metals (Cu, Pb, Zn,. . .) have also been mining [1]. Gold mineralizations occur in outcrops with low ore/barren host rock ratio (e.g., the usual values of ore/host rock ratio for gold are in the range of part per million). Therefore the mining process originates big volumes of dumps waste. In addition, as gold (and other metals) does not appear frequently in nature as native elements, but as part of ore minerals, it is necessary to use some extraction methods, typically amalgamation with mercury or cyanidation [2]. Material from which gold was separated, mixed with residue of chemical products used during extraction processes, was overturned in tailing impoundment being potential sources of contamination.

The use of unsupervised and supervised pattern recognition techniques provide several avenues for exploratory assessment of water quality sets and grouping of water qualities [3–5]. These techniques make it possible to extract information from analytical parameters, allowing (a) to verify associations among variables,

* Corresponding author. Tel.: +34 958243327; fax: +34 958243328.
E-mail addresses: mgbagur@ugr.es (M.G. Bagur), smorales@ugr.es (S. Morales), mlopezc@ugr.es (M. López-Chicano).

0039-9140/$ – see front matter © 2009 Elsevier B.V. All rights reserved.
doi:10.1016/j.talanta.2009.06.075

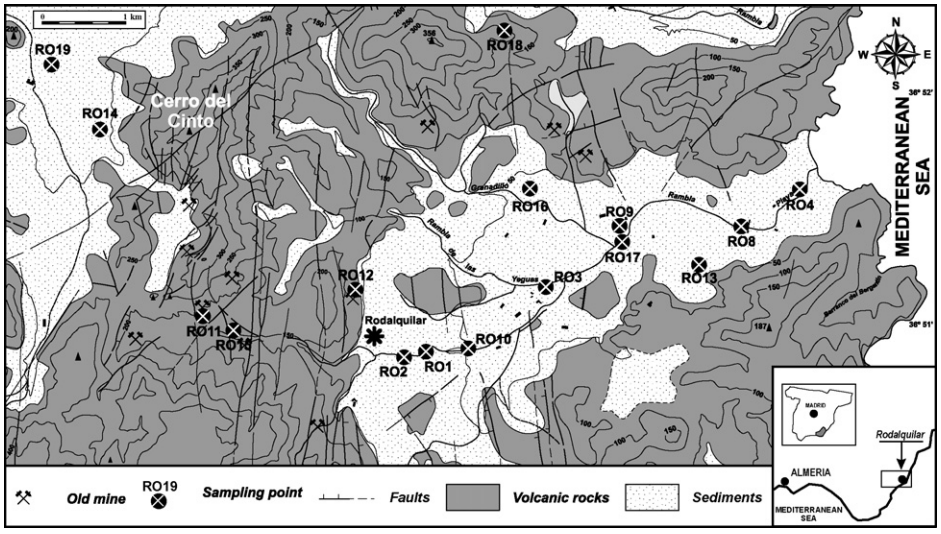


Fig. 1. Location of sampling points on Rodalquilar mining district.

(b) to group or to clusters samples (objects) with respect to comparable chemical descriptors, and (c) to search multivariate data classification on the basis of known class membership of those objects.

In this paper, a data matrix is subjected to different pattern recognition techniques to extract the information about the similarities or dissimilarities between sampling sites, to group the mining area waters in clusters, to identify the important discriminant variables, to classify them in order to evaluate the environmental contamination which could affect in the Rodalquilar mining district.

2. Materials and methods

2.1. Study area

The Rodalquilar gold mining district (Almería, SE Spain) [1] is now an abandoned mining area in which different types of metallic mineralizations appear related with volcanic rocks. In general, mineralizations are quartz veins with different metals (Pb–Zn–Cu–Ag–Au), usually in the form of sulphides or native elements. The area (Fig. 1) is characterized by the presence of small hills of different volcanic materials, often fractured, surrounded in the lower areas of porous sediments. These structures allow the movement of surface waters as well as a permeable behaviour of the rocks, so much by percolation through sediments and also movement through fractures. In the area, some small rivers or streams descend from volcanic rocks (topographically higher than sediments) until the sea crossing the sediments. They received locally the name of "ramblas". Due to the arid climate of the area, watercourses have a particular behaviour: normally there is very little water in the rivers, getting even to be dry, and, occasionally, coinciding with episodes of strong rains, watercourses reach high levels producing avenues and overflows.

From an extractive point of view, this zone has been mining for metals more or less continuously since mid-nineteenth century until 1990 [2], with a maximum between 1943 and 1966, when the mining activity stopped. In the zone, Au was the main exploited ore, but other minor metals (Pb, Ag,. . .) were also mining. The method of benefit of the gold changed throughout the time, from the initial stages of amalgamation with Hg *in situ* or close to mine entrance (until 1930), up to a process with cyanidation tanks (1930–1970, approx.) or using batch leaching (1973–1990). As consequence of this activity, in the zone it is possible to find numerous products with remains of the mining exploitation: dumps, tailings impoundments, two great tailing disposals, situated in the east zone (from cyanidation tanks process) and in the western part (from batch leaching process), etc. (Fig. 1).

In order to study the effect of this mining activity on waters, a field campaign was carried out for sampling. Bearing in mind the zone is quite arid (average annual temperature 18.5 °C, average annual precipitation 150 mm [6]), it was quite difficult to obtain water samples. Nevertheless, there were inspected nineteen points of sampling. Of them, it was impossible to take samples in three cases, whereas sixteen cases turned out to be effective for sampling (see location in Fig. 1 and description in Table 1). These cases reflect diverse activities or phenomena related to the water and cover a wide range: one sample proceeding from a water well, five samples from drill holes, three samples from waterwheel, one sample of a coastal lagoon, one sample of a little pool at foot of a pile of mine waste, one from the nowadays accumulated rainfall in a empty dam used formerly for process with batch leaching of cyanidation, one sample from a domestic cistern, two samples from windlassed wells, and finally one sample from a spring (known locally like "El Granadillo"). These waters have diverse uses: domestic use (although they are not consumed like drink water), irrigation or rural use, ecological (wetland maintenance). In other cases they are waters without use, which in some occasions they have had a former domestic use (even probably like drink water), for irrigation and livestock consumption.

2.2. Monitored parameters and analytical methods

Sampling, preservation and transportation of the water samples to the laboratory were as standard methods [7]. The monitored parameters were the concentrations of Mn, Ba, Co, Cu, Zn, As, Cd, Sb, Hg, Au and Pb. They have been selected according the mineralogy of the zone as possible contamination indicators. The analysis of the samples was done by ICP-MS, the instrument used was a PerkinElmer Sciex-Elan 5000 ICP-mass spectrometer (PerkinElmer, Überlingen, Germany) equipped with quartz torch, nickel sampler and skimmer cones, a peristaltic pump (maintaining a 1 mL min^{-1}) sample uptake rate), a cross-flow type pneumatic nebulizer and a double pass Scott-type spray chamber. Operating conditions are summarized in Table 2. The results obtained expressed as arithmetic means of three replicate of each determination are summarized in Table 3.

Table 1
Sampling points on the Rodalquilar mining district, Southern Spain.

Sample	Brief description	Use
RO-1	Windlassed dug shaft	Without use. Old use for domestic and livestock consumption
RO-2	Domestic cistern	Domestic use, not drinking
RO-3	Well drilled with electric pump	Domestic use in hotel, not drinking
RO-4	Coastal lagoon at the end of the watercourse	Ecological use. Wetland maintenance
RO-8	Excavated well for waterwheel	Without use. Old use for domestic, irrigation and livestock supply
RO-9	Excavated well for waterwheel	Without use. Old use for domestic, irrigation and livestock supply
RO-10	Well drilled with electric pump	Use for irrigation
RO-11	Little pool "at foot" of a pile of mine waste	Without use
RO-12	Well close to installations for gold recovery processes	Use for irrigation. Old public supply of Rodalquilar
RO-13	Well drilled with electric pump with a close irrigation storage reservoir	Use for irrigation
RO-14	Nowadays accumulated rainfall in a empty dam used formerly for process with batch leaching of cyanidation	Without use
RO-15	Excavated well close to a gully	Without use. Old use for domestic consumption
RO-16	Excavated well for waterwheel	Rural use
RO-17	Well drilled with electric pump	Use for domestic, irrigation and livestock supply
RO-18	"El Granadillo" spring	Use for irrigation
RO-19	Windlassed excavated well	Without use. Old use for domestic, irrigation and livestock supply

2.3. Chemical reagents and standards

All ICP-MS standards were prepared from ICP single element standard solutions (Merck, Darmstadt, Germany) after appropriate dilution with 10% HNO_3. For calibration, two sets of multielement standards containing all the analytes of interest at five levels concentrations were prepared using Rhodium as internal standard (based on repeatability variation of the measurements).

HNO_3 acid used (Merck) was analytical grade. All solutions were prepared using Milli-Q ultra pure water (18.2 MΩ cm^{-1}). All the plastic and glassware were cleaned by soaking in dilute HNO_3 and then rinsed with ultra pure water prior to analysis.

2.4. Data treatment and multivariate statistical methods

Assuming environmental data show in general a spatial dependence not normally distributed and they are subject to many potential sources of error involved in sampling, sample preparation and analysis, i.e. detection limit problems, precision–concentration relationship (values are less precise at very low and very high concentrations), and data outliers (some samples with unusually high concentrations) the standardized values of skewness and kurtosis were determined [8]. The statistical analysis of data showed that all of them are not normally distributed and are skewed (the standardized skewness and kurtosis estimated varied from 2.05 to 6.53 and from 0.55 to 13.06, respectively). The Kolmogorov–Smirnov test was used to check the data fit to a normal distribution the test concluded that not all the variables were normally distributed with a 95% confidence interval. This fact made us to study the matrix of the data in detail, observing four anomalous sampling points (RO-04, RO-08, RO-11 and RO-14), in which the values of certain concentrations were excessively high and inconsistent in relation with the other points. These points could be considered different to the rest of sampling points, so they were rejected for this study. Concretely, RO-04 corresponds to a seasonal lagoon, located inside the watercourse, developed in periods of desiccation of the watercourse. This lagoon has around 40–50 m in length and is placed at the end of the watercourse. Thus, the anomalous high values of metals can be considered as a combination of two factors: (i) its location, which could favour the gathering of metals through the crossed materials, and (ii) the local concentration of metals transported in the water, due to its accumulation in the lagoon from evaporation processes of immobilized waters. RO-08 belongs to a deserted waterwheel near the previous one, where filtration processes from the mentioned lagoon are recognized; RO-11 corresponds to a sample of water taken in a little pool located on a pile foot of the mine waste, and subsequently the sample is loaded in metals coming from the leaching of this dump; RO-14 also corresponds to a sample of rainwater, which was accumulated seasonally in a empty dam. This empty dam was used in the last period of the mining operations, for processing with batch leaching of cyanidation.

Table 2
ICP-MS operating conditions.

RF power (W)	1000
Plasma argon (L min^{-1})	15
Nebulizer flow (L min^{-1})	0.9–1
Nebulizer	Cross-flow
Data acquisition	Peak hop transit
Resolution	Normal
Dwell time (ms)	50
Number of replicates	3

The statistical analysis of the remained data showed that, once again, all of them were not normally distributed and were skewed (the standardized skewness and kurtosis estimated varied from 0.22 to 4.89 and from −1.13 to 8.46, respectively). Box–Cox transformation was used to transform the data set into normal form [2,9–11]. The transformation procedure was designed to determine an optimal transformation for Y to fit a linear regression model:

$$W = \beta_0 + \beta_1 X + \varepsilon \quad (1)$$

where W is the transformed variable, X is the regression variable, β_0 and β_1 are the unknown parameters and ε is the error. The dependent variable W is related to Y according to equation:

$$W = 1 + \frac{(Y+\lambda_2)^{\lambda_1} - 1}{\lambda_1 G^{\lambda_1 - 1}} \quad \text{for } \lambda_1 \neq 0 \quad (2)$$

$$W = G\ \ln(Y+\lambda_2) \quad \text{for } \lambda_1 = 0 \quad (3)$$

where λ_1 and λ_2 are the transformation parameters and G is the geometric mean of $Y+\lambda_2$. The optimal transformation is the one that minimizes the mean squared error (MSE) for W. In all the cases, the normality tests used (Kolmogorov–Smirnov; Shapiro–Wilks and skewness score) showed that Box–Cox transformation applied to the analysed metals concentration in the 12 sampling point selected, adjusts them to a normal distribution for a 90% confidence (Table 4). In which, the mean squared error (MSE) diminished in each case when the applied transformations was depicted.

To study the correlation structure between normalized variables the Spearman rank-order correlations (Spearman R coefficient) were used, due the samples are less sensitive to outliers than the Pearson coefficients.

In all the cases, the statistical treatment of the data was performed using with Statgraphich Plus for windows v. 5.1 [12].

Table 3
Mean values of analytes concentrations in the water samples analysed.

Sample	Analyte[a]										
	Mn	Ba	Co	Cu	Zn	As	Cd	Sb	Hg	Au	Pb
RO01											
Mean value	**19.84**	**32.03**	**0.42**	**3.2**	**93.21**	**18.46**	**0.82**	**2.96**	**0.59**	**0.16**	**0.47**
% RSD ($n = 3$)	7.22	8.99	0.68	10.55	6.90	9.28	8.44	2.70	3.84	1.30	4.69
RO02											
Mean value	**14.88**	**6.18**	**0.16**	**16.0**	**105.97**	**21.26**	**0.53**	**0.15**	**0.59**	**0.20**	**0.19**
% RSD ($n = 3$)	5.15	1.79	3.46	2.41	2.31	8.72	3.08	8.18	2.69	9.92	9.68
RO03											
Mean value	**551.97**	**28.58**	**0.25**	**7.78**	**46.74**	**8.97**	**0.13**	**0.10**	**4.75**	**0.31**	<DL
% RSD ($n = 3$)	7.52	5.32	1.36	8.16	7.21	7.27	6.49	4.19	4.09	10.48	
RO04											
Mean value	**135.63**	**129.81**	**1.96**	**80.23**	**493.95**	**304.59**	**2.77**	**3.63**	**0.51**	**1.20**	**1.69**
% RSD ($n = 3$)	3.20	3.07	5.98	7.49	6.48	5.72	2.08	8.11	0.14	1.99	1.72
RO08											
Mean value	**552.44**	**152.19**	**1.10**	**7.02**	**110.21**	**1081.62**	**0.52**	**4.32**	**0.51**	**0.67**	**0.48**
% RSD ($n = 3$)	3.47	1.92	0.48	1.82	9.65	0.88	5.93	2.28	5.80	8.72	4.66
RO09											
Mean value	**10.11**	**49.76**	**0.51**	**6.35**	**55.58**	**11.83**	**0.25**	**0.23**	**2.19**	**0.19**	**0.08**
% RSD ($n = 3$)	1.89	5.53	10.56	9.04	2.48	11.20	2.51	2.02	3.05		11.02
RO10											
Mean value	**39.41**	**24.50**	**0.35**	**9.08**	**16.21**	**11.13**	**0.18**	**1.86**	**1.79**	**0.06**	**0.49**
% RSD ($n = 3$)	11.90	8.10	1.02	9.31	7.17	11.82	6.84	10.16	1.25	7.44	8.88
RO11											
Mean value	**4731.12**	**2.20**	**5155.50**	**10617.88**	**50270.00**	**834.61**	**990.57**	**1.56**	**7.51**	**0.69**	**1.19**
% RSD ($n = 3$)	10.83	3.83	11.36	10.82	10.89	7.90	5.04	1.18	2.86	5.60	5.55
RO12											
Mean value	**1019.87**	**8.92**	**4.67**	**14.24**	**797.24**	**17.17**	**3.32**	**0.78**	**2.91**	**0.09**	**3.15**
% RSD ($n = 3$)	5.14	1.24	9.64	3.87	3.22	3.96	5.45	15.64	2.10	2.49	2.82
RO13											
Mean value	**223.98**	**48.29**	**149.09**	**22.80**	**203.29**	**81.34**	**9.092**	**2.60**	**0.27**	**0.20**	**2.70**
% RSD ($n = 3$)	1.45	3.06	4.4	0.93	5.40	9.11	10.20	6.95	4.33	5.99	4.47
RO14											
Mean value	**31.03**	**16.90**	**0.48**	**117.09**	**13.99**	**1990.91**	**0.15**	**78.52**	**4.33**	**0.69**	**0.75**
% RSD ($n = 3$)	5.81	4.19	6.16	2.29	2.53	3.63	0.47	1.71	5.42	3.98	9.15
RO15											
Mean value	**91.42**	**22.32**	**1.40**	**39.59**	**301.45**	**10.67**	**3.40**	**0.25**	**0.28**	**0.06**	**1.96**
% RSD ($n = 3$)	9.36	7.44	1.19	5.70	5.10	5.39	2.83	4.14	2.30	4.42	2.53
RO16											
Mean value	**7.33**	**12.17**	**0.07**	**3.83**	**9.67**	**3.24**	**0.05**	**0.14**	**0.50**	<DL	**0.86**
% RSD ($n = 3$)	5.86	4.08	0.95	10.05	2.34	9.27	7.08	7.42	2.05		9.85
RO17											
Mean value	**19.33**	**6.11**	**0.46**	**10.04**	**48.32**	**10.77**	**0.13**	**0.15**	**1.14**	**0.13**	**0.61**
% RSD ($n = 3$)	2.40	8.69	8.37	10.38	6.31	4.11	5.75	5.74	7.64	10.26	6.04
RO18											
Mean value	**7.32**	**49.66**	**0.22**	**8.07**	**34.40**	**15.22**	**0.17**	**0.13**	**0.62**	<DL	<DL
% RSD ($n = 3$)	1.60	6.51	4.41	2.99	7.29	6.25	6.18	8.76	12.02		
RO19											
Mean value	**968.13**	**54.57**	**0.61**	**2.16**	**22.16**	**19.52**	**0.03**	**0.09**	**0.66**	**0.02**	**0.15**
% RSD ($n = 3$)	0.85	1.31	9.06	7.56	3.46	3.41	5.18	9.83	8.34	16.24	7.24

[a] Concentration expressed as ng/mL (ppb).

2.5. Unsupervised pattern recognition methods

2.5.1. Cluster analysis

Hierarchical agglomerative CA [13] was performed on the normalized data set by means of Manhattan (city-block) distance as similarity measurement and Ward's method as the amalgamation rule. These criterion have been selected with two objectives: (i) to find at each stage those two clusters whose merger gives the minimum increase in the total within group error sum of squares (Ward objective) and, (ii) to dampen the effect of outliers bearing in mind using city-block distance the average differences across dimensions are not squared. The distance between two monitoring point locations using Manhattan distance is given by [12]

$$d(x, y) = \sum_{i=1}^{n} \left| x_i - y_i \right| \tag{4}$$

where $d(x, y)$ denotes the city block distance, i.e. the average difference across dimensions, between two objects represented by x_i, y_i and n the dimensional space of the variables. This distance is a special case of Minkowski distance with $\lambda = 1$ (taxicab geometry).

Table 4
Box–Cox transformation applied to the analytes concentrations in the water samples analysed.

Variable	Univariate non-normal distribution	Optimun Box–Cox transformation	% MSE[a] diminished	Normality test for the transformation
Mn	Standardized skewness: 2.13 Typified kurtosis: 0.56	λ_1: 0.21 λ_2: 0.0 G = 57.70	92.53	$\chi_{\text{lack of fit}}$ = 6.33 (p = 0.501)[b] $W_{(\text{Shapiro–Wilks})}$ = 0.905 (p = 0.175) Z_{score}(asymmetry) = 0.26 (p = 0.790)
Ba	Standardized skewness: 0.23 Typified kurtosis: −1.13	λ_1: 0.46 λ_2: 0.0 G = 22.10	10.11	$\chi_{\text{lack of fit}}$ = 11.33 (p = 0.124) $W_{(\text{Shapiro–Wilks})}$ = 0.9 (p = 0.170) Z_{score}(asymmetry) = 0.24 (p = 0.811)
Co	Standardized skewness: 4.89 Typified kurtosis: 8.47	λ_1: −0.35 λ_2: 0.0 G = 0.70	99.94	$\chi_{\text{lack of fit}}$ = 4.67 (p = 0.700) $W_{(\text{Shapiro–Wilks})}$ = 0.98 (p = 0.920) Z_{score}(asymmetry) = 0.15 (p = 0.880)
Cu	Standardized skewness: 2.99 Typified kurtosis: 3.41	λ_1: −0.43 λ_2: 0.0 G = 10.36	60.13	$\chi_{\text{lack of fit}}$ = 6.33 (p = 0.501) $W_{(\text{Shapiro–Wilks})}$ = 0.97 (p = 0.890) Z_{score}(asymmetry) = 0.04 (p = 0.970)
Zn	Standardized skewness: 3.78 Typified kurtosis: 5.41	λ_1: −0.15 λ_2: 0.0 G = 66.32	86.33	$\chi_{\text{lack of fit}}$ = 8 (p = 0.333) $W_{(\text{Shapiro–Wilks})}$ = 0.99 (p = 0.990) Z_{score}(asymmetry) = 0.06 (p = 0.950)
As	Standardized skewness: 4.34 Typified kurtosis: 7.14	λ_1: −0.14 λ_2: 0.0 G = 14.30	73.2	$\chi_{\text{lack of fit}}$ = 8 (p = 0.333) $W_{(\text{Shapiro–Wilks})}$ = 0.89 (p = 0.130) Z_{score}(asymmetry) = −0.065 (p = 0.950)
Cd	Standardized skewness: 2.09 Typified kurtosis: 0.51	λ_1: −0.08 λ_2: 0.0 G = 0.37	83.1	$\chi_{\text{lack of fit}}$ = 3 (p = 0.89) $W_{(\text{Shapiro–Wilks})}$ = 0.95 (p = 0.604) Z_{score}(asymmetry) = 0.06 (p = 0.952)
Hg	Standardized skewness: 2.41 Typified kurtosis: 1.93	λ_1: −0.25 λ_2: 0.0 G = 0.91	63.52	$\chi_{\text{lack of fit}}$ = 11.33 (p = 0.124) $W_{(\text{Shapiro–Wilks})}$ = 0.944 (p = 0.52) Z_{score}(asymmetry) = 0.107 (p = 0.91)
Au	Standardized skewness: 0.77 Typified kurtosis: −0.23	λ_1: 0.48 λ_2: 0.0 G = 0.06	28.54	$\chi_{\text{lack of fit}}$ = 4.67 (p = 0.700) $W_{(\text{Shapiro–Wilks})}$ = 0.96 (p = 0.78) Z_{score}(asymmetry) = −0.4 (p = 0.69)
Sb	Standardized skewness: 2.00 Typified kurtosis: 0.31	λ_1: −0.48 λ_2: 0.0 G = 0.34	85.73	$\chi_{\text{lack of fit}}$ = 6.33 (p = 0.501) $W_{(\text{Shapiro–Wilks})}$ = 0.89 (p = 0.145) Z_{score}(asymmetry) = 0.43 (p = 0.670)
Pb	Standardized skewness: 1.88 Typified kurtosis: 0.28	λ_1: 0.24 λ_2: 0.0 G = 0.28	76.44	$\chi_{\text{lack of fit}}$ = 6.33 (p = 0.501) $W_{(\text{Shapiro–Wilks})}$ = 0.97 (p = 0.880) Z_{score}(asymmetry) = −0.17 (p = 0.860)

[a] Mean squared error.
[b] p value for probability level of 90%.

Cluster analysis was applied to the Box–Cox transformed monitoring (normalized) matrix data set in order to observe the natural grouping of the sampling sites (spatial variability) which are spread over the tested/sampling region.

2.5.2. Principal component (PCA)

PCA is a projection method that reduces the dimensionality in a data matrix while retaining most signification information. The technique transforms the variables into a smaller set of independent (uncorrelated) variables (principal components) without losing much information [13,14]. A reliable model requires a number of PCs, so that over 75% of the total variation can be explained.

As in CA, PCA was applied to the Box–Cox transformed matrix data set in order to display the structure of the normalized data using information about latent relationship within them.

2.5.3. Factor analysis (FA)

FA is a technique of data reduction that examines the interdependence of variables providing knowledge of the underlying structure of data. In this case the factorization type used was principal components which supposes that all the variability (variance) of the data corresponds exclusively to common factors. The orthogonal rotation of the axis defined by PCA, and obtained maximizing (Varimax rotation) produces new groups of variables called varifactors (VFs), which usually group the studied variables in accordance with common features which can include unobservable, hypothetical and/or latent variables [15].

2.6. Supervised pattern recognition methods

These methods permit to obtain suitable classification rules assuming a prior knowledge of the number of groups as well as the group membership of each sample.

2.6.1. Linear discriminant analysis (LDA)

It builds up a discriminant function for each group operating on raw data. The discriminant function has the form:

$$f(G_i) = k_i + \sum_{j=1}^{n} w_{ij} p_{ij} \quad (5)$$

where "i" is the number of groups (G_i), k_i is the constant inherent to each group, n is the number of variables/parameters used to classify a set of data into a given group, w_{ij} the weight coefficient, assigned by LDA to a given selected parameter (p_{ij}). As well as, in the model the classification functions associated to each group established can be used to determine to which group each object/case most likely belongs. Each function allows computing classification scores for each case for each group, by applying the equation:

$$S_i = c_i + \sum_{j=1}^{m} w_{im} x_j \quad (6)$$

where S_i is the resultant classification score, "i" denotes the respective group; c_i is a constant for the i^{th} group, n is the number of

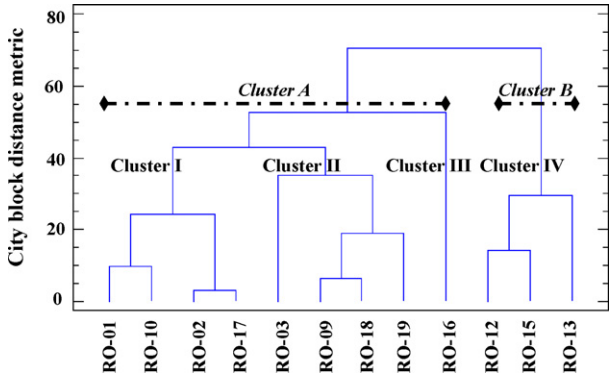


Fig. 2. Dendogram of clustering of sampling according its tributaries using Ward's method and city block distance method.

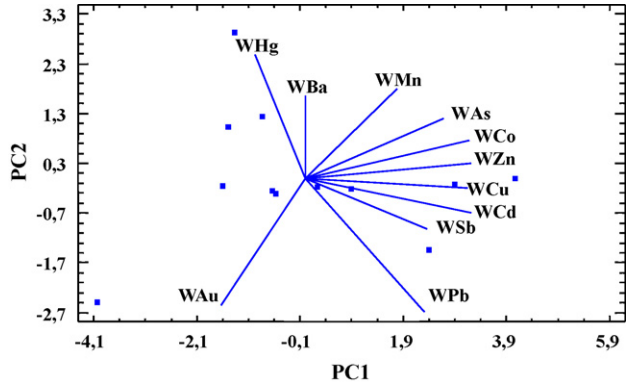


Fig. 3. Principal components biplot on the first and the second PCs.

variables/parameters used to classify the set of data, w_{ij} the weight for the j^{th} variable in the computation of classification score for the i^{th} group; x_j is the observed value for the respective object/case for the j^{th} variable. Subsequently the classification of a case is made assigning it to the group for which it has the highest classification score [16]. In this study LDAs were performed on the Box–Cox transformed monitoring data.

3. Results and discussion

3.1. Spatial similarity and site grouping

The Dendogram of the location pattern resulting from CA (Manhattan distance and Ward's agglomerative method) of normalized data set is represented in Fig. 2. It shows that the sampling points could be initially grouped into two main clusters, Cluster A and Cluster B. Nevertheless, in our opinion it would be possible to distinguish among "*four secondary*" clusters labelled as Clusters I to IV in Fig. 2. Cluster I formed by the sampling points RO-01, RO-10, RO-02 and RO-17, Cluster II by RO-03, RO-09, RO-18 and RO-19. Cluster III formed by RO-16, it is not exactly a cluster due it is an ungrouped sampling point but considered by us as "a group" bearing in mind that would represent a sample with a metals different from the rest. Finally Cluster IV formed by RO-12, RO-15 and RO-13. The grouping of these classes varies with the significance level. It is clearly seen that Cluster II is characterized by the biggest city-block distance (high significance clustering).

The geographical and geological locations of sampling points permit us to associate each group with a possible type of influence of mining activity over the water. Cluster I, Cluster II and Cluster III (Cluster A) all constituted by waters sampled from porous sediments with different metal concentrations. Clusters I and II are located next to main metallic mining area. Cluster I is constituted by samples from sediments located in a watercourse around mineralized areas. This watercourse collected the drained water from mineralized volcanic rocks and canalised downstream. Watercourse is limited by rocks less impermeable that difficult the free movement of waters and, subsequently, these rocks favour a higher accumulation of metals. Cluster II are samples from sediments located in watercourses collecting waters from mineralized areas but with an open circulation that permit dilution of metal concentrations. Cluster III represents a sample located in sediment from a watercourse located in a position less favourable to receive waters coming from main mineralizing areas. In addition, this sampling point is located at the foot of volcanic rock with non-metallic mining activity (alums). Cluster IV (Cluster B) are samples located inside the volcanic rocks and, consequently, conditioned by the regional background of metals characteristic for these volcanic rocks containing the mineralized veins.

3.2. Data structure determination and source identification

Principal component analysis was applied to the normalized data set (11 variables) to compare the composition patterns between the analysed water samples and to identify the factors that influence each one. On the basis of eigenvalues >1 criterion three principal components were developed explaining about 75, 94% of the total variance. This facilitated the explanation, of all the sampling points for the Box–Cox transformed original 11 variables, in a reduced space by three sets of calculated principal components (PCs). Fig. 3 shows the biplot corresponding to our data explaining. The analysis of the data shows that: (a) PC1, which explain the 46.19% of the total variance, is mainly influenced by the normalized concentration of Cd, Zn, Co, Cu, As, Sb and Pb, (b) PC2 (16.33% of the total variance) is influenced by Hg, Mn, Ba, Au and Pb, and (c) PC3 is influenced by Hg, Zn, Cd, As and Ba. This last component explains the 13.43% of the total variance.

The scatter plot (Fig. 4) for the first two calculated factors on the basis on PCA shows four groups of waters in complete accordance with CA. It can be seen also that Group I (Cluster I) is characterized by low values from PC1 and PC2; Group II by negative values for PC1 and high positive values for PC2; Group III by highest negative values for PC1 and PC2, and finally Group IV characterized by high positive values for PC1 and negative values for PC2.

The rotation Varimax of the axes defined by PCs (FA) explains again the 75, 94% of the variability of the normalized data but it partially modifies the weight of the normalized variables in the three varifactors obtained (Fig. 5). It can be seen that: (a) VF1 is mainly influenced by the normalized concentration of Cd, Zn, Cu, Pb, Co and As, (b) VF2 is influenced by Ba, As, Co, and Mn, and (c) VF3

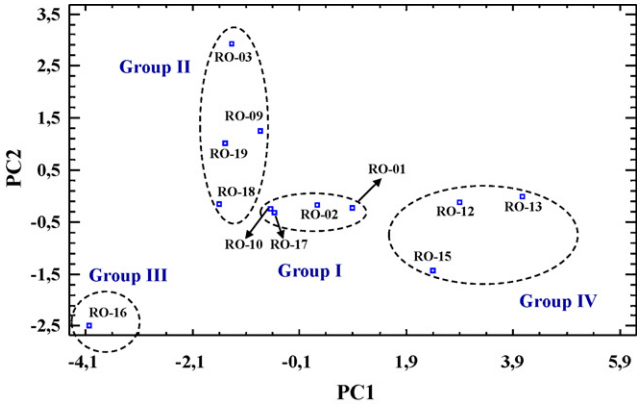


Fig. 4. Scatter plot of the principal components scores for Box–Cox transformed monitoring data.

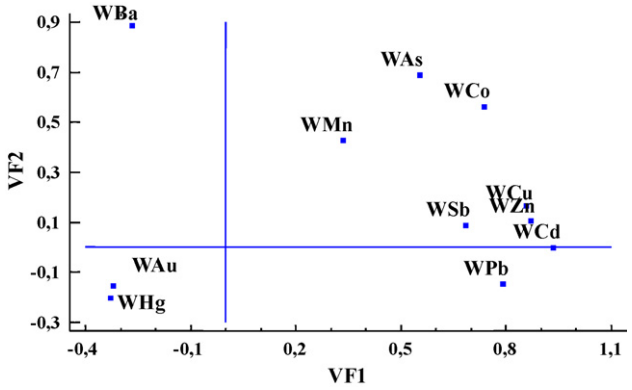


Fig. 5. Varifactors biplot on the first and the second VFs.

is influenced by Hg and Au. The scatter plot (Fig. 6) for the first two varifactor calculated, confirms the existence of two main groups of water samples (denoted initially in CA by Clusters A and B) although do no permit distinguish so clearly the four groups confirmed by PCA.

On the other hand, the Varimax rotation of the axes permits us to assign an influence of the mining activities happened in the studied area over the water samples analysed. Then, VF1 is determined by the behaviour of a group of elements that could come from the metallic mineralization extracted during different stages of the mining in the area. According with bibliography [17], different types of metallic mineralization appears in the area. In this sense, although the mining activity was focused mainly in gold, the veins are bearing of different metallic minerals associated with this element. In short, galena –PbS–, sphalerite –ZnS–, and copper sulphides (mainly chalcopyrite –$CuFeS_2$– and occasionally bornite –Cu_5FeS_4– or digenite –Cu_9S_5–), and also Cu-bearing sulphosalts (tennantite –$(Cu,Fe)_{12}As_4S_{13}$– or tetrahedrite –$(Cu,Fe)_{12}Sb_4S_{13}$–) have been described in the area. Also, it is very possible that this varifactor is not only reflecting the primary phases, but also reflects a group of alteration minerals formed by transformation of the primary phases – supergenic transformation or by way of acid mining drainage – e.g., copper carbonates, azurite –$Cu_3(CO_3)_2(OH)_2$–, malachite –$Cu_2(CO_3)(OH)_2$–, Pb-carbonates, cerusite –$PbCO_3$–, Pb-sulphates, anglesite –$PbSO_4$–, etc., more soluble in water even that the corresponding primary sulphides. The presence of Cd in this component can be justified by the frequent association in the nature of Cd as minor element in the sphalerite structure, being substituted Zn by Cd. That is why this varifactor could reflect the environmental pollution attributable to the mining activity of the zone.

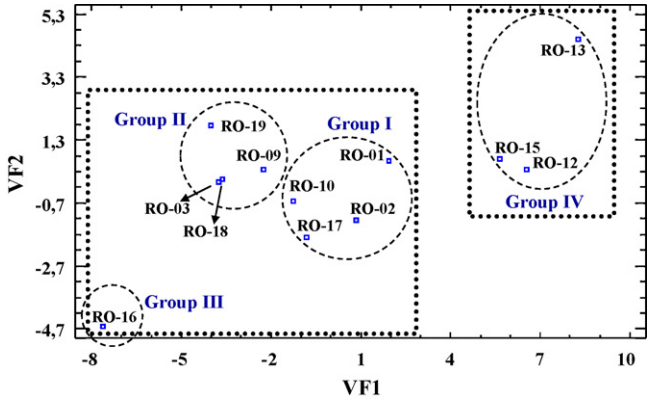


Fig. 6. Scatter plot of the varifactors loadings for Box–Cox transformed monitoring data.

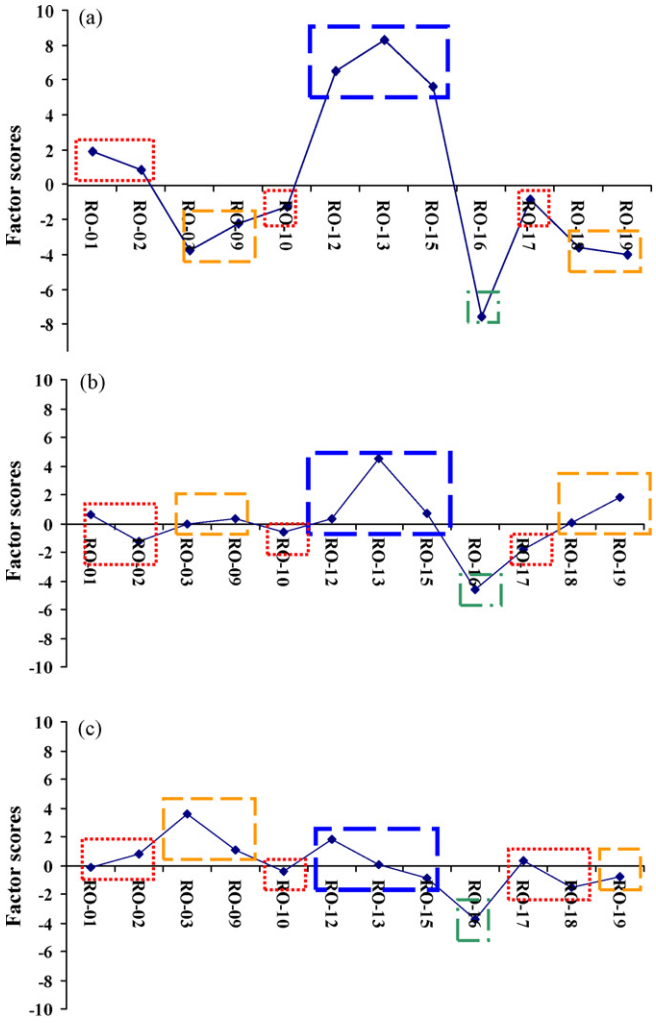


Fig. 7. Factor scores versus sampling points: (a) VF1; (b) VF2; (c) VF3.

VF2 can be justified by the action of acid drainage, as consequent of interaction between sulphides present in mineralized rocks and water. This drainage could mobilize not only Ba but also other metals present in host rock and mineralization (e.g., As, Co and Mn).

VF3 could be clearly anthropogenic, since the amalgamation with Hg was used like method of benefit of Au in different times. This process also could partially amalgamate a portion of Zn and, therefore, the associated with Cd as trace element in the sphalerite.

Fig. 7 shows the representation of the varifactor scores versus sampling location, which may be used in order to identify the pollution sources. In this sense, high scores correspond to high influence of the varifactor on the sampling site. In general the majority of water analysed samples presents an elevated metallic contribution as consequence of the mining activity of the zone. Varifactors 1 and 2 are crucial in water samples included in Group IV, which would indicate that these waters are more affected by the mining activity (Varifactor 1) and the effect of the acid drainage (Varifactor 2). Both varifactors are also important in Group II. Finally, Varifactor 3 is crucial in some water samples belonging to Group II, concretely those that are located in the influence area of the eastern tailing disposal. This fact support an idea about where spread the environmental impact originated by the chemical treatment which the mineral was submitted for the recovery of gold. This varifactor also presents an important load in a well located in the main mining area (RO-12).

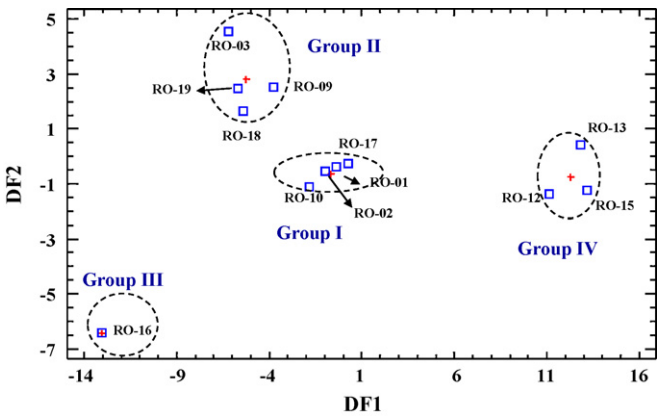


Fig. 8. Representation of the discriminant functions found from analyte concentrations for water samples analysed.

Finally, in order to verify the natural grouping obtained by unsupervised pattern recognition techniques (CA, PCA and FA), a LDA was performed. The discriminant functions were calculated considering the Box–Cox normalized metal concentrations that mainly affect to VF1 (mining activity). On these bases, i.e. WCd, WZn, WCu, WPb, WCo and WAs, three discriminant, orthogonal functions were calculated from which DF1 and DF2 contribute 99.65% to the total discriminant power, although only DF1 is statistically significant with a *p*-value of 0.008 for 95% confidence interval. Fig. 8 shows the scatterplot of monitoring samples locations using the two discriminant functions as axes. It can be observed that these two discriminant functions distinguish perfectly among the four natural groups defined by the non-supervised pattern recognition methods used previously. In this case, Group I is characterized by DF1 and DF2 values close to zero, Group II is characterized by negative DF1 values and highest positive DF2 values, Group III is characterized by the highest negative values for DF1 and DF2 and finally Group IV characterized by the highest positive values for DF1. However, to establish the model as a valid general one, more data should be included in the study.

4. Conclusions

The use of Box–Cox transformation to adjust the geochemical data set (eleven metal(loids) concentrations closely related to sulphide mining activity) in normal distribution form has been shown as a very useful tool to study the environmental impact of mining activity of water samples of the Rodalquilar mining district. Unsupervised pattern recognition methods, as hierarchical CA, grouped samples into four clusters closely related with the geographical and geological locations of the water samples analysed. Also, PCA and FA have allowed confirming this fact. Particularly, FA has been allowed to identify different sources of environmental pollution caused by the abandoned mining industry, i.e., (1) the mining activity developed in the zone—metal(loids) strongly associated with sulphides, (2) the acid drainage, and, (3) the chemical treatment used for the benefit of gold. Finally, the use of LDA as a supervised pattern recognition method has permit to obtain a discriminant function considering the elements associated with the mining activity, which generates classification scores from those it is possible to confirm the natural grouping obtained previously.

Acknowledgments

This work was supported by the project of excellence P05-RNM-0736 (Consejería de Innovación, Ciencia y Empresa, Junta de Andalucía, Spain).

References

[1] A. Arribas, Mapa Geológico del Distrito Minero de Rodalquilar (Almería), Instituto Tecnológico Geominero de España, 1993.
[2] F. Hernandez Ortíz, www.usc.es/estaticos/congresos/histec05/b16_hernandez_or tiz.pdf, 2005.
[3] P.R. Kannel, S. Lee, S.R. Kanel, S.P. Khan, Anal. Chim. Acta 582 (2007) 390.
[4] T. Kowalkowsky, R. Zbytnieweski, J. Szpejna, B. Buszewski, Water Res. 40 (2006) 744.
[5] K.P. Singh, A. Malik, S. Sinha, Anal. Chim. Acta 538 (2005) 355.
[6] www.inm.es.
[7] American Public Health Association, Standard Methods for the Examination of Water and Wastewater, 20th ed., APHA, Washington, DC, 1998.
[8] C. Reinmann, P. Filzmoser, Environ. Geol. 39 (9) (1999) 1001.
[9] G.E.P. Box, D.R. Cox, J. Roy. Stat. Assoc. B26 (1964) 211.
[10] M. Meloun, J. Militký, M. Forina, Chemometrics for analytical chemistry. In PC-Aided Statistical Data Analysis, vol.1, Ellis Horwood, Chichester, 1992.
[11] M. Meloun, M. Sáňka, P. Němec, Soňa Křítiková, K. Kupka, Environ. Poll. 137 (2005) 273.
[12] Statgraphich Plus for Windows v. 5.1, Statistical Graphics System by Statistical Graphic Corp., STSC Inc, Rockville, MD, 1994–2000, http://www.statgraphics.com.
[13] D.A. Wunderlin, M. Díaz, M.M.V. Ame, S.F. Pesce, A.C. Hued, M. Bistoni, Water Res. 35 (2001) 2881.
[14] K.P. Singh, A. Malik, D. Mohan, S. Sinha, Water Res. 38 (2004) 3980.
[15] C. Pérez-López, Estadística Práctica con STATGRAPHICS®, Pearson Education S.A., Madrid, 2002.
[16] http://www.statsoft.com/textbook/stathome.html?stdiscan.html&1.
[17] M.A. Fernandez, J. Gröbner, Mineralogía, in: A. Arribas Jr., F. Hernández, M.A. Fernández, J. Gröbner, G. Leal (Eds.), Rodalquilar. El oro del Cabo del Ágata. Bocamina, 2005, pp. 12–79.

Talanta 80 (2009) 385–389

Contents lists available at ScienceDirect

Talanta

journal homepage: www.elsevier.com/locate/talanta

Towards a hybrid micro-device allowing the selective detection of hydrogen fluoride vapours in a complex mixture

Jean-Baptiste Sanchez*, Franck Berger

LCPR-AC, UMR CEA E4, Université de Franche-Comté, Bâtiment Propédeutique, 16 route de Gray, 25030 Besançon Cedex, France

ARTICLE INFO

Article history:
Received 9 March 2009
Received in revised form 29 June 2009
Accepted 1 July 2009
Available online 9 July 2009

Keywords:
GC micro-column
SnO_2
Hydrogen fluoride
VOC

ABSTRACT

In this work, design and fabrication of a hybrid micro-device dedicated to the selective detection of hydrogen fluoride vapours is reported. This micro-device is composed by a gas chromatographic micro-column positioned in front of a tin dioxide-based gas sensor. The efficiency of this hybrid micro-system regarding to reproducibility and reversibility for various HF concentrations was investigated. The influence of the HF concentration on the electrical responses of the sensor is also studied. The experimental results show that this hybrid micro-system is efficient since it allows the elution, separation and detection of hydrogen fluoride at a low temperature close to ambient.

© 2009 Elsevier B.V. All rights reserved.

1. Introduction

Nowadays, there are increasing demands for the control of toxic chemical compounds in the atmosphere. Environmental standards have made it imperative to develop adequate methods for the analysis of gaseous substances or substances that can be converted to the gaseous state. Among the dangerous chemical compounds for both human and the environment, one can distinguish hydrogen fluoride (HF). HF is involved in a very specific chemical process and can be released in the atmosphere. In this case, it is essential to be able to quickly analyse this molecule in order to prevent possible risks of pollution. Some studies have dealt with the detection of hydrogen fluoride. In the literature, we can find works based on optical method to evaluate and quantify the presence of hydrogen fluoride [1,2]. Moreover, some studies have dealt with the use of chemical gas sensors for the detection of HF. In particular, we notice the use of field-effect gas sensor [3–5], surface acoustic wave sensor [6] or cantilever [7]. At the present time, only two studies have dealt with the use of tin oxide-based gas sensor for the detection of this chemical compound [8,9]. The detection limit of these sensors range from 30 ppm to 50 ppb. Generally, these works allowed to detect this molecule in a controlled atmosphere i.e. without any interfering gases in the surrounding atmosphere of the chemical gas sensor. It is evident that this experimental configuration does not correspond to the real conditions (complex atmosphere).

Since the development of semi-conductor gas sensors, various studies have shown that these chemical gas sensors are sensitive to a wide range of chemical compounds (O_3, CH_4, Volatil Organic Compounds (VOC), H_2, ...). Previous studies completed in our laboratory have shown that SnO_2-based gas sensor is very sensitive to hydrogen fluoride in a controlled atmosphere [9]. The detection limit is a low 50 ppb. Nevertheless, the typical lack of intrinsic selectivity of these chemical gas sensors does not allow using these devices in the presence of interfering pollutants (one or more). In order to detect hydrogen fluoride vapours in a complex atmosphere we developed a gas chromatographic micro-column (GC micro-column) which was positioned in front of the SnO_2-based gas sensor. This GC micro-column was developed in a clean room using the standard techniques of silicon's micro-machining.

The present paper provides a comprehensive description of the performances of a hybrid micro-system for the selective detection of hydrogen fluoride in a VOC complex sample. First a brief description of the GC micro-column used in this experiment will be exposed. Then results obtained for the detection of hydrogen fluoride in presence of some VOC will be presented in order to specify the advantage induced by the coupling of a GC micro-column and a semi-conductor gas sensor (SnO_2).

2. Experimental

2.1. Design and realization of the gas chromatographic micro-column

In this section, we present briefly the miniaturised fluidic device developed in our laboratory in order to eluate and separate chem-

* Corresponding author. Tel.: +33 3 81 66 65 06.
E-mail address: jbsanche@univ-fcomte.fr (J.-B. Sanchez).

0039-9140/$ – see front matter © 2009 Elsevier B.V. All rights reserved.
doi:10.1016/j.talanta.2009.07.003

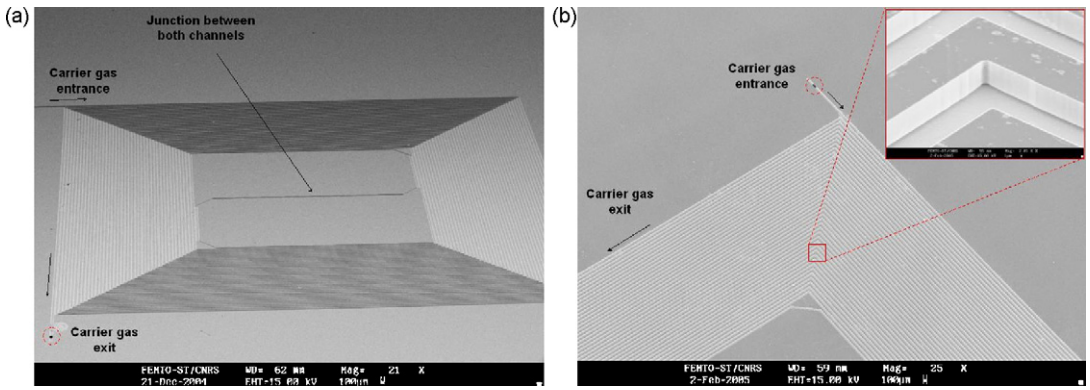


Fig. 1. SEM pictures of the etched micro-structure obtained after the step 1.

ical compounds from gas or vapour mixtures. More details in the manufacturing of this GC micro-column can be found in a previous research paper [10]. We dealt with a column about 2 m long, 50 μm wide and 50 μm deep. The geometry retained for this micro-structure is a rectangular spiral configured as two interlocking structures in order to reduce the final dimensions on the silicon wafer. Three principal steps were involved for the realization of the GC micro-column. The first step is the etching of the silicon substrate. Fig. 1 shows two SEM pictures of the etched micro-structure.

The second step consisted in the anodic bonding of a Pyrex wafer with the etched silicon structure to obtain the final three-dimensional micro-structure. Before this operation, a thin SiO_2 layer was deposited on the silicon substrate allowed the grafting of the future stationary phase. The last step concerned the filling of the GC micro-column with a specific stationary phase (cf. Fig. 2). The chemical formulation of the stationary phase has been obtained by mixing two metal-alkoxyde precursors: Tetraethoxysilane (TEOS) and 1H, 1H, 2H, 2H-perfluorooctyltriethoxysilane (F13-TEOS). The first precursor (TEOS) allowed the formation of a silica matrix grafted onto the internal walls of the GC micro-column. The second precursor (F13-TEOS) was used in particularly to functionalize the whole stationary phase. The principal interest to functionalize the stationary phase with fluorinated groups is to form a chemical compound with a composition identical to Teflon®. The Teflon® is well known for its chemical inertia with respect to HF.

2.2. Experimental set-up

In order to study the possibility of selective detection of HF vapours in a mixture, a special assembly was carried out. Fig. 3 shows the general architecture retained for the analysis of a gas mixture by coupling a GC micro-column with a SnO_2 gas sensor. In this approach, we used synthetic air as carrier gas (80% N_2, 20% O_2, free of moisture). Considering the very small inner volume of the GC micro-column, the volume of sample to be injected into the carrier gas must be very small. Then, the sampling was realized by a chromatographic injector equipped with a split device enabling a high dilution of the analytes before to reach the GC micro-column. For all the studies, we sampled liquid hydrogen fluoride (40%). The high temperature of the injector (250 °C) completely vapourized every chemical compounds that could be contained in the sample.

The separation step is obtained with the GC micro-column positioned into an oven in order to hold the GC micro-structure to a precise temperature. Each chromatographic analysis is carried out in isothermal mode. Previous studies completed in our laboratory have shown that using this gas chromatographic micro-column, best results in terms of separations of the chemical compounds, were obtained at temperature close to 30 °C [11]. The linear velocity of the carrier gas is an important experimental factor that controls the effectiveness of a chromatographic system. Using the chromatographic injector, the carrier gas flow rate in the GC micro-column directly depends on the inlet pressure of the carrier gas applied. Thus, an increase in the pressure imposed, induced an increase in the carrier gas flow rate. This experiment set-up deals with very low linear velocity of the carrier gas. For this experiment, we fixed the carrier gas flow rate at 0.25 mL × min^{-1} (4 bars). This value corresponds to the optimal velocity for the elution and separation of chemical compounds with this GC micro-column [12].

The last part of the experimental device concerns the detection unit. A SnO_2 gas sensor is positioned directly at the end of the GC micro-column and is used as a chromatographic detector. Tin oxide is an ntype semiconductor material, which at typical working temperatures ranging from 200 °C and 500 °C adsorbs oxygen from the surrounding atmosphere leading to an electron-depleted zone. Its

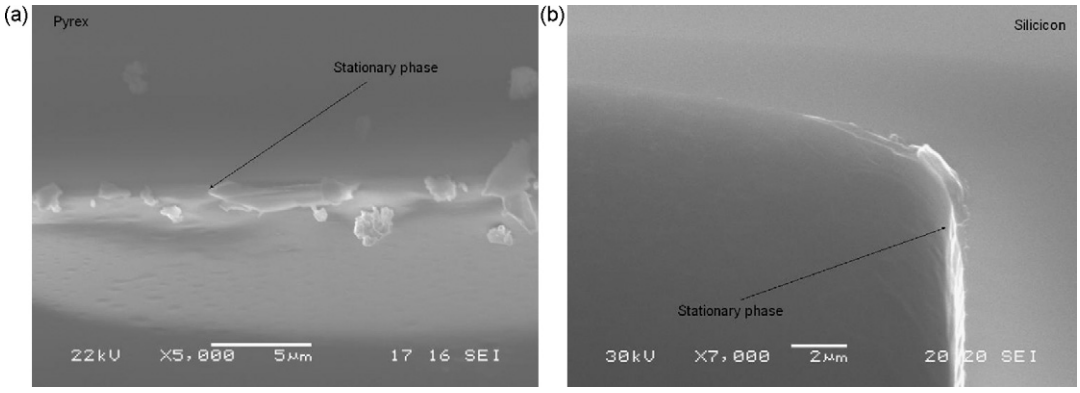


Fig. 2. SEM pictures of the GC micro-column cross section with the deposited stationary phase.

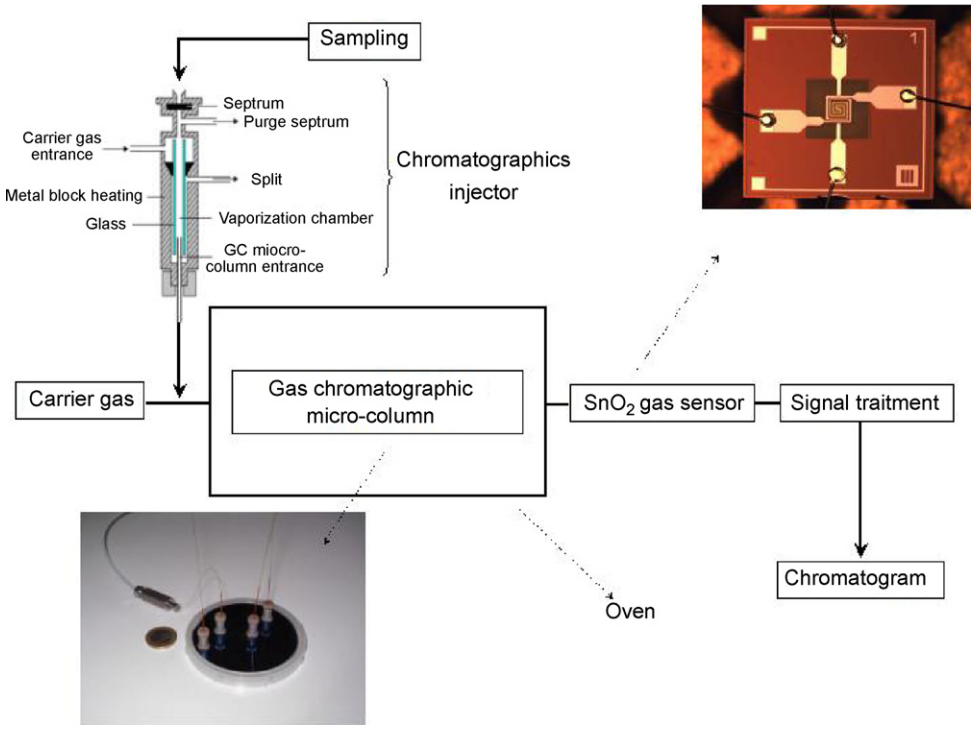


Fig. 3. General achitecture of the experimental set-up used.

electrical resistance decreases in the presence of reducing gases, which react with the pre-adsorbed oxygen leading to an increase in the electronic concentration. The measurement of the change in the resistive value of the sensitive layer due to the chemical reaction induced by gas adsorption serves as sensing signal. The electrical conductance variations of the layer (SnO_2) are connected both with the gas concentration and with the physical–chemical properties of the detected gas. The gas sensor used includes a semi-conducting metal oxide layer (SnO_2) and a silicon substrate with an integrated heater. Before conducting experiments, each sensor was exposed to constant pure air flow for 24 h (conditioning process). This 24 h protocol consists in a linear heating program of the sensitive layer (2.2 °C s^{-1}) for temperatures ranging between 25 °C and 500 °C. This process allowed for the desorption of pollutants chemical compounds adsorbed during the storage stage (organic compounds, water). Fig. 4 represents a 2-h sequence of the conditioning process of a tin dioxide-based gas sensor. We notice a rapid decrease and stabilisation of the gas sensor's conductance. In our

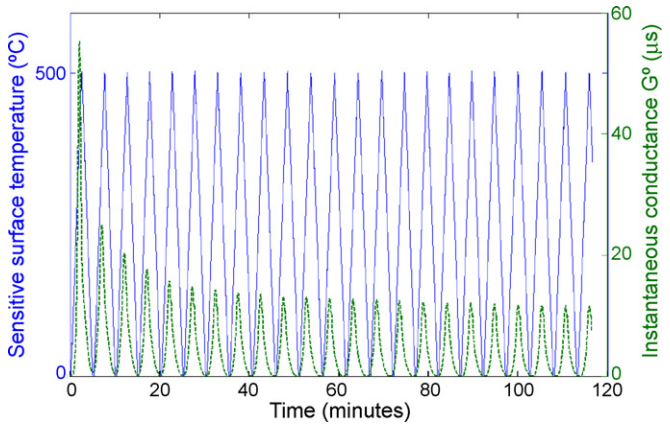


Fig. 4. A 2-hour stage of the conditioning process. Solid line : temperature of the sensitive layer, dash line : instantaneous conductance (µS).

experimental configuration (cf. Fig. 3), the effect of gases on the sensor's electrical properties is recorded by monitoring the variations in the sensor's instantaneous conductance versus time, for a temperature of the sensitive element (SnO_2) fixed at 500 °C [11–12].

3. Results and discussion

3.1. Elution of hydrogen fluoride

After having conditioned the gas sensor and fixed the various experimental parameters (column's temperature and inlet pressure of the carrier gas), one can study the elution and detection of HF with the hybrid micro-system. For this experiment, the sample was made from a hydrogen fluoride solution at 40% which is vapourized inside the injector before its migration in the GC micro-column.

Different dilutions with water have been realized in order to study the influence of the concentration in the sensor's electrical response. Fig. 5 summarized the main chromatograms obtained for the elution of such samples.

These results principally showed that the coupling between a chromatographic micro-column and a SnO_2-based gas sensor allows to first, eluate hydrogen fluoride and second, detect this chemical compound. Let us note two important points regarding these results:

- First, the retention time is very short (15 s) for this chemical compound.
- Second, the temperature of the GC micro-column (30 °C) is very low. This last point is very important particularly for the development of embarked devices.

From this graph, we noticed that the electrical responses of the gas sensor are directly dependant on the hydrogen fluoride concentrations. Higher concentrations give higher electrical responses, exactly like a chromatographic detector. Between each acquisition with the same gas sensor (i.e. for each concentration), no surface

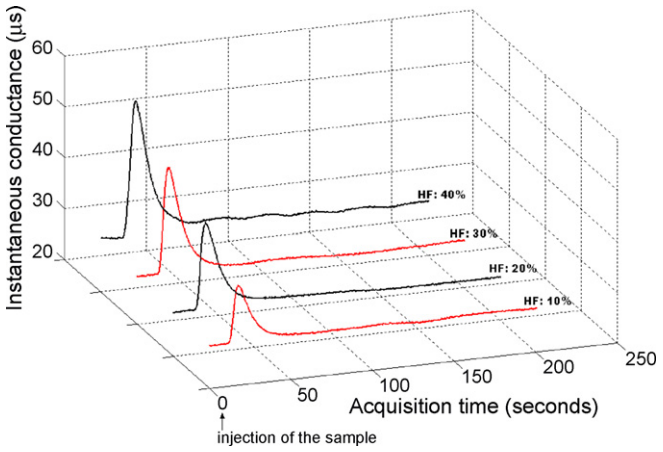


Fig. 5. Chromatograms showing the elution and detection of various hydrogen fluoride concentrations.

treatment of the sensitive layer was made. The sensor's sensitive surface is always maintained at 500 °C under an air flow. Let us specify however that the low temperature of the GC micro-column (30 °C) causes the recondensation of water present in the sample. Thus, water remains "trapped" ahead of the chromatographic micro-column and thus is not detected by the SnO_2 gas sensor. The sensor's electrical response will thus not be disturbed by the presence of water in the SnO_2 surrounding surface.

3.2. Comparison with classic GC

In order to underline the performance of the hybrid micro-system developed in our laboratory, we compared results obtained in the preliminary work completed with a commercial packed chromatographic column filled with a stationary phase which present the same chemical properties (Teflon® stationary phase) [11]. The packed column is 3 m long with a diameter equal to 1/8 in. Fig. 6 represents the hydrogen fluoride's elution peaks for each chromatographic column used (micro-column and packed column). For each experiment, sensor's temperature is equal to 500 °C and synthetic air carrier gas was used. Only the temperature and the linear velocity of the carrier gas of the chromatographic columns are different. For the packed column, the temperature is fixed at 100 °C with a carrier gas flow rate equal to 20 mL × min^{-1}. For the packed column, an injection loop was used to inject 300 µL of hydrogen fluoride at 9.91 ppm in air [11]. In comparison with the classical column for which working temperatures is about 100 °C (optimum condition

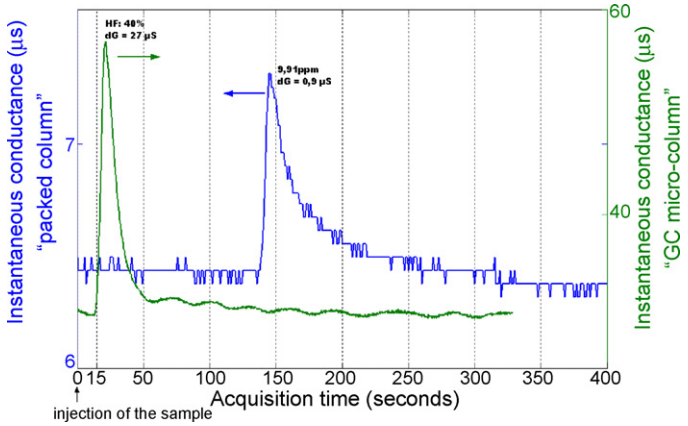


Fig. 6. Elution peaks of hydrogen fluoride from the GC micro-column and a packed column.

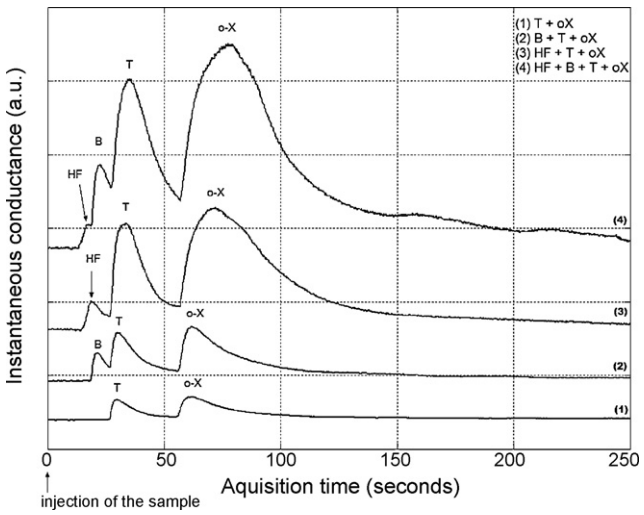


Fig. 7. Chromatograms of VOC mixture and hydrogen fluoride using the GC micro-column coupled with a tin oxide-based gas sensor.

of separation), our GC micro-column works at lower temperature (30 °C). At 30 °C, it is impossible to obtain elution peaks with the packed column. Moreover, the important result obtained with the use of this GC micro-column is the short analysis time for this chemical compound. Fifteen seconds for the GC micro-column against more than 2 min for the classic packed column.

3.3. Separation of hydrogen fluoride in a complex sample

For a complete study of our hybrid micro-system, we prepared various complex samples including volatile organic compounds and hydrogen fluoride. Pure toluene, ortho-xylene and benzene were used in this experimental section. First, samples consisted in an equivolumic mixture of liquid toluene, o-xylene and benzene. Chromatograms obtained when 0.1 µL of these solutions were injected in the chromatographic injector are represented in Fig. 7 (1 and 2). These chromatograms clearly show the presence of peaks, respectively corresponding to each chemical compounds injected ahead of the GC micro-column.

The retention time is the same for each chemical compound. Then, we studied samples constituted of an equivolumic mixture of liquid HF, toluene, o-xylene and benzene. The same volume as previously was injected ahead of the GC micro-column. Chromatograms in Fig. 7 (3 and 4) show the efficient elution and then the detection of the VOC's and hydrogen fluoride in a low isothermal mode (30 °C) for the micro-fluidic device. The first chemical compound emerging from the GC micro-column and detected is hydrogen fluoride. The retention time is, once again, very low for these chemical compounds. These chromatograms do not show any shift in the retention time for each chemical compounds analysed. With this experimental set-up, constituted a GC micro-column and a SnO_2 gas sensor, it is possible to obtain a highly selective gas sensor for various chemical compounds including hydrogen fluoride vapours.

4. Conclusion

The aim of this work was to validate the use of a GC micro-column positioned in front of a semi-conductor gas sensor for the selective detection of hydrogen fluoride vapours in a complex sample. The various tests conducted in this study showed a high selectivity and a good reproducibility in addition to a short response time. This hybrid micro-system provides rapid and discriminative analyses. In comparison with a packed chromatographic

column filled with a Teflon® stationary phase (operating temperature = 100 °C), the GC micro-column developed in this study presents best performances at lower temperature (30 °C). The next step of this study will consist of the development of a micro preconcentrator unit positioned in front of the GC micro-column in order to directly inject sample's vapours in the GC micro-column and determine the detection limit of the system for various pollutants.

Acknowledgement

This work was supported by the Commissariat à l'Energie Atomique Centre Valduc (France).

References

[1] S.E. Létant, M.J. Sailor, Adv. Mater. 12 (5) (2000) 355–359.
[2] J.G. Knowleset, J.H. Holloway, Talanta 13 (1966) 1219–1221.
[3] A. Vasiliev, W. Moritz, V. Fillipov, L. Bartholomaus, A. Terentjev, T. Gabusjan, Sens. Actuators B 49 (1998) 133–138.
[4] W. Moritz, S. Krause, A.A. Vasiliev, D.Y. Godovski, V.V. Malyshev, Sens. Actuators B 24–25 (1995) 194–196.
[5] W. Moritz, L. Bartholomaus, U. Roth, V. Filippov, A. Vasiliev, A. Terentjev, Anal. Chim. Acta 393 (1999) 49–57.
[6] V. Blondeau-Patissier, S. Ballandras, M.-H. Nadal, et al., Proceeding WCU, Paris, September 2003, pp. 7–10.
[7] J. Mertens, E. Finot, M.-H. Nadal, V. Eyraud, O. Heintz, E. Bourillot, Sens. Actuators B 99 (2004) 58–65.
[8] D.Y. Godovski, A.A. Vasiliev, E.V. Dorofeev, Sens. Actuators B 18–19 (1994) 483–485.
[9] J.-B. Sanchez, F. Berger, M. Fromm, M.-H. Nadal, V. Eyraud, Thin Solid Films 436 (2003) 132–136.
[10] J.-B. Sanchez, F. Berger, W. Daniau, P. Blind, M. Fromm, M.-H. Nadal, Sens. Actuators B 113 (2006) 1017–1024.
[11] J.-B. Sanchez, F. Berger, M. Fromm, M.-H. Nadal, Sens. Actuators B 106 (2004) 823–831.
[12] J.-B. Sanchez, F. Berger, M. Fromm, M.-H. Nadal, Sens. Actuators B 119 (2006) 227–233.

Talanta 80 (2009) 390–399

Contents lists available at ScienceDirect

Talanta

journal homepage: www.elsevier.com/locate/talanta

Short communication

Profiling ABA metabolites in *Nicotiana tabacum* L. leaves by ultra-performance liquid chromatography–electrospray tandem mass spectrometry

Veronika Turečková *[,1], Ondřej Novák [1], Miroslav Strnad

Laboratory of Growth Regulators, Palacký University & Institute of Experimental Botany ASCR, Šlechtitelů 11, CZ-783 71, Olomouc, Czech Republic

ARTICLE INFO

Article history:
Received 17 December 2008
Received in revised form 4 June 2009
Accepted 9 June 2009
Available online 17 June 2009

Keywords:
Abscisic acid
Ultra-performance liquid chromatography (UPLC)
Tandem mass spectrometry (MS/MS)

ABSTRACT

We have developed a simple method for extracting and purifying (+)-abscisic acid (ABA) and eight ABA metabolites – phaseic acid (PA), dihydrophaseic acid (DPA), neophaseic acid (neoPA), ABA-glucose ester (ABAGE), 7′-hydroxy-ABA (7′-OH-ABA), 9′-hydroxy-ABA (9′-OH-ABA), ABAaldehyde, and ABAalcohol – before analysis by a novel technique for these substances, ultra-performance liquid chromatography–electrospray ionisation tandem mass spectrometry (UPLC–ESI-MS/MS). The procedure includes addition of deuterium-labelled standards, extraction with methanol–water–acetic acid (10:89:1, v/v), simple purification by Oasis® HLB cartridges, rapid chromatographic separation by UPLC, and sensitive, accurate quantification by MS/MS in multiple reaction monitoring modes. The detection limits of the technique ranged between 0.1 and 1 pmol for ABAGE and ABA acids in negative ion mode, and 0.01–0.50 pmol for ABAGE, ABAaldehyde, ABAalcohol and the methylated acids in positive ion mode. The fast liquid chromatographic separation and analysis of ABA and its eight measured derivatives by UPLC–ESI-MS/MS provide rapid, accurate and robust quantification of most of the substances, and the low detection limits allow small amounts of tissue (1–5 mg) to be used in quantitative analysis. To demonstrate the potential of the technique, we isolated ABA and its metabolites from control and water-stressed tobacco leaf tissues then analysed them by UPLC–ESI-MS/MS. Only ABA, PA, DPA, neoPA, and ABAGE were detected in the samples. PA was the most abundant analyte (ca. 1000 pmol/g f.w.) in both the control and water-stressed tissues, followed by ABAGE and DPA, which were both present at levels ca. 5-fold lower. ABA levels were at least 100-fold lower than PA concentrations, but they increased following the water stress treatment, while ABAGE, PA, and DPA levels decreased. Overall, the technique offers substantial improvements over previously described methods, enabling the detailed, direct study of diverse ABA metabolites in small amounts of plant tissue.

© 2009 Elsevier B.V. All rights reserved.

1. Introduction

Abscisic acid (ABA) is an isoprenoid plant hormone that regulates embryonic development and physiological adaptation to various environmental stresses, including water deficiency, osmotic stress, and low temperature [1]. Hence, plant tissue ABA concentrations change under stress and during physiological processes [2].

In plants, ABA can be metabolised by three types of reaction: oxidation, conjugation, and reduction [3,4]. The major oxidative pathway of natural ABA [(+)-S-enantiomer] is through 8′hydroxylation, forming 8′-hydroxyABA, which in turn spontaneously isomerizes to phaseic acid (PA). PA can then be reduced to the major product dihydrophaseic acid (DPA), with minor amounts of *epi*-dihydrophaseic acid (*epi*-DPA). The minor oxidation pathway includes the formation of (+)-7′-hydroxy-ABA (7′-OH-ABA), while the minor reductive pathway produces the unstable ABA 1′,4′-diol [2,4]. A novel ABA 9′-hydroxylation pathway has also been reported [5], yielding the metabolites 9′-hydroxy ABA (9′-OH-ABA) and its cyclised product, neophaseic acid (neoPA). In addition, ABA and its metabolites may be conjugated with glucose, thereby forming corresponding glucose esters at C-1 (ABAGE) or glycosides at C-1′ or C-4′ [2,4]. Two new glucose conjugates, namely *epi*-DPA-β-D-glucoside and 8′-hydroxy-ABA-β-D-glucoside, have also been identified in avocado seeds [6]. Furthermore, a compound identified as 8′-oxoABA has been isolated from corn cell suspension cultures [7]. The isolation and characterization of several new ABA metabolites (8′-oxoDPA, 8′-oxoDPA-GS, 5′-hydroxy-8′-oxoDPA, and 5′-hydroxyDPA) in plums (*Prunus domestica* L.) have also been reported [8].

ABA and its metabolites can be relatively easily and sensitively analysed. For instance, ABA has been detected and quantified in plant tissues by diverse techniques [9], including

* Corresponding author. Tel.: +420 585634862; fax: +420 585634870.
E-mail address: hradeckav@post.cz (V. Turečková).
[1] These authors contributed equally to this work.

0039-9140/$ – see front matter © 2009 Elsevier B.V. All rights reserved.
doi:10.1016/j.talanta.2009.06.027

radioimmunoassays (RIA) [10–12], enzyme-linked immunosorbent assays (ELISA) [13,14], reversed-phase high performance liquid chromatography (HPLC) with ultraviolet (UV) detection [15–18], gas chromatography with electron capture detection (GC/ECD) [19,20], GC–mass spectrometry (GC–MS) in either selected ion monitoring (SIM) [21,22] or multiple ion monitoring (MIM) modes [23], and LC–ESI-MS via either direct quantification [24,25] or following several purification steps [26,27]. Its metabolites have also been analysed by several techniques (albeit much less frequently than ABA) including: HPLC/UV detection to determine PA and DPA [28,29]; GC/ECD for PA, DPA, *epi*-DPA and ABAGE [19,20], and the cited GC–MS and LC–MS modes for ABAGE [21–27]. However, there is still a need for a convenient, efficient purification procedure prior to their analysis. Purification approaches that have been commonly applied include liquid-phase extraction (LPE) [30], solid-phase extraction [31–34], and solid-phase microextraction [35]. A purification procedure involving use of immunoaffinity chromatography (IAC) prior to single ion monitoring by liquid chromatography electrospray ionisation–mass spectrometry (LC–ESI-MS) analysis has also been recently described [36]. All of these approaches, for both purification and subsequent analysis have some advantages, but also various limitations.

In addition, in recent years, HPLC–tandem mass spectrometry (HPLC–MS/MS) in multiple reaction monitoring mode (MRM) has become increasingly popular for analysing ABA and its metabolites, due to its selectivity and sensitivity. This approach has been used: to measure ABA in *Arabidopsis thaliana* leaves [37] and *Citrus reticulata* leaves and roots [38]; to monitor changes in levels of ABA metabolites during seed development and germination in *Brassica napus* siliques [32], lettuce seeds [31], Western white pine seeds [39,40] and Douglas fir seeds [41]; and to evaluate ABA's role in developmental switches in *Marsilea quadrifolia* [42]. An analytical protocol for quantifying ABA by LC–MS/MS, using non-exchangeable isotope-labelled ABA analogues as internal standards, has also been developed [43] and used to analyse metabolites in the ABA catabolic pathway [39,40,44]. Furthermore, new ultra-performance liquid chromatography (UPLC)-based methods for purifying ABA in plant extracts have been developed very recently [45,46], but no applications of UPLC for analysing ABA metabolites have been previously described.

Here we report the development of an approach (optimised using deuterated internal standards) for isolating, purifying, and measuring ABA and its metabolites (see Fig. 1 for the structures) by UPLC followed by ESI-MS/MS. The method yielded a 10-fold increase in throughput compared to conventional LC–MS analysis, reducing the total time of the analytical procedure for sample preparation and analysis of ABA and its metabolites to just a few hours, rather than days. Thus, the new technique appears to offer fast, highly sensitive, selective, and simultaneous profiling and quantification of ABA and its diverse metabolites in plant tissues.

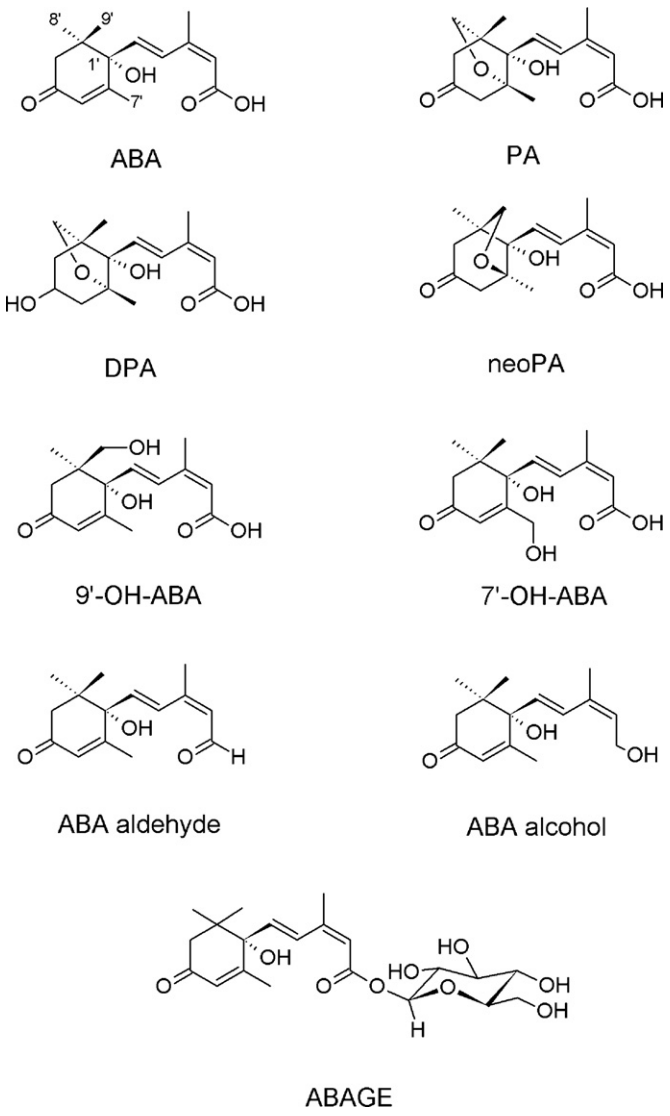


Fig. 1. The structures of ABA and its metabolites.

2. Experimental

2.1. Chemicals

(+)-*cis*,*trans*-ABA was obtained from Sigma (St. Louis, MO, USA); (−)-phaseic acid, (−)-dihydrophaseic acid, (±)-abscisylaldehyde, (±)-abscisylalcohol, (+)-neophaseic acid, (±)-7′-OH-ABA, (+)-9′-OH-ABA, $^{2}H_2$-ABAalcohol, $^{2}H_2$-ABAaldehyde, [(−)-7′,7′,7′-$^{2}H_3$-phaseic acid] (d_3-PA), [(−)-7′,7′,7′-$^{2}H_3$-dihydrophaseic acid] (d_3-DPA), [(−)-8′,8′,8′-$^{2}H_3$-neophaseic acid] (d_3-neoPA), [(+)-4,5,8′,8′,8′-$^{2}H_5$-ABAGE] (d_5-ABAGE), and [(−)-5,8′,8′,8′-$^{2}H_4$-7′-OH-ABA] (d_4-7′-OH-ABA) were kindly provided by Prof. S. Abrams (National Research Council, Saskatoon, Canada). (+)-*cis*,*trans*-ABA methyl ester (ABAMe) and (±)-abscisyl-β-D-glucosylester were generous gifts from Olchemim Ltd. (Czech Republic). Deuterium-labelled (+)-*cis*,*trans*-abscisic acid [(+)-3′,5′,5′,7′,7′,7′-$^{2}H_6$-ABA)] (d_6-(+)ABA) was synthesised using a previously described method [47]. Methanol (HPLC grade) and acetic acid were supplied by Sigma–Aldrich (St. Louis, MO, USA), formic acid by MERCK (Darmstadt, Germany), and Oasis® HLB cartridges (60 mg) by Waters (Milford, USA). The PBS buffer used contained 7.8 g $NaH_2PO_4{\cdot}2H_2O$ and 0.877 g NaCl per liter, adjusted to pH 7.2 using 0.1 M NaOH. Deionised (Milli-Q) water, obtained from a Simplicity 185 system (Millipore, Bedford, MA, USA), was used to prepare all aqueous solutions. The polyclonal antibody based immunoaffinity gel used for the IAC was prepared, used and stored as described previously [36].

2.2. Instrumentation

An Acquity UPLC™ System (Waters, Milford, MA, USA), including a Binary solvent manager, sample manager, and 2996 PDA detector, combined with a Micromass Quattro micro™ API mass spectrometer (Waters MS Technologies, Manchester, UK), was used to analyse ABA and its metabolites. All data acquired were processed using the QuanLynx™ module within the MassLynx™ software (version 4.1, Waters, Milford, MA, USA).

2.3. Biological material

Nicotiana tabacum L. plants were cultivated in a greenhouse at +20 °C under 12-h dark/12-h light cycles. Leaves were harvested from well-watered 8-week-old plants and corresponding plants from which water had been withheld for 4 days prior to sampling. The leaf samples were immediately frozen in liquid nitrogen after harvesting, and then stored at −80 °C until preparation.

2.4. Purification of ABA and its metabolites

The tobacco leaf tissues (1–50 mg f.w.) were powdered using a MM 301 vibration mill at a frequency of 30 Hz for 3 min (Retsch GmbH & Co. KG, Haan, Germany) after adding 3-mm tungsten carbide beads (Retsch GmbH & Co. KG, Haan, Germany). Samples were extracted for 1 h in 750 μL of ice-cold methanol/water/acetic acid (10/89/1, v/v) containing sodium diethyldithiocarbamate (400 $\mu g\,g^{-1}$ d.w.) as an antioxidant. Internal standard mixtures, containing 20 pmol each of d_2-ABAalcohol, d_2-ABAaldehyde, d_3-PA, d_3-DPA, d_3-neoPA, d_4-7′-OH-ABA, d_5-ABAGE, and d_6-(+)ABA were also added to the samples. The homogenates were centrifuged (21 000 × *g*, 10 min, 4 °C) after 1 h of extraction, and the resultant pellets were then re-extracted in the same way for 30 min. The combined extracts were transferred by a pipette onto 3 mL Oasis® HLB cartridges (60 mg, Waters, Milford, MA, USA), that had been conditioned with 2 mL methanol and equilibrated with 2 mL methanol/water/acetic acid (10/89/1, v/v). The samples (ca. 1.5 mL) were loaded onto the cartridges, washed with 1 mL methanol/water/acetic acid (10/89/1, v/v) and eluted with 3 mL methanol/water/acetic acid (80/19/1, v/v), then the eluates were dried under vacuum.

Four purification procedures were tested. In the first, the evaporated samples were directly analysed by UPLC–ESI(−/+)-MS/MS. In the second, the samples were purified with a preimmune column and processed by (+)ABA-specific IAC, as previously described [36]. The purified samples were then evaporated to dryness in a Speed-Vac (UniEquip) and analysed by UPLC–ESI(−/+)-MS/MS. In the third procedure, the extracts were methylated using excess diazomethane for 10 min at room temperature, then dried under a nitrogen stream and finally analysed by UPLC–ESI(+)-MS/MS. In the last procedure, the evaporated samples were methylated, purified by IAC [36], and analysed by UPLC–ESI(+)-MS/MS.

2.5. Immunoaffinity purification

An immunoaffinity gel (IAG) containing immobilized anti-ABA antibodies was used to purify the ABA metabolites in the samples, as previously described [36]. Initially, the capacity of the IAG was tested using standard solutions, in triplicate, containing eight methylated ABA standards in equal amounts at concentrations (per standard) ranging from 5 to 300 pmol in ethanol:PBS buffer (5:95, v/v). The eluates were analysed by UPLC–ESI-MS/MS, and the whole experiment was repeated twice.

2.6. UPLC–ESI-MS/MS conditions

The dried samples were reconstituted in 30 μL of mobile phase (initial conditions), and 15 μL of each sample was then injected onto a reversed-phase column (BEH C18, 2.1 mm × 150 mm, 1.7 μm; Waters) coupled to an ESI-MS/MS system. The fractions containing ABA and the related acids were analysed in negative ion mode $[M-H]^-$, ABAGE was measured in negative and positive modes, while ABAalcohol, ABAaldehyde, and the methylated acids were determined solely in the positive ion mode $[M+H]^+$. In the first and second purification approaches, non-methylated compounds were separated by a linear gradient of methanol (A) and 10 mM formic acid (B), from 30:70 A:B (v/v) to 50:50 (v/v) over 7.5 min. Finally, the column was washed with 100% methanol (1 mL) and equilibrated to initial conditions (30:70 A:B, v/v) for 3.5 min. The retention time of ABA was 8.85 ± 0.02 min, and those of its metabolites DPA, ABAGE, PA, 9′-OH-ABA, 7′-OH-ABA, neoPA, ABAalcohol and ABAaldehyde were 4.44 ± 0.03, 5.25 ± 0.02, 5.39 ± 0.03, 5.97 ± 0.01, 6.83 ± 0.02, 7.39 ± 0.03, 8.01 ± 0.01, 8.20 ± 0.01 min, respectively. Methylated samples generated using the third and fourth purification procedures (see above) were separated using a linear methanol gradient, from 35 to 65% over 8 min, after which the column was washed with 100% methanol (1 mL) and equilibrated to initial conditions for 3.5 min. The retention times of ABAGE, DPAMe, ABAalcohol, PAMe, ABAaldehyde, 7′-OH-ABAMe, neoPAMe and ABAMe were 4.11 ± 0.02, 5.48 ± 0.01, 5.76 ± 0.01, 6.09 ± 0.01, 6.22 ± 0.01, 6.82 ± 0.01, 7.51 ± 0.01 and 8.56 ± 0.01 min, respectively. Calibration curve were created from triplicate analysis of free and methylated ABA metabolites by plotting the known concentration of each unlabeled analyte against the calculated response area of the analyte/IS ratio 0.15, 0.75, 1.5, 7.5, 15, 75 and 150 pmol/7.5 pmol and 0.015, 0.075, 0.15, 0.75, 1.5, 7.5, 15, 75

Table 1
Optimised product ion scans, diagnostic transitions, cone voltages (CV), collision energies (CE), and dwell times (DT) for the electrospray interface-mass spectrometry (in positive and/or negative ion modes) for the analyses of ABA and ABA metabolites.

	Transition	CV (V)	CE (eV)	DT (s)		Transition	CV (V)	CE (eV)	DT (s)
DPA	281>237	25	14	0.17	ABAGE	427>247	20	14	0.17
d_3-DPA	284>240	25	14		d_5-ABAGE	432>252	20	14	
ABAGE	425>263	25	14	0.08	DPAMe	279>175	27	16	0.08
d_5-ABAGE	430>268	25	14		d_3-DPAMe	282>175	27	16	
PA	279>205	25	10		ABAalcohol	249>121	17	15	
d_3-PA	282>208	25	10		d_2-ABAalcohol	251>123	17	15	
9′-OH-ABA	279>205	22	10	0.08	PAMe	277>159	27	19	0.08
7′-OH-ABA	279>151	20	15		d_3-PAMe	280>162	27	19	
d_4-7′-OH-ABA	283>155	20	15		ABAaldehyde	233>149	22	14	
neoPA	279>205	20	15		d_2-ABAaldehyde	235>151	22	14	
d_3-neoPA	283>208	22	10		7′-OH-ABAMe	277>127	23	16	0.17
ABAalcohol	249>121	17	15	0.08	d_4-7′-OH-ABAMe	281>127	23	16	
d_2-ABAalcohol	251>123	17	15						
ABAaldehyde	233>149	22	14		neoPAMe	277>159	30	20	0.17
d_2-ABAaldehyde	235>151	22	14		d_3-neoPAMe	280>159	30	20	
ABA	263>153	25	10	0.17	ABAMe	261>187	24	14	0.17
d_6-ABA	269>159	23	10		d_6-ABAMe	267>191	24	14	

and 150 pmol/7.5 pmol, respectively, where IS concentration is the known amount of the internal standard added.

For both non-methylated and methylated analytes, the column temperature and flow rate were kept constant at 40 °C and 0.20 mL min^{-1}, respectively, the eluant was introduced into a UV-diode array detector (scanning range: 210–400 nm, resolution: 1.2 nm, sampling rate: 10 spectra s^{-1}) and the MS/MS without post-column splitting. The eluting parent ions and the appropriate product ions were measured by MRM in either negative ion mode ($[M-H]^-$), for ABAGE and the free ABA acids, or positive ion mode (ABAGE as $[M+H]^+$; ABAalcohol, ABAaldehyde, and the methylated ABA acids as $[M+H-H_2O]^+$). The optimised conditions for the selective MRM analyses were: capillary voltage: 1.0 kV, source/desolvation gas temperature: 100/350 °C, cone/desolvation gas: 2.0/500 L h^{-1}, LM/HM resolution: 12.5, ion energy 1: −0.3 V, ion energy 2: −1.5 V, entrance and exit potentials: 2.0 V, and multiplier voltage: 650 eV. The collision cell pressure was 5.10^{-3} mbar (maintained using argon), and the dwell time, cone voltage, and collision energies depended on the compounds under investigation (see Table 1). In addition, the dwell time of each MRM channel was calculated to provide 16 scan points per peak, with an inter channel delay of 0.1 s.

3. Results and discussion

3.1. Immunoaffinity chromatography of ABA metabolites

A mixture of high affinity C1ABA1 and C1ABA2 antibodies was used to prepare the IAG, which has been previously shown to bind up to 1.7 ± 0.2 nmol (+)-*cis*,*trans*-ABA and 8.0 ± 0.9 nmol of (+)-*cis*,*trans*-ABAMe in the presence of a single free competitor [36]. However, for the immunoaffinity isolation of ABA metabolites to provide reliable results when several cross-reacting metabolites are present, the capacity and recovery must remain high for each of the target metabolites. Hence, since the previous cross-reactivity study only investigated antibody binding parameters in the presence of a single free competitor, we used IAC–UPLC–ESI-MS/MS to determine the extent of cross-reactivity when the immobilized antibody was exposed to a mixture of potentially cross-reacting compounds. For this purpose, solutions containing mixtures of eight equal amounts of methylated ABA acids and metabolites at levels ranging from 5 to 300 pmol (Fig. 3B) were purified using 500 μL IAC gel, as described in [36], and the resultant eluates were analysed by UPLC–ESI-MS/MS. This procedure allowed the effects of competition between the compounds with differing affinities on their recoveries to be determined (Fig. 2).

The following five ligands were retained with high recoveries over the concentration range tested: ABAMe, its glucosylester, 7′-OH-ABAMe, PAMe, and neoPAMe, and all of these substances showed slow concentration-dependent losses. The binding capacity of the IAC gel was estimated to be about 1.1 nmol/mL gel for the tested standard mixture. Metabolites that had extremely low affinity for the sorbent (detection limits <5 pmol) included DPAMe; the IAG showed little (if any) concentration-dependent binding of this substance, and only trace amounts of it were detected in the eluate by the UV and MS systems (data not shown). Virtually no retention of ABAaldehyde and ABAalcohol was observed at 5 pmol either, but both became temporarily coupled at levels exceeding 50 pmol. Recoveries higher than 90% were obtained for ABAMe in the range 5–50 pmol, and the recoveries were still higher than 50% up to 300 pmol. However, the recovery of ABAMe declined very rapidly beyond this limit. The results of these experiments indicated that the IAC gel's maximum capacity for ABAMe, and hence its recovery, may vary depending on the other ABA-type ligands present in natural samples. In addition, the capacity per mL of our

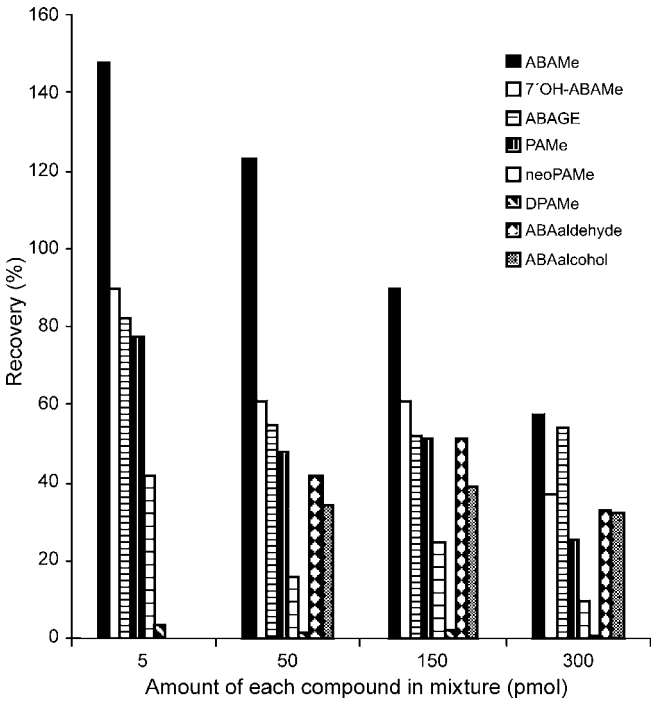


Fig. 2. Binding capacities of anti-ABA antibodies for eight methylated ABA metabolite standards in mixtures containing various, equimolar concentrations of the metabolites.

gel, expressed according to [48], was similar to previously published values [49–51]. On the other hand, at all concentrations tested, the differences in individual metabolite capacities were not fully parallel with previous observations of the metabolites' cross-reactivities in ELISAs (see [36] for comparison), hence the binding capacity of the antibodies appears to be influenced by their immobilization to varying degrees, depending on the metabolite. The binding capacities were also probably influenced by the high availability of free antibody binding sites at the low tested concentrations. The cross-reactivity parameters for a complex mixture may differ from those of the primary antigen for a number of reasons, including: (1) differences between the K_a values of antibodies for the cross-reacting substance and the antigen, (2) differences in the binding parameters of the immobilized antibodies on the gel, and (3) differences in the concentrations (relative and absolute) amongst cross-reacting substances in real samples [49]. Nevertheless, there are several reported advantages of using IAC for purifying ABA from plant tissue extracts, notably the immunoaffinity purification can significantly increase the selectivity and sensitivity (more than 10-fold) of subsequent LC–ESI-MS analysis [36]. Furthermore, we have shown the IAC gel to be highly specific for ABA, certain C1-ABA metabolites, and other structurally related compounds, making it highly useful for purifying ABA-like substances in complex plant extracts, which is often essential since total amounts of ABA metabolites in non-stressed plant material range from 5 to 50 pmol per gram fresh weight. Unfortunately, however, this approach cannot be used to isolate ABA metabolites like DPA, neoPA, and 7′-OH-ABA, due to their low affinity for the IAC gel.

3.2. Extraction and purification procedure

In order to identify and quantify ABA and its metabolites in plant tissue the samples must first be homogenized and extracted with a suitable solvent. These substances have generally been extracted using methanol or acetone acidified with 0.5–2% acetic acid (70–100%) [24,32,43,52,53], although other solvents, such as

Table 2
Levels of ABA and its metabolites in water-stressed *Nicotiana tabacum* L. leaves. Plant tissues (50 mg f.w.) were extracted with methanol/water/acetic acid (10/89/1, v/v), purified by HLB column chromatography and (a) directly analysed by UPLC–ESI(−/+)-MS/MS, (b) purified by immunoaffinity chromatography and analysed by UPLC–ESI(−/+)-MS/MS, (c) methylated and analysed by UPLC–ESI(+)-MS/MS, or (d) methylated, processed by immunoaffinity chromatography, and analysed by UPLC–ESI(+)-MS/MS. Data shown are means ± SE of three replicates.

	(a) (pmol/g f.w.)	Recovery (%)	(b) (pmol/g f.w.)	Recovery (%)	(c) (pmol/g f.w.)	Recovery (%)	(d) (pmol/g f.w.)	Recovery (%)
ABA	70 ± 2	76 ± 6	69 ± 3	57 ± 3	77 ± 8	51 ± 1	87 ± 13	46 ± 5
ABAGE	194 ± 19	63 ± 1	133 ± 8	59 ± 4	162 ± 2	57 ± 1	163 ± 8	21 ± 2
PA	754 ± 78	64 ± 2	n.c.[b]	–	772 ± 39	23 ± 0.2	844 ± 49	19 ± 5
DPA	172 ± 16	57 ± 3	n.c.	–	166 ± 9	16 ± 0.2	n.d.	<0.1
neoPA	n.d.[a]	114 ± 3	n.c.	–	31 ± 4	110 ± 4	n.d.	1 ± 0.1
7′-OH-ABA	n.d.	74 ± 5	n.c.	–	n.d.	34 ± 0.4	n.d.	<0.1
ABAaldehyde	n.d.	44 ± 2	n.d.	51 ± 3	n.d.	30 ± 2	n.d.	26 ± 1
ABAalcohol	n.d.	47 ± 5	n.d.	14 ± 1	n.d.	82 ± 3	n.d.	6 ± 1

[a] n.d.—not detected.
[b] n.c.—no cross-reactivity with anti-ABA antibodies.

40% ethanol [36] and water [36,38], have also been used. We extracted ABA and its metabolites from water-stressed *N. tabacum* leaves using acidified 10% methanol, and then purified them using Oasis® HLB columns (see Tables 2 and 3). This procedure gave practically identical results to the classical method of 80% methanol extraction followed by purification using C18 cartridges (compare data presented in column (a) of Table 2 to the following values obtained following extraction by acidified 80% methanol: 84 ± 4, 203 ± 12, 848 ± 84 and 168 ± 23 pmol/g f.w. for ABA, ABAGE, PA and DPA, respectively). Furthermore, extraction by 10% methanol recovered 67% of the added internal standards, on average (Table 2), whereas recoveries of around 55% were obtained using the more commonly applied 80% methanol (data not shown). Extraction with an aqueous solution of methanol with a higher water content was also preferred due to the relatively low pigment content of our crude plant extracts, which is very advantageous for subsequent LC–ESI-MS/MS analysis when no immunoaffinity purification procedure is applied. Consequently, the 10% methanolic solvent was used for extraction in all subsequent optimisation procedures.

Samples usually require purification after extraction, which can be performed by reversed-phase chromatography, to remove lipids and chlorophyll, or by immunoaffinity columns, which allow almost complete purification of the samples. Furthermore, ABA and its metabolites have been purified using Oasis® HLB cartridges [31,32]. An Oasis® HLB can also be used to purify other plant hormones, such as gibberellins and indole-3-acetic acid [32]. Therefore, in the presented study purifications with both Oasis® HLB cartridges and an IAC gel were tested to examine their influence on subsequent UPLC–ESI-MS/MS analysis, again using the water-stressed *N. tabacum* leaves.

The yield and efficiency of the following purification protocols were compared (Table 2): (a) purification with Oasis® HLB cartridges, (b) combined Oasis® HLB and IAC, (c) Oasis® HLB purification followed by methylation, and (d) Oasis® HLB combined with methylation and the IAC step. The levels of ABA metabolites in *N. tabacum* leaves, determined by UPLC–ESI-MS/MS following each of these purification approaches are shown in Table 2. ABA and ABAGE concentrations detected by UPLC–ESI-MS/MS following all of the purification procedures (a–d) varied between 69 ± 2 and 87 ± 13 pmol/g f.w. and 133 ± 2 and 194 ± 19 pmol/g f.w., respectively. PA levels determined following three of the purification methods (a, c, d) ranged from 754 ± 39 pmol/g to 844 ± 78 pmol/g f.w., but this metabolite was undetectable after purification with the second method (b). DPA was only detected after use of the first and third purification methods (a and c), which did not involve an IAC step. Endogenous neoPA (31 ± 4 pmol/g f.w.) was detected only in those samples subjected to Oasis® HLB purification and methylation (c). The other metabolites, such as 7′-OH-ABA, 9′-OH-ABA, ABAalcohol, and ABAaldehyde, were undetectable in the *N. tabacum* leaf samples.

We also compared the recoveries of the internal standards from the samples. About 67% of the internal standards were recovered following the first purification procedure (Table 2a), which involved direct analysis of crude *N. tabacum* tissues by UPLC–ESI-MS/MS; similar to the values obtained by Zhou et al. [32]. The second purification procedure yielded recoveries of ca. 57% of

Table 3
Levels of ABA and its metabolites in varied amounts of tobacco leaves. Plant tissues were extracted with methanol/water/acetic acid (10/89/1, v/v), purified by HLB column chromatography and either (A) directly analysed by UPLC–ESI(−/+)-MS/MS or (B) methylated by ethereal diazomethane and then analysed by UPLC–ESI(+)-MS/MS. NeoPA, 7′-OH-ABA, ABAaldehyde, and ABAalcohol were not detected (n.d.) in tobacco leaves.

Weight (mg f.w.)	Content of ABA and its metabolites (pmol/in sample)			
	ABA	ABAGE	PA	DPA
A				
1	n.d.	n.d.	n.d.	n.d.
5	0.40 ± 0.05	0.90 ± 0.22	4.26 ± 0.60	n.d.
10	0.76 ± 0.06	1.50 ± 0.23	8.99 ± 0.81	2.08 ± 0.27
20	1.17 ± 0.06	2.80 ± 0.21	20.03 ± 1.43	3.75 ± 0.29
40	2.10 ± 0.04	5.93 ± 0.05	35.14 ± 2.56	5.82 ± 0.32
Weight (mg f.w.)	Content of ABA and its metabolites (pmol/in sample)			
	ABAMe	ABAGE	PAMe	DPAMe
B				
1	0.10 ± 0.01	0.24 ± 0.01	0.85 ± 0.15	0.10 ± 0.01
5	0.54 ± 0.17	0.90 ± 0.09	4.10 ± 0.27	0.89 ± 0.10
10	1.07 ± 0.31	1.91 ± 0.16	8.06 ± 0.15	1.71 ± 0.12
20	1.94 ± 0.17	3.55 ± 0.03	19.34 ± 2.20	3.30 ± 0.44
40	3.14 ± 0.21	7.11 ± 0.37	37.32 ± 0.71	6.26 ± 0.30

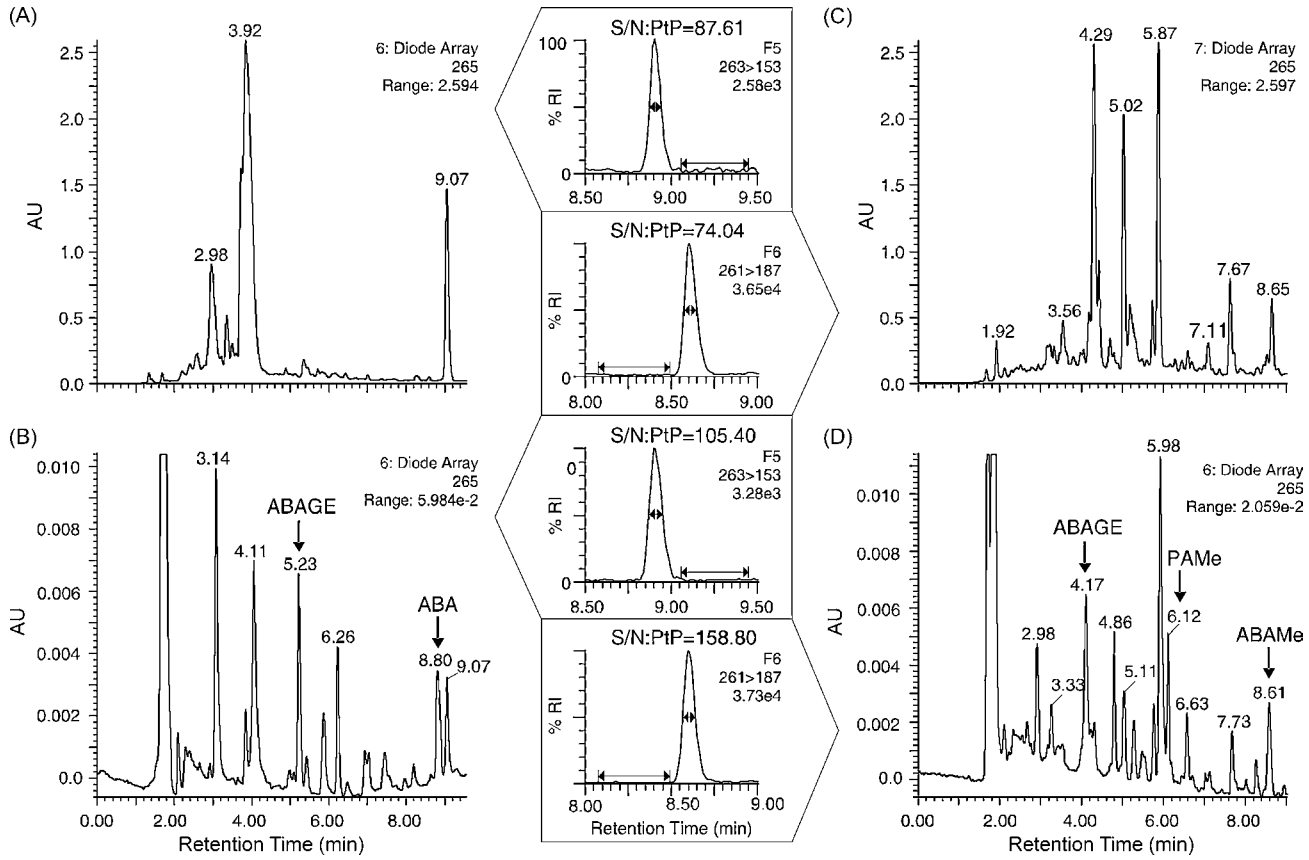


Fig. 3. Effects of immunoaffinity purification on the selectivity and sensitivity of subsequent ESI-MS/MS analysis. Comparison of UV (265 nm) and MRM chromatograms of authentic ABA present in 50 mg *Nicotiana tabacum* non-methylated (A and B) and methylated (C and D) extracts, before (A and C) and after using IAC (B and D).

the labelled d_6-(+)ABA, 59% of d_5-ABAGE, 51% of d_2-ABAaldehyde, and 14% of d_2-ABAalcohol (Table 2b). The other ABA metabolites could not be detected following this procedure due to the negligible cross-reactivity of the polyclonal anti-ABA-antibodies with PA, DPA, neoPA and 7′-OH-ABA [36]. Therefore, the combination of IAC and solid-phase extraction was wholly unsuitable for purifying these weakly immunoaffinity-binding analytes. The third procedure, based on purification of methylated samples by Oasis® HLB, recovered about 50% of each of the internal standards, while the subsequent introduction of the IAC step (4th procedure) resulted in only ca. 31% recoveries (Table 2c and d). Thus, once again, using IAC after sample methylation hindered measurement of metabolites other than ABAMe, ABAGE, and PAMe. On the other hand, non-significant variations were seen in the estimated levels of the analytes following each of the four purification protocols (as illustrated in Table 2). The rapid purification by each of these approaches, validated by the internal standardization procedure, allowed such differences to be accounted for, thereby enabling accurate quantification of endogenous ABA metabolites by UPLC–ESI-MS/MS. Adding labelled analogues to the extracts further facilitated the detection of natural ABA and the metabolites, providing better resolution of analytes eluting close together and

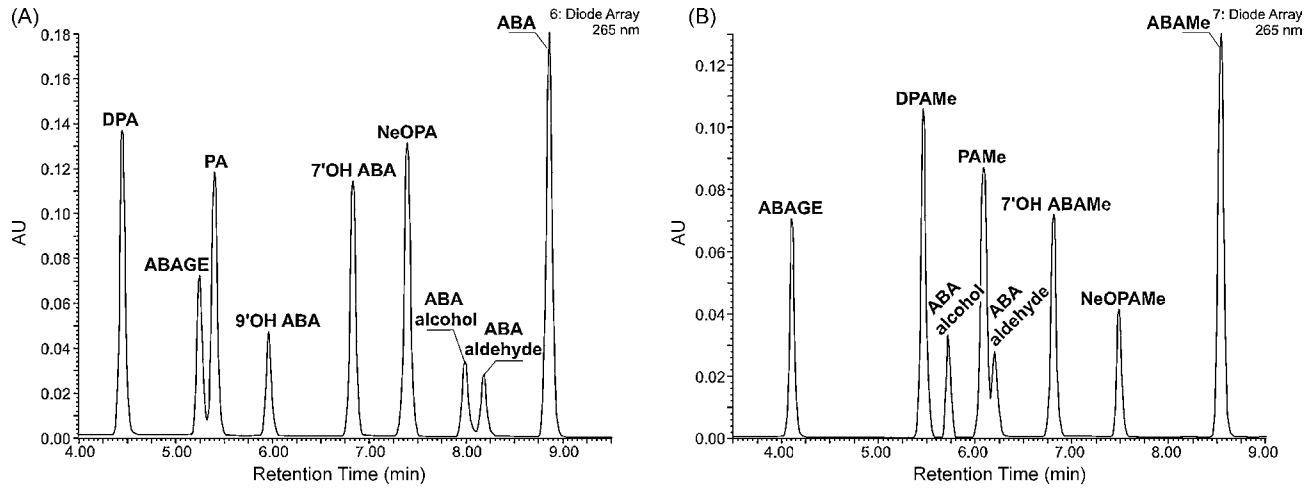


Fig. 4. Separation of ABA and its metabolites by ultra-performance liquid chromatography (UPLC). UPLC-UV chromatogram (265 nm) of free (A) and methylated (B) standard mixtures.

Table 4
Limits of detection, dynamic range, linearity (correlation coefficients, R^2), recovery, and analytical accuracy for the estimation of ABA and its metabolites by UPLC–ESI(−/+)-MS/MS.

	LOD[a] (pmol)	Dynamic range (pmol)	R^2	Recovery[b] (%)	Analytical accuracy[b] (%)
Negative mode					
ABA	0.1	0.25–0	0.9985	79.3 ± 2.2	113.3 ± 1.8
ABAGE/ESI(−)	0.25	0.5–150	0.9975	54.5 ± 2.2	105.2 ± 2.3
PA	0.75	1.0–150	0.9988	63.5 ± 6.0	124.5 ± 3.3
DPA	0.5	0.75–150	0.9991	55.0 ± 1.6	116.4 ± 2.6
neoPA	0.5	0.75–150	0.998	86.3 ± 2.8	126.2 ± 5.7
7′-OH-ABA	1	2.5–150	0.9987	95.8 ± 5.4	116.1 ± 25.5
9′-OH-ABA	1	2.5–150	0.9987	105.9 ± 2.7	120.9 ± 24.7
Positive mode					
ABAGE/ESI(+)	0.1	0.25–150	0.9992	32.1 ± 4.6	93.2 ± 3.1
ABAaldehyde	0.25	0.5–150	0.9994	79.4 ± 1.5	104.6 ± 10.4
ABAalcohol	0.5	0.75–150	0.999	16.1 ± 5.9	95.4 ± 16.1
ABAMe	0.01	0.025–150	0.9991	97.3 ± 7.1	124.4 ± 1.5
PAMe	0.01	0.025–150	0.999	58.6 ± 6.9	125.7 ± 7.5
DPAMe	0.01	0.025–150	0.9994	31.8 ± 2.9	81.3 ± 3.2
neoPAMe	0.05	0.1–150	0.9993	102.1 ± 18.8	129.0 ± 3.0
7′-OH-ABAMe	0.01	0.025–150	0.9993	64.0 ± 5.5	116.6 ± 1.7

[a] Limit of detection, defined as a signal-to-noise ratio of 3:1.
[b] Mean value of four independent measurements ± standard deviation.

measures of their recovery throughout the purification procedure. The results also corroborate the value of using specific recovery markers for each hormone metabolite measured [31].

However, the results also showed that the IAC step enhanced the purification of ABA, ABAGE and PA (Fig. 3), despite the losses of certain compounds (DPA and neoPA) from the profile of analysed tobacco leaf ABA metabolites. The UPLC chromatograms obtained before (0.1–2.5 AU) and after (0.001–0.01 AU) IAC purification confirmed that large proportions of potentially interfering UV-absorbing substances present in the plant extracts were removed. IAC also increased the selectivity and sensitivity of the subsequent high-throughput UPLC–ESI-MS/MS analysis, and reduced the need for frequent system clean-up, since interference by the sample matrix was reduced, resulting in an increased signal-to-noise ratios (e.g. 88/105 and 74/159 for ABA and ABAMe, respectively). Similar trends were observed for ABAGE and PA, although the IAC did not isolate all of the ABA metabolites (Table 2). The advantages of using IAC prior to LC–ESI-MS for the analysis of ABA, as well as other plant hormones, have been described in previous studies [36,47,54].

3.3. Optimisation of the UPLC–ESI-MS/MS methods

The masses of the diagnostic precursor-to-product ions for (non)methylated ABA, its metabolites, and their internal standards are shown in Table 1, while corresponding UPLC chromatograms are shown in Fig. 4. Fig. 4A shows the separation of a mixture of nine standards on a short reversed-phase column (2.1 mm × 150 mm) over 9 min, as monitored by diode array detection at 265 nm. The whole series of standards was eluted in 5 min, starting with DPA at 4.44 ± 0.03 min and ending with ABA at 8.85 ± 0.02 min, and the method provided baseline separation of all of the ABA compounds under investigation. Fig. 4B shows the separation of the standard mixture on the same reversed-phase column after methylation. In accordance with the mobile and solid phases used, the most polar ABA conjugate (ABAGE) was eluted in the first retention window and the polarity of the eluted compounds decreased as the chromatographic process continued. The polarity of the ABA acids was decreased by methylation, so ABAGE, ABAalcohol, and ABAaldehyde eluted earlier in the UPLC separation using the methanol gradient (see Fig. 4). Furthermore, the run-time of the analysis was reduced up to 3-fold compared to the previously published HPLC method (30 min in [36]). The retention times were also much more consistent (with RSDs between 0.1 and 0.7% for all compounds) than those of the previously published LC method (e.g. the mean and standard deviations of the ABA and ABAMe retention times were 13.53 ± 0.03 and 17.01 ± 0.04 min, respectively). This allowed the chromatographic runs to be split into five retention windows for non-methylated compounds (4.0–4.8, 4.8–5.7, 5.7–7.7, 7.7–8.5, 8.5–9.5 min) and six retention windows for methylated compounds (3.0–4.6, 4.6–5.9, 5.9–6.4, 6.4–7.1, 7.1–8.0, 8.0–9.0 min), which increased the sensitivity of the subsequent ESI-MS/MS measurements.

The MS parameters (ion mode, capillary voltage, cone voltage, collision energy, and dwell times) were optimised to maximise the overall sensitivity of the analysis, according to the analyte peak areas, and strong consistency was found between the MRM transitions obtained here and those previously acquired for ABA, ABAGE, and 7′-OH-ABA [31,37,43]. In the presented study, ABAGE and the free acids were measured in negative ion mode, which yields strong molecular deprotonated $[M-H]^-$ ions of these substances. Conversely, positive ion mode had more advantages for measuring ABAalcohol, ABAaldehyde, ABAGE and ABA acid methylesters. In positive ion mode, the most intense parent ions for these analytes were $[M+H]^+$ ions, followed by $[M+H-H_2O]^+$, and $[M+Na]^+$ ions. However, while the $[M+Na]^+$ ions were the most prominent, their high stability hindered their fragmentation and thus their utility as precursor ions in MRM analysis (data not shown). Hence, the second most prominent ions were chosen as precursors; $[M+H]^+$ for ABAGE and $[M+H-H_2O]^+$ for ABAalcohol, ABAaldehyde, and the methylesters. Product ion scans of each of the selected precursor ions showed several product fragments similar to those observed by other groups [31,37], and the predominant fragment generated from each precursor was chosen as a corresponding product ion for MRM transition. Each analyte, and the corresponding deuterated analogue, was scanned to confirm its retention time and optimised MRM transition characteristics (Table 1).

Limits of detection (LOD) and quantification (LOQ), defined as concentrations yielding signal-to-noise ratios of 3 and 10, respectively, were determined for the UPLC–ESI-MS/MS analysis of ABA and all of the investigated analytes. Analysis of ABA by IAC–LC–ESI(+)/MS has been previously described, with detection limits of 0.25 and 0.1 pmol for ABA and ABAMe, respectively [36]. The UPLC–ESI-MS/MS method presented here provided LODs ranging between 0.1–1.0 and 0.01–0.05 pmol for the free and methylated analytes, respectively (Table 4), while the LOQs ranged from 0.025 pmol (ABAaldehyde) to 2.5 pmol (7′-OH-ABA, 9′-OH-ABA). In comparison, ABA has been previously analysed by LC–ESI(−)-MS/MS in *B. napus* siliques [32], *A. thaliana* leaves [37] and *C.*

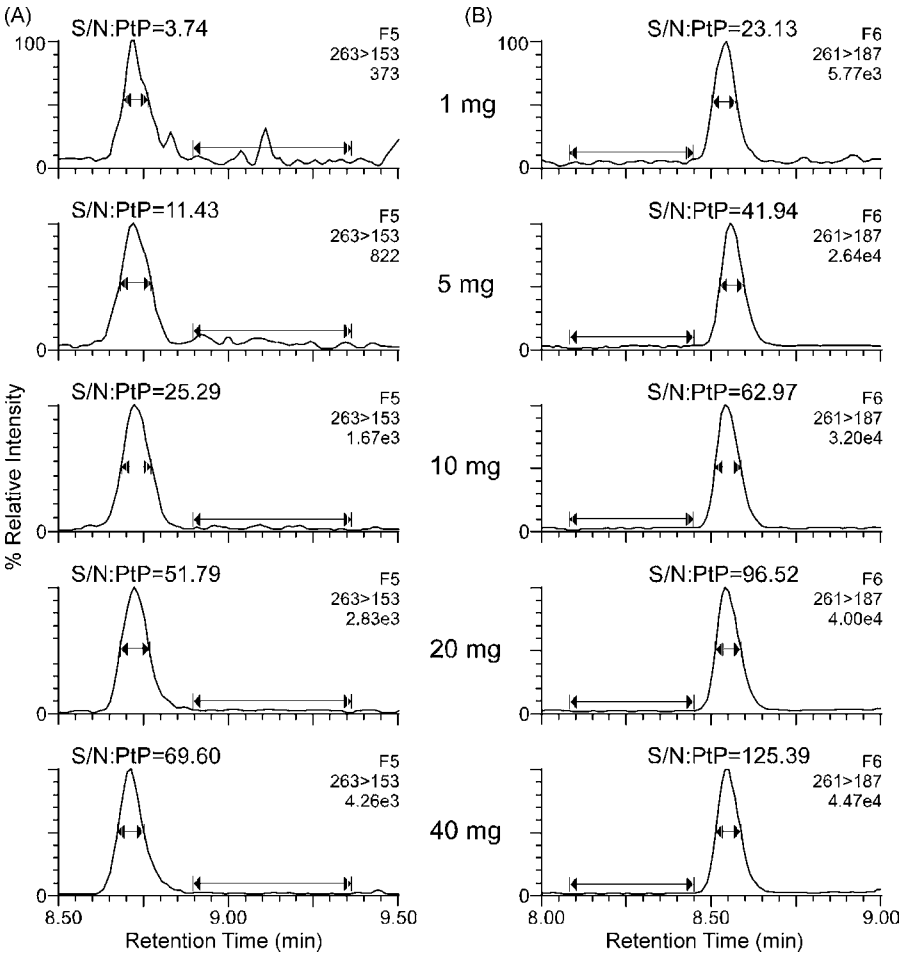


Fig. 5. Chromatograms showing the increase in sensitivity of subsequent UPLC–ESI(+)-MS/MS analysis afforded by the methylation of analytes in small amounts of tobacco plant tissues (1, 5, 10, 20, and 40 mg f.w.).

reticulata leaves and roots [38], with reported detection limits of 0.76, 3.8 and <50 pmol/g d.w., respectively. The cited study of *B. napus* siliques also reported detection limits for ABAGE, PA and DPA of 6.32, 1.79 and 2.49 pmol/g d.w., respectively [32].

Finally, the sensitivity of the analytical procedure for analyses of real plant tissue samples was examined by extracting samples of tobacco leaf material ranging from 1 to 40 mg (f.w.) in the presence of an internal standard mixture (20 pmol per standard). The samples were then purified by Oasis® HLB columns alone, and subjected to either direct analysis by UPLC–ESI(−/+)-MS/MS or UPLC–ESI(+)-MS/MS following methylation. The results of these experiments, presented in Table 3, show that methylation of the samples considerably increased the analytical sensitivity of UPLC–ESI(+)-MS/MS (Fig. 5). In addition, the use of small amounts of plant tissue reduced the analyte ion-suppressing effects of the matrix, and in combination with the methylation step enhanced the signal-to-noise ratios of the MS/MS measurements up to 6-fold. Furthermore, the results demonstrate that less than 5 mg of tissue is sufficient for determining ABA, ABAGE, and PA, although DPA analysis would require 10 mg of tissue (Table 3A). The results of analyses following Oasis® HLB purification and methylation (Table 3B) show that the minimum amount of tissue required for detecting all the analytes found in the material (ABA, ABAGE, PA and DPA) using this preparation procedure was 1 mg. Therefore, the analysis of ABA and its metabolites should be carried out with a minimum of 1 mg plant tissue when methylation is used, and 10 mg when it is not. In comparison, relatively high amounts (20–1000 mg) of fresh plant tissue [see, for example [36,37,55]], or 10–100 mg of dry seeds [32,33,39,43,46], have to be used to obtain measurable amounts of the ABA analytes when using the LC technique. Furthermore, LC requires a complex purification procedure involving several steps.

3.4. Validation of the UPLC–MS/MS method

To validate the UPLC method for the analysis of tissue samples, endogenous ABA and its metabolites were measured in replicates ($n = 4$) of water-stressed *N. tabacum* leaf extracts, using calibration curves generated from analyses of solutions with varied amounts of each unlabelled analyte and fixed amounts of the corresponding deuterium-labelled internal standards. This method gave a broader linear range with the methylated compounds, spanning at least four orders of magnitude. Furthermore, the resultant calibration curves were mostly linear, across concentration ranges of 0.25–2.5 to 150 pmol for the free substances and 0.025–0.5 to 150 pmol for the methylated analytes, with correlation coefficients (R^2) varying between 0.9975 and 0.9994 (Table 4).

The results demonstrate that either Oasis® HLB chromatography followed by UPLC–ESI(−/+)-MS/MS or Oasis® HLB purification followed by methylation and UPLC–ESI(+)-MS/MS can be used to reduce sample matrix effects and enhance the analytical accuracy sufficiently to reliably determine levels of the analytes in small samples of *N. tabacum* tissue (25 mg f.w., Table 4). Furthermore, the

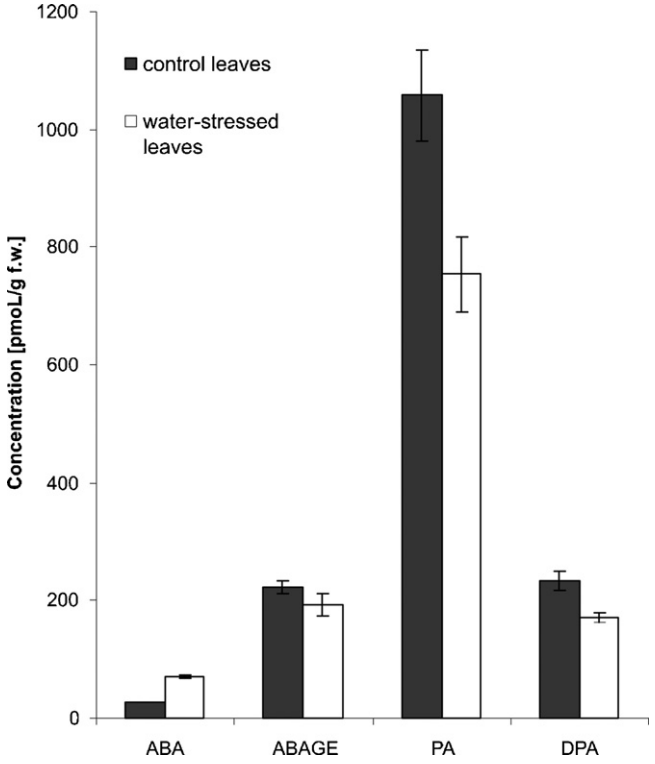


Fig. 6. Levels of ABA and its metabolites (ABAGE, PA and DPA) in control and water-stressed *Nicotiana tabacum* L. leaves (mean ± SE, $n = 3$).

accuracy of the method was validated by the "standard addition method", using two sets of samples: purified extracts of tobacco leaves (25 mg of 4 days water-stressed leaves) with and without the addition of a standard mixture (50 and 150 pmol each). The UPLC–ESI-MS/MS measurements were practically identical, regardless of the inclusion of the methylation step, as shown by the average results obtained using the two procedures in Table 4. The percentages of the analytes recovered were also calculated for ESI-MS/MS analysis in both positive and negative ion modes ($n = 4$), and were found to be 60 ± 7 and 77 ± 3%, on average, respectively. Hence, the data show that the method was satisfactory for measuring these trace components in a complex plant matrix [56]. Assessments of analytical accuracy using spiked tobacco extracts showed that estimated amounts of the ABA metabolites (after adjustments based on the results for the standards) were generally within ±25% of the true amounts.

3.5. Quantification of abscisic acid and its metabolites in water-stressed tobacco leaves

Levels of abscisic acid and its metabolites in leaves of control and 4 days water-stressed tobacco plants were quantified using the UPLC–ESI-MS/MS method in conjunction with standard isotope dilution measurements, which generally provide quantitative results with high accuracy and precision [57]. As shown in Fig. 6, the samples from the control and stressed leaves had ABA concentrations of 27 and 70 pmol/g f.w., respectively. Conversely, the control plants contained higher levels of ABAGE, PA, and DPA than the water-stressed plants. PA was the most abundant ABA metabolite in both control and water-stressed plants, followed by ABAGE and DPA, which were present at approximately 5-fold lower concentrations. Furthermore, ABA levels were at least 100-fold lower than PA concentrations, but its endogenous levels increased after water stress, while ABAGE, PA, and DPA concentrations decreased. The other ABA metabolites such as neoPA, 7′-OH-ABA, 9′-OH-ABA, ABAalcohol and ABAaldehyde were not detected, even in the water-stressed plants. Previous authors have reported contents of ABA and related compounds (PA, DPA, neoPA, ABAGE and 7′-OH-ABA) in seeds of various species, including western white pine (*Pinus monticola*) seeds during dormancy breakage (by moist chilling) and germination [39,40], thermodormant and germinating lettuce (*Lactuca sativa* L.) seeds [31], and in canola (*B. napus*) siliques (valves and seeds) [32]. In addition, the effect of parasitism on ABA metabolism during the early development of Douglas fir seeds has been described [41]. However, this is the first published study in which endogenous ABA and its metabolites have been analysed in leaves of *N. tabacum*, or any other species.

4. Conclusion

In the presented study we developed a UPLC–ESI-MS/MS method and combined it with a convenient procedure for extracting and purifying plant samples. This method was then successfully applied to the analysis of ABA and its metabolites in water-stressed *N. tabacum* leaves, and unstressed controls. The extraction procedure, which combines solvent extraction followed by solid-phase purification, allows samples to be prepared much more simply and rapidly than possible using previous protocols, permitting more than 70 samples per day to be extracted and purified. Overall, the methodology is less time-consuming and much more effective than other LC techniques. The liquid chromatographic separation and analysis of nine ABA derivatives by UPLC–ESI-MS/MS also provides accurate and reproducible quantification of most ABA metabolites. Furthermore, the approach enables the detailed and direct study of ABA and various ABA metabolites in small amounts of leaf tissues, which was not previously possible. Therefore, this newly developed UPLC–ESI-MS/MS method should be useful for studying the physiological roles, metabolism, and modes of action of ABA derivatives in plants.

Acknowledgements

This research was supported by the Ministry of Education, Youth, and Sports of the Czech Republic, Grant No. 6198959216, and the Grant Agency of the Czech Academy of Sciences, Grants No. KAN200380801. We would like to thank Sees-Editing Ltd. for linguistic correction of the text.

References

[1] J. Leung, J. Giraudat, Annu. Rev. Plant Physiol. Mol. Biol. 49 (1998) 199.
[2] J.A.D. Zeevaart, Abscisic acid metabolism and its regulation, in: P.J.J. Hooykaas, M.A. Hall, K.R. Libbenga (Eds.), Biochemistry and Molecular Biology of Plant Hormones, Elsevier Science, Amsterdam, The Netherlands, 1999, pp. 189–207.
[3] A. Cutler, J. Krochko, Trends Plant Sci. 4 (1999) 472.
[4] T. Oritani, H. Kiyota, Nat. Prod. Red 20 (2003) 414.
[5] R. Zhou, A.J. Cutler, S.J. Ambrose, M.M. Galka, K.M. Nelson, et al., Plant Physiol. 134 (2004) 361.
[6] M.R. Ramos, G. Jerz, S. Villanueva, F. Lopez-Dellamary, R. Waibel, et al., Phytochemistry 65 (2004) 955.
[7] L.I. Zaharia, Y. Gay, K.M. Nelson, S.J. Ambrose, S.R. Abrams, Phytochemistry 65 (2004) 3199.
[8] H. Kikuzaki, S. Kayano, N. Fukutsuka, A. Aoki, K. Kasamatsu, et al., J. Agric. Food Chem. 52 (2004) 344.
[9] E. Montero, J. Sibole, C. Cabot, C. Poschenreider, J. Barcelo, J. Chromatogr. A 658 (1994) 83.
[10] E.W. Weiller, Planta 144 (1979) 255.
[11] E.W. Weiller, Planta 148 (1980) 262.
[12] D.C. Walton, W. Dashek, E. Galson, Planta 146 (1979) 139.
[13] J. Daie, R. Wyse, Anal. Biochem. 119 (1982) 365.
[14] E.W. Weiller, Physiol. Plant 54 (1982) 510.
[15] A.J. Ciha, M.L. Brenner, W.A. Brun, Plant Physiol. 59 (1977) 821.
[16] N.L. Cargile, R. Borchert, J.D. McChesney, Anal. Biochem. 97 (1979) 331.
[17] I.B. Taylor, S. Rossal, Planta 154 (1982) 1.
[18] S. Mapelli, P. Rocchi, Ann. Bot. 52 (1983) 407.
[19] M.A. Harrison, D.C. Walton, Plant Physiol. 56 (1975) 250.

[20] J.A.D. Zeevaart, B.V. Milborrow, Phytochemistry 15 (1976) 493.
[21] A.G. Netting, B.V. Milborrow, A.M. Duffield, Phytochemistry 21 (1982) 385.
[22] P.H. Duffield, A.G. Netting, Anal. Biochem. 289 (2001) 251.
[23] S.J. Neill, R. Horgan, J.K. Heald, Planta 157 (1983) 371.
[24] L.R. Hogge, G.D. Abrams, S.R. Abrams, P. Thibault, S. Pleasance, J. Chromatogr. 623 (1992) 255.
[25] G. Schneider, F. Ziethe, J. Schmidt, Chromatographia 45 (1997) 78.
[26] F. Vilaró, A. Canela-Xandri, R. Canela, Anal. Bioanal. Chem. 386 (2006) 306.
[27] V. Hlaváčková, P. Krchňák, J. Nauš, O. Novák, M. Špundová, M. Strnad, Planta 225 (2006) 235.
[28] R.C. Durley, T. Kannangara, G. Simpson, J. Chromatogr. 236 (1982) 181.
[29] N. Hirai, K. Koshimizu, Agric. Biol. Chem. 47 (1983) 365.
[30] A. Durgbanshi, V. Arbona, O. Pozo, O. Miersch, J.V. Sancho, A. Gómez-Cadenas, J. Agric. Food Chem. 53 (22) (2005) 8437.
[31] S.D.S. Chiwocha, S.R. Abrams, S.J. Ambros, A.J. Cutler, M. Loewen, A.R.S. Ross, A.R. Kermode, Plant J. 35 (2003) 405.
[32] R. Zhou, T.M. Squires, S.J. Ambrose, S.R. Abrams, A.R.S. Ross, A. Cutler, J. Chromatogr. A 1010 (2003) 75.
[33] P.I. Dobrev, M. Kamínek, J. Chromatogr. A 950 (2002) 21.
[34] P.I. Dobrev, L. Havlíček, M. Vágner, J. Malbeck, M. Kamínek, J. Chromatogr. A 1075 (2005) 159.
[35] H.-T. Liu, Y.-F. Li, T.-G. Luan, Ch-Y. Lan, W.-S. Shu, Chromatographia 66 (2007) 515.
[36] V. Hradecká, O. Novák, L. Havlíček, M. Strnad, J. Chromatogr. B 847 (2) (2007) 162.
[37] M. López-Carbonell, O. Jáuregui, Plant Physiol. Biochem. 43 (2005) 407.
[38] A. Gómez-Cadenas, O.J. Pozo, P. García-Augustín, J.V. Sancho, Phytochem. Anal. 13 (2002) 228.
[39] J.A. Feurdato, S.J. Ambrose, A.J. Cutler, A.R.S. Ross, S.R. Abrams, A.R. Kermode, Planta 218 (2004) 630.
[40] J.A. Feurtado, J. Yang, S.J. Ambrose, A.J. Cutler, S.R. Abrams, A.R. Kermode, J. Plant Growth Regul. 26 (2007) 46.
[41] S.D.S. Chiwocha, G. Rouault, S.R. Abrams, P. von Aderkas, Sex Plant Reprod. 20 (2007) 19.
[42] B.-L. Lin, H.-J. Wang, J.-S. Wang, L.I. Zaharia, S.R. Abrams, J. Exp. Bot. 56 (2005) 2935.
[43] A.R.S. Ross, S.J. Ambrose, A.J. Cutler, J.A. Feurtado, A.R.ET-AL Kermode, Anal. Biochem. 392 (2004) 324.
[44] L.I. Zaharia, M.K. Walker-Simmon, C.N. Rodriguez, S.R. Abrams, J. Plant Growth Regul. 24 (2005) 274.
[45] T. Naito, T. Yamashino, T. Kiba, N. Koizumi, M. Kojima, H. Sakakibara, T. Mizuno, Biosci. Biotechnol. Biochem. 71 (5) (2007) 1269.
[46] R. Zentella, Z.-L. Zhang, M. Park, S.G. Thomas, A. Endo, K. Murase, Ch.M. Fleet, Y. Jikumaru, E. Nambara, Y. Kamiya, T.-P. Sun, Plant Cell 19 (2007) 3037.
[47] E. Prinsen, P. Redig, W. Vandongen, E.L. Esmans, H.A. van Ockelen, Rapid Commun. Mass Spectrom. 9 (1995) 948.
[48] G.C. Davis, M.B. Hein, D.A. Chapman, B.C. Neely, C.R. Sharp, R.C. Durley, D.K. Biest, B.R. Heyde, M.G. Carnes, Plant Growth Subst., Springer-Verlag, Heidelberg, 1985, pp. 44–51.
[49] B. Nicander, U. Stahl, P.O. Bjorkman, E. Tilberg, Planta 189 (1993) 312.
[50] T.L. Wang, S.K. Cook, J.P. Knox, Phytochemistry 26 (1987) 2447.
[51] R. Vaňková, A. Gaudinová, H. Süssenbeková, P. Dobrev, M. Strnad, J. Holík, J. Lenfeld, J. Chromatogr. A 811 (1998) 77.
[52] M. Okamoto, K.I. Takahashi, T. Doi, Rapid Commun. Mass Spectrom. 7 (1993) 1067.
[53] A. Gómez-Cadenas, F.R. Tadeo, M. Talón, E. Primo-Millo, Plant Physiol. 112 (1996) 401.
[54] O. Novák, E. Hauserová, P. Amakorová, K. Doležal, M. Strnad, Phytochemistry 69 (2008) 2214.
[55] A. Müller, P. Düchting, E.W. Weiler, Planta 216 (2002) 44.
[56] J.A. van Rhijn, H.H. Heskamp, E. Davelaar, W. Jordi, M.S. Leloux, U.A.T. Brinkman, J. Chromatogr. A 929 (2001) 31.
[57] K. Ljung, G. Sandberg, T. Moritz, Methods of plant hormone analysis, in: P.J. Davies (Ed.), Plant Hormones: Biosynthesis, Signal Transduction, Action!, Kluwer Academic Publishers, Dordrecht, 2004, pp. 671–694.

Talanta 80 (2009) 400–402

Contents lists available at ScienceDirect

Talanta

journal homepage: www.elsevier.com/locate/talanta

Short communication

Solid-phase microcolumn extraction and gas chromatography–mass spectrometry identification of volatile organic compounds emitted by paper

Ján Hrivňák[a,1], Peter Tölgyessy[b,*], Soňa Figedyová[c], Svetozár Katuščák[c]

[a] Expertise and Analytical Services, Astrová 46, 821 01 Bratislava, Slovak Republic
[b] Water Research Institute, Nábrežie L. Svobodu 5, 812 49 Bratislava, Slovak Republic
[c] Faculty of Chemical and Food Technology, Slovak University of Technology, Radlinského 9, 812 37 Bratislava, Slovak Republic

ARTICLE INFO

Article history:
Received 19 March 2009
Received in revised form 10 June 2009
Accepted 15 June 2009
Available online 21 June 2009

Keywords:
Gas chromatography
Solid-phase microcolumn extraction
Paper
Volatile organic compounds
Adsorption
Tenax

ABSTRACT

A rapid non-destructive sampling technique for the analysis of volatile organic compounds (VOCs) emitted by paper sheets is described. A capillary, which is connected to a microcolumn packed with Tenax TA, is inserted between two sheets at the centre of a paper stack encapsulated inside a PET/Al/PE composite foil. The other end of the microcolumn is connected to a gas-tight syringe and an appropriate volume of gaseous phase is aspirated. The microcolumn is then thermally desorbed in a modified GC inlet (modification is presented) and analysed by gas chromatography–mass spectrometry (GC–MS). In the chromatogram from the analysis of artificially aged paper sample 21 compounds were identified. Advantages of the method including the short sampling time (1 min), simplicity and economic aspect are discussed.

© 2009 Elsevier B.V. All rights reserved.

1. Introduction

Paper emits a complex mixture of volatile organic compounds (VOCs) as it ages. Its composition depends on the nature of the paper, the degree of its degradation, and the pathway by which it degrades [1]. Identification, determination and evaluation of the ratios of different degradation products can be used for the evaluation of condition of aged paper material and it can be suitable for the comparison of the used and newly developed paper modification processes.

Analytical methods applied for the evaluation of paper material condition and degree of its degradation can be divided into destructive (size-exclusion chromatography, viscosity measurements, etc.) and non-destructive ones (e.g. headspace methods) [2]. However, the non-destructive ones are the most suitable for examination of valuable artefacts. Recently, a non-destructive solid-phase microextraction (SPME) method has been applied to the trapping and analysis of VOCs emitted during ageing of books [3,4]. The contact SPME coupled to GC–MS allowed the characterisation of more than 50 individual organic constituents and enabled to monitor relative abundances of the main degradation products.

The aim of this work was the application of another recently introduced non-destructive sampling technique, the headspace solid-phase microcolumn extraction (HS-SPMCE), for the analysis of VOCs emitted by paper [5–7]. In the presented method, the loaded microcolumn was thermally desorbed in a modified GC inlet and VOCs were separated and detected by GC–MS.

2. Experimental

2.1. Sample and sampling procedure

A sample of a newsprint paper (Jihočeské papírny, Větřní, Czech Republic) was conditioned for 24 h according to ISO 187 at 23 ± 1 °C, and at relative air humidity of 50 ± 1% [8]. Seventy-five sheets of paper (A5 format) were then encapsulated inside a polyethylene terephthalate/aluminium/polyethylene (PET/Al/PE) composite foil (Tenofan Al/116S) using Polystar 30D impulse tong sealer (Rische + Herfurth, Hamburg, Germany). The sample was submitted to accelerated temperature ageing at 98 ± 2 °C during 15 days according to the ASTM D 6819-02 standard test method [9] in which sealed glass tubes were replaced by the PET/Al/PE foil.

The PET/Al/PE foil was pierced and a deactivated fused silica capillary column (12 cm long, 0.25 mm I.D.) equipped with a glass press-fit connector (to protect the paper surface) was inserted

* Corresponding author. Tel.: +421 2 59343466; fax: +421 2 54418047.
E-mail addresses: janhrivnak@post.sk (J. Hrivňák), Tolgyessy@vuvh.sk (P. Tölgyessy), sona.figedyova@stuba.sk (S. Figedyová), svetozar.katuscak@stuba.sk (S. Katuščák).
[1] Tel.: +421 903707897.

0039-9140/$ – see front matter © 2009 Elsevier B.V. All rights reserved.
doi:10.1016/j.talanta.2009.06.035

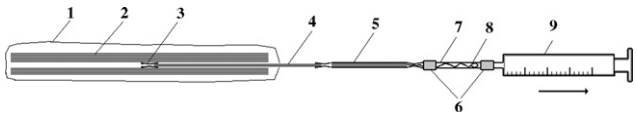


Fig. 1. Sampling procedure: (1) PET/Al/PE foil, (2) sheets of paper, (3) press-fit connector, (4) fused silica capillary, (5) sorbent-packed microcolumn, (6) short flexible tubing, (7) glass tube, (8) wire for microcolumn manipulation and (9) gas-tight syringe.

10 cm deep between two sheets at the centre of a paper stack (Fig. 1). The exit end of the capillary was gas-tightly connected to the entrance end of the microcolumn. The other end of the microcolumn was attached to a 20-mL all-glass gas-tight syringe (Poulten & Graf, Wertheim, Germany) and 10 mL of gaseous phase was aspirated through it.

2.2. Apparatus

Analyses were conducted using a Hewlett–Packard 6890GC–5972 MS system (Palo Alto, CA, USA) combination equipped with a modified split/splitless (S/SL) inlet. The inlet modification is shown in Fig. 2A (see also in [7]) and the Tenax TA (30 mg) packed glass microcolumn (specified in [5]) and the parts employed are shown in Fig. 2B. The inside of the entrance end of the microcolumn is conically broadened (as in glass press-fit connectors) to make a gas-tight connection when it is put on the end of a capillary column inserted into the bottom part of a glass tube chamber. To place a loaded microcolumn into the glass tube chamber, the modified upper part of the S/SL insert weldment with tubing has previously to be taken out and then replaced. For the separation of analytes a 60 m × 0.32 mm I.D. fused silica HP-VOC/MS capillary column with a film thickness of 1.8 μm was used. The GC column was temperature programmed from 50 °C (2 min) to 120 °C at 7 °C/min and then to 270 °C (10 min) at 14 °C/min. Desorption of the loaded microcolumn was accomplished at the inlet temperature of 250 °C and a carrier gas (helium) pressure of 5 kPa during 1 min. After desorption, the carrier gas pressure was increased to 50 kPa at 100 kPa/min and maintained at this value for the rest of the analysis. The split ratio in the modified inlet was adjusted to 100:1. Gas chromatographically separated compounds were detected by MS operating in the scan mode scanning from 10 μ to 300 μ at 2.59 scans/s. Temperatures of the MS ion source and of the GC–MS interface were 170 °C and 280 °C, respectively. Identification of mass spectra of the detected compounds was carried out by computer matching against an Agilent Wiley7n mass spectra library (Agilent Technologies, USA).

3. Results and discussion

As an example of the method application, a chromatogram from the analysis of the headspace of the artificially aged paper sample is shown in Fig. 3A. In 10 mL of the gaseous phase that had been in contact with the paper stack, 21 organic compounds were identified. The chromatogram (Fig. 3B) of the blank SPMCE–GC–MS analysis of 10 mL of air taken from the empty composite foil bag was clean. The obtained qualitative data together with information on relative abundances of degradation products can be used for the characterisation of the paper condition [2–4]. So far, no method is available in the literature which would allow the determination of the VOCs content in paper material quantitatively on the basis of their concentration in the gaseous phase. For the quantitative VOCs analysis in paper destructive methods can be used, too. However, those are not appropriate for the testing of valuable historic documents.

The advantage of using microcolumn adsorption lies in short sampling times (in our case 1 min) in comparison with the SPME

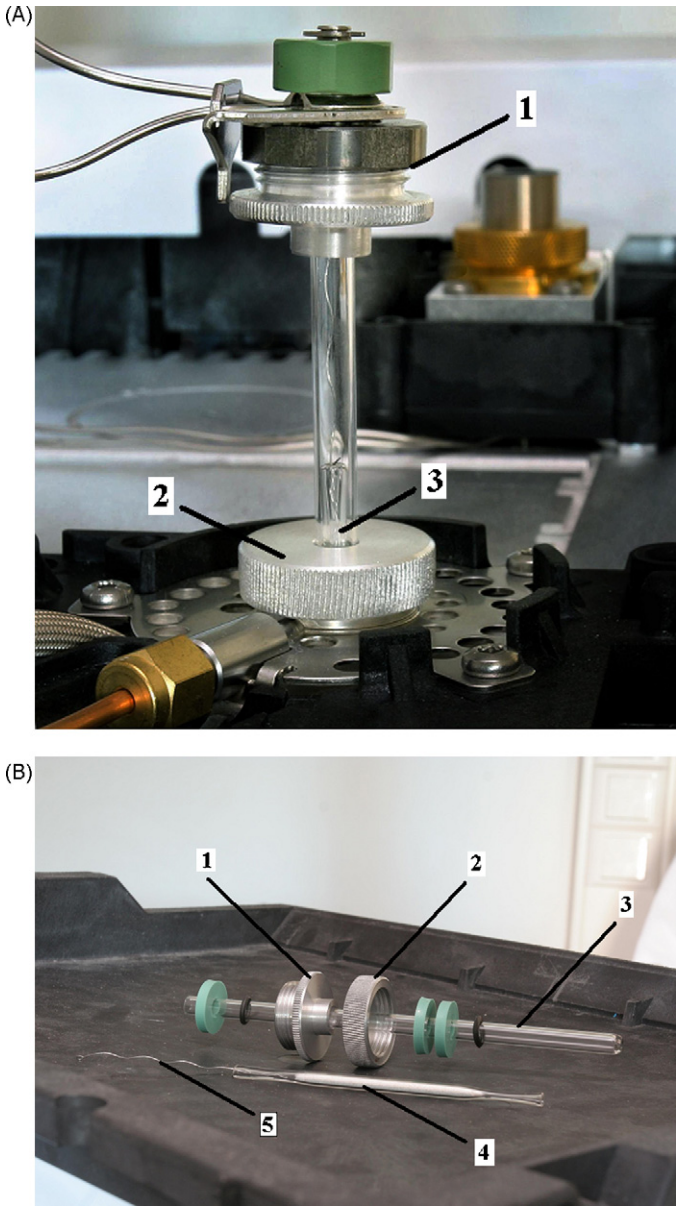


Fig. 2. (A) The split/splitless inlet modification for thermal desorption of a microcolumn: (1) upper part of S/SL insert weldment with tubing, (2) lower nut, (3) inserted microcolumn. (B) The sorbent-packed glass microcolumn and parts employed: (1) upper nut, (2) lower nut, (3) glass tube chamber, (4) microcolumn and (5) wire for microcolumn manipulation.

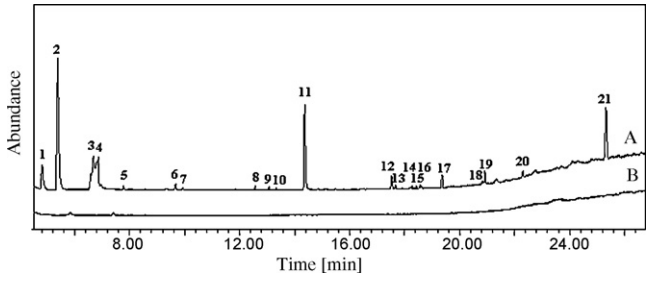


Fig. 3. Chromatograms from the SPMCE–GC–MS analysis (A) of the headspace of the artificially aged paper sample and (B) of the blank run. Peaks: (1) acetone; (2) methyl acetate; (3) 2,3-butanedione; (4) acetic acid; (5) methyl propanoate; (6) 2,3-pentanedione; (7) pentanal; (8) toluene; (9) octane; (10) hexanal; (11) furfural; (12) decane; (13) 2-pentylfuran; (14) alpha-terpinene; (15) 1,2,3,4-tetramethylbenzene; (16) limonene; (17) undecane; (18) benzoic acid; (19) dodecane; (20) tridecane; (21) 1-methylethyl tetradecanoate.

method, in which sampling takes tens of minutes. In the studies [3,4] describing the use of contact SPME for the analysis of VOCs emitted by naturally aged book, the applied sampling times varied from hours to several days, which is not convenient for practical purposes. Another advantage of a method operating up to the adsorbent packing breakthrough capacity, is that the amount ratios of analytes trapped in the microcolumn are comparable with the ratios in the aspirated gaseous phase. In the case of SPME the ratios of the fibre-sorbed analytes depend on the sampling time and the equilibrium is shifted towards the higher boiling components with increasing time. As a result, the use of the microcolumn method is more advantageous for trapping of more volatile compounds.

The simple modification of the GC inlet presents an inexpensive alternative to the commercially available thermal desorption systems. The modified inlet can be reversed to its initial S/SL status in a few minutes. During the analysis run, the microcolumn remains inside the GC inlet and is flushed by the carrier gas, so there is no need of subsequent conditioning of the adsorbent. In the case of analysis of higher concentrations of less volatile compounds, the carryover can be eliminated by repeating the thermal desorption of the microcolumn. The microcolumn makes it possible to analyse hundreds of samples without significant distortion.

References

[1] T. Doering, P. Fischer, G. Banik, U. Binder, J. Liers, Adv. Print. Sci. Technol. 27 (2001) 27–39.
[2] A. Lattuati-Derieux, S. Bonnassies-Termes, B. Lavédrine, J. Cult. Herit. 7 (2006) 123–133.
[3] A. Lattuati-Derieux, S. Bonnassies-Termes, B. Lavédrine, J. Chromatogr. A 1026 (2004) 9–18.
[4] M. Strlič, I.K. Cigić, J. Kolar, G. de Bruin, B. Pihlar, Sensors 7 (2007) 3136–3145.
[5] P. Tölgyessy, J. Hrivňák, J. Chromatogr. A 1127 (2006) 295–297.
[6] P. Tölgyessy, B. Vrana, J. Hrivňák, Chromatographia 66 (2007) 815–817.
[7] J. Hrivňák, E. Král'ovičová, P. Tölgyessy, J. Ilavský, J. Occup. Health 51 (2009) 173–176.
[8] ISO 187:1990, Paper, Board and Pulps. Standard Atmosphere for Conditioning and Testing and Procedure for Monitoring the Atmosphere and Conditioning of Samples, International Organization for Standardization, Geneva, Switzerland.
[9] ASTM D6819-02:2002, Standard Test Method for Accelerated Temperature Ageing of Printing and Writing Paper by Dry Oven Exposure Apparatus, American Society for Testing and Materials, West Conshohocken, PA, USA.

Talanta 80 (2009) 403–406

Contents lists available at ScienceDirect

Talanta

journal homepage: www.elsevier.com/locate/talanta

Short communication

Glucose biosensor based on immobilization of glucose oxidase in platinum nanoparticles/graphene/chitosan nanocomposite film

Hong Wu[a], Jun Wang[a], Xinhuang Kang[a], Chongmin Wang[a], Donghai Wang[a], Jun Liu[a], Ilhan A. Aksay[b], Yuehe Lin[a,*]

[a] Pacific Northwest National Laboratory, Richland, WA 99352, USA
[b] Department of Chemical Engineering, Princeton University, Princeton, NJ 08544, USA

ARTICLE INFO

Article history:
Received 1 May 2009
Received in revised form 17 June 2009
Accepted 17 June 2009
Available online 2 July 2009

Keywords:
Graphene
Platinum nanoparticles
Nanocomposite
Biosensor
Glucose

ABSTRACT

The bionanocomposite film consisting of glucose oxidase/Pt/functional graphene sheets/chitosan (GOD/Pt/FGS/chitosan) for glucose sensing is described. With the electrocatalytic synergy of FGS and Pt nanoparticles to hydrogen peroxide, a sensitive biosensor with a detection limit of 0.6 μM glucose was achieved. The biosensor also has good reproducibility, long-term stability and negligible interfering signals from ascorbic acid and uric acid comparing with the response to glucose. The large surface area and good electrical conductivity of graphene suggests that graphene is a potential candidate as a sensor material. The hybrid nanocomposite glucose sensor provides new opportunity for clinical diagnosis and point-of-care applications.

© 2009 Published by Elsevier B.V.

1. Introduction

Graphene has recently emerged as an interesting material in a myriad of applications because of its unique mechanical and electronic properties [1–5]. Most of the graphene studies have focused on its physical properties, such as its electronic properties, and these studies have demonstrated some applications in gas sensors [6,7] and pH sensors [8]. However, using graphene for biosensors has not received much attention. Graphene exhibits excellent electrical conductivity, high surface area, and strong mechanical strength [2,4,9]. Such properties indicate that graphene may be a good support for electrocatalysts. Recently, we developed a new approach for producing functionalized graphene sheets (FGSs) in mass quantities through the thermal expansion of graphite oxide to yield single graphene sheets with epoxy, hydroxyl, and carboxyl groups as well as Stone-Wales and 5–8–5 lattice defects [10]. Such functional groups and their lattice defects may play a significant role in preparing graphene-based electrocatalysts. Furthermore, these FGSs are more dispersible and biocompatible than other carbon-based materials due to their functional groups. These advantages of FGSs make them an ideal material for sensor and fuel cell applications. In fact, due to their planar morphology and thus larger accessible surface area, FGSs may perform better than any other carbon-based electrode as a sensor material. Another advantage of graphene is its potential low manufacturing cost as compared to other nanostructured carbon materials, such as carbon nanotubes. Recently, graphene has been used as electrode material for direct electrochemistry of glucose oxidase, battery, and fuel cell [11–13].

Noble nanoparticles (NPs), such as platinum, exhibit electrocatalytic behavior to hydrogen peroxide (H_2O_2) and have been widely used for sensing applications [14–16]. It will be attractive to prepare nanoparticle-functionalized FGS, e.g., platinum nanoparticles (Pt NP)/FGS nanocomposite, because such a functionalized FGS may generate synergy on electrocatalytic activity and thus enhance the sensitivity of the biosensor.

In this work, we report a FGS-based bionanocomposite film and demonstrate its application for sensitive glucose sensing. This bionanocomposite film was prepared by the following routes: chemically controlled modification of FGSs by electrodeposition of Pt NPs followed by physical modification of the Pt/FGS nanocomposite with enzymes. The FGS used here was prepared as described elsewhere [10]. The FGSs were first dispersed in a solution containing 0.2% chitosan and then cast on a glassy-carbon electrode (GCE). By using the potentiostatic electrodeposition in a platinum-containing solution, platinum nanoparticles were modified on the FGS/chitosan/GCE. Then glucose oxidase (GOD) was immobilized on Pt/FGS/chitosan/GCE, forming a bionanocomposite film.

* Corresponding author at: Pacific Northwest National Laboratory, 902 Battelle Blvd., PO Box 999, Richland, WA 99352, USA. Tel.: +1 509 376 0529; fax: +1 509 376 5106.
E-mail address: yuehe.lin@pnl.gov (Y. Lin).

0039-9140/$ – see front matter © 2009 Published by Elsevier B.V.
doi:10.1016/j.talanta.2009.06.054

2. Experimental

2.1. Chemicals

GOD, D-glucose, chitosan, phosphate buffer saline, potassium chloride, acetic acid, chloroplatinic acid, sulfuric acid, H_2O_2, ascorbic acid, and uric acid were all purchased from Sigma–Aldrich (St. Louis, USA). All solutions used in the experiments were prepared with ultra-pure water (18.3 MΩ cm, Nanopure, Barnstead, USA).

2.2. Materials

The graphene used in our study was made by thermal exfoliation of graphite oxide [10], which starts with the chemical oxidation of graphite flakes to increase the *c*-axis spacing from 0.34 nm to 0.7 nm. The resulting graphite oxide is split apart through rapid thermal expansion to yield a single but wrinkled graphene sheet functionalized with hydroxyl and epoxy sites.

2.3. Preparation of FGS/chitosan/GCE

The suspension of FGS was prepared by dispersing 1 mg graphene in 1 mL of 0.2% chitosan solution (pH 5). The mixture was sonicated 1 h to obtain a homogeneous dispersion. The FGS suspension was cast on the surface of a GCE (∅ = 3 mm) to prepare the FGS-modified electrode. Six microliters of 1 mg/mL FGS suspension was cast on the pretreated GCE and dried at room temperature.

2.4. Preparation of Pt/FGS/chitosan/GCE

Platinum nanoparticles were electrochemically deposited on the FGS/chitosan/GCE with constant potential at −0.25 V for a desired time in a 5-mL solution containing 1 mM H_2PtCl_4 and 0.5 M H_2SO_4. After the deposition, the electrode was thoroughly rinsed with water and allowed to dry at room temperature for further modification.

2.5. Preparation of GOD/Pt/FGS/chitosan/GCE

GOD was dissolved in a 0.2% chitosan solution, and the GOD concentration was 10 mg/mL. Six microliters of the solution were cast on the as-prepared Pt NP/FGS/chitosan/GCE. Right after casting, the GOD-modified electrode was moved into a refrigerator and kept at 4 °C to dry overnight. During the experimental period, the modified electrodes were stored at 4 °C until use.

2.6. Instrumentation

Cyclic voltammetric and amperometic measurements were performed on a CHI 824 electrochemical workstation (CHI Instruments, Inc., Austin, TX) connected to a personal computer. A three-electrode cell (10 mL) was employed with a modified GCE as the working electrode, an Ag/AgCl electrode as the reference electrode, and platinum wire as the auxiliary electrode. An amperometric response of the GOD/Pt/FGS/chitosan/GCE to the sequential addition of a desired amount of glucose was measured at +0.4 V with continuous gentle stirring in a 5-mL buffer solution containing 0.01 M PBS. The transmission electron microscope (TEM) images were recorded on a JEOL JEM 2010 microscope with a specified point-to-point resolution of 0.194 nm. The operating voltage on the microscope was 200 keV. The FGS sample was prepared by dropping a diluted FGS suspension onto the Cu–C grid. The Pt/FGS/chitosan nanocomposite sample was prepared by peeling the hybrid Pt/FGS/chitosan nanocomposite off the GCE and was transferred to a Cu–C grid. All images were digitally recorded with a slow-scan charge-coupled device camera (image size 1024 × 1024 pixels), and image processing was carried out using a Digital Micrograph (Gatan).

3. Results and discussion

The chitosan dispersed FGSs were prepared and characterized with TEM. Fig. 1(A) shows an image of FGSs dispersed in chitosan. As shown in this figure, the FGSs exhibit wrinkled graphene sheets. This wrinkled nature of FGSs is highly beneficial in maintaining a high surface area on the electrode since the sheets cannot readily collapse back to a graphitic structure. The inset in Fig. 1(A) displays a selected-area electron diffraction (SAED) of the nanocomposite material, yielding a double six-spot-ring pattern from a graphene sheet [17].

Pt nanoparticles were electrochemically deposited on FGS/chitosan film. Fig. 1(B) is a TEM image of Pt NP-modified FGSs. It can be seen from this figure that Pt NPs are uniformly deposited on the graphene surface with a size of less than 50 nm.

In the current study, the electrochemical response of the graphene-based glucose biosensor was coming from the anodic oxidation current of the enzymatic product H_2O_2. It is well known that H_2O_2 undergoes electrochemical oxidation processes at the solid electrodes, but the oxidation or reduction occur at relatively high potentials that cause high background current and interference from other electroactive compounds. Noble nanoparticles, such as platinum, have been widely used as electrocatalysts for oxidation and reduction of H_2O_2. To study the electrocatalytic effect of the FGS/chitosan and Pt/FGS/chitosan films to H_2O_2, cyclic

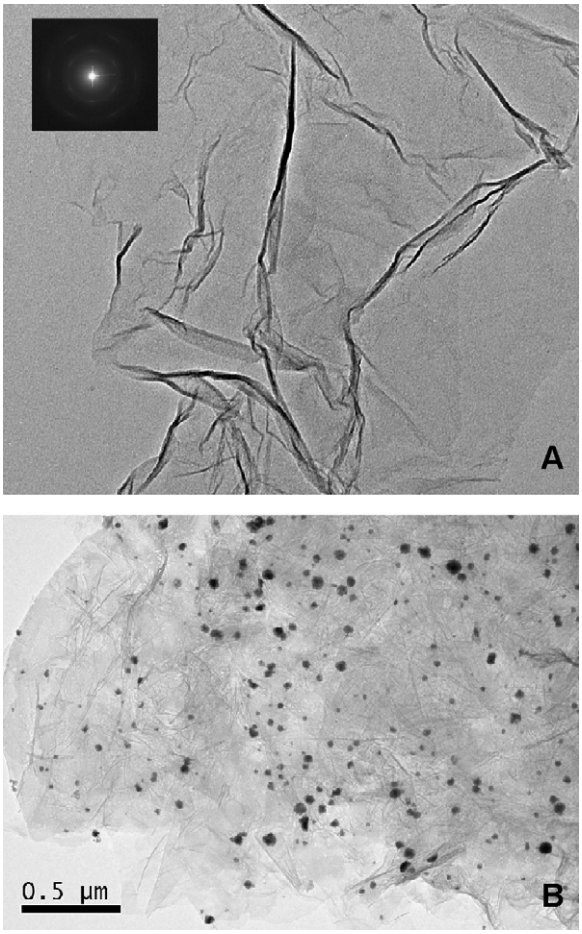


Fig. 1. (A) TEM image of FGS (inset: SAED of FGS). (B) TEM image of platinum nanoparticles deposited on a graphene sheet.

voltammetry was performed. Fig. 2(A) shows the cyclic voltammograms obtained at the modified GCE with a hybrid Pt/FGS/chitosan nanocomposite film in a 10-mM phosphate-buffered saline (PBS) solution containing 1.5 mM H_2O_2 in comparison with a bared GCE and FGS/chitosan GCE. The electrochemical responses of all these electrodes are negligible in the solution in the absence of H_2O_2 (data not shown). As shown in this figure, the oxidation and reduction currents from H_2O_2 at the bare GCE are quite small, and the oxidation of H_2O_2 at the bare GCE starts at 0.6 V. However, the electrochemical responses obtained at the FGS/chitosan/GCE and the Pt/FGS/chitosan/GCE are much larger than that obtained at the GCE. Moreover, it can be seen that the oxidation of H_2O_2 started at ~0.3 V, and the oxidation current increased as the potential increased at these modified electrodes. It can also be seen that the reduction of H_2O_2 started at 0.1 V at the modified electrode, and the reduction current increased as the potential decreased. The decrease of the overpotential of H_2O_2 is ascribed to the electrocatalytic activity of the platinum NP and graphene. Furthermore, it can be seen that the magnitude of the electrochemical response at these different electrodes increased in the following order: Pt/FGS/chitosan/GC > FGS/chitosan/GC > GC. It was concluded that the hybrid nanocomposite film with both graphene and platinum nanoparticles showed a synergistic effect on the electrocatalytic activity to H_2O_2. Therefore, the hybrid Pt/FGS/chitosan/GCE exhibited the highest electrocatalytic activity toward H_2O_2. The data from hydrodynamic voltammograms shown in Fig. 2(B) further confirmed the results in Fig. 2(A). Fig. 2(B) illustrates that the FGS-modified electrode improved the electrocatalytic activity to H_2O_2 (Curve b) compared with that at the GCE (Curve a). It can be seen that the Pt/FGS/chitosan nanocomposite had the highest electrochemical response to H_2O_2 and showed a significant synergistic effect on the electrocatalytic activity to H_2O_2 (Curve c).

The effect of the Pt electrodeposition time on the electrocatalytic activity of Pt/FGS/chitosan/GCE to H_2O_2 was studied. The electrocatalytic activity of the prepared electrode was measured at 0 V in a solution containing 0.6 mM H_2O_2. It was found that the response current increased as the deposition time increased until it reached the plateau at 200-s deposition. Then the signal started to decrease with more deposition time, which may be ascribed to the reduced electrochemical active surface area because large-sized particles may be deposited on the electrode surface with a long deposition time. A 200 s deposition time was chosen for this work.

Amperometric technique was used for the evaluation of the graphene-based biosensor for glucose detection. Fig. 3(A) shows the typical amperometric response of GOD/Pt/FGS/chitosan/GCE to successive additions of 0.15 mM glucose with an applied potential at 0.4 V. As can be seen from Fig. 3(A), the electrochemical response increased as the glucose concentration increased. From the inset in Fig. 3(A), it can be seen that the sensor is responsive to a low

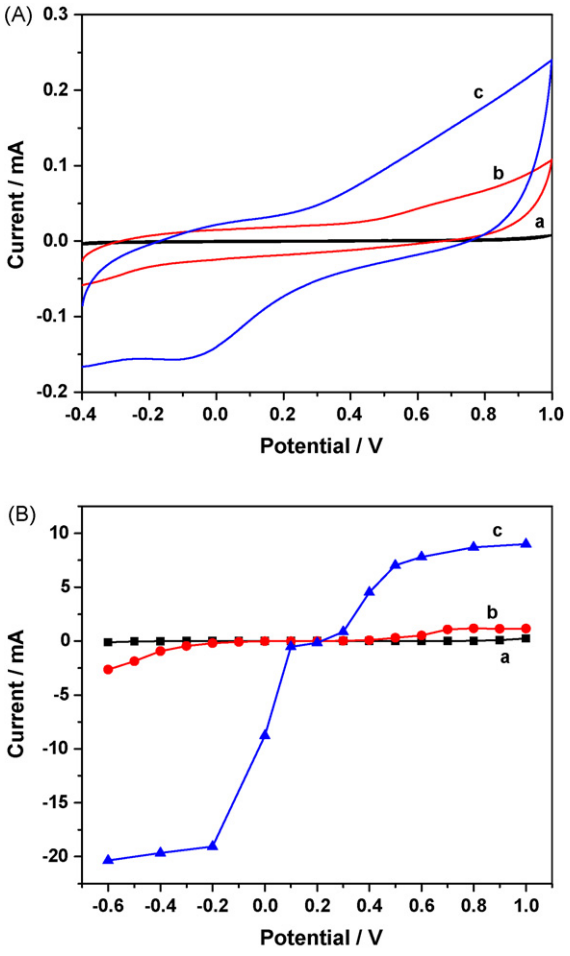


Fig. 2. (A) Cyclic voltammograms obtained at (a) bare GCE; (b) FGS/chitosan/GCE; (c) Pt/FGS/chitosan/GCE in 10 mM PBS buffer solution containing 1.5 mM H_2O_2. (B) Hydrodynamic voltammograms obtained at (a) bare GCE; (b) FGS/chitosan/GCE; (c) Pt/FGS/chitosan/GCE in 10 mM PBS buffer solution containing 0.12 mM H_2O_2.

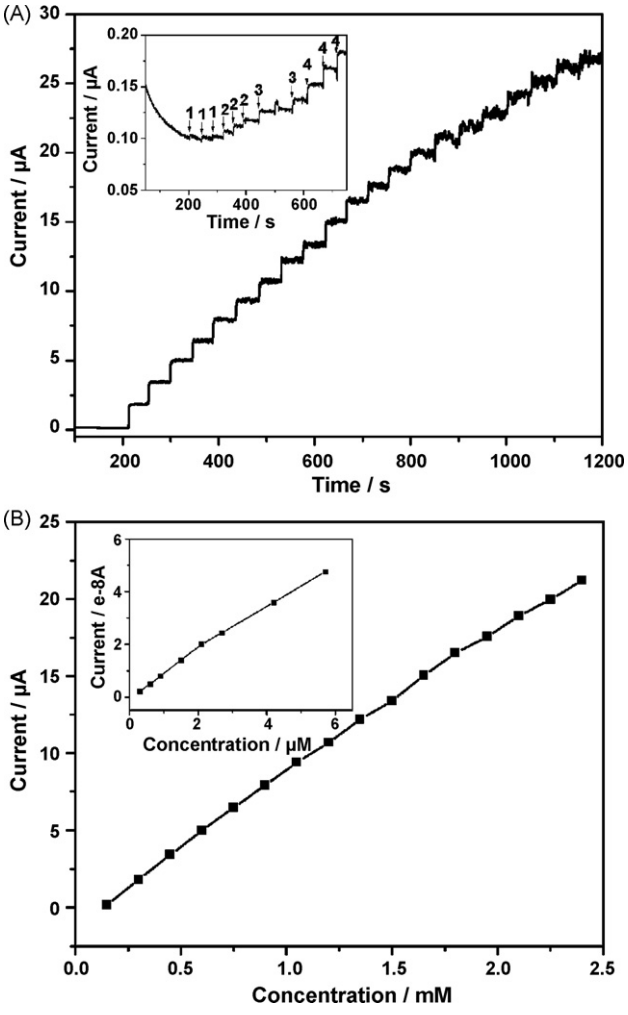


Fig. 3. (A) Amperometric response of GOD/Pt/FGS/chitosan/GCE to sequential addition of a series of glucose concentrations from 0.15 mM to 4.2 mM at +0.4 V. Inset (a) amperometric response to the sequential addition of (1) 0.3 μM, (2) 0.6 μM, (3) 1.5 μM, and (4) 3 μM glucose. (B) The calibration curve from (A). Inset (b) is the lower range of the calibration curve.

concentration of glucose, such as 0.6 μM glucose. Fig. 3(B) displays the plot of the electrochemical response vs. the glucose concentration. It can be seen from this figure that this sensor shows a wide linear range from sub-μM to 5 mM glucose. The detection limit of the glucose sensor is 0.6 μM based on the three times of signal-to-noise ratio. Such a sensitivity of the biosensor might be attributed to a large surface area, a fast electron transfer activity of FGS, and the electrocatalytic synergy from platinum and graphene. Within the nanocomposite, GOD can contact both graphene and platinum, which facilitates the fast electron transfer with a relatively low barrier between the enzyme and the electrode. The glucose sensor based on Pt NP/FGSs achieved a better detection limit in comparison with the Pt/Pb alloy NP/carbon nanotube-based glucose sensor [16] (a detection limit of 7 μM) and the Pt nanowire/carbon nanotube-based glucose sensor [15] (a detection limit of 3 μM). The sensitive biosensor was also accompanied with good reproducibility. The relative standard deviation (RSD) of the biosensor in response to 15 μM glucose was 6% for five different electrodes, indicating the good reproducibility of the biosensor. The long-term stability of the glucose sensor was examined with two electrodes for 2 weeks. The data showed that the enzyme maintained 86% of its activity during the first week and 75% during the second week. We also evaluated the potential interference from other electroactive biomolecules, such as ascorbic acid and uric acid, with concentrations similar to physiological fluid. Results indicate that the responses from these interferents are negligible. The sensor was also validated with glucose-spiked human plasma samples, and the recovery of the spike sample was 101%. These results indicate that the biosensor developed in this work has high sensitivity and selectivity for detecting blood glucose level.

4. Conclusion

We present a novel bionanocomposite film consisting of GOD/Pt/FGS/chitosan for glucose sensing. The biosensor exhibits good sensitivity with a detection limit of 0.6 μM glucose. Such a sensitivity is attributed to the synergy of FGS and Pt nanoparticles on the electrocatalytic activity to H_2O_2. The glucose biosensor has good responses because of the large surface area and fast electron transfer of graphene and Pt nanoparticles. The biosensor also has good reproducibility and long-term stability. The interfering signals from ascorbic acid and uric acid are negligible compared with the response to glucose. Human plasma samples were tested with the glucose sensor, and good recovery was achieved with the spiked samples. This work shows that the hybrid GOD/Pt/FGS/chitosan nanocomposite-based biosensor has great potential for clinical utility and home care for a rapid monitoring of glucose. The graphene-based biosensor fabrication method demonstrated in this work is readily applicable to the fabrication of other biosensors based on oxidases, such as biosensors for cholesterol, alcohol, lactate, acetylcholine, hypoxanthine, and xanthine [18,19].

Acknowledgements

This work was supported by a laboratory-directed research and development program at Pacific Northwest National Laboratory (PNNL). The work was performed at the Environmental Molecular Sciences Laboratory, a national scientific user facility sponsored by the U.S. Department of Energy (DOE) and located at PNNL. PNNL is operated by Battelle for DOE under Contract DE-AC05-76RL01830. Ilhan A. Aksay acknowledges support from Army Research Office (ARO)/Multidisciplinary Research Initiative (MURI) under grant number W911NF-04-1-0170 and the Directed Technologies, Inc.

References

[1] A.K. Geim, K.S. Novoselov, Nat. Mater. 6 (2007) 183.
[2] M. Wilson, Phys. Today 59 (2006) 21.
[3] C. Stampfer, E. Schurtenberger, F. Molitor, J. Guttinger, T. Ihn, K. Ensslin, Nano Lett. 8 (2008) 2378.
[4] D. Li, R.B. Kaner, Science 320 (2008) 1170.
[5] N.M.R. Peres, F. Guinea, A.H. Castro Neto, Phys. Rev. B 73 (2006) 125411.
[6] O. Leenaerts, B. Partoens, F.M. Peeters, Phys. Rev. B 77 (1–6) (2008) 125416.
[7] B. Huang, Z. Li, Z. Liu, G. Zhou, S. Hao, J. Wu, B. Gu, W.H. Duan, J. Phys. Chem. C 112 (2008) 13442.
[8] P.K. Ang, W. Chen, A.T.S. Wee, K.P. Loh, J. Am. Chem. Soc. 130 (2008) 14392.
[9] R.M. Westervelt, Science 320 (2008) 324.
[10] (a) H.C. Schniepp, J.-L. Li, M.J. McAllister, H. Sai, M. Herrera-Alonso, D.H. Adamson, R.K. Prud'homme, R. Car, D.A. Saville, I.A. Aksay, J. Phys. Chem. B 110 (2006) 8535;
(b) M.J. McAllister, J.-L. Li, D.H. Adamson, H.C. Schniepp, A.A. Abdala, J. Liu, M. Herrera-Alonso, D.L. Milius, R. Car, R.K. Prud'homme, I.A. Aksay, Chem. Mater. 19 (2007) 4396.
[11] C. Shan, H. Yang, J. Song, D. Han, A. Ivaska, L. Niu, Anal. Chem. 81 (2009) 2378.
[12] D. Wang, D. Choi, J. Li, Z. Yang, Z. Nie, R. Kou, D. Hu, C. Wang, L.V. Saraf, J. Zhang, I.A. Aksay, J. Liu, ACS Nano 3 (2009) 907.
[13] R. Kou, Y. Shao, D. Wang, M.H. Engelhard, J.H. Kwak, J. Wang, V. Viswanathan, C. Wang, Y. Lin, Y. Wang, I.A. Aksay, J. Liu, Electrochem. Commun. 11 (2009) 954.
[14] X. Chu, D. Duan, G. Shen, R. Yu, Talanta 71 (2007) 2040.
[15] F. Qu, M. Yang, G. Shen, R. Yu, Biosens. Bioelectron. 22 (2007) 1749.
[16] H. Cui, J. Ye, W. Zhang, C. Li, J.H.T. Luong, F. Sheu, Anal. Chim. Acta 594 (2007) 175.
[17] K.S. Novoselov, A.K. Geim, S.V. Morozov, D. Jiang, Y. Zhang, S.V. Dubonos, I.V. Grigorieva, A.A. Firsov, Science 306 (2004) 666.
[18] J. Wang, Y. Lin, Trends Anal. Chem. TrAC 27 (2008) 619.
[19] M. Jiang, Y. Lin, in: C.A. Grimes, E.C. Dickey, M.V. Pishko (Eds.), Encyclopedia of Sensors, vol. 2, American Scientific Publishers, Stevenson Ranch, CA, 2006, pp. 25–51.

Talanta 80 (2009) 407–410

Contents lists available at ScienceDirect

Talanta

journal homepage: www.elsevier.com/locate/talanta

Short communication

Detection of microcystins in environmental samples using surface plasmon resonance biosensor

Chenlin Hu[a,b], Nanqin Gan[a], Yuanyuan Chen[c], Lijun Bi[c], Xianen Zhang[c], Lirong Song[a,*]

[a] State Key Laboratory of Freshwater Ecology and Biotechnology, Institute of Hydrobiology, Chinese Academy of Sciences, Donghu Nanlu 7, Wuchang, Wuhan 430072, PR China
[b] Graduate School of Chinese Academy of Sciences, Beijing 100049, PR China
[c] Analytical Biotechnology of State Key Laboratory of Macromolecules, Institute of Biophysics, Chinese Academy of Sciences, Beijing 100101, PR China

ARTICLE INFO

Article history:
Received 19 January 2009
Received in revised form 19 June 2009
Accepted 19 June 2009
Available online 27 June 2009

Keywords:
Microcystins
Surface plasmon resonance (SPR)
Biosensor
ELISA

ABSTRACT

An indirect inhibitive surface plasmon resonance (SPR) immunoassay was developed for the microcystins (MCs) detection. The bioconjugate of MC-LR and bovine serum albumin (BSA) was immobilized on a CM5 sensor chip. A serial premixture of MC-LR standards (or samples) and monoclonal antibody (mAb) were injected over the functional sensor surface, and the subsequent specific immunoreaction was monitored on the BIAcore 3000 biosensor and generated a signal with an increasing intensity in response to the decreasing MCs concentration. The developed SPR immunoassay has a wide quantitative range in 1–100 $\mu g\,L^{-1}$. Although not as sensitive as conventional enzyme-linked immunosorbent assay (ELISA), the SPR biosensor offered unique advantages: (1) the sensor chip could be reusable without any significant loss in its binding activity after 50 assay-regeneration cycles, (2) one single assay could be accomplished in 50 min (including 30-min preincubation and 20-min BIAcore analysis), and (3) this method did not require multiple steps. The SPR biosensor was also used to detect MCs in environmental samples, and the results compared well with those obtained by ELISA. We conclude that the SPR biosensor offers outstanding advantages for the MCs detection and may be further developed as a field-portable sensor for real-time monitoring of MCs on site in the near future.

© 2009 Published by Elsevier B.V.

1. Introduction

Microcystins (MCs) are a family of cyclic heptapeptides produced mainly by some freshwater cyanobacteria such as *Microcystis*, and are hazardous to humans and animals due to their hepatotoxicity and tumor-promoting activity [1,2]. Among the MCs variants, MC-LR is the most common and well investigated. To reduce the adverse effects on humans and animals, World Health Organization (WHO) has established a maximum permissible concentration of 1 $\mu g\,L^{-1}$ of MC-LR in drinking water [3]. It is therefore necessary to develop a rapid and reliable method for MCs detection in environmental monitoring. Recently, a series of biochemical and physicochemical methods have been developed for MCs detection such as protein phosphatase inhibition assay (PPiA), enzyme-linked immunosorbent assay (ELISA), high-performance liquid chromatography (HPLC) and liquid chromatography with mass spectrometry (LC/MS) [4]. However, these methods require either complex operation or expensive materials and devices. To circumvent these drawbacks, several research groups have made the attempts to develop biosensors for MCs detection, such as molecularly imprinted polymer (MIP)-based sensor [5], electrochemical immunosensors [6–9], and evanescent wave all-fiber immunosensors [10,11]. There have been the reports that described the application of test strips for rapid MCs analysis *in situ* [12,13]; however, it is still challenging to develop a simple, rapid, and sensitive method for MCs analysis.

Recently, the optical biosensor based on the surface plasmon resonance (SPR) has received more and more attention because of its own outstanding advantages: allowing rapid and real-time analysis, owning reusable sensor chip, and requiring low amounts of reagents without chemical labels. And it has been successfully and widely employed to detect small molecules of biomedical, food and environmental interest [14]. In this paper, we developed an indirect inhibitive SPR immunoassay for the MCs detection. The sensor chip was firstly functionalized by the amine-coupling method, and then the MCs detection was performed with indirectly measuring the inhibition by MCs in samples. The regeneration of the sensor chip was investigated. Moreover, the SPR biosensor was also used to detect MCs in environmental samples, the results were discussed and compared with the conventional ELISA.

* Corresponding author. Tel.: +86 27 68780806 fax: +86 27 68780871.
E-mail address: lrsong@ihb.ac.cn (L. Song).

0039-9140/$ – see front matter © 2009 Published by Elsevier B.V.
doi:10.1016/j.talanta.2009.06.044

2. Experimental

2.1. Materials and sample preparation

MC-LR with >95% purity (HPLC-grade), the (MC-LR)–BSA bioconjugate, and anti-(MC-LR) monoclonal antibody (mAb) were prepared in our laboratory, the cross-reactivity of mAb with MCs variants has been tested in our previous work [15]. *N*-hydroxysuccinimide (NHS), 1-ethyl-3-(3-dimethylaminopropyl)-carbodiimide hydrochloride (EDC), ethanolamine, and Tween-20 were purchased from BIAcore (Amersham Pharmacia Biotech, Uppsala, Sweden). All other chemicals used in the experiment were of analytical grade. All the solutions were prepared using deionized water (18.2 MΩ cm), which was obtained from a Milli-Q System (Millipore, Bedford, MA).

Natural water samples and fish tissue extractions were collected, pretreated, and extracted according to our previous procedure [16].

2.2. Instrumentation

The SPR immunoassay was performed with a BIAcore™ 3000 instrument (BIAcore, Uppsala, Sweden). The molecular weight (MW) of BSA and (MC-LR)–BSA were determined by matrix-assisted laser desorption/ionization time-of-flight mass spectrometry (MALDI-TOF-MS) instrument (Bruker Daltonic Reflex™ III mass spectrometer, Bruker Doltonic, Bremen, Germany).

2.3. Immobilization protocol

Before the immobilization, the molecular weight (MW) of BSA and (MC-LR)–BSA were determined to be 66,354 and 68,708, respectively. The difference of MW between BSA and (MC-LR)–BSA (2354) indicated that the molar ratio of MC-LR to carrier protein BSA was 2.4 in this work, which was suitable for further immobilization. Then the CM5 sensor chip was functionalized by the EDC–NHS amine coupling as follows: the sensor chip was activated twice by mixing equal volumes of NHS (0.1 M) and EDC (0.4 M) and injecting the mixture over the sensor chip for 10 min at a flow rate of 10 μL min^{-1}. (MC-LR)–BSA (100 μg mL^{-1}) was dissolved in sodium acetate buffer (10 mM, pH 4.3) and injected over the sensor chip surface at a flow rate of 5 μL min^{-1}. NaOH (25 mM) was injected to wash the surface, and capping of the unreacted sites was achieved by injection of ethanolamine (1 M, pH 8.0) for 7 min.

2.4. SPR immunoassay and indirect competitive ELISA (ic ELISA)

The SPR immunoassay was performed in the indirect inhibitive immunoassay format. MC-LR standards or samples (40 μL) were incubated with an equal volume of mAb for 30 min at room temperature. The equilibrated mixture was then injected over the functional surface at a flow rate of 5 μL min^{-1}; the remaining free mAb was captured by (MC-LR)–BSA on the surface. Real-time monitoring will be displayed in a sensorgram as the optical response (RU) versus time (in seconds). To convert the response back to baseline, the sensor chip was regenerated by injecting NaOH (40 mM) at a flow rate of 20 μL min^{-1}. The next sample was analyzed at random. A typical sensorgram for the real-time detection of MCs could be seen in Fig. 1.

To evaluate the reliability of the SPR immunoassay, MCs in the same samples were detected by the indirect competitive ELISA (ic ELISA) and the SPR immunoassay. The ic ELISA was performed according to our previous report [16].

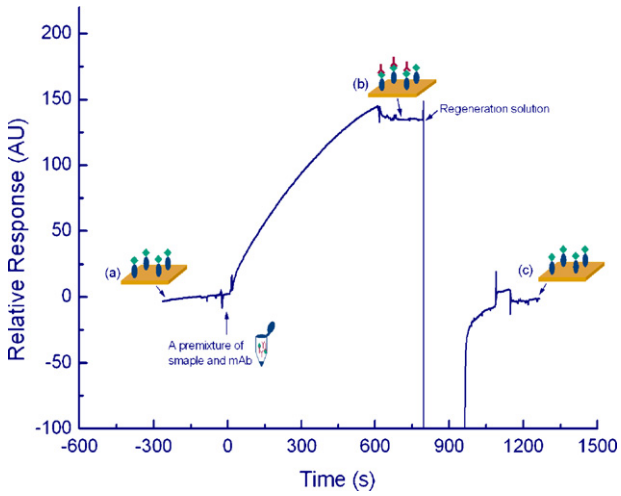


Fig. 1. The representative SPR response in real-time detection: PBS buffer was injected over the sensor chip surface immobilized with (MC-LR)–BSA, and a baseline of the SPR response was obtained (a); a premixture of samples and mAb was injected over the functional sensor chip for 10 min, and free mAb was captured by MC-LR on the sensor chip surface; the corresponding response was recorded (b); and the captured antibodies were removed using NaOH solution (40 mM) for the regeneration, the response returned to the baseline (c).

3. Results and discussion

3.1. The (MC-LR)–BSA bioconjugate immobilization

In the inhibitive SPR immunoassay, it is crucial to obtain a high bioconjugate immobilization level (amount), or rather a high hapten immobilization level because high amount of hapten generally means a potent capacity of antibody binding for the surface. The optimal immobilization level in this work was obtained through the preconcentration assay, as a result, a nearly saturated coverage level (approx. 9000 RU) was observed by using (MC-LR)–BSA solution (100 μg mL^{-1}) in 10 mM sodium acetate (pH 4.3). Subsequently, the capacity of mAb binding at the 9000 RU-immobilization level was further checked by injecting the mAb solution (15 μg mL^{-1}) over the functional surface, yielding a 218 RU-capacity of mAb binding, similar to the results in the other developed inhibitive immunoassays: 80 RU- and 300 RU-capacities of the antibody binding were generated at the same high bioconjugate immobilization level (10,000 RU) [17,18]. Actually, in a certain immunoassay, the capacity value of antibody binding on the surface should be evaluated rationally based on the used antibody affinity, working concentration, and especially, the effective hapten immobilization level. The surface with the high immobilization level did not necessarily yield a high capacity value of antibody binding. To be exact, only the high immobilization simultaneous with high molar ratio of hapten to carrier protein could contribute to the high surface antibody-binding capacity. Miura and co-workers previously reported the relative high capacity of antibody binding by using HBP–BSA bioconjugate with high molar ratio of HBP to BSA (n = approx. 54) [19], 22.5-fold more than that in this work (the molar ratio of MC-LR to BSA in this work, n = 2.4).

3.2. Detection of MCs using SPR biosensor and regeneration efficiency

According to the indirect inhibitive immunoassay format, MC-LR (0–100 μg L^{-1}) was incubated with mAb for 30 min; the mixture was then injected over the functional sensor chip. As observed in Fig. 2A, the binding response was inversely proportional to MC-LR concentration, which further supported the results obtained

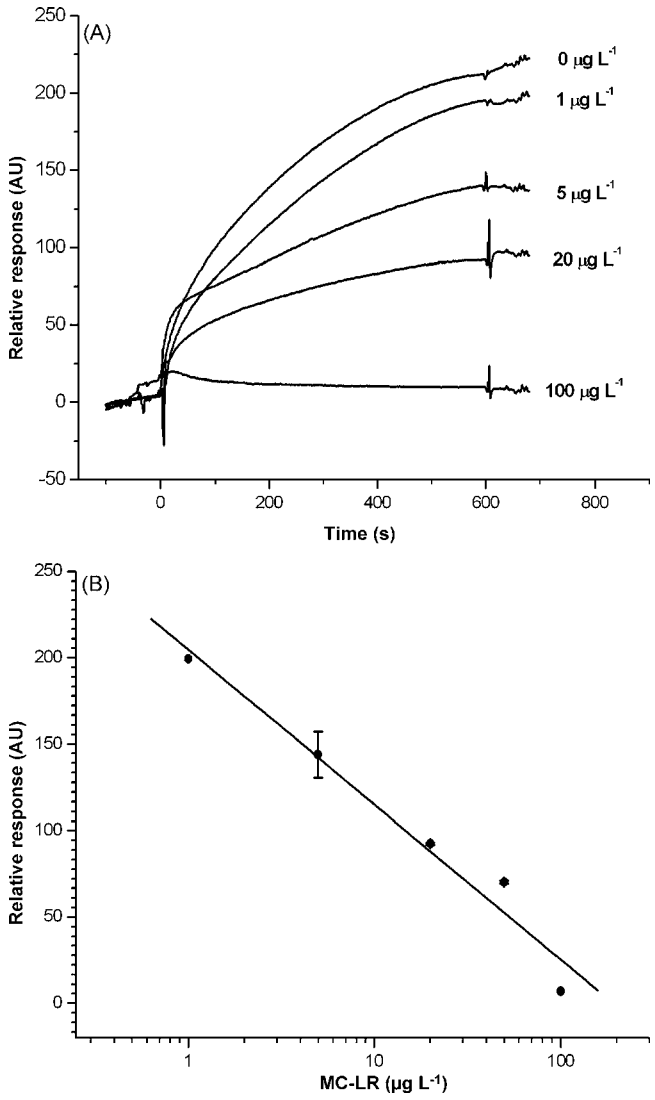


Fig. 2. (A) Sensorgram generated by injecting the solution mixture of monoclonal antibody and MC-LR at various concentrations (0, 1, 5, 20, and 100 μg L^{-1}) on the functional CM5 sensor chip and (B) standard curve for the detection of MCs by the SPR biosensor.

using the indirect inhibitive format. On the basis of these results, a dose–response curve was generated (Fig. 2B). The results indicated a good linearity (r^2 = 0.9667) in the wide quantitative range of 1–100 μg L^{-1}. And it has reached the permissive MCs concentration in drinking water (1 μg L^{-1}) by WHO [3]. In our previous work, sensitive time-resolved fluorescence (TRF) and chemiluminescence (CL) techniques were employed to improve the assay sensitivity, and exhibited the wide quantitative range of 0.01–10 and 0.05–10 μg L^{-1}, respectively [15,16], superior to the present SPR immunosensor sensitivity. However, the SPR immunosensor offered several important advantages over the above immunoassays: (1) compared to the ELISA, TRFIA, and CL immunoassays in our previous report, the SPR immunoassay could be rapidly accomplished in 50 min, whereas the immunoassays (ELISA, TRFIA, and CL immunoassays) required 2 h or more, (2) the entire SPR assay analysis is simple without any labeling and cumbersome washing that are indispensable for the above immunoassays, and (3) importantly the SPR sensor chip could be regenerated.

Furthermore, a comparison of the other biosensors for MCs detection is summarized in Table 1, in contrast to the other techniques such as the electrochemical and evanescent wave all-fiber biosensors for MCs detection [7,9,11–13], the present SPR immunosensor was not as highly sensitive as the biosensors above, which may be due to the different antibodies, assay strategies, and technique platforms. However, there is still further scope of the SPR immunoassay sensitivity improvement since antibody-amplification strategies have been successfully applied in other biochemical molecules analyses [21,22]. As an important parameter, the BIAcore analysis time could be 20 min, moreover, the whole analysis time including the preincubation and BIAcore analysis time was approximately 50 min, and could be also competitive with or better than other techniques in Table 1.

3.3. Regeneration efficiency

After one sample analysis, the antigen–antibody complex on the surface should be dissociated using a regeneration solution for the next analysis. In the present study, NaOH (40 mM) was found to be suitable for regeneration (Fig. 1). After 50 assay-regeneration cycles, the capacity of mAb binding for the functional chip was determined to be 179 RU compared with 218 RU-capacity of the original mAb binding, indicating that decrease in the binding capacity of the functional CM5 sensor chip was less than 20% of the initial binding capacity, which was an acceptable loss of binding capacity according to the validation parameters for the SPR biosensor [20].

3.4. Application of SPR immunoassay for environmental samples

In the present study, the reliability of the SPR immunoassay was evaluated by the conventional ELISA. The results are summarized in Table 2 [maximum relative standard deviation (RSD) for ELISA in the present study, 6.6%]. The results obtained by the biosensor and ELISA were in fairly good agreement, supporting the feasibility of the application of the SPR biosensor to detect

Table 1
Comparison of the biosensors and strips developed for the detection of MC-LR.

Analytical technique of the biosensor	Assay format	The working range (μg L^{-1})	The whole analysis time[a]	Reference
Piezoelectric sensor	Molecularly imprinted polymer-based specific recognition	NA[b]	Approx. 25 min	Chiallena et al. [5]
Electrochemical immunosensor	Protein phosphatase-based inhibition	NA[b]	NA[b]	Campàs and Marty [6]
Electrochemical immunosensor	Competitive immunoassay	10^{-4}–10^{2} (mAb); 10^{-1}–10^{2} (pAb)	Approx. 2 h 30 min	Campàs et al. [7]
Electrochemical immunosensor	Enzyme inhibition	37–188	Approx. 50 min	Campàs et al. [8]
Capacitive immunosensor	Immunoassay based on mAb	10^{-5}–1	Approx. 38 min	Loyprasert et al. [9]
Evanescent wave immunosensor	Indirect competitive immunoassay	NA[b]	Approx. 40 min	Long et al. [10]
Evanescent wave immunosensor	Indirect competitive immunoassay	0.1–10.1	Approx. 40 min	Long et al. [11]
Fluorescent immunochromatographic assay	Competitive immunoassay	0.125–2	Approx. 15 min	Kim et al. [12]
Electronical enzyme immunoassay strip	Competitive immunoassay	0.01–3.16	10 min 30 s	Zhang et al. [13]
SPR immunosensor	Indirect competitive immunoassay	1–100	Approx. 50 min	This work

[a] The whole analysis time was evaluated from each experiment section in the literatures.
[b] NA, not available.

Table 2
Microcystins determined by SPR biosensor and ic ELISA in environmental samples.

Sample code[a]	SPR biosensor ($\mu g\,L^{-1}$), mean ± SD[b]	ic ELISA ($\mu g\,L^{-1}$)
1	<1	0.49
2	<1	1.12
3	1.8 ± 0.3	1.66
4	2.4 ± 0.2	2.70
5	2.8 ± 0.1	2.50
6	14.5 ± 1.2	10.17

[a] Samples 1–3 were water samples, the pretreatment of samples was seen in Section 2. Samples 4–6 were fish tissues; MCs extracted from the samples were dissolved in 1 mL aliquot of ultrapure water; SPE extracts were diluted to perform the MCs analysis (if necessary).

[b] Data were mean ± SD from triplicate analyses for each sample.

MCs in environmental samples. Therefore, the SPR biosensor could be reliable and practical for the MCs analysis in environmental samples.

4. Conclusion

We have developed an inhibitive SPR immunoassay for MCs detection in environmental samples. The immunosensor chip was functionalized with (MC-LR)–BSA by amine coupling. Using this chip, a wide linear range ($1–100\,\mu g\,L^{-1}$) was achieved, which reached the permissive MCs concentration in drinking water ($1\,\mu g\,L^{-1}$) by WHO, meanwhile, only $40\,\mu L$ of samples were required and the whole assay can be analyzed in 50 min. Additionally, the functional sensor chip was favorable as its binding ability was not significantly affected after 50 assay-regeneration cycles. The SPR biosensor was applied to environmental samples, the results compared well with those by the conventional ELISA. This work has demonstrated that SPR immunosensor is simple, rapid, and suitable for the detection of MCs in environmental samples. Meanwhile, since less expensive portable SPR devices become increasingly popular and useful, presently, our further effort may be made to miniaturize the SPR biosensor to monitor field samples *in situ* for MCs detection.

Acknowledgments

The authors greatly acknowledge the financial support from National Natural Science Foundation of China (No. 20407017) and Chinese Academy of Sciences (KZCX-1-YW-14-1).

References

[1] W.W. Carmichael, Adv. Bot. Res. 27 (1997) 211.
[2] C. MacKintosh, K.A. Beattie, S. Klumpp, P. Cohen, G.A. Codd, FEBS Lett. 264 (1990) 187.
[3] WHO, Guidelines for Drinking Water Quality, Addendum to Vol. 1, 2nd ed., World Health Organization, Geneva, 1998.
[4] T.A.M. Msagati, B.A. Siame, D.D. Shushu, Aquat. Toxicol. 78 (2006) 382.
[5] I. Chiallena, S.A. Piletsky, I.E. Tothill, B. Chen, A.P.F. Turner, Biosens. Bioelectron. 18 (2003) 119.
[6] M. Campàs, J.L. Marty, Biosens. Bioelectron. 22 (2007) 1034.
[7] M. Campàs, D. Szydłowska, M. Trojanowicz, J.L. Marty, Biosens. Bioelectron. 20 (2005) 1520.
[8] M. Campàs, D. Szydłowska, M. Trojanowicz, J.L. Marty, Talanta 72 (2007) 179.
[9] S. Loyprasert, P. Thavarungkul, P. Asawatreratanakul, B. Wongkittisuksa, C. Limsakul, K. Kanatharana, Biosens. Bioelectron. 24 (2008) 78.
[10] F. Long, M. He, H. Shi, A. Zhu, Biosens. Bioelectron. 23 (2008) 952.
[11] F. Long, M. He, A.N. Zhu, H.C. Shi, Biosens. Bioelectron. 24 (2009) 2346.
[12] Y.M. Kim, S.W. Oh, S.Y. Jeong, D.J. Pyo, E.Y. Choi, Environ. Sci. Technol. 37 (2003) 1899.
[13] F. Zhang, S.H. Yang, T.Y. Kang, G.S. Cha, H. Nam, M.E. Meyerhoff, Biosens. Bioelectron. 22 (2007) 1419.
[14] D.R. Shankaran, K.V. Gobi, N. Miura, Sens. Actuators B 121 (2007) 158.
[15] L. Lei, Y. Wu, N. Gan, L. Song, Clin. Chim. Acta 348 (2004) 177.
[16] C. Hu, N. Gan, Z. He, L. Song, Int. J. Environ. Anal. Chem. 84 (2008) 267.
[17] M. Miyashita, T. Shimada, H. Miyashita, M. Akamatsu, Anal. Bioanal. Chem. 381 (2005) 667.
[18] G.J. Keating, J.G. Quinn, R. O'Kennedy, Anal. Lett. 32 (1999) 2163.
[19] S.J. Kim, K.V. Gobi, R. Harada, D.R. Shankarna, N. Miura, Sens. Actuators B 115 (2006) 349.
[20] R.L. Wong, D. Mytych, S. Jacobs, R. Bordens, S.J. Swanson, J. Immunol. Methods 209 (1997) 1.
[21] J.S. Mitchell, Y.Q. Wu, C.J. Cook, L. Main, Anal. Biochem. 343 (2005) 125.
[22] X. Liu, Y. Sun, D. Song, Q. Zhang, Y. Tian, H. Zhang, Talanta 68 (2006) 1026.

Contents lists available at ScienceDirect

Talanta

journal homepage: www.elsevier.com/locate/talanta

Corrigendum

Corrigendum to "Single-step microwave digestion of food and biological samples for the quantitative conversion of Se into the +4 oxidation state" [Talanta 78 (2009) 753–758]

R. Toniolo, F. Tubaro, S. Bin, A. Pizzariello, S. Susmel, N. Dossi, G. Bontempelli *

Department of Chemical Science and Technology, University of Udine, via Cotonificio 108, I-33100 Udine, Italy

The authors regret that during the processing of the above paper an error occurred in the indication of the optimised NaCl concentration in sample digestion media. In fact, a concentration of 1.3 g mL^{-1} has been reported at both line 2 from the bottom at p. 756 (left-hand column) and line 3 form the bottom in the caption of Fig. 1 (reported at p. 756 either) for a typewriting mistake, while the correct concentration is instead 0.3 g mL^{-1}.

The authors would like to apologise for any inconvenience this may have caused to the readers of the journal.

DOI of original article: 10.1016/j.talanta.2008.12.045.

* Corresponding author. Tel.: +39 0432 558842; fax: +39 0432 558803.
E-mail address: Gino.Bontempelli@uniud.it (G. Bontempelli).

0039-9140/$ – see front matter © 2008 Elsevier B.V. All rights reserved.
doi: 10.1016/j.talanta.2009.06.043

Talanta 80 (2009) 413–421

Contents lists available at ScienceDirect

Talanta

journal homepage: www.elsevier.com/locate/talanta

Review

Recent developments in homogeneous and dispersive liquid–liquid extraction for inorganic elements determination. A review

Aristidis N. Anthemidis*, Kallirroy-Ioanna G. Ioannou

Laboratory of Analytical Chemistry, Department of Chemistry, Aristotle University, Thessaloniki 54124, Greece

ARTICLE INFO

Article history:
Received 5 August 2009
Received in revised form 27 August 2009
Accepted 3 September 2009
Available online 8 September 2009

Keywords:
Homogeneous liquid–liquid extraction
Dispersive liquid–liquid microextraction
Metal
Metalloid

ABSTRACT

This review aims to provide an overview of homogeneous liquid–liquid extraction (HLLE) and dispersive liquid–liquid microextraction (DLLME) methods and their potential use in inorganic analysis. Relevant applications to the determination of metal ions, metalloids and organometals are included. The phase separation mechanisms of these unconventional solvent extraction techniques are discussed. The new trends in the field of miniaturization and automation are presented, while proposing future trends and potential new areas for their application.

© 2009 Elsevier B.V. All rights reserved.

Contents

1. Introduction 413
2. How do HLLE and DLLME work? 414
3. Applications HLLE and DLLME for metal determination 416
   3.1. HLLE based on temperature separation 416
   3.2. HLLE based on salting-out phenomenon with salt 416
   3.3. HLLE based on salting-out with auxiliary solvent 417
   3.4. HLLE based on pH-dependent phase separation with $PFOA^-$ 417
   3.5. HLLE based on pH-dependent ternary solvent systems 419
   3.6. HLLE based on ion-pair formation 419
   3.7. Dispersive liquid–liquid microextraction (DLLME) 419
4. Automation of DLLME 420
5. Conclusions 421
   References 421

1. Introduction

Transportation of materials from one phase to another is the most fundamental procedure for the separation of a chemical species from the matrix or from other coexisting components. Liquid–liquid or solvent extraction is based on the principle that a solute or analyte can distribute itself in a certain ratio between two immiscible solvents, one of which is usually water (aqueous phase) and the other an organic solvent (organic phase). In certain cases the analyte can be more or less completed moved into the organic phase.

Sample pre-treatment is often the bottleneck in a measurement process, as they tend to be slow and labor-intensive. In routine analysis, liquid–liquid extraction (LLE) is the most widely used sample preparation technique, whose goal is cleanup, enrichment and signal enhancement. However, some shortcomings like the use of extensive amounts of hazardous organic solvents and sample volumes, the generation of large amounts of pollutants make this procedure time consuming, expensive, environmentally unfriendly, tedious, laborious and hence potentially prone to sample contamination when ultra-trace determinations are required [1,2].

* Corresponding author. Tel.: +30 2310997826; fax: +30 2310997719.
E-mail address: anthemid@chem.auth.gr (A.N. Anthemidis).

0039-9140/$ – see front matter © 2009 Elsevier B.V. All rights reserved.
doi:10.1016/j.talanta.2009.09.005

Modern trends in analytical chemistry are towards the simplification and miniaturization of sample preparation procedures as they lead inherently to a minimum solvent and reagent consumption and drastic reduction of laboratory wastes [3,4]. Under this context, unconventional LLE methodologies have been arisen like: single drop microextraction (SDME), wetting film extraction (WFE), cloud point extraction (CPE), homogeneous liquid–liquid extraction (HLLE), dispersive liquid–liquid microextraction (DLLME) and dispersive liquid–liquid microextraction based on solidification of a floating organic drop (DLLME-SFO).

SDME is based on a droplet of organic solvent, which is suspended at the tip of a microsyringe needle and immersed into the aqueous sample, which can be stagnant or moving. Recently, an automatic SDME method performing on-line metal preconcentration coupled with ETAAS has been presented [4]. A micro-drop of di-isobutyl ketone (DIBK) is generated and suspended at a glass capillary tip into the flow-through microextraction cell. As the fresh metal complex flows continuously around the micro-droplet, the analyte is extracted into the solvent. Subsequently, the micro-drop is retracted back into the holding coil for measuring. Xu et al. [5] overviewed the basic extraction principles of SDME as well as its latest developments and applications. WFE concept is based on the formation of a thin layer coating of organic phase on the inner walls of a PTFE extraction coil, as a result of the hydrophobic interactions between solvent and coil. The theoretical aspects as well as fundamental stages of the renewable phase WFE technique have been well presented by Miro et al. in a recent review [3]. Once the metal complex species have been preconcentrated a small plug of a suitable solvent or back-extraction solution is pumped into the coated reactor to strip out the isolated analyte, which thereafter is delivered to the detector for quantification. The CPE procedure is based on the phase separation, which occurs in aqueous solutions of non-ionic surfactants when heated above the so-called cloud point temperature. At this point the initial solution separates into a surfactant rich phase of small volume containing the metal trapped by organized structures and a bulk aqueous phase [6].

On the other hand, homogeneous liquid–liquid extraction (HLLE) utilizes the phase separation phenomenon from a homogeneous solution and simultaneously extracting the target solutes into the separated phase [7,8]. It can be considered, that the surface area of the interface between the two phases (aqueous and organic) initial is infinitely large. Consequently, vigorous shaking or mixing is not necessary. Generally, HLLE has been applied through binary [9,10] and ternary component miscible solvent systems [11,12]. In these cases, phase separation is based on salting-out phenomenon, on temperature, on pH of perfluorinated surfactant systems and on ion-pair formation. HLLE is a simple and powerful preconcentration method that reduces reagent consumption, extraction time, cost of analysis and the exposure to the organic solvents [11].

Recently, Assadi and co-workers [13] presented a microextraction technique, termed dispersive liquid–liquid microextraction (DLLME) based on ternary component solvent systems. An appropriate mixture of an extraction solvent and a disperser solvent, with high miscibility in both aqueous and organic phase (extraction solvent) is rapidly injected into the sample solution (aqueous phase). By this procedure a cloudy solution (high turbulence) is produced, which is consisted of fine droplets of the extraction solvent, dispersed throughout the aqueous solution. Consequently, the analyte is extracted into the fine droplets of extraction solvent usually through complex formation. After centrifugation, the fine droplets are settled down at the bottom of the conical test tube, removed by a syringe and analyzed by various analytical techniques like gas chromatography (GC) [14,15], gas chromatography–mass spectrometry (GC–MS) [16], high-performance liquid chromatography (HPLC) [17–19], electrothermal atomic absorption spectrometry (ETAAS) [20–22] and FAAS [23,24]. The applications of this new procedure have been reviewed recently by Bosch-Ojeda and Sanchez-Rojas [25] and Zang et al. [26]. DLLME has been performed in manually (batch) mode and only one study has been presented in on-line sequential injection mode up today. DLLME has been applied for determination of organic compounds [13,17–19] as well as for metals [14,15,20–24,27] and metalloids [14,28,29] in various types of samples but mainly in water samples. The principal advantage of HLLE and DLLME is that the initial surface area between extraction solvent and aqueous sample is very large, thus the equilibrium state is achieved quickly and the extraction time is very short.

An alternative DLLME procedure named DLLME-SFO has been presented by Leong and Huang for organic compounds determination. This method based on the solidification of floating organic droplet by cooling the glass tube in an ice bath for 5 min. The organic solvent was then transferred into a conical vial; melted quickly at room temperature and injected into gas chromatography [30,31] for analysis.

This review presents an update on progress in implementing the HLLE and DLLME for preconcentration of metal and metalloid species hyphenated with various detection systems such as atomic spectrometry, UV–vis spectophotometry, X-ray fluorescence spectrometry and polarography including the new trends and applications.

2. How do HLLE and DLLME work?

In LLE, certain solvents such as acetonitrile, acetone, 2-propanol, propylene carbonate, methanol, ethanol, and dimethylsulphoxide cannot be used as extracting solvents because they are miscible with water in all proportions. Also they are omitted from use as extractants from aqueous solution, although their high dielectric constants, donor numbers, and solubility parameters would make them helpful if they could be employed [28,32]. It is obvious that if some ways could be found to separate these solvents as organic phases from aqueous solutions, the versatility of solvent extraction would be greatly increased.

Murata et al. [33] proposed a method for the extraction of iron(III) in propylene carbonate from aqueous phase, based on the high solubility of organic solvent in water in higher temperature. At room temperature, the two phases are present heterogeneously, but at the elevated temperature they change into a homogeneous solution, which separates into the two phases again upon cooling. During these sequential procedures, the species in the aqueous phase transfers into the organic phase. The effectiveness of the homogeneous liquid–liquid extraction is attributed just to the higher reaction temperature.

Matkovich and Christian [34] have separated acetone as an organic phase by using the salting-out effect, and the organic phase thus obtained served not only to extract certain metal chelates but also to improve the performance characteristics of the flame-emission or atomic absorption spectrophotometry for metals determination. The best salting-out agents of the 79 studied, were calcium chloride, magnesium chloride and sucrose, but the metal impurities in the salts and the high viscosity in the aqueous phase produced by the sucrose caused problems in analysis.

Two relatively simple and similar theories have been used to explain salting-out phenomena, one postulating decreased mutual solubility of the solvents and the other postulating removal of one solvent via solvation processes [34]. The former assumes that compounds, not necessarily ionic in nature, are preferentially solvated by one of the solvents, making this solvent unavailable for dissolving the second. The latter theory, which applies only to ionic compounds, assumes that the more polar of the two solvents (e.g., water) preferentially congregates around the salt because of electrostatic attrac-

tion, leading to nonideal behaviour. A combination of these two processes is obviously possible, but the salt effect will probably predominate with ionic salting-out compounds. Three factors should be considered when evaluating a salt and its potential salting-out effect on acetone [34]. (1) The solubility of the salt in acetone must be negligible. Salts such as the lithium halides, which might be expected to cause phase separation based on the other parameters, showed no separation because they were soluble in acetone. (2) The solubility in water must be large in order to have maximum interaction with the water molecules. (3) The ability of ions to precipitate water loving substances (gels), according the lyotropic series ($Mg^{2+} > Ca^{2+} > Sr^{2+} > Ba^{2+} > Li^{+} > Na^{+} > K^{+} > Rb^{+} > Cs^{+}$). Various salts have been used for acetonitrile phase separation for metal determination, like: calcium chloride [35], sodium nitrate [36], ammonium sulphate [37], and sodium bromide [38].

In case of ternary solvent (water/methanol/chloroform) the phase separation of the extracting solvent (chloroform) from aqueous phase can also be accomplished by salt addition [39]. By this procedure, fine particles of the extraction phase were sedimented in the bottom of a conical test tube by centrifugation. In this case the volume of the sedimented phase is very small about 11 μL.

A similar HLLE method called "single phase" using ternary solvent system (water/ethanol/methylisobutylketone) [12], (acetonitrile/chloroform/HCl aqueous solution) [40] and (water/ethanol/chloroform) [41] has been proposed for metal extraction and determination. After preparing this single-phase solution, the homogeneous three component solvent system is "broken down" by the addition of an excess of water. By this procedure the homogeneous solution is separated into two liquid layers.

There is also the procedure of Fujinaga and Hori [32] that used, instead of the salting-out effect, the addition of a small volume of a third solvent to promote the separation of an immiscible ternary phase (water/acetonitrile/chloroform), made up almost entirely of the water-miscible solvent. Although such auxiliary solvents need to be found empirically, once a suitable one has been found and the phase diagrams for the ternary system have been constructed, the phases obtainable by use of various ternary solvent compositions can be used for solvent extraction as easily as the solvent pairs in conventional solvent extraction systems.

Igarashi and Yotsuyanagi [8] proposed an alternative homogeneous liquid–liquid extraction method based on pH-dependent phase separation. Neutralization of perfluorooctanoate ion ($PFOA^{-}$) in water-miscible organic solvent solution (such as acetone, 1,4-dioxane and tetrahydrofuran) induces phase separation, providing a small volume (down to 0.1 mL, depending on the amount of $PFOA^{-}$ which has been added) of an oily and transparent water-immiscible liquid phase, from a large volume of the aqueous solution. This phase separation was reversible with the pH change in the solution, corresponding to below and above the pK_{α}, value of perfluorooctanoic acid (HPFOA). The above method has been applied for organic and inorganic analytes [42–48].

The $PFOA^{-}$, pH dependent, method needs usually strongly acidic condition (pH < 1) and thus is difficult to be applied to the separation and concentration of biologically active substances, due to the fact that these substances easily hydrolyse the substituents and cause denaturation of the protein. In order to solve these problems, phase separation in the neutral pH region has been achieved using Zonyl FSA (the Du Pont trade name for $CF_3(CF_2)_n–CH_2CH_2–SCH_2CH_2–COOH$, $n = 6 \pm 8$), which induced the methylene group as a spacer of the fluorosurfactant [49]. The pH-dependent phase separation with Zonyl FSA has been applied as a preconcentration for the spectrofluorometric determination of chlorophyll-A [49] and recently for analysis of 14 elements with ICP-AES [50].

Table 1
Classification of the reported HLLE methods according the miscible solvent system and the phase separation mode.

Binary miscible solvent system
By temperature [33,55]
By salting-out with salt [11,39,56]
By salting-out with third solvent [32]
By pH with $PFOA^{-}$ [42–44,46–48]
By ion-pair formation [53,54,9]
Ternary miscible solvent system
By auxiliary solvent (excess of water) [12,41]
By pH-dependent ternary systems [51,52]

Moreover, a homogeneous liquid–liquid extraction method using the pH-dependent phase separation in the water/acetic acid/chloroform ternary solvent system was reported for copper(II) and palladium(II) determination [51,52]. It is postulated that the state of the homogeneous solution in water/acetic acid/chloroform dissolved in water is due to the solvation of the acetic acid molecule for small amounts of chloroform. When sodium hydroxide (4.5 mL, 10 mol L^{-1} NaOH) is added to this system, acetic acid converts to acetate ion due to the acid–base reaction of acetic acid, and consequently its function as a solvation molecule was absent. Hence, water-immiscible chloroform is formed in the aqueous solution by phase separation [51]. Extracting solvent selection in this case is an important factor and it has to meet the following characteristics: (a) it should be heavier than water, (b) it should form a ternary homogeneous system with water and acetic acid, (c) it should dissolve the analyte more than water and (d) it should be sedimented after adding a phase-separation agent (NaOH solution).

The ion-pair formation of tetrabutylammonium ion (TBA^{+}) and perfluorooctanoate ion ($PFOA^{-}$) in a homogeneous solution of water/sodium acetate has been used for extraction and spectrophotometric determination of uranium(VI) [53].

Recently, an ion-pair formation pH-independent phase separation method was established using a homogeneous ternary solvent system (water/TBA^{+}–ClO_4^{-}/chloroform) for iron(II), cobalt, copper and nickel determination, based on ion-pair formation of TBA^{+} and perchlorate ion (ClO_4^{-}) [54,9].

The classification of the reported HLLE separation modes from binary or ternary component solvent systems are summarized in Table 1.

Dispersive liquid–liquid microextraction (DLLME) is a miniaturized sample pre-treatment preconcentration technique based on ternary component solvent systems and salting-out phenomenon similar with as HLLE/Ternary miscible solvent system. The main difference between the above two techniques is that in HLLE, the mixture of solvents firstly produce a homogeneous form prior to the separation of the two phases by adding either a salt or an auxiliary solvent. In addition in HLLE much larger volumes of organic solvents are usually used. On the other hand, in DLLME the phase separation is accomplished instantly by adding rapidly the mixture of disperser and extraction solvent into the aqueous solution. No homogeneous form is appeared. Actually, it is a modified solvent extraction method and its acceptor-to-donor phase ratio is greatly reduced comparing with the other methods [20]. Thereby, cloudy solution is formed. In fact, the cloudy state results from the formation of fine droplets of the extraction solvent, which disperse in the sample solution. Then, this cloudy solution shall be centrifuged and the fine droplets will be sedimented at the bottom of the conical test tube as it is shown in Fig. 1. The determination of analytes in sedimented phase can be performed by various detection systems. By this procedure any component in the solution, directly or indirectly after previous (or simultaneous) derivatization reaction, interacts with the fine droplets of the extraction solvent and consequently get extracted from the initial aqueous

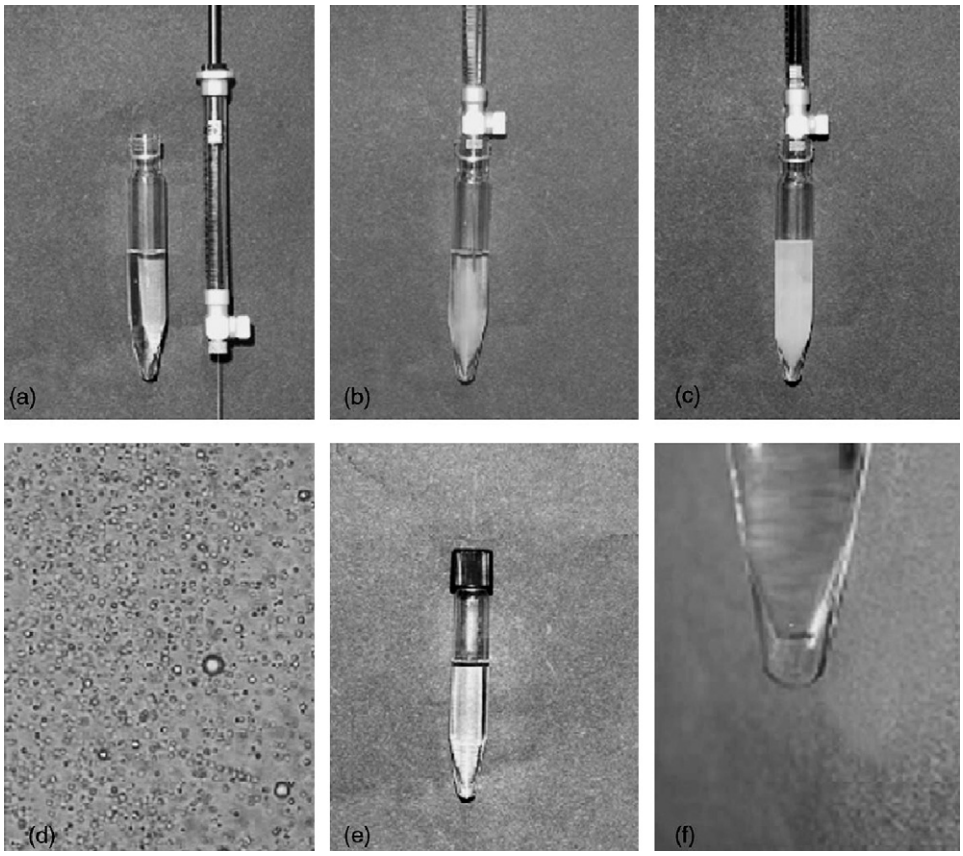


Fig. 1. Photography of different steps in DLLME: (a) before injection of mixture of disperser solvent (acetone) and extraction solvent (C_2Cl_4) into sample solution, (b) starting of injection, (c) end of injection, (d) optical microscopic photography, magnitude 1000 (that shows fine particles of C_2Cl_4 in cloudy state), (e) after centrifuging and (f) enlarged view of sedimented phase [13].

solution and concentrated in the small volume of the sedimented organic phase.

The miscibility of disperser solvent in aqueous and organic phase (extraction solvent) is an essential point for its selection. Acetone, acetonitrile, methanol and ethanol have been successfully used for this purpose. In addition, the volume of the disperser solvent plays an important role, due to the fact that variation of the amount causes changes in the sedimented phase volume, through the salting-out effect. At low volume of disperser solvent, the dispersion of the extraction solvent is not properly and the cloudy solution is not formed completely, while at high volume, the solubility of analytes in water increases, therefore, the extraction efficiency decreases [15].

The selection of a suitable organic solvent for DLLME is also a very important task. It should able to form a cloudy solution system with water and disperser solvent. Also it should have highly immiscibility with aqueous phase (sample solution), high extraction efficiency, selectivity and hydrophobicity [27]. Chloroform, chlorobenzene and carbon tetrachloride have been employed. In manual (batch) mode, organic solvents are selected on the basis of higher density rather than water, in order to facilitate the sedimentation with the centrifuging. In addition, they should have extraction capability of the interested compounds, and in some cases, good gas chromatography behaviour. Increasing the volume of the extraction solvent, the volume of the sedimented phase increases, resulting thus to a decreasing of the enrichment factor [15].

In contrast to manual DLLME systems, in the on-line procedure, organic solvent is not required to be heavier than water, due to the fact that the formation of the cloudy solution takes place in a moving stream and the retention of the fine droplets on the sorbent material is based on its hydrophobic nature. It means that the separation of the organic phase is based on the retention and not on the centrifuging [27].

3. Applications HLLE and DLLME for metal determination

The relevant applications of the two liquid–liquid extraction techniques, HLLE and DLLME, which have been discussed above in inorganic analysis including metals and metalloids, are summarized in Tables 2 and 3, respectively.

3.1. HLLE based on temperature separation

Murata and Ikeda used propylene carbonate ($PrCO_3$) with an aqueous phase at 80 °C for Mo(IV) and Fe(III) spectrophotometric determination [33,55]. This method is based on the high solubility of organic solvent in water at higher temperature and is characterized by immediate formation of the complex upon attaining a state of homogeneous solution consisting of water and the organic solvent during the procedure. At room temperature the two phases are present heterogeneously, but at the elevated temperature they change into a homogeneous solution, which separates into the two phases again upon cooling. However, no application data are given for real samples.

3.2. HLLE based on salting-out phenomenon with salt

By the use of the salting-out effect, Matkovich and Christian [34] were able to separate acetone from aqueous solutions with either saturated calcium chloride or 65% m/v sucrose. Several metals like Sc(III), Cr(III), Mn(II), Fe(II), Fe(III), Co(II), Ni(II), Cu(II) and Zn(II) as

Table 2
Analytical performance characteristics and optimal conditions of relevant HLLE methods for metals and metalloids determination.

Analyte	Solvent system	Separation mode	Chelating system	Detection system	Linear range ($\mu g\,L^{-1}$)	Detection limit ($\mu g\,L^{-1}$)	Ref.
Cu(II)	Water/acetonitrile	Salting-out/$(NH_4)_2SO_4$	NH_4SCN	Polarographic	2.25–5.0	–	[37]
In(III)	Water/acetonitrile	Salting-out/NaBr	–	Polarographic	183.6–574	9.18	[38]
Co(II); Ni(II)	Water/acetonitrile	Salting-out/Na_2CO_3–$CH_3COONa\cdot 3H_2O$	2,2′-Bipyridine	Polarographic	100–10,000	–	[56]
Mo(VI)	Water/ethanol/chloroform	Salting-out/excess of water	NH_4SCN	UV–vis	0.1–8.0	–	[41]
Ag; Co; Ni; Cu; Pd; Hg; Sb; Au; Bi; Se; Mo	Water/acetone	pH-dependent/$PFOA^-$	DDTC	XRF	29.5–589 (Co) 104.5–2090 (Bi)	0.59 (Co) 2.1 (Bi)	43]
Ur(VI)	Water/acetone	pH-dependent/$PFOA^-$	TOPO	UV–vis	–	–	[47]
Mo(VI)	Water/acetone	pH-dependent/$PFOA^-$	ABO	UV–vis	–	–	[46]
Cu	Water/acetic acid/chloroform	pH-dependent	TPyP	HPLC	1.27–25.4 5.3–85.1	0.318 0.851	[51]
Pd							
Cu	Water/acetic acid/chloroform	pH-dependent	8-Hydroxy quinoline	FAAS	10–2000	1.74	[52]
U(VI)	Water/sodium acetate aqueous solution	Ion-pair formation/TBA^+–$PFOA^-$	–	UV–vis	7.85–643	0.143	[53]
Fe(II)	Water/chloroform	Ion-pair formation/TBA^+–ClO_4^-	1,10-phen	ETAAS	0.060–125	–	[54]
Co	Water/chloroform	Ion-pair formation/TBA^+–ClO_4^-	K-4-BPDC	FAAS	20–1500	10	[9]
Cu					15–2000	5	
Ni					35–1600	15	

Acronyms: FAAS: flame atomic absorption spectrometry; ETAAS: electrothermal atomic absorption spectrometry; HPLC: high-performance liquid chromatography; XRF: X-ray fluorescence; $PFOA^-$: perfluorooctanoate ion; TOPO: tri-*n*-octylphosphine oxide; ABO: α-benzoin oxime; DDTC: diethyldithicarbamate; 1,10-phen: 1,10-phenanthrolne; DFO: desfer-rioxamine B; DFB: desfer-rioxamine B; TBA^+: tetrabutylammonium ion; K-4-BPDC: 4-benzylpiperidinedithiocarbamate potassium salt; TPyP: 5,10,15,20-tetrakis(4N-pyridyl)porphine.

complexes with ammonium l-pyrrolidinecarbodithioate and dithizone were successfully extracted from calcium chloride solutions into the acetone phase while metal oxine chelates were extracted from sucrose solutions and analyzed by FAAS. Nagaosa and Fujinaga separated the acetonitrile phase, and applied for extraction and polarographic determination of some metal ions like Cu(II), In(III), Ni(II), Co(II) and Cd(II) [37,38,56,57], without any application in real samples.

3.3. HLLE based on salting-out with auxiliary solvent

This technique was first applied by da Silva and Martins [12] for the extraction and spectrophotometric determination of Fe(III), Cu(II), Co(II), Ni(II) and Pb(II). More recently, it has been used as an analytical tool by de Andrade et al. [41] for single-phase extraction of Mo(VI) with α-benzoin oxime in a mixture of water–ethanol–chloroform homogeneous ternary solvent system. Then Mo(VI) is spectrophotometrically determined with thiocyanate in the same solvent system. The calibration graph was linear up to 8.00 mg L^{-1}, according to the equation $A = 0.005 + 0.143$ [Mo(VI)] ($r^2 = 0.9999$). The accuracy of the proposed method was evaluated by comparing with standard samples determined by atomic absorption spectrometry and the applicability was tested by analyzing two commercial stainless steel samples with satisfactory results.

3.4. HLLE based on pH-dependent phase separation with $PFOA^-$

In a strongly acidic aqueous solution, desfer-rioxamine B (DFB) forms 1:1 complex with Ti(IV), Zr(IV), V(V), Nb(V), Ta(V), Mo(IV), and W(VI) at room temperature [42]. These metal chelates were preconcentrated by HLLE using perfluorooctanoic acid (HPFOA). Under the optimum conditions the volume of sedimented phase was 0.1 mL and the extraction procedure was varied in the range 83–98%. The metals were determined by X-ray fluorescence spectrometry the linear range of calibration curve for Ti(IV), Zr(IV), V(V), Nb(V), Ta(V) was up to 2.0×10^{-6} mol L^{-1} and the detection limits were at 10^{-8} mol L^{-1}. The proposed method was applied only in a synthetic sample for Ti(IV), Zr(IV) and V(V) determination.

Igarashi et al. reported two HLLE methods for 36 metal ions with diethyldithiocarbamate [43], 1-10-phenanthroline and desfer-rioxamine B [44] as complexing agents. Moreover, the proposed method was utilized as a preconcentration method for X-ray fluorescence analysis of these metals. The recovery of each metal was ca. 83–100%. The detection limits were at the 10^{-8} mol L^{-1} levels and the relative standard deviations were below 5%. The developed method was used for the determination of contaminants in a synthetic Al-based alloy sample and for the analysis of an Au–Pd alloy wire sample. The results were satisfactory.

In a weak acidic solution (pH ~ 2), acetone as a water-soluble organic solvent, 1,10-phenanthroline as chelate-forming agent and Zonyl FSA as a phase separating reagent 14 elements such as Al, Cu and Ti were determined with ICP-AES. The volume of the separated phase was 100 μL and the recovery of each element was at least 95% or more [50]. Although the proposed method could be applied in a wide range of practical fields, no application data are presented.

Ghiasvand et al. demonstrate the usefulness of HLLE combined with UV-spectrophotometer for determination of uranium(VI) [47] and molybdenum(VI) [46] using tri-*n*-octylphosphine oxide (TOPO) and α-benzoin oxime (ABO) as complexing agents, respectively, and perfluorooctanoate ion (PFOA) as a phase-separator agent under strongly acidic conditions. The maximum concentration factor was 5000-fold for Ur(VI) and 125-fold for Mo(VI). The methods were applied successfully in the analysis of natural water samples and also for spinach and lucerne samples.

Table 3
Analytical performance characteristics and optimal conditions of relevant DLLME methods for metals and metalloids determination.

Analyte	Disperser solvent	Extraction solvent	Chelating system	Detection system	Linear range ($\mu g\,L^{-1}$)	Enrichment factor	Detection limit ($\mu g\,L^{-1}$)	Centrifugation conditions		Ref.
								min	rpm	
Cd	Methanol	CCl_4	APDC	ETAAS	0.002–0.020	100	0.006	2	5000	[20]
Au	Acetone	C_6H_5Cl	Victoria Blue R	ETAAS	0.03–0.5	388	0.005	2	4000	[21]
Pd	Ethanol	CCl_4	DDTC	ETAAS	0.1–5	156	0.0024	5	3000	[22]
Cu	Methanol	$CHCl_3$	8-Hydroxy quinoline	FAAS	10–2000	42–48	3	5	1000	[23]
Pb	Methanol	CCl_4	DDTP	FAAS	1–70	1000	0.5	2	3800	[24]
Pd	Ethanol	$C_6H_4Cl_2$	PAN	FO-LADS	2–100	162	0.25	2	2500	[58]
Co					1–70	165	0.2	2	5000	
Co	Ethanol	$CHCl_3$	PAN	UV–vis	2–50	125	0.5	2	5000	[59]
Sm; Eu; Gd; Dy	Methanol	$CHCl_3$	PAN	ICP-AES	–	80; 100; 103; 78	–	60	3000	[60]
Pb	Acetone	CCl_4	DDTP	ETAAS	0.05–1.0	150	0.02	2	5000	[61]
Pb	Ethanol	CCl_4	PMBP	ETAAS	0.1–20	78	0.039	5	3000	[62]
Co	Acetone	CCl_4	PAN	ETAAS	–	101	0.021	2	4000	[63]
Ni					–	200	0.033	2	4000	
Hg	Acetone	[Hmim][Tf_2N]	TMK	UV–vis	12–140	18.8	3.9	6	5000	[64]
Cd	Methanol	CCl_4	Salen	ETAAS	0.002–0.021	122	0.005	2	5000	[65]
Se(IV)	Ethanol	CCl_4	APDC	ETAAS	0.1–3	70	0.05	2	5000	[28]
As(III)	Methanol	CCl_4	APDC	ETAAS	0.06–2	115	0.01	2	5000	[29]
Sb(III)					0.05–5		0.05			
Se(IV) 5-nitropiazselenol	Ethanol	C_6H_5Cl		GC–ECD	0.15–10	122	0.005	2	5000	[14]
Butyl-; phenyl-tin	Ethanol	CCl_4	–	GC–FPD	0.0005–1	825–1036	0.0002–0.001	2	5000	[15]
Cu	Methanol	xylene	DDPA	On-line-FAAS	0.16–12.0	560	0.04		NO	[27]
Pb					2.3–160.0	265	0.54		NO	

Acronyms: FAAS: flame atomic absorption spectrometry; ETAAS: electrothermal atomic absorption spectrometry; ICP-AES: inductively coupled plasma atomic emission spectrometry; GC–ECD: gas chromatography–electron-capture detection; GC–FPD: gas chromatography-flame photometric detection; UV–vis: UV–vis spectrophotometry; FO-LADS: fiber optic-linear array detection spectrophotometry; DDTP: diethyldithiophosphoric acid; DDTC: diethyldithicarbamate; DDPA: ammonium diethyldithiophosphate; APDC: ammonium pyrrolidine dithiocarbamate; PAN: 1-(2-pyridylazo)-2-naphthol; PMBP: 1-phenyl-3-methyl-4-benzoyl-5-pyrazolone; TMK: 4,4′-bis(dimethylamino)thiobenzophenone; [Hmim][Tf_2N]: 1-hexyl-3-methylimmidazolium bis(trifluormethylsulfonyl)imid; Salen: Salen(N,N′-bis(salicylidene) ethylenediamine).

Thirteen lanthanoids were extracted from a strong acid solution (pH ~ 1) by HLLE (water/HPFOA/acetone) and phosphoric acid di(2-ethlyhexyl)ester (D2EHPA) as extractant [48]. The concentration of lanthanoids(III) ion in the aqueous phase was determined by ICP atomic emission spectrometry and the recovery was varied in the range 85–95%. No application data were given for real samples.

3.5. HLLE based on pH-dependent ternary solvent systems

Igarashi et al. [51] and Farajzadeh et al. [52] applied the pH-dependent phase-separation process in a ternary solvent system (water/acetic acid/chloroform) for the preconcentration of copper and palladium by HPLC and for copper determination by FAAS, respectively. In order to obtain a water-immiscible phase of a small volume of chloroform, sodium hydroxide was added to a homogeneous aqueous solution which consisted of water, chloroform and acetic acid. The relative standard deviations for the central value of the calibration graph were 3.2% for Cu(II) and 3.7% for Pd(II) while the detection limits were 5×10^{-9} mol L^{-1} for Cu(II) and 8×10^{-9} mol L^{-1} for Pd(II) by HPLC. For FAAS determination the relative standard deviation was 7.6%, while the limit of detection and the limit of quantification of the method were 1.74 and 6 μg L^{-1}, respectively. The methods were applied in the analysis of natural water samples with satisfactory results.

3.6. HLLE based on ion-pair formation

Takahashi et al. [53] reported for the first time the ion-pair phase separation mode using $PFOA^-$ and tetrabutylammonium ion (TBA^+) for uranium(VI) extraction from weakly acidic acetate solution. The proposed method was applied as a preconcentration method for the spectrophotometric determination of uranium(VI) with arsenazo III, in sea-water samples. The uranium(VI) extraction was 96% and the maximum concentration factor was approximately 330-fold. The relative standard deviation was 1.4% and the detection limit was 6.0×10^{-10} mol L^{-1}. It was clearly shown that the volume of the sedimented phase depends on the concentration of $PFOA^-$. As it was proved, the phase separation phenomenon was observed at concentrations lower than the critical micelle concentration (CMC) of $PFOA^-$. Hence, this phenomenon could not be attributed to the micellar phase separation [53].

A HLLE method based on phase separation phenomenon which occurred by an ion-pair formation of TBA^+ and perchlorate ion was established using a water/chloroform solvent system for Fe(II) determination using 1,10-phenanthroline complex formation and ETAAS as detector [54]. A concentration factor of 260 was achieved in a linear range varied from 0.060 to 125 μg L^{-1} for Fe(II). However, no applications are reported for the proposed method.

Recently, a FAAS method presented for cobalt, copper and nickel determination after the formation of complex with 4-benzylpiperidinedithiocarbamate potassium salt (K-4-BPDC) using (water/tetrabutylammonium ion (TBA^+)/chloroform) as a ternary component system [9]. The phase separation phenomenon occurred by an ion-pair formation of TBA^+ and perchlorate ion. The detection limits were 10, 5, and 15 μg L^{-1} for Co(II), Cu(II), and Ni(II), respectively. The reliability of the developed method for Co, Cu and Ni determination was tested in natural water samples.

3.7. Dispersive liquid–liquid microextraction (DLLME)

Dispersive liquid–liquid microextraction (DLLME) as a simple and fast microextraction technique has been proved to be a suitable preconcentration procedure for gas chromatography (GC), liquid chromatography (LC), flame and electrothermal atomic absorption spectrometry (FAAS, ETAAS), as well as for inductively coupled plasma atomic emission spectrometry (ICP-AES) and UV–vis spectrophotometry. However, this technique is limited to a small number of extractants, which should efficiently extract the analytes of interest, since the required conditions, i.e., to have higher density rather than water, form a stable cloudy solution and be easily removed from the bottom of the conical vial after centrifugation, are met by a few organic solvents.

Firstly, DLLME has been demonstrated for cadmium determination in water samples by Jahromi et al. [20]. In this extraction method, 500 μL methanol (disperser solvent) containing 34 μL carbon tetrachloride (extraction solvent) and ammonium pyrrolidine dithiocarbamate (chelating agent) was rapidly injected by syringe into the water sample containing cadmium ions. Thereby, a cloudy solution is formed. After 2 min centrifugation at 5000 rpm, 20 μL of the sedimented phase was determined by ETAAS. The calibration graph was linear in the range of 2–20 ng L^{-1} with detection limit of 0.6 ng L^{-1}, requiring 5.00 mL volume of sample. The relative standard deviation (R.S.D.) was 3.5%. The analytical performance characteristics of the proposed method were compared with other reported preconcentration methods with adequate results and it was applied in the analysis of tap, sea and river water samples.

Shokoufi et al. [58] combined DLLME and fiber optic-linear array detection spectrophotometry (FO-LADS) using a cylindrical micro-cell for simultaneous preconcentration and determination of palladium and cobalt. Under the optimum conditions, the calibration graphs were linear in the range of 2–100 and 1–70 μg L^{-1} with detection limit of 0.25 and 0.2 μg L^{-1} and enhancement factors of 162 and 165 for palladium and cobalt, respectively. The method was applied to the analysis of several real and synthetic samples with satisfactory results.

Shamsipur and Ramezani [21] used DLLME–ETAAS ultra-trace amounts of Au(III) determination in tap water and silicate ore samples. The method is based on separation and preconcentration of gold by Victoria Blue R into fine droplets of chlorobenzene. A preconcentration factor of 388 and a detection limit of 0.005 μg L^{-1} were obtained for the system. The figures of merit of the proposed method were compared with other reported methods for Au(III) determination with sufficient results.

Farajzadeh and Jonsson [23] combined DLLME with FAAS for copper determination in natural water samples. 8-Hydroxy quinoline was used as a chelating agent and chloroform as extracting solvent. The effect of various experimental parameters was investigated using two optimization methods, one variable at a time and central composite design. The experimental design was performed at five levels of the operating parameters and the obtained results were almost similar using both methods. The calibration graph was linear over the range 0.050–2.0 mg L^{-1}. The relative standard deviation was 5.1% and the detection limit was 3 μg L^{-1}.

Preconcentration and spectrophotometric determination of Co(II) in tap and river water samples by DLLME was reported using 1-(2-pyridylazo)-2-naphthol (PAN) as complexing agent [59]. Enhancement factor of 125 was obtained from 50 mL of water sample, and the detection limit was 0.5 mg L^{-1}.

Mallah et al. [60] presented a DLLME method for simultaneous preconcentration of lanthanides such as samarium, europium, gadolinium and dysprosium based on the complex formation with the 1-(2-pyridylazo)-2-naphthol (PAN). After phase separation, the precipitate phase was dried (80 °C) and diluted to 0.5 mL by 1 mol L^{-1} HNO_3. Determination of the ions was accomplished using ICP-AES. However, no application of the method in real samples has been reported.

Naseri et al. [61] reported an application of DLLME to the determination of ultra-trace amounts of lead in tap, well, mineral and sea-water samples using diethyldithiophosphoric acid (DDTP) as chelating agent, with ETAAS. Enrichment factor of 150-fold was obtained from 5.00 mL water sample while the detection limit was 0.02 μg L^{-1}. In order to establish the validity of the

recommended procedure, the method was applied to the lead determination in a TM-23.3 certified reference water sample. The obtained result was in agreement with the certified value. The same group combined DLLME with FAAS by using microsample introduction system for the first time [24]. This novel introduction system was employed for the microvolume nebulization of the non-flammable chlorinated organic extracts. The calibration graph was linear in the range of 1–70 $\mu g\,L^{-1}$ with a detection limit of 0.5 $\mu g\,L^{-1}$. The relative recoveries of lead in tap, well, river and sea-water samples at the spiking level of 20 $\mu g\,L^{-1}$ ranged from 93.8 to 106.2%.

Liang et al. employed DLLME with ETAAS for lead [62] and palladium [22] determination using 1-phenyl-3-methyl-4-benzoyl-5-pyrazolone (PMBP) and diethyldithiocarbamate (DDTC) as complexing agents, respectively. For lead the detection limit was 39 $ng\,L^{-1}$ and the enrichment factor was 78 while for palladium the detection limit was 2.4 $ng\,L^{-1}$ and the enrichment factor reached at 156. The methods were applied successfully for the determination of lead in human urine and natural water samples and for palladium determination in river, lake and tap waters.

A method combining DLLME and ETAAS for the determination of trace Co and Ni in environmental and food samples was proposed by Jiang et al. using 1-(2-pyridylazo) 2-naphthol (PAN) as chelating reagent [63]. The enrichment factors were 101 and 200 and the detection limits of the method were 21 and 33 $ng\,L^{-1}$ for Co and Ni, respectively. Two certified reference materials of Environment Water (GSBZ50009-88) and NIES No.10-b rice flour were analyzed for validation purposes. Also the method was applied to the determination of Co and Ni in lake and river samples with good recoveries.

Gharehbaghi et al. [64] combined DLLME with small amounts of a hydrophobic ionic liquid. Ionic liquid (IL) named 1-hexyl-3-methyl-immidazolium-bis(trifluormethylsulfonyl)imid ([Hmim][Tf_2N]), were used as an extraction solvent, which is dissolved in acetone (disperser solvent) and then dispersed into the sample solution (aqueous phase), which contains sodium dodecyl sulphate (SDS), an anti-sticking agent to prevent sticking of IL to the test tube wall. Thus, a cloudy solution of fine droplets of IL appeared and sedimented at the bottom of a conical test tube by centrifuging. The performance of DLLME technique based on IL was illustrated for mercury determination in water samples by using spectrophotometric detection.

Bidari and Assadi [28] demonstrate the application of DLLME combined with iridium-modified graphite tube atomizer atomic absorption spectroscopy for determination of selenium in water samples. Ammonium pyrrolidine dithiocarbamate (APDC) was elaborated as chelating agent and carbon tetrachloride as extraction solvent. Enrichment factor of 70 was obtained from 5.00 mL of water sample. The calibration graph was linear in the range of 0.1–3 $\mu g\,L^{-1}$ with detection limit of 0.05 $\mu g\,L^{-1}$. The relative recoveries of selenium in tap, river and sea-water samples at spiking level of 2.00 $\mu g\,L^{-1}$ were 106, 96 and 98%, respectively. The same authors used a derivatization reaction with Se(IV) and the application of the DLLME method for the microextraction of the formed piazselenol in environmental water samples by gas chromatography–electron-capture (GC–ECD) detection system [14]. The selenium derivative was extracted using a mixture of ethanol (disperser solvent) and chlorobenzene (extraction solvent). Enrichment factor of 122 and detection limit of 0.005 $\mu g\,L^{-1}$ was obtained from 5.00 mL water sample.

Birjandi et al. [15] was focused on the suitability of dispersive liquid–liquid microextraction and gas chromatography–flame photometry (DLLME–GC–FPD) for speciation and determination of butyl- and phenyl-tin compounds in water samples after derivatization with $NaBEt_4$. Some important parameters, such as pH, amount of $NaBEt_4$, derivatization time, kind and volume of extraction solvent and disperser solvent, extraction time and salt effect were investigated and optimized.

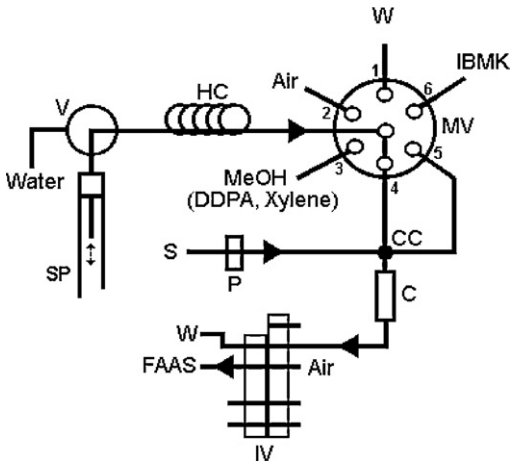


Fig. 2. Schematic manifold for SI-DLLME metal determination by FAAS. S, sample; MeOH, solution containing 2.0% (v/v) xylene and 0.3% (m/v) DDPA; W, waste; P, peristaltic pump; SP, syringe pump; MV, multiposition valve; IV, injection valve in "load" position; V, valve in "out" position; HC, holding coil; C, microcolumn; CC, confluence connector [27].

Recently, Rivas et al. [29] presented a DLLME method combined with ETAAS for the determination of inorganic arsenic (III, V) and antimony (III, V) in water samples using ammonium pyrrolidine dithiocarbamate (APDC). Total inorganic As and Sb are determined after the reduction of the pentavalent forms with sodium thiosulphate. The detection limits are 0.01 and 0.05 $\mu g\,L^{-1}$ for As(III) and Sb(III), respectively, with an enrichment factor of 115. The procedure has been applied to the speciation of inorganic As and Sb in bottled, tap and sea-water samples.

4. Automation of DLLME

Automatic on-line hydrodynamic analytical systems could be exploited with a view to enhancing the inherent properties of conventional measurement procedures. Up to date, the combination of the flow injection technique with DLLME or HLLE has appeared only in one publication [27], describing sequential injection dispersive liquid–liquid microextraction (SI-DLLME) system for metal preconcentration and determination using FAAS. The effectiveness and efficiency of the proposed SI-DLLME system has been demonstrated for copper and lead determination in environmental water samples. The method was evaluated by analysis of the certified reference material NIST CRM 1643e (National Institute of Standard and Technology, Trace elements in water). Ammonium diethyldithiophosphate (DDPA) was selected as chelating agent due to its good selectivity in strong acidic medium. The microcolumn for retention of the extraction solvent and the derivative chelate complex M–DDPA, was packed with a hydrophobic material, PTFE-turnings [65]. The manifold and its operation for on-line sequential injection dispersive liquid–liquid microextraction (SI-DLLME) metal determination by FAAS is presented schematically in Fig. 2. The xylene droplets, which contain the metal complexes, were retained on the PTFE-turnings into the microcolumn. In the next step, a segment of 300 μL isobutylmethylketone (IBMK) is pumped through C eluting the analyte. The eluent forwarded to the nebulizer for atomization and measuring.

Opposition to conventional (off-line) DLLME systems, extraction solvent is not necessary to have higher density than water, due to the fact that the formation of the cloudy solution takes place in a moving stream and the retention of the extraction fine droplets was based on the hydrophobicity of the sorbent material. It means

that the separation of the organic phase is based on the retention and not on the centrifugation. Chloroform, carbon tetrachloride, dichloromethane, hexane, benzene, xylene, toluene, IBMK, and diisobutyl ketone (DIBK) were compared as extraction solvent.

5. Conclusions

An overview of two unconventional liquid–liquid extraction procedures, HLLE and DLLME based on the mutually solubility of solvents and the separation of organic phase from a binary or ternary component solvent system is presented. Homogeneous liquid–liquid extraction is simple preconcentration method that reduces the extraction time and disposal costs. Although it seems to be promising for various determinations, the reported applications in real samples are limited. The miniaturization of solvent extraction procedures leads inherently to a minimum solvent, sample and reagent consumption and dramatic reduction of laboratory wastes. From commercial, economical and environmental point of view DLLME offers several important advantages over conventional solvent extraction methods: simplicity of operation, rapidity, low cost, high recovery and enrichment factor, low consumption of organic solvents, easier manipulation and less stringent requirements for separation. It shows increased wide applications in the field of trace analysis. The future trends of DLLME could be summarized in the following aspects: Applications in the analysis of samples with complex matrix, since, up to date, most of the analytes are detected in relatively simple samples matrices. Broadening of the range of used extraction solvents in order to increase the extraction capability of the method. Most of the extraction solvents, which have been reported, are halogenated hydrocarbons. Applications for determination of inorganic elements using the recent developed DLLME-SFO technique. New perspectives are to be certainly opened in the near future for trace-metal monitoring by hyphenation of miniaturized on-line DLLME systems with various detection systems especial with ICP-AES/ICP-MS for multielemental determinations.

References

[1] A.N. Anthemidis, M. Miro, Appl. Spectrosc. Rev. 44 (2009) 140.
[2] F. Pena-Pereira, I. Lavilla, C. Bendicho, Spectrochim. Acta Part B 64 (2009) 1.
[3] M. Miro, J.M. Estela, V. Cerda, Curr. Anal. Chem. 1 (2005) 329.
[4] A.N. Anthemidis, I.S.I. Adam, Anal. Chim. Acta 632 (2009) 216.
[5] L. Xu, C. Basheer, H.K. Lee, J. Chromatogr. A 1152 (2007) 184.
[6] E.K. Paleologos, D.L. Giokas, M.I. Karayannis, Trends Anal. Chem. 24 (2005) 426.
[7] C.E. Matckovich, G.D. Christian, Anal. Chem. 46 (1974) 102.
[8] S. Igarashi, T. Yottuyanagi, Mikrochim. Acta 106 (1992) 37.
[9] M.R. Jamali, Y. Assadi, F. Shemirani, Sep. Sci. Technol. 42 (2007) 3503.
[10] A.R. Ghiasvand, S. Shadabi, E. Mohagheghzaden, P. Hashemi, Talanta 66 (2005) 912.
[11] H. Ebrahimzadeh, Y. Yamini, F. Kamarei, S. Shariati, Anal. Chim. Acta 594 (2007) 93.
[12] J.F. da Silva, W. Martins, Talanta 39 (1992) 1307.
[13] M. Razaee, Y. Assadi, M.-R.M. Hosseini, E. Aghaee, F. Ahmadia, S. Berijani, J. Chromatogr. A 1116 (2006) 1.
[14] A. Bidari, P. Hemmatkhah, S. Jafarvand, M.R.M. Hosseini, Y. Assadi, Microchim. Acta 163 (2008) 243.
[15] A.P. Birjandi, A. Bidari, F. Rezaei, M.R.M. Hosseini, Y. Assadi, J. Chromatogr. A 1193 (2008) 19.
[16] W.-C. Tsai, S.-D. Huang, J. Chromatogr. A 1216 (2009) 5171.
[17] M.A. Farajzadeh, M. Bahrama, J.A. Jonsson, Anal. Chim. Acta 591 (2007) 69.
[18] Q. Wu, C. Wang, Z. Liu, C. Wu, Z. Wang, J. Chromatogr. A 1216 (2009) 5504.
[19] Q. Wu, Y. Li, C. Wang, Z. Liu, X. Zang, Z. Xin, Z. Wang, Anal. Chim. Acta 638 (2009) 139.
[20] E.Z. Jahromi, A. Bidari, Y. Assadi, M.R.M. Hosseini, M.R. Jamali, Anal. Chim. Acta 585 (2007) 305.
[21] M. Shamsipur, M. Ramezani, Talanta 75 (2008) 294.
[22] P. Liang, E. Zhao, F. Li, Talanta 77 (2009) 1854.
[23] M.A. Farajzadeh, M. Bahram, B.G. Mehr, J.A. Jonsson, Talanta 75 (2008) 832.
[24] M.T. Naseria, P. Hemmatkhaha, M.R. Milani Hosseinia, Y. Assadi, Anal. Chim. Acta 610 (2008) 135.
[25] C. Bosch-Ojeda, F. Sanchez-Rojas, Chromatographia 69 (2009) 1149.
[26] X.-H. Zang, Q.-H. Wu, M.-Y. Zhang, G.-H. Xi, Z. Wang, Chin. J. Anal. Chem. 37 (2009) 161.
[27] A.N. Anthemidis, K.-I.G. Ioannou, Talanta 79 (2009) 86.
[28] A. Bidari, E. Zeini Jahromi, Y. Assadi, M.R.M. Hosseini, Microchem. J. 87 (2007) 6.
[29] R.E. Rivas, I. López-García, M. Hernández-Córdoba, Spectrochim. Acta Part B 64 (2009) 329.
[30] M.-I. Leong, S.-D. Huang, J. Chromatogr. A 1211 (2008) 8.
[31] H. Xua, Z. Dingb, L. Lv, D. Song, Y.-Q. Feng, Anal. Chim. Acta 636 (2009) 28.
[32] T. Hori, T. Fujinaga, Talanta 32 (1985) 735.
[33] K. Murata, Y. Yokoyama, S. Ikeda, Anal. Chem. 44 (1972) 805.
[34] C.E. Matkovich, G.D. Christian, Anal. Chem. 45 (1973) 1915.
[35] C.E. Matkovich, G.D. Christian, Anal. Chem. 46 (1974) 102.
[36] H. Kawamoto, H. Akaiwa, Chem. Lett. (1973) 259.
[37] Y. Nagaosa, Microchim. Acta I (1979) 495.
[38] Y. Nagaosa, Talanta 26 (1979) 987.
[39] L. Tavakoli, Y. Yamini, H. Ebrahimzadeh, S. Shariati, J. Chromatogr. A 1196–1197 (2008) 133.
[40] Y. Takagai, T. Kubota, R. Akiyama, E. Aoyama, S. Igarashi, Anal. Bioanal. Chem. 380 (2004) 351.
[41] J.C. de Andrade, C.J. Cuelbas, S. de Paula Eiras, Talanta 47 (1998) 719.
[42] A. Takahashi, H. Yamaguchi, S. Igarashi, Bunseki Kagaku 46 (1997) 55.
[43] A. Takahashi, S. Igarashi, Y. Ueki, H. Yamaguchi, Fresen. J. Anal. Chem. 368 (2000) 607.
[44] S. Igarashi, A. Takahashi, Y. Ueki, H. Yamaguchi, Analyst 125 (2000) 797.
[45] A. Manaka, S. Igarashi, H. Suzuki, Bunseki Kagaku 52 (2003) 635.
[46] A.R. Ghiasvand, S. Shadabi, E. Mohagheghzdeh, P. Hashemi, Talanta 66 (2005) 912.
[47] A.R. Ghiasvand, E. Mohagheghzadeh, Anal. Sci. 20 (2004) 917.
[48] J. Fuchimukai, H. Yamaguchi, Y. Mugero, T. Kubota, S. Igarashi, Solvent Extr. Res. Dev., Jpn. 13 (2006) 139.
[49] T. Sudo, S. Igarashi, Talanta 43 (1996) 233.
[50] H. Yamaguchi, S. Itoh, S. Igarashi, T. Kobayashi, Bunseki Kagaku 54 (2005) 227.
[51] S. Igarashi, N. Ide, Y. Takagai, Anal. Chim. Acta 424 (2000) 263.
[52] M.A. Farajzadeh, M. Bahram, S. Zorita, B.G. Mehr, J. Hazard. Mater. 161 (2009) 1535.
[53] A. Takahashi, Y. Ueki, S. Igarashi, Anal. Chim. Acta 387 (1999) 71.
[54] S. Oshite, S. Igarashi, Anal. Sci 17 (2001) i1329.
[55] K. Murata, S. Ikeda, J. Inorg. Nucl. Chem. 32 (1970) 267.
[56] Y. Nagaosa, Anal. Chim. Acta 115 (1980) 81.
[57] T. Fujinaga, Y. Nagaosa, Chem. Lett. (1978) 587.
[58] N. Shokoufi, F. Shemirani, Y. Assadi, Anal. Chim. Acta 597 (2007) 349.
[59] M. Gharehbaghi, F. Shemirani, M. Baghdadi, Int. J. Environ. Anal. Chem. 88 (2008) 513.
[60] M.H. Mallah, F. Shemirani, M. Ghannadi Maragheh, J. Radioanal. Nucl. Chem. 278 (2008) 97.
[61] M.T. Naseri, M.R. Milani Hosseini, Y. Assadi, A. Kiani, Talanta 75 (2008) 56.
[62] P. Liang, H. Sang, Anal. Biochem. 380 (2008) 21.
[63] H. Jiang, Y. Qin, B. Hu, Talanta 74 (2008) 1160.
[64] M. Gharehbaghi, F. Shemirani, M. Baghdadi, Int. J. Environ. Anal. Chem. 89 (2009) 21.
[65] A.N. Anthemidis, G.A. Zachariadis, J.A. Stratis, J. Anal. Atom. Spectrom. 17 (2002) 1330.

Talanta 80 (2009) 422–427

Contents lists available at ScienceDirect

Talanta

journal homepage: www.elsevier.com/locate/talanta

Effect of variation in argon content of calibration gases on determination of atmospheric carbon dioxide

Deullae Min[a,b], Namgoo Kang[a,*], Dong Min Moon[a], Jin Bok Lee[a], Dong Soo Lee[b], Jin Seog Kim[a]

[a] Center for Gas Analysis, Division of Metrology for Quality of Life, Korea Research Institute of Standards and Science, 1 Doryong-Dong, Yuseong-Gu, Daejeon 305-340, Republic of Korea
[b] Department of Chemistry, Yonsei University, 262 Seongsanno, Seodaemun-Gu, Seoul 120-749, Republic of Korea

ARTICLE INFO

Article history:
Received 30 December 2008
Received in revised form 4 March 2009
Accepted 4 March 2009
Available online 19 March 2009

Keywords:
Greenhouse gases
Calibration gas mixture
Matrix effect
MFC
NDIR
GC

ABSTRACT

Carbon dioxide (CO_2) is a greenhouse gas that makes by far the largest contribution to the global warming of the Earth's atmosphere. For the measurements of atmospheric CO_2 a non-dispersive infrared analyzer (NDIR) and gas chromatography are conventionally being used. We explored whether and to what degree argon content can influence the determination of atmospheric CO_2 using the comparison of CO_2 concentrations between the sample gas mixtures with varying Ar amounts at 0 and 18.6 mmol mol^{-1} and the calibration gas mixtures with Ar at 8.4, 9.1, and 9.3 mmol mol^{-1}. We newly discovered that variation of Ar content in calibration gas mixtures could undermine accuracy for precise and accurate determination of atmospheric CO_2 in background air. The differences in CO_2 concentration due to the variation of Ar content in the calibration gas mixtures were negligible ($<\pm 0.03$ μmol mol^{-1}) for NDIR systems whereas they noticeably increased ($<\pm 1.09$ μmol mol^{-1}) especially for the modified GC systems to enhance instrumental sensitivity. We found that the thermal mass flow controller is the main source of the differences although such differences appeared only in the presence of a flow restrictor in GC systems. For reliable monitoring of real atmospheric CO_2 samples, one should use calibration gas mixtures that contain Ar content close to the level (9.332 mmol mol^{-1}) in the ambient air as possible. Practical guidelines were highlighted relating to selection of appropriate analytical approaches for the accurate and precise measurements of atmospheric CO_2. In addition, theoretical implications from the findings were addressed.
© 2009 Elsevier B.V. All rights reserved.

1. Introduction

Carbon dioxide (CO_2) is a greenhouse gas that makes the key contribution to the global warming of the Earth's atmosphere. The atmospheric concentration of CO_2 remarkably increased from approximately 280 μmol mol^{-1} (ppmv) during the pre-industrial era to a global average of 379 μmol mol^{-1} in 2005. Atmospheric CO_2 monitoring started in 1958 to establish that the CO_2 concentration was rising and to document its rate of increase. During the past decade, increase in CO_2 is responsible for 84% of the increase in global radiative forcing. Such increase is due primarily to emissions from fossil fuel combustion [1].

Although CO_2 monitoring has been conducted in many parts of the world and on a voluntary basis, a number of strict criteria exist in order to establish and maintain the data quality for atmospheric CO_2 measurements. The Global Atmospheric Watch (GAW) under the World Meteorological Organization (WMO) has set the target precision of the atmospheric CO_2 measurement programme to 0.1 μmol mol^{-1} (parts per million as volumetric fraction) in the Northern Hemisphere and 0.05 μmol mol^{-1} in the Southern Hemisphere [2,3].

There are at least 3 major quality elements for guaranteeing CO_2 data reliability: (i) best available analytical method to ensure repeatability and reproducibility (precision, measurement uncertainty); (ii) the closeness of measured data to true values (accuracy); and (iii) establishment of a chain to be capable of tracing any sources of systematic errors from true values (traceability) [4].

Valid analytical approaches need to be well established prior to applications to real observations of atmospheric CO_2. Any valid method for the determination of CO_2 in gas mixtures requires basically not only calibration gas mixtures but also appropriate analytical equipment. Quantitative determination of CO_2 in gas mixtures is realized by comparison of instrumental response signals from calibration and sample gas mixtures using appropriate equipment [5].

The available analytical systems frequently used in practice to date for the measurement of atmospheric CO_2 are a non-dispersive infrared analyzer (NDIR) and a gas chromatograph (GC) equipped with a methanizer and a flame ionization

* Corresponding author. Tel.: +82 42 868 5221; fax: +82 42 868 5344.
E-mail address: nkang@kriss.re.kr (N. Kang).

0039-9140/$ – see front matter © 2009 Elsevier B.V. All rights reserved.
doi:10.1016/j.talanta.2009.03.019

detector (FID) or with thermal conductivity detector (TCD) [6,7].

Potential sources of measurement uncertainties for CO_2 measurements come mostly from sample gas mixtures, calibration gas mixtures, instrumental drift, changes of environmental conditions, and matrix effects due to the interactions among these factors [8]. As far as CO_2 calibration gases are concerned, it is impossible in reality to prepare such calibration gases in which background composition is exactly identical to that of natural ambient air due to the presence of a number of minor constituents including Ne (18.2 μmol mol^{-1}), CH_4 (1.5 μmol mol^{-1}), and Xe (0.1 μmol mol^{-1}), and other trace elements. CO_2 calibration gases therefore must best simulate natural atmospheric composition as possible. In practice, simulated air is gravimetrically prepared with the mixture of N_2 and O_2 near to the levels found in dried ambient air (0.78083 mol mol^{-1} N_2 and 0.20944 mol mol^{-1} O_2). Depending on analytical goals, argon (Ar), an important noble gas found in ambient air, may need to be added (approximately 10 mmol mol^{-1}) to the mixture of N_2 and O_2. The best accurate value for Ar content in dried ambient air is reportedly 9.332 mmol mol^{-1} [9].

In order to guarantee high precision and accuracy of the measured data in gas analysis, it is of great importance to apply the identical amounts of sample and calibration gas mixtures to an analytical system for every run. For this goal, it is imperative to maintain flow rates of a sample gas as constant as possible. A mass flow meter and/or controller (MFC) are thus commonly used to minimize the variation of gas flow rates. Thermal mass flow controller (TMFC) is widely used to control due to merits that it is possible to directly measure relatively small mass flow rate of a gas with high precision and that no calibration needed against temperature and pressure. It is to be recognized that different gas species may result in different volumetric flow rates due to the nature of a thermal mass flow controller (TMFC) and that as a consequence, a gas species with different matrices are subject to different volumetric flow rates. In other words, if TMFC is used for different gas or different composition of a gas mixture from the initially calibration gas (e.g., N_2), the TMFC could lead to an important source of measurement uncertainty. In other words, depending on varying composition of gas mixtures, the gas flow rates are subject to change through the TMFC. The TMFCs should be calibrated prior to its usage for gas analysis [10]. As long as appropriate calibrations are conducted against the specific gas mixtures, the TMFC can maintain the mass flow rate of a gas unchanged throughout gas analysis. Without additional calibrations, the volumetric flow rate of an analyte through the TMFC may be altered by different matrices of gas mixtures depending upon the presence and the levels of other constituents. Best accuracy can ensure solely by conducting calibration processes appropriately under real operating conditions. However, it is not unusual to apply the TMFC to an analytical system without additional calibration because commercially available TMFCs in the market are initially one-point calibrated against high-purity inert gas (e.g., N_2). Moreover, it is practically impossible to calibrate the TMFC as to a number of different samples prior to analysis and to prepare all RMs with the identical matrices to those of the sample gas mixtures to be analyzed.

We report for the first time the initial findings from the investigation on whether and to which degree Ar as a matrix constituent (ranging from 0 to 18.6 mmol mol^{-1}) can influence CO_2 determination in gas mixtures using calibration gas mixtures prepared in different matrices through comparisons between analytical systems. This study explored a total of 5 different analytical systems after some modifications made to conventional systems, aiming at probing potential effects of Ar on instrumental sensitivity and precision of atmospheric CO_2 determination: (i) a conventional NDIR analyzer; (ii) a modified NDIR; (iii) a conventional GC-FID; and (iv) a modified GC-FID; and (iv) a modified GC-TCD. Based on these findings, practical implications and reliable analytical approach to the measurements of atmospheric CO_2 were suggested.

2. Experimental

2.1. Preparation of calibration and sample gas mixtures

The gravimetric method is officially a primary method that ensures international traceability for the preparation of calibration gas mixtures. A total of 5 gas mixtures (3 calibration gas mixtures and 2 sample gas mixtures) containing atmospheric-level CO_2 were prepared in the 30-L stainless-steel gas cylinders under ambient conditions (1.0 atm, 25 ± 2 °C) by a gravimetric technique [11]. Detailed description of the preparation procedures by this technique is found elsewhere [12]. A total of 4 source gases were used as the mother gases for each constituent. All source gases were of high purity grade: CO_2 (0.9999 mol mol^{-1} Matheson Co., USA), N_2 (0.9999 mol mol^{-1}, Deokyang Energen Co., South Korea); O_2 (0.99999 mol mol^{-1}, Prexair Co., Rep. South Korea), and Ar (0.99999 mol mol^{-1} Deokyang Energen Co., South Korea). The compositions and concentrations of gaseous impurities contained in the mother gases were determined as summarized in Supporting Information. A total of 6 calibration and sample gas cylinders were used in this study. The compositions and concentrations of the calibration and sample gas mixtures prepared by this technique are presented in Table 1. R and S stand for calibration and sample gas mixtures, respectively. The second calibration gas mixture ($R_{2,NDIR}$) was used exclusively for the NDIR whereas $R_{2,GC}$ for the GC systems only. $R_{2,GC}$ is a standard reference material (SRM) purchased from the Global Monitoring Division (GMD) under the National Oceanic & Atmospheric Administration (NOAA; Boulder, Colorado, USA) in September 2001. For of the SRM, the GMD/NOAA indicated that the SRM has CO_2 at 383.36 ± 0.04 μmol mol^{-1} as the World Meteorological Organization (WMO) mole fraction scale [4]. Information on the gravimetric concentrations for N_2 and O_2 (GMD/NOAA) were not available from the provider. The cylinders contain 4 major constituents in common: CO_2 (380–392 μmol mol^{-1}), N_2 (0.775–0.783 mol mol^{-1}), O_2 (0.205–0.216 mol mol^{-1}), and Ar (zero-18.6 mmol mol^{-1}). The sample gas mixtures were prepared in the different Ar matrices (0 and 18.6 mmol mol^{-1}). The amount of Ar in S_1 indicates only trace amount (<0.022 mmol mol^{-1}) estimated from the impurities analysis. For the calibration gas mixtures, the expanded uncertainty values ($U = ku_c$) at a coverage factor (k) of 2 for the preparation of 5 different CO_2 concentrations using a computer software (GUM Workbench Version 2.3) fall within 0.06 μmol mol^{-1} [13,14].

2.2. NDIR analytical systems

The modified NDIR analytical system is identical to the conventional one except a pressure control system (Fig. 1). The system compartments are comprised of an NDIR analyzer (Siemens Ultramat 6, Germany), two commercially available TMFCs (Brooks 5850E, Japan), and the pressure control system. The NDIR analyzer for measuring atmospheric CO_2 used in this study is of an open-path cell type. The NDIR analyzer determine the amount of CO_2 with a characteristic wavelength region of 2349 ± 50 cm^{-1} by measuring the difference in the intensities in the infrared radiation (2349 ± 50 cm^{-1}) passing through a sample cell relative to that through a reference cell. The TMFC has been initially calibrated against N_2 at a volumetric flow rate of 1000 mL min^{-1} by the manufacturer. The modified NDIR analyzer adopted a pressure control system which consists of a damping chamber and a pressure controller (a pressure sensor, an indicator, and a pressure relief valve). To make corrections for the drift of the instrumental signals during

Table 1
The composition and gravimetric concentrations of constituents contained in the calibration (R) and sample (S) gas mixtures.

Symbol	Cylinder ID	Gravimetric composition			
		CO_2 (μmol mol^{-1})	N_2 (mol mol^{-1})	O_2 (mol mol^{-1})	Ar (mmol mol^{-1})
R_1	ME5599	392.258	0.78007	0.21112	8.408
$R_{2,NDIR}$	ME5653	380.527	0.78036	0.21014	9.120
$R_{2,GC}$	CA04886	383.740	NA	NA	9.33
R_3	ME5501	385.570	0.78090	0.20942	9.285
S_1	ME5590	386.884	0.78328	0.21633	<0.022
S_2	ME5502	384.294	0.77568	0.20532	18.613

NA = data not available; see Section 2.1 for details.

the analytical time, we applied an analytical order of (R_1-S_1-$R_{2,NDIR}$-S_2-R_3)-R_1. As a means to increase the instrumental sensitivity, the volumetric flow rates for sample and calibration gas mixtures were maintained at 800 mL min^{-1}. Instrumental sensitivity (S) can be defined as the ratio of increment in the magnitude of response signal in the instrument (ΔR) to a unit increment in CO_2 concentration ($\Delta[CO_2]$):

$$S = \frac{\Delta R}{\Delta[CO_2]} \quad (1)$$

The analytical conditions used for this NDIR system were 700 °C for IR source temperature. While CO_2 at 350 μmol mol^{-1} in N_2 balance from the zero gas cylinder passed through the reference cell, a calibration or a sample gas mixture passed through the sample cell. All analytical runs were conducted at least in triplicates under the laboratory environmental conditions at 23 °C and 1 atm.

2.3. GC analytical systems

The modified GC-methanizer-FID system is identical to the conventional one except a flow restrictor (Fig. 2). The system compartments are a gas chromatograph (GC, Agilent 6890N, USA), a methanizer (Agilent, USA) and a flame ionization detector (FID). The methanizer were installed between the column injection port and the FID. A FID is generally used for analyses of organic compounds containing carbon atoms (e.g., hydrocarbons).

Gas chromatography separates inorganic carbon gases (CH_4, CO, and CO_2) from other gases in the gas mixtures. Following the GC separation, CO_2 and CO were passed in a stream of carrier gas (He, 99.999%). In order to detect oxidized carbon gases (CO and CO_2) using FID, these molecules must first be reduced to CH_4. The CO an CO_2 undergo chemical transformation (methanization) from CO_2 and CO to CH_4 by catalytic reduction reactions in the flame generated by hydrogen-rich oxygenated carrier gas (e.g., a mixture of H_2 and air) in the presence of a hot nickel catalyst. The overall chemical reaction schemes for the methanization can be summarized [15,16]:

$$CO_2 + 4H_2 \overset{260^oC,\,Ni}{\longrightarrow} CH_4 + 2H_2O \quad (2)$$

$$CO + 3H_2 \overset{260^oC,\,Ni}{\longrightarrow} CH_4 + H_2O \quad (3)$$

Since the calibration coefficient for CO_2 determination using FID after methanization depends on the catalytic activity of the catalyst (Ni) and its temperature, recalibrations using calibration gases are needed prior to analysis. The catalytic conversion efficiency from CO_2 to CH_4 was virtually close to 1.0 as long as the system is stabilized, indicating that CH_4 and CO_2 molecules yield nearly identical sensitivity to the FID. Potential variation in this coefficient can be disregarded because atmospheric CO_2 in the sample gases was determined by comparison with the calibration gas mixtures.

A single TMFC (Brooks 5850E, Japan) of the same model as those used in the NDIR analyzers was installed before the sample loop for maintaining flow rates constant. The initial state of the TMFC available in the market has been calibrated against N_2 at a volumetric flow rate of 500 mL min^{-1}. While minimizing possibility of leaking and dead volume, the liner of the injection port was removed and the mixture of the carriers gas (He) and sample gas from the sample loop were directly introduced into the packed column. The electronic pressure controller in the inlet part of the column was installed before the 6-port valve in order to keep the flow rate of the carrier gas constant.

The sample loop is installed inside the valve box of which temperature remains nearly constant at 100 °C (constant T). The

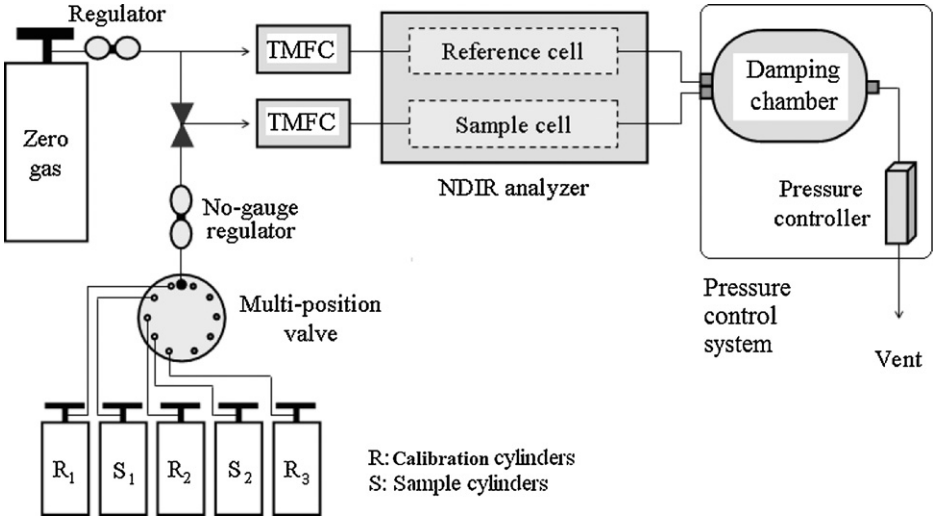


Fig. 1. A schematic representation of the modified NDIR analytical system for atmospheric CO_2 determination.

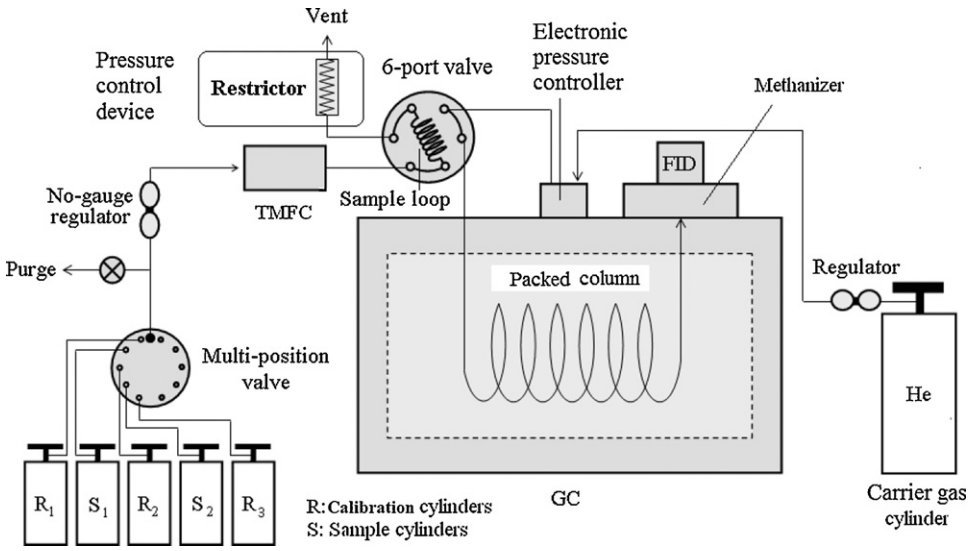


Fig. 2. A schematic representation of the modified GC-methanizer-FID system for atmospheric CO_2 determination.

Table 2
The analytical conditions used for the GC-FID systems.

Attribute	Condition
Packed Column	Resteck Porapak Q 80/100 mesh 4 m, 1/8 in. SUS
Sample loop volume (mL)	0.25
FID temperature (°C)	250
H_2 flow rate (mL min^{-1})	40
Air flow rate (mL min^{-1})	450
Methanizer temperature (°C)	375
Oven temperature (°C)	35, isothermal
Carrier gas	Helium 99.999%
Carrier gas flow rate (mL min^{-1})	28
Sample flow rate (mL min^{-1})	100

identical volume (constant V) of the loop was applied for analyses of both calibration and sample gas mixtures.

The modified GC-methanizer-FID system adopted a flow restrictor (Valco Instruments Co. Inc., USA) as the additional pressure control device. The restrictor was installed at the end of the sample vent line in the modified GC-FID system in order to maximize instrumental sensitivity (e.g., response peak area) and to enhance stability of instrumental signals as well. To make corrections for any drift of response signals during the analytical time period, we applied an analytical order of (R_1-S_1-R_1-S_2-R_1-$R_{2,GC}$-R_1-R_3)-R_1. All analytical runs were conducted at least in triplicates under the laboratory environmental conditions at 23 °C and 1 atm.

In addition, a modified GC-TCD (thermal conductivity detector) system with a restrictor was examined as another GC technique. The analytical conditions for the GC-FID and GC-TCD systems are respectively listed in Tables 2 and 3.

Table 3
The analytical conditions used for the GC-TCD system.

Attribute	Condition
Packed Column	Resteck Porapak Q 80/100 mesh 4 m, 1/8 in. SUS
Sample loop volume (mL)	3
TCD temperature (°C)	250
He reference flow rate (mL min^{-1})	45
Oven temperature (°C)	35, isothermal
Carrier gas	Helium 99.999%
Carrier gas flow rate (mL min^{-1})	26
Sample flow rate (mL min^{-1})	100

3. Results and discussion

A total of 5 different analytical systems were explored in this study: (1) an NDIR analyzer with no sharing of the outlets without a pressure control system (conventional NDIR); (2) an NDIR analyzer in which the two outlets of the sample and the calibration cells are shared, and which is equipped with a pressure control system (modified NDIR); (3) a GC-methanizer-FID system without a flow restrictor (conventional GC-FID); (4) a GC-methanizer-FID system with the restrictor (modified GC-FID); and (5) a GC-TCD system with a restrictor (modified GC-TCD).

Fig. 3 shows whether and to which degree Ar, a matrix constituent, can influence the determination of CO_2 concentrations in the 2 sample gas mixtures prepared in the different Ar matrices (0 and 18.6 mmol mol^{-1}) from the calibration gas mixtures prepared in the simulated air containing 8.4, 9.1 or 9.3 mmol mol^{-1} of Ar by the 5 different analytical systems.

To evaluate the nearness of a measured value to the true value (accuracy), $\Delta[CO_2]$ were obtained from the difference in CO_2 concentration between the measured value and the gravimetrically prepared value (true value) using each analytical system:

$$\Delta[CO_2] = [CO_2]_{measured} - [CO_2]_{gravimetric} \quad (4)$$

Each data point represents an arithmetic mean from at least triplicate measurements for one sample gas mixture. The $\Delta[CO_2]$ from the NDIR systems were within ±0.03 μmol mol^{-1}, suggesting no noticeable matrix effect. To ensure accurate and precise measurements of CO_2, its amount (mol) should be under control. Volumetric flow rates of CO_2 are first controlled via the TMFCs before entering the reference and sample cells. A practical way is to maintain the pressure values inside the two different cells as equal as possible throughout measurements. For this purpose, the outlets of a sample cell and a reference cell were combined into a damping chamber within the modified NDIR system. The pressure values insides the reference and the sample cells can be equal due to the shared outlets of both the sample and the reference cells. Since the pressure control device was installed at the end to the outlet of the damping chamber, the overall pressure in the reference and the sample cells can be readily stabilized. Potential differences in the volumetric flow rates of CO_2 due to different matrices of calibration and sample gas mixtures can be thus prevented. As long as the pressures within the sample and the reference cells are equal in the NDIR systems, reliable determination of atmospheric CO_2 would not be hampered

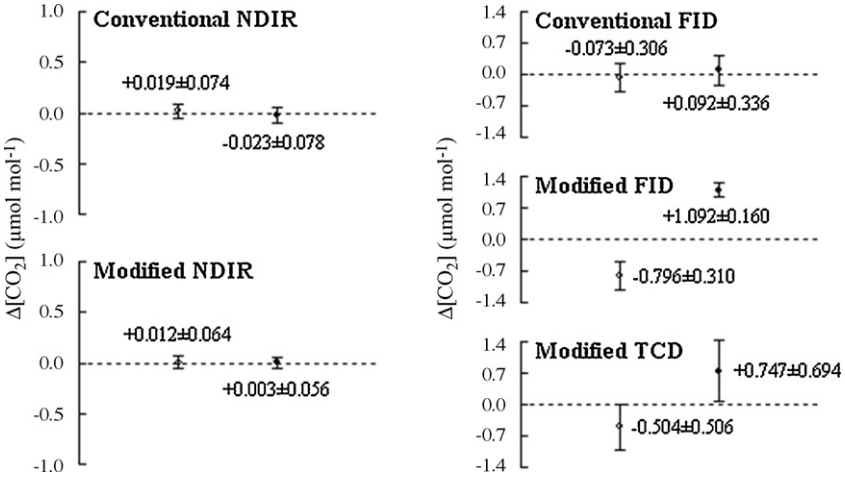


Fig. 3. Difference in CO_2 concentration between the measured and the gravimetric values of the calibration and sample gas mixtures with different mole fractions of Ar (open circle ○ from sample gases containing <0.022 mmol mol^{-1} Ar; filled circle ● from those containing 18.613 mmol mol^{-1} Ar).

significantly by the presence of Ar. The conventional NDIR analyzer is of the open path type capable of keeping the reference and sample cells at the ambient level, thereby little affected by varying flow rates. This characteristic is conducive to reliable monitoring of real atmospheric CO_2 by most GAW laboratories under WMO that use conventional NDIR analyzers.

GC modifications may be especially susceptible to variations in Ar content in calibration gases for determination of atmospheric CO_2. The value for the experimentally measured difference was the largest (1.09 μmol mol^{-1}) for the modified GC-FID system whereas the second largest value (0.75 μmol mol^{-1}) was observed for the modified GC-TCD system. Provided that there is no noticeable effect of system compartments other than the TMFC, the maximum limit of the predicted differences in CO_2 determination caused by variation in Ar content ($\Delta[CO_2]$) is ±1.16 μmol mol^{-1}. Comparison of the predicted differences with the measured ones indicates that the two values are at least comparable. These results support the first working hypothesis that the effect of variation in Ar content of calibration gases (i.e., matrix effect of Ar) on $\Delta[CO_2]$ can be directly caused by the role of TMFC. This hypothesis was tested by comparison of $\Delta[CO_2]$ between the observed values and predicted ones estimated by the principle of TMFC. However, such effect due to the TMFC appeared in the modified GC-FID system only, suggesting that this effect is closely associated with the presence of the flow restrictor. The second working hypothesis is that potential variations in the gas pressure inside the sample loop would be indicative of such effect because of the ideal gas law indicating that variations in gas amount (mol) are linearly proportional to those in gas pressure (atm) under constant volume and temperature. The second hypothesis was experimentally investigated further. Both the theoretical aspects and the experimental results demonstrated that these hypotheses are valid under the experimental conditions investigated in this study. Details are as described in Supporting Information.

In addition, to check the reproducibility (precision) of the measured concentrations of CO_2, uncertainty budgets were evaluated based on the international guides [13,14]. Each error bar indicates an expanded uncertainty ($U = ku_c$) at a coverage factor (k) of 2. Using the computer software (GUM Workbench, Version 2.3), standard combined uncertainties (u_c) were estimated for the NDIR systems and the GC systems, taking both the preparation of the calibration gas mixtures and the measurement by the three-point and the two-point calibration processes, respectively. Uncertainty sources were not only from measurement itself but also from the preparation of the CO_2 calibration gas mixtures. Results show that the measurement uncertainty values for the NDIR systems are much smaller than those for the GC systems. The U values for the NDIR systems fall <0.08 μmol mol^{-1} ($k = 2$), whereas those for the GC-FID systems were <0.31 μmol mol^{-1} ($k = 2$) and that for the modified GC-TCD system was <0.70 μmol mol^{-1} ($k = 2$). Details on the uncertainty estimates are presented in Supporting Information.

4. Conclusions

Based on our findings, we can draw some important implications. Under the explored experimental conditions, the NDIR systems were typically less susceptible to potential matrix effects due to the association of the TMFC as compared to the GC systems. Some practical implications and recommendations need to be addressed. In general, one should check whether an available analytical system with TMFCs can affect determination of the analyte due to different matrices between calibration and sample gas mixtures. In particular, for reliable monitoring of real atmospheric CO_2 samples and for the verification of gravimetrically prepared CO_2 calibration gas mixtures, one should use calibration gas mixtures that contain Ar content close to the level (9.332 mmol mol^{-1}) in the ambient air as possible.

One of the best options we recommend is to use the modified NDIR system without a trade-off between enhancing sensitivity and high accuracy and precision. The second best option would be the conventional NDIR. Unless NDIR analytical systems are available, the next option is the conventional GC-FID system. Since the sensitivity of TCD to CO_2 detection is generally low relative to that of the FID, the conventional GC-TCD system would not be the preferred choice for accurate and precise determination of atmospheric CO_2. The modified GC-TCD would be not be of desirable choice because the results showed the second largest difference from the true value (1.09 μmol mol^{-1}) and the largest measurement uncertainty (0.75 μmol mol^{-1}).

This research has just opened a great horizon for CO_2 determination by focusing the current research scope on fairly narrow concentrations of atmospheric CO_2 in background air. We will further investigate potential matrix effects on CO_2 concentrations far beyond atmospheric levels (up to emission or stack levels). It is anticipated that this extension would provide a deeper understanding and practical significance on reliable measurement of CO_2 in various applications.

Acknowledgements

This research was supported by KRISS through basic research funding on Chemical Metrology and Standards and a National Agenda Project entitled Development of Environmental Measurement Techniques for Low Carbon and Green Growth.

Appendix A. Supplementary data

Supplementary data associated with this article can be found, in the online version, at doi:10.1016/j.talanta.2009.03.019.

References

[1] World Meteorological Organization Global Atmosphere Watch, WMO Global Atmospheric Watch (GAW) Strategic Plan: 2008–2015, A contribution to the implementation of the WMO strategic plan: 2008–2011, No. 172, WMO TD NO. 1384, 2008.
[2] World Meteorological Organization Global Atmosphere Watch, Strategy for the Implementation of the Global Atmosphere Watch Programme (2001–2007), A contribution to the implementation of the WMO long-term plan, No. 142, WMO TD No. 1077, 2001.
[3] World Meteorological Organization Global Atmosphere Watch, Report of the Eleventh WMO/IAEA Meeting of Experts on Carbon Dioxide Concentration and Related Tracer Measurement Techniques, No. 148, 2003.
[4] C.L. Zhao, P.P. Tans, J. Geophys. Res. 111 (2006), D08S09.
[5] International Organization for Standardization, Gas analysis—comparison methods for determining and checking the composition of calibration gas mixtures, ISO 6143, International Organization for Standardization, Geneva, Switzerland, 2001 (E).
[6] M. Sega, E. Amico Di Meane, M. Plassa, Annali di Chimica 92 (2002) 897–902.
[7] M. Kamiński, R. Kartanowicz, D. Jastrzebski, M.M. Kamiński, J. Chromatogr. A 989 (2002) 277–283.
[8] E. Amico Di Meane, M. Sega, Anali di Chimica 93 (2003) 583–587.
[9] S.Y. Park, J.S. Kim, J.B. Lee, M.B. Esler, R.S. Davis, R.I. Wielgosz, Metrologia 41 (2004) 387–395.
[10] International Organization for Standardization, Measurement of fluid flow in closed conduits—thermal mass flowmeters, ISO 14511, International Organization for Standardization, Switzerland, 2001.
[11] International Organization for Standardization, Gas analysis—preparation of calibration gas mixtures—gravimetric method, ISO 6142, International Organization for Standardization, Geneva, Switzerland, 2001 (E).
[12] J.-Y. Lee, H.-S. Yoo, K. Marti, D.M. Moon, J.B. Lee, J.S. Kim, J. Geophys. Res 111 (2006), D05302.
[13] BIPM/IEC/ISO/IUPAC/IUPAP/OIML, Guide to the Expression of Uncertainty in Measurement, 1st ed., International Organization for Standardization, Switzerland, 1993.
[14] EURACHEM/CITAC Guide, Quantifying Uncertainty in Analytical Measurement, 2nd ed., 2000.
[15] P.C. Novelli, Chemosphere 1 (1999) 115–126.
[16] M. Prokopowicz, E. Lubock, J. Namieśnik, J.F. Biernat, A. Przyjazny, Talanta 44 (1997) 1551–1561.

Talanta 80 (2009) 428–433

Contents lists available at ScienceDirect

Talanta

journal homepage: www.elsevier.com/locate/talanta

Biomonitoring of metal contamination in a marine prosobranch snail (*Nassarius reticulatus*) by imaging laser ablation inductively coupled plasma mass spectrometry (LA-ICP-MS)

Mirian C. Santos[b], Martin Wagner[c], Bei Wu[a,d], Jessica Scheider[c], Jörg Oehlmann[c], Solange Cadore[b], J. Sabine Becker[a,*]

[a] Central Division of Analytical Chemistry, Forschungszentrum Jülich, D-52425 Jülich, Germany
[b] Group of Atomic Spectrometry, Chemistry Institute, State University of Campinas, P.O. Box 6154, 13083-970 Campinas, SP, Brazil
[c] Department Aquatic Ecotoxicology, Goethe University Frankfurt, D-60054 Frankfurt am Main, Germany
[d] Department of Environmental Engineering, Zhejiang University, Hangzhou 310029, China

ARTICLE INFO

Article history:
Received 1 January 2009
Received in revised form 26 June 2009
Accepted 30 June 2009
Available online 8 July 2009

Keywords:
Biomonitoring
Imaging mass spectrometry
Laser ablation ICP-MS
Metal contamination
Snail tissues

ABSTRACT

An imaging mass spectrometric method using laser ablation inductively coupled plasma spectrometry (LA-ICP-MS) was developed to determine Cu, Zn, Cd, Hg and Pb and metal distribution in longitudinal tissue sections of the marine snail *Nassarius reticulatus* (Gastropoda, Prosobranchia). Snails were sampled in northern Brittany (France) at three stations with different contamination levels.

The quantification of metal distribution (imaging or mapping) in a thin slice of the snail tissue was carried out using different strategies: by one-point calibration and via matrix-matched laboratory standards using different biological materials (BCR 278, snail tissue, and rat brain). Together with the imaging of metals the distribution of two non-metals (carbon and sulfur) was analyzed. The imaging LA-ICP-MS analysis yielded an inhomogeneous distribution for all elements investigated. The detection limits for the distribution analysis of Cu, Zn, Cd, Hg and Pb measured by LA-ICP-MS were in the low $\mu g\,g^{-1}$ range.

© 2009 Elsevier B.V. All rights reserved.

1. Introduction

Laser ablation inductively coupled plasma mass spectrometry (LA-ICP-MS) has been established as a promising powerful technique for the determination of elements in solid samples with high sensitivity and low detection limits [1–3]. The advantages of laser ablation ICP-MS include direct trace, bulk and isotope analysis of solids without any chemical procedures for the dissolution of samples. Therefore, the risk of contamination or analyte loss is reduced. Furthermore, the elemental and isotope analysis of very small samples including a spatially resolved analysis can be performed. The latter is of interest for the study of inhomogeneities of elements, e.g. in geological samples, metals, alloys or ceramics, layered systems or tissues. LA-ICP-MS allows a spatially resolved characterization of heterogeneities in solid materials or tissues with lateral and in-depth resolution in the μm range (from 200 μm down to 5 μm, e.g. micro-local analysis and in-depth profiling for single particle characterization and surface mapping) [1,3–5].

The determination of element concentrations, as well as their distribution in different kinds of biological tissues (e.g. brain, liver, plant section, etc.), is a challenging task in analytical chemistry and of great importance in different areas of biological research [6–11]. A deficit of essential elements within tissues (e.g. Fe, Cu, Se, Zn, Mn, Mo and Ni) results in different diseases. Some undesired metals can also catalyze cytotoxic reactions, which lead to DNA modification (such as the Fenton reaction), or toxic processes at high concentrations, which could be involved during tumor progression. Due to the fact that all essential and toxic elements tend to be inhomogeneously distributed in biological tissues, imaging studies require powerful analytical tools with good spatial resolution and low detection limits. Recently, imaging analysis has been used in studies to evaluate bioactivity, transport processes, distribution, and contamination, as well as to monitor environmental exposure using indicator organisms [2].

The distribution and quantity of elements involved in biological processes have been analyzed using different analytical techniques [11,12]. Not only are element concentrations in tissue of interest, but so are their precise spatial allocation (mapping or imaging) in organs, tissues and even single cells [6,11]. At the moment, a number of analytical techniques are available for imaging elements in biological tissues [13,14]. Some of these techniques offer exceptional spatial resolution, but poor detection limits and vice versa. However, for imaging studies on biological tissues, a powerful analytical technique with both good spatial resolution and high sensitivity

* Corresponding author. Tel.: +49 2461 612698; fax: +49 2461 612560.
E-mail address: s.becker@fz-juelich.de (J.S. Becker).

0039-9140/$ – see front matter © 2009 Elsevier B.V. All rights reserved.
doi:10.1016/j.talanta.2009.06.080

is essential. Frequently used methods for element imaging in tissues are histochemical staining techniques [8], which, however, do not provide multi-element competence. Other surface analytical techniques, such as scanning electron microscopy with energy dispersive X-ray analysis (SEM-EDX) [13], proton-induced X-ray emission (PIXE) [14] or autoradiography [15], are generally less sensitive for trace analysis. Secondary ion mass spectrometry (SIMS) allows ion images of the distribution of chemical elements in tissue to be produced with a spatial resolution in the low μm to sub-μm range. However, a major problem in SIMS analysis is the strong matrix dependence of the ion yields, which makes the quantification of analytical data very difficult due to inherent matrix effects [16–18].

The application of LA-ICP-MS with its multi-elemental capability of imaging metals and non-metals in thin cross-sections of biological samples, is currently the most suitable approach for imaging metals, metalloids and non-metals, due to its high sensitivity, fewer matrix effects (compared to SIMS), low detection limits, and relatively simple quantification and sample preparation procedures [19,20].

For the quantification of analytical data in LA-ICP-MS, different strategies [1] can be applied (e.g. using certified reference materials (CRM) from the same or a similar matrix). If no suitable SRM is available, matrix-matched laboratory standards [21,22] can be prepared and analyzed together with the sample or an isotope dilution technique or solution-based calibration in LA-ICP-MS can be applied [23,24].

The netted whelk *Nassarius reticulatus* (L., 1758) is a marine prosobranch gastropod inhabiting most European coasts [25]. *N. reticulatus* is a well-established bioindicator for marine pollution, especially for organotin compounds [26–29]. Within the organotins, tributyltin (TBT) compounds are mainly used as antifouling biocides. They induce a masculinisation syndrome in prosobranch species, termed imposex [30]. Imposexed females develop male sex organs (penis and vas deferens) and may eventually be sterilized by a blockade of the vaginal opening or other malformations of the oviduct [31–33]. This phenomenon has been described for more than 150 species worldwide [34] and is used to monitor the TBT biological effects on a routine basis [35,36]. Due to the fact that *N. reticulatus* spends most of its life cycle burrowed in the sand and other soft sediments, it is suitable for the biomonitoring of marine sediments [37,38].

The aim of this work is to study the element distribution in *N. reticulatus* by imaging LA-ICP-MS in order to biomonitor the metal pollution in such species. Different calibration procedures were studied to quantify the analytical data.

2. Experimental

2.1. LA-ICP-MS instrumentation and measurement procedure

LA-ICP-MS measurements of elemental distribution in sections of snail tissues were performed using a quadrupole-based ICP mass spectrometer (ICP-QMS, Agilent 7500 ce) coupled to a laser ablation system (New Wave UP 266). The thin sections of biological tissues were ablated using a Nd:YAG laser (wavelength: 266 nm, repetition frequency: 20 Hz, spot size: 160 μm) and then transported by argon as the carrier gas into the inductively coupled plasma (ICP). The ions formed in the ICP were extracted in the quadrupole mass spectrometer and separated according to their mass-to-charge ratios. The experimental parameters of LA-ICP-MS were optimized with respect to the maximum ion intensity of $^{63}Cu^+$ using a well homogenized synthetic laboratory standard with known Cu concentration. Maximum ion intensity for $^{63}Cu^+$ was observed at an rf ICP power of 1500 W and a carrier gas flow rate of 1.2 L min^{-1} for the transport of ablated material to the ICP source. By means of two-dimensional (2D) imaging of biological tissues, a defined sample area (less than 1 cm^2) of a thin section of snail tissue (thickness: 20 μm) was ablated line by line with a focused laser beam. The distribution of metals in the sections of *N. reticulatus* was investigated by LA-ICP-MS under the optimized experimental parameters as summarized in Table 1.

Table 1
Optimized operating conditions for the developed imaging LA-ICP-MS procedure for the determination of the lateral distribution of Cu, Zn, Cd, Hg and Pb in thin cross-sections of snails.

ICP-MS	ICP-QMS, Agilent 7500 ce
Rf power (W)	1500
Carrier gas flow rate (mL min^{-1})	1.2
Sweeping/reading	1
Readings/replicate	Changeable
Laser ablation system	New Wave UP 266
Wavelength of Nd-YAG laser (nm)	266
Laser power density (W cm^{-2})	10^9
Ablation mode	Scanning (line per line)
Laser pulse duration (ns)	20
Repetition frequency (Hz)	20
Number of passes	1
Scan speed (μm s^{-1})	40
Laser spot size (μm)	160

Samples and calibration standards were arranged in a commercial laser ablation chamber (NewWave UP266, Fremont) in order to allow imaging LA-ICP-MS analysis be performed under the same experimental conditions. Thin sections of snail tissues were investigated to determine the elemental distribution of Cu, Zn, Cd, Hg and Pb. The background intensities of the analytes of interest were determined directly by LA-ICP-MS in a snail tissue ("blank") obtained from a reference site (C).

In all measurements $^{13}C^+$ ion intensity was used for internal standardization of mass spectrometric measurements. In addition, as internal standard element manganese (with the certified value of 7.3 ppm) was used for semi-quantitative analysis of metals in tissue when one-point calibration was used [1]. A multi-element analysis by LA-ICP-MS was carried out directly on standard discs fixed on the glass slides with special target-holder tape together with the snail tissue.

2.2. Samples and sample preparation

2.2.1. Certified reference materials

Reference mussel tissue from the Community Bureau of Reference (BCR CRM 278) with certified metal concentration for the selected analytes was employed to evaluate the analytical data using one-point calibration in the semi-quantitative modus.

This powder biological certified reference material (mussel tissue BCR CRM 278) was pressed into discs with a diameter of 3 mm at 8 atm. The LA-ICP-MS method was used to determine essential and toxic metals by measuring $^{63}Cu^+$, $^{66}Zn^+$, $^{111}Cd^+$, $^{202}Hg^+$ and $^{208}Pb^+$ in mussel tissue and snail sample that had been dried, ground and pressed into discs.

2.2.2. Field samples and sample preparation

Adult specimens of *N. reticulatus* (shell height of 2.2–3.9 cm) were collected in spring 2007 at different locations in northern Brittany, near Roscoff (France). One sampling site (site A) represents a heavily polluted area (harbor: 48°43′33.2″N 3°58′39.2″W). A second site (site B, 2.2 km west of the harbor: 48°43′51.0″N 4°0′22.0″W) is contaminated to a lesser extent due to the tidal transport of pollutants from the harbor. The third sampling site (site C, Beg en Fry: 48°42′4.2″N 3°43′1.2″W) is more remote from anthropogenic influence and therefore serves as reference site. The vas

deferens sequence index (VDSI), as a measure for imposex intensities (maximum value: 4.0 in *N. reticulatus*) and thus for the degree of TBT exposure [26] in the sampled snails, was 3.94, 0.78 and 0 at the sites A, B and C, respectively. These values demonstrate the different contamination levels of the sampling stations [39].

The snails were transported to the Frankfurt laboratory and housed in glass aquaria (60 L) with reconstituted sea water [40]. Prior to further analysis, they were kept under starvation for at least 2 weeks to remove remaining food particles from the alimentary tract. After this time, the snails were narcotized in 7.5% $MgCl_2$ solution for 2 h. Shell and aperture height were measured. The shell was broken with a vice and carefully removed. Morphological parameters were analyzed as reported previously [39]. The imposex stage was determined according to Stroben et al. [26,27]. Immediately after morphometrical analysis, the single specimen were embedded in Tissue-Tek (Sakura Finetek Europe B.V., Zoeterwoude, The Netherlands), frozen in liquid nitrogen and stored at −80 °C.

Female snails from site A with pronounced imposex (VDSI stage 3) and snails from the less contaminated site B (no imposex) were dissected in 50 μm frozen sections using a cryostat (Microtom HM 50 O, Walldorf, Germany). Serial section slices were thaw-mounted on microscope slides, air-dried and measured at Forschungszentrum Jülich by developed imaging LA-ICP-MS method. Furthermore, whole snail tissue from site C (reference site) was used as "Blank" to prepare matrix-matched laboratory standards to quantify the analytical data (via standard addition strategy) and calculate the background.

2.3. Semi-quantitative analysis via one-point calibration using certified reference material

Strategy 1: Certified reference materials (CRMs) are mainly applied to validate the analytical procedure developed for routine analysis in order to determine the accuracy of analytical data, the recovery of selected elements, the uncertainty of element determination and the detection limits [1]. In LA-ICP-MS, the one-point calibration has been employed as a possible calibration strategy using CRMs to obtain semi-quantitative data. In our work, the relative sensitivity coefficients (RSCs) of elements, defined as the ratio of the experimentally measured concentration to the certified (true) concentration of an element in a given matrix [41,42], are determined using the reference material of mussel tissue (BRC CRM 278). Manganese with a known concentration (certified value) present in a matrix was used as an internal standard element. In LA-ICP-MS, the RSCs correction of measured values is a quantification method that uses only one reference material.

2.4. Quantitative trace metal analysis

The distribution profiles of the essential and toxic trace metals of interest in snail tissues using LA-ICP-MS were quantified using synthetic laboratory standards:

Strategy 2: Synthetic laboratory standards were prepared from mussel tissue BRC 278 doped with trace elements with defined concentrations. Milli-Q water or standard solutions with known concentrations of analytes (Cu, Zn, Cd, Hg and Pb) were added to the mussel tissue. After absorption for 48 h, the materials were dried, ground into a fine powder and pressed under 8 atm. The final metal concentrations in these laboratory standards were determined by ICP-MS (Elan 6100) after digestion with HNO_3 and H_2O_2 in a microwave oven (range of concentration between 0.5 and 25 $\mu g\,g^{-1}$ for all elements).

Strategy 3: Matrix-matched synthetic laboratory standards were prepared from the reference snail tissue (C) spiked with standard solutions containing the elements of interest (Cu, Zn, Cd, Hg and Pb). A laboratory standard without spike was used as the "blank". Each standard was homogenized and centrifuged for 5 min. After this, the samples were frozen, cut and placed onto the glass slides as described in Ref. [8]. The final concentrations in these standards measured by ICP-MS were in the range of 0.5–30 $\mu g\,g^{-1}$ for all the analytes.

Strategy 4: Another series of synthetic laboratory standards were prepared from a rat brain tissue doped with standard solutions with well-defined analyte concentrations. The procedures were the same as described above. The final metal concentrations in the brain tissue standards were in the range of 0.5–10 $\mu g\,g^{-1}$ for all elements.

Calibration curves were produced by measuring the ion intensities of analytes in several lab standards by LA-ICP-MS.

All calibration strategies were applied to quantify the interested elements (Cu, Zn, Cd, Hg and Pb) in the snail samples. The accuracy of the strategies was evaluated with a corresponding analysis of the same samples digested by ICP-MS.

2.5. Measurement procedure for imaging Cu, Zn, Cd, Hg and Pb by LA-ICP-MS

Thin biological tissue sections of *N. reticulatus* were analyzed using developed imaging LA-ICP-MS method together with the synthetic laboratory standards under the same experimental conditions. To obtain two-dimensional images of element distribution, the region of interest in the sample was scanned line by line by a focused laser beam. LA-ICP-MS data files for each element analyzed were converted into .txt files and used to create 2D images of element distribution. The images were plotted using in-house computing software.

3. Results and discussion

3.1. Comparison of different calibration strategies

The quantification of the analytes in the solid sample is a fundamental aspect of acquiring the best possible results from mass spectrometric measurements [1]. In accordance with this fact, in this work we investigated different methods for the quantification of the potentially toxic elements in the tissues from field samples of the marine prosobranch *N. reticulatus*.

A semi-quantitative measurement is often used for a quick analysis of a sample in respect to a rough determination of matrix, major and trace element concentrations, and can be performed as the first step before the quantitative analysis. Firstly, a semi-quantitative multi-element analysis was performed by LA-ICP-MS using Mn as an internal standard element with a known concentration (certified value: 7.3 $\mu g\,g^{-1}$) whereby the concentrations of analytes in the sample were calculated from the ion intensities measured with respect to the known concentration of internal standard element using the following analysis equation (1):

$$c(x) = \frac{c(v) \cdot I(x) \cdot A(v)}{I(v) \cdot A(x)} \quad (1)$$

where x is the element to be determined, v is the internal standard element, c is the element concentration, I is the ion intensity measured, and A is the isotopic abundance [1].

The element concentration in the mussel tissue (BCR 278) measured by LA-ICP-MS was corrected using experimentally determined relative sensitivity coefficient (RSC) of a chemical element. The RSC [defined as the ratio of measured (experimental) to certified (true) element concentrations in a given matrix] of chemical elements depend on the analytical procedure applied. The same matrix or a similar matrix composition should therefore be compared to the sample (under identical experimental conditions) [1,41]. In this case, RSCs were measured on pressed discs of

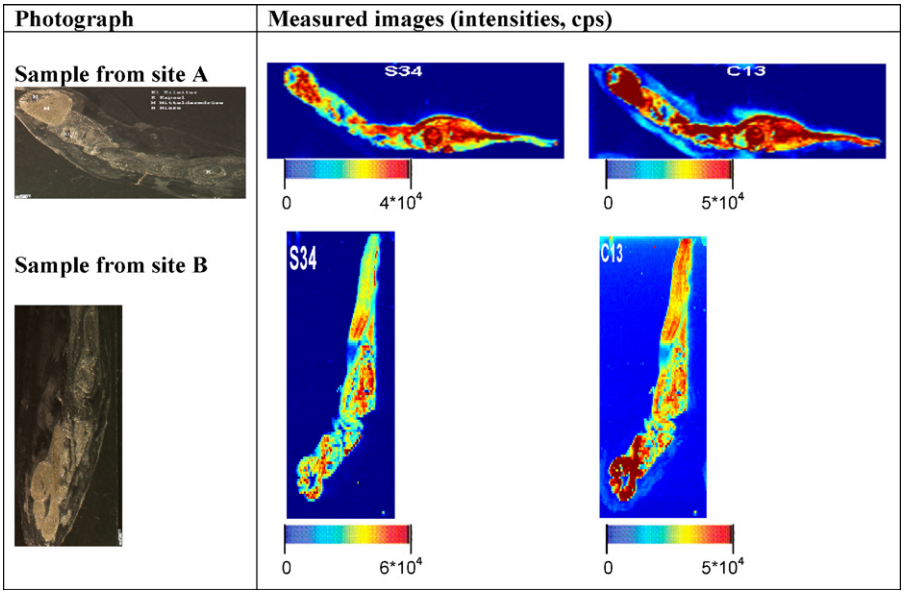


Fig. 1. Photograph and ion images of analyzed thin section of snail samples from site A and site B.

Table 2
Relative sensitivity coefficients in LA-ICP-MS determined using pressed discs of the certified reference material (CRM) of mussel tissue (BRC 278) and the certified concentrations [$\mu g\,g^{-1}$].

Element	Isotope measured	RSC	Certified values [$\mu g\,g^{-1}$]
Cu	63	2.7	9.6 ± 0.16
Zn	66	0.4	76 ± 2
Cd	111	1.8	0.34 ± 0.02
Hg	202	1.6	0.188 ± 0.007
Pb	208	1.9	1.91 ± 0.04

reference mussel tissue (BCR CRM 278), the values of RSCs together with the certified values are presented in Table 2.

The RSCs for the investigated elements varied from 0.4 to 2.7, therefore a semi-quantitative determination of these metals by LA-ICP-MS is possible with an error factor in this range. Using the RSC as correction factors of measured data of real samples in the semi-quantitative mode is often sufficient for a first survey analysis on the sample analyzed. The pressed disc of mussel tissue sample (BCR 278) was used for the calibration in order to study the performance in this mode of one-point calibration for the snail sample and mussel tissue by LA-ICP-MS. The results of analytical data in a snail sample and mussel tissue using different calibration strategies: one point calibration compared to the use of synthetic laboratory standards for calibration are summarized in Table 3 and were compared with ICP-MS solutions analysis ($n = 3$). A semi-quantitative multi-element analysis is limited in accuracy and precision. Semi-quantitative trace metal analysis by LA-ICP-MS via one-point calibration was compared with ICP-MS analysis and the values for Hg, Cd and Pb were found to be in agreement. However, LA-ICP-MS values for Cu and Zn are on average 65% and 26% higher than ICP-MS analysis, respectively. Reliable data were obtained for the determination of Hg, Cd and Pb in snail sample and mussel tissue using BCR 278 in the semi-quantitative approach.

In the next step the quantitative analyses of Cu, Zn, Cd, Hg and Pb were performed using three types of synthetic laboratory standards with three types of biological matrix. The quantification in LA-ICP-MS using all calibration strategies with synthetic laboratory standards yielded a good linearity in the calibration graphs, with linear correlation coefficients (R^2) better than 0.99 for all three calibration strategies in Table 3.

Table 3
Results of trace metal analysis in snail-sample and mussel-tissue using different strategies for calibration: (A) one-point calibration (semi-quantitative); (B) synthetic matrix-matched solid standard (mussel tissue SRM 278); (C) matrix-matched laboratory synthetic standard (snail blank); (D) matrix-matched laboratory synthetic standard (rat brain).

		Calibration strategy			
Elements	ICP-MS analysis	Strategy 1 [$\mu g\,g^{-1}$]	Strategy 2 [$\mu g\,g^{-1}$][a]	Strategy 3 [$\mu g\,g^{-1}$][a]	Strategy 4 [$\mu g\,g^{-1}$][a]
Mussel tissue					
Cu	8.9 ± 0.2	15 ± 3	8.7 ± 0.3	8.5 ± 0.3	10.6 ± 0.4
Zn	64 ± 4	80 ± 10	73 ± 8	63 ± 4	67 ± 6
Cd	0.4 ± 0.0	0.3 ± 0.1	0.2 ± 0.1	0.3 ± 0.1	0.3 ± 0.1
Hg	n.d.	0.5 ± 0.1	0.4 ± 0.1	0.4 ± 0.0	0.5 ± 0.1
Pb	1.8 ± 0.3	2.0 ± 0.7	2.4 ± 0.1	1.7 ± 0.3	2.3 ± 0.4
Snail sample					
Cu	72 ± 5	131 ± 15	78 ± 8	76 ± 7	95 ± 9
Zn	64 ± 6	82 ± 13	75 ± 7	64 ± 7	69 ± 7
Cd	3.8 ± 0.7	4.9 ± 0.7	3.5 ± 0.4	3.9 ± 0.4	4.7 ± 0. 6
Hg	0.9 ± 0.3	1.1 ± 0.3	0.8 ± 0.2	1.0 ± 0.4	1.1 ± 0.4
Pb	2.5 ± 0.4	3.1 ± 0.8	3.6 ± 0.5	2.3 ± 0.5	3.3 ± 0.5

n.d.: not determined; $n = 3$.

[a] The correlation coefficients for calibration curves (R^2) varied for all analytes investigated in the different calibration strategies between 0.997 (for Cd) and 0.999 (for Pb).

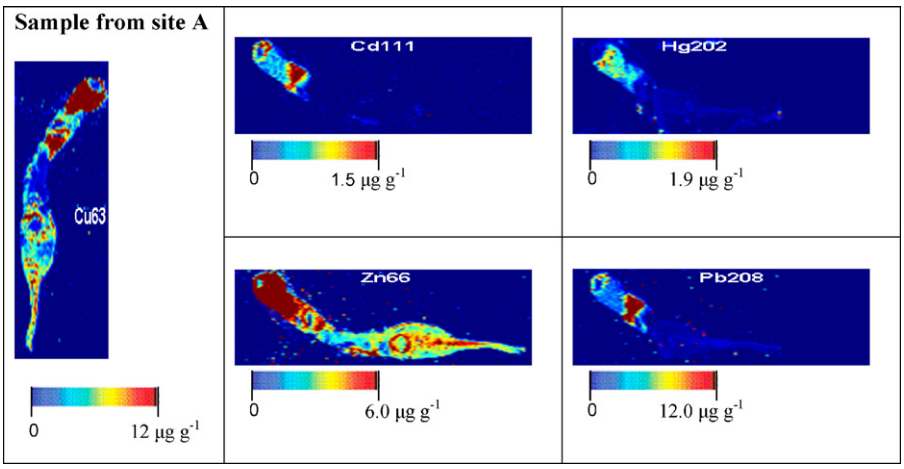


Fig. 2. Cu, Cd, Hg, Zn, and Pb images in a cross-section of snail tissue from site A. The analyzed area was 34 mm × 9 mm; the measured isotopes are given in the images.

The accuracy of the investigated methods was verified by comparing the results obtained with the values from ICP-MS analysis using the Student's *t*-test. We concluded that there was no significant difference at a confidence level of 95% between the values determined by LA-ICP-MS (all quantitative strategies) and those determined by ICP-MS analysis for all elements investigated. However, the best strategy was found to be the use of matrix-matched synthetic laboratory standards of snail tissue (strategy 2).

The analytical results obtained in the semi-quantitative and quantitative calibration modes are compared in Table 3. Generally good agreement of the data sets was obtained by quantitative calibration via calibration curves and one-point calibration by LA-ICP-MS, when compared to ICP-MS analysis. The analysis of the snail sample and mussel tissue using calibration curves for quantification (for three cases) yielded a better accuracy overall compared to the semi-quantification using RSCs. However, this technique was more time-consuming and required matrix-matched certified standard reference materials.

The concordant results obtained using the investigated calibration technique (strategy 2) and ICP-MS analysis indicates that the use of matrix-matched laboratory standards is the method of choice for the bio-imaging of metals.

With respect to calibration strategies, synthetic pressed-powder pellets (strategy 1) and another kind of artificial matrix were not sufficiently similar in either physical structure or chemistry to be ablated in the same way as the real field samples.

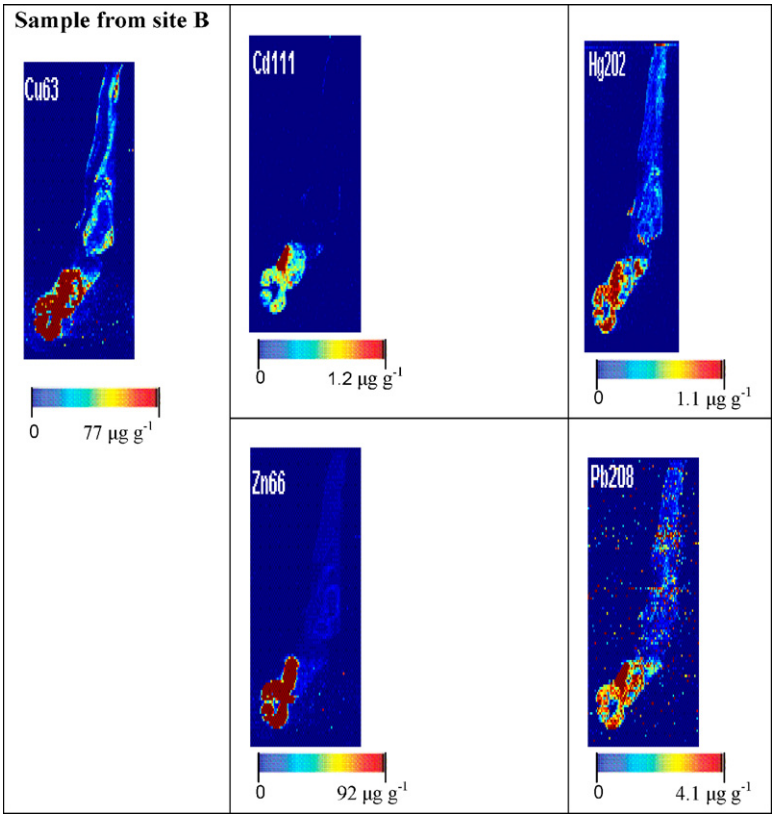


Fig. 3. Images of Cu, Cd, Hg, Zn, and Pb in a cross-section of snail tissue from site B. The analyzed area was 34 mm × 12 mm; the measured isotopes are given in the images.

3.2. Quantitative two-dimensional mapping of Cu, Zn, Cd, Hg and Pb in analyzed thin sections of snail tissue

Laser ablation ICP-MS was applied to produce images of element distribution in sections of *N. reticulatus* collected at sampling sites with a different degree of pollution. Fig. 1 shows the distribution of two essential non-metals (S and C). For anatomical orientation, photomicrographs of the sections (posterior part of the snail on the left side, anterior on the right) are shown together with LA-ICP-MS images of S and C. Sulfur and carbon are distributed uniformly across the snail's body. The elemental images obtained by LA-ICP-MS correlated very well with the anatomical structure of snail tissue shown in the photographs.

The quantification of the distribution of metals in snail samples was performed by measuring matrix-matched synthetic laboratory standards with well-defined element concentrations (under the same experimental conditions as the tissue sections) using LA-ICP-MS according to the developed method (strategy 2). Two-dimensional distributions of Cu, Cd, Hg, Pb and Zn were determined in the cross-sections of three snail tissues (Figs. 2 and 3).

Figs. 2 and 3 show a heterogeneous distribution of all elements analyzed by LA-ICP-MS. There are no pronounced differences between animals collected at the different sampling sites, indicating that *N. reticulatus* collected at site B are still contaminated with the toxic elements. High concentrations of copper (77 $\mu g\,g^{-1}$) and zinc (92 $\mu g\,g^{-1}$) were found in the female *N. reticulatus* from site B. In snails collected at the contaminated site A, much lower levels of Cu and Zn were measured. This gave rise to the assumption that the harbor (site A) may not be the only source of pollution for Cu and Zn. Cadmium, mercury and lead were detected in low $\mu g\,g^{-1}$ range with one exception: lead concentration in the female collected at site A (26 $\mu g\,g^{-1}$) is much higher compared to the lead concentrations in the male from the same site and the female from site B. Metal concentrations are frequently determined in marine clams mainly for reasons of food safety [43,44]. It is difficult to compare these total concentrations with the data presented here, since whole tissue is conventionally analyzed by ICP-MS [45,46]. In our work, metal concentrations were presented with a lateral resolution at the 160 μm range of the tissue section within the snail body using the developed bio-imaging LA-ICP-MS technique.

In general, the highest metal concentrations were found in the visceral mass of the snails, where the digestive and reproductive organs were located. All elements seemed to accumulate mainly in the digestive gland. Copper and zinc were distributed most broadly and were also found in the reproductive tract in parts of the testis (male) and oviduct (female) but not in the ovary. Cadmium and mercury accumulation was restricted to the digestive gland, whereas lower levels of lead were also found in the testis and ovary. Furthermore, copper, cadmium and lead were detected in the kidney, the gland and the mantle epithelium. The anterior part of the mantle epithelium (high concentrations of Cu, Cd and Pb) contained ectodermic cells secreting the shell material. The accumulation of metals in this body region may be a first step for their storage and thus detoxification in the gastropod shell.

4. Conclusions

An imaging mass spectrometric technique was developed for the quantitative determination of essential and toxic metals in biological tissues using LA-ICP-QMS. Several quantification procedures, e.g. using certified reference materials or synthetic matrix-matched laboratory standards, were established for selected metals in LA-ICP-MS. With the ability to analyze thin sections of biological tissues with sufficient sensitivity, as well as a relatively short analysis time, LA-ICP-MS is a very powerful technique for the quantitative multi-elemental imaging analysis of tissues sections to study the uptake and transport of metals. The technique presented here is promising for a wide applications ranging from environmental research and toxicology to drug development and the basic life sciences.

Acknowledgments

The first author wishes to express her appreciation to DAAD/CAPES for financial support of this research.

References

[1] J.S. Becker, Inorganic Mass Spectrometry: Principles and Applications, John Wiley and Sons, Chichester, 2007.
[2] J.S. Becker, M. Zoriy, B. Wu, A. Matusch, J.Su. Becker, J. Anal. At. Spectrom. 23 (2008) 1275–1280.
[3] J.S. Becker, H. Sela, J. Dobrowolska, M. Zoriy, J.Su. Becker, Int. J. Mass Spectrom. 270 (2008) 1–7.
[4] B. Fernández, F. Claverie, C. Pécheyran, O.F.X. Donard, Trends Anal. Chem. 26 (2007) 951–966.
[5] R.E. Russo, X. Mao, H. Liu, J. Gonzalez, S.S. Mao, Talanta 57 (2002) 425–451.
[6] J. Feldmann, A. Kindness, P. Ek, J. Anal. At. Spectrom. 17 (2002) 813–818.
[7] M.V. Zoriy, A. Kayser, A. Izmer, C. Pickhardt, J.S. Becker, Int. J. Mass Spectrom. 242 (2005) 297–302.
[8] J.S. Becker, M.V. Zoriy, C. Pickhardt, N. Palomero-Gallagher, K. Zilles, Anal. Chem. 77 (2005) 3208–3216.
[9] J.S. Becker, A. Matusch, C. Depboylu, J. Dobrowolska, M.V. Zoriy, Anal. Chem. 79 (2007) 6074–6080.
[10] J.S. Becker, N. Jakubowski, Chem. Soc. Rev. 38 (2009) 1969–1983.
[11] J.S. Becker, J. Anal. At. Spectrom. 20 (2005) 1173–1184.
[12] J.T. Elliston, S.E. Glover, R.H. Filby, J. Radioanal. Nucl. Chem. 263 (2005) 301–306.
[13] V. Mizuriha, H. Hasegawa, M. Notoya, Acta Histochem. 30 (1997) 277–301.
[14] J. Mesjasz-Przybylowicz, W.J. Przybylowicz, Nucl. Instrum. Methods Phys. Res. B 189 (2002) 470–481.
[15] A. Takeda, H. Tamano, S. Enomoto, N. Oku, Cancer Res. 61 (2001) 5065–5069.
[16] S. Chandra, Appl. Surf. Sci. 679 (2003) 203–204.
[17] G.H. Morrison, I. Gay, S. Chandra, Scanning Microsc. 8 (1994) 359–370.
[18] D. Touboul, F. Halgand, A. Brunelle, R. Kersting, E. Tallarek, B. Hagenhoff, O. Laprevote, Anal. Chem. 76 (2004) 1550–1559.
[19] J.S. Becker, M.V. Zoriy, J.S. Becker, J. Dobrowolska, A. Matusch, J. Anal. At. Spectrom. 22 (2007) 736–744.
[20] M.V. Zoriy, M. Dehnhardt, A. Matusch, J.S. Becker, Spectrochim. Acta B 63 (2008) 375–382.
[21] B. Wu, Y. Chen, J.S. Becker, Anal. Chim. Acta 633 (2009) 165–172.
[22] J.Su. Becker, M. Zoriy, C. Pickhardt, M. Przybylsky, J.S. Becker, Int. J. Mass Spectrom. 242 (2005) 135–144.
[23] C. Pickhardt, M. Zoriy, A. Izmer, J.S. Becker, Int. J. Mass Spectrom 248 (2006) 136–141.
[24] J.Su. Becker, M. Zoriy, M. Przybylski, J.S. Becker, J. Anal. At. Spectrom 22 (2007) 63–68.
[25] V. Fretter, A. Graham, J. Mol. Stud. Suppl. 15 (1985) 435–556.
[26] E. Stroben, J. Oehlmann, P. Fioroni, Mar. Biol. 113 (1992) 625–636.
[27] E. Stroben, J. Oehlmann, P. Fioroni, Mar. Biol. 114 (1992) 289–296.
[28] G.W. Bryan, G.R. Burt, P.E. Gibbs, P.L. Pascoe, J. Mar. Biol. Assoc. U K 73 (1993) 913–929.
[29] R. Barreiro, R. Gonzáles, M. Quintela, J.M. Ruiz, Mar. Ecol. Progr. Ser. 218 (2001) 203–212.
[30] B.S. Smith, J. Appl. Toxicol. 1 (1981) 141–144.
[31] P.E. Gibbs, G.W. Bryan, J. Mar. Biol. Assoc. U K 66 (1986) 767–777.
[32] J. Oehlmann, E. Stroben, P. Fioroni, J. Mol. Stud. 57 (1991) 375–390.
[33] J. Oehlmann, P. Fioroni, E. Stroben, B. Markert, Sci. Total Environ. 188 (1996) 205–223.
[34] P. Fioroni, J. Oehlmann, E. Stroben, Zool. Anz. 226 (1991) 1–26.
[35] M. Huet, P. Fioroni, J. Oehlmann, E. Stroben, Hydrobiologia 309 (1995) 29–35.
[36] J. Oehlmann, E. Stroben, U. Schulte-Oehlmann, B. Bauer, P. Fioroni, B. Markert, Fresenius J. Anal. Chem. 354 (1996) 540–545.
[37] M. Duft, C. Schmitt, J. Bachmann, C. Brandelik, U. Schulte-Oehlmann, J. Oehlmann, Ecotoxicology 16 (2007) 169–182.
[38] J. Oehlmann, P. Di Benedetto, M. Tillmann, M. Duft, M. Oetken, U. Schulte-Oehlmann, Ecotoxicology 16 (2007) 29–43.
[39] G. Wirzinger, C. Vogt, J. Bachmann, M. Hasenbank, C. Liers, C. Stark, S. Ziebart, J. Oehlmann, Cah. Biol. Mar. 48 (2007) 85–94.
[40] J. Oehlmann, U. Schulte-Oehlmann, M. Tillmann, B. Markert, Ecotoxicology 9 (2000) 383–397.
[41] J.S. Becker, C. Pickhardt, H.-J. Dietze, Microchim. Acta 135 (2000) 71–80.
[42] J.Su. Becker, C. Pickhardt, N. Hoffmann, H. Hocker, J.S. Becker, At. Spectrosc. 23 (2002) 1–6.
[43] C. Skinner, N.J. Turoczy, P.L. Jones, D. Barnett, R. Hodges, Food Chem. 85 (2004) 351–356.
[44] J.C. Amiard, C. Amiard-Triquet, L. Charbonnier, A. Mesnil, P.S. Rainbow, W.X. Wang, Food Chem. Toxicol. 46 (2008) 2010–2022.
[45] F. Cubadda, A. Raggi, Microchem. J. 79 (2005) 91–96.
[46] J. Zukowska, M. Biziuk, J. Food Sci. 73 (2008) R21–R29.

Talanta 80 (2009) 434–439

Contents lists available at ScienceDirect

Talanta

journal homepage: www.elsevier.com/locate/talanta

Ultrasound energy focused in a glass probe: An approach to the simultaneous and fast extraction of trace elements from sediments

Silvia Fdez-Ortiz de Vallejuelo, Ana Barrena, Gorka Arana, Alberto de Diego*, Juan Manuel Madariaga

Department of Analytical Chemistry, University of the Basque Country, P.O. Box 644, E-48080 Bilbao, Basque Country, Spain

ARTICLE INFO

Article history:
Received 24 March 2009
Received in revised form 29 June 2009
Accepted 1 July 2009
Available online 9 July 2009

Keywords:
Sediments
Trace elements
Ultrasound focused energy
Sample treatment

ABSTRACT

The 3051 USEPA method (or alternatively, the 3051A) can be considered nowadays as a reference method to extract metals from sediments. However, after microwave heating, the sample must be allowed to cool down, which results in a considerable lengthening of the whole analytical process. Microwave ovens and their maintenance are, in addition, expensive, and its use is relatively dangerous. The use of ultrasound focused energy to assist the extraction of chemicals from solid samples is a safe and relatively cheap technique. In this work we propose a new method to extract simultaneously several elements from sediments using ultrasound energy focused in a glass probe to accelerate the process, and check its possibilities to become an alternative to the EPA3051(A) approach. The optimised procedure allows extracting 13 elements in only 6 min, with similar recoveries and, in general, better repetitivities than the EPA3051. In addition, the suspension is only slightly heated during the leaching process.

© 2009 Elsevier B.V. All rights reserved.

1. Introduction

Metals, specifically arsenic, and their compounds are included in the indicative list of main pollutants of the EU water framework directive [1]. They are present in natural aquatic systems at trace and ultratrace levels [2]. There is a continuous exchange of trace elements between sediments and water in oceans, estuaries, rivers and lakes [3]. This exchange plays an important role in the biogeochemical cycle of these pollutants and usually determines their availability to living organisms [4,5]. In addition, sediments serve as reservoir of trace elements and, due to the long residence times involved, they can be used to investigate historical pollution in selected areas [4,6]. In this context, the need of measuring the concentration of trace metals in sediments becomes evident.

The analysis of trace and ultratrace elements in sediments is a long process which involves several steps. Nowadays, extraction of the analytes from the matrix constitutes the bottleneck of the analysis in terms of time, reproducibility and accuracy [7]. A quantitative extraction requires the total dissolution of the sample, which is only attained using hydrofluoric acid or any of its derivatives (usually combined with other strong acids and/or oxidants) as extractant. In many cases, however, the determination of total concentrations is not mandatory, and the result obtained after the extraction of the analytes using strong mineral acids such as nitric and hydrochloric acids (or mixtures of them, e.g., *aqua regia*) is enough for toxicological purposes. The so-called "pseudo-total" metal content (or acid leachable fraction) is usually well up the bioavailable fraction and has been frequently used, for instance, in environmental monitoring programs [8] and toxicological risk assessment [9].

Solid–liquid acid leaching has become, consequently, the most popular technique to extract trace elements from sediments. The conventional hot-plate procedure [10] is long and tedious. The methods recommended by the International Organization for Standardisation (ISO 11466 [11]) and the U.S. Environmental Protection Agency (EPA 3050B [12]) use a reflux condenser, mixtures of mineral acids and oxidants, and still take several hours. Different approaches, such as pressure-bombs [13], ultrasound baths [14] and both focused [15] or pressurised [16] microwave ovens, have been investigated to accelerate the process. By far, the last option has been the most popular one over the last 10 years. The EPA method (EPA 3051) describes the microwave assisted HNO_3 extraction of sediments for metal analysis [17]. Its alternative, the EPA 3051A [18] allows using HNO_3–HCl mixtures to improve the performance for several elements. Microwave assisted leaching, however, is affected by several and serious limitations, such as relatively long extraction time and low reproducibility. The sample is subjected to high temperature and pressure and must be allowed to cool down before going on with the general procedure. Last generation microwave ovens and their maintenance, in addition, are relatively expensive, and must be manipulated by well trained personal.

Ultrasound energy has been used to accelerate the extraction of organics, metals and also organometals from environmental solid samples [19,20]. Ultrasound baths provide a simple and cheap way to deliver ultrasound energy. They allow using a large variety of

* Corresponding author. Fax: +34 946013500.
E-mail address: alberto.dediego@ehu.es (A. de Diego).

0039-9140/$ – see front matter © 2009 Elsevier B.V. All rights reserved.
doi:10.1016/j.talanta.2009.07.002

solvents as extractants. However, the irradiation power is poor, the reproducibility is low and the ultrasonic efficiency is not homogeneously distributed in the bath [21]. Focused ultrasound systems overcome those problems. The ultrasound energy is focused in the tip of a probe, typically made in titanium, which is immersed in the solution to be irradiated. The irradiation power is up to 100 times higher than that provided by a bath. Only long irradiation times result in a constant but modest increase in temperature of the irradiated system. Use of focused ultrasound produces relatively short, quantitative and reproducible extractions of pollutants from solid samples of different origin [19,22,23]. The use of concentrated strong mineral acids as extractant, however, is not recommended by manufacturers, because the half-life of the titanium probe is considerably reduced. Consequently only a few works, all of them appeared before 2000, have been published on the extraction of metals from sediments using an ultrasonic probe [24–26]. In all the cases, short extraction times (less than 5 min) and diluted HNO_3 (up to 10%, v/v) were used, and recoveries of 60%, 54–69%, 15% and 75–95% were obtained, respectively, for Cu, Pb, Cr and Cd. From these results it becomes evident that the impossibility of using concentrated acids seriously limits the applicability of the technique.

The commercialisation of a glass probe as an alternative to the classical titanium one is recent. Glass is chemically resistant to strong concentrated acids and becomes an excellent candidate to be used in the extraction of metals from solid samples. There is no restriction regarding irradiation time and acid concentration. In addition, potential contamination of the samples with impurities contained in the titanium probe is eliminated [21]. As a drawback, the ultrasound power and amplitude delivered by a glass probe are limited, due to the low mechanical resistance of glass compared to titanium. There is only one work dealing with the extraction of eight metals from solid samples (sewage sludge) for using industrial ultrasound focused on a glass sonotrode to accelerate the process [27]. To our knowledge, this technique has not been yet used in the analysis of sediments.

In this work we check the possibilities of the ultrasound energy focused in a glass probe as an alternative to the microwave assisted leaching of trace elements from sediments. The results obtained have allowed us proposing a very fast procedure (6 min of irradiation time) for the simultaneous extraction of several elements (Al, As, Co, Cr, Cu, Fe, Mg, Mn, Ni, Pb, Sn, V and Zn) from sediments and their simultaneous detection and quantification by ICP/MS.

2. Experimental

2.1. Materials and reagents

Calibrant solutions of the analytes all together were prepared by weight in 1% HNO_3 from individual commercial stock solutions of Al, As, Co, Cr, Cu, Fe, Mg, Mn, Ni, Pb, Sn, V and Zn (1000 mg L^{-1} in 5% HNO_3, Specpure, Alfa Aesar, Ward Hill, MA, USA). Be^9, Sc^{45}, In^{115} and Bi^{209} stock standard solutions (1000 mg L^{-1} in 5% HNO_3, Specpure, Alfa Aesar) were added to blank, standard and sample solutions to yield at 10 μg L^{-1} in concentration as internal standard. Preparation of calibrants and analysis of samples were performed in a "class 100" clean room.

Efficiency of the extraction method was checked using the certified reference materials NIST 1646a (estuarine sediment, National Institute of Standards and Technology, Gaithersburg, USA).

Hydrochloric acid (37%, Tracepur), acetic acid (100%, Pro analysis) and nitric acid (69%, Tracepur) were purchased from Merck (Darmstadt, Germany). Milli-Q quality water ($\kappa < 0.05$ μS cm^{-1}, Millipore, Billerica, MA, USA) was used throughout.

All plastic and crystal materials in contact with calibrants or samples were first cleaned with water and soap, rinsed with deionised water and finally left in a 10% nitric acid bath for 24 h. Afterwards, it was thoroughly rinsed with deionised and MilliQ water before use.

Chemometric analysis of data was carried out with The Unscrambler 9.2 (Camo Process, Oslo, Norway) and Multisimplex 1.0 (Grabitech, Sundsvall, Sweden).

2.2. Instrumentation

Weighing solid samples and preparation of calibrants were carried out by means of an analytical balance AE200 (Mettler Toledo, Columbus, OH, USA) with a precision of ±0.00001 g.

An HD 2070 Sonopuls Ultrasonic Homogenizer (Bandelin, Germany) equipped with a GM 2070 generator (70 W, 20 kHz), an UW 2070 ultrasonic converter and either a SH 70G horn and MS 73 titanium probe (3 mm) or, alternatively, a SH 70 GQ horn and GS 6 glass probe (6 mm) was used in the extraction step. A variable power setting (0–100%) allows controlling amplitude of the delivered ultrasound. A maximum power of 35% is recommended by the manufacturer when using the glass probe. In some experiments, the sample was continuously stirred during extraction by means of an Asincro magnetic stirrer (Selecta, Barcelona, EU).

Trace element analysis was carried out with an Elan 9000 ICP/MS (PerkinElmer, Ontario, Canada), provided with Ryton cross-flow nebulizer, Scott-type double pass spray chamber and standard nickel cones. Preparation of calibrants and analysis of samples were done inside a clean room (class 100). Argon (99.999%, Praxair, Spain) was used as carrier gas in the ICP/MS measurements.

2.3. Experimental procedure

2.3.1. Ultrasound assisted extraction of sediments

Previously freeze-dried and sieved (<75 μm) sediment collected in December 2005 in the estuary of the Nerbioi-Ibaizabal River (Bilbao, Bay of Biscay, Basque Country, N 43°19′04.5″; W 02°59′35.1″), *NI0512*, was used in all the experiments. Design of experiments (DoE) was used to study the influence of several variables on the extraction efficiency and to optimise the extraction process. DoE addresses several advantages when compared to the classical "one-experiment-at-a-time" approach: (i) it is possible to investigate simultaneously the effect of several factors as well as interactions among them, (ii) the ratio between obtained information and experimental effort is optimised, and (iii) DoE allows modelling mathematically the system under study.

An exact amount of dry sediment (0.2–0.5 g) was transferred to a polyethylene cylindrical extraction vessel together with an appropriate volume of extractant (10–20 mL). In some experiments a stir bar was added to the vessel. The probe (titanium or silica–glass) was placed inside the suspension (0.5–2 cm), the magnetic stirrer was switched on (when applicable) and sonication was applied at a fixed power (10–100%) and cycles (1–9 or continuous) during a fixed time (5–3540 s). To avoid cross-contamination the probe was rinsed several times with MilliQ water and then air dried between sample runs. After sonication, the suspensions were filtered through PVDF 0.45 μm filters using plastic syringes. In some experiments, the extract was separated from the residual solid by centrifugation at 2500 rpm during 10 min (2×) and the supernatant was filtered through PVDF 0.45 μm filters before analysis. Two different dilutions of the extract were prepared in water to measure, respectively, minor and major elements. In both of them HNO_3 and HCl concentrations were adjusted to 1% and 0.45% respectively by adding the appropriate amounts of concentrated HNO_3 and HCl. All dilutions were made by weight. In both dilutions, Be^9, Sc^{45}, In^{115} and Bi^{209} were added (10 μg L^{-1} each) as internal standard before analysis. Blanks were processed in a similar way.

Table 1
Experimental conditions used in the ICP/MS analysis.

Nebulization flow	0.94 L min^{-1}
Plasma flow	15 L min^{-1}
Auxiliary flow	1.2 L min^{-1}
Sample flow	1 L min^{-1}
Measured isotopes	^{27}Al, ^{75}As, ^{59}Co, ^{52}Cr, ^{63}Cu, ^{57}Fe, ^{24}Mg, ^{55}Mn, ^{60}Ni, ^{208}Pb, ^{120}Sn, ^{51}V, ^{66}Zn
Radiofrequency power	1000 W
Integration time	1000 ms
Replicates	3–4

2.3.2. Analysis of extracts and calibrants

The concentrations of Al, As, Co, Cr, Cu, Fe, Mg, Mn, Ni, Pb, Sn, V and Zn in the dilutions of the extracts and calibrant solutions were simultaneously measured by ICP/MS using the external calibration method with internal standard correction [28]. The experimental conditions are summarised in Table 1. All measurements were run in triplicate. The accuracy of the analysis was checked using the NIST 1640 standard reference material (Natural water, National Institute of Standards and Technology, Gaithersburg, USA) with satisfactory results.

3. Results and discussion

3.1. Influence of several variables on extraction efficiency

In a first approach, the influence of several variables, e.g., sonication time (t), amplitude of the ultrasound (A), length of probe immersed in the suspension (l), and cycle (cy; cy indicates a pulsed mode; for instance, $cy = 4$ means a 0.4 s active period followed by a 0.6 s passive period) was studied using different solutions as extractants. In each case, experiments were organised according to a full factorial design with variables at two different levels and four replicates of the central point. Experiments were always run in a random order. About 0.2 g of sediment was weighted in a conical (flat) bottom extraction vessel and extraction was performed as described in Section 2, without stirring, under the experimental conditions defined in the design. The suspension was filtered before dilution and ICP/MS analysis. Analysis of variance (ANOVA) of the results was carried out by means of Unscrambler to decide if the variables considered or any combination among them significantly influenced the extraction of each element at a 95% confidence level.

First, acetic acid was checked as extractant using the titanium probe to focus the ultrasound energy. In this case, t (5–600 s), A (10–100%), l (0.5–2 cm), cy (1–9 or continuous) and concentration of acetic acid (c_{HAc}, 0.1–3 mol dm^{-3}) were studied. A total of 36 experiments were run as suggested by a full factorial design $2^5 + 4$. ANOVA showed that only the influence of c_{HAc} was significant (and positive) for all the elements considered. Irradiation time, t, only affected significantly in a positive way the extraction of As, Cu and Mn. The rest of variables and combination of variables did not influence the extraction efficiency.

In a next step, t (5–600 s), A (10–35%), cy (1–9 or continuous) and concentration of nitric acid (c_{HNO_3}, 0.01–15 mol dm^{-3}) were considered ($2^4 + 4$, 20 experiments) using HNO_3 aqueous solutions as extractant and the silica–glass probe. The probe was immersed 1.5 cm in the suspension. It was concluded that only c_{HNO_3} influenced positively the extraction of all the elements, being the influence highly significant. Like in the case of HAc, irradiation time also affected positively the extraction of several elements, As, Fe, Mg and Mn. The rest of variables and combinations were not significant.

Finally, a $2^4 + 4$ full factorial design with 20 extraction experiments was used to study how t (5–600 s), A (10–35%), cy (1–9 or continuous) and proportion of HNO_3 in the extractant (%HNO_3, 0–100%) affected the extraction of metals when aqueous mixtures of HNO_3 and HCl are used as extractants and the silica–glass probe to focus the ultrasound energy. The probe was immersed 1.5 cm in the suspension, and 69% HNO_3 and 36% HCl were used to prepare the extractant solution at the proportion defined in the design, in a way that %HNO_3 = 0, 50 and 100 results, respectively, in an aqueous solution of HCl 13.2 mol dm^{-3}, an aqueous mixture of HNO_3 7.1 mol dm^{-3} and HCl 6.6 mol dm^{-3}, and an aqueous solution of HNO_3 14.2 mol dm^{-3}. ANOVA showed that it is possible to define two groups of elements: those which are better extracted with HNO_3 rich solutions (Al, Co, Cu, Mg, Pb and Zn), and those which prefer HCl rich solutions (As, Fe, Mn, Ni, Sn and V). Extraction of Cr is not clearly influenced by this variable. In addition, extractions of Al, As, Co, Cu, Fe, Mg, Mn and Ni are positively affected by irradiation time, t. The rest of variables and combination showed no clear trend.

For each design, the concentration of each element in the leachate was estimated under the best possible experimental conditions using the mathematical models provided by Unscrambler after ANOVA of the results. Concentrations were compared with those obtained after analysis of the sediment according to the EPA 3051 method [17] with a Mars Xpress microwave oven from CEM Corporation, Matthews, NC, USA. The extraction efficiencies calculated in this way are shown in Fig. 1a. The best recoveries were always obtained with a mixture of HNO_3–HCl as extractant, except for Fe and Mg. In those cases, extraction with HAc offered better results, probably due to the fact that the use of the titanium probe allowed delivering ultrasound energy of higher amplitude.

To check the effect of agitation on extraction efficiency, analysis of the *NI0512* sediment was repeated with ($n = 4$) and without ($n = 4$) magnetic stirring. About 0.4 g of sample was weighed in a flat bottom extraction vessel, a magnetic bar was added (in experiments with agitation) and it was processed as described before using 20 mL of HNO_3 2.8 mol dm^{-3}–HCl 3.1 mol dm^{-3} as extractant and the silica–glass probe. The leachate was separated from the solid residue by filtration. The rest of variables was fixed as follows: $t = 1800$ s, $A = 35\%$, $l = 1.5$ cm and $cy = 5$. As it can be observed in Fig. 1b, extraction efficiency was systematically higher in experiments with agitation. Similar experiments showed that separating the leachate from the solid residue by filtration or centrifugation did not significantly affect the result of the analysis. Consequently, in all the next experiments the suspension was magnetically stirred during extraction and the leachate was separated by filtration.

3.2. Optimisation of the extraction step

After the preliminary experiments described in the previous section it was concluded that the variables with higher influence on the extraction of the elements considered from sediments using ultrasound energy focused in a silica–glass probe were irradiation time, t, as well as proportion, %HNO_3, and concentration, c_{acid}, of acids in the HNO_3–HCl aqueous mixture used as extractant. A central composite design (CCD) with three variables at five different levels and four repetitions of the central point (18 experiments run in a random order) was used to find the optimal experimental conditions for the extraction of each element considered. t, %HNO_3 and c_{acid} were varied from 0.5 to 59 min, 8–92% and 0.01–11.8 mol L^{-1}, respectively ($-\alpha$ to $+\alpha$ levels). In all the experiments, about 0.4 g of the *NI0512* sediment was suspended in about 20 mL of extractant, the suspension was magnetically stirred along the extraction process, the glass probe was immersed 1.5 cm in the solution and ultrasound amplitude of 35% was applied with a cycle of 5. The extract was separated from the solid residue by filtration. Regression analysis of the obtained results allowed defining the response surface for each element, and observation of these surfaces led to the best experimental conditions summarised in Table 2.

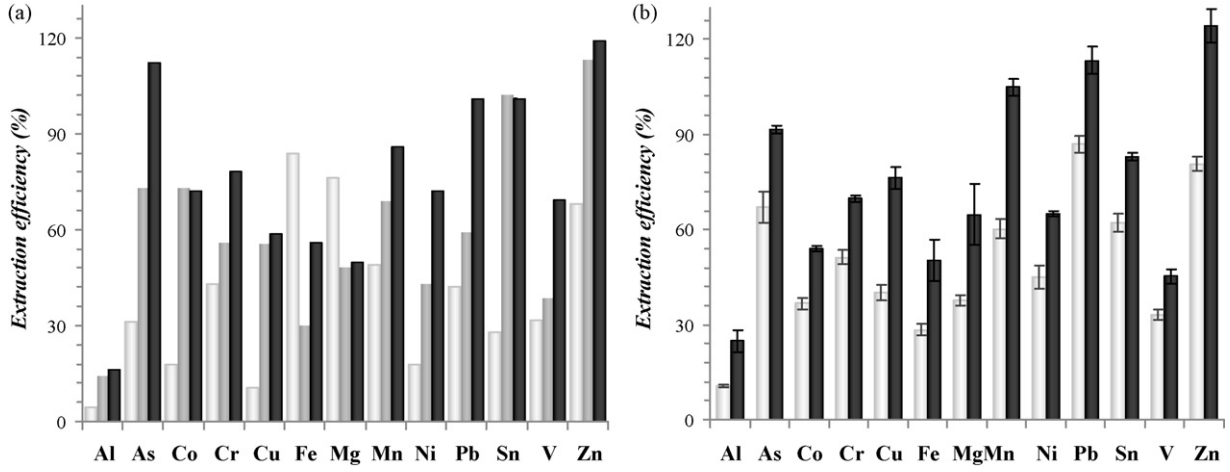


Fig. 1. Extraction efficiencies (as percentage referred to the EPA 3051 method) found for each element considered: (a) using the combination HAc/titanium (white), HNO_3/silica–glass (dark grey) and HNO_3–HCl/silica–glass (black) as extractant/probe. The sediment used in the experiments was the *NI0512* collected in the estuary of the Nerbioi-Ibaizabal River in December 2005; (b) after analysis of the same sediment with ($n = 4$, black) or without ($n = 4$, white) stirring the suspension during ultrasound assisted extraction with a silica–glass probe and HNO_3–HCl as extractant.

The extraction efficiencies calculated at those conditions are shown in the last row of Table 2, using as reference the EPA 3051 method (Mars Xpress unit from CEM was used).

3.3. Best conditions for a simultaneous extraction of the elements considered

The experimental conditions that provide the best extraction efficiency substantially differs from element to element, as observed in Table 2. One of the goals of this work was to propose a method for the simultaneous analysis of trace elements in sediments so, the next step consisted on looking for a combination of t, $\%HNO_3$, and c_{acid} able to provide an equilibrated, and as high as possible, extraction efficiency for all the elements considered. MultiSimplex helped us in this task. MultiSimplex is a modification of the Simplex algorithm [29] that allows optimizing simultaneously more than one response (extraction efficiency of each element) by changing the values of multiple variables (t, $\%HNO_3$, and c_{acid}). In this case, the optimisation process was simulated using the mathematical models provided by The Unscrambler (after regression analysis of the results obtained in the CCD, previous section) to calculate the extraction efficiency obtained at each combination of variables proposed by MultiSimplex. The same statistical weight was assigned to all the elements. The best set of variables found was as follows: $t = 6$ min, $\%HNO_3 = 45\%$ and $c_{acid} = 6.8$ mol L^{-1}. The extraction efficiencies estimated at these conditions are shown in the first column of Table 3. As observed, they are only slightly lower than those provided in Table 2. For many elements the recoveries are close (As, Mn and Sn) or even over (Pb and Zn) those obtained by the EPA 3051 method. Other ones (Co, Cr, Cu, Mg, and Ni) show acceptable recoveries (55%–75%) and only for Al, Fe and V the recovery is below 50%.

Table 3
Extraction efficiency (%, compared with the EPA 3051 method) estimated for the elements considered at different experimental conditions. t: irradiation time; $\%HNO_3$: proportion of HNO_3 in the HNO_3–HCl used as extractant; c_{acid}: concentration of the HNO_3 and HCl aqueous solution used to prepare the solution used as extractant.

	$t = 6$ min; $\%HNO_3 = 45\%$; $c_{acid} = 6.8$ mol L^{-1}	$t = 0.5$ min; $\%HNO_3 = 8\%$; $c_{acid} = 8.2$ mol L^{-1}	$t = 0.5$ min; $\%HNO_3 = 55\%$; $c_{acid} = 6.3$ mol L^{-1}
Al	22 ± 2	17 ± 2	21 ± 2
As	95 ± 9	100 ± 10	96 ± 9
Co	56 ± 6	61 ± 6	57 ± 6
Cr	72 ± 5	71 ± 5	72 ± 5
Cu	67 ± 3	56 ± 2	66 ± 3
Fe	45 ± 5	39 ± 5	43 ± 5
Mg	56 ± 5	46 ± 4	54 ± 5
Mn	98 ± 10	83 ± 9	94 ± 9
Ni	68 ± 5	70 ± 5	69 ± 5
Pb	107 ± 6	90 ± 5	105 ± 6
Sn	88 ± 5	98 ± 6	90 ± 6
V	48 ± 5	54 ± 3	49 ± 2
Zn	119 ± 7	106 ± 6	117 ± 7

An USF based extraction strategy will be a valid alternative to the microwave classical approach only if the method is effective and comparatively fast. The second and third columns of Table 3 show the extraction efficiencies estimated using an irradiation time as short as 0.5 min and two different acid mixtures as extractant (HNO_3 poor mixture (8%) and HNO_3 rich mixture (55%)). In general, the extraction efficiencies obtained in each case are very similar to those reported in the first column of the Table, especially in the case of the HNO_3 rich mixture. This result suggests that the influence of irradiation time on the extraction efficiency is important only at the very beginning of the extraction process (first 0.5–1 min), reaching a plateau very fast.

Table 2
Best experimental conditions found for the ultrasound assisted extraction of each element considered. t: irradiation time (min); $\%HNO_3$: proportion of HNO_3 in the HNO_3–HCl used as extractant; c_{acid}: concentration (mol L^{-1}) of the HNO_3 and HCl aqueous solutions used to prepare the extractant. EE: extraction efficiency (compared with the EPA 3051 method).

	Al	As	Co	Cr	Cu	Fe	Mg	Mn	Ni	Pb	Sn	V	Zn
t	31	2	59	58	30	29	30	29	1	30	59	21	29
$\%HNO_3$	66	8	8	54	53	44	52	45	10	47	92	92	47
c_{acid}	8.4	8.3	8.5	7.0	6.9	8.5	7.1	7.4	8.0	6.6	6.5	6.1	6.7
EE	23	100	61	73	70	46	59	104	70	112	99	45	122

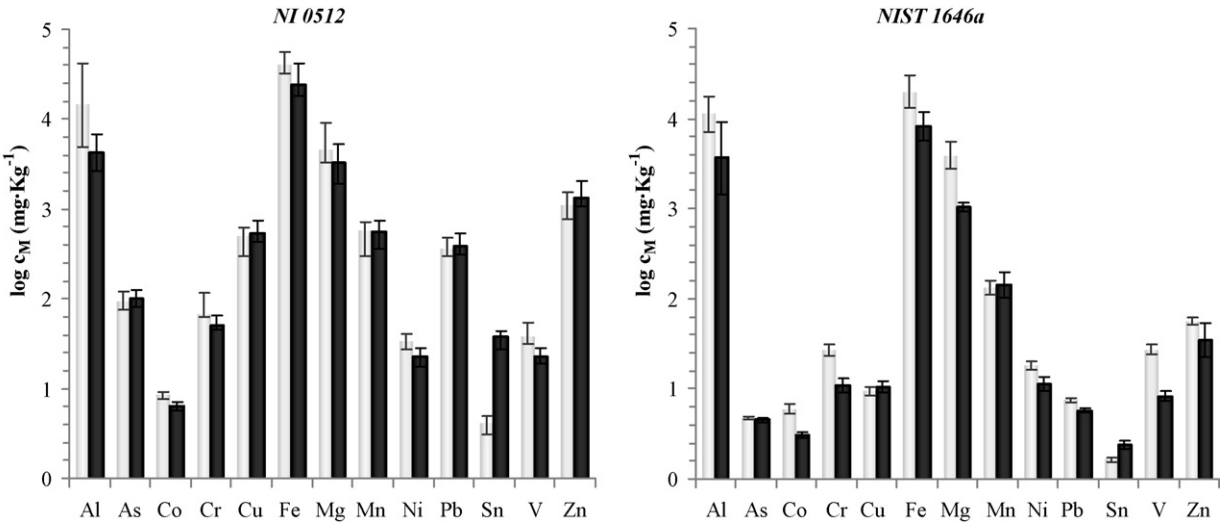


Fig. 2. Comparison between the results obtained after the analysis of the *NI0512* sediment and the NIST 1646a certified reference material (estuarine sediment) using the ultrasound assisted method proposed in this work (t = 6 min, %HNO_3 = 45%, c_{acid} = 6.8 mol L^{-1}, black) and the EPA 3051 method (white). Error bars represent the standard deviation of 8 replicate analyses.

Table 4
Recoveries (calculated with respect to certified values) obtained after the analysis of the NIST 1646a reference material according to the EPA 3051 method (n = 8).

	Al	As	Co	Cr	Cu	Fe	Mg	Mn	Ni	Pb	Sn	V	Zn
Mean recovery (%)	38.2	87.1	93.8	53.7	118.5	78.1	77.4	52.5	64.3	60.9	146.8	18.0	93.3
Standard deviation	4.8	3.0	1.8	2.8	5.1	4.8	2.8	5.0	1.4	1.9	10.3	0.5	10.4

3.4. Validation of the proposed method

3.4.1. Accuracy

The extraction efficiencies provided in Tables 2 and 3 are result of an estimation using mathematical models. In order to compare experimentally the efficiencies of the methods, the *NI0512* sediment and certified reference material (*NIST 1646a*) sediment were analysed using the ultrasound based method (n = 8) proposed here (t = 6 min, %HNO_3 = 45%, c_{acid} = 6.8 mol L^{-1}) and the EPA 3051 method (n = 8). This time the MW extractions were carried out using an Multiwave 3000 microwave oven from Anton Paar. Previous experiments demonstrated that the results obtained with the Anton Paar oven did not differ significantly (95% confidence level) from those obtained with the CEM unit. The results obtained are compared in Fig. 2. The recoveries (related to certified total concentrations) obtained after the analysis of the NIST 1646a with the EPA 3051 are also provided in Table 4. No significant difference between both methods (MW *vs* USF) was observed, except in the case of tin. It is worth noting that only a non-certified value is provided for tin in the certificate of the NIST 1646a material.

3.4.2. Uncertainty

The uncertainty of the optimised ultrasound based method (t = 6 min, %HNO_3 = 45%, c_{acid} = 6.8 mol L^{-1}) was checked by analysis of the *NI0512* sediment in 4 consecutive days. In addition, in the first day four replicates of the analysis were carried out. For comparability, analysis of the same sediment was repeated eight times the same day by the EPA 3051 method (Anton Paar unit). The results, expressed as relative standard deviations are shown in Table 5. As it can be observed, the precision obtained by the USF method was considerably better in most of the cases, with RSDs always below 5%.

3.4.3. Detection limit

The detection limit of the method was estimated after replicate analysis (n = 8) of a blank. The results obtained for each element, expressed as concentration of element in the sediment in mg kg^{-1} (for 0.5 g of sediment processed), are shown in Table 5. It is worth noting that the detection limit is higher when the measurement by ICP/MS is done in the second dilution rather than in the first one (this is the case when the concentration of the element in the extract is higher than about 100 mg L^{-1}).

Table 5
Uncertainty (calculated after replicate analysis of the *NI0512* sediment) of the USF based proposed method and the MW assisted EPA 3051, together with the detection limits for the USF proposed method (calculated after analysis of 8 blanks).

	Uncertainty (RSD, %)			Detection limit (mg kg^{-1})
	USF		MW	USF
	Within day (n = 4)	Between days (n = 4)	Within day (n = 8)	
Al	2.0	2.9	11.2	18
As	1.2	3.7	5.1	0.9
Co	2.2	4.0	3.0	0.2
Cr	2.3	2.5	12.8	0.5
Cu	0.7	1.7	3.1	23
Fe	3.3	4.2	3.2	12
Mg	2.1	3.3	7.9	6.0
Mn	3.2	4.7	3.0	0.9
Ni	1.5	2.6	5.4	4.0
Pb	0.9	1.1	4.9	1.0
Sn	1.2	2.2	13.6	1.9
V	1.8	3.5	10.1	0.3
Zn	2.0	2.0	4.7	4.0

4. Conclusions

Ultrasound energy focused in a glass probe is a good alternative to accelerate the simultaneous extraction of elements from sediments. The process is highly repetitive and extremely fast. The recoveries obtained are comparable to those of the microwave assisted EPA 3051 method. In addition, the suspension of the sediment in the extractant is only slightly heated during the process. As a consequence: (i) possible losses of analytes by evaporation are minimised and (ii) the extract must not be allowed to cool down before going on with the general analysis procedure. The equipment involved and its maintenance is cheap, and operation safe and extremely simple. As a drawback of the technique, it should be mentioned that samples must be treated one by one but, since the analyst can go on with the general procedure as soon as the extraction process is finished, sample throughput is similar to that of a standard microwave oven. The method proposed here is appropriate for monitoring purposes, ecotoxicological studies and risk assessment.

Acknowledgment

This work has been financially supported by the ETORTEK Programme of the Basque Government through the BERRILUR II project (Ref. IE06-179).

References

[1] European Commission Off., J. Eur. Commun. L327 (2000) 1–72.
[2] C. Reimann, P. de Caritat, Chemical Elements in the Environment, 1st ed., Springer-Verlag, Berlin, 1998.
[3] G.A. Van Den Berg, J.P.G. Loch, L.M. Van Der Heijdt, J.J.G. Zwolsman, Trace Elements–Their Distribution and Effects in the Environment in: B. Marker, K. Friese (Eds.), Trace Metals in the Environment Series, vol. 4, Elsevier, Amsterdam, 2000, pp. 517–533.
[4] J.E. Rae, Biogeochemistry of Intertidal Sediments in: T.D. Jickells, J.E. Rae (Eds.), Cambridge Environmental Chemistry Series, vol. 9, Cambridge University Press, Cambridge, 1997, pp. 16–41.
[5] W.J.G.M. Peijnenburg, M.G. Vijver, Pure Appl. Chem. 79 (2007) 2351–2366.
[6] M.J. Charles, R.A. Hites, Sources and Fates of Aquatic Pollutants, in: R.A. Hites, S.J. Eisenreich (Eds.), Advances in Chemistry Series, vol. 216, Oxford University Press, Oxford, 1987, pp. 365–389.
[7] J.M. Cook, M.J. Gardner, A.H. Griffiths, M.A. Jessep, J.E. Ravenscroft, R. Yates, Mar. Pollut. Bull. 34 (1997) 637–644.
[8] M. Jayaprakash, M.P. Jonathan, S. Srinivasalu, S. Muthuraj, V. Ram-Mohan, N. Rajeshwara-Rao, Estuar. Coastal Shelf Sci. 76 (2008) 692–703.
[9] A. Sahuquillo, A. Rigol, G. Rauret, TRAC Trend. Anal. Chem. 22 (2003) 152–159.
[10] N.R. McQuaker, D.F. Brown, P.D. Kluckner, Anal. Chem. 51 (1979) 1082–1084.
[11] International Organization for Standardisation, Soil quality, extraction of trace elements soluble in aqua regia, ISO 11466, 1995.
[12] U.S. Environmental Protection Agency (EPA), Method 3050B, Acid Digestion of Sediments, Sludges and Oils, 1996.
[13] J.C. Woo, D.M. Moon, H. Kawaguchi, Anal. Sci. 12 (1996) 195–200.
[14] H. Güngör, A. Elik, Microchem. J. 86 (2007) 65–70.
[15] J. Sanz, A. de Diego, J.C. Raposo, J.M. Madariaga, Anal. Chim. Acta 508 (2004) 107–117.
[16] A. Robbat Jr., R.L. Simpson, Fresenius J. Anal. Chem. 364 (1999) 305–312.
[17] U.S. Environmental Protection Agency (EPA), Method 3051, Microwave Assisted Acid Digestion of Sediments, Sludges, Soils and Oils, 1994.
[18] U.S. Environmental Protection Agency (EPA), Method 3051A, Microwave Assisted Acid Digestion of Sediments, Sludges, Soils and Oils, 2007.
[19] J.L. Capelo, A.M. Mota, Curr. Anal. Chem. 1 (2005) 193–201.
[20] M. Zabaljauregui, A. Delgado, A. Usobiaga, O. Zuloaga, A. de Diego, J.M. Madariaga, J. Chromatogr. A 1148 (2007) 78–85.
[21] H.M. Santos, J.L. Capelo, Talanta 73 (2007) 795–802.
[22] M. Gallego-Gallegos, M. Liva, R.M. Olivas, C. Cámara, J. Chromatogr. A 1114 (2006) 82–88.
[23] J. Sanz-Landaluze, L. Bartolomé, O. Zuloaga, L. González, C. Dietz, C. Cámara, J. Anal. Atom. Spectrom. 384 (2006) 1331–1340.
[24] J.L. Capelo, I. Lavilla, C. Bendicho, J. Anal. Atom. Spetrom. 13 (1998) 1285–1290.
[25] L. Amoedo, J.L. Capelo, I. Lavilla, C. Bendicho, J. Anal. Atom. Spetrom. 14 (1999) 1221–1226.
[26] E.C. Lima, F. Barbosa Jr., F.J. Drug, M.M. Silva, M.G.R. Vale, J. Anal. Atom. Spetrom. 15 (2000) 995–1000.
[27] D. Hristozov, C.E. Domini, V. Kmetov, V. Stefanova, D. Georgieva, A. Canals, Anal. Chim. Acta 516 (2004) 187–196.
[28] S. Fernández, U. Villanueva, A. de Diego, G. Arana, J.M. Madariaga, J. Mar. Sys. 72 (2008) 332–341.
[29] J.A. Nelder, R. Mead, Comp. J. 7 (1965) 308–313.

Talanta 80 (2009) 440–447

Contents lists available at ScienceDirect

Talanta

journal homepage: www.elsevier.com/locate/talanta

Determination of soil amino acids by high performance liquid chromatography-electro spray ionization-mass spectrometry derivatized with 6-aminoquinolyl-N-hydroxysuccinimidyl carbamate

Songmei Hou[a,c], Hongbo He[a], Wei Zhang[a], Hongtu Xie[a], Xudong Zhang[a,b,*]

[a] Key Laboratory of Terrestrial Ecological Process, Institute of Applied Ecology, Chinese Academy of Sciences, Shenyang 110016, China
[b] National Field Research Station of Shenyang Agroecosystems, Shenyang 110016, China
[c] Supervision and Test Center for Pesticide Safety Evaluation and Quality Control, Shenyang 110021, China

ARTICLE INFO

Article history:
Received 6 February 2009
Received in revised form 30 June 2009
Accepted 2 July 2009
Available online 9 July 2009

Keywords:
6-Aminoquinolyl-N-hydroxysuccinimidyl carbamate
High performance liquid chromatography
Mass spectrometry
Amino acid
Soil

ABSTRACT

Determination of amino acids by mass spectrometry (MS) is an important technique to investigate soil nitrogen transformation and cycling as amino acids being the major nitrogen-containing compounds in soil organic matter. However, researchers have long faced a critical problem in coupling an efficient separation technique to a sensitive MS detection system simultaneously. In this context, we established a new method of liquid chromatography coupled to mass spectrometry based on the 6-aminoquinolyl-N-hydroxysuccinimidyl carbamate (AQC) derivatization method for convenient and accurate quantification of amino acids in soil samples. Baseline separation of 17 amino acid AQC-derivatives was achieved on an XTerra^R MS C_{18} column using ammonium formate as a mobile phase modifier. The concentration of ammonium formate and the pH of the mobile phase were optimized in order to obtain sensitive MS signals. The response curves were linear over the range of 50–800 $\mu mol\,L^{-1}$ amino acids. The detection limits were 0.20–0.60 $pmol\,\mu L^{-1}$ on column and 0.07–0.24 $\mu g\,g^{-1}$ soil under the optimized conditions. The method has been applied successfully for the first time to determine amino acids in 4 types of soil samples, in which 15 amino acids were quantified by MS detector but methionine and cystine were below the detection limits. Both the recovery and the precision were satisfactory. Hence, this proposed technique shows a potential for the identification of amino acids in soil as well as tracing the transformation of soil amino acids with isotope dilution technique in nitrogen cycling investigation.

© 2009 Elsevier B.V. All rights reserved.

1. Introduction

Amino acids are the main component in soil organic matter and play important roles in soil nitrogen (N) biogeochemical cycling in terrestrial ecosystems [1]. Quantitatively speaking, around 20–50% of total N in soil organic matter was found in the form of amino acids, which are mainly present in peptide or protein and can be released by acid hydrolysis [2–5]. Hence, the determination of amino acids in soil and tracing the transformation process of amino acids became a powerful tool in characterizing N turnover in soil.

Although various methods have been applied to quantify amino acids in soil samples, mass spectrometry (MS) is still a promising technique especially for the selective measurement of the compounds at low concentrations in complex matrix and has a great potential for the application to the compound-specific isotope enrichment investigation [6,7]. Theoretically, it is unnecessary to separate the target compounds in MS detection; however, there are still some limitations mainly occurred in the following three cases: (1) the isomass compounds cannot be separated by mass; (2) the "chemical suppression" phenomenon in ion trap is brought when several molecules are co-eluted and ionized together; and (3) in a lesser extent, the presence of isotopes can interfere with other molecules, especially when the mass difference is 1 or 2 only [8]. Therefore, the good chromatography separation is still essential for sensitive MS analysis.

Gas chromatography–mass spectrometry (GC–MS) has been used to identify amino acids and trace isotope enrichment in target compounds [9–13]. However, a complex and laborious derivatization procedure has to be conducted before GC determination. For example, two steps of reactions at 110 and 150 °C are required to form pentafluoropropionyl isopropyl ester derivatives of amino acids. Even though, it is still difficult to ensure complete derivatization of arginine and histidine. As a result, the reproducibility of the

* Corresponding author at: Key Laboratory of Terrestrial Ecological Process, Institute of Applied Ecology, Chinese Academy of Sciences, Shenyang 110016, China. Tel.: +86 24 83970375; fax: +86 24 83970376.
E-mail address: xdzhang@iae.ac.cn (X. Zhang).

0039-9140/$ – see front matter © 2009 Elsevier B.V. All rights reserved.
doi:10.1016/j.talanta.2009.07.013

derivatization is not always satisfied under such rigorous reaction conditions [13].

Compared with GC–MS, liquid chromatography–mass spectrometry (LC–MS) is more convenient for both amino acid separation and isotope enrichment measurement due to easier sample preparation. Traditionally, amino acid isolation can be achieved by ion-exchange liquid chromatography [14–16], but the high salt concentration in modifier is not suitable for MS detection. Hence, amino acid analyses without derivatization have been re-updated for MS detector [16] and the separation under this condition is usually achieved by ion-pair reversed-phase liquid chromatography [8,17–22]. Although the procedure without derivatization can reduce the errors introduced by side reactions and reagent interferences, there are still some notable disadvantages that cannot be overcome at present. Firstly, because the molecular weight of most amino acids is below 200, the interference from the mobile phase and sample matrix are obvious for the fragmentation acquirement of individual amino acids [8,17,19,23]. Hence the specific MS/MS detection has to be adopted for a satisfactory quantification of amino acids in the complex matrix, for instance soil samples [17,23]. Secondly, the detection limits of most amino acids are bigger than 1 pmol, much higher than that of UV or fluorescence detection [23]. Thirdly, some widely used ion-pair reagents, such as perfluoroheptanoic acid (PFHA) [19] can be accumulated in the column slowly. PFHA would change the surface of the stationary phase of the column, and furthermore, influence the reproducibility and separation significantly. As a result, the column has to be flushed frequently with pure organic solvent during analysis process, and this prolongs the analysis time and makes the process more complicated.

In this context, the pre-column derivatization method is more promising for amino acid analysis by liquid chromatography. The commonly used derivatization reagents include *ortho*-phthalaldehyde (OPA) [24,25], phenyl isothiocyanate (PITC) [26–29], 2-(9-fluorenyl)-ethyl chloroformate (FMOC-Cl) [30–33], 2-(9-carbazole)-ethyl chloroformate (CEOC) [34] and 6-aminoquinolyl-N-hydroxysuccinimidyl carbamate (AQC) [35]. The AQC derivatization technique for the analysis of amino acids was established by Cohen and Michard [35] and was commercialized by the Waters Co. Ltd. Notable advantages of this method included rapid, sensitive, quantitative and linear reactions [36]. In the past 15 years, AQC derivatization has been used in a wide variety of samples including amino acid nutrients in feed grain hydrolyzates [37,38], non-amino acid analytes such as polyamines [39] and incompletely hydrolyzed peptides [40,41] as well as nicotianamine and amino acids in some metal-hyperaccumulating plants [42]. Compared with other derivatization reagents, the compatibility of derivatization in the presence of salts makes the AQC reagent as the preferred choice for the amino acid analysis in complex samples. However, the identification and quantification of AQC–amino acid derivatives with mass spectrometer has not been reported until today, especially in soil samples. The reason, to our knowledge, is just due to the use of the non-volatile modifier in the mobile phase for obtaining good separation [35–37]. The non-volatile components will bring noisy background, and consequently, decrease the sensitivity of the MS system and affect the accuracy of quantification seriously [43]. In practice, the non-volatile modifiers in mobile phase are either removed by using on-line membrane suppressor or replaced by volatile modifier in order to be compatible with MS, but unfortunately, this attempt does not always give identical resolution for the analyzed compounds.

In a word, there is still a need to optimize the mobile phase for achieving both good resolution and high sensitivity of amino acid identification and quantification if AQC-derivatization technique is applied. Our objective is, therefore, to develop a new LC–MS method for the determination of amino acids in soil samples, providing a new choice for tracing the dynamics of amino acids in soil.

2. Experimental

2.1. Soils and reagents

2.1.1. Soils

Four types of surface soil samples (0–20 cm) were collected in 2006 across four provinces in China for amino acid determination. The physical and chemical characteristics of the tested soils are significantly different and main properties were listed in Table 1.

2.1.2. Reagents

AccQ. Fluor reagent kit (consisting of AQC reagent, acetonitrile and 0.2 mmol L^{-1} sodium borate buffer, pH 8.8) as well as glass reaction tubes (6 × 50 mm) were provided by Waters Co. Ltd. (Milford, MA, USA). Amino acid standard solution was purchased from Pierce (Rockford, IL, USA) and it contains 17 amino acids including alanine (Ala), arginine (Arg), aspartic acid (Asp), cystine (Cys–Cys), glutamic acid (Glu), glycine (Gly), histidine (His), isoleucine (Ile), leucine (Leu), lysine (Lys), methionine (Met), phenylalanine (Phe), proline (Pro), serine (Ser), threonine (Thr), tyrosine (Tyr), and valine (Val). The concentration of each amino acid is 2.5 mmol L^{-1}. Ultra-pure water was generated using a Milli-Q water purification system (Millipore, Milford, MA, USA). HPLC-grade acetonitrile (ACN) and formic acid (>96.0%) were purchased from DIKMA Tech. Inc. (Richmond Hill, ON, USA). L-2-aminobutyric acid (AABA) (>99.0%) and Dowex 50WX8 cation exchange resin (100–200 mesh) was bought from Sigma–Aldrich Inc. (St. Louis, MO, USA). Parafilm® was the product of Alcan Packaging Co. Ltd. (Neenah, WI, Canada). Ammonium formate was purchased from Yili fine chemical Co. Ltd. (China). HCl, $NH_3{\cdot}H_2O$ and oxalic acid were also purchased in China and are all analytical-grade (Shenyang, LN, China).

2.2. Pre-column derivatization with AQC

A set of amino acid standard mixture solutions containing 200 μmol L^{-1} of internal standard was prepared at a concentration range of 50–800 μmol L^{-1}. A portion of 10 μL of each standard mixture solution was pipetted into the bottom of a glass tube, and then 110 μL sodium borate buffer (0.2 mmol L^{-1} at pH 8.8) was added. After 15 μL of AQC (10 mmol L^{-1} in acetonitrile) was added, the glass tube was closed with Parafilm^R and heated for 20 min at 55 °C to form AQC–amino acid. Thereafter, the solution was cooled down to room temperature and 10 μL portion of each solution was injected into the HPLC-ESI-MS system for amino acid analysis without further purification. It was reported that di-AQC substituted derivatives were dominantly formed for lysine and cystine, while the other tested amino acids reacted with AQC at 1:1 ratio [42].

2.3. Samples hydrolysis and purification

Soil amino acids in bound forms were liberated by acid hydrolysis and the hydrolyte was purified before derivatization to remove the interfering organic components and metal ions in soil matrix. The hydrolysis and purification process was conducted according to the method of Amelung and Zhang [13]. Briefly, 200–250 mg of the air-dried and sieved (< 0.25 mm) soil samples was weighted accurately, and then hydrolyzed with 20 mL of 6 mol L^{-1} HCl for 12 h (105 °C). After 80 μL of 2.5 mmol L^{-1} L-2-aminobutyric acid addition, the hydrolyte was filtered. The filtrate was dried using a rotary evaporator (<45 °C) and the residue was re-dissolved in 4 mL of 0.05 mol L^{-1} HCl. The solution was then transferred into a polypropylene column of 25 mL (BioRad Laboratories, Munich, Germany), which was filled with 3 g Dowex 50WX8 cation exchange

Table 1
Some properties of the soil samples studied.

Soil types (based on FAO classification)	Sampling site (city, province)	Location	Content of total organic carbon (g kg^{-1})	Content of total nitrogen (g kg^{-1})	pH (water:soil = 2.5:1)
Ultisol	Yingtan, Jiangxi	115°50′E 28°46′N	7.68	1.07	5.5
Alfisol	Shenyang, Liaoning	123°24′E 41°31′N	11.34	1.21	6.0
Inceptisol	Gongzhuling, Jilin	124°40′E 43°36′N	12.51	1.52	7.1
Mollisol-1	Hailun, Heilongjiang	126°38′E 47°26′N	29.32	2.42	6.3
Mollisol-2 (fertilized)	Hailun, Heilongjiang	126°38′E 47°26′N	35.50	3.14	6.0

resin for sample purification. After being rinsed with 5 × 5 mL of 0.1 mol L^{-1} oxalic acid (pH 1.6–1.8, adjusted with $NH_3{\cdot}H_2O$), 5 × 5 mL of 0.01 mol L^{-1} HCl and 5 mL of de-ionized water in turn, the amino acids were eluted with 5 × 5 mL of 2.5 mol L^{-1} $NH_3{\cdot}H_2O$. The eluted solution was also dried by rotary evaporator (<45 °C), and re-dissolved in 4 mL 0.1 mol L^{-1} HCl. After being centrifuged, the supernatant was freeze-dried and then was dissolved with 700 μL of 0.02 mol L^{-1} HCl. Finally, a portion of 10 μL solution was used for derivatization as described in Section 2.2.

2.4. LC–MS system

The Waters 2695 LC–MS systems (USA) was used and it is equipped with four pumps, Waters 996 photodiode array detector for ultraviolet detection and ion trap mass spectrometer with electrospray ionization (ESI) source (Waters micromass ZQ4000, USA). Waters MassLynx 3.5 software was used for data analysis. The separation of amino acid derivatives was carried out on an XTerra^R MS C_{18} column (3.5 μm, 150 mm × 2.1 mm I.D.) maintained at 35 °C. L-2-aminobutyric acid was used as internal standard and the injection volume of sample solution was 10 μL. The mobile phase consisted of three solvents: 1.5 mmol L^{-1} ammonium formate in water (solvent A, pH 3.0, adjusted with formic acid), acetonitrile (solvent B), and water (solvent C). The gradient profile was listed in Table 2. The wavelength λ = 248 nm was used for ultraviolet detection and the analysis time was 50 min.

The operation conditions of MS detector were optimized using a 17 AQC–amino acid standard at 50 μmol L^{-1} and the derivatives were infused into the ESI-MS system with the flow rate of mobile phase at 0.2 mL min^{-1}. The MS detection conditions were set as: capillary voltage, 3000 V; cone voltage, 25 V; extractor and RF lens voltage, 4 and 0.4 V, respectively; ion source temperature, 105 °C; desolvation temperature, 120 °C; desolvation gas flow (N_2), 2.5 L min^{-1}; and cone gas flow (N_2), 1.7 L min^{-1}. Under the full scan mode (the mass range was 220–900), the signal intensity of m/z $[M+H]^+$ on the positive ion mode was maximal for most amino acids, but for lysine and cystine derivatives, m/z 244 and 291 was the most abundant, respectively.

2.5. Quantification technique and method validation

The internal standard method was applied for amino acid quantification and it was done by calculating the ratio between the integration of the most abundance peak (i.e., m/z $[M+H]^+$) of the target amino acid and that of AABA, but m/z 244 for lysine and 291 for cystine were better than m/z $[M+H]^+$. The same procedure was employed to plot calibration curves and six standard mixtures at concentrations of 50, 100, 200, 400, 600 and 800 μmol L^{-1} were prepared for the linearity calculation of the MS detector. The detection limits (LOD) were determined by the direct injection of the amino acids standard solution at 5 μmol L^{-1} and then calculated based on the signal to noise ratio of 3. Ten μL of 2.5 mmol L^{-1} amino acid standard mixture solution was spiked to a Mollisol-1 sample to evaluate the recovery of individual amino acids. The determination procedure of amino acids in the spiked soil was the same as described above.

In addition, the amino acids in soil samples was determined by a amino acid auto analyzer (Hitachi L-8800, Japan), an independent technique, to test the accuracy of the proposed MS method. The operation conditions of the instrument were set as follows: column type: 4.6 mm × 60 mm (#2622 resin); analysis column temperature: 50 °C; reaction column temperature: 135 °C; flow rate of the buffer: 0.4 mL min^{-1}; flow rate of chromogenic agent (Ninhydrin): 0.35 mL min^{-1}; injection volume: 20 μL; detection wavelength: 570 nm (440 nm for proline).

Table 2
Gradient profiles for the optimized separations of AQC–amino acids.

Time (min)	Mobile phase A (%)	Mobile phase B (%)	Mobile phase C (%)	Curve[a]
0	100	0	0	1
0.5	99	1	0	11
21	91	9	0	6
25	85	15	0	6
35	83	17	0	6
37	0	60	40	11
40	100	0	0	11

[a] Curve 6 is a linear segment; curve 1 and 11 are two of the step functions.

3. Results and discussion

3.1. Preliminary modification of the AQC derivatization method

As developed by the Waters Co. Ltd., sodium acetate (CH_3COONa) used in the traditional AQC method [35] has been replaced by ammonium acetate (CH_3COONH_4) for coupling to MS detector and the mobile phase contained 140 mmol L^{-1} CH_3COONH_4 (pH 4.95–5.05, titrated with acetic acid), acetonitrile and water, respectively. Unfortunately, under such conditions, no intensive MS response was acquired at the scan mode although the separation was excellent (Fig. 1). If CH_3COONH_4 was no longer used, while other conditions were kept unchanged, the intensity of MS response was enhanced significantly. However, the separation of 17 AQC–amino acids became poor (see Fig. 2). The findings indicated that 140 mmol L^{-1} CH_3COONH_4 at pH 4.95–5.05 was essential for good resolution of AQC–amino acids, but the MS response of the derivatives was restrained significantly due to high concentration CH_3COONH_4 addition. Therefore, more work should be conducted to optimize the pH and volatile modifier of the mobile phase in order to improve both the sensitivity of MS response and the resolution of AQC–amino acids.

3.2. Effect of the mobile phase pH on MS response and separation of AQC–amino acid derivatives

Mass spectrometry is a universal detection mode, and the ionization of a compound is the precondition for determination. Among different ionization modes, ESI is especially appropriate for the ionization of polar or ionic compounds such as amino acids [44]. Unlike most of other ionization processes occurring in the gas phase,

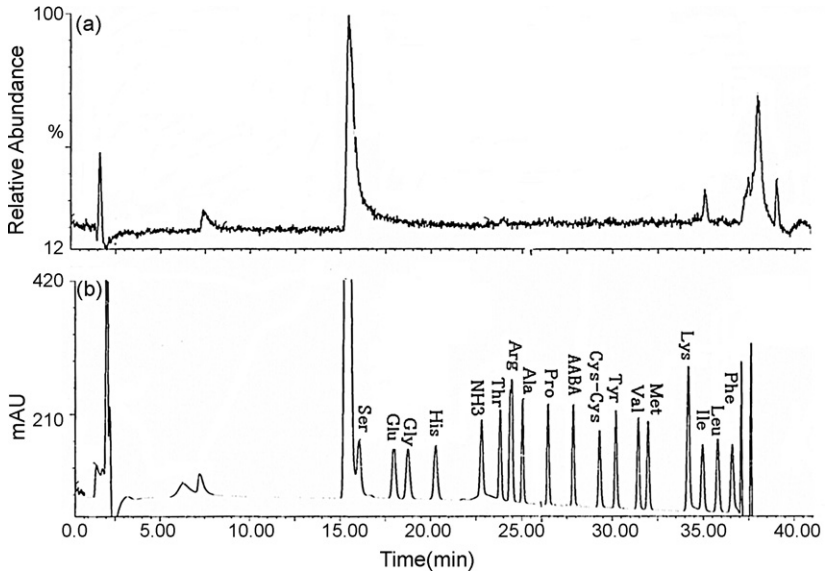


Fig. 1. LC-UV-MS analysis of AQC–amino acids (a) MS detection and (b) ultraviolet detection. Mobile phase: (A) 140 mmol L^{-1} of ammonium acetate in water (pH 4.95–5.00, titrated with acetic acid); (B) acetonitrile; and (C) water. Gradient: Initial = 100% A, 0.5 min = 99% A and 1% B, 18 min = 95% A and 5% B, 19 min = 91% A and 9% B, 29.5 min = 83% A and 17% B, hold for 4.5 min, washed with 60% acetonitrile in water for 3 min, and equilibrate with 100% A for 9 min before subsequent injection (step gradient at 0.5 min, wash and equilibration steps, liner steps for all other elution).

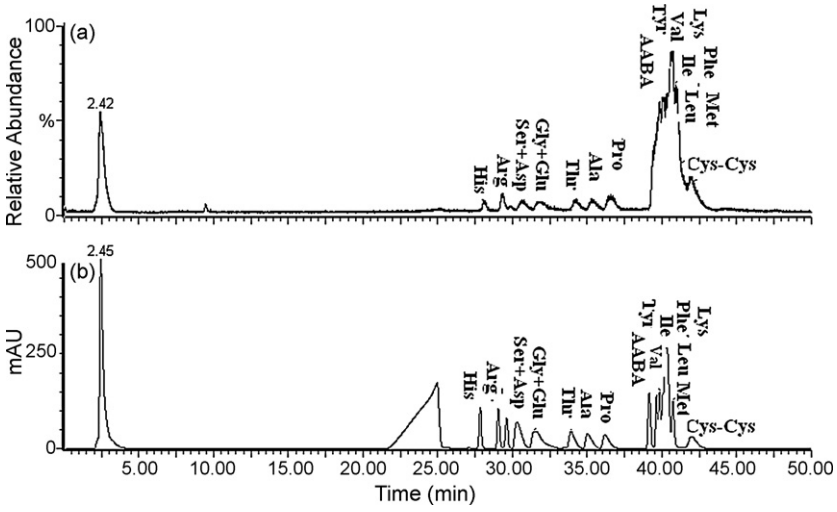


Fig. 2. Primarily modified LC-UV-MS analysis of AQC–amino acids (a) MS detection and (b) ultraviolet detection. Mobile phase: A, water solution (pH 4.95–5.00, adjusted with acetic acid); B, acetonitrile; and C, water. Gradient: Initial = 100% A, 0.5 min = 99% A and 1% B, 18 min = 95% A and 5% B, 19 min = 91% A and 9% B, 29.5 min = 83% A and 17% B, hold for 4.5 min, washed with 60% acetonitrile in water for 3 min, and equilibrate with 100% A for 9 min before subsequent injection (step gradient at 0.5 min, wash and equilibration steps, liner steps for all other elution).

electrospray ionization is the transfer of the ions present in a liquid phase into their gas phase [44]. Therefore, a prerequisite for the ionization with ESI is that the analyte exist in ion form in the solution, i.e., the AQC–amino acids in the mobile phase should be ionized intensively in order to obtain the sensitive MS response. On the basis of the reaction principle, the AQC–amino acid derivatives contain both NH and COOH groups (Fig. 3) and the ionization of the compounds was highly depended on solution pH [42]. When the pH of mobile phase A (water in this case) was adjusted by formic acid or $NH_3 \cdot H_2O$ and other conditions were kept the same as shown in Fig. 1, the ionization degree of AQC–amino acids was affected by the pH of the mobile phase A. As shown in Fig. 4, when the pH value was increased from 2.5 to 9.9, the intensity of MS signal changed greatly and the highest response was obtained between

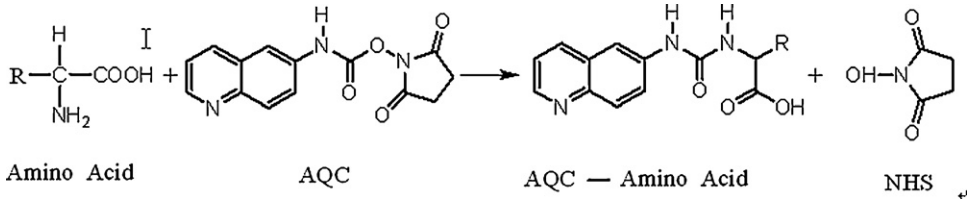


Fig. 3. The derivatization reaction model of AQC and amino acids.

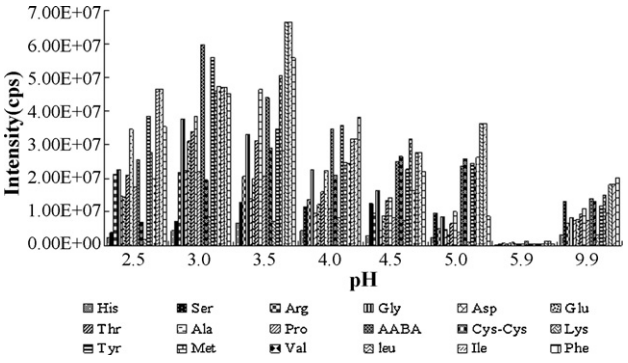


Fig. 4. The effect of mobile phase pH on MS detection of AQC–amino acid derivatives. Mobile phase: (A) water solution with pH from 2.5 to 9.9, adjusted with formic acid or $NH_3{\cdot}H_2O$; (B) acetonitrile; and (C) water.

pH 3 and 3.5, while the lowest was found at pH 5.9, suggesting that pH was a key factor to influence the sensitivity of MS response due to the occurrence of isoelectric point in amino acids. Hence lower pH of the mobile phase enhanced the ionization of the AQC–amino acids to produce positive ions in the solution [35,36]. According to the results in Fig. 4, the pH of the mobile phase was optimal between 3 and 3.5 for the MS detection of AQC–amino acid derivatives.

Not only ionization but also the retention behavior of AQC–amino acids on the column was highly related to the mobile phase pH. The separation of amino acids was improved significantly when the pH of the mobile phase was decreased from 5.0 to 3.5 even without any modifier addition. Ten of the 17 amino acids in the standard mixture were fully separated under the same gradient condition, while Arg, Ser, Ile, Leu, and Phe were partly separated and the other two pairs were co-eluted (Cys–Cys with Lys and Val with Met) (Fig. 5a). It is known that Leu and Ile should be separated absolutely for accurate quantification because they cannot be distinguished by their mass in MS detector. When the pH of the mobile phase was decreased to 3.0, only Met and Val were still co-eluted, while Leu, Ile and the other AQC–amino acids were all in the baseline separation (Fig. 5b). The results showed that pH 3.0 of mobile phase A is optimal, but the overall separation is still unacceptable, hence further optimization should be done.

3.3. Effect of ammonium formate in mobile phase on the resolution and MS response

In principle, it is unnecessary for the target compound to be totally separated from the co-eluted components when identified by MS due to different m/z acquirement, but the co-eluted ions may severely disturb the ionization process of the analyte to be measured due to so called chemical suppression effect, and consequently, it might influence the accuracy of quantification. Therefore, the baseline separation was preferred by adjusting the modifier in mobile phase. Considering excess inorganic ion can deteriorate the MS response severely even if it was volatile and beneficial to the resolution of amino acid derivatives, we attempted to add low concentration gradients of volatile modifier such as ammonium formate (the concentration is 1.0–2.5 mmol L^{-1}) to solvent A to improve the resolution of the AQC–amino acids. It was found that the separation of Cys–Cys-, Lys-, Tyr-, Met-, and Val-AQC derivatives was improved significantly with the modifier addition at 1.5–2.0 mmol L^{-1} and the sensitive MS response was also acquired at the same time (data not shown). Therefore, the concentration of 1.5 mmol L^{-1} of ammonium formate was preferred for the derivative resolution and MS detection. The determination of AQC–amino acids in both standard and soil hydrolysate under the optimized conditions was shown in Fig. 6. The separation of individual amino acids was improved due to the enhanced hydrophobic character of AQC–amino acids which results in increased retention on a C_{18} column [42]. Consequently, the interference of mobile phase on the ionization of AQC–amino acids was reduced because of the significant increase in the derivative mass (246–581) [8,17,19,23].

3.4. Validation and applicability of the method

The validation of our method was conducted at the optimized condition, i.e., the pH of mobile phase A was 3.0 by using 1.5 mmol L^{-1} ammonium formate as the modifier. In the concentration range of 50–800 μmol L^{-1}, the MS response of the AQC-amino acids showed excellent linearity (r^2 = 0.988–0.999, as listed in Table 3). The detection limits were determined by using a 5 μmol L^{-1} of a standard mixture of 17 AQC–amino acids and calculated based on the signal to noise ratio of 3. The detection limits for all amino acids were in the range of 0.20–0.60 pmol μ L^{-1} (Table 3).

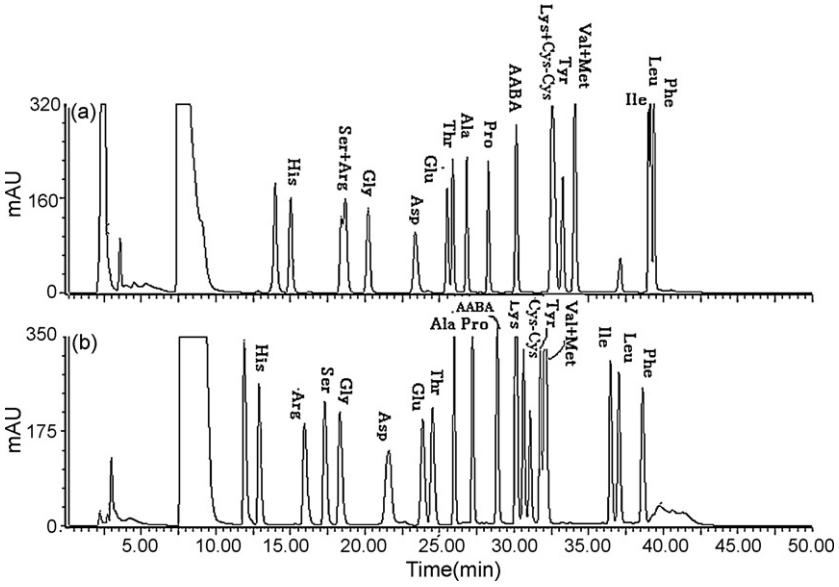


Fig. 5. Effect of mobile phase pH on the separation of AQC–amino acid derivatives at (a) pH 3.5 and (b) pH 3.0 by ultraviolet detection. Mobile phase: (A) water solution (pH 3.0 or pH 3.5, adjusted with formic acid); (B) acetonitrile; and (C) water.

Table 3
Calibration linearity, precision and detection limits of the MS method for the determination of AQC–amino acids.

Amino acid	[M + H] + ion of AQC–amino acid derivative (m/z)[a]	Calibration linearity (r^2)	Detection limit (pmol μL^{-1})	Precision (RSD%)	
				Intraday ($n = 6$)	Interday ($n = 6$ in 3 days)
His	326	0.988	0.35	3.0	4.1
Ser	276	0.996	0.23	1.9	7.3
Arg	345	0.998	0.35	3.4	7.3
Gly	246	0.989	0.60	3.6	5.0
Asp	304	0.993	0.49	2.5	2.3
Glu	318	0.993	0.55	1.8	5.4
Thr	290	1.000	0.57	2.5	8.0
Ala	260	0.999	0.42	1.5	6.1
Pro	286	0.996	0.43	3.0	6.8
Cys–Cys	581	0.999	0.35	3.1	6.3
Lys	487	0.998	0.33	4.0	3.3
Tyr	352	0.991	0.24	1.9	3.2
Met	320	0.996	0.20	3.0	8.7
Val	288	0.994	0.41	2.1	4.4
Ile	302	0.997	0.42	1.8	5.8
Leu	302	0.997	0.30	1.1	3.4
Phe	336	0.999	0.27	1.2	5.9

[a] The molecule weight of AQC combined with amino acid is 171.

Furthermore, we spiked a mixture of amino acid standard (10 μL of 2.5 mmol L^{-1} amino acid) to Mollisol-1 sample and the mean recovery of all amino acids ranged from 82.8% to 111.0% (Table 4). On the basis of the LOD on column, recovery and aliquot of hydrolyte solution for derivatization, the calculated detection limits of amino acids in the soil samples were in the range of 0.07–0.24 μg g^{-1} soil (Table 4), suggesting that the proposed MS method is sensitive and quantitative. The precision of the method was firstly tested using a mixed standard of 17 AQC–amino acids at the concentration of 100 μmol L^{-1}. The mixture was analyzed for six consecutive times in 1 day (intraday, $n = 6$) and 6 times in three different days (interday, $n = 6$). The relative standard deviation (RSD%) for the intraday and interday analyses ranged from 1.1% to 4.0% and from 2.3% to 8.7%, respectively (Table 3). The RSD of the LC–MS determination of the soil samples ($n = 4$) among different assays was below 10% (except tyrosine) for the very heterogeneous and complex matrix, indicating that this method was highly precise (Table 4).

AABA was recommended for the quantification of amino acids by LC analysis, while the application in MS detection should be further validated due to the possible chemical suppression in complex samples which may affect the reliability of quantification. When AABA concentration was kept as 200 μmol L^{-1} and amino acid standard in the range of 50–800 μmol L^{-1}, the intensity ratio between the selected ion of the target amino acid and AABA was strictly proportional to the corresponding concentration. And furthermore, the purification of soil amino acids was effective and the baseline AQC–AA separation was obtained in our method, which enables the quantitative determination of amino acids in soil samples. Thereby, we recommend using AABA as an internal standard without isotope labeling for routine analysis. Nevertheless, the correction of chemical suppression by stable isotope labeled amino acids is still preferred; especially when the target compounds were not well separated from their complex matrix.

Table 4
Recovery, precision and detection limit of amino acids in soil samples and concentrations of amino acids detected by MS and UV in Mollisol-1.

Amino acid	Precision (RSD%)	Recovery (%)	Detection limit (μg g^{-1} soil)	Concentrations of amino acids (μg g^{-1} soil)		
				MS detection	UV detection	MS/UV
His	10.0	82.8[a]	0.15[b]	40.7 ± 4.8[c]	33.4 ± 5.3	0.82
Ser	8.6	95.1	0.07	139.6 ± 17.3	135.4 ± 11.6	0.97
Arg	9.8	87.7	0.17	70.2 ± 7.7	64.6 ± 7.8	0.92
Gly	6.7	100.0	0.13	203.7 ± 7.3	232.2 ± 14.9	1.14
Asp	5.9	111.0	0.18	294.6 ± 44.8	309.3 ± 34.0	1.05
Glu	6.3	107.7	0.23	215.5 ± 18.1	219.8 ± 22.4	1.02
Thr	8.7	101.0	0.19	132.5 ± 18.6	143.1 ± 15.2	1.08
Ala	6.4	101.6	0.10	196.5 ± 21.6	218.1 ± 20.9	1.11
Pro	8.1	97.4	0.14	95.3 ± 9.9	102.9 ± 9.5	1.08
Cys–Cys	–	108.7	0.24	–[d]	–	–
Lys	9.9	94.4	0.13	144.6 ± 14.2	157.7 ± 26.2	1.09
Tyr	12.5	94.0	0.12	13.8 ± 1.8	12.7 ± 1.3	0.92
Val	5.9	101.8	0.08	91.9 ± 12.1	99.2 ± 8.9	1.08
Met	–	97.2	0.13	–	–	–
Ile	5.7	103.1	0.15	43.6 ± 1.7	42.2 ± 4.0	0.97
Leu	4.9	109.9	0.11	90.3 ± 9.0	89.4 ± 9.5	0.99
Phe	6.3	104.1	0.12	49.6 ± 6.9	50.6 ± 7.0	1.02

[a] The recovery evaluation was conducted by adding a amino acid standard with known concentration to the soil samples and then to determine total amount of the amino acids in the spiked samples and the same soil samples without spiking were also determined in the same manner. The recovery was calculated by the following formula: recovery% = the amount of AAs in the spiked soils/(the amount of AAs in the original soil plus that of added AA) × 100%.

[b] The detection limits of amino acids in soil samples were calculated based on the detection limit on column and the recovery of amino acids in soil samples as well as the aliquot of hydrolyte solution for derivatization.

[c] The soil samples were determined in four replicates (n = 4) and the confidence level was 95%.

[d] Concentrations were below detection limits.

Table 5
Concentrations of amino acids in four different soils determined by the proposed method (data 1) and amino acid automatic analyzer (data 2).

Amino acid	Concentration of amino acids ($\mu g\,g^{-1}$ soil)							
	Ultisol		Alfisol		Inceptisol		Mollisol-2	
	Data 1	Data 2	Data 1	Data 2	Data 1	Data 2	Data 1	Data 2
His	25.7 ± 2.8[a]	28.5 ± 2.7	20.1 ± 2.7	23.2 ± 2.6	94.4 ± 9.1	93.6 ± 7.7	59.9 ± 6.1	60.6 ± 5.9
Ser	78.4 ± 7.5	73.0 ± 6.1	109.5 ± 12.9	119.6 ± 11.5	275.7 ± 17.6	271.4 ± 21.2	383.6 ± 29.9	372.6 ± 27.6
Arg	58.5 ± 4.8	51.4 ± 5.1	98.1 ± 7.5	111.1 ± 10.9	251.5 ± 16.6	283.7 ± 20.4	226.1 ± 15.4	202.9 ± 14.6
Gly	83.2 ± 8.5	89.1 ± 8.4	166.4 ± 17.0	178.4 ± 14.3	455.6 ± 28.2	421.1 ± 26.1	875.3 ± 36.8	937.8 ± 76.9
Asp	113.7 ± 11.1	109.5 ± 9.2	233.7 ± 18.7	244.7 ± 17.1	630.7 ± 44.1	548.2 ± 46.0	1140.7 ± 54.8	1098.0 ± 59.3
Glu	151.8 ± 17.3	137.9 ± 12.7	236.3 ± 19.4	234.4 ± 17.3	592.7 ± 48.6	548.2 ± 37.3	990.0 ± 39.4	949.1 ± 47.5
Thr	70.7 ± 8.5	69.1 ± 6.4	102.7 ± 7.2	115.1 ± 9.4	284.2 ± 21.0	307.4 ± 17.8	491.4 ± 31.4	480.6 ± 43.3
Ala	110.2 ± 10.6	102.4 ± 8.6	151.4 ± 15.4	164.6 ± 12.5	409.9 ± 29.5	389.2 ± 24.1	978.0 ± 66.5	947.5 ± 70.1
Pro	74.5 ± 8.2	74.8 ± 6.1	91.9 ± 8.6	100.4 ± 10.4	258.8 ± 23.8	315.0 ± 23.3	536.3 ± 45.0	538.5 ± 44.2
Cys–Cys	–[b]	–	–	–	–	–	–	–
Lys	96.2 ± 12.1	88.7 ± 9.0	137.3 ± 8.5	150.1 ± 16.5	351.5 ± 24.6	279.3 ± 24.6	228.3 ± 17.8	210.6 ± 19.0
Tyr	74.3 ± 10.8	71.9 ± 6.9	76.7 ± 6.9	38.0 ± 4.7	154.1 ± 9.9	86.9 ± 8.7	215.4 ± 17.7	208.5 ± 17.5
Met	–	–	–	–	–	–	–	–
Val	64.5 ± 6.1	66.5 ± 7.0	157.8 ± 15.1	137.7 ± 8.3	392.7 ± 29.8	340.3 ± 19.7	720.7 ± 41.8	742.5 ± 56.4
Ile	33.7 ± 3.8	36.4 ± 3.5	112.0 ± 8.3	124.8 ± 10.5	156.4 ± 9.7	207.3 ± 11.6	498.0 ± 30.9	536.8 ± 44.0
Leu	107.6 ± 11.4	99.2 ± 8.3	46.0 ± 5.2	52.6 ± 5.8	360.2 ± 30.3	361.6 ± 29.7	966.8 ± 61.9	891.6 ± 69.5
Phe	54.8 ± 6.4	52.0 ± 4.9	109.8 ± 9.0	101.8 ± 8.6	223.0 ± 20.5	214.1 ± 15.0	580.7 ± 32.5	550.4 ± 45.1

[a] The soil samples were determined in three replicates ($n = 3$) and the confidence level was 95%.
[b] Concentrations were below the detection limits (not reliable enough).

To test the applicability of the method for a broad range of soils, we analyzed amino acids in five samples representing different types of soil with significantly different properties, especially soil organic matter (SOM) and total nitrogen (TN) contents. The soil samples are classified as Ultisol, Alfisol, Inceptisol, and Mollisols (Mollisol-1 and 2), respectively. The amino acid contents in the soil samples were determined firstly by our MS method (Table 5) and it was found that the concentration of all amino acids was in different range, which is accordant with that from other studies [5]. In order to test the reliability of the method, the amino acids in Mollisol-1 sample was also analyzed by the UV detector online with the MS detector on the same condition (see Table 4). Both total and individual amino acid concentrations determined by the two detectors were very close, suggesting that the quantitative results by the MS detector are reliable. In addition, the contents of amino acids in soil samples were determined independently by using a widely accepted method, the amino acid automatic analyzer. We found that the concentrations of most amino acids are identical between the two independent methods, though significant difference was observed for lysine, isoleucine and tyrosine (Table 5). The reason, to our opinion, is mainly derived from the different principles for amino acid determination. Each amino acid was quantified by the selective ion ($[M+H]^+$ or the fragment with the most abundance) in our method, while it was evaluated by the total area of its chromatogram peak in the amino acid automatic analyzer technique. The separation of isoleucine was excellent in both standard and soil samples under the two detection techniques, but its concentrations in the Inceptisol was significantly higher detected by amino acid automatic analyzer. This might have been attributed to the interference from the co-elution of soil impurities because not all the impurities in soil hydrolysis can be removed during purification. If this happens, it is known for sure that the quantification from amino acid automatic analyzer detection should be influenced more significantly than those from our MS detection. In this context, the amino acid automatic analyzer method could result in overestimation of isoleucine. On the other hand, chemical suppression may influence the accuracy of MS quantification for the co-eluted amino acids (lysine and tyrosine in our case), especially for those with low concentrations, so the concentration of tyrosine might be erratically determined by our MS method. However, tyrosine is a minor amino in soils and its quantification result does not influence the interpretation of the whole picture of soil amino acids. The concentrations of cystine and methionine in the tested soils were below detection limits from both methods, but the recoveries and sensitivity of the two amino acids were quite high, inferring that it is still possible to quantify the two amino acids while increasing soil sample amounts.

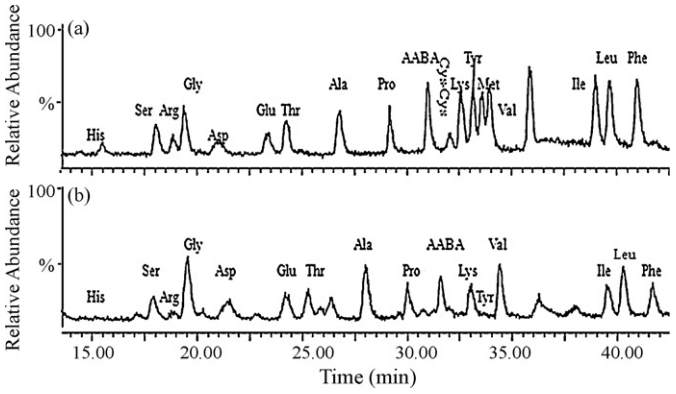


Fig. 6. The total ion current chromatogram of amino acids in standard (a) and soil samples (b) under the optimized mobile phase conditions. Mobile phase: (A) 1.5 mmol L^{-1} of ammonium formate in water (pH 3.0, titrated with formic acid); (B) Acetonitrile; and (C) water. Gradient conditions: Initial = 100% A, 0.5 min = 99% A and 1% B, 21 min = 91% A and 9% B, 25 min = 85% A and 15% B, 35 min = 83% A and 17% B, hold for 2 min, washed with 60% acetonitrile in water for 3 min, and equilibrate with 100% C for 10 min before subsequent injection (step gradient at 0.5 min, wash and equilibration steps, liner steps for all other elution). The flow rate of mobile phase was set at 0.2 mL min^{-1} and the analysis time was 50 min.

4. Conclusion

A new method of liquid chromatography coupled to mass spectrometry was established for convenient and accurate quantification of amino acids in soil samples. The method is based on the use of pre-column AQC derivatization as well as the optimization of mobile phase conditions, especially of pH and ammonium formate concentration. In addition, the sensitivity, linearity and detection limits of amino acids by using MS detector were assessed strictly. Finally, the method is validated by the calculation of the recoveries of the amino acids in the spiked soil and the comparison of the results quantified by the MS detector and UV detector as well as by the two independent methods. All findings indicate that the

proposed MS method can be practically applied for the determination of amino acids in a wide range of soil samples. It is the first time that 15 amino acids in soil have been quantified by HPLC-MS and thus, the technique shows a potential for tracing the transformation of soil amino acids with isotope technique for N transformation and cycling investigation.

Acknowledgements

This work was jointly funded by the Natural Science Foundation of China (Project No. 40535028) and Major State Basic Research Development Program of China (973 Program) (No. 2009CB118607).

References

[1] W. Amelung, J. Plant Nutr. Soil Sci. 166 (2003) 677.
[2] R. Aldag, R. Kickuth, J. Plant Nutr. Soil Sci. 136 (1973) 193.
[3] F.J. Stevenson, Soil Sci. Am. Proc. 20 (1956) 204.
[4] E. Scheller, Soil Fertility and Examination, in: T.V. Ostergarrd (Ed.), IFOAM Internation Scientific Conference. Proceedings, IFOAM International Copenhagen, vol. 1, 1996, p. 47.
[5] Z.N. Senwo, M.A. Tabatabai, Biol. Fertil. Soil 26 (1998) 235.
[6] W.B. Silvester, R. Parsons, P.W. Watt, New Phytol. 132 (1996) 617.
[7] X.D. Zhang, H.B. He, W. Amelung, Soil Biol. Biochem. 39 (2007) 2785.
[8] P. Chaimbault, K. Petritis, C. Elfakir, M. Dreux, J. Chromatogr. A 855 (1999) 191.
[9] M.J. Nozal, J.L. Bernal, M.L. Toribio, J.C. Diego, A. Ruiz, J. Chromatogr. A 1047 (2004) 137.
[10] R. Wolfe, Radioactive and Stable Isotope Tracers in Biomedicine: Principles and Practice of Kinetic Analysis, Wiley–Liss, New York, 1992.
[11] D.C. Marquez, S.T. Weintraub, P.C. Smith, J. Chromatogr. B 658 (1994) 213.
[12] B. Patterson, X. Zhang, Y. Chen, S. Klein, R. Wolfe, Metabolism 46 (1997) 943.
[13] W. Amelung, X. Zhang, Soil. Biol. Biochem. 33 (2001) 553.
[14] L.E. Welch, W.R. Lacourse, D.A. Mead Jr., D.C. Johnson, Anal. Chem. 61 (1989) 555.
[15] P. Luo, F. Zhang, R.P. Baldwin, Anal. Chem. 63 (1991) 1702.
[16] J.M. Marioli, L.E. Sereno, J. Liq. Chromatogr. Rel. Technol. 19 (1996) 2505.
[17] K. Petritis, E. Claire, D. Michel, J. Chromatogr. A 961 (2002) 9.
[18] P. Chaimbault, K. Petritis, C. Elfakir, M. Dreux, J. Chromatogr. A 870 (2000) 245.
[19] J. Qu, Y.M. Wang, G.A. Luo, Z.P. Wu, C.D. Yang, Anal. Chem. 74 (2002) 2034.
[20] Y.R. Song, M.S. Wu, S.L. Zhao, D.Y. Hou, Y.M. Liu, J. Chromatogr. A 1091 (2005) 102.
[21] R.G.J. Van Leuken, G.T.C. Kwakkenbos, A.L.L. Duchateau, J. Chromatogr. 647 (1993) 131.
[22] K. Petritis, P. Chaimbault, C. Elfakir, M. Dreux, J. Chromatogr. A 833 (1999) 147.
[23] K. Petritis, P. Chaimbault, C. Elfakir, M. Dreux, J. Chromatogr. A 896 (2000) 253.
[24] D. Kutlan, P. Presits, I. Molnar-Perl, J. Chromatogr. A 949 (2002) 235.
[25] M.H. Hans van Eijk, R.D. Rooyakkers, B.P. Soeters, E.P. Nicolaas Deutz, J. Anal. Biochem. 271 (1999) 8.
[26] P.S.L. Janssen, J.W. van Nispen, P.A.T.A. Melgers, H.W.M. van den Bogaart, R.L.A.E. Hamelinck, B.C. Goverde, Chromatographia 22 (1986) 345.
[27] J.F. Davey, R.S. Ersser, J. Chromatogr. 528 (1990) 9.
[28] K.R. Anumula, P.B. Taylor, Anal. Biochem. 197 (1991) 113.
[29] M.J. Spiro, R.G. Spiro, Anal. Biochem. 204 (1992) 152.
[30] S. Einarsson, J. Chromatogr. 348 (1985) 213.
[31] S. Einarsson, S. Folestad, B. Josefsson, S. Lagerekvist, Anal. Chem. 58 (1986) 1638.
[32] K.C. Chan, G.M. Janini, G.M. Muschik, H.J. Issaq, J. Chromatogr. A 653 (1993) 93.
[33] J. Kirschbaum, B. Luckas, W.D. Beinert, J. Chromatogr. A 661 (1994) 193.
[34] X.E. Zhao, Y.R. Suo, Talanta 76 (2008) 690.
[35] S.A. Cohen, D.P. Michard, Anal. Biochem. 211 (1993) 279.
[36] H.J. Liu, J. Chromatogr. A 670 (1994) 59.
[37] S.A. Cohen, K.M. De Antonis, J. Chromatogr. 661 (1994) 25.
[38] H.J. Liu, B.Y. Chang, H.W. Yan, F.H. Yu, X.X. Liu, J. AOAC Int. 78 (1995) 736.
[39] S. Merali, A.B. Clarkson Jr., J. Chromatogr. 675 (1996) 321.
[40] K.M. De Antonis, P.R. Brown, Y.F. Cheng, S.A. Cohen, J. Chromatogr. A 661 (1994) 279.
[41] G. Li, J. Yu, I.S. Krull, S. Cohen, J. Liq. Chromatogr. 18 (1995) 3889.
[42] D.L. Callahan, S.D. Kolev, R.A.J. O'Hair, D.E. Salt, A.J.M. Baker, New Phytol. 176 (2007) 836.
[43] S. Bajic, C. Woodward, J. Chromatogr. 554 (1991) 27.
[44] R. Willoughby, E. Sheehan, S. Mitrovich (Eds.), A Global View of LC/MS, Global View Publishing, Pittsburgh, PA, 2002, p. 62.

Talanta 80 (2009) 448–453

Contents lists available at ScienceDirect

Talanta

journal homepage: www.elsevier.com/locate/talanta

Sensitive determination of verticine and verticinone in *Bulbus Fritillariae* by ionic liquid assisted capillary electrophoresis–electrochemiluminescence system

Ying Gao[a,b,*], Yuanhong Xu[b], Bingyan Han[b], Jing Li[b], Qian Xiang[a]

[a] *Department of Applied Chemistry, Changchun Institute of Technology, Changchun 130021, China*
[b] *State Key Laboratory of Electroanalytical Chemistry, Changchun Institute of Applied Chemistry, Chinese Academy of Sciences, Changchun 130022, China*

ARTICLE INFO

Article history:
Received 7 February 2009
Received in revised form 1 July 2009
Accepted 2 July 2009
Available online 10 July 2009

Keywords:
Electrochemiluminescence
Capillary electrophoresis
Verticine
Verticinone
Ionic liquids

ABSTRACT

CE/Ru(bpy)$_3^{2+}$ electrochemiluminescence (ECL) system with the assistance of ionic liquids (ILs) was successfully established for sensitive determination of verticine and verticinone in *Bulbus Fritillariae* for the first time. Migration behavior of alkaloid largely relies on the hydrogen bonding interactions between alkyl imidazolium cations in ILs and the alkaloids. Running buffer containing 40 mmol/L 1-butyl-3-methylimidazolium tetrafluoroborate ($BMImBF_4$) IL–8 mmol/L phosphate resulted in significant changes in separation selectivity for alkaloids with similar structures. The highest sensitivity of the detection was obtained by maintaining the detection potential at 1.2 V. Under the optimized conditions, relative standard derivations of the ECL intensity and the migration time were 3.27 and 2.84% for verticine and 4.42 and 1.69% for verticinone, respectively. The standard curves were linear between 1×10^{-8} and 1×10^{-6} mol/L for verticine and between 5×10^{-8} and 1×10^{-6} mol/L for verticinone, respectively. Detection limits of 1.25×10^{-10} mol/L for verticine and 1×10^{-10} mol/L for verticinone were obtained (S/N = 3). Developed method was successfully applied to determine the amounts of alkaloids in *Bulbus Fritillariae*.

© 2009 Elsevier B.V. All rights reserved.

1. Introduction

In the last few decades, the research and development of bioactive ingredients of traditional medicines has attracted international scientific attention [1,2]. *Bulbus Fritillariae* is a famous Chinese crude herb, which has been used as one of the most important antitussive and expectorant drugs thousands of years ago. Pharmacological studies demonstrate that verticine and verticinone in *Bulbus Fritillariae* are the primary active ingredients responsible for the antitussive activity [3,4]. Then, work on the quality control and quantitative analysis of verticine and verticinone in *Bulbus Fritillariae* is very necessary.

Verticine and verticinone are non-chromophoric, which makes the use of direct UV detection without pre- or post-column derivatization impossible. Molecular structures of verticine and verticinone are shown in Fig. 1. Ding et al. [5] and Li et al. [6] analyzed major pharmacologically active alkaloids of *Fritillaria* species by a HPLC method with prederivatization. Also, a method of pre-column derivatization GC was developed for the determination of major steroidal alkaloids in *Bulbus Fritillariae* [7]. Liu et al. [4] and Jin et al. [8] described high-speed counter-current chromatography coupled with evaporative light scattering approach used for the separation and purification of verticine and verticinone from *Bulbus Fritillariae thunbergii*. However, no detection limits for verticine and verticinone were given in their methods. By using HPLC-evaporative light scattering detection in combination with a low-temperature adapter, Li et al. determined the major biologically active isosteroidal alkaloids in *Bulbus Fritillariae* [9]. In addition, HPLC–MS [10] and direct GC method [11] were used for the analysis of *Fritillaria* alkaloids. However, a major drawback of the methods mentioned above appears to be low sensitivity and time-consuming due to necessary derivatization although the several alkaloids could be detected simultaneously in such procedures. Therefore, it is necessary to establish sensitive, rapid and effective methods for the quantization of verticine and verticinone in *Bulbus Fritillariae*.

Electrochemiluminescence is a means of converting electrical energy into radiative energy [12]. Among a wide range of ECL reagents, Ru(bpy)$_3^{2+}$ ECL has received considerable attention as a sensitive detection technique in chemical analysis because of its excellent stability and high efficiency in the aqueous phase. ECL based on Ru(bpy)$_3^{2+}$ has found many applications such as in immunoassays and for detection of a number of biologically important species without derivatization [13–15].

Abbreviations: $EMImBF_4$, 1-ethyl-3-methylimidazolium tetrafluoroborate; $BMImBF_4$, 1-butyl-3-methylimidazolium tetrafluoroborate; $BMImPF_6$, 1-butyl-3-methylimidazolium hexafluorophosphate; $OMImBF_4$, 1-octyl-3-methylimidazolium tetrafluoroborate; $HMImBF_4$, 1-hexadecyl-3-methylimidazolium tetrafluoroborate; ECL, electrochemiluminescence; CE–ECL, capillary electrophoresis–Ru(bpy)$_3^{2+}$ electrochemiluminescence; ILs, ionic liquids.

* Corresponding author at: Department of Applied Chemistry, Changchun Institute of Technology, No. 395 Kuanping Street, Changchun 130021, China.
Tel.: +86 431 85711660; fax: +86 431 85689711.
E-mail address: gaoy@ciac.jl.cn (Y. Gao).

0039-9140/$ – see front matter © 2009 Elsevier B.V. All rights reserved.
doi:10.1016/j.talanta.2009.07.012

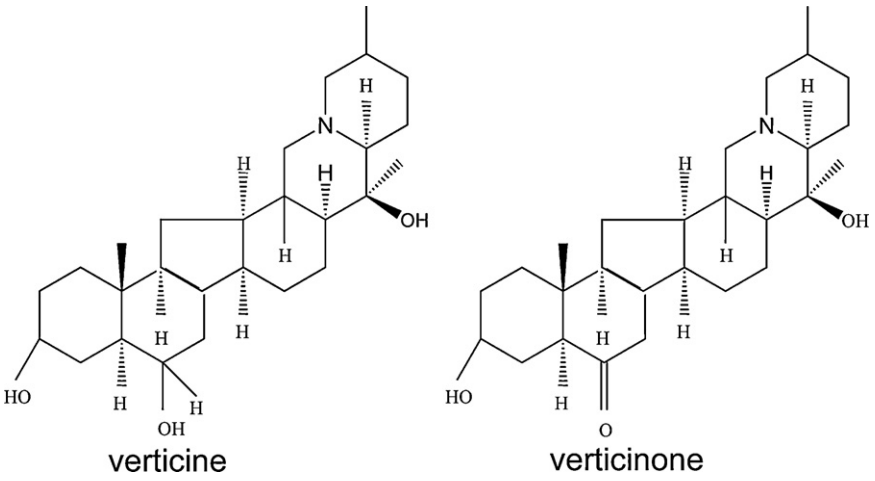


Fig. 1. Molecular structures of verticine and verticinone.

Capillary electrophoresis–Ru(bpy)$_3^{2+}$ electrochemiluminescence method (CE–ECL) has been proved as a highly efficient and sensitive analytical technique for the determination of medicines and biomaterials containing no strong chromophores. The technique has been applied to the measurement of active ingredients in Chinese traditional medicine [16–20].

IL is a new advanced material with potential use in various fields of modern chemistry because of its special chemical and physical properties [21–23]. ILs are frequently used as electrolyte since it shows reasonable ionic conductivity, hydrophobicity, polarity and selectivity. Due to higher conductivity and lower viscosity of 1-ethyl-3-methylimidazolium tetrafluoroborate (EMImBF$_4$) among ILs, it was once chosen as a representative to investigate the effect of ILs on ECL behavior of alkaloids in Chinese traditional medicine [17]. However, the influences of chain lengths and anions of ILs on CE separation and ECL behavior of alkaloids were seldom investigated.

In this paper, the coupling of CE–ECL method was employed to detect verticine and verticinone in *Bulbus Fritillariae*. Several ILs with different chain lengths and different anions were studied. BMImBF$_4$ was finally selected as the optimum running buffer for the separation of analytes. It was demonstrated to be an efficient separation system for alkaloids determination in Chinese traditional medicine. All separation and detection parameters were optimized in order to achieve good resolution and high sensitivity.

2. Experimental

2.1. Chemicals and materials

Verticine and verticinone standard samples were purchased from National Institute for the Control of Pharamaceutical and Biological Products, Ministry of Health (Beijing, China). The purity of the verticine and verticinone standards is over 99%, and they can be used directly in the experiment without further purification. Tris(2,2′-bipyridyl) ruthenium (II) chloride hexahydrate was purchased from Aldrich Chemical Co. (Milwaukee, WI, USA). Chinese herb *Bulbus Fritillariae* was obtained from various areas of China and from National Institute for the Control of Pharmaceutical and Biological Products, Ministry of Health (Beijing, China). EMImBF$_4$, BMImBF$_4$, 1-octyl -3-methylimidazolium tetrafluoroborate (OMImBF$_4$), 1-hexadecyl-3-methylimidazolium tetrafluoroborate (HMImBF$_4$) and 1-butyl-3-methylimidazolium hexafluorophosphate (BMImPF$_6$) used in this work were synthesized by Centre for Green Chemistry and catalysis, Lanzhou Institute of Chemical Physics, Chinese Academy of Sciences following the procedure described elsewhere [24], and the starting materials were obtained from Sigma–Aldrich (Steinheim, Germany). Borax, phosphate, sodium hydroxide, acetonitrile, ethanol, methanol, chloroform and ammonia were from Beijing Chemical Reagent Factory (Beijing, China). All reagents used in the analysis were of analytical purity and used without further purification.

2.2. Preparation of standard solutions

The stock solutions of verticine and verticinone were prepared by dissolving the standard samples in methanol and stored at 4 °C in a refrigerator. A series of standard solutions with suitable concentrations were prepared by diluting the solution with methanol. Other various running buffers with different concentrations were prepared with double-distilled water.

2.3. Extraction of verticine and verticinone from Bulbus Fritillariae

The crude alkaloid extracts were from seven *Fritillaria* species: *Fritillaria hupehensis*, *Fritillaria walujewii*, *Fritillaria cirrhosa*, *F. thunbergii*, *Fritillaria ussuriensis*, *Fritillaria pallidiflora and Fritillaria przewalskii.* About 0.2 g herbal medicine powdered was weighted accurately, alkalinized with 0.2 ml ammonia, extracted for 30 min with 3 ml of chloroform as the extraction in an ultrasonic bath. The extraction was repeated two times. The extracts were combined and evaporated at room temperature. The dry residue was resolved in 1 mL methanol and filtered through a 0.45 μm membrane before use.

2.4. Apparatus and analysis conditions

The detection of analytes was employed by an ECL system (Xi'an Remax Electronics Co. Ltd, Xi'an, China). Electrophoresis was driven by a high-voltage power supply (Spellman Electronics Corp., Plainview, NY). A three-electrode configuration was used in the detection system consisting of a 500 μm Pt disk as a working electrode, Ag/AgCl as a reference electrode and Pt wire as a counter electrode. The end-column ECL detection was employed by using a wall-jet configuration. Detection voltage was set at 1.2 V. The distance 150 μm between working electrode and separation capillary was aligned setting with the aid of an optical microscope. The voltage of photomultiplier tube for collecting the ECL signal was set at 800 V. ECL detection reservoir used herein is the same as that reported previously [25]. In the reservoir, a solution of 5 mmol/L Ru(bpy)$_3^{2+}$ and 50 mmol/L phosphate buffer was replaced once for 2 h.

Separations were performed in a 58 cm long fused-sillica capillary (Yongnian Optical Fabric Factory Hebei, China) with a 50 μm internal diameter and 360 μm outer diameter. Methanol was used as solvent for verticine and verticinone. Electrokinetic injections were performed at 16 kV for 3 s. Separation voltage was set at 16 kV. A new capillary was filled with 0.1 mol/L NaOH overnight. At the beginning of experiment each day, the capillary was activated with 0.1 mol/L NaOH for 5 min, followed by double-distilled water for 5 min and running buffer for 5 min so as to maintain an active and reproducible inner surface. 40 mmol/L $BMImBF_4$–8 mmol/L phosphate (pH 8.00) was used as a running buffer. Every run was repeated at least three times under the same conditions.

3. Results and discussion

3.1. Method optimization

3.1.1. Selection of detection potential

Preliminary static experiments are necessary to acquire useful information about verticine and verticinone. Cyclic voltammetries under the static conditions were performed. As is shown in Fig. 2 inset, the oxidation current of $Ru(bpy)_3^{2+}$ (solid line) increased to a peak at about 1.18 V. In the presence of verticine (dash line), rise in the anodic current and fall in the cathodal current, a marker of catalytic effect of $Ru(bpy)_3^{2+}$, were observed as the potentials were scanned to +1.19 and −1.10 V, respectively. In addition, similar catalytic effect produced by verticinone (dash line) was observed. Fig. 2 shows the corresponding ECL responses. It can be seen that the enhancement to $Ru(bpy)_3^{2+}$ ECL by verticine and verticinone is quite similar. The possible reason is two alkaloids have the similar structures. The $Ru(bpy)_3^{2+}$ ECL intensity increased by about 5 times for verticine and verticine, respectively. The results showed that the ECL method was sensitive for verticine and verticinone detection.

In CE–ECL system, the intensity of light depends on the rate of light-emitting reaction and the reaction rate is decided by the applied potential. Therefore, the influence of applied potential on ECL intensity was studied in the range from 0.9 to 1.4 V, and the results were illustrated in Fig. 3. No evident ECL signal was observed below 1.0 V. The ECL intensities of two alkaloids enhanced with the increasing of potential from 1.0 to 1.2 V and then decreased after 1.2 V. The most sensitive detection potential for verticine and verticinone should be maintained at 1.2 V.

3.1.2. Effects of injection condition

Electrokinetic injection volume is directly proportional to the injection voltage and the injection time, respectively. Effect of injection time and injection voltage was studied by increasing the injection time ranging from 2 to 8 s and by adjusting injection voltage from 10 to 18 kV, respectively. Long injection time and excessive injection voltage led to strong ECL signal and low resolution between verticine and verticinone due to the introduction of more analytes. However, when shorter injection time and lower injection voltage were used, it was difficult to obtain favorable ECL intensity of analytes though high column efficiency could be achieved. Then, electrokinetic injection for 3 s at 16 kV was used as a compromise in this experiment.

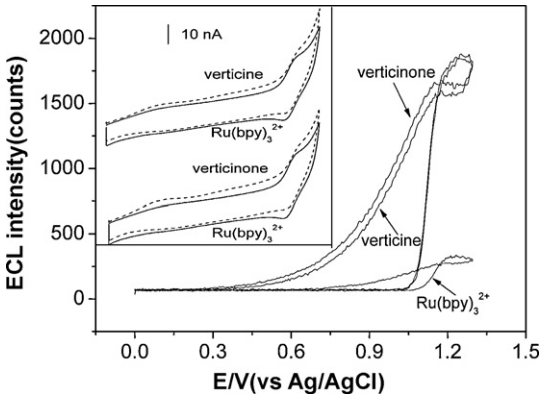


Fig. 2. Electrochemical and ECL responses of $Ru(bpy)_3^{2+}$ and alkaloids on cyclic scanning. BGE, 3 mmol/L $Ru(bpy)_3^{2+}$ in 25 mmol/L phosphate buffer at pH 8.0; analytes concentration: verticine, 1×10^{-7} mmol/L; verticinone, 1×10^{-7} mmol/L; Scan rate, 0.1 V/s.

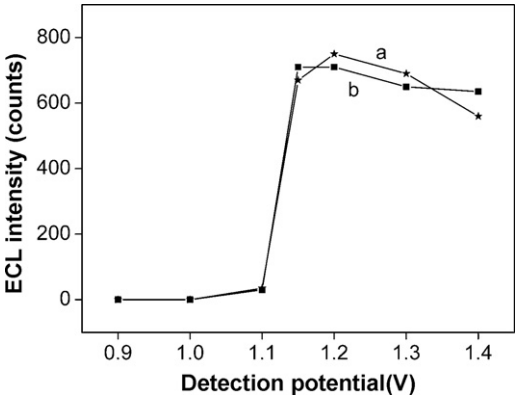


Fig. 3. Selection of detection potential: (a) ECL intensity of 1×10^{-6} mol/L verticine and (b) ECL intensity of 1×10^{-6} mol/L verticinone. 5 mmol/L $Ru(bpy)_3^{2+}$ and 50 mmol/L phosphate buffer in the detection cell; electrokinetic injection, 3 s at 16 kV; separation voltage, 16 kV.

3.1.3. Selection of solvent

At first, water was used as sample solvent, but the experimental results showed that the sensitivities of verticine and verticinone in water were not satisfactory. Verticine and verticinone are poorly soluble in water. However, they have good solubility in alcohols. To obtain the high sensitivity and good separation efficiency, the solvent was chosen from ethanol and methanol. It can be seen that the sensitivity and resolution can be improved markedly by use of alcohols. Lee et al. studied the effect of organic solvents on the chemiluminescence intensity between $Ru(bpy)_3^{3+}$ and carbamazepine [26]. The results show the chemiluminescence signal was enhanced in the presence of alcohols, and the chemiluminescence signal in methanol system was higher than that in ethanol system. Similar to their results, methanol was found to give high ECL intensities of verticine and verticinone in our experiment. The reason is that the alcohols may improve the solubility of verticine and verticinone and result in field-amplified sample stacking in CE. Therefore, methanol was used as solvent for verticine and verticinone.

3.2. Choice of running buffer and the use of ILs

Separation in CE is generally based on differences of the charge/size ratio of the analytes in running buffer. Initial separation investigation of analytes was carried out using various buffer systems such as phosphate, borate, phosphate–borate and acetonitrile–phosphate buffers in order to study resolution and sensitivity of analytes. But only one overlapped peak was found in the electropherograms.

As the resolution of analytes in these buffer systems was not sufficient for the determination of verticine and verticinone, several ILs with different anions and different alkyl chain lengths were used for investigating the effects of ILs on CE separation.

$BMImPF_6$ and $BMImBF_4$ were elected representatives to investigate the effects of ILs with different anions on CE separation. Due

to the high viscosity and low ionic conductivity of hydrophobic $BMImPF_6$, addition of even a small quantity of $BMImPF_6$ to the electrolyte leads to increases both in the migration times and overlapped peaks. However, by employing hydrophilic $BMImBF_4$, there was significant change in separation selectivity.

ILs with different alkyl chain lengths such as $EMImBF_4$ containing ethyl alkyl chain, $BMImBF_4$ with butyl alkyl chain, $OMImBF_4$ with octyl alkyl chain and $HMImBF_4$ with hexadecyl alkyl chain were used to study the effect on the separation of verticine and verticinone. As the alkyl chain length of ILs increases, the solubility in aqueous media decreases [27]. Because of poor solubility of $HMImBF_4$ in aqueous media, it cannot be used for separation of analytes. By using $EMImBF_4$, the peaks of verticine and verticinone overlapped completely, only one peak was observed on the electrophoregram. But employing $BMImBF_4$ or $OMImBF_4$, the two peaks separated and similar ECL intensity of analytes was achieved. Compared with ILs with short alkyl chain, $OMImBF_4$ with longer alkyl chain provided better resolution between analytes. However, the improved resolution was obtained at the expense of longer analyses time.

Analogous to previously reported polyphenols separations using ILs [28], the separation mechanism largely relies on the hydrogen bonding interactions between alkyl imidazolium cations and the alkaloids. Cation in ILs is a little larger than anion in ILs and its electrostatic attraction with negative charged capillary surface would change the net charge in capillary channel. Accordingly, it would reduce EOF in electrophoresis and lead to too long migration time of verticine and verticinone, thereby affording more opportunity for the analytes to associate with the alkyl imidazolium cation. Despite the very similar structures of verticine and verticinone, favorable interactions between the alkaloids and the imidazolium cations result in different migration times for analytes and caused significant changes in separation selectivity. To maintain high resolution with a suitable analysis time, $BMImBF_4$ was finally selected for further experiments. While using $BMImBF_4$ in the running buffer, not only baseline separation of verticine and verticinone was guaranteed, but also shorter separation time than that of using $OMImBF_4$ was achieved.

The effect of $BMImBF_4$ concentration on the separation and ECL intensity of the alkaloids was studied in a concentration range from 10 to 60 in 10 mmol/L units. With increasing $BMImBF_4$ concentration, the resolution between analytes was improved gradually. When $BMImBF_4$ concentration was higher than 40 mmol/L, resolution of alkaloids changed no longer sequentially, while ECL intensity of analytes decreased. Thus phosphate with different concentrations was added into $BMImBF_4$ buffer in order to shorten analyte migration time. Effect of phosphate concentration on resolution and migration time of verticine and verticinone is shown in Fig. 4. With increasing phosphate concentration, the migration time of analytes reduced gradually and resolution between analytes increased remarkably. Finally, buffer containing 40 mmol/L $BMImBF_4$ and 8 mmol/L phosphate at pH 8.00 was found to be optimum condition for the separation of these analytes in CE–ECL system.

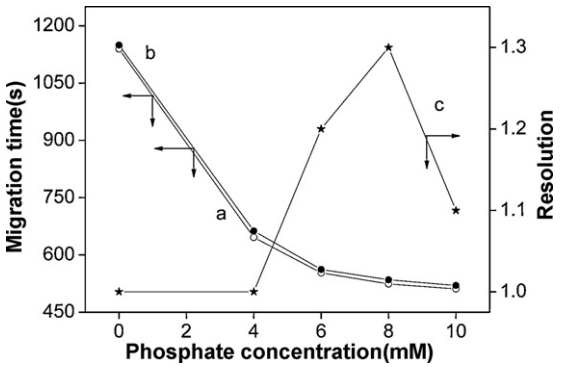


Fig. 4. Effect of phosphate concentration on resolution and migration time. (a) Migration time of verticinone, (b) migration time of verticine and (c) resolution between verticine and verticinone. Condition: detection voltage, 1.2 V; electrokinetic injection, 3 s at 16 kV; 40 mmol/L $BMImBF_4$; separation voltage, 16 kV.

3.3. Repeatability, linearity, detection limit of verticine and verticinone

Under the optimized conditions: ECL detection at 1.2 V, electrokinetic injection for 3 s at 16 kV, separation voltage at 16 kV, 5 mmol/L $Ru(bpy)_3^{2+}$ and 50 mmol/L phosphate buffer at pH 7.48 in the detection cell, 40 mmol/L $BMImBF_4$–8 mmol/L phosphate (pH 8.00) as running buffer, the reproducibility of this method was tested by six identical injections of 1×10^{-6} mol/L verticine and verticinone standard solution. Relative standard derivations of the ECL intensity and the migration time were 3.27 and 2.84% for verticine and 4.42 and 1.69% for verticinone, respectively. To investigate the detection linearity of verticine and verticinone, a series of standard mixture solutions containing verticine and verticinone were tested using CE–ECL system. The standard curves were linear between 1×10^{-8} and 1×10^{-6} mol/L for verticine and between 5×10^{-8} and 1×10^{-6} mol/L for verticinone, respectively. The calibration equations and regression coefficients were $y = 1.29 \times 10^9 x + 93.08$ and $R = 0.998$ for verticine, $y = 9.15 \times 10^8 x + 272.50$ and $R = 0.997$ for verticinone in terms of peak height response as a function of analyte concentration. Detection limits of 1.25×10^{-10} mol/L for verticine and 1×10^{-10} mol/L for verticinone were obtained (S/N = 3). Comparison of the proposed method with other methods is listed in Table 1. The developed method significantly improved limits of detection for two alkaloids between 10^2- and 10^4-fold more sensitive than those existing analytical methods and provided an appropriate linear range. The high sensitivity analysis method is better suited than existing methodology for the target analytes and sample type with sensitive, precise and reproducible performance. Further studies on the quantitative determinations of related alka-

Table 1
Comparison of various methods for determination of verticine and verticinone.

Method	Detection limit (μg/ml)		Linear range (μg/ml)		Reference
	Verticine	Verticinone	Verticine	Verticinone	
HPLC-UV	1	1	15–135	15–135	[5]
GC–FID	0.88	1.20	17.6–528.0	24.0–720.0	[7]
HPLC-ELSD	0.70	0.63	1.0–27.4	0.9–23.7	[9]
HPLC–MS	0.0036	0.0063	1.115–223	0.185–108.5	[10]
GC-FID	0.50	–	3.1–93.5	–	[11]
HSCCC-ELSD	–	–	–	–	[4]
HSCCC-ELSD	–	–	–	–	[8]
CE–ECL	1.25×10^{-10} mol/L (~0.000054 μg/ml)	1.0×10^{-10} mol/L (~0.000043 μg/ml)	1.0×10^{-8} to 1.0×10^{-6} mol/L (~0.0043–0.43 μg/ml)	5.0×10^{-8} to 1.0×10^{-6} mol/L (~0.021–0.43 μg/ml)	This paper

Table 2
Recoveries and contents of verticine and verticinone in sample analysis ($n = 3$)[a].

Sample	Ingredient	Amount (mg/L)			Recovery (%)	Content (%)
		Original	Added	Found		
F. hupehensis	Verticine	5.40	8.64	13.86	97.9	0.0032
	Verticinone	7.18	8.60	15.38	95.3	0.0043
F. walujewii	Verticine	10.80	8.64	19.11	96.2	0.0021
	Verticinone	–	8.60	8.83	102.7	–
F. cirrhosa	Verticine	7.25	8.64	15.75	98.4	0.0092
	Verticinone	7.94	8.60	16.33	97.6	0.0030
F. thunbergii	Verticine	12.35	8.64	20.48	94.1	0.024
	Verticinone	8.07	8.60	16.30	95.7	0.016
F. ussuriensis	Verticine	6.95	8.64	15.12	94.6	0.0013
	Verticinone	5.66	8.60	13.66	93.0	0.0026
F. pallidiflora	Verticine	9.31	8.64	17.64	96.4	0.0057
	Verticinone	–	8.60	8.39	97.6	–
F. przewalskii	Verticine	7.03	8.64	15.36	96.4	0.00091
	Verticinone	–	8.60	8.33	96.9	–

[a] CE–ECL conditions is the same as in Fig. 5.

loid in *Fritillariae* species by using the presently developed CE–ECL method are currently in progress in our research laboratories.

3.4. Applications

The proposed CE–ECL method was applied to the determination of verticine and verticinone in the extract of *Bulbus Fritillariae* under the optimized conditions. Identification of the analytes in herbal extracts was confirmed by comparing the electropherograms of diluted extracts with that of diluted extracts spiked with verticine and verticinone, where the increase of peak height at certain migration time was directly proportional to the amount spiked with verticine and verticinone. We collected seven plant samples such as *F. hupehensis*, *F. walujewii*, *F. cirrhosa*, *F. thunbergii*, *F. ussuriensis*, *F. pallidiflora and F. przewalskii.* All plant samples were detected by using standard addition method, the contents and recovery of the individual constituents in seven herbs were summarized in Table 2. The typical electropherograms including *F. hupehensis and F. walujewii* are shown in Figs. 5 and 6, respectively. The results showed the presently developed CE–ECL in combination with ILs is sensitive and efficient on the quantitative analysis of verticine and verticinone in *Bulbus Fritillariae.* Investigations into the fingerprinting

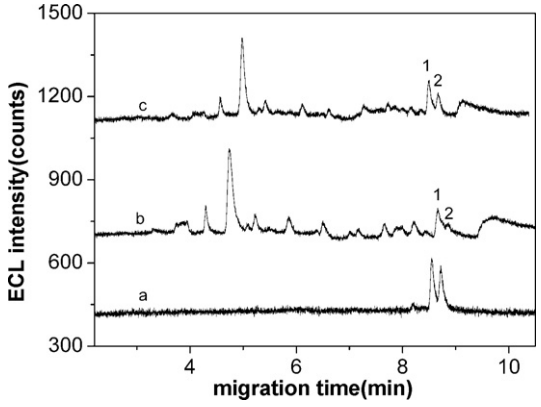


Fig. 5. Electropherograms of (a) 1×10^{-7} mol/L verticine and 1×10^{-7} mol/L verticinone standard solution; (b) *F. hupehensis* sample solution; (c) the sample solution spiked with 2.5×10^{-7} mol/L verticine and 2.5×10^{-7} mol/L verticinone standard solution; ECL intensities of (1) verticinone and (2) verticine; Condition: buffer, 40 mmol/L $BMImBF_4$–8 mmol/L phosphate (pH 8.00); other conditions are the same as in Fig. 4.

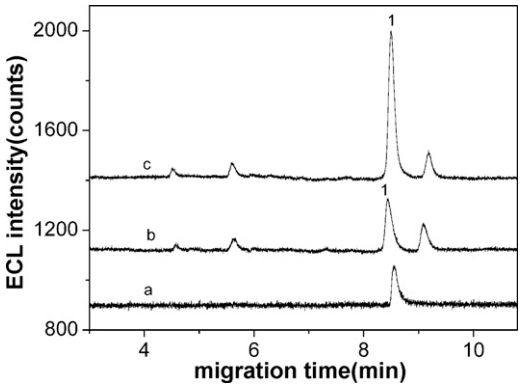


Fig. 6. Electropherograms of (a) 1×10^{-8} mol/L verticine standard solution (b) *F. walujewii* sample solution; (c) the sample solution spiked with 1×10^{-6} mol/L verticine standard solution; (1) ECL intensity of verticine; other conditions are the same as in Fig. 4.

application of the proposed approach are currently in progress in our research laboratories and the results will be reported separately.

4. Concluding remarks

In this work, it was observed that the presently developed CE–ECL in combination with ILs is more sensitive and efficient than conventional HPLC and GC methods on the quantitative analysis of verticine and verticinone in *Bulbus Fritillariae.* It significantly improved limits of detection for two alkaloids between 10^2- and 10^4-fold more sensitive than those existing analytical methods. The excellent sensitivity allows quantification of low levels of alkaloids in complex *Fritillariae* species extracts. The hydrogen bonding interactions between alkyl imidazolium cations in ILs and the alkaloids caused significant changes in separation selectivity for alkaloids with similar structures. The assay is proved sensitive, simple and practicable, which is valuable addition to existing analytical tools and may be used for the determination of verticine and verticinone in *Bulbus Fritillariae*.

Acknowledgements

This project was supported by the National Natural Science Foundation of China (No. 20675078) and the Scientific and Technological Developing Scheme of Jilin Province (No. 20070555).

References

[1] H.Y. Cheung, W.P. Lai, M.S. Cheung, F.M. Leung, D.J. Hood, W.F. Fong, J. Chromatogr. A 989 (2003) 303.
[2] H.T. Liu, K.T. Wang, X.G. Chen, Z.D. Hu, Biomed. Chromatogr. 18 (2004) 288.
[3] P. Li, H. Ji, S. Zhou, Chin. Trad. Herbal Drugs 24 (1993) 475.
[4] Z. Liu, Y. Jin, P. Shen, J. Wang, Y. Shen, Talanta 71 (2007) 1873.
[5] K. Ding, G. Lin, Y.-P. Ho, T.Y. Cheng, P. Li, J. Pharm. Sci. 85 (1996) 1174.
[6] W. Li, K. Bi, Y. Qiao, L. Ning, X. Luo, J. Chin. Pharm. Sci. 5 (1996) 213.
[7] S.-L. Li, S.-W. Chan, P. Li, G. Lin, G.-H. Zhou, Y.-J. Ren, F.C.-K. Chiu, J. Chromatogr. A 859 (1999) 183.
[8] Y. Jin, P. Shen, J. Zhang, C. Zhuo, C. Xu, Y. Yu, Res. Inf. Tradit. Chin. Med. 7 (2005) 13.
[9] S.-L. Li, G. Lin, S.-W. Chan, P. Li, J. Chromatogr. A 909 (2001) 207.
[10] J.-L. Zhou, P. Li, H.-J. Li, Y. Jiang, M.-T. Ren, Y. Liu, J. Chromatogr. A 1177 (2008) 126.
[11] S.-L. Li, P. Li, G. Lin, S.-W. Chan, Y.-P. Ho, J. Chromatogr. A 873 (2000) 221.
[12] M.M. Richter, Chem. Rev. 104 (2004) 3003.
[13] K.A. Fähnrich, M. Pravda, G.G. Guilbault, Talanta 54 (2001) 531.
[14] Y. Du, E. Wang, J. Sep. Sci. 30 (2007) 875.
[15] B.A. Gorman, P.S. Francis, N.W. Barnett, Analyst 131 (2006) 616.
[16] Y. Gao, Y. Tian, E. Wang, Anal. Chim. Acta 545 (2005) 137.
[17] Y. Gao, Q. Xiang, Y. Xu, Y. Tian, E. Wang, Electrophoresis 27 (2006) 4842.
[18] J. Yin, Y. Xu, J. Li, E. Wang, Talanta 75 (2008) 38.
[19] M. Zhou, Y. Ma, X. Ren, X. Zhou, L. Li, H. Chen, Anal. Chim. Acta 587 (2007) 104.
[20] J. Li, Y. Chun, H.J. Ju, Electroanalysis 19 (2007) 1569.
[21] Y. Xu, Y. Gao, T. Li, Y. Du, J. Li, E. Wang, Adv. Funct. Mater. 17 (2007) 1003.
[22] M. Koel, Crit. Rev. Anal. Chem. 35 (2005) 177.
[23] S. Pandey, Anal. Chim. Acta 556 (2006) 38.
[24] P. Bonhote, A.P. Dias, N. Papageorgiou, K. Kalyanasundaram, M. Gratzel, Inorg. Chem. 35 (1996) 1168.
[25] J. Liu, X. Yang, E. Wang, Anal. Chem. 74 (2003) 3637.
[26] S.H. Lee, M. Li, J.K. Suh, Anal. Sci. 19 (2003) 903.
[27] S.M. Mwongela, N. Siminialayi, K.A. Fletcher, I.M. Warner, J. Sep. Sci. 30 (2007) 1334.
[28] E.G. Yanes, S.R. Gratz, M.J. Baldwin, S.E. Robison, A.M. Stalcup, Anal. Chem. 73 (2001) 3838.

Talanta 80 (2009) 454–458

Contents lists available at ScienceDirect

Talanta

journal homepage: www.elsevier.com/locate/talanta

Biotin induced fluorescence enhancement in resonance energy transfer and application for bioassay

Shan Hu, Hai Yang, Ruxiu Cai, Zhenshi Liu, Xiangliang Yang*

College of Life Science and Technology, Huazhong University of Science and Technology, Luoyu Road 1037, Wuhan 430074, China

ARTICLE INFO

Article history:
Received 14 February 2009
Received in revised form 28 June 2009
Accepted 2 July 2009
Available online 10 July 2009

Keywords:
FRET
Biotin–streptavidin system
Fluorescence enhancement
One-step competitive assay

ABSTRACT

A novel method to significantly enhance fluorescence resonance energy transfer (FRET) signal which occurred from fluoresceine isothiocyanate (FITC) to Dylight 549 was studied in this paper. Streptavidin was labeled with the donor fluorophore FITC and biotinamide was conjugated to the acceptor Dylight 549. When biotinamide bound to streptavidin, FRET would occur from FITC to Dylight 549 while a remarkable fluorescence enhancement of streptavidin–FITC was observed. The fluorescence enhancement of streptavidin–FITC in the presence of biotin was utilized in the FRET system to obtain higher fluorescence signal. Increase of fluorescence intensity of FITC and decrease of Dylight 549 depended on the concentration of competitive biotin. A homogeneous analysis method was established based on the fluorescence recovery of FITC in the FRET system with fluorescence enhancement. This method is highly sensitive and simple to determine the concentration of biotin. The detection limit for biotin was 0.5 nM and the linear range of the assay was 0.8–9.8 nM. The response time is no more than 15 min during the one-step assay due to the high affinity between streptavidin and biotin.

© 2009 Elsevier B.V. All rights reserved.

1. Introduction

Fluorescence resonance energy transfer (FRET) is a non-radioactive process without the appearance of a photon. It occurs between a donor molecule in the excited state and an acceptor molecule in the ground state. The donor molecules typically emit at shorter wavelength that overlap with the absorption spectrum of the acceptor. The rate of energy transfer depends on the extent of spectral overlap of the emission spectrum of the donor with the absorption spectrum of the acceptor, the quantum yield of the donor, the relative orientation of the donor and acceptor transition dipoles, and the distance between the donor and acceptor molecules [1].

As FRET efficiency is sensitive to the distance between the donor and the acceptor, typically no more than 10 nm, it can be used as a 'spectroscopic ruler' to calculate the nanoscale distance [2]. The classic application of FRET is to study the structure of biomacromolecules and their interaction, like proteins [3] and nucleic acid [4,5]. One example of this application is to determine the conformation of an apolipoprotein when bound to lipids [6]. Krull et al. have demonstrated the potential for a simultaneous two-color diagnostic scheme for nucleic acids operating on the basis of FRET [5]. Organic dyes, fluorescent proteins (e.g. green fluorescent protein) and quantum dots [7–11] are commonly used as energy donors or acceptors with the linker such as immunocomplex [9,12,13], maltose binding protein [7,8] and streptavidin–biotin complex [14]. Streptavidin–biotin is a perfect linker in FRET owing to the strong interaction between streptavidin and biotin (Kd$\sim 10^{-15}$ mol/L) [14]. It is also a useful technique that is commonly utilized in the area of quantitative assay. FRET combined with immunoassay has been developed to detect antigens, such as β-estradiol [15,16], thyronine [17], biotin [14], urinary albumin [18] and immunoglobulin G. Su et al. have studied FRET between two quantum dots with immunocomplex of antigen and antibody as a linker and applied for the determination of the concentration of immunoglobulin G with a linear range of 0.1–20.0 mg/L [9]. A novel method combining FRET and flow-injection analysis has been proposed for the determination of vitamin B_{12} by Tang and his co-workers, with a detection limit of 1.65 μM [2]. Compared with conventional chemical analytical methods, FRET-based analysis has higher sensitivity and convenience in detection of ligand–receptor binding [19].

As a traditional fluorescent dye, fluoresceine isothiocyanate (FITC) is widely used in fluorescence analysis. It has many good properties such as high fluorescent efficiency and easy to label to proteins. Therefore, FITC can be applied as an energy donor in FRET assays. It is seldom used as an energy acceptor due to its relative short emission wavelength. Zhao et al. have investigated FRET between FITC (donor) [20] and quantum dots (acceptor) and provided a new trail of the thought for FRET research based on quantum dots. FITC served as an energy donor for quantitative analysis, for gastric cancer cell imaging [21] with tetramethyl rhodamine isothiocyanate (TRITC) as an acceptor or for DNA hybridization study [22]

* Corresponding author. Tel.: +86 27 87794520; fax: +86 27 87794517.
E-mail address: yangxl@mail.hust.edu.cn (X.L. Yang).

0039-9140/$ – see front matter © 2009 Elsevier B.V. All rights reserved.
doi:10.1016/j.talanta.2009.07.011

with Light Cycler-Red 640 as an acceptor. FITC has also been used in assays based on fluorescence enhancement. Al-Hakiem et al. have discovered that fluorescence of FITC labeled to avidin enhanced in the presence of biotin and developed simple fluorimetric assays for avidin and biotin [23]. Smith-Palmer et al. have utilized the fluorescence enhancement of avidin–FITC by biotin to develop a flow-injection method for biotin assay [24]. However, to our knowledge, few studies have been focused on the combination of FRET and fluorescence enhancement. Dylight 549 NHS ester is a product of Pierce Biotechnology. It fluoresces over a broad pH range, matches the output wavelengths of common fluorescence instrumentation and can be excited by the emission of FITC so as to be an efficient energy acceptor with FITC donor. Additionally, the water solubility of the reagent allows a high fluor-to-protein ratio without precipitation during conjugation [25].

Herein, our overall objective of this study is to establish a simple feasible quantitative assay based of FRET as a model for the determination of biotin. Streptavidin–biotin conjugate was used as a linker in the FRET assay. FITC and Dylight 549 were selected as energy donor and acceptor, respectively. The specific binding of streptavidin–FITC and biotinamide–Dylight 549 brought the two fluorophores close enough to induce energy transfer from FITC to Dylight 549. Therefore, the fluorescence intensity of Dylight 549 enhanced while that of FITC reduced. In the presence of competitive biotin, the fluorescence intensity of Dylight 549 would reduce while that of FITC would recover. The change of fluorescence intensity could be applied for quantitative analysis of biotin. The fluorescence enhancement of streptavidin–FITC with biotin was first applied in FRET assay in our research and proved to improve the sensitivity of the method.

2. Experimental

2.1. Reagents

FITC was purchased from Amresco. Dylight 549-NHS Ester, a novel high quantum yield water soluble fluorophore, was purchased form Piece Biotechnology. Streptavidin was obtained from Promega and N-(2-aminoethyl)biotinamide from Invitrogen Corporation. D-biotin was purchased from Kangjie Biotechnology Limited Company (Shanghai, China). Sephadex G25 was the product of GE Healthcare.

2.2. Apparatus

Fluorescence experiments were recorded by a Hitachi F-4500 fluorescence spectrophotometer. Fluoroimmunoassays were carried out by a PerkinElmer 1420 multilabel counter.

2.3. Methods

2.3.1. Conjugation of fluorophores to streptavidin and biotinamide

FITC and Dylight 549, which composed the FRET fluorophore pair, were conjugated to streptavidin and biotinamide, respectively.

FITC labeled streptavidin was prepared by mixing 37.5 μL of 1 mg/mL solution of FITC in DMSO with 150 μL of 2 mg/mL solution of streptavidin in carbonate buffer (0.1 M, pH 9.10). After 2-h reaction at room temperature, the product was separated from unconjugated FITC by gel filtration on a column (1.2 cm × 10 cm) of Sephadex G25 that was equilibrated and eluted with carbonate buffer.

Dylight 549 labeled biotin was prepared by mixing 50 μL of 1 mg/mL solution of Dylight 549 in DMF with 200 μL of 1 mg/mL solution of biotinamide in carbonate buffer (0.1 M, pH 9.10). After 2-h reaction at room temperature, the reaction was terminated by adding 10 μL 1 M β-mercaptoethanol.

The fluor-to-protein ratio of streptavidin–FITC was calculated by the following formula:

$$\text{Moles dye per mole protein} = \frac{A_{\max} \text{ of the labeled protein}}{\varepsilon_{\text{flour}}} \times \text{protein concentration}\,(M)$$

Calculate protein concentrations as follows:

$$\text{Protein concentration}\ (M) = \frac{A_{280} - A_{\max} \times \text{CF}}{\varepsilon_{\text{protein}}} \times \text{dilution factor}$$

$\varepsilon_{\text{protein}}$ = protein molar extinction coefficient; CF = correction factor = $A_{280}/A_{\max}$

The fluor-to-protein ratio of streptavidin–FITC was 2.0 and the concentration of streptavidin was 7.52 μM.

The conjugate biotinamide–Dylight 549 was not purified by gel filtration because of the low molecular weight of biotinamide. The fluor-to-biotin ratio of biotinamide–Dylight 549 was assumed as 1, which was the reactive ratio of biotinamide to Dylight 549.

2.3.2. Biotin induced fluorescence enhancement of streptavidin–FITC

D-biotin solutions of various concentrations were dispensed (50 μL) into a microtitration plate. To each well 50 μL of streptavidin–FITC (0.7 μM streptavidin) was added. The final molar ratio of D-biotin to streptavidin ranged from 0.1 to 8. After 15-min reaction at room temperature, the fluorescence was measured by a PerkinElmer 1420 multilabel counter at excitation wavelength of 485 nm and emission wavelength of 535 nm.

FITC solution of 1 mg/mL was prepared in DMSO and placed overnight at room temperature so that FITC could not be labeled to proteins (–SCN of FITC was inactivated and could not react with $-NH_2$ of proteins). 1.4 μM FITC solution was obtained by diluting the 1 mg/mL FITC using carbonate buffer (0.1 M, pH 9.10). D-biotin solutions of various concentrations were dispensed (50 μL) into a microtitration plate. To each well 25 μL of streptavidin (0.7 μM) and 25 μL of FITC (1.4 μM) was added. The final molar ratio of D-biotin to streptavidin ranged from 0.1 to 8. After 15-min reaction at room temperature, the fluorescence was measured by a PerkinElmer 1420 multilabel counter at excitation wavelength of 485 nm and emission wavelength of 535 nm.

2.3.3. FRET and one-step competitive assay for determining biotin

Biotinamide–Dylight 549 solutions of various concentrations were dispensed (50 μL) into centrifuge tubes, ranging from 0 to 4.5 μM. To each tube 50 μL of streptavidin–FITC solution (0.7 μM) was added. After 15-min reaction at room temperature, 10 μL of D-biotin solution (14.1 μM) was added. Then the fluorescence was measured by a Hitachi F-4500 fluorescence spectrophotometer at excitation wavelength of 480 nm and emission wavelength ranging from 490 to 650 nm.

D-biotin solutions of various concentrations were dispensed (10 μL) into centrifuge tubes, ranging from 0 to 20.5 μM. To each tube 50 μL of biotinamide–Dylight 549 solution (biotinamide 2.8 μM) was added, followed by 50 μL of streptavidin–FITC solution (0.7 μM). After 15-min reaction at room temperature, the fluorescence was measured by a Hitachi F-4500 fluorescence spectrophotometer at excitation wavelength of 480 nm and emission wavelength ranging from 490 to 650 nm.

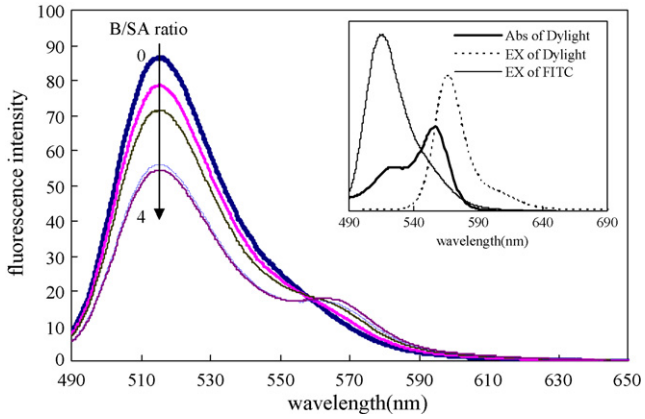


Fig. 1. The process of fluorescence resonance energy transfer between streptavdin–FTIC and biotinamide–Dylight 549. Ratios of biotinamide to streptavidin were 0, 1, 2, 3 and 4, respectively. The insert displays spectral properties of the donor FITC and the acceptor Dylight 549. The emission spectrum of FITC (excited at 480 nm), the emission spectrum of Dylight 549 (excited at 520 nm) and the absorbance spectrum of Dylight 549.

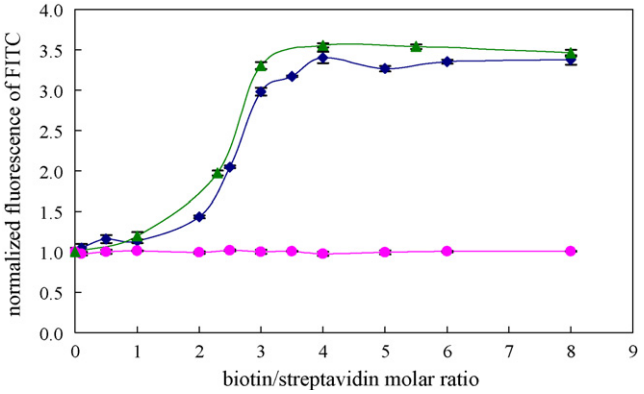


Fig. 2. The enhanced effect of biotin to the fluorescence of streptavidin–FITC. The relationship between the fluorescence of FITC and ratios of biotin to streptavidin when FITC was labeled to streptavidin (♦) and when FITC was free (●). The normalized fluorescence intensity of FITC conjugated to streptavidin in the presence of biotinamide (▲).

3. Result and discussion

3.1. Spectra characteristics of FRET system

The absorbance spectrum of Dylight 549 is from about 520 to 550 nm (Fig. 1), which mostly overlaps with the emission spectrum of FITC. So Dylight 549 can be excited effectively by the emission of FITC. Besides, Dylight 549 is emitting maximum from about 560–580 nm as shown in Fig. 1, separating from the emission spectrum of FITC. Therefore, FITC can be used as an energy donor and Dylight 549 as an acceptor in a FRET system.

FRET occurred between streptavidin–FITC and biotinamide–Dylight 549 when biotinamide specifically bound to streptavidin with FITC as an energy donor and Dylight 549 as an acceptor. The fluorescence intensity of FITC reduced while that of Dylight 549 increased as shown in Fig. 1. In order to enhance the fluorescence intensity of streptavidin–FITC to the same extent, D-biotin was added after mixing streptavidin–FITC and biotinamide–Dylight 549 for 15 min. Interaction between biotin and streptavidin was strong ($Kd \sim 10^{-15}$ mol L^{-1}), so D-biotin would not compete with biotinamide–Dylight 549 to bind to streptavidin.

3.2. The enhanced effect of biotin to the fluorescence of streptavidin–FITC

The specific binding of streptavidin and biotin enhanced the fluorescence intensity of FITC that was labeled to streptavidin. Fig. 2 showed that the enhancement of fluorescence intensity of FITC increased with the addition of molar ratio ($1 \leq$ molar ratio ≤ 4) of biotin to streptavidin. When the molar ratio of biotin to streptavidin was below 1, the fluorescence intensity of FITC was not affected. When the molar ratio increased to 4 and more, FITC reached a maximal intensity and remained the same despite a further increase in molar ratio. This phenomenon could be related to the quadrovalent nature of streptavidin (one molecule of streptavidin could bind to maximum four molecules of biotin). The fluorescence of streptavidin–FITC was enhanced by biotin to a maximum extent of about 3 to 4 fold. The fluorescence intensity of free FITC would not enhance when streptavidin and biotin mixed with it. So only the fluorescence intensity of labeled FITC can be enhanced. This can be utilized to improve the sensitivity of fluorescent quantitative analysis based on FRET.

Biotinamide would also enhance the fluorescence of streptavidin–FITC as shown in Fig. 2. The fluorescence intensity of streptavidin–FITC was enhanced by biotinamide to a maximum extent of about 3.5 fold. The trend of the curve of enhancement was similar to that of biotin on streptavidin–FITC. Thus, the enhancement by biotinamide had the same effect as by biotin. It was expected that biotinamide in the conjugate biotinamide–Dylight 549 would enhance the fluorescence of streptavidin–FITC. In the one-step competitive assay below, the molar ratio of biotinamide to streptavidin (B/SA) in all competition assays was 4:1, which would saturate the fluorescence enhancement of streptavidin–FITC. Therefore, the change of fluorescence signal was only caused by FRET between streptavidin–FITC and biotinamide–Dylight 549.

3.3. One-step competitive assay based on FRET for biotin determination

Competitive assay was carried out by mixing D-biotin and biotinamide–Dylight 549 first and then adding streptavidin–FITC. When streptavidin–FITC was added to the mixture of D-biotin and biotinamide–Dylight 549, D-biotin competed with biotinamide–Dylight 549 to bind to streptavidin–FITC. So the number of the complex FITC–streptavidin–biotinamide–Dylight 549 reduced and the probability of FRET reduced accordingly. Compared with the normal process of FRET (Fig. 1), the fluorescence intensity of FITC recovered and that of Dylight 549 reduced. The fluorescent enhancement of FITC and decrease of Dylight 549 were related to the concentration of competitive D-biotin. It was shown in Fig. 3a that the fluorescence intensity of FITC increased with the increase of the concentration of competitive D-biotin. The area under fluorescence peak of Dylight 549 was inversely proportional to the concentration of competitive biotin. It was not as expected that the fluorescence intensity of Dylight 549 reduced with the increase of the concentration of competitive D-biotin, because the fluorescence intensity of Dylight 549 was not as strong as that of FITC. So the area under fluorescence peak of Dylight 549 was used instead of fluorescence intensity.

Competitive curve for D-biotin assay was obtained by measuring the area under the fluorescence peak of Dylight 549 for different D-biotin concentrations. The fluorescence intensity of Dylight 549 was not as strong as that of FITC, so the fluorescence of FITC would influence that of Dylight 549 slightly. The concentration of D-biotin was inversely proportional to the fluorescence of Dylight 549 that was

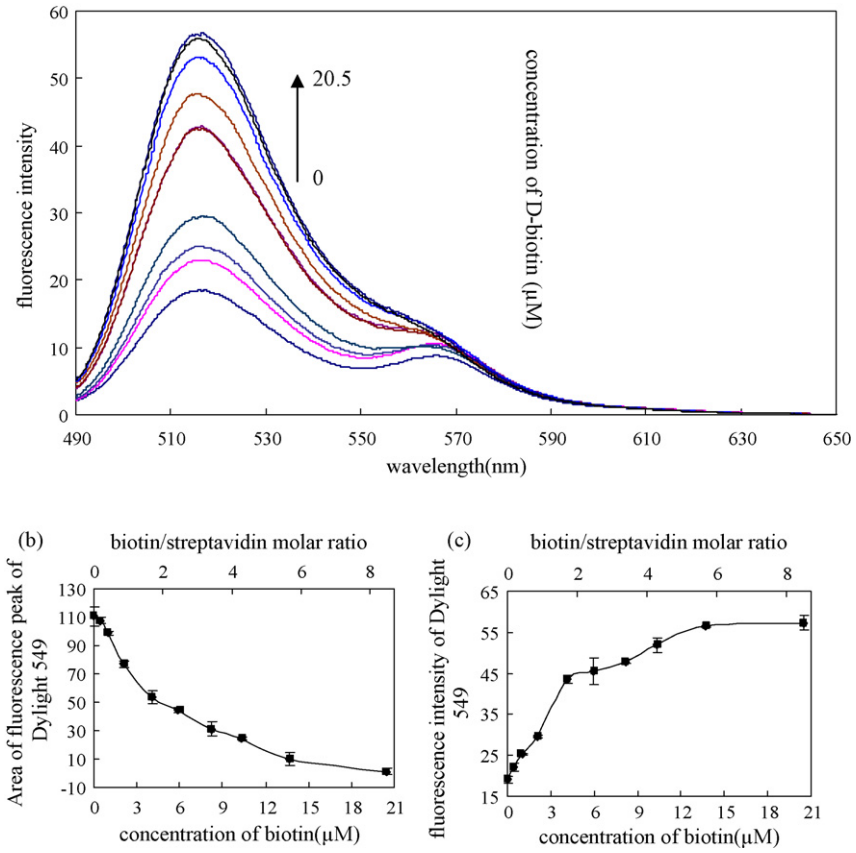


Fig. 3. (a) The relationship between fluorescence intensity of streptavidin–FITC mixed with biotinamide–Dylight 549 and different amounts of D-biotin. Concentrations of D-biotin in the samples were 0, 0.4, 1.0, 2.1, 4.1, 5.9, 8.2, 10.3, 13.7, 20.5 μM, respectively. (b) The competitive curve of D-biotin in the FRET system of streptavidin–FITC and biotinamide–Dylight 549. (c) Relationship between competitive D-biotin and the fluorescence intensity of FITC. Data were presented as average ± SD from four repeated measurements.

labeled with biotinamide as presented in Fig. 3b. The fluorescence intensity of FITC was strong enough to be used as detection signals. The concentration of D-biotin was proportional to the fluorescence intensity of FITC labeled to streptavidin as shown in Fig. 3c. Therefore, both fluorescence signals of energy donor (FITC) and acceptor (Dylight 549) can be utilized for quantitative analysis of D-biotin.

3.4. Sensitivity of the one-step homogeneous assay and analysis of real samples

The detected signals were low and the operation was complex in Hitachi F-4500 fluorescence spectrophotometer, so PerkinElmer 1420 multilabel counter was used to simplify the operation and improve the detected signals. Therefore, the sensitivity of the assay was improved.

In this experiment, the capability of quantitative analysis of D-biotin based on the streptavidin–FITC/biotinamide–Dylight 549 FRET system was investigated. Standard curve (Fig. 4) for D-biotin was obtained by measuring the fluorescence intensity of FITC while the amount of streptavidin–FITC was 7.5 nM and biotinamide–Dylight 549 was 30 nM. The reduced concentration of streptavidin–FITC and biotinamide–Dylight 549 led to low detection limits of biotin. However, streptavidin–FITC and biotinamide–Dylight 549 could not be diluted infinitely owing to detection limit of the instrument. The lowest concentrations of streptavidin–FITC and biotinamide–Dylight 549 were 7.5 and 30 nM, respectively. The lineal regression equation is $Y = 0.0451X + 1.1309$, with the regression coefficient $R = 0.9959$. In this equation, X and Y represent D-biotin contents and the normalized fluorescence intensity of FITC (in conjugate streptavidin–FITC). The linear range of D-biotin concentration is from 0.8 to 9.8 nM. For the blank test, the mixture of streptavidin–FITC and biotinamide–Dylight 549 was used as the sample and the detection limit for the proposed method is 0.5 nM based on the 3δ criterion ($n = 19$). R.S.D. of intra-assay ($n = 4$) and inter-assay ($n = 3$) of various D-biotin concentrations were less than 3.51% and 9.87%, respectively.

Pure milk purchased from native market was detected with this system. 1 mL milk was treated with 3 mL H_2SO_4 (1 M) and centrifuged at 12,000 g. The upper clear solution was adjusted to pH 9.1

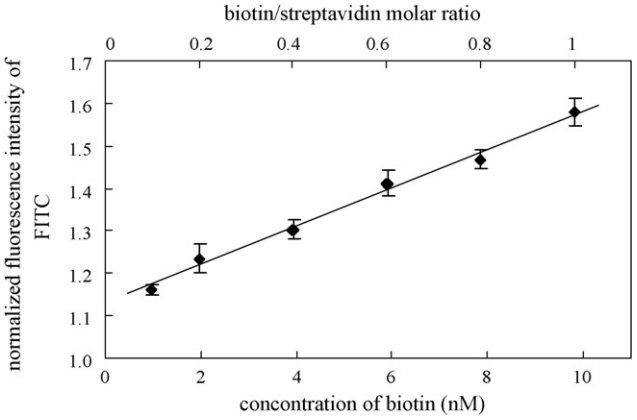


Fig. 4. Standard curve for biotin assay by measuring the fluorescence intensity of FITC based on the FRET system of streptavidin–FITC and biotinamide–Dylight 549. Data were presented as average ± SD from four repeated measurements.

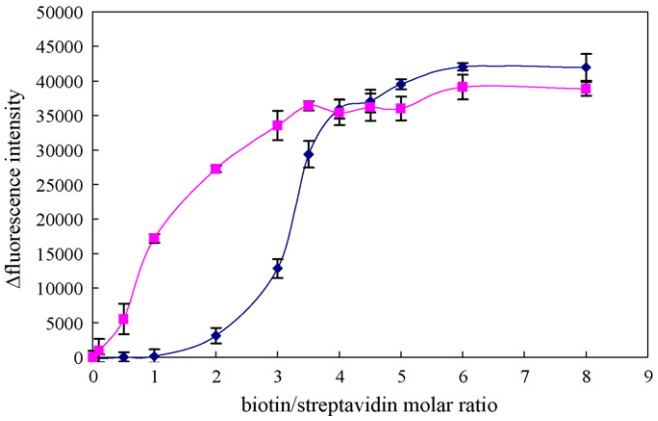


Fig. 5. The relationship between fluorescence intensity of FITC and ratios of biotin to streptavidin by the method of fluorescence enhancement (♦) and FRET based on fluorescence enhancement (■). Data were presented as average ±SD from four repeated measurements.

by NaOH (4 M). The milk was diluted about 5 times during the disposal procedure. The results showed that D-biotin contained in pure milk was about 36.5 nM (n = 4, R.S.D. = 4.19%). The results demonstrated that the proposed method can provide precise data when real life samples are analyzed.

3.5. Comparison of methods of fluorescence enhancement and FRET with fluorescence enhancement

The sensitivity of the assay could be improved due to the fluorescence enhancement by biotin to streptavidin–FITC. B/SA in all competitive assays was higher than 4, which would saturate the fluorescence enhancement of streptavidin–FITC. Thus, the fluorescence change of streptavidin–FITC was only related to FRET effect other than fluorescence enhancement by competitive D-biotin.

The method of FRET with fluorescence enhancement has the potential of lower detection limit, broader measurable range and higher sensitivity than that of the method of fluorescence enhancement to determine D-biotin. As shown in Fig. 5, there was no fluorescence change in the method of fluorescence enhancement when the B/SA is less than 1. However, obvious change emerged in the same range by the method of FRET competition assay with fluorescence enhancement. This indicated that the method of FRET with fluorescence enhancement is more sensitive to detect D-biotin and has lower detection limit.

4. Conclusion

We have demonstrated a novel competitive homogeneous analysis method based on fluorescence resonance energy transfer between FITC and Dylight 549 with fluorescence enhancement. The method is a fast, simple method and reaches a high sensitivity with the detection limit of 0.5 nM for biotin. The assay has the advantage of double-labeled detection, which means the fluorescence recovery of donor and decrease of acceptor can both be utilized for quantitative assays. The fluorescence enhancement introduced into the assay significantly improves the sensitivity. The results also demonstrate that FRET is a powerful tool for sensitive, precise and prompt quantitative analysis of some important biomolecules when it combines with fluorescence enhancement and homogeneous immunoassay. As a homogeneous assay, the procedure is more simple with only one step than that of Enzyme Linked Immunosorbent Assay which includes many washing steps. Such FRET system can be applied as immunosensor with antigen–antibody as linkers to detect more antigen or antibody. The FRET system can also be carried out by utilizing other fluorescent materials, such as quantum dots or lanthanide, which have anti-photobleaching fluorescent characteristics or long stock shift and long fluorescent life.

Acknowledgement

This work was financially supported by the National Natural Science Foundation of China (Grant No. 20075009).

References

[1] J.R. Lakowicz, Principles of Fluorescence Spectroscopy, Springer Science, Baltimore, Maryland, USA, 2006.
[2] H. Xu, Y. Li, C. Liu, Q. Wu, Y. Zhao, L. Lu, H. Tang, Talanta 77 (2008) 176.
[3] D.M. Willard, L.L. Carillo, J. Jung, A. Van Orden, Nano Lett. 1 (2001) 469.
[4] Y.-P. Ho, H.H. Chen, K.W. Leong, T.-H. Wang, J. Control. Release 116 (2006) 83.
[5] W.R. Algar, U.J. Krull, Anal. Chim. Acta 581 (2007) 193.
[6] H.H. Li, D.S. Lyles, M.J. Thomas, W. Pan, S.T. MG, J. Biol. Chem. 275 (2000) 37048.
[7] A.R. Clapp, I.L. Medintz, J.M. Mauro, B.R. Fisher, M.G. Bawendi, H. Mattoussi, J. Am. Chem. Soc. 126 (2004) 301.
[8] A.R. Clapp, I.L. Medintz, B.R. Fisher, G.P. Anderson, H. Mattoussi, J. Am. Chem. Soc. 127 (2005) 1242.
[9] Q. Ma, X.G. Su, X.Y. Wang, Y. Wan, C.L. Wang, B. Yang, Q.H. Jin, Talanta 67 (2005) 1029.
[10] E.R. Goldman, I.L. Medintz, J.L. Whitley, A. Hayhurst, A.R. Clapp, H.T. Uyeda, J.R. Deschamps, M.E. Lassman, H. Mattoussi, J. Am. Chem. Soc. 127 (2005) 6744.
[11] N. Hildebrandt, L.J. Charbonnière, M. Beck, R.F. Ziessel, H.-G. Löhmannsröben (Eds.), Angew. Chem. Int. 44 (2005) 7612.
[12] Q.D. Chen, Q. Ma, Y. Wan, X.G. Su, Z.B. Lin, Q.H. Jin, Luminescence 20 (2005) 251.
[13] Y. Li, Q. Ma, X. Wang, X. Su, Luminescence 22 (2007) 60.
[14] T. Kokko, L. Kokko, T. Soukka, T. Lögren, Anal. Chim. Acta 585 (2007) 120.
[15] T. Kokko, L. Kokko, T. Lövgren, T. Soukka, Anal. Chem. 79 (2007) 5935.
[16] K. Kuningas, T. Ukonaho, H. Pakkila, T. Rantanen, J. Rosenberg, T. Lovgren, T. Soukka, Anal. Chem. 78 (2006) 4690.
[17] G. Wang, J. Yuan, X. Hai, K. Matsumoto, Talanta 70 (2006) 133.
[18] Q.P. Qin, O. Peltola, K. Pettersson, Clin. Chem. 49 (2003) 1105.
[19] W. Li, X. Yang, K. Wang, W. Tan, H. Li, C. Ma, Talanta 75 (2008) 770.
[20] J.-H. Wang, T.-C. Liu, Y.-C. Cao, X.-F. Hua, H.-Q. Wang, H.-L. Zhang, X.-Q. Li, Y.-D. Zhao, Colloids Surf. A: Physicochem. Eng. Aspects 302 (2007) 168.
[21] X. He, J. Ge, K. Wang, W. Tan, H. Shi, C. He, Talanta 76 (2008) 1199.
[22] J. Schüein, B. Graβl, J. Krause, C. Schulze, C. Kugler, P. Müler, W.M. Bertling, J. Hassmann, Talanta 56 (2002) 875.
[23] M.H.H. Al-Hakiem, J. Landon, D.S. Smith, R.D. Nargessi, Anal. Biochem. 116 (1981) 264.
[24] T. Smith-Palmer, M.S. Barbarakis, T. Cynkowski, L.G. Bachas, Anal. Chim. Acta 279 (1993) 287.
[25] http://www.piercenet.com/Products/Browse.cfm?fldID=9AA97866-4822-4AFE-B36D-49F7E1D7D653.

Talanta 80 (2009) 459–465

Contents lists available at ScienceDirect

Talanta

journal homepage: www.elsevier.com/locate/talanta

Peroxidase activity–structure relationship of the intermolecular four-stranded G-quadruplex–hemin complexes and their application in Hg^{2+} ion detection

De-Ming Kong[a,b,*], Jing Wu[b], Na Wang[b], Wei Yang[b], Han-Xi Shen[b]

[a] Key Laboratory of Functional Polymer Materials, Ministry of Education, Nankai University, Tianjin 300071, PR China
[b] Research Centre for Analytical Sciences, Department of Chemistry, Nankai University, Tianjin 300071, PR China

ARTICLE INFO

Article history:
Received 6 March 2009
Received in revised form 29 June 2009
Accepted 2 July 2009
Available online 10 July 2009

Keywords:
DNAzyme
G-quadruplex
Hemin
Peroxidase
Mercury ion detection

ABSTRACT

The peroxidase activities of the complexes of hemin and intermolecular four-stranded G-quadruplexes formed by short-stranded $X_nG_mX_p$ sequences (X = A, T or C), especially $T_nG_mT_p$ sequences, were compared. The results, combining with those of circular dichroism (CD) spectra and acid–base transition study for DNA–hemin complexes, provide some important information about DNAzymes based on G-quadruplex–hemin complexes, such as the formation of a G-quadruplex structure is an important factor for determining whether a DNA sequence can enhance the catalytic activity of hemin; both intramolecular parallel G-quadruplexes and intermolecular four-stranded parallel G-quadruplexes can enhance the catalytic activity of hemin; the addition of T nucleotides to the 5′-end of a G-tract confers corresponding G-quadruplex greatly enhanced catalytic activity, whereas the addition of T nucleotides to the 3′-end of the G-tract has little effect; the high catalytic activity of hemin in the presence of some short-stranded G-rich sequences may be a result of the reduction of the acidity of the bound hemin cofactor. These studies provide more information for the DNA–hemin peroxidase model system, may help to elucidate the structure–function relationship of peroxidase enzymes and to develop novel, highly efficient peroxidase-liking DNAzymes. As a sequence of such an investigation, a new Hg^{2+} detection method was developed.

© 2009 Elsevier B.V. All rights reserved.

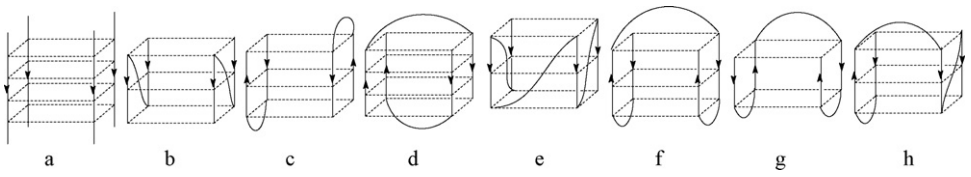
1. Introduction

DNAzymes are catalytically active DNA molecules that could show different enzymatic activities. With all else being equal, DNAzymes should be superior to many protein-based enzymes because DNAzymes are relatively less expensive to produce and more readily to mutate and self-replicate. [1,2]. Therefore, the development of DNAzymes with interesting activities attracted increasing interest [3,4].

An important development in the field of DNAzymes has been the discovery of the peroxidase-like activity of some DNA–hemin complexes. It has been reported that the complexes formed by hemin and some G-quadruplexes can reveal enhanced peroxidase activity [5,6]. This class of DNAzymes has been used in the detection of telomerase activity [7,8], hemin [9] and cofactor units of DNAzymes (e.g. Pb^{2+} ions, L-histidine and AMP) [10,11], the screening of G-quadruplex ligands [12] and the development of DNA sensors [13–15]. Compared with application studies, the basic studies (e.g. structure–function relationship study) on this class of DNAzymes are relatively backward. In DNA–hemin peroxidase model system studies, the most widely used catalytic DNA apatmer is PS2.M. PS2.M originally resulted from an in vitro selection for a reaction (porphyrin metallation) very different from peroxidation [16–19]. Travascio et al. reported that PS2.M–hemin can show peroxidase activity two orders of magnitude higher than that of hemin [6]. The ability of PS2.M to enhance the catalytic activity of hemin is attributed to the formation of a specific DNA structure, that is, a G-quadruplex. G-quadruplexes are unique higher-order structures formed by G-rich nucleic acid sequences based on stacked arrays of G-quartets connected by Hoogsteen-type base pairing. These structures are stabilized by monovalent cations (especially K^+) and can have different types dependent on the number of associated DNA strands, such as intermolecular four-stranded quadruplex formed by the association of four nucleic acid strands possessing a single poly(dG) domain, intermolecular dual-stranded quadruplex formed by two nucleic acid strands possessing two poly(dG) domains, and intramolecular single-stranded quadruplex formed by a nucleic acid strand possessing four or more than four poly(dG) domains [20]. Even with the same number of associated molecules, G-quadruplexes can reveal many topological structures differing by mutual strand orientation (Scheme 1) [21].

* Corresponding author at: Key Laboratory of Functional Polymer Materials, Ministry of Education, Nankai University, Tianjin 300071, PR China.
Tel.: +86 22 23505091; fax: +86 22 23502458.
E-mail address: kongdem@nankai.edu.cn (D.-M. Kong).

0039-9140/$ – see front matter © 2009 Elsevier B.V. All rights reserved.
doi:10.1016/j.talanta.2009.07.010



Scheme 1. Schematic representation of different types of G-quadruplex. (a) intermolecular four-stranded parallel quadruplex; (b) intermolecular two-stranded parallel quadruplex; (c and d) intermolecular two-stranded antiparallel quadruplex; (e) unimolecular parallel quadruplex; (f and g) unimolecular antiparallel quadruplex; (h) unimolecular mixed-parallel quadruplex. arrows indicate 5′–3′ polarity.

It is generally accepted that PS2.M can fold to a G-quadruplex, but the details of the folded and catalytically active structure of PS2.M have not been adequately elucidated to date. In most cases, such G-quadruplexes are described as a unimolecular quadruplex with antiparallel structure [10,11,13,14], but no evidence for this structure was presented yet. Lee et al. constructed two closely related structural models for the folded PS2.M, which both contained two guanine quartets [22]. But it seems that these two models cannot be supported by results of circular dichroism (CD) spectroscopy. Majhi and Shafer concluded the catalytically active form of PS2.M may be the multistranded parallel quadruplex rather than the unimolecular antiparallel structure [23]. This conclusion issues a challenge to the most applications of these DNAzymes because of the slow formation kinetics of multistranded quadruplexes. Recently, we demonstrated that the catalytically active form of CatG4 (5′-$TG_3TAG_3CG_3TTG_3AAA$), a 21-nucleotide oligonucleotide that has similar sequence to PS2.M and has been demonstrated to be able to enhance the peroxidase activity of hemin [13], is a unimolecular parallel quadruplex rather than a multistranded parallel quadruplex [24]. In summary, the basic knowledge of DNA–hemin peroxidase model system is relatively inadequate, which may seriously hinder the development of new DNA aptamers with higher catalytic activities and the discovery of new analytical applications for this kind of DNAzyme.

Herein, the peroxidase activities of the complexes formed by hemin and different four-stranded G-quadruplexes were compared to provide more information for the DNA–hemin peroxidase model system. The four-stranded G-quadruplexes are formed by different short-stranded DNAs that have a single G-tract with different numbers of T residues attached at the 5′ or/and 3′-ends. The results demonstrated that some four-stranded G-quadruplexes can increase the peroxidase activity of hemin to some extent, and the position of T residues in the sequence has a great influence on the level of activity.

2. Experimental

2.1. Materials

All Oligonucleotides that were used in this study were purchased from Jinsite Co., Ltd. (China). The concentrations of these oligonucleotides were represented as single-stranded concentrations. Single-stranded concentrations were determined by measuring the absorbance at 260 nm. Molar extinction coefficients were determined using a nearest neighbor approximation (http://www.idtdna.com/analyzer/Applications/OligoAnalyzer). H_2O_2, 2,2′-azinobis(3-ethylbenzothiozoline)-6-sulfonic acid (ABTS), Triton X-100 and hemin were obtained from Sigma. All chemical reagents were of reagent grade and used without further purification.

2.2. Peroxidase activity measurements

DNA solutions (0.86, 1.72 and 3.44 μM for one-stranded, two-stranded and four-stranded G-quadruplexes, respectively) were prepared in buffer A (10 mM Tris–HCl, pH 8.0, 16 mM KCl, 0.8 mM $MgCl_2$, 0.0017% (v/v) Triton X-100). In order to ensure the formation of G-quadruplex structures, the mixtures were heated to 90 °C for 5 min, cooled slowly to room temperature, and then incubated at room temperature for 30 min. 1.72 μM of hemin was added to the mixtures. The reaction mixtures were held for another 1 h at room temperature, then 1.28 mM of ABTS and 1.28 mM of H_2O_2 were added. The color of the reaction mixtures was recorded by a digital camera, and the absorption intensity at λ = 414 nm was followed using a TU-1901 UV–vis spectrophotometer.

2.3. Circular dichroism (CD) study

CD spectra were measured on a Jasco J-820 spectropolarimeter at room temperature. DNA solutions (0.86, 1.72 and 3.44 μM for one-stranded, two-stranded and four-stranded G-quadruplexes, respectively) were prepared in buffer A. To ensure the formation of quadruplex structures, the solutions were heated to 90 °C for 5 min, cooled slowly to room temperature, and then incubated at room temperature overnight. Spectra were recorded between 200 and 320 nm in 1 mm pathlength cuvettes. Spectra were averaged from three scans, which were recorded at 50 nm/min with a response time of 1 s and a bandwidth of 0.2 nm.

2.4. Acid–base transition study for DNA–hemin complexes

The mixtures of 1.72 μM hemin and individual DNAs (0.86, 1.72 and 3.44 μM for one-stranded, two-stranded and four-stranded G-quadruplexes, respectively) were prepared in different buffers: glycine–HNO_3 (pH 2.0–4.0), MES–Tris (pH 4.6–7.0), HPO_4^{2-}–$H_2PO_4^-$ (pH 5.8–6.8), Tris–HNO_3 (pH 7.0–8.9), and glycine–OH^- (pH 8.5–10.5). The electronic absorption spectra of various DNA–hemin complexes were recorded between 300 and 600 nm. The ratio of A_{360}/A_{404} was plotted as a function of pH value, and corresponding p*K*a value was determined from the position of the maximum of the first derivative of the plot.

2.5. Detection of Hg^{2+} ion

Aliquots of 3.44 μM T_4G_3 (5′-TTTTGGG) solutions containing 10 mM Tris–HCl (pH 8.0), 16 mM KCl, 0.8 mM $MgCl_2$, 0.0017% (v/v) Triton X-100 were heated to 90 °C for 5 min, cooled slowly to room temperature. Then, different concentration of Hg^{2+} ion was added and the mixtures were incubated at room temperature for 30 min. 1.72 μM of hemin was added to the mixtures and the reaction mixtures were held for another 1 h at room temperature. Then 1.28 mM of ABTS and 1.28 mM of H_2O_2 were added. 10 min later, the absorption spectra of the reaction product $ABTS^+$ were recorded. The absorbance at 414 nm (the maximal absorption of $ABTS^+$) was used for quantitative analysis.

Table 1
Potential G-quadruplex-forming sequences used in this work.

DNA aptamers	Sequences	G-quadruplex structure[a]
PS2.M	5′-GTGGGTAGGGCGGGTTGG	e
Apt	5′-$G_2T_2G_2TGTG_2T_2G_2$	g
Hum21	5′-$G_3(TTAG_3)_3$	h
Hum12	5′-$(T_2AG_3)_2$	b
Oxy12	5′-$G_4T_4G_4$	d
TG_4T	5′-TG_4T	a
T_4G_4	5′-T_4G_4	a

[a] Refers to Scheme 1.

3. Results and discussion

3.1. Catalytic activity and structural studies of various DNAs

Although the structure of the DNA aptamers that can provide hemin with enhanced peroxidase activity is unclear, it is generally acknowledged that they may form a G-quadruplex structure. The peroxidase activity of hemin in the presence of seven different G-quadruplexes (Table 1) was compared to investigate the abilities of these G-quadruplexes to enhance the peroxidase activity of hemin. The results are shown in Fig. 1, where it can be seen that PS2.M and T_4G_4 have markedly enhanced peroxidase activity compared with hemin alone. They catalyze the oxidation of 2,2′-azinobis(3-ethylbenzothiozoline)-6-sulfonic acid (ABTS) by H_2O_2, and the absorption intensity of reaction mixtures at $\lambda = 414$ nm are greatly increased. TG_4T enhances the peroxidase activity of hemin much less than PS2.M and T_4G_4. The other four G-quadruplexes induce very little enhancement of peroxidase activity.

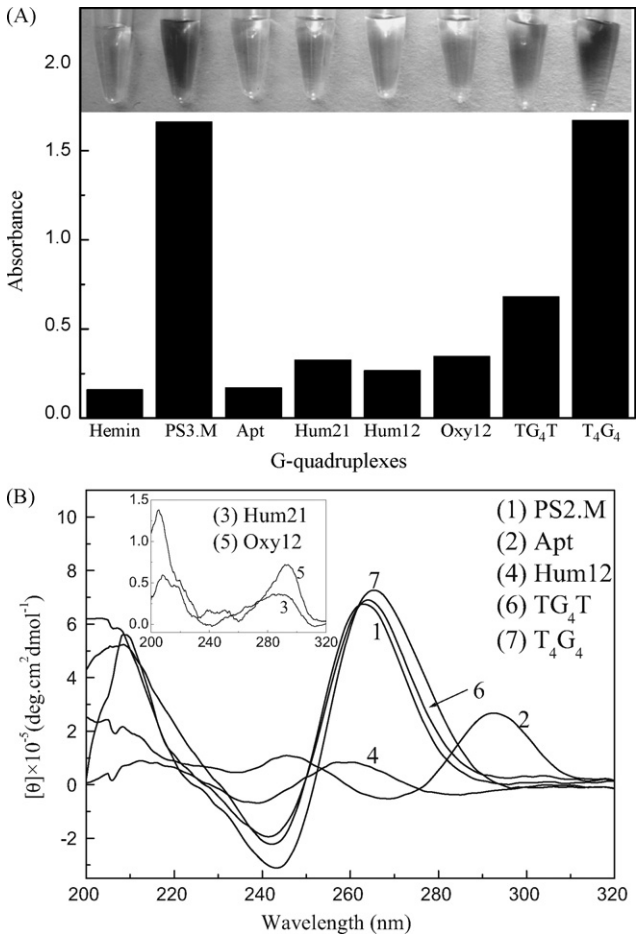


Fig. 1. (A) Oxidation of ABTS by H_2O_2 in the presence of hemin and the DNAs listed in Table 1, and (B) the CD spectra of corresponding DNAs. For clarity, the CD spectra of Hum21 and Oxy12 were given in the inset figure. Corresponding color figures can be found in supporting information.

The CD spectra of the seven G-quadruplexes were recorded in order to investigate whether there is any relationship between the peroxidase activity of a G-quadruplex and its conformation. Earlier studies showed that the CD spectra of quadruplexes can be used to indicate whether they fold in a parallel or an antiparallel conformation. The CD spectrum of a parallel G-quadruplex has a positive peak near 265 nm and a negative peak near 240 nm, whereas an antiparallel G-quadruplex has a positive peak near 295 nm and a negative peak near 265 nm [25]. The results shown in Fig. 1B suggest that Apt and Oxy12 can form antiparallel quadruplexes, whereas PS2.M, T_4G_4, TG_4T and Hum12 can form parallel quadruplexes. The CD spectrum of Hum21 has a positive peak at around 295 nm and a negative peak at around 240 nm, suggesting the co-existence of parallel and antiparallel conformations in solution, or the presence of a hybrid structure containing both *syn* and *anti* bonds as in Scheme 1h [26–29]. It is interesting that the three G-quadruplexes (PS2.M, T_4G_4 and TG_4T) that can enhance the peroxidase activity of hemin adopt the parallel G-quadruplex conformation and have a strong positive peak at around 265 nm in CD spectra. This result suggests that the conformation of G-quadruplexes may be an important factor in determining their effect on peroxidase activity.

3.2. Catalytic activity and structural studies of $T_nG_mT_p$ sequences

The results described above indicate that both unimolecular parallel G-quadruplexes and intermolecular four-stranded parallel G-quadruplexes can enhance the catalytic activity of hemin. A detailed study of the catalytic activity of four-stranded quadruplexes formed by $T_nG_mT_p$ sequence is reported here for the first time.

3.2.1. G_4T_n and T_nG_4

G_4 has little effect, and G_4T_n and T_nG_4 ($n = 0$–5) enhance the catalytic activity of hemin to different extents (Fig. 2). The increase is much greater in the presence of T_nG_4 sequences than that in the presence of G_4T_n sequences; i.e. the addition of T residues to G_4 increases the catalytic activity of hemin, and the greatest effect is obtained when the T residues are added to the 5′-end. However, the number of T nucleotides added to the same side of G_4 has little effect on the catalytic activity.

The CD spectra of the oligonucleotides with sequences of G_4T_n and T_nG_4 are shown in Fig. 2. The CD spectra of both T_nG_4 and G_4T_n sequences have a major positive peak around 265 nm and a minimum around 240 nm, which is typical of a parallel arrangement of the strands. These results suggest that the ability of the intermolecular G-quadruplexes to enhance the catalytic activity of hemin is correspond not only to G-quadruplex structure, but also to the position of added T nucleotides.

3.2.2. $T_4G_4T_n$ and $T_nG_4T_n$

The results described above show that the position of T nucleotides in the sequence has a marked influence on the catalytic activity. Two experiments were done to further investigate the effect of the location of the T nucleotides. In the first experiment, different numbers of T nucleotides were added to the 3′-end of T_4G_4, and the catalytic activity of the resulting $T_4G_4T_n$ sequences ($n = 0$–5) was determined (Fig. 3). The addition of T nucleotides at the 3′-end dramatically decreases the catalytic activity of T_4G_4, but there was little difference in the effect when different numbers of T nucleotides were added. In the second experiment, the catalytic activity of the $T_nG_4T_n$ sequences ($n = 0$–4) was investigated. As shown in Fig. 3, the $T_nG_4T_n$ sequences have a level of catalytic activity comparable to that of the $T_4G_4T_n$ sequences. That is to say,

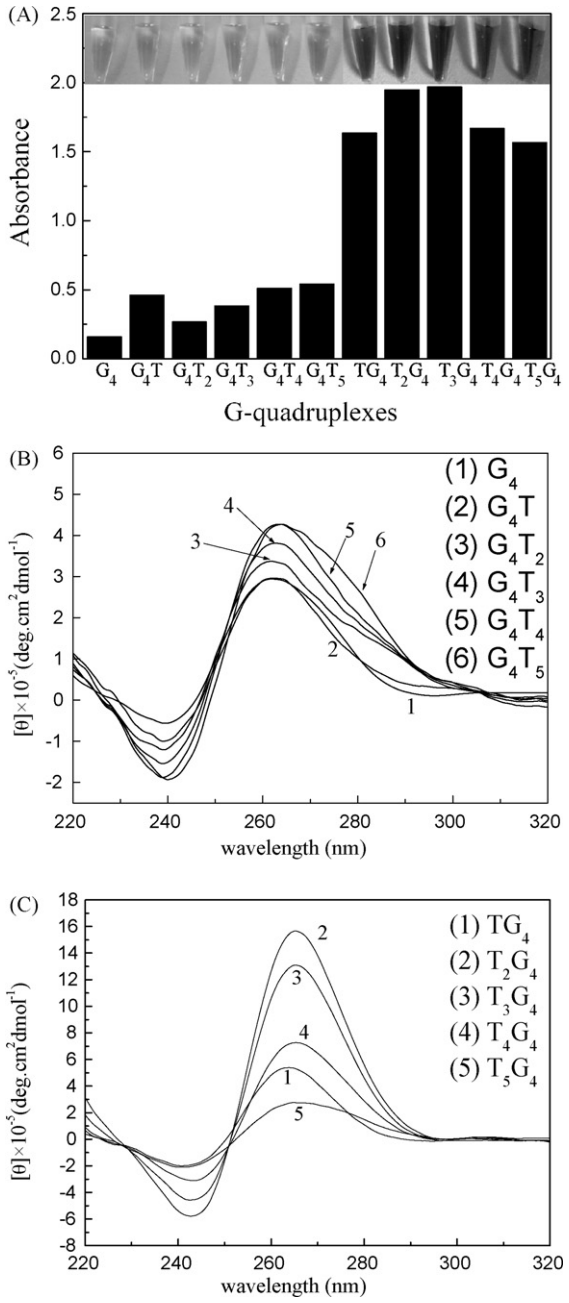


Fig. 2. Oxidation of ABTS by H_2O_2 in the presence of hemin and G_4T_n or T_nG_4 (A), and the CD spectra of G_4T_n (B) and T_nG_4 (C). Corresponding color figures can be found in supporting information.

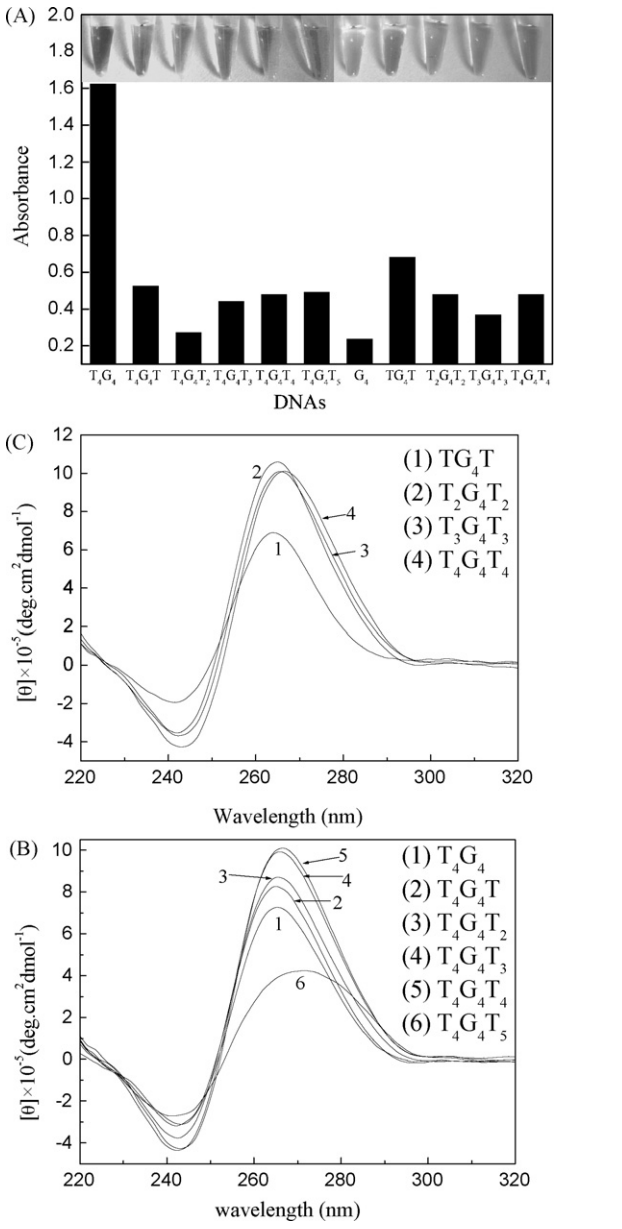


Fig. 3. Oxidation of ABTS by H_2O_2 in the presence of hemin and $T_4G_4T_n$ or $T_nG_4T_n$ (A), and the CD spectra of $T_4G_4T_n$ (B) and $T_nG_4T_n$ (C). Corresponding color figures can be found in supporting information.

although the $T_nG_4T_n$ sequences have slightly higher catalytic activity than G_4, it is much weaker than those of the T_nG_4 sequences ($n = 1$–4).

The CD spectra of both $T_4G_4T_n$ and $T_nG_4T_n$ sequences have a major positive peak around 265 nm with a minimum around 240 nm, indicating that all of the G-quadruplexes formed by these sequences adopt the parallel quadruplex conformation.

On the basis of the results described above, the catalytic activity of the $T_nG_4T_m$ sequences is ranked in the order: $T_nG_4 > G_4T_n \approx T_nG_4T_m$ ($m > 0$) $> G_4$

3.2.3. T_4G_n

The number of quarterts in a G-quadruplex is an important factor in determining the stability of the G-quadruplex. From the results described above, it can be seen that the addition of T nucleotides to the 5′-end of a G tract can provide corresponding G-quadruplexes with strong catalytic activity. So, in this experiment, the position of the T nucleotides was fixed at the 5′-end of the G tract, the number of T nucleotides was fixed at 4, and the number of G nucleotides in the G tract was changed from 3 to 9, and the catalytic activity and CD spectra of the resulting T_4G_n sequences ($n = 3$–9) were compared. As shown in Fig. 4, T_4G_3 has no catalytic activity, whereas each of the other T_4G_n sequences has very strong catalytic activity, which increases as the number of G nucleotides increases from 4 to 6; after that, the catalytic activity reaches a plateau and there is no change as the number of G nucleotides increases.

T_4G_3 did not show any CD signal in the range of wavelengths studied here, implying that it cannot form a G-quadruplex structure. Under the same conditions, as the CD spectra display a positive peak around 265 nm with a minimum around 240 nm, the T_4G_4–T_4G_9 sequences can form a typical parallel G-quadruplex structure.

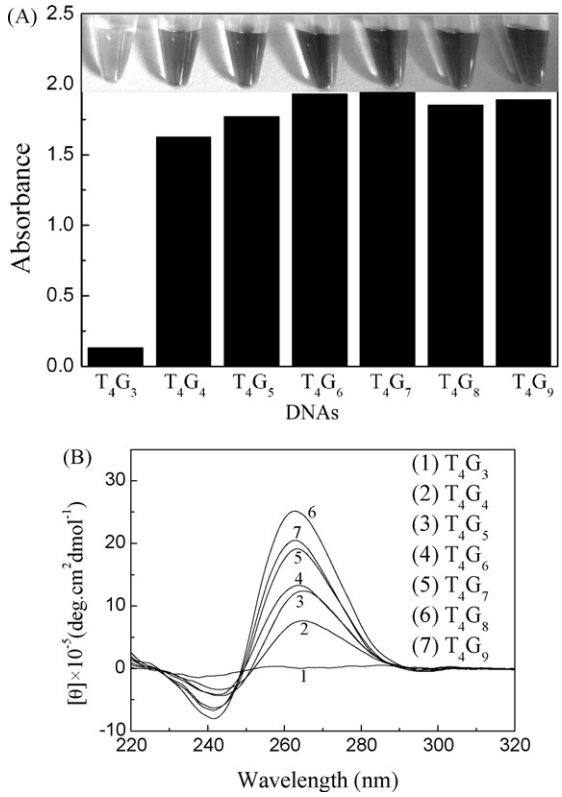


Fig. 4. Oxidation of ABTS by H_2O_2 in the presence of hemin and the T_4G_n (A), and the CD spectra of T_4G_n (B). Corresponding color figures can be found in supporting information.

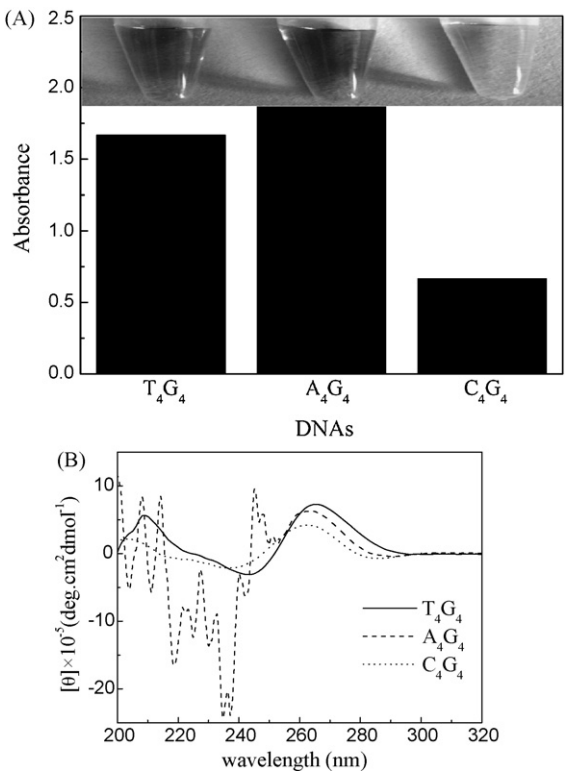


Fig. 5. Oxidation of ABTS by H_2O_2 in the presence of hemin and the X_4G_4 (A), and the CD spectra of X_4G_4 (B). Corresponding color figures can be found in supporting information.

From these results, it can be concluded that: (1) the formation of a stable G-quadruplex structure is an important factor for determining whether T_4G_n sequences can enhance the catalytic activity of hemin; (2) stable intermolecular four-stranded G-quadruplexes cannot be formed when the number of G nucleotides in the G tract is less than 4; (3) in the range of $n = 4$–6, the catalytic activity of the T_4G_n sequences gradually increased as n increased. Any further increase of n has very little effect on the catalytic activity.

3.3. Catalytic activity and structural studies of X_4G_4 (X = T, A or C) sequences

The catalytic activity of the X_4G_4 sequences (X = A, T or G) were compared to investigate the effect of the identity of the nucleotide that was added to the 5′-end of the G tract. As shown in Fig. 5, both T_4G_4 and A_4G_4 have strong catalytic activity, and the activity of A_4G_4 is a little higher than that of T_4G_4. The catalytic activity of C_4G_4 is much lower than that of either T_4G_4 or A_4G_4.

The CD spectrum of T_4G_4 has a positive peak around 265 nm with a minimum around 240 nm, indicating that T_4G_4 adopts a parallel G-quadruplex structure. The CD spectrum of C_4G_4 shows a positive peak at 263 nm, and a negative peak is at 235 nm. The secondary structure of C_4G_4 cannot be determined directly from the CD spectrum. It is well known that the presence of divalent cations (e.g., Mg^{2+}) will aid the formation of duplex DNAs, and the presence of monovalent cations (especially K^+) will aid the formation of G-quadruplex structures. Under the buffer conditions used here (0.8 mM Mg^{2+}; 16 mM K^+), both duplex and G-quadruplex structures may be formed, but only the G-quadruplex DNA can enhance the catalytic activity of hemin. Therefore, the catalytic effect of the C_4G_4 sequence is smaller than that of either T_4G_4 or A_4G_4. The CD spectrum of the A_4G_4 sequence has a positive peak at 263 nm, but fluctuates sharply at short wavelengths, so it is difficult to identify the presence of the G-quadruplex structure. Considering that no base-pair can be formed between A and G, it is very possible that the A_4G_4 sequence will adopt the intermolecular parallel G-quadruplex structure. Considering that two hydrogen bonds may be formed between T and G, and the stability of the T:G mismatch is the highest of all base mismatches, the possibility of the formation of the G-quadruplex structure for A_4G_4 is even higher than that for T_4G_4. That is to say, the possibility of the formation of G-quadruplex structures for the three sequences follows the order: $A_4G_4 > T_4G_4 \gg C_4G_4$, which is quite consistent with the results of catalytic activity studies.

3.4. The "acid–base transition" of the DNA–hemin complexes

Recently, Travascio et al. demonstrated that the high catalytic activity of PS2.M may be a result of the reduction of the acidity of the bound hemin cofactor (e.g., a water molecule coordinated to the iron atom of the hemin that is bound to the DNAzyme scaffolds) [16]. Here, the acid–base titrations for hemin and DNA–hemin complexes were also followed by monitoring the absorption curve at various pH values, and corresponding pK_a values could be derived from A_{360}/A_{404}–pH plots. As shown in Fig. 6 (and see supporting information Fig. S6), regardless of hemin or the DNA–hemin complexes, the absorbance ratio of A_{360}/A_{404} increases greatly with increasing pH, and pK_a can be determined from the position of the maximum of the first derivative of the transition curves. According to the relationship between catalytic activities and pK_a values (Table 2), hemin and the DNA–hemin complexes that were studied can be clearly divided into two groups (Fig. 7). Hemin has a pK_a value of 4.36 ± 0.15, which is very similar to those of the DNA–hemin complexes (pK_a < 6.50) whose catalytic activities are comparable to hemin itself, but is much lower than those of the DNA–hemin complexes (pK_a > 7.20) that have much higher catalytic activities. Our results are gen-

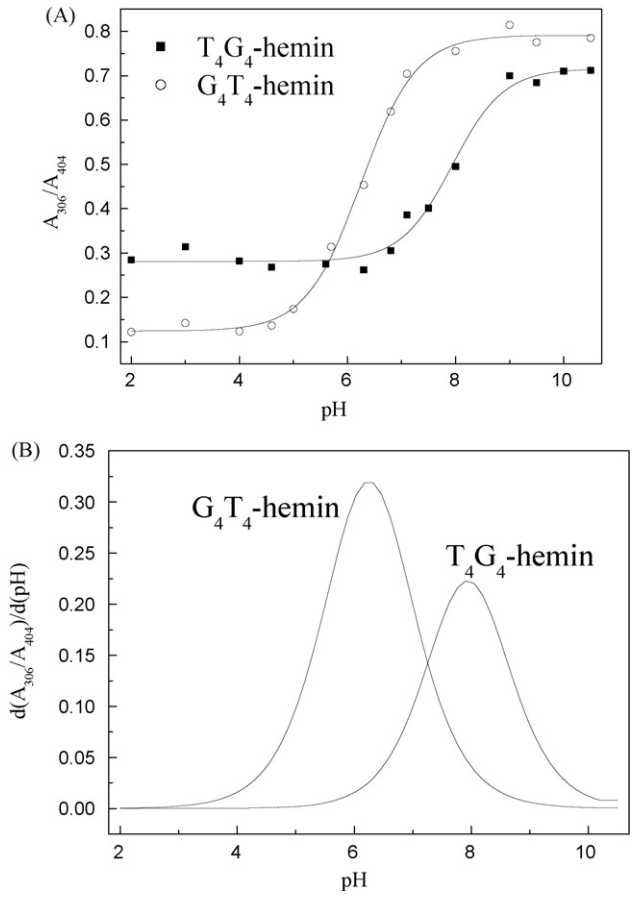


Fig. 6. Spectrophotometric titration to determine the p*K*a of the water molecule ligated to T_4G_4–hemin and G_4T_4–hemin complexes from the ratio of absorptions at 360 and 404 nm. (A) Titration plots; (B) first derivative of the titration plots.

erally consistent with the conclusion drawn by Travascio et al. It is noteworthy that the pK_a values of T_nG_m–hemin complexes are much higher than those of G_4T_n–hemin and $T_nG_4T_m$–hemin complexes, suggesting that the acidicity of the bound hemin cofactor may be an important factor in determining the abilities of $T_nG_mT_p$ sequences to enhance the catalytic activity of hemin. More experiments are needed to elucidate why the addition of T residues to different sides of the G_4 sequence results in very different pK_a values for the corresponding DNA–hemin complexes.

Table 2
Derived pK_a values for the acid-base transitions of various hemin complexes.

Enzyme (hemin complex)	pK_a	Catalytic activity
Hemin	4.36 ± 0.15	Very low
PS2.M–hemin	8.63 ± 0.08	High
Apt–hemin	4.80 ± 0.12	Very low
Hum21–hemin	5.38 ± 0.12	Low
Oxy12–hemin	5.48 ± 0.12	Low
Hum12–hemin	5.33 ± 0.25	Low
TG_4–hemin	7.19 ± 0.06	High
T_3G_4–hemin	7.46 ± 0.05	High
T_4G_4–hemin	7.94 ± 0.12	High
T_4G_6–hemin	8.03 ± 0.12	High
T_4G_9–hemin	7.69 ± 0.11	High
G_4T–hemin	5.41 ± 0.37	Low
G_4T_3–hemin	6.01 ± 0.05	Low
G_4T_4–hemin	6.25 ± 0.05	Low
TG_4T–hemin	6.45 ± 0.06	Low
$T_3G_4T_3$–hemin	6.11 ± 0.08	Low
$T_4G_4T_3$–hemin	6.34 ± 0.09	Low
$T_4G_4T_5$–hemin	6.29 ± 0.08	Low
A_4G_4–hemin	8.08 ± 0.10	High

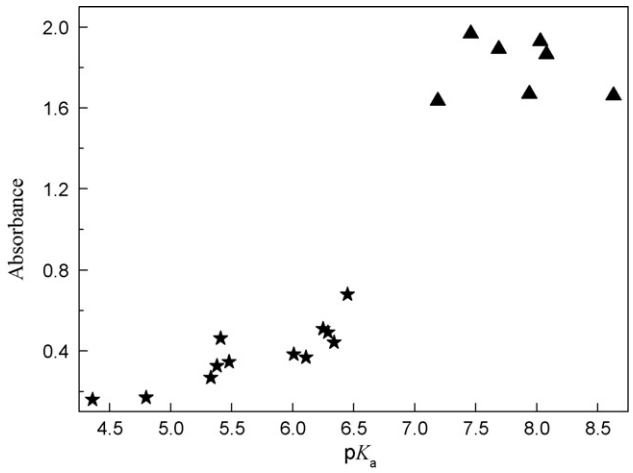
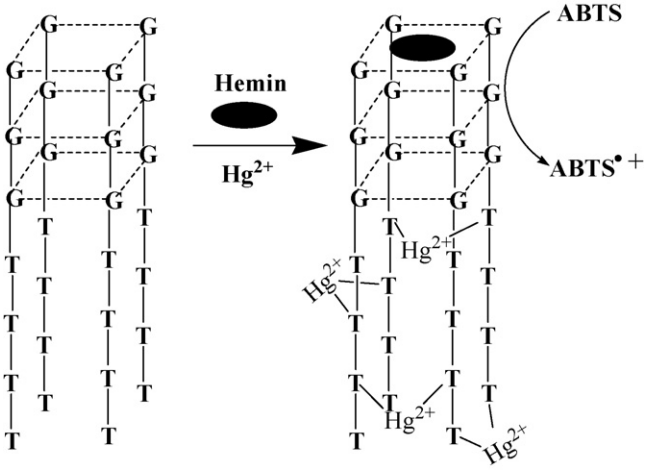


Fig. 7. The relationship between catalytic activities versus pK_a values. The catalytic activities of hemin and the DNA–hemin complexes were represent as the absorption intensities for the reaction solutions of ABTS oxidation by H_2O_2.

3.5. Application in Hg^{2+} ion detection

Mercury is an important toxic pollutant in the environment, and it is attractive to develop a reliable sensing system for mercury detection. To date, numerous studies concerning Hg^{2+} ion assays have been reported [30]. Many of them are based on the fact that Hg^{2+} ion can bind to two thymine (T) and stabilize T–T mismatches in a DNA duplex. Recently, Li et al. reported a new Hg^{2+} ion detection method utilizing the Hg^{2+}-mediated T–T base pair to destroy the G-quadruplex structure and to inhibit corresponding catalytic activity [31]. Although this method gave a good detection result, from the sensing point of view, this is not a "turn-on" sensor. The results mentioned above indicate that the addition of T nucleotides to the 5′-end of the G-tract can confer enhanced catalytic activity, but the prerequisite is that a stable G-quadruplex can be formed. In the intermolecular G-quadruplex formed by T_nG_m sequences, four T_n tails locate at the 5′-terminals of the G-quadruplex. The addition of Hg^{2+} ion can promote the formation of T–Hg^{2+}–T base pairs. The formation of T–Hg^{2+}–T base pairs may strength the intermolecular G-quadruplexes, resulting in the increase of catalytic



Scheme 2. Intermolecular G-quadruplex-based DNAzyme as sensing platform for colorimetric detection of Hg^{2+} ion.

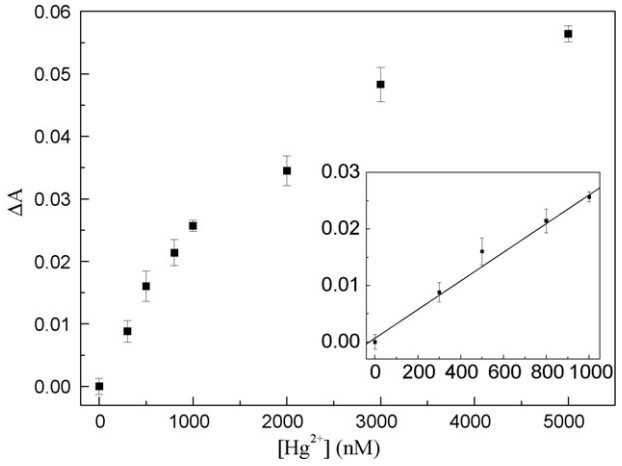


Fig. 8. Hg^{2+} ion concentration-dependent increase in the absorbance at $\lambda = 414$ nm. ΔA represents the difference between A_{414} and the background absorption imparted by hemin catalysis. The insert shows the change of ΔA value as a function of Hg^{2+} ion concentration in the n range of 0–1000 nM. The solid line represents linear fit to the data.

activity (Scheme 2). To test this idea, the catalytic activity of the T_4G_3–hemin complex as a function of Hg^{2+} ion concentration was investigated. As shown in Fig. 8, upon increasing addition of Hg^{2+} ion, the catalytic activity gradually enhanced. After subtracting the background absorption due to the intrinsic catalytic activity of hemin, the ΔA values at 414 nm increased linearly with Hg^{2+} ion concentration up to 1 μM with a detection limit of 52 nM based on 3α/slope.

4. Conclusions

The catalytic activity and the secondary structure of short-stranded $X_nG_mX_p$ sequences (X = A, T or C), especially $T_nG_mT_p$ sequences, were investigated. The results of these experiments suggest that: (1) both intramolecular parallel G-quadruplexes and intermolecular four-stranded parallel G-quadruplexes can enhance the catalytic activity of hemin. (2) When the number of G nucleotides in the G-tract is fixed at 4, the catalytic activity of the $T_nG_4T_m$ sequence follows the order:

$$T_nG_4 > G_4T_n \approx T_nG_4T(m > 0) > G_4$$

That is to say, the addition of T nucleotides to the 5′-end of the G-tract confers greatly enhanced catalytic activity, whereas the addition of T nucleotides to the 3′-end of the G-tract has little effect on the catalytic activity. (3) As for T_4G_n, when the number of G nucleotides in the G-tract is 3, no stable G-quadruplex structure can be formed and the sequence is unable to enhance the catalytic activity of hemin. When the number of G nucleotides exceeds 4, stable intermolecular parallel G-quadruplexes can be formed, and greatly enhanced catalytic activity can be observed. (4) The catalytic activity of X_4G_4 follows the order $A_4G_4 > T_4G_4 \gg C_4G_4$, which may be correlated with the competitive formation of G-quadruplex and duplex structures. (5) The high catalytic activity of hemin in the presence of some short-stranded G-rich sequences may be a result of the reduction of the acidity of the bound hemin cofactor. These studies may help to elucidate the structure–function relationship of peroxidase enzymes and the ways in which a DNAzyme might work to enhance the intrinsic activity of hemin. Also, these studies may be helpful for the development of novel, highly efficient DNAzymes with peroxidase activity. Based on these studies, a "turn-on" Hg^{2+} ion detection method with a detection limit of 52 nM was developed.

Acknowledgment

This work was supported by the National Basic Research Program of China (no. 2006CB705700), the National Natural Science Foundation of Tianjin (no. 08JCZDJC21200), and the Natural Science Foundation of China (no. 20675041).

Appendix A. Supplementary data

Supplementary data associated with this article can be found, in the online version, at doi:10.1016/j.talanta.2009.07.010.

References

[1] A.M. Rojas, P.A. Gonzalez, E. Antipov, A.M. Klibanov, Biotechnol. Lett. 29 (2007) 227.
[2] Y. Ito, H. Hasuda, Biotechnol. Bioeng. 86 (2004) 73.
[3] D. Sen, C.R. Geyer, Curr. Opin. Chem. Biol. 2 (1998) 680.
[4] R.R. Breaker, Science 290 (2002) 2095.
[5] P. Travascio, A.J. Bennet, D.Y. Wang, D. Sen, Chem. Biol. 6 (1999) 779.
[6] P. Travascio, Y. Li, D. Sen, Chem. Biol. 5 (1998) 505.
[7] V. Pavlov, Y. Xiao, R. Gill, A. Dishon, M. Kotier, I. Willner, Anal. Chem. 76 (2004) 2152.
[8] Y. Xiao, V. Pavlov, T. Niazov, A. Dishon, M. Kotler, I. Willner, J. Am. Chem. Soc. 126 (2004) 7430.
[9] T. Li, B. Li, S. Dong, Anal. Bioanal. Chem. 389 (2007) 887.
[10] J. Elbaz, B. Shlyahovsky, I.A. Willner, Chem. Commun. (2008) 1569.
[11] D. Li, B. Shlyahovsky, J. Elbaz, I. Willner, J. Am. Chem. Soc. 129 (2007) 5804.
[12] D.-M. Kong, W. Jing, Y.-E. Ma, H.-X. Shen, Analyst 133 (2008) 1158.
[13] Y. Xiao, V. Pavlov, R. Gill, T. Bourenko, I. Willner, ChemBioChem 5 (2004) 374.
[14] I. Willner, Z. Cheglakov, Y. Weizmann, E. Sharon, Analyst 133 (2008) 923.
[15] M. Deng, D. Zhang, Y. Zhou, X. Zhou, J. Am. Chem. Soc. 130 (2008) 13095.
[16] P. Travascio, D. Sen, A.J. Bennet, Can. J. Chem. 84 (2006) 613.
[17] Y. Li, C.R. Geyer, D. Sen, Biochemistry 35 (1996) 6911.
[18] Y. Li, D. Sen, Nat. Struct. Biol. 3 (1996) 743.
[19] Y. Li, D. Sen, Biochemistry 36 (1997) 5589.
[20] H. Zhu, F.D. Lewis, Bioconjugate Chem. 18 (2007) 1213.
[21] T. Simonsson, Biol. Chem. 382 (2001) 621.
[22] H.-W. Lee, D.J.-F. Chinnapen, D. Sen, Pure Appl. Chem. 76 (2004) 1537.
[23] P.R. Majhi, R.H. Shafer, Biopolymers 82 (2006) 558.
[24] D.-M. Kong, L.-L. Cai, J.-H. Guo, J. Wu, H.-X. Shen, Biopolymers 91 (2009) 331.
[25] S. Paramasivan, I. Rujan, P.H. Bolton, Methods 43 (2007) 324.
[26] D. Monchaud, P. Yang, L. Lacroix, M.-P. Teulade-Fichou, J.-L. Mergny, Angew. Chem. Int. Ed. Engl. 47 (2008) 4858.
[27] A. De Cian, G. Cristofari, P. Reichenbach, E. De Lemos, D. Monchaud, M.P. Teulade-Fichou, K. Shin-Ya, L. Lacroix, J. Lingner, J.L. Mergny, Proc. Natl. Acad. Sci. U.S.A. 104 (2007) 17347.
[28] A. Ambrus, D. Chen, J. Dai, T. Bialis, R.A. Jones, D. Yang, Nucleic Acids Res. 34 (2006) 2723.
[29] K.N. Luu, A.T. Phan, V. Kuryavyi, L. Lacroix, D.J. Patel, J. Am. Chem. Soc. 128 (2006) 9963.
[30] E.M. Nolan, S.J. Lippard, Chem. Rev. 108 (2008) 3443.
[31] T. Li, S.J. Dong, E.K. Wang, Anal. Chem. 81 (2009) 2144.

Talanta 80 (2009) 466–472

Contents lists available at ScienceDirect

Talanta

journal homepage: www.elsevier.com/locate/talanta

Measurement uncertainty in analytical studies based on surface plasmon resonance

Praskovia M. Boltovets, Boris A. Snopok*

V. Lashkaryov Institute of Semiconductor Physics, NAS Ukraine, 41 Nauky Prospect, Kyiv 03028, Ukraine

ARTICLE INFO

Article history:
Received 10 March 2009
Received in revised form 2 July 2009
Accepted 2 July 2009
Available online 10 July 2009

Keywords:
Sensor
Biosensor
Surface plasmon resonance
Sensitivity
Measurement uncertainty

ABSTRACT

The sensitivity of surface plasmon resonance (SPR) transducers depends on the thickness and spatial organization of interfacial structures at their surfaces. This is because the response of the SPR sensor is determined by integrating the distance-dependent refractive index (spatial interfacial architectures), weighted by the square of the electromagnetic field, from zero to infinite distance. The effect of SPR transducer sensitivity variation on the accuracy of SPR analysis is considered. Our quantitative estimation (based on the results of refractometric studies) gave a value for sensitivity variation of about 3% for the formation of a self-assembled thiocyanate layer or a trypsin-soybean trypsin inhibitor surface complex. The estimated accuracy in measured variation (*i.e.*, by 0.01) for the refractive index of the external medium was 3×10^{-4}. This restriction, which follows immediately from the physical mechanism of the SPR phenomenon, should be taken into account when analyzing data obtained with the above technique.

© 2009 Elsevier B.V. All rights reserved.

1. Introduction

The surface plasmon resonance (SPR) phenomenon is a basis of many optical nondestructive analytical techniques [1–5]. Typically, the technique involves the excitation of surface plasmon–polariton waves by a polarized laser beam on a gold film employing the Kretschmann configuration for achieving an attenuated total reflection [6,7]. This effect (that manifests itself as an abrupt drop of reflected light intensity at certain angles or wavelengths in conventional setups) can be easily measured with high precision. The parameters of the SPR plot (*e.g.*, the dependence of reflectivity R *versus* the incidence angle, θ) are modified in the presence of the adsorbed particles, molecules, *etc*. In particular, the binding of an analyte to the sensor surface may be monitored in real time if the analyte has a different refractive index than the bulk solution. This is the basis for SPR sensor applications [6,8]. This method is widely used for the registration of protein adsorption on the surface, protein–protein interactions, reactions of proteins with small molecules, DNA, *etc*. [9–11] using many available commercial single- and multi-channel SPR systems [4].

The main advantage of the SPR technique is possibility of direct registration of surface interactions without any additional procedures or labels [12]. Real time response registration enables the investigation of interaction kinetics and, thereby, tracking of a system's evolution on a nanometer scale [12,13]. This is the result of the fact that the dielectric-metal interface is being probed with high sensitivity because the effective path length is increased as the plasmons, being guided waves, propagate along the surface [14]. The plasmon–polariton wave, which decays exponentially with moving off the surface, has penetration depth approximately equal to half of the incident wavelength, so the SPR excitation angle depends on environmental optical parameters adjacent to the metal layer. Therefore, the response of the SPR sensor is determined by integrating the distance-dependent refractive index (interfacial particles architectures), weighted by the square of the electromagnetic field, from zero to infinite distance [15,16]. The physical phenomena of surface plasmon resonance is relatively well understood and widely discussed in the literature [6,13,17,18].

In general, an optoelectronic technique measuring parameters depend on interfacial structure in nonlinear manner since evanescent wave distribution at the interface depends strongly on variations in the permittivity within interfacial architectures on a nanometer scale and, consequently, on the presence of different spatial organizations of analyte or other molecules that are introduced [19,20]. Thus, both the interface conditions and the characteristics of the metal film may affect functionality of optoelectronic transducers based on surface effects. In particular, for SPR transducers, parameters of the metal film that support propagation of a guided optical plasmon–polariton mode may influence the sensor's response through variations in the performance characteristics of the instrument [21]. However, in fact, the details of these processes are not fully understood at the present time. Although

* Corresponding author. Tel.: +38 0445255246.
E-mail address: snopok@isp.kiev.ua (B.A. Snopok).

0039-9140/$ – see front matter © 2009 Elsevier B.V. All rights reserved.
doi:10.1016/j.talanta.2009.07.009

the SPR facilities are widely used, there is relatively little information concerning the accuracy of the technique and conditions for its adequate application in routine researches. Most of the latest publications are related to the theoretical estimations [14] and determination of the limit of detection of SPR for specific systems. Several papers have previously addressed some aspects of the quantitative interpretation of SPR signals in terms of structural parameters of adlayers in the so-called linear-response regime [22]. This approach can be efficiently used for the adsorbed films that are thinner than the decay length of the evanescent field [23]. A few papers have addressed the response to thicker films, beyond the linear regime [24,25], but generally theoretically. Also, careful analysis of nonlinearity of SPR calibration plots presented in Ref. [20] cannot be implemented in convential analytical practice because of the necessary estimation a characteristic decay length of the evanescent electromagnetic field at the interface. At the same time, various publications during the last few years have addressed SPR research of bacteria and virus particles, high-molecular weight proteins nanoparticles and so on without any comments regarding accuracy of the measurements, *i.e.*, "closeness of the agreement between the result of measurement and a true value of the measured" [26]. In particular, no experiments have been reported to date in which the role of biofilms has been investigated from the point of measurement uncertainty (the width of a confidence interval for the relative measurements as used here) in SPR analysis. In line with that, the purpose of this paper is to examine critically the accuracy of the SPR measurements in the presence of different interfacial layers, and, in particular, to quantify the uncertainty in the measurement of the refractive index of several binary solutions of glycerol/water with a range of concentration in contact with different sensor surfaces.

First we consider a simple analytical model for surface-type physical transducers with the idealized linear calibration plot. Relative variations (changes of SPR angle and analyte concentration) of the measurement process serve as informative parameters of the model. Then we analyze the methods of determination of the minimum of SPR resonance curve, as well as the procedure for obtaining the calibration equation. After this, we present experimental data on variation of SPR sensor sensitivity in the case of treatment of the gold film surface with a strong oxidizing agent and adsorption of low- and high-molecular compounds onto the film surface. At the end of this work, we give a generalized analysis of the results obtained, as well as estimation of the uncertainty in the SPR measurements that depends on the surface condition and formation of interfacial architectures at it.

2. Experimental

Spectra were acquired on a scanning SPR spectrometer "Plasmon" [1,7,10,27] developed at the V. Lashkaryov Institute of Semiconductor Physics of the National Academy of Sciences of Ukraine (Kyiv). A GaAs laser, $\lambda = 670$ nm, was used as excitation source. Glass plates (refractive index $n = 1.61$) with a 50 nm gold layer evaporated on a 1.5 nm chromium interlayer were fixed at a supporting glass prism ($n = 1.61$) using immersion liquid (polyphenyl ether, $n = 1.6$) [1,10,28]. "Piranha" solution ($1H_2O_2$ (30%):$3H_2SO_4$ (37%), v/v) was used to clean the surface. A solution of sodium thiocyanate, NaSCN (40 μM, Sigma, USA) was prepared, using distilled water, immediately before application [29]. Soybean trypsin inhibitor (STI) (Radomed, Hungary) and trypsin (Radomed, Hungary) were dissolved in distilled water (100 μg/ml) [30]. The refraction coefficients of glycerol solutions in water (2.5–10 vol.%) were determined with a commercial refractometer IRF-23 [31].

Winspall 2.0 software (Max-Planck-Institute for Polymer Research, Mainz, Germany) was used to calculate the SPR curves and approximate the experimental dependences with an optical model within the framework of Maxwell macroscopic approach [6]. To approximate the curves and linear dependences, we applied the standard procedures of OriginPro 7.5 (OriginLab Corporation).

3. A simple model of an SPR transducer with linear calibration equation

A rapid proliferation and diversity of SPR systems has led to a lack of understanding in defining some of their performance criteria. General characteristics of SPR sensors are common to different types of transducers [32,33]. However just the efficiency of SPR sensors for detection the process over the extended interfacial architectures like dextran films or multilayer structures is determined by sensitivity variations in the sensor in the course of measurements. Indeed, for SPR sensors, when a linear calibration is applied it is usually assumed that this calibration does not vary in the course of analysis [34]. However, taking into account the features of evanescent wave distribution at interface (exponential decay of intensity from the surface [35]), it seems reasonable to expect variation of SPR sensors' sensitivity if the interface architecture is changed.

Owing to some discussion regarding the meaning of the analytical sensitivity S [36–38], we note that use IUPAC defines S as the slope of the calibration curve, *i.e.*, $(y–y_0)$ *versus* x, where x refers to the analyte amount, and responses y corrected for a background signal y_0 [26]. The following simple phenomenological model demonstrates how the uncertainty in the measured analyte amount on the surface depends on variation of sensitivity S.

A measurement system is assumed to give an output response, y, for a given value of the input variable of interest, x. Fig. 1 includes two hypothetical calibration plots, depicted by square ("Q") and circle ("C") symbols, with different sensitivities and similar measurement errors (y) for two hypothetical situations on the transducer surface. A fixed measurement error was used in the example for sake of simplicity. The combined effects of the sensitivities and measurement errors can be quantified by projections of the error bars onto the analyte concentration axis (x axis). These projections show that the measurement uncertainty (confidence interval for direct measurements) for the absolute value of x for "C"

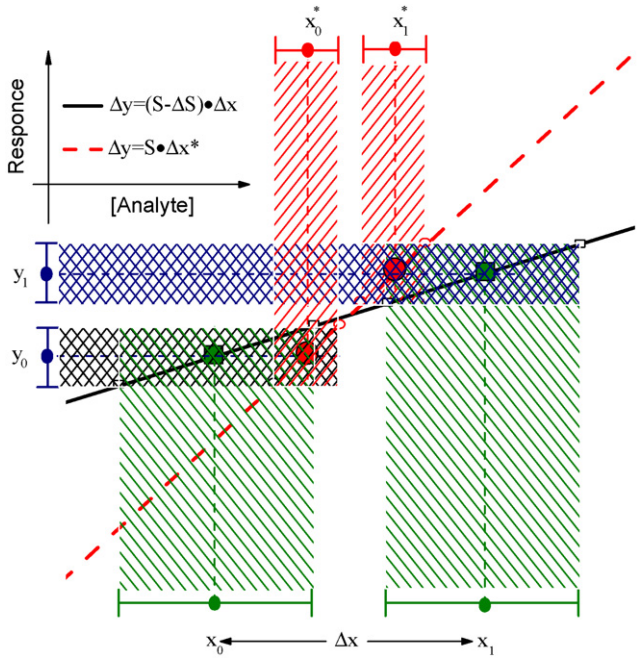


Fig. 1. Effects of sensitivity and measured error on the measurement accuracy.

case is smaller than for "Q" one, the reason being that "C" is more sensitive than "Q". Thus, the increasing of a quantitative resolution in relative measurements for more sensitive sensors is the reason to improve the sensitivity of SPR transducers [39].

Consider the case where the initial sensitivity, S ("C") changes by ΔS ("Q") due to some modification of the surface or formation an interfacial layer (Fig. 1). In this case for the same value of SPR response $\Delta y = y_1 - y_0$, we would determine two different values for the change in refractive index for the same solution in contact with the sensor surface, Δx and Δx^*:

$$\Delta y = S(x_1 - x_0) = S\Delta x, \quad (1)$$

$$\Delta y = (S - \Delta S)(x_1^* - x_0^*) = (S - \Delta S)\Delta x^*. \quad (2)$$

The difference between the determined Δx and Δx^* values is

$$\delta x = \Delta x^* - \Delta x = \left(\frac{\Delta y}{S}\right)\left(\frac{\Delta S}{(S - \Delta S)}\right) = \left(\frac{\Delta y}{S}\right)\left(\frac{\Delta S/S}{(1 - \Delta S/S)}\right). \quad (3)$$

Taking into account Eq. (1), we get

$$\delta x = \Delta x \frac{(\Delta S/S)}{(1 - \Delta S/S)} \quad (4)$$

Eq. (4) makes it possible to estimate directly the absolute (δx) or relative ($\delta x/\Delta x$) error that arises due to variation of transducer sensitivity ΔS. One can see from Fig. 2 that $\delta x/\Delta x$ is rapid-growing function of $\Delta S/S$ because of the asymptote that is approached as $\Delta S \to S$. This fact has to be accounted for when solving the problems of analysis related to estimation of the true value of analyte amount on the surface from the sensor response. To obtain quantitative estimation of the absolute (δx) or relative ($\delta x/\Delta x$) errors one must determine the $\Delta S/S$ value experimentally. To do this, we used the results of analysis of variations of SPR transducer sensitivity under different conditions at the gold film surface obtained from the refractometric measurements.

4. Results and discussion

To apply SPR sensing for the monitoring of interfacial processes, some method must be available to extract from raw SPR data a quantitative measurement of the surface concentration [9,38] of the adsorbed layer or refractive index of the "infinitely thick" medium in contact with the sensor surface. For example, the analyte surface concentration Γ (surface coverage, in units of mass/area, *i.e.*, ng/mm^2) can be calculated from experimental data (the change in the thickness d and the refractive index Δn near the surface) *via* a linear approach for homogeneous or inhomogeneous surface-adsorbed layers or for low-concentration solutions [38,39]. However, despite the wide application of SPR, no simple yet general method has been proposed for transformation the SPR response in some variation of refractive index. The reason for that lies in the complex procedure for SPR calibration plot measurement that generates compounding errors and use some assumptions regarding the form of fitting functions. Indeed, the measurement accuracy of the analyte surface concentration, *etc*. depends on:

1) *the instrumental errors* related to the determination of the value of
   a) incident angle, and
   b) reflection intensity;
2) *the data processing errors* related to
   a) the effectiveness of the asymmetric SPR curve-fitting procedure for determination the curve minimum, and
   b) the standard errors indicating the deviation from linearity of the calibration plot obtained using the values of SPR curve minima, and
3) *the truncation errors* related to
   a) the assumption of linear calibration plot for SPR sensor, and
   b) the values of the refractive index increment [38] or other constants used for conversion procedure.

It is necessary to stress that the errors arising from modern instrumental facilities (1a and 1b) are at least an order of magnitude less than one related to (2). The value of constants (3b) results in systematic errors in surface concentration of analyte. Thus, the main sources of uncertainly in SPR measurements arising from both data processing and, possibly, assumption of linearity for the calibration plot.

4.1. Selection curve-fitting equation for the accurate determination of SPR resonance angle

In real time SPR measurements various procedures based on analytical functions for finding the resonance angle in the SPR curve are applied, for example, polynomial approximation, centroid algorithms, Lorentzian approximation, *etc*. [40]. Most used methods are just within "minima hunt" techniques in the SPR curve. Procedures based on multilayer Fresnel equations are much more time-consuming and are unacceptable in real time measurements. To determine the position of minimum in the SPR curve $R(\theta)$ (Fig. 3) we used the following approaches that are applied most often:

I. direct determination of the absolute minimum in the curve $R(\theta)$,
II. calculation of the minimum by approximating the curve as a parabola $(\theta - \theta_{SPR})^2$ (ii) or third-order polynomial $(a_1\theta^3 + a_2\theta^2 + a_3\theta + a_4)$ (iii) in the vicinity of the minimum of angular dependence $(\theta_{SPR} \pm \Delta\theta)$,
III. numerical simulation of $R(\theta)$ using an optical model using multilayer Fresnel equations.

One should note that accuracy of determination of the minimum increases with the number of the experimental points used for calculation (N) because stochastic noise decreases as $\sqrt{N}$ if approximating function has been chosen adequately. Therefore, choosing the widest possible approximation range enables one to obtain the most valid estimates for θ_{SPR}.

The effectiveness of the approximation methods for θ_{SPR} determination was examined using the curve-fitting routine of OriginPro 7.5. Origin's nonlinear regression method is based on the Levenberg–Marquardt algorithm and is the most widely used algorithm in nonlinear least squares fitting. Shown in Fig. 3b are typical examples of approximation of angular dependence of the SPR

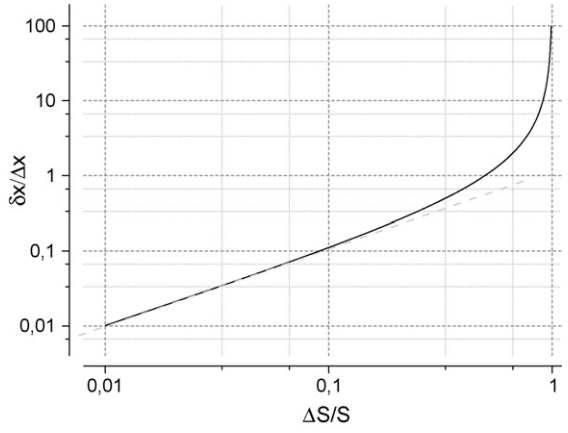


Fig. 2. Relative error of Δx determination, $\delta x/\Delta x$, as function of relative variation of transducer sensitivity, $\Delta S/S$. Dashed line indicates the semilinear region of the curve.

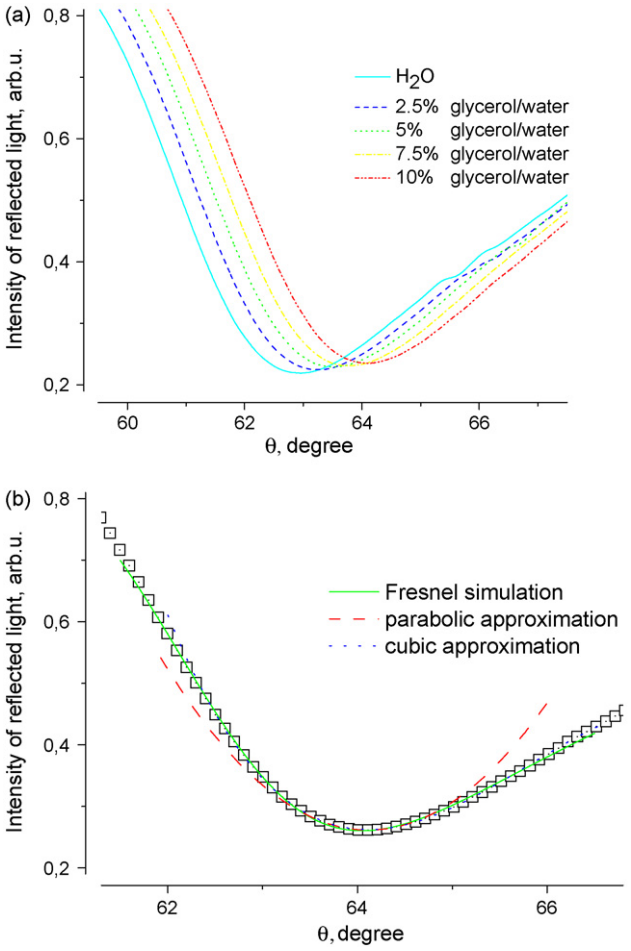


Fig. 3. Measured SPR response for an untreated gold surface (a) and an example of approximation by different functions for sample with 10 vol.% of glycerol in water (b).

reflection curve for a sample of glycerol solution in water (volume concentration of 10.0%). The parabolic approximation of angular dependence is adequate only in a narrow angle range (no wider than $\theta_{SPR} \pm 0.5^\circ$) near the minimum, owing to asymmetry of $R(\theta)$ about θ_{SPR}. As the range is increased up to $\theta_{SPR} \pm 2.0^\circ$, approximation with a third-order polynomial is adequate. The best results are given by numerical simulation of the response curve based on an optical model for interface structure within the framework of the Maxwell macroscopic approach.

The numerical characteristics of the approximation procedure are given in Table 1. The data presented in Fig. 3b and Table 1 enable one to conclude that, to determine θ_{SPR} in the range no more than $\theta_{SPR} \pm 2.0^\circ$, it is reasonable to approximate the minimum with third-order polynomials. Thus, this procedure was used for the analysis that follows. It is necessary to stress that the presented results are relatively common for many different situations including both measurements of solutions and thin interfacial films owing to the ubiquity of SPR curve form for various situations.

4.2. SPR response to bulk solutions: experimental technique of refractometric analysis

For bulk solutions the SPR response is the shift of SPR angle associated with changes in the index of refraction of the medium in contact with the surface of SPR device. Sufficiently accurate refractometric measurements require the absence of the processes of solution components (in our case, binary solutions glycerol/water with a range of concentrations) adsorbing on the surface. In an optimal situation, this usually assumes that the change in SPR angle due to difference in adsorption between different solutions is small compared to the measured shift, which is dominated by changes in the bulk index of refraction of these solutions. To elucidate this problem, we performed a number of methodological experiments (see Fig. 4). In the first set of measurements, the solutions were replaced in series one after another, while in the second set, the surface was washed in distilled water after each sample.

In both series of experiments, the gold film surface was untreated. As expected, the response in both cases was fairly linear over narrow range of refractive index of used solutions (up to 10% of glycerol). Thus, over a narrow range, the response to changes in bulk index of refraction, in the absence of adsorption from the solution, can be approximated as linear. Similar results have been reported repeatedly previously [19,41]. As can be seen from Fig. 4c, the distinction between the results of measurements is within the experimental error (1×10^{-4} for the refractometer and 2×10^{-4} for SPR spectrometer). At the same time, the above results confirm that the adsorption of glycerol on the gold surface is reversible for concentrations of 2.5–10 vol.%. However, to exclude a possible shift of the instrument's baseline, all following experiments were performed with sensor surface washing after each solution.

It should be noted that difference in sensitivity might not be related only to the problems concerning approximation accuracy. To avoid inaccuracies resulting from gold surface nonuniformity and variations of its optical parameters within a chip, the measurements were made at the same place.

4.3. Measured calibration plot for bulk solutions: effect of SPR curve-fitting equation

To check how the type of approximation of the SPR curves affects the parameters of calibration plot, we compared sensitivities S for different approximation techniques. The data presented in Table 1 enable one to conclude that the biggest deviation from linearity (largest standard error and smallest r^2 value) appeared in the calibration plot based on the values determined from the curves' absolute minima (method i). Curves based on the parabolic approximation (method ii) introduced a systematic bias, overestimating the sensitivity compared to other approaches (apparently

Table 1
Comparison of methods used for determination of position of angular dependence minimum when studying linearity of the SPR transducer calibration plot.

Approximation function	r^2 (approximation of angular dependences $R(\theta)$)	Sensitivity (tangent of angle of slope of calibration plot)	r^2 (linearity of calibration curve)
Absolute minimum of angular dependence	–	94.9 ± 7.1	0.994
Parabolic approximation $\theta_{SPR} \pm 0.5^\circ$	0.985–0.994	98.6 ± 2.7	>0.999
Third-order polynomial approximation $\theta_{SPR} \pm 0.5^\circ$	>0.998	93.7 ± 3.6	>0.998
Third-order polynomial approximation $\theta_{SPR} \pm 1.0^\circ$	>0.999	93.0 ± 2.1	>0.999
Third-order polynomial approximation $\theta_{SPR} \pm 2.0^\circ$	>0.998	92.8 ± 1.2	>0.999
Model curve (Fresnel) $\theta_{SPR} \pm 0.5^\circ$	>0.999	92.4 ± 2.4	>0.999
Model curve (Fresnel) $\theta_{SPR} \pm 1.0^\circ$	>0.999	92.9 ± 2.7	>0.999
Model curve (Fresnel) $\theta_{SPR} \pm 2.0^\circ$	>0.999	92.6 ± 3.5	>0.999

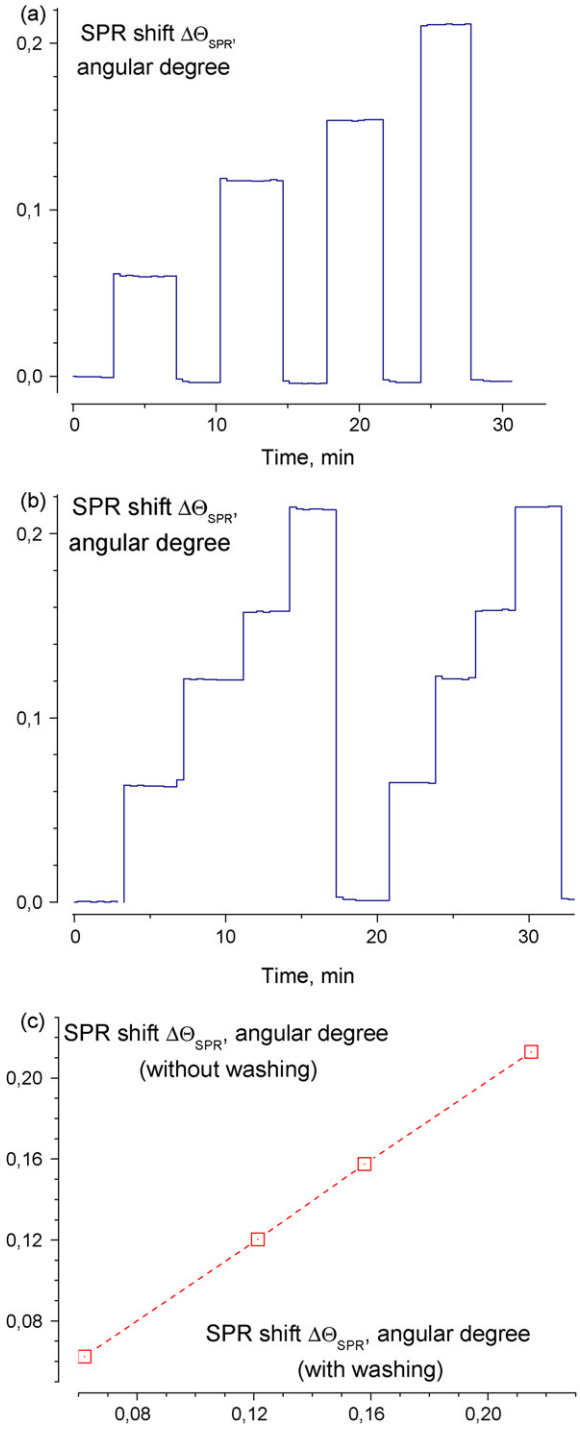


Fig. 4. Variation of SPR minimum position with concentration of glycerol solution for an untreated sensor surface for experiments with (a) and without (b) washing by water before use of each new glycerol solution (with increased concentration: 2.5, 5.0, 7.5 and 10.0 vol.%) and their cross correlation (c). The symbol size indicates the measurement uncertainty.

due to $R(\theta)$ asymmetry). The calibration based on approximating the experimental SPR curves with third-order polynomials (method iii) demonstrate that, in the $\theta_{SPR} \pm 2.0^\circ$ angle range, the sensitivity and linearity of this method are comparable to those obtained with numerical simulation in accordance with the optical model of the system. The last method is the most accurate one in the widest-angle range but requires numerically solving Maxwell's equations for the optical model of the system with known layer parameters.

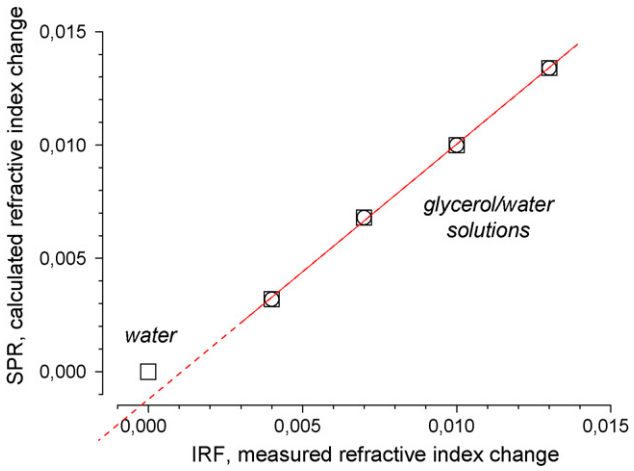


Fig. 5. Comparison of the refraction coefficient values for (different) samples: measured (with refractometer IRF-23) and calculated from SPR data (Winspall 2.0). Numerical simulation of the SPR curves was performed in the region $\theta_{SPR} \pm 2.0^\circ$ using a single-layer optical model: a semi-infinite prism ($1.61 + 0i$), a gold film (with effective thickness of 280 nm and refractive index $0.229 + 4.208i$) and a semi-infinite sample ($n_r + 0i$). The symbol size indicates the measurement uncertainty.

These results show that application of third-order polynomials is the most convenient and adequate procedure for construction of calibration equation for SPR transducers in the case of conventional measurements. Some additional information regarding the procedures for the determination of SPR resonance angle can be found in Ref. [40].

4.4. Calculating the refraction coefficient for external medium from SPR data

Shown in Fig. 5 are the calculated values of indices of refraction for the binary glycerol–water samples. They were obtained using numerical simulation (Winspall 2.0) of the SPR response curves near the minimum ($\theta_{SPR} \pm 2.0^\circ$), within the framework of a single-layer optical model of the system: a semi-infinite prism ($n = 1.61 + 0i$), a gold film with effective thickness of 280 nm ($n_{eff} = 0.23 + 4.21i$) and a semi-infinite sample ($n_r + 0i$)). One can see that the results of calculation (based on SPR curves) agree well with those measured using a standard refractometer. These observations enable us to stress that the application of angular dependence measurements in the analysis of SPR data makes it possible to take into account the features of the spatial distribution of the evanescent wave at the interface. At the same time, one should note that variation of instrument's baseline for different chips mounting in an immersion layer on the supporting prism surface can change the values of calculated parameters. One of the simplest and admissible ways to take into account such variations in the instrument parameters is the use of effective parameters of a thin gold film for numerical calculations.

It should be noted that the refractive indices for water and aqueous solutions of glycerol, measured by the SPR technique or by refractometry, also do not demonstrate linear dependence. The SPR technique overestimates the refractive index for water if we compare one with the linear calibration curve constructed from four values for glycerol solutions (2.5–10 vol.%, $r^2 > 0.999$).

The observed effect seems to be related to a process of nonspecific adsorption of glycerol on the surfaces. This process is reversible but it leads to formation of a dynamic Langmuir adsorption layer on the surface. This is the reason for effective overestimation of the calculated refractive index of the external medium by the SPR.

The above observation shows that one should be careful when choosing calibration solutions. It is desirable to take systems of

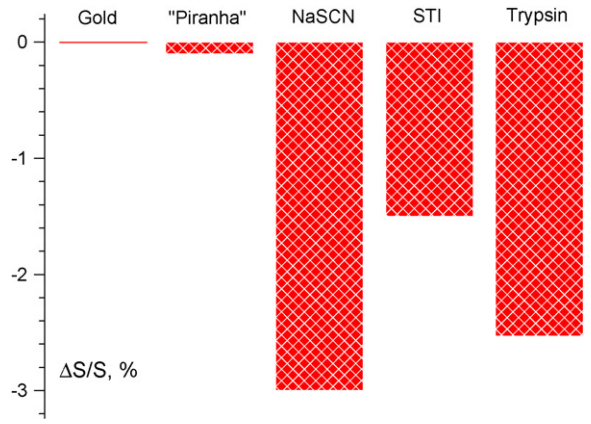


Fig. 6. Variation of SPR transducer sensitivity determined from the refractometric measurements data (5–10 vol.% glycerol in water) for different conditions at the interface: after treatment in "piranha" solution for 5 s. ("Piranha"), modification in NaSCN (4×10^{-5} M) solution for 5 min. ("NaSCN"), after adsorption of STI from 100 μg/ml solution ("STI"), and after interaction with 100 μg/ml trypsin ("Trypsin").

similar composition, with minimal amounts of surface-active components and narrow concentration range.

4.5. Dependence of SPR sensor sensitivity on surface structure formation

To study how the modification of SPR transducer with low-molecular weight compounds and subsequent interfacial biospecific reactions affect the sensitivity, we considered the results of refractometric analysis made with glycerol solutions made with increasing concentrations (5, 7.5 and 10 vol.%), washing the sensor after each measurement. For all the approximation methods, r^2 was over 0.998 and the standard error was less than 3%.

The results were obtained for the following surfaces: (1) an untreated gold surface without any additional molecular layers; (2) a gold film treated with an oxidizing etchant ("piranha" solution); (3) surface 1 modified with a NaSCN (4×10^{-5} M) solution; (4) surface 1 after STI (100 μg/ml) immobilization; and (5) surface 4 after interaction of immobilized STI with trypsin of the same concentration. It was shown (Fig. 6) that, in all cases, sensitivity variation depended on surface pretreatment.

It is necessary to stress that the variations of analysis sensitivity are of the same order as the standard error of S determination (2–3%). At the same time, the following two features are observed in the data set presented in Fig. 6. First is that formation of a thiocyanate layer on the gold film results in considerable sensitivity variations. This seems reasonable because the properties of gold film – the carrier of plasmon oscillations – change near the maximum of the electric field at the surface. Second is the reduction of analytical sensitivity as the thickness of a protein layer on the surface grows (such as in the case of the formation of an initial STI layer and then its complex with trypsin). This effect results from a decrease in the overlap area of the evanescent wave field and the sample (in this case, the external medium) owing to formation of a dielectric layer at the interface as discussed above [42]. The absence of any effect of treatment in "piranha" solution (a few seconds' exposure to minimize gold etching) on refractometric sensitivity seems to be because we used freshly prepared gold samples for analysis that should have only minimal organic surface contamination.

5. Some concluding remarks

The experimental variation of SPR transducer sensitivity (about 3%) at formation of interfacial biospecific architecture based on two proteins (molecular mass of about 20–25 kDa, diameter of several nanometers) enables one to estimate the measurement uncertainty of refractive index variation at the interface when performing analytical studies. The value obtained is, of course, the lower limit for the SPR transducer sensitivity variation because it does not take into account the accuracy in the refractive index based on refractometric measurements (2–3%). Therefore, the total error of sensitivity determination will be bigger owing to convolution of these factors. This fact is of particular importance when comparing the results of a series of experiments obtained with different SPR transducers as well for multilayer measurements.

Eq. (4) enables one to estimate the absolute measurement uncertainty arising at Δx measurements with the SPR technique. For instance, if the sample's refractive index is changed by 0.1 (Δx) and the sensitivity changes by 3% (say, due to formation of an interfacial protein structure), then the absolute error δn (δx) will be about 3×10^{-3}, and at $\Delta x = 0.01$, it will be $\delta x = 3 \times 10^{-4}$. One should take into account that sizes of both STI and trypsin are considerably below those of different specific immunoglobulins most often used for analysis. Therefore, the above values are lower limits for the error in determination of the refraction coefficient of external medium with the SPR technique. It is of interest that the estimated error we calculate is larger than the traditionally used value (about 10^{-4}) for variation of the refraction coefficient of water at temperature change by 1 K [43].

All these restrictions enable one to conclude that parameters of most of the present-day commercial SPR spectrometers are better than the above estimates. Therefore, we believe that further development of the SPR technique should involve not only increasing the sensitivity of optoelectronic transducers (which facilitates only better quantitative resolution of the method) but also developing the simple procedures for unification and standardization of the SPR chips. Moreover, it seems reasonable to apply various methods for initial signal amplification using selective agents (of biological [44] as well as inorganic [45] nature), analytical procedures [46], biochemical reactions [47] or even fluorescent labels [15,16] or light scattering techniques [2,20].

Acknowledgements

The authors wish to thank V.Lyapin and C.Blanford for helpful comments and help preparing this manuscript. National Academy of Sciences of Ukraine supported this work.

References

[1] P.M. Boltovets, B.A. Snopok, V.R. Boyko, N.S. Dyachenko, Yu.M. Shirshov, J. Virol. Methods 121 (2004) 101–106.
[2] A. Savchenko, E. Kashuba, V. Kashuba, B. Snopok, Anal. Chem. 79 (2007) 1349–1355.
[3] D.R. Shankaran, K.V. Gobi, N. Miura, Sens. Actuators B 121 (2007) 158–177.
[4] R. Mukhopadhyay, Anal. Chem. 77 (2005) 313A–317A.
[5] M. Seidel, R. Niessner, Anal. Bioanal. Chem. 391 (2008) 1521–1544.
[6] H. Raether, Surface Plasmons on Smooth and Rough Surfaces and on Gratings, Springer-Verlag, Berlin, 1985.
[7] B.A. Snopok, K.V. Kostyukevych, O.V. Rengevych, Yu.M. Shirshov, E.F. Venger, I.N. Kolesnikova, E.V. Lugovskoi, Quantum Electron. Optoelectronics 1 (1998) 121–134.
[8] T.R. Barlas, N.L. Dmitruk, N.V. Kotova, O.I. Mayeva, V.R. Romanyuk, Superlatices Microstruct. 38 (2005) 130–141.
[9] B. Snopok, E. Kostukevich, Anal. Biochem. 348 (2006) 222–231.
[10] B.A. Snopok, P.N. Boltovets, F.J. Rowell, Theor. Exp. Chem. 42 (2006) 210–216.
[11] A. Savchenko, M. Yurchenko, B. Snopok, E. Kashuba, Mol. Biotechnol. 41 (2008) 270–277.
[12] W. Barnes, J. Opt. A 8 (2006) S87–S93.
[13] W. Barnes, A. Dereux, T. Ebbesen, Nature 424 (2003) 824–831.
[14] E.M. Yeatman, Biosens. Bioelectron. 11 (1996) 635–649.
[15] S. Ekgasit, C. Thammacharoen, W. Knoll, Anal. Chem. 76 (2004) 561–568.
[16] S. Ekgasit, F. Yu, W. Knoll, Sens. Actuators B 104 (2005) 294–301.
[17] J. Homola, Chem. Rev. 108 (2008) 462–493.
[18] R. Marx, C. Lowe, D. Cullen (Eds.), Handbook of Biosensors and Biochips, Willey and Sons, NY, 2007.

[19] L.S. Jung, C.T. Campbell, T.M. Chinowsky, M.N. Mar, S.S. Yee, Langmuir 14 (1998) 5636–5648.
[20] A. Savchenko, E. Kashuba, V. Kashuba, B. Snopok, Sens. Lett. 6 (2008) 705–713.
[21] B.A. Snopok, K.V. Kostyukevich, S.I. Lysenko, P.M. Lytvyn, O.S. Lytvyn, S.V. Mamykin, S.A. Zynyo, P.E. Shepelyavyj, E.F. Venger, S.A. Kostyukevich, Yu.M. Shirshov, Quantum Electron. Optoelectronics 4 (2001) 56–69.
[22] X. Caide, S.-F. Sui, Sens. Actuators B 66 (2000) 174–177.
[23] E. Stenberg, B. Persson, H. Roos, C. Urbaniczky, J. Colloid Interf. Sci. 143 (1991) 513–526.
[24] B. Liedberg, I. Lundström, E. Stenberg, Sens. Actuators B 11 (1993) 63–72.
[25] W. Lukosz, Biosens. Bioelectron. 12 (1997) 175–184.
[26] R.P. Buck, E. Lindner, Pure Appl. Chem. 66 (1994) 2527–2537.
[27] G.V. Beketov, Yu.M. Shirshov, O.V. Shynkarenko, V.I. Chegel, Sens. Actuators B 48 (1998) 432–438.
[28] B.A. Snopok, K.V. Kostyukevich, G.V. Beketov, S.A. Zynio, Yu.M. Shirshov, E.F. Venger, S.V. Verevka, Quantum Electron. Optoelectronics 3 (2000) 59–69.
[29] P.M. Boltovets, B.A. Snopok, Yu.M. Shirshov, N.S. Dyachenko, Rep. Natl. Acad. Sci. 11 (2001) 137–144.
[30] P.M. Boltovets, S.V. Verevka, N.S. Dyachenko, B.A. Snopok, Yu.M. Shirshov, Ukrainian Biochem. J. 74 (2002) 71–75.
[31] N.P. Yevlampieva, B. Dardel, P. Lavrenko, R. Deschenaux, Chem. Phys. Lett. 382 (2007) 32–40.
[32] D.R. Thevenot, K. Tóth, R.A. Durst, G.S. Wilson, Pure Appl. Chem. 71 (1999) 2333–2349.
[33] J. Inczedy, T. Lengyel, A.M. Ure, IUPAC Compendium of Analytical Nomenclature, Blackwell Science, Oxford, 1998.
[34] S. Chah, M.R. Hammond, R.N. Zare, Chem. Biol. 12 (2005) 323–328.
[35] M.H.F. Meyer, M. Hartmann, M. Keusgen, Biosens. Bioelectron. 21 (2006) 1987–1990.
[36] R. Ekins, P. Edwards, Clin. Chem. 43 (1997) 1824–1831.
[37] S. Manghani, J. Ramsden, J. Biol. Phys. Chem. 3 (2003) 11–17.
[38] V. Ball, J. Ramsden, Biopolymers 46 (1998) 489–492.
[39] H.L. Pardue, Clin. Chem. 43 (1997) 1831–1837.
[40] K. Kurihara, K. Nakamura, K. Suzuki, Sens. Actuators B 86 (2002) 49–57.
[41] B. Liedberg, C. Nylander, I. Lundström, Biosens. Bioelectron. 10 (1995) I–IX.
[42] J. Homola, Anal. Bioanal. Chem. 377 (2003) 528–539.
[43] I.T. Kim, K.D. Kihm, Opt. Lett. 32 (2007) 3456–3458.
[44] B. Nguyen, F.A. Tanious, W.D. Wilson, Methods 42 (2007) 150–161.
[45] S.V. Kolotilov, P.N. Boltovets, B.A. Snopok, V.V. Pavlishchuk, Theor. Exp. Chem. 42 (2006) 211–216.
[46] A. Zybin, D. Boecker, V.M. Mirsky, K. Niemax, Anal. Chem. 79 (2007) 4233–4236.
[47] Y. Li, H.J. Hye, R.M. Lee, Anal. Chem. 79 (2007) 1082–1088.

Talanta 80 (2009) 473–478

Contents lists available at ScienceDirect

Talanta

journal homepage: www.elsevier.com/locate/talanta

Nir-chemical imaging study of acetylsalicylic acid in commercial tablets

Jordi Cruz [a], Manel Bautista [a], José Manuel Amigo [b], Marcel Blanco [a,*]

[a] Unidad de Química Analítica, Departamento de Química, Facultad de Ciencias, Universitat Autónoma de Barcelona, 08193 Bellaterra, Barcelona, España, Spain
[b] Department of Food Science, Quality & Technology, University of Copenhagen, Rolighedsvej 30, DK-1958 Frederiksberg-C, Denmark

ARTICLE INFO

Article history:
Received 24 March 2009
Received in revised form 30 June 2009
Accepted 2 July 2009
Available online 10 July 2009

Keywords:
NIR-CI
Hyperspectral imaging
Acetylsalicylic acid
Aspirin tablets
MCR-ALS

ABSTRACT

Near Infrared Chemical Imaging (NIR-CI) is demonstrating an increasing interest in pharmaceutical research since it meets the challenging analytical needs of pharmaceutical quality and may serve as a versatile adjunct to conventional NIR spectroscopy in many fields.

The direct analysis of samples by using hyperspectral imaging techniques, which provide a NIR spectrum in each pixel of the image, generates a big amount of information from one sample. Focusing the interest in pharmaceutical research, several chemometric algorithms are demonstrating their usefulness extracting the relevant information (i.e. quantitative determination of the component in one sample) in tablets with only one sample and without damaging it.

In this work, a quantitative method to analyze different commercial Acetylsalicylic acid tablets is proposed by using Multivariate Curve Resolution-Alternating Least Squares (MCR-ALS) method to the hyperspectral image and without any previous calibration model. For this purpose, a large concentration range of active pharmaceutical ingredient (ASA, Acetylsalicylic acid in this work), between 82% and 12%, was covered depending on the manufacturer. MCR-ALS allowed obtaining a concentration maps for acetylsalicylic acid and therefore, consequent analysis of the ASA distribution in the tablet was developed by using the histograms of the distribution of concentration.

Results certified the good distribution of ASA despite the different origins of the tablets. Moreover, the obtained values of concentration showed a very good concordance with the nominal value of ASA. As a matter of fact, the quality of the results demonstrated the useful of encompassing NIR-CI techniques with MCR-ALS and, consequently, the well development on the production of Acetylsalicylic acid tablets.

© 2009 Elsevier B.V. All rights reserved.

1. Introduction

Once conventional spectroscopy techniques have been demonstrated to be a useful tool in pharmaceutical technology providing a high number of publications praising this technique [1–4], hyperspectral imaging techniques have appeared with the aim not only to cover weak points in conventional spectroscopic techniques but also to extend the knowledge in this field [5–8]. Hyperspectral imaging techniques result especially attractive because of the possibility of providing huge spectral and spatial information of one sample (up to 82,000 spectra per sample) in a short time analysis.

Among all Imaging techniques, Near Infrared-Chemical Imaging (NIR-CI) has been confirmed to be an excellent tool to extract information of high quality of the sample surfaces, being applied in very diverse fields [9–14].

The greatest capacity of NIR-CI technique has drawn attention within the pharmaceutical field where robust methods are continuously demanded to obtain information of the quality of products in all the stages of the manufacturing process. Concerning this aspect, the final assessment of the quality in the final tablet (i.e. obtaining both quantitative and information about the spatial distribution of the components) is becoming a key-point in where NIR-CI is starting to gain importance [15].

Despite the benefits of NIR-CI in pharmaceutical research, there exists still a gap between the acquisition of the hyperspectral image and the treatment of such amount of information. In this sense some multivariate models have been previously used and tested, as Principal Component Analysis (PCA) [5,16,17], providing valuable initial information that helps to focus the further quantitative analysis.

On the other hand, quantitative analysis of pharmaceutical samples using NIR-CI has been performed using techniques as Partial Least Squares Regression (PLS) or PLS-Discriminant Analysis (PLS-DA) [18–21]. However, these techniques require a complete calibration set of samples with the corresponding time consuming until the calibration model is performed and adequately tested.

Concerning the quantification purposes without needing a previous calibration model, Classical Least Squares (CLS) may be presented as an alternative, since CLS only requires the pure spectra

* Corresponding author.
E-mail address: marcel.blanco@uab.cat (M. Blanco).

0039-9140/$ – see front matter © 2009 Elsevier B.V. All rights reserved.
doi:10.1016/j.talanta.2009.07.008

Table 1
Description of the 10 commercial ASA tablets analyzed.

Commercial brand	Nominal ASA (mg)	Diameter (mm)	Tablet weight (g)	Calculated concentration (%)	Main excipient
A.A.S 100	100	82	0.227	44.13	Manitol
A.A.S 500	500	134	0.864	57.88	Manitol
Bayer 500	500	120	0.609	82.06	MCC
Adiro 100	100	72	0.135	73.86	MCC
Adiro 300	300	102	0.409	73.28	MCC
Aspirina C*	400	258	3.235	12.37	–
Dolmen*	500	242	3.399	14.71	–
Aspirine Nicholas	500	120	0.624	80.13	MCC
Bioplak 250	250	70	0.348	71.84	MCC
Bioplak 125	125	100	0.173	72.09	MCC

MCC = microcrystalline cellulose.
* Effervescent tablets.

of all the components of the tablet. This is not a problem in tablets manufacturing, in where the pure spectra of the components are commonly available. Nevertheless, typical phenomena as interaction between analytes, illumination noise or moisture contributions are important drawbacks that may CLS not to be as robust as it can be expected since the pure analytes do not recover the experimental variation [20].

One alternative that does not require a specific calibration set of samples has been recently proposed. Multivariate Curve Resolution-Alternating Least Squares (MCR-ALS) and its augmented version have been successfully applied to extract quantitative information of NIR Chemical Images in pharmaceutical samples [20,22,23]. This augmented version consists in providing information to the initial sample, helping the method to solve the inherent drawbacks of the Chemical Imaging measurement. Therefore, this technique presents a welcome alternative to quantify different components in tablets without needing a specific calibration model.

The objective of this paper is demonstrating the capability of the NIR-CI to extract information of different samples without the application of chemical quantitative information studying the distribution of Acetylsalicylic acid in commercial tablets. For this purpose, commercial tablets of Aspirin from 10 different manufacturers and different content of Acetylsalicylic acid were selected and studied by means of Multivariate Curve resolution-Alternating Least Squares. The consequent distribution of ASA content in each different commercial tablet surface was also studied and compared by using histograms.

2. Experimental

2.1. Reagents and instrumentation

2.1.1. Samples

10 commercial tablets of Aspirin were used in this study and purchased at the pharmacies. The ASA concentration for all the tablets was obtained by dividing the nominal content by the weight for each tablet. The nominal concentrations of ASA in the different tablets covered a wide range of concentration, from 82% to 12%.

The composition of the formulations is unknown and only the information, indicated in the brochure accompanying the different pills each box or in the Vademecum guide [24], has been used in this study. Table 1 shows the main features of each tablet.

Microcrystalline Celullose (MCC) is the main excipient in 6 of the preparations; whereas manitol is the main excipient in the other 2 tablets. *Dolmen* and *Aspirina C* are effervescent tablets and also content ascorbic acid as active component and other known excipients used in the formulation as citric acid, sodium carbonate and sodium bicarbonate anhydrous.

2.1.2. Instrumentation

All tablets were measured obtaining a hyperspectral image of the surface for each sample by using a "Think Spectrally Roda-25" NIR Hyperspectral Imaging Spectrophotometer (*Think Spectrally*, Valencia, Spain). This instrument is a Focal Plane array (FPA) and it is composed by a Liquid Crystal Tunable Filter (LCTF) monochromator

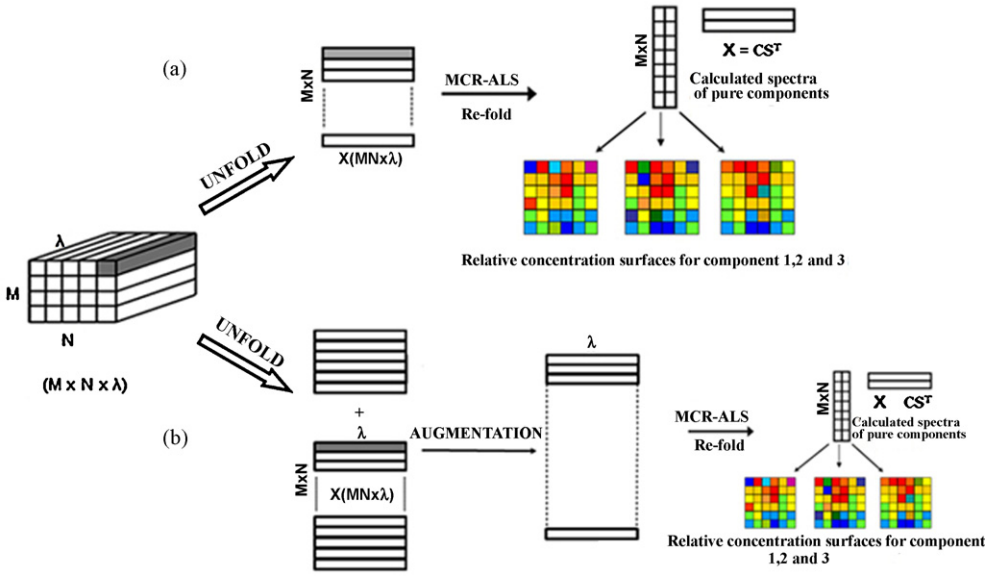


Fig. 1. Scheme of MCR-ALS analysis (a) and augmented MCR-ALS (b) application to the hyperspectral cube.

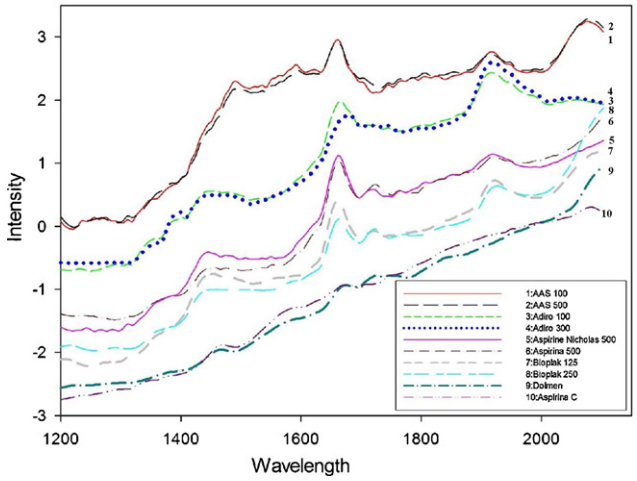


Fig. 2. Average spectra for each tablet after SNV pretreatment. Note: spectra have been shifted up or down in intensity in order to observe significant differences between them.

and a Mercury Cadmium Telluride (MCT) detector which provides a spectral range between 1000 and 2400 nm with 7 nm of spectral resolution and a spatial resolution of 100 μm × 100 μm each pixel.

Three different areas of image were used depending on the size of the tablets: 15 × 15, 8 × 8 and 5 × 5 mm^2. The total time of image acquisition was about 2 min. The lighting to the sample is a very relevant parameter in order to obtain quality images avoiding noise related to a bad illumination. Therefore, 4 halogen lamps were focused to the sample place with a 45° orientation. Prior to the registration of the images the calibration of the instrument was performed by using 6 standards (FOSS *AP-0200 NIR*) covering reflectance values from 99% to 0.2%.

2.1.3. Software

All the spectral pretreatments were applied by using home-made routines programmed in MATLAB code (MATLAB v 7.0, *The MatWorks*, Massachussetts) [18] and they are available via web [25]. MCR-ALS software from the reference [26] working under MATLAB was used.

2.2. Hyperspectral images pretreatment

When a sample is registered with a Hyperspectral image device a three-dimensional array, X ($M \times N \times \lambda$) is obtained being the M and N axis the spatial information and the λ axis represents the spectral information. The three-dimensional structure of the hyperspectral data cube requires a previous unfolding step to a bi-dimensional matrix, adapting the image for further pretreatments or any other method.

Once the images were unfolded several spectral pretreatments were applied to avoid the influence of undesirable phenomena commonly found in NIR measurements. Thus, Standard Normal Variation (SNV), 1st and 2nd Savitzky–Golay Derivatives and also smoothing were applied.

2.3. MCR-ALS in imaging data

Multivariate Curve Resolution-Alternating Least Squares (MCR-ALS) [17,27] decomposes the unfolded matrix X ($MN \times \lambda$) into the product of two matrices, C ($MN \times A$), containing the concentration profiles and S^T ($A \times \lambda$), containing the spectral profiles for each A component (Fig. 1a) (Eq. (1)):

$$X = CS^T + E \quad (1)$$

where E ($MN \times \lambda$) corresponds to the experimental error matrix. The ALS optimization stops when the relative difference in lack of fit (%LOF) values between consecutive iterations is below than a threshold value where e is each mnth element of the residual matrix E, and x is each mnth element of the X matrix. The threshold value

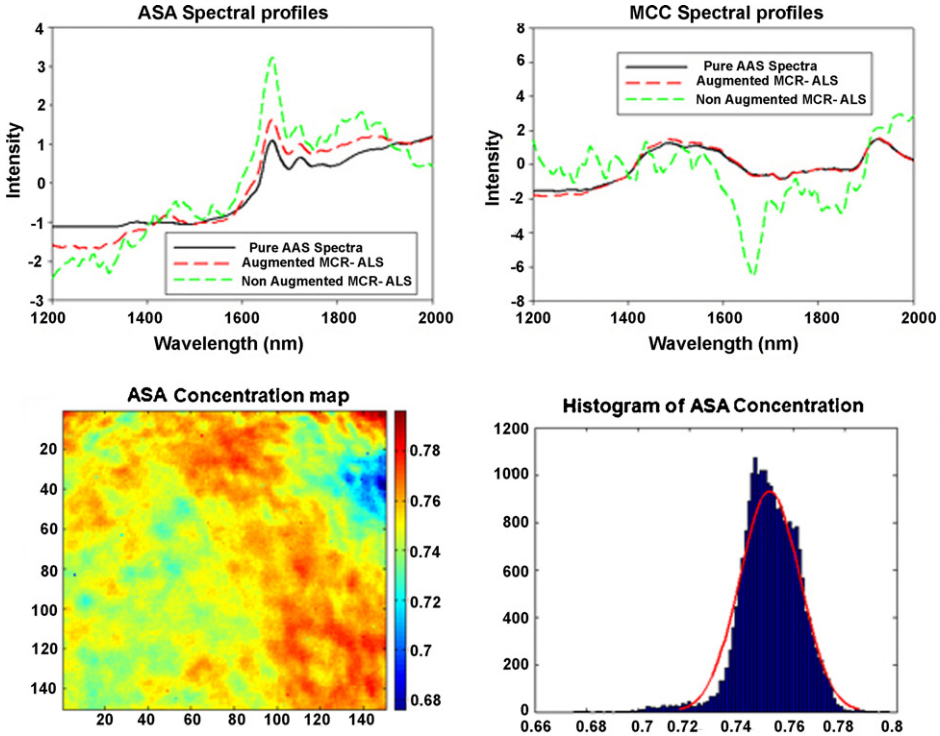


Fig. 3. Augmented MCR-ALS results for one commercial tablet (Aspirine Nicholas 500). (a) Spectral profiles for ASA; (b) spectral profiles for MMC; (c) concentration ASA map; (d) histogram of ASA concentrations.

Table 2
Results obtained for the 10 commercial tablets by using augmented MCR-ALS.

Tablet	Nominal concentration (%)	Augmented MCR-ALS concentration (%)	Difference (%)	Correlation ASA	Correlation MCC	Correlation manitol
A.A.S 100	44.13	53.32	9.19	0.984	–	0.946
A.A.S 500	57.88	54.87	−3.01	0.966	–	0.926
Bayer 500	82.06	81.57	−0.49	0.988	0.998	–
Adiro 100	73.86	76.47	2.61	0.948	0.994	–
Adiro 300	73.28	70.91	−2.37	0.949	0.977	–
Aspirina C*	12.37	12.95	0.58	0.97	–	–
Dolmen*	14.71	16.44	1.73	0.951	–	–
Aspirine Nicholas	80.13	76.96	−3.17	0.963	0.997	–
Bioplak 250	71.84	71.34	−0.5	0.993	0.997	–
Bioplak 125	72.09	67.84	−4.25	0.986	0.994	–

* Effervescent tablets.

of LOF should be selected according to the noise in the spectra (Eq. (2)):

$$\%\mathrm{LOF} = 100 \times \sqrt{\frac{\sum_m^M \sum_n^N e_{mn\lambda}^2}{\sum_m^M \sum_n^N x_{mn\lambda}^2}} \quad (2)$$

where $e_{mn\lambda}$ and $x_{mn\lambda}$ represent each point of the residuals and original three way array, respectively. A very used criterion is to stop the iterations when the difference between two consecutive %LOF values is below 0.1%.

Before starting the iterations, initial estimates are required to help the algorithm to converge to the absolute minimum error. Using the pure spectra of the components (if they are available) as initial estimations becomes one of the most attractive ways of including information about the sample. Other constraints can be used to correctly decompose the matrix when chemical images are analyzed: (1) non-negativity in concentration and/or spectral profiles, which imposes that concentration profiles of the components are supposed to be always positive; and (2) closure, where each pixel can be supposed to accomplish a constant mass balance of 1, representing the totality of the concentration.

However, the quality of the images, which depends on the spatial and also spectral resolution, could be a disadvantage when MCR-ALS is applied since there could be lack of selectivity in the surface of the image. To overcome this problem an alternative has already been formulated: The augmentation of the original sample with

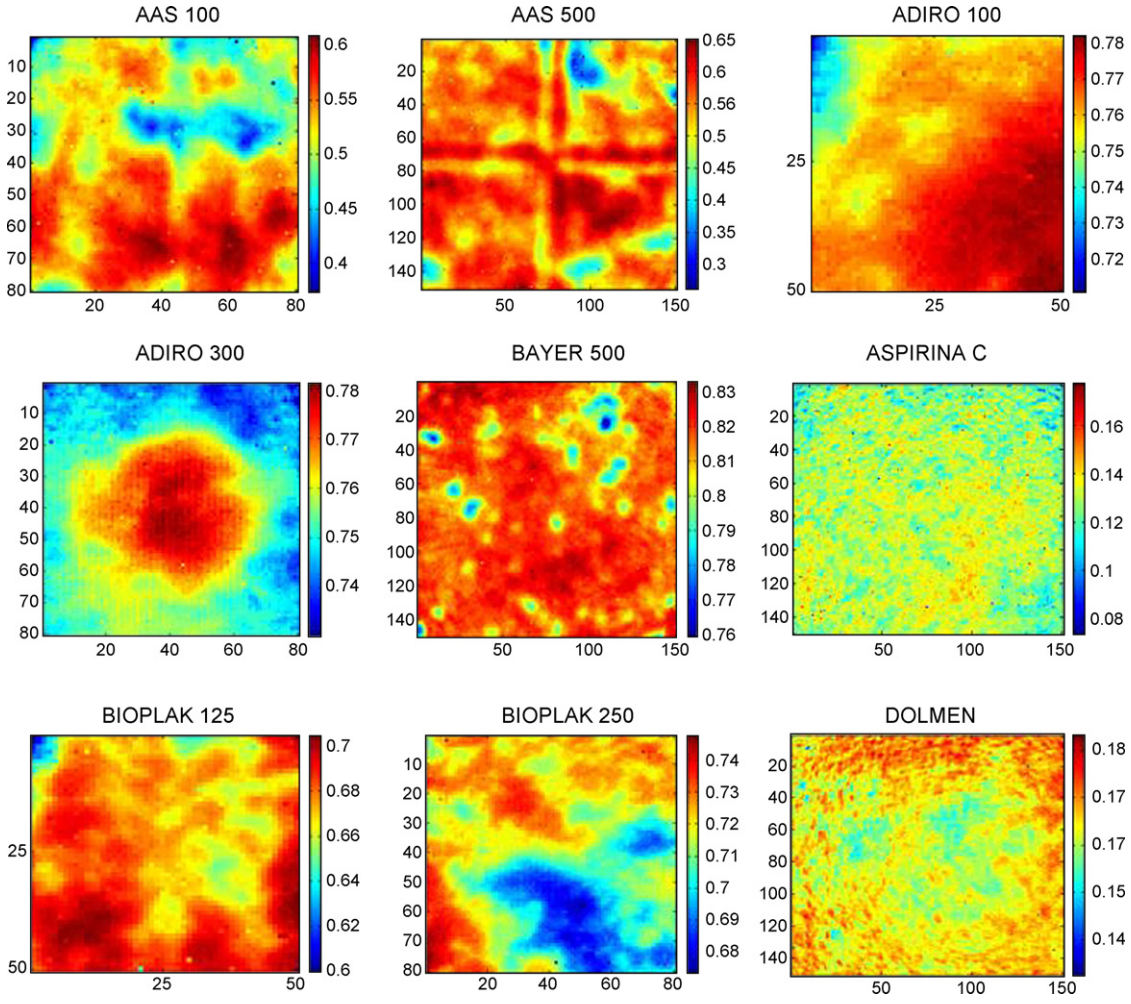


Fig. 4. Concentration maps for ASA obtained by using Augmented MCR-ALS.

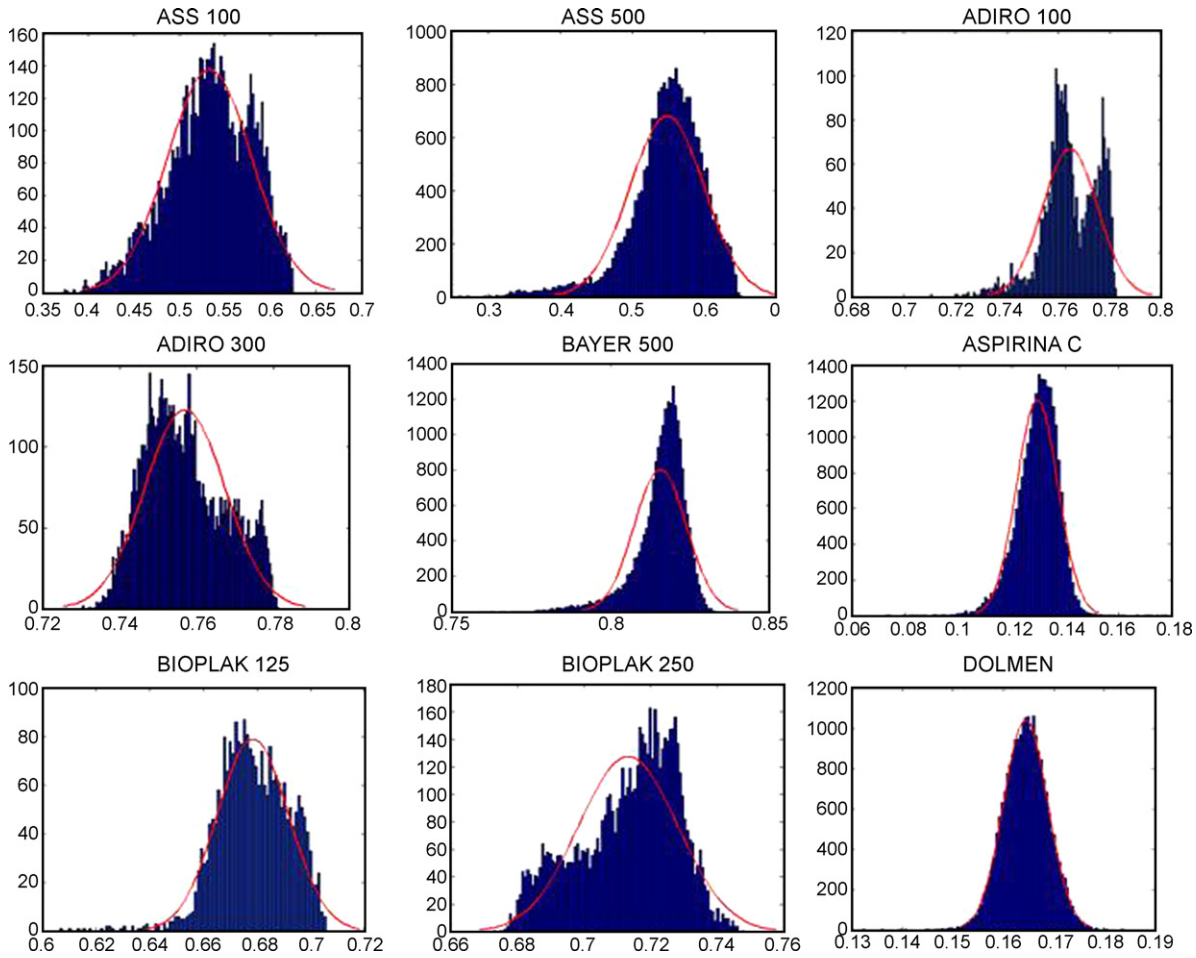


Fig. 5. Histograms for the ASA distribution on the surface tablets.

images of the pure analytes (Fig. 1b). The original idea consisted analyzing several samples simultaneously by augmenting all the images [17]. In the present work, the augmentation is performed by inserting images of pure components as it is shown in Amigo and Ravn [20]. These images of pure components can be easily measured in the same way as the commercial tablet. This approach helps to minimize the problem and offers valuable information to the algorithm.

3. Results and discussion

3.1. MCR-ALS and augmented MCR-ALS analysis

Fig. 2 offers a first impression of the main differences between tablets; these differences are expected since the composition of each tablet depends on the different excipients; however, the spectral band of ASA (around 1680 nm) can be observed in all spectra. Moreover, the tablets *AAS*, *Adiro* and *Bioplak* can be distinguished in depending on the different origins, because they present very similar spectra between them and can be clearly distinguished from other formulations. On the other hand, *Dolmen* and *Aspirina C* mean spectral profiles are very similar despite the fact that they come from different manufacturers.

Several pretreatments were tested with the images, and the combination of SNV and smoothing average with a window size of 7 points provided the best results. Prior to apply MCR-ALS, non-negativity of concentration profiles and closure constraint were applied as constraints. Despite the fact that the tablets were comprised by a different number of components, closure constraint was applied taking into consideration the Active Pharmaceutical Ingredient (ASA) and the main excipients for each of the tablet (MCC or Manitol for 8 tablets and the whole formulation for *Dolmen* and *Aspirina C*). Therefore, the spectral profiles obtained by MCR-ALS will provide information about the goodness of the decomposition of images. Moreover, ASA and the excipients used in this study provided the highest spectral information and were used to perform the MCR-ALS analysis, while the minor excipients may be related with the residual matrix. The pure spectra of the main components were included as initial estimations to start the iterations. The same methodology has been followed when the augmented version of MCR-ALS was applied, including 10 spectra for both analytes (ASA and major excipient) to the unfolded matrix in order to improve the decomposition. To test the MCR-ALS decomposition, %LOF and correlation coefficient between pure spectra and obtained spectral profile were used.

As an example, the %LOF of the MCR-ALS model applied to *Aspirine Nicholas 500* was 2.79%, explaining 99% of variance, indicating the goodness of the model. Moreover, quantitative results from this tablet were accurate compared to the formulation percentage (77.5% for ASA while theoretical value is 80.1%). Nevertheless, the correlation coefficient between the obtained spectral profile for ASA and MMC with the pure spectrum was lower than 1 (0.76 and 0.51 respectively).

To overcome this problem, the augmented version of MCR-ALS was applied. The augmentation was developed by including selective information (10 pure spectra) for each component in the image. The same pretreatments for the image and restrictions were applied. The model obtained with Augmented-MCR

ALS showed quite similar values for %LOF (3.55) and explained variance (99.87%), providing also quite good results in the quantitative analysis. As it can be seen in Fig. 3a and b, the spectral profiles obtained with the augmented version of MCR-ALS perfectly matched with the pure spectra of each compound. Correlations coefficients between these spectra, shown in Table 2, are closed to 1.

The concentration map calculated for ASA using this model showed the distribution on the surface of the tablet and some regions with different concentrations of ASA. At first sight, ASA could be thought not to be well distributed in the tablet. However, the colour scale of this image showed a narrow range, between 0.70 and 0.78. Therefore, the ASA content in each pixel was similar as showed the histogram of the concentration map with a distribution close to a Gaussian distribution (Fig. 3d).

3.2. Results for all the commercial tablets

Table 2 shows the quantitative results for the 10 tablets obtained by using augmented MCR-ALS. The concentration for ASA in the surface of the tablets was similar to the calculated value confirming the goodness of the quantitative analysis. Good results were obtained for almost all of the samples (the spectral correlation between pure ASA spectrum and the spectral profile for ASA in all samples was close to 1 confirming the goodness of the application of augmented MCR-ALS). Tablets with Manitol as the main significant excipient showed not so good results for the determination of ASA content. Looking at their correlation coefficients with Manitol, they were not so close to 1. It might be caused by the influence of another excipient with a high spectral relevance providing information to the image, but avoiding the correct decomposition of the data matrix.

On the other hand, samples where the ASA content was lower could be waited to show bad predictive results. However, the use of all pure spectra allowed obtaining quite good results. Taking into account the fact that closure constraint was applied and in these samples, ASA is not the most relevant spectral compound, the decomposition of the image could have been less successful.

Despite of using all the compounds in the analysis of *Dolmen* and *Aspirina C*, the correlation coefficients obtained were not of high quality. For *Aspirina C* the correlation coefficients obtained were 0.851 for Citric Acid, 0.957 for Ascorbic Acid and 0.995 for Carbonate whereas for *Dolmen* the coefficients obtained were 0.856 and 0.823 for Ascorbic Acid and Carbonate respectively. However, ASA concentration obtained in both tablets was truly similar with real values.

All the concentration maps for ASA are depicted in Fig. 4, where different distributions of the ASA were observed. As already described for the *Aspirine Nicholas 500*, the first impression might be misleading, because of the scale of the colour maps. Therefore, the histogram for each ASA concentration map was depicted in Fig. 5 for better interpretation. Ideally, one would expect a histogram whose values were around the prediction values, and with a narrow variation, implying that the whole surface of the tablet contained the same amount of ASA.

Looking at the histograms of the local concentration it was possible to correctly visualize tablets with best ASA distributions. Thus, the tablets with narrowest ASA distribution were: *Aspirine C*, *Dolmen*, *Bayer 500* (according to the prior conclusion). Although the range for ASA 100 tablet was not as narrow as for the other 3 samples, the distribution of concentration values remained close to a normal distribution. For the other samples, the visual inspection of the concentration maps and the representation of histograms confirmed a less regular distribution for the ASA in the surface.

4. Conclusions

Intact commercial tablets were analyzed by NIR-Chemical Imaging in order to determine de distribution of ASA and its ASA concentrations for each tablet using the MCR-ALS decomposition. The quantification results in combination with the spectral profiles obtained provided information about of the 10 commercial tablets quality.

MCR-ALS decomposition de applied to images to obtain accurate information of the surface demonstrated to be an appropriate tool to obtain quantitative information of ASA content on the surface of the tablets. In addition, the augmented version of MCR-ALS demonstrated to be an outstanding methodology to overcome the problems of MCR-ALS decomposition itself.

The distribution of ASA in the surface and the mean concentration were correctly calculated without needing a calibration model with reference values. The quantitative results obtained were of quality, especially for the tablets whose major ingredient was ASA.

The low time of analysis without altering the sample and the good results obtained, make the combination of NIR-Imaging and MCR-ALS a very interesting approach in the pharmaceutical field for the quality control assessment of final preparations.

Acknowledgement

The authors are grateful to Spain's MCyT for funding this research within the framework of Project CTQ2006-12923.

References

[1] J. Luypaert, D.L. Massart, Y.V. Heyden, Talanta 72 (2007) 865.
[2] M. Blanco, M. Bautista, M. Alcala, Journal of Pharmaceutical Sciences 97 (2008) 1236.
[3] S.S. Sekulic, H.W. Ward, D.R. Brannegan, E.D. Stanley, C.L. Evans, S.T. Sciavolino, P.A. Hailey, P.K. Aldridge, Analytical Chemistry 68 (1996) 509.
[4] O. Berntsson, L.G. Danielsson, B. Lagerholm, S. Folestad, Powder Technology 123 (2002) 185.
[5] L. Zhang, M.J. Henson, S.S. Sekulic, Analytica Chimica Acta 545 (2005) 262.
[6] F.C. Clarke, M.J. Jamieson, D.A. Clark, S.V. Hammond, R.D. Jee, A.C. Moffat, Analytical Chemistry 73 (2001) 2213.
[7] J. Medendorp, R.A. Lodder, Journal of Chemometrics 19 (2005) 533.
[8] F. Clarke, Vibrational Spectroscopy 34 (2004) 25.
[9] E.N. Lewis, J. Schoppelrei, E. Lee, Spectroscopy 19 (2004).
[10] R.C. Lyon, D.S. Lester, E.N. Lewis, E. Lee, L.X. Yu, E.H. Jefferson, A.S. Hussain, AAPS PharmSciTech 3 (2002) 1.
[11] E.N. Lewis, J.D. Carroll, F.M. Clarke, NIR News 12 (2001) 16.
[12] N. Jovanovic, A. Gerich, A. Bouchard, W. Jiskoot, Pharmaceutical Research 23 (2006) 2002.
[13] T. Furukawa, H. Sato, H. Shinzawa, I. Noda, S. Ochiai, Analytical Sciences 23 (2007) 871.
[14] N. Elkhider, K.L.A. Chan, S.G. Kazarian, Journal of Pharmaceutical Sciences 96 (2007) 351.
[15] E.N. Lewis, L.H. Kidder, E. Lee, Innovations in Pharmaceutical Technology (2006).
[16] P. Geladi, H. Grahn, Multivariate Image Analysis, John Wiley & Son Ltd., New York, 1997.
[17] A. de Juan, R. Tauler, R. Dyson, C. Marcolli, M. Rault, M. Maeder, Trac-Trends in Analytical Chemistry 23 (2004) 70.
[18] J.M. Amigo, J. Cruz, M. Bautista, S. Maspoch, J. Coello, M. Blanco, Trac-Trends in Analytical Chemistry 27 (2008) 696.
[19] C. Ravn, R. Bro, E. Skibsted, Journal of Pharmaceutical and Biomedical Analysis 48 (2008) 554.
[20] J.M. Amigo, C. Ravn, European Journal of Pharmaceutical Sciences, doi:10.1016/j.ejps.2009.01.001 (accepted for publication).
[21] C. Gendrin, Y. Roggo, C. Collet, Talanta 73 (2007) 733.
[22] B.O. Budevska, S.T. Sum, T.J. Jones, Applied Spectroscopy 57 (2003) 124.
[23] K. Awa, T. Okumura, H. Shinzawa, M. Otsuka, Y. Ozaki, Analytica Chimica Acta 619 (2008) 81.
[24] http://www.vademecum.es.
[25] http://www.models.kvl.dk/users/jose_manuel_amigo/index.htm.
[26] J. Jaumot, R. Gargallo, A. de Juan, R. Tauler, Chemometrics and Intelligent Laboratory Systems 76 (2005) 101.
[27] A. de Juan, R. Tauler, Critical Reviews in Analytical Chemistry 36 (2006) 163.

Talanta 80 (2009) 479–483

Contents lists available at ScienceDirect

Talanta

journal homepage: www.elsevier.com/locate/talanta

One step to detect the latent fingermarks with gold nanoparticles

Dongmei Gao[a], Fei Li[a], Jixia Song[a], Xiaoyu Xu[a,b,**], Qixian Zhang[a], Li Niu[a,*]

[a] State Key Laboratory of Electroanalytical Chemistry, Changchun Institute of Applied Chemistry and Graduate University of the Chinese Academy of Sciences, Chinese Academy of Sciences, Changchun 130022, PR China
[b] Department of Public Security of Jilin Province, Changchun 130051, PR China

ARTICLE INFO

Article history:
Received 27 April 2009
Received in revised form 27 June 2009
Accepted 2 July 2009
Available online 10 July 2009

Keywords:
Gold nanoparticles
Glucose
One-step single-metal nanoparticles deposition
Latent fingermarks

ABSTRACT

A simple and environment friendly chemical route for detecting latent fingermarks by one-step single-metal nanoparticles deposition method (SND) was achieved successfully on several non-porous items. Gold nanoparticles (AuNPs) synthesized using sodium borohydride as reducing agent in the presence of glucose, were used as working solution for latent fingermarks detection. The SND technique just needs one step to obtain clear ridge details in a wide pH range (2.5–5.0), whereas the standard multi-metal deposition (MMD) technique requires six baths in a narrow pH range (2.5–2.8). The SND is very convenient to detect latent fingermarks in forensic scene or laboratory for forensic operators. The SND technique provided sharp and clear development of latent fingermarks, without background staining, dramatically diminished the bath steps.

© 2009 Elsevier B.V. All rights reserved.

1. Introduction

Hitherto, fingermarks constitute one of the most important categories of physical evidence in the forensic science. In past decades, methods of visualization of fingermarks have been developed significantly, such as iodine fuming, ninhydrin, silver nitrate [1], and cyanoacrylate fuming [2–4]. Recently, nanoparticles were widely used in this filed, e.g. CdS [5–8], CdTe [9], SiO_2 [10], and AuNPs. Multi-metal deposition method (MMD), as a useful mean to detect latent fingermarks on porous and non-porous items, was first proposed by Saunders in 1989 [11,12]. It is a two-step wet chemical process for latent fingermarks detection, combining the principles of small particles reagent with AuNPs and following a silver physical developer (AgPD). It is an equivalent, and usually superior to the well-known methods of cyanoacrylate fuming [2–4] and vacuum metal deposition [13] on various kinds of items. Schnetz and Margot used smaller AuNPs to take further studies on MMD procedure, yielding better results [14]. They explored the influence of particle size, pH value, concentration of the colloidal gold solution and the concentration of Tween 20 on detecting latent fingermarks. Mandler and Almog [15] proposed AuNPs stabilized by n-alkanethiols according to Brust et al. [16] to detect latent fingermarks on porous items in petroleum ether. Meanwhile, they probed the relationship among the thiol chain length, concentration of AuNPs, and fingermark enhancement. Becue et al. developed a new MMD technique of modifying AuNPs with mercaptocyclodextrin as a host for organic dye. This technique reduced the bath numbers and enhanced the latent fingermarks through utilizing organic dye instead of AgPD [17]. Stauffer et al. presented a single-metal deposition (SMD) to visualize latent fingermarks [18]. In the second step, they replaced the AgPD with tetrachloroauric acid and hydroxylamine hydrochloride to enhance the fingermark detection. Actually the SMD technique is quite similar to the standard MMD technique. Latent fingermarks detection techniques, as described above, suffer from restrictive experimental conditions, such as bothersome processes to prepare precursors (AuNPs), many baths, high cost preparation, and even some harmful solvents involved. So far, latent fingermarks detection only with AuNPs through one-step has not been reported yet.

AuNPs have received considerable attention for potential applications in the fields of physics, chemistry, optics, biology, electronics, and materials science [19]. A variety of methods have been reported and reviewed for preparation of AuNPs [10,20–23]. The most commonly used method is chemical reduction of gold salts by various reductants, such as sodium citrate [22], thiocyanate [20], and sodium borohydride [10]. Several forensic science laboratories [12,14–16,20] have also concluded that colloidal gold is a particularly effective reagent on detecting latent fingerprints.

In this work, glucose stabilized AuNPs were synthesized and utilized as working solution to detect latent fingermarks. Two methodologies, the SND and MMD, were applied in fingermarks detection under the same condition. The influence of pH values

* Corresponding authors. Tel.: +86 0431 85262425; fax: +86 0431 85262800.
** Corresponding author. Fax: +86 0431 85262800.
E-mail addresses: xyxu@ciac.jl.cn (X. Xu), lniu@ciac.jl.cn (L. Niu).

0039-9140/$ – see front matter © 2009 Elsevier B.V. All rights reserved.
doi:10.1016/j.talanta.2009.07.007

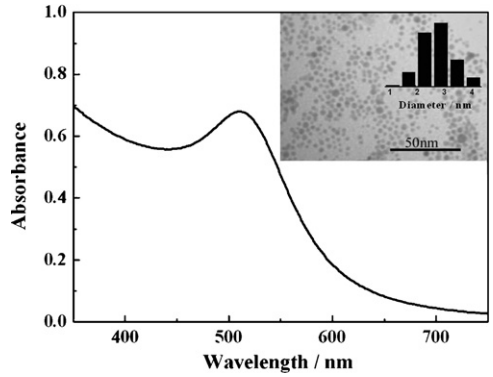


Fig. 1. UV–vis absorption spectrum, TEM image, and corresponding particle size distribution histogram (inset) of the glucose stabilized AuNPs (concentration of tetrachloroauric acid is 1.0 mM).

on detecting latent fingermarks was also explored. It was found that the SND technique provided sharp and clear development of latent fingermarks, without background staining, dramatically diminished the bath steps in a wide pH range.

2. Experimental

2.1. Chemicals

Chloroauric acid tetrahydrate, sodium borohydride, and sodium hydroxide were purchased from Sinopharm Chemical Reagent Co. (Shanghai, China). Citric acid was purchased from Beijing Chemicals (Beijing, China). Glucose was purchased from Aldrich (USA). All of the chemical reagents were used without any further purification. All glassware used in the following procedures was cleaned in a bath of freshly prepared 3:1 HCl/HNO_3 (v/v), and rinsed thoroughly with double distilled water prior to use. All the experiments were carried out at room temperature.

2.2. Preparation of AuNPs

Glucose stabilized AuNPs were prepared according to the following procedures: 2×10^{-5} mol chloroauric acid tetrahydrate and 2×10^{-4} mol glucose were dissolved in 18 ml deioned water in a flask with stirring. 30 min later, a freshly prepared 2 ml ice-water solution of sodium borohydride (1×10^{-4} mol) was added dropwise into the above solution under vigorous stirring. Color of the solution changed immediately from straw yellow to wine red, indicating the formation of AuNPs. After stirring for 1 h, the prepared AuNPs were used for detecting latent fingermarks.

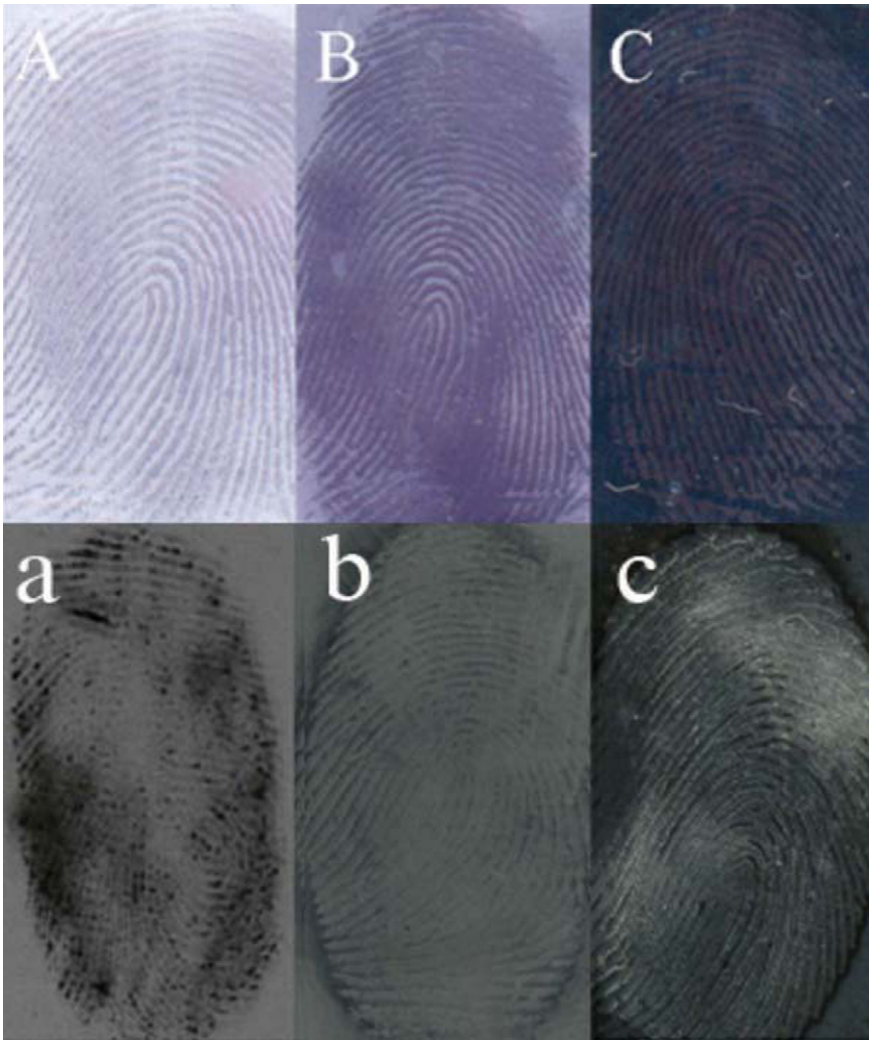


Fig. 2. Latent fingermarks were developed with the SND technique using glucose stabilized AuNPs on (A) glass slide, (B) plastic, and (C) tin foil; and with the standard MMD technique on (a) glass slide, (b) plastic, and (c) tin foil.

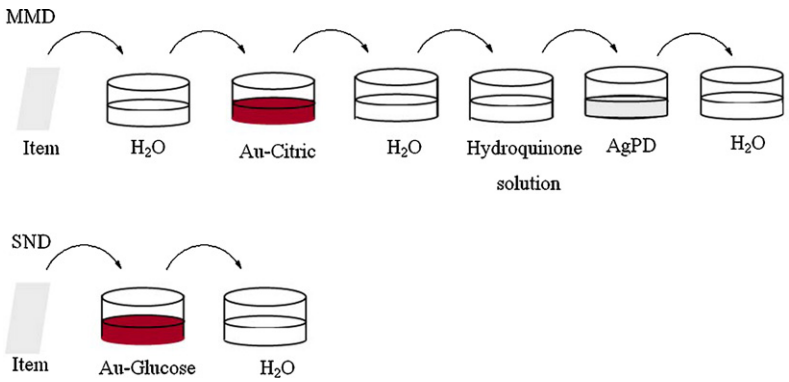


Fig. 3. Schematics of the standard MMD and the SND technique.

2.3. Detection of latent fingermarks

Latent fingermarks were obtained all from one volunteer by rubbing fingers against the forehead and stamping them onto glass slides, plastic and tinfoil at the same condition, respectively. The obtained latent fingermarks are similar to real samples on the same items.

Citric acid (1 M) and sodium hydroxide (1 M) solution were used to adjust the pH value of the prepared AuNPs. Then, the items bearing latent fingermarks were immersed into the working solution, removed from the solution 40 min later, rinsed with deioned water, and dried with nitrogen steam. Clear ridges of prints were obtained.

Control experiments were carried out at pH 2.8, using the SND and the standard MMD [14].

The influence of the pH on detecting latent fingermarks was further investigated. Different pH was adjusted with citric acid (1 M) and sodium hydroxide (1 M) (2.0, 2.5, 3.0, 3.5, 4.0, 5.0, 5.5, 6.0, and 7.0) to detect latent fingermarks at room temperature.

2.4. Instrumentations

UV–vis measurement was carried out on a Cary 50 UV–vis spectrophotometer (Varian, USA). TEM measurement was performed on a JEOL 2010 transmission microscopy operated at an accelerating

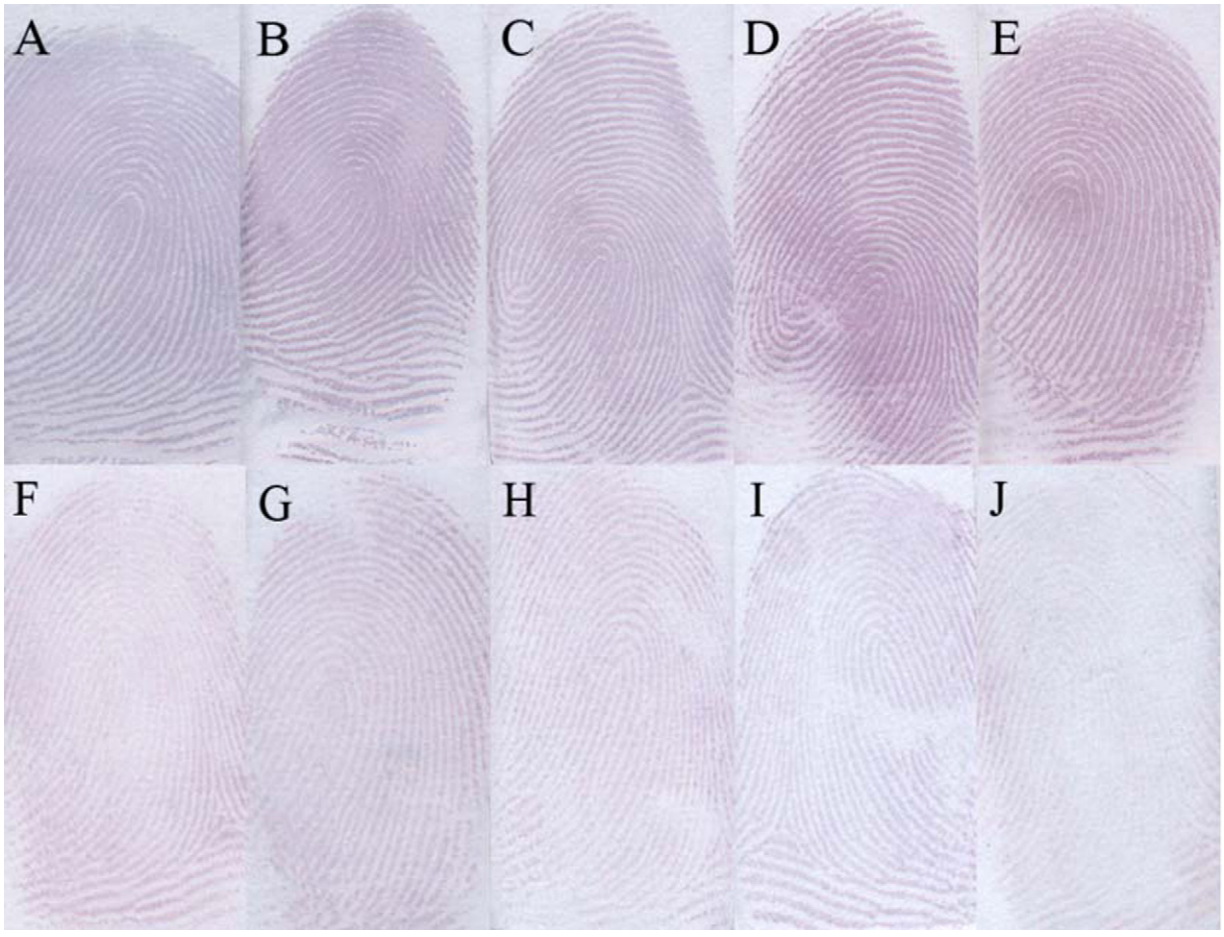


Fig. 4. The pH influence of colloidal gold solution on the fingermarks detection on glass slides: (A) 2.0, (B) 2.5, (C) 3.0, (D) 3.5, (E) 4.0, (F) 4.5, (G) 5.0, (H) 5.5, (I) 6.0, and (J) 7.0, respectively.

voltage of 200 kV. The sample for TEM measurement was prepared by placing a drop of as-prepared AuNPs solution onto a carbon-coated copper grid and dried at room temperature. SEM and EDAX measurement was taken on a FE-SEM, S-4800, Hitachi Scanning Electron Microscopy. Photos were taken with Nikon D100 made by Nikon Corporation.

3. Results and discussion

AuNPs were prepared using sodium borohydride as the reducing agent in the presence of glucose. The UV–vis spectrum and TEM image were used to confirm the formation of AuNPs (Fig. 1). The UV–vis spectrum of the AuNPs shows an absorption peak at 511 nm, assigned to the characteristic surface plasmon resonance [19]. TEM image was applied to further confirm the AuNPs formation. Inset of Fig. 1 displays the AuNPs are generally well-separated from each other. The size distribution histogram shown in the inset reveals an average diameter of 2.5 nm, as judged from more than 200 individual particles, which is much smaller than particles in Schnetz and Margot's work (14 nm).

Control experiments were carried out between the SND and the standard MMD technique. The items bearing latent fingermarks were immersed into the glucose stabilized AuNPs at pH 2.8 for 40 min, and washed with deioned water to remove redundant AuNPs, natural drying. On glass slide, plastic and tinfoil, high quality prints were developed and shown in Fig. 2A–C. Meanwhile, control experiments were carried out according to the MMD procedure [14]. Correspondingly, Fig. 2a, b, and c were the results developed on glass slide, plastic, and tin foil, at the same condition as above. Comparatively, both of the two methods can obtain quasi-identical ridge details of fingermarks. Nevertheless, the SND procedure has no background interference and shows much clearer ridge details than the MMD procedure (Fig. 2). The color of fingermarks detected by the SND is reddish while the other is black with MMD procedure.

The standard MMD and the SND technique procedures were schematically depicted in Fig. 3. The standard MMD is seldom used in forensic laboratories, due to its labor intensive, time consuming, and only producing dark grey or black fingermarks. The MMD laboratory procedures are consisted of six consecutive baths into which the items were immersed for different time (upper in Fig. 3). The first three baths assure the deposition of gold colloids, while the other three baths were the reduction of silver on the gold colloids to enhance the detected latent fingermarks to be grey or black. The SND technique was carried out in two baths, with no reinforcing reagent (as AgPD or organic dye) just glucose stabilized AuNPs (lower in Fig. 3). The SND has significantly diminished the number of laboratory operations, and cut the cost for detecting latent fingermarks. So the procedure might be an attractive alternative to the MMD procedure.

The influence of pH on detecting fingermarks was further explored. Latent fingermarks were immersed in different pH solutions of glucose stabilized AuNPs (2.0, 2.5, 3.0, 3.5, 4.0, 5.0, 5.5, 6.0, and 7.0) for 40 min, washed with deioned water, and dried with nitrogen steam (as shown in Fig. 4). In a wide pH range, marks on glass surfaces could be visualized well. At a low pH value, the synthesized AuNPs are unstable and aggregated easily, so the fingermarks are light blue (Fig. 4A and B). At high pH value, there are not enough protons to activate the protein or peptide included in the latent fingermarks. So the obtained results are not as good as those in lower pH solution. In the neutral condition (pH 7.0), there were almost no ridge details obtained. From these points we conclude that the favorable pH range for latent fingermarks detection is around 2.5–5.0, which is obviously wider than traditional MMD (only working for pH 2.5–2.8). It is much convenient for workers to detect latent fingermarks in forensic science or laboratory.

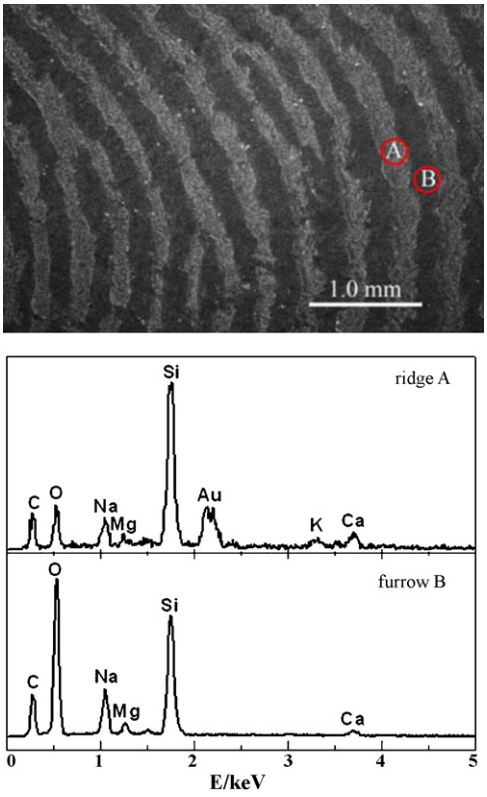


Fig. 5. SEM image of detected fingermarks with glucose stabilized AuNPs on silicon wafer and EDAX analysis for the ridges (region A in SEM image) and furrows (region B).

The binding mode of the AuNPs to the fingermark residues remains misunderstood, even if the electrostatic attraction is the most widely accepted one. The theory is that proteins or amino acid containing components within a fingermark can be protonated under acidic conditions and thus charged positively. Negatively charged AuNPs are deposited preferentially onto the fingermark ridges through electrostatic interactions or non-covalent interaction [6]. There are more components, like oil, protein and salt, on the ridges of the fingermarks than on the furrows [7]. So there are more AuNPs attracted on the ridges. Hence, latent fingermarks can be revealed. Fingermarks detected by glucose stabilized AuNPs on silicon wafer was characterized by SEM and EDAX (Fig. 5). Au element appeared on the ridges of the developed latent fingermarks (Fig. 5 ridge A), while no Au element on the furrows (Fig. 5 furrow B).

4. Conclusion

In this report, a one-step single-metal nanoparticles deposition method (SND) has been proposed for detecting latent fingermarks on non-porous items. AuNPs stabilized by glucose have been successfully synthesized and suggested to be utilized as the working solution to detect latent fingermarks. The SND technique could obtain even better results in a wide pH range compared with the standard MMD. It is a simple method to detect latent fingermarks only with AuNPs and just in one step rather than tow or more. This technique has dramatically diminished the baths, operated simply and expediently, and enlarged the pH range for detecting latent fingermarks. These may establish a new possibility for the detection of latent fingermarks in forensic science.

Acknowledgements

This work is financially supported by Ministry of Science and Technology (no.2007AA03Z354 and 2007BAK26B06). And the authors are thankful to Mr. Chuang Li (Department of Public Security of Jilin Province) for his assistance.

References

[1] D. Burow, D. Seifert, A.A. Cantu, J. Forensic Sci. 48 (2003) 1094.
[2] L. Lewis, R. Smithwick, G. Devault, B. Bolinger, S. Lewis, J. Forensic Sci. 46 (2001) 241.
[3] J.A. Prahlow, P.E. Lantz, J. Forensic Sci. 38 (1993) 1507.
[4] J. Zhang, D.A. Gong, Forensic Sci. Int. 52 (1991) 31.
[5] J.J. Yu, J.L. Yun, P.L. Guo, L. Jie, F.W. Yuan, Q.Y. Rui, T.L. Wen, Forensic Sci. Int. 179 (2008) 34.
[6] R.Q. Yang, Q.Y. Zhou, Y.F. Wang, Y.J. Jin, Chin. J. Inorg. Chem. 24 (2008) 1874.
[7] E.R. Menzel, M. Takatsu, R.H. Murdock, K. Bouldin, K.H. Cheng, J. Forensic Sci. 45 (2000) 770.
[8] K.K. Bouldin, E.R. Menzel, M. Takatsu, R.H. Murdock, J. Forensic Sci. 45 (2000) 1239.
[9] K.H. Cheng, J. Ajimo, W. Chen, J. Nanosci. Nanotechnol. 8 (2008) 1170.
[10] M.J. Choi, T. Smoother, A.A. Martin, A.M. McDonagh, P.J. Maynard, C. Lennard, C. Roux, Forensic Sci. Int. 173 (2007) 154.
[11] M.J. Choi, A.M. McDonagh, P. Maynard, C. Roux, Forensic Sci. Int. 179 (2008) 87.
[12] H.C. Lee, R.E. Gaebsslen, in: H.C. Lee, R.E. Gaebsslen (Eds.), Advances in Fingerprint Technology, New York, 2001, pp. 105-177.
[13] N. Jones, M. Stoilovic, C. Lennard, C. Roux, Forensic Sci. Int. 115 (2001) 73.
[14] B. Schnetz, P. Margot, Forensic Sci. Int. 118 (2001) 21.
[15] M. Sametband, I. Shweky, U. Banin, D. Mandler, J. Almog, Chem. Commun. (2007) 1142.
[16] M. Brust, M. Walker, D. Bethell, D.J. Schiffrin, R. Whyman, J. Chem. Soc. Chem. Commun. (1994) 801.
[17] A. Becue, C. Champod, P. Margot, Forensic Sci. Int. 168 (2007) 169.
[18] E. Stauffer, A. Becue, K.V. Singh, K.R. Thampi, C. Champod, P. Margot, Forensic Sci. Int. 168 (2007) e5.
[19] S.K. Ghosh, T. Pal, Chem. Rev. 107 (2007) 4797.
[20] N. Chandrasekharan, P.V. Kamat, J.Q. Hu, G. Jones, J. Phys. Chem. B 104 (2000) 11103.
[21] M.C. Daniel, D. Astruc, Chem. Rev. 104 (2004) 293.
[22] G. Frens, Nat. Phys. Sci. 241 (1973) 20.
[23] A.C. Templeton, M.P. Wuelfing, R.W. Murray, Acc. Chem. Res. 33 (2000) 27.

Talanta 80 (2009) 484–488

Contents lists available at ScienceDirect

Talanta

journal homepage: www.elsevier.com/locate/talanta

Electrochemical determination of melamine using oligonucleotides modified gold electrodes

Qian Cao [a], Hong Zhao [a,*], Lixi Zeng [a], Jian Wang [a], Rui Wang [b], Xiaohui Qiu [b], Yujian He [a,c,*]

[a] College of Chemistry and Chemical Engineering, Graduate University of Chinese Academy of Sciences, 19A YuQuan Road, Beijing 100049, China
[b] National Center for Nanoscience and Technology, Beijing 100190, China
[c] State Key Laboratory of Natural and Biomimetic Drugs, Peking University, Beijing 100191, China

ARTICLE INFO

Article history:
Received 7 May 2009
Received in revised form 30 June 2009
Accepted 2 July 2009
Available online 10 July 2009

Keywords:
Oligonucleotides
Melamine
Differential pulse stripping voltammetry
Electrochemical impedance spectrometry

ABSTRACT

A novel and simple electrochemical method for determination of melamine is developed based on oligonucleotides film modified gold electrodes. The electrochemical probe of ferricyanide was used to investigate the interactions between oligonucleotides and melamine. Results of cyclic voltammetries, differential pulse stripping voltammetries, electrochemical impedance spectrometry and atomic force microscope, proved that melamine might interact with oligonucleotides mainly through electrostatic and hydrogen-bonding interactions. The interactions between oligonucleotides and melamine lead to the increase in the peak currents of ferricyanide, which could be used for electrochemical sensing of melamine. The redox peak currents of ferricyanide were linear with the concentration of melamine in the range from 3.9×10^{-8} to 3.3×10^{-6} M with a linear coefficiency of 0.990. The detection limit was 9.6×10^{-9} M. The proposed electrochemical biosensor is rapid, convenient and low-cost for effective sensing of melamine. Particularly, the proposed method was applied successfully to the determination of melamine in milk products, and the recovery was 95%.

© 2009 Elsevier B.V. All rights reserved.

1. Introduction

Melamine, a kind of triazine analogue with three amino groups (Fig. 1), is widely used as an industrial chemical in the production of melamine resins, which are used in laminates, glues, adhesives, and plastics. Melamine can be found as a contaminant in a variety of foods from food-contact materials. When added to milk powder, melamine increases the nitrogen concentration, which suggests a false increase in protein concentration. When meeting strong acids or alkali, melamine yields ammeline, ammelide and cyanuric acid by hydrolysis. Melamine could form insoluble complexes with cyanuric acid, depending on urine pH, which could lead to crystallization and subsequent tissue injury [1], such as urolithiasis and bladder cancer. Recently many young children have suffered from renal stone caused by melamine in the milk powder, so significant efforts have been made on the fast and effective detection of melamine.

Up to now, some methods, such as gas chromatography (GC) [2], high performance liquid chromatography (HPLC) [3], high performance liquid chromatography/mass spectrum (HPLC/MS) [4], surface enhanced raman spectroscopy [5] and capillary zone electrophoresis/mass spectrum (CE/MS) [6] have been employed for the determination of melamine. However, complicated preconcentration, time-consuming steps and high-cost instruments limit the application of the existing methods. Hence, there have been increasing demands for new, fast, simple, convenient and sensitive methods for the determination of melamine. Compared to those existing methods, much importance has been attached to the electrochemical sensors due to their simplicity, low-cost, accurateness, sensitivity and high stability. Unfortunately, so far few of papers have been reported concerned about electrochemical methods to determine melamine at solid electrodes.

In this paper, surface electrochemical method based on an oligonucleotide ($d(T)_{20}$) film modified electrode is developed for the determination of melamine (Fig. 2). Due to complementary triamino triazine unit, melamine can be immobilized onto the oligonucleotides modified electrode via electrostatic interaction and hydrogen-bonding [7]. The morphologic differences between melamine and melamine interacted with oligonucleotides were observed by AFM. The electrochemical probe of $[Fe(CN)_6]^{3-/4-}$ was used to investigate the interaction between melamine and oligonucleotides since melamine is non-electroactive over the potential range studied. The peak currents of the electrochemical probe evaluated by differential pulse stripping voltammetry (DPSV) were linear with the concentrations of melamine in the range from 3.9×10^{-8} to 3.3×10^{-6} M with a linear coefficiency of 0.990. The detection limit was 9.6×10^{-9} M. On the other hand, electrochemical impedance spectrometry is a useful

* Corresponding authors. Tel.: +86 010 88256141; fax: +86 010 88256141.
E-mail addresses: hongzhao@gucas.ac.cn (H. Zhao), heyujian@gucas.ac.cn (Y. He).

0039-9140/$ – see front matter © 2009 Elsevier B.V. All rights reserved.
doi:10.1016/j.talanta.2009.07.006

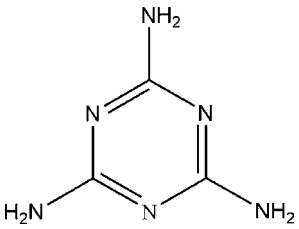


Fig. 1. The structure of melamine.

method to study the interfacial properties of modified electrode [8–12]. The immobilization of materials on the electrode surface might probably alter the interfacial electron transfer features at the electrode surface. Therefore, in this study, electrochemical impedance spectrometry was further used to study the interaction between oligonucleotides and melamine. The proposed method was applied successfully to the determination of melamine in milk products, and the recovery was 95%. To the best of our knowledge, the proposed method has not been reported, which will have great implications in the determination of melamine in food.

2. Experimental

2.1. Chemicals and materials

Melamine, analytical grade, was purchased from Sigma (USA). Oligonucleotides ($d(T)_{20}$) containing a 6-mercaptohexyl linker at the 5′ end was obtained from Shanghai Invitrogen Corporation (China). The $d(T)_{20}$ stock solution (20 μM) was prepared by dissolving the $d(T)_{20}$ powder in 0.01 M phosphate buffer solution (pH 7.0) containing 0.5 M NaCl and stored at 4 °C. Other chemicals were of analytical reagent grade and used as received. All aqueous solutions were prepared with distilled water.

2.2. Apparatus and equipments

Electrochemical measurements were carried out by a CHI 760C electrochemical workstation (CHI Instrument Company, Shanghai, China). A three-electrode system was used in the measurements, composed of a bare gold electrode (d = 2 mm) or $d(T)_{20}$/Au as the working electrode, a saturated calomel electrode (SCE) as the reference electrode and the Pt wire as the counter electrode. All the pH measurements were performed with PB-10 pH meter (Sartorius, Germany). The images of atomic force microscope (AFM) were obtained by Veeco Dimension 3100 (Digital Instrument, USA) in the tapping mode in air.

2.3. Preparation of $d(T)_{20}$ modified electrodes

Gold electrode was cleaned by exposure to warm piranha solution (70% concentrated sulfuric acid, 30% peroxide solution (30%)) for 10 min, and rinsed ultrasonically with ethanol and water. Then the electrode was cycled between 0.2 and 1.5 V in 0.1 M H_2SO_4 at 100 mV/s until reproducible voltammograms were obtained.

Self-assembled monolayer was prepared by transferring 15 μL $d(T)_{20}$ solution onto the gold electrode's surface. After the 16 h immobilization period, the electrode was soaked in sterilized water for 2 h to remove any un-adsorbed $d(T)_{20}$, and dried with a nitrogen stream. Thus, the $d(T)_{20}$ modified gold electrode($d(T)_{20}$/Au) was obtained.

2.4. Atomic force microscopy

Cleaned mica substrates were dried under a stream of N_2, and a drop of melamine phosphate buffer solution (pH = 7.0) was deposited on the freshly mica surface. Half an hour later the excess solution was gently cleaned with a jet of distilled water, and the mica with adsorbed melamine molecules was then dried in a sterile atmosphere. Afterwards a drop of $d(T)_{20}$ phosphate buffer solution (pH = 7.0) was deposited on the positively charged melamine-modified substrates for 1–4 h as incubation time, and the excess solution was gently cleaned with a jet of distilled water. After the mica substrate was completely dried, the morphology of the resulting surfaces was characterized using atomic force microscopy.

3. Results and discussion

3.1. Atomic force microscopy evaluation of melamine–$d(T)_{20}$ interaction

Atomic force microscopy is another common method to study the interaction between small molecules and oligonucleotides [13–15]. Therefore, it is used to further investigate the interaction between melamine and $d(T)_{20}$. Mica was chosen as substrate because of its atomically flat surface over a large area. A drop of melamine solution spreads rapidly across the mica surface in a thin layer because of the high hydrophilicity of the mica surface when it is deposited on a freshly cleaved mica surface. Cationic melamine can be easily adsorbed on the negatively charged mica surface by electrostatic attractive force (Fig. 3A). Firstly we changed the incubation time to evaluate the effect of incubation time on $d(T)_{20}$ immobilization. Fig. 3B and C show the AFM images of $d(T)_{20}$ molecules absorbed on the melamine-modified mica surface for 1–2 h incubation time, respectively. The $d(T)_{20}$ molecules which carry negatively charged phosphate groups were immobilized onto positively charged melamine-modified mica surface via electrostatic attractions, while the negatively charged $d(T)_{20}$ molecules can hardly absorb onto the mica surface. The thickness of the $d(T)_{20}$ layer on the positively charged melamine-modified surfaces was 8.2 nm during the first 1 h, and increased to around 32.8 nm in 2 h. Obviously, the $d(T)_{20}$ molecules formed much more clusters to form a higher surface coverage with the increasing incubation time. The effect of concentration on the thick-

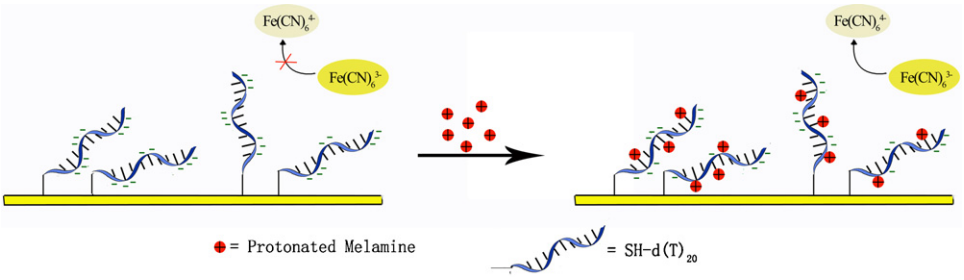


Fig. 2. Schematic representation of the sensing processes.

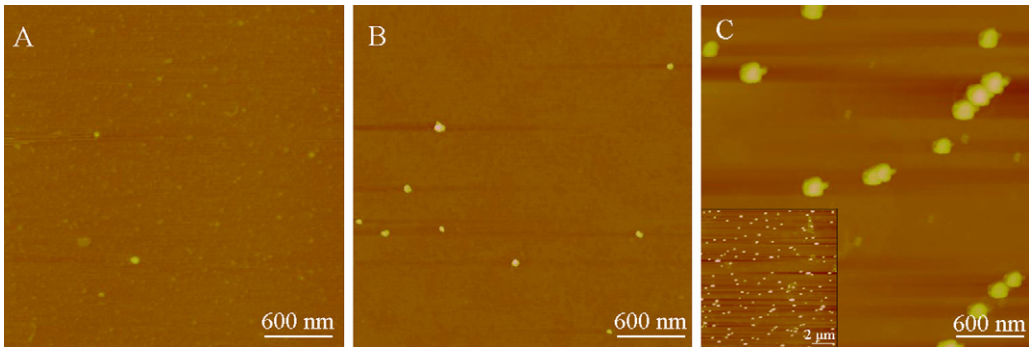


Fig. 3. AFM images (3 μm × 3 μm) of melamine-modified mica surface for different incubation time with $d(T)_{20}$: (A) 0 h, (B) 1 h, (C) 2 h. ($d(T)_{20}$ concentration: 2.2×10^{-5} M). Inset in Fig. 3C shows AFM image (10 μm × 10 μm) of melamine-modified mica surface incubated with 2.2×10^{-5} M $d(T)_{20}$ for 2 h.

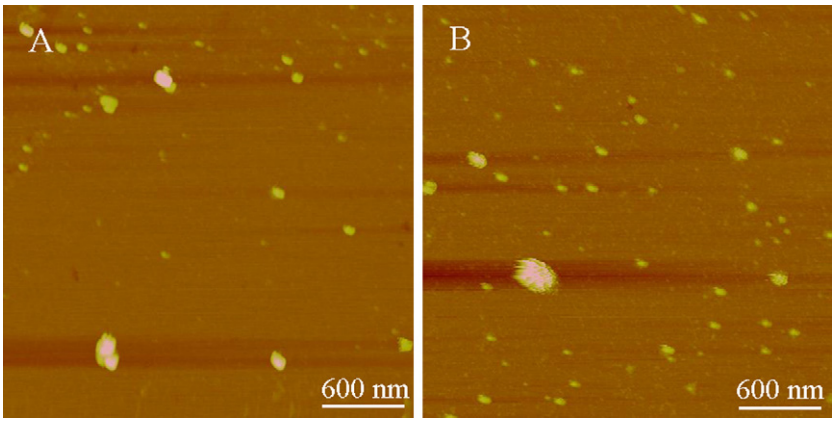


Fig. 4. AFM images (3 μm × 3 μm) of two different surfaces for different concentration of $d(T)_{20}$: (A) 5.4×10^{-6} M, (B) 1.1×10^{-5} M (Incubation time: 4 h).

nesses of the $d(T)_{20}$ overlayers formed on the positively charged melamine-modified surfaces was investigated by applying different concentration of $d(T)_{20}$ solutions (5.4×10^{-6} and 1.1×10^{-5} M, in pH 7.0 phosphate buffer solution) at room temperature. As seen from Fig. 4, more clusters formed on the melamine-modified mica surface with the increasing $d(T)_{20}$ solution concentration since the assembly becomes more convenient at higher concentration of $d(T)_{20}$.

3.2. Optimum conditions for melamine determination

3.2.1. Effect of the amount of $d(T)_{20}$

The electrochemical impedance spectroscopy was used to select a suitable $d(T)_{20}$ concentration for the electrochemical measurements. With increasing $d(T)_{20}$ concentration from 1 to 40 μM, the semicircle diameter in EIS initially increased and then became a plateau at 20 μM or higher. And the large semicircle diameter confirms the high surface density of $d(T)_{20}$ on the gold electrode when the concentration of $d(T)_{20}$ is selected as 20 μM. Therefore, 20 μM of $d(T)_{20}$ was employed for further assay.

3.2.2. Effect of accumulation potential and time

The electrochemical probe of $[Fe(CN)_6]^{3-/4-}$ was used in PBS buffer solution (pH7.0) containing 1.6 μM melamine by DPSV, varying the accumulation potential from 0.2 to 1.0 V, with 30 s accumulation time. The peak current increased with increasing accumulation potential and reached the highest at 0.8 V. Therefore, we select 0.8 V as the optimum accumulation potential.

In the same solution as above, the accumulation time changed from 0 to 300 s when the accumulation potential went to 0.8 V. The peak current value increased slowly with the time, so we selected 30 s as accumulation time to realize the rapid detection.

3.2.3. The pH effect on the melamine–$d(T)_{20}$ interaction

Fig. 5 displays the pH effect on the interaction between $d(T)_{20}$ and melamine. The strength of the interaction between melamine and $d(T)_{20}$/Au electrode is pH dependent. At pH 8.0, melamine is electrically neutral so its electrostatic interaction with the $d(T)_{20}$ is weakened (likely to be due to deprotonation of the amino groups

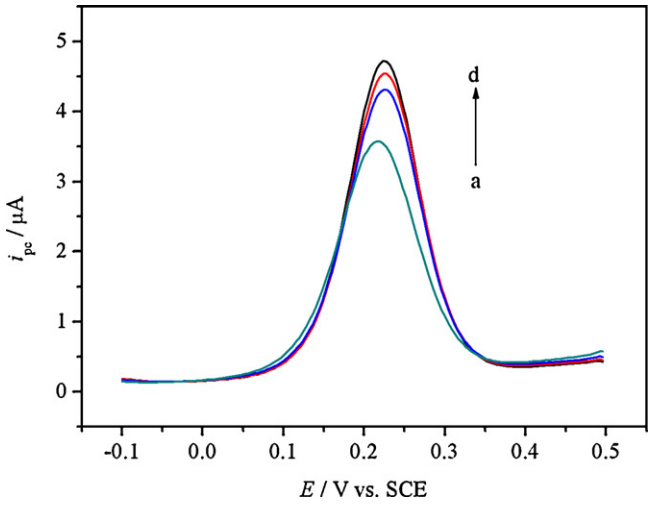


Fig. 5. Differential pulse stripping voltammograms of 1.0 mM $K_3Fe(CN)_6$ mixed with 7.6×10^{-8} M melamine in PBS buffer of different pH values (a–d: the pH values are 8.0, 7.0, 6.0, 5.0) at $d(T)_{20}$/Au.

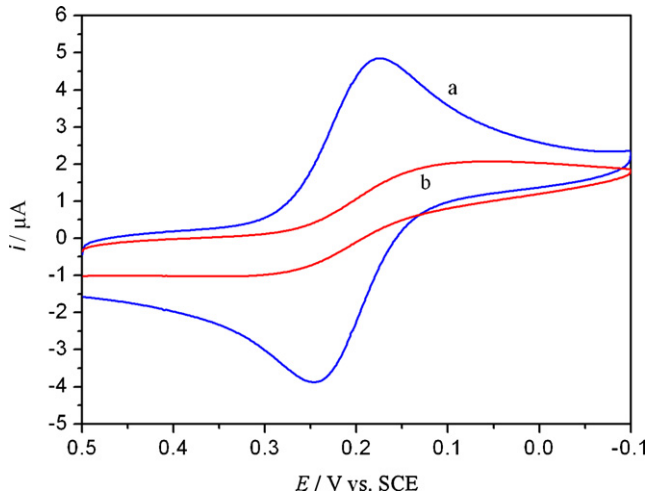


Fig. 6. Cyclic voltammograms of 1.0 mM $K_3Fe(CN)_6$ in pH 7.0 PBS buffer at the bare gold (a) and $d(T)_{20}$/Au (b) with a scan rate of 0.05 V/s.

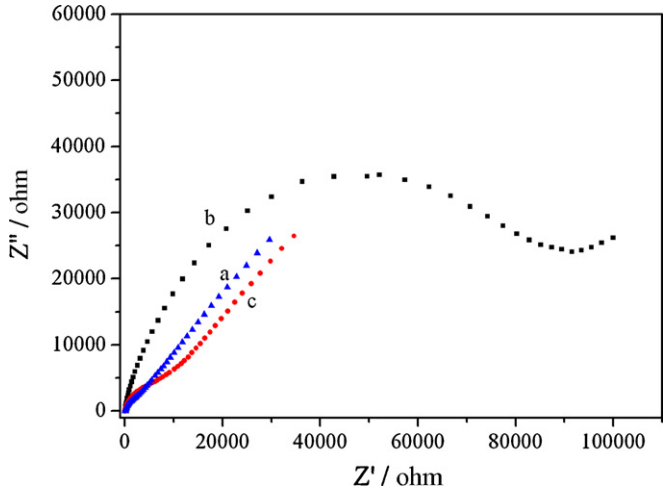


Fig. 7. AC impedance plots of 1.0 mM $K_3Fe(CN)_6$ in pH 7.0 PBS buffer at the bare gold (a), $d(T)_{20}$/Au (b) and $d(T)_{20}$/Au dealed with 6.7×10^{-7} M melamine by DPSV(c).

in melamine). With the decreasing of pH value the peak currents increased, especially from pH 8.0 to pH 7.0. Thus, it is indicated that the interaction becomes stronger in low pH condition, and we presume that the electrostatic interaction between $d(T)_{20}$ and melamine is predominate. To be close to the physiological condition (pH 7.4), we selected pH 7.0 for experiments.

3.3. Electrochemical characteristics of the $d(T)_{20}$/Au

3.3.1. Cyclic voltammograms

The electrochemical behavior of the modified electrode was characterized by cyclic voltammetry using $[Fe(CN)_6]^{3-/4-}$ as an electroactive probe. As shown in Fig. 6, a pair of reversible redox peaks was observed on the bare gold electrode. Compared with the bare gold electrode, the anodic peak potential (E_{pa}) on the $d(T)_{20}$ modified gold electrode shifted from 0.25 to 0.32 V, and the cathodic peak potential (E_{pc}) from 0.17 to 0.06 V, demonstrating that the potential separation between anodic and cathodic peaks ($\Delta E_p = E_{pa} - E_{pc}$) was larger than that of on the bare gold electrode. And the amperometric response of the modified electrode decreased. These results showed that the electron transfer kinetics of $[Fe(CN)_6]^{3-/4-}$ redox reactions was perturbed when the bare gold electrode was modified with the $d(T)_{20}$, confirming that the $d(T)_{20}$ was successfully assembled on gold surface through the Au-S bond.

3.3.2. Impedance analysis

Fig. 7 shows the electrochemical impedance spectroscopy (EIS) at the bare gold electrode and the electrode modified with $d(T)_{20}$. The impedance change of the electrode surface can characterize the stepwise-assemble process of the surface-modified electrode. The typical impedance spectrum (presented in the form of the Nyquist plot) includes a semicircle portion at higher frequencies corresponding to the electron-transfer-limited process and a linear part at lower frequency range representing the diffusion-limited process. The semicircle diameter in the impedance spectrum equals the electron-transfer resistance, R_{et}, which is related to the electron-transfer kinetics of the redox probe at the electrode surface. The response of electrochemical impedance spectroscopy at the bare gold electrode is a straight line (Fig. 7a), revealing there is almost no heterogeneous charge-transfer resistance on bare gold electrode surface, while the impedance response at the modified electrode (Fig. 7b) is much larger, illustrating the immobilization of $d(T)_{20}$ on the electrode. Due to the non-conductivity of $d(T)_{20}$, the introduction of $d(T)_{20}$ layer forms a barrier for electron transfer between the redox probe in the electrolyte solution and the electrode. On the other hand, the negatively charged phosphate groups on $d(T)_{20}$ can also resist the access of the $[Fe(CN)_6]^{3-/4-}$ redox couple to the electrode surface. These results are in good agreement with the results of cyclic voltammetry in Fig. 6.

3.4. The electrochemical determination of melamine

The electrochemical probe of $[Fe(CN)_6]^{3-/4-}$ was used to investigate the interaction between $d(T)_{20}$ and melamine by DPSV. Fig. 8A shows the reductive peak current value of $[Fe(CN)_6]^{3-/4-}$ at $d(T)_{20}$/Au increased with the increasing concentration of melamine in the range from 3.9×10^{-8} to 3.3×10^{-6} M. Fig. 8B shows the linear relationship between the reductive peak current and the concentration of melamine from 3.9×10^{-8} to 3.3×10^{-6} M with a coefficiency of 0.990. The detection limit is up to 9.6×10^{-9} M. These results are attributed to the interaction between melamine and $d(T)_{20}$ on the electrode surface. As we know, the pK_a of melamine is 8.0 [16], hence, the amino groups of melamine could be protonated in pH7.0 PBS solution. Thus, protonated melamine interacted with the negatively charged phosphates of the $d(T)_{20}$ through electrostatic attraction. This suggests that the presence of melamine gives rise to partial charge screening (neutralization) of the negative charges of the phosphate groups of $d(T)_{20}$, which facilitates the electrochemical reaction of $[Fe(CN)_6]^{3-/4-}$ at the $d(T)_{20}$/Au electrode. Meanwhile, melamine can bind to the thymine base through its complementary triamino triazine unit by hydrogen-bonding [17] and specifically combine to the $d(T)_{20}$. Therefore, we presume that the interactions between melamine and $d(T)_{20}$ including electrostatic interaction and hydrogen-bonding. The results of electrochemical impedance spectroscopy can further prove the interaction of $d(T)_{20}$ and melamine (Fig. 7). The radius of the semicircle of $d(T)_{20}$/Au after the interaction with melamine became smaller obviously than that of before the interaction, but it was still lager than that of bare Au. The EIS results indicated that melamine can absorb on the electrode modified with $d(T)_{20}$ and reduce the electron-transfer resistance.

3.5. The selectivity for melamine detection

The influences of some foreign substances on the determination of 9.6×10^{-7} M melamine were investigated. The proposed method showed a good selectivity for melamine detection. For example, 100 fold K^+, Na^+, NH_4^+, Cl^-, PO_4^{3-}, SO_4^{2-}, Ac^-, glucose, alanine, arginine, tyrosine, and monosodium glutamate barely interfere in the determination of melamine.

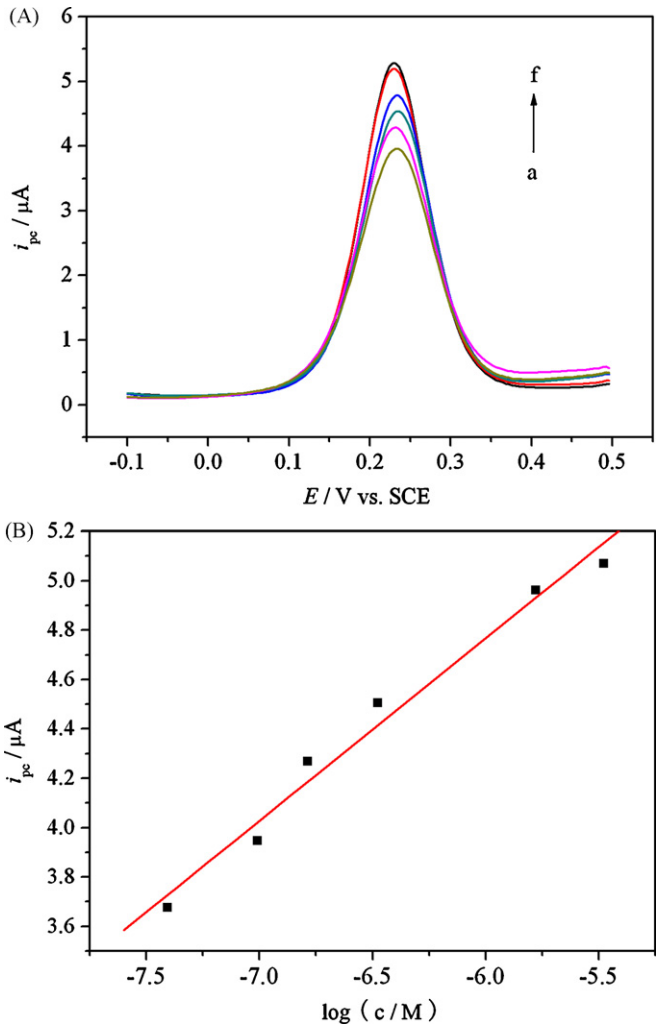


Fig. 8. (A) Differential pulse stripping voltammograms of 1.0 mM $K_3Fe(CN)_6$ in the mixture of melamine in pH 7.0 PBS buffer at $d(T)_{20}$/Au (a–f: the concentration of melamine is 3.9×10^{-8} M, 9.8×10^{-8} M, 1.6×10^{-7} M, 3.3×10^{-7} M, 1.7×10^{-6} M, 3.3×10^{-6} M). (B) Linear relationship between the reductive peak current and the concentration of melamine.

3.6. Stability and reproducibility of $d(T)_{20}$/Au

The stability of the $d(T)_{20}$/Au was examined. After keeping it in refrigerator for two weeks, the current response of the electrode did not remarkably change, showing that the $d(T)_{20}$/Au has good stability.

The reproducibility of the current response for the $d(T)_{20}$/Au was examined in 1.0 mM $K_3Fe(CN)_6$ solution containing 4.8×10^{-7} M melamine. The relative standard deviation was 1.9% for 10 independent determinations.

3.7. Analytical application in milk

To assess its applicability, the proposed method was applied to the analysis of melamine in liquid milk bought from supermarket. The liquid milk was pretreated according to the general procedure. Briefly, 5 g milk was first mixed with 5 mL of 61 mM trichloroacetic acid and 35 mL of 4.9 M methanol solution. After 15 min sonication and 10 min shaking, the mixture was centrifuged at 10000 rpm/min for 10 min, and then the supernatant was filtrated. Next, the filtrate was condensed to give a total volume of 5 mL and filtered through a 0.45 μm filter membrane to obtain the samples for detection. Because the existing milk in the market is free of melamine, the sample was spiked with certain amounts of melamine standard solution directly. The concentration of melamine was calculated to be 3.8×10^{-7} M by standard addition method. The recovery rate was calculated to be 95%, demonstrating the accuracy of the proposed method.

4. Conclusions

In conclusion, we have developed a rapid, simple and reliable method to study the interaction between $d(T)_{20}$ and melamine by using $K_3Fe(CN)_6$ as an electrochemical indicator. Melamine might interact with $d(T)_{20}$ in two modes, electrostatic attraction and hydrogen-bonding. The proposed electrochemical sensor has a good sensitivity for the detection of melamine, and the peak current of $K_3Fe(CN)_6$ linearly increased with the increasing concentration of melamine over a range from 3.9×10^{-8} to 3.3×10^{-6} M. The detection limit of the proposed sensor is lower than that of traditional methods. The proposed method was applied successfully to the determination of melamine in milk products, and the recovery was 95%. Thus this sensor is expected to have a potential application in food inspection.

Acknowledgments

This work was supported by the National Natural Science Foundation of China (Grant Nos. 20571085 and 20877099), 973 Project (Grant No. 2007CB935900), the State Key Laboratory of Natural and Biomimetic Drugs (Grant No. 20080208), President Fund of GUCAS (Grant No. 065101HM03) and (water special project (Grant No. 2008ZX07527-007)).

References

[1] B. Puschner, R.H. Poppenga, L.J. Lowenstine, M.S. Filigenzi, P.A. Pesavento, J. Vet. Diagn. Invest. 19 (2007) 616.
[2] R.A. Yokley, L.C. Maye, R. Rezaaiyan, M.E. Manuli, M.W. Cheung, J. Agric. Food Chem. 48 (2000) 3352.
[3] S. Ehling, S. Tefera, I.P. Ho, Food Addit. Contam. 24 (2007) 1319.
[4] B. Kim, L.B. Perkins, R.J. Bushway, S. Nesbit, T. Fan, R. Sheridain, V. Greene, J. AOAC Int. 91 (2008) 408.
[5] M. Lin, L. He, J. Awika, L. Yang, D.R. Ledoux, H. Li, A. Mustapha, J. Food Sci. 73 (2008) T129.
[6] H.A. Cook, C.W. Klampfl, W. Buchberger, Electrophoresis 26 (2005) 1576.
[7] L. Strekowski, B. Wilson, Mutation Res. 623 (2007) 3.
[8] M.L. Guo, J.H. Chen, L.H. Nie, S.Z. Yao, Electrochim. Acta 49 (2004) 2637.
[9] A. Mehdinia, S.H. Kazemi, S.Z. Bathaie, A. Alizadeh, M. Shamsipur, M.F. Mousavi, J. Pharm. Biomed. Anal. 49 (2009) 587.
[10] S.D. Keighley, P. Li, P. Estrela, P. Migliorato, Biosens. Bioelectron. 23 (2008) 1291.
[11] M. Yang, J.B. Hu, Q.L. Li, Anal. Lett. 40 (2007) 2758.
[12] D.L. Li, X.Q. Zou, Q. Shen, S.J. Dong, Electrochem. Commun. 9 (2007) 191.
[13] T. Hugel, M. Seitz, Macromol. Rapid Commun. 22 (2001) 989.
[14] G.B. Demirel, T. Çaykara, Appl. Surf. Sci. 255 (2009) 6571.
[15] O. Corduneanu, A.M. Chiorcea-Paquim, M. Garnett, A.M. Oliveira-Brett, Talanta 77 (2009) 1843.
[16] H.Y. Shen, Y.G. Zhang, L.P. Wang, Q.F. Mao, Chin. Chem. Soc. (2009) 341.
[17] P.G.A. Janssen, J. Vandenbergh, J.L.J. van Dongen, E.W. Meijer, A.P.H.J. Schenning, J. Am. Chem. Soc. 129 (2007) 6078.

Talanta 80 (2009) 489–492

Contents lists available at ScienceDirect

Talanta

journal homepage: www.elsevier.com/locate/talanta

Determination of oleic acid in sunflower seeds by infrared spectroscopy and multivariate calibration method

Miguel A. Cantarelli[a,b], Israel G. Funes[c], Eduardo J. Marchevsky[b,d], José M. Camiña[a,d,*]

[a] Facultad de Ciencias Exactas y Naturales, Universidad Nacional de La Pampa, Av. Uruguay 151 (6300) Santa Rosa, La Pampa, Argentina
[b] Instituto de Química de San Luis (INQUISAL), Chacabuco y Pedernera (5700) San Luis, Argentina
[c] Laboratorio de Control de Calidad, Gente de La Pampa S.A. Ruta 1 km 171.5 (6330) Catriló, La Pampa, Argentina
[d] Consejo Nacional de Investigaciones Científicas y Técnicas (CONICET), Av. Rivadavia 1917 (C1033AAJ) Ciudad de Buenos Aires, Argentina

ARTICLE INFO

Article history:
Received 8 June 2009
Received in revised form 1 July 2009
Accepted 2 July 2009
Available online 10 July 2009

Keywords:
Sunflower
Seed
Oleic acid
PLS
Infrared spectroscopy

ABSTRACT

A method for the determination of oleic acid in sunflower seeds is proposed. One hundred samples of sunflower seeds were analyzed by near-infrared diffuse reflectance spectroscopy (NIRDRS). The direct measures were realized in ground and sifted seeds. The PLS multivariate calibration model was obtained using first derivate absorbance values as response matrix, while the oleic acid concentration matrix was obtained analyzing the seed samples by gas chromatography with a flame ionization detector (GC-FID). The NIRDRS-PLS model was validated externally using unknown samples of sunflower seeds. The accuracy and precision of the method was evaluated using GC as reference method. The following figures of merit (FOM) were obtained: LOD = 3.4% (w/w); LOQ = 11.3% (w/w); SEN = 8×10^{-5}; SEL = 0.15; analytical sensibility (γ) = 1.5 and linear range (LR) = 18.1–89.2% (w/w). This method is useful for the fast determination of oleic acid in sunflower seeds and for quality control of raw materials.

© 2009 Elsevier B.V. All rights reserved.

1. Introduction

In Argentina, sunflower crops represent an important agricultural, industrial and commercial activity due to the high production of this grain. In the year 2007, the total world production of sunflower grains was 2.7×10^7 ton; Argentina occupied the 3rd place in the production of sunflower seeds, with 3.5×10^6 ton, after Russia and Ukraine, with a sunflower cultivated area for the first country of 2.44×10^6 ha [1].

Since 1975, when the crop was introduced in Argentina, varieties of sunflower have been cultivated, with high content of oleic acid, higher than 77% of the total content of fatty acids, higher than the traditional sunflower whose range of oleic acid is 15–25%. Due to its high content of oleic acid, the high oleic sunflower varieties are very much requested by edible oil factories to obtain oils with high oleic acid concentration, which have a higher commercial price in comparison with the rest of the common edible oils. For this reason, the oleic acid analysis is crucial to define the final price of the raw material.

On the other hand, the production of biodiesel around the world involves the use of vegetable and animal oils, including traditional and high oleic sunflower varieties [2]. In previous works, the use of sunflower oil in biodiesel production was reported, including the production of biodiesel at room temperature [3], optimization of biodiesel production from vegetable oils [4] and the study of blended vegetable oils for production of biodiesel [5]. Sunflower oil is frequently used for biodiesel production and, as in the case of edible oil factories, the cost of sunflower raw material depends on the content of oleic acid in the seed.

The percentage of oleic acid in seeds is determined by gas chromatography, which is the more classical method for this determination [6]. The technique requires an important time of analysis, including the sample preparation and chromatographic times, which result in a critical aspect in the commercialization of seeds for biodiesel production and edible oil factories. Since the percentage of oleic acid determines the final price of the raw material, it is an important fact to find a single and fast method that may allow analyzing the content of oleic acid by direct measure on seeds, without chemical pretreatment of samples, reducing considerably the analysis time.

Oleic and fatty acids analysis were widely studied in previous works. In this way, a physiological study of the stearic synthesis and oleic acids in developing high-oleic sunflower seeds has been reported by use of TLC and radio-isotope scanning in biological assays [7]. Nevertheless, spectroscopic methods have been the preferred ones for analysis of fatty and organic acids in different kinds of samples. On the other hand, near-infrared diffuse reflectance

* Corresponding author. Tel.: +54 2954 436787; fax: +54 2954 432535.
E-mail addresses: jcaminia@exactas.unlpam.edu.ar, jcaminia@yahoo.com (J.M. Camiña).

0039-9140/$ – see front matter © 2009 Elsevier B.V. All rights reserved.
doi:10.1016/j.talanta.2009.07.004

spectroscopy (NIRDRS) has been proved to be a convenient and fast quantitative method for complex samples and its properties have been improved by means of the multivariate calibration methods [8]. Near-infrared reflectance hyperspectral imaging and multivariate calibration methods were used to determine the concentration of oleic acid in corn kernel [9]. An automated method for the determination of total fatty acids and peroxide value by FTIR with spectral reconstitution was reported [10]. In a previous work, the determination of total fatty acids in poultry feed by FTIR and attenuated total reflectance was reported [11]. Also, fatty acids composition in intact seed of perilla was studied using NIRS and PLS [12]. The profile of fatty acids was determined in cotyledon soybean seeds by reflectance NIR and PLS [13]. A study of acidity and peroxide index in edible oil was carried out by near-infrared spectrometry and PLS [14]. The determination of trans isomers of fatty acids was carried out for edible oil by FTIR and spectral reconstitution procedure [15]. The monitoring of oleic, linoleic, un-saturated, mono-unsaturated and poly-unsaturated fatty acids in virgin olive oil and FTIR and PLS was proposed [16]. The determination of oleic, linoleic, total saturated and unsaturated fatty acids was carried out in edible oils samples by IR spectroscopy, second derivate data and multivariate calibration analysis [17]. Also, a work has been reported that uses the second derivate spectra of NIRS and PLS to estimate the content of total free fatty acids in high oleic sunflower seeds, using a titrimetric method as reference [18] and there is a preliminary technical report that uses NIRS and PLS for the estimation of oleic and linoleic acids in sunflower seed using a special device for seeds analysis and absorbance measures without preprocessing [19]. On the other hand, previous works have been reported related to the classification of edible oils by use of multivariate calibration methods to evaluate quality/authenticity [6,20], designation of origin [21] and a study of oxidative index for determination of aging of edible oils by NIRS and chemometric methods [22].

This paper discusses a fast and complete method to quantify a wide range of oleic acid concentrations in all varieties of sunflower seeds, by near-infrared reflectance diffuse spectroscopy (NIRDRS) and data evaluation using the partial least square regression (PLS) multivariate calibration method. In comparison with previous works, the proposed method was of easy application, because it requires a very simple treatment of sunflower seed samples and simple modeling, and also because it uses only 100 variables (first derivate absorbance spectra) and 2 PLS components. Another important contribution of this method is the report of the complete study of analytical properties: accuracy, precision and figures of merit (FOM) of the NIRDRS-PLS method. FOM have not been reported previously for the determination of oleic acid in sunflower seeds by infrared spectroscopy. The reported FOM include limit of detection (LOD), limit of quantification (LOQ), sensibility (SEN), selectivity (SEL) and analytical sensibility (γ) and linear range (LR) [23–24].

2. Experimental

2.1. Instrumental

The chromatographic analysis was carried out with a Varian Gas Chromatograph model GC 3900 (CA, USA) with a Varian flame ionization detector (FID). A capillary column Varian factor FOUR VF-23 (cyanopropyl stationary phase, 30 m, 0.25 mm ID) was used.

Diffuse reflectance infrared measures were taken by a Brimrose NIRS model Luminar (MA, USA) with acoustic–optic tuning filter (AOTF) and a rotator cup as sample cell.

The Unscrambler 6.11 by CAMO-AS (Trondheim, Norway) software was used for the PLS-1 modeling and the figures of merit were calculated using the MVC1 software [25].

2.2. Reagents

A 1000 $\mu g\,mL^{-1}$ of fatty acid Supelco 31 mix FAME (MO, USA) standard solution was used for the chromatographic analysis. Heptane and methanol were provided by Merck (Darmstad, Germany) and potassium hydroxide was provided by Sigma (MO, USA). The N_2 gas carrier and H_2 and air (chromatographic quality) were provided by Air Liquid (Buenos Aires, Argentina).

2.3. Sampling and sample treatment

The varieties of sunflower seeds (from low to high oleic acid content) were obtained from different places of Argentina and harvested from 2007 to 2008. Validation was carried out with 20 samples, different from those used to obtain the model. The criteria for selection of samples for the calibration step covered a wide range of oleic acid concentrations, from low to high oleic sunflower varieties, to improve the predictive ability of the model. For the validation step all samples were selected randomly.

The chromatographic analysis was carried out following the ISO 5590 method for the determination of fatty acids methyl esters by gas chromatography. A portion of 20.00 g of whole seeds was weighted in an OHaus analytical balance (NJ, USA) and pressed in a hydraulic press (Jack, Argentina). A weight of 0.50 g of obtained oil was transferred to a 10 mL volumetric flask, dissolved with 5 mL of n-heptane, added with 0.2 mL of 2 mol L^{-1} potassium hydroxide in methanol, stirred for 20 s and diluted with n-heptane to mark. After phase separation, the supernatant was collected for gas chromatography analysis [26]. This esterification method is recommended due to its low reagent toxicity and cost [27].

For the NIRDRS analysis, whole sunflower seeds, free from dust, samples were ground in a Dalvo grinder, model MCI. The fraction $\leq$2 mm was obtained by passing through a 2 mm sieve and placed in the sample rotator cup.

3. Results and discussion

3.1. Chromatographic analysis

Calibration solutions of oleic acid were prepared by adequate dilutions of 1000 $\mu g\,mL^{-1}$ standard of fatty acids. Five triplicates concentration levels were analyzed, obtaining a calibration fit with an r^2 coefficient of 0.995. Then, the analysis of 100 sunflower samples was carried out to obtain the necessary concentration matrix to build the PLS model for the calibration step. Chromatographic parameters were the following: injection volume: 1 μL; temperature program: 150 °C during 4 min, 3 °C/min to 190 °C, 1 °C/min to 200 °C; final temperature 200 °C during 3 min; detector temperature: 225 °C; injector temperature: 275 °C; gas carrier flow: N_2, 1 mL min^{-1}; split: 1:20; total run time: 30 min and oleic acid time: 12 min.

3.2. Near-infrared diffuse reflectance spectroscopy (NIRDRS)

A portion of the same samples used for chromatographic analysis was analyzed by infrared spectroscopy. A weight of 20 g of whole ground and sifted sample seeds were placed in the rotator cup and the NIRDRS spectra were obtained. The total spectral range went from 1100 to 2200 nm every 2 nm. The sample rotator cup with the samples was irradiated with NIR radiation, and detected by acousto-optic tunable filter (AOTF). The instrumental system is based on the measurement of the relative beam intensities produced when a 45° plane polarized beam of radiation passes through a sample cell and is directed to the entrance window of the AOTF. The AOTF filter uses an anisotropic crystal of TeO_2, producing two planar and orthogonally polarized beams. The presence of an optically active sample

causes the polarization plane to rotate and a consequent difference in the intensities of the AOTF diffracted beams is registered as a function of the optical activity of the sample. Thirty scans were obtained for every standard and sample seeds and the total number of scans collected from every sample was averaged by Brimrose software into a single spectrum, which was used in the response matrix. Measurements were carried out at room temperature.

3.3. PLS model: calibration step

The concentration of oleic acid obtained by the GC method was used as the concentration matrix for the NIRDRS-PLS model. The response matrix was obtained using the first derivate absorbance values from the NIRDRS spectrum (a single averaged spectrum for every sample was used). The first derivate absorbance signal was preferred due to the fact it had yielded better results in the previous multivariate models in comparison with the second derivate and conventional absorbance signal. The range from 1596 to 1794 nm was selected by analysis of the correlation coefficient and important variables as function of wavelength [28]. This selected range produced a response matrix with 100 variables (wavelength) and 100 objects (calibration samples). Fig. 1 shows the first derivate spectral data of 100 calibration samples. With the selected range of wavelength, the final model was built using internal validation (cross-validation method), where the model leaves out one standard of the calibration set every time. Then, the calibration and validation model error was calculated through root mean square of calibration (RMSEC) and root mean square of prediction (RMSEP), finding a minimum value for both cases in the second PLS component: for this component, RMSEC and RMSEP showed a value of 4.65 and 4.72 respectively. The explained variance, obtained in the calibration and validation processes for the NIRDRS-PLS model, were 99.46 and 99.45% respectively, using 2 PLS components, which are in agreement with the minimum value found for the RMSEC and RMSEP. With this 2 PLS components for the NIRDRS-PLS model, the observed-predicted concentrations plot for oleic acid was obtained, showing an r^2 coefficient = 0.995, abscise and slope (mean ± standard deviation): 0.63 ± 1.10 and 0.99 ± 0.02 respectively, which suggest a good fit of the model (ideal values of $r^2 = 1$, abscise = 0 and slope = 1).

3.4. External validation set: accuracy and precision

In order to corroborate the predictive ability of the model, 20 triplicates of the unknown samples were predicted by the NIRDRS-PLS method and the obtained concentrations were compared with gas chromatography analysis. Table 1 shows the mean values with standard deviation of 20 validation samples. The accuracy of the method was evaluated by the elliptical joint confidence region (EJCR) test, which is frequently used to evaluate accuracy of new analytical methods [29,30]. This ellipse must contain values of abscise = 0 and slope = 1, which indicate the absence of systematic errors [31,32]. The ellipse for oleic acid includes these theoretical values (1, 0) at a level of confidence of 95%, which indicates absence of systematic errors of the IR-PLS method in comparison with gas chromatography.

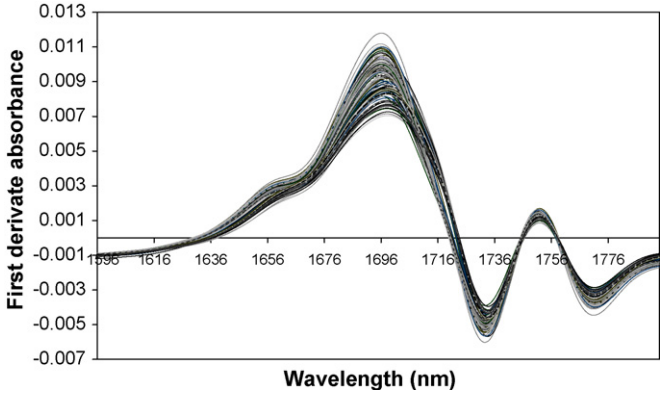


Fig. 1. Spectra data plot. First derivate absorbance – from 1596 to 1794 nm – for 100 calibration samples of sunflower seeds.

Table 1
Results of validation test set.

Sample	GC[a]	NIRDRS-PLS[a]	Sample	GC[a]	NIRDRS-PLS[a]
1	20.5 ± 0.1	21.2 ± 0.3	11	69.7 ± 0.2	69.0 ± 0.7
2	27.2 ± 0.1	27.0 ± 0.4	12	27.5 ± 0.1	28.4 ± 0.3
3	30.2 ± 0.2	29.0 ± 0.5	13	42.3 ± 0.1	44.1 ± 0.4
4	26.9 ± 0.1	25.4 ± 0.4	14	81.9 ± 0.3	82.2 ± 0.9
5	59.8 ± 0.2	55.7 ± 0.6	15	51.3 ± 0.2	49.2 ± 0.5
6	85.5 ± 0.3	86.0 ± 1.0	16	89.2 ± 0.3	90.1 ± 1.1
7	82.7 ± 0.2	85.3 ± 0.6	17	25.5 ± 0.1	24.2 ± 0.3
8	65.8 ± 0.2	63.5 ± 0.7	18	79.6 ± 0.2	75.9 ± 0.7
9	27.5 ± 0.1	28.4 ± 0.3	19	75.7 ± 0.2	78.4 ± 0.6
10	72.9 ± 0.3	76.2 ± 1.0	20	48.5 ± 0.1	46.4 ± 0.4

[a] Concentration of oleic acid (%, w/w) ± standard deviation ($n = 3$).

Precision of the NIRDRS-PLS model was evaluated using the F test, through the analysis of 10 replicates of the same sample, analyzed by both, gas chromatography and the NIRDRS-PLS methods. The critical value is $F = 4.026$ ($n_1 - 1 = 9$ and $n_2 - 1 = 9$). The calculated F value was 3.810, lower than the F critical value, which indicates that the proposed method was precise in comparison to the classical chromatographic method. The percentage of precision obtained for a same day (intra-day precision) was 1.2%, while the precision found for a week (inter-day precision) was 2.0%.

3.5. Figures of merit (FOM)

The method's calculated figures of merit (FOM) were: limit of detection (LOD), limit of quantification (LOQ), sensibility (SEN_k), selectivity (SEL_k) and analytical sensibility (γ_k). SEN_k is described as:

$$SEN_k = \frac{1}{\|\mathbf{b}_k\|}$$

where $\mathbf{b}_k$ is the vector of regression coefficient for the k analytes. LOD is defined as:

$$LOD = 3.3 \|\delta_r\| \|\mathbf{b}_k\|$$

where $\|\delta_r\|$ is a measure of instrumental noise. LOQ is defined as:

$$LOQ = 3LOD$$

SEL_k is defined as:

$$SEL_k = \frac{\|\mathbf{s}_k^*\|}{\|\mathbf{s}_k\|}$$

Table 2
Figures of merit (FOM) calculated for the NIRDRS-PLS method.

Figures of merit	Value
Limit of detection (LOD)	3.4% (w/w)
Limit of quantification (LOQ)	11.3% (w/w)
Sensibility (SEN)	0.00008
Selectivity (SEL)	0.15
Analytical sensibility (γ)	1.5
Linear range	18.1–89.2% (w/w)

Table 3
Comparative table for the determination of oleic acid and other analytes by infrared spectroscopy reported in previous works.

IR method	Sample	Analyte	Reported FOM
NIR-reflact–multiv. cal [9]	Corn kernel	Oleic acid	Non-reported
FTIR–spect. reconst. [10]	Edible oils	Total fatty acids and peroxide value	Non-reported
FTIR-ATR [11]	Poultry feed	Total fatty acids	Non-reported
NIR and mult. cal. [12]	Perilla seed	Palmitic, stearic, oleic, linoleic, linolenic acids	Non-reported
NIR reflectance–multiv cal. [13]	Soybean cotyledons	Palmitic, stearic, oleic, linoleic, linolenic acids	Non-reported
NIR-PLS [14]	Edible oil	Peroxide and acidity index	LOD
FTIR-ATR [15]	Edible oil	Trans fatty acids	Non-reported
FTIR-PLS [16]	Virgin olive oil	Oleic, linoleic, unsaturated, mono-unsaturated, poly-unsaturated fatty acids	LOD, LOQ, SEN, γ and SEL
FTIR-PLS [17]	Edible oil	Oleic, linoleic, unsaturated and saturated fatty acids	Non-reported
NIRS-PLS [18]	Sunflower seed	Total free fatty acids	Non-reported
NIRS-PLS [19]	Sunflower seed	Oleic and linoleic acids	Non-reported

where $\mathbf{s}_k$ is the vector of spectral sensitivities of k components in the pure form, while $\mathbf{s}_k^*$ is the projection onto the net analyte signal space [24]. Finally, analytical sensibility is defined as:

$$\gamma_k = \frac{\mathrm{SEN}_k}{\left\|\delta_r\right\|}$$

The figures of merit for determination of oleic acid in sunflower seeds by the proposed NIDRS-PLS method are shown in Table 2. Table 3 shows a summary of the determination of oleic acid and other analytes using infrared spectroscopy, reported in previous works for edible oil and seed samples.

4. Conclusions

This paper shows the result of a complete research for the determination of oleic acid by direct analysis in sunflower seeds, using near-infrared diffuse reflectance spectroscopy and data evaluation by partial least square multivariate calibration. The proposed method is fast, accurate and precise in comparison to the gas chromatography classical method and figures of merit were presented. Due to the fact that pretreatment of solid samples was minimal, this method can be useful for the fast analysis of oleic acid in sunflower seeds, and also for quality control of raw material in edible and biodiesel oil factories.

Acknowledgements

The authors wish to thank to Prof. Roberto Olsina (Universidad Nacional de San Luis) for providing The Unscrambler 6.11 software and the financial support from Consejo Nacional de Investigaciones Científicas y Técnicas (CONICET).

References

[1] FAO, Food and Agriculture Organization of the United Nations, FAOSTAT database. http://faostat.fao.org/.
[2] G. Vicente, M. Martínez, J. Aracil, Energy Fuel 20 (2006) 394.
[3] G. Guan, N. Sakurai, K. Kusakabe, Chem. Eng. J. 146 (2009) 302.
[4] A. Bouaid, M. Martinez, J. Aracil, Chem. Eng. J. 134 (2007) 93.
[5] B. Mosser, Energy Fuel 22 (2008) 4301.
[6] M. Hajimahmoodi, Y. Vander Heyden, N. Sadeghi, B. Jannat, M.R. Oveisi, S. Shahbazian, Talanta 66 (2005) 1108.
[7] R. Pleite, E. Martinez-Force, R. Garces, J. Agric. Food Chem. 54 (2006) 9383.
[8] Y. Hao, W. Cai, X. Shao, Spectrochim. Acta A 72 (2009) 115.
[9] B.A. Weinstock, J. Janni, L. Hagen, S. Wrigth, Appl. Spectrosc. 60 (2006) 9.
[10] X. Yu, S. Du, F. van der Voort, T. Yue, Z. Li, Anal. Sci. 25 (2009) 627.
[11] S.T.H. Sherazi, S.A. Mahesar, M.I. Bhanger, F.R. van De Voort, J. Sedman, J. Agric. Food Chem. 55 (2007) 4928.
[12] K.S. Kim, S.H. Park, M.G. Choung, J. Agric. Food Chem. 55 (2007) 1679.
[13] C.A. Roberts, C. Ren, P.R. Beuselinck, H.R. Benedict, K. Bilyeu, Appl. Spectrosc. 60 (2006) 1328.
[14] S. Armenta, S. Garrigues, M. de la Guardia, Anal. Chim. Acta 596 (2007) 330.
[15] F.R. van der Voort, J. Sedman, S.T. Sherazi, J. AOAC Int. 90 (2007) 446.
[16] R.R. Maggio, T.S. Kaufman, M.D. Carlo, L. Cerretani, A. Bendini, A. Cichelli, D. Compagnone, Food Chem. 114 (2009) 1549.
[17] A.A. Christy, P.K. Egeberg, Chemometr. Intell. Lab. 82 (2006) 130.
[18] C.R. Moschner, B. Biskupek-Korell, Eur. J. Lipid Sci. Tech. 108 (2006) 606.
[19] Brimrose, Report # 7, determination of percent oleic and linoleic acid in sunflower seeds using AOTF-NIR spectroscopy.
[20] F. Fernandes Gambarra-Neto, G. Marino, M.C. Ugulino Araújoa, R. Kawakami Harrop Galvão, M.J. Coelho Pontesa, E.P. de Medeiros, R. Sousa Lima, Talanta 77 (2009) 1660.
[21] S. López-Feria, S. Cárdenas, J.A. García-Mesa, M. Valcárcel, Talanta 75 (2008) 937.
[22] Y. Le Dréau, N. Dupuy, J. Artaud, D. Ollivier, J. Kister, Talanta 77 (2009) 1748.
[23] A.C. Olivieri, N.M. Faber, J. Ferré, R. Boqué, J.H. Kalivas, H. Mark, Pure Appl. Chem. 78 (2006) 633.
[24] A. Lorber, K. Faber, B.R. Kowalsky, Anal. Chem. 69 (1997) 1620.
[25] A.C. Olivieri, H.C. Goicoechea, F.A. Inón, Chemometr. Intell. Lab. 73 (2004) 189.
[26] ISO, International Organization for Standardization 1978, International Standard ISO 5509, p. 1.
[27] M.C. Milinsk, M. Matsushita, J.V. Visentainer, C.C. de Oliveira, N.E. de Souza, J. Braz. Chem. Soc. 19 (2008) 1475.
[28] V.A. Lozano, J.M. Camiña, M.S. Boeris, E.J. Marchevsky, Talanta 73 (2007) 282.
[29] M.J. Culzoni, M.M. De Zan, J.C. Robles, V.E. Mantovani, H.C. Goycochea, J. Pharm. Biomed. 39 (2005) 1068.
[30] M.A. Cantarelli, R.G. Pellerano, E.J. Marchevsky, J.M. Camiña, Food Chem. 115 (2009) 1128.
[31] J. Riu, F.X. Rius, Anal. Chem. 68 (1996) 1851.
[32] J. Riu, F.X. Rius, Trend Anal. Chem. 16 (1997) 211.

Talanta 80 (2009) 493–498

Contents lists available at ScienceDirect

Talanta

journal homepage: www.elsevier.com/locate/talanta

Determination of phenylurea herbicides in aqueous samples using partitioned dispersive liquid–liquid microextraction

Tso-Ying Chou, Shu-Ling Lin, Ming-Ren Fuh*

Department of Chemistry, Soochow University, No. 70 Lin-hsi Road, Shihlin, Taipei 111, Taiwan

ARTICLE INFO

Article history:
Received 21 May 2009
Received in revised form 3 July 2009
Accepted 3 July 2009
Available online 10 July 2009

Keywords:
Partitioned dispersive liquid–liquid microextraction (PDLLME)
Liquid chromatography
Phenylurea herbicides (PUHs)
Polar organic compounds

ABSTRACT

Partitioned dispersive liquid–liquid microextraction (PDLLME), using THF as the dispersive solvent and dichloromethane as the extraction solvent, was utilized to isolate and concentrate phenylurea herbicides (PUHs) from aqueous samples. In PDLLME, a dispersive solvent should be able to partition in the organic extractant droplets to effectively extract the polar organic compounds from aqueous samples. The mixture of the water-immiscible extractant and the partitioned dispersive solvent was obtained by centrifugation, dried under low pressure, reconstituted in methanol–water mixture (1:1), and injected into a HPLC system for the determination of PUHs. The enrichment factors of the PUHs ranged from 68 to 126 under the optimal conditions. The linear range was 0.5–100 ng ml^{-1} for each analyte, the relative standard deviations of PUHs were in the range of 1.5–5.9% (n = 5), and the detection limits (signal-to-noise ratio of 3) ranged from 0.10 to 0.28 ng ml^{-1} for the herbicides. The range of intraday precision (n = 5) for PUHs at the levels of 0.5, 5, and 50 ng ml^{-1} were 3.0–5.9%, 1.8–3.3%, and 2.2–3.6%, respectively. The range of interday precision (n = 5) at 0.5, 5, and 50 ng ml^{-1} were 0.4–1.8%, 1.2–2.4%, and 0.9–2.3%, respectively. The recoveries of PUHs from three spiked river water samples, at a level of 10 ng ml^{-1}, were 91.2–104.1%. Due to its rapidity, ease of operation, and high recovery, PDLLME can be utilized to isolate and concentrate organic environmental contaminants such as PUHs from aqueous samples.

© 2009 Elsevier B.V. All rights reserved.

1. Introduction

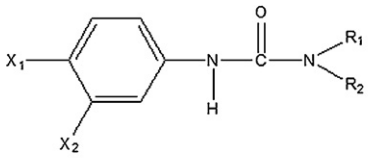
Phenylurea herbicides (PUHs) are commonly used in agriculture for weed control by inhibiting their photosynthesis pathways. There are quite a few of PUHs reported to be potential carcinogens [1–3]. Herbicides including PUHs can enter environment through various pathways such as washing and leaching into surface and ground waters, which may be slowly accumulated and lead to toxic levels. These concerns urge the need of monitoring herbicides in environment as well as establishing an admissible limit for any individual herbicide. The European Union regulates the use of PUHs and allows a permissible limit of 0.1 μg l^{-1} of any single herbicides in drinking water [4].

A number of publications have reported the determination of PUHs in water and crops by various analytical techniques. Gas chromatography (GC) can achieve efficient separation and quantitative determination for many small organic molecules. However, derivatization is necessary for thermally unstable PUHs to be determined by GC [5,6]. High performance liquid chromatography (HPLC) provides the advantage of direct analysis of PUHs without derivatization prior to chromatographic separation. A variety of publications utilized HPLC for determining the amount of PUHs in water samples [4,7–9], crops [10,11], and soil [12,13]. Several detection methods have been coupled to HPLC for the determination of PUHs, including post-column derivatization with fluorescence detection [8,9,11], mass spectrometry (MS) [10,14], and UV detection [4,7,12]. Although UV detection does not provide superior sensitivity for quantitative analysis, the absence of labeling process and the relatively low cost for equipment setup make UV detection an attractive detection method compared to fluorescence and MS.

A sample preparation technique, which can isolate and concentrate target analytes prior to separation, becomes desirable in order to allow UV detection for determining trace analytes. Most commonly used sample preparation techniques include solid phase extraction (SPE) [8,15], solid phase microextraction (SPME) [7,9,16], liquid–liquid extraction (LLE) [10,17], liquid phase microextraction (LPME) [18–20], and dispersive liquid–liquid microextraction (DLLME) [21–25]. Conventional LLE requires a large amount of organic solvent and is a time-consuming process. Although SPE greatly reduces the use of organic solvent for extracting analytes, the cost of purchasing solid phase particles can be expensive. SPME is a solvent-free extraction technique, which utilizes a section of polymer-coated fiber as the stationary phase to allow analytes partitioning between the sample matrix and the stationary phase.

* Corresponding author. Tel.: +886 2 28819471x6821; fax: +886 2 28812685.
E-mail address: msfuh@mail.scu.edu.tw (M.-R. Fuh).

0039-9140/$ – see front matter © 2009 Elsevier B.V. All rights reserved.
doi:10.1016/j.talanta.2009.07.005



Herbicides	X_1	X_2	R_1	R_2
1. Metoxuron	Cl	OCH_3	CH_3	CH_3
2. Monuron	Cl	H	CH_3	CH_3
3. Monolinuron	Cl	H	CH_3	OCH_3
4. Isoproturon	$(CH_3)_2CH$	H	CH_3	CH_3
5. Metobromuron	Br	H	CH_3	OCH_3
6. Buturon	Cl	H	CH_3	$CH(CH_3)CCH$
7. Linuron	Cl	Cl	CH_3	OCH_3
8. Chlorbromuron	Br	Cl	CH_3	OCH_3

Fig. 1. Structures of phenylurea herbicides.

However, the polymer-coated fiber is usually fragile, limited types of polymer coatings are commercially available, and SPME fibers are fairly expensive. Same as SPME, LPME generally requires a longer extraction time. DLLME, a relatively new sample preparation technique, provides the advantages of ease of operation, rapid extraction, and use of small volume of organic solvent. In DLLME, a water-immiscible organic extractant and a water-miscible dispersive solvent are two key factors to form fine droplets of the extractant, which disperse entirely in the aqueous solution, for extracting analytes. The cloudy sample solution is then subjected to centrifuge to obtain sedimented organic extractant containing target analytes. However, the partitioning of analytes in organic extractant may be decreased due to the increased solubility of analytes in aqueous phase as larger volumes of dispersive solvent are used [26]. This phenomenon becomes more critical for isolating polar organic compounds using DLLME. A recently developed sample preparation technique, partitioned dispersive liquid–liquid microextraction (PDLLME) [27], improves the extraction efficiency by choosing a dispersive solvent that can be partitioned in the extractant droplets. The polar nature of the dispersive solvent allows the partitioning of the polar analytes into the disperser, which increases the amount of analytes transferred into the extractant droplets, and leads to the increase in extraction efficiency by PDLLME.

In this study, we utilized PDLLME for the determination of PUHs in aqueous samples using HPLC coupled with UV detection. The type and volume of both extractant and dispersive solvent, salt addition, and pH adjustment were investigated as well as optimized to achieve efficient extraction of PUHs by PDLLME. Application of PDLLME was also demonstrated by determining PUHs in three river water samples.

2. Experimental

2.1. Materials and reagents

Analytical standards of phenylurea herbicides (metoxuron, monuron, metobromuron, isoproturon, monolinuron, buturon, linuron, and chlorbromuron), as shown in Fig. 1 and Table 1, were purchased from Riedel-de Haen (Seelze, Germany). Sodium chloride (NaCl) and hydrochloric acid (HCl) were also obtained from Riedel-de Haen. HPLC-grade organic solvents including acetone, isopropyl alcohol (IPA), acetonitrile (ACN), methanol, tetrahydrofuran (THF) and dichloromethane (DCM) were purchased from Mallinckrodt Baker, Inc. (Phillipsburg, NJ, USA). Chlorobenzene (CB; 99.5+%) was from Aldrich (Milwaukee, WI, USA). Tetrachloroethylene (C_2Cl_4; 99.9+%) was obtained from Sigma–Aldrich (Steinhelm, Germany). Deionized water was from a Milli-Q Plus water purification system (Millipore, Bedford, MA, USA). All herbicide stock solutions were prepared individually in methanol at a concentration of 1000 mg l^{-1} and stored at −20 °C. Working standard solution was prepared by spiking a stock solution into river water. Three river water samples were collected from Wai-Shuanghsi, Shuanghsi, and Keelung River in Taipei, Taiwan to serve as real environmental samples. All aqueous samples were filtered through a 0.45 μm Durapore membrane filters (Millipore, County Cork, Ireland) prior to extraction. Solvents and reagents used in this study were all HPLC or analytical grade.

2.2. Instrumentation and LC conditions

A HP-1100 HPLC system (Hewlett-Packard Co., Palo Alto, CA, USA) equipped with a quaternary pump, an online degasser, an autosampler, a photodiode array detector, and a reversed phase SymmetryShield™ RP18 column (2.1 mm × 50 mm, 3.5 μm; Waters, Ireland) was employed for determining the herbicides. ChemStation for LC3D (Rev. A. 10.02[1757], Agilent, USA) was used for controlling the HPLC system and data analysis. The solvent used for isocratic separation was 40% ACN in deionized water at a flow rate of 0.2 ml min^{-1}. Full scan UV spectra of herbicide standards were performed to develop proper LC separation and confirm the appearance of PUHs in real samples. The detection was then set at 243 nm for optimizing the extraction parameters. Fig. 2 shows the representative chromatograms of blank (bottom trace) and the spiked (1 ng ml^{-1}, top trace) sample solutions.

A Kubota centrifuge (Model 2420, Tokyo, Japan), a miVac DUO concentrator (Genevac Ltd., Ipswich, UK) operated under low pressure, and Hamilton syringes (100 μl and 2.5 ml; Reno, NV, USA) were utilized for the study. The screw-capped test tubes with conical bottom were used for extraction. The 2 ml sample vials with PTFE/red silicon rubber septa and 300 μl vial inserts with polymeric feet were purchased from Agilent and used to hold sample solutions for auto-injection.

Table 1
Physical and chemical properties of phenylurea herbicides.

Herbicides	Molecular weight[a]	Log K_{ow}[a,b]	Solubility in water[b] (μg ml^{-1}, 20–25 °C)	LD_{50}[a] (mg kg^{-1}) (oral, rats)
1. Metoxuron	228.7	1.6	678	1600
2. Monuron	198.7	2.0	230	1053
3. Monolinuron	214.7	2.2	735	1800
4. Isoproturon	206.3	2.5	65	>2000
5. Metobromuron	259.1	2.5	330	2000
6. Buturon	236.7	–	30	1791
7. Linuron	249.1	3.0	64	1146
8. Chlorbromuron	293.5	3.3	35	2150

[a] Material Safety Data Sheet (MSDS) from Sigma–Aldrich.
[b] C.D.S. Tomlin (Ed.), The Pesticide Manual, 11th ed., British Crop Protection Council, Surrey, UK, 1997.

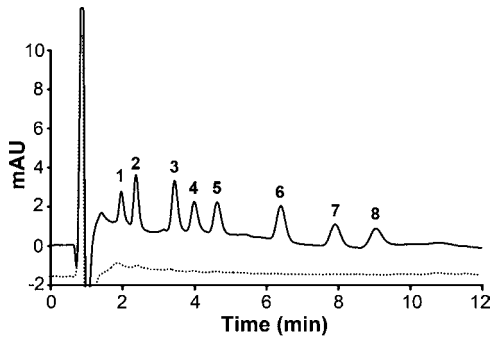


Fig. 2. Representative chromatograms of the blank and the spiked sample solutions. Experimental conditions are described in Section 2.2. Peak identification: (1) metoxuron, (2) monuron, (3) monolinuron, (4) isoproturon, (5) metobromuron, (6) buturon, (7) linuron, and (8) chlorbromuron.

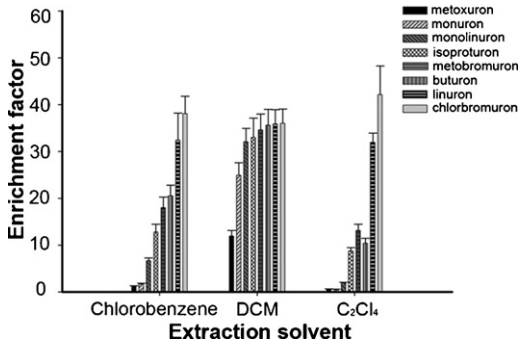


Fig. 3. Selection of organic extractant. Three measurements were performed for each set of experiments. Conditions: spiked sample solution (50 ng ml^{-1} each); organic extractant: 10 μl chlorobenzene, 70 μl DCM, 10 μl C_2Cl_4; dispersive solvent: 500 μl acetone. Refer to Section 3.1 for experimental details.

2.3. Extraction procedures

A 5 ml aqueous sample containing the target herbicides (in 0.5% NaCl, without adjusting pH) was placed in a conical-bottomed test tube. A 1 ml of DCM/THF (60/1000, v/v) mixture was rapidly injected into the sample using a 2.5 ml syringe and gently mixed the cloudy solution. The extracted herbicides in the mixed phase of DCM droplets and DCM-partitioned THF were collected by centrifugation (4000 rpm, 5 min) and the sedimented organic phase (~75 μl) was transferred into a 300 μl insert using a 100-μl syringe. The organic phase was dried under low pressure in a concentrator and reconstituted in a 30 μl methanol–water (1:1) mixture. Then 20 μl of the sample solution was auto-injected into the HPLC system for analysis.

2.4. Validation process

The following experiments were performed to validate the method used for quantifying the amount of PUHs remaining in river water samples for this study. Linearity was obtained by generating a calibration curve of individual herbicide concentration vs. peak area. Seven different concentrations (0.5, 1, 5, 10, 30, 50, and 100 ng ml^{-1}) of individual herbicide were spiked in river water collected from Wai-Shuanghsi to mimic the matrix effect in river water and five runs of each sample were performed. The limit of detection (LOD) was defined as the signal-to-noise ratio of 3. The precision and accuracy, including intra-day and inter-day experiments, were obtained at three different concentrations (0.5, 5, and 50 ng ml^{-1}) by calculating the relative standard deviations and the relative recoveries of individual herbicide, respectively. Five runs of each sample were performed. The relative recovery was determined by comparing the measured extracted concentration with the initially spiked concentration of each analyte.

3. Results and discussion

3.1. Selection of organic extractant and dispersive solvent

Selecting an appropriate organic extractant (also called as extraction solvent) is an important issue for performing PDLLME. A suitable extractant needs to meet the following criteria: (1) immiscible in water, (2) with higher density than that of water, (3) having high extraction capability for target analytes. For the selection of dispersive solvent, a suitable candidate has to be miscible with both organic extractant and water as well as to form a cloudy phase when injected with a selected extractant into an aqueous solution. Based on these criteria, chlorobenzene, DCM, and C_2Cl_4 were chosen to be the candidates of organic extractant when acetone was used as

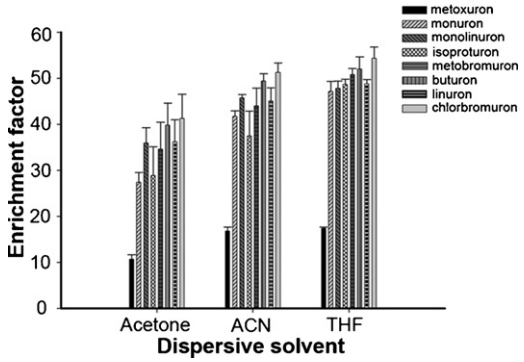


Fig. 4. Selection of disperser solvent. Three measurements were performed for each set of experiments. Conditions: spiked sample solution (50 ng ml^{-1} each); organic extractant: 70 μl DCM; dispersive solvent: acetone, ACN, and THF (500 μl each). Refer to Section 3.1 for experimental details.

dispersive solvent for the study. In the cases of chlorobenzene and C_2Cl_4, 10 μl of the organic extractant was mixed with 500 μl acetone and 500 μl of the organic mixture was rapidly injected into a 5 ml spiked aqueous solution (50 ng ml^{-1} each) for extraction. However, in the case of DCM, no phase separation was observed when the volume of DCM was lower than 70 μl. This phenomenon might be due to the relatively high solubility of DCM in water. Therefore, 70 μl of DCM was used to investigate the extraction efficiency of individual herbicide. The extraction efficiency was determined by calculating the enrichment factor (EF) of each analyte, where $EF = C_{ex}/C_0$ (C_{ex} and C_0 are the concentration of an extracted analyte and the initial concentration of the target analyte, respectively). According to the experimental results shown in Fig. 3, DCM was cho-

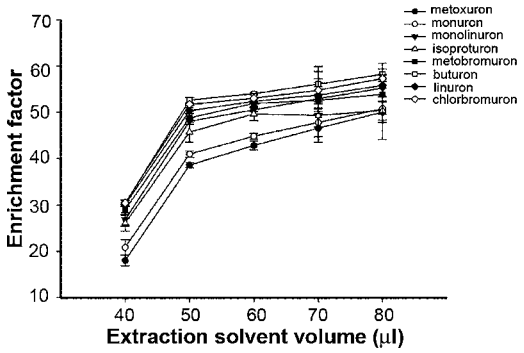


Fig. 5. Effect of extraction solvent volume. Three measurements were performed for each set of experiments. Conditions: spiked sample solution (50 ng ml^{-1} each); dispersive solvent: 500 μl THF. Refer to Section 3.2 for experimental details.

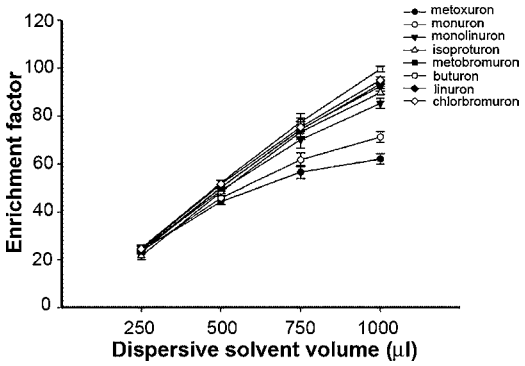


Fig. 6. Effect of disperser solvent volume. Three measurements were performed for each set of experiments. Conditions: spiked sample solution (50 ng ml^{-1} each); organic extractant: 70 μl DCM. Refer to Section 3.2 for experimental details.

sen as the extraction solvent due to the high EF value obtained for most target herbicides.

In addition, methanol, IPA, acetone, ACN, and THF (500 μl each) were utilized as the dispersive solvents while DCM (70 μl) served as the extraction solvent. Same as the procedures mentioned above, the DCM–dispersive solvent mixture was rapidly injected into a spiked sample to form a cloudy phase. However, no phase separation after centrifugation was observed in both cases of methanol and IPA. An increase in the volume of the settled phase (compared with the volume of DCM applied) was observed when THF was used as the dispersive solvent. This volume increase may be due to the partition of THF in the organic extractant droplets, which can effectively extract the polar organic compounds from aqueous samples [27]. Due to the increase in the volume of the settled phase, the EFs calculated based on the volume of the settled phase will decrease proportionally [22]. To improve EF, the settled phase was dried and the residue was reconstituted in LC compatible solvent with a fixed volume. Therefore, the influence of the settled phase volume in EF became negligible. For the selection of dispersive solvent, results shown in Fig. 4, highest EFs were found for all selected PUHs using THF as the dispersive solvent compared to the EFs obtained using acetone or ACN. Similar to the trend with THF, the EFs attained using ACN increased with the increasing volume of ACN (data not shown). However, the EFs (5–32) obtained using ACN were lower than the EFs (22–100) obtained using THF. In the case of acetone, no phase separation was observed when the volume of acetone reached 750 μl or higher. Therefore, THF was chosen as the dispersive solvent for further investigations. The variation in the volume of the extract, using 60 μl DCM and increased volumes of THF (250–1000 μl), ranged from 5 to 10%.

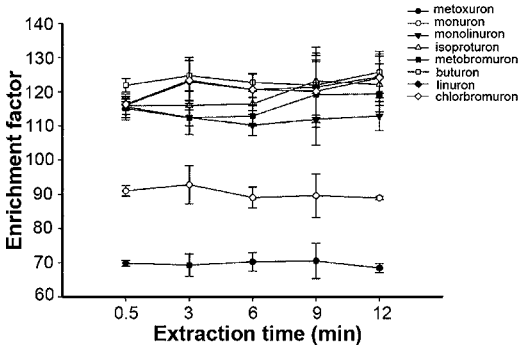


Fig. 7. Effect of extraction time on PDLLME efficiency. Three measurements were performed for each set of experiments. Experimental conditions: spiked sample solution (50 ng ml^{-1} each); organic extractant: 60 μl DCM; dispersive solvent: 500 μl THF. Refer to Section 3.3 for experimental details.

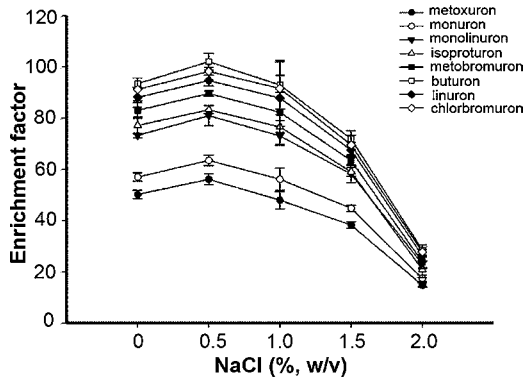


Fig. 8. Effect of ionic strength on PDLLME efficiency. Three measurements were performed for each set of experiments. Conditions: spiked sample solution (50 ng ml^{-1} each); organic extractant: 60 μl DCM; dispersive solvent: 1000 μl THF. Refer to Section 3.4 for experimental details.

3.2. Volume effect of organic extractant and dispersive solvent

To investigate the volume effect of organic extractant on extraction efficiency, several different volumes of DCM (40, 50, 60, 70, and 80 μl; no phase separation after centrifugation was observed as DCM volume was smaller than 40 μl) were applied to perform PDLLME. As shown in Fig. 5, a dramatic increase of EFs was observed on all target analytes as the extraction solvent volume was increased from 40 to 50 μl. For most analytes, except for isoproturon, the EFs were slightly increased with increasing DCM volume (from 50 to 80 μl). However, in the case of isoproturon, a small decrease in EF was found when DCM volume was increased from 60 to 70 μl. According to these observations, a volume of 60 μl DCM was applied for the subsequent experiments.

The dispersive solvent volume is another important factor that affects extraction efficiency in PDLLME. At low disperser volume, the organic extractant droplets cannot form properly which leads to low EFs. At high disperser volume, the solubility of polar organic analytes in aqueous phase will increase due to the increasing partitioning of THF in water. In order to optimize the THF volume, a fixed DCM volume (60 μl) was mixed with a series of THF in different volumes, 250–1000 μl at a 250 μl interval, was utilized to perform PDLLME. The settled phase became unstable at 1250 μl and no phase separation was observed when THF volume reached 1500 μl. Fig. 6 shows that the EFs were increased for all analytes as the THF volume increased from 250 to 1000 μl. Therefore, 1000 μl THF was mixed with 60 μl DCM and 1 ml of the mixture was rapidly injected into an aqueous sample to perform PDLLME for further experiments.

3.3. Effect of extraction time

The importance of extraction time on EF was also investigated to optimize the experimental conditions of PDLLME. After injecting

Table 2
Numerical results of the calibration of PUHs by PDLLME from aqueous samples.

Herbicides	Calibration equation	Regression (R^2)	RSD (%)	LOD (ng ml^{-1})
Metoxuron	$y = 20.45x - 0.11$	0.9998	2.7–4.8	0.18
Monuron	$y = 31.01x - 0.40$	0.9997	3.4–4.9	0.10
Monolinuron	$y = 52.58x - 0.12$	0.9995	1.8–5.9	0.12
Isoproturon	$y = 49.33x - 0.16$	0.9999	1.5–4.3	0.11
Metobromuron	$y = 46.59x - 0.25$	0.9999	1.4–3.4	0.10
Buturon	$y = 49.54x + 0.02$	0.9995	1.9–4.9	0.15
Linuron	$y = 42.19x - 0.31$	0.9997	1.7–5.2	0.24
Chlorbromuron	$y = 41.02x + 0.22$	0.9996	2.5–5.8	0.28

Table 3
Precision and accuracy (intraday vs. interday) of PUHs by PDLLME from aqueous samples.

Herbicides	Concentration (ng ml^{-1})	Intraday (n = 5)		Interday (n = 5)	
		RSD (%)	Accuracy (%)	RSD (%)	Accuracy (%)
Metoxuron	0.5	3.0	100.3	1.7	99.1
	5	2.7	102.5	2.2	101.4
	50	2.9	100.5	1.9	98.6
Monuron	0.5	4.9	100.8	0.7	100.8
	5	3.4	100.9	1.4	100.1
	50	3.6	98.7	2.3	100.7
Monolinuron	0.5	5.9	101.2	0.9	99.8
	5	2.5	99.1	2.0	99.8
	50	3.3	98.2	1.3	100.0
Isoproturon	0.5	4.3	100.4	0.4	100.2
	5	1.8	99.6	1.2	100.4
	50	2.6	100.9	1.5	99.5
Metobromuron	0.5	3.2	100.5	1.3	101.2
	5	1.9	101.0	1.9	101.3
	50	3.4	101.4	0.9	100.0
Buturon	0.5	4.9	100.6	0.9	100.0
	5	2.4	98.1	1.9	100.2
	50	2.2	102.0	1.5	100.5
Linuron	0.5	5.2	101.4	1.2	99.9
	5	2.5	97.3	2.4	99.0
	50	3.4	101.7	1.4	100.8
Chlorbromuron	0.5	5.8	99.2	1.8	100.5
	5	3.3	97.4	1.5	99.7
	50	2.6	98.8	2.1	99.8

the extractant–disperser mixture, the extraction was carried out for five different time intervals (0.5, 3, 6, 9, and 12 min) prior to centrifugation. No significant differences in EFs were observed for all target analytes by increasing extraction time. The experimental results are presented in Fig. 7. This observation implied that the mass transfer of analytes from a sample solution was fast to quickly reach extraction equilibrium due to the considerably large surface area between extractant droplets and sample solution. Similar observations were also reported by other researchers [23,24]. This short extraction time provides a remarkable advantage to perform PDLLME for sample preparation.

3.4. Effect of ionic strength and pH

To assess the influence of ionic strength on extraction efficiency of PDLLME, a series of experiments were performed by increasing NaCl concentration in the range of 0–2% (w/v) at an interval of 0.5% in sample solution. The experimental results (Fig. 8) showed that EFs were increased as 0.5% NaCl was applied and started being decreased for all analytes when NaCl concentration was higher than 0.5%. In all cases, it was also observed that the organic phase became less dense (occupied the upper layer after centrifugation) when 2.5% or more NaCl was added into the system. Therefore a salt concentration of 0.5% was utilized for the subsequent studies.

The pH value of each original sample solution was measured prior to PDLLME. The pH of all sample solutions ranged from 5 to 6. The evaluation of pH effect on PDLLME efficiency was therefore performed within pH 4–pH 9 at an interval of pH 1. The pH value was adjusted by adding 0.1 M HCl or 0.1 M NaOH in spiked river water. No obvious EF changes in the pH range of 4–9 (data not shown) for all target herbicides. Similar pH effect on the determination of PUHs was also reported by Huang's group [7]. As a result, no pH adjustment was done for extracting PUHs from river water.

3.5. Quantitative features

Linearity, LOD, precision, and accuracy were investigated to validate PDLLME for the quantitative analysis of PUHs in river water samples under optimal conditions (60 μl DCM as extraction solvent, 1 ml THF as dispersive solvent, containing 0.5% NaCl, without pH adjustment). The validation procedures were described in Section 2.4. A fairly linear relationship in the concentration range of 0.5–100 ng ml^{-1} was observed with a linear regression coefficient higher than 0.9995 for each target herbicide. The numerical results of the calibration are summarized in Table 2. The precision and accuracy (including intra-day and inter-day experiments) of PDLLME were also examined under optimal conditions. The experimental results are presented in Table 3. The intraday and interday precisions of PUHs were in the range of 1.8–5.9% and 0.4–2.4%, respectively. The method accuracy defined as relative recovery was observed in the range of 97.3–102.5%. In addition, the extraction efficiency of PDLLME for each analyte was investigated and found the enrichment factors of the PUHs ranged from 68 to 126 under the optimal conditions.

3.6. Application of PDLLME

Three aqueous environmental samples collected from Wai-Shuanghsi, Shuanghsi, and Keelung River (close to Soochow University, Taipei, Taiwan) were utilized to demonstrate the capability of PDLLME under optimized conditions. According to our preliminary results, the properties of these 3 matrices, such as pH and ionic strength, were quite similar. They also showed similar chromatographic patterns after extraction. The experimental results (data not shown) showed that the residual PUHs were under their detection limits (see Table 2) in all three samples. In order to examine the matrix effect in real samples, river waters were spiked with PUHs at a level of 10 ng ml^{-1}. Table 4 shows high recoveries of PUHs (91.2–104.1%) from the spiked river waters. The high recoveries indicated a negligible matrix effect on PDLLME efficiency in different aqueous samples from environment.

In addition, two aqueous samples collected from rice fields, one in northern Taiwan (before harvest) and the other in central Taiwan (after harvest), were also examined (data not shown). In brief,

Table 4
Standard deviations and recoveries of PUHs from spiked river water samples.

Herbicides (10 ng ml^{-1})	Wai-Shuanghsi		Shuanghsi		Keelung River	
	Found mean ± S.D. (ng ml^{-1})	Recovery (%)	Found mean ± S.D. (ng ml^{-1})	Recovery (%)	Found mean ± S.D. (ng ml^{-1})	Recovery (%)
Metoxuron	10.3 ± 0.5	102.5	10.4 ± 0.4	103.7	9.6 ± 0.4	96.4
Monuron	10.3 ± 0.2	102.5	10.4 ± 0.2	104.1	10.1 ± 0.1	100.6
Monolinuron	10.1 ± 0.3	100.9	10.1 ± 0.3	100.5	9.7 ± 0.3	96.7
Isoproturon	9.7 ± 0.3	96.7	9.1 ± 0.3	91.2	10.0 ± 0.2	100.3
Metobromuron	9.9 ± 0.5	99.0	9.6 ± 0.5	96.3	10.4 ± 0.3	104.0
Buturon	9.5 ± 0.3	94.6	9.8 ± 0.3	97.7	9.8 ± 0.3	97.8
Linuron	9.7 ± 0.3	96.9	10.1 ± 0.4	100.7	10.0 ± 0.2	99.7
Chlorbromuron	10.1 ± 0.5	101.2	10.3 ± 0.2	103.0	9.7 ± 0.2	97.3

Table 5
Comparison of the present PDLLME technique with SPE [15] and SPME [7] techniques for determining PUHs in aqueous samples.

Comparison parameter	Technique		
	SPE	SPME	PDLLME
Sample volume (ml)	500	3	5
Extraction time (min)[a]	>60	40	Few seconds
Cost of extraction	Sorbents + solvent	Polymeric fibers + solvent	Solvent only
Linear range (ng ml^{-1})	0.05–2	5–1000	0.5–100
Recovery (%)	70–90	85–113	91–104
Detection limit (ng ml^{-1})	0.02–0.04	0.5–5.1	0.10–0.28

[a] Time of centrifugation, evaporation, and reconstitution is not included.

both samples showed negligible matrix effect. However, both contained an unknown component overlapped with metobromuron in HPLC chromatogram without spiking. The full UV spectrum of the unknown was performed to exclude the possibility of the appearance of metobromuron in the two samples from rice fields. Therefore, no further experiments were done with spiked PUHs.

4. Conclusions

In this study, we demonstrated the capability of PDLLME for determining phenylurea herbicides in aqueous environmental samples. The comparison of PDLLME with SPE [15] and SPME [7] techniques for determining PUHs in aqueous samples is also summarized in Table 5. This PDLLME method showed acceptable linear range (0.5–100 ng ml^{-1}), low detection limits (0.10–0.28 ng ml^{-1}), good intraday/interday precision (1.8–5.9% and 0.4–2.4%, respectively), high recovery (97.3–102.5%), and short extraction time for quantifying PUHs in aqueous solutions. Due to its rapidity, ease of operation, and high recovery, PDLLME can be an alternative to isolate and concentrate organic environmental contaminants such as PUHs from aqueous samples.

Acknowledgement

This work was supported by the National Science Council of Taiwan.

References

[1] D.E. Amacher, I. Zelljadt, Carcinogenesis 4 (1983) 291.
[2] C.R. Elcombe, J. Odum, J.R. Foster, S. Stone, S. Hasmall, A.R. Soames, I. Kimber, J. Ashby, Environ. Health Perspect. 110 (2002) 363.
[3] L. Fava, P. Bottoni, A. Crobe, E. Funan, Chemosphere 41 (2000) 1503.
[4] S.R. Ruberu, W.M. Draper, S.K. Perera, J. Agric. Food Chem. 48 (2000) 4109.
[5] F.P.M. Karg, J. Chromatogr. 634 (1993) 87.
[6] A.C. Gerecke, C. Tixier, T. Bartels, R.P. Schwarzenbach, S.R. Müller, J. Chromatogr. A 930 (2001) 9.
[7] H.-H. Lin, Y.-H. Sung, S.-D. Huang, J. Chromatogr. A 1012 (2003) 57.
[8] A.M. de la Paña, M.C. Mahedero, A. Bautista-Sánchez, Talanta 60 (2003) 279.
[9] A.R. Mughari, P.P. Vázquez, M.M. Galera, Anal. Chim. Acta 593 (2007) 157.
[10] M. Hiemstra, A. de Kok, J. Chromatogr. A 1154 (2007) 3.
[11] R.-X. Mou, M.-X. Chen, J.-L. Zhi, J. Chromatogr. B 875 (2008) 437.
[12] C. Molins, E.A. Hogendoorn, E. Dijkman, H.A.G. Heusinkveld, R.A. Baumann, J. Chromatogr. A 869 (2000) 487.
[13] I. Ferrer, D. Barceló, E.M. Thurman, Anal. Chem. 71 (1999) 1009.
[14] R. Romero-González, A.G. Frenich, J.L.M. Vidal, Talanta 76 (2008) 211.
[15] R. Carabias-Martínez, E. Rodríguez-Gonzalo, E. Herrero-Hernández, J. Hernández-Méndez, Anal. Chim. Acta 517 (2004) 71.
[16] M. Giardina, L.H. Ding, S.V. Olesik, J. Chromatogr. A 1060 (2004) 215.
[17] T. Gunnar, S. Mykkänen, K. Ariniemi, P. Lillsunde, J. Chromatogr. B 806 (2004) 205.
[18] E.M. Gioti, D.C. Skalkos, Y.C. Fiamegos, C.D. Stalikas, J. Chromatogr. A 1093 (2005) 1.
[19] E. Zhao, L. Han, S. Jiang, Q. Wang, Z. Zhou, J. Chromatogr. A 1114 (2006) 269.
[20] M. Khalili-Zanjania, Y. Yaminia, N. Yazdanfarb, S. Shariatia, Anal. Chim. Acta 606 (2008) 202.
[21] M.B. Melwanki, M.-R. Fuh, J. Chromatogr. A 1198 (2008) 1.
[22] M.A. Farajzadeh, M. Bahram, J.Å. Jönsson, Anal. Chim. Acta 591 (2007) 69.
[23] Y. Li, G. Wei, J. Hu, X. Liu, X. Zhao, X. Wang, Anal. Chim. Acta 615 (2008) 96.
[24] A.S. Yazdi, N. Razavi, S.R. Yazdinejad, Talanta 75 (2008) 1293.
[25] H. Sereshti, M. Karimi, S. Samadi, J. Chromatogr. A 1216 (2009) 198.
[26] M. Rezaee, Y. Assadi, M.-R.M. Hosseini, E. Aghaee, F. Ahmadi, S. Berijani, J. Chromatogr. A 1116 (2006) 1.
[27] M.B. Melwanki, M.-R. Fuh, J. Chromatogr. A 1207 (2008) 24.

Talanta 80 (2009) 499–503

Contents lists available at ScienceDirect

Talanta

journal homepage: www.elsevier.com/locate/talanta

Online process control of acidic texturisation baths with ion chromatography

Martin Zimmer*, Antje Oltersdorf, Jochen Rentsch

Department PV Production Technology and Quality Assurance, Fraunhofer Institute for Solar Energy Systems, Heidenhofstrasse 2-4, 79110 Freiburg, Germany

ARTICLE INFO

Article history:
Received 11 March 2009
Received in revised form 3 July 2009
Accepted 4 July 2009
Available online 14 July 2009

Keywords:
Acidic texturisation
Ion chromatography
Online process control
Silicon solar cell manufacturing

ABSTRACT

Etching of silicon with mixtures of hydrofluoric acid and nitric acid is a widely used process in silicon solar cell fabrication. One precondition for an optimized usage of the acidic etching baths is the exact knowledge of the chemical bath composition. In this paper, we investigated a fast and online-capable method for the total analysis of all bath constituents by ion chromatography. The chromatographical system consists of a low-volume injection valve, which injects the concentrated samples directly into the KOH-based eluent. After separation and detection of nitrate and fluoride, a post-column derivatization with sodium molybdate is applied to detect the hexafluorosilicic acid, which enriches in the texturisation bath during the etching process. The results of the presented approach are discussed and compared with already published chromatographical and titration methods found in literature.

© 2009 Elsevier B.V. All rights reserved.

1. Introduction

Acidic texturisation of multicrystalline silicon wafers is a widely used process step in solar cell fabrication [1,2]. The dissolution of silicon in a solution of hydrofluoric acid (HF) and nitric acid (HNO_3) removes the saw damage from the wafer surface and creates a surface structure which improves the light coupling into the solar cell and therefore the cell efficiency. The dissolution of silicon is commonly described by the following equation [3]:

$$3Si + 4HNO_3 + 18HF \rightarrow 3H_2SiF_6 + 8H_2O + 4NO \quad (1)$$

The etching rate as well as the surface morphology mainly depends on the chemical composition of the texturisation bath [3–5]. Hence, maintaining a constant process requires a fast and reliable online-capable analysis method for determination of the main components.

Recently, several analysis techniques for the measurement of HF, HNO_3 and H_2SiF_6 have been published. Two titrimetric methods were proposed, in which the total analysis is achieved in two steps [6]. In a first pH-titration, the total acid amount and the concentration of dissolved silicon are determined. In method 1, this step is followed by a non-aqueous acid–base titration using a methanolic solution of cyclohexylamine as titrant to determine the amount of nitric acid, the concentration of HF is then calculated as difference between the total acid amount and the concentrations of H_2SiF_6 and HNO_3. Method 2 uses a fluoride sensitive electrode (F-ISE) for the determination of the total fluoride concentration. The HF concentration is then calculated as difference between the total fluoride content and the fluoride originating from the H_2SiF_6, the nitric acid content is calculated as difference between the total acid amount and the concentrations of H_2SiF_6 and HF. Method 1 delivers a higher reliability with respect to the recovery rate, but it includes a precipitation step which needs approximately 2 h for the separation of dissolved silicon which prevents an application as industrial process control. Method 2 is fast enough for industrial purposes, but the uncertainty of the measured HF content increases with increasing silicon contents.

Adjacent to the titrimetric analysis, a method for the analysis of acidic texturisation baths by ion chromatography was presented [7]. The nitric acid amount is directly measured as nitrate in the ion chromatography, the concentrations of HF and H_2SiF_6 are both calculated from the measured fluoride concentration. Therefore, a precipitation step, where the SiF_6^{2-} is removed from the solution is needed. The HF concentration can be determined in the filtrate, the H_2SiF_6 concentration is calculated from the fluoride concentration of the re-dissolved and hydrolyzed precipitate.

All three presented approaches stick out due to their high accuracy, but the high expenditure of time avoids an implementation as online process control method. A much faster approach is the ion chromatographical determination of fluoride and nitrate with a post-column derivatization (PCD) of the present silicate with sodium molybdate [8]. This method enables the simultaneous measurement of all components in acidic texturisation baths. In this paper, we describe a fully automated online-method for total analysis of acidic texturisation baths with ion chromatography, where a measurement cycle of 8 min is reached.

* Corresponding author. Tel.: +49 761 4588 5479; fax: +49 761 4588 9250.
E-mail address: martin.zimmer@ise.fraunhofer.de (M. Zimmer).

0039-9140/$ – see front matter © 2009 Elsevier B.V. All rights reserved.
doi:10.1016/j.talanta.2009.07.019

2. Experimental

2.1. Ion chromatography system

All experiments were performed with an ICS-2000 System with an integrated eluent generation, an ASRS 300 self-regenerating suppressor and conductivity measurement cell (Dionex, Sunnyvale, USA). Separation was achieved with a 4 mm × 50 mm IonPac AG11-HC guard column and a 4 mm × 250 mm AS11-HC separation column (Dionex, Sunnyvale, USA). The conductivity measurement outlet was connected via a mixing tee (Dionex, Sunnyvale, USA), wherein the post-column derivatization reagent is added to a reaction coil (self-made from PTFE tube 1.06 mm × 10 m), and then to an ICS-3000 VWD UV/VIS detector (Dionex, Sunnyvale, USA). Post-column reagent delivery was performed with an AXP-pump with a high pressure pulse damper DXP-DX 100 (Dionex, Sunnyvale, USA). The offline samples and validation samples were injected with an ICS-3000 AS autosampler (Dionex, Sunnyvale, USA) with variable injection volume.

2.2. Post-column derivatization

The post-column reagent is an acidified sodium molybdate solution, which was prepared by dissolving 19.36 g sodium molybdate (p.a., Sigma–Aldrich, Taufkirchen, Germany) in a graduated beaker in approximately 2 l of deionized water, 50 ml concentrated nitric acid (>69%, puranal, Honeywell, Seelze, Germany) and 6.00 g sodium laurylsulfate are added, after stirring, the solution is filled up to a volume of 4.00 l.

2.3. Measurement conditions

All measurements were performed with an eluent flow rate of 1.3 ml/min; the eluent concentration was 30 mM KOH. Suppressor current was adjusted to 100 mA. Post-column reagent was added with a flow rate of 0.5 ml/min, the resulting silicomolybdate was detected in the UV–vis channel at 390 nm.

2.4. Calibration

A sodium nitrate solution with a concentration of 1.00 g/l (Sigma–Aldrich, Taufkirchen, Germany) was used for the calibration of nitrate. The fluoride and hexafluorosilicate calibration was performed with a 1:10 dilution of an ammonium hexafluorosilicate solution with a silicon concentration of 1.000 g/l Si, which is equivalent to a fluoride concentration of 4.058 g/l F^- (Merck, Darmstadt, Germany). The calibration was performed by varying the injection volume of the standard solution. The volumes for the calibration can be calculated from the concentration range in the texturisation bath, the concentrations of the standard solutions and the injection volume of the online injection valve by Eq. (2):

$$V_{\text{standard}} = \frac{c_{\text{texturization}}}{c_{\text{standard}}} V_{\text{inline injection loop}} \quad (2)$$

The acidic texturisation bath, used in the investigation, contains up to 120 g/l HF and 500 g/l HNO_3. In our laboratory environment, the silicon amount enriches up to 40 g/l, texturisation baths in industrial applications reach concentrations up to 60 g/l. Regarding these concentration ranges and the injection volume of 0.1 μl, the calibration was carried out with the following volumes:

Fluoride/silicate (SiF_6^{2-}): 1, 2, 4, 8, 16, 32 μl

Nitrate (NO_3^-): 25, 30, 35, 40, 45 μl

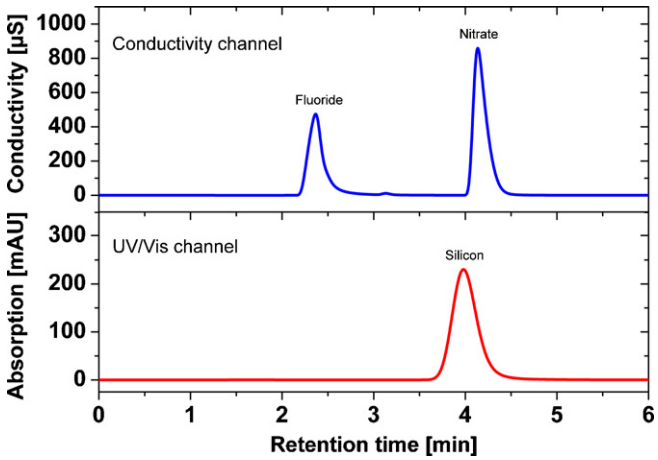


Fig. 1. Online-measured chromatogram of an acidic texturisation bath. Fluoride and nitrate are detected in the conductivity channel, molybdosilicic acid, generated in the post-column derivatization from the hexafluorosilicic acid, is observed in the UV–vis channel at 390 nm.

2.5. Reference samples

Certified reference samples are not commercially available for acidic texturisation baths, hence, we prepared reference samples from pure hydrofluoric acid, nitric acid (puranal, Honeywell GmbH, Seelze, Germany) and hexafluorosilicic acid (20–25%, Sigma–Aldrich, Taufkirchen, Germany). The concentrations of the concentrated acids were exactly determined by titration against sodium hydroxide, whose concentration was adjusted by titration of potassium hydrogen phthalate (primary standard material, traceable to NIST reference material, Merck, Darmstadt, Germany). The reference samples were prepared as 1:100 dilutions by pipetting the respective amounts of each acid into a 50 ml volumetric flask and filling up with deionized water. An error propagation calculation, including the errors of weighting, pipetting and titration gave an estimation of the relative error of $1\sigma = 1.0\%$ for the concentrations in the prepared reference samples. An amount of 8 μl was injected for each sample.

2.6. Online-measurement

Texturisation experiments were carried out with an inline saw damage etching tool (Gebr. Schmid, Freudenstadt, Germany) with a production capacity of 1000 wafers per hour and a process bath volume of 175 l. Silicon enrichment was achieved by etching multicrystalline silicon wafers.

The delivery of the process medium in online-measurement mode was carried out by a Reglo Digital MS-2/12 peristaltic pump (ISMATEC, Wertheim-Mondfeld, Germany), for the sample injection, a separate injection valve with an injection volume of 0.1 μl (Valco Instruments, Houston, USA) was used.

3. Results and discussion

3.1. Calibration

Fig. 1 shows an online-measured chromatogram of an acidic texturisation solution. Fluoride and nitrate are detected in the conductivity channel, the molybdosilicate is registrated in the UV–vis channel. Due to the column overloading, a more or less pronounced deviation from the linear relation between peak area and calibration volume is observed, hence a quadratic function was selected as calibration curve for each species. Using these calibration

Table 1
Correlation coefficients and relative standard deviations for the calibration curves of fluoride, nitrate and silicon from hexafluorosilicate.

No.	Peak name	Calibration curve type	Number of samples	Relative standard deviation	Correlation coefficient
1	Fluoride	Quadratic with offset	10	0.66%	99.98%
2	Nitrate	Quadratic with offset	10	0.21%	99.99%
3	Silicate	Quadratic with offset	10	0.52%	99.99%

The relative standard deviation is calculated from the residuals with respect to the measured peak area.

Table 2
Recovery rate for the nitric acid concentration, calculated from the nitrate amount, and the common hydrofluoric acid concentration, calculated from the fluoride amount.

Sample ID	HNO_3			HF common		
	Initial [g/l]	Analyzed [g/l]	Recovery	Initial [g/l]	Analyzed [g/l]	Recovery
Reference 1	594	584 ± 4	98%	135	136 ± 1	101%
Reference 2	632	625 ± 4	99%	150	148 ± 1	99%
Reference 3	314	316 ± 2	101%	180	182 ± 1	101%
Reference 4	421	418 ± 3	99%	175	175 ± 1	100%
Reference 5	354	354 ± 3	100%	120	119 ± 1	99%
Reference 6	416	414 ± 3	100%	93	92 ± 1	98%
Reference 7	357	358 ± 3	100%	112	114 ± 0	102%
Reference 8	380	379 ± 3	100%	160	162 ± 0	101%
Reference 9	389	388 ± 1	100%	165	168 ± 0	102%
Average			100%			100%

The nine 1:100 diluted reference samples (see Section 2.5) were injected via autosampler. All measurement uncertainties are given as 1σ ($n = 10$).

functions, good correlation coefficients and relative standard deviations are reached (see Table 1).

3.2. Reference samples

Nine 1:100 diluted reference samples, which cover the range of possible bath compositions, were prepared from the pure acids. The initial and analysed concentrations as well as the recovery rates are listed in Tables 2 and 3. Nitric acid concentration as well as the total hydrofluoric acid amount are found with a mean recovery rate of 99.6 ± 0.7% and 100.3 ± 1.2%, respectively. The silicon recovery rate, analyzed with post-column derivatization, was 98.7 ± 2.9%. The high deviation is due to the low concentrations of samples *Reference* 5 and *Reference* 6, where the low silicon content is associated with a relatively high uncertainty during the sample preparation.

The most challenging concentration is the one of free hydrofluoric acid. This concentration is calculated as difference from the total fluoride amount and the silicon concentration (Eq. (3)):

$$c_{\mathrm{HF_{free}}} = c_{\mathrm{HF_{total}}} - 6\frac{M_{\mathrm{HF}}}{M_{\mathrm{Si}}}c_{\mathrm{Si}} \tag{3}$$

Assuming constant relative uncertainties for the total HF concentration as well as for the silicon concentration, the relative

Table 3
Recovery rate for dissolved silicon, measured with post-column derivatization, and free hydrofluoric acid, calculated from total hydrofluoric acid amount and silicon concentration.

Sample ID	Free HF			Si		
	Initial [g/l]	Analyzed [g/l]	Recovery	Initial [g/l]	Analyzed [g/l]	Recovery
Reference 1	69	71 ± 1	102%	15.4	15.3 ± 0.1	99%
Reference 2	124	124 ± 1	99%	6.0	5.8 ± 0.1	97%
Reference 3	71	71 ± 1	101%	25.6	25.9 ± 0.2	101%
Reference 4	134	135 ± 1	101%	9.6	9.4 ± 0.1	98%
Reference 5	112	111 ± 1	99%	2.0	1.9 ± 0.0	97%
Reference 6	88	87 ± 1	99%	1.2	1.1 ± 0.0	93%
Reference 7	44	46 ± 0	105%	16.0	16.0 ± 0.1	100%
Reference 8	17	16 ± 0	98%	33.6	34.2 ± 0.3	102%
Reference 9	56	57 ± 0	102%	25.6	25.9 ± 0.1	101%
Average			101%			99%

Table 4
Comparison between online-measurements and taken samples, measured with autosampler after a dilution of 1:100; m denotes the number of replicated injections for the offline-measured samples.

Sample	Online				Offline					Difference			
	HF tot. [g/l]	Free HF [g/l]	HNO_3 [g/l]	Si [g/l]	HF tot. [g/l]	Free HF [g/l]	HNO_3 [g/l]	Si [g/l]	m	HF tot.	Free HF	HNO_3	Si
Sample 1	123.7	121.2	474.4	0.59	125.6	123.0	467.3	0.63	3	1.5%	1.4%	−1.5%	5.9%
Sample 2	122.7	120.2	494.3	0.58	120.5	117.9	487.4	0.60	3	−1.8%	−1.9%	−1.4%	3.9%
Sample 3	120.5	106.0	470.8	3.39	119.5	104.9	467.8	3.42	3	−0.8%	−1.1%	−0.6%	0.9%
Sample 4	122.1	109.2	498.8	3.01	123.4	110.5	503.6	3.02	3	1.1%	1.2%	0.9%	0.6%
Sample 5	136.7	98.5	480.4	8.94	134.8	97.2	475.8	8.79	2	−1.4%	−1.3%	−1.0%	−1.7%
Sample 6	171.0	104.0	425.6	15.66	165.7	100.3	416.6	15.29	3	−3.2%	−3.7%	−2.2%	−2.4%
Average										−0.8%	−0.9%	−1.0%	1.2%

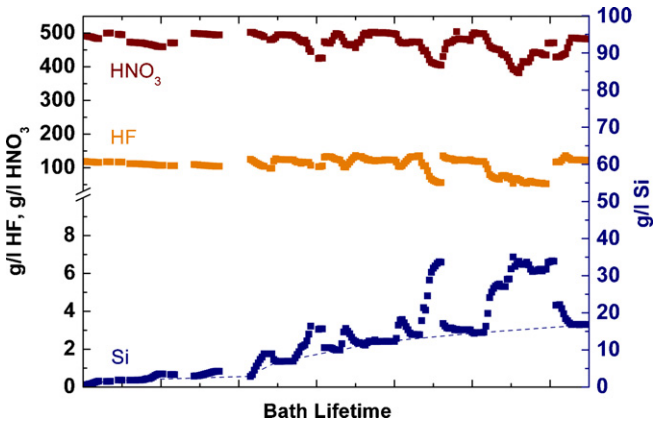


Fig. 2. Enrichment of silicon during the lifetime of a texturisation bath in the PV-Tec laboratory of Fraunhofer ISE.

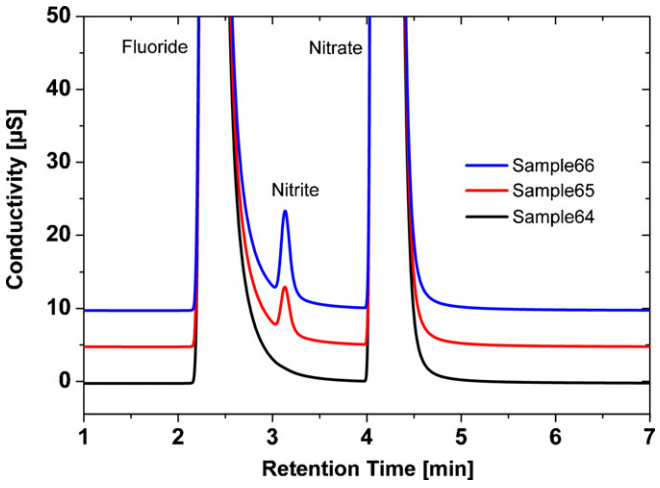


Fig. 3. Online-measured chromatograms of an acidic texturisation bath before (sample 64) and after (samples 65 and 66) addition of silicon. The rising nitrite peak summarizes the total amount of N(III) species in the etching bath.

uncertainty of the free HF concentration increases with increasing silicon and decreasing free HF content. This manifests itself in a higher variation of the recovery rate on the one hand and in a high relative standard deviation for the free HF concentration in sample *Reference* 8 on the other hand. Despite this, the reached recovery rates of $100.6 \pm 2.2\%$ are comparable to the existing ion chromatographic and titration methods and suitable for the industrial process control.

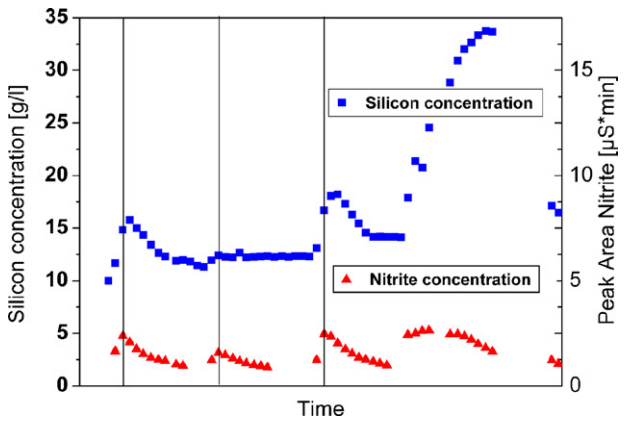


Fig. 4. Peak area of nitrate plotted together with the silicon amount in the texturisation bath. A high etching activity, corresponding to a high slope in the silicon concentration, correlates with an increasing nitrite peak area.

3.3. Online-measurement

In a first step, the exact volume of the 0.1 µl injection loop was determined. Therefore, a sample, consisting 1 g/l fluoride and 1 g/l nitrate was measured five times with the 0.1 µl injection loop. Thereafter, 8 µl of a 1:100 dilution of this sample was injected five times via the autosampler. The exact volume was calculated from the ratio between the peak areas to 0.0792 ± 0.0008 µl.

Industrial application for process control requires a stable calibration during at least one shift. Therefore, the stability of the system was tested with a solution of HF, HNO_3 and H_2SiF_6, which was measured continuously with the online-mode. Over a period of 8 h, the concentrations were stable in a range of 1% relatively for total HF, HNO_3 and silicon; the free HF concentration had a relative standard deviation of 2%.

To validate the accuracy of the online-measurement, six samples were taken during a texturisation process and – after a 1:100 dilution – measured via the autosampler. The assignment to the online-samples was made using the timestamps of the online- and offline-measurements. The comparison of the online- and offline-measurements is shown in Table 4, no significant differences are observed.

The new method was used to observe the silicon enrichment in an acidic texturisation bath in the Photovoltaic Technology Evaluation Center (PV-Tec) at Fraunhofer ISE. During the experiment, broken silicon wafers were dissolved in a texturisation bath, while the concentrations of HF and HNO_3 were kept constant by dosing the pure acids. At certain silicon concentrations, multicrystalline silicon wafers were textured to study the influence of hexafluorosilicic acid on the surface structure. The development of the bath concentrations is shown in Fig. 2.

During the etching of silicon, an additional peak raised at a retention time of 3.1 min (Fig. 3). This peak was identified as nitrite.

Table 5
Comparison of the presented method with existing methods regarding accuracy, measurement cycle time and online capability.

	Titration method 1 [6]	Titration method 2 [6]	IC [7]	IC with PCD [this paper]
Recovery rate HF	103.5%[a]	107.1%[a]	104.3%[a,b]	100.6%
Uncertainty HF (1σ)	1.9%	1.5%	1.5%	0.9%
Recovery rate HNO_3	100.1%	95.8%	98.4%	99.6%
Uncertainty HNO_3 (1σ)	1.1%	3.7%	0.1%	0.7%
Recovery rate H_2SiF_6	98.1%	98.1%	98.4%	98.7%
Uncertainty H_2SiF_6	0.6%	0.6%	0.7%	0.7%
Measurement time	>2 h	~10 min	>2 h	8 min
Online capability	–	+	–	+

[a] Calculated from the presented data; only sample series S1 (dissolving of SiO_2 in HF/HNO_3) was considered.
[b] Data from *route a* was taken for the calculation.

Nitrogen oxides are produced as intermediate reaction products in the etching process. In the alkaline environment of the ion chromatography, they decompose into nitrite ions. These nitrogen oxides have a very strong influence on the etching rate and hence on the texturisation results [9] on the one hand, and on the other hand, they are a very sensitive parameter to monitor the etching activity of the texturisation bath. This can be seen in a time dependent plot of the silicon concentration and the peak area of the nitrate peak (Fig. 4). In those regions, where the silicon concentration is increasing, the areas of the nitrite peaks show a maximum. Regions with a constant silicon concentration and no etching reaction show a slight decreasing of the peak area. This is due to the destruction of nitrogen(III) oxides by oxidation and disproportionation, according to Eq. (4):

$$N_2O_3 + O_2 \rightarrow 2NO_2 \quad (4)$$

$$2NO_2 + H_2O \rightarrow HNO_2 + HNO_3$$

4. Conclusions

The described method enables an online determination of the acidic texturisation bath components. Table 5 shows a comparison of the presented method with the cited titration and chromatographic methods. Precision and accuracy of the two ion chromatographical methods are in the same range and seems to be more accurate than titration. Considering the online capability, only titration method 2 [6] seems to be suitable for a fully automated process control in solar cell fabrication. Compared to this method, inline ion chromatography with silicon detection by means of post-column derivatization enables a very fast measurement cycle of only 8 min with enhanced precision and accuracy. Due to the high flexibility of ion chromatography, a further measurement of additives for advanced texturisation solutions like sulfuric or phosphoric acid is possible. In addition to the concentrations of hydrofluoric acid, nitric acid and hexafluorosilicic acid, the total amount of N(III)-species like NO_2^- can be monitored as nitrite peak. These species are expected to be an indicator for the bath activity.

References

[1] R. Einhaus, E. Vazsonyi, J. Szlufcik, J. Nijs, R. Mertens, Proceedings of the 26th IEEE PV Specialists Conference, Anaheim, CA, 1997.
[2] Y. Nishimoto, T. Ishihara, K. Namba, J. Electrochem. Soc. 146 (2) (1999) 457.
[3] H. Robbins, B. Schwartz, J. Electrochem. Soc. 106 (6) (1959) 505.
[4] B. Schwartz, H. Robbins, J. Electrochem. Soc. 123 (12) (1976) 1903.
[5] W. Weinreich, J. Acker, I. Gräber, Semicond. Sci. Technol. 21 (2006) 1278.
[6] A. Henßge, J. Acker, Talanta 73 (2007) 220.
[7] J. Acker, A. Henßge, Talanta 72 (2007) 1540.
[8] A. Oltersdorf, M. Zimmer, J. Rentsch, Proceedings of the 23rd EUPVSEC, Valencia, 2008.
[9] M. Steinert, J. Acker, A. Henßge, K. Wetzig, J. Electrochem. Soc. 152 (12) (2005) C843.

Talanta 80 (2009) 504–510

Contents lists available at ScienceDirect

Talanta

journal homepage: www.elsevier.com/locate/talanta

Development of a methodology for the simultaneous determination of inorganic and organolead compounds using supercritical fluid extraction followed by gas chromatography–mass spectrometry and its application to environmental matrices

M.C. Zúñiga [a,b,*], E. Jover [a], V. Arancibia [b], J.M. Bayona [a]

[a] Environmental Chemistry Department, I.I.Q.A.B.-C.S.I.C., Jordi Girona 18-26, E-08034 Barcelona, Spain
[b] Facultad de Química, Pontificia Universidad Católica de Chile, Santiago 7820436, Chile

ARTICLE INFO

Article history:
Received 13 February 2009
Received in revised form 3 July 2009
Accepted 6 July 2009
Available online 9 August 2009

Keywords:
Supercritical CO_2–CH_3OH extraction
Organolead compounds
Gas chromatography–mass spectrometry
Multivariate optimization

ABSTRACT

A method for the extraction of triethyl lead (TEL^+), trimethyl lead (TML^+), and Pb^{2+} from sand was developed using supercritical modified CO_2–CH_3OH extraction and *in situ* complexation with sodium diethyldithiocarbamate (NaDDTC) using a 2^5 factorial exploratory design is described. The screened variables were (i) pressure (69–193 bar), (ii) temperature (40–150 °C), (iii) ligand amount (0–100 mg), (iv) methanol volume (0.0–0.5 mL) and (v) static time (0–45 min). The optimum extraction conditions found were as follow: pressure, 193 bar; temperature, 40 °C; amount of NaDDTC, 100 mg; methanol volume, 0.5 mL; static time 45 min; and CO_2 flow rate, 1 mL min^{-1}. Under these conditions the following recoveries were obtained (TML^+ 97 ± 2%, TEL^+ 70 ± 5%, and Pb^{2+} 100 ± 4%). The presence of NaDDTC is not necessary for the extraction of TML^+ and TEL^+, but it is a very significative parameter for Pb^{2+}. A second experimental design 2^2 + star for temperature and pressure was realized, but the results were not better than those of the first model. SFE extract derivatization was achieved with pentylmagnesium bromide, and target analyte determination was carried out by gas chromatography–mass spectrometry. Detection limits in the full-scan mode were 4, 10, and 39 pg as lead for TMPeL, TEPeL and $PbPe_4$, respectively. The method was validated with urban dust containing TML^+ (CRM 605. Pb 7.9 ±1.2 μg kg^{-1}) and river sediment containing inorganic lead (GBW08301. Pb 79.0 ± 12.0 mg kg^{-1}) as reference materials. The proposed method was applied to lead analysis in sand collected from an oil-polluted beach in Chile.

© 2009 Published by Elsevier B.V.

1. Introduction

Inorganic lead is introduced into the natural environment from several sources, but organolead compounds are mainly exhausted into the air from the petroleum industry and automobiles, and then they contaminate soil and water sources. Organolead compounds such as tetramethyl lead and tetraethyl lead have been widely used as antiknocking agents in fuels [1]. In 1990, leaded gasoline (latter a.k.a. gas) represented over 57% of the global world gasoline market. Consumption decreased to 40% in 1996, 20% in 2000, and 8% by the end of 2005. A 2007 report from the International Fuel Quality Center [2] stated that approximately 25 countries worldwide were still using leaded gasoline: Bosnia, Kazakhstan, Macedonia, Serbia, Tajikistan, Turkmenistan, Uzbekistan, Korea, Algeria, Morocco, Tunisia, Western Sahara, Afghanistan, Iraq, Jordan, Palestine, and Yemen. In America, Cuba and Venezuela are the only countries still using leaded gasoline [2]. In Chile leaded car gasoline was eliminated toward the end of 2000, but aviation gasoline (100/130 n-octane) still contains 1.06 mL of tetraethyl lead per liter [3].

Aviation gasoline is currently the fuel with the highest alkyl lead content, ranging from 5.4×10^{-4} to 1.07 g of lead per liter [4,5]. Only TEL is used in aviation gasoline and very recently the US EPA has filed a claim requesting to limit lead emissions from aircraft [6]. Alkyl lead (tetraethyl lead and tetramethyl lead) is one of 12 chemicals identified as Level 1 priority called *Persistent*, *Bioaccumulative*, and *Toxic* (PBT) pollutants. Nowadays sources of alkyl lead emissions include airport fuel terminals, bulk aviation gasoline plants, bulk leaded racing and other non-road vehicle gasoline plants, spills from fuel loading, transfer storage, and fuelling. Once released into the environment, progressive dealkylation takes place leading to the formation of inorganic lead [7].

Tetraalkyl lead is a fat-soluble compound and consequently it is easily absorbed by living organisms (through the skin, lungs, or intestinal tract). Alkyl lead absorption depends on the nature of the compound, exposure time, and type of organism. It has been

* Corresponding author at: Facultad de Química, Pontificia Universidad Católica de Chil, Santiago 7820436, Chile. Tel.: +56 2 6864723; fax: +56 2 6864744.
E-mail address: mczuniga@uc.cl (M.C. Zúñiga).

0039-9140/$ – see front matter © 2009 Published by Elsevier B.V.
doi:10.1016/j.talanta.2009.07.017

confirmed that chronic exposure of alkyl lead compounds is more toxic than inorganic lead compounds to human beings. Once in the body, organolead compounds are degraded by the liver to ionic alkyl lead or Pb^{2+}, and these metabolites are excreted in urine [8–12].

In the soil it has been reported that TML^+ degrades rapidly in the forest floor with a half-life of 33.5 days, while in wetland soil it is 421 days, and in mineral soil it is 612 days [13,14]. Toxicity decreases with decreasing number of ethyl or methyl moieties or with decreasing number of carbon atoms (e.g., from ethyl lead to methyl lead). The toxicity of alkyl lead compounds decreases according to the following sequence: $R_4Pb > R_3Pb^+ > R_2Pb^{2+}$, with R = $-CH_3$ or $-C_2H_5$ [15,16]. Therefore, urban dust, sediments, and rainwater are still currently monitored to assess the levels of alkyl lead.

Lead speciation of various matrices has traditionally been carried out by several techniques, including a combination of complexation–extraction–derivatization, and separation–quantitation by gas chromatography (GC) coupled with selective detectors (e.g., atomic absorption, atomic emission, mass spectrometry) [17].

Supercritical fluid extraction (SFE) with modified CO_2 could be a feasible method for the simultaneous extraction of inorganic and organometallic lead compounds from solid samples [18–21]. A method for the supercritical fluid extraction of TML^+, TEL^+ and DEL^{2+} from solid samples in the absence of ligand has been reported [22]. The sediment samples analyzed contained about 45 $\mu g\,g^{-1}$ as Pb^{2+}, however the extraction of inorganic lead was avoided adding EDTA in the extractor cell. The objective of our work was the simultaneous extraction of inorganic and organolead compounds.

SFE of ionic compounds cannot be carried out with neat supercritical CO_2 or CO_2 modified with methanol due to the charge neutralization requirement and weak solute–solvent interaction. However, when ionic compounds are bound to ligands like NaDDTC with *in situ* complexation, their solubility in supercritical fluids is increased significantly. Extraction of inorganic compounds with *in situ* complexation (β-diketonates, diethyldithiocarbamates, fluorinated derivatives) has been successfully carried out with methanol-modified CO_2. For example, the extraction of Cu^{2+}, Co^{2+}, Cd^{2+}, and Zn^{2+} from filter paper, sand, and silica gel, and heavy metals including As, Cd, Cu, Mn, Pb, Se, and Zn in environmental or biological samples have been extracted prior *in situ* complexation with ligands such as tetrabutylammonium diethyldithiocarbamate, dibutyldithiocarbamate, or diethyldithiophosphate [23–30].

Before the determination, the chromatographic behavior of alkyl lead can be improved by its derivatization using a Grignard reagent [11,35–39]. For instance, ionic alkyl lead has been extracted as neutral complexes into organic solvents and propylated [31–34]. The organolead determination has been carried out with GC combined with different detectors including microwave-excited-helium-plasma detection (MWPD) [40,41], microwave induced plasma atomic emission spectrometry (MIP-AES), inductively coupled plasma time-of-flight mass spectrometry (ICP-TOFMS) [42], atomic emission spectrometry (AES) [43], mass spectrometry (MS) [44]. GC–MS with electron impact source, despite its widespread availability as a commercial GC detector and its usefulness in confirming the structure of derivatized compounds, has seldom been used in lead speciation [8].

The aim of this work was to develop and optimize an extraction method based on SFE with simultaneous *in situ* complexation of TEL^+, TML^+ and Pb^{2+} using NaDDTC as complexing agent and methanol as CO_2 modifier. Speciation of organolead compounds has been investigated, but the benefits of including Pb^{2+} in the determination have not been studied thoroughly. On the other hand, this method may be potentially used for other organic and inorganic trace elements like Hg and As.

Separation and detection of the target analytes have been carried out with GC–MS after penthylation using a Grignard reagent. Some publications on organolead compounds indicate that inorganic lead, usually present in much higher concentration than organolead compounds, interferes with the derivatization reaction with NaDDTC, and for that reason the validation was carried out with reference material with low organolead content and high inorganic lead content. The materials chosen were urban dust containing TML^+ with $7.9 \pm 1.2\ \mu g\,kg^{-1}$ of lead (CRM 605) and river sediment containing $79.0 \pm 12.0\ mg\,kg^{-1}$ of lead (GBW08301). The method was applied to the analysis of these compounds in sand samples from a Chilean beach located near a petroleum refinery that includes an automobile gasoline plant, storage tanks for crude and refined oil, asphalt plants, etc., that has been in operation for 80 years.

2. Experimental

2.1. Reagents and solutions

All aqueous solutions were prepared with Milli-Q water (18.2 MΩ). Trimethyl lead and triethyl lead chloride stock solutions (≈5 $mg\,L^{-1}$ as Pb) were prepared by dissolving appropriate amounts of the corresponding alkyl lead salts in methanol (CRM, Karlsruhe, Germany). A standard solution of triphenylamine (200 $\mu g\,L^{-1}$) was prepared in hexane. These working solutions were prepared when needed and kept at −20 °C in the dark Standard stock solutions with different Pb^{2+} concentrations were prepared from standard Pb^{2+} 1000 $mg\,L^{-1}$ solution (Merck, Darmstadt, Germany). All solvents used were obtained from Merck. NaDDTC, hydrochloric acid, and anhydrous sodium sulfate were analytical-reagent grade (Merck). White sand quartz (50–70 mesh) used for the optimization of the methodology was obtained form Sigma–Aldrich. SFE grade liquid carbon dioxide was obtained from Praxair (Barcelona, Spain). Urban dust reference material (CRM 605) was obtained from the Community Bureau of Reference (Brussels, Belgium) and river sediment (GBW08301) from the China National Analysis Center for Iron & Steel.

2.2. Instrumentation

All the experiments were carried out in an SFE-400 extractor (Supelco, Bellefonte, PA, USA). The extraction cell (6.94 mL, Keystone Scientific, Bellefonte, PA, USA) was filled with raw sand samples (5.0 g). The flow rate of liquid was adjusted with a micro mite forged metering valve to approximately 1.0 $mL\,min^{-1}$, holding the temperature at 50 °C.

A trace GC–MS from Thermo Finnigan (Austin, TX, USA) fitted with a splitless injector and a ZB-5ms fused silica capillary column (5% phenyl, 95% methyl-polysiloxane, 30 m, 0.25 mm i.d.; 0.25 μm film thickness) was used for the separation of the organolead compounds (Phenomenex, Torrance, CA. USA).

2.3. Procedures

2.3.1. Sand sampling and treatment

The sand samples were obtained from an Chilean beach (center zone). It has a length of 800 m, with sampling points every 120 m from which samples were obtained at three different depths (0–27, 50–80, and 100–140 cm), since the pipeline transporting crude and refined oil from the beach to the storage area is deeper than 1.5 m. Sand samples were collected with metallic collectors, returned to the laboratory in polyethylene bags, and stored at 4 °C. Before analysis the sand samples (about 10 kg) were spread and dried at ambient temperature. The dried samples were homogenized and sifted through a 2-mm stainless steel sieve.

Table 1
Results obtained in the first design of extraction optimization (2^5).

Pressure (bar)	Temperature (°C)	Ligand mass (mg)	MeOH volume (mL)	Static time (min)	TML^+ % recovery	TEL^+ % recovery	Pb^{2+} % recovery
69	40	100	0.5	45	22	10	73
69	150	0	0.5	0	57	36	63
69	150	100	0.0	0	17	5	29
193	40	100	0.5	0	1	1	73
193	150	100	0.5	0	19	14	20
193	40	0	0.0	45	12	7	76
193	150	100	0.0	45	61	33	95
193	150	0	0.5	0	47	38	68
69	150	0	0.0	0	0	0	60
69	150	100	0.5	45	14	3	68
69	40	0	0.0	45	2	2	47
193	40	0	0.5	45	35	25	45
69	40	100	0.5	0	92	72	101
69	150	100	0.0	45	2	0	101
69	40	0	0.5	45	34	51	8
131	95	50	0.25	22.5	9	5	47
131	95	50	0.25	22.5	7	4	34
193	150	0	0.0	0	9	7	21
69	150	0	0.0	45	0	0	27
69	150	0	0.5	45	2	5	20
193	150	0	0.0	45	18	4	43
193	40	100	0.0	45	17	10	55
69	40	0	0.5	0	57	77	22
193	40	100	0.0	0	30	14	72
193	40	100	0.5	45	97	70	100
193	150	100	0.5	45	40	27	79
131	95	50	0.25	22.5	13	6	38
193	150	0	0.5	45	40	44	33
193	150	100	0.0	0	13	5	92
193	40	0	0.5	0	100	93	55
69	40	0	0.0	0	2	2	9
69	40	100	0.0	45	18	2	101
193	40	100	0.0	0	2	1	38

2.3.2. Supercritical fluid extraction optimization

To carry out the extraction optimization, white sand quartz was spiked with a mixture of TELCl, TMLCl and $PbCl_2$ (ca. 100 ng g^{-1}). In a first step triphenyl lead was used as surrogate, but a large number of signals of phenyl lead compounds were seen in the chromatograms, because during the derivatization step the triphenyl lead degrades, since it is an exothermic reaction and the phenyl groups form other organolead compounds. The spiked samples were equilibrated during 24 h in a refrigerator at 4 °C before extraction. *In situ* complexation was performed with NaDDTC. The extracts containing complexed inorganic and organolead compounds were depressurized in a vial containing 6 mL of hexane. Volatilization of the target analytes was avoided using a cryogenic trap (acetone–dry ice). The selected parameters to be optimized were pressure, temperature, ligand amount, methanol volume, and static extraction time. The first optimization step was a 2^5 factorial design, and 35 experiments were carried out choosing two levels (high and low), with the central point repeated three times (Table 1). This design was used as an exploratory experimental design using STATGRAPHICS Centurion XV program. Statistical validation was performed by an ANOVA test with 95% confidence level. Then, a central 2^2 + star composite design was carried out optimizing pressure and temperature. Experiments were performed using a star experimental design for which 11 extractions were made, including the central point three times in triplicate (Table 2).

2.3.3. Derivatization reaction

For the preparation of penthylated standards, 100 μL of TMPbCl (5.26 μg mL^{-1} as lead), 100 μL of TEPbCl (4.97 μg mL^{-1} as lead), and 100 μL of $PbCl_2$ (5.26 μg mL^{-1} as lead) in the presence of NaDDTC were added to a dry 100 mL round-bottom flask placed in a vortex mixer. The Grignard reagent was added slowly (3.0 mL of 2.0 mol L^{-1} PeMgBr). Once addition was completed, the mixture was stirred for 1 min and allowed to stand for 20 min for complete reaction. Excess Grignard reagent was destroyed by dropwise addition of deionized water, followed by the addition of concentrated HCl solution to solubilize the salts formed. The reaction mixture was transferred to a separatory funnel and the organic layer was separated, dried with kiln-fired anhydrous sodium sulfate, and extracted with aliquots of hexane. The extracts were concentrated down to 1 mL (≈500 ng mL^{-1}) in a gentle stream of nitrogen. The SFE extracts recovered from the samples were processed in a similar way.

2.3.4. Determination of lead compounds by GC–MS

Triphenylamine (TPA) in hexane (5 ng) was used as internal standard and added to ≈1 mL of extract. The oven temperature was programmed from 60 °C (1 min) to 90 °C at 5 °C min^{-1}, then from 90 to 220 °C (10 min) at 4 °C min^{-1} and finally from 220 to 280 °C (5 min) at 5 °C min^{-1}. Injections were made in the splitless mode keeping the injector, transfer line, and ion source tempera-

Table 2
Results obtained in the second design of extraction optimization (2^2 + star).

Pressure (bar)	Temperature (°C)	TML^+ % recovery	TEL^+ % recovery	Pb^{2+} % recovery
69	100	47	21	104
88	60	66	38	96
88	140	53	25	101
137	50	72	52	109
137	100	90	40	108
137	150	62	49	83
186	60	90	57	81
186	140	79	34	61
206	100	82	71	95
137	100	97	54	110
137	100	64	30	86

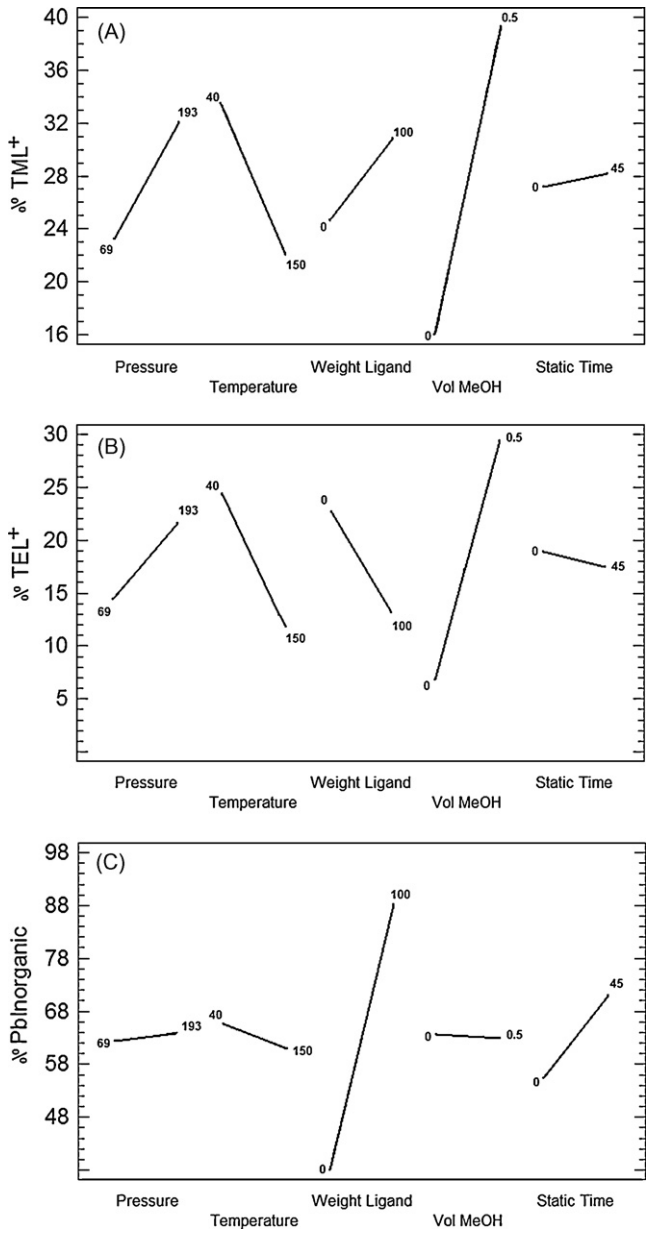


Fig. 1. Influence of the main factors on response in the 2^5 factorial design for optimization of experimental variables. (A) TML^+, (B) TEL^+, and (C) Pb^{2+}.

ture at 250, 280 and 200 °C, respectively. Helium was used as carrier gas at a constant flow rate of 1.2 mL min^{-1}. The injection volume was 2 μL and the solvent delay was of 5 min. The MS operating conditions were the following: positive electron ionization (EI^+) mode with an electron energy of 70 eV, and the scan range was m/z 50–550 with full scan acquisition type. Quantification was carried out using external calibration with $R^2 > 0.99$ for all the target analytes.

2.3.5. Method validation

The accuracy of the developed method was checked by analyzing two certified reference materials. For the validation of the methodology with respect to the extraction and analysis of TML^+, a certified urban dust sample reference material (CRM 605) was used (3.00 g). No reference material was found for TEL^+ determination. On the other hand, the inorganic lead content was validated with a certified river sediment reference material (100 mg) (GBW08301).

3. Results and discussion

3.1. Optimization of the SFE method

The effect of five main variables on supercritical methanol-modified CO_2 extraction was studied simultaneously using a five-factor exploratory design, with two levels for each factor (low (−1), and high (+1)) and middle point (0) in triplicate. The selected factors were extraction pressure (bar), temperature (°C), ligand amount (mg of NaDDTC), modifier (mL of methanol), and static extraction time (min). The ranges of the selected values were pressure from 69 to 193 bar, temperature from 40 to 150 °C, static extraction time from 0 to 45 min, methanol volume from 0.0 to 0.5 mL, and ligand amount from 0 to 100 mg. The responses considered for evaluation were extraction yields (in %) for three compounds (TML^+, TEL^+ and Pb^{2+}). Table 1 shows the parameters selected and the results obtained. For a better understanding of the importance of each variable, the relevant coefficients are plotted in Fig. 1.

Fig. 1C shows that for inorganic lead the most important factor was the amount of ligand, because to obtain good extraction recovery the charge of the metal ion must be neutralized. On the other hand, static time has a positive effect because it is necessary to form the complex. Chakrabarti and co-workers [45] and Nenenka and Branica [46] reported the stoichiometry and stability constants of the complexes between NaDDTC and organic or inorganic lead: $Pb(DDTC)_2$ ($\log K \approx 18$), TML(DDTC) ($\log K \approx 5$), and TEL(DDTC) ($\log K \approx 6$). However, the presence of ligand was not necessary for the quantitative extraction of TML^+ and TEL^+. The ligand has a small positive effect for TML^+ and a negative for TEL^+. This would indicate that these compounds are soluble in supercritical CO_2–CH_3OH and are extracted as ion pairs. The most important parameter for organolead compounds (Fig. 1A and B) was methanol volume, because the presence of modifier increases fluid polarity and can solubilize these ionic compounds neutralized with an anion present in synthetic or real samples. Considering the individual results shown in Table 1 and the average extraction percentages of the three analytes, the best conditions were the following:

	Pressure (bar)	Temperature (°C)	Ligand mass (mg)	MeOH volume (mL)	Static time (min)	% Ex TML^+	% Ex TEL^+	% Ex Pb^{2+}
13	69	40	100	0.5	0	92	72	101
25	193	40	100	0.5	45	97	70	100

On the other hand, good recoveries of TML^+ and TEL^+ were obtained in the absence of ligand, but its presence did not interfere with the extraction.

	Pressure (bar)	Temperature (°C)	Ligand mass (mg)	MeOH volume (ml)	Static time (min)	% Ex TML^+	% Ex TEL^+	% Ex Pb^{2+}
23	69	40	0	0.5	0	57	77	22
30	193	40	0	0.5	0	100	93	55

Pressure had a small positive effect for TML^+ and TEL^+ because it increases fluid density and solvating power. Static extraction time and temperature had a negative effect because these organolead compounds can be degraded during extraction. Therefore, higher temperature and long extraction times can contribute to degradation of the compounds.

The results of the first design showed that the amount of NaDDTC and the volume of methanol were the most significant factors. However, for these two parameters a compromise was found, because at higher levels of NaDDTC as ligand the SFE restrictor was clogged and it was necessary to repeat some extractions. The NaDDTC is not necessary for quantitative extraction of TML^+ and TEL^+, and therefore it was lowered from 100 to 70 mg. On the other hand, for greater

methanol volume the extraction is not carried out under supercritical conditions of temperature, and therefore it was increased only to 0.7 mL, which corresponds to about 10% in a 6.94-mL cell. Because extraction time has a negative effect on organolead compounds and good results were obtained to shorter times. The time was lowered from 45 to 25 min. After this exploratory design, the two main SFE parameters (pressure and temperature) were optimized more precisely.

Then, to find the optimum temperature and pressure values under these new conditions of NaDDTC amount (70 mg), methanol volume (0.7 mL), and static extraction time (25 min), a central composite (2^2 + star) design was used. Pressure ranged from 69 to 207 bar and temperature from 50 to 150 °C. Table 2 shows the parameters selected and the results obtained. The response obtained for the different target analytes was fitted with a polynomial regression considering quadratic and first order interactions:

$$\%R^{+}_{TML} = 83.4(\pm6.7) + 12.2X_1(\pm4.1) - 4.9X_2(\pm4.1) + 0.5X_1X_2(\pm5.8) - 7.9X_1^2(\pm4.9) - 6.6X_2^2(\pm4.9)$$

$$\%R^{+}_{TEL} = 41.7(\pm7.5) + 12.3X_1(\pm4.6) - 4.9X_2(\pm4.6) - 2.7X_1X_2(\pm6.5) - 0.3X_1^2(\pm5.4) + 1.9X_2^2(\pm5.4)$$

$$\%R^{2+}_{Pb} = 108.9(\pm10.4) - 8.6X_1(\pm6.3) - 8.2X_2(\pm6.3) - 6.3X_1X_2(\pm8.9) - 8.7X_1^2(\pm7.6) - 7.6X_2^2(\pm7.6)$$

Considering the individual results shown in Table 2 and the average extraction percentage of analytes, the best conditions were:

	Pressure (bar)	Temperature (°C)	% Ex TML^+	% Ex TEL^+	% Ex Pb^{2+}
5	138	100	90	40	108
9	207	100	82	71	95
10	138	100	97	54	110

However, the results obtained in the second model (2^2 + star) were not better than those of the first model (2^5). Temperature and/or pressure affected the recovery of TML^+ and TEL^+, and Pb^{2+} extraction was better than 100% due to decomposition of organolead to inorganic lead.

The response surface for each analyte is shown in Fig. 2, where it is seen that the plots of TML^+, TEL^+ and Pb^{2+} are different. The extraction yield of TML^+ increases with increasing pressure up to 186 bar, but decreases with increasing temperature, reaching maximum values around 170 bar and 90 °C. In the same way, the extraction yield of TEL^+ increases with increasing pressure and decreases with increasing temperature, reaching a maximum extraction yield at 200 bar and 50 °C. For inorganic lead, the extraction yield increases with increasing pressure and temperature at low values, but decreases with increasing pressure and temperature at medium and high values, reaching maximum values at 120 bar and 85 °C. A different behavior was seen for inorganic lead compared to organolead compounds. For TML^+ and TEL^+ the effect of pressure was positive, an increase in pressure at constant temperature increasing the density of the fluid, and solvating power is higher as in the previous design. The effect of temperature was negative because these compounds have low thermal stability. On the other hand, for inorganic lead high pressure and temperature show a negative effect.

Briefly, the best parameters for the simultaneous extraction of TML^+, TEL^+, and Pb^{2+} were 200 bar pressure, 100 °C temperature, 70 mg of NaDDTC, 0.7 mL of methanol (6.94 mL cell), and 25 min of static extraction time. Dynamic extraction time was 10 min, sufficient for complete flushing of the methanol out of the extractor. Considering that TEL^+ has the lowest yields under all the experimental conditions, the chosen parameters were the best for this compound. Under these conditions, extraction yields were TML^+ 82 ± 3%, TEL^+ 71 ± 5%, and Pb^{2+} 94 ± 8%.

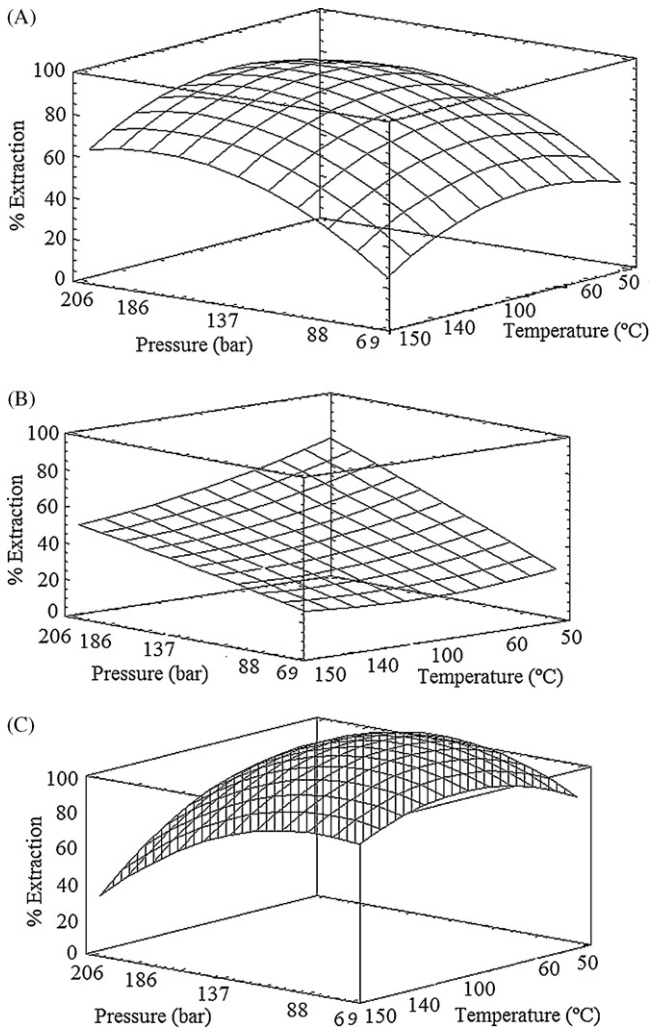


Fig. 2. Response surfaces for extraction in %. Plot as a function of pressure and temperature. (A) TML^+, (B) TEL^+, and (C) Pb^{2+}.

3.2. Determination of lead compounds by GC–MS

Organolead compounds were analyzed by GC–MS as penthylated derivatives and identified by combining the use of retention time data with mass spectral data. Retention times of TMPeL, TEPeL, Pe_4Pb, and TPA (internal standard) were 10.57, 17.03, 24.87, and 24.45 min, respectively, as shown in Fig. 3. The quantification ions for TMPeL, TEPeL, Pe_4Pb, and TPA were 253, 279, 279, and 245 m/z, respectively, as shown in Table 3. This method may be potentially used for other mono and dialkyl lead compounds.

Limits of detection and quantitation (LODs and LOQs) were 10 and 34 pg for TEPeL, 4 and 14 pg for TMPeL, 39, and 131 pg of Pe_4Pb for a 2 μL volume injection. These LODs are lower than those

Table 3
List of the GC–MS ions and retention times of the target analytes. Quantification ions are underlined.

Compound	m/z quantification underlined	Retention time (min)
TMLPe	208, 253, 209	10.65
TELPe	208, 237, 279, 337	17.03
$PbPe_4$	208, 279, 421	24.87
TPA (internal standard)	77, 167, 245	24.92

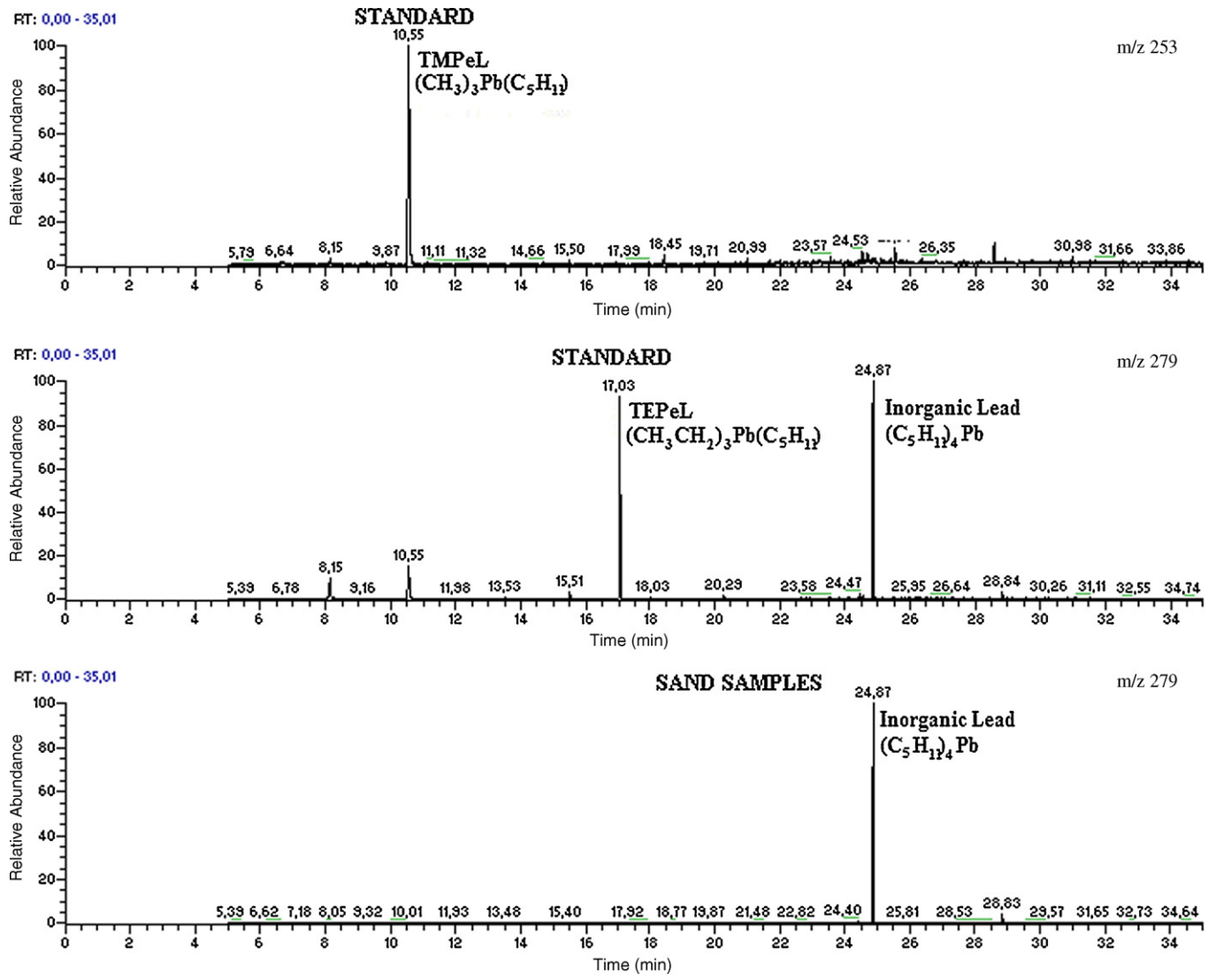


Fig. 3. GC–MS of standards and sand sample: *m/z* 253 (TMPeL); *m/z* 279 (TEPeL), and *m/z* 279 ($PbPe_4$).

reported previously using different techniques: GC-FAAS: 1.5 ng; GC-AF: 0.3 ng; GC-quartz-furnace-AAS: 0.1 ng; GC-quartz-furnace-suspended-flame: 0.09 ng, and GC-electrothermal-AAS: 0.03 ng for organolead compounds (1–5 μL injection volume) [47].

3.3. Validation of the developed method

The validation study was carried out by analyzing reference materials under the optimum conditions by triplicate. The value obtained with the certified urban dust (CRM 605) was $7.1 \pm 2.1\ \mu g\ kg^{-1}$ (certified value $7.9 \pm 1.2\ \mu g\ kg^{-1}$), while the result obtained for inorganic lead in river sediment (GBW08301) was $80.0 \pm 6.7\ mg\ kg^{-1}$ (certified value $79.0 \pm 12.0\ mg\ kg^{-1}$) calculated as Pb. The results obtained were satisfactory and not interference due to high concentration of inorganic lead was found.

3.4. Application to environmental samples

The method was applied to the determination of organolead and inorganic lead in sand samples collected from a Chilean beach (see Section 2.3.1). The vertical profiles obtained are given in Fig. 4, which shows that only inorganic lead was found in all the samples and that its concentration is usually higher on the surface. It could indicate that the lead pollution of this beach is attributable to recent industrial sources (i.e., oil refinery).

The surface sand analyzed was the most highly contaminated part. In fact, Moss and Constanzo [48] reported metal concentration values in sediments to establish baseline or reference values for heavy metals in the sediments of Queensland water. They considered $15\ mg\ kg^{-1}$ as allowed limits for Pb in this zone, and in our

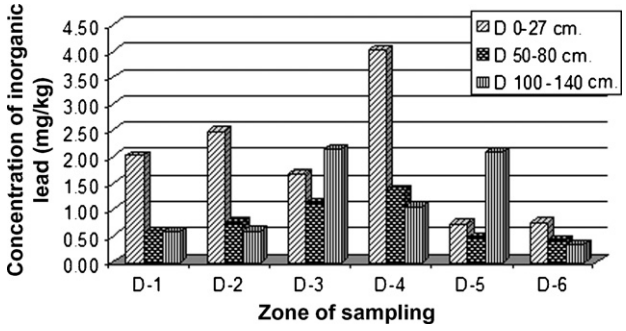


Fig. 4. Lead concentration in sand samples according to depth (0–27; 50–80, and 100–140 cm depths).

study the highest value was 4.0 mg kg^{-1}. Accordingly, the evaluation of contamination by organic or inorganic lead in this populated beach is not worrisome.

4. Conclusion

The suitability of SFE and GC–MS for the simultaneous determination of inorganic and organolead compounds in sand samples has been shown. The presence of inorganic lead does not interfere with the organolead analysis. With respect to supercritical fluid extraction, the amount of methanol was only relevant for organolead compounds, while the amount of ligand was the most important parameter for inorganic lead. This method is an alternative to GC-ICP-AS or GC-ICP-MS, frequently used for the separation and analysis of organolead compounds. This method may be potentially used for other mono and dialkyl lead compounds, and for organic and inorganic trace elements, e.g., Hg and As.

Accurate results were obtained in the validation with CRM 605 urban dust for TML^{+} and GBW08301 river sediment for inorganic lead certified materials. All the environmental samples analyzed contained only inorganic lead attributable to organolead degradation over time. Although tetraethyl lead in car gasoline was eliminated about 5 years ago in Chile but is still in use today in aviation fuel, the only occurrence of inorganic lead in the sand samples analyzed may indicate that aviation is a small input source, and the inorganic lead concentrations found can be attributable to an historical contamination.

Acknowledgements

Financial support from FONDECYT Project 1080524 and a PhD grant from CONICYT and the Pontificia Universidad Católica de Chile (Facultad de Química) are gratefully acknowledged.

References

[1] M. Bragadin, D. Marton, S. Manente, J. Inorg. Biochem. 101 (2007) 876.
[2] IFQC (International Fuel Quality Center), Special Report: Global–Current Status of Gasoline Lead Phase-Out May 24, 2007.
[3] NCh 1897. Of1996, Gasolina-Determinación de plomo-Método por Espectrometría de Absorción Atómica.
[4] D. Seyferth, Organometallics 22 (2003) 5154.
[5] Emissions Inventory of Section 112C (6) Pollutants, The U.S. Environmental Protection Agency (USEPA) 1990.
[6] http://www.epa.gov/fedrgstr/EPA-AIR/2007/November/Day-16/a22456.htm.
[7] PBT National Action Plan for Alkyl-lead. The US EPA Persistent, Bioaccumulative, and Toxic (PBT) Chemical Program, June 2002.
[8] I.A. Leal-Granadillo, J.I. Garcia, A. Sanz-Medel, Anal. Chim. Acta 423 (2000) 21.
[9] A. Seeber, E. Kiesswetter, B. Neidhart, M. Blaszkewicz, Neurotoxicol. Teratol. 12 (1990) 653.
[10] M. Blaszkewicz, G. Baumhoer, B. Neidhart, Z. Fresen, Anal. Chem. 325 (1986) 129.
[11] B. Pons, A. Carrera, C. Nerín, J. Chromatogr. B 716 (1998) 139.
[12] M. Blaszkewicz, G. Baumhoer, B. Neidhart, R. Ohlendorf, M. Linscheid, J. Chromatogr. 439 (1988) 109.
[13] J.-H. Huanga, K. Kalbitzb, E. Matznerb, Soil Sci. Soc. Am. J. 72 (2008) 978.
[14] J.-H. Huanga, E. Matznerb, Biogeochemistry 71 (2004) 125.
[15] K. Pyrzynska, Mikrochim. Acta 122 (1996) 279.
[16] C. Gallert, J. Winter, Water Res. 36 (2002) 3130.
[17] P. Quevauviller, R. Harrison, F. Adams, L. Ebdon, Trends Anal. Chem. 19 (2000) 195.
[18] J.M. Bayona, Trends Anal. Chem. 19 (2000) 107.
[19] I. Fernández-Escobar, J.M. Bayona, Anal. Chim. Acta 355 (1997) 269.
[20] G.P. Foy, G.E. Pacey, Talanta 61 (2003) 849.
[21] G. Centineo, E. Blanco, A. Sanz-Medel, J. Chromatogr. A 1034 (2004) 191.
[22] M. Johansson, T. Berglof, D.C. Baxter, W. Frech, Analyst 120 (1995) 755.
[23] M. Wai, S. Wang, J. Chromatogr. A 785 (1997) 369.
[24] M. Ashraf-Khorassani, M.T. Combs, L.T. Taylor, J. Chromatogr. A 774 (1997) 37.
[25] N.G. Smart, T. Carleson, T. Kast, A.A. Clifford, M.D. Burford, C.M. Wai, Talanta 44 (1997) 137.
[26] C. Erkey, J. Supercrit. Fluids 17 (2000) 259.
[27] S. Wang, S. Elshani, C.M. Wai, Anal. Chem. 67 (1995) 919.
[28] C.M. Cowey, K.D. Bartle, M.D. Burford, A.A. Clifford, S. Zhu, N.G. Smart, N.D. Tinker, J. Chem. Eng. Data 40 (1995) 1217.
[29] V. Arancibia, A. López, M.C. Zúñiga, R. Segura, Talanta 68 (2006) 1567.
[30] V. Arancibia, R. Segura, J. Leiva, R. Contreras, M. Valderrama, J. Chromatogr. Sci. 38 (2000) 21.
[31] Y. Cai, R. Alzaga, J.M. Bayona, Anal. Chem. 66 (1994) 1161.
[32] Y. Lin, V. Lopez-Avila, M. Alcaraz, W.R. Beckert, Anal. Chem. 66 (1994) 3788.
[33] Y. Liu, V. Lopez-Avila, M. Alcaraz, W.R. Beckert, J. High Resolut. Chromatogr. 16 (1993) 106.
[34] R. Alzaga, J.M. Bayona, J. Chromatogr. A 655 (1993) 51.
[35] D. Chakraborti, W.R.A. De Jonghe, W.E. Van Mol, R.D.J. Van Cleuvenbergen, F.C. Adams, Anal. Chem. 56 (1984) 2692.
[36] C.N. Hewitt, R.M. Harrison, Anal. Chim. Acta 167 (1985) 277.
[37] D. Chakraborti, W. Dirkx, R. Van Cleuvenbergen, F. Adams, Sci. Total Environ. 84 (1989) 249.
[38] Y.K. Chau, Analyst 117 (1992) 571.
[39] Y.K. Chau, P.T.S. Wong, G.A. Bengert, J.L. Dunn, Anal. Chem. 56 (1984) 271.
[40] S.A. Estes, P.C. Uden, R.M. Barnes, Anal. Chem. 53 (1981) 1336.
[41] Y.K. Chan, P.T.S. Wong, O. Kramar, Anal. Chim. Acta 46 (1983) 211.
[42] J.R. Baena, M. Gallego, M. Valcárcel, Anal. Chem. 73 (2001) 3927.
[43] A. Sadiki, D.T. Williams, Chemosphere 32 (1996) 1983.
[44] R. Zufiaurre, B. Pons, C. Nerin, J. Chromatogr. A 779 (1997) 299.
[45] R. Scharfe, V. Sastri, C. Chakrabarti, Anal. Chem. 45 (1973) 413.
[46] M. Nenenka, M. Branica, Electroanalysis 6 (1994) 37.
[47] B. Radziuk, Y. Thomassen, L.R.P. Butler, J.C. Van Loon, Y.K. Chau, Anal. Chim. Acta 108 (1979) 31.
[48] A. Moss, S. Contanzo, Environment technical report vol. 20, Department of Environment of Queensland Government ISSN 1037-4671 (1998) RE200, February 1998.

Talanta 80 (2009) 511–518

Contents lists available at ScienceDirect

Talanta

journal homepage: www.elsevier.com/locate/talanta

Smart electrochemical sensor for some neurotransmitters using imprinted sol–gel films

Nada F. Atta*, Ali M. Abdel-Mageed

Department of Chemistry, Faculty of Science, University of Cairo, 1 Al Gamaa Street, Post Code 12613, Giza, Egypt

ARTICLE INFO

Article history:
Received 2 May 2009
Received in revised form 2 July 2009
Accepted 6 July 2009
Available online 3 August 2009

Keywords:
Molecular imprinting
Recognition
Surface template
Thin films
Spin coating
Neurotransmitters
EIS

ABSTRACT

A hybrid sol–gel material formed by acid hydrolysis of a mixture of tetraethylorthosilicate (TEOS) and phenyltriethylorthosilicate (PTEOS) as functional monomers was imprinted by tyramine and dopamine as template molecules for the purpose of molecular recognition. Imprinted materials were spin coated as thin films on the surface of glassy carbon electrodes and then were characterized using cyclic voltammetry (CV). After extraction of the encapsulated molecules, imprinted films were tested in solutions of their templates and other molecules. Rebinding experiments were followed by electrochemical characterization using square wave voltammetry (SWV). Imprinted films showed higher affinities toward their template molecules compared to other structurally similar molecules especially for tyramine imprinted film. With the exception of tyramine and norepinephrine, the interference level did not exceed 5% for all compounds studied for dopamine-imprinted films. Tyramine-imprinted films however showed high affinity to tyramine with dopamine 40% interference. Some factors related to the rebinding ability process like pH of solution, concentration of template were studied. The sensing surface lifetime extended to 2 weeks with decay in response signal that ranged from 22%, 40% to 60% for dopamine, tyramine and norepinephrine, respectively. The standard deviation from the mean of measurements for the repeated experiments is 7.4%. Electrochemical impedance spectroscopy (EIS) measurements confirmed the results obtained by electrochemical measurements. Morphological characteristics of the imprinted thin films and their thickness were investigated using scanning electron microscope (SEM).

© 2009 Elsevier B.V. All rights reserved.

1. Introduction

Molecular imprinting has been widely studied and applied in the last two decades as an innovative tool for various technological and scientific fields. The first approach to molecular imprinting was not well known until 1949 when Dicky succeeded to create complementary molecular cavities for certain dye molecules. Dickey's silicates could be considered as the first molecularly imprinted material [1].

In general, molecular imprinting process involves the formation of molecular cavities inside the polymer matrix being imprinted which are of complementary structural, functional group orientation and geometrical features with respect to the molecule being imprinted. Specifically, the molecular cavities are created by the incorporation of the template molecule during the polymerization process in such a way that a three-dimensional network is formed around the molecule being imprinted. Upon the extraction of the molecular moiety (template) from the polymer matrix, molecular cavities with specific shape, size and electrostatic features, remain in the cross-linked host material [2–4]. The imprinted material can be used to rebind the template molecules with very high degree of selectivity.

Because of its unique properties, molecularly imprinted materials have been widely utilized for a lot of applications and in various fields. They were applied in high performance liquid chromatography [5], food analysis [6], capillary chromatography, solid phase extraction [7] and drug delivery systems [8].

One of the most important applications of the imprinting technique is the molecular recognition. Biosensors prepared by imprinting methods could introduce good solution for the recognition of a variety of biologically active molecules. Recognition mechanism of the molecules is largely similar to what happens in living organisms. In our bodies, there are a large number of different molecules, and cells, without which we cannot survive. These molecules are able to work cooperatively and integrally in such a way that certain functions are carried out very precisely and accurately. For example, the receptors on the surface of cell membranes bind hormones specifically and selectively. When the receptor binds a hormone, its conformation is changed and a message of the hormone is transferred in terms of a conformational change in such away that the function is achieved. In molecular recognition, the molecules being imprinted can rebind to their

* Corresponding author. Tel.: +20 0237825266; fax: +20 0235727556.
E-mail address: Nada_fah1@yahoo.com (N.F. Atta).

0039-9140/$ – see front matter © 2009 Elsevier B.V. All rights reserved.
doi:10.1016/j.talanta.2009.07.014

molecular cavities with very high degree of selectivity and specificity, so these materials may be named as artificial antibodies.

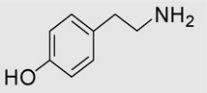
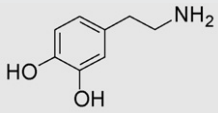
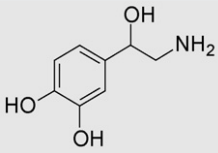
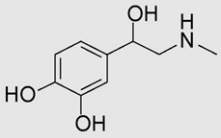
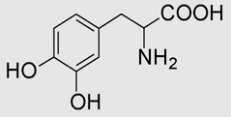
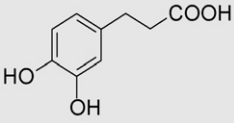
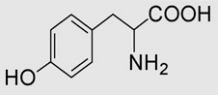
Sol–gel materials have been extensively used for the purposes of molecular imprinting. The imprinting of hybrid sol–gel materials has found great interest in the last few years [9–12] due to their unique properties. In this work, a hybrid sol–gel material synthesized by hydrolysis of a mixture of tetraethylorthosilicate (TEOS) and phenyltriethylorthosilicate (PTEOS) was molecularly imprinted with tyramine and dopamine for sensing applications in aqueous medium. Imprinted sol–gel materials were spin coated on the surfaces of glassy carbon electrodes at 2500 rpm for 45 s. The modified electrodes were electrochemically characterized using cyclic voltammetry for the imprinted molecules. Rebinding experiments were carried out by adsorption from solutions of the imprinted molecules and other test molecules followed by electrochemical characterization by SWV. Electrochemical impedance measurements were carried out to confirm the voltammetric results.

2. Experimental

2.1. Reagents

Tetraethylorthosilicate (TEOS) (>99%) and phenyltriethylorthosilicate (PTEOS) (>99%) were used as functional monomers for polymerization process. Dopamine (≥99%), tyramine (≥99%), dopa (≥99%), dopac (≥99.0%), tyrosine (≥99%), catechol (≥98%), epinephrine (≥99%), norepinephrine (≥99%), and catechol (≥98%) were used as template molecules in the imprinting process and as test molecules for rebinding experiments. Phosphate buffer solution (PBS) (pH 7.2 and 10 mmol L^{-1}) was prepared from sodium dihydrogen phosphate and disodium hydrogen phosphate. 2-Ethoxyethanol and absolute ethyl alcohol were used as solvents for dissolving template molecules and monomers for polymerization process. Hydrochloric acid and distilled water were used for hydrolysis of functional monomers in polymerization process. All chemicals were supplied by Aldrich Chem Co. (Milwaukee, WI, USA). Chemicals were used as received. Table 1 contains the chemical structures of template molecules and test molecules being studied.

Table 1
List of compounds studied in this work.

Molecule	Structure	Molecular volume (Å^3)
Tyramine		131.1
Dopamine		146.0
Norepinephrine		149.2
Epinephrine		166.1
Dopa		169.1
Dopac		157.4
Tyrosine		159.9

2.2. Equipments

Glassy carbon electrodes from BAS (USA) with 3 mm diameter were used as working electrodes. A platinum wire, 4 cm long with a diameter 0.5 mm, was used as counter electrode. All cell potentials were measured against saturated Ag/AgCl as a reference electrode. One compartment, three electrodes cell, made of glass (30 mL), fitted with gas bubbler was used for all electrochemical measurements. Electrochemical characterization including cyclic voltammetry (CV) and square wave voltammetry (SWV) were carried out using a BAS-100B electrochemical analyzer (Bioanalytical Systems, West Lafayette, USA). Electrochemical impedance spectroscopy (EIS) measurements were performed using a Gamry-750 system and a lock-in amplifier in conjunction with a personal computer used as data acquisition system and simulations. JEOL JSM-T330A scanning electron microscope (SEM) was used for all measurements.

2.3. Electrode preparation and procedures

2.3.1. Imprinted film preparation

The electrodes were polished well using 0.05 μL alumina slurry on Buehler felt pads and rinsed thoroughly with deionized water and ethanol. Electrodes were then electrochemically activated before spin coating. Glassy carbon electrode was activated by polarization at +1.6 V for 60 s and at −1.6 V for the same period. Electrodes were then cycled between +1.0 and −0.2 till a stable CV was obtained [13,14]. Then, 400 μL (1.791 mmol) tetraethylorthosilicate were mixed with 65 μL (0.351 mmol) phenyltriethylorthosilicate in 3.0 mL of 2-ethoxyethanol, and then solution was stirred till a homogeneous is obtained. This was followed by adding 100 μL of 0.1 mol L^{-1} HCl solution drop-wise with continuous stirring, and 90 μL H_2O were added in the same manner. The mixture was stirred gently for 2.5 h. A 1.0 mL portion of the prepared sol–gel mixture was mixed with 300 μL of 0.1 mol L^{-1} tyramine or 350 μL of 0.05 mol L^{-1} dopamine in order to prepare tyramine- or dopamine-imprinted surfaces, respectively. The resulting mixtures were stirred for another 2 h. The imprinted sol–gel materials were spin coated on the surfaces of glassy carbon electrodes at spinning rate 2500 rpm for 45 s. The electrodes were allowed to dry overnight, and then they were electrochemically characterized by cyclic voltammetry (CV) between −200 mV and +1000 mV at a scan rate 100 mV/s. Template molecules were extracted form the imprinted film by repeated CV and the decay in current response was followed as indicator for the extraction procedure. Electrodes were allowed to dry overnight before rebinding experiments were carried out.

2.3.2. Rebinding experiments

Modified electrodes were dipped for 15 min in rebinding solutions for different test molecules of concentration 50 μmol L^{-1} each, and then followed by electrochemical characterization with

square wave voltammetry. The incubation time for rebinding experiments was selected in such a way that high sensitivity and stability of the current response was obtained.

3. Results and discussion

3.1. Sol–gel synthesis and characterization

Tetraalkylorthosilicates monomers are hydrolyzed in the presence of either acid of base catalyst. Acid catalyst was the best to be used for a lot of applications especially for the design of sensing elements [15–18]. The hydrolysis step is followed by a condensation step of the hydrolyzed monomers. It was reported that strong concentrated acids produces highly cracked and slightly shrunken aerogels. On the other hand, very dilute acids results in monolithic and well shrunken aerogels [19]. In this work silica gel material was polymerized using dilute hydrochloric acid (0.1 mol L^{-1}). Condensation between completely hydrolyzed monomers occurs by the elimination of water while incompletely hydrolyzed monomers may condense by elimination of alcohol molecules.

In order to obtain the best imprinted material with good physicochemical properties, water content has to be adjusted in the start mixture before synthesis step. The ratio of water and alkyl orthosilicates monomers was determined experimentally to be 4.5:1 (water:silane). This ratio was found to be sufficient for complete hydrolysis of all monomer units before the start of condensation step which was necessary to enhance the process of incorporation of template molecules into the sol–gel material before the growth of the polymeric networks around them.

The use of hybrid sol–gel matrix is very crucial factor for material design. A hybrid monomer solution composed of TEOS and PTEOS was hydrolyzed using 0.1 mol L^{-1} HCl solution. The phenyl group inserted in the sol–gel material is of great importance. This group allows for non-polar interaction with the imprinted molecules which all carry benzene rings so it could act as a Pi–Pi interaction center with the template molecules through further steps. Also, it was reported that a combination of functional monomers enhances and promotes the rebinding ability of template molecules to the imprinted films [20–22].

The modified electrodes coated with the imprinted sol–gel films were characterized electrochemically using CV. An applied potential window between −0.2 V and +1.0 V at scan rate of potential 100 mV/s, was sufficient to cover the oxidation potentials of all the template and test molecules rebinding to the imprinted film. Cyclic voltammetry characterization was carried out in PBS (10 mM and pH 7.2). Fig. 1(A and B) illustrates the CVs of sol–gel films imprinted with tyramine and dopamine, respectively.

The extraction process of template molecules was carried out through repeated CV in phosphate buffer solution followed by dipping in PBS only for a relatively short period of time (ca. 1.0 h) to confirm the complete extraction of the molecules from the imprinted films. Repeated cycling between −0.2 V and +1.0 V, at scan rate 100 mV/s, was applied to the surface till complete disappearance of the template current response was attained.

The mechanism of the extraction of template molecules by repeated cycling can be understood in terms of oxidation–reduction properties of the neurotransmitter molecules. For example;

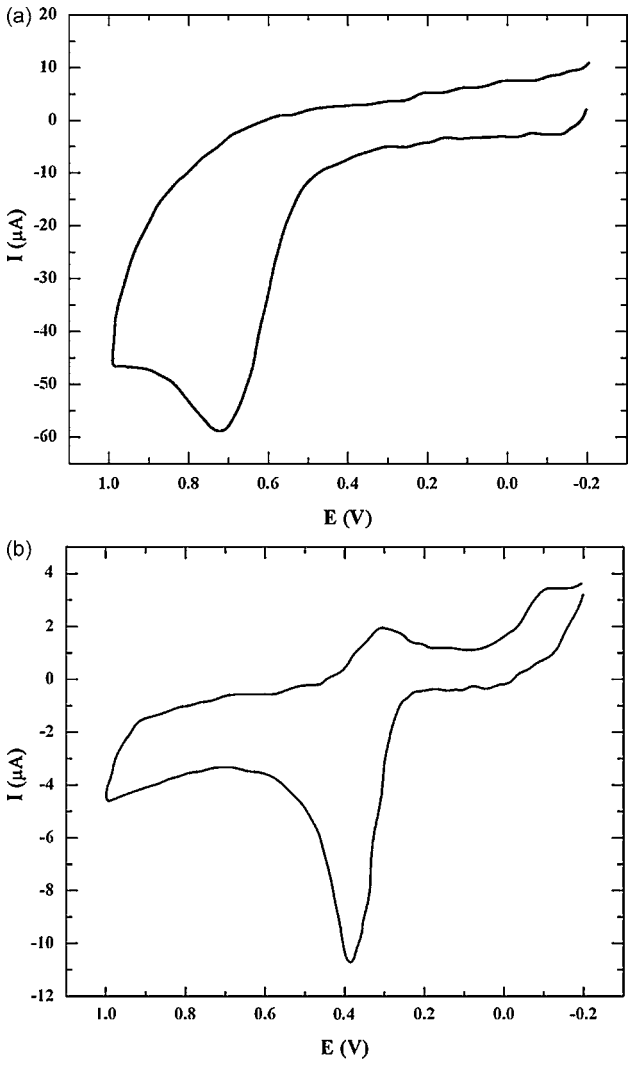
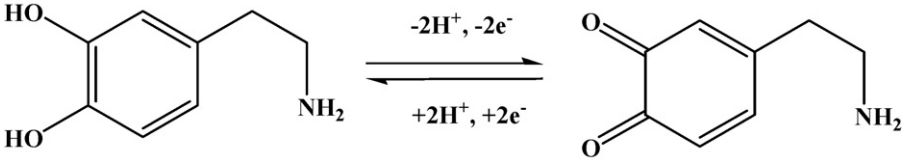


Fig. 1. Cyclic voltammograms of tyramine (A) and dopamine (B) molecularly imprinted sol–gel films spin coated on the surface of glassy carbon electrodes cycled in PBS (pH 7.2 and 10 mmol L^{-1}) versus Ag/AgCl reference electrode.

dopamine is electrochemically oxidized by losing two electrons and two protons. Oxidation reaction was found to be quasi-reversible process; as a result of this behavior, the structure of the molecules is changed during its oxidation process. The change in chemical structure makes the template molecule less bound to the molecular cavity (ca. the transformation of the two hydroxyl groups that affect the extent of hydrogen bonding) which in turn helps its extraction out of the molecular cavity inside the solution with repeated cycling.



3.2. Molecular recognition and selectivity of the imprinted films

3.2.1. Tyramine-imprinted film

Tyramine (p-hydroxy-phenylethylamine) is naturally occurring in animals and plants. In foods, it is produced via decarboxylation of amino acid tyrosine, so considerable amounts in food stuffs indicate potentially an expired product. The molecule increases the release

of neurotransmitters stored in the body. To the best of our knowledge, this is the first time that tyramine is molecularly imprinted. Rebinding experiments for tyramine-imprinted film were carried out from template solution of different molecules of concentration 50 μmol L^{-1} prepared in PBS. Rebinding experiments as mentioned in the above section were followed by electrochemical characterization using SWV. Tyramine molecularly imprinted films showed a preferential adsorption for their imprinted molecules compared to other molecules. The high affinity of the imprinted films toward its template was attributed to the fact that the molecular cavities created inside these films are correctly sized and shaped and appropriately functionalized in the way that they bind these molecules or allow the passage of any moiety which may be analogous in size or geometry into them [23–25]. It is also perceived that the recognition ability of molecularly imprinted materials comes from the functional group orientation inside the molecular cavities created during polymerization which enhances the ability of these template molecules to interact well with these molecular cavities. As shown in Fig. 2A tyramine-imprinted film showed relatively high current response for tyramine compared to other molecules. Although dopamine has larger molecular size than tyramine, it is found to be partially adsorbed into the surface imprinted with tyramine. The appreciable interference of dopamine into the tyramine cavities is largely attributed to the similarity of their functionality beside the fact that the molecular size of dopamine is not extremely larger than tyramine. On the other hand, norepinephrine showed relatively smaller interference to tyramine-imprinted film compared to dopamine. This is certainly due to larger molecular size of norepinephrine and the extra hydroxyl group which changed the average electron density around the molecule and in turn decreased the possibility of electrostatic interaction with the molecular cavity oriented functional groups. As illustrated in the same figure other molecules including epinephrine, dopa, dopac, tyrosine, and catechol showed almost no rebinding ability with respect to tyramine-imprinted film. All molecules except catechol are characterized by larger molecular size in addition to relatively different functionality. It is interesting to notice that although catechol is smaller in size compared to tyramine, it could not rebind to the imprinted film to any extent. This is attributed mainly to the fact that catechol is missing the amino group present in tyramine which inhibit its electrostatic interaction with the imprinted film. Therefore, we can conclude that the selectivity of imprinted films depends on the size of template molecule and its ability for electrostatic interaction with the functional groups oriented inside these cavities during polymerization. Moreover, it is important to mention that all measurements were carried out using three independent electrodes to ensure reproducibility of the results.

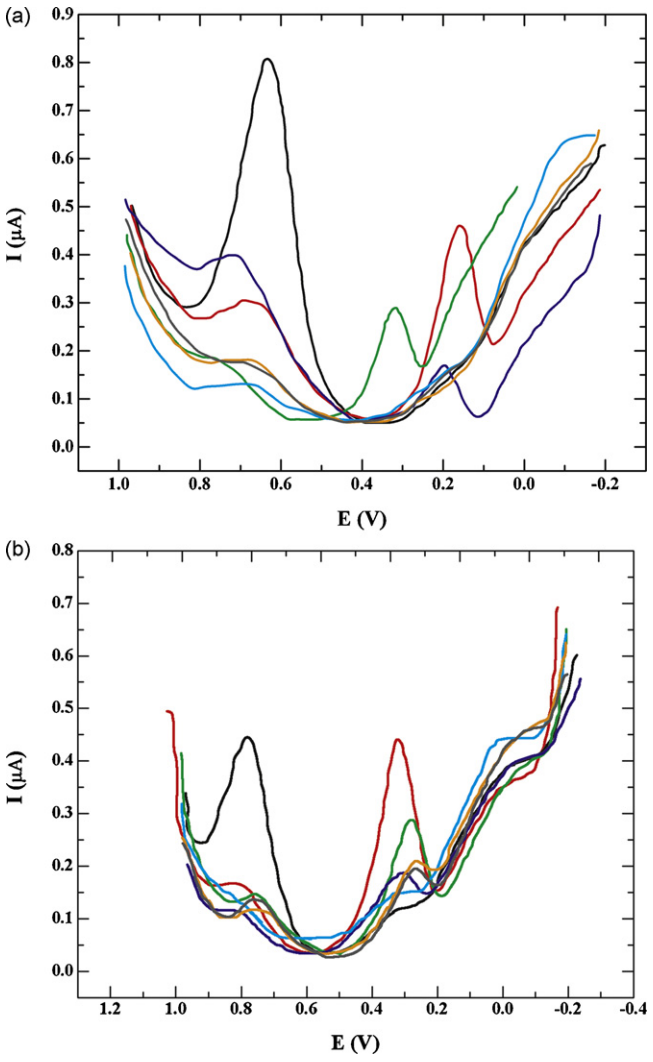


Fig. 2. (A) Square wave voltammograms of tyramine and other test molecules with respect to tyramine-imprinted film. Rebinding experiments are carried out by dipping electrodes in 50 μmol L^{-1} solutions of the tested molecules prepared in PBS: tyramine (—), dopamine (—), norepinephrine (—), epinephrine (—), tyrosine (—), dopa (—), dopac (—). (B) Square wave voltammograms of dopamine and other test molecules with respect to dopamine imprinted film. Rebinding experiments are carried out by dipping electrodes in 50 μmol L^{-1} solutions of the tested molecules prepared in PBS: tyramine (—), dopamine (—), norepinephrine (—), epinephrine (—), tyrosine (—), dopa (—), dopac (—).

3.2.2. Dopamine imprinted film

Dopamine is a neurotransmitter found in various animals whether vertebrates or invertebrates. It is produced in various areas in the brain and activates five types of receptors. As illustrated in Fig. 2B, current response after rebinding tyramine to dopamine-imprinted film is relatively high when compared to the current response after dopamine rebinding to its imprinted film. This is due to the smaller molecular size of tyramine which facilitates the diffusion of tyramine into the dopamine imprinted cavities. Although norepinephrine is larger in molecular size than dopamine, it gives relatively high rebinding current response. This is mainly due to the similarity of functional groups of both molecules which implies very similar electron density and as a result of this, strong electrostatic interactions arise between them and the molecular cavities oriented functional groups. Also, it is observed from the results that norepinephrine interferes with dopamine-imprinted film nearly to the same percentage of interference of dopamine to tyramine-imprinted film. Other molecules interfere to dopamine film with less than 5% as depicted in Fig. 2B.

It is to be mentioned here that non-imprinted sol–gel films were prepared following the same procedure as the imprinted films but without the addition of the template solution to the sol mixture during the polymerization process and were tested for rebinding of different test molecules. Percentage adsorption to non-imprinted films is negligible which confirms the fact that rebinding process mainly takes place into the imprinted surface sites.

3.3. Binary mixture analysis

One important challenge for the effective use of imprinted materials in molecular recognition processes is the ability of the imprinted film for selective recognition of imprinted template in the presence of other molecules. As an example dopamine molecularly imprinted film was tested for selective adsorption

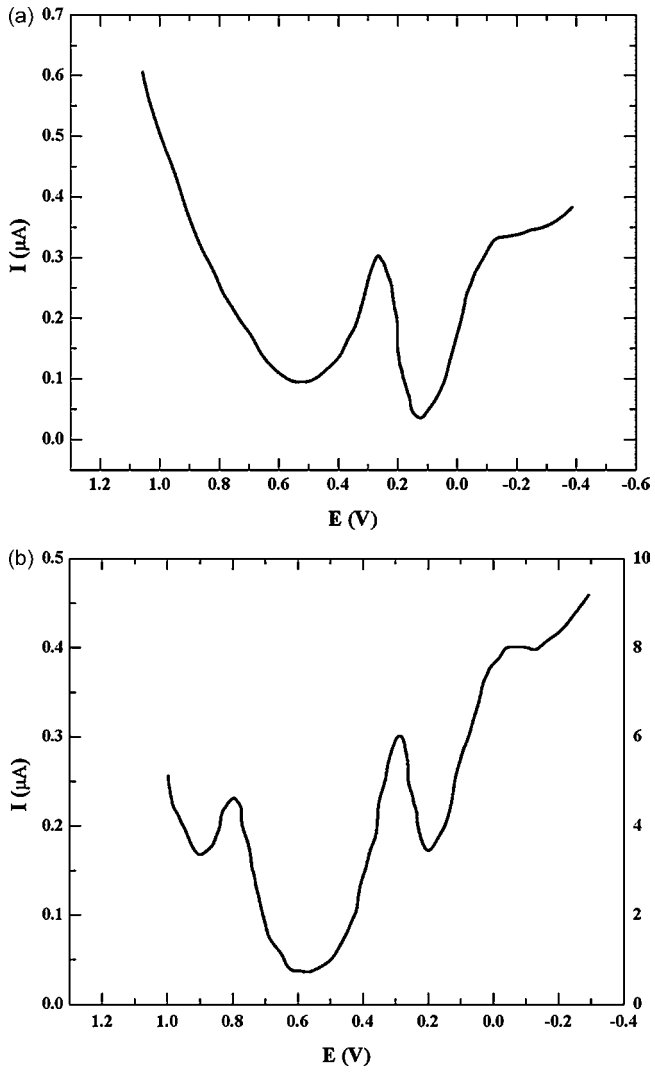


Fig. 3. SWV signal characteristic for dopamine imprinted film after dipping in (A) binary mixture of dopamine and tyrosine and (B) binary mixture of dopamine and tyramine. Rebinding binary solutions are 50 μmol L^{-1} with respect to template molecules.

(recognition) of a binary mixture of equal concentrations of tyrosine and dopamine (50 μmol L^{-1}). Dopamine-imprinted film showed high selectivity for dopamine in presence of tyrosine. As illustrated in Fig. 3A, dopamine showed relatively high current response at 250 mV while tyrosine showed almost no current response after the rebinding process. On the other hand, when the imprinted film was tested in a binary mixture of tyramine and dopamine, tyramine could rebind to the imprinted film and showed relatively appreciable current response at 780 mV with respect to dopamine imprinted film as shown in Fig. 3B. The results of rebinding experiments in binary mixture of dopamine and tyramine are similar to those obtained previously (cf. Section 3.2) in single rebinding runs. Thus, with the exception of tyramine that showed appreciable interference, dopamine imprinted film showed excellent selective recognition for dopamine in presence of other interfering molecules.

3.4. Effect of pH of the template solution on rebinding process

Virtually all drug-like molecules are weak acids or bases. This means that they contain at least one site that can reversibly disas-

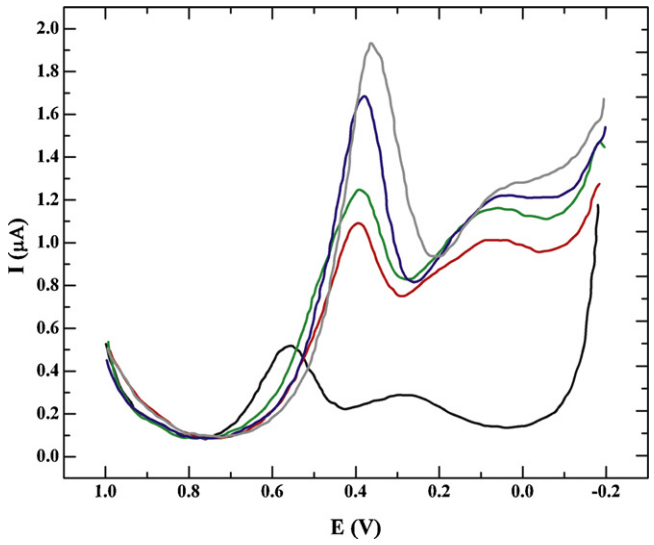


Fig. 4. SWVs of dopamine imprinted film after dipping in 100 μmol L^{-1} of dopamine solutions at different values of pH: 1.0 (—), 3.0 (—), 5.0 (—), 7.0 (—), 9.0 (—).

sociate or associate a proton (a hydrogen ion) to form a negatively charged anion or a positively charged cation. Molecules that disassociate protons are acids, and those that associate protons are bases. The reversibility means that a sample is always in equilibrium with some fraction protonated and the rest deprotonated.

$$HA \Leftrightarrow H^+ + A^- \text{ or } HB \Leftrightarrow H^+ + B^-$$

By varying the availability of protons, i.e. the acidity of the media, the balance of the equilibrium can be shifted. Alternatively, the p*K*a-values of a site can be thought of the pH at which the protonated and deprotonated fractions are equal. Experiments were carried out from different pH solutions on dopamine imprinted surface. All pH measurements were carried out from 100 μmol L^{-1} with respect to dopamine. As illustrated in Fig. 4, the current response increases with the increase in pH value. At pH-values lower than pKa_1 (8.57), the protonated form of dopamine predominates than the unprotonated zwitter ion form. On the other hand, at pH-values higher than pKa_2 (10.08) the deprotonated (phenoxide ion) form is higher than unprotonated zwitter ion. Between pKa_1 and pKa_2, the zwitter ion form predominates over the charged form [26]. This argument clarifies the fact that the protonated dopamine molecule is less interacting with the oriented functional groups in the molecular cavities while the neutral form is best fitted to the imprinted sites so by increasing the pH values current response enhances.

On the other hand, there was an increase in the oxidation potential value of the adsorbed species on the imprinted surface with the increase of pH value. This result could be explained from the fact that, positively charged molecules due to protonation of dopamine at lower pH values needs higher polarization potential (overvoltage) for oxidation. This is because the average electronic charge on the molecules is lowered, therefore it is more difficult to withdraw electrons at such a lower potential, while at higher pH values the molecule is either neutral or negatively charged which increases its electro-oxidation. This study was not extended to pH values higher than 9 because the glassy silicon film could decompose under the effect of strong alkaline medium.

3.5. Sensitivity versus electrode selectivity and lifetime

One important factor regarding the molecularly imprinted materials is the stability of the geometry of molecular cavities cre-

Table 2
Comparison of the rebinding results of dopamine imprinted film at the beginning and at the end of 2 weeks. Adsorption experiments were carried out from 50 μM solution with respect to dopamine prepared in PBS.

Molecule	I (10^{-7} A) Immediately after preparation	I (10^{-7} A) After 2 weeks	Percentage of decrease in current response signal (%)
Dopamine	3.35	2.59	22.3
Tyramine	3.01	1.82	40
Norepinephrine	1.93	0.71	63.5

ated inside the sol–gel material which in turn affects both the selectivity and the sensitivity of the imprinted material for template molecules on the long term. Dopamine imprinted films were tested in dopamine solution and in solutions of the other molecules being studied, then the electrodes were left in a dry place for relatively long period (ca. 2 weeks). The electrodes were tested again in dopamine solution and in solutions of other molecules at the end of the 2 weeks for rebinding process in order to test the selectivity and stability of the response. Measurements were carried out using three independent glassy carbon electrodes prepared in the same way to ensure repeatability of measurements. The standard deviation from the mean of measurements for the repeated experiments is 7.4%.

Current response for different test solutions was found to decrease after 2 weeks of drying with varying percentages. The most interesting point here is the incremental decrease in current response ascending from dopamine down to catechol. It was found that dopamine current response after 2 weeks, decreased by 22%. Tyramine signal decreased by 40% and norepinephrine by 63.5% of the original current response signal as indicated in Table 2. Rebinding current response disappeared completely for the remaining of the group of molecules being tested. It is concluded that the selectivity of the imprinted film increases appreciably for imprinted film if compared to other molecules, by increasing the time between drying and measurement.

Moreover, although the selectivity of the imprinted film toward its template compared to other structurally related molecules is enhanced, there is an appreciable decrease in the current response of the template itself. In other words meanwhile the selectivity of imprinted films toward its template molecule increases, the sensitivity of the imprinted films decreases. More extensive studies may help in the future to achieve a compromise between selectivity and sensitivity of molecularly imprinted materials.

3.6. The effect of concentration of the template molecule on the rebinding ability

In this part, we studied the relationship between the concentration of template molecule in the solution from which the template rebinds to the imprinted film, and the electrochemical current response after rebinding to the film. The imprinted films showed fairly linear rebinding response over the concentration range from 100 μmol L^{-1} down to 10 μmol L^{-1} as illustrated in Fig. 5. Beyond this concentration range; over the 100 μmol L^{-1} limit deviation from linearity was observed, while below 10 μmol L^{-1} the imprinted films are not sensitive for the template molecules. The linearity of the process confirms again that the rebinding process occurs specifically on selected sites created during the imprinted process in this concentration region.

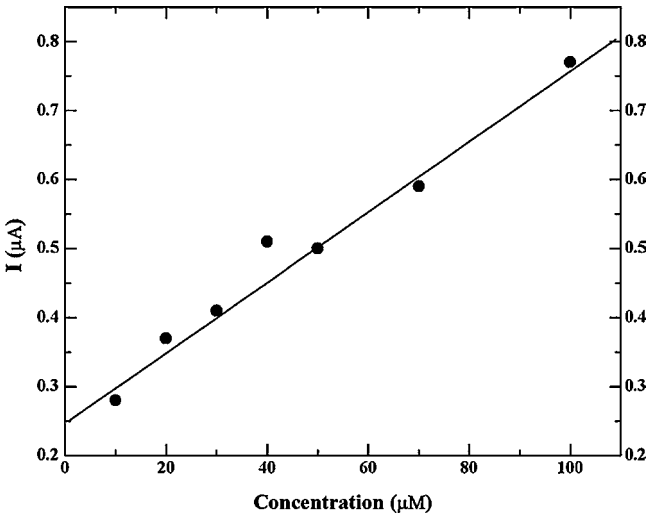


Fig. 5. Current response (SWV) of dopamine imprinted film as a function of the concentration of dopamine in the rebinding solution.

3.7. Electrochemical impedance characterization of the imprinted film

Impedance measurements were carried out over a frequency range from 0.5 Hz to 10^5 Hz with an applied AC voltage of 5 mV. Excitation DC voltages were predetermined using cyclic voltammetry for the molecules being tested against the imprinted films. Work was carried out at DC potentials 330 mV for dopamine, 720 mV for tyramine, and 550 mV for tyrosine. Previous studies showed that the imprinted film swells upon the association with their template molecules, which in turn enhances their electrical permittivity with respect to the electrolyte [27,28]. As a result of this, the electron transfer process is facilitated across the double layer. In case of dopamine-imprinted film that was incubated in dopamine solution the swelling effect of the imprinted film occurs due to rebinding of the template to its film. Fig. 6A illustrates Nyquist plots of dopamine films in case of incubation in dopamine solution and in PBS, respectively. Lines in Nyquist plot represent the calculated and fitted data for the equivalent circuit components while symbols represent the experimental data. Triangle symbols in the diagrams represent the signal after incubation of the imprinted film into its template solution while the square symbols represent the impedance signal of the imprinted film after incubation in buffer solution (buffer background).

Dopamine and tyramine-imprinted films were incubated in a solution containing a different molecule like tyrosine which showed no rebinding affinity to the imprinted film. The slope of Nyquist plots in both cases did not change appreciably for the incu-

Table 3A
EIS results of the equivalent circuit for dopamine imprinted film (a) incubated in 50 μM dopamine solution prepared in PBS (b) incubated in PBS. EIS work was carried out over a frequency range 0.5 Hz to 100 kHz at AC voltage with an excitation DC voltage 330 mV.

Impedance component	R_p (10^5 Ω cm^{-2})	R_u (10^3 Ω cm^{-2})	C_f (10^{-6} F cm^{-2})	W (10^5 Ω s$^{-1/2}$)	CPE (10^6 F cm^{-2})	n
(a)	0.0254	0.6030	6.3260	2.3670	1.9270	0.898
(b)	3.0640	1.0800	3.1090	8.8520	6.5020	0.902

Table 3B
EIS results of the equivalent circuit for dopamine imprinted film (a) incubated in 50 μM tyrosine solution prepared in PBS (b) incubated in PBS buffer. EIS work was done over a frequency range 0.5 Hz to 100 kHz at AC voltage with an excitation DC voltage 550 mV.

Impedance component	R_p ($10^4\ \Omega\,cm^{-2}$)	R_u ($10^2\ \Omega\,cm^{-2}$)	C_f (10^{-6} F cm^{-2})	W ($10^5\ \Omega\,s^{-1/2}$)	CPE (10^6 F cm^{-2})	n
(a)	4.6110	6.831	1.095	5.4470	2.6900	0.952
(b)	4.4790	6.762	1.279	5.4670	3.0460	0.9616

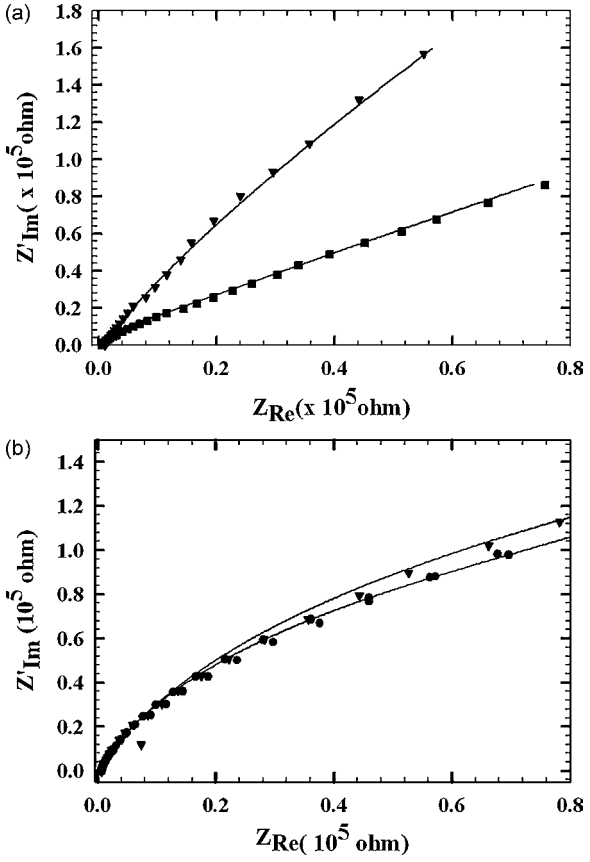


Fig. 6. (A) Nyquist plots of dopamine imprinted films tested in dopamine solution compared to the signal after testing in PBS. (B) Nyquist plots of dopamine imprinted films tested in tyrosine solution compared to the signal after testing in PBS.

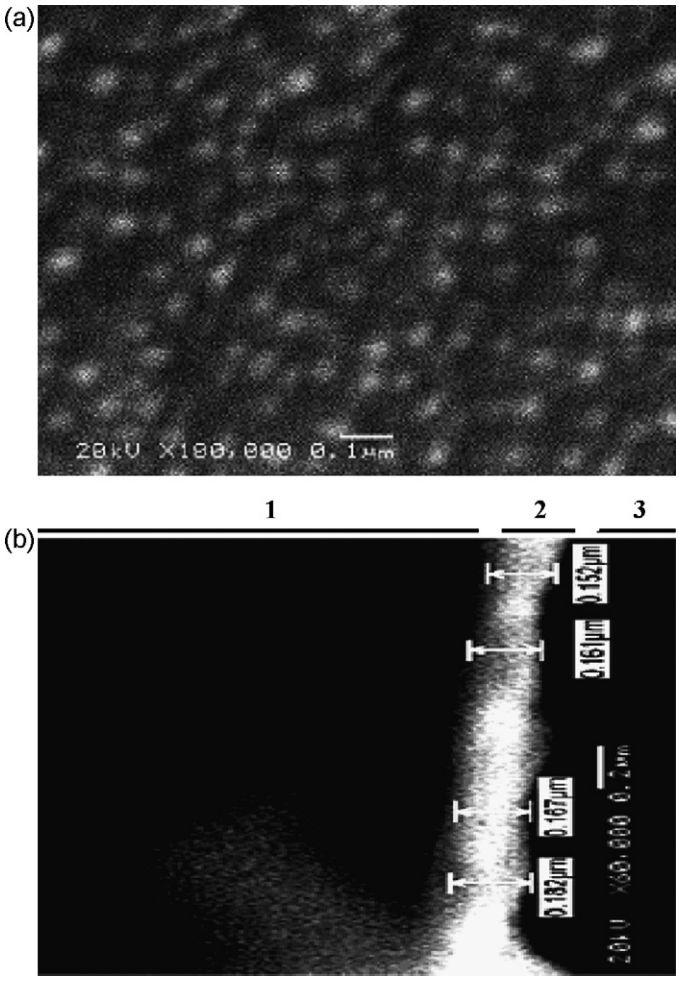


Fig. 8. Scanning electron microscope image of (A) sol–gel material used in the imprinting processes and (B) the side image of the sol–gel film coated on the surface of glassy carbon electrode. (1) Substrate edge, (2) sol–gel film and (3) air.

bation of the imprinted films in tyrosine solution compared to the incubation in PBS for the same period of time which is shown in Fig. 6B. This result indicated that tyrosine did not rebind into the molecular cavities of either tyramine or dopamine. From the foregoing results, it is confirmed again that imprinted sites are able to rebind their template molecules while molecules of largely different molecular structures and shape are unable to rebind.

The fitted electrochemical equivalent circuit is formed of five components connected in a specific way that they fit the impedance measurements carried out across the interface between the imprinted film coated on the electrode surface and the solution. Equivalent circuit designed for the molecularly imprinted film is indicated in Fig. 7. This circuit is formed of five components. R_u is the solution resistance, R_p is polarization resistance, C_f is capacitance component while CPE is another capacitance component called constant phase element. Constant phase element is more accurate component in describing the capacitance behavior of the double layer. W is Warburg component which describe the diffusion behavior of electro-active species with respect to the electrode surface.

Tables 3A and 3B lists the best fitting components calculated for the equivalent circuit for dopamine after testing in dopamine and in

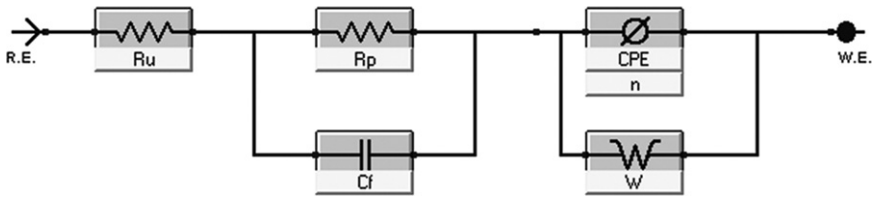


Fig. 7. Electrochemical equivalent circuit for EIS measurements.

tyrosine solutions, respectively. The circuit components decreased in case of incubation in dopamine solution compared to incubation in PBS. On the other hand these components did not change appreciably in case of incubation in tyrosine which confirms the experimental results described in Fig. 6(A and B).

3.8. Surface characterization

Sol–gel material synthesized for imprinting was characterized using scanning electron microscope at magnification power 100,000. The sol–gel particles were distributed very homogeneously and uniformly on the surface of substrate. The average particle size was found to be in the range of 38–45 nm as indicated in Fig. 8A. In this work, molecularly imprinted thin films were made using spin coating with spinning rate 2500 rpm as an optimized time in such away that it could allow the highest adsorption (recognition) capacity of the template molecules. The uniformity of the particles is mainly attributed to carrying spinning process at this high speed. Thin films were then allowed to dry to give a chance for complete polymerization of free hydroxyl groups on the film surface which may increase non-specific adsorption toward different molecular species by increasing the probability of H-bonding between the amino and hydroxyl groups of catecholamine compounds and these free hydroxyl groups.

We determined the average film thickness using side imaging of the coated electrode by scanning electron microscope [29] as illustrated in Fig. 8B. The film thickness ranged between 152 nm and 180 nm with an average value of 165 nm. The sensitivity as noticed in the high current responses of the modified electrode is highly affected by the film thickness. Thin films facilitate the diffusion of the template inside the molecular cavities compared to relatively thicker films [9].

4. Conclusions

Tyramine and dopamine molecules were imprinted successfully in a hybrid sol–gel material and then were spin coated as thin films on the surfaces of glassy carbon electrodes. The modified electrodes were used for sensing of the template molecules electrochemically. Selectivity of the electrodes for dopamine or tyramine was found to depend largely on the shape and size of the molecular cavity created during polymerization of sol–gel material in addition to the functional group orientation inside the cavities with respect to the template molecules.

Acknowledgments

The authors would like to acknowledge the financial support from Cairo University through the Vice President Office for Research Funds. We also like to thank “Mubarak City for Scientific Research and Technology Applications” for SEM measurements.

References

[1] F.H. Dickey, Natl. Acad. Sci. U.S.A. 35 (1949) 227.
[2] N.K. Raman, M.T. Anderson, C.J. Brinker, Chem. Mater. 8 (1996) 1682.
[3] S. Mann, S.L. Burkett, S.A. Davis, C.E. Fowler, N.H. Medelson, S.D. Sims, D. Walsh, N.T. Whilton, Chem. Mater. 9 (1997) 2300.
[4] D. Kriz, O. Ramstrom, K. Mosbach, Anal. Chem. (1997) 345A.
[5] Q. Fu, H. Sanbe, C. Kagawa, K.K. Kunimoto, J. Haginaka, Anal. Chem. 75 (2003) 191.
[6] O. Ramstrom, K. Skuder, J. Haines, P. Patel, O. Bruggeman, J. Agric. Food Chem. 49 (2001) 2105.
[7] P. Spegel, L. Schweitz, S. Nilsson, Anal. Chem. 75 (2003) 6608–6613.
[8] A.G. Mayes, M.J. Whitcombe, Adv. Drug Deliv. Rev. 57 (2005) 1742–1778.
[9] S. Firenman-Shoresh, I. Turyan, D. Mandler, D. Avir, S. Marx, Langmuir 22 (2005) 7842.
[10] T. Shiomi, M. Matsui, M. Mizukami, K. Sakaguchi, Biomaterials 26 (2005) 5564.
[11] Z. Zhang, Y. Long, L. Nie, S. Yao, Biosens. Bioelectron. 21 (2006) 1244.
[12] R.G. de Costa, F. Augusto, J. Chromatogr. A 1114 (2006) 216.
[13] I. Turyan, D. Mandler, Anal. Chem. 69 (1997) 894.
[14] G. Shustak, S. Marx, I. Turyan, D. Mandler, Electrocatalysis 15 (2003) 398.
[15] M.E. Brown, D.A. Puleo, Chem. Eng. J. 137 (2008) 97.
[16] K. Lee, R.R. Itharaju, D.A. Puleo, Acta Biomater. 3 (2007) 515.
[17] X. Jiang, W. Tian, C. Zhao, H. Zhang, N. Liu, Talanta 72 (2007) 119–125.
[18] X. Jiang, C. Zaho, N. Jiang, H. Zhang, M. Liu, Food Chem. 108 (2008) 1061.
[19] A.V. Rao, G.M. Pajonk, N.N. Parvathy, J. Mater. Sci. 29 (1994) 1807.
[20] S. Marx, Z. Liron, Chem. Mater. 13 (2002) 3624.
[21] S. Fireman-Shoresh, D. Avnir, S. Marx, Chem. Mater. 15 (2003) 3607.
[22] S. Marx, A. Zaltsman, Int. J. Environ. Anal. Chem. 83 (2003) 671.
[23] K. Farrington, F. Regan, Biosens. Bioelectron. 22 (2007) 1138.
[24] D. Silvestri, N. Barbani, C. Cristallini, P. Giusti, G. Ciardelli, J. Membr. Sci. 282 (2006) 284.
[25] Oliver K. Castell, Christopher J. Allender, David A. Barrowb, Biosens. Bioelectron. 22 (2006) 526.
[26] M.T.I.W. Schüsler VanHees, G.M.J. Beijersbergen Van Henegouwen, M.F.J. Driever, Pharm. Weekbl. [Sci.] 5 (1983) 102.
[27] M. Watanabe, T. Akahoshi, Y. Tabata, D. Nakayama, J. Am. Chem. Soc. 120 (1998) 5577.
[28] J. Matsui, K. Akamatsu, S. Nishiguchi, D. Miyoshi, H. Nawafune, K. Tamaki, N. Sugimoto, Anal. Chem. 76 (2004) 1310.
[29] H.-J. Liang, T.-R. Ling, Rick F. Jo, J.-C. Choub, Anal. Chim. Acta 542 (2005) 83.

Talanta 80 (2009) 519–525

Contents lists available at ScienceDirect

Talanta

journal homepage: www.elsevier.com/locate/talanta

Voltammetric performance and application of a sensor for sodium ions constructed with layered birnessite-type manganese oxide

Murilo T. Martinez[a], Alex S. Lima[a], Nerilso Bocchi[b], Marcos F.S. Teixeira[a,*]

[a] Department of Physics, Chemistry and Biology, Faculty of Science and Technology, University of State of Sao Paulo (UNESP), Rua Roberto Simonsen, 305, CEP 19060-900, Presidente Prudente, SP, Brazil
[b] Departamento de Química, Universidade Federal de São Carlos, São Carlos, SP, Brazil

ARTICLE INFO

Article history:
Received 27 May 2009
Received in revised form 3 July 2009
Accepted 6 July 2009
Available online 5 August 2009

Keywords:
Birnessite
Manganese oxide
Insertion electrochemical
Sodium determination
Urine sample

ABSTRACT

The preparation and electrochemical characterization of a carbon paste electrode modified with layered birnessite-type manganese oxide for use as a sodium sensor is described. The effects of powder synthesis process (sol–gel and redox precipitation) for birnessite on the electrochemical activity of the sensor was investigated by cyclic voltammetry. The carbon paste electrode modified with birnessite-type manganese oxide that was synthesized by the sol–gel method showed a best electrochemical for sodium ions. The detection is based on the measurement of anodic current generated by oxidation of Mn(III) to Mn(IV) at the surface of the electrode and consequently the sodium ions extraction into the birnessite structure. The best voltammetric response was obtained for an electrode composition of 15% (w/w) birnessite oxide in the paste, a TRIS buffer solution of pH 8.0 and a scan rate of 50 mV s^{-1}. A sensitive linear voltammetric response for sodium ions was obtained in the concentration range of 7.89×10^{-5} to 3.49×10^{-4} mol L^{-1} with a slope of 37.5 μA L $mmol^{-1}$ and a detection limit (3σ/slope) of 3.43×10^{-5} mol L^{-1} using cyclic voltammetry. Under the working conditions, the proposed method was successfully applied to determination of sodium ions in urine samples.

© 2009 Elsevier B.V. All rights reserved.

1. Introduction

Porous manganese oxides are a class of materials that combine the high surface area/selectivity properties of zeolites with the redox capacity of manganese. Birnessite is a common manganese oxide mineral found in soils, ore deposits, and marine manganese nodules [1–5]. It has a two-dimensional layered structure that consists of edge-shared MnO_6 octahedra with cations and water molecules occupying the interlayer region, as indicated in Fig. 1. The interlayer distance in birnessite is typically 7 Å, but further hydration can increase this spacing to produce a closely related 10 Å birnessite variant known as buserite [6–9].

Manganese oxide forms various structures, including spinel (hausmannite), layered (birnessite, buserite), and one-dimensional tunnel (hollandite, todorokite). It also contains manganese atoms of different valencies, dependent on the molar ratio of manganese and oxygen, the defects in the crystals, or the content of other metal ions such as alkali metals [10]. Birnessite is an important ion-exchange material [11] and a precursor to todorokite (a class of octahedral molecular sieves containing 3×3 MnO_6 units) [12–14]. Birnessite can be used in rechargeable battery materials [15] and is also a promising catalytic material [16].

A lowering of the electrolytic concentration of sodium ions in the blood to a serum concentration below 136 mmol L^{-1} results in hyponatremia, an electrolytic disturbance in hospitalized patients. This reflects a water balance disturbance associated to hyposmolality [17,18]. The official method for analyzing sodium ion concentration is flame photometry [19]. Several reports demonstrate alternative procedures for the determination of sodium concentration that employ different analytical systems in various pharmaceutical, environmental and clinical samples [20–22]. However, the majority of the studies proposed in literature are based on spectrophotometric techniques [23–25].

In this paper, the construction of a carbon paste electrode modified with birnessite-type manganese oxide is proposed. The influence of various parameters such as electrode composition, pH, potential scan rate and interference in potential was studied by cyclic voltammetry.

2. Experimental

2.1. Apparatus

The cyclic voltammetric measurements were carried out with μAutolab III, controlled by a PC using GPES 4.9.7 software. The

* Corresponding author. Tel.: +55 18 32295355; fax: +55 18 32215682.
E-mail address: funcao@fct.unesp.br (M.F.S. Teixeira).

0039-9140/$ – see front matter © 2009 Elsevier B.V. All rights reserved.
doi:10.1016/j.talanta.2009.07.015

measurements were performed in a glass cell containing three electrodes: a modified carbon paste electrode (CPEM) as the working electrode, a saturated calomel electrode (SCE) as the reference electrode and a platinum wire as the auxiliary electrode. During the measurements, the solution in the cell (TRIS buffer solution at pH 8.0) was not stirred.

2.2. Reagents and solutions

All solutions were prepared using deionized water. Chemicals of analytical-reagent grade were used without further purification. The supporting electrolyte used for all experiments was a 0.1 mol L^{-1} tris(hydroxymethyl) aminomethane (TRIS) buffer solution at pH 8.0. A stock solution of 1.0×10^{-2} mol L^{-1} sodium ion was prepared daily by dissolving sodium chloride (Aldrich) in 100 mL of 0.1 mol L^{-1} TRIS buffer solution (pH 8.0). Graphite powder (1-2 μm particle size, Aldrich) and mineral oil (Aldrich), both of high purity, were used in the preparation of the carbon paste.

2.3. Synthesis of birnessite-type manganese oxide

The synthesis of birnessite-MnO_2 through a sol–gel method was realized by the procedure previously described [26], in the following way: 3.0 g of $NaMnO_4 \cdot H_2O$ dissolved in 50 mL of distilled water was added to 5.0 g of glucose dissolved in 20 mL of distilled water. The resulting mixture was swirled vigorously for 50 s and then allowed to stand without further agitation. The exothermic reaction produced a reddish sol that became a brown gel within 90 s of the initial mixing. The gel was allowed to cool at room temperature for 30 min before being dried at 110 °C overnight. Calcination of the resulting brown xerogel at 400 °C for 2 h produced an ash, which was ground into a fine brown/black powder. The crude product was stirred in water overnight before being isolated by filtration, washed with water and dried at 110 °C.

The synthesis of birnessite-MnO_2 though a redox precipitation method was realized by the procedure previously described [27], in the following way: a solution of 13.5 g of $MnSO_4 \cdot H_2O$ and 3.95 g of $MgSO_4 \cdot 7H_2O$ in 160 mL of deionized distilled water (DW) was added slowly to a solution of 40 g of sodium hydroxide in 180 mL of DW with vigorous agitation to form pink gels of $Mn(OH)_2$. A solution of 5.1 g of $KMnO_4$ in 160 mL of DW was then added slowly into the gel during vigorous agitation to produce a black suspension of MnO_x. This suspension was aged at room temperature and at atmospheric pressure. The resultant product was filtered and washed.

2.4. Structural characterization of birnessite-type manganese oxide

The powder of birnessite oxide was characterized by X-ray diffraction (XRD) using a D5000 X-ray diffractometer with Cu Kα radiation and monochromatic graphite. Samples were spread onto glass slides and scanned at 2° 2θ/min between 5° at 75°. The comparison with JCPDS card 23-1046 confirmed the peaks of greater intensity characteristic of the structure of birnessite-type manganese oxide.

2.5. Construction of the carbon paste electrode

The modified carbon paste electrode was prepared manually by carefully mixing the dispersed graphite powder with birnessite oxide at several mass ratios and subsequently adding a fixed quantity of 150 mg of mineral oil (15%, w/w). Those mixtures were mixed by magnetic agitation in a 50 mL beaker containing 10 mL of hexane. The final paste was obtained via evaporation of the solvent. The modified carbon paste was packed into an electrode body consisting of a plastic cylindrical tube (i.d. 3 mm) equipped with a stainless steel rod serving as an external electric contact.

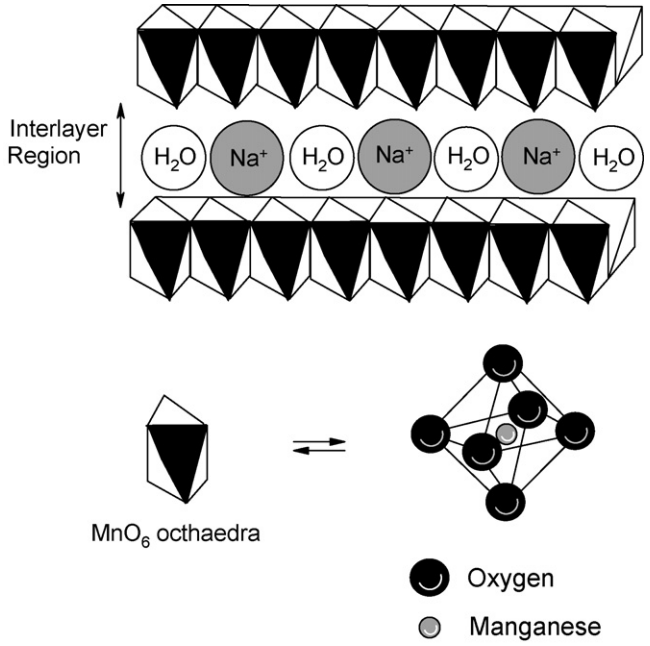


Fig. 1. Schematic representation of the birnessite-type manganese oxide.

3. Results and discussion

3.1. XRD characterization of birnessite-type manganese oxide

The birnessite-MnO_2 synthesized by the sol–gel and redox precipitation methods provided XRD spectra with many peaks. Among them were two structural phases of higher importance: one with an interlayer distance of 0.7 nm ($2\theta = 12°$) and another with a layer spacing of 0.55 nm ($2\theta = 25.0°$). The XRD patterns of the birnessite oxides synthesized by the sol–gel and redox precipitation methods are shown in Fig. 2, respectively. Prolonged stirring of this product mixture in water converts the 0.55 nm form into the 0.7 nm form [26]. Layered manganese oxides with spacing near 0.55 nm have previously been observed and characterized as dehydrated forms of 0.7 nm birnessite [28–31].

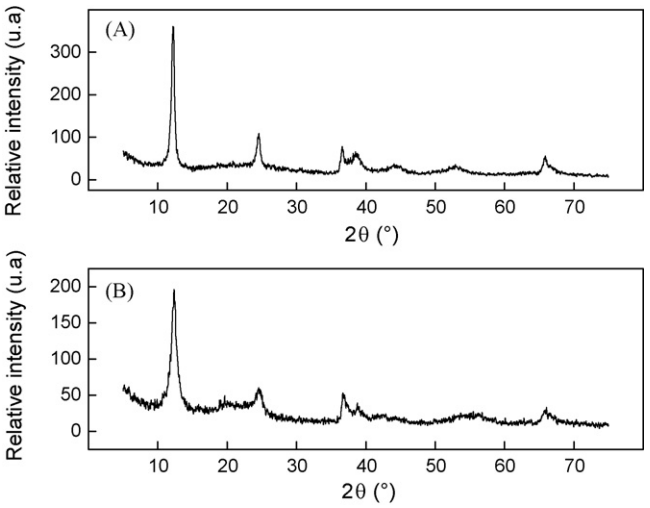


Fig. 2. The XRD patterns of birnessite synthesized by the sol–gel (A) and redox precipitation methods (B).

In terms of structural organization and crystallinity, some differences were observed between the oxides synthesized by the two methods. The sol–gel method yielded a diffractogram with narrower, more defined peaks, indicating good structural organization of the birnessite oxide. The redox precipitation method yielded a diffractogram with more phases, represented by characteristic signal located in the peaks of crystalline reflection: $2\theta = 12.43^\circ$; 19.86°; 24.75°; 55.45° and 65.97°. Although they have minor intensities, the presence of several allotropic phases of manganese oxide reduces the sensor's active region of electrochemical response, which is indicated by relative proportion Mn(III)/Mn(IV) of birnessite-MnO_2 contain in the interlayer region with distance of 0.7 nm. This space region is responsible for the intercalation/deintercalation reaction of sodium ions of layer conformation of birnessite manganese oxide, due to the higher negative charge density of MnO_6 octahedra.

However, the birnessite manganese oxide synthesized by the sol–gel method was the modifier utilized in the elaboration of this sensor. The carbon paste electrode modified with birnessite-type manganese oxide that was synthesized by the sol–gel method showed a best electrochemical for sodium ions. This performance is related to the degree of crystallinity, the homogeneity of the oxide and the ideal interlayer distance for the sodium ions.

3.2. Voltammetric behavior of the CPEM

The characteristics of the carbon paste electrode modified (CPEM) with birnessite-type manganese oxide were studied by cyclic voltammetry. Fig. 3 shows a typical cyclic voltammogram obtained for the CPEM with birnessite-type manganese oxide in 0.1 mol L^{-1} TRIS buffer (pH 8.0), both in the presence of 1.67×10^{-3} mol L^{-1} of sodium ions (indicated by curve **B**) and the absence of sodium ions (indicated by curve **A**). The potential was scanned between −0.50 and 1.0 V versus SCE; an anodic potential peak was observed at +0.57 V (peak **I**) and a cathodic potential peak was observed at +0.04 V (peak **II**). This electrochemical activity was due to the topotactic extraction process of the sodium ions from the birnessite structure, which occurs according to [32]:

$$NaMn^{3+}Mn^{4+}O_x + H_2O \rightarrow HMn_2{}^{4+}O_x(OH) + Na^+ + e^- \quad (\text{peak I}) \tag{1}$$

$$HMn_2{}^{4+}O_x(OH) + Na^+ + e^- \rightarrow NaMn^{3+}Mn^{4+}O_x + H_2O \quad (\text{peak II}) \tag{2}$$

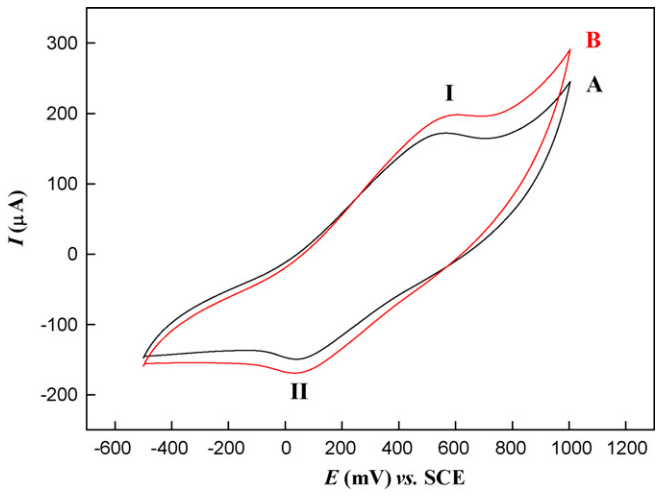


Fig. 3. Cyclic voltammogram at a scan rate of 15 mV s^{-1} for the CPEM with birnessite-type manganese oxide in TRIS buffer solution (pH 8.0) in the absence of sodium ions (A) and in the presence of 1.67×10^{-3} mol L^{-1} sodium ions (B).

Reaction (1) represents the electrochemical response of the correspondent electrode, an oxidation reaction of Mn(III) to Mn(IV) with concomitant departure of the sodium ions from the birnessite structure. Reaction (2) represents the electrochemical response of the correspondent electrode, a reduction reaction of Mn(IV) to Mn(III) with intercalation of the sodium ions into the birnessite structure. The entrance and exit of water molecules in the birnessite-MnO_2 interlayer region is essential for oxidation and reduction of the manganese atom, respectively [33]. The electrochemical response is illustrated in Scheme 1. The enhanced response to sodium occurs because the cathodic polarization of the CPEM with birnessite-type manganese oxide is enough to reduce the manganese in the solid phase. Consequently, the sodium ions from the adjacent solution are able to diffuse through the birnessite structure to maintain the electroneutrality principle. In the absence of sodium ions (curve A—Fig. 3), the voltammetric profile of the modified electrode shows a redox peak. Supposedly, that behavior can be related with the vestige of sodium ions in the birnessite-type manganese oxide occurred during its preparation.

3.3. Electrode composition effect

The amount of manganese oxide in the carbon paste had a significant influence on the voltammetric response. The peak currents increased according the elevation on amount of birnessite-type manganese oxide up to 25% (w/w). For amounts of manganese oxide greater than 30% (w/w), the anodic peak current decreased significantly. This occurs because of a decrease of the graphite content in the paste and, consequently, a reduction of conductive area at the electrode surface. The best carbon paste composition was found to be an electrode composition of 15% (w/w) modified birnessite-type manganese oxide, 70% (w/w) graphite and 15% (w/w) mineral oil.

3.4. Effect of pH

The voltammetric response of the carbon paste electrode modified with birnessite-type manganese oxide was studied over a pH range between 5.0 and 10.0, controlled with TRIS buffer in the presence (1.67×10^{-3} mol L^{-1}) and absence of sodium ions. The results obtained indicated that the values difference current of anodic peaks are strongly influenced and reached a maximum value at pH values near 8.0, as shown in Fig. 4.

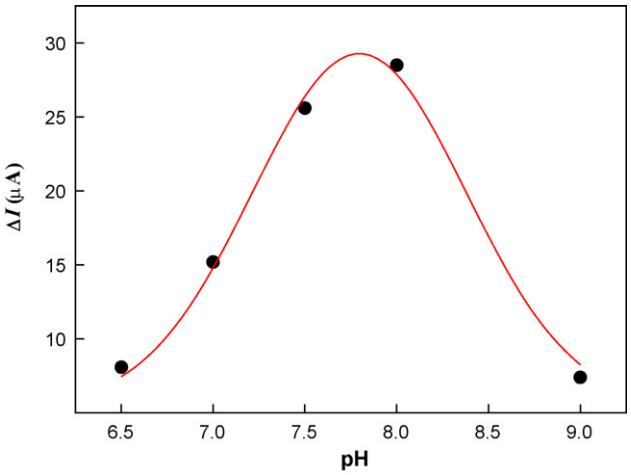
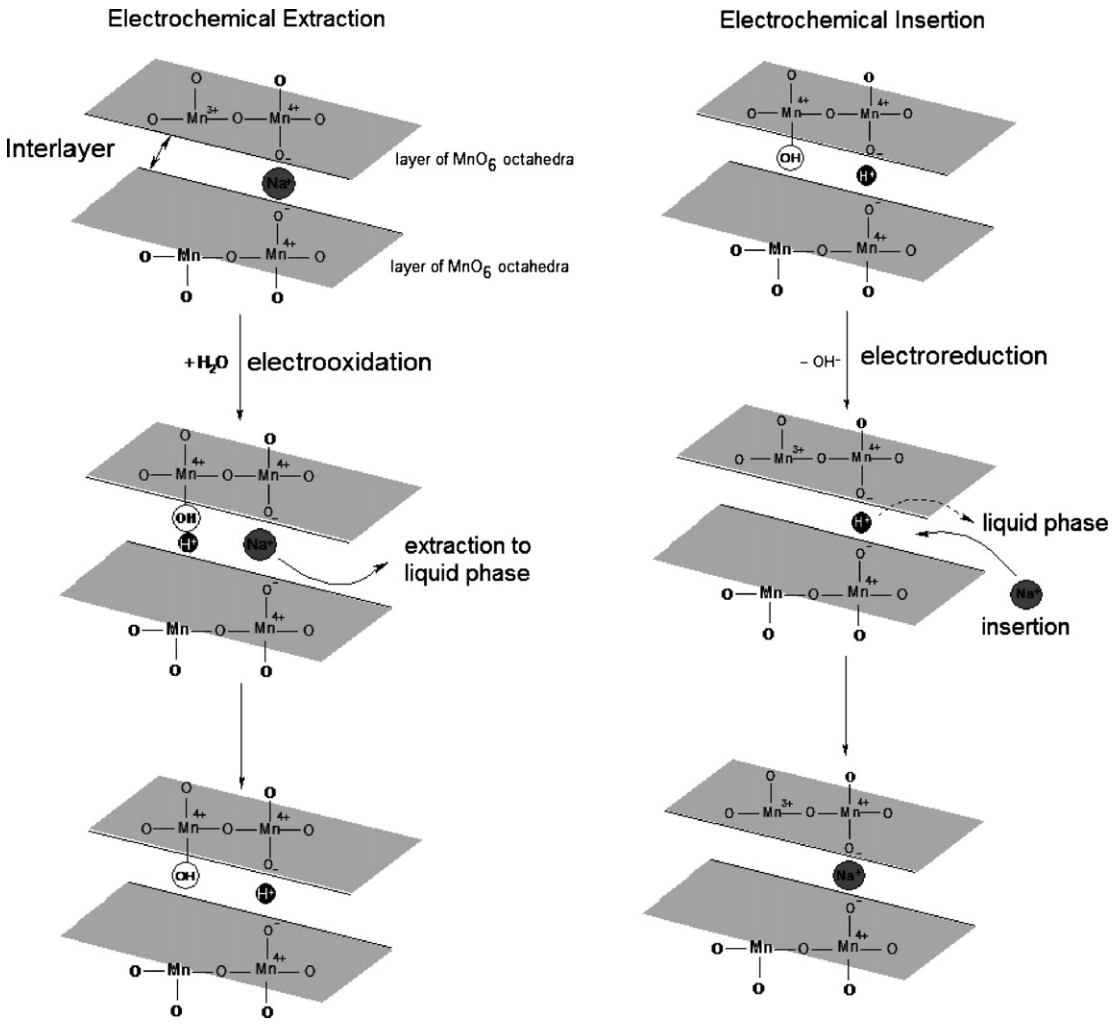


Fig. 4. pH dependence of the voltammetric response of the carbon paste electrode modified with 15% (w/w) birnessite at a scan rate of 50 mV s^{-1} in TRIS buffer solution containing 1.67×10^{-3} mol L^{-1} sodium ions. The anodic peak current (ΔI_{pa}) was obtained from the difference of the currents in the absence and presence of sodium ions.



Scheme 1. Schematic representation of the electrode modified with layered birnessite-type manganese oxide. Electrochemical extraction/insertion reactions of sodium ions from the birnessite structure. Adapted from Ref. [42].

At pH values under 8.0, the surface disproportion reaction proposed by Hunter [34] and Sato et al. [35] (represented in Eq. (3)) could explain the pH dependency of the peak current.

$$2Na[Mn^{3+}Mn^{4+}]O_{4(s)} + 4H_3O^+_{(aq)} \rightarrow 3HMn^{4+}O_2(OH)_{(s)} + 2Na^+_{(aq)} + Mn^{2+}_{(aq)} + 3H_2O_{(l)} \quad (3)$$

For pH values of 9.0 and 10.0, the values of the peak current decrease again, probably due to another surface formation of pyrochroite ($Mn(OH)_2$) and/or non-electroactive spinel-type oxide (Mn_3O_4-hausmannite) [36,37]. Therefore, only a TRIS buffer of pH 8.0 was used in further studies.

3.5. Studies on the ion extraction process

The time it takes to extract sodium ions from birnessite-type manganese oxide is an important parameter; with this parameter, one can obtain an oxide with a smaller proportion of sodium in the layered and two-dimensional structures of birnessite. Therefore, this parameter was studied in the hopes of obtaining an oxide with a better electrochemical performance. Oxide samples were agitated in 1 mol L^{-1} nitric acid over different cationic extraction periods (24, 48, 72 and 96 h) and evaluated in the CPEM in 0.1 mol L^{-1} TRIS buffer (pH 8.0) – both in the absence and presence of sodium ions ($[Na^+] = 1.67 \times 10^{-3}$ mol L^{-1}) – by cyclic voltammetry. A higher variation in the anodic peak current was obtained with the birnessite oxide sample that was subjected to 48 h of sodium ion extraction (Table 1). The cyclic voltammogram of the sample subjected to 72 h of cationic extraction, however, presented the best voltammetric profile, and this oxide was used in all further studies.

3.6. Effect of the scan rate

The effect of the scan rate on the voltammetric response of CPEM with birnessite-type manganese oxide in a solution containing 1.67×10^{-3} mol L^{-1} of sodium ions was investigated in the range of 5–100 mV s^{-1}. For scan rates higher than 50 mV s^{-1}, an increase in the values of the anodic peak currents was accompanied with a

Table 1
Effect of the extraction of sodium ions from birnessite-type manganese oxide in the anodic peak current (ΔI_{pa})[a] of the sensor in the presence of 1.67×10^{-3} mol L^{-1} sodium ions.

Cationic extraction periods (h)	ΔI_{pa} (μA)
24	22.4
48	70.8
72	54.2
96	40.0

[a] The values of anodic current were obtained by difference of the currents in the presence and absence of sodium ion in solution.

broadening and distortion of the peaks. When the values of the peak currents for both anodic peaks were plotted against the square root of the scan rate, a linear relationship was observed. These results show that the charge transfer reaction ($Mn^{3+} \rightarrow Mn^{4+} + e^-$) is controlled by diffusion of the sodium ions in the solid phase [38]. The linear relationship obtained was:

$$I_{pa}(\mu A) = 56.9 + 1322.6\,\nu^{1/2}(V^{1/2}s^{-1/2}) \quad r = 0.9993,\ n = 6 \qquad (4)$$

$$I_{pc}(\mu A) = -37.0 - 855.4\,\nu^{1/2}(V^{1/2}s^{-1/2}) \quad r = 0.9977,\ n = 6 \qquad (5)$$

The apparent electrochemical rate constant (k_e) and the electron-transfer coefficients (α_{anodic} and $\alpha_{cathodic}$) were calculated for the CPEM birnessite-MnO_2 according to the method described by Larivon [39]. It has been shown by Laviron that for a surface redox couple, α_a and α_c, k_e can be determined from the variation of E_{pa} and E_{pc} with scan rate. For large enough scan rates, the E_p versus $\log \nu$ plots gave two straight lines with slopes of $-2.303RT/\alpha_c nF$ for the cathodic branch and $2.303RT/(1-\alpha_a)nF$ for the anodic branch, where R is the gas constant, T is the absolute temperature, F is the Faraday constant, and n is the number of electrons involved in the redox process. Considering that the number of electrons involved in the redox process is 1, the calculated values for the coefficients α_a and α_c are 0.54 and 0.18, respectively. These results suggest that the redox process tends an almost irreversible system. The apparent electrochemical rate constant for anodic peak can then be determined applying the equation $k_e = 2.303\alpha_a nF\nu_o/RT$, in which the value of the scan rate (ν_o) is determined by extrapolation of the linear branch at higher scan rates to its intersection with the constant peak potential, represented by the peak of the voltammogram at the lower scan rate. From the equation, the observed value for k_e was $2.42 \times 10^{-1}\ s^{-1}$.

3.7. Effect of interference

For this study, cyclic voltammograms for the CPEM with birnessite-type manganese oxide were carried out in 0.10 mol L^{-1} TRIS buffer solution (pH 8.0) containing 1.67×10^{-3} mol L^{-1} of Li^+, K^+, Rb^+, Mg^{2+}, Ca^{2+}, Sr^{2+} and Ba^{2+}. Fig. 5 shows the effect of these different cations in the voltammetric response of the sensor. The relative current (%) was calculated by the difference in the peak currents in the presence and absence of the cations. The values of the anodic peak current decreased with the increase of the ionic radius of the cation. For ions with an ionic radius of less than 1.13 Å, current values were observed to be higher for bivalent ions than for monovalent ions. These results suggest that ions with a greater charge and smaller ionic radius easily insert into the birnessite-type manganese dioxide matrix. The magnesium ion was interference serious in the voltammetric response of CPEM. The magnitude of this interference was correlated with the high capacity of the magnesium ion to insert into the interlayer region of the birnessite oxide. This capacity is related to the high charge density (ion charge/ionic radius = 3.08) of the magnesium ion; for comparison, the charge density of a sodium ion is 1.05 [40].

3.8. Effect of the pre-concentration time

The dependence of the anodic peak currents on the pre-concentration time is presented in Fig. 6. The voltammetric responses of the CPEM with birnessite-type manganese oxide in a solution containing 1.63×10^{-3} mol L^{-1} sodium ions, after pre-concentration at −0.2 V, range 0 at 100 s was available. The values of the anodic peak currents increased linearly with the pre-concentration time (Fig. 6). This is because the birnessite-type manganese oxide structure enables accumulation of sodium ions through the oxide's larger superficial area, in comparison with respective areas for other manganese oxides (spinel-MnO_2) [41].

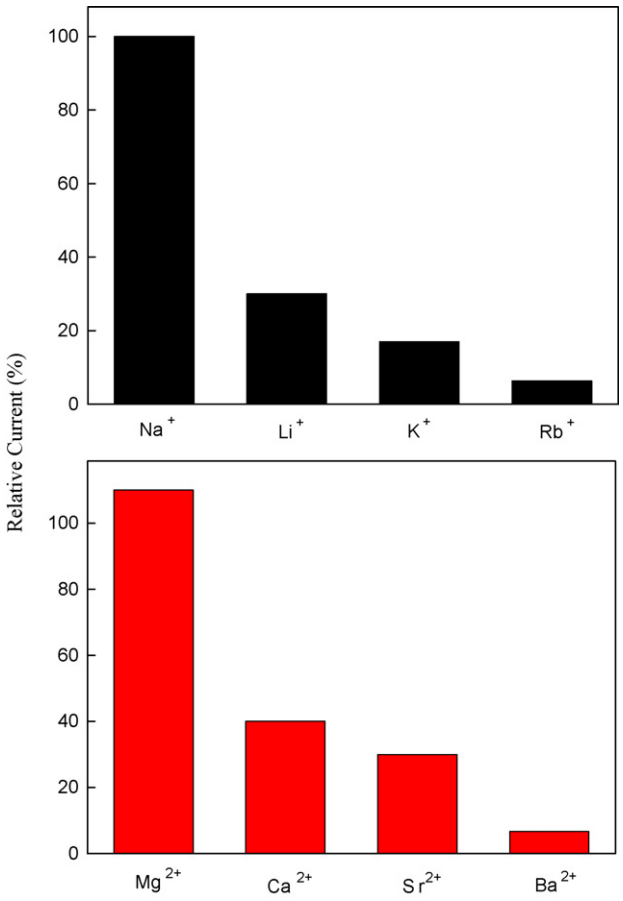


Fig. 5. Interference dependence of the voltammetric responses of the CPEM with birnessite-type manganese oxide in TRIS buffer solution (pH 8.0) containing 1.67×10^{-3} mol L^{-1} of Li^+, K^+, Rb^+, Mg^{2+}, Ca^{2+}, Sr^{2+} and Ba^{2+} ions. Scan rate = 50 mV s^{-1}.

Hence, for all subsequent measurements, a pre-concentration time of 100 s was employed.

3.9. Calibration graph and precision of the sensor

Under the optimized conditions previously studied–including composition of the electrode (15%, w/w), pH (8.0) and scan rate

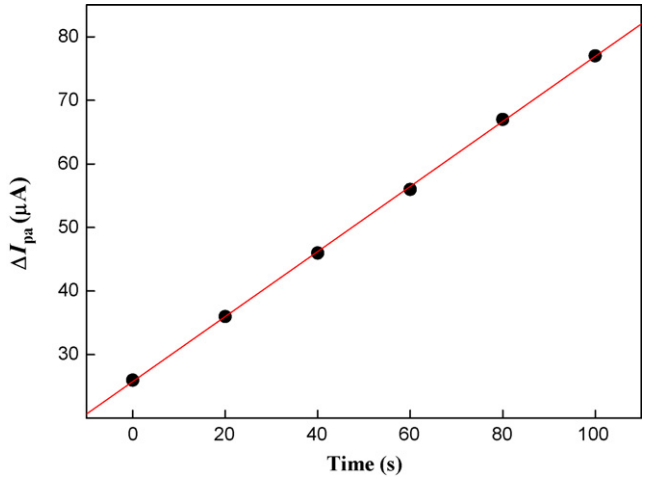


Fig. 6. Pre-concentration time dependence of the voltammetric responses of the CPEM with birnessite-type manganese oxide in TRIS buffer solution (pH 8.0) containing 1.67×10^{-3} mol L^{-1} of sodium ions after pre-concentration at −0.2 V vs. SCE. Scan rate = 50 mV s^{-1}.

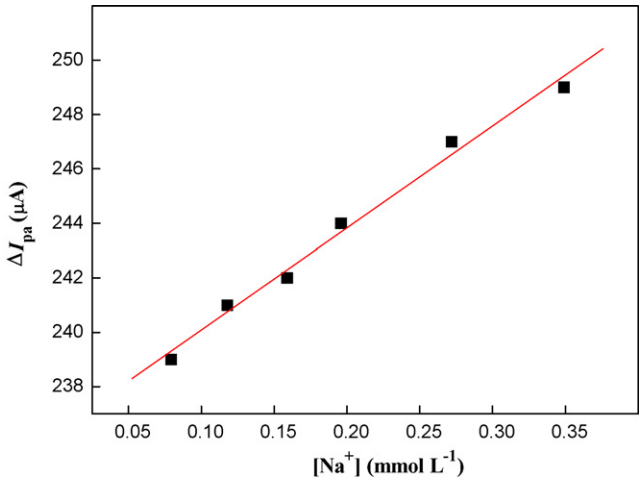


Fig. 7. Analytical curve for sodium ions in 0.1 mol L^{-1} TRIS buffer solution (pH 8.0) using the CPEM with 15% (w/w) birnessite-MnO_2, with a pre-concentration time at −0.2 V vs. SCE of 100 s. Scan rate = 50 mV s^{-1}.

(50 mV s^{-1})—cyclic voltammetrics were carried out in the buffered solution containing varying sodium ion concentrations in order to obtain the analytical curve of the CPEM. A linear relationship was obtained when the anodic peak current values were plotted against sodium ion concentrations in the range of 7.89×10^{-5} to 3.49×10^{-4} mol L^{-1} (I_{pa} (μA) = 236.3 + 37.5 [Na^+(mmol L^{-1})]; $r = 0.9948$; $n = 6$), as illustrated in Fig. 7. The sodium ion concentration detection limit (3σ/slope) was 3.43×10^{-5} mol L^{-1}.

The precision of the method was tested by analyzing six voltammograms of CPEM in 0.1 mol L^{-1} TRIS buffer solution at pH 8.0 containing 1.67×10^{-3} mol L^{-1} of sodium ions. A small increase in the peak current was observed with the increase of the number of cycles. This behavior can be related with the ionic capture capacity of oxides with bigger superficial areas.

3.10. Determination of sodium ions in urine samples

The sodium ions concentrations of three different human urine samples were determined by cyclic voltammetric using the CPEM with birnessite-type manganese oxide under the previously optimized experimental conditions. The urine samples were pre-treated with ammonium hydroxide to eliminate calcium and magnesium ions by precipitating them in the form of $Ca(OH)_2$ and $Mg(OH)_2$, respectively. The ammonia in the pre-treated samples was eliminated by heating. The sample solution was prepared in the TRIS buffer solution (pH 8.0) prior to analysis. The sodium ions concentration was determined by the standard addition method and compared with the values obtained by atomic absorption spectrophotometry at a wavelength of 589 nm. Relevant analyses are summarized in Table 2. The statistical calculations for the assay results show significant precision for the proposed method.

In the addition and recovery study, five different sodium concentrations (3.98, 7.94, 1.18, 15.7 and 19.6×10^{-4} mol L^{-1}) were added in triplicate in the urine sample. The results are showed in the Table 3. Recoveries between 92.7% and 107% of sodium ion were obtained using the sensor; it suggests the absence the interference of matrix effect in the procedure proposed.

Table 2
Comparative results for the determination of sodium ions content in urine samples using the voltammetric methodology and atomic absorption spectrophotometry.

Samples	Sodium ions (μg mL^{-1})		
	Spectrophotometry	Voltammetry	E_r (%)
1	4.783	4.702	5.7
2	4.836	4.734	7.2
3	4.812	4.725	6.1

E_r = relative error, voltammetric method vs. spectrophotometric method.

Table 3
Results of addition-recovery experiments using voltammetric procedure for three different standard concentrations of sodium ion.

Sodium ion* ($\times 10^{-4}$ mol L^{-1})		
Added	Found	Recovery (%)
3.98	3.69	92.7
7.94	8.20	103
11.8	12.6	107
15.7	15.6	99.4
7.94	8.70	97.4

* $n = 3$.

4. Conclusion

The present study demonstrates that the carbon paste electrode modified (CPEM) with birnessite-type manganese oxide can be used for the determination of sodium ion concentrations in the presence of several alkali metals. The electrochemical behavior of the CPEM with birnessite-type manganese oxide was well defined and stable. The best voltammetric response was obtained for an electrode composition of 15% (w/w) birnessite-type manganese oxide in the paste, a 0.1 mol L^{-1} tris(hydroxymethyl) aminomethane buffer solution at a pH of 8.0, a scan rate of 50 mV s^{-1}, an accumulation potential of −0.2 V versus SCE, and a pre-concentration time of 100 s. Under these experimental conditions, the proposed methodology responds to sodium ions in the concentration range of 7.89×10^{-5} to 3.49×10^{-4} mol L^{-1}, with a detection limit of 3.43×10^{-5} mol L^{-1}. The lifetime of the proposed sensor was at least six months (more than 100 determinations was performed using the same electrode surface and more than 600 determinations was done when the surface was renewed). The determination of sodium ions in urine using the proposed procedure is characterized by precision and selectivity. This makes the procedure applicable for the analysis and quality control of clinical samples.

Acknowledgements

The financial support of CNPq (474367/2004-5) and FAPESP (2005/01296-4) is gratefully acknowledged. The scholarships granted by FAPESP (2007/00600-7) to M.T. Martinez are gratefully acknowledged. The authors thank SJT.

References

[1] L.H.P. Jones, A.A. Milne, Miner. Mag. 31 (1956) 283.
[2] F.V. Chukhrov, A.I. Groshkov, R. Trans, Soc. Edinburgh: Earth Sci. 72 (1981) 195.
[3] M.D. Siegel, S. Turner, Science 219 (1983) 172.
[4] E. Paterson, J.L. Bunch, D.R. Clark, Clay Miner. 21 (1986) 949.
[5] R.G. Burns, V.M. Burns, Mineralogy, in: G.P. Glasby (Ed.), Marine Manganese Deposits, Elsevier, Amsterdam, 1977, p. 11, Chapter 7.
[6] Y.F. Shen, R.P. Zerger, R.N. Deguzman, S.L. Suib, L. Mccurdy, D.I. Potter, C.L. O'Young, Science 260 (1993) 511.
[7] D.C. Golden, J.B. Dixon, C. Chen, Clays Clay Miner. 34 (1986) 511.
[8] J.E. Post, D.R. Veblen, Am. Miner. 75 (1990) 477.
[9] R.M. McKenzie, Miner. Mag. 38 (1971) 493.
[10] R.G. Burns, V.M. Burns, Recent structural data for manganese (IV) oxides, in: B. Schumm, H.M. Joseph, A. Kozawa (Eds.), Proceedings of the Manganese Dioxide Symposium, vol. 2, Electrochemistry Society Publication, Tokyo, 1980, pp. 97–112.
[11] S. Turner, P.R. Buseck, Science 203 (1979) 456.
[12] S. Ching, K.S. Krukowska, S.L. Suib, Inorg. Chim. Acta 294 (1999) 123.
[13] X.H. Feng, W.F. Tan, F. Liu, Y.S. Xu, Bull. Miner. Petro. Geochem. 22 (2003) 184.
[14] Q. Feng, K. Yanagisawa, N. Yamasaki, J. Porous Mater. 5 (1998) 153.
[15] M. Nakayama, T. Kanaya, J.W. Lee, B.N. Popov, J. Power Sources 179 (2008) 361.

[16] S.P. Jiang, W.R. Ashton, A.C.C. Tseung, J. Catal. 131 (1991) 88.
[17] R.A. Irving, T.D. Noakes, R. Buck, R. van Zyl Smit, J. Godlonton, R.J. Norman, J. Appl. Physiol. 70 (1991) 342.
[18] T. Post, B.D. Rose, Clinical Physiology of Acid-base and Electrolyte Disorders, McGraw-Hill, New York, 2000, p. 651.
[19] K. Helrich, Official Methods of Analysis of the Association of Official Analytical Chemists, 15th ed., AOAC, Arlington, 1990, p. 503.
[20] P. Akhtar, C.O. Too, G.G. Wallace, Anal. Chim. Acta 339 (1997) 211.
[21] W. Hu, K. Hasebe, A. Iles, K. Tanaka, Analyst 126 (2001) 555.
[22] G.N. Doku, V.P.Y. Gadzekpo, Talanta 43 (1996) 735.
[23] A. Krejcova, T. Cernohorsky, E. Curdova, J. Anal. At. Spectrom. 16 (2001) 1002.
[24] I. Nemcova, S. Cihelník, P. Rychlovský, L. Antalova, Anal. Lett. 37 (2004) 2721.
[25] B. Budic, J. Anal. At. Spectrom. 13 (1998) 869.
[26] S. Ching, D.J. Petrovay, M.L. Jorgensen, S.L. Suib, Inorg. Chem. 36 (1997) 883.
[27] J. Luo, A. Huang, H.P. Ssang, L.S. Steven, C. O'young, Chem. Mater. 10 (1998) 1561.
[28] R. Chen, P. Zavalij, M.S. Whittingham, J. Chem. Mater. 8 (1996) 1275.
[29] P. Le Goff, N. Baffier, S. Bach, J.P. Pereira-Ramos, R. Messina, Solid State Ionics 61 (1993) 309.
[30] S. Hirano, R. Narita, S. Naka, Mater. Res. Bull. 19 (1984) 1229.
[31] S. Bach, J.P. Pereira-Ramos, N. Baffier, J. Solid State Chem. 70 (1995) 120.
[32] H. Kanoh, W. Tang, Y. Makita, K. Ooi, Langmuir 13 (1997) 6845.
[33] E.A. Johnson, J.E. Post, Am. Miner. 91 (2006) 609.
[34] J.C. Hunter, Solid State Chem. 39 (1981) 142.
[35] K. Sato, D.M. Poojary, A. Clearfield, M. Kohno, Y.J. Inoue, J. Solid State Chem. 131 (1997) 84.
[36] S. Bakardjieva, P. Bezdicka, T. Grygar, J. Solid State Electrochem. 4 (2000) 306.
[37] C. Cachet-Vivier, S. Bach, J.P. Pereira-Ramos, Electrochim. Acta 44 (1999) 2705.
[38] A.J. Bard, L.R. Faulkner, Electrochemical Methods: Fundamentals and Applications. New York, 1980, p. 215.
[39] E. Laviron, J. Electroanal. Chem. 101 (1979) 19.
[40] J.R. Nightingale, J. Phys. Chem. 63 (1959) 1381.
[41] M.F.S. Teixeira, M.F. Bergamini, N. Bocchi, Talanta 62 (2004) 603.
[42] Q. Feng, H. Kanoh, K. Ooi, J. Mater. Chem. 9 (1999) 319.

Talanta 80 (2009) 526–531

Contents lists available at ScienceDirect

Talanta

journal homepage: www.elsevier.com/locate/talanta

Salt-assisted liquid–liquid microextraction with water-miscible organic solvents for the determination of carbonyl compounds by high-performance liquid chromatography

Manju Gupta, Archana Jain, Krishna K. Verma *

Department of Chemistry, Rani Durgavati University, Pachpedi, Jabalpur 482001, Madhya Pradesh, India

ARTICLE INFO

Article history:
Received 5 April 2009
Received in revised form 4 July 2009
Accepted 6 July 2009
Available online 14 July 2009

Keywords:
Liquid–liquid microextraction
Phase separation by salt
Carbonyl compounds
2,4-Dinitrophenylhydrazones
HPLC

ABSTRACT

A simple and rapid method has been reported for the determination of carbonyl compounds involving reaction with 2,4-dinitrophenylhydrazine and extraction of hydrazones with water-miscible organic solvent acetonitrile when the phase separation occurs by addition of ammonium sulphate, a process called salt-assisted liquid–liquid microextraction. The extract was analyzed by high-performance liquid chromatography with UV detection at 360 nm. The procedure has been optimized with respect to solvent suitable for extraction, salt for phase separation between water and organic solvent, reaction temperature and reaction time. The method has been validated when a linear dynamic range was obtained between the amount of analyte and peak area of hydrazones in the range 7 μg–15 mg L^{-1}, the correlation coefficient over 0.9964–0.9991, and the limit of detection in the range 0.58–3.2 μg L^{-1}. Spiked water samples have been analyzed with adequate accuracy, and application of the method has been demonstrated in the analysis of benzaldehyde formed as oxidation product in pharmaceutical preparation where benzyl alcohol is used as preservative, and for a keto drug dexketoprofen.

© 2009 Elsevier B.V. All rights reserved.

1. Introduction

Carbonyl compounds, aldehydes and ketones, are ubiquitous pollutants because of their toxicity and potential to react with other pollutants to form carcinogenic compounds [1–3]. In the troposphere, these compounds are formed mainly by photochemical oxidation of anthropogenic and biogenic hydrocarbons [4]. They are major contributors to urban photochemical smog, being significant source of free radicals in the atmosphere and acting as precursors to the formation of organic aerosols. Many carbonyl compounds are recognized irritants of skin and eyes, while formaldehyde even at concentration of 50 μg L^{-1} causes respiratory tract sickness and is a confirmed animal carcinogen and a suspected human carcinogen [5,6]. In Japan, formaldehyde is regulated below 80 μg L^{-1} in tap water [7]. Additionally, carbonyl compounds have been detected as drug metabolic products in urine, plasma, serum, amniotic fluid, etc. [8]. Many low molecular mass carbonyl compounds arise from the pyrolysis of cigarette and stimulate the sense organs and respiratory system of humans. Formaldehyde and acetaldehyde in cigarette smoke are deposited directly in the blood after inhalation and cause biological complication [9]. Aldehydes are considered as potential markers for enhanced oxidative stress and have been proposed to diagnose the status of cancer [10,11].

The high reactivity and volatility of low molecular mass carbonyl compounds impose the need for derivatization prior to their detection by a spectroscopic or chromatographic technique. The commonly used methods to determine aldehydes and ketones involve the reaction of carbonyl group with substituted amine, hydrazine or hydroxylamine, used as reagents, to form a Schiff base, hydrazone or oxime [12]. Hydrazines constitute the most popular group of derivatizing agents for formation of hydrazones of carbonyl compounds that are suitable for analysis by gas and liquid chromatography. Such reagents include 2,4-dinitrophenylhydrazine (DNPH) [13–15], 2,4,6-trichlorophenylhydrazine [16], 2,3,4,5,6-pentafluorophenylhydrazine [17], 5-dimethylaminonaphthalene-1-sulphohydrazide (dansylhydrazine) [18–20] and methylhydrazine [21]. Hydroxylamine derivatives, such as *O*-(2,3,4,5,6-pentafluorobenzyl)hydroxylammonium chloride (PFBHA) [22,23], where an oxime is formed, have also gained popularity due to its facile reaction chemistry and analysis by gas chromatography (GC). 2-Aminoethanethiol (cysteamine) [24,25], and Hantzsch reagents [26] have also been employed in GC for carbonyl compounds.

DNPH is the most extensively used reagent for hydrazone formation, and the precision obtained with it in high-performance liquid chromatography (HPLC) is better than that obtained with volatile oximes in GC. Carbonyl compounds in air were collected on DNPH coated cartridge and analyzed after elution by capillary

* Corresponding author. Tel.: +91 761 2605103.
E-mail address: arichna@sancharnet.in (K.K. Verma).

0039-9140/$ – see front matter © 2009 Elsevier B.V. All rights reserved.
doi:10.1016/j.talanta.2009.07.021

electrochromatography-diode array detection [27]. The influence of sampling volume and concentration of atmospheric carbonyl compounds on collection by DNPH impregnated cartridge was investigated when the method was found to be affected more by the concentration levels of analytes [14]. DNPH treated filters were developed as convenient device for collection of carbonyl compounds in cigarette smoke [28]. A C_{18} precolumn was used in place of sample loop in the injector into which was introduced DNPH treated sample, any unreacted DNPH was removed by washing the precolumn and then the hydrazones were transferred to HPLC column for analysis [7].

The sample preparation step in an analytical process typically consists of an extraction procedure that results in the isolation, clean-up and enrichment of components of interest from the sample matrix. Extraction can vary in degree of selectivity, speed and convenience and depends not only on the approach and conditions used but also on the geometric configuration of the extraction phase [29]. The traditional extraction methods based on liquid–liquid extraction (LLE) are time-consuming and need a large amount of organic solvents, which are dangerous for human health and the environment. Impelled by the need to address these drawbacks, microextraction gradually evolved as a popular technique. Compared with LLE, solid-phase microextraction (SPME) is a solvent free process that includes simultaneous extraction and preconcentration of analytes by immersion of fibre into aqueous samples or by keeping it in the sample headspace. However, SPME is expensive, its fibres are fragile and have limited lifetime, and sample carry-over could be a problem [30]. As miniaturized LLE technique, single drop microextraction (SDME) has attracted great attention due to its merits of being simple, rapid and utilizing microlitre volumes of organic solvents [31–36]. However, attention is required to avoid drop instability due to evaporation or dislodgement under gravity or at higher stirring rate of sample [37]. SDME may be time-consuming due to slow attainment of equilibrium [36,38] and is less sensitive as the final extract is small (1–3 μL).

Salting-out is a process of addition of electrolytes to an aqueous phase in order to increase the distribution ratio of a particular solute. The term also connotes reduction of mutual miscibility of two liquids by addition of electrolytes. Weak intermolecular forces, *e.g.*, hydrogen bonds, between organic molecules or nonelectrolytes and water are easily disrupted by the hydration of electrolytes. The separation of acetone from aqueous solution for performing solvent extraction was first demonstrated by Matkovich and Christian [39] using salting-out of the acetone for phase separation. This method was later used for the extraction of several metal chelates with dithiocarbamate, dithionate and oxine using calcium chloride or sucrose for salting-out acetone [40]. Based on this phase separation phenomenon, a liquid–liquid extraction technique using acetonitrile as organic phase was developed [41]. Water and acetonitrile, which are miscible in all proportions, were made immiscible by the addition of an electrolyte such as tetrabutylammonium perchlorate [41], ammonium sulphate [42] or magnesium sulphate [43]. Acetonitrile was found promising extracting solvent owing to its compatibility with reversed-phase HPLC. However, there are a few methods available utilizing sample preparation by salting-out phase separation and HPLC. Secondly, all reported methods [41,42,44] used large volumes (typically 3–21 mL) of extracting solvent or diluted the extract with water before injection [43]. Injection of a part of extract decreased sensitivity, and to avoid this, the extract was evaporated and the residue dissolved in smaller volume (2 mL) of solvent and analyzed by HPLC [42]. The aim of the present work was to use microlitre volume (typically 500 μL) of water-miscible organic solvent and to optimize the experimental conditions of salt-assisted liquid–liquid microextraction (SALLME) of $\mu g\,L^{-1}$ level of carbonyl compounds after derivatization with DNPH, and analysis by HPLC. As an application of this method, determination of a keto drug dexketoprofen in pharmaceutical formulations, and benzaldehyde formed upon oxidation of benzyl alcohol, used as preservative, in drug formulations (injections) has been demonstrated.

2. Experimental

2.1. Instrumentation

The chromatographic system consisted of a Shimadzu (Tokyo, Japan) HPLC (LC-5A) isocratic pump and an SPD-2A spectrometric detector (8 μL flow-through cell). Detection was carried out at 360 nm. A Rheodyne Model 7010 valve (Alltech, Deerfield, IL, USA) equipped with a 10 μL sample loop was used for sample injection. Data processing was carried out with an HP 3395 integrator (Hewlett-Packard, Palo Alto, CA, USA). The analytical column, 25 cm × 4.6 mm i.d., packed with octadecylsilane (ODS, 5 μm particle size) (Princeton, Rankem, New Delhi, India) was used.

2.2. Reagents and solvents

Acetone (Rankem, New Delhi, India), benzaldehyde, furfural, ethylmethyl ketone, iso-propylmethyl ketone and cyclohexanone were obtained from Merck, Mumbai, India. The derivatizing agent DNPH was obtained from (BDH, Poole, England). HPLC grade or high purity solvents methanol, water, ethyl acetate and ethanol were obtained from Rankem, New Delhi, India. Ammonium sulphate, potassium chloride, sodium chloride, dipotassium hydrogenphosphate, potassium dihydrogenphosphate, ammonium chloride, sodium sulphate and sodium nitrate were from Merck, Mumbai, India.

2.3. Reagent and standards

The reagent solution was prepared by stirring together 10 mg of DNPH and about 0.5 mL of concentrated sulphuric acid to effect salt formation, dissolving the solid in methanol (carbonyl compounds free), filtering and diluting up to 10 mL in a standard flask. Less concentrated solution of reagent was made by sequential dilution with methanol and stored in a cool place.

Standard solutions, $1000\,mg\,L^{-1}$, of each carbonyl compound were prepared in methanol (carbonyl free) and stored in refrigerator when not in use. Working solutions were prepared by sequential dilution of the stock solution. Formaldehyde solution was standardized using Romijn hypoiodite method [45]. In this method a known volume of formaldehyde solution was treated with a measured excess of iodine solution in alkaline medium. Sodium hypoiodite formed *in situ* oxidized formaldehyde to formate ion. The surplus of hypoiodite after oxidation was determined iodimetrically by acidifying the solution and titrating the liberated iodine with standardized sodium thiosulphate solution using 1% starch as indicator near the end-point.

For the preparation of 2,4-dinitrophenylhydrazones of carbonyl compounds, about 200 mg of DNPH was treated with 0.2–0.3 mL of concentrated sulphuric acid, stirred to effect formation, cooled in crushed ice bath, and the solid was dissolved in about 4 mL of carbonyl free methanol. About 150 mg (or 0.2 mL) of the carbonyl compound was added, the reaction mixture heated in a boiling water bath for about 5 min and then cooled to the room temperature. If no precipitate appeared, distilled water was added dropwise until cloudiness appeared. The product was filtered, washed with 1% sulphuric acid and then with distilled water. The yield was quantitative and the product recrystallized from ethanol–water mixture was almost pure.

2.4. Chromatographic conditions

The flow rate of the mobile phase was set to 1 mL min^{-1} in all experiments. Initially all the compounds were eluted with methanol–water (containing 0.5% acetic acid), 60:40 (v/v), and their retention time were recorded to find the order of elution. The peaks were well separated but analysis time was long (about 22 min). The mobile phase of methanol–water (containing 0.5% acetic acid), 80:20 (v/v), resulted in adequate separation of peaks and the analysis was complete within 14 min. UV detector wavelength was set at 360 nm for the detection of hydrazones of carbonyl compounds. Peak area was used for quantitation.

2.5. Extraction and derivatization of carbonyl compounds

To 3 mL portion of aqueous sample solution containing 7 μg–15 mg L^{-1} of each carbonyl compound, 0.2 mL of 4% sulphuric acid and 100 μL of DNPH was added and the reaction mixture was heated in a water bath at 50–60 °C for 5 min. The mixture was cooled to room temperature and mixed with 500 μL of acetonitrile when a homogeneous phase was formed. The mixture was diluted to 5 mL with water and mixed with 0.5 g portions each of ammonium sulphate, shaking after addition, until the solution was saturated and a small amount of salt remained undissolved. Immediately, two phases separated out clearly, the top phase being about 150 μL of acetonitrile containing the derivatives. About 100 μL of extract was withdrawn with a Hamilton syringe and collected in the injection vial. A 10 μL portion of extract was injected on to the column.

2.6. Method for the determination of dexketoprofen in drugs

A known number of tablets of dexketoprofen were weighed, ground into a fine powder and a mass equivalent to a tablet was treated with 2–3 mL of 5% sodium hydrogencarbonate solution (to dissolve the carboxylic acid drug), stirred and filtered into a 100 mL standard flask. The residue on filter-paper was washed with water. The combined filtrate and washings were diluted to the mark with deionized water. A 1–2 mL portion of this solution was subjected to analysis as described in Section 2.5.

2.7. Method for the determination of benzaldehyde in drugs

The contents of a known number of ampoules for injection were combined and a volume equivalent to one injection was diluted to 10 mL with methanol in a standard flask. For analysis, 0.5 mL of this solution was taken through the procedure as described in Section 2.5.

3. Results and discussion

Fig. 1 shows the standard chromatogram of carbonyl compounds obtained by derivatization to their 2,4-dinitrophenylhydrazones and SALLME. Two peaks of unequal intensity were observed for 2,4-dinitrophenylhydrazones of unsymmetrical carbonyl compounds, viz., furfural, ethylmethyl ketone, benzaldehyde, iso-propylmethyl ketone and dexketoprofen corresponding to syn (*Z*) and anti (*E*) isomers [46]. The anti-isomer predominated owing to its higher thermodynamic stability and molar absorptivity.

3.1. Optimization of reaction conditions

Derivatization and extraction of hydrazones were two discrete steps that required optimization. For the first step, the amount of acid added and length of reaction time played critical role, while for the second step the nature and the volume/amount of water-miscible organic solvent and inorganic salt used for phase separation were important parameters. An aliquot of 200 μL of 4% sulphuric acid was found optimum for derivatization. The peak areas of hydrazones increased substantially with reaction temperature, but decreased with length of reaction time. The latter effect was apparently due to loss of carbonyl compounds formed by acid hydrolysis of hydrazones at longer reaction time. Reaction temperature in range 50–60 °C and heating for 5 min was optimum.

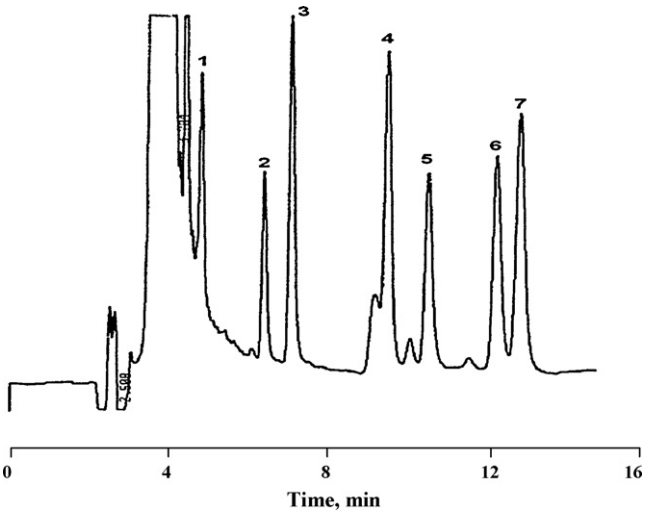


Fig. 1. Standard chromatogram of carbonyl compounds after derivatization with DNPH and SALLME. Experiment conditions, aqueous sample volume 4.5 mL, 500 μL of extracting solvent acetonitrile and 2.5 g of ammonium sulphate. Peaks identification (as their 2,4-dinitrophenylhydrazones; concentration of carbonyl compound), 1 = formaldehyde (0.5 mg L^{-1}), 2 = furfural (0.3 mg L^{-1}), 3 = acetone (0.5 mg L^{-1}), 4 = ethylmethyl ketone (1.0 mg L^{-1}), 5 = benzaldehyde (0.5 mg L^{-1}), 6 = iso-propylmethyl ketone (1.5 mg L^{-1}), and 7 = cyclohexanone (0.75 mg L^{-1}). AFS, 0.16.

3.2. Optimization of extraction system

Ammonium sulphate and dipotassium hydrogenphosphate gave better phase separation between water and water-miscible organic solvents in comparison to other salts used for this purpose, viz., potassium chloride, potassium dihydrogenphosphate, ammonium chloride, sodium sulphate and sodium nitrate. Methanol, ethanol, acetonitrile and ethyl acetate were examined for the extraction of hydrazone derivatives of carbonyl compounds when the best extraction and phase separation was found with acetonitrile (Fig. 2). Ethyl acetate was better for some hydrazones but the chromatographic performance (peak shape) was poor. Methanol–water mixtures did not show any phase separation. For clear phase separa-

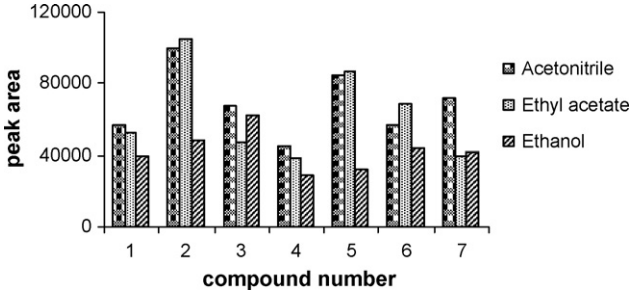


Fig. 2. Effect of organic solvents for SALLME of 2,4-dinitrophenylhydrazones of 2 mg L^{-1} of each carbonyl compounds. Experiment conditions, aqueous sample volume 4.5 mL, extracting solvent 500 μL and 2.5 g, 0.75 g and 3.2 g of ammonium sulphate used for extraction with acetonitrile, ethyl acetate and ethanol, respectively. The separated organic phase analyzed by HPLC. Peaks identification as in Fig. 1.

Table 1
Figures of merit in the SALLME and HPLC-UV for the determination of carbonyl compounds as their 2,4-dinitrophenylhydrazones.

Compound	Range (mg L^{-1})	r^2 [a]	RSD (%)[b]	RSD (%)[c]	LOD[d] (μg L^{-1})
Formaldehyde	0.012–10	0.9964	3.4	4.8	1.2
Furfural	0.007–15	0.9971	5.1	4.6	0.65
Acetone	0.012–10	0.9971	4.4	4.0	1.3
Ethylmethyl ketone	0.024–12	0.9977	5.3	7.5	2.5
Benzaldehyde	0.012–15	0.9970	3.9	1.6	0.58
Iso-propylmethyl ketone	0.022–15	0.9982	3.8	7.7	3.2
Cyclohexanone	0.012–10	0.9991	6.0	4.3	2.4

[a] Based on 10 concentration levels over the calibration range.
[b] Six replicate analyses on 40 μg L^{-1} of carbonyl compounds.
[c] Six replicate analyses on 2 mg L^{-1} of carbonyl compounds.
[d] Limit of detection (S/N = 3).

tion of water–ethanol, water–acetonitrile and water–ethyl acetate mixtures containing 4.5 mL of water and 0.5 mL of water-miscible organic solvent, respectively 3.2, 2.5 and 0.75 g of ammonium sulphate were required to be added. The volume of organic solvent rich phase/water rich phase after separation were 0.6 mL/5.8 mL, 0.2 mL/5.2 mL and 0.4 mL/4.8 mL, respectively. In comparison to results obtained by direct injection of standards of equivalent concentration, the solvent extraction recovery of hydrazones ranged 92–99% when acetonitrile was used as solvent. A 1 mL aliquot of mixture containing 1 mg L^{-1} of each carbonyl compound was subjected to hydrazone formation, the total volume of reaction mixture being adjusted to 3.0, 3.5, 4.0 and 4.5 mL by addition of deionized water, cooled to room temperature and mixed respectively with 2.0, 1.5, 1.0 and 0.5 mL of acetonitrile and treated with 1.0–2.5 g of ammonium sulphate. Each experiment gave adequate phase separation. The recovered organic solvent, 1.8, 1.3, 0.8 and 0.2 mL, respectively, was analyzed by HPLC. As expected, smaller volume of organic solvent, 0.5 mL, led to higher preconcentration of analytes and better sensitivity (Fig. 3). An aliquot of 4.5 mL of sample containing 1 mg L^{-1} of each carbonyl compound was mixed with 500 μL of acetonitrile and 2.0–3.5 g of ammonium sulphate. The optimum recovery was obtained by 2.5 g of ammonium sulphate and remained practically unchanged with higher amounts (Fig. 4). The overall precision in extraction with 0.5 mL of acetonitrile was 1.5% (range 0.8–3.4%) when a test sample containing 1 mg L^{-1} of each carbonyl compound was analyzed by six separate derivatizations and extractions. Extracting solvent volume less than 0.5 mL was difficult to handle in the present method, and was not used. In subsequent experiments, acetonitrile as water-miscible organic solvent and ammonium sulphate as phase separating salt were used. Three standards containing each carbonyl compound at 50 μg L^{-1}, 1 mg L^{-1} and 10 mg L^{-1} were analyzed by the present method. The volume of sample was in range 5–50 mL, and of extracting solvent acetonitrile in range 0.5–5 mL. Ammonium sulphate required for separation of extracting phase was in range 2.5–14 g. The enrichment factor, as found relative to injection of standards without extraction, was in range 160–850. A 2 mL aliquot containing 1 mg L^{-1} of each carbonyl compound was diluted to 5–50 mL with deionized, derivatized and extracted as above. The extract obtained in each case was diluted to 0.5 mL with acetonitrile and analyzed by HPLC. Over the tested range of sample volume, the areas of carbonyl compounds were within 10% of the average value. The extraction time, range tested 5–20 min, did not have any effect on recovery. The recommended condition for analysis used 5 mL of sample, 0.5 mL of acetonitrile and 2.5 g of ammonium sulphate.

3.3. Calibration graph and detection limits

The dependence of the chromatographic signal on concentration of analytes was verified under optimum conditions of SALLME and LC-UV. The figures of merit in the analysis of diverse carbonyl compounds are summarized in Table 1. A linear dynamic range 7 μg–15 mg L^{-1} of analytes was obtained after derivatization to their 2,4-dinitrophenylhydrazones, overall the correlation coefficient, r^2, was 0.9975, relative standard deviation, 4.7%, and the limit of detection (S/N = 3), 1.69 μg L^{-1}.

Low molecular weight carbonyl compounds are volatile and require special attention in preparing their standard solutions. 2,4-Dinitrophenylhydrazones of carbonyl compounds, which are crystalline products, dissolved in methanol or acetonitrile, could be used as standards in the construction of calibration graph. Analysis of equimolar amounts of carbonyl compounds involving derivatization to hydrazones produced recoveries that ranged 94–102% with RSD in range 2–5% in comparison to when pre-prepared respective 2,4-dinitrophenylhydrazone was used.

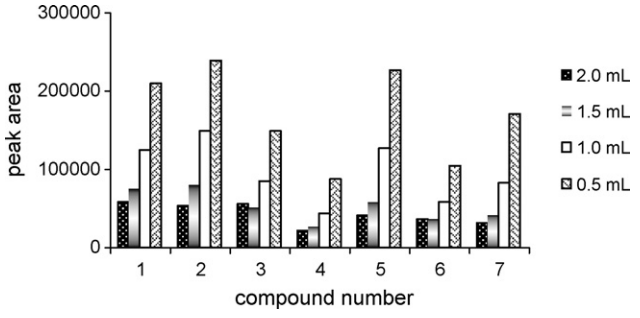


Fig. 3. Effect of volume of extracting organic solvent, 0.5–2.0 mL of acetonitrile, used in the SALLME of 2,4-dinitrophenylhydrazones of 1 mg L^{-1} of each carbonyl compound; sample volume 3.0–4.5 mL and ammonium sulphate 1.0–2.5 g. Peaks identification as in Fig. 1.

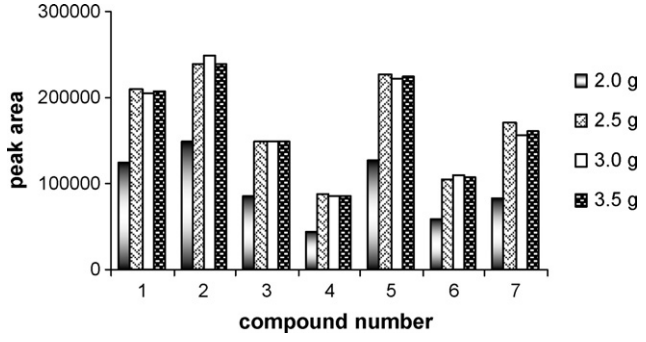


Fig. 4. Effect of amount of ammonium sulphate, 2.0–3.5 g, used in the SALLME of 2,4-dinitrophenylhydrazones of 1 mg L^{-1} of each carbonyl compound; aqueous sample volume 4.5 mL and extracting solvent acetonitrile 500 μL. Peaks identification as in Fig. 1.

Table 2
Recovery of carbonyl compounds spiked to river and tap water samples.

Compound	Recovery (%)					
	10 mg L^{-1} Narmada Water	Tap water	1 mg L^{-1} Narmada water	Tap water	30 μg L^{-1} Narmada water	Tap water
Formaldehyde	97.2	94.5	98.2	94.6	94.7	90.4
Furfural	89.5	94.5	92.6	95.5	95.7	92.9
Acetone	96.5	96.2	95.6	92.9	93.6	91.4
Ethyl methyl ketone	96.9	101.8	97.4	95.8	89.9	92.1
Benzaldehyde	96.6	91.6	94.8	91.7	90.2	92.5
Iso-propylmethyl ketone	95.3	103.6	90.6	91.5	94.8	91.0
Cyclohexanone	94.8	105.2	97.0	94.2	97.4	94.5

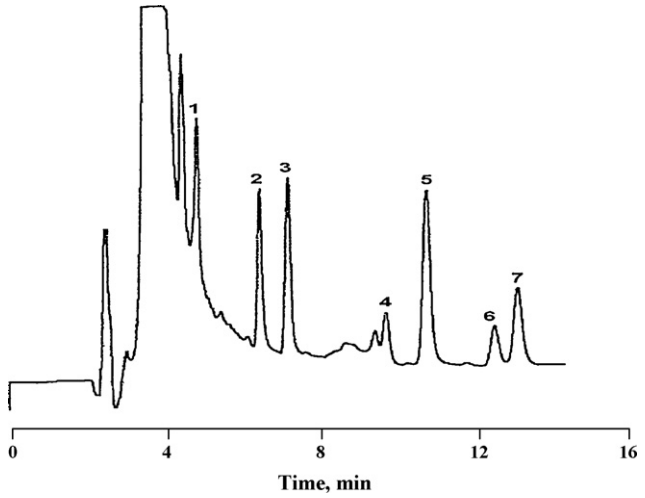


Fig. 5. Chromatogram for carbonyl compound spiked to the Narmada river water, Jabalpur, derivatization with DNPH and SALLME. Experiment conditions, sample volume 4.5 mL, 500 μL of extracting solvent acetonitrile and 2.5 g of ammonium sulphate. Peaks identification (as their 2,4-dinitrophenylhydrazones; concentration of carbonyl compound), 1 = formaldehyde (20 μg L^{-1}), 2 = furfural (10 μg L^{-1}), 3 = acetone (12 μg L^{-1}), 4 = ethylmethyl ketone (20 μg L^{-1}), 5 = benzaldehyde (40 μg L^{-1}), 6 = iso-propylmethyl ketone (60 μg L^{-1}), and 7 = cyclohexanone (30 μg L^{-1}). AFS, 0.04.

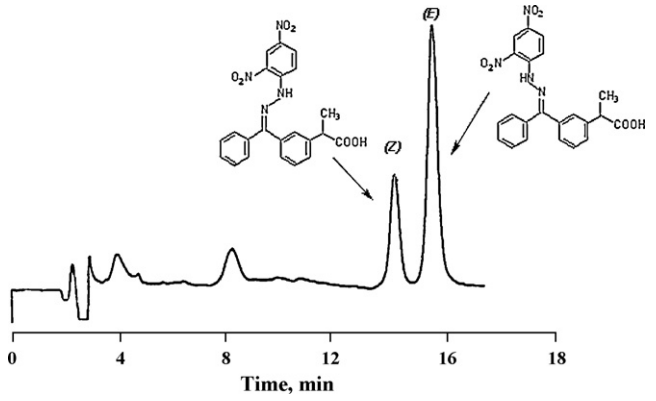


Fig. 6. Chromatogram of 0.5 mg L^{-1} of dexketoprofen, after derivatization to its 2,4-dinitrophenylhydrazone and SALLME. Experiment conditions, sample volume 4.5 mL, 500 μL of extracting solvent acetonitrile and 2.5 g of ammonium sulphate. AFS, 0.16.

4. Application to real samples

4.1. Environmental samples

The present method was validated by analyzing two water samples, viz., the Narmada river water, Jabalpur, and city tap water, Jabalpur, that were spiked with known amount of carbonyl compounds. Fig. 5 shows the chromatogram for Narmada river water spiked with 10–60 μg L^{-1} of carbonyl compound obtained after hydrazone formation, SALLME and HPLC. None of unspiked samples showed any peak for carbonyl compounds. Average recoveries of three replicate measurements on three concentration levels spiked to tap water and Narmada river water samples are given in Table 2. The results demonstrate that in samples matrices had practically no adverse effect on derivatization of carbonyl compounds and their SALLME.

4.2. Drug samples

Two pharmaceutical formulations were analyzed, dexketoprofen, a keto compound, in drug tablets and trace quantities of benzaldehyde in injectable formulations of Vitamin B-complex. Benzaldehyde is the oxidation product of widely used preservative and co-solvent benzyl alcohol in injectable formulations, and is toxic.

Dexketoprofen was determined under the recommended optimized conditions as its 2,4-dinitrophenylhydrazone. Though high level of drug in tablets does not require preconcentration, sample preparation was simplified by SALLME. The therapeutic dose of

Table 3
Comparison of salient features of diverse HPLC methods for the determination of carbonyl compounds as their 2,4-dinitrophenylhydrazones.

Sample/pre-treatment method	Linear range	LOD (μg L^{-1})	Ref.
Water, drugs/SALLME of hydrazones with 500 μL of acetonitrile	0.007–15 mg L^{-1}	0.58–3.2	This work
Formaldehyde in presence of acetone/extraction with chloroform	1.5–40 mg L^{-1}	51	[48]
Air/collection on C_{18} cartridge loaded with DNPH	0.1–2 mg L^{-1}	0.08–0.1	[49]
Water/on-line C_{18} preconcentration column in HPLC	0–44 μg L^{-1}	0.13	[7]
Cigarette smoke/DNPH coated Cambridge filters	4–34 μg L^{-1}	0.027	[28]
Air, 2,4-dinitro-3,5,6-trideuterophenylhydrazine reagent/no pre-treatment	15 μg L^{-1}-?	3–12	[50]
Water/headspace in-drop derivatization and preconcentration	0.01–15 mg L^{-1}	1.7–24.1	[13]
Water/DNPH coated C_{18} cartridge in flow injection system	0.5–200 μg L^{-1}	0.1–1.0	[51]
Human saliva/polymer monolithic capillary microextraction	1.5–540 μg L^{-1}	0.43–1.4	[52]
Wine/no pre-treatment method	0.005–89.6 mg L^{-1}	1.3–7.5	[53]
Air/off-line DNPH coated C_{18} cartridge	0.05–10 mg L^{-1}	3	[54]
Fuel ethanol/no pre-treatment method	5–400 μg L^{-1}	1.7–2.0	[55]

The '?' refers to the upper limit in the linear range.

dexketoprofen is reported to be 1–5 μg mL^{-1} [47]. A linear dynamic range was obtained between the amount of dexketoprofen and peak area of hydrazone in the range 0.035–5.0 mg L^{-1}, the correlation coefficient was 0.9958 and the limit of detection was 15.5 μg L^{-1}. The average relative standard deviation for three concentration levels was found to be 6.4%. A standard chromatogram for hydrazone derivative of dexketoprofen is shown in Fig. 6, where cis (*Z*) and trans (*E*) isomers showed baseline separation.

For analysis of benzaldehyde in injectable formulation, appropriate known quantities of benzaldehyde was spiked to sample. Each spiked and unspiked samples were subjected to derivatization and extraction, and triplicate injections of each were made into the HPLC. Benzaldehyde found in a formulation was 8.5 μg L^{-1} with RSD of 3.2%.

5. Conclusions

In this study SALLME has been demonstrated as viable means of extracting trace level of carbonyl compounds in real samples after their conversion into 2,4-dinitrophenylhydrazones. SALLME integrates sampling, extraction and clean-up in a single step. Quick phase separation, rapid partition equilibrium, minimum amount and less toxicity of extracting solvent, and compatibility of extract with subsequent analysis by HPLC are advantages of SALLME. Furthermore, this method has benefit of its simplicity, high sensitivity, short preconcentration time and freedom from memory effects. A comparison of salient features of diverse HPLC methods [7,13,28,48–55] for the determination of carbonyl compounds as their 2,4-dinitrophenylhydrazones, as given in Table 3, suggests that SALLME is a simple sample preparation technique and can be used as an alternative to solid-phase extraction with DNPH loaded cartridge. In comparison to dispersive LLME [56], SALLME is more suitable for HPLC owing to the use of water-miscible extraction solvents.

Acknowledgement

Thanks are due to the Council of Scientific and Industrial Research, New Delhi, for award of Research Associateship to M.G.

References

[1] K. Villberg, A. Veijanen, Anal. Chem. 73 (2001) 971.
[2] X. Pang, X. Mu, Atmos. Environ. 40 (2006) 6313.
[3] S. Garcia-Alonso, R.M. Perez-Pastor, Anal. Chim. Acta 367 (1998) 93.
[4] R.J. Kieber, M.F. Rhines, J.D. Willey, G.B. Avery, Atmos. Environ. 33 (1999) 3659.
[5] M.I. Khoder, A.A. Shakour, S.A. Farag, A.A.A. Hameed, J. Environ. Monit. 2 (2002) 123.
[6] E.B. Bakeas, D.I. Argyris, P.A. Siskos, Chemosphere 52 (2003) 805.
[7] K. Takeda, S. Katoh, N. Nakatani, H. Sakugawa, Anal. Sci. 22 (2006) 1509.
[8] D.A. Cancilla, S.S.Q. Hee, J. Chromatogr. 627 (1992) 1.
[9] L. Rau, Hypertension 90 (1991) 13S.
[10] M. Phillips, K. Gleeson, J.M.B. Hughes, J. Greenberg, R.N. Cataneo, L. Baker, W.P. McVay, Lancet 353 (1999) 1930.
[11] H.J. O'Neill, S.M. Gordon, M.H. O'Neill, R.D. Gibbons, J.P. Szidon, Clin. Chem. 34 (1988) 1613.
[12] R.H. Brandenberger, H. Brandenberger, in: K. Blau, J.M. Halket (Eds.), Handbook of Derivatives for Chromatography, John Wiley & Sons, Chichester, 1993, pp. 131–140.
[13] A.K.K.V. Pillai, K. Gautam, A. Jain, K.K. Verma, Anal. Chim. Acta 632 (2009) 208.
[14] R. Pal, K.H. Kim, Anal. Chim. Acta 610 (2008) 289.
[15] J.Z. Dong, S.C. Moldoveanu, J. Chromatogr. A 1027 (2004) 25.
[16] Y.C. Fiamegos, C.D. Stalikas, Anal. Chim. Acta 609 (2008) 175.
[17] E.E. Stashenko, M.A. Puertas, W. Salgar, W. Delgado, J.R. Martynez, J. Chromatogr. A 886 (2000) 175.
[18] W. Schmied, M. Przewosnik, K. Baechmann, Fresenius' Z. Anal. Chem. 335 (1989) 464.
[19] N. Binding, H. Klaning, U. Karst, W. Potter, P.A. Czeschinski, U. Witting, Fresenius' J. Anal. Chem. 362 (1998) 270.
[20] J. Zhang, L. Zhang, Z. Fan, V. Ilacqua, Environ. Sci. Technol. 34 (2000) 2601.
[21] K.J. Dennis, T. Shibamoto, Lipids 25 (1990) 460.
[22] E.D. Hudson, K. Okuda, P.A. Ariya, Anal. Bioanal. Chem. 388 (2007) 1275.
[23] H.-G. Schmarr, T. Potouridis, S. Ganß, W. Sang, B. Kopp, U. Bokuz, U. Fischer, Anal. Chim. Acta 617 (2008) 119.
[24] M.N. Lau, J.D. Ebeler, S.E. Ebeler, Am. J. Enol. Viticult. 50 (1999) 324.
[25] H. Kataoka, T. Kondo, A. Sumida, Anal. Chim. Acta 358 (1998) 269.
[26] F. Reche, M.C. Garrigos, A. Sanchez, A. Jimenez, J. Chromatogr. A 896 (2000) 51.
[27] E. Dabek-Zlotorzynska, E.P.C. Lai, J. Chromatogr. A 853 (1999) 487.
[28] T.L. Wang, H.W. Tong, X.Y. Yan, L.Q. Sheng, J. Yong, S.M. Liu, Chromatographia 62 (2005) 631.
[29] J. Pawliszyn, Anal. Chem. 75 (2003) 2543.
[30] P. Helena, Z.K. Locija, Trends Anal. Chem. 18 (1999) 272.
[31] M. Gupta, A. Jain, K.K. Verma, Talanta 71 (2007) 1039.
[32] J.L. Manzoori, M. Amjadi, J. Abulhassani, Talanta 77 (2009) 1539.
[33] Q. Xiao, B. Hu, M. He, J. Chromatogr. A 1211 (2008) 135.
[34] E.A. Herrador, R. Lucena, S. Cardenas, M. Valcarcel, J. Chromatogr. A 1209 (2008) 76.
[35] H. Ebrahimzadeh, Y. Yamini, A. Gholizade, A. Sedighi, S. Kasraee, Anal. Chim. Acta 626 (2008) 193.
[36] E.G. Amvrazi, N.G. Tsiropoulos, J. Chromatogr. A 1216 (2009) 2789.
[37] G. Shen, H.K. Lee, Anal. Chem. 74 (2002) 648.
[38] F. Ahmadi, Y. Assadi, M.R.M. Hosseini, M. Rezaee, J. Chromatogr. A 1101 (2006) 307.
[39] C.E. Matkovich, G.D. Christian, Anal. Chem. 45 (1973) 1915.
[40] C.E. Matkovich, G.D. Christian, Anal. Chem. 46 (1974) 102.
[41] Y. Nagaosa, S. Segawa, Fresenius' J. Anal. Chem. 345 (1993) 753.
[42] Y. Cai, Y. Cai, Y. Shi, J. Liu, S. Mou, Y. Lu, Microchim. Acta 157 (2007) 73.
[43] J. Zhang, H. Wu, E. Kim, T.A. El-Shourgbagy, Biochem. Chromatogr. 23 (2009) 419.
[44] H. Wu, J. Zhang, K. Norem, T.A. El-Shourbagy, J. Pharm. Biomed. Anal. 48 (2008) 1243.
[45] S. Siggia, J.G. Hanna, Quantitative Organic Analysis via Functional Groups, John Wiley & Sons, New York, 1979, p. 136.
[46] C.N. Konidari, T.S. Giannopoulos, C.G. Nanos, C.D. Stalikas, Anal. Biochem. 338 (2005) 62.
[47] R. Regenthal, M. Krueger, C. Koeppel, R. Priess, J. Clin. Monit. 15 (1999) 529.
[48] X.H.H. Huang, H.S.S. Ip, J.Z. Yu, Anal. Chim. Acta 604 (2007) 134.
[49] R. Pal, K.-H. Kim, Anal. Chim. Acta 610 (2008) 289.
[50] G. Zurek, U. Karst, J. Chromatogr. A 869 (2000) 251.
[51] C.-E. Banos, M. Silva, Talanta 77 (2009) 1597.
[52] H.-J. Zhang, J.-F. Huang, H. Wang, Y.-Q. Feng, Anal. Chim. Acta 565 (2006) 129.
[53] R.J. Elias, V.F. Laurie, S.E. Ebeler, J.W. Wong, A.L. Waterhouse, Anal. Chim. Acta 626 (2008) 104.
[54] A. Sakuragawa, T. Yoneno, K. Inoue, T. Okutani, J. Chromatogr. A 844 (1999) 403.
[55] A.A. Saczk, L.L. Okumura, M.F. Oliveira, M.V.B. Zanoni, Chromatographia 63 (2008) 45.
[56] Q. Wu, Y. Li, C. Wang, Z. Liu, X. Zang, X. Zhou, Z. Wang, Anal. Chim. Acta 638 (2009) 139.

Talanta 80 (2009) 532–538

Contents lists available at ScienceDirect

Talanta

journal homepage: www.elsevier.com/locate/talanta

An efficient thiourea-based colorimetric chemosensor for naked-eye recognition of fluoride and acetate anions: UV–vis and ^{1}HNMR studies

Arvind Misra*, Mohammad Shahid, Pratibha Dwivedi

Nucleic Acids Research Laboratory, Department of Chemistry, Faculty of Science, Banaras Hindu University, Varanasi 221005, UP, India

ARTICLE INFO

Article history:
Received 27 April 2009
Received in revised form 3 July 2009
Accepted 6 July 2009
Available online 14 July 2009

Keywords:
Anion recognition
Colorimetric sensor
Thiourea

ABSTRACT

An efficient colorimetric chemosensor with a thiourea binding site and 2-amino-6-nitrobenothiazole as a signaling unit has been synthesized by dithiocarbamate approach. The chemosensor has been utilized for selective recognition of fluoride and acetate anions in dry DMSO solution by UV–vis and ^{1}H NMR titration experiments. The chemosensor has shown naked-eye sensitivity for both the anions in solution.

© 2009 Elsevier B.V. All rights reserved.

1. Introduction

The selective recognition and sensing of anions via artificial organic chemosensor molecule/probe, containing a suitable receptor site, have attracted considerable attention for chemists in past decades [1]. Anions especially, fluoride and carboxylate play significant roles in chemical, environmental and biochemical processes [2–8], hence their recognition is important. The ionic recognition can be confirmed by different analytical methods like electrochemical methods – by variation in the redox potential, by change in chemical shifts in ^{1}H NMR signal or by change in fluorescence intensity signal – utilizing fluorescence spectroscopy [9]. The non-covalent ionic recognition generally, governs by the energy of the receptor–anion interaction, geometry, basicity of the employed anion and nature of the solvent systems. In fact, the strongest hydrogen-bond interactions are established with anions that contain the most electronegative atoms, such as, fluoride and carboxylate, and that display the most pronounced basic strength in a particular solvent. Recently, major impetus is given on strategies to develop colorimetric sensors for ionic species by utilizing binding site-signaling unit approach, in which an appropriate chromophore is attached to a specific anion receptor [10–18], to make sensitive recognition behaviors simple and convenient through naked-eye. The designing of such kind of chemosensor usually involves the covalent linking of a chromogenic fragment to a neutral receptor that should be capable in establishing selective interaction with the envisaged anion either by directional hydrogen bonding or by donation of one or more hydrogen of N–H fragment to the anions–deprotonation. In this sense several synthetic receptors (also referred as host) have been designed, to include, urea [19–23], thiourea [24–28], amides [29,30], macrocyclic ammonium/guanidinium [31], phenylhydrazone [32,33], indole [34], pyrrole [35–37] and phenol [38] units for interaction study with negatively charge ionic species (also referred as guest). The phenylhydrazone and indole type of receptors is neutral and the synthetic chemistry involved to synthesize these kinds of molecule is also simpler. Moreover, such kind of receptor molecule could recognize anions through color change, which is visible to naked-eye in aqueous medium.

In continuation of anion recognition by neutral receptors, urea and thiourea subunits, owing to their ability to act as hydrogen-bond donors have also been extensively utilized to produce chemosensors [39–41]. In fact, urea is capable for donating two hydrogen bonds to get an orientation complementary to Y-shaped oxoanions, parallel to carboxylates [42]. Further, by incorporating N–H unit into the chromogenic subunit, it is reasonable to have modification in the dipole and associated charge transfer transition in the influence of anions. Consequently, the ultimate negative charge being developed on the receptor will modulate UV–vis spectrum and thus, a prominent color change of medium that could be visible through naked-eye. To make chemosensor and recognition phenomenon more sensitive, presence of electron-withdrawing substituent on the chromophoric unit is useful. The presence of electron withdrawing group, like $-NO_2$, $-CF_3$, persuades for more acidity to the anion binding subunit—receptor site or more polarization in the N–H bond to facilitate more promising hydrogen-bond donating or interaction tendency, to support further an "incipient"

* Corresponding author. Tel.: +91 542 2307321x104/6702503; fax: +91 542 2368127/2368175.
E-mail address: arvindmisra2003@yahoo.com (A. Misra).

0039-9140/$ – see front matter © 2009 Elsevier B.V. All rights reserved.
doi:10.1016/j.talanta.2009.07.020

and "frozen" proton-transfer phenomenon [43]. Although, both urea and thiourea-based neutral-receptor are efficient for bifurcate H-bond interaction with anions however, thiourea (pK_a = 21.1 in DMSO) specifically, due to more acidic nature generates stronger interaction with anions rather than urea (pK_a = 26.9) [44] and under typical circumstances both urea and thiourea-based receptor on interaction with very strong basic anions such as F^- increases the possibility of deprotonation at N–H fragment.

Keeping these perspective in mind, we have designed a new class of thiourea-based receptor **6**, [1-(naphthalen-2-yl)-3-(6-nitrobenzothiazol-2-yl)]-thiourea, to elucidate recognition for F^- and AcO^- anions through naked-eye visible color changes. The thiourea subunit, speculated to be a receptor-site and suitable to interact with the anions, has been appended in between naphthyl and 2-amino-6-nitrobenzothiazole units. The covalently linked benzothiazole moiety intends to act as a chromogenic signaling unit. The presence of electron withdrawing nitro substituent at benzothiazole moiety ensures low energy absorption bands for receptor as well as formation of anionic charged species due to more polarization at the N–H bond and hence associated prominent red-shift through extended conjugation in the system and consequent visible color change for naked-eye recognition.

2. Experimental

2.1. Reagents

All the anions in the form of tetrabutylammonium salts were purchased from Sigma–Aldrich Chemical Co. stored in a desiccator under vacuum containing self-indication silica, and used without further purification. Solvents like dimethylsulphoxide (DMSO) and tetrahydrofuran (THF) were purified prior to use. Spectroscopic grade solvents were used for titration studies. Commercial grade chemicals and solvents were used as such unless stated otherwise. Silica Gel G was used for thin layer chromatography (TLC).

2.2. Synthesis of

2.2.1. Isothiocyanates

1-Naphthylamine (0.28 g, 2 mmol) and triethylamine (0.9 ml, 6.2 mmol) were taken in anhydrous THF (5 ml) under nitrogen (N_2) atmosphere and cooled the reaction mixture on an ice-bath. To the well stirred cold reaction mixture, carbon disulfide (CS_2) (0.12 ml, 2 mmol) was added slowly (1 h). After complete addition reaction mixture was allowed to come at room temperature and stirred overnight and monitored (on TLC). ^{1}H NMR of an aliquot indicated incomplete conversion into the dithiocarbamate **2**. The reaction mixture was again cooled down and sodium hydride (0.048 g, 2 mmol) was added to the reaction and stirred for 1 h under atmosphere of N_2. CS_2 (0.12 ml, 0.2 mmol) was again added. The dithiocarbamate **2** was obtained in good yield after further stirring the reaction mixture at r.t. for 2–3 h as was evident on TLC with consumption of starting material.

Similarly, 2-amino-6-nitrobenzothiazole (0.39 g, 2 mmol) in *N*,*N*′-dimethylformamide (DMF) (4 ml) was reacted with CS_2 (0.12 ml, 2 mmol) in presence of sodium hydroxide (NaOH) (0.09 g, 2.2 mmol) under anhydrous condition. After completion of reaction (on TLC), chloroform ($CHCl_3$) was added to the reaction mixture. The orange color solid so obtained was filtered and washed again with $CHCl_3$ to get corresponding dithiocarbamate **5** in 97% yield.

The unpurified dithiocarbamic salts (**2** and **5**) were cooled on an ice-bath, tosyl chloride (0.42 g, 2.2 mmol) was added and reaction was allowed to warm at room temperature with continuous stirring for 1.5–2 h. 1N hydrochloric acid (HCl) (10 ml) was added to the reaction mixture and extracted with diethylether (4 times). The organic layer was pooled, kept over anhydrous sodium sulphate and concentrated in vacuum to obtain 1-naphthylisothiocyanate (**3**) as a brown color solid with in 65% yield (0.24 g, 1.3 mmol), m.p. 55 °C. The IR spectra have shown a strong band in 2095 cm^{-1} region corresponding to the cumulated double bond of isothiocyanate.

2.2.2. Synthesis of receptor [1-(naphthalen-2-yl)-3-(6-nitrobenzothiazol-2-yl)]thiourea **6**

2.2.2.1. Method 1. 2-Amino-6-nitrobenzothiozole (0.156 g, 0.8 mmol) and sodium hydride (NaH) (0.019 g, 0.8 mmol) in THF (3 ml) were stirred at room temperature for 2 h. 1-Naphthylisothiocyanate (0.148 g, 0.8 mmol), dissolved in THF (5 ml) was added drop-wise (0.5 h) and then refluxed the reaction mixture for 2–3 h. After completion of reaction (on TLC), reaction mixture was concentrated in vacuum to get orange color solid. The crude product was washed with water (10 ml, 4 times) and dried under vacuum to afford the pure thiourea compound in 55% yield (0.167 g, 0.44 mmol).

2.2.2.2. Method 2. Dithiocarbamate **5** (0.293 g, 1 mmol) and 1-naphthylamine (0.143 g, 1 mmol) were dissolved in DMF (3 ml) and stirred for 2 h at 60 °C. After completion of reaction (on TLC) excess amount of water was added to the reaction mixture, filtered and dried to get same compound in 65% yield (0.247 g, 0.65 mmol).

M.p. 137–140 °C. R_f 0.65 (EtOAc:hexane:: 4:6, v/v); IR (ν_{max}, KBr, cm^{-1}): 3325, 3166, 3056, 1568, 1511, 1445, 1329, 1228, 778; ^{1}H NMR (DMSO-d_6) δ (ppm): 10.40 (Br, 1H, NH), 9.72 (br, 1H, NH), 8.64 (s, 1H, benzothiazole), 8.01–7.98 (d, 1H, J = 8.1 Hz, benzothiazole), 7.96–7.93 (d, 1H, J = 7.8 Hz, naphthyl), 7.93 (t, 1H, J = 7.5 and 8.1 Hz, naphthyl), 7.79–7.76 (d, 1H, J = 7.5 Hz, naphthyl), 7.66–7.63 (d, 1H, J = 8.1 Hz, benzothiazole), 7.59–7.44 (m, 3H, naphthyl), 7.41–7.39 (d, 1H, J = 8.1 Hz); ^{13}C NMR ($CDCl_3$, 75.45 MHz.) δ (ppm): 156.2, 153.9, 142.7, 134.4, 131.8, 128.6, 127.3, 127.1, 126.7, 125.8, 125.6, 125.5, 122.1, 121.8, 121.6, 118.6, 117.3; Anal. Calc. for $C_{18}H_{12}N_4O_2S_2$; C, 56.83; H, 3.18; N, 14.73%. Found: C, 56.35; H, 3.41, N, 14.84%.

2.3. General methods

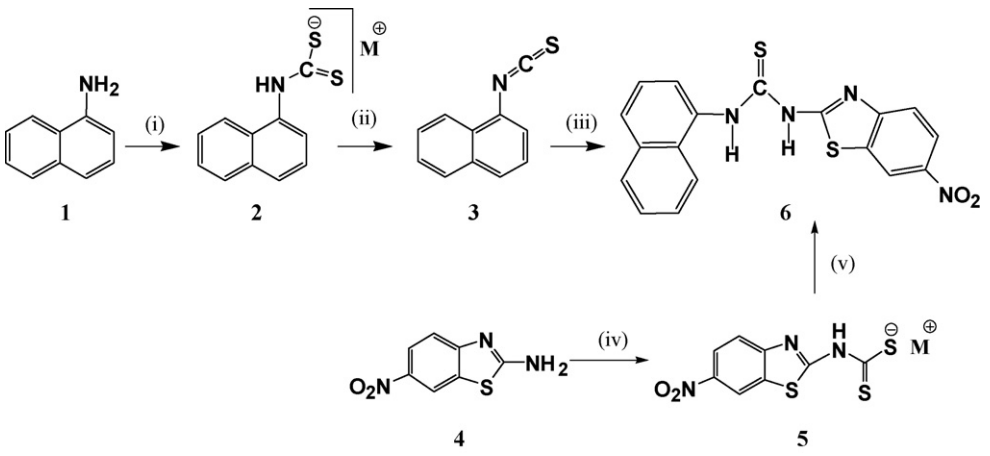
All the experiments were carried out at room temperature. The UV–vis spectra were recorded on a Shimadzu 1700 spectrophotometer using a quartz cuvette (path length = 1 cm). Infrared (IR) spectra in potassium bromide (KBr) were recorded on a Varian-3100 FTIR spectrophotometer. ^{1}H NMR spectra (chemical shifts in δ ppm) were recorded on a JEOL AL 300 FT-NMR (300 MHz) spectrometer, using tetramethylsilane (TMS) as internal standard. Elemental analysis was carried out on CE-440 CHN Analyser (Exeter Analytical Inc.). Melting points were recorded by open glass capillary method and are uncorrected.

2.4. Absorption titration studies

The binding stability of receptor or chemosensor for acetate and halide anions (as tetrabutylammonium salts) was investigated by UV–vis absorption spectroscopy in DMSO solution keeping a constant host concentration (2×10^{-5} mol l^{-1}) and increasing concentrations of anions by stepwise addition of different equivalents (10 μl for 1 equiv. of 6×10^{-3} M solution).

2.5. ^{1}H NMR titrations

Chemosensor **6** (1.02×10^{-2} mol l^{-1} in DMSo-d_6) was titrated with acetate and fluoride anions (as tetrabutylammonium salts) by addition of increasing equivalents of anion in DMSO-d_6.



Scheme 1. Synthesis of receptor molecule **6**. (i) CS_2/NaH/THF; (ii) TsCl/2h; (iii) **4**, NaH/THF/60 °C/2h; (iv) CS_2/NaOH/DMF; (v) **1**, DMF/60 °C/2h.

3. Results and discussion

The synthesis (Scheme 1) of receptor molecule was carried out by generating dithiocarbamic acid salt of 1-naphthylamine and 2-amino-6-nitrobenzothiazole in the presence of strong base followed by slow addition of carbon disulphide (2 h) under anhydrous condition for 2–3 h. To generate isothiocyanate active group, tosyl chloride (TsCl) was added to the well stirred suspension of derived unpurified salt under colder condition and then continued the stirring for further 0.5–1 h at room temperature. Naphthyl-1-isothiocyante **3** was isolated in 65% yield. The IR spectra have shown a strong band at 2095 cm^{-1} region corresponding to the cumulated double bond of isothiocyanate functional group. However, in case of 2-amino-6-nitrobenzothiazole **5** we were not able to convert dithiocarbamic acid salt to isothiocyanate derivative in good yield. Receptor **6**, was obtained by refluxing either dithiocarbamic acid salt, **5** with 1-naphthylamine or by refluxing 1-naphthyl isothiocyanate, **3** with 2-amino-6-nitrobenzothiazole in presence of sodium hydride in good yield.

3.1. UV–vis experiments

The anion binding affinity of present thiourea-base receptor was determined by UV–vis absorption spectra in the absence and presence of different anions such as Br^-, Cl^-, F^-, I^-, SCN^-, AcO^- (as tetrabutylammonium salts). The experiment was performed by preparing 2×10^{-5} mol l^{-1} solution of receptor in dimethylsulphoxide (DMSO) solution followed by addition of particular tetrabutylammonium anionic salts separately. In the absence of anions, the spectrum of chemosensor **6** showed two characteristic absorption peaks λ_{max} at 392 nm (ε = 26,100 mol^{-1} l cm^{-1}) and 325 nm. The low energy band (392 nm) was expected to intramolecular charge transfer (ICT) transition while the second high energy peak at 325 nm corresponds to $\pi \rightarrow \pi^*$ electronic transitions. Upon the addition of AcO^- or F^- to **6**, a prominent change was observed in UV–vis absorption spectra due to complexation between host–guest molecules. The ICT band at 392 nm as shown in Fig. 1, disappeared with the formation of a new peak in yellow region of spectra at 457 nm. The electronic excitation with considerable red-shift of 65 nm is attributed to the charge transfer from receptor site to acceptor substituent ($-NO_2$) of chromophoric moiety. On addition of other anionic species as their tetrabutylammonium salts no significant modulation in the UV–vis absorption spectra was observed thus, showing the specificity of the chemosensor for selective binding interaction with AcO^- and F^- anions.

In order to estimate the specific concentration for selective anions and its associated colorimetric changes, chemosensor **6** was titrated by successive increment of number of equivalents for acetate and fluoride ion separately and monitored the UV–vis absorption spectra. From UV–vis titration spectra (Fig. 2) it can be seen that as the number of equivalents of AcO^-, as $[Bu_4N]AcO$ salt increases, the absorption bands, appeared at 392 and 325 nm wavelengths gradually reduced and new bands appeared at 457 and 330 nm with concomitant development of two isosbestic points at 424 and 347 nm wavelengths. The formation of isosbestic points shows the presence of two ionic species in the medium. In titration experiment the observed change at high energy band, 325 nm was less peculiar with a small red-shift of 5 nm. This is attributed to intramolecular charge transfer (ICT) towards electron deficient $-NO_2$ group of benzothiazole moiety from anionic –NH fragment of receptor in the influence of AcO^- anion. Further, from Fig. 2 it is also evident that on addition of 5.5 equiv. of AcO^- anion, a saturation point reached with a marked visible color change of the sensor solution from light yellow-green to red. To know the stoichiometry between the guest (AcO^-) and host (receptor) molecule in DMSO solution Job's plot (Fig. 2, inset) has been drawn that shows the maxima at 0.5 molar fraction, for 1:1 stoichiometry between the two interacting species for which association constant (K_{ass}), determined by non-linear fitting of spectroscopic titration curve [45] was found $K_{ass} = 5.27 \pm 0.45$ log unit.

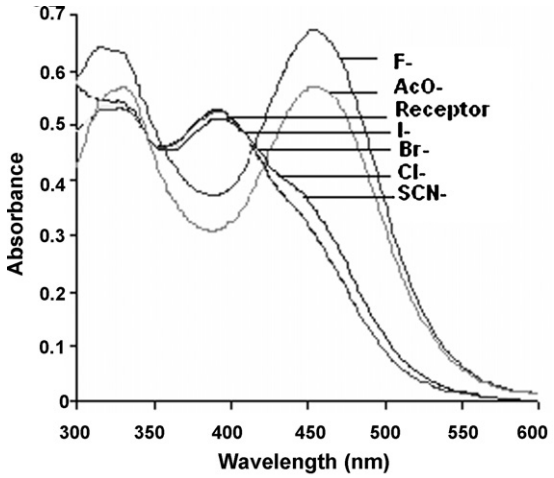


Fig. 1. Change in UV–vis spectra for the receptor **6** (2×10^{-5} mol l^{-1}) in DMSO solution with addition of different anions as their tetrabutylammonium salt.

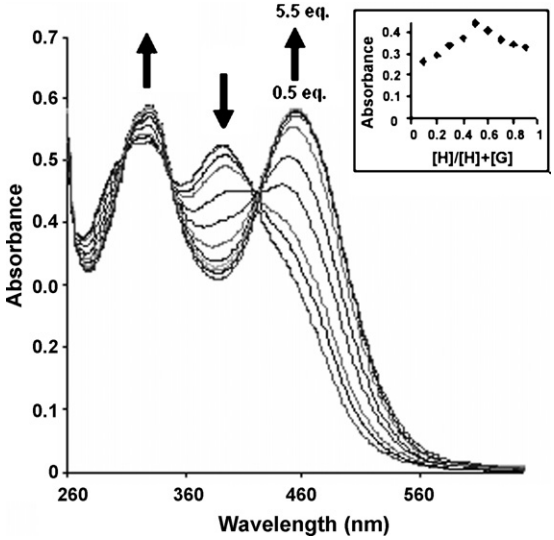


Fig. 2. Change in UV–vis spectra for the receptor **6** (2×10^{-5} mol l^{-1}) in DMSO solution with sequential addition of [Bu_4N]AcO from 0 to 5.5 equiv. Inset: Job's plot for receptor 1 with AcO^-.

Similarly, spectrophotometric behavior of receptor molecule with fluoride was monitored by titrating solution of chemosensor **6** with [Bu_4N]F. The change in spectral pattern (Fig. 3) was almost same as observed in case of AcO^- anion. The only difference being that the change in absorption bands appeared at 392 and 325 nm wavelengths gets modulated to new bands at 457 and 330 nm, rapidly with concomitant development of prominent isosbestic points at 424 and 347 nm wavelengths, respectively. The new lower energy band at 457 nm, representing the deprotonated form of chemosensor, reaches to a saturation point on addition of 2 equiv. of F^- anion. The isosbestic points observed with F^- was more prominent than AcO^- anion on addition of less number of equiv. of anions along with higher absorption intensity. This shows the presence of two ionic species in the medium with pronounce affinity for F^- compare to AcO^- anion, as is evident from Job's plot (Fig. 3, inset) and association constant determined to have $K_{ass} = 6.73 \pm 0.33$ log unit value.

The above discussed results indicate the occurrence of equilibrium between the host and guest molecule in which a proton is abstracted from one of the N–H fragments of the thiourea-based chemosensor and bridges two fluoride ions, to result the

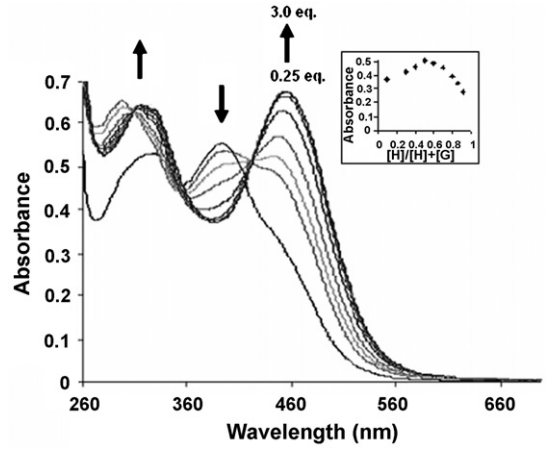


Fig. 3. Change in UV–vis spectra for the receptor **6** (2×10^{-5} mol l^{-1}) in DMSO solution with sequential addition of [Bu_4N]F from 0 to 3.5 equiv. Inset: Job's plot for receptor 1 with F^-.

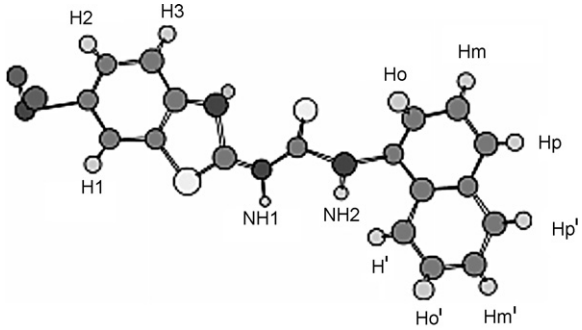


Fig. 4. Optimized geometry of receptor molecule, **6**.

hydrogen difluoride H-bond self-complex as shown in following equation.

$$[LH + 2F^- \rightleftarrows L^- + HF_2^-]$$

3.2. ^1H NMR titrations

On the basis of spectrophotometric investigations it is difficult to predict whether the prominent changes involve formation of complex between host and guest through hydrogen bonding or deprotonation of host by sufficient basic strength of guest molecules. To affirm the real phenomenon we have carried out ^1H NMR titration experiment with receptor molecule in DMSO-d_6 ($c = 1.05 \times 10^{-2}$ mol l^{-1}) by stepwise addition of equivalents of AcO^- and F^- as their [Bu_4N]AcO and [Bu_4N]F salts. The ^1H NMR spectrum of chemosensor **6**, shows two characteristic broaden peaks at 10.40 and 9.72 ppm corresponding to thiourea fragment protons designated as NH1 and NH2 protons. The assigned positions of respective protons have been demonstrated in the model picture for receptor molecule (Fig. 4). On addition of 0.5 equiv. of AcO^- both singlet signals for N–H protons are shifted towards downfield with broadening in signals (Figs. 5 and 6). On addition of 0.5 equiv. of AcO^- the signal for N-H2 proton shifted downfield from 9.72 to 9.73 ppm which on further successive addition of AcO^- significantly shifted towards more downfield (10.1 ppm) region. Additionally, at 2.5 equiv. of acetate ion, N-H1 proton attached to benzothiazole moiety disappeared. The H1 (8.64 ppm) and H2 (8.01 ppm, $J = 8.1$ Hz) peaks of benzothiazole moiety appeared as singlet and doublet, respectively, are due to an increase as well as decrease in electron density on benzothiazole and naphthyl units, respectively. The H1 proton shifted towards upfield while the H2 proton towards the downfield with broadening at 4.0 equiv. of AcO^- ion. This attributes the shielding and de-shielding electronic environments by through-bond propagation mechanism on respective protons. The H3 proton of benzothiazole moiety appeared at 7.66–7.63 ppm ($J = 8.1$ Hz) as a doublet and Hm proton of naphthyl unit appeared at 7.93 ppm as a triplet ($J = 9.3$ Hz, $J = 8.1$ Hz), remain unaffected after addition of AcO^-. The two characteristic peaks of H′ and H2 protons initially, were partially overlapped, and by the addition of AcO^- anion (1.5 equiv.) gets separated to appear at 7.96 ppm ($J = 7.8$ Hz) as a doublet. All the signals corresponding to aromatic protons get broadened and shifted toward downfield could be due to the deshielding affect caused by a polarization of C–H bonds or induced by through-space effect on interaction with AcO^- ion. The second triplet for Hp′ proton at 7.81–7.76 ppm of naphthyl unit on addition of salt reappears as doublet at 7.79–7.76 ppm ($J = 7.5$ Hz) and finally merged with other aromatic protons of naphthyl unit at 4 equiv. of AcO^-. A multiplet resonance signal for Hm′, Hp and Ho′ protons was appeared at 7.59–7.47 ppm along with merged Ho proton signal at 7.4 ppm. The Ho proton reappeared as a doublet

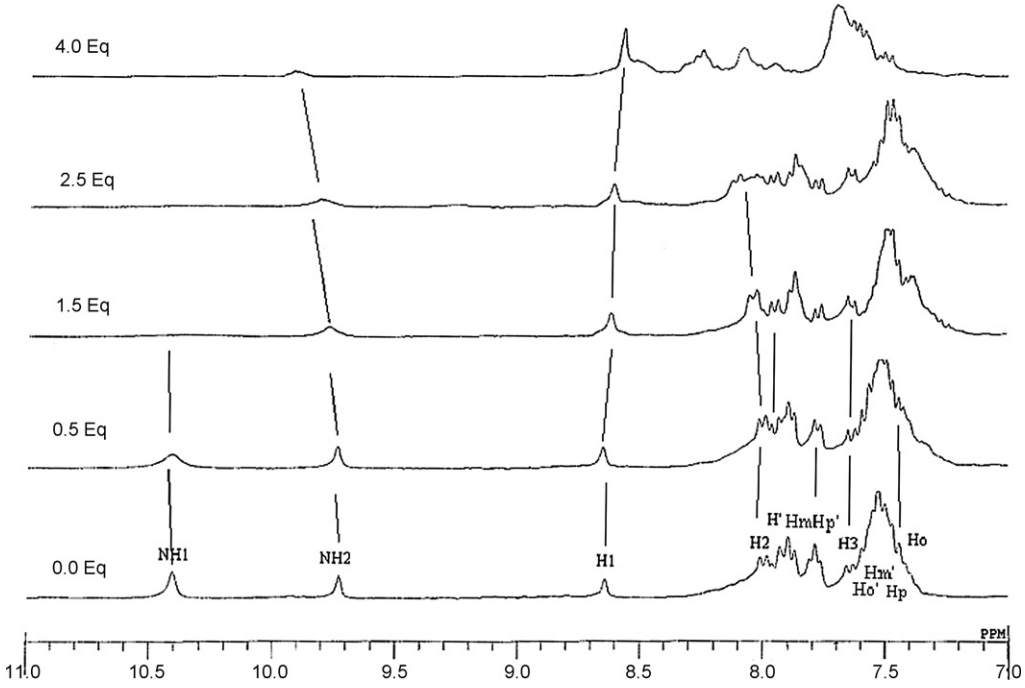


Fig. 5. Changes in ^{1}H NMR titration spectra for chemosensor **6** (1.05×10^{-2} M) in DMSO-d_6 solution with gradual addition of equiv. of [Bu_4N]AcO.

by the addition of 0.5 equiv. of AcO^- and initially shifted upfield at 7.38 ppm and disappeared after the addition of 2.5 equiv. of AcO^-.

These results clearly indicate that chemical shifts are varying in narrow range with pronounced broadening and all the aromatic protons close to anionic receptor site are moving towards the upfield via a through-bond propagation mechanism. Such features can be deduced for complexation between guest and host through H-bond formation as indicated in Scheme 2. The peculiar broadening in resonance signal obtained as a result of complex formation is due to restricted relative rotation of naphthyl and benzothiazole rings. Since, in ^{1}H NMR most of the broadening occurs in the benzothiazole ring's proton hence, is more closure to the nitrogen atoms of thiourea fragment and in turn closure to H-bound acetate. However, whatever the case, on H-bond complexation between chemosensor and AcO^-, the electron density is transferred more on the receptor site, causing more shielding effect and hence accounting the distinct chemical shifts in the proton signals. Moreover, as speculated, with the transfer of more electron on receptor site, modulation in dipole moment occurs in such a fashion that the extent of optical transition becomes equivalent to the state of deprotonation and we observed the respective changes in ^{1}H NMR titration spectra. On the other hand, by considering H-bonding interaction as an incipient proton transfer from donor to acceptor, these results are supporting the proton transfer from an early transition state with strongly basic AcO^-, and hence the electronic properties of receptor molecule in complexation state become close to those of deprotonation form. These facts has been observed in Fig. 3 (inset) that on addition of 2.5 equiv. of AcO^- there is case of H-bond complexation between the receptor and anion which on further addition of AcO^- disappeared showing the deprotonation state (Scheme 2).

Similarly, significant variations in chemical shifts were observed on performing ^{1}H NMR titration experiment in case of fluoride-induced deprotonation of chemosensor, **6** (Figs. 7 and 8). The

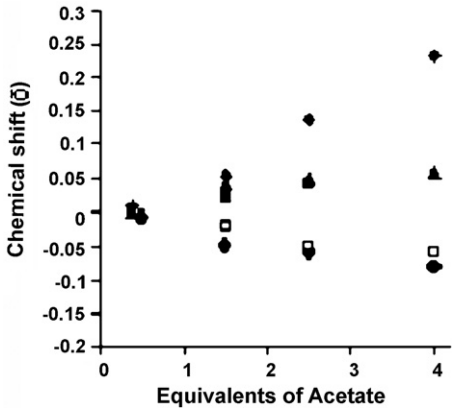
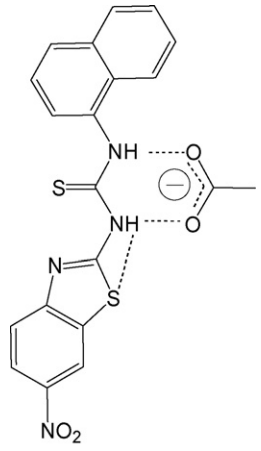


Fig. 6. Changes in chemical shifts in ^{1}H NMR titration with equiv. of [Bu_4N]AcO (diamond, NH2; square, NH1; triangle, H2; circle, H1 and hollow square, Ho).



9

Scheme 2. Proposed deprotonation mechanism for thiourea-based chemosensor, **6** with AcO^- ion.

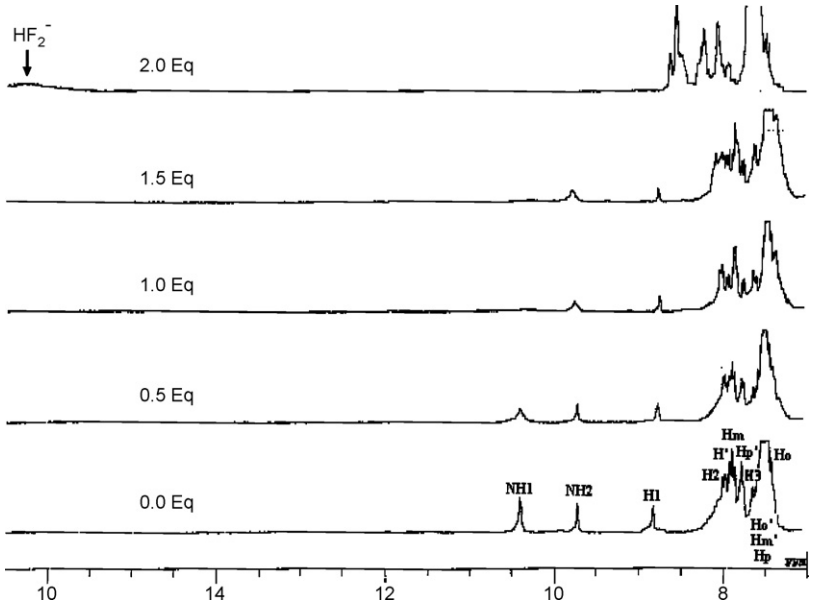


Fig. 7. Changes in ^{1}H NMR titration spectra for chemosensor **6** (1.05×10^{-2} M) in DMSO-d_6 solution with gradual addition of equiv. of [Bu_4N]F.

spectral pattern obtained over the course of titration in DMSO-d_6 solution of receptor **6** with [Bu_4N]F was very much similar to that of AcO^-. The difference being that the chemical shifts corresponding to NH1 (10.40 ppm) and NH2 (9.72 ppm) protons get affected by addition of less equivalents of F^- anion. The association constant, was determined from UV–vis titration spectra, of 6.73 ± 0.33 log unit value and frequent chemical shifts corroborate greater affinity of chemosensor for F^-, compare to AcO^-. In case of fluoride the NH1 proton of receptor **6** on addition of 1 equiv. of F^- disappeared while the resonance signal for NH2 proton become broaden and shifted toward lowfield due to more shielded electronic environment effect. On successive addition of 1.5 equiv. of F^- NH2 proton further shifted toward downfield and disappeared on addition of 2 equiv. F^-. Thus, the initial broadening in the ^{1}H NMR signal of the amino peaks of the receptor molecule attributes interaction between guest and host molecules through the hydrogen bonding which on increasing the amount of F^- (1 equiv.) deprotonated first, more acidic proton (N-H1), close to the benzothiazole unit, thereby generating HL^- species in the reaction medium. On addition of more amount of F^- broadening in the N-H2 proton signal of receptor occured and at 2.0 equiv. of F^-, resonance signal corresponding to N-H2 proton almost become flattened or disappeared.

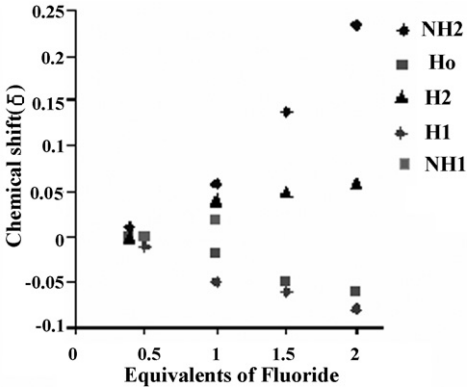
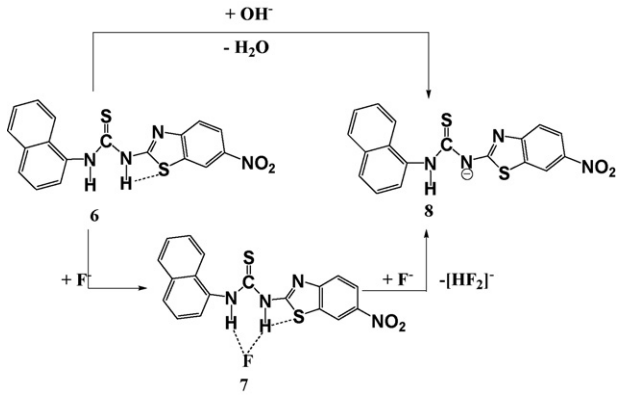


Fig. 8. Changes in chemical shifts in ^{1}H NMR titration with equiv. of [Bu_4N]F; (diamond, NH2; square, NH1; triangle, H2; circle, H1 and hollow square, Ho).



Scheme 3. Proposed deprotonation mechanism for thiourea-based chemosensor, **6** with F^- ion.

This indicates that the receptor molecule is in deprotonated dianionic (L^{2-}) state (Scheme 3). The resonance signal for formation of HF_2^- complex has been started after the addition of 1.5 equiv. of F^- and appeared prominently at 16.32 ppm chemical shift after addition of 2.0 equiv. of F^- and subsequent color change of chemosensor solution, that was visible to naked-eye from light yellow-green to red (Fig. 9).

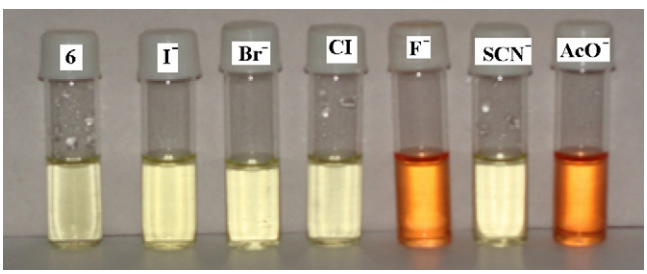


Fig. 9. Color changes of chemosensor **6**, in DMSO solution (2×10^{-5} M) after addition of 5 equiv. of different anions.

4. Conclusion

To sum up, a new colorimetric chemosensor has been synthesized via dithiocarbamate synthetic strategy and by keeping in mind binding site-signaling unit approach in which an appropriate chromophore was attached to a specific anion receptor to make sensitive recognition behaviors simple and convenient through naked-eye. The sensor has demonstrated successfully, recognition for fluoride and acetate and expected to have other opportunities for detection of anions.

Acknowledgement

Authors are thankful to Department of Science and Technology, New Delhi for financial support.

References

[1] H.D. Paduka Ali, P.E. Kruger, T. Gunnlaugsson, New J. Chem. 32 (2008) 1153.
[2] K.L. Kirk, Biochemistry of the Halogens and Inorganic Halides, Plenum Press, NY, 1991, p. 58.
[3] B.L. Riggs, Bone and Mineral Research; Annual 2, Elsevier, Amsterdam, 1983, p. 366.
[4] M. Kleerekoper, Endocrinol. Metab. Clin. North Am. 27 (1998) 441.
[5] A. Wiseman, Handbook of Experimental Pharmacology XX/2, Springer-Verlag, Berlin, 1990, p. 48, part 2.
[6] J.A. Weatherall, Handbook of Experimental Pharmacology XX/1, Springer-Verlag, Berlin, 1969, p. 141, part 1.
[7] S.Y. Kim, J.-In. Hong, Org. Lett. 9 (2007) 3109.
[8] T. Gunnlaugsson, A.P. Davis, J.E. O'Brien, M. Glynn, Org. Lett. 4 (2002) 2449.
[9] M. Mei, S. Wu, New J. Chem. 25 (2001) 471.
[10] A.P. deSilva, H.Q.N. Gunarantane, T. Gunnlaugsson, A.J.M. Huxley, C.P. McCoy, J.T. Rademacher, T.E. Rice, Chem. Rev. 97 (1997) 1515.
[11] R. Martinez-Manez, F. Sancenon, Chem. Rev. 103 (2003) 4419.
[12] A.P. deSilva, D.B. Fox, A.J.M. Huxley, T.S. Moody, Coord. Chem. Rev. 205 (2000) 41.
[13] Kimura, Acc. Chem. Res. 34 (2001) 171.
[14] T. Gunnlaugsson, M. Glynn, G.M. Tocci, P.E. Kruger, F.M. Pfeffer, Coord. Chem. Rev. 250 (2006) 3094.
[15] T. Gunnlaugsson, H.D.P. Ali, M. Glynn, P.E. Kruger, G.M. Hussey, F.M. Pfeffer, C.M.G. dosSantos, J. Tireney, J. Fluores. 15 (2005) 287.
[16] G.J. Mohr, Sens. Actuators 107 (2005) 2.
[17] R. Martinez-Manez, F. Sancenon, J. Fluores. 15 (2005) 267.
[18] E.J. Cho, J.W. Moon, S.W. Ko, J.Y. Lee, S.K. Kim, J. Yoon, K.C. Nam, J. Am. Chem. Soc. 125 (2003) 12376.
[19] E. Quinlan, S.E. Matthews, T. Gunnlaugsson, J. Org. Chem. 72 (2007) 7497.
[20] K. Ghosh, G. Masanta, A.P. Chattopadhyay, Tetrahedron Lett. 48 (2007) 6129.
[21] F.M. Pfeffer, A.M. Buschgens, N.W. Barnett, T. Gunnlaugsson, P.E. Kruger, Tetrahedron Lett. 46 (2005) 6579.
[22] D.R. Turner, M.J. Paterson, J.W. Steed, J. Org. Chem. 71 (2006) 1598.
[23] D.R. Turner, B. Smith, E.C. Spencer, A.E. Goeta, I.R. Evans, D.A. Tocher, J.A.K. Howard, J.W. Steed, New J. Chem. 29 (2005) 90.
[24] A.J. Lowe, F.A. Dyson, F.M. Pfeffer, Org. Biomol. Chem. 5 (2007) 1343.
[25] T. Gunnlaugsson, A.P. Davis, J.E. O'Brien, M. Glynn, Org. Lett. 4 (2002) 2449.
[26] T. Gunnlaugsson, A.P. Davis, M. Glynn, Chem. Commun. (2001) 2556.
[27] D.E. Gómez, L. Fabbrizzi, M. Licchelli, E. Monzani, Org. Biomol. Chem. 3 (2005) 1495.
[28] M. Bonizzoni, L. Fabbrizzi, A. Taglietti, E. Tiengo, Eur. J. Org. Chem. (2006) 3567.
[29] S.O. Kang, R.A. Begum, K. Bowman-James, Angew. Chem. Int. Ed. 45 (2007) 7882.
[30] S.O. Kang, Md.A. Hossain, K. Bowman-James, Coord. Chem. Rev. 250 (2006) 3038.
[31] K. Niikura, A. Metzger, E.V. Anslyn, J. Am. Chem. Soc. 120 (1998) 8533.
[32] Y. Wang, H. Lin, J. Shao, Z.-S. Cai, H.-K. Lin, Talanta 74 (2008) 1122.
[33] J. Shao, H. Lin, M. Yu, Z. Cai, H.-K. Lin, Talanta 75 (2008) 551.
[34] G.W. Bates, Triyanti, M.E. Light, M. Albrecht, P.A. Gale, J. Org. Chem. 72 (2007) 8921.
[35] J.L. Sessler, N.M. Barley, G.D. Pantos, V.M. Lynch, New J. Chem. 31 (2007) 646.
[36] R. Li, L.S. Evans, D.S. Larsen, Ph.A. Gale, S. Brooker, New J. Chem. 28 (2004) 1340.
[37] P.A. Gale, P. Anzenbacher, J.L. Sessler, Coord. Chem. Rev. 222 (2001) 57.
[38] K.J. Winstanley, A.M. Sayer, D.K. Smith, Org. Biomol. Chem. 4 (2006) 1760.
[39] P.A. Gale, Encyclopedia of Supramolecular Chemistry, Marcel Dekker, New York, 2004, p. 31.
[40] P.D. Beer, P.A. Gale, Angew. Chem. 113 (2001) 502;
P.D. Beer, P.A. Gale, Angew. Chem. Int. Ed. 40 (2001) 486.
[41] F.P. Schmidtchen, M. Berger, Chem. Rev. 97 (1997) 1609.
[42] M. Boiocchi, L.D. Boca, D. Esteban-Gomez, L. Fabbrizzi, M. Licchelli, E. Monzani, Chem. Eur. J. 11 (2005) 3097.
[43] T. Steiner, Angew. Chem. Int. Ed. 41 (2002) 48.
[44] F.G. Bordwell, Acc. Chem. Res. 21 (1988) 456.
[45] K.A. Connors, Binding Constant, 1st ed., Wiley, New York, 1987.

Talanta 80 (2009) 539–543

Contents lists available at ScienceDirect

Talanta

journal homepage: www.elsevier.com/locate/talanta

A simple method for fabrication of sole composition nickel hexacyanoferrate modified electrode and its application

Wei Chen[a,b], Jian Tang[a], Han-Jun Cheng[a], Xing-Hua Xia[a,*]

[a] Key Laboratory of Analytical Chemistry for Life Science, School of Chemistry and Chemical Engineering, Nanjing University, Nanjing 210093, Jiangsu, China
[b] Department of Pharmaceutical Analysis, School of Pharmacy, Fujian Medical University, Fuzhou 350004, China

ARTICLE INFO

Article history:
Received 2 April 2009
Received in revised form 2 July 2009
Accepted 7 July 2009
Available online 15 July 2009

Keywords:
Nickel hexacyanoferrate
Chemical deposition
Solo composition
Stability
Sodium ion sensing
Electrocatalysis
Electrochemical analysis

ABSTRACT

Nickel hexacyanoferrate film modified gold electrode was prepared by a simple chemical deposition procedure from a fresh prepared solution containing ferricyanide, Ni^{2+}, and sodium nitrate. The resultant films have solo composition and are significantly stable as compared to the electrochemically deposited NiHCF films. For different concentrations of Na^+ in the solution, the formal potential values of NiHCF shift according to the Nernstian behavior with a slope of 48 mV in the range of 10^{-4} to 1.0 M. The NiHCF film was also used for the electrocatalytic oxidation of ascorbic acid. The anodic peak current observed in cyclic voltammetry increased with the ascorbic acid concentration. At a fixed potential under hydrodynamic conditions, the calibration plot was linear over the ascorbic acid concentration range 0.1–12 mM.

© 2009 Elsevier B.V. All rights reserved.

1. Introduction

Prussian blue (PB) and its related transition metal hexacyanoferrates (MHCFs), an important class of inorganic polymeric compounds, recently have attracted intense interests because of their attractive properties such as electrocatalysis, electrochromicity, ion sensing and magnetism [1–7]. Moreover, metal hexacyanoferrates have been widely studied as environmentally benign ion exchangers for the selective removal of radioactive ^{137}Cs from nuclear waste solutions containing high concentration of alkali metals because of their zeolitic structure and strong affinity for Cs^+ [8,9].

Nickel hexacyanoferrate (NiHCF) is an important analogue of PB. Among the cyanometallate systems, NiHCF can be considered as a material for certain fundamental and applied studies since NiHCF films show well-defined and reproducible voltammetric responses not only in K^+ containing electrolytes, but also in other alkali metal cations such as Li^+, Na^+, Rb^+ or Cs^+. Unlike Prussian blue and many of its metal-substituted analogues, both the oxidized and reduced forms of NiHCF seem to be fairly open and allow an easy transport of alkali metal cations of different sizes while providing charge balance during the redox processes [10–12].

Although the electrochemical behaviors of MHCFs might be similar, it is still necessary to investigate such kinds of electroactive materials, since under different conditions the formation of MHCFs on electrode surface as well as the electrochemical behaviors may be different. NiHCF films can be easily formed on many conductive substrates by electrodeposited through potential cycling [10,11]. However, NiHCF films formed by potential cycling contain two different composites [11,13]. It is important to note that, for an ideal sensor or separation matrix, one would design the processing conditions that produce the NiHCF with predominantly one type of intercalation site or the other, rather than a mixture of both [14]. In this paper, we propose a novel method for the fabrication of NiHCF films on electrode substrates. The NiHCF was deposited by immersing conductive substrate in a fresh prepared solution containing ferricyanide, Ni^{2+}, and sodium nitrate. This approach is simple and effective for establishing electroactive NiHCF interface. The resultant NiHCF has solo composition and is significantly stable as compared to the electrochemically deposited NiHCF films. Compared with the electrochemical method, the present approach can modify many electrodes at the same time by just immersing them in the reaction solution. To verify the applicability of the proposed NiHCF interface, two important properties and potential applications of metal hexacyanoferrate, ion sensing and electrocatalysis, were then studied. Based on the established voltammetry and amperometry, sodium ion in blood and ascorbic acid in pharmaceuticals were successfully determined, respectively.

* Corresponding author. Tel.: +86 25 83697436; fax: +86 25 83697436.
E-mail address: xhxia@nju.edu.cn (X.-H. Xia).

0039-9140/$ – see front matter © 2009 Elsevier B.V. All rights reserved.
doi:10.1016/j.talanta.2009.07.022

2. Experimental

2.1. Electrode fabrication

NiHCF films were deposited on polished gold electrodes. Before deposition, the electrode surfaces were electrochemically cleaned in the potential region for oxygen and hydrogen evolution in 0.5 M H_2SO_4 by cyclic voltammetry. In chemical deposition, the gold electrodes were immersed in a freshly mixed solution of 1 mM $K_3Fe(CN)_6$, 1 mM $NiSO_4$ and 0.5 M $NaNO_3$ for 30 min. Then, the NiHCF-modified electrode was rinsed thoroughly by distilled water. The electrochemically deposited NiHCF films were fabricated in the same solution by cycling the potential from 0 to 850 mV for 20 cycles.

2.2. Electrochemistry

Cyclic voltammograms of the NiHCF modified electrodes were performed with a CHI model 1140 analyzer. A platinum wire was used as the counter electrode and all reported potentials are referenced to an Ag/AgCl reference electrode.

2.3. Sodium sensing

The formal potential of NiHCF modified electrode was measured by cyclic voltammetry at a scan rate of 1 mV/s. Serum and plasma from healthy volunteers were determined without any pretreatment.

2.4. Ascorbic acid detection

Quantitative determination of ascorbic acid was carried out amperometrically in a stirred PBS solution (pH 7.0, containing 1.0 M $NaNO_3$). The potential of the electrode was kept constant at +0.40 V, which corresponds to the peak potential for oxidation. The response was recorded by adding a series of standards of the analyte to the measuring solution.

3. Results and discussion

3.1. Electrochemical characterization

As an analogue of Prussian blue, NiHCF also contains electrochemically reversible iron centers that switch between the ferrous reducing and the ferric oxidizing states depending on applied potential. To maintain charge neutrality, reversible intercalation and deintercalation of charge-compensating alkali cations take place in the NiHCF electrochemical redox reaction. Fig. 1 indicates the voltammetric response of NiHCF films fabricated by chemically or electrochemically deposited in a 1.0 M KNO_3 or $NaNO_3$ aqueous solution. The observation of reproducible and well-behaved cyclic voltammetric peaks provides evidence for the attachment of the NiHCF film on the electrode surfaces. Since the Ni^{2+} cations in the modifying film are not expected to be electroactive in the potential range examined, the redox peaks present a single electron process of hexacyanoferrate (III/II) in the film. Positive currents correspond to the oxidation of NiHCF with the release of alkali cations from the matrix and negative currents denote the reduction with the uptake of alkali cations. The cyclic voltammograms show that the redox processes of both the electrodes are electrochemically reversible and the cations loading and unloading can be controlled by modulating the potential. However, it is noteworthy that different preparation procedures of the electrodes lead to different CV shapes. In electrolytes containing sodium or potassium, particularly in the presence of K^+ ions, voltammetric peaks of the electrodeposited NiHCF tend to undergo splitting, implying the coexistence of two stable forms of NiHCF and two overlapping redox reactions [11]. Fig. 1A, curve b shows the cyclic voltammogram of the electrodeposited NiHCF film modified Au electrode in a solution of 1.0 M KNO_3 at a scan rate of 25 mV/s. There are two pairs of well-defined redox peaks, namely redox couple I and redox couple II, appearing in the curve. The anodic (E_{pa}) and cathodic (E_{pc}) peak potentials are +492 and +482 mV, respectively, and the formal potential $E^{0'}$, which was defined as the mid-point potential of the anodic and cathodic peak potentials, is +487 mV for the redox couple I. The separation of the anodic and cathodic peak potentials, ΔE_p, is 10 mV. For the redox couple II, the values of E_{pa}, E_{pc}, $E^{0'}$ and ΔE_p are +618, +612, +615 and 6 mV, respectively. The respective redox reactions can be represented by Eqs (1) and (2) [11,13].

$$ANi[Fe^{III}(CN)_6] + A^+ + e^- = A_2Ni[Fe^{II}(CN)_6] \quad (1)$$

$$Ni_{1.5}[Fe^{III}(CN)_6] + A^+ + e^- = ANi_{1.5}[Fe^{II}(CN)_6] \quad (2)$$

where A is the intercalated alkaline cation, and A^+ is the corresponding alkaline cation in solution.

As compared to the electrodeposited hybrid NiHCF, the chemically deposited NiHCF films have the solo formation, which shows only one pair of redox peaks in potassium electrolytes (Fig. 1B).

Fig. 2A shows that the chemically deposited NiHCF on gold electrode has a chemically reversible redox couple in a 1.0 M $NaNO_3$ solution when cyclic voltammetry is performed at various scan rates over a range of 5–500 mV/s. It is observed that as the scan rate increases the peak current as well as the peak-to-peak separation increase. The peak-to-peak separation, ΔE_p, varies from 5 to 30 mV upon varying the scan rate from 5 to 500 mV/s. Fig. 2B shows the plot of I_p vs. scan rate. Both the anodic and cathodic peak currents are directly proportional to the scan rate up to 500 mV/s. The ratio of the anodic to cathodic peak current, I_{pa}/I_{pc}, is almost equal to unity. This behavior is as expected for diffusionless, surface-confined redox

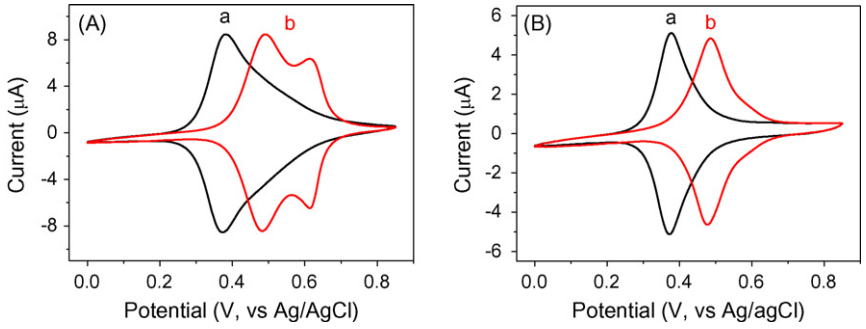


Fig. 1. Cyclic voltammograms of (A) an electrodeposited NiHCF film and (B) a chemically deposited NiHCF film on Au electrode in a 1.0 M (a) $NaNO_3$ and (b) KNO_3 solution at a scan rate of 25 mV/s.

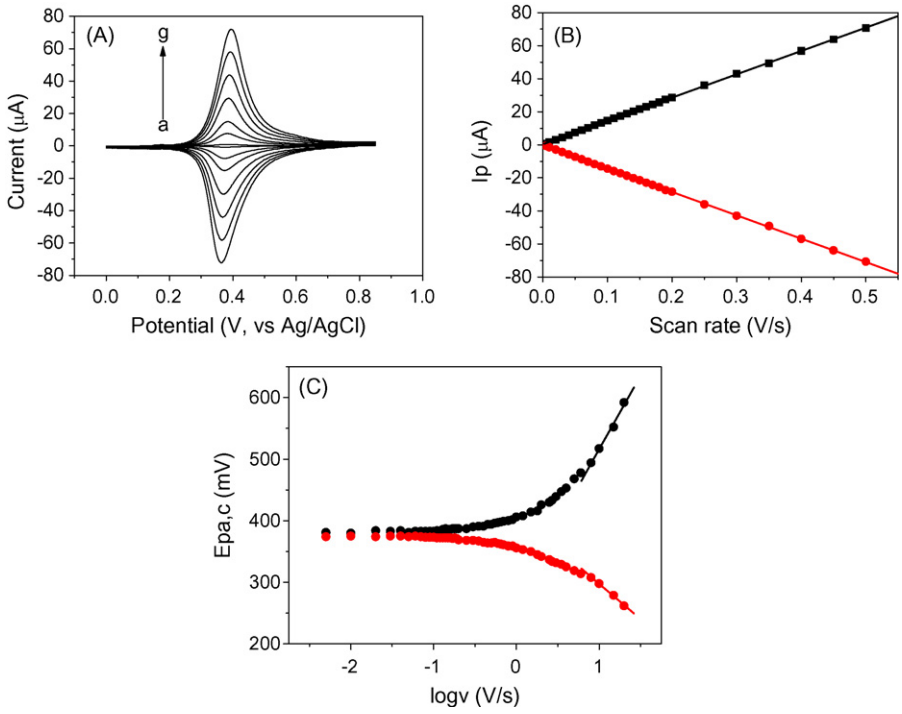


Fig. 2. (A) Cyclic voltammograms of the chemically deposited NiHCF on gold electrode in 1.0 M $NaNO_3$ at different scan rates: (a)–(g) 5, 50, 100, 200, 300, 400, 500 mV/s. (B) Plot of the anodic and cathodic peak currents vs. scan rate. (C) Plot of anodic and cathodic peak potentials as function of log ν.

systems. The peak current and scan rate are related as

$$I_p = \frac{n^2F^2\nu AG_0}{4RT} \quad (3)$$

where G_0, ν, A and I_p represent the surface coverage concentration, the scan rate, the electrode area, and the peak current, respectively. This result indicates that the redox process is confined to the surface of the NiHCF/Au electrode, confirming the immobilized state of the NiHCF.

As shown in Fig. 2C, the peak separation begins to increase at higher scan rates, indicating the limitation arising from charge transfer kinetics. The anodic and cathodic peak potentials are proportional to the logarithm of the scan rate for $\nu > 8000$ mV/s. Based on the Laviron theory [15], the electron transfer rate constant (k_s) as well as the transfer coefficient (α) can be calculated. For the anodic and cathodic peaks, the slope of E_p (E_{pa} and E_{pc}) vs. log ν is 239.3 and −114.6, respectively. The calculated value of α is 0.68. According to the following equation:

$$\log k_s = \alpha\log(1-\alpha)+(1-\alpha)\log\alpha-\log\left(\frac{RT}{nF\nu}\right)-\frac{\alpha(1-\alpha)nF\Delta E_p}{2.3RT} \quad (4)$$

From this Eq. (4), the electron transfer rate constant (k_s) was also calculated to be 19.3 s^{-1}.

3.2. Morphological characterization

Fig. 3 shows the morphology of the NiHCF fabricated by chemical and electrochemical methods on gold-CD electrode. In the case of electrochemical deposition, the resultant NiHCF film consists of irregular nanoparticles, which are equally distributed over the whole surface (Fig. 3A). In contrast, NiHCF nucleated sparsely on the gold substrate and quasi cubic structures formed in the chemical deposition process (Fig. 3B). This phenomenon could be ascribed to the different nucleation and crystal growth rates in these two methods.

3.3. Stability of the NiHCF modified electrodes

It has been described that the main drawback for hexacyanometallates-based chemically modified electrodes is the gradual dissolution during continuous potential scan, which is an important factor hindering their practical performances [16]. Therefore, the major concern regarding the use of PB and its

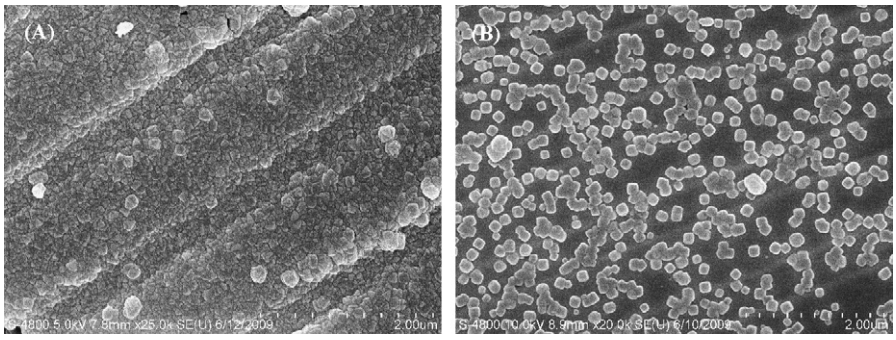


Fig. 3. Scanning electron micrographs of the NiHCF modified gold-CD electrode fabricated by (A) electrochemical and (B) chemical methods.

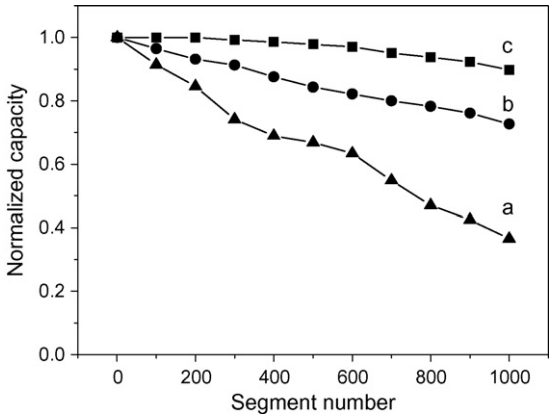


Fig. 4. Normalized capacity as a function of the potential scan cycles showing the electrochemical stability of NiHCF film on gold electrodes fabricated by (a) electrochemical deposition, (b) chemical deposition for 30 min, and (c) chemical deposition for 60 min. Data were obtained from the cyclic voltammograms of these modified electrodes in a 1.0 M $NaNO_3$ solution at a scan rate of 100 mV/s.

analogues for sensor and biosensor design is the enhancement of their stability. For this reason, some works have been carried out for improving the stability of NiHCF [17,18]. The stability of the as-prepared films was characterized using cyclic voltammetry in a 1.0 M $NaNO_3$ solution starting from 0 to 0.85 V at a scan rate 100 mV/s. The ion exchange capacities were estimated by the charge passed under the redox peaks [19], and the capacity values are normalized by their corresponding initial capacity. To shed light on the significance of the stability of the chemically deposited NiHCF film, results were also compared with a NiHCF film modified electrode prepared by a common electrochemically deposition method. As shown in Fig. 4, the fabrication process considerably influences the redox cycling stability of the NiHCF modified electrode. For the electrochemically deposited NiHCF, the ion exchange capacity decreases very quickly upon repeated potential cycling (Fig. 4, curve a). About 60% decrease in the ion exchange capacity is observed after 500 cycles of potential scan. On the contrast, the chemically deposited NiHCF films have a significant stability during potential cycling. The NiHCF films chemically deposited for 30 and 60 min remained 72.7% and 89.8% of the exchange capacity of their initial values after 500 cycles of potential scan, respectively (Fig. 4, curves b and c). This relative high stability could be attributed to the chemical composition of the NiHCF fabricated.

3.4. Na^+ sensing

Sodium ion is the most essential extracellular cation for maintaining osmotic pressure and electrodynamic cellular properties in living organism. Electrolyte disorders are frequently observed in clinical practice, and quantitative detection of sodium ion is routinely performed in biochemistry laboratories. Since the formal potential changes linearly with log[Na^+], the NiHCF films modified gold electrode were employed as sodium sensor by voltammetric determination of the formal potential of the nickel hexacyanoferrate film modified electrode.

Cyclic voltammograms of the chemically deposited NiHCF film on gold electrode in different concentrations of $NaNO_3$ are shown in Fig. 5A. When the concentration of $NaNO_3$ decreases from 1.0 to 0.0001 M, the redox peaks shifts towards less positive potential from 0.38 to 0.19 V with a simultaneous decrease in peak current. The gradual decrease in peak current can be explained by the Fick's first diffusion law [20]. Fig. 5B shows the plot of Na^+ ion concentration vs. formal potential. A linear graph with a slope of 48 mV is obtained in the range of 10^{-4} to 1.0 M.

The application of the NiHCF-modified electrode in the determination of sodium ion in blood was also examined. Table 1 compares the results obtained using the electrochemical method with that using flame emission spectrophotometry. Both methods show good reproducibility, low standard deviations and good agreement with each other. However, the electrochemical method has the significant advantages of ease of operation and low cost.

Table 1
Concentration of sodium ion (mM) in blood obtained by different analytical methods ($n = 5$).

Method	Sample	
	Serum	Plasma
Voltammetry	134.9 ± 0.3	140.1 ± 0.3
Flame emission spectrophotometry	135.1 ± 0.5	139.8 ± 0.4

3.5. Electrocatalytic oxidation of ascorbic acid

To validate the electrocatalytic property of the resultant NiHCF film, the electrooxidation of ascorbic acid on the modified electrode was studied. Fig. 6A shows the cyclic voltammograms of the chemically deposited NiHCF film modified Au electrodes in the absence and presence of ascorbic acid. As seen in Fig. 6A, the NiHCF film modified Au electrode in the blank solution (20 mM phosphate buffer, pH 7.0, 1.0 M $NaNO_3$) exhibits a well-behaved redox reaction at 430 mV (curve a). Upon the addition of ascorbic acid, an enhancement in the anodic peak current was observed and the cathodic peak current tends to disappear (curve b). This behavior is typical of that expected for mediated oxidation. The anodic peak current increases with increasing the ascorbic acid concentration in solution (curves b–d). A typical calibration curve based on the hydrodynamic amperometric measurement (Fig. 6B and C) shows a linear range in the concentration range 0.1–12 mM

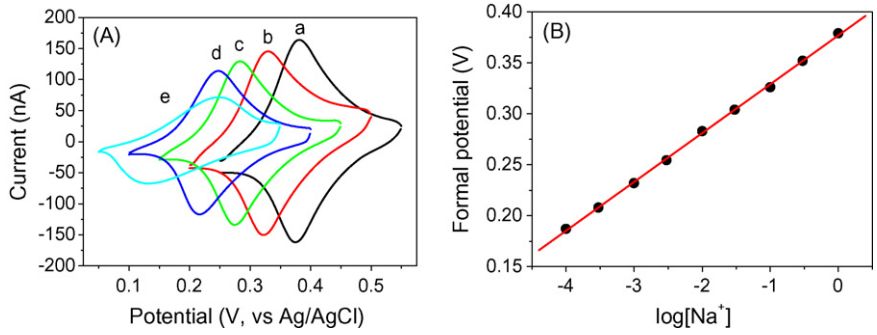


Fig. 5. (A) Cyclic voltammograms of the chemically deposited NiHCF film on gold electrode in (a) 1.0 M, (b) 0.1 M, (c) 0.01 M, (d) 0.001 M, and (e) 0.0001 M $NaNO_3$ solutions. Scan rate: 1 mV/s. (B) The plot of formal potential vs. log[Na^+].

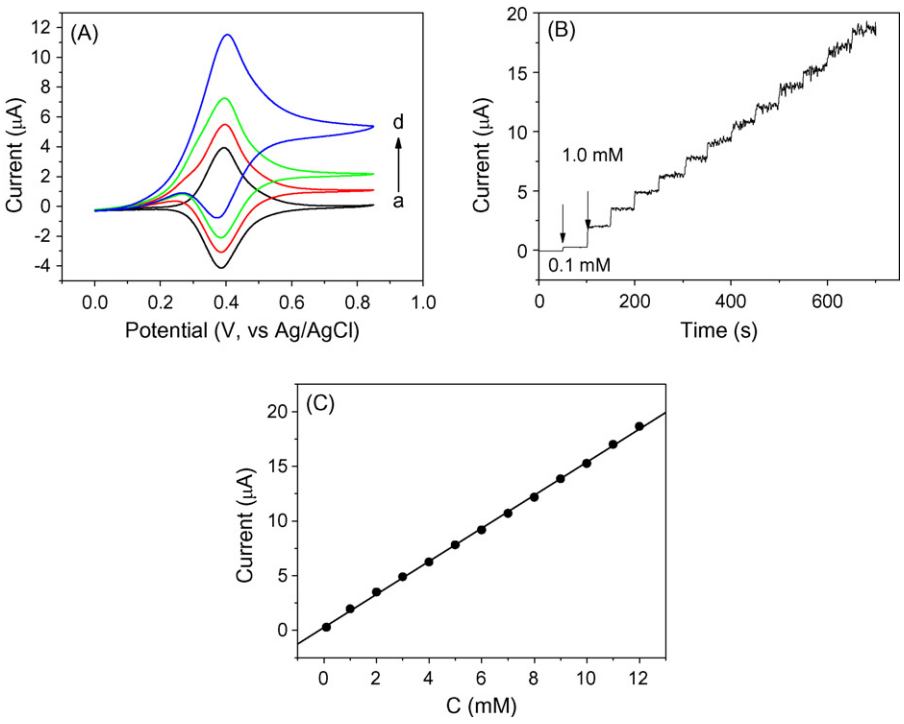


Fig. 6. (A) Cyclic voltammograms of a chemically deposited NiHCF film on Au electrode in the absence (a) and in the presence of ascorbic acid (b) 2.0, (c) 4.0, (d) 10.0 mM, respectively. Supporting electrolyte: 1.0 M $NaNO_3$ with 20 mM phosphate buffer (pH 7.0); potential scan rate: 25 mV/s. (B) Typical amperometric response of a chemically deposited NiHCF film on Au electrode to successive injection of ascorbic acid into a stirring PBS solution (pH 7.0, containing 1.0 M $NaNO_3$). The working potential was 0.4 V. (C) The calibration curve of ascorbic acid concentration at the modified electrode.

Table 2
Results for the determination of ascorbic acid in pharmaceuticals.

Sample	Amount of ascorbic acid[a]	
	Proposed method	Iodine titration method
Tablet (mg/tablet)	986.5 ± 16.3	994.7 ± 10.2
Injection (mg/ml)	255.1 ± 2.6	249.8 ± 3.3

[a] Average of five replicate determinations.

with a correlation coefficient over 0.9996. The detection limit is 0.025 mM.

To verify the present catalytic method, pharmaceutical dosage forms containing ascorbic acid including tablets and injections purchased from local sources were analyzed. The evaluation of the ascorbic acid concentration is carried out with the aid of a standard addition method. The results for the analysis of these preparations with the amperometric method compared favorably with those obtained by the iodine titration method (Table 2).

4. Conclusion

A novel chemical deposition method has been established for construction of NiHCF film on conductive substrates. The resultant NiHCF films have single chemical composition. Both alkaline ions response and electrocatalytic activity are favorable for these films. The ease of preparation and the relatively high stability of the film represent important factors for use in routine quantitative analysis.

Acknowledgements

This work was financially supported by the National Basic Research Program (2007CB714501), the National Natural Science Foundation of China (20535010, 20828006), the National Science Fund for Creative Research Groups (20821063), and Natural Science Foundation of Fujian Province of China (C0710024).

References

[1] M. Verdaguer, A. Bleuzen, V. Marvaud, J. Vaissermann, M. Seuleiman, C. Desplanches, A. Scuiller, C. Train, R. Garde, G. Gelly, C. Lomenech, I. Rosenman, P. Veillet, C. Cartier, F. Villain, Coord. Chem. Rev. 190–192 (1999) 1023.
[2] N.R. Tacconi, K. Rajeshwar, R.O. Lezna, Chem. Mater. 15 (2003) 3046.
[3] D.M. DeLongchamp, P.T. Hammond, Chem. Mater. 16 (2004) 4799.
[4] L.J. Amos, A. Duggal, E.J. Mirsky, P. Ragonesi, A.B. Bocarsly, Anal. Chem. 60 (1988) 245.
[5] R. Martinez-Garcia, M. Knobel, E. Reguera, J. Phys. Chem. B 110 (2006) 7296.
[6] M. Yamada, M. Arai, M. Kurihara, M. Sakamoto, M. Miyake, J. Am. Chem. Soc. 126 (2004) 9482.
[7] S.M. Chen, C.M. Chan, J. Electroanal. Chem. 543 (2003) 161.
[8] D.V. Ca, J.A. Cox, Microchim. Acta 147 (2004) 31.
[9] M.W.A. Raouf, J. Chem. Technol. Biotechnol. 79 (2004) 22.
[10] J. Joseph, H. Gomathi, G. Prabhakara Rao, Electrochim. Acta 36 (1991) 1537.
[11] J. Bacskai, K. Martinusz, E. Czirok, G. Inzelt, P.J. Kulesza, M.A. Malik, J. Electroanal. Chem. 385 (1995) 241.
[12] S. Sinha, B.D. Humphrey, A.B. Bocarsly, Inorg. Chem. 23 (1984) 203.
[13] S. Zamponi, M. Berrettoni, P.J. Kulesza, K. Miecznikowski, M.A. Malik, O. Makowski, R. Marassi, Electrochim. Acta 48 (2003) 4261.
[14] X. Hao, D.T. Schwartz, Chem. Mater. 17 (2005) 5831.
[15] E. Laviron, J. Electroanal. Chem. 101 (1979) 19.
[16] T.R.I. Cataldi, G.E. De Benedetto, J. Electroanal. Chem. 458 (1998) 149.
[17] Y. Lin, X. Cui, Chem. Commun. 5 (2005) 2226.
[18] W. Chen, X.H. Xia, Adv. Funct. Mater. 17 (2007) 2943.
[19] S.D. Rassat, J.H. Sukamto, R.J. Orth, M.A. Lilga, R.T. Hallen, Sep. Purif. Technol. 15 (1999) 207.
[20] P. Wang, Y. Yuan, X. Jing, G. Zhu, Talanta 53 (2001) 863.

Talanta 80 (2009) 544–550

Contents lists available at ScienceDirect

Talanta

journal homepage: www.elsevier.com/locate/talanta

Borate complexation-assisted field-enhanced sample injection for on-line preconcentration of *cis*-diol-containing compounds in capillary electrophoresis

Jing Liu, Feifei Zhu, Zhen Liu*

Key Lab of Analytical Chemistry for Life Science, School of Chemistry and Chemical Engineering, Nanjing University, 22 Hankou Road, Nanjing 210093, Jiangsu, China

ARTICLE INFO

Article history:
Received 11 May 2009
Received in revised form 3 July 2009
Accepted 13 July 2009
Available online 21 July 2009

Keywords:
cis-Diol-containing compounds
Borate complexation
Field-enhanced sample injection
On-line preconcentration
Capillary electrophoresis

ABSTRACT

A new on-line preconcentration technique called borate complexation-assisted field-enhanced sample injection (BCA-FESI) was proposed for preconcentrating *cis*-diol-containing compounds (CDCCs) in capillary electrophoresis (CE). The principle relies on amplification of the difference in the electrophoretic mobilities of CDCC in sample matrix and background electrolyte (BGE) through complexation of CDCC with borate in a sample matrix of basic pH and dissociation of the complex in a BGE of acidic pH. Meanwhile, CDCC and borate ions electro-injected into the capillary are finally in neutral state, which maintains the pre-filled low conductivity zone and thus allows for longer injection time. With catechol as a test compound, the principle and effectiveness of BCA-FESI was verified. As compared to conventional sample injection, BCA-FESI allowed for sensitivity enhancement of 1850-fold. The established method was further evaluated with three catechins, including (−)-epicatechin gallate (ECG), (−)-gallocatechin gallate (GCG), and (−)-epigallocatechin (EGC), in a standard mixture of trace content. The limit of detection (LOD) was found to be 1.4, 3.8, 17.5 nM (S/N = 3) for ECG, GCG, EGC, respectively. Finally, the BCA-FESI method was applied to a real sample of diluted tea beverage, in which the three catechins were detected.

© 2009 Elsevier B.V. All rights reserved.

1. Introduction

CE has become an important separation and analytical tool because of its significant advantages of high efficiency, short analysis time, low sample consumption and multiple modes. However, the major limitation of CE lies in insufficient concentration sensitivity with UV absorption detection due to its limited optical path and small sample volume. Many attempts have been focused on how to overcome this drawback. In addition to alteration of the hardware configuration, including the use of bubble-cell [1], Z-shaped capillary [2], mass spectrometry [3] and laser-induced fluorescence detection [4], on-line sample preconcentration [5] is a practical, simple and effective strategy to improve the detection sensitivity of CE. According to the focusing mechanism, the on-line sample preconcentration techniques can be grouped into four major principles: (1) sample stacking [6–8], (2) sweeping [9,10], (3) pH junction [11,12], and (4) transient isotachophoresis [13].

Sample stacking is in common use, on the basis of which several other modes have been developed, such as large-volume sample stacking (LVSS) and field-enhanced sample injection (FESI). The basic principle of sample stacking relies on conductivity-induced difference in the velocities of analytes in two distinct zones in the capillary: the sample zone, which is of low conductivity, and the remaining zone of BGE, which is of high conductivity. The analytes migrate at higher velocities in the sample zone but slow down when migrating into the BGE zone. Thus a relatively large sample plug can be introduced hydrodynamically into the capillary, and under an electric field applied to the capillary, the analytes are focused at the boundary between the sample zone and BGE. From this principle, the higher the difference in the conductivity between the two zones, the higher the concentration efficiency is. In practice, however, BGE of too high conductivity should be avoided in order to prevent excess Joule-heating. Moreover, generally the maximum sample volume allowed is not very large (usually 10% or so). Further increase in injected sample volume failed to focus the sample zone effectively, because the electric field enhancement gained across the sample zone becomes lower and ions migrating into this zone from BGE apparently increase the conductivity of the sample zone. A strategy for injecting a larger sample volume and keeping effective sample stacking is to remove the sample matrix during the process of sample stacking. Burgi and Chien [14] and other groups [15–17] proposed the technique LVSS, in which a reversed electroosmotic flow (EOF) is used to pump the sample matrix out of the capillary. However, the disadvantage of this method is the difficulty to exactly monitor the current change during the stacking process, which leads to irreproducible results. In regular sample stacking and LVSS, the sensitivity enhancement is limited by the sample volume injected. As the maximum sample volume allowed

* Corresponding author. Tel.: +86 25 8368 5639; fax: +86 25 8368 5639.
E-mail address: zhenliu@nju.edu.cn (Z. Liu).

0039-9140/$ – see front matter © 2009 Elsevier B.V. All rights reserved.
doi:10.1016/j.talanta.2009.07.023

is usually about 30–50% of the total capillary length, the sensitivity improvement is not very high, only 1–2 orders of magnitude. As a comparison, FESI is a more effective solution to reach higher sensitivity improvement. In FESI, the velocity difference of analytes between the low-conductivity zone and the high-conductivity zone is dramatically increased by amplifying the electric field at the capillary inlet. A short plug of low conductivity solution (usually water) is introduced hydrodynamically into the capillary inlet and the sample prepared in dilute buffer is injected electrokinetically. The electric field strength established across the low-conductivity zone is enhanced by a factor of up to several hundred times relative to that in normal CE [18]. FESI allows for pumping a large amount of analytes into a very narrow zone, obviating the limit on the sample volume injected. By FESI, the sensitivity can be improved by 2–3 orders of magnitude without degradation of separation efficiency. According to the principle of sample stacking, if difference in the velocity of analytes between the low-conductivity zone and the high-conductivity zone can be effectively enlarged by any means, then the detection sensitivity can be further improved [11].

It has been known that borate and boronate can form stable complexes with *cis*-diol-containing compounds (CDCCs) [19–22]. Boric acid and boronic acids form covalent bonds with 1,2- or 1,3-*cis*-diols to generate five- or six-membered cyclic esters in non-aqueous or basic aqueous media. When the pH of the environment is changed to an acidic condition, the complexation reversibly releases boronic acids and CDCC. This reversible specific chemical reaction leads to the successful applications in chemical sensing [23–26] and boronate affinity chromatography [27–32]. Boronate complexation-based new chromatographic techniques have been developed [33–36]. In CE, borate complexation has been a useful strategy for the separation of carbohydrates [22,37–39]. Also, it has been used as a carrier for preconcentrating of CDCC in sweeping [40,41] and sweeping-pH junction [42], where borate is present only in the BGE.

In this study, we propose a new on-line preconcentration technique, borate complexation-assisted FESI (BCA-FESI), for preconcentrating CDCC, by taking advantage of the pH-dependent reversible feature of the borate complexation as an additional means to increase the difference in the velocity of analytes in the low-conductivity zone and the high-conductivity zone. The principle is schematically illustrated in Fig. 1. CDCC are dissolved in borate buffer of low conductivity and high pH, while the BGE is of high conductivity and low pH. In the high pH sample matrix, CDCC associate with borate and become negatively charged, and thereby gain faster electrophoretic velocities as compared with the case without borate in the matrix; when the complexes migrate into the low-pH BGE, CDCC dissociate from the complexes and become completely neutral and therefore gain a zero velocity. Thus, the concentration efficiency of FESI can be effectively improved by the borate complexation. On the other hand, borate ions migrating to the water plug-BGE boundary from the sample matrix become boric acid due to the low local pH. The final neutral state of borate and CCDC, especially the former as it is plentiful in the sample matrix, helps maintain the water plug of low conductivity during the electro-injection process and thereby allows for injection of a larger amount of analytes. Due to the neural state feature of the preconcentrated analytes in BCA-FESI, separation mode for neutral analytes, such as micellar electrokinetic chromatography (MEKC) or capillary electrochromatography (CEC), is required for consequent separation of the preconcentrated analytes. In this study, we demonstrate the principle of BCA-FESI through combining it with MEKC (in which sweeping is involved, but is not the essential preconcentration effect). Due to the presence of BCA-FESI, the MEKC separation was performed under an acidic pH, which is different from general MEKC where a basic pH BGE is used.

Catechol, a 1,2-*cis*-diol-comtaining compound, was first selected as the test analyte to demonstrate the principle and to investigate the experimental factors that influenced the preconcentration efficiency, such as the water plug length and the sample injection time. The results indicate that the presence of borate complexation can apparently improve the sensitivity enhancement of FESI. Finally, the established method was applied to the preconcentration of three catechins in standard mixture solution of trace content and in diluted tea beverage.

2. Materials and methods

2.1. Instrumentation

CE experiments were performed on a PACE/MDQ system (Beckman Coulter, Fullerton, CA, USA) equipped with a DAD detector. The detection wavelength was set at 214 nm, and the temperature was kept constant at 25 °C. A bare fused-silica capillary (Yongnian Optical Fiber Factory, Hebei, China) of 30 cm (20 cm to detector) × 50 μm i.d. was used for the separations. The length of pre-filled water plug was calculated with the software CE expert from Beckman Coulter according to the experimental parameters used, with calibration using the measured travel time of a neutral marker (methanol or other organic solvent) from the capillary inlet to the detection window at the pressure under use. Dimethyl sulfoxide (DMSO) was used as EOF marker.

2.2. Chemicals

Catechol was purchased from Alfa-Aesar (Tianjin, China), while (−)-epicatechin gallate (ECG), (−)-epigallocatechin (EGC) and (−)-gallocatechin gallate (GCG) were from Sigma-Aldrich (St. Louis, MO, USA). Chemical structures for the three catechins are given in Fig. 2. Sodium dodecylsulfate (SDS) was bought from Bio-Rad (California, USA). Other chemicals were from Sinopharm Chemical Reagent Co. Ltd (Shanghai, China). All chemicals used were of analytical grade or higher. Ultrapure water produced by a Milli-Q advantage A10 system (Millipore, Milford, MA, USA) was used to prepare all solutions. Suntory Wulong Tea beverage (non-sugar containing) was bought from local supermarket in Nanjing.

2.3. Electrolyte and sample preparation

When measuring the effective mobility of catechol under different pH and sample matrix-BGE systems, two kinds of buffer were used: (1) 0.2 M boric acid containing 1 mM sodium dihydrogen phosphate and 6 mM sodium metabisulfite; (2) 5 mM sodium dihydrogen phosphate buffer containing 6 mM sodium metabisulfite. Borate buffers of 5, 12.5, 25, 50, 100, and 200 mM at pH 9.5 containing 6 mM sodium metabisulfite were used to investigate the effect of borate concentration on the effective mobility of catechol.

The non-micellar BGE was 50 mM phosphate buffer containing 100 mM sodium chloride, pH 2.0. The micellar BGE, contained 50 mM phosphate, 50 mM sodium chloride and 100 mM SDS, pH 2.0, the conductivity of which was measured to be the same as that of non-micellar BGE. For the separation of catechins, the non-micellar BGE and micellar BGE were prepared in a similar way with slight modification, where the concentrations of phosphate buffer and SDS were adjusted. All buffers were adjusted to the desired pH by sodium hydroxide or hydrochloric acid, and sonicated for 15 min in a water bath before use.

The stock solutions of catechol (5 mg/mL), ECG (1 mg/mL), EGC (1 mg/mL), and GCG (1 mg/mL) were prepared with ultrapure water. Then they were diluted by different sample matrix under various conditions. Sodium metabisulfite was added to the sample matrices

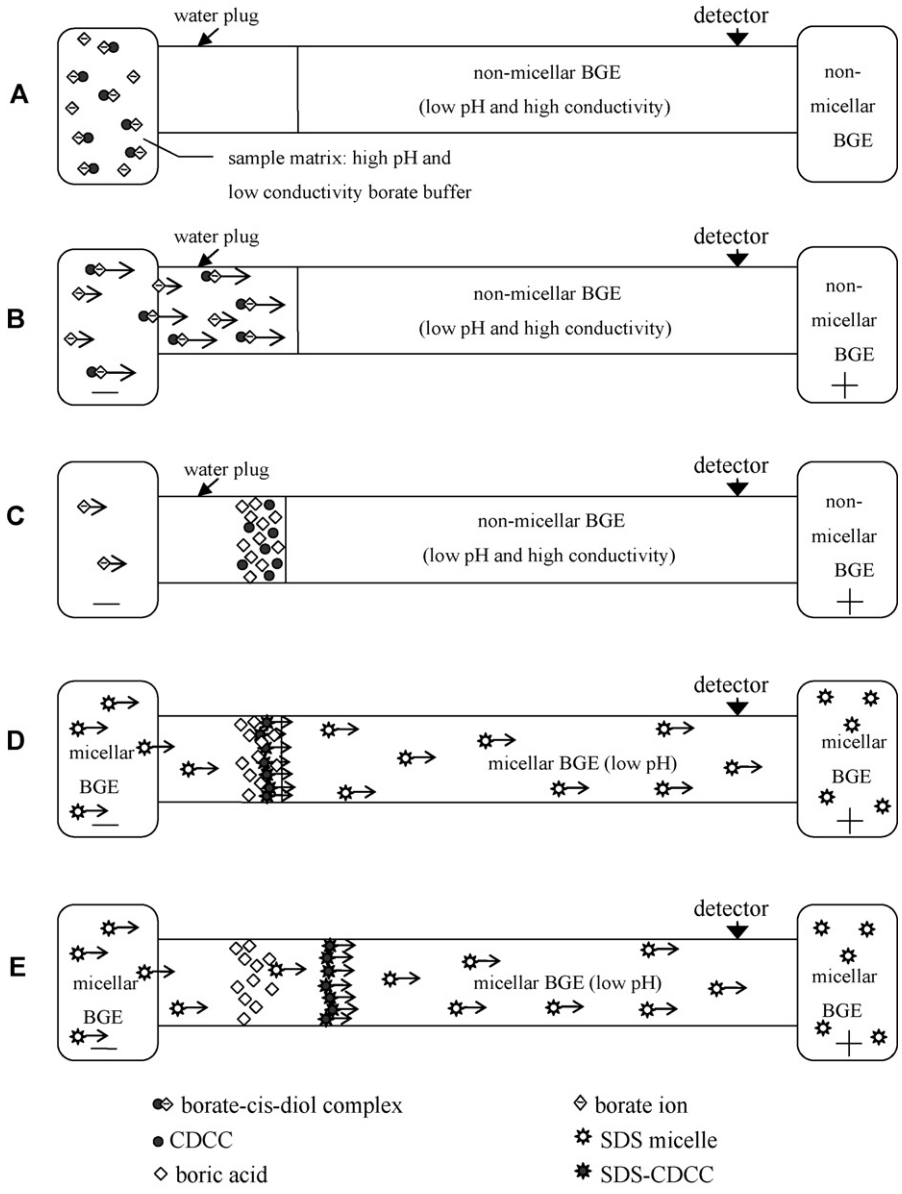


Fig. 1. Schematic of the principles of BCA-FESI (A–C) and its combination with MEKC (D and E): (A) a certain length of water plug is hydrodynamically injected into the capillary which is pre-filled with non-micellar BGE of low conductivity and high pH; the sample is prepared with borate buffer of high conductivity and low pH, and therefore contains the CDCC–borate complexes; (B) the complexes and excessive borate ions are electrokinetically injected into the capillary by applying a negative voltage, which migrate forward quickly within the water plug due to the enhanced electric field; (C) when they reach the boundary between the water plug and the non-micellar BGE, the complexes dissociate into free borate and free CDCC, and both borate and CDCC are neutralized and consequently stack into a narrow zone at the boundary; (D) the solutions at both capillary ends are replaced by micellar BGE, and a negative voltage is applied to the capillary for MEKC separation; the anionic SDS micelles sweep through the stacked sample zone and further preconcentrate the analytes; (E) the stacked analytes are separated in MEKC mode.

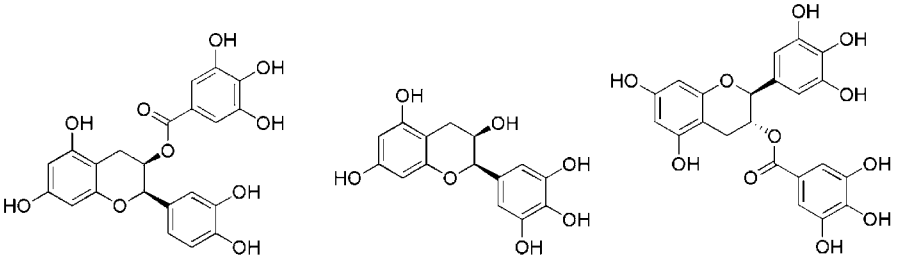


Fig. 2. Chemical structures of the three catechins used in this study.

and the BGE of basic pH as an antioxidant to avoid oxidation of CDCC in alkaline conditions.

2.4. CE conditions

At the beginning of each day, the capillary was preconditioned sequentially with 1.0 M sodium hydroxide, 0.1 M sodium hydroxide, water, and the separation buffer for 5 min each. Between runs the capillary was rinsed with 0.1 M sodium hydroxide, water, and the separation buffer, for 2 min each.

The BCA-FESI-MEKC process included three steps: (1) a certain length of water plug was first hydrodynamically introduced into the capillary, which was pre-filled with non-micellar BGE; (2) a constant negative voltage (−3.5 kV) was applied for the electrokinetic injection; (3) finally, a negative voltage (−12 kV) was applied to the capillary for separation, with the micellar BGE at both ends of capillary. Samples once used were replaced with fresh ones after each electro-injection, in order to avoid sample exhaustion.

3. Results and discussion

3.1. Effect of borate complexation on the electrophoretic mobility

Since the principle of BCA-FESI is based on the enhancement of the electrophoretic mobility of the analyte through borate complexation, the effect of borate complexation was first investigated. Fig. 3 illustrated the electrophoretic mobility of catechol in different sample matrix-BGE systems under different pH in the range of 8.5–11.0. When the sample matrix-BGE system was a borate–borate combination, the electrophoretic mobility of catechol kept nearly constant within the pH range investigated (trace A). When the BGE was changed to a phosphate buffer, the electrophoretic mobility of catechol was apparently reduced, which increased as the pH was increased (trace B). When sample matrix-BGE system was switched to a phosphate–phosphate combination, the electrophoretic mobility of catechol was further reduced, which also increased as elevating the pH (trace C). Clearly, as compared with

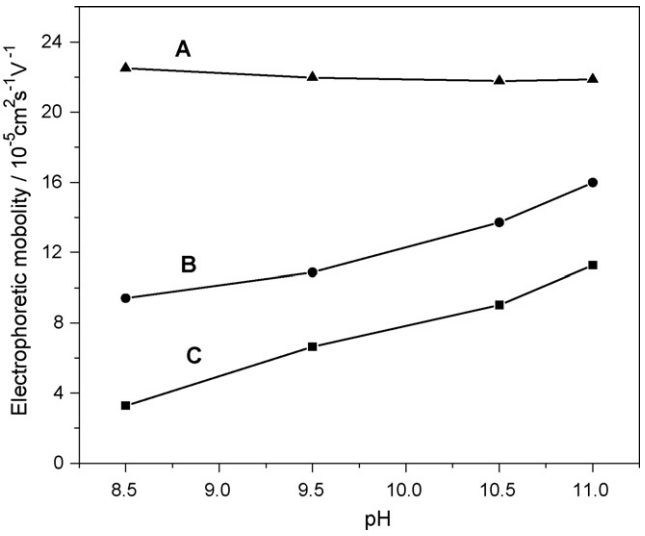


Fig. 3. Dependence of effective electrophoretic mobility of catechol on the pH in different sample matrix-BGE systems. Sample, 0.25 mg/mL catechol; sample matrix: (A) and (B) 0.2 M borate buffer containing 1 mM sodium dihydrogenphosphate and 6 mM sodium metabisulfite, (C) 5 mM phosphate buffer containing 6 mM sodium metabisulfite; BGE: (A) 0.2 M borate buffer containing 1 mM sodium dihydrogenphosphate and 6 mM sodium metabisulfite, (B) and (C) 5 mM phosphate buffer containing 6 mM sodium metabisulfite. Both sample matrix and BGE are at the same pH values ranging from 8.5 to 11.0. Sample injection, 0.3 psi × 3 s from the outlet end of the capillary; applied voltage, −20 kV.

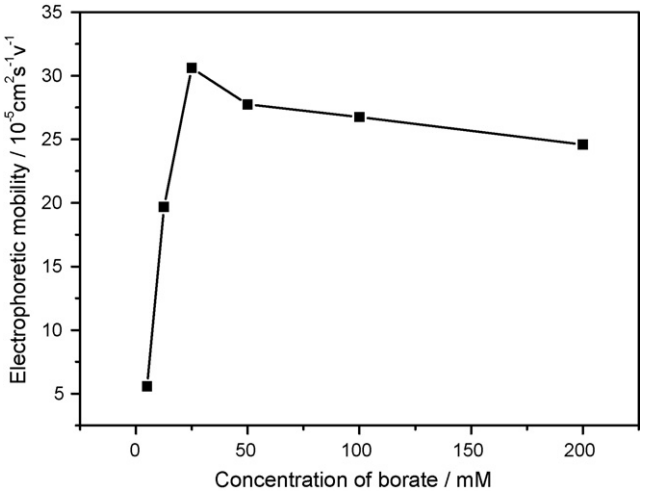


Fig. 4. Effect of borate concentration on effective electrophoretic mobility of catechol. Sample, 0.25 mg/mL catechol; sample matrix is the same as BGE; BGE, borate buffer (pH 9.5) with concentration ranging from 5, 12.5, 25, 50, 100, to 200 mM. Other conditions are the same as in Fig. 3.

that in the borate-free matrix-BGE system, the electrophoretic mobility of catechol can be apparently enhanced by addition of borate into the sample matrix. Although a higher pH favors the absolute electrophoretic mobility, pH 9.5 was chosen for further investigation because borate buffer has a highest buffer capacity among the pH values examined, at which the electrophoretic mobility of catechol was amplified by a factor of 1.6 by borate complexation.

3.2. Effect of borate concentration on the electrophoretic mobility

The influence of borate concentration on the electrophoretic mobility of catechol was investigated through changing the borate concentration in both the sample matrix and the BGE. As shown in Fig. 4, the electrophoretic mobility catechol increased as elevating the borate concentration from 5 to 25 mM, and then gradually slightly decreased as further increasing the borate concentration. Thus, 25 mM was chosen as the sample matrix for further investigate to ensure the maximum enhancement of the electrophoretic mobility.

3.3. Dissociation of borate complex in low-pH buffer

A prerequisite of BCA-FESI is that when the CDCC–borate complexes migrate to the BGE of acidic pH, they can dissociate quickly; otherwise, the preconcentration efficiency is poor. To confirm such a precondition, normal MEKC experiments were carried out with low pH BGE and high pH borate and phosphate matrices. The phosphate matrix was used as a comparison. If CDCC–borate complexes formed at high pH can dissociate into free CDCC and free borate ions when they encounter a low pH BGE, the peaks observed should have the same peak width as that in the control experiment. This is verified experimentally, as shown in Fig. 5.

3.4. Effect of water plug length

The water plug pre-injected plays a key role in FESI, which provides an enhanced electric field for the electro-injection. A general equation has been proposed to describe the relationship between the analyte amount injected and the experimental parameters in FESI [8]. According to this equation, the water plug length should as short as possible for the largest injection amount. However, if the water plug is too short, the introduced ionic analyte will increase

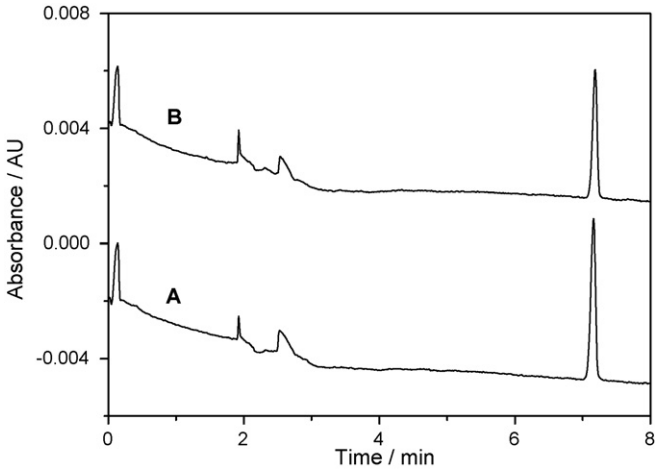


Fig. 5. Electrophoretograms of catechol dissolved in different sample matrix in MEKC mode under an acidic condition. Sample, 0.25 mg/mL catechol; sample matrix: (A) 25 mM borate and 6 mM sodium metabisulfite, pH 9.5, (B) 25 mM phosphate and 6 mM sodium metabisulfite, pH 9.5; sample injection, 0.3 psi × 3 s; the capillary is filled with non-micellar BGE-containing 50 mM phosphate buffer and 100 mM NaCl, pH 2.0. After injection, the vials at both ends are changed into micellar BGE-containing 50 mM sodium dihydrogenphosphate, 50 mM NaCl, and 100 mM SDS, pH 2.0. Separation voltage is −12 kV.

the conductivity of the water plug quickly, and as a result the stacking process will become feeble or even stop soon. Therefore, an optimal water plug length, which is usually millimeters in length, can be found experimentally. The effect of the water plug length was investigated. As illustrated in Fig. 6, there was an optimal water plug length under the conditions used, 2.4 mm (the corresponding injection pressure and time were 0.5 psi and 5 s), in terms of the dependence of the corrected peak area (peak area/migration time) and corrected peak height (peak height/migration time) for the preconcentrated analyte. This trend is in agreement with that reported previously [8].

3.5. *Effect of sample injection time and maintaining low conductivity*

The amount of analyte injected in FESI is dependent on the sample injection time if other experimental parameters, such as water plug length and injection voltage, are fixed. As mentioned above, in regular FESI, the water plug must be short enough, usually millimeters long. As stated in earlier context, the final neutral states of borate ion and analyte in BCA-FESI allow them serve as low conductivity maintainers, thus BCA-FESI permits longer sample injection time as compared with regular FESI. To demonstrate such a phenomenon, two water plugs of different length, 2.4 and 12.0 mm, were used for investigation on the effect of sample injection time. As shown in Fig. 7, at both water plugs, there was an optimal injection time, in terms of dependences of the corrected peak areas and the corrected peak heights of catechol on the injection duration. This means that beyond the optimal value, one cannot further improve the sensitivity by extending the injection time. However, BCA-FESI significantly extended the optimal injection time through using a longer water plug, from 15 min at 2.4 mm to 35 min at 12.0 mm, as can be seen in Fig. 7. Accordingly, the sensitivity enhancement was improved by use of the longer water plug. Under the optimal injection time at the water plug of 2.4 mm, the sensitivity enhancement factor was calculated to be 1080 according to the following equation:

$$\alpha = \frac{C_1 H_2}{C_2 H_1} \quad (1)$$

where α is the sensitivity enhancement factor; C_1 and C_2 are the analyte concentration used for conventional injection and on-line sample preconcentration, respectively; H_1 and H_2 are corresponding corrected peak height (peak height/migration time). On contrast, the value obtained at the water plug of 12.0 mm was 1850, which was nearly doubled.

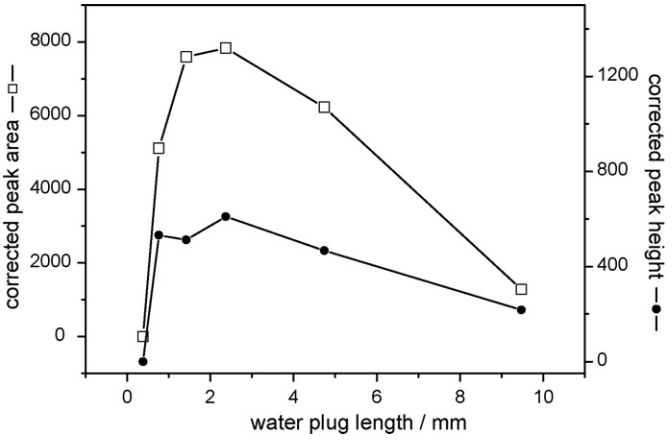


Fig. 6. Effect of water plug length on BCA-FESI-MEKC. Sample, 0.25 μg/mL catechol dissolved in 25 mM borate and 6 μM sodium metabisulfite, pH 9.5; injection, −3.5 kV × 90 s; the length of water plug, 0.4, 0.8, 1.4, 2.4, 4.7 and 9.5 mm. Other conditions are the same as in Fig. 5.

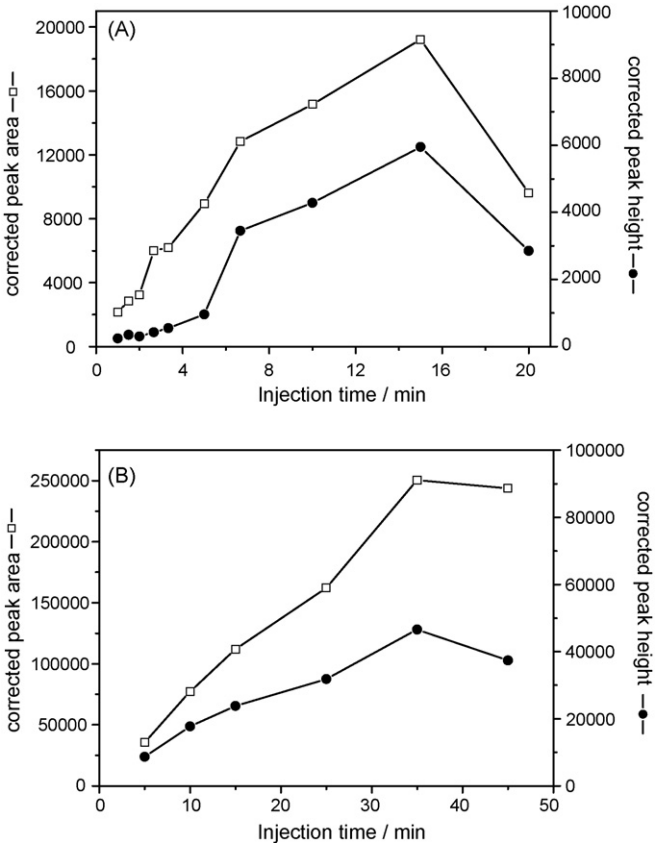


Fig. 7. Dependence of corrected peak area or peak on electrokinetic injection time with different length of water plug in BCA-FESI-MEKC. Sample, 0.25 μg/mL catechol dissolved in 25 mM borate and 6 μM sodium metabisulfite, pH 9.5; water plug length: (A) 2.4 mm; (B) 12.0 mm; injection voltage, −3.5 kV; injection time: (A) 1–20 min; (B) 5–45 min. Other conditions are the same as in Fig. 5.

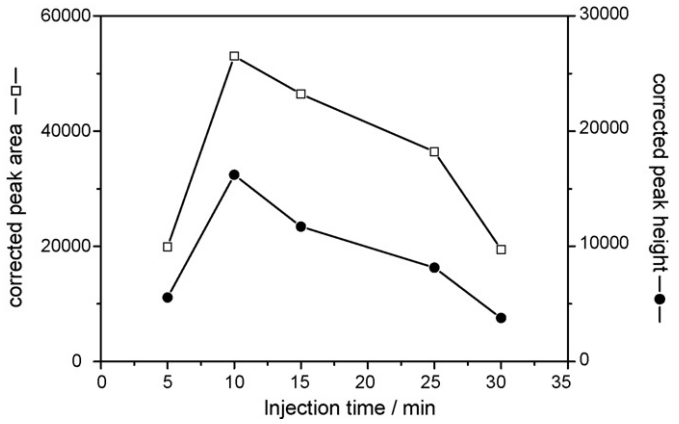


Fig. 8. Dependence of corrected peak area or peak on electrokinetic injection time in regular FESI-MEKC. Sample, 0.25 μg/mL catechol; water plug length, 12.0 mm; injection voltage, −3.5 kV; injection time, 5–45 min; sample matrix, 8 mM sodium metabisulfite and 6 μM sodium metabisulfite, pH 9.5. Other conditions are the same as in Fig. 5.

3.6. Comparison of BCA-FESI with regular FESI

The effectiveness of borate complexation assistance was investigated by comparison of the optimal sample injection time and the sensitivity enhancement factor calculated according to corrected peak height in BCA-FESI and regular FESI under otherwise identical conditions. In regular FESI, the optimal sample injected time was only 10 min, as can be seen from Fig. 8, and the sensitivity enhancement factor was 400. As a comparison, in BCA-FESI, the optimal sample injected time was 35 min and the sensitivity enhancement factor was 1850. The sensitivity in BCA-FESI was further improved by 4.6-fold on the basis of the best results of regular FESI. Clearly, the presence of borate complexation assistance allows for longer sample injection duration and therefore provides higher preconcentration efficiency, which can be supported by the electropherograms shown in Fig. 9.

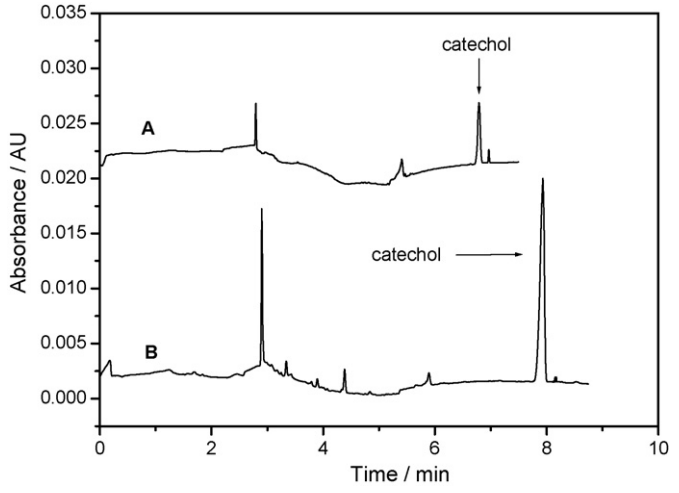


Fig. 9. Comparison of the preconcentration of catechol by regular FESI-MEKC (A) and BCA-FESI-MEKC (B). Sample: (A) 0.25 μg/mL catechol dissolved in 8 mM phosphate and 6 μM sodium metabisulfite, pH 9.5, (B) 0.25 μg/mL catechol dissolved in 25 mM borate and 6 μM sodium metabisulfite, pH 9.5; sample injection: electro-injection at −3.5 kV for 10 min (A) and 35 min (B), with a pre-filled water plug of 12.0 mm. Other conditions are the same as in Fig. 5.

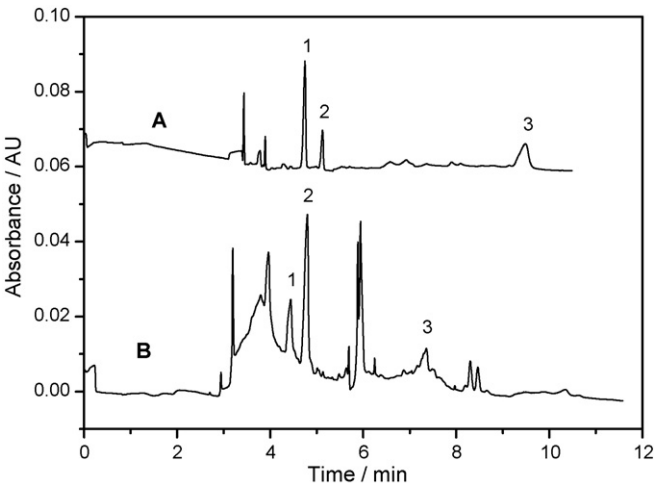


Fig. 10. BCA-FESI-MEKC of catechin standards (A) and real sample (B). Sample (A) a standard mixture containing 0.2 μg/mL ECG, 0.2 μg/mL GCG, and 0.4 μg/mL EGC; (B) 50-fold diluted tea beverage; sample matrices are both 25 mM borate and 0.24 mM sodium metabisulfite, pH 9.5; water plug length, 12.0 mm; injection, −3.5 kV × 35 min; the capillary is filled with non-micellar BGE-containing 37.5 mM phosphate buffer and 75 mM NaCl, pH 2.0. After injection, the vials at both ends are changed into micellar BGE-containing 50 mM sodium dihydrogenphosphate, 75 mM NaCl, and 50 mM SDS, pH 2.0. Other conditions are the same as in Fig. 4. Peak identities: 1, ECG; 2, GCG; 3, EGC.

3.7. Application to catechins and real sample

Catechins, polyphenolic compounds that contain *cis*-diol groups, are main components of tea leaves. More interestingly, catechins are found to be able to reduce or delay the risk of some major health problems such as stroke, aging, cancer and diabetes [43–47]. So it is important to determine the catechins level in tea products for quality control. Three catechins, including ECG, GCG, ECG, were used as test compounds to investigate the feasibility of the established methods for more complicated samples and real samples. Catechin standards in diluted sample that contains borate matrix at high pH were first examined. As shown in Fig. 10A, the three catechins were baseline separated with sharp peak shape and detectable at trace content level. The LOD was found to be 1.4, 3.8, 17.5 nM (S/N = 3) for ECG, GCG, EGC, respectively. Finally, this method was applied to a 50-fold diluted Wulong tea beverage, and the three catechins were clearly found in this real sample.

4. Concluding remarks

In this paper, a new on-line preconcentration method, BCA-FESI, has been developed and validated for preconcentrating CDCC in CE. By virtue of the assistance of borate complexation, the preconcentration efficiency of CDCC can be effectively improved on the basis of regular FESI. As compared with conventional FESI under optimized conditions, the sensitivity improvement is 4.6-fold higher. Although such an enhancement is not outstanding, it is of significance since it is on the basis of the best result of conventional FESI. The overall sensitivity improvement by BCA-FESI relative to conventional injection is usually of 3 orders of magnitude. The distinct features of BCA-FESI are its longer pre-filled water plug and longer sample injection time. As a great number of biologically active compounds contain one or more vicinal diol groups, such as carbohydrates, nucleotides, theaflavins, some vitamins and some flavonoids, BCA-FESI can be a promising on-line sample preconcentration technique for these compounds.

Acknowledgments

We gratefully acknowledge the financial support of the Key Grant (No. 20727004) from the National Natural Science Foundation of China, the Key Grant of 973 Program (No. 2007CB914102), the International Science & Technology Cooperation Grant (2008DFA01910) from the Ministry of Science and Technology of China, and the General Grant (No. KB2008258) from the Natural Science Foundation of Jiangsu Province to Z.L.

References

[1] Z. Liu, K. Otsuka, S. Terabe, J. Chromatogr. A 961 (2002) 285–291.
[2] S.E. Moring, R.T. Reel, R.E.J. van Soest, Anal. Chem. 85 (1993) 3454–3459.
[3] D. Figeys, R. Aebersold, Electrophoresis 19 (1998) 885–892.
[4] Y.F. Cheng, N.J. Dovichi, Science 242 (1988) 562–564.
[5] S.L. Simpson Jr., J.P. Quirino, S. Terabe, J. Chromatogr. A 1184 (2008) 504–541.
[6] A. Macia, F. Borrull, C. Aguilar, M. Calull, Electrophoresis 24 (2003) 2779–2787.
[7] S.H. Liu, Q.F. Li, X.G. Chen, Z.D. Hu, Electrophoresis 23 (2002) 3392–3397.
[8] Z. Liu, K. Otsuka, S. Terabe, Electrophoresis 22 (2001) 3791–3797.
[9] J.P. Quirino, S. Terabe, Science 282 (1998) 465–468.
[10] J.P. Quirino, S. Terabe, Anal. Chem. 580 (1999) 339–344.
[11] P. Britz-McKibbin, D.D.Y. Chen, Anal. Chem. 72 (2000) 1242–1252.
[12] P. Britz-McKibbin, G.M. Behault, D.D.Y. Chen, Anal. Chem. 72 (2000) 1729–1735.
[13] Z.K. Shihabi, Electrophoresis 23 (2002) 1628–1632.
[14] D.S. Burgi, R.L. Chien, Anal. Chem. 64 (1992) 1046–1050.
[15] M.W.F. Nielen, Trends Anal. Chem. 12 (1993) 345–356.
[16] D. Martinez, F. Borrull, M. Calull, J. Chromatogr. A 788 (1997) 185–193.
[17] M. Albert, L. Debusschere, C. Demesmay, J.L. Rocca, J. Chromatogr. A 757 (1997) 281–289.
[18] C.X. Zhang, W. Thormann, Anal. Chem. 68 (1996) 2523–2532.
[19] J.P. Advis, L. Hernandez, N.A. Guzman, Peptide Res. 2 (1989) 389–394.
[20] N.A. Guzman, C.M. Berck, L. Hernandez, J.P. Advis, J. Liq. Chromatogr. 13 (1990) 3843–3858.
[21] S. HGffstetter-Kuhn, A. Paulue, E. Gassmann, E.M. Widmer, Anal. Chem. 63 (1991) 1541–1547.
[22] S. Honda, S. Iwase, A. Makino, S. Fujiwara, Anal. Biochem. 176 (1989) 72–77.
[23] W.H. Wu, C. Greene, Clin. Chem. 32 (1986) 1193–11193.
[24] J.Y. Yoon, A.W. Czarnik, J. Am. Chem. Soc. 114 (1992) 5874–5875.
[25] M. Takeuchi, T. Imada, S. Shinkai, J. Am. Chem. Soc. 118 (1996) 10658–10659.
[26] E. Shoji, M.S. Freund, J. Am. Chem. Soc. 123 (2001) 3383–3384.
[27] R. Flueckiger, T. Woodtli, W. Berger, Diabetes 33 (1984) 73–76.
[28] C.J. Hawkins, M.F. Lavin, D.L. Parry, I.L. Ross, Anal. Biochem. 159 (1986) 187–190.
[29] S. Hjerten, J.P. Li, J. Chromatogr. 500 (1990) 543–553.
[30] X.C. Liu, W.H. Scouten, Methods Mol. Biol. 147 (2000) 119–128.
[31] W.L. Roberts, Clin. Chem. 53 (2007) 142–143.
[32] Q. Zhang, N. Tang, J.W.C. Brock, H.M. Mottaz, J. Proteome Res. 6 (2007) 2323–2330.
[33] J. He, Z. Liu, P. Dou, J. Liu, L. Ren, H.Y. Chen, Talanta 79 (2009) 746–751.
[34] L. Ren, Z. Liu, M. Dong, M. Ye, H. Zou, J. Chromatogr. A 1216 (2009) 4768–4774.
[35] P. Dou, L. Liang, J. He, Z. Liu, H.Y. Chen, J. Chromatogr. A, in press, doi:10.1016/j.chroma.2009.04.040.
[36] L. Ren, Z. Liu, Y. Liu, P. Dou, H.Y. Chen, Angew. Chem. Int. Ed., in press, doi:10.1002/anie.200902469.
[37] P.J. Oefner, C. Chiesa, G. Bonn, C. Horvath, J. Capil. Electrophor. 1 (1994) 5–26.
[38] P.J. Oefner, A.E. Vorndran, E. Grill, C. Huber, G.K. Bonn, Chromatographia 34 (1992) 308–316.
[39] S. Suzuki, S. Honda, Electrophoresis 19 (1998) 2539–2560.
[40] M.J. Markuszewski, P. Britz-McKibbin, S. Terabe, K. Matsuda, T. Nishioka, J. Chromatogr. A 989 (2003) 293–301.
[41] J.P. Quirino, S. Terabe, Chromatographia 53 (2001) 285–289.
[42] P. Britz-McKibbin, K. Otsuka, S. Terabe, Anal. Chem. 74 (2002) 3736–3743.
[43] K.Y. Chyu, S.M. Babbidge, X. Zhao, R. Dandillaya, Circulation 109 (2004) 2448–2453.
[44] A. Mittal, M.S. Pate, R.C. Wylie, T.O. Tollefsbol, S.K. Katiyar, Int. J. Oncol. 24 (2004) 703–710.
[45] S. Katiyar, C.A. Elmets, S.K. Katiyar, J. Nutr. Biochem. 18 (2007) 287–296.
[46] H. Gradisar, P. Pristovsek, A. Plaper, R. Jerala, J. Med. Chem. 50 (2007) 264–271.
[47] T. Murase, S. Haramizu, N. Ota, T. Hase, Am. J. Physiol. 295 (2008) R281–R289.

Talanta 80 (2009) 551–558

Contents lists available at ScienceDirect

Talanta

journal homepage: www.elsevier.com/locate/talanta

Dielectrophoresis assisted immuno-capture and detection of foodborne pathogenic bacteria in biochips

Liju Yang*

Biomanufacturing Research Institute and Technology Enterprise (BRITE), and Department of Pharmaceutical Sciences, North Carolina Central University, 1801 Fayetteville St, Durham, NC 27707, USA

ARTICLE INFO

Article history:
Received 30 April 2009
Received in revised form 12 July 2009
Accepted 13 July 2009
Available online 21 July 2009

Keywords:
Bacteria detection
Dielectrophoresis
Immuno-capture
Immunoassay
Biochip

ABSTRACT

This study integrated dielectrophoresis (DEP) with non-flow through biochips to enhance the immuno-capture and detection of foodborne pathogenic bacteria. It demonstrated two major functions provided by DEP to improve the chip performance: (i) concentrating bacterial cells from the suspension to different locations on the chip surface by positive and negative DEP; (ii) making the cells in close contact with the immobilized antibodies on the chip surface so that immuno-capture efficiency can be dramatically enhanced.

The microchip achieved the immuno-capture efficiencies of ~56.0% and ~64.0% to *Salmonella* cells with 15 and 30 min DEP, respectively, which were considerably higher than those of ~10.4% and ~17.6% for 15 and 30 min immuno-capture without DEP. The immuno-captured bacterial cells were detected by the sandwich format ELISA on the chips. The final absorbance signals were enhanced by DEP assisted immuno-capture by 64.7–105.2% for the samples containing 10^3–10^6 cells/20 μl. The integration of DEP with the biochips has the potential to advance the chip-based immunoassay methods for microbial detection.

© 2009 Elsevier B.V. All rights reserved.

1. Introduction

Foodborne pathogens have been a serious threat to the public health and food safety for decades and remain one of the major concerns of our society. In the United States of America, foodborne pathogens cause an estimated 76 million cases of foodborne diseases, resulting in 325,000 hospitalizations and more than 5000 deaths each year [1]. Today, there are more than 250 known diseases caused by different foodborne pathogenic microorganisms. Pathogenic bacteria are the most common foodborne pathogens, accounting for 91% of the total outbreaks of foodborne diseases in the USA [2,3].

Effective detection of pathogens in food products is the first control point for the prevention of fooodborne diseases. Although traditional microbiological methods have been a gold standard practice for the detection and identification of pathogens in food for nearly one century and continue to be a reliable standard for ensuring food safety, these methods are time-consuming and labor intensive, and are therefore not suitable for modern food quality assurance to make a timely response to possible risks. As a result, over the past 25 years, numerous rapid methods have been studied with the main purpose of reducing the assay time. Various biosensors and biochips have gained popularity in this field due to their rapid detection speed, high sensitivity, and reliability. Many biosensors and biochips are based on derived sandwich immunoassay formats, in which the immuno-capture of the target cells by the immobilized antibodies on the sensor surface is the critical step. This step determines the amount of the target cells bound to the sensor surface, and thus determine the sensitivity of the method. The detection limits of these biosensors/biochips typically range from 10^2 to 10^7 cells/ml with detection times ranging from tens of minutes to several hours [4–7].

It is becoming increasingly difficult to continue improving the detection limit of such biosensors and biochips for the detection of bacterial pathogens. There are two main reasons that can account for this difficulty: (i) the limited physical sensitivities of the transducers; and (ii) the low immuno-capture efficiency of the immobilized antibodies on the solid sensor/chip surfaces. Fortunately, the advances in microfabrication technology have made it possible to fabricate sensors with scales and dimensions similar to target cells, which can improve the physical sensitivity of the transducer to be able to sense a few cells or even a single cell binding to the sensor/chip surface [8]. However, the issue of the low capture efficiency of immobilized antibodies on sensor surfaces has not been well addressed. Since bacterial cells in suspensions do not diffuse as easy as small molecules, it is particularly difficult for the cells to access and interact with immobilized antibodies on the sensor surfaces. Researchers have attempted various approaches to make the immuno-capture on the sensor surface more efficient, mainly

* Tel.: +1 919 530 6704; fax: +1 919 530 6600.
E-mail address: lyang@nccu.edu.

0039-9140/$ – see front matter © 2009 Elsevier B.V. All rights reserved.
doi:10.1016/j.talanta.2009.07.024

including different antibody immobilization methods [9] and different immuno-reaction conditions [10]. For example, orientated immobilized antibody on a sensor surface can generally achieve a better capture efficiency than non-orientated antibody layer [9]. Although these efforts have achieved moderate improvement, the immuno-capture efficiencies of *Salmonella* and other foodborne bacteria cells are still limited, ranging from 0.01% to less than 20% [10,11]. Further improvement in the immuno-capture efficiency in biosensor and biochip settings required the integration of available technologies to develop new concepts and devices that can address the challenges.

Dielectrophoresis (DEP) is the electrokinetic motion of dielectrically polarized particles in non-uniform electric fields [12]. As most biological cells behave as dielectrically polarized particles in external electric field, DEP has been recognized as a powerful tool in manipulation of biological cells. Its typical applications are the separations of different types of mammalian cells based on the differences in their dielectric polarizabilities [13–19]. DEP has also been employed for the separation of viable and nonviable yeast cells [20,21], the trapping of viruses from fluid [22], and the separation of bacterial cells [23–28].

In addition to the typical separation function, DEP can also provide other attractive functions that can be integrated with biosensor and biochip platforms to improve the sensor performance. Gomez et al. [29] demonstrated DEP concentration of *Listeria* cells in a lab-on-a-chip impedance microbiology, achieving a concentration factor of 10^4–10^5. This DEP concentration step eliminated the long time growth-based enrichment steps that are usually used in traditional microbial methods. In our previous study [30], we used DEP in a flow through microchip to concentrate *Listeria monocytogenes* cells from the flow and used immobilized antibody to capture the cells in the microfluidic channel. This microfluidic chip achieved an improved immuno-capture efficiency of ~27% to *Listeria* cells. A latest study reported that the capture efficiency of *L. monocytogenes* by heat shock protein 60 (Hsp60) immobilized on silicon dioxide was increased by 60% when a DEP force was applied for 5 min at the beginning of the 1 h incubation step [31]. These studies have demonstrated that DEP can concentrate bacterial cells from the flow and help to increase the capture efficiency to bacterial cells in microfluidic chips.

In this study, we integrated DEP with non-flow through biochips to assist the immuno-capture of one of the major foodborne pathogenic bacteria—*Salmonella* Typhimurium, and coupled with absorbance measurement. We demonstrated two significant functions of DEP in the biochip platforms to improve the detection of *Salmonella*: (i) DEP can concentrate bacterial cells from the suspension to different locations on the chip surface, which make it very useful in manipulating bacterial cells in biosensors and biochips; (ii) DEP can make bacterial cells in close contact with the immobilized antibodies on the chip surface, which can effectively improve the immuno-capture efficiency. The immuno-captured cells were detected by absorbance measurements. The enhancement in the final absorbance signals resulted from the DEP assistance to the immuno-capture was investigated.

2. Materials and methods

2.1. Chemicals

Biotinylated bovine serum albumin (BSA) and streptavidin were purchased from Pierce (Rockford, IL). Biotinylated anti-*Salmonella* antibody and horse radish peroxidase (HRP) labeled anti-*Salmonella* antibody were purchased from Biodesign International (Saco, ME). Hydrogen peroxide (30%) and ammonium hydroxide (30%) were obtained from VWR (West Chester, PA). Phosphate buffered saline (PBS) solution (pH 7.0), containing 0.1 M sodium phosphate and 0.15 M sodium chloride, was prepared by dissolving one pack of PBS powder (JAW PBS pack from G Bioscience, St Louis, MO) into 1 L of deionized (DI) water according to the instruction. Millipore water (Milli-Q-System, 18.2 MΩ cm, Molsheim, France) was used throughout the experiments.

2.2. Preparation of bacterial samples

Salmonella Typhimurium culture was purchased from Carolina Biological Supply Company (Burlington, NC). The culture was grown in brain heart infusion (BHI) broth (TEKnova, Hollister, CA) at 37 °C for 16–18 h. When harvested, 1 ml of the culture was centrifuged (Eppendorf, Westbury, NY) at 6000 × *g* for 2 min, then the supernatant was removed in order to get rid of ionic residues from the growth medium. The cells were washed with DI water 3 times and resuspended in 1 ml sterilized DI water. The cell concentration in the suspension was determined by surface plating 0.1 ml of appropriate dilutions onto XLT4 agar plates (Difco, Sparks, MD). Colonies were counted after incubation of the plates at 37 °C for 24 h. The average cell concentration in a culture was at ~10^9 colony forming units per milliliter (cfu/ml). The cell suspension was serially (1:10) diluted with DI water to desired concentrations for further experiments.

2.3. Microchips

The non-flow through biochip was assembled by two parts: a gold interdigitated microelectrode (IME) on a glass substrate (ABtech Scientific, Inc., Richarmond, VA) and a micro-chamber right above the electrode area formed by poly dimethylsiloxane (PDMS) (Sylgard 184 Silicone Elastomer kit, Dow Corning Co., Midland, MI) (Fig. 1A). The insert in Fig. 1A shows the image of the IME chip with the rectangle (red line) showing the IME area. The IME contained 50 pairs of opposing gold finger electrodes with 15 μm of electrode width and space, and 5 mm of electrode length. The chips were cleaned with a solution of 1:1:5 (v/v) H_2O_2(30%)/NH_4OH(30%)/H_2O for 5 s, rinsed with DI water, and dried with air, before they were assembled with the PDMS chamber. The PDMS layer (approxi-

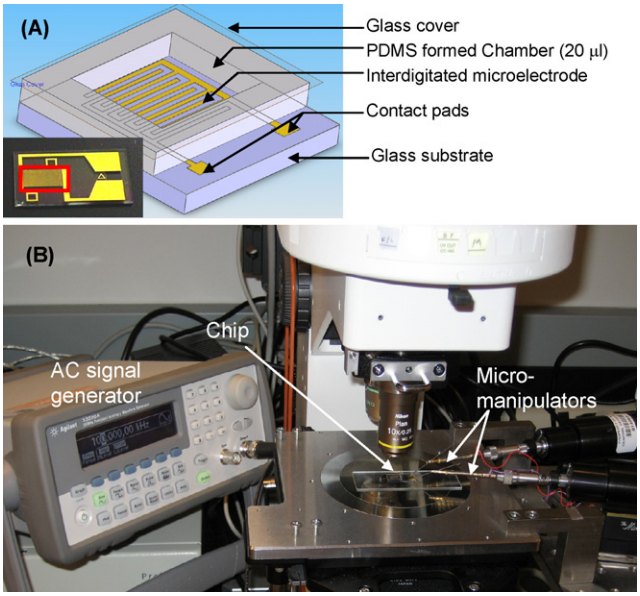


Fig. 1. (A) The non-flow through chip used in this study for DEP enhanced immuno-capture of *Salmonella* cells, which consists of a chamber formed by PDMS and a set of interdigitated microelectrodes (IMEs) on a glass substrate and (B) the experiment setup. The chip was placed on the stage of a microscope. An Agilent waveform generator was used to apply DEP voltage to the IME through a pair of micromanipulators.

mately 2 mm thick) was made by mixing the elastomer monomer: the curing agent at the ratio of 15:1 (w/w) and was cured at 70 °C overnight in a petri dish. The PDMS layer was then cut into 1 cm × 1 cm pieces. A rectangle shaped chamber (~3 mm × 5 mm, equivalent to the IME electrode area) was made in the center of each PDMS piece. The PDMS piece was then aligned with the IME chip and attached to the chip by gentle pressing to form a chamber right above the electrode area.

2.4. Antibody immobilization on the chips

Anti-*Salmonella* antibody was immobilized onto the chip surface through a sandwich structure consisting of biotinylated BSA – streptavidin – biotinylated anti-*Salmonella* antibody as previously reported [30]. In detail, an aliquot of 10 μl of 0.5 mg/ml biotinylated BSA in 0.1 M PBS was introduced into the chamber, and the chip was placed in a moisture chamber and kept at 4 °C overnight, allowing physical absorption of biotinylated BSA onto the chip surface. The chip was then rinsed with PBS for 2 min to remove unbound biotinylated BSA from the surface. Then, an aliquot of 10 μl of 0.25 mg/ml streptavidin in 0.1 M PBS was placed into the chamber and allowed to react at 4 °C for 2 h. The excess streptavidin was washed away with PBS. Finally, an aliquot of 10 μl of 0.25 mg/ml of biotinylated anti-*Salmonella* antibody in 0.1 M PBS was introduced into the chamber to react with streptavidin at 4 °C for 2 h. The chip was washed with PBS for 2 min and rinsed with DI water for 2 min before further use in the experiments.

2.5. DEP assisted immuno-capture of bacterial cells on the chip.

Fig. 1B shows the image of the experimental setup. The chip was mounted on a glass slide and was placed on the stage of the microscope. An Agilent 33120A arbitrary waveform generator (Agilent Technologies, Inc., Palo Alto, CA) was used to apply sinusoidal voltages (3 Vpp with different frequencies ranging from 1 Hz to 1 MHz) to the IME electrodes through a pair of micromanipulators (Micromanipulator, Carson city, NV).

The mechanism of DEP assisted immuno-capture of *Salmonella* cells on the chip in comparison with non-DEP assisted immuno-capture is shown in Fig. 2A and B. When *Salmonella* cell samples are placed in the chamber, if without DEP (Fig. 2A), the cells suspended in the solution generally move around in the solution and do not have sufficient opportunities to reach the surface of the chip and interact with the immobilized antibodies. Only a small population of cells can reach the chip surface by sediment, as a result, the capture efficiency of immobilized antibody is generally very low, especially when a small sensor is used in a large volume of sample. When a DEP voltage is applied, *Salmonella* cells can be pulled down to the chip surface from the suspension by the DEP forces, which results in much more cells reaching the chip surface, and the cells can make well contact with the immobilized antibodies on the chip surface (Fig. 2B). With such DEP assistance, an increased immuno-capture efficiency of the immobilized antibody to bacterial cells can be realized.

2.6. Determination of the immuno-capture efficiencies with and without DEP assistance by traditional plating method

Two sets of tests were performed in order to compare the immuno-capture efficiencies with and without DEP assistance: the control tests and the DEP assisted immuno-capture tests. In DEP-assisted immuno-capture, an aliquot of 20 μl of *Salmonella* cell suspension was introduced into the chamber. The chamber was covered with a glass cover (VWR, West Chester, PA) to prevent evaporation. A DEP voltage was applied to the IMEs with desired periods of time (15 or 30 min). The control tests were preformed in the same way but no DEP voltage was applied to the electrodes.

To examine the immuno-capture efficiencies, 10 μl of the sample in the chamber was taken after the immuno-capture with or without DEP and diluted with 90 μl sterilized DI water. Further serial 1:10 dilutions (100 μl sample + 900 μl DI water) of these samples were made. Appropriate dilutions were plated on XLT4 agar. Colonies were counted after the plates were incubated at 37 °C for 24 h, and the cell number was determined by the calculated cfu/ml. The immuno-capture efficiencies were estimated using the following equation:

$$\text{immuno-capture efficiency} = \frac{\text{cell number in original suspension} - \text{cell number in suspension after immuno} - \text{reaction}}{\text{cell number in original suspension}} \times 100 \quad (1)$$

2.7. Enzyme-linked immuno absorbance detection of the captured bacterial cells on chip

After the immuno-capture of cells on the chips either with or without DEP, non-specifically bound cells were washed out, the captured cells were further detected by using the derived sandwich ELISA on the chip (Fig. 2C). To produce a quantitative absorbance signal, HRP labeled secondary anti-*Salmonella* antibody was added to react with these captured cells. After washing out the excess secondary antibody, the substrate 3,3′,5,5′-tetramethylbenzidine (TMB) (VWR, West Chester, PA) was added to produce a color product which can be read by absorbance at 450 nm (Fig. 2C). In detail, the following steps were performed to detect the cells using absorbance: (1) the chips were washed with PBS, and HRP labeled secondary anti-*Salmonella* antibody (10 μl, 0.01 mg/ml) was added into the chamber and reacted with the captured cells for 30 min. (2) After washing with PBS, TMB (20 μl) was added and allowed to react for 5 min. The product (15 μl) was taken from the chamber and transferred into a microcentrifuge tube which already contained 15 μl of 1 M HCl in order to stop the enzymatic reaction. Twenty microliter of the yellow product was transferred into a 384-well ELISA plate (Corning, Lowell, MA), and the absorbance at 450 nm was read using Spectramax Plus^{384} plate reader (Molecular

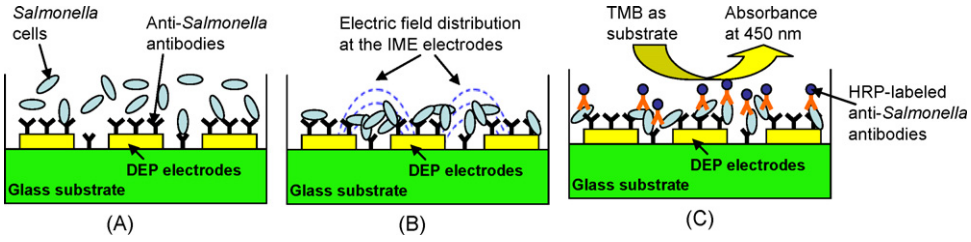


Fig. 2. The mechanisms of immuno-capture of *Salmonella* cells (A) without DEP and (B) with DEP assistance, and (C) the further sandwich ELISA detection of captured cells on the chip.

Devices, Sunnyvale, CA). The plate reader has a photometric range of 0–4000 OD (optical density), with photometric error for microplate <±1.0% and ±0.006 OD within 190–1000 nm (from manufacturer user guide).

2.8. Imaging

The fluorescent images were taken on a Nikon ECLIPSE E600FN fluorescence microscope (Japan) with a Coolsnap HQ camera (Roper Scientific, Inc.—Photometric, Tucson, AZ) using a FITC (Fluorescin isothiocyanate) filter. For visualization purposes, *S.* Typhimurium cells were stained with 3,3′-dihexyloxacarbocyanine iodide ($DiOC_6(3)$) dye (green) (Molecular Probes, Eugene, OR). To stain the cells, 3 μl of 1 μM $DiOC_6(3)$) dye was added to 1 ml of the cell sample and incubated at 37 °C for 10 min. The stained cells were centrifuged and washed with sterilized DI water 3–4 times to remove excess dye. Appropriate dilutions were made for further experiments.

Field emission scanning electron microscopic (FESEM) images were taken on a Hitachi S 4800 FESEM microscope (Tokyo, Japan). The acceleration voltage was at 2.0 kV. Images were acquired digitally using Quartz PCI v. software (Hitachi High-technologies Canada, Inc., Resdale, Ontario, Canada).

3. Results and discussion

3.1. Manipulating Salmonella cells on the chip by positive and negative DEP

When a particle experience DEP in a non-uniform electrical field, the time-averaged dielectrophoretic force acting on a spherical particle can be approximated as Eq. (2) [32]:

$$F_{DEP} = 2\pi r^3 \varepsilon_m \,\mathrm{Re}[f_{CM}(\omega)]\nabla E_{rms}^2 \quad (2)$$

where r is the particle radius; ε_m, the permittivity of the suspending medium; E_{rms}, the root mean square value of the electric field; and $\mathrm{Re}[f_{CM}(\omega)]$, the real part of the Clausius–Mossotti factor (f_{CM}), which is given by

$$f_{CM}(\omega) = \frac{\varepsilon_p^* - \varepsilon_m^*}{\varepsilon_p^* + 2\varepsilon_m^*} \quad (3)$$

where $\varepsilon_p^* = (\varepsilon_p - j\sigma_p)/\omega$ and $\varepsilon_m^* = (\varepsilon_m - j\sigma_m)/\omega$ are the complex permittivities of the particle and the medium, respectively, with σ the conductivity, ε the permittivity, ω the angular frequency of the applied electric field, and $j = \sqrt{-1}$.

The frequency dependence of $\mathrm{Re}[f_{CM}(\omega)]$ indicates that the force acting on the particle varies with the frequency. Depending on the relative polarizability of the particle with respect to the surrounding medium, the particle can experience positive DEP or negative DEP. When $\mathrm{Re}[f_{CM}] > 0$, the particle will experience positive DEP which will move the particle towards the region where the electrical field is the strongest. While $\mathrm{Re}[f_{CM}] < 0$, the particle will experience negative DEP which will move the particle towards the region where the electrical field is weak.

In this study, we used the designed IME to generate a non-uniform electrical field and to serve as DEP electrodes for capturing bacterial cells to the electrode surface. Fig. 3A shows the non-uniform electrical field generated by the IME. It has the strongest electrical field zones at the edges of the finger electrodes and the weakest electrical field zones at the centers of the finger electrodes and the gaps between the finger electrodes. Depending on the relative dielectric constant between the bacterial cells and the medium as well as the frequency of the applied voltage, *Salmonella* cells can either experience negative DEP which moves them towards the regions where the electric fields are the weakest, i.e. the centers of the finger electrodes or the gaps between the finger electrodes, or experience positive DEP which moves them to the regions where

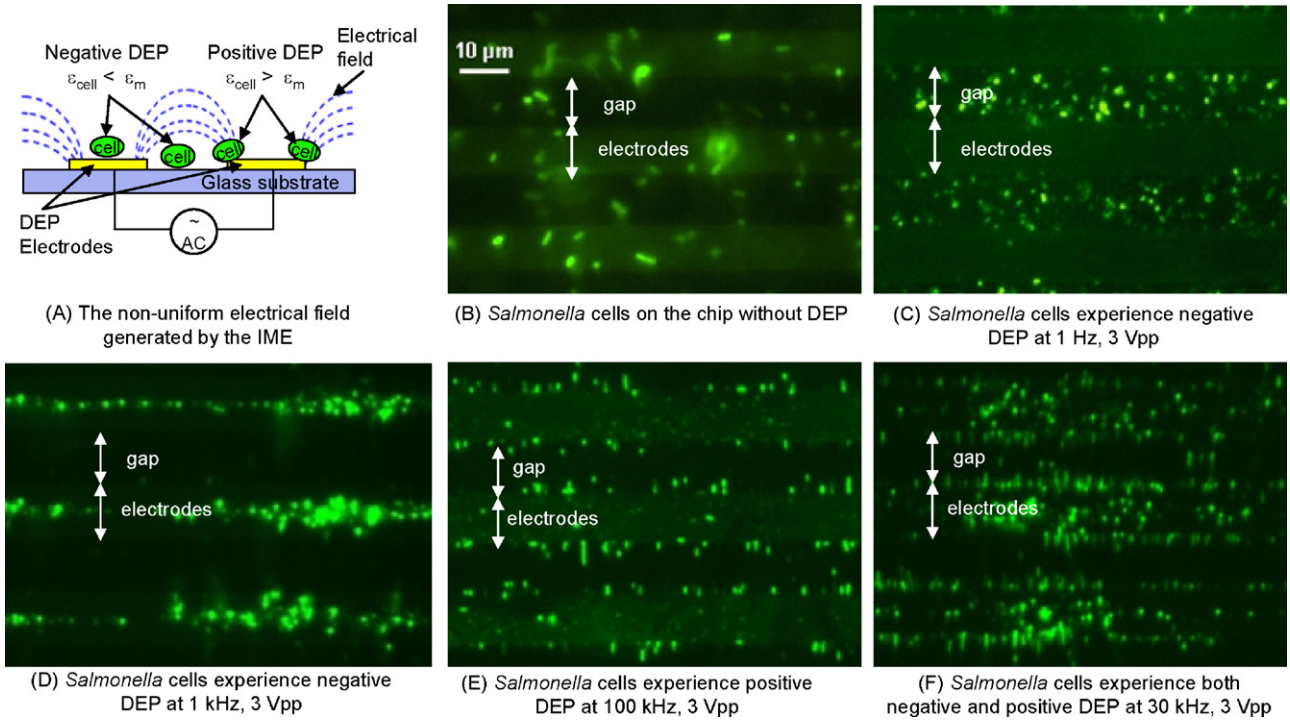


Fig. 3. (A) Schematic of the non-uniform electrical field generated by the interdigitated microelectrodes, and the positive and negative DEP for bacterial cells in this electrical field; and the fluorescence images of (B) *Salmonella* cells on the non-flow through chip without DEP; (C) cells collected in the gap between the finger electrodes by negative DEP at 1 Hz and 3 Vpp; (D) cells collected at the centers of the finger electrodes by negative DEP at 1 kHz and 3 Vpp; (E) cells collected at the edges of the finger electrodes by positive DEP at 100 kHz and 3 Vpp; and (F) cells exhibited positive or negative DEP at 30 kHz and 3 Vpp. The IMEs were with anti-*Salmonella* antibody immobilized on their surfaces. Green dots are *Salmonella* cells stained with $DiOC_6(3)$.

the electrical fields are the strongest, i.e. the edges of the finger electrodes.

Fig. 3B–E present the fluorescence microscopic images of *Salmonella* cells on the IMEs with anti-*Salmonella* antibody immobilized on their surfaces, when there was (B) no DEP, (C) negative DEP at 1 Hz and 3 Vpp, (D) negative DEP at 1 kHz and 3 Vpp, (E) positive DEP at 100 kHz and 3 Vpp (green dots are *Salmonella* cells stained with $DiOC_6(3)$. As shown in Fig. 3B, when there was no DEP voltage applied, *Salmonella* cells distributed randomly in the suspension. When DEP voltage was applied to the IME, cells were trapped at different locations depending on the applied frequency. Fig. 3C and D shows the fluorescence images of bacterial cells captured in the gaps between the finger electrodes and at the centers of the finger electrodes by negative DEP at 1 Hz, 3 Vpp, and 1 kHz, 3 Vpp, respectively. The results indicated that at frequencies no more than 1 kHz, *Salmonella* cells exhibited negative DEP, and depending on the applied frequency, cells could be captured at the two different locations where the electrical fields were the weakest. The trapped rod-shaped *Salmonella* cells looked like small round dots, suggesting that the cells were aligned upwards on the electrodes at these frequencies. When the applied frequency was increased to 100 kHz or higher, *Salmonella* cells exhibited positive DEP, and they were trapped at the edges of the finger electrodes (Fig. 3E). In between these frequencies, in the same sample, some cells exhibited negative DEP while other cells exhibited positive DEP due to the slight variations among these individual cells. Fig. 3F shows a representative image of *Salmonella* cells on the IME with some cells exhibiting positive DEP and some exhibiting negative DEP, when the applied DEP frequency was at 30 kHz. Our previous study indicated that DEP treatments (1 h or less) at all these frequencies would not affect the viability of bacterial cells [33].

This frequency-dependent positive and negative DEP of *Salmonella* cells is due to the relative dielectric properties of the cells with respect to that of the medium at different frequencies. Bacterial cells consist of adjacent structures of materials that have very different electrical properties. The cell membrane consists of a lipid bilayer containing many proteins, thus is highly insulating, while the inside of a cell, the cytoplasm, is complex and contains many dissolved charged molecules, and is therefore highly conductive. The conductivity of the cell membrane is around 10^{-7} S/m, whereas the conductivity of the interior of a cell can be as high as 1 S/m [13]. The medium, DI water, has its conductivity in a range from 1–2 μS/cm to about 10–15 μS/cm. In DEP manipulation, most likely, at low frequencies, the electrical field is mainly dropped across the outermost membranes of the cells. The cells behave as poorly conductive spheres having the permittivity of the cell membrane [26,34], hence negative DEP is expected. As the frequency increases, the applied field gradually penetrates into the cells. The cells then behave as more conductive spheres with the permittivity of the cell interior [26], and positive DEP is expected. In practice, the actual frequency at which *Salmonella* cells exhibit positive or negative DEP may vary case by case, because it is related to many factors including the medium, the physiological stages of the cells, the dimensions and the design of the electrodes.

This frequency-dependent positive and negative DEP manipulation of *Salmonella* cells allows us to trap cells at different regions on the chip. This would be particularly useful to address one of the technical challenges for detecting a few cells or a single cell in a sensor/chip setting, i.e. how to bring the cells to the sensor site. This problem has not been well addressed in most of the studies related to single cell detection. Gray et al. [35] demonstrated that DEP could register thousands of single mammalian cells on each of thousands of 3 μm diameter planar microelectrodes. However, trapping of single bacterial cells onto microelectrodes for detection has not been reported yet. The results here suggested that DEP could be a possible tool to drive a single bacterial cell to the desired locations on a sensor/chip, but the realization of single cell detection is also related to other factors such as the dimension, the effective area, and the physical sensitivity of the sensor.

Of particular interest in this study is the ability of DEP to pull cells from the suspension to the chip surface. As we can see in Fig. 3B, when there is no DEP, it is obvious that most cells did not have opportunities to reach the chip surface and to interact with the immobilized antibodies on the chip surface. All other images in Fig. 3 indicate that, with DEP, *Salmonella* cells were pulled to the chip surface by DEP forces, so that much more cells had the opportunities to react with the immobilized antibodies, thus an enhanced immuno-capture efficiency could be expected.

Fig. 4A shows the FESEM image of *Salmonella* cells captured by DEP on the chip surface at the high cell density region, clearly showing that the captured cells are in close contacts with the chip surface, which confirms that DEP can effectively make these cells in close contact with the immobilized antibodies on the chip surface, so that the antibodies can react to the cells more effectively, and thus the immuno-capture efficiency can be improved. Fig. 4B presents a FESEM image of captured *Salmonella* cells on the chip by positive DEP at the low cell density region. It can be seen that the cells trapped by positive DEP at the edges of the electrodes has the maximum value of the polarization at the two ends of the rod-shaped cells, and they tended to align as a 'pearl chain' parallel to the electrical field.

It should be noted that the planar interdigitated microelectrodes have a limited effective DEP region above its surface. Several research groups have developed mathematical models for calculation of the DEP forces on IMEs, and have found that the DEP forces decrease exponentially with the height from the electrode surface

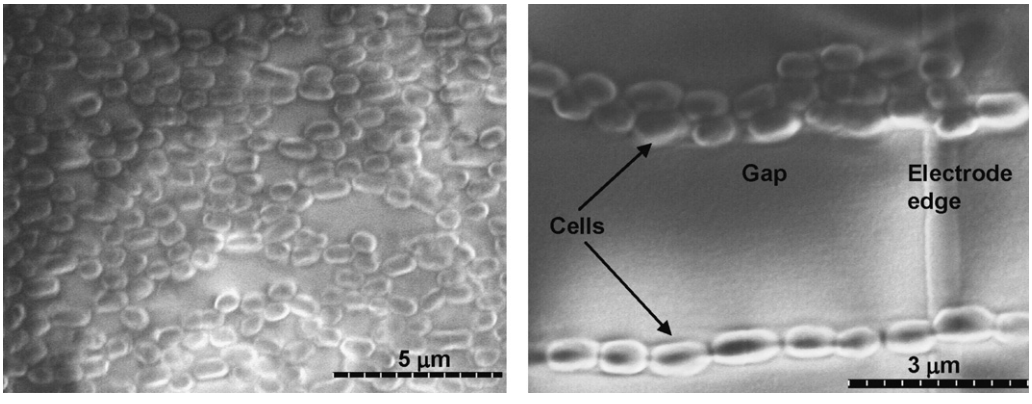


Fig. 4. The FESEM image of *Salmonella* cells captured by positive DEP at 100 kHz and 3 Vpp on the chip surface (A) in the high cell density region and (B) captured cells forming "pearl chains" at the edge of the finger electrode in the low cell density region.

[36–38]. Roughly, the effective DEP region for an IME is within the height equivalent to the electrode width from the electrode surface [36] (~15 μm in this study), therefore, a thin layer of cell sample right above the electrode surface is required for effective capture of the cells in the sample. As long as the cells move or settle down into the effective DEP region, they can be captured by DEP to the sensor surface.

3.2. DEP assisted immuno-capture of Salmonella cells in the chips

Fig. 5 presents the representative fluorescence images of *Salmonella* cells that were captured by immobilized antibodies on the chip with DEP treatment at 100 kHz and 3 Vpp for 5 min and without DEP. Images on the left side show the immuno-captured cells on the chips when 20 μl of the samples with concentrations at 1.2×10^8, 1.2×10^7, and 1.2×10^6 cfu/ml were placed on the chip with DEP treatment, while images on the right side show the immuno-captured cells without DEP treatment. It can be seen that almost all the cells being captured with positive DEP distributed at the edges of the finger electrodes, while without DEP treatment the cells distributed randomly on the chips. At each concentration, much more cells were captured by the immobilized antibodies with DEP treatment than without DEP. As evidenced by these fluorescence images, the immuno-capture efficiency of the immobilized antibody on the chips can be increased dramatically with DEP assistance. The enhanced immuno-capture are resulted from the two functions of DEP: one is that DEP pulls more cells down to the chip surface such that more cells have the opportunities to react with the immobilized antibodies, acting as a concentration step; and the other is that DEP helps these captured cells to make well contacts with the immobilized antibodies, so that the reaction between the cells and the antibodies are more efficient.

Table 1 shows the immuno-capture efficiency of the immobilized antibodies to *Salmonella* cells with DEP assistance in comparison with those without DEP, determined by the traditional surface plating method. As shown in Table 1, when 20 μl of a sample containing $\sim 1.93 \times 10^6$ cfu/ml was introduced into the chamber, after the 15 min DEP treatment at 100 kHz and 3 Vpp, the cell concentration in the suspension was found to be $\sim 8.50 \times 10^5$ cfu/ml. The reduced cell concentration in the suspen-

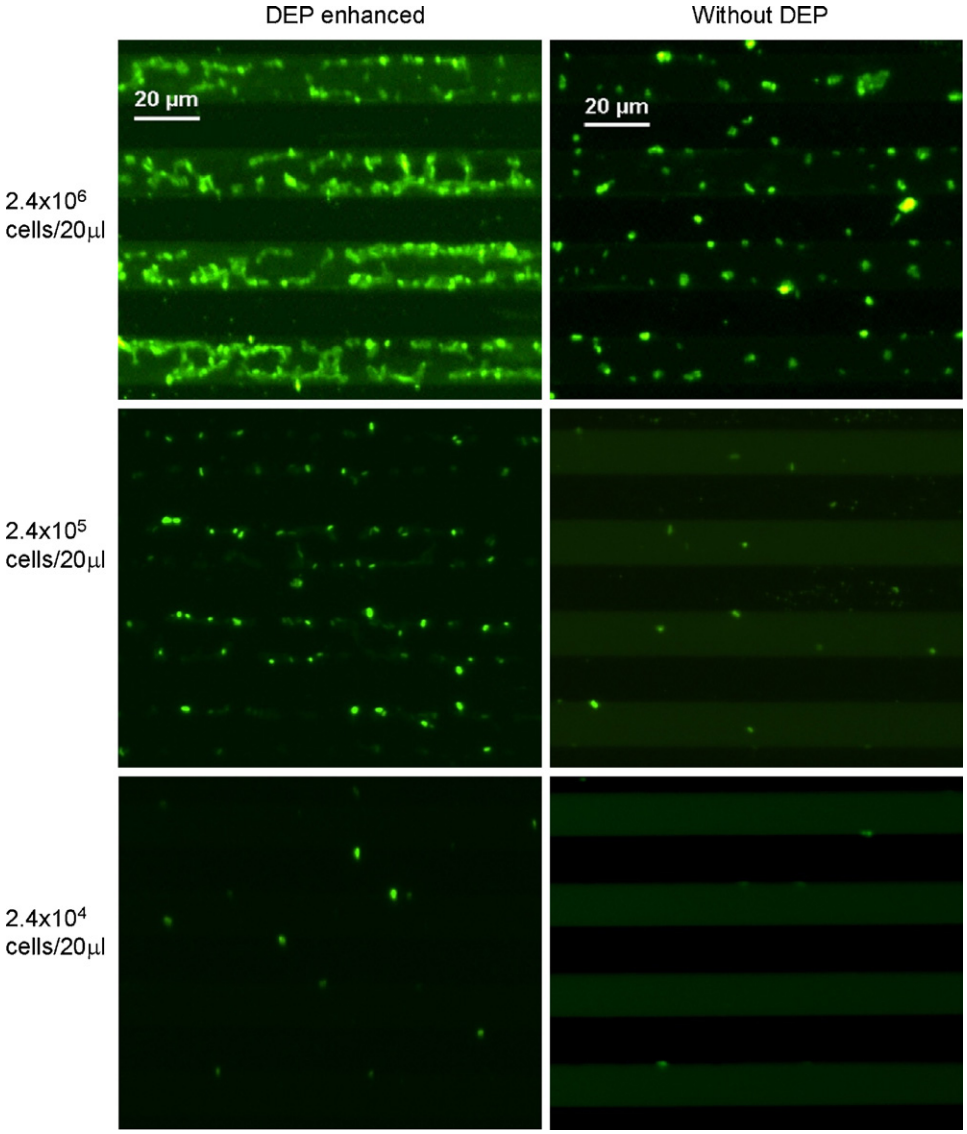


Fig. 5. The representative fluorescence images of *Salmonella* cells captured by immobilized antibodies on the chip with DEP treatment at 100 kHz and 3 Vpp for 5 min in comparison with those without DEP. Images on the left side are immuno-captured cells with DEP assistance, and the images on the right side are immuno-captured cells without DEP assistance. The three samples contained different cell concentrations at 2.4×10^6, 2.4×10^5, and 2.4×10^4 cells/20 μl.

Table 1
The immuno-capture efficiency of the immobilized antibody on the non-flow through chip to *Salmonella* cells with 15 and 30 min DEP assistance in comparison with those without DEP assistance.

Reaction time (min)	Cell concentration in suspension			
	Original sample (cfu/ml)	After immuno-reaction with DEP (cfu/ml)	After immuno-reaction without DEP (cfu/ml)	Immuno-capture efficiency (%)
15 min	$(1.93 \pm 0.21) \times 10^6$	$(8.5 \pm 0.48) \times 10^5$	–	~56.0%
	$(1.93 \pm 0.21) \times 10^6$	–	$(1.73 \pm 0.15) \times 10^6$	~10.4%
30 min	$(4.03 \pm 0.43) \times 10^6$	$(1.45 \pm 0.13) \times 10^6$	–	~64.0%
	$(1.42 \pm 0.46) \times 10^6$	–	$(1.17 \pm 0.33) \times 10^6$	~17.6%

DEP: 100 kHz and 3 Vpp.

sion was a result of the immuno-capture of cells by the immobilized antibodies on the chip. So the capture efficiency of the antibodies to the cells with DEP enhancement was approximately 56.0%. Whereas the 15 min immuno-reaction without DEP reduced the cell concentration to ~1.73×10^6 cfu/ml, and the capture efficiency was calculated to be approximately ~10.4%. The results demonstrated that the 15 min DEP assisted immuno-capture increased the immuno-capture efficiency by approximately 5-folds. We further investigated the immuno-capture efficiency with prolonged DEP treatment. The immuno-capture efficiency with a 30 min DEP treatment (100 kHz and 3 Vpp) was about 64.0% for the sample with cell concentration of ~4.03×10^6 cfu/ml, while the immuno-capture efficiency without DEP was ~17.6% for the control sample with similar cell concentration (1.42×10^6 cfu/ml) with 30 min immuno-reaction time. The data indicated that the prolonged reaction time could increase the capture efficiency of the immobilized antibodies on the chip regardless of with or without DEP. This is mostly due to the increased number of cells reaching the chip surface either because of DEP or sediment during the prolonged time. But it is still true that the immuno-capture efficiency with DEP assistance is much higher (>3-folds) than that without DEP.

In general, the immuno-capture efficiencies of antibodies immobilized on solid surfaces to bacterial cells are very low. For example, Brewster et al. [10] reported that the binding efficiency of anti-*Salmonella* antibodies immobilized on a roughened glassy carbon electrode surface was less than 0.01% by immersing the electrode into 1 ml solution containing 10^7 cells; it increased to ~0.5% by placing a droplet (containing ~10^5 cells) directly on the electrode surface. Ruan et al. [11] achieved a capture efficiency of ~16% of anti-*E. coli* antibody immobilized on an indium tin oxide (ITO) electrode surface to *E. coli* cells, when 50 μl of 6.0×10^6 cfu/ml sample was dropped on the sensor surface twice and incubated for 1 h at 37 °C. We achieved the capture efficiencies of 18–27% for *Listeria* cells with concentrations ranging from 10^1 to 10^3 cells in a flow through microchip with DEP at 1 MHz, 20 Vpp [30]. The results in this study demonstrated that DEP can effectively improve the immuno-capture efficiency to 56–64% with a considerable short reaction time (15–30 min) in the designed non-flow through microchip device.

When bacterial cells get into the electrical field, they get polarized and be captured very rapidly (within about microsecond) [39]. Generally, cells close to the electrodes are captured onto the electrodes' surface by DEP immediately (less than 1 s). Cells further from the electrodes can be captured by DEP when they move or settle down by gravity closer to the electrode surface into the effective DEP region. Therefore, with DEP, most bacterial cells in the suspension can be captured onto the sensor surface within a very short time, while without DEP, cells take much longer time to settle down onto the sensor surface. In this respect, DEP can effectively shorten the time required for bacterial cells to reach the antibodies immobilized on the chip surface, thus save the total assay time while still achieve high immuno-capture efficiency.

3.3. On chip ELISA detection of immuno-captured Salmonella cells

Fig. 6 shows the absorbance detection results of *Salmonella* cells on the chip captured with and without DEP. For samples with 5.0×10^3, 5.0×10^4, 4.7×10^5, and 5.0×10^6 cells/20 μl, the absorbance signals produced by the cells immuno-captured with DEP were 0.39 ± 0.084, 0.84 ± 0.11, 1.66 ± 0.20, and 2.66 ± 0.071, while the absorbance signals produced by the cells immuno-captured without DEP were 0.19 ± 0.071, 0.42 ± 0.049, 0.91 ± 0.066, and 1.65 ± 0.13. The absorbance signals with DEP assistance increased by 105.2%, 101.2%, 82.4%, and 64.7% compared with those without DEP. The enhancement in the absorbance decreased with the increasing cell concentrations in the samples. This is possibly due to the aggregation of cells on the chip surface during the DEP capture process for samples containing higher cell concentrations, and not all the cells can access to the antibodies on the chip surface, resulting in less effective capture enhancement (less increase in the final absorbance signal). While for samples with low cell concentrations, cells captured by DEP on the chip surface only form a monolayer, and all the captured cells can access to the immobilized antibodies, therefore resulting in a more effective DEP enhanced immuno-capture (larger increase in the final absorbance signal). Based on the data in Fig. 6, using the sample containing no bacteria as control, the detection limit of the on chip ELISA detection with DEP assistance was 5.0×10^3 cells/20 μl (2.5×10^5 cfu/ml), one order of magnitude better than that of without DEP (5.0×10^4 cells/20 μl or 2.5×10^6 cfu/ml). The results here demonstrated that DEP assisted immuno-capture of bacterial cells can provide a substantial enhancement in the finial detection signal and thus improve the detection limit of immuno-based detection of bacterial cells.

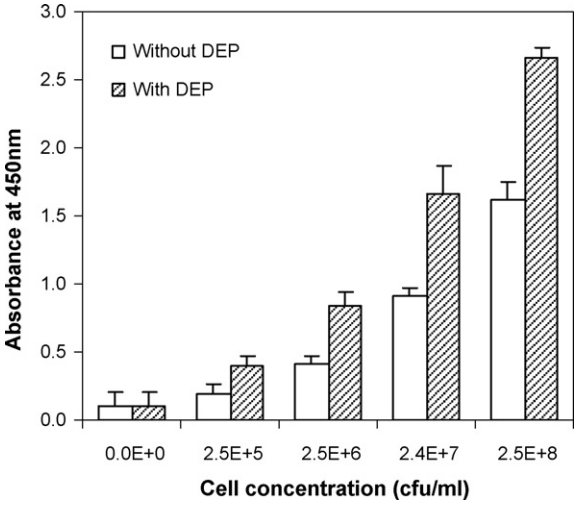


Fig. 6. The absorbance signals of the on-chip ELISA detection of the captured *Salmonella* cells with and without DEP assistance in the non-flow through chips.

DEP as the concentration step is very useful in both flow through and non-flow through microchip platforms for bacterial cell detection. Flow through microchips allow continuous injection/perfusion of bacterial samples and accumulation of the cells inside the fluidic chip even without additional concentration steps [40]. However, different concentration methods can be integrated with the flow through microchip to further help the accumulation/concentration of bacterial cells in the chips. For example, Varshney et al. [41] reported a microfluidic chip method that coupled antibody-coated magnetic nanoparticles as separation and concentration steps with an impedance sensor for detection of *E. coli* cells. The integration of DEP into flow through microchips can concentrate/accumulate bacterial cells in the chip for detection, and at the same time DEP also helps to improve the immuno-capture inside the fluidic chips [30]. The sample volume for fluidic chips can vary from several microliter to hundreds microliter, however, the larger the sample volume, the longer time it takes to inject the sample into the chips. The non-flow through microchip platforms usually use only one time addition of the sample. The sample volume is generally from several microliter to tens microliter. Therefore, it would be particularly useful to concentrate bacterial cells from the suspension to the chip surface to enhance the detection. This study demonstrated that the integration of DEP with non-flow through microchips could effectively concentrate bacterial cells from the suspension to the chip surface, and enhanced the immuno-capture efficiency by 3–5-folds in comparison with non-DEP assisted immuno-capture.

4. Conclusions

This study has demonstrated the successful integration of DEP with non-flow through biochips for immuno-capture and detection of foodborne pathogenic bacterial cells. DEP could serve two major functions in the biochips to significantly improve the chip performance: (i) concentrating bacterial cells from the suspension to different locations on the chip surface by positive and negative DEP; (ii) making the cells in close contact with the immobilized antibodies on the chip surface so that immuno-capture efficiency can be dramatically enhanced.

We have achieved the immuno-capture efficiencies of ~56.0% with 15 min DEP and ~64.0% with 30 min DEP to *Salmonella* cells in the non-flow through chip, which were 3–5-folds higher than ~10.4% and ~17.6% for 15 and 30 min immuno-capture without DEP, respectively. The captured bacterial cells were detected by the sandwich format ELISA on the chip. The final absorbance signals were enhanced by DEP assisted immuno-capture by 64.7–105.2% for the samples containing 10^3–10^6 cells/20 μl. The detection limit of the on chip ELISA detection with DEP assistance (5.0×10^3 cells/20 μl) was one order of magnitude better than that of without DEP (5.0×10^4 cells/20 μl).

This non-flow through microchip-based method integrated DEP, immuno-capture, and absorbance measurement, to detect foodborne pathogenic bacteria, and achieved enhanced detection signals. Microchips usually use very small sample volume, therefore capture of the cells from suspension to chip surface to enhance immuno-capture are particularly useful to improve the detection. Theoretically, the DEP assisted immuno-capture could be integrated with any other measurements to enhance final detection signals. This suggests that the integration of DEP with biochips has the potential to advance the state-of-the-art in chip-based immunoassay methods for microbial detections.

Acknowledgements

The author acknowledges the funding support from the Golden LEAF Foundation and the NCBIOIMPACT initiative of the state of North Carolina through the Biomanufacturing Research Institute & Technology Enterprise (BRITE) at North Carolina Central University.

References

[1] P.S. Mead, L. Slutsker, V. Dietz, L.F. McCaig, J.S. Bresee, C. Shapiro, P. Grifrm, R.V. Tauxe, Emerg. Infect. Dis. 5 (1999) 607–625.
[2] G.W. Beran, H.P. Shoeman, K.F. Anderson, Dairy Food Environ. Sanit. 11 (1991) 189–194.
[3] M.E. Potter, S. Gonzalez-Ayala, N. Silarug, Epidemiology of foodborne diseases, in: M.P. Doyle, L.R. Beuchat, T.J. Montville (Eds.), Food Microbiology: Fundamentals and Frontiers, ASM Press, Washington, DC, 1997.
[4] D. Ivnitsk, I. Abdel-Hamid, P. Atanasov, E. Wilkins, S. Stricker, Electroanalysis 12 (2000) 317–325.
[5] D. Ivnitsk, I. Abdel-Hamid, P. Atanasov, E. Wilkins, Biosens. Bioelectron. 14 (1999) 599–624.
[6] A.G. Rand, J. Ye, C.W. Brown, S.V. Letcher, Food Technol. 56 (2002) 32–39.
[7] X.L. Su, Y. Li, Biosens. Bioelectron. 19 (2004) 563–574.
[8] A. Gupta, D. Akin, R. Bashir, Appl. Phys. Lett. 84 (2004) 1976–1978.
[9] I.S. Park, N. Kim, N. Thiolated, Biosens. Bioelectron. 13 (1998) 1091–1097.
[10] J.D. Brewster, A.G. Gehring, R.S. Mazenko, L.J. Van Houten, C.J. Crawford, Anal. Chem. 68 (1996) 4153–4159.
[11] C. Ruan, L. Yang, Y. Li, Anal. Chem. 74 (2002) 4814–4820.
[12] H.A. Pohl, Dielectrophoresis, Cambridge University Press, Cambridge, 1979.
[13] R. Pethig, G.H. Markx, Trends Biotechnol. 15 (1997) 426–432.
[14] F.F. Becker, X.B. Wang, Y. Huang, R. Pethig, J. Vykoukal, P.R.C. Gascoyne, Proc. Natl. Acad. Sci. U.S.A. 92 (1995) 860–864.
[15] P.R.C. Gascoyne, X.B. Wang, Y. Huang, F.F. Becker, IEEE Trans. Ind. Appl. 33 (1997) 670–678.
[16] J. Cheng, E.L. Sheldon, L. Wu, M.J. Heller, J.P. O'Connell, Anal. Chem. 70 (1998) 2321–2326.
[17] E.G. Cen, C. Dalton, Y. Li, S. Adamia, L.M. Pilarski, K.V.I.S. Kaler, J. Microbiol. Methods 58 (2004) 387–410.
[18] M. Stephens, M.S. Talary, R. Pethig, A.K. Burnett, K.I. Mills, Bone Marrow Trans. 18 (1996) 777–782.
[19] S. Prasad, X. Zhang, M. Yang, Y. Ni, V. Parpura, C.S. Ozkan, M. Ozkan, J. Neurosci. Methods 135 (2004) 79–88.
[20] Y. Huang, R. Holzel, R. Pethig, X.B. Wang, Phys. Med. Biol. 37 (1992) 1499–1517.
[21] G.H. Markx, M.S. Talary, R. Pethig, Phys. Med. Biol. 37 (1992) 1499–1517.
[22] T. Schnelle, S. Muller, S. Fiedler, S.G. Shirley, K. Ludwig, A. Hermann, G. Fuhr, B. Wagner, U. Zimmerman, Naturwisswnschaften 83 (1996) 172–176.
[23] G.H. Markx, Y. Huang, X.F. Zhou, R. Pethig, Microbiology 140 (1994) 585–591.
[24] G.H. Markx, P.A. Dyda, R. Pethig, J. Biotechnol. 51 (1996) 175–180.
[25] W.B. Betts, Trends Food Sci. Technol. 6 (1995) 51–58.
[26] H. Li, R. Bashir, Sens. Actuators B: Chem. 86 (2002) 215–221.
[27] J. Suehiro, D. Noutomi, M. Shutou, M. Hara, J. Electrostat. 58 (2003) 229–246.
[28] J. Suehiro, M. Shutou, T. Hatano, M. Hara, Sens. Actuators B: Chem. 96 (2003) 144–151.
[29] R. Gomez, D.T. Morisette, R. Bashir, J. Microelectromech. Syst. 14 (2005) 829–838.
[30] L. Yang, P. Banada, R. Chatni, A. Bhunia, R. Bashir, Lab-on-a-Chip 6 (2006) 896–905.
[31] O.K. Koo, Y. Liu, S. Shuaib, S. Bhattacharya, M.R. Ladisch, R. Bashir, A.K. Bhunia, Anal. Chem. 81 (2009) 3094–3101.
[32] P.R.C. Gascoyne, J. Vykoukal, Electrophoresis 23 (2002) 1973–1983.
[33] L. Yang, P. Banada, A. Bhunia, R. Bashir, J. Biol. Eng. 2 (2008) 6.
[34] X. Wang, Y. Huang, P.R.C. Gascoyne, F.F. Becker, IEEE Trans. Ind. Appl. 33 (1997) 660–669.
[35] D.S. Gray, J.L. Tan, J. Voldman, C.S. Chen, Biosens. Bioelectron. 19 (2004) 1765–1774.
[36] H. Li, Y. Zheng, D. Akin, R. Bashir, J. Microelectromech. Syst. 14 (2005) 103–112.
[37] H. Morgan, A.G. Izquierdo, D. Bakewell, N.G. Green, A. Ramos, J. Phys. D: Appl. Phys. 34 (2001) 1553–1561.
[38] Y. Huang, X.B. Wang, F.F. Becker, P.R.C. Gascoyne, Biophys. J. 73 (1997) 1118–1129.
[39] R. Pethig, Application of A.C. electrical fields to the manipulation and characterization of cells, in: I. Karube (Ed.), Automation in Biotechnology, Elsevier, Miamisburg, OH, 1991, pp. 159–185.
[40] D.A. Boehm, P.A. Gottlieb, S.Z. Hua, Sens. Actuators B: Chem. 126 (2007) 508–514.
[41] M. Varshney, Y. Li, B. Srinivasan, S. Tung, Sens. Actuators B: Chem. 128 (2007) 99–107.

Talanta 80 (2009) 559–564

Contents lists available at ScienceDirect

Talanta

journal homepage: www.elsevier.com/locate/talanta

Statistical mixture design development of digestion methods for Oyster tissue using inductively coupled plasma optical emission spectrometry for the determination of metallic ions

R.M.W. Nano[a,b], R.E. Bruns[a], S.L.C. Ferreira[c], N. Baccan[a,d], S. Cadore[a,*]

[a] Institute of Chemistry – University of Campinas, P.O. Box 6154, 13083-970 Campinas, SP, Brazil
[b] Centro Federal de Educação Tecnológica, 40301-015 Salvador, BA, Brazil
[c] Instituto de Química-Universidade Federal da Bahia, 40170-290 Salvador, BA, Brazil
[d] Faculdade de Paulínia, 13140-000 Paulínia, SP, Brazil

ARTICLE INFO

Article history:
Received 20 April 2009
Received in revised form 10 July 2009
Accepted 13 July 2009
Available online 21 July 2009

Keywords:
Statistical mixture design
Simplex centroid design
Biological samples
Metallic ions
Atomic emission spectrometry

ABSTRACT

The quantitative determination of chemical elements in organic or biological samples is an important analytical problem. Normally the elements to be determined in the organic matrix must be transformed into a simple inorganic form. A digestion method by heating on a block digestor has been developed for the determination of Al, As, Ba, Ca, Cd, Co, Cu, Fe, Mg, Mn, V and Zn in Oyster tissue by ICP OES. A simplex centroid statistical mixture design has been used to study the effects of changing HNO_3, HCl and H_2O_2 reagent proportions on the digestion of these samples. Response surface and principal component analyses show that the species Ca, Cd, Cu, Fe, Mg, Mn and Zn have very similar analytical tendencies under this experiment. By means of mixture modeling maximum recoveries for these ions were predicted using 19%, 18% and 63% of the HCl, HNO_3 and H_2O_2 pseudocomponent mixtures, respectively. This corresponds to 21.4%, 30.8% and 47.8% of the HCl, HNO_3 and H_2O_2 commercial solutions. Furthermore the As, Co and V ions present large recoveries for these mixtures as well. The Al and Ba ion recoveries are seen to be independent of the mixture proportions. The analysis of Oyster tissue reference material (SRM 1566b – NIST) under optimized conditions at the selected wavelengths resulted in ion recoveries between 90% and 100%.
© 2009 Elsevier B.V. All rights reserved.

1. Introduction

Decomposition methods of biological samples are generally executed using two or more reagents because their different chemical properties can be exploited for the complete destruction of the organic material. Nitric and sulfuric acids, used individually or together with hydrogen peroxide are common digestion mediums. A reliable decomposition method that results in the complete solubilization of the biological sample while retaining the volatile components, reducing the contaminants, having low blank readings as well as an acceptable analytical frequency is one of the most critical steps of a spectrochemical analytical technique [1–4].

Biological materials rich in proteins and fats require high decomposition temperatures or the use of concentrated oxidizing mineral acid or a mixture of an oxidizing acid with hydrogen peroxide in open or closed systems with conventional or microwave heating [3].

Microwave (MW) radiation has become an analytical tool for sample decomposition. The use of high pressure flasks and oxidizing acids results in faster digestion permitting the processing of a larger number of samples while eliminating losses of volatile species. This technique, however, is sensitive to several factors such as sample mass, acid type, reagent proportions, temperature, pressure and heating time. Different researchers have employed MW ovens or steel bombs for the digestion of biological materials although sample mass and acid volumes were as small as possible to avoid a very acidic final solution as well as for safety reasons.

In these solutions trace elements are preferably determined using mass spectrometry with inductively coupled plasma (ICP-MS) [5] or atomic absorption spectrometry with electrothermal atomization (ET AAS) [6–8] but atomic emission spectrometry [9,10] can also be used.

Some researchers describe the use of acidic or alkaline solubilization [11,12] in open systems [13–16], with larger sample masses and reagent volumes than those used in closed systems, for the determination of trace elements in addition to major elements, although these processes are slow and inadequate to determine volatile elements.

Based on the above considerations the objective of this study is to optimize mixtures of an oxidizing (HNO_3) and non-oxidizing (HCl) acids and an auxiliary oxidizing agent (H_2O_2) to determine macro- and micro-constituents in Oyster tissue using block digestor heating under reflux (cold finger).

* Corresponding author. Tel.: +55 19 3521 3125; fax: +55 19 3521 3023.
E-mail address: cadore@iqm.unicamp.br (S. Cadore).

0039-9140/$ – see front matter © 2009 Elsevier B.V. All rights reserved.
doi:10.1016/j.talanta.2009.07.025

Unfortunately the optimum mixture of these components cannot be determined from chemical principles or existing information. For this reason statistical mixture designs are employed in this work to determine the mixture proportions that result in maximum percentage recoveries of the 12 metals from the organic material by inductively coupled argon plasma optical emission spectrometry (ICP OES) [17–20]. These designs are especially appropriate for this study since they not only permit a determination of the linear blending properties of each solution but also the second and third order synergic and antagonistic interaction effects among the mixture components for each of the metallic elements investigated.

2. Experimental

2.1. Reagents and solutions

All the solutions were prepared with analytical reagent grade and ultra pure water, obtained by a Milli-Q system (Millipore, USA, with a conductivity of 0.054 μS cm^{-1}). All the glassware and plastic flasks used were cleaned with a neutral detergent (5%, v/v), dilute nitric acid (10%, v/v for 24 h) and then with deionised water.

Multielement standards of Al, As, Ba, Ca, Cd, Co, Cu, Fe, Mg, Mn, V and Zn were prepared by dilution of 1000 μg L^{-1} standard solutions (Merck) of the elements. Analytical curves were made using the following concentrations of the analytes: (i) 0.5; 1.0; 2.0; 4.0; 6.0 μg mL^{-1} for Al, Cu and Fe; (ii) 0.02; 0.04; 0.10; 0.20; 0.40 μg mL^{-1} for As, Ba, Cd, Co, Mn, and V; (iii) 5.0; 10; 15; 20; 40 μg mL^{-1} for Ca, Mg and Zn.

2.2. Sample digestion

The solutions for each point of the mixture design were prepared weighing approximately 0.5000 ± 0.0001 g of reference material (SRM 1566b – NIST) in a digestion tube and adding volumes of 37% (v/v) HCl and 65% (v/v) HNO_3, as listed in Table 1. The tubes were put in a TECNAL model TE 040/25 block digestor. Cold finger condensors with water refrigeration were attached to the tubes. The system remained in operation overnight, at a temperature of 50 °C. After this step 30% (w/v) H_2O_2 was added and the temperature gradually raised until about 140 °C, with digestion occurring for 4 h at this temperature. After digestion the tubes were taken off the block digester and cooled to room temperature. The solutions were then transferred to a 25.0 mL volumetric flask with the volume being completed with ultra pure water [21]. The Al, As, Ba, Ca, Cd, Co, Cu, Fe, Mn, Mg, V and Zn concentrations were determined at the selected wavelengths shown in Table 2.

2.3. Statistical mixture design

Mixture properties are governed by reagent proportions and not by the total quantity of each reagent. The mixture proportions are not independent of one another since

$$f_{HCl} + f_{HNO_3} + f_{H_2O_2} = 1$$

where the f values are the volume fractions of the commercial grade acids. Since digestion is not recommended using pure acid or peroxide solutions only ternary mixtures of these solvents were investigated. To facilitate the statistical interpretation of the mixture models the component proportions were converted to pseudocomponents using the usual equation:

$$x_i = \frac{f_i - L_i}{1 - \sum L_i}$$

where L_i are the lower limits of the proportions of the components used in the mixture design, and f_i are the volume proportions. The subscript i represents HCl, HNO_3 and H_2O_2. The volumes of HCl, HNO_3 and H_2O_2 solutions used to make the mixtures and the corresponding pseudocomponent values are included in Table 1. Fig. 1 shows the compositions of the 10 mixtures investigated here. The vertices correspond to the pseudocomponent mixtures of the commercial solutions: (1) 10% HCl, 20% HNO_3 and 70% H_2O_2, (2) 70% HCl, 10% H_2O_2 and 20% HNO_3 and (3) 10% HCl, 10% H_2O_2 and 80% HNO_3. Since the pseudocomponents are linearly related to the volume proportions, model interpretation in terms of pseudocomponents is easily converted into laboratory values.

Mixture models are determined for each of the metallic ions being analyzed. The recovery value for each ion, y, is expressed as a function of the mixture pseudocomponents by linear, quadratic and special cubic models incorporated in the equation:

$$y = b_{HCl}x_{HCl} + b_{HNO_3}x_{HNO_3} + b_{H_2O_2}x_{H_2O_2} + b_{HCl-HNO_3}x_{HCl}x_{HNO_3} + b_{HCl-H_2O_2}x_{HCl}x_{H_2O_2} + b_{HNO_3-H_2O_2}x_{HNO_3}x_{H_2O_2} + b_{HCl-HNO_3-H_2O_2}x_{HCl}x_{HNO_3}x_{H_2O_2} + e$$

Table 2
Instrument operating conditions for the determination of metallic elements in Oyster tissue (SRM 1566b-NIST).

Sample flow rate (mL min^{-1})	1.0
Radio frequency power (kW)	1.4
Principal argon flow rate (L min^{-1})	15
Auxiliary argon flow rate (L min^{-1})	0.5
Nebulization flow rate (L min^{-1})	0.6
Read delay (s)	30
Auto integration (s, min.–max.)	1–5
Radial observation height (mm)	15
Replicates	3
Wavelengths (nm)	Al I: 396.152; As I: 188.977; Ba II: 455.403; Ca II: 315.887; Cd II: 226.502; Co II: 228.616; Cu I: 324.754; Fe II: 238.204; Mg II: 279.077; Mn II: 257.610; V II: 292.402; Zn I: 213.856;
Background correction	2 points

Table 1
Volume proportions and pseudocomponent values for the mixtures of the statistical design shown in Fig. 1.

Mixture	V_{HCl}	V_{HNO_3}	$V_{H_2O_2}$	x_{HCl}	x_{HNO_3}	$x_{H_2O_2}$
1,11	3.0	1.0	1.0	0.8333	0	0.1667
2,12	0.5	4.0	0.5	0	1	0
3,13	1.0	1.0	3.0	0.1667	0	0.8333
4,14	0.5	2.3	2.2	0	0.4167	0.5833
5,15	2.2	2.3	0.5	0.5833	0.4167	0
6,16	2.0	1.0	2.0	0.5	0	0.5
7,17	1.6	1.7	1.7	0.3888	0.2222	0.3888
8,18	2.8	1.1	1.1	0.7777	0.0283	0.1950
9,19	1.1	2.8	1.1	0.1950	0.6117	0.1950
10,20	1.1	1.1	2.8	0.1950	0.0283	0.7777

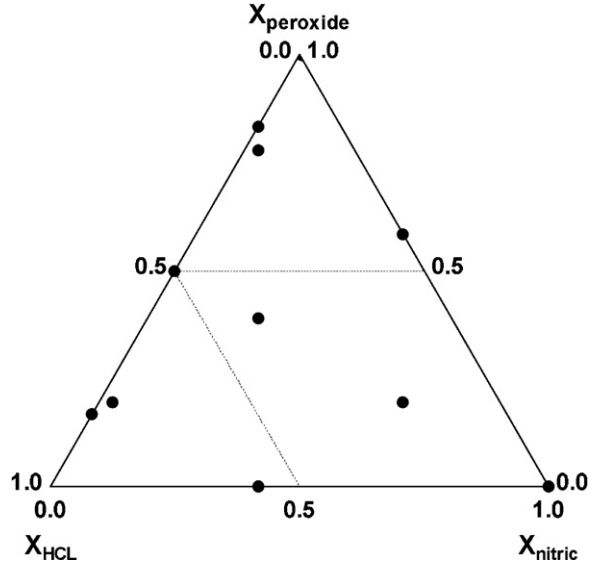


Fig. 1. Mixture design points, 1–10, of Table 1. The pseudocomponents correspond to the vertices of the inner triangle.

For additive mixture behavior a linear model including only the first three terms is adequate to describe percentage recovery. The b_{HCl}, b_{HNO_3} and $b_{H_2O_2}$ are linear blending terms reflecting the importance of each pure pseudocomponent on the percentage recovery. Synergic and antagonistic interactions between pairs of mixture pseudocomponents are given by the next three terms in the equation. Quadratic models contain all the terms in the above equation except the ternary mixture term that describes the interaction involving all three mixture components. The special cubic model includes all the terms in the above equation.

Linear, quadratic and special cubic models were determined for each of the metallic ions analyzed here, Al, As, Ba, Ca, Cd, Co, Cu, Fe, Mg, Mn, V and Zn. Attempts to obtain the best recovery percentage for all these ions involved determining individual linear, quadratic and special cubic models for each ion. These models were compared using ANOVA (ANalysis Of VAriance) and by calculating standard errors for each model coefficient. Models can be validated if they do not have statistically significant lack of fit at the 95% confidence level but have statistically significant regression results at this level. For those ions for which more than one model meets these criteria, the preferred model can be chosen based on the statistical significance of individual model coefficients.

The mixture that is optimum for the recovery of one element may not be optimum for the other ones. For this reason the validated models for all 12 ions must be examined to determine the most appropriate mixture for recovery of all the elements studied. In this case principal component analysis (PCA) and hierarchical cluster analysis (HCA) were used to treat all the experimental data simultaneously rather than individually. These methods allow the user to extract the maximum amount of useful information from multivariate data sets.

2.4. Instrumentation

The analytical measurements were made with a Perkin-Elmer Inductively Coupled Optical Emission Spectrometer, model Optima 3000DV (Norwalk, CT, USA), equipped with a peristaltic pump, a cross-flow nebulizer coupled to a Ryton double pass spray chamber (Scott type) and a ceramic central torch tube injector with an internal diameter of 2.0 mm. This instrument has a solid-state segmented array charge coupled device (SCD) detector and operates in radial and axial torch configurations. For the axial viewing mode a shear gas interface was used to strip off the cool plasma recombination area. The entire system is controlled with PE Winlab software. The spectrometer conditions [22] of operation are presented in Table 2.

3. Results and discussion

3.1. Statistical mixture design

Table 3 contains the recoveries percentage for Al, As, Ba, Ca, Cd, Co, Cu, Fe, Mg, Mn, V and Zn ions determined by digestion of the NIST 1556b reference material using the 10 mixtures of the statistical design. All determinations were performed in duplicate in order to validate the mixture models. Decompositions performed with the 2.8 mL HCl, 1.1 mL HNO_3 and 1.1 mL H_2O_2 solutions were not successful because the Oyster tissue was carbonized.

Linear, quadratic and special cubic models were determined for all the metallic ions. The coefficients and their standard errors for the preferred models for each ion are given in Table 4 for all ions except Al and Ba. The linear and quadratic models for Al suffered from statistical lack of fit at 95% confidence level whereas the special cubic model was not significant at that level. For the Ba ion all models showed insignificant regression results. As such the recoveries of the Al and Ba ions are predicted to be independent of the component proportions of the digestion mixture. Significant mixture models with no statistical lack of fit were found for all the other ions. Quadratic models were most adequate for describing the As, Ca, Cd, Cu, Fe, Mg, Mn and Zn ion recoveries. For all these models at least one binary interaction model coefficient was significant at the 95% confidence level. Furthermore none of the special cubic models for these ions had significant ternary interaction model coefficients. Linear models were validated for the Co and V ions. Their quadratic models did not contain any significant binary interaction model coefficients.

For each of these models the *F* distribution statistical for lack of fit was calculated using ANOVA. All the values given in Table 4 are much smaller than the 95% confidence critical *F* value demonstrating that the models accurately predict the recovery values within experimental error. Furthermore the *F* statistical values calculated for regression significance, also given in Table 4, are con-

Table 3
Percentage recoveries of the ions for the mixtures of statistical design.

Mixture	Al		As		Ba		Ca		Cd		Co		Cu		Fe		Mg		Mn		V		Zn	
1	53	46	85	78	86	63	96	88	96	87	54	54	97	88	88	82	94	86	93	84	78	78	92	84
2	54	39	78	76	112	68	75	74	62	68	14	40	70	69	70	71	76	74	74	73	26	69	73	75
3	55	36	94	89	94	55	101	94	105	95	121	54	94	89	93	86	98	94	98	92	87	69	97	91
4	75	61	106	97	139	117	97	94	97	92	81	52	88	86	87	87	93	92	90	90	60	67	92	89
5	15	38	74	72	**	68	89	79	83	77	40	40	81	73	80	69	86	79	84	77	34	59	86	78
6	40	18	86	83	31	**	96	97	96	94	80	54	90	90	91	89	94	94	93	92	77	86	92	92
7	57	88	90	93	93	**	98	95	97	94	81	67	89	85	92	89	96	92	94	90	69	78	94	90
9	39	41	89	90	54	37	94	93	90	91	54	54	85	85	87	88	91	91	89	89	52	78	89	88
10	38	47	88	95	42	67	87	101	86	98	120	67	80	91	80	92	84	97	85	95	78	78	81	96

Table 4
Model coefficients and their standard errors for the ion recoveries and calculated and reference *F*-distribution values for model validation.

Coefficient	As	Ca	Cd	Co	Cu	Fe	Mg	Mn	V	Zn
b_{HCl}	75.91 (±4.72)	84.41 (±6.32)	84.10 (±7.31)	47.48 (±12.54)	90.55 (±6.14)	74.56 (±6.22)	83.23 (±5.80)	81.57 (±5.54)	71.33 (±8.56)	82.14 (±6.23)
b_{HNO_3}	77.21 (±2.47)	75.27 (±3.31)	66.00 (±3.83)	31.01 (±10.57)	70.52 (±3.21)	71.32 (±3.26)	75.68 (±3.04)	74.22 (±2.90)	45.32 (±7.21)	74.51 (±3.26)
$b_{H_2O_2}$	91.03 (±4.21)	90.16 (±5.63)	91.72 (±6.51)	99.91 (±10.64)	85.37 (±5.47)	78.72 (±5.54)	88.46 (±5.17)	88.12 (±4.93)	82.83 (±7.26)	87.31 (±5.55)
$b_{HCl-HNO_3}$	−8.32 (±13.91)	19.82 (±18.61)	22.65 (±21.51)	–	-14.29 (±18.08)	13.02 (±18.31)	15.52 (±17.08)	14.22 (±16.30)	–	16.77 (±18.34)
$b_{HCl-H_2O_2}$	14.21 (±19.98)	40.70 (±26.74)	34.29 (±30.91)	–	11.83 (±25.98)	60.60 (±26.31)	36.14 (±24.54)	34.93 (±23.41)	–	31.40 (±26.35)
$b_{HNO_3-H_2O_2}$	72.66 (±13.23)	52.76 (±17.71)	62.86 (±20.47)	–	38.44 (±17.20)	53.88 (±17.43)	43.24 (±16.26)	36.86 (±15.51)	–	38.45 (±17.45)
$b_{HCl-HNO_3-H_2O_2}$	–	–	–	–	–	–	–	–	–	–
F_{faj}	0.96	0.81	2.02	0.17	1.95	1.35	1.33	1.42	0.54	0.80
F_{crit}	3.86	3.86	3.86	3.37	3.86	3.86	3.86	3.86	3.37	3.86
F_{Reg}	18.61	7.54	10.92	9.45	7.18	6.61	6.66	7.50	6.52	5.04
F_{crit}	3.11	3.11	3.11	3.68	3.11	3.11	3.11	3.11	3.11	3.11

Fig. 2. Principal component loading plot of the ion recoveries for the experiments of the mixture design. The cluster of points represents the Ca, Cd, Cu, Fe, Mg, Mn and Zn ions.

siderably higher than their corresponding critical values showing that recovery values indeed depend on the HCl, HNO_3 and H_2O_2 proportions.

The quadratic models in Table 4 contain some striking similarities. First, for all the ions except for As and Cu, $b_{H_2O_2} > b_{HCl} > b_{HNO_3}$. For the As model $b_{H_2O_2} > b_{HCl} = b_{HNO_3}$ and for Cu $b_{HCl} = b_{H_2O_2} > b_{HNO_3}$ within experimental error. Second, the HNO_3–H_2O_2 interaction coefficients are two to four times larger than the corresponding standard errors in each model with all these coefficients being significant at the 95% confidence level. The linear models for Co and V have some similarities to the quadratic models. Both models have $b_{H_2O_2} > b_{HCl} > b_{HNO_3}$ although no binary interaction terms were found to be significant.

The above similarities show that the percentage recoveries of these ions have similar dependencies on the HCl, HNO_3 and H_2O_2 proportions. The linear terms indicate that recoveries for these ions are highest for the H_2O_2 pseudocomponent (10% HCl, 20% HNO_3 and 70% H_2O_2 solution) followed by the HCl pseudocomponent (70% HCl, 10% H_2O_2 and 20% HNO_3) with the HNO_3 pseudocomponent (10% HCl, 10% H_2O_2 and 80% HNO_3) promoting the smallest recovery. The synergistic HNO_3–H_2O_2 interaction term provides significant contributions to the recoveries of As, Ca, Cd, Cu, Fe, Mg, Mn and Zn ions. The HCl–H_2O_2 binary interaction terms are positive for all these ion recoveries and usually are larger than their corresponding standard errors. However they are not significant at the 95% confidence level for any of these ions.

Principal component (PC) graphs are useful for illustrating the correlations between the analytical results of the different ions. Fig. 2 shows the loading graph for the first two principal components that represent 80% of the total variance of the data set in Table 4. The ion recoveries more adequately described by the quadratic models have almost identical loadings and their points form a tight cluster in the PC plot except for As point that is closer to this cluster than any of the other ion points. This indicates that ion recoveries for the experiments of the mixture design are highly correlated. Indeed correlation coefficients for all the ions in the tight cluster are 0.95 or more and between 0.72 and 0.78 for all these ions with the As ion. The V and Co ion points are close to each other and farther from the cluster. Their ion recoveries follow a linear model with $b_{H_2O_2} > b_{HCl} > b_{HNO_3}$ the same numerical ordering in the linear terms as have most of the quadratic models, but without any significant binary interaction. The Al and Ba ion recoveries with models indicating no dependence on the type of mixture used for

Table 5
Equivalent background concentration (BEC), limits of detection (LOD) and limits of quantification (LOQ) for the elements studied.

Element	Wavelength (nm)	Instrumental BEC ($\mu g\,mL^{-1}$)	BEC ($\mu g\,mL^{-1}$)	LOD ($\mu g\,mL^{-1}$)	LOQ ($\mu g\,mL^{-1}$)
Al	396.153	0.95	0.076	0.0025	0.0082
As	188.979	4.55	0.0028	0.012	0.04
Ba	455.403	0.04	0.018	0.00074	0.0025
Ca	315.887	0.73	0.00053	0.000022	0.000074
Cd	226.502	0.11	0.00015	0.000043	0.00014
Co	228.616	0.23	0.00014	0.000056	0.00019
Cu	324.754	0.18	0.00031	0.000022	0.000074
Fe	238.204	0.15	0.060	0.005	0.016
Mg	279.077	1.00	0.012	0.00046	0.0015
Mn	257.610	0.05	0.00039	0.00001	0.000034
V	292.402	0.25	0.00022	0.000084	0.00028
Zn	213.856	0.06	0.0083	0.00001	0.000033

digestion have loading points at the bottom right far removed from the other points.

The contour lines for the response surface for Cd recovery are shown in Fig. 3. It is representative of all the elements that are described by quadratic models for ions with points in the tight cluster. The vertex for the H_2O_2 pseudocomponent is predicted to have higher recoveries than those for HCl pseudocomponent. The HNO_3 pseudocomponent is predicted to have the smallest recovery value. However does exist a high plateau region in the upper portion of the triangle with ion recoveries expected to be 95% or more. The plateau represents mixtures for which the synergic binary interactions have important contributions that increase ion recovery. A maximum recovery is predicted for 19%, 18% and 63% of the HCl, HNO_3 and H_2O_2 pseudocomponents, respectively. This corresponds to 21.4%, 30.8% and 47.8% of the HCl, HNO_3 and H_2O_2 commercial solutions used here.

3.2. Figures of merits

BEC, SBR and LOD were calculated according to the literature [23], relating to the analyte concentration and SBR (analytical signal and signal background ratio). Limit of quantification was calculated as 3.3 LOD [24].

Table 5 presents the values of BEC, LOD and LOQ. Comparing the values of BEC from the manufacturer with those obtained experimentally it is possible to conclude that the instrumental conditions of this work were robust ones as can be seen by the MgII/MgI ratio of 9.2 and by the low background signal.

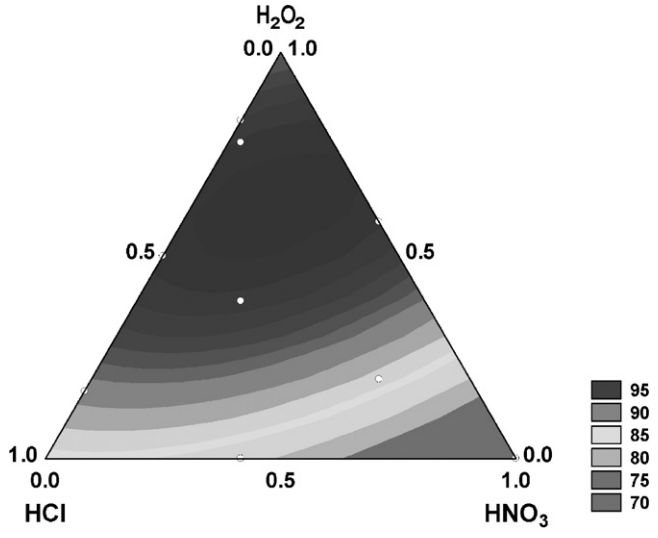


Fig. 3. Contour curves for the response surface of the Cd ion determined from the results of the mixture design.

Table 6
Concentration and recovery values for the analytes in the certified reference material (CRM 1566b).

Element	Concentration of CRM		Recovery (%)
	Declared value ($\mu g\,g^{-1}$)	Obtained value ($\mu g\,g^{-1}$)	
Al	197.2 ± 6.0	94 ± 8	47.9 ± 4.2
As	7.65 ± 0.65	7.52 ± 0.17	98.4 ± 2.2
Ba	8.6 ± 0.3	7.11 ± 0.39	92.9 ± 5.1
Ca	838 ± 20	877 ± 12	104.7 ± 1.4
Cd	2.48 ± 0.08	2.677 ± 0.56	108.0 ± 2.2
Co	0.371 ± 0.009	0.311 ± 0.017	83.8 ± 4.5
Cu	71.6 ± 1.6	72.8 ± 1.4	101.7 ± 1.9
Fe	205.8 ± 6.8	205.3 ± 2.7	99.8 ± 1.3
Mg	1085 ± 23	1106 ± 15	101.9 ± 1.4
Mn	18.5 ± 0.2	20.22 ± 0.47	109.3 ± 2.5
V	0.577 ± 0.023	0.393 ± 0.037	68.0 ± 6.4
Zn	1424 ± 46	1415 ± 61	99.3 ± 4.3

3.3. Validation of method

An evaluation of the accuracy of the digestion method using a digestion block was carried out under the optimized instrumental conditions. Table 6 shows good efficiency of digestion procedure with recoveries between 84% and 110%. Concentrations for Co and V in the certified reference material are lower than their LOQ values resulting in low recoveries. Aluminum also showed problems and this can be understood considering the need to add fluoridric acid in the sample for the recovery of aluminum since fluoride ion reacts with refractory oxides and forms a complex in order to increase the solubility [1].

Statistical tests using one-way ANOVA as well as the multiple Student and Newman–Keuls comparison methods were carried out to verify the existence of significant differences between results from the decomposition method with those of the reference material for the analyzed ions [25]. The null hypothesis indicating no significant difference at the 95% confidence level between the results of the proposed digestion method and the certified values was obtained for the As, Ba, Ca, Cd, Cu, Fe, Mg, Mn and Zn ions.

4. Conclusion

An optimum 21.4%, 30.8% and 47.8% mixture of HCl, HNO_3 and H_2O_2 commercial solutions was determined using a statistical simplex centroid design for the digestion of a biological sample and the subsequent determination of the Al, As, Ba, Ca, Cd, Co, Cu, Fe, Mn, Mg, V and Zn concentrations by ICP OES.

References

[1] J.F. Krug (ed.), Métodos de preparo de amostras; fundamentos sobre preparo de amostras orgânicas e inorgânicas para análise elementar, 1st ed., Piracicaba, 2008, 340 p.
[2] J.C.J. Silva, E.E. Garcia, A.R.A. Nogueira, J.A. Nobrega, Talanta 55 (2001) 847.

[3] E.N.V.M. Carrilho, A.R.A. Nogueira, J.A. Nobrega, G.B. de Souza, G.M. Cruz, Fresenius J. Anal. Chem. 371 (2001) 536.
[4] A.A. Momen, G.A. Zachariadis, A.N. Anthemidis, J.A. Stratis, Talanta 71 (2007) 443.
[5] R.A. de Sousa, A.S. Ribeiro, M.A. Vieira, A.J. Curtius, N. Baccan, S. Cadore, Microchim. Acta 159 (2007) 241.
[6] J. Sneddon, M.D. Vincent, Anal. Lett. 41 (2008) 1291.
[7] Y. Saavedra, A. González, P. Fernández, J. Blanco, Spectrochim. Acta Part B 59 (2004) 533.
[8] A. Sokolwski, A.S. Bawazir, M. Wolowicz, Arch. Environ. Sci. Toxicol. 46 (2004) 67.
[9] N.A.R. Pedro, E. de Oliveira, S. Cadore, Food Chem. 95 (2006) 94.
[10] J. Wang, T. Nakazato, K. Sakanishi, O. Yamada, H. Tao, I. Saito, Talanta 68 (2006) 1584.
[11] A.S. Ribeiro, M.A.Z. Arruda, S. Cadore, Microchim. Acta 141 (2003) 149.
[12] M.C. Santos, R.A. de Sousa, S. Cadore, J.A. Nobrega, R. Barnes, M. Tatro, Spectrochim. Acta Part B 61 (2006) 465.
[13] M.M. Storelli, G.O. Marcotrigiano, Environ. Monit. Assess. 102 (2005) 159.
[14] A.C. Tomazelli, L.A. Martinelli, W.E.P. Avelar, Braz. Arch. Biol. Technol. 46 (2003) 673.
[15] L.R. Astudillo, C.L. Yen, J. Agard, I. Bekele, R. Hubbard, Arch. Environ. Contamin. Toxicol. 42 (2002) 410.
[16] O.M. Pereira, M.B. Henriques, O. Zenebon, A. Sakuma, C.S. Kira, Rev. Inst. Adolfo Lutz 61 (2002) 19.
[17] J.A. Cornell, Experiments with Mixtures: Designs, Models and Analysis of Mixture Data, 2nd ed., Wiley, New York, 1990.
[18] R.E. Bruns, I.S. Scarminio, B.B. Neto, Statistical Design—Chemometrics, Elsevier, Amsterdam, 2006.
[19] F.R. Albuquerque, I.M. Santos, S.J.G. Lima, M.R. Cássia-Santos, L.E.B. Soledade, A.G. Souza, A.E. Martinelli Lima, Cerâmica 53 (2007) 300.
[20] C.B. Cano, M.L. Felsner, R.E. Bruns, J.R. Matos, L.B. Almeida-Muradian, J. Braz. Chem. Soc. 17 (2006) 588.
[21] R.M.W.N. Carvalho, Determinação de Íons Metálicos em Moluscos Bivalves do Manguezal da Região Petrolífera de São Francisco do Conde – Recôncavo Baiano (Doctoral Thesis)—Universidade Estadual de Campinas, Campinas, Brazil, 2006, 162 p.
[22] R.A. de Sousa, N. Baccan, S. Cadore, J. Braz. Chem. Soc. 16 (2005) 540.
[23] V. Thomsen, G. Roberts, K. Burgess, Spectroscopy 15 (2000) 33.
[24] V. Thomsen, D. Schatzlein, D. Mercuro, Spectroscopy 18 (2003) 112.
[25] J.H. Zar, Biostatistical Analysis, 4th ed., Prentice Hall Inc., Upper Saddle River, 1999.

Talanta 80 (2009) 565–571

Contents lists available at ScienceDirect

Talanta

journal homepage: www.elsevier.com/locate/talanta

Exploring fiber optic approach to sense humid environment over nano-crystalline zinc oxide film

S.K. Shukla [a,*], Ashutosh Tiwari [b,*], G.K. Parashar [c], A.P. Mishra [d], G.C. Dubey [e]

[a] Department of Polymer Science, Bhaskaracharya College of Applied Sciences, University of Delhi, New Delhi 110075, India
[b] Department of Mechanical Engineering, University of Wisconsin-Milwaukee, 3200 N Cremar St., Milwaukee 53211, WI, USA
[c] Swami Shradhanand College, University of Delhi, Delhi 110036, India
[d] Department of Science and Technology, Technology Bhawan, New Delhi 110016, India
[e] Institute of Defense Scientists and Technologists, C.F.E.E.S, S.K. Mazumdar Road, Delhi 110054, India

ARTICLE INFO

Article history:
Received 13 April 2009
Received in revised form 10 July 2009
Accepted 13 July 2009
Available online 21 July 2009

Keywords:
Molecular precursor
Nano-crystalline ZnO film
Fiber optics
Humidity sensor

ABSTRACT

A novel humidity sensor made up of nano-crystalline zinc oxide (ZnO) film, coated onto the U-shaped typical glass substrate as a wave guide, conjugated with an optical fiber and He–Ne un-polarized laser source. The nano-crystalline zinc oxide (ZnO) was synthesized using single molecular precursor method. The resulting material was characterized with Fourier transform infrared spectroscopy (FTIR), X-ray diffractometry (XRD), thermogravimetric-differential thermal analysis (TG-DTA) and scanning electron microscopy (SEM). In the thin film, ZnO particles exhibited the wurtzite phase structure with the particle size in a diameter range of 70–80 nm. The humidity sensing characteristic has been estimated by measuring the optical permeability (OP) as a function of percentage relative humidity (%RH) in the ranging from 5 to 90 inside a closed chamber. The OP decreases linearly with increase in %RH with a respond time of about 30 and recovery time of 35 s. The sensor exhibits the sensitivity of 0.45 in the %RH range 5–50 and 0.30 from 50 to 90.

© 2009 Elsevier B.V. All rights reserved.

1. Introduction

In the recent years, humidity sensors have been gained much attention of scientists because of their demand for the monitoring of humidity in the environment and also in various industrial processes including food, electronics, textile, and pharmaceuticals [1–4]. It is found that most of the existing humidity sensors are based on the modulation of range of materials in their electrical parameters like resistance, capacitance or conductance [5–7]; however, they are expensive, large in size, and sometimes cannot operate at room temperature. Thus, much attention has been paid lately to the development of compact, low-priced sensors that can detect humidity in real time at room temperature.

Particularly, with the advent of optical fiber technology, a considerable level of research has been focused on fiber optic based techniques especially for humidity sensing. The fiber optic based humidity sensors show additional features such as small size, immunity to electromagnetic interference, multiplexing, remote sensing capabilities and offer specificity and efficiency for the detection of wide range of analytes [8–12]. A fiber optic detection system, comprises: (1) a light source; (2) an optical sensitive layer; (3) an optical detector with optical connection. The optical fiber has a plurality of bends which follow a circuitous path and establishes a detection zone of the optical sensor [13–16].

In this context, the use of nano-materials to fabricate sensors is one of the most exciting approaches because nano-materials have a unique structure and high surface-to-volume ratio. The surfaces of nano-materials can also be tailored in the molecular scale in order to achieve various desirable properties [17]. Many attempts have been made to fabricate nano-crystalline ZnO of unique properties for versatile applications in the area of transparent electronics, light emitting diodes, piezo-electric devices, spin electronics and chemical sensors [17–20]. Further, nano-crystalline ZnO has stable structure with good chemical stability and favorable properties that are suitable for device fabrications [21–25]. In the past few years, many reports have been published on the fabrication of ZnO films of different surface morphologies such as single and multi-dimensional nano-structural shapes like nano-wire, nano-tube, nano-ring and nano-tetrapods using various film deposition techniques for example chemical vapor deposition, thermal evaporation, electro-deposition [26–30]. Although physical processes are prevailing for the synthesis of the nano-structured ZnO but the chemical methods such as electro-deposition, polymer assisted growth and sol–gel have been developed simultaneously. Among them, sol–gel methods have proven the easiest ways to form ZnO

* Corresponding authors. Tel.: +91 11 2785 9078; fax: +91 11 2508 7596.
E-mail addresses: sarojshukla2003@yahoo.co.in (S.K. Shukla), tiwari@uwm.edu, ashunpl@gmail.com (A. Tiwari).

0039-9140/$ – see front matter © 2009 Elsevier B.V. All rights reserved.
doi:10.1016/j.talanta.2009.07.026

Table 1
Comparison of the characteristics of nano-sized ZnO based humidity sensors.

ZnO based sensing materials	Analytes and sensor types	Linearity with HR	Response time and recovery time	Reference
ZnO nano-particles film	Humidity and fiber optic	5–90%	30 and 35 s	Present work
Gallium-doped ZnO	Humidity and impedancometric	30–90%	70 and 90 s	[46]
KCl-doped ZnO nano-fibers	Humidity and impedancometric	25–95%	2 and 1 s	[47]
p-ZnO/n-Si thin film	Humidity and conductometric	30–97%	12 and 36 s	[48]
Ag–Pd interdigitated electrodes loaded with ZnO nano-rods	Humidity and conductometric	11–95%	5 and 10 s	[49]
ZnO nano-rods of 75–300 nm	Humidity and conductometric	10–95%	–	[50]
ZnO nano-rods	Humidity and impedancometric	11–95%	5 and 10 s	[51]

nano-structures at relatively lower temperature and less rigorous synthesis conditions [31–33].

Recent development of nano-materials, with every imaginable combination of physical and chemical characteristics, has led to the fabrication of efficient humidity sensors that can be used for a wide range of applications. Zhou et al. reported fiber optics based humidity sensors using etched borosilicate optical fiber segment doped with $CoCl_2$ that sense humidity by in-line absorption technique [34]. Otsuki et al. have prepared rhodamine-B doped HPC film and they observed humidity sensing measurements with U-bent fiber [35]. Gupta et al. fabricated phenol red doped polymethyl methacrylate film based humidity sensor having limited detection range from 30 to 80%RH [36,37]. Also, the doped and undoped nano-structured ZnO were used to detect humidity using various transducers as listed in Table 1. Most of the reported humidity sensors are not widely adaptable due to their limited operational range, cost effectiveness and risky temperament. Therefore, it will be interested to prepare an efficient humidity sensor of a wider operational range using eco-friendly nano-materials such as nano-crystalline ZnO at room temperature.

This study investigates the feasibility of nano-crystalline ZnO film for a potential humidity sensor. A typical U-shaped nano-crystalline zinc oxide coated Pyrex glass rod has been used as sensing element, conjugated with an optical fiber, and He–Ne unpolarized laser source. The advantageous features of the present sensor include low price tag, ease of fabricated, sufficiently larger operational range, good stability and sensitivity.

2. Experimental

2.1. Materials

Zinc acetate dihydrate ($Zn(OAc)_2{\cdot}2H_2O$, 99%, Sigma–Aldrich), ethanol (99.5%, E. Merck), methanol (99.8%, E. Merck) and benzene (99.8%, Sigma–Aldrich) were used without further purifications.

2.2. Synthesis of precursor

To prepare the precursor solution, 50 mM of $Zn(OAc)_2{\cdot}2H_2O$ was dissolved in a 25 mL of anhydrous ethanol. Next, the resulting mixture was stirred for 2 h at room temperature until the $Zn(OAc)_2{\cdot}2H_2O$ flakes were completely dissolved. In the obtained homogeneous solution, added 5 mL of anhydrous benzene and again stirred at 60 °C for 24 h. The solution is then kept at standing for 72 h to ensure hydrolytic stability against any sort of precipitation, coagulation or suspension. The prepared precursor solution was used further for the fabrication of nano-crystalline ZnO films.

2.3. Preparation of precursor film

In our already ongoing laboratory programme for developing metal oxide thin film or coatings on variedly shaped complex substrate, we have preferred relatively convenient 'spin casting' or dip coating methodology. To facilitate prior physico-chemical and spectroscopic characterizations, we have also casted the precursor film on the glass substrate and then subjected it to thermal treatment through gradual heating up to ~500 °C. The thickness of representative nano-crystalline ZnO films was measured using profile-meter (SPN Technology).

2.4. Characterization

The produced film has been characterized using FTIR, TGA-DTA, XRD, and SEM techniques. FTIR spectra are recorded by a PerkinElmer (RK-1310) FTIR spectrometer by making pellet with dehydrated KBr at 10 ton pressure. The thermal analysis was carried out with a Rigaku Thermoflex PTC-10A thermal analyzer at 10 °C min^{-1} heating rate. The nano-sized crystalline structure of the ZnO film was studied by Rigaku Rotaflex (RAD/Max-200B) XRD spectrometer, Rigaku Corporation Japan at 1° min^{-1} scanning speed and JEOL-840 scanning electron microscope, JEOL Corporation Japan operated at 15 kV. The films were sputter-coated with a thin layer of gold (~20 nm) prior to the morphological examination.

2.5. Fabrication of film on U-shaped glass rod

The glass rod with the diameter of 1 mm has bent in U-shaped and dipped in the above prepared precursor solution, dried and then gradually heated again up to ~500 °C to obtain nano-crystalline ZnO cladding.

2.6. Device fabrication, assembly and sensing measurements

The nano-sized ZnO coated U-shaped Pyrex glass was fixed on the wall of a glass chamber (4 cm × 7 cm) via two holes. The resulting both arms of U-shaped glass were projected outside and coupled with optical fiber. The optical fiber was a standard single mode optical fiber at 1300 nm with core and cladding diameters of 8.3 and

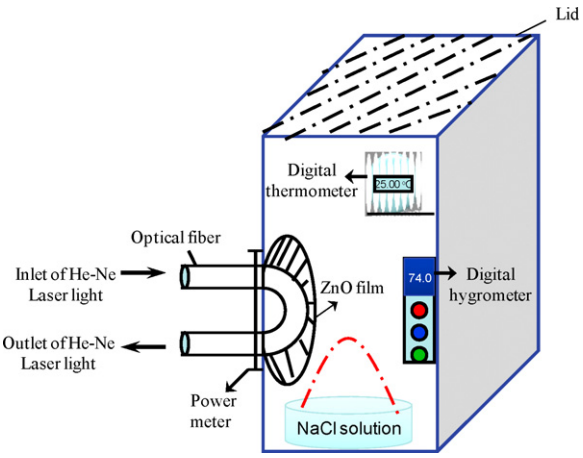


Fig. 1. Schematic illustration of optical fiber based humidity sensor using nano-crystalline ZnO film as a sensing element in a complex device assembly.

125 μm, respectively (cable type OFNR from Optical Cable). The unpolarized laser light from He–Ne laser source (2 mW) was passed from one end of the fiber and the output intensity was measured at the other end of the optical fiber. The photo-detector-II (Epitaxx InGaAs Photodetector, type ETX) was used to provide a reference for the optical power incident at the nano-crystalline ZnO film coating. The photo-detector-I (Anritsu Optical Power Meter ML93B) measured the reflected optical power. The saturated solution of KOH was used to control %HR of the glass chamber and also monitored by a reference hygrometer. During our experimental observations setup, the relative humidity inside the sensing chamber was variably controlled up to 90%. A thermometer with least count of 0.1 °C was also positioned together for monitoring the temperature inside the chamber. The complete experimental setup is shown in Fig. 1. All experiments were conducted at room temperature (~25 °C), with the same sensor used for each set of measurements. Prior to each measurement the sensor was heated in vacuum at 100 °C for 2 h to completely remove the adsorbed moisture. All measurements were carried out at 25 °C.

3. Results

The deposition of film specifically on a complex shaped substrate has been found relatively a difficult task often as the challenging ones, apart from being expensive as experienced by us in our previous studies. In the present study, U-shaped Pyrex glass rod was employed as a candidate to act as a prospective wave guide when carefully clad with nano-crystalline ZnO film with a desired as homogenous cast as possible. We prepared the nano-crystalline ZnO film as described in the literature [38]. To modify or if possible to work out in parallel methodology, where procuring nano-crystalline ZnO film on the above mentioned target could be made simple and cost effective. Thus, we happened to devise–design–develop and arrive at a method to prepare a precursor solution desirable for casting of ZnO thin film, coatable onto any complex shape of glass substrate, i.e., just by dipping substrate into the precursor solution, drying and then firing at a desired temperature to an optimum duration.

3.1. FTIR spectra

The soluble form of the precursor, coated on the glass substrate as a film at room temperature and subjected to a scratched portion of the film for the FTIR investigation in the region from 500 cm^{-1} to 4000 cm^{-1}. The spectrum given in Fig. 2A, clearly shows a broad

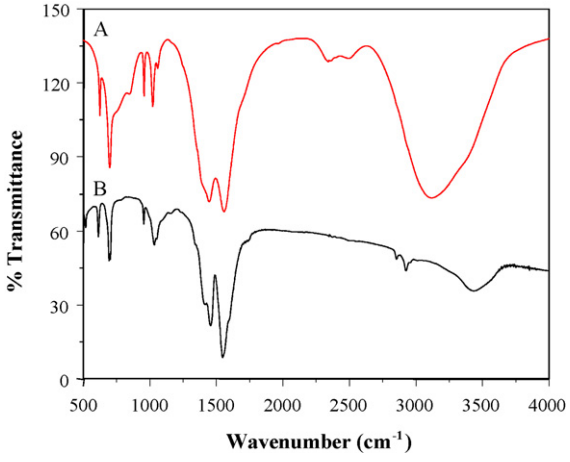


Fig. 2. FTIR spectra of the ZnO film prepared at: (A) room temperature and (B) after heat treatment at 500 °C.

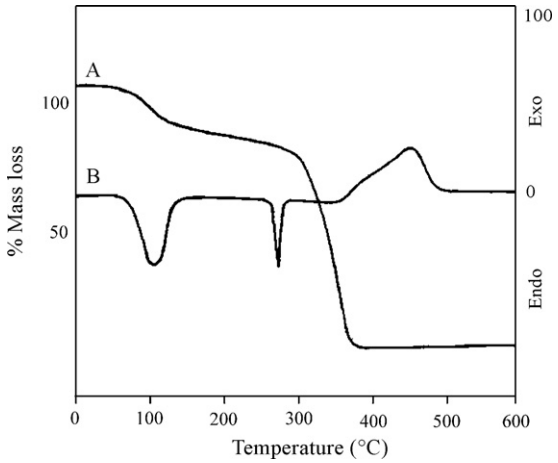


Fig. 3. (A) TGA and (B) DSC profiles of the prepared ZnO film.

strong band centered around 3130 cm^{-1} possibly due to the presence of –OH stretching vibrations contributed by the surrounding solvent molecules. The two bands appearing at 1554 cm^{-1} and 1440 cm^{-1} may attribute to the presence of anti-symmetric and symmetric C–O stretching vibrations, respectively, which confirm the presence of acetate group in the precursor. Though further investigations are required while ascertaining various modes of coordination involved in carboxylate bonding with the metal ions, the current individual positions and particularly the separation between the asymmetrical C–O (~1554 cm^{-1}) and symmetrical C–O (~1440 cm^{-1}) stretching vibrations probably indicate rather bridging modes of coordination involving in the acetate group surrounding the zinc metal ions.

In another supporting exercise, the above precursor film was subjected to gradual heating and maintained for some time at ~500 °C, cooled to room temperature and then subjected to FTIR investigations. The spectrum is given in Fig. 2B. It was observed that after treatment, the broad band at ~3130 cm^{-1} in Fig. 2A was found somehow completely missing in Fig. 2B. But appear a new band centered on ~3444 cm^{-1}. The individual position and separation between anti-symmetric and symmetric carboxylate stretching vibrations were again observed with a considerable shift at ~1546 cm^{-1} and 1458 cm^{-1}, respectively. It indicates that the surroundings of zinc metal ion including the modes with the carboxylate binding and resulted a positive change evolving through metal oxygen bonds. It suggests that after the gradual heating precursor film produces anhydrous zinc oxide film. Hence, heat treatment is a basic requirement for anhydrous fabrication of zinc oxide film.

3.2. Thermogravimetric analysis

Thermal behavior of a scratched portion of the ZnO precursor film has been recorded and is shown in Fig. 3. The TGA curve shows two-step mass losses, first at ~125 °C due to desolvation and second at ~320 °C due to decomposition of intermediate to form zinc oxide. The observed and calculated weight change of the precursor film at different steps is corresponding to the zinc acetate. The data is given in Table 2.

The DTA curve as in Fig. 3 is showing three peaks at temperatures 100.4 °C (endothermic), 256.7 °C (endothermic) and 452.3 °C (exothermic). The first endothermic peak is due to desolvation and second is because of the melting of precursor, while the third exothermic peak is associated for the decomposition of zinc acetate [39]. The thermogram indicates that decomposition of zinc acetate completed at ~400 °C. Therefore, in order to prepare a ZnO film, it

Table 2
Details of the TGA information of ZnO film.

Sl. no.	Temperature (°C)	Weight loss (observed)	Weight loss (calculated)	Inference
1	50–120	16.5	16.4	Desolvation
2	200–350	66.2	50.75	Decomposition

Table 3
Details of the DTA statistics of ZnO film.

Sl. no.	Temperature (°C)	Nature	Inference
1	100.4	Endothermic	Desolvation
2	256.7	Endothermic	Melting
3	425.3	Exothermic	Decomposition

is necessary to anneal the precursor film above 400 °C. The heating at 500 °C is done in the present study in order to ensure complete decomposition of zinc acetate precursor into ZnO. The transition temperatures, nature and inference about precursor film concluded from DTA curve is also tabulated Table 3.

3.3. XRD spectra

The ZnO precursor film, after heating at 500 °C has been examined by XRD and the diffraction pattern shown in Fig. 4. The observed peaks in XRD are matching with the reported diffraction peaks for ZnO for wurtzite hexagonal structure [39]. In the XRD pattern ZnO film shows the sharp X-ray reflection at $2\theta = 31^\circ$ (1 0 0), 34 (0 0 2), 36 (1 0 1), 47 (1 0 2), 56 (1 1 0), 62 (1 0 3), 66 (2 0 0), 67 (1 1 2), 69 (2 0 1), 72 (0 0 4), and 76° (2 0 2). These peaks correspond to nano-crystalline ZnO. The crystallite size of ZnO nano-particles was calculated using the Scherrer's equation [40] and was found to be in the range of 70–80 nm.

3.4. SEM study

SEM image of the ZnO film (after heat treatment at 500 °C) is shows as in Fig. 5. The microstructure of ZnO film illustrates a homogeneous distribution of globular particles in a porous film surface. The estimated value of ZnO particles in the film was measured in a range of ~70–80 nm. It appeared that some of the ZnO particles visualized bigger. It may happen due to the agglomeration of neighboring ZnO particles. In this context, the dip coated precursor of ZnO film can be converted into nano-crystalline ZnO film. The obtained film has a unique surface structure and can provide a high surface-to-volume ratio for the adsorption of humidity over the film.

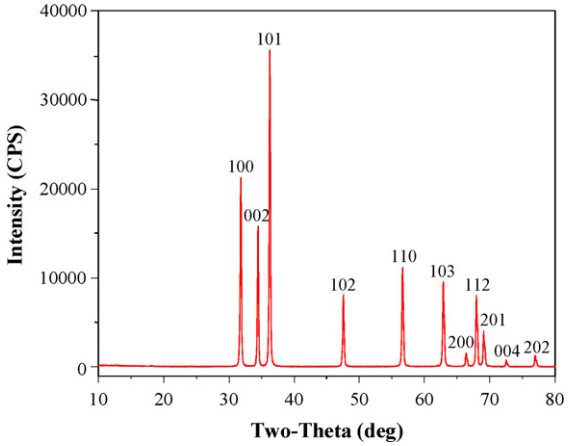


Fig. 4. XRD of the ZnO film after heat treatment at 500 °C.

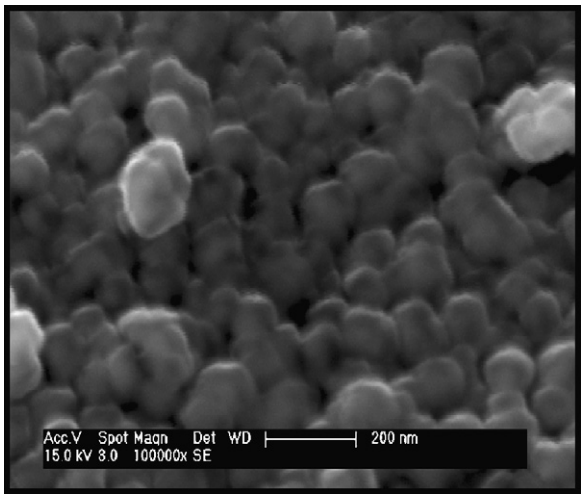


Fig. 5. SEM micrograph of the nano-crystalline ZnO film after heat treatment at 500 °C.

3.5. Humidity sensing behavior

The humidity sensing behaviors of nano-crystalline ZnO film (thickness of film = ~600 nm) were evaluated by the reported method [34]. The change in the optical permeability of the sensing probe, i.e., U-shaped nano-crystalline ZnO film as a function of %HR and time was recorded in a closed chamber at room temperature. Fig. 6 shows the variation of output Ir/Ii versus %RH profile of U-shaped nano-crystalline ZnO film with varying %RH in the presence and absence of interferences such as methanol and ethanol. The output Ir/Ii decreases with an increase in %RH ranging from 5 to 90. In general, the optical permeability of probe decreases

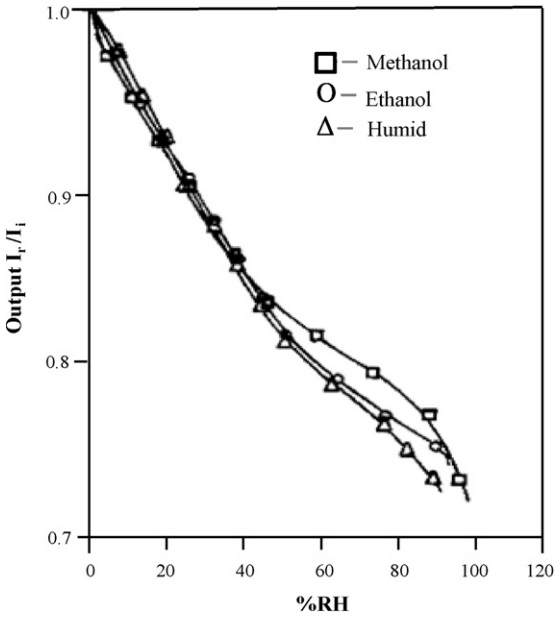


Fig. 6. Linear relationship between optical output and relative humidity content up to 90% at 25 °C.

Table 4
Effect of interference on the nano-crystalline ZnO humidity sensor at 25 °C.

Sl. no.	Analyte/interference	Output Ir/Ii
1.	75%HR	0.76
2.	75%HR + ethanol (80 mM)	0.77
3.	75%HR + methanol (80 mM)	0.80

linearly with increase in %RH and exhibits the sensitivity of 0.45 (%RH range 5–50) and 0.3 (%RH range 50–90). The effect of interferents (methanol and ethanol) was studied on the output Ir/Ii responses of the probe (Table 4). The volatile methanol (80 mM) and ethanol (80 mM) were added into the sensing chamber. It was found that the presence of interferents had a negligible effect at %RH ranging from 5 to 45 but after that optical response was obtained about 2–6% higher than those obtained from the standard method; therefore, using this probe, %HR can be detected negligible interference.

The sensitivity of the sensor was estimated from the measured value of output Ir/Ii (i.e., optical permeability) in the evacuated chamber or/and at a fixed %RH. The graph of changes in output Ir/Ii of the probe as a function of time is shown in Fig. 7. With exposure of humidity (%HR 80) to probes, the sudden decrease in output Ir/Ii was observed at 25 °C. The U-shaped nano-crystalline ZnO film was obtained a response time of ~30 s and a recovery time of about 35 s. Table 1 compares the characteristics of nano-sized ZnO based humidity sensors as reported in the literature. From this table it is clearly observed that most of the reported humidity sensors are not widely adaptable due to their limited operational range, cost effectiveness and risky temperament. Thus, present nano-crystalline ZnO probe exhibited as an efficient humidity sensor of a wider operational range with higher selectivity, sensitivity at room temperature. The lifetime of the nano-crystalline ZnO probe was determined by measuring the current up to ~6 months at an interval of 7 days. It was observed that the optical permeability decreased slowly with the increase in time period. After 6 months, the decrease in optical permeability was found to be about 18%.

The lowest detection limit of the %HR was found to be about ~0.45. The reproducibility of the response of the probe was investigated at a 45%RH. No significant decrease in optical response was observed after at least 10 uses in testing; thus, the sensing probe displayed good reproducibility. The relative standard deviation was found to be about ±4% determined by five successive measurements of a 45%RH standard using a single probe. In a series of 10 sensors using 10 different U-shaped nano-crystalline ZnO film sensing probes, a relative standard deviation of about ±5% was obtained for the individual optical response at constant 45%RH. Thus, a good reproducibility was observed with the sensor.

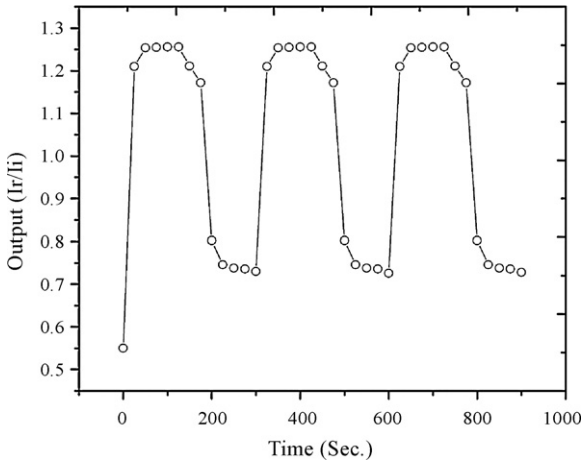


Fig. 7. Effect of time on the output power of the nano-crystalline ZnO film with 80% RH at 25 °C.

4. Discussion

During past few years, a great advancement has been ended in the field of optical fiber based humidity sensors [41,42]. In these devices, external perturbation involving physical forces such as temperature, pressure, composition of liquid and gas phase induces the change in intensity phase or polarization of magnetic wave propagating through the sensing element like optical fiber, glass plate or prism, etc. The magnitude of emerging light is related to changes in refractive index of optical fiber [43]. The change in refractive index depends on the cladding materials and adsorbed chemical species. It is known that, while entering the cross-section of the optical fiber, laser light obeys the Snell's law:

$$n_1 \sin\theta_1 = n_2 \ \sin\theta_2 \tag{1}$$

where, n_1 and n_2 are the refractive index (RI) of the first medium, i.e., air and the optical fiber respectively. θ_1 is the angle of incidence at the axis of the optical fiber where as θ_2 is the angle of emergence in the optical fiber. By using the basic optical geometry, one can show that:

$$\text{Numerical aperture (NA)} \ = \sin\theta_1 = \sqrt{n_c^2 - n_l^2} \tag{2}$$

Eq. (2) shows that NA is directly proportional to θ_1 which depends on n_c and n_l, i.e., RI of core of the optical fiber and that of cladding around the fiber which is nano-crystalline ZnO film in the present experimental setup. n_c is constant and n_l value is being changed in the experimental setup by varying the humidity around the nano-crystalline ZnO film on the optical fiber. Thus the net value of RI of the cladding and the humid medium is being denoted by n_{net} and Eq. (2) can be written as

$$\sin\theta_1 = \sqrt{n_c^2 - n_{net}^2} \tag{3}$$

Eq. (3) can also be interpreted using the elementary geometrical optics, that higher is the value of NA, more the cone of laser light will be able to enter the optical fiber and hence more intensity of light will be able to pass through the optical fiber.

The refractive index of glass is 1.5 and ZnO is ~2.0, therefore, the net refractive index or composite refractive index n_{net} of sensing element (U-shaped nano-crystalline ZnO film) is increased. It further decreases after adsorption of H_2O molecules with refractive index 1.33. In any medium, when water vapor content increases, the amount of oxygen and nitrogen decreases per unit volume and the density will decrease because the mass decreases as dry air is denser than the humid. It is also a common fact that in all transparent medium the optical density is in direct proportion to its mechanical density and also the RI of the medium. Since the optical density of the humid medium is inversely proportional to magnitude of its humidity. In other words, as the humidity of the medium increases, its rarity increases. This in turn causes n_{net} change as result of which NA will decrease (cf. Eq. (3)). Thus, on the other side of the optical fiber, less light will be able to pass through.

This expected result is in quite good agreement with our experimental results as shown in Fig. 6. The optical output power (OP) decreases linearly with increase in humidity content up to 90%. It may be because adsorption of water vapor on the surface of nano-crystalline ZnO film causes the change in refractive index and successively numerical aperture of used optical fiber. This also changes light output power emerging out from optical fibers. The ZnO films prepared by sol–gel technique are offered the fine particle on glass rod. The nano-sized ZnO particles on the surface of the glass rod enhances the surface activity of the film, and useful

for adsorbing polar molecules including water vapor. The sensitivity of the film was calculated from Fig. 6 and found to be 0.45 to the range of 5–50% and 0.3 for the range of 50–90%. It indicates better sensitivity in the lower range. The best linear fitting is observed in all the three cases: (1) with varying %RH, (2) with varying %RH in the presence of 80 mM ethanol and (3) with varying %RH in the presence of 80 mM methanol. It was found that the presence of interferents had a relative error of less than 4% in the optical method; therefore, this humidity sensor can detect %RH with negligible interference.

Fig. 7 shows the change output power with the time at 80% RH. The maximum change in output power was observed at ~30 s and this will be response time of sensor [44]. After then the graph shows a flat region up to 35 s and then increases to approximately original value which proves the good reversibility, recovery and reproducibility of the nano-crystalline ZnO coated optical fiber as a humidity sensing element, and the device as a humidity sensor after due calibration. The recovery of adsorbed moisture took place at 80% HR at 25 °C, while complete recovery of adsorbed moisture was observed after evacuating at 45 °C. Therefore, one can conclude that co-efficient of adsorption is proportional to the amount of humidity around the nano-crystalline ZnO film, which can be a versatile principle of fabricating a humidity monitoring device. This is because the adsorption of water molecules on cladding changes the effective refractive index of the wave guide, this change would shift the coupling angle and would be detected as an apparent absorbance [15].

There are various forces responsible for adsorption namely the physical and chemical forces [45]. The reversibility in R_f value is related to types of surface binding. If the H_2O is weakly bonded, i.e., physical adsorption, reversal of nano-crystalline ZnO surface is possible along with the change in R_f value after the change in vapor pressure in the surrounding. Further, if H_2O is strongly adsorbed on the nano-crystalline ZnO surface, it does not recover nano-crystalline ZnO surface because of change in water vapor pressure in surrounding of optical fiber. This may depend on the particle size, surface area, and the adsorption binding energy. In the present case, an isothermal TGA–DTA at 45 °C and 30 °C was recorded and observed the weight loss of moisture without any significant DTA peaks. It confirms the formation of very weak type of interaction appeared in between H_2O and nano-crystalline ZnO surface in the study.

Moreover, not all light, which is coupled or allowed into the fiber, will emerge from the fiber. Several attenuations take place during the course of transmission of light through the core for example light striking the core cladding interface at an angle larger than the critical angle (θ_c) is no longer completely transmitted. This microscopic non-uniformity of the RI partially scatters the light into much direction, known as Rayleigh loss. Here, in explaining the experimental results of our experiment, we are not concerned with any of the above mentioned losses, as they remain constant for any optical fiber in use. We are mainly concerned with the loss of intensity of light because of variation of numerical aperture due to variation in the value of RI of the humid medium around the cladding.

5. Conclusion

The sol–gel deposited ZnO film has been prepared with ZnO particles size 70–80 nm size, becoming sensitive for humidity adsorption application. It would be utilized for monitoring the change in humidity in the environment and can be employed safely in many possible applications. Also, nano-crystalline ZnO film was deposited on the U-shaped glass rod, where the change in optical output power corresponds to change in humidity. This can be calibrated as a humidity sensor element and are more convenient than the conventional humidity sensors. In conclusion, as the humidity around the cladding is increasing, output power is decreasing because the change in refractive index. This, perfectly, is in agreement with our experimental results and can be an underlying principle for humidity detecting devices.

Acknowledgements

Authors are grateful to Prof. M. Deb, Director, University Science Instrumentation Centre, University of Delhi, India for providing research facilities. S.K.S. and G.K.P. are thankful to the Principal, Bhaskaracharya College of Applied Sciences and Swami Shradhanand College, University of Delhi, India, respectively for their encouragements and ever inspiring gestures towards performing academic excellences.

References

[1] B.M. Kulwicki, J. Am. Ceram. Soc. 74 (1991) 697.
[2] M.K. Jain, M.C. Bhatnagar, G.L. Sharma, Sens. Actuators B: Chem. 55 (1999) 180.
[3] D.D. Lee, D.K. Lee, IEEE Sens. 1 (2001) 214.
[4] J. Ying, C. Wang, P. He, Sens. Actuators B: Chem. 62 (2000) 165.
[5] P.R. Wiederhold, Water Vapor Measurement, Marcel Dekker, 1997.
[6] C.Y. Lee, G.B. Lee, Sens. Lett. 3 (2005) 1.
[7] K. Nishizawa, T. Seiyama (Eds.), Chemical Sensor Technology-1, Kodausha, Tokyo, Japan, 1998.
[8] H. Dacres, R. Narayanswamy, Talanta 69 (2006) 631.
[9] Z.A. Ansari, R.N. Karekar, R.C. Aiyer, Thin Sold Film 305 (1997) 330.
[10] P. Mishra, R.K. Shukla, L.M. Bali, C.L. Gupta, G.C. Dubey, Sens. Actuators B: Chem. 94 (2003) 210.
[11] O.S. Wolfbeis, Anal. Chem. 76 (2004) 3269.
[12] M. Ando, H. Steffes, R. Chabicovsky, M. Haruta, G. Stangl, IEEE Sens. 4 (2004) 232.
[13] H.C. Hesse, East German Patent, 106 (1974) 86.
[14] J.R. Epstein, D.R. Wat, Chem. Soc. Rev. 32 (2003) 203.
[15] A.D. Kersey, Opt. Fiber Technol. 2 (1996) 291.
[16] H. Gunzler, A. William, Handbook of Analytical Techniques, vol. 2, Willey-VCH, 2001, p. 954.
[17] C. Jagadish, S. Pearton, Zinc Oxide Bulk, Thin Film and Nano Structure, Elsevier Limited, 2006.
[18] A. Dorfman, N. Kumar, J. Hahm, Langmuir 22 (2006) 4890.
[19] X.D. Bai, E.G. Wang, P.X. Gao, Z.L. Wang, Nano Lett. 3 (2003) 1147.
[20] Z.L. Wang, J.H. Sang, Science 312 (2006) 242.
[21] Z. Fan, J.G. Lu, J. Nanosci. Nanotechnol. 5 (2005) 1561.
[22] W. Wang, J. Zhang, Z. Zhu, J. Zh, Appl. Surf. Sci. 253 (2007) 3168.
[23] L. Liao, H.B. Lu, J.C. Li, H. He, D.F. Wang, D.J. Fu, C. Liu, W.F. Zhang, J. Phys. Chem. C 111 (2007) 1900.
[24] Z.L. Wang, X.Y. Kong, Y. Ding, P. Gao, W.L. Hughes, R. Yang, Y. Zhang, Adv. Funct. Mater. 14 (2004) 943.
[25] Z.J. Yan, D.W. Zeng, C.S. Xie, H.H. Wang, W.L. Song, Thin Solid Films 517 (2009) 1541.
[26] W. He, Y. Li, Z. Chen, Y. Wang, R. Zhang, Mater. Lett. 60 (2006) 2299.
[27] Y. Chen, R. Yu, Q. Shi, J. Quin, F. Zhang, Mater. Lett. 61 (2007) 4438.
[28] X.Y. Kong, Z.L. Wang, Nano Lett. 3 (2003) 1625.
[29] P.X. Gao, Y. Ding, Nano Lett. 3 (2003) 1315.
[30] B. Liu, H.C. Zheng, J. Am. Chem. Soc. 125 (2003) 4430.
[31] B.B. Lakshmi, P.K. Dorhout, C.R. Martin, Chem. Mater. 9 (1997) 857.
[32] P.X. Gao, Z.L. Wang, J. Phys. Chem. B108 (2004) 7534.
[33] B. Liu, H.C. Zeng, Langmuir 20 (2004) 4196.
[34] S.K. Shukla, G.K. Parashar, A.P. Mishra, P. Misra, B.C. Yadav, R.K. Shukla, L.M. Bali, G.C. Dubey, Sens. Actuators B: Chem. 98 (2004) 5.
[35] S. Otsuki, K. Adachi, T. Taguchi, Anal. Sci. 14 (1998) 633.
[36] S. Otsuki, K. Adachi, T. Taguchi, Sens. Actuators B: Chem. 53 (1998) 91.
[37] A. Vijayan, M. Fuke, R. Hawaldar, M. Kulkarni, D. Amalnerkar, R.C. Aiyer, Sens. Actuators B: Chem. 129 (2008) 106.
[38] P.O. Brien, T. Saeed, J. Knowles, J. Mater. Chem. 6 (1996) 1135.
[39] T. Arrie, A. Kishi, Thermochim. Acta 400 (2003) 175.
[40] H.P. Klug, L.E. Alexander, X-ray Diffraction Procedures for Polycrystalline and Amorphous Materials, 2nd ed., Wiley InterScience, 1974, (Chapter 9).
[41] M. Ando, Trends Anal. Chem. 25 (2006) 937.
[42] T.L. Yeo, T. Sun, K.T.V. Grattan, Sens. Actuators A: Phys. 144 (2008) 280.
[43] A. Banerjee, S. Mukherjee, R.K. Verma, B. Jana, T.K. Khan, M. Chakraborty, R. Das, S. Bisawas, A. Sexena, V. Singh, R.M. Hallen, R.S. Rajput, P. Tewari, S. Kumar, V. Saxena, A.K. Ghosh, J. John, P.G. Bhaya, Sens. Actuators B 123 (2007) 594.
[44] J.P. Brown, P.W. Haycock, L.M. Smith, A.C. Jones, E.W. Williams, Sens. Actuators B 63 (2000) 109.
[45] S. Brunauer, P.H. Emmett, E. Teller, J. Am. Chem. Soc. 60 (1938) 309.
[46] P.G. Su, J.Y. Tseng, Y.C. Huang, H.H. Pan, P.C. Li, Sens. Actuators B 137 (2009) 496.

[47] Q. Qi, T. Zhang, S. Wang, X. Zheng, Sens. Actuators B 137 (2009) 649.
[48] S. Majumdara, P. Banerji, Sens. Actuators B 140 (2009) 134.
[49] Y. Feng, S. Wang, B. Feng, R. Wang, Y. He, T. Zhang, Sens. Actuators A 152 (2009) 104.
[50] B.C. Yadav, R. Srivastava, C.D. Dwivedi, P. Pramanik, Sens. Actuators B 131 (2008) 216.
[51] Q. Qia, T. Zhanga, Q. Yu, R. Wang, Y. Zeng, L. Liu, H. Yang, Sens. Actuators B 133 (2008) 638.

Talanta 80 (2009) 572–580

Contents lists available at ScienceDirect

Talanta

journal homepage: www.elsevier.com/locate/talanta

An approach to identifying sequential metabolites of a typical phenylethanoid glycoside, echinacoside, based on liquid chromatography–ion trap-time of flight mass spectrometry analysis

Yuxin Wang[a], Haiping Hao[a,*], Guangji Wang[a,**], Pengfei Tu[b], Yong Jiang[b], Yan Liang[a], Liang Dai[a], Hao Yang[a], Li Lai[a], Chaonan Zheng[a], Qiong Wang[a], Nan Cui[a], Yitong Liu[a]

[a] Key Lab of Drug Metabolism & Pharmacokinetics, China Pharmaceutical University, No. 24, Tongjiaxiang Street, Nanjing 210009, China
[b] Department of Natural Medicines, School of Pharmaceutical Sciences, Peking University Health Science Center, Haidian District, Beijing 100083, China

ARTICLE INFO

Article history:
Received 9 April 2009
Received in revised form 12 July 2009
Accepted 13 July 2009
Available online 21 July 2009

Keywords:
Phenylethanoid glycoside
Echinacoside
LC/MS-IT-TOF
Metabolite identification

ABSTRACT

Metabolite identification for the compounds that undergo multiple and sequential metabolism is still a great challenge. Echinacoside (ECH), a typical phenylethanoid glycoside, contains multiple unstable chemical bonds and high reactive functional groups which are susceptible to multiple pathways of degradation and metabolism, leading great difficulties for its metabolite identification. This study proposed a novel approach for rapidly identifying the complicated and unpredictable metabolites of ECH, based on the powerful liquid chromatography hybrid ion trap and time of flight mass spectrometry (LC/MS-IT-TOF) analysis. Four degradation products were rapidly identified via the "fragmentation–degradation" comparisons. Five phase I and phase II metabolites of the degradation products were rapidly characterized via the crossover mass differences comparisons of their quasi-molecular ions with the potential precursors. Four direct phase I and phase II metabolites of the parent compound were identified by the mass differences analysis of the molecular ions between metabolites and the parent compound. Multiple stages of fragmentation patterns were used to confirm the metabolites characterizations. This study provides a novel approach to characterizing the complicated metabolites, and would be widely applicable for the metabolite identification of natural products.

© 2009 Elsevier B.V. All rights reserved.

1. Introduction

Phenylethanoid glycoside is a class of polyphenolic compound distributed in many plants. They are reported to posses cytostatic [1], cardioactive [2], hepatocyte protective [3], antibacterial, antioxidative [4], neuroprotective [5] effects and so on. In particular, echinacoside (ECH), a representative phenylethanoid glycoside contained in Herb Cistanchis [6], *Echinacea angustifolia* and *E. pallida* roots have been the best-selling herbal medicine in the United States and Europe as the immunostimulant [7]. It has been also observed to have various kinds of other pharmacological activities including antioxidant [8–10], neuroprotective [11] and anti-inflammatory [12].

In spite of the well defined pharmacological activities of phenylethanoid glycoside, very less is known about its pharmacokinetic and metabolic characteristics. Previous studies showed that no phenylethanoid glycoside was detected in human plasma after echinacea tablets ingestion [13] and the bioavailability of echinacoside in rat was only about 0.83% [14], suggesting poor membrane permeability and/or extensive presystemic metabolism.

The chemical structure of ECH is composed of three chemical moieties including cafffeic acid (CA), phenylethanoid aglycone (PhA, 3,4-dihydroxyphenethyl alcohol, hydroxytyrosol), and sugar. The chemical bonds linking these moieties and the multiple hydroxyl groups in ECH structure are susceptible to multiple and sequential routes of hydrolysis, phase I (oxidation and reduction) and/or phase II (glucuronic acid, sulfate, and methyl conjugation) metabolism. Thus, we hypothesized that ECH may be susceptible to extensive and multiple metabolism. In a recent study [15], eight phase II metabolites (methyl and glucuronic acid conjugations) of ECH were identified from the rat bile samples. Although this study resulted in an unambiguous identification of eight metabolites of ECH by using NMR, we hypothesized that there should have much other metabolites failed to be identified, in view of the characteristics of ECH chemical structure. The present study was thus aimed to characterize ECH metabolites from rat urine and feces as many as possible.

* Corresponding author. Tel.: +86 25 83271347; fax: +86 25 85306750.
** Corresponding author. Tel.: +86 25 83271128; fax: +86 25 83302827.
E-mail addresses: hhp_770505@yahoo.com.cn (H. Hao), guangjiwang@hotmail.com (G. Wang).

0039-9140/$ – see front matter © 2009 Elsevier B.V. All rights reserved.
doi:10.1016/j.talanta.2009.07.027

Table 1
Accurate mass measurements of pseudo-molecular and fragment ions of echinacoside.

Pseudo-molecular ion (PI)			Fragment ion (MS^2)		
Measured m/z (% base peak, mDa[a], ppm[b])	Calculated m/z	Formula	Measured m/z (% base peak, mDa, ppm)	Calculated m/z	Fomula
392.1228[c] (100.00, 1.0, 2.55)	392.1218[c]	$C_{35}H_{46}O_{20}$	135.0458 (58.27, 0.6, 4.44)	135.0452	$C_8H_8O_2$
785.2481 (5.39, −2.9, 3.69)	785.2510	$C_{35}H_{46}O_{20}$	161.0266 (24.47, 2.2, 13.66)	161.0244	$C_9H_6O_3$
			179.0349 (100.00, −0.1, 0.56)	179.0350	$C_9H_8O_4$
			311.0931[c] (20.77, −2.3, 7.39)	311.0954[c]	$C_{29}H_{36}O_{15}$
			315.1062 (1.3, −2.3, 7.30)	315.1085	$C_{14}H_{20}O_8$
			461.1656 (1.41, −0.6, 1.30)	461.1662	$C_{20}H_{30}O_{12}$
			477.1583 (3.12, −3.1, 6.50)	477.1614	$C_{20}H_{30}O_{13}$
			623.2182 (25.88, −1.1, 1.77)	623.2193	$C_{26}H_{40}O_{17}$

[a] Milli-Dalton, differences between the measured and calculated values.
[b] Differences between the measured and calculated values.
[c] $[M-2H]^{2-}$ ions in negative scan mode, while others were $[M-H]^-$ ions.

Despite the recent advancement of various analytical tools, the metabolite identification for the compounds undergoing multiple and unpredictable metabolism from the biological matrix remains still a great challenge. In the past few years, mass spectrometry (MS) coupled with chromatographic separation has become a powerful and frequently used technique for metabolite identification. For their low sensitivity in full scan mode, LC/MS or LC/MS/MS are challenged for complex biological samples containing many compounds [16]. In contrast, LC–TOF/MS characterized with a wide mass range, sensitivity in full scan mode, the high resolving power, and accurate mass measurement, enables to the powerful identification of non-target compounds at trace level [17,18]. In addition, LC–IT/MS is also a useful tool for identifying unknown compounds because of its ability to gain abundant fragment ions [19]. The LC/MS-IT-TOF and LC–QTOF/MS, a combination of these two techniques can provide structural information from fragmentation as well as elemental compositions from accurate mass measurement, which represents a powerful tool to analyze unknown compounds of trace levels in complex matrices [20–27].

The present study was thus designed to detect and identify the metabolites of ECH in urine and feces based on the powerful LC/MS-IT-TOF analysis. A generally applicable approach to identifying the complicated metabolites including the degradation products, the phase I/phase II metabolites of the parent compound and its degradation products has been proposed in this study.

2. Experimental

2.1. Chemicals and reagents

Echinacoside (powder, purity 96.4%) was separated and purified from an ethanol extract of Cistanche tubulosa (Schenk) R. Wight [14]. Verbascoside (powder, purity 98.8%) was purchased from Chengdu Push Bio-Technology Co., Ltd. (Chengdu, Sichuan, China). 3,4-Dihydroxyphenethyl alcohol (oil, purity 98.5%) was from Chengdu Biopurify Phytochemicals Ltd. (Chendu, Sichuan, China). Caffeic acid (CA, powder, purity >98%) was from National Institute for the Control of Pharmaceutical and Biological Products (Beijing, China). HPLC grade acetonitrile and methanol was obtained from sigma company, USA. Solid-phase cartridge was from Waters Chromatography (HLB 6cc, OasisTM, Waters, USA). Deionized water was purified using a mili-Q system (Milipore, Milford, MA, USA). Acetic acid and other chemicals and solvents used were all of analytical grade.

2.2. Drug administration and sample collection

Sprague–Dawley rats (230–250 g) were obtained from academy of military medical sciences (Beijing, China) and housed with unlimited access to food and water except for fasting 12 h before experiment. The rats were maintained on a 12 h light–dark cycle (light on from 8:00 to 20:00 h) at ambient temperature (22–24 °C) and ca. 60% relative humidity. After an oral administration of echinacoside 1.5 g/kg, urine was collected at 6, 12, 24, and 36 h in ice-bath. Feces were also collected at 24 and 36 h. All samples were stored at −80 °C immediately after collection.

2.3. Separation and extraction procedures

Solid phase extraction (SPE) was used to extract the metabolites from the biological samples. All samples were thawed in a water-bath at 37 °C. The 1:2 dilution of urine samples and the 1:10 dilution of feces homogenate samples were added onto the SPE cartridge, which had been previously activated with 4 mL methanol and equilibrated with 4 mL water. After the sample had been absorbed by the cartridge, the cartridge was washed with 2 mL water, and then eluted with 3 mL methanol. The elution was then evaporated under an air stream at 25 °C in a water-bath. The residue was reconstituted in 200 μL of methanol with vortex. After centrifugation at 20,000 × *g* for 10 min, 100 μL of supernatant was drawn and 5 μL was injected into the LC/MS-IT-TOF.

2.4. Instruments and analytical condition

LC experiments were conducted using a Shimadzu (Kyoto, Japan) HPLC system consisting of an LC-20AB binary pump, an SIL-20AC autosampler, a CTO-20AC column oven and an SPD-M20A PDA. Chromatographic separation of analytes was achieved using a 100 mm × 2.0 mm capcell pak C18 MG analytical column (Shiseido, Tokyo, Japan) protected by a Security guard (Phenomenex, USA). The column and autosampler tray temperatures were set at 25 and 4 °C, respectively. The mass detection was carried out using a hybrid Shimadzu ion trap/time-of-flight mass spectrometry (IT-TOF/MS) (Shimadzu, Kyoto, Japan), equipped with an electrospray ionization source. In automatic mode, all ions were firstly accumulated in octopole and then rapidly pulsed into IT for MS^n analysis according to the criteria settings. All ions produced were finally introduced into the TOF instrument for accurate mass determination. Data acquisition and analysis were performed with LC solution 3.0 software (Shimadzu, Kyoto, Japan).

A mobile phase composed of eluent A (0.1% acetic acid in water, v/v) and B (acetonitrile) with a gradient elution was employed for the separation. The mobile phase was programmed as follows: an isocratic elution of 5% B for the first 10 min, followed by a linear gradient elution of 5–10% B from 10 to 20 min, 10% B from 20 to 30 min, 10–30% B from 30 to 50 min and 30–70% B from 50 to 60 min. After holding the solvent composition of 70% B for the next 10 min, the gradient was returned to its starting conditions.

The optimized MS conditions were as follows: negative ion mode; electrospray voltage, −3.5 kV; CDL temperature, 200 °C;

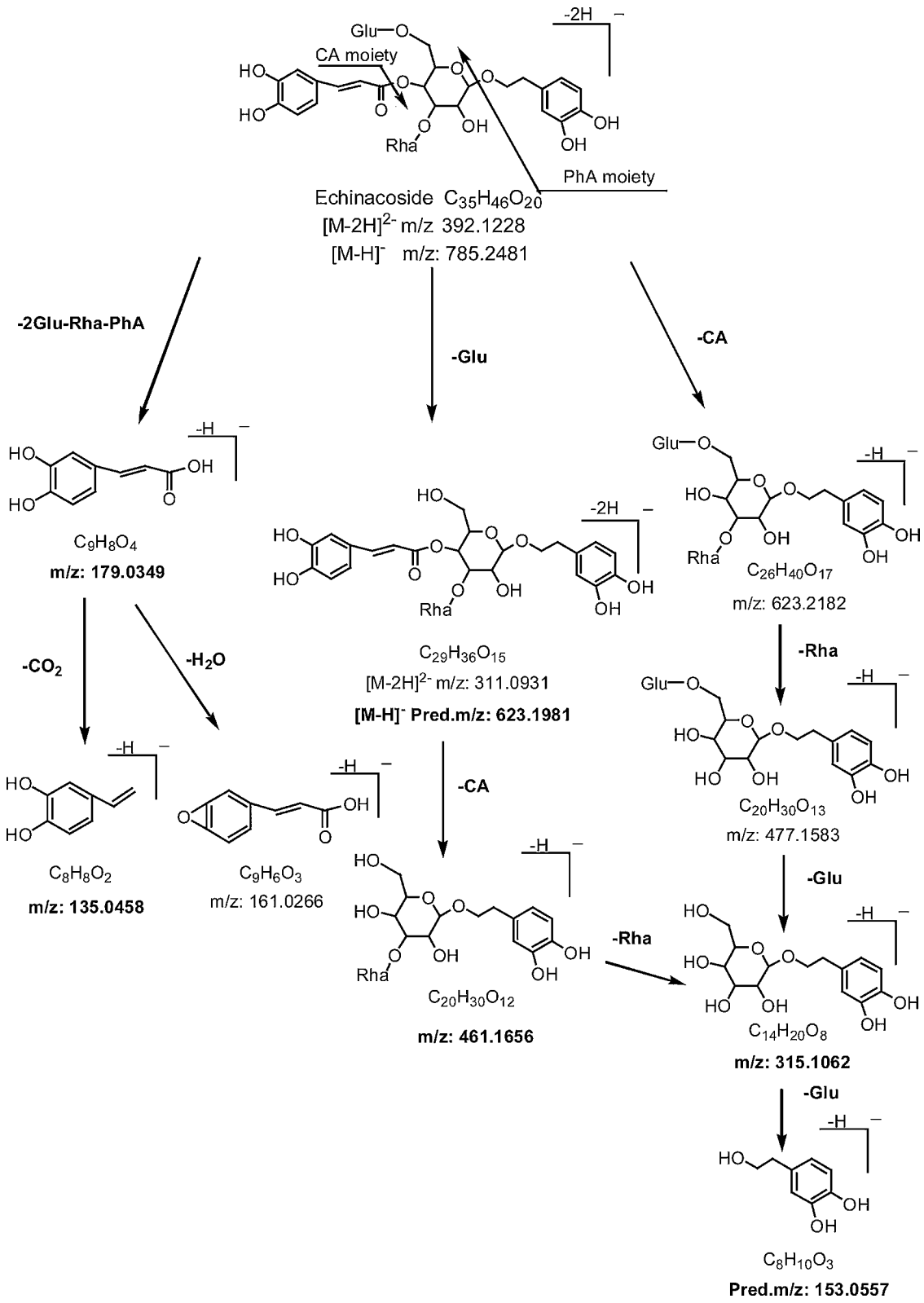


Fig. 1. Proposed fragmentation pathways of echinacoside.

Block Heater temperature, 200 °C; nebulizing gas (N_2), 1.5 L/min; drying gas (N_2) pressure, 0.1 MPa. Mass spectra were acquired in the range of *m/z* 100–1000 for MS^1, 100–1000 for MS^2. The MS^n data were collected in an automatic mode and the software could automatically select precursor ions for MS^n analysis according to criteria settings. Argon was used as the collision gas and the collision energy was set at 150% for MS^2. Prior to data acquisition, the instrument was calibrated with sodium TFA clusters against the entire mass range (*m/z* 50–5000) specified for the instrument.

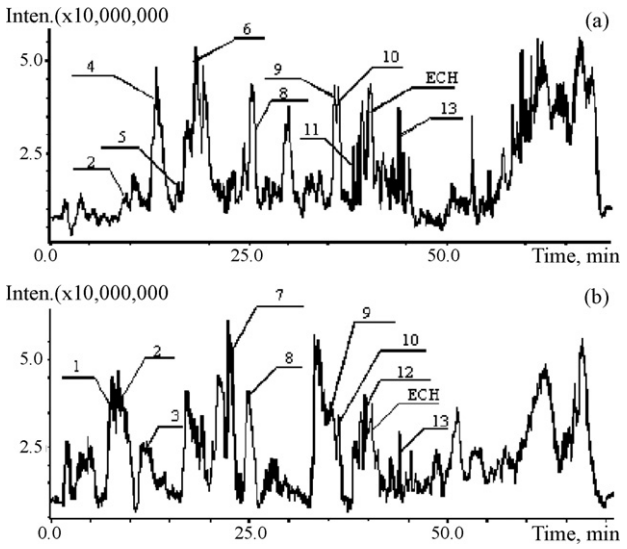


Fig. 2. Total ion chromatograms for the rat urine (a) and feces (b) samples after intragastric administration of echinacoside.

3. Results and discussion

3.1. Fragmentations of echinacoside

Since it has been well proven that the mass fragmentation patterns of metabolites are always similar to the parent compounds, and thus the fragmentation patterns analysis of parent compound is very helpful for the metabolite characterizations, we firstly conducted a detailed fragmentation study of the ECH authentic standard in LC/MS-IT-TOF. To ensure sufficient fragments production, 5 μg/mL of ECH authentic samples prepared in methanol was used for the fragmentation pattern study. Accurate mass measurements of pseudo-molecular and fragment ions of ECH are listed in Table 1. The $[M-2H]^{2-}$ ion at *m/z* 392.1228 ($C_{35}H_{46}O_{20}$) was observed as the predominant pseudo-molecular ion. The product ion at *m/z* 179.0349 ($C_9H_8O_4$) corresponding to CA moiety is one of the major fragments. The fragment at *m/z* 135.0458 ($C_8H_8O_2$) and *m/z* 161.0266 ($C_9H_6O_3$) was formed from the CO_2 and H_2O loss from CA moiety, respectively. The loss of a glucose (Glu) from the double deprotonated pseudo-molecular ion forms a fragment at *m/z* 311.0931 ($[M-2H]^{2-}$, $C_{29}H_{36}O_{15}$), which further losses a CA moiety and produces a fragment at *m/z* 461.1656 ($C_{20}H_{30}O_{12}$). The fragments at *m/z* 623.2182 ($C_{26}H_{40}O_{17}$), *m/z* 477.1583 ($C_{20}H_{30}O_{13}$), and *m/z* 315.1062 ($C_{14}H_{20}O_8$) are produced from the sequential CA, rhamnose (Rha) and Glu moiety loss from the molecular ion, respectively. The proposed fragmentation pattern of ECH is illustrated in Fig. 1.

3.2. Identification of metabolites in rat urine and feces

To ensure the detecting sensitivity of this method, the limit of detection (LOD) and the limit of quantification (LOQ) of quantifying ECH in the rat urine and feces had been validated. The determined LOD (defined as the concentration producing signal to noise ratio over 3) and LOQ (defined as the concentration producing signal to noise ratio over 10 and with the precision variations less than 20%) for quantifying ECH in both biological matrixes was 10 and 25 ng/mL, respectively, indicating that the present LC/MS-IT-TOF based method was sensitive enough to detect and identify the metabolites of ECH at trace level. The representative mass chromatograms for profiling the rat urine and feces samples after intragastric administration of ECH are shown in Fig. 2. The peaks corresponding to potential metabolites were determined from the

Table 2
Retention time (t_R) and accurate mass measurements of echinacoside and all metabolites in rat urine and feces samples.

Peak No.	t_R (min)	Pseudo-molecular ion *m/z* (formula, mDa[a], ppm[b])	Fragment ion *m/z* (mDa, ppm)	Identification
1	8.0	153.0561 ($C_8H_{10}O_3$, 0.4, 2.61)	123.0473 (2.1, 17.07)	3,4-Dihydroxyphenethyl alcohol
2	10.0	233.0119 ($C_8H_{10}O_6S$, −0.6, 2.57)	153.0577 (0.00, 0.00), 123.0467 (1.5, 12.19)	3,4-Dihydroxyphenethyl alcohol sulfate conjugate
3	12.0	461.1668 ($C_{20}H_{30}O_{12}$, 0.6, 1.30)	315.1054 (−3.1, −9.84), 161.0460 (0.5, 3.10)	Decaffeoyl verbascoside
4	12.7	405.1399 ($C_{17}H_{26}O_{11}$, −0.3, −0.74)	345.1187 (−0.4, −1.16), 165.0588 (3.1, 18.78)	Hydroxyl methyl 3,4-dihydroxyphenethyl glycoside
5	16.0	258.9923 ($C_9H_8O_7S$, 0.3, 1.16)	179.0381 (3.1, 17.32)	Caffeic acid sulfate conjugate
6	18.0	389.1457 ($C_{17}H_{26}O_{10}$, 0.4, 1.03)	329.1225 (0.4, 1.03), 167.0740 (−1.7, 5.17), 123.0472 (2.6, 15.56)	Methyl 3,4-dihydroxyphenethyl glycoside
7	23.0	179.0359 ($C_9H_8O_4$, 0.9, 5.03)	135.0474 (2.2, 16.29)	Caffeic acid
8	26.0	432.0996[c] ($C_{35}H_{46}O_{23}S$, 0.8, 1.85)	392.1205[c] (−1.3, 3.32), 179.0368 (1.8, 10.05), 703.1769 (0.8, 1.14), 215.0038 (1.8, 8.37)	Echinacoside sulfate conjugate I
9	35.8	432.1006[c] ($C_{35}H_{46}O_{23}S$, 0.2, 0.46)	703.1692 (−6.9, −9.82), 161.0253 (0.9, 5.59),	Echinacoside sulfate conjugate II
10	36.3	400.1196[c] ($C_{35}H_{46}O_{21}$, 0.3, 0.75)	391.112[c] (−1.1, −2.81), 179.0363 (−1.3, −7.26), 135.0479 (2.7, 19.99)	Hydroxyl echinacoside
11	38.8	480.1386[c] ($C_{41}H_{54}O_{26}$, 1.5, 3.12)	623.2241 (4.8, 7.70), 785.2481 (−2.9, 3.69), 392.1218[c] (0.0, 0.00)	Echinacoside glucuronide conjugate
12	39.7	432.1017[c] ($C_{35}H_{46}O_{23}S$, 1.3, 3.01)	258.9908 (1.0, 3.86)	Echinacoside sulfate conjugate III
13	44.2	623.2024 ($C_{29}H_{36}O_{15}$, 4.3, 6.90)	461.1688 (2.6, 5.64), 315.1116 (3.1, 9.48)	Verbascoside

[a] Milli-Dalton, differences between the measured and predicted values.
[b] Differences between the measured and predicted values.
[c] $[M-2H]^{2-}$ ions in negative scan mode, while others were $[M-H]^-$ ions.

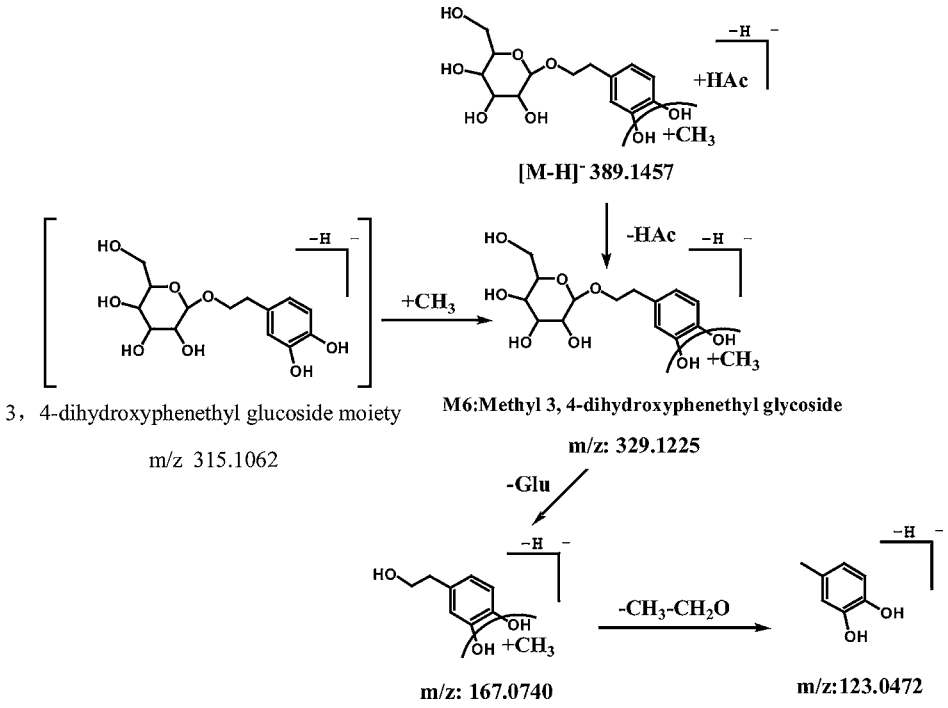


Fig. 3. Proposed fragmentation mechanism of M6.

automated mass chromatogram comparisons between the blank samples and the drug treated samples. The retention time, accurate mass data of the parent and fragment ions for the parent compound and all metabolites are collected in Table 2. A total of 13 metabolites were found from the rat urine and feces samples. The metabolites identification strategy and results were elucidated in detail as follows.

3.2.1. Identification of degradation products via direct fragment comparisons

The chemical structure of ECH is composed of three chemical moieties including CA, phenylethanoid aglycone (PhA, 3,4-dihydroxyphenethyl alcohol, hydroxytyrosol), and sugar. According to the current knowledge of drug metabolism, ECH are readily subject to hydrolysis under the biological conditions, especially cat-

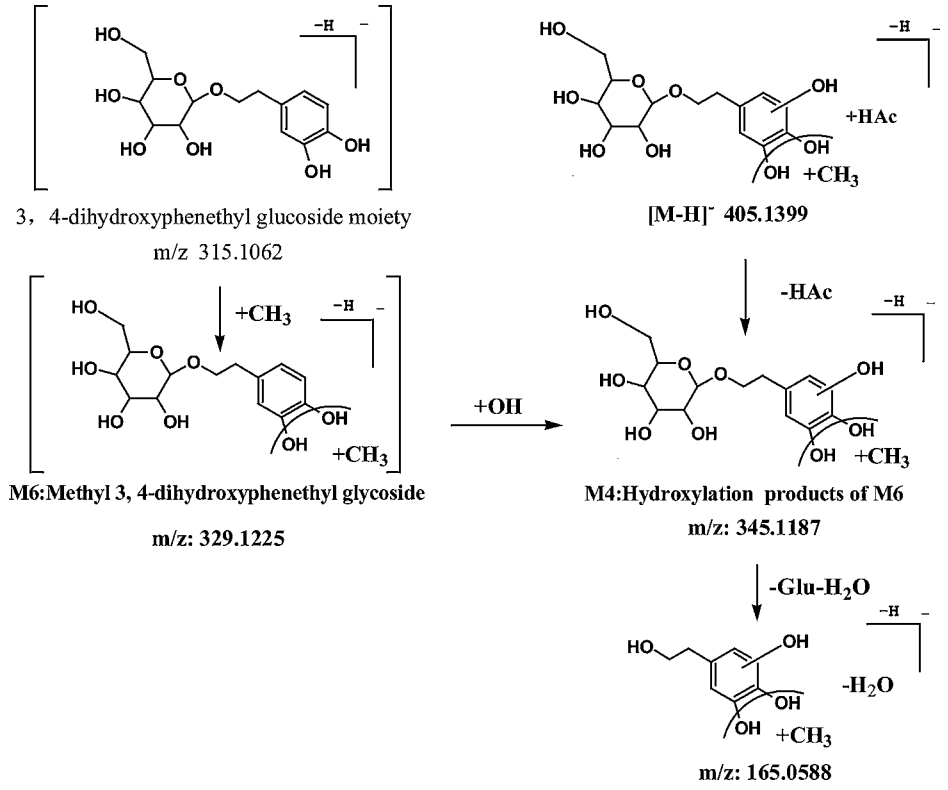


Fig. 4. Proposed fragmentation mechanism of M4.

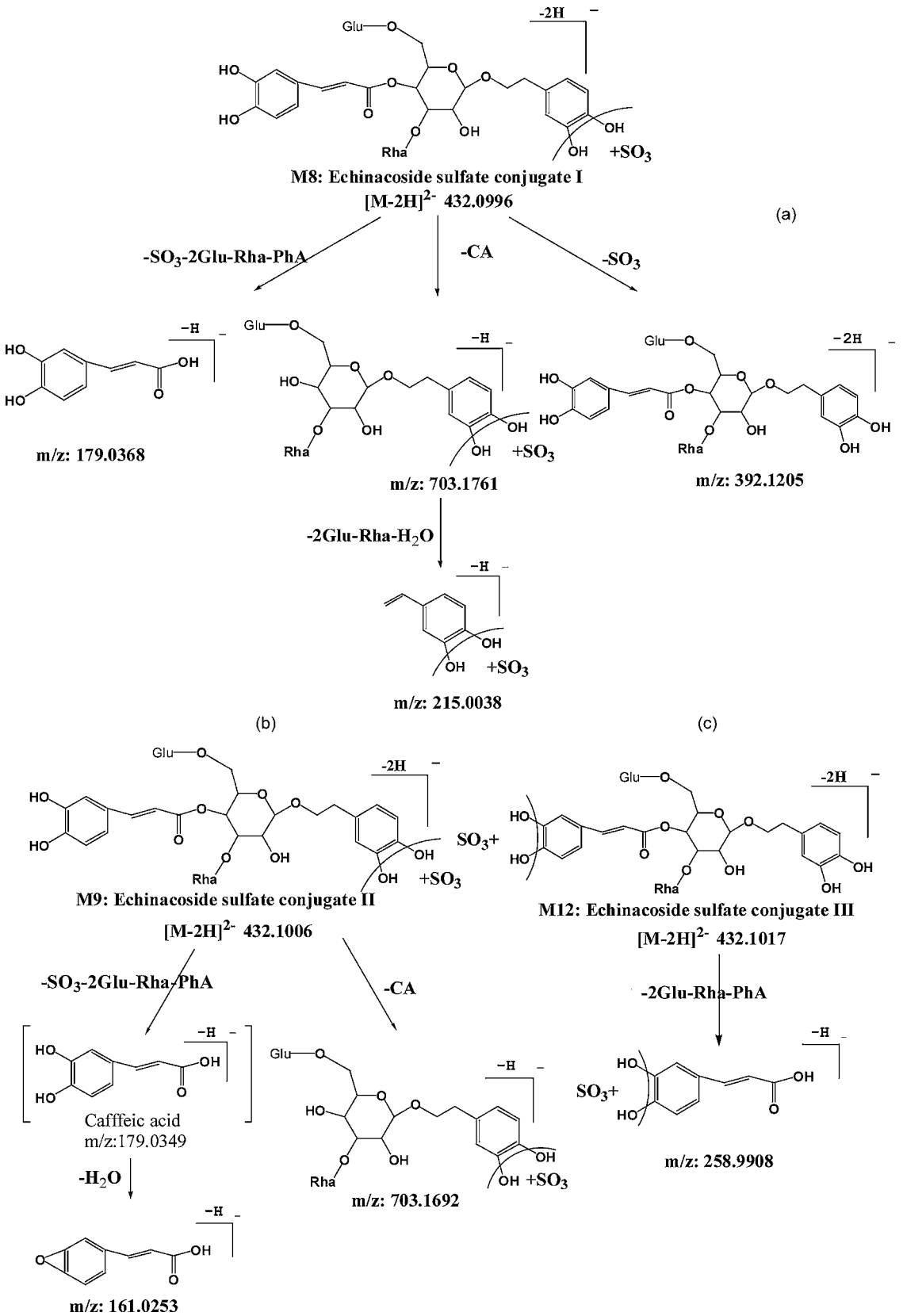


Fig. 5. Proposed fragmentation mechanism of M8 (a), M9 (b), M12 (c).

alyzed by the intestinal microflora. Therefore, we proposed that ECH may produce several degradation products in the rat gastrointestinal tract. Recently, García-Reyes et al. [28] proposed a "fragmentation–degradation" correlation strategy to identify the degradation products based on the fact that the compounds degradation pathways are always similar to the fragmentation patterns in the mass CID conditions. For this consideration, we applied such a strategy to search for the potential degradation prod-

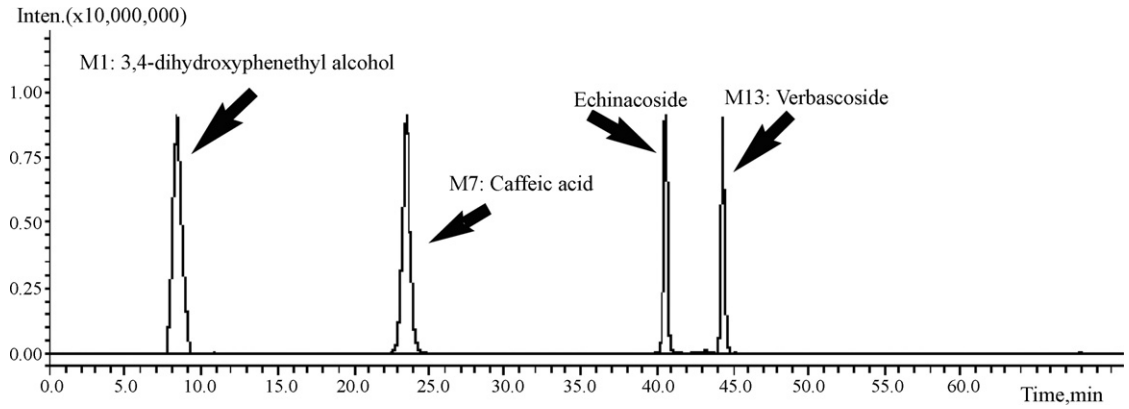


Fig. 6. Extracted ion chromatogram of 3,4-dihydroxyphenethyl alcohol, caffeic acid and verbascoside standards.

ucts of ECH using the determined fragments of ECH authentic standard.

The determined and predicted fragment ions of ECH were searched against the mass chromatograms of rat urine and feces samples. A total of four metabolites have been found to characterize the pseudo-molecular ions with same *m*/*z* and calculated elemental compositions to that of the ECH fragments. M7, eluted at 23.0 min, is characterized with the pseudo-molecular ion at *m*/*z* 179.0359 ($C_9H_8O_4$), which is actually identical to the ECH fragment ion at *m*/*z* 179.0349 ($C_9H_8O_4$, caffeic acid moiety). The major fragment ion determined at *m*/*z* 135.0474 ($C_8H_8O_2$) for M7 is also same to that of the caffeic acid moiety. Therefore, M7 is identified as a degradation product of echinacoside, caffeic acid. M13, eluted at 44.2 min, characterized with the deprotonated molecule ion at *m*/*z* 623.2024 ($C_{29}H_{36}O_{15}$) which is really close to the de-glucose fragment ion (*m*/*z* 623.1981) of ECH, is proposed to be the de-glucose product of ECH named as verbascoside. The major fragment ions of M13 (*m*/*z* 461.1688, *m*/*z* 315.1116) are also same to that from the verbascoside moiety. Based on this rule, M3 (Rt, 12.0 min; *m*/*z* 461.1668) and M1 (Rt, 8.0 min; *m*/*z* 153.0561) is identified as the decaffeoyl product of verbascoside and 3,4-dihydroxyphenethyl alcohol, respectively.

3.2.2. Phase I and phase II metabolites of degradation products

The degradation products can further undergo phase I and/or phase II metabolism. Since such metabolites are always produced from multiple metabolic reactions from the parent compound, it is relatively difficult to characterize their structures. In this study, we proposed a strategy for rapidly characterizing the phase I and phase II metabolites of the degradation products. Firstly, the pseudo-molecular ions of such metabolites were compared with those of the determined degradation products. With the benefit of accurate mass measurements by TOF, it is feasible to obtain the elemental composition differences between the target metabolites and their precursors (degradation products). Subsequently, the reasonable elemental composition difference could be determined based on the current understanding of the metabolic routes. Finally, the fragmentation patterns comparisons would help to confirm the characterizations. The observed quasi-molecular ion for M5, eluted at 16.0 min, was at *m*/*z* 258.9923, which was 80 Da over that of the degradation product M7, caffeic acid. The major fragment ion of M5 at *m*/*z* 179.0381 ($C_9H_8O_4$) confirms that M5 is caffeic acid sulfate conjugate. Similarly, M2 (Rt, 10.0 min) characterized with the quasi-molecular ion at *m*/*z* 233.0119 was readily identified as the sulfate conjugate of M1, 3,4-dihydroxyphenethyl alcohol.

However, some degradation products of the parent compound might be immediately and completely metabolized and thus could not be detected. The identification of such kind of metabolites when their precursors were not detected would be more difficult. In view that the degradation modes are always similar to the mass fragmentation patterns, we proposed here that the multiple crossover comparisons of the quasi-molecular ions with the fragments of the parent compound would help for characterizing such metabolites. As is in this study, M6 has been rapidly characterized following such a strategy. As shown in Fig. 3, M6 eluted at 18.0 min produced a predominant quasi-molecular ion at *m*/*z* 389.1457 ($C_{17}H_{26}O_{10}$), which was presumed to be an acetic adductive ion as evidenced from its elemental composition difference ($C_2H_4O_2$) from the deprotonated ion at *m*/*z* 329.1225 ($C_{15}H_{22}O_8$). Comparing the deprotonated molecular ion of M6 with that of the defined degradation products leaded to none of reasonable results, suggesting that M6 was not a subsequent metabolite of the detected degradation products. When matching the quasi-molecular ion of M6 with the fragments of parent compound, a 14 Da difference corresponding to a methyl group has been observed from a fragment at *m*/*z* 315.1062 ($C_{14}H_{20}O_8$), which was the 3,4-dihydroxyphenethyl glucoside moiety. Therefore, M6 was proposed to be a methyl 3,4-dihydroxyphenethyl glycoside. The fragmentation pattern of M6 supported such a characterization. The loss of a Glu from the deprotonated molecular ion produced a fragment ion at *m*/*z* 167.0740 ($C_9H_{12}O_3$), which further produced a fragment ion at *m*/*z* 123.0472 ($C_7H_8O_2$) by the CH_3 and CH_2O dissociation.

M4, eluted at 12.7 min, showed a major quasi-molecule ion at *m*/*z* 405.1399 ($C_{17}H_{26}O_{11}$) which was also presumed to be an acetic acid adduct ion since it also produced a deprotonated molecular ion at *m*/*z* 345.1187. The predicted elemental composition of $C_{15}H_{22}O_9$ for M4 is an oxygen atom more than that of the M6 and a CH_2O more than the fragment at *m*/*z* 315.1062 ($C_{14}H_{20}O_8$). Therefore, the M4 was tentatively presumed to be the subsequent hydroxylation products of M6. As shown in Fig. 4 the major fragment ion at *m*/*z* 165.0588 ($C_9H_{10}O_3$) presumed to be produced via losing a Glu moiety and a H_2O group from the deprotonated molecular ion of M4 supported such a characterization.

3.2.3. Phase I and phase II metabolites of echinacoside

The direct phase I and phase II metabolites of a compound are relatively easy to be characterized based on the fragmentation comparisons with the parent compound. M8, M9 and M12, characterized with similar quasi-molecular ion ($[M-2H]^{2-}$) mass at *m*/*z* 432.0996, *m*/*z* 432.1006 and *m*/*z* 432.1017 and same predicted elemental composition of $C_{35}H_{46}O_{23}S$, suggested that they were the sulfate conjugation products at different hydroxyl groups. The further fragmentation patterns and retention behavior analysis helped us to determine the sulfate conjugating positions for M8, M9 and M12. The fragment ion at *m*/*z* 703.1769 ($C_{26}H_{40}O_{20}S$) was a CA moiety loss from the molecular ion, which suggested that the sulfate conjugation position was not at the CA moiety for M8. In addition,

Table 3
Comparison of retention time (t_R) and accurate mass data for the metabolites proposed and their respective authentic standards.

Peak No.	Compound name	Metabolites			Standards		
		t_R (min)	Pseudo-molecular ion m/z (ppm)	Fragment ion m/z (ppm)	t_R (min)	Pseudo-molecular ion m/z (ppm)	Fragment ion m/z (ppm)
1	3,4-Dihydroxyphenethyl alcohol	8.0	153.0561 (2.61)	123.0473 (17.07)	8.3	153.0563 (3.92)	123.0462 (8.13)
7	Caffeic acid	23.0	179.0359 (5.03)	135.0474 (16.29)	23.4	179.0349 (−0.56)	135.0458 (4.44)
13	Verbascoside	44.2	623.2024 (6.90)	461.1688 (5.64), 315.1116 (9.48)	44.4	623.1999 (2.89)	461.1643 (−4.77), 315.1044 (5.40)

the fragment ion at m/z 215.0038 ($C_8H_8O_5S$) presumed to be a H_2O loss from 3,4-dihydroxyphenethyl alcohol sulfate conjugate (m/z 233.0119, $C_8H_{10}O_6S$), confirmed that the site of sulfate conjugant of M8 was at PhA moiety. For M9, the major fragment ion at m/z 703.1692 ($C_{26}H_{40}O_{20}S$) was formed through a CA moiety loss from the quasi-molecular ion, suggesting that the sulfate was conjugated with the hydroxyl group at PhA moiety. The sole fragment ion at m/z 258.9908 ($C_9H_8O_7S$) for M12 which was proposed to be the caffeic acid sulfate conjugate (m/z 258.9923, $C_9H_8O_7S$) supported that the sulfate conjugation was formed at the CA moiety. The fragmentation patterns of M8, M9 and M12 are illustrated in Fig. 5 separately.

M10, eluted at 36.3 min, showed the predominant quasi-molecular ion $[M-2H]^{2-}$ at m/z 400.1192 ($C_{35}H_{46}O_{21}$) that is an oxygen atom more than the parent compound ECH, suggesting that it was a hydroxylation product of ECH. The major fragment ion at m/z 391.1129 ($C_{35}H_{44}O_{20}$) was a H_2O loss from the quasi-molecular ion. The fragment ions found at m/z 179.0363 ($C_9H_8O_4$) and m/z 135.0479 ($C_8H_8O_2$) were same to that of the parent compound ECH, suggested that the hydroxylation position was not on the caffeic acid moiety. In addition, in view that the H_2O loss fragmentation for M10 has not been observed from the parent compound, we proposed that the hydroxylation was more likely to occur on the PhA moiety to form a benzenetriol structure.

M11, eluted at 38.8 min, was characterized with the major qausi-molecular ion $[M-2H]^{2-}$ at m/z 480.1386 ($C_{41}H_{54}O_{26}$). The double and mono-deprotonated fragment at m/z 392.1218 ($C_{35}H_{46}O_{20}$) and m/z 785.2481 ($C_{35}H_{46}O_{20}$) that was formed through a glucuronic acid (176 Da, $C_6H_8O_6$) loss from the parent ion of M11, supporting that M11 was a glucuronic conjugate of ECH. Due to the insufficient fragmentation information, we failed to determine the conjugation position.

3.2.4. *Metabolites identification verified by authentic standards*

To further confirm the metabolite identifications, three major metabolites M1, M7 and M13 that were proposed as 3,4-dihydroxyphenethyl alcohol, caffeic acid and verbascoside, respectively, were verified by using authentic standards. The three compounds were prepared in methanol at 5 μg/mL of each as a mixture and injected into the instrument which was run under same conditions as that used for the metabolites identification. The obtained extracted ion chromatogram is shown in Fig. 6 and the retention time and mass spectra data are summarized in Table 3. The retention times and accurate mass data comparisons showed that the metabolites proposed from the real world biological samples (rat urine and feces) matched well with their respective authentic standards, further supporting the original structure characterizations.

4. Conclusion

This study proposed a systematic approach for rapid metabolites identification of such compounds as ECH undergoing multiple and unpredictable metabolism from biological matrix, based on the LC/MS-IT-TOF analysis. Firstly, the degradation products of ECH were characterized via degradation and fragmentation relationship analysis. Based on the fragmentation patterns analysis of ECH, four degradation products were rapidly identified. Secondly, the further metabolites of the degradation products were characterized by the elemental composition differences analysis of the quasi-molecular ions between the metabolites and their precursors. Finally, the direct phase I and phase II metabolites of the parent compound were readily characterized by the quasi-molecular ion mass difference analysis. With the benefit from the sufficient fragments information, the metabolic positions can be determined in most cases. Using this approach, a total of 13 metabolites of ECH has

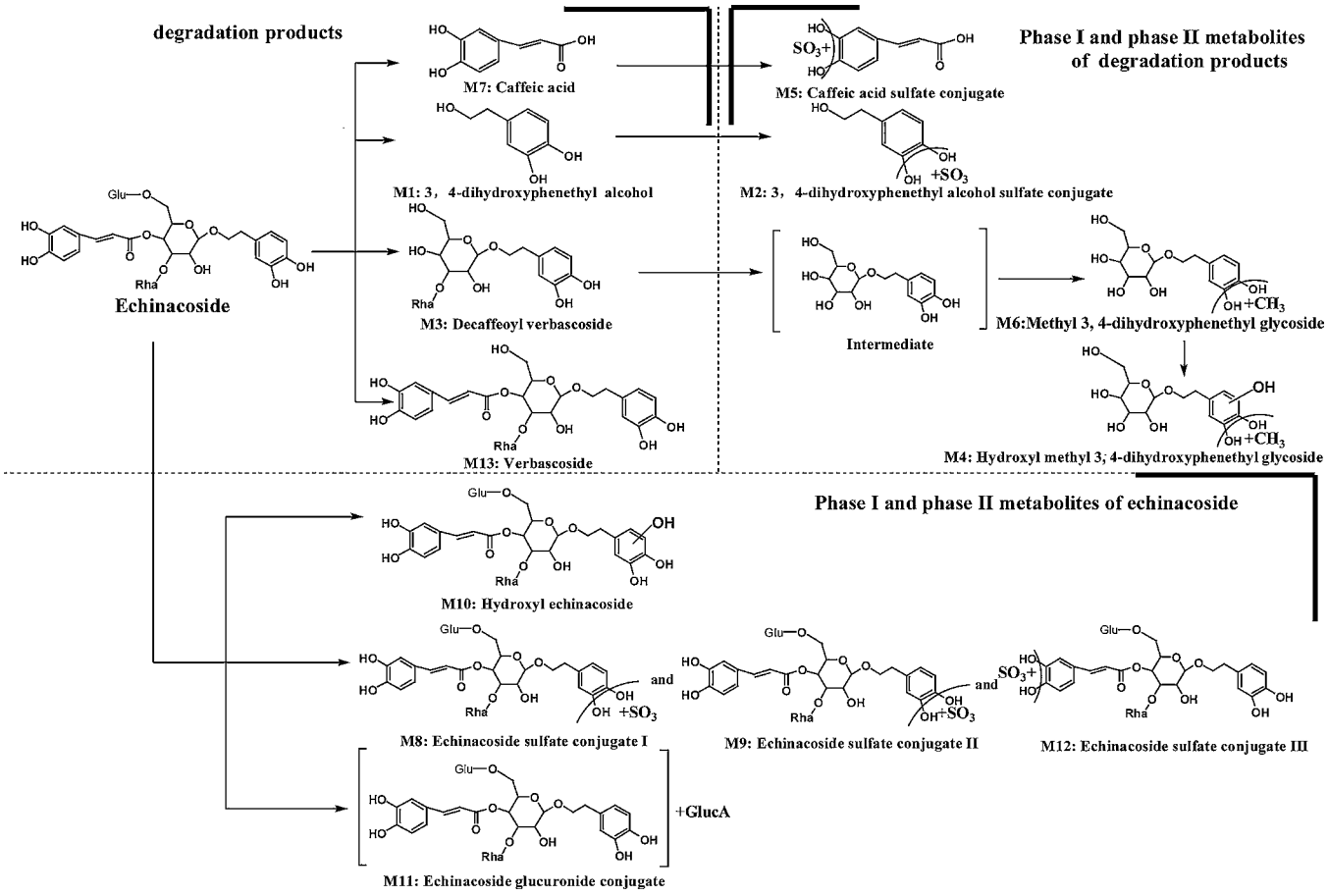


Fig. 7. Proposed metabolic pathways of echinacoside.

been identified from the rat urine and feces after an intragastric dosage. Fig. 7 depicts the identified metabolic pathways for ECH, including degradation products, and glucuronic acid, sulfate, and methyl conjugation of both parent compound and the degradation products.

In summary, the present study provides a more comprehensive map of ECH metabolism than that from the previously published results [15], where only eight phase II metabolites of the parent compound ECH had been identified. In addition, this study presents a feasible and generally applicable strategy for the complicated metabolites identification of natural products.

Acknowledgements

This work was financially supported by National Natural Science Foundation of China (No. 30630076) and "eleventh-five years" supporting program from the Ministry of Science and Technology of PR China (No. 2006BAI08B04-05).

References

[1] I. Saracoglu, M. Inoue, I. Calis, Y. Oglihara, Biol. Pharm. Bull. 18 (1995) 1396.
[2] M. Pennacchio, E. Alexander, Y.M. Syah, Euro. J. Pharmacol. 305 (1996) 169.
[3] Q.B. Xiong, K. Hase, Y. Tezuka, T. Tani, Planta Med. 64 (1998) 120.
[4] Q.B. Xiong, S. Kadota, T. Tani, T. Namba, Biol. Pharm. Bull. 19 (1996) 1580.
[5] M. Deng, J.Y. Zhao, P.F. Tu, Y. Jiang, Euro. J. Pharmacol. 505 (2004) 11.
[6] P.F. Tu, B. Wang, T. Deyama, Z.G. Zhang, Acta Pharm. Sin. 32 (1997) 294.
[7] N.B. Perry, E.J. Burgess, V.L. Glennie, J. Agric. Food Chem. 49 (2001) 1702.
[8] R. Cervellati, C. Renzulli, M.C. Guerra, E. Speroni, J. Agric. Food Chem. 50 (2002) 7504.
[9] C. Hu, D.D. Kitts, J. Agric. Food Chem. 48 (2000) 1466.
[10] F. Pellati, S. Benvenuti, L. Magro, M. Melegari, J. Pharm. Biomed. Anal. 35 (2004) 289.
[11] K.A. Koo, S.H. Sung, J.H. Park, S.H. Kim, Planta Med. 71 (2005) 778.
[12] E. Speroni, P. Covoni, S. Guizzardi, C. Renzulli, J. Ethnopharmacol. 79 (2002) 265.
[13] A. Matthias, R.S. Addison, K.G. Penman, R.G. Dickinson, Life Sci. 77 (2005) 2018.
[14] C.Q. Jia, H.M. Shi, X.M. Wu, J. Chromatogr. B 844 (2006) 308.
[15] C.Q. Jia, H.M. Shi, W. Jin, Drug Metab. Dispos. 37 (2009) 431.
[16] R.J. Steen, I. Bobeldijk, U.A. Brinkman, J. Chromatogr. A 915 (2001) 129.
[17] S. Lacorte, A.R. Fernandez-Alba, Mass Spectrom. Rev. 25 (2006) 866.
[18] I. Ferrer, E.M. Thurman, J. Chromatogr. A 1175 (2007) 24.
[19] E.M. Thurman, I. Ferrer, A.R. Fermandez-Alba, J. Chromatogr. A 1067 (2005) 127.
[20] E.M. Thurman, I. Ferrer, J.A. Zweigenbaum, J. Chromatogr. A 1082 (2005) 71.
[21] I. Ferrer, C.E. Heine, E.M. Thurman, Anal. Chem. 76 (2004) 1437.
[22] H.P. Hao, N. Cui, G.J. Wang, B.R. Xiang, Anal. Chem. 80 (2008) 8187.
[23] C.N. Zheng, H.P. Hao, X. Wang, G.J. Wang, J. Mass Spectrom. 44 (2009) 230.
[24] F.X. Zhang, Z.H. Jia, P. Gao, H.W. Kong, X. Li, J. Chen, Q. Yang, P.Y. Yin, J.S. Wang, X. Liu, F.M. Li, Y.L. Wu, G.W. Xu, Talanta 79 (2009) 836.
[25] H.Y. Zhang, X. Cheng, P. Hu, Q.L. Liang, X.P. Liang, Y.M. Wang, G.A. Luo, Talanta 79 (2009) 254.
[26] J. Zhang, Y. Jin, J. Dong, Y. Xiao, J. Feng, X. Xue, X. Zhang, X. Liang, Talanta 78 (2009) 513.
[27] R. Guo, Q. Zhou, Y. Cai, G. Jiang, Talanta 75 (2008) 1394.
[28] J.F. García-Reyes, A. Molina-Díaz, A.R. Fernandez-Alba, Anal. Chem. 79 (2007) 307.

Talanta 80 (2009) 581–585

Contents lists available at ScienceDirect

Talanta

journal homepage: www.elsevier.com/locate/talanta

A renewable copper electrode as an amperometric flow detector for nitrate determination in mineral water and soft drink samples

Juan C.M. Gamboa [a], Roselyn C. Peña [a], Thiago R.L.C. Paixão [b], Mauro Bertotti [a,*]

[a] Instituto de Química, Universidade de São Paulo, São Paulo, SP 05508-900, Brazil
[b] Centro de Ciências Naturais e Humanas, Universidade Federal do ABC, Santo André, SP 09210-170, Brazil

ARTICLE INFO

Article history:
Received 11 May 2009
Received in revised form 3 July 2009
Accepted 14 July 2009
Available online 21 July 2009

Keywords:
Nitrate
Nitrite
Flow injection analysis
Renewable copper surface
Mineral water
Soft drink

ABSTRACT

A novel approach was developed for nitrate analysis in a FIA configuration with amperometric detection ($E = -0.48$ V). Sensitive and reproducible current measurements were achieved by using a copper electrode activated with a controlled potential protocol. The response of the FIA amperometric method was linear over the range from 0.1 to 2.5 mmol L^{-1} nitrate with a detection limit of 4.2 μmol L^{-1} (S/N = 3). The repeatability of measurements was determined as 4.7% ($n = 9$) at the best conditions (flow rate: 3.0 mL min^{-1}, sample volume: 150 μL and nitrate concentration: 0.5 mmol L^{-1}) with a sampling rate of 60 samples h^{-1}. The method was employed for the determination of nitrate in mineral water and soft drink samples and the results were in agreement with those obtained by using a recommended procedure. Studies towards a selective monitoring of nitrite were also performed in samples containing nitrate by carrying out measurements at a less negative potential (−0.20 V).

© 2009 Elsevier B.V. All rights reserved.

1. Introduction

Nitrate can be found naturally in soil, water, vegetables and foods. In soil, the presence of nitrate is essential for the conversion of nitrogen unused by plants and its concentration is controlled by some processes like reduction by bacteria (denitrification), uptake by plants and decay of organic matter [1–3]. Anthropogenic sources of nitrate in soil are correlated to the intensive cultivation of lands and application of nitrogen fertilizers [1–3]. As a result of the high solubility of nitrate in water, this chemical species is easily leached down into groundwater, leading to a contamination of water supplies.

In the last years, concern has been expressed about the increasing levels of nitrate ion in drinking water, due to the toxicological problems associated with the formation of *N*-nitrous compounds [1–4]. Accordingly, these compounds are classified as carcinogenic hazard to humans and animals. Moreover, high levels of nitrate in water could result in disequilibrium of the freshwater ecosystem, due to a fast eutrophication process. The intake of large amounts of nitrate for infants could result in the "blue-baby syndrome", as a consequence of nitrate reduction in the organism to nitrite and further reaction of this metabolite with haemoglobin. Hence, the absorption and transfer of oxygen to cells is compromised. For this reason, nitrate levels (as N-NO_3^-) in potable water should not exceed 11 mg L^{-1} (or 0.8 mmol L^{-1}) and 10 mg L^{-1} (or 0.7 mmol L^{-1}), according to recommendations of the World Health Organization (WHO) [5] and the US Environmental Protection Agency (EPA) [6], respectively. Taking into account these aspects, it is clear that the development of fast and sensitive methods for quantification of nitrate in natural water samples is a pertinent topic in Analytical Chemistry.

Several procedures have been reported in the literature to quantify nitrate in different matrices and they were reviewed by Compton et al. [7]. Different techniques have been used such as UV/vis, chemiluminescence, fluorimetry, infrared, Raman and molecular cavity emission, chromatography, capillary electrophoresis and electrochemistry. In the case of electrochemical methods, copper [8–15], nickel [16], copper–nickel alloys [17], copper–cadmium alloys [18], copper–palladium alloys [1], platinum [19,20], lead [21], silver [22], rhodium [23], boron-doped diamond [24], gold [25] and polypyrrole nanowires [26] have been employed as substrate materials. The use of bare unmodified electrodes for the direct determination of nitrate is difficult owing to the slow kinetics of the charge transfer step. Hence, methods based on the direct reduction of nitrate are characterised by low sensitivity and irreproducibility and associated with surface passivation effects [27]. Nonetheless, procedures to increase the sensitivity in direct electroanalytical determinations of nitrate are generally associated with activation of the electrodic surface, especially when copper cathodes [13] are used. The indirect determination of nitrate

* Corresponding author. Fax: +55 11 3815 5579.
E-mail address: mbertott@iq.usp.br (M. Bertotti).

0039-9140/$ – see front matter © 2009 Elsevier B.V. All rights reserved.
doi:10.1016/j.talanta.2009.07.028

has been proposed after a derivatisation procedure [28], as also reported in a method for nitrite analysis [29].

The use of a copper surface as amperometric detector in a flow-through configuration has been already explored by our group in the determination of sulphite in alkaline conditions [30]. As fresh copper surfaces are more effective for cathodic reactions, we have also proposed the development of a renewable process for the activation of copper electrodes without the necessity to introduce copper ions into the sample [13]. However, as the majority of other published works involving the electroanalytical determination of nitrate, measurements were obtained in a batch mode with low analytical frequency. In the present work, we describe our efforts to associate the renewable copper surface with a mechanised process (flow injection analysis). The analytical applicability of this high-throughput proposed method was examined by measuring the nitrate content in mineral water and soft drink samples.

2. Experimental

2.1. Chemicals, materials and samples

All solid reagents were of analytical grade and were used without further purification. Sulphuric acid, sodium sulphate, potassium nitrite and potassium nitrate were obtained from Merck (Darmstadt, Germany). The supporting electrolyte for flow injection experiments was a 0.1 mol L^{-1} Na_2SO_4 solution, pH 2.0 (adjusted with H_2SO_4). In almost all cases the solutions were prepared by dissolving the reagents in deionised water processed through a water purification system (Nanopure Infinity, Barnstead). Samples of mineral water and soft drink were acquired from a local market. Carbon dioxide was removed from soft drink samples by thorough bubbling with argon. Nitrite solutions were standardised as reported in the literature [31].

2.2. Electrodes and instrumentation

An Autolab PGSTAT 30 (Eco Chemie) bipotentiostat with data acquisition software made available by the manufacturer (GPES 4.8 version) was used for electrochemical measurements. Experiments were done in a conventional electrochemical cell, a Ag/AgCl (saturated KCl) electrode and a stainless-steel tube being used as reference and counter electrodes, respectively. A copper sheet (Pertech® of Brazil) fabricated by copper electroplating in a substrate composed of paper and phenolic resin was used as working electrode (area = 56 mm^2). This copper sheet is used for fabrication of printed circuit boards. The flow injection apparatus consisted of an aquarium air pump (to propel the solution by pressurization), a homemade rotatory injection valve and an acrylic cell mounted in a thin layer configuration [32,33].

2.3. Activation of the electrode surface in FIA experiments

The working electrode surface is activated by two potential steps prior current measurements, Fig. 1. To drive copper dissolution, the working electrode is polarised at +0.50 V (step a). Then, the redeposition is carried out at −0.25 V (step b). Both steps are performed in absence of flow, otherwise, copper ions would escape from the diffusion layer after the anodic dissolution. These two steps (copper dissolution and redeposition) are required to produce a fresh copper layer with an active role concerning the cathodic reduction of nitrate, as previously demonstrated [13]. The optimisation of both time parameters involved in the pre-treatment potential program (steps a and b) was investigated as an attempt of enhancing the sensitivity of nitrate determinations. After the activation process, the electrode was polarised at the potential required for nitrate reduction. Three samples were injected after each activation step.

2.4. Spectrophotometric analysis

An evaluation of the accuracy of the proposed method for quantitative determinations of nitrate in mineral water samples was performed by UV-spectrophotometry without derivatisation at 220 nm in a Hitachi U-3000 spectrophotometer using a 1.00 cm optical pathlength quartz cuvette. As soft drink samples are more complex and contain large amounts of organic compounds (glucose), comparative measurements were obtained with the UV-spectrophotometry Griess assay. The reduction of nitrate to nitrite was accomplished by using a copperised cadmium reactor column prior to spectrophotometric measurements with the Griess method at 543 nm.

3. Results and discussion

Previous reports on the literature [8,12,13] have demonstrated that the reduction of nitrate can be promoted on a fresh copper surface, in accordance with Eq. (1):

$$NO_3^- + 10H^+ + 8e^- \rightleftharpoons 3H_2O + NH_4^+ \quad (1)$$

Taking into account the necessity of a fresh copper layer, a protocol involving the dissolution of the outer copper layer for further redeposition of copper ions is required. A schematic representation of the pre-treatment procedure used in the FIA system is shown in Fig. 1. At the activated detector surface, FIA experiments were carried out to investigate the best applied potential for nitrate reduction. From the results obtained in hydrodynamic voltammetric experiments (not shown), the working potential value −0.48 V was selected as the most appropriate to ensure complete analyte reduction at the copper sensor.

The optimisation of both parameters (dissolution and redeposition time) was also investigated. Data in Fig. 2, curve A, shows that no faradaic signal is obtained at a non pre-treated surface (i.e. bare copper electrode), a different situation being observed as the amount of copper ions redeposited during the cathodic process increases (for a constant dissolution time). In a similar way, the signal for nitrate reduction increases with the increase in the dissolution time (for a constant redeposition time) (Fig. 2, curve B). Optimal conditions were achieved by using 30 s, respectively, for the dissolution and redeposition steps, and this procedure was employed for all analytical determinations.

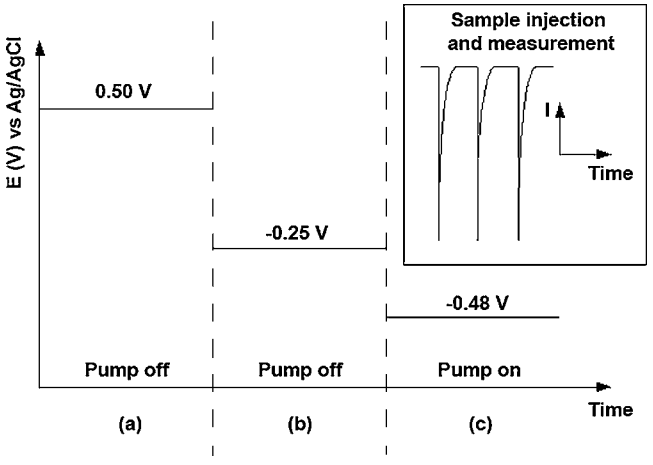


Fig. 1. Schematic representation of the copper surface activation protocol in the FIA system: copper dissolution (a); copper redeposition (b) and nitrate electroreduction (c). The inset shows the amperometric signal recorder after 3 injections of a nitrate solution in the FIA apparatus.

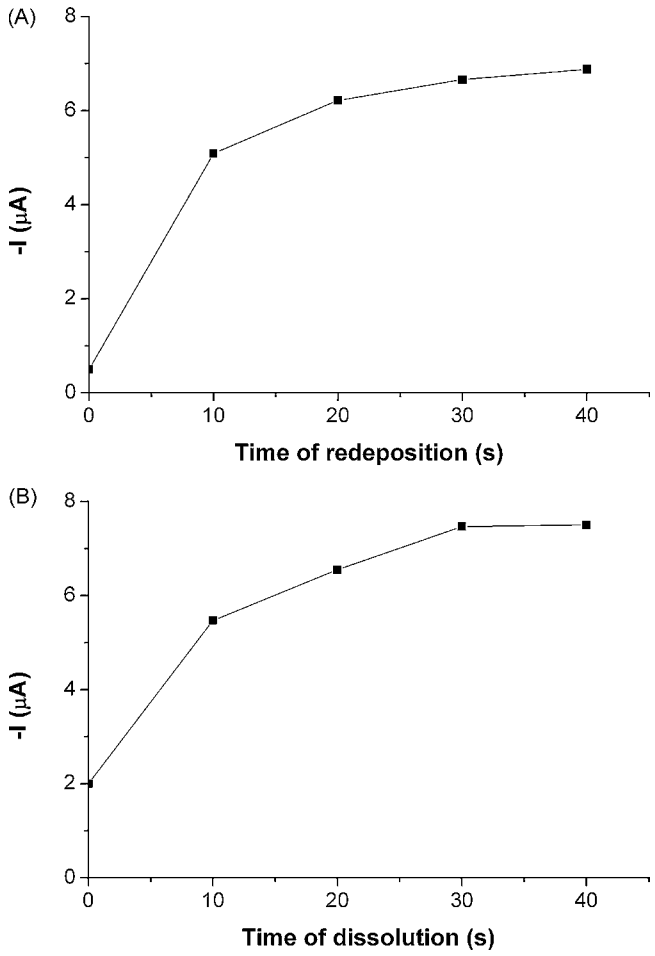


Fig. 2. Dependence of cathodic peak current values on the redeposition (A) and dissolution (B) time for injections of a 0.1 mol L^{-1} Na_2SO_4 + 1.0 mmol L^{-1} NO_3^- solution (pH 2.0). The dissolution time was 30 s for experiments represented by curve (A) and the redeposition time was 30 s for experiments represented by curve (B). Carrier solution: 0.1 mol L^{-1} Na_2SO_4 (pH 2.0), E = −0.48 V, number of measurements: 3, flow rate: 3.0 mL min^{-1}, sample volume: 150 μL.

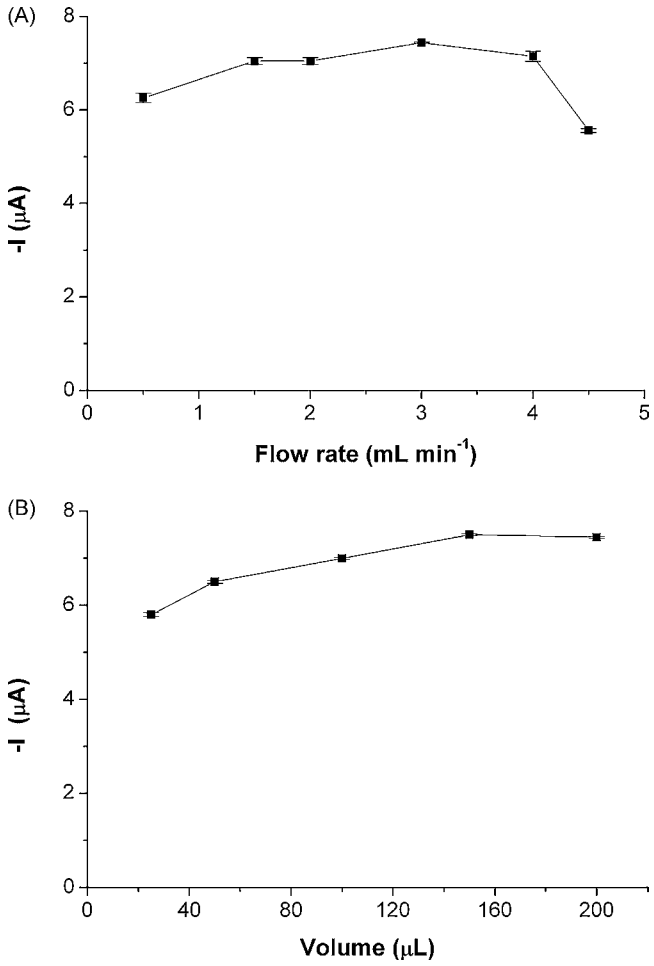


Fig. 3. Average current peak values (n = 3) recorded for a 1.0 mmol L^{-1} nitrate + 0.1 mmol L^{-1} de Na_2SO_4 solution (pH 2.0) at various flow rates (A) (sample volume 150 μL) and various sample volumes (B) (flow rate 2.0 mL min^{-1}). Carrier solution: 0.1 mol L^{-1} Na_2SO_4 (pH 2.0), E = −0.48 V.

To investigate the optimal conditions for the flow injection system performance, parameters such as sample volume and flow rate were varied using a 1.0 mmol L^{-1} nitrate solution. The effect of flow rate (studied from 0.5 to 4.5 mL min^{-1}) on the analytical signal was evaluated (Fig. 3A) and the current increased with flow rate up to 3.0 mL min^{-1}. This indicates that a kinetic limitation is prevalent at more efficient mass-transport conditions. Taking into account these aspects, a flow rate of 3.0 mL min^{-1} was selected as the most favourable. The effect of sample volume was evaluated using injection loops from 25 up to 200 μL, Fig. 3B. The amperometric signal increased almost linearly up to 150 μL, and then a slight decrease was noticed. Hence, a 150 μL sample volume was selected as the most appropriate, based on the best compromise between reproducibility and sampling rate.

In order to confirm the importance of surface activation on the repeatability of the measurements, two independent studies were performed. Firstly, nitrate solutions were injected in the FIA system after one activation procedure (30 s of dissolution and 30 s of redeposition, Fig. 4, curve B) at the beginning of experiment. A continuous current decrease was noticed, indicating the sensor activity loss during the experiment. On the other hand, by using the protocol described in Section 2 a completely different result was obtained (Fig. 4, curve A). In this case, 3 samples were injected after each activation step and the standard deviation (SD) for 9 injections was found to be 4.7% (60 samples per hour). No significant improve-

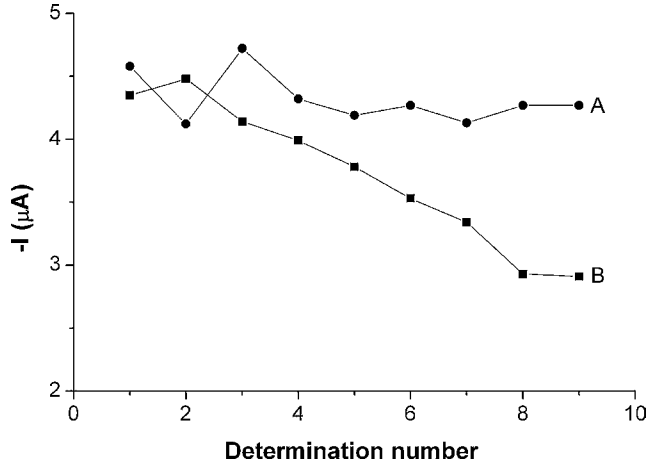


Fig. 4. Current peak values as a function of time for injections of a 0.1 mol L^{-1} Na_2SO_4 + 0.5 mmol L^{-1} NO_3^- solution (pH 2.0). Data were obtained by using the proposed protocol (pre-treatment of the copper electrode after each set of 3 injections) (A) and by pre-treating the electrode only in the beginning of the experiment (B). Carrier solution: 0.1 mol L^{-1} Na_2SO_4 (pH 2.0), E = −0.48 V, flow rate: 3.0 mL min^{-1}, sample volume: 150 μL.

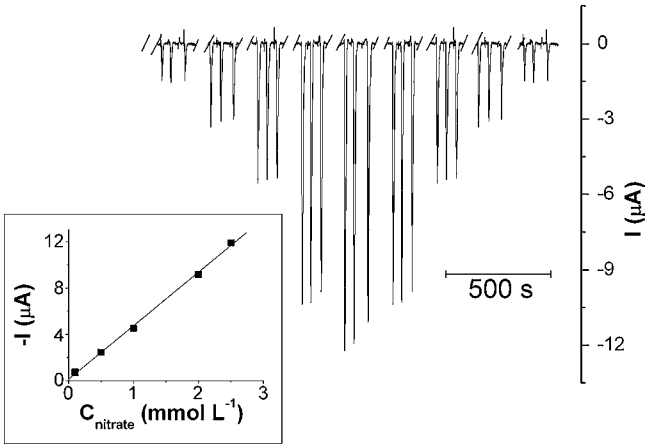


Fig. 5. Peaks recorded for injections of nitrate standard solutions at the optimised FIA conditions (0.1–2.5 mmol L^{-1}). The breaks (//) in the figure represent the pre-treatment gap (60 s). The inset shows the calibration curve. Carrier solution: 0.1 mol L^{-1} Na_2SO_4 (pH 2.0), E = −0.48 V, flow rate: 3.0 mL min^{-1}, sample volume: 150 μL.

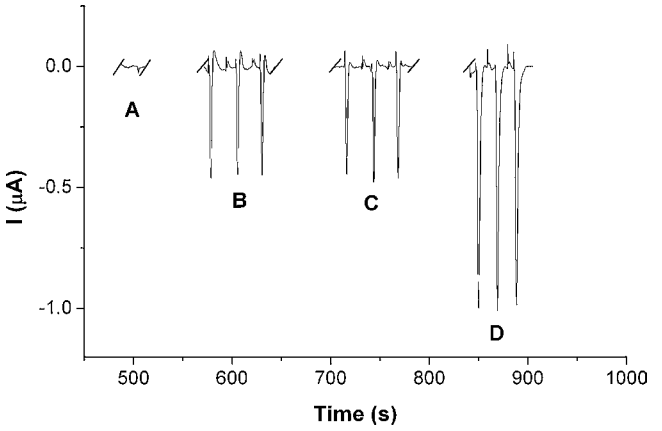


Fig. 6. Peaks recorded at the optimised FIA conditions for injections of 1.0 mmol L^{-1} nitrate (A), 0.05 mmol L^{-1} nitrite (B), a mixture of 1.0 mmol L^{-1} nitrate + 0.05 mmol L^{-1} nitrite (C) and a mixture of 1.0 mmol L^{-1} nitrate + 0.10 mmol L^{-1} nitrite. Carrier solution: 0.1 mol L^{-1} Na_2SO_4 (pH 2.0), E = −0.20 V, flow rate: 3.0 mL min^{-1}, sample volume: 150 μL.

Table 1
Analytical parameters for nitrate determination.

Analytical parameters	Batch mode [13]	Proposed method
Analytical frequency (h^{-1})	25	60
Detection limit (μmol L^{-1})	11.6	4.2
Quantification limit (μmol L^{-1})	38.7	14.0
Linear range (mmol L^{-1})	0.1–2.5	0.1–2.5
Sample volume (mL)	10	0.15

ment in the precision was noticed by injecting each nitrate sample after the activation step. Hence, in order to increase the analytical frequency without lose in precision, the second protocol (one activation step prior to 3 sample injections) was elected as the most convenient for all subsequent FIA experiments.

The relationship between the amperometric peak current and the concentration of nitrate was investigated in the range 0.1–2.5 mmol L^{-1} (Fig. 5). Using the optimised conditions previously reported, a linear response ($(-Ip/\mu A) = 0.13 + 4.6 (C_{nitrate}/mmol\ L^{-1})$, $R^2 = 0.9991$) was obtained. No memory effect was observed during the experiment, demonstrating that the adopted procedure is convenient. The detection (3 SD) and quantification (10 SD) limits were estimated as 4.2 and 14 μmol L^{-1}, respectively. In order to compare the results obtained by using the batch method [13] with those proposed in this work, figures of merit of both methods are summarised in Table 1. It is clearly seen that the limit of detection, sample volume and analytical frequency of the FIA proposed method are better, indicating its potentiality as an alternative method for routine analysis of nitrate.

The applicability of the renewable copper electrode as detector in a FIA configuration for the determination of nitrate in real samples was also performed. Table 2 shows the nitrate content in 3 mineral water and 3 soft drink samples. The results were in good agreement with those obtained by using standard methods [31] (for a 95% confidence level according to the Student's t-test). As an additional accuracy test of the proposed method, a set of recovery experiments in which nitrate was added directly to water samples was carried out. Recovery results were satisfactory and ranged from 90 to 97%. Accordingly, we can conclude that the proposed method is reliable for nitrate measurements in the investigated samples.

Table 2
Nitrate content (as $N\text{-}NO_3^-$) in mineral water and soft drink samples.

Sample	Standard method [31] (mg L^{-1})	Proposed method (mg L^{-1})
Aquana[1]	11.03 ± 0.04	11.3 ± 0.1
Schincariol[1]	10.49 ± 0.07	10.6 ± 0.1
Lindoya[1]	5.16 ± 0.02	5.7 ± 0.2
Soda Antártica[2]	6.30 ± 0.01	6.1 ± 0.1
Tônica Antártica[2]	17.60 ± 0.01	18.0 ± 0.2
Sprite[2]	15.27 ± 0.09	14.7 ± 0.6

Number of replicates = 3, 1 = mineral water, 2 = soft drink.

Previous experiments with the activated copper electrode [13] have shown the good resolution between nitrate and nitrite reduction current peaks in differential pulse voltammograms, respectively −0.48 and −0.20 V. In order to investigate the possibility of analysing nitrite in the presence of nitrate using the proposed FIA method, a standard solution of nitrite was injected under the optimised conditions for nitrate determination. However, experiments were carried out at −0.20 V, instead of −0.48 V. A transient signal for nitrite is observed (Fig. 6, injection B), no response being obtained for nitrate at the same experimental conditions (injection A). By injecting solutions containing both nitrate and nitrite, the current response (injection C) is similar to the one observed after injection of nitrite (injection B). The FIA response for nitrite is proportional to the analyte concentration, as can be observed by comparing peaks C and D. Data shown in this figure also demonstrate that the detector sensitivity for nitrite is good, as a suitable discrimination between signal and noise is observed for 0.05 mmol L^{-1} nitrite solutions (around 0.7 ppm N-nitrite). Accordingly, an interesting option for the simultaneous determination of both analytes in mixtures is envisaged by performing experiments using dual-detection. We are currently undertaking experiments on this subject, and determining low levels of nitrite in water samples with the proposed copper sensor is an expected challenge.

4. Conclusions

A renewable copper electrode was successfully used as an amperometric detector in a flow injection apparatus for nitrate determination. The system provides high throughput with good reproducibility and sensitivity, hence the analytical parameters are significantly improved in comparison with determinations performed using the batch method. Moreover, taking into account the principles of Green Chemistry, the proposed method is favoured as no carcinogenic compounds are required to convert the analyte. Finally, the possibility to differentiate nitrate and nitrite may consti-

tute a valuable tool in examining samples containing both analytes in a rapid, simple, inexpensive and safe way.

Acknowledgements

The authors are thankful to FAPESP (Fundação de Amparo à Pesquisa do Estado de São Paulo), CAPES (Coordenação de Aperfeiçoamento de Pessoal de Nível Superior) and CNPq (Conselho Nacional de Desenvolvimento Científico e Tecnológico) for the financial support.

References

[1] K. Soropogui, M. Sigaud, O. Vittori, Electroanalysis 18 (2006) 2354.
[2] T. Le Goff, J. Braven, L. Ebdon, N.P. Chilcott, D. Scholefield, J.W. Wood, Analyst 127 (2002) 507.
[3] M.C. Cann, C. Baird, Environmental Chemistry, W H Freeman & Co., 2005.
[4] P.M. Tucker, M.J. Waite, B.E. Hayden, J. Appl. Electrochem. 34 (2004) 781.
[5] W.H. Organization, Guidelines for Drinking Water Quality Recommendations, WHO, Paris, 1993.
[6] US, EPA Federal register 38668, vol. 59, 1994.
[7] M.J. Moorcroft, J. Davis, R.G. Compton, Talanta 54 (2001) 785.
[8] D. Pletcher, Z. Poorabedi, Electrochim. Acta 24 (1979) 1253.
[9] M. Shibata, K. Yoshida, N. Furuya, J. Electroanal. Chem. 387 (1995) 143.
[10] M. Shibata, K. Yoshida, N. Furuya, J. Electrochem. Soc. 145 (1998) 2348.
[11] N.G. Carpenter, D. Pletcher, Anal. Chim. Acta 317 (1995) 287.
[12] J. Davis, M.J. Moorcroft, S.J. Wilkins, R.G. Compton, M.F. Cardosi, Analyst 125 (2000) 737.
[13] T.R.L.C. Paixão, J.L. Cardoso, M. Bertotti, Talanta 71 (2007) 186.
[14] J. Davis, M.J. Moorcroft, S.J. Wilkins, R.G. Compton, M.F. Cardosi, Electroanalysis 12 (2000) 1363.
[15] A.G. Fogg, S.P. Scullion, T.E. Edmonds, B.J. Birch, Analyst 116 (1991) 573.
[16] J.O. Bockris, J. Kim, J. Electrochem. Soc. 143 (1996) 3801.
[17] M.J. Moorcroft, L. Nei, J. Davis, R.G. Compton, Anal. Lett. 33 (2000) 3127.
[18] M.E. Bodini, D.T. Sawyer, Anal. Chem. 49 (1977) 485.
[19] V. Mori, M. Bertotti, Anal. Lett. 32 (1999) 25.
[20] A. Hulanicki, W. Matuszewski, M. Trojanowicz, Anal. Chim. Acta 194 (1987) 119.
[21] J.D. Genders, D. Hartsough, D.T. Hobbs, J. Appl. Electrochem. 26 (1996) 1.
[22] D. Kim, I.B. Goldberg, J.W. Judy, Analyst 132 (2007) 350.
[23] J.W. Peel, K.J. Reddy, B.P. Sullivan, J.M. Bowen, Water Res. 37 (2003) 2512.
[24] P. Bouamrane, A. Tadjeddine, J.E. Butler, R. Tenne, C. LevyClement, J. Electroanal. Chem. 405 (1996) 95.
[25] Y.P. Chen, S.Y. Liu, F. Fang, S.H. Li, G. Liu, Y.C. Tian, Y. Xiong, H.Q. Yu, Environ. Sci. Technol. 42 (2008) 8465.
[26] S. Aravamudhan, S. Bhansali, Proceedings of the 14th International Conference on Solid-State Sensors, Actuators and Microsystems, Elsevier Science Sa, Lyon, France, 2007, p. 623.
[27] Z.F. Zhao, X.H. Cai, J. Electroanal. Chem. 252 (1988) 361.
[28] A.G. Fogg, S.P. Scullion, T.E. Edmonds, Analyst 114 (1989) 579.
[29] J. Davis, R.G. Compton, Anal. Chim. Acta 404 (2000) 241.
[30] D. Corbo, M. Bertotti, Anal. Bioanal. Chem. 374 (2002) 416.
[31] L.S. Clescerl, A.E. Greenberg, A.D. Eaton, Standard Methods for Examination of Water & Wastewater, Method 4500-NO_3^-, American Public Health Association, Washington, 1999.
[32] T.R.L.C. Paixão, R.C. Matos, M. Bertotti, Electrochim. Acta 48 (2003) 691.
[33] T.R.L.C. Paixão, R.C. Matos, M. Bertotti, Electroanalysis 15 (2003) 1884.

Talanta 80 (2009) 586–592

Contents lists available at ScienceDirect

Talanta

journal homepage: www.elsevier.com/locate/talanta

A single-wall carbon nanotubes modified edge plane pyrolytic graphite sensor for determination of methylprednisolone in biological fluids

Rajendra N. Goyal*, Sanghamitra Chatterjee, Anoop Raj Singh Rana

Department of Chemistry, Indian Institute of Technology Roorkee, Roorkee 247667, India

ARTICLE INFO

Article history:
Received 21 June 2009
Received in revised form 14 July 2009
Accepted 14 July 2009
Available online 21 July 2009

Keywords:
Methylprednisolone
Single-wall carbon nanotubes
Edge plane pyrolytic graphite electrode
Square wave voltammetry
Blood plasma

ABSTRACT

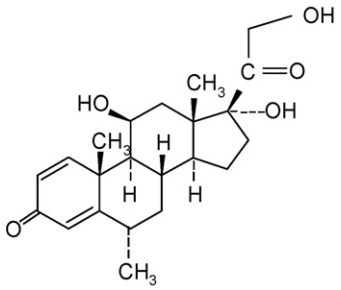
An electrochemical protocol based on reduction is developed to determine methylprednisolone using single-wall carbon nanotubes (SWNTs) modified edge plane pyrolytic graphite electrode (EPPGE). To obtain a good sensitivity, instrumental variables were studied using Square Wave Voltammetry (SWV). The voltammetric results indicate that SWNTs modified EPPGE remarkably enhances the reduction of methylprednisolone which leads to considerable improvement of peak current with shift of peak potential to less negative values. The voltammetric current showed a linear response for methylprednisolone concentration in the range 5–500 nM with a sensitivity of 98 nA nM^{-1}. The limit of detection was estimated to be 4.5×10^{-9} M. The developed method is used for the determination of methylprednisolone in pharmaceutical dosages and human blood plasma samples of patients undergoing treatment with methylprednisolone. The major metabolites present in blood plasma did not interfere with the present investigation as they did not exhibit reduction peak in the experimental range used. A comparison of results with high performance liquid chromatography (HPLC) indicates a good agreement.

© 2009 Elsevier B.V. All rights reserved.

1. Introduction

The last few years have signaled a remarkable evolution of the approach followed, at an international level, to control the abuse of drugs in competitive sports. A series of preventive actions and educational campaigns have been put in place by the World Anti-Doping Agency (WADA), to discourage the illicit use of performance-enhancing agents, thus complementing the traditional activities of the anti-doping laboratories. Glucocorticosteroids, anabolic steroids, beta-2 agonists are all included in the prohibited list of WADA [1]. Neale Greaves had his license suspended in the year 2009 racing season as his horse Double Agent was tested positive for methylprednisolone [2]. Brass Hat was disqualified for having trace amounts of methylprednisolone in the year 2006 [3]. The triple jumper Kenta Bell, who placed third at United States Championship in June 2007, accepted a first-offence suspension of three months as he tested positive for the banned substance methylprednisolone [4]. It is therefore mandatory for the accredited laboratories to develop an effective method which aims at the determination of methylprednisolone, a drug abused for doping.

Methylprednisolone **(I)** is a synthetic glucocorticosteroid which is readily absorbed from the gastrointestinal tract and is sold under the brand names Medrol, Depo-Medrol, Solu-Medrol, Phocenta and Cadista. It is primarily used in the therapeutic treatment, particularly for its anti-inflammatory and immunosuppressive actions [5,6]. It is used for the treatment of various conditions like allergic rhinitis, arthritis, blood diseases, respiratory problems, certain cancers, eye diseases, intestinal disorders, collagen and skin diseases [7–16]. It is used to achieve prompt suppression of inflammatory conditions like systemic lupus erythematosus, ulcerative colitis and Crohn's disease [17–20]. Systemic administration of methylprednisolone can reduce neurological deficits after acute spinal cord injury [21] and it is also used for the treatment of patients with multiple sclerosis [22] and proliferative lupus nephritis [23]. Thus, keeping in consideration the efficacy of the drug in pharmaceutical industry and its abuse for doping, a need was felt to develop a sensitive and rapid assay for the determination of methylprednisolone.



(I)

* Corresponding author. Tel.: +91 1332 285794 (O)/274454 (R); fax: +91 1332 273560.
E-mail addresses: rngcyfcy@iitr.ernet.in, rngcyfcy@rediffmail.com (R.N. Goyal).

0039-9140/$ – see front matter © 2009 Elsevier B.V. All rights reserved.
doi:10.1016/j.talanta.2009.07.029

Literature survey revealed that the analysis of methylprednisolone in the past years have been mostly based on the chromatographic methods. Liquid chromatography–tandem mass spectrometry [24], high performance liquid chromatography [25], high performance liquid chromatography–mass spectrometry [26], atmospheric pressure chemical ionization–liquid chromatography mass spectrometry [27], GC-ion-trap MS/MS [28] and ultra performance liquid chromatography [29] are some of the chromatographic techniques used for the determination of methylprednisolone. In spite of being sensitive, the chromatographic methods encounter problems like the low volatility of compounds, need for derivatisation, expensive instrumentation and time-consuming extraction procedures. Voltammetric oxidation of methylprednisolone has also been investigated using differential pulse voltammetry [30] and linear sweep voltammetry [31] but the drawback in these studies was the interference caused by the major metabolites present in biological fluids like uric acid, ascorbic acid, dopamine, etc. Therefore, the aim of the present work is to determine the electrochemical reduction of methylprednisolone using SWV which is a simple, rapid and sensitive technique. The studies have been performed at SWNTs modified EPPGE as edge plane pyrolytic graphite has been found to be a better substrate for modification in comparison to other conventional electrodes like glassy carbon electrode [32] due to its strong adsorption property and wide potential window. Methylprednisolone has been determined in pharmaceutical samples and human blood plasma following administration of therapeutic doses of the drug. The results obtained by the proposed method have also been compared with HPLC.

2. Experimental

2.1. Apparatus

The voltammetric experiments were performed using a three electrode single compartment cell equipped with SWNTs modified edge plane pyrolytic graphite electrode (~6 mm^2) as the working electrode, platinum wire as the counter electrode and an Ag/AgCl (3 M NaCl) reference electrode (BAS Model MF-2052 RB-5B). The edge plane pyrolytic graphite piece was obtained from Pfizer Inc., New York, USA and the electrode was prepared as reported in literature [32]. Experiments were carried out using a BAS CV-50 W voltammetric analyzer (Bioanalytical Systems, West Lafayette, IN, USA). All the potentials quoted are versus Ag/AgCl electrode at an ambient temperature of 25 ± 2 °C. The surface morphology of modified electrode was characterized by recording FE-SEM using Quanta 200 FE-SEM instrument. HPLC studies were performed on Agilent 1100 series system with RP-18e (5 μm) column. The method involved the systematic use of isocratic mobile phase of water and methanol in the ratio 40:60 at a flow rate of 1.4 mL min^{-1} and detection was carried out at 254 nm.

2.2. Chemicals

Methylprednisolone acetate injectable suspension USP was obtained from Pfizer Products India Private Limited, Mumbai, India and was used as received. SWNTs of purity > 95% was purchased from Bucky USA, Houston, TX, USA. Methylprednisolone containing tablets and injection marketed by different medical companies were purchased from the local market. Phosphate buffers (1 M) of different pH were prepared from analytical grade chemicals according to the reported method [33]. All other solvents and reagents used were of analytical grade. Double distilled water was used to prepare the solutions.

2.3. Procedure

Stock solution (1 μM) of methylprednisolone acetate was prepared by diluting the injection content (40 mg in 1 mL) with double distilled water. The solution was ultra sonicated for 30 min. Required amount of the stock solution was added to 3 mL of phosphate buffer solution (1.0 M, pH 7.2) and the total volume was made to 6.0 mL with double distilled water. Since oxygen is a major interference at negative measurement potential, high-purity nitrogen was bubbled for 12–15 min to deoxygenate the solutions before recording each voltammogram. The electrode surface was cleaned after each run by applying a potential of 200 mV for 60 s in the blank solution (3 mL of phosphate buffer solution and 3 mL of double distilled water). Instrumental conditions for square wave voltammetry were: Initial E: −800 mV, Final E: −1600 mV, Square wave amplitude (E_{sw}): 25 mV, Potential Step (E): 4 mV, Square wave frequency (f): 15 Hz.

Human blood plasma samples of normal person (control) were obtained from the Indian Institute of Technology hospital and used as control. The plasma samples of patients undergoing treatment with methylprednisolone were obtained from Matrichaya Nursing Home, Roorkee after centrifuging the whole blood with EDTA as anticoagulant for 15 min. The samples were obtained after 10 h of administration of 16 mg tablet of methylprednisolone. The biological samples did not exhibit any reduction peak on scanning from −0.8 to −1.6 V indicating thereby the absence of other reducible compounds in this potential window. The samples were therefore used for analysis without any dilution.

2.4. Preparation of SWNTs modified electrode

Prior to modification, the surface of bare EPPGE was rubbed on an emery paper and then rinsed with double distilled water and dried. A 0.5 mg/mL suspension was prepared by dispersing 0.5 mg SWNTs in 1.0 mL N,N-dimethylformamide (DMF) using ultrasonic bath. A known volume (40 μL) of this suspension was coated onto the surface of the bare EPPGE and the solvent was allowed to evaporate at room temperature. The working electrode surface with a well coated layer of SWNT was then ready for use after 4–6 h. A comparison of the surface morphology of bare and modified electrodes was studied by recording FE-SEM images as shown in Fig. 1. The image in Fig. 1(B) clearly indicates the deposition of SWNTs at the surface of the EPPGE.

3. Results and discussion

3.1. Determination of surface area

To determine the efficacy of surface modification procedure, the surface area of bare and SWNTs modified EPPGE was calculated. For this purpose, cyclic voltammograms were recorded for 1 mM $K_3Fe(CN)_6$ at different scan rates using 0.1 M KCl as the supporting electrolyte. Due to the presence of Fe^{+3}/Fe^{+2}, well defined redox couple was observed at both the electrodes. There was an enhancement in the peak current values at SWNTs modified electrode in comparison to the bare EPPGE. For a reversible process, the following equation applies:

$$i_p = 2.69 \times 10^5 A n^{3/2} D_R^{1/2} c_o \nu^{1/2}$$

where i_p refers to the peak current in Ampere and A is the electrode surface area in cm^2. For 1 mM $K_3Fe(CN)_6$, $n = 1$, $D_R = 7.6 \times 10^{-6}$ cm^2 s^{-1}, c_o is the concentration of $K_3Fe(CN)_6$ in M and ν is the scan rate in V s^{-1}. The slope of i_p versus $\nu^{1/2}$ plot was then used to calculate the surface area of bare and SWNTs modified EPPGE which were found as 0.08239 cm^2 and 0.22479 cm^2 respec-

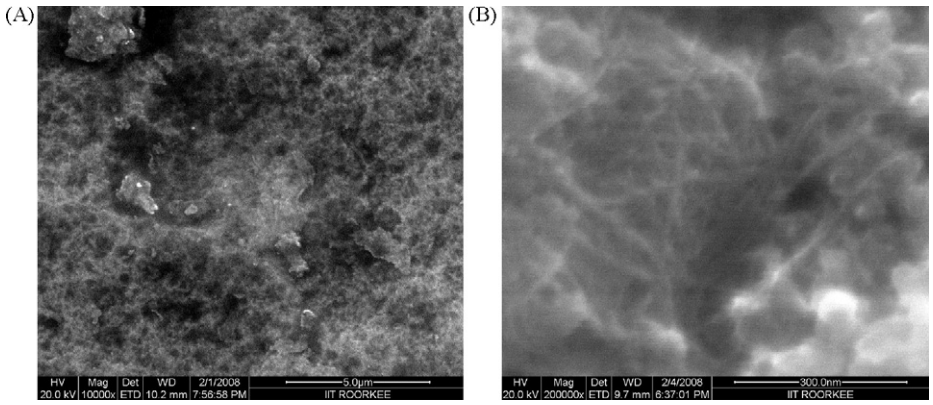


Fig. 1. A comparison of typical FE-SEM images of (A) bare and (B) SWNTs modified edge plane pyrolytic graphite electrode.

tively. The effective working area of the modified electrode is ~2.7 times larger than that of the bare EPPGE thereby indicating that the bare electrode has been modified efficiently by SWNT film. In recent studies, the increased dc current signals in cyclic voltammetry seen for the ferri/ferro cyanide at SWNTs modified glassy carbon electrode have been assigned to effect of diffusion within a porous thin layer [34]. Thus, apart from semi-infinite planar diffusion of ferri/ferro cyanide at the SWNTs modified electrode thin layer diffusion effects are also likely to operate.

3.2. Voltammetric behavior of methylprednisolone

3.2.1. Cyclic voltammetry

The cyclic voltammograms recorded for 0.3 μM methylprednisolone at the bare and SWNTs modified EPPGE in 1 M phosphate buffer solution at pH 7.2 are illustrated in Fig. 2. A well defined single reduction peak at ~−1312 mV was obtained at SWNTs modified EPPGE which shifted to more negative potentials (~−1458 mV) with a marked decrease in peak current at the bare EPPGE. These results clearly reveal that SWNTs acts as a very efficient promoter to enhance the kinetics of the electrochemical reduction of methylprednisolone. The absence of anodic peaks in the reverse scan clearly indicated that the reduction of methylprednisolone at this particular voltammetric sensor is irreversible in nature. To ascertain the nature of electrode reaction, sweep rate studies were performed in the range 10–1000 mV s^{-1}. The peak current was found to increase with increasing sweep rates and the plot of $i_p/v^{1/2}$ versus log v clearly indicated that the electrode process is adsorption controlled [35,36]. The peak potentials shifted to more negative potentials with increasing scan rate. The change in peak potential at different pH values was also studied and a linear plot was obtained between E_p and pH which obeyed the following equation:

$$-E_p(\text{pH } 2.4\text{–}11.0) = [889 + 60.50\,\text{pH}]\ \text{mV versus Ag/AgCl}$$

with a correlation coefficient of 0.9950. The slope clearly indicated that the total number of electrons and protons taking part in the charge transfer was the same. As SWV is considered to be a more sensitive technique in comparison to cyclic voltammetry, hence it is used for the determination of methylprednisolone.

3.2.2. Square wave voltammetry

Initially, square wave voltammograms were recorded for 100 nM methylprednisolone at pH 7.2 at the bare basal plane pyrolytic graphite electrode (BPPGE), bare EPPGE and SWNTs modified EPPGE. The working electrodes had almost the same surface area exposed to solution. Fig. 3 represents a comparison of square wave voltammograms observed for the drug at different working electrodes. In the case of bare BPPGE, a small peak is observed at ~−1395 mV which shifts to ~−1336 mV at bare EPPGE, thus indicating that the exposed edge plane sites in bare EPPGE contribute in making it a better substrate for modification than bare BPPGE. At SWNTs modified EPPGE, methylprednisolone gets reduced at ~−1285 mV with a significant increase in the peak current (Fig. 3). The increase in peak current confirms that the adsorption is much stronger on SWNTs modified EPPGE than bare EPPGE as reported

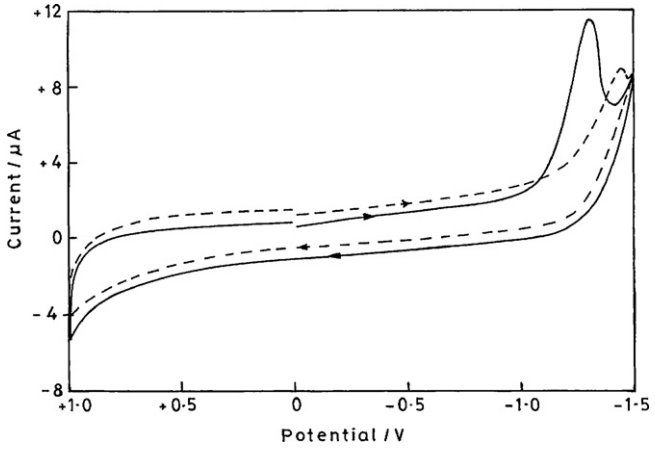


Fig. 2. Cyclic voltammograms obtained for 0.3 μM methylprednisolone at pH 7.2 at bare (- - - -) and SWNTs modified EPPGE (—) at 50 mV s^{-1}.

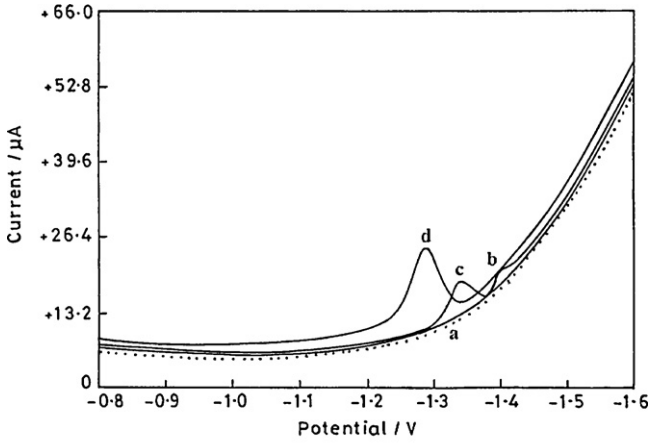


Fig. 3. A comparison of square-wave voltammograms of 100 nM methylprednisolone at pH 7.2 at bare BPPGE (b), bare EPPGE (c) and SWNTs modified EPPGE (d). (a) is the background phosphate buffer solution (pH 7.2) at SWNTs modified EPPGE.

earlier for other compounds [37–39]. Thus, the increase in current response along with the lowering of peak potential is a clear evidence of the electrocatalytic activity of SWNTs modified EPPGE towards the reduction of methylprednisolone. It has been reported that the electrocatalytic activity of SWNTs is due to the metallic impurities present in it [40,41]. Hence, further investigations were carried out at SWNTs modified EPPGE.

3.3. Influence of pH and square wave frequency

The electrochemical behaviour of methylprednisolone at different pH and square wave frequency were then studied at SWNTs modified EPPGE. The voltammetric reduction of 100 nM methylprednisolone was studied in the range 2.4–11.0 in phosphate buffer solution. The pH value strongly affects the peak potential of methylprednisolone, with the E_p shifting linearly towards more negative potential values with increase in pH. The relationship between $-E_p$ and pH is represented by the following equation:

$$-E_p(\text{pH } 2.4\text{–}11.0) = [842 + 62.85\ \text{pH}]\ \text{mV versus Ag/AgCl}$$

having correlation coefficient of 0.9969. The slope of 62 mV/pH indicates that the number of protons and electrons involved in the reduction process is equal. The results were thus found to be consistent with the previous studies performed using cyclic voltammetry.

The effect of square wave frequency on peak potential was examined in the range 5–200 Hz at pH 7.2 at SWNTs modified EPPGE. The plot of $-E_p$ versus log f was linear and is found to shift towards more negative potentials with increase in square wave frequency. The variation of $-E_p$ with log f can be expressed by the equation:

$$-E_p(\text{mV}) = 74.98\ \log f + 1197$$

with a correlation coefficient of 0.9937.

The peak current (i_p) for the reduction of methylprednisolone was found to increase linearly with the increase in square wave frequency in the range 5–200 Hz and the relation between i_p and f can be expressed by the relation:

$$i_p(10^{-5}\ \text{A}) = 0.139f - 0.329$$

having a correlation coefficient of 0.9933. These observations are in agreement with the properties of irreversible electrochemical process which is adsorption controlled [42–44]. The results supported the inferences obtained from cyclic voltammetry studies.

3.4. Concentration study

The quantitative analysis of the drug was based on the dependence of the peak current on the concentration of methylprednisolone. Typical square wave voltammograms depicting the systematic increase in the peak current values with an increase in the concentration in the range 5–500 nM is presented in Fig. 4 along with the linear calibration plot as the inset. The peak current is found to increase linearly with increasing concentration of methylprednisolone and the linear regression equation is expressed as:

$$i_p(10^{-5}\ \text{A}) = 0.0098C\,(\text{nM}) + 0.373$$

where C is the concentration of methylprednisolone. The correlation coefficient for the expression was 0.993. The current values are obtained by subtracting the background current and are reported as an average of at least three replicate determinations. The detection limit of the proposed method was calculated by using the formula $3\sigma/b$, where σ is the standard deviation of the blank and b is the slope of the calibration curve and it was found as 4.5×10^{-9} M. The sensitivity was estimated to be 98 nA nM^{-1}.

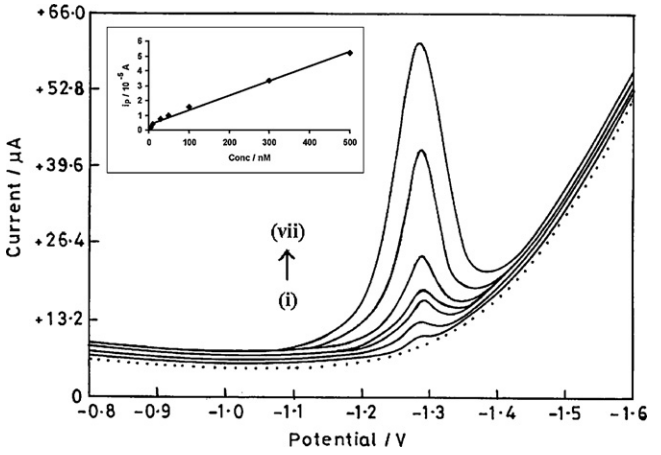


Fig. 4. Square wave voltammograms recorded for (a) phosphate buffer solution (background) at the modified electrode (...) and (b) increasing concentration of methylprednisolone at the modified electrode (—) [curves were recorded at (i) = 5; (ii) = 10; (iii) = 30; (iv) = 50; (v) = 100; (vi) = 300; (vii) = 500 nM concentration in phosphate buffer solution of pH 7.2] and observed calibration curve of peak current on methylprednisolone concentration (inset) measured at pH 7.2 at SWNTs modified EPPGE.

3.5. Effect of the amount of SWNTs

The effect of different quantity of SWNTs on the peak current response of methylprednisolone was examined. For this purpose, different volumes of the suspension prepared by dispersing SWNTs in N,N-dimethylformamide were casted on the bare electrode surface. It was observed that up to 40 μL there was an increase in the peak current response of 100 nM methylprednisolone at pH 7.2. At SWNTs volume more than 40 μL, the peak current response became almost constant. Therefore, it can be stated that the optimum amount of SWNTs required to catalyze the reduction of methylprednisolone is 40 μL and is used in the present investigation.

3.6. Reproducibility and stability of the SWNTs modified electrode

The reproducibility of the modified electrode has been evaluated by repetitive determinations of 100 nM methylprednisolone at pH 7.2. The results of six replicate measurements showed a relative standard deviation (R.S.D.) of 2.13% indicating that the results are reproducible. Further, inter-day precision was examined by measuring the current response of the modified electrode for six consecutive days for the same 100 nM concentration of methylprednisolone and the R.S.D. was found to be 3.02%. To confirm the reproducibility of the results further, four different modified electrodes with approximately the same exposed surface area were independently constructed. They showed an acceptable reproducibility with a R.S.D. of 1.67% for 100 nM methylprednisolone.

To characterize the stability of the SWNTs modified EPPGE, the voltammetric current response of fixed concentration of 100 nM methylprednisolone was measured after the modified electrode was stored over a period of 10 days. The electrode was used daily and stored in air. Only a minimal decrease of current sensitivity with a R.S.D. of about 3.62% was observed which can be attributed to the excellent stability of the modified electrode. Thus, the SWNTs modified EPPGE exhibits good stability and reproducibility for the determination of methylprednisolone.

Table 1
Determination of methylprednisolone in pharmaceutical formulations using SWNTs modified EPPGE.

Sample	Stated content	Determined content	Error (%)
Medrol	16 mg	15.65 mg	−2.2
Sterio-16	16 mg	15.78 mg	−1.4
Depo-Medrol (injection)	40 mg/mL	38.74 mg/mL	−3.1

The R.S.D. value for determination was less than 4.1% for $n = 3$.

3.7. Pharmaceutical formulations

The method was successfully implemented for the analysis of three commercial medicinal samples containing methylprednisolone, viz. Medrol (Pharmacia, Pfizer products India private limited, Jogeshwari, Mumbai), Sterio–16 (Welcure drugs and pharmaceutical limited, Ranipur, Haridwar) and Depo-Medrol (Pfizer products India private limited, Jogeshwari, Mumbai). Solutions obtained by dissolution of methylprednisolone tablets and injection were subsequently diluted so that methylprednisolone concentration lies in the range of calibration plot. Square wave voltammograms were then recorded and the concentration of methylprednisolone in the pharmaceutical preparations was determined. Results summarized in Table 1 show that the content for all assayed tablets and injection falls within the claimed amount indicating the good agreement with the proposed voltammetric method.

3.8. Quantification in real samples

The effectiveness of the proposed approach was evaluated on human blood plasma samples obtained from patients undergoing treatment with methylprednisolone. The samples were used for analysis without any dilution as the major metabolites present in human plasma such as ascorbic acid, uric acid and dopamine did not exhibit reduction peak in the range −0.8 to −1.6 V. Curve a in Fig. 5 represents a typical voltammogram which depicts human blood plasma of normal person used as control. The human blood plasma of patient obtained after 10 h of administration of Medrol tablet and the blood plasma of patient spiked with methylprednisolone are shown by curves b and c. A well-defined peak of methylprednisolone was observed at ∼−1285 mV and the results obtained are tabulated in Table 2.

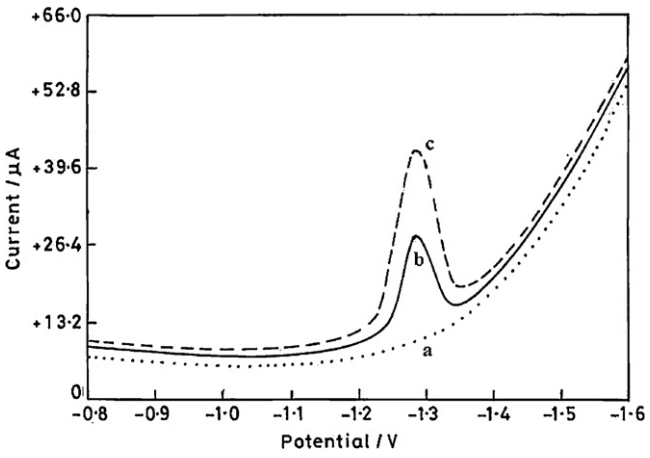


Fig. 5. Voltammograms observed for (a) normal blood plasma sample (. . .), (b) plasma sample of patient being treated with methylprednisolone (—) and (c) the patient sample spiked with methylprednisolone (- - - -) at pH 7.2 at SWNTs modified EPPGE.

Table 2
A comparison of observed concentration of methylprednisolone in human plasma after 10 h of methylprednisolone administration at SWNTs modified edge plane pyrolytic graphite electrode and by using HPLC.

Added (μM)	Found (μM)	Actual concentration (μM) by	
		Modified EPPGE	HPLC
Sample 1			
0.00	0.15	0.15	0.14
0.10	0.24	0.14	0.15
0.20	0.35	0.15	0.13
Sample 2			
0.00	0.16	0.16	0.15
0.10	0.25	0.15	0.14
0.20	0.35	0.15	0.15
Sample 3			
0.00	0.14	0.14	0.14
0.10	0.25	0.15	0.16
0.20	0.36	0.16	0.15

The R.S.D. value for determination was less than 2.3% for $n = 3$.

3.9. Comparison by HPLC

The results obtained by the voltammetric method were compared with HPLC analysis to prove the reliability of data obtained. For this purpose, various concentrations of methylprednisolone were analyzed using HPLC and the peak area was calculated. A well-defined peak is obtained at $R_t \sim 9.176$ min in the standard sample of methylprednisolone as shown in Fig. 6(A). Blood plasma sample of normal person used as control was then injected in HPLC and the peak of methylprednisolone was found to be absent as depicted in Fig. 6(B). Finally, the concentration of the drug was determined in the human blood plasma of patients undergoing treatment with methylprednisolone. Fig. 6(C) shows a typical HPLC chromatogram of Sample 1 of patient plasma. The peak at $R_t \sim 9.176$ min is due to methylprednisolone. However, no attempt was made to identify the

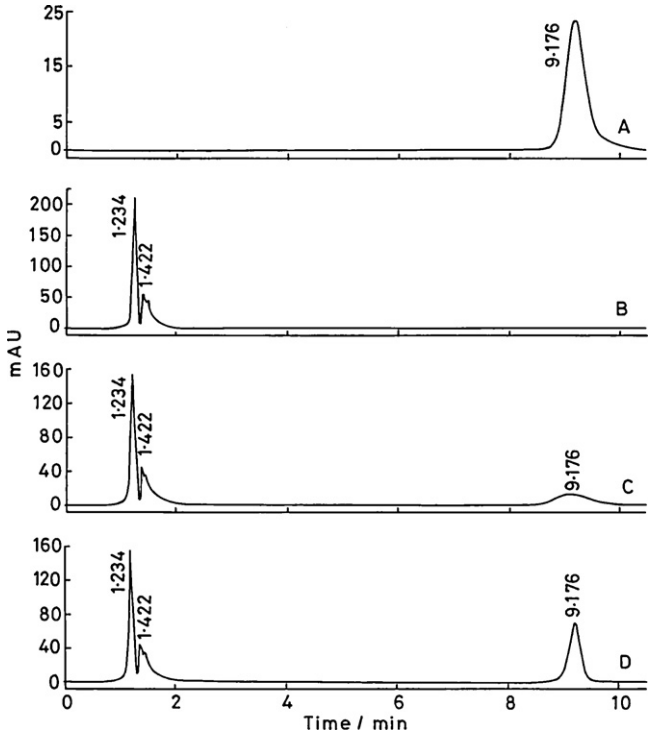
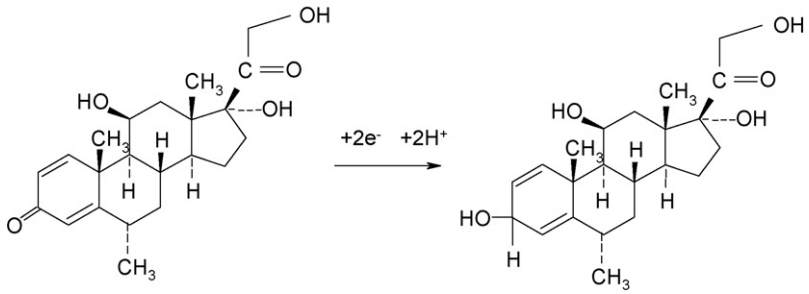


Fig. 6. Observed HPLC chromatograms of (A) standard methylprednisolone (B) normal human blood plasma used as control (C) plasma sample of patient being treated with methylprednisolone (D) methylprednisolone spiked in patient plasma.



Scheme 1. Tentative mechanism for the reduction of methylprednisolone.

rest of the peaks which are likely to be due to uric acid, ascorbic acid etc. The plasma sample of the patient was then spiked with methylprednisolone which is presented in Fig. 6(D). The chromatogram clearly indicates the increase in peak at $R_t \sim 9.176$ min. A calibration curve was obtained by plotting the peak area of the analyte peaks against the analyte concentration. The resulting calibration plot was linear. A comparison of the values obtained by HPLC and the proposed voltammetric method (as listed in Table 2) clearly indicated that the results obtained by two methods are in good agreement.

4. Conclusions

The purpose of the present investigation was to develop a specific and robust method for the determination of methylprednisolone in pharmaceutical formulations and real samples. The electrochemical reduction of the drug had an advantage over the voltammetric oxidation of methylprednisolone because the major metabolites like uric acid, ascorbic acid, dopamine etc. present in real samples did not interfere with the studies. These metabolites did not exhibit any reduction peak in the potential window of −0.8 V to −1.6 V. The voltammetric reduction of related corticosteroids was also investigated on the SWNTs modified EPPGE. It was found that prednisolone, triamcinolone and betamethasone showed reduction peaks at ∼−1332, ∼−1232 and ∼−1102 mV indicating that SWNTs modified EPPGE is specific for the reduction of methylprednisolone at ∼−1285 mV. The significant increase in current response for the ferri/ferro cyanide oxidation at SWNTs modified EPPGE cannot account for by the semi-infinite diffusion model alone and can also be attributed to the thin layer diffusion as reported earlier at SWNTs modified glassy carbon electrode by Streeter et al. [34]. The improvement of methylprednisolone voltammetric signal at the modified electrode also suggests the diffusion within porous layer in addition to semi-infinite diffusion. Also in addition to the increased surface area of the electrode, the improved adsorption efficiency of the electrode surface due to the presence of SWNTs plays a vital role as reported earlier [37–39]. Thus, the SWNTs modified EPPGE shows electrocatalytic activity towards the reduction of methylprednisolone leading to an increase in the current response and a shift of the reduction potential to lower values in comparison to bare BPPGE and bare EPPGE. The developed protocol has lower detection limit (4.5×10^{-9} M) as compared to the previously reported at gold nanoparticles modified indium tin oxide (2.68×10^{-7} M) [30] using differential pulse voltammetry.

The available sites for reduction in methylprednisolone are the keto groups present at positions 3 and 20. It is clearly stated in literature that in ketosteroids the carbonyl group conjugated with a double bond undergoes reduction preferably in comparison to the isolated keto group [45]. Thus, the most probable site for reduction in methylprednisolone is at position 3 where the keto group undergoes reduction in $2e^-$, $2H^+$ process to give a hydroxyl group as shown in Scheme 1.

Thus, the present method has been satisfactorily applied to the voltammetric determination of methylprednisolone in pharmaceuticals and human blood plasma samples obtained from patients being treated with the drug. A comparison of the results with HPLC indicates that the method is sensitive and the results are comparable. The developed protocol is simple, rapid, specific, reproducible and sensitive for the determination of methylprednisolone at SWNTs modified edge plane pyrolytic graphite electrode at the site of competitive games to detect the cases of doping.

Acknowledgements

Authors (SC and ARSR) are thankful to the Council of Scientific and Industrial Research, New Delhi and Department of Science and Technology, New Delhi for the award of Junior Research Fellowship. Authors are thankful to Dr. Ajay Panwar, M.D., Institute Medical Officer, IIT Roorkee for helpful discussions on pharmacokinetics of methylprednisolone and his help in providing blood samples of the patients undergoing treatment with methylprednisolone. Financial assistance for this work was provided by Department of Science and Technology, New Delhi vide grant no. SR/S1/IC-21/2007.

References

[1] http://www.wada-ama.org/en/prohibitedlist.ch2.
[2] http://www.trinidadexpress.com/index.pl/article_sports?id=161447846.
[3] http://news.surfwax.com/drugs/files/Methylprednisolone.html.
[4] http://www.nytimes.com/2007/07/31/sports/othersports/31sportsbriefsbell.html.
[5] J.D. Kelly, S.L. O'Hogan, S.R. Dillon, PCT Int. Appl. (2005) 52.
[6] R. Mehvar, R.O. Dann, D.A. Hoganson, J. Pharm. Biomed. Anal. 22 (2000) 1015–1022.
[7] Y. Hao, S. Chen, L. Zhang, X. Yang, Faming Zhuanli Shenqing Gongkai Shuomingshu (2009) 13.
[8] Y. Barenholz, Y. Naparstek, Y. Avnir, R. Ulmansky, PCT Int. Appl. (2006) 56.
[9] E. Kunter, A. Ilvan, N. Ozmen, E. Demirer, A. Ozturk, K. Avsar, O. Sayan, Z. Kartaloglu, Respiration 75 (2008) 145–154.
[10] S. D'Sa, K. Yong, C. Kyriakou, S. Bhattacharya, K.S. Peggs, B. Foulkes, M.J. Watts, S.J. Ings, K.M. Ardeshna, A.H. Goldstone, C.D. Williams, Br. J. Haematol. 125 (2004) 756–765.
[11] Y. Hao, L. Zhang, S. Chen, X. Yang, Faming Zhuanli Shenqing Gongkai Shuomingshu (2009) 10.
[12] A.B.S. Fernandes, W.A. Zin, P.R.M. Rocco, Braz. J. Med. Biol. Res. 38 (2005) 147–159.
[13] W.X. Yu, S.B. Li, F.Y. Hou, B.Q. Huang, H.L. Luo, Zhonghua Shenjingyixue Zazhi 6 (2007) 403–405.
[14] J.D. Dobak, PCT Int. Appl. (2008) 44.
[15] N. Otterbeck, PCT Int. Appl. (2000) 20.
[16] M. Petersen-Braun, S. Rabini, S. Glaeser, K. Kluthe, PCT Int. Appl. (2008) 36.
[17] A. Lavalle-Graef, L. Villegas-Acosta, C. Lavalle, Arch. Med. Res. 35 (2004) 421–426.
[18] J. Utikal, W.K. Peitsch, N. Kemmler, N. Booken, R. Hildenbrand, R. Gladisch, S. Goerdt, M. Goebeler, Br. J. Dermatol. 156 (2007) 764–766.
[19] G. Bresci, G. Parisi, A. Mazzoni, F. Scatena, A. Capria, J. Gastroenterol. Hepatol. 23 (2008) 1678–1682.
[20] P.M. Irving, R.B. Gearry, M.P. Sparrow, P.R. Gibson, Aliment Pharmacol. Ther. 26 (2007) 313–329.
[21] Y.T. Kim, J.M. Caldwell, R.V. Bellamkonda, Biomaterials 30 (2009) 2582–2590.
[22] S. Ozkan, N. Uzuner, C. Kutlu, D. Ozbabalik, G. Ozdemir, J. Clin. Neurosci. 13 (2006) 214–217.

[23] C. Grootscholten, F.J. Snoek, M. Bijl, H.C. Van Houwelingen, R.H.W.M. Derksen, J.H.M. Berden, J. Rheumatol. 34 (2007) 1699–1707.
[24] S.Q. Zhang, H.R. Thorsheim, S. Penugonda, V.C. Pillai, Q.R. Smith, R. Mehvar, J. Chromatogr. B: Analyt. Technol. Biomed. Life Sci. 877 (2009) 927–932.
[25] F. Li, Y. Hu, J. Zhang, Zhongguo Linchuang Yaoxue Zazhi 15 (2006) 52–54.
[26] Y. Qin, J. Zhang, X. Wang, X. Liu, Z. Wang, Zhongguo Yundong Yixue Zazhi 26 (2007) 620–623.
[27] M.I. Reddy, A. Beotra, R.B. Lal, R. Khanduja, S. Jain, T. Kaur, Indian J. Pharmacol. 39 (2007) 160–164.
[28] G. Ding, X. Xu, W. Zhong, Y. He, X. Li, Y. Zhang, Y. Sun, Sepu 25 (2007) 602–603.
[29] Q. Ma, C. Wang, X. Wang, H. Bai, W. Chen, T. Wu, X. Zhou, W. Yu, Sepu 25 (2007) 541–545.
[30] R.N. Goyal, M. Oyama, A.A. Umar, A. Tyagi, N. Bachheti, J. Pharm. Biomed. Anal. 44 (2007) 1147–1153.
[31] R.N. Goyal, N. Bachheti, A. Tyagi, A.K. Pandey, Anal. Chim. Acta 605 (2007) 34–40.
[32] R.N. Goyal, V.K. Gupta, S. Chatterjee, Biosens. Bioelectron. 24 (2009) 1649–1654.
[33] G.D. Christian, W.C. Purdy, J. Electroanal. Chem. 3 (1962) 363–367.
[34] I. Streeter, G.G. Wildgoose, L. Shao, R.G. Compton, Sens. Actuators B 133 (2008) 462–466.
[35] R.H. Wopshall, I. Shain, Anal. Chem. 39 (1967) 1514–1527.
[36] R.N. Goyal, A. Sangal, J. Electroanal. Chem. 521 (2002) 72–80.
[37] R.T. Kachoosangi, G.G. Wildgoose, R.G. Compton, Electroanalysis 20 (2008) 1714–1718.
[38] R.T. Kachoosangi, G.G. Wildgoose, R.G. Compton, Analyst 133 (2008) 888–895.
[39] R.T. Kachoosangi, G.G. Wildgoose, R.G. Compton, Anal. Chim. Acta 618 (2008) 54–60.
[40] C.E. Banks, A. Crossley, C. Salter, S.J. Wilkins, R.G. Compton, Angew. Chem. Int. Ed. 45 (2006) 2533–2537.
[41] R.N. Goyal, S.P. Singh, Carbon 46 (2008) 1556–1562.
[42] A. Radi, M.A. EL Ries, G.E. Bekhiet, Anal. Lett. 32 (1999) 1603–1612.
[43] M.R.C. Massaroppi, S.A.S. Machado, L.A. Avaca, J. Braz. Chem. Soc. 14 (2003) 113–119.
[44] S. Komorsky-Lovric, S. Gagic, R. Penovski, Anal. Chim. Acta 389 (1999) 219–223.
[45] P. Zuman, M. Kolthoff, Progress in Polarography, vol. 2, Interscience Publishers, New York, 1962.

Talanta 80 (2009) 593–599

Contents lists available at ScienceDirect

Talanta

journal homepage: www.elsevier.com/locate/talanta

Prion protein detection in serum using micromechanical resonator arrays

Madhukar Varshney[a,*], Philip S. Waggoner[a], Richard A. Montagna[b], Harold G. Craighead[a]

[a] School of Applied and Engineering Physics, Cornell University, Ithaca, NY 14853, United States
[b] Rheonix Inc., Ithaca, NY 14850, United States

ARTICLE INFO

Article history:
Received 25 May 2009
Received in revised form 15 July 2009
Accepted 16 July 2009
Available online 23 July 2009

Keywords:
Resonators
Cantilevers
Prion
Mass amplification
Nanoparticles
Prion protein

ABSTRACT

Prion proteins that have transformed from their normal cellular counterparts (PrP^c) into infectious form (PrP^{res}) are responsible for causing progressive neurodegenerative diseases in numerous species, such as bovine spongiform encephalopathy (BSE) in cattle (also known as mad cow disease), scrapie in sheep, and Creutzfeldt–Jakob disease (CJD) in humans. Due to a possible link between BSE and CJD it is highly desirable to develop non-invasive and *ante mortem* tests for the detection of prion proteins in bovine samples. Such *ante mortem* tests of all cows prior to slaughter will help to prevent the introduction of PrP^{res} into the human food supply. Furthermore, detection of PrP^{res} in donated blood will also help to prevent the transmission of CJD among humans through blood transfusion. In this study, we have continued development of a micromechanical resonator array that is capable of detecting PrP^c in bovine blood serum. The sensitivity of the resonators for the detection of PrP^c is further enhanced by the use of secondary mass labels. A pair of antibodies is used in a sandwich immunoassay format to immobilize PrP^c on the surface of resonators and attach nanoparticles as secondary mass labels to PrP^c. Secondary mass labeling is optimized in terms of incubation time to maximize the frequency shifts that correspond to the presence of PrP^c on the surface of resonators. Our results show that a minimum of 200 pg mL^{-1} of PrP^c in blood serum can be detected using micromechanical resonator arrays.

© 2009 Elsevier B.V. All rights reserved.

1. Introduction

Prions, discovered by Stanley Prusiner in 1982 [1], are proteins, which in mis-folded form are believed to be responsible for causing progressive neurodegenerative diseases in numerous species, such as bovine spongiform encephalopathy (BSE) in cattle (also known as mad cow disease), scrapie in sheep, and Creutzfeldt–Jakob disease (CJD) in humans. These are fatal diseases and currently untreatable. It is believed that these diseases are caused by the conversion of normal cellular prion proteins (PrP^c) into a mis-folded infectious form (PrP^{res}). Although the infectious form has the same amino acid sequence as the normal form, it is rich in beta-sheet structures as compared to the normal form which is rich in alpha helical structures [2].

The current state of technology to detect BSE relies upon the *post-mortem* detection of prions in homogenates of brain tissue removed from slaughtered cows. The numerous methods used to detect PrP^{res} in the brain homogenate are described below. Such *post-mortem* testing therefore is not suitable for routine screening of all animals, regardless of initial symptoms of BSE when animals cannot stand or walk. But, it has been shown that the animals not showing any symptoms of the disease could potentially be carrying the disease [3,4]. If these animals are not tested for PrP^{res}, they could conceivably make their way into the human food supply. Thus in order to improve the safety of human food, new technologies must be developed to allow *ante mortem* tests for PrP^{res} proteins in the body fluids of the cows. Blood is considered as the most appropriate body fluids, and is known to contain infectivity even before the onset of the clinical symptoms [5–7]. An important aspect of these *ante mortem* tests is the short detection time, so that all animals can be routinely screened prior to slaughter. Contraction of CJD in humans is not only attributed to the consumption of contaminated meat, but also to blood transfusions from an infected donor [5,8]. This is a serious problem, especially if an asymptomatic infected individual was not prevented from donating blood because of the lack of sufficiently sensitive screening tests [9–11]. Such presumed healthy humans could trigger the transmission of the disease to other humans through blood transfusion. Therefore the lack of routine testing of cattle is compounded by the lack of routine testing of human blood for transfusion, establishing a dangerous scenario whereby transmission of infectious prions from cattle to humans could lead to additional transmission of those infectious prions from one human to another via blood transmission.

There are several methods available for the detection of prion proteins in animals, namely, protein misfolding cyclic amplification,

* Corresponding author at: School of Applied and Engineering Physics, Cornell University, 212 Clark Hall, Ithaca, NY 14853, United States. Tel.: +1 607 255 6286; fax: +1 607 255 7658.
E-mail address: mv265@cornell.edu (M. Varshney).

0039-9140/$ – see front matter © 2009 Elsevier B.V. All rights reserved.
doi:10.1016/j.talanta.2009.07.032

conformation-dependent immunoassay, dissociation enhanced lanthanide fluorescent immunoassay, capillary gel electrophoresis, fluorescence correlation spectroscopy, flow microbead immunoassay, etc. [12]. Most of these techniques are intended to detect PrP^{res} in the brain homogenate and thus will not be suitable for routine blood screening based tests. Saa et al. [13] developed a method to detect PrP^{res} proteins in the blood of presymptomatic animals. The number of PrP^{res} proteins in the blood of infected hamsters was amplified by mixing them with normal brain homogenate and running protein misfolding cyclic amplification (PMCA) to convert PrP^{c} (in the normal brain homogenate) into PrP^{res}. Seven rounds of 144 PMCA cycles were performed in order to sufficiently amplify the initial low numbers of PrP^{res} to the detection level. The technique was sensitive to detect as low as 20–50 molecules of monomeric hamster PrP, however, the time of cyclic amplification alone was 525 h (7× 75 h). Another study based on cytometric methods demonstrated analytical sensitivity in the range of 10 aM or 0.24 fg mL^{-1} of PrP^{res} for serum samples [14]. The cytometric test, however, requires at least a 20 h incubation time, followed by flow cytometry. Both of these methods are highly sensitive to detect extremely small amounts of infectious prions in blood, but until either of these methods can be automated and performed in a faster manner, they will prove to be too complicated and time consuming to be practical for routine rapid screening of all cattles prior to slaughter.

Micromechanical resonators are considered as suitable candidate to develop sensitive and rapid blood based tests to detect prion proteins. Resonators have been used to detect attograms of masses [15]. They are suitable to detect variety of biomolecules, as the resonators can be functionalized with a number of different biorecognition molecules (antibody, nucleic acid, and other protein). Resonators can be fabricated with a variety of materials or coated with a particular material as suitable for the functionalization chemistry. These devices resonate at a frequency which decreases as mass is added to the surface. This frequency shift is measured to detect the presence of mass on the surface. The sensitivity of these resonators to mass detection depends on size, shape, thickness and the fabrication material [16–22]. In order to detect biomolecules of smaller masses, mass amplification techniques are used. Amplification is achieved by using secondary mass labeling with massive particles binding to the target analyte already present on the surface of resonators [23]. These amplification techniques are not time consuming as compared to PMCA or cytometry used for prion protein detection, although the amplification is limited by the background noise due to non-specific binding. In addition to this, the array format of the resonators makes it possible to run multiple tests on the same sample to improve the statistics of detection as well as to reduce false positives and negatives.

In the current work, we demonstrate the potential of these devices for the direct detection of prion proteins in blood serum. We have fabricated an array of paddlever shaped resonators for the detection PrP^{c} in blood samples. Secondary antibodies and nanoparticles were used for the mass amplification to detect the presence of small amounts of PrP^{c}. A sandwich immunoassay was used to immobilize PrP to the surface of resonators and subsequently add nanoparticles. Kinetic studies of secondary mass labeling have also been performed to improve the sensitivity of the resonators for detection of PrP^{c}. Due to the limitation of biosafety level of our research lab, we were able to work on non-infectious full length prion protein (PrP^{c}) and not infectious prion protein (PrP^{res}). We project this work to be successfully used with PrP^{res} in real world based on the affinity of the antibodies used, which have been claimed to be equally sensitive for the detection of both PrP^{c} and PrP^{res} (based on the information provided by the antibodies supplier).

2. Materials and methods

2.1. Reagents

Two antibodies were used for the sandwich assay. One is conjugated to the surface of the resonators (capture antibodies) while another is used to attach nanoparticles as additional mass labels (detection antibodies). Both antibodies are monoclonal and are produced in mice against different epitopes of bovine prion protein. Prion proteins used in this work are histidine tagged recombinant proteins and are full-length mature part of bovine PrP (25–244) expressed in *E. coli* BL21 (Millipore Inc.). Capture antibodies are against amino acids 23–237 of bovine prion protein (Millipore Inc.) and detection antibodies are against amino acids 123–136 and 140–160 of bovine prion protein (Abcam Inc.). Bovine serum albumin was used to block the surface of the resonators and was purchased from Sigma. Streptavidin conjugated nanoparticles (R&D Systems, Minneapolis, MN) of diameter 150 nm were used as secondary mass labels. These particles were irregularly shaped particles with diameters ranging from 80 nm to 200 nm (as analyzed with SEM). Deprionized fetal bovine serum was obtained from BioRad Laboratories. BioRad obtained fetal bovine serum from Biowest, Rau. Della Caille, Nuaille, France and origination of the product is from Canada. Deprionization was performed by BioRad Laboratories. Aliquots were made from the stock and were stored frozen until used. Before use the aliquots were thawed and vortexed. 3-Aminopropyl triethoxysilane (APTES, Sigma) was used to functionalize the surface of resonators with primary amine groups. Glutaraldehyde was used as a homo-bifunctional cross-linker to attach antibodies on the silanized surfaces. Glycine solution prepared in deionized (DI) water was used for quenching. Both of these chemicals were purchased from Sigma. Detection antibodies were modified with biotin to attach 5–7 biotin molecules per antibody molecule by using NHS-PEO_4-biotin (Pierce Chemicals). The biotin per antibody was determined by using EZ biotin quantification kit (Pierce Chemicals).

2.2. Resonator fabrication and functionalization

Resonators were fabricated as described in our previous work [24]. Briefly, a 150 nm thick layer of low-stress nitride was deposited on a thermally oxidized silicon wafer. The silicon nitride device layer was then patterned using an anisotropic reactive ion etch. Chips were then dipped in hydrofluoric acid in order to remove the 1.5 μm thick sacrificial silicon dioxide layer under the resonators and release them from the substrate. Release allows them to move freely and resonate. Resonators in this work were cantilevered structures with a 3 μm × 10 μm paddle at the free end, also called paddlevers, with typical resonant frequencies of approximately 4.6 MHz and quality factors of about 7000 for bare devices.

In this study, APTES (10% solution in dry toluene) was used to silanize the surface of the resonators. Glutaraldehyde (5% solution in 10 mM borate buffer pH 8.0) was used as a cross-linker between amine groups on capture antibodies (50 μg mL^{-1} in PBS buffer) and the surface of the resonators. The conjugation chemistry to modify the surface of resonator with capture antibodies is shown in Fig. 1. After a wash with DI water (95 rpm for 4 min, two times), the devices were quenched with glycine (50 mM solution in DI water, 30 min) to block unreacted amine group binding sites on the surface of the resonators followed by a blocking with 1% BSA (w/v) in PBS buffer (30 min). Blood serum obtained from BioRad laboratories was spiked with different concentrations of prion protein. Excess of prion protein was removed by washing with DI water (95 rpm for 4 min, two times). This was followed by a 10 min blocking step. Detection antibodies (50 μg mL^{-1} in PBS buffer) were used to label prion protein on the surface of resonators (80 min

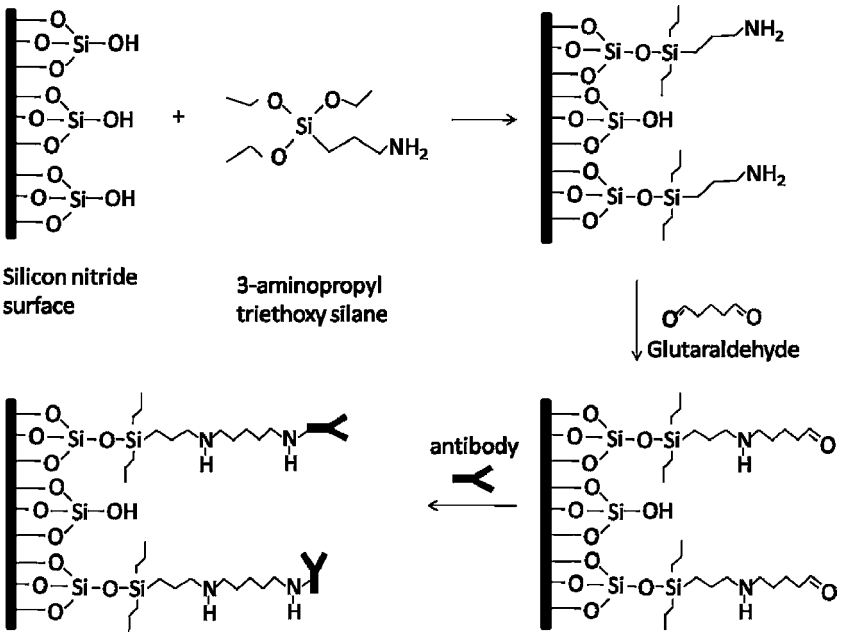


Fig. 1. Schematic diagram of the capture of antibodies on the surface of resonators. Amine groups were formed on the resonator surface by covalent reaction between 3-aminopropyl-triethoxy silane and silanol groups on silicon nitride surface. Glutaraldehyde was used as a cross linker between amine groups on the resonator surface and antibodies.

incubation time). After the removal of excess of detection antibodies (DI water wash, 95 rpm for 4 min, two times), the streptavidin conjugated nanoparticles were attached to biotin on the detection antibodies. Finally, excess nanoparticles were washed (DI water wash, 95 rpm for 4 min, two times). An orbital shaker was used for washing.

2.3. Frequency measurement

Resonators were both excited and sensed in vacuum using optical techniques as shown in Fig. 2a [18]. A 405 nm diode laser was modulated in intensity and used to excite the resonators by focusing the beam near its clamped end. Due to the higher thermal conductivity of the silicon nitride layer as compared to the underlying silicon dioxide layer, a temperature gradient is induced that is responsible for the inhomogenous thermal expansion of the device. Thermal expansion mismatch between the silicon nitride and oxide is ultimately responsible for actuation of the sensor. Resonant frequencies were determined interferometrically by measuring the reflectance variation from an incident HeNe red laser focused at the free end of the resonator. As the sensor moves in and out of the plane, the gap between the wafer and device layers changes in thickness. This dynamic film stack changes the degree of optical interference and modulates the intensity of reflected light at the mechanical resonant frequency of the device. The reflected signal was collected by a photodetector, and the resonant spectrum of the device extracted using a spectrum analyzer.

Resonators chips were dried under the stream of nitrogen gas before frequency measurements. They were loaded into a small vacuum chamber that was mounted to a motorized stepper stage and the resonant frequencies were measured. Computer control of the stage and spectrum analyzer allowed easy measurement of large arrays of resonators in a short amount of time. The chip consisted of blocks of arrays of the resonators, each containing 20 devices. All devices on the chip were alike and they gave similar response in terms of the resonant frequency and quality factor. For each concentration of PrP^c and control experiments (without PrP^c), 2 arrays of resonators (40 devices) per chip were chosen randomly on the chip and they were used for frequency measurement in a single test. The average values and errors were calculated based on frequency measurements from 40 resonators. These experiments were repeated on other day as well.

The paddlever shaped cantilevers were used for mass detection because the tip of the cantilever is sensitive to bound mass [22]. Paddlever design increases the area for binding in the tip region and in turn improves its sensitivity. Fig. 2b and c shows the conjugation of prion proteins and nanoparticles mass labels on the surface of resonators. The addition of mass decreases the resonant frequencies of resonators (Fig. 2d).

3. Results and discussion

3.1. Reaction kinetics of secondary mass labeling

Secondary mass labeling was optimized by varying the incubation time during the antibody and nanoparticles conjugation step. Separate experiments were performed for antibodies and nanoparticles to see the effect of each mass label on frequency shifts. The concentrations of PrP^c used for this purpose for antibodies and nanoparticles were 2 $\mu g\,mL^{-1}$ and 20 $ng\,mL^{-1}$, respectively. The incubation times for antibodies and nanoparticles were varied from 20 to 120 min and 10 to 60 min, respectively. The results showed that the frequency shifts (measured before and after secondary mass labeling) for control and sample increased with the increase in incubation time (data not shown). The optimum incubation time was determined based on the normalized frequency shift calculated by subtracting the frequency shift of the control sample from the frequency shift of the specimen being tested. The control devices had no PrP^c added to the blood serum. The results indicated that the incubation times of 80 min and 30 min were sufficient to maximize the effect (normalized frequency shifts) of secondary mass labeling for the detection of PrP^c in blood serum.

The first order Langmuir model is used to study adsorption kinetics of secondary antibodies and nanoparticles labeling. This model is based on the following assumptions—adsorption occurs only at specific localized sites on the surface and coverage of the surface takes place in the form of a monolayer of adsorbate. Our experimental conditions will sufficiently satisfy these conditions.

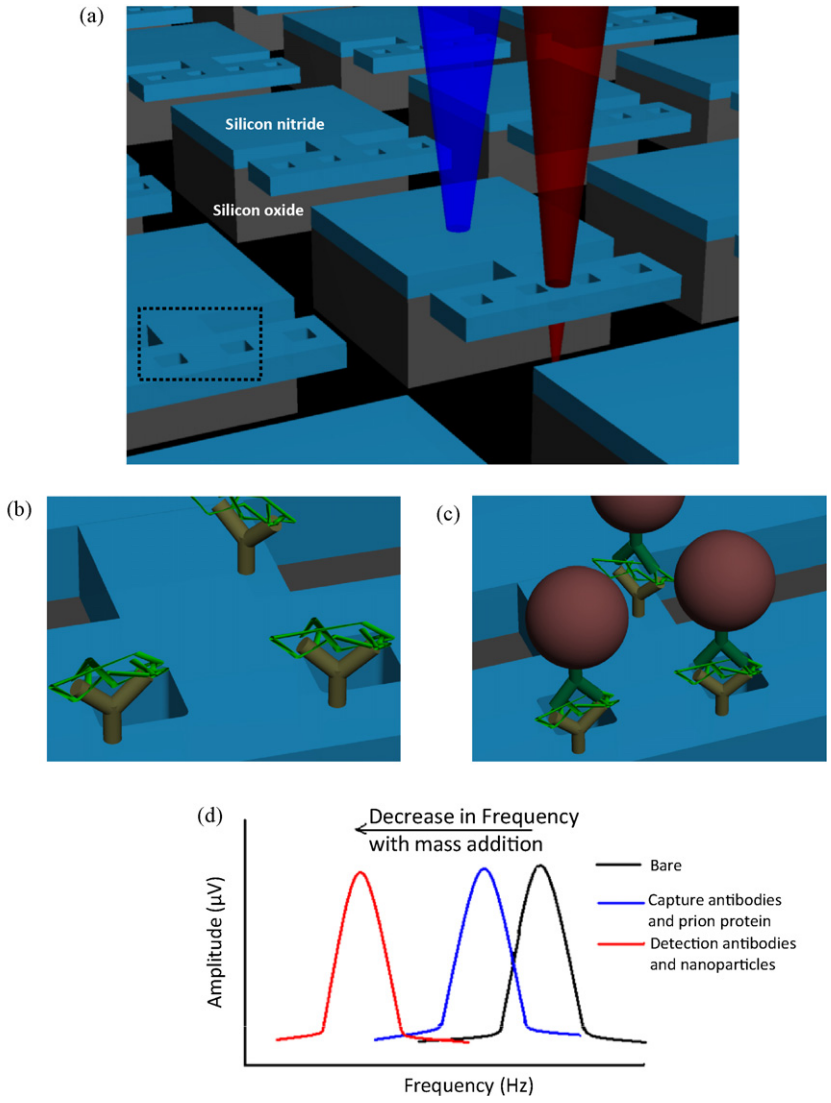


Fig. 2. Schematic diagrams of mechanism of actuation and detection of resonant frequencies and secondary mass labeling. (a) shows an array of bare resonators actuated and detected by blue and red laser, respectively. Dotted rectangle shows the area of the resonator shown in figures b and c; (b) shows the conjugation of prion protein on the surface using capture antibodies; (c) shows the secondary mass labeling with nanoparticles. Detection antibodies were used in between nanoparticles and prion protein; and (d) shows the change in resonant frequencies with mass addition. Antibodies, prion proteins and nanoaprticles are represented by Y-shape, intertwined ribbon, and spheres, respectively. Diagram is not drawn to scale.

As far as the localization of binding sites is concerned, secondary antibodies are developed against PrP and they will bind only to the location where PrP^c are present. Self-binding and non-specific binding of antibodies were minimum as shown by the presence of very small number of nanoparticles in the SEM image of the control (Fig. 3). The possibility of multiple layer formation during the addition of nanoparticles is also avoided by sequential addition of secondary antibodies and nanoparticles. Keeping in mind that there are multiple biotin molecules per antibody and streptavidin molecules per nanoparticles, cluster formation is minimized by the addition of nanoparticles after conjugation of secondary antibodies on the surface of the resonator. Assuming an irreversible adsorption of antibodies and nanoparticles on the surface of the resonator, the first order Langmuir model can be written as:

$$\theta = 1 - \exp^{-k_{obs}\tau} \tag{1}$$

where θ is the fraction of sites occupied by antibodies or nanoparticles at time τ, k_{obs} is the absolute rate constant observed for the molecules adsorbed on the surface. θ can also be represented in terms of n, the number of binding sites at time τ, and N, the maximum number of sites required to form a monolayer:

$$\theta = \frac{n}{N} \tag{2}$$

Since the frequency shift can be related to the mass change on the surface of the resonator by:

$$\frac{\Delta f}{f} = -\frac{1}{2}\frac{\Delta m}{m} \tag{3}$$

We can write

$$\Delta f \alpha\, n \quad \text{and} \quad \Delta f_\infty \alpha\, n \tag{4}$$

where Δf and Δf_∞ are the frequency shifts when surface is partially (with n number) and completely (with N number) covered with molecules. Rearranging Eq. (3) and putting the ratio of above two equations into n/N, we get:

$$\ln\left(\frac{\Delta f_\infty - \Delta f}{\Delta f_\infty}\right) = -k_{obs}\tau \tag{5}$$

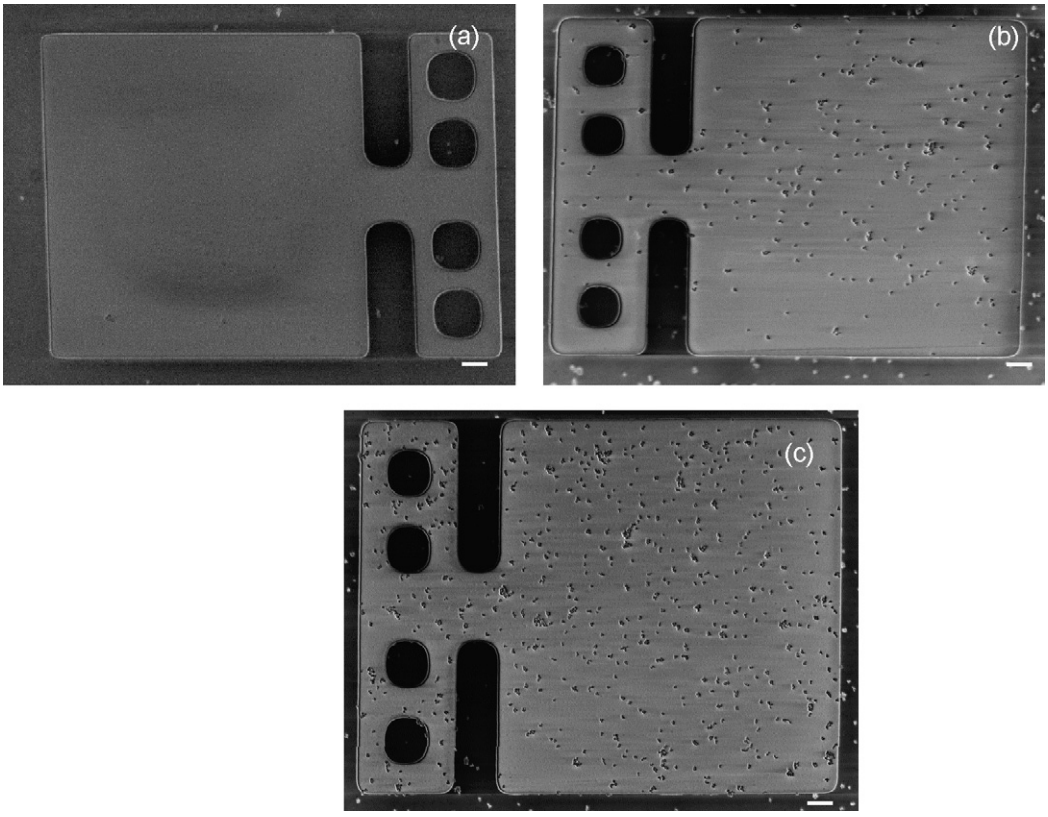


Fig. 3. Scanning electron micrographs of resonators with nanoparticle mass labeling for (a) control, and (b) 200 pg mL^{-1}, (c) 20 ng mL^{-1} of prion proteins in blood serum. Scale bar is 1 μm in length.

The plot of this equation with left hand side of the equation on y-axis and time (τ) on x-axis will determine the rate constant for the adsorption of antibodies and nanoparticles. Fig. 4 shows the plot of Eq. (5) for binding of secondary antibodies and nanoparticles. A linear curve fit results in a straight line with the equation $y = -mx$ where m represents the rate constant of adsorption. Based on the curve fit, we observed that the rate constant of adsorption of nanoparticles is twice as large as that of antibodies, which reveals that nanoparticles bind faster as compared to antibodies.

The total time of secondary mass labeling could have been reduced by preparing detection antibody–nanoparticle-conjugates before adding to the surface of the resonators. However, previous studies have shown that these conjugates form clusters and they are not uniform in size [25]. There are several biotin molecules per antibody and hundreds of streptavidin molecules per nanoparticle. As a result, several bonds are formed between antibodies and nanoparticles that give rise to the formation of clusters. The size of the cluster will depend on the relative concentrations of antibodies and nanoparticles and incubation time. Therefore, cluster formation will give non-uniform mass labeling and could also result in a higher variation in frequency shifts from one resonator to the other. Additionally, antibodies would not be available for binding with antigen due to physical entrapment into the clusters. Keeping these possibilities in mind, in the current study, we have added antibodies and nanoparticles in separate steps and have compromised on the total time for secondary mass labeling.

3.2. Prion protein detection in blood serum

The optimized conditions determined in the previous section were used to maximize the effect of secondary mass labeling to detect of PrP^c in blood serum. PrP^c was spiked in blood serum in a range of concentrations from 20 pg mL^{-1} to 200 ng mL^{-1}.

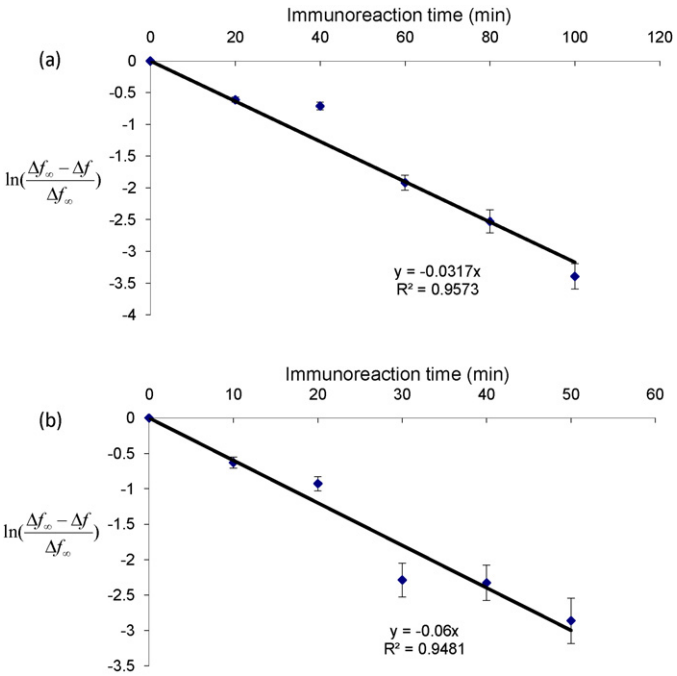


Fig. 4. Fitting of the Langmuir model to the change in the values of frequency shifts for the (a) secondary antibodies and (b) nanoparticles mass labeling with respect to immunoreaction time. Y-axis shows the left hand side of the equation $\ln\left(\frac{\Delta f_\infty - \Delta f}{\Delta f_\infty}\right) = -k_{obs}\tau$

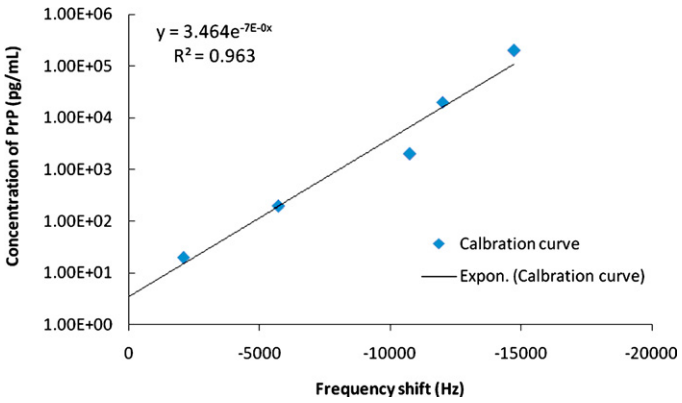


Fig. 5. Calibration curve for detection of unknown concentrations of prion proteins in blood serum by measuring the frequency shifts.

The frequency shift due to non-specific binding of non-targeted proteins in the blood serum was measured by using a control experiment with no PrP^c. This control experiment will also provide information about the presence of normal prion protein present in the fetal bovine serum. The frequency shift of the control experiments were -5519 ± 1201 Hz which matches clearly with the control experiments that were performed with buffers not with fetal bovine serum (shown in our previous work). It seems that the deprionization performed by BioRad Laboratories removed all prion proteins from fetal bovine serum. No information was made available to us about the deprionization protocol to make some specific comments about removal of PrP^c or PrP^{res} or both. The frequency shift for each concentration of PrP^c was determined by subtracting frequencies measured after PrP^c addition from that measured after nanoparticle addition. Such frequency shifts were measured for 40 resonators per chip and an average of these values was used to calculate the mean frequency shift for a concentration of PrP^c. Based on the comparison of mean values of frequency shifts for different concentrations of PrP^c and control sample, the minimum detection limit of PrP^c in blood serum was shown to be 200 pg mL^{-1}. Fig. 5 shows the calibration curve suitable for the measurement of an unknown concentration of PrP^c. The calibration curve is plotted with the frequency shifts on the x-axis and concentrations on a logarithmic scale on y-axis. It is observed that the frequency shifts and concentrations follow an exponential linear relationship with a function of $y = 3.464 \exp^{-7E-0x}$ and a coefficient of relationship (R^2) value of 0.963. In an application where we have a sample with unknown concentration of the PrP, we will experimentally determine two frequency shifts—control and sample. The normalized frequency shifts for the sample will be located on (x-axis) the calibration curve and tracked (on y-axis) for the unknown concentration of the PrP in the sample.

In order to show the conjugation chemistry of secondary mass labeling, SEM pictures are shown for two concentrations (20 pg mL^{-1} and 2 ng mL^{-1}) of PrP and the control sample (Fig. 3). It has been shown in our previous work that the number of nanoparticles increases with the increase in concentration of the PrP^c. The mass calculated from the number of particles counted on each resonator was not significantly different ($P > 0.05$) from the mass calculated using experimentally observed frequency shifts. Fig. 3 also shows that the numbers of nanoparticles increase with the increase in the concentrations of the PrP and the non-specific binding of antibodies and nanoparticles on the control is negligible as compared to samples. The number of nanoparticles on control represents the non-specific binding of antibodies and nanoparticles.

The current detection limit of PrP in blood is an order of magnitude lower than our previous work of detecting PrP in PBS buffer [24]. This can be attributed to the optimized protocol, thinner resonators and the blood serum proteins acting as blocking agents. Thinner resonators with smaller mass show large frequency shifts for the same change in mass on the surface, thus are more sensitive for the detection of small masses [16]. The albumin present in the bovine serum is most commonly used as blocking agent in immunoassays. Other blood serum proteins also act as blocking agent which may have reduced the non-specific binding of nanoparticles on the surface of resonators. The average frequency shift of the control sample in the current study was reduced by 25% as compared to the average frequency shift for the control in our previous work. Though these frequency shift values were not significantly different ($P > 0.05$).

The concentration of PrP^{res} in the buffy coat (a component of the blood) extracted from animals in their symptomatic and presymtomatic phase of the disease is expected to be 1 pg mL^{-1} and 0.1 pg mL^{-1}, respectively [6,11]. The resonators used in the present study could be used for the detection of such low concentrations of the PrP^{res} in the blood samples. Our current detection limit is not the fundamental limit of the system, rather is dependent on the capture efficiency of antibodies and uniform coating of antibodies on the surface. In one of our unpublished work, we have used cantilever array technology for the detection of fg/ml of similar mass of protein (prostate specific antigen). Thus antibodies and other reagents also play critical role in the detection low amounts of protein with this detection system. Moreover, thickness and shapes of the device can also play role in improving the detection limits. Concentration of PrP^{res} prior to detection could also be performed to detect low levels of PrP^{res} in the buffy coat of presymptomatic animals. Thus combining all these possibilities we are very confident that in the future current detection system could be used for the detection PrP in preclinical animals. The specificity of the system is a function of the antibodies. Although, our current system was developed for the detection of PrP^c, the same antibodies are also claimed to be sensitive for the detection of PrP^{res} (Product specification sheet, Chemicon Inc. and Abcam Inc.), and thus the current system could also be optimized for the detection of PrP^{res}. The combination of a concentration step, use of high density nanoparticles, thinner devices and different shapes of resonators could be instrumental in the detection of extremely low levels of infectious prion proteins in the blood of animals in the early stages of the disease. If so, resonators based system could serve as an industry standard to screen all animals going into the human food supply.

4. Conclusions

A detection system based on arrayed resonant sensors was successfully used to detect a minimum of 200 pg mL^{-1} of PrP^c in blood serum, and the response of the system was a linear exponential for a range of concentration from 20 pg mL^{-1} to 200 pg mL^{-1}. Additional effort will be required to improve the current detection limit and run appropriate field trials to detect infectious prions in the blood of animals at an early stage of the disease.

Acknowledgments

This material is based upon work supported by the Cooperative State Research, Education, and Extension Service, U.S. Department of Agriculture, under Award No. 2007-35603-17746. Any opinions, findings, conclusions, or recommendations expressed in this publication are those of the author(s) and do not necessarily reflect the view of the U.S. Department of Agriculture.

References

[1] S.B. Prusiner, Science 216 (1982) 136.

[2] K.M. Pan, M. Baldwin, J. Nguyen, M. Gasset, A. Serban, D. Groth, I. Mehlhorn, Z. Huang, R.J. Fletterick, F.E. Cohen, S.B. Prusiner, Proc. Natl. Acad. Sci. 90 (1993) 10962.
[3] P. Brown, Vox Sang. 89 (2005) 63.
[4] N. Hunter, J. Foster, A. Chong, S. McCutcheon, D. Parnham, S. Eaton, C. MacKenzie, F. Houston, J. Gen. Virol. 83 (2002) 2897.
[5] C.A. Llewelyn, P.E. Hewitt, R.S. Knight, K. Amar, S. Cousens, J. Mackenzie, R.G. Will, Lancet 363 (2004) 417.
[6] P. Brown, L. Cervenakova, H. Diringer, J. Lab. Clin. Med. 137 (2001) 5.
[7] F. Houston, J.D. Foster, A. Chong, N. Hunter, C.J. Bostock, Lancet 356 (2000) 999.
[8] A.H. Peden, M.W. Head, D.L. Ritchie, J.E. Bell, J.W. Ironside, Lancet 364 (2004) 527.
[9] Q. Schiermeier, Nature 409 (2001) 658.
[10] L. Ingrosso, V. Vetrugno, F. Cardone, M. Pocchiari, Trends Mol. Med. 8 (2002) 273.
[11] C. Soto, Nat. Rev. Microbiol. 2 (2004) 809.
[12] A. Sakuda, I. Nakamura, K. Ikuta, T. Onodera, J. Vet. Med. Sci. 69 (2007) 329.
[13] P. Saa, J. Castilla, C. Soto, Science 313 (2006) 92.
[14] L. Trieschmann, A.N. Santos, K. Kaschig, S. Torkler, E. Maas, H. Schatzl, G. Bohm, BMC Biotechnol. 5 (2005) 26.
[15] B. Ilic, H.G. Craighead, S. Krylov, W. Senaratne, C. Ober, P. Neuzil, J. Appl. Phys. 95 (2004) 3694.
[16] P.S. Waggoner, H.G. Craighead, Lab on a Chip, 7, 2007, p. 1238.
[17] A. Gupta, D. Akin, R. Bashir, J. Vac. Sci. Technol. B 22 (2004) 2785.
[18] B. Ilic, Y. Yang, K. Aubin, R. Reichenbach, S. Krylov, H.G. Craighead, Nano Lett. 5 (2005) 925.
[19] A.K. Gupta, P.R. Nair, D. Akin, M.R. Ladisch, S. Broyles, M.A. Alam, R. Bashir, Proc. Natl. Acad. Sci. 103 (2006) 13362.
[20] J. Tamayo, D. Ramos, J. Mertens, M. Calleja, Appl. Phys. Lett. 89 (2006) 224104.
[21] J. Fritz, M.K. Baller, H.P. Lang, H. Rothuizen, P. Vettiger, E. Meyer, H.-J. Güntherodt, C. Gerber, J.K. Gimzewski, Science 288 (2000) 316.
[22] P.S. Waggoner, H.G. Craighead, J. Appl. Phys. 105 (2009) 054306.
[23] M. Su, S. Li, V.P. Dravid, Appl. Phys. Lett. 82 (2003) 3562.
[24] M. Varshney, P.S. Waggoner, C.P. Tan, R.A. Montagna, H.G. Craighead, Anal. Chem. 80 (2008) 2141.
[25] M. Varshney, L. Yang, X. Su, Y. Li, J. Food Protect. 68 (2005) 1804.

Talanta 80 (2009) 600–606

Contents lists available at ScienceDirect

Talanta

journal homepage: www.elsevier.com/locate/talanta

Main fatty acid classes in vegetable oils by SB-ATR-Fourier transform infrared (FTIR) spectroscopy

S.T.H. Sherazi*, M. Younis Talpur, S.A. Mahesar, Aftab A. Kandhro, Sarfraz Arain

National Center of Excellence in Analytical Chemistry University of Sindh, Jamshoro 76080, Pakistan

ARTICLE INFO

Article history:
Received 19 June 2009
Received in revised form 15 July 2009
Accepted 16 July 2009
Available online 23 July 2009

Keywords:
SB-ATR-FTIR spectroscopy
Main fatty acid classes
Vegetable oils

ABSTRACT

The prospect of using single bounce attenuated total reflectance (SB-ATR)-Fourier transform infrared (FTIR) spectroscopy as a rapid quantitative tool to determine the main fatty acid groups present in different edible oils was investigated. Partial least squares (PLS) calibrations were developed using SB-ATR-FTIR spectra which were associated with fatty acid groups (saturated, *trans*, mono- and polyunsaturated) using quantitative data obtained by gas chromatography (GC). Good calibrations were obtained for all main four fat groups (saturated, mono, *trans* and polyunsaturated) with excellent precision. The coefficient of determination (R^2), root mean square error of prediction (RMSEP) and bias for validation set were obtained as 0.999, 2.43 and 0.998 for saturated; 0.999, 1.850 and 0.003 for mono; 0.999, 0.625 and −0.001 for *trans* while for poly the values were 0.999, 1.170 and 0.003, respectively. The results of 13 validation samples for total saturated, mono, *trans* and polyunsaturated fats by FI-IR were found in the range of 8.16–55.16, 37.62–74.75, 0.20–18.16 and 1.36–62.35%, respectively. The present study shows that it may well be possible to expand the utility of SB-ATR-FTIR spectroscopy not only to provide isolated *trans* data, but also serve as a simple, rapid and quantitative means of categorizing the main groups present in the edible oils. The information obtained would be useful for meeting the new lipid nutritional labeling requirements.

© 2009 Elsevier B.V. All rights reserved.

1. Introduction

The rapid determination of fatty acid groups i.e. saturated, monoene, *trans*, and polyunsaturated is an essential obligation to assess food material due to the consumers demand to get better quality of fat in the foods. The more concern in dietary fat has developed in the last few years with reference to *trans* fatty acids (TFAs), which are formed artificially by the industrial hydrogenation process [1]. The consumption of *trans* fat has been related with the increase in serum cholesterol levels and the risk of cardiovascular diseases [2,3]. Additionally, TFAs are linked with higher circulating markers of systemic inflammation and increased tumor necrosis factor (TNF) system activity among healthy women [4,5]. These vital concerns have strengthened the consideration of nutritionists and food manufacturers to manage the FA composition of food products. Therefore, a rapid, cheap and reliable method for the determination of fatty acid profile of edible oils is the increasing importance for manufacturers, consumers and standard control laboratories.

Concern in the development of a more versatile method was largely motivated by the intention of the FDA to mandate *trans* labeling of highly lipid containing foods. Traditionally, this issue starts from the legislation originally propagated in 1993, when the FDA issued a final rule entitled "Food Labeling: Mandatory Status of Nutrition Labeling and Nutrient Content Revision, Format or Nutrition Label" that prescribed how nutrition labeling was to be provided on foods that were regulated by the agency [6]. FDA also anticipated descriptions for claims and a proposed footnote statement [6–9]. Therefore consumers are also compelling to affirm fatty acid profile labeling so that they could know the fatty acid composition including TFA content of foods to make the right purchase decision. The regulations required the declaration of total fat, saturated fat, monounsaturated and polyunsaturated fat when claims are made about quality of oils. Since that time evidence has accumulated that *trans* fatty acids behave more like saturated acids and monounsaturated fatty acids have also become more prominent from a nutritional perspective. Hence the new legislation will mandate the inclusion of the *trans* content and its declaration. From a practical standpoint, processors will need to provide a quantitative breakdown of lipid composition with regard to four main categories; (a) saturated fatty acids, (b) monounsaturated fatty acids, (c) isolated *trans* fatty acids and (d) polyunsaturated fatty acids.

Abbreviations: SB-HATR, single bounce-heated attenuated total reflectance; FTIR, fourier transformed infrared; SFA, saturated fatty acid; MUFA, monounsaturated fatty acids; TFA, *trans* fatty acids; PUFA, polyunsaturated fatty acid; GC, gas chromatography; PLS, partial least squares; RMSEC, residual mean standard error of calibration; RMSEP, residual mean standard error of prediction; SD, standard deviation.

* Corresponding author. Tel.: +92 22771379; fax: +92 22771560.
E-mail address: tufail.sherazi@yahoo.com (S.T.H. Sherazi).

0039-9140/$ – see front matter © 2009 Elsevier B.V. All rights reserved.
doi:10.1016/j.talanta.2009.07.030

Information of this nature is usually obtained by gas chromatography (GC), which provides a complete fatty acid profile from which the respective amounts of each lipid component category can be calculated. Although a standardized methodology, GC is a cumbersome, time consuming and an expensive analytical methodology to implement, maintain and support, and it would be useful to have a simpler and more straightforward method by which to obtain the relative amounts of saturates, mono- and polyunsaturates including *trans* content in food lipids.

Fourier transform infrared (FTIR) spectroscopy is an excellent analytical tool, as it has already been shown to be a means of rapid determination of important quality parameters of vegetable oils [10–13]. Attenuated total reflectance (ATR) is widely used sample handling technique in mid-FTIR spectroscopy. ATR technique provides a simple approach that control many sample handling problems and explored the mid-IR spectroscopy as an analytical technique in a number of areas, including food samples [14]. ATR sample handling devices are based on the phenomenon of the total internal reflection of light [15]. When light passing in a medium of high refractive index hits an interface with a medium of lower refractive index at an angle equal to or greater than critical angle the light will totally internally reflect in the medium of higher refractive index. This results to an evanescent wave in the medium of lower refractive index whose amplitude decays exponentially with distance from interface. The attenuation of the evanescent wave is due to the absorption of energy of the totally internally reflected light beam. Thus, measurement of the energy of the totally internally reflected light as a function of frequency yields the absorption of these species. In single bounce (SB) ATR sampling devices, the sample is placed in contact with an "internal reflection element" (IRE) which is a crystal of an IR-transmitting material of high refractive index, such as zinc solenoid or germanium. Light from the infrared source impinges on the IRE and reaches the interface between the IRE and the sample at such an angle that the beam totally reflects in the IRE, thus, an evanescent wave emerges in the sample, the material of lower refractive index. The depth of penetration is very short: in the mid-IR region, it lies between 1 and 4 μm. When higher sensitivity is needed, the effective path length can be extended by using multiple-bounce ATR device, in which light is made to bounce through the IRE so that it undergoes multiple internal reflections. One of the most common ATR sampling accessories is the horizontal ATR (HATR, usually 1 cm × 8 cm), which can hold the sample volume between 0.2 and 0.5 ml. It is also possible to use temperature controlled HATR, which is particularly advantageous in the analysis of oil and fats [16–18]. This paper presents evidence that SB-ATR-FTIR spectroscopy has the prospective to quantitatively classify lipids into the broad categories and offer the information required for the revised nutritional labeling regulations proposed by the FDA.

2. Materials and methods

2.1. Samples and reagents

Twenty-one samples representing a broad range of saturation and unsaturation, including *trans* fat, such as palm, sunflower, soybean, canola, cotton seed, rice bran and partially hydrogenated oils were obtained from different edible oil industries, Karachi, Pakistan. All reagents, chemicals and solvents used were procured from E. Merck (Darmstadt, Germany). *Trans* and fatty acids methyl ester (FAME) standards (GLC 481-B and 607) were purchased from Nu-Check-Prep, Inc. (Elysian, MN).

2.2. GC–FID analysis

Fatty acid methyl esters (FAMEs) were prepared using standard (IUPAC method 2.301, 1979) and analyzed on a PerkinElmer gas chromatograph (8700) fitted with a RT-2560 biscyanopropylsiloxane capillary column (100 m × 0.25 mm i.d × 0.25 μm film thickness) and a flame ionization detector. Oxygen-free nitrogen gas was used as mobile phase. Oven temperature was programmed as follows: the column held initially at 130 °C for 2 min after injection increased to final temperature 220 °C with 4 °C/min heating holding for 5 min; injector temperature, 260 °C; detector (FID) temperature, 270 °C; column flow rate, 4 ml/min; split ratio, 40:1; injected volume, 1 μL. Elaidine methyl ester was identified by comparing the retention time of the authentic standard obtained from Nu-Check-Prep, Inc. (Elysian, MN). The integration was done by a built-in data-handling program provided by the manufacturer of the gas chromatography(PerkinElmer). Fatty acids were reported as relative percentage of the total peak area. Standards FAMEs for calibration, and samples were run on GC under the same conditions and parameters. The fatty acid composition was expressed as a percentage of the total fatty acid composition, which included minor fatty acids not accounted for by the standards.

2.3. FTIR spectral measurements

All infrared spectra were obtained using a ThermoNicolet Avatar 330 FTIR spectrometer equipped with a removable ZnSe crystal, deuterated triglycine sulfate (DTGS) detector and KBr optics, controlled by OMNIC software (Thermo Nicolet Analytical Instruments, Madison, WI). An SB-ATR accessory with heated demountable cell and time proportional temperature controller (Spectra-Tech, Shelton, CT) was used to control the temperature at constant value. All spectra were collected by co-addition of 32 scans at a resolution of 4 cm^{-1} in the range of 4000–650 cm^{-1}. The spectrum of each standard or sample was ratioed against a fresh background spectrum recorded from the bare ATR crystal; prior to collection of each background spectrum, the ATR crystal was carefully cleaned with propanol to remove any residual contribution of the previous sample, and remaining solvent was then evaporated using a stream of nitrogen gas.

2.4. FTIR calibrations/validations

The FTIR calibration set consisted of 21 oil samples spectra, which had been analyzed for their fatty acid composition by GC. These spectra, along with their respective reference fatty acid compositional data were input into the TQ Analyst program to develop partial least squares (PLS) calibrations. A set of PLS calibrations were developed for the determination of saturated, *trans*, mono, and polyunsaturated fatty acids by selecting their specific spectral regions from the mid-FTIR spectra. Correlation and variance spectra were generated to identify spectral regions that contained information related to the grouped and ungrouped data and these regions were subsequently explored for calibration development and refinement. The performance of the calibrations was assessed by linear regression, and evaluated by running the samples of known fatty acid profile. Therefore, in the calibration step, cross-validation and partial least square regression (PLSR) [19–21] were applied for developing the calibration models for the determination of saturated, mono, *trans* and polyunsaturated fatty acids. The number of calibration models and maximum number of PLS factors were set at 4 and 6, respectively. The latter is commonly depends on the following rule: one PLS factor per 10 samples of the training set plus 2. Statistic parameters as residual mean standard error of calibration (RMSEC) and the determination coefficient (R^2) were also employed. While in the validation, the validation set was introduced in the model, thus statistic parameters such as standard error prediction (SEP) and R^2 were obtained. Table 1 presents some statistical performance characteristics of each calibration/validation model obtained from mid-ATR-FTIR

Table 1
Mean composition (%) of vegetable oil samples in four different studied classes by GC.

Index	Spectrum title	Saturated (SFA)		Mono (MUFA)		Trans (TFA)		Poly (PUFA)	
		Mean	SD	Mean	SD	Mean	SD	Mean	SD
1	Sample1	8.80	0.3	66.10	0.60	0.50	0.10	24.6	0.4
2	Sample2	55.50	1.3	25.00	0.30	18.30	0.30	1.2	0.1
3	Sample3	20.50	0.6	55.80	0.90	5.00	0.30	18.7	0.3
5	Sample5	26.30	0.5	50.70	1.20	7.20	0.40	15.8	0.6
6	Sample6	23.40	0.3	53.30	0.70	6.10	0.60	17.3	0.4
7	Sample7	16.10	0.1	60.10	0.80	2.90	0.10	20.9	0.4
8	Sample8	12.50	0.3	63.40	0.50	1.40	0.10	22.8	0.7
9	Sample9	10.60	0.4	65.00	1.10	0.70	0.10	23.7	0.5
10	Sample10	40.90	0.4	38.00	0.40	12.60	0.30	8.5	0.3
11	Sample11	13.50	0.5	24.20	0.50	0.20	0.05	62.1	0.9
12	Sample12	11.70	0.3	44.80	0.70	0.60	0.06	43	0.4
13	Sample13	48.20	0.5	31.50	0.80	15.40	0.70	4.9	0.3

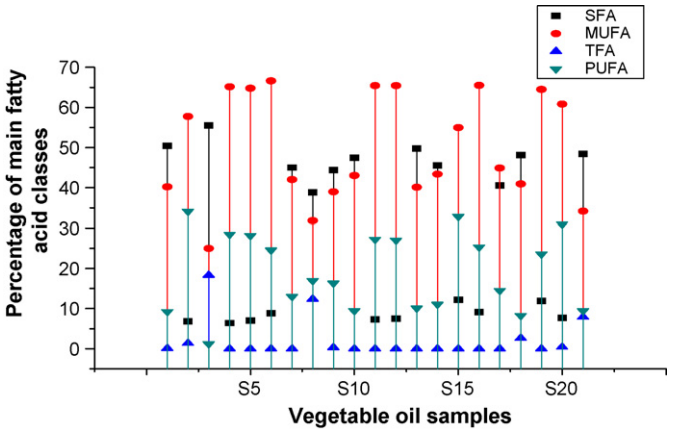


Fig. 1. Vertical drop line plot showing the distribution of SFA, MUFA, TTFA and PUFA as determined by GC analysis of 21 oil samples.

spectroscopy versus GC to assess the methodology for accuracy and reproducibility.

3. Results and discussion

3.1. Gas chromatography

The fatty acid composition of 21 vegetable oil samples was determined by capillary GC. As reported in Fig. 2 the sum of SFA (C14:0, C16:0, C18:0, C20:0, C22:0 and C24:0), MUFA (C16:1, C17:1, C18:1 and C20:1), *trans* (C18:1t) and PUFA (C18:2 and C18:3) were accounted for 28–55.49, 11.00–69.69, 1.00–18.31 and 5.00–64.27%, respectively. Usually in vegetable oils, palmitic (C16:0) and stearic acids (C18:0) are predominant among saturated fatty acids. In

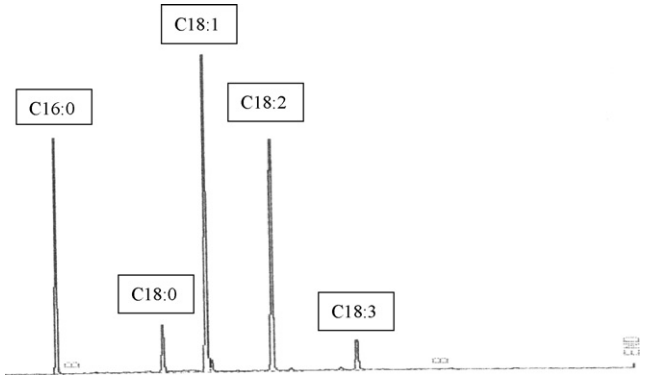


Fig. 2. A representative gas chromatogram of canola oil.

monounsaturated fatty acids (MUFA), oleic (C18:1c) acid and elaidic acid (C18:1t), while among the polyunsaturated fatty acids, linoleic (C18:2) and linolenic (C18:3) fatty acids were found in significant amount. Although technically elaidic acid is also a monounsaturated fatty acid, but for nutritional labeling purposes, only cis monounsaturated fatty acids are categorized as such, the same being true for any *trans* double bonds present in polyunsaturated fatty acids.

Gas chromatography provided the amount of all individual fatty acids for each analyzed oil sample. The information about fatty acids was grouped into saturated, mono, *trans* and polyunsaturated constituents by summation of the areas contributed by specific concerned peak. Representative gas chromatogram of the methyl esters of pure canola oil sample is shown as Fig. 2. The resultant fatty acid methyl ester peaks were identified by comparing the chromatogram of the samples with standards. From Fig. 2 it is evident that all the fatty acids methyl esters were well separated with good peak shapes under the adopted gas chromatographic conditions.

3.2. FTIR spectroscopy and general considerations

The infrared spectrum of an organic molecule is known to provide detailed information about its molecular structure, in effect providing a unique spectral fingerprinting. This unique fingerprint becomes unclear as more molecules with similar structural features are mixed together as is the case of fats and oils, which are complex mixtures of triacylglycerols. Besides, when fats are hydrogenated, new *trans* fatty acids can also be produced, these, however, are readily discerned by their unique and strong *trans* absorption at 966 cm^{-1}. Hence in the case of triacylglycerols, as glycerol is a constant molecular feature, the spectral variations observed in oils are largely the result of differences in overall fatty acid composition. In theory this spectral variation should be something which can be modelled and quantified through the use of advanced chemometric techniques such as partial least squares (PLS) regression techniques.

In Fig. 3 the spectra A–D illustrate the spectra of palm oil (containing high amount of saturated fatty acids), hydrogenated palm oil blended with canola oil (containing high amount of *trans* fatty acids), pure sunflower cooking oil (containing higher amount of polyunsaturated fatty acids) and canola oil (containing higher amount of monounsaturated fatty acids). These spectra have been collected on a heated SB-ATR accessory at 60 °C. These spectra, which are on-scale over the whole mid-IR range, appear very similar with some spectral differences, mainly in the CH, C=O and fingerprint regions. One of the main benefits of using a SB-HATR accessory is its simplicity in terms of sample handling, only requiring that a sample be placed on the crystal and the spectrum taken against the fresh background of the clean crystal.

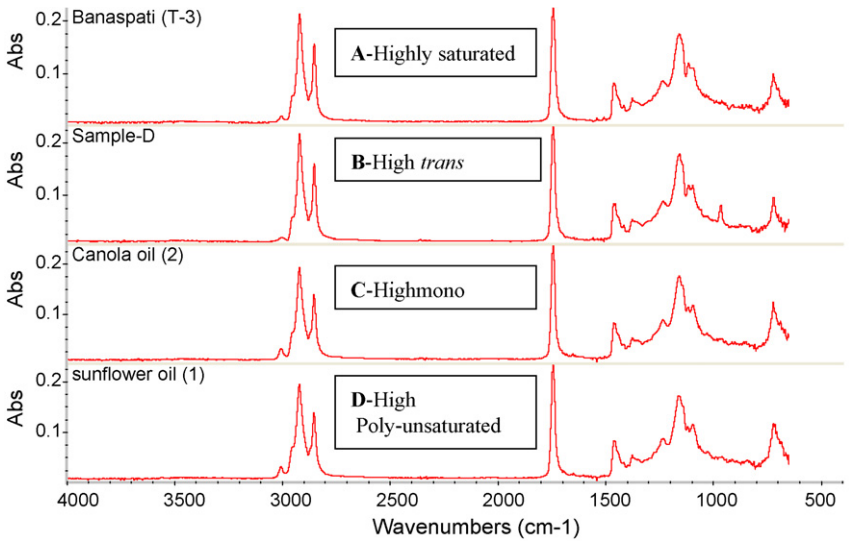


Fig. 3. Full Fourier transform mid-infrared spectra (4000–650 cm^{-1}) of high saturated-palm oil (A), high *trans*-partially hydrogenated palm oil (B), high monounsaturated-pure canola oil (C) and high polyunsaturated-sunflower oil (D).

It can be seen in Fig. 3A, that the highly saturated constituents do not show any significant cis unsaturated features around 2900 cm^{-1} as compared to the *trans* and saturated spectra. Which in turn differ in intensities in the regions of 964 and 700 cm^{-1}, respectively.

In order to obtain information, PLS calibrations were developed on full mid-FTIR spectral range of different type of vegetable oils, based on the main fatty acid classes of the 21 vegetable oil samples, determined by capillary GC analysis which are summarized in Fig. 1.

3.3. PLS calibration development

3.3.1. Saturated, monounsaturated, trans and polyunsaturated groupings

One of the advantages of working advanced chemometric techniques such as PLS is that as long as there is some relationship between the spectral information and a measurable property which could attribute the possibility of establishing a calibration. PLS is a sophisticated statistical practice in which complete or partial spectral region rather than single peak can be used. The algorithm is stand on the capability to precisely compare the spectral information to a property matrix while concurrently accounting for all other important spectral factors that perturb the spectrum.

In developing a PLS model, the group percent values for saturated, mono, *trans* and polyunsaturated fatty acid of different type of oils obtained from GC were put along with the spectra in the TQ Analyst program. The calibrations were developed for the determination of saturated, monoene, *trans* and polyunsaturated fatty acids using three different regions individually and in combination in a structured fashion, initially using cross-validation to assess the general predictive performance of each calibration, followed

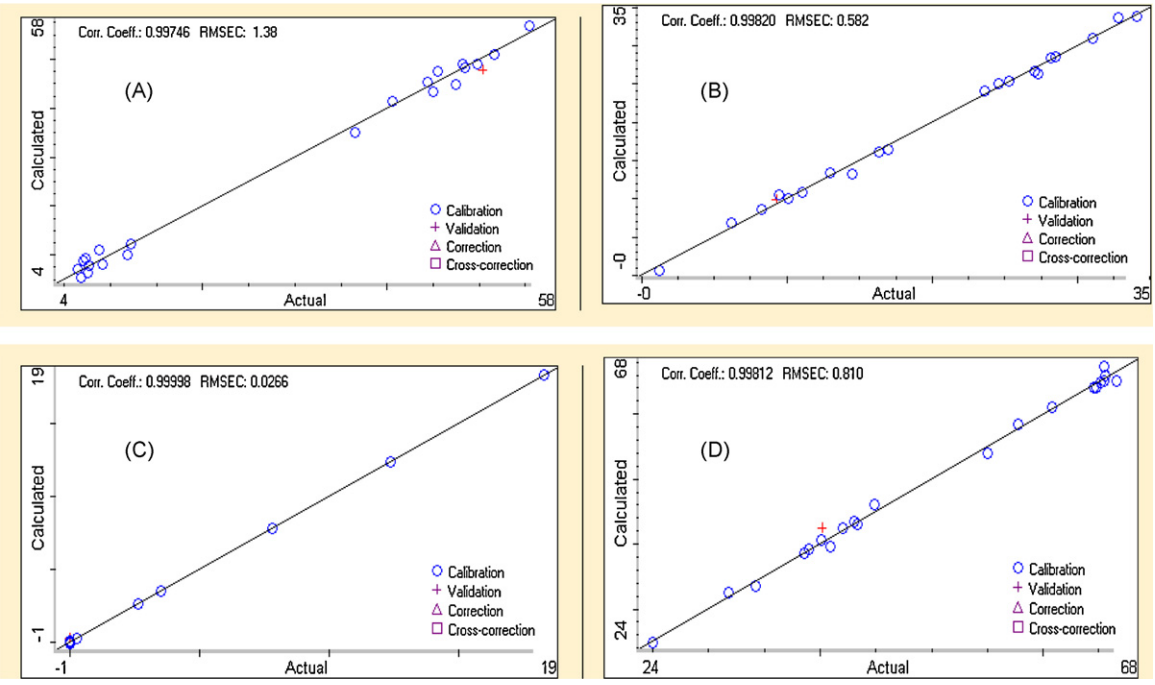


Fig. 4. GC–FID vs. FTIR-PLS calibrations for SFA (A), MUFA (B), TFA (C) and PUFA (D).

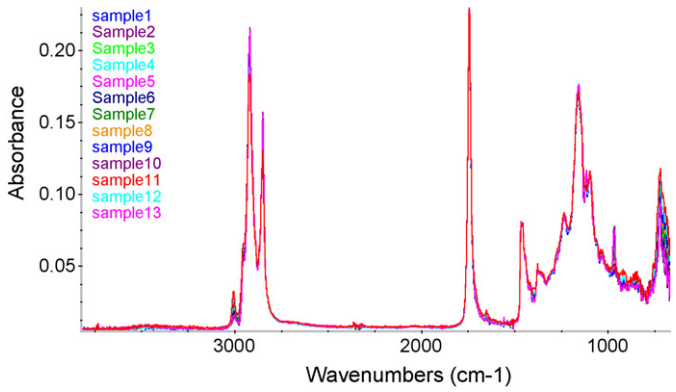


Fig. 5. Full mid-FTIR spectra (4000–650 cm^{-1}) blended with 13 different ratios of partially hydrogenated palm oil blended, canola and soybean oil.

by validation using a separate validation set. On this basis, the full mid IR region encompassing 4000–650 cm^{-1} combined with the 1000–900 and 827–665 cm^{-1} were used to produce good calibrations for all four groupings as shown in Fig. 4A–D.

In order to obtain the reproducibility of proposed developed method, 13 validation samples were run twice. The validation samples were obtained as a result of the mixing of canola, soybean and hydrogenated palm oil with known values of saturated, monoene, *trans* and polyunsaturated by GC. The amount saturated, mono, *trans* and polyunsaturated fatty acids of the freshly prepared mixtures were quantitatively calculated from the known values of their base oils. The GC values of 13 validation samples are presented in Table 1.

Fig. 5 presents 13 FTIR spectra of 13 validation samples with known values of saturated, monoene, *trans* and polyunsaturated. The pure component spectra reproduce the spectral uniqueness and such grouped constituents would have as a result of their numerical assignments, derived from the GC data. The FTIR spec-

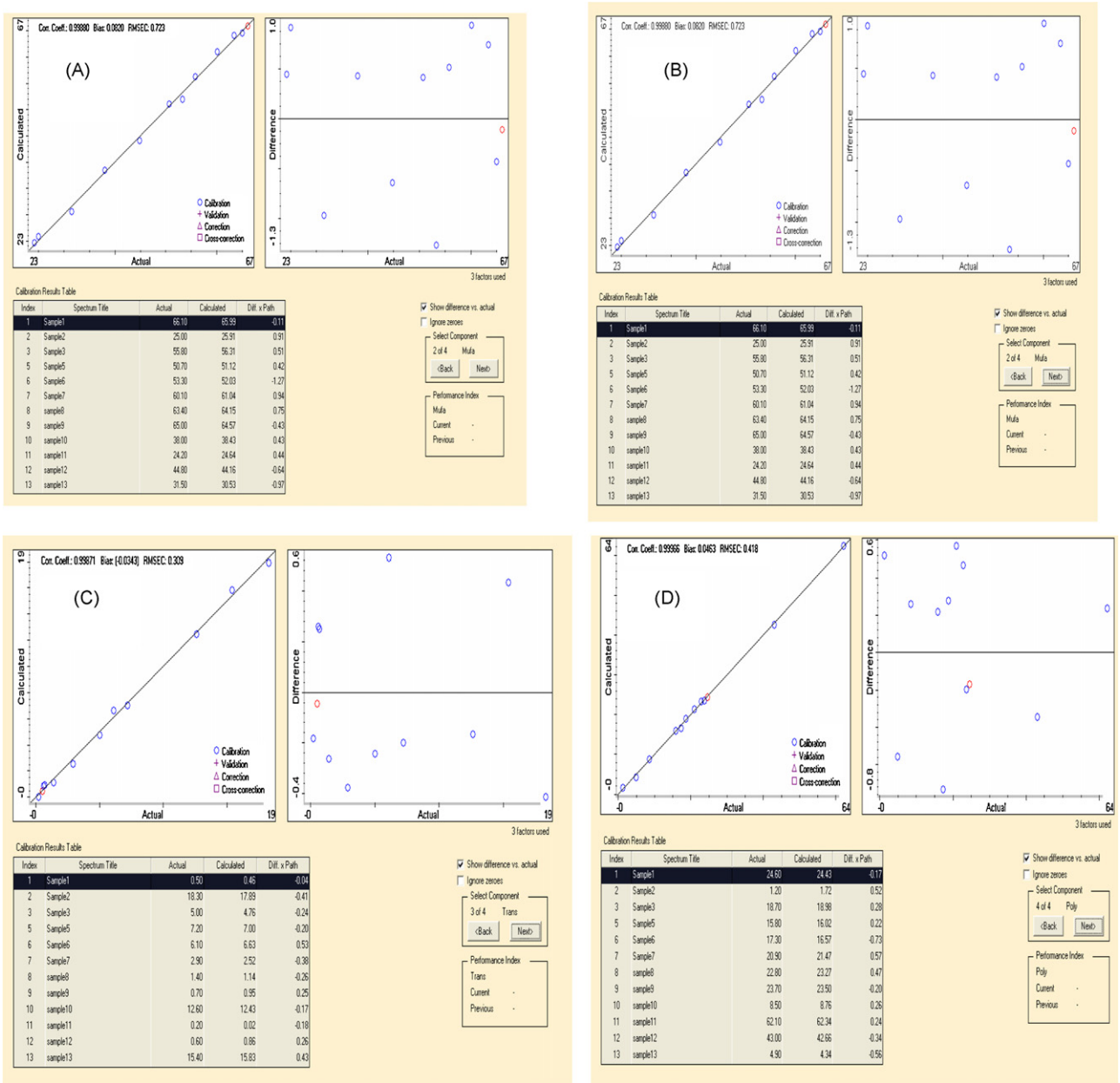


Fig. 6. GC–FID vs. FTIR-PLS cross-validations for SFA (A), MUFA (B), TFA (C) and PUFA (D).

Table 2
Statistical results of GC–FID vs. FTIR calibrations and validations of SFA, MUFA, TFA and PUFA.

Component	FA range (%)	Spectral range (cm^{-1})	Statistic					
			Calibration ($n = 21$)		Validation ($n = 13$)			
			R^2	RMSEC	R^2	RMSEC	RMSEP	Bias
SFA	6.32–55.49	1051–883	0.99746	1.38	0.99893	0.663	2.430	0.99893
MUFA	24.94–69.69	4000–650	0.99820	0.582	0.99913	0.584	1.850	0.00344
TFA	0.28–18.31	1000–900	0.99988	0.027	0.99905	0.252	0.625	−0.00122
PUFA	1.21–64.27	4000–650	0.99812	0.810	0.99982	0.334	1.170	0.00278

Table 3
Mean composition (%) of vegetable oil samples in four different studied classes by ATR-FTIR.

Index	Spectrum title	Saturated (SFA)		Mono (MUFA)		Trans (TFA)		Poly (PUFA)	
		Mean	SD	Mean	SD	Mean	SD	Mean	SD
1	Sample1	8.93	0.10	66.02	0.21	0.52	0.02	24.53	0.07
2	Sample2	55.16	0.17	25.29	0.12	18.16	0.05	1.36	0.02
3	Sample3	19.89	0.11	56.34	0.16	4.77	0.03	19.01	0.06
5	Sample5	26.02	0.13	50.97	0.17	7.07	0.07	15.94	0.03
6	Sample6	24.43	0.11	52.40	0.14	6.50	0.05	16.78	0.11
7	Sample7	15.19	0.10	60.86	0.11	2.60	0.04	21.36	0.12
8	Sample8	10.11	0.12	65.07	0.13	0.93	0.02	23.93	0.09
9	Sample9	8.16	0.13	66.75	0.23	0.20	0.02	24.9	0.06
10	Sample10	41.31	0.14	37.62	0.11	12.77	0.08	8.29	0.03
11	Sample11	12.99	0.11	24.66	0.15	–	–	62.35	0.21
12	Sample12	12.73	0.12	43.87	0.14	1.00	0.03	42.49	0.17
13	Sample13	45.75	0.16	33.61	0.13	14.56	0.08	6.08	0.03

tra of the prediction samples were subjected to the same spectral data pre-processing and before fitting in the calibration model the concentration of saturated, monoene, *trans* and polyunsaturated contents in the oil samples were determined by gas chromatography (Fig. 6).

From the calibration, the assessment of the errors was carried out by calculating the residual mean standard error of calibration (RMSEC) after comparing the actual concentration with the computed one for each component, the residual mean standard error of prediction (RMSEP) and bias according to reported method [19–21].

Table 2 lists the parameters that were used to assess statistically the results of calibration and prediction for the models to determine saturated, monoene, *trans* and polyunsaturated fatty acid by using normal mid-ATR-FTIR spectra. As observed, all four models performed properly for calibration, yielding very good correlation coefficients and low RMSEC values; predictions were also very satisfactory, in terms of RMSEP and bias values. These parameters were applied for evaluating the analytical quality of the proposed FTIR method with reference to GC.

The values of R^2 and bias were useful parameters for distinguishing the accuracy and studying the correlation between the GC values and the FTIR method. Table 2 clearly indicates that the cross-validated models could predict total saturated, monoene, *trans* and polyunsaturated fatty acids with residual mean standard error of prediction (RMSEP) of 2.430, 1.850, 0.625 and 1.170, respectively which proves that all calibrations developed were robust. The coefficient of determination (R^2), root mean and bias for validation set were 0.999, and 0.998 for saturated; 0.999, and 0.003 for mono; 0.999, and −0.001 for *trans* while for poly the values were 0.999, and 0.003, respectively. These parameters were evaluated for testing whether statistically they are close to 1 and 0, correspondingly. For all four models, the values for R^2 and bias were within the acceptable range.

The results of saturates, monoene, *trans* and polyunsaturated fatty acids obtained by single bounce ATR-FTIR using are shown in Table 3. The comparable results of FTIR and GC were revealed that SB-ATR-FTIR could be used as an alternate technique to GC for determination of main fatty acid classes in vegetable oils (Tables 1 and 3).

4. Conclusion

The results indicated that ATR-FTIR method can clearly track the total amount of saturated, mono, *trans* and polyunsaturated contents present in the oils and fats. Furthermore, no costly standards were used for the calibration and validation of saturated, monoene, *trans* and polyunsaturated fatty acids for FTIR calibration. Also sample preparation and use of organic solvents were totally avoided just to take the results quickly and not only to reduce the cost of toxic chemicals but also to save the natural environment. The use single bounce-heated ATR facilitated the both liquid and solid vegetable oil samples. For food labeling point of view the proposed method could be easily applied on oils and fats for the determination of total saturates, monoene, *trans* and polyunsaturated fatty acids as an alternative technique to GC.

Acknowledgments

The authors would like to thank the management of Shujabad Agro Industries (Pvt.) Limited, Karachi, Pakistan for providing the oil samples and the National Centre of Excellence in Analytical Chemistry, University of Sindh, Jamshoro, Pakistan for the financial support to carry out this research work.

References

[1] A. Kandhro, S.T.H. Sherazi, S.A. Mahesar, M.I. Bhanger, M.Y. Talpur, A. Rauf, Food Chem. 109 (2008) 207.
[2] A. Ascherio, W.C. Willet, Am. J. Clin. Nutr. 66 (1997) 1006.
[3] D. Mozaffarian, M.B. Katan, A. Ascherio, J.M. Stampfer, W.C. Willett, N. Engl. J. Med. 354 (2006) 1601.
[4] E. Lopez-Garcia, M.B. Schulze, J.B. Meigs, J.E. Manson, N. Rifai, M.J. Stampfer, W.C. Willett, F.B. Hu, J. Nutr. 135 (2005) 562.
[5] D. Mozaffarian, T. Pischon, S.E. Hankinson, N. Rifai, K. Joshipura, W.C. Willett, E.B. Rim, Am. J. Clin. Nutr. 79 (2004) 606.

[6] Department of Health and Human Services (DHHS)/Food Drug Administration (FDA), Fed. Regist. 64 (November) (1999) 62746–62825.
[7] DHHS/FDA, Fed. Regist. 65 (December) (2000) 75887–75888.
[8] DHHS/FDA, Fed Regist. 67 (November) (2002) 69171–69172.
[9] DHHS/FDA, Fed. Regist. 68 (July) (2003) 41433–41506.
[10] F.R. van de Voort, A.A. Ismail, J. Sedman, G. Emo, Food Res. Int. 25 (1992) 193.
[11] F.R. van de Voort, J. Sedman, G. Emo, A.A. Ismail, J. Am. Oil Chem. Soc. 69 (1992) 1118.
[12] F.R. van de Voort, J. Sedman, S.T.H. Sherazi, J. Assoc. Off. Anal. Chem. Int. 90 (2007) 446.
[13] S.T.H. Sherazi, A. Kandhro, S.A. Mahesar, M.I. Bhanger, M.Y. Talpur, S. Arain, Food Chem. 114 (2009) 323–327.
[14] J. Sedman, A.A. Ismail, A. Nicodemo, S. Kubow, F.R. van de Voort, Application of FT-IR/ATR differential spectroscopy for the monitoring of oil oxidation and antioxidant efficiency, in: F. Shahidi (Ed.), Natural Antioxidants, AOCS Press, Champaign, IL, 1996, pp. 358–378.
[15] N.J. Harrick, Internal Reflection Spectroscopy, Wiley-Interscience, New York, 1967.
[16] A.A. Ismail, F.R. van de Voort, J. Sedman, Fourier transform infrared spectroscopy: principles and applications, in: J.R.J. Paré, J.M.R. Bélanger (Eds.), Instrumental Methods in Food Analysis, Elsevier Science B.V., 1997, pp. 93–139.
[17] J. Sedman, F.R. van de Voort, A.A. Ismail, Attenuated total reflectance spectroscopy: principles and applications in infrared analysis of food, in: M. Mossoba (Ed.), Spectral Methods in Food Analysis, Marcel Dekker, New York, 1998, pp. 397–425.
[18] A.A. Ismail, A. Nicodemo, J. Sedman, F.R. van de Voort, I. Holzbaur, Infrared spectroscopy of lipids: principles and applications, in: Spectral Properties of Lipids, Sheffield Academic Press, 1999.
[19] M. Fuller, P.R. Griffiths, Anal. Chem. 50 (1988) 1906.
[20] O. Galtier, Y. Le Dreau, D. Ollivier, J. Kister, J. Artaud, N. Dupuy, Appl. Spectrosc. 62 (2008) 583.
[21] M.D. Guillén, N. Cabo, J. Am. Oil Chem. Soc. 74 (1997) 1281.

Talanta 80 (2009) 607–613

Contents lists available at ScienceDirect

Talanta

journal homepage: www.elsevier.com/locate/talanta

Triphenylmethane dyes as fluorescent probes for G-quadruplex recognition

Jun-Hong Guo [c], Li-Na Zhu [b], De-Ming Kong [a,c,*], Han-Xi Shen [c]

[a] Key Laboratory of Functional Polymer Materials (Nankai University), Ministry of Education, Nankai University, Tianjin 300071, PR China
[b] Department of Chemistry, Tianjin University, Tianjin 300072, PR China
[c] Research Centre for Analytical Sciences, Department of Chemistry, Nankai University, Tianjin 300071, PR China

ARTICLE INFO

Article history:
Received 27 April 2009
Received in revised form 14 July 2009
Accepted 17 July 2009
Available online 25 July 2009

Keywords:
Fluorescent probe
Triphenylmethane dye
G-quadruplex
Double-stranded DNA
Single-stranded DNA

ABSTRACT

Triphenylmethane (TPM) dyes normally render rather weak fluorescence due to easy vibrational deexcitation. However, when they stack onto the two external G-quartets of a G-quadruplex (especially intramolecular G-quadruplex), such vibrations will be restricted, resulting in greatly enhanced fluorescence intensities. Thus, TPM dyes may be developed as sensitive G-quadruplex fluorescent probes. Here, fluorescence spectra and energy transfer spectra of five TPM dyes in the presence of G-quadruplexes, single- or double-stranded DNAs were compared. The results show that the fluorescence spectra of four TPM dyes can be used to discriminate intramolecular G-quadruplexes from intermolecular G-quadruplexes, single- and double-stranded DNAs. The energy transfer fluorescence spectra and energy transfer fluorescence titration can be used to distinguish G-quadruplexes (including intramolecular and intermolecular G-quadruplexes) from single- and double-stranded DNAs. Positive charges and substituent size in TPM dyes may be two important factors in influencing the binding stability of the dyes and G-quadruplexes.

© 2009 Elsevier B.V. All rights reserved.

1. Introduction

As we know, genomic DNAs usually adopt a double-stranded helical form in living organisms, but they can also exist in other conformations. Particularly, guanine-rich nucleic acid sequences are capable of folding into four-stranded structures called G-quadruplexes [1–5]. G-quadruplexes are unique higher-order structures formed by G-rich nucleic acid sequences based on stacked arrays of G-quartets connected by Hoogsteen-type base pairs (Scheme 1). These structures are stabilized by monovalent cations, especially by potassium ion. G-quadruplex-forming sequences are prevalent in pivotal genomic regions, such as telomeres, promoters of oncogenes, and most growth control genes [6–8]. In addition, G-quadruplexes have been proposed to play a functional role in a variety of biological processes. For example, such structures are not only involved in the regulation of the telomerase activity but also associated with mechanisms of cancer, HIV, and other diseases [9–11]. Therefore, substantial research efforts have been devoted to develop a specific probe for distinguishing the quadruplex from other DNA conformations, especially the predominant double-stranded conformation [12–15].

Triphenylmethane (TPM) dyes such as malachite green (MG) normally render rather weak fluorescence due to easy vibrational deexcitation, but viscous, cold environments or MG aptamer have been demonstrated to enhance the fluorescence by restricting such vibrations [16,17]. Moreover, it is reported that MG becomes highly fluorescent upon mixing with intramolecular G-quadruplexes [18]. In our previous work, we studied the interactions between crystal violet (CV), another TPM dye, and G-quadruplexes, single- and double-stranded DNAs, and therefore concluded that CV could be developed as a specific probe for G-quadruplex recognition based on fluorescence spectra or energy transfer fluorescence spectra [19]. These exciting results promoted us to assume that other members of the TPM family may be applicable in G-quadruplex recognition. With this idea in mind, here the abilities of other three known TPM dyes—methyl violet (MV), ethyl violet (EV) and methyl green (MEG), to distinguish G-quadruplexes from single- and double-stranded DNAs were investigated and compared with those of MG and CV.

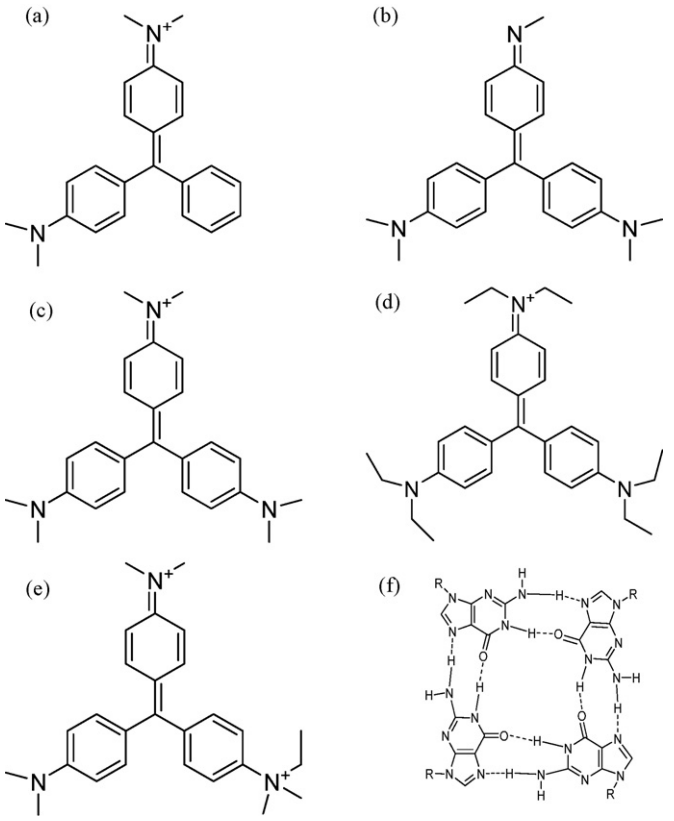
2. Experimental

2.1. Materials

All TPM dyes in this work were obtained from Sigma–Aldrich (St. Louis, MO) and were used as received without further purification. CtDNA was purchsed from Sangon Biotech. Co. Ltd. (Shanghai, China). The oligonucleotides were purchased from Etiwu Biotech. Co. Ltd. (Tianjin, China). The concentrations of these oligonu-

* Corresponding author at: Key Laboratory of Functional Polymer Materials (Nankai University), Ministry of Education, Nankai University, Tianjin 300071, PR China. Tel.: +86 22 23505091; fax: +86 22 23502458.
E-mail address: kongdem@nankai.edu.cn (D.-M. Kong).

0039-9140/$ – see front matter © 2009 Elsevier B.V. All rights reserved.
doi:10.1016/j.talanta.2009.07.034



Scheme 1. The structures of the triphenylmethane dyes used in this paper and a schematic representation of a G-quartet. (a) Malachite green (MG), (b) methyl violet (MV), (c) crystal violet (CV), (d) ethyl violet (EV), (e) methyl green (MEG), and (f) G-quartet.

cleotides were represented as single-stranded concentrations unless otherwise noted, which were determined by measuring the absorbance at 260 nm in a quartz cuvette. Molar extinction coefficients were determined using a nearest neighbor approximation (http://www.idtdna.com/analyzer/Applications/OigoAnalyzer). The DNAs we studied are listed in Table 1. The water was purified using a Millipore filtration system.

2.2. Fluorescence spectroscopy and energy transfer fluorescence spectroscopy

Fluorescence measurements were made using a Hitachi RF-4500 spectrofluorimeter. Oligonucleotide solutions were prepared in Tris–HCl buffer (25 mM, pH 7.0) containing KCl (100 mM). To ensure the formation of quadruplex structures, the solutions were heated to 95 °C for 5 min and then cooled slowly to room temperature. After incubation at room temperature overnight, the TPM dye (10 μM) was added. The mixtures were kept at 30 °C for 1 h before spectrometric detection. In fluorescence spectroscopy determination, the spectra were excited at 605 nm and monitored from 630 to 800 nm for MG, excited at 635 nm and monitored from 660 to 800 nm for MEG. When the other three TPM dyes were used, the excited wavelengths were, respectively, 570 nm for EV, 580 nm for MV and 580 nm for CV, and their spectra were monitored from 600 to 800 nm. In energy transfer fluorescence spectroscopy determination, the spectra were excited at 280 nm for MV, CV, MG and MEG and 270 nm for EV and monitored from 600 to 800 nm.

Table 1
Sequences of oligonucleotides used in this work.

Name	Oligonucleotide sequence
Hum21	5′-$G_3(T_2AG_3)_3$
Oxy28	5′-$G_4(T_4G_4)_3$
Hum12	5′-$(T_2AG_3)_2$
Oxy12	5′-$G_4T_4G_4$
CtDNA	
AT	5′-$(AT)_6$
LD	5′-$GCGCA_2T_2GCGC$
GC	5′-$(GC)_6$
ssDNA1	5′-GAGCTCTCGAAAGAGCTCCGATTA
ssDNA2	5′-TAGAGCACAGCCTGTCCGTG

2.3. The fluorescence titration and energy transfer fluorescence titration

The measurements were performed by keeping the concentration of the TPM dye at 10 μM while varying the DNA concentrations (from 1 μM to 18 μM for Hum21 and Oxy28, strand concentration; from 16 μM to 2.72 mM for CtDNA, base concentration; from 2 μM to 30 μM for other DNAs, strand concentration). The emission at 635 nm for MV, 640 nm for CV, 645 nm for EV, 680 nm for MG and MEG was monitored as a function of DNA concentration on a Hitachi RF-4500 spectrophotometer.

3. Results and discussion

3.1. Fluorescence spectra

In order to evaluate suitability of the 5 TPM dyes for the sensitive recognition of G-quadruplexes, the fluorescence spectra of these TPM dyes were measured in the presence of 10 different DNAs (Table 1). Hum21 and Oxy28 can fold into intramolecular G-quadruplex structures; Hum12 and Oxy12 can exist as intermolecular G-quadruplex conformations (Hum21 and Hum12 mimic the human telomeric sequence, Oxy28 and Oxy12 have the repeated subunits of Oxytricha telomeres); AT, GC and LD can form short double-stranded structures; CtDNA belongs to long double-stranded duplex DNA; ssDNA1 and ssDNA2 are single-stranded DNAs with a random DNA sequence. As shown in Fig. 1, all of the five dyes displayed rather faint intrinsic fluorescence, the addition of intramolecular G-quadruplexes (Hum21 and Oxy28) could greatly enhance the fluorescence of the dyes (except that the addition of Hum21 to EV only gave a very small fluorescence enhancement). When 10 μM of each dye was mixed with 5 μM Hum21 or Oxy28, the Hum21/MV mixture showed the maximal fluorescence enhancement compared with corresponding free dye, and the fluorescence enhancement could reach 80-fold. The Oxy28/CV mixture gave the minimal fluorescence enhancement, but the fluorescence enhancement could also reach 12-fold. These results indicate that all of the five triphenylmethane dyes can be used as sensitive intramolecular G-quadruplex fluorescence probes. The addition of intermolecular G-quadruplexes, single- or double-stranded DNAs could also increase the fluorescence of the dyes, but the fluorescence enhancements were much weaker. Except that the fluorescence intensities of MV and CV in the presence of intermolecular G-quadruplexes were always higher than those in the presence of single- or double-stranded DNAs, other three TPM dyes did not show any selectivity for intermolecular G-quadruplex DNAs over single- or double-stranded DNAs. For example, the addition of CtDNA to MG caused higher fluorescence enhancement than that of Hum12, and the addition of AT and LD to MG caused similar fluorescence enhancement to that of Oxy12. The fluorescence intensity of EV induced by ssDNA2 was similar to that by Oxy12. CtDNA, LD and AT had more effects on fluorescence of MEG than Oxy12 and Hum12. The results mentioned above suggest that MG, MV, CV and MEG may be developed as good

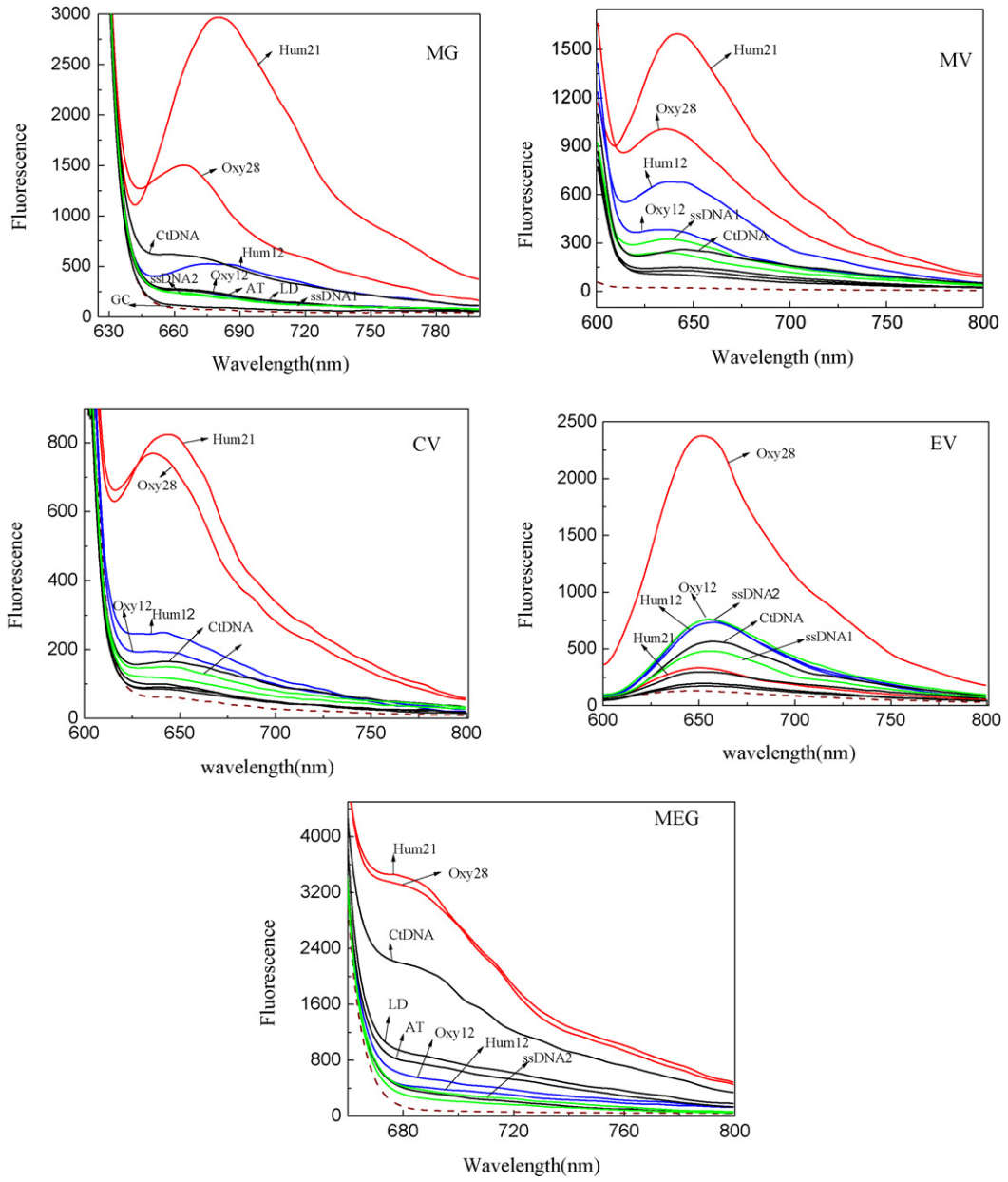


Fig. 1. Fluorescence spectra of the five TPM dyes in the presence of different DNAs. Free dye (purple, dotted lines), intramolecular G-quadruplexes (red), intermolecular G-quadruplexes (blue), duplex DNAs (black), single-stranded DNAs (green). [Hum21] = [Oxy28] = 5 μM; [Hum12] = [Oxy12] = [AT] = [LD] = [GC] = [ssDNA1] = [ssDNA2] = 10 μM; [CtDNA] = 240 μM (base concentration), [MG] = [MV] = [CV] = [EV] = [MEG] = 10 μM. (For interpretation of the references to color in this figure legend, the reader is referred to the web version of the article.)

fluorescent probes to discriminate intramolecular G-quadruplexes from intermolecular G-quadruplexes and to discriminate intramolecular G-quadruplexes from single- and double-stranded DNAs, but cannot give satisfactory results in discriminating intermolecular G-quadruplexes from single- and double-stranded DNAs. EV is not a good G-quadruplex probe because not all intramolecular G-quadruplexes we studied can increase the fluorescence of EV to a high level.

3.2. Energy transfer fluorescence spectra

The energy transfer fluorescence spectra of the 5 TPM dyes in the presence of the 10 DNAs were also studied in order to further investigate the ability of these 5 dyes to discriminate G-quadruplex DNAs from single- and double-stranded DNAs. As can be seen from Fig. 2, when excited at 270 or 280 nm, which is in the DNA absorption region [20], free dyes can only emit very weak fluorescence. However, the addition of intramolecular G-quadruplexes can greatly enhance the fluorescence of the dyes (except the addition of Hum21 to EV), indicating that efficient energy transfer occurs between the dyes and the intramolecular G-quadruplexes. Though the fluorescence emission intensities of the dyes were also enhanced in the presence of intermolecular G-quadruplexes, the enhancements were far lower compared with those in the presence of intramolecular G-quadruplexes, suggesting that energy transfer can also occur between intermolecular G-quadruplexes and the dyes, but the efficiencies of energy transfer are much weaker than those between the intramolecular G-quadruplexes and the dyes. It was previously demonstrated that energy transfer between DNA bases and a bound fluorescent ligand is only possible if the ligand is in close contact with the DNA bases [21]. This happens only when a fluorescent ligand is intercalated between stacked base pairs in duplex

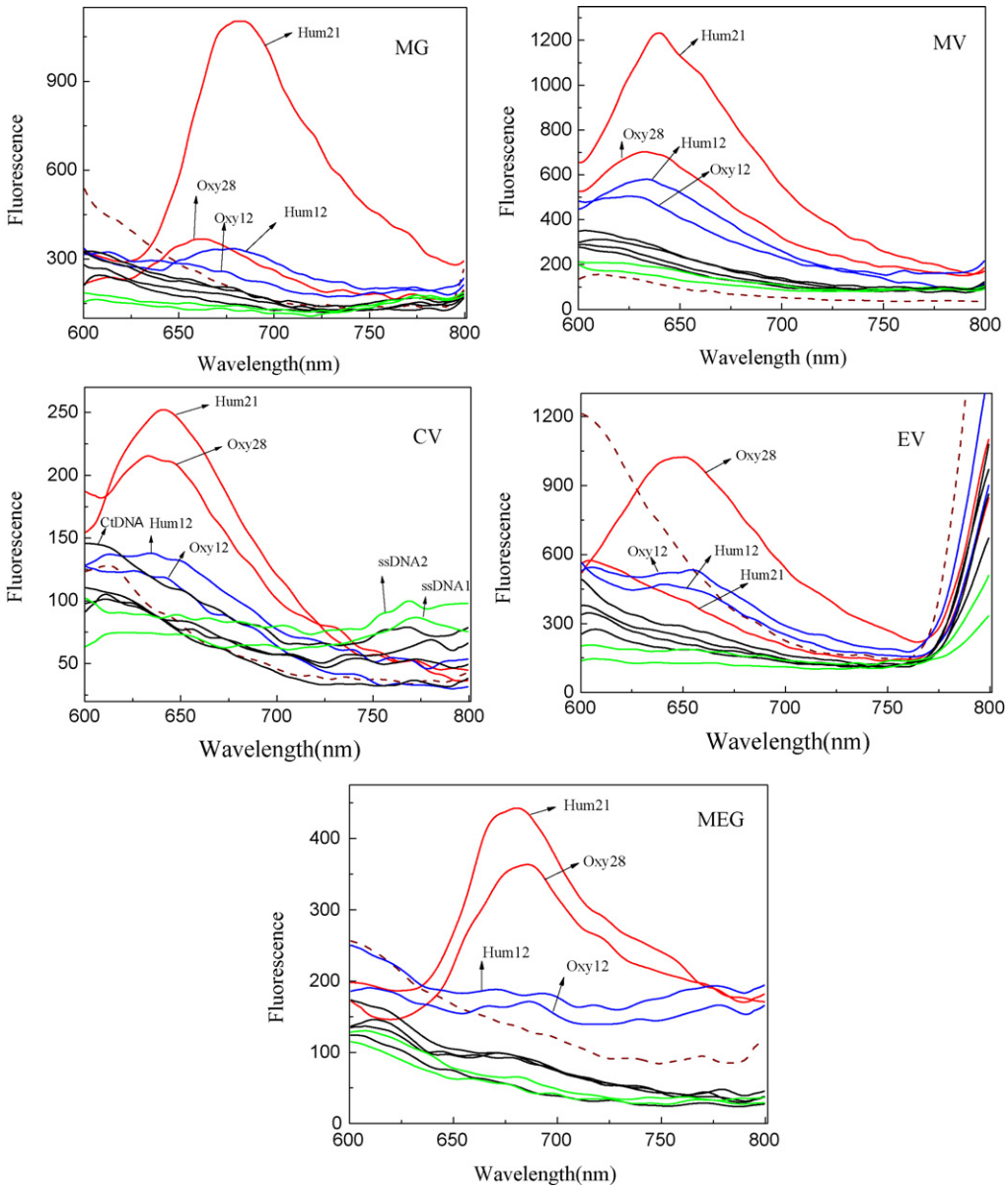


Fig. 2. Energy transfer fluorescence spectra of the five TPM dyes in the presence of different DNAs. Free dye (purple, dotted lines), intramolecular G-quadruplexes (red), intermolecular G-quadruplexes (blue), duplex DNAs (black), single-stranded DNAs (green). [Hum21] = [Oxy28] = 5 μM; [Hum12] = [Oxy12] = [AT] = [LD] = [GC] = [ssDNA1] = [ssDNA2] = 10 μM; [CtDNA] = 240 μM (base concentration), [MG] = [MV] = [CV] = [EV] = [MEG] = 10 μM. (For interpretation of the references to color in this figure legend, the reader is referred to the web version of the article.)

DNAs and G-quartets in G-quadruplex DNAs or stacked onto the two external G-quartets of quadruplexes. The above results surely indicated that the binding modes between the TMP dyes and the G-quadruplex DNAs were intercalation or external stacking but not outside binding. To the contrary, the fluorescence intensities of MG, CV, EV and MEG decreased upon addition of single- or double-stranded DNAs, indicating that no energy transfer occurs between the dyes and single- or double-stranded DNAs. It is not surprise because the added single- and double-stranded DNAs can compete with the dyes to absorb the energy of excitation light, causing the fluorescence of the dyes to decrease. Though all DNAs studied in this work could cause a large fluorescence enhancement for MV, the extents of fluorescence enhancement in the presence of G-quadruplexes (including intramolecular and intermolecular G-quadruplexes) were much higher than those in the presence of single- or double-stranded DNAs. The results mentioned above indicate that energy transfer fluorescence spectra are better than fluorescence spectra in differentiating DNAs with different conformations. According to the fluorescence change trends caused by the addition of DNAs, energy transfer fluorescence spectra can be used to distinguish G-quadruplexes (including intramolecular and intermolecular G-quadruplexes) from single- and double-stranded DNAs. According to the fluorescence change extents caused by the addition of DNAs, energy transfer fluorescence spectra can be used to discriminate intramolecular G-quadruplexes from intermolecular G-quadruplexes.

3.3. *Fluorescence titrations and energy transfer fluorescence titrations by different DNAs*

To gain further insight into the interactions between DNAs and the TPM dyes, the fluorescence titration and energy transfer fluorescence titration experiments were conducted. The fluorescence titration results are shown in Fig. 3, from which one can find that the fluorescence of each TPM dye initially increased greatly with increased concentrations of added intramolecular G-quadruplexes,

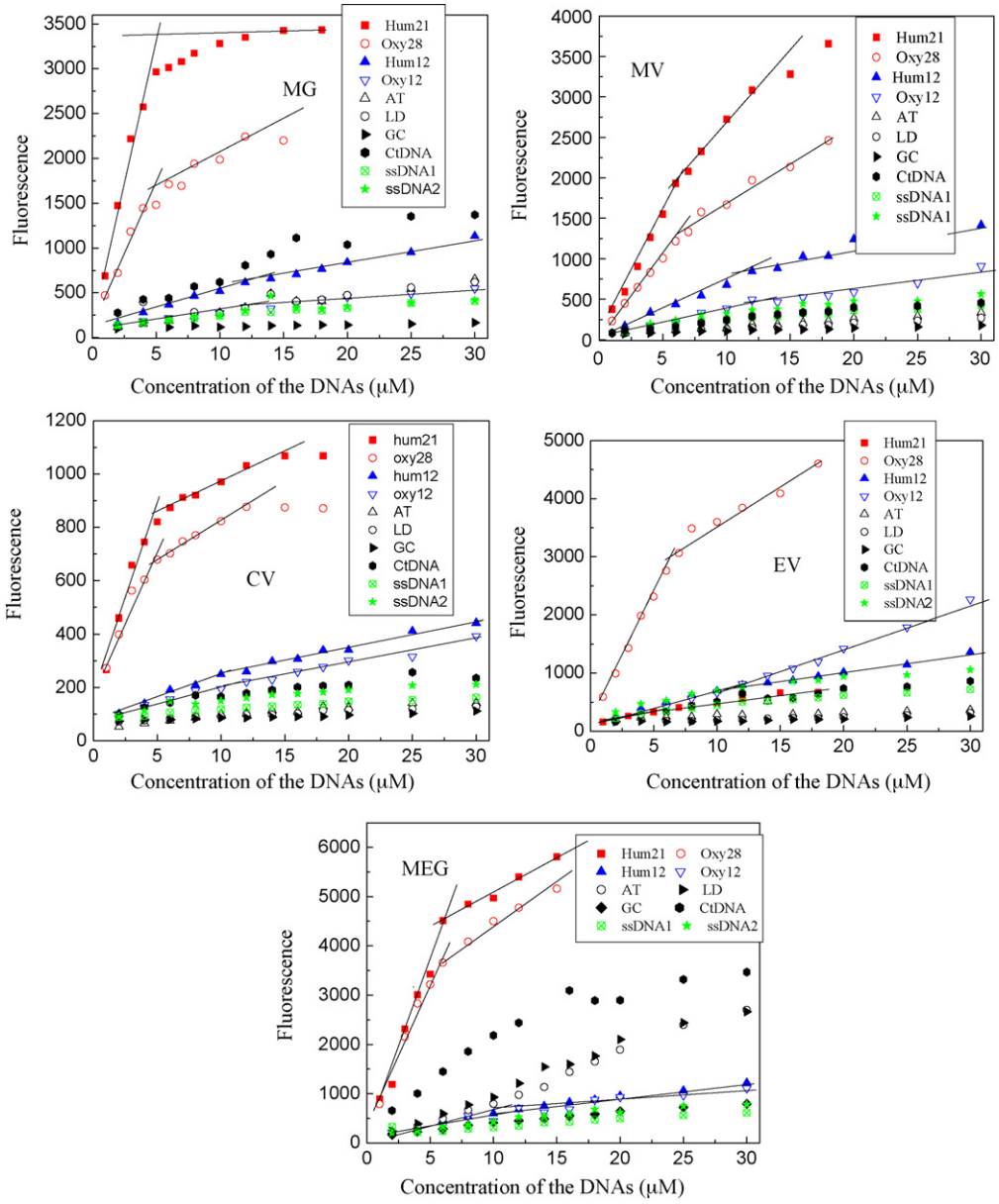


Fig. 3. Fluorescence titrations of the five TPM dyes by different DNAs. [MG] = [MV] = [CV] = [EV] = [MEG] = 10 μM. DNA concentration is expressed as strand concentration. The concentration of CtDNA is converted to the strand concentration of an oligonucleotide with 12-nucleotide.

and then leveled off or slowed down. A close examination of the fluorescence data indicated that the DNA concentrations (strand concentration) at the intersection points in the titration curves were about 5.0 μM for Hum21 and Oxy28 when the concentration of each dye was fixed at 10.0 μM, indicating that the binding stoichiometric ratios of the TPM dyes to the two intramolecular G-quadruplexes were all 2:1. This 2:1 stoichiometry is consistent with a binding mode based on stacking of the dye onto the two external G-quartets of the intramolecular quadruplexes [21–23]. Titration of the TPM dyes with intermolecular G-quadruplexes could result in similar fluorescence change trends (except that the fluorescence of EV continuously increased with the increase of Oxy12 concentration), but the fluorescence changes were much smaller and the intersection points in the titration curves were also not so clear. However, after a close examination of the fluorescence data, one can also find that 10.0 μM of each TPM dye can interact with 10.0 μM Hum12 or Oxy12. Considering that two strands of Hum12 (or Oxy12) can form a quadruplex, the binding stoichiometric ratios of the TPM dyes to the two intermolecular G-quadruplexes were also 2:1, indicating that the interaction of the TPM dyes with intermolecular G-quadruplexes also follows an external stacking mode. To the contrary, the fluorescence intensities of the dyes were continuously enhanced with increased concentrations of added single- or double-stranded DNAs, and no obvious inflexions were observed in the titration curves over the studied concentration range. The exceptional phenomenon appeared when MEG was mixed with CtDNA, whose fluorescence seemed to reach a platform with an increase in the concentration of CtDNA.

Fig. 4 shows the energy transfer fluorescence titration results. From this figure, one can find that the energy transfer fluorescence of the dyes firstly increased dramatically with increased concentrations of added intramolecular G-quadruplexes, then reached a maximum, and at last decreased abruptly. Such phenomenon could be well explained by the competition between the dyes and intramolecular G-quadruplexes for the absorption of excitation light. In the low DNA concentration range, the TPM dye was in excess. The addition of intramolecular G-quadruplexes was helpful in the formation of G-quadruplex–TPM complexes

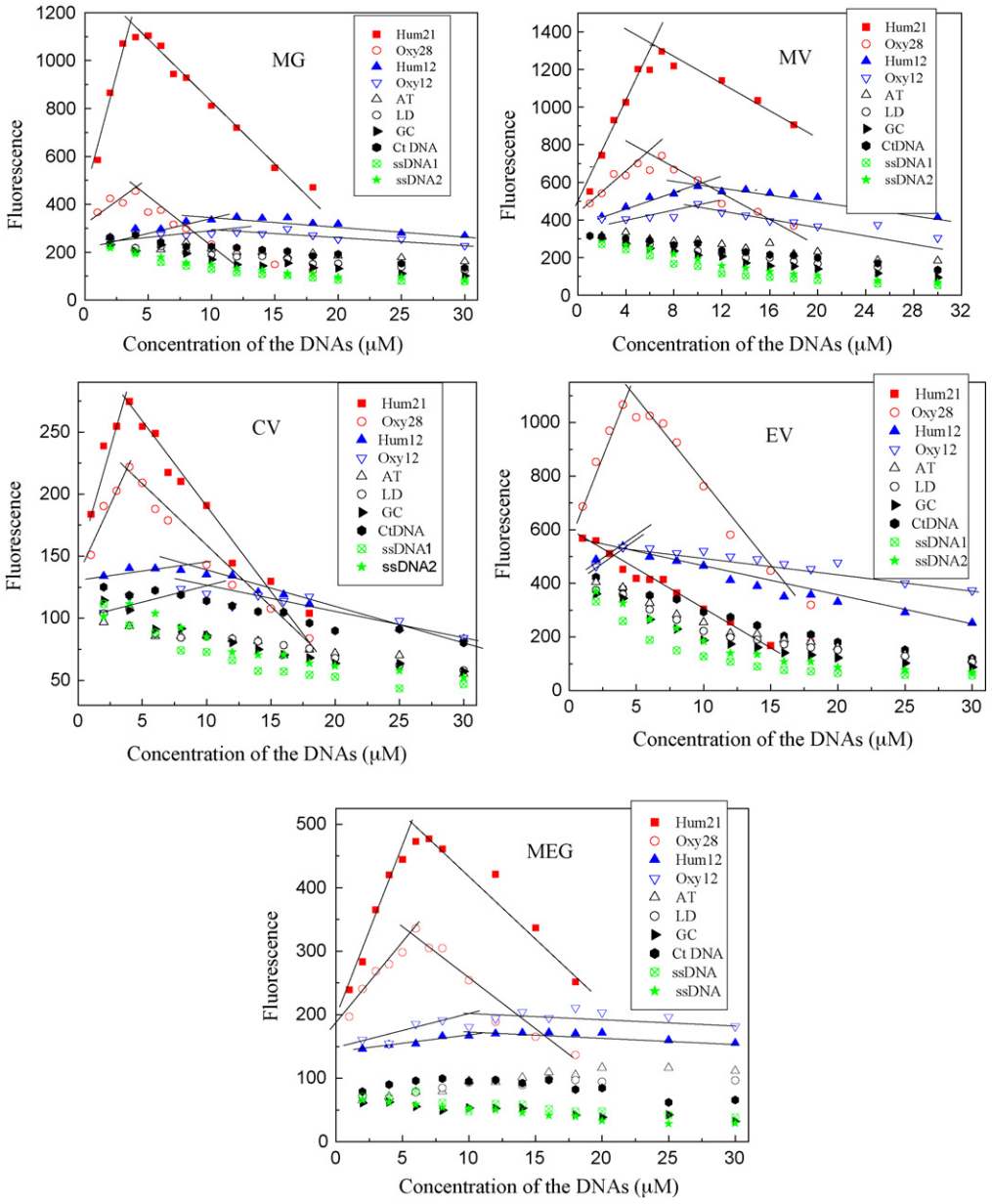


Fig. 4. Energy transfer fluorescence titrations of the five TPM dyes by different DNAs. [MG] = [MV] = [CV] = [EV] = [MEG] = 10 μM. DNA concentration is expressed as strand concentration. The concentration of Ct DNA is converted to the strand concentration of an oligonucleotide with 12-nucleotide.

as more and more energy was transferred from DNA to TPM, thus the fluorescence of TPM increased continuously. In the high DNA concentration range, the intramolecular G-quadruplexes were in excess. Free intramolecular G-quadruplexes competed with G-quadruplex–TPM complexes to absorb the energy of excitation light and, therefore, the fluorescence of the TPM dyes decreased sharply. Noting that the maxima occurred around 5.0 μM for the intramolecular G-quadruplexes, we could easily conclude that the binding stoichiometric ratios of the TMP dyes to intramolecular G-quadruplexes were all 2:1. Again, titration of the TPM dyes with intermolecular G-quadruplexes can result in similar energy transfer fluorescence change trends, and maximal points in the titration curves can also be observed clearly. According to the maximal points, the binding stoichiometric ratio of 2:1 can also be obtained for the interaction between TMP dyes and intermolecular G-quadruplexes. Unusually, the fluorescence emission of EV continuously went down as a consequence of addition of Hum21, and the binding stoichimetric ratios of EV to the two intermolecular G-quadruplexes seemed to be 4:1. Under the same conditions, mixing with single- or double-stranded DNAs resulted in a steady decrease in the fluorescence of the dyes, which also could be interpreted by the competitive absorbance of DNAs and dyes for excitation energy. The results mentioned above indicate that energy transfer fluorescence titration data are more suitable in studying the binding stoichiometric ratios of dyes to G-quadruplexes than fluorescence titration data due to the more obvious inflexions observed in the energy transfer fluorescence titration curves. In addition, they can also be used to distinguish G-quadruplexes from single- and double-stranded DNAs according to the trend in fluorescence change of dyes with the increase of DNA concentration.

3.4. Binding stability between dyes and G-quadruplexes

Based on the stoichiometric ratio of 2:1, the association constants (K_a) between the five dyes and the two intramolecular G-quadruplexes can be obtained by fitting the data in fluorescence

Table 2
The K_a (μM^{-1}) values of the intramolecular G-quadruplex–TPM complexes.

	Hum21	Oxy28
MV	0.0026(5)	0.0019(3)
EV	0.00078(26)	0.0064(15)
MG	0.45(18)	0.029(17)
CV	0.049(14)	0.025(5)
MEG	0.026(8)	0.019(6)

titration experiments using the equation we deduced [19]:

$$[G\text{-quadruplex}]_T = \frac{F - F_{\min}}{F_{\max} - F_{\min}} \times \frac{[\text{Dye}]_T}{n} + \frac{(F - F_{\min})(F_{\max} - F_{\min})^{n-1}}{nK_a(F_{\max} - F)^n[\text{Dye}]_T^{n-1}}$$

In which, $F_{\min}$, $F_{\max}$ and F represent the fluorescence of free dye, fully bound dye and partially bound dye, respectively. n is the number of the dye that one G-quadruplex can bind. Here, the value of [Dye] is 10 μM. The value of n is fixed at 2.

The fitting results are listed in Table 2. As for the interaction between Hum21 and the dyes, the K_a value follows the order of MG > CV > MEG > MV> EV; as for the interaction between Oxy28 and the dyes, the K_a value follows the order of MG > CV > MEG> EV > MV. In these five dyes, each MG, CV and EV carries one positive charge. The main difference among them is the number and the size of substituent moieties. MG has two dimethylamino substituents, CV has three dimethylamino substituents, and EV has three diethylamino substituents. That is, the size of substituents in triphenylmethane backbone as follows: MG < CV < EV, which is justly contrary to the order of the K_a values. When the dyes bind to G-quadruplexes, it is likely that the three phenyl rings of the dyes stack onto the two external G-quaterts of the G-quadruplex, and the pendent substituents intercalate into the grooves of the G-quadruplex [24]. Such opposite orders of the binding stability and the substituent size suggested that the increase of size could hinder the intercalation of substituents into the grooves, resulting in the decrease of binding stability. MV has two dimethylamino substituents and one methylamino substituent, the size of the substituents in MV is even smaller than that of CV, but the binding stability between MV and G-quadruplexes is lower than that between CV and G-quadruplexes, which may be attributed to the difference of positive charges the two dyes carry. CV carries one positive charge, but MV has none. The protonation of the methylamino substituent may provide MV a positive charge, but protonation needs acidic condition. Based on the results mentioned above, we conclude that positive charge and substituent size are two important factors in determining the binding stability of the intramolecular G-quadruplexes–TPM complexes. As for which one is more predominant, it is very possible that the presence of one positive charge is very important for improving the binding stability (this can be proved by the difference between CV and MV), but the presence of the second positive charge seems to have less influence than the size of the substituent, which can be deduced from the difference between CV and MEG. MEG has two positive charges and a larger substituent size, but its binding stability is weaker than CV.

4. Conclusions

In order to evaluate the suitability of the five TPM dyes to discriminate G-quadruplex DNAs from single- and double-stranded DNAs, the fluorescence and energy transfer fluorescence of the five TPM dyes in the presence of G-quadruplexes, single- or double-stranded DNAs were investigated in the present paper. The results indicate the fluorescence spectra of the TPM dyes except EV can be used to discriminate intramolecular G-quadruplexes from intermolecular G-quadruplexes as well as single- and double-stranded DNAs, but cannot be used to discriminate intermolecular G-quadruplexes from single- and double-stranded DNAs. The energy transfer fluorescence spectra (especially MG, CV and MEG) not only can be used to discriminate intramolecular G-quadruplexes from intermolecular G-quadruplexes but also can be used to discriminate G-quadruplexes (including intramolecular G-quadruplexes and intermolecular G-quadruplexes) from single- and double-stranded DNAs. The energy transfer fluorescence titration experiments can be used to distinguish G-quadruplex DNAs from single- and double-stranded DNAs according to the fluorescence change trend of dyes with the increase of DNA concentration. The interaction of the five TPM dyes with G-quadruplexes may follow an external stacking mode, and the binding stoichiometric ratios are all 2:1. Positive charges and substituent size in TPM dyes may be two important factors in influencing the binding stability of the dyes and G-quadruplexes. This study may provide some important information for the development of sensitive and specific G-quadruplex fluorescent probes.

Acknowledgments

This work was supported by the National Natural Science Foundation of China (No. 20801040), the National Basic Research Program of China (No. 2006CB705700), and the Natural Science Foundation of Tianjin (No. 08JCZDJC21200).

References

[1] P.A. Rachwal, I.S. Findlow, J.M. Werner, T. Brown, K.R. Fox, Nucleic Acids Res. 35 (2007) 4214.
[2] D. Yang, L.H. Hurley, Nucleosides Nucleotides Nucleic Acids 25 (2006) 951.
[3] T. Simonsson, Biol. Chem. 382 (2001) 621.
[4] C.C. Hardin, A.G. Perry, K. White, Biopolymers 56 (2001) 147.
[5] N. Smargiasso, F. Rosu, W. Hsia, P. Colson, E.S. Baker, M.T. Bowers, E. De Pauw, V. Gabelica, J. Am. Chem. Soc. 130 (2008) 10208.
[6] J. Seenisamy, E.M. Rezler, T.J. Powell, D. Tye, V. Gokhale, C.S. Joshi, A. Siddiqui-Jain, L.H. Hurley, J. Am. Chem. Soc. 126 (2004) 8702.
[7] A. Siddiqui-Jain, C.L. Grand, D.J. Bearss, L.H. Hurley, Proc. Natl. Acad. Sci. U.S.A. 99 (2002) 11593.
[8] S.L. Palumbo, R.M. Memmott, D.J. Uribe, Y. Krotova-Khan, L.H. Hurley, S.W. Ebbinghaus, Nucleic Acids Res. 36 (2008) 1755.
[9] A.M. Zahler, J.R. Williamson, T.R. Cech, D.M. Prescott, Nature 350 (1991) 718.
[10] S. Neidle, G. Parkinson, Nat. Rev. Drug Des. 1 (2002) 383.
[11] J.L. Mergny, J.F. Riou, P. Mailliet, M.P. Teulade-Fichou, E. Gilson, Nucleic Acids Res. 30 (2002) 839.
[12] H. Arthanari, S. Basu, T.L. Kawano, P.H. Bolton, Nucleic Acids Res. 26 (1998) 3724.
[13] C. Wei, G. Jia, J. Yuan, Z. Feng, C. Li, Biochemistry 45 (2006) 6681.
[14] Z.A.E. Waller, P.S. Shirude, R. Rodriguez, S. Balasubramanian, Chem. Commun. (2008) 1467.
[15] A. Bugaut, K. Jantos, J.L. Wietor, R. Rodriquez, J.K. Sanders, S. Balasubramanian, Angew. Chem. Int. Ed. 47 (2008) 2677.
[16] M.S. Baptista, G.L. Indig, J. Phys. Chem. B 102 (1998) 4678.
[17] J.R. Babendure, S.R. Adams, R.Y. Tsien, J. Am. Chem. Soc. 125 (2003) 14716.
[18] A.C. Bhasikuttan, J. Mohanty, H. Pal, Angew. Chem. Int. Ed. 46 (2007) 9305.
[19] D.M. Kong, Y. E Ma, J. Wu, H.X. Shen, Chem. Eur. J. 15 (2009) 901.
[20] D. Suh, J.B. Chaires, Bioorg. Med. Chem. 3 (1995) 723.
[21] I. Lubitz, N. Borovok, A. Kotlyar, Biochemistry 13 (2007) 12925.
[22] D.M. Kong, Y. E Ma, J.H. Guo, W. Yang, H.X. Shen, Anal. Chem. 81 (2009) 2678.
[23] E.S. Baker, J.T. Lee, J.L. Sessler, M.T. Bowers, J. Am. Chem. Soc. 128 (2006) 2641.
[24] J.E. Reed, A.A. Arnal, S. Neidle, R. Vilar, J. Am. Chem. Soc. 128 (2006) 5992.

Talanta 80 (2009) 614–621

Contents lists available at ScienceDirect

Talanta

journal homepage: www.elsevier.com/locate/talanta

Theoretical and experimental methods of determination of the breakthrough volume of SPE sorbents

Katarzyna Bielicka-Daszkiewicz*, Adam Voelkel

Poznań University of Technology, Institute of Technology and Chemical Engineering, Pl. M. Skłodowskiej-Curie 2, 60-965 Poznań, Poland

ARTICLE INFO

Article history:
Received 1 June 2009
Received in revised form 9 July 2009
Accepted 20 July 2009
Available online 28 July 2009

Keywords:
SPE
Breakthrough volume
Polymeric sorbents

ABSTRACT

Solid-phase extraction is one of the most popular sample preparation methods. The selection of the appropriate extraction system is an important stage in the elaboration of analytical procedure. In this case, the knowledge of the interactions between isolated compounds, sorbent and elution solvents seems to be important. The extraction ability of sorbents in the SPE bed depends also on: (i) the bed capacity; (ii) the volume of sample loaded, (iii) the nature and volumes of conditioning solvents and eluents. One of the important parameters is the breakthrough volume, which determines the maximum volume of water sample which can be introduced into the sorbent. In this work two methods of determination of the breakthrough volumes are presented: experimental method with frontal analysis, and theoretical method with computational applications. Both procedures were used for the characterization of nine polymeric sorbents based on divinylbenzene copolymers. Comparison of results allows to choose the computational procedure of breakthrough volume determination as the easier one and less time consuming.

© 2009 Elsevier B.V. All rights reserved.

1. Introduction

Solid-phase extraction (SPE) technique was invented in the 1970s. It is an alternative method to liquid–liquid extraction. This technique has spread very fast and found interest in different domains of research. The analytical procedures using SPE are applied very often in both science and industry. This technique is used in the analysis of different samples, e.g. environmental, biological, medical and many others. The use of SPE allows the isolation of different compounds, sample pre-concentration, change of the sample matrix and sample clean-up. Wide interest results from numerous advantages of this extraction method:

- it is fast and easy;
- small volumes of solvents are used;
- capability of automation of this technique;
- there are no problems related to emulsion formation during the extraction process;
- it is selective and effective;
- relatively inexpensive.

In the selection of the extraction system very important is the knowledge of the relations/interactions between isolated compounds, sorbent and elution solvents. Physicochemical properties: polarity, acidity, basicity and hydrophobicity of sorbents, isolated compounds and the solvents used in the extraction process affect mutual interactions and finally extraction efficiency.

The selection of the appropriate sorbent is an important stage in the elaboration of the analytical method. There are many sorbents used in this technique. This can be divided into three main groups: silica sorbents, polymeric sorbents and activated carbon or graphitized carbon black. All kinds of sorbents can be modified in different ways, to change their extraction properties. The series of papers were published in this field [1–9].

The SPE method development very often relies on trial-and-error procedures. As it is time consuming and arduous way, so the optimization methods are investigated. These are based on physicochemical and thermodynamical dependencies between sorbents, analytes and solvents. One of them is the solublility parameter system, used in the description of the interactions in the extraction systems, especially between analyte and sorbent and the selection of the appropriate eluent [10,11].

The physical characteristics of the sorbents: its surface area, particle size, pore size or pore volume are crucial sorbent properties. However, the extraction ability of sorbents in the SPE bed depends also on the bed capacity; the volume of sample loaded on the bed, the nature and volumes of conditioning solvents and eluents. These are some critical SPE parameters: breakthrough volume, volume of rinsing solvent, elution volume, which depends on the kinetic properties of the SPE bed, its hold-up volume and retention factor. The aim of this paper is the description and discussion of the theoretical background and methods of breakthrough volume determination.

* Corresponding author. Tel.: +48 61 665 3722; fax: +48 61 665 3649.
E-mail address: Katarzyna.Bielicka-Daszkiewicz@put.poznan.pl (K. Bielicka-Daszkiewicz).

0039-9140/$ – see front matter © 2009 Elsevier B.V. All rights reserved.
doi:10.1016/j.talanta.2009.07.037

2. Theory

The breakthrough volume (V_B) is one of the parameters characterizing the SPE sorbent bed. This parameter is defined in literature in different ways:

- the sample volume which can be loaded on the sorbent bed without the loss of the analytes;
- the sample volume over which the analytes are eluted by the sample matrix;
- the sample volume that can be loaded onto the a SPE bed providing a given ratio of outlet to inlet analyte concentration at a given temperature [12,13];
- maximum sample volume which can be applied with a theoretical 100% recovery [14];
- the volume of sample which has to flow through the sorbent in order to obtain a percent of retention of 99–95% [15];
- V_B expressed the capacity of a sampling column (sorbent bed) [16–18].

V_B depends on the concentration of analytes in the solution loaded to the sorbent, the temperature, the flow rate, the number of theoretical plates [12]. In the on-line method, the breakthrough depends on the flow rate, so it must be constant [19]. The breakthrough volume determines the amount of analyte that can be isolated, it depends on the kinetic properties of the extraction device [20].

The breakthrough volume can be described or presented by the breakthrough curve. It is the relationship between the sample concentration and the sample volume passed through the sorbent. Plotting the observed concentration of the analyte, against the corresponding aliquot volumes generates the breakthrough curve [19]. The breakthrough volume depends on kinetic parameters of sorbent and on the retention parameters as well as on the flow rate of the sample. The experiments with SPE disks [21] show that there is an optimum flow rate at which the breakthrough volume reach the maximum value. The breakthrough volume is reduced at very low and very high flow rates [21].

Another important parameter, which is connected with the breakthrough volume is the breakthrough level. This parameter is defined as the fraction of the total mass of analyte which has passed out of the sorbent and has been lost [13].

To treat the SPE as chromatographic process, one have to define the breakthrough level as the function of retention volume or retention time. Breakthrough volume can be than defined as the volume giving an assumed breakthrough level (the ratio of outlet to inlet concentration). More useful is the definition based on mass instead of the concentration, then the breakthrough level is defined as the fraction of total mass of analyte which has passed out of the column without adsorption. When the relationship is converted from time scale to volume scale, one can define the breakthrough volume as the function of the plate number of the column. Eq. (1) was proposed by Lövkvist and Jönsson [18] and cited many times [12,19,22–24].

$$V_B = V_R\left(a_0 + \frac{a_1}{N} + \frac{a_2}{N^2}\right)^{-1/2} \quad (1)$$

where V_R is the retention volume, $a_0 = (1-b)^2$ and give the correct asymptotic limit for large values of N, a_1, a_2 are complicated function of b and numerical values, a_1 was adjusted to provide a good fit for intermediate values of N, a_2 was found from equation for b when N tends toward zero, b is the breakthrough level [%], N is the number of theoretical plates.

The numerical value of a_0, a_1 and a_2 coefficients, determined for various values of "b", can be found in the literature [18].

Another relationship between breakthrough volume and number of theoretical plates was proposed by Werkhoven-Goëwie at al. [21,24,25].

$$V_B = V_R\left[\frac{\sqrt{N}-2}{\sqrt{N}}\right] \quad (2)$$

3. Experimental determination of the breakthrough volume

Breakthrough volume can be determined experimentally in several ways using on-line or off-line methods including frontal or elution chromatography.

3.1. Frontal chromatography [14,16,17,26,27]

It is the process where a solute (sample) is continually applied to the column (sorbent) until some of the analytes begins to appear in the effluent of the column (sorbent), breakthrough occurs when the capacity of the sorbent has been reached. The concentration of the analyte in the effluent can be measured by UV detector. The dependence between the concentration of the analyte in the effluent and volume of the sample passed through the sorbent gives the breakthrough curve on the diagram (Fig. 1) [15]. Under ideal conditions, the breakthrough curve has a bilogarithmic shape and the chromatographic parameters can be determined from the curve as follows:

- the inflection point of the curve corresponds to the retention volume V_R of the analyte;
- V_B is defined as the volume of the mobile phase, that corresponds (on the breakthrough curve) to 1% of max concentration of the analyte in the effluent;
- V_M – hold-up volume – is defined as the volume of the mobile phase, that corresponds (on the breakthrough curve) to 99% of max concentration of the analyte in the effluent.

Under real conditions the retention parameters can be determined from the diagram as seen in [26,27]:

Breakthrough volume V_B is defined as:

$$V_B = V_R - 2\sigma_V \quad (3)$$

where V_R is the retention volume, can be determined graphically from the diagram, it corresponds to 0.5 of the average value of maximum analyte concentration in the effluent (C_E); it can be expressed

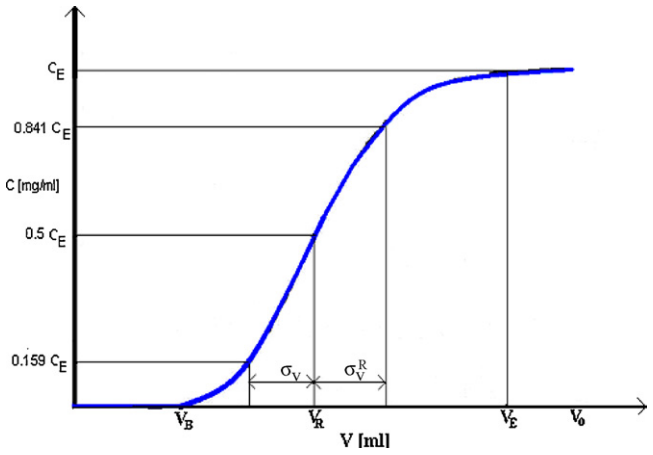


Fig. 1. Breakthrough curve.

analytically by the well known equation:

$$V_R = V_M(1+k) \tag{4}$$

where k is the retention (capacity) factor of the solute (for the analyte in the sample) [21,24], σ_V, σ_V^* are the standard deviations of the derivative curve determined graphically from the breakthrough curve; due to its asymmetry these are given suitably as values corresponding to 0.159 and 0.841 of the average value of max concentration of analyte in the effluent (C_E), respectively.

It can be given as follows [14,19,28]:

$$\sigma_V = V_M \frac{1+k}{\sqrt{N}} \tag{5}$$

V_E is the equilibrium volume defined as:

$$V_E = V_R + 2\sigma_V^* \tag{6}$$

The breakthrough volume depends on plate number (N) of the sorbent. For small plate number ($4 < N < 9$) the V_B can be described by Eq. (1) or (2). For plate number $N > 9$ the breakthrough volume is described by the following functions:

$$V_B = V_R - 3\sigma_V \tag{7}$$

or

$$V_B = \left[1 - \left(\frac{3}{\sqrt{N}}\right)\right] V_R \tag{8}$$

For the sorbent beds with large plate number, the breakthrough volume can be given as in Eq. (9) at the 1% breakthrough level [12–14]:

$$V_B = V_R \left(1 - \frac{2.3}{\sqrt{N}}\right) \tag{9}$$

3.2. Off-line methods [19,27,29–32]

In this kind of experimental method, the sample is introduced into the sorbent in aliquots. The sorbent should be conditioned earlier. The volume of the individual aliquot (fraction) varies from 5 to 10 ml. Each sample aliquot is collected in separate vial, and analyzed with spectroscopic or chromatographic techniques [29,30] to measure the concentration of the analyte in each aliquot of the sample. If liquid chromatography is used as analytical technique, the water sample can be analyzed directly. However, when the gas chromatography is used, the additional extraction of the effluents is necessary to change the sample matrix [30].

3.3. On-line methods

One of the on-line methods is elution chromatography, where SPE cartridge is treated as chromatographic column, water is the mobile phase, and the analyte is injected into the column in a microliter volume. The concentration of the analyte in the effluent can be measured by UV detector [14,17,26].

Another method is when the SPE sorbent is applied as a precolumn in SPE–HPLC system. A solution containing a constant concentration of analyte is pumped at a constant flow rate through the sorbent (column). The effluent from the sorbent goes directly to the detector. The appearance of the analyte is recorded [19]. The relationship between the peak area against the sample volume is linear. When the breakthrough of analyte begins, this relationship starts to deviate from linearity [33].

Another on-line method of determining the breakthrough volume is the connection of the sorbent packed tube with GC/FID or GC/MS system. In this method, the breakthrough volume can be determined in the whole temperature range (from −10 to 170 °C) by using microtrap technology [12,34]. The measurement of breakthrough volume can be carried out in the appropriate system [35]. The sorbent tube is placed in the GC oven or in a separate unit – in the thermal desorber. In this method the specific breakthrough volume (in given temperature) is determined. The dimension of the specific breakthrough volume is ml/g, it is the volume of gas per gram of adsorbent.

3.4. Plate number

The plate number depends on column parameters (diameter, length) and on the physicochemical properties of the sorbent.

The plate number (N) is related to mobile and stationary phase properties [18] or can be calculated from the breakthrough curve [13,19,25,27,36].

The number of theoretical plates corresponds to the efficiency of the SPE column.

Approximate plate number can be calculated using reduced values of mobile phase velocity (ν) and plate height (h) [18,37,38].

3.5. Retention factor

Retention factor is an essential parameter describing the sorption properties of the SPE bed. It is determined for each solute, extracted with the SPE system. The retention factor influences extraction process, it can describe the minimum amount of sorbed analyte, the elution volume or sample volume. It is related to the most important extraction parameter – recovery [19].

The value of retention factor can be determined from the breakthrough curve or by using the method based on the equilibration of the solutes between the SPE sorbent and the model solution [19,27,28].

Generally, the retention factor can be defined as ratio of amount of moles of analyte adsorbed in the stationary phase (n_s) and amount of moles present in the mobile phase (n_E):

$$k = \frac{n_s}{n_E} \tag{10}$$

$$n_E = c_E V_M \tag{11}$$

C_E is defined as:

$$c_E = \frac{n_0 - n_s}{V_0 + V_M} \tag{12}$$

Then retention factor is given as:

$$k = \frac{n_s(V_0 + V_M)}{V_M(n_0 - n_s)} \tag{13}$$

If one defines n_0 as number of moles in aqueous solution V_0, than retention factor is given as:

$$k = \frac{n_0 - c_E(V_0 + V_M)}{c_E V_M} \tag{14}$$

V_0 – is defined as the sample volume – volume of the solute used to determine breakthrough curve.

Recovery can be expressed by the following relationship when using the retention factor [27,28]:

$$r = \frac{V_M k}{V_0} 100\% \tag{15}$$

It is for the solutes when the value of sample volume is:

$$V_0 > V_R + 2\sigma_V \tag{16}$$

3.6. Estimation of the breakthrough volume with short experiment

Experimental determination of breakthrough volume, particularly by using off-line methods, is time consuming. The theory of frontal chromatography allows to deduce a relationship between

the breakthrough volume and the properties of the SPE device: plates number, hold-up volume of the sorbent bed and retention factor of the analyte.

Combining the relationships described above, one can try to approximate the breakthrough volume with only short experiment necessary to determine the recovery.

In this work the relationships described above were used for the characterization of several polymeric sorbents – nine divinylbenzene copolymers. The breakthrough volume was determined experimentally by using frontal analysis and theoretical relationship described by equations given above. The aim of this work was to compare theoretical and experimental methods for the determination of breakthrough volume for some polymeric sorbents, to compare the values of plates number and breakthrough volume obtained in these two different ways. The final effect of this work should be the procedure of the estimation of breakthrough volume after a short experiment. Three aromatic compounds were use as analytes: phenol, hydroquinone and benzoquinone. These compounds can be found in water solutions after phenol oxidation process. The development of analytical procedures for phenol and its degradation products determination allow to describe phenol degradation pathway and degree.

4. Experimental

4.1. Chemicals

Methanol p.a., acetonitryle p.a. and dichloromethane were obtained from POCh (Gliwice, Poland). Phenol (99%), hydroquinone (99%), benzoquinone (98%) were obtained from Sigma–Aldrich, Chimie GmbH (Steinheim, Germany).

4.2. Sorbents

Nine divinylbenzene copolymers were used as SPE sorbents. There were five commercial sorbents:

- SDB-1 – styrene-divinylbenzene copolymer, J.T. Baker (Deventer, Holland, supplied by Witko, Łódź, Poland);
- Strata-X – styrene-divinylbenzene copolymer modified with butyrlactame, interaction: reversed phase;
- Strata-X-C – styrene-divinylbenzene copolymer modified with sulphonic groups, interaction: strong cation exchange and reversed phase;
- Strata-X-CW – styrene-divinylbenzene copolymer modified with carboxylic groups, interaction: weak cation exchange and reversed phase;
- Strata-X-AW – styrene-divinylbenzene copolymer modified with diamine, interaction: weak anion exchange and reversed phase.

All Strata-X sorbents were from Phenomenex® (USA, supplied by Shim-Pol "A.M. Borzymowski", Poland).

All commercial sorbents mass were of 200 mg weight. They were placed into polypropylene cartridges of 6 ml (SDB-1) and 3 ml volume.

Four non-standard polymeric sorbents were also examined:

- BM-DVB (sorbent mass: 193 mg);
- DMN-DVB (sorbent mass: 133 mg);
- MEDDE-DVB (sorbent mass: 191 mg);
- MEMDE-DVB (sorbent mass: 170 mg).

The non-standard polymeric materials were synthesized by the suspension copolymerization of 4,4′-bis(maleimido)diphenylmethane (BM) and divinylbenzene (DVB) and by combined suspension–emulsion copolymerization of divinylbenzene (DVB) with di(methacryloxymethyl)naphthalene (DMN), p,p′-dihydroxydiphenylmethane diglycidyl methacrylic ester (MEMDE), p,p′-dihydroxydiphenylpropane diglycidyl methacrylic ester (MEDDE). Synthesis of monomers (BM, DMN, MEMDE and MEDDE) and the extraction properties of divinylbenzene copolymers were described earlier in literature [39–41].

New synthesized polymeric resins were placed into 6 ml polypropylene cartridges, produced by J.T. Baker (Deventer, Holland, supplied by Witko, Łódź, Poland).

Physical characteristic of sorbents is given in Table 1.

4.3. SPE experiments

SPE experiment was carried out as follows: 25 ml of solution (concentration 0.08 mg/ml) was introduced into SPE sorbent conditioned with methanol (10 ml) and water (10 ml), then the sorbent was dried with air and then analytes were eluted using 5 ml of dichloromethane. Eluate was analyzed by GC–FID.

For each compound (phenol, hydroquinone and benzoquinone) frontal analysis was carried out as follows.

4 mg of analyte were diluted in 500 ml of ultra pure water (Maxima, Ultra Pure Water) then the solute was given to the sorbent in aliquots of 5 ml. From each aliquot the 1 ml sample of effluent was analyzed with HPLC. Breakthrough curves were determined as the relationship between concentration in the water sample after extraction and the total volume of water sample passed through the sorbent. For each sorbent/analyte system the retention parameters were determined from the appropriate curve.

Retention factor k (Eq. (15)) and retention volume V_R (Eq. (4)) were determined.

The plate number was determinated from breakthrough curve using following equation:

$$N = \frac{V_R(V_R - \sigma_V)}{\sigma_V^2} \tag{17}$$

Number of theoretical plates in calculating way was determined as follows:

Table 1
Physical characteristic of sorbents.

Sorbent	Sorbent mass (mg)	Surface area (m^2/g)	Pore diameter (Å)	Pore volume (cm^3/g)	Particle size (μm)
DMN-DVB	157.9	105.5	85	0.26	20–30
BM-DVB	187.2	35.0	155	0.12	30–50
MEDDE-DVB	193.7	21.5	–	0.33	20–40
MEMDE-DVB	186.3	68.3	–	0.36	20–30
SDB-1	200	299.0	90	0.77	43–123
Strata-X	200	800	85	1.2	30
Strata-X-C	200	800	85	1.2	30
Strata-X-CW	200	800	85	1.2	30
Strata-X-AW	200	800	85	1.2	30

First the mobile phase reduced velocity was calculated as:

$$\nu = \frac{ud_p}{D_M} \quad (18)$$

where d_p is the particle diameter and D_M is the diffusion coefficient in mobile phase.

The reduced plate height (h) was determined from the Knox equation [18,37,38]:

$$h = A\nu^{1/3} + \frac{B}{\nu} + C\nu \quad (19)$$

where A, B, C are the constants; for sorbents with particle size near 20 μm $A = 1$; $B = 2$; $C = 0.1$, and ν is the mobile phase reduced velocity.

The relation between plate height and reduced plate height is described as:

$$H = hd_p \quad (20)$$

Then the plate number was calculated from equation:

$$N = \frac{L}{H} \quad (21)$$

where L is the column length and H is the plate height.

Finally the breakthrough volume was calculated from Eqs. (1), (2) or (9) depending on plate number.

The breakthrough level (b) was determined as the fraction of total mass of analyte which has passed out of the column without adsorption, parameters a_0, a_1, a_2 were taken from literature [18]. The number of theoretical plates was calculated using Eq. (17) (for frontal analysis), and using equations given above. Retention parameters (k, V_R, V_M) were determined in frontal analysis and without experiment using Eqs. (15) and (4). The hold-up volume V_M value was determined using the value to multiply pore volume and sorbent mass. Recovery was determined as the ratio of mass of analyte introduced to the sorbent bed and mass of analyte indicated in the eluent, multiplied by 100%.

4.4. Chromatographic analysis

4.4.1. HPLC

Qualitative and quantitative analysis of effluent samples was carried out with the use of liquid chromatograph HPLC HP 1100. Conditions of HPLC experiment were as follows: Ultra Aqueous C18 5 μm column, 250 mm × 4.6 mm i.d. (Restek), acetonitrile as mobile phase at a flow rate of 1 ml/min; UV-DAD detector. The column was thermostated during analysis at 45 °C. For quantitative analysis the calibration curves were determined for each compound in the range from 0.0005 to 5 mg/ml.

4.4.2. GC

Gas chromatograph HP 5890II was used with capillary column RTX-1701 (Restek) 0.25 μm, 30 m × 0.32 mm, helium was used as carrier gas at flow rate 1.5 ml/min, and a head pressure of 150 kPa. Flame-ionization detector (FID) and split/splitless injector were used. Analyses were carried out in a programmed temperature: the column temperature was held at initial temperature of 60 °C for 2 min, then ramped at 10 °C/min to 125 °C, then at 70 °C/min to 250 °C where it was held for 5 min total analysis time was 15.30 min.

5. Results and discussion

Extraction process of phenol, hydroquinone and benzoquinone from water samples by means of SPE with the use of series of polymeric sorbents might be characterized by the parameters collected in Tables 2–4. Significant similarities were found when these data were analyzed. For all analytes better efficiency of SPE columns (cartridges) given by the number of theoretical plates corresponded to the highest breakthrough volume. Strata-X-AW sorbent was found to be the most efficient sorbent for phenol: the number of theoretical plates is higher than 100 and breakthrough volume is equal to 243.1 ml. The most efficient sorbent for hydroquinone is Strata-X where the number of theoretical plates is very high and equal to 188 and the breakthrough volume equal to 159.1 ml. Strata-X-CW was the most efficient sorbent for benzoquinone ($N = 31$ and $V_B = 121.6$ ml). The highest efficiency and the highest breakthrough volume corresponds to a large surface area of the sorbent. All sorbents from the Strata-X group have large surface areas (800 m^2/g), and these sorbents are efficient in the extraction of phenol, hydroquinone and benzoquinone. The information on sorption properties of the sorbent may be deduced from the maximum concentration of analyte in the effluent (C_E). High C_E values indicate weak sorption properties for given analyte and it results in

Table 2
Parameters determined for phenol on different sorbents in frontal analysis.

Sorbent	Breakthrough volume, V_B (ml)	Retention volume, V_R (ml)	Equilibrium volume, V_E (ml)	σ_V (ml)	σ_V^* (ml)	Number of theoretical plates, N
DMN-DVB	36.5 ± 1.8	82.7 ± 4.1	232.7 ± 11.6	23.1	75.0	9 ± 0.5
BM-DVB	1.6 ± 0.1	14.4 ± 0.7	90.0 ± 4.5	6.4	37.8	3 ± 0.2
MEDDE-DVB	1.6 ± 0.1	14.4 ± 0.7	90.0 ± 4.5	6.4	37.8	3 ± 0.2
MEMDE-DVB	9.1 ± 0.5	50.0 ± 2.5	195.4 ± 9.8	20.5	72.7	18 ± 0.9
SDB-1	>500	–	–	–	–	–
Strata-X	168.3 ± 8.4	229.1 ± 11.5	261.9 ± 13.1	30.4	16.4	50 ± 2.5
Strata-X-C	78.2 ± 3.9	234.0 ± 11.7	389.8 ± 19.5	77.9	77.9	6 ± 0.3
Strata-X-CW	89.5 ± 4.5	110.5 ± 5.5	194.7 ± 9.7	10.5	21.1	99 ± 5.0
Strata-X-AW	243.1 ± 12.2	263.9 ± 13.2	330.3 ± 16.5	10.4	33.2	–

Table 3
Parameters determined for hydroquinone on different sorbents in frontal analysis.

Sorbent	Breakthrough volume, V_B (ml)	Retention volume, V_R (ml)	Equilibrium volume, V_E (ml)	σ_V (ml)	σ_V^* (ml)	Number of theoretical plates, N
DMN-DVB	2.4 ± 0.1	28.0 ± 1.4	156.0 ± 7.8	12.8	64.0	3 ± 0.2
BM-DVB	4.0 ± 0.2	10.6 ± 0.5	117.2 ± 5.9	3.3	53.3	7 ± 0.4
MEDDE-DVB	2.6 ± 0.1	50.0 ± 2.5	128.9 ± 6.4	23.7	39.5	2 ± 0.1
MEMDE-DVB	19.6 ± 1.0	45.6 ± 2.3	89.1 ± 4.5	13.0	21.7	9 ± 0.5
SDB-1	50.1 ± 2.5	83.3 ± 4.2	140.4 ± 7.0	16.6	28.6	20 ± 1.0
Strata-X	159.1 ± 8.0	185.2 ± 9.3	216.5 ± 10.8	13.0	15.6	–
Strata-X-C	41.1 ± 2.1	58.8 ± 2.9	141.1 ± 7.1	8.8	41.2	37 ± 1.9
Strata-X-CW	42.1 ± 2.1	68.4 ± 3.4	121.0 ± 6.1	13.2	26.3	22 ± 1.1
Strata-X-AW	36.8 ± 1.8	73.7 ± 3.7	136.8 ± 6.8	18.4	31.6	12 ± 0.6

Table 4
Parameters determined for benzoquinone on different sorbents in frontal analysis.

Sorbent	Breakthrough volume, V_B (ml)	Retention volume, V_R (ml)	Equilibrium volume, V_E (ml)	σ_V (ml)	σ_V^* (ml)	Number of theoretical plates, N
DMN-DVB	16.1 ± 0.8	51.7 ± 2.6	258.7 ± 12.9	17.8	103.5	6 ± 0.3
BM-DVB	11.9 ± 0.6	19.7 ± 1.0	32.9 ± 1.6	3.9	6.6	20 ± 1.0
MEDDE-DVB	10.5 ± 0.5	18.4 ± 0.9	37.8 ± 1.9	3.9	9.7	17 ± 0.9
MEMDE-DVB	2.2 ± 0.1	19.6 ± 1.0	58.7 ± 2.9	8.7	19.6	3 ± 0.2
ST-DVB	35.2 ± 1.8	92.8 ± 4.6	230.9 ± 11.5	28.8	69.0	7 ± 0.4
Strata-X	75.0 ± 3.8	130.6 ± 6.5	183.3 ± 9.2	27.8	26.4	18 ± 0.9
Strata-X-C	52.7 ± 2.6	78.9 ± 3.9	152.5 ± 7.6	13.1	36.8	4 ± 0.2
Strata-X-CW	121.6 ± 6.1	181.3 ± 9.1	319.4 ± 16.0	29.9	98.9	31 ± 1.6
Strata-X-AW	80.3 ± 4.0	110.7 ± 5.5	158.6 ± 7.9	15.2	24.0	46 ± 2.3

low breakthrough volume. When C_E is low then sorption properties are better and the breakthrough volume is higher. These relationships are illustrated in Fig. 2 for phenol, in Fig. 3 for hydroquinone and in Fig. 4 for benzoquinone.

The plate number determined for some sorbents are too high (these values are impossible for SPE columns), it is connected with imprecise determination of retention volume (V_M) from the breakthrough curve.

The aim of this work was to find simple and fast method to approximate the breakthrough volume using only short experiment. V_B values might be calculated from Eq. (1) [18] and Eq. (2) [21,24,25]. The values of breakthrough volume given in Tables 5–7 were obtained using V_R and N calculated from linear velocity and reduced plate height, using Eqs. (20), (18) and (19). These values are compared with V_B determined in the frontal analysis (V_B exp.). For phenol and hydroquinone these values are determined for all sorbents and for hydroquinone the data are given only for three sorbents: Strata-X with very good extraction properties and MEMDE-DVB and MEDDE-DVB being rather weak sorbents.

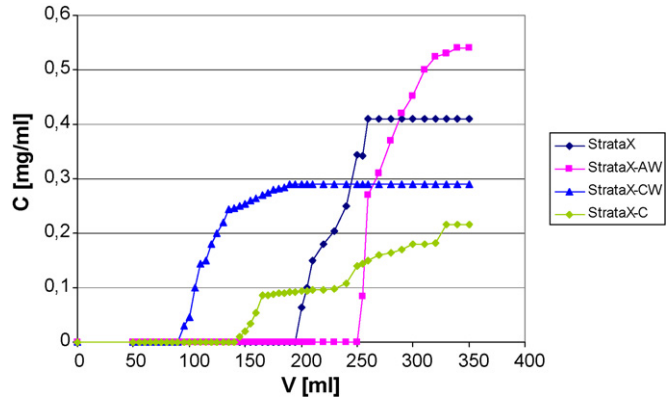


Fig. 2. Comparison of breakthrough curves determined for phenol on polymeric sorbents.

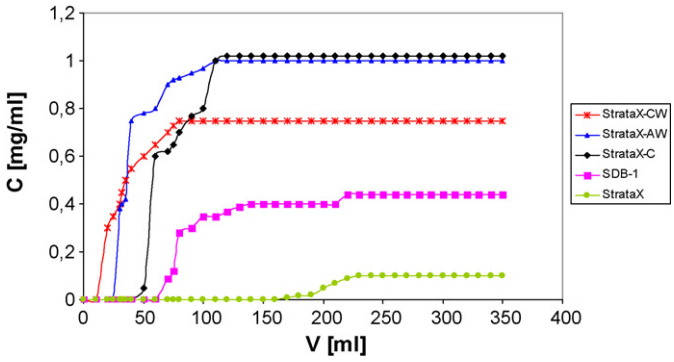


Fig. 3. Comparison of breakthrough curves determined for hydroquinone on polymeric sorbents.

Comparison of the breakthrough volume values determined using Eq. (1) or (2) with those found experimentally show that for all analytes V_B determined from Eq. (2) do not differ significantly from experimental data. The differences are much lower than those obtained when Lövkvist equation was applied. The existence of such large differences can be connected with the use of a_0, a_1, a_2 factors taken from literature. These factors depend only on breakthrough level (b), and they are the same for all sorbents. The determination of V_B by using equations proposed by Werkhoven-Goëwie is therefore easier and more precise and it was used in further calculations.

The breakthrough values determined using Eqs. (1) and (2) (or (9)) are similar to V_B values determined experimentally especially for sorbents from Strata-X group. However, differences between both the theoretical and experimental values of discussed parameters for other sorbents are higher. It can be connected with different values of V_R and N determined experimentally (from breakthrough curve) and determined theoretically using recovery and retention factor k.

When the absolute and relative errors are analyzed (Tables 5–7) it can be found that differences between the values of breakthrough volume determined in computational and experimental methods for some sorbents are in error range, e.g. for Strata-X-AW sorbent in phenol separation. The precision of computational method is determined with the precision of recovery determination.

The efficiency of SPE sorbents (expressed by N) determined for phenol, hydroquinone and benzoquinone to a large extent depends on their specific surface area. The large surface area of the sorbent is "accompanied" by high N values while small surface area corresponds to lower efficiency (N value). It means that the sorbent efficiency is not identical with its extraction properties given by recovery.

Comparison of two methods used for the determination of the breakthrough volume is presented in Fig. 5. It is clear that calculating way is shorter and more precise. The required experiment

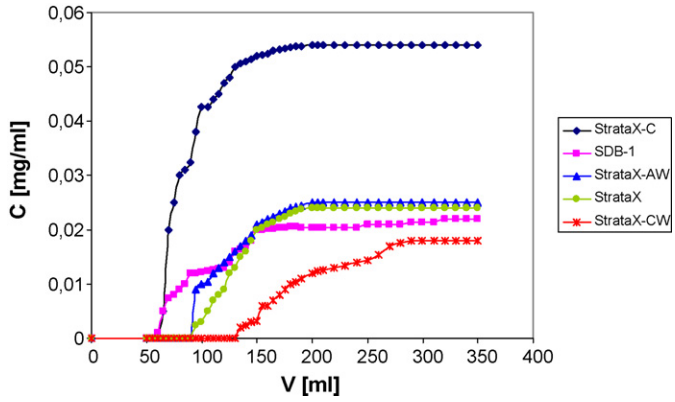


Fig. 4. Comparison of breakthrough curves determined for benzoquinone on polymeric sorbents.

Table 5
The value of recovery, breakthrough level retention volume calculated for phenol.

Sorbent	Recovery			Breakthrough level, b (%)	V_R (ml)	N	V_B Eq. (1)[a] (ml)	V_B Eq. (2)[a] (ml)	V_B exp.[b] (ml)
	%	σ	RSD (%)						
DMN-DVB	80.0	4.7	5.9	1	240.2 ± 12.0	9.7 ± 0.5	115.9 ± 5.8	88.3 ± 5.2	36.5 ± 1.8
BM-DVB	5.3	2.2	41.7	1	16.0 ± 0.8	3 ± 0.2	1.8 ± 0.1	–	1.6 ± 0.1
MEDDE-DVB	52.4	0.1	0.3	1	158.8 ± 7.9	7 ± 0.4	17.6 ± 0.9	38.8 ± 0.1	1.6 ± 0.1
MEMDE-DVB	47.5	7.6	15.9	1	142.6 ± 7.1	17 ± 0.9	35.3 ± 1.8	38.8 ± 6.1	9.1 ± 0.5
SDB-1	52.6	4.4	8.4	0.5	263.3 ± 13.2	4.2 ± 0.2	168.6 ± 8.4	6.3 ± 0.5	–
Strata-X	81.5	4.4	5.4	1	285.6 ± 14.3	38.9 ± 1.9	226.2 ± 11.3	148.4 ± 8.1	168.3 ± 8.4
Strata-X-C	50.4	1.5	6.0	1	176.7 ± 8.8	21.8 ± 1.1	117.7 ± 5.9	63.7 ± 1.9	78.2 ± 3.9
Strata-X-CW	59.5	5.1	8.5	1	208.4 ± 10.4	21.8 ± 1.1	138.9 ± 7.0	75.1 ± 6.4	89.5 ± 4.5
Strata-X-AW	98.8	11.4	11.5	0.5	345.9 ± 17.3	21.8 ± 1.1	230.5 ± 11.5	197.7 ± 22.7	243.1 ± 12.2

[a] V_B Eq. (1), V_B Eq. (2) – breakthrough volume calculated with Eqs. (1) and (2) or (9) using values of V_R and N determined theoretically.
[b] V_B exp. – breakthrough volume determined experimentally in frontal analysis.

Table 6
The value of recovery, breakthrough level and retention volume calculated for benzoquinone.

Sorbent	Recovery			Breakthrough level, b (%)	V_R (ml)	N	V_B Eq. (1)[a] (ml)	V_B Eq. (2)[a] (ml)	V_B exp.[b] (ml)
	%	σ	RSD (%)						
DMN-DVB	85.8	3.4	4.0	1	257.3 ± 12.9	9.4 ± 0.5	124.1 ± 6.2	13.2 ± 0.5	16.1 ± 0.8
BM-DVB	80.9	4.8	5.9	1	242.6 ± 12.1	3 ± 0.2	59.0 ± 3.0	–	11.9 ± 0.6
MEDDE-DVB	57.0	3.9	6.9	1	96.6 ± 4.8	6.8 ± 0.3	39.0 ± 2.0	23.6 ± 1.6	10.5 ± 0.5
MEMDE-DVB	47.3	2.6	5.5	1	93.5 ± 4.7	16.5 ± 0.8	10.4 ± 0.5	25.5 ± 1.4	2.2 ± 0.1
SDB-1	99.7	4.8	5.6	1	299.3 ± 15.0	4.1 ± 0.2	87.6 ± 4.4	3.7 ± 0.2	35.2 ± 1.8
Strata-X	99.7	3.4	3.4	1	349.2 ± 17.5	37.9 ± 1.9	274.7 ± 13.7	235.8 ± 8.0	75.0 ± 3.8
Strata-X-C	92.5	4.3	4.6	1	324.1 ± 16.2	21.2 ± 1.1	265.9 ± 13.3	111.9 ± 5.2	52.7 ± 2.6
Strata-X-CW	100.5	7.2	7.2	0.5	327.5 ± 16.4	21.2 ± 1.1	214.7 ± 10.7	113.1 ± 8.1	121.6 ± 6.1
Strata-X-AW	100.1	6.4	6.4	1	329.6 ± 16.5	21.2 ± 1.1	216.1 ± 10.8	113.8 ± 7.3	80.3 ± 4.0

[a] V_B Eq. (1), V_B Eq. (2) – breakthrough volume calculated with Eqs. (1) and (2) or (9) using values of V_R and N determined theoretically.
[b] V_B exp. – breakthrough volume determined experimentally in frontal analysis.

Table 7
The value of recovery, breakthrough level and retention volume calculated for hydroquinone.

Sorbent	Recovery			Breakthrough level, b (%)	V_R (ml)	N	V_B Eq. (1)[a] (ml)	V_B Eq. (2)[a] (ml)	V_B exp.[b] (ml)
	%	σ	RSD (%)						
MEDDE-DVB	90.3	9.1	10.1	1	270.8 ± 13.5	6.6 ± 0.3	30.0 ± 1.5	66.1 ± 3.3	2.6 ± 0.1
MEMDE-DVB	84.6	12.6	14.9	1	254.0 ± 12.7	17.5 ± 0.9	154.0 ± 7.7	69.2 ± 3.5	19.6 ± 1.0
Strata-X	94.4	6.3	6.7	0.5	330.4 ± 16.5	40.0 ± 2.0	294.9 ± 14.7	171.7 ± 8.6	159.1 ± 8.0

[a] V_B Eq. (1), V_B Eq. (2) – breakthrough volume calculated with Eqs. (1) and (2) or (9) using values of V_R and N determined theoretically.
[b] V_B exp. – breakthrough volume determined experimentally in frontal analysis.

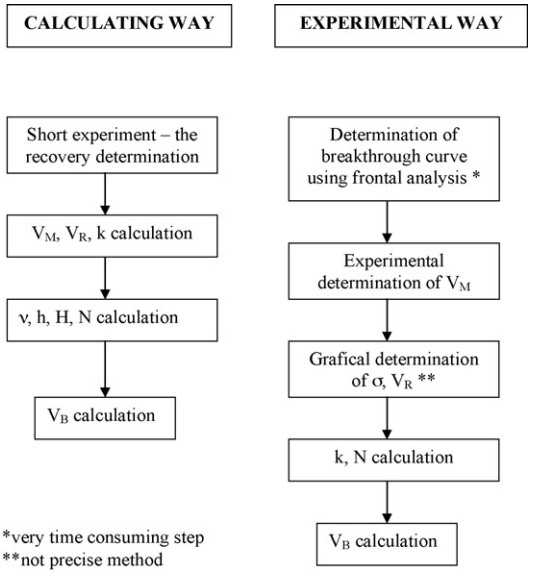


Fig. 5. Two ways of breakthrough volume determination.

is limited by the recovery determination only, the other steps are computational. In experimental way the first step is very time consuming as breakthrough curve determination in frontal chromatography is rather long. Some parameters must be determined graphically from breakthrough curve, and it can cause relatively large error.

Both methods – experimental and calculating – gave satisfactory results during the estimation of breakthrough volume and the efficiency of SPE sorbents but calculating way is somewhat quicker and more precise.

6. Conclusion

The method proposed in this work allows to determine the breakthrough volume with short experiments. The compared experimentally and computationally achieved values are close. It shows that these two ways of determining the breakthrough volume of SPE sorbents are equivalent. The computational way is more suitable as it is non-time consuming and easy. The method allows to estimate the sorbents' properties in a sufficient way.

Computational methods seem to be useful. However, one should take into account other, e.g. kinetic factors, influencing the SPE

process. The success of calculating procedure depends on the precise and reproducibility determination of recovery.

Acknowledgement

This work was supported from DS 32/045/2009 PUT grant.

References

[1] I. Rodriguez, M.P. Llompart, R. Cela, J. Chromatogr. A 885 (2000) 291.
[2] M.E. Leon-Gonzalez, L.V. Perez-Arribas, J. Chromatogr. A 902 (2000) 3.
[3] N. Fontanalas, R.M. Marcé, M. Galià, F. Borrull, J. Polym. Sci. Part A: Polym. Chem. 41 (2003) 1927.
[4] N. Fontanalas, M. Galiá, R.M. Marcé, F. Borrull, J. Chromatogr. A 1030 (2004) 63.
[5] M. Hrubý, J. Hradil, M.J. Beneš, React. Funct. Polym. 59 (2004) 105.
[6] S. Le Moullec, L. Truong, C. Montauban, A. Begos, V. Pichon, B. Bellier, J. Chromatogr. A 1139 (2007) 171.
[7] B. Filiz Senkal, M. Ince, E. Yavuz, M. Yaman, Talanta 72 (2007) 962.
[8] S. Guenu, M.-C. Hennion, J. Chromatogr. A 737 (1996) 14.
[9] G. Zgórka, J. Chromatogr. A 1120 (2006) 230.
[10] J. Poerschmann, F.-D. Kopinke, Environ. Sci. Technol. 35 (6) (2001) 1142.
[11] F.-D. Kopinke, J. Poerschmann, U. Stottmeister, Environ. Sci. Technol. 29 (1995) 941.
[12] P. López, R. Batlle, C. Nerín, J. Cacho, V. Ferreira, J. Chromatogr. A 1139 (2007) 36.
[13] L. Ortega, R. López, J. Cacho, V. Ferreira, J. Chromatogr. A 931 (2001) 31.
[14] M.-C. Hennion, J. Chromatogr. A 856 (1999) 3–54.
[15] R. Ferrer, J.L. Beltran, J. Guiteras, Anal. Chim. Acta 346 (1997) 253.
[16] L.E. Vera-Avila, J.L. Gallegos-Perez, E. Camacho-Frias, Talanta 50 (1999) 509.
[17] E.M. Thurman, M.S. Mills, Solid-Phase Extraction. Principles and Practice, A Wiley–Interscience Publication, New York, 1998.
[18] P. Lövkvist, J.Å. Jönsson, Anal. Chem. 59 (1987) 818.
[19] C.F. Poole, A.D. Gunatilleka, R. Sethuraman, J. Chromatogr. A 885 (2000) 17.
[20] C.F. Poole, Trends Anal. Chem. 22 (2003) 362.
[21] M.L. Larrivee, C.F. Poole, Anal. Chem. 66 (1994) 139.
[22] C.F. Poole, S.K. Poole, D.S. Seibert, C.M. Chapman, J. Chromatogr. B 689 (1997) 245.
[23] K.G. Miller, C.F. Poole, J. High Resol. Chromatogr. 17 (1994) 125.
[24] W. Peter, N. Fernando, M.L. Larrivee, C.F. Poole, Anal. Chem. 65 (1993) 588.
[25] C.E. Werkhoven-Goëwie, U.A.Th. Brinkman, R.W. Frei, Anal. Chem. 53 (1981) 2072.
[26] M.-C. Hennion, V. Pichon, Environ. Sci. Technol. 28 (1994) 576A.
[27] A. Gelencsér, G. Kiss, Z. Krivácsy, Z. Varga-Puchony, J. Chromatogr. A 693 (1995) 217.
[28] A. Gelencsér, G. Kiss, Z. Krivácsy, Z. Varga-Puchony, J. Hlavay, J. Chromatogr. A 693 (1995) 227.
[29] S.K. Poole, C.F. Poole, Analyst 120 (1995) 1733.
[30] P.J. Dumont, J.S. Fritz, J. Chromatogr. A 691 (1995) 123.
[31] M.L. Mayer, S.K. Poole, C.F. Poole, J. Chromatogr. A 697 (1995) 89.
[32] M.S. Dopico-García, J.M. López-Vilariño, M.V. González-Rodríguez, Talanta 66 (2005) 1103.
[33] D. Puig, D. Barcelo, J. Chromatogr. A 733 (1996) 371.
[34] A. Kroupa, J. Dewulf, H. Van Langehove, I. Víden, J. Chromatogr. A 1038 (2004) 215.
[35] http://www.sisweb.com/index/referenc/resin10.htm.
[36] V. Ferreira, I. Jarauta, L. Ortega, J. Cacho, J. Chromatogr. A 1025 (2004) 147.
[37] J.H. Knox, J. Chromatogr. A 831 (1999) 3.
[38] J.H. Knox, J. Chromatogr. A 960 (2002) 7.
[39] K. Bielicka-Daszkiewicz, A. Voelkel, M. Szejner, J. Osypiuk, Chemosphere 62 (2006) 890.
[40] B. Gawdzik, T. Matynia, J. Osypiuk, Chromatographia 47 (1998) 509.
[41] B. Gawdzik, J. Osypiuk, J. Chromatogr. A 898 (2000) 13.

Talanta 80 (2009) 622–630

Contents lists available at ScienceDirect

Talanta

journal homepage: www.elsevier.com/locate/talanta

Potentialities of two solventless extraction approaches—Stir bar sorptive extraction and headspace solid-phase microextraction for determination of higher alcohol acetates, isoamyl esters and ethyl esters in wines

R. Perestrelo[a,b], J.M.F. Nogueira[b,c], J.S. Câmara[a,*]

[a] Centro de Química da Madeira, Universidade da Madeira, Departamento de Química, Campus Universitário da Penteada, 9000-390 Funchal, Portugal
[b] Universidade de Lisboa, Faculdade de Ciências, Departamento de Química e Bioquímica, Campo Grande Ed. C8, 1749-016 Lisboa, Portugal
[c] Universidade de Lisboa, Faculdade de Ciências, Centro de Química e Bioquímica, Campo Grande Ed. C8, 1749-016 Lisboa, Portugal

ARTICLE INFO

Article history:
Received 14 April 2009
Received in revised form 15 July 2009
Accepted 20 July 2009
Available online 28 July 2009

Keywords:
Solid-phase microextraction
Stir bar sorptive extraction
Higher alcohol acetates
Isoamyl esters
Ethyl esters
Wine
Gas chromatography–quadrupole mass spectrometry

ABSTRACT

A stir bar sorptive extraction with liquid desorption followed by large volume injection coupled to gas chromatography–quadrupole mass spectrometry (SBSE-LD/LVI-GC–qMS) was evaluated for the simultaneous determination of higher alcohol acetates (HAA), isoamyl esters (IsoE) and ethyl esters (EE) of fatty acids. The method performance was assessed and compared with other solventless technique, the solid-phase microextraction (SPME) in headspace mode (HS). For both techniques, influential experimental parameters were optimised to provide sensitive and robust methods. The SBSE-LD/LVI methodology was previously optimised in terms of extraction time, influence of ethanol in the matrix, liquid desorption (LD) conditions and instrumental settings. Higher extraction efficiency was obtained using 60 min of extraction time, 10% ethanol content, *n*-pentane as desorption solvent, 15 min for the back-extraction period, 10 mL min^{-1} for the solvent vent flow rate and 10 °C for the inlet temperature. For HS-SPME, the fibre coated with 50/30 μm divinylbenzene/carboxen/polydimethylsiloxane (DVB/CAR/PDMS) afforded highest extraction efficiency, providing the best sensitivity for the target volatiles, particularly when the samples were extracted at 25 °C for 60 min under continuous stirring in the presence of sodium chloride (10% (w/v)). Both methodologies showed good linearity over the concentration range tested, with correlation coefficients higher than 0.984 for HS-SPME and 0.982 for SBES-LD approach, for all analytes. A good reproducibility was attained and low detection limits were achieved using both SBSE-LD (0.03–28.96 μg L^{-1}) and HS-SPME (0.02–20.29 μg L^{-1}) methodologies. The quantification limits for SBSE-LD approach ranging from 0.11 to 96.56 μg $L^{-}$and from 0.06 to 67.63 μg L^{-1} for HS-SPME. Using the HS-SPME approach an average recovery of about 70% was obtained whilst by using SBSE-LD obtained average recovery were close to 80%. The analytical and procedural advantages and disadvantages of these two methods have been compared.

Both analytical methods were used to determine the HAA, IsoE and EE fatty acids content in "Terras Madeirenses" table wines. A total of 16 esters were identified and quantified from the wine extracts by HS-SPME whereas by SBSE-LD technique were found 25 esters which include 2 higher alcohol acetates, 4 isoamyl esters and 19 ethyl esters of fatty acids. Generally SBSE-LD provided higher sensitivity with decreased analysis time.

© 2009 Elsevier B.V. All rights reserved.

1. Introduction

Aroma compounds are important in wine as they contribute to the quality of the final product, hence to the consumer acceptance [1]. The wine volatile fraction can be composed by over 800 different compounds [1,2], but only several tens of which can be odour active [3] and must be considered for differentiation purposes. These compounds belong to different chemical families, including *higher alcohols*, *ethyl esters*, *fatty acids*, *acetates*, *isoamyl esters*, *carbonyls*, *sulphurs*, *furanics*, *monoterpenols*, C_{13}-*norisoprenoids* and *volatile phenols*, presenting different polarities, volatilities and moreover, are found in a wide range of concentrations from ng L^{-1} to mg L^{-1} [4,5]. They proceed from four major sources, like (i) grapes; (ii) processing of the grapes (namely crushing, pressing, *etc.*) by chemical, enzymatic-chemical and thermal reaction in grape must; (iii) fermentation process, and (iv) chemical reactions during maturation of wine (wood, commonly oak). An important part of wine aroma arises during the alcoholic fermentation of grape sugars by the wine yeast, which produces ethanol, carbon dioxide and a number of by-products including

* Corresponding author. Tel.: +351 291705112; fax: +351 291705149.
E-mail address: jsc@uma.pt (J.S. Câmara).

0039-9140/$ – see front matter © 2009 Elsevier B.V. All rights reserved.
doi:10.1016/j.talanta.2009.07.038

higher alcohols and esters [6], whose formation is closely related to the particular yeast species involved. Acetates, such as ethyl acetate, hexyl acetate, isoamyl acetate and 2-phenylethyl acetate are recognised as very important flavour compounds in wine and other grape-derived alcoholic beverages. In general, these volatile compounds have a pleasant odour and a low perception threshold, which allows the assumption that they contributed to the wine aroma even present in small concentrations. The main esters in commercial wines used to be ethyl and 3-methylbuthyl esters of short-chain fatty acids [7].

The analysis of volatile and semi-volatile organic compounds that contribute to wine aroma has been carried out following different methodologies, such as liquid–liquid extraction [4,8,9], purge and cold trapping extraction [10], simultaneous distillation–extraction [11], supercritical fluid extraction [12], solid-phase extraction [13] and ultrasound extraction [14]. However, most of these approaches present several disadvantages, including expensive equipment requirements, significant amounts of environmentally unfriendly solvents, multiple handling steps that increase error, and the need for a concentration step to achieve detectable levels. Nowadays, there are available solventless alternatives to these classical methodologies, which may overcome all those disadvantages such as the well-known solid-phase microextraction (SPME), developed by Pawliszyn et al. [15,16] and more recently, stir bar sorptive extraction (SBSE) proposed by Baltussen et al. [17]. The latter methodology uses the Twister™, a glass stir bar onto which is bonded a polydimethylsiloxane (PDMS) phase, in quantities far in excess of those found on SPME fibres [18]. The SBSE extraction takes place when the aqueous sample begins to be stirred by the bar during a period of time until the volatile or semi-volatile compounds reach the equilibrium and after enrichment, are thermally desorbed (TD) followed by gas chromatography analysis usually coupled to mass spectrometry (GC–MS) [19–21]. These sorptive extraction approaches showed great advantages when compared with other conventional enrichment methodologies, since eliminate the use of toxic organic solvents, allow the determination of a large number of analytes with low limits of detection and good linear dynamic ranges, combine extraction, concentration and instrumental analysis into a single step, require no or little manipulation/sample preparation, reduce substantially the analysis time, are simple and faster methods, cover a wide range of sampling techniques, including field, *in situ* and air matrices and can be performed by immersing the polymeric coatings into sample medium or in the headspace (HS). In general, the accepted disadvantages are relatively lot-to-lot variations, sensitivity against organic solvents and the limited range of commercially available specific stationary phases [22,23].

In the last years, SBSE have becoming more accepted since present remarkable sensitivity and accuracy than SPME in particular, during trace analysis of complex matrices such as wine samples [18,24,25]. For instance, it was already demonstrated that SBSE-TD is an analytical technique much more powerful than HS-SPME, which allowed higher ability for profiling trace and ultra-trace compounds for Madeira wine characterisation [18]. Nevertheless, the TD systems are expensive devices and many times, are not the best option to analyse particular thermolabile constituents, due to the very high desorption temperature requirements with possible occurrence of artefacts. Moreover, the TD mode does not offer the opportunity of multiple injections, which is an important issue in many studies during validation purposes. More recently, we proved that SBSE-LD is a remarkable alternative presenting interesting features to overcome these limitations [20,21,26]. In this approach, the analytes are trapped followed by removal through back-extraction with a small volume (typically microliters) of a convenient organic solvent prior to GC–MS analysis. Furthermore, if we combine large volume injection (LVI) to enhance sensitivity with suitable desorption solvents under optimised conditions [19], volatile compounds can be easily analysed in wine matrices, as was reported lately [27]. Although HS-SPME [28,29] and SBSE-LD methodologies can be easily applied in any laboratory since they do not need special instrumental requirements, both procedures were never compared in terms of analytical advantages, selectivity and sensitivity.

The purpose of the present work is to compare the performance of two solventless sorptive extraction approaches: HS-SPME/GC–MS versus SBSE-LD/LVI-GC–MS, for the determination of volatile compounds in wines, using HAA, IsoAE and EE as model compounds. The optimisation, validation and application of both methodologies, as well as the advantages observed are fully discussed using commercial wines from different grape varieties produced in Madeira Island.

2. Experimental

2.1. Reagents and standards

Methanol (MeOH), acetonitrile (ACN) and acetone purchased from Fluka (Buchs, Switzerland) were of HPLC grade. 2-Phenylethyl acetate, ethanol, diethyl ether and *n*-pentane were supplied from Riedel-de Haën (Barcelona, Spain). Isoamyl acetate, 2-propanol, ethyl hexanoate, octanoate and ethyl salicylate and clear glass vials were purchased from Sigma-Aldrich Química S.A. (Madrid, Spain). Ethyl decanoate, dodecanoate, cinnamate, benzoate, lactate, 2-furoate and ethyl butyrate were supplied from Acros (Geel, Belgium). Isoamyl hexanoate and isoamyl octanoate were obtained from SAFC (Steinheim, Germany). Pure water was obtained from a Milli-Q purification system (Millipore, Bedfords, MA, USA). Sodium hydroxide (NaOH, 98%) and sodium chloride (NaCl, 98.5%) were purchased from Panreac (Barcelone, Spain). The SPME fibres, the manual SPME holder and the PTFE coated-silicone caps, were purchased from Supelco (Bellefonte, PA, USA). The glass vials (30 ml) were obtained from Macherey-Nagel, (Düren, Germany). The manual crimper was obtained from Agilent Technologies (Little Falls, DE, USA) and the Variomag Multipoint komet agitation plate from Thermo Fisher Scientific Inc. (Waltham, MA, USA). The stir bars (Twister; Gerstel, Müllheim a/d Ruhr; Germany) containing PDMS (0.5 mm film thickness, 10 mm in length) with a volume of 24 μL were used. Ultrasonic equipment, Branson 3510, was purchased from Branson Ultrasonic Corporation (Danbury, CT, USA).

Individual stock standard solutions of each target compound were prepared by weight in ethanol. A global stock standard solution, containing all the analytes under study, was prepared in a synthetic wine matrix (120 ml L^{-1} of ethanol, 5 g L^{-1} of tartaric acid and pH 3.3 adjusted with NaOH). Working solutions were prepared by diluting different amounts of the global standard solution in a synthetic wine. All solutions were stored at 4 °C. For calibration purposes five different levels of concentration, covered the concentration ranges expected in wines, were prepared. Three replicates of each level were analysed. The average and the relative standard deviation (R.S.D.) were calculated.

2.2. Wine samples

All varieties used were *Vitis vinifera* L. species. The most important and most representative commercial "Terras Madeirenses" wines from Madeira Island (Portugal), produced according to standard procedures, were selected. The grapes were crushed, de-stemmed, racked and pressed. The musts were fermented in stainless-steel containers at 22 °C with spontaneous yeast. The white wines, Enxurros (ENX) and Palmeira (PAL) of 2005 vintage and Quinta do Moledo Reserva (QMR) of 2004 vintage, were produced using Verdelho & Arnsburguer, Verdelho & Bual & Arns-

Table 1
Calibration and sensitivity data of the 14 examined compounds obtained with HS-SPME and SBSE-LD methodologies.

Ion (*m*/*z*)	Kovats index	Volatile compounds	Concentration range ($\mu g\,L^{-1}$)		R^2		Slope ($\mu g\,L^{-1}$)		Intercept ($\mu g\,L^{-1}$)	
			SPME	SBSE	SPME	SBSE	SPME	SBSE	SPME	SBSE
Higher alcohol acetates										
43	1008	Hexyl acetate	34.84–696.80	5.81–929.07	0.995	0.999	3.24×10^{6}	7.15×10^{7}	-1.25×10^{5}	6.37×10^{5}
104	1238	2-Phenylethyl acetate	2.00–120.00	1.37–549.33	0.997	0.993	1.18×10^{7}	1.81×10^{7}	-4.60×10^{4}	-5.86×10^{5}
Isoamyl esters										
43	925	Isomayl acetate	120.00–4800.00	40.00–2666.67	0.996	0.997	3.15×10^{6}	1.88×10^{7}	-6.14×10^{5}	1.15×10^{6}
70	1233	Isoamyl hexanoate	1.00–40.00	0.67–20.00	0.985	0.998	6.88×10^{8}	1.81×10^{8}	-2.21×10^{6}	-2.58×10^{5}
70	1431	Isoamyl octanoate	1.00–40.00	0.67–20.00	0.998	0.992	2.18×10^{9}	1.38×10^{8}	-3.04×10^{6}	5.61×10^{4}
Ethyl esters										
71	778	Ethyl butanoate	40.00–1600.00	–	0.984	–	8.33×10^{5}	–	5.50×10^{3}	–
88	1006	Ethyl hexanoate	20.00–1200.00	0.66–666.67	0.998	0.997	1.36×10^{7}	1.65×10^{7}	-4.70×10^{5}	9.67×10^{4}
95	1038	Ethyl 2-furoate	222.88–4457.60	37.23–1489.33	0.995	0.998	7.15×10^{6}	3.92×10^{6}	-2.61×10^{6}	-1.90×10^{5}
105	1091	Ethyl benzoate	40.00–2000.00	26.67–2666.67	0.993	0.995	6.03×10^{6}	4.59×10^{7}	-5.25×10^{5}	-7.84×10^{5}
88	1205	Ethyl octanoate	20.00–2400.00	0.67–1178.33	0.998	0.997	1.04×10^{8}	1.12×10^{8}	-3.58×10^{4}	8.90×10^{5}
120	1240	Ethyl salicylate	20.00–600.00	153.19–1477.14	0.990	0.982	7.93×10^{7}	4.02×10^{7}	-2.00×10^{6}	3.43×10^{6}
88	1410	Ethyl decanoate	20.00–800.00	0.67–666.67	0.991	0.997	9.30×10^{7}	2.94×10^{8}	2.24×10^{6}	-2.74×10^{6}
131	1441	Ethyl cinnamate	200.00–2400.00	0.67–666.67	0.990	0.989	7.58×10^{6}	1.14×10^{8}	8.39×10^{4}	-3.56×10^{6}
88	1607	Ethyl dodecanoate	9.00–300.00	0.81–80.06	0.995	0.994	1.49×10^{8}	1.72×10^{8}	-1.30×10^{6}	2.13×10^{5}

R^2: determination coefficient; (–) not determined by SBSE (solvent delay higher than its retention time).

burguer and Verdelho grapes, respectively. Therefore, Verdelho grapes were the main composition of white wines studied. The Colombo (COL) red wine of 2004 vintage was produced using Tinta Negra Mole grape variety. The grapes were harvested at optimum maturity evaluated by indices of sugar and acid content. All samples were taken from bottled wines (750 ml) and stored at −28 °C until analysis. In all cases, analysis was performed in triplicate and the values were averaged. For the optimisation of HS-SPME extraction methods, Enxurros (ENX) young white wine from 2005 harvest was used.

2.3. Extraction procedure

2.3.1. SPME assays

Six different coating fibres: 75 μm carboxen-poly(dimethylsiloxane) (CAR/PDMS), 65 μm carbowax-divinylbenzene (CW/DVB), 50/30 μm divinylbenzene-carboxen-poly(dimethylsiloxane) (DVB/CAR/PDMS), 100 μm poly(dimethylsiloxane) (PDMS), 85 μm polyacrylate (PA) and 65 μm poly(dimethylsiloxane)-divinylbenzene (PDMS/DVB) were assessed to evaluate their performance for the study of HAA, IsoAE and EE in wines. The fibres were conditioned following the manufacturer instructions by inserting them into the GC injector port. Before the first daily analysis the fibres were conditioned for 6 min at 240 °C in the GC injector. A blank test was performed to check possible carry-over. Besides the fibre type, some other SPME parameters that influence the extraction process were optimised, namely extraction time (5, 15, 30, 60 and 75 min), temperature (25, 30, 40 and 60 °C), ionic strength (0, 10, 20 and 30% NaCl (w/v)) and matrix effects (12, 15, 17 and 19% (v/v) of ethanol). For each HS-SPME assay, aliquots of 10 mL of wines were placed into a 20 mL clear glass vial, to which 10% (w/v) of NaCl was added, and hermetically sealed with a PTFE coated-silicone cap, after addition of a small stirring bar. The extractions were carried out at wine pH (3.3). The vial was placed in a thermostat block on a stirrer. The SPME fibre was inserted into the HS at the sampling time during the sampling extraction time. All solutions were stirred at constant speed (800 rpm). After sampling, the fibre was retracted, removed from the sample vial and manually introduced into the GC injection port. Each assay was performed in triplicate.

2.3.2. SBSE assays

Each wine sample was introduced into a glass vial (30 mL); a stir bar with PDMS coating film (0.5 mm thick; 10 mm long, 24 μL) was immersed, and the vial was closed with a seal (aluminium seals with PTFE septa) using a manual crimper. Assays were performed in a 15th agitation point plate at room temperature (25 °C), using an extraction time of 60 min and a rotation speed of 800 rpm. For back-extraction purposes, the stir bars were placed into 250 μL glass flat-bottom inserts filled with 200 μL of *n*-pentane inside a glass vial. The back-extraction was performed by using ultrasonic treatment and desorption time of 15 min at constant temperature (25 °C). After back-extraction, the stir bars were removed by means of a magnetic rod and the vials were closed with seals, using a manual crimper, and placed into the automatic liquid sample (ALS) tray for LVI-GC–MS analysis. After each extraction, the stir bars were cleaned to dryness under a stream of purified nitrogen followed by a cleaning with ACN. All the experiments were performed in triplicate.

2.4. GC–MS analysis

After sampling the SPME fibre containing the volatile compounds were introduced into the GC injection port at 260 °C and kept for 6 min for thermal desorption. Desorbed volatile compounds were separated in an Agilent Technologies 6890 gas chromatograph equipped with a 30 m × 0.25 mm (i.d.) × 0.25 μm film thickness TRB-5MS fused silica capillary column (95% dimethyl, 5% diphenylpolysiloxane; Teknokroma, Spain), connected to an Agilent 5973N quadrupole mass selective detector (Agilent 7683, Agilent Technologies, Little Falls, DE, USA). The carrier gas used was helium N60 (Air Liquid, Portugal) at 3.5 mL min^{-1} with a column-head pressure of 21 psi and splitless injections were used (6 min). The GC oven temperature was programmed as follows: initial oven temperature 40 °C, then increased in two steps: 40–175 °C at 2 °C min^{-1} and 175–220 °C at 10 °C min^{-1} (5 min) in a 77 min running time. The quadrupole operating in electronic ionisation (70 eV) and the acquisition was made in full scan mode (35–550 *m*/*z*) using the selected ions illustrated in Table 1. The quadrupole detector was set as follows: transfer line temperature 280 °C; ion source temperature 230 °C and quadrupole analyzer temperature 150 °C. The analysis from the SBSE-LD assays were performed using the GC–MS conditions as above with the exception of the inlet port for which an Agilent 7683 ALS and a programme temperature vapourizing (PTV) injector having a baffled liner and a septumless head (SLH; Gerstel, Mülheim a/d Ruhr, Germany) were used. LVI using the solvent vent mode and liquid nitro-

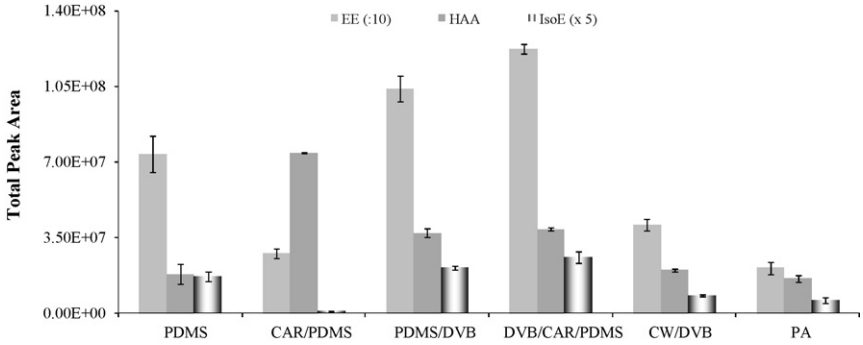


Fig. 1. Influence of the polymeric fibre coating on the HS-SPME yields of higher alcohol acetates (HAA), isoamyl esters (IsoE) and ethyl esters (EE) in wines (other extraction conditions: 60 min and 25 °C).

gen as inlet cooling was operating according to previous work [19]. The solvent vent injection mode was performed (vent time: 0.30 min; flows: 10 mL min^{-1}; pressure: 0 psi; purge: 60 mL min^{-1} at 2 min), for which the inlet temperature was ramped from 10 °C (0.35 min) to 300 °C at a rate of 600 °C min^{-1} and subsequently decreased to 200 °C (held until end) at a rate of 50 °C min^{-1}. The injection volume and speed were 20 μL and 100 mL min^{-1}, respectively.

The mass spectra data were compared with the Wiley library reference spectral bank (G1035B; Rev D.02.00; Agilent Technologies, USA) and confirmed with the retention indices (RI) of standards when they were available. Data recording and instrument control were performed by the MSD ChemStation software (G1701CA; version C.00.00; Agilent Technologies, USA). For the determination of the retention indices (RI) a C8–C20 *n*-alkanes series was used.

2.5. Method validation

Calibration plots constructed using suitable dilution of the global solutions were obtained by the least-square linear regressions of ratio of the peak area of each compound versus the added amount of the targets.

The proposed analytical methods were evaluated in relation to linearity, repeatability (precision, expressed as relative standard deviation (R.S.D.)), evaluation of the recovery of known quantities of substance (accuracy) and detection and quantification limits. The detection (LOD) and quantification (LOQ) limits were calculated as the concentration of the analyte that produce a signal-to-noise ratio of 3 and 10 times, that is $3S_{y/x}/b$ and $10S_{y/x}/b$, respectively, where $S_{y/x}/b$ is the blank standard deviation and b is the slope of the regression plot. The linear range experiments provide the essential information to determine the detections and quantifications limits, from lowest concentration point on the linear calibration curve. For recovery studies, ENX wine was spiked with target volatiles and six replicates of the original and spiked wines were assayed (HS-SPME and SBSE-LD) and analysed by GC–MS. The area increments between spiked and original wines were interpolated in the calibration graphs and the experimental concentration calculated. The recovery was determined according to the following relation:

$$\text{Recovery } (\%) = \frac{C_1 - C_0}{C_2} \times 100$$

where C_0 is the concentration in the ENX wine, C_1 is the concentration found in spiked wine and C_2 is the concentration added. The repeatability of the method was calculated by six consecutive extractions of the spiked synthetic wines. For each assay the average values and R.S.D. were determined.

3. Results and discussion

To compare the performance of both HS-SPME and SBSE-LD analytical methodologies, 15 volatile components were selected as model compounds, *i.e.* 3 HAA, 2 IsoE and 10 EE in order to optimise the experimental conditions.

3.1. HS-SPME optimisation

In the beginning we investigated for the best fibre coating for HS-SPME, followed by optimisation of the extraction time and temperature, ionic strength and matrix effects, using a constant magnetic stirring (800 rpm). Six types of SPME fibres, differing in the polarity and thickness of the stationary phase, were tested in order to compare their extraction yields towards higher alcohol acetates and esters. The data presented in Fig. 1 showed that the DVB/CAR/PDMS fibre performed the best extraction efficiency for all EE and IsoE. The CAR/PDMS fibre achieved almost two times higher efficiency for acetates than PDMS/DVB and DVB/CAR/PDMS ones, but did not show better extraction efficiency for the ester compounds. On the other hand, the lowest extraction efficiency was obtained by PA. Therefore, the PDMS/CAR/PDMS fibre was selected as the most convenient polymeric phase for HS-SPME analysis of EE and HAA in commercial wines.

Subsequently, the extraction time profile for the 15 compounds was also performed and the data obtained are depicted in Fig. 2a. Since HS-SPME is a distribution process of the analytes between the wine matrix, vapour phase and polymeric phase (three-phase system), it is very important to establish the most convenient time to reach the equilibrium [30]. In order to investigate the sorption behaviour of wine HAA, IsoE and EE using a DVB/CAR/PDMS fibre, assays were performed at five different extraction times, *i.e.* 5, 15, 30, 60 and 75 min (25 °C). For almost all compounds, the extraction yields increased with time until 60 min. However, after this period, the extraction efficiency decreases slightly due probably to the phenomena competition as this type of fibres present capacity limitations. On the basis of the results obtained, 60 min of extraction time were selected for further assays.

During HS-SPME analysis, the distribution constant of an analyte between the sample and the fibre coating is influenced very much by the extraction temperature, which depends on the matrix composition and the polymeric phase selected. Since SPME is an exothermic process, when temperature arises the sorption process reduces enhancing HS concentrations but, on the other hand, decreases the partition coefficients due to the thermodynamic effect. According to Carvalho et al. [30], excessive increment of temperature can cause premature desorption of the analytes. Therefore, the effect of temperature on the extraction efficiency was also evaluated by sampling an ENX wine at 25, 30, 40 and 60 °C, with the

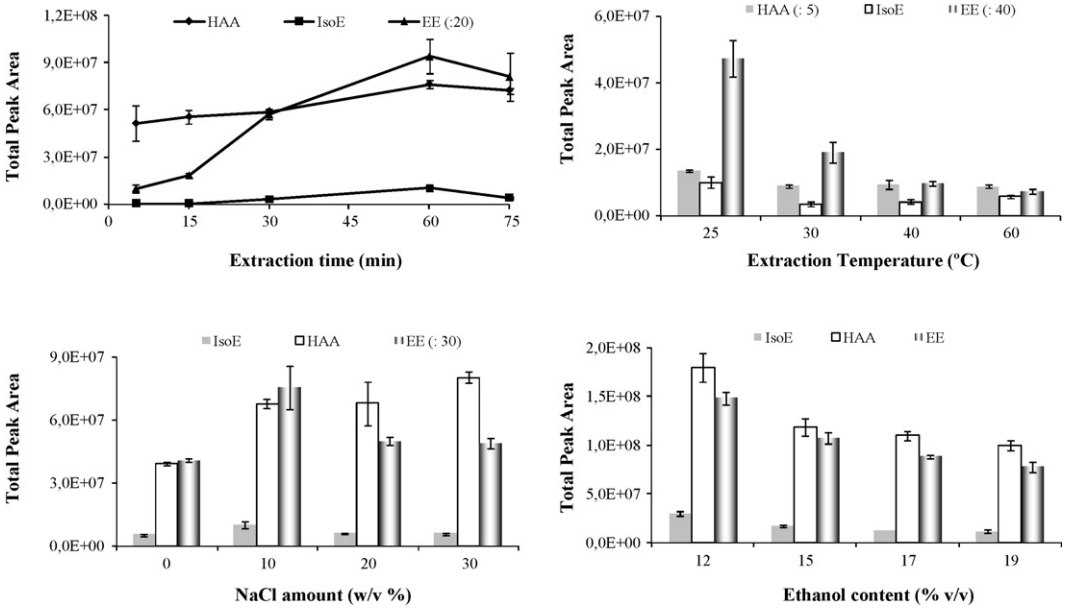


Fig. 2. Influence of the extraction time (a), temperature (b), ionic strength (c) and ethanol content (d) on the extraction efficiency of HAA, IsoE and EE in wines by HS-SPME using a DVB/CAR/PDMS fibre.

DVB/CAR/PDMS fibre incubated for 60 min (extraction of salt saturated sample: 10% NaCl (w/v)). As can be observed in Fig. 2b, the temperature increment leads to a decrease in the extraction yield for the IsoE and EE, although the HAA content increased. As a consequence, 25 °C was selected for further optimisation. Another parameter that must be taken into consideration is the ionic strength once this greatly influences the partitioning coefficient of the solutes between the liquid and vapour phases. An increment of salt concentration increases the extraction efficiency due to the decrease of analytes solubility, which improves sensitivity by promoting higher enrichment into the stationary phase [31]. Thus, the ionic strength was tested at 0, 10, 20 and 30% of NaCl (w/v) using the DVB/CAR/PDMS fibre (60 min at 25 °C) and the results obtained are depicted in Fig. 2c. With the exception of EE for which better yields were obtained with 10% of salt, for the remaining chemical families (HAA and IsoE), the analytical response increased with higher salt levels. In general, the addition of 10% NaCl promotes the best results and therefore, this amount was chosen to all wine samples prior to analysis. The distribution constant between the polymeric coating and the sample are

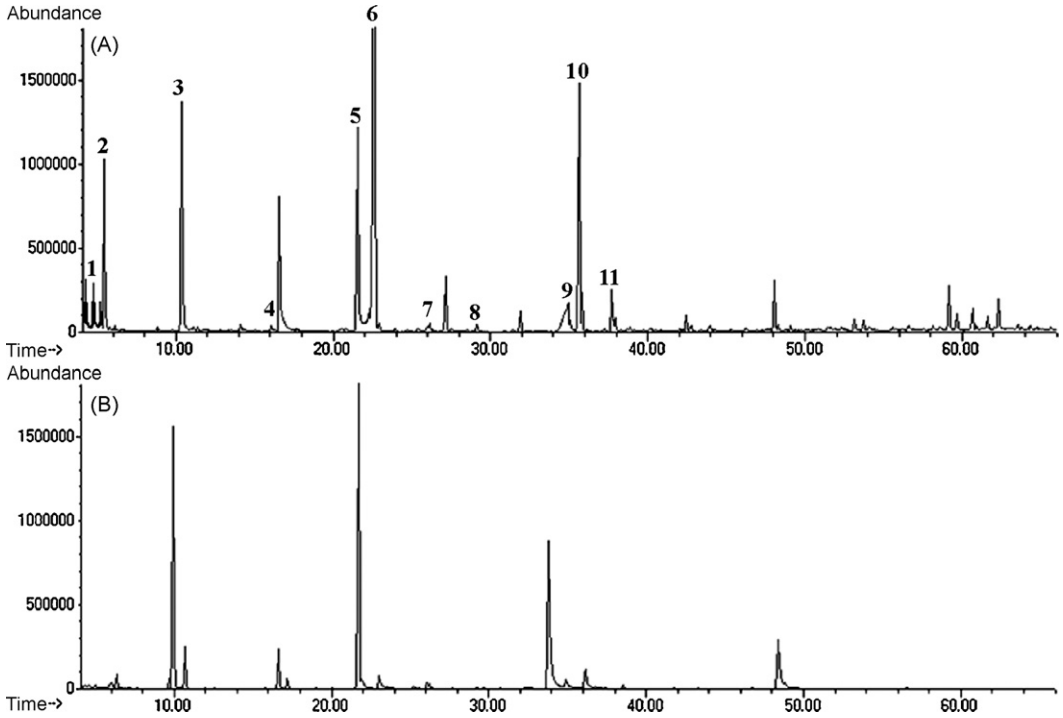


Fig. 3. Typical total ion chromatograms of volatile profiles of COL red wines analysed by (a) SBSE-LD/LVI-GC–qMS and (b) HS-SPME$_{DVB/CAR/PDMS}$/GC–qMS methodologies. Peak identification: 1: ethyl 2-methylbutanoate + ethyl 3-methylbutanoate; 2: isoamyl acetate; 3: ethyl hexanoate; 4: ethyl heptanoate; 5: diethyl succinate; 6: ethyl octanoate; 7: 2-phenylethyl acetate; 8: ethyl nonanoate; 9: ethyl 9-decenoate + decanoic acid; 10: ethyl decanoate; 11: ethyl succinate.

Table 2
HS-SPME and SBSE-LD performance characteristics.

Compounds	LOD ($\mu g\,L^{-1}$)		LOQ ($\mu g\,L^{-1}$)		R.S.D. (%)		% Recovery ± R.S.D.	
	SPME	SBSE	SPME	SBSE	SPME	SBSE	SPME	SBSE
Higher alcohol acetates								
Hexyl acetate	4.35	1.16	14.49	3.87	11.02	9.05	97.04 ± 6.31	79.07 ± 5.10
Ethyl 2-phenyl acetate	0.42	0.07	1.41	0.22	12.41	11.74	50.09 ± 9.55	83.91 ± 9.42
Isoamyl esters								
Isoamyl acetate	20.29	18.37	67.63	61.24	15.87	8.21	57.42 ± 7.87	83.81 ± 6.66
Isoamyl hexanoate	0.02	0.10	0.06	0.34	4.10	10.31	38.43 ± 9.00	108.04 ± 10.98
Isoamyl octanoate	0.06	0.21	0.21	0.73	11.51	8.76	21.78 ± 7.12	106.95 ± 7.75
Ethyl esters								
Ethyl butanoate	6.5	–	21.6	–	9.82	–	89.19 ± 6.63	–
Ethyl hexanoate	1.67	0.13	5.56	0.45	11.12	15.28	25.02 ± 7.47	32.49 ± 2.45
Ethyl 2-furoate	7.91	0.53	26.38	1.75	14.03	12.03	117.27 ± 5.97	84.08 ± 6.18
Ethyl benzoate	2.61	5.56	8.71	18.53	12.76	15.51	76.87 ± 7.30	90.79 ± 5.84
Ethyl octanoate	6.12	0.20	20.39	0.67	6.98	13.76	72.09 ± 6.26	90.38 ± 7.20
Ethyl salicylate	1.71	28.96	5.68	96.56	10.59	16.52	71.12 ± 9.54	78.02 ± 4.89
Ethyl decanoate	5.60	0.07	18.69	0.23	8.70	9.79	100.38 ± 13.96	83.91 ± 9.98
Ethyl cinnamate	19.60	0.03	65.32	0.11	10.04	17.88	68.70 ± 14.59	65.91 ± 8.59
Ethyl dodecanoate	1.46	0.23	4.87	0.77	11.78	16.24	87.87 ± 13.96	93.60 ± 11.03

LOD: limit of detection; LOQ: limit of quantification; R.S.D.: relative standard deviation; (–) not determined by SBSE (solvent delay higher than their retention time).

strongly dependent on the matrix effects. For instance, the ethanol content in wines appears to interfere very much during the HS-SPME analytical procedure [23]. Thereby, to check the effect of ethanol content on the HS-SPME extraction yields, four solutions having different contents (12, 15, 17 and 19% (v/v)) and spiked with the same amounts of volatile compounds were assayed using DVB/CAR/PDMS fibre (extraction of salt sample: 10% NaCl (w/v) during 60 min at 25 °C). Fig. 2d compares the data obtained for HAA, IsoE and EE on that media, where the peak area decreases as the ethanol content increases for all of the studied chemical families. As a consequence no advantages were observed by increasing the ethanolic content.

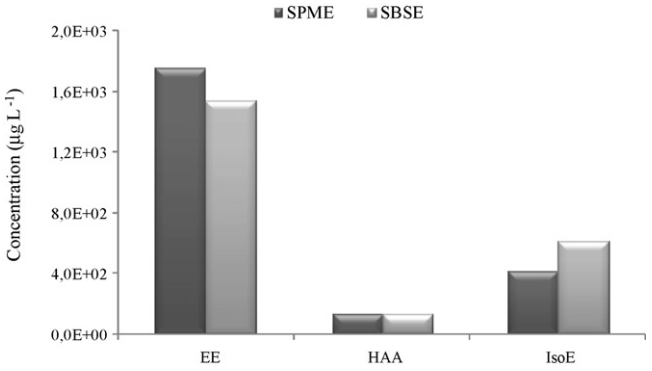


Fig. 4. Comparison of extraction efficiency performance of SBSE and SPME for the analysis of HAA, IsoE and EE.

3.2. SBSE-LD/LVI optimisation

By using the SBSE-LD/LVI approach the extraction time, ethanol content, LD conditions and instrumental settings were established, according to a methodology previously optimised [19]. Therefore 10 volatile compounds, representative of the main chemical families of wine, were used, *i.e.* guaiazulene, (*E*, *E*)-farnesol, β-ionone, geranylacetone, ethyl decanoate, β-citronellol, 2-phenylethanol, linalool, hexyl acetate and *n*-hexanol were selected for SBSE-LD optimisation. During our assays, stir bars coated with 24 μL of PDMS were chosen, once this polymer is the only one commercially available, more effective to non-polar compounds, and needs a low amount of back-extraction solvent (<200 μL) inside an insert, which is a key role during the liquid desorption step. The use of a minimum amount of solvent for LD is very convenient since avoid the undesirable solvent evaporation step usually performed for sensitivity enhancement and minimizes possible losses of volatiles. The best solvents used for LD should be the ones that must desorbs the analytes from the PDMS phase and simultaneously present low boiling points for LVI under solvent vent mode avoiding losses of volatiles. For this purposes, several solvents were already tested, namely, ACN, MeOH, *n*-pentane, acetone, diethyl ether, propan-2-ol and azeotropic mixtures. According to the data obtained, *n*-pentane was chosen as the best back-extraction solvent during the LD process, because all standards were detected and the peaks did not present fronting, consequently, more reproducibility was obtained. The time for the back-extraction used was 15 min, since higher period of time did not bring any advantages. For LVI purposes, the chromatographic performance is also very dependent of the He flow rate against solvent used, due to the dependence of the inlet purge flow rate and temperature in the solvent vent mode. Better performance was observed with flow rate of 10 mL min^{-1} and therefore, was selected as the purge vent. Different inlet purge temperatures were also tested because solvent vent mode is also a critical parameter. According to previous data [19], the recovery of the volatile compounds seems to present higher reproducibility and recovery when the analysis carried out at 10 °C. Since SBSE was used in a two-phase system (liquid sample-stir bar) and is time dependent, we have decided to use 60 min at 800 rpm.

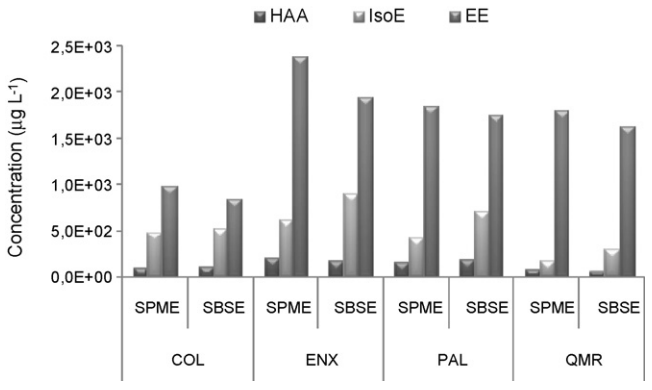


Fig. 5. Concentration of HAA, IsoE and EE. found in commercial wines by HS-$SPME_{DVB/CAR/PDMS}$/GC–MS and SBSE-LD/LVI-GC–MS methodologies.

Table 3
Comparison of the SBSE-LD results with those obtained by HS-SPME for higher alcohol acetates, isoamyl esters and ethyl esters found in "Terras Madeirenses" commercial wines.

Compounds	Concentration ($\mu g\,L^{-1}$)							
	COL		ENX		PAL		QMR	
	SPME	SBSE	SPME	SBSE	SPME	SBSE	SPME	SBSE
Higher alcohol acetates								
Hexyl acetate	56.26 ± 0.50	25.43 ± 0.61	168.98 ± 10.72	95.14 ± 4.66	111.17 ± 5.52	97.57 ± 3.84	64.93 ± 5.27	25.35 ± 1.49
Ethyl 2-phenyl acetate	42.08 ± 3.77	86.13 ± 12.00	39.42 ± 5.29	72.98 ± 15.17	43.59 ± 2.24	84.08 ± 13.71	15.35 ± 0.99	48.37 ± 4.14
Isoamyl esters								
Isoamyl acetate	474.98 ± 45.63	525.06 ± 52.99	608.00 ± 61.29	881.91 ± 98.62	404.64 ± 52.70	694.14 ± 47.71	159.56 ± 19.06	270.51 ± 12.21
Isoamyl hexanoate	1.09 ± 0.03	0.25 ± 0.03	2.67 ± 0.04	0.93 ± 0.06	2.57 ± 0.02	0.91 ± 0.08	2.56 ± 0.01	0.45 ± 0.03
Isoamyl octanoate	1.17 ± 0.04	2.07 ± 0.14	6.29 ± 0.04	8.13 ± 1.65	6.22 ± 0.03	8.12 ± 1.08	6.23 ± 0.01	9.86 ± 0.87
Isoamyl decanoate	–	1.42 ± 0.56	–	8.72 ± 0.77	–	8.18 ± 0.87	–	8.30 ± 1.15
Ethyl esters								
Ethyl butanoate	165.82 ± 13.52	–	329.25 ± 41.43	–	211.89 ± 15.48	–	162.68 ± 10.24	–
Ethyl 2-methylbutanoate	–	3.95 ± 0.50	–	1.67 ± 0.13	–	1.97 ± 0.28	–	2.11 ± 0.15
Ethyl 3-methylbutanoate	3.54 ± 0.41	1.63 ± 0.43	1.87 ± 0.38	0.68 ± 0.22	1.41 ± 0.61	0.75 ± 0.14	3.15 ± 0.92	3.01 ± 0.36
Ethyl hexanoate	118.43 ± 25.66	160.44 ± 5.04	316.95 ± 45.94	338.43 ± 29.68	263.03 ± 21.45	288.76 ± 10.26	219.10 ± 51.82	246.66 ± 27.09
Ethyl 2-hexenoate	–	1.52 ± 0.05	–	1.54 ± 0.06	–	2.10 ± 0.04	–	2.07 ± 0.11
Ethyl heptanoate	–	2.73 ± 0.07	–	1.73 ± 0.05	–	1.81 ± 0.03	–	2.11 ± 0.13
Methyl octanoate	1.93 ± 0.88	0.35 ± 0.02	2.01 ± 0.12	0.58 ± 0.06	1.46 ± 0.06	0.48 ± 0.02	1.45 ± 0.21	0.33 ± 0.07
Diethyl succinate	163.47 ± 19.87	112.77 ± 8.19	125.87 ± 8.21	46.37 ± 5.66	116.36 ± 7.29	70.16 ± 6.32	209.32 ± 32.88	100.58 ± 4.89
Ethyl octanoate	381.21 ± 20.39	351.37 ± 22.92	915.83 ± 83.07	943.47 ± 76.25	804.57 ± 34.48	866.90 ± 7.07	744.68 ± 36.71	813.13 ± 9.36
Ethyl phenylacetate	–	48.69 ± 2.75	–	22.53 ± 0.52	–	26.63 ± 0.74	–	39.74 ± 0.92
Ethyl nonoate	2.57 ± 0.13	0.49 ± 0.04	1.54 ± 0.06	0.31 ± 0.12	1.44 ± 0.07	0.28 ± 0.04	1.48 ± 0.03	1.48 ± 0.08
Methyl decanoate	–	9.94 ± 0.02	–	9.86 ± 0.02	–	9.74 ± 0.02	–	9.63 ± 0.03
2-Methylpropyl octanoate	14.73 ± 1.04	9.40 ± 0.00	38.77 ± 6.05	25.55 ± 0.01	28.64 ± 2.05	19.50 ± 0.01	16.74 ± 1.05	16.51 ± 0.02
Ethyl 9-decenoate	1.44 ± 0.15	1.72 ± 0.09	4.78 ± 0.66	1.76 ± 0.09	9.81 ± 0.78	3.48 ± 0.26	1.81 ± 0.40	1.76 ± 0.07
Ethyl decanoate	110.27 ± 17.83	61.43 ± 2.04	630.94 ± 67.39	457.43 ± 18.94	391.55 ± 24.23	371.95 ± 16.74	422.11 ± 12.69	355.42 ± 45.30
Ethyl succinate	–	20.61 ± 0.12	–	36.21 ± 0.04	–	51.55 ± 0.06	–	14.64 ± 0.02
Ethyl 3-hydroxyoctanoate	–	1.57 ± 0.12	–	4.15 ± 0.48	–	2.83 ± 0.13	–	2.26 ± 0.11
Ethyl dodecanoate	9.96 ± 0.02	3.11 ± 0.02	21.72 ± 0.62	27.09 ± 1.27	19.77 ± 0.75	13.95 ± 0.75	17.40 ± 0.12	10.02 ± 0.86
Butyl hexadecanoate	–	14.54 ± 1.90	–	4.38 ± 0.75	–	6.46 ± 0.91	–	3.38 ± 0.14
Butyl octadecanoate	–	34.88 ± 5.81	–	22.98 ± 3.77	–	8.83 ± 0.83	–	1.70 ± 0.44

(–) Not determined by SBSE (solvent delay higher than their retention time).

Fig. 3 compares total ion chromatograms of wine samples obtained by HS-SPME$_{DVB/CAR/PDMS}$/GC–MS (a) and SBSE-LD/LVI-GC–MS (b) methodologies, under optimised experimental conditions. As it can be observed, both methods present good performance besides the latter approach showed much better overall sensitivity in particular to detect minor constituents.

3.3. Validation and comparison of SPME and SBSE methodologies

In a first approach, both methodologies are very easy to work-up without special instrumental needs, which make them potential analytical tools to analyse wines in any conventional laboratory. Although SBSE-LD presents a much higher capacity and therefore better sensitivity than HS-SPME, the selectivity concerning the polar characteristics of the analytes under study, seems to be better performed by the latter since we have the possibility to choose the more suitable polymeric phase and in the former case, only PDMS is available. In the experimental point of view, SBSE-LD is a technique much more robust than HS-SPME, without any polymeric damage during analytical manipulation, do not need salt addition to increase the vapour tension or suitable temperature control and if the right desorption solvent is combined with LVI, present a remarkable performance as it was successfully demonstrated to the particular case of acetates and esters in wines.

In Tables 1 and 2, the calibration parameters (linearity, repeatability (precision, expressed as R.S.D.), recovery of known quantities of substance (accuracy), LODs and LOQs, are given for both methodologies. Calibration plots constructed using suitable dilutions of the global solutions were obtained by the least-square linear regressions of ratio of the peak area of each compound versus the added amount of the targets. Both methodologies showed good linearity over the concentration ranges tested with all determination coefficients (r^2) higher than 0.982. Regarding the detection purposes, some differences were observed between both analytical approaches since ethyl lactate and ethyl butanoate were not found by SBSE-LD. Detection and quantification limits (Table 2) were achieved by extrapolation of the lowest concentrations points from the standard plots (3 and 10 times the R.S.D. of blanks, respectively). Therefore, LODs ranged between 0.02 $\mu g\,L^{-1}$ (isoamyl hexanoate) and 20.29 $\mu g\,L^{-1}$ (isoamyl acetate) were found for HS-SPME methodology, whereas for SBSE-LD ranged from 0.03 $\mu g\,L^{-1}$ (ethyl cinnamate) to 28.96 $\mu g\,L^{-1}$ (ethyl salicylate). In average the LOD's values obtained by SBSE-LD were lower than those obtained by HS-SPME. LOQs ranged from 0.06 $\mu g\,L^{-1}$ (isoamyl hexanoate) to 67.63 $\mu g\,L^{-1}$ (isoamyl acetate) and 0.11 $\mu g\,L^{-1}$ (ethyl cinnamate) to 96.56 $\mu g\,L^{-1}$ (ethyl salicylate) for HS-SPME and SBSE-LD, respectively. The repeatability has been evaluated by means of a series of six extractions from the same wine. The results indicated that the methods had good repeatability. For HS-SPME good within-day precision was noticed with R.S.D. values between 4.10% (isoamyl hexanoate) and 15.87% (isoamyl acetate). For SBSE-LD methodology the R.S.D. values ranges between 8.21% (isoamyl acetate) and 17.88% (ethyl cinamate). In order to check the accuracy of the proposed methods, a recovery study was carried out by fortifying an ENX wine sample. For HS-SPME approach, the recoveries of the higher alcohol acetates, isoamyl esters and ethyl esters from spiked samples varied from 21.78% (isoamyl octanoate) to 117.27% (ethyl 2-furoate) with an average recovery of 69 ± 8%, while by using SBSE-LD approach the recoveries ranging between 32.49% (ethyl hexanoate) to 108.04% (isoamyl hexanoate) with an average of 81 ± 8%. These results corroborate the higher accuracy of SBSE.

3.4. SBSE and SPME application to wines

Six samples of each wine (one red and three white wine) were analysed by SBSE and SPME methodologies under optimised conditions. As expected, the recovery of EE depends on the enrichment methodology used. Qualitative and quantitative differences were definitely observed in the chromatographic profiles obtained by both approaches (Fig. 3). A higher number of HAA, IsoE and EE were detected in the sample studied by means of SBSE. A total of 25 target compounds were identified and quantified from the analysed wines by SBSE-LD/LVI-GC–qMS, while by HS-SPME/GC–qMS only 16 compounds were identified. The compounds included 20 EE, 2 HAA and 4 IsoE. The results obtained for these samples are shown in Table 3. SBSE-LD/LVI-GC–MS provided higher efficiency in the extraction of HAA (31.1%) and IsoE (1.2%) than HS-SPME/GC–MS (21.6% and 0.3%, respectively). The latter methodology showed a better efficiency extraction of EE (78.2%) than the former (67.7%). This analysis allows the conclusion that the SBSE-LD approach is generally a more sensitive methodology than HS-SPME in extracting these chemical classes of volatile compounds (Fig. 4). However, these methodologies can be complementary because some volatile compounds with low log $K_{O/W}$ values (ethyl butanoate) are not detected by SBSE-LD.

Among HAA, isoamyl acetate highlighted with their higher concentrations. Hexyl acetate and 2-phenylethyl acetate were found as well, but at lower amounts. As can be seen (Table 3), SBSE-LD exhibits better sensitivities than HS-SPME for IsoE and 2-phenylethyl acetate. However, hexyl acetate shows better extraction efficiency by HS-SPME than that SBSE-LD. According to their mean contents (Fig. 5), the ENX, PAL and COL wines had higher concentrations (559.40–816.40 $\mu g\,L^{-1}$ (HS-SPME) and 636.62–1050.03 $\mu g\,L^{-1}$ (SBSE-LD) than QMR wines (239.84 $\mu g\,L^{-1}$ (HS-SPME) and 328.23 $\mu g\,L^{-1}$ (SBSE-LD)). In general, these compounds are responsible for the "fruity" and "floral" characteristics of young wines.

The fatty acids EE are produced enzymatically during yeast fermentation from ethanolysis of acylCoA which is formed from fatty acids synthesis or degradation. Their concentration is dependent on several factors mainly: yeast strain, fermentation temperature, aeration degree and sugar contents. Among the EE identified, the major compounds were, ethyl octanoate, ethyl hexanoate and ethyl decanoate. HS-SPME showed higher sensitivities for this chemical group than SBSE-LD approach.

As can be seen in Table 3, SBSE-LD exhibits better sensitivities than HS-SPME for IsoE. It has been observed that their mean values were very similar and they did not present significant differences between ENX, PAL and QMR wines using HS-SPME and SBSE-LD approaches. The COL wine presents the lowest concentration of IsoE, namely 2.26 and 3.74 $\mu g\,L^{-1}$ for HS-SPME and SBSE-LD methods, respectively. Among the identified IsoE, the isoamyl octanoate were at higher concentrations in the four types of wines.

4. Conclusions

HAA, IsoE and EE of red and white commercial wines extracted using the two analytical methods headspace solid-phase microextraction and stir bar sorptive extraction–liquid desorption, were determined by GC–MS. These methodologies are sensitive, fast, easy, reliable, solventless techniques and an alternative to the traditional methods to characterize volatiles in wines.

The SBSE-LD method showed higher sensitivity than HS-SPME for the selected volatile compounds. Twenty-five esters were identified by SBSE-LD using *n*-pentane as solvent back-extraction whereas only 16 esters were identified by the HS-SPME method.

Both analytical methods showed good linearity, precision, detection and quantification limits that allow their application in real samples. Quantitatively, EE of fatty acids, namely ethyl hexanoate, octanoate and decanoate were the major volatile compounds found in studied wines. Their concentration, higher than LPO, enables their contribution to wine sensory proprieties with

"fruit" and "cheese/fatty" odours. Both approaches are highly sensitive and can be applied to a wide variety of food matrices.

Acknowledgments

The authors are grateful to the Interreg IIIB-MAC and FEDER, for the financial support provided to ANTIVINMAC 05/MAC/2.3/M28 Project.

References

[1] S.M. Rocha, P. Coutinho, I. Delgadillo, M.A. Coimbra, J. Chromatogr. A 1150 (2007) 155.
[2] J.S. Câmara, P. Herbert, J.C. Marques, M.A. Alves, Anal. Chim. Acta 513 (2004) 203.
[3] D. Komes, D. Ulrich, T. Lovric, Eur. Food Res. Technol. 222 (2006) 1.
[4] R. Perestrelo, A. Fernandes, F.F. Albuquerque, J.C. Marques, J.S. Câmara, Anal. Chim. Acta 563 (2006) 154.
[5] Y. Kotseridis, R. Baumes, J. Agric. Food Chem. 48 (2000) 400.
[6] A. Rapp, H. Mandery, Experientia 43 (1986) 873.
[7] J.C.R. Demyttenaere, J.I.S. Martínez, R. Verhé, P. Sandra, N. Kimpe, J. Chromatogr. A 985 (2003) 221.
[8] J.S. Câmara, J.C. Marques, R.M. Perestrelo, F. Rodrigues, L. Oliveira, P. Andrade, M. Caldeira, J. Chromatogr. A 1150 (2007) 198.
[9] W. Wardencki, J. Curylo, J. Namiesnik, J. Biochem. Biophys. Meth. 70 (2007) 275.
[10] M. Liu, Z. Zeng, Y. Tian, Anal. Chim. Acta 540 (2005) 341.
[11] M. Shimoda, T. Shibamoto, A.C. Noble, J. Agric. Food Chem. 41 (1993) 1664.
[12] P. Karásek, J. Planeta, E.V. Ostrá, M. Mikesová, J. Golias, M. Roth, J. Vejrosta, J. Chromatogr. A 1002 (2003) 13.
[13] G. Giraudi, L. Anfossi, C. Baggiani, C. Giovannoli, C. Tozzi, J. Chromatogr. A 1175 (2007) 174.
[14] S. Cabredo-Pinillos, T. Cedrón-Fernández, M. González-Briongos, L. Puente-Pascual, C. Sáenz-Barrio, Talanta 69 (2006) 1123.
[15] H. Lord, J. Pawliszyn, J. Chromatogr. A 885 (2000) 153l.
[16] L. Arthur, J. Pawliszyn, Anal. Chem. 62 (1990) 2145.
[17] E. Baltussen, P. Sandra, F. David, C. Cramers, J. Microcol. Sep. 11 (1999) 737.
[18] R.F. Alves, A.M.D. Nascimento, J.M.F. Nogueira, Anal. Chim. Acta 546 (2005) 11.
[19] E. Coelho, R. Perestrelo, N.R. Neng, J.S. Câmara, M.A. Coimbra, J.M.F. Nogueira, S.M. Rocha, Anal. Chim. Acta 624 (2008) 79.
[20] P. Serôdio, J.M.F. Nogueira, Anal. Chim. Acta 517 (2004) 21.
[21] P. Serôdio, M.S. Cabral, J.M.F. Nogueira, J. Chromatogr. A 1141 (2007) 259.
[22] A. Zalacain, J. Marín, G.L. Alonso, M.R. Salina, Talanta 71 (2007) 1610.
[23] F. Rodrigues, M. Caldeira, J.S. Câmara, Anal. Chim. Acta 609 (2008) 82.
[24] C. Dietz, J. Sanz, C. Cámara, J. Chromatogr. A 1103 (2006) 183.
[25] F. David, P. Sandra, J. Chromatogr. A 1152 (2007) 54.
[26] A.R.M. Silva, F.C.M. Portugal, J.M.F. Nogueira, J. Chromatogr. A 1209 (2008) 10–16.
[27] E. Coelho, M.A. Coimbra, J.M.F. Nogueira, S.M. Rocha, Anal. Chim. Acta 635 (2009) 214.
[28] R. Perestrelo, M. Caldeira, F. Rodrigues, J.S. Câmara, J. Sep. Sci. 31 (2008) 1841.
[29] L. Ferreira, R. Perestrelo, J.S. Câmara, Talanta 77 (2009) 1087.
[30] P.N. Carvalho, L.F. Pinto, M.C.P. Basto, M.T.S.D. Vasconcelos, J. Microchem. 87 (2007) 147.
[31] C. Pizarro, N. Pérez-del-Notario, J.M. González-Sáiz, J. Chromatogr. A 1143 (2007) 26.

Talanta 80 (2009) 631–635

Contents lists available at ScienceDirect

Talanta

journal homepage: www.elsevier.com/locate/talanta

Modification of carbon screen-printed electrodes by adsorption of chemically synthesized Bi nanoparticles for the voltammetric stripping detection of Zn(II), Cd(II) and Pb(II)

Mª Ángeles Granado Rico [a], Mara Olivares-Marín [b], Eduardo Pinilla Gil [a,*]

[a] Department of Analytical Chemistry, University of Extremadura, Av. de Elvas, s/n, E-06071 Badajoz, Spain
[b] Department of Organic and Inorganic Chemistry, University of Extremadura, Av. de Elvas, s/n, E-06071 Badajoz, Spain

ARTICLE INFO

Article history:
Received 15 April 2009
Received in revised form 8 July 2009
Accepted 20 July 2009
Available online 28 July 2009

Keywords:
Screen-printed electrodes
Bismuth nanoparticles
Heavy metals
Stripping voltammetry
Water samples

ABSTRACT

A simple procedure for the chemical synthesis of bismuth nanoparticles and subsequent adsorption on commercial screen-printed carbon electrodes offer reliable quantitation of trace zinc, cadmium and lead by anodic stripping square-wave voltammetry in nondeareated water samples. The influence of two hydrodynamic configurations (convective cell and flow cell) and the effect of various experimental variables upon the stripping signals at the bismuth-coated sensor are explored. The square-wave peak current signal is linear over the low ng mL^{-1} range (120 s deposition), with detections limits ranging from 0.9 to 4.9 ng mL^{-1} and good precision. Applicability to waste water certified reference material and drinking water samples is demonstrated. The attractive behaviour of the new disposable Bi nanoparticles modified carbon strip electrodes, coupled with the negligible toxicity of bismuth, hold great promise for decentralized heavy metal testing in environmental and industrial effluents waters.

© 2009 Elsevier B.V. All rights reserved.

1. Introduction

The development of "green", "sustainable" or "environmentally friendly" analytical procedures is an active and growing research field [1]. Increasing concern about the side impact of chemical waste derived from analytical methodologies have promoted new method design strategies, based on reduction or suppression of toxic reagents used for sample pretreatment and analytical signal measurement. Green analytical chemistry is especially relevant when the methodologies are intended for use in the field or in decentralized laboratories, where dangerous waste processing is less available, or directly absent. This is usually the case in field environmental monitoring. Electrochemical methods of analysis have been especially sensitive to this trend in recent years, so they have moved greener in different ways. A wide set of electrochemical sensor that fulfils the environmental friendly requirements are available [2–4], and several of them are commercially available or in advanced prototype stages for water monitoring [5,6].

Replacement of conventional electrochemical cells by screen-printed electrodes (SPEs) connected to miniaturized potentiostats is a main trend in the shift of lab electrochemical equipments to hand-held field analyzers. SPEs produced by printing different inks on plastic or ceramic supports are gaining widespread applicability for electrochemical monitoring, especially in the environmental, biomedical and industrial fields. An increasing number of SPE types are commercially available, but they are also amenable for lab production since screen-printed technology is cheap and easily accessible. Unmodified and modified carbon and metallic working electrode surfaces have been explored [7,8]. The specific applicability of SPE to the determination of heavy metals has been reviewed [9].

From the original work of Wang et al. [10], modification of carbon electrodes, especially glassy carbon supports, with metallic bismuth for anodic stripping of heavy metals has been widely explored as an environmentally friendly alternative to the well-known mercury film electrode [11,12]. Applicability of other supporting materials has been described, including carbon fibres [13], carbon films [14], edge plane pyrolytic graphite [15], and a variety of modified carbon pastes [16,17]. Screen-printed carbon working electrodes (SPCEs) have been also explored as supports for Bi modification, including Bi codeposition (so called "in situ" Bi film) and preplated Bi (so called "ex situ" Bi film) approaches. Wang et al. [18] described anodic stripping procedures for lead on home-made Bi preplated disposable SPCEs for the quantification of trace Pb(II) in drinking water by anodic stripping with a detection limit of 0.3 ng mL^{-1}. Kadara and Tothill [19,20] fabricated single use Bi preplated SPCEs for the voltammetric stripping analysis of Pb(II) and Cd(II), obtaining detection limits of 8 and 10 ng mL^{-1} in soil extracts and waste waters for Cd(II) and Pb(II) respectively,

* Corresponding author.
E-mail address: epinilla@unex.es (E.P. Gil).

0039-9140/$ – see front matter © 2009 Elsevier B.V. All rights reserved.
doi:10.1016/j.talanta.2009.07.039

with a deposition time of 120 s. Zaouak et al. [21] have modified screen-printed carbon microband electrodes by preplating a Bi film and demonstrated application to the detection of labile cadmium in river water. Microelectronic Bi-film electrode preparation have been also described [22,23]. About "in situ" Bi films for heavy metals determination on SPCE, Chuanuwatanakul et al. [24] have described a stopped flow system for Zn(II), Cd(II) and Pb(II) in water samples. Our group has recently described the simultaneous determination of the same elements at a novel cell design with improved convective accumulation by "in situ" bismuth codeposition on commercial SPCE strips [25].

Some authors have attempted the modification of SPEs with metallic nanoparticles before stripping analysis of heavy metals, in order to benefit from unique advantages over macroelectrodes: enhancement of mass transport, catalysis, high effective surface area and control over electrode microenvironment [26]. Two groups have reported electrode modification with Bi nanoparticles before voltammetric stripping of heavy metals, based on electrochemical synthesis of the metallic particles on thick film printed electrodes [27], electrode modification with Bi nanopowder synthesized by a levitational gas condensation (LGC) method [28] and sono-melting of Bi powder in octane [29]. We propose here a simpler and easier way to modify commercial SPCEs with metallic Bi nanoparticles, consisting on chemical synthesis on the particles by a procedure based on a method previously reported by Zhao et al. [30], and passive adsorption of the modifying material onto the carbon working electrode surface. We have tested the procedure for the determination of Zn(II), Cd(II) and Pb(II) in water samples.

2. Experimental

2.1. Materials

All chemicals used for the preparation of stock and standard solutions were of analytical grade. 1000 mg L^{-1} stock solutions of Zn(II), Cd(II), Pb(II) and Bi(III) were supplied by Scharlab (Spain). Working solutions were prepared by dilution with ultrapure water obtained from a MilliQ (Millipore) system. Dilute standards were adjusted to pH 2 with subboiled HNO_3. 0.1 M buffer solutions were prepared with HPLC grade acetic acid and sodium acetate (Merck). Multielement test solutions and real samples were adjusted to pH 4.5 with acetate buffer. 10^{-2} M potassium chloride (Merck) was added for better performance of the Ag strip reference electrode. Bismuth granules (99.99%, 100 mesh, Sigma), paraffin oil (Panreac, Spain) and chloroform (Merck) were used as for the preparation of bismuth nanoparticles.

Samples of the SPS-WW2 waste water certified reference material obtained from Spectrapure Standards A.S. (Norway) were used as received for accuracy evaluation. The drinking water samples were collected from a running water tap in our lab at the Department of Analytical Chemistry, University of Extremadura.

2.2. Instrumentation

Square-wave voltammetric measurements were taken by a computerized hand-held, battery-powered PalmSens potentiostat/galvanostat (Palm Instruments BV, The Netherlands) interfaced with a laptop. The whole analytical procedure is controlled by the Palm Sens PC software, including stirring of the samples by a standard stirrer and magnetic bar. Screen-printed three electrode strips were purchased from Drop Sens (Spain). They include a three electrode configuration printed on the same strip. The strips present a 4 mm diameter disk screen-printed carbon working electrode (SPCE) and a counter electrode, both printed on alumina substrate using heat curing carbon composite inks, and a silver pseudo-reference electrode. An insulating layer serves to delimit the working area and electric contacts. Ink formulation and production characteristics of commercial SPCEs are regarded by the manufacturers as proprietary information. A specific connector allows the connection of the electrochemical strip to the potentiostat.

The Bi modified electrochemical strips were mounted on two different supporting systems for accumulation and stripping measurements:

(a) *Accumulation by conventional stirring*: a novel cell configuration recently described by our group was used [25]. The cell allows fast and highly efficient convective accumulation by conventional stirring. Briefly, the Bi modified screen-printed strip is inserted face down through a partially cut 16 mm diameter (10 mL volume) plastic tube, leaving the electrical connection pads out of the tube. The stirring bar is placed in the bottom of the tube, close and parallel to the working electrode surface for highly effective convection. The planar screen-printed surface is parallel to the plane described by the stirring bar movement, so a very significant increasing of the accumulation efficiency is obtained at the proposed convective cell compared with the sample drop approach commonly used for voltammetric measurements on SPEs.
(b) *Flow cell*: Analyte accumulation was also performed by inserting the Bi modified screen-printed strips in a commercial (Drop Sens, Spain) wall jet (90° jet angle) electrochemical flow cell. The flow cell consists of two pieces of methacrylate fixed together by magnets; the upper part has the inlet and outlet flow channels, and the lower part has an insert for the screen-printed strip, the electrochemical cell volume being defined by an o-ring. A peristaltic pump (Perimax Spetec, Germany) was used in connection with the flow cell.

A PerkinElmer ELAN 9000 ICP-MS was used for accuracy check of the electrochemical results.

The morphology of bismuth particles adsorbed on the modified electrodes was observed by scanning electron microscopy (SEM) on a FE-SEM Hitachi S-4700 microscope.

2.3. Procedures

2.3.1. Chemical synthesis of the Bi nanoparticles

Bismuth nanoparticles were prepared by a modification of an extremely simple one-step solution dispersion method starting from bulk metal described by Zhao et al. [30]. Briefly, 50 mg bismuth granules were dispersed in 30 mL paraffin oil. The vessel was a sealed and the mix then was heated for 10 h at 230 °C for bismuth melting under vigorous stirring. After cooling, the supernatant was transferred to a tube and centrifuged for 30 min. The bismuth particles residue was washed several times with chloroform to eliminate any paraffin, and finally dried under N_2 stream. The dark grey powder obtained was stored in a sealed vial at room temperature.

2.3.2. Electrode modification with Bi nanoparticles

Electrode modification was performed according to an experimental procedure previously described by Lee et al. [28]. 2.5 mg of the synthesized Bi nanopowder was dispersed in 50 mL ultrapure water under ultrasonic radiation for 1 h. 10 μL of the dispersion was placed onto the carbon working electrode of a screen-printed strip. After solvent evaporation at room temperature, the electrode was stored for future use.

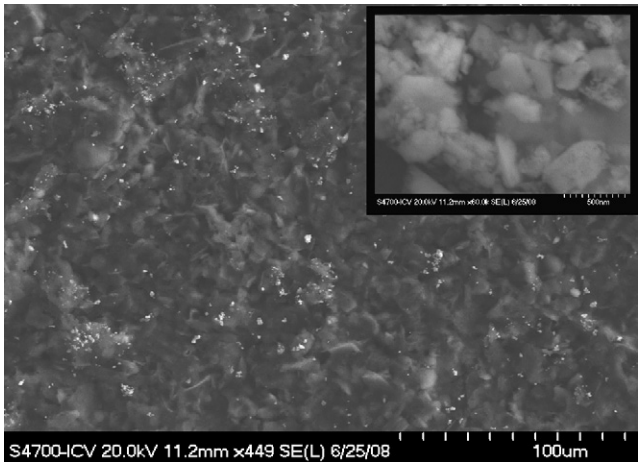


Fig. 1. Scanning electron microscopy (SEM) image of the Bi nanoparticles modified screen-printed carbon working electrode surface.

2.3.3. Voltammetric measurements

Convective (at stirred or flowing sample solutions) accumulation of Zn, Cd and Pb on the SPCE was carried out at a deposition potential of −1.4 V at variable rotation speed or flowing rates. After the accumulation time and 10 s equilibration, the anodic voltammetric curves were registered in the quiescent solution by square-wave voltammetry with frequency of 20 Hz, step potential of 5 mV and amplitude of 25 mV. The potential sweep was ended at −0.6 V (vs Ag/AgCl). The rest potential between experiments was set at −0.6 V to avoid damage of the Bi nanoparticles modification.

3. Results and discussion

3.1. SEM characterization of the modified electrodes

The simple and fast adsorption procedure employed in this work produces ready to use Bi modified electrodes without the need of special instrumentation used in previously described methodologies [22,23,28]. Fig. 1 shows a SEM image of a modified screen-printed carbon electrode. A nearly homogeneous dispersion of irregularly shaped adsorbed Bi particles was observed on the carbonaceous surface, with a size range within 0.25 and 5 μm. The large particle size distribution is probably caused by the broad size distribution of bismuth droplets formed in solvent by stirring effect [30]. Quantitative microanalysis of bismuth by scanning electronic microscopy with energy dispersion X ray (Fig. 2), confirmed the presence and purity of bismuth nanoparticles. Carbon and oxygen signals are also observed due to the nature of the electrode supporting material. A similar EDX spectrum has been reported for a similar Bi nanoparticles synthesis procedure based on reducing bismuth chloride with hydrazine hydrate in the presence of sodium oleate [31].

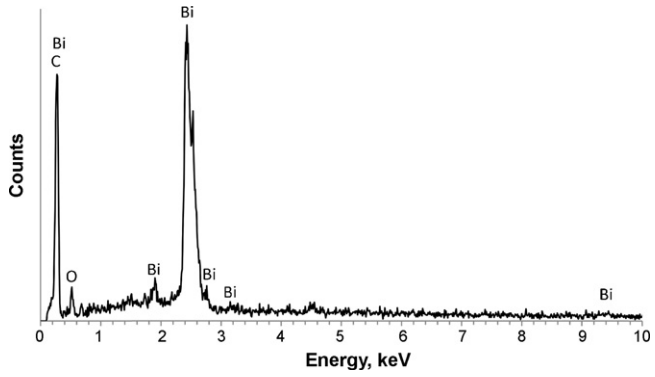


Fig. 2. Energy dispersion X ray (EDX) pattern of the Bi nanoparticles modified screen-printed working electrode surface.

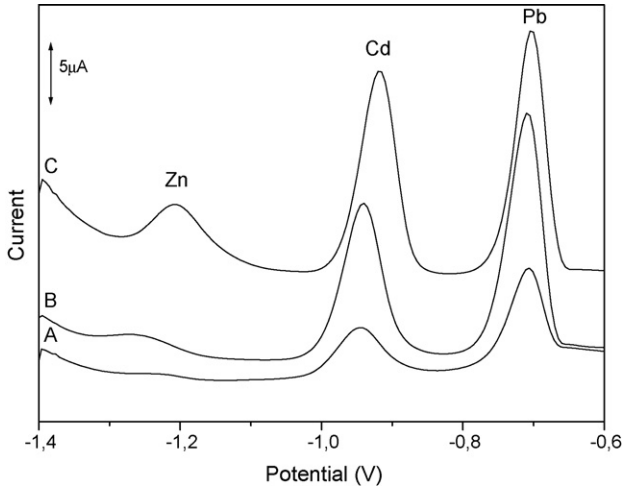


Fig. 3. Stripping voltammograms for 80 ng mL^{-1} Zn(II), Cd(II) and Pb(II) at the Bi nanoparticles modified screen-printed electrode. pH 4.5 0.1 M acetate buffer. Square-wave voltammetric stripping scan with a frequency of 20 Hz, step potential 5 mV, and amplitude 25 mV. (A) Unmodified electrode. (B) Convective cell with 500 r.p.m. stirring speed and 120 s deposition time. (C) Flow cell with 2,3 mL min^{-1} flow rate and 120 s deposition time.

3.2. General voltammetric behaviour and signal stability

The voltammetric stripping behaviour and signal stability of the ready to use Bi modified nanoparticles SPCEs for the detection of Zn(II), Cd(II) and Pb(II) was first inspected. Two hydrodynamic configurations as described in 2.2 were used to enhance analyte deposition during the accumulation step, based on convection by stirring (convective cell) and by flow (flow cell). Consecutive runs were carried out on the same Bi nanoparticles modified electrode on a pH 4.5 0.1 M acetate buffer solution containing 80 ng mL^{-1} Zn(II), Cd(II) and Pb(II). Fig. 3 shows the typical response obtained at both hydrodynamic configurations. Intense, well-resolved and clearly defined peaks were obtained, with enhanced signals with respect to the electroanalytical response on unmodified electrodes. The overall response is comparable with previously reported voltammetric stripping results at in situ [24,25] and preplated [18,19] Bi-film SPCEs. No significant differences in terms of peak height or potential were observed between the convective cell (Fig. 3, solid line) and the flow cell (Fig. 3, dashed line), apart from a slightly higher Zn(II) signal at the flow cell.

Signal stability was first inspected as a key parameter to test the practical usability of the proposed beforehand prepared Bi modified SPCE electrodes. Since electrode modification is based on passive adsorption of Bi sumicroparticles on the carbon screen-printed surface, erosion of the modified layer by repeated cycles of stirring or flowing accumulation could be expected, with the consequent lose of electrode activity. As seen in Fig. 4, analytical signals are stable for some measuring cycles, so a single modified electrode can be used for a complete set of blank measurement, sample run and standard additions if necessary. Electrode stability was found to be dependent on experimental conditions, especially the deposition potential. A somewhat better stability was found for the Pb signal. Signal stability is similar for both the convective cell and the flow cell hydrodynamic configurations. An experiment was conducted to test the repeatability of the modification procedure by assaying a set of 8 electrodes modified in parallel. The rela-

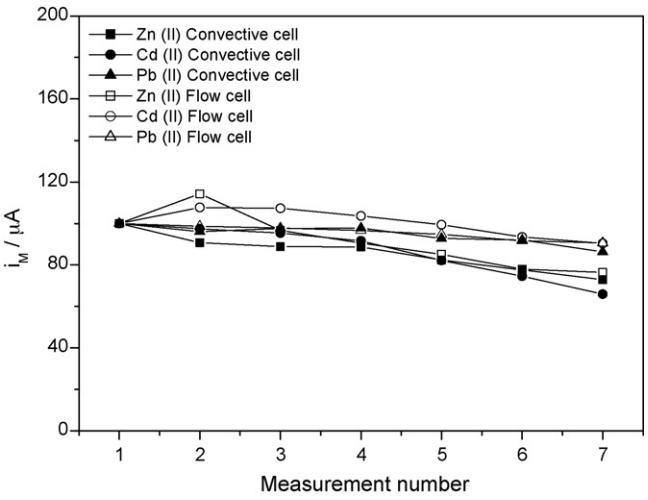


Fig. 4. Stability of peak currents for 80 ng mL^{-1} Zn(II), Cd(II) and Pb(II) at the Bi nanoparticles modified screen-printed electrode. pH 4.5 0.1 M acetate buffer. Square-wave voltammetric stripping scan with a frequency of 20 Hz, step potential 5 mV, and amplitude 25 mV. Convective cell with 500 r.p.m. stirring speed and 120 s deposition time. Flow cell with 2,3 mL min^{-1} flow rate and 120 s deposition time.

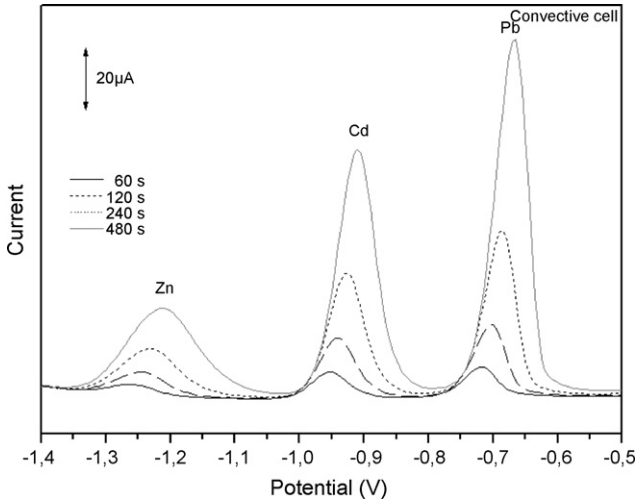


Fig. 5. Stripping voltammograms for 80 ng mL^{-1} Zn(II), Cd(II) and Pb(II) at the Bi nanoparticles modified screen-printed electrodes. pH 4.5 0.1 M acetate buffer. Square-wave voltammetric stripping scan with a frequency of 20 Hz, step potential 5 mV, and amplitude 25 mV. Convective cell with 500 r.p.m. stirring speed. Variable deposition times as indicated.

tive standard deviations were 6% for Zn, 7.5% for Cd, and 10.5% for Pb.

3.3. Instrumental variables

Stirring speed and flow rate were studied as hydrodynamic instrumental variables for the Bi modified SPCE placed in the convective cell and the flow cell, respectively, using a model solution containing 80 ng mL^{-1} Zn(II), Cd(II) and Pb(II). The influence of stirring speed on the analytical signals was inspected in the range from 0 to 900 r.p.m. Increased sensitivity was observed up to a point where turbulent conditions caused an unstable response, so an optimal value of 500 r.p.m. was selected. Increasing flow rates from 0.7 to 4.5 mL min^{-1} produced increasing peak currents at the flow cell. The effect of deposition time was studied in the range from 30 to 480 s, for Bi modified SPCE placed both at the convective and in the flow cell. Sample voltammograms are shown in Fig. 5 for the convective cell configuration. Linear correlations between peak currents and deposition times were obtained for Zn, Cd and Pb.

3.4. Calibration data

Calibration data for Zn, Cd and Pb by using the proposed Bi nanoparticles modified screen-printed electrodes were estimated by analyzing multistandars solutions of increasing concentrations, both at the convective cell and at the flow cell, the results being summarized at Table 1. Detection limits were calculated according to Long and Winefordner [32]. Somewhat better values were obtained for Zn(II) Cd(II) and Pb(II) at the flow cell with respect to the convective cell. The results were better than those previously described for stripping analysis on "in situ" Bi modified screen-printed electrochemical strips with convective accumulation on sample drops [25]. SWASV on modified thick film electrodes, prepared by electrochemical synthesis of Bi nanoparticles on thick film printed electrodes [27] gave somewhat lower detection limits: 0.52 ng mL^{-1} for Zn (II), 0.45 ng mL^{-11} for Cd (II) and 0.41 ng mL^{-1} for Pb (II), but the modification procedure is more complicated than our approach. Lee et al. [28] have reported the lowest to date voltammetric stripping detection limits for Cd (0.15 ng mL^{-1}) and Pb (0.07 ng mL^{-1}) on Bi nanoparticles modified electrodes, by using SWASV on a glassy carbon electrode modified with Bi nanopowder synthesized by a complex levitational gas condensation (LGC) method, using 10 min accumulation time. Five aliquots of a synthetic standard solution containing 12 ng mL^{-1} Zn(II) and 8 ng mL^{-1} Cd(II) and Pb(II), were assayed by the proposed methods. The recoveries obtained at the convective cell were in the range 101.3–118.3%, with RSD between 2.7 and 7.4%. The recoveries obtained at the flow cell were in the range 101.7–105.5%, with RSD between 2.1 and 7.5%.

3.5. Certified reference materials and real samples

The SPS-WW2 waste water certified reference material was assayed to test the applicability of the proposed Bi modified elec-

Table 1
Calibration data for the determination of Zn(II), Cd(II) and Pb(II) on screen-printed carbon electrodes modified by Bi nanoparticles. Square-wave voltammetric stripping scans with a frequency of 20 Hz, step potential 5 mV, and amplitude 25 mV. Convective cell with 500 r.p.m. stirring speed and 120 s deposition time. Flow cell with 2.3 mL min^{-1} flow rate and 120 s deposition time.

Metal ion	Regression	R^2	Linearity (%)	Analytical sensitivity	Detection limit (ng mL^{-1})
(a) Convective cell					
Zn(II)	$y = 0.044x + 0.036$	0.993	94	2.0	4.9
Cd(II)	$y = 0.106x - 0.002$	0.987	93	0.6	1.7
Pb(II)	$y = 0.941x - 0.029$	0.980	93	0.6	1.3
(b) Flow cell					
Zn(II)	$y = 0.037x - 0.004$	0.999	99	0.1	2.6
Cd(II)	$y = 0.238x - 0.144$	0.986	94	0.6	1.3
Pb(II)	$y = 0.172x + 0.050$	0.993	96	0.5	0.9

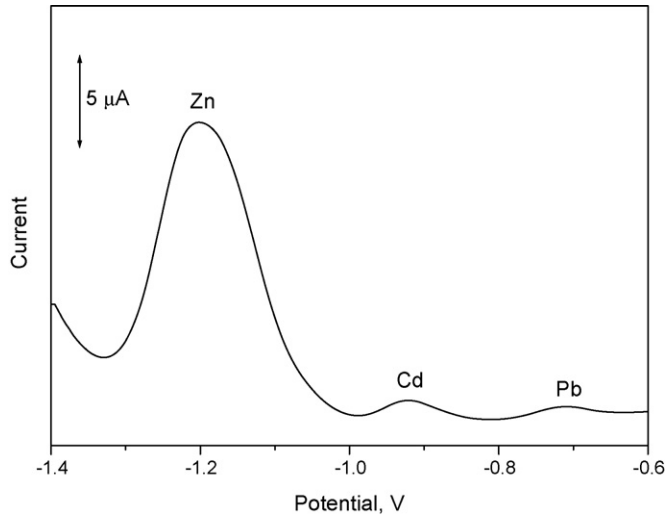


Fig. 6. Stripping voltammogram for a tap water sample at the Bi nanoparticles modified screen-printed electrodes. pH 4.5 0.1 M acetate buffer. Square-wave voltammetric stripping scan with a frequency of 20 Hz, step potential 5 mV, and amplitude 25 mV. Convective cell with 500 r.p.m. stirring speed. 120 s deposition time.

Table 2
Determination of Zn(II), Cd(II) and Pb(II) on screen-printed carbon electrodes modified by Bi nanoparticles in drinking water. Square-wave voltammetric stripping scans with a frequency of 20 Hz, step potential 5 mV, and amplitude 25 mV. Convective cell with 500 r.p.m. stirring speed and 120 s deposition time. Flow cell with 2.3 mL min^{-1} flow rate and 120 s deposition time.

Metal ion	SWASV convective cell (ng mL^{-1})	SWASV flow cell (ng mL^{-1})	ICP-MS (ng mL^{-1})
Zn(II)	212.3 ± 11.0	212.3 ± 29.7	216.1 ± 2.6
Cd(II)	11.6 ± 2.8	7.3 ± 0.9	11.1 ± 0.5
Pb(II)	3.7 ± 0.6	3.2 ± 0.1	3.3 ± 0.2

trodes and voltammetric methods. Five replicates were analyzed after 1/10 dilution and pH adjustment with acetate buffer. It was only possible to quantify Pb in the samples by the standard additions method; Zn and Cd were not measurable, probably due to high level of interfering ions like Cu(II) (2 mg/L), as previously described [12,19,33]. A concentration of 497 ± 24 ng mL^{-1} Pb(II) was measured by using the convective cell with the optimized experimental conditions (see Table 1); 461 ± 103 ng mL^{-1} Pb(II) was found by using the flow cell. The certified value is 500 ng mL^{-1}.

Tap water samples obtained at the lab were also assayed to test the proposed methodologies, using ICP-MS as the reference technique. The only treatment was pH adjustment with acetate buffer and Cd(II) addition to obtain a measurable level. Fig. 6 shows a typical voltammetric response obtained for the real sample at the convective cell. Table 2 presents the metal concentrations measured by the SWASV methods at the convective and flow cell, and the corresponding ICP-MS results. An overall acceptable agreement was found between both methodologies, showing potential applicability of the proposed methods for real sample analysis.

4. Conclusions

Passive adsorption of metallic bismuth chemically synthesized nanometric particles is a simple and useful protocol to modify screen-printed carbon electrodes for the voltammetric stripping detection of Zn(II), Cd(II) and Pb(II) in liquid samples. The placement of microlitre amounts of an aqueous Bi dispersion onto the working electrode followed by solvent evaporation to dryness resulted in stable adsorption of Bi nanoparticles, without the need of sophisticated instrumentation. This procedure allows easy and fast modification of multiple electrodes beforehand analysis, without the need of Bi preplating or addition of Bi(III) to the sample solution. Optimization of chemical and instrumental variables, including accumulation under convective and flow configurations using disposable three electrode screen-printed electrochemical strips gave detection limits in the low ng mL^{-1} with a good recovery and reproducibility. The performance of the proposed method was tested with a certified reference sample (waste water) and tap water, with overall acceptable results but affected by interferences when high Cu(II) concentrations were present, suggesting potential applicability for decentralized electrochemical sensing of heavy metals in water samples.

Acknowledgements

Financial support from Junta de Extremadura, Spain (project PDT07A016) is gratefully acknowledged. Mara Olivares acknowledges a grant from A.G. Siderurgia Balboa, Spain.

References

[1] S. Armenta, S. Garrigues, M. de la Guardia, Trends Anal. Chem. 27 (2008) 497.
[2] G. Hanrahan, D.G. Patila, J. Wang, J. Environ. Monit. 6 (2004) 657.
[3] J. Buffle, M.L. Tercier-Waeber, Trends Anal. Chem. 24 (2005) 172.
[4] W. Yantasee, Y. Lin, K. Hongsirikarn, G.E. Fryxell, R. Addleman, C. Timchalk, Environ. Health Perspect 115 (2007) 1683.
[5] I.J. Allan, B. Vrana, R. Greenwood, G.A. Mills, B. Roig, C. Gonzalez, Talanta 69 (2006) 302.
[6] M. Farré, L. Kantiani, S. Pérez, D. Barceló, Trends Anal. Chem. 28 (2009) 170.
[7] J.P. Hart, A. Crew, E. Crouch, K.C. Honeychurch, R.M. Pemberton, Anal. Lett. 37 (2004) 789.
[8] O. Domínguez Renedo, M.A. Alonso-Lomillo, M.J. Arcos Martínez, Talanta 73 (2007) 202.
[9] K.C. Honeychurch, J.P. Hart, Trends Anal. Chem. 22 (2003) 456.
[10] J. Wang, J. Lu, S. Hocevar, P. Farias, B. Ogorevc, Anal. Chem. 72 (2000) 3218.
[11] J. Wang, Electroanalysis 17 (2005) 1341.
[12] A. Economou, Trends Anal. Chem. 24 (2005) 334.
[13] E.A. Hutton, S.B. Hocevar, B. Ogorevc, Anal. Chim. Acta 537 (2005) 285.
[14] R. Pauliukaite, C.M. Brett, Electroanalysis 17 (2005) 1354.
[15] R.T. Kachoosangi, C.E. Banks, X. Ji, R.G. Compton, Anal. Sci. 23 (2007) 283.
[16] L. Baldrianova, I. Svancara, S. Sotiropoulos, Anal. Chim. Acta 599 (2007) 249.
[17] N.G. Naseri, S.J. Baldock, A. Economou, N.J. Goddard, P.R. Fielden, Anal. Bioanal. Chem. 391 (2008) 1283.
[18] J. Wang, J. Lu, S.B. Hocevar, B. Ogorevc, Electroanalysis 13 (2001) 13.
[19] R.O. Kadara, I.E. Tothill, Anal. Bioanal. Chem. 378 (2004) 770.
[20] R.O. Kadara, I.E. Tothill, Anal. Chim. Acta 623 (2008) 76.
[21] O. Zaouak, L. Authier, C. Cugnet, A. Castetbon, M. Potin-Gautier, Electroanalysis 21 (2009) 689.
[22] C. Kokkinos, A. Economou, I. Raptis, C. Efstathiou, Electrochim. Acta 53 (2008) 5294.
[23] Z. Zou, A. Jang, E. MacKnight, P. Wu, J. Do, P.L. Bishop, C.H. Ahn, Sens. Actuators B 134 (2008) 18.
[24] S. Chuanuwatanakul, W. Dungchai, O. Chailapakul, S. Motomizu, Anal. Sci. 24 (2008) 589.
[25] M.A. Granado Rico, M. Olivares-Marín, E. Pinilla Gil, Electroanalysis 20 (2008) 2608.
[26] C.M. Welch, R.G. Compton, Anal. Bioanal. Chem. 384 (2006) 601.
[27] N.A. Malakhova, N.Y. Stojko, K.Z. Brainina, Electrochem. Commun. 9 (2007) 221.
[28] G.J. Lee, H.M. Lee, C.K. Rhee, Electrochem. Commun. 9 (2007) 2514.
[29] S. Ward-Jones, A.O. Simm, C.E. Banks, R.G. Compton, Ultrason. Sonochem. 13 (2006) 261.
[30] Y. Zhao, Z. Zhang, H. Dang, Mater. Lett. 58 (2004) 790.
[31] Y. Wang, J. Zhao, X. Zhao, L. Tang, Y. Li, Z. Wang, Mater. Res. Bull. 44 (2009) 220.
[32] G.L. Long, J.D. Winefordner, Anal. Chem. 55 (1983) 712A.
[33] P. Masawat, S. Liawruangrath, J.M. Slater, Sens. Actuators B 91 (2003) 52.

Talanta 80 (2009) 636–642

Contents lists available at ScienceDirect

Talanta

journal homepage: www.elsevier.com/locate/talanta

Optimization of clean-up procedure for patulin determination in apple juice and apple purees by liquid chromatography

Francisco M. Valle-Algarra [a], Eva M. Mateo [a], Jose V. Gimeno-Adelantado [b], Rufino Mateo-Castro [b], Misericordia Jiménez [a,*]

[a] Dpto. de Microbiología y Ecología, Universidad de Valencia, Dr. Moliner 50, E-46100, Burjassot, Valencia, Spain
[b] Dpto. de Química Analítica, Universidad de Valencia, Dr. Moliner 50, E-46100, Burjassot, Valencia, Spain

ARTICLE INFO

Article history:
Received 29 April 2009
Received in revised form 9 July 2009
Accepted 20 July 2009
Available online 28 July 2009

Keywords:
Liquid chromatography
Patulin
Mycotoxins
Apple juice
Apple puree

ABSTRACT

Patulin (PAT) is a mycotoxin produced in fruits, mainly in apples, by several fungal species that can be carried into industrial apple juice by-products during factory processing. An analytical method for determination of PAT in apple juice and another one for determination of this compound in apple purees and apple compotes by liquid chromatography are proposed in the present paper. These methods have better precision and sensitivity than previously reported methods and focus mainly on extraction and clean-up. To accomplish analytical methods with higher accuracy, lower limits of detection and simpler procedures for application in quality control of the goods, different extraction and clean-up procedures for PAT were comparatively studied. PAT recoveries in apple juice spiked with 1.0 mg PAT/kg varied between 52.3% and 81.0%. The highest PAT recovery in apple puree spiked with 0.1 mg PAT/kg was 82.9%. Addition of NaH_2PO_4 during the extraction phase here reported for the first time has the advantage of keeping the pH slightly acidic, thus avoiding PAT degradation.

© 2009 Elsevier B.V. All rights reserved.

1. Introduction

Patulin {4-hydroxy-4H-furo[3,2-c]pyran-2(6H)-one} (PAT) is a polyketide lactone produced by certain *Penicillium*, *Aspergillus*, and *Byssochlamys* species, principally by *Penicillium expansum*, on fruits, such as apples, and apple products [1–3]. It has also been determined in oranges, peaches, apricots and tomatoes and its by-products [4,5]. It is considered immunotoxic, genotoxic, embryotoxic, and neurotoxic [6], but no adequate evidence exists for carcinogenicity in experimental animals. Recent studies have demonstrated that micromolar concentrations of PAT induce a rapid and dramatic decrease of transepithelial resistance of human epithelial intestinal cell lines without major signs of toxicity as assessed by the lactate dehydrogenase release assay [7].

PAT carryover during factory processing into industrial apple juice concentrates and subsequently into commercial apple juices as well as in a variety of apple products is a cause of food safety concern [8]. Based on a no-observed-effect level (NOEL) of 43 μg/kg body weight (bw)/day and a safety factor of 100, a provisional maximum tolerable daily intake (PMTDI) of 400 ng/kg bw was established by the JECFA and recently endorsed by the Scientific Committee for Food (SCF) [9,10].

PAT is considered a marker of the quality of apples entering the processing factory, and levels in the final product are subjected to legislative regulatory control. Maximum levels for this mycotoxin in fruity foodstuffs have been established by the European Commission. They are 50 μg/kg, for apple fruit juice and apple juice ingredients in other beverages, 50 μg/kg in spirit drinks, ciders and other fermented drinks, 25 μg/kg for solid apple products, such as apple puree, and 10 μg/kg for apple products intended for infants and young children [11]. The new regulation shows a separate limit for baby food to protect infants and young children who have a higher fruity foodstuffs consumption compared to adults [12].

Some methods have been developed to quantify PAT in apple juice concentrate [8,13–18]. They are based on TLC, GC and LC [19,20]. Among them, LC, coupled with UV detection, is particularly well suited to the determination of PAT. GC/MS and LC/MS are also used [21–24]. There are no commercial enzyme-linked immunosorbent assay kits available for testing PAT. For sample pretreatment, conventional methods such as multistep liquid–liquid extraction with ethyl acetate, the most common extraction solvent, and purification by $NaHCO_3$ solution have been widely used [8,11,19,25]. Liquid–liquid extraction (LLE) is time-consuming owing to the use of large amounts of organic solvents that imply environmental disposal problems [4]. Clean-up procedures using Na_2CO_3 deactivate PAT because this compound (a lactone) is more stable in acidic medium. In recent years, new methods of extraction and clean-up using SPE cartridges have been validated and

* Corresponding author. Tel.: +34 963543144; fax: +34 963544570.
E-mail address: misericordia.jimenez@uv.es (M. Jiménez).

0039-9140/$ – see front matter © 2009 Elsevier B.V. All rights reserved.
doi:10.1016/j.talanta.2009.07.040

published [19,20,25–29]. These methods are reportedly more reliable, repeatable with increased throughput, better recoveries, and increased sensitivity, enabling the determination of much lower levels of toxin [30]. In 2006, a simplified LLE procedure prior to LC separation and UV detection was reported [31]. This procedure is even simpler than those that use SPE columns [22]. However, more suitable analytical methods with high accuracy, low limits of detection and simple procedures are needed for application in quality control of the goods.

The method adopted by the European Committee for Standardization as European Standard for PAT determination in clear and cloudy apple juice and in apple puree is a LC method that has been validated by a collaborative trial at levels equal or higher than 25 μg PAT/kg [32,33]. This method has been recently modified to permit the determination of PAT at a level of 10 μg/kg or lower, and has been validated by a collaborative study [34].

The aim of this study was to develop an optimized analytical method for the determination of PAT in apple products (apple juice and apple puree) using LC-UV. A goal was to improve precision and sensitivity over previously reported methods. Comparison of the better existing methods and changes in some of them were performed to get the optimized one.

2. Experimental

2.1. Chemicals and reagents

The following standards were purchased for the analysis: PAT, 5-hydroxymethyl furfural (HMF), dihydrated monosodium phosphate and sodium hydrogencarbonate (Sigma–Aldrich, Alcobendas, Spain), sodium carbonate, anhydrous sodium sulfate, sodium acetate and acetone (Panreac, Barcelona, Spain), acetonitrile, methanol, hexane, ethyl acetate, acetic acid, SPE–C_{18} cartridges, and SPE–silica cartridges (J.T. Baker, Deventer, The Netherlands). All solvents were LC grade. Whatman No. 4 filter paper (Whatman, Maidstone, UK) were as well used. Milli-Q water (Milli-Q, Millipore, Milford, MA, USA) was generated in situ. Acetic acid/acetate buffer solution (AABS) was prepared by addition of 0.45 ml of acetic acid and 0.15 g of sodium acetate to 40 ml of water, the pH was adjusted to 4.0 with acetic acid. The volume was finally brought to 50 ml and the solution was stored in the dark.

2.2. Samples

Fifty-four samples of juices, solid products, including compotes and puree, and products for infants and young children containing apple and/or pear as the main component were studied. Samples were acquired in different supermarkets and stores located in Spain. Twenty-eight of them belonged to juices, 5 to compotes, nectars and jams made of apple, and the remaining samples to foods for young children. These samples were stored in their original packages at 4 °C until the moment of analysis. The samples were thoroughly homogenized and opened the same day of the analysis.

2.3. Preparation of standards

A 10-ml solution of PAT (1.0 mg/ml) in ethyl acetate was prepare and stored at −20 °C. A 0.2-ml aliquot of this PAT solution was poured into a 10-ml volumetric flask and evaporated to dryness under a stream of N_2. Immediately absolute ethanol was added to dissolve the residue, and after dilution to volume, the absorption of this standard stock solution was measured at 276 nm. The concentration of the mycotoxin was calculated according to the AOAC Official Method 974.18C [35].

Working standards were prepared by evaporation of the appropriate volume of the stock solution under a stream of N_2 at room temperature. Furthermore, they were solved in the corresponding volume of AABS. Calibration curves were made by LC analysis of these standard solutions.

2.4. Extraction and clean-up

The extraction and clean-up procedures described below have been applied to apple product samples that had been previously analyzed by official methods to check that they had no detectable PAT levels. Suitable volumes of PAT standard solution were added to blank matrices using a precision syringe to obtain concentrations of 0.02, 0.05, 0.1, and 1.0 mg of PAT/kg. The spiked samples were allowed to stand overnight and extracted as described below (Sections 2.4.1–2.4.7).

2.4.1. LLE–$NaHCO_3$ procedure

The method is based on the procedure reported by Iha and Sabino [31]. Apple juice was homogenized and 5 g was placed in a 50-ml centrifuge tube, together with 0.5 g of $NaHCO_3$ and 5 ml of ethyl acetate–hexane (96:4, v/v). The sample was shaken for 10 min in an orbital shaker at 250 rpm, and then centrifuged for 3 min at 3000 rpm. A 3-ml volume of the organic phase was transferred to a glass tube, together with 30 μl of acetic acid, and then the solvent was evaporated just to dryness under a gentle N_2 stream at room temperature. Immediately, 1 ml of AABS was added and the mixture was vigorously vortexed for 1 min. Finally, 50 μl was injected into the chromatographic system.

2.4.2. C_{18}–SPE procedure

It is based on the procedure reported by Li et al. [27]. C_{18} SPE cartridges were preconditioned with: (i) 10 ml of methanol, (ii) 3 ml of 10% methanol in aqueous solution, and (iii) 10 ml of water. The columns were not allowed to be dry. One gram of apple juice sample with 0.5 ml of AABS solution was transferred to a C_{18} SPE cartridge and the solution was pushed at 2–3 ml/min with a plunger. Next, 5 ml of hexane was added and then the column was dried with air stream for 15 min. Eluates were discarded and the cartridge was successively eluted (three times) with 5 ml of different mixtures of hexane–ethyl acetate–acetone where the proportion changed in the order 1:5:4, 1:4:5, and 1:3:6. The flow of each portion was stopped for 1 min to allow enough contact time with the packing material of the cartridge. The eluates were combined. Then, 30 μl of acetic acid was added to the solution and the solvent was evaporated just to dryness under a gentle N_2 stream at 30 °C. The extract was immediately dissolved with 1 ml of AABS and 50 μl was injected into the LC system.

2.4.3. Modified Arranz procedure

The method is based on the collaborative study performed by Arranz et al. [34] with some modifications: (i) sea sand was not added where LLE was accomplished because it was not necessary; (ii) purified sample was dissolved with AABS instead of water (pH 4). Briefly, 15 g of Na_2SO_4 and 2 g of $NaHCO_3$ were added to a 50-ml screw cap conical flask and homogenized. Then, 10 ml of ethyl acetate–hexane (60:40, v/v) was added and shaken softly. Ten grams of apple product sample was transferred to the conic tube, which was vortexed for 30 s and then shook in an orbital shaker at 250 rpm for 5 min. Then, the sample was centrifuged at 3000 rpm for 3 min to separate phases. A 2.5-ml aliquot of the organic phase was transferred to a SPE–silica cartridge without preconditioning. The eluate was collected at a flow of a drop per second in a glass vial containing 50 μl of acetic acid. Immediately, the cartridge was washed with 3 ml of ethyl acetate–hexane (60:40, v/v) to elute PAT in the same vial. The solvent was evaporated just to dryness in a gentle N_2 stream at 30 °C. After drying, 1 ml of AABS was quickly

added, the extract was vortexed for at least 1 min, and 50 μl was injected into the LC system.

2.4.4. MacDonald procedure

This is the AOAC Official Method 2000.02 for PAT in clear and cloudy apple juices and apple puree [32]. Ten grams of cleaned juice sample and 20 ml of ethyl acetate were put in a 250-ml separatory funnel and the mixture was shaken for 1 min. The extraction was repeated two more times and the organic phases were mixed in the separatory funnel. The tube that contained the organic phase extract was rinsed with 5 ml of ethyl acetate, which were also added to the separatory funnel. Four milliters of an aqueous solution of Na_2CO_3 (1.5%) was added and the mixture was shaken for 30 s. The aqueous phase was left in a conical flask and the organic phase was filtered through a filter paper that contained 15 g of anhydrous sodium sulfate into a balloon flask. The aqueous phase was transferred to the separatory funnel again, the conical tube was rinsed with 10 ml of ethyl acetate and this liquid was added to the separatory funnel. Then, it was shaken, let stand and once the two phases were separated, the aqueous phase was discarded and the organic phase was filtered through filter paper containing anhydrous sodium sulfate into a balloon flask. Finally, the separatory funnel was washed twice with 10 ml of ethyl acetate and the rinsing solvent was added to the flask. The obtained solution was evaporated just to dryness under a gentle N_2 stream at room temperature. The remaining solid was quickly solved in 1 ml of AABS solution, and a 50-μl aliquot was injected into the LC system.

2.4.5. LLE–NaH_2PO_4 procedure

This procedure is similar to the LLE–$NaHCO_3$ procedure (Section 2.4.1), but $NaHCO_3$ was substituted by the same amount of NaH_2PO_4.

2.4.6. LLE–NaH_2PO_4–silica procedure

It is applied to apple juice. The first part of the extraction until the collection of 3 ml of organic phase coincides with the LLE–NaH_2PO_4 procedure (Section 2.4.5). The difference is that the 3-ml aliquot (without acetic acid addition) was transferred to a non-preconditioned silica SPE cartridge and the eluate was collected at a drop per second in a glass vial with 50 μl of acetic acid. Immediately, the cartridge was washed with 3 ml of ethyl acetate–hexane solution (60:40, v/v) to quantitatively elute PAT of the column in the same vial. The solvent was evaporated just to dryness under a gentle N_2 stream at 30 °C. Then, 1 ml of AABS was immediately added, the extract was vortexed during at least 1 min and 50 μl was injected into the LC system.

2.4.7. LLE–NaH_2PO_4–C_{18} procedure

The apple product sample was homogenized and 5 g was placed in a 50-ml centrifuge tube containing 1 g of NaH_2PO_4, 5 g of anhydrous Na_2SO_4 and 5 ml of ethyl acetate–hexane (96:4, v/v). The tube was shaken in an orbital shaker (250 rpm, 10 min) and later centrifuged (3000 rpm, 3 min). Three milliliters of the organic phase was transferred to a glass tube containing 30 μl of acetic acid, and the solvent was evaporated just to dryness under a gentle N_2 stream at room temperature. Immediately, 2× 1 ml of AABS was added and the mixture was transferred to a C_{18} SPE cartridge, previously conditioned with 5 ml of ethyl acetate–hexane (80:20, v/v) and then with 5 ml of water. The redissolved extract was passed through the cartridge at a speed of 2–3 ml/min with the help of a plunger. Immediately, the cartridge was washed with 5 ml of hexane and then dried with a flow of air during about 15 min. These eluates were discarded and the column was washed with 4 ml of ethyl acetate–hexane (80:20, v/v). The eluate was collected in a 10-ml screw cap tube. Thirty microliters of acetic acid was added to the eluate and the solvent was evaporated just to dryness under a gentle N_2 stream at 30 °C. The solid was quickly dissolved with 0.5 ml of AABS and 50 μl was injected into the LC system.

2.5. Patulin determination

The obtained aliquots were analyzed by liquid chromatography. The LC system was a Waters 600 quaternary pump, with a Waters 717 autosampler and a Waters 996 UV–visible diode array detector. Millennium 32 (version 3.05.01) software was used to control the system and to process the obtained signals (Waters, Milford, MA, USA). The separation was performed at 30 °C in a C18 Agilent Zorbax XDB-C18® reversed-phase column (150 mm × 4.6 mm, 5 μm particle size) connected to an Agilent Zorbax® guard column (4 mm × 3 mm, 5 μm particle size) filled with the same stationary phase.

To optimize the separation column, 50 μl of AABS containing 2 μg of HMF/ml and 50 ng of PAT/ml was injected. HMF and PAT should elute as two completely separated peaks. The content of acetonitrile in the LC mobile phase is generally increased to achieve this objective. The two peaks can be separated satisfactorily using acetonitrile–water as a mobile phase. The elution was carried out at a flow of 1 ml/min with a mixture of acetonitrile (solvent A) and water (solvent B) applying the following gradient program: (i) initial solvent: 99% B, maintained for 2 min, (ii) lineal variation of B from 99% to 90% for 11 min, (iii) lineal variation of B from 90% to 1% for 3 min, (iv) 1% of B for 1 min, and (v) return to the initial conditions in 1 min. Detection wavelength was 276 nm.

2.6. Validation of analytical methods

The analytical methods used for PAT were assessed for selectivity, linearity, and precision from the regulated minimum of 0.010–5.0 μg/ml. Selectivity was checked by injecting three times 50 μl of PAT standard solution before injecting extracted samples and comparing the peak retention times and the UV spectra of the substances that produce these peaks. Linearity was assessed by performing triplicate injections of standard solutions whose concentrations were 0.01, 0.02, 0.05, 0.1, 0.25, 0.5, 1.0, 5.0, 10.0 and 15.0 μg PAT/ml. Standard curves were generated by linear regression of peak areas against concentrations.

Precision and recovery were established for each method by determination of PAT in apple juice and apple puree, covering the range of the method (0.02, 0.05, 0.1, and 1.0 mg/kg). Recovery was determined by comparing the absolute responses of PAT obtained from the apple juice samples with the absolute responses of calibration standards. Recovery ratios between 70% and 105% and RSD < 15% for precision were considered as acceptable.

The limit of detection (LOD) was considered as the PAT concentration that provides a signal equal to $b + 3S_b$, where b is the intercept of the calibration curve and S_b is the standard error of the estimate assuming to be the blank, and the limit of quantification (LOQ) was considered equal to 3× LOD [36].

3. Results and discussion

3.1. Comparison of procedures for apple juice

The analytical methods chosen for this comparative study are the most common at present. Comparison involve two official methods [32,34] and two other more recent and simple methods (developed by Li et al. [27] and Iha and Sabino [31]). In addition, variations of some of the previous methods were included in this study. For comparative purposes the study has been centered mainly on the following aspects: recovery, limit of detection (LOD),

Table 1
Average recoveries, relative standard deviations ($N = 3$) and limits of detection of PAT by different procedures in apple juices contaminated with 0.02, 0.05, 0.1 and 1.0 mg of mycotoxin/kg.

Procedure	Spiking level (mg/kg)	Recovery (%)	RSD (%)	LOD (μg/kg)
LLE–$NaHCO_3$	0.02	69.3	7.3	2.1
	0.05	72.3	4.2	
	0.1	74.3	1.7	
	1.0	72.1	3.1	
C18–SPE	0.02	72.4	12.5	6.6
	0.05	65.5	7.3	
	0.1	68.3	9.9	
	1.0	72.5	11.0	
Modified Arranz	0.02	70.1	10.3	2.5
	0.05	68.3	7.1	
	0.1	64.2	4.5	
	1.0	68.9	5.3	
MacDonald	0.02	72.4	6.2	1.8
	0.05	78.4	9.4	
	0.1	73.2	8.5	
	1.0	81.0	12.3	
LLE–NaH_2PO_4	0.02	71.6	6.8	2.0
	0.05	73.6	5.6	
	0.1	82.9	3.1	
	1.0	77.0	1.7	
LLE–NaH_2PO_4–silica	0.02	62.4	9.3	2.1
	0.05	63.9	5.8	
	0.1	67.8	4.0	
	1.0	69.2	4.9	
LLE–NaH_2PO_4–C_{18}	0.02	65.4	8.2	1.3
	0.05	62.3	6.4	
	0.1	55.1	6.2	
	1.0	52.3	8.0	

and selectivity (possible interferences that can appear in the analyzed samples). As shown in Table 1, it can be found that recoveries in apple juice spiked with 0.1 mg PAT/kg varied between 55.1% for the LLE–NaH_2PO_4–C_{18} procedure and 82.9% for the LLE–NaH_2PO_4 procedure. Although PAT recovery is below the required minimum value (60%) for the LLE–NaH_2PO_4–C_{18} procedure, its LOD is the lowest (1.3 μg/kg) of all the procedures. This is due to the higher sample pre-concentration ratio (6:1), which is generally superior to the one for the other methods.

The best recoveries in apple juices spiked with 0.05 mg PAT/kg were obtained using the methods of MacDonald (78.4%) and LLE–NaH_2PO_4 (73.6%) (Table 1). Although the MacDonald method provided good recoveries, the obtained RSD is relatively high (9.4%) and the LOD (1.8 μg/kg) is not significantly lower than those attained by the other methods. The sample is concentrated in a 10:1 ratio by the MacDonald method, whereas this ratio is 3:1 by the LLE–$NaHCO_3$ method, whose LOD is 2.1 μg/kg. This is because, although the sample is very concentrated, many impurities may be co-eluted due to the more complex liquid–liquid extraction step. Other disadvantages of the MacDonald method are the time-consuming extraction step and the cost of solvents, since it uses more volume of organic solvent than other methods (see Section 2.4.4), which also involves environmental problems. The LLE–NaH_2PO_4 method is fast, simple, has a low LOD (2.0 μg/kg) and a low RSD that provides good repeatability and is accurate enough. This method provided the best results among all the studied methods. According to what has been indicated, extraction in basic medium is used to eliminate acidic compounds. Nevertheless, any interference originating a peak near PAT, or any increase of the background noise that could influence the result of PAT determination was not observed following the LLE–NaH_2PO_4 method. In addition, PAT is more stable in slightly acidic medium than in basic medium. For this reason, it is reasonable to think that this procedure must have a higher PAT recovery.

Table 2
Average recoveries and relative standard deviations for PAT in apple juice spiked at 0.02 and 0.1 mg/kg obtained by change in the proportions of the extraction solvent mixture used in the LLE–$NaHCO_3$ procedure ($N = 3$).

	Spiking level 0.02 mg PAT/kg		Spiking level 0.1 mg PAT/kg	
	Recovery (%)	RSD (%)	Recovery (%)	RSD (%)
98:2	61.9	9.0	63.1	5.3
96:4	75.2	7.3	73.4	2.3
90:10	59.8	8.2	67.0	6.4
80:20	60.1	11.2	63.8	6.1
60:40	28.4	8.3	39.2	6.7

With the purpose of improving the LLE–$NaHCO_3$ method, different ethyl acetate–hexane ratios were assayed to improve the LLE step (Table 2). The best toxin recoveries were 75.2% and 73.4%, for spiking levels of 0.02 and 0.1 mg PAT/kg, respectively, when the original ethyl acetate–hexane ratio (96:4) was used.

At a spiking level of 0.1 mg PAT/kg the recoveries obtained by the C_{18}–SPE method were lower than those obtained by the LLE–$NaHCO_3$ method (68.3% and 74.3%, respectively) (Table 1). In addition, the RSD of the C18–SPE method is higher (9.9%), thus being less precise. The LOD of the C_{18}–SPE method (6.6 μg/kg) is the highest, because sample concentration ratio is 1:1. Moreover, the chromatograms obtained by this method were the noisiest. Some changes in the elution solvent were assayed to improve the procedure for PAT elution out of the C_{18} cartridge (Table 3). A series of three mixtures hexane–ethyl acetate–acetone of different composition used by Li [27], was substituted by a unique mixture of two solvents (ethyl acetate–hexane) which implies an easier and fast procedure. When ethyl acetate–hexane (96:4) (the mixture used in the Iha extraction procedure) was used, PAT was not recovered (Table 3). However, when the polarity was lowered (ethyl acetate–hexane, 80:20), the recovery obtained was not significantly different ($p < 0.05$) from that obtained by the original C_{18}–SPE method. This modification led to less solvent consumption and lower run time, but it was unable to improve recovery and LOD.

Finally, the modified Arranz method and the LLE–NaH_2PO_4–silica method gave recovery ratios of 68.3% and 63.9%, respectively, for apple juices spiked with 0.05 mg PAT/g. These values are not significantly different between them ($p < 0.05$). For this reason, the modification carried out in the LLE–NaH_2PO_4–silica procedure did not produce any significant improvement.

Fig. 1 shows the chromatograms obtained for an apple juice sample spiked with PAT (0.1 mg/kg) by the methods of LLE with NaH_2PO_4 (Fig. 1A), modified Arranz (Fig. 1B), and LLE–NaH_2PO_4–C_{18} (Fig. 1C). The peak of PAT eluted at about 13.3 min. Moreover, in all except the LLE–NaH_2PO_4–C_{18} method, another peak that can interfere with the analyte, usually appeared

Table 3
Average recoveries and relative standard deviations ($N = 3$) for PAT in apple juice spiked with 0.05 and 1.0 mg of mycotoxin/kg, obtained by change in the SPE solvent mixture using the C_{18}–SPE procedure.

	Spiking level 0.05 mg/kg		Spiking level 1.0 mg/kg	
	Recovery (%)	RSD (%)	Recovery (%)	RSD (%)
Li method (hexane–EtAc–acetone in variable proportion)[a]	68.4	11.5	75.3	10.2
EtAc–hexane (96:4)	–	–	–	–
EtAc–hexane (80:20)	68.1	9.3	71.4	8.4
EtAc–hexane (60:40)	53.5	12.4	46.7	7.2

[a] See Section 2.4.2.

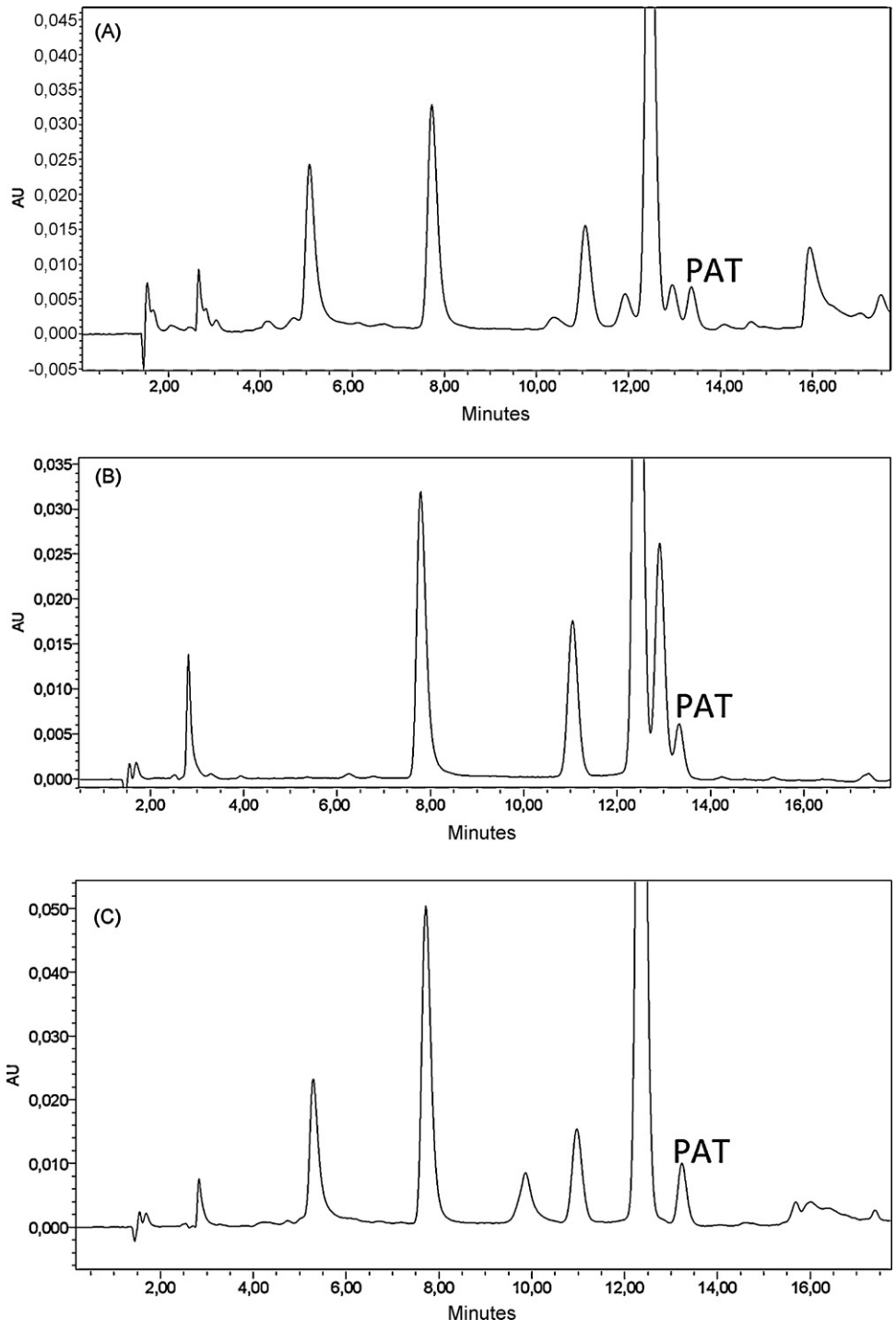


Fig. 1. Chromatograms of an apple juice sample contaminated with 0.10 mg PAT/kg using three procedures for sample preparation: (A) LLE–NaH_2PO_4, (B) modified Arranz, and (C) LLE–NaH_2PO_4–C_{18}.

at 12.8 min. The LLE–NaH_2PO_4–C_{18} procedure eliminates this interfering peak, although the recoveries were below 70%.

3.2. Comparison of procedures for solid apple products

Comparison of procedures was limited to the Modified Arranz and LLE–NaH_2PO_4–C_{18} methods that can be applied to semisolid samples, such as purees. The other procedures are only applicable to juices and when they are used for apple purees and compotes the chromatograms show several interfering peaks. The recovery ratios and LOD obtained by these two procedures are listed in Table 4, which shows that PAT recoveries were always slightly higher when the LLE–NaH_2PO_4–C_{18} procedure was performed. Nevertheless, the LOD of the LLE–NaH_2PO_4–C_{18} procedure (1.4 μg/kg) was lower than the LOD of the Modified Arranz one (2.4 μg/kg). This may be due to the different pre-concentration ratio of the sample before being injected in the chromatograph, as commented for apple juice (Section 3.1). It is worth taking into account that, when the LLE–NaH_2PO_4–C_{18} procedure is used, the peak that can interfere with PAT detection does not appear (Fig. 2) and, hence, the determination is free from this error. The chromatogram for the sample of puree of apple and banana for infant consumption spiked with

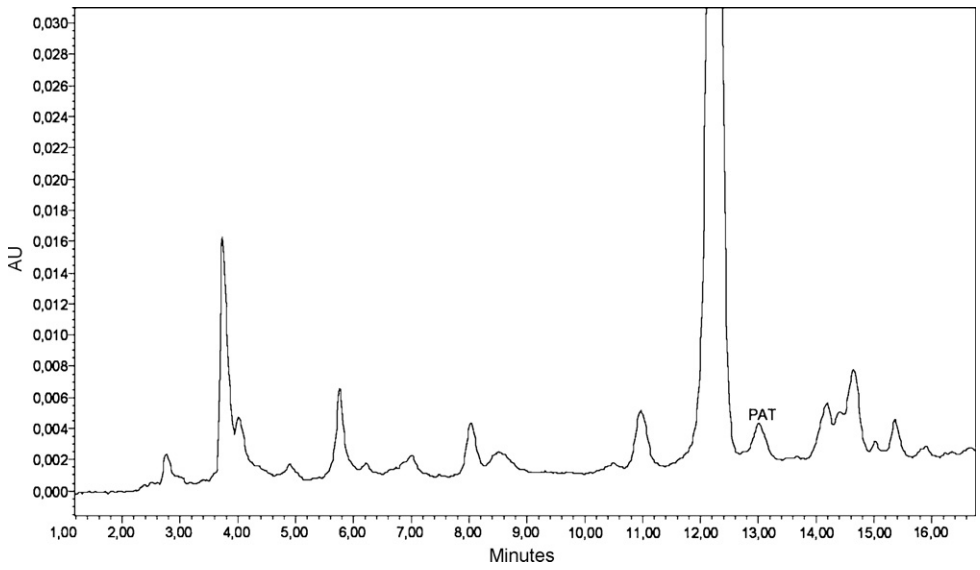


Fig. 2. Chromatogram of an apple/banana puree sample destined to infant consumption contaminated with 0.02 mg PAT/kg using the LLE–NaH_2PO_4–C_{18} procedure for sample preparation.

0.02 mg PAT/kg using the LLE–NaH_2PO_4–C_{18} procedure is observed in Fig. 2. Moreover, addition of NaH_2PO_4 in the LLE–NaH_2PO_4–C_{18} procedure makes slightly acidic the sample pH, which hinders the lactone ring opening.

This method is valid for compotes and apple puree products but its application to dried solid apple products, as performed by Katerere et al. [29], has not been assayed.

3.3. Occurrence of patulin in apple samples

The PAT levels in the apple samples determined by applying the Iha–NaH_2PO_4 method for juices, and the Iha–C_{18} method for apple puree and fruity products for young children were always below the LOQ. However, there were two juice samples that contained PAT concentrations over the LOD (between 2 and 6 μg/kg). Therefore, none of the analyzed samples appears to contain PAT concentrations surpassing the maximum levels fixed by the European Union. Although the risk of PAT intake by the Spanish population is apparently small, it cannot be ruled out. These results should be confirmed by a broader study and, if PAT seemed to be a problem, the apple product manufacturing industries should implant strict control systems to avoid the contamination with this mycotoxin.

In another survey concerning apple juices and apple products performed in Spain [37], PAT was detected in 2 out of 13 samples. The maximum concentration was 7.5 ng/g, which is slightly higher than the levels determined in our analyses, where the highest toxin level was only slightly above the LOD. In that survey [37], PAT was not detected in purees and apple compotes although one out of 59 infant food samples was found to contain 5 ng/g. In all the samples, PAT concentrations were below the limits permitted in the European Union. However, other authors [38] found PAT in 66 out of 100 apple juice samples with an average of 19.4 ng/ml and a maximum value of 118.70 ng/ml. Similar values were obtained in other surveys in Spain [39–41]. Prieta et al. [39] carried out a survey of PAT in 100 samples of commercial apple juice and 12 samples of apple food for children. In apple juice, PAT was detected in 82% of samples, and the maximum concentration found was 170 μg/l with a mean level of 13.8 μg/l, and 7 samples had PAT levels above 50 μg/l. However, children's apple food samples were free of PAT. Rovira et al. [40] found this mycotoxin in only one of the 18 apple juices analyzed with a level higher than 50 μg/l, and 15 samples of them were positives to PAT with a mean value of 20.2 μg/l. González-Osnaya et al. [41] analyzed 53 apple-containing products and detected PAT in 26.4% of the samples in the 1.5–50.9 μg/l range, and 6 samples surpassed the maximum permitted level in the European Union.

Although the results from different authors do not agree, it can be observed that contamination with PAT of apple products has occurred during the past years in Spain. Control of products intended for infant consumption is being stricter but in any case, a greater effort to reduce the incidence of PAT in apple-based food is needed to minimize the toxicological risk.

Table 4
Average recoveries, relative standard deviations ($N = 3$) and limits of detection for PAT in fruity foods for young children containing mainly apple puree at spiking levels of 0.02, 0.05, 0.1 and 1.0 mg of mycotoxin/kg by two procedures.

Procedure	Spiking level (mg/kg)	Recovery (%)	RSD (%)	LOD (μg/kg)
Modified Arranz	0.02	69.0	7.4	2.4
	0.05	72.8	8.1	
	0.1	68.3	7.3	
	1.0	65.3	6.5	
LLE–NaH_2PO_4–C_{18}	0.02	70.1	8.7	1.4
	0.05	74.3	6.2	
	0.1	71.6	8.9	
	1.0	69.3	5.7	

4. Conclusions

An easy and fast sample preparation procedure for the determination of PAT in apple juices has been proposed. It uses NaH_2PO_4 [30] instead of $NaHCO_3$ and involves a simple liquid–liquid extraction and has a low LOD (2.0 μg/kg) to be applied in the frame of the European Union regulation. This procedure is carried out at acidic pH thus avoiding PAT degradation during manipulation. Another procedure for the determination of PAT in apple purees and apple compotes is suggested. It is similar to that applied to apple juices, but there is an additional clean-up step with C_{18} SPE cartridge to eliminate impurities that were not removed during the liquid–liquid extraction step.

Acknowledgements

The authors wish to thank financial support from FEDER and Spanish Government "Ministerio de Ciencia e Innovación" (Project AGL2007-66416-C05-01/ALI and a research grant).

References

[1] V. Gökmen, J. Acar, J. Chromatogr. A 815 (1998) 99–102.
[2] N.L. Leggott, G.S. Shephard, Food Control 12 (2001) 73–76.
[3] L. Wu, J. Hyg. Res. 21 (1992) 101.
[4] V. Gökmen, J. Acar, K. Sarioğlu, Anal. Chim. Acta 543 (2005) 64–69.
[5] P. Majerus, K. Kapp, Reports on tasks for scientific cooperation, task 3.2.8. Assessment of dietary intake of patulin by the population of EU Member States. Brussels: SCOOP Report, 2002. http://europa.eu.int/comm/food/fs/scoop/3.2.8.en.pdf.
[6] M.M. Moake, O.I. Padilla-Zakour, R.W. Worobo, Compr. Rev. Food Sci. Food Saf. 1 (2005) 8–21.
[7] R. Mahfoud, M. Maresca, N. Garmy, J. Fantini, Toxicol. Appl. Pharmacol. 181 (2002) 209–218.
[8] G.S. Shephard, N.L. Leggott, J. Chromatogr. A 882 (2000) 17–22.
[9] M.F.A, Wouters, G.J.A. Speijers, Food Additives Series 35. Toxicological evaluation of certain food additives and contaminants, World Health Organization, Geneva, 1996, p. 337. http://www.inchem.org/documents/jecfa/jecmono/v35je16.htm.
[10] SCF, Scientific Committee on Food, Minutes of the 120th meeting, Brussels, 2000. http://ec.europa.eu/food/fs/sc/scf/out55_en.pdf.
[11] Commission Regulation (EC) No. 1881/2006 of 19 December 2006 setting maximum levels for certain contaminants in foodstuffs. Official Journal of the European Union L 364, 5–24.
[12] L. Piemontese, M. Solfrizzo, A. Visconti, Food Addit. Contam. 22 (2005) 437–442.
[13] V. Gökmen, J. Acar, J. Chromatogr. A 730 (1996) 53–58.
[14] V. Gökmen, J. Acar, J. Chromatogr. A 847 (1999) 69–74.
[15] V. Sewram, J.J. Nair, T.W. Nieuwoudt, N.L. Leggott, G.S. Shephard, J. Chromatogr. A 897 (2000) 365–374.
[16] J.Y. Song, G.F. Yu, X.H. Wei, Chin. J. Health Lab. Technol. 9 (1999) 227–228.
[17] S.M. Wang, W.L. Yang, Biotechnology 13 (2003) 18.
[18] K.Q. Zhou, Foreign Med. Sci. Sect. Hyg. 28 (2001) 29–32.
[19] G. Boonzaaijer, I. Bobeldijk, W.A. van Osenbruggen, Food Control 16 (2005) 587–591.
[20] M.W. Trucksess, Y.F. Tang, J. AOAC Int. 82 (1999) 1109–1113.
[21] R. Ito, H. Yamazaki, K. Inoue, Y. Yoshimura, M. Kawaguchi, H. Nakazawa, J. Agric. Food Chem. 52 (2004) 7464–7468.
[22] H.S. Marks, J. AOAC Int. 90 (2007) 881–885.
[23] H.S. Rupp, S.B. Turnipseed, J. AOAC Int. 83 (2000) 612–620.
[24] M. Sulyok, F. Berthiller, R. Krska, R. Schuhmacher, Rapid Commun. Mass Spectrom. 20 (2006) 2649–2659.
[25] A.R. Brause, M.W. Trucksess, F.S. Thomas, S.W. Page, J. AOAC Int. 79 (1996) 451–455.
[26] T.A. Eisele, M.Z. Gibson, J. AOAC Int. 86 (2003) 1160–1163.
[27] J. Li, R. Wu, Q. Hu, J. Wang, Food Control 18 (2007) 530–534.
[28] M.W. Trucksess, Y. Tang, Method Mol. Biol. 157 (2001) 205–213.
[29] D.R. Katerere, S. Stockenström, G.S. Shephard, Food Control 19 (2008) 389–392.
[30] D.R. Katerere, S. Stockenström, G. Balducci, G.S. Shephard, J. AOAC Int. 90 (2007) 162–166.
[31] M.H. Iha, M. Sabino, J. AOAC Int. 89 (2006) 139–143.
[32] S. MacDonald, M. Long, J. Gilbert, I. Felgueiras, J. AOAC Int. 83 (2000) 1387–1394.
[33] CEN (European Committee for Standardization). Determination of patulin in clear and cloudy apple juice and puree – HPLC method with liquid/liquid partition clean-up. CEN/TC 275/WG5. Food analysis – Biotoxins – Foodstuffs – EN 14177, Brussels: CEN, 2003.
[34] I. Arranz, J. Stroka, K. Kroeger, M. Derbyshire, C. Mischke, E. Anklam, Validation of an analytical method to determine the content of patulin in apple juice and fruit puree: Collaborative trial. Euroreport: EUR 21008, Brussels: European Commission, 2004.
[35] Official Methods of Analysis, 17th ed., AOAC International, Gaithersburg, MD, 2000, Methods 974.18 and 995.10.
[36] N. Miller, C. Miller, Statistics and Chemometrics for Analytical Chemistry, 4th ed., Prentice Hall, Upper Saddle River, NJ, USA, 2000.
[37] T.M. Legarda, P.A. Burdaspal, Alimentaria 368 (2005) 69–79.
[38] M. Murillo-Arbizu, S. Amézqueta, E. González-Peñas, A. López de Cerain, Food Chem. 113 (2009) 420–423.
[39] J. Prieta, M.A. Moreno, S. Díaz, G. Suárez, L. Domínguez, J. Agric. Food Chem. 42 (1994) 1701–1703.
[40] R. Rovira, F. Ribera, V. Sanchis, R. Canela, R.J. Agric, Food Chem. 41 (1993) 214–216.
[41] L. González-Osnaya, J.M. Soriano, J.C. Moltó, J. Mañes, Food Addit. Contam. 24 (2007) 1268–1274.

Talanta 80 (2009) 643–650

Contents lists available at ScienceDirect

Talanta

journal homepage: www.elsevier.com/locate/talanta

Optimisation and validation of programmed temperature vaporization (PTV) injection in solvent vent mode for the analysis of the 15 + 1 EU-priority PAHs by GC–MS

José Ángel Gómez-Ruiz [1], Fernando Cordeiro, Patricia López, Thomas Wenzl *

European Commission, Joint Research Centre, Institute for Reference Materials and Measurements (IRMM), Retieseweg 111, B-2440 Geel, Belgium

ARTICLE INFO

Article history:
Received 29 April 2009
Received in revised form 3 July 2009
Accepted 20 July 2009
Available online 28 July 2009

Keywords:
15 + 1 EU-priority polycyclic aromatic hydrocarbons (PAHs)
Large volume injection (LVI)
Programmed temperature vaporization (PTV)
Gas chromatography mass spectrometry (GC–MS)
Food

ABSTRACT

This paper presents the optimisation of a programmed temperature vaporization solvent vent (PTV-SV) injection gas chromatographic mass spectrometric (GC–MS) method for the analysis of the 15 + 1 EU-priority PAHs in food extracts. Three operation parameters (vent time, vent flow and vent pressure) were optimised by applying a D-optimal experimental design. Among these variables, vent time showed the highest effect on the analytical response (signal intensity) of the target PAHs.

The 15 + 1 EU-priority PAHs were analysed in solvent solutions and in extracts of fortified sausage. In addition, blank lamb meat extracts were prepared and spiked with the target PAHs prior to GC–MS analysis. The performance of the optimised PTV-SV injection GC–MS method was scrutinised for linearity, precision, matrix effects and robustness. All parameters were found satisfactorily. Compared to PTV injection in splitless mode, the PTV-SV injection method provided an enhancement of sensitivity for all target PAHs. Especially significant was the improvement of the S/N ratios of the compounds with the highest molecular mass.

© 2009 Elsevier B.V. All rights reserved.

1. Introduction

Polycyclic aromatic hydrocarbons (PAHs) are a large group of organic compounds containing two or more fused aromatic rings constituted of carbon and hydrogen atoms. PAHs constitute a large class of environmental contaminants. They are emitted from diesel engines, but also stationary sources, e.g. different kinds of industries [1]. The main source of exposure to PAHs for non-smoking humans is food. Food might be contaminated by PAHs through the environment or via formation during processing. The dietary intake of PAHs is of concern because some of them can cause cancer in humans [2]. The Scientific Committee on Food (SCF) assessed in 2002 the toxicity of 33 PAHs and concluded that 15 of them are potentially genotoxic and carcinogenic to humans [3]. In 2005, the Joint FAO/WHO Expert Committee on Food Additives (JECFA) identified an additional PAH (benzo[*c*]fluorene) as probably carcinogenic [4]. The joint set of PAHs is recognized as the 15 + 1 EU-priority PAHs (Table 1). This terminology serves to distinguish them from the 16 PAHs highlighted in the 1970s by the US Environmental Protection Agency (EPA) [5]. Though eight of the 15 + 1 EU-priority PAHs are identical with PAHs of the US-EPA list they are challenging from the analytical point of view. Difficulties are related to both separation efficiency and sensitivity.

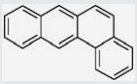
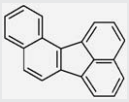
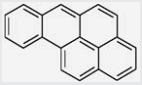
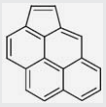
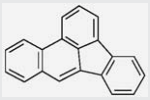
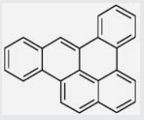
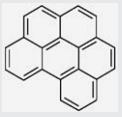
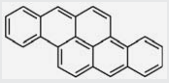
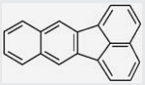
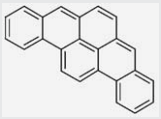
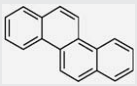
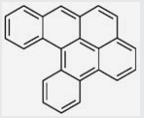
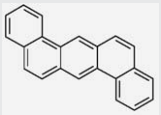
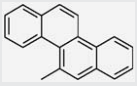
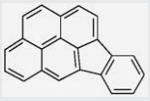
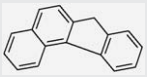
High discrimination of the signal intensities of low and high molecular weight compounds is a common problem in the analysis of PAHs by gas chromatography [6,7]. The lower abundance of the heavier compounds causes also smaller signal-to-noise (S/N) ratios which result in the increase of the limits of detections (LOD). Among the 15 + 1 EU-priority PAHs are four dibenzopyrenes (Table 1), which are especially susceptible to discrimination of signal intensities due to their high molecular mass.

Large-volume injection (LVI) techniques such as programmed-temperature-vaporization (PTV) and cool-on-column (COC) injection can be used to increase method sensitivity through the injection of larger volumes of the final extract. PTV injection has also been used to reduce discrimination of certain analytes compared to classical split–splitless injection [8]. In addition, PTV injection is preferred to on-column injection when the analyses involve complex samples [9]. Several studies have been recently reported using PTV methods for the determination of trace pollutants, such as phenols [10], pesticides [11] and polychlorinated biphenyls [12]. Likewise, PAHs have been also determined in environmental samples [12–17] and foodstuff [18,19] using PTV injection. However, it

* Corresponding author. Tel.: +32 14 571 320; fax: +32 14 571 783.
E-mail address: Thomas.Wenzl@ec.europa.eu (T. Wenzl).
[1] Current address: Instituto de Fermentaciones Industriales, Consejo Superior de Investigaciones Científicas (CSIC), C/ Juan de la Cierva 3, 28006 Madrid, Spain.

0039-9140/$ – see front matter © 2009 Elsevier B.V. All rights reserved.
doi:10.1016/j.talanta.2009.07.041

Table 1
15 + 1 EU-priority PAHs under investigation (with acronyms). The right part of the table (in bold) shows those PAHs that are not included in the 16 EPA PAHs.

1	Benz[*a*]anthracene (BaA) (Mw 228)		9	**Benzo[*j*]fluoranthene (BjF)** (Mw 252)	
2	Benzo[*a*]pyrene (BaP) (Mw 252)		10	**Cyclopenta[*cd*]pyrene (CPP)** (Mw 226)	
3	Benzo[*b*]fluoranthene (BbF) (Mw 252)		11	**Dibenzo[*a*,*e*]pyrene (DeP)** (Mw 302)	
4	Benzo[*ghi*]perylene (BgP) (Mw 276)		12	**Dibenzo[*a*,*h*]pyrene (DhP)** (Mw 302)	
5	Benzo[*k*]fluoranthene (BkF) (Mw 252)		13	**Dibenzo[*a*,*i*]pyrene (DiP)** (Mw 302)	
6	Chrysene (CHR) (Mw 228)		14	**Dibenzo[*a*,*l*]pyrene (DlP)** (Mw 302)	
7	Dibenz[*a*,*h*]anthracene (DhA) (Mw 278)		15	**5-Methylchrysene (5MC)** (Mw 242)	
8	Indeno[1,2,3-*cd*]pyrene (IcP) (Mw 276)		+1	**Benzo[*c*]fluorene (BcL)** (Mw 216)	

must be stressed that none of the cited studies covered the whole set of 15 + 1 EU-priority PAHs.

PTV injection offers more operating parameters than split/splitless injection. Hence the optimum combination of parameter settings needs to be identified for each analysis task individually. Some authors [11,13] tackled the optimisation of the PTV injection by univariate procedures, whereas others applied multivariate statistical experimental designs for that purpose [12,14,16,20]. From the latter, only Yusà et al. [14] and León et al. [20] focused in their studies on the determination of PAHs, which however covered only a part of the analytes dealt with in this paper.

The use of statistically based experimental designs (two-level full factorial designs, fractional factorials, central composite or Plackett-Burman designs) can simplify the optimisation of PTV injection through the use of a selected number of experiments that randomly combines the desired variables. This approach provides a method for the simultaneous investigation of multiple variables, estimating any interaction among them, and requires fewer experiments to complete the optimisation [14].

Only a few papers have been published on the optimisation of PTV injection for the determination of PAHs by GC–MS. They reported a significant increase in sensitivity by the use of PTV injection if compared to splitless injection [13,14,16]. These studies however have focused only on few selected PAHs [14] or on the 16 EPA PAHs [13,16]. A study has been published recently concerning the determination of high molecular mass PAHs by application of PTV injection GC–MS [21]. This paper reported on the measurement of 15 out of the 15 + 1 EU-priority PAHs in solvent solution and edible oil extracts by using PTV injection (1 μL) in splitless mode [21]. However PTV injection in splitless mode has the same limitations with regard to tolerated solvent volume as conventional splitless injection. If the solvent volume exceeds a certain level peak distortions have to be taken into account. PTV injection in solvent vent mode (PTV-SV) in contrary offers the possibility to perform large volume injection and gain thereby extra sensitivity. The limitation of this injection technique is provided by the larger amount of matrix that is injected into the instrument, which might interfere with the analyte signal. However, no studies are currently available that focus on the employment of PTV-SV injection for the GC–MS analysis of the 15 + 1 EU-priority PAHs in food samples.

The aim of the present study was the optimisation of a PTV-SV injection method for the GC–MS analysis of the 15 + 1 EU-priority PAHs in foodstuff. The optimisation of different operating parameters of the PTV injection was carried out by application of a statistically based experimental design. Sausage samples prepared with oil fortified with the 15 + 1 EU-priority PAHs and non-contaminated lamb meat samples were used throughout the study. Different performance parameters such as linearity, precision, and matrix effects were evaluated for the optimised PTV-SV injection GC–MS analysis method. Sensitivity and discrimination of signal

intensities were compared to standard PTV injection in pulsed splitless injection mode (PTV-PSL).

2. Materials and methods

2.1. Reagents and reference materials

All solvents were purchased in chromatographic grade from VWR International (Leuven, Belgium). The drying material poly(acrylic acid), partial sodium salt-graft-poly(ethylene oxide) was obtained from Aldrich (Milwaukee, USA) and Ottawa sand from Acros Organics N.V. (Geel, Belgium).

The analytes benz[*a*]anthracene (BaA) CAS#56-55-3, chrysene (CHR) CAS#218-01-9, 5-methylchrysene (5-MC) CAS#3697-24-3, benzo[*b*]fluoranthene (BbF) CAS#205-99-2, benzo[*j*]fluoranthene (BjF) CAS#205-82-3, benzo[*k*]fluoranthene (BkF) CAS#207-08-9, benzo[*a*]pyrene (BaP) CAS#50-32-8, indeno[1,2,3-*cd*]pyrene (IcP) CAS#193-39-5, dibenz[*a,h*]anthracene (DhA) CAS#53-70-3, benzo[*ghi*]perylene (BgP) CAS#191-24-2, dibenzo[*a,l*]pyrene (DlP) CAS#191-30-0, dibenzo[*a,e*]pyrene (DeP) CAS#192-65-4, dibenzo[*a,i*]pyrene (DiP) CAS#189-55-9, dibenzo[*a,h*]pyrene (DhP) CAS#189-64-0, were commercially available BCR certified reference materials (IRMM, Geel, Belgium). Cyclopenta[*cd*]pyrene (CPP) CAS#27208-37-3, purity >99.0% by GC, was manufactured on request (Biochemisches Institut für Umweltkarzinogene, Großhansdorf, Germany). Benzo[*c*]fluorene (BcL) CAS#205-12-9, purity 99.99%, was purchased from Dr. Ehrenstorfer GmbH (Augsburg, Germany). The isotopically labelled compounds benz[*a*]anthracene (^{13}C6, 99%), benzo[*a*]pyrene (^{13}C6, 99%), benzo[*b*]fluoranthene (^{13}C6, 99%), benzo[*ghi*]perylene (^{13}C12, 99%), benzo[*k*]fluoranthene (^{13}C6, 99%), chrysene (^{13}C6, 99%), dibenz[*a,h*]anthracene (^{13}C6, 99%), dibenzo[*a,e*]pyrene (^{13}C6, 99%), dibenzo[*a,i*]pyrene (^{13}C12, 99%), indeno[1,2,3-*cd*]pyrene (^{13}C16, 99%) and pyrene (^{13}C3, 99%), which was used as internal standard for BcL, were obtained from LGC Promochem GmbH (Wesel, Germany). 9-Fluorobenzo[*k*]fluoranthene, used as injection standard, was purchased from Chiron AS (Trondheim, Norway). Stock solutions of the individual PAHs were gravimetrically prepared in toluene. The different working solutions containing the 15 + 1 EU-priority PAHs were prepared by mixing appropriate volumes from the individual stock solution and adding toluene to achieve the desired concentrations (6 different levels between 15 ng/mL and 80 ng/mL).

2.2. Sample preparation

Contaminated sausage samples were prepared at the Max-Rubner-Institut (MRI), Bundesforschungsinstitut für Ernährung und Lebensmittel, Institut für Sicherheit und Qualität bei Fleisch (Kulmbach, Germany) by applying spiked olive oil for the production of sausages. The sausage samples were split into portions of 50 g each and packed into aluminium cans. The final analyte contents ranged from 3.9 $\mu g\,kg^{-1}$ to 9.9 $\mu g\,kg^{-1}$. Benzo[*a*]pyrene, the only PAH regulated by current EU legislation, was present at a level of 5.3 $\mu g\,kg^{-1}$, a value slightly above the maximum level specified in Commission Regulation (EC) No 1881/2006 (5 $\mu g\,kg^{-1}$) [22].

Blank meat extracts were prepared from commercial minced lamb meat. They were fortified with the 15 + 1 EU-priority PAHs prior to the GC–MS analysis in order to evaluate matrix effects of the optimised PTV-SV method. The blank extracts were fortified to a concentration of 50 ng mL^{-1} for each PAH, a concentration similar to that expected in the final extract of the sausage sample considering sample intake and analyte enrichment.

2.2.1. Pressurised liquid extraction (PLE)

Extraction was carried out in accordance with the method described by Jira et al. [23]. Briefly, 5 g of homogenised sausage was mixed with the same amount of poly(acrylic acid), partial sodium salt-graft-poly(ethylene oxide) and 15 g of Ottawa sand. After adding 200 μL of the ^{13}C-labelled standard solution, the mix was placed into 33 mL extraction cells with cellulose filters at the bottom. The extraction was performed with *n*-hexane (at 100 °C and 100 bars at a static time of 10 min) in an ASE 300 pressurised liquid extraction system (Dionex, Amsterdam, The Netherlands). The flush volume was 60% and the purge time 120 s. Two static extraction cycles were performed per sample. Afterwards, the extractant was evaporated in a Turbo Vap® workstation (Zymark, Hopkinton, USA) at 40 °C using a stream of nitrogen.

2.2.2. Gel permeation chromatography (GPC)

The evaporated PLE-extract was dissolved in approximately 5 mL of cyclohexane:ethyl acetate (1:1 v/v) and filtered through PTFE filters of 5 μm pore size (Millipore, Bedford, USA). GPC clean up was carried out on a GPC column (25 mm internal diameter and 320 mm length) filled with 50 g Bio-Beads S-X3 (Bio-Rad Laboratories, Nazareth-Eke, Belgium) applying a GPC Ultra instrument (LCTech, Dorfen, Germany) connected to a FW-20 detector (LCTech) that was operated at 254 nm. Chromatographic separation was achieved with cyclohexane:ethyl acetate (1:1 v/v) at a flow rate of 4 mL min^{-1}. The PAHs containing fraction eluted between 35 min and 80 min. The volume of this fraction was reduced to 4.5 mL by using an automated concentrator (CPC 2000-II Vacuubrand, Wertheim, Germany) that was integrated in the GPC system. The sensitivity of the UV detector was not sufficient to detect the elution of the PAHs. As an alternative the elution of toluene, which got into the extract as a residue of the spiking with internal standards dissolved in toluene, and the elution of the fat fraction were monitored for quality control purposes. Toluene eluted shortly after the fat fraction and directly in front of the first target analyte, benzo[*c*]fluorene.

2.2.3. Solid phase extraction (SPE)

The GPC eluate was further reduced with a stream of nitrogen to 200 μL. Then 800 μL of cyclohexane were added and the mix was quantitatively loaded onto a preconditioned silica SPE cartridge (500 mg/4 mL, Alltech, Deinze, Belgium). The PAHs were eluted with 10 mL of cyclohexane.

2.2.4. Preparation for GC–MS analysis

Toluene (200 μL) was added as a keeper to the SPE eluate, which was then concentrated to a volume of about 200 μL. Afterwards, 300 μL of toluene containing 9-fluorobenzo[*k*]fluoranthene was added, which served for monitoring the variability of injection.

2.3. Instrumentation and analytical conditions

A gas chromatograph HP 6890N from Agilent Technologies (Waldbronn, Germany) with a programmable-temperature vaporization (PTV) injection port (septumless head) was used for the analysis of the target PAHs. The GC was coupled to an Agilent 5975B single quadrupole mass spectrometer (Agilent Technologies) operated in electron ionization (EI) mode at 70 eV. The analyses were performed in selected ion monitoring (SIM) mode recording the molecular ion of each compound (Table 1). Transfer line temperature and ion source temperature were maintained at 325 °C and 300 °C, respectively. The mass spectrometer was equipped with a 6 mm ultra large aperture draw out lens (Agilent Technologies). Injection was carried out using an automated GC PAL injection system (CTC Analytics, Zwingen, Switzerland).

PTV-PSL injection was performed to set reference values on which basis the performance characteristics of the PTV-SV injection method were evaluated. The parameters of the PTV-PSL injection method were: injection volume 1 μL, injection pulse pressure 30 psi

for 0.3 min, and injection port temperature 300 °C. The purge valve was opened after 1 min (purge flow 30.5 mL min^{-1}).

The parameters of the PTV-SV injection were subject of the optimisation process and are discussed later in this paper.

All analyses were carried out on a DB-17MS column 60 m × 0.25 mm internal diameter, 0.25 μm film thickness (Agilent Technologies, Diegem, Belgium). The oven temperature programme was 80 °C (hold 1 min), to 250 °C at 40 °C min^{-1}, to 305 °C at 25 °C min^{-1}, to 315 °C at 2 °C min^{-1}, to 330 °C at 40 °C min^{-1} and hold for 35 min. Helium was used as carrier gas at 1.5 mL min^{-1} flow rate.

2.4. Statistical software

Dedicated software for the design of experiments and optimisation, MODDE version 8.0 (Umetrics, Umeå, Sweden), was used for building up the parameter matrix and further evaluation of the results.

3. Results and discussion

3.1. Optimisation of PTV-SV injection

All standards and sample extracts were prepared in toluene. Although toluene is not the preferred solvent for large volume injection due to its rather high boiling point, it is the most suitable solvent to dissolve PAHs with high molecular mass (i.e. dibenzopyrenes). Its application was also recommended to prevent the adsorption of micro-contaminants to glassware [24].

Large volume injection into a PTV injector can be done in different modes: *at-once* (i), or using *multiple injection* (ii) [25]. In mode (i), the sample is introduced at relatively high speed, whereas in mode (ii) the sample is introduced at a rate that is theoretically equal to that of evaporation.

At-once injection was applied for this study. Different speeds were tested and the best results were obtained by injecting the sample at a speed of 5 μL s^{-1}.

3.1.1. Selection of the inlet liner

The most appropriate PTV inlet liner has to be identified prior to the optimisation of operating parameters, as this device has a crucial role in the trapping and transfer of the analytes. The optimisation was carried out using a step-wise approach. Four different PTV inlet liners were tested in this study: the single-baffle, the single-baffle packed with glass wool, the multi-baffle, and the sintered glass inlet liner. Another type of liner, which is filled with Tenax was not considered in this study since it has been reported that their use can provoke problems during the transfer of high boiling compounds to the column, leading to peak distortion and losses among other negative effects [9].

Standard solutions containing 100 ng mL^{-1} of each target analyte were injected ten times into each liner applying PTV-SV injection, and repeatability of injection was evaluated. An injection volume of only 1 μL was selected to avoid chromatographic problems stemming from the, at that point of time, non-optimised PTV-SV injection.

The sintered glass inlet liner showed the worst performance in terms of mass transfer and was therefore excluded from further studies. Fig. 1 shows the respective chromatograms for the baffle inlet liner (A) and the sintered glass inlet liner (B). As can be seen strong discrimination in terms of peak height occurred especially for the compounds with the highest molecular weight, the dibenzopyrenes.

Table 2 shows the relative standard deviations (RSDs) obtained under repeatability conditions for the other three inlet liners. The

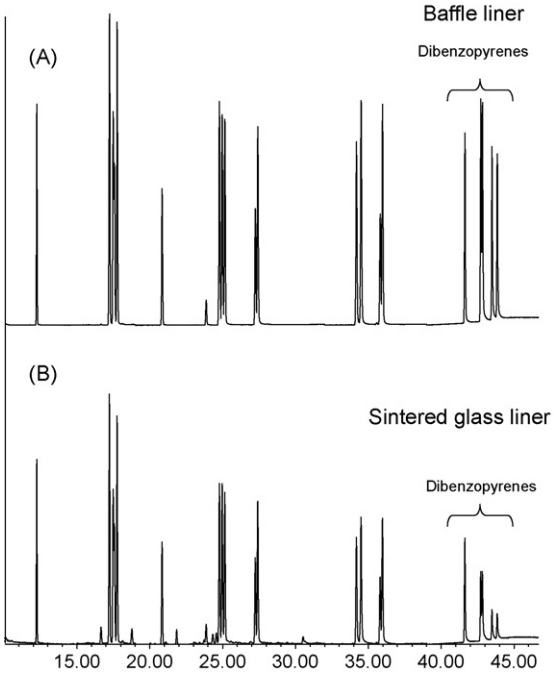


Fig. 1. Chromatograms of the 15 + 1 EU-priority PAHs on a DB-17MS column 60 m × 0.25 mm internal diameter, 0.25 μm film thickness applying a PTV baffle liner (A) and a PTV sintered glass liner (B).

multi-baffle inlet liner provided the best results in terms of precision for all compounds, although a similar level of precision was obtained with the single-baffle inlet liner for the compounds with low and medium molecular mass (from BcL to BaP). However the performance of the multi-baffle liner was superior for analytes with high molecular mass.

The results obtained with the single-baffle inlet liner packed with glass wool were generally worse than those obtained with the other two baffle inserts. Noticeably high RSDs were found for BcL and for high molecular weight compound like DiP and DhP. This might be caused by losses of BcL during the solvent evaporation phase, and irreversible adsorption of the heavy PAHs on active sites of the glass wool.

When increasing the injection volume from 1 μL up to 5 μL, peak symmetry was maintained only with the multi-baffle inlet liner.

Therefore, the multi-baffle inlet liner was applied for further optimisation of the PTV-SV injection.

3.1.2. Injection volume

The maximum tolerable injection volume of toluene was determined for the multi-baffle inlet liner by injecting different volumes of toluene into the PTV injector without connecting the column. The carrier gas flow was turned on in that experiment. According to Godula et al. [26] the injection volume can be increased until a solvent drop is observed at the exit of the inlet liner. A volume of 10 μL of toluene was injected into the multi-baffle inlet liner without visible overflow of the liquid and hence further-on used in this study.

3.1.3. Initial inlet temperature

The initial injector temperature plays an important role in large volume injection in solvent vent mode. It has to be set to allow fast removal of the solvent without losses of the analytes. The temperature of the injection port was set in the described experiments to 55 °C because higher temperatures caused losses of the most volatile target analyte, benzo[*c*]fluorene. This temperature reflects also the minimum temperature that can be reached in a

Table 2
Repeatability expressed as RSD % obtained for the injection of 1 μL of a standard solution containing the 15 + 1 EU-priority PAHs in toluene in a DB-17MS column 60 m × 0.25 mm internal diameter, 0.25 μm film thickness (100 ng/mL, $n = 10$). The RSD (%) of three different liners is shown.

	Single-baffle liner	Single-baffle packed with glass wool liner	Multi-baffle liner
			
	RSD (%)		
Benzo[*c*]fluorene	1.32	37.84	3.13
Benz[*a*]anthracene	1.73	2.43	1.81
Cyclopenta[*c,d*]pyrene	1.37	5.07	1.51
Chrysene	2.38	8.45	2.10
5-Methylchrysene	1.54	1.62	1.46
Benzo[*b*]fluoranthene	1.10	4.57	0.61
Benzo[*k*]fluoranthene	1.43	1.58	0.85
Benzo[*j*]fluoranthene	1.63	5.01	1.13
Benzo[*a*]pyrene	1.27	0.88	0.39
Indeno[1,2,3-*cd*]pyrene	3.01	3.09	0.90
Dibenz[*a,h*]anthracene	5.05	9.38	0.99
Benzo[*ghi*]perylene	2.98	3.98	0.77
Dibenzo[*a,l*]pyrene	3.95	2.76	1.65
Dibenzo[*a,e*]pyrene	6.01	2.40	1.19
Dibenzo[*a,i*]pyrene	6.61	24.19	1.96
Dibenzo[*a,h*]pyrene	6.20	26.18	2.33

reasonable period of time without applying cryogenic inlet cooling. Compressed air was used as replacement of cryogenic gases for facilitating the cooling process of the PTV injector. Consequently less than 5 min were necessary after each run to reach the initial inlet temperature.

3.1.4. Optimisation of PTV operating parameters

The PTV-SV injection can be divided into four different phases: the injection, the solvent vaporization, the transfer of analytes and the cleaning phase. During the injection the split valve is open (solvent vent mode) and the sample is introduced into the injection port set at a temperature below the boiling point of the carrier solvent. The following step, the solvent vaporization, is critical with regard to the analyte transfer onto the column and its effect on the quality of separation. The aim of the solvent vaporization is to eliminate the excess of solvent without loosing the analytes. If the residual solvent volume is too high a long flooded zone is formed in the front part of the column leading to peak distortion (a phenomenon known as "peak band broadening in space") [27]. Too excessive elimination of solvent will lead to losses of the most volatile compounds. Hence a small quantity of remaining solvent that is later-on transferred onto the column is desirable, not only to prevent analyte losses, but also to form a film at the front part of the column that traps and thereby focuses early eluting compounds [26].

The solvent elimination is influenced by different parameters that were considered in the optimisation process. They were in particular vent flow, vent time, vent pressure, and initial inlet temperature. The initial inlet temperature was set to 55 °C, as detailed before. Hence the focus was put onto the other three variables. Previous reported studies [28] and own investigations revealed that a high final temperature of the injection port enhanced the transfer of the analytes with high molecular mass onto the column, while the slope of the temperature increase in the PTV injection port did not have any significant influence. Accordingly, the final temperature of the injection port was maintained throughout the study at 400 °C and the temperature ramp at the maximum value of 600 °C min^{-1}. Regardless the conditions selected during optimisation, the split valve was opened after 3 min (purge time) and kept in this position for 15 min at 400 °C (cleaning step).

Vent time, vent flow and vent pressure were the variables that had to be optimised in order to maximise the analytical response (peak area) of the different PAHs.

The type of experimental design was selected taking into consideration the number of experiments to be performed and hence the time needed for measurements and the information level gained, which is expressed by the efficiency of the design. A full factorial experimental design including the three variables at two levels would consist of eight analyses, but would only allow the set up of linear models. Any non-linear relationships cannot be identified at two levels. A full factorial experimental design at three levels would consist without replication of 27 (3^3), and at four levels even of 64 (4^3) experiments. The advantage of full factorial designs is that all main effects and all multi-factor interactions can be described. However, if higher order factor interactions are not considered important fractional factorial experimental designs such as the D-optimal design may be applied. This is a computer generated design which consists of N runs out of all runs of the full factorial design, select in a way that maximum information can be gained with a minimum number of analyses [29]. The D-optimal design applied in the current work comprised 21 randomized chromatographic runs (10 corner experiments to which 11 axial points were added) out of 64 possible runs that span maximally the experimental region.

Table 3 shows the parameter settings employed for each variable in the D-optimal experimental design.

The correlation matrix obtained from the experimental data indicated an extremely high correlation between the responses obtained for all PAHs, which justifies the application of one single model for all the 15 + 1 EU-priority PAHs. The data was fitted by means of partial least square regression (PLS-R) providing an independent multivariate regression curve (model) for each PAH. No significant lack-of-fit was identified for any of the responses. Among the selected factors, vent time showed the highest influence on the analytical responses (negatively correlated with all the 15 + 1 EU-priority PAHs) followed by vent pressure and vent flow. Contour surface plots were used to visualise the modelled region and to assist in finding the optimal experimental conditions. Fig. 2 shows the contour plots of the response variable for the most volatile compound within the set of target analytes (BcL),

Table 3
Experimental conditions employed for the optimisation of the programmed temperature vaporization (PTV) injection in solvent vent mode by applying a D-optimal experimental design.

Parameter	Level		
	Minimum	Intermediate	Maximum
Vent time (min)	0.5	1 and 1.5	2
Vent flow (mL min^{-1})	25	50 and 75	100
Vent pressure (bar)	0.25	0.5 and 1	1.5

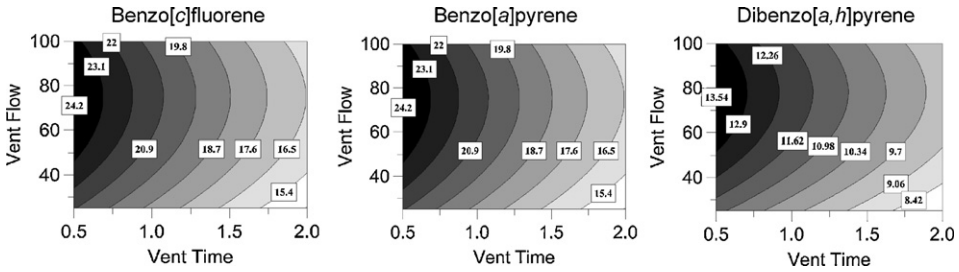


Fig. 2. Contour surface plots of BcL, BaP and DhP for two independent variables (vent time and vent flow) at a constant value of the other independent variable (vent pressure = 0.5 bar). Values inside the plots represent analytical responses in arbitrary units.

for BaP, for which maximum levels in food are specified in EU legislation, and for the last eluting PAH (DhP) for the two independent variables vent time and vent flow at a constant value of the vent pressure (0.5 bar). The contour plots show that small variations in vent time provoke significant changes in the analytical response of the PAHs (the response decreases as the vent time increases). A minimum value of the vent time (0.5 min) combined with vent flow values ranging between 60 mL min^{-1} and 100 mL min^{-1} maximised the analytical response of all compounds. Long vent times showed a negative effect on the response even though the vent flow was kept low.

The optimisation of the response for the individual analytes is not the way to success if the target is performance at the best for the whole set of analytes, because parameter settings to maximise performance for the volatile target analytes might be improper for the six-ring PAHs, which show low volatility. Therefore, the optimiser and the prediction list (two features provided by MODDE software) were used to predict the best experimental conditions considering that the response variables for all 15 + 1 EU-priority PAHs have the same importance. This is done by optimising an overall desirability function that is combining the individual desirability for each response. However, a finding that is not reflected in the models was that broad and fronting chromatographic peaks were obtained when short vent times were combined with low vent flows. Similar responses were gained for vent flows in the range of 60 mL min^{-1} to 100 mL min^{-1} when combined with low vent time (0.5 min) (Fig. 2). Therefore it was decided to set for the optimisation of the model the vent flow to the highest value to ensure adequate solvent elimination. Hence the following parameter settings were found most appropriate for the PTV-SV injection of PAH solutions: vent time 0.5 min, vent flow 100 mL min^{-1} and vent pressure 0.5 bar.

3.2. Method validation

The optimised PTV-SV method was validated to assess its applicability for the analysis of the 15 + 1 EU-priority PAHs in different samples. Different parameters such as linearity, precision (repeatability and intermediate precision), influence of matrix effects, and robustness of the PTV-SV injection method were evaluated.

3.2.1. Linearity

The linearity of the optimised PTV-SV injection GC–MS method was evaluated in the range of 15 ng mL^{-1} to 80 ng mL^{-1} from calibration standards applying Mandel's fitting test. All calibration functions were found linear. Table 4 presents performance characteristics of the method that were determined from replicate injections of six PAH standard solutions, respectively sausage extracts. The coefficients of determination of the calibration functions were for all 15 + 1 EU-priority PAHs higher than 0.99.

3.2.2. Precision and matrix effects

The precision of the PTV-SV method was evaluated both under repeatability and intermediate precision conditions. Standard solutions in solvent (toluene) and sausage extracts containing the 15 + 1

Table 4
Performance characteristics of the optimised PTV injection in solvent vent mode – GC–MS analysis method.

Compound	PTV injection in solvent vent mode					
	Solvent solution			Meat extracts		
	Calibration function R^2	Repeatability[a] RSD_r (%)	Intermediate precision[a] RSD_i (%)	Repeatability[b] RSD_r (%)	Intermediate precision[b] RSD_i (%)	Recovery[c] (%)
Benzo[*c*]fluorine	0.997	3.34	3.60	3.94	9.95	98.6 ± 2.3
Benz[*a*]anthracene	0.996	1.32	2.45	3.09	3.09	99.1 ± 2.2
Cyclopenta[*cd*]pyrene	0.998	1.62	2.15	2.38	3.77	102.5 ± 2.5
Chrysene	0.998	0.77	2.42	2.92	3.63	98.1 ± 1.9
5-Methylchrysene	0.996	3.34	4.92	5.30	5.30	98.8 ± 3.6
Benzo[*b*]fluoranthene	0.996	2.85	3.49	3.09	3.44	99.3 ± 3.7
Benzo[*k*]fluoranthene	0.998	1.79	2.50	3.34	3.34	97.5 ± 2.6
Benzo[*j*]fluoranthene	0.998	1.36	2.12	3.98	4.08	98.3 ± 2.6
Benzo[*a*]pyrene	0.998	0.93	2.57	2.84	4.01	97.5 ± 2.0
Indeno[1,2,3-*cd*]pyrene	0.993	2.47	5.56	3.43	3.86	97.5 ± 2.5
Dibenz[*a,h*]anthracene	0.998	1.69	2.45	4.38	4.53	98.8 ± 1.9
Benzo[*ghi*]perylene	0.998	1.20	2.91	1.53	4.74	97.7 ± 1.9
Dibenzo[*a,l*]pyrene	0.998	1.45	1.79	3.60	4.30	100.0 ± 2.4
Dibenzo[*a,e*]pyrene	0.999	1.71	3.67	3.39	3.39	98.3 ± 2.0
Dibenzo[*a,i*]pyrene	0.992	3.05	3.07	4.38	4.94	95.2 ± 2.1
Dibenzo[*a,h*]pyrene	0.996	3.54	4.00	3.84	13.64	104.6 ± 3.4

R^2: coefficient of determination from the analysis of 6 different concentrations in the range 15–80 ng mL^{-1}.

[a] 50 ng mL^{-1} standard mix of the 15 + 1 EU-priority PAHs.

[b] Sausage meat extract (3.9 μg kg^{-1} to 9.9 μg kg^{-1} for the 15 + 1 EU-priority PAHs).

[c] Average recovery (%) plus standard deviation calculated from triplicate analysis of blank lamb meat extracts (n = 3) fortified with the 15 + 1 EU-priority PAHs (50 ng mL^{-1}) prior to their analysis by GC–MS.

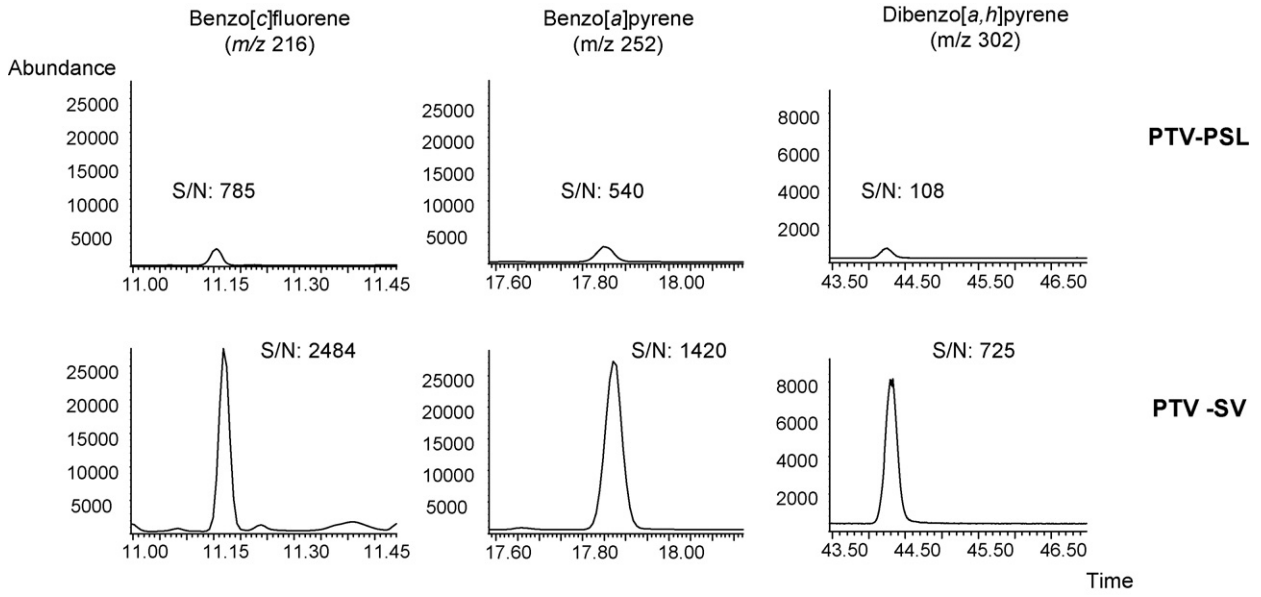


Fig. 3. SIM chromatograms of BcL (*m*/*z* 216), BaP (*m*/*z* 252) and DhP (*m*/*z* 302) obtained with PTV-SV and PTV-PSL injection of an extract of sausage fortified with the 15 + 1 EU-priority PAHs (concentration ranging from 3.9 μg kg^{-1} to 9.9 μg kg^{-1}). Concentration of the presented compounds were 3.9 μg kg^{-1}, 5.3 μg kg^{-1} and 9.9 μg kg^{-1} for BcL, BaP and DhP, respectively.

EU-priority PAHs were analysed. Repeatability was calculated from analysis results of three consecutive injections on the same day of either one PAH standard solution in toluene (50 ng mL^{-1} of each analyte), or one sausage extract sample (3.9 μg kg^{-1} to 9.9 μg kg^{-1} of the different PAHs), while intermediate precision was evaluated performing one-way ANOVA of three consecutive injections of both samples on three different days. Hence the calculated precision estimates reflect only the contribution of the GC–MS measurements on the overall precision of the analysis method.

The relative repeatability standard deviations (RSD_r) of the PTV-SV injection GC–MS measurements were satisfactory for the PAH solution in toluene, ranging between 0.77% for CHR and 3.54% for DhP. The respective relative intermediate precision standard deviation (RSD_i) ranged between 1.79% for DlP and 5.56% for IcP (Table 4).

The influence of matrix effects on the GC–MS measurement can be deduced from the precision estimates of the sausage sample. For most analytes the intermediate precision was of the same order of magnitude as the repeatability, which indicates that the gradual accumulation of co-extractives in the injection liner did not negatively impact precision. They were significantly different only for BcL and DhP (Table 4). The precision estimates for the sausage samples were somewhat higher than the respective estimates for the solvent solution, which was to be expected. However the vaporization of the analytes from food extracts was not significantly different to that from solvent solutions. This was confirmed by the replicate injection of blank lamb meat extract samples that were spiked with the target analytes to a level of 50 ng mL^{-1} just before injection and comparison of the results to those for solvent solutions. The ratio of the results for the meat sample and of the solvent solution would indicate matrix effects, if it was significantly different from one. The last column of Table 4 contains this information, expressed as percent recovery. Most of the results were close to 100%, which reveals the absence of matrix interferences in the analysis of meat samples applying this particular combination of sample preparation and PTV-SV-injection-GC–MS analysis.

3.2.3. Robustness

The robustness of the optimised PTV-SV method was evaluated using a screening fractional factorial design. Robustness measures the capacity of the method to remain unaffected by small but deliberate variations in the method parameters [30]. Assuming that the precision of the temperature control and of the control of pneumatics of the PTV injector is better than 5%, this value was selected for testing of the robustness of the PTV-SV injection. Therefore, values between 0.475 min and 0.525 min were selected for vent time, between 95 mL min^{-1} and 105 mL min^{-1} for vent flow and between 0.475 bar and 0.525 bar for vent pressure. A *t*-test was used to estimate the significance of each effect relative to the random variability (expressed as the observed standard deviation obtained under repeatability conditions at the centre of the experimental region). The PTV-SV method was considered robust since none of the three investigated factors had a statistically significant effect at the 95% confidence level on the analytical response of the different PAHs.

3.3. PTV in solvent vent mode and PTV splitless injection. Sensitivity of the optimised method

The performance of the optimised PTV-SV injection method was compared to the PTV-PSL injection (injection volume 1 μL) in terms of the signal-to-noise (S/N) ratios of two different samples: a standard solution containing the 15 + 1 EU-priority PAHs (15 ng mL^{-1}) and a sausage sample fortified with the 15 + 1 EU-priority PAHs (concentration ranging from 3.9 μg kg^{-1} to 9.9 μg kg^{-1}). A PTV-PSL injection method was already published by Bordajandi et al. [21]. The aim of the current experiments was to identify potential improvements of sensitivity of the PTV-SV injection method (10 μL) compared to the pulsed splitless injection method (1 μL). Fig. 3 shows selected SIM chromatograms of both PTV-SV injection and PTV-PSL injection of the meat extract for the ions with *m*/*z* 216, 252 and 302 corresponding to the base peak ions of BcL, BaP and DhP, respectively. The S/N ratios were for all analytes much higher in the chromatograms recorded after injection of the meat extract with the optimised PTV-SV method. Significantly increased was the sensitivity obtained for DhP, with an almost seven-fold higher S/N ratio after PTV-SV injection compared to PTV-PSL injection.

The gain of sensitivity with the PTV-SV injection was noticeable also for the other six-ring PAHs (Table 5). An increase in S/N ratios

Table 5
Signal-to-noise (S/N) ratio of GC–MS analysis applying the optimised PTV injection in solvent vent mode (PTV-SV) and PTV injection in pulsed splitless mode (PTV-PSL) for the analysis of both a solution of the 15 + 1 EU-priority PAHs in solvent (15 ng mL^{-1} in toluene) and an extract of a sausage samples fortified with the15 + 1 EU-priority PAHs (content ranging from 3.9 μg kg^{-1} to 9.9 μg kg^{-1}).

Compound	S/N ratio				S/N ratios for the sausage extract normalised to BaP	
	Solvent solution		Sausage extract		PTV-SV	PTV-PSL
	PTV-SV	PTV-PSL	PTV-SV	PTV-PSL		
Benzo[*c*]fluorene	538	246	2484	785	1.75	1.45
Benz[*a*]anthracene	7938	241	1439	590	1.01	1.09
Cyclopenta[*c,d*]pyrene	5918	176	1111	426	0.78	0.79
Chrysene	2902	299	2017	578	1.42	1.07
5-Methylchrysene	975	70	1231	221	0.87	0.41
Benzo[*b*]fluoranthene	5072	265	2013	327	1.42	0.61
Benzo[*k*]fluoranthene	541	191	1722	378	1.21	0.70
Benzo[*j*]fluoranthene	3489	205	2779	550	1.96	1.02
Benzo[*a*]pyrene	3551	175	1420	540	1.00	1.00
Indeno[1,2,3-*cd*]pyrene	926	136	1155	330	0.81	0.61
Dibenz[*a,h*]anthracene	4597	118	1794	368	1.26	0.68
Benzo[*ghi*]perylene	585	127	1202	221	0.85	0.41
Dibenzo[*a,l*]pyrene	779	43	608	119	0.43	0.22
Dibenzo[*a,e*]pyrene	811	46	643	105	0.45	0.19
Dibenzo[*a,i*]pyrene	483	37	380	62	0.27	0.11
Dibenzo[*a,h*]pyrene	442	33	725	108	0.51	0.20

ranging between 5.1 and 6.7 times was observed. This is particularly important with regard to the typical discrimination of signal intensities that is observed in the analysis of PAHs by GC–MS [6,7]. However the effect of the injection technique on the discrimination of the signal intensities was visualised by determining relative signal-to-nose ratios in order to demonstrate that the enhancement of signal-to-noise ratios in PTV injection in solvent vent mode was not only the consequence of the higher amount of analyte introduced into the instrument. For that purpose the S/N ratio of the analytes were normalised to the S/N ratio of BaP (Table 5). For the last eluting PAHs (DiP and DhP) a 2.5-fold increase of the normalised S/N ratios was observed when applying PTV-SV injection compared to PTV-PSL injection. Likewise, the normalised S/N values of the other two dibenzopyrenes (DlP, DeP) as well as the rest of PAHs (except for BaA and CPP that showed similar values) were improved when the PTV-SV injection was used. Therefore, the PTV-SV injection does not only improve the sensitivity of the 15 + 1 EU-priority PAHs, it is moreover also able to reduce the discrimination of signal intensities between the low- and the high-molecular weight compounds.

4. Conclusions

A PTV method in solvent mode (PTV-SV) for the analysis of the 15 + 1 EU-priority PAHs has been optimised and validated. The use of statistical experimental design simplified the optimisation of the most important parameters governing the PTV injection. As compared to PTV injection in splitless mode, the optimised PTV-SV method provided higher sensitivity for all studied analytes, irrespective of the type of injected sample being it a solvent solution of the target analytes or an extract of a fortified sausage sample. Especially significant was the improvement in the S/N ratio of the compounds with the highest molecular weight (more than six-fold increase for DeP, DiP and DhP). The optimised PTV-SV injection showed very good performance in terms of linearity, precision, and robustness. Matrix effects were not experienced in the analysis of meat extract samples.

References

[1] K. Ravindra, R. Sokhi, R. Van Grieken, Atmos. Environ. 42 (2008) 2895.
[2] International Agency for Research on Cancer (IARC), IARC Monographs on the Evaluation of Carcinogenic Risks to Humans, vol. 32, IARC, Lyon, France.
[3] European Commission, Opinion of the Scientific Committee on Food, 2002. http://europa.eu.int/comm/food/fs/sc/scf/out153_en.pdf.
[4] Joint FAO/WHO Expert Committee on Food Additives (JECFA), 2006. http://www.who.int/ipcs/food/jecfa/summaries/summary_report_64_final.pdf.
[5] Environmental Protection Agency (EPA) of the United States of America (1999), Compendium Method TO-13A, EPA, Cincinnati, OH, USA.
[6] E. Martínez, M. Gros, S. Lacorte, D. Barceló, J. Chromatogr. A 1047 (2004) 181.
[7] A. Filipkowska, L. Lubecki, G. Kowalewska, Anal. Chim. Acta 547 (2005) 243.
[8] F. Poy, S. Visani, F. Terrosi, J. Chromatogr. 217 (1981) 81.
[9] E. Hoh, K. Mastovska, J. Chromatogr. A 1186 (2008) 2.
[10] A. Vermeulen, K. Welvaert, J. Vercammen, J. Chromatogr. A 1071 (2005) 41.
[11] D. Štajnbaher, L. Zupančič-Krajl, J. Chromatogr. A 1190 (2008) 316.
[12] A. Esteve-Turrillas, E. Caupos, I. Llorca, A. Pastor, M. de la Guardia, J. Agric. Food Chem. 56 (2008) 1797.
[13] F.M. Norlock, J.-K. Jang, Q. Zou, T.M. Schoonover, A. Li, J. Air Waste Manage. Assoc. 52 (2002) 19.
[14] V. Yusà, G. Quintas, O. Pardo, A. Pastor, M. de la Guardia, Talanta 69 (2006) 807.
[15] B.S. Crimmins, J.E. Baker, Atmos. Environ. 40 (2006) 6764.
[16] V. Fernández-González, E. Concha-Graña, S. Muniategui-Lorenzo, P. López-Mahía, D. Prada-Rodríguez, Talanta 74 (2008) 1096.
[17] J.L. Pérez Pavón, M. del Nogal Sánchez, M.E. Fernández Laespada, B. Moreneo Cordero, J. Chromatogr. A 1202 (2008) 196.
[18] E. Ballesteros, A. García Sánchez, N. Ramos Martos, J. Chromatogr. A 1111 (2006) 89.
[19] R. Rodil, M. Schellin, P. Popp, J. Chromatogr. A 1163 (2007) 288.
[20] N. León, V. Yusá, O. Pardo, A. Pastor, Talanta 75 (2008) 824.
[21] L.R. Bordajandi, M. Dabrio, F. Ulberth, H. Emons, J. Sep. Sci. 31 (2008) 1769.
[22] Commission Regulation (EC) No 1881/2006 of 19 December 2006 setting maximum levels for certain contaminants in foodstuffs, Off. J. Eur. Union L 364 (2006) 5–24.
[23] W. Jira, K. Ziegenhalsa, K. Speerb, Food Addit. Contam. 25 (2008) 704.
[24] A. Covaci, S. Voorspoels, J. De Boer, Environ. Int. 29 (2003) 735.
[25] A. Covaci, J. de Boer, J.J. Ryan, S. Voorspoels, P. Schepens, Anal. Chem. 74 (2002) 790.
[26] M. Godula, J. Hajslova, K. Mastouska, J. Krivankova, J. Sep. Sci. 24 (2001) 355.
[27] K. Grob, J. Chromatogr. 213 (1981) 3.
[28] B. Veyrand, A. Brosseaud, L. Sarcher, V. Varlet, F. Monteau, P. Marchand, F. Andre, B. Le Bizec, J. Chromatogr. A 1149 (2007) 333.
[29] L. Delgado-Moreno, A. Peña, M.D. Mingorance, J. Hazard. Mater. 162 (2009) 1121.
[30] Citac/Eurochem, Guide to Quality in Analytical Chemistry—An Aid to Accreditation, Edition 2002, p. 31. http://www.eurachem.org/.

Talanta 80 (2009) 651–655

Contents lists available at ScienceDirect

Talanta

journal homepage: www.elsevier.com/locate/talanta

Isolation of novel indole-3-acetic acid conjugates by immunoaffinity extraction

Aleš Pěnčík[a,1], Jakub Rolčík[a,*,1], Ondřej Novák[a], Volker Magnus[b], Petr Barták[c], Roman Buchtík[a], Branka Salopek-Sondi[b], Miroslav Strnad[a]

[a] Laboratory of Growth Regulators, Faculty of Science, Palacký University and Institute of Experimental Botany ASCR, Šlechtitelů 11, CZ-78371 Olomouc, Czech Republic
[b] Ruđer Bošković Institute, Bijenička cesta 54, HR-10000 Zagreb, Croatia
[c] Department of Analytical Chemistry, Faculty of Science, Palacký University, Tř. Svobody 8, CZ-77146 Olomouc, Czech Republic

ARTICLE INFO

Article history:
Received 12 May 2009
Received in revised form 9 July 2009
Accepted 20 July 2009
Available online 28 July 2009

Keywords:
Immunoaffinity extraction
High-performance liquid chromatography (HPLC)
Tandem mass spectrometry (MS/MS)
Indole-3-acetic acid (IAA)
Auxin conjugates
Helleborus niger L.

ABSTRACT

An analytical protocol for the isolation and quantification of indole-3-acetic acid (IAA) and its amino acid conjugates was developed. IAA is an important phytohormone and formation of its conjugates plays a crucial role in regulating IAA levels in plants. The developed protocol combines a highly specific immunoaffinity extraction with a sensitive and selective LC–MS/MS analysis. By using internal standards for each of the studied compounds, IAA and seven amino acid conjugates were analyzed in quantities of fresh plant material as low as 30 mg. In seeds of *Helleborus niger*, physiological levels of these compounds were found to range from 7.5 nmol g^{-1} fresh weight (IAA) to 0.44 pmol g^{-1} fresh weight (conjugate with Ala). To our knowledge, the identification of IAA conjugates with Gly, Phe and Val from higher plants is reported here for the first time.

© 2009 Elsevier B.V. All rights reserved.

1. Introduction

Indole-3-acetic acid (IAA), referred to as auxin, is an important phytohormone. It plays crucial roles in many aspects of the regulation of plant growth and development, including cell elongation [1], tropisms [2] and the establishment of apical-basal polarity in both individual cells and the whole plant [3]. Such wide-ranging regulation of developmental processes by IAA requires that its concentration in cells and tissues is rapidly and sensitively regulated in both space and time. One of the mechanisms by which IAA level in plants is regulated is by conjugation of free IAA with amino acids, giving rise to either biologically inactive, but hydrolyzable, conjugates with alanine (IAAla) and leucine (IALeu) or to unhydrolyzable conjugates with aspartic acid (IAAsp) and glutamic acid (IAGlu). These two groups of conjugates are believed to have a storage function or to precede degradation of excessive IAA, respectively [4].

Although plant materials consist of a very complex matrix containing large amounts of ballast compounds, quantification of IAA – the quantities of which per gram of fresh weight (FW) vary typically between tens and hundreds of pmol – is not too difficult to perform. In current practice, raw extract is usually purified by solid-phase extraction [5] and analyzed by GC–MS [6] following methylation [7], trimethylsilylation [6] or other kind of derivatization [8,9]. Analysis by HPLC coupled to tandem mass detection is also an option, both with [10] or without [11] prior derivatization.

Compared with free IAA analysis, the quantification of IAA amino acid conjugates is much more elaborate due to the significantly lower levels of the analytes present in plant material. Thus in *Arabidopsis thaliana*, a model organism often used in plant biology, Kowalczyk and Sandberg [12] have described, together with free IAA (the amounts of which ranged between 40 and 130 pmol per gram of fresh material) conjugates with the following four amino acids: Asp, Glu (both present at picomolar level), Leu (hundreds fmol g^{-1} FW) and Ala, with quantities as low as 20 fmol g^{-1} FW. The extracts from *A. thaliana* were subjected to solid-phase (SPE) extraction and after methylation analyzed by HPLC linked to tandem mass detection. The protocol appeared to be notably simpler than that of Tam and coworkers [13] who used preparative HPLC before quantification of IAAsp and IAGlu by GC–MS.

Recently, an analytical protocol for the quantification of IAA and its conjugates in rice (*Oryza sativa*) has been described [14], which consists of SPE and subsequent HPLC–MS/MS analysis without prior derivatization. The protocol allows quantification of IAA conjugates with these amino acids: Ala, Asp, Glu, Leu, Phe and Val. It was applied to rice samples of 20–100 mg in fresh weight.

* Corresponding author. Tel.: +420 585 634 864; fax: +420 585 634 870.
E-mail address: jakub.rolcik@seznam.cz (J. Rolčík).
[1] These authors contributed equally to this work.

0039-9140/$ – see front matter © 2009 Elsevier B.V. All rights reserved.
doi:10.1016/j.talanta.2009.07.043

Table 1
Selected parameters of HPLC–MS/MS analysis of methyl esters of IAA and seven IAA amino acid conjugates. In parentheses, transitions of ^{15}N- and/or $^{2}H_5$-labeled standards are described.

RT (min)	Analyte	Transition	CV (V)	CE (eV)	LOD (fmol)	Dynamic range (pmol)	Calibration curve	R^2
8.60	IAGly-Me	247.2 > 130.1 (253.2 > 134.1)	19	22	0.2	0.004–2.5	$y = 0.9744x + 0.3592$	0.9998
11.41	IAAla-Me	261.2 > 130.1 (267.2 > 134.1)	21	19	0.7	0.004–2.5	$y = 0.9853x + 0.4162$	0.9995
12.53	IAAsp-Me_2	319.2 > 130.1 (325.2 > 134.1)	21	25	0.7	0.2–125	$y = 0.9829x + 0.3599$	0.9993
14.19	IAGlu-Me_2	333.2 > 130.1 (339.2 > 134.1)	21	35	0.6	0.04–25	$y = 1.0132x + 0.2683$	0.9998
16.19	IAA-Me	190.2 > 130.1 (195.2 > 134.1)	21	13	1.2	0.2–125	$y = 0.9693x + 0.1860$	0.9996
17.42	IAVal-Me	289.2 > 130.0 (295.2 > 134.1)	23	22	0.3	0.004–2.5	$y = 0.9962x + 0.4024$	0.9998
19.86	IALeu-Me	303.2 > 130.1 (309.2 > 134.0)	25	24	1.0	0.004–2.5	$y = 0.9888x + 0.3500$	0.9992
20.36	IAPhe-Me	337.2 > 130.0 (343.1 > 134.1)	16	27	0.6	0.004–2.5	$y = 0.9680x + 0.3064$	0.9998

However, only conjugates with Ala, Asp and Glu were detected in the selected plant material.

In this paper we introduce a complex analytical protocol suitable for isolation and quantification of IAA and a broad range of its amino acid conjugates. Based on a polyspecific anti-IAA immunoaffinity purification, it may be used to study novel (previously undescribed) naturally occurring IAA conjugates. Since we used internal standards for each of the analyzed compounds, we were able to quantify four known and three novel derivatives over a wide range of concentrations in which they are present in plant material.

2. Experimental

2.1. Reagents and materials

Indole-3-acetic acid and other indole compounds were obtained from OlChemIm (Olomouc, Czech Republic). ^{15}N- and/or $^{2}H_5$-labeled internal standards were prepared according to Ilić et al. [15]. Affi-Gel 10 was ordered from Bio-Rad (Hercules, CA, USA). Other reagents and solvents were provided by Sigma–Aldrich (St. Louis, MO, USA). Water was purified by the Simplicity 185 water purification system (Millipore, Bedford, MA, USA).

2.2. Preparation of antibodies and their use in immunoaffinity extraction

Polyspecific polyclonal antibodies against IAA and its conjugates were obtained by immunizing rabbits with an IAA–protein conjugate. To couple IAA to bovine serum albumin (BSA) through its carboxyl group, the procedure described by Weiler [16] was used, resulting in a hapten:protein molar ratio of 23. Purification of the antibodies and the preparation of immunoaffinity columns and their use were essentially as described earlier [17]. Capacity and recovery of the columns estimated by application of various amounts of indole-3-acetamide was about 3 nmol and 95–100%, respectively.

2.3. Sample processing and LC–MS/MS analysis

The extraction and subsequent SPE were similar to those used by Karin Ljung (personal communication). Approximately 30 mg (fresh weight) of plant material frozen in liquid nitrogen was ground with pestle and mortar and extracted for 5 min with 1 ml of cold phosphate buffer (50 mM; pH 7.0) containing 0.02% sodium diethyldithiocarbamate and the following ^{15}N- and/or $^{2}H_5$-labeled internal standards: [$^{2}H_5$]IAA, [^{15}N,$^{2}H_5$]IAAla, [^{15}N,$^{2}H_5$]IAAsp, [^{15}N,$^{2}H_5$]IAGlu, [^{15}N,$^{2}H_5$]IAGly, [^{15}N,$^{2}H_5$]IALeu, [^{15}N,$^{2}H_5$]IAPhe, and [^{15}N,$^{2}H_5$]IAVal.

After centrifugation (36,000 × *g*; 10 min; +4 °C), each sample was transferred into an eppendorf tube, acidified with 1 M HCl to pH 2.7 and applied on a C8 column (Bond Elut, 500 mg, 3 ml; Varian) pre-washed with 2 ml of methanol and equilibrated with 2 ml of formic acid (1%; v/v). The column was washed with 2 ml of methanol (10%; v/v) acidified with formic acid (1%; v/v) and retained analyte was eluted with 2 ml of methanol (70%; v/v) acidified with formic acid (1%; v/v). The eluate was evaporated to dryness *in vacuo*.

Samples were reconstituted in 100 μl of methanol acidified with concentrated hydrochloric acid (1 μl per ml of methanol) and methylated with 300 μl of ethereal solution of diazomethane. After 10 min the reaction mixture was evaporated under a stream of gaseous nitrogen (40 °C).

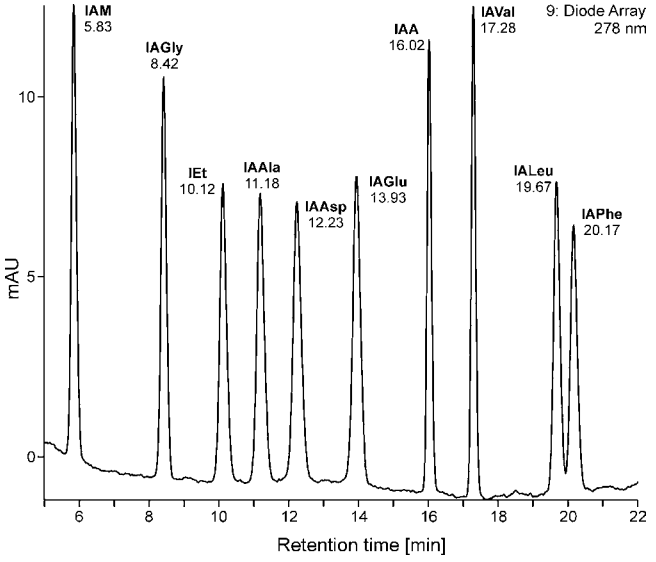


Fig. 1. HPLC–UV chromatogram (278 nm) of methyl esters of IAA, seven IAA conjugates and two other indole compounds retainable by a polyspecific anti-IAA immunoaffinity extraction: Indole-3-acetamide (IAM) and indole-3-ethanol (IEt).

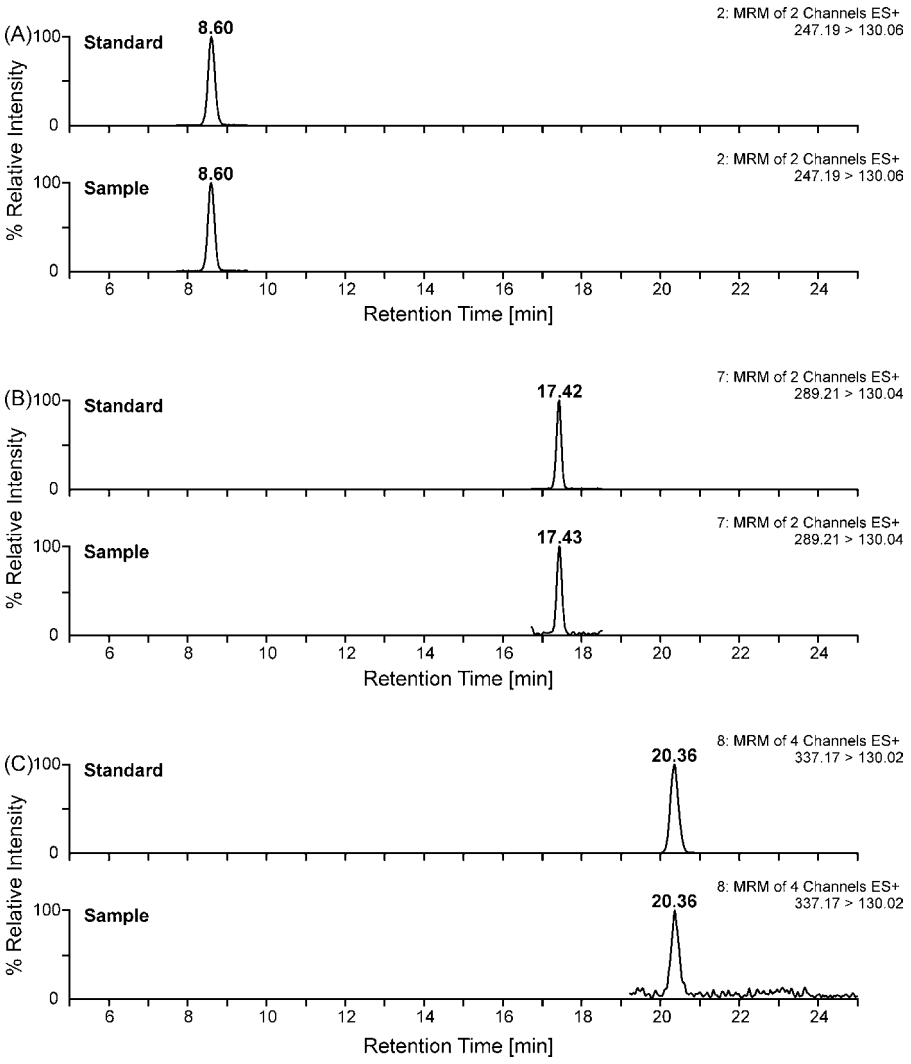


Fig. 2. Chromatograms of the newly discovered IAA amino acid conjugates compared with chromatograms of the corresponding authentic compounds: IAGly (A), IAVal (B) and IAPhe (C).

Prior to immunoaffinity purification, the sample was dissolved in 50 μl of ethanol (70%; v/v) and 450 μl of phosphate buffer (20 mM NaH_2PO_4; 15 mM NaCl; pH 7.2) and passed through a pre-column containing gel with immobilized BSA. The pre-column was then washed with 0.5 ml phosphate buffer and pooled effluent was applied on an immunoaffinity column with immobilized polyspecific rabbit polyclonal antibody against IAA. The application of the solution was repeated five-times. The immunoaffinity column was then washed three-times with 3 ml of H_2O and the analyte was subsequently eluted with 3 ml of methanol (−20 °C). The eluate was evaporated to dryness under nitrogen (40 °C).

Final analysis was done by HPLC coupled to tandem MS/MS detection with the use of a triple-quadrupole mass spectrometer. Separation was performed on an Acquity UPLC System (Waters) equipped with a Symmetry C18 column (5 μm, 2.1 mm × 150 mm; Waters) at 30 °C by gradient elution with a flow-rate of 250 μl min^{-1}. The mobile phase consisted of 10 mM aqueous formic acid and methanol containing 10 mM formic acid. The content of methanol kept at 25% during the first minute was then increased linearly to 38% (at 7 min), 40% (12 min), 58% (15 min), and 60% (26 min). The effluent was introduced into the ion source of a Quatro micro API tandem quadrupole mass spectrometer (Waters). The capillary voltage was set to +500 V, desolvation gas flow was 500 l h^{-1}, desolvation temperature was 350 °C and source block temperature was 100 °C. Other settings of the instruments, together with multiple reaction monitoring (MRM) transitions of individual compounds, are listed in Table 1.

3. Results and discussion

3.1. Anti-auxin polyspecific immunoaffinity purification

Immuno-based sample preparation techniques have extraordinary potential for trace analysis [18] and have been successfully utilized in analytical protocols used for quantification of various phytohormones including IAA [19,20], cytokinins [10,21–25] and abscisic acid [20,26,27].

In our study of IAA and its conjugates, we exploited the polyspecificity of anti-IAA antibodies. These were obtained by immunizing rabbits with a BSA conjugate in which IAA was linked to the protein through its carboxyl group (IAA-C1′-BSA). Such antibodies are capable of interacting specifically not only with IAA itself but also with other indole compounds substituted in position 3, such as indole-3-acetamide and indole-3-acetonitrile [28]. Furthermore, such antibodies have been reported [16] to cross-react in radioimmunoassays with the IAA homologues indole-3-propionic and indole-3-butyric acid and with IAA conjugated with aspartic

acid. However, this relatively high cross-reactivity is contingent on the free acids being transformed into their methyl esters. Hence, it is necessary to treat samples with diazomethane prior to analysis by an immunomethod [16,29].

An extensive study of our rabbit anti-IAA antibodies, performed by ELISA, has corroborated their polyspecificity. Compared to methylated IAA, cross-reactivities of 3-substituted indoles, including indole-3-acetamide, indole-3-acetonitrile, indole-3-ethanol and methyl esters of IAA conjugates, range typically between 85% and 210%. This allows the antibodies to be used in specific immunoaffinity purification of diverse IAA derivatives. We successfully used immunoaffinity extraction based on these antibodies to isolate and subsequently quantify IAA conjugates with Ala, Asp, Glu and Leu. Furthermore, we succeeded in isolating from a vascular plant and identifying novel naturally occurring IAA conjugates with the three amino acids: Gly, Val and Phe.

3.2. HPLC–MS/MS analysis

Using a linear methanol gradient acidified with formic acid, we achieved base-line separation (see Fig. 1) of a mixture containing methyl esters of IAA and seven IAA conjugates and also two other indole derivatives retainable by the developed immunoaffinity extraction: indole-3-acetamide and indole-3-ethanol (data not shown). In Table 1 the methyl esters are listed in order of their retention time.

Positive ESI tandem mass detection was run in multiple reaction monitoring (MRM) mode. Diagnostic transitions were similar to those used by Kowalczyk and Sandberg [12]: The parent ion of the protonated molecule $[M+H]^+$ fragments to a quinolinium ion of m/z 130.

To cover various recoveries of individual analytes, which may vary depending on the plant material being analyzed, we used internal standards corresponding to each of the studied compounds. All the standards comprised the indole skeleton labeled with five deuterium atoms; additionally, in standards of the conjugates the amino acid was ^{15}N-labeled. Thus values of m/z of internal standard parent ion differed by six units (or by five in the case of IAA) from those of the corresponding unlabeled compounds. Collision-induced dissociation yielded fragments of m/z = 135, 134 and 133. We used the fragment of m/z 134, the most intensive one, to perform MRM detection of labeled IAA and its conjugates. We achieved limits of detection (for signal-to-noise ratio of 3) around 1 fmol per injection. Detailed parameters together with other MS settings are listed in Table 1.

3.3. Identification of novel IAA conjugates

A recent study by Staswick et al. [30] has revealed the capability of *Arabidopsis* GH3 enzymes to catalyze synthesis of IAA conjugates with a wide range of amino acids, thus raising the question of whether IAA conjugates other than those with Ala, Asp, Glu and Leu exist. The question gains significance as Ludwig-Müller et al. [31] have very recently identified IAA conjugate with Val in non-vascular plant (moss *Physcomitrella patens*) grown on medium supplemented with IAA.

In our screening for putative IAA conjugates we concentrated on immature seeds of the Christmas rose (*Helleborus niger* L.), in which we had previously detected very high levels of free IAA (around 10 nmol g^{-1} FW). Alongside IAA and the conjugates described earlier [12] we identified novel IAA conjugates with Gly, Phe and Val.

In Fig. 2, chromatograms of newly discovered IAA conjugates are compared with chromatograms of the corresponding authentic compounds. Each pair of chromatograms is characterized by practically identical retention times of peaks for the standard and for the putative compound isolated from plant material. Each pair of chromatograms was obtained in MRM mode where the m/z of the parent ion corresponds to the m/z of the pseudomolecular ion $[M+H]^+$ of the respective IAA conjugate, while an m/z equal to 130 for the daughter ion corresponds to an m/z of the quinolinium ion, which is typical of fragmentation of IAA and its conjugates.

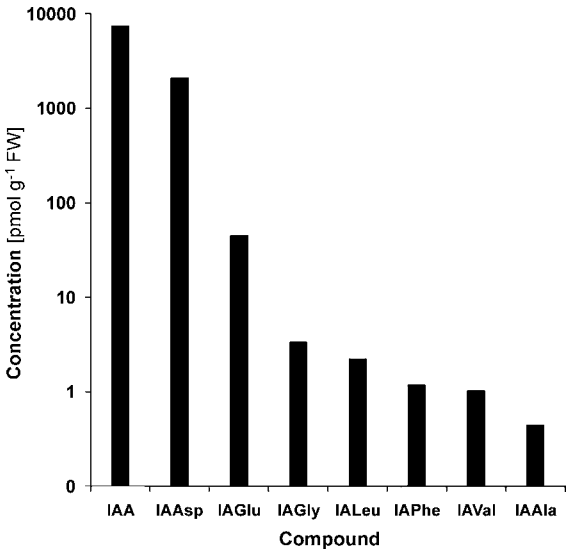


Fig. 3. Semi-logarithmic overview of IAA and seven IAA amino acid conjugates quantified in immature seeds of the Christmas rose (*Helleborus niger* L.).

The identity of the conjugates analyzed in *H. niger* seeds seems to be further verified by the fact that they passed through a preceding immunoaffinity purification designed to interact specifically with (3-substituted) indole skeleton. Thus, to our knowledge, for the first time naturally occurring IAA conjugates with Gly, Phe and Val have been identified in vascular plant.

3.4. Quantification of IAA and its conjugates in milligram amounts of plant material

Combination of the highly specific immunoaffinity extraction described above and a sensitive and selective LC–MS/MS – together with the application of internal standards for each of the studied compounds at the initial phase of sample processing – allowed us to reliably quantify IAA and a wide spectrum of its amino acid conjugates. Amounts of fresh plant material required for such an analysis typically lie between 25 mg and 40 mg.

On the basis of our previous experience, we supply the analyzed samples with amounts of internal standards corresponding to expected levels of respective native compounds. In a parallel manner we construct calibration curves which cover typical physiological levels of individual analytes in plant material. The curves

Table 2
Indole-3-acetic acid and its amino acid conjugates as quantified by HPLC–MS/MS in immature seeds and pericarp of *Helleborus niger*.

Analyte	Content in plant tissue (pmol g^{-1} FW)[a]	
	Immature seeds	Pericarp
IAA	7378 ± 17	313 ± 16
IAAsp	2089 ± 79	62.5 ± 3.7
IAGlu	44.9 ± 1.2	2.86 ± 0.05
IAGly	3.35 ± 0.19	n.d.[b]
IALeu	2.24 ± 0.11	1.60 ± 0.14
IAPhe	1.17 ± 0.17	n.d.
IAVal	1.02 ± 0.13	n.d.
IAAla	0.44 ± 0.02	n.d.

[a] Mean value of three independent analyses ± standard deviation.
[b] n.d.: not detected.

extend to a little under three orders of magnitude, with good linearity and correlation coefficients (R^2) between 0.9992 and 0.9998 (see Table 1).

Fig. 3 shows the results of an analysis of IAA and its conjugates performed on immature seeds of *H. niger*. The semi-logarithmic plot of the results demonstrates clearly the vast difference (of about four orders of magnitude) between the contents of free IAA (7.5 nmol g^{-1} fresh weight) and IAAla, the least abundant of quantified conjugates (0.44 pmol g^{-1} fresh weight). The value found for IAA itself is comparable to that estimated by Matsuda et al. [14], who analyzed auxins in seeds of rice (*O. sativa*).

Detailed results of our quantification are listed in Table 2 together with the results obtained by analysis of *H. niger* pericarp (husk). Levels of IAA and its conjugates with Asp, Glu and Leu in the pericarp were remarkably lower than those found in seeds, while conjugates with Ala, Gly, Phe and Val were below their limits of detection.

4. Conclusion

We developed a highly specific protocol for analysis of IAA and its amino acid conjugates in small quantities (about 30 mg) of fresh plant material. The protocol is based on a combination of polyspecific anti-IAA immunoaffinity extraction and a sensitive LC–MS/MS method. We successfully used the protocol for quantification of IAA and its conjugates in immature seeds and in the pericarp of *H. niger*. Furthermore, we isolated three novel naturally occurring conjugates of IAA with Gly, Phe and Val and confirmed their identity by analysis of corresponding synthesized standards.

Acknowledgements

We wish to thank Jarmila Greplová for an excellent technical assistance. We are grateful to Prof David A. Morris for careful revision of the manuscript. This work was supported by the Ministry of Education, Youth and Sports of the Czech Republic (MSM 6198959216), the Grant Agency of the Academy of Sciences CR (GAČR 522/08/H003 and KAN200380801) and the Croatian Ministry of Science, Education and Sports (Grant No. 098-0982913-2829).

References

[1] A. Hager, J. Plant Res. 116 (2003) 483.
[2] C.A. Esmon, U.V. Pedmale, E. Liscum, Int. J. Dev. Biol. 49 (2005) 665.
[3] J. Friml, P. Benfey, E. Benková, M. Bennett, T. Berleth, N. Geldner, M. Grebe, M. Heisler, J. Hejátko, G. Jürgens, T. Laux, K. Lindsey, W. Lukowitz, C. Luschnig, R. Offringa, B. Scheres, R. Swarup, R. Torres-Ruiz, D. Weijers, E. Zažímalová, Trends Plant Sci. 11 (2006) 12–14.
[4] A.W. Woodward, B. Bartel, Ann. Bot. 95 (2005) 707.
[5] J. Rolčík, J. Řečinská, P. Barták, M. Strnad, E. Prinsen, J. Sep. Sci. 28 (2005) 1370.
[6] A. Edlund, S. Eklof, B. Sundberg, T. Moritz, G. Sandberg, Plant Physiol. 108 (1995) 1043.
[7] A. Müller, P. Düchting, E.W. Weiler, Planta 216 (2002) 44.
[8] C. Birkemeyer, A. Kolasa, J. Kopka, J. Chromatogr. A 993 (2003) 89.
[9] F.M. Perrine, B.G. Rolfe, M.F. Hynes, C.H. Hocart, Plant Physiol. Biochem. 42 (2004) 723.
[10] E. Prinsen, W. Van Dongen, E.L. Esmans, H.A. Van Onckelen, J. Chromatogr. A 826 (1998) 25.
[11] S.J. Hou, J. Zhu, M.Y. Ding, G.H. Lv, Talanta 76 (2008) 798.
[12] M. Kowalczyk, G. Sandberg, Plant Physiol. 127 (2001) 1845.
[13] Y.Y. Tam, E. Epstein, J. Normanly, Plant Physiol. 123 (2000) 589.
[14] F. Matsuda, H. Miyazawa, K. Wakasa, H. Miyagawa, Biosci. Biotechnol. Biochem. 69 (2005) 778.
[15] N. Ilić, V. Magnus, A. Östin, G. Sandberg, J. Labelled Compd. Radiopharm. 39 (1997) 433.
[16] E.W. Weiler, Planta 153 (1981) 319.
[17] J. Rolčík, R. Lenobel, V. Siglerová, M. Strnad, J. Chromatogr. B 775 (2002) 9.
[18] M.C. Hennion, V. Pichon, J. Chromatogr. A 1000 (2003) 29.
[19] B. Sundberg, G. Sandberg, A. Crozier, Phytochemistry 25 (1986) 295–298.
[20] P. Redig, O. Shaul, D. Inze, M. Van Montagu, H. Van Onckelen, FEBS Lett. 391 (1996) 175.
[21] P. Redig, T. Schmulling, H. Van Onckelen, Plant Physiol. 112 (1996) 141.
[22] J.A. van Rhijn, H.H. Heskamp, E. Davelaar, W. Jordi, M.S. Leloux, U.A.T. Brinkman, J. Chromatogr. A 929 (2001) 31.
[23] O. Novák, P. Tarkowski, D. Tarkowská, K. Doležal, R. Lenobel, Strnad M, Anal. Chim. Acta 480 (2003) 207.
[24] E. Hauserová, J. Swaczynová, K. Doležal, R. Lenobel, I. Popa, M. Hajdúch, D. Vydra, K. Fuksová, M. Strnad, J. Chromatogr. A 1100 (2005) 116.
[25] O. Novák, E. Hauserová, P. Amakorová, K. Doležal, M. Strnad, Phytochemistry 69 (2008) 2214.
[26] T. Kannangara, A. Wieczorek, D.P. Lavender, Physiol. Plant 75 (1989) 369.
[27] V. Hradecká, O. Novák, L. Havlíček, M.M. Strnad, J. Chromatogr. B 847 (2007) 162.
[28] P. Ulvskov, J. Marcussen, R. Rajagopal, E. Prinsen, P. Rüdelsheim, H.A. Van Onckelen, Plant Cell Physiol. 28 (1987) 937.
[29] P. Ulvskov, J. Marcussen, P. Seiden, C.E. Olsen, Planta 188 (1992) 182.
[30] P.E. Staswick, B. Serban, M. Rowe, I. Tiryaki, M.T. Maldonado, M.C. Maldonado, W. Suza, Plant Cell 17 (2005) 616.
[31] J. Ludwig-Müller, S. Jülke, N.M. Bierfreund, E.L. Decker, R. Reski, New Phytol. 181 (2009) 323.

Talanta 80 (2009) 656–663

Contents lists available at ScienceDirect

Talanta

journal homepage: www.elsevier.com/locate/talanta

Differential pulse voltammetric simultaneous determination of noradrenalin and acetaminophen using a hematoxylin biosensor

Navid Nasirizadeh, Hamid R. Zare*

Department of Chemistry, Yazd University, P.O. Box 89195-741, Yazd 89195-741, Iran

ARTICLE INFO

Article history:
Received 21 April 2009
Received in revised form 20 July 2009
Accepted 22 July 2009
Available online 30 July 2009

Keywords:
Noradrenalin
Acetaminophen
Differential pulse voltammetry
Biosensor
Hematoxylin

ABSTRACT

A highly efficient noradrenalin (NA) biosensor was fabricated on the basis of hematoxylin electrodeposited on a glassy carbon electrode, GCE. The cyclic voltammetric responses of the hematoxylin biosensor at various scan rates, which were obtained in a 0.25 mmol L^{-1} NA solution, showed the characteristic shape typical of an EC_{cat} process. The kinetic parameters such as electron transfer coefficient, α, the catalytic electron transfer rate constant, k', and the standard catalytic electron transfer rate constant, k^0, for oxidation of NA at the hematoxylin biosensor surface were estimated using cyclic and RDE voltammetry. The peaks of differential pulse voltammetric (DPV) for NA and acetaminophen (AC) oxidation at the hematoxylin biosensor surface were clearly separated from each other when they co-exited in the physiological pH (pH 7.0). It was, therefore, possible to simultaneously determine NA and AC in the samples at a hematoxylin biosensor. Linear calibration curves were obtained for 5.0×10^{-1} to 65.40 μmol L^{-1} and 65.40–274.20 μmol L^{-1} of NA, and for 12.00–59.10 μmol L^{-1} and 59.10–261.70 μmol L^{-1} of AC. The sensitivities of the biosensor to NA in the absence and presence of AC were found virtually the same, which indicates the fact that the electrocatalytic oxidation processes of NA are independent of AC and, therefore, simultaneous or independent measurements of the two analytes (NA and AC) are possible without any interference. The results of 16 successive measurements show an average voltammetric peak current of 1.13 ± 0.03 μA for an electrolyte solution containing 5.00 μmol L^{-1} NA. The hematoxylin biosensor has been satisfactorily used for the determination of NA and AC in pharmaceutical formulations. The results obtained, using the biosensor, are in very good agreement with those declared in the label of pharmaceutical inhalation products.

© 2009 Elsevier B.V. All rights reserved.

1. Introduction

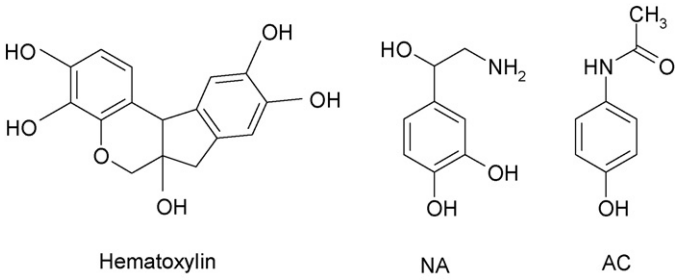
The chemical modifications of bare electrodes with a thin film of a suitable electroactive species offer significant advantages in the design and development of electrochemical sensors and biosensors. In practice, electrode surface modification has been tried as a means of reducing the overvoltage and overcoming the slow kinetics of many electrode processes [1–4]. A further advantage of chemically modified electrodes is that they are usually less exposed to surface fouling than bare electrodes are. Also, modified electrodes can sometimes separate the electroanalytical signals of solution components whereas, at bare electrode surfaces, the signals appear at potentials close to each other [5–11].

The electrochemical determination of biomolecules has been intensively studied over the past two decades. Noradrenalin (NA) is a very important catecholamine neurotransmitter in the mammalian central nervous system. Many diseases are related to the changes of NA concentration. Thus, the determination of its concentrations in biological systems provides useful information. The determination of NA is usually executed by high-performance liquid chromatography [12–14], gas chromatography [15], ion chromatography [16], capillary electrophoresis [17], and spectrophotometry [18]. NA is also an electroactive compound that can be detected by electrochemical oxidation on various electrodes. The electrochemical oxidation of NA has led to the development of useful methods for measuring NA concentrations [7,19–21].

In addition, acetaminophen (AC) is a widely used analgesic antipyretic drug with actions similar to aspirin. It is a suitable alternative for the patients who are sensitive to aspirin and is safe up to therapeutic doses. Unfortunately, easy availability has resulted in its increased use in attempted suicides. Hence, the need has arisen for the development of rapid and reliable methods for the determination of AC concentration. Many methods have been used for the determination of AC in pharmaceutical formulations and biological fluids including titrimetry [22], UV–vis spectrophotometry [23,24], spectrofluorimetry [25], near infrared transmittance spectroscopy [26], and chromatography [27,28]. Also, electrochemical methods

* Corresponding author. Tel.: +98 351 8122669; fax: +98 351 8210991.
E-mail address: hrzare@yazduni.ac.ir (H.R. Zare).

0039-9140/$ – see front matter © 2009 Elsevier B.V. All rights reserved.
doi:10.1016/j.talanta.2009.07.044



Scheme 1. Structures of hematoxylin, noradrenalin (NA) and acetaminophen (AC).

have attracted much attention because of their quick response, high sensitivity, as well as ability to miniaturize [29–33].

It is known that on a bare electrode, the oxidation peaks of NA and AC are nearly at the same potential, which results in overlapped voltammetric responses making their discrimination highly difficult. Therefore, the establishment of a simple, economical, and accurate analytical method for the simultaneous determination of NA and AC would be useful to medical manufacturers.

Although there are some studies on NA [7,19–21] or AC [29–33] electrochemical oxidation alone, to the best of our knowledge there are no reports about the simultaneous determination of NA and AC using electrochemical or other techniques in the literature. A published paper has reported that AC administrated in high doses results in increased serotonin (5-HT) levels in rat forebrains [34]; 5-HT is known to play a role in NA release in the brain [35]. Also, researchers have investigated the effect of AC and aspirin on the brain [36] and the posterior cortex [37]. The results show that AC administration alone significantly increase NA levels in the forebrain [36] and the posterior cortex [37]. Since so many over-the-counter analgesic preparations contain AC, we decided to investigate the simultaneous determination of NA and AC by electrocatalytic oxidation. Also, there are a few reports concerning the electrocatalytic activity or electrochemical properties of hematoxylin [38–40]. As a follow-up of our studies to prepare modified electrodes for the simultaneous determination of important biological compounds [41–43], we employed a hematoxylin biosensor for NA electrocatalytic oxidation and the simultaneous determination of NA and AC in the physiological pH (pH 7.0). Our findings indicate that a hematoxylin biosensor offers several distinct advantages including extraordinary stability, high surface charge transfer rate constant, and good limit of detection for NA. Differential pulse voltammetry (DPV) was also used to evaluate the analytical performance of the biosensor in quantification of NA in the presence of AC. Finally, to evaluate the utility of the hematoxylin biosensor for analytical applications, it was used for the simultaneous voltammetric determination of NA and AC in real samples.

2. Experimental

2.1. Reagents and apparatus

NA, 4-(2-amino-1-hydroxyethyl)benzene-1,2-diol hydrochloride (see Scheme 1 for structure) was purchased from Aldrich and used without purification. Hematoxylin and AC, 4′-hydroxyacetanilide (see Scheme 1 for their structures) and other reagents were of analytical grade from Merck and used as received. NA injection solution (from Bio&Pharma Companies, Brussels, Belgium), AC oral solution and AC tablet (from Pharma Chemi, Iran) were purchased in a local drugstore. All the solutions were prepared with doubly distilled water. NA and AC solutions were prepared just prior to use.

All the electrochemical experiments were carried out using a potentiostat PGSTAT 30 model from Autolab (Ecochemie, Netherlands), interfaced with a personal computer. The geometrical area of the bare glassy carbon working electrode (Metrohm, Switzerland) was 0.031 cm^2. All the electrochemical experiments were carried out in a conventional three-electrode cell at room temperature. A platinum electrode and a saturated calomel electrode (SCE) were used as the counter and reference electrodes respectively. All the potentials were reported with respect to this reference electrode. pH was measured with a Metrohm model 691 pH/mV meter. Also, the experiments were carried out inside a Faraday cage at room temperature (ca. 25 °C).

2.2. Preparation of the hematoxylin biosensor

The glassy carbon electrode, GCE, was first polished mechanically with 0.05 μm alumina in water slurry using a polishing cloth and then rinsed with doubly distilled water. The electrochemical activation of the electrode was performed by a continuous potential cycling from −1.4 to 1.6 V at a sweep rate of 100 mV s^{-1} in a sodium bicarbonate (0.1 mol L^{-1}) solution until a stable voltammogram was obtained. For modification, the activated electrode was placed in a 0.10 mmol L^{-1} solution of hematoxylin in a 0.15 mol L^{-1} phosphate buffer (pH 7.0), and it was modified by eight cycles of potential sweep between −0.4 and 0.5 V at 50 mV s^{-1}.

3. Results and discussion

3.1. Electrochemical behavior of the hematoxylin biosensor

The mechanism of electrodeposition of *o*- or *p*-hydroquinone derivatives, such as hematoxylin, as modifiers on the surface of an activated GCE has already been discussed [44,45]. Indeed, electrochemical treatment of an electrode surface leads to the formation of some reactive functional groups which can react as nucleophiles with the *o*-quinone produced during the electro-oxidation of the modifier. Fig. 1A shows the cyclic voltammograms of a hematoxylin biosensor in a 0.15 mol L^{-1} phosphate buffer solution (pH 7.0) as the supporting electrolyte at various scan rates. When the potential was scanned between −30 and 300 mV, a surface immobilized redox couple with a formal potential ($E^{0'}$) value of 104 mV was observed. In addition, the formal potential, $E^{0'}$, was almost independent of the potential scan rate for sweep rates ranging from 10 mV to 2000 mV s^{-1}, suggesting facile charge transfer kinetics over this range of sweep rate. The peak-to-peak potential separation ($\Delta E_p = E_{pa} - E_{pc}$) was small, and about 70 mV for the sweep rates below 1000 mV s^{-1}. Also, the electrochemical responses of the biosensor were those anticipated for a surface-confined redox couple because the anodic and cathodic peak currents were directly proportional to the scan rate (not shown), as predicted for the deposited chemical species at the electrode surface. The ratio of cathodic to anodic peak currents at various scan rates was almost constant. The electron transfer coefficient, α, between the electrode and the surface-confined redox couple can be evaluated in cyclic voltammetry from the variation of the anodic and cathodic peak potentials with the logarithm of scan rates, according to the method described by Laviron [46]. For high scan rates, this theory predicts a linear dependence of E_p upon $\log \nu$, which can be used to extract the kinetic parameter of α from the slope of such plots. We found that for the scan rates above 3 V s^{-1} the value of E_{pa} and E_{pc} were proportional to the $\log \nu$ (Fig. 1B). Using these plots at pH = 7.0, the value of $\alpha = 0.59$ was obtained.

3.2. Electrocatalytic oxidation of NA at the hematoxylin biosensor

The cyclic voltammetric responses of the bare GCE in a 0.15 mol L^{-1} phosphate buffer (pH 7.0), without and with NA in solution, are shown in Fig. 2 (curves c and d respectively). If a

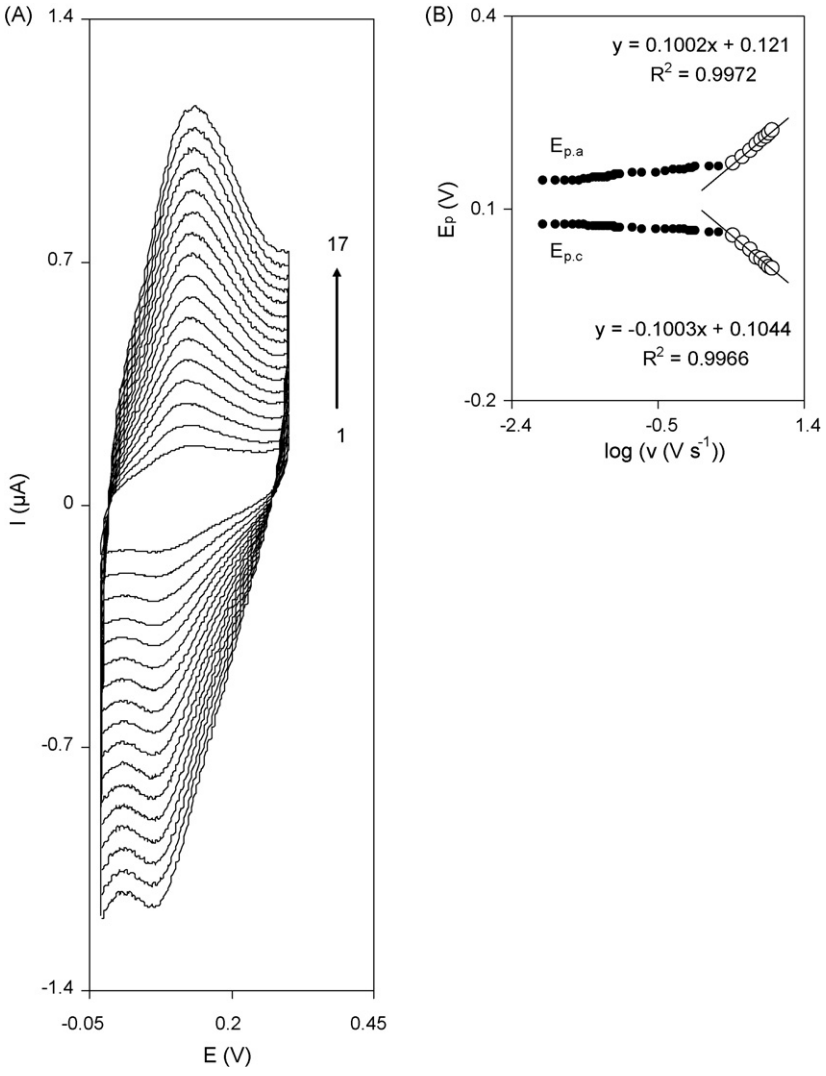


Fig. 1. (A) Cyclic voltammograms of the hematoxylin biosensor in a 0.15 mol L^{-1} phosphate buffer (pH 7.0) at various scan rates. The numbers 1–17 correspond to 10, 15, 20, 25, 30, 35, 40, 45, 50, 55, 60, 65, 70, 75, 80, 85 and 90 mV s^{-1}, respectively. (B) Variation of E_p versus the logarithm of the scan rate.

hematoxylin biosensor is placed into the same NA containing an electrochemical cell, a large anodic peak is observed without a cathodic counterpart (Fig. 2, curve b). That the current observed is associated with the NA oxidation and not only with the oxidation of surface-attached hematoxylin is demonstrated by comparing the current in curve b with that in curve a. Fig. 2, curve a, shows the cyclic voltammetric behavior of the hematoxylin biosensor in a NA-free electrolyte (0.15 mol L^{-1} phosphate buffer with pH 7.0). It is apparent that the anodic current associated with the surface-attached materials is significantly lower than that obtained in the solution containing NA. The anodic peak potential for the oxidation of NA at the hematoxylin biosensor is about 150 mV (Fig. 2, curve b), while NA starts to oxidize at about 570 mV (Fig. 2, curve d) at the bare GCE under identical conditions. So, a decrease in an overpotential of about 420 mV is observed.

The cyclic voltammograms of the hematoxylin biosensor at various scan rates obtained in a 0.15 mol L^{-1} phosphate buffer solution (pH 7.0) containing 0.25 mmol L^{-1} NA are shown in Fig. 3A. As shown in Fig. 3A inset, curve a, the oxidation currents increase linearly with the square root of the scan rate, suggesting that at a sufficient overpotential the reaction is mass transport controlled. From the slope of the I_P versus $v^{1/2}$ plot can be obtained the number of electrons in the overall reaction. According to the following equation for a totally irreversible diffusion controlled processes [47]:

$$I_p = 3.01 \times 10^5 n[(1-\alpha)n_\alpha]^{1/2} A C_b D^{1/2} v^{1/2} \quad (1)$$

and considering $(1-\alpha)n_\alpha = 0.69$ (see below), $D = 5.8 \times 10^{-6}$ cm^2 s^{-1} (D was determined by chronoamperometry), and $A = 0.0314$ cm^2, it is estimated that the total number of electrons involved in the anodic oxidation of NA is $n = 2.1 \cong 2$. Also, the plot of the scan rate-normalized current ($I_p/v^{1/2}$) versus the scan rate (Fig. 3A inset, curve b) exhibits a characteristic shape typical of an EC_{cat} process. These results show that the overall electrochemical oxidation of NA at the biosensor might be controlled by the cross exchange process between the redox site of the hematoxylin and the diffusion of NA. Under these conditions for EC catalytic mechanism, Andrieux and Saveant theoretical model [48] can be used to calculate the catalytic rate constant between NA and hematoxylin, k'. According to the approach of Andrieux and Saveant and using Fig. 1 in their theoretical paper [48], the average value of k' was calculated to be $(3.64 \pm 0.49) \times 10^{-3}$ cm s^{-1}.

The inset of Fig. 3B shows a Tafel plot that was drawn from the data of the rising part of the current–voltage curve recorded at a scan rate of 30 mV s^{-1} (Fig. 3B). This part of voltammogram, known as Tafel region, is affected by the electron transfer kinetics between the substrate (NA) and the surface-confined hematoxylin,

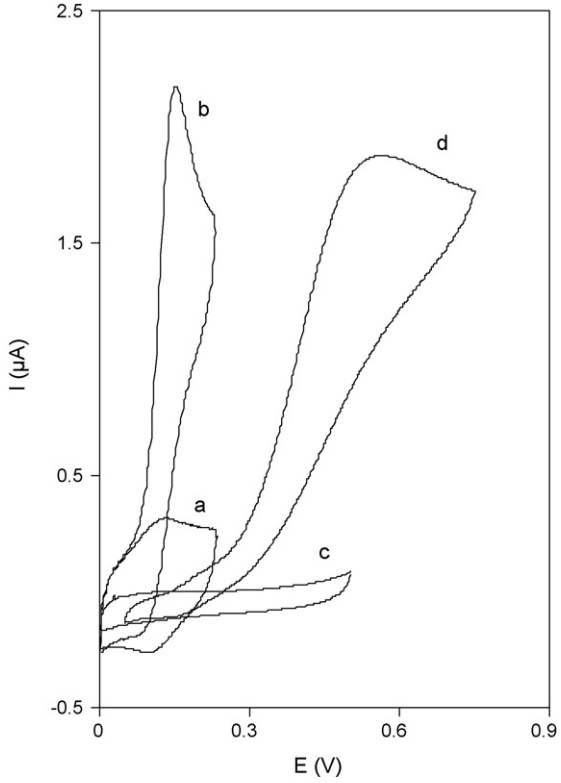


Fig. 2. Cyclic voltammograms of the hematoxylin biosensor in a 0.15 mol L^{-1} phosphate buffer (pH 7.0) solution in the absence (a) and presence (b) of 0.15 mmol L^{-1} NA. (c) As (a) and (d) as (b) for a bare GCE. In all cases the scan rate was 20 mV s^{-1}.

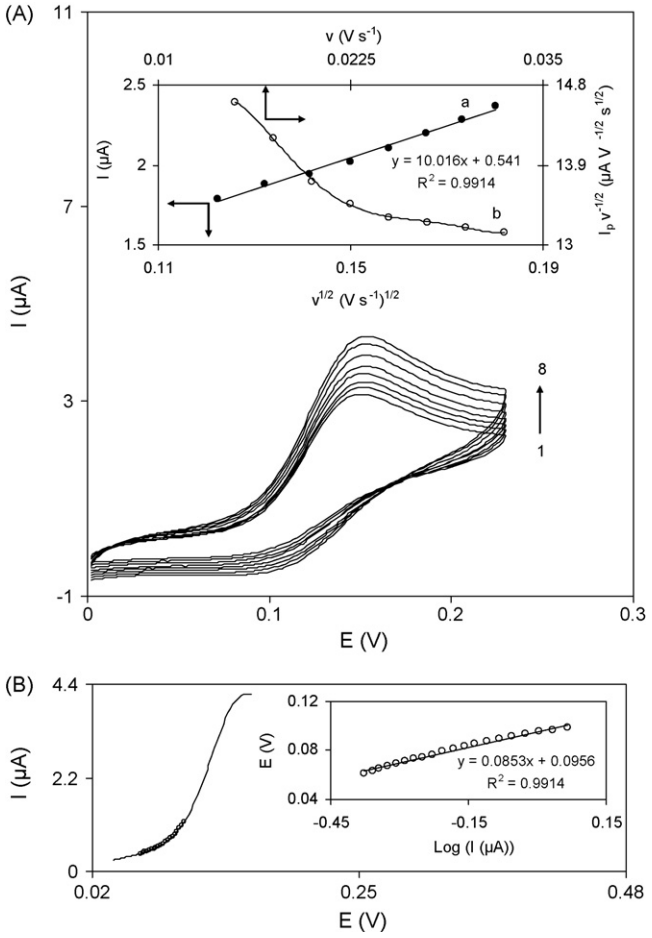


Fig. 3. (A) Cyclic voltammograms of the hematoxylin biosensor in a 0.15 mol L^{-1} phosphate buffer (pH 7.0) containing 0.25 mmol L^{-1} NA at different scan rates. The numbers of 1–8 correspond to 15, 17.5, 20, 22.5, 25, 27.5, 30 and 32.5 mV s^{-1}, respectively. Inset shows the plot (a) variation of the electrocatalytic peak current (I_p) with the square root of sweep rate and (b) variation of the sweep rate-normalized current ($I_p/v^{-1/2}$) with the sweep rate. (B) Linear sweep voltammogram recorded at 30 mV s^{-1}. Inset shows the Tafel plot derived from the linear sweep voltammogram.

assuming the deprotonation of the substrate as a sufficiently fast step. In this condition, the number of electrons involved in the rate-determining step can be estimated from the slope of Tafel plot. A slope 0.0853 V decade^{-1} is obtained indicating a one-electron transfer in the rate-determining step of the electron transfer process, assuming a charge transfer coefficient of $\alpha = 0.31$ [49].

The catalytic oxidation of NA with a hematoxylin biosensor was also studied by chronoamperometry. The chronoamperometric measurements of different concentrations of NA at a biosensor were done by setting the working electrode potential at 200 mV. In chronoamperometric studies, based on Cottrell equation [49], we have determined the diffusion coefficient of NA. Fig. 4A shows the experimental plots of I verses $t^{-1/2}$ with the best fit for different concentrations of NA employed. The slopes of the resulting straight line were then plotted versus the NA concentration (Fig. 4B), from whose slope we calculated a diffusion coefficient of 5.8×10^{-6} cm^2 s^{-1} for NA.

In order to elucidate the kinetics of NA oxidation at a hematoxylin biosensor, RDE measurements were performed at different rotation speeds in a 0.15 M phosphate buffer (pH 7.0) containing various concentrations of NA. Fig. 5 represents a typical example of RDE voltammograms of a 0.50 mmol L^{-1} NA at the biosensor as a function of the electrode rotation rates. Levich plots obtained at 220 mV for different concentrations of NA are shown in Fig. 5, inset A. According to Levich plots, the current increases with increasing electrode rotation speed but was found to be nonlinear. The clear lack of linearity immediately suggests that the reaction is limited by kinetics and not by transport [49]. In addition, we again conclude that the reaction between NA and the electrodeposited hematoxylin is the sole rate-limiting step [50]. In such cases, the currents are conveniently analyzed by plots of I^{-1} versus $\omega^{-1/2}$ [49]. Fig. 5, inset B, presents such plots (so-called Koutecky–Levich plots) and, in this case, well behaved linear responses are obtained. The value of catalytic reaction rate constant, k', between the oxidized form of the deposited hematoxylin and NA can be calculated from the intercepts of Koutecky–Levich plots [49]. From the values of the intercept of various plots, the mean values of k' dependent on potentials of 140, 160, 180, 200, and 220 mV are calculated and the results are shown in Table 1. As it can be seen in Fig. 5, inset C, and Table 1, the rate constant, k', is strongly potential dependent and k' increases with the increase of the potential which is considered for obtaining Koutecky–Levich plots. The kinetic parameters of the standard heterogeneous rate constant, k^0, and transfer coefficient, α, can be evaluated from the intercept and the slope of the plot of $\ln k'$ versus $E - E^{0'}$ (Fig. 5, inset C), according to the following equation described in [49]:

$$k'(E) = k' = k^0 \exp\left[\frac{n_\alpha(1-\alpha)F(E-E^{0'})}{RT}\right] \quad (2)$$

where E and $E^{0'}$ are the potentials which are considered for the obtained Koutecky–Levich plot and the formal potential of

Table 1
The relationship between the heterogeneous electron transfer rate constant, k', and the considered potential, E, in drawing the Koutecky–Levich plots.

E (mV)	140	160	180	200	220
$\times 10^3\, k'$ (cm s^{-1})	2.79	4.65	7.71	14.10	24.2

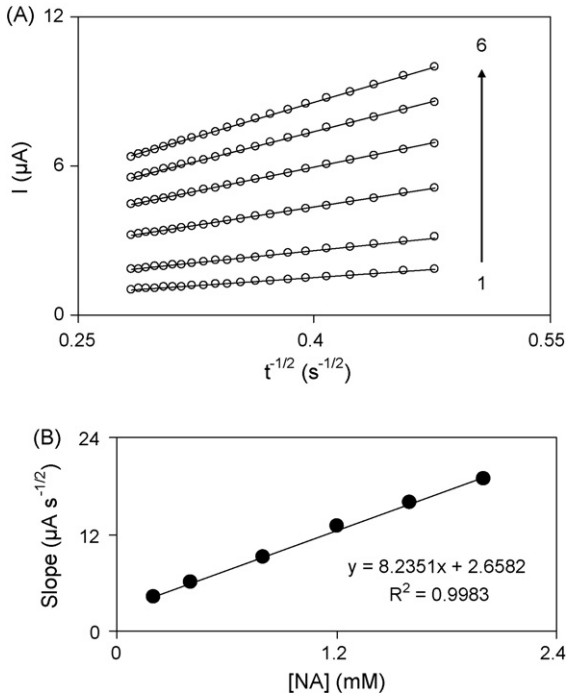


Fig. 4. (A) Plots of I versus $t^{-1/2}$ obtained from chronoamperometric experiments for the hematoxylin biosensor in a 0.15 mol L^{-1} phosphate buffer (pH 7.0) at a potential step 200 mV for different concentrations of NA. The numbers of 1–6 correspond to 0.20, 0.40, 0.80, 1.20, 1.60 and 2.00 mmol L^{-1} of NA. (B) Plot of the slope of straight lines against the NA concentration.

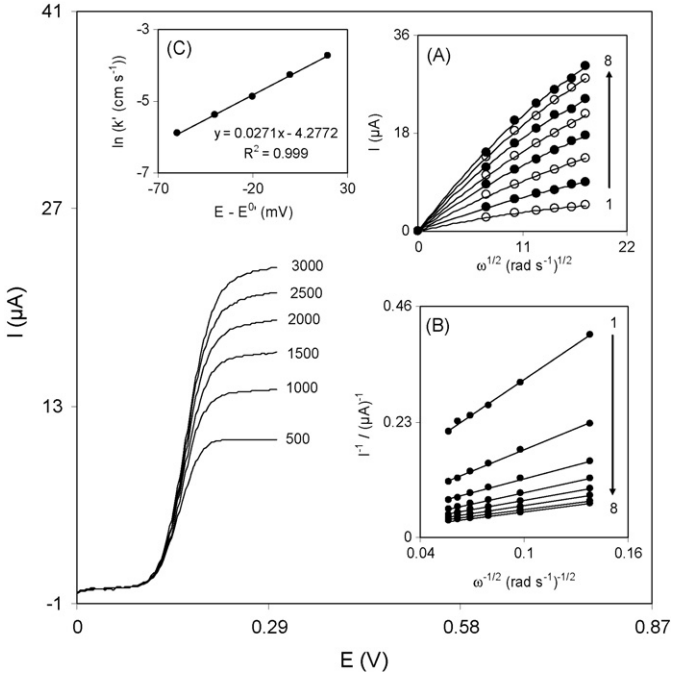


Fig. 5. Voltammograms of a rotating disk hematoxylin biosensor in a 0.15 M phosphate buffer (pH 7.0) containing 0.50 mmol L^{-1} NA at the various rotation rates indicated for each voltammograms. Insets: (A) Levich plots constructed from the modified RDE voltammograms and using current for E_{disk} = 220 mV of different concentrations of NA. The numbers of 1–8 correspond to 0.10, 0.20, 0.30, 0.40, 0.50, 0.60, 0.70 and 0.80 mmol L^{-1} of NA. (B) Koutecky–Levich plots obtained from Levich plots shown in inset (A). (C) Plot of the ln k' versus the $E - E^{0'}$. E and $E^{0'}$ are the potentials which were considered for obtaining the Koutecky–Levich plot and the formal potential of hematoxylin.

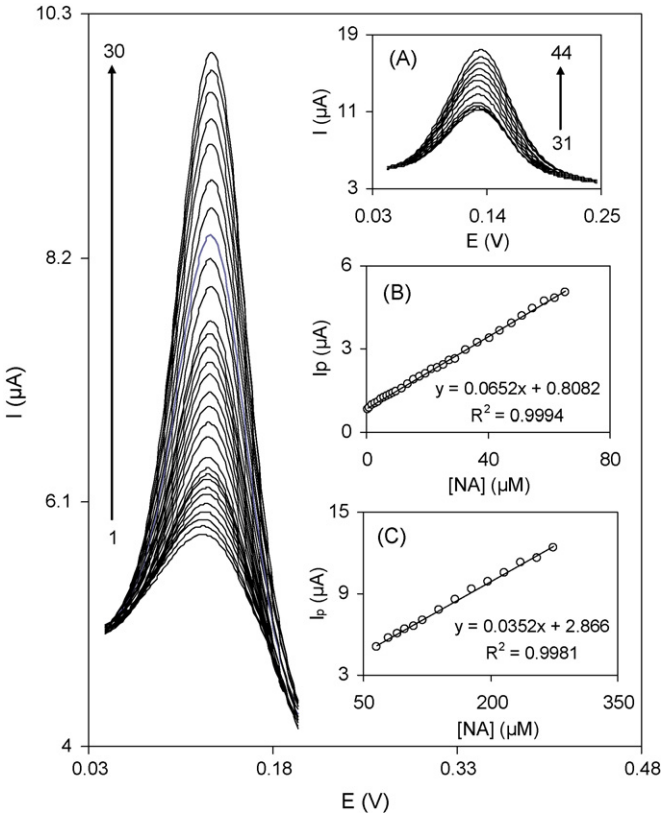


Fig. 6. Differential pulse voltammograms of the hematoxylin biosensor in a 0.15 mol L^{-1} phosphate buffer solution (pH 7.0) containing different concentrations of NA. The numbers of 1–30 correspond to 5.0×10^{-1} to 65.40 μmol L^{-1} of NA. Insets: (A) DPVs of the hematoxylin biosensor in solution containing 65.40–274.20 μmol L^{-1} of NA. (B) and (C) shows the plots of the electrocatalytic peak current as a function of NA concentration in the range of 5.0×10^{-1} to 65.40 and 65.40–274.20 μmol L^{-1} of NA, respectively.

hematoxylin respectively. The slope of 0.0271 mV^{-1} was obtained, indicating that a one-electron process is involved in the rate-determining step, $n_\alpha = 1$, assuming a charge transfer coefficient of $\alpha = 0.30$. This value of α is very close to that obtained from Tafel plot previously discussed. Also, the value of k^0 is found to be 1.02×10^{-3} cm s^{-1} from the intercept of Fig. 5, inset C. The value obtained for k^0 indicates that the electron transfer between the electrodeposited hematoxylin and NA is fast enough. Thus, hematoxylin can be used as a good electron transfer mediator for NA electrocatalytic oxidation.

3.3. Differential pulse voltammetric detection of NA and AC at the hematoxylin biosensor

The main objective in this study was the development of a biosensor capable of the electrocatalytic oxidation of NA and simultaneous detection of NA and AC. Since differential pulse voltammetry (DPV) has a much higher current sensitivity than cyclic voltammetry, it was used to estimate the lower limit of detection and the linear range of NA. In addition, the charging current contribution to the background current, which is a limiting factor in the analytical determination, is lower in DPV mode. The effects of increasing the concentration of NA on the voltammograms are presented in Fig. 6 (in range of 5.0×10^{-1} to 65.40 μmol L^{-1}) and its inset A (in range of 65.40–274.20 μmol L^{-1}). Also, insets B and C of Fig. 6 clearly show that the plot of the peak current versus the NA concentration is constituted of two linear segments (5.0×10^{-1} to 65.40 μmol L^{-1} and 65.40–274.20 μmol L^{-1}) with different slopes.

Table 2
Comparison of analytical parameters of several biosensors for NA determination.

Modifier	Method[a]	Linear range (μmol L^{-1})	Detection limit (μmol L^{-1})	Refs.
Polycalconcarboxylic acid	DPV	0.63–62.50	0.1	[7]
Poly(isonicotinic acid)	DPV	0.40–10.00 10.0–200.0	0.006	[20]
Tetrakis-(2-aminopheny) porphyrin	CV	1.0–7.0 7.0–50.0	–	[21]
C60-[dimethyl-(b-cyclodextrin)]$_2$	CV	50.0–800.0	8.0	[46]
β-Cyclodextrin	CV	1.0–300.0	0.50	[47]
Hematoxylin	DPV	0.50–65.40 65.40–274.20	0.14	This work

[a] DPV: differential pulse voltammetry, CV: cyclic voltammetry.

The plot of the average peak current of three replicates of DPVs versus NA concentration in the range of 5.0×10^{-1} to 4.00 μmol L^{-1} (not shown) was used to estimate the lower limit of NA detection at the biosensor. For these low concentrations, a linear correlation with a slope of 0.0673 μA μmol^{-1} L and a correlation coefficient 0.9943 are observed between the measured average current and the NA concentration. From the analysis of these data, we estimate that the lower limit of detection ($X_{\text{l.o.d.}}$) of NA is 0.14 μmol L^{-1} according to the definition $X_{\text{l.o.d.}} = (Y_{\text{l.o.d.}} - Y_{\text{bl.}})/m$ [51]. The lower detection limit of NA obtained in this method is lower than those previously reported for other biosensors [17,52–54]. The average voltammetric peak current and the precision estimated in terms of the coefficient of variation for 16 repeated measurements ($n = 16$) of 5.00 μmol L^{-1} NA at the hematoxylin biosensor were 1.13 ± 0.03 μA and 2.6% respectively. The coefficient of variation value indicates that the biosensor is stable and does not undergo surface fouling during the voltammetric measurements. This also demonstrates the fact that the results obtained at the biosensor are reproducible in analytical applications. In Table 2, some of the response characteristics obtained in this work are compared with those previously reported by others [7,20,21,52,53]. These data show that the responses of the proposed biosensor are superior in most cases to those of the previously reported biosensors.

The next attempt was made to detect NA and AC simultaneously by using a hematoxylin biosensor. Fig. 7 shows the differential pulse voltammetric responses which were gained by varying either the NA (Fig. 7A) or AC (Fig. 7B) concentration while the concentration of the other compound was kept constant. As shown in Fig. 7A, the electrochemical response of NA in the presence of a constant concentration of 5.0×10^{-1} mmol L^{-1} AC increased linearly with the increase of the NA concentration, while the response of AC remaining almost constant. Similarly, Fig. 7B shows DPVs obtained by increasing the concentrations of AC in the presence of 2.0×10^{-1} mmol L^{-1} NA. As it can be seen, an increase in the peak current of AC is observed with increasing AC concentration, while the voltammetric peak of NA is almost unchanged during the oxidation of AC. It can also be noted from these results that the responses to NA and AC at the biosensor are relatively independent. On the other hand, Fig. 7C shows the DPV of a mixture of 1.0×10^{-1} mmol L^{-1} NA and 4.0×10^{-1} mmol L^{-1} AC at the bare GCE. As shown, the bare GCE could not separate the voltammetric signals of NA–AC, and only one broad voltammetric signal at around 304 mV was obtained.

The utilization of the hematoxylin biosensor for the simultaneous determination of NA and AC was demonstrated by simultaneously changing the concentrations of NA and AC. The DP voltammetric results show that the simultaneous determination of NA and AC with two well distinguished anodic peaks at potentials of 127 and 300 mV, corresponding to the oxidation of NA and AC, is possible at the biosensor (Fig. 8). Fig. 8, inset A, shows that the linear range of NA concentration is 7.5×10^{-1} to 65.40 μmol L^{-1}. Also insets B and C of Fig. 8 clearly show that the plot of the peak current versus the AC concentration is constituted of two linear segments of 12.00–59.10 μmol L^{-1} and 59.10–261.70 μmol L^{-1} with different slopes, corresponding to two different ranges of substrate concentration. The decrease of sensitivity (slope) in the second linear range (Fig. 8, inset C) is likely to be due to kinetic limitation. Comparing Fig. 6, inset B, to Fig. 8, inset A, the sensitivities to NA in the absence and presence of AC were found to be 0.0652 (absence of AC) and 0.0697 (presence of AC) μA μmol^{-1} L. It is very interesting to note that the sensitivities of the biosensor to NA in the absence and presence of AC are virtually the same, which indicates the fact that the oxidation processes of NA at the hematoxylin biosensor are independent and, therefore, simultaneous or independent measurements of the two analytes are possible without any interference. If the NA signal was affected by AC, the above-mentioned slopes would be different.

Table 3
Determination of NA and AC in pharmaceutical formulations using calibration plots and with the hematoxylin biosensor[a].

Samples	Added (μmol L^{-1})		Found[a] (μmol L^{-1})		RSD (%)		Recovery (%)	
	NA	AC	NA	AC	NA	AC	NA	AC
Injection solution of NA	–	–	4.74	–	2.8	–	–	–
	5.00	40.00	9.99	38.63	1.2	1.6	103	97
	10.00	50.00	14.60	51.10	1.7	2.0	99	102
Oral solution of AC	–	–	–	15.46	–	3.0	–	–
	8.00	15.00	8.08	31.32	2.3	2.0	101	103
	12.00	30.00	12.39	46.22	1.5	1.8	103	102
Tablet of AC	–	–	–	20.88	–	3.0	–	–
	10.00	20.00	9.79	42.16	1.9	1.0	98	103
	15.00	40.00	14.83	61.67	2.1	2.0	99	101

[a] Three replicate measurements were made on the same samples.

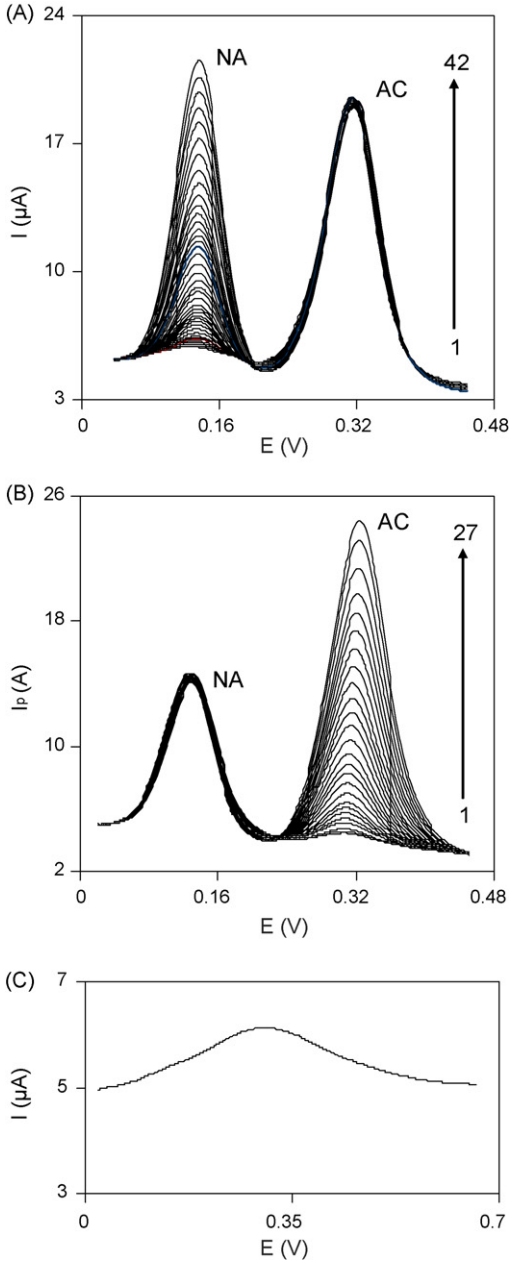


Fig. 7. (A) Differential pulse voltammograms of the hematoxylin biosensor in a 0.15 mol L^{-1} phosphate buffer solution (pH 7.0) containing 5.0×10^{-1} mmol L^{-1} AC and different concentrations of 5.0×10^{-1} to 488.00 μmol L^{-1} of NA. (B) Differential pulse voltammograms of the hematoxylin biosensor in a 0.15 mol L^{-1} phosphate buffer solution (pH 7.0) containing 2.0×10^{-1} mmol L^{-1} of NA and different concentrations of 12.00–1150.00 μmol L^{-1} of AC. (C) Shows the response at a bare GCE for the oxidation of a mixed solution of 1.0×10^{-1} mmol L^{-1} of NA and 4.0×10^{-1} μmol L^{-1} of AC.

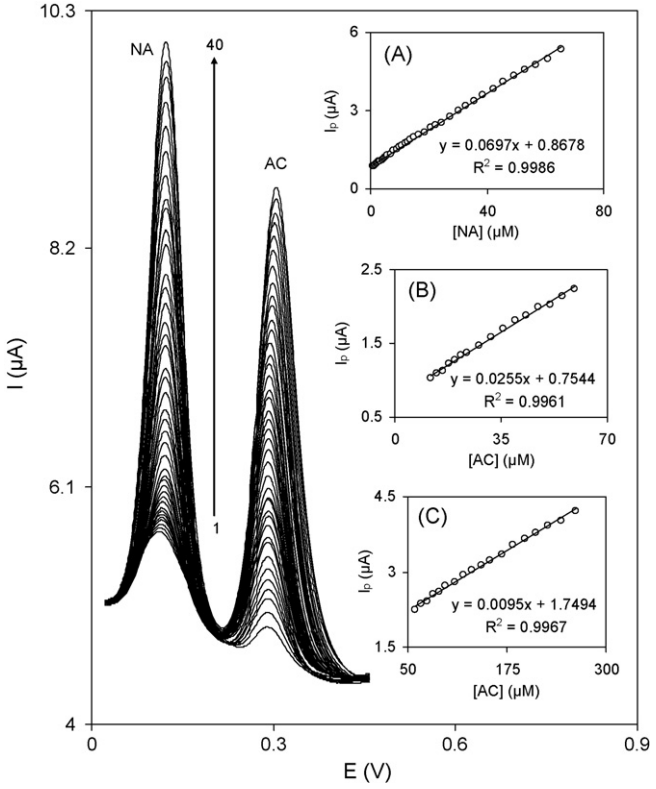


Fig. 8. Differential pulse voltammograms of the hematoxylin biosensor in a 0.15 mol L^{-1} phosphate buffer solution (pH 7.0) in mixed solutions of (from inner to outer): 7.5×10^{-1} to 65.40 μmol L^{-1} for NA and 12.00–261.70 μmol L^{-1} for AC. Insets: (A) plot of the peak currents as a function of NA concentration in the linear range of 7.5×10^{-1} to 65.40 μmol L^{-1}. (B) and (C) Plots of the peak currents as a function of concentration of AC in two linear ranges of 12.00–59.10 and 59.10–261.70 μmol L^{-1}.

3.4. Application of the hematoxylin biosensor for determination of NA and AC in real samples

The utility of the present hematoxylin biosensor for determination of NA and AC in pharmaceutical formulations was tested by measuring the NA concentration in an injection solution and the AC concentration in an oral solution and tablet samples. The NA injection solution and the AC oral solution were diluted 10^3 and 10^4 times respectively. Also one tablet of AC (0.4356 g), after dissolving in 1 L doubly distilled water was diluted 100 times with a phosphate buffer solution before the measurements. The differential pulse voltammograms of various real samples solutions are shown in curve (a) Fig. 9A–C. The measurements were performed using the calibration plots which are shown in Fig. 8, insets, and the results obtained are listed in Table 3. To authenticate the validity of the results, the samples were spiked with certain amounts of NA and AC at levels similar to those found in the samples themselves. The results in Table 3 show that the relative standard deviations (RSD%) and the recovery rates of the spiked samples were acceptable. Thus, the proposed biosensor can be efficiently used for the simultaneous determination of NA and AC in pharmaceutical samples. The reliability of the proposed biosensor was also evaluated by comparing the obtained results with those declared in the label of the pharmaceutical inhalation products. The data in Table 4 demonstrate that the results obtained by a differential pulse voltammetric method (utilizing the biosensor) are in very good agreement with the values declared in the label of the analytes.

Table 4
Comparison of the total values of NA and AC of various formulations obtained using the hematoxylin biosensor with those declared in the label of the pharmaceutical inhalation products[a].

Samples	Declared value	Found value	RSD (%)
Injection solution of NA (mg mL^{-1})	1.0	0.98	3.1
Oral solution of AC (mg mL^{-1})	24.0	23.37	3.0
Tablet of AC (mg g^{-1})	725.3	724.62	2.9

[a] The total values (average of three measurements) were obtained by multiplying the measured values by the appropriate dilution factor and number of sample assayed was three.

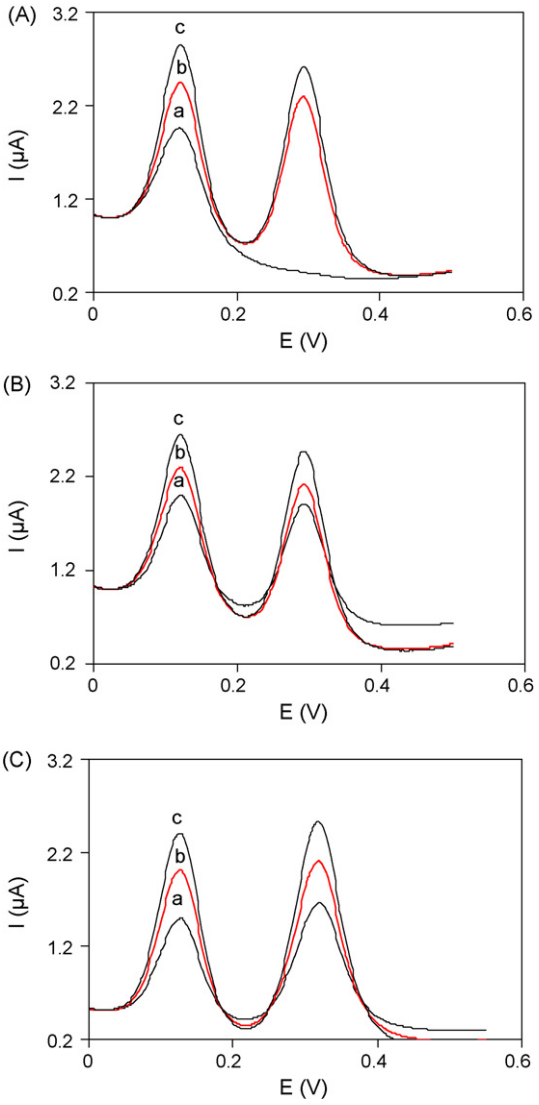


Fig. 9. Voltammograms of (a) are shown the differential pulse voltammograms of the hematoxylin biosensor in a 0.15 mol L^{-1} phosphate buffer solution (pH 7.0) containing a concentration of the real samples which indicated in Table 3 for (A) an NA injection solution, (B) AC oral solution and (C) AC tablet. In all cases, for voltammograms of (b) and (c), different concentrations of NA and AC added to the real samples according to the data which reported in Table 3.

4. Conclusions

In this study, a simple and fast procedure was used for the electrodeposition of hematoxylin on a GCE. The electrodeposited hematoxylin layers on the GCE exhibited excellent electrocatalytic activity toward the electro-oxidation of NA, which appeared as a reduced overpotential and an increase in the peak current. The transfer coefficient, α, the catalytic rate constant, k', the standard catalytic rate constant, k^0, and the overall number of electrons involved in the electrocatalytic oxidation of NA at a hematoxylin biosensor surface were determined using voltammetric methods. The diffusion coefficient of NA was calculated as 5.8×10^{-6} cm^2 s^{-1} for experimental conditions, using chronoamperometric results. The hematoxylin biosensor could successfully separate the voltammetric peaks of NA and AC, which are indistinguishable on a bare GCE. The precision of the differential pulse voltammetry (DPV) method was found to be 2.6% for the replicate determination of a 5.00 μmol L^{-1} solution of NA ($n = 16$). Also, in DPV measurements, two linear calibration ranges were obtained for NA and AC. The sensitivities of NA and AC determination at the biosensor surface were obtained 0.0697 and 0.0255 μA μmol^{-1} L respectively. The proposed hematoxylin biosensor has been applied to the simultaneous determination of NA and AC in an injection solution of NA, an oral solution of AC, and a tablet of AC with satisfactory results. Thus, the reliability and stability of the biosensor offers a good possibility for applying the technique to a routine analysis of NA and AC in pharmaceutical formulations.

References

[1] A. Salimi, A. Noorbakhsh, M. Ghadermarzi, Sen. Actuators B 123 (2007) 530.
[2] S.M. Golabi, H.R. Zare, M. Hamzehloo, Electroanalysis 14 (2002) 611.
[3] H.R. Zare, Z. Sobhani, M. Mazloum-Ardakani, Sen. Actuators B 126 (2007) 641.
[4] H.R. Zare, N. Nasirizadeh, Electroanalysis 18 (2006) 507.
[5] J. Huang, Y. Liu, H. Hou, T. You, Biosens. Bioelectron. 24 (2008) 632.
[6] J.M. Zen, C.T. Hsu, Y.L. Hsu, J.W. Sue, E.D. Conte, Anal. Chem. 76 (2004) 4251.
[7] A.L. Liu, S.B. Zhang, W. Chen, X.H. Lin, X.H. Xia, Biosens. Bioelectron. 23 (2008) 1488.
[8] H.R. Zare, N. Rajabzadeh, N. Nasirizadeh, M. Mazloum-Ardakani, J. Electroanal. Chem. 589 (2006) 60.
[9] J. Li, X.-Q. Lin, Anal. Chim. Acta 596 (2007) 222.
[10] G. Hu, Y. Ma, Y. Guo, S. Shao, Electrochim. Acta 53 (2008) 6610.
[11] L. Lin, J. Chen, H. Yao, Y. Chen, Y. Zheng, X. Lin, Bioelectrochemistry 73 (2008) 11.
[12] V. Carrera, E. Sabater, E. Vilanova, M.A. Sogorb, J. Chromatogr. B 847 (2007) 88.
[13] H. Wang, H. Jin, H.S. Zhang, Fresenius J. Anal. Chem. 365 (1999) 682.
[14] N. Aoyama, M. Tsunoda, K. Imai, J. Chromatogr. A 1074 (2005) 47.
[15] D.L. Kuhlenbeck, T.P.O. Neill, C.E. Mack, S.H. Hoke, K.R. Wehmeyer, J. Chromatogr. B 738 (2000) 319.
[16] C.L. Guan, J. Quyang, Q.L. Li, B.H. Liu, W.R.G. Baeyens, Talanta 50 (2000) 1197.
[17] S. Wei, G. Song, J.M. Lin, J. Chromatogr. A 1098 (2005) 166.
[18] M. Zhu, X.M. Huang, J. Li, H.X. Shen, Anal. Chim. Acta 357 (1997) 261.
[19] G. Wang, X. Liu, B. Yu, G. Luo, J. Electroanal. Chem. 567 (2004) 227–231.
[20] H. Zhao, Y. Zhang, Z. Yuan, Anal. Chim. Acta 454 (2002) 75.
[21] H. Jeong, H. Kim, S. Jeon, Microchem. J. 78 (2004) 181.
[22] K.G. Kumar, R. Letha, J. Pharm. Biomed. Anal. 15 (1997) 1725.
[23] V. Rodenas, M.S. Garcia, C. Sanchez-Pedreno, M.I. Albero, Talanta 52 (2000) 517.
[24] N. Erk, Y. Ozkan, E. Banoglu, S.A. Ozkan, Z. Senturk, J. Pharm. Biomed. Anal. 24 (2001) 469.
[25] J.L. Vilchez, R. Blanc, R. Avidad, A. Navalon, J. Pharm. Biomed. Anal. 13 (1995) 1119.
[26] A. Eustaquio, M. Blanco, R.D. Jee, A.C. Moffat, Anal. Chim. Acta 383 (1999) 283.
[27] J.L. Perez, M.A. Bello, Talanta 48 (1999) 1199.
[28] D.J. Speed, S.J. Dickson, E.R. Cairns, N.D. Kim, J. Anal. Toxicol. 25 (2001) 198.
[29] M. Li, L. Jing, Electrochim. Acta 52 (2007) 3250.
[30] F.S. Felix, C.M.A. Brett, L. Angnes, J. Pharm. Biomed. Anal. 43 (2007) 1622.
[31] S.F. Wang, F. Xie, R.F. Hu, Sens. Actuators B 123 (2007) 495.
[32] M.L.S. Silva, M.B.Q. Garcia, J.L.F.C. Lima, E. Barrado, Anal. Chim. Acta 573 (2006) 383.
[33] M. Boopathi, M.S. Won, Y.B. Shim, Anal. Chim. Acta 512 (2004) 191.
[34] S. Daya, S. Anoopkumar-Dukie, Life Sci. 67 (2000) 235.
[35] S.L. Xi-Ming, K.W. Perry, D.T. Wong, Neuropharmacology 42 (2002) 181.
[36] H. Maharaj, D.S. Maharaj, K.S. Saravanan, K.P. Mohanakumar, S. Daya, Metabol. Brain Dis. 19 (2004) 71.
[37] Naunyn-Schmiedeberg's Arch. Pharmacol. 364 (2001) 534.
[38] H.R. Zare, N. Nasirizadeh, M. Mazloum-Ardakani, M. Namazian, Sens. Actuators B 120 (2006) 288.
[39] H.R. Zare, N. Nasirizadeh, Electrochim. Acta 52 (2007) 4153.
[40] A.M.H. El-Askalany, A.M.A. El-Magd, Chem. Pharm. Bull. 43 (1995) 1791.
[41] H.R. Zare, F. Memarzadeh, M. Mazloum-Ardakani, M. Namazian, S.M. Golabi, Electrochim. Acta 50 (2005) 3495.
[42] H.R. Zare, N. Nasirizadeh, S.M. Golabi, M. Namazian, M. Mazloum-Ardakani, D. Nematollahi, Sens. Actuators B 114 (2006) 610.
[43] H.R. Zare, N. Nasirizadeh, M. Mazloum-Ardakani, J. Electroanal. Chem. 577 (2005) 25.
[44] F. Pariente, F. Tobalina, M. Darder, E. Lorenzo, H.D. Abruna, Anal. Chem. 68 (1996) 3135.
[45] H.R. Zare, S.M. Golabi, J. Electroanal. Chem. 464 (1999) 14.
[46] E. Laviron, J. Electroanal. Chem. 101 (1979) 19.
[47] S. Antoniadou, A.D. Jannakoudakis, E. Theodoridou, Synth. Met. 30 (1989) 295.
[48] C.P. Andrieux, J.M. Saveant, J. Electroanal. Chem. 93 (1978) 163.
[49] A.J. Bard, L.R. Faulkner, Electrochemical Methods, Fundamentals and Applications, Wiley, New York, 2001.
[50] R.D. Rocklin, R.W. Murray, J. Phys. Chem. 85 (1981) 2104.
[51] J.N. Miller, J.C. Miller, Statistics and Chemometrics for Analytical Chemistry, 4 ed., Pearson Education Ltd., Harlow, UK, 2000.
[52] M. Wei, M. Li, N. Li, Z. Gu, X. Duan, Electrochim. Acta 47 (2002) 2673.
[53] G. Wang, X. Liu, B. Yu, G. Luo, J. Electroanal. Chem. 567 (2004) 227.
[54] Y. Baoxian, X. Ping, L. Lin, Microchem. J. 64 (2000) 125.

Talanta 80 (2009) 664–669

Contents lists available at ScienceDirect

Talanta

journal homepage: www.elsevier.com/locate/talanta

Solid phase extraction–spectrophotometric determination of fluoride in water samples using magnetic iron oxide nanoparticles

H. Parham*, N. Rahbar

Department of Chemistry, College of Science, Shahid Chamran University, Ahvaz, Iran

ARTICLE INFO

Article history:
Received 1 May 2009
Received in revised form 20 July 2009
Accepted 22 July 2009
Available online 30 July 2009

Keywords:
Magnetic iron oxide nanoparticles
Fluoride
Solid phase extraction
Spectrophotometric determination

ABSTRACT

A new, sensitive, fast and simple method using magnetic iron oxide nanoparticles (MIONs), as an adsorbent has been developed for extraction, preconcentration and determination of traces of fluoride ions. The determination method is based on the discoloration of Fe(III)–SCN complex with extracted fluoride ions which was subsequently monitored spectrophotometrically at λ_{max} = 458 nm. Various parameters affecting the adsorption of fluoride by the MIONs have been investigated, such as pH of the solution, type, volume and concentration of desorbing reagent, amount of adsorbent and interference effects. A linear response for the determination of fluoride was achieved in the concentration range of 0.040–1.250 μg mL^{-1}. The limit of detection (LOD) and limit of quantification (LOQ) for fluoride based on 3 times and 10 times the standard deviation of the blank ($3S_b$, $10S_b$) were 0.015 and 0.042 μg mL^{-1} (n = 20) for fluoride ion, respectively. A preconcentration factor of 50 was achieved in this method. The proposed procedure has been applied for determination of fluoride concentration in various water samples. The results obtained from this method were successfully compared with those provided by standard SPADNS method.

© 2009 Elsevier B.V. All rights reserved.

1. Introduction

Fluoride is widely distributed in natural water at low concentrations. In unpolluted fresh and sea waters, it generally exists in the range of 0.01–0.30 and 1.2–1.5 μg mL^{-1}, respectively. A fluoride concentration of approximately 1.0 μg mL^{-1}, in drinking water effectively reduces dental caries without harmful effects on health. Some fluorosis may occur when the fluoride level exceeds the recommended limits [1]. Acute toxicity, generally due to ingestion of fluoride-containing rat poisons, includes gastrointestinal symptoms and neurological signs of hypocalcemia presumably related to the calcium-binding properties of fluoride. Due to the adverse effects of fluoride, the World Health Organization (WHO) has limited the maximum fluoride concentration acceptable in drinking water to 1.5 mg L^{-1} [2]. Therefore continuous monitoring of the fluoride levels in water samples is important to ensure good water quality.

Several analytical methods have been developed and described for fluoride determination in water including potentiometry [3–6], spectrophotometry [7–12], ion chromatography [13,14], fluorometry [15,16], capillary electrophoresis [17] and polarography [18]. Methods based on flow injection analysis have also been reported, using different detection techniques [19–21].

Among all the techniques mentioned above, for both potentiometric methods with fluoride ion selective electrode and standard colorimetric methods proved to be the most popular. Spectrophotometric methods for instance are widely used due to their simplicity, low cost and reliability. In most of these methods, fluoride ions displace organic ligands from colored complexes of metal ions such as zirconium and thorium. However both methods (potentiometric and colorimetric) do suffer from drawback, e.g. interfering effects from ions like sulphate, phosphate, chloride, iron and aluminum and it may be necessary to distill the sample. Thus lengthy distillation process (up to 80 min) is required prior to sample analysis. Additionally, this step is considered hazardous due to the strong acids required throughout the process [1]. Chromatographic methods are also time consuming and expensive to run.

Nanoscale materials have recently utilized in methods development and validation. The unique properties of nanoscale materials offer excellent prospects for designing new methods and instrumentation for chemical analysis [22,23]. Their small particle size will increase the surface area-to-volume ratio thus generating new electrical, magnetic, and optical properties among others [24–26].

Among many nanomaterials investigated, systems made from magnetic iron oxide nanoparticles (MIONs), proved to be useful in variety applications such as biomedicine, bioseparation and waste water treatment [27–31]. Moreover, these nanoparticles are known to be capable of sorption of some ligands, dyes, metal ions, anions, cations and use of them is thus becoming very attractive in a

* Corresponding author. Tel.: +98 611 3360018; fax: +98 611 3337009.
E-mail address: hoparham@yahoo.com (H. Parham).

0039-9140/$ – see front matter © 2009 Elsevier B.V. All rights reserved.
doi:10.1016/j.talanta.2009.07.045

new area of adsorption, recovery or removal of some ions [32–37]. A major advantage of using MIONs is the possibility of recovering the particles through the application of a magnetic field. This makes magnetic nanoparticles, excellent candidates for combining adsorption properties with ease of phase separation.

In this work, a new method has been proposed for solid phase extraction (SPE) and determination of fluoride, without particular interference, using MIONs as solid phase extractor. Extraction of fluoride ion is based on adsorption of analyte as Fe(III)–fluoride complex on MIONs and desorption by NaOH solution. After neutralization of the alkalinity, the extracted fluoride ions react with colored Fe–SCN complex and form FeF_6^{3-} colorless anionic complex which causes discoloration of Fe–SCN complex. As the amounts of fluoride ions increase, the color of the reaction mixture becomes progressively lighter. The optimum conditions for quantitative recoveries of fluoride were investigated and application of this method for analysis of water samples was established.

This analytical approach provides a selective, sensitive, simple, rapid and low cost colorimetric method for the determination of fluoride in water samples. The results of analysis by the proposed method compared favorably with results by standard SPADNS method [20].

2. Experimental

2.1. Instrumentation

The spectrophotometric measurements were carried out with a Cintra 101 spectrophotometer (GBC SCIENTIFIC EQUIPMENT, Australia). A transmission electron microscope (906E, LEO, Germany), pH-meter (632 Metrohm, Herisau, Switzerland) and a magnet (1.2 T, 10 cm × 5 cm × 2 cm) were used.

2.2. Reagents

All reagents and standards were of analytical grade unless otherwise stated, and all dilutions have been carried out with doubly distilled water. A 1000 μg mL^{-1} stock solution of fluoride was prepared from NaF (Merck, Darmstadt, Germany). Ammonium thiocyanate, ammonia solution (25%, m/m), hydrochloric acid (37%, m/m), acetic acid (99.9%, m/m), $FeCl_3$ (96%, m/m), $FeCl_2{\cdot}4H_2O$ (99.9%, m/m) were purchased from Merck (Darmstadt, Germany). pH adjustments were performed with 0.01–1.0 mol L^{-1} HCl and NaOH solutions. A formate buffer (pH = 2.5) was prepared by mixing formic acid (1.0 mol L^{-1}) and NaOH (1.0 mol L^{-1}) solutions.

2.3. Preparation of MIONs

The magnetite iron oxide nanoparticles, Fe_3O_4, (MIONs) were synthesized by coprecipitation of a stoichiometric mixture of ferrous and ferric chlorides (molar ratio 1:2) in an ammonium hydroxide solution with constant stirring [38]. The nanoparticles were collected by the magnet and thoroughly washed with distilled water to remove excess amounts of ammonium hydroxide. Experimental conditions such as temperature, addition rate of ammonia and stirring rate are of critical parameters that can affect the size of nanoparticles. The average size of the nanoparticles obtained was about 80 nm as shown in the transmission electron micrograph (TEM) image (Fig. 1).

2.4. Extraction and determination procedure

The extraction procedure was carried out in a batch process. A 250 mL solution containing 0.040–1.250 μg mL^{-1} of fluoride ion, 0.75 mL of 0.1 mol L^{-1} $FeCl_3$ and 5 mL of formate buffer solutions was stirred with 0.25 g damped MIONs for 2 min in a beaker.

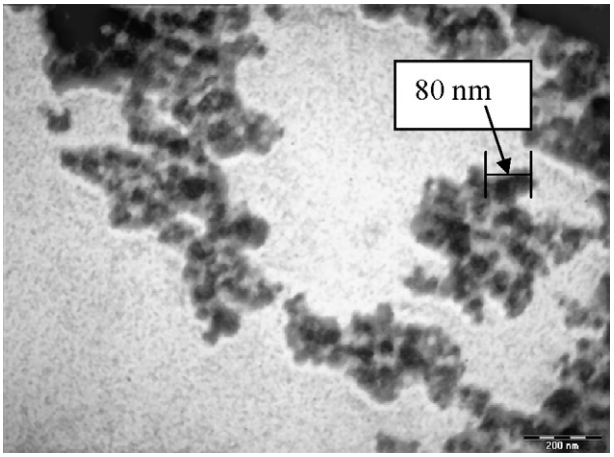


Fig. 1. TEM image of magnetic iron oxide nanoparticles (MIONs).

The beaker was placed on the magnet and nanoparticles were collected. After decanting the supernatant solution the collected MIONs have been washed with 2 mL of 1.0 mol L^{-1} NaOH solution in order to desorb the adsorbed fluoride ions by stirring for 3 min. The alkalinity of the extracted solution was neutralized with 1.1 mL of 2.0 mol L^{-1} of HNO_3 solution and transferred into the 5 mL volumetric flask containing 0.6 mL of reagent mixture (0.3 mL of 0.01 mol L^{-1} $FeCl_3$ solution and 0.3 mL of 0.1 mol L^{-1} NH_4SCN solution) and diluted to the mark with distilled water. Finally the absorption of the Fe–SCN complex solution containing the preconcentrated fluoride ion was measured spectrophotometrically at λ_{max} = 458 nm. A blank solution was also run under the optimized conditions without adding the analyte.

2.5. Method validation

The method was validated for linearity, precision, accuracy, extract recovery and selectivity according to the FDA guideline for validation of bioanalytical methods [39]. Validation runs were conducted on six consecutive days. The absorbance measurements of desorbing solution containing the preconcentrated fluoride amounts of quality control (QC) samples were interpolated from the calibration curve on the same day to give concentrations of the analyte. The results from QC samples in three runs were used to evaluate the precision and accuracy of the method developed.

The calibration curve of F^- ions was constructed using standard desorbing sample solutions at eight concentrations in the range of 0.040–1.250 μg mL^{-1} with least squares linear regression method. The limit of quantification (LOQ) is defined as the lowest concentration on the calibration curve at which an acceptable accuracy (R.E.) within ±20% and a precision (R.S.D.) below 20% can be obtained.

In order to test the reproducibility and repeatability of the proposed method, the intra-day precision and accuracy were evaluated by determining a replicate analysis of QC samples of fluoride ions on the same day. The run consisted of a calibration curve and five replicates of each low, mid, and high concentration quality control samples. For determining the inter-day accuracy and precision, analysis of three batches of QC samples was performed on different days.

The solid phase extraction efficiency of F^- was determined by analyzing five replicates of water sample solutions at three QC concentration levels of F^-. The recovery was calculated by comparing the absorbance of the preconcentrated F^- (spiked into blank water, extracted and 50-fold preconcentrated) in the desorbing solution (1.0 mol L^{-1} NaOH solution) with those obtained from F^- standard solutions in 1.0 mol L^{-1} NaOH solution.

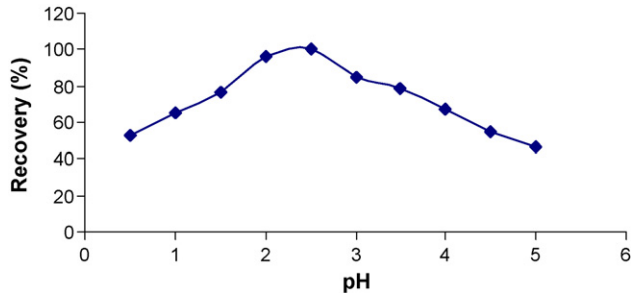


Fig. 2. The effect of pH on the recovery percentage of 0.2 μg mL^{-1} of fluoride ion (conditions—volume of 0.1 mol L^{-1} of $FeCl_3$ solution: 0.75 mL; sample volume: 250 mL; amount of adsorbent: 0.25 g).

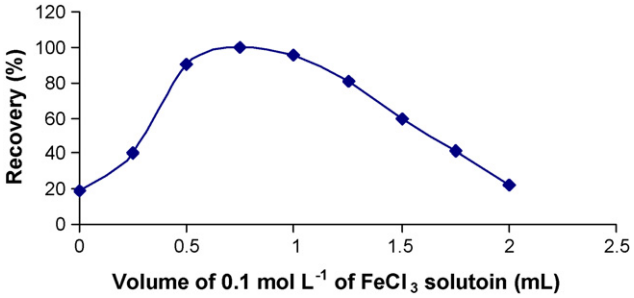


Fig. 3. The effect of Fe(III) concentration in Fe–fluoride complex formation and its sorption on MIONs (conditions—pH = 2.5; sample volume: 250 mL; amount of adsorbent: 0.25 g).

3. Results and discussion

Fe(III)–SCN complex has been known for a long time and used for spectrophotometric determination of Fe(III) ions [40]. On the other hand, primary experiments showed that adsorption of fluoride ions complex (FeF_6^{3-}) on the surface of MIONs took place in acidic solutions. Therefore, the uptake of this complex by MIONs, can take place via the surface complex formation mechanism due to adsorption affinity of surface hydrated ferric oxide at low pHs [36]. The optimum conditions for extraction and determination of traces of fluoride on magnetite nanoparticles were investigated. Preliminary experiments carried out with two levels full factorial designs showed that there is no significant interaction between significant parameters such as pH and adsorbent amount; pH and Fe(III) concentration; adsorbent amount and Fe(III) concentration. Therefore, these parameters were optimized by the one-factor at a time method.

3.1. Effect of pH

The influence of pH on the adsorption of fluoride ion on MIONs was investigated. The pH of each solution was adjusted to values ranging from 1 to 5 with HCl solutions. According to the results (Fig. 2), maximum recovery for the analyte was obtained at pH = 2.5. Additional experiments on type and volume of suitable buffer showed that 5 mL of formate buffer solution (pH = 2.5) gives the best result. However, at pH values higher than 2.5, adsorption of fluoride ion was diminished due to decrease of active surface area of hydrated ferric oxides. At lower pH values, the amount of MIONs was decreased because of high solubility of nanoparticles in stronger acidic solutions and also lower stability of FeF_6^{3-} complex.

3.2. Effect of Fe(III) concentration on the adsorption of F^- on MIONs

Early experiments showed that the adsorption of fluoride ion is very low without the presence of free Fe^{3+} ion in the test solution. It seems that the adsorption of fluoride on nanoparticles occurs via Fe(III)–fluoride complex (FeF_6^{3-}). Therefore, in order to determine the optimum concentration of Fe(III) for quantitative adsorption and recovery of fluoride, the proposed method was applied using different volumes of $FeCl_3$ (0.1 mol L^{-1}) solution. According to Fig. 3, 0.75 mL of 0.1 mol L^{-1} solution of $FeCl_3$ was recommended as optimum reagent volume for quantitative recovery of fluoride ion.

3.3. Effect of the type, concentration and volume of the desorbing solution

In order to choose the best solvent for desorption of the adsorbed fluoride ion on MIONs many reagent solutions were investigated. Among these reagents, NaOH solution provided the maximum recovery. The concentration of the NaOH solution was optimized and the results indicated that highest recovery was obtained by using 1 mol L^{-1} of NaOH solution. Since the desorbing NaOH solution contains high concentration of hydroxyl ions, we propose that OH^- ions can exchange and desorb the analyte (fluoride) from the surface of iron nanoparticles via the formation of highly stable iron hydroxide particles. Subsequent experiments showed that 2 mL of 1 mol L^{-1} solution of NaOH was the optimum volume for desorbing the fluoride from MIONs (Fig. 4). It must be mentioned that higher amounts of NaOH solution cause lower desorption and recovery of fluoride which may be due to formation of colloidal particles of iron oxides (decreasing the active surface area of the nanoparticles) and also entrapment of fluoride between the particles.

3.4. Effect of the adsorbent amount

In order to choose the optimum amount of adsorbent (MIONs) required for quantitative recoveries for fluoride ions, different quantities of pretreated MIONs (damped) were used in this testing ranging between 0.125 and 1.000 g. The maximum recovery percentage (recovery %) was obtained at 0.250 g of MIONs as shown in Fig. 5. Above this point the recovery percentage started to decrease due to high surface area of nanoparticles and the small volume of desorbing solvent. The repeatability of the preparation procedure of MIONs was evaluated by repeating the synthesis of magnetic nanoparticles for 8 times and each time 0.250 g of freshly prepared adsorbent was used for adsorption of fluoride ion. The validity of preparation procedure of magnetic adsorbent was checked by recovery tests carried out for adsorption and desorption of 0.2 and 1.0 μg mL^{-1} of F^-. Mean recovery percent values for 0.2 and 1.0 μg mL^{-1} of F^- test solutions were estimated to be 97.5 and 98.1, respectively. The R.S.D. values for eight adsorp-

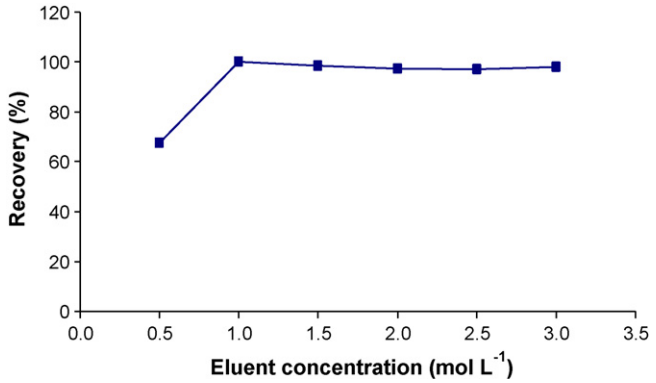


Fig. 4. The effect of NaOH concentration as desorbing eluent on the recovery percentage of 0.2 μg mL^{-1} of fluoride ion (conditions—pH = 2.5; volume of 0.1 mol L^{-1} of $FeCl_3$ solution: 0.75 mL; sample volume: 250 mL; amount of adsorbent: 0.25 g).

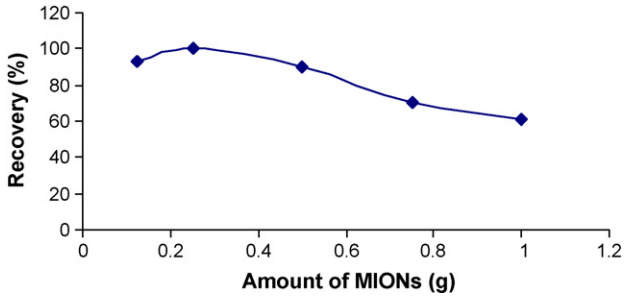


Fig. 5. The effect of the magnetic iron oxide nanoparticles (MIONs) adsorbent amount on the recovery percentage of 0.2 μg mL^{-1} of fluoride ion (conditions—pH = 2.5; volume of 0.1 mol L^{-1} of $FeCl_3$ solution: 0.75 mL; sample volume: 250 mL).

tion and desorption processes with freshly prepared MIONs for two mentioned concentrations are 3.50 and 2.74, respectively.

3.5. The effect of sample volume on the recovery percent and preconcentration factor

In order to carry out solid phase extraction procedure on natural water samples leading to high preconcentration factor, the sample volume need to be optimized. In this case the effect of sample volume on the adsorption of fluoride ions on MIONs was investigated. By using different feed volumes of water samples ranging between 50 and 300 mL, each of which containing fixed amounts of MIONs (0.250 g) and fluoride ions (50 μg), the maximum sample volume with high recovery percentage for the process was determined. As can be seen in Fig. 6, the recoveries of fluoride were quantitative up to 250 mL of sample volume. By applying of 250 mL sample volume under optimum conditions and as stated previously, desorbing of fluoride ions with 2 mL of 1.0 mol L^{-1} NaOH solution and dilution to 5 mL (the final volume of desorbed solution is 5 mL as mentioned in Section 2.4), the preconcentration factor of 50 was obtained.

3.6. Effect of interfering ions

Prior to the application of proposed method on real samples it was vital to investigate the effect of some of the interfering ions on the recovery percentage of fluoride. The adsorption–desorption of fluoride ion was tested in the presence of spiked known amounts of interfering ions. The tolerance limit was defined as the amount of the foreign ion causing a change of ±5% in the absorbance reading. The tolerable limits of interfering ions are given in Table 1. The results showed that most of the investigated ions do not interfere in the adsorption–desorption and determination of traces of fluoride in water samples.

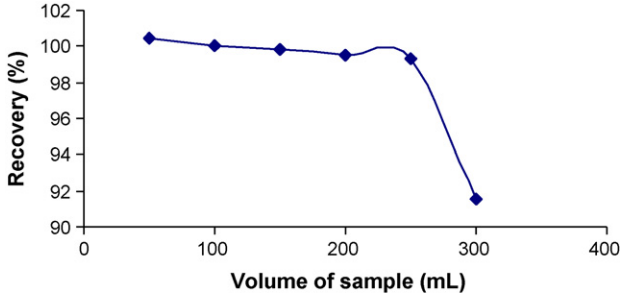


Fig. 6. The effect of sample volume on the recovery percentage of 0.2 μg mL^{-1} of fluoride ion (conditions—pH = 2.5; volume of 0.1 mol L^{-1} of $FeCl_3$ solution: 0.75 mL; desorbent volume: 2 mL of 1 mol L^{-1} of NaOH solution; amount of adsorbent: 0.25 g).

Table 1
The effect of foreign ions on adsorption–desorption and recovery percentage of fluoride ion (0.20 μg mL^{-1}) on MIONs.

Ion	Tolerance limit (mg L^{-1})
Na^+, K^+, Cl^-	5000
NO_3^-, SO_4^{2-}	250
Ca^{2+}, Mg^{2+}, CO_3^{2-}, HPO_4^{2-}	150
Cr^{3+}	20
Al^{3+}	1

Conditions—pH = 2.5; volume of 0.1 mol L^{-1} of $FeCl_3$ solution: 0.75 mL; sample volume: 100 mL; desorbent volume: 2 mL of 1 mol L^{-1} of NaOH solution; amount of adsorbent: 0.25 g.

Table 2
Precision and accuracy data for SPE of F^- from water solution by using MIONs (intra-day: $n = 5$; inter-day: $n = 5$ runs per day, 6 days).

F^- concentration (μg mL^{-1})		R.S.D. (%)		R.E. (%)
Added	Found (mean ± S.D.)	Intra-day	Inter-day	
0.200	0.191 ± 0.007	3.5	7.9	−3.6
0.400	0.415 ± 0.014	3.7	7.6	+3.0
0.800	0.781 ± 0.042	2.2	8.8	−2.6

3.7. Loading capacity

The loading capacity of MIONs was determined by batch method. The adsorbent (0.250 g) was mixed with 250 mL solution containing 5 μg mL^{-1} of fluoride using a stirrer for 1 h period under optimal experimental conditions. After removing the supernatant, the MIONs nanoparticles were collected and washed by 8 mL of 1 mol L^{-1} NaOH solution in four steps prior to the determination of the fluoride concentration. The loading capacity calculated from the measurement process was found to be 0.204 mg g^{-1}.

3.8. Analytical performance and method validation

In order to show the validation of the proposed method, the analytical features of the method such as linear range of the calibration curve, limit of detection (LOD), limit of quantification (LOQ), accuracy and precision were examined. Two calibration curves were obtained for determination of fluoride ion. The calibration graphs were linear in the ranges of

Table 3
Determination of fluoride content and recovery test of fluoride ion in tap (100 mL), river (100 mL) and sea (25 mL) water samples with the proposed method ($n = 5$).

Sample	Added F^- (μg mL^{-1})	Found F^-[a] (μg mL^{-1})	Recovery (%)
Tap water[b]	–	0.141 ± 0.002	–
Tap water	0.1	0.243 ± 0.003	99.7
Tap water	0.2	0.342 ± 0.003	100.1
River water[c]	–	0.139 ± 0.002	–
River water	0.1	0.236 ± 0.002	97.0
River water	0.2	0.343 ± 0.003	99.9
Sea water[d]	–	0.217 ± 0.002	–
Sea water	0.1	0.309 ± 0.003	96.0
Sea water	0.2	0.423 ± 0.003	100.1

Conditions—pH = 2.5; volume of 0.1 mol L^{-1} of $FeCl_3$ solution: 0.75 mL; sample volume: 100 mL; desorbent volume: 2 mL of 1 mol L^{-1} of NaOH solution; amount of adsorbent: 0.25 g.

[a] $x \pm s$ ($n = 5$).

[b] Tap water components: $Ca^{2+} = 52$; $Mg^{2+} = 29$; $Na^+ = 37$; $CO_3^{2-} = 61$; $Cl^- = 24$; $SO_4^{2-} = 25$; $NO_3^- = 9$ μg mL^{-1}; pH = 7.3; EC = 853.

[c] River water main components: $Ca^{2+} = 82$; $Mg^{2+} = 49$; $Na^+ = 68$; $CO_3^{2-} = 91$; $Cl^- = 44$; $SO_4^{2-} = 35$; $NO_3^- = 9$ μg mL^{-1}; pH = 7.1; TDS = 387; EC = 1340.

[d] Sea water main components: $Ca^{2+} = 400$; $Mg^{2+} = 900$; $Na^+ = 11{,}058$; $CO_3^{2-} = 150$; $Br^- = 68$; $Cl^- = 17{,}000$; $SO_4^{2-} = 2400$; $K^+ = 400$ μg mL^{-1}; pH = 7.6; EC > 4500 (25 mL of sea water was diluted to the final volume of 100 mL).

Table 4
Determination of fluoride ion in water samples with the proposed and standard SPADNS methods ($n = 5$).

Water sample	Proposed method ($\mu g\,mL^{-1}$)	Standard SPADNS method ($\mu g\,mL^{-1}$)
Tap water	0.141 ± 0.002	0.143 ± 0.002
River water	0.138 ± 0.003	0.136 ± 0.002
Sea water	0.217 ± 0.002	0.205 ± 0.001

Conditions—pH = 2.5; volume of 0.1 mol L^{-1} of $FeCl_3$ solution: 0.75 mL; sample volume: 100 mL; desorbent volume: 2 mL of 1 mol L^{-1} of NaOH solution; amount of adsorbent: 0.25 g.

0.04–0.20 and 0.20–1.25 $\mu g\,mL^{-1}$ of fluoride ion. The equations for these calibration graphs were $\Delta A = 0.971C_F - 0.0122$ ($R^2 = 0.9967$) and $\Delta A = 0.337C_F + 0.1051$ ($R^2 = 0.9971$), respectively (ΔA is the absorbance difference between blank and sample solution and C_F is the concentration of fluoride in $\mu g\,mL^{-1}$). The limit of detection (LOD) and limit of quantification (LOQ) based on 3 times and 10 times the standard deviation of the blank ($3S_b$, $10S_b$) [41], under optimum experimental conditions were 0.015 and 0.042 $\mu g\,mL^{-1}$ for fluoride ($n = 20$), respectively. The relative standard deviations (R.S.D.) for 0.2 and 0.8 $\mu g\,mL^{-1}$ of fluoride ($n = 10$) were 3.1 and 2.0%, respectively.

Intra- and inter-day precision and accuracy data (showing reproducibility and repeatability terms) for SPE of fluoride by MIONs from quality control (QC) samples are summarized in Table 2. The precision and accuracy of the present method conform to the criteria for the analysis of biological samples according to the guidance of FDA where the R.S.D. determined at each concentration level is required not exceeding 15% (20% for LOQ) and R.E. within ±15% (±20% for LOQ) of the actual value [39].

The extraction recoveries from QC samples of plasma solutions containing low, middle and high concentrations of F^- (0.20, 0.40 and 0.80 $\mu g\,mL^{-1}$) were 96.4 ± 3.6, 97.0 ± 3.0, and 97.4 ± 2.6%, respectively. No significant matrix effect for SPE of F^- by MIONs was observed indicating that no co-adsorbing substance could influence the separation and determination of the analyte.

Table 5
The comparison of the proposed method (magnetic solid phase extraction–spectrophotometric, MSPES) with other reported methods of F^- determination.

Detection method[a]	Detection limit ($\mu g\,mL^{-1}$)	Time of analysis (min)	Recovery (%)	Ref.
P	NR[b]	15	99	[3]
P	0.19	1.5	101	[4]
P	0.08	NR	97	[5]
P	0.004	10	98	[6]
SPE	0.8	10	NR	[7]
S	0.02	>20	99	[8]
S	0.002	>10	101	[9]
S	NR	>60	NR	[10]
S	0.06	20	100	[11]
S	2.5	NR	NR	[12]
IC	–	NR	–	[13]
IC	0.008	10	NR	[14]
S	0.08	NR	99	[15]
SES	0.018	>10	100	[16]
FIA-CE	NR	NR	NR	[17]
V	0.008	>20	90	[18]
FIAS	0.01	10	96	[19]
FIAS	0.1	NR	NR	[20]
FIAS	0.04	>10	98	[21]
MSPES	0.015	8	99	Proposed

[a] Potentiometric (P), voltammetric (V), spectrophotometric (S), ion chromatographic (IC), solvent extraction–spectrophotometric (SES), solid phase extraction (SPE), flow injection analysis-spectrophotometric (FIAS) and FIA-capillary electrophoresis (FIA-CE).
[b] NR = not recorded.

3.9. Application on real sample

In order to test the validity of the method, the proposed procedure was applied to determination of fluoride ion in water samples. Recovery tests were used to examine the reliability and accuracy of the method, different amounts of fluoride were spiked into the tap (100 mL), river (100 mL) and sea (25 mL) water samples and fluoride content of each sample was determined at optimum conditions. The fluoride content of different samples and recoveries of added analyte were evaluated and the results showed that it is possible to determine the fluoride concentration in real sample solutions using the proposed method outlined in this investigation (Table 3). The results achieved were comparable with those obtained by the SPADNS method [20] (Table 4).

4. Conclusion

The proposed methodology was simple, sensitive and cheap, especially if more sophisticated techniques such as spectrofluorometry or ion chromatography are not available. In addition, it is notable that both the adsorption and desorption of fluoride are fast and could be completed within 5 min. LOD and linear dynamic range of the method are comparable or better than some of the previously reported methods [3–5,7,8,10–13,15,17–21]. The proposed method was successfully applied for determination of fluoride in water samples and concentration values obtained are in agreement with those of standard SPADNS method (CRM was not available). No use of toxic compounds, short time of the procedure (total time of a single determination is about 8 min) and low LOD are the main advantages of the proposed methods. Table 5 shows a comparison of the proposed method with other reported methods. Some reported values for LOD [6,9,14,18,19] are better than that of the proposed method, but total time of analysis of this method is short. The proposed method shows good and comparable recovery values with respect to other reported methods.

Acknowledgement

The authors wish to thank Shahid Chamran University Research Council for financial support of this work (Grant 1386).

References

[1] Standard Methods for the Examination of Water and Wastewater, 21st ed., 2005, pp. 4–79.
[2] World Health Organization (WHO), Guidelines for Drinking Water Quality, vol. 1, 2nd ed., World Health Organization, Geneva, 1993.
[3] A. Ruiz-Payan, M. Ortiz, M. Duarte-Gardea, Microchem. J. 81 (2005) 19.
[4] A.C. Conceicao, M.M. Correia dos Santos, M.L.S. Alves, F.J.V. Santos, Talanta 50 (2000) 1245.
[5] A.C. Conceicao, M.M. Correia dos Santos, M.L.S. Alves, Talanta 76 (2008) 107.
[6] A. Yuchi, K. Matsunaga, T. Niwa, H. Terao, H. Wada, Anal. Chim. Acta 388 (1999) 201.
[7] O.A. Zaporozhets, L.Y. Tsyukalo, Anal. Chim. Acta 597 (2007) 171.
[8] M.E. Khalifa, M.A.H. Hafez, Talanta 47 (1998) 547.
[9] C.Q. Zhu, J.L. Chen, H. Zheng, Y.Q. Wu, J.G. Xu, Anal. Chim. Acta 539 (2005) 311.
[10] S.M. Maliyekkal, A.K. Sharma, L. Philip, Water Res. 40 (2006) 3497.
[11] X. Gao, H. Zheng, G. Shang, J.G. Xu, Talanta 73 (2007) 770.
[12] J. Ramkumar, Talanta 68 (2006) 902.
[13] Y. Miyake, N. Yamashita, P. Rostkowski, M.K. So, S. Taniyasu, P.K.S. Lam, K. Kannan, J. Chromatogr. A 1143 (2007) 98.
[14] E.N. Kapinus, I.A. Revelsky, V.O. Ulogov, Y.A. Lyalikov, J. Chromatogr. B 800 (2004) 321.
[15] H. Matsunaga, C. Kanno, H. Yamada, Y. Takahashi, T.M. Suzuki, Talanta 68 (2006) 1000.
[16] J. Nishimoto, T. Yamada, M. Tabata, Anal. Chim. Acta 428 (2001) 201.
[17] P. Kuban, B. Karlberg, Anal. Chem. 69 (1997) 1169.
[18] L. Guanghan, W. Qiongling, W. Xiaogang, Z. Tong, Y. Xin, Food Chem. 66 (1999) 519.
[19] K. Shimada, T. Shimoda, H. Kokusen, S. Nakano, Talanta 66 (2005) 80.
[20] J.A. Arancibia, A. Rullo, A.C. Olivieri, S.D. Nezio, M. Pistonesi, A. Lista, B.S. Fernández Band, Anal. Chim. Acta 512 (2004) 157.
[21] P.D. Tzanavaras, D.G. Themelis, Anal. Chim. Acta 467 (2002) 83.

[22] M. Trojanwicz, Trends Anal. Chem. 25 (2006) 480.
[23] J. Wang, Analyst 130 (2005) 421.
[24] S.C. Tjong, H. Chen, Rep.: A Rev. J. 45 (2004) 1.
[25] P.M. Ajayan, Chem. Rev. 99 (1999) 1787.
[26] M.C. Daniel, D. Astruc, Chem. Rev. 104 (2006) 293.
[27] E.H. Kim, Y. Ahn, H.S. Lee, J. Alloys Compd. 434–435 (2007) 633.
[28] C.C. Berry, S. Wells, S. Charles, A.S.G. Curtis, Biomaterials 24 (2003) 4551.
[29] D.B. Shieh, F.Y. Cheng, C.H. Su, C.S. Yeh, M.T. Wu, Y.N. Wu, C.Y. Tsai, C.L. Wu, D.H. Chen, C.H. Chou, Biomaterials 26 (2005) 7183.
[30] Y.Y. Liang, L.M. Zhang, W. Li, R.F. Chen, Colloid Polym. Sci. 285 (2007) 1193.
[31] V. Rocher, J.M. Siaugue, V. Cabuil, A. Bee, Water Res. 42 (2008) 1290.
[32] A. Uheida, G. Salazar-Alvarez, E. Björkman, Z. Yu, M. Muhammed, J. Colloid Interface Sci. 298 (2006) 501.
[33] S.Y. Mak, D.H. Chen, Dyes Pigments 61 (2004) 93.
[34] P. Li, D. Miser, S. Rabiei, R.T. Yadav, M.R. Hajaligol, Appl. Catal. B: Environ. 43 (2003) 151.
[35] J.T. Mayo, C. Yavuz, S. Yean, L. Cong, H. Shipley, W. Yu, J. Falkner, A. Kan, M. Tomson, V.L. Colvin, Sci. Technol. Adv. Mater. 8 (2007) 71.
[36] L.M. Blaney, S. Cinar, A.K. Sen Gupta, Water Res. 41 (2007) 1603.
[37] K. Hristovski, P. Westerhoff, T. Moller, P. Sylvester, W. Condit, H. Mash, J. Hazard. Mater. 152 (2008) 397.
[38] P. Berger, N. Adelman, K. Beckman, J. Chem. Ed. 76 (1999) 943.
[39] Guidance for Industry: Bioanalytical Method Validation, US Department of Health and Human Services, Food and Drug Administration, Center for Drug Evaluation and Research, Rockville, MD, 2001, Available from: http://www.fda.gov/CVM.
[40] R.B. Fischer, D.G. Peters, A Brief Introduction to Quantitative Chemical Analysis, W. B. Saunders, Philadelphia, 1969.
[41] J.C. Miller, J.N. Miller, Statistics and Chemometrics for Analytical Chemistry, 5th ed., Parson Education, England, 2005.

Talanta 80 (2009) 670–675

Contents lists available at ScienceDirect

Talanta

journal homepage: www.elsevier.com/locate/talanta

A centrifugal microanalysis system for the determination of nitrite and hexavalent chromium

Angela LaCroix-Fralish[a,b], Jennifer Clare[a,b], Cameron D. Skinner[a], Eric D. Salin[b,*]

[a] Department of Chemistry and Biochemistry, Concordia University, 7141 Sherbrooke St. W., Montreal, QC, Canada H4B 1R6
[b] Department of Chemistry, McGill University, 801 Sherbrooke St. W., Montreal, QC, Canada H3A 2K6

ARTICLE INFO

Article history:
Received 19 May 2009
Received in revised form 21 July 2009
Accepted 22 July 2009
Available online 30 July 2009

Keywords:
Microanalysis
Centrifugal microfluidics
Nitrite
Hexavalent chromium
Environmental analysis

ABSTRACT

A centrifugal microanalysis system using spectrophotometric detection has been developed for the determination of nitrite and chromium VI. The system was designed to illustrate the potential of centrifugal microfluidic systems for on-site (field) analysis of waters. The performance was significantly better than manual/visual field test systems and approaches that of bench top systems with detection limits of 0.008 mg L^{-1} NO_2^--N and 0.03 mg L^{-1} Cr^{6+}. The system used pre-loaded solid reagents on the disc, providing ease of use, and could process up to 24 samples simultaneously. Precision was enhanced by the use of a multiwavelength ratiometric blank estimation technique.

© 2009 Elsevier B.V. All rights reserved.

1. Introduction

In environmental studies there may be considerable advantage to be had if the analysis can be done on-site. Bulk transport problems are eliminated as well as concerns over changes in chemical form (*e.g.* nitrite to nitrate), degradation, or concentration (*e.g.* VOCs). Additionally, in some cases, contamination risks may be minimized by on-site analysis. There may also be an additional logistic advantage if the analysis can provide immediate feedback to a process at hand, such as a site remediation. Thus there appear to be considerable advantages to the development of analytical techniques which can be used on-site to provide accurate results in a timely manner and at low cost.

Recently, there has been an increase in the development of methods for analyzing samples in the field including: a portable GC for analyzing VOC's [1], a mass spectrometer for field gases [2], and an electrochemical instrument for heavy metal mapping [3]. Field-portable instruments can often be very specialized, require a large financial investment and entail extensive operator training. To address these limitations, user-friendly, rugged systems have been developed that can analyze multiple analytes on-site [4,5]. This is especially important for water and wastewater contaminants as supplying unadulterated, potable, recreational and economic water supplies becomes an ever increasing issue.

For several years, the advantages of small size, minimal reagent consumption, and the low power requirements of microfluidics have been seen as a gateway to meeting the needs for developing field-portable systems. Several review papers discuss the use of microfluidic manifolds for environmental analysis [1,6,7]. The majority of methods available, however, have several drawbacks including the requirement for external sample preparation (*e.g.* pre-concentration, filtering, separation), high power demand, complex procedures or high cost.

In the present work, we demonstrate microanalysis instrumentation that is applicable to a variety of environmentally significant analyses. The technique is demonstrated with two different model analytes, nitrite and hexavalent chromium.

Contamination of natural waters from anthropogenic sources of nitrogen is a widespread problem. Nitrite is often found in industrial effluent as a byproduct of corrosion inhibitors in boiler systems, as a curing agent for meat, and in the production of explosives. It is also used extensively in agriculture for crop fertilization. Excess nitrite nutrients can cause eutrophication of lakes, rivers and estuaries leading to an imbalance in the natural food and life cycles of organisms. Nitrite can also fuel algal blooms that result in high levels of cyanobacteria and other toxic microorganisms leading to dead zones, unusable recreational waterways, and commercial fish kills.

Chromium(VI) is a compound with demonstrated carcinogenic effects for both humans and animals [8]. Natural and drink-

* Corresponding author at: Department of Chemistry, McGill University, 801 Sherbrooke St. W., Montreal, QC, Canada H3A 2K6. Tel.: +1 514 398 6236; fax: +1 514 398 3797.
E-mail address: Eric.salin@mcgill.ca (E.D. Salin).

0039-9140/$ – see front matter © 2009 Elsevier B.V. All rights reserved.
doi:10.1016/j.talanta.2009.07.046

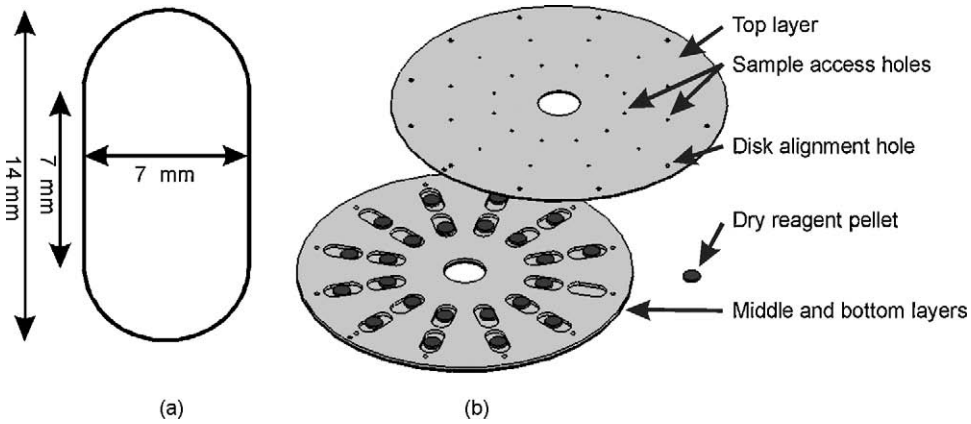


Fig. 1. Disc used for the derivatization and detection of nitrite and/or hexavalent chromium using pressed powder reagent pellets; (a) illustrates the size and dimensions of cells made by machining the center layer of the composite disc, and (b) shows a partially assembled disc. All of the cells, except for one, have the dry reagent pellet in place.

ing waters can become contaminated with Cr(VI) as a result of untreated, or under treated, industrial effluent discharged into waterways. The US EPA has imposed a limit of 0.05 mg L^{-1} for Cr(VI) in drinking water.

This paper demonstrates the detection of both NO_2^- and Cr(VI) on a simple microfluidic/microanalysis centrifugal disc system. Incorporation of measured amounts of dry reagents on the disc allows storage of the disc for long periods of time and facile, quantitative analyte derivatization and measurement. Centrifugal force is used to rapidly mix the dry reagents and sample followed by spectrophotometric detection on the device. The discs can be fabricated inexpensively and provide analytical results that approach those of bench top instruments.

2. Experimental

2.1. Reagents

The modified Griess reaction was used for the detection of nitrite. The reaction consisted of a coupling reaction between chromatropic acid and the diazonium ion formed in acidic solution after a stoichiometric reaction with the nitrite in the sample [9,10]. Chromium(VI) was detected using the classic 1,5-diphenylcarbazide reaction [11,12].

All standards were prepared with deionized water by mass in appropriately cleaned containers. Nitrite solutions were diluted from a 100 mg L^{-1} NO_2^--N (nitrite as nitrogen) stock solution (SPEX, Metuchen, NJ, USA) to appropriate concentrations. Chromium standards were made daily from a 100 mg L^{-1} $K_2Cr_2O_7$ solution (SCP Science, Baie D'Urfé, QC, Canada) in clean, 30 mL plastic bottles. The reagents for both derivatization reactions were purchased from Hach Corporation (Loveland, OH, USA) in the form of sealed foil/plastic "pillow packets". According to the manufacturer, the nitrite reagent (Nitriver3®) consisted of chromatropic acid disodium salt, sodium sulfanilate, potassium pyrosulfate, monobasic potassium phosphate, 1,2-cyclohexanediaminetetraacetic acid trisodium salt. The chromium reagent (Chromaver3®) consisted of potassium pyrosulfate magnesium sulfate and 1,5-diphenylcarbohydrazide.

2.2. Microfluidic/microanalysis disc design

The microfluidic discs were fabricated using a combination of computer numerically controlled (CNC) micro-milling machining and xurography as previously described by Bartholomeusz et al. [13]. The body of the 120 mm diameter microfluidic disc was made using commercially available uncoated polycarbonate discs of two thicknesses: a 1200 μm thick disc used in the manufacture of compact discs (CD) and a 600 μm thick disc normally used in the manufacture of digital video discs (DVD) (U-Tech Media Corporation, Taiwan). These relatively simple microfluidic discs consisted of a 1200 μm thick disc as an internal layer that provided the depth, and hence volume, for the solution reservoirs. The top and bottom layers/covers were made using the 600 μm thick discs to reduce the overall thickness and weight of the system and minimized the optical window thickness. The disc was assembled using 2 alignment holes and sealed using 101.6 μm thick pressure sensitive acrylic adhesive layers (FLEXcon, Spencer, MA, USA) by cold pressing with a Sidewinder Roller Laminator (Desert Laminator, Palm Springs, CA, USA). Considerable additional detail on aspects of the design and experiments is available elsewhere [14].

The disc comprised 24 individual cells with injection holes (Fig. 1a). The reaction/detection cell consisted of two 7 mm diameter half-circles connected by a 7 mm × 7 mm square. The nominal sample pathlength for spectroscopic measurements was 1400 μm (a 1200 μm thick disc plus two 101.6 μm thick adhesive layers) but variances in disc construction and sealing, may introduce a few percent error in the pathlength and necessitates calibration with standard solutions on each disc.

A pellet containing all the reagents needed for analysis was inserted into the disc prior to sealing (Fig. 1b). The metal surfaces of the pellet press were either covered with Parafilm or replaced with

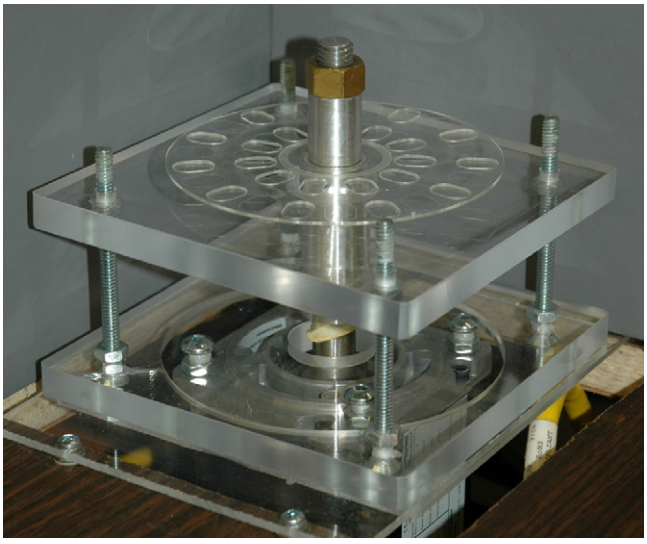


Fig. 2. An image of the servo motor system, and spindle used to spin the disc.

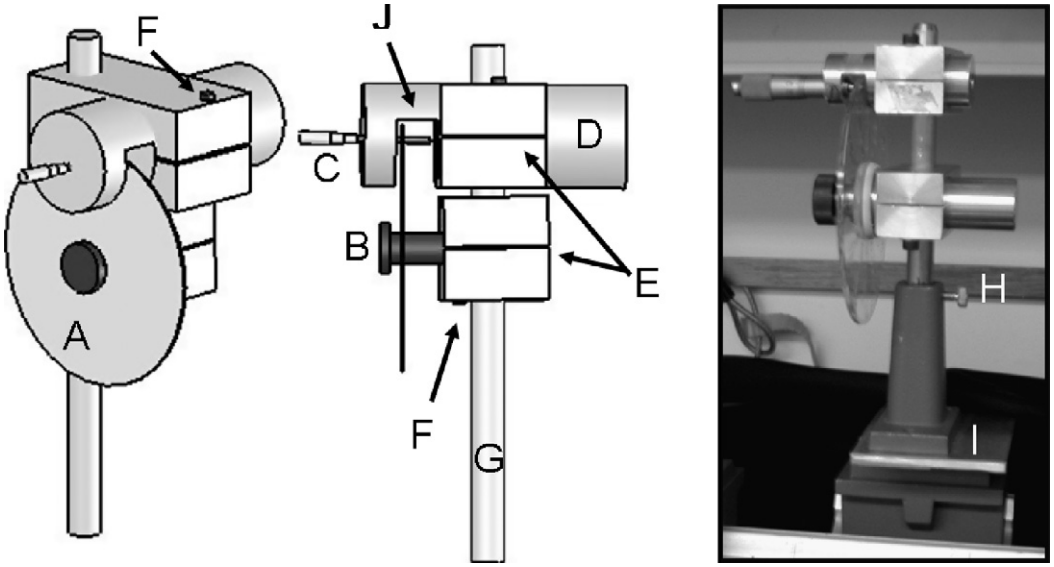


Fig. 3. The disc (A) fits onto a cylinder fitted with a tightening screw (B) and is locked into position with a micrometer (C). D and B provide the *X*-axis adjustment by sliding through two blocks (E) that are fitted with tension screws (F). The blocks (E) also individually slide along G, which provides movement along the *Z*-axis for different sizes of discs. *Z*-axis adjustment is also provided by adjusting H, which allows the whole assembly to slide along the *Z* (up/down) axis. The entire apparatus is mounted on I, which provides adjustment in the *X*-axis, using a typical optical rail mount. A portion of D has been cut-away (J) to allow proper positioning.

Teflon to avoid metal contamination of the pellets. After sealing the disc, vinyl adhesive was used to seal the access ports/openings to the cell and the entire disc was placed in a desiccator until use.

2.3. Instrumentation configuration

The disc was mounted on a servo motor (Parker Automation Servo Motor with Aries Servo Drive, Parker Hannifin Corp., Rohnert Park, CA) using a lab constructed spindle designed to accept the disc. The speed, direction and duration of the motor were all controlled via a National Instruments Motion Controller (Model# UMI-7764) and software written in LabView (National Instruments, Quebec, Canada). An image of the system is shown in Fig. 2. The system is also described in detail by Duford et al. [15].

For spectral measurements the disc was removed from the spindle and installed in the optical path of the spectrometer system using the disc holder, shown in Fig. 3, which was designed for maximum flexibility and is adjustable in three axes allowing for multiple thicknesses, sizes and disc designs. The open design of the holder allowed for easy placement of the entire sample cell area in the optical path and minimized reflective materials, reducing the amount of light scatter (see Fig. 4). Evenly spaced stabilization/alignment holes on the periphery of the disc provided reproducible disc placement and aligned the cells in the optical path (not shown but approximately at the 4 o'clock position on the disc). New cells were positioned in the path by loosening the micrometer and rotating the disc to the next alignment hole.

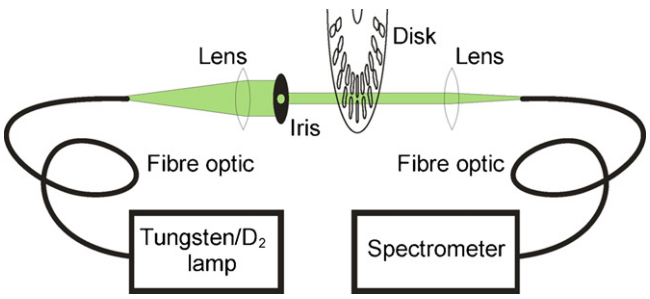


Fig. 4. Overall schematic of the optical detection system showing the relative positioning of the source and receiving fiber optics and the lenses. The adjustable iris limited illumination to the central area of the reaction/detection cell while preventing scatter from the milled cell walls.

The detection apparatus shown in Fig. 4, consisted of a Tungsten-Halogen/Deuterium light source (DT-MINI-2-GS, Ocean Optics, Dunedin, FL) that provided radiation in both the visible and ultraviolet region. The light was transferred to the disc using a 300 μm × 1 m, solarization resistant fiber optic (QP300-1-SR, Ocean Optics, Dunedin, FL). The light was collimated using a 4 cm focal length quartz lens, truncated to a 6 mm diameter beam with an iris, directed through the sample cell on the disc in the holder apparatus and focused by a matching lens onto the detection fiber optic. This fiber optic was connected to a USB compatible asymmetric crossed Czerny-Turner type miniature spectrometer with a linear charged coupled device (CCD) photodiode array detection system (USB4000-UV-VIS, Ocean Optics, Dunedin, FL).

2.4. Procedure and measurement

Standard or sample (100 μL) was pipetted into the disc and the seal over the injection hole was replaced. The reagent pellet was dissolved by mounting the disc on the spindle and programming the motor to rotate the disc by alternating direction every half turn for 180 s at 150 rpm. After mixing was complete the disc was held at rest for the 20 min reaction period and placed in the disc holder for absorbance measurements.

The "reference (large scale) experiment" consisted of preparing standards and reagents according to the manufacturer's suggested protocol with 10 mL volumes and measuring the resulting spectra with a bench top spectrometer using the same calculation technique as spectra taken using the disc. These absorbance measurements were made using a 1 cm optical grade, plastic cell from Ocean Optics (Dundin, FL, USA) and an Agilent 8453 spectrometer.

To establish the length of time the reagent pellet was stable and whether pellet size affected the absorbance a single disc was constructed using normal procedures, sealed and placed in a desiccator until use. Several cells with known pellet mass were tested over a 31-day period using a fresh solution of approximately 0.5 mg L^{-1} $NO_2{}^{-1}$-N. The final absorbance was adjusted for any difference in standard concentration.

In order to overcome the path length and absorbance imprecision associated with using plastic discs as both reaction chamber and detection cell window, a ratiometric method was used to estimate the blank. The blank absorbance signal can be estimated directly from a sample spectrum provided that the sample does not absorb over the entire available spectral range. First, several sample spectra were taken and the wavelength(s) at which the analyte absorbs (λ_1) and at which the analyte does not absorb (λ_2) were found. Second, a blank spectrum was taken. The ratio of the blank signal (I) at the analyte absorbing wavelength (λ_1) to the blank signal at the sample's non-absorbing wavelength (λ_2) was found from the blank spectrum using the following equation.

$$\text{Ratio} = \frac{I_{\lambda_{1\text{blank}}} - I_{\lambda_{1\text{dark}}}}{I_{\lambda_{2\text{blank}}} - I_{\lambda_{2\text{dark}}}} \quad (1)$$

When a sample was run, the measured signal at the non-absorbing wavelength (λ_2) was multiplied by the ratio to give an estimated signal of the blank at the absorbing wavelength (λ_1). The modified transmittance equation is:

$$T = \frac{I_{\lambda_{1\text{sample}}} - I_{\lambda_{1\text{dark}}}}{\text{Ratio}(I_{\lambda_{2\text{sample}}} - I_{\lambda_{2\text{dark}}})} \quad (2)$$

A single blank spectrum per disc was taken during each set of measurements and used to provide the ratio. For the nitrite calculations, the average absorbance from 499 to 540 nm was used for the absorbing wavelength and 603 to 624 nm for the non-absorbing wavelength. For chromium, the ratio was calculated using 530–560 nm for the absorbing wavelengths and 758–786 nm for the non-absorbing wavelengths.

3. Results and discussion

3.1. Centrifugal microfluidics

Centrifugal microfluidics is a relatively unexplored research avenue in the pantheon of analytical methodologies and offers many appealing features to the analytical chemist developing new instrumentation, especially if field portability is the ultimate goal. Some of the key aspects of a field-portable instrument that centrifugal microfluidics have are: simplicity, robust and reliable mechanisms, minimal sample, and reagent handling, low power consumption and versatility. Although closely related to microfluidics, centrifugal microfluidics has the advantage for portable instrumentation due to its operational simplicity, freedom in choice of fabrication materials and operating conditions. Centrifugal microfluidics excels when multiplexed analyses are implemented on the same disc. Scaling an analysis up into a multiplexed assay is easy, because the driving and mixing forces on a rotating disc are a function of radial position. This provides uniform conditions for all positions/devices on the disk that are located at the same radial position.

In the present implementation, we have made the simplest of multiplexed discs: an array of reaction/detection cells, but more complicated manifolds have been presented in the literature [16]. The motor system that we used allowed the disc to be oscillated by 1/2 turns for 180 s under programmed control and ensured rapid dissolution of the dry reagent pellet in the sample solution and initiation of the reaction.

It became apparent early in testing that there were disc to disc variations which resulted in spectral differences that would introduce appreciable variance into any analysis. We attributed these differences to small pathlength and disc transparency changes that an appropriate blank measurement would largely eliminate. Analytically, the best blank measurement utilizes the sample cell filled with a blank solution; however, in centrifugal systems this is impractical so estimation of the blank signal (at the analyte wavelength) using non-analyte wavelengths was the next best alternative.

By using the ratio method, only one blank spectrum per disc was needed to establish the appropriate ratios to apply to all samples on that disc. This reduced the analysis time significantly and improved precision and accuracy by taking a simultaneous measurement for both wavelengths through the same optical window. During the Cr(VI) experiments, there was poor performance due to inconsistencies caused by fiber optic movement. In this prototype instrument, the fiber optics were not permanently secured and the transmittance of different wavelengths of light through the fiber varied based on the position of the fiber optic. Blank spectra were taken throughout the experiments to insure that the ratio was correct. Results were similar to the classical method, but suffered from higher detection limits and a lower replicate precision. In this case, superior results were calculated by using the classic manner using the averaged blank signal taken before and after each sample.

3.2. Stability study

The stability study was performed to determine how long a disc, with reagent pellets included, could be stored and still provide reliable results. In this experiment we chose to use the nitrite assay because the reagents are known to be sensitive to water vapor [9] and should prove to be the most sensitive to storage effects. The disc sampling holes were sealed using a plastic adhesive and stored in a desiccator for the 31-day test period. There was a 7.91% relative standard deviation for the concentration adjusted absorbance (*i.e.* the absorbance was adjusted for the small changes in the concentration of the standard nitrite solution that was made fresh daily). It is important to note that both the nitrite and Cr(VI) methods are designed to use excess reagents and that all of the pellets used were of sufficient mass to ensure that this excess was obtained [14]. The precision might be further improved with more consistent pellet mass and by better sealing of the injection holes or construction of the disc in a low humidity environment. Importantly, this data shows that on-disc dry reagent pellets can provide a stable long term solution for a portable device.

3.3. Nitrite

The visual color comparison method is a widely used field method for detecting nitrite, and Cr(VI), in water because it is simple, cost effective, and very portable. The human eye is a log-normal detector and can discriminate a large range of colors and intensities; however, depending on the person, the color and intensity is

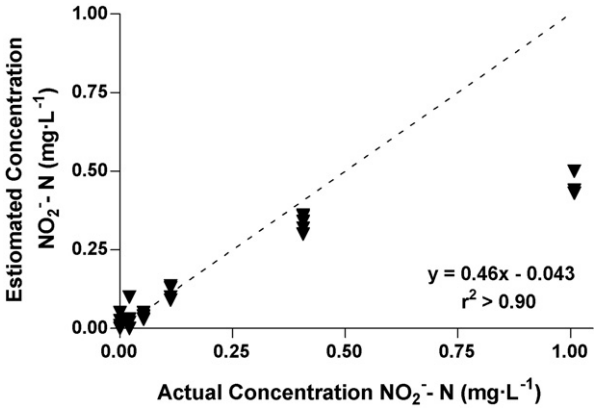


Fig. 5. Comparison of standard nitrite concentrations to visually estimated concentrations using a Hach conventional field analysis test kit, $n = 5$.

Table 1
Summary of calibration parameters for the detection of nitrite (NO_2^--N) using the disc-based microanalysis and the reference procedures.

Analysis method	Pathlength (cm)	Slope (AU/mg L^{-1})	DL (mg L^{-1})	Upper calibration limit (mg L^{-1})
Visual field test	1.2	N/A	0.1	0.5
Bench top	1.0	2	0.006	1
Disc	0.14	0.27	0.008	5

open to subjective assessment [17]. The results of visual tests using a Hach NI-12 color wheel based system for nitrite are illustrated in Fig. 5. The non-linear response is evident and, of course, detection limits are much higher than those obtained with bench top instruments. The manufacturer states "accurate to ±10% or ± the smallest increment, subject to individual color perception".

It is generally accepted that analyses performed in the controlled laboratory environment provide the maximum in precision, accuracy and dynamic range for most analytical methods. To compare our method to the US EPA Standard Method 4500, we used an Agilent HP8542 bench top spectrometer and the Hach reagents to obtain a linear calibration (Table 1) with a precision of 1% at the 0.5 mg L^{-1} level ($n = 6$). These results are of course superior to those of the visual field test but the real question is: how do the disc-based measurements compare to these two measurement strategies?

The analytical figures of merit for the linear calibration ($r^2 > 0.99$) of the microanalysis disc are presented in Table 1. Recall that the bench top instrument uses a 1 cm pathlength cell which should make the measurement more sensitive than the disc. We verified that the slope was proportional to pathlength. Of greater significance than the method sensitivity, the precision ranged from 0.2 to 3% RSD ($n = 3$–9 cells/disc) at the 0.5 mg L^{-1} level, a performance that is comparable to a bench top instrument. After some investigation, we found that small bubbles sometimes formed in some of the cells during reaction and these bubbles affect the apparent transmittance. Most bubbles could be removed by gently tapping the disc to dislodge them; however, some remained causing slightly degraded precision.

These results suggest several possible improvements to the disc design with the goals of increasing the sensitivity, to further lower the detection limit, and elimination of bubbles from the optical path to improve precision. Increasing the method sensitivity, with this reagent system, will require longer pathlengths. This can be easily achieved by making the middle disc layer thicker than the currently used 1.4 mm or by modifying the light path using internal reflection methods previously described [18,19]. In this analysis, sample consumption is not a limitation so both the sample and disc volume could easily be scaled-up by an order of magnitude. However, minimizing reagent and sample consumption is beneficial for some analyses, so a using a smaller diameter sample cell is a viable alternative with a thicker disc or a folded optical path of the type shown by Steigert et al. [20].

Loss of analytical performance within microfluidic systems due to bubbles is an established problem [21,22] but modifying the disc surface to be more hydrophilic or including surface tension reducing surfactants in the reaction mixture may be sufficient to eliminate some of the precision damaging bubble problems.

Environmental field testing is often used to guide and evaluate contamination remediation efforts. In these cases, the accuracy, precision, ability to measure many samples simultaneously, and speed of analysis is a clear advantage of the disc-based system over the visual field and laboratory-based strategies. When measuring nitrite, the promptness with which samples can be measured is especially important since nitrite is easily converted to other nitrogen species, mainly by oxidation to nitrate, so the delays introduced by transporting samples to a lab facility may significantly bias results and should be avoided.

3.4. Chromium(VI) results

To simplify the hexavalent chromium experiments and result comparisons, only the Ocean Optics spectrometer was used for measurements (*i.e.* the fiber optics were connected to either an Ocean Optics 1 cm cell holder or the disc holder). Using the Hach recommended procedure with a 5 mL sample and a 1 cm cell, a linear calibration curve from 0.01 to 1.5 mg L^{-1} Cr(VI) was calculated (Table 2). Measurement of Cr(VI) using the disc-based approach, with 1.5–2.2 mg pellets of Chromaver3, yielded an extinction coefficient (approximately 40,000 L g^{-1} cm^{-1} Cr(VI)) and spectral shape that are in close agreement with the literature [12,23]. The calculated slope was the expected one order of magnitude smaller than that of the 1 cm path cell. Despite this loss of sensitivity, the detection limit only increased by a factor of 2 to 0.03 mg L^{-1}. The decreased sensitivity of the disc-based measurement was accompanied by a corresponding increase in the linear dynamic range to 5 mg L^{-1} Cr(VI) suggesting that further improvements in detection limit can be achieved by increasing the pathlength as discussed above.

The current disc-based detection limit is considered acceptable for industrial point-of-source monitoring. However, the limit of quantification (0.1 mg L^{-1} Cr(VI)) is not adequate to meet the 0.05 mg L^{-1} US EPA/Health Canada drinking water limits [24] and would need to be improved by at least a factor of two. Incorporation of a longer pathlength, or reduction of blank noise, on the disc would be beneficial and should address this issue.

To demonstrate the potential for analysis of realistic samples several spiked waste water samples, collected from a waste water management company, were analyzed. As before, samples were injected onto a disc containing reagent pellets and calibrated using simple aqueous standards. The results produced approximately 130% recovery from the spiked recovery measurements. The high recovery may be due to the organic matrix in the samples and suggests that standard additions may be needed. The high time and labor costs associated with standard additions make a very powerful argument for parallel sample analysis that is easily achieved with the present disc-based approach. With 24 reactions operating in parallel already demonstrated, it is easy to conceive of a disc that apportions a single sample into an array of reaction cells

Table 2
Summary of calibration parameters for hexavalent chromium (Cr^{6+}) using the developed system, a common field instrument and the reference procedure.

Analysis method	Pathlength (cm)	Slope (AU/mg L^{-1})	DL (mg L^{-1})	Upper calibration limit (mg L^{-1})
Visual field test	1.2	N/A	N/A	1.5
Bench top	1.0	0.7	0.01	1.5
Disc	0.14	0.07	0.03	5

[25] with increasing amounts of analyte and fixed amounts of the derivatization reagents. Reading the results from the array would provide a standard additions calibration while mitigating the negative aspects of this calibration strategy.

4. Conclusions

It is possible to quantify nitrite-nitrogen and hexavalent chromium using a centrifugal microfluidic platform suitable for on-site analysis. The procedure requires 100 μL of sample or standard. By incorporating the dry reagents on disc, derivatization and detection can be performed in one step and directly on disc. In the current design, 24 individual cells are available on one disc and would permit calibration and multiple sample measurements on a single disc. Both reactions showed molecular extinction coefficients similar to those reported in the literature with detection limits of 0.008 mg L^{-1} NO_2^--N and 0.03 mg L^{-1} Cr(VI). Reproducibilities of 0.2–3% ($n = 3$) and 7% ($n = 3$) RSD respectively for mid-range samples, are within the range required for industrial and environmental applications for both analytes. The analytical performance is also adequate for detection of both analytes in drinking water as the detection limits are below the maximum permissible drinking water limits (Section 1); however, the quantification limit for Cr(VI) is above the permissible limit. Increasing the pathlength of the disc should provide the required increase in sensitivity and allow performance nearly equivalent to bench top instrumentation.

Multiwavelength measurements allowed the use of the ratio technique for the blank estimation that produced improved precision and a decreased analysis time, as only one blank measurement was needed. In a portable system designed for a single species, this could be inexpensively done with two appropriate wavelength light emitting diode sources and one detector. However, the multiwavelength source and detection system provides an extremely flexible system capable of measuring multiple reactions on a single disc.

Other single step reaction kits for environmentally important species such as orthophosphate, sulfate and molybdenum are commercially available and may be good candidates for single step centrifugal microfluidic discs.

Acknowledgements

The authors wish to acknowledge support under the Natural Sciences and Engineering Research Council Strategic Grants Program.

References

[1] Q. Zhong, W.H. Steinecker, E.T. Zellers, Analyst 134 (2009) 283–293.
[2] J.A. Diaz, C.F. Giese, W.R. Gentry, Field Anal. Chem. Technol. 5 (2001) 156–167.
[3] K. Christidis, P. Robertson, K. Gow, P. Pollard, Instrum. Sci. Technol. 34 (2006) 489–499.
[4] T.M. Chinowsky, S.D. Soelberg, P. Baker, N.R. Swanson, P. Kauffman, A. Mactutis, M.S. Grow, R. Atmar, S.S. Yee, C.E. Furlong, Biosens. Bioelectron. 23 (2007) 149.
[5] T.M. Chinowsky, S.D. Soelberg, P. Baker, N.R. Swanson, P. Kauffman, A. Mactutis, M.S. Grow, R. Atmar, S.S. Yee, C.E. Furlong, Biosens. Bioelectron. 22 (2007) 2268–2275.
[6] A.G. Crevillén, M. Hervás, M.A. López, M.C. González, A. Escarpa, Talanta 74 (2007) 342–357.
[7] L. Marle, G.M. Greenway, TrAC-Trends Anal. Chem. 24 (2005) 795–802.
[8] V. Gómez, M.P. Callao, TrAC-Trends Anal. Chem. 25 (2006) 1006–1015.
[9] Hach Company, Nitrite Diazotization Method LR, Method 8507, 1st ed., 2005.
[10] J.P. Griess, Ber. Dtsch. Chem. Ges. 12 (1879) 426.
[11] Hach Company, Hexavalent Chromium 1,5-Diphenylcarbohydrazide DR/4000 procedure 0–0.700 mg/L, Method 8023, 11th ed., 2005.
[12] A.E. Greenberg, L.S. Clesceri, E.W. Rice (Eds.), Standard Methods for Examination of Water and Wastewater, 21st edition, Port City Press, Baltimore, 2005.
[13] D.A. Bartholomeusz, R.W. Boutte, J.D. Andrade, J. Microelectromech. Syst. 14 (2005) 1364–1374.
[14] A. LaCroix-Fralish, Msc Thesis Chemistry and Biochemistry, Concordia University, Montreal, QC, 2008.
[15] D.A. Duford, D.D. Peng, E.D. Salin, Anal. Chem. 81 (2009) 4581–4584.
[16] J. Ducree, S. Haeberle, S. Lutz, S. Pausch, F. Von Stetten, R. Zengerle, J. Micromech. Microeng. 17 (2007) S103–S115.
[17] L.D. Albright, A.J. Both, International Lighting in Controlled Environments Workshop, University of Wisconsin, Madison, WI, 1994, pp. 281–297 (CP-3309).
[18] M. Grumann, J. Steigert, L. Riegger, I. Moser, B. Enderle, K. Riebeseel, G. Urban, R. Zengerle, J. Ducrée, Biomed. Microdevices 8 (2006) 209–214.
[19] J. Steigert, M. Grumann, T. Brenner, L. Riegger, J. Harter, R. Zengerle, J. Ducrée, Lab on a Chip-Miniaturisation Chem. Biol. 6 (2006) 1040–1044.
[20] J. Steigert, M. Grumann, T. Brenner, K. Mittenbühler, T. Nann, J. Rühe, I. Moser, S. Haerberle, L. Riegger, J. Riegler, W. Bessler, R. Zengerle, J. Ducrée, JALA-J. Assoc. Lab. Automation 10 (2005) 331–341.
[21] J.H. Kang, Y.C. Kim, J.K. Park, Lab on a Chip-Miniaturisation Chem. Biol. 8 (2007) 176–178.
[22] D.D. Meng, J. Kim, C.J. Kim, J. Micromech. Microeng. 16 (2006) 419–424.
[23] T.L. Allen, Anal. Chem. 30 (1958) 447–450.
[24] Health Canada. E.a.W. Health, Ottawa, 1986, pp. 1–6.
[25] M. Madou, J. Zoval, G. Jia, H. Kido, J. Kim, N. Kim, Annu. Rev. Biomed. Eng. (2006) 601–628.

Talanta 80 (2009) 676–684

Contents lists available at ScienceDirect

Talanta

journal homepage: www.elsevier.com/locate/talanta

Measurement of total Zn and Zn isotope ratios by quadrupole ICP-MS for evaluation of Zn uptake in gills of brown trout (*Salmo trutta*) and rainbow trout (*Oncorhynchus mykiss*)☆

Ruth E. Wolf[a,*], Andrew S. Todd[a,*], Steve Brinkman[b], Paul J. Lamothe[a], Kathleen S. Smith[a], James F. Ranville[c]

[a] *U. S. Geological Survey, Denver Federal Center, MS 964D Denver, CO, USA*
[b] *Colorado Division of Wildlife, Aquatic Research, 317 W. Prospect Road, Fort Collins, CO, USA*
[c] *Colorado School of Mines, Department of Chemistry and Geochemistry, Golden, CO, USA*

ARTICLE INFO

Article history:
Received 5 May 2009
Received in revised form 23 July 2009
Accepted 23 July 2009
Available online 6 August 2009

Keywords:
Zinc isotopes
Zinc tracer studies
Biotic ligand model
Zinc toxicity and trout
ICP-MS determination of zinc isotope ratios

ABSTRACT

This study evaluates the potential use of stable zinc isotopes in toxicity studies measuring zinc uptake by the gills of brown trout (*Salmo trutta*) and rainbow trout (*Oncorhynchus mykiss*). The use of stable isotopes in such studies has several advantages over the use of radioisotopes, including cost, ease of handling, elimination of permit requirements, and waste disposal. A pilot study using brown trout was performed to evaluate sample preparation methods and the ability of a quadrupole inductively coupled plasma mass spectrometer (ICP-MS) system to successfully measure changes in the $^{67}Zn/^{66}Zn$ ratios for planned exposure levels and duration. After completion of the pilot study, a full-scale zinc exposure study using rainbow trout was performed. The results of these studies indicate that there are several factors that affect the precision of the measured $^{67}Zn/^{66}Zn$ ratios in the sample digests, including variations in sample size, endogenous zinc levels, and zinc uptake rates by individual fish. However, since these factors were incorporated in the calculation of the total zinc accumulated by the gills during the exposures, the data obtained were adequate for their intended use in calculating zinc binding and evaluating the influences of differences in water quality parameters.

Published by Elsevier B.V.

1. Introduction

The level and mechanism of aqueous zinc uptake in fish is a topic of recent research efforts. As a micronutrient, zinc is found at naturally high levels in fish tissues. Although zinc uptake primarily occurs through the diet, at elevated zinc levels in water uptake can also occur via the gills causing morphological alterations and toxicity [1–4]. Zinc is thought to competitively disrupt calcium uptake across the gills that can lead to acute hypocalcemia and eventual death, depending on the zinc concentrations [2,5]. Rainbow trout (*Oncoryhnchus mykiss*), and to a lesser extent brown trout (*Salmo trutta*), are susceptible to increased concentrations of waterborne zinc, for example, in streams impacted by acid rock drainage [5–7]. In some cases, zinc toxicity is sufficient that popular recreational fishing streams must be routinely restocked to compensate for fish losses due to exposure to waters with high zinc concentrations [5].

Previous toxicological studies on the uptake of zinc in fish have utilized radio-labeled ^{65}Zn to differentiate the comparatively low levels of zinc accumulated via waterborne exposure versus the larger pool of endogenous zinc [1–4]. Although an effective means of studying zinc uptake, the use of radioactive isotopic spikes has several disadvantages, including: cost, handling requirements, and disposal of radioactive waters from fish exposure studies. These earlier radioisotope studies utilized atomic absorption spectrometry for total zinc determinations and gamma spectrometry to determine uptake of the radioactive zinc isotopes. With current inductively coupled plasma mass spectrometer (ICP-MS) instrumentation, it is possible to use enriched stable (i.e., non-radioactive) zinc isotopes to perform these types of studies, eliminating the concerns and costs involved in employing methods that utilize radioactive isotopic methods. A recent review article by Stürup et al. [8] discusses the use of a variety of enriched stable isotopes, including zinc, as tracers in biological systems. Since the main goal in such studies is to measure an enriched isotopic ratio and not to perform quantitative isotopic measurements, these

☆ **Disclaimer**: Any use of trade, product, or firm names is for descriptive purposes only and does not imply endorsement by the U.S. Government.

* Corresponding authors. Tel.: +1 303 236 2470; fax: +1 303 236 3200.
E-mail addresses: rwolf@usgs.gov (R.E. Wolf), atodd@usgs.gov (A.S. Todd).

0039-9140/$ – see front matter. Published by Elsevier B.V.
doi:10.1016/j.talanta.2009.07.048

types of measurements can generally be performed as long as precisions of 1% RSD or better can reasonably be achieved. Another review by Cloquet et al. [9] specifically discusses the use of stable zinc isotopic tracers in biological systems. Croteau et al. have reported the use of Cu, Cd, and Cr stable isotopes to examine biological uptake rates in freshwater bivalves and gastropods [10,11]. With the advent of multi-collector ICP-MS systems, the precision of zinc isotope ratios has improved dramatically to better than 0.01% RSD [8,9], allowing many more biochemical and geochemical applications to be realized. In the geochemical realm, multi-collector ICP-MS measurements are often utilized to examine the fractionation of Zn isotopes by geochemical processes because the shifts in isotopic abundances can be very small [12–14]. However, most of these applications require the Zn isotopes to be chemically separated from other elements in the sample matrix prior to analysis, and these methods require tedious sample clean-up procedures. Balcaen et al. [15] used a high-resolution sector-field ICP-MS to perform a double-spiking study on water fleas (*Daphnia magna*) using ^{67}Zn and ^{68}Zn isotopic spikes and reported precisions for ^{67}Zn/^{66}Zn of 1.3% RSD and 0.7% RSD for high-resolution ICP-MS and quadrupole ICP-MS, respectively.

In this study, we examine the use of a quadrupole ICP-MS system to determine changes in ^{67}Zn/^{66}Zn ratios in gills extracted from brown trout and rainbow trout exposed to various Zn concentration levels and exposure times in ^{67}Zn-enriched exposure media. Due to its low natural abundance (4.1%) and availability, ^{67}Zn was selected as the spiking isotope in order to maximize the ability to detect a change in the measured ratio as a result of the exposure. The data will ultimately be used to evaluate the influence of water chemistry parameters on acute fish toxicity and will be used to determine physical constants that can be incorporated into the Biotic Ligand Model (BLM), which can be used to estimate the acute toxicity of metal exposure to fish populations [16].

2. Materials and methods

2.1. Reagents

Unless otherwise noted, all reagent and stock solutions were prepared in 20% (v/v) nitric acid made from de-ionized water (Millipore, Billerica, MA, USA, 18 MΩ) and double-distilled HNO_3 (prepared via sub-boiling distillation, Milestone subPUR, Shelton, CT, USA), in order to match the acid matrix resulting from the sample preparation procedure. Zinc metal enriched in ^{67}Zn (^{67}Zn (89.6%), ^{64}Zn (1.56%), ^{66}Zn (3.88%), ^{68}Zn (4.91%), ^{70}Zn (0.05%)) was obtained (Isoflex, San Francisco, CA, USA) and was dissolved in double-distilled HCl and diluted with de-ionized water to prepare a ^{67}Zn-enriched spiking solution of 995 mg/L in 5% HCl. This spiking solution was used to prepare the exposure solutions for both the pilot study and the rainbow trout study.

2.2. Fish care

Two groups of fish were used in our study. The first was a group of approximately 50 juvenile brown trout (*S. trutta*) included in a pilot study performed in order to test the various laboratory methods employed in the full-scale exposure study. Brown trout were selected for the pilot study due to their availability, similarity to the planned test species, and because they are known to be less susceptible to metal toxicity than rainbow trout; so, if differences were observed in the brown trout, they should also be observed in the planned test species. The second group of approximately 300 juvenile rainbow trout (*O. mykiss*) was used in the primary zinc exposure study. Fish for both groups were obtained from the Colorado Division of Wildlife Research Hatchery (Bellevue, CO) and were transported to the Colorado Division of Wildlife Aquatic Toxicology Laboratory in Fort Collins, CO, USA. Dim fluorescent lighting provided a 16-h:8-h light:dark photoperiod. Trout were fed twice daily using appropriately sized trout food (Rangen Inc., Buhl, ID, USA) at an estimated rate of 2% body weight per day. Feeding was ended 48 h prior to test exposures, a common practice in acute toxicity testing, to avoid problems caused by feeding, such as possible alteration of toxicant concentration, build-up of metabolic wastes, and possible increased oxygen demand. Water temperature was maintained at $12 \pm 0.7\,^{\circ}C$ during holding and all experiments using a recirculating chiller.

For the pilot study, the brown trout were maintained in Fort Collins municipal tap water (~44 mg/L $CaCO_3$ total hardness) until the test exposure. Fish weights ranged from 2.5 g to 4.5 g with an overall average weight of 3.15 g.

For the rainbow trout exposure, fish were maintained in water matching the hardness of the hatchery water (201 mg/L $CaCO_3$). Prior to testing, the trout were divided equally into two aerated acclimation tanks and the water hardness adjusted gradually (~10 mg/L per day) to the test hardness of ~30 mg/L $CaCO_3$ for soft water and ~140 mg/L $CaCO_3$ for hard water testing, respectively. Trout were maintained at the test hardness for 14 days prior to testing. The average mass of hard water acclimated trout was 8.3 ± 2.7 g while the soft water trout were slightly larger at an average weight of 9.9 ± 3.3 g.

2.3. Isotopic exposures

The primary objective of the pilot study was to determine if the changes in the ^{67}Zn/^{66}Zn ratios in the gill material would be large enough to be measured at the exposure times planned. Additional objectives included determining the optimum parameters for ICP-MS detection, evaluating the efficacy of the digestion method, and determining any necessary sample pretreatment (e.g., rinsing) of the dissected gill material prior to digestion.

For the pilot scale study, the brown trout were allowed to acclimate for several weeks in water of the same hardness and chemical composition as the exposure water. A control group of fish ($n = 8$) was harvested before the exposure. The remaining fish were exposed to water spiked with ~600 μg/L of the enriched ^{67}Zn solution. Ten fish were harvested after 3 h and 24 h of exposure. At the end of each exposure time sequence, the selected number of fish were randomly netted and placed into a bucket containing a lethal dose, 1 g/L, of an anesthetic solution MS-222 (Tricaine Methanesulfonate, Argent Chemical Laboratories, Redmond, WA). Post mortem, the gills from five fish in each exposure group were "rinsed" with a stream of de-ionized water applied through the mouth over the gills for approximately 5–10 s, while the gills from another set of five fish in the same exposure group remained "unrinsed".

An additional 20 fish were harvested after 3 h of exposure and their gills excised, rinsed, and composited. Composited samples were used to estimate the size fish that would be necessary in the event that the differences in zinc isotope ratios were undetectable in the gills from individual fish. One half of the composite sample was used to approximate a 30 g fish, one quarter was used to approximate a 15 g fish and one-eighth was used to approximate a 7.5 g fish. Fish were refrigerated until dissection. Fish gills were removed and separated from gill rakers within 24 h after fish death using high-quality corrosion-resistant stainless steel instruments. The gills were subsequently frozen ($-80\,^{\circ}C$) until sample digestion.

For the rainbow trout exposure study, calculated amounts of the enriched ^{67}Zn stock solution discussed previously were added to fully aerated 30-L static exposure tanks to achieve nominal concentrations in hard water (75 μg/L, 150 μg/L, 250 μg/L, 500 μg/L, and 1000 μg/L) and soft water (25 μg/L, 50 μg/L, 75 μg/L, 150 μg/L,

Table 1
Measured water quality parameters for rainbow trout exposure study experiments in hard and soft waters. Measured values are expressed as means (standard deviation). Additional information on measurement of water quality values can be found in Todd et al. [18].

Parameter	Hard water	Soft water
Hardness (as mg/L $CaCO_3$)	144 (1.2)	31.7 (1.3)
Alkalinity (as mg/L $CaCO_3$)	88 (5.1)	29.2 (1.6
Temperature (°C)	12.4 (0.2)	12.1 (0.2)
pH	7.7 (0.3)	7.2 (0.2)
Dissolved oxygen (mg/L)	8.5 (0.5)	8.5 (0.9)
Ca^{2+} (mg/L)	35.6 (1.2)	7.9 (0.4)
Mg^{2+} (mg/L)	10.3 (0.4)	1.7 (0.1)
Na^{+} (mg/L)	12.7 (3.2)	5.5 (0.1)
K^{+} (mg/L)	1.0 (0.16)	0.4 (0.12)
SO_4^{2-} (mg/L)	42.3 (0.8)	10.1 (0.3)
Cl^{-} (mg/L)	21.3[a] (7.4)	4.8 (0.2)
Dissolved organic carbon (DOC) (mg/L)	3.1[b] (0.9)	2.3[b] (0.8)

[a] Chloride values varied significantly as a result of the HCl in the metal stock solution.
[b] Average DOC concentration calculated from measurements in accumulation tanks at all time intervals. DOC started low and was observed to increase over the course of the exposure.

250 μg/L, and 500 μg/L). Prior to the addition of the zinc spikes, the pH value of each solution was adjusted back to that of the dilution water with NaOH. Average water quality parameters for the soft and hard waters used can be found in Table 1. Thirty rainbow trout were transferred from the acclimation tanks to each static exposure tank. Ten rainbow trout were harvested from each acclimation tank as controls. At sampling times of 0.75 h, 1.5 h, 3 h, 24 h, 48 h, and 72 h, five fish from each aquarium were randomly netted and placed into buckets containing a lethal dose of the anesthetic solution, MS 222. The rationale for the exposure times and concentrations selected was, in part, to allow for comparison with the radioisotope study by Alsop and Wood [3] and is discussed in Todd et al. [18]. At each sampling time, a water sample was also taken from each aquarium for total zinc and zinc isotope analysis. Post mortem, the gills of each fish were rinsed for approximately 10 s with a stream of de-ionized water through the mouth, as discussed previously, to remove Zn present in the gill mucus. After rinsing, the gills were dissected and frozen (−80 °C) in polypropylene sample vials until sample digestion.

Additionally, the gills of a wild-caught adult lake trout (*Salvelinus namaycush*) not used in the Zn exposure study were rinsed, removed, and composited for use as an analytical quality control (QC) sample. A large adult fish was used in order to obtain enough gill material (approximately 3.5 g) so the same material could be analyzed periodically with the exposed rainbow trout gill tissues to estimate the long-term analytical precision of the method. The lake trout was selected due to its size and availability. A portion of this composited gill QC sample (approximately 0.150 g) was weighed out and prepared with each sample preparation batch.

2.4. Sample preparation

The frozen gill tissue samples were weighed to the nearest 0.0001 g and transferred to acid-washed 50 mL perfluoroalkoxy polymer (PFA) microwave digestion vessels. The samples were digested using 4 mL of double-distilled HNO_3 and 2 mL of ultrapure H_2O_2 (Seastar, Inc., Vancouver, BC, Canada) in a microwave digestion system equipped to handle 48 samples (Multiwave 3000 with Rotor 48MF50, Anton Paar, Graz, Austria). The microwave temperature/pressure sensor was located in vessel number 1. The microwave digestion program consisted of a heating step at 1400 W power at the lowest fan speed with a ramp time of 10 min followed by a hold time of 10 min. After the heating program completed, the power was reduced to zero and the fan speed increased to the medium setting for 10 min, followed by an additional 30-min cooling step at the highest fan speed. After this program completed, the samples were allowed to sit in the digestion vessels until they cooled to room temperature. This procedure resulted in a complete digestion (no residue) for all samples, except three samples from the pilot study where small portions of gill raker remained attached to the gill and were not digested. The resulting clear sample solutions were quantitatively transferred to 50 mL polypropylene centrifuge tubes (Becton Dickenson Labware, Franklin Labs, NJ, USA) and diluted to 20 mL, using the scribed volume marks on the tubes, with de-ionized water. Prior to dilution, the accuracy of the scribed volumetric markings on a series of tubes ($n = 10$) were checked by weight and were found to be accurate to within 2% of the marked volume. The final sample solutions contained approximately 20% (v/v) nitric acid and were directly analyzed by ICP-MS for both total elemental content as well as zinc isotopic ratios.

2.5. Instrumentation

It was desirable that the final analysis protocol not require any complicated sample pretreatments, such as those described by Borrok et al. [14], for multi-collector ICP-MS analysis of zinc isotopes due to the large number of samples (>600) that would eventually require isotopic analysis. For this reason, the use of quadrupole ICP-MS was investigated for determination of the zinc isotope ratios and total zinc concentrations, although the laboratory also has at its disposal both multi-collector ICP-MS and high-resolution sector-field ICP-MS instruments. The instrument used was an ELAN DRC II ICP-MS system (PerkinElmer LAS, Inc., Waltham, MA, USA) equipped with a quartz cyclonic spray chamber and 2 mm quartz injector. Due to the limited sample volume available, the system was equipped with a glass concentric nebulizer (Type TR-50-C1, Meinhard Glass Products, Golden, CO) and was operated at a sample uptake rate of approximately 0.35 mL/min. A detector deadtime correction value of 60 ns was determined using the procedure recommended by the instrument manufacturer. Other instrument operating parameters are given in Table 2.

Considerations in using quadrupole ICP-MS for the analysis of Zn include the impacts of both isobaric and polyatomic interferences on particular zinc isotopes. As illustrated by Table 3, ^{64}Zn can be

Table 2
General ICP-MS instrument operating conditions (ELAN DRC II).

RF power	1100 W
Lens (total Zn)	Autolens
Lens (Zn isotopes)	Static, 7.5 V
Nebulizer flow (total Zn)	0.74 mL/min, optimized for $CeO^{+}/Ce^{+} < 3\%$
Nebulizer flow (Zn isotopes)	0.78 mL/min, optimized for maximum ^{67}Zn
Nebulizer type	Glass type TR-50-C1
Peristaltic pump (total Zn)	0.889 mm i.d. tubing for sample and internal standard, total flow rate ~ 0.7 mL/min
Peristaltic pump (Zn isotopes)	0.889 mm i.d. tubing for sample, total flow rate ~ 0.35 mL/min
Spray chamber	Quartz cyclonic
Injector	Quartz 2 mm i.d.
Data acquisition (total Zn)	Dwell times 10–100 ms/isotope, 15 sweeps, 3 replicates, 80 masses monitored, total time 2:10 min
Isotopes monitored (Zn isotopes)	^{64}Zn, ^{66}Zn, ^{67}Zn, ^{68}Zn, ^{70}Zn, ^{60}Ni
Detector mode (Zn isotopes)	Pulse only (short settling time not used)
Deadtime correction	60 ns
Data acquisition (Zn isotopes)	Dwell 20 ms/isotope, 500 sweeps, 10 replicates, total acquisition time/isotope = 10 s, total time 11:30 min

Table 3
Common interferences affecting Zn isotope measurements. Interferences with high abundance will have greater impact on Zn isotopes than those with lower interference abundance, given equal concentrations.

Mass affected	Exact mass	Zn isotope abundance (%)	Interference	Exact mass[a]	Interference abundance (%)	Estimated resolving resolution[b]
$^{64}Zn^+$	63.92915	48.63	$^{64}Ni^+$	63.92797	0.93	54,200
$^{64}Zn^+$	63.92915	48.63	$^{31}P^{16}O_2H^+$	63.97141	99.37	1,550
$^{64}Zn^+$	63.92915	48.63	$^{32}S^{16}O_2^+$	63.96189	94.56	1,950
$^{66}Zn^+$	65.92604	27.90	$^{34}S^{16}O_2^+$	65.95769	4.19	2,100
$^{66}Zn^+$	65.92604	27.90	$^{40}Ar^{26}Mg^+$	65.94498	0.11	3,450
$^{67}Zn^+$	66.92713	4.10	$^{34}S^{16}O_2H^+$	66.96552	4.19	1,750
$^{68}Zn^+$	67.92485	18.75	$^{36}S^{16}O_2^+$	67.95690	0.02	2,150
$^{68}Zn^+$	67.92485	18.75	$^{136}Ba^{2+}$	67.95228	0.002[c]	2,500
$^{70}Zn^+$	69.92532	0.62	$^{70}Ge^+$	69.92425	21.23	65,450

[a] *Source*: Isotope Chart, Nu Instruments, Ltd., Wrexham, UK.
[b] Rounded to nearest 50.
[c] Estimated by multiplying abundance by 0.03 (instrument optimized for $Ba^{2+}/Ba^+ < 0.03$).

impacted by several major interferences, particularly in biological matrices which may contain high levels of sulfur or phosphorus. Preliminary studies on the use of dynamic reaction cell (DRC) technology available on the quadrupole ICP-MS used in our laboratory to eliminate the various interferences on the Zn isotopes, using ammonia as the reaction gas, resulted in attenuation of the Zn signal. Since lower signal levels would require longer analysis times for the isotope ratio analysis and the total volume of sample available for both the total Zn analysis and the Zn isotopic analysis was limited to 20 mL, standard (non-DRC) conditions were utilized for this study. Preliminary estimates based on counting statistics indicated that precisions of 0.5% RSD or less could be achieved if the zinc concentrations were 10 μg/L or greater.

Although in most geochemical studies the $^{67}Zn/^{64}Zn$ ratio is reported, due to the potential interferences on ^{64}Zn from nickel, sulfur, and phosphorus, there could be significant error in measured ^{64}Zn values. For this study, the $^{67}Zn/^{66}Zn$ ratio was determined since ^{67}Zn and ^{66}Zn measurements are not affected by nickel and phosphorus interferences (see Table 3) and the potential impact of any sulfur present in the sample is greatly reduced. As is illustrated in Table 3, the abundances of the $^{34}S^{16}O_2^+$ and $^{34}S^{16}O_2H^+$ species that interfere with ^{66}Zn and ^{67}Zn measurements, respectively, are approximately only 4% as compared to the 94% abundance of the $^{32}S^{16}O_2^+$ species that interferes with ^{64}Zn measurement. Therefore, by using the $^{67}Zn/^{66}Zn$ ratio the impact of any sulfur interferences on the measurements should be reduced. In order to verify this, the contributions on the ^{64}Zn, ^{66}Zn, ^{67}Zn, ^{68}Zn, and ^{70}Zn signals were measured using separate solutions containing 10 mg/L of phosphorus and sulfur and 10 μg/L nickel. In Table 4, these signals are compared to the signals obtained from 10 μg/L solutions of zinc (JMC 30749 and HP 403518). As Table 4 indicates, the contributions at masses 66 and 67 from the 10 mg/L sulfur solution are 116 cps and 21 cps (counts per second), respectively. This contribution is within the observed average standard deviations at masses 66 and 67 of 150 cps and 27 cps, respectively, from measurement of the 10 μg/L zinc solutions. Likewise, the contributions at masses 66 and 67 from the 10 mg/L phosphorus solution are 64 cps and 17 cps, respectively. This contribution is also within the observed average standard deviations at masses 66 and 67 from measurement of the 10 μg/L zinc solutions. Since the digested fish gill samples yielded solutions containing less than 10 mg/L phosphorus or sulfur (see Table 6 for average concentration information) with a total Zn concentration of approximately 20 μg/L or more, the impact of the sulfur and phosphorus interferences on the signals for ^{66}Zn and ^{67}Zn would be indistinguishable as compared to the short-term reproducibility of the zinc measurements. Furthermore, the data in Table 4 also illustrate that the contributions from the sulfur interferences on the measurement of ^{64}Zn and ^{68}Zn and of the phosphorus interference on ^{68}Zn are significantly larger than the standard deviation of the measurement of the 10 μg/L zinc standards and would be of significant concern, if these isotopes were used for monitoring the change in the zinc isotopic ratios in the fish gills. It was therefore concluded that the quadrupole ICP-MS instrument could be used for the zinc isotopic measurements in our study, if the $^{67}Zn/^{66}Zn$ ratios were used, instead of the more traditional $^{67}Zn/^{64}Zn$ ratio.

2.6. Elemental and total zinc analysis

In order to verify that the total zinc concentrations were sufficient (>10 μg/L) for isotope ratio analysis using established measurement conditions, each gill digestate was analyzed for total Zn content and for the concentrations of approximately 40 other elements for informational purposes prior to the zinc isotopic analyses. Multi-element calibration standards were prepared by appropriate dilution of single and multi-element stock solutions purchased commercially (High Purity Standards, Charleston, SC, USA) and the matrix stock solution in 20% HNO_3 (v/v) as detailed in Table 5. The matrix stock solution containing the major cations typically found in a wide variety of sample matrices was added to the multi-element stock solutions to bring the concentrations up to acceptable levels for multi-point calibration of these elements and to minimize any ionization effects that the presence of these elements might have on other elements in the calibration. The matrix stock solution was also used to provide high-level calibration standards for the matrix elements, which were monitored for possible use in performing ratios of selected trace elements, such as Zn, to biological matrix elements, such as Mg, K, and Ca to identify any

Table 4
Measured effects of potential interferences from sulfur, phosphorus, and nickel on measured zinc isotope intensities. Int is the measured intensity of the solution at the mass or isotope listed using the developed isotope ratio method. The standard deviations of the 10 individual replicates in each analysis are given in parentheses.

Test solution	$Int^{64}Zn$ (SD)	$Int^{66}Zn$ (SD)	$Int^{67}Zn$ (SD)	$Int^{68}Zn$ (SD)	$Int^{70}Zn$ (SD)
20% HNO_3 blank ($n = 3$)	172 (117)	102 (76)	22 (12)	795 (42)	243 (9)
JMC 30749 (10 μg/L Zn)	21,521 (250)	13,410 (135)	2,080 (25)	10,623 (131)	599 (11)
HP 403518 (10 μg/L Zn)	21,177 (238)	13,087 (164)	2,018 (29)	10,286 (142)	583 (9)
10 mg/L S	762 (46)	116 (6)	21 (1)	739 (22)	230 (6)
10 mg/L P	155 (22)	64 (3)	17 (2)	717 (32)	220 (3)
10 μg/L Ni	240 (13)	58 (3)	14 (1)	754 (28)	235 (6)

Table 5
Stock solution concentrations and working standard concentrations for elemental and total Zn analysis.

Solution ID	Element(s)–concentration (units)
Matrix stock	Na, Mg, K, Ca, Fe–30 mg/L, Al–100 mg/L, Si, Ti, Mn–5 mg/L, P–1 mg/L
Stock A	Li, Be, Na, Mg, Al, P, K, Ca, V, Cr, Mn, Fe, Co, Ni, Cu, Zn, Ga, As, Se, Rb, Sr, Cd, Cs, Ba, La, Ce, Pr, Nd, Sm, Eu, Tb, Gd, Dy, Ho, Er, Tm, Yb, Lu, Tl, Pb, Bi, Th, U–10 mg/L
Stock B	Si, Ti, Ge, Zr, Nb, Mo, Ag, Sb, Ta, W, Hf, Sn, Te–10 mg/L
Calibration Standard 1	All elements from calibration Stocks A and B–5 μg/L, no matrix stock
Calibration Standard 2	Stock A elements–20 μg/L, Stock B elements–10 μg/L, 1:1000 dilution of matrix stock
Calibration Standard 3	Stock A elements–100 μg/L, Stock B elements–50 μg/L, 1:5 dilution of matrix stock
Calibration Standard 4	Matrix stock solution, undiluted
Calibration Standard 5	1:2 dilution of matrix stock solution
Calibration Standard 6	SO_4^{2-}–141.2 mg/L, Na–50 mg/L, Ca–25 mg/L

possible trends based on changes in sample weight. Finally, sulfur, a possible interference, was monitored after calibration with Standard 6 in Table 5. An internal standard solution containing 500 μg/L ^{6}Li, 20 μg/L Rh, and 20 μg/L Ir was prepared in 20% HNO_3 (v/v). The internal standard solution was mixed on-line with the sample solution using the peristaltic pump on the ICP-MS instrument and a polypropylene barbed T-connector (Cole-Parmer Instrument Company, Part. No. WU-30506-15, Vernon Hills, IL, USA) with 0.889 mm i.d. pump tubing (Meinhard Glass Products, Golden, CO). Sample usage for the total Zn analysis was approximately 2 mL, including sample uptake and stabilization times.

In order to obtain accurate total Zn concentrations, the ^{64}Zn, ^{66}Zn, ^{67}Zn, and ^{68}Zn isotopes were added together using the elemental equations portion of the instrument software to compensate for the increasing amount of ^{67}Zn present in the samples as exposure times increased. The calibration curve for zinc was based on the total intensity (Int) of the four major zinc isotopes summed together: $Int^{total}Zn = Int^{64}Zn + Int^{66}Zn + Int^{67}Zn + Int^{68}Zn$. The ^{70}Zn isotope was not used in the determination of total Zn due to its low abundance (0.6%) and the presence of Ge, which has an isotope of major abundance (21.2%) at mass 70, in the multi-element calibration standards. The accuracy of the total zinc measurements using the summed zinc isotopes by ICP-MS was verified by a separate analysis of a subset of the samples ($n = 52$) by inductively coupled plasma atomic emission spectrometry (ICP-AES). A comparison of the ratio of the ICP-OES results to the ICP-MS results gave an average ratio of 0.99 ± 0.06, indicating the results were within acceptable agreement. A summary of the results for the total Zn measurements and for other elements of interest in the gill digests is given in Table 6. All other elements that were monitored were not detected at concentrations above 1 μg/L in the sample digests, including Ba, which is also identified in Table 3 as a potential interference on ^{68}Zn measurements. As illustrated by Table 6, the average concentrations sulfur and phosphorus, key elements that could potentially cause interferences affecting the measurement of the ^{67}Zn/^{66}Zn ratios, are both less than 10 mg/L in the digested solutions that were analyzed directly without dilution. In addition, the concentration of Mg, which could potentially cause an interference on ^{66}Zn was less than 0.5 mg/L in all solutions. Since the calculated abundance of the potential interference from Mg is very low, 0.11, as illustrated in Table 3, the potential for this molecular species causing significant impact on the measured ^{67}Zn/^{66}Zn ratios was considered to be quite low.

2.7. Isotopic Zn analysis

Since no certified natural abundance zinc isotope reference material was available, mass-bias corrections were performed using a natural abundance Zn standard, JMC Zinc (Johnsen Matthey batch 3-0749-L), which has previously been characterized by several laboratories [12–14]. Due to the limited availability of this particular standard, a secondary zinc standard, HP 403518, (1000 mg/L Zn, High Purity Standards, Lot 403518) of "natural" abundance was cross-correlated to the JMC Zinc values for use as a secondary isotopic standard. The HP 403518 standard was then run approximately every 15–20 samples during the isotopic analysis run and appropriate mass-bias corrections were applied to the sample data between bracketing standards. Although the standard-sample bracketing technique is traditionally run for each sample, i.e., the isotopic standard is run before and after every sample, the large number of sample analyses required (over 600 individual samples) us to modify this procedure in order to maintain suitable sample throughput. The JMC Zinc solution was also analyzed as a check periodically throughout the rainbow trout study sample run. It should be noted that the measured isotopic ratios are relative to the standards, JMC Zinc and HP 403518, used for mass-bias correction and are not absolute isotopic ratios, since there is no internationally agreed upon isotopic standard for zinc at the current time. However, since we are only interested in measuring observed changes in the zinc ratios due to exposure of our test organisms to enriched ^{67}Zn waters, this matter is of no consequence to the results of our study.

In order to obtain suitable precision for the zinc isotope analysis, a total integration time of 10 s was used per isotope. All five zinc isotopes, ^{64}Zn, ^{66}Zn, ^{67}Zn, ^{68}Zn, and ^{70}Zn were measured as well as ^{60}Ni, as indicated in Table 2 along with other operational parameters. Although we decided to use the ^{67}Zn/^{66}Zn ratios for this study, the ^{67}Zn/^{64}Zn ratios were also monitored. All isotope ratios were automatically calculated using the instrument software. The relative internal precision (% RSD) of the 10 replicate ^{67}Zn/^{66}Zn or ^{67}Zn/^{64}Zn measurements for each individual sample was of the order of 0.2–0.4%. Due to the long total analysis time of 15 min (including sample uptake and stabilization times) for the isotope ratio measurements, a low sample uptake rate was necessary in order to have enough solution to perform both the total Zn analysis and the Zn isotope analysis. The sample introduction system (nebulizer and peristaltic pump) was adjusted to obtain a sample flow rate of ~0.35 mL/min, requiring approximately 6 mL of sample solution per isotopic analysis.

Table 7 gives a summary of the figures of merit for the method. The expected ^{67}Zn/^{64}Zn ratio of 0.0822 and the calculated

Table 6
Average concentrations and standard deviations (in parentheses) of elements detected in digests from rainbow trout gills ($n = 196$) with concentrations greater than 1 μg/L.

Element	Na (mg/L)	Mg (mg/L)	Al (μg/L)	P (mg/L)	S (mg/L)	K (mg/L)	Ca (mg/L)	Fe (μg/L)
Mean (SD)	4.6 (1.9)	0.4 (0.1)	4.4 (7.1)	7.0 (2.8)	5.2 (1.8)	6.5 (2.3)	1.8 (1.1)	120 (50)
Element	Zn (μg/L)	Rb (μg/L)	Sr (μg/L)	Se (μg/L)	Cr (μg/L)	Mn (μg/L)	Ni (μg/L)	Cu (μg/L)
Mean (SD)	160 (120)	5.4 (2.0)	5.9 (3.5)	1.6 (0.5)	0.7 (0.3)	2.8 (1.4)	0.4 (0.6)	1.5 (0.6)

Table 7
Figures of merit/analytical performance, where *N* = number of samples analyzed.

	N	Total Zn	$^{67}Zn/^{66}Zn$ analysis
Sample volume required (mL)	–	2	6
Detection limit (3σ) (μg/L)	8	0.03	–
Total Zn concentration for accurate $^{67}Zn/^{66}Zn$ (<0.5% RSD)	–	–	10 μg/L
Short-term analytical precision (standards), %RSD, <2 h	4	1.1	0.2
Short-term analytical precision (control gills), % RSD, <2 h	20	1.6	0.2
Long-term analytical precision (standards), % RSD, 96 h	9	1.7	1.0
Long-term analytical precision (composite gill QC sample), %RSD, 96 h	8	1.5	0.7
Accuracy (JMC Zinc), 96 h, mean (SD), %error	4	–	0.1450 (0.0013), 0.3

$^{67}Zn/^{66}Zn$ ratio of 0.1455 for the JMC Zinc standard were obtained from the values last reported by Bermin et al. [13]. The expected values for the HP 403518 standard (0.0804 for $^{67}Zn/^{64}Zn$ and 0.1442 for $^{67}Zn/^{66}Zn$) were obtained by running this sample immediately after mass-bias calibration with the JMC Zinc standard. The precisions obtained over the shorter 15-h runs for the HP 403518 standard were of the order of 0.5–1.5% RSD for the $^{67}Zn/^{64}Zn$ ratio and 0.1–0.2% RSD for the $^{67}Zn/^{66}Zn$ ratio. For the 96-h long analysis of the rainbow trout gill tissue samples, the precisions obtained for both the JMC Zinc and the HP 403518 standards were of the order of 4% RSD for the $^{67}Zn/^{64}Zn$ ratio and 1% RSD for the $^{67}Zn/^{66}Zn$ ratio. It is possible that the higher RSDs for the $^{67}Zn/^{64}Zn$ ratios could be the result of the effects of the various interferences impacting the measurement of ^{64}Zn, including the correction for ^{60}Ni, as was discussed previously. The better precisions obtained for the $^{67}Zn/^{66}Zn$ ratios supported our decision to use this ratio for the study instead of the more traditional $^{67}Zn/^{64}Zn$ measurement.

As illustrated in Table 7, the short-term analytical precision of the isotope ratio method for both the zinc standards and the rainbow trout gills from the two sets of 10 exposure control samples (for hard and soft water exposures) is of the order of 0.2% RSD during the 2 h time period it took to analyze these groups of samples. In order to estimate long-term analytical precision over the course of the 96 h of total analysis time, the ratios for the zinc standards analyzed every 15–20 samples for mass-bias correction and for the composited gill QC samples in each sample preparation batch were averaged and the standard deviations calculated. As shown in Table 7, the long-term analytical precision for the mass-bias correction standards and the composited gill QC samples were 1.0% RSD and 0.7% RSD, respectively. The use of the composited gill QC sample allows the long-term analytical precision of the method to be calculated without any effects due to differences between individual fish, such as amount of endogenous zinc present, zinc uptake rate, amount of gill mucus, and gill weights. The error of the measured $^{67}Zn/^{66}Zn$ ratio over the entire 96-h period was 0.3% for the JMC Zinc standard.

3. Results and discussion

3.1. Pilot study–Brown trout

3.1.1. Determination of total Zn by ICP-MS

A summary of the results for the total Zn analysis on a gill wet-weight basis (in μg Zn/g gill), for the pilot study gill samples is given in Fig. 1. Initial studies and calculations based on counting statistics indicated that in order to obtain usable isotope ratio analyses using 10-s integration times, the zinc concentrations in the digestates needed to be 10 μg/L or greater. Total Zn concentrations in the pilot study ranged from 18 μg/L to 110 μg/L in the gill digests for individual fish and from 115 μg/L to 475 μg/L in the composited samples.

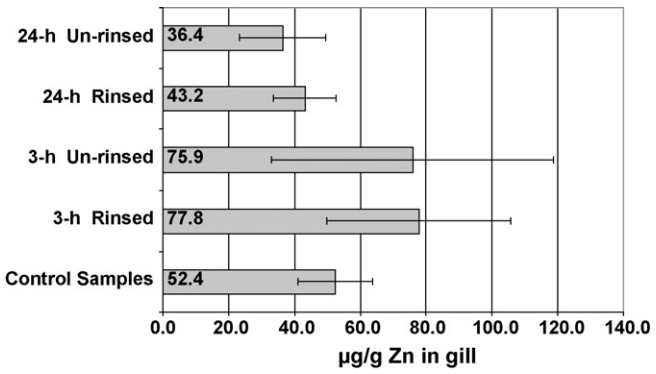


Fig. 1. Summary of total Zn content in gills (μg/g) from the brown trout pilot study, mean values are given at the base of each bar. Error bars are ±1standard deviation of measured values for each exposure group ($n = 8$ for control samples, $n = 5$ for all 3-h and 24-h exposures).

One of the considerations in the experimental design was to evaluate whether rinsing the dissected gill tissues would be necessary to remove Zn that was contained in the gill mucus and not actually bound to the gill. Earlier studies [17] had used physical means, e.g., wiping the gill material with a laboratory tissue, to remove mucus from the gill. This was identified as a possible source of contamination since leaching studies performed on laboratory wipes indicated a significant amount of Zn present (~0.9 μg/g). As the data in Fig. 1 indicate, the values of zinc found in the rinsed gills appear to have slightly less variation (based on smaller standard deviation values) than did the un-rinsed samples, presumably because any additional Zn present in the mucus or from residual exposure water was being rinsed off. However, the mean values for the rinsed and un-rinsed samples are not statistically different. From this study, it was concluded that rinsing was not a detrimental practice and could reduce the variability in the total zinc values and should be used in the rainbow trout exposure study.

In addition, as shown in Fig. 1, the error (plotted as ±1standard deviation of the mean value) on the total Zn measurement for each exposure group is quite large. It is believed this is due to the significant amount of endogenous zinc present in the gill tissues, which can vary widely from fish to fish. In fact they are so large that no significant differences can be discerned between each exposure group, confirming that the use of total Zn measurements to estimate Zn uptake in the gills would lead to inconclusive results.

3.1.2. Determination of Zn isotopes by ICP-MS

The results for the isotope ratio analyses for the pilot study are summarized in Fig. 2. Fig. 2 shows the mean $^{67}Zn/^{66}Zn$ ratio along with the error (plotted as ±1standard deviation) for each exposure group. Preliminary analysis of the ratios in Fig. 2 indicate that there is an increase in $^{67}Zn/^{66}Zn$ ratios in fish exposed to the ^{67}Zn-enriched water after just 3 h time and an even more significant increase after 24 h of exposure. However, in order to determine if the differences in the ratios were significant, a statistical analysis was performed using a two-tailed *t*-test for samples with unequal variances (MINITAB Release 14.13, State College, PA, USA). Compared to the control group that was not exposed to the ^{67}Zn-enriched water, both the 3-h rinsed and un-rinsed groups resulted

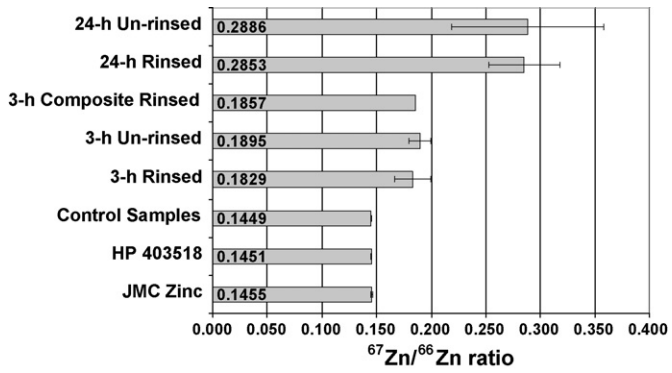


Fig. 2. Summary $^{67}Zn/^{66}Zn$ ratios for brown trout pilot exposure test results. Mean values for each exposure group are given at the base of the bar. Error bars are ±1standard deviation of measured values for each exposure group ($n = 8$ for control samples, $n = 3$ for 3-h composite group, $n = 5$ for all other 3-h and 24-h exposures).

in increases in the $^{67}Zn/^{66}Zn$ ratio that were statistically different ($p < 0.05$). Likewise, the 24-h rinsed and un-rinsed groups showed $^{67}Zn/^{66}Zn$ ratios that were significantly different than those from the 3-h rinsed and un-rinsed groups, respectively. However, comparisons of the rinsed and un-rinsed sample ratios from both the 3-h and 24-h exposures were not significantly different from one another ($p > 0.05$), although errors did vary somewhat, but not conclusively. Based on the Zn ratio data in Fig. 2, it would seem that rinsing would be unnecessary. However, as discussed in the section above, rinsing did make a difference in the variation of the total zinc values, which are also necessary for the calculations that will be ultimately be performed on the data to estimate gill Zn uptake.

For the brown trout control samples ($n = 10$) in Fig. 2, it should be noted that the mean value does not vary significantly (within the standard error) from the values obtained for the zinc standards (JMC Zinc and HP 403518) used for mass-bias correction. For the control samples, the precision obtained was 0.3% RSD. This indicates that the differences, if any, that might be occurring due to the various interferences possible in the digested gill matrix, including those from phosphorous and sulfur, are small.

It is believed that the errors observed for the measured zinc ratios in the different exposure groups are due to a number of factors, including the amount of endogenous Zn present, the small sample sizes (~20 mg of gill tissue was harvested from each fish), variation in sample size, variability in individual fish zinc uptake rates, and the relatively low number of fish ($n = 5$) in each exposure. The observed precision of 0.2% RSD for the three 3-h Composite samples in Fig. 2 is significantly smaller than the 9% RSD and 6% RSD that were obtained for the 3-h Rinsed and 3-h Unrinsed groups, respectively. This is an indication that many factors affecting overall precision are due to differences between individual fish, as discussed above. In the composited sample, these variations from individual fish have been removed by homogenization of the samples. The 3-h Rinsed and 3-h Unrinsed groups each contain five fish, averaging 3.5 g in total weight, with individual gill weights that ranged from 0.008 to 0.030 g each and an average gill weight of 0.018 g. This high variation in individual gill weights could lead to significant errors in the measured zinc isotopic ratios depending on the amount of endogenous zinc present on the gills, which would also vary on a per fish basis. The data in Fig. 2 illustrate that improved precision in the isotope ratios might be obtained if either larger fish or composited samples could be used. However, both these options have limitations, including availability of suitable numbers of stock of the same age and size, cost, space available, and predation issues (particularly with larger fish).

3.2. Rainbow trout exposure study

3.2.1. Determination of total Zn

As in the pilot study discussed previously, all gill digests were analyzed for total Zn content prior to isotopic analysis. Zinc concentrations in the gills ranged from 22.42 ± 6.43 μg/g to 80.82 ± 37.48 μg/g for the soft water exposures and from 23.47 ± 6.78 μg/g to 77.21 ± 56.22 μg/g for the hard water exposures (see Table S1 in the electronic supplement for details). All sample digests were above the minimum concentration of 10 μg/L required for the zinc isotopic analysis.

3.2.2. Determination of Zn isotope ratios

Summary data for the determination of the isotopic ratios for $^{67}Zn/^{66}Zn$ are given in Fig. 3a and b for soft water and hard water exposures, respectively. In general, a trend can be seen where the mean $^{67}Zn/^{66}Zn$ ratios increase with increased exposure concentration and time for both soft and hard water exposures. However, statistical analysis (see Table S2 in the electronic supplement for detailed data and statistics) indicates that while all exposure means differ significantly from the control means, only a few exposures in each exposure concentration group differ significantly from the exposure time immediately preceding it. Specifically, for the soft water exposures (Fig. 3a), a significant difference is only observed between the ratio means for the 3-h and 24-h exposures for the

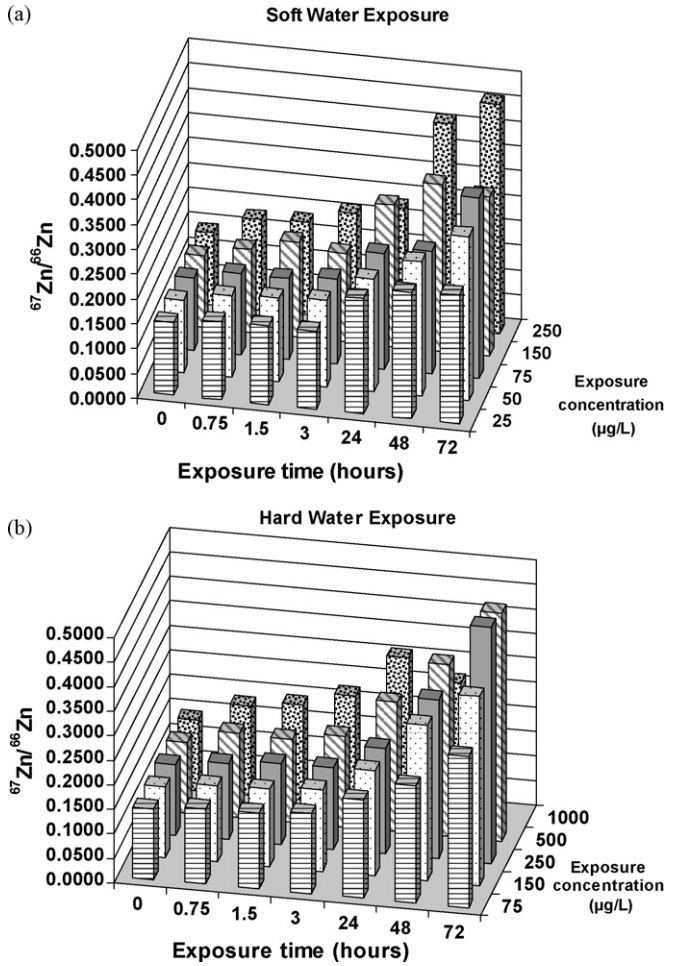


Fig. 3. (a) Summary data for $^{67/66}Zn$ ratio (mass-bias corrected) for rainbow trout exposure study using soft water. Detailed data, including statistics are available in Table S2(a). (b) Summary data for $^{67/66}Zn$ ratio (mass-bias corrected) for rainbow trout exposure study using hard water. Detailed data, including statistics are available in Table S2(b).

25 μg/L, 75 μg/L, and 150 μg/L exposure concentrations. For the hard water exposures (Fig. 3b), there is a statistical difference between the means for the 3-h and 24-h exposures at all concentrations, except for the highest exposure at 1000 μg/L. In addition, there are differences between the 3-h and 1.5-h exposures at the lowest zinc concentration, 75 μg/L, and between the 48-h and 24-h exposures at the 150 μg/L and 250 μg/L exposure concentrations. Although a general upward trend in the measured ratios was observed, as expected, the close proximity of the time intervals and concentrations could be a factor in the lack of statistically significant differences between adjacent time and concentration groupings. In addition, after 24 h, there may be complicating factors such as non-specific sorption of Zn onto the gills that result in a leveling off of the observed increase in the $^{67}Zn/^{66}Zn$ ratio, particularly in the soft waters.

Although the precision obtained for the control samples in both hard and soft waters was 0.2% RSD, for subsequent exposure times and zinc concentrations the precision of the measured values increased from 2% RSD to as much as 50% RSD (see Table S2 for detailed data). A generalized trend of increasing uncertainty with increased exposure concentrations and times was observed. Uncertainties greater than 10% RSD were observed for soft water exposure groups greater then 75 μg/L Zn and for hard water exposure groups greater than 500 μg/L Zn. Because long-term reproducibility of the measured ratios in the composited gill QC samples was very good (0.7% RSD over 96 h) the increasing relative standard deviations in the exposure groupings must be related to differences between individual fish. As stated previously, the reproducibility of the measured zinc isotope ratios is influenced by the low sample number ($n = 5$ in most cases), the high degree of variability in the total Zn concentration in each fish based on sample weight (see Table S1 in the electronic supplement for details), and the different zinc uptake rates for individual fish. These three factors result in a relatively high variance in the measured zinc ratios in each individual fish because the observed change in the $^{67}Zn/^{66}Zn$ ratios is greatly affected by the variability in the amount of total endogenous zinc on the gills as compared to the sample weight. The levels of endogenous zinc present may have greater effect on longer exposure times as zinc is ultimately exchanged between various tissues in the fish or if other effects such as increased mucus production (a stress response) occur. Nevertheless, these uncertainties should be an important consideration in any inferences made based on the calculated amount of bound zinc, particularly for longer exposure times at higher exposure concentrations.

3.2.3. Determination of accumulated zinc

The ultimate goal of the total zinc and zinc isotopic analysis was to use the measured values to determine the total zinc accumulated or bound onto the gills of each individual fish during the various exposures. The amount of bound zinc was calculated for each fish using the equation

$$Zn_{accum} = \frac{Zn_{total}(f_{67-nat} - (R_{final} \times f_{66-nat}))}{R_{final}(f_{66-enr} - f_{66-nat}) + f_{67-nat} - f_{67-enr}}$$

where Zn_{total} = total zinc post exposure in gill tissue; Zn_{accum} = total accumulated zinc in gill tissue; R_{final} = final $^{67}Zn/^{66}Zn$ ratio in gill tissue; f_{x-enr} = fraction of given isotope in exposure media; f_{x-nat} = fraction of given isotope in control gill tissue.

Calculation of total estimated analytical error on the determination of accumulated zinc using the equation above, based on measurement error propagation, results in an estimated analytical error of 2.4% on the calculated accumulated zinc values. Summarized results for calculated accumulated zinc in each exposure grouping are given in Fig. 4a and b. The mean values for accumulated zinc in all exposures for both soft and hard waters were statistically different (see Table S3 in the electronic supplement for details and statistics) from the control group. In the soft waters, all exposure concentrations show a significant difference between amount of zinc accumulated between the 3-h and 24-h exposures and the 24-h and 48-h exposures. In addition at the lowest exposure concentration, 25 μg/L, the amount of accumulated zinc is significantly different for all exposures longer than 0.75 h.

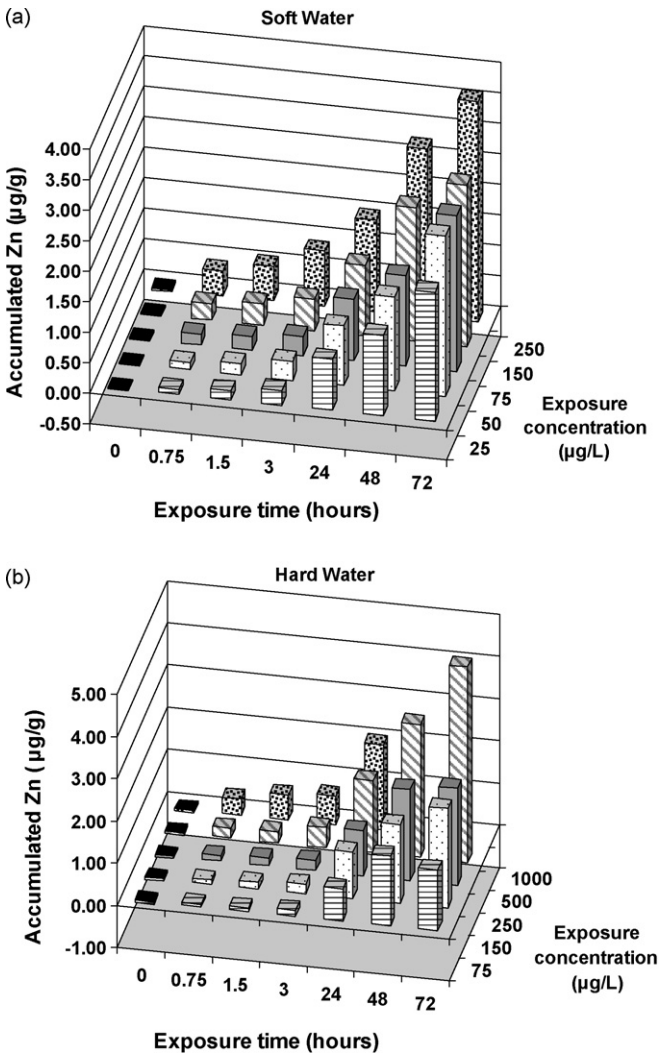


Fig. 4. (a) Summary data for accumulated zinc (μg/g) in soft water rainbow trout exposures. Detailed data, including statistics, are available in Table S3(a). (b) Summary data for accumulated zinc (μg/g) in hard water rainbow trout exposures. Detailed data, including statistics, are available in Table S3(b).

For the hard waters illustrated in Fig. 4b, all exposure concentrations show significantly different amounts of accumulated zinc between the 3-h and 24-h exposure times. In addition, the amounts of accumulated zinc also differ significantly between the 24-h and 48-h exposure times at the lower exposure concentrations (75 μg/L, 150 μg/L, and 250 μg/L).

However, the most significant result is that the amounts of accumulated zinc in the 75 μg/L, 150 μg/L, and 250 μg/L exposure concentrations differ significantly between the soft and hard exposures, as is indicated in Fig. 5. It should be noted that the error bars in Fig. 5 are the standard deviations of the average value of calculated accumulated zinc for each exposure group which were obtained from individually calculated accumulated zinc values for each fish in the study. These observed differences between exposure concentrations as a function of water hardness are important in evaluating the potential effects of water chemistry parameters, such as hardness, on fish toxicity. The use of these data is further discussed in

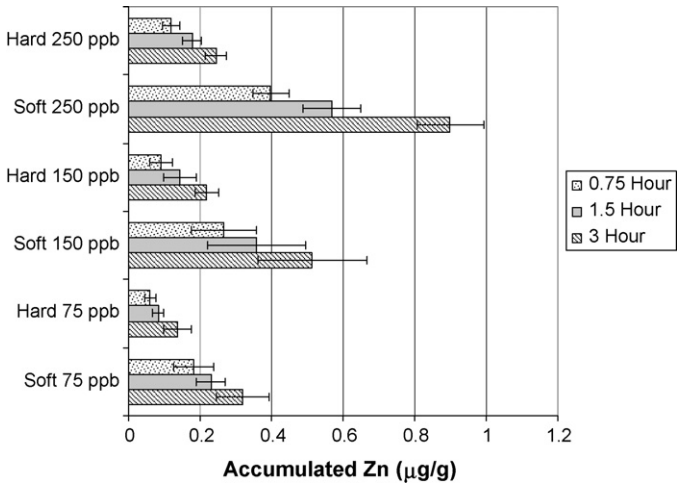


Fig. 5. Comparison of accumulated zinc in rainbow trout gills for exposures ≤3 h for both soft and hard waters. Error bars are ±1standard deviation of mean values of individually calculated values of accumulated zinc.

Todd et al. [18] for evaluating the impact of water chemistry on toxicity models, such as the Biotic Ligand Model (BLM).

4. Conclusion

The results from the pilot study indicate that the sample preparation and methods of analysis for both total Zn and Zn isotopic analysis described were suitable for use on the rainbow trout exposure study. The $^{67}Zn/^{66}Zn$ ratio was found to be less susceptible to interferences and demonstrated better precision than the more traditionally used $^{67}Zn/^{64}Zn$ ratio. As a result, the $^{67}Zn/^{66}Zn$ ratio was used in the subsequent rainbow trout exposure study. The measured $^{67}Zn/^{66}Zn$ ratios for the fish control samples did not vary significantly from those obtained for the zinc standards, indicating that any possible effects due to the presence of phosphorus and sulfur in the sample digests on the $^{67}Zn/^{66}Zn$ ratio was minimal. A key finding of the pilot study is that statistically significant differences in the $^{67}Zn/^{66}Zn$ ratios can be seen in individual fish in exposures times as short as 3 h. Another finding was that the use of composited samples could possibly improve the precision of the measured isotope ratios significantly, by eliminating differences between individual fish in each exposure group due to variables such as zinc uptake rate and endogenous since levels, if required for future studies.

The methods discussed in the pilot study were successfully used in the rainbow trout exposure study. The isotope ratio method was found to have a long-term analytical precision of 0.7% RSD for the composited gill QC samples. However, it was found that the high variability of factors such as levels of endogenous zinc, zinc uptake rate, and gill weight among individual fish in each exposure grouping resulted in widely varying total zinc concentrations and isotope ratios in the individual gill digests. This led to higher standard deviations and more uncertainty in the measured $^{67}Zn/^{66}Zn$ ratio than anticipated for each exposure grouping, particularly at longer exposure times and higher exposure concentrations. However, the calculations to determine the amount of zinc accumulated by individual fish incorporated these variances and the resulting values for accumulated zinc showed significant differences between 3-h and 24-h exposures as well as between 24-h and 48-h exposures for most exposure concentrations in both soft and hard waters. Most significant was the difference in accumulated zinc in exposure media of the same concentration in soft and hard waters. This supports other findings [1–6] that water chemistry parameters such as hardness have an important effect on aquatic toxicity results. The data obtained in this study are further discussed in relationship to the biotic ligand model and in comparison to earlier studies performed using radioactive ^{65}Zn in a companion paper by Todd et al. [18].

Acknowledgement

This work was funded by the United States Geological Survey Mendenhall Program.

Appendix A. Supplementary data

Supplementary data associated with this article can be found, in the online version, at doi:10.1016/j.talanta.2009.07.048.

References

[1] D.H. Alsop, C.M. Wood, Can. J. Fish. Aquat. Sci. 56 (1999) 2112–2119.
[2] D.H. Alsop, J.C. McGreer, D.G. McDonald, C.M. Wood, Environ. Toxicol. Chem. 18 (1999) 1014–1025.
[3] D.H. Alsop, C.M. Wood, Environ. Toxicol. Chem. 19 (2000) 1911–1918.
[4] J.C. McGeer, C. Szebedinszky, D.G. McDonald, C.M. Wood, Aquat. Toxicol. 50 (2000) 245–256.
[5] A.S. Todd, D.M. McKnight, C.L. Jaros, T. Marchitto, Environ. Monit. Assess. 130 (2007) 111–127.
[6] S. Brinkman, N.M.K. Vieira, Effect of embryo–larval incubation temperature on the toxicity of zinc to brown trout (*Salmo trutta*), Water Pollution Studies, Federal Aid Project F-243-R13, 2006, Colorado Division of Wildlife, Fort Collins, CO, June 2006. Available at: http://wildlife.state.co.us/NR/rdonlyres/B72E3667-E8DC-4E3D-8640-F00898D4D9F2/0/2006brinkmanvieiracomplete.pdf.
[7] S. Brinkman, N.M.K. Vieira, A comparison of the acute sensitivity of two strains of rainbow trout (*Oncorhynchus mykiss*) to zinc, Water Pollution Studies, Federal Aid Project F-243-R13, 2006, Colorado Division of Wildlife, Fort Collins, CO, June 2006. Available at: http://wildlife.state.co.us/NR/rdonlyres/B72E3667-E8DC-4E3D-8640-F00898D4D9F2/0/2006brinkmanvieiracomplete.pdf.
[8] Stefan Stürup, Helle Rüsz Hansen, Bente Gammelgaard, Anal. Bioanal. Chem. 390 (2008) 541–554, doi:10.1007/s00216-007-1638-8.
[9] Christophe Cloquet, Jean Carignan, Mortiz F. Lehmann, Frank Vanhaecke, Anal. Bioanal. Chem. 390 (2008) 451–463, doi:10.1007/s00216-007-1635-y.
[10] Marie-Noële Croteau, Samuel N. Luoma, Brent R. Topping, Cary B. Lopez, Environ. Sci. Technol. 38 (2004) 5002–5009.
[11] Marie-Noële Croteau, Samuel N. Luoma, Bastien Pellet, Aquat. Toxicol. 83 (2007) 116–125.
[12] Chloé Nadia Maréchal, Philippe Télouk, Francis Albarède, Chem. Geol. 156 (1999) 251–273.
[13] J. Bermin, D. Vance, C. Archer, P.J. Statham, Chem. Geol. 226 (2006) 280–297.
[14] D.M. Borrok, R.B. Wanty, W.I. Ridley, R. Wolf, P.J. Lamothe, M. Adams, Chem. Geol. 242 (2007) 400–414.
[15] Lieve I.L. Balcaen, Karel A.C. De Schamphelaere, Colin R. Janssen, Luc Moens, Frank Vanhaecke, Anal. Bioanal. Chem. 390 (2008) 555–569, doi:10.1007/s00216-007/-1620-5.
[16] Dominic M. Di Toro, Herbert E. Allen, Harold L. Bergman, Joseph S. Meyer, Paul R. Paquin, Robert C. Santore, Environ. Toxicol. Chem. 20 (2001) 2383–2396.
[17] James F. Ranville, Colorado School of Mines, 2007, personal communication.
[18] Andrew S. Todd, Stephen Brinkman, Ruth E. Wolf, Paul J. Lamothe, Kathleen S. Smith, James F. Ranville, Use of an enriched stable-isotope approach to determine the gill-zinc binding properties of juvenile rainbow trout (*Oncorhynchus mykiss*) during acute zinc exposures in hard and soft waters, Environ. Toxicol. Chem. 28 (2009) 1233–1243, doi:10.1897/08-252.1.

Talanta 80 (2009) 685–693

Contents lists available at ScienceDirect

Talanta

journal homepage: www.elsevier.com/locate/talanta

Determination of cobalt ions at nano-level based on newly synthesized pendant armed macrocycle by polymeric membrane and coated graphite electrode

Ashok K. Singh*, Prerna Singh, G. Bhattacharjee

Department of Chemistry, Indian Institute of Technology-Roorkee, Roorkee 247 667, India

ARTICLE INFO

Article history:
Received 23 June 2009
Received in revised form 24 July 2009
Accepted 24 July 2009
Available online 3 August 2009

Keywords:
Macrocyclic ligands
Cobalt selective sensor
Polymeric membrane electrode
Coated graphite electrode

ABSTRACT

Poly(vinylchloride) (PVC) based membranes of macrocycles 2,3,4:9,10,11-dipyridine-1,3,5,8,10,12-hexaazacyclotetradeca-2,9-diene (L_1) and 2,3,4:9,10,11-dipyridine-1,5,8,12-tetramethylacrylate-1,3,5,8,10,12-hexaazacyclotetradeca-2,9-diene (L_2) with NaTPB and KTpClPB as anion excluders and dibutylphthalate (DBP), benzyl acetate (BA), dioctylphthalate (DOP), *o*-nitrophenyloctyl ether (o-NPOE) and tri-n-butylphosphate (TBP) as plasticizing solvent mediators were prepared and investigated as Co^{2+} selective electrodes. The best performance was observed with the membranes having the composition L_2:PVC:TBP:NaTPB in the ratio of 6:39:53:2 (w/w; mg). The performance of the membrane based on L_2 was compared with polymeric membrane electrode (PME) and coated graphite electrode (CGE). The PME exhibits detection limit of 4.7×10^{-8} M with a Nernstian slope of 29.7 mV decade^{-1} of activity between pH 2.5 and 8.5 whereas CGE exhibits the detection limit of 6.8×10^{-9} M with a Nernstian slope of 29.5 mV decade^{-1} of activity between pH 2.0 and 9.0. The response time for PME and CGE was found to be 11 and 8 s, respectively. The CGE has been found to work satisfactorily in partially non-aqueous media up to 35% (v/v) content of methanol, ethanol and 25% (v/v) content of acetonitrile and could be used for a period of 4 months. The CGE was successfully applied for the determination of Co^{2+} in real and pharmaceutical samples and as an indicator electrode in potentiometric titration of cobalt ion.

© 2009 Elsevier B.V. All rights reserved.

1. Introduction

The increasing use of ion sensors in the fields of environmental, agricultural and medicinal analysis is putting more and more pressure on analytical chemists to develop new sensors for the fast, accurate, reproducible and selective determination of various species. During the past few decades, many intensive studies on the design and synthesis of highly selective ionophores as sensory molecules for ion-selective electrodes have been reported and much interest has been focused on macrocyclic compounds. The design and function of synthesized macrocyclic carriers for cation selective membrane sensors are usually based on such diverse parameters as the structure and cavity size of ion carrier, the stability and its ability to extract the target ion into the membrane phase. Currently, a great deal of attention is being focused on macrocyclic ligands because they play an important role in many aspects of chemistry, medicine and the chemical industry.

The need of selective determination of heavy metal ions has increased immensely during the last few decades due to the growing environmental problems. Among heavy metals, the pollution caused by cobalt is of considerable concern. Determination of cobalt assumes importance because of its widespread occurrence in sea as well as in fresh water, earth crust, meteorites, animals and plants. It is a vital trace element in animal nutrition and widely distributed in the body with high concentration in liver, bone and kidney. Cobalt is used in high-temperature alloys, in permanent magnets and its salts are useful in paint dryers as catalysts, abrasion resistant glasses, ceramics, batteries and in production of numerous pigments like cobalt blue and cobalt green, in ground coats for porcelain enamels and in electroplating industry. Cobalt, in the form of cobalamin, is an essential component of Vit. B_{12} required for the production of red blood cells and prevention of pernicious anaemia [1]. Deficiency of cobalt may cause anaemia, retarted growth and loss of apetite. On the other hand, if consumed in large doses, cobalt may be toxic and cause diarrhea, irritation of gastrointestinal tract and vomiting. Exposure to cobalt may cause lung effects, which include respiratory irritation, coughing, asthma, pulmonary edema and pneumonia. The maximum dietary tolerable level of cobalt for common livestock species is 10 ppm [2].

A number of sophisticated methods such as flame atomic absorption [3], electrochemiluminescence [4], thin film sequential injection [5], graphite furnace-atomic absorption spectrometry (GF-AAS) [6], electrothermal-atomic absorption spectrometry [7], differential pulse anodic stripping voltammetry [8] have been reported for the determination of cobalt. However, these methods are disadvantageous as they are time consuming, involves sample

* Corresponding author. Tel.: +91 1332 285798.
E-mail address: akscyfcy@iitr.ernet.in (A.K. Singh).

0039-9140/$ – see front matter © 2009 Elsevier B.V. All rights reserved.
doi:10.1016/j.talanta.2009.07.049

manipulation, relatively expensive and require large infrastructure back up. Selective analytical methodologies, which are easily operated and involve harmless reagents, cost effective equipment, have therefore been proposed as alternative to standard methods. Potentiometric sensors based on ion-selective electrodes are especially suited for such determination because they offer advantages such as selectivity, sensitivity, good precision, simplicity and low cost [9,10].

A literature survey revealed that the sensors developed for cobalt make use of chelates [11], macrocycles [12–17], extractants [18], organic resins [19,20], mercapto compounds [21], OXCDD (diamide) [22], Schiff base [23,24], isothiazole [25], calixarenes [26,27] and variety of other ligands [28,29]. However, most of these sensors suffer from disadvantages such as narrow working concentration range. With a near or non-Nernstian response, exhibit high response time, poor reproducibility.

The purpose of the present work is to explore the polymeric membrane electrode (PME) and coated graphite electrode (CGE) as Co^{2+} selective sensors based on two newly synthesized macrocyclic ligands (L_1 and L_2).

2. Experimental

2.1. Reagents

Reagent grade sodium tetraphenylborate (NaTPB), potassium tetrakis *p*-(chloro phenyl)borate (KTpClPB), dibutylphthalate (DBP), tri-n-butylphosphate (TBP), benzyl acetate (BA), dioctylphthalate (DOP), *o*-nitrophenyloctyl ether (*o*-NPOE), tetrahydrofuran (THF) and high molecular weight poly(vinylchloride) were purchased from E. Merck (Germany) and used as received. Ethylenediamine and 2,6-dichloropyridine were procured from Aldrich (USA). The nitrate salts of all the cations used were of analytical grade and used without any further purification. The solutions of metal salts were prepared in doubly distilled water and standardized whenever necessary.

2.2. Synthesis of macrocyclic ligand 2,3,4:9,10,11-dipyridine-1,3,5,8,10,12-hexaaza-cyclotetradeca-2,9-diene (L_1)

The macrocyclic ionophore L_1 (Fig. 1) was synthesized by dissolving equimolar amounts of ethylenediamine (0.01 M) and 2,6-dichloropyridine (0.01 M). Ethylenediamine was dissolved in minimum quantity of methanol and to this solution 2,6-dichloropyridine dissolved in methanol was added dropwise with stirring. The resulting mixture was refluxed for 10 h and then was concentrated to half of its original volume on a water bath, followed by cooling and keeping aside for 1 day. A white crystalline product was obtained. Yield: 72%. M.pt.: 138 °C. Anal. calcd. for [$C_{14}H_{18}N_6$] (%): C, 62.19; H, 6.69; N, 31.12; Observed (%): C, 62.20; H, 6.71; N, 31.09, ^{1}H NMR (MeOH, 500 MHz) δ_{ppm}: 7.02–7.64 (m, H–Ar, 6H), 2.64–2.67 (m, –C–NH–C–, 4H), 2.32 (s, –N–CH_2–C, 8H). FT-IR (KBr, cm^{-1}): 3268 (–NH str.).

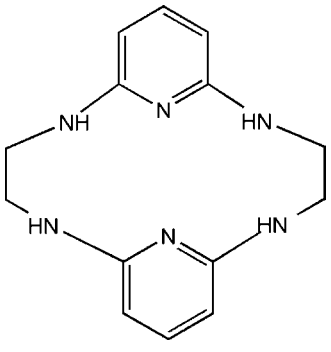


Fig. 1. Structure of macrocyclic ligand 2,3,4:9,10,11-dipyridine-1,3,5,8,10,12-hexaazacyclotetradeca-2,10-diene (L_1).

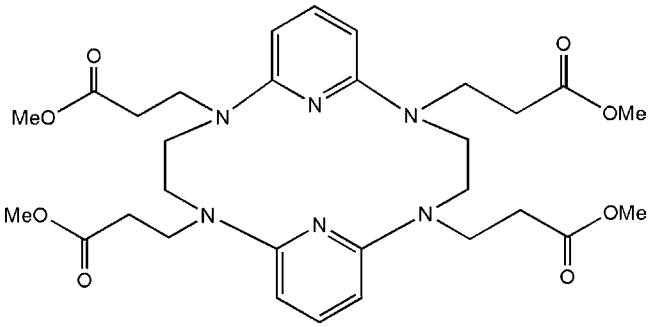


Fig. 2. Structure of macrocyclic pendant ligand 2,3,4:9,10,11-dipyridine-1,5,8,12-tetramethylacrylate-1,3,5,8,10,12-hexaazacyclotetradeca-2,10-diene (L_2).

2.2.1. Synthesis of macrocyclic ligand 2,3,4:9,10,11-dipyridine-1,5,8,12-tetramethylacrylate-1,3,5,8,10,12-hexaazacyclotetradeca-2,9-diene (L_2)

The macrocyclic pendant ligand L_2 (Fig. 2) was synthesized from macrocycle L_1. To a stirred solution of the macrocycle L_1 (1 mmol) in 10 mL saturated solution of anh. K_2CO_3 in anhydrous MeOH, 5 mL methylacrylate (excess amount) was added drop by drop and then it was stirred overnight and refluxed for 24 h. Then the volume was reduced half of its initial amount and was kept in a refrigerator overnight. A creamish coloured oily product was obtained. Yield: 43%. Anal. calcd. for [$C_{30}H_{42}N_6O_8$] (%): C, 58.60; H, 6.88; N, 13.67; O, 20.85; Observed (%): C, 58.62; H, 6.89; N, 13.67; O, 20.82. ^{1}H NMR (MeOH, 500 MHz) δ_{ppm}: 6.90–7.22 (m, H–Ar, 8H), 2.97–3.25 (m, –N–CH_2–C–, 8H), 2.52 (s, N–CH_2–CH_2–N, 8H), 2.38–2.42 (m, –C–CH_2–COOMe, 8H), 1.36 (s, –OCH_3, 12H), FT-IR (KBr, cm^{-1}): 2930 (asymmetric –CH_2– str.), 2848 (symmetric –CH_2– str.), 1747 (ester C=O str.), 1570–1382 (aromatic C=C and C=N str.), 1163 (OC–OCH_3 str.), 1109 (–OCH_3 str.).

2.3. Electrode preparation

The nature and amount of ionophore, nature of plasticizers, plasticizer/PVC ratio and especially the nature of lipophilic additives used, are known to significantly influence the sensitivity and selectivity. Varying amount of the ion-active phase and anion excluder KTpClPB and NaTPB were dissolved with an appropriate amount of PVC in 3 mL THF. To these, solvent mediators, *viz*. DBP, TBP, BA, DBS and *o*-NPOE were added to get membranes of different compositions. The mixture was shaken vigorously with a glass rod. When the solution became viscous it was poured in acrylic ring placed on smooth glass plate. The solution was then allowed to evaporate for 24 h at room temperature. Transparent membranes of about 0.1 mm thickness were obtained, which were then cut to size and glued to one end of a pyrex glass tube with araldite. The ratio of membrane ingredients, time of contact and concentration of equilibrating solution were optimized so that the potential recorded were reproducible and stable within the standard deviation. Membrane to membrane reproducibility was assured by carefully following the optimum condition of fabrication. The membrane that gave reproducible results and showed best performance was selected for further studies.

To prepare the coated graphite electrodes, spectroscopic grade graphite rods 10 mm long and 3 mm in diameter were used. A

Table 1
Formation constants for cobalt ion-selective electrode.

Interfering cations	Formation constant ($\log \beta_{IL_n}$)* ± SD	Interfering cations	Formation constant ($\log \beta_{IL_n}$)* ± SD
Co^{2+}	6.73 ± 0.01	Sr^{2+}	1.52 ± 0.07
La^{3+}	4.55 ± 0.05	Cu^{2+}	5.74 ± 0.03
Ce^{3+}	4.71 ± 0.13	Zn^{2+}	5.41 ± 0.12
Na^{+}	4.21 ± 0.03	Ni^{2+}	5.02 ± 0.08
K^{+}	4.11 ± 0.14	Ba^{2+}	3.64 ± 0.02
Ag^{+}	3.44 ± 0.04	Pb^{2+}	3.89 ± 0.06
NH_4^{+}	3.32 ± 0.08	Al^{3+}	2.50 ± 0.03
Cd^{2+}	2.98 ± 0.07	Hg^{2+}	3.14 ± 0.11
Cr^{3+}	2.77 ± 0.02	Fe^{3+}	1.89 ± 0.01
Ca^{2+}	2.21 ± 0.14	Mg^{2+}	1.12 ± 0.05

* Mean value ± standard deviation (three measurements).

shielded copper wire was glued to one end of the graphite rod, and the electrode was sealed into the end of a PVC tube of about the same diameter with epoxy resin. The working surface of the electrode was polished with fine alumina slurries on a polishing cloth, sonicated in distilled water and dried in air. The polished graphite electrode was dipped into the membrane solution mentioned above, and the solvent was evaporated. A membrane was formed on the graphite surface, and the electrode was allowed to stabilize overnight.

2.4. Equilibration of membranes and potential measurements

The time of contact and concentration of equilibrated solutions were optimized so that the sensors generated stable and reproducible potentials at relatively short response times. The polymeric membrane electrodes and coated graphite electrodes were equilibrated for 4 days and 2 days, respectively in a 1.0×10^{-1} M $Co(NO_3)_2$ solution. The potentials were measured by varying the concentration of $Co(NO_3)_2$ in test solution in the range 1.0×10^{-9} to 1.0×10^{-1} M. Standard $Co(NO_3)_2$ solution was obtained by gradual dilution of 0.1 M $Co(NO_3)_2$ solution. The emf measurements with the polymeric membrane electrode and the coated graphite electrode were carried out on a Orion 4 pH meter at 25 ± 0.1 °C using saturated calomel electrode (SCE) as reference electrode with the following cell assemblies:

$Hg/Hg_2Cl_2|KCl$ (satd.)|internal solution (0.1 M $Co(NO_3)_2$)||PVC membrane||sample solution|$Hg\text{-}Hg_2Cl_2$, KCl (satd.) (PME).

CGE||test solution||$Hg\text{-}Hg_2Cl_2|KCl$ (satd.)

Activity coefficients were calculated according to the Debye–Huckel procedure, using the following equation [30].

$$\log \gamma = -0.511 z^2 \left[\frac{\mu^{1/2}}{(1 + 1.5\mu^{1/2}) - 0.2\mu} \right] \quad (1)$$

where μ is the ionic strength and z the valency.

2.5. Determination of formation constant

Formation constant of the ion–ionophore complex within the membrane phase is a very important parameter that indicates the practical selectivity of the sensor. In this method, two membrane segments are fused together, with only one containing the ionophore, to give a concentration-polarized sandwich membrane. A membrane potential measurement of this transient condition reveals the ion activity ratio at both interfaces, which translates into the apparent binding constants of the ion–ionophore complex [31]. In this method complex formation constants were obtained by neglecting ion pairing. As reported, the membrane potential E_M was determined by subtracting the cell potential for a membrane without ionophore from that for the sandwich membrane. The formation constant was then calculated from the following equation:

$$\beta_{IL_n} = \left(L_T - \frac{nR_T}{Z_I} \right)^{-n} \exp\left(\frac{E_M z_I F}{RT} \right) \quad (2)$$

where L_T is the total concentration of ionophore in the membrane segment, R_T is the concentration of lipophilic ionic site additives, n is the ion–ionophore complex stoichiometry, and R, T and F are the gas constant, the absolute temperature, and the Faraday constant. The ion I carries a charge of z_I. The determined formation constants ($\log \beta_{IL_n}$) for the examined different complexes are recorded in Table 1. The elapsed time between sandwich fusion and exposure to electrolyte was typically <1 min. The potential was recorded as the mean of the last minute of a 5 min measurement period in the appropriate salt solution. The potential of such sandwich membranes remained free of diffusion-induced potential drifts for about 20 min. Standard deviations were obtained based on the measurements of sets of at least three replicate membrane disks that were made from the same parent membrane. A careful analysis of the data in Table 1 reveals that cobalt ion has significant cation-binding characteristics.

Table 2
Optimization of membrane compositions and their potentiometric response for Co^{2+} ion-selective membrane based on ionophore L_1.

S.no.	Composition of membrane (w/w; mg)									Working concentration range (M)	Slope (mV decade^{-1} of activity)	Detection limit (M)
	L_1	NaTBP	KTpClPB	DBP	BA	DOP	NPOE	TBP	PVC			
1	7	–	–	–	–	–	–	–	93	3.4×10^{-5} to 1.0×10^{-1}	28.2	1.9×10^{-5}
2	7	–	–	55	–	–	–	–	38	3.9×10^{-5} to 1.0×10^{-1}	24.7	2.1×10^{-5}
3	7	–	–	–	55	–	–	–	38	3.1×10^{-5} to 1.0×10^{-1}	33.5	1.1×10^{-5}
4	7	–	–	–	–	55	–	–	38	7.6×10^{-7} to 1.0×10^{-1}	32.0	5.2×10^{-7}
5	7	–	–	–	–	–	55	–	38	9.5×10^{-6} to 1.0×10^{-1}	31.2	4.5×10^{-6}
6	7	–	–	–	–	–	–	55	38	8.7×10^{-6} to 1.0×10^{-1}	26.7	2.1×10^{-6}
7	7	3	–	–	–	55	–	–	35	5.5×10^{-7} to 1.0×10^{-1}	31.0	3.6×10^{-7}
8	7	–	3	–	–	55	–	–	35	4.6×10^{-7} to 1.0×10^{-1}	29.9	2.2×10^{-7}
9	6	–	3	–	–	55	–	–	36	9.9×10^{-7} to 1.0×10^{-1}	34.3	7.6×10^{-7}
10	8	–	3	–	–	55	–	–	34	6.7×10^{-6} to 1.0×10^{-1}	27.9	5.4×10^{-6}
11	7	–	2	–	–	55	–	–	36	2.2×10^{-6} to 1.0×10^{-1}	25.3	1.1×10^{-6}
12	7	–	4	–	–	55	–	–	34	8.8×10^{-5} to 1.0×10^{-1}	28.7	6.3×10^{-5}

Table 3
Optimization of membrane compositions and their potentiometric response for Co^{2+} ion-selective membrane based on ionophore L_2.

S.no.	Composition of membrane (w/w; mg)									Working concentration range (M)	Slope (mV decade^{-1} of activity)	Detection limit (M)
	L_2	NaTBP	KTpClPB	DBP	BA	DOP	NPOE	TBP	PVC			
13	6	–	–	–	–	–	–	–	94	2.6×10^{-5} to 1.0×10^{-1}	27.8	1.2×10^{-5}
14	6	–	–	53	–	–	–	–	41	2.2×10^{-6} to 1.0×10^{-1}	23.6	8.1×10^{-7}
15	6	–	–	–	53	–	–	–	41	9.8×10^{-7} to 1.0×10^{-1}	22.0	4.8×10^{-7}
16	6	–	–	–	–	53	–	–	41	9.1×10^{-6} to 1.0×10^{-1}	31.1	4.1×10^{-6}
17	6	–	–	–	–	–	53	–	41	8.3×10^{-6} to 1.0×10^{-1}	27.3	3.0×10^{-6}
18	6	–	–	–	–	–	–	53	41	8.1×10^{-8} to 1.0×10^{-1}	30.0	7.2×10^{-8}
19	6	2	–	–	–	–	–	53	39	6.0×10^{-8} to 1.0×10^{-1}	29.7	4.7×10^{-8}
20	6	–	2	–	–	–	–	53	39	1.8×10^{-7} to 1.0×10^{-1}	27.1	9.7×10^{-8}
21	7	2	–	–	–	–	–	53	38	4.3×10^{-7} to 1.0×10^{-1}	25.7	2.5×10^{-7}
22	5	2	–	–	–	–	–	53	40	8.7×10^{-7} to 1.0×10^{-1}	28.4	6.2×10^{-7}
23	6	1	–	–	–	–	–	53	40	1.0×10^{-7} to 1.0×10^{-1}	32.2	8.6×10^{-8}
24	6	3	–	–	–	–	–	53	38	9.8×10^{-7} to 1.0×10^{-1}	26.7	5.1×10^{-7}

3. Results and discussion

3.1. Optimization of membrane composition

The selectivity, linearity and sensitivity obtained for a given ionophore depend significantly on the membrane composition, nature of plasticizers and additive used [32–34]. The potentials of membranes of two macrocyclic ligands L_1 and L_2 were investigated as a function of cobalt ion concentration and the results are summarized in Tables 2 and 3, respectively. The optimization of membrane sensor is known to be highly dependent on the incorporation of additional membrane components. In order to guarantee a good membrane performance, an adequate plasticizer must show sufficient lipophilicity, no crystallization and exudation in the membrane phase. It is now well established that the plasticizer plays a vital role in the sensor performance as it is responsible for ionophore salvation and distribution in the membrane matrix, thus controlling the detection limit affecting the selectivity and sensitivity and giving the plastic membrane its proper elasticity and strength. It can be seen from Fig. 3 that the sensor no. 1 having membrane of L_1 without plasticizer exhibits linear response over a working concentration range of 3.4×10^{-5} to 1.0×10^{-1} M with a slope of 28.2 mV decade^{-1} of activity. Similarly, sensor no. 13 (Fig. 4) having the membrane of L_2 without plasticizer exhibits working concentration range of 3.6×10^{-5} to 1.0×10^{-1} M with a slope of 27.8 mV decade^{-1} of activity. The slopes of the membranes are near Nernstian and the working concentration ranges narrow.

Several membranes of varying composition were fabricated to improve the performance characteristics of the electrode by adding different plasticizers such as DBP, BA, DOP, o-NPOE and TBP as shown in Fig. 3 (for L_1) and Fig. 4 (for L_2) and the results are compiled in Tables 2 and 3, respectively. The electrodes based on L_1 and L_2 exhibited good Nernstian behaviour with DOP and TBP, respectively.

It is well known that the incorporation of lipophilic additive can significantly improve the selectivity of an ion sensor by decreasing the membrane resistance and co-ion interference [35]. In our experiments, we examined the effect of NaTPB and KTpClPB as suitable lipophilic additives in conjugation with ionophores L_1 and L_2 on the potentiometric response of Co(II) selective electrode. As is obvious from Tables 2 and 3, the use of 3 mg KTpClPB (for L_1) and 2 mg NaTPB (for L_2) significantly improves the performance characteristics of the membrane sensors.

The variation in potential with different amounts of ionophores was also examined as shown in Table 2 (sensor nos. 8–10) and Table 3 (sensor nos. 19, 21, 22). In this case of carrier type ion-selective electrodes, the extraction equilibrium in the vicinity of the interface between the membrane and aqueous layer affects the potentiometric response of membrane. Inspite of these considerations, a carrier content of 7 mg for L_1 and 6 mg for L_2 was chosen as the optimum ionophore amount, because the surface conditions of the PVC membrane deteriorated on decreasing and

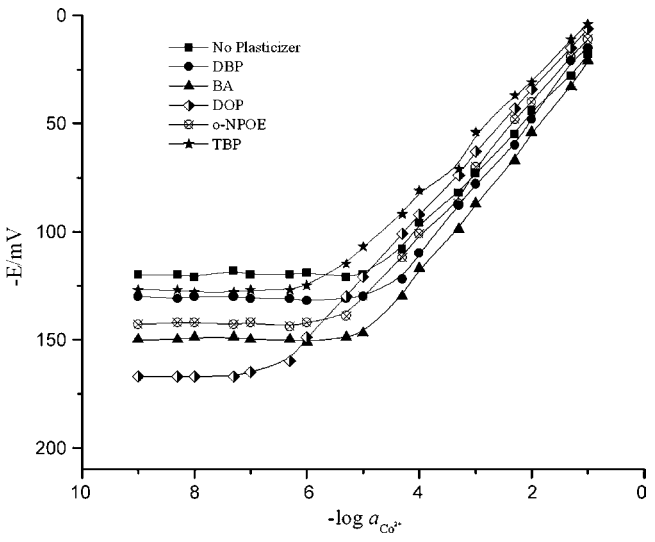


Fig. 3. Plots showing variation of membrane potential with the concentration of Co^{2+} ions based on L_1 with different plasticizers.

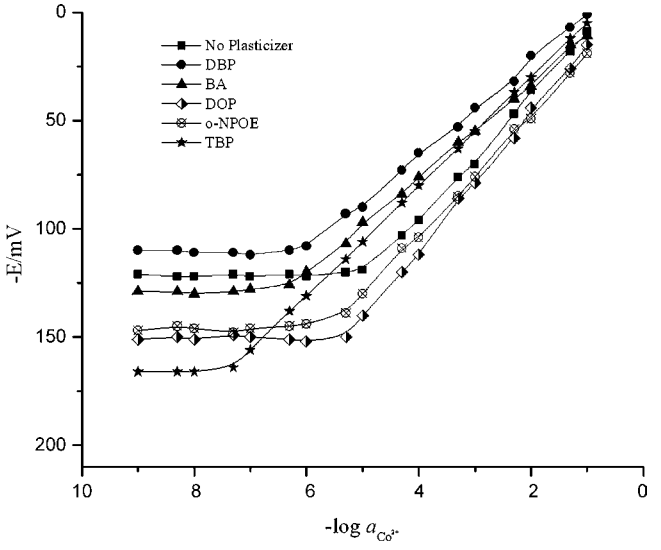


Fig. 4. Plots showing variation of membrane potential with the concentration of Co^{2+} ions based on L_2 with different plasticizers.

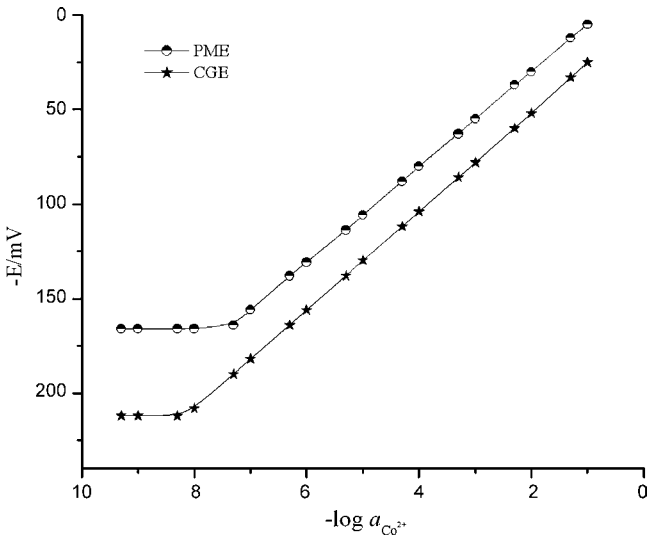


Fig. 5. Calibration characteristics of Co^{2+} selective electrodes (PME and CGE) based on L_2.

increasing the carrier content. Hence the membrane obtained with L_1:PVC:DOP:KTpClPB in the ratio of 7:32:58:3 (w/w; mg) (sensor no. 8) and L_2:PVC:TBP:NaTPB ratio as 6:39:53:2 (w/w: mg) (sensor no. 19) showed Nernstian slope over wide Co^{2+} concentration range.

3.2. Potentiometric response characteristics of the best electrode

The result thus obtained indicate that the best electrode (no. 8) (Table 2) based on L_1 exhibits a Nernstian slope (29.9 ± 0.2 mV decade^{-1} of activity) and a concentration range of 4.6×10^{-7} to 1.0×10^{-1} M with a limit of detection 2.2×10^{-7} M while the best results are shown by the electrode (no. 19) (Table 3) based on L_2 which exhibits a good Nernstian slope (29.7 ± 0.2 mV decade^{-1} of activity) over a wide concentration range of 6.0×10^{-8} to 1.0×10^{-1} M with a limit of detection 4.7×10^{-8} M.

3.3. Effect of internal solution

The proposed electrodes were also examined at different concentration of inner reference solution (1.0×10^{-1} to 1.0×10^{-3} M) and potential response of the electrodes based on L_1 and L_2 membrane have been observed. It was found that the best results in terms of slope and working concentration range has been obtained with internal solution of activity 1.0×10^{-1} M. Thus, 1.0×10^{-1} M concentration of the reference solution was quite appropriate for the smooth functioning of the proposed electrodes.

3.4. Response characteristics of polymeric membrane electrode (PME) and coated graphite electrode (CGE)

The investigations on PVC based membrane of two macrocyclic ligands, *viz.* L_1 and L_2 have shown that they act as Co^{2+} selective sensors. However, of the two ligands, the sensor no. 19 based on (L_2) containing TBP as solvent mediator with the composition L_2:PVC:TBP:NaTPB in the ratio of 6:39:53:2 (w/w; mg) exhibit widest working concentration range (6.0×10^{-8} to 1.0×10^{-1} M), Nernstian compliance (29.7 ± 0.2 mV decade^{-1} of activity), low detection limit (4.7×10^{-8} M) and high selectivity for Co^{2+} ions. The performance of this membrane based on L_2 was compared with polymeric as well as coated graphite electrode. Thus, sensor no. 19, *i.e.* membrane containing TBP as plasticizer was selected to prepare both the PME and CGE for the Co^{2+} ion.

The EMF response of the PME and CGE (Fig. 5) indicates their Nernstian behaviour over a wide concentration range. A comparison of data given in Table 4 revealed the superiority of CGE with respect to concentration range (1.3×10^{-8} to 1.0×10^{-1} M), detection limit (6.8×10^{-9} M) and Nernstian slope (29.5 mV decade^{-1} of activity) over PME. The improved performance characteristics of the CGE over those of PME presumably originate from the coated graphite technology, where an internal 1.0×10^{-1} M $Co(NO_3)_2$ solution, in case of PME, has been replaced by a copper wire of much higher electrical conductivity, in case of CGE. It is well known that the higher limit of detection of PME than that of CGE is mainly due to some leakage of the internal solution into the test solution via. polymeric membrane [36].

3.5. Effect of soaking time and lifetime

The lifetime of the electrodes were determined by soaking both PME and CGE in 0.1 M $Co(NO_3)_2$ solution for interval ranging from 2 to 120 days till the electrode lost its Nernstian behaviour. This behaviour attributed to the decomposition of the ionophore and loss of other components in the membrane phase that was in contact with aqueous test solution containing cobalt ion. The response of both electrodes has been measured by recording the calibration graph at 25 °C at different intervals. The results listed in Table 5 show the effect of soaking time on slope, detection limit and concentration range. It can be seen that the lifetime measured in this way was found to be 3 months for PME and 4 months for CGE during which the slope of electrode, showed only a slight change from 29.7 ± 0.2 to 23.1 ± 0.2 mV decade^{-1} of activity for PME and 29.5 ± 0.1 to 24.5 ± 0.1 mV decade^{-1} of activity for CGE.

3.6. Dynamic response time behaviour of the proposed sensors

Dynamic response time is an important factor for any ion-selective electrodes. To measure the dynamic response time of the proposed electrode the concentration of the test solution was

Table 4
Response characteristics of the cobalt ion-selective electrodes based on PME and CGE.

Properties	Values/range	
	PME	CGE
Optimized membrane composition	(L_2) (6 mg):PVC (39 mg):BA (53 mg):NaTPB (2 mg)	(L_2) (6 mg):PVC (39 mg):BA (53 mg):NaTPB (2 mg)
Conditioning time	4 days in 0.1 M $Co(NO_3)_2$	2 days in 0.1 M $Co(NO_3)_2$
Working concentration range (M)	6.0×10^{-8} to 1.0×10^{-1}	1.3×10^{-8} to 1.0×10^{-1}
Detection limit (M)	4.7×10^{-8}	6.8×10^{-9}
Slope (mV decade^{-1} of activity)	29.7	29.5
S.D. of slope	±0.2	±0.1
Response time (s)	11	8
Life span	3 months	4 months
pH range	2.5–8.5	2.0–9.0

Table 5
Effect of soaking time on the potential response of the cobalt selective electrode.

Soaking time	Slope (mV decade^{-1} of activity)	Working concentration range (M)	Detection limit (M)
PME			
2 days	29.7	6.0×10^{-8} to 1.0×10^{-1}	4.7×10^{-8}
10 days	29.7	6.5×10^{-8} to 1.0×10^{-1}	4.9×10^{-8}
25 days	29.4	7.0×10^{-8} to 1.0×10^{-1}	5.3×10^{-8}
45 days	29.2	7.9×10^{-8} to 1.0×10^{-1}	6.0×10^{-8}
70 days	28.9	8.4×10^{-8} to 1.0×10^{-1}	7.1×10^{-8}
90 days	28.5	9.7×10^{-8} to 1.0×10^{-1}	7.9×10^{-8}
95 days	23.1	4.2×10^{-7} to 1.0×10^{-1}	2.3×10^{-7}
CGE			
2 days	29.5	1.3×10^{-8} to 1.0×10^{-1}	6.8×10^{-9}
10 days	29.4	1.8×10^{-8} to 1.0×10^{-1}	7.0×10^{-9}
25 days	29.2	2.6×10^{-8} to 1.0×10^{-1}	7.3×10^{-9}
45 days	29.0	3.1×10^{-8} to 1.0×10^{-1}	7.9×10^{-9}
70 days	28.9	4.8×10^{-8} to 1.0×10^{-1}	8.4×10^{-9}
90 days	28.6	6.1×10^{-8} to 1.0×10^{-1}	8.8×10^{-9}
105 days	28.4	7.4×10^{-8} to 1.0×10^{-1}	9.0×10^{-9}
120 days	28.2	9.1×10^{-8} to 1.0×10^{-1}	9.8×10^{-9}
125 days	24.5	1.5×10^{-7} to 1.0×10^{-1}	9.4×10^{-8}

successively changed from 1.0×10^{-6} to 1.0×10^{-1} M. The average time required for the electrodes to reach a potential response within ±1 mV of the final equilibrium value after successive immersion in a series of Co^{2+} ion solution, each having a 10-fold difference in concentration was 11 s for PME (Fig. 6) and 8 s for CGE (Fig. 7). Potentials generated by the developed sensors remained stable for more than ~5 min after which a slow divergence was recorded. The much higher electrical conductivity of the copper wire (in CGE) than that of the internal solution (in PME) is expected to result in lower response time of the CGE in comparison with the PME.

3.7. Influence of pH on sensor performance

The pH dependence of both PME and CGE has been tested over the pH range 1.0–10.0 for 1.0×10^{-3} and 1.0×10^{-4} M for the Co^{2+} ion. The pH was adjusted by using 0.1 M solution of either HCl or NaOH and the results are shown in Fig. 8. It can be seen that potential response for PME remains constant over pH range 2.5–8.5 and 2.0–9.0 for CGE. Therefore, the same was taken as the working pH range of the electrodes. The significant change in potential response observed at lower pH can be reasonably related to the response of the sensor to the hydrogen ions. On the other hand, the observed potential drift at higher pH values could be due to the formation of some hydroxyl complexes of Co^{2+} in solution.

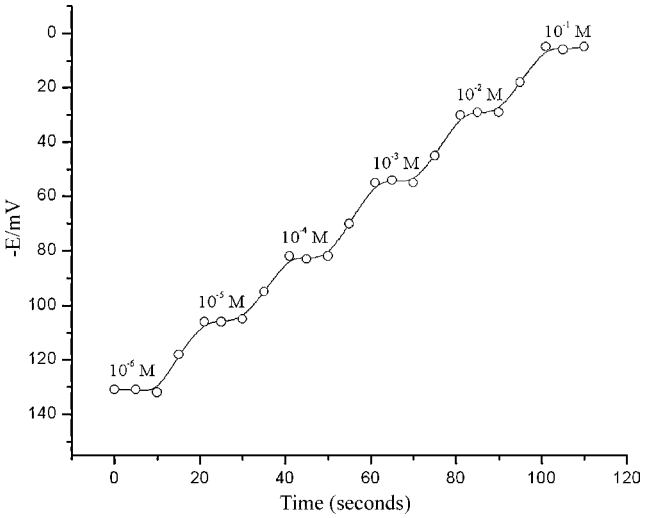


Fig. 6. Dynamic response of polymeric membrane electrode based on L_2.

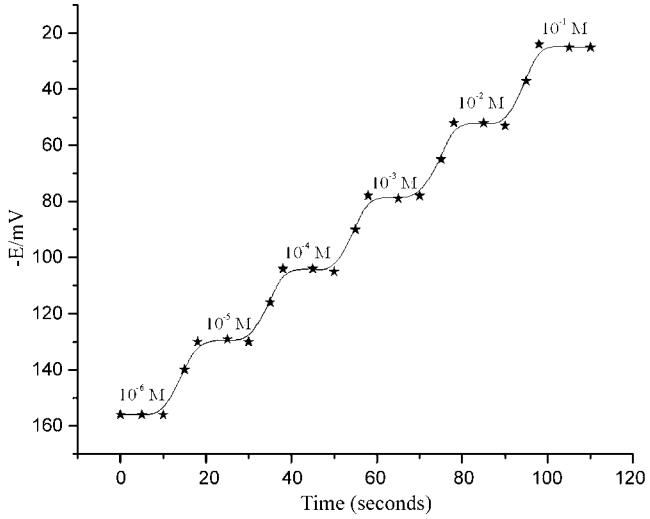


Fig. 7. Dynamic response of coated graphite electrode based on L_2.

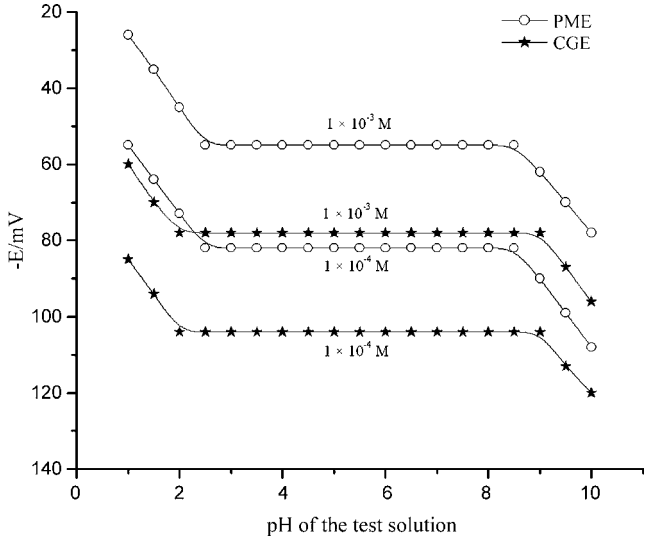


Fig. 8. Effect of pH of the test solutions on the potential responses of the PME and CGE.

3.8. Effect of interfering ions on sensor performance

Selectivity is an important characteristic of an electrode that delineates the extent to which the device may be used in the estimation of analyte ion in the presence of other ions and extent of utility of any electrode in real sample measurement. In this work, the selectivity coefficients of the electrode towards different cationic species were evaluated by using the fixed interference method (FIM) [37] and matched potential method (MPM) [38]. In the matched potential method, the selectivity coefficient was determined by measuring the change in potential upon increasing the primary ion activity from an initial value of a_A to a'_A and a_B represents the activity of interfering ion added to the reference solution of primary ion of activity a_A which also brings about same potential change. It is given by expression:

$$K^{pot}_{A,B} = \frac{\Delta a_A}{a_B} = \frac{a'_A - a_A}{a_B}$$

In the present studies a_A and a'_A were kept at 1.0×10^{-3} and 3.0×10^{-3} M Co^{2+} and a_B was experimentally determined.

However, in the FIM, the selectivity coefficient was evaluated from potential measurement on solutions containing a fixed concentration of interfering ion (1.0×10^{-2} M) and varying amount of Co^{2+} ions. The selectivity coefficient was calculated from the following equation:

$$K^{pot}_{A,B} = \frac{a_A}{(a_B)^{z_A/z_B}}$$

where a_A is the activity of primary ion A (Co^{2+}) at the lower detection limit in the presence of interfering ion B, a_B, the activity of interfering ion B and z_A and z_B are their respective charges.

The values of selectivity coefficient so determined for PME and CGE are compiled in Table 6. It is quite obvious from the corresponding table that Co (II) ion-selective electrodes are highly selective w.r.t. other common cations. The data in Table 6 revealed that, in all cases, the selectivity coefficients obtained for CGE are lower than those for the PME, emphasizing the superiority of CGE in this respect as well and hence further studies were carried out with it only.

Table 6
Selectivity coefficient of various interfering ions for Co^{2+} selective electrodes.

Metal ions	Selectivity coefficient ($K^{MPM}_{A,B}$)			
	PME		CGE	
	FIM	MPM	FIM	MPM
La^{3+}	4.9×10^{-2}	5.6×10^{-2}	3.8×10^{-3}	4.9×10^{-3}
Ce^{3+}	4.1×10^{-2}	5.2×10^{-2}	3.2×10^{-3}	4.5×10^{-3}
Na^{+}	5.3×10^{-2}	5.9×10^{-2}	4.1×10^{-3}	5.2×10^{-3}
K^{+}	5.7×10^{-2}	6.6×10^{-2}	4.5×10^{-3}	5.8×10^{-3}
Ag^{+}	7.1×10^{-2}	7.9×10^{-2}	6.2×10^{-3}	7.0×10^{-3}
NH_4^{+}	7.8×10^{-2}	8.1×10^{-2}	6.7×10^{-3}	7.6×10^{-3}
Cd^{2+}	8.9×10^{-2}	8.8×10^{-2}	8.2×10^{-3}	8.6×10^{-3}
Cr^{3+}	9.3×10^{-2}	9.5×10^{-2}	9.1×10^{-3}	9.4×10^{-3}
Ca^{2+}	1.8×10^{-3}	2.3×10^{-3}	2.5×10^{-4}	3.1×10^{-4}
Sr^{2+}	2.7×10^{-3}	3.5×10^{-3}	4.1×10^{-4}	4.9×10^{-4}
Cu^{2+}	2.6×10^{-2}	3.1×10^{-2}	1.6×10^{-3}	2.7×10^{-3}
Zn^{2+}	3.2×10^{-2}	4.6×10^{-2}	2.3×10^{-3}	3.2×10^{-3}
Ni^{2+}	3.8×10^{-2}	4.9×10^{-2}	2.9×10^{-3}	3.8×10^{-3}
Ba^{2+}	6.6×10^{-2}	7.4×10^{-2}	5.9×10^{-3}	6.6×10^{-3}
Pb^{2+}	6.4×10^{-2}	6.9×10^{-2}	5.6×10^{-3}	6.1×10^{-3}
Al^{3+}	9.7×10^{-2}	9.9×10^{-2}	9.7×10^{-3}	9.8×10^{-3}
Hg^{2+}	8.5×10^{-2}	8.6×10^{-2}	7.3×10^{-3}	8.3×10^{-3}
Fe^{3+}	2.2×10^{-3}	2.9×10^{-3}	3.7×10^{-4}	4.3×10^{-4}
Mg^{2+}	3.0×10^{-3}	4.2×10^{-3}	5.2×10^{-4}	5.7×10^{-4}

Table 7
Effect of partially non-aqueous medium on the working of Co^{2+} selective sensor (CGE).

Non-aqueous content (%; v/v)	Working concentration range (M)	Slope (mV decade^{-1} of activity)
0	1.3×10^{-8} to 1.0×10^{-1}	29.5
Methanol		
10	1.3×10^{-8} to 1.0×10^{-1}	29.5
20	1.3×10^{-8} to 1.0×10^{-1}	29.5
30	1.4×10^{-8} to 1.0×10^{-1}	29.4
35	1.6×10^{-8} to 1.0×10^{-1}	29.2
40	3.3×10^{-7} to 1.0×10^{-1}	26.5
Ethanol		
10	1.3×10^{-8} to 1.0×10^{-1}	29.5
20	1.3×10^{-8} to 1.0×10^{-1}	29.5
30	1.5×10^{-8} to 1.0×10^{-1}	29.3
35	1.8×10^{-8} to 1.0×10^{-1}	29.1
40	5.2×10^{-7} to 1.0×10^{-1}	25.2
Acetonitrile		
10	1.3×10^{-8} to 1.0×10^{-1}	29.5
20	1.6×10^{-8} to 1.0×10^{-1}	29.4
25	1.9×10^{-8} to 1.0×10^{-1}	29.1
30	1.0×10^{-7} to 1.0×10^{-1}	24.7

3.9. Effect of non-aqueous content

The real samples may also contain non-aqueous component, and the performance of the sensor was also investigated in partially non-aqueous media using 10%, 20%, 30%, 35% and 40% (v/v) methanol–water, ethanol–water and acetonitrile–water mixtures (Table 7). It was found that the membranes did not show any appreciable change in working concentration range and slope in methanol–water and ethanol–water mixtures up to 35% (v/v) non-aqueous contents, whereas in acetonitrile–water mixture, membrane could tolerate up to 25% (v/v) non-aqueous content. However, above these mentioned non-aqueous contents, the slope and working concentration range decreased appreciably, consequently reliable measurements could not be obtained. The drift in potentials in the organic phase may probably be due to swelling in membrane and made it mechanically weak and leaching of ionophore from membrane to non-aqueous solution took place.

3.10. Effect of ionic and nonionic surfactants

It is commonly known that both ionic and nonionic surfactants interact with the polymer membrane being divided between the aqueous phase and the membrane phase and result in increased background potential and lower binding ability for the ionophore [39]. Such effects should result in deteriorated detection limits, reduced response slopes and lower selectivity for the primary ions.

In the present paper, we examined the effect of cationic (tetrabutylammonium chloride, TBC), anionic (sodium dodecyl sulfate, SDS) and nonionic (Triton X-100) surfactants on the potentiometric properties of proposed CGE based on the macrocyclic pendant ligand L_2 and the results obtained are compiled in Table 8. It was observed that the content of surfactants up to 1.0×10^{-4} M does not cause any significant change in the response characteristics of the proposed electrode. However, concentration of the surfactants above 1.0×10^{-4} M adversely affected the performance of the electrode as the selectivity, slope and working concentration range were observed to decrease.

4. Analytical application

The analytical applicability of the electrode was evaluated by carrying out potentiometric titration of 20 mL of 5.0×10^{-3} M Co(II) ions against 1.0×10^{-2} M EDTA at pH 6 using CGE as an indicator

Table 8
Effect of different surfactants on the performance of Co(II) selective electrode.

Interfering ions	−log (selectivity coefficients)			
	Without surfactant	With >10^{-4} M CTAB	With >10^{-4} M SDS	With >10^{-4} M Triton X-100
La^{3+}	2.42	2.01	2.47	2.32
Ce^{3+}	2.49	2.51	2.37	2.11
Na^{+}	2.38	1.92	2.03	2.21
K^{+}	2.34	2.30	2.22	1.98
Ag^{+}	2.20	2.15	2.05	2.13
NH_4^{+}	2.17	1.83	2.11	2.23
Cd^{2+}	2.05	2.10	2.18	2.00
Cr^{3+}	2.04	2.01	1.31	1.57
Ca^{2+}	3.60	3.57	3.17	3.22
Sr^{2+}	3.38	3.13	2.95	3.07
Cu^{2+}	2.79	2.98	2.15	2.38
Zn^{2+}	2.63	2.42	2.52	2.20
Ni^{2+}	2.53	2.61	2.49	2.01
Ba^{2+}	2.22	2.38	2.00	1.51
Pb^{2+}	2.25	2.11	1.67	1.01
Al^{3+}	2.01	1.83	1.94	2.11
Hg^{2+}	2.13	2.01	1.95	1.61
Fe^{3+}	3.43	3.71	3.05	2.77
Mg^{2+}	3.28	3.30	3.18	2.96
Slope (mV decade^{-1} of activity)	29.5	33.2	26.7	21.1
Detection limit (M)	6.8×10^{-9}	3.7×10^{-7}	5.3×10^{-6}	7.1×10^{-5}
Working concentration range (M)	1.3×10^{-8} to 1.0×10^{-1}	6.2×10^{-7} to 1.0×10^{-1}	9.9×10^{-6} to 1.0×10^{-1}	8.7×10^{-5} to 1.0×10^{-1}

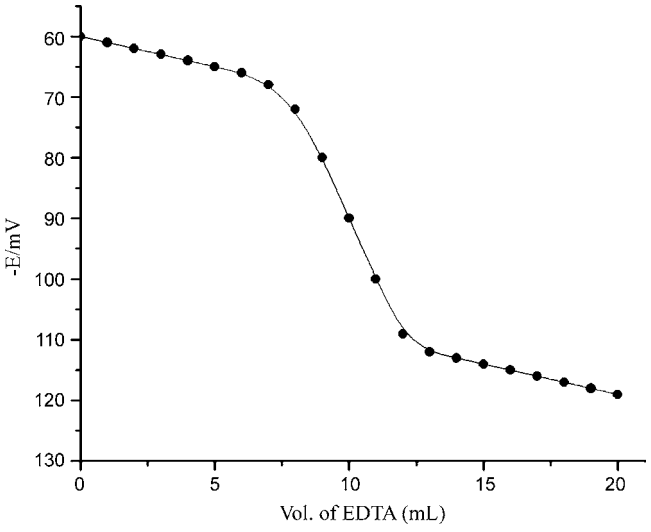


Fig. 9. Potentiometric titration curve of 20 mL of 5.0×10^{-3} M solution of Co^{2+} ion with 1.0×10^{-2} M EDTA at pH 6.0 using CGE as indicator electrode.

electrode. The titration plot shown in Fig. 9 is of sigmoid shape that is also an indication of selectivity of electrode. The inflexion point of the plot corresponds to 1:1 stoichiometry of Co-EDTA complex.

The proposed coated graphite electrode (CGE) was successfully applied for the direct determination of cobalt in different water samples. The results are given in Table 9. It was found that the cobalt contents obtained from triplicate measurements were in satisfactory agreement with those obtained by using AAS method.

Table 9
Potentiometric determination of Co^{2+} ions in different water samples by CGE.

Samples	ISE[a] (mg/mL)	AAS[a] (mg/mL)
Fresh water	0.58 ± 0.01	0.61 ± 0.03
River water	6.47 ± 0.02	6.46 ± 0.02
Sea water	13.26 ± 0.01	13.22 ± 0.02

[a] Results of triplicate measurements.

The cobalt selectivity exhibited by the membrane electrode makes it potentially useful for monitoring the concentration of Co^{2+} in real samples. In this regard, experiments were performed to measure Co^{2+} in beer samples. Cobalt is present in trace amounts in virtually all-living tissues and thus the raw materials used for brewing barley, corn, rice and hops, are no exception. As a consequence, commercial beer normally contains a minute concentration of cobalt, usually a few hundredths of a part per million. So there is need to develop a method to check whether a beer sample contains added cobalt or not. An amount of 1 mL of 18N H_2SO_4 was added to 50 mL of degassed beer, evaporated to dryness and 10 mL of distilled water was added. The pH was adjusted to 6.0 using either 0.1N HCl or 0.1N NaOH. The solution was filtered and finally diluted to 50 mL with water. A beer containing known amount of cobalt was chosen. Aliquots of the working solution were added to 50 mL samples of this beer, to give known concentration of added cobalt ranging from about 0.6–1.5 ppm. The concentration of added cobalt was then determined for each sample by CGE that is presented in Table 10.

The accuracy and applicability of the proposed CGE was also evaluated by its application for the determination of cobalt in various pharmaceutical samples. A sample each of injectable Neurobion (Merck, India) and Sioneuron (Albert David Ltd., India) was digested with nitric acid in a covered beaker. The residue of the sample was leached with dil. H_2SO_4 and diluted to the mark in a calibrated flask. Working solutions were prepared by taking an appropriate amount of the sample and its cobalt content was determined by the proposed electrode. The results obtained are compiled in Table 11 and were found to be in good agreement with those obtained by AAS, thereby reflecting the utility of this sensor for determination of cobalt in real samples.

Table 10
Potentiometric determination of Co^{2+} ion in beer by CGE.

Added to beer (ppm)	Found by analysis (ppm)	Recovery (%)
0.60	0.59 ± 0.02	98
0.85	0.84 ± 0.01	99
1.00	1.00 ± 0.02	100
1.20	1.18 ± 0.03	98
1.50	1.50 ± 0.02	100

Table 11
Quantitative determination of cobalt in pharmaceutical samples by CGE.

S.no.	Samples	Certified value (ppm)	Cobalt found (ppm)	
			Proposed method	AAS method
1	Neurobion (Inj.) Merck, India	21.74	21.73 ± 0.01	21.71 ± 0.02
2	Sioneuron (Inj.) Albert David Ltd., India	10.86	10.84 ± 0.02	10.82 ± 0.02

Table 12
Comparison of the proposed Co^{2+} selective electrode with the reported electrode.

Ref. no.	Carrier name	Linear range (M)	Detection limit (M)	Slope (mV decade^{-1} of activity)	pH range	Response time (s)
[13]	5,7,7,12,14,14-Hexamethyl-1,4,8,11-tetraazacycloterradeca-4,11-dienediperchlorate	8.0×10^{-6} to 1.0×10^{-1}	8.0×10^{-6}	29.0	2.8–7.3	20
[14]	Dibenzopyridino-substituted macrocyclic diamide	7.0×10^{-7} to 1.0×10^{-2}	2.0×10^{-7}	29.1 ± 0.1	3.0–8.5	10
[15]	Benzosubstituted macrocyclic diamide	2.0×10^{-6} to 1.0×10^{-2}	6.0×10^{-7}	29.45 ± 0.5	3.0–8.0	10
[17]	2,3,4-Pyridine-1,3,5,8,11,14-hexaazacyclohexadeca-2-ene	6.3×10^{-6} to 1.0×10^{-1}	8.5×10^{-7}	30.0	2.5–6.5	15
[21]	(2-Mercapto-4-methylphenyl)-2-benzamido-3-phenyl-thiopropenolate	4.0×10^{-7} to 1.0×10^{-2}	1.0×10^{-7}	30.0 ± 1.0	5.0–8.0	> 5
[22]	OXCCD	1.0×10^{-6} to 1.0×10^{-1}	9.0×10^{-7}	29.8	3.5–8.0	> 25
[23]	5-((4-Nitrophenyl)azo)-N-(2′,4′-dimethoxyphenyl)salicylaldimine	9.0×10^{-7} to 1.0×10^{-2}	8.0×10^{-7}	29.0 ± 1.0	3.5–6.0	5-10
[24]	N,N′-bis(salicylidene)-3,4-diaminotoluene	7.9×10^{-8} to 1.0×10^{-1}	5.0×10^{-8}	30 ± 0.2	2.0–9.0	12
[25]	5-Amino-3-methylisothiazole	6.3×10^{-7} to 1.0×10^{-1}	3.9×10^{-7}	29.5 ± 0.2	3.3–9.0	15
[26]	4-Tert-butylthiacalix[4]arene	5.3×10^{-6} to 1.0×10^{-1}	0.3 ppm	30 ± 0.1	2.5–6.0	10
[27]	p-(4-n-Butylphenylaza)calix[4]arene	9.2×10^{-6} to 1.0×10^{-1}	4.0×10^{-6}	29.0 ± 1.0	4.0–7.2	25
This work	2,3,4:9,10,11-Dipyridine-1,5,8,12-tetramethylacrylate-1,3,5,8,10,12-hexaazacyclotetradeca-2,10-diene (L_2)	1.3×10^{-8} to 1.0×10^{-1}	6.8×10^{-9}	29.5	2.0–9.0	8

5. Conclusion

The investigations on PVC based membrane of two macrocyclic ligands *viz.* (L_1) and (L_2) shows that they are Co^{2+} selective sensors. However, of the two ligands, the sensor no. 19 based on L_2 with membrane composition L_2:PVC:TBP:NaTPB in the ratio of 6:39:53:2 (w/w; mg) exhibited widest working concentration range (6.0×10^{-8} to 1.0×10^{-1} M), Nernstian compliance (29.7 mV decade^{-1} of activity) and high selectivity for cobalt ions. The performance of the membrane based on L_2 was compared with PME as well as with CGE. Comparison of data (Table 4) revealed that CGE was superior to PME with regard to detection limit (6.8×10^{-9} M), response time (8 s) and selectivity. The proposed sensor is superior to the reported sensors (Table 12). Thus, the CGE was used as indicator electrode in the potentiometric titration of Co^{2+} ions with EDTA and in determination of cobalt ions in real and pharmaceutical samples.

Acknowledgement

Ms. Prerna Singh is highly thankful to Defence Research and Development Organisation (DRDO) for providing financial assistance to undertake this work.

References

[1] O.R. Kirk, F.D. Othmer, Encyclopedia of Chemical Technology, vol. 5, Wiley, 1982, p. 851.
[2] I. Pais, J. Benton Jr., The Handbook of Trace elements, St. Lucie Press, Florida, 1996, p. 240.
[3] S. Cadore, R.D. Goi, N. Baccan, J. Braz. Chem. Soc. 165 (2005) 957.
[4] L. Zhang, J. Zhou, Y. Hao, P. He, Y. Fang, Electrochim. Acta 50 (2005) 3414.
[5] J.F. Vanstaden, R.E. Talijaard, Talanta 64 (2004) 1203.
[6] M.A. Belarra, C. Crespo, M.P. Martinez-Garbayo, M. Resano, Spectrochim. Acta B 10 (2003) 1847.
[7] N. Todorovska, I. Karadjova, S. Arpadjan, Acta Pharm. 53 (2003) 83.
[8] X. Lu, Z. Geng, J. Kang, J. Gao, Talanta 52 (2000) 411.
[9] H.K. Wipfe, L.A.R. Pioda, Z. Stefanac, W. Simon, Helv. Chim. Acta 51 (1968) 377.
[10] R.S. Hutchins, L.G. Bachas, Anal. Chem. 67 (1995) 1654.
[11] A.A. Ombetko, E.M. Rakhman'ko, V.L. Lomako, Zh. Anal. Khim. 45 (1990) 1592.
[12] Y. Su, G. Wang, Z. Jiang, D. Wang, Fenxi Huaxue 18 (1990) 15.
[13] A.K. Jain, V.K. Gupta, L.P. Singh, U. Khurana, Analyst 122 (1997) 583.
[14] M. Shamsipur, S. Rouhani, T. Poursaberi, M.R. Ganjali, H. Sharghi, M.R. Ganjali, H. Sharghi, K. Niknam, Electroanalysis 14 (2002) 729.
[15] M. Shamsipur, T. Poursaberi, S. Rouhani, K. Niknam, H. Sharghi, M.R. Ganjali, Anal. Sci. 17 (2009) 1049.
[16] A.K. Singh, P. Saxena, S. Mehtab, A. Panwar, Anal. Sci. 531 (2004) 20.
[17] A.K. Singh, R.P. Singh, P. Saxena, Sens. Actuators B 114 (2006) 578.
[18] S.P. Awasthi, T.C. Thembi, V.T. Kulkarni, M. Sundareson, J. Electrochem. Soc. Ind. 49 (1991) 23.
[19] A.M. Volovik, V.N. Tomlachev, L.V. Microshnik, Zh. Anal. Khim. 40 (1985) 481.
[20] U.S. Lal, M.C. Chattopadhyaya, A.K. Dey, Electrochim. Acta 26 (1981) 283.
[21] M.H. Mashhadizadeh, A. Momeni, R. Razavi, Anal. Chim. Acta 462 (2002) 245.
[22] M.R. Ganjali, F. Mizani, M. Emami, M. Darjezini, M.R. Darvich, M. Yousefi, Anal. Sci. 20 (2004) 531.
[23] M.H. Mashhadizadeh, I. Sheikhshoaie, Anal. Bioanal. Chem. 375 (2003) 708.
[24] V.K. Gupta, A.K. Singh, S. Mehtab, B. Gupta, Anal. Chim. Acta 566 (2006) 5.
[25] A.K. Singh, S. Mehtab, P. Saxena, Sens. Actuators B 120 (2007) 455.
[26] V.K. Gupta, A.K. Jain, M. Al Khayat, S.K. Bhargava, J.R. Raisoni, Electrochim. Acta 53 (2008) 5409.
[27] P. Kumar, Y.B. Shim, Talanta 77 (2009) 1057.
[28] H.R. Pouretedal, M.H. Keshavarz, Chem. Res. Chin. Univ. 21 (2005) 28.
[29] V.K. Gupta, S. Chandra, S. Agarwal, H. Lang, Proc. Ind. Nat. Sci. Acad. 70 (2004) 399.
[30] T. Katsu, K. Ido, K. Takaishi, H. Yokosu, Sens. Actuators B 87 (2002) 331.
[31] M.M. Shultz, O.K. Stefanova, S.B. Mokrov, K.N. Mikhelson, Anal. Chem. 74 (2002) 510.
[32] D. Siswanta, K. Nagatska, H. Yamada, K. Kumakura, H. Hisamoto, Y. Shichi, K. Toshima, K. Suzuki, Anal. Chem. 68 (1996) 4166.
[33] N. Tavakkoli, M. Shamsipur, Anal. Lett. 29 (1996) 2269.
[34] M. Javanbakht, M.R. Ganjali, H. Sharghi, M. Shamsipur, Electroanalysis 11 (1999) 81.
[35] W.E. Morf, G. Kohr, W. Simon, Anal. Lett. 7 (1974) 9.
[36] J.B. Harrell, A.D. Jones, G.R. Choppin, Anal. Chem. 41 (1969) 1459.
[37] F.J. Sa'ez de Viteri, D. Diamond, Analyst 119 (1994) 749.
[38] Y.P.Y. Gadzekpo, G.D. Christian, Anal. Chim. Acta 164 (1984) 279.
[39] H.J. Oh, G.S. Cha, H. Nam, Bull. Korean Chem. Soc. 24 (1) (2003) 37.

Talanta 80 (2009) 694–702

Contents lists available at ScienceDirect

Talanta

journal homepage: www.elsevier.com/locate/talanta

Quercetin molecularly imprinted polymers: Preparation, recognition characteristics and properties as sorbent for solid-phase extraction

Xingliang Song[a,c], Jinhua Li[b], Jiangtao Wang[a,*], Lingxin Chen[b,**]

[a] Key Laboratory of Marine Chemistry Theory and Technology, Ministry of Education, Ocean University of China, Qingdao 266100, China
[b] Yantai Institute of Coastal Zone Research for Sustainable Development, Chinese Academy of Sciences, Chunhui Road 17, Laishan District, Yantai 264003, China
[c] Department of Chemistry, Linyi Normal University, Linyi 276005, China

ARTICLE INFO

Article history:
Received 9 May 2009
Received in revised form 18 July 2009
Accepted 25 July 2009
Available online 3 August 2009

Keywords:
Molecularly imprinted polymers
Quercetin
Molecular recognition
Solid-phase extraction
HPLC
Cacumen platycladi

ABSTRACT

Molecular imprinted polymers (MIPs) were prepared through thermal polymerization by using quercetin as the template molecule, acrylamide (AA) as the functional monomer and ethylene glycol dimethacrylate (EDMA) as the cross-linker in the porogen of tetrahydrofuran (THF). The synthesized MIPs were identified by both Fourier transform infrared (FTIR) and scanning electron microscope (SEM). Systematic investigations of the influences of key synthetic conditions, including functional monomers, porogens and cross-linkers, on the recognition properties of the MIPs were conducted. Scatchard analysis revealed that the homogeneous binding sites were formed in the polymers. Besides quercetin, two structurally similar compounds of rutin and catechol were employed for molecular recognition specificity tests of MIPs. It was observed that the MIPs exhibited the highest selective rebinding to quercetin. Accordingly, the MIPs were used as a solid-phase extraction (SPE) sorbent for the extraction and enrichment of quercetin in cacumen platycladi samples, followed by HPLC-UV analysis. The application of MIPs with high affinity and excellent stereo-selectivity toward quercetin in SPE might offer a novel method for the enrichment and determination of flavonoid compounds in the natural products.

© 2009 Elsevier B.V. All rights reserved.

1. Introduction

Molecular imprinting technique (MIT) is an attractive synthetic approach to mimic natural molecular recognition [1–4], which exhibits a high affinity and selectivity toward a particular target compound (template molecule). The MIT utilizes template molecules to assemble their own recognition sites by interacting with complementary functional groups of appropriate monomers. The technique is schematically depicted in Fig. 1. In the process, the selected template molecules (quercetin) are first allowed to establish binding interactions with functional monomers (acrylamide, AA), in which the polymerizable functional monomers are pre-arranged around a template molecule in porogenic solvent. The resulting complexes are then copolymerized with an excess of cross-linkers (ethylene glycol dimethacrylate, EDMA) in the presence of a free radical initiator (2,2′-Azobisisobutyronitrile, AIBN) by thermal polymerization. Subsequent removal of the template molecules creates specific binding sites with the precise spatial arrangement of the functional groups in the polymer network together with the shape [5]. Thus, reversible re-binding and high selective recognition of the target molecules are realized. Since it was invented by Wuff and Sarhan [6], MIT has been exploited extensively in many fields including chiral resolution [7], biosensor [8], biochemical separation [9–11], antibody simulation [12], enzyme catalysis simulation [13], etc. So, molecularly imprinted polymers (MIPs) display excellent application prospects. In particular, MIPs used as adsorbents of solid-phase extraction (SPE) are being widely involved in the concentration and determination of drug molecules, and the extraction of active components from natural products [2,14–16].

Quercetin (3,3′,4,5,7-penta-hydroxy flavone) is the most active compound in flavone family, widely occurring in leaves, fruits, and flowers of many plants [17]. Quercetin has now become the topic of increasing interest based on its various bioactivities such as inoxidability, antiviral property, antitumor and adjusting the immune function [18], as well as its chemical applications, e.g., quercetin is immobilized on silica gel and used as a solid-phase reagent for tin (IV) determination [19]. The determination of quercetin is typically performed with HPLC-UV [15,20,21], besides electrogenerated chemiluminescence (ECL) [22] and capillary electrophoresis (CE) [23]. Because of the existence of quercetins in nature at low concentrations, the complexity of the sample matrices and the structural similarity to other flavonols, selective sample preparation methods are necessary

* Corresponding author. Tel.: +86 532 66782506; fax: +86 532 66782506.
** Corresponding author. Tel.: +86 535 2109130; fax: +86 535 2109000.
E-mail addresses: jtwang@ouc.edu.cn (J. Wang), lxchen@yic.ac.cn (L. Chen).

0039-9140/$ – see front matter © 2009 Elsevier B.V. All rights reserved.
doi:10.1016/j.talanta.2009.07.051

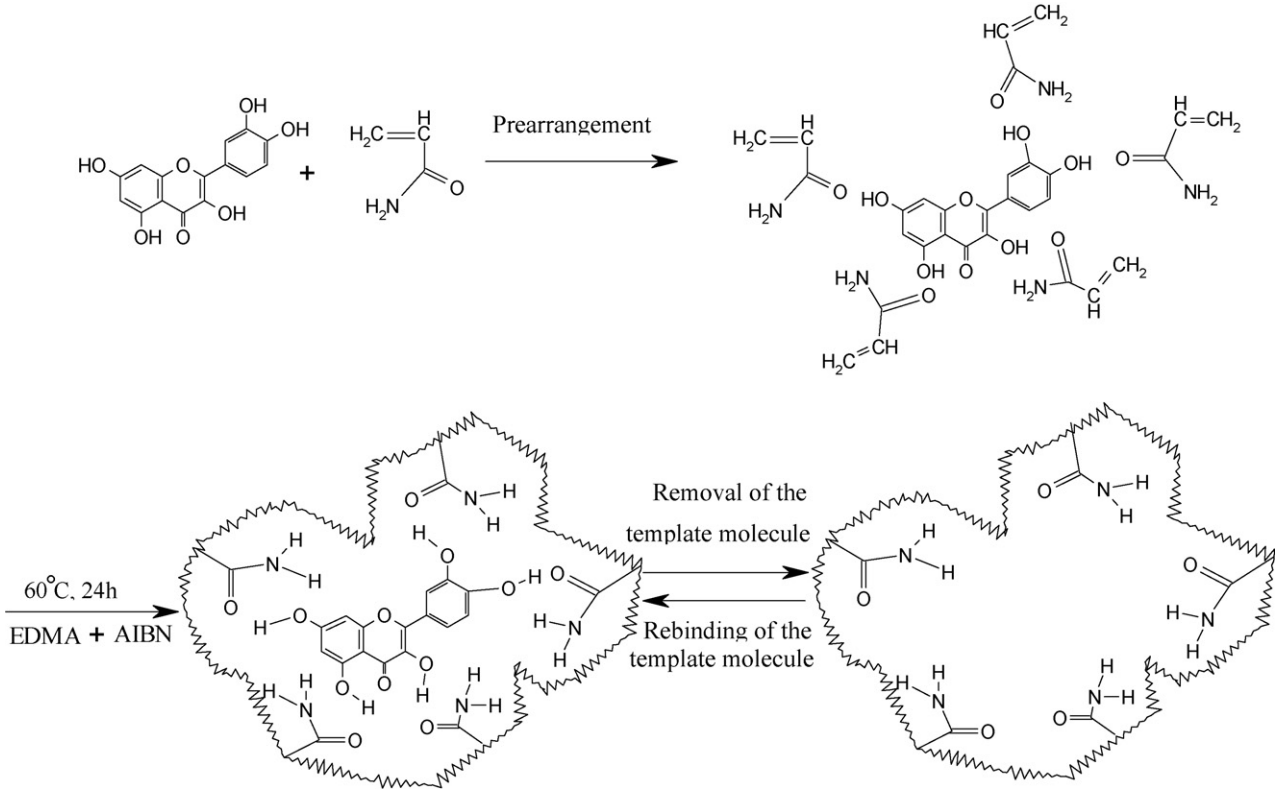


Fig. 1. Schematic representation of MIPs for quercetin.

prior to chromatographic analysis. Preconcentration and/or separation of the compounds are frequently conducted by using SPE [20,21], in which new selective materials employing molecular recognition mechanisms might guarantee selective analyte separation from complex real world matrices. This mechanism can improve significantly the method specificity and sensitivity. Related works on quercetin determination and separation by using MIT have been reported [5,24,25]. Weiss et al. reported that MIPs for quercetin was prepared by using quecertin as template molecule, 4-vinylpyridine as functional monomer and EDMA as cross-linker [5]. The prepared MIP showed excellent performance on quercetin separation. Yan et al. also prepared effective MIPs for quercetin by using AA as a functional monomer [24]. He and Deng reported the effectiveness of MIPs prepared by using different functional monomers including methacrylic acid (MAA), AA and 2-vinylpridine, and found the properties of MIPs for quercetin were varying in different functional monomers [25].

In this work, the feasibility of preparing quercetin imprinted polymers and the utilization of the selective membranes as sorbent for SPE were demonstrated. The influences of porogenic solvents, functional monomers and cross-linkers on the adsorption specificity for quercetin of the MIPs were investigated and the stabilization energy calculated by computational quantum chemical analysis (CQCA) was adopted to support the analysis. The synthesized MIPs were characterized by Fourier transform infrared (FTIR) and scanning electron microscope (SEM). HPLC-UV and Scatchard method were used to evaluate the adsorption properties and recognition mechanism of the MIPs. Structurally similar compounds including rutin and catechol were utilized for verifying the molecular selectivity and characterizing the recognition capability of the MIPs. The MIP–SPE was testified to be applicable for the preconcentration and determination of cacumen platycladi samples.

2. Experimental

2.1. Chemicals

Quercetin, rutin and catechol were purchased from Shanghai Sinopharm Chemical Reagent Co., Ltd. Fig. 2 shows their chem-

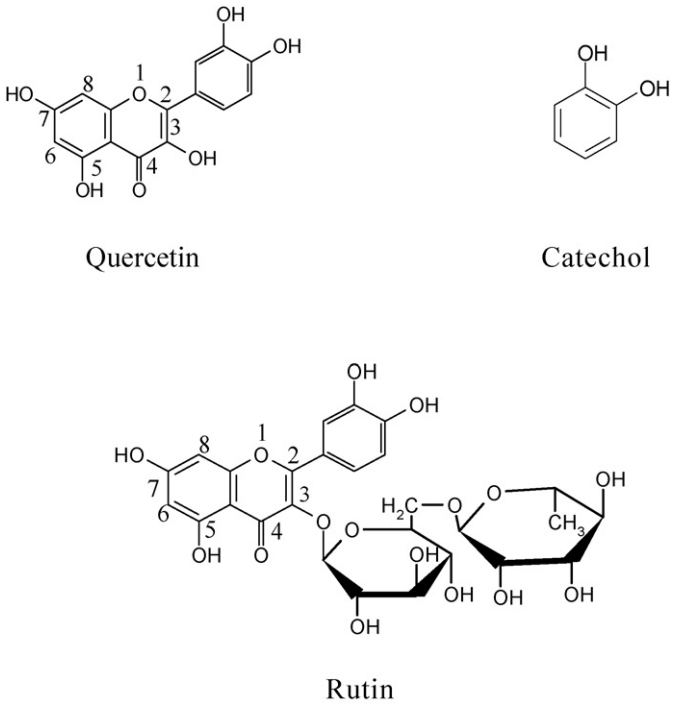


Fig. 2. Chemical structures of quercetin, catechol and rutin.

ical structures. AA was supplied from Tianjin Chemical Research Institute. EDMA, divinylbenzene (DVB), pentaerythritol triacrylate (PTA) and N,N′-methylenebisacrylamide (BisAA) were purchased from Sigma–Aldrich (Taufkirchen, Germany). AIBN was obtained from Shanghai Chemical Reagent Company. HPLC-grade tetrahydrofura (THF), acetone, acetonitrile (ACN), 1,4-dioxane, methanol (MeOH) and anhydrous acetic acid were all from Merck (Darmstadt, Germany).

2.2. Preparation of the MIPs and NIPs

The MIPs were prepared with a slight modification according to the published procedures [24]. Briefly, 0.13 g (0.40 mmol) of template molecules (quercetins) and 0.20 g (2.8 mmol) of functional monomers (AA) were dissolved in 5 mL different porogenic solvents including 1,4-dioxane, THF, acetone and ACN in four corked test tubes, respectively. After oscillating for 30 min, 3.5 mL (18.5 mmol) of cross-linkers (EDMA) and 0.01 g initiators (AIBN) were added. The solutions were degassed in a sonicating bath for 15 min and filled with nitrogen for 15 min and sealed. The test tubes were immersed into isothermal water bath and the mixtures were thermally polymerized at 60 °C for 24 h. The resultant polymers were then grinded and sieved through a 105 μm sieve. The polymer particles were extracted with a mixture of MeOH/acetic acid (9:1, v/v) in Soxhlex extractor for 24 h to remove the template molecules (quercetins) and then were rinsed with MeOH. After removing acetic acid, the MIPs were dried at 60 °C under vacuum for 24 h and stored in a desiccator for further use. As references, the non-imprinted polymers (NIPs) in the absence of template molecules were prepared and treated by using the above same method. The compositions of MIPs (M1–M4) and NIPs (N1–N4) are shown in Table 1.

2.3. FTIR measurements

FTIR spectroscopic measurements were performed on model Avatar 370 FTIR Spectrometer (Thermo Nicolet Corporation, USA) with KBr pellet method. The wave numbers of FTIR measurement range were controlled from 500 to 4000 cm^{-1}, and collected at one data point per 2 cm^{-1} with sample scanning for 32 times.

2.4. Adsorption determination of MIPs and NIPs for quercetins

The adsorption experiments were carried out to confirm the rebinding performance and the subsequent Scatchard analysis of the polymers as follows.

The MIPs and NIPs (Table 1) of 100 mg were added into eight 50 mL conical flasks, respectively, and were mixed with 25 mL of solution containing a known concentration of 20 μg mL^{-1} quercetins in MeOH. Then, these mixtures were shaken at 20 °C by using SHA-B Water Bath Isothermal Shaker (Jiangsu Jintan Medical Instrument Factory) and centrifuged using a high-speed centrifuge. 20 μL of the supernatant was taken out for HPLC analysis to measure the free concentration of quercetin and determine the adsorption quantity of quercetin in different time intervals.

In the other hand, the M2 and N2 (Table 1) of 100 mg, respectively, were added into 50 mL conical flasks, and were mixed with 25 mL of a known initial concentration of quercetin (0.01–0.1 μmol mL^{-1}) in MeOH solution. The mixtures were oscillated by using a SHA-B Water Bath Isothermal Shaker at 20 °C for 24 h, and then were centrifugated for 10 min. The concentration of quercetin in the solution was analyzed using HPLC-UV. And thus, the saturated extents of adsorption of MIPs and NIPs for quercetins were obtained. The selectivity of MIPs was investigated by using quercetin adsorption on the MIPs and NIPs.

Table 1
Compositions of MIPs and NIPs.

Polymers	Quercetin (g)	AA (g)	EDMA (mL)	AIBN (g)	Porogenic solvents
M1	0.13	0.2	3.5	0.01	1,4-Dioxane
M2	0.13	0.2	3.5	0.01	THF
M3	0.13	0.2	3.5	0.01	Acetone
M4	0.13	0.2	3.5	0.01	ACN
N1	–	0.2	3.5	0.01	1,4-Dioxane
N2	–	0.2	3.5	0.01	THF
N3	–	0.2	3.5	0.01	Acetone
N4	–	0.2	3.5	0.01	ACN

2.5. Computational quantum chemical analysis (CQCA)

Molecular simulation as a promising technology of computational chemistry is also a useful tool in the studies of molecular imprinting technology, so the stabilization energy by solvent was often used to evaluate the interaction strength of molecular template with solvent, monomer or cross-linker with solvent. In this study according to calculation method of Gaussian 98, B3LYP/6-31+G**, the stabilization energy of quercetin and AA with different solvents was obtained through calculating the interaction energy between gas and solvent. The simulation of solvent effect is based on the Onsager self-consistent reaction field (SCRF) technique [26], which supposes that the solute molecule is embedded into a spherical cavity with radius a_0 surrounded, and the solvent is characterized by a given dielectric constant. The gas-phase geometry of quercetin and functional monomer or cross-linker is used as its initial guess to start the full optimizations at the same level of B3LYP/6-31+G** with different dielectric constants of porogenic solvents. The radius a_0 automatically resorted from quantum mechanical procedures. After stationary points were located, vibrational frequencies were calculated in order to ascertain that each structure was characterized to be the stable structure (no imaginary frequencies). All calculations were carried out with the Gaussian 98 program on a Pentium IV computer using the default convergence criteria. The stabilization energy of solvents is calculated as $E_{solvation} = E_{in\ solvent} - E_{in\ gas}$. The $E_{solvation}$ is the energy stabilized by a solvent, namely the relative energy difference of a complex in the solvent and that in a gas phase.

2.6. MIP–SPE procedures

A PTFE frit (10 μm in porosity size) was placed on the bottom of an empty polypropylene SPE cartridge (5 mL in total volume and 8 mm in diameter) purchased from Agilent Technologies (USA), which was employed as the MIP–SPE column, packed with 500 mg of quercetin-MIPs in 5 mL MeOH solution using a wet packing method. Then another frit was placed on the top of the cartridge. Prior to loading the sample, the cartridge was washed with a mixture of MeOH/acetic acid (9:1, v/v) until quercetin could not be detected by the HPLC analysis in the filtrate. Then the cartridge was conditioned with 10 mL of MeOH.

Considering the solubility of quercetin and its structurally similar compounds (rutin or catechol), a mixture containing quercetin and its analogues in MeOH was prepared. Then, 2–4 mL of the different concentration mixtures were loaded onto the SPE cartridge at 1 mL min^{-1}. Subsequently, the cartridge was consecutively rinsed with 3 mL of MeOH and 3 mL of the mixed solution of MeOH/acetic acid (v/v, 9:1). The collected column-solution, rinsed solution and eluates were evaporated to dryness under nitrogen and the residues were redissolved in 1 mL of MeOH, respectively, for HPLC-UV analysis.

In this work, the enrichment factor (EF) was introduced and it was defined as the ratio of the analyte concentration in the con-

centrated phase (C_{con}, μmol mL^{-1}) and the initial concentration of analyte within the sample (C_0, μmol mL^{-1}):

$$EF = \frac{C_{con}}{C_0}.$$

The C_{con} was obtained from the HPLC analysis for the analyte in eluates after being redissolved in 1 mL of MeOH.

2.7. Preparation of cacumen platycladi

The preparation of cacumen platycladi was consulted to previous work [27,28]. In brief, 1.0 g of cacumen platycladi was placed into a 100 mL of conical flask, followed by 50 mL of 50% MeOH, stewing for 6 h; subsequently the flask was marinated into a water bath at 80 °C for 6 h. The resultant leaching liquors were filtrated with a 0.45 μm membrane filter, and then evaporated to dryness under low fire. The extracts were dissolved in doubly distilled deionized (D.D.I.) water and extracted by 25 mL of saturated ethyl acetate for three times. The three aliquots of extraction solutions were pooled and dried with anhydrous sodium sulfate, and then they were transferred to a 250 mL of round flask for reduced pressure distillation. The residues were dissolved with anhydrous MeOH for use.

2.8. HPLC-UV analysis

The HPLC-UV analysis was performed using EasySepTM-1010 HPLC (Unimicro Technologies Co., Ltd., Shanghai, China) with a 1010 LC liquid delivery pump and a 1010 UV ultraviolet/visible variable wavelength detector with a spectral range from 190 to 700 nm. Column was C-18 column (2.1 mm × 250 mm). The analytical procedure was conducted according to reported work [29,30] with necessary modification. Briefly, the column was rinsed with a mobile phase until a stable baseline was obtained, which consisted of ACN and 0.1% (w/v) H_3PO_4 aqueous solution (36:64, v/v). The detection was carried out with wavelength at 365 nm. Column oven temperature was controlled at 25 °C. The flow-rate was maintained at 0.5 mL min^{-1} and 20 μL of sample was injected.

3. Results and discussion

3.1. Preparation and characterization of the quercetin-MIPs

Quercetin was dissolved in THF at the usual imprinting concentration, and AA was selected as the functional monomer because it was favorable for hydrogen-bonding interaction in the solvent [24]. Thus, a stable donor–receptor complex between template and functional monomer is formed in the imprinting process shown in Fig. 1. The existence of such a complex leads to the formation of well-defined specific binding sites in the MIPs. Then a thermal polymerization was followed, in which AIBN was used as free radical initiator and its half-life at 60 °C was around 10 h and proper for polymerization. The cross-linker, EDMA, formed a "frozen" spatial structure. The quercetin molecule contains five hydroxyl groups and one carbonyl group, which can form hydrogen bonds with functional groups such as hydroxyl, amino and carbonyl groups. From the structure of quercetin shown in Fig. 2, both the γ-OH (No. 3) and ε-OH (no. 5) of the quercetin molecule can form strong intramolecular hydrogen bonds with the δ-carbonyl group (no. 4), and therefore the inter-molecular interaction between the template and monomer is weakened. The remained three hydroxyl groups as main imprinting functional groups supply strong inter-molecular hydrogen bonds with the polymer and control the precise imprinting sites. So, there are less five apparent selective binding sites in the quercetin molecule. After removal of the template molecule, the specific imprinting sites will be maintained. These sites will selectively adsorb quercetin molecules.

To further ensure that the quercetin-MIPs had been made, we performed additional FTIR analysis (see Fig. 3). Fig. 3a shows the FTIR spectrum of quercetin. A strong and broad stretching vibration absorbance peak of hydroxyl groups was found at 3299 cm^{-1}, suggesting there are a few hydroxyl groups in the quercetin molecule, which might form the intra- and/or inter-molecular hydrogen bonds. A stretching vibration peak of carbonyl group was found at 1656 cm^{-1} [31], moving toward the low wave number region in the conjugated system. In addition, stretching vibration peaks of cyclobenzene skeleton in the quercetin molecule was found at 1615, 1512 and 1432 cm^{-1} [32]. Fig. 3b shows the FTIR spectrum of AA (monomer). The main absorption bands of AA situating around 3356 (and 3188), 1673, and 1613 cm^{-1} were assigned to the following vibrations: N–H stretching, being characteristic absorption peaks of primary acylamide, C=O stretching and C=C stretching, respectively.

For MIPs, shown in Fig. 3c, the peak at 1732 cm^{-1} was attributed to C=O stretching vibration absorbance, because the MIPs were synthesized by the polymerization of EDMA and AA, and the cross-linked polymers must carry the repeated cross-linking units of EDMA. At 1637 cm^{-1}, the weak absorbance peak of C=C suggests that most AA were cross-linked and only a few ones were remained. The broad peak at 3441 cm^{-1} was assigned to the asymmetric stretching vibration of N–H in acylamide. Moreover, the stretching vibration peak of methyl or methylene was found at 2990 cm^{-1}, and C–O stretching vibration of asymmetric ester was found at 1154.37 cm^{-1}. For NIPs shown in Fig. 3d, the characteristic signals of FTIR were almost the same, except for the intensity of the

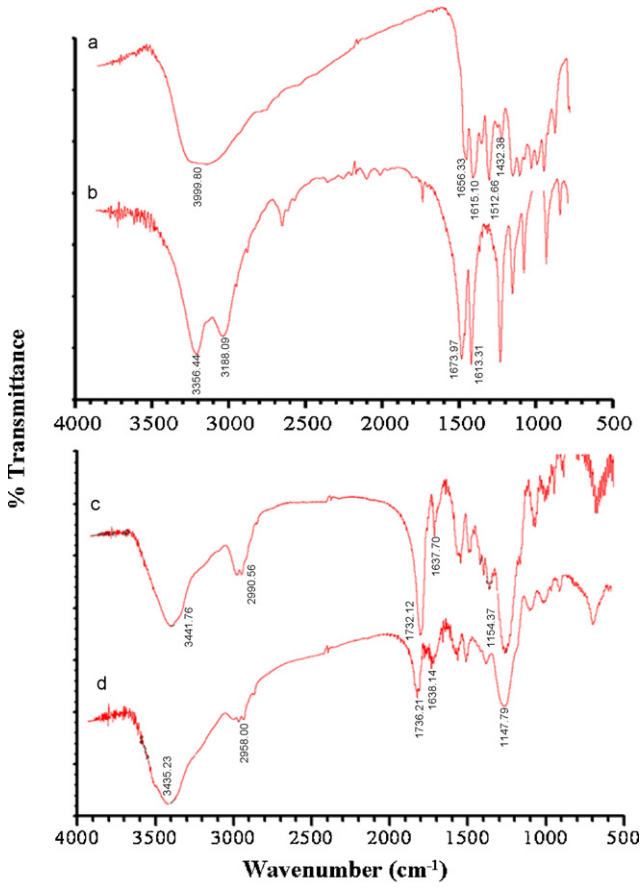


Fig. 3. FTIR spectra of quercetin (a), AA (b), MIPs removal of the template molecule (c), and NIPs (d).

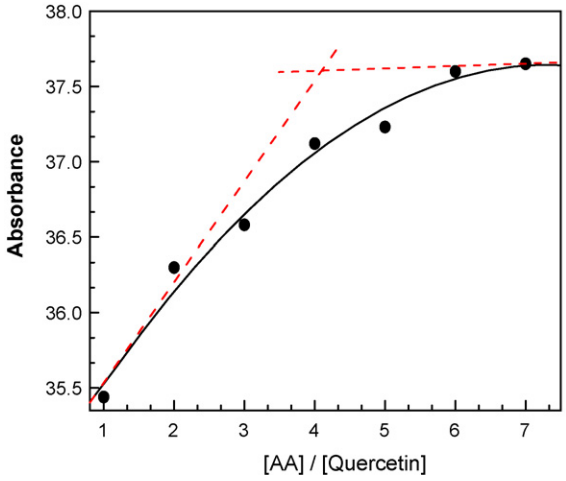


Fig. 4. Absorbance curve in different ratios of [AA]/[Quercetin].

stretching vibration peak of C=O (1736 cm^{-1}), distinctly lower than that for MIPs. The possible reason was that the template molecules which were assembled with monomer via the hydrogen-bonded interaction in preparing MIPs, helpful for the co-polymerization of monomer and cross-linker, and thus stable imprinting cavities was formed by ordered distribution of functional groups containing carbonyl group. The result of FTIR confirmed that obviously there were functional groups in the MIPs which would interact with the template molecule, namely acylamide group in the quercetin-MIPs.

3.2. Influence of polymerization conditions on adsorption properties of MIPs

3.2.1. Functional monomers

For non-covalent MIPs, the complementary inter-molecular reactions between the template and the functional monomer are crucial for the subsequent affinity and selectivity of the MIPs [33]. It is therefore important to search for a suitable functional monomer that can strongly interact with the template and form specific "donor–receptor" or "antibody–antigen" complexes prior to polymerization. Due to the higher specific binding but the lower non-specific adsorption of the resultant MIPs, AA was thus selected as the functional monomer for preparing the MIPs [24].

The molar ratio of functional monomer to template is important in terms of its interaction strength, which will have an effect on the number and property of MIP recognition sites [34]. The intensity and ratio range of the MIPs were estimated by absorption measurement. As shown in Fig. 4, the equilibrium absorbance of the complex increases with the ratio of AA to template (M/T) increasing, suggesting that the quercetin molecules form super-molecular structure with AA via non-covalent inter-cavity mode in the THF solution. At 7:1, the plot begins to level off, indicating that almost all the template molecules had been bound with the functional monomers. The coordination number was expected 4 (Fig. 4); from the quercetin structure (Fig. 2), it is clear that the number of the apparent selective binding sites was less 5. The molar ratio should be higher than 4:1. At lower content monomer, it is difficult to form stable imprinting sites. An excess of functional monomers can cause more non-selective adsorption sites with random distribution in the MIPs and result in self-association of the monomers, which will reduce the selective adsorption sites and increase the adsorption mass transfer resistance. So, the optimum ratio of M/T at 7:1 was chosen for preparing the maximum specific-selective MIPs in the following investigations.

3.2.2. Porogens

It is essential for the adsorption properties of MIPs that the functional monomer and imprinting molecules can form stable complexes. Strong interaction between imprinting molecules and functional monomers produces excellent stability of the resultant complex, which therefore results in high recognition specificity of the MIPs. On the other hand, weak interaction often causes inefficiency of MIPs. So, it is important to investigate the influence of porogens. The porogens generally act as dispersion media and pore forming agents in the polymerization process. The solvent is very important for providing the synthesis environment of MIPs. The polarity of solvents will affect the interaction between template molecule and functional monomer, and thereby the adsorption properties of MIPs.

As shown in Table 2, the interactions between solvent and quercetin or AA increased with increasing polarity of solvents, while the specific recognition capacity of the MIPs decreased. Higher polar solvents competed more efficiently with template molecules for binding the recognition sites of the functional monomers and thus weakened the interaction between the latter two compounds. This leads to forming fewer imprinting sites in MIPs and reduces its adsorption effectiveness for quercetin. In addition, quercetin was not easily dissolved and its floccule was easily observed in ACN, likely causing phase separation. This resulted in unfavorable MIPs with inhomogeneous pores and reduced internal surface area. For less polar solvent having less interaction with either template molecule or functional monomer, in which the interaction of template molecule and functional monomer is strong, however, the formed MIPs are easily precipitated due to less solubility in the less polar solvent. Only when the solvent has medium polarity, does it have proper interactions with quercetin or AA. And for the medium polar THF, it also offers better dissolving capacity for the quercetin-template and the initial polymers, which maintains the pore dimension, specific surface area and mass transfer rate, and therefore facilitates synthesizing the MIPs with homogeneous pores and high specific surface area. This assists to form uniform imprinting sites in MIPs. So, THF was selected as the porogenic solvent to produce better MIPs.

Meanwhile, the surface morphologies of MIPs prepared in different solvents were studied by using SEM (Fig. 5). Although all have rough surfaces, the MIPs from THF and acetone seemed more dense and homogenous with more and larger-dimension pores (Fig. 5a and b) than that from ACN and 1,4-dioxane (Fig. 5c and d). It can be evaluated that the surface of the MIPs in THF exhibits bigger dimension of the pore and bigger volume rough structure than that of the MIPs in acetone. The uniform and more open structure is obviously favorable for the embedding of the template molecules and mass transfer.

3.2.3. Cross-linkers

The basic structures of the polymers synthesized via cross-linkers and function monomers play a key role for preparing MIPs. Because the specificity of the template cavity is not controlled by the template molecules but is mainly dependent on the network spatial array of MIPs, the structural optimization is vital for the selectivity of MIPs. In the polymerization, cross-linkers are employed to control matrix stability and solid shapes of imprinting binding sites after removal of template molecules. The cross-linkers of DVB, EDMA, PTA and BisAA were introduced to investigate their influences on the adsorption properties of MIPs.

Fig. 6 shows the effects of solvation energy of cross-linkers on the imprinting factors of the four MIPs. DVB and EDMA are both better cross-linkers in the polymerization. The molecular chains of MIPs linked by EDMA are suitably feasible while the polymers containing DVB are of considerable rigidity but sometime they do not facilitate the rebinding of template molecules with MIPs.

Table 2
Specific adsorption properties of MIPs in different porogenic solvents.

Solvents	ε	$E_{solvation,\ AA}$ (kJ mol^{-1})	$E_{solvation,\ quercetin}$ (kJ mol^{-1})	Q_{MIP} (μg g^{-1})	$Q_{control}$ (μg g^{-1})	Imprinting factor (α)
1,4-Dioxane	2.25	3.23	4.78	372	354	1.05
THF	7.58	4.00	6.90	480	400	1.20
Acetone	20.7	7.25	9.78	409	381	1.07
ACN	37.5	9.18	11.2	309	300	1.03

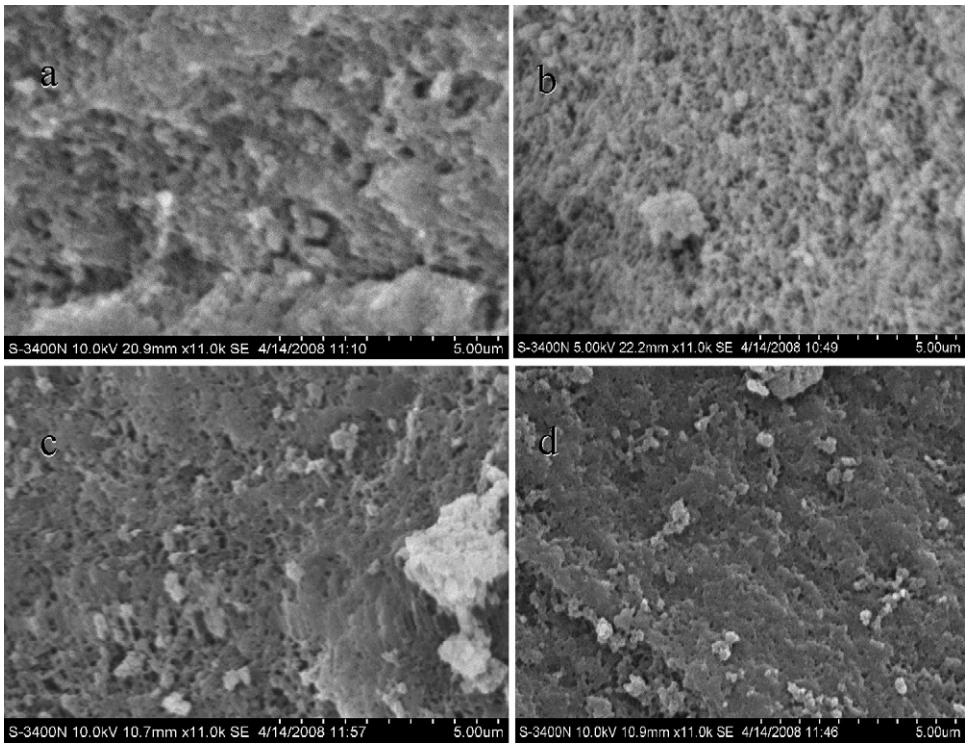


Fig. 5. SEM microphotographs of MIPs prepared in different porogens. (a) THF, (b) acetone, (c) ACN and (d) 1,4-dioxane.

Enhancement of the interaction between cross-linkers and template molecules will benefit the formation of selective template cavity. Increasing interaction between cross-linkers and solvents will increase the competition and therefore weaken the interaction between cross-linkers and template molecules. This is adverse to immobilize the binding sites and the mobility of sites will bring down the recognition specificity of MIPs.

In order to improve the recognition performance of the MIPs prepared by using EDMA, a series of polymers have been synthesized by increasing the molar percentage ratio of EDMA to quercetin (C/T) in the polymerization mixture. As shown in Fig. 7, the adsorption properties of MIPs are remarkably affected by the content change of cross-linkers, where Q_e (μg g^{-1}) is the equilibrium adsorption amount at each concentration. Increasing cross-linkers will increase the rigidity of MIPs and decrease the swelling in solvents, and thus will reduce the change of the spatial structure and the binding groups in the polymerization and recognition, which will facilitate forming stable binding sites and therefore improve the selectivity of MIPs. It is observed that for the MIPs, at the ratios of 10:1 to 25:1, the specific adsorption amounts were rapidly increased and the MIPs exhibited the better selectivity and

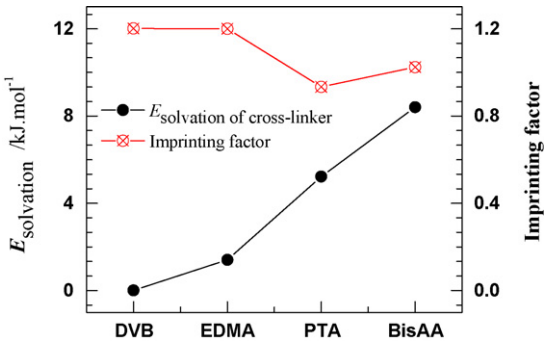


Fig. 6. Effects of the solvation energy of cross-linkers on the specific adsorption of MIPs.

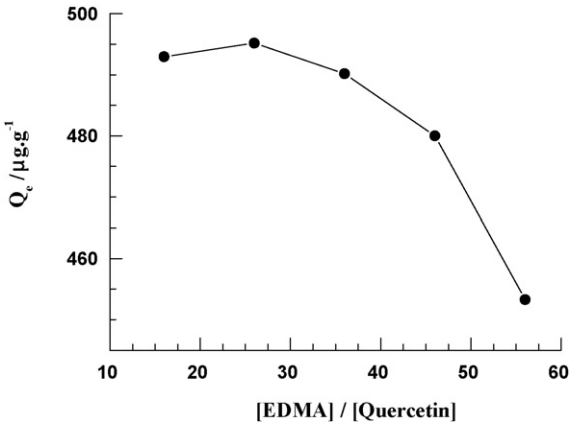


Fig. 7. Effects of the amounts of cross-linkers on the equilibrium adsorption amounts of MIPs.

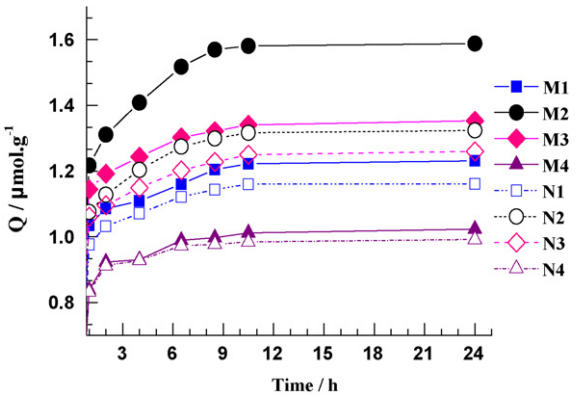


Fig. 8. Dynamic curves for the adsorption of quercetins onto MIPs and NIPs.

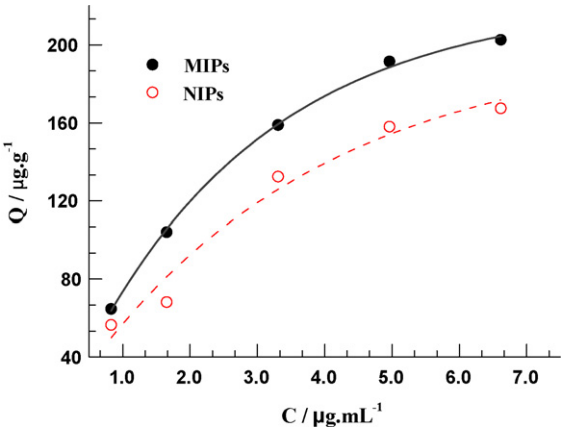


Fig. 9. Adsorption isotherms of polymers using THF as solvent.

recognition capacity. The high cross-linking degree will contribute to stabilize the recognition sites of MIPs. While the ratio of *C*/*T* is increased especially to 40:1, the specific adsorption and specific binding capacity of the resultant MIPs rapidly decay. At high concentrations of cross-linkers, the binding sites in MIPs are too mobile, which will reduce the orderliness of matrix arrangement of MIPs and increase non-specific cavity, resulting in high non-specific binding and low affinity.

3.3. Adsorption analysis and recognition mechanism

Fig. 8 shows the dynamic curves for the adsorption of quercetin onto the MIPs and NIPs in four different solvents, where *Q* is the amounts of quercetins adsorbed at any time. It is observed that the amounts of quercetins both adsorbed onto MIPs and bound to NIPs increased with time and nearly reached saturation state within 10 h. For the adsorption equilibrium, the adsorption time was set for 24 h in the following experiments. It is assumed that the high adsorption rate within 6 h might result from the preferential and rapid adsorption of template molecules onto the recognition sites in the surface of MIPs. When these imprinted sites in the surface were occupied, it became difficult for quercetin to implant into the MIPs. This would cause the adsorption to slow down. The various contributions of polymers on the template molecular recognition would be attributed to the hydrogen bonds between template and monomer, and the comprehensive functions of resultant microenvironment and complementary cavity to the template molecules [35]. It is also observed that both M2 and N2 have the largest adsorption amounts in THF among the MIPs and NIPs, respectively. Although NIPs show similar trend to MIPs on the quercetin adsorption (Fig. 8), their adsorption capacities are much lower. This might be likely because of the non-specific adsorption of NIPs caused by van der Waals force, due to the absence of imprinting procedure and thereafter lacking suitable recognition sites and imprinting cavities in the NIPs. However, there were numerous and precise imprinting sites in the MIPs, resulting in specific adsorption, and thus they produced higher adsorption capacity. So, the presence of complementary cavities to the template molecules in the MIPs is vital for the specific adsorption.

Fig. 9 shows the adsorption isotherms of quercetins onto the MIPs and NIPs using THF as recognition medium. The curves were obtained by plotting the saturated adsorption amounts with equilibrium concentrations of the quercetins in MeOH solution. In other words, the adsorption capacity (*Q*) of quercetin increased quickly with the increase of initial concentration. At higher equilibrium concentration than 6.0 μg mL^{-1}, adsorption of MIPs became stable and its recognition sites were almost saturated. NIPs had the same trend as MIPs with lower saturated adsorption amounts. Thus, adsorption isotherms are important for describing how adsorbates interact with adsorbent [36].

Scatchard analysis was employed to further analyze the binding isotherms, which is an approximate model commonly used to estimate the binding parameters of MIPs [2,26]. The Scatchard equation can be expressed as, $Q/C = (Q_{max} - Q)/K_d$, where K_d (μmol mL^{-1}) is defined as the equilibrium dissociation constant of the binding sites, Q (μmol g^{-1}) is the amount of quercetin bound to the polymer, Q_{max} (μmol g^{-1}) is the maximum adsorption amounts of quercetin on the polymer, and C (μmol mL^{-1}) is equilibrium concentration of quercetin in the solution. Fig. 10 shows the Scatchard plots of the binding of quercetin to MIPs and NIPs, respectively. It is clear that the Scatchard plot for MIPs is a single straight line. The linear regression equation was, $Q/C = -32.32Q + 98.30$ ($R^2 = 0.9903$), suggesting that the homogeneous recognition sites for quercetins were formed in the MIPs, namely the adsorption interaction was nearly equivalent for the four binding sites. From the slope (-32.32 ($1/K_d$)) and intercept (98.30 (Q_{max}/K_d)), K_d and Q_{max} for the affinity binding sites were calculated to be 0.03 μmol mL^{-1} and 3.04 μmol g^{-1}, respectively. For NIPs, the non-linearity indicated that there were not selective adsorption sites for quercetins on them. From the Scatchard analysis, it could be assumed that the rebinding sites in the MIPs are mainly dependent on hydrogen bonding, while the interaction between NIPs and quercetins was mainly from non-specific adsorption such as van der Waals.

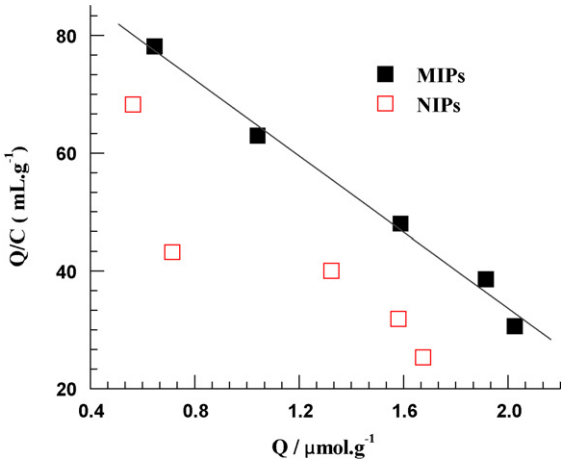


Fig. 10. Scatchard plots of MIPs and NIPs.

Table 3
Distribution coefficient (K_d) and ratio (β) of distribution coefficients between two tested substrates.

Sorbents	Initial conc. ($\mu g\,g^{-1}$)		Final conc. ($\mu g\,mL^{-1}$)		K_d ($mL\,g^{-1}$)		β
	Quercetin	Rutin	Quercetin	Rutin	Quercetin	Rutin	
MIPs	20	20	16.9	18.2	46.1	25.1	1.84
NIPs	20	20	19.0	19.1	13.2	12.5	1.06

3.4. Molecular selectivity of MIPs

The selective adsorption of MIPs was evaluated by using quercetin and its structurally similar compounds, rutin and catechol, as substrates in THF. Rutin and catechol were chosen as references for investigating the static adsorption specific selectivity and MIP–SPE specific selectivity, respectively. The static adsorption distribution coefficient K_d was utilized to evaluate the molecular selectivity of polymers [24]. K_d is defined as follows, $K_d = C_P/C_S$, where C_P ($\mu g\,g^{-1}$) is the concentration of the tested substrates adsorbed on the MIPs and C_S ($\mu g\,mL^{-1}$) is the equilibrium concentration of substrates in solution. Table 3 shows the K_d and the separation factor, β, namely the ratio of K_d of the two tested substrates. It is seen that the adsorption capacities of NIPs are very close for both rutin and quercetin because there are not selective recognition sites in the NIPs and the adsorption for substrates are non-selective. On the other hand, obviously, the MIPs offer better selectivity for quercetins since the MIPs present the β value about 1.7 times of that for the corresponding NIPs. The molecular recognition of MIPs mainly depends on two factors, molecular dimension of template and matching degree of the bonding sites [25]. For the rutin molecule, it has a large substitution group in γ-OH position of quercetin. Different molecular dimensions cause the rutin not complementary to the imprinting cavities of the quercetin-MIPs and therefore weak interactions. As a result, the MIPs gave a lower selectivity for rutin than that for quercetin.

Table 4 shows the comparisons of MIP–SPE properties between quercetin and catechol. As seen, the MIPs exhibit much stronger binding affinity for quercetin even if the concentration of catechol is 15 times of querectin, while both have the same adsorption trend in different solvents, namely strongest in THF and weakest in ACN. Since the molecular dimension of catechol is smaller than that of quercetin, the molecule maybe easily enters the MIP cavity. Also, because it contains two phenolic hydroxyl groups, the molecules could form two hydrogen bonds with the amino groups of AA in the MIPs. However, the smaller structure of catechol makes it poorly match the cavities induced by quercetin, resulting in weaker binding interaction and lower selectivity.

3.5. SPE specificity of the MIPs for quercetin

The prepared quercetin-polymer was employed as the sorbent of SPE column for the pretreatment of quercetin and structurally similar rutin. Fig. 11 shows the HPLC-UV chromatograms of the standard mixtures. Good baseline separation was obtained for them without SPE procedure and rutin was eluted first (Fig. 11a). Not any apparent peak is observed in Fig. 11b for determining

Table 4
Comparisons of two analogues before and after MIP–SPE.

Solvents	Before SPE ($\mu g\,mL^{-1}$)		After SPE ($\mu g\,mL^{-1}$)		K_d ($mL\,g^{-1}$)	
	Quercetin	Catechol	Quercetin	Catechol	Quercetin	Catechol
1,4-Dioxane	2	30	0.56	15.0	17.1	6.67
THF	2	30	0.28	12.3	41.0	9.59
Acetone	2	30	0.40	12.9	26.7	8.84
ACN	2	30	0.74	15.6	11.4	6.15

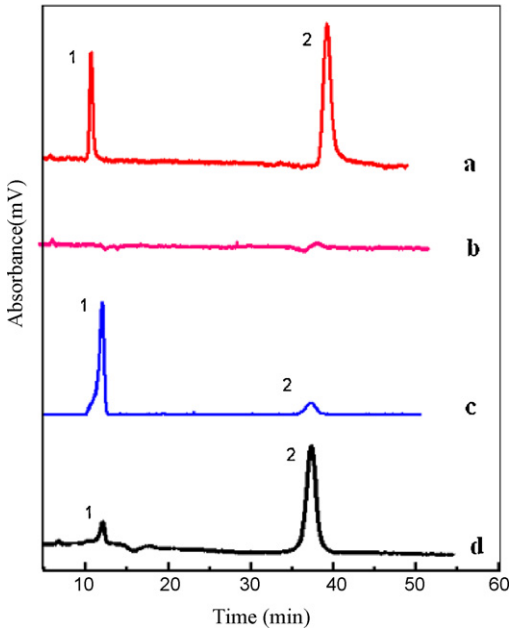


Fig. 11. Chromatograms of the standard mixture. (a) Initial solutions before MIP–SPE, (b) solutions after MIP–SPE, (c) solutions after rinsing with MeOH, and (d) eluates after washing with MeOH/acetic acid (9:1, v/v). (1) Rutin and (2) Quercetin.

the solutions after the MIP–SPE, which indicates quercetin and rutin were almost completely adsorbed onto the MIPs. Fig. 11c shows that almost all the rutins were eluted with only minor quercetins by rinsing the MIP–SPE column with MeOH; quercetin was not easily eluted with MeOH. Then using the more polar eluting solutions, namely MeOH/acetic acid (9:1, v/v), quercetins were nearly all eluted, shown in Fig. 11d. The linking of a rutinose group (α-L-mannopyranosyl-β-D-glucopyranosyl) in rutin causes a larger space volume than that of quercetin, and it is therefore most difficult for the rutin to be embedded into the cavity of the quercetin-MIPs, so it was easily eluted with MeOH. However, the quercetins adsorbed onto the MIPs through the specific recognition effects could be destroyed only by the strongly polar solvents containing acetic acid. Thus the MIPs are highly structural-selective toward quercetins.

In addition, quercetins in two eluates were analyzed after the above same MIP–SPE procedure for the standard mixture of quercetin and rutin of 2 mL at 20 $\mu g\,mL^{-1}$ and 5 mL at 4 $\mu g\,mL^{-1}$, respectively. The molar ratios of quercetin to rutin were both 2 to 1 before SPE, and then they became 8 to 1 and 143 to 1, respectively, for the two aliquots. The EF of quercetin compared to rutin was improved by at least 4–71.5 times. Therefore, under the suitable conditions of loading, rinsing and eluting, the MIPs with high selectivity can be employed not only to separate some structurally similar compounds, but also to excellently concentrate and clean up the trace analytes.

Fig. 12 shows the chromatograms of the solutions from cacumen platycladis. The peaks of quercetin and rutin were identified with the comparison of chromatographic retention times with those of the spiked standards shown in Fig. 11. It is supposed that querceins mainly exist in the cacumen platycladis. Also, a relatively large peak appeared between ca. 16–20 min shown in Fig. 12a, which is not surprising in the extracts before the MIP–SPE, and they were not identified. On the other hand, by the same MIP–SPE pretreatment as that for Fig. 11d, quercetin is predominantly present and there is only a minor of impurities and rutin is hardly observed (Fig. 12b). The MIP–SPE is not only high selective for quercetin but also offers cleanup and enrichment effects for the real samples. The obtained unique profile demonstrates

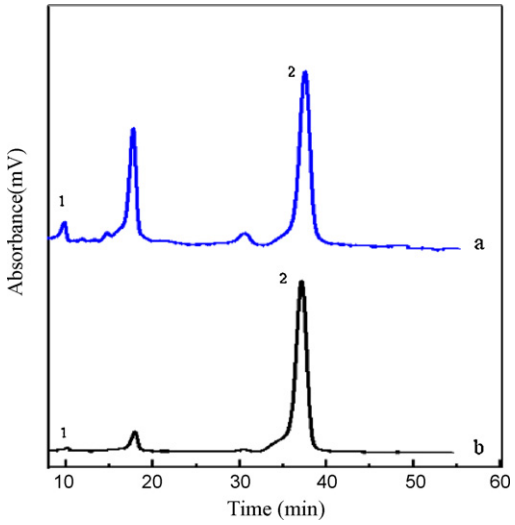


Fig. 12. Chromatograms of the solutions from cacumen platycladis. (a) Solutions before MIP-SPE and (b) eluates after MIP–SPE. (1) Rutin and (2) Quercetin.

the endogenous quercetins could be efficiently separated from the extracts of cacumen platycladis. It provides an effective method for the separation and determination of active ingredients from cacumen platycladis and further for flavonoid compounds in the traditional Chinese medicine. Besides for the SPE application, the quercetin-MIPs have been also employed in diverse fields. To take two examples, quercetin-MIPs immobilized silica gel could be used as a solid-phase reagent for the tin determination by using sorption-spectroscopic method [19] and quercetin-MIPs could be developed into sensors by self-assembling monolayer/mediator system for analyzing biomolecules and drug molecules [37]. Thus, further analysis and applications of quercetin-MIPs are under on the way.

4. Conclusions

The prepared quercetin-MIPs were confirmed by both FTIR and SEM, characterized by HPLC-UV, and applied for the SPE of a natural product (cacumen platycladi). Optimal imprinting parameters for enhanced recognition properties of MIPs toward quercetin were attained, which were very important for the successful preparation and application of the MIPs. The resultant MIPs displayed fast adsorption dynamics and high adsorption capacity. And they could contain single selective adsorption sites for quercetin. The molecular selectivity of the MIPs was also evaluated by using rutin and catechol as references. The high specific binding could be attributed to a large population of sites of high affinity for the templates. Selective recognition for the isolation of quercetin from cacumen platycladi samples was achieved, and thus the MIPs would powerfully be applied for the preconcentration of traditional Chinese medicines. Further research will focus on developing new imprinting materials for the separation and determination of quercetins from natural products, and extending to more flavonoid compounds, as well as using the promising quercetin-MIPs as an analytical tool for various potential applications.

Acknowledgements

This work was supported by the Department of Science and Technology of Shandong Province of China (2008GG20005005), One Hundred Person Project of the Chinese Academy of Sciences (20090462), the Natural Science Foundation of Shandong Province of China (Y2007B38), and a grant from the Major State Basic Research Development Program of China (973 Program) (2010CB428701).

References

[1] R. Gupta, A. Kumar, Biotechnol. Adv. 26 (2008) 533.
[2] T. Yang, Y.H. Li, S. Wei, Y. Li, A.P. Deng, Anal. Bioanal. Chem. 391 (2008) 2905.
[3] C. Cacho, L. Schweitz, E. Turiel, C. Conde, J. Chromatogr. A 1179 (2008) 216.
[4] Y.G. Tan, Z.L. Zhou, P. Wang, L.H. Nie, S.Z. Yao, Talanta 55 (2) (2001) 337.
[5] R. Weiss, A. Molinelli, M. Jakusch, B. Mizaikoff, Bioseparation 10 (2002) 379.
[6] G. Wuff, A. Sarhan, J. Angew. Chem. Int. Ed. Engl. 11 (3) (1972) 341.
[7] M. Quaglia, L.E. De, C. Sulitzky, G. Massolini, B. Sellergren, Analyst 126 (9) (2001) 1495.
[8] B.S. Ebarvia, C.A. Binag, F. Sevilla, Anal. Bioanal. Chem. 378 (5) (2004) 1331.
[9] M.L. Zhang, J.P. Me, Q. Zhou, G.Q. Chen, Z. Liu, J. Chromatogr. A 984 (2003) 173.
[10] T.W. Tan, X.J. He, W.X. Du, J. Chem. Ind. Eng. (China) 52 (2001) 176.
[11] C. Baggiani, G. Giraudi, F. Trotta, C. Giovannoli, A. Vanni, Talanta 51 (1) (2000) 71.
[12] L. Ye, K. Mosbach, React. Funct. Polym. 48 (12) (2001) 149.
[13] G. Wulff, Chem. Rev. 102 (1) (2002) 1.
[14] E. Turiel, A.M. Esteban, P. Fernandez, C.P. Conde, C. Caĭmara, Anal. Chem. 73 (2001) 5133.
[15] L.L. Zhu, X.J. Xu, J. Chromatogr. A 991 (2003) 151.
[16] E. Turiel, J.L. Tadeo, A.M. Esteban, Anal. Chem. 79 (2007) 3099.
[17] Y.F. Wang, X.H. Wang, Y.T. Zhu, Nat. Prod. Res. Dev. 15 (2) (2003) 171.
[18] N. Russo, M. Toscano, N. Uccella, J. Agric. Food Chem. 48 (2000) 3232.
[19] O.A. Zaporozhets, L.S. Ivanko, I.V. Marchenko, E.V. Orlichenko, V.V. Sukhan, Talanta 55 (2) (2001) 313.
[20] J.C. Xie, L.L. Zhu, H.P. Luo, L. Zhou, C.X. Li, X.J. Xu, J. Chromatogr. A 934 (2001) 1.
[21] G. Theodoridis, M. Laskov, V. Kov, A. Tegou, N. Giantsiou, P. Jandera, J. Sep. Sci. 29 (2006) 2310.
[22] R. Lei, X. Xu, F. Yu, N. Li, H.W. Liu, K.A. Li, Talanta 75 (4) (2008) 1068.
[23] S. Zhang, S.Q. Dong, L.Z. Chi, P.G. He, Q.J. Wang, Y.Z. Fang, Talanta 76 (4) (2008) 780.
[24] L.S. Yan, J. Jing, Z.M. Huang, Z.D. Wen, F.T. Liu, Chin. J. Anal. Lab. 25 (5) (2006) 97.
[25] J.F. He, Q.Y. Deng, J. Chin. Med. Mater. 30 (5) (2007) 588.
[26] M.W. Wong, M.J. Frisch, K.B. Wiberg, J. Am. Chem. Soc. 13 (1991) 4776.
[27] M.W. Wang, G.J. Liang, L.P. Zhang, W.P. Wang, W.Y. Tang, Chin. Guizhou Agric. Sci 34 (1) (2006) 24.
[28] H.S. Hu, Y.Y. Yu, C.H. Wan, B. Yan, Z.X. Long, Chin. Mod. Sci. Instrum. 5 (2008) 61.
[29] M.M. Zhang, S.Y. Du, Chin. J. Chin. Mater. Med. 32 (1) (2007) 64.
[30] Y.P. Luo, L.W. Guo, F.J. Zhu, Chin. Trad. Patent Med. 31 (4) (2009) 582.
[31] X.Z. Yang, D.C. Wu, Z.L. Du, R.X. Li, X.L. Chen, X.H. Li, J. Agric. Food Chem. 57 (2009) 3431.
[32] T.L. Lin, B.Z. Yan, G.F. Hu, M. Wang, Chin. J. Spectrosc. Lab. 23 (3) (2006) 431.
[33] J.F. He, Q.H. Zhu, Q.Y. Deng, Spectrochim. Acta A 67 (2007) 1297.
[34] R. Rajkumar, A. Warsinke, H. Mohwald, F.W. Scheller, M. Katterle, Talanta 76 (5) (2008) 1119.
[35] T. Takeuchi, J. Haginak, J. Chromatogr. B 728 (1999) 1.
[36] Y.Q. Xia, T.Y. Guo, M.D. Song, B.H. Zhang, B.L. Zhang, React. Funct. Polym. 66 (2006) 1.
[37] P.Y. Chen, P.C. Nien, C.T. Wu, T.H. Wu, C.W. Lin, K.C. Ho, Anal. Chim. Acta 643 (2009) 38.

Talanta 80 (2009) 703–709

Contents lists available at ScienceDirect

Talanta

journal homepage: www.elsevier.com/locate/talanta

Improved selection of LMW over HMW proteins from human plasma by mesoporous silica particles with external modification

Yanxia Qi[a,1], Junying Wei[b,1], Hua Wang[a], Yangjun Zhang[b], Jing Xu[a], Xiaohong Qian[b], Yafeng Guan[a,*]

[a] Department of Instrumentation and Analytical Chemistry, Key Laboratory of Separation and Analysis, Dalian Institute of Chemical Physics, Chinese Academy of Sciences, 457 Zhongshan Road, Dalian 116023, PR China
[b] State Key Laboratory of Proteomics, Beijing Proteome Research Center, Beijing Institute of Radiation Medicine, No. 33 Life Science Park Road, Changping District, Beijing 102206, PR China

ARTICLE INFO

Article history:
Received 24 May 2009
Received in revised form 19 July 2009
Accepted 25 July 2009
Available online 3 August 2009

Keywords:
Selective extraction
Low molecular weight proteins
External modification
Mesoporous material
Human plasma

ABSTRACT

Selective extraction of low molecular weight (LMW) proteins and peptides from complex biological samples plays an important role in the discovery of useful biomarkers and signaling molecules. Various methods, such as solid-phase extraction (SPE), ultrafiltration, and size-exclusion chromatography have been developed for such extraction purpose. In this study, we present, to our knowledge, the first demonstration of alkyl-diol@SiO_2 mesoporous material MCM-41 (alkyl-diol group on the external surface of mesoporous material) for selective extraction of LMW proteins and peptides from complex biological samples. The adsorption kinetics of LMW proteins, the influence of pH on adsorption and the desorption recovery by different elution solvents were investigated by using standard proteins as model samples. It was demonstrated that the modification of alkyl-diol group on the external surface could efficiently decrease the adsorption of HMW protein and increase the desorption recovery of LMW protein. Furthermore, the mesoporous materials were applied to selectively extract LMW proteins and peptides (<10 kDa) from crude human plasma. And the modified MCM-41 material had much better extraction selectivity and efficiency for LMW proteins and peptides than unmodified one.

© 2009 Elsevier B.V. All rights reserved.

1. Introduction

In the past decade, selective extraction of low molecular weight (LMW) proteins and peptides from complex biological samples, such as plasma and tissue extracts, drew more and more interest due to their important roles in elucidation of biological and pathological variations, as well as in the discovery of useful biomarkers and signaling molecules [1–4]. Various extraction methods, such as solid-phase extraction (SPE), ultrafiltration, acetonitrile precipitation, and size-exclusion chromatography have been developed [5–7]. Moreover, the combination of selective extraction with mass spectrometry (MS) analysis becomes a powerful tool to achieve high-throughout separations and identifications of LMW proteins and peptides from complex matrixes [5,8–10]. However, one of the major difficulties in extraction of LMW proteins and peptides is that their concentration is much lower compared with other proteins with high molecular weight (HMW). Therefore, the specific and efficient extraction of LMW proteins and peptides from complex sample solutions still presents challenges [11]. Orvisky et al. applied denaturing ultrafiltration to extract proteins and peptides smaller than 50 kDa from plasma and serum, followed by MALDI MS profiling and identifications of the peptides smaller than 5 kDa [6]. However, the selectivity of denaturing ultrafiltration was poor and Aristoteli et al. have demonstrated that SPE was another efficient approach among various extraction methods [5].

Various materials with different retention mechanisms had been developed to improve the efficiency and specificity of SPE method, such as chromatographic separation materials [7], magnetic beads [4], organic or inorganic polymers [12,13] and C60-fullerene silica [14] with reversed-phase or ion-exchange group. Yang and co-workers applied nanozeolite materials and $CaCO_3$–poly(methyl methacrylate) nanoparticles for adsorption and separation of low abundance peptides [10,15]. But these materials cannot be used to enrich LMW proteins and peptides exclusively from complex protein mixtures. MCM-41 material is a member of M41S family, and discovered by the scientists of Mobil Oil Corporation in 1992. These materials have high pore surface area, very ordered pore structure, narrow pore-size distribution, and relatively high chemical and mechanical stability [16,17]. The MCM-41 materials have been widely used to adsorb proteins and environment contaminations [18–24]. Tian et al. applied mesoporous silica MCM-41 particles with a pore size of 20.5 Å to selective

* Corresponding author. Tel.: +86 411 84379590; fax: +86 411 84379570.
E-mail addresses: guanyafeng@dicp.ac.cn, guan_yafeng@yahoo.com.cn (Y. Guan).
[1] These authors contributed equally to the work.

0039-9140/$ – see front matter © 2009 Elsevier B.V. All rights reserved.
doi:10.1016/j.talanta.2009.07.050

enrichment peptides with a range from 1 to 12 kDa from plasma [9]. It was demonstrated that the unique pore structure of this material makes it efficient to enrich LMW proteins and peptides from complex matrixes. Though critical pore can repel most large proteins, the external surface of the material can also adsorb some HMW proteins, which greatly decreases the enrichment selectivity, and the adsorbed proteins on the external surface of the material can further prevent the LMW proteins and peptides from reaching the interior surface of the mesopores by steric exclusion. Katiyar and Ji investigated the adsorption of bovine serum albumin (BSA) on MCM-41 and Al-MCM-41 materials. They demonstrated that the characteristic of external surface can strongly influence the adsorption capacity, and the adsorption on the external surface may be misinterpreted as the adsorption on the interior surface of MCM-41 materials [18,19].

It is well known that the external surface of restricted access materials (RAM) is usually modified with electroneutral alkyl-diol group to eliminate the unspecific adsorption of protein matrixes, which makes it capable to extract small molecular objects directly from untreated biological fluid [25,26]. So in this study, we modified the external surface of mesoporous silica material with alkyl-diol group to improve the efficiency and specificity of the enrichment of LMW proteins and peptides. It was demonstrated that the alkyl-diol group modification on the external surface of mesoporous material could efficiently decrease the HMW protein adsorption and increase the desorption recovery in different elution solvents. The mesoporous material modified on external surface also showed much better extraction selectivity and efficiency for LMW proteins than the unmodified one when crude human plasma was applied. And the extraction efficiency increases about 1200 times for some LMW peptides and proteins by using the alkyl-diol@SiO_2 MCM-41 material.

2. Experimental

2.1. Materials

Tetraethoxysilane (TEOS) and [3-(2,3-epoxypropoxy)propyl] trimethoxysilane were from Meryer chemical technology Co. Ltd. (Shenzhen, China). Cetyltrimethyl ammonium bromide (CTAB) was from Aoboxing Biological Technology Co. Ltd. (Beijing, China). NH_4OH (25%), disodium hydrogen phosphate (Na_2HPO_4), sodium hydroxide (NaOH), and toluene were from Tianjing Kemael Chemical Reagents Center (Tianjing, China). Citric acid was from Shenyang Fourth Chemical Plant (Shenyang, China). Ovalbumin (from chicken egg white), insulin (from bovine pancreas) and a-cyano-4-hydroxycinnamic acid (CHCA) were obtained from Sigma (St. Louis, MO, USA). Human blood plasma was obtained from Beijing PLA 307 hospital. Trifluoroacetic acid (TFA) was purchased from Acros (Morris plains, NJ, USA). HPLC-grade acetonitrile (ACN) was obtained from Mallinckrodt Baker Inc. (Phillipsburg, NJ, USA). Deionized water (R > 18.2 MΩ) used for all experiments was purified by Millipore purification system (Billerica, MA, USA). Matrix CHCA (5 mg/mL) was dissolved in acetonitrile/water (50/50, v/v) solution containing 0.1% TFA.

2.2. Instrumentation

MALDI MS experiments were performed on an Applied Biosystems 4800 Proteomics Analyzer instrument (Framing, MA) in the positive reflector mode for low molecular weight peptides and proteins (m/z 700–3500) and in the linear mode for the proteins with m/z 3000–90 000 (linear middle mass range, m/z 3000–10 000, linear high mass range, m/z 10 000–90 000), respectively. Each mass spectrum was typically summed with 1000 laser shots after being calibrated using an internal calibration by using ion signal of peptide mixtures of myoglobin. All the MALDI MS experiments were performed in CHCA matrix.

2.3. Synthesis and modification of the mesoporous materials

The reactant mixture for the synthesis of SiO_2 mesoporous material consisted of CTAB, TEOS, $NH_3{\cdot}H_2O$, NaOH and H_2O with molar ratio of 0.1:1:6:0.3:80. The synthesis was performed according to the previously published methods [16,17,27]. After the mixture reacting at room temperature for 3 h, the formed gel was transferred to a Teflon bottle and kept at 100 °C for 120 h. The resultant product was filtered, washed, and dried.

External surface modifications of the mesoporous particles were performed following the procedures as previously reported [28–31], which was carried out by two steps: the first is grafting of (2,3-epoxypropoxy)propyl group on the external surface of the mesoporous material containing the template species; the second is extraction of the template CTAB and conversion of the (2,3-epoxypropoxy)propyl group to alkyl-diol group by acidified ethanol (Scheme 1). Generally, 1 g of the as-synthesized MCM-41 silica sample was suspended in 30 mL toluene, then 3 mL of [3-(2,3-epoxypropoxy)propyl]trimethoxysilane was added under nitrogen protection. After refluxing for 24 h, the suspension was filtered, washed with toluene and ethanol, respectively, and dried at 100 °C under vacuum. The surfactant (CTAB) in the unmodified and modified materials was extracted by acidified ethanol according to the published methods [29,32]. Briefly, 100 mL ethanol including 1.5 mL aqueous HCl (37%) was added to per 1 g material and refluxed at 60 °C for 8 h, followed by drying at 100 °C under vacuum overnight. The resultant materials were designated as unmodified MCM-41 and alkyl-diol@SiO_2 MCM-41 material, respectively.

2.4. Characterizations of the mesoporous materials

X-ray diffraction (XRD) was used to identify the crystal phases of the materials. The data were recorded using a X′ Pert PRO (PANalytical, Holland) vertical goniometer with Cu Kα radiation (λ = 1.5406 Å), at 40 kV, 40 mA. XRD patterns were set as scan for 2θ ranging from 0.5° to 10° with a step size of 0.033° and a time step of 40 s.

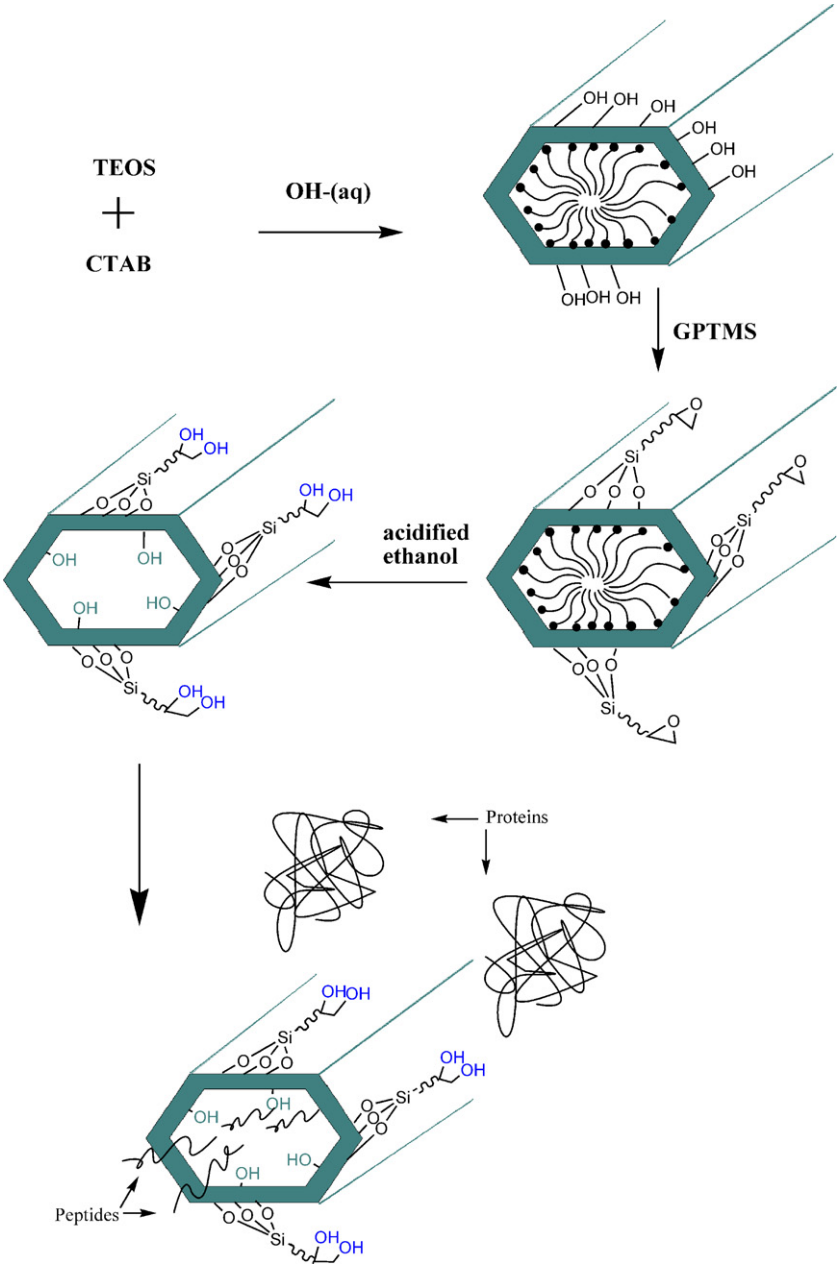
Nitrogen adsorption and measurements were performed at 77 K on a NOVA 2200e surface area & pore size analyzer (Quantachrome, USA). The specific surface area was obtained by using the BET method, and the pore-size distribution was based on BJH methods [33,34].

Transmission electron microscope (TEM) was performed using a FEI Tecnai G^2 Spirit TEM instrument (Philips, Holland) operating at 120 kV. Samples were prepared on a copper grid by placing a small aliquot of a suspension of ground sample in ethanol on the grid, followed by drying at ambient conditions.

Fourier transform infrared (FT-IR) spectroscopy was performed on Spectrum 100/100N (PerkinElmer, USA) with the scan range of 4000–400 cm^{-1} at room temperature. Spectra were acquired at 4 cm^{-1} resolution and the scan rate was set as 0.20 cm/s. Spectrum ES software (version 6.1.0) was used in the manipulation of spectra data.

2.5. Protein adsorption on external surface of mesoporous materials

Ovalbumin (MW: 43 kDa, MD: 4.0 nm × 5.0 nm × 7.0 nm) [22] was selected as model HMW protein due to its relatively large dimension compared with the pore size of the adsorbents. To investigate the influence of pH on HMW proteins adsorption, 10 mg of mesoporous adsorbents were mixed with 1 mL of ovalbumin



Scheme 1. Synthesis of alkyl-diol@SiO_2 MCM-41 and its application of selectively adsorption of LMW proteins. TEOS: tetraethoxysilane, CTAB: cetyltrimethyl ammonium bromide, GPTMS: [3-(2,3-epoxypropoxy)propyl]trimethoxysilane.

solutions prepared in Na_2HPO_4–citric acid buffer with pH 2.8, 4.9 and 7.8, respectively. After 12 h incubation, the protein concentration of each supernatant was determined by UV–vis spectrometer (Lambda 35, PerkinElmer, USA) and the amounts of ovalbumin adsorbed were calculated by the difference of the concentration of the protein before and after adsorption [18–20]. Calibration experiment was done before ovalbumin adsorption process.

2.6. Determinations of adsorption kinetics and desorption recovery of LMW protein

Insulin was used as LMW protein to determine the adsorption kinetics and desorption recovery of the mesoporous materials. First, adsorption kinetics was investigated at pH 2.8. Briefly, the adsorption kinetics was investigated by mixing 5 mg of each mesoporous adsorbent with 8 mL of insulin solution (0.25 mg/mL). The resulting mixture was vigorously agitated in an Environmental Incubator Shaker at 180 rpm at room temperature. 500 μL supernatant was removed from mixture at the time point of 10, 30, 120, 300, 420, 600, 720 and 1440 min, respectively. The protein concentration of each supernatant was determined by UV adsorption [18–20] as described above. Then, the desorption recovery was also determined. Briefly, 3 mL of insulin solution (0.2 mg/mL, pH 2.8) was mixed with 5 mg of mesoporous adsorbents. The mixture was vigorously agitated at room temperature until equilibrium. Then the suspension was centrifugated, and the supernatant was collected. The mesoporous particles were washed with 1 mL deionized water for three times. Then, 500 μL 50% aqueous ACN (containing 0.1% TFA) was added to elute adsorbed insulin from the mesoporous particles. The protein concentration in supernatant and eluate were both determined by UV adsorption. Calibration experiment was done before insulin adsorption and desorption process. The recov-

ery (R) was calculated by the following formula:

$$R = \frac{C_e \times V_e}{(C_t - C_s) \times V_s}$$

C_e represents the protein concentration in eluate, V_e represents the volume of eluate, C_t represents the protein concentration before adsorption, C_s represents the protein concentration after adsorption, and V_s represents the volume of adsorption mixture.

In order to study the effect of eluents on the desorption recovery, different eluents: 50% ethanol solution, 1 M NaCl aqueous solution, and Na_2HPO_4–citric acid buffer with pH 7.8 were also investigated by the same way.

2.7. Extraction LMW proteins from human plasma

To extract LMW proteins and peptides from plasma, 10 mg of each mesoporous material was mixed with 0.5 mL deionized water and 0.5 mL plasma. The mixture was vigorously agitated at room temperature for 7 h. Then, the suspension was centrifugated and the supernatant was discarded. The mesoporous particles were washed with 1 mL deionized water for three times. Finally, 1 M NaCl was used to elute the adsorbed proteins. The NaCl eluates were exchanged to 50% ACN solution containing 0.1% TFA using C_{18} Ziptip and spiked with a double ^{18}O labelled standard peptide (FEDGVLDPDYPR, m/z = 1426.53). All the eluates were analyzed by MALDI MS [35,36], which were performed in CHCA matrix.

3. Results and discussion

3.1. Characterizations of the mesoporous materials

Fig. 1 shows three distinct diffraction peaks (d100, d110, d200) for both MCM-41 materials, which reflect the hexagonal pore structure of MCM-41 materials in X-ray diffraction (XRD) analysis [16]. Powder XRD patterns of alkyl-diol@SiO_2 MCM-41 mesoporous particles showed some a little less sharp peaks comparing with the unmodified ones, which can be well explained by the fact that the presence of the organic component can decrease the intensity of the XRD patterns [37], implying a successful external modification. The transmission electron microscope (TEM) images of unmodified and alkyl-diol@SiO_2 MCM-41 are shown in Fig. 2. It can be found that the mesopores of alkyl-diol@SiO_2 MCM-41 are well organized as those of unmodified MCM-41 material. The XRD analysis and TEM image implied that the external surface modification had little influence on the order of mesoporous structure, which is important for the high specific extraction of the LMW proteins from complex samples. The measurement of N_2 adsorption/desorption of alkyl-diol@SiO_2 MCM-41 shows a well-defined step associated with the filling of the mesopores due to capillary condensation, and the pore size is centered at 2.19 nm, and the corresponding surface area is 781 m^2/g (shown in Fig. 2b), which are a little smaller than those of unmodified MCM-41 (2.76 nm and 843 m^2/g, as shown in Fig. 2a). And it may be attribute to the modification on the external surface and inlet of mesopores. The FT-IR spectra of unmodified and modified materials were shown in Fig. 3. The bands near 1080 and 800 cm^{-1} are assigned to the Si–O–Si stretching mode of the mesoporous silica framework. 460, 960 and 3400 cm^{-1} correspond to Si–O–Si bending mode, Si–OH stretching mode, and O–H stretching mode, respectively. The FT-IR spectra of alkyl-diol@SiO_2 MCM-41 have some differences from the unmodified one, the bands near 1460 and 1380 cm^{-1} are assigned to the C–H bending mode, and the bands near 2960, 2930 and 2850 cm^{-1} become stronger due to the introduction of alkyl group.

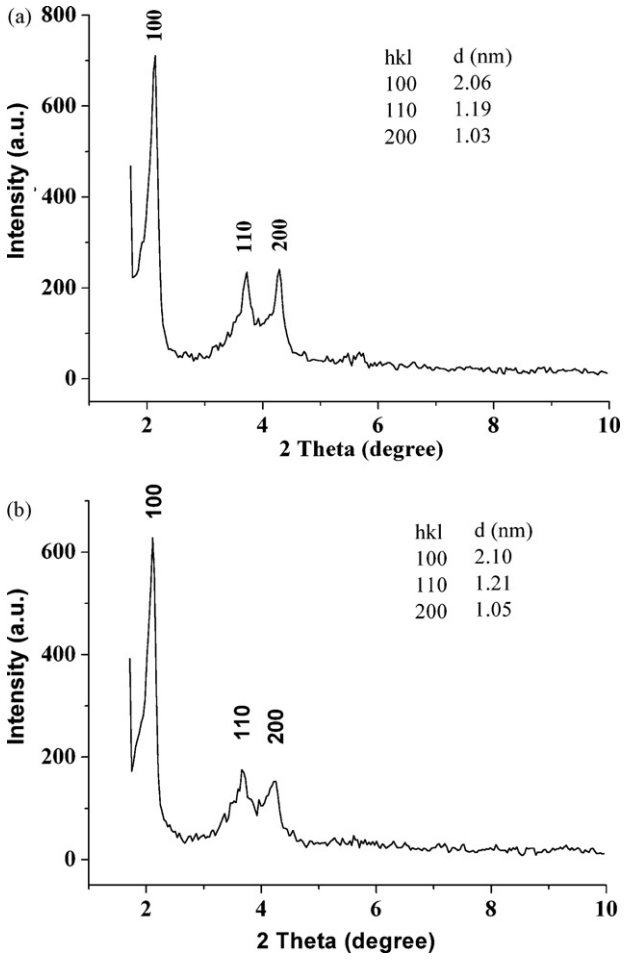


Fig. 1. Power XRD patterns of (a) unmodified and (b) alkyl-diol modified MCM-41 mesoporous materials.

3.2. Exclusion effectiveness on HMW proteins

Highly ordered mesoporous silica particles, especially MCM-41, have been demonstrated to be a useful adsorbent for selective enrichment of LMW proteins and peptides based on the effect of size-exclusion. However, the undesired adsorption of HMW proteins on the external surface was adverse to the selectivity of the enrichment. Therefore, we modified the external surface of MCM-41 material with alkyl-diol groups. To study the exclusion effectiveness of alkyl-diol group on HMW proteins, we used ovalbumin as a model HMW protein due to its larger dimension than the pore size of the adsorbents.

The HMW protein adsorptions were conducted into Na_2HPO_4–citric acid buffers at pH 2.8, 4.9 and 7.8 and the results are shown in Table 1. The adsorption amounts of HMW protein decreased at all of the pH after alkyl-diol group modification on external surface of material. Obviously, it is efficient to reduce the adsorption of HMW protein by introducing the electroneutral alkyl-diol group onto the external surface of mesoporous material. Compared with the adsorption amount by unmodified MCM-41 at pH 4.9, the adsorption amounts decrease 16.98% at pH 2.8, and 21.32% at pH 7.8, respectively. This result consisted with that, when the pH of the buffer is set as the pI of the protein, the highest adsorption capacity by unmodified mesoporous material can be obtained due to the hydrophobic interaction [19]. When the alkyl-diol@SiO_2 MCM-41 was applied, the adsorption amounts had little change when the pH was under the pI and decreased

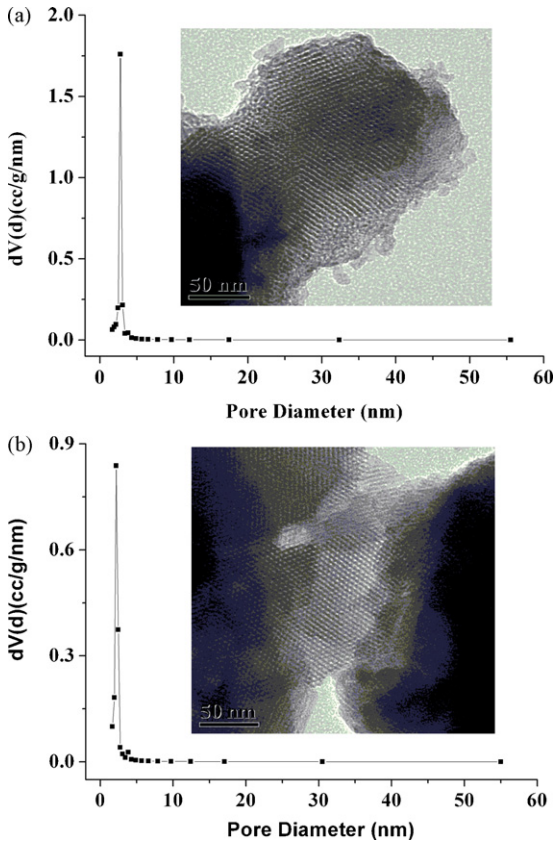


Fig. 2. Differential pore-size distributions calculated from nitrogen adsorption isotherms (inset: TEM image) of (a) unmodified and (b) alkyl-diol modified MCM-41 mesoporous materials.

greatly when the pH was above the pI. The highest adsorption capacity of modified MCM-41 materials was not obtained at the pI of protein, which might be attributed to that the introduction of alkyl-diol group would decrease the hydrophobicity of exterior of the material.

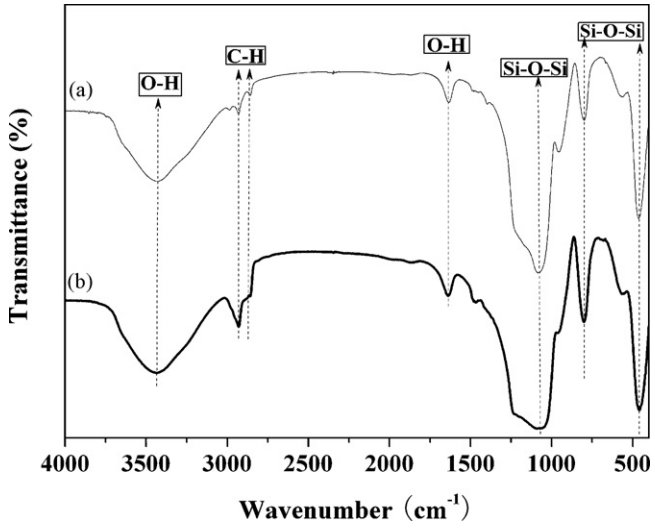


Fig. 3. FT-IR spectra of (a) unmodified and (b) alkyl-diol modified MCM-41 mesoporous materials.

Table 1
Comparison of adsorption efficiency for ovalbumin by unmodified and modified MCM-41 ($n = 3$)[a].

	Adsorption amounts (mg/g)[b]		(RSD (%))[c]
	pH 2.8	pH 4.9	pH 7.8
MCM-41	32.67 (0.8)	39.35 (2.8)	30.96 (0.3)
Modified MCM-41	25.63 (4.8)	24.61 (2.2)	13.63 (1.8)

[a] Protein/silica (wt/wt) = 0.1.
[b] The amounts of ovalbumin adsorbed on external surface (12 h) of the three mesoporous materials, which were obtained by subtracting the amounts in supernatant from the total amount, respectively.
[c] Each adsorption experiment was conducted three times, and the RSDs were given within the parentheses.

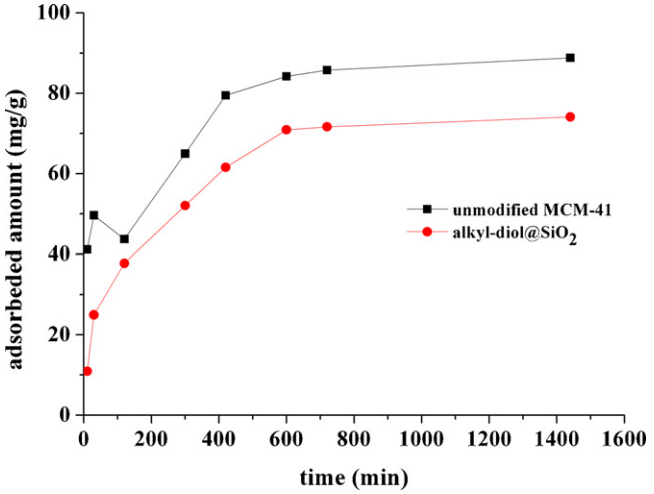


Fig. 4. Adsorption amounts of insulin as a function of time on the two mesoporous materials (protein/silica (wt/wt) = 0.4). The value of each spot was the average of three replicate measurements.

3.3. LMW protein adsorption kinetics and desorption recovery on different mesoporous materials

Desorption recovery is an important parameter for adsorbents in highly efficient extraction. Insulin (MW: 5.7 kDa) was used as a model LMW protein to investigate the adsorption kinetics and the desorption recovery of the mesoporous materials. The adsorption kinetics conducted in Na_2HPO_4–citric acid buffer at pH 2.8 is shown in Fig. 4. After equilibrium for 12 h, the unmodified MCM-41 had higher loading capacity than the modified material due to its stronger external surface adsorption. The desorption recovery of insulin by different elution conditions was also investigated and the results are shown in Table 2. It can be seen that most insulin could not be desorbed from the unmodified and alkyl-diol@SiO_2 MCM-41 materials by using organic solvents (50% ACN or ethanol). However, when 1 M NaCl solution was used, good desorption recovery (over 70%) was achieved for both the materials, and the better one was obtained for alkyl-diol@SiO_2 MCM-41 (91.77%). This might

Table 2
Recovery of insulin for unmodified and modified MCM-41 by using different eluents ($n = 3$).

	Recovery (%) (RSD (%))[a]			
	50% ACN	50% ethanol	1 M NaCl	Na_2HPO_4–citric acid (pH 7.8)
MCM-41	8.69 (9.7)	15.96 (7.9)	75.56 (3.9)	35.59 (12.8)
Modified MCM-41	40.78 (0.5)	44.57 (6.4)	91.77 (6.6)	56.05 (4.5)

[a] Each experiment was conducted three times, and the RSDs were given within the parentheses.

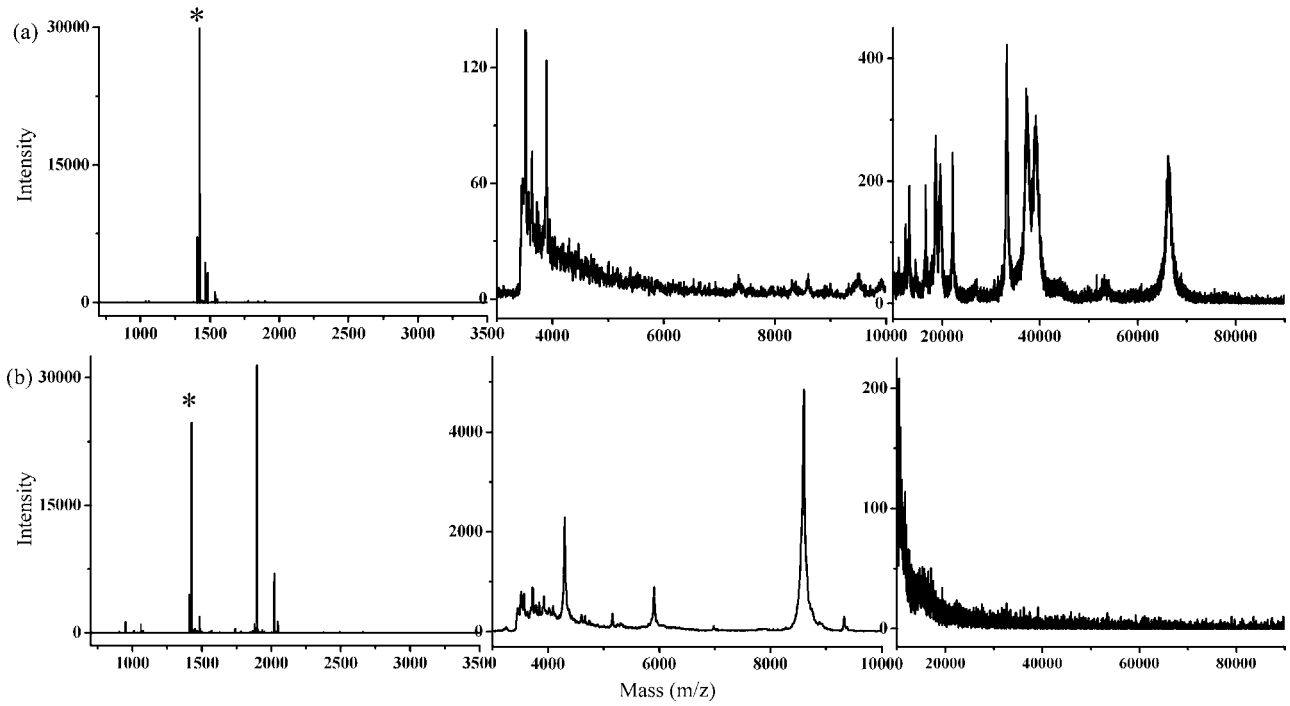


Fig. 5. MALDI MS spectra of human plasma extracts by using (a) unmodified and (b) alkyl-diol modified MCM-41 mesoporous materials. MALDI MS analysis was performed in the m/z range of 0.7–3.5, 3.0–10 and 10–90 kDa. CHCA was used as the matrix. The bound proteins and peptides on mesoporous materials were desorbed by 1 M NaCl. The peaks marked with * represent the internal standard (double ^{18}O labelled standard peptide FEDGVLDPDYPR, m/z = 1426.53).

be attributed to that the protein adsorbed onto the external surface could block the mesopores and influence the desorbing of proteins adsorbed onto the internal surface. Last, the elution by using Na_2HPO_4–citric acid buffer at pH 7.8 was also performed. The results were not better than that by 1 M NaCl (see Table 2). These results can be explained by the ion-exchange mechanism of Si–OH group. Therefore, it is obvious that alkyl-diol group modification on the external surface of mesoporous material can increase the desorption recovery due to eliminating of the adsorption on external surface.

3.4. LMW protein extraction efficiency and selectivity for human plasma

Human plasma is a complex biological sample comprised of tens of thousands of proteins and peptides, most of which is made up of high abundant species, such as albumin, immunoglobulins and so on [38]. However, some low abundant LMW proteins and peptides also play an important role in elucidation of biological and variation and discovery of useful biomarkers [1–4], and their identification is always interfered by high abundant species. Therefore, we applied the mesoporous material to repel high abundant proteins in plasma and selectively extract LMW proteins and peptides. The eluates by 1 M NaCl were desalted by C_{18} Ziptip and analyzed by MALDI MS. To measure the relative amounts of enriched LMW peptide, we added a double ^{18}O labelled standard peptide (FEDGVLDPDYPR, m/z = 1426.53) into the eluate as internal standard. When the unmodified MCM-41 material was applied, about 50 peaks were detected in the m/z range 800–10 000 (S/N > 10), and 8 peaks were observed in the m/z range 10 000–90 000 as shown in Fig. 5a, which indicates that the selectivity of LMW proteins extraction is poor due to the external surface adsorption. It could be also seen that extracted peptides have relative low intensity compared with the standard peptide and the relative area to standard peptide is 0.17 for extracted peptide with MW 1896.1 (assuming z = 1). When alkyl-diol@SiO_2 MCM-41 material was applied, about 100 peaks were detected in the m/z range 800–10 000 (S/N > 10), and few peaks were observed in the m/z range 10 000–90 000 as shown in Fig. 5b, which demonstrates the good selectivity of the external surface modified material for LMW proteins. Not only much more peaks are obtained in the m/z range 800–10 000, but the intensity is also much higher compared with that by unmodified MCM-41 material. As standard peptide was also added, the relative areas of peptides with MW 1896.1 and 2021.1 (assuming z = 1) to standard peptide are 209.45 and 42.55. Compared with the unmodified MCM-41, the extraction efficiency increases about 1200 times (209.45/0.17) for alkyl-diol@SiO_2 MCM-41 material. Obviously, alkyl-diol group modification on the external surface of MCM-41 materials is an efficient strategy to eliminate unspecific adsorption on external surface as well as increase the extraction selectivity and efficiency.

Mesoporous material is a new type of adsorbent for selectively extraction of LMW proteins and peptides from complex biological samples. However, the unspecific adsorption on external surface would decrease the extracting selectivity and desorbing recovery. Therefore, we selectively modified the external surface of the mesoporous MCM-41 particles with biocompatible alkyl-diol groups in this study. Compared with the unmodified MCM-41, the mesoporous material of alkyl-diol@SiO_2 has much higher extracting selectivity and efficiency for LMW proteins and peptides from crude plasma. It could be attributed to that the alkyl-diol group could eliminate the interference of HMW proteins, and the adsorbed HMW proteins would decrease the selectivity as well as block the mesopores and decrease the desorbing recovery of LMW proteins and peptides.

4. Conclusion

New mesoporous material (alkyl-diol@SiO_2) was synthesized and applied to extract LMW proteins and peptides from biological samples. It was demonstrated that the alkyl-diol group modification on the external surface could efficiently decrease the unspecific

HMW protein adsorption, and increase the extraction selectivity and efficiency for LMW proteins and peptides. The extraction efficiency of some LMW proteins and peptides increases about 1200 times by alkyl-diol@SiO_2 MCM-41 material compared with that by unmodified MCM-41 material. Therefore, alkyl-diol@SiO_2 MCM-41 material is suitable for selective extraction of LMW proteins and peptides from complex biological samples, making the approach promising for use in biological separation and the discovery of useful biomarkers.

Acknowledgments

The authors thank the National Natural Science Foundation of China (No. 20635010) for financial support of this work. We also thank Dr. Peng Tian and Dr. Wei Han for helpful discussion in the synthesis of mesoporous silica materials and thank Dr. Hao Cheng for helpful discussions in the measurements of N_2 adsorption/desorption.

References

[1] E.P. Diamandis, J. Proteome Res. 5 (2006) 2079–2082.
[2] H. Tammen, H. Kreipe, R. Hess, M. Kellmann, U. Lehmann, A. Pich, N. Lamping, P. Schulz-Knappe, H.-D. Zucht, R. Lilischkis, Br. Cancer Res. Treat. 79 (2003) 83–93.
[3] J. Villanueva, D.R. Shaffer, J. Philip, C.A. Chaparro, H. Erdjument-Bromage, A.B. Olshen, M. Fleisher, H. Lilja, E. Brogi, J. Boyd, M. Sanchez-Carbayo, E.C. Holland, C. Cordon-Cardo, H.I. Scher, P. Tempst, J. Clin. Invest. 116 (2006) 271–284.
[4] J. Villanueva, J. Philip, D. Entenberg, C.A. Chaparro, M.K. Tanwar, E.C. Holland, P. Tempst, Anal. Chem. 76 (2004) 1560–1570.
[5] L.P. Aristoteli, M.P. Molloy, M.S. Baker, J. Proteome Res. 6 (2007) 571–581.
[6] E. Orvisky, S.K. Drake, B.M. Martin, M. Abdel-Hamid, H.W. Ressom, R.S. Varghese, Y. An, D. Saha, G.L. Hortin, C.A. Loffredo, R. Goldman, Proteomics 6 (2006) 2895–2902.
[7] T. Stroink, G. Wiese, J. Teeuwsen, H. Lingeman, J.C. Waterval, A. Bult, G.J. Jong, W.J. Underberg, Electrophoresis 24 (2003) 897–903.
[8] H. Tammen, I. Schulte, R. Hess, C. Menzel, M. Kellmann, P. Schulz-Knappe, Comb. Chem. High Throughput Screen. 8 (2005) 725–733.
[9] R. Tian, H. Zhang, M. Ye, X. Jiang, L. Hu, X. Li, X. Bao, H. Zou, Angew. Chem. Int. Ed. 46 (2007) 962–966.
[10] Y. Zhang, X. Wang, W. Shan, B. Wu, H. Fan, X. Yu, Y. Tang, P. Yang, Angew. Chem. Int. Ed. 44 (2005) 615–617.
[11] N.L. Anderson, N.G. Anderson, Mol. Cell. Proteomics 1 (2002) 845–867.
[12] E. Bonneil, J. Li, T.-L. Tremblay, J.J. Bergeron, P. Thibault, Electrophoresis 23 (2002) 3589–3598.
[13] N. Lion, V. Gobry, H. Jensen, J.S. Rossier, H. Girault, Electrophoresis 23 (2002) 3583–3588.
[14] R.M. Vallant, Z. Szabo, S. Bachmann, R. Bakry, M. Najam-ul-Hag, M. Rainer, N. Heigl, C. Petter, C.W. Huck, G.K. Bonn, Anal. Chem. 79 (2007) 8144–8153.
[15] W. Jia, X. Chen, H. Lu, P. Yang, Angew. Chem. Int. Ed. 45 (2006) 3345–3349.
[16] C.T. Kresge, M.E. Leonowicz, W.J. Roth, J.C. Vartuli, J.S. Beck, Nature 359 (1992) 710–712.
[17] J.S. Beck, J.C. Vartuli, W.J. Roth, M.E. Leonowicz, C.T. Kresge, K.D. Schmitt, C.T-W. Chu, D.H. Olson, E.W. Sheppard, S.B. McCullen, J.B. Higgins, J.L. Schlenker, J. Am. Chem. Soc. 114 (1992) 10834–10843.
[18] A. Katiyar, L. Ji, P.G. Smirniotis, N.G. Pinto, Micropor. Mesopor. Mater. 80 (2005) 311–320.
[19] L. Ji, A. Katiyar, N.G. Pinto, M. Jaroniec, P.G. Smirniotis, Micropor. Mesopor. Mater. 75 (2004) 221–229.
[20] J.F. Díaz, K.J. Balkus Jr., J. Mol. Catal. B: Enzym. 2 (1996) 115–126.
[21] W. Xiao, D. Xiao, Talanta 72 (2007) 1288–1292.
[22] M. Hartmann, Chem. Mater. 17 (2005) 4577–4593.
[23] M.L. Kim, J.D. Stripeikis, M.B. Tudino, Talanta 77 (2009) 1068–1074.
[24] X. Feng, G.E. Fryxell, L.-Q. Wang, A.Y. Kim, J. Liu, K.M. Kemner, Science 276 (1997) 923–926.
[25] W.R.G. Baeyens, G.V. Weken, J. Haustraete, H.Y. Aboul-Enein, S. Corveleyn, J.P. Remon, A.M. García-Campaña, P. Deprez, Biomed. Chromatogr. 13 (1999) 450–454.
[26] K. Wagner, T. Miliotis, G. Marko-Varga, R. Bischoff, K.K. Unger, Anal. Chem. 74 (2002) 809–820.
[27] Q. Cai, W.-Y. Lin, F.-S. Xiao, W.-Q. Pang, X.-H. Chen, B.-S. Zou, Micropor. Mesopor. Mater. 32 (1999) 1–15.
[28] B.F. Juan, E. Ruiz-Hitzky, Adv. Mater. 12 (2000) 430–432.
[29] M. Park, S. Komarneni, Micropor. Mesopor. Mater. 25 (1998) 75–80.
[30] D.R. Radu, C.-Y. Lai, J.W. Wiench, M. Pruski, V.S.-Y. Lin, J. Am. Chem. Soc. 126 (2004) 1640–1641.
[31] F. Hoffmann, M. Cornelius, J. Morell, M. Frőba, Angew. Chem. Int. Ed. 45 (2006) 3216–3251.
[32] M.H. Lim, C.F. Blanford, A. Stein, J. Am. Chem. Soc. 119 (1997) 4090–4091.
[33] E.P. Barrett, L.G. Joyner, P.P. Halenda, J. Am. Chem. Soc. 73 (1951) 373–380.
[34] S. Brunauer, P.H. Emmett, E.J. Teller, Am. Chem. Soc. 60 (1938) 309–319.
[35] M. Gaspari, M.M.-C. Cheng, R. Terracciano, X. Liu, A.J. Nijdam, L. Vaccari, E. Fabrizio, E.F. Petricoin, L.A. Liotta, G. Cuda, S. Venuta, M. Ferrari, J. Proteome Res. 5 (2006) 1261–1266.
[36] L. Trojer, G. Stecher, I. Feuerstein, G.K. Bonn, Rapid Commun. Mass Spectrom. 19 (2005) 3398–3404.
[37] W. Zhang, J. Shi, H. Chen, Z. Hua, D. Yan, Chem. Mater. 13 (2001) 648–654.
[38] C.A. Burtis, E.R. Ashwood (Eds.), Tietz Fundamentals of Clinical Chemistry, 5th ed., W.B. Saunders Co., Philadelphia, PA, 2001.

Talanta 80 (2009) 710–715

Contents lists available at ScienceDirect

Talanta

journal homepage: www.elsevier.com/locate/talanta

Coffee aroma—Statistical analysis of compositional data

M. Korhoňová[a,*], K. Hron[b,*], D. Klimčíková[a], L. Müller[a], P. Bednář[a], P. Barták[a]

[a] Department of Analytical Chemistry, Faculty of Science, Palacky University, 17. listopadu 12, 711 46 Olomouc, Czech Republic
[b] Department of Mathematical Analysis and Applications of Mathematics, Faculty of Science, Palacky University, 17. listopadu 12, 771 46 Olomouc, Czech Republic

ARTICLE INFO

Article history:
Received 17 February 2009
Received in revised form 23 July 2009
Accepted 27 July 2009
Available online 3 August 2009

Keywords:
Coffee aroma
Solid-phase microextraction
SPME
Compositional data
Principal component analysis
Cluster analysis

ABSTRACT

Solid-phase microextraction in headspace mode coupled with gas chromatography–mass spectrometry was applied to the determination of volatile compounds in 30 commercially available coffee samples. In order to differentiate and characterize Arabica and Robusta coffee, six major volatile compounds (acetic acid, 2-methylpyrazine, furfural, 2-furfuryl alcohol, 2,6-dimethylpyrazine, 5-methylfurfural) were chosen as the most relevant markers. Cluster analysis and principal component analysis (PCA) were applied to the raw chromatographic data and data processed by centred logratio transformation.

© 2009 Elsevier B.V. All rights reserved.

1. Introduction

Standard multivariate statistical methods, like principal component analysis (PCA), are widely used to analyze results of chemical measurements. The main objective of PCA is to reduce high-dimensional data sets by preserving as much as possible of the variation, contained in the data. PCA is designed to transform the original variables into new, uncorrelated variables (axes), called the principal components, such that the new axes lie along the directions of maximum variance. PCA provides an objective way of finding indices of this type so that the variation in the data can be accounted as concisely as possible. The results of PCA, both loadings and scores, can be advantageously visualized using biplot [1] with the corresponding interpretation. On the other hand, too many variables in the original data set (often with only low concentrations) can cause a kind of 'pollution' of the PCA results because of the variability, presented in these variables. As a consequence, the results can be misleading or even completely useless. A standard way to overcome this undesirable effect is to omit such variables, which are not necessary for the further considerations, by using an expert knowledge before the analysis begins.

The most common way of expressing chemical data is to present them as percentages. That means the data contain only relative information (have relative scale) or, more precisely, contain only the relevant information among the ratios of the variables [2]. Unfortunately, this obvious and natural property of the data (called in the following compositional data, or shortly compositions) is in contradiction to the procedures of standard multivariate statistics, where the scale is absolute. This holds among others also for covariance structure of the data and leads to its undesirable behaviour. Concretely, leaving one or more compositional variables (parts), the covariance structure can completely change. Let us illustrate this situation on the example, arranged from [3].

Consider two scientists A and B interested in some chemical samples, which have been divided into aliquots. For each aliquot A records a 4-part composition, B works without recording the last element and arrives at a 3-part composition. Let us further assume for simplicity the ideal situation where the aliquots in each part are identical and where the two scientists are precise in their determination. Then clearly B's 3-part composition $[s_1, s_2, s_3]$ for an aliquot will be a subcomposition for A's 4-part composition $[x_1, x_2, x_3, x_4]$ for the corresponding aliquot related by

$$[s_1, s_2, s_3] = \frac{[x_1, x_2, x_3]}{(x_1 + x_2 + x_3)}.$$

This is then obvious that any statements that A and B make about the three common parts should agree. This is the nature of so-called subcompositional coherence [3]. Let us consider the simple data

* Corresponding authors.
E-mail addresses: korhonovam@seznam.cz (M. Korhoňová), hronk@seznam.cz (K. Hron).

0039-9140/$ – see front matter © 2009 Elsevier B.V. All rights reserved.
doi:10.1016/j.talanta.2009.07.054

set:

Full compositions$[x_1, x_2, x_3, x_4]$	Subcompositions$[s_1, s_2, s_3]$
[0.1, 0.2, 0.1, 0.6]	[0.25, 0.50, 0.25]
[0.2, 0.1, 0.1, 0.6]	[0.50, 0.25, 0.25]
[0.3, 0.3, 0.2, 0.2]	[0.375, 0.375, 0.25]

Scientist A would report the correlation between first two elements as $\mathrm{corr}(x_1, x_2) = 0.5$ whereas B would report $\mathrm{corr}(s1, s2) = -1$. There is thus incoherence of the correlation between raw components as a measure of dependence. Note, however, that the ratio of two components remains unchanged when we move from composition to subcomposition: $s_i/s_j = x_i/x_j$, so that, as long as we express all our statements about compositions in terms of ratios, we shall be subcompositional coherent.

Another serious requirement within compositions is that any statistical method, convenient for compositional data analysis, should respect their relative scale property. Its basic idea is to distinguish between the following two pairs of concentrations in a chosen compositional part, 0.50 and 0.51 together with 0.01 and 0.02. In the first one, the growth of an element's concentration is only negligible (the increase is by a factor 1.02) in contrary to the second case, when 0.02 is double of the previous size (i.e. increase by a factor 2). Thus, although the data pairs visually have the same distance (because we are thinking in terms of Euclidean distances), a distance between the second pair of compositions (with unaltered ratios of concentrations in the other parts) should be essentially greater than between the first one. Unfortunately again, standard methods, working with Euclidean distance, do not take this requirement into account. As a way out a new distance measure, or more generally, new geometry should be introduced, respecting this property as well as the necessity of the mentioned subcompositional coherence.

In the following section we give solutions for the above mentioned challenges like subcompositional coherence or relative scale preserving for compositional data introducing a family of so-called logratio transformations. Specially, we show how to use the logratio approach for cluster analysis and PCA of compositional data.

Consequently, the results will be applied to the analysis of coffee samples. As it is known, coffee aroma is composed of an extensive group of volatile compounds. Chemical composition of individual coffee products, accompanying coffee aroma, depends on several factors including species of green coffee beans (e.g. Arabica vs. Robusta variety) [4,5], geographical origin [6,7] and processing conditions [8–13], especially roasting, packaging and stocking of products. More than 800 significant volatile compounds have been identified, but the number of discovered aromatic compounds has been increasing. As a principal classes of aroma compounds [14–18], which are generated during a roasting process of green coffee beans, are presented aducts and derivatives of aldehydes, ketones, phenols, sulphur compounds, pyrazines, pyridines, pyrolles and furans as well. The aim of the study is to find out a relatively small group of compounds (major compounds, mainly formed during the roasting process), which could distinguish different coffee origins. Evidently, the perception of coffee aroma depends on both, the concentration of the compound and its odor threshold. So, the application of PCA and cluster analysis has been used to chromatographic results, obtained by headspace solid-phase microextraction (HS-SPME) in connection with gas chromatography–mass spectrometry (GC–MS). Simultaneously, the verification and the comparison between the standard statistical analysis and the introduced logratio approach were performed as well.

2. Theoretical considerations

As already mentioned in the previous section, D-part compositions are by their definition vectors $\boldsymbol{x} = [x_1, x_2, \ldots, x_D]$, rows of a data matrix $\boldsymbol{X}$, when all its components are strictly positive real numbers and they carry only relative information [2,19]. Indeed, the property that compositional information is relative is implicitly stated in the units, as they are always parts of a whole, like volume percent or molar fraction. It means that a composition and its positive real multiple convey essentially the same information. As a consequence, a way to simplify use of compositions is to represent them in closed form, i.e. as positive vector with constant sum k (usually 1 or 100 in case of percentages) of the parts. A set of all compositions with a constant sum k (also called closed data) forms a simplex, sample space of compositional data. An apparent problem is hidden in the requirement of nonzero values in the compositional parts. In compositional data we distinguish two kinds of zeros: essential zeros – or absolute of the part in the observation – and rounded zeros – or presence of a component, but below a detection limit [20]. Its different nature implies that the treatment of the two kinds of zeros should be different. When we consider that one component has a rounded zero, what represents apparently a more common problem in chemical data sets, i.e. when we consider that this value does not denote that the part is completely absent, but rather that no quantifiable proportion could be recorded to the accuracy of the measurement process, it seems reasonable, and is done traditionally, to replace them by a suitable small value. Possible problems of this approach (that do not occurs in the following) as well as proposed solutions are available in [20].

As mentioned above, the usual correlation analysis is not meaningful in the case of compositional data. For this reason, dispersion in compositional data sets can be described by *variations* [2], defined as

$$\tau_{ij} = \mathrm{var}\left(\ln \frac{x_i}{x_j}\right), \quad i, j = 1, \ldots, D.$$

It is possible to see that the problem of subcompositional incoherence does not occur more here as the ratio of two compositional parts x_i and x_j remains unchanged when taking only a subcomposition instead of the whole composition. However, the interpretation is different from the standard correlation measure. The values of τ_{ij} close to zero refers that the ratio x_i/x_j is nearly a constant and that the two parts, x_i and x_j, can be assumed to be redundant [21]. Generally, also a correlation analysis for compositional data in some cases is possible [22], but requires some more theoretical considerations.

In practice, regarding the above mentioned, standard statistical methods can lead to questionable results if they are directly applied to the original, closed data. The main reason is another geometry of compositional data on the simplex, called Aitchison geometry [19], in contrast to the standard multivariate data, represented by the well known Euclidean approach in real space. As a way out, the family of logratio one-to-one transformations from the simplex to the real space has been introduced [2,23]. For the purposes of the paper, we will consider so-called *centred logratio* (*clr*) *transformation* [2], where the compositions $\boldsymbol{x}$ are transformed to data $\boldsymbol{y}$, with

$$\boldsymbol{y} = [y_1, y_2, \ldots, y_D] = \left[\ln \frac{x_1}{\sqrt[D]{\prod_{i=1}^{D} x_i}}, \ldots, \ln \frac{x_D}{\sqrt[D]{\prod_{i=1}^{D} x_i}}\right].$$

The clr transformated data are already standard multivariate data, what enable us to use the mentioned PCA for data reduction. Moreover, clr transformation preserve distances among original compositions. Thus, the cluster analysis to reveal groups formed by the observations can be performed immediately when the data are transformed. Although this transformation has also some drawbacks like singularity of the data (the sum of the transformed variables y_i equals 0, see [2] for details), it treats all components symmetrically by dividing by the geometrical mean and the interpretation of the resulting values thus seems to be in some cases easier than by other members of the logratio transformations family (here for PCA of compositional data).

A way to perform PCA for compositional data is the following [19]. Consider the compositional data matrix $\boldsymbol{X}$ with n rows and D columns. Thus, D measurements have been obtained from each of n samples. Transform the rows of the matrix $\boldsymbol{X}$ with clr transformation to data matrix $\boldsymbol{Y}$. Then, for the purpose of better interpretation of the PCA results using biplot, centre the rows of matrix $\boldsymbol{Y}$, i.e. subtract the corresponding columns' means from each of elements of $\boldsymbol{Y}$. Note that $\boldsymbol{Y}$ is of the same order as $\boldsymbol{X}$, i.e. it has n rows and D columns and recall that clr transformation preserves distances. Thus, we can apply standard PCA procedure to $\boldsymbol{Y}$ in order to obtain resulting loadings and scores.

According to the relative scale of compositional data, the compositional parts with only small concentrations can contain a significant part of the total variability of the compositional data set and thus depreciate the results of PCA after clr transformation. For this reason, it is recommended, even more than in the case of standard multivariate data, to leave out such parts, not necessary for the further considerations, before the analysis is performed.

Anyhow when taking standard PCA, also in case of clr transformed compositions the loadings and scores can be visualized simultaneously using biplot, with interpretation of the loadings corresponding to the nature of compositional data [25]. Namely, the links (distances) between rays, representing the loading plot, approximate the variations. Thus, if the vertices of the rays coincide, or nearly so, this means that the ratio x_i/x_j is constant, or nearly so.

3. Experimental

3.1. Samples

Thirty commercially available roasted coffee samples of different origins, processed by different technologies were obtained in local supermarket. Different sort of coffee, including both, Arabica (16 samples) and Robusta coffee (3 samples), as well as various blends of them (11 samples), were examined in this study.

3.2. HS-SPME and GC/MS analyses

A commercially available carboxen/polydimethylsiloxane fiber (CAR/PDMS, 75 μm) was used for SPME analyses. At the first, the SPME fiber was reconditioned for 10 min in the GC injection port at 250 °C, and then was inserted into septum-sealed flask (40 mL) containing 2.00 g of ground coffee sample. The fiber was exposed for 60 min in the headspace at the laboratory temperature. All analyses were performed on a HP 6890 Series GC system with an Agilent 5973 N Mass Selective Detector (Agilent, Palo Alto, CA, USA), equipped with a Rtx-5Sil MS capillary column (30 m × 0.25 mm I.D. ×0.25 μm film thickness). SPME fibers were loaded in manual mode. The following conditions were used for the experiment: desorption temperature 250 °C, 4 min; splitless injection, temperature program 40 °C (2 min) – 5 °C/min – 200 °C (5 min), a carrier gas was helium (99.998%; velocity 0.9 mL/min; SIAD, Bergamo, Italy). MS scans were recorded within the range 29–370 m/z using electron ionization (energy 70 eV).

3.3. Data processing

Statistical analysis was accomplished by the statistical software R [24]. R is a free software environment that provides a wide variety of statistical (linear and nonlinear modelling, classical statistical tests, time-series analysis, classification, clustering, etc.) and graphical techniques, and is highly extensible.

4. Results and discussion

The HS-SPME analysis connected with GC–MS technique was used for the identification and quantification of the volatile compounds in commercially available coffee varieties (16 Arabica, 3 Robusta and 11 blends, denoted as A, R and AR, respectively). A multipurpose carboxen/polydimethylsiloxane SPME fiber has been applied to the determination of volatile compounds in coffee aroma. In qualitative analysis, 15 volatile flavor compounds were identified by the comparison with mass spectra in the NIST mass spectra library. These compounds could be essential for specification of coffee aroma in a particular coffee product. As promising descriptors of coffee aroma were selected following compounds: acetic acid, 1-hydroxy-2-propanone, pyrazine, pyridine, 2-methylpyrazine, furfural, furfuryl alcohol, 1,2-ethanediol diacetate, 2,6-dimethylpyrazine, 2-ethylpyrazine, 5-methylfurfural, furfuryl acetate, 2-ethyl-6-methylpyrazine, 3-ethyl-2,5-dimethylpyrazine, 1-furfuryl pyrrole. The representation of particular chemical components in each coffee sample is presented as relative contents in Table 1. An expertise mathematical consideration and examination of major volatile compounds made out to avoid the probable 'pollution' caused by compounds (compositional parts) with low concentrations, that cover, however, from the properties of Aitchison geometry, an extensive proportion of total variability of the data set. Only six flavor markers were selected from a number of alternative volatile compounds in coffee by the statistical approach: acetic acid (1), 2-methylpyrazine (2), furfural (3), 2-furfuryl alcohol (4), 2,6-dimethylpyrazine (5), 5-methylfurfural (6). These six compounds cover over 80% of the average relative amount of volatile compounds detected in the coffee samples. It could be stated that these flavor compounds observed in coffee samples are significant for distinguishing coffee variety or geographical origin, that was also reported by other authors [7,26].

The statistical evaluation of chromatographic data has been elaborated by the standard statistical analysis as well as the centred logratio transformation followed by both, cluster analysis and principal component analysis. Firstly, hierarchical clustering (using the complete agglomeration method) was applied to both raw and clr transformed data and the results were displayed using dendrogram (Fig. 1). As can be seen in Fig. 1, the standard cluster analysis causes that the data structure is not clearly visible. Arabica and blend samples are grouped together and only the group of Robusta coffees is quite well separated (Fig 1, upper plot). Performing clr transformation that turns out the compositions into the Euclidean geometry, the considered three groups (Arabica, Robusta and blends) are already distinguished. Now only few adjacent objects are assigned to wrong clusters (Fig. 1, lower plot), namely A1, A4 and A9 to blends and AR5, AR9 and AR11 to Arabica group. This effect can be explained by the unknown properties of the coffee samples, such as a composition of blended coffee (ratio of each coffee species in AR samples), coffee origin and quality. It is worth to mention, for example, that the manufacture process may affect on the part of coffee quality. For instance Arabica sample A16 and mixture AR11 were manufactured by the same producer and both samples were assigned to the same group in the dendrogram.

Table 1
Relative representation of volatile compounds in coffee ($\times 10^4$), nd—not detected.

	Acetic acid (1)	1-Hydroxy-2-propanone	Pyrazine	Pyridine	2-Methylpyrazine (2)	Furfural (3)	Furfuryl alcohol (4)	1,2-Ethanediol diacetate	2,6-Dimethyl-pyrazine (5)	2-Ethylpyrazine	5-Methylfurfural (6)	Furfuryl acetate	2-Ethyl-6-methylpyrazine	3-Ethyl-2,5-dimethyl-pyrazine	1-Furfuryl-pyrrole
R1	4.8	172.4	121.7	598.8	973.4	335.3	1530.6	121.4	707.8	229.3	320.2	367.9	244.6	15.6	49.4
R2	6.4	177.9	157.1	853.8	801.1	259.6	1520.1	113.6	533.2	173.8	170.2	290.4	174.4	98.8	52.6
R3	8.2	207.1	147.6	535.9	975.5	412.8	1273.3	156.7	685.8	213.5	449.6	285.1	236.5	180.0	52.6
A1	832.4	174.9	72.4	496.6	910.3	451.7	1770.0	313.5	579.9	173.5	620.0	481.8	201.6	104.5	36.9
A2	1155.1	256.6	24.3	94.5	358.4	1195.7	1699.2	152.9	396.1	137.5	792.9	206.4	124.1	73.1	26.0
A3	1783.5	203.8	10.8	73.6	135.5	722.2	1682.6	107.2	41.6	22.6	378.2	97.3	4.5	3.2	12.6
A4	862.7	213.0	72.0	533.9	603.7	1011.1	1757.1	192.3	434.8	115.7	589.8	353.3	119.5	86.7	22.9
A5	1341.0	328.2	74.7	307.5	660.2	1634.5	1226.7	178.5	484.8	122.3	1193.8	231.1	115.4	58.9	27.5
A6	1455.1	353.5	59.5	242.7	603.4	1641.9	1365.5	nd	478.5	159.6	955.0	219.6	124.6	61.5	28.0
A7	1142.2	195.8	33.3	297.1	382.7	897.9	1300.0	194.7	355.3	153.5	793.7	367.4	85.1	20.8	24.6
A8	1325.3	334.0	14.6	136.1	327.9	858.1	1229.2	194.4	275.7	44.6	624.1	176.9	55.8	22.2	14.9
A9	762.7	178.6	50.0	425.7	584.5	554.1	1003.2	198.9	497.3	163.4	672.4	369.0	98.6	44.1	31.5
A10	1305.0	279.2	44.3	361.9	479.6	1295.8	1875.6	196.4	414.2	90.4	804.7	344.3	95.0	58.8	22.8
A11	1442.1	300.9	27.4	114.6	420.8	1911.6	1258.4	156.7	396.2	121.8	1156.2	185.5	89.5	47.3	12.2
A12	1208.7	226.7	39.0	211.5	107.8	1517.3	2236.9	213.0	422.4	11.0	991.8	327.0	107.1	63.9	12.8
A13	1237.9	252.9	35.3	297.5	390.3	1295.4	2038.3	213.2	310.9	103.6	1027.0	279.8	107.5	36.8	27.2
A14	1496.7	289.8	32.0	208.0	302.1	1733.5	1925.6	207.8	310.9	103.6	1027.0	279.8	82.2	27.0	30.9
A15	1352.0	250.7	21.2	236.8	320.1	1365.5	1876.6	216.8	349.4	36.0	940.4	300.7	91.0	42.3	29.7
A16	343.5	66.9	15.3	118.5	190.9	558.2	573.3	8.5	168.1	38.1	388.1	102.4	23.7	11.9	nd
AR1	1106.4	375.6	127.4	218.0	886.8	1140.3	1414.0	163.7	560.9	2.0	853.7	178.9	135.4	72.8	30.6
AR2	1103.6	370.8	201.3	244.1	1197.4	1364.7	1642.1	204.2	526.2	191.4	747.5	171.8	157.1	125.1	44.2
AR3	1124.9	217.9	66.2	322.1	489.9	464.1	1294.9	172.3	359.9	148.2	385.6	267.9	112.2	55.1	28.8
AR4	601.7	170.7	107.1	423.7	691.1	240.0	769.5	12.9	488.9	204.7	263.3	236.5	170.6	71.1	29.9
AR5	1301.7	270.2	7.4	190.0	516.3	1522.1	896.0	163.0	456.9	187.5	939.3	191.1	135.6	43.9	23.9
AR6	975.9	282.2	109.1	158.2	859.0	669.3	985.5	153.5	588.9	240.0	520.2	128.7	149.2	66.0	22.2
AR7	1083.1	269.0	95.5	188.3	722.6	901.2	1025.4	147.6	519.2	192.8	804.1	151.0	135.1	68.9	26.9
AR8	389.6	167.0	73.5	374.2	644.5	393.4	865.9	118.5	489.8	191.7	362.8	232.0	133.7	73.3	14.6
AR9	1266.1	312.1	31.4	162.8	447.0	1554.2	874.1	93.4	409.0	137.3	872.4	174.4	93.7	34.2	9.4
AR10	1099.2	236.9	76.8	267.7	612.3	463.7	1649.9	183.9	471.9	82.2	558.0	299.1	123.3	71.1	50.0
AR11	322.9	67.2	6.5	149.5	215.2	463.5	543.3	17.4	200.2	57.9	357.9	116.4	7.4	11.1	8.8

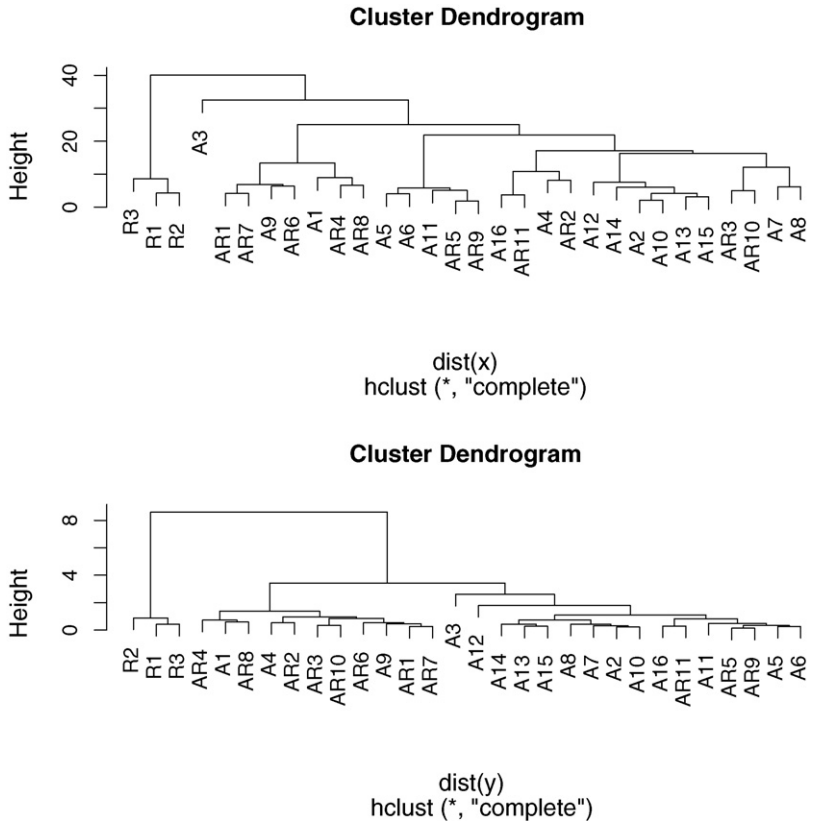


Fig. 1. Dendrograms for the raw coffee data (upper figure) and after clr transformation (lower figure).

Whereas the cluster analysis was able to distinguish particular groups of coffee, the PCA statistical analysis was performed to indicate similarities or differences within the complex odors, to establish the relation between varieties and particular volatile compounds. The results of PCA are presented in the widely used form of biplot [1] that displays both loadings and scores, with interpretation corresponding to compositional data [25] in the case of clr transformed compositions. Applying standard PCA to the data matrix consisting of the relative amounts of the 6 analytical variables (chosen major compounds) and 30 objects (coffee samples), the first two principal components were extracted. The total variance of initial data explain for 84.28%, where the first principal component (PC1) accounts 61.43% and the second principal component (PC2) accounts 22.85%, see Fig. 2. However, regarding the results of cluster analysis, the corresponding scores (representing objects) do not sufficiently meet the data structure (mixed A and AR samples). Thus the interpretation of this biplot could lead to misleading results.

On the other hand, the PCA for clr transformed data seems to produce much more interpretable results, presented again in the form of biplot (Fig. 3). The first two principal components account even for 96.01% of the total variance of the data; PC1 explains 88.79% of the variance in the clr transformed data set and PC2 explains 7.21%. Now, the scores illustrate very good resolution of groups of coffee and the reliability of the result is supported by high proportion of explained variability in the data set (96%) using the first two principal components. The loadings, represented by rays, refer to more or less constant ratio between the compounds (compositional parts). One can point out the role of acetic acid that forms the main source of differentiation of the Robusta variety by PC1. The groups of Arabica coffee and mixed coffee varieties are then measurably discriminated by PC2. If it is evident that the latter ones are divided into two groups, the second principal component might be interpreted as 'a factor of quality'. The resolution of these two coffee varieties is visualized through delimitated groups, however 'polluted' by objects, corresponding to the problematic samples revealed by the cluster analysis (A1, A4, A9 and AR5, AR9 and AR11, respectively, see Figs. 1 and 3).

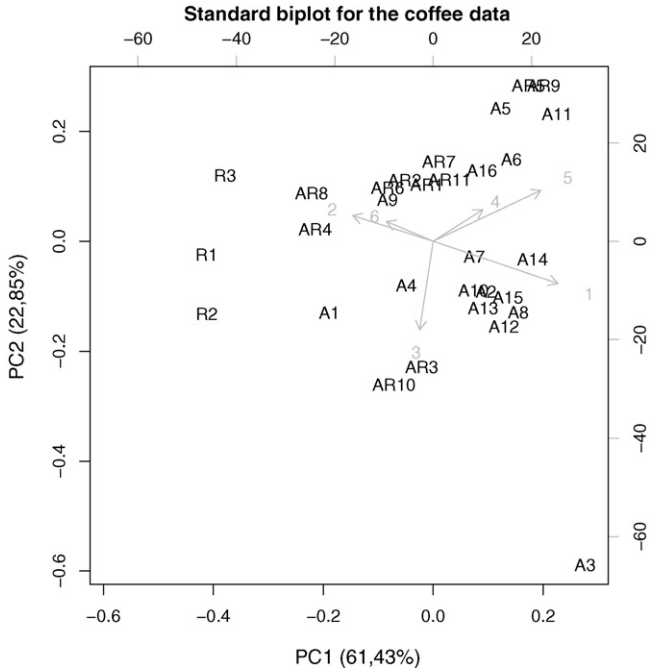


Fig. 2. Standard biplot for the coffee data.

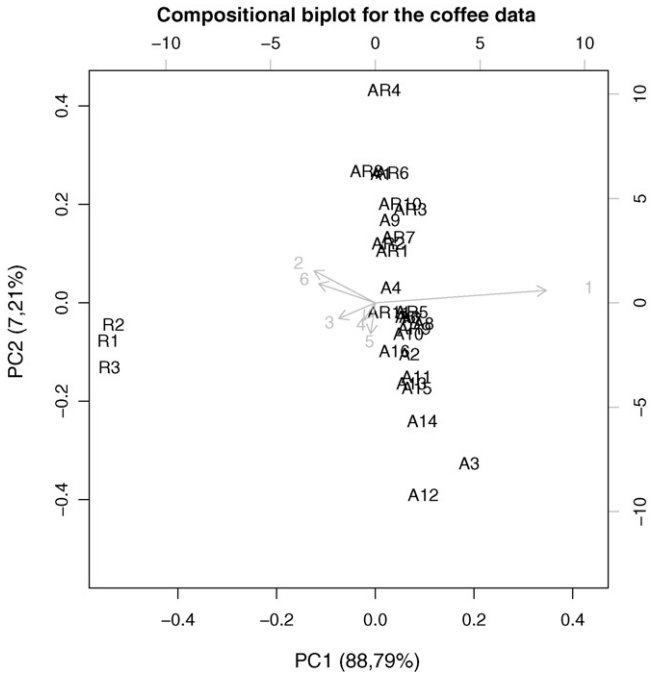


Fig. 3. Compositional biplot for the coffee data.

5. Conclusions

A comparison of the proposed centred logratio transformation and standard statistical approach of cluster analysis and principal component analysis has been applied on the data set concerning compounds of aroma profile of coffee samples. Two important conclusions have resulted from this study: (i) only 6 major volatile compounds (acetic acid, 2-methylpyrazine, furfural, 2-furfuryl alcohol, 2,6-dimethylpyrazine, 5-methylfurfural) provide sufficient differentiation of 30 roasted coffee samples under investigation. (ii) Application of centred logratio transformation provides better results in comparison to the standard statistical procedure (PC1 and PC2 explain 96% of total variability and provide better interpretation of the compositional data set).

Acknowledgement

The financial support by grants No. MSM 6198959214, MSM 6198959216, of the Ministry of Education, Youth and Sport of Czech Republic is gratefully acknowledged.

References

[1] K.R. Gabriel, Biometrika 58 (1971) 453–467.
[2] J. Aitchison, The Statistical Analysis of Compositional Data, Chapman & Hall, London, 1986.
[3] J. Aitchison, CoDaWork'08, Girona, Spain, 2008.
[4] M.S. Valdenebro, M. León-Camacho, F. Pablos, A.G. Gonzáles, M.J. Martín, Analyst 124 (1999) 999–1002.
[5] A.B. Rubayiza, M. Meurens, J. Agric. Food Chem. 53 (2005) 4654–4659.
[6] A.M.C. Freitas, A.I. Mosca, Food Res. Int. 32 (1999) 565–573.
[7] A.S. Risticevic, E. Carasej, J. Pawliszyn, Anal. Chim. Acta 617 (2008) 72–84.
[8] M. Czerny, W. Grosch, J. Agric. Food Chem. 48 (2000) 868–872.
[9] E. Nebesny, G. Budryn, J. Kula, T. Majda, Eur. Food Res. Technol. 225 (2007) 9–19.
[10] C.A.B. DeMaria, L.C. Trugo, R.F.A. Moreira, C.C. Werneck, Food Chem. 50 (1994) 141–145.
[11] W. Baltes, G. Hochmann, J. Agric. Food Chem. 35 (1987) 340–346.
[12] H. Kallio, M. Leino, K. Koullias, S. Kallio, J. Kaitaranta, Food Chem. 36 (1990) 135–148.
[13] M. Leino, J. Kaitaranta, H. Kallio, Food Chem. 43 (1992) 35–40.
[14] J. Stoffelsma, G. Sipma, D.K. Kettenes, J. Pypker, J. Agric. Food Chem. 16 (1968) 1000–1004.
[15] C. Sanz, D. Ansorena, J. Bello, C. Cid, J. Agric. Food Chem. 49 (2001) 1364–1369.
[16] O.G. Vitzthum, P. Werkhoff, J. Agric. Food Chem. 23 (1975) 510–516.
[17] H.A. Bondarovich, P. Friedel, V. Krampl, J.A. Renner, F.W. Shephard, M.A. Gianturco, J. Agric. Food Chem. 15 (1967) 1093–1099.
[18] J.C. Spadone, G. Takeoka, R. Liardon, J. Agric. Food Chem. 38 (1990) 226–233.
[19] V. Pawlowsky-Glahn, J.J. Egozcue, J. Tolosana-Delgado, Lect. Notes Composit. Data Anal. (2008), http://hdl.handle.net/10256/297, February 2009.
[20] J.A. Martín-Fernández, C. Barceló-Vidal, V. Pawlowsky-Glahn, Math. Geol. 35 (2003) 253–278.
[21] J. Daunis-i-Estadella, C. Barceló-Vidal, A. Buccianti, in: A. Buccianti, G. Mateu-Figueras, V. Pawlowsky-Glahn (Eds.), Compositional Data Analysis in the Geosciences: From Theory to Practice, Geological Society, London, Special Publications 264 (2006) 161–174.
[22] P. Filzmoser, K. Hron, Math. Geosci., in press, doi:10.1007/s11004-008-9196-y.
[23] J.J. Egozcue, V. Pawlowsky-Glahn, G. Mateu-Figueraz, C. Barceló-Vidal, Math. Geol. 35 (2003) 279–300.
[24] R development core team, Vienna, 2008, http://www.r-project.org/ (February 2009).
[25] J. Aitchison, M. Greenacre, Appl. Stat. 51 (2002) 375–392.
[26] C.P. Bicchi, O.M. Panero, G.M. Pellegrino, A.C. Vanni, J. Agric. Food Chem. 45 (1997) 4680–4686.

Talanta 80 (2009) 716–722

Contents lists available at ScienceDirect

Talanta

journal homepage: www.elsevier.com/locate/talanta

The problem of arsenic interference in the analysis of Cd to evaluate its extractability in soils contaminated by arsenic

Christophe Waterlot*, Francis Douay

Groupe ISA, Laboratoire Sols et Environnement, 48 Boulevard Vauban, 56046 Lille Cedex, France

ARTICLE INFO

Article history:
Received 21 April 2009
Received in revised form 17 July 2009
Accepted 27 July 2009
Available online 3 August 2009

Keywords:
Cadmium
Arsenic
Interference
ICP-AES
FAAS
GFAAS

ABSTRACT

The arsenic (As) spectral interference observed in the determination of cadmium (Cd) by inductively coupled plasma atomic emission spectrometry (ICP-AES) was studied in atomic absorption spectrometry (AAS) using flame (FAAS) and graphite furnace (GFAAS) as atomizers. The soils of 15 kitchen gardens located near two smelters in the North of France were selected according the ratio As/Cd. Four different extracting solutions usually used to evaluate the mobility of Cd were chosen to extract Cd from these soil samples: citric acid 0.11 M, acetic acid 0.11 M, calcium chloride 0.01 M and water. The quantitative determinations of Cd in the 15 soils for each solvent were investigated by ICP-AES at two lines (228.802 and 214.438 nm) and by FAAS or GFAAS with two-way background compensation. Compared to the Cd concentrations measured in the acid solutions and in the $CaCl_2$ solution after the addition of a chemical modifier, it was clearly demonstrated that the high-speed self-reversal background compensation (HSSR-method) was the method of choice to eliminate the spectral interference of As during Cd determination by FAAS and by GFAAS. In water, it was shown that the deuterium lamp used for the background compensation (D_2-method) was able to eliminate the most of the As interference. In comparison with Cd concentrations in water after adding a chemical modifier, those obtained with the HSSR-method were similar and a very good correlation was obtained between these two methods ($R^2 = 0.995$). It was therefore established that the HSSR-method would be able to replace the chemical modifiers to eliminate As interference in the determination of Cd-extractable from As contaminated soils.

© 2009 Elsevier B.V. All rights reserved.

1. Introduction

Since several metals are generally present in trace concentrations in complex matrix such as agricultural soils, urban soils, dust and plants, sensitive and selective methods are necessary to determine the metal concentrations [1–6]. FAAS and GFAAS are the most widely used general techniques for the analysis of metallic elements. This is attributed on the one hand, to the low initial and running costs of the instrument compared to the ICP-AES and on the other hand, to the high sensitivity of the GFAAS. However, as is the case with emission spectrometry, FAAS and GFAAS suffer from several types of interferences, which can be explained by the variability in the surface tension and the viscosity characteristics of samples, and which change the rate of the sample aspiration and affect the analyte atomization efficiency [7]. The latter changes according to the variability in ionization and chemical characteristics between samples too. Another class of interferences is the molecular and particular absorptions which overlap with the analytical line [8]. This phenomenon is explained by the scattering of the source beam due to incompletely atomized particles. Well known common types of spectral interferences in emission techniques are the mass interferences [9–12] and the atomic interferences which are due to the line overlap of the analyte and an element of the matrix [13–16]. For specific elements, some particular techniques have been developed. Based on the treatment of samples before analysis or using specific equipment [1,17–19], these techniques are used for the background compensation.

Atomic interference is a less common type of spectral interference in AAS. However some specific studies, concerning for example interferences between iron (Fe) and zinc (Zn), have recently been conducted. To eliminate spectral interferences between these two elements, some authors described a pretreatment of samples [20–23] while others developed an online elimination and/or preconcentration procedures before AAS determination [24–27] or used other techniques such as flow injection analysis (FIA), thermospray flame atomization or simultaneous electrothermal atomic absorption spectrometry (SIMAAS) [28–31]. However, the atomic interferences in AAS cannot always be fully resolved by the optical system of a spectrophotometer when spacing between the lines of the element and its interferent is less than the size of the slit width.

* Corresponding author. Tel.: +33 03 28 38 48 48; fax: +33 03 28 38 48 47.
E-mail address: c.waterlot@isa-lille.fr (C. Waterlot).

0039-9140/$ – see front matter © 2009 Elsevier B.V. All rights reserved.
doi:10.1016/j.talanta.2009.07.053

Nowadays, analytical procedures require instruments obtaining reliable and reproducible quantification of the element with a minimum effort in time-consuming sample pre-treatment. For this, different background compensations are widely used to solve molecular and atomic interference problems generated by samples. In almost all cases, they concern the deuteriumlamp- and Zeeman-effect-based methods. The third is the Smith–Hieftje method (H–S method) which can operate in a single-beam mode and uses only a single source, the hallow cathode lamp in a double pulsed mode [32]. More recently, a new approach has been developed [33]. This one is based on the broadening, which occurs in the resonance lines when a hollow cathode lamp is operated in a pulsed mode with a high frequency (100 Hz) at high current, up to a maximum of 600 mA. This background compensation method is called high-speed self-reversal method (HSSR-method) and was described as a universal technique used in a flame and graphite furnace atomization covering the entire wavelength range from 190 to 900 nm [33].

The determination of trace amounts of Cd in the presence of large amounts of As by FAAS and GFAAS following the guidelines suggested by the manufacturers, which specify using a 1.0-nm slit width, is prone to overestimate or underestimate the Cd concentrations. The reason for this is that the more sensitive Cd atomic adsorption line at 228.802 nm is only 0.01 nm from the weakly absorbing arsenic line at 228.812 nm [34]. Moreover, in the extracting solutions from soils, interferences between Fe and Cd may occur because of two iron lines, which are closely positioned next to the Cd line at 228.802 nm with a difference of only 0.04 and 0.08 nm, respectively in FAAS using the deuterium technique [35] or using the Zeeman-effect background compensation system in ETAAS [36].

The purpose of the present work is to evaluate the HSSR-method as background compensation (BGC) developed by Shimadzu for its AAS to determine Cd-extractable of soils. Firstly, Cd concentration was measured in test solutions containing increasing As concentrations. Secondly, the objective was to validate the HSSR-method for the Cd determination in the soil of 15 kitchen gardens after single extractions with citric acid, acetic acid, calcium chloride and water using FAAS and ETAAS for which Fe interferences may exist.

2. Experiments

2.1. Reagents and solutions

All solutions were prepared from analytical grade reagents unless specified otherwise. Double distilled (Val de Reuil, France) water with a specific conductibility of 0.1 $\mu S\,cm^{-1}$ was used to prepare all aqueous solutions and dilutions.

2.1.1. Extractants

Calcium chloride 0.01 M was prepared by dissolving 1.47 g of calcium chloride dihydrate reagent for analysis (Acrōs Organics, Noisy-le-Grand, France) in 1000 ml of double distilled water. A solution of acetic acid 0.11 M was obtained by diluting of a glacial acetic acid (Acrōs Organics) used for trace metal analysis. Citric acid monohydrate for analysis (23.11 g) (Acrōs Organics) was dissolved in 1000 ml of double distilled water to obtain a solution of citric acid 0.11 M.

2.1.2. Metal ion stock solutions

The Cd metal stock solutions, 1, 2 and 5 $mg\,l^{-1}$ in 2% HNO_3 (C.P.A. groupe A.C.S.D., Voisins le Bretonneux, France) were used to prepare the other solutions. Test solutions containing As were prepared from 1000 $mg\,l^{-1}$ standard solution in 1 M HCl (Reagecon, Shannon, Ireland).

2.1.3. Test solutions of Cd + As

Test solutions containing Cd and As were prepared from the stock solutions described above. Samples were analysed in pairs to allow for machine drift, for example, Cd 1 $\mu g\,l^{-1}$; Cd 1 $\mu g\,l^{-1}$ + As 0 $mg\,l^{-1}$; Cd 1 $\mu g\,l^{-1}$; Cd 1 $\mu g\,l^{-1}$ + As 0 $mg\,l^{-1}$, etc.

2.2. Studied soils

Between 2003 and 2004, 15 kitchen gardens were chosen in an area contaminated by the past atmospheric emissions of two smelters in the North of France. The soils were sampled up to a depth of 25 cm with a hand auger. Depending on the site surface, a composite sample of the ploughed layer of the soils was made starting from about 10 sub-samples taken in a random fashion from the area of the kitchen garden. These sub-samples were then mixed and homogenized to constitute a representative sample of the site surface. Care was taken to avoid the proximity of pathways, vehicle tracks or roads. In these soils, agronomic parameters and the total concentration of 18 pollutants were determined following protocols detailed in the literature [37]. Data were detailed by Douay et al. [38]. The highest Cd and As contents in soils were 26.5 and 65.1 $mg\,kg^{-1}$, respectively, while the lowest Cd and As measured contents were 4.0 and 4.4 $mg\,kg^{-1}$. The maximum value of the ratio As/Cd was 3.6 and the minimum value was 0.5.

2.3. Soil extraction procedures

The preparation of the 15 topsoil samples was carried out according to standard NF ISO 11464. Samples were air-dried and crushed to pass through a 2-mm stainless steel sieve. After drying at a temperature less than 40 C, an automatically sieve was conducted with an ultra centrifugal mill <250 μm (Retsch type ZM 200, Hann, Germany) to obtain a representative sub-sample (100 g) for each of the 15 samples of soil. Sub-samples were then used for the determination of metals in extracting solutions.

2.3.1. Microwave-assisted digestion

The digestion of dry samples was conducted using a microwave oven (Berghof Speedwave™ MWS-2, Eningen, Germany) with a system to control the temperature inside the reactor pressure. This system, integrated into the microwave oven, is an infrared thermometer that permits the temperature radiation emitted by the digestion solution to be quickly determined and regulated. The analytical solutions were obtained by digesting of 300 mg of air-dry soil in a mixture of 1.5 ml nitric acid (70%) and 4.5 ml sulphuric acid (70%). Before beginning the digestion, the reactors were agitated to promote the formation of carbon dioxide and then closed with an aluminium rupture disc, a TFM lid and a coupling cap. The reactors were placed in the rotor and the system was inserted into the oven and connected in the centre to a vent PFA tube. Quality control was based on the use of a certified sample (BCR CRM 141R).

2.3.2. Single extractions of Cd and As from soils

Selective extractions with citric acid 0.11 M, acetic acid 0.11 M, calcium chloride 0.01 M and water were performed in three replicates. For this, 3 g of a representative soil sub-sample that had been crushed and sieved to pass through a 250 μm sieve were taken. The aliquots were shaken with a soil/extractant ratio of 1/10 (w/v). A circular agitation of the samples with the chemical extractants was carried out using a rotor disc (10 rpm) for 16 h in the case of acid extracts and for 2 h in the case of calcium chloride and water extracting solutions. The extract was separated from the solid residue by centrifugation (4 530 rpm) over 20 min at room temperature and the solution was filtered on an acetate Millipore membrane (Millipore, 0.45 μm porosity). The solution was put into

Table 1
Temperature programme for GFAAS.

Furnace programme step	Temperature (°C)[a]	Hold time (s)	Ramp rate (°C s^{-1})	Argon gas flow rate (ml min^{-1})
Dry-1	120 (150)[b]	5	24	1
Dry-2	250 (250)[b]	5	26	1
Pyrolysis-1	300 (500)[b]	5	10	1
Pyrolysis-2	300 (500)[b]	3	0	0
Atomization	1800 (2200)[b]	6	Maximum	0
Cleaning	2300 (2400)[b]	3	Maximum	0

[a] Temperature programme used in absence of chemical modifier.
[b] Temperature programme used in presence of chemical modifier.

a polypropylene container, acidified with 92 μl of nitric acid solution (65%) and stored at 4 °C for analysis.

2.4. Apparatus

An ICP-AES (Varian, Mulgrave, Australia) was used to determine the pseudo-total Cd and As contents and the concentration of these elements in the single extractions from the soils. Characteristics and detection limits of this material were described by Abbasse et al. [39]. All samples analysed using ICP-AES were also analysed by FAAS or by GFAAS using the same set of standards for calibration. For atomic absorption determination, a Shimadzu AA-6800 (Tokyo, Japan) was operated under guidelines by the manufacturer using a 1.0 nm slit width, an ASC-6100 autosampler (Tokyo, Japan) and two techniques of background compensation. For graphite furnace investigations, the ASC-6100 autosampler (Tokyo, Japan) in combination with an ASK-6100 autodiluter (Tokyo, Japan) was used and the Shimadzu AA-6800 was fitted with a digital control technology graphite furnace atomizer (GFA-EX7, Tokyo, Japan) that had been fitted with a high-density graphite tube.

2.4.1. Background compensation used in AAS

The first BGC used is this study was based on the D_2-method which required a single element (Cd) hollow cathode lamp (Hamamatsu, Iwata, Japan) for the element specific absorption and a deuterium lamp (Hamamatsu, Iwata, Japan) for the background absorption. This method is one of the most popular and is available as a standard method in all Shimadzu atomic spectrometers. For this method, the hallow cathode lamp current was 8 mA.

The second BGC was based on the HSSR-method which is available on the Shimadzu AA-6800. To apply the technique of the self-reversal background compensation, the single Cd hollow cathode lamp current is modulated in two modes: a low current mode (8 mA) and a high current mode (100 mA). Because the high current mode measures only the background absorption, the difference between the absorption of both types of light provides accurate background compensation and measurement of the atomic absorption of the studied element.

2.4.2. Temperature programme for GFAAS

In absence of chemical modifier, the furnace programme was optimized for the determination of water or calcium chloride Cd-extractable from the studied soils (Table 1). The charring temperature was 300 °C [23,40] and the furnace temperature on atomization step was 1800 °C to obtain a maximum peak area absorbance value [23,41]. In presence of chemical modifier, the furnace temperature program was operated under guidelines by the manufacturer. The temperature applied for the atomization step was 2200 °C.

2.5. Statistical analysis

A Mann–Whitney *U* test was used to determine the influence of As on the determination of Cd concentrations in the test solutions. For each extractant and analytical techniques a Bonferroni, a Tuckey and a Fischer post hoc test were conducted to determine significant differences among Cd concentrations according to the analytical techniques and the background compensations. Moreover, a Dunnett-ANCOVA was carried out with datasets by choosing the data obtained by AAS with the HSSR-method as control. All statistical tests were performed using Statistica 6.0 for Windows.

3. Results and discussion

3.1. Analytical performance of the AAS

The measuring conditions used in FAAS were the same as those described by the manufacturers and in the literature [33,42]. For the graphite furnace, some modifications were made. The atomization conditions are summarized in Table 1. The limits of detection (LOD) and the limits of quantification (LOQ), respectively defined as the concentration equivalent to three times and to 10 times standard deviation of the reagent blank ($n = 10$) were determined for Cd using FAAS, GFAAS and the two methods of background compensation described above. Two methods of standard calibration were applied. In the case of FAAS, six standard solutions, in the 2–25 μg l^{-1} concentration range, were injected *via* the autosampler. For GFAAS, the same calibration procedure was applied injecting 20 μl of solutions, in the 0.025–4 μg l^{-1} concentration range. The results, expressed in molar concentration units, are shown in Table 2. Moreover, this one shows the characteristic mass, defined as $m_0 = (0.0044\ CV)/(A_1 - A_2)$ in which C is the analyte concentration, V is the introduced volume and A_1 and A_2 are the integrated absorbance of the sample and blank, respectively [43]. Values in Table 2 indicate clearly that the detection sensitivity using D_2-method was superior to that of the HSSR-method, making it ideal for analyses of Cd requiring high sensitivity in simple matrix. Nevertheless, the LOD, which were lower with the HSSR-

Table 2
Linear working range, equation of calibration curves, limits of detection (LOD), limits of quantification (LOQ) and characteristic mass (m_0) for Cd in GFAAS.

Techniques	Calibration range (μg l^{-1})	Equation of calibration curves	LOD (μg l^{-1})	LOQ (μg l^{-1})	m_0 (pg)
FAAS with D_2-method	2–25	$A = 0.57000\ [Cd] + 0.00097$, $R^2 = 0.9996$	6.4	21.3	
FAAS with HSSR-method	2–25	$A = 0.18381\ [Cd] - 0.00014$, $R^2 = 0.9998$	2.1	7.0	
GFAAS with D_2-method	0.025–4	$A = 0.19300\ [Cd] + 0.00190$, $R^2 = 0.9999$	0.0328	0.109	0.46
GFAAS with HSSR-method	0.025–4	$A = 0.11743\ [Cd] + 0.00058$, $R^2 = 0.9997$	0.0185	0.061	0.75

A means integrated absorbance and [Cd] is in μg l^{-1}. Units for slopes are in l μg^{-1}.

Table 3
Mean, minimum, maximum values and standard deviation (SD) of Cd concentrations determined by ICP-AES at 228.802, 226.502 and 214.439 nm in the presence of varying amounts of As.

	Cd (0 mg l^{-1})		Cd (0.5 mg l^{-1})		Cd (1 mg l^{-1})	
	Cd only	Cd + As	Cd only	Cd + As	Cd only	Cd + As
λ = 228.802 nm						
Mean	0.004	0.480	0.504	0.948	0.993	1.438
Min	−0.001	0.008	0.479	0.525	0.896	0.893
Max	0.011	2.203	0.519	2.308	1.054	3.150
SD	0.005	0.749	0.013	0.628	0.046	0.722
λ = 226.502 nm						
Mean	0.001	0.001	0.496	0.524	0.983	0.969
Min	−0.001	0.001	0.475	0.492	0.875	0.873
Max	0.004	0.002	0.519	0.558	1.036	1.034
SD	0.002	0.000	0.016	0.019	0.064	0.070
λ = 214.439 nm						
Mean	0.001	0.002	0.494	0.522	0.982	0.968
Min	0.000	0.001	0.476	0.490	0.869	0.867
Max	0.002	0.002	0.516	0.555	1.041	1.039
SD	0.001	0.000	0.012	0.019	0.065	0.071

Table 4
Mean, minimum, maximum values and standard deviation (SD) of Cd concentrations determined by FAAS at 228.802 nm in the presence of varying amounts of As ($1 \leq As \leq 500$ mg l^{-1}) using D_2-method and HSSR-method.[a].

	Cd (0 mg l^{-1})		Cd (0.5 mg l^{-1})		Cd (1 mg l^{-1})	
	Cd only	Cd + As	Cd only	Cd + As	Cd only	Cd + As
D_2-method						
Mean	0.008	0.031	0.513	0.555	1.022	1.029
Min	−0.005	0.008	0.505	0.531	1.004	1.009
Max	0.023	0.055	0.522	0.602	1.042	1.061
SD	0.010	0.017	0.007	0.021	0.015	0.016
HSSR-method						
Mean	−0.011	−0.008	0.492	0.504	0.994	1.000
Min	−0.014	−0.014	0.489	0.495	0.987	0.986
Max	−0.008	−0.002	0.499	0.522	0.998	1.025
SD	0.002	0.004	0.004	0.009	0.003	0.013

[a] Measurement results were detailed in Ref. [44].

method, indicated that this background compensation method was more efficient than with the D_2-method.

3.2. Determination of Cd in test solutions

Initial investigations of ICP-AES showed that interference by As at 228.812 nm was significant. Its magnitude depended on the concentration of As and on the As/Cd ratio (Table 3). For the two other lines available for determination of Cd (226.502 and 214.438 nm) interference by As was not observed (Table 3). This result is in accordance with the strategy recommended by Lambkin and Alloway [34] for Cd determination in soils contaminated by As. Other investigations using the D_2-method and the HSSR-method in FAAS showed that arsenic interference was not significant when Cd >1 mg l^{-1} [44]. Moreover, from the summarized data given in Table 4, it was established that the lower was the Cd concentration, the higher the interference by As and it was shown that the interference was more significant when the D_2-method was used [44,45].

The graphite furnace atomization method is used to determine low Cd concentrations. It is a more sensitive technique than flame atomization and its detection limits are lower (Table 2). That is why interferences should be more prevalent with this device. The results obtained by measuring Cd with various amounts of As are summarized in Table 5. For each Cd concentration, the investigation showed that As spectral interference was minimized using the HSSR-method. Moreover, the Mann–Whitney *U* test showed that

Table 5
Mean, minimum, maximum values and standard deviation (SD) of Cd concentrations determined by GFAAS at 228.802 nm in the presence of varying amounts of As ($0.01 \leq As \leq 100$ mg l^{-1}) using D_2-method and HSSR-method.[a].

	Cd (0 μg l^{-1})		Cd (1 μg l^{-1})		Cd (2 μg l^{-1})	
	Cd only	Cd + As	Cd only	Cd + As	Cd only	Cd + As
D_2-method						
Mean	−0.012	0.045	1.024	1.210	1.992	2.268
Min	−0.017	0.016	1.013	1.005	1.963	2.069
Max	−0.003	0.068	1.039	1.470	2.008	2.536
SD	0.004	0.018	0.008	0.136	0.015	0.165
HSSR-method						
Mean	−0.010	0.040	0.982	1.082	1.982	2.112
Min	−0.015	0.001	0.969	1.003	1.954	2.039
Max	−0.005	0.074	0.997	1.174	2.014	2.213
SD	0.003	0.023	0.011	0.055	0.019	0.061

[a] Measurement results were detailed in Ref. [44].

As interferences were not significant when As <50 mg l^{-1} and the ratio As/Cd was inferior to 50,000.

3.3. Cadmium and arsenic in acid solutions

3.3.1. Cadmium measurements in citric and acetic acid solutions

Citric and acetic acid solutions are very used to evaluate the mobility of trace elements in contaminated soils. Some applications of the first acid were for the removal of metals from contaminated soils [46,47]. This acid was used on the other hand to simulate the condition of root environment of the plant [48] and to study the interaction of Cd with low molecular weight organic acids in soils [49,50]. Acetic acid is included in the SM&T Programme for metal fractionation in environmental solid samples. It is regularly used to evaluate the metal extractable in acidic conditions [51,52] and to estimate the metal bioavailability [53,54]. Therefore, it seems to be interesting to study in these extracting solutions the possible interference of As in the determination of Cd by ICP-AES and AAS.

Of the three lines available for the Cd determination by ICP-AES, only two lines were used. The 228.802 nm line coincides with the As line at 228.812 nm causing a spectral interference (Table 3) and the Cd line at 214.438 with Al line. The third line, at 226.502 nm, is less sensitive and it is subject to broad-interference by iron [34]. The same solutions were analyzed by FAAS at 228.802 nm using the D_2-method and the HSSR-method (see supplementary data). In almost all of the acid solutions, Cd concentrations were elevated when ICP-AES at 228.802 nm and AAS with D_2-method were used. This was mainly the case for the extractions with citric acid for which ANCOVA (Bonferroni, Fischer and Tuckey post hoc tests) statistical analysis showed that Cd concentrations obtained with these two analytical methods were not significant ($P < 0.05$). According to these tests, the statistical results showed significant differences between Cd concentrations measured after applying the D_2-method and this method with a chemical modifier in the solution. This result can be explained by the As interferences and the possible Fe interferences which can induce a underestimation of Cd concentrations [33]. On the other hand, differences between Cd concentration obtained with the D_2-method after adding a chemical modifier and those obtained with the self-reversal background compensation without modifier were not significant. This interesting result was confirmed considering the Cd concentrations obtained with a chemical modifier as control. In these conditions, the Dunett post hoc test indicated a non-significant difference between the control and concentrations obtained with the HSSR-method ($P < 0.05$). These results showed that the As spectral interferences were not significant for the Cd-extractable with citric acid using the HSSR-method. Moreover, as shown in a previous study [33], the HSSR-method is an efficiency

Table 6
Determination of As, Fe and Cd (mg kg^{-1}) in CRM 141R and in the urban topsoils.

References	Total As	Total Fe	Total Cd	Pseudo-total Cd	Recovery of Cd[a]
CRM 141R[b]	8.84 ± 0.43[c]	n.d.[d]	14.6 ± 0.5	14.0 ± 0.4[e]	95.9
CRM 141R	8.12 ± 0.43[f]	23,164 ± 1085[f]	n.d.[d]	13.3 ± 0.1[g]	n.d.[d]
03-159	44.2	8374.5	23.9	23.5	98.2
03-161	65.1	15165.5	26.5	26.1	98.5
03-163	17.9	5870.0	11.5	11.1	96.7
03-164	30.2	10758.2	23.1	21.7	94.1
03-165	54.4	8920.9	24.9	24.0	96.5
04-170	13.2	6780.0	6.9	6.8	99.7
04-171	25.2	9891.7	10.8	10.4	96.3
04-172	15.4	7906.5	12.7	12.6	99.2
04-173	51.9	9150.1	14.5	14.2	98.1
04-174	15.1	8140.0	21.7	21.3	97.8
04-175	8.6	8230.0	17.2	16.9	98.4
04-176	12.6	6500.0	4.0	3.8	94.4
04-177	4.4	7660.0	8.7	8.1	93.8
04-178	21.0	11000.0	21.6	21.3	98.5
04-179	16.4	8030.0	9.3	9.1	97.4

[a] Recovery (%) = ([mean measured value]/[certified or reference value]) × 100.
[b] Certified value.
[c] Pseudo-total concentration from Bettinelli et al. [60].
[d] Not determined.
[e] From Bettinelli et al., Cd concentration after inter-laboratory analysis by GFAAS is 13.6 ± 0.4 [61].
[f] Pseudo-total concentration, number of replicates: $n = 5$.
[g] Number of replicates ($n = 5$).

background compensation method to eliminate the possible Fe interferences. For some soil samples, the same remarks can be made about acetic acid used as extractant. Nevertheless, the differences between Cd concentrations obtained by ICP-AES and AAS were lower than those obtained using citric acid as extractant. This observation can be explained by the probable existence of molecular interferences between Cd and hydroxy groups or carboxy function [55–57] coming from the low molecular weight organic acids in soils during extractions with acids [58,59].

3.3.2. *Validation of aqua regia digest procedure for the Cd determination*

A certified reference material of soil (BCR CRM 141R), contaminated in particular with Cd and As, was systematically digested with the 15 studied kitchen garden soils by microwave-acid digestion followed by GFAAS measurements. The results are presented in Table 6.

For the certified reference material, the mean value and the standard deviation of replicates are indicated. Concerning reproducibility, the standard deviation values obtained with the application of *aqua regia* microwave digestions were lower than 5%. Compared to the average value obtained in a previous work, whose aim was to compare analytical techniques, the recovery was about 98.5% [60,61]. This result validates our procedure, *aqua regia* digests of soils, and the Cd determinations using GFAAS with the HSSR-method.

For the studied kitchen garden soils, Cd contents in *aqua regia* digests were compared to the total Cd determined by the INRA Laboratory of Soil Analysis (Table 6). The good values obtained in all *aqua regia* matrix indicate a complete dissolution of Cd contents of soil samples and the absence of interference problems by As and Fe during the Cd measurements using GFAAS with the HSSR-method.

3.4. *Cadmium and arsenic in aqueous solutions*

3.4.1. *Cadmium measurements in calcium chloride 0.01 M*

Many authors regularly use a solution calcium chloride 0.01 M to evaluate the phytoavailability of Cd in soils [62–64]. In fact, this procedure provides information concerning the phytoavailability of Cd without growing plants in greenhouses. However, this procedure can be perturbed by the presence of As in soils, such as those around smelters. It is so very important to obtain a good determination of Cd in a centimolar calcium chloride solution, which also probably contains As due to the multi-contamination of soils. In this extracting solution, systematic higher Cd values were observed using ICP-AES in comparison with those observed in GFAAS (see supplementary data). Regarding the latter technique, the Cd values were highest when deuterium lamp background compensation was applied. This point can be explained by the molecular interference of chloride ion with Cd [65]. The use of palladium as a chemical modifier to reduce the chloride interference was investigated using the D_2-method [66] and the results were compared with those measured after using the HSSR-method (Fig. 1). Based on the correlation between the obtained results ($R^2 = 0.933$), it has been established that the HSSR-method is an efficient technique to correct the As spectral interference for the Cd determination. Moreover, the HSSR-method seemed to correct the chloride interference observed using the D_2-method as background compensation.

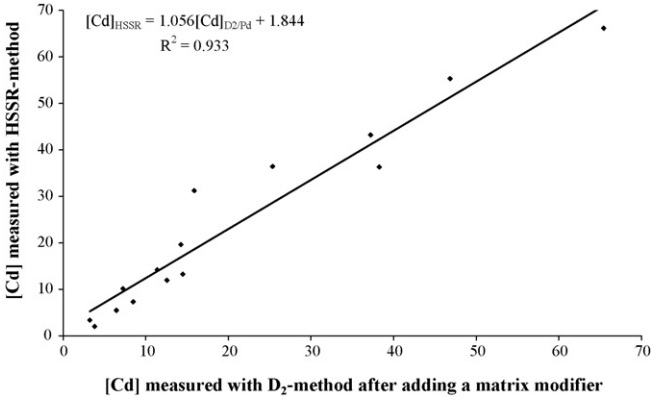


Fig. 1. Linear correlation between Cd concentrations (μg l^{-1}) in calcium chloride extract measured with GFAAS using the HSSR-method and those obtained after adding a chemical modifier and applying the D_2-method.

3.4.2. Cadmium measurements in water

In the last decades, a lot of work has been carried out in order to investigate the metal toxicity, such as that caused by Cd, collected near tailing mines, around metallurgical smelters and incinerators. Biotests have been also developed to assess the toxicity of metals and the results were then compared to the water-extractable metal concentrations of soils [67,68]. In many cases, Cd concentrations measured in water extracts of soil samples are very low. Thus, the determination of Cd requires analytical techniques exhibiting low detection limits for this element which has been designated a human carcinogen [69]. That is why new methods have recently been developed prior to the Cd measurements in water extracts by AAS [70,71]. The obtained results showed that the Cd concentrations measured using ICP-AES were systematically higher than those measured using GFAAS (see supplementary data). For some soils, the ratio between the two methods can even reach 80. For the line at 228.802 nm, this result can be explained firstly by the mean value of water-extractable As (2.72 mg kg^{-1}), which is approximately 250-fold higher than that of Cd.

For almost all of the samples, the Cd concentrations obtained using GFAAS with deuterium lamp for the background compensation were near those obtained with the HSSR-method. The statistical post hoc tests were not very clear because significant differences were found between these two methods using the Tukey test, and no difference was found using the Bonferroni and Fischer tests ($P < 0.05$) (see supplementary data). Then, the Cd measurements obtained using the HSSR-method were considered as control values and a Dunett post hoc test was conducted in order to compare the control values and those obtained after the background compensation with the D_2-method. Statistical results showed significant differences between the two background compensation methods ($P < 0.05$). These results may be explained by the As concentration in solution and probably by the high mean value of the water-extractable Fe (507 mg kg^{-1}), corresponding to an average concentration of 51 mg l^{-1}. According to the study led with the same scheme as the one described in this paper for As and Cd, a large overestimation (up to 55%) of the measured concentrations of Cd using the D_2-method can be obtained especially when the ratio Fe/Cd is 100,000. This result is explained by the closely positioned two lines to the Cd line at 228.802 nm (differences 0.04 and 0.08 nm). Using the HSSR-method for the background compensation, the overestimation corresponding to a ratio Fe/Cd = 100,000 calculated from [Cd] = 2 μg l^{-1} and [Fe] = 100 mg l^{-1} is lower than 25%. Taking into account of these data, the difference between Cd concentrations measured by AAS and ICP at 228.802 nm can be only explained by the As interference. On the other hand, differences between concentrations obtained using the HSSR- and D_2-methods can be explained by As and Fe interferences. But, according to the Dunett post hoc test, there was no significant difference between Cd concentrations found with the HSSR-method and those obtained with the D_2-method after adding a solution of palladium nitrate, used as a chemical modifier, into the water. As shown in Fig. 2, a very good linear correlation ($R^2 = 0.995$) was obtained between Cd concentrations obtained with these last two methods. These results confirm that the HSSR-method is an efficient background compensation of the spectral interferences caused by As during the Cd measurements using GFAAS. Moreover, it seems that the HSSR-method greatly reduces the Fe interferences during the Cd determination by ETAAS.

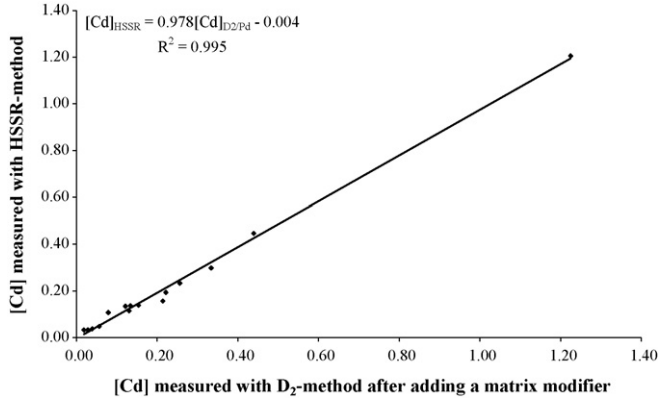


Fig. 2. Linear correlation between Cd concentrations in water (μg l^{-1}) measured with GFAAS using the HSSR-method and those obtained after adding a chemical modifier and applying the D_2-method.

4. Conclusion

Extractability of 15 kitchen garden soils contaminated by cadmium and arsenic were conducted using citric acid, acetic acid, calcium chloride and water as extractants. From our investigation, it has been observed that the HSSR-method is a versatile technique for quantitative determinations of Cd-extractable from As contaminated soils. The Cd concentration values in citric acid solutions depend on the method for the background compensation. Compared to the Cd concentrations measured using the D_2-method after adding a chemical modifier, those obtained using the HSSR-methods were not significantly different. The HSSR-method appears also as an accurate method for the background compensation in the studied case even if the differences between Cd concentrations measured using the HSSR-method and the D_2-method in acetic acid solutions are very low. In ETAAS, the obtained results are very clear and unambiguous. The high-speed self-reversal method appears so as an universal technique and using the Shimadzu atomic absorption spectrometer which is equipped with both D_2 and HSSR-methods as a standard configuration, As spectral interferences in the determination of Cd in complex matrix seem to be compensated in almost all studied cases.

Appendix A. Supplementary data

Supplementary data associated with this article can be found, in the online version, at doi:10.1016/j.talanta.2009.07.053.

References

[1] R.N. Sah, P.H. Brown, Plant Soil 193 (1997) 15–33.
[2] M.J. Nash, J.E. Maskall, S.J. Hill, J. Environ. Monit. 2 (2) (2000) 97–109.
[3] I. De Gregori, H. Pinochet, E. Fuentes, M. Potin Gautier, J. Anal. Atom. Spectrom. 16 (2001) 172–178.
[4] O.A. Farghaly, M.A. Ghandour, Environ. Res. 97 (2005) 229–235.
[5] M. Harper, B. Pacolay, M.E. Andrew, J. Environ. Monitor. 7 (2005) 592–597.
[6] A.B. Tabrizi, Food Chem. 100 (2007) 1698–1703.
[7] J.-L. Todolì, J.-M. Mermet, Spectrochim. Acta B 54 (1999) 895–929.
[8] M.M. Shafer, M. Siker, S.T. Overdier, P.C. Ramsl, M. Teschler Nicola, P.M. Farrell, Sci. Total Environ. 401 (2008) 144–161.
[9] L.L. Yu, R.D. Vocke, K.E. Murphy, C.M. Beck II, Fresen. J. Anal. Chem. 370 (2001) 834–837.
[10] B. Planer Friedrich, B.J. Merckel, Environ. Sci. Technol. 40 (2006) 3181–3187.
[11] B. Bocca, S. Caimi, P. Smichowski, D. Gomez, S. Caroli, Sci. Total Environ. 358 (2006) 255–264.
[12] J. Wang, T. Nakazato, K. Sakanishi, O. Yamada, H. Tao, I. Saito, Talanta 68 (2006) 1584–1590.
[13] J.P. Rybarczyk, C.P. Jester, D.A. Yates, S.R. Kolrtyohann, Anal. Chem. 54 (1982) 2162–2170.
[14] P. Pohl, A. Lesniewicz, W. Zyrnicki, Int. J. Environ. Anal. Chem. 83 (2003) 963–970.
[15] M. Raessler, J. Rothe, I. Hilke, Sci. Total Environ. 337 (2005) 83–90.
[16] B. Li, H. Yan, L. Yang, B. Huang, Anal. Bioanal. Chem. 376 (2003) 923–927.
[17] R. Payling, N.V. Brown, S.A. Gower, J. Anal. Atom. Spectrom. 9 (1994) 363–368.
[18] Z. Chen, J. Anal. Atom. Spectrom. 14 (1999) 1823–1828.
[19] C. Camara, Anal. Bioanal. Chem. 381 (2005) 277–278.
[20] K. Čundeva, T. Stafilov, Talanta 44 (1997) 451–456.
[21] M.A. Taher, Talanta 52 (2000) 181–188.

[22] D.L. Giokas, E.K. Paleologos, M.I. Prodromidis, M.I. Karayannis, Talanta 56 (2002) 491–498.
[23] T. Stafilov, D. Zendelovska, G. Pavlovska, K. Čundeva, Spectrochim. Acta B 57 (2002) 907–917.
[24] W.N.L. dos Santos, C.M.C. Santos, S.L.C. Ferreira, Microchem. J. 75 (2003) 211–221.
[25] P.S. Roldan, I.L. Alcântara, C.C.F. Padilha, P.M. Padilha, Fuel 84 (2005) 305–309.
[26] J.A. Sweileh, E.M. El-Nemma, Anal. Chim. Acta 523 (2004) 287–292.
[27] A. Efendioğlu, M. Yağan, B. Batir, J. Hazard. Mater. 149 (2007) 160–165.
[28] S. Zhao, X. Xia, G. Yu, B. Yang, Talanta 46 (1998) 845–850.
[29] E.V. Alonso, A.G. de Torres, J.M.C. Pavón, Talanta 55 (2001) 219–232.
[30] C.C. Nascentes, M.A.Z. Aruda, A.R.A. Nogueira, J.A. Nóbrera, Talanta 64 (2004) 912–917.
[31] P.R.M. Correia, E. Oliveira, P.V. Oliveira, Anal. Chim. Acta 458 (2002) 321–329.
[32] S.B. Smith, G.M. Hieftje, Appl. Spectrosc. 37 (1983) 419–424.
[33] U. Oppermann, J. Schram, D. Felkelay, Spectrochim. Acta B 58 (2003) 1567–1572.
[34] D.C. Lambkin, B.J. Alloway, Sci. Total Environ. 256 (2000) 77–81.
[35] P.L. Larkins, Spectrochim. Acta B 43 (1988) 1175–1186.
[36] X.-F. Yin, G. Schlemmer, B. Welz, Anal. Chem. 59 (1987) 1462–1466.
[37] T. Sterckeman, F. Douay, N. Proix, H. Fourrier, E. Perdrix, Water Air Soil Pollut. 135 (2002) 173–194.
[38] F. Douay, C. Pruvot, H. Roussel, H. Ciesielski, H. Fourrier, N. Proix, C. Waterlot, Water Air Soil Pollut. 188 (2008) 247–260.
[39] G. Abasse, B. Ouddane, J.C. Fisher, J. Anal. Atom. Spectrom. 17 (2002) 1354–1358.
[40] C.S. Nomura, P.R.M. Correia, P.V. Oliveira, E. Oliveira, J. Braz. Chem. Soc. 15 (2004) 75–82.
[41] A. Zacharia, S. Gucer, B. Izgi, A. Chebotarev, H. Karaaslan, Talanta 72 (2007) 825–830.
[42] Shimadzu Cook Handbook, Atomic Absorption Spectrophotometry Cookbook Section 3, Measuring Conditions by Element of Flame Atomic Absorption Spectrophotometry, Shimadzu Corporation, Kyoto, Japan, 2005, 45 pp.
[43] M.Y. Kamogawa, A.N.A. Nogueira, L.M. Costa, E.E. Garcia, J.A. Nóbrega, Spectrochim. Acta B 56 (2001) 1973–1980.
[44] C. Waterlot, F. Douay, J. Environ. Eng. Sci., submitted for publication.
[45] C. Waterlot, G. Bidar, F. Douay, F. Daurangeon, Spectra Anal. 261 (2008) 48–52.
[46] A. Majid, S. Argue, Miner. Eng. 14 (2001) 1513–1525.
[47] A.P. Khodadoust, K.R. Reddy, K. Maturi, J. Hazard. Mater. 117 (2005) 15–24.
[48] I. Ahumada, P. Escuredo, L. Ascar, J. Mendoza, P. Richter, Commun. Soil Sci. Plant Anal. 35 (2004) 1615–1634.
[49] D.-M. Zhou, H.-M. Chen, S.-Q. Wang, C.-R. Zheng, Water Air Soil Pollut. 145 (2003) 109–121.
[50] F. Qin, X.-Q. Shan, B. Wei, Chemosphere 57 (2004) 253–263.
[51] M. Pueyo, G. Rauret, J.R. Bacon, A. Gomez, H. Muntau, P. Quevauviller, J.F. Lopez-Sanchez, J. Environ. Monitor. 3 (2001) 238–242.
[52] M. François, H.-C. Dubourguier, D. Li, F. Douay, Aquat. Sci. 66 (2004) 78–85.
[53] J.E. Morgan, A.J. Morgan, Appl. Soil Ecol. 13 (1999) 9–20.
[54] M. Žemberiová, J. Barteková, M. Závadska, M. Šišoláková, Talanta 71 (2007) 1161–1668.
[55] J.-L. Todolì, J.-M. Mermet, A. Canals, V. Hernandis, J. Anal. Atom. Spectrom. 13 (1998) 55–62.
[56] A. Canals, L. Gras, H. Contreras, J. Anal. Atom. Spectrom. 17 (2002) 219–226.
[57] Y. Cho, Y. Nam Pak, Bull. Korean Chem. Soc. 26 (2005) 1415–1420.
[58] E. Meers, G. Du Laing, V. Unamuno, A. Ruttens, J. Vangronsveld, F.M.G. Tack, M.G. Verloo, Geoderma 141 (2007) 247–259.
[59] F. Qin, X.Q. Shan, B. Wei, Chemosphere 57 (2004) 253–263.
[60] M. Bettinelli, C. Baffi, G.M. Beone, S. Spezia, Atom. Spectrosc. 21 (2000) 60–70.
[61] M. Bettinelli, C. Baffi, G.M. Beone, S. Spezia, Atom. Spectrosc. 21 (2000) 50–59.
[62] I. Novozamsky, T.M. Lexmond, V.G.J. Houba, Int. J. Environ. Anal. Chem. 51 (1993) 47–58.
[63] A. Perez de Mora, E. Madejon, P. Burgos, F. Cabrera, Sci. Total Environ. 363 (2006) 38–45.
[64] P. Burgos, A. Perez de Mora, P. Madejon, F. Cabrera, E. Madejon, Environ. Geochem. Health 30 (2008) 109–114.
[65] S.M. Fraser, A.M. Ure, M.C. Mitchell, T.S. West, J. Anal. Atom. Spectrom. 1 (1986) 19–21.
[66] J. Creed, T. Martin, L. Lobring, J. O'Dell, Environ. Sci. Technol. 26 (1992) 102–106.
[67] A. Boularbah, C. Schwartz, G. Bilton, J.L. Morel, Chemosphere 63 (2006) 802–810.
[68] M. Heinlaan, A. Karhu, K. Kasemets, I. Kurvet, C. Waterlot, K. Sepp, H.-C. Dubourguier, F. Douay, Alter. Lab. Anim. 35 (2007) 101–110.
[69] International Agency for Research on Cancer (IARC), Beryllium, Cadmium, Mercury, and Exposures in the Glass Manufacturing Industry, IARC Monographs on the Evaluation of Carcinogenic Risks to Humans, vol. 58, International Agency for Research on Cancer, Lyon, France, 1987, p. 10.
[70] H. Parham, N. Pourreza, N. Rahbar, J. Hazard. Mat. 163 (2009) 588–592.
[71] A.M.H. Shabani, S. Dadfarnia, F. Motavaselian, S.H. Ahmadi, J. Hazard. Mater. 162 (2009) 373–377.

Talanta 80 (2009) 723–729

Contents lists available at ScienceDirect

Talanta

journal homepage: www.elsevier.com/locate/talanta

A new easy method for specific measurement of active myeloperoxidase in human biological fluids and tissue extracts

T. Franck[a,b,*], S. Kohnen[b], K. Zouaoui Boudjeltia[c], P. Van Antwerpen[g], A. Bosseloir[d], A. Niesten[b], O. Gach[e], M. Nys[f], G. Deby-Dupont[b], D. Serteyn[a,b]

[a] Department of General Anaesthesia and Surgical Pathology of Large Animals, Veterinary Institute B 41, University of Liege, Sart Tilman, BE-4000 Liège, Belgium
[b] Centre of Oxygen, Research and Development, Institute of Chemistry B 6a, University of Liege, Sart Tilman, BE-4000 Liège, Belgium
[c] Laboratory of Experimental Medicine, University of Brussels, U 222, ISPPC, CHU André Vésale, B-6110, Montigny-le-Tilleul, Belgium
[d] Zentech S.A., Liege Science Park, Av. Pré Aily, 10, B-4031 Angleur, Belgium
[e] Department of Cardiology, CHU B 35, University of Liege, Sart Tilman, BE-4000 Liège, Belgium
[f] Department of Anaesthesiology and Intensive Care, CHU B 35, University of Liege, Sart Tilman, BE-4000 Liège, Belgium
[g] Laboratory of Pharmaceutical Chemistry, Institute of Pharmacy, Universite Libre de Bruxelles, Brussels, Belgium

ARTICLE INFO

Article history:
Received 22 April 2009
Received in revised form 22 July 2009
Accepted 27 July 2009
Available online 3 August 2009

Keywords:
Human neutrophils
Myeloperoxidase
Peroxidase activity
Immunological extraction
Enzymatic detection
Amplex Red
Nitrite

ABSTRACT

The SIEFED ("Specific Immunological Extraction Followed by Enzymatic Detection") method already developed for the specific detection of the activity of equine myeloperoxidase (MPO) was adapted for the specific measurement of active human MPO in biological fluids or tissue extracts. The method consists of the extraction of MPO from aqueous solutions by immobilized anti-MPO antibodies followed by a washing (to eliminate the extraction medium and the biological fluid with their possible interfering molecules) and the measurement of the activity of MPO with a detection system containing a fluorogenic substrate, H_2O_2 and nitrite ions as reaction enhancer. The SIEFED was applied to study active MPO in human biological fluids (plasma, bronchoalveolar lavage fluid and supernatant from carotids extracts). The SIEFED for human MPO has a sensitivity limit of 0.080 mU/mL and showed good precision with intra- and inter-assay coefficients of variation below 10 and 20% respectively within a broad range of MPO activities establish from 0.156 to 473 mU/mL. The SIEFED for human MPO will be useful for the specific detection of active MPO in complex fluids and can be complementary to an ELISA to determine an active/total MPO ratio in healthy volunteers and patients especially in case of chronic or acute inflammatory diseases.
© 2009 Elsevier B.V. All rights reserved.

1. Introduction

Neutrophil myeloperoxidase (MPO) is involved in the intracellular bacterial destruction by producing potent oxidant molecules, mainly hypochlorous acid (HOCl) [1,2]. MPO is released in the extracellular milieu by dying or highly stimulated neutrophils in pathological conditions of acute and chronic inflammations [2–6]. In these conditions, MPO is able to exert a deleterious oxidant activity on neighbouring cells and tissues, and a therapeutic target should be to modulate its activity. Increased blood levels of MPO are now considered as markers of neutrophil activation and degranulation [7,8] and are measured by immunological methods (ELISA or RIA), which quantify the total concentration of the enzyme [9,10] without reflecting its true enzymatic activity. The activity of MPO is currently measured by the direct addition in the medium of H_2O_2 and a chromogenic or fluorogenic substrate as electron donors [11–13]. The oxidation of these electron donors is monitored by spectrophotometry or fluorimetry as a probe of the MPO activity [14,15]. Although these methods are suitable for measuring the activity of MPO *in vitro* in simple mixtures [13], they lack sensitivity, are cumbersome for cohort measurements and are not easily applicable to complex biological samples such as blood, plasma, or tissues, because of interferences with components endowed with peroxidasic activity (e.g. haemoglobin) [16,17], proteins (e.g. albumin, lipoproteins, ceruloplasmin) [18,19], reducing agents (e.g. ascorbic acid, glutathione) [16]. The physicochemical characteristics (pH, viscosity, etc.), the redox status or the colour of the biological fluids also interfere with the reading of the colorimetric or fluorescence response.

We designed a new technique, the SIEFED (for "Specific Immunological Extraction Followed by Enzymatic Detection") to measure the activity of an enzyme in biological fluids, and firstly developed it for equine MPO [20]. The major advantage of the SIEFED technique is its rapidity and an easy extraction of MPO out of the sample or reaction mixture by specific immobilized antibodies. The MPO binding to antibodies is followed by a washing

* Corresponding author at: Anesthésiologie et Pathologie Chirurgicale des Grands Animaux, Institut Vétérinaire, B 41, Université de Liège, Sart Tilman, BE-4000 Liège, Belgium. Tel.: +32 4 3663314; fax: +32 4 3662866.
E-mail address: t.franck@ulg.ac.be (T. Franck).

0039-9140/$ – see front matter © 2009 Elsevier B.V. All rights reserved.
doi:10.1016/j.talanta.2009.07.052

step that eliminates the solution and its potential interfering capacity, before starting the detection of MPO enzymatic activity. In human, increasing evidence indicated that MPO plays important roles in the initiation and progression of arthritis, carcinogenesis, pulmonary, kidney, neurodegenerative, inflammatory bowel and especially cardiovascular diseases in which the enzyme is taken as an inflammatory marker and a prognostic agent [6]. In these diseases, an important clinical aspect is to know the active part of MPO, which is the real witness of the oxidant potential of the enzyme. We describe here the development and optimization of the SIEFED technique for the specific detection of the enzymatically active human MPO in complex media [plasma, bronchoalveolar fluids (BALs)] and tissue extracts (carotids). The SIEFED technique is based on the immunological capture of the antigen by antibodies. An interesting point of this study was to compare the active MPO content measured by SIEFED with the total MPO content measured by ELISA to determine an active/total MPO ratio for the tested samples.

2. Experimental

2.1. Reagents

Analytical grade phosphate salts, sodium and potassium chlorides, sodium hydroxide, sodium acetate, H_2O_2 (30%, w/v), ethanol and Tween 20 and human myeloperoxidase (Calbiochem) were purchased from Merck (VWR International, Leuven, Belgium). Bovine serum albumin (BSA) and sodium nitrite were purchased from Sigma–Aldrich (Bornem, Belgium). 96-Wells microtiter plates (Combiplate 8 EB) were from Thermo Scientific (Breda, The Netherlands). The fluorogenic substrate, Amplex Red (10-acetyl-3,7-dihydroxyphenoxazine), was purchased from Molecular Probes (Invitrogen) (Merelbeke, Belgium).

2.2. Purification of human MPO and rabbit anti-human MPO polyclonal antibodies

MPO was purified from human neutrophils by detergent enhanced extraction followed by two steps of chromatography, and antisera were obtained by rabbit immunization against the pure human MPO emulsified with complete Freud adjuvant as previously described [9,21]. Polyclonal antibody (IgG), purified from rabbit antisera by affinity chromatography on Protein A sepharose (GE Healthcare, The Netherlands), was characterized for its specificity and stability and firstly used to develop a radioimmunoassay for total MPO assay in human plasma [9].

2.3. Methodology of the SIEFED technique

Three buffers were used. The coating buffer was 20 mM K and Na phosphates (pH 7.4), 137 mM NaCl and 2.7 mM KCl. The blocking buffer was obtained by addition of 5 g/L BSA to the coating buffer. The diluting buffer was the blocking buffer added with 0.1% Tween 20. The washing solution was 154 mM NaCl with 0.1% Tween 20. Microtitration wells were coated overnight, at 4 °C with 100 μL/well of serial dilutions of a rabbit IgG solution (62.5–500 ng/well) diluted with the coating buffer to determine the optimal IgG concentration to be used in the SIEFED assay. After removing the coating solution, the blocking buffer was added, the plates were incubated for 150 min at room temperature and washed three times. Serial dilutions of a standard MPO solution (pure human MPO) or unknown samples were added (100 μL/well) and incubated for 1 or 2 h either at 22 °C or at 37 °C or for 20 h at 4 °C. After three washings, the peroxidasic activity of MPO was detected by adding 100 μL of a 40 μM Amplex Red solution freshly prepared in phosphate buffer (50 mM) at pH 7.5 and added with 10 μM H_2O_2 and 10 mM nitrite. After incubation in the darkness (30 min, 37 °C), the fluorescence was read with a Fluoroscan Ascent (Thermo Scientific) with excitation and emission wavelengths set at 544 and 590 nm, respectively. Controls (blank) were performed with the dilution buffer. The fluorescence value was directly proportional to the quantity of active MPO present in the sample.

2.4. Validation of the SIEFED technique

The stability of the reference human MPO (from Calbiochem) was tested after its dilution in phosphate buffer saline (PBS) or PBS added with 5 g/L BSA and 0.1% Tween 20 (dilution buffer) and either incubated for 2 h at 37 °C or submitted to several freezing–thawing cycles.

The cross-reactivity of the anti-MPO antibodies with albumin, haemoglobin, elastase or eosinophil peroxidase was measured as previously described [9]. The detection limit was defined as the lowest active MPO concentration (mean value ± SD) that was statistically different from the value obtained with buffer alone. The standard curve was calculated and plotted point to point by using the Ascent Software for Multiscan Ascent (Thermo Labsystems). The precision and reproducibility were estimated by the coefficients of variation (CV) within or between assays calculated for several determinations of the same sample in the same assay or in different assays performed on different days. Accuracy was estimated by the recovery of known amounts of purified MPO added to the samples (plasma, BALs and carotid extracts).

To assure that the SIEFED technique could be reproduced with other anti-MPO antibodies, the immunoreactivity of our antibody was compared with that of the primary MPO-antibody (polyclonal antibody from rabbit) used in the MPO-ELISA kit (ELIZEN MPO) purchased from the Zentech company (Belgium).

2.5. Sampling technique

To test the stability of the neutrophils in blood after sampling, blood was drawn from five healthy donors without anticoagulant and on three anticoagulants with centrifugation (10 min, 22 °C, 1000 × *g*) 1 or 3 h after sampling. The anticoagulants were EDTA (1.8 mg/mL blood, in 3.5 mL vacutainer tubes; Venosafe, Terumo, Belgium), lithium heparin (15 IU/mL blood), or citrate (3.2% Na-citrate solution). Blood in plain tubes was allowed to clot (3 h) at room temperature (22 °C) before serum collection. For all the other studies with healthy and pathological subjects, venous peripheral blood samples were obtained in vacutainer tubes on EDTA (1.8 mg/mL blood), and centrifuged within 30 min after drawing.

Bronchoalveolar lavages (BALs) were performed in intensive care patients for therapeutic purpose (bacterial agent determination) via the endotracheal tube, with four aliquots of 50 mL warm sterile 0.9% NaCl solution as previously described [22]. The first aliquot was discarded and the second used for bacterial studies. The aspirated liquids of the third and the fourth aliquots were strained through sterile gauze and centrifuged (10 min, 4 °C, 300 × *g*); the supernatant was used for SIEFED assay.

Carotid atherosclerotic plaques were collected during surgery for carotid thrombo-endatherectomy and rinsed with 0.9% NaCl solution before their freezing at −20 °C. After thawing, the carotid plaques were homogenised on ice in 20–25 mL of cold 10 mM Tris-buffer, pH 7.4. The extract was centrifuged (20 min, 4 °C, 17,000 × *g*) and the supernatant was used for SIEFED assay.

Plasma samples, supernatants from BALs and carotid extracts were freshly used or kept frozen in small aliquots at −20 °C. Immediately before the SIEFED assay, samples were thawed and diluted with the diluting buffer before loading into the wells.

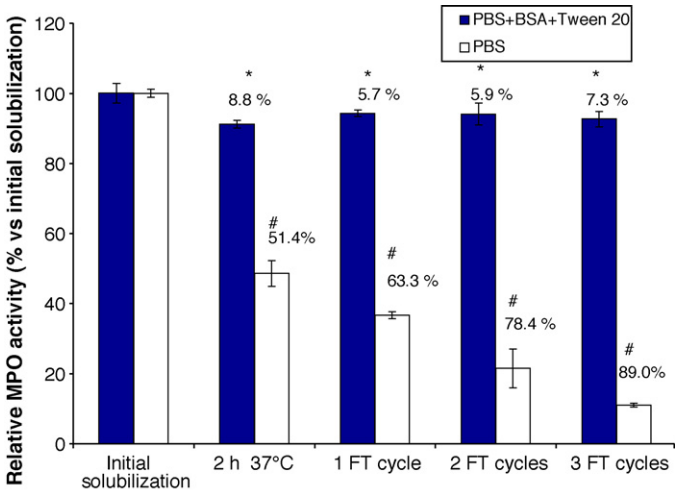


Fig. 1. Stability of human MPO activity in PBS buffer or PBS buffer + BSA + Tween 20 after an incubation period of 2 h at 37 °C or after several freezing–thawing (FT) cycles. The test performed directly after MPO dilution was taken as 100%. Mean ± SD, $n = 3$, ANOVA $^{*}p < 0.05$ versus initial solubilization in PBS + BSA + Tween 20; $^{\#}p < 0.05$ versus initial solubilization in PBS.

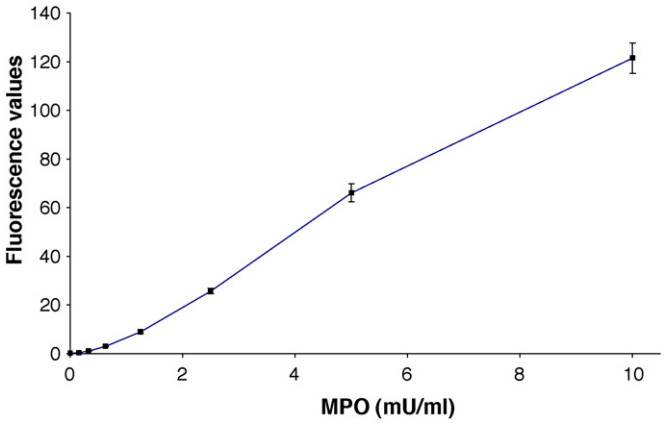


Fig. 2. Standard curve for the measurement of the activity of human MPO by the SIEFED technique (mean ± SD, $n = 5$).

Optimal dilution was determined by testing serial dilutions (1:1, 1:2.5, 1:5, 1:10, 1:20, 1:40, 1:80) of the samples in the dilution buffer.

2.6. Total MPO assay by a sandwich ELISA

To compare active MPO to the total content of the enzyme, total (active and non-active) MPO was measured with a sandwich human myeloperoxidase ELISA kit (ELIZEN MPO, Zentech SA, Belgium). Before the ELISA, plasma samples, and carotid extracts were diluted 20 times and BAL samples 50 times with the diluting buffer furnished by the ELISA kit.

2.7. Statistical analysis

SigmaStat 3.5 software (Systat, San Jose, CA) was used for the analysis. Data are presented as the mean ± SD and were evaluated by a one-way ANOVA.

3. Results

3.1. Stabilization of the reference human MPO

According to the supplier (Calbiochem), human MPO specific activity ranged from 180 to 220 U/mg proteins: we took the mean value, 200 U/mg proteins, as MPO specific activity. Fig. 1 shows that MPO diluted in PBS was not stable: the enzyme lost 51.4 ± 3.7% of its activity after 2 h at 37 °C and 89.0 ± 0.5% after three freezing thawing cycles. In PBS with 5 g/L BSA and 0.1% Tween 20, MPO remained stable, with only a slight loss of activity of 8.8 ± 1.1 and 7.3 ± 2.2% respectively after 2 h at 37 °C or three freezing thawing cycles.

3.2. Calibration curve and detection limit of the SIEFED technique

The standard curve was obtained by plotting the fluorescence values as a function of the known activity of the reference MPO, from 0.156 to 10 mU/mL (Fig. 2). Table 1 shows the fluorescence data measured for a typical active MPO reference curve (mU/mL) with the corresponding reference concentrations of the pure human MPO in ng/mL. The intra-assay CVs did not exceed 8%. The detection limit of the test (0.080 mU/mL) was determined as the lowest active MPO concentration (mean value ± SD) statistically different from the value obtained with buffer alone.

3.3. SIEFED method for MPO measurement in biological samples

Based on the detection limit and the slope of the standard curve, we chose 250 ng per well (or 2.5 μg/mL) as the optimal concentration of the coating antibody. After blocking and washing, the coated plates could be stored at 4 °C under dry conditions for up to 4 weeks. The binding of purified MPO to the coated antibodies increases with time and is similar at 37 °C and room temperature (RT) (Fig. 3). The activity of the samples measured after the incubation at RT are generally lower than after the incubation at 37 °C but, interestingly, the activity obtained after an overnight incubation at 4 °C or after 1 or 2 h incubation at 37 °C are similar (CV < 10%) (results not shown). The incubation at 4 °C does not disturb the activity of MPO and its binding to the antibody. The rapidity of the test being a priority factor, a 2 h incubation time at 37 °C was chosen for further studies.

As previously described [20], to reach a high sensitivity of the SIEFED technique for its application to biological samples, we used as peroxidase substrate, the Amplex Red molecule, which is transformed into the fluorescent resorufin upon its peroxidase-

Table 1
Standard curve values for the measurement of active human MPO by the SIEFED technique.

Human MPO (mU/mL)	Human MPO (ng/mL)	Mean fluorescence value ($n = 5$)	SD	CV (%)
0	0	0.149	0.002	1.3
0.156	0.78	0.441	0.025	5.7
0.3215	1.56	1.067	0.069	6.5
0.625	3.125	3.003	0.107	3.6
1.25	6.25	8.976	0.656	7.3
2.5	12.5	25.737	1.123	4.4
5	25	66.083	3.701	5.6
10	50	121.429	6.213	5.1

Mean ± SD, $n = 5$. The detection limit of the test was 0.080 mU/mL.

Table 2
Effect of the delay between blood collection and centrifugation on the activity of MPO measured by SIEFED in anticoagulated plasma and serum.

Collecting tube	Time between blood collection and centrifugation (h)	Mean MPO activity (mU/mL)	SD (mU/mL)	CV (%)
Citrate	1	1.4	0.3	23.2
	3	2.5	1.0	39.0
EDTA	1	1.9	0.2	11.7
	3	3.4	0.3	7.9
Li-heparin	1	2.9	0.7	23.4
	3	6.3	2.1	32.4
Dry (serum)	3	19.9	5.1	25.8

Mean ± SD of five healthy donors, $n = 5$.

catalyzed oxidation by H_2O_2 [23]. The optimal working conditions to measure the activity of MPO were reached with a freshly prepared 40 μM Amplex Red solution and 10 μM H_2O_2. The addition of 10 mM sodium nitrite ($NaNO_2$) in the reaction mixture increased 4–5-folds the sensitivity of the SIEFED [20].

3.4. Sampling conditions: effects of the anticoagulant and the delay in blood centrifugation

When centrifugation was done 1 h after blood sampling, the lowest mean MPO activity was observed for blood drawn on citrate and the highest one for blood drawn on Li-heparin (Table 2). After a delay of 3 h before centrifugation, the MPO activity values increased 1.8 times for EDTA and citrate and 2.1 times for Li-heparin. Interestingly, the lowest CVs, both after 1 and 3 h before blood centrifugation, were obtained for the EDTA plasmas what suggested that the neutrophils remained stable with time. For citrate and Li-heparin samples, the high CVs were unacceptable. A high mean value of MPO activity was observed for serum (Table 2). On the basis of these results, it was decided to use preferably EDTA anticoagulated blood for all the other studies; citrated samples obtained after blood centrifugation within 1 h can also be used, but we excluded the serum samples.

3.5. Application of the SIEFED technique to biological samples

The dilution of the sample improved the MPO activity till the dilution 1:10, undoubtedly by improving the binding between MPO and the primary antibody (Fig. 4). At higher dilutions, the measured values were stabilized and reached a plateau for most samples at the dilution 1:20 and for some samples at the dilution 1:40. But at this dilution, the limit of sensitivity is reached for samples with low content of active MPO. Linearity of the assay was determined by evaluating dilutional parallelism. Percentages of recovery calculated from observed-to-expected values for two plasmas, two BALs and two carotid extracts at two dilution factors (1:10 and 1:20) ranged from 94.1 to 130.0% (mean ± SD: 113.4 ± 12.2%; Table 3).

The accuracy of the assay was evaluated by determining the spiking recovery in two plasmas, two BALs and two carotid extracts. Percentages of recovery for seven spiking concentrations of active MPO added to the samples ranged from 72.6 to 113.1% (mean ± SD: 93.5 ± 9.2%; Table 4). A lack of recovery above 20% was observed for the highest active MPO concentrations (2.5 and 5 mU/mL) added to the plasma samples, but not to BALs and carotid extracts.

The intra-assay precision of the SIEFED technique estimated by repeated measurements within the same run on three different types of biological fluids with MPO activities ranging from 2.6 to 473.0 mU/mL showed CVs that did not exceed 10%. The mean CV value for all the samples ($n = 45$) was 3.8 ± 2.7% (Table 5).

Inter-assay precision was estimated by duplicate or triplicate assays of the biological fluids performed in different runs over a period of 4, 3 or 2 days. The MPO activities ranged from 1.8 to 118.1 mU/mL and the CVs did not exceed 20%. The mean CV value for all the samples ($n = 49$) was 10.2 ± 4.8% (Table 5).

In the plasma of 19 healthy donors, the total and active MPO contents were measured by ELISA (ELIZEN MPO, Zentech, Belgium) and by SIEFED respectively after checking that the primary antibody used in the kit had a similar response for the capture of active MPO than our antibody, and by diluting the samples in the same manner for the ELISA and the SIEFED. The mean total MPO value was 42.0 ± 15.0 ng/mL, while the mean active MPO value was 15.1 ± 5.2 ng/mL corresponding to 3.0 ± 1.0 mU/mL (Table 6). The active/total MPO ratio indicates that about 40 ± 9% of total plasmatic MPO was active in the healthy donors. The values of active and total MPO in five pathological plasmas, ranged from 80.5 to 210.7 ng/mL for active MPO and from 87.1 to 235.4 ng/mL for total MPO, were higher than the mean value obtained in healthy donors

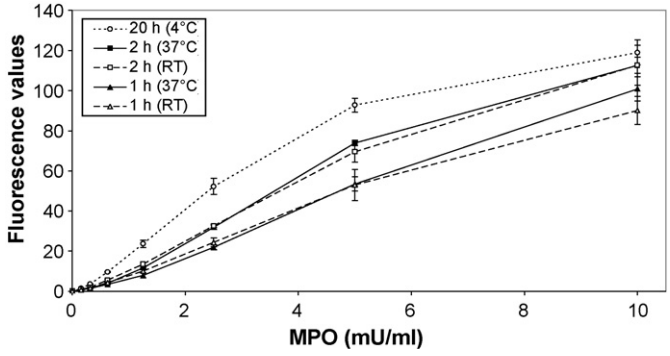


Fig. 3. Effects of incubation time and temperature on the MPO binding to its antibodies (mean ± SD, $n = 3$).

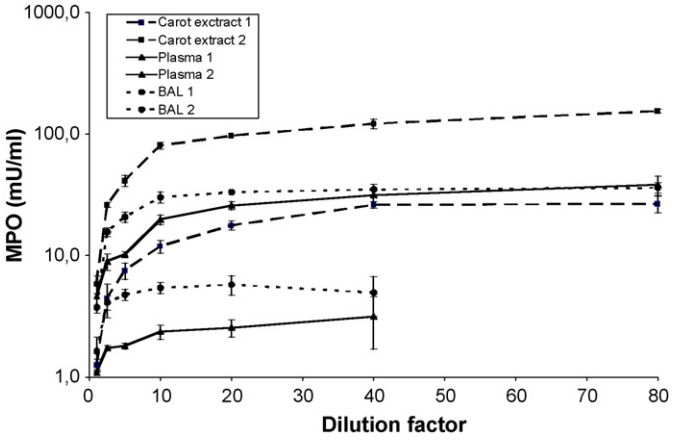


Fig. 4. Curves obtained with serial dilutions of plasma, carotid extracts and BALs (mean ± SD, $n = 5$).

Table 3
Active MPO values measured by SIEFED for dilutional parallelism of plasma, carotid extracts and BALs (mean ± SD, $n = 3$).

Samples	Dilution factor	MPO observed value (mU/mL)	MPO expected value (mU/mL)	Recovery (%)
Plasma 1	1:10	0.53		
	1:20	0.30	0.27	111.1
Plasma 2	1:10	1.71		
	1:20	1.04	0.85	122.3
Carotid 1	1:10	9.04		
	1:20	5.88	4.52	130.0
Carotid 2	1:10	0.42		
	1:20	0.23	0.21	110.0
BAL 1	1:10	10.23		
	1:20	5.77	5.12	112.6
BAL 2	1:10	0.34		
	1:20	0.16	0.17	94.1

Table 4
Recovery of spiked active human MPO measured by SIEFED in plasma, carotid extracts, and BALs.

Samples	Initial active MPO (mU/mL)	Added active MPO (mU/mL)	MPO expected (mU/mL)	MPO observed (mU/mL)	Recovery (%)
Plasma 1 (dilution 1:20)	0.843	0.078	0.92	0.90	97.8
		0.156	1.00	0.96	96.0
		0.312	1.16	1.18	101.7
		0.625	1.47	1.38	93.9
		1.25	2.09	1.86	89.0
		2.5	3.34	2.79	83.5
		5	5.84	4.33	74.1
Plasma 2 (dilution 1:10)	2.73	0.078	2.81	2.80	99.6
		0.156	2.89	2.82	97.6
		0.312	3.04	2.87	94.4
		0.625	3.36	3.02	89.9
		1.25	3.98	3.41	85.7
		2.5	5.23	4.12	78.8
		5	7.73	5.61	72.6
Carotid 1 (dilution 1:20)	5.8	0.078	5.84	6.24	106.9
		0.156	5.91	6.21	105.1
		0.312	6.07	6.22	102.5
		0.625	6.38	6.58	103.1
		1.25	7.01	6.82	97.3
		2.5	8.26	7.95	96.3
		5	10.76	9.73	90.4
Carotid 2 (dilution 1:10)	0.53	0.078	0.61	0.69	113.1
		0.156	0.69	0.69	100.0
		0.312	0.84	0.86	102.4
		0.625	1.16	1.31	112.9
		1.25	1.78	1.84	103.4
		2.5	3.03	2.94	97.0
		5	5.53	5.11	92.4
BAL 1 (dilution 1:20)	0.53	0.078	0.61	0.56	91.8
		0.156	0.69	0.66	95.7
		0.312	0.84	0.80	95.2
		0.625	1.16	1.02	87.9
		1.25	1.78	1.47	82.6
		2.5	3.03	2.42	79.9
		5	5.53	4.48	81.0
BAL 2 (dilution 1:10)	1.565	0.078	1.64	1.55	94.2
		0.156	1.72	1.56	90.8
		0.312	1.88	1.75	93.5
		0.625	2.19	2.01	91.6
		1.25	2.82	2.44	86.6
		2.5	4.07	3.50	86.1
		5	6.57	6.00	91.4

(Table 6). The active/total MPO ratio was also higher than in healthy controls, with a range from 0.5 to 0.9 (Table 6). In the five carotid and three BAL samples, the ratio of active versus total MPO showed that the active part of the enzyme varied from 20 to 90% of total MPO amount (Table 6), but no comparison was possible with healthy carotid and BAL samples.

4. Discussion

Owing to our experience with equine MPO [20] and RIA assay of human MPO [21], we developed a SIEFED technique for the specific and rapid measurement of the enzymatically active form of human MPO in complex biological samples. This technique has five inter-

Table 5
Intra- and inter-assay reproducibility of the SIEFED technique for active MPO measurements in human plasma, carotid extracts and BALs.

Samples	n[a]	Mean MPO activity (mU/mL)	SD (mU/mL)	CV (%)
Intra-assay				
Plasma 1	4	16.0	0.2	1.3
Plasma 2	4	9.5	0.1	1.1
Plasma 3	3	6.3	0.0	0.6
Plasma 4	3	16.3	0.5	3.1
Plasma 5	2	5.9	0.3	5.1
Plasma 6	2	15.3	0.4	2.6
Carotid 1	4	119.5	11.9	10.0
Carotid 2	4	167.3	12.0	7.2
Carotid 3	3	4.2	0.1	2.4
Carotid 4	2	61.7	1.7	2.8
Carotid 5	2	473.0	26.0	5.5
BAL 1	4	4.3	0.1	2.3
BAL 2	4	30.9	2.2	7.1
BAL 3	2	17.6	0.4	2.3
BAL 4	2	2.6	0.1	3.8
Samples	n[b]	Mean MPO activity (mU/mL)	SD (mU/mL)	CV (%)
Inter-assay				
Plasma 7	4	2.9	0.5	17.2
Plasma 8	4	15.5	0.5	3.2
Plasma 9	3	10.7	1.1	10.2
Plasma 10	3	24.4	2.4	9.8
Plasma 11	2	6.9	0.6	8.7
Plasma 12	2	19.8	3.2	16.1
Carotid 6	4	1.8	0.3	16.7
Carotid 7	4	54.7	2.4	4.3
Carotid 8	3	16.8	2.3	13.7
Carotid 9	3	88.4	9.5	10.7
Carotid 10	2	118.1	4.5	3.8
Carotid 12	2	4.4	0.4	9.1
BAL 5	4	5.5	0.9	16.3
BAL 6	4	31.0	2.8	9.0
BAL 7	3	29.0	2.9	3.4
BAL 8	2	50.8	5.6	11.0

CV = coefficient of variation, SD = standard deviation.
[a] Number of sample measurement during the same assay.
[b] Number of assays with the sample measured in duplicate or triplicate in each assay.

esting characteristics: (i) the easy immuno-capture of MPO out of a biological sample (or a reaction mixture containing MPO) without any preparation of the sample (no partial purification or precipitation of the enzyme), which is simply diluted, loaded into the antibody-coated wells and discarded after the incubation period during which MPO binding has occurred, (ii) the washing after the immuno-capture of MPO to eliminate the sample with its compounds potentially able to interfere with the enzymatic detection step, (iii) the specificity since the specific antibodies will only capture human MPO so that the detection system will disclose only the MPO activity, (iv) the high sensitivity of the test reached by the combined used of Amplex Red, a stable fluorogenic substrate for detection of peroxidases [12], and nitrite as an enhancer of the reaction, (v) the measurement of the activity by referring to a calibration curve made with pure human MPO.

As previously described, the success of the SIEFED technique depends on a good compromise between a strong binding of MPO and a low inhibition of its activity by the antibodies [20]. We obtained the best conditions to bind active MPO by coating the wells with 250 ng of rabbit anti-MPO IgG. The use of a polyclonal antibody increased the possibilities to capture MPO by different epitopes, but also the risk to inhibit the enzyme as observed in different models with MPO in solution [24,25]. We thus expected an inhibitory effect of immobilized antibodies on the MPO activity, but the MPO activities measured in the tested samples are calculated from a calibration curve, in which the reference human MPO is submitted to the same inhibitory effect of the antibody.

Good conditions for MPO incubation with the primary antibody were established at 37 °C for 2 h. Interestingly, the values obtained after an overnight incubation at 4 °C or a 2 h incubation at 37 °C were similar (CV < 10%): the overnight incubation at 4 °C can thus be used as an alternative condition for the SIEFED technique.

A good sensitivity of the test was obtained with the fluorogenic substrate Amplex Red, which is transformed during the peroxidasic cycle of MPO into the fluorescent resorufin in the presence of H_2O_2 [12,23]. We succeeded to greatly increase the sensitivity of the reaction by adding nitrite to the reaction mixture [20]. This increasing effect can be firstly explained by a cooperation of nitrite and Amplex Red for the turn over of the peroxidasic reaction of MPO. Burner et al. [26] showed that nitrite is a good substrate to reduce the compound I of MPO provided that a good electron donor is present to reduce the compound II. Amplex Red could play the role of the second electron donor for compound II. But, the oxidation of nitrite by the compound I mediates nitrogen dioxide, a reactive radical which can react with fluorescent probes [27]. Thus a second way to explain the amplification role of nitrite is the reduction of nitrogen dioxide by Amplex Red allowing both the formation of resorufin and the recycling of nitrite for the turnover of the peroxidasic cycle.

The study of the blood sampling conditions revealed that consistently higher MPO activity was measured in samples collected on heparin and in serum than in samples on EDTA or citrate. The delay between blood sampling and centrifugation increased the MPO activity values for all the anticoagulants, but the increase

Table 6
Concentration (ng/mL) of active and total MPO measured by SIEFED and ELISA and active/total MPO ratio in plasma of 19 healthy donors (mean ± SD) and in 5 plasmas, 5 carotid extracts and 3 BALs of pathological subjects.

	Active MPO (mU/mL)	Active MPO (ng/mL)	Total MPO (ng/mL)	Active MPO/total MPO
Mean plasmatic value for 19 healthy donors	3.0 ± 1.0	15.1 ± 5.2	42.0 ± 15.0	0.4 ± 0.1
Plasma 1	19.8	99.1	139.6	0.7
Plasma 2	26.1	130.6	235.4	0.6
Plasma 3	42.1	210.7	415.2	0.5
Plasma 4	23.1	115.3	170.1	0.7
Plasma 5	16.1	80.5	87.1	0.9
Carotid 1	4.6	22.8	26.0	0.9
Carotid 2	63.0	315.1	530.3	0.6
Carotid 3	5.3	26.5	97.1	0.3
Carotid 4	5.6	27.9	131.9	0.2
Carotid 5	18.6	93.0	442.8	0.2
BAL 1	3.4	16.8	61.2	0.3
BAL 2	21.9	109.5	251.2	0.4
BAL 3	2.6	13.2	71.4	0.2

was similar for citrate and EDTA and more pronounced for heparin. These results are in agreement with previous studies showing higher total MPO contents in heparin plasma and serum than in citrate and EDTA plasma [28,29].

The SIEFED method allows reliable quantification of MPO activity from 0.156 to 10 mU/mL, what corresponds to 0.78–50 ng/mL pure MPO. The dilution buffer stabilizes the enzyme during the incubation time and freezing–thawing cycles, because BSA and Tween 20 are known to prevent adhesion and aggregation of proteins [30]. The intra-assay coefficients of variation of the reference curve do not exceed 8%. The detection limit of the assay (0.080 mU/mL) allows an easy measurement of active MPO in diluted biological fluids. Like for ELISA, the dilution of the samples increases the sensitivity of the test by reducing the interactions between MPO and other biomolecules of the sample and by improving the binding of MPO to the primary antibody. The polyclonal antibody could also recognize the precursor of MPO, which is active in human [31]. The dilutions of 1:10 to 1:20 are adequate for most of the samples, but we cannot exclude that higher dilutions will be necessary for pathological samples.

We calculated the mean normal value of active MPO measured in EDTA plasmas as 15.1 ± 5.2 ng/mL or 3.0 ± 1.0 mU/mL, but the number of tested normal plasmas will be increased by further studies. In pathological samples, we measured MPO activities ranging from 2.9 to 42.1 mU/mL for plasmas, 1.8 to 473.0 mU/mL for carotid extracts and 2.6 to 50.8 mU/mL for BALs with good intra-assay CVs (below 10%) and acceptable inter-assay CVs (below 20%). These preliminary results indicate that the SIEFED technique will be useful to measure the active MPO in biological fluids or extracts from patients suffering from inflammatory pathologies with neutrophil activation and infiltration [6,22,32,33]. In theses pathologies, the measurement of total MPO by ELISA is often taken as a marker of neutrophil activation, but we compared the total and active MPO contents in samples and found in plasma an active/total MPO ratio of 0.4 ± 0.1 in healthy donors and a higher but variable ratio of 0.5–0.9 in pathological subjects. A still higher variability of this ratio (from 0.2 to 0.9) was observed for carotid extracts and BALs from pathological subjects. These original results suggest an important variability of active MPO contents in pathological samples probably linked to the activation status of neutrophils, the inhibitory capacity of the fluids towards the enzyme or other disease conditions. The results obtained with the SIEFED technique emphasized the importance of measuring the active part of MPO, which is the real witness of the oxidant potential of the enzyme that is not taken into consideration by a classical ELISA. Indeed, the presence of free active MPO increases the risk of cytotoxicity, as the enzyme is taken up by cells or binds on the cell surface with an *in situ* production of oxidant species [34,35], which are involved in chlorination and nitration of proteins [2,6], and surely contribute to the pathogenesis of the disease [2,6] or to the modulation of the inflammation reaction [36].

In conclusion, the SIEFED technique that we developed for human MPO opens news perspectives for the study of pathologies accompanied by the release of active MPO. The SIEFED is a method of choice to measure easily, reliably, quantitatively, and specifically the active part of MPO present in biological samples or tissue extracts. Moreover, SIEFED and ELISA can be used as complementary immunological techniques to determine with accuracy the active/total MPO ratio in biological samples, what constitutes a new prospect in clinical research.

Acknowledgement

The SIEFED technique is protected by an international patent (PCT/BE2005/00017).

References

[1] N. Borregaard, J.B. Cowland, Blood 89 (1997) 3503.
[2] S.J. Klebanoff, J. Leukoc. Biol. 77 (2005) 598.
[3] G. Deby-Dupont, C. Deby, M. Lamy, Intensivmed 36 (1999) 500.
[4] K.A. Kaminski, T.A. Bonda, J. Korecki, W.J. Musial, Int. J. Cardiol. 86 (2002) 41.
[5] A. Hoy, B. Leininger-Muller, D. Kutter, G. Siest, S. Visvikis, Clin. Chem. Lab. Med. 40 (2002) 2.
[6] M.J. Davies, C.L. Hawkins, D.I. Pattison, M.D. Rees, Antioxid. Redox Signal. 10 (2008) 1199.
[7] M.L. Brennan, S.L. Hazen, Curr. Opin. Lipidol. 14 (2003) 353.
[8] C.C. Wu, J.S. Chen, W.M. Wu, T.N. Liao, P. Chu, S.H. Lin, C.H. Chuang, Y.F. Lin, Nephrol. Dial. Transpl. 20 (2005) 1134.
[9] J. Pincemail, G. Deby-Dupont, C. Deby, A. Thirion, G. Torpier, M.E. Faymonville, P. Damas, M. Tomassini, M. Lamy, P. Franchimont, J. Immunol. Methods 137 (1991) 181.
[10] S. Neumann, G. Gunzer, H. Lang, M. Jochum, H. Fritz, Fresenius J. Anal. Chem. 324 (1986) 325.
[11] P.C. Andrews, N.I. Krinsky, Anal. Biochem. 127 (1982) 346.
[12] R. Haughland, Handbook of Fluorescent Compounds and Research Products, ninth ed., Molecular Probes, Inc., 2002.
[13] E. Malle, P.G. Furtmüller, W. Sattler, C. Obinger, Br. J. Pharmacol. 152 (2007) 838.
[14] Peroxidase, in: V. Worthington (Ed.), Worthington Enzyme Manual, 1972, p. 43.
[15] J. de la Harpe, C.F. Nathan, J. Immunol. Methods 78 (1985) 323.
[16] G. Graff, D.A. Gamache, M.T. Brady, J.M. Spellman, J.M. Yanni, J. Pharmacol. Toxicol. Methods 39 (1998) 169.
[17] E. Monzani, B. Bonafè, A. Fallarini, C. Redaelli, L. Casella, L. Minchiotti, M. Galliano, Biochim. Biophys. Acta 1547 (2001) 302.
[18] M. Segelmark, B. Persson, T. Hellmark, J. Wieslander, Clin. Exp. Immunol. 108 (1997) 167.
[19] A.C. Carr, M.C. Myzak, R. Stocker, M.R. McCall, B. Frei, FEBS Lett. 487 (2000) 176.
[20] T. Franck, S. Kohnen, G. Deby-Dupont, S. Grulke, C. Deby, D. Serteyn, J. Vet. Diagn. Invest. 18 (2006) 326.
[21] G. Deby-Dupont, J. Pincemail, A. Thirion, C. Deby, M. Lamy, P. Franchimont, Experientia 47 (1991) 952.
[22] M. Nys, D. Ledoux, J.L. Canivet, P. De Mol, P. Lamy, P. Damas, Crit. Care Med. 28 (2000) 2825.
[23] J.G. Mohanty, J.S. Jaffe, E.S. Schulman, D.G. Raible, J. Immunol. Methods 202 (1997) 133.
[24] S.V. Griffin, P.T. Chapman, E.A. Lianos, C.M. Lockwood, Kidney Int. 55 (1999) 917.
[25] R.J. Falk, M. Becker, R. Terrell, J.C. Jennette, Clin. Exp. Immunol. 89 (1992) 274.
[26] U. Burner, P.G. Furtmüller, A.J. Kettle, W.H. Koppenol, C. Obinger, J. Biol. Chem. 275 (2000) 20597.
[27] P. Wardman, Free Radic. Biol. Med. 43 (2007) 995.
[28] T. Franck, S. Grulke, G. Deby-Dupont, C. Deby, H. Duvivier, F. Peters, D. Serteyn, J. Vet. Diagn. Invest. 17 (2005) 412.
[29] J. Shih, S.A. Datwyler, S.C. Hsu, M.S. Matias, D.P. Pacenti, C. Lueders, C. Mueller, O. Danne, M. Möckel, Clin. Chem. 54 (2008) 1076.
[30] L. Kreilgaard, L.S. Jones, T.W. Randolph, S. Frokjaer, J.M. Flink, M.C. Manning, J.F. Carpenter, J. Pharm. Sci. 87 (1998) 1597.
[31] R.L. Olsen, C. Little, Biochem. J. 222 (1984) 701.
[32] S. Baldus, J.P. Eiserich, M.L. Brennan, R.M. Jackson, C.B. Alexander, B.A. Freeman, Free Radic. Biol. Med. 33 (2002) 1010.
[33] O. Gach, C. Biemar, M. Nys, G. Deby-Dupont, J.P. Chapelle, C. Deby, M. Lamy, L.A. Pierard, V. Legrand, Coron. Artery Dis. 16 (2005) 59.
[34] M. Mathy-Hartert, G. Deby-Dupont, P. Melin, M. Lamy, C. Deby, Experientia 52 (1996) 167.
[35] H. Omi, N. Okayama, M. Shimizu, M. Okouchi, S. Ito, T. Fukutomi, M. Itoh, J. Diab. Complicat. 16 (2002) 201.
[36] D. Lau, H. Mollnau, J.P. Eiserich, B.A. Freeman, A. Daiber, U.M. Gehling, J. Brümmer, V. Rudolph, T. Münzel, T. Heitzer, T. Meinertz, S. Baldus, Proc. Natl. Acad. Sci. U.S.A. 102 (2005) 431.

Talanta 80 (2009) 730–737

Contents lists available at ScienceDirect

Talanta

journal homepage: www.elsevier.com/locate/talanta

Optimization of FLEC®-SPME for field passive sampling of VOCs emitted from solid building materials

Jérôme Nicolle[a,b], Valérie Desauziers[a,*], Pierre Mocho[b], Olivier Ramalho[c]

[a] Laboratoire Génie de l'Environnement Industriel, Ecole des Mines d'Alès, Hélioparc, 2 avenue Pierre Angot, 64053 Pau Cedex 9, France
[b] Laboratoire Thermique Energétique et Procédés, Université de Pau et des pays de l'Adour, B.P. 1155, 64000 Pau, France
[c] Université Paris-Est, Centre Scientifique et Technique du Bâtiment, 84 avenue Jean Jaurès, Champs-sur-Marne, 77447 Marne-la-Vallée Cedex 2, France

ARTICLE INFO

Article history:
Received 13 February 2009
Received in revised form 24 July 2009
Accepted 27 July 2009
Available online 7 August 2009

Keywords:
Indoor air
Building material
VOC
SPME
Passive sampling
Emission cell

ABSTRACT

The FLEC®-SPME sampler, described in a previous paper, consists of an emission cell coupled with solid phase microextraction (SPME) for passive sampling of VOCs emitted from building materials. It represents an interesting alternative to standard dynamic sampling protocol as it is easier to implement. If standard dynamic sampling determines emission rates, passive FLEC®-SPME aims to the determination of the concentration in air at the material surface. That could be assumed provided that material/air equilibrium is reached. Thus, VOCs emission kinetics were studied for 3 different materials (pine wood panel, carpet and PVC floor) to determine equilibrium times. Then, the relevance of the method has been assessed using new materials through a 3-day emission test. Qualitative results were compared to those obtained from the standard method to check the ability of FLEC®-SPME to detect the most toxic compounds, named "VOCs of interest" and listed in the French regulation. Minor differences were observed, so this methodology seems promising, especially for field studies aiming in the identification of VOCs sources in buildings. Moreover, the concentration at the material surface combined to emission modeling could be used to predict indoor VOCs concentrations helping in indoor air quality diagnostic.

© 2009 Elsevier B.V. All rights reserved.

1. Introduction

In order to reduce VOCs levels in indoor air, a major strategy relies on the control of emission from sources, especially building materials [1,2]. In France as in a few European countries, new products, such as floor coverings, can be evaluated through a time-consuming procedure involving a 28-day emission test in an environmental chamber or in an emission cell [3]. The test involves a dynamic sampling mode to transfer the VOCs emitted from the solid material to an adsorbent tube and is covered by ISO standards [4,5]. Thus, the sampling step of this procedure needs clean air supply, air flow meters and a long sampling duration (60 min) to concentrate the low quantity of VOCs emitted by the materials. To increase sampling frequency, microchambers, inspired from the emission cell described above, were developed for automated control of material emissions [6]. It requires specific and expensive equipment (Microchamber/Thermal Extractor) hyphenated to the chromatographic system and hence, is only suitable to laboratory samplings.

Several works [7–12] and national (or European) guides [2,3,13] use dynamic sampling to test single materials under laboratory conditions (fixed temperature, air flow-rate and relative humidity). These data are very useful to determine if the sample complies with labeling criteria or to compare it with other similar products. However, they may not be enough to predict the material behavior in the field because of the established effects of temperature, air exchange rate and relative humidity on the concentration–time profile of the VOCs specific emission rate (SER) [14]. For this purpose, on-site sampling must be developed by implementing simpler and faster sampling methods. Passive sampling, only based on VOCs diffusion, seems to be adapted as no pump or flow control is required. Recently, a sorption-based sampling technique, the Sorptive Tape Extraction (STE), was developed [15]: a polydimethylsiloxane (PDMS) tape is used to recover VOCs at the solid surface by direct contact. Although it is very simple and attractive, this method cannot be representative of emission in air because of the direct transfer of VOCs from the material to the PDMS which would favor low volatile compounds. Another device, the "Passive Flux sampler" (PFS) [16,17] seems to be more representative of material emissions. It consists of a glass Petri dish (inner diameter: 36 mm; depth: 10 mm) whose bottom is covered by an adsorbent layer. The PFS is simply placed on the surface to be studied and the VOCs diffuse to the adsorbent. The emission rate can be determined as described in the following Eq. (1) (from

* Corresponding author. Tel.: +33 5 59 30 99 92; fax: +33 5 59 30 63 68.
E-mail addresses: jerome.nicolle@ema.fr (J. Nicolle), valerie.desauziers@ema.fr (V. Desauziers), pierre.mocho@univ-pau.fr (P. Mocho), olivier.ramalho@cstb.fr (O. Ramalho).

0039-9140/$ – see front matter © 2009 Elsevier B.V. All rights reserved.
doi:10.1016/j.talanta.2009.07.063

first Fick law under steady state conditions) [16]:

$$F = -D\frac{dC}{dx} = -D\frac{C_a - C_{as}}{L} \quad (1)$$

where F is the emission rate of the target VOC ($\mu g\,m^{-2}\,s^{-1}$), D, the diffusion coefficient ($m^2\,s^{-1}$), C_a the concentration in indoor air ($\mu g\,m^{-3}$), C_{as} the gas phase concentration at the material surface ($\mu g\,m^{-3}$), L the thickness of the gas phase boundary layer (m).

Studies with PFSs showed that the emission rates measured were proportional to those determined by the standard chamber method ($r^2 = 0.96$) [16]. These low cost and simple samplers are relevant for field measurements, especially for multipoint samplings. However, the sampling times are long (at least 4 h) to reach a sufficient sensitivity. Moreover, analysis requires collecting and introducing a part of the adsorbent in an empty tube for thermal desorption [17]. This supplementary step could be a source of experimental errors and complicates the protocol.

As an alternative, another passive sampling method has been developed in our laboratory [18]. It consists of coupling a standard FLEC® emission cell [19] with SPME [20] for rapid sampling and simple thermal desorption, directly performed in GC injector. As other passive samplings, this method could be more representative of the material in use than dynamic sampling procedures which require a fixed air flow-rate in the emission cell [21]. Moreover, during the standardized dynamic sampling, the air turbulences in the emission cell could lead to inhomogeneous surface emission and then to an inaccurate estimation of the VOC emission. So, the first part of this paper presents the modeling of the air flow turbulences in the emission cell under standard operating conditions to assess the relevance of the passive sampling considered in this study.

FLEC®-SPME sampling involves two steps: first, VOCs diffusion from the material to the gas phase (FLEC® headspace) and second, after introduction of SPME in the FLEC®, the VOCs transfer from the gas phase to the PDMS-Carboxen fiber. This latter step was already studied using standard gas and is detailed elsewhere [18]. In this paper, the first step (material to gas phase diffusion) will be studied on three different materials (pine wood panel, carpet and PVC floor). Assuming equilibrium is reached in the FLEC®, the headspace concentration could be assimilated to the gas phase concentration at the material surface, C_{as} (Eq. (1)). Unlike the standard evaluation procedure, all parameters (air velocity, relative humidity and temperature) could be adjusted according to field conditions to be as representative as possible of the studied building.

Then, the optimized method is applied to identify and quantify, respectively by gas chromatography–mass spectrometry (GC–MS) and gas chromatography-flame ionization detection (GC-FID), the VOCs emitted by the three studied materials. Qualitative results were compared to those obtained with the standard evaluation method to assess the ability of FLEC®-SPME to detect the VOCs of interest based on toxicological reference values and listed in the French AFSSET protocol [3].

2. Materials and methods

2.1. Modeling of fluid flow in the FLEC cell

Computational fluid dynamics (CFD) was used to study the fluid in the FLEC® cell using the Fluent 6.0 software (ANSYS, Canonsburg, USA), which solves mass and momentum conservation equations according to Navier–Stokes equation. The parameters used are summarized in the Table 1.

Table 1
Fluent simulation main parameters.

Cell structure	Tetrahedral
Cell size (m)	7×10^{-4}
Cell number	588886
Inlet pressure (Pa)	1.01×10^5
Temperature (°C)	20
Volumetric flow ($L\,min^{-1}$)	0.3
Model	k-epsilon standard
Turbulence intensity (%)	10
Hydraulic diameter (m)	4.67×10^{-3}
Wall roughness height (m)	0
Wall roughness constant	0.5

2.2. Material samples

The emission of VOCs from three material samples provided by CSTB (Scientific and technical Center for Building) was studied in this paper. A PVC floor tile (300 mm × 300 mm × 1 mm), a polyamide carpet (250 mm × 250 mm × 4 mm) and a natural raw pine wood panel (300 mm × 300 mm × 9 mm) with no varnish samples were studied for quantification.

Carpet and pine wood panel were also used to compare FLEC®-SPME procedure with the standard methodology. To avoid bias due to the variation of emission in time and the heterogeneity of material samples, dynamic and FLEC®-SPME samplings were performed successively the same day on the same material plate, at the CSTB laboratory. Thermal desorption, involved in the standard method, requires a specific analytical configuration (Automated Thermal Desorber on-line with GC). Hence, these analyses were carried out in the CSTB laboratory. Since this apparatus is dedicated to routine analysis, it was not possible to change its configuration for the SPME thermal desorption. Thus, SPME analyses were performed in our laboratory within 3 days after sampling ensuring a good preservation of the fibers [22].

2.3. Sampling methods

Both SPME and standard samplings were performed using the Field and Laboratory Emission Cell: *FL-0001* (FLEC®) (Fondis Electronic, Guyancourt, France).

2.3.1. Dynamic sampling (standard method)

The sampling was carried out according to ISO-16000-10 standard (Fig. 1A). Clean air was swept through the emission cell at a 300 mL min^{-1} flow rate, 50% RH (relative humidity) and 23 ± 2 °C. At the cell outlet, the air flow was divided in order to perform the preconcentration in duplicate with two adsorbent tubes filled with Tenax® TA. For each tube, the flow rate was fixed at 85 mL min^{-1} (FLEC Air pump 1001) (Chematek, Denmark) and the sampling time was 60 min.

2.3.2. Passive FLEC®-SPME sampling

The principle consists in sweeping clean and dry air, at 23 ± 2 °C and at 300 mL min^{-1}, through the emission cell, just a few seconds to replace the previous headspace (Fig. 1B). Then, the valves are closed to let the VOCs diffuse from the solid material to the gas phase (FLEC® headspace). Once the equilibrium is reached (see kinetics study in the following paragraphs), a 75 μm PDMS-Carboxen fiber (Supelco, Bellefonte, PA, USA) is introduced in the cell for passive sampling. Considering sensitivity [18], a 20 min sampling time was used. The comparative study between the standard and the SPME methods was performed in the CSTB laboratory under the same operating conditions that means that the cell was flushed in the two cases by clean air at 300 mL min^{-1} flow rate and 50% RH.

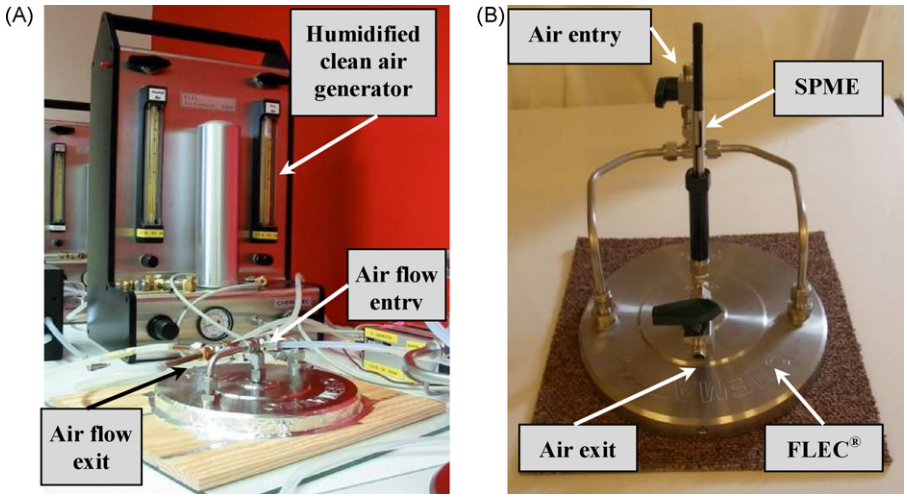


Fig. 1. (A) Dynamic sampling mode (standard protocol assembly) and (B) modified device for passive FLEC®-SPME sampling.

2.4. Chromatographic methods

Analyses were performed using GC-FID for quantification and GC–MS for identification of VOCs emitted from material surfaces. Parameters are grouped in Table 2.

GC-FID calibration was carried out using standard gas generated in laboratory. The FLEC® was placed on a glass plate and headspace was filled with the standard atmospheres before passive SPME sampling [18]. Calibration curves were plotted for fourteen VOCs and concentrations ranging from 2 to 10 mg m^{-3} according to a 20 min sampling time. These calibration curves were also used to calculate the concentrations of compounds belonging to the same chemical family as standard VOCs, according to the estimation method of the response factors [23]. The following relationship was applied (Eq. (2)):

$$EC_i = EC_{ref} \times MW_i \times \frac{c_{ref}}{c_i} \quad (2)$$

where EC_i is the concentration of the studied compound (μg m^{-3}), EC_{ref} is the emission concentration of the reference compound

Table 2
Analytical parameters for the standard and FLEC®-SPME methods.

Step	Parameter	Standard method	FLEC®-SPME method
Adsorbent conditioning		ATD[a] 400 (PerkinElmer, Courtaboeuf, France)	3800 GC injector (Varian, Les Ulis, France)
	Duration	40 min	10 min, 2 h (new fiber)
	Temperature	250 °C (10 min) + 300 °C (10 min) + 330 °C (10 min) + 350 °C (10 min)	300 °C
	Gas flow	Nitrogen 100 mL min^{-1}	Helium (split 50)
Thermal desorption		ATD 400	3800 GC injector
Primary desorption	Purge time	1 min	/
	Desorption time	15 min	4 min
	Desorption temperature	260 °C	320 °C
	Cold trap temperature	−30 °C	/
	Desorption flow	Helium 50 mL min^{-1}	Helium (splitless)
Secondary desorption	Desorption time	10 min	/
	Temperature	280 °C at 40 °C s^{-1}	/
	Transfer line	220 °C	/
GC separation		3800 GC	3800 GC
	Carrier gas	Helium	
	Gas flow	2 mL min^{-1} (constant pressure)	2 mL min^{-1} (constant flow)
	Column	VF5 ms (Varian) 60 m × 0.25 mm × 1 μm	VF5 ms (Varian) 60 m × 0.25 mm × 1 μm
	Oven temperature	40 °C per 5 min, 2.5 °C min^{-1} up to 170 °C 7.5 °C min^{-1} up to 250 °C and 250 °C per 13 min	40 °C per 4 min, 5 °C min^{-1} up to 140 °C 10 °C min^{-1} up to 240 °C 25 °C min^{-1} up to 290 °C and 290 °C per 14 min
Identification (MS)		Saturn 2000 (ion trap) (Varian, les Ulis, France)	1200 Q (quadrupole) (Varian, les Ulis, France)
	Transfer line temperature	270 °C	280 °C
	Ion source temperature	150 °C	250 °C
	Ionization mode	Electron-impact (EI)	Electron-impact (EI)
	Acquisition rate	0.8 scan s^{-1}	0.5 scan s^{-1}
	Acquisition mass range	33–425 a.m.u	30–250 a.m.u
	Filament delay	/	4 min
Quantification (FID)		3800 GC (Varian)	3800 GC (Varian)
	Temperature	270 °C	300 °C

[a] ATD: Automated Thermal Desorber.

Table 3
Reference compounds used for VOCs quantification by GC-FID (LOD and LOQ were determined using standard gas for 20 min FLEC®-SPME sampling time).

VOC families	VOCs of reference	LOD ($\mu g\,m^{-3}$)	LOQ ($\mu g\,m^{-3}$)
Monocyclic aromatic hydrocarbons	Toluene	10	30
	Styrene	0.7	2
Aliphatic hydrocarbons	n-Decane	1.8	5
Terpenes	α-Pinene	1.0	3
Alcohols	Ethanol	12	36
	n-Butanol	5	14
	2-Ethyl-1-hexanol	2.8	8
Aldehydes	Hexanal	2.4	7
	Benzaldehyde	2.4	7
Ketones	Acetone	12	36
	Methyl vinyl ketone	3.9	12
	Cyclohexanone	16	48
Acids	Acetic acid	1.4	4
Esters and Lactones	Methyl metacrylate	0.6	2

($\mu g\,m^{-3}$), MW_i is the molecular weight of the studied compound, C_{ref} and C_i are the number of effective carbons, respectively in the compound of reference and in the studied compound.

For the different chemical families of VOCs, the model compounds used as references are described in Table 3. Limit of detection (LOD) and quantification (LOQ) in GC-FID for a 20 min sampling time are also presented. LOD and LOQ were determined according to Eqs. 3.

$$\mathrm{LOD} = \frac{3.3\delta_b}{a}, \quad \mathrm{LOQ} = \frac{10\delta_b}{a} \tag{3}$$

where δ_b is the standard deviation of the y-intercept for the calibration curve and a is the slope of the calibration curve.

3. Results and discussion

3.1. Dynamic or passive sampling

The fluid flow in the FLEC® under the dynamic conditions used in the standard method was characterized with CFD to assess its influence in the VOC mass transfer from the material to the gas phase. Main results of the simulation are shown in Fig. 2.

Turbulence intensity represents the relative deviation between local and mean velocities.

Contours of turbulence intensity show a relatively low turbulence level in the FLEC® cell (<21%), so the flow rate profile is quite uniform. However, central and peripheral areas of the material are exposed to a lower turbulence level which is unfavorable to an efficient mass transfer. In the future, it would be interesting to optimize the geometry of the cell to improve the contact between fluid and material.

Regarding these results, passive sampling seems to be an interesting alternative due to the homogeneous diffusion of VOCs to the gas phase. Moreover, this sampling mode corresponding to free convection could be easier to adapt to indoor conditions.

3.2. Kinetics of VOC emission from materials: determination of the equilibrium time

To optimize the sampling conditions, the passive diffusion of the VOCs from the solid sample to the headspace of the FLEC® was studied to determine the time required to reach equilibrium concentrations in the emission cell headspace (so-called "equilibrium time"). This study was performed on the 3 building materials (pine wood panel, carpet and PVC floor) which were left uncovered for 3 days according to the 3-day emission test. Before introduction of the SPME fiber, the FLEC® was placed on each material sample and flushed by clean air (see Section 2.3.2). Then, the valves are closed to let the VOCs diffuse from the solid material to the headspace for different times ranging from 5 to 60 min. Then, a 20 min SPME sampling was applied. This duration was chosen as a compromise between a short sampling time and a good reproducibility (relative standard deviation, RSD) ranging from 5% (α-pinene) to 16% (hexanal) for quantitative results. Under these conditions, LOD and LOQ are in the $\mu g\,m^{-3}$ range (Table 3). Relative standard deviations (RSD) were calculated from 3 replicates, applying 45 min material/gas phase diffusion in the FLEC® and 20 min SPME sampling. The RSD ranges from 9% (phenol) to 28% (acetic acid).

For readability, only results for four VOCs are shown in Fig. 3, considering, e.g. the two lower and the two higher emitted concentrations for each material.

For carpet, Fig. 3 shows that the material/FLEC® headspace equilibrium is reached after 25 min (5 min material/gas phase diffusion + 20 min SPME sampling) for all considered compounds and whatever the concentration level (from 20 to 200 $\mu g\,m^{-3}$).

For PVC floor, equilibrium is reached after 35 min (15 material/gas phase diffusion + 20 min SPME sampling) (Fig. 3). The longer equilibrium time is observed for pine wood panel: 65 min (45 material/gas phase diffusion + 20 min SPME sampling) (Fig. 3).

For all materials, the equilibrium time seems to only depend on the material and not on the compound. Actually, acetic acid equilibrium step was obtained for 25 min (carpet), 35 min (PVC) and 65 min (pine wood). This finding was also noted for 1-butanol comparing carpet (25 min) and pine wood (65 min) and for 2-ethyl-1-hexanol in the carpet (25 min) and PVC flooring (35 min).

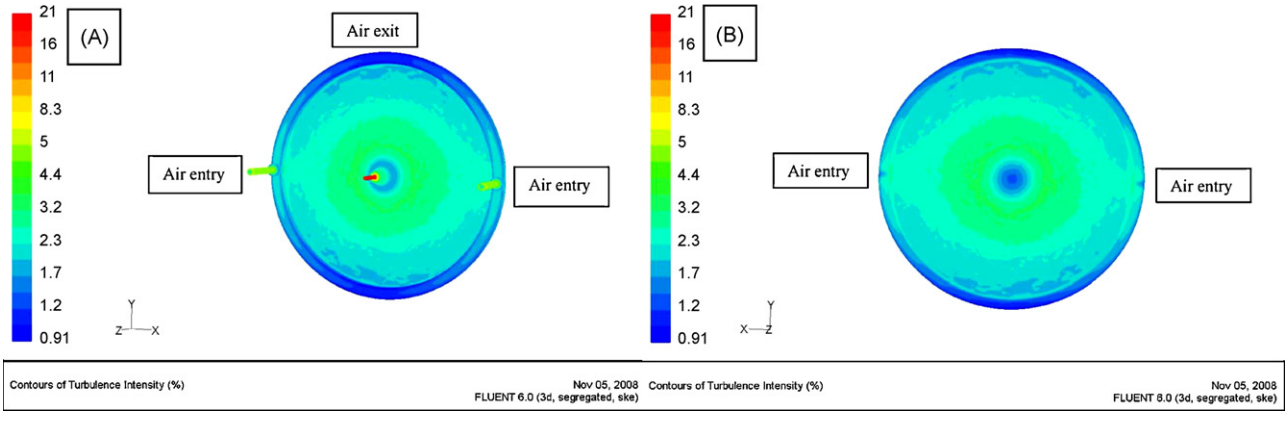


Fig. 2. Contours of turbulence intensity with a 0.3 L min^{-1} air flow: (A) top view; (B) underneath view.

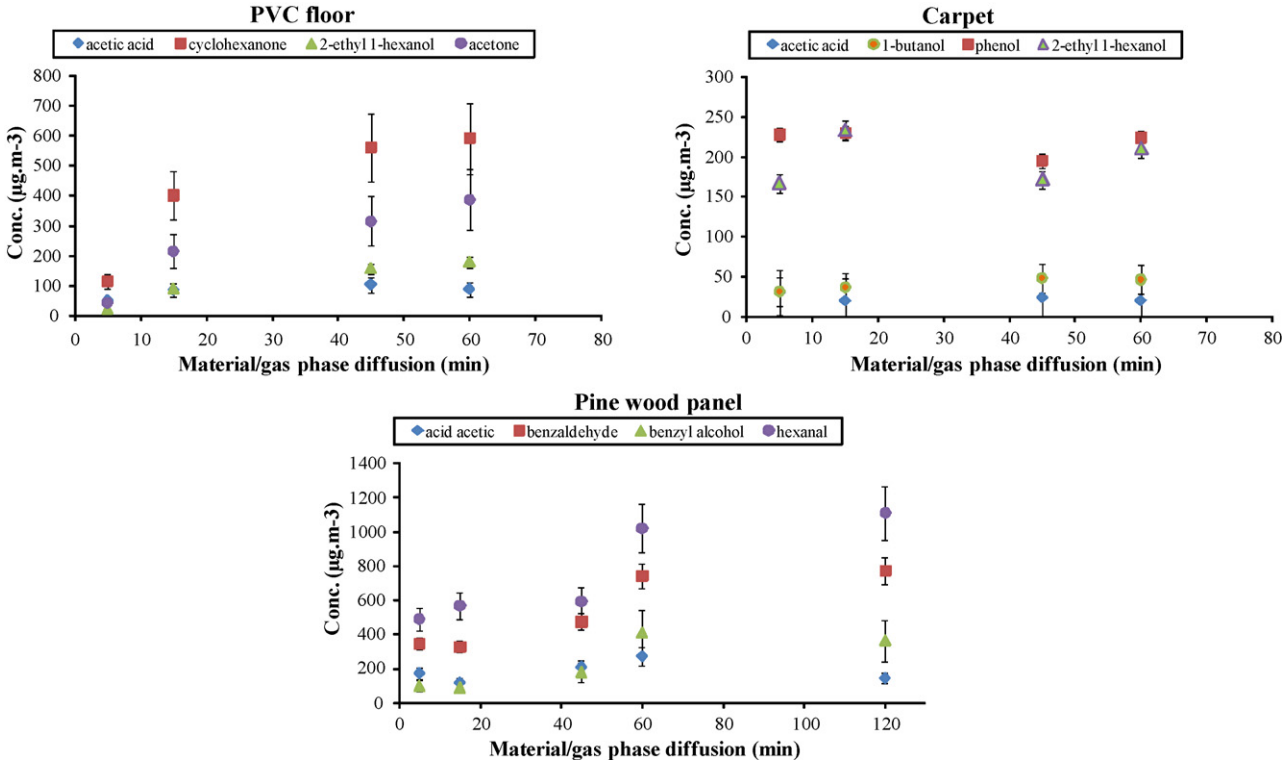


Fig. 3. Kinetic of VOCs emission from materials (PVC floor, carpet and pine wood panel).

Moreover, the equilibrium time does not seem to be related to the emission concentration. For example, equilibrium concentration of acetic acid reached 20 $\mu g\,m^{-3}$ for the carpet against 100 $\mu g\,m^{-3}$ for the PVC (Fig. 3). In the same way, the concentrations of 2-ethyl-1-hexanol determined for these two materials are similar (200 $\mu g\,m^{-3}$) (Fig. 3) but three more time is needed to reach equilibrium for PVC. These results also show that emission concentration at equilibrium does not depend on compound volatility. Thus, for PVC, the concentration of the most volatile VOC (acetone, 22 800 Pa at 20 °C) [24] is close to 200 $\mu g\,m^{-3}$ compared to 450 $\mu g\,m^{-3}$ for cyclohexanone (4700 Pa at 20 °C) [25]. From these results, it can be expected that the transfer of VOCs from the material to the gas phase is probably governed by diffusion in the material and not by surface evaporation.

A complementary study was performed to check that concentration equilibrium remains constant in the headspace even after SPME sampling. Hence, two successive SPME extractions were carried out for 45 min material/gas phase diffusion and 20 min SPME sampling on the pine wood panel. This material was chosen because of the longer associated equilibrium time, compared to carpet and PVC floor.

The average difference between concentrations at the material surface (C_{as}) obtained for the two successive SPME samplings is 4% and ranges from 0.5% (acetone) to 13% (α-pinene). So, these data suggest that the equilibrium between the building materials and the FLEC® headspace is sufficiently stable to perform quantitative analyses.

3.3. Application of the developed method to the three building materials

The three building materials (carpet, PVC and pine wood panel) were analyzed according to the longer equilibrium time determined in the previous paragraph. Results are summarized in Table 5.

Among the VOCs identified, a lot of them are shared by two or three of the materials studied. For example, acetone, acetic acid and 1-butanol were detected in the three materials. Pentanal, phenol and 2-ethyl-1-hexanol were found in pine wood panel and PVC. The other quantified compounds are specific of a material and often belong to the same families. Thus, the main families encountered in pine wood are aldehydes and terpenes. For the PVC floor studied, alcohol, ketone, glycol ester and glycol ether are the major substances. Finally, the carpet mainly emitted acids, alcohols and esters.

To conclude, this methodology allows the identification and quantification of VOCs in a wide range of physico-chemical properties and concentrations (Table 4). Hence, VOCs emission profiles could be drawn up. It could be an interesting tool to identify sources in indoor environments.

3.4. Evaluation of the SPME method for identification of VOCs of interest

The AFSSET protocol defines concentration limits for material labeling. Thus, a total VOCs concentration ([TVOC]) higher than 10 $mg\,m^{-3}$ for a 3 days test does not allow labeling. Then, a similar test is done after 28 days of conditioning. Compounds of interest are defined for observed concentrations higher than 5 $\mu g\,m^{-3}$. For each compounds of interest, a ratio (R) between the concentration after 28 days ([J28]) and the lowest concentration of interest (LCI) proposed in the protocol [3], is calculated. The health risks associated with the emission of VOCs from the material is considered to be low when both individual R ratios and their sum remain below 1.

As previously stated, the VOCs concentrations determined by passive and dynamic samplings cannot be directly compared, because of the different modes of mass transfer. So, the new FLEC®-SPME procedure was only evaluated for the identification of the VOCs of interest. It was applied to two materials (carpet

Table 4
Substances emitted from materials after 3 days—FLEC®-SPME passive sampling (45 min material/gas phase diffusion + 20 min SPME sampling)—identification by GC–MS; quantification by GC-FID.

		PVC C ($\mu g\,m^{-3}$)	Pine wood panel C ($\mu g\,m^{-3}$)	Carpet C ($\mu g\,m^{-3}$)
1	Toluene	<LOQ	<LOQ	/
2	2-Methylbutane	184.7	/	/
	2-Methylhexane	157.5	/	/
	Methylcyclohexane	4.2	/	/
	Tetradecane	/	/	31.0
	Pentadecane	/	/	27.2
$\Sigma[VOC_2]$		346.4	/	58.2
3	α-Pinene	/	42.8	/
	Longifolene	/	<LOQ	/
	Caryophyllene	/	<LOQ	/
$\Sigma[VOC_3]$		/	42.8	/
4	1-Butanol	3.9	164.6	48.6
	2-Hexanol	/	8.3	/
	1-Pentanol	/	1.4	/
	2-Ethyl-1-hexanol	228.0	/	171.7
$\Sigma[VOC_4]$		231.9	174.3	220.3
5	Phenol	506.9	/	195.1
	Benzyl alcohol	/	242.9	33.1
	BHT[a]	<LOQ	/	/
$\Sigma[VOC_5]$		506.9	242.9	228.2
6	2-(2-Hydroxypropoxy)-1-propanol	<LOQ	/	/
	Dipropylene glycol monomethyl ether	<LOQ	/	/
	1-(2-Methoxypropoxy)-2-propanol	<LOQ	/	/
	2-(2-Butoxyethoxy)-ethanol	/	/	<LOQ
	n-Butyric acid 2-ethylhexyl ester	<LOQ	/	/
	TXIB[b]	/	/	<LOQ
7	Pentanal	17.5	98.8	/
	Hexanal	/	628.8	/
	Heptanal	/	19.2	/
	Octanal	/	13.6	/
	Nonanal	/	37.1	/
	Decanal	/	23.8	<LOQ
	Benzaldehyde	/	476.3	/
$\Sigma[VOC_7]$		17.5	1297.6	/
8	Acetone	309.5	82.1	165.3
	Methylisobutylketone	5.2	/	/
	Cyclohexanone	553.9	/	/
$\Sigma[VOC_8]$		868.6	82.1	165.3
9	Acetic acid	103.1	208.1	23.9
	2-Ethyl-1-hexanoic acid	/	/	69.9
$\Sigma[VOC_9]$		103.1	208.1	93.8
10	Trichloroethene	<LOQ	/	/
11	Caprolactam	/	/	17.4
[TVOC]		2074.4	2047.8	783.2

1: monocyclic aromatic hydrocarbons; 2: aliphatic hydrocarbons; 3: terpenes; 4: alcohols; 5: aromatic alcohols; 6: glycols, glycol ethers and esters; 7: aldehydes; 8: ketones; 9: acids; 10: halogenated hydrocarbons; 11: other chemical families.

[a] Butylated hydroxytoluene.

[b] 2,2,4-Trimethyl-1,3-pentanediol diisobutyrate.

and pine wood panel) after 3 days. The VOCs of interest were defined according to the standard method. Results are presented in Tables 5 and 6. It can be noted that the sum of R ratios for the carpet is over 1 ($R = 3.05$), meaning that emissions of this flooring material could present health risks. If we look at individual R-values, it appears that the health impact would be mainly due to two compounds: caprolactam and phenol ($R = 1.64$ and 1.09, respectively). For pine wood panel, all the individual R ratios are below 1 and their sum just reaches 1, which suggests that the product does not present a significant health risk.

Table 5
Potential of passive FLEC®-SPME for GC–MS identification of VOCs of interest emitted by the carpet sample (5 min material/gas phase diffusion + 20 min SPME sampling).

Identified VOC		Boiling point (°C)	FLEC®-SPME		Standard method		$R_{[J28]}$
			Signal/noise	Signal/noise	[J3] ($\mu g\,m^{-3}$)	[J28] ($\mu g\,m^{-3}$)	
1	Tetradecane	253	45	261	50.7	10.7	0.001
	Pentadecane	269	27	367	26.2	8.5	0.001
	Phenylundecane	316	nd	179	23.1	16.0	0.020
2	2-Ethylhexanol	184	123	3,102	76.9	20.1	0.009
3	Phenol	182	1802	16,978	478.6	173.8	1.086
	Benzyl alcohol	205	65	1,723	69.2	13.4	0.038
4	2-(2-Butoxyethoxy)-ethanol	231	106	333	142.0	21.1	0.020
	TXIB*	280	96	237	49.6	28.5	0.028
5	1-Methyl-2-pyrrolidone	202	71	600	56.2	11.3	0.014
	Alkenes (C12)		3	302	46.9	8.4	0.036
	Alkenes (C12)		41	313	45.1	8.2	0.055
	Alkenes (C12)		4	48	34.3	5.7	0.052
	Alkenes (C12)		14	237	29.4	8.8	0.051
	Caprolactam	267	307	195	125.2	65.7	1.643
Average signal/noise			193	1670			
[TVOC]					1253.4	400.2	
ΣR							3.054

1: aliphatic hydrocarbons; 2: alcohols; 3: aromatic alcohols; 4: glycols, glycol ethers and esters; 5: other chemical families; nd: not detected; [J3]: VOC concentration at Day 3; $R_{[J28]}$ = [J28]/LCI; *2,2,4-trimethyl-1,3-pentanediol diisobutyrate.

Table 6
Potential of passive FLEC®-SPME for GC–MS identification of VOCs of interest emitted by the pine wood panel sample (45 min material/gas phase diffusion + 20 min SPME sampling).

Identified VOCs		Boiling point (°C)	FLEC®-SPME		Standard method		$R_{[J28]}$
			Signal/noise	Signal/noise	[J3] ($\mu g\,m^{-3}$)	[J28] ($\mu g\,m^{-3}$)	
1	Toluene	111	19	82	3.3	5.2	0.017
3	1-Butanol	118	910	1,489	34.2	5.5	0.004
4	Benzyl alcohol	205	3197	39,002	211.9	95.3	0.238
5	Hexanal	124	3183	3,160	41.0	17.8	0.028
	Benzaldehyde	179	2235	4,647	76.4	32.2	0.366
	Nonanal	195	280	3,252	14.7	6.4	0.010
	Decanal	208	165	1,650	9.3	5.0	0.008
7	Acetic acid	118	469	953	294.6	96.3	0.385
Average Signal/noise		1307	6779				
[TVOC]					685.4	263.7	
ΣR							1.056

1: monocyclic aromatic hydrocarbons; 2: terpenes; 3: alcohols; 4: aromatic alcohols; 5: aldehydes; 6: ketones; 7: acids; [J3]: VOC concentration at Day 3; $R_{[J28]}$ = [J28]/LCI.

The comparison with the standard procedure shows that FLEC®-SPME did not detect all the VOCs identified by the standard protocol: thirteen compounds of seventeen for the carpet and twenty-one out of thirty two for the pine wood panel. This is mainly due to the lower sensitivity of the whole methodology compared to the standard evaluation method which is five to eight times better. This may be explained by several differences in the analytical protocols (Table 2), but the most influencing parameter is probably the difference between the adsorbent masses: around 200 μg for Carboxen® SPME fiber and 200 mg for Tenax® tubes. However, despite this lack of sensitivity, all the compounds of interest (Tables 5 and 6) are identified by the FLEC®-SPME method, except phenylundecane for the carpet. For this compound, adsorption affinity with Carboxen® is better than with Tenax®, leading to poor desorption efficiency [26]. Nevertheless, caprolactam was better detected with the SPME methodology: this can be explained by the higher desorption temperature applied (320 °C).

To summarize, the FLEC®-SPME methodology is able to determine 96% of the compounds of interest defined by the AFSSET protocol (concentration >5 $\mu g\,m^{-3}$), so it is relevant for the identification of the most toxic compounds emitted by materials.

4. Conclusion

A new FLEC®-SPME passive sampling method, firstly developed on standard gas in a previous study, was optimized to analyze VOCs emitted from solid building materials.

The fluid flow study in FLEC® emission cell puts in evidence low turbulences (central and peripheral areas of the material surface) when applying the standard dynamic sampling procedure. As this could lead to heterogeneous diffusion of VOCs from material to the gas phase, passive FLEC®-SPME was considered relevant because it better represents VOCs surface emissions and transfer to indoor air. To optimize the experimental procedure, VOCs diffusion from the solid material to the FLEC® cell headspace was studied and equilibrium conditions were determined for three materials. It was shown that equilibrium time only depends on the material type (25 min for carpet, 35 min for PVC floor and 65 min for pine wood panel). The longest sampling time is in the same order of the

standard dynamic sampling (60 min) and a factor four is gained compared to other passive sampling methods (several hours). Hence, this new method combined easy implementation and time-saving.

Comparison with the standard dynamic sampling protocol showed the potential of FLEC®-SPME in identifying the VOCs of interest defined by the AFSSET protocol. Quantification of VOCs is also possible by determining concentrations at the material/air interface. Therefore, this new method seems well adapted to field sampling and would be helpful for identification and rating of sources in indoor environments. Moreover, combined with emission modeling, it could become an interesting support tool to decision making in applications such as indoor air quality diagnostic and health advocacy.

Acknowledgements

Authors acknowledge ADEME (Agency for Environment and Energy Management) and the Aquitaine Region Council for financial support.

References

[1] ECA, Indoor Air Quality & Its Impact On Man, Report 18, Evaluation of VOC Emissions from Building Materials, Office for Official Publications of the European Communities, Luxembourg, 1997.
[2] AgBB, Health-related Evaluation Procedure for Volatile Organic Compounds (VOC and SVOC) from Building Products, 2008.
[3] AFSSET, Procédure de qualification des produits de construction sur la base de leurs émissions de COV et de formaldéhyde et de critères sanitaires, Rapport du groupe de travail Afsset "COV et produits de construction", saisine 2004/011, Agence Française de Sécurité Sanitaire de l'Environnement et du Travail (AFSSET), Paris, 2006.
[4] ISO 16000-9, Indoor Air—Part 9: Determination of the Emission of Volatile Organic Compounds from Building Products And Furnishing—Emission Test Chamber Method, International Organization for Standardization, Geneva, 2006.
[5] ISO 16000-9, Indoor Air—Part 10: Determination of the Emission of Volatile Organic Compounds from Building Products and Furnishing—Emission Test Cell Method, International Organization for Standardization, Geneva, 2006.
[6] T. Schripp, B. Nachtwey, J. Toelke, T. Salthammer, E. Uhde, M. Wensing, M. Bahadir, Anal. Bioanal. Chem. 387 (2007) 1907–1919.
[7] B. Lundgren, B. Jonsson, B. Ek-Olausson, Indoor Air 9 (1999) 202–208.
[8] L.Z. Zhang, J.L. Niu, Intern. J. Heat Mass Transf. 46 (2003) 2415–2423.
[9] O. Wilke, O. Jann, D. Brödner, Indoor Air 14 (2004) 98–107.
[10] H. Järnström, K. Saarela, P. Kalliokoski, A.L. Pasanen, Atmos. Environ. 40 (2006) 7178–7191.
[11] H. Järnström, K. Saarela, P. Kalliokoski, A.L. Pasanen, Atmos. Environ. 41 (2007) 2290–2302.
[12] H. Järnström, K. Saarela, P. Kalliokoski, A.L. Pasanen, Environ. Int. 34 (2008) 420–427.
[13] ECA-IAQ, Harmonisation of Indoor Material Emissions Labelling Systems in the EU: Inventory of Existing Schemes, Report No 24, EUR 21891 EN, Office for Official Publications of the European Communities, Luxembourg, 2005.
[14] C.-C. Lin, K.-P. Yu, P. Zhao, G. Whei-May Lee, Build. Environ. 44 (2009) 525–533.
[15] C. Bicchi, C. Cordero, E. Liberto, P. Rubiolo, B. Sgorbiniand, P. Sandra, J. Chromatogr. A 1148 (2007) 137–144.
[16] N. Shinohara, M. Fujii, A. Yamasakic, Y. Yanagisawa, Atmos. Environ. 41 (2007) 4018–4028.
[17] N. Shinohara, Y. Kai, A. Mizukoshi, M. Fujii, K. Kumagai, Build. Environ. 44 (2009) 859–863.
[18] J. Nicolle, V. Desauziers, P. Mocho, J. Chromatogr. A 1208 (1–2) (2008) 10–15.
[19] P. Wolkoff, P.A. Clausen, P.A. Nielsen, L. Gunnarsen, Indoor Air 3 (1993) 291–297.
[20] J. Pawliszyn, Solid phase microextraction: theory and practice, Wiley-VCH, New York, 1997.
[21] E. Uhde, A. Borgschulte, T. Salthammer, Atmos. Environ. 32 (1998) 773–781.
[22] V. Larroque, V. Desauziers, P. Mocho, J. Chromatogr. A 1124 (2006) 106–111.
[23] C. Badol, A. Borbon, N. Locoge, T. Léonardis, J.C. Galloo, Anal. Bioanal. Chem. 378 (2004) 1815–1827.
[24] INRS, Toxicological Data Sheet FT3, URL http://www.inrs.fr (accessed in June 2009), 2008.
[25] INRS, Toxicological Data Sheet FT39, URL http://www.inrs.fr (accessed in June 2009), 2006.
[26] J.J. Manure, Calculation and Use of Breakthrough Volume Data, http://www.sisweb.com (accessed in January 2009), 1996.

Talanta 80 (2009) 738–743

Contents lists available at ScienceDirect

Talanta

journal homepage: www.elsevier.com/locate/talanta

Simple water analysis of golf link pesticides by means of batch-wise adsorption and supercritical fluid extraction

Hiroaki Chikushi[a,b], Kazutoshi Hirota[a], Natsuko Yoshida[a], Takuya Edamura[b], Kei Toda[a,*]

[a] Department of Chemistry, Kumamoto University, 2-39-1 Kurokami, Kumamoto 860-8555, Japan
[b] Institute of Environmental Analysis, Nodaichi-Denshi Co., 335 Yoyasu, Kumamoto 860-0823, Japan

ARTICLE INFO

Article history:
Received 27 March 2009
Received in revised form 26 July 2009
Accepted 27 July 2009
Available online 5 August 2009

Keywords:
Golf link pesticides
Supercritical fluid extraction
Water analysis
Octadecylsilane (ODS)
Styrene-divinylbenzene copolymer (XAD)

ABSTRACT

Here, a simple new method is proposed to evaluate water for the presence of pesticides. Specifically, pesticides for golf link maintenance were used as the targets for this investigation. Water samples containing the pesticides were mixed with particulate adsorbent, after which the pesticides were extracted from the adsorbents using supercritical fluid carbon dioxide and then analyzed by gas chromatography–mass spectrometry. The recoveries of pesticides were examined with several types of adsorbents and found to be related to their octanol/water partition coefficients (K_{ow}) for most of the adsorbents. Good recoveries were obtained when the water samples were mixed with octadecylsilane (ODS) and stylene-divinylbenzene copolymer (XAD) resins for 15 and 30 min, respectively. In the supercritical fluid extraction, extraction pressure affected the efficiency of extraction from XAD while a little effect on extraction from ODS, probably due to the internal structure of the adsorbents. The limit of detection ranged from 0.002 to 2.3 $\mu g\,L^{-1}$ and the method is suitable for the measurement of golf link pesticides in $\mu g\,L^{-1}$ order to 100 $\mu g\,L^{-1}$. The procedure of the proposed method was simpler than the conventional solid-phase extraction method. Finally, the method presented here was used to identify pesticides present in actual wastewater from golf links.

© 2009 Elsevier B.V. All rights reserved.

1. Introduction

Although agricultural chemicals such as herbicides, germicides and insecticides (pesticides) are necessary to improve agricultural productivity, they can exert adverse effects on the ecosystem once they flow into natural or public water systems [1]. Therefore, the use of these chemicals is controlled by agricultural chemical regulation laws. In Japan, provisional guidelines for golf link pesticides that provide determination methods and acceptable limits of these concentrations were provided in May of 1990 in an attempt to prevent water pollution. The number of target chemicals covered by these guidelines was increased to 45 in December 2001 [2]. The provisional guidelines state that golf link chemicals should be determined by liquid–liquid extraction (LLE) [3] or solid-phase extraction (SPE), which both especially LLE require harmful organic solvents. Liquid–liquid microextraction is one of the new ways to reduce the use of organic solvent [4]. Conventional LLE and SPE require a great deal of time and special skills to conduct the extraction and refining processes. Furthermore, the results obtained using these methods can be affected by the sample and experimental conditions. In most modern water contaminant analyses, the compounds are trapped by solid-phase cartridges [5,6] or solid-phase disks [7,8] and then extracted using organic solvents to enable their subsequent analysis by gas chromatography (GC). Guardia-Rubio et al. applied the SPE–GC method to the multi-residue analysis of three groups of pesticides in wash waters [9]. Supercritical fluid chromatography is also a powerful tool for analysis after SPE [10]. However, in real water analyses, suspended materials such as algae sometimes clog the SPE cartridge, which can make it difficult to push water through the cartridge at a high flow rate during the extraction.

Residual pesticides in agricultural products can be screened using simple whole analyses [11]. Recently, solid-phase microextraction (SPME) was coupled with GC analysis [12–14] or HPLC analysis [15] to measure the levels of pesticides in water and juice samples, and stir-bar-sorptive extraction–thermal desorption was also applied to water analysis [16]. However, due to the limited surface area and adsorbing capacity of these micro-solid devices, the recoveries are generally not very good. As a result, the SPME devices are primarily used to identify specific species.

Supercritical fluid extraction (SFE) is known to be a useful method of pretreating samples for subsequent screening [17–19] and analysis for the presence of specific pesticides such as rotenone [20]. Ong and Hites developed a low solvent method comprising solid extraction disks and subsequent SFE [21]. SFE provides an advantageous extraction because the extraction medium is highly

* Corresponding author.
E-mail address: todakei@sci.kumamoto-u.ac.jp (K. Toda).

0039-9140/$ – see front matter © 2009 Elsevier B.V. All rights reserved.
doi:10.1016/j.talanta.2009.07.061

soluble as a liquid and has a high diffusion rate as a gas. Generally, CO_2 is a good medium for SFE because it goes to supercritical state at relatively low temperatures (32 °C and 7.4 MPa), inert and will not affect chromatographic analyses. Therefore, SFE with CO_2 is preferable for the analysis of thermally unstable compounds such as pesticides.

Glazkov et al. developed a method for the direct extraction of organic compounds from water by SFE [22]. In their method, the water sample was placed in a SFE cell, after which high-pressure CO_2 fluid was introduced and the extracts were trapped with glass wool. Although this direct extraction for analytical purpose is very simple, small number of papers on this subject has been published [23] while its usefulness for the remediation of polluted water is currently being evaluated [24]. Unstable compounds such as pesticides tend to decompose in response to exposure to water in the supercritical fluid, and SFE is often used to induce the degradation of water contaminants [25]. Indeed, it is well known that water adsorbent is placed in the SFE cell to prevent water catalyzed decomposition. Therefore, a strategy comprising the collection of pesticides by solid adsorbents and subsequent extraction from the adsorbents would be better for the analysis of pesticides than the direct SFE from water samples. Previous studies have utilized SPME devices [26] and disks [21] as pre-collection devices prior to SFE. In this study, adsorbent resin powders were placed directly in the water samples to enable quantitative adsorption.

Here, we present a simple method to evaluate the pesticides contained in water samples. We investigated the use of simple and solvent free pretreatment for the determination of golf link pesticides based on batch-wise adsorption and SFE. In the batch-wise adsorption, solid adsorbents were simply added to the water samples; therefore, special equipment such as syringe pumping systems was not required. Then we optimized the adsorbents and adsorption conditions, after which we applied the system to real water analyses.

2. Experimental

2.1. Chemicals

A standard solution of golf link pesticides (10 mg mL^{-1}) was obtained from Kanto Kagaku (Tokyo). The standard solution contained 27 kinds of pesticide which were measurable by gas chromatography. Adsorbents were used as purchased or after pretreatment as follows. One gram of octadecylsilane adsorbent (ODS, Bondesil-C18, 40 μm) obtained from Varian (Palo Alto, CA) or Tenax GR obtained from GL Science (Tokyo) was placed in a 100-mL beaker, after which 5 mL of acetonitrile and 5 mL of acetone were added. The adsorbents were then allowed to dry at room temperature for 15 min. Activated carbon powder (acid treated) and silica gel 60 for column chromatography, which were both obtained from Nacalai Tesque (Kyoto), were heated at 200 °C for 2 h and then cooled in a desiccator. A styrene-divinylbenzene copolymer adsorbent (XAD, Amberlite XAD-4, Φ 0.49–0.69 mm, 750 m^2 g^{-1} dry, pore 12 nm) obtained from Sigma–Aldrich (St. Louis, MO) was washed with acetone with a help of ultrasonication just before use. Activated alumina 200 and diatomaceous earth both from Nacalai Tesque were used without any treatment. For comparison, two SPME devices coated with 100 μm polydimethylsiloxane (PDMS) or 75 μm polyacrylate (PA) both obtained from Supelco (Bellefonte, PA) were utilized for collection of the pesticides in water.

2.2. Analytical procedure

One gram of adsorbent (2.0 g in case of XAD) and a Teflon stir-bar (4 cm in length) were placed in a 100-mL glass beaker, after which 50 mL of water standard (containing each pesticide at a concentration of 20 μg L^{-1}) or of water sample were added. The samples were then stirred on a six-stage-multi-stirrer for 15 or 30 min. Next, the absorbents were collected on a cellulose membrane filter (1.0 μm, Φ 47 mm, Advantec, Tokyo) and then dried in a vacuum desiccator with silica gels overnight. All of the adsorbent was then transferred to a 50-mL beaker and mixed with 2.0 g of diatomaceous earth as wet support. Round sand, the adsorbent/wet support mixture, and the wet support were then placed in an extraction cell in this order, after which 1 mL of methanol was added as a modifier. The cell was then placed in the SFE instrument (SE-30; Isco). The typical SFE conditions were a temperature of 50 °C, a pressure of 3000 psi, static 15 min and dynamic 15 min, and a restrictor temperature of 60 °C. The extracts were then collected by bubbling through 5 mL of acetone in a test tube. Next, the solution volume was adjusted to 1 mL by vaporization induced by blowing of nitrogen, after which 2 μL of the solution was injected in split-less mode (injector temperature: 250 °C) into a gas chromatograph equipped with a mass spectrometer (GC–MS, Agilent 6890N/5973 or Thermo Electron GC ultra DSQ). An InertCap 5MS/sil separation column (0.25 mm i.d. × 30 m, 0.25 μm thick) obtained from GL Science was used and helium was applied at 1.0 mL min^{-1} as a carrier gas. The column oven temperature was initially 50 °C for 2 min, after which it was ramped to 120 °C at 20 °C min^{-1} and then to 270 °C at 5 °C min^{-1}. Each compound was measured using selected ion monitoring in accordance to the library PEST provided from Agilent. For calibration, from 0.5 to 5 mL of acetone solution containing 1-mg L^{-1} standards were added to 50 mL water, and treated in the same way as sample waters.

2.3. Recovery test and sample water analysis

Water samples were collected from golf link wastes and rivers and then stored in a refrigerator until analysis, which was conducted within one week. The pesticides contained in the 50-mL samples were then determined as described in Section 2.2. The pesticides were also concurrently evaluated using the conventional SPE–GC–MS method [2,27] for comparison. To accomplish this, a 200–500 mL of sample water was allowed to flow through a SPE cartridge (Sep-PaK VAC 500 mg, Waters) at a rate of 10 mL min^{-1} with the aid of a syringe pump (Sep-Pak concentrator N10003, Waters). The inside of the cartridge was then dried by allowing nitrogen to flow through the cartridge, after which the analytes were extracted with 10 mL of acetone and 5 mL of acetonitrile. Next, 0.5 mL of 2% diethylene glycol acetate was added to the extract and the sample was concentrated to a volume of 1 mL using a rotary evaporator. The volume of the sample was then adjusted to 2 mL by the addition of acetone to prepare it for GC–MS analysis. For recovery tests, 1 mL of standard solution (each concentration was 1 mg L^{-1}) was added to the water samples to give final concentrations of 20 μg L^{-1}.

3. Results and discussion

3.1. Investigation of adsorbents

Several types of adsorbents were tested for use with batch-wise adsorption/SFE. Fig. 1 shows the results obtained using a 15-min adsorption time plotted against the octanol–water partition coefficient (K_{ow}). Interestingly, the recoveries were related to K_{ow} for most of the adsorbents, which suggests that the adsorption onto these materials was based on the hydrophobic interaction between the pesticides and materials. Even for the silica gel and alumina, the recovery increased as K_{ow} increased. For the relatively hydrophilic materials, it is reasonable to assume that the molecular–matrix interaction between these two materials increases as the molec-

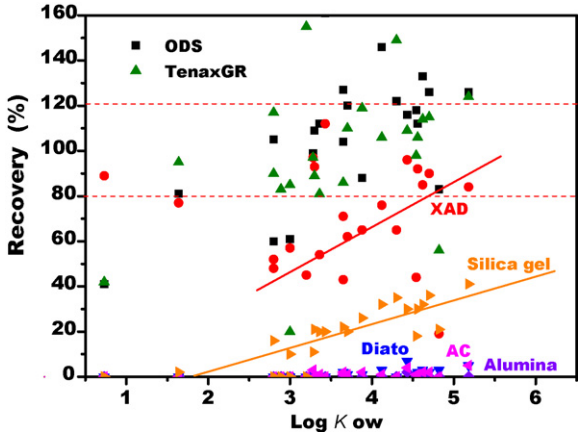


Fig. 1. Recoveries of the pesticides obtained using the batch-wise adsorption plotted against log K_{ow}. The following seven materials were tested: (■) ODS, (●) XAD, (▲) Tenax GR, (▲) silica gel, (▼) diatomaceous, (▲) activated carbon and (▲) activated alumina.

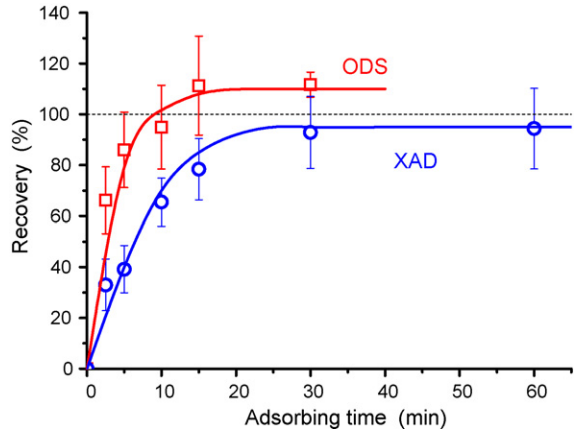


Fig. 2. Recoveries of pesticides as a function of adsorbing time for ODS and XAD.

ular size increases which subsequently affects K_{ow}. In the case of ODS, the recoveries were around 100%, which indicates a good adsorption of pesticides. These findings are similar to the results previously obtained using ODS in a study conducted by Junk and Richard [28]. Conversely, recovery was found to be a function of K_{ow} for XAD when the same adsorption time was used. In addition, a partial adsorbing equilibrium was observed after 15 min when the XAD resins were used, whereas complete equilibrium could be achieved after 30 min of treatment (Fig. 2). Based on the results shown in Fig. 1, ODS, Tenax GR and XAD were considered to be good adsorbing materials. However, Tenax GR is an expensive material and was therefore not used in the subsequent experiments. This was because the cost of the material is an important factor since the adsorbents can only be used once. As a result, ODS and XAD were chosen as optimal adsorbents for this study.

Fig. 2 shows the change in recovery with the adsorbing time. For both ODS and XAD, the recoveries initially increased as the adsorbing time increased and then reached the constant values after 15 or 30 min. The time required to reach the steady equilibrium was shorter for the ODS than the XAD. The typical diameters of ODS and XAD were 0.04 and 0.6 mm, respectively. Therefore, the apparent spherical surface area to volume ratio of ODS is 15 times greater than that of XAD. This high apparent surface area ratio was advantageous for the short-time collection. In addition, adsorptions only occur on the surface of ODS particles, whereas molecules are adsorbed inside the micropores of the XAD resins. As a result, the actual adsorbing area per mass of XAD was 3000 times greater than that of ODS, and more time was required to enable the molecules to enter the pores of the XAD resins. Accordingly, the optimal adsorbing times were determined to be 15 and 30 min for ODS and XAD, respectively.

We also evaluated the use of SPME for pesticide analysis in the same stirring condition to compare the adsorbing performance. SPME is a well-known tool for the analysis of organic compounds contained in water and has been successfully applied to a variety of compounds [12,15,26]. The recoveries after 60 min of SPME collection ranged from 10 to 30% for the eight compounds (diazinon, tolclofosmethyl, dithiopyr, chlorpyrifos, pendimethalin, butamifos, trichlopyr butoxyethyl, and isoxathion) evaluated in this study. In addition, for most of the pesticides, the recoveries were lower than 1% with the same stirring conditions. Taken together, these results indicate that ODS and XAD particulates are superior than the thin PDMS film on the SPME device based on the interactions with the organic compounds, adsorbing capacity and adsorbing area. As a result, it can be said that the conventional SPE and the present batch-wise collection are more suitable for multi-compound analysis of aqueous pesticides.

3.2. Conditions of supercritical fluid extraction

The conditions of SFE were examined to determine their effects on the extraction of pesticides from ODS and XAD resins. First, the effects of each modifier that was added to the SFE cell were examined to determine if it improved the extraction efficiency. Methanol and acetone were tested and methanol was found to be a better modifier than acetone. Some of the pesticides, such as trichlopyr-2-butoxyethyl ether, were extracted well even without the modifier.

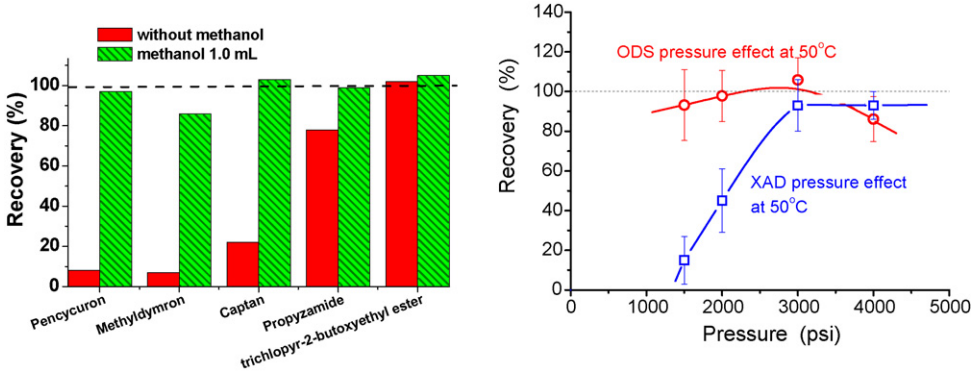


Fig. 3. Examination of extraction conditions. Effect of methanol as a modifier (left) and effect of extraction pressure (right). In the right panel, 19 pesticides were selected whose recoveries were 100 ± 20% at 3000 psi and average of recoveries are plotted with deviation against the extraction pressure at extraction temperature of 50 °C for XAD and ODS.

Table 1
Pesticides tested and their detection limits and correlation in determination of calibration curves.

Pesticide	m/z	$\log K_{ow}$	Guide-line[a]	ODS		XAD	
				LOD[a]	R^2	LOD[a]	R^2
Pencycuron	180, 209	4.82	400	0.040	0.9956	2.294	0.8962
Simazine	201, 186	0.73	30	0.010	0.9938	0.064	0.9949
Propyzamide	173, 254	3.28	80	0.008	0.9974	0.012	0.9989
Chlorothalonil	266, 264	2.89	40	0.007	0.9914	0.157	0.9292
Diazinon	179, 304	3.30	50	0.020	0.9980	0.099	0.9938
Terbucarb	205, 220		200	0.003	0.9982	0.005	0.9987
Tolclofosmethyl	265, 267	4.56	800	0.002	0.9978	0.025	0.9995
Metalaxyl	206, 249	1.64	500	0.092	0.9989	0.061	0.9982
Bensulide	131, 141	4.22	1000	-	-	-	-
Dithiopyr	354, 306	4.43	80	0.004	0.9982	0.963	0.9991
Fenitrothion	277, 125	3.43	30	0.071	0.9717	0.023	0.9988
Chlorpyrifos	197, 314	4.70	40	0.019	0.9973	0.044	0.9911
Pendimethalin	252, 281	5.18	500	0.043	0.9690	0.016	0.9994
Methyldymron	107, 119	3.00	300	0.019	0.9956	0.285	0.9949
Isofenphos	213, 255	4.12	10	0.011	0.9952	0.035	0.9991
Captan	79, 149	2.80	3000	0.160	0.9792	1.576	0.9882
Butamifos	286, 200	4.62	40	0.069	0.9629	0.049	0.9991
Napropamide	271, 128	3.36	300	0.013	0.9976	0.078	0.9997
Flutolanil	173, 281	3.70	2000	0.004	0.9975	0.007	0.9989
Isoprothiolane	290, 231	2.80	400	0.015	0.9974	0.191	0.9995
Trichlopyrbutoxyethyl	210, 212	4.30	60	0.034	0.9977	0.075	0.9995
Isoxathion	177, 313	3.88	80	0.079	0.9814	0.445	0.9776
Mepronil	119, 269	4.54	1000	0.013	0.9958	0.044	0.9997
Propiconazole	259, 173	3.65	500	0.033	0.9961	0.048	0.9997
Pyridaphenthion	340, 199	3.2	20	0.011	0.9952	0.029	0.9999
Iprodione	314, 316	3.00	3000	0.013	0.9935	0.418	0.9993

[a] Guidelines and LODs are shown in $\mu g\,L^{-1}$.

However, the extraction performance was dramatically improved in response to the addition of the modifier for most of the pesticides, especially pencycuron and methyldymron (Fig. 3, left).

Next, the effects of temperature and pressure on the extractions were examined. The recovery was almost constant as the extraction temperature changed from 30 to 50 °C at a constant pressure of 3000 psi for both ODS and XAD. Conversely, different effects on the recovery were observed in response to changes in pressure. Specifically, pressure exerted a small effect on the extraction conducted using ODS, whereas the recoveries were very poor at pressures lower than 2000 psi in the case of XAD as shown in Fig. 3, right. Furthermore, the recovery obtained using the XAD resins increased in proportion to the pressure up to 3000 psi. These findings reveal an interesting behavior in the SFE process. Extraction from flat surfaces

Table 2
Recoveries from real water samples. Standard addition level was $20\,\mu g\,L^{-1}$.

Pesticide	Guideline	Recovery (%)				
	$\mu g\,L^{-1}$	XAD		ODS		SPE
		GW	GCW	GW	GCW	RW
Pencycuron		18 ± 1	24 ± 2	87 ± 9	98 ± 23	89 ± 4
Simazine	30	61 ± 1	84 ± 12	28 ± 2	32 ± 10	68 ± 5
Propyzamide	80	92 ± 6	143 ± 24	82 ± 11	88 ± 35	78 ± 3
Chlorothalonil	40	7 ± 1	17 ± 12	2 ± 1	3 ± 0	0 ± 0
Diazinon	50	80 ± 1	114 ± 16	91 ± 13	100 ± 24	78 ± 3
Terbucarb	200	69 ± 12	66 ± 38	176 ± 43	73 ± 38	79 ± 6
Tolclofosmethyl	800	92 ± 10	133 ± 19	92 ± 12	108 ± 27	76 ± 4
Metalaxyl	500	62 ± 6	87 ± 17	66 ± 5	69 ± 17	79 ± 1
Bensulide	1000	ND	ND	ND	ND	ND
Dithiopyr	80	98 ± 7	138 ± 17	99 ± 13	111 ± 27	66 ± 5
Fenitrothion	30	101 ± 7	144 ± 30	111 ± 18	99 ± 25	61 ± 3
Chlorpyrifos	40	94 ± 1	129 ± 22	102 ± 12	107 ± 29	59 ± 4
Pendimethalin	500	113 ± 4	154 ± 26	114 ± 14	131 ± 36	57 ± 4
Methyldymron	300	57 ± 3	79 ± 10	81 ± 9	90 ± 21	98 ± 6
Isofenphos	10	101 ± 6	132 ± 23	119 ± 15	126 ± 31	78 ± 7
Captan	3000	59 ± 3	84 ± 17	85 ± 8	89 ± 22	64 ± 8
Butamifos	40	128 ± 9	165 ± 38	122 ± 16	118 ± 32	70 ± 6
Napropamide	300	56 ± 7	71 ± 14	121 ± 14	121 ± 29	79 ± 6
Flutolanil	2000	77 ± 5	104 ± 17	108 ± 12	119 ± 28	70 ± 2
Isoprothiolane	400	54 ± 6	79 ± 12	102 ± 10	111 ± 25	80 ± 2
Trichlopyr butoxyethyl	60	72 ± 1	83 ± 17	93 ± 10	90 ± 27	75 ± 5
Isoxathion	80	73 ± 9	91 ± 23	84 ± 13	90 ± 21	50 ± 5
Mepronil	1000	57 ± 1	72 ± 13	88 ± 11	105 ± 27	102 ± 7
Propiconazole	500	59 ± 3	76 ± 12	80 ± 7	98 ± 25	83 ± 11
Pyridaphenthion	20	54 ± 13	73 ± 15	110 ± 11	97 ± 25	0 ± 0
Iprodione	3000	ND	ND	ND	ND	ND

GW: groundwater, GCW: golf course wastewater, RW: river water and ND: not detectable.

occurs independently of the extraction pressure. Conversely, higher pressure is required for extraction from materials with complicated structures. Because adsorption occurs on the surface of ODS, but inside the XAD particles, XAD requires a higher pressure for the extraction. Based on these data, the optimum conditions were determined to be 50 °C at 3000 psi with the modifier methanol.

3.3. Performance of the method

After optimization, the method was tested with standard solutions which containing 0, 1, 5, 10, 20, 40 (or 50) and 100 μg L^{-1} pesticides. The series of measurements were repeated 3 times for the each concentration sample. In both ODS and XAD adsorption methods, the calibration curves were straight up to 100 μg L^{-1} for all pesticides investigated except pencycuron with XAD (sigmoid). Some chromatogram peaks were small below 5 μg L^{-1} for such as pencycuron, simazine, chlorothalonil, methyldymron, isofenfos, isoprothiolane, isoxathion, propiconazole with ODS adosorption. In case of XAD, same downward curve in low concentrations was observed only for isoxathion. For the other compounds, good linearities were obtained and good coefficient of determination (R^2) was obtained (Table 1). Sensitivity of the proposed method was comparable to that of conventional SPE method. When 200 mL of water sample was used in the SPE method, slope of calibration curve would be double of the proposed method for 50 mL sample. If same volume was used in the two methods, the proposed method gives twice sensitivity compared to the SPE method. Detection limits were determined from 3 times of deviation of blank signals; they ranged from 0.002 to 2.3 μg L^{-1}. The guidelines specify that the allowable limits of the pesticides range from tens to thousands of μg L^{-1} (Table 1). The method described here had sensitivity sufficient to detect pesticides present at concentrations lower than the guideline levels when only a 50 mL sample of water was analyzed.

3.4. Water sample analysis

The applicability of this method was confirmed by comparing the recovery of pesticides from natural water that had been spiked with golf link pesticides at a concentration of 20 μg L^{-1} using the method described here with the recovery obtained using the conventional SPE method [2,28]. As shown in Table 2, good recoveries were obtained for most of the pesticides using the method described in the present study. For some pesticides, recoveries were too high (>120%) in case of XAD. It can be said that the resin matrix might be extracted from XAD in SFE process to interfere the results. This can be observed in the chromatogram for blank sample with XAD (Fig. 4). This effect was small in analysis with ODS. In the conventional SPE analyses, recoveries were mostly lower (71% in average) compared to the present method for 20 μg L^{-1} pesticides whereas they were quantitative when water containing 1 mg L^{-1} pesticides was determined with the conventional SPE. Recoveries for some of pesticides such as simazine ($\log K_{ow}$ 0.73), terbucarb and metalaxyl ($\log K_{ow}$ 1.64) were relatively low even in the present method. Values of K_{ow} for these compounds were low compared to those of the other compounds ($10^{2.8–5.18}$). Bensulide and iprodione were not detected in the examined concentrations. These compounds were difficult to detect even in direct injection of acetone solution and guideline levels are very high compared to the examined concentrations.

In our prefecture, pesticides are rarely detected in water samples. However, several water samples evaluated in this study were found to contain pesticides. The results obtained using the method described here agreed with the data generated by the conventional SFE method as shown in Table 3. Also, chromatograms for the standard (20 μg L^{-1}) and water sample which was found to contain propyzamide are shown in Fig. 4. Determinations by the two

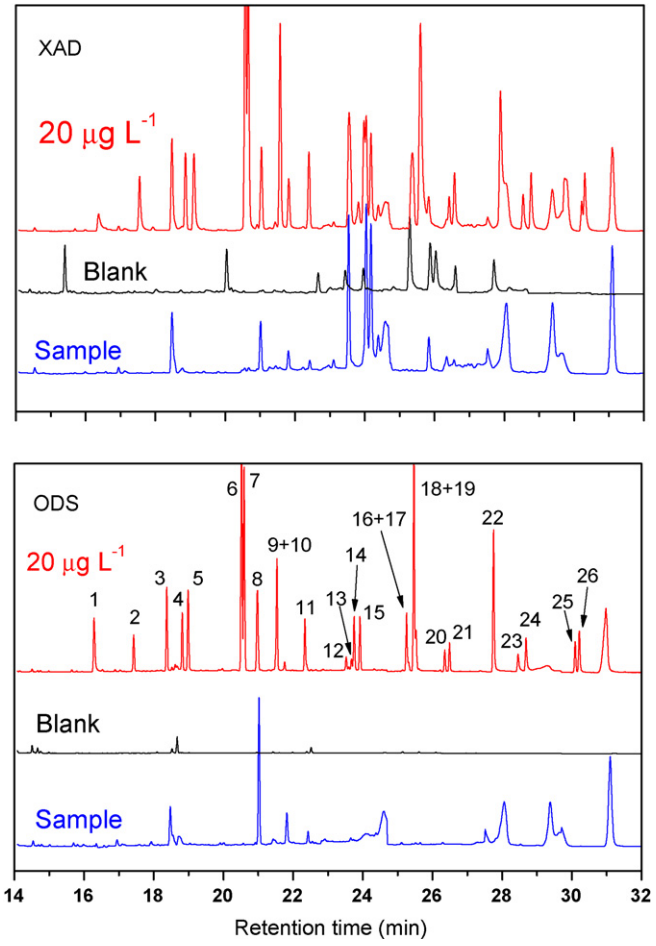


Fig. 4. Chromatograms for the sample and standard solutions. (1) pencycuron, (2) simazine, (3) propyzamide, (4) diazinon, (5) chlorothalonil, (6) terbucarb, (7) tolclofosmethyl, (8) metalaxyl, (9) dithiopyr, (10) fenitrothion, (11) chlorpyrifos, (12) pendimethalin, (13) captan, (14) methyldymron, (15) isophenphos, (16) naprozamide, (17) butamifos, (18) flutolanil, (19) isoprothiolane, (20) trichlopyrbutoxyethyl, (21) isoxathion, (22) mepronil, (23) iprodione, (24) propiconazole, (25) iprodione and (26) pyridaphenthion.

Table 3
Results of wastewater analysis.

Sample no.	Propyzamide found (μg L^{-1})		
	SFE cartridge	Batch ODS	Batch XAD
1	11.7 ± 0.7	11.3 ± 2.7	9.0 ± 0.9
2	5.8 ± 0.3	4.5 ± 0.8	5.3 ± 1.2
3	3.3 ± 0.1	3.0 ± 0.3	3.5 ± 0.2
4	3.1 ± 0.8	2.6 ± 0.4	3.0 ± 0.4

methods were performed in the same day or in two days. As can be seen in Fig. 4, there were interference peaks in the blank signals in case of XAD. On the other hand, flat chromatogram for the blank was obtained in ODS method. For low level analysis such in μg L^{-1} order, ODS was preferred in this method rather than XAD. The XAD resin would be suitable for high concentration samples because particles are relatively large and treatment was easier in the adsorption/extraction processes.

4. Conclusions

Supercritical fluid extraction was found to be useful for water analysis when it was coupled with batch-wise adsorption. Indeed, the results of this study revealed that the pesticides were adsorbed

onto the particulate adsorbents very simply using only a stirrer in a small beaker. Although the adsorption characteristics of the pesticides are related to their octanol/water partition coefficients, K_{ow}, good recoveries were obtained when a sufficient adsorbing time was adopted. Additionally, the recoveries obtained using this method with ODS and XAD are compatible with those obtained using the conventional SPE method. ODS was better than XAD resins due to lower interference and shorter adsorbing time. Finally, the operation time and cost of operation of the proposed method were lower than those associated with conventional SPE.

References

[1] M. Sudo, T. Kunimatsu, T. Okubo, Water Res. 36 (2002) 315.
[2] Standard Method of Waste Water Analysis (Multi-Analysis of Pesticides), in: Provisional Guideline for Preventing Water Pollution with Golf Link Chemicals (in Japanese), Ministry of Environment, Government of Japan, pp. 93–96 (http://www.env.go.jp/water/dojo/noyaku/law_data/f402kansuido0077.pdf).
[3] P. Ormad, S. Cortés, J. Sarasa, A. Martín, A. Puig, J.L. Ovellerio, J. Chromatogr. A 733 (1996) 159.
[4] Q. Zhou, L. Pang, G. Xie, J. Xiao, H. Bai, Anal. Sci. 25 (2009) 73.
[5] S.D. Scullion, M.R. Clench, M. Cooke, A.E. Ashcroft, J. Chromatogr. A 733 (1996) 207.
[6] C. de la Colina, A. Peña, M.D. Mingorance, F.S. Rasero, J. Chromatogr. A 733 (1996) 275.
[7] E. Viana, M.J. Redondo, G. Font, J.C. Moltó, J. Chromatogr. A 733 (1996) 267.
[8] G.A. Peñuela, D. Barceló, J. Chromatogr. A 754 (1996) 187.
[9] M. Guardia-Rubio, A. Ruiz-Medina, M.I. Pascual-Reguera, M.L. Fernández-de Córdova, Microchem. J. 85 (2007) 257.
[10] L. Toribio, M.J. del Nozal, J.L. Bernal, J.J. Jiménez, M.L. Serna, J. Chromatogr. A 823 (1998) 163.
[11] Determination Methods of Pesticides, Animal Food Additives, and Animal Medicines Resided in Foods (in Japanese), Notification of Food Safety No. 01241001, Ministry of Health, Labor and Welfare, Administration of Food Safety, 2005 (http://www.mhlw.go.jp/topics/yunyu/hassyutu/dl/174.pdf).
[12] X. Xu, H. Yang, L. Wang, B. Han, X. Wang, F.S. Lee, Anal. Chim. Acta 591 (2007) 87.
[13] J. Wu, T. Luan, C. Lan, T.W.H. Lo, G.Y.S. Chan, Food Control 18 (2007) 466.
[14] R. Eisert, K. Levsen, J. Chromatogr. A 733 (1996) 143.
[15] G. Sagratini, J. Mañes, D. Giardiná, P. Damiani, Y. Picó, J. Chromatogr. A 1147 (2007) 135.
[16] E. Bonet-Domingo, S. Grau-González, Y. Martin-Biosca, M.J. Medina-Hernández, S. Sagrado, Anal. Bioanal. Chem. 387 (2007) 2537.
[17] A.R. Valverde-García, M. Fernández-Alba, A. Contreras, Agüera, J. Agric. Food Chem. 44 (1996) 1780.
[18] V. Camel, Analysis 26 (1998) 99.
[19] Š. Hartík, J. Tekel, J. Chromatogr. A 733 (1996) 217.
[20] J.S. Ho, W.L. Budde, Anal. Chem. 66 (1994) 3716.
[21] V.S. Ong, R.A. Hites, Environ. Sci. Technol. 29 (1995) 1259.
[22] I.N. Glazkov, I.A. Revelsky, I.P. Efimov, Y.A. Zoltov, J. Microcol. Sep. 11 (1999) 729.
[23] J. Yu, Water Res. 36 (2002) 1095.
[24] V. Janda, M. Mikešová, J. Vejrosta, J. Chromatogr. A 733 (1996) 35.
[25] R. Fuoco, A. Ceccarini, M. Onor, L. Marrara, J. Chromatogr. A 846 (1999) 387.
[26] S.H. Salleh, Y. Saito, K. Jinno, Anal. Chim. Acta 418 (2000) 69.
[27] Solid-phase extraction, <http://www.epa.gov/osw//hazard/testmethods/sw846/pdfs/3535a.pdf>.
[28] G.A. Junk, J.J. Richard, Anal. Chem. 60 (1988) 451.

Talanta 80 (2009) 744–748

Contents lists available at ScienceDirect

Talanta

journal homepage: www.elsevier.com/locate/talanta

Six orders of magnitude dynamic range in capillary electrophoresis with ultrasensitive laser-induced fluorescence detection

Colin D. Whitmore, David Essaka, Norman J. Dovichi*

Department of Chemistry, University of Washington, Box 351700, Seattle, WA 98195-1700, United States

ARTICLE INFO

Article history:
Received 3 May 2009
Received in revised form 26 July 2009
Accepted 27 July 2009
Available online 5 August 2009

Keywords:
Capillary electrophoresis
Dynamic range
Linear range
Laser induced fluorescence

ABSTRACT

An ultrasensitive laser-induced fluorescence detector was used with capillary electrophoresis for the study of 5-carboxy-tetramethylrhodamine. The raw signal from the detector provided roughly three orders of magnitude dynamic range. The signal saturated at high analyte concentrations due to the dead time associated with the single-photon counting avalanche photodiode employed in the detector. The signal can be corrected for the detector dead time, providing an additional order of magnitude dynamic range. To further increase dynamic range, two fiber-optic beam-splitters were cascaded to generate a primary signal and two attenuated signals, each monitored by a single-photon counting avalanche photodiode. The combined signals from the three photodiodes are reasonably linear from the concentration detection limit of 3 pM to 10 μM, the maximum concentration investigated, a range of 3,000,000. Mass detection limits were 150 yoctomoles injected onto the capillary.

© 2009 Elsevier B.V. All rights reserved.

1. Introduction

Capillary electrophoresis provides outstanding resolution and near-Gaussian peaks. As a result, trace components can be detected in the presence of interfering compounds present at many orders of magnitude higher concentration. The dynamic range of the detector limits the ability to determine simultaneously the amounts of both trace and abundant components.

In capillary electrophoresis, absorbance measurements are limited to two or three orders of magnitude in dynamic range, whereas fluorescence detectors are able to achieve perhaps four orders of magnitude dynamic range. The latter tend to employ photomultiplier tubes as photodetectors with 16-bit analog-to-digital converters (ADC). The ADCs are typically operated so that the noise in the measurement is larger than the least significant digit in the ADC. A single measurement will typically have a dynamic range of less than 10,000; averaging the signal from many measurements in the presence of uncorrelated noise can improve the dynamic range to a limited extent [1]. Higher dynamic range ADC converts are becoming available but are seldom employed in fluorescence detection.

In principle, photon-counting detectors can achieve an arbitrary dynamic range limited only by the size of the register used to accumulate counts. However, photon counters have a finite dead time during which they do not respond to a second photon [2]. In a paralizable detector, the arrival of a second photon restarts the dead time. At very high incident rates, the detector will saturate and record no signal at all. For commercial avalanche photodiode photon counters, the dead time is on the order of 50 ns, and the detector will saturate as the incident photon rate approaches 20 MHz. The dead-time characteristic of detectors has received significant attention from the atomic and nuclear physics communities, and a number of models are available to correct for dead-time effects [3,4].

There are cases where very high-dynamic range is desirable, for example when detecting minute amounts of enzymatic product in the presence of a very large excess of substrate [5,6]. We report a simple method to increase dynamic range without limit in fluorescence detection and employ this method to produce over six orders of magnitude dynamic range while retaining yoctomole detection limits. In this system, fluorescence generated in a sheath-flow cuvette is collected by a microscope objective and imaged onto a gradient index-coupled fiber optic. The light captured by the fiber is sent to a cascade of fiber-optic beam-splitters, repeatedly dividing the signal into successively lower intensity channels. These beam-splitters require no alignment, are robust, and are inexpensive.

Each channel is equipped with a dedicated avalanche photodiode photon counting module. The highest intensity signal is used to characterize components present at very low levels and the most attenuated signal is used to characterize the highly abundant components. In principle, an arbitrary number of splitters can be

* Corresponding author. Tel.: +1 206 543 7835; fax: +1 206 685 8665.
E-mail addresses: cwhitmor@u.washington.edu (C.D. Whitmore), edachris@u.washington.edu (D. Essaka), dovichi@chem.washington.edu (N.J. Dovichi).

0039-9140/$ – see front matter © 2009 Elsevier B.V. All rights reserved.
doi:10.1016/j.talanta.2009.07.060

cascaded to generate an arbitrary dynamic range measurement; we demonstrate this approach with a cascade of two splitters and three photodiodes.

2. Materials and methods

2.1. Reagents

Unless specified, reagents were from Sigma. Water was from a Barnstead Nanopure water supply. 5-Carboxy-tetramethyl rhodamine (TAMRA) was from Invitrogen. Capillaries were from Polymicro Technologies.

2.2. Capillary electrophoresis

The capillary electrophoresis system was similar to others developed by this group [7–9]. Briefly, a 23-cm long, 20-μm ID, and 150-μm OD uncoated fused silica capillary was used for the separation. The separation was performed using a running buffer composed of 10 mM sodium tetraborate, 35 mM sodium deoxycholate, and 5 mM methyl-β-cyclodextrin. The running voltage was 18 kV. Injection was for 1 s at 1 kV. Counts were recorded at 50 Hz.

2.3. High-dynamic range, ultrasensitive laser-induced fluorescence detector

The instrument was equipped with a post-column sheath-flow cuvette for fluorescence detection [10,11]. The optical design of the high-dynamic range detector is shown in Fig. 1. The majority of the system was identical to that described earlier. Excitation was provided with a 10 mW diode-pumped solid-state (DPSS) laser at 532 nm (Coherent) that was focused in a sheath-flow cuvette. Fluorescence was collected by a 0.45 NA microscope objective, passed through a 580 DF40 bandpass filter, and imaged onto a GRIN-lens coupled fiber optic.

We employed fiber-optic beam-splitters to divide the fluorescence into two channels; one channel retained most of the original intensity and the second presented an attenuated version. The beam-splitters (Thorlabs) have a nominal 99:1 split ratio at 850 ± 40 nm. However, the split ratio degraded at the 580 nm wavelength of the fluorescence. One splitter generated a split ratio of ~15:1 and the other generated a split ratio of ~4:1. The splitters were placed in series, where the intense output of the first splitter was directed to a single-photon counting avalanche photodiode (APD1) and the attenuated output was directed to the second splitter. The outputs of that splitter were connected to two additional single-photon counting avalanche photodiodes (APD2 and APD3). PerkinElmer SPCM single-photon counting modules were employed in the experiment; all three had nominal dead time of 55 ns.

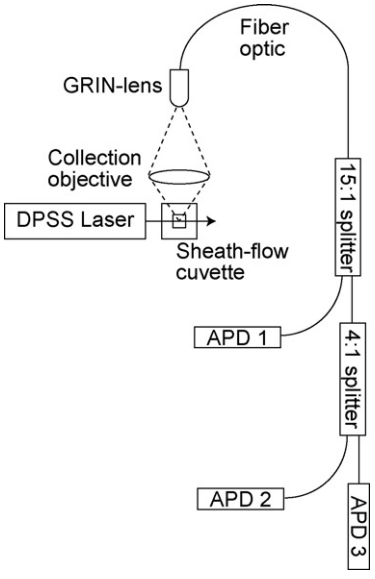


Fig. 1. Optical diagram. Fluorescence is divided with a cascade of fiber-optic beam-splitters into three channels. APD 1 provides the highest sensitivity but saturates at relatively low signals. APD 3 provides the poorest sensitivity but saturates at relatively high signals.

The fiber-optic cables attached to these beam-splitters are relatively transparent in the visible portion of the spectrum. Room light striking the fibers will increase the dark count. We cover the fibers with an opaque plastic sheet to eliminate this source of background signal.

The outputs of the photodiodes were digitized at 50 Hz by counters (National Instruments) in a PC. The data were then processed on a Macintosh computer using Matlab. Data were treated with a three point median filter to remove spikes due to light scatter from particles, and then convoluted with a 44-point wide Gaussian function with 5-point (100 ms) standard deviation. The MatLab routine cftool was used to fit a Gaussian function to the TAMRA peak; peak area was estimated by multiplying the peak amplitude with the standard deviation.

3. Results and discussion

3.1. Single avalanche photodiode detector

We employed the most sensitive photodiode of Fig. 1 to construct a calibration curve for the injection of 45 pL of various concentrations of 5-carboxy-tetramethylrhodamine. The data were treated with a 3-point median filter to remove the occasional noise spike associated with the passage of a particle through the detector and then convoluted with a 100 ms wide Gaussian filter, which matched the width of the electrophoretic peak.

Determining the linearity of wide dynamic range signals is not straightforward. We measured the signal for samples prepared by tenfold serial dilution. A simple plot of signal *vs.* concentration is virtually guaranteed to generate a high correlation coefficient in a least-squares plot. Instead, we inspect the slope of the least-squares fit of a straight line to the logarithm of concentration *vs.* the logarithm of signal; the slope should be close to 1.0 if the signal is linearly related to concentration.

Fig. 2 presents a log–log plot of the calibration data. The signal indeed increased linearly with concentration from 10 pM to 10 nM; the log–log plot generated a slope of 0.92 ± 0.04. The signal saturated at higher concentrations.

The concentration detection limit (3 s) was 3.4 pM and the mass detection limit was 150 ymol (100 copies) injected onto the capillary. The linear dynamic range from the detection limit to the start of the nonlinear portion of the calibration curve was 3000. The peaks in the linear portion of the calibration curve generated 300,000 ± 20,000 theoretical plates.

3.2. Paralizable detector

The observed photon count rate, N_{obs}, from a paralizable detector is related to the true photon count rate, N_{true}, and the detector dead time, t_d [4].

$$N_{obs} = N_{true} e^{-N_{true} t_d} \quad (1)$$

A plot of the incident and observed count rates predicted from Eq. (1) is shown in Fig. 3 for a paralizable photodetector with a 55-ns dead time, the nominal dead time for our photodiodes. The

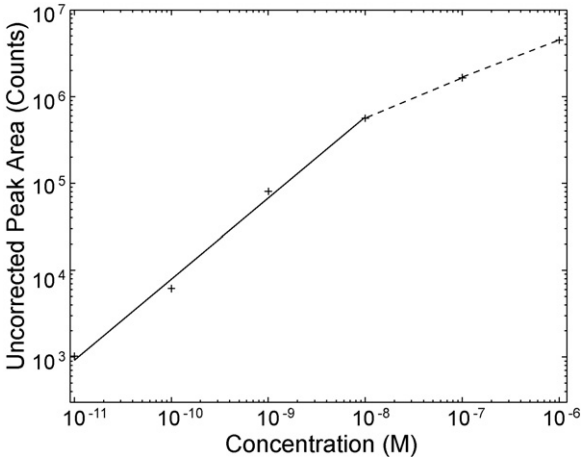


Fig. 2. Log–log calibration curve for uncorrected peak area for diode 1. The straight line is the result of a linear regression analysis to the log-log data for concentrations of 10^{-11}, 10^{-10}, 10^{-9}, and 10^{-8} M; slope = 0.92 ± 0.04, r = 0.9980. The dashed lines are to guide the eye.

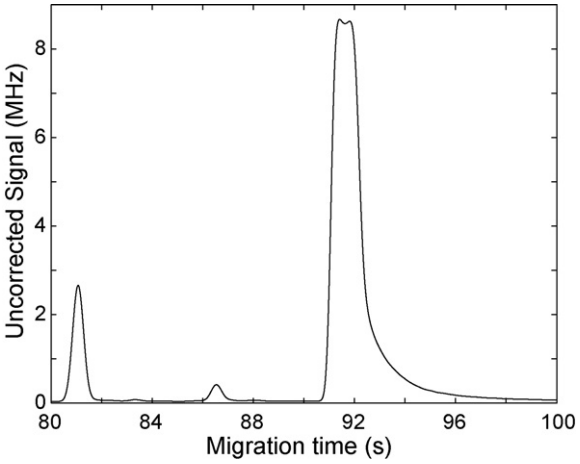


Fig. 4. Uncorrected electropherogram of a 1 μM solution of TAMRA recorded with photodiode 1. Data were treated with a 3-point median filter and then convoluted with a Gaussian filter with a standard deviation of 100 ms. Note the dip at the center of the peak at 92 s due to detector saturation.

observed count rate is within 5% of the true count rate for signals less than 1 MHz, but becomes highly nonlinear at higher count rates. The observed signal reaches a maximum at an incident count rate equal to $1/t_d$ and then decreases at higher count rates. The maximum signal is $1/(t_d\, e)$.

Fig. 4 presents the electropherogram generated by a 1 μM TAMRA solution. The lower amplitude impurity peaks at 81 and 86.5 s are Gaussian in shape, whereas the main peak is severely distorted, showing a truncated peak with a dip at the center. This dip occurs because N_{obs} is not monotonically related to N_{true}; the true count rate near the dip exceeds $1/t_d$. The signal exceeds the maximum predicted for a 55-ns dead-time detector; Eq. (1) is not accurate for very high signals.

An inverse function can be used to estimate N_{true} for $N_{true} < 1/t_d$. Several models have been presented for the inverse function. The most common correction function is [12]

$$N_{true} \approx \frac{N_{obs}}{1 - N_{obs} t_d} \tag{2}$$

A second order term can be included, which improves the accuracy of the inverse function [4].

$$N_{true} \approx \frac{N_{obs}}{1 - N_{obs} t_d - (N_{obs} t_d)^2} \tag{3}$$

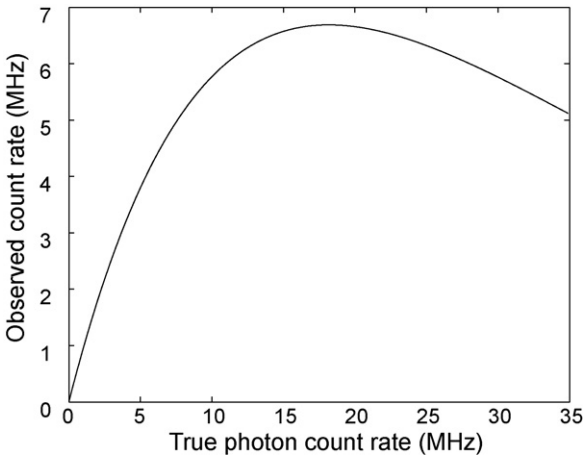


Fig. 3. Plot of Eq. (1) for a paralizable detector with a dead time of 55 ns. The observed count rate maximizes near 6 MHz and decreases at more intense signals.

The latter correction is accurate to within 2% for $N_{true} < 0.65/t_d$ ($N_{obs} < 0.34/t_d$).

We employed Eq. (3) with t_d = 55 ns to correct the nonlinear response of the photodiode. The resulting calibration curve was reasonably linear from the detection limit to 100 nM concentration (slope of the log–log plot = 0.91 ± 0.04, r = 0.9974). The non-monotonic relationship between N_{true} and N_{obs} prevented an accurate correction of the 1 μM data. The detection limit was not affected by this procedure, and the linear dynamic range was increased to ~30,000.

3.3. Fiber-optic beam-splitter cascade

We employed a cascade of two fiber-optic beam-splitters to divide the fluorescence intensity. The first beam-splitter divided the intensity in ~15:1 ratio; the second divides intensity by ~4:1. The splitting ratios were determined by first correcting the signal from each photodiode for detector dead time and then comparing the signal intensity of low concentration samples. The first photodiode received the vast majority of the fluorescence signal and was useful for the lowest amplitude signals; the third diode received only 2% of the fluorescence signal and was useful for higher amplitude signals.

The beam-splitters have some loss. We measured the baseline signal with the APD directly connected to the GRIN lens and the signal after going through the beam-splitters. The signal from photodiode 1 was attenuated by about 35%. 5% of that loss was due to light directed to the other photodiodes and could be recovered by summing the photodiode signals. The detection limit of a shot-noise limited experiment scales inversely with the square-root of the signal. A 30% decrease in signal corresponds to 20% degradation in detection limit. That loss of performance is accompanied by a two order of magnitude increase in dynamic range and should be acceptable in most experiments.

Fig. 5 presents the electropherogram generated by the 1 μM sample as observed by the three photodiodes. The traces have been corrected for the detector dead time with Eq. (3) and scaled based on the measured fiber-optic beam-splitter ratio. Although the peak signal from photodiode 1 could not be corrected by Eq. (3), the lower amplitude signals were well within the linear range of the photodiode. The corrected signal from photodiode 3 was multiplied by 10,000 to highlight trace components, and the corrected and scaled signal from photodiode 2 was multiplied by 100 to highlight intermediate amplitude components. The trace component at 77 s was

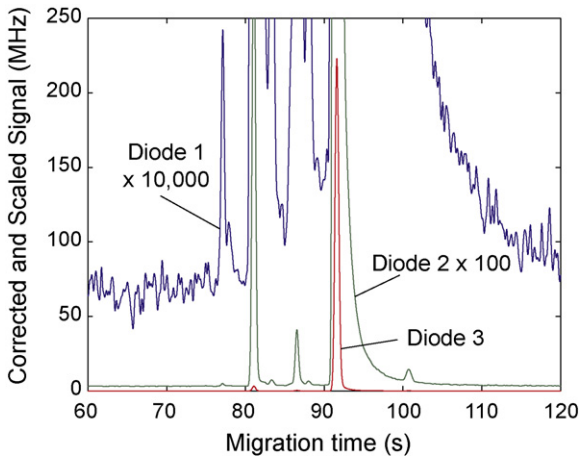


Fig. 5. Corrected electropherogram of a 1 μM solution of TAMRA and recorded with three photodiodes. The signals from the photodiodes have been filtered and corrected for detector dead time. The signals from photodiodes 2 and 3 have also been scaled to account for the attenuation introduced by the fiber-optic beam-splitter cascade. Finally, the corrected signal from diode 1 has been multiplied by 10,000 and the corrected and scaled signal from diode 2 has been multiplied by 100 to highlight low and medium abundance components.

roughly four orders of magnitude less intense than the main TAMRA peak.

The high-dynamic range allows a detailed characterization of peak shape. In particular, the main peak shows a modest amount of tailing in the photodiode 3 signal, which becomes much more prominent in the higher sensitivity signal of photodiode 1. That tailing is not the result of the convolution filter employed to treat the data. The convolution function is symmetrical and cannot introduce tailing. The effect of the filter is shown in Fig. S1 of the supporting information for this paper.

Fig. 6 presents the calibration curves generated by combining the scaled peak areas from the three diodes; photodiode 1 was used for corrected and scaled signals up to 1 MHz, photodiode 2 was used for corrected and scaled signals between 50 kHz and 100 MHz, and photodiode 3 was used for signals between 50 kHz and 1 GHz. The combined calibration curve generated a log–log slope of 0.93 ± 0.02, $r = 0.9981$ ($n = 20$), ranging from the detection limit of 3×10^{-12} M to 1×10^{-5} M, a range of 3,000,000 in concentration. The slope is not within experimental error of unity; the origin of that discrepancy is not clear, but may be associated with the photophysical phenomena described below. Because the slope is not unity, it is necessary to construct a calibration curve using at least two concentrations of analyte to determine the slope. In practice, the splitter combination should be evaluated across a wide concentration range to characterize its performance.

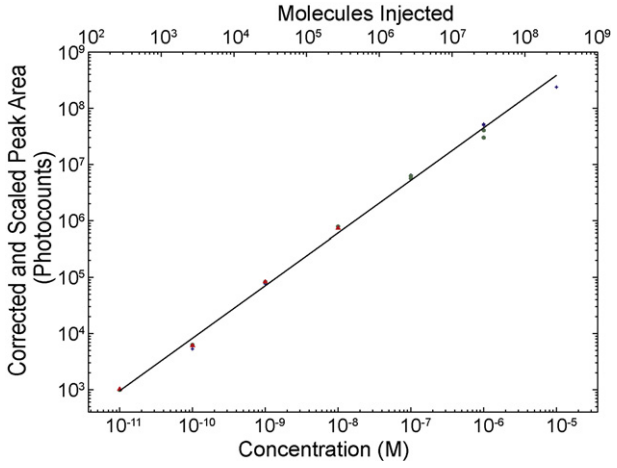


Fig. 6. Log–log calibration curve combining peak area for the three diodes. Red "Δ" is the corrected area for diode 1 (from 10^{-11} to 10^{-7} M), green "o" is the corrected and scaled area for diode 2 (from 10^{-10} to 10^{-6} M), and black "+" is the corrected and scaled area for diode 3 (from 10^{-10} to 10^{-5} M). The line is a least-squares fit of a line to the log–log data; the slope is 0.93 ± 0.02, $r = 0.9981$, $n = 20$. (For interpretation of the references to colour in this figure legend, the reader is referred to the web version of the article.)

Of course, additional beam-splitters and detectors can be added to the system to increase the dynamic range to higher concentrations. However, we are near the limits provided by the electrophoretic and spectroscopic properties of this dye. There are three phenomena that occur at higher analyte concentrations to generate nonlinear responses. First, dimer formation occurs at sub-millimolar concentrations of highly conjugated aromatic dye molecules [13]. These dimers have different molar absorptivity than the free dye and will lead to deviations from Beer's law. Antonov has reported a dimer dissociation constant of 3×10^{-4} M for rhodamine 6G, a similar dye to TAMRA. Second, capillary electrophoresis peak shapes become distorted as the ionic strength of the sample approaches the ionic strength of the buffer; in our system, analyte concentration can be increased to ~1 mM before electrophoretic phenomena distort peak shape. Finally, the fluorescence signal will become nonlinear when absorbance across the stream radius becomes significant, which again will become important for tetramethyl rhodamine concentration greater than a few hundred micromolar.

We also point out that Merz and Mort employed a liquid-crystal programmable attenuator in the emission channel of a fluorescence detector [14]. This device was used to keep the fluorescence intensity within the linear dynamic range of their photodetector and was particularly useful at high analyte concentrations. Unfortunately, a calibration curve was not generated to evaluate the performance of this system.

Finally, the dynamic range of the instrument can be improved at lower concentrations. Most simply, the capillary inner diameter can be increased, allowing an increase in injection volume by at least one order of magnitude. As the ultimate improvement, a beam-splitter cascade can be incorporated into a single molecule detector [15], which would allow the widest possible dynamic range in fluorescence detection—nine or ten orders of magnitude should be possible, limited only by the photochemistry of the dye molecule.

Acknowledgements

This work was supported by a grant from the National Institutes of Health (R01NS061767). CDW acknowledges an American Chemical Society—Division of Analytical Chemistry Graduate Fellowship. We thank one of the reviewers who brought Ref. [14] to our attention.

Appendix A. Supplementary data

Supplementary data associated with this article can be found, in the online version, at doi:10.1016/j.talanta.2009.07.060.

References

[1] G. Horlick, Reduction of quantization effects by time averaging with added random noise, Anal. Chem. 47 (1975) 352–354.
[2] X.L. Sun, F.M. Davidson, Photon-counting with silicon avalanche photodiodes, Lightwave Technol. 10 (1992) 1023–1032.
[3] M. Blackman, J.L. Michiels, Efficiency of counting systems, Proc. Phys. Soc. London 60 (1948) 549–561.
[4] M.T. Madsen, R.J. Nickles, Method for correcting count-rate losses in scintillation cameras, Med. Phys. 13 (1986) 344–349.

[5] C.D. Whitmore, U. Olsson, E.A. Larsson, O. Hindsgau, M.M. Palcic, N.J. Dovichi, Yoctomole analysis of ganglioside metabolism in PC12 cellular homogenates, Electrophoresis 28 (2007) 3100–3104.
[6] C.D. Whitmore, O. Hindsgaul, M.M. Palcic, R.L. Schnaar, N.J. Dovichi, Glycosphingolipid metabolism in single cells, Anal. Chem. 79 (2007) 5139–5142.
[7] Y.F. Cheng, N.J. Dovichi, Subattomole amino-acid analysis by capillary zone electrophoresis and laser-induced fluorescence, Science 242 (1988) 562–564.
[8] S.L. Wu, N.J. Dovichi, High-sensitivity fluorescence detector for fluorescein isothiocyanate derivatives of amino-acids separated by capillary zone electrophoresis, J. Chromatogr. 480 (1989) 141–155.
[9] J.R. Kraly, M.R. Jones, D.G. Gomez, J.A. Dickerson, M.M. Harwood, M. Eggertson, T.G. Paulson, C.A. Sanchez, R. Odze, Z.D. Feng, B.J. Reid, N.J. Dovichi, Reproducible two-dimensional capillary electrophoresis analysis of Barrett's esophagus tissues, Anal. Chem. 78 (2006) 5977–5986.
[10] N.J. Dovichi, J.C. Martin, J.H. Jett, R.A. Keller, Attogram detection limit for aqueous dye samples by laser-induced fluorescence, Science 219 (1983) 845–847.
[11] N.J. Dovichi, J.C. Martin, J.H. Jett, M. Trkula, R.A. Keller, Laser-induced fluorescence of flowing samples as an approach to single-molecule detection in liquids, Anal. Chem. 56 (1984) 348–354.
[12] E.H. Turner, K. Lauterbach, H.R. Pugsley, V.R. Palmer, N.J. Dovichi, Detection of green fluorescent protein in a single bacterium by capillary electrophoresis with laser-induced fluorescence, Anal. Chem. 79 (2007) 778–781.
[13] L. Antonov, G. Gergov, V. Petrov, M. Kubista, J. Nygren, UV–vis spectroscopic and chemometric study on the aggregation of ionic dyes in water, Talanta 49 (1999) 99–106.
[14] J.A. Merz, J.A. Mort, A computer-controlled variable light attenuator for protection and autoranging of a laser-induced fluorescence detector for capillary zone electrophoresis, Electrophoresis 19 (1998) 2239–2242.
[15] D.Y. Chen, N.J. Dovichi, Single-molecule detection in capillary electrophoresis: molecular shot noise as a fundamental limit to chemical analysis, Anal. Chem. 68 (1996) 690–696.

Talanta 80 (2009) 749–753

Contents lists available at ScienceDirect

Talanta

journal homepage: www.elsevier.com/locate/talanta

Kinetic approach for evaluation of total antioxidant activity

Elena E. Karyakina[a], Darya V. Vokhmyanina[a], Natalya V. Sizova[b], Aytugan N. Sabitov[a], Anastasiya V. Borisova[a], Tatyana G. Sazontova[b], Yury V. Arkhipenko[b], Vsevolod A. Tkachuk[b], Yury A. Zolotov[a], Arkady A. Karyakin[a,*]

[a] Chemistry Faculty of M.V. Lomonosov Moscow State University, Lenin Hills, 119991 Moscow, Russia
[b] Basic Medicine Faculty of M.V. Lomonosov Moscow State University, Lenin Hills, 119991 Moscow, Russia

ARTICLE INFO

Article history:
Received 7 May 2009
Received in revised form 27 July 2009
Accepted 27 July 2009
Available online 5 August 2009

Keywords:
Antioxidant activity
Kinetics
Hydrogen peroxide scavenging

ABSTRACT

We propose a novel approach for assessment of total antioxidant activity by monitoring kinetics of hydrogen peroxide (H_2O_2) scavenging after its injection into liquid sample under study. H_2O_2 is known to be the strongest oxidant, really presented in human body in contrast to the majority of the model oxidative systems used for evaluation of antioxidant activity. In addition, kinetic approach, being more informative than the commonly used determination of the final product, obviously provides better discrimination of potential antioxidants. Prussian Blue based sensor due to its high sensitivity and operational stability allowed to monitor kinetics of hydrogen peroxide consumption in turbid and colored samples. The pseudo-first order kinetic constants of hydrogen peroxide scavenging in the presence of different food additives correlated with total antioxidant activity of these samples evaluated via standard procedure based on lipid peroxidation. However, in contrast to the standard method, the proposed kinetic approach is expressed and does not require fresh biological tissues.

© 2009 Elsevier B.V. All rights reserved.

1. Introduction

Recent attention of clinical chemists is paid to a so-called oxidative stress, recognized as one of the major risk factors in progression of disease-related pathological complications in diabetes, atherosclerosis, renal disease, cancer, aging and other conditions [1–5]. Oxidative stress arises due to imbalance between oxidative and reductive processes, and in particular due to imbalance in the antioxidant status. This provides an interest to the compounds, which are able to decrease the rate of oxidizing reactions, usually referred to as antioxidants.

Methods to estimate the antioxidant activity can be divided in the two general groups [6]. One group involves analysis of oxidized products, for example of lipid peroxidation, in the presence of the samples or individual substances under study [6]. However, this approach is time consuming and requires fresh biological tissues. This provided the interest for determination of antioxidant activity by addition of powerful oxidants and investigation of their decomposition by the samples under study [6–8]. Among the most widely used tests are: total radical-trapping antioxidant parameter (TRAP) based on generation of free radicals by thermal decomposition of 2,2-azo-bis-2-amidinopropane hydrochloride with subsequent measurement or luminol-enhanced chemiluminescence [9,10], scavenging of diphenylpicrylhydrazyl radical (DPPH) [11–13], a procedure based on inhibition of the production of the ABTS (2,2a-azinobis(3-ethylbenzthiazoline)-6-sulfonic acid) radical cation [14], the ferric reducing antioxidant power (FRAP) method [15,16], based on the reduction of a Fe^{3+} complex of tripyridyltriazine, the latter monitored by means of spectrophotometry, etc. Unfortunately, the spectrophotometric and luminescence assays used in the majority of tests have limits raised by color and turbidity of real samples. A separate group of antioxidant tests is based on investigation of redox properties of the samples (compounds) under study in most cases by means of electrochemistry [17].

The major disadvantage of the known methods for accessing of total antioxidant activity is that the majority of the used oxidizing compounds do not present in human body. This makes doubtful any correlation between their reactivity with potential antioxidants and, hence, the usefulness of the latter.

Hydrogen oxides are involved in biochemical reaction pathways. Strategies have been developed for measuring the antioxidant activity as the ability to scavenge free radicals generated in aqueous and lipophilic phases. However, the lifetime of the natural free radicals is extremely low, so their concentration in biological liquids is almost negligible. Hydrogen peroxide is much more stable than hydroxide radicals. It can be recognized as a natural oxidant, since it is detected in blood [18]. Hydrogen peroxide is definitely more powerful oxidant than oxygen; the difference in the correspondent electrochemical potentials exceeds 1 V

* Corresponding author.
E-mail address: aak@analyt.chem.msu.ru (A.A. Karyakin).

0039-9140/$ – see front matter © 2009 Elsevier B.V. All rights reserved.
doi:10.1016/j.talanta.2009.07.059

[19]. Moreover, thermodynamically hydrogen peroxide in neutral media is similarly powerful oxidant as hydroxide radical [19]. On the other hand, H_2O_2 is less reactive compared to free radicals providing the latter also to be decomposed by the compounds able to consume hydrogen peroxide.

Hydrogen peroxide scavenging measured by photometric or fluorometric assays has been used in combination with the accepted methods for evaluation of antioxidant activity (lipid peroxidation, ABTS, DPPH tests) [20–22]. A positive correlation has been reported [21].

Another disadvantage of the accepted assays for evaluation of antioxidant activity *in vitro* is the detection of the final product rather than the kinetics of its accumulation/consumption. The choice, however, was dictated by the analytical protocols used. On the contrary, kinetic approach is much more informative, which would obviously allow better discrimination of potential antioxidants.

We propose the new method for estimation of total antioxidant activity based on kinetics of hydrogen peroxide scavenging in the presence of potential antioxidants. A choice of hydrogen peroxide as an oxidant is provided by the knowledge that H_2O_2 is the most powerful oxidant presented in human body (see above).

The proposed approach for estimation of total antioxidant activity involves application of electrochemical sensor for hydrogen peroxide for measurement of H_2O_2 (as oxidizing compound) added to food samples. Starting from 1994 our team pioneered the use of electrochemically deposited films of Prussian Blue (ferric hexacyanoferrate) for development of chemical and biological sensors with amperometric detection [23–25]. During the last 15 years the fundamental research work has been carried out in order to achieve the most advantageous H_2O_2 transducer. Compared to the most widely used platinum, Prussian Blue modified electrodes are characterized by: (i) three orders of magnitude higher electrochemical rate constant in both H_2O_2 reduction and oxidation and (ii) three orders of magnitude improved selectivity in hydrogen peroxide reduction [26]. The electrochemical rate constant is proportional to sensitivity if the latter is limited by the electrochemical reaction rather than diffusion. Even in case of ultramicroelectrodes operating in improved diffusion conditions, the Prussian Blue modified ones provide at least the 100 times improved responses compared to platinum.

Even in case of conventional electrodes the improved electrocatalytic properties of Prussian Blue allow low-potential H_2O_2 detection with advantageous analytical characteristics: (i) the sensitivity of 1–2 A M^{-1} cm^{-2}, which is at the upper limiting sensitivity level [27], (ii) the detection limit of 1×10^{-7} M in FIA mode, and (iii) linear calibration range starting from the detection limit and extending over more than three orders of magnitude of hydrogen peroxide concentration [24–26]. Moreover, on the basis of Prussian Blue based nano-electrode arrays [28] the record electrochemical sensor has been elaborated [29].

In current study we propose to assess the antioxidant activity by evaluating the kinetic constants of H_2O_2 consumption. The approach is advantageous over existing systems because of both the use of natural oxidant and monitoring the kinetics of its scavenging, which obviously provides better screening of potential antioxidants. Antioxidant activity evaluated in course of the proposed method and a standard protocol of lipid peroxidation were found to be in a good agreement. However, in contrast to the latter the proposed approach is express, simple and cheap, which opens a wide area for it's use in screening of food products.

2. Experimental

Experiments were carried out with MilliQ water from a Millipore MilliQ system. All inorganic salts, and hydrogen peroxide (30% solution) were obtained at the highest purity from Reakhim (Moscow, Russia) and used as received. Perfluorosulfonated ionomer (Nafion analogue) was purchased from Plastpolymer (St. Petersburg, Russia) as 8% solution in iso-propanol.

Samples of juices and wines were bought in a local supermarket. Sublimated fresh juices of cranberry, carrot, sea-buckthorn, beet were kindly supported by LTD "Victoria" (Russia). Bergenia extract was produced by LTD "Provantsal" (Russia).

Lipid membrane samples were prepared by homogenization of rat cerebral cortex in 20 mM TRIS buffer, pH 7.4 with the ratio of tissue-buffer of 10. Then the homogenate was centrifuged ($3600 \times g$, 10 min, 4 °C) using Eppendorf (Germany) 5417R centrifuge. Protein concentration was determined according to Lowry method.

Peroxidation of cerebral cortex was carried out at 37 °C upon continuous stirring by injection of 50 μM of hydrogen peroxide. Products of lipid peroxidation were detected according to their reaction with 2-thiobarbituric acid [30–32] monitoring optical density at 532 nm with spectrophotometer Cintra 10e GBS (UK).

Prussian Blue based screen-printed sensors for hydrogen peroxide were obtained from "Rusens" LTD (Moscow, Russia). Sensor contained carbon auxiliary electrode encircling working disk (Ø2 mm), the latter modified with Prussian Blue, and Ag|AgCl reference. Analytical characteristics in H_2O_2 detection were: sensitivity 0.4–0.5 A M cm^{-2}, detection limit 1×10^{-7} M. For stabilization of H_2O_2 sensor a 2 μl drop of 1% iso-propanol solution of perfluorosulfonated ionomer was applied to working electrode surface and dried at a room temperature.

Monitoring of hydrogen peroxide with screen-printed sensors has been carried out upon stirring using PalmSens electrochemical interface interfaced to an IBM PC. Operational stability of Prussian Blue modified electrodes was investigated in flow-through system consisted of a Cole Parmer (Vernon Hills, IL) peristaltic pump (7519-10), homemade flow-through wall-jet cell with 0.5-mm nozzle positioned at 1–2-mm distance from the surface of disk electrode. Amperometric batch measurements were performed in stirred solutions of food samples (20 ml) with applied potential of 0 mV *vs* Ag|AgCl. Once a stable baseline current was reached (within 5–10 min), an aliquot of H_2O_2 sample solution ($2–5 \times 10^{-5}$ M) was injected. After achieving of maximum response (within 10 s) the kinetics of current decay was investigated. A supporting electrolyte used was 0.025 M phosphate buffer, pH 6.0, containing 0.1 M KCl.

Concentration of hydrogen peroxide in stock solutions was controlled by optical density at 230 nm with an LKB-Ultraspec UII spectrophotometer (Broma, Sweden).

3. Results and discussion

3.1. Operational stability of Prussian Blue based hydrogen peroxide sensors

Prussian Blue films onto the electrode surfaces are stable in cyclic voltammetric conditions. However, operational stability of Prussian Blue modified electrodes is affected by both (i) thermodynamic instability of the reduced form of the electrocatalysis, Prussian White, and (ii) an ability of the hydroxyl anions, the product of H_2O_2 reduction, to solubilize the inorganic polycrystal [26].

To investigate operational stability of H_2O_2 sensors a continuous flow of hydrogen peroxide in wall-jet cell was chosen. Despite for investigation of kinetics of H_2O_2 consumption the batch regime is more convenient, the harder conditions providing faster inactivation of the electrocatalyst ensures a validity of the kinetic study in batch regime.

Operational stability of Prussian Blue based hydrogen peroxide sensors was investigated under continuous flow of 0.1 mM of H_2O_2

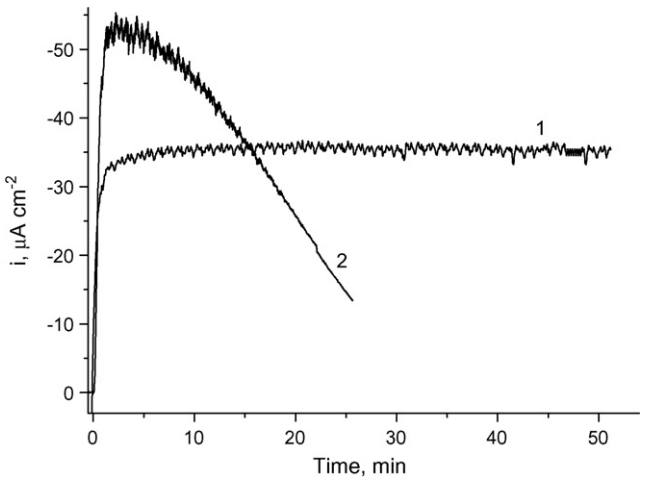


Fig. 1. Operational stability of Prussian Blue modified electrodes under continuous flow (0.7 ml min^{-1}) of 0.1 mM H_2O_2 in wall-jet cell: (1) Prussian Blue covered with 1% perfluorosulfonated ionomer and (2) naked Prussian Blue.

in wall-jet cell. A seen in Fig. 1, the naked Prussian Blue based sensor in such hard conditions maintains its maximum current only within 3–4 min. Afterwards a rather sharp decay occurs, and after 20 min the sensor loses 50% of its initial sensitivity. In order to stabilize the sensor a drop of perfluorosulfonated ionomer solution (1% in isopropanol) was applied onto the top surface of Prussian Blue film. Operational stability of the sensor stabilized with polymer film was investigated in similar conditions. As seen in Fig. 1, despite the 1.5 times lower sensitivity, the resulting sensor displayed a completely stable response in such hard conditions for more, than 50 min. Taking into account, that flow-through wall-jet regime provides faster inactivation of the electrocatalyst, we conclude, that such operational stability is enough for investigation of kinetics of hydrogen peroxide consumption is batch regime.

3.2. Kinetics of hydrogen peroxide consumption

Electrochemical sensor for hydrogen peroxide with high sensitivity and high operational stability allowed to monitor kinetics of hydrogen peroxide consumption (H_2O_2 scavenging activity) in turbid and colored samples which was previously impossible using photometric or fluorometric assays.

Kinetics of hydrogen peroxide consumption monitored by means of perfluorosulfonated ionomer stabilized Prussian Blue based sensors was investigated in batch regime under stirring. After injection of hydrogen peroxide to a final concentration of $2–5 \times 10^{-5}$ M in buffer solution a stable baseline was achieved (data not shown). This is not surprising taking into account excellent operational stability of the stabilized Prussian Blue based sensors in much harder conditions—continuous flow of 0.1 mM of H_2O_2 (see above).

Since easily oxidizable compounds are able to generate anodic (positive current) response of the Prussian Blue based sensors, the kinetics of H_2O_2 consumption was investigated as follows. First, the sensor was immersed in food sample under study, and operated until a stable baseline achieved. Afterwards, hydrogen peroxide was injected in the sample to a final concentration of $2–5 \times 10^{-5}$ M. Since the sensor is completely stable under such conditions, the decay of the current response is only due to H_2O_2 consumption. An ability of food samples to inactivate the electrocatalyst was independently checked controlling sensor sensitivity in buffer solutions before and after exposing.

Fig. 2 displays the usual continuous monitoring of hydrogen peroxide after its injection using the Prussian Blue based sensor. A seen, some food products do not show an ability to decompose hydrogen peroxide. In case of cranberry juice sublimate after injection of hydrogen peroxide a stable cathodic current is observed. However, beet juice displayed high hydrogen peroxide scavenging activity. After injection of hydrogen peroxide, the current has sharply increased, and then exponentially decreased (Fig. 2a). We have found that hydrogen peroxide is unstable in the majority of food samples: dry red and white grape wines, grape, apple, grapefruit, orange juices, food additives (sublimated sea-buckthorn, bergenia, beet juices).

Current decay in chronoamperograms of H_2O_2 sensors in the presence of food samples can be for simplicity assumed to obey pseudo-first order kinetics. Indeed, in some cases treatment of the decay in semi-logarithmic plots gives perfect linearization (Fig. 2b). For samples, which do not display a straight line in semi-logarithmic plots in the whole time scale, an initial slope has been taken for consideration. From the slope in semi-logarithmic plots the kinetic constant k of hydrogen peroxide elimination is determined (the example in Fig. 2b gives $k \approx 2 \times 10^{-3}$ s^{-1}).

We propose to use the kinetic constant of hydrogen peroxide elimination as a relative indicator of total antioxidant activity. Obviously, the higher the kinetic constant is, the more powerful is the antioxidant. The kinetic constants of hydrogen peroxide elimination have been found to be quite different in various food samples (Table 1). As expected, freshly squeezed grapefruit juice is more powerful antioxidant than the juice commercially available. Orange juices from different suppliers display significant differ-

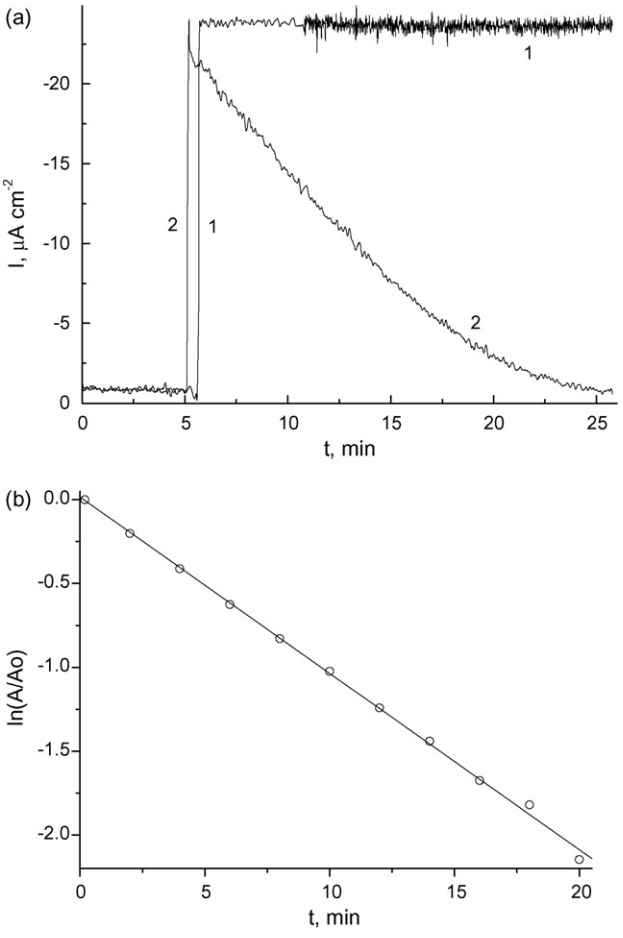


Fig. 2. (a) Response of the Prussian Blue based hydrogen peroxide sensor after addition of 5×10^{-5} M of H_2O_2 in 0.1 M phosphate buffer, pH 6.0 phosphate buffer containing sublimates of cranberry (1) and beet juice (2); (b) relative (to peak current) current decay in semi-logarithmic plots.

Table 1
Antioxidant activity of different food samples.

Sample	k ($\times 10^3$ s^{-1})
Grapefruit juice, freshly prepared	4.0 ± 0.3
Grapefruit juice, Rich (Russia)	2.0 ± 0.3
Orange juice, Rich (Russia)	1.2 ± 0.3
Orange juice, Dobryi (Russia)	0.4 ± 0.1
White dry wine "Baron de Valls" (France)	1.8 ± 0.3
Red dry wine "La Bifora Rosso" (Italy)	1.0 ± 0.3
White dry wine "Tsinandali" (Georgia)	0.08± 0.01
Bergenia juice sublimate	5.0 ± 0.5
Sea-buckthorn juice sublimate	2.2 ± 0.3
Beet juice sublimate	2.1 ± 0.4
Cranberry juice sublimate	$<1 \times 10^{-5}$
Carrot juice sublimate	$<1 \times 10^{-5}$

ence in antioxidant activity. Wine samples display sufficiently high antioxidant power, except for 'Tsinandali' wine. Solutions of juice sublimate display as the highest antioxidant activity (bergenia), as the absence of an ability to decompose hydrogen peroxide (cranberry). The significant variation in kinetic constants of H_2O_2 elimination in food samples points to its potential use as a relative indicator of antioxidant activity.

3.3. Validation of the kinetic approach for accessing of antioxidant activity

Certainly, any approach for accessing of antioxidant activity cannot be accepted without correlation with the direct protocol based on lipid peroxidation. Since the highest variation in kinetic constant of H_2O_2 elimination was found for sublimates of juices (Table 1), these particular food additives were taken for validation of the proposed kinetic approach.

As seen in Fig. 3, optical density at 532 nm in the presence of juice sublimates in incubation mixture was always lower than in control series. The lower optical density at the certain time indicates the higher antioxidant activity. The total antioxidant activity of juice sublimates accessed by the direct method can be presented as a row:

bergenia ≈ cranberry > beet > sea-buckthorn > carrot

Comparing this row with the results of proposed kinetic approach (Table 1), we conclude, that except for cranberry juice sublimate, both protocols give similar relative antioxidant activity. The difference in antioxidant activity of cranberry can be explained considering different mechanisms of inhibition of lipid peroxidation. Indeed, the latter can be inhibited by both a decrease of peroxidation reaction rate, as well as by a decrease of oxidant penetration in lipid phase. Cranberry juice sublimate having a minor activity in peroxide elimination, can affect transport properties of the oxidant. Indeed, the antimicrobial effect of cranberry juice with one of the mechanisms affecting lipid membranes is known [33,34].

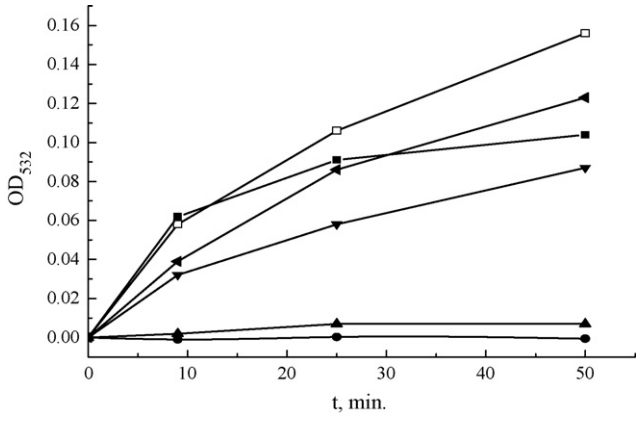


Fig. 3. Peroxidation kinetics of cerebral cortex homogenate (□ – control) and in the presence of juice sublimates (0.1 mg/ml): ◄ – carrot; ■ – sea-buckthorn; ▼ – beet; ▲ – cranberry; ● – bergenia; oxidation by 50 μM H_2O_2.

Hence, the kinetic approach for accessing of total antioxidant activity based on hydrogen peroxide scavenging is correlated with the standard direct method based on lipid peroxidation.

4. Conclusion

The proposed kinetic approach for accessing of total antioxidant activity shows positive correlation with the standard protocol based on lipid peroxidation, which confirms the possibility for its use for express screening of potential antioxidants. The use of natural oxidant (hydrogen peroxide) for this aim is obviously advantageous.

The proposed approach is based on kinetics of oxidant scavenging, rather than on the detection of the final products, which is obviously much more informative. We believe that monitoring of free radicals scavenging would also improve the accepted antioxidant activity tests.

Acknowledgements

The authors are grateful for financial support to Russian Foundation for Basic Research (RFBR), project 06-03-33013-a and Federal Agency of Science and Innovation.

References

[1] P.A. MacCarthy, A.M. Shah, Coronary Artery Disease 14 (2) (2003) 109–113.
[2] R. Rodrigo, G. Rivera, Free Radical Biology and Medicine 33 (3) (2002) 409–422.
[3] R.S. Sohal, R.J. Mockett, W.C. Orr, Free Radical Biology and Medicine 33 (5) (2002) 575–586.
[4] T.T.C. Yang, S. Devaraj, I. Jialal, Journal of Clinical Ligand Assay 24 (1) (2001) 13–24.
[5] M.A. Yorek, Free Radical Research 37 (5) (2003) 471–480.
[6] M. Antolovich, P.D. Prenzler, E. Patsalides, S. McDonald, K. Robards, Analyst 127 (1) (2002) 183–198.
[7] S. Gorinstein, O. Martin-Belloso, E. Katrich, A. Lojek, M. Ciz, N. Gligelmo-Miguel, R. Haruenkit, Y.S. Park, S.T. Jung, S. Trakhtenberg, Journal of Nutritional Biochemistry 14 (3) (2003) 154–159.
[8] M.S. Fernandez-Panchon, D. Villano, A.M. Troncoso, M.C. Garcia-Parrilla, Critical Reviews in Food Science and Nutrition 48 (7) (2008) 649–671.
[9] R. Luukkainen, R. Aejmelaeus, H. Alho, T. Metsa-Ketela, S.R. Ikonen, M.K. Salo, Free Radical Research 30 (3) (1999) 189–197.
[10] D.D.M. Wayner, G.W. Burton, K.U. Ingold, S. Locke, FEBS Letters 187 (1) (1985) 33–37.
[11] F. Bonina, C. Puglia, A. Tomaino, A. Saija, N. Mulinacci, A. Romani, F.F. Vincieri, Journal of Pharmacy and Pharmacology 52 (10) (2000) 1279–1285.
[12] U. Krings, R.G. Berger, Food Chemistry 72 (2) (2001) 223–229.
[13] M. Ohnishi, H. Morishita, H. Iwahashi, S. Toda, Y. Shirataki, M. Kimura, R. Kido, Phytochemistry 36 (3) (1994) 579–583.
[14] C.A. Rice-Evans, N.J. Miller, Total Antioxidant Status in Plasma and Body-Fluids, in: Oxygen Radicals in Biological Systems, Pt D, 1994, pp. 279–293.
[15] I.F.F. Benzie, J.J. Strain, Analytical Biochemistry 239 (1) (1996) 70–76.
[16] I.F.F. Benzie, J.J. Strain, Methods in Enzymology, Oxidants and Antioxidants (1999) 15–27.
[17] H. Paulova, H. Bochorakova, E. Taborska, Chemicke Listy 98 (4) (2004) 174–179.
[18] B. Halliwella, M.V. Clementb, L.H. Longa, FEBS Letters 486 (2000) 10–13.
[19] D. Dobos, Electrochemical Data, Akademiai Kiado, Budapest, 1975.
[20] P. Pinto, M. Saraiva, S. Reis, J. Lima, Analytica Chimica Acta 531 (1) (2005) 25–32.
[21] Z. Sroka, W. Cisowski, Food and Chemical Toxicology 41 (6) (2003) 753–758.
[22] M. Martinez-Tome, A.M. Jimenez, S. Ruggieri, N. Frega, R. Strabbioli, M.A. Murcia, Journal of Food Protection 64 (9) (2001) 1412–1419.
[23] A.A. Karyakin, O.V. Gitelmacher, E.E. Karyakina, Analytical Chemistry 67 (14) (1995) 2419–2423.
[24] A.A. Karyakin, E.E. Karyakina, Sensors and Actuators B B57 (1999) 268–273.
[25] A.A. Karyakin, E.E. Karyakina, L. Gorton, Analytical Chemistry 72 (7) (2000) 1720–1723.
[26] A.A. Karyakin, Electroanalysis 13 (10) (2001) 813–819.
[27] T. Ruzgas, E. Csoregi, J. Emneus, L. Gorton, G. Marko-Varga, Analytica Chimica Acta 330 (1996) 123–138.
[28] A.A. Karyakin, E.A. Puganova, I.A. Budashov, I.N. Kurochkin, E.E. Karyakina, V.A. Levchenko, V.N. Matveyenko, S.D. Varfolomeyev, Analytical Chemistry 76 (2) (2004) 474–478.

[29] A.A. Karyakin, E.A. Puganova, I.A. Bolshakov, E.E. Karyakina, Angewandte Chemie-International Edition 46 (40) (2007) 7678–7680.
[30] H. Ohkawa, N. Ohishi, K. Yagi, Analytical Biochemistry 95 (1979) 351–358.
[31] K. Kikugawa, T. Kojima, S. Yamaki, H. Kosugi, Analytical Biochemistry 202 (1992) 249–255.
[32] T.G. Sazontova, Hypoxia Medical Journal 1–2 (2002) 2–9.
[33] R. Puupponen-Pimia, L. Nohynek, H.L. Alakomi, K.M. Oksman-Caldentey, Applied Microbiology and Biotechnology 67 (1) (2005) 8.
[34] D.A. Vattem, Y.T. Lin, R.G. Labbe, K. Shetty, Process Biochemistry 39 (12) (2004) 1939.

Talanta 80 (2009) 754–762

Contents lists available at ScienceDirect

Talanta

journal homepage: www.elsevier.com/locate/talanta

Determination of pK_a values of tenoxicam from ^{1}H NMR chemical shifts and of oxicams from electrophoretic mobilities (CZE) with the aid of programs SQUAD and HYPNMR

Damaris Rodríguez-Barrientos[a], Alberto Rojas-Hernández[a,b,*], Atilano Gutiérrez[a], Rosario Moya-Hernández[b], Rodolfo Gómez-Balderas[b], María Teresa Ramírez-Silva[a]

[a] Universidad Autónoma Metropolitana-Iztapalapa, Departamento de Química, Área de Química Analítica, Apartado Postal: 55-534, 09340 México, D. F., Mexico
[b] Universidad Nacional Autónoma de México, Facultad de Estudios Superiores-Cuautitlán, Unidad de Investigación Multidisciplinaria, Laboratorio de Fisicoquímica Analítica, 54714 Cuautitlán Izcalli, Edo. de México, Mexico

ARTICLE INFO

Article history:
Received 12 May 2009
Received in revised form 25 July 2009
Accepted 27 July 2009
Available online 5 August 2009

Keywords:
Oxicams
SQUAD
HYPERQUAD
HYPNMR
pK_a values
^{1}H NMR chemical shifts
CZE
Electrophoretic mobility

ABSTRACT

In this work it is explained, by the first time, the application of programs SQUAD and HYPNMR to refine equilibrium constant values through the fit of electrophoretic mobilities determined by capillary zone electrophoresis experiments, due to the mathematical isomorphism of UV–vis absorptivity coefficients, NMR chemical shifts and electrophoretic mobilities as a function of pH. Then, the pK_a values of tenoxicam in H_2O/DMSO 1:4 (v/v) have been obtained from ^{1}H NMR chemical shifts, as well as of oxicams in aqueous solution from electrophoretic mobilities determined by CZE, at 25 °C. These values are in very good agreement with those reported by spectrophotometric and potentiometric measurements.
© 2009 Elsevier B.V. All rights reserved.

1. Introduction

Capillary electrophoresis technique has been in development over the last three decades, it has been widely used for compound mixture resolution. Comparing with other methods of separation, capillary electrophoresis offers high resolution, is convenient for aqueous solutions, employs small volumes and needs shorter times for analysis [1–3]. In contrast with the extensive use of capillary zone electrophoresis (CZE) as a separation method, few reports have been published on its application to obtain acid dissociation constants. Although some clear advantages can be identified over other methods, for instance: non-high purity samples can be treated, concentrations as low as 10^{-5} M might be employed, to increase the selectivity it is possible to add organic modifiers to the aqueous solutions [1–6].

One of the main advantages of CZE is that some level of impurities do not interfere with the pK_a value determination, because it depends only on the migration time of the peak of the substance under study [7,8].

Non-steroidal anti-inflammatory drugs (NSAIDs) are a well-known class of drugs that present anti-inflammatory, analgesic and antipyretic properties. In general, they are used to reduce pain in different arthritis and other post-operative conditions as well as chemopreventive and chemosuppresive effects in some kind of cancers such as colon cancer, lung cancer, breast cancer, etc. A group of NSAID, the oxicams (Fig. 1), is particularly important because they reduce the side effects, due to prostaglandins inhibitions, such as gastrointestinal toxicity. Oxicams drugs were designed under the isosteric replacement paradigm; i.e. groups or molecular fragments are replaced for other molecular moieties with similar stereo-electronic features looking for pharmacological activity enhancement [9]. These drugs are also important because their great therapeutic potential as well as their chemical properties, which result in dynamic features extremely sensitive to the micro environment [10].

It is well known that acid–base character is very important in pharmacology, the physicochemical characterization of compounds that display biological activity includes the determination of their acidity constants [11].

In this contribution we demonstrate that the behavior of absorbance, chemical shifts and effective mobility of a Brønsted acid–base system, as a function of pH, is mathematically equivalent

* Corresponding author.
E-mail address: suemi918@xanum.uam.mx (A. Rojas-Hernández).

0039-9140/$ – see front matter © 2009 Elsevier B.V. All rights reserved.
doi:10.1016/j.talanta.2009.07.058

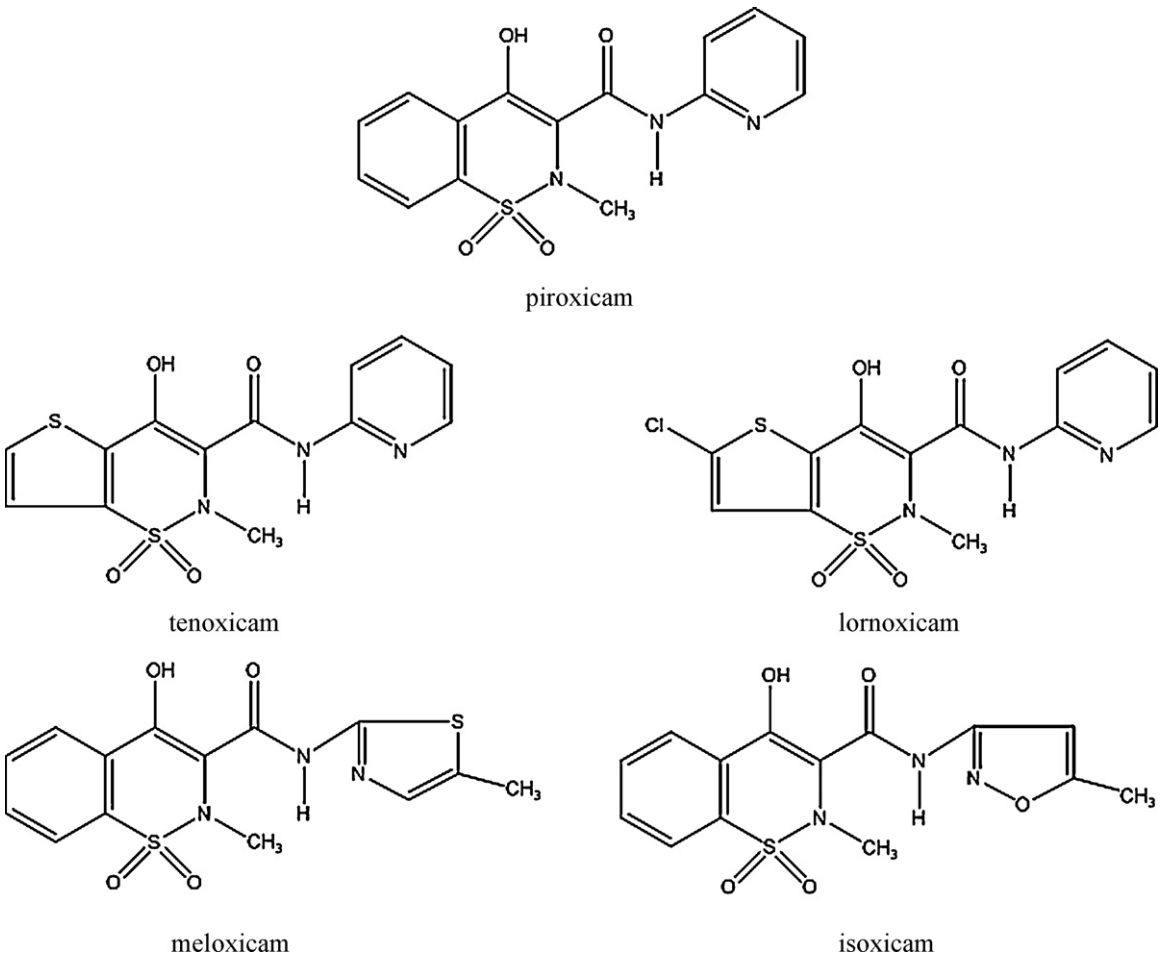


Fig. 1. Chemical structure for all the oxicams included in this study.

for the three properties. Then we report the use of SQUAD [12,13] and HYPNMR [14,15] (developed to refine equilibrium constants through the input of absorbances and NMR chemical shifts, respectively) to refine equilibrium constants through chemical shifts and effective mobility values, without any modification to the programs. This work shows that, as long as the measured property gives similar curves as a function of the pH, we can introduce the experimental data to any of these programs. We apply these programs to obtain the acid dissociation constants of tenoxicam in H_2O/DMSO 1:4 (v/v) from ^1H NMR chemical shifts. On the other hand, the programs are also employed to refine the pK_a values of five oxicams, from electrophotetic mobilities determined by capillary zone electrophoresis data at 25 °C with aqueous phosphates buffers. The pK_a refined by this way are comparable to those calculated from spectrophotometric and potentiometric measurements [9,16].

2. Theory

2.1. Properties with a linear dependence with concentration or species fractions

There are several physicochemical properties (or responses to a perturbation, R) that, in some controlled conditions, have a linear behavior with concentrations of the species that produce them. This linearity may be described by Eq. (1).

$$R = R_1 + R_2 + \cdots + R_n = k_1C_1 + k_2C_2 + \cdots + k_nC_n \quad (1)$$

where R is the overall response of the system, R_i, C_i and k_i are the contribution to the overall response, the concentration and the response factor (independent of the species concentrations and responses) of the i-esim species, respectively.

If the species are related through fast chemical equilibria or kinetic exchange, the overall response may be understood as a weighed mean of the contribution of all the present species, with weights equal to some kind of fractions of the species.

For example, if the species $L^{z_L}, HL^{(z_L+1)}, \ldots, H_jL^{(z_L+j)}, \ldots, H_nL^{(z_L+n)}$ are related by the global formation equilibria, defined by Eq. (2):

$$L^{z_L} + jH^+ \rightleftarrows H_jL^{(z_L+j)} \quad \text{with} \quad \beta_j \quad \text{where} \quad j \in \{1, 2, \ldots, n\} \quad (2)$$

It is possible to calculate the molar species fractions [17], given by

$$f_o = f_L \equiv \frac{[L^{z_L}]}{[L']} = \left(\frac{1}{1 + \beta_1[H^+] + \beta_2[H^+]^2 + \cdots + \beta_j[H^+]^j + \cdots + \beta_n[H^+]^n} \right) \quad \text{and} \quad f_j = f_{H_jL} \equiv \frac{\left[H_jL^{(z_L+j)}\right]}{[L']} = f_o\beta_j[H^+]^j \quad (3)$$

where $[L']$ represents the sum of the concentrations of the $(n+1)$ species of the component L in the system. The fractions of the species given by Eq. (3) may be the weights in the weighed mean of some properties, as it is explained in de following sections.

2.2. Absorbance in spectrophotometry

In the common way, spectrophotometry requires the accomplishment of the ideal Beer's and additive laws for the absorbance of the existent chemical species. Then, the absorbance of the system, at a given wavelength ($A^{(\lambda)}$) and optic path length (ℓ), follows Eq. (4) [18]:

$$\begin{aligned} A^{(\lambda)} &= A_L^{(\lambda)} + A_{HL}^{(\lambda)} + \cdots + A_{H_jL}^{(\lambda)} + \cdots + A_{H_nL}^{(\lambda)} \\ &= \epsilon_L^{(\lambda)}\ell[L^{z_L}] + \epsilon_{HL}^{(\lambda)}\ell[HL^{(z_L+1)}] + \cdots + \epsilon_{H_jL}^{(\lambda)}\ell[H_jL^{(z_L+j)}] + \cdots + \epsilon_{H_nL}^{(\lambda)}\ell[H_nL^{(z_L+n)}] \\ &= \epsilon_L^{(\lambda)}\ell f_L[L'] + \epsilon_{HL}^{(\lambda)}\ell f_{HL}[L'] + \cdots + \epsilon_{H_jL}^{(\lambda)}\ell f_{H_jL}[L'] + \cdots + \epsilon_{H_nL}^{(\lambda)}\ell f_{H_nL}[L'] \\ &= (\epsilon_L^{(\lambda)}f_L + \epsilon_{HL}^{(\lambda)}f_{HL} + \cdots + \epsilon_{H_jL}^{(\lambda)}f_{H_jL} + \cdots + \epsilon_{H_nL}^{(\lambda)}f_{H_nL})\ell[L'] = \epsilon_{L'}\ell[L'] \end{aligned} \tag{4}$$

Thus, Eq. (4) demonstrates that absorbance or molar absorptivity coefficient of L' may be written as the weighed mean through molar fractions of all species in the system.

2.3. Chemical shifts in NMR with fast kinetic chemical exchange

In NMR, when a fast chemical exchange of the H^+ (or OH^-) is present in the equilibria (Eq. (2)), the chemical shifts of the same nuclei (N_i, different to acids H nuclei) in L' show also a linear behavior given by Eq. (5) [14]

$$N_i\delta_{L'} = N_i\delta_L f_L + N_i\delta_{HL}f_{HL} + \cdots + N_i\delta_{H_jL}f_{H_jL} + \cdots + N_i\delta_{H_nL}f_{H_nL} \tag{5}$$

because the chemical shifts are the weighed mean through the relative abundance of species, due to the nuclei respond to the mean chemical environment surrounding them.

2.4. Equivalent conductivity and electrophoretic mobility

The electrophoretic mobility (u_{H_jL}) of an electrically charged species ($L^{z_{H_jL}}$) is given by Eq. (6) [19]:

$$z_{H_jL}\lambda_{H_jL} = Fu_{H_jL} \tag{6}$$

where z_{H_jL} is the electric charge of the species $H_jL^{z_{H_jL}}$, λ_{H_jL} is its equivalent conductivity and F is the constant of Faraday.

Then, for a set of species defined by equilibria of Eq. (2) faster than its motion into an electric field, electrophoretic mobility follows Eq. (7) [20]:

$$u_{L'} = u_L f_L + u_{HL}f_{HL} + \cdots + u_{H_jL}f_{H_jL} + \cdots + u_{H_nL}f_{H_nL} \tag{7}$$

and introducing Eq. (6) in Eq. (7) it can be demonstrated that:

$$u_{L'} = \frac{z_L\lambda_L}{F}f_L + \frac{z_{HL}\lambda_{HL}}{F}f_{HL} + \cdots + \frac{z_{H_jL}\lambda_{H_jL}}{F}f_{H_jL} + \cdots + \frac{z_{H_nL}\lambda_{H_nL}}{F}f_{H_nL} \tag{8}$$

Eq. (7) shows that electrophoretic mobility of L' is a weighed mean of electrophotetic mobilities of species, with weights equal to the molar species fractions.

Even more, if the equivalent conductivities of each one of species are nearly equal between them,

$$\frac{\lambda_L}{F} \approx \frac{\lambda_{HL}}{F} \approx \cdots \approx \frac{\lambda_{H_jL}}{F} \approx \cdots \approx \frac{\lambda_{H_nL}}{F} = \frac{\lambda}{F} \tag{9}$$

Eq. (8) accepts the approximation given in Eq. (10).

$$u_{L'} \approx (z_L f_L + z_{HL}f_{HL} + \cdots + z_{H_jL}f_{H_jL} + \cdots + z_{H_nL}f_{H_nL})\frac{\lambda}{F} \approx \bar{z}\frac{\lambda}{F} \tag{10}$$

Eq. (10) presents electrophotetic mobility of L' as a weighed mean with weights equal to the electric charge fractions of species and also shows that it is, in principle, directly proportional to mean number of electric charge ($\bar{z}$).

3. Experimental

3.1. NMR experiments for tenoxicam

3.1.1. Instrumentation

All the spectra were obtained on a Bruker AVANCE DMX 500 NMR spectrometer, using a 5 mm ID *z*-gradient probe.

3.1.2. Reagents

DMSO-d_6 (Sigma–Aldrich), D_2O (Sigma–Aldrich), IUPAC pH 4.000 and 7.000 buffers (Radiometer), 1 M HCl and 1 M NaOH aqueous solutions (Titrisol, Merck).

3.1.3. Solutions

50 mg of tenoxicam were solved in 1 mL of D_2O/DMSO-d_6 1:4 (v/v), due to the low solubility of tenoxicam in water. To this solution aliquots of HCl or NaOH solutions were added to change pH of the solutions, as required.

3.1.4. pH measurements

pH values were measured in accord with the procedure described by Mukerjee and Ostrow [21], with a radiometer potentiometer PHM210 equipped with a Ag/AgCl/glass combined microelectrode PHC3359-8.

3.1.5. Spectroscopic procedures

One-dimensional ^1H and ^{13}C NMR spectra, DEPT (135° and 90°), *z*-gradient-HSQC and gradient-HMBC ^1H–^{13}C correlation spectra, were acquired for unequivocal assignment. The chemical shifts of ^1H or ^{13}C were related to tetramethylsilane (TMS) or DMSO-d_6, respectively as internal standards.

3.2. CZE experiments for oxicams

3.2.1. Instrumentation

Experiments were carried out using a P/ACE MDQ Beckman system with DAD, employing a fused silica capillary of 50 μm I.D. × 50.2 cm (effective length: 40 cm); the sample was injected under pressure for 10 s at 1.0 psi, a constant voltage of 20 kV was applied at 25 °C. For pH lower than 4 reverse polarity was employed. Acetone marker was used to take into consideration the electroosmotic flow (eof). The wavelength for the main channel of the UV detector were 245 nm, 255 nm, 260 nm, 250 nm and 240 nm, for piroxicam, tenoxicam, meloxicam, lornoxicam and isoxicam, respectively. The acetone marker and the oxicam under study were simultaneously monitored. The buffer pH was measured with a combined glass electrode connected to a MettlerToledo pH/Ion analyzer, after calibration with pH 4, 7 and 10 buffer solutions.

3.2.2. Conditioning of capillary

Prior sample injection, capillary was conditioned with 0.1 M NaOH solution for 5 min, then deionized water passed through for 5 more minutes, finally it was rinsed for 15 min with phosphates buffer solution of pH 7. Between consecutive runs, capillary was successively rinsed for 1 min with 0.1 M NaOH solution and water, buffer solution at the corresponding pH was then passed for 2 min. Capillary is stored full of deionized water.

3.2.3. Reagents

Piroxicam, tenoxicam and isoxicam were purchased from Sigma, Boehringer Ingelheim laboratories supply meloxican, lornoxicam was directly extracted from tablets (Bosporon, 8 mg), purchased from Tedec-Meiji Farma, S.A., NaH_2PO_4 and Na_2HPO_4 were used as supplied (99% of purity) by Fluka, H_3PO_4 (J.T. Baker)

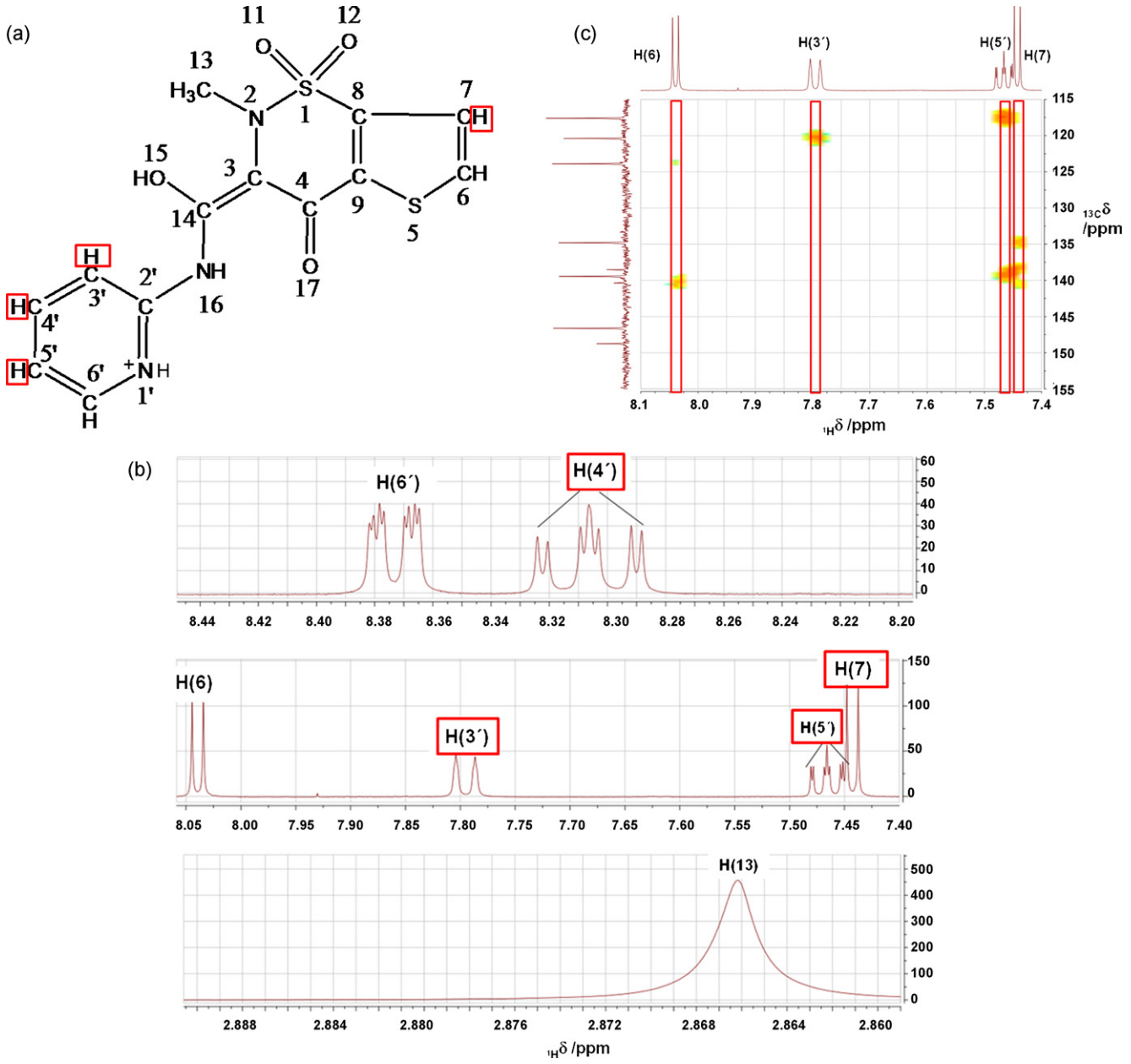


Fig. 2. (a) Developed formula of the fully protonated tenoxicam species (H_2Tenox^+), with numbering to each nucleus, or each set of nuclei, given elsewhere [22]. Hydrogen atoms in positions 3′, 4′, 5′ and 7 – H(3′), H(4′), H(5′) and H(7) – have been marked with a rectangle. (b) One-dimensional ^{1}H NMR spectrum for tenoxicam with the assignation of each nucleus given to each signal: pH < 1. (c) Partial two-dimensional gradient-HMBC spectrum for tenoxicam that permits to give the unequivocal assignment of the nuclei to the structure: pH < 1.

was used without further purification (85.4%). Water was deionized using a MilliQ deionizer in order to obtain a resistivity of 18.2 MΩ cm.

3.2.4. Solutions

Phosphates buffer solutions 50 mM were made from H_3PO_4, $H_2PO_4^-$, HPO_4^{2-} and PO_4^{3-} 0.5 M stock solutions, adjusting to the required pH value with NaOH and HCl (0.1 M).

For all oxicams individual solutions were prepared by solving 5 mg of the drug in 0.5 mL of NaOH (0.1 M) adding deionized water up to a final volume of 10 mL, all the injected samples contained acetone (5% v/v) as electroosmotic flow marker.

3.2.5. Procedure

For all the oxicam solutions at every pH value a set of at least three runs was made. The effective electrophoretic mobilities ($u_{Ox'} = u_{eff}$) were computed as the difference between the oxicam apparent mobility (u_{app}) and the neutral marker mobility (u_{eof}), taking into account the total and effective capillary lengths (50.2 and 40.0 cm, respectively) as well as the applied voltage [2–4]. When inverse polarity voltage was applied, an effective length of 10.2 cm was considered. Each reported mobility is the mean over all the carried out for each pH. The equation used to determine u_{eff} from experimental electropherograms is the operating definition given by Eq. (11).

$$u_{eff} = u_{app} - u_{eof} = \frac{L_t L_d}{V}\left(\frac{1}{t_{Ox'}} - \frac{1}{t_{eof}}\right) \quad (11)$$

where L_t is the total length of the capillary, L_d is the effective length (from injection to detector), V is the applied voltage, $t_{Ox'}$ the migration time of the oxicam peak and t_{eof}

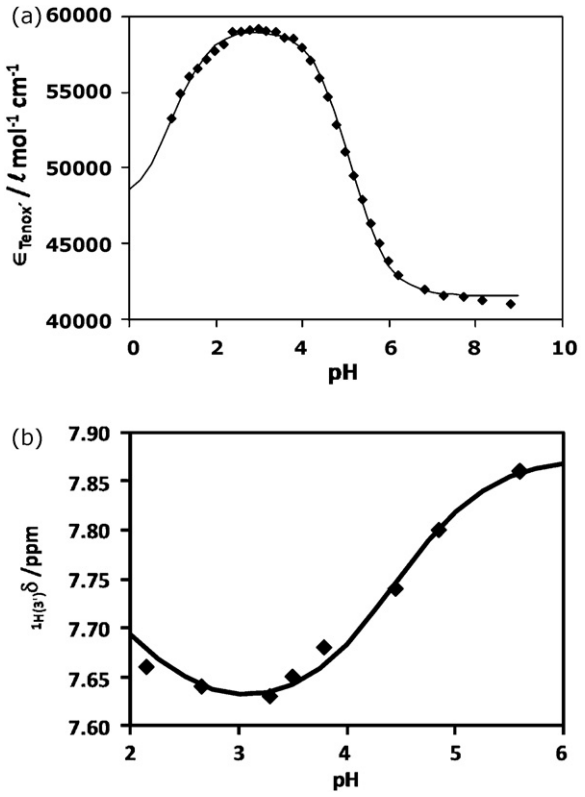


Fig. 3. (a) Mean molar absorptivity coefficients of tenoxicam (from 1.0×10^{-4} M in aqueous solutions) as a function of pH at 350 nm and 25 °C [23,24]. (b) ^{1}H(3′) chemical shifts of tenoxicam (from 0.09 M in H_2O/DMSO 1:4 (v/v) solutions) as a function of pH at 25 °C.

the time related to the migration due to the electroosmotic flow.

4. Results and discussion

4.1. Sigmoidal functions of absorbances and ^{1}H chemical shifts as a function of pH

Eqs. (4) and (5) indicate that absorbances and chemical shifts of a set of species related by the chemical equilibria given in Eq. (2), as functions of pH, should look very similar.

Given the chemical structure (Fig. 1), the oxicams studied here may present up to two pK_a values. In order to obtain these values for tenoxicam, its mean absorptivity coefficients or chemical shifts of any H nucleus (Fig. 2) may be plotted versus the solution pH (Fig. 3).

Fig. 3 clearly shows that the shape of this kind of functions is a superposition of sigmoid curves. The markers represent experimental results while solid lines the fitting achieved with SQUAD [12,13] or HYPNMR [14] programs, in agreement with Eqs. (4) (Fig. 3a) and (5) (Fig. 3b), and the refined values are presented in Table 1.

It is important to remember that the code of the program SQUAD, in FORTRAN, has been published by Legget [13] and is completely free for any one that could compile it. HYPNMR may be acquired from Protonic Software [15].

Fig. 3a shows the behavior of molar absorptivity coefficients (for a wavelength of 350 nm) of tenoxicam at different pH values. Experimental details are found elsewhere [23,24].

Fig. 3b shows the behavior of chemical shifts of ^{1}H(3′) nuclei (see Fig. 2) for 0.09 M tenoxicam mixtures in water 20%–DMSO 80% (H_2O/DMSO 1:4 (v/v)) at several pH values. Chemical shifts

Table 1
pK_a values of tenoxicam obtained with the aid of SQUAD and HYPNMR for data shown in Fig. 3. During the refining also are estimated the molar absorptivity coefficients or chemical shifts of each one of the species involved.

From spectrophotometric data		
Tenoxicam aqueous solutions (Fig. 3a)*		
SQUAD (σ_{reg} = 430 ℓ mol^{-1} cm^{-1})**	p$K_{ai} \pm \sigma$	$\epsilon^{(380)} \pm \sigma$ (ℓ mol^{-1} cm^{-1})
$H_2Tenox^+ \rightleftarrows HTenox + H^+$	1.074 ± 0.025	
$HTenox \rightleftarrows Tenox^- + H^+$	5.142 ± 0.027	
$Tenox^-$		41481 ± 110
HTenox		58728 ± 150
H_2Tenox^+		47500 (fixed)
HYPNMR (σ_{reg} = 400 l mol^{-1} cm^{-1})**		
$H_2Tenox^+ \rightleftarrows HTenox + H^+$	1.008 ± 0.027	
$HTenox \rightleftarrows Tenox^- + H^+$	5.117 ± 0.020	
$Tenox^-$		41520 ± 450
HTenox		59090 ± 700
H_2Tenox^+		47500 (fixed)
From ^{1}H NMR data		
Tenoxicam in DMSO 80% solutions (Fig. 3b)		
SQUAD (σ_{reg} = 0.012 ppm)**	p$K_{ai} \pm \sigma$	$_{1_{H(3')}}\delta \pm \sigma$ (ppm)
$H_2Tenox^+ \rightleftarrows HTenox + H^+$	1.923 ± 0.151***	
$HTenox \rightleftarrows Tenox^- + H^+$	4.422 ± 0.069	
$Tenox^-$		7.8745 ± 0.0093
HTenox		7.6106 ± 0.0064
H_2Tenox^+		7.79 (fixed)
HYPNMR (σ_{reg} = 0.012 ppm)**		
$H_2Tenox^+ \rightleftarrows HTenox + H^+$	1.923 ± 0.152***	
$HTenox \rightleftarrows Tenox^- + H^+$	4.422 ± 0.069	
$Tenox^-$		7.874 ± 0.012
HTenox		7.611 ± 0.007
H_2Tenox^+		7.79 (fixed)

* The refining of each pK_a value was made by separating the input data.
** σ_{reg} is the standard deviation of the regression.
*** Obtained by Hess's law from logarithmic global formation constants refined: $pK_{a1} = \log \beta_2 - \log \beta_1$.

of H nuclei in the different solutions were determined experimentally in this paper from the corresponding spectra (similar to that of Fig. 2b).

In order to process the relevant information shown in Fig. 3 and obtain the results given in Table 1, molar absorptivity coefficients or chemical shifts were input to SQUAD and HYPNMR, respectively, as the common practice. Besides we fed SQUAD with chemical shifts and HYPNMR with absorptivity coefficients, modified by a constant factor when necessary. In the same way a value equal to unity is

Table 2
Oxicams pK_a values, at 25 °C, obtained using SQUAD and HYPNMR.

SQUAD	pK_{a1}	pK_{a2}
Piroxicam	2.119 ± 0.030	5.309 ± 0.025
Tenoxicam	1.342 ± 0.059	5.268 ± 0.026
Lornoxicam	0.980 ± 0.117	5.131 ± 0.034
Meloxicam	–	4.170 ± 0.011
Isoxicam	–	3.781 ± 0.062
HYPNMR	**pK_{a1}**	**pK_{a2}**
Piroxicam	2.118 ± 0.037	5.303 ± 0.023
Tenoxicam	1.335 ± 0.069	5.261 ± 0.031
Lornoxicam	0.743 ± 0.109	5.130 ± 0.033
Meloxicam	–	4.170 ± 0.011
Isoxicam	–	3.814 ± 0.065

The values obtained consider at least three repetitions of the experimental CZE method.

Table 3
Effective electrophoretic mobilities (10^8 m^2 V^{-1} s^{-1}) calculated by SQUAD and HYPNMR.

SQUAD	H_2Ox^+	HOx	Ox^-
Piroxicam	1.72*	0*	−1.724 ± 0.073
Tenoxicam	1.78*	0*	−1.789 ± 0.075
Lornoxicam	1.65*	0*	−1.650 ± 0.102
Meloxicam	–	0*	−1.730 ± 0.021
Isoxicam	–	0*	−1.757 ± 0.275
HYPNMR	H_2Ox^+	HOx	Ox^-
Piroxicam	1.72*	0*	−1.722 ± 0.053
Tenoxicam	1.78*	0*	−1.786 ± 0.061
Lornoxicam	1.65*	0*	−1.650 ± 0.053
Meloxicam	–	0*	−1.730 ± 0.094
Isoxicam	–	0*	−1.767 ± 0.037

* This parameter has been estimated from the approximation given by Eq. (10) and maintained constant during refining.

placed in the location of concentrations of the corresponding component present in the system. It is remarkable that the processing of this information can be achieved without any modification of the code of the programs. On the other hand, the standard deviation of the regression (σ_{reg}) in Table 1 for chemical shifts has been obtained by refining with SQUAD or HYPNMR the signals of the four protons marked as H(3′), H(4′), H(5′) and H(7) in Fig. 2.

The results given in Table 1 also demonstrate that both programs (SQUAD and HYPNMR) arrive practically to the same set of pK_a values and species absorption parameters, from a statistical point of view. It is due to the mathematical isomorphism of the last row of Eq. (4) with Eq. (5).

Then, the refining of equilibrium constants and species mobility values through experimental electrophoretic mobilities – determined by CZE experiments – should be well achieved with the aid of both programs (as it is demonstrated in the present paper for oxicams), due to the isomorphism of Eq. (7) with the last row of Eqs. (4) and (5).

4.2. Sigmoidal functions of electrophoretic mobilities with pH

Effective mobility of oxicams is plotted as a function of the solution pH in Fig. 4.

Jiménez et al. have indicated that for each inflexion point that occurs in the curve a pK_a value should be expected [3]. On the other hand, sigmoid curves with at least one or two inflexion points are expected in agreement with Eqs. (7), (8) and (10).

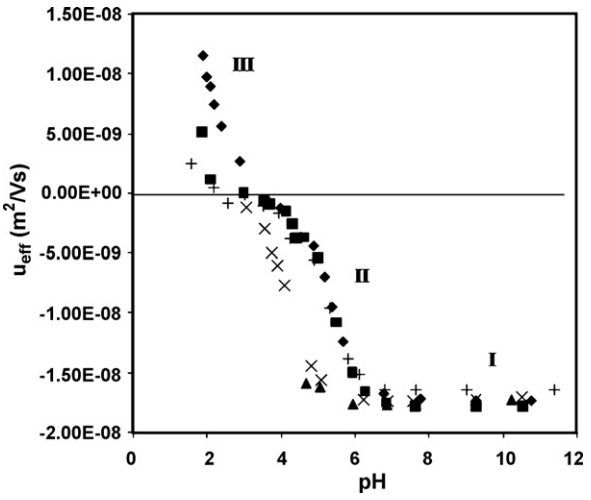


Fig. 4. Effective mobility (u_{eff}) vs. pH, piroxicam (♦), tenoxicam (■), lornoxicam (+), meloxicam (×) and isoxicam (▲).

Observing Fig. 4 we can notice two inflexion points, far enough to point out the presence of two pK_a values. Isoxicam is an exception because of its low solubility in acid solutions, however in a different solvent this possibility is not ruled out. In the high pH region (I) the mobility takes almost constant negative values, indicating the predominance of an anionic species. As the pH decreases a new species with zero electric charge is formed, increasing the system effective mobility and given place to the first inflexion point (region II). This increase continues until mobility reaches a value close to zero. Finally, a last very substantial change in mobility is observed in the acid pH (region III) for piroxicam, tenoxicam and lornoxicam, indicating the apparition of a mono-positive charged species and the second pK_a value for the system. Beyond this region a constant value for mobility is expected, which would indicate the positive ion predominance. The two inflexion points in pH confirm that piroxicam, tenoxicam and lornoxicam have two pK_a values, as it was previously pointed out from their chemical structure. Meloxicam and isoxicam have lost its electrophoretic signal below an acid pH value, relatively high (pH < 3.0 for meloxicam and pH < 4.6 for isoxicam).

Isoxicam and meloxicam are hardly soluble in acid solutions (pH < 5), limiting the experimental pK_a determination to one of the two values in water solutions. Because of the similar chemical structure of the studied oxicams, it is possible to propose a general set of acid–basic equilibria to rationalize the observed experimental behavior.

Considering the general case of an oxicam (HOx), which presents two dissociation equilibria, with constants K_{a1} and K_{a2} that involve one single positive, one zero and one single negative charged species:

$$H_2Ox^+ \rightleftarrows HOx + H^+ \quad K_{a1}$$

$$HOx \rightleftarrows Ox^- + H^+ \quad K_{a2}$$

as well as the global formation equilibria

$$Ox^- + H^+ \rightleftarrows HOx \quad \beta_1 = \frac{1}{K_{a2}}$$

$$Ox^- + 2H^+ \rightleftarrows H_2Ox^+ \quad \beta_2 = \frac{1}{(K_{a1}K_{a2})}$$

Then, Eq. (7) may be particularized to this set of species:

$$u_{eff} = u_{Ox'} = u_{Ox^-}f_{Ox^-} + u_{HOx}f_{HOx} + u_{H_2Ox^+}f_{H_2Ox^+}$$
$$= u_{Ox^-}f_{Ox^-} + u_{H_2Ox^+}f_{H_2Ox^+} \quad (12)$$

Table 4
Equivalent conductivities (λ_i) for anionic and cationic oxicam species at 25 °C from Eq. (6), and limiting equivalent conductivities (λ_i°), reported in scientific literature, at the same temperature.

Species	$\lambda \times 10^3$ (m^2 S^{-1} equiv^{-1})		λ (cm^2 S^{-1} equiv^{-1})	
	H_2Ox^+	Ox^-	H_2Ox^+	Ox^-
Piroxicam	1.660*	1.663 ± 0.070	16.60*	16.63 ± 0.70
Tenoxicam	1.717*	1.697 ± 0.071	17.17*	16.97 ± 0.71
Lornoxicam	1.592*	1.565 ± 0.096	15.92*	15.65 ± 0.96
Meloxicam	–	1.641 ± 0.020	–	16.41 ± 0.20
Isoxicam	–	1.670 ± 0.260	–	16.70 ± 2.60

Ion reported	Reference	λ° (cm^2 S^{-1} equiv^{-1})
Picrate (Pi^-)	[25]	30.39
n-Tetrabutylammonium (Bu_4N^+)	[25]	19.13
Hydrogentartarate ($HTar^-$)	[26]	31.75
Nicotinate (Nic^-)	[27]	34.61 ± 0.18
Hydrogenglutarate ($HGlut^-$)	[28]	19.10 ± 1.34
Glutarate ($Glut^{2-}$)	[28]	55.89 ± 0.84

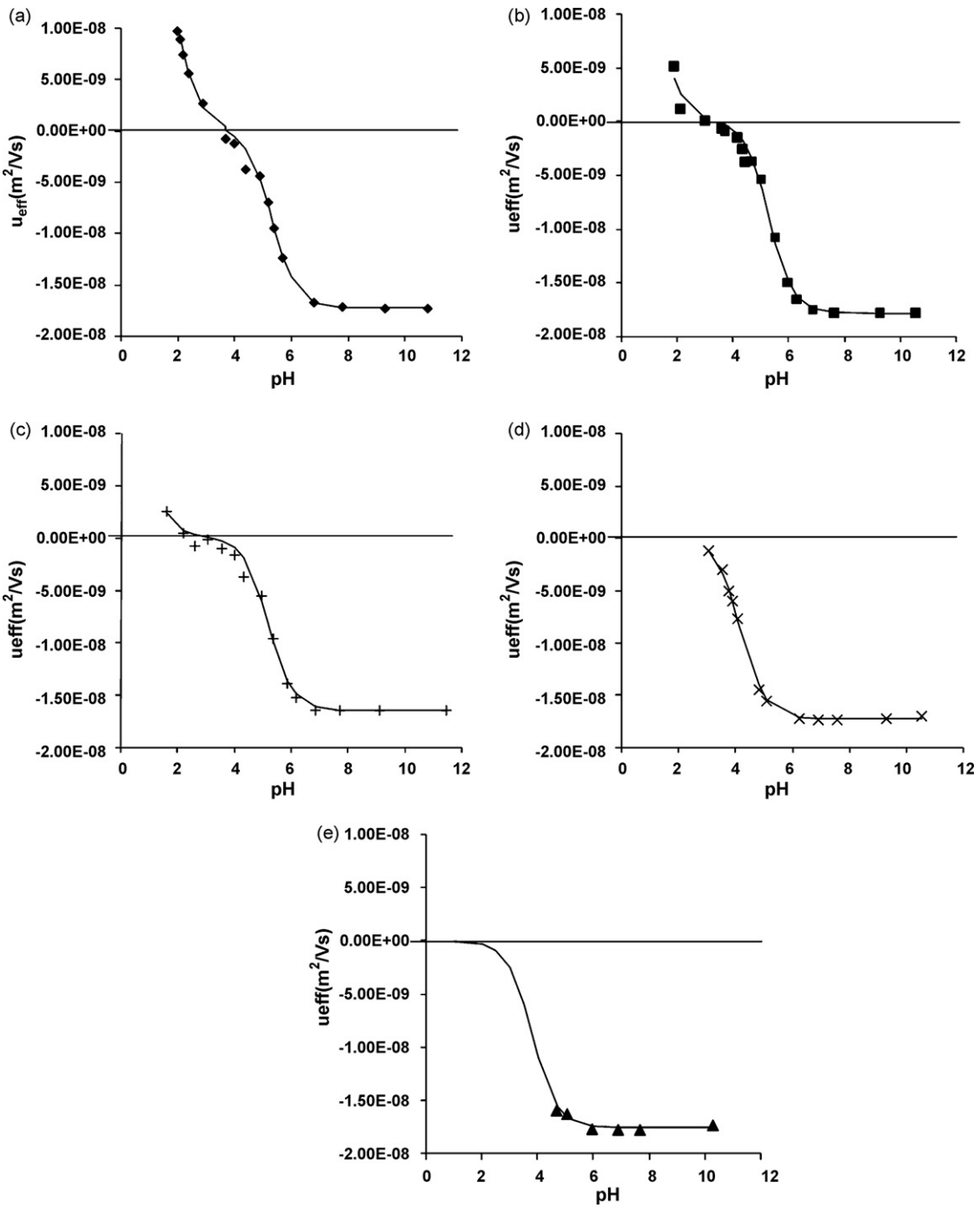


Fig. 5. Predicted behavior employing the chemical model (solid line) compared to the experimental mobility measured for (a) piroxicam, (b) tenoxicam, (c) lornoxicam, (d) meloxicam, (e) isoxicam.

The last member in Eq. (12) may be written due to the electrophoretic mobility of any zero charged species is equal to zero.

Introducing the set of Eqs. (3) into Eq. (12) it can be demonstrated that

$$u_{eff} = u_{Ox'} = \frac{u_{Ox^-} + \beta_2[H^+]^2 u_{H_2Ox^+}}{1 + \beta_1[H^+] + \beta_2[H^+]^2} \quad (13)$$

where u_{Ox^-} and $u_{H_2Ox^+}$ are the individual mobilities for the deprotonated and protonated species of the oxicam, respectively.

Employing Eq. (13) the proposed acid–base model may be used to fit the experimental effective mobilities as a function of pH. The global formation constants used in Eq. (13), given in Table 2, were refined by fitting the experimental data with SQUAD [12,13] or HYPNMR [14] programs. The effective mobilities calculated for the anionic species in the same refinement process are shown in Table 3. In all cases it was assumed that the effective mobility of the cationic species is equal to the corresponding absolute value of the anionic species, as it is assumed in Eq. (10). The experimental observations are well reproduced by the model, as it is shown in Fig. 5.

From the effective electrophoretic mobility of each species in Table 3 it is possible to obtain its equivalent conductivity, according to Eq. (6), as it can be seen in Table 4. A comparison of these

Table 5
Literature reported pK_a values for the oxicams.

	pK_{a1}	pK_{a2}	Method	Conditions	Reference
Piroxicam	1.86	5.46	UV	H_2O	[16]
		5.26 ± 0.01	P	H_2O/EtOH 1:1 (v/v)	[9]
	2.12 ± 0.04	5.31 ± 0.03	CZE	H_2O	This work*
Tenoxicam	1.07	5.34	UV	H_2O	[16]
		4.95 ± 0.02	P	H_2O/EtOH 1:1 (v/v)	[9]
	1.92 ± 0.15	4.42 ± 0.07	^{1}H NMR	H_2O/DMSO 1:4 (v/v)	This work*
	1.34 ± 0.07	5.26 ± 0.03	UV	H_2O	This work*
Lornoxicam	0.85 ± 0.06	5.59	UV	H_2O	[9]
		4.69 ± 0.01	P	H_2O/EtOH 1:1 (v/v)	[9]
	0.86 ± 0.11	5.13 ± 0.03	CZE	H_2O	This work*
Meloxicam	1.09	4.18	UV	H_2O	[29]
		4.24 ± 0.01	P	H_2O/EtOH 1:1 (v/v)	[9]
	–	4.17 ± 0.11	CZE	H_2O	This work*
Isoxicam		3.93	UV	H_2O	[16]
		4.85 ± 0.01	P	H_2O/EtOH 1:4 (v/v)	[9]
	–	3.80 ± 0.07	CZE	H_2O	This work*

UV: spectrophotometric, P: potentiometric, CZE: capillary zone electrophoresis, ^{1}H NMR: proton NMR.
* The values obtained in this work and reported in this table are averages of those shown in Tables 1 and 2.

values with those of similar species reported in scientific literature [25–28]; demonstrate that they are plausible enough as it is shown in the same Table 4.

Even though the equivalent conductivity is an important parameter because it indicates the ion capacity by one equivalent for transporting charge, it is rarely reported in literature on electrophoresis methods.

Table 5 compiles literature pK_a experimental values reported by different analysis methods for oxicams in aqueous solution and solvent mixtures. A comparison of the pK_a reported values by Bernhard and Zimmermann [9] with those determined in the present work allows establishing that they are in good agreement for both pK_a values in the case of piroxicam, tenoxicam and lornoxicam, even in those cases where the solvent mixture is H_2O/EtOH [16].

For meloxicam and isoxicam Bernhard and Zimmermann [9] as well as Tsai et al. [16] have found only one pK_a value, using spectrophotometric and potentiometric methods, respectively. We also found only one pK_a value as it was discussed before and it is in agreement with both cited works.

The use of effective electrophoretic mobilities obtained from CZE has shown several advantages such as small analysis time, few quantity and low purity of the substance under study, acceptable precision and good agreement with other experimental methods. Moreover, from the mobility values it is straightforward calculating properties like charge and equivalent conductivity of ions. The charge of ions is particularly important in order to propose the number of species involved in the system.

5. Conclusions

In this work we have determined the pK_a values of tenoxicam in H_2O/DMSO 1:4 (v/v) from ^{1}H NMR chemical shifts. Moreover, by employing experimental data derived from CZE, the pK_a values have been refined for the drugs: piroxicam, tenoxicam, lornoxicam, and one pK_a for meloxicam and isoxicam in aqueous solutions at 25 °C, with the aid of the programs SQUAD and HYPNMR. The values obtained are in good agreement with those reported by spectrophotometric and potentiometric methods. In fact, even though the use of SQUAD and HYPNMR to obtain pK_a values from effective electrophoretic mobilities has been demonstrated for oxicams, it may be applied to other molecules [30,31].

Acknowledgments

The authors are indebted with UNAM through PAPIIT-IN218408 and PACIVE CONS111 projects as well as CONACyT through 46124 project, by partial financial support. The authors also grateful to A. Vacca and P. Gans the copy of program HYPNMR, Rafael García-Barrera for the samples of meloxicam, and J. Havel and A. Soto-Guerrero for helpful comments. DR-B and AR-H want to acknowledge CONACyT by scholarship to follow postgraduate studies and support for sabbatical leave on FESC-UNAM during 2009, respectively.

References

[1] F. Foret, Capillary Zone Electrophoresis, VCH, Weinheim, 1993.
[2] D. Barrón, E. Jiménez-Lozano, A. Irles, J. Barbosa, J. Chromatogr. A 871 (2000) 381.
[3] E. Jiménez, I. Marqués, D. Barrón, J.L. Beltrán, J. Barbosa, Anal. Chim. Acta 464 (2002) 37.
[4] R. Weinberger, Practical Capillary Electrophoresis, Academic Press, New York, 1993.
[5] S.F.Y. Li, Capillary Electrophoresis: Principles, Practice and Applications (Journal of Chromatography Library), vol. 52, Elsevier, Amsterdam, 1993.
[6] C. Foulon, C. Danel, C. Vaccer, S. Yous, J.-P. Bonte, J.-F. Goossens, J. Chromatogr. A 1035 (2004) 131.
[7] Z. Jia, Curr. Pharm. Anal. 1 (2005) 41.
[8] V. de Nogales, R. Ruiz, M. Rosés, C. Ràfols, E. Bosch, J. Chromatogr. A 1123 (2006) 113.
[9] E. Bernhard, F. Zimmermann, Arzneim-Forsch. 34 (1984) 647.
[10] H. Chakraborty, R. Banerjee, M. Sarkar, Biophys. Chem. 104 (2003) 315.
[11] G. Garrido, C. Rafols, E. Bosch, Eur. J. Pharm. Sci. 28 (2006) 118.
[12] D.J. Legget, W.A.E. McBryde, Anal. Chem. 47 (1975) 1065.
[13] D.J. Legget, Computational Methods for Determination of Formation Constants, Plenum Press, New York, 1985.
[14] Ch. Frassineti, S. Ghelli, P. Gans, A. Sabatini, M.S. Moruzzi, A. Vacca, Anal. Biochem. 231 (1995) 374.
[15] Protonic Software, http://www.hyperquad.co.uk/, Page visited on July 2009.
[16] R.S. Tsai, P.A. Carrupt, N. El-Tayar, Y. Giroud, P. Andrade, B. Testa, Helv. Chim. Acta 76 (1993) 842.
[17] R. Moya-Hernández, J.C. Rueda-Jackson, M.T. Ramírez, G.A. Vázquez, J. Havel, A. Rojas-Hernández, J. Chem. Educ. 79 (2002) 389.
[18] H.H. Willard, L.L. Merritt, J.A. Dean, F.A. Settle, Instrumental Methods of Analysis, Wadsworth, Belmont, 1998.
[19] A.J. Bard, R. Faulkner, Electrochemical Methods: Fundamentals and Applications, John Wiley & Sons, New York, 1980.
[20] S. Poole, S. Patel, K. Dehring, H. Workman, C.F. Poole, J. Chromatogr. A 1037 (2004) 445.
[21] P. Mukerjee, J.D. Ostrow, Tetrahedron Lett. 39 (1998) 423.
[22] S. Defazio, R. Cini, Polyhedron 22 (2003) 1355.
[23] M.R. Moya-Hernández, Ph.D. Thesis, Universidad Autónoma Metropolitana, Unidad Iztapalapa, México, 2003, p. 27.
[24] M.R. Moya-Hernández, A. Mederos, S. Domínguez, A. Orlandini, C.A. Ghilardi, F. Cecconi, E. González-Vergara, A. Rojas-Hernández, J. Inorg. Biochem. 95 (2003) 131.

[25] H.M. Daggett Jr., E.J. Bair, Ch.A. Kraus, J. Am. Chem. Soc. 73 (1951) 799.
[26] M. Bešter-Rogač, R. Neueder, J. Barthel, A. Apelblat, J. Sol. Chem. 26 (1997) 537.
[27] Z. Orekhova, M. Ben-Hamo, E. Manzurola, A. Apelblat, J. Sol. Chem. 34 (2005) 687.
[28] A. Apelblat, E. Manzurola, Z. Orekhova, J. Sol. Chem. 36 (2007) 1023.
[29] P. Luger, K. Daneck, W. Engel, G.W. Trummlitz, S. Klaus, Eur. J. Pharm. Sci. 4 (1996) 175.
[30] J.M. Islas-Martínez, D. Rodríguez-Barrientos, A. Galano, E. Ángeles, L.A. Torres, F. Olvera, M.T. Ramírez-Silva, A. Rojas-Hernández, J. Phys. Chem. B (2009), doi:10.1021/jp904474m.
[31] V.H. Abrego, L.A. Torres, E. Ángeles, L. Martínez, J.L. Marroquín-Pascual, R. Moya-Hernández, H.A. Amaro-Recillas, J.C. Rueda-Jackson, D. Rodríguez-Barrientos, A. Rojas-Hernández, Bioorg. Chem., submitted for publication.

Talanta 80 (2009) 763–769

Contents lists available at ScienceDirect

Talanta

journal homepage: www.elsevier.com/locate/talanta

Flexible NH_3 sensors fabricated by *in situ* self-assembly of polypyrrole

Pi-Guey Su*, Chi-Ting Lee, Cheng-Yi Chou

Department of Chemistry, Chinese Culture University, Taipei 111, Taiwan

ARTICLE INFO

Article history:
Received 20 May 2009
Received in revised form 25 July 2009
Accepted 27 July 2009
Available online 5 August 2009

Keywords:
Flexible NH_3 sensor
Polypyrrole (PPy)
In situ self-assembly
Layer-by-layer (LBL)

ABSTRACT

Novel flexible NH_3 gas sensors were formed by the *in situ* self-assembly of polypyrrole (PPy) on plastic substrates. A negatively charged substrate was prepared by the formation of an organic monolayer (3-mercapto-1-propanesulfonic acid sodium salt—MPS) on a polyester (PET) substrate using a pair of comb-like Au electrodes. Two-cycle poly(4-styrenesulfonic acid) sodium salt/poly(allylamine hydrochloride) (PSS/PAH) bilayers (precursor layer) were then layer-by-layer (LBL) deposited on an MPS-modified substrate. Finally, a monolayer of PPy self-assembled *in situ* and PPy multilayer thin films self-assembled LBL *in situ* on a $(PSS/PAH)_2$/MPS/Au/Cr/PET substrate. The thin films were analyzed by atomic force microscopy (AFM). The effects of the precursor layer (PSS), the deposition time of the monolayer of PPy and the number of PPy multilayers on the gas sensing properties (response) and the flexibility of the sensors were investigated to optimize the fabrication of the film. Additionally, other sensing properties such as sensing linearity, reproducibility, response and recovery times, as well as cross-sensitivity effects were studied. The flexible NH_3 gas sensor exhibited a strong response that was comparable to or even greater than that of sensors that were fabricated on rigid substrate at room temperature.

© 2009 Elsevier B.V. All rights reserved.

1. Introduction

The fabrication of organic electronic devices on plastic substrates has attracted much interest recently, because of the proliferation of handheld portable consumer electronics. Plastic substrates have many attractive characteristics, such as biocompatibility, flexibility, lightness, shock resistance, softness and transparency [1]. A new trend towards the direct integration of sensors on flexible substrates has become evident. Flexible multisensor platforms that support temperature, humidity and gas detection will be manufactured at very low-cost and integrated into smart textiles or radio frequency identification (RFID) tags for logistics applications [2,3]. The development of sensors should be consistent with the future goal of the development of the completely plastic RFID tag, and extensible to the sensing of various gases. The main challenge is not only their manufacture, but also the stability of their mechanical, electrical and gas sensing properties.

Conducting polymers such as polythiophene, polypyrrole (PPy) and polyaniline have been intensively studied because of their remarkable mechanical and electrical properties, which can be exploited in actuators, sensors and electrochromic devices [4–6]. Among conducting polymers, PPy has attracted much particular interest because it is easily synthesized; it has relatively good environmental stability, and its surface charge characteristics can easily be modified by changing the dopant species in the material during synthesis.

Many approaches for fabricating PPy films have been proposed. They include chemical deposition by dip-coating [6,7], vapor deposition polymerization [8], UV-photopolymerization [9], deposition of Langmuir–Blodgett film [10], and electrochemical deposition [11,12]. The layer-by-layer (LBL) self-assembly of multilayer films based on sequential adsorptions of ionized polyelectrolytes and oppositely charged materials in aqueous solutions has been developed [13,14]. LBL self-assembly has many advantages over other methods, including simplicity, low-cost, low temperature of deposition, controllable thickness (from nanometers to micrometers) and the lack of any need for complex equipment. Therefore, the preparation of PPy multilayered films using LBL and *in situ* self-assembly has been studied [15–18]. Notably, the surfaces coated by PPy in these studies were deposited on rigid substrates, such as ceramics or SiO_2/Si. Recently, Ferrer-Anglada et al. [19] adopted the electrochemical method to prepare PPy and polyaniline on plastic substrate as a pH sensor. However, no attempt has been made to form a flexible NH_3 gas sensor based on PPy thin films by LBL *in situ* self-assembly. In this work, flexible NH_3 gas sensors were fabricated by the *in situ* self-assembly of monolayer of PPy and the LBL *in situ* self-assembly of PPy multilayer thin films on a flexible substrate (polyester film—PET). Poly(styrenesulfonic acid) sodium salt (PSS) assembled with poly(allylamine hydrochloride) (PAH) was a precursor layer before the PPy thin film was self-assembled *in situ*. The thin films were observed by atomic force microscopy (AFM). The effects of the precursor layer (PSS), the deposition time

* Corresponding author. Tel.: +886 2 28610511x25332; fax: +886 2 28614212.
E-mail address: spg@faculty.pccu.edu.tw (P.-G. Su).

0039-9140/$ – see front matter © 2009 Elsevier B.V. All rights reserved.
doi:10.1016/j.talanta.2009.07.057

of the monolayer of PPy and the number of PPy multilayers on the gas sensing properties (response) and the flexibility of the sensors were investigated. The other gas sensing properties, such as sensing linearity, reproducibility, response and recovery times, as well as cross-sensitivity effects were also investigated.

2. Experimental

2.1. Materials

3-Mercapto-1-propanesulfonic acid sodium salt (MPS), poly(allylamine hydrochloride) (PAH; Mw = 15,000), poly-(styrenesulfonic acid) sodium salt (PSS; Mw = 70,000), pyrrole monomer (98%), *p*-toluene sulfonic acid (*p*-TSA) and ferric chloride ($FeCl_3$) were obtained from Aldrich. All used deionized water (DIW) were prepared using a Milli-Q Millipore (Bedford, MA, USA) purification system, and the resistivity of water was above 18.0 MΩ/cm.

2.2. Preparation of substrates

The structure of the flexible NH_3 gas sensors was the same as that in our earlier study [20]. The interdigited gold electrodes (IDE) were made by sputtering first Cr (50 nm thick) and then Au (250 nm thick) at temperature from 120 to 160 °C. The gap between electrodes was 0.2 mm. The substrates were first immersed in a bath that contained a solution of H_2O_2/H_2SO_4 (1:2 volume ratio) for 3 min. The substrates were thoroughly rinsed with DIW after each step. This process made the substrates hydrophilic. The negatively charged MPS/Au surface was prepared by immersing the hydrophilic Au/Cr/PET substrate in 2.0 mM aqueous MPS for 24 h, rinsing it with DIW and then drying it at 80 °C. A cyclic PSS/PAH bilayer film architecture was produced by alternately depositing PAH (pH 4) and PSS (pH 1) aqueous solution onto the negatively charged MPS-modified substrate. For each layer produced, the immersion time was about 10 min and rinsing and drying followed each immersion. Therefore, a two-cycle PSS/PAH bilayers film was fabricated by repeating the above processes, yielding, a negatively charged $(PSS/PAH)_2$/MPS/Au/Cr/PET substrate.

2.3. Preparation of monolayer of PPy and PPy multilayered films

The active solution for use in PPy contained the oxidizing agent ($FeCl_3$) and *p*-TSA, and was later adjusted to pH 1 by adding HCl; then the pyrrole monomer was added. The optimal film of PPy was produced using a solution of 0.006 M $FeCl_3$, 0.026 M *p*-TSA and 0.02 M pyrrole, as described in the literature [16,18]. The active solution was stirred for 15 min. A monolayer PPy was self-assembled *in situ* as a thin film on the $(PSS/PAH)_2$/MPS/Au/Cr/PET substrate. The PPy multilayered thin films, composed of $(PPy/PSS)_n$, were deposited on the $(PSS/PAH)_2$/MPS/Au/Cr/PET substrate in the same manner as the PSS/PAH multilayered thin films, where *n* is the number of coated layers. The optimal deposition time in PPy active solution and PSS solution was 5 and 10 min, respectively. Table 1 presents the various compositions of interest. Fig. 1(a) schematically depicts an *in situ* self-assembly of a PPy monolayer film on PET substrate over time. Fig. 1(b) schematically depicts an LBL *in situ* self-assembly of a PPy/PSS multilayered thin film on a PET substrate. Fig. 2 presents the flexibility of the PPy multilayer thin film assembled on a PET substrate.

2.4. Instruments and analysis

The surface microstructure of the thin film that was coated on a PET substrate was investigated using a field emission scanning electron microscope (FE-SEM, JEOL, JSM 6335F) and an atomic force

Table 1
Compositions of precursor layer and PPy thin films used to prepare flexible NH_3 sensors.

Sample number	Precursor layer	PPy layer	
	PSS concentration (mg/mL)	Deposition time (min)	Numbers of PPy/PSS bilayer
1	0.5	5	1
2	1	5	1
3	2	5	1
4	1	10	1
5	1	15	1
6	1	30	1
7	1	5	2
8	1	5	5

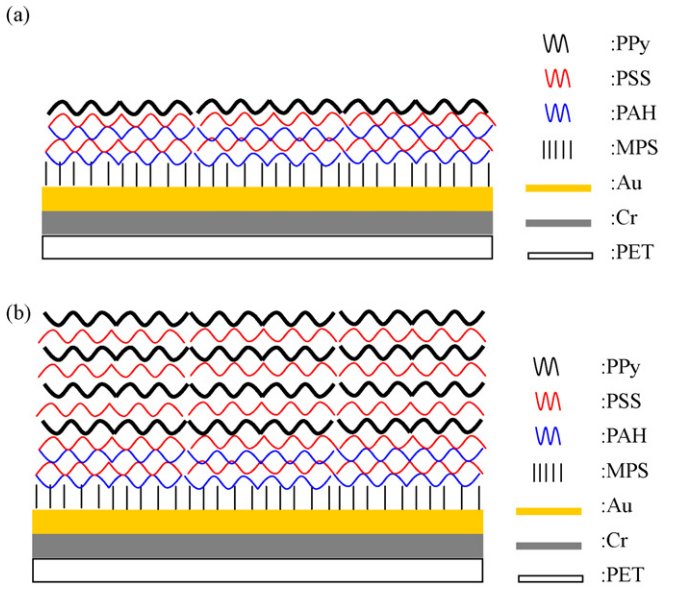


Fig. 1. Schematic diagram of PPy thin films assembled *in situ* on modified PET substrate; (a) *in situ* self-assembly of monolayer of PPy on PSS surface at various times and (b) LBL *in situ* self-assembly of PPy with PSS.

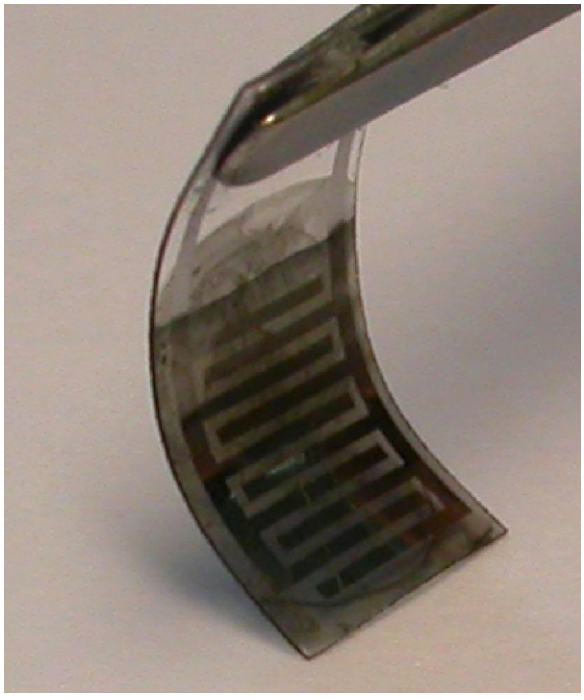


Fig. 2. Photograph of bent flexible NH_3 gas sensor based on PPy thin film assembled *in situ* on modified PET substrate.

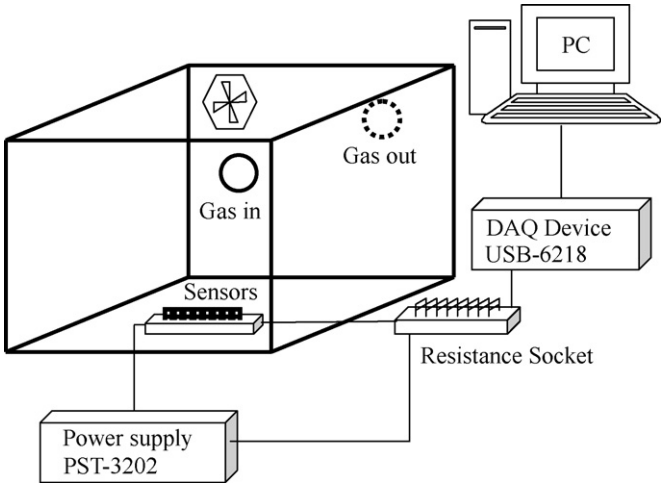


Fig. 3. Measurement system for testing gas sensors.

microscope (AFM, Ben-Yuan, CSPM 4000) in tapping mode. The electrical and sensing characteristeristics were measured using a bench system at room temperature, as shown in Fig. 3. Each sensor was connected in series with a load resistor and a fixed 5 V was continuously supplied to the sensor circuit from a power supply (GW, PST-3202). The resistance of the sensor was determined from the voltage at the ends of the load resistor using a DAQ device (NI, USB-6218) in various concentrations of gas. The desired NH_3 gas concentrations, obtained by mixing a known volume of standard NH_3 gas (100,000 ppm) with N_2, were injected into the chamber. The cross-sensitivity experiment was performed by measuring the resistance of the sensor upon controlled concentration of 5, 200 and 1000 ppm for NO_2, CO and H_2 gases, respectively. The gas inside the chamber was uniformly distributed using a fan. After some time, the chamber was purged with air and the experiment was repeated for another cycles. All experiments were performed at room temperature, and the relative humidity was 53 ± 3 RH%. Flexibility experiments were performed in which the sensors were bent to various degrees as their responses were monitored as a function of the period of exposure to NH_3 gas. The bending angle was measured using a goniometer.

3. Results and discussion

3.1. Microstructure of surface

Fig. 4 presents the surface morphology of the *in situ* self-assembled of manolayer of PPy and PPy multilayered thin films on a modified PET substrate, analyzed using tapping-mode AFM. The size of each image is 5 μm × 5 μm. Table 2 presents the roughness and sphere size of various PPy thin films that were deposited on the modified PET substrate. Fig. 4(a)–(c) (Samples 1–3) presents the surface morphology of *in situ* self-assembled films of a monolayer of PPy fabricated on a modified PET substrate using various PSS concentrations. The PPy films all had typical granular patterns and the size of spheres ranged from 50 to 58 nm. Fig. 4(a) (Sample 1) indicates that less PPy *in situ* self-assembled as films on modified PET substrate than in Samples 2 and 3 (Fig. 4(b) and (a)) because the charge on the previously grown layer of Sample 1 was lower than that of Samples 2 and 3. Therefore, Sample 1 exhibited some imperfections in packing. Fig. 4(b) and (d)–(f) (Samples 2 and 4–6) presents the surface morphologies of the *in situ* self-assembled films of monolayers of PPy at various times. Clearly, the surface roughness and sphere size increased from 12.4 to 35.3 and from 50 to 78 nm, respectively, as the deposition time of the monolayer of PPy increased. The films of PPy were completely covered with fine grains after 5 min. Fig. 4(b), (g) and (h) (Samples 2, 7 and 8) presents the surface morphologies of LBL *in situ* self-assembled films of PPy multilayers for various numbers of PPy/PSS bilayers. The surface topography of the alternate PPy and PSS deposited LBL film reveals a similar structure is similar to that of monolayer of PPy films. The size of the spheres of PPy multilayered exceeded that of single-layered PPy thin films. The surface roughness and sphere size increased from 12.4 to 42.6 and from 50 to 82 nm, respectively, as the number of PPy/PSS bilayers increased. This difference between the surface morphologies of the *in situ* self-assembled monolayer of PPy and the PPy multilayered thin films may be associated with the different molecular orientations of PPy [16,17].

Table 2
Roughness and sphere size of various PPy thin films deposited on a modification of PET substrate.

Sample number	RMS (nm)	Size cluster circular (Φ) (nm)
1	10.6	58 ± 25
2	12.4	50 ± 22
3	11.7	53 ± 25
4	14.8	52 ± 30
5	20.1	68 ± 47
6	35.3	78 ± 42
7	38.0	74 ± 50
8	42.6	82 ± 60

3.2. Flexibility and response properties of monolayer of PPy and PPy multilayered thin films

Fig. 5 plots the effect of the concentration of PSS, the deposition time of the monolayer of PPy and the number of PPy/PPS bilayers in the *in situ* self-assembled PPy thin films on their flexibility characteristics. At each bending angle, the sensors were exposed to 50 ppm NH_3 gas. Table 3 presents the corresponding responses. The sensor response (S) was given by $S = (R_{gas} - R_{air})/R_{air}$ ($\Delta R/R_{air}$), where R_{gas} and R_{air} are the electrical resistances of the sensor in the tested gas and air, respectively.

3.2.1. Effect of concentration of PSS on flexibility and response of monolayer of PPy thin films

Fig. 5(a) plots the effect of the concentration of PSS on the flexibility characteristics of the *in situ* self-assembled PPy thin monolayer films. When the concentration of PSS exceeded 1 mg/mL, the deviations of the responses of Samples 2 and 3 were both under 10% when the sensors were bent downward at an angle of up to 60° from horizontal. In the LBL *in situ* self-assembly process, before the PPy monolayer and the PPy/PSS multilayered coating systems were constructed, two-cycle PSS/PAH bilayers (precursor layer) were deposited on the MPS-modified substrate to improve the combinability of the surface and the first monolayer of the film of PPy. Additionally, the polyanion PSS layer on the substrates is importantly involved in the formation of the PPy thin film, which involves the simultaneous polymerization of the pyrrole monomer and oxidation of the PPy molecules [16–18]. Therefore, in a more dilute PSS solution, less charge remained on the previously grown layer, and so less Fe^{3+} is adsorbed on the PSS, causing poorer polymerization of PPy on the surface [16]. In a more concentrated PSS solution, some PPy molecules aggregate and become entangled with each other (as observed in Fig. 4(c)), increasing the size of the spheres. Therefore, Sample 2 had a higher response than Sample 3 (Table 3).

3.2.2. Effect of deposition time of PPy on flexibility and response of monolayer of PPy thin films

Fig. 5(b) plots the effect of deposition time of PPy on the flexibility characteristics of the *in situ* self-assembled monolayer of PPy

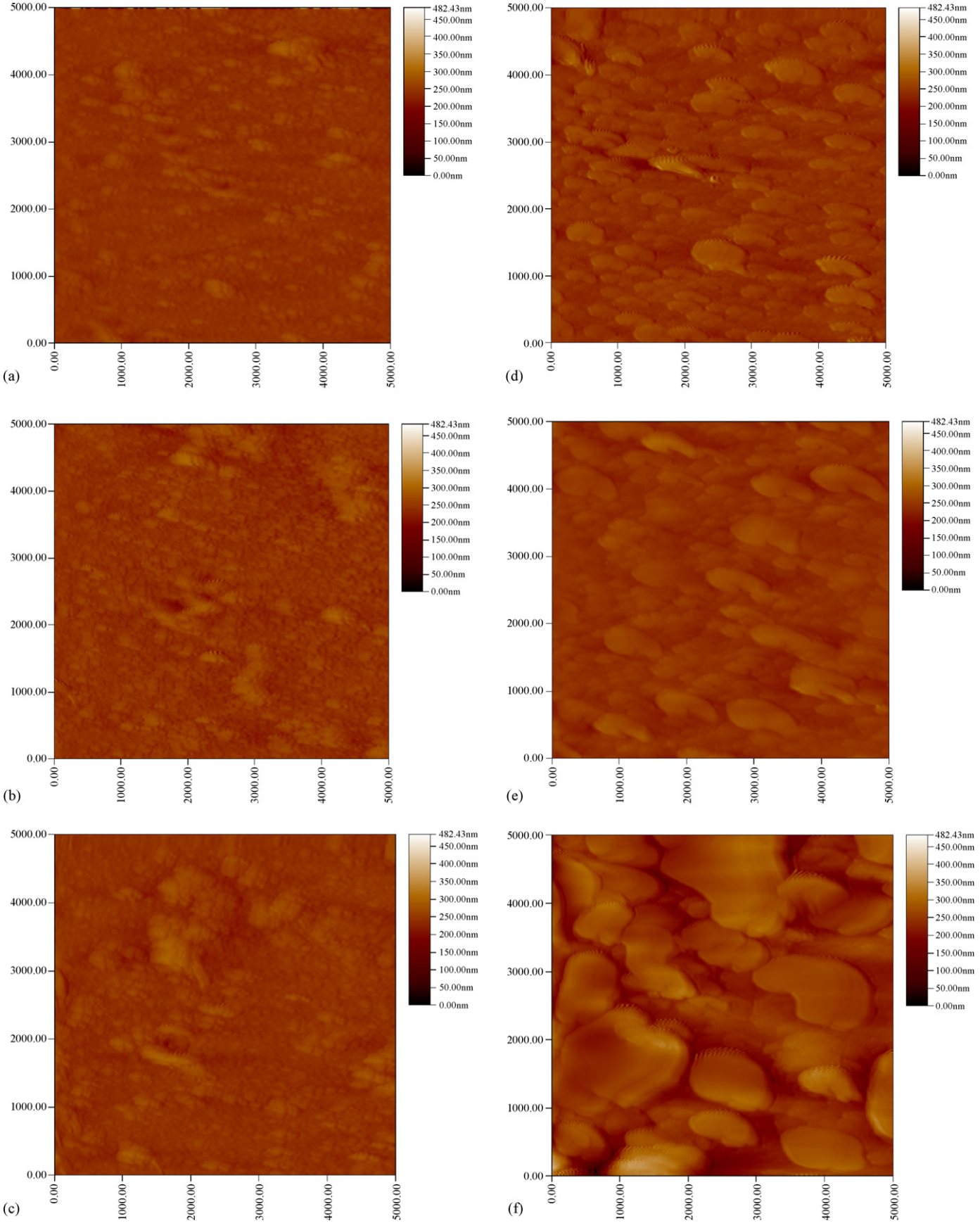


Fig. 4. AFM micrographs of various PPy thin films assembled *in situ* on modified PET substrate (compositions as shown in Table 1); (a) Sample 1, (b) Sample 2, (c) Sample 3, (d) Sample 4, (e) Sample 5, (f) Sample 6, (g) Sample 7 and (h) Sample 8.

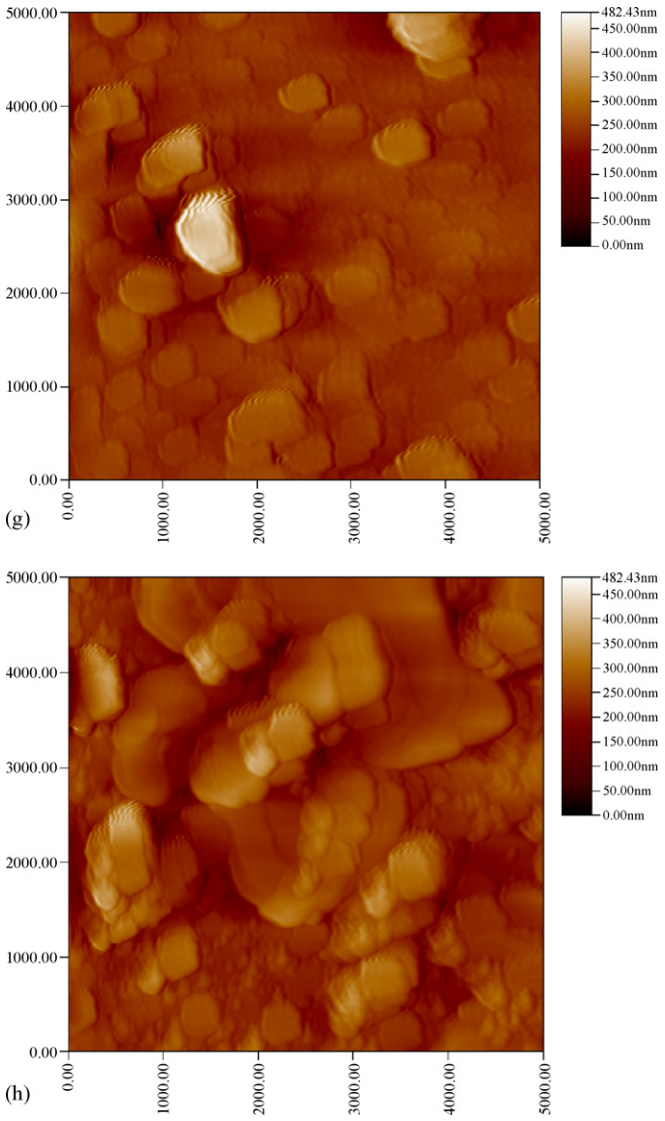


Fig. 4. (*Continued*).

thin films. When the sensors were bent downward at an angle of up to 60° from horizontal, the response deviation increased with the deposition time of the monolayer of PPy on a modified PET substrate increased (Samples 2 and 4–6). In the LBL *in situ* self-assembly process, the PSS layer, acting as an intermediate electrostatic adhesive, helped to maintain the positions of PPy, even when the substrate was bent. Consequently, a large PPy adheres to the PET surface less strongly than a small PPy (as observed in Figs. 4(b) and (d)–(f); Table 2). The sensor response decreased as the deposition time of the monolayer of PPy on the modified PET substrate increased (Table 3). Therefore, PPy in the thin film assemblies was small, so the surface area was large, favoring the adsorption of gas molecules.

Table 3
Response to NH_3 of various PPy thin films deposited on a modification of PET substrate.

Sample number	Response[a]
1	42.66
2	77.75
3	58.01
4	54.76
5	38.40
6	29.38
7	33.40
8	29.33

[a] Sensor response at 50 ppm NH_3 gas.

3.2.3. *Effect of number of PPy/PPS bilayers on flexibility and response of PPy multilayer thin films*

Fig. 5(c) plots the effect of the number of PPy/PPS bilayers on the flexibility of the LBL *in situ* self-assembled PPy multilayer thin films. In the PPy/PSS multilayer thin film, PPy was reinforced by two adjacent PSS layers as intermediate electrostatic glue and therefore, the PSS molecules helped to keep the PPy in their positions even when the substrate was bent. However, the spheres of multilayered PPy were too large to adhere to the PET surface when the substrate was bent (as observed in Fig. 4(b), (g) and (h); Table 2). Therefore, the $(PPy/PSS)_1$ multilayer thin film (Sample 2) was more flexible than that of $(PPy/PSS)_2$ (Sample 7) and $(PPy/PSS)_5$ (Sample 8). The sensor response decreased as the number of PPy/PPS bilayers increased (Table 3). This result was reasonable because of the effect of the size of PPy (as described in Section 3.2.2). Sample 2 showed the highest response (77.75) and greatest flexibility (within 8%), and so Sample 2 was chosen to study the other gas sensing properties.

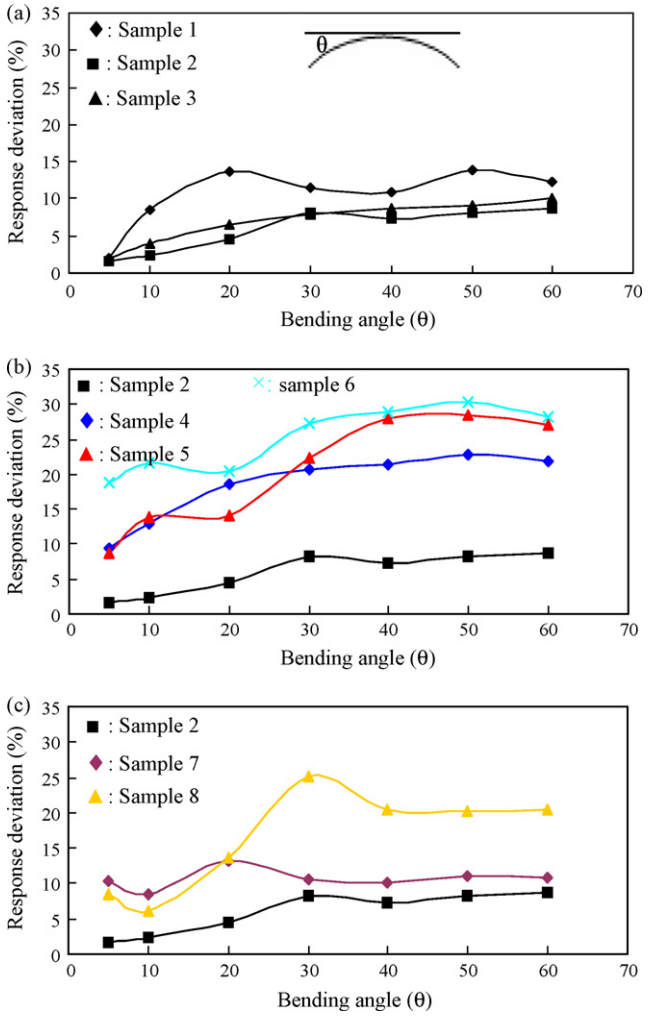


Fig. 5. Flexibility of various PPy thin films assembled *in situ* on modified PET substrate in response to 50 ppm NH_3 gas (compositions as shown in Table 1); (a) effect of concentration of PSS, (b) effect of deposition time of monolayer of PPy and (c) effect of number of PPy/PPS bilayers.

3.3. Gas sensing characteristics of flexible gas sensor

Fig. 6 plots the responses of Sample 2 to various concentrations of NH_3. Fig. 7 plots the results of calibration curve of Sample 2, and the slope and linear correlation coefficient were calculated, as shown in Table 4. The linear sensing characteristics in the ranges 5–50 ppm and 50–200 ppm differed. A steep decrease in slope

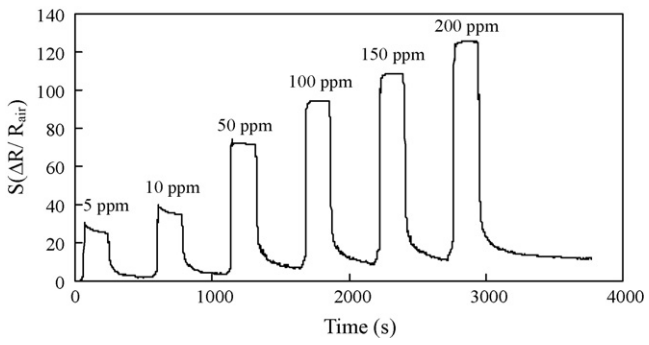


Fig. 6. Response (S) as a function of time (s) for various concentrations of NH_3 gas on Sample 2 sensor (with compositions as shown in Table 1).

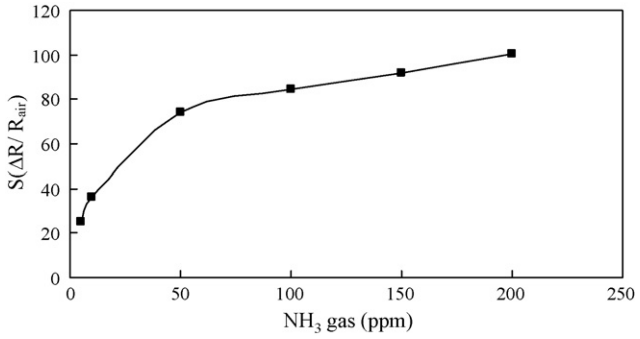


Fig. 7. Response (S) of Sample 2 sensor as function of concentration of NH_3 gas (with compositions as shown in Table 1).

Table 4
Linear sensing characteristics of Sample 2 sensor at different concentrations of NH_3 gas.

Concentration (ppm)	Sensing characteristics	
	Slope	Linearity[a]
5–50	1.036	0.9857
50–200	0.1646	0.9996

[a] Correlation coefficient.

was observed from 50 to 200 ppm of NH_3 gas. This behavior was related to the adsorption of NH_3 gas molecules on the surface of the PPy film. Therefore, at the concentration of NH_3 increased (50–200 ppm), suggesting the absence of active sites for adsorption, causing the steep decrease in the slope. Therefore, the respondent sensitivity of Sample 2 to a low concentration of NH_3 gas was much higher than that to a high concentration of NH_3 gas. The NH_3 gas sensing properties of the present flexible NH_3 sensor were compared with the sensor fabricated on rigid substrate in Table 5. The response of Sample 2 exceeded that of sensors made from electrosynthesized and chemical polymerized PPy film on Al_2O_3 or SiO_2 substrate: Sample 2 had a detection limit of 5 ppm of NH_3 gas [10,21–26]. Fig. 8 plots the real-time response of Sample 2. The response (RT_{90}) and recovery time of Sample 2 were 12 and 52 s, respectively, at the testing concentration of 50 ppm of NH_3. Moreover, five gas on/off cycles produced similar responses, indicating the reproducibility of Sample 2. Table 6 presents the results on the cross-sensitivity effects of NO_2, CO and H_2 gases on the sensor. NO_2, CO and H_2 gases may be regarded as having undesirable cross-sensitivity effects with NH_3.

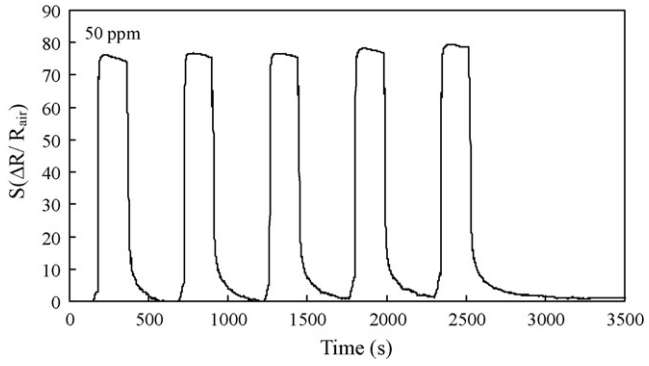


Fig. 8. Reproducibility of response of Sample 2 sensor to NH_3 gas (with compositions as shown in Table 1).

Table 5
Flexible NH_3 sensor performance of this work compared with the literatures.

Sensor substrate	Sensing material	Fabrication method	Detection limit (ppm)	References
PET	PPy	LBL self-assembly	5	This work
Glass	PPy–$LiClO_4$	Electrochemical deposition	10	[21]
Glass	PPy	Langmuir–Blodgett	100	[10]
Al_2O_3	PPy/poly(vinyl alcohol)	Electrochemical deposition	50	[22]
Glass	polypyrrole/sulfonated polyaniline	Electrochemical deposition	20	[23]
Glass	PPy/carbon nanofiber	Vapor deposition polymerization	10	[24]
SiO_2	PPy/single walled carbon nanotubes	Chemical oxidation	10	[25]
SiO_2	PPy	Electrochemical deposition	8	[26]

Table 6
Response (S) of Sample 2 sensor to various gases.

NH_3 (50 ppm)	NO_2 (5 ppm)	CO (200 ppm)	H_2 (1000 ppm)
77.75	19.16	0.21	0.46

4. Conclusions

A novel flexible NH_3 gas sensor was successfully fabricated by layer-by-layer *in situ* self-assembly of a PPy thin film on a modified PET substrate. The gas sensing properties (response) and flexibility characteristics of the fabricated sensors depended strongly on the architecture of the PPy layer. A precursor layer was optimally fabricated with 1 mg/mL concentration of PSS, a deposition time of PPy of 5 min and an *in situ* self-assembled monolayer PPy thin film for use in a novel flexible NH_3 gas sensor for future low-cost and flexible applications. The novel flexible NH_3 gas sensor had very high flexibility, a very high response and acceptable linearity ($R^2 = 0.9976$) between 5 and 50 ppm, a very fast response (12 s), a short recovery time (52 s), high reproducibility and an undesirable cross-sensitivity effect. The flexible NH_3 gas sensor exhibited a sensing performance that is comparable to or even greater than that of the sensors fabricated on the rigid substrate at room temperature.

Acknowledgements

The authors thank the National Science Council (Grant Nos. NSC 97-2221-E-034-002 and 98-2113-M-034-001-MY2) of Taiwan for support.

References

[1] M.C. Mcalpine, H. Ahmad, D. Wang, J.R. Heath, Nat. Mater. 16 (2007) 379.
[2] E. Abad, S. Zampolli, S. Macro, A. Scorzoni, B. Mazzolai, A. Juarros, D. Gómez, I. Elmi, G.C. Cardinali, J.M. Gómez, F. Palacio, M. Cicioni, A. Mondini, T. Becker, I. Sayhan, Sens. Actuators B 127 (2007) 2.
[3] A. Vergara, E. Llobet, J.L. Ramírez, P. Ivanov, L. Fonseca, S. Zampolli, A. Scorzoni, T. Becker, S. Marco, J. Wöllenstein, Sens. Actuators B 127 (2007) 143.
[4] E. Smela, J. Micromech. Microeng. 9 (1999) 1.
[5] R.H.M. van de Leur, A. van der Waal, Syn. Met. 102 (1999) 1330.
[6] J.H. Cho, J.B. Yu, J.S. Kim, S.O. Sohn, D.D. Lee, J.S. Huh, Sens. Actuators B 108 (2005) 389.
[7] S. Brady, K.T. Lau, W. Megill, G.G. Wallace, D. Diamond, Syn. Met. 154 (2005) 25.
[8] E. Stussi, S. Cella, G. Serra, G.S. Venier, Mater. Sci. Eng. C 4 (1996) 27.
[9] P.G. Su, L.N. Huang, Sens. Actuators B 123 (2007) 501.
[10] M. Penza, E. Milella, M.B. Alba, A. Quirini, L. Vasanelli, Sens. Actuators B 40 (1997) 205.
[11] Q. Fang, D.G. Chetwynd, J.A. Covington, C.S. Toh, J.W. Gardner, Sens. Actuators B 84 (2002) 66.
[12] J.N. Barisci, G.G. Wallace, M.K. Andrews, A.C. Partridge, P.D. Harris, Sens. Actuators B 84 (2002) 252.
[13] G. Decher, J.D. Hong, J. Schmitt, Thin Solid Films 210 (1992) 831.
[14] G. Decher, Science 277 (1997) 1232.
[15] A.C. Fou, M.F. Rubner, Macromolecules 28 (1995) 7115.
[16] M.K. Ram, M. Adami, P. Faraci, C. Nicolini, Polymer 41 (2000) 7499.
[17] M. Onoda, K. Tada, A. Shinkuma, Thin Solid Films 499 (2006) 61.
[18] H. Tai, Y. Jiang, G. Xie, J. Yu, M. Zhao, Intern. J. Environ. Anal. Chem. 87 (2007) 539.
[19] N. Ferrer-Anglada, M. Kaempgen, S. Roth, Phys. Stat. Sol. 243 (2006) 3519.
[20] P.G. Su, C.S. Wang, Sens. Actuators B 123 (2007) 1071.
[21] M. Brie, R. Turcu, C. Neamtu, S. Pruneanu, Sens. Actuators B 37 (1996) 119.
[22] C.W. Lin, B.J. Hwang, C.R. Lee, Mater. Chem. Phys. 58 (1999) 114.
[23] H. Bai, Q. Chen, C. Li a, C. Lu, G. Shi, Polymer 48 (2007) 4015.
[24] J. Jang, J. Bae, Sens. Actuators B 122 (2007) 7.
[25] N.V. Hieu, N.Q. Dung, P.D. Tam, T. Trung, N.D. Chien, Sens. Actuators B 140 (2009) 500.
[26] S. Carquigny, J.B. Sanchez, F. Berger, B. Lakard, F. Lallemand, Talanta 78 (2009) 199.

Talanta 80 (2009) 770–776

Contents lists available at ScienceDirect

Talanta

journal homepage: www.elsevier.com/locate/talanta

A block copolymer covalent coating acting as surfactants in separation of 2-[hydroxy(4-nitrophenyl)methyl]-cyclopent-2-enone and 4-nitrobenzaldehyde by capillary electrophoresis

Juan Qiao[a,b], Li Qi[a,*], Huimin Ma[a], Huwei Liu[c], Jun Yang[a,b], Yi Chen[a], Gengliang Yang[d]

[a] Beijing National Laboratory of Molecular Science, Laboratory of Analytical Chemistry for Life Science, Institute of Chemistry, Chinese Academy of Sciences, No. 2 Beiyijie, Zhongguancun, Beijing 100190, China
[b] Graduate School, Chinese Academy of Sciences, Beijing 100049, China
[c] College of Chemistry and Molecular Engineering, Peking University, Beijing 100871, China
[d] College of Pharmacy, Hebei University, Baoding 071002, China

ARTICLE INFO

Article history:
Received 22 May 2009
Received in revised form 24 July 2009
Accepted 27 July 2009
Available online 5 August 2009

Keywords:
Block copolymer
Surfactant
Capillary coating
Covalent bonding

ABSTRACT

An innovative block copolymer capillary coating P(MAn-alt-St)$_{127}$-b-PSt$_{592}$, synthesized by maleic anhydride and styrene, was developed as a new kind of coating for capillary electrophoresis. The covalent bond coating was effectively applied in the separation of raw material (4-nitrobenzaldehyde) and production (2-[hydroxy(4-nitrophenyl)methyl]-cyclopent-2-enone) in a Baylis–Hillman reaction using ammonium acetate with 20% tetrahydrofuran (v/v) as the buffer solution. Electroosmotic flow measurement gave an instantly stable value after 70 times continued injection in 5 days and showed that P(MAn-alt-St)$_{127}$-b-PSt$_{592}$ coatings could suppress electroosmotic flow effectively compared with the bare capillary. The effects of tetrahydrofuran and the pH of buffer on the separation were investigated. The characteristics of the coatings to form micelles similar to surfactants were detected by atomic force microscopy. Moreover, the superiority of this coating was further applied in the separation of four aromatic amines.

© 2009 Elsevier B.V. All rights reserved.

1. Introduction

Capillary electrophoresis (CE) is a separation technique with high efficiency, short analysis time, a small amount of sample and reagent consumption, which has been widely utilized for analysis. An understanding and control of the chemistry of capillary surface is essential to exploit the power of CE.

Since surfactant coatings are inexpensive, flexible and easy to apply in manipulating the surface charge of the capillary, they have become increasingly popular in capillary coatings [1–3]. Numerous types of surfactant coatings have been employed, including: "aggregate coating" and "semi-permanent coating" [4].

However, for "aggregate coatings", some of the surfactant monomers must be present in the running buffer to maintain the coatings; the major shortcoming is that free surfactant molecules in the background electrolyte could interfere with the separation or detection scheme. Furthermore, the presence of surfactant would suppress ionization in mass spectrometry (MS) detection, and thus would make these surfactant coated capillaries incompatible with this increasingly popular and powerful method. For "semi-permanent coating", attributed to form bilayer at the capillary wall [3], the coatings are sufficiently stable and the excess surfactants are removed from the capillary, so separations are performed with no surfactant in the running buffer. But perhaps the main drawback is their irreproducibility.

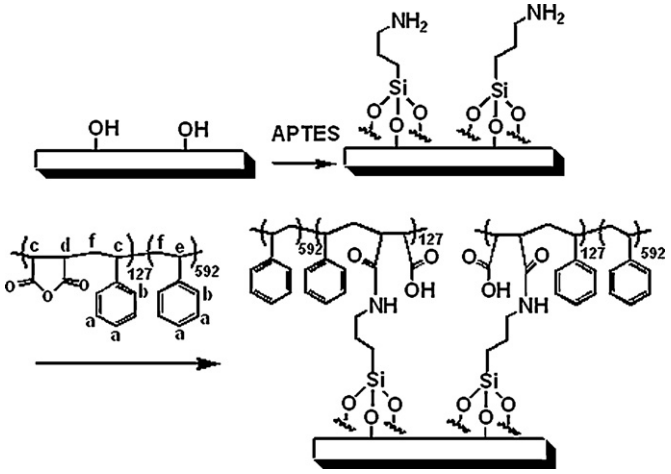
Many kinds of block copolymer have been used in capillary coatings as an alternative choice in recent years [5,6]. Some block copolymers have played an important role in the separation of proteins, deoxyribonucleic acids and oligonucleotides as separation medium [7,8]. The most interesting thing is that these block copolymer coatings have high sieving ability and can self-assemble to transient networks with appropriate mesh sizes or star like micelle structures [9] in selective conditions and the driving force mainly comes from the hydrophobicity in one of the blocks.

Among these block copolymers, only few of them such as the amphiphilic triblock copolymer $E_{99}P_{69}E_{99}$ (F127) forming micelles

Abbreviations: CE, capillary electrophoresis; MS, mass spectrometry; HPCE, high performance capillary electrophoresis; NMR, nuclear magnetic resonance; GPC, gel permeation chromatography; AFM, atomic force microscopy; SEM, scanning electron microscope; EOF, electroosmotic flow; *R*s, resolution; MEKC, micellar electro kinetic capillary chromatography; CMC, critical micellar concentration; RSDs, relative standard deviations; CTAB, cetyltrimethylammonium bromide; MAn, maleic anhydride; St, styrene; THF, tetrahydrofuran; SDS, sodium dodecyl sulfate; SDC, sodium deoxycholate; DMSO, dimethylsulfoxide; AIBN, azo-bis-isobutryonitrile; BTBA, (S)-benzyl dithiobenzoate; APTES, 3-aminopropyltriethoxysilane; HNE, 2-[hydroxy(4-nitrophenyl)methyl]-cyclopent-2-enone; NBA, 4-nitrobenzaldehyde.

* Corresponding author. Tel.: +86 10 82627290; fax: +86 10 62559373.
E-mail address: qili@iccas.ac.cn (L. Qi).

0039-9140/$ – see front matter © 2009 Elsevier B.V. All rights reserved.
doi:10.1016/j.talanta.2009.07.056



Scheme 1. Coating processes of P(MAn-alt-St)$_{127}$-b-PSt$_{592}$ block copolymer.

in solution [9] and block copolymer consisting of polyethylene glycols end-capped with micelle-forming fluorocarbon tails [10] used as surfactants in CE separation. Some other block copolymers also can form micelles on Si [11] or SiO_2 [12] but not in capillary. Unfortunately, these block copolymers are physically adsorbed or dynamically coated in capillary with low reproducibility. However, covalent bonding has been reported as an effective measure to improve reproducibility of polymer coatings [13–15]. Therefore, exploring new kinds of covalent bonded block copolymer acting as surfactants will be an active area of research.

In this work, a novel covalent bonded block copolymer coating in the capillary, which can be expected to play the role of surfactants in the CE separation, has been investigated. We have synthesized a well-defined block copolymer having alternating segments constituted by maleic anhydride (MAn) and styrene (St): P(MAn-alt-St)$_m$-b-PSt$_n$ (Scheme 1). The segment in the block copolymer can easily be hydrolyzed resulting in an amphiphilic block copolymer which can form uniform nanoscale structures by self-assembly. The architectural particles in nanoscale size were constructed by PSt segment as a hydrophobic head group and P(MAn-alt-St) segment as a hydrophilic tail, which was similar to the configuration of surfactants. Thus the innovative capillary coatings have been developed and applied in the separation of the raw material (4-nitrobenzaldehyde) (NBA) and production (2-[hydroxy(4-nitrophenyl)methyl]-cyclopent-2-enone) (HNE) [16] in the Baylis–Hillman reaction. In addition, the separation of four kinds of aromatic amines by the coated capillary has further confirmed that the copolymers indeed play the role as surfactants.

2. Experimental

2.1. Instrumentation

A 1229 high performance capillary electrophoresis (HPCE) analyzer (Beijing Institute of New Technology and Application, Beijing, China) was used to carry out all electrophoretic experiments. Unless stated otherwise, separations were performed at 25 °C in block copolymer coated capillaries (Yongnian Optical Fiber Factory, Hebei, China) of 75 μm I.D. × 70 cm (55 cm effective).

Capillary coating process was as follows: The bare capillary was washed [17] with 1.0 M NaOH for 2 h, followed with pure water, 1.0 M HCl for 10 min, then with pure water and acetone. After complete removal of acetone by nitrogen, tetrahydrofuran (THF) and 3-aminopropyltriethoxysilane (APTES) (50/50, v/v) were flowed through the capillary and kept at room temperature (25 °C) for 12 h. After the reaction, the modified capillary was washed repeatedly with chloroform for 5 min. The modified capillary was coated by rinsing with the block copolymer solution (30.0 mg block copolymer dissolved in 1.0 mL chloroform) for 1 h. Then it was placed at room temperature for 3 h before rinsing with methanol for 2 min. A detection window (about 2 mm width) was made directly by burning off the block copolymer inner capillary and polyimide coating outside.

Prior to injection, the coated capillaries were sequentially rinsed with water and running buffer for 2 min each. A sample was separated at +20 kV and siphoned for 10.0 s in 15.0 cm height. The separated bands were detected by UV absorption at 254 nm and acquired at 4 Hz. Peaks were identified by spiking relative standard HNE, NBA and aromatic amines in sample solutions and the peaks with increased height were considered to be the targets.

Elemental analysis was carried out on FLASH EA1112 (Thermo, America) and the characterization of polymer coating was detected by an S-4300 scanning electron microscope (SEM, Hitachi, Japan). Atomic force microscopy (AFM) phase images were obtained by a Nano-Scope III MultiMode AFM Digital Instruments at room temperature. Si tips were used with a resonance frequency of approximately 300 kHz and a spring constant of about 40 N m^{-1}. The scan rate was in the range 0.5–1.2 Hz. Three flat glass of similar material to the capillary were coated with block copolymer for AFM measurements in air.

Gel permeation chromatography (GPC) was performed on a set of a Hitachi L-2130 pump with a Waters 2410 refractive index detector, and a Waters 2487 ultraviolet detector with the combination of Hersteller MZ-Gel SDplus 5 μm, porosity 10^3, 10^4, 10^5, and 10^6 Å. THF was used as the eluent with a flow rate of 1.0 mL/min and polystyrene standards were used for calibration.

^{1}H nuclear magnetic resonance (^{1}H NMR) observation of the block copolymers was performed on Bruker Avance 400 spectrometer (Bruker biospin, Switzerland) (400 MHz). A 4.0-mg block copolymers dissolved in 0.5 mL deuterated chloroform containing 0.03% tetramethylsilane for NMR measurements.

2.2. Chemicals

APTES was purchased from Acros (New Jersey, USA). P-phenylenediamine, aniline, 4-bromoanilines, α-naphthylamine, NBA, THF, dimethyl sulfoxide (DMSO), chloroform, sodium dodecyl sulfate (SDS), cetyl trimethyl ammonium bromide (CTAB) and other chemicals were analytical reagent grade and obtained from Beijing Chemical Factory (Beijing, China). Sodium deoxycholate (SDC) was purchased from Beijing Aoboxing Biological Technology Ltd. (Beijing, China). Azo-bis-isobutryonitrile (AIBN) was purchased from Shanghai Chemical Plant (Shanghai, China) and MAn was obtained from Guangfu reagent (Tianjin, China). They were re-crystallized before use. Styrene (St) was got from Shanghai Chemical Plant (Shanghai, China) and (S)-benzyl dithiobenzoate (BTBA) utilized without further purification. HNE was synthesized in our laboratory [16]. DMSO was used as the neutral marker in the electroosmotic flow (EOF) determination.

2.3. Solutions preparation

All solutions were prepared in triply distilled water produced by a distillation apparatus model SZ-97 (Yarong Biochemical Instrument Co., Shanghai, China) and stored at 4 °C. CE running buffers, unless stated otherwise, were composed of 30.0 mM boric acid, and adjusted to pH 10.5 with 1.0 M NaOH or 30.0 mM ammonium acetate, adjusted to pH 7.0 with 1.0 M ammonia before THF was added. Before use, all the running buffers were filtered through a membrane filter with 0.45 μm pores and degassed by sonication for 2 min.

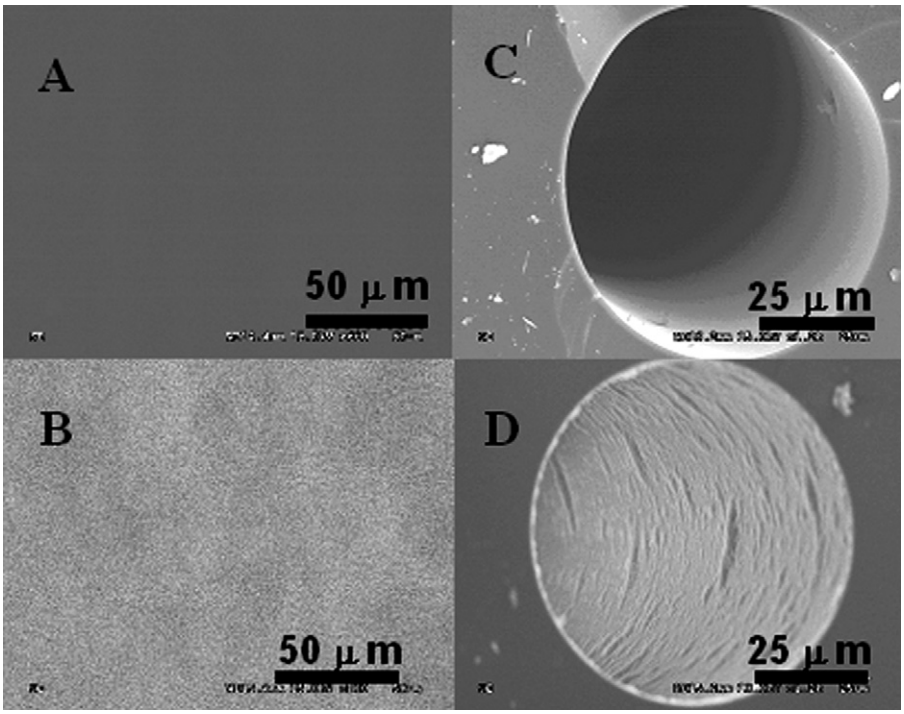


Fig. 1. Scanning electron micrograph of glasses and capillaries. (A) Bare glass; (B) glass coated by P(MAn-alt-St)$_{127}$-b-PSt$_{592}$ block copolymer; (C) bare capillary; (D) capillary coated by P(MAn-alt-St)$_{127}$-b-PSt$_{592}$ block copolymer.

Standard stock solutions of HNE and NBA stock solutions were prepared in 50% THF at concentrations of 0.1 and 0.5 M, respectively. Standard stock solutions of aromatic amines were dissolved in 50% THF at a final concentration of 1.0 mg/mL. Working solutions were diluted from the stock solutions with 50% THF by 10–10^4-fold; these were stored in the dark at −20 °C.

2.4. Synthesis of the block copolymer

A typical reversible addition-fragmentation chain transfer initiating [18] system was used in the combination of BTBA and AIBN. The copolymerization took place in a 50.0 mL boiling flask-3-neck under nitrogen. $[MAn]_0:[St]_0:[BTBA]_0:[AIBN]_0 = 100:1000:1:0.2$ in molar ratio, $[MAn]_0 = 10.0$ mM, in 5.0 mL 1,4-dioxane, magnetic stirring at 60 °C for 38 h. When the reaction was completely finished, purity process of the block P(MAn-alt-St)$_m$-b-PSt$_n$ copolymer was as follows: the polymer sample was first dissolved in 15.0 mL 1,4-dioxane, then after adding polymer solution into an excess of ether, the polymer was precipitated, filtered, and dried at 50 °C in a vacuum oven for 24 h. Finally, 3.3 g P(MAn-alt-St)$_m$-b-PSt$_n$ copolymer was produced by this procedure.

2.5. Coating on glass

To investigate the mechanism of the coated block copolymer on the separation, a coating on glass was carried out. The pretreatment of the glass (1 cm × 1 cm, microscopic slides purchased from Sail Brand, China) was as follows: washed with water, 1.0 M NaOH aqueous solution for 2 h and then with 1.0 M HCl for 10 min, followed by washing with pure water and acetone. The THF and APTES (50/50, v/v) were coated on the glass after the glass dry and kept at room temperature (25 °C) for 12 h. The block copolymer solution (30.0 mg/mL, 50.0 μL) was tiled on the glass and dry.

3. Results and discussion

3.1. Preparation of block copolymer coating

The preparation of the P(MAn-alt-St)$_m$-b-PSt$_n$ block copolymer was described in Section 2.4. In order to characterize the structure and the average size of the block copolymer, elemental analysis, ^{1}H NMR and GPC were measured.

^{1}H NMR results based on the following signal assignment δ (ppm): 7.4 (CH, cycle, a in Scheme 1), 6.9 (CH, cycle, b in Scheme 1), 3.8 (CH, c in Scheme 1), 2.6–2.4 (CH, d in Scheme 1), 2.2–1.9 (CH, e in Scheme 1), 1.8–1.3 (CH_2, f in Scheme 1). The result of elemental analysis showed that C was 79.7%, H was 6.4%. On the basis of the results above and GPC data (Mn is 9.4 × 10^4 and polydispersity is 1.1), it has been known the structure of the block copolymer is P(MAn-alt-St)$_{127}$-b-PSt$_{592}$ (Scheme 1). All of the results demonstrated that a well-defined block copolymer of P(MAn-alt-St)$_{127}$-b-PSt$_{592}$ with narrow polydispersities has been obtained.

The anhydride groups on the MAn of the block copolymer reacted with the amido of APTES and carboxylic groups can be electronegative in basic buffer solution. This process was illustrated in Scheme 1.

SEM has been utilized successfully for the purpose of observing the morphologies of coatings in capillary and films on glass. The morphologies of block copolymer coatings on the capillary surface are important parameters to evaluate the coating stability and reproducibility. In this regard, the morphologies of the block copolymer coated on the glass and in capillary were observed by SEM. Fig. 1 shows the SEM micrographs of capillaries and glasses before and after coated by P(MAn-alt-St)$_{127}$-b-PSt$_{592}$ block copolymer. Fig. 1 indicates that the coated glass (Fig. 1B) was whiter than the uncoated (Fig. 1A). The possible reason was that the block copolymer coating altered the refraction. Furthermore, this result also proved that the copolymer coating on the glass was very smooth. On the other hand, the SEM results shows that a uniform and dense polymer coating had attached onto the capillary inner

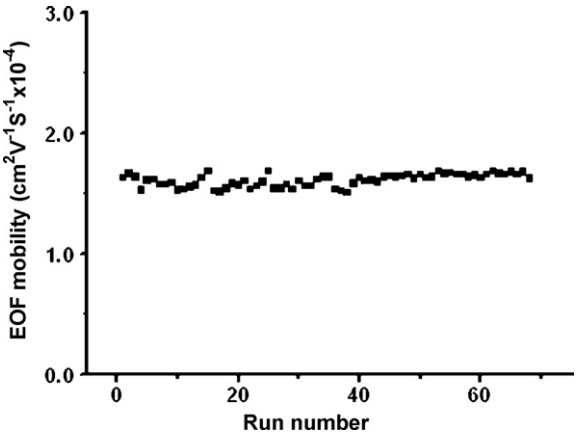


Fig. 2. Coating stability of the block copolymer reflected as EOF mobility vs continuous run for 5 days. Experimental conditions: buffers, 30.0 mM borate (pH 10.5)/THF (80/20) (v/v); neutral marker, 1.0% DMSO. Capillary: 75 μm I.D. × 70 cm (55 cm effective); injection: siphoned for 10.0 s in 15.0 cm height; voltage: +20 kV; UV detection: 254 nm.

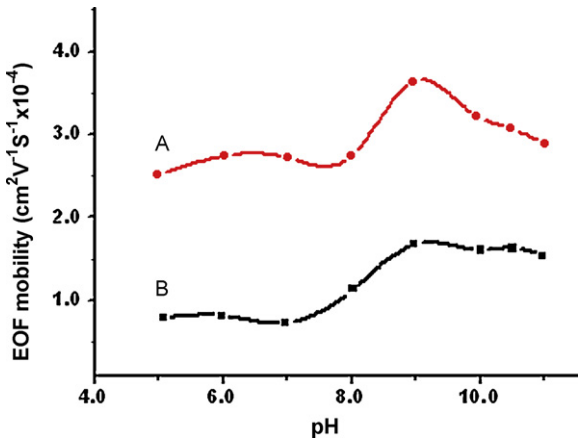


Fig. 3. Effect of changing pH on EOF mobility measured (A) in a bare capillary, and (B) in P(MAn-alt-St)$_{127}$-b-PSt$_{592}$ block copolymer coated capillary. Experimental conditions: pH 5.0–7.0: 30.0 mM ammonium acetate/THF (80/20) (v/v); pH 8.0–10.5: 30.0 mM borate/THF (80/20) (v/v); other conditions are the same as in Fig. 2 except for different pH.

wall with a wrinkly surface (Fig. 1D), which is much different from bare capillary (Fig. 1C).

3.2. Stability of the coated capillary

In order to confirm the further application value, stability test was performed by continuous run and the results are shown in Fig. 2. EOF measurements under a number of conditions could indirectly determine the stability of coated capillaries. The reproducibility was evaluated using the relative standard deviations (RSDs) of the EOF. In the tests, the 30.0 mM borate (pH 10.5)/THF (80/20) (v/v) buffer solution and 1.0% DMSO as a neutral marker were used, respectively. The P(MAn-alt-St)$_{127}$-b-PSt$_{592}$ block copolymer coated capillary could endure more than 70 consecutive electrophoresis runs with good repeatability and result in a RSD value of 3.4% (n = 70). The capillary-to-capillary RSD was obtained by using 35 runs (7 consecutive runs performed in 5 different capillaries) and resulted in a RSD value of 3.3%. All RSDs of the EOF were below 3.5%, and thus, very good reproducibility was observed. Though the lifetime of covalently bonded capillaries was longer than 3 months, it should be mentioned that the capillaries must be filled with water and sealed once they were taken off from the equipment.

In consideration of the importance of EOF in the evaluation of coated capillary, the effect of pH on the EOF mobility has been investigated. Fig. 3 shows the effect of pH on EOF mobility in coated capillary and in bare capillary at pH values ranging from 5.0 to 11.0. Compared with the bare capillary, the copolymer coated capillary generated a low EOF mobility because the carboxylic groups of the copolymers could effectively cover on the capillary wall. Furthermore, the EOF mobility could also be restrained by the addition of THF. In addition, the copolymer coating showed an excellent performance in EOF, which is stable in basic solution.

3.3. Separation of HNE and NBA with block copolymer coated capillary

In our early study of the Baylis–Hillman reaction, micellar electrokinetic chromatography (MEKC) in capillary has been used to detect the raw material NBA and production HNE [16]. Thus the new method has been expected to find whether the block copolymer coatings can replace the surfactants in CE, which can provide the possibility of the combination of CE and MS without desalting in the future.

3.3.1. Optimization of organic additive

Because the copolymer can self-assemble to nanoscale [18] structure, the optimization concentration of organic additive in the buffer solution should be an important factor. The organic additive can affect critical micelle concentrations (CMCs) of block copolymers [19] and the separation selectivity as the copolymer coating is strongly influenced by the organic additive in the solution. Furthermore, the P(MAn-alt-St) segment in the block copolymer can easily be hydrolyzed [18] and as a result the block copolymer can form uniform nanoscale structures by self-assembling. These nanoscale structures constructed by PSt segment as a hydrophobic head group, and P(MAn-alt-St) segment as a hydrophilic tail which provided reactive anhydride or carboxylic groups on the surface of head group. Thus, several kinds of organic solvent have been investigated according to their polarities (data were not shown). The polarities of the organic solutions are as follows [20]: acetonitrile, 11.8; acetone, 9.0; ethanol, 5.8; tetrahydrofuran, 5.8; methanol, 5.7; 2-propanol, 5.5; and 1,4-dioxane, 1.5. Among the eight kinds of organic solvent, only THF and ethanol as additives can contribute to the block copolymer coating forming micelles at a certain extent and redound to the separation of HNE and NBA.

In this section, various THF concentrations in the running buffer (borate and ammonium acetate) were tested to study their effects on the system. The data in Table 1 show that the optimal THF concentrations for the two kinds of buffer were both 20% (v/v). For borate, with the concentration of THF increased from 10% to 20% (v/v), the resolution of HNE and NBA increased distinctly. However, when THF concentration exceeded 20% (v/v), the resolution decreased and finally HNE and NBA cannot be well resolved. The trend for THF concentration in ammonium acetate was similar with that in borate (Table 1, line 3). This phenomenon may be due to the

Table 1
Effect of THF concentrations on the separation of HNE and NBA[a].

	THF (%)						
	10	15	18	20	21	25	30
Rs							
Borate	0.6	1.2	1.3	1.7	1.5	0.6	0.4
Ammonium acetate	1.5	1.5	1.4	1.7	1.6	1.5	1.4

[a] Experimental conditions: 30.0 mM borate (pH 10.5) and THF at different ratio; 30.0 mM ammonium acetate (pH 7.0) and THF at different ratio. Capillary: 75 μm I.D. × 70 cm (55 cm effective); injection: siphoned for 10.0 s in 15.0 cm height; voltage: +20 kV; UV detection: 254 nm. *Rs*: resolution between HNE and NBA.

Table 2
Influence of buffer concentrations and pH on the resolutions of HNE and NBA[a].

Buffer	Concentration (mM)	*Rs*	pH	*Rs*
Ammonium acetate	10.0	1.6	4.8	0.5
	20.0	1.6	5.0	1.3
	30.0	1.7	7.0	1.7
	40.0	1.6	9.0	1.6
	50.0	1.4	10.5	1.6
	60.0	1.5	10.7	1.2
Borate	10.0	1.4	8.0	0.7
	20.0	1.5	9.0	0.8
	30.0	1.9	9.3	1.6
	40.0	2.1	9.8	1.7
	50.0	1.7	10.5	2.1
	60.0	1.9	11.0	0.9

[a] Experimental conditions: ammonium acetate (pH 7.0)/THF (80/20) (v/v), and borate (pH 10.5)/THF (80/20) (v/v) at different concentrations; 30.0 mM buffer/THF (80/20) (v/v), at different pH values, other conditions are the same as in Table 1.

THF at a lower concentration assisting the block copolymer in forming micelles which resemble surfactants in the separation process. Therefore the hydrophobic analytes were enveloped in the micelles and different analytes were separated similar to the separation process in MEKC. However, excess THF in the buffer solution will make the analytes be extracted from the micelles and result in decreased resolution. This phenomenon that the resolution of the analytes decreased when THF was added to the buffer solution was also observed in MEKC using bare capillary.

The experiment results also showed that the baseline separation was achieved when the additive of ethanol concentration was as high as 50% (v/v) and the migration time was prolonged about 21 min. Thus, 20% THF in the buffer solution (v/v) was finally selected.

3.3.2. *Optimization of buffer solution*

In order to investigate the influence of the buffer composition in the separation of the HNE and NBA, experiments were performed on buffer concentration and pH.

The influence of different kinds of buffer solution and their concentrations were investigated in detail. Results in Table 2 show that baseline resolution, low conductivity (current $\leq$70 μA) and high reproducibility were achieved for ammonium acetate and borate buffer solutions. Only minor improvements in the resolution of HNE and NBA were obtained when the buffer concentration increased from 10.0 to 60.0 mM with the cost of the high conductibility instead. Consequently, 30.0 mM was selected for further experiments.

On the other hand, the influence of buffer pH on the resolution was evaluated respectively ranging from 4.8 to 10.7 for ammonium acetate buffer and 8.0 to 11.0 [21] for borate buffer (Table 2). Table 2 shows that the resolution increased with the increasing of pH before 10.5 and decreased at 11.0, thus the optimum pH at 10.5 was chosen for the borate buffer in the separation. Ammonium acetate buffer at pH 7.0 [22] could yield baseline separation and provide the possibility of the combination of CE and MS without desalting in the future. So the ammonium acetate buffer at pH 7.0 was finally selected for the separation.

The temperature effect on the separation was also investigated [23] ranging from 20 to 40 °C. Although the resolution has not been improved, the migration time decreased with the increasing of temperature. Furthermore, in consideration of yielding lower current and smaller Joule heat, 25 °C was selected.

Therefore, a baseline separation of HNE and NBA was carried out (Fig. 4) by using P(MAn-alt-St)$_{127}$-b-PSt$_{592}$ block copolymer coated capillary and 30.0 mM ammonium acetate (pH 7.0) added with 20% (v/v) THF as buffer solution.

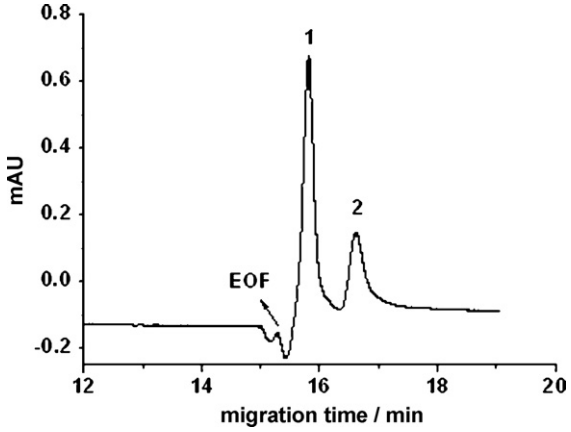


Fig. 4. Electropherogram of HNE and NBA samples in P(MAn-alt-St)$_{127}$-b-PSt$_{592}$ block copolymer coated capillary. Experimental conditions: 30.0 mM ammonium acetate (pH 7.0)/THF (80/20) (v/v), others are the same as in Fig. 2. Peak identity: 1. HNE, 10.0 mM; 2. NBA, 5.6 mM.

3.3.3. *The separation of HNE and NBA by using the coated and bare capillary*

In order to prove that the P(MAn-alt-St)$_{127}$-b-PSt$_{592}$ block copolymer coating acted as surfactants, the influence of different kinds of common surfactants (CTAB, SDS and SDC) and varies concentration using bare capillary was investigated (Fig. 5). Compared with the chromatograms obtained from the coated capillary (Fig. 4), it indicated that HNE was always in front of NBA in the block copolymer coated capillary but behind it in the bare capillary with surfactants. On the basis of observed result, all subsequent experiments were performed on the effect of surfactants concentration to resolution. The most widely used method for resolution (*Rs*) calculation is the tangent method as follows [24]: $Rs = 2(t_2 - t_1)/(W_2 + W_1)$, where t_1 and t_2 are the migration times of the two components, and W_1 and W_2 are the corresponding widths of the peaks.

Fig. 5 also shows that the resolution increased with the concentration of surfactants and baseline separation ($Rs = 1.5$) occurred at concentration 12.2 mM for SDS, 2.0 mM for CTAB and 5.0 mM for SDC, respectively. According to the literature, the CMCs of the three surfactants were 8.1 mM for SDS [25], 1.3 mM for CTAB [25] and 3.1 mM for SDC [26], respectively. From these data, it was concluded that baseline separation was obtained only when the concentrations of the surfactants were above the CMCs. It was found that the block copolymer coating had formed micelles in the buffer solu-

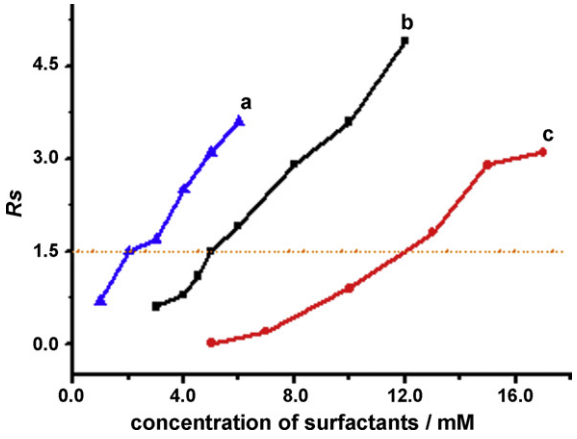


Fig. 5. Effect of varying surfactants and concentrations on the separation of HNE and NBA using bare capillary. Experimental conditions: 30.0 mM borate (pH 10.5); (a) CTAB, (b) SDS, (c) SDC, others are the same as in Fig. 2.

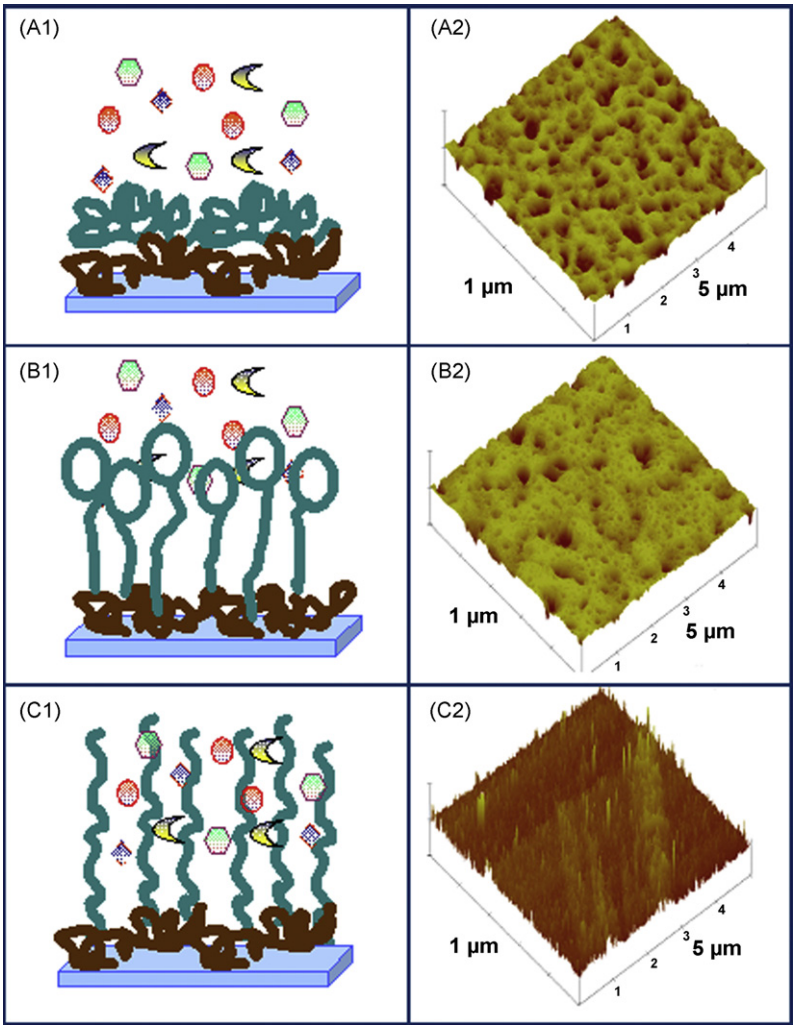


Fig. 6. Schematic illustration of block copolymer morphologies in different CE procedure (A1–C1); AFM images of block copolymer coating after dipping in water for 5 min (A2); coating after dipping in 20% THF for 30 min (B2); coating after dipping in 100% THF for 30 min (C2).

tion and the concentration of the copolymer coating micelles was approximately equivalent to or higher than CMCs of those surfactants when the *R*s was 1.5 (Fig. 5). The resolution results obtained from the coated capillary (Fig. 4) also showed that the copolymers indeed play the role as surfactants.

3.3.4. *Effect of copolymer morphologies on separation*

As described in Section 3.3.1, THF was used as an organic additive and played an important role in self-assembling of the block copolymer. PSt is soluble in some organic solvents independent of pH while MAn is soluble in water when it is protonated. Although P(MAn-alt-St) segment provides reactive anhydride which turns into carboxylic groups in the basic buffer solution, P(MAn-alt-St)$_{127}$-b-PSt$_{592}$ block copolymer are insoluble in a buffer solution without organic solvents. When there was no THF in the buffer solution, the block copolymer like dendritic tentacles docked on the inner wall of capillary. However, when THF was used as an organic additive and added into the buffer solution, micelles with hydrophobic head group and hydrophilic tail were formed spontaneously. The phenomenon was similar to F127, which could self-assemble to star like micelle structures above its critical micelle concentration with the P blocks forming the core and the E blocks dangling outside [9].

It has been reported that images of some double-chained quaternary ammonium surfactants reveal the presence of spherical aggregates spaced uniformly over the silica surface. To determine whether this micelle-type coating formed on the capillary surface during CE, Baryla and co-workers employed AFM imaging to study surfactant adsorption in a common electrophoretic buffer [1].

Therefore, to reveal the relationship between resolution and morphology, the copolymers morphologies in different solution were investigated by AFM (Fig. 6). Generally, when the length of the copolymer is invariable, the morphologies of micelle formed by block copolymers in solutions can be easily tuned by change of THF concentration. Fig. 6A2 shows that after the coating on glass dipped in water for 5 min, the P(MAn-alt-St)$_{127}$-b-PSt$_{592}$ block copolymer formed a film, and the copolymer was insoluble since the hydrophobic block of PSt dominated the composition of the block copolymer in this situation. However, when dipped in 20% THF (v/v) for 30 min, the film expanded obviously (Fig. 6B2) due to the dendrite tentacles of copolymers being extended, meanwhile, the height of the copolymer coating increased obviously because the coating layer became 60.0 nm thicker than that formed in Fig. 6A2. After the coating was dipped in 100% THF for 30 min, it became more compact (Fig. 6C2); the reason might be that the formed micelle cores of block copolymers (Fig. 6B2) had been disrupted by THF. The results of AFM indicate that the coatings could form micelles and could play the role of surfactants in the analytes separation.

Fig. 6A1–C1 shows the schematic illustration of the separation procedure of copolymers according to the AFM results. The mechanism of this block copolymer coating in the separation process

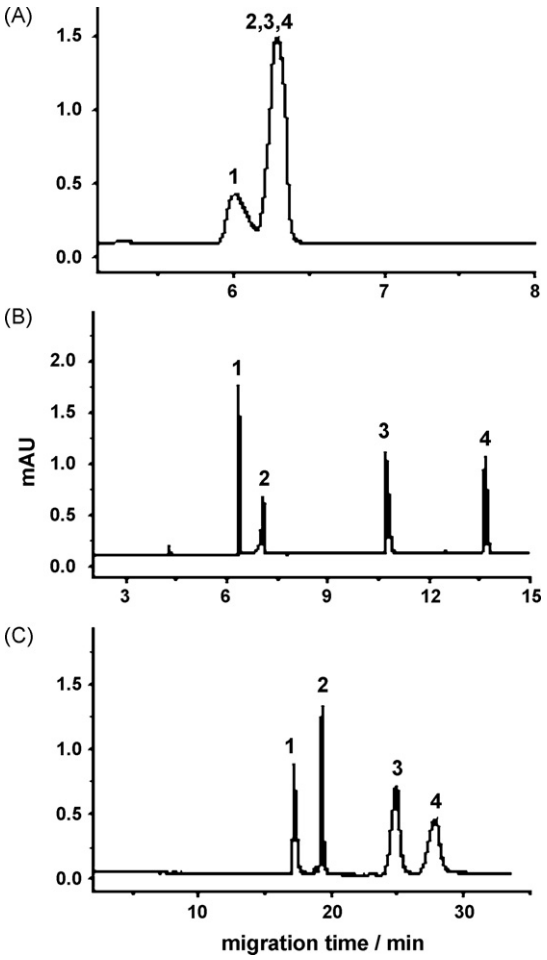


Fig. 7. Electropherograms of amines samples in bare capillary and P(MAn-alt-St)$_{127}$-b-PSt$_{592}$ block copolymer coated capillary. Experimental conditions: (A) bare capillary, 30.0 mM NaH_2PO_4 (pH 7.0)/THF (90/10) (v/v); (B) bare capillary, 30.0 mM NaH_2PO_4 (pH 7.0, 15.0 mM SDS); (C) capillary coated by P(MAn-alt-St)$_{127}$-b-PSt$_{592}$ block copolymer, buffer is same as (A).Other conditions are the same as in Fig. 2. Peak identity: 1. P-phenylenediamine, 0.6 mM; 2. aniline, 0.5 mM; 3. 4-bromoanilines, 1.0 mM; 4. α-naphthylamine, 0.7 mM.

was also displayed that P(MAn-alt-St)$_{127}$-b-PSt$_{592}$ block copolymer could form micelles and assist in the separation. Thus a novel covalently bonded block copolymer acting as surfactants was developed.

3.4. Separation of aromatic amines

The separation of four UV-absorbing organic amines shown in Fig. 7 was performed using the block copolymer coated (Fig. 7C) and uncoated (Fig. 7A and B) capillaries. When using the buffer solution of 30.0 mM NaH_2PO_4 (pH 7.0)/THF (90/10) (v/v), the four organic amines cannot be well separated on the bare capillary. However, using the same buffer solution on the coated capillary, all the analytes were baseline separated. In order to show that the coating polymer acts as surfactants, different concentrations of SDS were added to the buffer solution of 30.0 mM NaH_2PO_4 [27] (pH 7.0). As a result, 15.0 mM SDS reached the resolution (Fig. 7B) comparing with the coated capillary (Fig. 7C). This result further testified the former supposition that coating block copolymer play the similar role as surfactants when THF as an additive in the buffer solution.

4. Conclusion

A novel block copolymer coating was developed and proposed as a valid alternative to surfactants in the separation of the raw material and production in a Baylis–Hillman reaction. Compared with using surfactants in the bare capillary for the separation, the main features of the coating were the excellent chemical stability, a very good capillary-to-capillary and run-to-run repeatability, and the possibility of CE-MS detection without desalting of the buffer solution in the future. The efficacy of the developed coating was also proven at the separation of four amines, obtaining baseline separation and further testified the function of copolymer coating similarly to surfactants. This remarkable analytical result was validated by testing the optimum organic solution as an additive and observing morphology using SEM and AFM. This integrated approach could be considered as an alternative strategy for simplify operating process of CE-MS detection and providing possibility of the online detection in reactions and separations.

Acknowledgements

We gratefully acknowledge the financial support from NSFC (No. 20875091 and No. 90813032), Ministry of Science and Technology of China (No. 2007CB714504 and No. 2008AA02Z206), and Chinese Academy of Sciences. We also thank Dr. Zhenpeng Guo and Shuai Zhao for their kind assistance.

References

[1] N.E. Baryla, J.E. Melanson, M.T. McDermott, C.A. Lucy, Anal. Chem. 73 (2001) 4558–4565.
[2] C. Wang, C.A. Lucy, Electrophoresis 25 (2004) 825–832.
[3] C.A. Lucy, A.M. MacDonald, M.D. Gulcev, J. Chromatogr. A 1184 (2008) 81–105.
[4] J.E. Melanson, N.E. Baryla, C.A. Lucy, Anal. Chem. 72 (2000) 4110–4114.
[5] V. Barbier, B.A. Buchholz, A.E. Barron, J.L. Viovy, Electrophoresis 23 (2002) 1441–1449.
[6] H. Liu, R.H. Shi, W.M. Wan, R.M. Yang, Y.M. Wang, Electrophoresis 29 (2008) 2812–2819.
[7] B. Chu, D. Liang, J. Chromatogr. A 966 (2002) 1–13.
[8] R.L. Rill, Y. Liu, D.H. Van Winkle, B.R. Locke, J. Chromatogr. A 817 (1998) 287–295.
[9] C. Wu, T. Liu, B. Chu, D.K. Schneider, V. Graziano, Macromolecules 30 (1997) 4574–4583.
[10] S. Menchen, B. Johnson, M.A. Winnik, B. Xu, Electrophoresis 17 (1996) 1451–1459.
[11] K. Emoto, Y. Nagasaki, K. Kataoka, Langmuir 15 (1999) 5212–5218.
[12] J. Hahn, S.E. Webber, Langmuir 20 (2004) 1489–1494.
[13] S. Liu, L. Gao, Q. Pu, J.J. Lu, X. Wang, J. Proteome Res. 5 (2006) 323–329.
[14] J. Charvátová, V. Kašička, Z. Deyl, V. Král, J. Chromatogr. A 990 (2003) 111–119.
[15] H. Sirén, K. Vuorensola, J. Microcolumn Sep. 13 (2001) 126–133.
[16] L. Qi, K. Cui, J. Qiao, G.L. Yang, Y. Chen, J. Sep. Sci. 32 (2009) 1480–1486.
[17] M. Borissova, M. Vaher, M. Koel, M. Kaljurand, J. Chromatogr. A 1160 (2007) 320–325.
[18] M.Q. Zhu, L.H. Wei, M. Li, L. Jiang, F.S. Du, Z.C. Li, F.M. Li, Chem. Commun. 4 (2001) 365–366.
[19] S.Y. Park, Y. Kawakami, Macromol. Chem. Phys. 206 (2005) 533–539.
[20] C. Reichardt, Solvents and Solvent Effects in Organic chemistry, second ed., VCH, New York, 1988, p. 408.
[21] W.W. Bia, S.R. Lei, X.P. Yanga, Z.M. Xua, H.Y. Yuan, D. Xiao, M.M.F. Choic, Talanta 78 (2009) 1167–1172.
[22] A. Vassort, D.A. Barrett, P.N. Shaw, P.D. Ferguson, R. Szucs, Electrophoresis 26 (2005) 1712–1723.
[23] W.L. Wei, B.Y. Guo, J.M. Lin, Electrophoresis 30 (2009) 1380–1387.
[24] D. Song, J. Wang, J. Pharm. Biomed. Anal. 32 (2003) 1105–1112.
[25] C. Reichardt, Solvents and Solvent Effects in Organic Chemistry, second ed., VCH, New York, 1988, p. 40.
[26] M. Kato, S. Ozawa, R. Hayashi, Lipids 32 (1997) 1229–1230.
[27] C.E. Lin, Y.T. Chen, T.Z. Wang, J. Chromatogr. A 837 (1999) 241–252.

Talanta 80 (2009) 777–780

Contents lists available at ScienceDirect

Talanta

journal homepage: www.elsevier.com/locate/talanta

Detection of ozone gas using gold nanoislands and surface plasmon resonance

Aleksey N. Pisarenko, Wolfgang U. Spendel, Richard T. Taylor, Jordan D. Brown, James. A. Cox, Gilbert E. Pacey*

Miami University Center for Nanotechnology, Miami University, Oxford, OH 45056, United States

ARTICLE INFO

Article history:
Received 27 April 2009
Received in revised form 27 July 2009
Accepted 28 July 2009
Available online 7 August 2009

Keywords:
Ozone detection
Gold nanoislands
Surface plasmon resonance

ABSTRACT

Gold nanoislands interact with gaseous ozone to produce a surface plasmon resonance shift, similarly to the interaction of ozone and gold nanoparticles in water. Gold nanoislands are produced by sputtering, which significantly simplifies the synthesis and produces controlled size for the gold nanoislands. The shift of surface plasmon resonance peak was monitored while gold nanoislands were exposed to variable concentration of gaseous ozone. The shift was then correlated with ozone concentration. Our current results indicate sensing gaseous ozone at concentration of as low as 20 μg/L is achievable. Gold nanoislands were reversed to their original wavelength and were able to cycle between the wavelengths as ozone was introduced and removed. Potentially, this system can be useful as a sensor that identifies the presence of ozone at low part-per-billion concentrations of ozone in gaseous media.

© 2009 Elsevier B.V. All rights reserved.

1. Introduction

The objective is to develop an ozone sensor for the drinking water industry and other industries that electrolytically produce gaseous ozone. Tighter control of the generation system will produce significant energy cost savings while maximizing the efficacy of the ozone treatment. Up to now this task has been complicated by the complex nature of the ozone decomposition pathways and the irreversible oxidization of the reagents/sensing element [1,2]. Electrochemically based measurements have also been problematic due to poor sensitivity and electrode fouling [2].

In a previous paper this group reported that aqueous solutions of gaseous ozone produced a shift in the surface plasmon resonance of colloidal gold nanoparticles [3]. This was surprising on two fronts. First, in ozone methods, ozone irreversibly oxidizes the analytical reagent(s) thereby making a reversible sensor impossible. Even in prior gold surface interactions utilizing gold crystals and monolayer surfaces the ozone decomposed on the surface, but the surface was unaffected by the ozone [4–6]. Surface spectroscopy indicated that oxygen covered the surface and that an electron transfer from the Au substrate into the oxygen adlayer occurred [4]. The oxygen could be removed by heating the surface to 600 K; this desorption exhibits first-order kinetics. The Au–O bond dissociation energy is about 58 kcal/mol. Other papers confirmed the need for high temperature and that the ozone decomposes on the metallic surface [6–8]. Based on UV–Vis spectral data observing the 254 nm ozone peak from the gold colloidal solutions, the decomposed ozone does not produce surface oxygen.

The second surprising finding was that the shift in the surface plasmon resonance from the colloidal gold nanoparticles was reversed to the original wavelength upon removal of ozone. This is unexpected since most reports of analytical utilization of surface plasmon resonance claimed irreversibility since the plasmonic shift was due to irreversible aggregation of the gold nanoparticles or other surface modifications. It was observed that the colloidal gold nanoparticles were able to reproducibly cycle between the surface plasmon resonances wavelength as ozone was introduced and removed. Based on particle size experiments there was no evidence of aggregation. Since our long-term goal is a reversible gaseous ozone sensor, the surface plasmon resonance signal was usable, but the colloidal solution had to be replaced by a solid state system.

Initially, gold nanoislands were made using vapor deposition followed by thermal curing. As was the case in the aqueous system, the surface plasmon resonance of the gold nanoislands exhibited a cycling effect when gaseous ozone was introduced and removed. The difficulty with this production approach was that the process to make the nanoislands was not very reproducible both in size and distribution of the gold nanoislands. This paper discusses an alternative solid state system and the characterization of the gold nanosurface, the gold nanosurface interaction with ozone, the desirable performance characteristic(s) of the sensor, the optimal size for gold nanosurface, the current sensor configuration, and the sensor performance characteristics.

* Corresponding author. Tel.: +1 513 529 2875; fax: +1 513 529 5715.
E-mail address: paceyge@muohio.edu (G.E. Pacey).

0039-9140/$ – see front matter © 2009 Elsevier B.V. All rights reserved.
doi:10.1016/j.talanta.2009.07.062

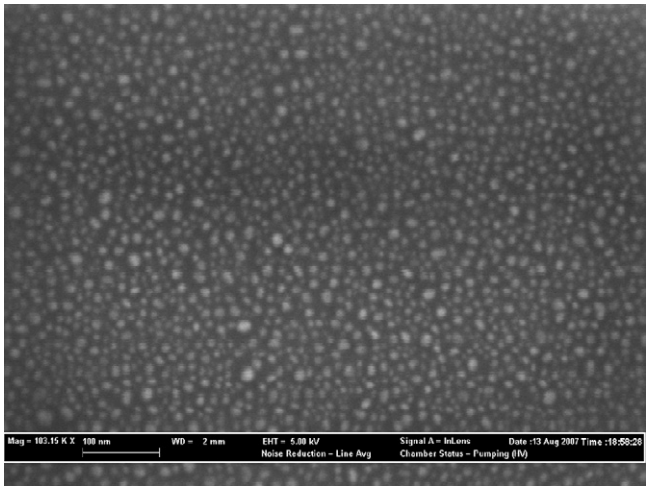


Fig. 1. SEM images of typical gold nanoislands produced by sputtering process on a polished aluminum substrate.

2. Experimental

Ozone generation was performed using a water-cooled Ozone Research Equipment Corporation Model O3B9-0 generator. The cooling water and fan are turned on first. Oxygen pressure from the oxygen cylinder is reduced down to 6 psi by a regulator. The generator is turned on and the electric current set to 1.3 amps. This setting should produce approximately 9 g per hour of ozone. Ozone concentration was determined by measuring absorbance at 254 nm on HP 8453 Photodiode UV–Vis. Molar absorptivity of 3300 M^{-1} cm^{-1} was used to calculate the concentration of ozone. A 10 cm quartz sample cuvette was used to lower the detection limit of ozone. PerkinElmer, Lambda 950 Reflectance Spectrophotometer, employing an integrating sphere was used to collect absorbance spectra of gold nanoislands. Varian's Cary 50 spectrophotometer was used to collect UV–Vis spectra of gold nanoislands sputtered onto transparent substrates, such as polished quartz and indium tin oxide-coated glass plates.

Previously (1), the gold nanoislands were produced using Physical Vapor Deposition (PVD) onto glass or indium tin oxide-coated glass. The current work uses a sputtering procedure to produce gold nanoislands. This greatly reduces synthesis time and it also provides very good control of sputtering parameters, which improves reproducibility. Gold nanoislands were generated using Anatech Hummer V Sputter Coater. Typical settings for the sputter coater: 70–80 mtorr vacuum, high voltage set to generate current above 10 mA and coating time: 1–5 min. The next step is to anneal the gold coating at 375 °C for 15 min. This temperature was selected to reduce the time to produce nanoislands. Lower temperatures require longer annealing time but can be used as well.

3. Results and discussion

In the prior vapor deposition investigation, the gold nanolayers where reproducible, but the thermal curing to produce gold nanoislands did not produce consistent nanoisland surfaces. By using sputtering technology it was possible to reproducibly make the desired gold nanoislands. To prove that gold nanoislands were produced by the sputtering technique, the surfaces were subjected to AFM and SEM imaging. It should be noted that in most vapor deposition techniques for gold, a thin chromium layer is first placed upon the substrate surface to enhance the mechanical stability of the gold layer. For sputtering, the initial chromium layer was not needed. Fig. 1 shows a typical SEM image of sputtered gold nanoislands on a polished aluminum substrate. Unlike the vapor deposition work, the sputtered nanoislands are evenly distributed across the surface. Fig. 2 shows the AFM image of 25 nm (a) and 14 nm (b) gold nanoislands on quartz substrate.

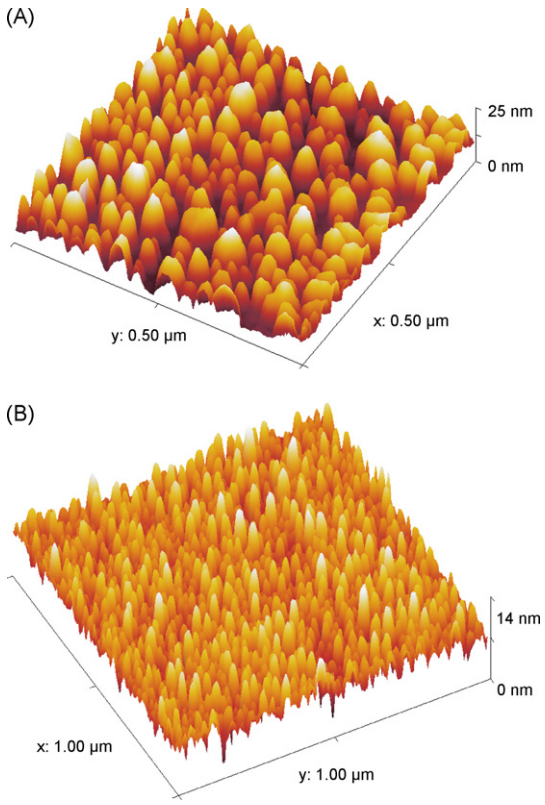


Fig. 2. AFM images of 25 nm (a) and 14 nm (b) gold nanoislands on quartz substrate.

For comparison purposes Fig. 3 shows the spectra for a gold thin film (top line) that produces a broad absorbance after 600 nm and exhibits no surface plasmon resonance, sputtered gold nanoislands exhibiting surface plasmon resonance, and sputtered nanoislands exhibiting a red-shift in surface plasmon resonance from 520 to 540 nm in response to gaseous ozone. The presence and concentration of ozone was monitored by measuring the ozone absorbance peak at 254 nm. Upon ozone depletion, the surface plasmon resonance peak for the gold nanoislands completely return to the

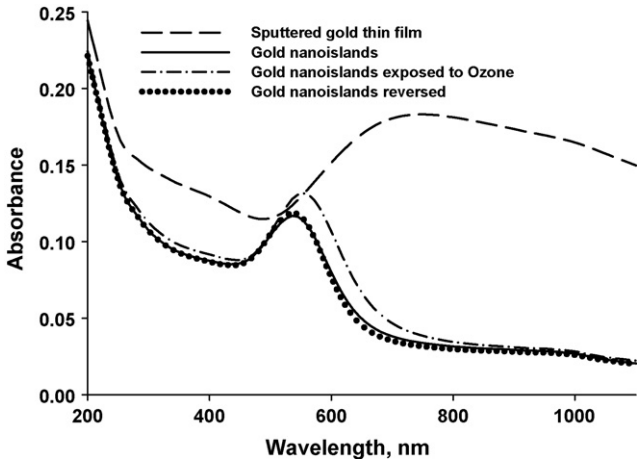


Fig. 3. Overlaid UV–Vis spectra of: dashed line, gold thin film on quartz; solid line, gold nanoislands; dot-dashed line, gold nanoislands exposed to ozone gas; dotted line, gold nanoislands reversed by heating at 375 °C for 15 min.

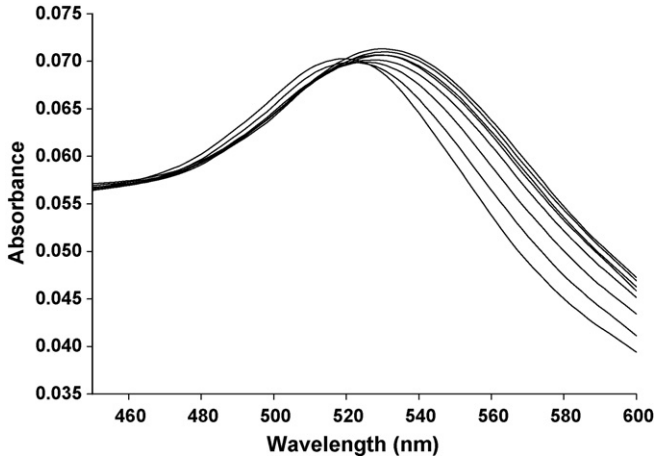


Fig. 4. Overlaid UV–Vis spectra of 25 nm gold nanoislands with surface plasmon absorbance max at 520 nm exposed to concentrations of ozone, increased in increments form 20.9 μg/L to 166.1 μg/L. Ozone causes a red-shift in the surface plasmon absorbance max.

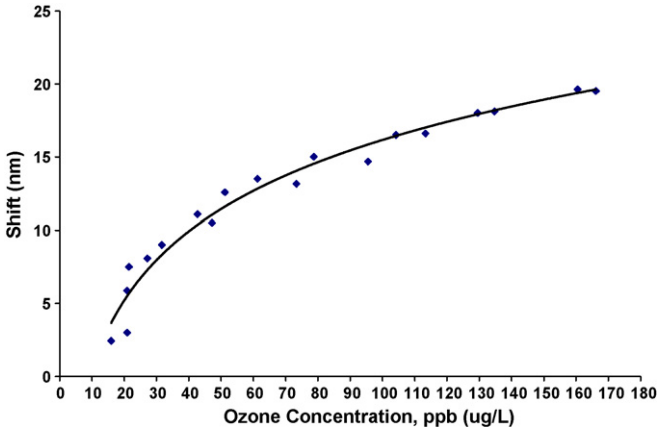


Fig. 5. Shift of the 25 nm gold nanoislands surface plasmon max (520 nm) as a function of ozone concentration.

original position and intensity at 520 nm. For comparison purposes aqueous colloidal suspension of gold nanoparticles produced a surface plasmon shift from 519 to 540 nm, for vapor deposited chromium/gold the shift was from 549 to 565 nm, and for ITO with gold vapor deposited the shift was from 558 to 583 nm upon exposure to gaseous ozone. Comparison among the various gold nanodomain systems show that the nanoislands reported in this work produced about 50% more sensitivity toward gaseous ozone.

Based on the spectral evidence it appears that the mechanism suggested for a thin gold film of ozone to oxygen decomposition that is adhered to the metal surface is not the same for nanoislands. For nanoislands as long as the ozone 254 nm peak persists, the surface plasmon shift is observed. Once the ozone peak disappears, the surface plasmon shift reverses. In addition unlike gold thin films, high temperatures are not needed to promote the surface plasmon reversal. Clearly, the ozone is directly influencing the surface plasmon resonance and when it decomposes, the oxygen that is produced does not interact with the gold nanoislands. This was further verified by testing pure oxygen's interaction with the gold nanoisland. No surface plasmon shifts were observed and after oxygen treatment the nanoislands still produced a surface plasmon shift when ozone was introduced.

The desirable performance characteristic(s) of an ozone sensor are described in the "Disinfectant Residual Measurement Methods" reference [9]. The ideal method/technique would be specific for only ozone itself and not respond to its decomposition products. It needs to be selective over possible interferences by at least 500. A detection limit of 0.01 mg/L for ozone with a precision of at least 0.1% and an accuracy of at least 0.5% is needed. The system must be easily, absolutely calibrated. A working linear range of five orders of magnitude is desirable but not mandatory for all situations. The system cannot require dilution of the water or gas sample to mask or minimize potential interferences. The system must work equally well (and satisfy the above requirements) in batch and automated modes of operation. The system must be operable by a technician and not require specialized skills or unusual or ultra-complex instruments. The measurement should be made in less than 1 min. The whole process must be relatively cost-effective.

The response of the gold nanoislands sensor to gaseous ozone was investigated by exposing it to different ozone concentrations. Fig. 4 shows the spectra exhibiting the amount of red-shift, in nm, with increasing ozone concentration. Fig. 5 is a calibration plot of spectral shift (nm) of the gold nanoislands surface plasmon resonance peak versus ozone concentration. The calibration plot shows that with the current design, the detection of gaseous ozone at concentration of less than 20 ppb (μg/L) is possible. Starting with the 20 ppb data point, a curve with an equation of $y = 6.8\ln(x) - 15.19$ produced a correlation coefficient of 0.9659. Comparison between the vapor deposition nanoislands and the sputtered nanoislands show that the sputtered nanoislands are about two orders of magnitude more sensitive to ozone.

Based on this group's aqueous gold nanoparticle investigations, it is expected that the size and density of gold nanoislands affects the response performance of the sensor. The current work shows evidence that different size and density of gold nanoislands may in fact affect the observed wavelength for the sensor. Direct comparison of ~25 nm versus ~50 nm nanoislands showed that the larger nanoislands were less sensitive to ozone. The absorbance maximum of the surface plasmon shifts from 520 to 532 nm was identical. The smaller particles increase in sensitivity may be due to the fact that they are more densely packed and thus interparticle distance is smaller. The interparticle distance is known to affect the surface plasmon shift. This finding suggests that the useful range of the sensor can be controlled by nanoisland size. The majority of this work was performed with 20–30 nm gold nanoislands.

Potential interfering gases like oxygen and nitrogen did not produce a surface plasmon resonance shift. However, as was the case with solution nanoparticles, the nanoisland surface was destroyed by nitrous oxide. The presences of the non-interfering gases during the reversal of the gold nanoislands did not affect surface plasmon resonance reversibility.

Future sensor designs will place gold nanomaterials in a substrate material that is resistant to ozone, cost-effective, and interference-free to the detection scheme. The substrate does not need to be transparent in the UV–Vis region of electromagnetic spectrum, since a reflective mode can be used to collect absorbance spectra of the gold nanoislands. The substrate should also provide open access to the surface of gold nanoislands.

4. Conclusions

It has been demonstrated that fabrication of a fast and cheap sensor material that can be used for detection of ozone is possible. The observed ozone-induced surface plasmon resonance shift of gold nanoislands is reversible. The surprising aspect of this material is it stability to ozone. The observed ozone response and reversibility is very reproducible an ozone detection limit of 20 μg/L was achieved.

References

[1] H. Tomiyasu, H. Fukutomi, G. Gordon, Inorg. Chem. 24 (19) (1985) 2962.
[2] G. Gordon, W. Cooper, R. Rice, G. Pacey, Disinfectant Residual Measurement Methods, AWWARF, Denver, CO, 1987, p. 815.
[3] S.D. Puckett, J.A. Heuser, J.D. Keith, W.U. Spendel, G.E. Pacey, Talanta 66 (2005) 1242–1246.
[4] N. Saliba, D. Parker, B. Koela, Surf. Sci. 8 (1998) 270.
[5] A. Krozer, M. Rodahl, Vac. Sci. Technol. 15 (3) (1997) 1704.
[6] G. Poirier, T. Herne, C. Miller, M. Tarlov, J. Am. Chem. Soc. 121 (1999) 9703.
[7] D. King, Vac. Sci. Technol. 13 (3) (1995) 1247.
[8] P. Lee, D. Meisel, Phys. Chem. 86 (1982) 3391.
[9] G. Gordon, W. Cooper, R. Rice, G. Pacey, Disinfectant Residual Measurement Methods, AWWARF, Denver, CO, 1987, pp. 267–268.

Talanta 80 (2009) 781–788

Contents lists available at ScienceDirect

Talanta

journal homepage: www.elsevier.com/locate/talanta

Cyclodextrin-MEEKC for the analysis of oxybutynin and its impurities

Iacopo Giannini[a], Serena Orlandini[a], Roberto Gotti[b], Sergio Pinzauti[a], Sandra Furlanetto[a,*]

[a] Department of Pharmaceutical Sciences, University of Florence, Via U. Schiff 6, 50019 Sesto Fiorentino, Florence, Italy
[b] Department of Pharmaceutical Sciences, University of Bologna, Via Belmeloro 6, 40126 Bologna, Italy

ARTICLE INFO

Article history:
Received 16 April 2009
Received in revised form 28 July 2009
Accepted 30 July 2009
Available online 8 August 2009

Keywords:
Cyclodextrin
Doehlert design
Impurities
MEEKC
Mixture design
Oxybutynin

ABSTRACT

The development of a cyclodextrin-MEEKC method for the analysis of oxybutynin and five related impurities is described. Experimental design strategies were applied in order to reach baseline separation of the compounds in a short analysis time. Mixture design made it possible to find the best composition for the microemulsion acting as pseudostationary phase, which was constituted by 89.1% 10 mM borate buffer pH 9.2, 1.7% *n*-heptane, 9.2% SDS/*n*-butanol in 1:2 ratio. The addition of (2-hydroxypropyl)-β-cyclodextrin to the background electrolyte was found to improve analysis performance. A Doehlert design, for the factors cyclodextrin concentration and voltage, was carried out and Derringer desirability function led to the identification of 18 mM and 29 kV as the optimal values. Applying the optimum conditions, separation of all the compounds, including the enantiomers of impurity 1, was obtained in less than 12 min. The method was validated according to ICH guidelines for drug assay and determination of impurities and was applied to oxybutynin tablet analysis.

© 2009 Elsevier B.V. All rights reserved.

1. Introduction

Capillary electrophoresis is today a well established technique applied in pharmaceutical quality control [1] since it combines high resolution power, high speed and reduced cost of analysis [2–4]. The plain environment used in capillary zone electrophoresis and the continuous improvement of instrumentation make it possible to obtain good repeatability and reliability of analysis. Nevertheless, when pseudostationary phases are used, the complexity of the environment can give repeatability problems which can in turn lead to a lack of confidence during method application. This is probably the main reason why up to now only a few papers have appeared concerning the use of microemulsion electrokinetic capillary chromatography (MEEKC) in pharmaceutical quality control [5–11]. Nevertheless, the methods that have been proposed have been validated showing satisfactory performances and indicating MEEKC as a powerful tool for drug analysis.

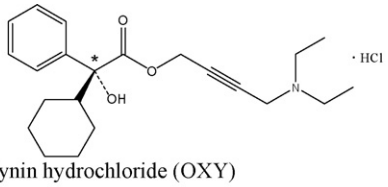
In the present paper a cyclodextrin-MEEKC method is reported which was developed for the determination of oxybutynin and five related impurities in drug substance and drug product. Oxybutynin hydrochloride (4-(diethylamino)but-2-ynyl(RS)-2-cyclohexyl-2-hydroxy-2-phenylacetate hydrochloride, OXY) is a tertiary amine antimuscarinic which is used for the management of urinary frequency, urgency, and incontinence in neurogenic bladder disorders and in idiopathic detrusor instability [12]. According to the information provided by the producer (Sanofi-Aventis, Sisteron, France), OXY is administered as racemate and may present five principal impurities (reported in Fig. 1), with different acid–base properties.

Determination of OXY has been carried out in pharmaceuticals [13–16] and in biological samples [17–19], and OXY plasma protein binding was examined enantioselectively by high-performance frontal analysis [20]. Other methods were also developed for the separation of OXY enantiomers [21,22] and for the determination of OXY and its major metabolite desethyloxybutynin in biological samples [23–25].

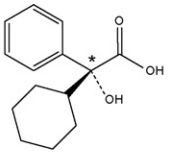
To the best of our knowledge, no method has been reported for the determination of oxybutynin and its impurities in drug substance and/or drug product, apart from the HPLC methods reported in the current Ph. Eur. [26] and USP [27]. Using capillary electrophoresis with MEEKC operative mode for this purpose is the analytical novelty described in this paper. Due to the different acid–base properties of the compounds, an electrokinetic capillary chromatographic method was considered suitable to approach the problem. In particular, the optimized method used a microemulsion system as background electrolyte to which (2-hydroxypropyl)-β-cyclodextrin was added to improve the separation. The presence of a complex system made the use of a multivariate strategy necessary for the optimization of the variables [28,29]. In a previous paper [9], the advantages of using mixture design [29] to optimize a MEEKC method were demonstrated for the first time. In the present work, mixture design

* Corresponding author. Tel.: +39 055 4573717; fax: +39 055 4573779.
E-mail address: sandra.furlanetto@unifi.it (S. Furlanetto).

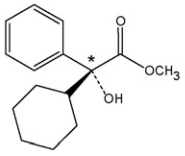
0039-9140/$ – see front matter © 2009 Elsevier B.V. All rights reserved.
doi:10.1016/j.talanta.2009.07.071



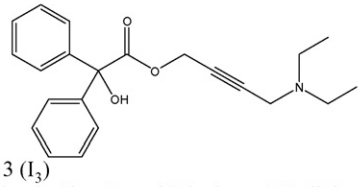
Oxybutynin hydrochloride (OXY)



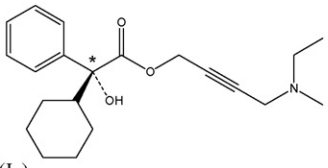
Impurity 1 (I_1)
(*RS*)-2-cyclohexyl-2-hydroxy-2-phenylacetic acid
(phenylcyclohexylglycolic acid)



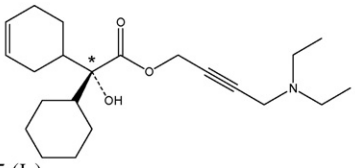
Impurity 2 (I_2)
(*RS*)-2-cyclohexyl-2-hydroxy-2-phenylacetic methyl ester



Impurity 3 (I_3)
4-(diethylamino)but-2-ynyl 2-hydroxy-2,2-diphenylacetate
(diphenyl analogue of oxybutynin)



Impurity 4 (I_4)
4-(ethylmethylamino)but-2-ynyl (*RS*)-2-cyclohexyl-2-hydroxy-2-phenylacetate (methylethyl analogue of oxybutynin)



Impurity 5 (I_5)
4-(diethylamino)but-2-ynyl (*RS*)-2-(cyclohex-3-enyl)-2-cyclohexyl-2-hydroxyacetate

Fig. 1. Molecular structures of oxybutynin and related impurities.

was again used to optimize the microemulsion composition and Doehlert design [29] was applied to optimize the process factors voltage and cyclodextrin concentration. Validation of the method was then carried out following ICH guidelines [30].

2. Experimental

2.1. Chemicals

All chemicals used in this study were of analytical-reagent grade with no further purification. Sodium tetraborate decahydrate was from BDH Laboratory Supplies (Poole, UK). *n*-heptane, *n*-butanol, sodium dodecyl sulphate (SDS), β-cyclodextrin, methyl-β-cyclodextrin, (2-hydroxypropyl)-β-cyclodextrin (HPβCD), (2-hydroxypropyl)-γ-cyclodextrin (HPγCD), heptakis(2,3,6-tri-O-methyl)-β-cyclodextrin were from Sigma–Aldrich (St. Louis, MO, USA). Methanol (HPLC grade) was obtained from Riedel-de Haën (Seelze, Germany), sodium hydroxide from Merck (Darmstadt, Germany).

Working standards of OXY and its impurities, Ditropan® tablets (labelled to contain 5 mg OXY) and excipients (lactose anhydrous, microcrystalline cellulose, calcium stearate) were kindly donated by Sanofi-Aventis (Sisteron, France). Flufenamic acid (FLU), employed as internal standard, was obtained from Sigma–Aldrich (St. Louis, MO, USA).

A Simplicity 185 system (Millipore, Billerica, MA, USA) was employed to purify water previously treated by electrode ionisation using an Elix system (Millipore) and ultrapure water was used throughout this study.

2.2. Solutions, microemulsions and sample preparation

Standard stock solutions of OXY (40 mg/mL), FLU (internal standard, 10 mg/mL) and OXY impurities (1 mg/mL each) were prepared in methanol. All these solutions were stored at 4 °C and used within one week. Working standard solutions were prepared daily by diluting the appropriate volume of each of the stock solutions with 10 mM sodium borate pH 9.2 directly in a vial to 500 μL.

The aqueous phase of the microemulsion system was constituted by 10 mM sodium borate pH 9.2 and was prepared adding an accurately weighed amount of sodium borate to a volumetric flask. Microemulsions were prepared by mixing in a beaker the aqueous phase with a proper amount of cosurfactant (*n*-butanol), then adding an accurately weighed amount of surfactant (SDS) and finally an appropriate amount of oil (*n*-heptane). The addition of each component was made only after reaching a complete dissolution of the previously mixed compounds and all mixtures were continuously stirred to obtain optically transparent microemulsion systems. All microemulsions were prepared on a w/w basis.

The considered percentage of the microemulsion components was 88.0–93.9% for the aqueous phase, 0.1–2.0% for the oil phase and 6.0–10.0% for the mixture surfactant/cosurfactant in 1:2 ratio. The optimized microemulsion consisted of 89.1% 10 mM borate buffer, 1.7% *n*-heptane, 9.2% SDS/*n*-butanol in 1:2 ratio. The optimum BGE was obtained by adding to this microemulsion an appropriate weighed amount of HPβCD in order to reach a concentration value of 18 mM.

The optical transparency of the microemulsions was verified in a previous paper [9] by measuring their transmittance at 550 nm [31]. All microemulsions were filtered before use through 0.45 μm cellulose acetate syringe filters and further stirred for at least 5 min.

The solution for tablet assay was prepared as follows: 20 tablets were weighed and finely powdered. An accurately weighed portion of the powder, corresponding to about 80 mg of OXY, was transferred into a 25 mL beaker. The contents were diluted adding by a manual pipette 10.000 mL of methanol solution containing 0.5 mg/mL internal standard, then sonicated for 10 min and shaken again. An aliquot of 1 mL of the mixture was then centrifuged and 500 μL of the supernatant were introduced into a vial for analysis. The final test concentration of OXY was about 8 mg/mL.

2.3. Equipment and capillary electrophoretic conditions

A 300 Ultrasonik ultrasonic bath (Ney Company, Bloomfield, USA) was used to sonicate solutions and a Metrohm 691 pH Meter (Metrohm, Herisau, Switzerland) was employed to measure pH. Microemulsions were stirred with a multiple magnetic stirrer Multipoint HP15 (Variomag, Daytona Beach, FL, USA).

CE analyses were performed by an Agilent Technologies ^{3D}CE system (Agilent Technologies, Waldbronn, Germany), driven by ^{3D}CE ChemStation software (Rev. A.09.01, Agilent Technologies) and equipped with an on-column UV–visible diode-array detector and an air thermostating system. The vial carousel was at room temperature.

The separations were carried out in an uncoated fused-silica capillary (50 μm inner diameter, 375 μm outer diameter) which was 48.5 cm long (40.0 cm to the detector), purchased from Composite Metal Services (Ilkley, UK). The detection wavelength was 195 nm.

The separation run was carried out in positive polarity mode. Sample introduction was performed hydrodynamically from the inlet side and the injection time of both the sample and the subsequent buffer plug was 5 s at 50 mbar.

Prior to the first use, the capillary was conditioned by flushing, sequentially, 1 M NaOH and water for 5 min each. At the beginning of each day, the capillary was rinsed with 0.1 M NaOH for 2 min and then with water for 2 min. Between the runs, the capillary was flushed as follows: 1 min with methanol, 1 min with 1 M NaOH, 1 min with 0.1 M NaOH, 2 min with water and finally 4 min with run buffer. Due to the particular complexity of the background electrolyte, in order to maintain good system performance, particular care had to be taken in instrument maintenance and cleaning, with special regard to capillary, electrodes and prepunchers.

2.4. Calibration curves

The corrected peak area ratios (analyte to internal standard) were plotted against the corresponding concentration of analyte in order to obtain the calibration graphs. For the calibration curve of impurity 1, which corresponded to two enantioseparated peaks in the electropherogram, the sum of I_1 enantiomers corrected areas/internal standard corrected area ratio was plotted versus I_1 concentration.

Five different concentrations of each analyte were prepared and the solutions were analysed twice. FLU concentration was kept constant at 0.5 mg/mL throughout all the experiments. The regression curve for OXY ranged from 3.2 to 9.6 mg/mL (40–120% of the test concentration) and the considered ranges for the impurities were from the respective LOQ to 0.08 mg/mL (1% of the test concentration).

2.5. Calculations and software

Resolution value R_5 (I_3/I_4) was calculated according to the formula

$$R = 2(t_{RB} - t_{RA}/w_B + w_A)$$

where t_{RA} and t_{RB} are the migration times and w_A and w_B are the corresponding widths at the bases of adjacent peak pairs, respectively [32].

Due to the different characteristics of the last migrating peaks, for which different concentration values of the analytes were involved (OXY, 8 mg/mL; I_4 and I_5, 0.08 mg/mL), resolution values R_6 (I_4/OXY) and R_7 (OXY/I_5) were calculated using the statistical method [33,34]:

$$R = \frac{M1_b - M1_a}{w_{Sb} + w_{Sa}}$$

where $M1_a$ and $M1_b$ are the mean migration times for adjacent peak pairs (first statistical moment), w_{Sa} and w_{Sb} are the widths derived from statistical moments $= \sqrt{(M2)}$, where $M2$, the second statistical moment, is the peak variance which is a measure of lateral spreading. The detailed information for this calculation method is summarised in the software manual [33].

Experimental design was generated and statistical analysis of experimental data was performed using NEMROD-W software package [35]. During optimization, the electrophoretic experiments were run in a randomized order using a test solution containing 8 mg/mL OXY, 0.08 mg/mL OXY impurities and 0.5 mg/mL FLU (internal standard).

3. Results and discussion

Experimental design [28,29] is the methodology of planning and carrying out experiments in order to extract the maximum amount of information from the data in the lowest number of runs. In general, when applying this technique to the optimization of analytical methods, some preliminary experiments have to be carried out depending on the investigated analytes to obtain information on the behaviour of the system under study and, thus, to efficiently plan the experiments to be run.

In the present work, the analytes were three basic (OXY, I_4, I_5), one acid (I_1) and one neutral (I_2) chiral substances, and one achiral basic substance (I_3). Due to the presence of analytes with different acid–base properties, the possibility of using a pseudostationary phase was taken into account. In a first step, MEKC using different surfactants was tested but failed to obtain good separations. Therefore, it was decided to test a microemulsion system optimized in a previous paper by the authors for the determination of ketorolac and its related substances [9]. Microemulsions are thermodynamically stable, transparent, isotropic dispersions composed of oil (O) and water (W) stabilized by an interfacial film of surfactant (S) molecules, suitably combined with a cosurfactant (CoS) [36]. In this case the microemulsion was made up of 90.0% 10 mM borate buffer pH 9.2, 2.0% *n*-heptane, and 8.0% SDS/*n*-butanol in 1:2 ratio. Using this system as pseudostationary phase, and performing a CE run on a mixture of the analytes kept at low concentrations (0.04 mg/mL), promising results were obtained as a good separation was achieved for all the peak pairs in about 11 min. However, the obtained resolution was not high enough to be maintained performing the analysis on the test sample, where the concentration of OXY (8 mg/mL) was 100 times the concentration of OXY impurities (0.08 mg/mL).

Therefore, needing to improve the separation, the use of a suitable neutral cyclodextrin was taken into consideration as an additional component of the BGE, due to the ability of cyclodextrins (CDs) in inclusion complexation of a number of drugs. Neutral CDs, having no charge and presenting a hydrophilic external surface, are not expected to interact with the anionic oil droplets [2]. The CDs could be though completely distributed into the aqueous phase of the bulk solution to give a second pseudostationary phase which acts in competition with the anionic oil droplet of the microemulsion [37]. This phase migrates with an identical velocity with the bulk solution and is capable of solubilizing selectively certain types of solutes depending on their size, shape and hydrophobicity [2].

Different CDs, reported in Section 2, were tested and HPβCD and HPγCD were found the most suitable on the basis of selectivity. However, the use of different concentration levels of HPγCD resulted in an inversion of the migration order of the analytes.

This behaviour could lead to problems when applying experimental design since resolution cannot be univocally measured. For this reason, HPγCD was discarded and HPβCD was preferred as this problem was not evidenced with the latter.

Adding 15 mM HPβCD to the microemulsion system, the resulting migration order was: I_{1A}, I_{1B}, FLU, I_2, I_3, I_4, OXY, I_5. The first two peaks, I_{1A} and I_{1B}, corresponded to the enantioseparation of I_1. This separation was presumably due to the fact that this acidic compound, negatively charged, has a low affinity for the negatively charged oil droplets, and conversely presents a significant interaction with the chiral cyclodextrin. It is worthwhile noting that for the aims of this work the chiral separation of OXY impurities was not required and it could even constitute a drawback. In fact, by splitting the peak in two the related heights become lower and this worsens the LOD and LOQ concentration values.

The following step of the work concerned the multivariate optimization of the microemulsion system by mixture design and the optimization of the process factors concentration of cyclodextrin and voltage. The experiments were performed using a test sample made up of 8 mg/mL OXY, 0.08 mg/mL OXY impurities and 0.5 mg/mL FLU.

3.1. Optimization of microemulsion composition by mixture design

The microemulsion system, from a statistical point of view, is a mixture and its study involves mixture design, *i.e.* a special response surface study where the response is a function of the different proportions of the components [29,38,39]. In this design each component can range between 0 and 1 according to the values assumed by the other components and the investigated experimental domain has a triangle shape. When upper and lower boundaries are present, the size of the experimental region is restricted. In the present study the component constraints were selected according to the literature [40,41] and corresponded to the values considered in a previous work by the authors for the analysis of ketorolac and its impurities [9]. The investigated experimental domain was inside the existence field of the microemulsion and no phase-diagram was used.

The ranges for the mixture variables were: x_1, 10 mM sodium borate (aqueous phase, W), 88.0–93.9%; x_2, *n*-heptane (oil phase, O), 0.1–2.0%; x_3, SDS/*n*-butanol in 1:2 ratio (surfactant, S/cosurfactant, CoS) 6.0–10.0%. For the presence of constraints, the size of the experimental region was restricted and a transformation of components (x_i) into new variables, called pseudocomponents (z_i), was necessary [29,38]. The pseudocomponents are combinations of the original components that rescale the constrained data area so that the minimum allowable amount of each component is zero. This transformation allows a more accurate estimation of model coefficients to be obtained with respect to that obtainable using the original component system [29,38].

The optimization of the system involved the critical resolution values among the analytes and analysis time (t), measured as migration time of the last peak (I_5).

In order to optimize the microemulsion system, a Scheffé special cubic regression model [29,38] was hypothesised among the response and the pseudocomponents:

$$y = \beta_1 z_1 + \beta_2 z_2 + \beta_3 z_3 + \beta_{12} z_1 z_2 + \beta_{13} z_1 z_3 + \beta_{23} z_2 z_3 + \beta_{123} z_1 z_2 z_3$$

where β_i terms are called the linear blending terms and correspond to the responses at the vertices, *i.e.* represent the expected response from a pure mixture of x_i and all other components set at zero. The quadratic terms β_{ij} are called nonlinear blending terms and are estimated at experimental points representing a 50:50 mixture of two components [39]. The cubic term β_{ijz} is estimated from a mixture of the three components and represents the interaction among them [39].

Table 1
Mixture design experimental plan and responses.

Exp. no.	W (% w/w)	O (% w/w)	S/CoS (% w/w)	R_5	R_6	R_7	t (min)
1	93.90	0.10	6.00	0.01	0.25	0.01	8.37
2	92.00	2.00	6.00	0.01	0.13	0.01	8.80
3	89.90	0.10	10.00	1.57	1.45	1.58	17.13
4	88.00	2.00	10.00	1.31	1.52	2.12	16.03
5	92.95	1.05	6.00	0.01	0.01	0.01	9.07
6	91.90	0.10	8.00	0.01	0.01	0.01	11.45
7	90.00	2.00	8.00	0.70	1.10	1.92	12.08
8	88.95	1.05	10.00	2.53	1.95	2.75	15.79
9	90.95	1.05	8.00	1.60	1.56	2.48	12.75
10	92.43	0.58	7.00	0.94	0.98	2.08	11.38
11	91.47	1.53	7.00	0.76	0.89	1.96	11.39
12	90.43	0.58	9.00	2.01	1.71	2.65	13.64
13	89.48	1.53	9.00	1.90	1.67	2.59	13.74
14	90.95	1.05	8.00	1.04	1.33	2.04	12.69
15	90.95	1.05	8.00	0.588	0.90	1.87	12.05
16	90.95	1.05	8.00	1.30	1.22	2.15	12.78

The model coefficients were calculated by a 13-run mixture design with three replicate experiments at the centre for estimating the experimental variance. The experimental plan that defined the percentage of the components to be used to prepare the different microemulsions is reported in Table 1 with the measured responses. The experiments were run keeping HPβCD concentration at 15 mM and voltage at 27 kV. No problems were observed for the resolutions between I_1 and FLU, FLU and I_2, I_2 and I_3. For these responses a resolution value above 3 was observed in all electropherograms, thus it was decided to discard them for the statistical treatment. Critical resolution values were observed for the last migrating peaks, thus the responses R_5 (I_3/I_4), R_6 (I_4/OXY) and R_7 (OXY/I_5) were maintained for the statistical treatment. For these responses the coefficients of the postulated model were calculated and the analysis of variance (ANOVA) [29,42] showed that for all the considered responses the regression model was significant and valid.

It was then possible to draw the contour plots in order to study the relationship between the response and the component proportions (Fig. 2). In these plots the response is projected onto a plane of the factors by means of isoresponse curves, where the isoresponse lines correspond to the same predicted values of the considered response. By examining the contour plots it is possible to find the proportions among the components in order to optimize the response, considering that moving towards one vertex the percentage of the relative component increases until the maximum permitted with the consequent reduction of the other components.

As regards response R_5, the obtained isoresponse lines are reported in Fig. 2a. In this case a maximization of the response is obtained by moving towards high levels of S/CoS and low levels of borate buffer. As for the oil phase, using high percentages of S/CoS, resolutions higher than 1.5 can be obtained in the whole investigated domain. The same trend can be observed for the other two resolutions R_6 (Fig. 2b) and R_7 (Fig. 2c): high values of S/CoS and low values of aqueous phase are necessary to obtain a baseline separation. As for analysis time, for which the contour plot is represented in Fig. 2d, this response is speeded up by using high percentages of water and low percentages of S/CoS, while the oil effect is not important in the investigated experimental domain.

Thus, there was a clear conflict between the conditions required to maximize the responses related to resolution and those required to minimize analysis time. In order to overcome this conflict and to find a good compromise among the responses, Derringer's desirability function (D) was used [29]. To apply this tool, each response has to be transformed into a partial desirability function d_i cor-

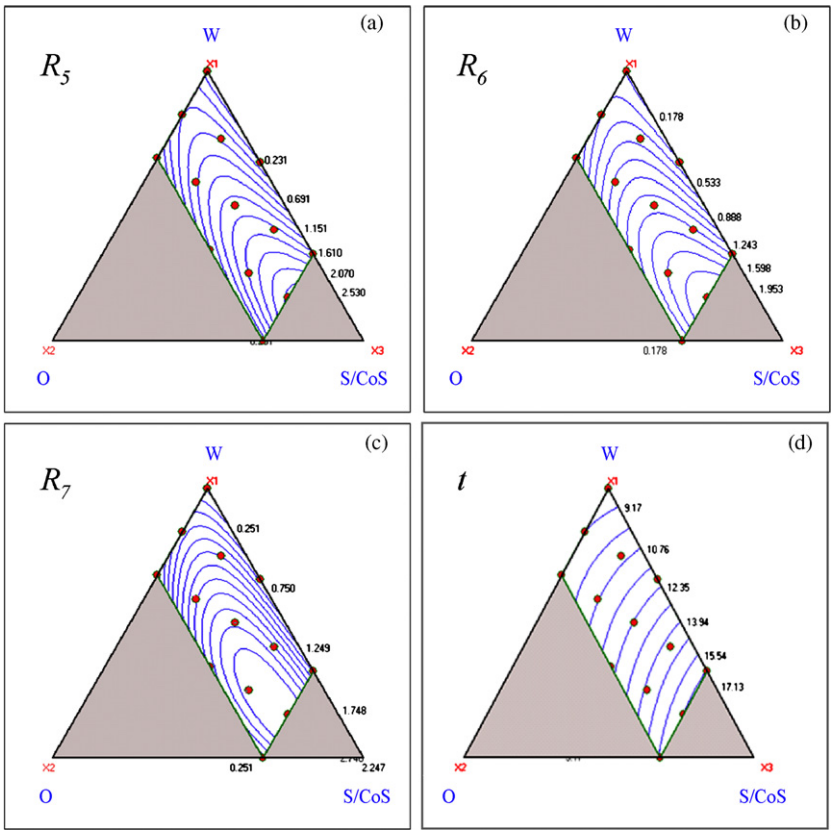


Fig. 2. Contour plots: (a) response I_3/I_4 resolution (R_5); (b) response I_4/OXY resolution (R_6); (c) response OXY/I_5 resolution (R_7); (d) response analysis time (t).

responding to defined optimization criteria and then an overall desirability function D is calculated by way of the geometric mean. For the resolution responses R_5, R_6 and R_7 a minimum and desired value of 1.5 was set, while for the response analysis time only values below 14 min were accepted. From the total desirability function, calculated as $D = \sqrt[4]{d_1 d_2 d_3 d_4}$, the most effective formulation in terms of both selectivity and analysis time was found to consist in 89.1% aqueous phase, 1.7% oil phase and 9.2% S/CoS. The selected microemulsion showed good technological properties with regard to stability and gave a good separation of the analytes, as shown in Fig. 3.

3.2. Optimization of voltage and CD concentration by Doehlert design

After finding the optimal microemulsion composition, with the aim of speeding up the analysis while maintaining a good separation among the compounds, experimental design was applied to optimize the values of the process factors voltage (V) and concentration of cyclodextrin (CD conc.). Having to deal with only two variables, a response surface study [29] was deemed suitable. Applying this approach, a map of the experimental domain span by the selected ranges of considered factors is determined by means of a quadratic polynomial model.

In this study the following quadratic model was assumed:

$$y = \beta_0 + \beta_1 x_1 + \beta_2 x_2 + \beta_{11} x_1^2 + \beta_{22} x_2^2 + \beta_1 x_1 x_2 + \varepsilon$$

where y represents the experimental response, x_i the independent evaluated factors, β_0 the intercept, β_i the model coefficients obtainable by multiple regression and ε the experimental error.

Estimation of the coefficients of this model can be carried out using different designs such as central composite design, Box-Behnken design, and Doehlert design [29]. In general, a good optimization strategy produces a set of experimental conditions that provide the optimum response with the smallest possible number of trials. From this point of view, Doehlert design is an efficient design and it was selected for this study. In fact, this kind of matrix makes it possible to study the problem in-depth and to

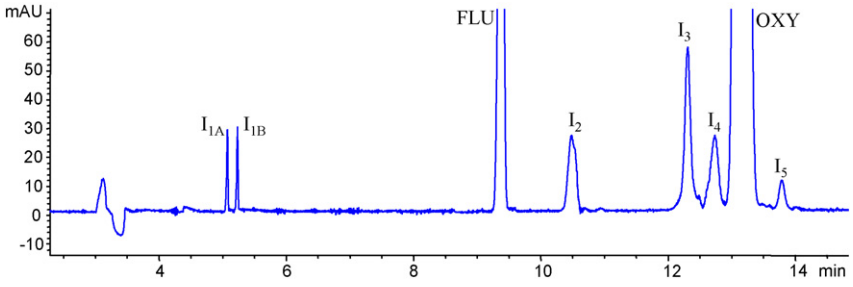


Fig. 3. Electropherogram of OXY and its impurities referring to the optimal microemulsion composition: voltage, 27 kV; temperature, 20 °C. BGE: microemulsion constituted by 89.1% 10 mM borate, 1.7% *n*-heptane, 9.2% SDS/*n*-butanol in a ratio of 1:2; 15 mM HPβCD. Hydrodynamic injection: 50 mbar, 5 s. Detection wavelength: 195 nm.

Table 2
Doehlert design experimental plan and responses.

Exp. No.	CD conc. (mM)	V (kV)	R_5	R_6	R_7	t (min)
1	20	27	1.17	1.80	2.68	12.60
2	12	27	2.83	1.47	2.00	13.74
3	18	30	2.24	1.75	1.66	10.11
4	14	24	2.66	1.87	2.71	17.45
5	18	24	1.68	2.27	3.58	16.86
6	14	30	2.86	1.62	1.89	10.36
7	16	27	2.02	1.62	2.17	12.47
8	16	27	1.61	2.24	2.55	13.13
9	16	27	2.19	1.92	2.78	12.98
10	16	27	2.04	1.81	2.68	13.26

draw the relative response surfaces, requiring a number of experiments equal to $k^2 + k + n$, where k is the number of factors and n is the number of replicates at the centre of experimental domain. It also offers the advantage of allowing the factors to be studied at a different number of levels, and permitting the study of some factors in a more in-depth way. In this study, the effect of cyclodextrin concentration on the responses was more deeply evaluated fractionating its range of variation, 12–20 mM, into five levels, while voltage, ranging from 24 to 30 kV, was studied at three levels.

The experimental plan, comprehensive of four replicates at the centre of the experimental domain, is reported in Table 2 together with the responses. In most of the 10 obtained electropherograms, good separations were achieved.

The response surfaces, as a function of concentration of HPβCD and voltage, are reported in Fig. 4. The best results for response R_5 were obtained by setting high voltages and low concentrations of CD (Fig. 4a). In any case, the most important effect was due to HPβCD concentration, which had to be set at low values in order to maximize the response. For the responses R_6 (Fig. 4b) and R_7 (Fig. 4c), low voltages and high concentrations of CD were necessary to obtain the maximization. For the response analysis time, represented in Fig. 4d, its minimization is obtained using high voltages and any concentration of CD.

Also in this case desirability function, as represented in Fig. 5, allowed the best conditions to be found. For the resolutions, a target value above 1.5 was again set as target; for analysis time, the desired response had to be 12 min or less. The plots showed that voltage was critical and high values were required. Fixing voltage at 29 kV, almost every concentration of cyclodextrin yielded good results. The selected optimal conditions were concentration of HPβCD 18 mM and voltage 29 kV.

Applying the optimized conditions, the analysis of OXY and the impurities was run in about 12 min, as shown in the related electropherogram (Fig. 6). Validation of calculated models was carried out by evaluating the agreement between the predicted value and the measured value for every response, thus confirming the predictive ability of the models.

3.3. Validation

Validation was carried out according to ICH guidelines [ICH]. The performance parameters selectivity, robustness, linearity, range, accuracy and precision were evaluated and, for the impurities, also limits of detection and quantitation were assessed. The test mixture for validation process consisted of 8 mg/mL OXY and 0.08 mg/mL for each of the related substances (corresponding to 1%, w/w with respect to the main component), unless otherwise described.

3.3.1. Selectivity

A baseline resolution of all the analytes was obtained, and the critical resolution values were calculated as the following ($n = 4$, $\alpha/2 = 0.025$): R_5, 2.22 ± 0.25; R_6, 1.66 ± 0.24; R_7, 1.73 ± 0.31. No

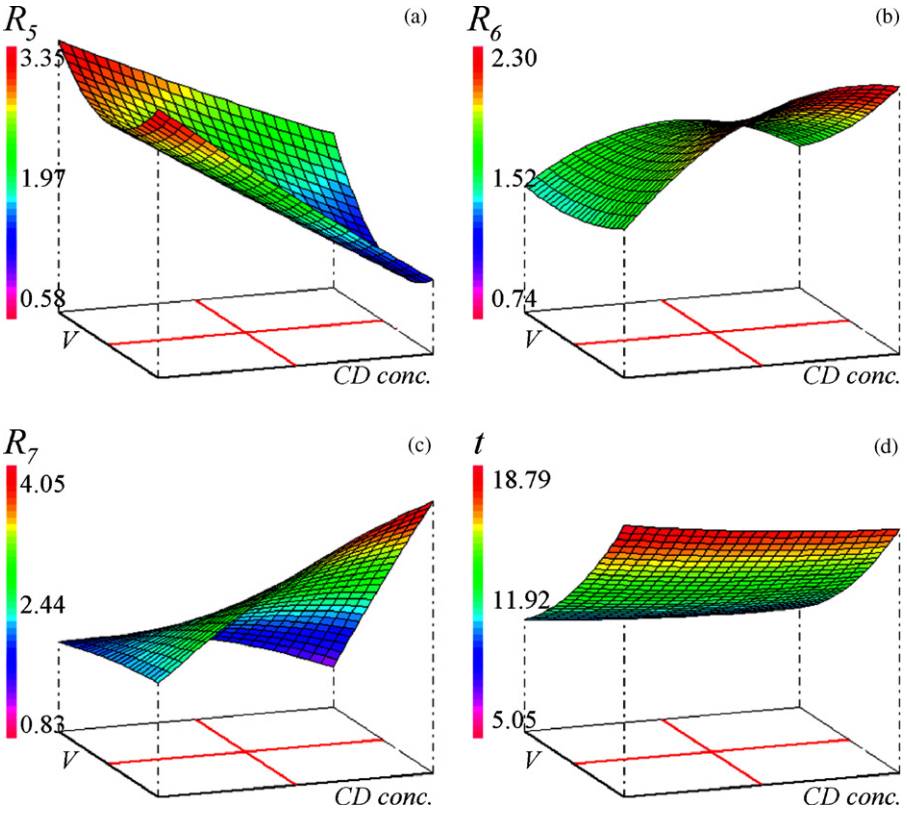


Fig. 4. Response surfaces obtained by plotting HPβCD concentration *vs.* voltage: (a) response I_3/I_4 resolution (R_5); (b) response I_4/OXY resolution (R_6); (c) response OXY/I_5 resolution (R_7); (d) response analysis time (t).

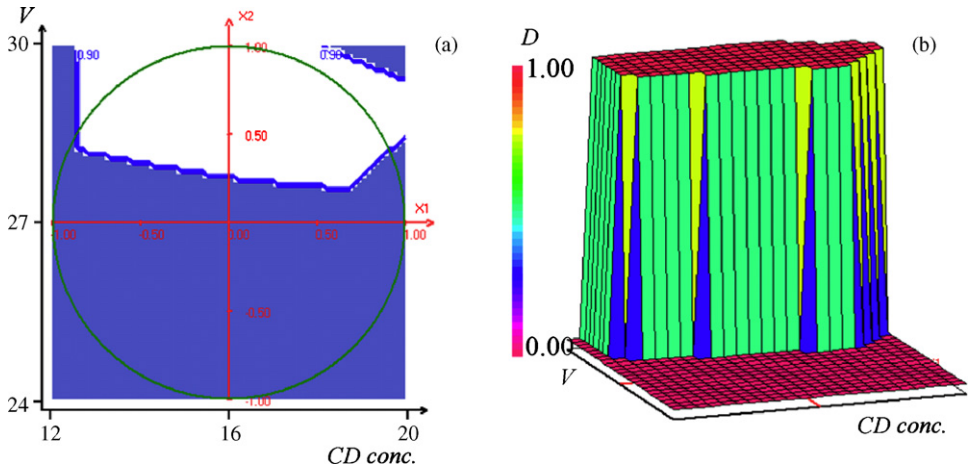


Fig. 5. Desirability function (a) 2D and (b) 3D graph obtained by plotting HPβCD concentration *vs.* voltage.

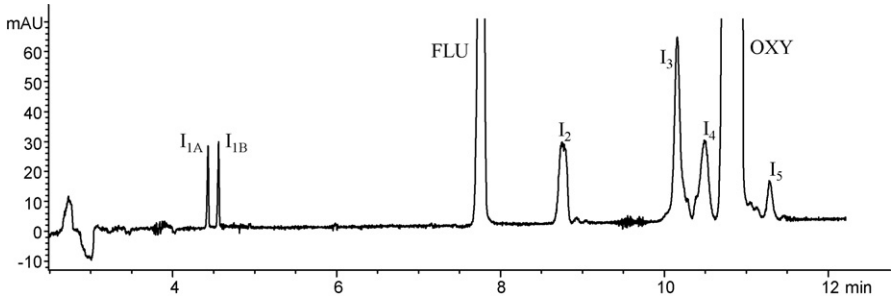


Fig. 6. Electropherogram of OXY and its impurities referring to optimal conditions: voltage, 29 kV; temperature, 20 °C. BGE: microemulsion constituted by 89.1% 10 mM borate, 1.7% *n*-heptane, 9.2% SDS/*n*-butanol in a ratio of 1:2; 18 mM HPβCD. Hydrodynamic injection: 50 mbar, 5 s. Detection wavelength: 195 nm.

interference in the electropherogram was observed due to the presence of the excipients of the dosage form.

3.3.2. Robustness

Robustness was tested by means of full factorial design, where the combinations of *k* factors are investigated at two levels consisting of 2^k experiments [29].

The selected responses were the same taken into consideration during the optimization phase, *i.e.* the critical resolutions R_5, R_6, R_7 and analysis time. As for the selected factors, mixture components were not considered as the optimal microemulsion composition was located in wide zones of the response surfaces where the responses were near constant. On the other hand, the effect of a small variation of the process factors voltage and HPβCD concentration, with the addition of temperature, was evaluated considering the following ranges, symmetric around the optimized values: X_1, CD conc., 17–19 mM; X_2, voltage (V), 28–30 kV, X_3, temperature (T), 19–21 °C. The experiments planned for the three factors describe the corners in a cube and are reported in Table 3 with the measured responses.

Table 3
Robustness testing full factorial design experimental plan and responses.

Exp. No.	CD conc. (mM)	V (kV)	T (°C)	R_5	R_6	R_7	t (min)
1	17	28	19	1.97	1.72	2.43	15.59
2	19	28	19	1.66	1.60	1.88	13.88
3	17	30	19	1.81	1.72	2.20	12.95
4	19	30	19	1.67	1.55	1.90	11.16
5	17	28	21	1.62	1.49	1.52	14.30
6	19	28	21	1.79	1.70	2.39	14.60
7	17	30	21	1.94	1.83	1.42	10.80
8	19	30	21	1.81	1.63	1.78	11.62

Graphic interpretation of effects [43] is reported in Fig. 7, where each bar is related to an effect. The length of the bar is proportional to the absolute value of the effect and the critical factors can be identified as those exceeding the reference lines. In this case only voltage exerted a negative effect on response analysis time.

3.3.3. Migration time and peak area precision

System repeatability was evaluated performing six replicate injections in three consecutive days for a total of $n = 18$ runs. Within-day RSD ranges were 0.6–0.8% for OXY and 1.5–3.8% for

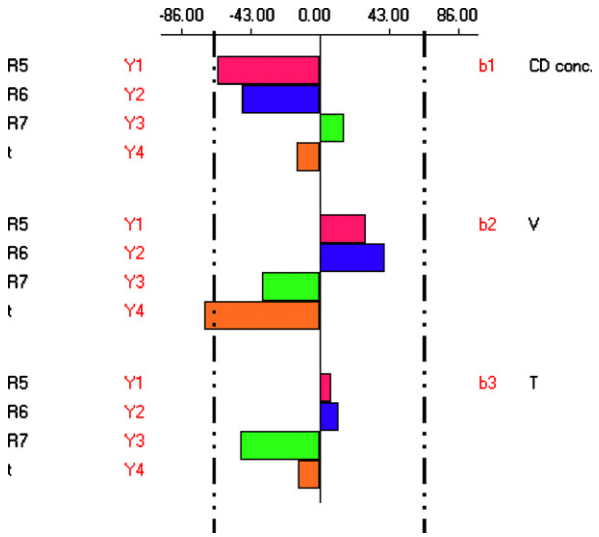


Fig. 7. Robustness testing graphic analysis of effects.

OXY-related substances. Between-day RSD were 1.5% for OXY and 11.4% for OXY-related substances. As concerns analysis time, the calculated within-day RSD values were included in the range 1.8–5.6% and between-day RSD was 8.4%.

3.3.4. LODs and LOQs

The LOD and LOQ of the impurities were calculated from S/N of approximately 3:1 and 10:1, respectively. The obtained values for LOD were: I_1, 12 μg/mL; I_2, 3 μg/mL; I_3, 4 μg/mL; I_4, 5 μg/mL, I_5, 4 μg/mL. As concerns LOQ, the following values were found: I_1, 20 μg/mL (0.250%, w/w); I_2, 5 μg/mL (0.0625%, w/w); I_3, 8 μg/mL (0.100%, w/w); I_4, 7 μg/mL (0.0875%, w/w); I_5, 8 μg/mL (0.100%, w/w). Values of LOQ were validated measuring the RSD corrected area of eight replicate injections keeping each impurity at LOQ concentration, and values in the range 2.9–5.6% were obtained.

3.3.5. Linearity

The linearity range for OXY was 3.2–9.6 mg/mL (40–120% of the test concentration) and the corresponding equation was $y = 1.5171x - 0.6319$ ($R_2 = 0.9989$). For OXY-related substances the linearity range was from the respective LOQ values to 0.08 mg/mL, corresponding to 1% (w/w) with respect to the main component. Values of correlation coefficients ranged from 0.9961 to 0.9973.

Accuracy and precision were evaluated by three replicate runs at three concentration values covering the linearity range, performing the assay of a known added amount of analyte in the sample. For OXY the obtained recoveries were from $99.0 \pm 1.5\%$ to $101.2 \pm 1.9\%$ and the maximum RSD was 0.7%. For OXY impurities, the recoveries were included in the interval ranging from $98.3 \pm 4.7\%$ to $101.5 \pm 2.9\%$, with a maximum observed RSD equal to 3.7%.

3.3.6. System suitability test

System suitability criteria were established choosing the critical resolution values as performance parameters and selecting as limits the lowest and the highest resolution values measured during system precision study [44,45], corresponding to: $2.10 < R_5 < 2.45$, $1.48 < R_6 < 1.72$, $1.54 < R_7 < 1.88$.

3.4. Application

The developed method was applied to a real sample of Ditropan® tablets, labelled to contain 5 mg OXY. The obtained results ($n = 4$, $\alpha/2 = 0.025$) were in agreement with the declared composition. Recovery was $97.4 \pm 1.5\%$ with RSD 1.2% and no OXY impurity was detected.

4. Conclusions

A cyclodextrin-MEEKC method was developed by means of a multivariate strategy involving, first, mixture design for optimizing microemulsion composition and, secondly, response surface study for selecting the optimal values for process factors. Baseline separation of the parent compound and its related substances was obtained in less than 12 min. The experimental plan used for optimizing the proportions of the microemulsion components can be proposed for a general use in MEEKC. Good results were obtained in terms of selectivity and analysis time, thus demonstrating the validity and versatility of the proposed approach. The analysis performances were then further improved by means of Doehlert design, which took into account voltage and cyclodextrin concentration and made it possible to find the optimum by applying desirability function.

Acknowledgements

The authors gratefully acknowledge Sanofi-Aventis (Sisteron, France) for the gift of oxybutynin and its related substances as reference samples.

References

[1] K. Altria, A. Marsh, C. Sanger-van de Griend, Electrophoresis 41 (2006) 2263.
[2] S.F.Y. Li, Capillary Electrophoresis, Elsevier, Amsterdam, 1992.
[3] B. Chankvetadze, Capillary Electrophoresis in Chiral Analysis, John Wiley & Sons Ltd., Chichester, 1997.
[4] C.F. Poole, The Essence of Chromatography, Elsevier, Amsterdam, 2003.
[5] K.D. Altria, J. Chromatogr. A 844 (1999) 371.
[6] M.S. Aurora-Prado, C.A. Silva, M.F.M. Tavares, K.D. Altria, J. Chromatogr. A 1051 (2004) 291.
[7] M. Broderick, S. Donegan, J. Power, K. Altria, J. Pharm. Biomed. Anal. 37 (2005) 877.
[8] S.H. Hansen, Z.A. Sheribah, J. Pharm. Biomed. Anal. 39 (2005) 322.
[9] S. Furlanetto, S. Orlandini, A.M. Marras, P. Mura, S. Pinzauti, Electrophoresis 27 (2006) 805.
[10] Y. Bitar, U. Holzgrabe, J. Pharm. Biomed. Anal. 44 (2007) 623.
[11] T. Wen, X. Zhao, G. Luo, J. Wang, Y. Wang, B. Yao, J. Zhao, J. Zhu, Z. Yu, Talanta 71 (2007) 854.
[12] S.C. Sweetman (Ed.), Martindale, The Complete Drug Reference, 35th edn., Pharmaceutical Press, London, 2007, pp. 1985–1986.
[13] J.A. De Schutter, P. De Moerloose, J. Chromatogr. 450 (1988) 337.
[14] M.V.S. Varma, A.M. Kaushal, S. Garg, J. Pharm. Biomed. Anal. 36 (2004) 669.
[15] R. Jain, K. Radhapyari, N. Jadon, J. Colloid Interface Sci. 314 (2007) 572.
[16] Y. Liu, H. Nguyen, S. Wang, J. Yeh, J. Pharm. Biomed. Anal. 43 (2007) 1654.
[17] B. Lindeke, H. Brotell, B. Karlen, G. Rietz, A. Vietorisz, Acta Pharm. Suec. 18 (1981) 25.
[18] K.S. Patrick, J.S. Markowitz, E.J. Jarvi, A.B. Straughn, M.C. Meyer, J. Chromatogr.: Biomed. Appl. 487 (1989) 91.
[19] R. Massoud, G. Federici, S. Cascinai, S.M. Di Stasi, G. Fucci, A. Giannantoni, C. Cortese, J. Chromatogr. B 734 (1999) 163.
[20] A. Shibukawa, N. Ishizawa, T. Kimura, Y. Sakamoto, K. Ogita, Y. Matsuo, Y. Kuroda, C. Matayatsuk, T. Nakagawa, I.W. Wainer, J. Chromatogr. B 768 (2002) 177.
[21] D. Bylund, A. Bergens, S.P. Jacobsson, Chromatographia 44 (1997) 74.
[22] T.A. Walker, J. Liq. Chromatogr. Relat. Technol. 23 (2000) 841.
[23] T. Alebic-Kolbah, A.P. Zavitsanos, J. Chromatogr. A 759 (1997) 65.
[24] H. Kim, S.B. Han, J. Pharm. Biomed. Anal. 31 (2003) 341.
[25] P. de Fonseca, L.A.P. de Freitas, L.F.R. Pinto, C.R. Pestana, P.S. Bonato, J. Chromatogr. B 875 (2008) 161.
[26] European Pharmacopoeia 6.0, vol. 2, Council of Europe, Strasbourg, 2008, pp. 2585–2587.
[27] The United States Pharmacopeia, 32nd Rev., vol. 3, The United States Pharmacopeial Convention, Rockville, MD, 2009, pp. 3161–3162.
[28] D.L. Massart, B.G.M. Vandeginste, L.M.C. Buydens, S. de Jong, P.J. Lewi, J. Smeyers-Verbeke, Handbook of Chemometrics and Qualimetrics: Part A, Elsevier, Amsterdam, 1997.
[29] G. Lewis, D. Mathieu, R. Phan-Tan-Luu, Pharmaceutical Experimental Design, Marcel Dekker, New York, 1999.
[30] ICH Harmonised Tripartite Guideline, Q2(R1); Validation of Analytical Procedures: Text and Methodology, 2005.
[31] H.J. Gi, S.-N. Chen, J.-S. Hwang, C. Tien, M.T. Kuo, Chin. J. Phys. 30 (1992) 665.
[32] The United States Pharmacopeia, 32nd Rev., vol. 1, The United States Pharmacopeial Convention, Rockville, MD, 2009, p. 236.
[33] Agilent Chemstation: Understanding your ChemStation, Agilent Technologies, Waldbronn, 2001.
[34] S. Orlandini, I. Giannini, R. Gotti, S. Pinzauti, E. La Porta, S. Furlanetto, Electrophoresis 28 (2007) 395.
[35] D. Mathieu, J. Nony, R. Phan-Tan-Luu, NEMROD-W, LPRAI sarl, Marseille.
[36] S.P. Moulik, B.K. Paul, Adv. Colloid Interface Sci. 78 (1998) 99.
[37] R. Pomponio, R. Gotti, J. Fiori, V. Cavrini, J. Chromatogr. A 1081 (2005) 24.
[38] J.A. Cornell, Experiments and Mixtures. Designs, Models and the Analysis of Mixture Data, 2nd edn., John Wiley & Sons, New York, 1990.
[39] R.G. Brereton, Chemometrics: Data Analysis for the Laboratory and Chemical Plant, John Wiley & Sons, Chichester, 2003.
[40] K.D. Altria, J. Chromatogr. A 892 (2000) 171.
[41] S.H. Hansen, C. Gabel-Jensen, D.T.M. El-Sherbiny, S. Pedersen-Bjergaard, Trends Anal. Chem. 20 (2001) 614.
[42] R. Carlson, Design and Optimisation in Organic Synthesis, Elsevier Science B.V., Amsterdam, 1992.
[43] D. Mathieu, R. Phan-Tan-Luu, M. Sergent, Criblage et Étude des Facteurs, LPRAI, Marseille, 1996.
[44] J. Ermer, J.H.McB. Miller (Eds.), Method Validation in Pharmaceutical Analysis—A Guide to Best Practice, Wiley, Weinheim, 2004.
[45] European Pharmacopoeia 6.0, vol. 1, Council of Europe, Strasbourg, 2008, p. 81.

Talanta 80 (2009) 789–796

Contents lists available at ScienceDirect

Talanta

journal homepage: www.elsevier.com/locate/talanta

Development and characterization of a new polyampholyte–surfactant complex applied to the solid phase extraction of bisphenol-A

J.M. Lázaro Martínez [a], M.F. Leal Denis [b], L.R. Denaday [b], V. Campo Dall' Orto [b,*]

[a] Departamento de Química Orgánica, Facultad de Farmacia y Bioquímica, Universidad de Buenos Aires, Junín 956 (C1113AAD), Ciudad Autónoma de Buenos Aires, Argentina
[b] Departamento de Química Analítica y Fisicoquímica, Facultad de Farmacia y Bioquímica, Universidad de Buenos Aires, Junín 956 (C1113AAD), Ciudad Autónoma de Buenos Aires, Argentina

ARTICLE INFO

Article history:
Received 29 April 2009
Received in revised form 27 July 2009
Accepted 30 July 2009
Available online 7 August 2009

Keywords:
Polyampholyte
Surfactant
NMR
Solid phase extraction
Sorption
Bisphenol-A

ABSTRACT

This paper presents a material that has both hydrophilic and hydrophobic domains, obtained by combination of a polyampholyte with a surfactant. This material was fully characterized by different spectroscopic techniques and microscopy.

Bisphenol-A (BPA) was chosen as a model molecule to study the interaction with compounds of intermediate polarity. We explored the kinetics and equilibrium of BPA on the surface of the polyampholyte–surfactant complex and found a significantly high loading capacity (2.02 mmol g^{-1}) and complete binding from solutions at concentration levels below 100 μmol L^{-1}.

The complex was encapsulated in agarose gel to be used as solid phase for extraction of BPA from food simulants in contact with polycarbonate bottles under different treatments. Bisphenol was preconcentrated, extracted and analysed by liquid chromatography with an amperometric detector. The instrumental detection limit of the technique was 10 μg L^{-1}, which was lowered to 0.14 μg L^{-1} by the preconcentration step. The BPA released from baby bottles was 2.1 ng cm^{-2} (σ_{n-1}: 0.1) in the first use with distilled water.

© 2009 Elsevier B.V. All rights reserved.

1. Introduction

Bisphenol-A (BPA), 2,2-bis(4-hydroxyphenyl) propane, is a chemical substance used mainly in the production of polycarbonate and epoxy resins [1]. A great variety of materials (storage containers, milk bottles, infant feeding bottles, microwave ovenware) derived from polycarbonate cause environmental contamination when they are in contact with water or food due to the leakage of non-polymerized monomers or residues from hydrolysis.

It has been reported that BPA has a weak affinity for estrogen receptors [2], has potential for disrupting thyroid hormone action [3], affects the proliferation of human prostate cancer cells [4] and blocks testosterone synthesis [5] at ng L^{-1} doses.

Due to these toxicological properties, many analytical methodologies, including sample preparation, separation and detection of BPA, have been developed [1].

In 2004, the EU Commission established a specific migration limit (SML) of BPA from food plastic materials of 600 ng g^{-1} [6]. Migration testing is usually carried out with food simulants instead of food, because its analysis usually presents some drawbacks. Simulants have been selected to model different categories of food (aqueous, acidic, alcoholic and fatty) to simplify the testing and evaluate whether a plastic is suitable for a given application [7].

Separation, identification and quantitation of BPA are reliably carried out with mass spectrometric methods, namely liquid chromatography–tandem mass spectrometry [8] and gas chromatography–tandem mass spectrometry [9]. Other methods such as liquid chromatography coupled to fluorescence or electrochemical detection and immunochemical methods have also been reported [1]. When food simulants are used, the sample preparation consists of a preconcentration step by solvent evaporation, liquid–liquid extraction, solid phase extraction (SPE), solid phase microextraction or stir bar sorptive extraction [1].

SPE is by far the most widely used technique for the extraction of BPA-containing liquids [9–12]. The technique uses a copolymer formed with the hydrophilic *N*-vinylpyrrolidone, which acts as a hydrogen acceptor, and the hydrophobic divinylbenzene, which provides reversed-phase retention (Oasis HLB).

A number of different approaches have been used to prepare new sorbents in order to improve particular features such as selectivity or capacity. Synthetic strategies such as the molecularly imprinting technique or the construction of immunoaffinity monoliths have been applied to generate selective binding sites in bulk or surfaces of polymeric matrixes [13–15].

* Corresponding author. Tel.: +54 1149648263; fax: +54 1149648263.
E-mail addresses: lazarojm@ffyb.uba.ar (J.M. Lázaro Martínez), mfldenis@ffyb.uba.ar (M.F. Leal Denis), lisandro01@hotmail.com (L.R. Denaday), vcdall@ffyb.uba.ar (V. Campo Dall' Orto).

0039-9140/$ – see front matter © 2009 Elsevier B.V. All rights reserved.
doi:10.1016/j.talanta.2009.07.065

This paper presents a material that combines a hydrophilic network with hydrophobic regions, and exhibits a notably high loading capacity for BPA. The network is a polyampholyte obtained by reaction of methacrylic acid, ethylene glycol, diglycidyl ether and 2-methylimidazole (poly(EGDE–MAA–2MI)) [16–18], following a new synthetic procedure. The acid form of this polymeric material binds dodecyl sulfate on the surface. The interactions between surfactants and polyelectrolytes have been well reviewed [19–21] and the dominating factor that influences binding is the electrostatic charged neutralization of the polyion by oppositely charged surfactants. The electrostatic binding is an endothermic process driven by entropy. The positive entropy is attributed to the recovery of translational entropy of released counterions by the bound surfactant.

The new material was fully characterized by spectroscopy (^{13}C Nuclear Magnetic Resonance in the solid-state, Fourier Transform-Infrared), thermogravimetry, elemental analysis, nitrogen adsorption and scanning electron microscopy.

The kinetics and sorption equilibrium of BPA on the surface were also studied. The material was also encapsulated in agarose beads and tested as sorbent for the BPA released from baby bottles into food simulants, under different treatments. The analysis was completed by liquid chromatography with electrochemical detection (HPLC-ED), and the performance of the method is discussed.

2. Materials and methods

2.1. Reagents

2-Methylimidazole (2MI; 99 wt%; pK_a: 7.86), bisphenol-A (BPA 99 wt%, MW: 228.29), methacrylic acid (MAA; 99 wt%; pK_a: 4.66), ethylene glycol diglycidyl ether (EGDE; 50 wt% in ethylene glycol dimethyl ether), phenol (99 wt%), methylparaben (99 wt%), propylparaben (99 wt%) and diethyl phthalate (99 wt%) were purchased from Sigma–Aldrich, and benzoyl peroxide from Fluka. Sodium dodecylsulfate (SDS; MW: 288.38; solubility at 20 °C: 10 g in 100 g of water; critical micelle concentration (CMC): 8.2 mmol L^{-1}) and dodecylbenzene sulfonic acid sodium salt (SBDS; MW 348.5; solubility at 20 °C: 32.8 g in 100 g of water; CMC: 1.2 mmol L^{-1}) were purchased from ICN Biomedical.

Baby bottles (250 cm^3) from one brand made of polycarbonate were washed twice with distilled water before use; no further treatment was performed.

Acetonitrile, isopropyl alcohol and methanol from Baxter were HPLC grade. BPA-free distilled water was used for all aqueous solutions. Spectroscopic grade potassium bromide was used for infrared pellets. Hydrochloric acid, sodium chloride, sodium hydroxide, disodium hydrogen phosphate and potassium hydrogen phosphate were of analytical grade.

2.2. Synthesis of the polyampholyte modified with the surfactant

The polyampholyte was synthesized according to previous reports [16–18], from methacrylic acid, ethylene glycol diglycidyl ether and 2-methylimidazole. Then it was washed with water, dried at 60 °C for 24 h and milled in particles with an average diameter of 200 μm. The particles were treated with 0.1 mol L^{-1} HCl to obtain the acid form of the polyampholyte (poly(EGDE–MAA–2MIH$^+$)), and 50 mg were put in contact with three aliquots of 4 mL of 20 mmol L^{-1} sodium dodecyl sulfate (SDS) solution. The adsorption of dodecyl sulfate (DS) on the surface of the poly(EGDE–MAA–2MIH$^+$) was expected to take place under these conditions (Scheme 1). The complex poly(EGDE–MAA–2MIH$^+$)–DS was rinsed with distilled water, filtered, and let to dry at room temperature. Sodium dodecylbenzene sulfonate (SDBS) was also used for the formation of the complex since it absorbs radiation at 273 nm and can be monitored spectrophotometrically.

2.3. Characterization of the poly(EGDE–MAA–2MIH$^+$)–DS complex

The Fourier Transform-Infrared (FTIR) spectra of poly(EGDE–MAA–2MIH$^+$)–DS and polyampholyte were recorded on a Spectrum 1000 PerkinElmer spectrometer using KBr pellets. The material was dried and placed in a desiccator at 20 °C prior to pellet preparation.

High-resolution ^{13}C Nuclear Magnetic Resonance (NMR) solid-state spectra were recorded using the ramp $\{^1H\} \rightarrow \{^{13}C\}$ CP-MAS (cross-polarization and magic angle spinning) sequence with proton decoupling during acquisition. All the solid-state NMR experiments were performed at room temperature in a Bruker Avance II-300 spectrometer equipped with a 4-mm MAS probe. The operating frequency for carbons was 75.46 MHz and the spinning rate was 10 kHz. Samples of two batches of each material were studied.

Thermogravimetric measurements were carried out with a TA Instrument SDT Q600, under nitrogen flux over a temperature range from 30 to 400 °C with a heating rate of 10 °C min^{-1}. The average sample size was 10 mg and the measurements were carried out in triplicate.

The surface of two batches of each polymer was characterized using a scanning electron microscope Field Emission SEM (Zeiss Gemini DSM 982) operated at a 0.3 kV acceleration voltage.

Elemental analysis was performed with a CE440 Elemental Analyser device (Exeter Analytical).

The nitrogen adsorption isotherm was collected at 77 K on a Micromeritics Gemini 2360 system. Specific surface area was calculated using the Brunauer–Emmett–Teller equation (BET).

2.4. Surfactant adsorption isotherms

For binding studies, SDS was replaced with SDBS, whose concentration was determined by UV measurements.

Kinetic experiments were performed with a 4 mmol L^{-1} SDBS standard solution under forced convection.

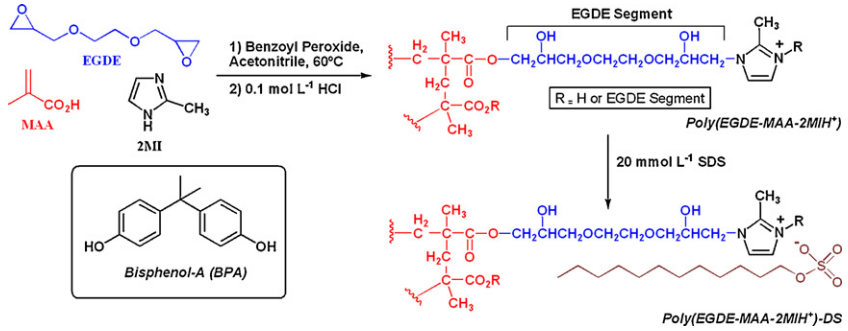
The adsorption isotherm was performed with aliquots of 80 mg of acid polyampholyte dispersed in 10.0 mL of SDBS standard solutions in a concentration range between 0.20 and 8.0 mmol L^{-1}. The suspensions were mixed and thermostated at 20.0 ± 0.5 °C for 16 h to reach equilibrium. The SDBS concentration in the supernatant and standard solutions was analysed spectrophotometrically at 273 nm.

2.5. Bisphenol-A (BPA) uptake

BPA in solution was analysed by liquid chromatography with electrochemical detection (HPLC-ED). The chromatographic system consisted of an HPLC SpectraSYSTEM Isocratic Pump P100, a Rheodyne injection valve (Model 7125) with a 20-μL sample loop, a guard column, and a C-18 bonded column (Hewlett-Packard) 5 μm, 200 mm × 4.6 mm. The mobile phase was methanol:aqueous solution containing 10 mmol L^{-1} KNO_3 and 0.25 mmol L^{-1} H_2SO_4 as supporting electrolyte in a proportion of 55:45, at a flow rate of 0.8 mL min^{-1}.

Amperometric detection was performed with a microprocessor-controlled electrochemical analyser. A thin-layer cell (7 μL volume), equipped with a glassy carbon working electrode (BAS, 7 mm^2 area) and a stainless steel block as auxiliary electrode, operated at +1 V vs. Ag/AgCl.

Stainless steel, PTFE and PEEK were used for the flow system connections.



Scheme 1. Chemical structure of bisphenol-A (BPA) and synthesis of the poly(EGDE–MAA–2MIH$^+$) and poly(EGDE–MAA–2MIH$^+$)–DS complex.

The linear range for BPA was verified up to 800 μg L^{-1}. All the samples were filtered and properly diluted for HPLC analysis.

Kinetic experiments of BPA sorption on the complex were carried out with 50 mg of poly(EGDE–MAA–2MIH$^+$)–DS in contact with 125 mL of 500 μmol L^{-1} BPA (114 mg L^{-1}) dissolved in 10:90 methanol:water, under forced convection.

The sorption isotherm experiments were performed with aliquots of 40 mg of poly(EGDE–MAA–2MIH$^+$)–DS dispersed in 200 mL of BPA standard solutions in a concentration range between 75 and 800 μmol L^{-1} (17 and 183 mg L^{-1}), in the same medium. The suspensions were mixed and thermostated at 20.0 ± 0.5 °C for 1 h.

For the adsorption isotherm of BPA on the polyampholyte without surfactant, 200 mg of polymer and 25 mL of BPA aqueous solution in the range between 3.7 and 216 μmol L^{-1} were used.

2.6. Preconcentration and analysis of BPA released from baby bottles

The linear concentration range of the HPLC-ED analytical technique was examined injecting BPA solutions prepared in 60:40 isopropanol:methanol, with five concentration levels (0.050, 0.100, 0.200, 0.300 and 0.500 mg L^{-1}), in triplicate.

The detection and the quantification limits (LoD and LoQ) were calculated as 3 and 10 times the standard deviation of five replicate runs of the procedure blank, respectively.

The extraction process of BPA from baby bottles consisted of a migration assay by using food-simulating liquids, and a preconcentration step prior to detection. A new extraction sorbent was prepared by including poly(EGDE–MAA–2MIH$^+$)–DS in agarose gel. Sorbent beads were obtained by mixing 200 μL of 1% agarose solution at 60 °C with 50 mg of poly(EGDE–MAA–2MIH$^+$)–DS in 4 mm × 4 mm cavities, and cooling at room temperature.

In a first assay (treatment A1), the extraction process was performed following the MERCOSUR Regulations [22], which indicate that distilled water should be used as food-simulating liquid for plastic containers to be used with milk. The regulation also indicates that the samples tested have to complete a final contact surface of 600 cm^2. For this reason, three new baby bottles filled up to 250 mL were used in each experiment. They were filled with boiling distilled water and kept in contact at 100 °C at atmospheric pressure for 30 min. The extract was cooled at room temperature, completed to volume with distilled water (for loss due to evaporation), and then a 300-mL aliquot was mixed with 2.0 mL of 30:70 methanol:water. Four sorbent beads were put in contact with this mixture in a stainless steel basket under convection for 1 h. The beads were then dried with tissue paper and put in contact with 4.0 mL of 60:40 isopropanol:methanol in a tube with cap under agitation at 30 °C in a thermostated bath to extract BPA for HPLC analysis. For recovery experiments the water extract was spiked with BPA standard by replacing 2.0 mL of 30:70 methanol:water by 2.0 mL of 0.400 mg L^{-1} BPA standard in the same solvent and thus making a 2.65 μg L^{-1} BPA spike (final concentration of 0.200 mg L^{-1} in the alcoholic extract). The analysis of the sample with and without the BPA spike was carried out in triplicate.

A blank was carried out with 300 mL of distilled water instead of the extract.

The beads were washed three times with 4.0 mL of 60:40 isopropanol:methanol for reutilization.

A comparison of the retention behaviour of BPA was made with Oasis HLB cartridges of 200 mg (60 μm particle size, purchased from Waters) after pretreatment with methanol and pure water. A 300-mL aliquot of the extract and another sample of distilled water spiked with 1.67 μg L^{-1} of BPA were, respectively loaded on the solid phase column at 3 mL min^{-1}. Each sample was eluted with 4.0 mL of 60:40 isopropanol:methanol. The analyses of both the extract and the water spiked with BPA were carried out in triplicate.

Then three used baby bottles were rinsed with distilled water and the extraction procedure was repeated (treatment A2). They were then subjected to 10 cycles of simulated use by boiling for 10 min in tap water and washing with a brush, after which the migration assay was repeated (treatment A3).

In order to validate the method, other treatments and liquids were used on new baby bottles. Tap water 1 from the laboratory with pH 6.9 and 59 mg L^{-1} of total alkalinity was kept in contact with the bottles for 10 min at 100 °C in treatment B. Tap water 2 with pH 7.6 and 499 mg L^{-1} of total alkalinity was kept in contact with the bottles for 10 min at 100 °C in treatment C, and the sample was diluted 5-fold with recently distilled water (pH 7.0) for preconcentration. A blank was carried out with 300 mL of each tap water instead of the extract, and BPA was not detected.

In treatment D, distilled water was kept in contact with new bottles for 30 min at 100 °C and was then spiked with 1.2 μg L^{-1} (8.0 nmol L^{-1}) methylparaben, 1.2 μg L^{-1} (6.9 nmol L^{-1}) propylparaben, 5.3 μg L^{-1} (57 nmol L^{-1}) phenol and 0.2 μg L^{-1} (1 nmol L^{-1}) diethyl phthalate.

In treatments B, C and D, the analysis of each sample was carried out in triplicate. The recovery figures for a 2.65 μg L^{-1} BPA spike were obtained in triplicate in treatments C and D.

3. Results and discussion

3.1. Characterization of the poly(EGDE–MAA–2MIH$^+$)–DS complex

Fig. 1 exhibits the FTIR spectra for the polyampholyte, SDS and the polyampholyte–DS complex. The results show a clear evidence of dodecyl sulfate (DS) adsorption on the surface of the poly(EGDE–MAA–2MIH$^+$). The polymer bands previously reported [16] were: 1730 cm^{-1} (carbonyl symmetric stretching); 1570 cm^{-1} (carboxylate asymmetric stretching); 1640 (C=C and/or C=N stretching vibrations), 750 and 670 cm^{-1} (2-methylimidazole ring stretching); 1450 cm^{-1} (C=C and/or C=N stretching vibrations

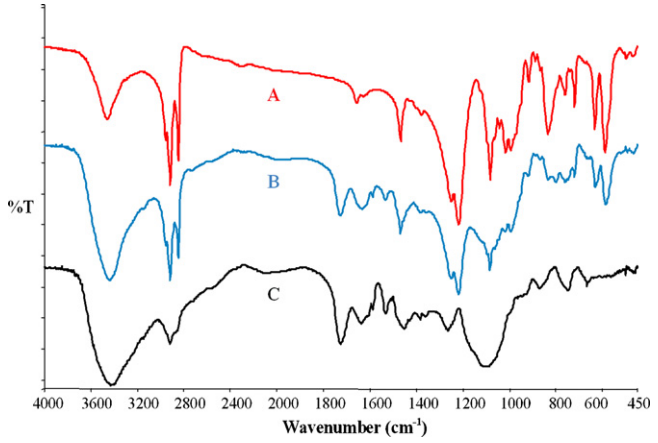


Fig. 1. FTIR spectra for SDS (A), the poly(EGDE–MAA–2MIH$^+$)–DS complex (B) and poly(EGDE–MAA–2MIH$^+$) (C).

and ether groups); 1100 cm^{-1} (ether groups); 2930 cm^{-1} (C–H) and 3435 cm^{-1} (O–H). The main signals for SDS were: 1469 and 1220 cm^{-1} (SO_2 stretching); 1253 and 1185 cm^{-1} (asymmetric and symmetric stretching of $ROSO_3Na$); 837 and 760 cm^{-1} (asymmetric and symmetric stretching of S–O–C); 635 and 591 cm^{-1} (SO_3 flexion).

In the FTIR spectrum of the polyampholyte–DS complex strong bands related to DS appeared at 2950, 1230, 635 and 591 cm^{-1}, and the bands associated with the polyampholyte network were weaker.

The ^{13}C CP-MAS signals for SDS were assigned tentatively according to the results reported by Ferruglio and co-workers in solution [23], and those for the polyampholyte were assigned as previously reported [18] (Fig. 2). The solid-state results indicate that important changes in the chemical environment occurred upon sorption with the DS surfactant. Fig. 3 clearly shows the effects on the chemical shifts associated with the carbons 3–9 of the DS molecule and for the signals of the carbons near the positive sites of the disubstituted imidazole ring in the polymer (C3, C4 and C6).

The thermogravimetric curves (TG and DTG) for the polymer and the polyampholyte–DS complex are shown in Fig. 4. The thermal

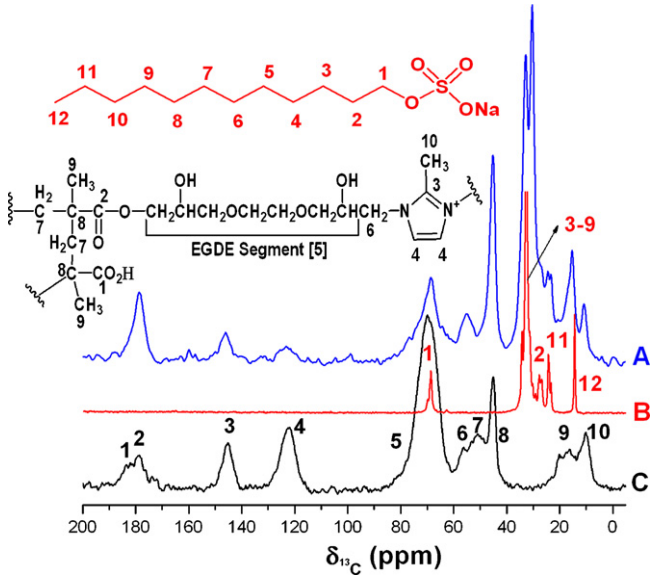


Fig. 2. Solid-state ^{13}C spectra for the poly(EGDE–MAA–2MIH$^+$)–DS complex (A), SDS (B) and poly(EGDE–MAA–2MI) (C). Operating frequency: 75.46 MHz. Spinning rate: 10 kHz.

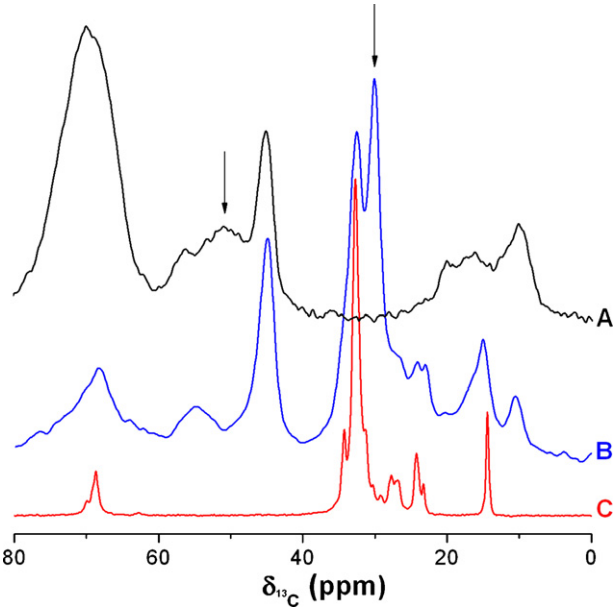


Fig. 3. Changes in the ^{13}C chemical shift for poly(EGDE–MAA–2MI) (A), the poly(EGDE–MAA–2MIH$^+$)–DS complex (B) and SDS (C).

behaviour of this kind of polymer matrixes has been previously studied [18]. The results showed an initial loss of weight due to the evaporation of water in the complex. Also, the anionic surfactant interacted electrostatically and hydrophobically through the $ROSO_3^-$ group and the hydrocarbon chain with the polymer backbone, respectively. The most important interaction was located between the positive charges of the imidazolium units and the disubstituted imidazole ring of the matrix with the negative domain of the DS [18,24]. That association produced the low thermal stability of the complex against the polyampholyte matrix and partial degradation of the DS molecules, as a consequence of the disruption in the electronic density in the polymer backbone with the concomitant weakness of the chemical bonds [18].

The scanning electron microscopy (SEM) images exhibit the modifications produced by the DS adsorption on the polyampholyte particles. This coverage had left rows of macropores with an average diameter of 85 nm, sharing the same direction over a restricted region (Fig. 5).

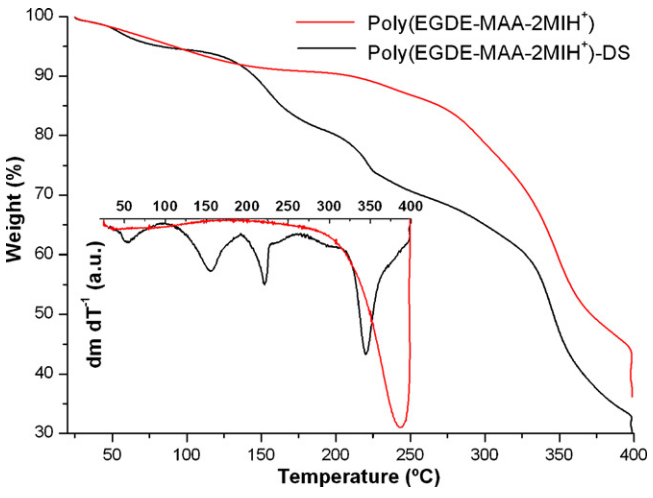


Fig. 4. TG and DTG curves for poly(EGDE–MAA–2MI) and the poly(EGDE–MAA–2MIH$^+$)–DS complex. Heating rate: 10 °C min^{-1}. Operating under nitrogen flux. Sample size: 10 mg.

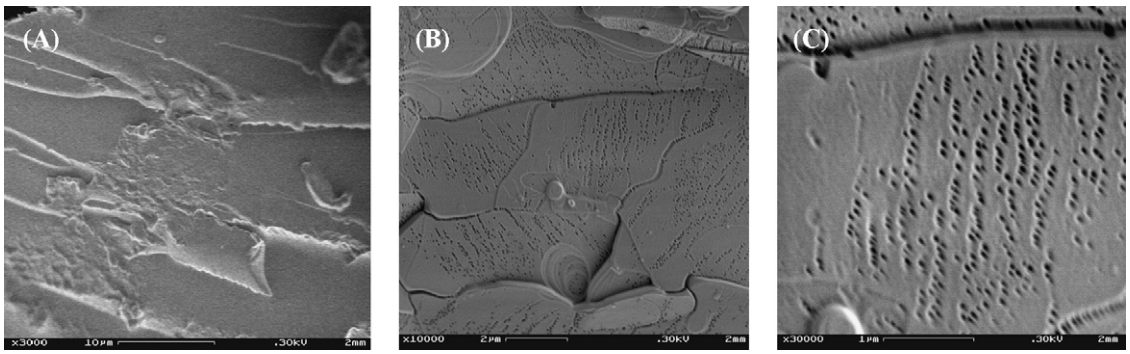


Fig. 5. SEM images for poly(EGDE–MAA–2MIH$^+$) (A), the poly(EGDE–MAA–2MIH$^+$)–DS complex (B) and the poly(EGDE–MAA–2MIH$^+$)–DS complex with magnification (C). Acceleration voltage: 0.3 kV.

The average nanopore width and the equivalent specific surface area obtained from the nitrogen adsorption isotherm were 36.8 Å and 3.04 $m^2\,g^{-1}$, respectively (the value for the polymer without DS is 0.6 $m^2\,g^{-1}$). These results were consistent with an increase in the specific surface area as a consequence of the increase in the hydrophobic segments from the interaction with DS.

3.2. Surfactant uptake

Kinetics and equilibrium studies were carried out with SDBS instead of SDS.

The results of the kinetics studies indicated that the binding equilibrium was reached in 5 min under forced convection at 20 °C.

The binding isotherm of dodecyl benzenesulfonate (DBS) to poly(EGDE–MAA–2MIH$^+$) is exhibited in Fig. 6. The experimental data fitted properly with Langmuir model with a regression coefficient (R) of 0.9911, a maximum loading capacity estimated in 1.5 ± 0.2 mmol g^{-1} (0.54 ± 0.07 g DBS g^{-1}) and a dissociation constant of $2.1 \pm 0.5 \times 10^{-3}$. This well-known model is based on the interaction of a ligand and a finite number of active sites available on the sorbent surface. In this case the nature of the interaction is mainly electrostatic: the ligand provides a negative charge and the polyampholyte presents regions of positive charge in protoned 2-methylimidazole terminal residues together with fixed positive charges in disubstituted 2-methylimidazole [16,17]. A hydrophobic interaction between the hydrocarbon chain of DS and the polymer backbone may take place to a lesser extent.

Even if the initial concentration of SDBS in the experiment in most of the experimental points of the isotherm was above the CMC, the interaction with the polymer was well described by Langmuir model, involving the uptake of one DBS molecule per site.

Then, a second binding experiment was performed as described in Section 2.2, using high amounts of SDS and SBDS. The elemental analysis of poly(EGDE–MAA–2MIH$^+$)–DS gave 4.992% of sulfur, equivalent to 1.557 mmol DS per gram of complex and 2.653 mmol DS per gram of polyampholyte. In the same way, 0.66 g of DBS (1.9 mmol) per gram of polyampholyte were adsorbed in this experiment, an amount higher than the binding predicted by Langmuir model. These results led us to conclude that some degree of aggregation took place, as expected for the interaction of polymers with surfactants [21]. Here, the concentration of the surfactant was far above the CMC, so an equilibrium between free micelles and the micelles bound to the polyampholyte must be taken into account.

3.3. Studies of interaction between the complex and bisphenol-A (BPA)

Poly(EGDE–MAA–2MIH$^+$)–DS was prepared following the procedure described in Section 2.2. Under that treatment, the polyampholyte was assumed to adsorb individual DS molecules to a larger extent and DS micelles.

The results of the kinetic experiments of BPA uptake are presented in Fig. 7. These results fit well with a first-order empiric model (R, 0.9962):

$$[\mathrm{BPA}] = [\mathrm{BPA}]_\infty + [\mathrm{BPA}]_b \times e^{-k \times t} \quad (1)$$

where $[\mathrm{BPA}]_\infty$ is the free amount in equilibrium, $[\mathrm{BPA}]_b$ the total amount of BPA withdrawn from the solution by sorption

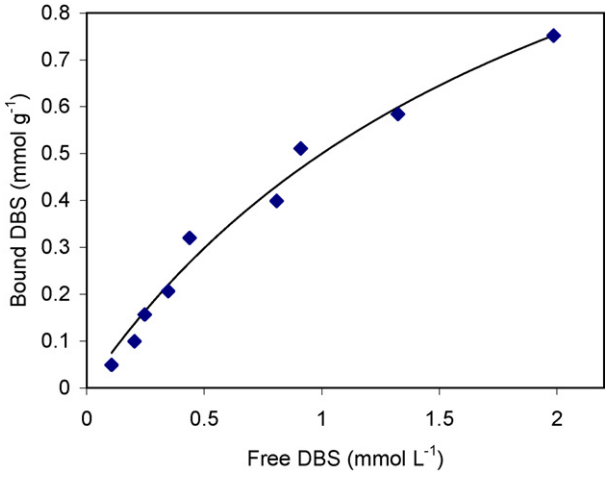


Fig. 6. Adsorption isotherm of DBS to poly(EGDE–MAA–2MIH$^+$). DBS concentration range: 0.2–8.0 mmol L^{-1}. Temperature: 20.0 ± 0.5 °C.

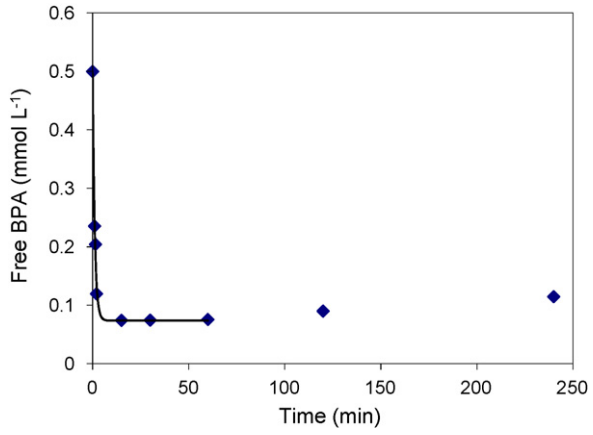


Fig. 7. Concentration of BPA for the solution in contact with poly(EGDE–MAA–2MIH$^+$)–DS as a function of time. Weight of the complex: 50 mg. Initial BPA concentration: 114 mg L^{-1} (500 μmol L^{-1}); solution volume: 125 mL; medium: 10:90 methanol:water.

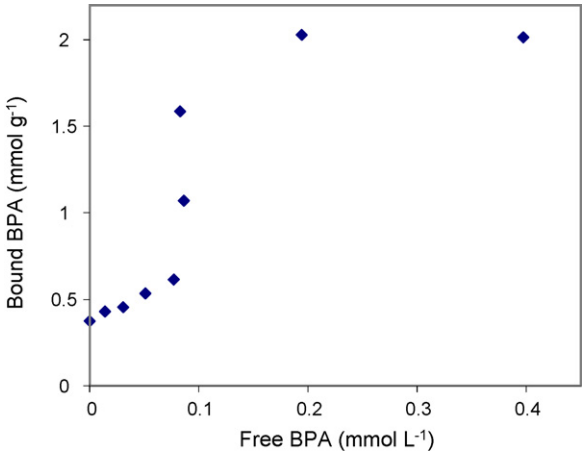


Fig. 8. Sorption isotherm of BPA to poly(EGDE–MAA–2MIH$^+$)–DS. Weight of the complex: 40 mg. BPA concentration range: 75–800 μmol L^{-1}; sample volume: 200 mL; medium: 10:90 methanol:water. Temperature: 20.0 ± 0.5 °C.

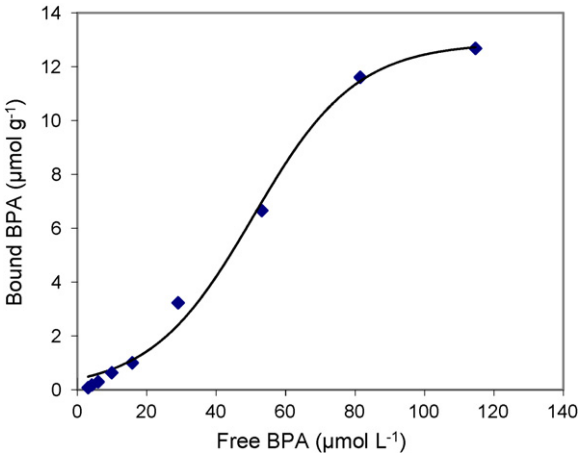


Fig. 9. Adsorption isotherm of BPA to poly(EGDE–MAA–2MIH$^+$). Polymer weight: 200 mg. BPA concentration range: 3.7–216 μmol L^{-1}; aqueous sample volume: 25 mL. Temperature: 20.0 ± 0.5 °C.

to the matrix, and k the pseudo first-order kinetic constant for the decrease in BPA in solution. The estimated parameters were: $[BPA]_\infty$: 7.38×10^{-5} mol L^{-1} (σ_{n-1}: 9.4×10^{-6}); $[BPA]_b$: 4.26×10^{-4} mol L^{-1} (σ_{n-1}: 1.9×10^{-5}); k: 0.929 min^{-1} (σ_{n-1}: 0.081).

This model properly describes the behaviour of this system for the first hour of contact between the matrix and the BPA solution. After this, a slow increase in BPA in solution was observed and attributed to the desorption of DS micelles from the polyampholyte surface. The contact time for BPA preconcentration on the polyampholyte–DS complex surface was then set in 60 min.

The results for BPA binding equilibrium gave a type-H4 isotherm (Fig. 8) in the classification of Giles et al. [25]. In this case the solute has such high affinity for the matrix that it was completely bound or there was no free measurable amount in equilibrium in diluted solutions (below 0.1 mmol L^{-1}). The first plateau corresponds to the formation of the first "monolayer". One possible mechanism for solute–sorbent interaction is hydrogen bonding between hydroxyl groups from BPA and the hydroxyl and carboxylic groups on the polyampholyte surface, forming isolated clusters of BPA molecules on the most active sites. Another possible mechanism of sorption is the partition of BPA into the hydrophobic environment of the hydrocarbon chains electrostatically bound to the polyampholyte. These simultaneous mechanisms would account for the complete solute uptake at low concentration levels. Electrostatic attraction is discarded under this experimental condition since BPA is expected to be neutral.

At total BPA concentrations above 0.2 mmol L^{-1} there was a sharp increase in sorption, indicating a complete saturation of the active surface of the polymer. In this second step, the solute molecules could be partitioned in the DS micelles sorbed on the polymer, and hydrogen bonding between BPA molecules on the sorbent could also be considered. The amount of BPA bound in the first step was 0.450 mmol g^{-1} (103 mg), and that in the second step 2.02 mmol g^{-1} (461 mg), representing a significantly high loading capacity for this new matrix as compared with other sorbents [14,15,26]. Then, in conditions of saturation, 2.02 mmol BPA can be bound to a gram of complex that contains 2.653 mmol of DS.

These results were compared with the isotherm for BPA adsorption on the polyampholyte without DS (Fig. 9). In this case, a sigmoidal or S-type isotherm was obtained with an R of 0.9975 for non-linear regression. This indicates cooperative adsorption, meaning that at low concentrations of BPA the interaction is weak but the adsorption becomes easier as the concentration of BPA increases. This behaviour is expected when the solute molecule is adsorbed as a single unit (not a micelle), has a moderate degree of intermolecular attraction by π–π interaction (which determines a vertical orientation in a regular arrangement), and presents strong competition with water for active sites on the surface of the polyampholyte [25]. In this case, BPA probably interacts by hydrogen bonding with carboxylic groups and the hydroxyl groups on the network resulting from the epoxide opening. Hydrogen bonding between BPA molecules could contribute to sorption at high solute concentrations.

The modification of the polyampholyte surface with DS significantly improved the uptake of BPA. The maximum binding capacity of the complex (2.02 mmol g^{-1}) was 160 times higher than the value observed for the polyampholyte (12.9 ± 0.5 μmol g^{-1}). When the concentration of BPA was lower than 100 μmol L^{-1}, a complete uptake of BPA on the complex was observed.

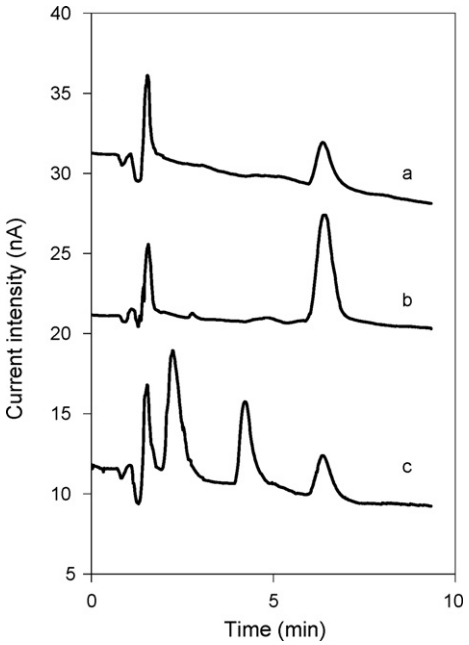


Fig. 10. Chromatograms of the sample in treatment A1 (a), the sample in treatment A1 with spiking of 0.200 mg L^{-1} BPA (final concentration in alcoholic extract) (b) and the sample in treatment D (c). Mobile phase: 55:45 methanol:aqueous solution of 10 mmol L^{-1} KNO_3 and 0.25 mmol L^{-1} H_2SO_4. Injection volume: 20 μL. Flow rate: 0.8 mL min^{-1}. Electrode potential: +1 V vs. Ag/AgCl.

Table 1
BPA concentration in extracts from baby bottles.

Sample treatment for extraction of BPA	BPA in extracts ($\mu g\,L^{-1}$)	Recovery[a] (%)
(A1) Distilled water at 100 °C for 30 min	1.70 (σ_{n-1}: 0.09)	96 (σ_{n-1}: 4)
(A2) Second sequence (after rinsing)	0.52	–
(A3) Third sequence (after 10 cycles of boiling for 10 min with tap water 1 and brushing)	3.6	–
(B) Tap water 1 at 100 °C for 10 min	3.7 (σ_{n-1}: 0.1)	–
(C) Tap water 2 at 100 °C for 10 min	9.1 (σ_{n-1}: 0.2)	95 (σ_{n-1}: 5)
(D) Distilled water at 100 °C for 30 min, and then spiking with other pollutants	1.7 (σ_{n-1}: 0.1)	98 (σ_{n-1}: 5)

[a] Recovery from a 2.65 $\mu g\,L^{-1}$ BPA spike.

3.4. Preconcentration and analysis of BPA released from baby bottles

The HPLC-ED system presented linearity for BPA tested in a concentration range up to 0.500 mg L^{-1} with a sensitivity of 667 nCoulombs L mg^{-1} (σ_{n-1}: 10) and a correlation coefficient of 0.9986. The repeatability of the technique was also good as the relative standard deviation for the standard BPA replicates of each concentration level was less than 4%.

The instrumental detection and quantification limits of the technique were 10 and 35 $\mu g\,L^{-1}$, respectively, and the preconcentration step allowed lowering the limits of the method to 0.14 and to 0.46 $\mu g\,L^{-1}$, respectively.

The new material was used as solid phase for preconcentration of BPA released by polycarbonate baby bottles to food-simulating liquids. The extraction sorbent was prepared by including poly(EGDE–MAA–2MIH$^+$)–DS in agarose gel as described in Section 2.6. Several sample treatments were carried out.

The first migration assay was performed following the MERCOSUR Regulations [22], using distilled water at 100 °C for 30 min as food simulant for milk (treatment A1). The BPA in the simulant was preconcentrated on the new sorbent and released to the alcoholic mixture for analysis by HPLC-ED. Fig. 10 shows the chromatogram of the sample (a) and the sample spiked with BPA in a final concentration of 0.200 mg L^{-1} (b). The retention time for BPA was 5.6 min and the released BPA was 2.1 ng cm^{-2} (σ_{n-1}: 0.1) using the new phase, and 2.3 ng cm^{-2} (σ_{n-1}: 0.1) using Oasis HLB phase for preconcentration. The amounts were in the same order as the results obtained by evaporation of the simulant liquid as strategy for preconcentration [27], and lower than the SML established by the Mercosur (4.8 $\mu g\,cm^{-2}$) [22] or the SML established by the EU Commission (750 ng cm^{-2}).

Table 1 presents the concentrations of BPA found in the food simulants and the recoveries for the 2.65 $\mu g\,L^{-1}$ BPA spike (final concentration of 0.200 mg L^{-1} in the alcoholic extract). The recovery of BPA with treatment A1 was 96% (σ_{n-1}: 4) with the new sorbent for a 2.65 $\mu g\,L^{-1}$ BPA spike, and 97% (σ_{n-1}: 4) with Oasis HLB for a 1.67 $\mu g\,L^{-1}$ BPA spike, indicating that the performance of the new matrix is good in comparison with the best sorbent [1,12].

The particularly high loading capacity of this new phase allowed the detection of released BPA by an amperometric technique with a relatively high LoD (10 $\mu g\,L^{-1}$) [1].

The sorbent beads were reused twice with new baby bottles and the relative difference between each replicate and the mean value found for BPA was lower than 7%.

The release of BPA into hot distilled water diminished in a successive test [28] as observed with treatment A2 (Table 1). Then, with treatment A3, the same polycarbonate baby bottles were subjected to simulated use by boiling in tap water and brushing in order to create scratches on the inner surface and increase the wettability of the wall. This fact could have contributed to the deposit of residual limescale which further dissolved in the food stimulant and promoted the degradation of the polymer [29,30]. Table 1 exhibits the release of 3.6 $\mu g\,L^{-1}$ BPA from these aged baby bottles into distilled water kept at 100 °C for 30 min.

Biedermann-Brem and Grob [30] found that hot water at high pH degraded the polycarbonate causing an increase in the amount of the released BPA. In treatments B and C we used tap water of different pH and alkalinity as food simulants. Tap water 1 was kept boiling in the bottle for 10 min, the pH rose from 6.9 to 7.3 and 3.7 $\mu g\,L^{-1}$ of BPA were released after 10 min. With tap water 2, the pH rose from 7.6 to 8.1 by loss of carbon dioxide causing the hydrolysis of polycarbonate and the release of 9.1 $\mu g\,L^{-1}$ of BPA, as expected [30].

In treatment D, we repeated the migration test on new bottles with distilled water at 100 °C for 30 min, and then four organic pollutants (phenol, methylparaben, propylparaben and diethyl phthalate) were added to the water extract prior to the preconcentration step. Parabens are a homologous series of hydroxybenzoic acid esterified at the C-4 position used as an antimicrobial in foods, beverages, pharmaceuticals and cosmetics [31]. Phenol is usually present in polluted water samples. The phenolic compounds were uptaken together with BPA on the new phase and later detected electrochemically. Fig. 10 exhibits their signals in chromatogram c; phenol had a retention time of 1.4 min and parabens coeluted at 3.4 min. Diethyl phthalate is a plasticizer designed to increase the durability and flexibility of plastics. Since plasticizers are not chemically bound to the polymer they can leach from the plastic into the environment [32]. Even if diethyl phthalate was expected to be preconcentrated on the new adsorbent, it is not electroactive and was not detected at +1 V vs. Ag/AgCl. The preconcentration of BPA on the sorbents tested was not affected by the presence of other structurally similar compounds in the matrix at the same concentration level. The concentration of BPA released to the simulant in treatment D did not differ from treatment A1 and the recovery figures were optimal.

4. Conclusions

The surface of a synthetic polyampholyte was modified with a surfactant in order to change its chemical and physical properties. The new material, which combines hydrophobic domains with hydrophilic functionality, was exhaustively characterized by spectroscopic and microscopic techniques.

BPA was chosen as a model molecule of intermediate polarity to evaluate the efficiency of this matrix as a solid phase for extraction. The sorption of this analyte was significantly improved by the presence of a surfactant and was complete at low concentration levels. The particularly high loading capacity of this new phase allowed the detection of released BPA by an amperometric technique with a relatively high LoD. The new complex was tested with different food simulants (distilled water, tap water and a model solution containing phenolic pollutants and a plasticizer) and the recovery figures were optimal. The use of this encapsulated sorbent was simple, not expensive and adequate for this application.

Acknowledgements

The authors thank the financial support from Universidad de Buenos Aires (UBACyT 04-07/B037 and B062, and UBACyT 08-10/B058), CONICET, ANPCyT (BID 1728/PICT 01778). María Florencia Leal Denis thank University of Buenos Aires for her research fellowship for undergraduate students. Juan Manuel Lázaro Martínez thank CONICET for his doctoral fellowships.

References

[1] A. Ballesteros-Gómez, S. Rubio, D. Pérez-Bendito, J. Chromatogr. A 1216 (2009) 449.
[2] A.V. Krishnan, P. Stathis, S.F. Permuth, L. Tokes, D. Feldman, Endocrinology 132 (1993) 2279.
[3] R.T. Zoeller, R. Bansal, C. Parris, Endocrinology 146 (2005) 607.
[4] Y.B. Wetherill, C.E. Petre, K.R. Monk, A. Puga, K.E. Knudsen, Mol. Cancer Ther. 7 (2002) 515.
[5] B.T. Akingbemi, C.M. Sottas, A.I. Koulova, G.R. Klinefelter, M.P. Hardy, Endocrinology 145 (2004) 592.
[6] Commission Directive 2004/19/EC, of 1 March 2004, relating to plastic materials and articles intended to come into contact with foodstuffs, Official Journal of the European Communities L71 8.
[7] EU, Commission of the European Communities 97/48/EC, and United Kingdom HB1996-0200 from the Minis, Off. J. Eur. Commun. L222 (1997) 10.
[8] I.-C. Beck, R. Bruhn, J. Gandrass, W. Ruck, J. Chromatogr. A 1090 (2005) 98.
[9] A. Hibberd, K. Maskaoui, Z. Zhang, J.L. Zhou, Talanta 77 (2009) 1315.
[10] T. Yoshida, M. Horie, Y. Hoshino, H. Nakazawa, Food Addit. Contam. 18 (2001) 69.
[11] J.-H. Kang, F. Kondo, Res. Vet. Sci. 73 (2002) 177.
[12] B. Shao, H. Han, J. Hu, J. Zhao, G. Wu, Y. Xue, Y. Ma, S. Zhang, Anal. Chim. Acta 530 (2005) 245.
[13] J. Ou, L. Hu, L. Hu, X. Li, H. Zou, Talanta 69 (2006) 1001.
[14] X. Jiang, W. Tian, C. Zhao, H. Zhang, M. Liu, Talanta 72 (2007) 119.
[15] L. Li, J. Wang, S. Zhou, M. Zhao, Anal. Chim. Acta 620 (2008) 1.
[16] M.F. Leal Denis, R.R. Carballo, A.J. Spiaggi, P.C. Dabas, V. Campo Dall' Orto, J.M. Lázaro Martínez, G.Y. Buldain, React. Funct. Polym. 68 (2008) 169.
[17] J.M. Lázaro Martínez, M.F. Leal Denis, V. Campo Dall' Orto, G.Y. Buldain, Eur. Polym. J. 44 (2008) 392.
[18] J.M. Lázaro Martínez, A.K. Chattah, G.A. Monti, M.F. Leal Denis, G.Y. Buldain, V. Campo Dall' Orto, Polymer 49 (2008) 5482.
[19] E.D. Goddard, K.P. Ananthapadmanaban, Interactions of Surfactants with Polymer and Proteins, CRC Press, Boca Raton, FL, 1993.
[20] J.C.T. Kwak, Polymer–Surfactant Systems, Surfactant Science Series, vol. 77, Marcel Dekker, New York, 1998.
[21] K.C. Tama, E. Wyn-Jones, Chem. Soc. Rev. 35 (2006) 693.
[22] Normas Mercosur, De la Canal y Asociados, SRL, MERCOSUR-GMC-Res No. 030/92.
[23] L. Bernazzani, S. Borsacchi, D. Catalano, P. Gianni, V. Mollica, M. Vitelli, F. Asaro, L. Feruglio, J. Phys. Chem. B 108 (2004) 8960.
[24] V. Schmidt, C. Giacomelli, V. Soldi, Polym. Degrad. Stabil. 87 (2005) 25.
[25] C.H. Giles, T.H. MacEwan, S.N. Nakhwa, D. Smith, J. Chem. Soc. (1960) 3973.
[26] Y. Jin, M. Jiang, Y. Shi, Y. Lin, Y. Peng, K. Dai, B. Lu, Anal. Chim. Acta 612 (2008) 105.
[27] A. D'Antuono, V. Campo Dall'Orto, A. Lo Balbo, S. Sobral, I. Rezzano, J. Agric. Food Chem. 49 (2001) 1098.
[28] Y. Sun, M. Wada, O. Al-Dirbashi, N. Kuroda, H. Nakazawa, K. Nakashima, J. Chromatogr. B 749 (2000) 49.
[29] J.H. Petersen, K.H. Lund, Food Addit. Contam. A 20 (2003) 1178.
[30] S. Biedermann-Brem, K. Grob, Eur. Food Res. Technol. 228 (2009) 679.
[31] M.G. Soni, I.G. Carabin, G.A. Burdock, Food Chem. Toxicol. 43 (2005) 985.
[32] H. Fromme, T. Kuchler, T. Otto, K. Pilz, J. Muller, A. Wenzel, Water Res. 36 (2002) 1429.

Talanta 80 (2009) 797–802

Contents lists available at ScienceDirect

Talanta

journal homepage: www.elsevier.com/locate/talanta

Gold nanoparticles-induced enhancement of the analytical response of an electrochemical biosensor based on an organic–inorganic hybrid composite material

M. Barbadillo [a], E. Casero [a,*], M.D. Petit-Domínguez [a], L. Vázquez [b], F. Pariente [a], E. Lorenzo [a,*]

[a] Departamento de Química Analítica y Análisis Instrumental, Universidad Autónoma de Madrid, Campus de Cantoblanco, 28049 Madrid, Spain
[b] Instituto de Ciencia de Materiales de Madrid (CSIC), C/Sor Juana Inés de la Cruz N°3, 28049 Madrid, Spain

ARTICLE INFO

Article history:
Received 12 June 2009
Received in revised form 29 July 2009
Accepted 30 July 2009
Available online 7 August 2009

Keywords:
Gold nanoparticles
Sol–gel technology
Glucose oxidase
Electrochemical biosensor
AFM
SEM

ABSTRACT

The design and characterization of a new organic–inorganic hybrid composite material for glucose electrochemical sensing are described. This material is based on the entrapment of both gold nanoparticles (AuNPs) and glucose oxidase, which was chosen as a model, into a sol–gel matrix. The addition of spectroscopic grade graphite to this system, which confers conductivity, leads to the development of a material particularly attractive for electrochemical biosensor fabrication. The characterization of the hybrid composite material was performed using atomic force microscopy and scanning electron microscopy techniques. This composite material was applied to the determination of glucose in presence of hydroxymethylferrocene as a redox mediator. The system exhibits a clear electrocatalytic activity towards glucose, allowing its determination at 250 mV vs Ag/AgCl. The performance of the resulting enzyme biosensor was evaluated in terms of sensitivity, detection limit, linear response range, stability and accuracy. Finally, the enhancement of the analytical response of the resulting biosensor induced by the presence of gold nanoparticles was evaluated by comparison with a similar organic–inorganic hybrid composite material without AuNPs.

© 2009 Elsevier B.V. All rights reserved.

1. Introduction

Development of sensors based on enzyme immobilization onto transducer surfaces has become one of the most promising research areas in the field of bionanotechnology, mainly due to its potential applications in the development of analytical devices. In general, the retention of the enzymatic activity after the immobilization process is one of the most important issues in this field. The interaction between the enzyme and the solid surface can induce conformational changes in the adsorbed enzymes. The alteration of the three-dimensional conformation leads to a diminution of the catalytic activity and hinders the enzyme functionality.

During the last years, numerous works have been published concerning the use of the silica sol–gel technology as a strategy to preserve the catalytic activity of enzymes after the immobilization step [1–4]. In this sense, the polymeric network generated by sol–gel technology can be used as an adequate matrix [5,6] in which several compounds, including biological material, can be encapsulated through physical entrapment rather than by covalent bonding leading to a non aggressive approach. Particularly, the sol–gel network provides a biocompatible environment for enzyme protection exhibiting additional advantages such as simplicity of preparation, chemical inertness, high stability, physical rigidity, renewable surface and tuneable properties. The final properties of the sol–gel matrix play a key role in the biosensor performance and can be easily controlled by varying some parameters such as the precursor or the preparation conditions (pH, ratio of compounds, etc). Various precursors have been reported in the literature for the preparation of the sol–gel network, but among them the most used for enzyme encapsulation are oxysilanes such as methyltrimethoxysilane (MTMOS), tetramethoxysilane (TMOS), 3-aminopropyltriethoxysilane (APTOS) and tetraethoxysilane (TEOS) [7–12].

Recently, the integration of nanomaterials into (bio)sensors has become an attractive method for improving the properties of the resulting analytical device. From a practical point of view, gold nanoparticles (AuNPs) are widely used due to their interesting physicochemical properties, which are essentially different to those of bulk gold [13]. In particular, several works have demonstrated that AuNPs exhibit highly attractive catalytic properties toward several compounds in solution indicating an enhancement of the electrical communication with the electrode surface [14,15]. Other key properties of AuNPs are their large surface area in

* Corresponding authors.
E-mail addresses: elena.casero@uam.es (E. Casero), encarnacion.lorenzo@uam.es (E. Lorenzo).

0039-9140/$ – see front matter © 2009 Elsevier B.V. All rights reserved.
doi:10.1016/j.talanta.2009.07.064

conjunction with an excellent biocompatibility. Both characteristics make this nanomaterial suitable to immobilize biomolecules, particularly enzymes, allowing the retention of the biological activity for a long period of time. Since the recognition of the use of nanoparticles is a versatile strategy for biomolecules immobilization [16], a great interest has been addressed to the development of biosensors based on AuNPs as a strategy of improving the biosensor performance [17].

In the present work we describe the preparation and characterization of a new organic–inorganic hybrid composite material from a three-dimensional silica polymer network, obtained by means of the sol–gel technology using tetraethoxysilane as precursor. This matrix provides an excellent network allowing the encapsulation of gold nanoparticles (AuNPs), a conductive material (graphite powder, C) and a biosensing molecule such as glucose oxidase (GOx), chosen as a model since it is a stable, inexpensive and well-studied enzyme. Moreover, GOx presents a wide range of applications in many fields such as biofuell cells [18] or clinical glucose determination [7,9,19,20]. The resulting hybrid materials were characterized by means of scanning electron microscopy (SEM) and atomic force microscopy (AFM) techniques. Both techniques allow obtaining information about not only the morphological properties of the surface but also about its compactness degree, homogeneity, rigidity and roughness. Finally, the analytical parameters of the resulting integrated glucose biosensor were studied.

2. Experimental

2.1. Reagents

Glucose oxidase (GOx, EC 1.1.3.4 from *Aspergillus niger*), lyophilized powder containing 15,200 U/g solid, was obtained from the Sigma Chemical Co. (St. Louis, MO). D-(+)-Glucose (99.5%) and Colloidal Gold (AuNPs, 20 nm particle size) were also purchased from Sigma Chemical Co. Tetraethoxysilane (TEOS), hydroxymethylferrocene (HMF, 97%) and polyethylene glycol (PEG, MW 400) were provided from Aldrich. Ultra pure spectroscopic graphite powder (C, particle size 50–50.3 μm) was from United Carbon Products Co. Inc. (Bay City, MI, USA). Other chemicals used in this work, such as sodium phosphate, acetaminophen, uric acid and ascorbic acid were reagent grade quality and used as received without additional purification steps. Sodium phosphate was employed for the preparation of buffer solutions (0.1 M, pH 7.0). Water was purified with a Millipore Milli-Q-System. All solutions were prepared just prior to use.

2.2. Experimental techniques

2.2.1. Scanning electron microscopy measurements

The scanning electron microscope was an ISI (DS-130C) operating at 40 kV. Measurements were carried out under high vacuum conditions.

2.2.2. Atomic force microscopy measurements

The atomic force microscope was a Nanoscope IIIa from Digital Instruments (DI, Santa Barbara, CA) used with D and J scanners (maximal scan range of ~14 μm and ~125 μm, respectively). Measurements were carried out in tapping-mode using Si cantilevers from Veeco. The samples were imaged with different cantilevers in order to ensure that the imaged structures were not due to tip artefacts. All measurements were carried out under ambient conditions.

2.2.3. Electrochemical measurements

All electrochemical measurements were performed on an Ecochemie Autolab PGSTAT12 system (Utrecht, The Netherlands). Experiments were carried out in an electrochemical cell with standard Teflon cover. All potentials are reported against a Ag/AgCl (Metrohm, 3.0 M KCl) reference electrode. The auxiliary electrode was a platinum wire and TEOS/GOx/C or TEOS/GOx/AuNPs/C composite electrodes were used as the working electrode. Cyclic voltammetry (CV) was the electrochemical technique applied to study the response of the composite electrodes in the presence of HMF (which acts as soluble mediator) and in the presence or absence of glucose. Solutions were deaerated with nitrogen gas before use, and the gas flow was kept over the solutions during experiments. Instrumental parameters were as follows: potential range from −0.1 V to 0.5 V and scan rate 10 mV s^{-1}.

2.3. Procedures

2.3.1. Sol–gel solution preparation

The sol–gel solution was prepared mixing 1.6 mL of TEOS with 1.0 mL of water and 200 μL of 0.1 M HCl. This solution was sonicated using an Ultrasons bath (P-Selecta) for 15 min at room temperature and stored overnight at 4 °C.

2.3.2. Activation of the graphite powder

The graphite powder used in the electrode preparation was previously activated by washing it with acetone, then with a mixture of HCl and HNO_3 (1:3) and finally with distilled water. The resulting paste was subsequently dried during 4 h at 400 °C [21].

2.3.3. Preparation of the biosensing organic–inorganic hybrid composite material

Two different kinds of biosensing organic–inorganic hybrid composite materials were prepared depending on the compounds encapsulated into the sol–gel three-dimensional network. The biosensing composite material denoted as TEOS/GOx/C was obtained by mixing 0.6 mL of the sol–gel solution with 0.4 g of graphite powder previously modified with enzyme. To obtain the glucose oxidase modified graphite, an amount of the conditioned graphite powder was mixed with GOx in phosphate buffer solution (PBS, pH 7) to adsorb the enzyme on the powder's surface after solvent evaporation (80 mg of GOx/0.5 g of graphite). This enzyme-modified graphite powder was allowed to dry for a week into a desiccator before being mixed with the sol–gel solution. The biosensing composite material including gold nanoparticles, denoted as TEOS/GOx/AuNPs/C, was prepared in a similar way, but using the gold colloidal solution (AuNPs, 20 nm average particle size) instead of water in the sol–gel solution preparation.

2.3.4. Electrode preparation procedure

The preparation of the electrode can be summarized as follows: 0.5 mL of the sol–gel solution was mixed with 0.4 g of graphite powder previously conditioned. The resulting inorganic composite material was packaged firmly into a glass body (15 mm large × 2 mm i.d.), leaving a little empty cavity (3 mm large × 2 mm i.d.) in one of the extremes. This was allowed to dry for five days at room temperature to achieve an adequate consistency. Subsequently, the little empty cavity was filled up tightly with the corresponding biosensing organic–inorganic hybrid composite material, leaving a little extra mixture sticking out of the tip to make easy the ulterior polishing step. Finally, a 0.5 mm diameter copper wire was inserted to the opposite extreme using silver tincture to establish the electrical contact and ensure the adhesion. The final electrode was allowed to dry for one day at room temperature and the surface was polished to remove any extra composite material, rinsed thoroughly with ultra pure water.

Before electrochemical measurements were made, electrode surfaces were conditioned by immersion during 2 h into 1 mM HMF

solution in PBS. This treatment avoids a posterior increment of the signal due to a mediator's adsorption.

3. Results and discussion

3.1. Optimization of parameters

As mentioned above, the first step involved in the preparation of the biosensing organic–inorganic hybrid composite material consists in a polymeric network generation by sol–gel technology, in which all the components integrating the biosensor will be subsequently encapsulated. The final properties of the resulting three-dimensional matrix depend strongly on both the chemical structure of the oxysilane precursor and the composition of the sol–gel solution. In this sense, two different silicon alcoxides (MTMOS and TEOS) were evaluated in order to study their influence on the final sol–gel properties. Among them, TEOS was selected as the most adequate because its use as precursor allows obtaining homogeneous sol–gel solutions without phase separation, relative short gelation times and adequate viscosity. Likewise, several volume ratios TEOS:H_2O were tested concluding that the optimal volume ratio TEOS:H_2O to reach the above requirements was 1.6:1.0. Under these conditions, the sol–gel process results in a homogeneous and transparent solution only under acid conditions using 200 μL of 0.1 M HCl as catalyser and ultrasonic agitation during 15 min. The obtained sol–gel solution is kept overnight at 4 °C and subsequently used to prepare the TEOS/GOx/C and TEOS/GOx/AuNPs/C composite electrodes. This preparation consists in thoroughly hand-mixing of the sol–gel solution with spectrographic graphite powder that is then allowed to gelify and to dry [21]. Different relations between graphite and sol–gel solution, unmodified and modified with GOx, were tested in order to obtain a uniform and suitable paste for its posterior packaging into the adequate electrode body. The optimal relation found were 0.4 g of graphite and 0.5 mL of sol–gel solution (0.8%, w/v), since the use of different ratios, 0.7% (w/v) and 0.5% (w/v), gives rise to a resulting paste whose consistency is not adequate for packaging into the glass tube. In the case of graphite modified with the enzyme, it was necessary to increase the volume of sol–gel solution up to 0.6 mL to ensure a good compactness, which is provided by the silicate continuum, without the necessity of any organic binder. The resulting composite material was packaged firmly into an electrode body. Among the diverse materials evaluated as candidates for electrode body, -plastic, Teflon and glass-, the last one was selected as the best material since, when the electrode body is filled up tightly with the sol–gel–graphite paste, the sol–gel solution bonds to the glass body, which results in an hermetic structure that only has contact with solutions through the electrode surface.

As mentioned above, gold nanoparticles are of extreme current interest since they have proved to be highly conductive (fast electron transfer) nanomaterials. In the preparation of TEOS/GOx/AuNPs/C composite electrodes, two different methods were used to achieve the objective of AuNPs incorporation in the composite: adsorption on graphite microparticles after solvent evaporation or direct incorporation in sol–gel precursors. In this case, although both methods were effective, the last one was selected because of its simplicity.

On the other hand, according to several authors, polyethylene glycol (PEG) enhances the hydrophilic character and permeability of the composite while reducing the sol–gel shrinkage over time [3,22]. After soaking in aqueous solution it forms microchannels within the composite because PEG leaches from the electrode. Thanks to the formation of these microchannels, PEG could be considered as "diffusion enhancer" of the analyte giving a higher current response [23,24]. In this sense, a volume of 250 μL of 10% (v/v) PEG was added to the sol–gel precursors but in this case, the AFM assays (discussed below) did not show significant structural differences between the two types of composites (in absence and in presence of PEG). As a consequence, PEG was not added to the sol–gel precursors.

3.2. Morphological characterization

As mentioned above, AFM and SEM techniques are very useful tools to obtain information about the morphological properties of the resulting surface obtained after each step involved in the ceramic composite electrodes preparation. The first step, the sol–gel formation, involves hydrolysis and polycondensation reactions leading to a SiO_2 lattice. Both the composition of the sol–gel mixture and the chemical structure of the precursor have a great influence on the morphological characteristics of the resulting surface, in particular roughness and size of pores. Fig. 1A shows a SEM image of a 40 μm × 40 μm sol–gel area, prepared as described above, which results to be rather flat and almost featureless. Fig. 1B and C shows AFM images taken on one of these flat areas. From these data a surface roughness in the 0.3–0.7 nm range is obtained, confirming the flatness of the surface. The higher resolution image displayed in Fig. 1C reveals a nanoporous surface with a typical external pore diameter of ~10 nm. The size and distribution of pores in the resulting sol–gel matrix is a relevant factor for enzyme encapsulation [25]. The pore diameter value obtained from the higher resolution AFM image confirms that the sol–gel preparation methodology leads to size pore diameters that will be not wide enough to allow the enzyme leakage, but adequate to facilitate the substrate permeation. As mentioned above, the influence of PEG addition to the sol–gel precursor on the final surface morphology was also evaluated by AFM (data not shown). In this case, the AFM measurements show that both preparation procedures (in absence and in presence of PEG) of the sol–gel lattice lead to a similar morphology of the resulting surface.

The addition of graphite powder to the sol–gel solution allows us to obtain a material (TEOS/C) that consists of a robust silica backbone entrapping interconnected carbon microparticles, which impart electronic conductivity to the material. As can be observed in Fig. 2A, it can be concluded that the addition of the graphite powder to the sol–gel solution causes a dramatic change on the micro-morphology of the surface. Large grains (between 25 μm and 50 μm of size) are observed on the surface, which correspond to those also observed by SEM on the raw graphite powder (data not shown). This rough morphology turns difficult the AFM measurements. It should be noted that the samples analyzed in this work were not specifically prepared for AFM characterization but they were the real surfaces generated by the sol–gel process. Notwithstanding, it is possible to carry out AFM analysis on restricted areas provided that special care is addressed to preserve the cantilever condition, particularly the tip size and shape during the imaging process. Under these conditions, images as that shown in Fig. 2B can be obtained. This figure shows micro and nanocrystalline flat graphite regions on top of one of the large grains observed in the SEM image. On one of these regions, we were able to obtain atomic resolution AFM images (Fig. 2C). The characteristic 0.25 nm graphite hexagonal lattice periodicity is clearly observed [26]. As mentioned above, we have essayed different ratios between graphite powder and sol–gel solution (0.8%, 0.7% and 0.5% (w/v)) to obtain the TEOS/C material. Subsequently, we have performed AFM measurements of the resulting composites. AFM images corresponding to TEOS/C material obtained by using graphite powder/sol–gel solution ratios of 0.7% and 0.5% (w/v) (data not shown) are similar than that presented in Fig. 2C for a 0.8% (w/v) ratio. Therefore, it can be concluded that a moderate change in the graphite powder/sol–gel solution ratio did not affect the final morphological characteristics of the resulting composite material.

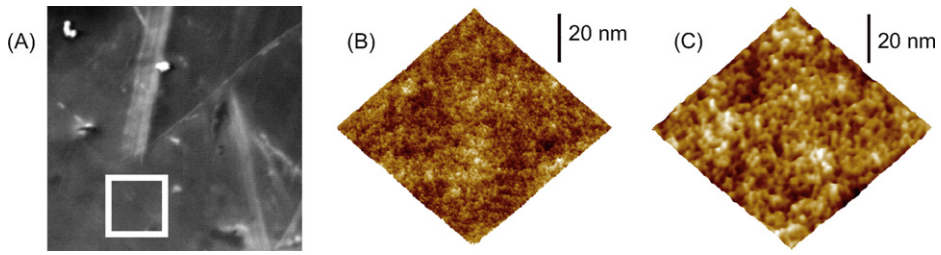


Fig. 1. (A) 40 μm × 40 μm SEM image of the sol–gel surface. (B) 7.5 μm × 7.5 μm and (C) 420 nm × 420 nm AFM images taken on a flat region as that marked in (A).

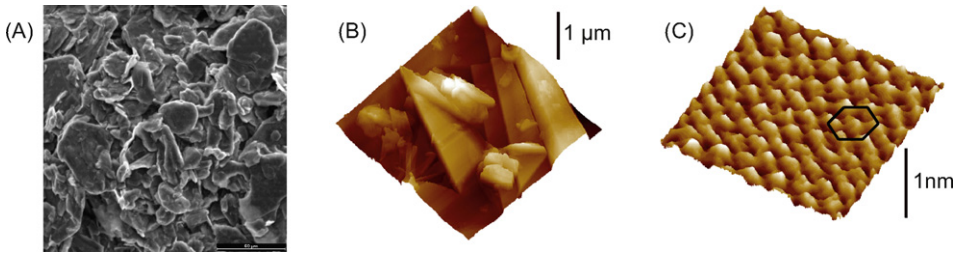


Fig. 2. (A) 150 μm × 150 μm SEM image of the TEOS/C surface. (B) 7.5 μm × 7.5 μm AFM image taken on a large grain. (C) 1.7 nm × 1.7 nm atomic resolution AFM image taken on a flat region of figure (B). The hexagonal graphite lattice, with a lateral side of 0.25 nm, is marked.

The presence of the enzyme (TEOS/GOx/C) implies a further change in the surface morphology of the sample at the micrometer scale (Fig. 3A) since it is formed by flat platelets delimited by deep crevices. Fig. 3B is an AFM image on two neighboring platelets separated by a deep groove in the middle of the image. At this scale, the platelet surface is rough and it is formed by rounded structures (Fig. 3C) that correspond to the globular GOx enzymes and aggregates covering the electrode surface. The measured lateral dimension of the smallest globular structures (14–16 nm) is in good agreement with the typical dimensions of GOx (6.0 nm × 5.2 nm × 7.7 nm) reported in the literature [27] taking into account tip widening effects due to the tip geometry and applied force. It is worth noting that AFM studies of the inner part of such sample, which was previously fractured, did show also globular structures. This fact indicates that the enzyme was successfully incorporated into the hybrid sol–gel matrix proving that the resulting sol–gel matrix is a good material for enzyme loading.

Finally, in order to assess the influence of the nanoparticles addition on the electrode nano-morphology we have compared the images obtained for the TEOS/GOx/AuNPs/C system (Fig. 4) with those obtained for the TEOS/GOx/C system (Fig. 3). From this comparison it is clear that both systems are analogous at the micron (Figs. 3A and 4A) and nano (Figs. 3B–C and 4B–C) scales.

3.3. Electrochemical performance of the glucose biosensor

Glucose biosensor is based on glucose oxidase, which in presence of oxygen catalyzes the oxidation of glucose into gluconolactone and hydrogen peroxide. The activity of the immobilized GOx can be electrochemically detected by monitoring the H_2O_2 produced in the enzymatic reaction. Accordingly, we have obtained the cyclic voltammetric response from −0.1 V to +0.8 V at 10 mV/s for the TEOS/GOx/AuNPs/C electrode in a 0.1 M pH 7.0 phosphate buffer solution containing 10 mM of hydrogen peroxide in order to test whether this strategy is adequate to glucose determination. The resulting cyclic voltammetric response (data not shown) exhibits an irreversible anodic wave with a peak potential at about +0.7 V. Therefore, the determination of glucose in real samples, such as blood, by direct oxidation of the hydrogen peroxide generated in the enzymatic reaction do not represent an adequate strategy because it can be affected by potential interfering species present in the sample, which could also be oxidized at the high potential required for H_2O_2 amperometric detection. In order to minimize the contribution of interfering substances to the glucose biosensor response, one of the most important approaches reported in the literature is based on the replacement of the natural electron acceptor (O_2) by an artificial mediator such as polyneutral red [11], celestin blue [20], or prussian blue [28,29]. Based on our previous experience with other oxidases [30], we have studied the ability of the hydroxymethylferrocene (HMF) to act as a redox mediator in solution. Fig. 5 (curve a) shows the cyclic voltammetric response from −0.1 V to +0.5 V at 10 mV/s for the TEOS/GOx/AuNPs/C electrode in a 0.1 M pH 7.0 phosphate buffer solution containing 1.0 mM of HMF in the absence of glucose. The redox response of the ferrocene/ferrocinium process in aqueous media is observed. Addition of glucose to a final concentration of 2.0 mM (curve b) leads to an enhancement of the anodic peak current concomitant with a decrease of the cathodic peak current consistent with a clear elec-

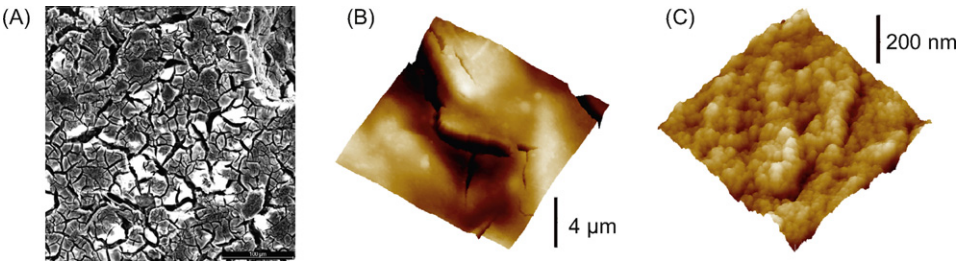


Fig. 3. (A) 350 μm × 350 μm SEM image of the TEOS/GOx/C surface. (B) 7.5 μm × 7.5 μm and (C) 1.0 μm × 1.0 μm AFM images taken on a platelet region.

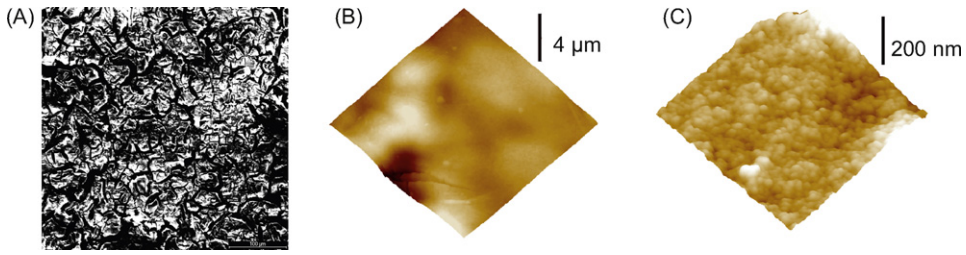


Fig. 4. (A) 350 μm × 350 μm SEM image of the TEOS/GOx/AuNPs/C surface. (B) 7.5 μm × 7.5 μm and (C) 1.0 μm × 1.0 μm AFM images taken on a platelet region.

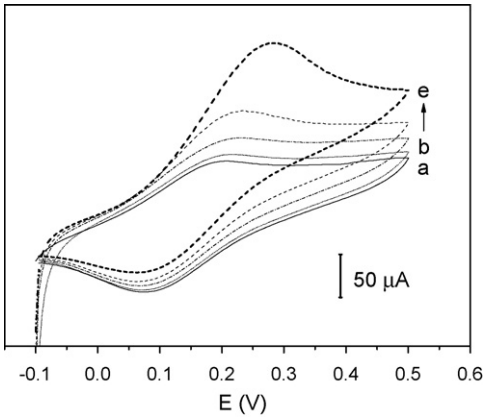


Fig. 5. (A) Cyclic voltammetric response at 10 mV/s for a TEOS/GOx/AuNPs/C composite electrode in a deareated solution of 1.0 mM HMF in 0.1 M phosphate buffer (pH 7.0) as a function of glucose concentration: (a) 0.0 mM, (b) 2.0 mM, (c) 7.0 mM, (d) 25 mM, (e) 55 mM.

trocatalytic effect. Fig. 5 (curves c–e) shows the increment of the magnitude of the catalytic current as a consequence of increasing the amount of glucose (final concentrations of 7 mM, 25 mM and 55 mM, respectively).

In order to ascertain the influence of the AuNPs on the enhancement of the analytical response of the designed organic–inorganic hybrid composite material, we have also obtained the voltammetric response (data not shown) of a similar composite material containing GOx but free of gold nanoparticles (TEOS/GOx/C). As one would expect, in this case the catalytic wave obtained after addition of 2.0 mM of glucose is smaller and less defined than that obtained when gold nanoparticles are present. Fig. 6 depicts typical calibration curves, in which catalytic current obtained from CV measurements was plotted vs glucose concentration for (A) TEOS/C, (B) TEOS/GOx/C and (C) TEOS/GOx/AuNPs/C ceramic carbon electrodes, respectively. Catalytic current was obtained by subtracting the current response in the absence of glucose to the response in the presence of glucose at a potential of +0.25 V. As one would expect, the response obtained (in the same conditions) for a hybrid composite material without enzyme (TEOS/C) is completely different. In this case, upon addition of glucose no catalytic waves are observed, confirming both the role of the enzyme in the catalytic response to substrate and the biocompatibility of the developed hybrid sol–gel material for immobilization of enzymes that retain their activity in a large extent. The analytical properties – linear response, sensitivity and detection limit – of both TEOS/GOx/C and TEOS/GOx/AuNPs/C biosensors were obtained from the linear part of the current vs glucose concentration plot. As shown in Fig. 6, the calibration plots were linear over a wide concentration range, 1–20 mM and 0.5–55 mM for TEOS/GOx/C and TEOS/GOx/AuNPs/C biosensors, respectively. The sensitivity values, calculated from the slope of the plot, were of 1.73 μA mM^{-1} and 2.43 μA mM^{-1}, respectively. The detection limit, calculated as the ratio between three times the standard deviation of background current and the sensitivity, was 1.9 mM for TEOS/GOx/C and 1.3 mM for TEOS/GOx/AuNPs/C. Since the normal glucose concentration in blood is in the 4.4–6.6 mM range [31], the detection limit obtained for the TEOS/GOx/AuNPs/C biosensor is medically useful for glucose level monitoring in blood. The accuracy of both TEOS/GOx/C and TEOS/GOx/AuNPs/C biosensors was evaluated from the relative standard deviation (R.S.D.) of eight different measurements of a 5 mM glucose concentration with the same biosensor. The R.S.D. values were 1.1% and 0.5%, respectively. As can be seen in Table 1, most of the analytical properties corresponding to both TEOS/GOx/C and TEOS/AuNPs/GOx/C are comparable or even better than results reported in the literature for similar sol–gel-based glucose biosensors [9,11,28,29,32–36]. The storage stability was also investigated by measuring the magnitude of the current response for a 10 mM glucose concentration every 5 days during a period of 30 days, keeping the biosensor stored at 4 °C between measurements. When the biosensor is reused, a gradual decay in the signal is observed, leading to a loss of 50% of the initial response after 30 days. Moreover, the developed biosensor exhibited a high degree of robustness since changes in the experimental conditions such as temperature, pH and electrolyte concentration do not critically affect its response.

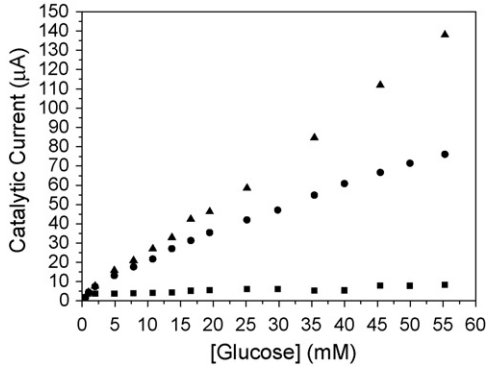


Fig. 6. Catalytic current vs glucose concentration for the following composite electrodes: (■) TEOS/C, (●) TEOS/GOx/C and (▲) TEOS/GOx/AuNPs/C. Data were obtained from cyclic voltammetric measurements at 10 mV/s in a deareated solution of 1.0 mM HMF in 0.1 M phosphate buffer (pH 7.0) for increasing glucose concentration.

In order to test the utility of the developed biosensors in the determination of glucose present in a real sample, we have carried out an exhaustive study of the influence of the more usual potential interferences. In this sense, we have obtained the biosensor response to 5 mM of glucose in absence and presence of several substances, which can be usually present in blood samples, such as acetaminophen (0.1 mM), ascorbic acid (0.1 mM) and uric acid (0.2 mM). While the presence of acetaminophen has a negligible effect to the biosensor response, addition of ascorbic acid or uric acid (both of them easily oxidized at electrodes) results in an increase of the catalytic current of 6% and 7%, respectively. These results, comparable or even better than other reported in the literature for similar biosensors [7,28,32,37], suggest that the developed

Table 1

Biosensor	Sensitivity ($\mu A\,mM^{-1}$)	Linear range (mM)	Applied potential (V)	Accuracy (R.S.D.)
TEOS/GOx/C (present work)	1.73	1–20	+0.25	1.1% ($n=8$)
TEOS/AuNPs/GOx/C (present work)	2.43	0.5–55	+0.25	0.5% ($n=8$)
Sol–gel/chitosan/GOx [32]	0.27	Up to 14	+0.35	2% ($n=7$)
Fc/Ormosil/GOx/GP [33]	1.76	Up to 35	+0.35	–
Sol–gel/CNT/GOx/Bppg [9]	0.20	0.2–20	+0.3	1.8% ($n=10$)
Sol–gel/GOx/chitosan/PB/GC [29]	0.42	0.05–26	−0.05	3.8% ($n=8$)
Sol–gel/PNR/GOx [11]	0.06	0.05–0.6	−0.25	–
Sol–gel/GOx/PtNPs-CNT [34]	0.28	1–25	+0.1	5.1% ($n=10$)
Sol–gel/PVA/GOx/SPE [35]	0.44	0–4.1	−0.5	–
Sol–gel/GOx/PB/GC [28]	0.84	0.01–5.8	0	1.8% ($n=8$)
Sol–gel/GOx/CNT/chitosan/PtNP/GC [36]	2.08	0.001–6.0	0.1	–

device can be successfully used to measure glucose concentrations in presence of possible interfering substances.

In the light of the results obtained concerning the performance of both TEOS/GOx/C and TEOS/AuNPs/GOx/C biosensors (summarized in Table 1), it is clear that addition of gold nanoparticles to the hybrid composite material improves the analytical properties of the resulting biosensor, particularly sensitivity, linear range concentration and accuracy. This improvement is a consequence of the advantages obtained through the combined use of gold nanoparticles and a biocompatible organic–inorganic hybrid material with a porous and open framework.

4. Conclusions

In this paper, we develop a novel organic–inorganic hybrid composite material for glucose electrochemical sensing based on integration of a biosensig element (GOx), nanomaterials (AuNPs) and graphite powder (C) into a sol–gel matrix. This composite material combines the advantages induced from both the silica matrix, which enables the incorporation of the other elements while keeping the enzymatic activity of the assembly, and the presence of nanostructures, which enhances the electroactive area. As a consequence, the resulting biosensor TEOS/AuNPs/GOx/C exhibits a wider linear range concentration, higher sensitivity and higher accuracy, when compared with a similar composite containing GOx but free of AuNPs (TEOS/GOx/C). Taking into account the good performance of the resulting biosensor, this approach is a promising route for designing a wide range of biosensors.

Acknowledgments

This work has been supported by Comunidad Autónoma de Madrid/Universidad Autónoma de Madrid (project No. CCG08-UAM/SEM-4074), Ministerio de Ciencia e Innovación (projects No. CTQ2008-05775, FIS2006-12253-C06-03 and Consolider No. CSD2007-00010). M.B. gratefully appreciates financial support from Universidad Autónoma de Madrid through FPU Grant.

References

[1] S. Braun, S. Rappoport, R. Zusman, D. Avnir, M. Ottolenghi, Mater. Lett. 10 (1990) 1–5.
[2] B.C. Dave, B. Dunn, J.S. Valentine, J.I. Zink, Anal. Chem. 66 (1994) 1120A–1127A.
[3] L. Rabinovich, O. Lev, Electroanalysis 13 (2001) 265–275.
[4] W. Jin, J.D. Brennan, Anal. Chim. Acta 461 (2002) 1–36.
[5] C. Cabello-Carramolino, M.D. Petit-Domínguez, Anal. Chim. Acta 614 (2008) 103–111.
[6] C. Cabello-Carramolino, M.D. Petit-Domínguez, Microchim. Acta 164 (2009) 405–410.
[7] B. Wang, B. Li, Q. Deng, S. Dong, Anal. Chem. 70 (1998) 3170–3174.
[8] A. Walcarius, Electroanalysis 13 (2001) 8–9.
[9] A. Salimi, R.G. Compton, R. Hallaj, Anal. Biochem. 333 (2004) 49–56.
[10] A. Kumar, R.R. Pandey, B. Brantley, Talanta 69 (2006) 700–705.
[11] R. Pauliukaite, A.M.C. Paquim, A.M. Oliveira-Brett, C.M.A. Brett, Electrochim. Acta 52 (2006) 1–8.
[12] S. Singh, R. Singhal, B.D. Malhotra, Anal. Chim. Acta 582 (2007) 335–343.
[13] J.H. Fendler, Nanoparticles and Nanostructured Films, Wiley-VCH, Weinheim, Germany, 1998.
[14] A.I. Abdelrahman, A.M. Mohammad, T. Okajima, T. Ohsaka, J. Phys. Chem. B 110 (2006) 2798–2803.
[15] M. Chirea, C.M. Pereira, F. Silva, J. Phys. Chem. C 111 (2007) 9255–9266.
[16] A. Rembaum, W.J. Dreyer, Science 208 (1980) 364–368.
[17] N. Zhou, J. Wang, T. Chen, Z. Yu, G. Li, Anal. Chem. 78 (2006) 5227–5230.
[18] T. Chen, S.C. Barton, G. Binyamin, Z. Gao, Y. Zhang, H.H. Kim, A. Heller, J. Am. Chem. Soc. 123 (2001) 8630–8631.
[19] R. Wilson, A.P.F. Turner, Biosens. Bioelectron. 7 (1992) 165–185.
[20] A. Noorbakhsh, A. Salimi, E. Sharifi, Electroanalysis 20 (2008) 1788–1797.
[21] M. Siswana, K.I. Ozoemena, T. Nyokong, Talanta 69 (2006) 1136–1142.
[22] Z. Ji, A.R. Guadalupe, Electroanalysis 11 (1999) 167–174.
[23] S. Sampath, O. Lev, Anal. Chem. 68 (1996) 2015–2021.
[24] G. Shustak, S. Marx, I. Turyan, D. Mandler, Electroanalysis 15 (2003) 398–408.
[25] A.M. Chiorcea-Paquim, R. Pauliukaite, C.M.A. Brett, A.M. Oliveira-Brett, Biosens. Bioelectron. 24 (2008) 297–305.
[26] M. Enachescu, D. Schleef, D.F. Ogletree, M. Salmeron, Phys. Rev. B 60 (1999) 16913–16919.
[27] H.J. Hetch, H.M. Kalisz, J. Hendle, R.D. Schmid, D. Schomburg, J. Mol. Biol. 229 (1993) 153–172.
[28] R. Liang, J. Jiang, J. Quiu, Electroanalysis 20 (2008) 2642–2648.
[29] X. Tan, Y. Tian, P. Cai, X. Zou, Anal. Bioanal. Chem. 381 (2005) 500–507.
[30] A. Parra, E. Casero, L. Vázquez, F. Pariente, E. Lorenzo, Anal. Chim. Acta 555 (2006) 308–315.
[31] G. Reach, G.S. Wilson, Anal. Chem. 64 (1992) 381A–386A.
[32] X. Chen, J. Jia, S. Dong, Electroanalysis 15 (2003) 608–612.
[33] P.C. Pandey, S. Upadhyay, N.K. Shukla, S. Sharma, Biosens. Bioelectron. 18 (2003) 1257–1268.
[34] M. Yang, Y. Yang, Y. Liu, G. Shen, R. Yu, Biosens. Bioelectron. 21 (2006) 1125–1131.
[35] S. Zuo, Y. Teng, H. Yuan, M. Lan, Sens. Actuators B 133 (2008) 555–560.
[36] X. Kang, Z. Mai, X. Zou, P. Cai, J. Mo, Talanta 74 (2008) 879–886.
[37] J. Lu, I. Do, L.T. Drzal, R.M. Worden, I. Lee, ACS Nano 2 (2008) 1825–1832.

Talanta 80 (2009) 803–808

Contents lists available at ScienceDirect

Talanta

journal homepage: www.elsevier.com/locate/talanta

An immunoassay for bisphenol A based on direct hapten conjugation to the polystyrene surface of microtiter plates

Yi Feng[a,1], Baoan Ning[b,1], Pu Su[b], Hongyong Wang[b], Caihong Wang[b], Fusheng Chen[a,**], Zhixian Gao[a,b,c,*]

[a] College of Food Science and Technology, Huazhong Agricultural University, Wuhan 430070, China
[b] Institute of Hygiene and Environmental Medicine, Tianjin 300050, China
[c] Tianjin Key Laboratory of Risk Assessment and Control Technology for Environment & Food Safety, Tianjin, 300050, China

ARTICLE INFO

Article history:
Received 17 April 2009
Received in revised form 27 July 2009
Accepted 30 July 2009
Available online 8 August 2009

Keywords:
Bisphenol A
Antibodies
Hapten
Immunoassay
Silane coupling agents

ABSTRACT

Based on direct hapten coated format a competitive indirect enzyme-linked immunosorbent assay (ciELISA) for bisphenol A (BPA) was developed. Polystyrene surface was modified by 3-Aminopropyltriethoxysilane (APTES) to produce amino groups after H_2SO_4/HNO_3-pre-treatment. 4,4-bis (4-hydroxyphenyl) valeric acid (BVA) which is analogue of BPA, was successfully immobilized on the surface of microtiter plates by N,N′-dicyclohexylcarbodiimide (DCC) method. The essential steps of the assay were optimized, especially blocking procedure which is key step to prevent unspecific binding of antibody. The results indicated that compared with hapten-protein coated format (IC_{50} = 176.67 ng ml^{-1}, LOD = 15.90 ng ml^{-1}), the direct hapten coated format (IC_{50} = 23.50 ng ml^{-1}, LOD = 0.27 ng ml^{-1}) could improve assay sensitivity and the detection ranges were 2.30 ng∼157.60 ng ml^{-1} with good signal reproducibility (P value > 0.05) after careful optimization of assay conditions. Tap water samples and seawater samples were spiked with a known amount of BPA and measured by ciELISA. The average recoveries were between 70 and 142%. As far as we are aware this is the most sensitive ELISA for BPA yet reported.

© 2009 Published by Elsevier B.V.

1. Introduction

In recent years, the issues of environmental endocrine disruptors (EEDs) have attracted more and more public attention. Bisphenol A (BPA) (Table 1) which is widely used for the production of plastics, belongs to EEDs. Since Krishnan firstly reported that BPA had weak estrogenic property [1], many studies have verified its effect on animals and human beings [2,3]. Thus, it is urgent to develop highly sensitive, selective, large-scale and rapid analytical methods to routinely monitor BPA level in the environment.

Enzyme-linked immunosorbent assays (ELISAs) have been developed and used widely to detect EEDs [4–6] due to their fast, portable and cheap characteristics.

Competitive ELISAs are always employed to determine EEDs because most of EEDs are low-molecular-weight compounds (hapten) without multi-epitopes compared with macromolecules.

In competitive ELISAs there are two assay formats—the antibody-immobilized-format and the antigen-immobilized-format [7].

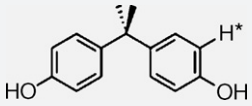
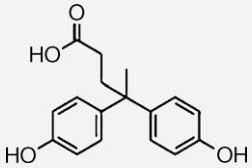
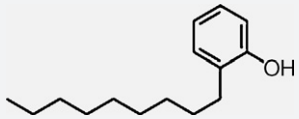
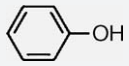
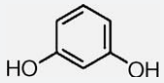
In the antibody-immobilized-format antibody was coated on polystyrene surface by passive adsorption owing to intermolecular attraction forces (hydrophobic interactions). However, most of the antibodies were denatured in this process. Butler determined that over 90% of monoclonal antibodies and about 75% of polyclonal antibodies against fluorescein could not recognize hapten upon adsorption onto polystyrene surfaces [8]. Moreover, it is difficult to prepare hapten–enzyme conjugate because enzyme has fewer coupling site than albumins and the conjugation could deactivate enzyme.

Hapten–protein conjugate was always used as coating protein in the antigen-immobilized-format. Based on hydrophobic interactions hapten–protein was immobilized on polystyrene surfaces. However, the immobilization must involve significant conformational changes to create large-scale hydrophobic contacts. Conformational change would influence hapten presentation for the reason that low-molecular-weight compounds with small size could be easily screened by macromolecular. On the other hand, the reaction between hapten and protein was not always reproducible, which is unfavorable to make assay standardization.

* Corresponding author at: College of Food Science and Technology, Huazhong Agricultural University, Wuhan 430070, China. Tel.: +86 022 84655191; fax: +86 022 84655191.
** Corresponding author. Tel.: +86 027 87282927; fax: +86 027 87282927.
E-mail addresses: chenfs@mail.hzau.edu.cn (F. Chen), gaozhx@163.com (Z. Gao).
[1] These authors contributed equally to this work.

0039-9140/$ – see front matter © 2009 Published by Elsevier B.V.
doi:10.1016/j.talanta.2009.07.070

Table 1
Cross-reactivities of the inhibition assays with selected compounds.

Compounds	Structure	Cross-reactivity (%)
Bisphenol A		100
BVA		75
Nonylphenol		<0.1
Phenol		<0.1
Resorcinol		<0.1

These drawbacks could be avoided by the new format—direct hapten linkage to the polystyrene surface. The polystyrene surface without reactive groups could be modified by silane coupling agents to produce various functional groups such as hydroxyl, amino, carbonyl, carboxyl, etc. Functional silane compounds are available from a number of commercial sources, which include Gelest, Aldrich, and others. There are some commonly used silane agents such as carboxyethylsilanetriol, 3-aminopropyltriethoxysilane (APTES), 3-glycidoxypropyltrimethoxysilane (GOPTS), isocyanatopropyltriethoxysilane (ICPTES), *N*-(trimethoxysilylpropyl)ethylenediamine triacetic acid (TMS-EDTA) etc. In our study, we developed an efficient and convenient method to modify the polystyrene surface by APTES to produce reactive amino group. One commercially available reagent, 4,4-bis(4-hydroxyphenyl) valeric acid (BVA) (Table 1) which is analogue of BPA, was used to link to modified surface based on DCC method. The results revealed that direct hapten coated format showed higher degree of assay sensitivity than hapten–protein format.

2. Experimental

2.1. Materials

APTES, BPA, BVA, GOPTS, native bovine serum albumin (nBSA), and ovalbumin (OVA) were purchased from Sigma (St. Louis, MO, USA). *N*,*N*′-Dicyclohexylcarbodiimide (DCC) and *N*-hydroxysuccinimide (NHS) were obtained from Pierce (Rockford, IL, USA). Goat anti-mouse IgG–HRP conjugate was from Sino-American Biotechnology Company (Beijing, China). Dimethylformamide (DMF) and other organic solvents were purchased from Sino-pharm Chemical Reagent Company (Shanghai, China). The anti-BPA monoclonal antibody was a kind gift from Dr. Gerardo R. Marchesini and Prof. Willem Haasnoot (RIKILT-Institute of Food-Safety, P.O. Box 230, 6700 AE Wageningen, The Netherlands).

2.2. Hapten–protein conjugates preparation

Preparation of Hapten–BSA conjugates for coating protein was carried out by the previous method [9] with some modifications. The coupling reaction was performed at pH 7.4 according to the following procedure. NHS (10 mg in 750 μl DMF) was mixed with DCC (20 mg in 750 μl DMF) and BVA (10 mg in 500 μl DMF) for 24 h at 25 °C. Of this mixture, 200 μl was added drop wise to 2 ml of a BSA solution (10 mg ml^{-1} in 0.1 M PBS buffer at pH 7.4). After 2 h incubation at 25 °C, the products were dialyzed against PBS for 72 h and the solution was lyophilized. Then the white crystal obtained was stored at −20 °C.

2.3. Direct hapten immobilization on polystyrene surface modified by APTES

Direct hapten immobilization followed by the method [10] with some modifications. The reaction mechanism of direct hapten immobilization on polystyrene surface modified by APTES is shown in Fig. 1. In brief, plates were first treated with 47% (v/v) HNO_3 in concentrated H_2SO_4 for 30 min at room temperature to generate $-NO_2$ groups on polystyrene surface. Then each well was treated with 250 μl 5% aqueous APTES solution at pH 5.5 by incubating at room temperature (RT) for 2 h. After washing wells two times with double distilled water (DDW), the plates reacted at 70 °C for 2 h to stabilize thin monolayer of APTES on polystyrene microtiter plates and incubated overnight at 4 °C. The unbound amines were blocked with 0.2 M formaldehyde by incubating the plates for 2 h at 37 °C.

Protein–hapten conjugates (BVA–BSA) coated on the surface of microtiter plate by adding 100 μl conjugate (50 ng ml^{-1} in carbonate buffer) per well and incubating overnight at 4 °C. To solve non-specific adsorption problem, plates were treated with blocking buffer (0.1 mol/l phosphate buffered saline, pH 7.4, containing 0.05% Tween 20, 1.0% BSA, 0.5% casein, 0.01% sodium azide) at 37 °C for 2 h and washed three times with washing solution (0.1 mol/l phosphate buffered saline, pH 7.4, containing 0.05% Tween 20, PBST) for further reaction.

2.4. Competitive inhibition ELISA protocol

The procedure of competitive inhibition ELISA was similar to routine methods [11] with some modifications. Briefly, treated plate was washed three times with washing solution for each well and decanted. Then 50 μl of antibody against BPA (1/6000) in antibody dilution buffer (0.1 mol/l phosphate buffered saline, pH 7.4, containing 0.05% Tween 20, 0.1% BSA, 0.01% sodium azide) and 50 μl various concentrations (10^{-2}, 10^{-1}, 10^{0}, 10^{1}, 10^{2}, 10^{3}, 10^{4} ng ml^{-1}) of analytes were added to each well and incubated at 37 °C for 2 h. After washing five times, 100 μl of goat anti-mouse IgG–HRP conjugate (1/2000) in secondary antibody dilution buffer (0.1 mol/l phosphate buffered saline, pH 7.4, containing 0.05% Tween 20, 1.0% BSA, 0.01% sodium azide) was added into each well and incubated at 37 °C for 1 h. Then 100 μl of 3,3′,5,5′-tetramethylbenzidine (TMB) substrate was added after washing the plate six times and incubated at 37 °C for 15 min. The reaction was terminated by the addition of 2 mol l^{-1} sulfuric acid. Absorbance at 450 nm was determined in a Multiskan MK3 ELISA reader (Thermo, China).

2.5. Immunoassay sensitivity and specificity

Briefly, after the polystyrene plates were coated by BVA–BSA and blocked with our blocking buffer, 50 μl of antibody against BPA (1/8000) in antibody dilution buffer (0.1 mol/l phosphate buffered saline, pH 7.4, containing 0.05% Tween 20, 0.1% BSA, 0.01% sodium azide) and 50 μl various concentrations (10^{-2}, 10^{-1}, 10^{0}, 10^{1}, 10^{2}, 10^{3}, 10^{4} ng ml^{-1}) of analytes were added to each well and incubated at 37 °C for 1 h. The subsequent steps were as described in Section 2.4.

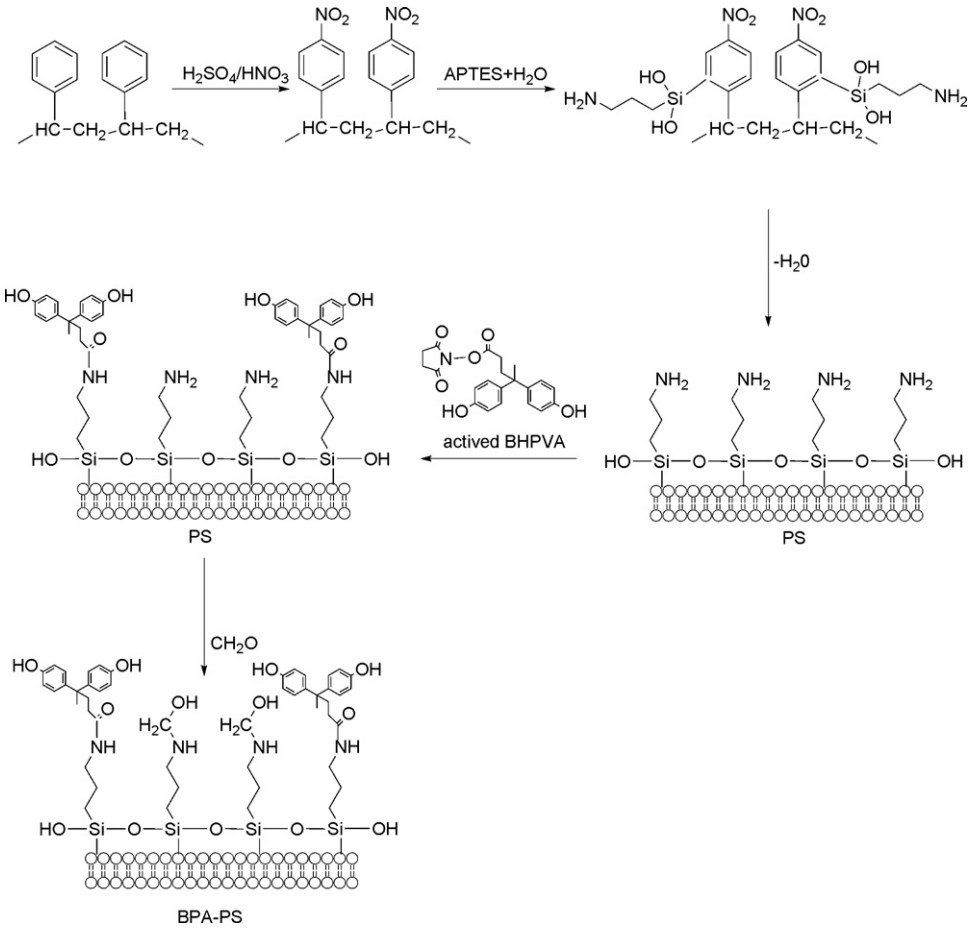


Fig. 1. Reaction mechanism of direct immobilization of BHPVA on PS surface modified with APTES.

Data analysis was performed using normalized assay signals % B/B_0 using the following formula:

$$\%\frac{B}{B_0} = 100 \times \frac{A - A_{ex}}{A_0 - A_{ex}}$$

where A is the absorbance of hapten at standard concentration; A_0 the absorbance at zero hapten concentration; and A_{ex} is the absorbance at excessive hapten concentration surface.

IC_{50} value was the half maximal (50%) inhibitory concentration of a substance and was determined in the competitive experiment described above. The cross-reactivity values were calculated according to the formula: $\frac{IC_{50\,hapten}\,(ngml^{-1})}{IC_{50\,BPA\,analogs}\,(ngml^{-1})} \times 100\%$

2.6. Matrix effect studies

Different natural water samples (tap water (Tianjin city), seawater (Tianjin coast)) were collected and used to assess the performance of the indirect ELISA method.

3. Results and discussion

3.1. Determination of BVA–BSA conjugates by UV spectrophotometer and mass spectrum

From UV–vis spectra (Fig. 2), we could observe that BVA–BSA conjugates had maximum absorption peak wavelength in 279 nm which is similar with BSA. Furthermore, the results also indicated that the absorption peak strength of BVA–BSA (1 mg ml^{-1}) in 279 nm was stronger than BSA (1 mg ml^{-1}) in same wavelength. This might result from BVA in the conjugate since BVA has maximum absorption peak wavelength at 277 nm.

MW of BVA–BSA was 71,127 determined by mass spectrum as shown in Fig. 3 and the coupling ratio was found to be 15:1.

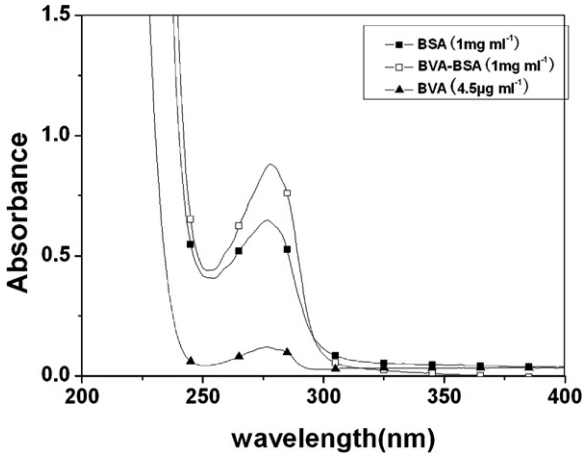


Fig. 2. The UV–vis spectra of 4.5 μg/ml BVA, 1.0 mg/ml BPA-BSA and 1.0 mg/ml BVA–BSA in 10% methanol solution.

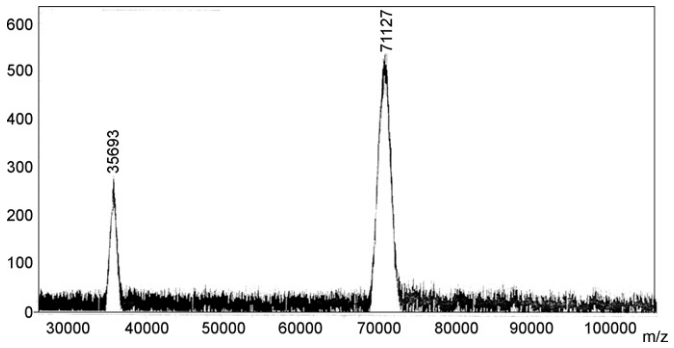


Fig. 3. Mass spectrograms of BVA–BSA.

3.2. Detection of specificity of antibodies by indirect competitive ELISA

In this study, cross-reactivities (CR) of two phenolic compounds (BPA, BVA) and three simple phenolic compounds (phenol, nonylphenol, resorcinol) were evaluated for competitive inhibition ELISA and were calculated as CR (%) = ($IC_{50\ BPA}$)/($IC_{50\ BPA\ analogs}$) × 100. From the result (Table 1), it could be clearly seen that the cross reactions of BPA and BVA were 100% and 75%, respectively, while the cross reactions of the other three compounds were all much lower than 1%. The common part of the structure of BPA and BVA is the two phenolic rings bridged through a carbon atom. Thus we believed that the produced antibody specifically recognized such a bisphenolic group. Interestingly BPA showed higher affinity than BVA with antibody. The results may be due to the influence of carboxy group of BVA on the antigen–antibody reaction.

3.3. Optimization of the essential steps of the assay

100 μl activated BVA solution at serial concentrations (40, 80, 160, 320, 640, 1280, 2560, 5120 nmol ml^{-1}) was added into each well with modified by APTES and incubated overnight at 4 °C. It could be clearly seen that with increasing of concentration of activated BVA solution OD_{450} value increases. The result indicated that the hapten was successfully immobilized on the polystyrene surface with modified by APTES.

To prevent the antibody from unspecific binding to the surface a blocking step is required. In hapten–protein format, blocking buffer (0.1 mol/l phosphate buffered saline, pH 7.4, containing 0.05% Tween 20, 1.0% BSA, 0.5% casein, 0.01% sodium azide) was added into well to block blank site on the surface before competition step. Our results (Fig. 4) showed that compared with blocking buffer without casein (IC_{50} = 206.34 ng ml^{-1}), assay with our blocking buffer (IC_{50} = 176.67 ng ml^{-1}) could improve assays sensitivity. However, BSA/OVA pre-treatment was not effective to prevent unspecific binding of the antibody in direct hapten coated format. Different blocking reagents were tested for their effectiveness–BSA, OVA, skimmed milk, trehalose. All were unable to prevent unspecific binding of the secondary antibody. Our study found that unspecific binding problem could be effectually solved only while the primary antibody and the secondary antibody were diluted in PBS + 0.1% BSA (W/V).

Chequerboard titration has been used for selecting an optimum of antigen–antibody reaction. Fig. 5 showed the chequerboard titration results for the antibody. From the result the titers of the antibody were found to be 1:6000, and the optimal concentration for activated BVA was 640 nmol/ml. Furthermore, it was interesting to note that with increasing coating hapten concentration A_0 signals showed a drop beyond 640 nmol/ml. Previous studies [12–14] also described a similar phenomenon. The extraordinary

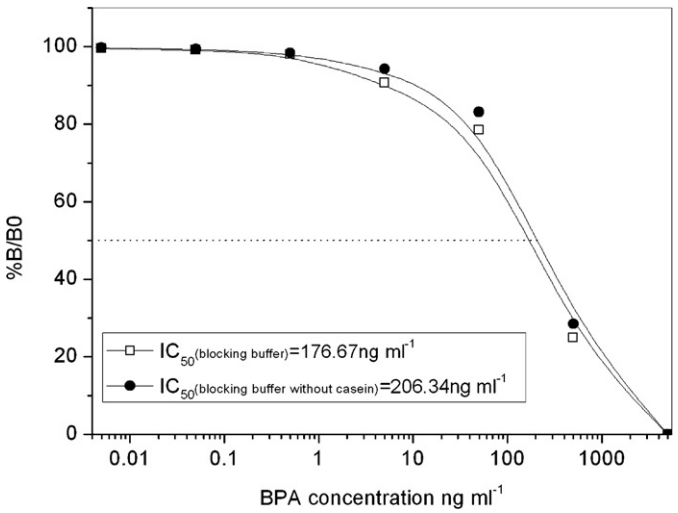


Fig. 4. Effect of different blocking buffers on ELISA sensitivity (IC_{50}).

results may be due to steric effects which could influence reaction between the primary antibody and surface-immobilized hapten. Steric effects arise from the fact that each atom with a molecule occupies a certain amount of space. If atoms are brought too close together, there is an associated cost in energy duo to overlapping electron clouds, and this may affect the molecule preferred shape (conformation) and reactivity. Based on steric effects theory, we proposed an explanation of decreasing A_0 signals beyond 640 nmol ml^{-1} that excessive surface-immobilized hapten would involve its conformational changes which was unfavorable to make the primary antibody recognize hapten. On the other hand, a change of the binding mechanism from univalent to bivalent might also be a factor. Thus in our study we chose 640 nmol/ml or below as coating hapten concentration.

3.4. Immunoassay sensitivity

The procedure of indirect competitive ELISA (icELISA) was similar to that mentioned in Section 2.4 with some modifications. Briefly, after the polystyrene plates were coated and blocked as described in Section 2.3, 50 μl of suitable diluent antibodies (1/3000) were added to each well and then 50 μl of serial concentrations (10^{-2}, 10^{-1}, 10^{0}, 10^{1}, 10^{2}, 10^{3}, 10^{4} ng ml^{-1}) of BPA

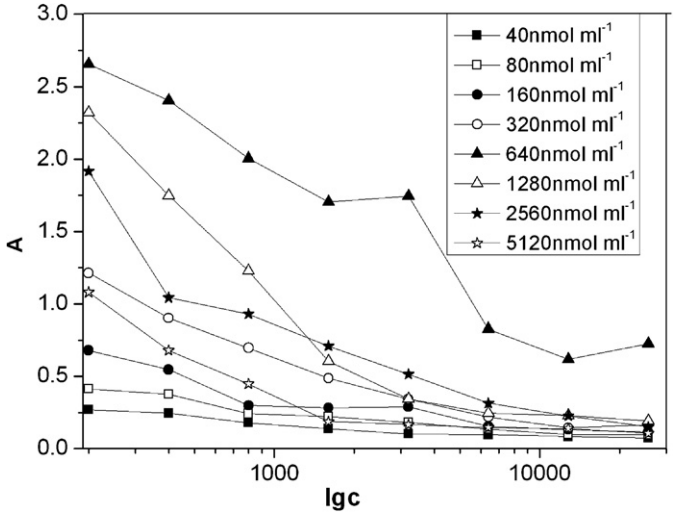


Fig. 5. The results of chequerboard titration.

Table 2
Parameters of optimized ELISA for two formats.

Format	Equation	R^2	IC_{50} (ng ml^{-1})	LOD (ng ml^{-1})	Working range (ng ml^{-1})
Hapten coated	$y = 445{,}077 + 97.6935/(1 + (x/32.7328)^{0.69812})$	0.993	23.50	0.27	2.30–157.60
Hapten–protein BSA	$y = -4.93161 + 103.31184/(1 + (x/201.77856)^{0.95583})$	0.997	176.67	15.90	4068–1289.70

Table 3
Based on direct hapten coated ELISA and hapten–protein coated ELISA the recovery has been determined by spiking BPA in PBS, tap water and seawater.

Format	Compels added (ng ml^{-1})	Seawater			Tap water			PBS		
		Found (ng ml^{-1})	% recovery	CV%	Found (ng ml^{-1})	% recovery	CV%	Found (ng ml^{-1})	% recovery	CV%
BVA coated	250	332	132	3.9	290	116	6.7	312	124	7.6
	50	57	114	12.3	43	96	8.4	53	106	9.7
	10	12	120	5.8	7	70	13.6	9	90	9.9
BVA–BSA coated	400	536	134	0.4	528	132	9.3	480	120	9.8
	100	142	142	10.8	123	123	5.0	132	132	112
	25	31	124	5.4	20	80	3.4	29	110	12.9

in 10% methanol solution were added and incubated at 37 °C for 1 h. The subsequent steps were as described in Section 2.4. However, there were some gaps between direct hapten coated format and hapten–protein coated format. First, in hapten–protein coated format blocking buffer was used to prevent the antibody from unspecific binding to the surface before competition step. In our study we found that the blocking procedure mentioned above was not effective to prevent unspecific binding of the antibody in direct hapten coated format. The antibody (include the primary antibody and the secondary antibody) solution diluted in PBS + 0.1% BSA could effectively decrease $A_{background}$ for direct hapten coated format. Second, hapten–antibody reaction time was extended to 2 h in direct hapten coated format compared with hapten–protein coated format. The explanations for this were that hapten–protein coated format was favorable to hapten presentation due to BSA or OVA with the large specific surface area as carrier protein.

Based on two types of coated formats, competitive ELISA was performed at optimum antibody concentration of 0.6 μg ml^{-1} (direct hapten coated format) and 0.15 μg ml^{-1} (hapten–protein coated format). From the results (Fig. 6; Table 2), we could observe that for hapten–protein coated format the IC_{50} values (50% B/B_0) and the limit of detection for BPA were approx. 176.67 and 15.90 ng ml^{-1}, respectively. However, immunoassay sensitivity and the limit of detection were up to 23.50 and 0.27 ng ml^{-1} with the direct hapten coated for BPA. As far as we are aware this is the most sensitive ELISA for BPA yet reported.

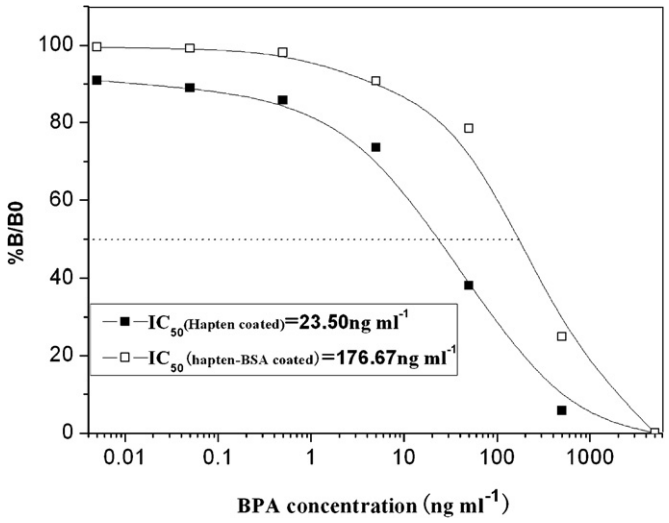


Fig. 6. The competitive inhibition curve of antibody against BPA.

Hapten–protein conjugate was always used as coating protein in the antigen-immobilized-format. Based on hydrophobic interactions hapten–protein was immobilized on polystyrene surfaces. However, the immobilization must involve significant conformational changes to create large-scale hydrophobic contacts. Conformational change would influence hapten presentation for the reason that low-molecular-weight compounds with small size could be easily screened by macromolecular. On the other hand, the reaction between hapten and protein was not always reproducible perhaps for above reasons, which is unfavorable to make assay standardization.

In competitive ELISAs hapten–protein was always used as coating protein to determine low-molecular-weight compounds (hapten). However, hapten–protein coated format had some drawbacks. First, the reaction between hapten and protein always involved severe precipitation for the reason that hydrophobic hapten would screen hydrophilic group (–COOH or $–NH_3$) of carrier protein in the reaction. Second, even when performing at same reaction condition, conjugation was not always reproducible which is unfavorable to make assay standardization. The explanation might be that different coupling ratios of hapten–protein conjugate would make different hapten densities on the polystyrene surfaces, and consequently different assay sensitivities. Finally, based on hydrophobic interactions hapten–protein was adsorbed on polystyrene surfaces. However, the immobilization must involve significant conformational changes to create large-scale hydrophobic contacts. As a result, Conformational change would influence hapten presentation because low-molecular-weight compounds with small size could be easily screened by macromolecular.

3.5. Matrix effect studies and assay validation

No significant matrix effect was observed when the ELISA was applied to measure the spiked tap water samples. But for seawater samples, a 1:10 dilution with PBS was necessary to obtain quantitative recoveries. As a result, the LODs for seawater shifted to 159 (hapten–protein coated format) and 2.7 ng ml^{-1} (direct hapten coated format). The recovery results were shown in Table 3.

4. Conclusions

In conclusion, this paper described a simple and efficient method to directly immobilize hapten with carboxy group on the polystyrene surface of microtiter plates.

Compared with hapten–protein coated format, immunoassay sensitivity increased seven folds up to 23.50 ng ml^{-1} with the direct hapten coated for BPA after careful optimization of assay con-

ditions. Tap water samples and Seawater samples were spiked with known amount of bisphenol A and measured by the competitive ELISA. Recoveries were between 70% and 142%. On the other hand, general applicability was important advantage for this format. Based on DCC method, we could immobilize hapten with carboxy group on the APTES layer. In further study various types of organo-siloxane layers with different functional groups could be constructed on the polystyrene surface of microtiter plates using Silane Coupling Agents such as GOPTS, ICPTES, etc. Thus, reactive polystyrene surface could be employed to fix different hapten by different conjugate techniques.

Acknowledgements

The authors gratefully acknowledge the financial support by the National High Technology Research and Development Program of China (No. 2007AA06Z419), Natural Science Foundation of China (No. 30771810) and Tianjin science and technology support project plan (09ZCKFSH02700), Tianjin applied-basic & cutting-edge reaserch program (09JCZDJC17700).

References

[1] A.V. Krishnan, P. Stathis, S.F. Permuth, L. Tokes, D. Feldman, Endocrinology 132 (1993) 2279.
[2] R. Steinmetz, N.A. Mitchner, A. Grant, D.L. Allen, R.M. Bigsby, N. Ben-Jonathan, Endocrinology 139 (1998) 2741.
[3] J.C. Gould, L.S. Leonard, S.C. Maness, B.L. Wagner, K. Conner, T. Zacharewski, S. Safe, D.P. McDonnell, K.W. Gaido, Mol. Cell. Endocrinol. 142 (1998) 203.
[4] M.-P. Zhao, Y.-Z. Li, Z.-Q. Guo, X.-X. Zhang, W.-B. Chang, Talanta 57 (2002) 1205.
[5] B. Mickova, T. Kovalczuk, P. Rauch, M.J. Moreno, A. Abad, A. Montoya, E. Ferri, F. Fini, S. Girotti, Anal. Chim. Acta 528 (2005) 243.
[6] Y.J. Kim, Y.A. Cho, H.-S. Lee, Y.T. Lee, Anal. Chim. Acta 494 (2003) 29.
[7] P. Tijssen, Practice and Theory of Enzyme Immunoassays, Elsevier, Amsterdam, 2005.
[8] J.E. Butler, L. Ni, W.R. Brown, K.S. Joshi, J. Chang, B. Rosenberg, Voss Jr., Mol. Immunol. 30 (1993) 1165.
[9] G.R. Marchesinia, E. Meulenberga, W. Haasnoot, H. Irth, Anal. Chim. Acta 528 (2005) 37.
[10] J. Kaur, R.C. Boro, N. Wangoo, K.R. Singh, C.R. Suri, Anal. Chim. Acta 528 (2005) 37.
[11] F.S. Chen, X.C. Luo, Q. Zhou, G.J. Li, Mycosystema 18 (1999) 409.
[12] H. Holthues, U. Pfeifer-Fukumura, I. Hartmann, W. Baumann, J. Anal. Chem. 371 (2001) 897.
[13] M.H. Wortberg Goodrow, S.J. Gee, B.D. Hammock, J. Agric. Food Chem. 44 (1996) 2710.
[14] S. Yonezawa, A. Kambegawa, S. Tokudome, J. Immunol. Methods 166 (1993) 55.

Talanta 80 (2009) 809–814

Contents lists available at ScienceDirect

Talanta

journal homepage: www.elsevier.com/locate/talanta

Simultaneous determination of antioxidants at a chemically modified electrode with vitamin B_{12} by capillary zone electrophoresis coupled with amperometric detection

Shuqing Dong, Langzhu Chi, Pingang He, Qingjiang Wang*, Yuzhi Fang*

Department of Chemistry, East China Normal University, Shanghai 200062, China

ARTICLE INFO

Article history:
Received 12 May 2009
Received in revised form 30 July 2009
Accepted 30 July 2009
Available online 8 August 2009

Keywords:
Vitamin B_{12} chemically modified electrode
Antioxidants
Oranges and tomatoes
Capillary zone electrophoresis
Amperometric detection

ABSTRACT

In the paper, a new kind of vitamin B_{12} (acquo-cobalamine) chemically modified electrode was fabricated and applied in capillary zone electrophoresis coupled with amperometric detection (CZE-AD) for simultaneous determination of six antioxidants in fruits and vegetables. The catalytic electrochemical properties of the chemically modified electrode could obviously enhance oxidation peak heights responses by about five times to glutathione, ascorbic acid, vanillic acid, chlorogenic acid, salicylic acid, and caffeic acid compared with common carbon disk electrode. Furthermore, the effects of working electrode potential, pH and concentration of running buffer, separation voltage and injection time on CZE-AD were investigated. Under the optimum conditions, the six analytes could be completely separated and detected in a borate–phosphate buffer (pH 8.4) within 15 min. Their linear ranges were from 2.5×10^{-7} to 1.0×10^{-4} mol L^{-1} and the detection limits were as low as 10^{-8} mol L^{-1} magnitude ($S/N = 3$). The proposed method has been successfully employed to monitor the six analytes in practical samples with recoveries in the range 96.0–106.0% and RSDs less than 5.0%. Above results demonstrate that capillary zone electrophoresis coupled with electrochemical detection using vitamin B_{12} modified electrode as detector is of convenient preparation, high sensitivity, good repeatability, and could be used in the rapid determination of practical samples.

© 2009 Elsevier B.V. All rights reserved.

1. Introduction

Free radicals are very unstable molecules arising physiologically during cellular aerobic metabolism, and their harmful effects for human health have been more and more concerned in recent years [1]. They react quickly with other compounds, causing chain reactions. Once the process starts, it can cascade, finally results in disruption of a living cell or in molecular and cellular DNA damage. So, free radicals have been indicated as probable pathogenesis determinants of many degenerative and chronic diseases that develop with age, such as cancer, cardiovascular disease, cataract, and immunity system dysfunctions [2]. For their potential role in preventing such diseases, natural compounds with antioxidant activity have attracted the attention of researchers and nutritionists. Estimation of the antioxidant contents is becoming, in fact, an evaluation parameter for the nutritional quality of foods.

A large number of fresh fruits and vegetables are primary sources of antioxidants. Oranges and tomatoes, two kinds of them, contribute to the daily intake of a significant amount of antioxidants [3]. They contain different classes of substances with antioxidant properties, such as ascorbic acid, phenolics, glutathione, etc. It is well known that ascorbic acid is a soluble vitamin widely present in oranges and tomatoes, which is commonly used to supplement inadequate dietary intake for antioxidants [4–6], and widely used for the prevention and treatment of common cold, mental illness, infertility, and in some clinical manifestations of HIV infections [7]. The major phenolics in oranges and tomatoes are vanillic acid, chlorogenic acid, salicylic acid, caffeic acid, etc. These phenolic compounds are located in the lipid–water interface of the membrane because of their lipophilic–hydrophilic structure. This location allows them to scavenge free radicals inside and outside the cell. Glutathione, which is also found to exist in both oranges and tomatoes, is a physiologically significant aqueous antioxidant, capable of scavenging reactive oxygen and nitrogen species which is thought to contribute to induce many diseases including cancer, heart attack, stroke, arthritis [8,9].

The most widely used method for the analysis of antioxidants in plants and fruits is high-performance liquid chromatography (HPLC) with photodiode array (PDA) detection [10–13]. HPLC coupled with mass spectrometric detection for analyzing polyphenols in plant extracts and food has also been explored [14]. However,

* Corresponding authors. Tel.: +86 21 62233508; fax: +86 21 62233508.
E-mail addresses: qjwang@chem.ecnu.edu.cn (Q. Wang), yuzhi@online.sh.cn (Y. Fang).

0039-9140/$ – see front matter © 2009 Elsevier B.V. All rights reserved.
doi:10.1016/j.talanta.2009.07.069

HPLC has some shortcomings including time-consuming sample pretreatment and short column lifetime. Owing to its advantages of short-analysis time, small-consuming sample, simple-experiment operation, and high separation efficiency [15], capillary zone electrophoresis (CZE) has been increasingly recognized as an important analytical separation technique for charged compounds and partially charged organics. In combination with electrochemical detection (ED), CZE-ED offers high sensitivity, good selectivity, free derivatization, and low cost for the analytes. However, the success in the electrochemical detection is strongly dependent on the choice of the working electrode materials. Different electrodes, such as carbon, sol–gel, platinum, gold, nickel, etc. have been used for different analytes [16–20]. In the past few years, there has been an explosion of research activity in the area of chemically modified electrodes. This area of research has attracted such interest because the chemical modification electrodes with redox active thin films, offer significant advantages in the design and development of electro-catalyst, enhance the sensitivity and extend further the applicability of capillary electrophoresis with electrochemical detection.

Vitamin B_{12} is a naturally cobalt (III) corrin complex or aquocob(III)alamine. Its electrochemical property has been studied extensively by many authors, including polarographie studies [21] and cyclic voltammetry [22]. These studies have demonstrated that vitamin B_{12} exhibits a rich redox chemistry centred on the cobalt atom. Vitamin B_{12a} (with Co (III)) can be reduced reversibly to vitamin B_{12r} (having Co (II)), and be further reduced to give vitamin B_{12s} that contains Co (I). Zagal's group has reported that vitamin B_{12} adsorbs on ordinary pyrolytic graphite (OPG) electrodes to investigate oxygen reduction kinetics, and the active for the electro-oxidation of cysteine and glutathione [23–25]. Therefore, immobilization of vitamin B_{12} on an electrode is a potential method for developing novel chemical conversion devices to improve further the detection sensitivity in some trace analysis.

In this regard, we are now investigating the method of immobilizing the vitamin B_{12} on an electrode by electropolymerization and manage to provide an easy and feasible method to improve the detection limits of ascorbic acid, phenolics, and glutathione in fruits and vegetables. It is found that under the optimum conditions, the six main antioxidants in vegetables and fruits could be completely separated and detected in a borate–phosphate buffer (pH 8.4) within 15 min. Their linear ranges were from 2.5×10^{-7} to 1.0×10^{-4} mol L^{-1} and the detection limits were as low as 10^{-7} or 10^{-8} mol L^{-1} magnitude ($S/N = 3$). Furthermore, the proposed method has been successfully employed to monitor the six analytes in practical samples with recoveries in the range 96.0–106.0% and RSDs less than 5.0%. Above results demonstrated that capillary zone electrophoresis coupled with electrochemical detection using vitamin B_{12} modified electrode as detector was of convenient preparation, high sensitivity, good repeatability, and could be used in the rapid determination of practical samples. It is possible to get new insights in the quality control of foods.

2. Experimental

2.1. Apparatus

The CZE-AD system was laboratory-built [26,27]. Electrophoresis was driven by a high-voltage power supply (±30 kV, Shanghai Institute of Nuclear Research, Shanghai, China). The high-voltage end of the system was housed in a plexiglas box equipped with an interlock for operator safety. Separations were performed in a fused silica capillary (Polymicro Technologies, Phoenix, AZ, USA) with 25 μm I.D., 360 μm O.D. and 70 cm long. Potential control and current output were achieved with a CH-2 amperometric detector (Jiangsu Electrochemical Analytical Instrumental Factory, China). Electropherograms were recorded by use of a chart recorder (Shanghai Dahua Instrument Factory, China). Electrochemical experiments were carried out with a CHI 830b electrochemical analyzer (CHInstruments, Austin, TX, USA). A three-electrode system was used, a vitamin B_{12} modified working electrode, a saturated calomel reference electrode (SCE), and a platinum wire counter electrode.

2.2. Reagents

Glutathione and ascorbic acid were obtained from First Chemical Reagent Factory (Shanghai, China). Vanillic acid, chlorogenic acid, salicylic acid, and caffeic acid were purchased from Shanghai Leechdom Inspection Agency (Shanghai, China) without further purification. Tomatoes and oranges were purchased from a local supermarket. All the other chemicals including carrier electrolytes were of analytical reagent grade. Doubly distilled water was used throughout the experiments.

The six standard analytes were accurately weighed and dissolved in anhydrous ethanol to furnish 1.0 mmol L^{-1} stock solutions of each; these were stored in the dark at 4 °C. Before CZE experiment they were diluted with the pH 8.4 borate–phosphate buffer. All solutions were filtered through 0.22 μm polypropylene acrodisc syringe filter (Xinya Purification Instrument Factory, Shanghai, China) and degassed by agitation in an ultrasonic bath for 5 min to remove bubbles.

2.3. Procedures

2.3.1. Preparation of modified electrodes

First, the working electrode was constructed by inserting 300 μm diameter carbon disk into a disposable polypropylene pipette tip with 3–5 mm protruding out and then sealing with epoxy glue (GC Electronics, Rockford, IL). Electrical contact was established via a copper wire, which was threaded into the opposite end of the electrolyte body. To smooth the resulting relatively rough surface, it was further subjected to sequential polishing on a polishing cloth covered with alumina powder of 1.0, 0.3 and 0.05 mm particle size (Buehler, USA) for 5, 10 and 20 min, respectively. To remove any adherent Al_2O_3 particles the electrode surface was rinsed thoroughly with doubly distilled water and cleaned in an ultrasonic bath for 5 min. Finally, the electrode was pretreated electrochemically by scanning in a 0.1 Na_2HPO_4/NaOH buffer solution (pH 12.0) between −1.2 and 0.6 V versus SCE until five subsequent scans were identical.

Then, the vitamin B_{12} electrochemically modified electrode was prepared by electropolymerization, and it was achieved by repetitive cycling of the electrode between −0.6 and 1.6 V at 0.05 V s^{-1} in a 1.0×10^{-3} mol L^{-1} dichloromethane solution of vitamin B_{12} and 0.1 mol L^{-1} tetrabutylammonium tetrafluoroborate. The growth of the film was observed by monitoring the increase in the charge attributed to the reversible redox couple of the metal centre Co (III)/(II) located at −0.85 V [28].

The modified working electrode was arranged in a wall-jet configuration in which the modified carbon disk electrode was inserted into the cathode compartment of the CE instrument and then positioned up against the capillary outlet as close as possible. In this configuration, the CE effluent impinged directly onto the disk-shaped electrode and then flowed radially outward across its surface.

2.3.2. Cyclic voltammetry experiments

Cyclic voltammetry (CV) was used to investigate the current responses of six analytes (glutathione, ascorbic acid, vanillic acid, chlorogenic acid, salicylic acid, and caffeic acid) on the modified

working electrodes in borate–phosphate solutions (pH 8.4). The scan rate was 50 mV s^{-1}.

2.3.3. CZE experiments

Before each run in CZE experiments, the capillary was sequentially rinsed with a self-made washing system, with 0.1 mol L^{-1} hydrochloric acid, doubly distilled water, 0.1 mol L^{-1} sodium hydroxide, doubly distilled water, 5 min for each and running buffer for 10 min, which was necessary for obtaining a reproducible electroosmotic flow (EOF). CZE was performed at the separation voltage of 17 kV with 0.05 mol L^{-1} borate–0.10 mol L^{-1} phosphate mixture solution (pH 8.4) as running buffer. The potential applied to the working electrode was 0.85 V (versus SCE). Samples were electrokinetically injected at 17 kV for 10 s. All experiments were carried out at room temperature. Currents were allowed to reach a stable baseline prior to doing experiments.

2.4. Sample preparation

One kind of orange and two kinds of tomatoes were obtained from local supermarket. The orange of Sunkist brand was planted in America, and the two kinds of tomatoes were nontransgenic and transgenic (cherry-tomato), respectively. A precisely weighed quantity of the samples was dissolved in 10 mL of anhydrous ethanol and sonicated for 30 min, then filtered through a cellulose filter and thereafter stored at 4 °C. The stock solution was diluted three times with 0.05 mol L^{-1} borate–0.10 mol L^{-1} phosphate buffer (pH 8.4) and filtered with 0.22 μm polypropylene acrodisc syringe filter, then sonicated before the analysis of CZE-AD.

3. Results and discussion

3.1. Electrochemistry experiments

Cyclic voltammetry was employed to investigate the electrochemical characteristics of the six anlytes at the modified electrode. As an example, Fig. 1 shows cyclic voltammograms of 50 μM chlorogenic acid in the borate–phosphate buffer solution at the bare carbon electrode (curve a) and vitamin B_{12} modified electrode (curve b), respectively. It could be seen that there was weak oxidation peak current response at about 0.2 V at the bare carbon disk electrode, while at the modified electrode, the oxidation currents

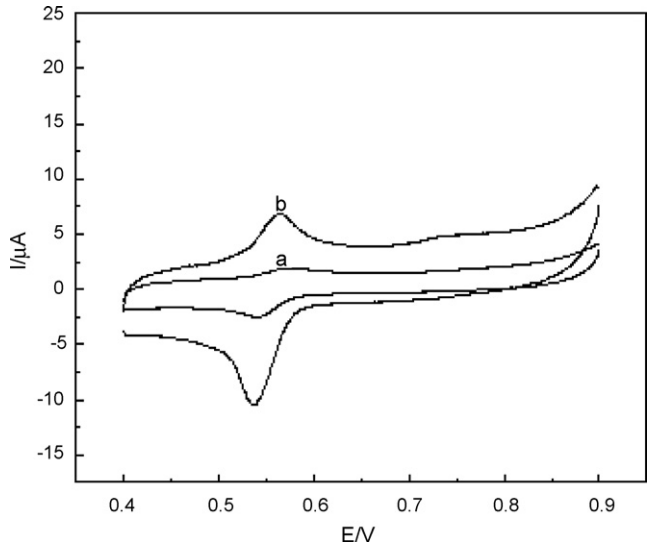


Fig. 1. Cyclic voltammetry of borate–phosphate buffer solution (pH 8.4) in the presence of 1.0×10^{-5} mol L^{-1} chlorogenic acid at (a) bare carbon disk electrode, (b) vitamin B_{12} modified electrode. Scan rate, 50 mV/s.

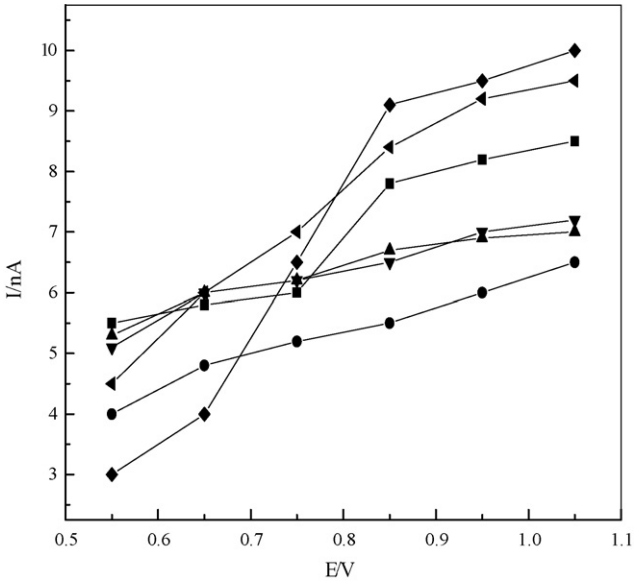


Fig. 2. Hydrodynamic voltammograms with a concentration of 2.0×10^{-5} mol L^{-1} glutathione (■), 1.0×10^{-5} mol L^{-1} ascorbic acid (●), 1.0×10^{-5} mol L^{-1} vanillic acid (▲), 2.0×10^{-5} mol L^{-1} chlorogenic acid (▼), 1.0×10^{-5} mol L^{-1} salicylic acid (♦), and 1.0×10^{-5} mol L^{-1} caffeic acid (◄), under the optimal CZE-AD conditions.

responses increased evidently about five times. The phenomenon can be explained by that vitamin B_{12}, the macrocyclic cobalt complexes, decreased the over potential with high current efficiency, since the cobalt complex can afford the ability to the analytes oxidation by Co(I), Co(II) and Co(III) surface states [29,30]. Analogous electrochemical behaviours were seen for other five investigated analytes. The modified electrode was chosen as working electrode for the study of capillary zone electrophoresis performance.

3.2. Effect of the detection potential

In amperometric detection, the potential applied to the working electrode directly affects the sensitivity, detection limit and stability of this method. Fig. 2 illustrates the hydrodynamic voltammograms (HDVs) for the six analytes at the modified working electrode. The curves were recorded step by step over the +0.55 to +1.05 V range, using a separation voltage of 17 kV. It was found that the current responses of these analytes increased with the applied potential increasing and got leveling at about +0.95 V. However, when applied potential was greater than +0.85 V (versus SCE), both the baseline noise and the background current increased, resulting in an unstable baseline, which was a disadvantage for sensitive and stable detection. Therefore, the applied potential of +0.85 V (versus SCE) was selected as the most suitable detection potential in this experiment, where the background current was not too high and the *S*/*N* ratio was the highest.

3.3. Optimization of capillary electrophoresis conditions

3.3.1. Effect of buffer pH and concentration

In order to improve the resolution and sensitivity, borate, phosphate, borate–phosphate mixture were employed as running buffer in this CZE separation respectively, and the best result was got with borate–phosphate mixture buffer.

The effects of pH and concentration of the buffer on the electrophoretical separation of the six analytes were evaluated in order to select the optimum separation conditions. The pH dependence of the migration time was investigated in the pH range of 5.0–10.0. When the running buffer pH increased, the resolution of

all compounds was improved. It was clear that when pH was 8.4, the six analytes could be separated completely. However, the peak height was low and the peak shape became poorer at pH value above 8.4. Therefore, pH 8.4 was chosen as the running buffer in considering of the peak height, resolution and the analytical time in the experiments.

Besides the pH value, the running buffer concentration is also an important parameter. The effect of the concentration of borate–phosphate mixture buffer was investigated. Several different concentrations of the buffer (0.05, 0.10, 0.20, 0.30, 0.40, 0.50, 0.60, 0.70 mol L^{-1} of borate mixed with 0.10, 0.20, 0.30, 0.40, 0.50, 0.60, 0.70, 0.80 mol L^{-1} of phosphate, respectively) were tested in order to choose the best one. The results showed that with the increase of the concentration of borate–phosphate buffer, the separation efficiency was much better. However, higher buffer concentrations also have negative effects on the detection limit, because the peak height of six analytes decreased and the effect of Joule heating became more pronounced. So 0.05 mol L^{-1} borate −0.10 mol L^{-1} phosphate buffer (pH 8.4) was finally chosen as the optimum running buffer concentration in this work, on the basis of the peak height, resolution, analysis time, and buffer capacity.

3.3.2. Effect of the separation voltage and injection time

The separation efficiency of CZE was investigated within the separation voltage range from 10 to 22 kV. The migration time of the analytes was significantly shortened and their corresponding current peaks were sharpened as the separation voltage was increased. However, if the separation voltage was higher than 18 kV, more Joule heat was produced because of the higher current inside the capillary, which caused peak broadening and reduced separation efficiency. As a compromise, 17 kV was selected as the optimum separation voltage in the experiments. Moreover, in order to make the process stable and obtain the best separation results, the same high-voltage was chosen for separation and injection.

Electrokinetic injection was used in the CZE experiment. The effect of injection time was investigated by selecting different injection time (4, 6, 8, 10 and 12 s at a voltage of 17 kV). It was found that when the injection time was prolonged, the peak height increased correspondingly. However, the current response peaks of the analytes were obviously broadened if the injection time was more than 12 s. So, 10 s was selected as the injection time in the experiments and satisfactory results were obtained under these conditions.

3.4. Analytical performance

Through the experiments above, the optimum conditions of CZE-AD for determining glutathione, ascorbic acid, vanillic acid, chlorogenic acid, salicylic acid, and caffeic acid were detection potential 0.85 V (versus SCE), separation voltage 17 kV, electrokinetic injection time 10 s (voltage 17 kV) and 0.05 mol L^{-1} borate–0.10 mol L^{-1} phosphate running buffer (pH 8.4). Fig. 3 shows the electropherograms of a standard six analytes mixture solution under the optimum conditions. It was clear that a very good base-lined separation was achieved for the six analytes within 15 min.

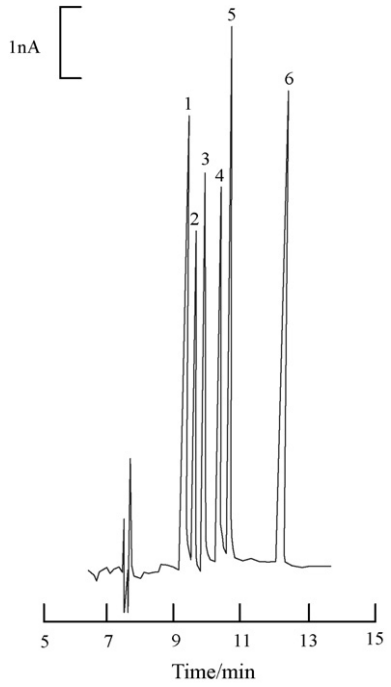


Fig. 3. Electropherograms of a standard solution containing 2.0×10^{-5} mol L^{-1} glutathione, 1.0×10^{-5} mol L^{-1} ascorbic acid, 1.0×10^{-5} mol L^{-1} vanillic acid, 2.0×10^{-5} mol L^{-1} chlorogenic acid, 1.0×10^{-5} mol L^{-1} salicylic acid, and 1.0×10^{-5} mol L^{-1} caffeic acid by CZE-AD at the vitamin B_{12} modified working electrode under the optimal conditions of detection potential 0.85 V (versus SCE), separation voltage 17 kV, electrokinetic injection time 10 s (voltage 17 kV) and 0.05 mol L^{-1} borate–0.10 mol L^{-1} phosphate running buffer (pH 8.4): (1) glutathione, (2) ascorbic acid, (3) vanillic acid, (4) chlorogenic acid, (5) salicylic acid, and (6) caffeic acid.

3.5. Repeatability, linearity and detection limits

A standard mixture solution was used to determine the repeatability of the current response and migration time under the optimum conditions in this experiment. The relative standard deviations (RSDs) of peak height and migration time are 2% and 3% for glutathione, 3% and 4% for ascorbic acid, 4% and 2% for vanillic acid, 3% and 4% for chlorogenic acid, 2% and 2% for salicylic acid, and 3% and 2% for caffeic acid, respectively. After the analysis was repeated five times under the same conditions, the peak signals only decreased slightly, which demonstrated that this method was of good repeatability.

A series of standard mixture solutions of glutathione, ascorbic acid, vanillic acid, chlorogenic acid, salicylic acid, and caffeic acid ranging from 2.5×10^{-7} to 1.0×10^{-4} mol L^{-1} were tested to determine the linearity of this detection method. Table 1 summarizes the regression equation, correlation coefficient and detection limit according to the 3 sb/m criterion [31], where m is the slope of the calibration curve and sb the standard deviation. Their detection limits were 2.9×10^{-7}, 2.2×10^{-7}, 1.6×10^{-7}, 3.9×10^{-7}, 7.5×10^{-8}, and 7.8×10^{-8} mol L^{-1}, respectively, which are lower than using a carbon disc working electrode. Table 2 compared

Table 1
The regression equations and the detection limits of glutathione, ascorbic acid, vanillic acid, chlorogenic acid, salicylic acid and caffeic acid.

Analytes	Concentration range (10^{-6} mol L^{-1})	Regression equation C (10^{-3} mol L^{-1}); I (nA)	Correlation coefficient	Detection limit (10^{-6} mol L^{-1})
Glutathione	1.0–100.0	$I = 388C - 0.018$	0.9998	0.29
Ascorbic acid	0.5–100.0	$I = 546C - 0.113$	0.9973	0.22
Vanillic acid	0.5–100.0	$I = 675C - 0.079$	0.9996	0.16
Chlorogenic acid	1.0–100.0	$I = 299C + 0.096$	0.9968	0.39
Salicylic acid	0.25–50.0	$I = 965C - 0.051$	0.9995	0.075
Caffeic acid	0.25–50.0	$I = 957C + 0.018$	0.9992	0.078

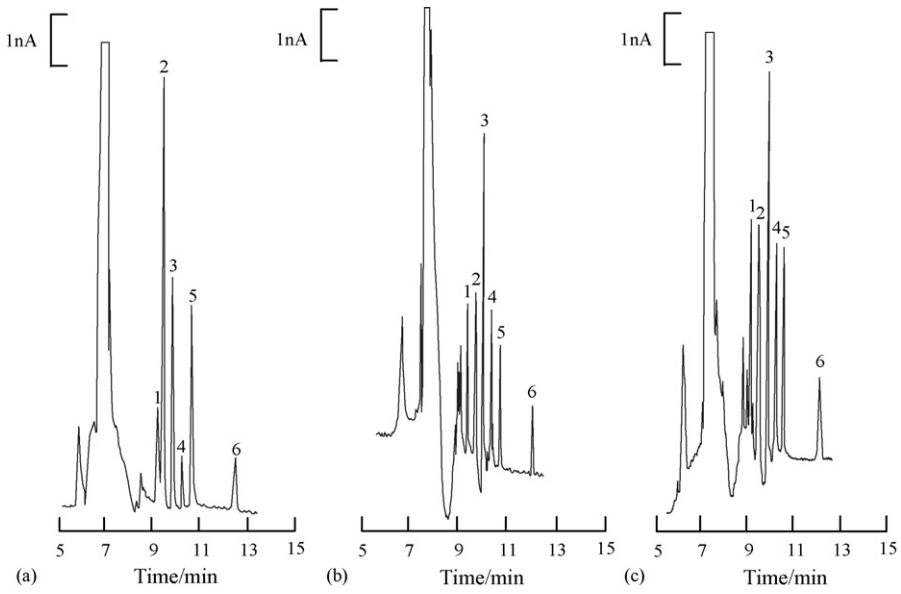


Fig. 4. Electropherograms of 10 mg orange was dissolved and extracted by 1 mL^{-1} anhydrous ethanol solutions at modified electrode under the optimal CZE-AD conditions: (a) Sunkist orange, (b) nontransgenic tomato, (c) transgenic tomato (cherry-tomato): (1) glutathione, (2) ascorbic acid, (3) vanillic acid, (4) chlorogenic acid, (5) salicylic acid, and (6) caffeic acid.

Table 2
The contrast of the six analytes detection limits in this experiment with the relevant reported in the literatures.

Analytes	Detection limit[a] (10^{-6} mol L^{-1})	Detection limit[b] (10^{-6} mol L^{-1})
Glutathione	0.29	2.5 [32]
Ascorbic acid	0.22	1.0 [33]
Vanillic acid	0.16	1.5 [34]
Chlorogenic acid	0.39	1.5 [35]
Salicylic acid	0.075	0.16 [36]
Caffeic acid	0.078	0.39 [37]

[a] Detection limits of the six analytes in this experiment.
[b] Detection limits of the six analytes in the relevant literatures.

different detection limits of the six analytes with reported in the relevant literatures [32–37]. The results demonstrate that the vitamin B_{12} modified working electrode is suitable for the detection of the six analytes, allowing a reproducible and more sensitive quantification of mixtures containing the six analytes.

3.6. Sample analysis

In order to demonstrate the practical application of the modified electrode by present analytical method, the determination of active ingredients in Sunkist orange and tomatoes practical samples was conducted by CZE-AD at the modified electrode under the selected optimum conditions. Typical electropherograms of the samples are shown in Fig. 4. By comparing the migration time of analytes with the electropherogram of the standard mixture solution and standard addition approach was used for further demonstration. The results showed that the active ingredients were (1) glutathione, (2) ascorbic acid, (3) vanillic acid, (4) chlorogenic acid, (5) salicylic acid, and (6) caffeic acid, indeed. The prolonged migration time of some analytes can be explained that in the practical samples, some organic acids such as citric acid, malic acid, tartaric acid, etc. are contained, which might influence the migration time of the active ingredients. From the sample electropherograms, it can be found that large amount of ascorbic acid in Sunkist orange (Fig. 4a), while large amount of phenolics compounds in tomato

Table 3
Determination results of the recoveries for this method in orange and tomatoes sample ($n = 5$).

Samples	Active ingredients	Original amount (10^{-5} mol L^{-1})	Added (10^{-5} mol L^{-1})	Found (10^{-5} mol L^{-1})	Recovery (%)	RSDs (%)
Orange	Glutathione	0.54	1.0	1.58	104.0	3.6
	Ascorbic acid	1.61	1.0	2.59	98.0	3.2
	Vanillic acid	0.73	1.0	1.78	105.0	4.2
	Chlorogenic acid	0.47	1.0	1.50	103.0	3.8
	Salicylic acid	0.48	1.0	1.45	97.0	3.9
	Caffeic acid	0.11	1.0	1.09	98.0	3.3
Tomato	Glutathione	0.90	1.0	1.92	102.0	4.5
	Ascorbic acid	0.72	1.0	1.70	98.0	4.1
	Vanillic acid	0.52	1.0	1.48	96.0	4.6
	Chlorogenic acid	1.17	1.0	2.20	103.0	3.9
	Salicylic acid	0.36	1.0	1.40	104.0	3.2
	Caffeic acid	0.14	1.0	1.12	98.0	4.4
Cherry-tomato	Glutathione	0.70	1.0	1.65	95.0	4.5
	Ascorbic acid	0.60	1.0	1.62	102.0	4.7
	Vanillic acid	0.95	1.0	2.01	106.0	3.8
	Chlorogenic acid	0.99	1.0	1.95	96.0	4.2
	Salicylic acid	0.28	1.0	1.25	97.0	3.9
	Caffeic acid	0.10	1.0	1.15	105.0	4.1

and cherry-tomato (Fig. 4b and c). Therefore, in order to maintain physical well being, it is necessary for us to intake them every day. Accurate amounts of glutathione, ascorbic acid, vanillic acid, chlorogenic acid, salicylic acid, and caffeic acid were added to the sample solutions, and the recovery values were obtained using their peak height from the calibration curve under the same conditions. The average recoveries and RSDs for the six analytes are listed in Table 3. The results indicate that this method is accurate for the analytes.

4. Conclusion

This work demonstrates that the modified vitamin B_{12} electrode showed excellent catalytic activity towards the antioxidants of glutathione, ascorbic acid, vanillic acid, chlorogenic acid, salicylic acid, and caffeic acid and can be used as amperometric detector for capillary zone electrophoresis to detect simultaneously. The results show that this method is of high separation efficiency, short-analysis time, and convenience of analysis. Under the optimum conditions, the six analytes are separated completely within 15 min and good linearity, repeatability and recovery results are obtained. Their detection limits are low to 10^{-8} mol L^{-1}, which are lower than using a carbon disc working electrode. From the present study, it can be concluded that the modified vitamin B_{12} electrode successfully employed in capillary zone electrophoresis provides a new methodology for the CZE-AD.

Acknowledgement

This work is financially supported by the National Nature Science Foundation of China (No. 20575022).

References

[1] A.P. Wickens, Respir. Physiol. 128 (2001) 379.
[2] A.Y. Kuresh, S.H. Barbara, A.J. James, Free Radic. Biol. Med. 37 (2004) 1683.
[3] Y.Y. Peng, Y.W. Zhang, J.N. Ye, J. Agric. Food Chem. 56 (2008) 1838.
[4] T. Akihiro, G. Eiichi, J. Chromatogr. B 853 (2007) 214.
[5] P. Stratil, B. Klejdus, V. Kubáň, Talanta 71 (2007) 1741.
[6] A.M. Yu, H.Y. Chen, Anal. Chim. Acta 344 (1997) 181.
[7] O. Arrigori, C.D. Tullio, Biochim. Biophys. Acta 1569 (2002) 1.
[8] B. Srinivas, H. Michael, K. Deepinder, R. Subramanian, K.A. Julie, Biochem. Pharmacol. 64 (2002) 1037.
[9] W.G. Kirlin, J. Cai, S.A. Thompson, D. Diaz, T.J. Kavanagh, D.P. Jones, Free Radic. Biol. Med. 27 (1999) 1208.
[10] Y.C. Shen, S.L. Chen, C.K. Wang, J. Agric. Food Chem. 55 (2007) 6475.
[11] Y. Zuo, H. Chen, Y. Deng, Talanta 57 (2002) 307.
[12] J. Riber, C. de la Fuente, M.D. Vazquez, M.L. Tascón, P. Sánchez Batanero, Talanta 52 (2000) 241.
[13] U. Justesen, P. Knuthsen, T. Leth, J. Chromatogr. A 799 (1998) 101.
[14] I. Nicoletti, A.D. Rossi, G. Giovinazzo, D. Corradini, J. Agric. Food Chem. 55 (2007) 3304.
[15] Z.M. Liu, O. Niwa, R. Kurita, T. Horiuchi, J. Chromatogr. A 891 (2000) 149.
[16] S. Sloss, A.G. Ewing, Anal. Chem. 65 (1993) 577.
[17] M. Chicharro, A. Zapardiel, E. Bermejo, A. Sánchez, Anal. Chim. Acta 469 (2002) 243.
[18] X. Huang, W.T. Kok, J. Chromatogr. A 716 (1995) 347.
[19] P.L. Weber, S.M. Lunte, Electrophoresis 17 (1996) 302.
[20] S.K. Moccelini, S.C. Fernandes, T.P. de Camargo, A. Neves, I.C. Vieira, Talanta 78 (2009) 1063.
[21] B. Jaselkis, H. Diehl, J. Am. Chem. Soc. 76 (1954) 4345.
[22] R.H. Silvia, G.R. Gustavo, C.G. Héctor, Talanta 61 (2003) 743.
[23] J. Zagal, J. Sturm, Bol. Soc. Chil. Quire. 31 (1986) 106.
[24] C. Pfiez, A. Prelle, S.U. Zaartu, J. Zagai, Bol. Soc. Cifil. Quim. 35 (1990) 299.
[25] J.H. Zagal, M.J. Aguirre, C.G. Parodi, J. Sturm, J. Electroanal. Chem. 374 (1994) 215.
[26] S.Q. Dong, S. Zhang, X. Cheng, P.G. He, Q.J. Wang, Y.Z. Fang, J. Chromatogr. A 1161 (2007) 327.
[27] Q. Wang, F. Ding, N. Zhu, H. Li, P. He, Y. Fang, J. Chromatogr. A 1016 (2003) 123.
[28] J. Obirai, N.P. Rodrigues, F. Bedioui, T. Nyokong, J. Porphyrins Phthalocyanines 7 (2003) 508.
[29] H. Aga, A. Aramata, Y. Hisaeda, J. Electroanal. Chem. 437 (1997) 111.
[30] J.H. Zagal, M.J. Aguirre, M.A. Pfiez, J. Electroanal. Chem. 437 (1997) 45.
[31] M. Chicharro, A. Sánchez, A. Zapardiel, M.D. Rubianes, G. Rivas, Anal. Chim. Acta 523 (2004) 185.
[32] A. Wang, L. Zhang, S. Zhang, Y. Fang, J. Pharm. Biomed. Anal. 23 (2000) 429.
[33] T. Wu, Y. Guan, J. Ye, Food Chem. 100 (2007) 1573.
[34] Y. Cao, C. Lou, Y. Fang, J. Ye, J. Chromatogr. A 943 (2001) 153.
[35] Y. Cao, Y. Wang, J. Ye, J. Pharm. Biomed. Anal. 39 (2005) 60.
[36] G. Zhou, Y. Guan, H. Chen, J. Ye, J. Chromatogr. A 1142 (2007) 236.
[37] Z. Tang, Y. Zhou, Y. Zeng, S. Zang, P. He, Y. Fang, J. Pharm. Biomed. Anal. 40 (2006) 484.

Talanta 80 (2009) 815–820

Contents lists available at ScienceDirect

Talanta

journal homepage: www.elsevier.com/locate/talanta

Electrochemical study of mono-6-thio-β-cyclodextrin/ferrocene capped on gold nanoparticles: Characterization and application to the design of glucose amperometric biosensor

Ming Chen, Guowang Diao*

College of Chemistry and Chemical Engineering, Yangzhou University, Yangzhou 225002, People's Republic of China

ARTICLE INFO

Article history:
Received 17 May 2009
Received in revised form 30 July 2009
Accepted 31 July 2009
Available online 8 August 2009

Keywords:
Cyclodextrin
Ferrocene
Gold nanoparticles
Mediator
Glucose biosensor

ABSTRACT

A novel amperometric glucose sensor based on inclusion complex of mono-6-thio-β-cyclodextrin/ferrocene capped on gold nanoparticles (GNPs/CD–Fc) and glucose oxidase (GOD) was described. The inclusion complex of mono-6-thio-β-cyclodextrin/ferrocene capped on gold nanoparticles played an effective role of an electron shuttle and allowed the detection of glucose at 0.25 V (versus SCE), with dramatically reduced interference from easily oxidizable constituents. The sensor (GNPs/CD–Fc/GOD) showed a relatively fast response time (5 s), low detection limit (15 μM, S/N = 3), and high sensitivity (ca. 18.2 mA M^{-1} cm^{-2}) with a linear range of 0.08–11.5 mM of glucose. The excellent sensitivity was possibly attributed to the presence of the GNPs/CD–Fc film that can provide a convenient electron tunneling between the protein and the electrode. In addition, the biosensor demonstrated high anti-interference ability, stability and natural life. The good stability and natural life can be attributed to the following two aspects: on the one hand, the fabrication process was mild and no damage was made on the enzyme molecule, on the other hand, the GNPs possessed good biocompatibility that could retain the bioactivity of the enzyme molecules immobilized on the electrode.

© 2009 Elsevier B.V. All rights reserved.

1. Introduction

Amperometric enzyme electrodes possess the advantages of combining the specificity of the enzyme for recognizing particular target molecules with the direct transduction of the rate of reaction into the current [1]. Enzyme electrodes, particularly the glucose electrode, have been subject to numerous studies devoted to their optimization for both biomedical and bioprocess control applications [2]. For glucose sensors, this enzyme is well-studied, inexpensive, stable and particularly applied in clinical and chemical analysis [3]. Nevertheless, there is need to improve the sensitivity and stability of glucose sensors due to the great demand for blood glucose measurements in control and treatment of diabetes. Recently, Adam Heller and Ben Feldman have given a wonderful review about electrochemical glucose sensors and their applications in diabetes management [4].

The oxidase-based amperometric biosensors previously relied on the immobilization of oxidase enzymes on the surface of various electrodes. However, electron transfer efficiency of redox enzymes is poor in the absence of mediator, because enzyme active sites are deeply embedded inside the protein. The sensitivity of resulted biosensors can be significantly improved by the immobilization of mediators in the matrices [5–9]. Among the different mediators described in the literature, ferrocene (Fc) and its derivatives, first reported by Cass et al. [5], have proved to be the most efficient electron transfers for the GOx enzymatic reaction. There are a lot of cases about ferrocene (Fc) and its derivatives introduced to enzyme biosensor as the mediator [10–16]. However, leakage has been a main problem for the entrapment of mediators due to their low molecular weight in polymer matrices [8]. In order to prevent the leakage of mediator, mediator can be linked covalently with polymer or with high molecular weight compounds before immobilization on the surface of electrode [8,17]. Gorton et al. [18] studied ferrocene-containing siloxane polymer modified electrode surface with a poly (ester-sulfuric acid) cation-exchanger to improve the stability of the mediator. Another alternative method is to synthesize a few Fc derivatives with specific functional groups [19,20], but the preparation methods are complicated. For instance, Jönsson et al. [19] used hydroxymethyl Fc and anthracene carboxylic acid to synthesize anthracene substituted ferrocene.

The other alternative method to increase the stability of Fc and its derivatives is the formation of inclusion complex with cyclodextrin (CD), a class of torpidly shaped cycloamyloses with a hydrophilic outer surface and a hydrophobic inner cavity, which makes the dissolubility of Fc decrease. Several investigations have been made to study the characterization of interacting Fc–CD

* Corresponding author. Tel.: +86 514 87975436; fax: +86 514 87975244.
E-mail address: gwdiao@yzu.edu.cn (G. Diao).

0039-9140/$ – see front matter © 2009 Elsevier B.V. All rights reserved.
doi:10.1016/j.talanta.2009.07.068

system and their roles [21–23]. Liu et al. [21] developed the sensitive biosensor for glucose by immobilizing glucose oxidase in β-cyclodextrin via cross-linking and by including ferrocene in the cavities of dextrin polymer via host–guest reaction. Zhang et al. [22] successfully used ferrocene with β-cyclodextrin to prepare β-CD/Fc inclusion complex modified carbon paste electrode. The water-soluble inclusion complex of 1,1-dimethylferrocene with (2-hydroxypropyl)-β-CD has been used in bioelectrocatalysis [23].

Recently, nanomaterials, such as gold (Au) [24–27] and magnetic nanoparticles have attracted much interest in the construction of biosensors due to their unique chemical and physical properties. Gold nanoparticles, in particular, have been widely used to construct biosensors because of their excellent ability to immobilize biomolecules and at the same time retain the biocatalytic activities of those biomolecules. In this paper, gold nanoparticles were capped by inclusion complex between mono-6-thio-β-cyclodextrin and ferrocene through –SH, which resulted into stable fixation of ferrocene on the surface of gold nanoparticles. Then, the glucose biosensors were constructed by using GNPs/CD–Fc as the building block. The composite nanoparticles showed excellent efficiency of electron transfer between the GOD and the electrode for the electrocatalysis of glucose.

2. Experimental

2.1. Reagents

Glucose oxidase (GOD) (EC1.1.3.4, Type VII-S, 108 U/mg) from *Aspergillus niger* was purchased from Amresco. Ferrocene was obtained from the Shanghai Chemical Reagent Pharmaceutical Factory. Hydrogen tetrachloroaurate tetrahydrate ($HAuCl_4{\cdot}4H_2O$) and sodium borohydride ($NaBH_4$) were purchased from Shanghai Chemical Reagents Company. Mono-6-thio-β-cyclodextrin was synthesized according to the literature [28]. Other reagents used in this paper were of analytical grade and used as commercially available. Double distilled and sterilized water was used to prepare all solution.

2.2. Apparatus

The film of GNPs/CD–Fc/GOD was characterized by scanning electron microscope (SEM). SEM was taken by Philips XL-30ESEM operating at an accelerating voltage of 20 kV. The morphology and size of GNPs/CD–Fc after adding glucose oxidase aqueous solution were investigated on a Philips TECNAI-12 transmission electron microscope (TEM) instrument operated at an accelerating voltage of 120 kV. Images of GOD in GNPs/CD–Fc organized assemblies were observed by TEM after negative staining with sodium phosphotungstate. All electrochemical experiments were carried out with a CHI660c electrochemical workstation (Chenghua, Shanghai) with a three-electrode cell. A platinum disk electrode (diameter: 1 mm) was used as a working electrode. The reference electrode was a saturated calomel electrode (SCE). All potentials reported in this paper were against SCE. A platinum wire was used as the counter electrode. All measurements were carried out in a thermostated cell at 25 °C. The aqueous electrolyte solutions were prepared in 0.1 M PBS buffers (Na_2HPO_4–NaH_2PO_4) in which the pH was measured as 7.0 using a PHs-25 pH-meter (Leizi Instrumental Factory, Shanghai). Electrolytic solutions were purged with highly purified nitrogen for at least 20 min prior to the series of experiments.

2.3. Construction of the GNPs/CD–Fc/GOD modified electrode

Firstly, the inclusion complex was synthesized. Mono-6-deoxy-6-(*p*-tolylsulfonyl)-β-cyclodextrin (β-CD–SH) (0.5 g) and Fc (1.6 g) were dissolved by 20 mL DMF in a 100 mL conical flask. Then, the solution should be stirred continually at least 24 h at room temperature. Finally, 20 mL ethanol was added into the solution. Immediately, a great deal of yellow crystal precipitate was occurred, which was the inclusion complex of Fc with β-CD–SH. The solubility of inclusion complex was weak in ethanol. The inclusion complex was obtained by filtrating and washed with ethanol and water for three times in turn, respectively, to clean the residual guest and host monomers. Then it was dried in a vacuum oven at 50 °C for 24 h.

Secondly, CD–Fc capped gold nanoparticles were prepared by the reduction of $AuCl_4^-$ with a similar method described before [28]. $NaBH_4$ and CD–Fc were dissolved in 10 mL of DMF, and $HAuCl_4$ in 10 mL of DMF was quickly added into the mixture of $NaBH_4$ and CD–Fc. The molar ratio of [CD–Fc]/[$HAuCl_4$] was 1:1. After 24 h stirring at room temperature, the precipitate was collected by centrifugation and washed with 25 mL of DMF for three times and then with 25 mL ethanol/water (9:1 in volume) for four times. At last, the precipitate, GNPs/CD–Fc, was dried at 60 °C in a vacuum oven for 24 h and characterized by TEM.

Finally, the working electrode (diameter: 1 mm) was polished to a mirror with 0.05 μm alumina aqueous slurry and rinsed with water in an ultrasonic cleaning bath before use. GOD was also dissolved in deionized and decarbonated water with a concentration of 5 mg mL^{-1}. The colloidal suspension of GNPs/CD–Fc (1 mg mL^{-1}) was prepared by dispersing GNPs/CD–Fc in deionized and decarbonated water. A defined amount of the aqueous mixture (GOD and GNPs/CD–Fc) was spread on the surface of the platinum disk electrode. The coating was dried in air at room temperature. Finally, the film was equilibrated under stirring for about 20 min in a phosphate buffer solution in order to allow hydrogel formation and remove unadsorbed enzyme. All electrodes were stored in PBS at 4 °C.

3. Results and discussion

3.1. Characterization of the GNPs/CD–Fc/GOD films

Fig. 1 shows SEM images of GNPs/CD–Fc film and GNPs/CD–Fc/GOD composite film. From Fig. 1A, GNPs/CD–Fc was found to form the three-dimensional island structure of film. However, when enzyme was absorbed onto GNPs/CD–Fc, the composite film was multi-layer and multi-pore structure which indicated that the composite film was highly porous in nature (Fig. 1B). At larger magnification in Fig. 1C, the distribution of the enzyme on the composite film can be clearly observed. The enzyme congregated and formed global congregation (diameter: 100–500 nm). The multi-layer and multi-pore structure of the GNPs/CD–Fc/GOD composite film would be of benefit to the fast electron shuttle among enzyme, mediator and substrate.

The morphology of GOD and GNPs/CD–Fc in aqueous solution may be obtained by TEM images. The image of GNPs/CD–Fc was shown in Fig. 2A. Because there were enough –SH to cap on the surface of the gold nanoparticles, stable gold nanoparticles with uniform distribution were obtained. However, when GOD was added into the solution of GNPs/CD–Fc, the gold nanoparticles were congregated and formed abnormal structure shown as in Fig. 2B. Because the morphology of biomacromolecules cannot be observed directly by TEM, specimen must be negative staining with heavy metal salt to increase contrast. Therefore, in order to observe the morphology of GOD, the specimen was negative staining with sodium phosphotungstate for 60 s. Fig. 2C showed that a mass of GOD were congregated together and a lot of gold nanoparticles were deeply embed into the congeries. The electron transfer between the redox center of GOD and electrode would be effectively promoted through the combination mode between GOD and GNPs/CD–Fc.

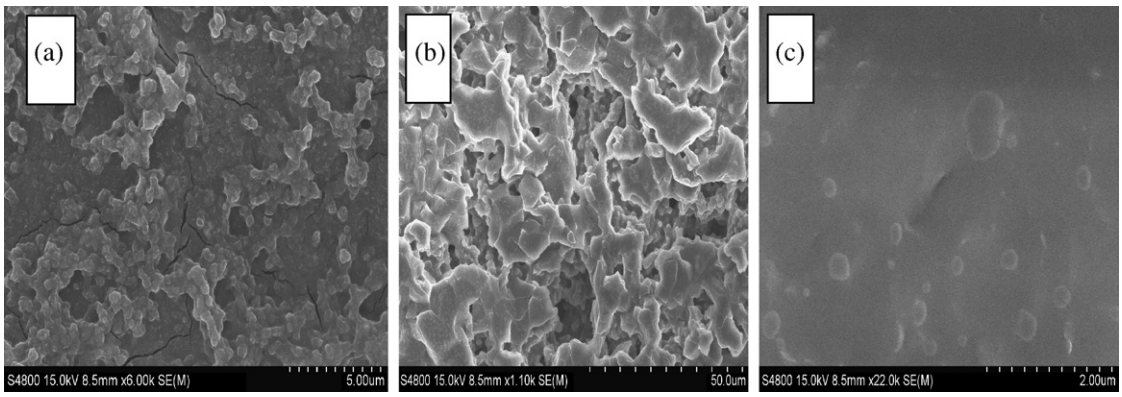


Fig. 1. SEM images of (A) GNPs/CD–Fc, and GNPs/CD–Fc/GOD with different magnifications of (B) 1100 and (C) 22,000.

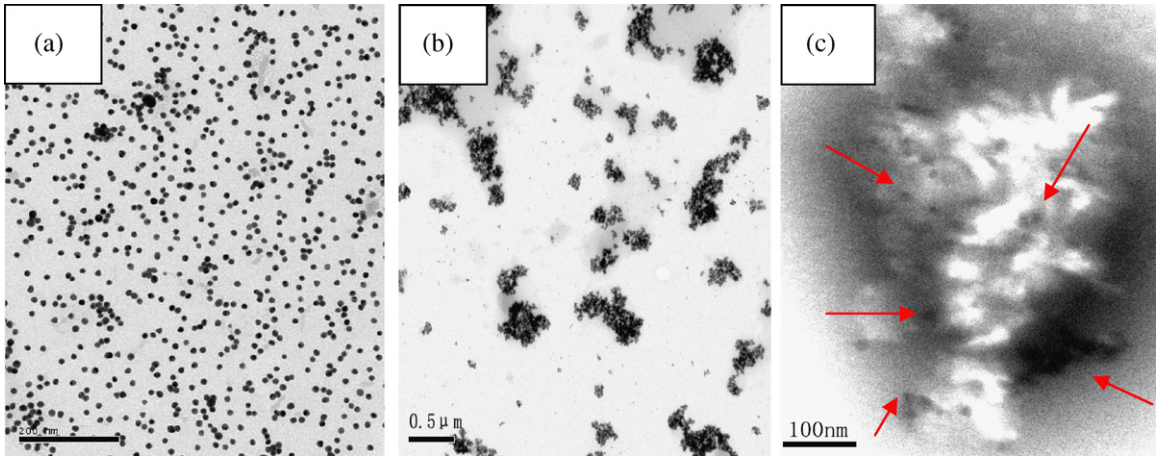


Fig. 2. TEM images of (A) GNPs/CD–Fc; (B) GNPs/CD–Fc/GOD without negative staining; (C) GNPs/CD–Fc/GOD negative staining with sodium phosphotungstate.

3.2. *Electrocatalytic oxidation of glucose at biosensor of GNPs/CD–Fc/GOD*

The GNPs/CD–Fc modified platinum electrode was cycled continuously in the potential range of −0.1 to 0.5 V (versus SCE) in 0.1 M PBS buffers. The current finally reached a steady state after 10 cycles. From Fig. 3A, there were well-defined anodic and cathodic peaks with the mean potential $\Delta E = (E_{pa} - E_{pc})$ at 75 mV (curve a in Fig. 3A). It corresponded to the reversible single electron oxidation of Fc to Fc^+, which indicated that the electrochemistry reaction was close to quasi-reversible state. Next, at the same condition, cyclic voltammogram of the enzyme electrode was carried out. In Fig. 3A, curve b showed well-defined anodic and cathodic peaks. Under the same conditions, neither glucose nor glucose oxidase showed any observable electrochemistry, so the peaks were still attributed to the redox reaction of Fc. Compared with the voltammogram of GNPs/CD–Fc modified platinum electrode, the anodic peaks shifted from 0.194 to 0.258 V and the ΔE increased 30 mV. When GOD was

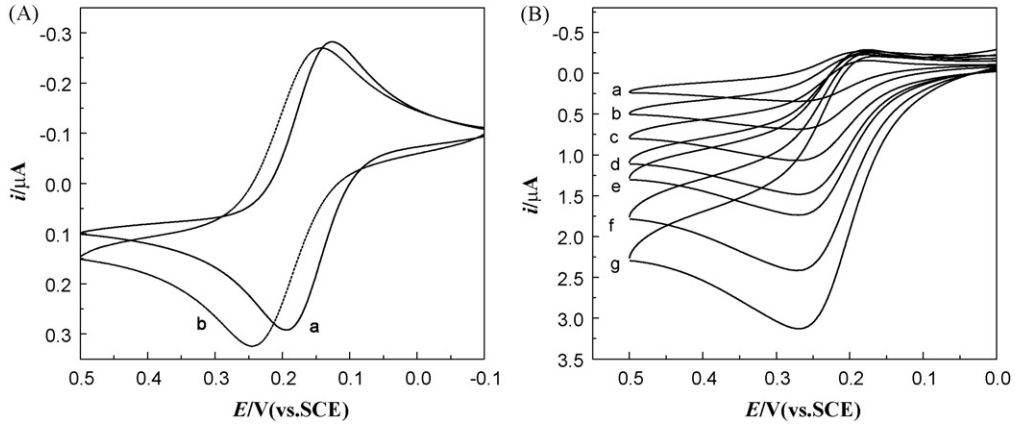


Fig. 3. (A) The cyclic voltammograms of (a) GNPs/CD–Fc (b) GNPs/CD–Fc/GOD modified electrode in 0.1 M PBS (pH 7.0) buffer solution. (B) The cyclic voltammograms on GNPs/CD–Fc/GOD modified electrode in 0.1 M PBS (pH 7.0) buffer solution with different concentration of glucose (mM): (a) 0; (b) 0.05; (c) 0.1; (d) 0.2; (e) 0.5; (f) 0.8; (g) 1.0. $t = 25\,^{\circ}C$, v: 10 mV s^{-1},

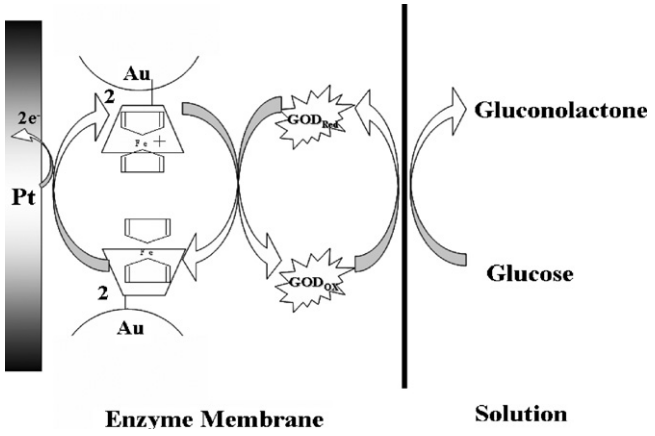


Fig. 4. Schematic illustration of sensing mechanism for electrocatalytic glucose on the GNPs/CD–Fc/GOD modified platinum electrode surface.

immobilized in the composite film, protein molecule blocked the charge transfer, which led to the positive shift of anodic peak and the value of ΔE increase. The phenomenon about the shifting of E_p upon immobilization of GOD was also observed in ferrocene-containing Nafion film [29]. At the same time, the current of anodic peak was larger than that of cathodic peak. The phenomenon was also observed in ferrocene-containing Nafion film. Upon the addition of glucose to the test solution, a very strong catalytic effect was observed: a dramatic increase in the oxidation current that was simultaneous with a gradual decrease of the reduction current (curves b–g in Fig. 3B). The decrease of the cathodic current was attributed to the reduction of oxidized form of Fc (Fc^+) by the reduced form of the enzyme (GODred), which was more efficient than the electro-reduction of the former at the base electrode. The oxidation wave was enhanced, since the reduced form of the mediator (Fc) was regenerated and then reoxidized at the base electrode. In this case, the mechanism of electron transfer from glucose to mediator was known to be of the "ping-pong" type which was shown in Fig. 4.

3.3. Optimization of experimental variables

In order to optimize the performance of the glucose biosensor based on GNPs/CD–Fc/GOD modified electrode, various experimental variables affecting the amperometric determination of glucose, such as the concentration ratio of GNPs/CD–Fc and GOD, GOD loading and pH of the solution, were investigated.

3.3.1. Influence of GOD loading

First, the effect of concentration ratio of GNPs/CD–Fc and GOD was studied. The response currents reached the maximum when the mass ratio of GOD and GNPs/CD–Fc was 1:5. The effect of GOD loading activity on the response characteristics of GNPs/CD–Fc/GOD modified electrode was examined in the presence of 1.0 mM glucose. The results showed that the current increased with the enzyme loading and the response currents reached the maximum when the GOD loading located at 12.7 $\mu g\,mm^{-2}$. However, when the GOD loading continuously increased, the current gradually decreased, which was due to the increasing resistance of the biomembrane. Furthermore, it is well known that enzyme denaturation often causes a considerable reduction in loss of biosensor response. Considering the response stability of the GNPs/CD–Fc/GOD biosensor, GOD loading for each test strip was set at 12.7 $\mu g\,mm^{-2}$ in this study.

3.3.2. Influence of pH

The value of pH is known to be one of the most important factors affecting the enzyme activity and stability, and hence the performance of enzyme electrodes. Lukachova et al. [29] also stated that pH values between 5.5 and 7 should be considered as being more appropriate for biosensors application, since most oxidases have pH optima in the neutral pH region. Thus, effects of pH on the current of the biosensor were determined in the range of pH 5–9 in the presence of glucose (1.0 mM). The results show that the highest response current can be obtained at pH 7. The pH value of the highest activity for GOD is 5.5 as reported by the supplier. In the case, the optimal pH value is larger than that for GOD highest activity (ca. pH 5.5), which is attributed to the presence of GNPs/CD–Fc, which may change the microenvironment of the enzyme and the surface charge distribution of the enzyme [30]. The experiment result also shows that the current sharply decreases at higher pH values. Wilson and Turner [31] ever reported that catalytic activity of GOD was rapidly lost below 2 or above 8 for pH. This result suggested that GNPs/CD–Fc addition may have no benefit to preventing GOD from alkaline inactivation. Moreover, the physiological pH value of blood is known to be near 7. As a consequence, pH 7 was selected for evaluating the performance of the glucose biosensor based on the GNPs/CD–Fc/GOD modified electrode.

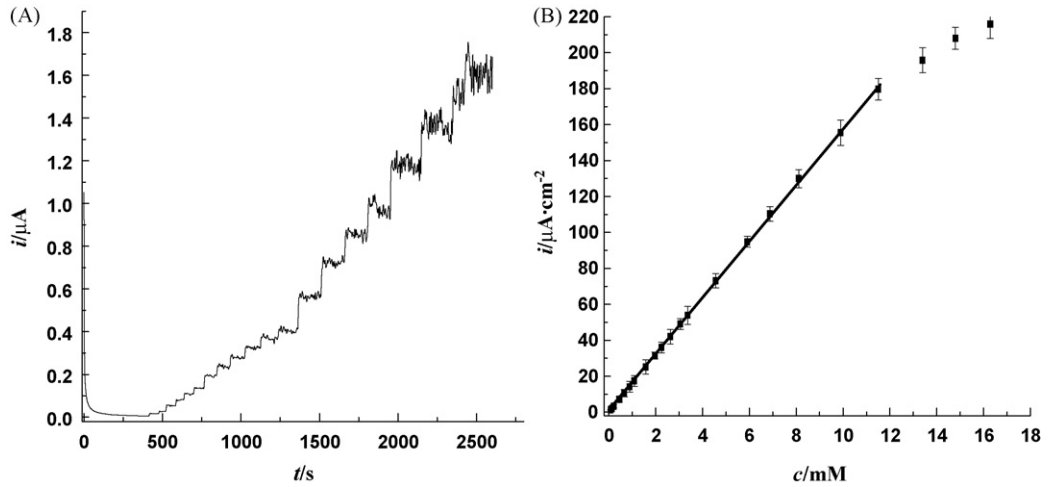


Fig. 5. (A) The i–t plot of GNPs/CD–Fc/GOD electrode response for glucose, under the optimum conditions; (B) Calibration curves of GNPs/CD–Fc/GOD for glucose, under the optimum conditions (0.1 M phosphate buffer solution with pH 7.0, at 25 °C, E_{app} = 0.25 V).

3.4. Performance of the chronoamperometric glucose biosensors

The electrocatalytic oxidation of glucose at GNPs/CD–Fc/GOD modified platinum electrode was also studied by amperometry. The potential of 0.25 V (versus SCE) was chosen as the applied potential for the amperometric determination of glucose. Fig. 5A showed the typical response curves for the GNPs/CD–Fc/GOD modified platinum electrode on successive injections of glucose to the stirring PBS at pH 7.0. Fig. 5B showed the corresponding linear range of the calibration curve obtained via the GNPs/CD–Fc/GOD modified platinum electrode. A clearly defined oxidation current proportional to the concentration of glucose was observed. The biosensor achieved 95% of the steady-state current within 5 s, with a linear range of 8×10^{-5} to 11.5×10^{-3} M. This kind of biosensor had a low detection limit of 1.5×10^{-5} M based on S/N = 3 and a high sensitivity of 18.2 mA M^{-1} cm^{-2}. The high sensitivity of the enzyme electrode can be attributed to the excellent adsorption ability, high electrocatalytic activity and good biocompatibility of the GNPs/CD–Fc composite nanoparticles. The apparent Michaelis–Menten constant (K_M) can be obtained by the analysis of the slope and the intercept of the plot of the reciprocals of the steady-state current versus glucose concentration. K_M value for GNPs/CD–Fc/GOD modified platinum electrode was 6.42 mM.

3.5. Effects of the interferences on the response of mediated enzyme biosensors

Generally, the influence of the presence of easily oxidizable endogenous and exogenous interferences was examined at their physiological normal levels on the biosensor response to glucose as reported in literature [32,33]. However, the normal concentration of these interferences (0.1 mM for ascorbic acid, 0.5 mM for uric acid, 0.2 mM for dopamine, 0.05 mM for *p*-acetaminophenol, and 0.02 mM for L-cysteine) was rather low compared with that of glucose (5.6 mM). The experiment results were shown in Table 1. Except for uric acid, the influences of ascorbic acid, dopamine, *p*-acetamidophenol and L-cysteine were quite weak. This was ascribed to the efficiency of the electrocatalytic process in the whole structure of the GNPs/CD–Fc composite film and also to the value of the low operating potential of 0.25 V versus SCE.

3.6. Reproducibility and stability of GNPs/CD–Fc/GOD biosensors

The reproducibility of biosensor was estimated by five GNPs/CD–Fc/GOD electrodes, which were prepared under the same condition and used to detect the current response of 1 mM glucose. The results revealed that the biosensors possessed satisfying reproducibility with a relative standard deviation (RSD) of 5.87% for 50 successive measurements (each sensor was performed 50 measurements). The storage stability of enzymatic biosensor in storage conditions (phosphate buffer of pH 7.0 at 4 °C) was investigated in the same phosphate buffer solution containing 1.0 mM glucose. In the storage stability test, 5 measurements of each biosensor were performed in each day during the period of the 30 days. The corresponding result showed that 82% response current was still retained after 30 days. The good stability can be attributed to the following aspects. Firstly, the fabrication process was mild and no damage was made on the enzyme molecule. Secondly, the GNPs possessed good biocompatibility that can retain the bioactivity of the enzyme molecules immobilized on the electrode. Finally, GOD can be immobilized efficiently on the film, which maintained a porous environment likely to impart fast mass transport issues into the composite film and thereby good sensitivity to the biosensor.

Table 1
Influence of interfering compounds on the response of GNPs/CD–Fc/GOD electrode.

Interfering compound	Physiological concentration (mM)	$(i_{G+I} - i_G)/i_G$ (%)
Ascorbic acid	0.1	3
Uric acid	0.5	18
3-Hydroxytyramine hydrochloride	0.2	5
p-Acetamidophenol	0.05	4
L-Cysteine	0.02	1.5

i_G: current response to 5.6 mM glucose; i_{G+I}: current response to 5.6 mM glucose in presence of interfering compound.

Table 2
Glucose content determination in serum sample.

Samples	Content determined by local hospital (mM)	Content determined by current method (average of five times) (mM)	Relative error (%)
1	4.17	4.35	−4.1
2	6.19	5.97	+3.7
3	4.88	4.99	−2.2
4	5.83	5.67	+2.8
5	4.26	4.43	−3.8

3.7. Real sample analysis

Human plasma samples were assayed to demonstrate the practical use of the GNPs/CD–Fc/GOD electrode. Fresh plasma samples were first analyzed in the local hospital with Olympus AU2700 biochemistry analyzer (Japan). The samples were then reassayed with the GNPs/CD–Fc/GOD electrode. A plasma sample (0.5 mL) was added into 5 mL PBS (pH 7.0), and the response was obtained at +0.25 V. The contents of glucose in blood can then be calculated from the calibration curve. The results, which were shown in Table 2, were satisfactory and agreed closely with those measured by the biochemical analyzer done by local hospital, indicating that the fabricated glucose biosensor had practical potential.

4. Conclusions

GOD can be effectively immobilized on GNPs/CD–Fc modified electrode. The immobilized GOD maintained its bioactivity and native structure. Fc was fitted on the surface of GNPs through inclusion complex with CD. This construction of the GNPs/CD–Fc/GOD modified electrode can decrease the leakage of mediator and improve the reproducibility and stability of GNPs/CD–Fc/GOD biosensors. From the cyclic voltammetry and amperometric measurements, the entrapped Fc was demonstrated to be redox active and function as electron shuttling agent between GOD and electrode. The use of artificial electron mediators to shuttle electrons from the redox center of the enzyme to the surface of the working electrode can effectively reduce the operating potential (0.25 V) and hence enhance selectivity and sensitivity.

Acknowledgements

The authors acknowledge the financial support from the National Natural Science Foundation of China (Grant Nos. 20773107 and 20810102054), the Natural Science Key Foundation of Educational Committee of Jiangsu Province of China (Grant No. 07KJA15015), the Foundation of Jiangsu Provincial Key Program of Physical Chemistry in Yangzhou University and the Foundation of the Educational Committee of Jiangsu Provincial Universities Excellence Science and Technology Invention Team in Yangzhou University. The authors also thank Professor Xue and Dr Shan for their useful suggestions about this work. The authors also thank Dr. Gao and Dr. Kong provided with human plasma samples and comparison data from SuBei People's Hospital.

References

[1] W.J. Albery, P.N. Bartlett, J. Electroanal. Chem. 194 (1985) 211.
[2] M. Koudelka, S. Gernet, N.F. de Rooij, Sens. Actuators 18 (1989) 157.
[3] P.S.J. Cheetham, A. Wiseman, Handbook of Enzyme Biotechnology, Wiley, New York, 1985.
[4] H. Adam, F. Ben, Chem. Rev. 108 (2008) 2482.
[5] A.E.G. Cass, G. Davis, G.D. Francis, H.A.O. Hill, W.J. Aston, I.J. Higgins, E.V. Plotkin, L.D.L. Scott, A.P.F. Turner, Anal. Chem. 56 (1984) 667.
[6] J. Okuda, J. Wakai, N. Yuhashi, K. Sode, Biosens. Bioelectron. 18 (2003) 699.
[7] J. Wu, Y.H. Zou, N. Gao, J.H. Jiang, G.L. Shen, R.Q. Yu, Talanta 68 (2005) 12.
[8] V.B. Kandimalla, V.S. Tripathi, H.X. Ju, Biomaterials 27 (2006) 1167.
[9] X.Y. Wang, H.F. Gu, F. Yin, Y.F. Tu, Biosens. Bioelectron. 24 (2009) 1527.
[10] S.J. Dong, B.X. Wang, B.F. Liu, Biosens. Bioelectron. 7 (3) (1992) 215.
[11] Z.R. Zhang, W.F. Bao, C.C. Liu, Talanta 41 (1994) 875.
[12] A. Chaubey, B.D. Malhotra, Biosens. Bioelectron. 17 (2002) 441.
[13] M. Nakayama, T. Ihara, K. Nakano, M. Maeda, Talanta 56 (2002) 857.
[14] D. Shan, W.J. Yao, H.G. Xue, Biosens. Bioelectron. 23 (2007) 432.
[15] B. Serra, J. Zhang, M.D. Morales, A. Guzmán-Vázquez de Prada, A.J. Reviejo, J.M. Pingarrón, Talanta 75 (2008) 1134.
[16] J.D. Qiu, W.M. Zhou, J. Guo, R. Wang, R.P. Liang, Anal. Biochem. 385 (2) (2009) 264.
[17] C.G. Tsiafoulic, A.B. Florou, P.N. Trikalitis, T. Bakas, M.I. Prodromidis, Electrochem. Commun. 7 (2005) 781.
[18] L. Gorton, H.I. Karan, P.D. Hale, T. Inagaki, Y. Okamoto, T.A. Skotheim, Anal. Chim. Acta 228 (1990) 23.
[19] G. Jönsson, L. Gorton, L. Pettersson, Electroanalysis 1 (1989) 49.
[20] N.C. Foulds, C.R. Lowe, Anal. Chem. 60 (1988) 2473.
[21] H.Y. Liu, H.B. Li, T.L. Ying, K. Sun, Y.Q. Qin, D.Y. Qi, Anal. Chim. Acta 358 (1998) 137.
[22] G.R. Zhang, X.L. Wang, X.W. Shi, T.L. Sun, Talanta 51 (2000) 1019.
[23] P.M. Bersier, J. Bersier, B. Klingert, Electroanalysis 3 (1991) 443.
[24] J. Liu, Y. Lu, J. Am. Chem. Soc. 125 (2003) 6642.
[25] R.N. Goyal, V.K. Gupta, M. Oyama, N. Bachheti, Talanta 72 (2007) 976.
[26] H.P. Wu, C.C. Huang, T.L. Cheng, W.L. Tseng, Talanta 76 (2008) 347.
[27] H. Zhu, X.Q. Lu, M.X. Li, Y.H. Shao, Z.W. Zhu, Talanta 79 (2009) 1446.
[28] G.W. Diao, C. Qian, M. Chen, Y.J. Huang, Supramol. Chem. 18 (2) (2006) 117.
[29] L.V. Lukachova, A.A. Karyakin, Y.N. Ivanova, E.E. Karyakina, S.D. Varfoloneyev, Analyst 123 (10) (1998) 1981.
[30] L. Goldstein, Methods in Enzymology, vol. 19, Academic Press, New York, 1970, p. 935.
[31] R. Wilson, A.P.F. Turner, Biosens. Bioelectron. 7 (1992) 165.
[32] K. Wang, J.J. Xu, H.Y. Chen, Biosens. Bioelectron. 20 (7) (2005) 1388.
[33] J. Yu, S. Liu, H. Ju, Biosens. Bioelectron. 19 (4) (2003) 401.

Talanta 80 (2009) 821–825

Contents lists available at ScienceDirect

Talanta

journal homepage: www.elsevier.com/locate/talanta

Molecularly imprinted polymer as SPE sorbent for selective extraction of melamine in dairy products

Huang-Hao Yang[a,*], Wen-Hui Zhou[b], Xiu-Chun Guo[b], Fa-Rong Chen[b], Heng-Qiang Zhao[b], Li-Ming Lin[c], Xiao-Ru Wang[b]

[a] The Key Lab of Analysis and Detection Technology for Food Safety of the MOE, College of Chemistry and Chemical Engineering, Fuzhou University, Fuzhou, PR China
[b] The First Institute of Oceanography, SOA, Qingdao 266061, PR China
[c] Technological Center, Shandong Entry-Exit Inspection & Quarantine Bureau, Qingdao 266002, PR China

ARTICLE INFO

Article history:
Received 19 May 2009
Received in revised form 28 July 2009
Accepted 31 July 2009
Available online 8 August 2009

Keywords:
Melamine
Molecularly imprinted polymers
Dairy products
Solid-phase extraction

ABSTRACT

In this paper, a highly selective sample cleanup procedure combining molecular imprinting and solid-phase extraction (MI-SPE) was developed for the isolation of melamine in dairy products. The molecularly imprinted polymer (MIP) was prepared using melamine as the template molecule, methacrylic acid as the functional monomer and ethylene glycol dimethacrylate as the cross-linking monomer. The melamine imprinted polymer was used as selective sorbent for the solid-phase extraction of melamine from dairy products. An off-line MI-SPE method followed by high-performance liquid chromatography with diode-array detection for the detection of melamine was also established. The mean recoveries of melamine from ultra-heat treatment (UHT) milk and milk powders were 92.9–98.0% and 91.6–102.8%, respectively. Good linearity was obtained from 0.5 μM to 10 μM ($r > 0.999$) with a quantitation limit of 0.5 μmol/L (0.06 ppm) which was sufficient to analyse melamine at the maximum level permitted by U.S. Food and Drug Administration (1 ppm) in dairy products. It was demonstrated that the proposed MI-SPE-HPLC method could be applied to direct determination of melamine in dairy products.

© 2009 Elsevier B.V. All rights reserved.

1. Introduction

Melamine, known as tripolycyanamide, is an industrial chemical in the production of melamine resins, which are used in laminates, glues, adhesives, and plastics. Melamine can be found at ppm levels in food and beverages due to migration from melamine-containing resins [1], or as a metabolite product of cyromazine, an insecticide used on animals and crops [2]. When added to milk intentionally, melamine can increase the nitrogen concentration, which suggests a false increase in protein concentration (by Kjeldahl method [3]). Though, low level melamine does not pose any danger to humans, intentional adulteration by a high melamine level can induce renal failure and even death in humans especially babies and children. Therefore, a reliable method is needed to determine melamine residues in food and particularly in dairy products for children.

High-performance liquid chromatography (HPLC) [4–8] particularly reversed-phase liquid chromatography (RPLC), gas chromatography [9,10] and capillary electrophoresis (CE) [11,12] have been developed for the analysis of melamine in different matrices. In view of the complexity of the bio-matrix, pretreatment in order to concentrate and purify melamine for analysis should be executed. Solid-phase extraction (SPE) is an extraction method that uses a solid phase and a liquid phase to isolate one, or one type, of analyte from a solution. SPE is usually used to cleanup a sample before using a chromatographic or other analytical method to quantitate the amount of analyte(s) in the sample. One of the main disadvantages of the classical SPE sorbents (C_8, C_{18}, etc.) is low selectivity. New sorbents such as molecular imprinting polymers (MIPs) and immunosorbents were increasingly developed to meet the need of selectivity. Coupling MIPs with SPE is possible to combine the advantages of both molecular recognition and traditional separation methods. Thus, molecularly imprinted solid-phase extraction (MI-SPE) presents the high specificity, selectivity and sensitivity of the molecular recognition mechanism and the high resolving power of separation methods [13].

In the present work, melamine imprinted polymer was prepared through bulk polymerization method using melamine as template molecule, methacrylic acid (MAA) as the functional monomer and ethylene glycol dimethacrylate (EGDMA) as the cross-linking agent. The obtained imprinted polymer showed high affinity to melamine and was successfully applied as special SPE sorbent for selective extraction of melamine from dairy products. The method had been validated and applied to determine melamine from dairy products with satisfactory results. To our knowledge, this work represents

* Corresponding author.
E-mail address: hhyang@fio.org.cn (H.-H. Yang).

0039-9140/$ – see front matter © 2009 Elsevier B.V. All rights reserved.
doi:10.1016/j.talanta.2009.07.067

the first attempt of using MIPs as selective SPE sorbents for the determination of melamine in dairy products.

2. Experimental

2.1. Materials

Methacrylic acid (MAA), ethylene glycol dimethacrylate (EGDMA) were purchased from Alfa and distilled to remove the polymerization inhibitor before use. Azobis(isobutyronitrile) (AIBN) was the product of Sinopharm Chemical Reagent Beijing Co., Ltd. (Beijing, China) and was recrystallized prior to use. Acetonitrile and methanol are all of HPLC grade and from Merck. All water used was obtained from a Millipore Milli-Q purification system. UHT milk and milk powders were purchased from a local supermarket.

A 1.0×10^{-3} mol/L melamine (Sigma) stock solution was prepared in methanol and placed in the dark. More dilute standards were prepared by appropriate dilution.

2.2. HPLC and ESI-TOF/MS conditions

HPLC analysis was performed on an Agilent 1100 series HPLC system containing a G1322A Vacuum Degasser, a G1312A Binary Pump, a G1313A ALS Autosampler, a G1316A Column Compartment, and a G1315B diode-array detector. Separation was carried out on a Luna HILIC (hydrophilic interaction liquid chromatography) column (250 mm × 4.6-mm-i.d., particle size 5 μm, Phenomenex Inc., USA). The column thermostat was set at room temperature. The mobile phase was water–acetonitrile (10:90, v/v) containing 0.01 mol/L ammonium acetate, and its flow rate was set at 1.0 mL/min.

ESI-TOF/MS analysis was performed on a 6210 time-of-flight mass spectrometer (Agilent, USA) equipped with an electrospray ionization (ESI) interface. The mass spectrometer conditions were optimized for melamine detection as follows. The collision induced dissociation (CID) voltage was set at 100 V. A spray voltage of 4.0 kV was employed and the velocity of drying gas was 10.0 L/min. The temperature of the heated transfer capillary was 340 °C. The mass spectrometer was scanned from m/z 100 to 300 in full scan mode.

2.3. Preparation of MIP

MIP was prepared using bulk polymerization method by dissolving 0.5 mmol of melamine, 6 mmol of functional monomer MAA, 30 mmol of cross-linker EGDMA in 5 mL of ethanol and 1.5 mL of water in a 20 mL borosilicate glass bottle, equipped with a rubber cap. This mixture was stirred over night at 50 °C for the formation of a complex of imprint molecule and monomers. After added 0.25 mmol of AIBN, the solution was saturated with dry nitrogen for 5 min and the bottle was placed in a thermostated oil bath at 60 °C for 24 h. After polymerization, the polymer was ground with a mortar and pestle, and sieved between 200 mesh and 400 mesh screens to give particles with size dimensions between 37 μm and 74 μm and then repeatedly suspended in acetone to remove the small particles. The product was extracted with ethanol containing 10% acetic acid using a Soxhlet apparatus for 48 h. Then the product was washed with ethanol for three times and dried under vacuum at room temperature.

The non-imprinted polymer (NIP) particles were prepared and washed using the same recipe but without the addition of the template melamine.

2.4. Steady-state binding studies

An amount of 10 mg of the bulk polymer particles was weighed and put into a 4 mL vial. Then 2 mL of melamine solution with known concentration was mixed with the polymer. The mixture was slightly shaken on a horizontal shaker for 5 h at room temperature and then filtered. Final melamine concentrations were determined by HPLC using UV detection at 240 nm. The amount of melamine bound to the polymer was calculated by subtracting the amount of free melamine from the initial amount added to the mixture.

2.5. Preparation of MI-SPE column

MI-SPE column was prepared by packing the dry MIP (100 mg) in a 1.0 mL glass syringe (2 cm × 0.9 cm i.d.). The syringe tube was thoroughly cleaned and dried, and attached with two sieve plates at the bottom end and the top end, respectively. Prior to loading the sample, the MI-SPE column was washed with water containing 5% acetic acid to remove residual melamine from the synthetic procedure, until melamine could not be detected in the filtrate.

2.6. Sample preparation

Five milliliters of UHT milk was transferred to a 30 mL centrifuge tube. Then, 10 mL of acetonitrile was added, and this tube was thoroughly shaken for 1 min to achieve proteins precipitation. After centrifugation at 10,000 rpm for 3 min, the buttermilk was spiked with melamine.

5 g of milk powder was mixed with 15 mL of MeOH, and stirred to a homogeneous status with a glass rod and then ultrasonicated for 10 min at room temperature. The mixture was centrifuged at 10,000 rpm for 3 min, and the supernatant was collected and spiked with melamine.

2.7. SPE for melamine standard solutions

Before loading analyte, the MI-SPE column was previously conditioned with 2 mL of deionized water and methanol, successively. After melamine standard solutions at different concentrations were passed through the columns at a flow rate of 0.25 mL/min, the columns were washed with 2 mL of water and 2 mL of methanol at the same flow rate. The analyte retained on the sorbent was eluted with 3 mL methanol containing 5% ammonium hydroxide. The eluent was evaporated to dryness under vacuum at 25 °C, and

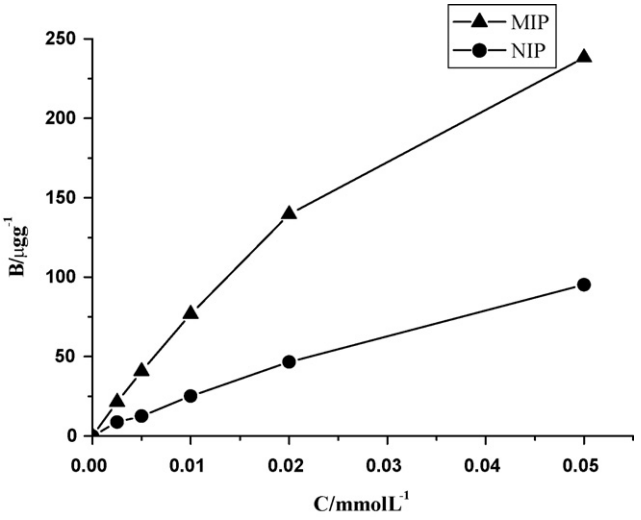


Fig. 1. Binding isotherm for molecularly imprinted polymer (MIP, ▲) and non-molecularly imprinted polymer (NIP, ●) particles. Experiment was conducted by the addition of 10 mg of particles in 2 mL of melamine in methanol at room temperature.

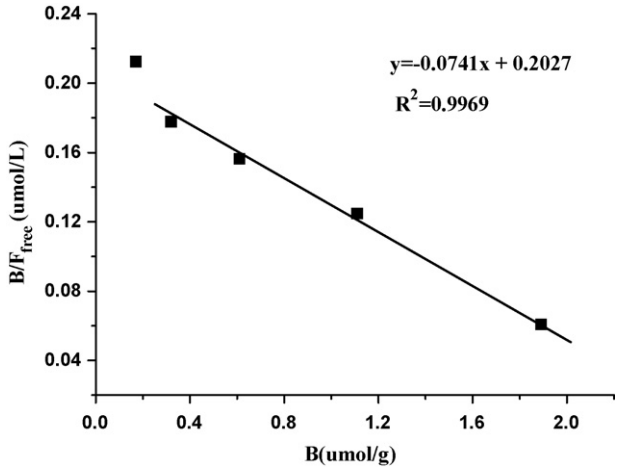


Fig. 2. Scatchard plot over 2.5–50 μmol/L (0.3–6 ppm) concentration range. Curve-fitting gives a dissociation constant K_d of 13.5 μmol/L with a saturation capacity of 2.74 μmol/g.

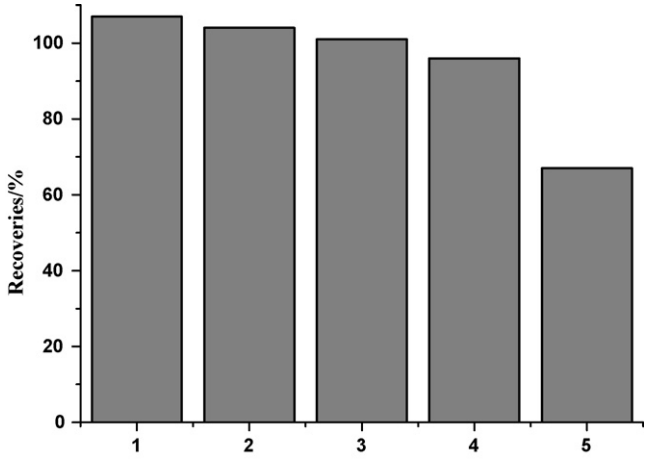


Fig. 3. The recoveries of melamine in standard solutions with an enrichment factor of 5.

the residue was reconstituted into 1 mL of mobile phase for further HPLC analysis.

2.8. SPE for spiked UHT milk and milk powders

To validate the performance of MI-SPE for the bio-matrix, the MIP and corresponding NIP were packed individually into cartridges to compare their efficiency of extracting melamine from UHT milk and infant formula. 5 mL of the dairy products sample spiked at 1 μmol/L (0.12 ppm) of melamine was passed through the MI-SPE (or NI-SPE) column as described above. Finally, the elution fractions were dried under a gentle nitrogen stream, the residues were reconstituted with methanol to final volume of 1 mL for subsequent HPLC analysis and extraction recoveries were calculated using the constructed calibration curve, respectively.

3. Results and discussion

3.1. Preparation of MIPs

Melamine is an organic base and a trimer of cyanamide, with a 1,3,5-triazine skeleton. The melamine imprinted polymer has not been synthesized though several MIPs for triazine herbicides have been prepared [14]. In order to synthesis melamine MIP, MIPs prepared in non-polar solvents, polar solvents and mixed medium with different molar ratios between template and functional monomer were investigated in our experiment, while the molar ratio of monomer to cross-linker was selected at 1:5 to ensure the formation of defined recognition sites with polymers [15]. Due to solubility limitations of melamine, melamine imprinted polymer could not be synthesized successfully in non-polar solvents. Coupled with restrictions of mechanical strength of the MIPs, only the melamine MIP prepared in the ethanol–water system with the molar ratio between template and functional monomer at 1:12 was successful (data not shown).

3.2. Evaluated the recognition efficiency of MIP

After MIP and NIP synthesis, equilibrium binding experiments were performed at room temperature with MIP and NIP. Fig. 1 shows experimental binding isotherms of MIP (and NIP) amount versus melamine concentrations. In the 2.5–50 μmol/L (0.3–6 ppm) melamine concentration range, the MIP exhibits a higher capacity for melamine than the NIP. The weak adsorption of template on NIP is due to non-specific interaction with the polymer matrix.

The data of the static absorption experiment were further processed with the Scatchard equation to estimate the binding parameters of the MIPs. Scatchard plot was constructed by plotting the ratios of bound amount to free melamine concentration against the bound concentration. As shown in Fig. 2, one straight line fitting the Scatchard equation, $B/F = (B_{max} - B)/K_d$, can be drawn, and gave two typical binding parameters. A dissociation constant (13.5 μmol/L) and a maximum number of binding sites (2.74 μmol/g) for MIP were calculated from the Scatchard

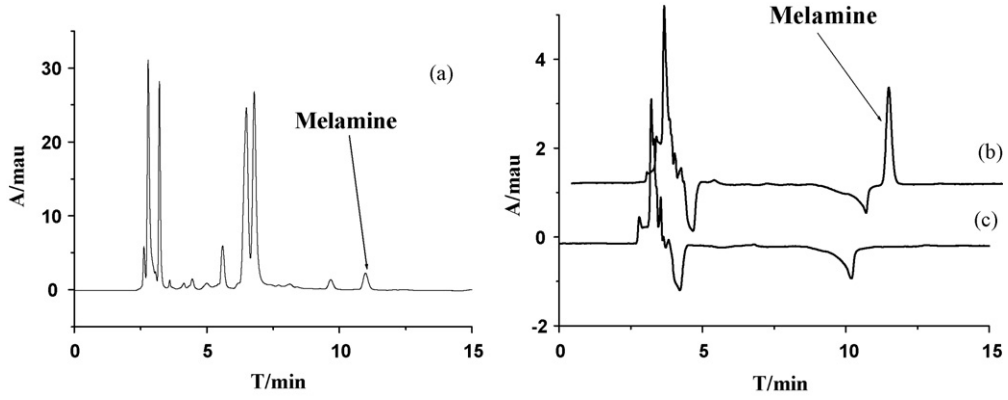


Fig. 4. HPLC chromatograms of (a) UHT milk extract after addition of 5 μmol/L (0.6 ppm) of melamine and after extraction of the UHT milk extract containing 1 μmol/L (0.12 ppm) melamine on MIP-SPE column (b) and NIP-SPE column (c).

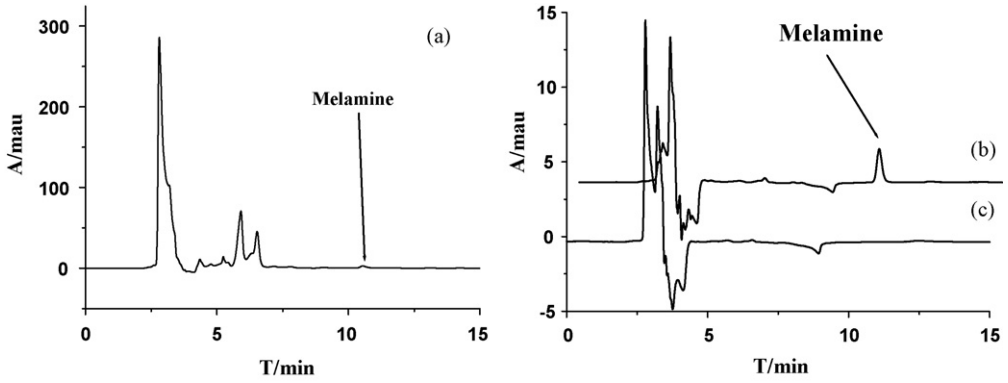


Fig. 5. HPLC chromatograms of (a) milk powder extract after addition of 5 μmol/L (0.6 ppm) of melamine and after extraction of the milk powder extract containing 1 μmol/L (0.12 ppm) melamine MIP-SPE column (b) and NIP-SPE column (c).

equation. Meanwhile a dissociation constant (107.5 μmol/L) and a maximum number of binding sites (2.54 μmol/g) for NIP were calculated from the NIP binding data. A large dissociation constant means low affinity to the target. When compared to NIP, the MIP has similar binding capacity but higher affinity to melamine. The difference in melamine binding affinity to the MIP and blank polymer clearly indicates the role of the imprinting process in the formation of specific binding sites.

3.3. SPE for melamine standard solutions

The recoveries of melamine in standard solutions were calculated and plotted in Fig. 3. It is clear that MI-SPE columns have good recoveries for melamine at different concentrations except for high concentration. A standard calibration curve for melamine analysis was constructed, which was linear ($R^2 > 0.999$) over the concentration range from 0.5 μM to 10 μM with a quantitative limit of 0.5 μmol/L (0.06 ppm). Thus, this method could be used to detect some polluted dairy products samples.

3.4. SPE for spiked UHT milk

To validate the performance of MI-SPE for the bio-matrix, the MIP and corresponding NIP were packed individually into cartridges to compare their efficiency of extracting melamine from UHT milk. Fig. 4a is the HPLC chromatogram of buttermilk of

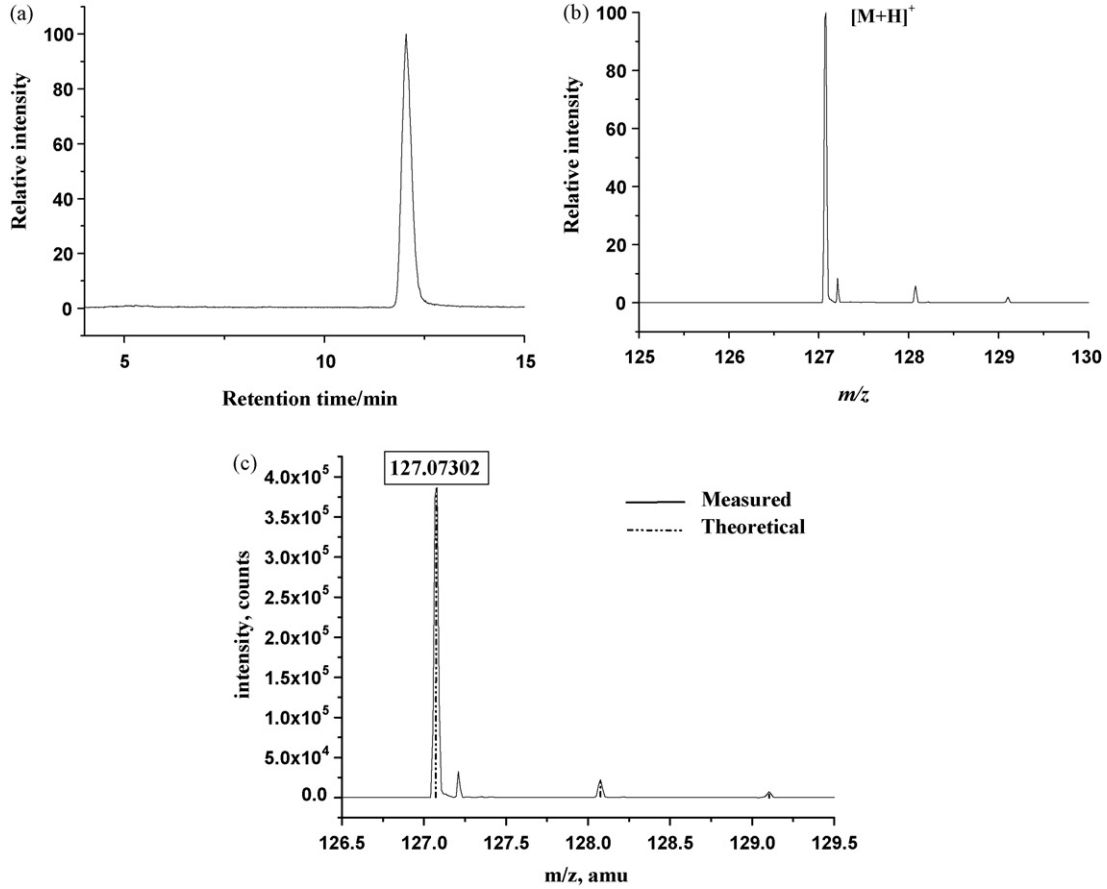


Fig. 6. The extracted ion chromatogram (EIC, a) of the elution fraction from milk powders; MS spectra (b) of the peak at 12 min in the positive mode; Observed mass ($[M+H]^+$) of melamine and its isotopics compared with calculated isotopics (c).

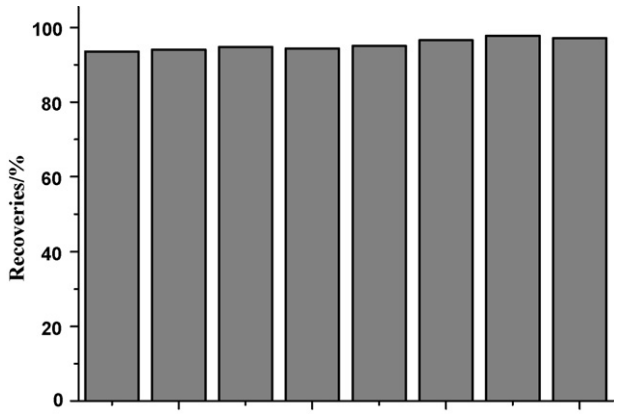


Fig. 7. Regeneration property experiment of the MI-SPE column (repeat 8 times).

UHT milk after addition of 5 μmol/L (0.6 ppm) of melamine, in which the complexity of the UHT milk matrix background is evident. The extraction on MIP column can successfully cleanup the UHT milk matrix, thus allowing the extraction of melamine with high selectivity (Fig. 4b). The result showed that the recovery of 1 μmol/L (0.12 ppm) melamine in UHT milk was 95.3 ± 1.1% (n = 3). Contrary to this, NIP column showed no such selectivity (Fig. 4c).

3.5. SPE for spiked milk powders

Milk powder constitutes a very complex matrix (Fig. 5a). The extraction on MIP column can successfully cleanup the milk powder matrix, thus allowing the extraction of melamine with high selectivity (Fig. 5b). The recovery of 1 μmol/L melamine in milk powder was also high enough for real sample analysis (95.2 ± 7.9%, n = 3). The high percentage recovery indicate that no interferences from milk powder that might be found in different formulations, which evaluates the high efficiency of extraction procedure.

Hence MIP offers itself as a simple and straightforward technique for the direct analysis of melamine in dairy products without lengthy sample cleanup.

3.6. Identification of melamine by HPLC-ESI-TOF/MS

In order to confirm the extraction of melamine on MIP column, ESI-TOF/MS analysis was performed on a 6210 time-of-flight mass spectrometer equipped with an ESI interface. The extracted ion chromatogram (EIC, 127–127.2 m/z) and MS spectra of peak at 12.05 min of the elution fraction from milk powder is shown in Fig. 6. The peak at 12.05 min observed on total ion chromatogram (TIC, not shown) was attributed to m/z 127 (EIC), meanwhile was not found from blank. Positive mass spectra of peak at 12.05 min showed its molecular ion peaks, $[M+H]^+$:m/z 127.1, in agreement with the molecular weight of melamine being 126. The typical isotopic pattern of the melamine was calculated by the isotope calculator and was found to be consistent (including position and intensity) with the pattern obtained from the main distribution in the spectrum (Fig. 6c). This provides a direct evidence for the extraction of melamine on MIP column.

3.7. Reproducibility of the MI-SPE column

Regeneration property is one of the important advantages of MIPs. MIPs can be used again to adsorb the interested analyte after regeneration. In order to reuse the polymers after each extraction, a short regeneration step was performed by washing with 3 mL of water: acetic acid (95:5, v/v). The results (see Fig. 7) showed that the MIP could be used many times and maintained their adsorption capacity at an almost constant value. This confirmed the reliability and efficacy of the proposed method for the analysis of melamine residues in real samples.

4. Conclusion

The melamine imprinted polymer was prepared by bulk polymerization using MAA and EGDMA as the functional monomer and cross-linker, respectively. The obtained MIP showed good selectivity and affinity for melamine. Accordingly, a method was successfully developed for analysis of melamine in dairy products by using the obtained MIP as the SPE sorbent coupled with HPLC. The high recoveries and satisfied precisions for analyte proved that the proposed method was valid for the analysis of melamine in different matrixes (UHT milk, infant formula). The limit of quantitation of the proposed method was 0.5 μmol/L (0.06 ppm), which is below the maximum residue limits established by U.S. FDA.

Acknowledgments

This project was supported by the National Natural Science Foundation of China (Nos. 20775019 and 20735002), the Hi-Tech Research and Development Program of China (No. 2006AA09Z168), the Natural Science Foundation of Shandong Province (No. Y2006B01) and the Natural Science Foundation of Qingdao City of China (08-1-3-32-JCH).

References

[1] H. Ishiwata, T. Inoue, T. Yamazaki, K. Yoshihira, J. Assoc. Off. Anal. Chem. 70 (1987) 457.
[2] J.V. Sancho, M. Ibanez, S. Grimalt, O.J. Pozo, F. Hernandez, Anal. Chim. Acta 530 (2005) 237.
[3] P.G. Wiles, I.K. Gray, R.C. Kissling, J. AOAC Int. 81 (1998) 620.
[4] P. Cabras, M. Meloni, L. Spanedda, J. Chromatogr. 505 (1990) 413.
[5] T. Ding, J. Xu, J. Li, C. Shen, B. Wu, H. Chen, S. Li, Chin. J. Chromatogr. 26 (2008) 6.
[6] M.S. Filigenzi, B. Puschner, L.S. Aston, R.H. Poppenga, J. Agric. Food Chem. 56 (2008) 7593.
[7] M.S. Filigenzi, R.E. Tor, R.H. Poppenga, A.L. Aston, B. Puschner, Rapid Commun. Mass Spectrom. 21 (2007) 4027–4032.
[8] J.V. Sancho, M. Ibañez, S. Grimalt, O.J. Pozo, F. Hernañdez, Anal. Chim. Acta 530 (2005) 237.
[9] J. Litzau, G. Mercer, K. Mulligan, GC–MS screen for the presence of melamine, ammeline, ammelide and cyanuric acid (version 2.1), May 22, 2007; http://www.fda.gov/cvm/GCMSMelamine.htm (accessed October 18, 2008).
[10] R.A. Yokley, L.C. Mayer, R. Rezaaiyan, M.E. Manuli, M.W. Cheung, J. Agric. Food Chem. 48 (2000) 3352.
[11] H.A. Cook, C.W. Klampfl, W. Buchberger, Electrophoresis 26 (2005) 1576.
[12] N. Yan, L. Zhou, Z.F. Zhu, X.G. Chen, J. Agric. Food Chem. 57 (2009) 807.
[13] F. Puoci, M. Curcio, G. Cirillo, F. Iemma, U.G. Spizzirri, N. Picci, Food Chem. 106 (2008) 836.
[14] J. Matsui, K. Fujiwara, S. Ugata, T. Takeuchi, J. Chromatogr. A 889 (2000) 25.
[15] S.T. Wei, A. Molinelli, B. Mizaikoff, Biosens. Bioelectron. 21 (2006) 1943.

Talanta 80 (2009) 826–832

Contents lists available at ScienceDirect

Talanta

journal homepage: www.elsevier.com/locate/talanta

Simultaneous determination of 15 steroids in rat blood via gas chromatography–mass spectrometry to evaluate the impact of emasculation on adrenal

Jun Chen [a], Qionglin Liang [a,*], Haiyin Hua [a], Yiming Wang [a], Guo'an Luo [a,**], Mingqiu Hu [b], Yanqun Na [b]

[a] Key Laboratory of Bioorganic Phosphorus Chemistry & Chemical Biology (Ministry of Education), Department of Chemistry, Tsinghua University, Beijing 100084, China
[b] Department of Urology, Institute of Urology, Peking University First Hospital, Beijing 100034, China

ARTICLE INFO

Article history:
Received 1 June 2009
Received in revised form 31 July 2009
Accepted 31 July 2009
Available online 8 August 2009

Keywords:
Adrenal
Emasculation
Steroids
Gas chromatography
Mass spectrum

ABSTRACT

Adrenal was believed to affect the prostate tumor tissue growth by its secretion of adrenal androgens. However, the mechanisms regulating these effects were not fully understood. In this work, a sensitive and specific method for the determination of 15 steroids in blood via gas chromatography–mass spectrometry in selective ion storage detection mode was established to evaluate the impact of emasculation on adrenal steroids metabolism. Steroids were isolated by solid-phase extraction using Oasis HLB cartridge, and then derivated with heptafluorobutyric anhydride before analysis. The limits of detection were between 0.15 and 1.0 ng/mL and limits of quantification were between 0.62 and 2.6 ng/mL. The recoveries of steroids were above 83%, and both the intra-day and inter-day precisions (RSD%) were lower than 8%. Pregnenolone, progesterone, 17α-hydroxyprogesterone (17αP), 17α-hydroxypregnenolone (17αH), dehydroepiandrosterone (DHEA), estrone, 17β-estradiol, dihydrotestosterone (DHT), testosterone (T), 4-androstenedione (4-A), 1,4-androstadiene-3,17-dione, 11-deoxycortisol, 11-deoxycorticosterone, cortisol and aldosterone were quantified in 156 major male SD rats at 0, 1, 2, 4, 7 days, 2, 4, 6, 8, 10, 12, 14, and 16 weeks following emasculation. T and DHT decreased by 86.2% and 73.4%, respectively in the first 7 days following emasculation, but adrenal androgens (DHEA, 4-A) stabled at the normal level accordingly. Adrenal androgens and their precursors (17αH, 17αP) increased from the 2nd week along with the increase of androgens and the decrease of mineralocorticoids. These facts revealed that adrenal possibly enhanced its function of producing adrenal androgens from the 2nd week responding to the low androgens level induced by emasculation.

© 2009 Elsevier B.V. All rights reserved.

1. Introduction

Recently, Prostate cancer (PCa) is a focused issue in men's health especially in the Europe and USA [1]. Based on the androgen dependence of prostate growth, medical and/or surgical emasculation was the main therapy for PCa, but it failed when the PCa became so-called androgen independent procedure [2]. Though the initial decrease of androgens levels responding to the androgen-deprivation therapy (ADT) was inspiring, those in blood and PCa tissue still increased after a period of time [3]. It was believed that adrenal played a role in the procedure because it was another important gland for steroids production [4]. In normal, adrenal produced corticoids and adrenal androgens, but not androgens and estrogens. However, the adrenal androgen, dehydroepiandrosterone (DHEA) and 4-androstenedione (4-A), could be converted to testosterone (T) and dihydrotestosterone (DHT) in periphery tissue, such as prostate [4]. In addition, it was reported that the adrenal tumor induced by emasculation was able to function as gonad [5]. Therefore, the evaluation of adrenal function after emasculation was valuable for the clinical PCa therapy. Based on the androgen metabolic pathway, the most important markers for evaluating adrenal function responding to emasculation were DHEA and 4-A. Meanwhile, the whole steroid metabolic pathway in adrenal also should be taken into consideration.

For steroids quantitation, immunoassays [6] and gas chromatography with mass spectrometry (GC–MS) [7] were the most preferred methods. Immunoassays were especially suitable for the screening of a large amount of samples for a few kinds of substances with great sensitivity, while GC–MS was superior in the screening of limited samples for a multiplicity of substances. Gas chromatography with mass spectrometry detection was widely used in the detection of steroids owing to its sensitivity and selectivity [8]. In order to endow GC with the detectability of steroids, and to further improve sensitivity and selectivity, target analytes had always been

* Corresponding author. Fax: +86 10 62772263.
** Corresponding author. Fax: +86 10 62781688.
E-mail addresses: liangql@tsinghua.edu.cn (Q. Liang), luoga@tsinghua.edu.cn (G. Luo).

0039-9140/$ – see front matter © 2009 Elsevier B.V. All rights reserved.
doi:10.1016/j.talanta.2009.07.066

Table 1
Analysis parameters for 15 steroids.

Compounds	Retention time (min)	Fragments (amu)	Calibration curve	r^2	Linear range (ng/mL)
Ald	17.45	542, 483[a], 105	$Y = 142.4X + 42.58$	0.9999	0.62–100
T	21.06	467, 451[a], 320	$Y = 59.57X - 56.21$	0.9982	1.4–180
E_2	21.43	468, 451[a], 237	$Y = 210.7X - 125.1$	0.9973	1.30–170
1,4-A	21.71	480[a]	$Y = 93.66X + 98.77$	0.9977	1.00–120
4-A	22.62	482[a], 467	$Y = 40.09X - 27.25$	0.9973	1.8–230
DHEA	22.72	270[a], 255, 199	$Y = 54.58X - 59.50$	0.9973	0.81–100
E_1	22.95	466, 422[a], 410	$Y = 20.82X - 63.62$	0.9971	2.6–130
DHT	24.10	414[a], 399	$Y = 21.32X - 18.25$	0.9989	1.8–230
17αH	24.73	528, 510, 467[a]	$Y = 266.4X + 41.78$	0.9998	1.7–220
17αP	24.76	526, 508, 465[a]	$Y = 305.0X + 82.15$	0.9984	1.8–230
Pr	27.02	510[a], 425, 296	$Y = 293.4X - 55.70$	0.9999	1.6–210
P	27.02	512, 298[a], 283	$Y = 198.2X - 22.62$	0.9997	1.8–230
RS	27.98	465[a], 369	$Y = 169.0X - 35.48$	0.9992	1.2–160
C	28.18	463[a], 169	$Y = 83.85X + 267.6$	0.9999	1.0–160
H	30.27	523, 491, 355[a]	$Y = 80.71X + 58.77$	0.9980	1.2–150

In the calibration curve, Y means the peak-area, and X means the compound concentration.
[a] Means the quantitative fragment ion of each compound.

derivatized. N,O-bis(trimethylsilyl)trifluoroacetamide (BSTFA) [9], N-methyl-N-(trimethylsilyl trifluoroacetamide) (MSTFA) [10,11] and heptafluorobutyric anhydride (HFBA) [11–14] were the preferred derivatization agents which had been used to react with the hydroxyl or keto functional groups in steroids. Scherer et al. [15] reported a method for the determination of T in human hair by GC–MS, proposing that the derivatization with HFBA gave rise to high mass increments thus diminishing background noise and that these derivatives tended to have shorter retention times than those of O-methoxime/trimethylsilyl (MO–TMS) ethers. Recently, solid-phase micro extract technology (SPME) combined with GC–MS was used in the determination of some anabolic steroids which could be analyzed without derivation [16]. Since Oasis HLB (hydrophilic–lipophilic balance) solid-phase extraction (SPE) cartridge was widely employed for its efficacy in steroids' extraction [17–20], Oasis HLB SPE cartridge was adopted in sample preparation.

Based on the art research, there were some reports on the study of specific steroids hormones classes such as androgens [9,17,21], estrogens [19,22], corticoids [23] and progestogens [24], but we found few reports on the simultaneous determination of the above four classes of steroids hormones. In this study, a sensitive method was established for the simultaneous determination of 15 steroids derivated with HFBA in rat's blood at 0, 1, 2, 4, 7 days, 2, 4, 6, 8, 10, 12, 14, and 16 weeks following emasculation, aiming to evaluate the impact of emasculation on adrenal function. Significant changes of steroids metabolism in adrenal occurred from the 2nd week to 4th week following emasculation when adrenal androgen levels were elevated and mineralocorticoid levels were decreased. These facts revealed that the enhancement of adrenal androgens' production was possibly due to the adrenal's compensation for the low androgen levels induced by emasculation, which should be paid more attention to in PCa patients undergoing surgical and/or medical emasculation.

2. Materials and methods

2.1. Animals

156 male Sprague–Dawley (SD) rats, weighing 250 ± 10 g, were housed at 21–23 °C with a relative humidity of 50–55%. They were maintained under a 12 h:12 h light:dark regime and fed commercial rat food and water. The experiment was performed in the animal research laboratory at Peking University. All experi-

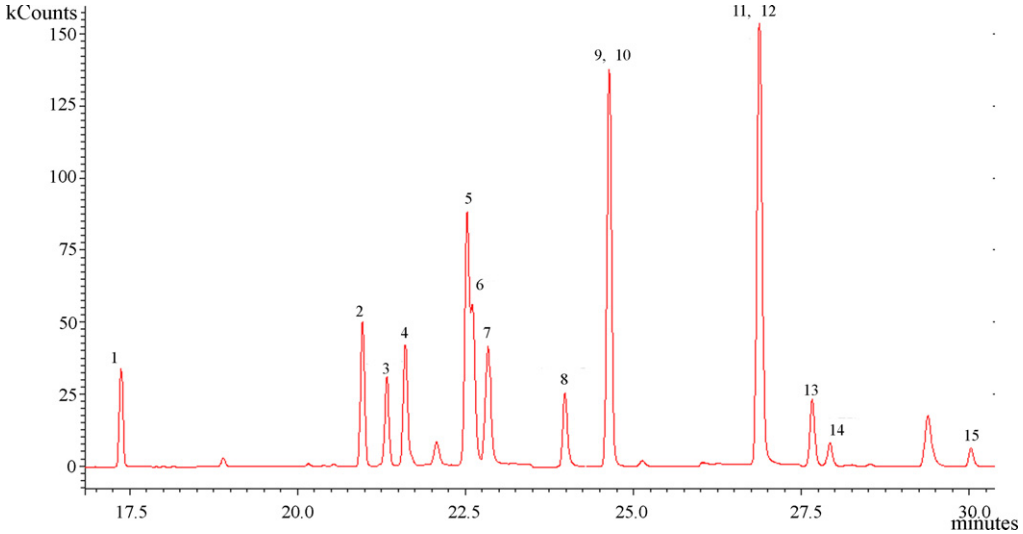


Fig. 1. Gas chromatography of 15 steroids. 15 Steroids were detected via mass spectrometry in selected ion storage mode after been derivated by heptafluorobutyric anhydride: (1) aldosterone; (2) testosterone; (3) 17β-estradiol; (4) 1,4-androstadiene-3,17-dione; (5) 4-androstenedione; (6) dehydroepiandrosterone; (7) estrone; (8) dihydrotestosterone; (9) 17α-hydroxypregnenolone; (10) 17α-hydroxyprogesterone; (11) progesterone; (12) pregnenolone; (13) 11-deoxycortisol; (14) cortisol; (15) 11-deoxycorticosterone.

mental protocols were approved by the Institutional Animal Care Committee.

156 rats were divided into 13 groups. Each group stood for one time point. Adrenal tissues were retained before emasculation, and at 1, 2, 4, 7 days, 2, 4, 8, 10, 12, 14, and 16 weeks after emasculation. All adrenal tissues were taken at 8–10 a.m.

2.2. Chemical and reagents

Pregnenolone (P, 98%), progesterone (Pr, cell culture tested), 17α-hydroxyprogesterone (17αP, 95%), 17α-hydroxypregnenolone (17αH, 95%), dehydroepiandrosterone (DHEA, 99%), 1,4-androstadiene-3,17-dione (1,4-A, 98%), 11-deoxycortisol (RS, 98%), 11-deoxycorticosterone (H, 99%), cortisol (C, 99.8%), aldosterone (Ald, 98%), estrone (E_1, 98%), and 17β-estradiol (E_2, 98%) were purchased from Sigma (St.

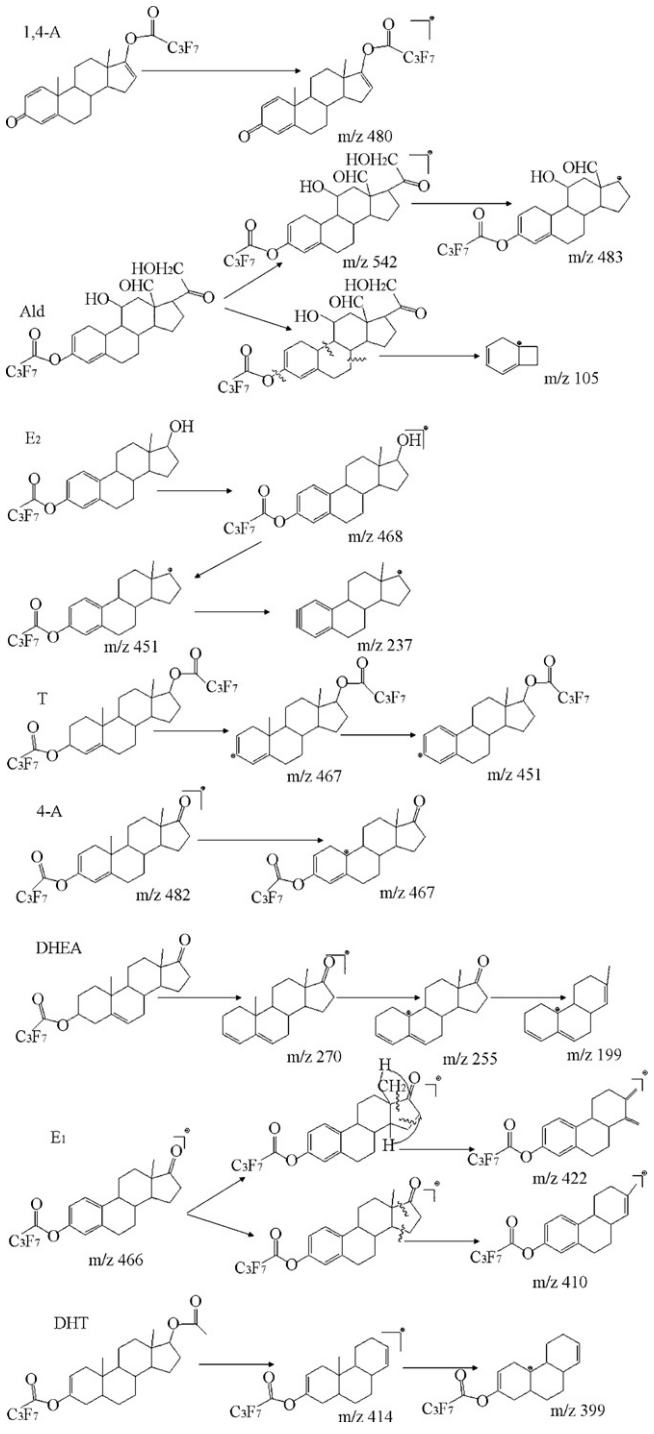


Fig. 2. Mass fragmentation of 15 steroids in full-scan mode of gas chromatography with mass spectrometry.

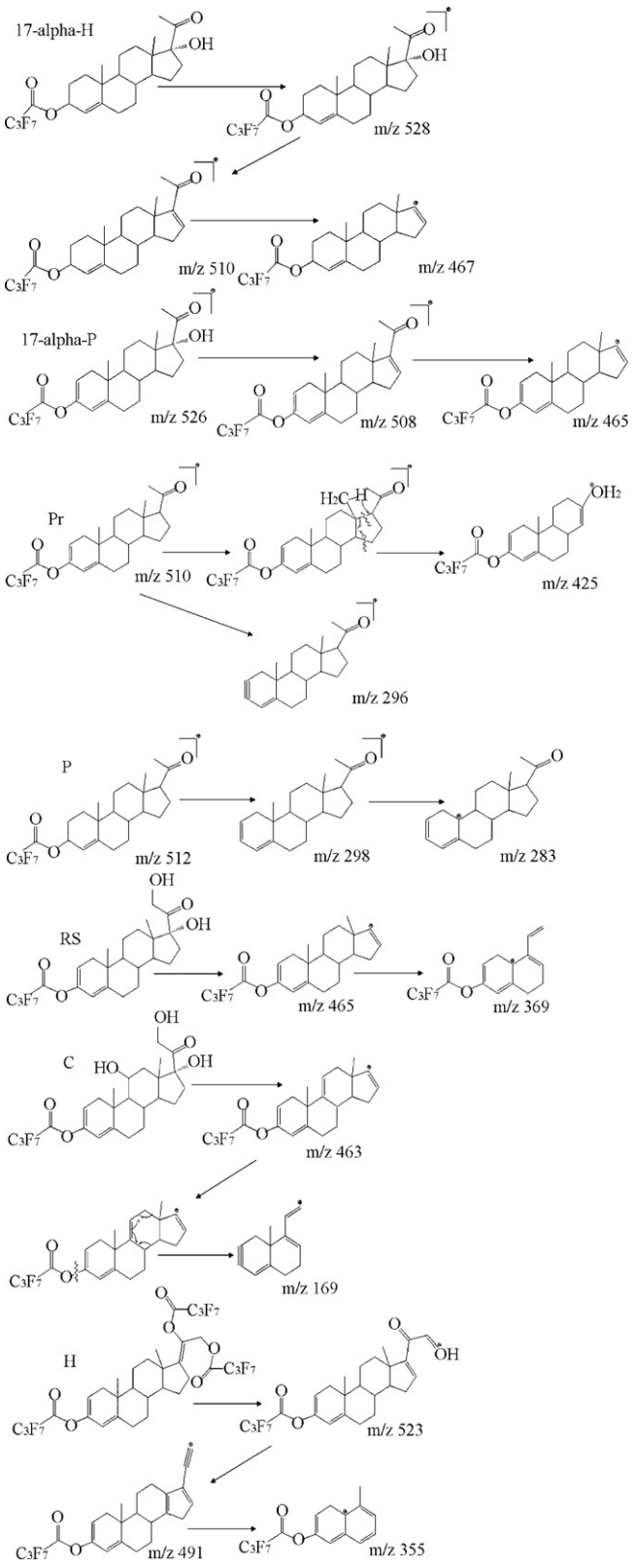


Fig. 2. (*Continued*)

Table 2
Intra-day precision and recoveries of 15 steroids ($n = 6$).

Compounds	Spiked concentration (ng/mL)	Measured concentration (means ± S.D.) (ng/mL)	RE (%)	Recovery (%)
Ald	80.0	84.3 ± 3.6	4.2	105
	10.0	8.85 ± 0.52	5.9	88.5
	2.50	2.56 ± 0.14	5.1	102
T	181	163 ± 9.2	6.0	90.0
	22.6	19.8 ± 1.2	6.0	87.3
	7.27	6.84 ± 0.19	3.2	94.1
E_2	166	155 ± 8.0	5.1	93.2
	20.8	17.7 ± 0.58	3.2	85.4
	5.19	5.12 ± 0.24	4.6	98.8
1,4-A	127	123 ± 8.5	6.9	97.4
	15.8	16.4 ± 0.58	3.5	103
	3.96	4.16 ± 0.17	4.1	105
4-A	233	218 ± 14	6.7	93.6
	29.1	26.4 ± 1.3	4.8	90.5
	7.28	6.86 ± 0.54	7.9	94.2
DHEA	104	99.4 ± 6.2	6.3	95.5
	13	12.0 ± 0.46	3.8	92.6
	3.25	3.30 ± 0.17	5.2	102
E_1	168	157 ± 7.9	5.0	93.4
	20.5	19.1 ± 1.3	6.8	93.2
	5.2	5.4 ± 0.22	4.1	104
DHT	232	194 ± 13	6.4	83.6
	29.1	26.0 ± 0.72	2.8	89.5
	7.27	6.86 ± 0.26	3.9	94.3
17αH	215	197 ± 10	5.2	91.6
	26.9	26.3 ± 1.5	5.8	97.8
	6.72	5.94 ± 0.32	5.4	88.4
17αP	226	226 ± 11	5.0	100
	28.2	29.0 ± 1.3	4.6	103
	7.06	6.88 ± 0.31	4.5	97.4
Pr	209	197 ± 13	6.4	94.7
	26.1	25.1 ± 0.90	3.6	96.2
	6.53	5.99 ± 0.32	5.4	91.7
5P	233	226 ± 14	6.0	97.1
	29.1	24.4 ± 1.4	5.8	84.0
	7.27	6.16 ± 0.26	4.2	84.8
RS	160	164 ± 4.4	2.7	102
	20.0	19.6 ± 0.89	4.5	98.0
	5.00	4.57 ± 0.28	6.2	92.3
C	129	111 ± 5.2	4.6	86.0
	16.1	16.7 ± 0.92	5.4	104
	4.03	3.82 ± 0.26	6.8	94.8
H	150	130 ± 7.0	5.3	86.8
	18.8	15.9 ± 0.86	5.4	84.8
	4.69	4.06 ± 0.25	6.1	86.7

Table 3
Inter-day precision and recoveries of 15 steroids ($n = 6$).

Compounds	Spiked concentration (ng/mL)	Measured concentration (means ± S.D.) (ng/mL)	RE (%)	Recovery (%)
Ald	80.0	82.7 ± 4.3	5.2	103
	10.0	8.79 ± 0.57	6.5	87.9
	2.50	2.44 ± 0.19	7.0	97.6
T	181	161 ± 7.6	5.0	89.0
	22.6	20.4 ± 1.3	6.6	90.3
	7.27	6.77 ± 0.14	2.4	93.1
E_2	166	152 ± 7.9	5.2	91.6
	20.8	17.6 ± 0.21	1.2	84.6
	5.19	5.12 ± 0.10	2.0	98.6
1,4-A	127	125 ± 8.8	7.0	98.4
	15.8	16.2 ± 0.37	2.3	102
	3.96	4.10 ± 0.16	3.9	104
4-A	233	208 ± 13	6.4	89.3
	29.1	27.4 ± 1.0	3.8	94.2
	7.28	7.21 ± 0.11	1.5	99.0
DHEA	104	101 ± 5.0	4.9	97.1
	13	12.4 ± 0.20	1.6	95.4
	3.25	3.16 ± 0.10	3.1	97.2
E_1	168	154 ± 5.3	3.4	91.7
	20.5	20.9 ± 1.1	5.3	102
	5.2	4.8 ± 0.12	2.5	92.3
DHT	232	194 ± 13	6.5	83.6
	29.1	26.3 ± 0.37	1.4	90.4
	7.27	6.80 ± 0.18	2.7	93.5
17αH	215	204 ± 6.4	3.1	94.9
	26.9	26.3 ± 0.82	3.1	97.8
	6.72	5.99 ± 0.091	1.5	89.1
17αP	226	223 ± 11	5.0	98.7
	28.2	27.2 ± 0.97	3.4	96.4
	7.06	6.98 ± 0.29	4.1	98.9
Pr	209	202 ± 7.86	3.9	96.6
	26.1	24.9 ± 0.54	2.2	95.4
	6.53	6.24 ± 0.42	6.7	95.6
P	233	212 ± 10	4.8	91.0
	29.1	24.4 ± 1.5	6.2	83.8
	7.27	6.21 ± 0.20	3.3	85.4
RS	160	165 ± 3.8	2.3	103
	20.0	19.5 ± 0.58	3.0	97.5
	5.00	4.51 ± 0.24	5.2	90.2
C	129	111 ± 4.9	4.4	86.0
	16.1	17.2 ± 0.68	3.9	107
	4.03	3.67 ± 0.14	3.9	91.1
H	150	129 ± 4.5	3.5	86.0
	18.8	15.8 ± 0.82	5.2	84.0
	4.69	4.76 ± 0.10	2.5	101

Loius, MO, USA), dihydrotestosterone (DHT, 99%) was purchased from TCI-EP (Tokyo, Japan), testosterone (T, 99%) and 4-androstenedione (4-A, 99%), heptafluorobutyric anhydride (HFBA, 99%) were purchased from ACROS (Geel, Belgium). SPE cartridge (Oasis HLB, 3 mL) was purchased from Waters (Milford, Mass, USA), and HPLC-grade methanol and hexane were purchased from Fisher (Fair Lawn, NJ, USA). DI water was generated by the MilliQ system (Millipore, Bedford, MA, USA).

2.3. Apparatus

The GC–MS experiment was performed on a Varian CP-3800 series gas-chromatograph with mass spectrometric detector Saturn 2200. GC condition was as follows: splitless injection mode; 5% phenyl methyl siloxane; 95% dimethylpolysiloxane capillary column [Varian, VF-5m, 30 m × 0.25 mm (i.d.); 0.25 μm film thickness]; injection port temperature, 280 °C; carrier gas, helium; flow rate, 1 mL/min; column temperature, 95 °C, hold 6 min, then increased to 210 °C at 30 °C/min, increased to 250 °C at 2 °C/min, and then increased to 290 °C at 10 °C/min, hold 5 min. Mass spectrometry was in SIS (select ion storage) mode, ion trap temperature, 200 °C; transfer line temperature, 270 °C; multiplier temperature, 40 °C.

2.4. Sample preparation

Samples were stored in liquid nitrogen, thawed prior to analysis. Before analysis, 200 μL of serum was mixed with 400 μL of methanol for deproteinization, thoroughly vortex-mixed and cen-

trifuged at 1500 × *g* for 30 min, kept the supernatant, discarded the pellet, then 500 μL DI water was added to the supernatant. The supernatant was then loaded with the flow rate of 2–3 drops/s onto the SPE cartridge which has been activated by 1 mL methanol, 1 mL H_2O, 1 mL methanol–H_2O (v:v = 1:1), and then extraction was performed with 2 mL 50% methanol/water, 1 mL 100% methanol in turn with the flow rate of 3–4 drops/s. Collected methanol wash-off liquor was evaporated with gentle nitrogen at 60 °C, and then mixed with 200 μL of acetone to resolute the pellet, added 40 μL HFBA to the solution. The reaction took place at 60 °C for 60 min, then evaporated with gentle nitrogen at 60 °C after the reaction, added 100 μL hexane to resolute the pellet and 2 μL was injected for analysis.

2.5. Standards and controls

Stock solutions of 0.5 mg/mL of each analyte were prepared in methanol. These stock solutions were mixed and diluted to give a series of stock solutions of all analytes.

3. Results and discussion

3.1. Method validation

3.1.1. Retention times and specificity

The retention times of 15 steroids were shown in Table 1. Though retention times of 4-A and DHEA, 17αH and 17αP, Pr and P were nearly the same, based on the fragmentation difference, high specificity was achieved in the select ion storage (SIS) mode employed in this quantitative method. An unknown 467 amu fragment was also detected at 21 min near the retention time of testosterone, thus 451 but not 467 amu was chosen as the quantitative ion of testosterone. The gas chromatography of 15 steroids was shown in Fig. 1.

3.1.2. Mass spectra

The main fragments of 15 steroids in full-scan EI (electronic ionization) mode were shown in Table 1. The molecular ions of 13 steroids derivated by HFBA were detected except DHEA and H. DHEA–HFBA was prone to lose a molecule of HFBA to obtain a strong 270 amu fragmentation, and H was suspected to react with three molecular HFBA to obtain a 918 amu H-$(HFBA)_3$ which exceeded the 650 amu maximum mass range of GC–MS. Fragments were mostly resulted from the cleavage of the D ring, especially at the 17 carbon connecting a side chain. For HFBA mostly reacted with the 3-hydroxyl group, the A ring cleavage was to lose HFBA. The B and C rings were split to obtain some low molecular ions at C7-8, C9-10, and C12–13, C8-14, respectively. The mechanism of fragmentation was illustrated in Fig. 2.

3.1.3. Optimized reaction condition

Reaction conditions such as volume of HFBA (10–90 μL), reaction time (30–90 min) and reaction temperature (25–75 °C) were tested. Recoveries of steroid would be better along with the increase of HFBA volume (<60 μL), reaction time (<60 min) and reaction temperature (<60 °C). But excessive HFBA volume, too long reaction time, and too high reaction temperature would also induce side reaction to reduce steroid recoveries. In this study, that samples reacting with 60 μL HFBA at 60 °C for 60 min was the optimized condition.

3.1.4. Calibration and sensitivity

The linear regression analysis was constructed by plotting the peak-area of analytes versus analyte concentration (ng/mL). The retention time, main fragments, regression equation of these curves, square of correlation coefficients (*r*), and linear range for each steroid were shown in Table 1. Signals 3 and 10 times higher than the peak noise were considered as the limit of detection (LOD) and quantification (LOQ) for all the 15 steroids. The LOQ were ranging from 0.62 to 2.6 ng/mL, and the LOD were ranging from 0.15 to 1.0 ng/mL.

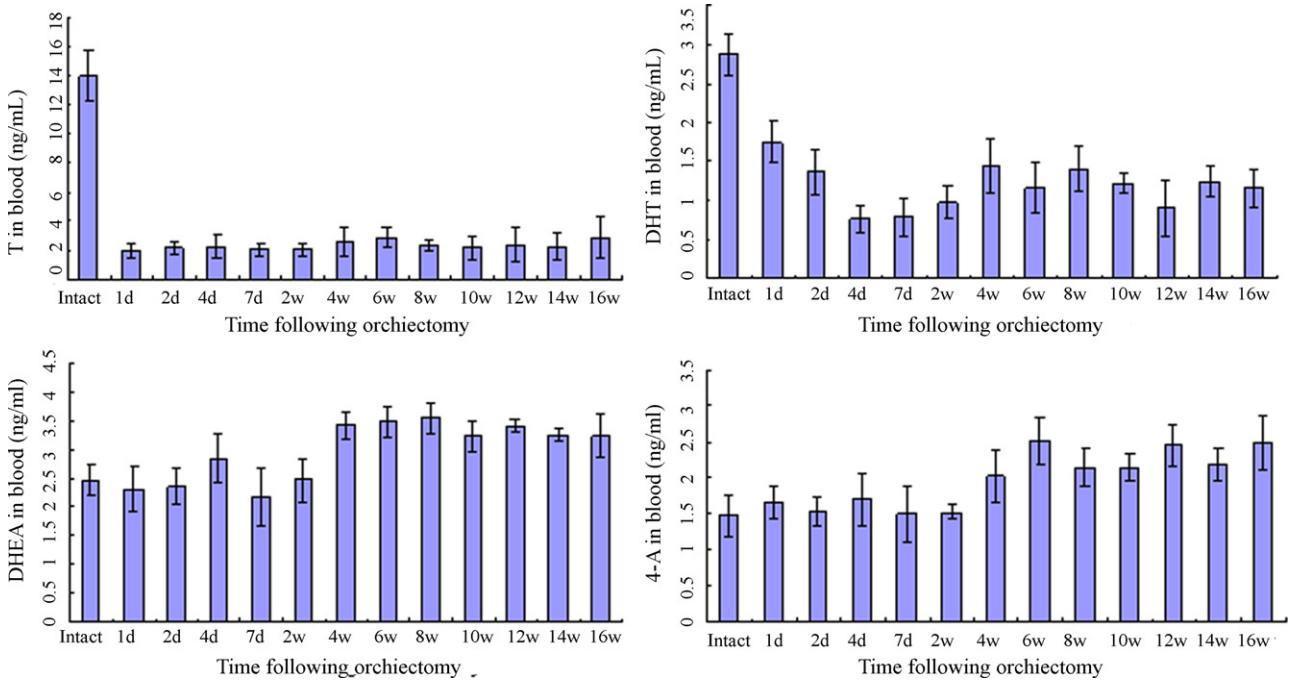


Fig. 3. Androgens and adrenal androgens levels in blood before and after emasculation. Androgens were decreased more than 70% while adrenal androgens (DHEA and 4-A) were nearly remain the same as normal level in the first 7 days following emasculation. But both androgens and adrenal androgens were rising from the 2nd week following emasculation.

3.1.5. Recoveries and stability

The extraction recoveries were determined at three concentration levels. The recoveries ranged from 83% to 107%, and the results were shown in Table 2. The background response in blank sample was subtracted.

The stability of 15 steroids was evaluated by determining a sample repeatedly at 0 h, 6 h, 12 h, 24 h with a RSD <7% ($n = 3$), which showed that the derivatives of these steroids had a good stability within 24 h.

3.1.6. Accuracy and precision

A total of 12 mL normal rat serum sample was divided into 60 portions as 200 μL each. All these portions were detected throughout 3 days, 18 portions per day. Then the intra-assay variation and the inter-assay variation of the method were determined, whose RSD% were both below 10%. We determined the extraction recovery by measuring a blank serum sample and the same serum sample enriched with synthetic compounds at three concentration levels. Results were shown in Tables 2 and 3.

3.2. Steroids in blood of castrated rat

Androgens, adrenal androgens, and progestogens were quantified, but estrogens, cortisol, 11-dehydrocortisol and 1,4-androstadiene-3,17-dione were under the limit of determination in blood of castrated rat.

3.2.1. Androgens in blood of castrated rat

After emasculation, T levels in blood descended dramatically from a normal level of 14.02 ± 1.78 to 1.96 ± 0.52 ng/mL, whose descending extent was about 86.2% ($p < 0.05$). Despite the initial drastic drop, T levels were stable ranging from 2.02 ± 0.43 to 2.19 ± 0.81 ng/mL during the first 2 weeks, while a gentle increase occurred from the 4th to 16th week, where the T levels were about 15.1–20.3% of normal manner. A successive descent of DHT levels occurred in the first 4 days, whose descending extent was about 73.4% at the 4th day compared to normal level ($p < 0.05$). From the 4th to 16th week, DHT levels were higher than that of the 2nd week ($p < 0.05$), ranging from 1.27 ± 0.13 to 1.59 ± 0.19 ng/mL which were about 72.9–90.9% of normal level. Since androgen was mainly produced by gonad, emasculation could reduce androgen level in blood immediately as it took place. The increase from the 4th week after emasculation implied emasculation was not a lasting effective way to reduce androgen level [3]. In addition, for adrenal was the primary gland for steroids production after emasculation, androgens after the 4th week were supposed to be adrenal source [4].

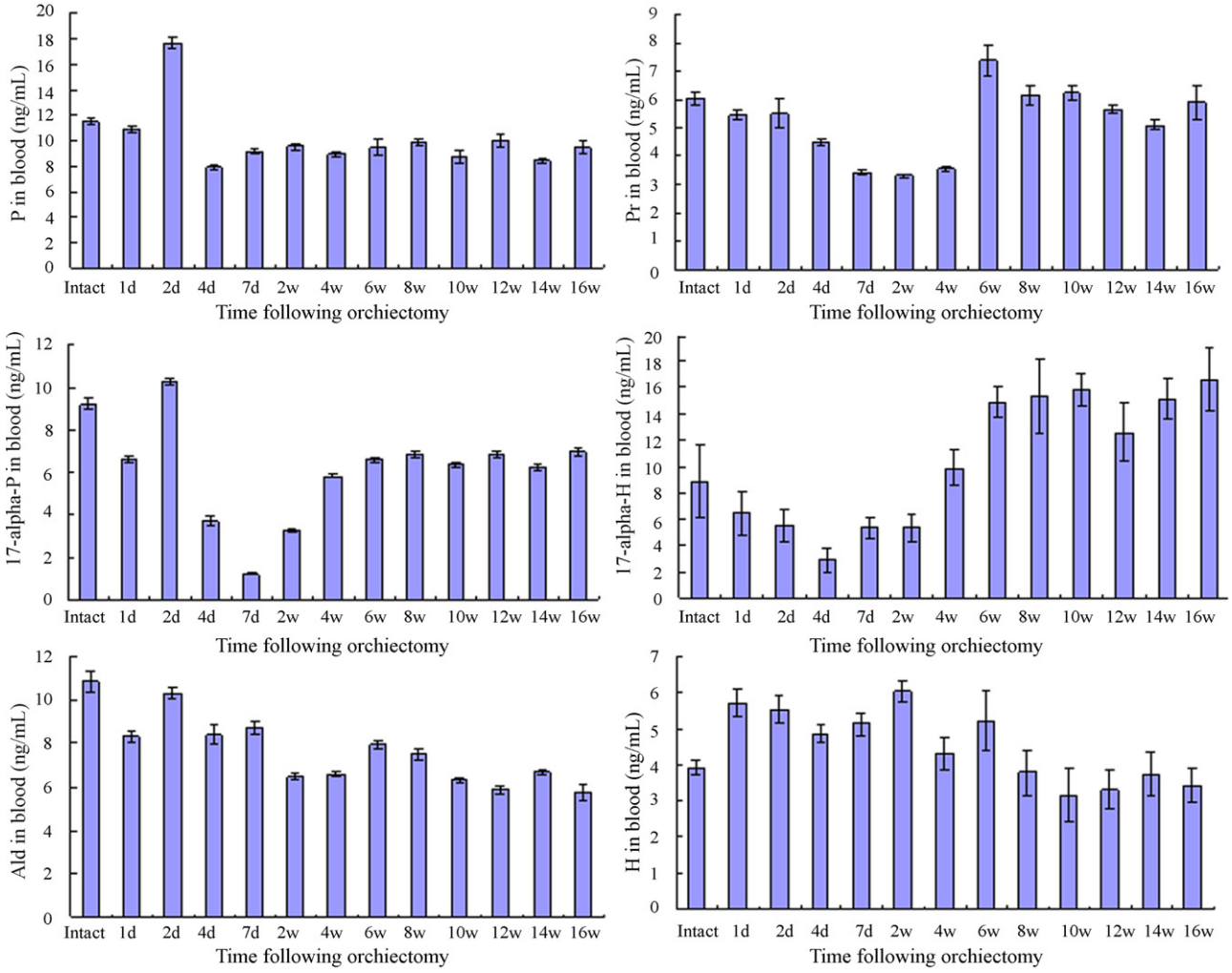


Fig. 4. Progestogens and corticoids levels in blood before and after emasculation. Progestogens decreased in the first 7 days to 2 weeks after emasculation, but then initiated a increasing procedure. Aldosterone decrease slightly in the first 7 days, but dramatically from the 2nd week, while 11-deoxycorticosterone (H) was above than normal till the 6th week, then a decrease initiated.

3.2.2. Adrenal androgens in blood of castrated rat

There was no obvious change of DHEA in the first 2 weeks with concentrations ranging from 2.15 ± 0.50 to 2.84 ± 0.43 ng/mL. It then escalated from the 4th to the 16th week compared to the 2nd week, ranging from 3.23 ± 0.27 to 3.54 ± 0.28 ng/mL which were 31.7–44.4% higher than the normal manner ($p < 0.05$). Similar to DHEA, 4-A levels were stable in the first 2 weeks. Compared to the normal level 1.47 ± 0.30 ng/mL, there was no significant difference of 4-A in the first 2 weeks ranging from 1.50 ± 0.38 to 1.70 ± 0.38 ng/mL. After 4 weeks, the concentrations of 4-A were higher than the normal manner by about 37.7%–70.5% ($p < 0.05$), ranging from 2.02 ± 0.36 to 2.51 ± 0.33 ng/mL. DHEA and 4-A which could be converted to androgens in periphery tissue were considered as adrenal androgens [4]. The increase of both of them from the 4th week was possibly a result of enhanced expression of CYP17 in adrenal induced by emasculation [25–27] (Fig. 3).

3.2.3. Progestogens and mineralocorticoids in blood of castrated rat

P stabled at concentrations lower than normal level except for the 2nd day. A successive descending occurred for Pr in the first 7 days, and stabled at half of the normal level from the 7th day to 4th week, but increased since the 6th week ranging from 8.41 ± 0.21 to 9.87 ± 0.32 ng/mL, 72.9–86.2% of normal level. 17αP descended successively till the 7th day at 1.20 ± 0.02 ng/mL, 13.1% of normal level, and then ascended till the 6th week to stable at 6.20 ± 0.14 to 6.96 ± 0.17 ng/mL, 67.5–75.8% of normal level. Nearly the same as 17αP, 17αH descended successively till the 4th day at 2.87 ± 0.95 ng/mL, 32.5% of normal level, and then ascended till the 6th week to stable at 12.5 ± 2.2 to 16.5 ± 2.4 ng/mL, 141–186% of normal level. Ald descended significantly from the 2nd week ($p < 0.05$), and H was above normal level at 3.92 ± 0.20 ng/mL before the 6th week ($p < 0.05$) ranging from 4.30 ± 0.43 to 6.03 ± 0.27 ng/mL, and descended till lower than normal level from the 8th week ranging from 3.17 ± 0.72 to 3.79 ± 0.62 ng/mL (Fig. 4). That 17αP and 17αH increased along with their metabolites DHEA and 4-A from the 2nd week implied that the enhancement of DHEA and 4-A production possibly occurred, while the decrease of Ald and H from the 2nd week implied that the production of mineral corticoids was weakened in adrenal responding to emasculation.

3.2.4. Impact of emasculation on adrenal

Despite androgen-deprivation therapy being the standard treatment of advanced prostatic cancer, the effect of emasculation on adrenal was poorly understood. For adrenal androgens was believed to be important in the prostate cancer therapy, we need to illuminate the changes of adrenal source androgens after emasculation.

Both T and DHT decreased significantly after emasculation, but DHEA and 4-A were stable in the first 2 weeks. These four hormones increased at the 4th week, and stabled since the 6th week. DHEA and 4-A, which could be converted to T and DHT in periphery tissue, were thought to be the primary source of androgens after emasculation. In addition, the levels of DHEA and 4-A were above normal from the 4th week, while the levels of 17αP and 17αH, precursors of DHEA and 4-A, respectively, both increased from the 2nd week and stabled since the 6th week. As DHEA and 4-A were mainly produced by adrenal, the increase of the both and their precursors from the 2nd week suggested that adrenal enhanced its production of adrenal androgens, presumably leading to the decrease of mineralocorticoids. Based on these facts, adrenal was suggested to increase adrenal androgens production and decrease aldosterone production from the 2nd week responding to the low androgens level induced by emasculation, which possibly resulted in the increase of DHT and T from the 4th week.

4. Conclusion

Different from the current study which usually focused on several specific analytes among steroids classes, the present study established a GC–MS method for the simultaneous determination of as many as 15 analytes covering 4 classes of endogenous steroids hormones such as androgens, estrogens, corticoids and progestogens. The utilization of HLB solid-phase extraction in the pretreatment of biological samples had significant merits in improving the recoveries, reducing the treatment time and also avoiding the usage of some solvents for liquid–liquid extraction such as ethyl acetate and chloroform. The method was applied to the study of evaluating adrenal function after emasculation. In the first 7 days after emasculation, androgens decreased dramatically but adrenal androgens stabled. Adrenal androgens and their precursor increased from the 2nd week along with the decrease of mineralocorticoids and the increase of androgens. These facts revealed that adrenal possibly enhanced its function of producing adrenal androgens which could further influence the androgens level. More efforts should be made to investigate these steroids in adrenal tissue after emasculation to illuminate the differentiate process of adrenal function.

Acknowledgments

This work was sponsored by National Natural Science Foundation of China (30772169, 20805026, 90709045), and National Basic Research Program (973 Program) of China (2005CB523503, 2007CB714505, 2007CB511903)

References

[1] B.A. Hellerstedt, K.J. Pienta, CA-Cancer J. Clin. 52 (2002) 154–179.
[2] R.D. Samuel, T.I. John, Nature 2 (2002) 389–392.
[3] F.H. Yoon, S.L. Gardner, C. Danjoux, G. Morton, P. Cheung, R. Choo, J. Urol. 180 (2008) 1438–1443.
[4] F. Labrie, V. Luu-The, A. Bélanger, S.X. Lin, J. Simard, G. Pelletier, C. Labrie, J. Endocrinol. 187 (2005) 169–196.
[5] N. Tsutomu, I. Toshihiko, H. Yutaka, W. Koichi, T. Kota, J. Urol. 178 (2007) 1282–1288.
[6] S.K. Makela, G. Ellis, Clin. Chem. 34 (1988) 2070–2075.
[7] K. Shimada, K. Mitamura, T. Higashi, J. Chromatogr. A 935 (2001) 141–172.
[8] B.G. Wolthers, G.P.B. Kraan, J. Chromatogr. A 843 (1999) 247–274.
[9] M.A.S. Marques, L.A. Lima, C.H.B. Bizarri, F.R. Aquino-Neto, J.N. Cardoso, J. Anal. Toxicol. 22 (1998) 367–373.
[10] B.L. Bizec, M.P. Montrade, F. Monteau, F. Andre, Anal. Chim. Acta 275 (1993) 123–133.
[11] M.R. Fuh, S.Y. Huang, T.Y. Lin, Talanta 2 (2004) 408–414.
[12] G. Casademont, B. Pérez, R.J.A. García, J. Chromatogr. B 686 (1996) 189–198.
[13] E. Daeseleire, R. Vandeputte, P.C. Van, Analyst 123 (1998) 2595–2598.
[14] M.H. Choi, B.C. Chung, W. Lee, U.C. Lee, Y. Kim, Rapid Commun. Mass Spectrom. 13 (1999) 376–380.
[15] C. Scherer, U. Wachter, S.A. Wudy, Analyst 123 (1998) 2661–2663.
[16] Z.M. Zhang, H.B. Duan, L. Zhang, X. Chen, W. Liu, G.A. Chen, Talanta 78 (2009) 1083–1089.
[17] R. Manfred, G. Michael, R. Wolfgang, G.D. Helmuth, Steroids 71 (2006) 450–458.
[18] K. Geoge, T. Geogios, N.P. Ioannis, D. Themistoklis, J. Agric. Food Chem. 55 (2007) 8325–8330.
[19] P. Marta, B. Francesc, P. Eva, M.R. Maria, Talanta 78 (2009) 1327–1331.
[20] J. Chen, Q.L. Liang, H. Li, G.A. Luo, Y.M. Wang, Chem. J. Chin. Univ. 29 (2008) 2155–2158.
[21] L. Lootens, P.V. Eenoo, P. Meuleman, G. Leroux-Roels, W.V. Thuyne, F.T. Delbeke, J. Chromatogr. A 1178 (2008) 223–230.
[22] I. Garcia, L. Sarabia, M.C. Ortiz, J.M. Aldama, Anal. Chim. Acta 526 (2004) 139–146.
[23] E. Pujos, M.M. Flament-Waton, O. Paisse, M.F. Grenier-Loustalot, Anal. Bioanal. Chem. 381 (2005) 244–254.
[24] H. Chang, S.M. Wu, J.Y. Hu, M. Asami, S. Kunikane, J. Chromatogr. A 1195 (2008) 44–51.
[25] W. Wang, Y.X. He, J. Chen, X. Li, G.A. Luo, Y.M. Wang, Chem. J. Chin. Univ. 29 (2008) 1349–1351.
[26] N.A. Rahman, S. Kiiveri, A. Rivero-Müller, J. Levallet, S. Vierre, J. Kero, D.B. Wilson, M. Heikinheimo, I. Huhtaniemi, Mol. Endocrinol. 18 (2004) 2553–2569.
[27] B.D. Looyenga, G.D. Hammer, Mol. Endocrinol. 20 (2006) 2848–2863.

Talanta 80 (2009) 833–838

Contents lists available at ScienceDirect

Talanta

journal homepage: www.elsevier.com/locate/talanta

Geographical classification of some Australian wines by discriminant analysis using HPLC with UV and chemiluminescence detection

S.A. Bellomarino[a], X.A. Conlan[a,b], R.M. Parker[c], N.W. Barnett[a], M.J. Adams[c,*]

[a] School of Life and Environmental Sciences, Deakin University, Geelong, Vic. 3217, Australia
[b] Institute for Technology Research and Innovation, Deakin University, Geelong, Vic. 3217, Australia
[c] Applied Chemistry, School of Applied Sciences, RMIT University, GPO Box 2476V, Melbourne, Vic. 3001, Australia

ARTICLE INFO

Article history:
Received 15 May 2009
Received in revised form 3 August 2009
Accepted 3 August 2009
Available online 8 August 2009

Keywords:
HPLC
Wine classification
Chemiluminescence
Chemometrics
Principal components analysis
Discriminant analysis

ABSTRACT

HPLC with UV and acidified potassium permanganate chemiluminescence detection, combined with multivariate data analysis techniques, were used for the geographical classification of some Australian red (Cabernet Sauvignon) and white (Chardonnay) wines from two regions (Coonawarra and Geelong). Identification of the wine constituents prominent in the chromatography was performed by mass spectrometry. Principal components analysis and linear discriminant analysis were used to classify the wines according to region of production. Separation between regions was achieved with both detection systems and key components leading to discrimination of the wines were identified. Using two principal components, linear discriminant analysis with UV detection correctly classified 100% of the Chardonnay wines and, overall 91% of the Cabernet Sauvignon wines. With acidified potassium permanganate chemiluminescence detection, 75% of the Chardonnay wines and 94% of the Cabernet Sauvignon wines were correctly classified using two factors.

© 2009 Elsevier B.V. All rights reserved.

1. Introduction

There is increasing interest from consumers for food products from known geographical origins, and product pricing is often related to region or country of origin. Considerable research has been devoted to applications of analytical science for food authentication and quality assurance with a number of reviews appearing in recent years [1–3]. Modern analytical techniques including spectroscopic [4–9], chromatographic [10–11], mass spectrometry [11–13], sensor [14] and isotopic methods [12,15] have been used for the determination of food authenticity. Combining these analytical methodologies with appropriate chemometric analysis offers the most promising approach for distinguishing geographic origin of foods [16].

In particular, classification of wines according to their denomination of origin has received considerable attention in the scientific literature and has been performed by elemental metals analysis using atomic absorption and atomic emission spectrometry and isotopic analysis [12,17]. Molecular spectroscopic techniques have also been extensively studied for wine analysis and classification, with UV–vis spectroscopy being employed in a number of publications. Urbano et al. have reported the use of UV–vis spectroscopy with pattern recognition methods as an inexpensive screening method for differentiation and classification of Spanish wines [4]. Principal components analysis (PCA) and modelling (SIMCA) were used for exploratory data analysis and development of classification models respectively. Acevedo et al. [5] examined the classification of Spanish red and white wines using UV–vis spectrophotometric analysis and novel classification methods such as support vector machines as a means of achieving improved classification rates. Liu et al. employed visible–near infrared (NIR) spectroscopies in an attempt to classify Spanish and Australian Tempranillo red wines as well as commercial Riesling wines from Australia, New Zealand, France and Germany [6,7]. PCA, linear discriminant analysis (LDA), partial least squares discriminant analysis (PLSDA), and stepwise linear discriminant analysis were examined as classification tools. The results clearly demonstrated that visible–NIR spectra contain information that when used with chemometrics allows discrimination between wines from different countries. The feasibility of visible–NIR spectroscopy for discriminating Australian white wines (Chardonnay and Riesling) of different varietal origin using PCA, principal components regression and PLSDA has also been reported [8]. Although successful classification models were developed, the authors recommended caution in extending the techniques to other wine varieties. The varietal discrimination of Australian wines by means of mid-infrared spectroscopy has been described by Bevin et al. [9]. Three red wine varieties (Cabernet Sauvignon, Shiraz and Merlot) and four white wine varieties (Chardonnay, Riesling, Sauvignon Blanc and Viognier) from different Australian wine regions were

* Corresponding author. Tel.: +61 3 9925 3358; fax: +61 3 9925 3747.
E-mail address: mike.adams@rmit.edu.au (M.J. Adams).

0039-9140/$ – see front matter © 2009 Elsevier B.V. All rights reserved.
doi:10.1016/j.talanta.2009.08.001

successfully discriminated according to variety using LDA. Chemometrics with mass spectrometric analysis is exemplified by the work of Cozzolino et al. using an electronic nose with PCA and PLSDA to classify Australian wines [13]. Isotopic ratios determined by SNIF-NMR and mass spectrometry methods have been used in combination with chemometric methods for the detection of wine chaptalisation and differentiation of wines according to the geographical origin [18].

Much of the molecular spectroscopy work involves non-specific analytes. Greater specificity is afforded when some form of separation science is involved in the procedure, and hyphenated techniques have proved successful for classification of wines. Ballabio et al. performed classification of wine samples using dynamic headspace gas chromatography mass spectrometry [19] and Brescia et al. have examined high-performance ion chromatography exclusion, ICP optical emission spectrometry and NMR measurements [20]. Phenolic compounds are important components in wines and have been successfully employed for characterising commercial wines [1,21]. Rodriguez-Delgado et al. have studied the phenolic profiles attributable to 15 polyphenols in 55 samples of red wine using HPLC with UV and fluorescence detection [22]. Good differentiation among the wines examined according to production region was achieved using PCA and LDA. With the aid of HPLC–MS, La-torre et al. classified Marsala wines according to their polyphenol and carbohydrate levels using discriminant analysis [23]. The results showed that the wines were correctly classified according to their phenolic and sugar content. Heberger et al. employed ion-exchange chromatography with PCA and LDA to classify Hungarian wines according to wine-making technology, geographic origin, grape variety, and year of vintage based on free amino acid and biogenic amine contents [24].

Due to the selective conditions attainable with individual reactions, chemiluminescence detection has been shown to be effective in the direct determination of a range of analytes in complex matrices. Acidified potassium permanganate [25], tris(2,2′-bipyridyl)ruthenium(II) [26] and luminol [27] chemiluminescence detection systems have been used to monitor a variety of analytes in wine that have been shown to be significant for geographical discrimination such as proline, polyphenols including resveratrol, and sulfite.

In this study we report for the first time the use of HPLC with both UV detection and chemiluminescence detection of the eluent stream for differentiation and classification of some Australian red and white wine varieties with multivariate data analysis techniques. Identification of the components significantly attributing to separation and classification has been undertaken using mass spectrometry.

2. Experimental

2.1. Samples

Finished high-quality Cabernet Sauvignon ($n = 34$) and Chardonnay ($n = 22$) wines were collected from the Geelong (Cabernet Sauvignon, $n = 10$, Chardonnay, $n = 11$) and Coonawarra (Cabernet Sauvignon, $n = 24$, Chardonnay, $n = 11$) wine regions of Australia from the 2003 (Cabernet Sauvignon, $n = 15$, Chardonnay, $n = 9$) and 2004 (Cabernet Sauvignon, $n = 19$, Chardonnay, $n = 13$) vintages with a total of 21 different wineries involved in the study. The wine samples were placed in centrifuge tubes and stored at −18 °C until required. Before analysis the samples were thawed and visually examined to confirm no precipitation, for example of tartaric acid, had formed and then equilibrated at room temperature and mixed thoroughly, using a vortex mixer, prior to filtering through a 0.45 μm nylon membrane filter (Acrodisc PSF syringe filters; Pall Australia, Vic., Australia). All wines were sampled in duplicate, providing for a total of 112 wine analyses.

2.2. Chromatographic analysis

Chromatographic runs were performed using a Hewlett Packard 1100 series liquid chromatograph equipped with a quaternary pump, solvent degasser, diode-array detector (DAD) and autosampler (Agilent Technologies, Forest Hill, Vic., Australia). The HPLC was fitted with a Chromolith Performance RP-18e 100 mm × 4.6 mm column, a 5 mm monolithic guard column (Merck, Kilsyth, Vic., Australia). The eluent from the DAD (254 nm) was then merged with a chemiluminescent reagent prior to the chemiluminescence detector [25]. Thus the column eluent was propelled sequentially through each detector. Control of the HPLC pump, DAD, and data acquisition from the chemiluminescence detector was achieved using Hewlett Packard Chemstation Software (Agilent Technologies). Wines were analysed by injecting 20 μL aliquots of the samples and separated at a flow rate of 3 mL min^{-1}. Solvent composition of 3% methanol in an aqueous solution of trifluoroacetic acid (0.1%, v/v) was increased to 30% methanol over 12 min, which was then raised to 70% methanol for a further 10 min. These conditions were based on an earlier study reported by Adcock et al. [28]. Duplicate runs were performed on all samples.

2.3. Mass spectrometry

The characterisation of the prominent wine constituents was obtained with the aid of high-resolution mass spectrometry. In order to gain an optimum signal in negative ion mode the chromatography was repeated without trifluoroacetic acid. Since the 3 mL min^{-1} flow rate is too fast for the formation of a stable electrospray, the sample stream was split 50% post chromatographic separation with a portion sent to the mass spectrometer. A 6210 MSDTOF mass spectrometer (Agilent Technologies) was used with the following conditions: drying gas, nitrogen (7 mL min^{-1}, 350 °C); nebulizer gas, nitrogen (16 psi); capillary voltage, 4.4 kV; vaporizer temperature, 350 °C; and cone voltage, 60 V.

2.4. Chemicals

HPLC grade methanol was obtained from BDH (Poole, UK). All mobile phases were filtered through a 0.45 μm nylon membrane filter. The permanganate chemiluminescence reagent was made by dissolving potassium permanganate (5×10^{-4} M, Ajax; Auburn, Australia) in a 1% (w/v) sodium polyphosphate (Sigma–Aldrich; Castle Hill, NSW, Australia) solution and the pH adjusted to 2.0 using sulfuric acid (Rhone-Poulenc; Melbourne, Australia).

2.5. Multivariate data analysis

All data manipulation and analysis algorithms were implemented in-house using Matlab (V 7.4, Mathworks Inc., USA) and the PLS Toolbox (V 4.0.2 Eigenvector Research Inc., USA).

Pre-processing involved removing the solvent peak, aligning, binning and normalising the data. Alignment was performed using correlation optimised warping (COW) [29–31]. The algorithm is a piecewise or segmented data pre-processing method aimed at aligning a sample data vector towards a reference vector by piecewise linear stretching and compression. The reference vector is selected by finding the sample with the maximum cumulative product of the correlation coefficients. COW requires two user input parameters, the segment length and slack size, which are selected in order to optimise the overall correlation between the sample and reference. Alignment is achieved by dividing the sample and

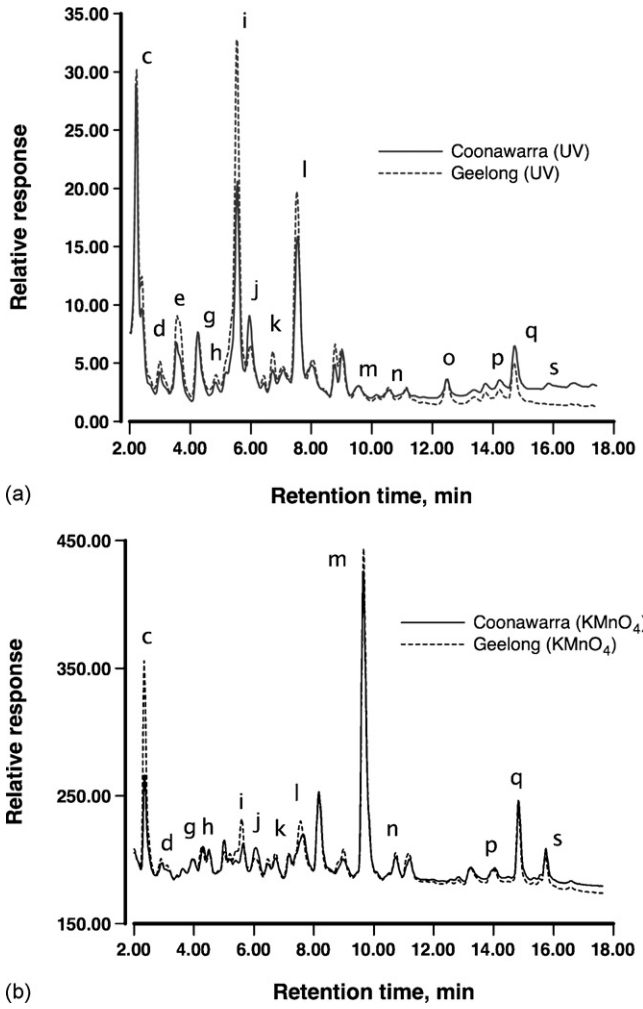


Fig. 1. The average chromatogram for Chardonnay wines from the Coonawarra and Geelong regions using (a) UV detection and (b) potassium permanganate chemiluminescence detection. Peak assignments are provided in Table 1.

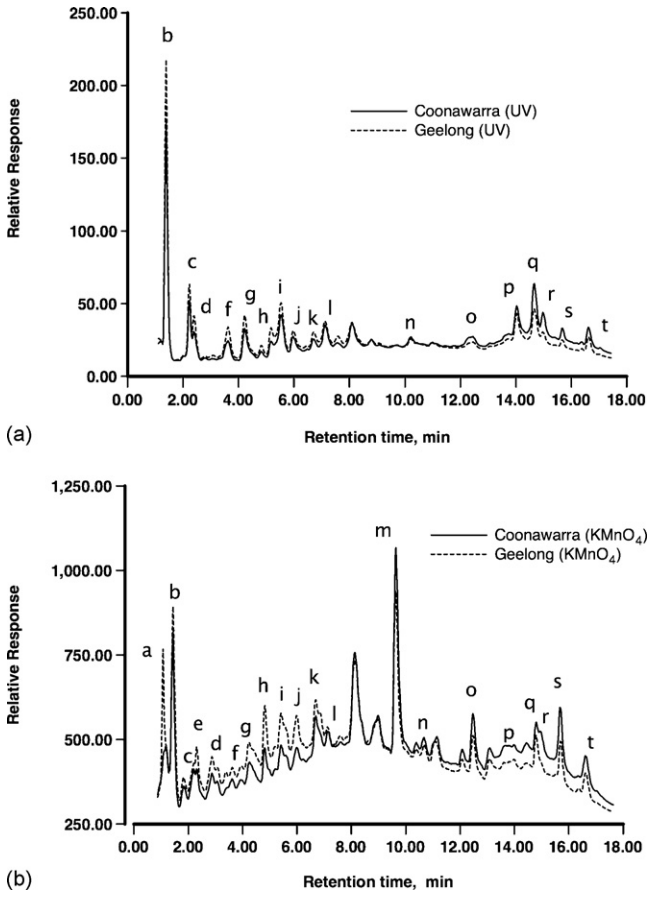


Fig. 2. The average chromatogram for Cabernet Sauvignon wines from the Coonawarra and Geelong regions using (a) UV detection and (b) potassium permanganate chemiluminescence detection. Peak assignments are provided in Table 1.

reference data into segments and warping each section by stretching and compressing within the designated slack range [30,31]. The multivariate data analysis methods employed were PCA and LDA. PCA was applied to mean-centred data and was used to reduce the dimensionality of the data and gain visual insight into possible grouping of the samples according to geographic origin. LDA assumes class data follow a multivariate normal distribution and seeks to maximise the ratio of between class variance and minimise the ratio of within class variance in order to select the boundary that achieves maximum separation between the two groups [16]. LDA was performed on the first two PCs and the classification model was developed and validated using the 'leave-one-out cross-validation' method.

3. Results and discussion

The characteristic chromatograms for Chardonnay and Cabernet Sauvignon produced with 254 nm UV detection and acidified potassium permanganate from the two wine growing regions are shown in Figs. 1 and 2. Peak assignments and analyte identification were achieved by mass spectrometry, as discussed previously and summarised in Table 1. Variation can be observed between the wine varieties from the two regions. In general the intensity of the chromatographic peaks is higher between 0 and 8 min for the Geelong region with the Coonawarra wines presenting a greater intensity for the peaks after 8 min. Based on the reversed-phase chromatography employed this may indicate that the Geelong wines contain higher concentrations of smaller water–soluble phenols and fewer less soluble polyphenolic tannins than those from Coonawarra. When comparing the average Chardonnay and Cabernet Sauvignon UV chromatograms (Figs. 1a and 2a) the Cabernet Sauvignon contain greater quantities of polyphenols as indicated by the greater

Table 1
Mass spectrometric peak assignments and retention times associated with the observed chromatographic peaks.

Peak	Retention time (min)	Compound
a	1.01	Cinnamic acid
b	1.48	Tartaric acid
c	2.09	Gallic acid
d	2.22	Gallocatechin
e	2.95	Vanillic acid
f	3.81	Quercetin hexoside-gallate
g	4.14	Catechin
h	4.91	Epigallocatechin
i	5.47	Coumaric acid
j	6.03	Caffeic acid
k	6.73	Sinapic acid
l	7.00	Epicatechin
m	9.81	Myricetin
n	10.80	Syringic acid
o	12.60	Procyanidin B
p	13.69	Procyanidin A
q	14.03	Resveratrol
r	14.22	Picied
s	15.80	Morin
t	16.60	Malvidin

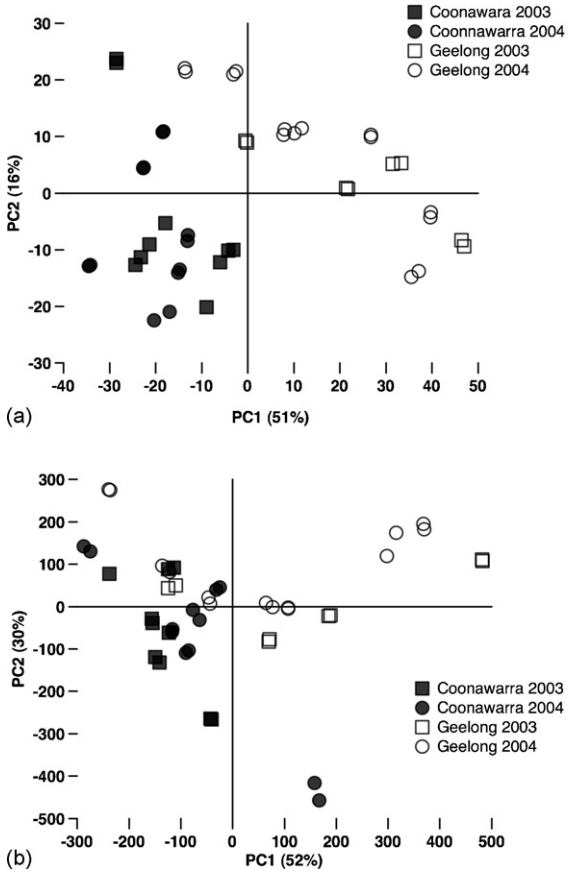


Fig. 3. The scores plot on the first two principal components for the Chardonnay wines using (a) UV detection and (b) potassium permanganate chemiluminescence detection.

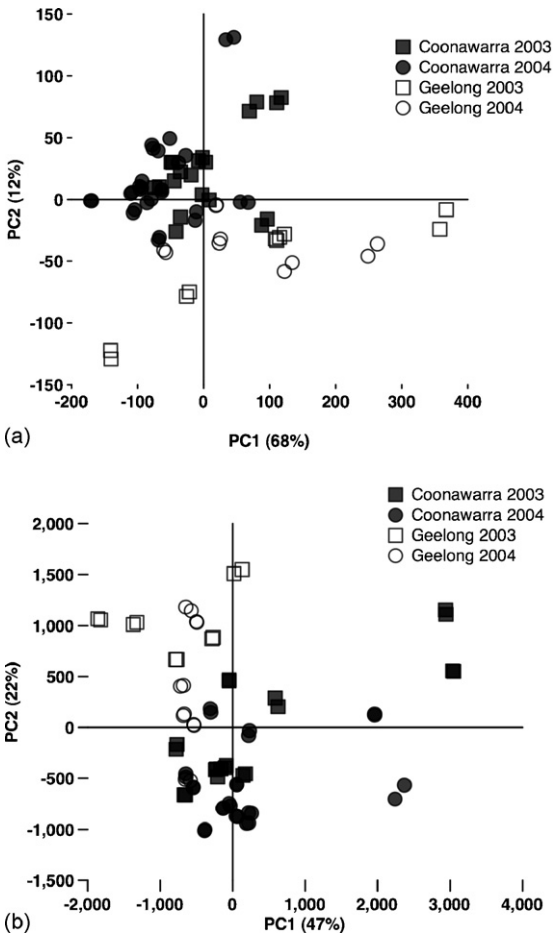


Fig. 4. The scores plot on the first two principal components for the Cabernet Sauvignon wines using (a) UV detection and (b) potassium permanganate chemiluminescence detection.

relative intensity of peaks later in the separation. This difference is not observed when comparing the acidified potassium permanganate chromatograms of Chardonnay and Cabernet Sauvignon (Figs. 1b and 2b). It has been found that polyphenols elicit a greater response than simple phenols with chemiluminescent detection. Chemiluminescence is more sensitive to polyphenols [32] than the smaller phenols as demonstrated by the observed response to myricetin (peak *m*), the peak of which is barely discernable with UV detection. Myricetin contains many hydroxy moieties making it an ideal candidate for reactivity with acidified potassium permanganate. The chemical structure of myricetin is similar to that of quercetin (myricetin has an extra hydroxyl moiety) that has been shown to have an exceptionally high response with permanganate chemiluminescence [25].

PCA was performed on the UV and acidified potassium permanganate data from both Chardonnay and Cabernet Sauvignon samples. The scores plots for the first two PCs are presented in Figs. 3 and 4. The percent variance explained by each component is noted on each axis, and these results show clustering of the wines according to production region. Details of the vintage (2003 and 2004) are also shown. It is evident that under the analytical conditions employed here that vintage plays no role in the classification.

Discrimination between the Geelong and Coonawarra regions was obtained using PCA–LDA and Table 2 summarises the LDA results for the Chardonnay and Cabernet Sauvignon wines as so-called confusion matrices. The tables present the true class identities in rows and the predicted classes in columns. The diagonal elements represent misclassified samples. The tables also present the accuracy of the classifier as the percentage of correctly classified samples in a given class compared to the total number of

Table 2
Results of linear discriminant analysis classification, with two principal components, of Chardonnay and Cabernet Sauvignon wines according to production region, using UV and chemiluminescence detection.

	Coonawarra	Geelong	Total	Accuracy
(a)				
Chardonnay UV detection				
Coonawarra	22	0	22	100%
Geelong	0	22	22	100%
Overall accuracy				100%
Chardonnay $KMnO_4$ detection				
Coonawarra	19	3	22	86%
Geelong	8	14	22	64%
Overall accuracy				75%
(b)				
Cabernet Sauvignon UV detection				
Coonawarra	45	3	48	94%
Geelong	3	17	20	85%
Overall accuracy				91%
Cabernet Sauvignon $KMnO_4$ detection				
Coonawarra	46	2	48	96%
Geelong	2	18	20	90%
Overall accuracy				94%

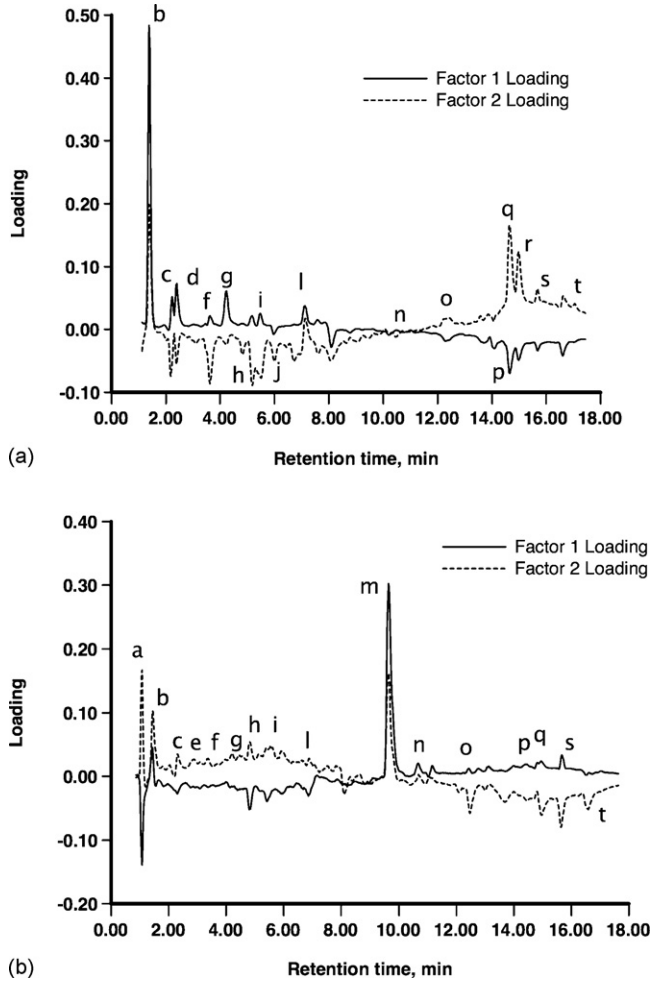


Fig. 5. The loadings (Factor 1 solid line and Factor 2 dashed line) associated with the first two principal components from the Chardonnay wines using (a) UV detection and (b) potassium permanganate chemiluminescence detection. Peak assignments are provided in Table 1.

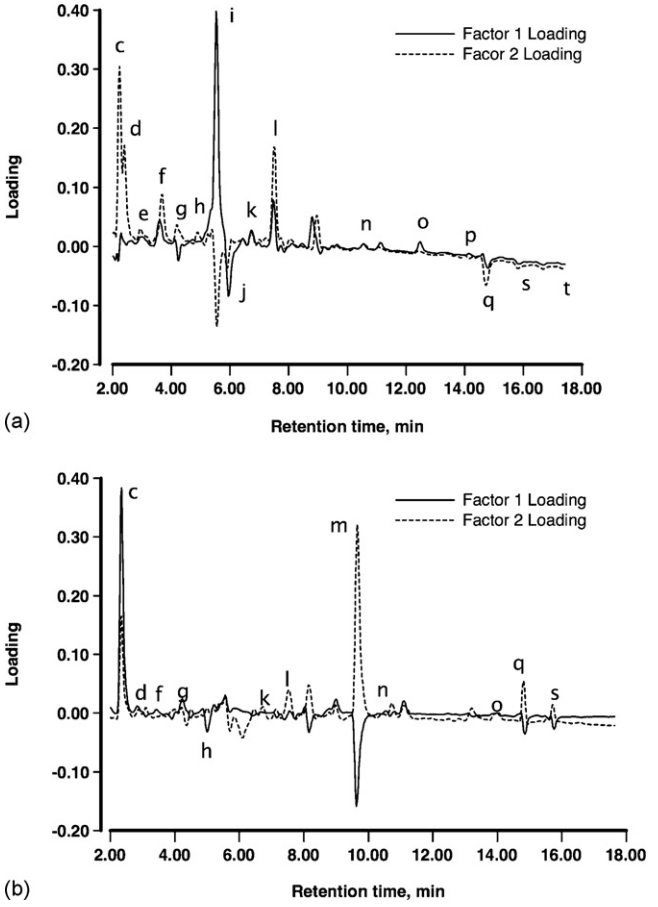


Fig. 6. The loadings (Factor 1 solid line and Factor 2 dashed line) associated with the first two principal components from the Cabernet Sauvignon wines using (a) UV detection and (b) potassium permanganate chemiluminescence detection. Peak assignments are provided in Table 1.

samples in that class. The overall accuracy of the classifier is also presented. Using two PCs, the UV data was able to correctly classify 100% of the Coonawarra and Geelong Chardonnays. while the acidified potassium permanganate was able to correctly classify 86% and 64% respectively. For the Cabernet Sauvignon the acidified potassium permanganate afforded marginally better discrimination, correctly identifying overall 94% compared with 91% for the UV.

The Chardonnay UV loadings data (Fig. 5a) show that the main species responsible for geographic discrimination are the simple phenolic acids, coumaric acid (peak *i*) and gallic acid (peak *c*), and epicatechin (peak *l*). The concentrations of these species are known, and have been shown to vary according to geographic origin [33]. Arvanitoyannis et al. have also shown that coumaric acid is a significant marker in chemical profiling of variety and ageing of wines [1]. Coumaric acid is a volatile phenol that can contribute to the aroma of wine and is a key component in the development of wine by yeast [34]. The loadings data for the acidified potassium permanganate (Fig. 5b) also highlights gallic acid (peak *c*) as a key marker compound and, along with myricetin (peak *m*), serves to discriminate the Chardonnay wines. Although myricetin is more commonly associated with red wines [35] its high sensitivity using chemiluminescent detection enables it to play a significant role here.

The Cabernet Sauvignon UV loadings data (Fig. 6a) identifies tartaric acid (peak *b*) and resveratrol (peak *q*) as significant marker compounds for identification of geographic origin. Tartaric acid is one of the most common acids found in red wine and is a key component responsible for the acidity of wine. Resveratrol concentrations in wine have been shown to vary considerably between regions, with significantly less resveratrol present in wines from warmer climates, such as Australia [36].

As found with the Chardonnay samples, the Cabernet Sauvignon acidified potassium permanganate loadings (Fig. 6b) highlight myricetin (peak *m*), cinnamic acid (peak *a*) and tartaric acid (peak *b*) as significant compounds in the classification of these red wines.

4. Conclusion

Acidified potassium permanganate chemiluminescence and UV detection systems when combined with HPLC were both found to be suitable for the geographical determination of some Australian wines. The UV detection highlighted that coumaric acid, gallic acid, and epicatechin were important for geographical determination of Chardonnay, whereas tartaric acid and resveratrol were found to be important for Cabernet Sauvignon samples. The acidic potassium permanganate detection showed that for both Chardonnay and Cabernet Sauvignon, the major constituents responsible for geographical determination, were differing concentrations of myricetin, cinnamic acid and tartaric acid.

Using two principal components, linear discriminant analysis with UV detection it was possible to correctly classify 100% of the

Chardonnay samples and 91% of the Cabernet Sauvignon samples, compared with acidified potassium permanganate chemiluminescence detection that afforded the correct classification of 75% of the Chardonnay samples and 94% of the Cabernet Sauvignon samples.

Acknowledgments

The authors would like to thank the following wineries for their generous donations of wines for analysis: Punters Corner Wines, Wynns Coonawarra Estate, Brand's of Coonawarra, Balnaves of Coonawarra, Wingara Wine Group, Hollick Wines Pty. Ltd., Rymill Winery, Majella Wines, Di Giorgio Family Wines Pty. Ltd., Flint's of Coonawarra, Redman Wines, Leconfield, Moorabool Estate, Provenance Wines, Scotchmans Hill, Bannockburn Vineyards, Pettavel Pty. Ltd., Eagles Rise, Clyde Park Vineyard, and Lethbridge Wines.

References

[1] I.S. Arvanitoyannis, M.N. Katsota, E.P. Psarra, E.H. Soufleros, S. Kallithraka, Trends in Food Science & Technology 10 (1999) 321.
[2] D.M.A.M. Luykx, S.M. van Ruth, Food Chemistry 107 (2008) 897.
[3] L.M. Reid, C.P. O'Donnell, G. Downey, Trends in Food Science & Technology 17 (2006) 344.
[4] M. Urbano, M. Luque de castro, P. Perez, J. Garcia-olmo, M. Gomez-nieto, Food Chemistry 97 (2006) 166.
[5] F.J. Acevedo, J. Jimenez, S. Maldonado, E. Diminguez, Journal of Agriculture and Food Chemistry 55 (2007) 6842.
[6] L. Liu, D. Cozzolino, W.U. Cynkar, R.G. Dambergs, L. Janik, B.K. O'Neill, C.B. Colby, M. Gishen, Food Chemistry 106 (2008) 781.
[7] L. Liu, D. Cozzolino, W.U. Cynkar, M. Gishen, C.B. Colby, Journal of Agriculture and Food Chemistry 54 (2006) 6754.
[8] D. Cozzolino, H. Smyth, M. Gishen, Journal of Agriculture and Food Chemistry 51 (2003) 7703.
[9] C. Bevin, R.G. Dambergs, A. Fergusson, D. Cozzolino, Analytica Chimica Acta 621 (2008) 19.
[10] A. González, F. Pablos, M. Martın, M. León-Camacho, M. Valdenebro, Food Chemistry 73 (2001) 93.
[11] K. Nagy, D. Bongiorno, G. Avellone, P. Agozzino, L. Ceraulo, K. Vekey, Journal of Chromatography A 1078 (2005) 90.
[12] C. Almeida, M. Vasconcelos, S.D. Teresa, Journal of Analytical Atomic Spectrometry 16 (2001) 607.
[13] D. Cozzolino, H. Smyth, W.U. Cynkar, R.G. Dambergs, M. Gishen, Talanta 68 (2005) 382.
[14] C. Steine, F. Beaucousin, C. Siv, G. Peiffer, Journal of Agriculture and Food Chemistry 49 (2001) 3151.
[15] S. Garcia-Ruiz, M. Moldovan, G. Fortunata, S. Wunerli, J.I.G. Alonso, Analytica Chimica Acta 590 (2007) 55.
[16] L.A. Berrueta, R.M. Alonso-Salces, K. Héberger, Journal of Chromatography A 1158 (2007) 196.
[17] S. Frias, J.E. Conde, J.J. Rodrigez-Bencomo, Talanta 59 (2003) 335.
[18] I.J. Kosir, M. Kocjancic, N. Ogrinc, J. Kidric, Analytica Chimica Acta 429 (2001) 195.
[19] D. Ballabio, T. Skov, R. Leardi, R. Bro, Journal of Chemometrics 22 (2008) 457.
[20] M.A. Brescia, I.J. Kosir, V. Caldarola, J. Kidric, A. Sacco, Journal of Agriculture and Food Chemistry 51 (2003) 21.
[21] M.S. Dopico-García, A. Fique, L. Guerra, J.M. Afonso, Talanta 75 (2008) 1190.
[22] M. Rodriguez-Delgado, G. Gonzalez-Hernandez, J. Conde-Gonzalez, J. Perez-Trujillo, Food Chemistry 78 (2002) 523.
[23] G. La-torre, L. La pera, R. Rando, V. Lo-turco, G. Di-bella, M. Saitta, G. Dugo, Food Chemistry 110 (2008) 729.
[24] K. Heberger, E. Csomos, L. Simon-Sarkadi, Journal of Agriculture and Food Chemistry 51 (2003) 8055.
[25] J.W. Costin, N.W. Barnett, S.W. Lewis, D.J. McGillivery, Analytica Chimica Acta 499 (2003) 47.
[26] J.W. Costin, N.W. Barnett, S.W. Lewis, Talanta 64 (2004) 894.
[27] Y.L. Huang, J.M. Kim, R.D. Schmid, Analytica Chimica Acta 266 (1992) 317.
[28] J.L. Adcock, N.W. Barnett, J.W. Costin, P.S. Francis, S.W. Lewis, Talanta 67 (2008) 585.
[29] N.P.V. Nielsen, J.M. Carstensen, J. Smedsgaard, Journal of Chromatography A 805 (1998) 17.
[30] T. Skov, F. Van Den Berg, G. Tomasi, R. Bro, Journal of Chemometrics 20 (2006) 484.
[31] G. Tomasi, F. Van Den Berg, C. Andersson, Journal of Chemometrics 18 (2004) 231.
[32] J.L. Adcock, P.S. Francis, N.W. Barnett, Analytica Chimica Acta 601 (2007) 36.
[33] D.M. Goldberg, E. Tsang, A. Karumanchiri, G.J. Soleas, American Journal of Enology and Viticulture 49 (1998) 142.
[34] P.X. Etievant, S.N. Issanchou, S. Marie, V. Ducruet, C. Flanzy, Sciences des Aliments (France) 91 (1989) 19.
[35] H. Vuorinen, K. Maatta, R. Torronen, Journal of Agriculture and Food Chemistry 48 (2000) 2675.
[36] Diamandis, A. Karumanchiri, G.J. Soleas, A.L. Waterhouse, American Journal of Enology and Viticulture 46 (1995) 159.

Talanta 80 (2009) 839–845

Contents lists available at ScienceDirect

Talanta

journal homepage: www.elsevier.com/locate/talanta

Selective pressurized liquid extraction of polybrominated diphenyl ethers in fish

S. Losada, F.J. Santos*, M.T. Galceran

Department of Analytical Chemistry, University of Barcelona, Avda. Diagonal 647, E-08028 Barcelona, Spain

ARTICLE INFO

Article history:
Received 9 June 2009
Received in revised form 30 July 2009
Accepted 3 August 2009
Available online 8 August 2009

Keywords:
PBDEs
Pressurized liquid extraction
GC–ITMS–MS
Flame retardants
Fish

ABSTRACT

A fast and simple method for the analysis of polybrominated diphenyl ethers (PBDEs) in fish samples was developed using a one-step extraction and clean-up by means of pressurized liquid extraction (PLE) combined with gas chromatography–ion trap tandem mass spectrometry (GC–ITMS–MS). The selective PLE method provided to obtain ready-to-analyse extracts without any additional clean-up step, using a sorbent as fat retainer inside the PLE cell. Several PLE operating conditions, such as solvent type, extraction temperature and time, number of cycles and type of fat retainer, were studied. Using Florisil as fat retainer, maximum recoveries of PBDEs (83–108%) with minimum presence of matrix-interfering compounds were obtained using a mixture of n-hexane:dichloromethane 90:10 (v/v) as solvent, an extraction temperature of 100 °C and a static extraction time of 5 min in combination with three static cycles. Quality parameters of the method were established using standards and fish samples. Limits of detection and quantification ranged from 10 to 34 pg g^{-1} wet weight and between 34 and 68 pg g^{-1} wet weight, respectively. In addition, good linearity (between 1 and 500 ng ml^{-1}) and high precision (RSD % < 15%) were achieved. The method was validated using the standard reference material SRM-1945 (whale blubber) and was then applied to the analysis of PBDEs in fish samples.

© 2009 Elsevier B.V. All rights reserved.

1. Introduction

Polybrominated diphenyl ethers (PBDEs) are a class of chemicals extensively used as flame retardant additives in a wide variety of commercial and industrial products [1,2]. They are released into the environment both during the production, use and recycling of products containing PBDEs, and during disposal in domestic waste, landfill, and incineration [3–5]. The presence of PBDEs in the environment is a cause of concern due to their persistence, lipophilic character and the ease with which they bioaccumulate in wildlife and humans through the food web [6]. They have been detected as environmental contaminants with widespread global distribution [7] in both biotic and abiotic matrices [8,9], and they accumulate in serum [10,11], adipose tissue [11,12] and human breast milk [13,14]. Due to the significant bioaccumulation of PBDEs in animals and humans, their detection in increasing concentrations during the last decade, and the adverse health effects reported (e.g., reproductive toxicity, endocrine disruption, and neurodevelopment effect in animals) [15–18], the use of Penta-BDE and Octa-BDE technical mixtures in consumer products have been regulated in Europe since 2004 [19]. In addition, restrictions in electrical and electronic equipment that contains these compounds became effective in 2006 [20].

Since an important human exposure route of PBDEs is through the diet, recent studies on PBDE levels in food [21–24] have demonstrated that fish consumption significantly contributed to the total human exposure. Due to these findings, efforts have been undertaken to develop reliable methods to analyse these compounds in biota samples. PBDEs are currently analysed using similar methods to those applied for polychlorinated biphenyls (PCBs) and other persistent organic pollutants [9]. These methods generally involve the extraction of the analytes from biological matrices using Soxhlet [25,26] or sonication with apolar solvents [27]. Alternative extraction techniques, such as pressurized liquid extraction (PLE) [28–30], microwave assisted extraction (MAE) [31], SFE [32] and matrix solid-phase dispersion (MSPD) [33,34], have also been used. All these extraction methods often require extensive clean-up procedures after extraction to remove matrix-interfering compounds and are usually time-consuming. In order to reduce the handling time, simultaneous PLE extraction and clean-up have been developed for the analysis of persistent organic pollutants such as polychlorinated biphenyls (PCBs) [35,36], polychlorinated dibenzo-*p*-dioxins and dibenzofurans (PCDD/Fs) [37,38], polychloronaphtalenes (PCNs) [39,40] and also PBDEs [41–44] in environmental samples. For fish samples, only two PLE methods

* Corresponding author. Tel.: +34 93 403 48 74; fax: +34 93 402 12 33.
E-mail address: javier.santos@ub.edu (F.J. Santos).

0039-9140/$ – see front matter © 2009 Elsevier B.V. All rights reserved.
doi:10.1016/j.talanta.2009.08.002

using alumina as fat retainer have been proposed for the analysis of PBDEs [43,44].

Gas chromatography coupled to mass spectrometry (GC–MS) is the technique commonly used for the determination of PBDEs [9,45,46]. Negative chemical ionisation (NCI) is the most popular ionisation mode for determination of these compounds by low resolution MS. This technique provides higher sensitivity than that of electron ionisation (EI) but is less selective, since only bromine ions are monitored. In addition, less accuracy in quantification is obtained since isotope dilution cannot be used. GC–HRMS in EI mode provides the most selective and sensitive method for the determination of these compounds [22,29,47,48] and it is recommended by the U.S. EPA for the analysis of PBDEs [49]. Nevertheless, since this technique is relatively expensive and requires skilled personnel and heavy maintenance to ensure proper functioning, low resolution mass spectrometry is preferred. Gas chromatography coupled to ion trap mass spectrometry working in tandem mode (GC–ITMS–MS) has shown to be a low-cost, rapid and reliable alternative to HRMS for the analysis of PBDEs in environmental and biological samples [13–15,50–54].

The aim of this study was to develop a simple and rapid PLE method in combination with gas chromatography coupled to GC–ITMS–MS for the analysis of PBDEs at low concentrations in fish samples. A one-step extraction and clean-up method was optimized in order to reduce the analysis time and solvent consumption. For this purpose, several fat retainers were studied and PLE parameters were optimized. In addition, MS–MS working conditions that provided maximum sensitivity and selectivity for the analysis of PBDEs were established. To validate the whole analytical method, a certified reference material was analysed. In addition, the method developed was used for the analysis of PBDEs in fish samples.

2. Experimental

2.1. Chemicals and standards

A standard solution of PBDEs (BDE-LMS, Lake Michigan Study) containing the BDE congeners 28, 47, 66, 85, 99, 100, 138, 153 and 154 at a concentration of 10 μg/ml in nonane was purchased from AccuStandard (New Haven, USA). For quantification, a standard solution of isotopically $^{13}C_{12}$-labelled BDEs 47, 99 and 153 (BDE-MXA), supplied by Wellington Laboratories (Guelph, Canada), at 5 μg ml^{-1} of each congener was used as internal standard. In addition, a standard solution of isotopically $^{13}C_{12}$-labelled BDE 139 at a concentration of 5 μg ml^{-1} (Wellington Labs) was used as syringe standard for recovery determination. Seven calibration standard solutions containing a mixture of the nine PBDE congeners at concentrations ranging from 2 to 400 ng ml^{-1} and the isotopically labelled internal standards for recovery and quantification at 100 ng ml^{-1} were prepared by dilution of the corresponding standard stock solutions in isooctane.

Dichloromethane and isooctane of Pestanal grade were purchased from Riedel-de Haën (Sigma–Aldrich Laborchemikalie, Seelze, Germany) and n-hexane of residue analysis grade was obtained from Fluka Chemie (Bucks, Switzerland). Hydromatrix was supplied by Varian (Palo Alto, USA) and glass fibre filters for the extracting cell came from Dionex Corp. (Sunnyvale, CA). Sulphuric acid (95–97%), sodium hydroxide and anhydrous sodium sulphate (purity > 99%) of residue analysis grade were obtained from Merck (Darmstadt, Germany). Florisil (0.15–0.25 mm) of residue analysis grade, silica gel (Gel 60) and aluminium oxide 90 active neutral (activity stage I) of chromatographic analysis quality were also obtained from Merck (Darmstadt, Germany). Before use, the silica gel and Florisil were baked at 600 °C for 10 h, while the alumina was activated at 300 °C for 10 h. Silica gel modified with sulphuric acid (44%, w/w) was prepared by slowly adding an appropriate amount of sulphuric acid to the activated silica at room temperature. All glass materials were cleaned with AP-13 Extran alkaline soap (Merck, Darmstadt, Germany) for 24 h, rinsed consecutively with Milli-Q water (Millipore Corp., Bedford, MA) and acetone, and dried overnight.

2.2. Samples and sample preparation

Fish samples (trout, salmon and horse mackerel) were purchased from a local supermarket and were selected for the analysis of PBDEs since they cover a wide range of lipid content and are among the fish products most frequently found in the Spanish diet [55]. Trout and salmon were of aquaculture origin, while horse mackerel were caught in the Mediterranean Sea. Each fish was washed and the non-edible parts were removed to obtain clean tissues. The muscle tissue was triturated, homogenized, frozen and lyophilized for 2 days. Then, the dried tissue was ground in a glass mortar to a fine powder, and stored in glass vials in dark at 4 °C before analysis.

A standard reference material, SRM-1945 (whale bubbler), obtained from the National Institute of Standards and Technology (NIST, Boulder, Colo, USA) was used to validate the whole method (on-line PLE/clean-up and GC/ITMS–MS) for PBDE analysis.

2.3. GC–MS instrumentation

A Trace GC 2000 Series gas chromatograph (ThermoFisher, Milan, Italy) coupled to a GCQ-Polaris (ThermoFisher, Austin, TX, USA) ion trap mass spectrometer equipped with an AS2000 autosampler was used for PBDE determination. The chromatographic separation of these compounds was performed using a DB-5MS (5% phenyl, 95% methyl polysiloxane) fused-silica capillary column (J&W Scientific, Folsom, USA) 30 m × 0.25 mm I.D., 0.25 μm of film thickness. The oven temperature was programmed from 90 °C (held for 1 min) to 200 °C at 15 °C min^{-1} and then to 280 °C at 2 °C min^{-1} and finally to 310 °C at 15 °C min^{-1} (held for 20 min). Helium was used as carrier gas at a constant flow-rate of 1 ml min^{-1} held by electronic pressure control at 90 °C. Injector temperature was kept at 280 °C and 1 μl of samples and standards was injected in the splitless injection mode (1 min). The MS operating conditions were the following: electron ionisation mode using automatic gain control (AGC) with electron energy of 70 eV and an emission current of 250 μA. The ion source and transfer line temperatures were kept at 200 °C and 280 °C, respectively. The instrument was tuned using perfluorotributylamine (FC-43) according to the manufacturer's recommendations in order to achieve the highest sensitivity. Electron multiplier voltage was set to 1450 V (10^5 gain) by automatic tuning. In MS–MS mode, for native and $^{13}C_{12}$-labelled PBDEs the most intense ion of the molecular and the $[M-2Br]^{+\bullet}$ cluster ions of each homologue group were investigated as precursor ion. After optimization, the $[M+4]^{+\bullet}$ ion of each homologue group was selected as precursor ion, except for tri-BDEs and hexa-BDEs where the $[M+2]^{+\bullet}$ and $[M+6]^{+\bullet}$ ions, respectively were selected (Table 1). For quantitative purposes, the product ions corresponding to the loss of two ^{79}Br atoms and one ^{79}Br and one ^{81}Br atoms of native and $^{13}C_{12}$-labelled compounds were monitored. After optimization, the resonance excitation voltages, which produce the maximal yield in the abundance of the corresponding product ions for all the compounds, was 1.20 V (Table 1). Other optimum MS–MS parameters were the following: maximum excitation energy, q_z, 0.3; isolation window of precursor ion, 2 m/z; isolation time, 10 ms; excitation time, 15 ms. The MS–MS acquisition method was time-programmed in five segments to determine tri- to hexa-PBDEs. Xcalibur version 2.0 software was used for data acquisition and

Table 1
MS–MS transitions selected and excitation voltage for each homologue group of PBDEs in GC–ITMS–MS method.

Homologue	Congener	Time window (min)	Transition $[M]^{+\bullet} \rightarrow [M-2Br]^{+\bullet}$				Transition $[M-2Br]^{+\bullet} \rightarrow [M-2Br\text{-}COBr]^{+}$			
			Precursor ion (m/z)		Product ion (m/z)	Excitation voltage (V)	Precursor ion (m/z)		Product ion (m/z)	Excitation voltage (V)
Tri-BDE	BDE 28	15–18.5	406	$[M+2]^{+\bullet}$	246 + 248	1.2	246	$[M-2Br]^{+\bullet}$	139	1.2
TetraBDEs	BDE 47	18.5–24.2	486	$[M+4]^{+\bullet}$	326 + 328	1.2	326	$[M+2-2Br]^{+\bullet}$	217 + 219	1.35
	BDE 66									
^{13}C-Tetra-BDE	$^{13}C_{12}$-BDE 47	18.5–24.2	498	$[M+4]^{+\bullet}$	338 + 340	1.2	338	$[M+2-2Br]^{+\bullet}$	229 + 231	
Penta-BDE	BDE 100	24.2–29.1	564	$[M+4]^{+\bullet}$	404 + 406	1.2	404	$[M+2-2Br]^{+\bullet}$	297 + 299	1.4
	BDE 99									
	BDE 85									
^{13}C-Penta-BDE	$^{13}C_{12}$-BDE 99	24.2–29.1	576	$[M+4]^{+\bullet}$	416 + 418	1.2	416	$[M+4-2Br]^{+\bullet}$	337 + 339	1.4
Hexa-BDE	BDE 138	29.1–33.6	644	$[M+6]^{+\bullet}$	484 + 486	1.2	484	$[M+6-2Br]^{+\bullet}$	375 + 377	1.6
	BDE 154									
	BDE 153									
^{13}C-Hexa-BDE	$^{13}C_{12}$-BDE 153	29.1–33.6	654	$[M+4]^{+\bullet}$	494 + 496	1.2	496	$[M+6-2Br]^{+\bullet}$	387 + 389	1.6
	$^{13}C_{12}$-BDE 139									

processing of the results. Quantification of PBDEs was carried out by isotope dilution using $^{13}C_{12}$-labelled PBDE congeners as internal standards.

2.4. PLE extraction and clean-up

The simultaneous extraction and clean-up of the lyophilized fish samples was performed on an ASE 100 Accelerated Solvent Extractor System (Dionex, Sunnyvale, CA). Before PLE extraction, an adequate amount of the isotopically $^{13}C_{12}$-labelled PBDEs (BDE-MXA) was added to 0.5 g of the freeze-dried fish sample, which was left overnight at room temperature to equilibrate. The sample was then mixed with sodium sulphate at a fish/Na_2SO_4 ratio of 1:20 (w/w) in a mortar until a homogenous mixture was obtained. Florisil (20 g) and alumina were tested as fat retainer material. The extraction cell was loaded by inserting a glass fibre filter into the cell outlets, followed by the fat retainer and the sample, using Hydromatrix to fill up the dead volume of the extraction cell. After sealing the cell with the top cell cap, the extraction cell was placed in the ASE system. Fish samples were extracted at 100 °C with a solvent mixture of n-hexane:dichloromethane (95:5, v/v) and working at a pressure of 1500 psi, a flush volume of 100% and a purge time of 290 s for a 100 ml PLE cell. Further details about the optimization of the extraction parameters are described in Section 3. The final extracts were then rotary evaporated to approximately 2 ml adding 100 μL of isooctane as a keeper. Afterwards, the final extract was carefully concentrated under a gentle nitrogen stream up to 25 μL and analysed by GC–ITMS–MS after adding an adequate amount of $^{13}C_{12}$-BDE 139 as internal standard.

The fat content of fish was determined gravimetrically by evaporation of the extract obtained from a PLE process (without fat retainer) of an additional sub-sample (2.5 g of freeze-dried fish). A solvent mixture of n-hexane:dichloromethane (1:1, v/v) was used. The percentage of fat determined for the fish samples (wet weight) was as follows: 0.68% for trout, 2.1% for horse mackerel and 16.9% for salmon.

2.5. Quality control criteria

A daily isomer-specific GC separation test, sensitivity test and calibration test were carried out. Procedural blanks (both instrumental and method) were routinely performed during the analysis, and quality control fish samples were periodically analysed in order to ensure that the analytical method was maintained under control. A salmon sample with non-detectable amounts of the PBDEs spiked at 1 ng g^{-1} ww was used as quality control sample. The certified reference material SRM-1945 was used for validation.

3. Results and discussion

3.1. Optimization of MS–MS conditions

Different MS–MS working conditions and strategies on the selection of the precursor and product ions have been proposed for the analysis of PBDEs, even using similar instruments. Therefore, experiments conducted to determine the optimum MS–MS parameters, especially those depending on the instrument for achieving the best sensitivity and selectivity in the PBDE analysis, were carried out. Before optimization, the precursor ions and the corresponding transitions were selected. Some authors [51,53,56] propose the use of $[M-2Br]^{+\bullet}$ ions as precursors since they are the most abundant ions on the EI-MS spectra for most tetra- to octa-BDEs, except for non-ortho-substituted congeners, BDE-35, BDE-37, BDE-77 and BDE-126, for which the $[M]^{+\bullet}$ cluster ions are predominant [57,58]. Selecting $[M-2Br]^{+\bullet}$ as precursor ions, the most abundant product ions obtained after CID collision correspond to the loss of COBr• ($[M-2Br-COBr]^{+}$) while $[M-3Br]^{+}$ and $[M-4Br]^{+\bullet}$ fragment ions were obtained at lower abundance. Other authors propose the use of $[M]^{+\bullet}$ ions instead of $[M-2Br]^{+\bullet}$ as precursor ions [11,12,52,54,59]. In this case, the fragment ions corresponding to the loss of two bromine atoms from the molecular cluster ions were selected as product ions. To determine the precursor ion which provides the best sensitivity on the MS–MS analysis, the performance of both strategies was examined. Table 1 shows the precursor and product ions selected for each transition studied. For this purpose, MS–MS parameters such as excitation voltage, excitation time, excitation energy and isolation mass window, were optimized for each CID transition evaluated. The effect of each parameter upon the MS–MS process was studied varying only one of the parameters while keeping the others constant. For these experiments, a standard mixture of native and $^{13}C_{12}$-isotopically labelled PBDE congeners (100 ng g^{-1}) was used. The best results were obtained using an excitation time of 15 ms and a mass isolation window of 2 m/z. The effect of the excitation voltage on the product ion yield was also studied and Table 1 shows the optimum values for both MS–MS transitions. The influence of the excitation energy (q_z parameter) on the fragmentation yield and the stabilization of the product ions was studied at three q_z levels, 0.225 (low), 0.300 (medium) and 0.450 (high). Maximum abundances of the product ions were observed at the medium q_z value (0.30) using both $[M]^{+\bullet}$ and $[M-2Br]^{+\bullet}$ as precursor ions. Fig. 1 shows the abun-

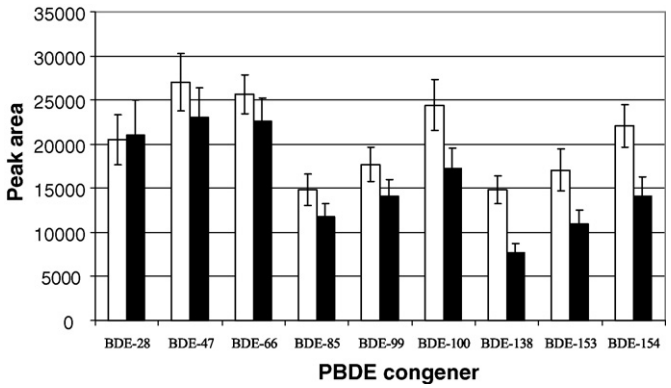


Fig. 1. Peak area of the product ions corresponding to the $[M]^{+\bullet}$ (white bars) and $[M-2Br]^{+\bullet}$ ions (black bars) selected as precursor ions. Error bars correspond to the standard deviation ($n = 7$).

dances of the product ions expressed as peak area ($n = 7$) obtained from the two precursor ions $[M]^{+\bullet}$ and $[M-2Br]^{+\bullet}$. As can be seen, the use of the most abundant ion of the molecular cluster ion of each homologue group as the precursor ion provided the highest response on the product ions for PBDE congeners, mainly for higher brominated ones (hexa-BDEs). Therefore, the $[M]^{+\bullet} \rightarrow [M-2Br]^{+\bullet}$ transitions are recommended for achieving maximum sensitivity for PBDEs analysis. Potential interferences on the determination of PBDEs by GC–ITMS/MS were also evaluated. The presence of several chlorinated compounds in the PBDE extracts could interfere on the isolation of precursor ions of PBDEs, but due to the transition selected any effect on the response of the product ions occurred. Other interfering compounds present in biotic samples such as polybrominated biphenyls (PBBs) did not cause any interference on the PBDE quantification because the contribution on the selected precursor ions of PBDEs is negligible (0.00002% of the most intense peak of the molecular or $[M-2Br]^{+\bullet}$ cluster ions). Methoxylated tetra-PDEs (MeO-tetr-BDEs) have also been reported as potential interfering compounds of $^{13}C_{12}$-penta-BDEs, but the fragments corresponding to the loss of CH_3Br from MeO-tetra-BDE congeners only interfere with the $[M+4-2Br]^{+\bullet}$ of $^{13}C_{12}$-penta-BDEs and these ions were not selected in our study. In addition, the molecular ions of hexabromocyclododecane (HBCD) could also interfere to hexa-BDE congeners, but these ions are not present in the EI spectrum of HBCD.

Instrumental quality parameters of the GC–ITMS–MS method were determined using standard solutions. To study the linearity, seven-point calibration standard solutions ranging from 5 to 400 ng ml^{-1} for native PBDEs and containing isotopically $^{13}C_{12}$-labelled PBDE congeners at a concentration of 100 ng ml^{-1} were used. Good linearity in the concentration range was obtained for all the compounds, with correlation coefficients (r) higher than 0.9990. Limits of detection (LODs), defined as the concentration that produces a signal to noise ratio (S/N) greater than 3, were determined experimentally using standard solutions at low concentrations (2.0 ng ml^{-1}). Under these conditions, instrumental LODs ranged from 0.8 to 2.5 pg injected. For run-to-run and day-to-day precisions, a standard mixture of PBDE congeners at a concentration of 20.0 ng ml^{-1} were analysed in quintuplicate on 1 day and on 3 days, respectively. Good run-to-run and day-to-day precisions were achieved with RSDs (%) between 4% and 9% and from 6% to 10%, respectively.

3.2. Simultaneous PLE extraction and clean-up

In order to set up a PLE method to simultaneously perform in-cell extraction and purification, several sorbents as fat retainers were evaluated. Preliminary studies were carried out using an off-line method based on a PLE extraction followed by a clean-up step with sorbents, such as Florisil, silica modified with sulphuric acid and alumina, often used in conventional analytical methodology for the clean-up of a wide range of environmental and biological samples [9]. For this purpose, 1 g of a lyophilized salmon sample spiked with the target PBDE congeners at a concentration of 5 ng g^{-1} dry weight (0.3 ng g^{-1} wet weight) and the $^{13}C_{12}$-labelled PBDEs (BDE-MXA) was used. The spiked sample was kept overnight at room temperature to equilibrate before PLE extraction and then mixed with anhydrous sodium sulphate (10 g) and Hydromatrix (around 4 g). Extraction was carried out using PLE (34-ml cell) without fat retainer. The extraction was carried out at 100 °C using hexane:dichloromethane 1:1 (v/v) as extraction solvent and applying 3 static cycles of 5 min each and a flush volume of 100% (90 s of purge). To clean-up of the PLE extracts, glass columns filled with different amounts of the sorbents (30 g of modified silica, 20 g of Florisil and 20 g of alumina) were studied. n-Hexane and several mixtures of n-hexane:dichlorometane (9:1, 8:2 and 7:3, v/v) were tested as elution solvents. Using modified silica, acceptable recoveries of the target compounds were obtained using n-hexane:dichlorometane 7:3 (v/v), but the presence of lipids and fat degradation products in the final extract was detected (Fig. 2A), causing a high variability in the GC–ITMS–MS determination (RSD % > 40%). Both Florisil and alumina using a mixture of hexane:dichloromethane 95:5 (v/v) allowed to obtain extracts clean enough for GC–ITMS–MS determination of the target compounds, achieving recoveries between 85% and 95%. Therefore, these sorbents were selected as potential fat retainers for the simultaneous extraction and clean-up in-cell method. Fig. 2B shows the GC-MS chromatogram of a salmon sample spiked with the target compounds where the lipid content was completely removed using Florisil.

The next step in the optimization process was to incorporate the fat retainer into the extraction cell in order to evaluate the capability of PLE for the analysis of the target compounds. Experiments were conducted to select the most adequate fat retainer with the aim of obtaining the maximum efficiency for the extraction of PBDEs with the minimum presence of interfering compounds. The efficiency of alumina and Florisil as fat retainers was tested using a similar amount of sorbent (10 g) in a 100 ml PLE cell, using 0.5 g of freeze-dried fish sample (a salmon spiked at 5 ng g^{-1} dry weight), an extraction temperature of 100 °C, a solvent mixture of n-hexane:dichloromethane 95:5 (v/v) and 2 static cycles of 10 min each (flush volume of 100%). At these conditions, recoveries obtained for all PBDE congeners and for each sorbent ranged from 65% to 85%, but a high variability on the results (RSD % > 30%) was obtained using alumina, even using higher amounts of sorbent (>10 g). The poor precision achieved with alumina could be attributed to the incomplete lipid removal that drastically affected the GC–ITMS–MS response. In contrast, when Florisil was used, an important improvement on the precision was obtained. Although alumina has been reported as fat retainer for on-line PLE extraction [9], it has always been used in GC–NCI–MS, which seems to be less affected than GC–ITMS–MS by lipid contamination. Therefore, Florisil was selected as fat retainer for the simultaneous extraction/clean-up in-cell of fish samples.

Several PLE parameters such as the amount of fat retainer, type of extraction solvent, number of extraction cycles, extraction temperature and static extraction time were optimized. For this, different amounts of Florisil were used, from 10 to 25 g, maintaining constant the other PLE parameters (n-hexane:dichloromethane 95:5 (v/v), 2 static cycle of 10 min). As a result, 25 g of Florisil were selected because this material provided the highest cleanness of the extract with a relatively high recovery of the analytes. We then examined the influence of the static extraction time (from 3 to 10 min), the number of cycles (between 2 and 4 cycles) and the

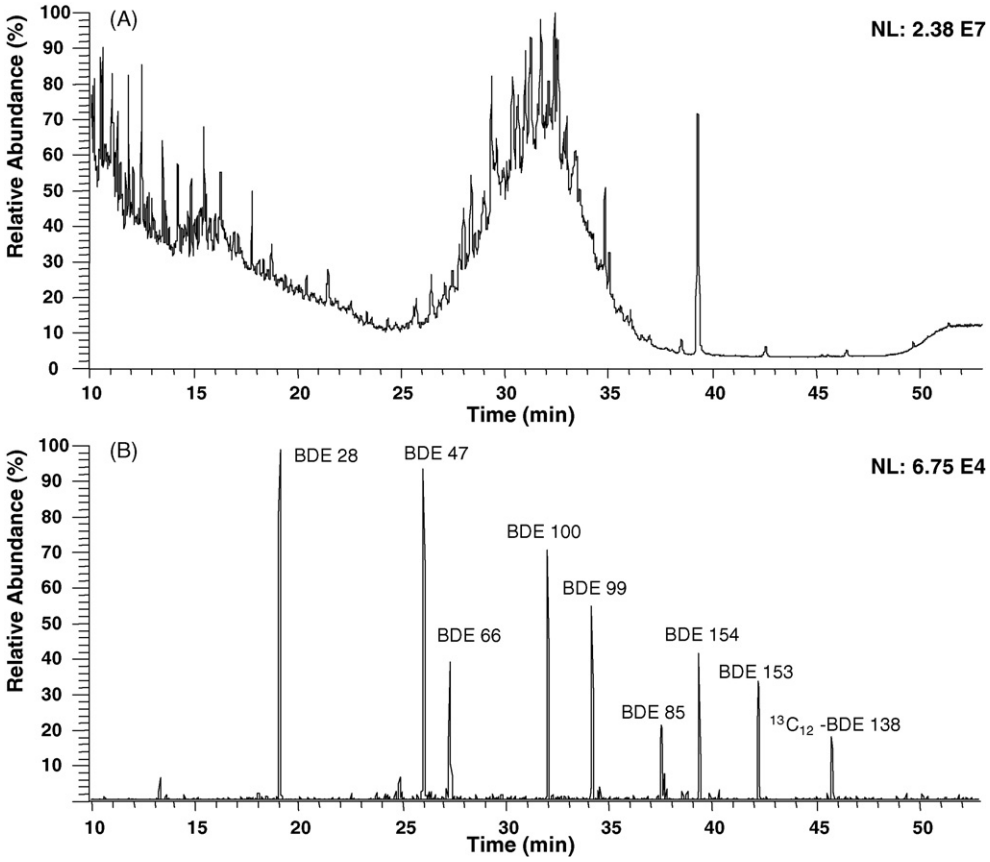


Fig. 2. GC–MS chromatogram (TIC) obtained in full-scan mode of a spiked salmon sample (0.3 ng g^{-1} ww) after simultaneous PLE extraction and purification with (A) silica modified with sulphuric acid, and (B) Florisil.

extraction temperature (at 50 °C and 100 °C) on the recovery of the analytes. For all experiments, a flush volume of 100% and a purge time of 290 s were used. After optimization, the best results were obtained using an extraction temperature of 100 °C and a static extraction time of 5 min in combination with 3 static cycles. Finally, we examined the effect of the composition of the extraction solvent on the recovery of the analytes. Several solvent mixtures of n-hexane:dichloromethane (95:5, 90:10, 80:20, 70:30 and 60:40, v/v) were tested using the optimized PLE parameters above mentioned. Generally, a rise in the proportion of dichloromethane in the extraction solvent increased the recovery of the target compounds. Solvent mixtures with percentages of dichloromethane higher than 30% provided coloured extracts with high lipid content. For the other mixtures, similar recoveries of the PBDE congeners were obtained, but the amount of lipids extracted increased with the percentage of dichloromethane. For this reason, the mixture n-hexane:dichloromethane 90:10 (v/v) was selected as optimum extraction solvent. Table 2 shows the recoveries (%) obtained for the spiked salmon samples using 25 g of Florisil as fat retainer under the optimized PLE conditions. High extraction efficiencies were obtained, with recoveries ranging between 83% and 108%.

Limits of detection and quantification of the simultaneous extraction and clean-up in-cell combined with GC–ITMS–MS determination were estimated using fish samples with low concentration levels. The LODs ranged from 10 to 34 ng g^{-1} wet weight, depending on the compound, while the LOQ of the method ranged between 34 and 68 pg g^{-1} wet weight. These results are in agreement with those reported in the literature for fish samples [9]. In order to evaluate the accuracy of the whole developed method, a whale blubber standard reference material, NIST SRM-1945, was

Table 2
Recovery (%), method limits of detection (mLOD) and quantification (mLOQ) and concentrations determined of PBDEs in whale bubbler (NIST SRM-1945).

Compound	Recovery (%)[a]	mLOD	mLOQ	SRM-1945 (ng g^{-1} wet weight)	
	Mean ± s.d.	(pg g^{-1} ww)	(pg g^{-1} ww)	Mean ± s.d.[a]	Certified value ± uncertainty[b]
BDE-28	108 ± 8	18	60	2.2 ± 0.1	–
BDE-47	106 ± 6	14	47	39.4 ± 3.2	39.6 ± 0.2
BDE-66	107 ± 8	10	35	nd	–
BDE-85	106 ± 12	10	36	nd	–
BDE-99	101 ± 6	11	34	18.5 ± 2.1	18.9 ± 2.3
BDE-100	115 ± 12	13	36	11.3 ± 1.5	10.3 ± 1.1
BDE-138	87 ± 7	14	50	nd	–
BDE-153	83 ± 12	30	64	8.2 ± 0.7	8.34 ± 0.55
BDE-154	93 ± 10	34	68	12.7 ± 1.3	13.3 ± 1.7

nd: below limit of detection.
[a] $n = 3$.
[b] Expanded uncertainly.

Table 3
Concentrations of PBDEs (ng g^{-1} wet weight) obtained using on-line PLE and GC–ITMS–MS in fish samples.

Compound	Concentration (ng g^{-1} wet weight)[a]					
	Trout		Horse Mackerel		Salmon	
	Mean ± s.d.	RSD %	Mean ± s.d.	RSD %	Mean ± s.d.	RSD %
BDE-28	2.8 ± 0.3	11	6.1 ± 0.9	15	6.3 ± 0.9	14
BDE-47	16.9 ± 1.9	11	91.3 ± 8.5	9	46.6 ± 4.1	9
BDE-66	2.9 ± 0.4	14	nd	–	3.9 ± 0.5	13
BDE-85	2.4 ± 0.3	13	nd	–	1.8 ± 0.2	11
BDE-99	10.7 ± 1.1	10	6.7 ± 1.0	15	11.6 ± 1.3	11
BDE-100	5.1 ± 0.5	10	32.7 ± 3.6	11	9.6 ± 1.1	11
BDE-138	nd	–	nd	–	nd	–
BDE-153	3.3 ± 0.1	15	0.39 ± 0.05	13	nd	–
BDE-154	0.95 ± 0.14	15	7.1 ± 0.9	13	2.5 ± 0.3	12
∑PBDEs	45.0		144.3		82.3	

nd = below limit of detection.
[a] $n = 3$.

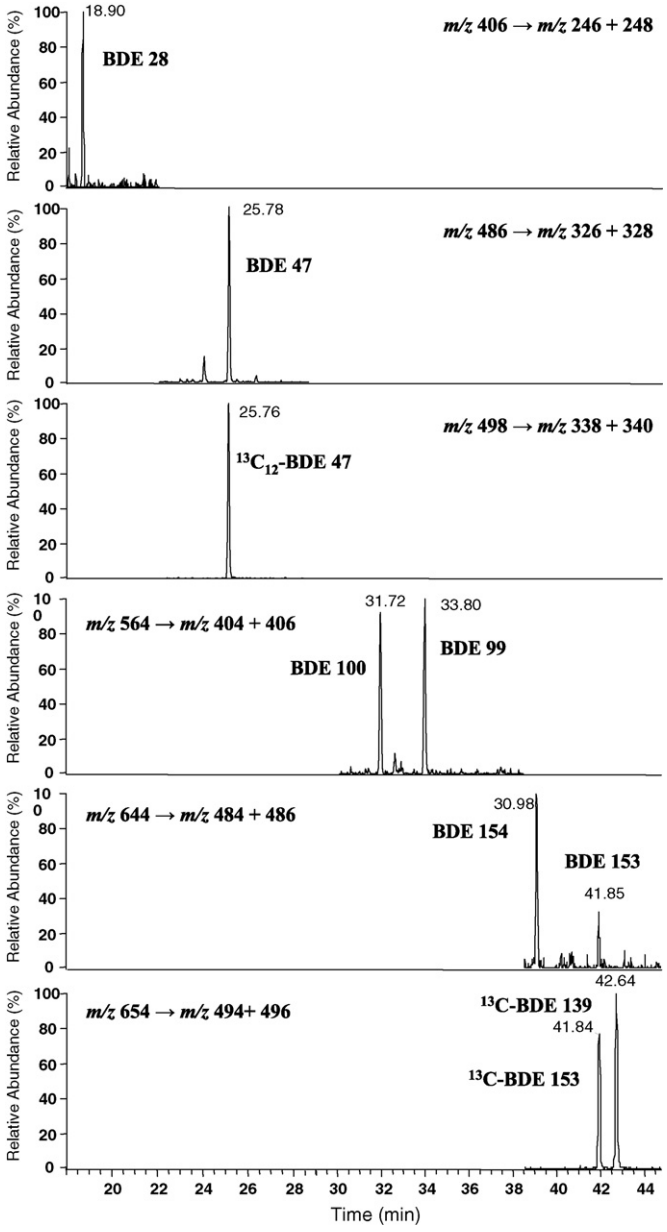


Fig. 3. GC–ITMS–MS chromatograms of a horse mackerel sample obtained using the simultaneous PLE extraction and clean-up developed with Florisil as fat retainer.

analysed. Triplicate analyses were carried out following the on-line PLE and GC–ITMS–MS method developed. The results obtained agreed with the certified values of the material (Table 2), achieving relative standard deviations lower than 13%. These results show that the proposed method can be considered as an attractive alternative method for the analysis of PBDEs in fish samples.

3.3. Analysis of PBDEs in fish samples

The proposed method was used for the determination of PBDEs at low concentrations in several fish samples (trout, horse mackerel and salmon) which cover a wide range of lipid content. Table 3 shows the PBDE concentration mean values obtained with their corresponding relative standard deviation (%). As an example, Fig. 3 shows the GC–ITMS–MS chromatograms obtained for a horse mackerel sample from the Mediterranean Sea. As can be seen, high selectivity and good signal-to-noise ratio were obtained using the proposed method. Concentration of the PBDE congeners ranged from 0.95 to 16.9 ng g^{-1} wet weight for trout, from 0.39 to 91.3 ng g^{-1} wet weight for horse mackerel and between 2.5 and 46.6 ng g^{-1} wet weight for salmon, with relative standard deviations (RSD %) ranging from 9% to 15% (Table 3). Total PBDE levels expressed as a sum of the nine PBDE congeners were respectively 45.0 ng g^{-1} ww, 144.3 ng g^{-1} ww and 82.3 ng g^{-1} ww for trout, horse mackerel and salmon. In all samples, the BDE-47 was the predominant congener followed by BDE-99 and BDE-100, which are the primary components of the commonly used Penta-BDE formulation. Generally, the results obtained in this study are consistent with data published in the literature for similar fish species. For instance, PBDE levels found in trout from the Laurentian Great Lakes (27–95 ng g^{-1} ww) [47] and four Swiss Lakes (1.6–7.4 ng g^{-1} ww) [60] are in agreement with those obtained in this work. Nevertheless, reported levels of PBDEs in horse mackerel from several markets in Fukuoka (Japan) (473.6 ng g^{-1} ww) were fourfold higher than those determined in this paper. For salmon, PBDE levels found in this work were similar to those reported for similar samples [61–63] and can be considered as fish samples with a medium contamination level.

4. Conclusion

A fast, simple and accurate on-line PLE extraction/clean-up method combined with GC–ITMS–MS has been proposed for the analysis of PBDEs in fish samples at low concentration levels. The use of Florisil as fat retainer in the PLE cell provided quantitative recoveries of PBDEs and extracts ready to GC–ITMS–MS determination. In contrast, the use of alumina did not provide extracts clean enough for PBDE determination and important variations in the results were obtained. Using the proposed on-line PLE procedure, a considerable reduction in the extraction time (around 30 min) and solvent consumption (100 ml) was obtained compared with conventional or PLE methods that employ an off-line clean-up. In addition, the accurate optimization of GC–ITMS–MS conditions allowed maximum sensitivity and selectivity on the PBDE determination. The whole method provided low limits of detection (10–34 pg g^{-1} wet weight) and good precisions (lower than 15%). Therefore, the PLE method combined with GC–ITMS–MS can be proposed for the analysis of PBDEs at low concentration levels in fish samples.

Acknowledgements

The authors gratefully acknowledge the financial support by the Ministerio de Ciencia y Tecnología of the Spanish Government

under the project CTM2006-00753/TECNO. S. Losada is grateful to the Ministerio de Ciencia y Tecnología for a FPI PhD grant.

References

[1] M. Alaee, P. Arias, A. Sjödin, A. Bergman, Environ. Int. 29 (2003) 683.
[2] Environmental Health Criteria 162: Brominated Diphenyl Ethers, World Health Organization, IPCS, Geneva, Switzerland, 1994.
[3] F. Rahman, K.H. Langford, M.D. Scrimshaw, J. Lester, Sci. Total Environ. 275 (2001) 1.
[4] R.C. Hale, M.J. La Guardia, E.P. Harvey, M.O. Taylor, T.M. Mainor, W.H. Duff, Nature 412 (2001) 140.
[5] J.-J. Kim, M. Osako, S. Sakai, Chemosphere 65 (2006) 506.
[6] C.A. de Wit, Chemosphere 46 (2002) 583.
[7] A. Sjödin, D.G. Patterson, A. Bergman, Environ. Int. 29 (2003) 829.
[8] R.J. Law, C.R. Allchin, J. de Boer, A. Covaci, D. Herzke, P. Lepom, S. Morris, J. Tronczynski, C.A. de Wit, Chemosphere 64 (2006) 187.
[9] A. Covaci, S. Voorspoels, L. Ramos, H. Neels, R. Blust, J. Chromatogr. A 1153 (2007) 145.
[10] C. Thomsen, E. Lundanes, G. Becher, Environ. Sci. Technol. 36 (2002) 1414.
[11] B. Gómara, L. Herrero, L.R. Bordajandi, M.J. González, Rapid Commun. Mass Spectrom. 20 (2006) 69.
[12] C. Naert, S. De Saeger, C. van Peteghem, Rapid Commun. Mass Spectrom. 18 (2004) 2317.
[13] S. Lacorte, M.G. Ikonomou, Chemosphere 74 (2009) 412.
[14] R.A. Hites, Environ. Sci. Technol. 38 (2004) 945.
[15] P. Eriksson, E.J. Akobsson, A. Fredriksson, Environ. Health Perspect. 109 (2001) 903.
[16] H. Viberg, A. Fredriksson, P. Eriksson, Toxicol. Sci. 67 (2002) 104.
[17] T. Zhou, M.M. Taylor, M.J. De Vito, K.M. Crofton, Toxicol. Sci. 66 (2002) 105.
[18] I. Branchi, F. Capone, E. Alleva, L.G. Costa, Neurotoxicology 24 (2003) 449.
[19] Directive 2003/11/EC of the European Parliament and of the Council of 6 February 2003 amending for the 24th time Council Directive 76/769/EEC relating to restrictions on the marketing and use of certain dangerous substances and preparations (pentabromodiphenyl ether, octabromodiphenyl ether) Official Journal L 42/45, 15/02/2003.
[20] Directive 2002/95/EC of the European Parliament and the Council of 27 January 2003 on the restriction of the use of certain hazardous substances in electrical and electronic equipment. Official Journal L037, 13/02/2003.
[21] I. Sioen, M. Bilau, F. Verdonck, W. Verbeke, J.L. Willems, S. De Henauw, J. Van Camp. Mol. Nutr. Res. 52 (2008) 250.
[22] S.A. Tittlemier, D. Forsyth, K. Breakell, V. Verigin, J.J. Ryan, S. Hayward, J. Agric. Food Chem. 52 (2004) 7740.
[23] J.L. Domingo, A. Bocio, G. Falcó, J.M. Llobet, Environ. Sci. Technol. 40 (2006) 4394.
[24] J.L. Domingo, J. Chromatogr. A 1054 (2004) 321.
[25] D.C.G. Muir, S. Backus, A.E. Derocher, R. Dietz, T.J. Evans, G.W. Gabrielsen, J. Nagy, R.J. Norstrom, C. Sonne, I. Stirling, M.K. Taylor, R.J. Letcher, Environ. Sci. Technol. 40 (2006) 449.
[26] B. Johnson-Restrepo, K. Kannan, D.P. Rapaport, B.D. Rodan, Environ. Sci. Technol. 39 (2005) 5177.
[27] M.N. Jacobs, A. Covaci, A. Gheorghe, P. Schepens, J. Agric. Food Chem. 52 (2004) 1780.
[28] D.R. Oros, D. Hoover, F. Rodigari, D. Crane, J. Sericano, Environ. Sci. Technol. 39 (2005) 33.
[29] C. Pirard, E. de Pauw, J.F. Focant, J. Chromatogr. A 1115 (2006) 125.
[30] E. Björklund, S. Sporring, K. Wiberg, P. Haglund, C. Von Holst, Trends Anal. Chem. 25 (2005) 318.
[31] S. Bayen, H.K. Lee, J.Ph. Obbard, J. Chromatogr. A 1035 (2004) 291.
[32] H. Wolkers, M.O. Hammill, B. van Bavel, Environ. Pollut. 142 (2006) 476.
[33] A. Martínez, M. Ramil, R. Montes, D. Hernanz, E. Rubí, I. Rodríguez, R. Cela-Torrijos, J. Chromatogr. A 1072 (2005) 83.
[34] B. Gómara, L. Herrero, M.J. González, Environ. Sci. Technol. 40 (2006) 7541.
[35] S. Sporring, E. Björklund, J. Chromatogr. A 1040 (2004) 155.
[36] S. Sporring, C. von Holst, E. Björklund, Chromatographia 64 (2006) 553.
[37] K. Wiberg, S. Sporring, P. Haglund, E. Björklund, J. Chromatogr. A 1138 (2007) 55.
[38] M. Nording, S. Sporring, K. Wiberg, E. Björklund, P. Haglund, Anal. Bioanal. Chem. 381 (2005) 1472.
[39] K. Saito, A. Sjodin, C.D. Sandau, M.D. Davis, H. Nakazawa, Y. Matsuki, D.G. Patterson, Chemosphere 57 (2004) 373.
[40] I. Wiater-Protas, B. Van Bavel, A. Parczewski, Chem. Anal. 47 (2002) 659.
[41] S. Harrad, S. Hazrati, C. Ibarra, Environ. Sci. Technol. 40 (2006) 4633.
[42] A. de la Cal, E. Eljarrat, D. Barceló, J. Chromatogr. A 1021 (2003) 165.
[43] E. Eljarrat, A. de la Cal, D. Raldúa, C. Duran, D. Barceló, Environ. Sci. Technol. 38 (2004) 2603.
[44] L. Webster, M. Rusell, F. Adefehinti, E.J. Dalgarno, C.F. Moffat, J. Environ. Monit. 10 (2008) 463.
[45] H.M. Stapleton, Anal. Bioanal. Chem. 386 (2006) 807.
[46] J. de Boer, D.E. Wells, Trends Anal. Chem. 25 (2006) 364.
[47] J.M. Luross, M. Alaee, D.B. Sergeant, C.M. Cannon, D. Michael Whittle, K.R. Solomon, D.C.G. Muir, Chemosphere 46 (2002) 665.
[48] H.-B. Moon, K. Kannan, S.-J. Lee, M. Choi, Chemosphere 66 (2007) 243.
[49] US EPA Method 1614: Brominated Diphenyl Ethers in waste soil, sediment and tissue by HRGC/HRMS. US Environmental Protection Agency. Office of Water. Office of Science and Technology Engineering and Analysis Division. Washington, DC, 2007 (EPA-821-R-07-005).
[50] C. Naert, C. Van Peteghem, J. Kupper, L. Jenni, H. Naegeli, Chemosphere 68 (2007) 977.
[51] Q. Luo, M. Wong, Z. Cai, Talanta 72 (2007) 1644.
[52] L. Zhu, B. Ma, X. Liang, Rapid Commun. Mass Spectrom. 22 (2008) 394.
[53] V. Yusá, O. Pardo, A. Pastor, M. de la Guardia, Anal. Chim. Acta 557 (2006) 304.
[54] M. Polo, G. Gómez-Noya, J.B. Quintanilla, M. Llompart, G. García-Jares, R. Cela, Anal. Chem. 76 (2004) 1054.
[55] Fish and Marine Cultures Market (FROM). Ministerio de Medio Ambiente y Medio Rural y Marino. Summary of the survey of the Spanish population's fishery product purchasing, storage and consumption habits–2007. Madrid, 2007.
[56] C. Pirard, E. de Pauw, J.-F. Focant, J. Chromatogr. A 998 (2003) 169.
[57] M. Alaee, D.B. Sergeant, M. Ikonomou, J.M. Luross, Chemosphere 44 (2001) 1489.
[58] G. Marsh, J. Hu, E. Jakobsson, S. Rahm, A. Bergman, Environ. Sci. Technol. 33 (1999) 329.
[59] D. Wang, Z. Cai, G. Jiang, M.H. Wong, W.K. Wong, Rapid Commun. Mass Spectrom. 19 (2005) 83.
[60] M. Zennegg, M. Kohler, A.C. Gerecke, P. Schmid, Chemosphere 51 (2003) 545.
[61] J.B. Manchester-Neesvig, K. Valters, W.C. Sonzogni, Environ. Sci. Technol. 35 (March) (2001) 1072.
[62] R.A. Hites, J.A. Foran, S.J. Schwager, B.A. Knuth, M.C. Hamilton, D.O. Carpenter, Environ. Sci. Technol. 38 (2004) 4945.
[63] P. Schmid, M. Kohler, E. Gujer, M. Zennegg, M. Lanfranchi, Chemosphere 67 (2007) S16.

Talanta 80 (2009) 846–852

Contents lists available at ScienceDirect

Talanta

journal homepage: www.elsevier.com/locate/talanta

Correction of structured molecular background by means of high-resolution continuum source electrothermal atomic absorption spectrometry—Determination of antimony in sediment reference materials using direct solid sampling

Rennan G.O. Araujo[a], Bernhard Welz[a,b,*], Fabiola Vignola[a], Helmut Becker-Ross[c]

[a] Departamento de Química, Universidade Federal de Santa Catarina, 88040-900 Florianópolis - SC, Brazil
[b] INCT de Energia e Ambiente do CNPq, Brazil[1]
[c] ISAS - Institute for Analytical Sciences, Department of Interface Spectroscopy, Albert-Einstein-Str. 9, 12489 Berlin, Germany

ARTICLE INFO

Article history:
Received 28 June 2009
Received in revised form 1 August 2009
Accepted 4 August 2009
Available online 13 August 2009

Keywords:
Antimony determination
Sediment analysis
Direct solid sampling
Electrothermal AAS
High-resolution continuum source AAS

ABSTRACT

A simple, fast and accurate procedure is proposed for the determination of antimony in certified sediment reference materials using direct solid sampling high-resolution continuum source electrothermal atomic absorption spectrometry and iridium as a permanent modifier. The less sensitive resonance line at 231.147 nm has been used in order to allow the introduction of larger sample mass. Six certified reference materials, one river, one estuarine and four marine sediments have been analyzed. The use of iridium as a permanent modifier caused an increase of 30% in sensitivity and stabilized antimony in the sediment to a pyrolysis temperature of 1100 °C. Significant background absorption with pronounced rotational fine structure was observed at the optimum atomization temperature of 2100 °C, which coincided with the analyte atomic absorption in time. This background was found to be due to the electron excitation spectra of mostly the SiO and in part the PO molecules, and could be eliminated by applying a least-squares background correction algorithm. A characteristic mass of 28 pg Sb was obtained, and the limit of detection (3σ, $n=10$) was 0.02 $\mu g\,g^{-1}$, calculated for 0.2 mg of sample. The results obtained for six certified reference materials with concentrations between 0.40 and $11.6 \pm 2.6\ \mu g\,g^{-1}$ Sb were in agreement with the certified values according to a Student's *t*-test for a 95% confidence level, using aqueous standards for calibration. The precision, expressed as relative standard deviation, ranged between 7% and 17% ($n=5$).
© 2009 Elsevier B.V. All rights reserved.

1. Introduction

In contrast to other toxic elements, such as arsenic, cadmium, lead or mercury, antimony came into the focus of environmental and health concern only less than a decade ago, maybe because no big environmental accident, such as the Minamata disaster in Japan or the arsenic poisoning in Bangladesh, was associated to antimony intoxication. Antimony and many of its compounds are toxic, bio-accumulative and persistent in the environment and its behavior and transport depend on its chemical form [1–3]. Antimony is generally more toxic than lead due to its higher solubility in lipids, which increases the potential for biological uptake and bio-accumulation. Its presence in the environment is due to natural processes and anthropogenic activities [4–6]. Antimony is increasingly being used in the semiconductor industry, in a wide variety of alloys and as a flame retardant [7,8]. Industries such as smelters, coal-fired plants and refuse incinerators can release relatively high amounts of antimony in the air. When released to air, antimony can attach itself to very small particles and may stay in the atmosphere for many days and be transported over long distances. In soil, antimony is strongly associated with particles containing iron, manganese or aluminum. In water it usually adheres to sediments [9].

The determination of trace elements in sediment is particularly difficult because of the complexity of the matrix. The total analyte concentration can only be determined after a fusion with sodium carbonate [10], lithium tetraborate [11] or lithium metaborate [12–14], or after acid digestion in the presence of hydrofluoric acid and frequently also perchloric acid [15,16]. These digestion procedures are relatively time-consuming and certainly not without problems. The high reagent concentration requires regular blank controls to be performed, and frequently the calibration solutions have to be matched to the matrix content. Moreover

* Corresponding author at: Departamento de Química, Universidade Federal de Santa Catarina, 88040-900 Florianópolis - SC, Brazil. Tel.: +55 48 9983 1344; fax: +55 48 3721 6850.
E-mail address: welz@qmc.ufsc.br (B. Welz).
[1] www.inct.cienam.ufba.br.

0039-9140/$ – see front matter © 2009 Elsevier B.V. All rights reserved.
doi:10.1016/j.talanta.2009.08.004

the high salt concentration can lead to interferences in the final determination. Digestions in hydrofluoric or perchloric acid are dangerous, and next to silicon, which should be removed in this manner, a number of elements, including antimony, form volatile fluorides which might be lost during sample preparation.

Owing to these problems, instead of a total digestion or fusion, it is common in environmental analysis to use a leaching with *aqua regia* [17,18]. This method is based on the assumption that heavy metals that are so strongly bound to the mineral matrix that they do not go into solution under these conditions will also not be taken up by plants and cannot be dissolved by water or bacteria. Even if this assumption might be true for many elements and matrices, such an extraction cannot replace a determination of the total content of an analyte in all situations. In addition, the resulting matrix can cause serious interferences in most spectrometric techniques unless the solutions are strongly diluted, which is often not possible in trace element determinations, or the analyte is extracted, which is another time-consuming procedure.

Due to the difficulties of bringing environmental samples, such as sediments, into solution and due to the complexity of the resulting solutions, which might need additional treatment before they can be analyzed, direct solid sampling (SS) using electrothermal atomic absorption spectrometry with a graphite tube furnace (GF AAS) might be an attractive alternative [19]. However, the complex and refractory matrix of sediments might also cause problems in SS-GF AAS. Although non-spectral interferences can usually be controlled using the Stabilized Temperature Platform Furnace (STPF) concept [20], spectral interferences and the limited background correction capability of conventional line source atomic absorption spectrometers might be the major obstacle in the application of this technique [21]. The introduction of high-resolution continuum source AAS (HR-CS AAS) has brought about a significant change in this direction due to its unsurpassed background correction capabilities [22]. It has been demonstrated that a number of trace elements in a wide variety of complex sample matrices can be determined by SS-HR-CS GF AAS using aqueous standards for calibration, i.e., without any interference [23].

Chemical modifiers are routinely used in GF AAS as part of the STPF concept in order to thermally stabilize volatile analytes and enable the use of higher pyrolysis temperatures to remove the majority of the matrix prior to the atomization stage [24]. In SS-GF AAS the addition of a modifier in solution over the solid sample prior to every determination obviously complicates the procedure. Permanent chemical modifiers, which are usually applied as kind of a surface coating on the SS platform, have therefore been investigated intensively and have been shown to stabilize the analyte in a similar way as when it is applied in solution [25–29]. The mechanism of operation is believed to be a migration of the analyte to the modifier in the pyrolysis stage, as it has been demonstrated that the analyte is released from the sample well below its melting point [30]. Platinum group metals, mainly those with high melting points, i.e., Rh, Ru and Ir, have typically been used as permanent modifiers for the stabilization of volatile elements. The use of permanent modifiers also reduces blank values, as the modifier is purified during its thermal deposition, resulting in better limits of detection and quantification [17].

The goal of this work has been to develop a fast routine procedure for the determination of total antimony in sediments using SS-HR-CS GF AAS. The visibility of the spectral environment at high resolution in HR-CS AAS has also been used as a diagnostic tool in order to investigate spectral interferences that might impede the determination of antimony in sediment using conventional line source GF AAS. The investigation of permanent chemical modifiers has been included in the study for obvious reasons in order to simplify the procedure.

2. Experimental part

2.1. Instrumentation

All experiments were carried out with a prototype high-resolution continuum source atomic absorption spectrometer, built at ISAS Berlin, based on an AAS 6 Vario (Analytik Jena AG, Jena, Germany), from which the entire optical compartment, including detector and associated controls, was removed and replaced by a double monochromator, similar to that described by Heitmann et al. [31]. This monochromator consists of a pre-dispersing prism monochromator and an echelle grating monochromator, both in Littrow mounting, resulting in a spectral resolution of $\lambda/\lambda\Delta \approx 140\,000$. A xenon short-arc lamp XBO 301 (GLE, Berlin, Germany) with a nominal power of 300 W, operating in a *hot-spot* mode, was used as the continuum radiation source. A UV-sensitive charge coupled device (CCD) detector, model S7031-0906 (Hamamatsu Photonics, Japan), with 512×58 pixels operating in full vertical binning mode was used, resulting in a spectral bandwidth per pixel of about 2 pm at 231.147 nm. 200 pixels are used for analytical purposes, which corresponds to a spectral environment of about ±0.20 nm around the center pixel. Details of this equipment and its specific features have been described previously [22,32]. Atomic absorption has been measured at the secondary resonance line of antimony at 231.147 nm, which is about a factor of 2.4 less sensitive than the primary resonance line at 217.581 nm. Three pixels have been used for signal evaluation, corresponding to a spectral interval of ~6 pm, as the best signal-to-noise ratio has been obtained under these conditions. The absorbance values obtained this way are denominated Peak Volume Selected Absorbance (PVSA, $A_{\Sigma 3,\mathrm{int}}$), i.e., the integrated absorbance summated over three pixels [33]. The integrated absorbance values obtained with direct solid sampling have been normalized for 1.0 mg of sample, as it is impossible and unnecessary to weigh always the same sample mass.

The conventional transversely heated graphite tube atomizer supplied by Analytik Jena together with the AAS 6 Vario has been used throughout. All experiments were carried out using pyrolytically coated SS graphite tubes without a dosing hole (Analytik Jena, Part No. 07-8130325) and SS graphite platforms (Analytik Jena, Part No. 407-A81.312). Samples were weighed on a M2P microbalance (Sartorius, Göttingen, Germany) directly onto the SS platforms and inserted into the graphite tube using a pre-adjusted pair of tweezers, which is part of the SSA 5 accessory for manual SS (Analytik Jena). Argon 99.996% (White Martins, São Paulo, Brazil) was used as purge and protective gas. The temperature program adopted for aqueous standards (calibration) and for solid samples is shown in Table 1. In all figures in which time-resolved absorbance is shown,

Table 1
Graphite furnace temperature program for the determination of Sb in sediment samples by SS-HR-CS GF AAS using Ir as a permanent modifier.

Program stage	Temperature (°C)	Ramp (°C s^{-1})	Hold (s)
Drying 1	90	10	10
Drying 2	130	5	5
Pyrolysis	1100	50	15
Auto Zero[a]	1100	0	1
Atomization[a]	2100	3000	7
Cleaning	2500	1000	5

[a] Purge gas (argon) flow rate 2 L min^{-1} in all stages, except during Auto Zero and atomization, where the gas flow was interrupted.

Table 2
Graphite furnace temperature program for the deposition of iridium as a permanent modifier on the SS graphite platform.

Step	Temperature (°C)	Ramp (°C s^{-1})	Hold (s)
1	130	10	40
2	160	10	50
3	1000	20	25
4	1400	100	5
5	2000	100	5

recording starts with the 'Auto Zero' stage, i.e., 1 s prior to the atomization stage.

2.2. Reagents and samples

Analytical grade reagents were used throughout. The nitric acid 65% (Merck, Germany), used to prepare aqueous calibration standards, was further purified by sub-boiling distillation in a quartz apparatus (Kürner Analysentechnik, Rosenheim, Germany). Distilled, deionized water with a resistivity of 18 MΩ cm from a Milli-Q water purification system (Millipore, Bedford, MA, USA) was used for the preparation of aqueous calibration standards. The antimony stock solution was prepared from Sb_2O_3 (SPEX, Edison, NJ, USA). Iridium stock solution with 1000 mg L^{-1} Ir in 1 mol L^{-1} nitric acid (Fluka, Buchs, Switzerland) was used as provided for coating of the platform.

The following certified reference materials (CRM) were used for validation of the method: NIST SRM 8704 (Buffalo River Sediment), NIST SRM 2702 (Inorganics in Marine Sediment), NIST SRM 2703 (Sediment for Solid Sampling Analytical Techniques) and NIST SRM 1646a (Esturine Sediment) (all from National Institute of Standards and Technology, Gaithersburg, MD, USA); Marine Sediment MESS-3, HISS-1 and PACS-2 from National Research Council of Canada (NRCC, Ottawa, Canada).

2.3. Procedure

Iridium was thermally deposited onto the platform surface using 10 repetitive injections of 40 μL of the 1000 mg L^{-1} Ir stock solution as described previously [34]. After each injection, the temperature program shown in Table 2 was applied. One coating has been sufficient for the lifetime of a SS platform. For the determination of Sb, sediment samples were ground in an agate mortar and passed through a polyester sieve for particle size <50 μm. Aliquots containing between 0.02 and 1.1 mg were weighed directly onto the SS platforms and inserted into the graphite tube with the SSA 5 accessory. Calibration solutions (20 μL) were injected manually onto the SS platforms using a micro-pipette. The analysis of one sample including five repetitive weighings and determinations takes less than 10 min, making possible the analysis of about 50 samples per working day.

3. Results and discussion

3.1. Pyrolysis and atomization temperatures

All method development and optimization experiments were carried out using an aqueous standard and NIST SRM 8704 (Buffalo River Sediment). Fig. 1 shows the pyrolysis curves obtained for the sediment CRM (Fig. 1a) and the aqueous standard (Fig. 1b) without a modifier and with iridium as a permanent modifier. Without a modifier antimony is partially lost above 800 °C from the aqueous standard and above 900 °C from the sediment CRM. In the presence of the permanent modifier a pyrolysis of 1100 °C can be used for the sediment, and an even higher pyrolysis temperature would be possible for the aqueous standard. A pyrolysis temperature of 1100 °C has been selected for all further experiments. The atomization temperature has been optimized in a similar way considering sensitivity and signal shape, and a temperature of 2100 °C has finally been selected.

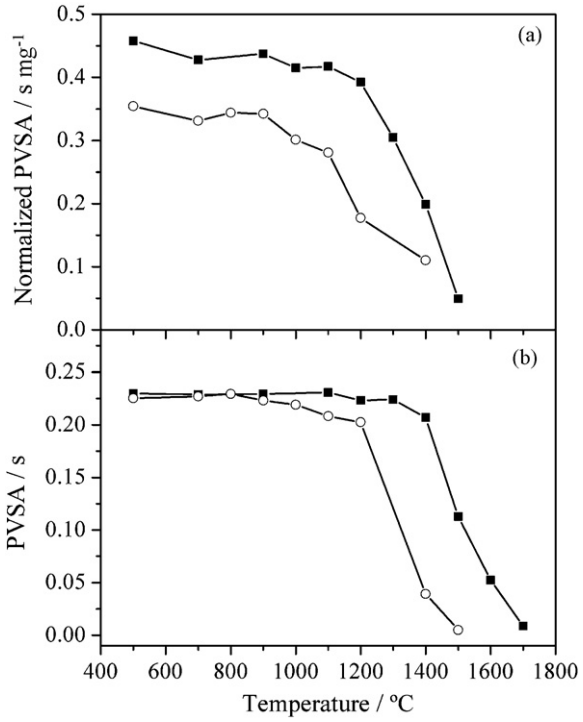


Fig. 1. Pyrolysis curves for Sb –○– without modifier and –■– with 400 μg Ir as permanent modifier; atomization temperature: 2100 °C; (a) NIST SRM 8704 (Buffalo River Sediment), PVSA ($A_{\Sigma 3,int}$) normalized for 1 mg of sample; (b) aqueous standard containing 1.3 ng Sb in 0.5% (v/v) HNO_3.

3.2. Background absorption and background correction

In HR-CS AAS 'continuous' background absorption, i.e., background absorption that does not exhibit any fine structure within the spectral range that is probed by the detector, such as radiation scattering or molecular absorption due to dissociation continua or polyatomic molecules, is corrected automatically and simultaneously with the measurement of atomic absorption using correction pixels. After this correction only discontinuous absorption, such as atomic absorption and molecular absorption due to diatomic molecules, which exhibits pronounced fine structure that can be resolved by the spectrometer, is displayed by the equipment.

The time- and wavelength-resolved absorption spectrum obtained for NIST SRM 8704 (Buffalo River Sediment) in the vicinity of the antimony line at 231.147 nm after automatic correction for continuous background is shown in Fig. 2. The Sb atomic absorption line and a secondary absorption line of Fe at 231.31 nm are marked with arrows; all the other lines are part of an electronic transition spectrum of one or more diatomic molecule(s) with pronounced rotational fine structure. There are actually three different phases within the time frame of the atomization stage. The first one is the appearance of very sharp peaks of a rotational fine structure at the onset of the atomization stage; the second set of molecular bands appears more or less together with the atomic absorption of Sb (and Fe), but does not return to the baseline; instead, towards the end of the atomization cycle, the molecular absorption increases rapidly to relatively high absorbance values. Due to the post-processing capability of the spectrometer it is possible to analyze the recorded spectrum after it has been stored in the computer in order to iden-

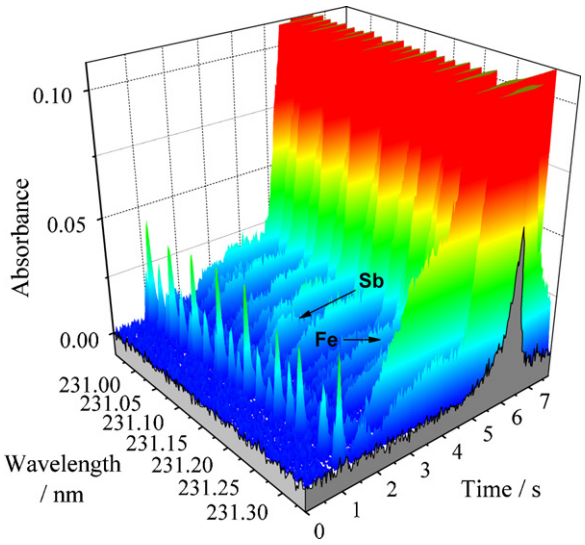


Fig. 2. Time- and wavelength-resolved absorbance spectrum recorded for NIST SRM 8704 (Buffalo River Sediment) in the vicinity of the Sb line at 231.147 nm after automatic correction for continuous background absorption; T_{pyr} = 1100 °C; T_{at} = 2100 °C; Ir as permanent modifier.

tify the molecular structures and to correct them using reference spectra and a least-squares algorithm [22].

Fig. 3a–c shows the three phases as wavelength-resolved absorbance spectra integrated over three time intervals, i.e., from 0 to 1.4 s, which are the first 0.4 s of the atomization stage, as signal recording starts with the Auto Zero stage (Fig. 3a); from 1.4 to

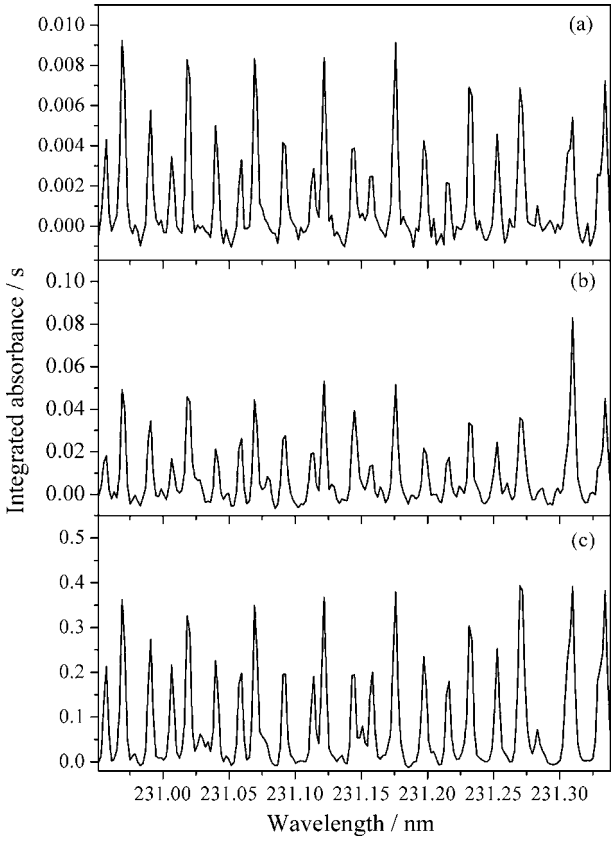


Fig. 3. Wavelength-resolved integrated absorbance spectrum in the vicinity of the Sb line at 231.147 nm for 0.092 mg of NIST SRM 8704 (Buffalo River Sediment); Ir as permanent modifier; T_{pyr} = 1100 °C; T_{at} = 2100 °C; (a) integration limits 0.0–1.4 s; (b) integration limits 1.4–4.2 s; (c) integration limits 4.2–7.0 s.

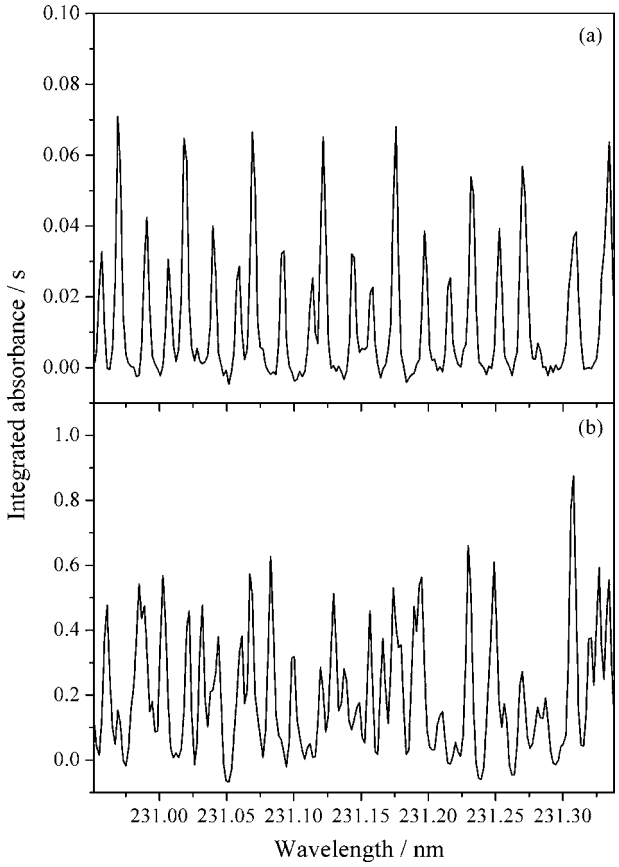


Fig. 4. Wavelength-resolved integrated absorbance spectrum in the vicinity of the Sb line at 231.147 nm; Ir as permanent modifier; T_{pyr} = 1100 °C; T_{at} = 2100 °C; (a) 0.116 mg of silica; (b) 150 μg P as $NH_4H_2PO_4$.

4.2 s, which is the period in time when the Sb atomic absorption signal appears (Fig. 3b); and from 4.2 to 7.0 s, which is the period after the Sb absorption signal returned to the baseline and the molecular absorption reaches fairly high levels (Fig. 3c). Although the spectra appear to be similar, they are not exactly identical. For this reason two reference spectra have been recorded, one for the silicon monoxide SiO, using pure silica (SiO_2), and one for the phosphorus monoxide PO, using ammonium dihydrogen phosphate ($NH_4H_2PO_4$), which are shown in Fig. 4a and b, respectively. The spectrum recorded for HISS-1 CRM, which has a very low antimony content (information value: 0.13 μg g^{-1}), has also been used for correction purposes in some cases, but is not shown here, as it is almost identical to that of SiO (Fig. 4a).

The spectrum shown in Fig. 3a, which appears at the onset of the atomization stage, has been identified as being exclusively due to SiO, and could be corrected to the baseline using the reference spectrum in Fig. 4a and least-squares background correction (LSBC). This is actually surprising, as this means that there is a silicon-containing compound in the sediment that is significantly more volatile than antimony, i.e., it cannot be mineral SiO_2; this early SiO absorption spectrum has been observed in all investigated sediment CRM. The molecular structures of the spectrum shown in Fig. 3b, which actually comprises the main atomization stage, could be removed reasonably well using LSBC and the spectrum of HISS-1 or SiO as reference spectrum; however, as can be seen in Fig. 5a, besides the atomic absorption peaks of antimony and iron, there are some irregularities in the baseline, indicating some correction problems, most likely due to a small amount of another diatomic molecule. Nevertheless, as these minor irregularities did not affect the analytical line, and were less than ±0.01 s in integrated absorbance,

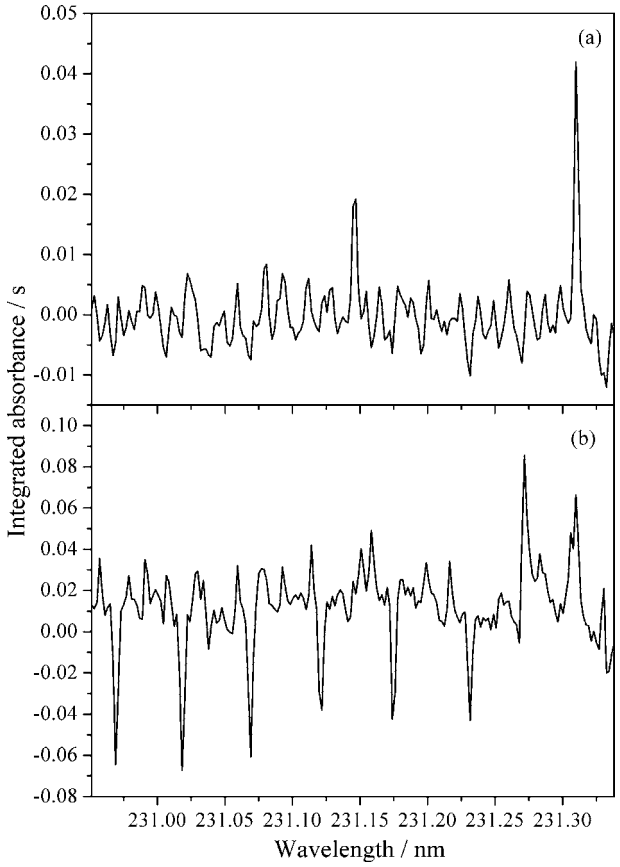


Fig. 5. Wavelength-resolved integrated absorbance spectrum in the vicinity of the Sb line at 231.147 nm for 0.092 mg of NIST SRM 8704 (Buffalo River Sediment) using HISS-1 CRM as reference spectrum for LSBC; Ir as permanent modifier; T_{pyr} = 1100 °C; T_{at} = 2100 °C; (a) integration limits 1.4–4.2 s; (b) integration limits 4.2–7.0 s.

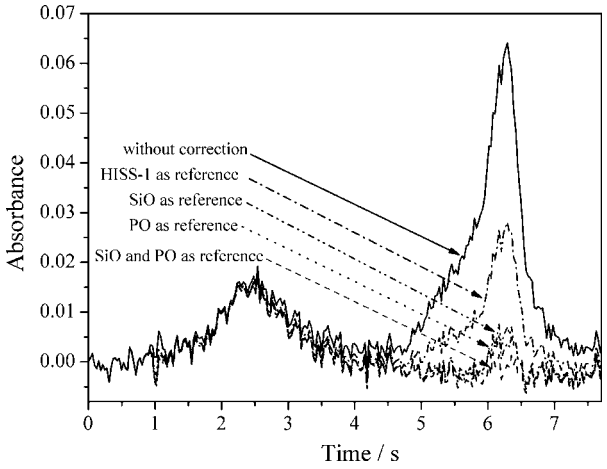


Fig. 6. Superimposed transient signals recorded at 231.147 nm for NIST SRM 8704 (Buffalo River Sediment) without LSBC (black line) and using the spectrum of HISS-1, SiO, PO, and SiO + PO, as reference for LSBC.

they have not been further investigated. The third section of the absorption spectrum, which is shown in Fig. 3c, is of no analytical interest, as it occurs in time after the atomization of antimony, but it might be of diagnostic interest in order to find out the source of this molecular absorption. A first attempt to correct for this molecular absorption using the spectrum of HISS-1 as a reference failed at least in part, as can be seen in Fig. 5b. There was a baseline offset of about 0.015 s in integrated absorbance, and pronounced negative peaks that coincided with the strongest absorption lines of SiO. The explanation for this phenomenon is straight-forward when we compare Fig. 3c with a maximum absorbance of about 0.4 s and Fig. 4a, where the maximum absorbance only reaches values of about 0.07 s. The intensity ratio between the strongest and the less intense absorption peaks in Fig. 4a is roughly 2:1, whereas in Fig. 3c it is less, indicating that the absorbance of the strongest peaks is already in the non-linear range, a task that cannot be solved by a least-squares algorithm.

This situation has therefore been investigated in more detail, primarily in the environment of the analytical line. Fig. 6 shows the absorbance signal over time recorded at the central pixel at 231.147 nm for the NIST SRM 8704 (Buffalo River Sediment) using different reference spectra for correction. Without LSBC there appears a strong molecular absorption after the antimony signal, which can only be corrected in part using the spectrum of HISS-1 CRM. The correction is much better using the reference spectrum of SiO, but there is still a residual signal that could only be corrected using the reference spectrum of PO in addition to that of SiO. This also explains why the spectrum of the HISS-1 CRM could not be used successfully for LSBC, at least not in this time interval. Whenever more than one molecule is contributing to such a spectrum, the reference spectra and the LSBC have to be applied sequentially for each molecule, unless the ratio between the two molecules is known and can be simulated in the reference spectrum, which is impossible in real sample analysis.

Obviously, this correction appears to be of no importance for the analyte signal, which returns to the baseline before the molecular absorption becomes significant. However, Fig. 6 only shows the situation at the central pixel, whereas the best S/N ratio is obtained using PVSA over three pixels; the results obtained for NIST SRM 8704 using this evaluation technique are shown in Table 3. It is obvious that a wrong result is obtained without using LSBC, as one of the rotational lines of the SiO molecular absorption is already overlapping significantly with the wing of the antimony absorption line. On the other hand there is little difference in the final result if HISS-1 is used for correction or SiO alone or together with PO, indicating the robustness of the method. The use of PO alone for LSBC does not give a satisfactory result, showing that this molecule has no significant contribution to the absorption spectrum during the first 4.2 s of the atomization stage. The fact that some correction has been achieved even with PO as the reference spectrum is due to some similarity of this spectrum with that of SiO (see Fig. 4a and b). The LSBC has therefore been in part successful to correct for the effect of SiO on the integrated absorbance of Sb using the spectrum of PO, although the final result is not within the confidence interval.

As a result of these investigations it would be of advantage to shorten the atomization stage to about 4 s in order to avoid the strong molecular absorption at the end of the atomization stage and remove these matrix components during the cleaning stage. A typical time- and wavelength-resolved absorbance spectrum recorded under these conditions, using LSBC for SiO and PO is shown in Fig. 7.

Table 3
Results obtained for antimony in NIST SRM 8704 (Buffalo River Sediment) (certified value: 3.07 ± 0.32 μg g^{-1} Sb) using different reference spectra for LSBC; integration interval: 0.5–4.5 s; T_{pyr} = 1100 °C; T_{at} = 2100 °C; Ir as permanent modifier.

Reference spectrum	Found value (μg g^{-1})[a]	Recovery (%)[b]
Without LSBC	4.61 ± 1.37	150 ± 35
HISS-1	2.96 ± 0.29	96 ± 9
SiO	2.77 ± 0.42	90 ± 14
PO	3.58 ± 0.86	117 ± 28
SiO + PO	2.81 ± 0.46	91 ± 15

[a] Average of five determinations ± confidence interval (at the 95% level).
[b] Recovery factor = (found value/certified value) × 100 ± confidence interval.

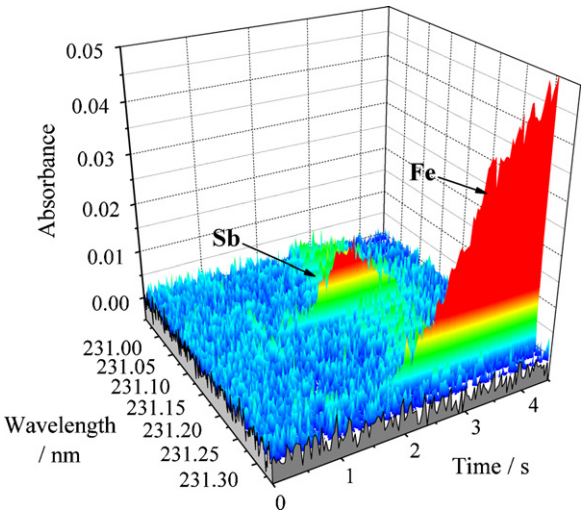


Fig. 7. Time- and wavelength-resolved absorbance spectrum recorded for 0.092 mg of NIST SRM 8704 (Buffalo River Sediment) in the vicinity of the Sb line at 231.147 nm after correction for continuous and discontinuous background absorption using the reference spectra of SiO and PO for LSBC; Ir as permanent modifier; T_{pyr} = 1100 °C; T_{at} = 2100 °C; integration interval: 0–4.5 s.

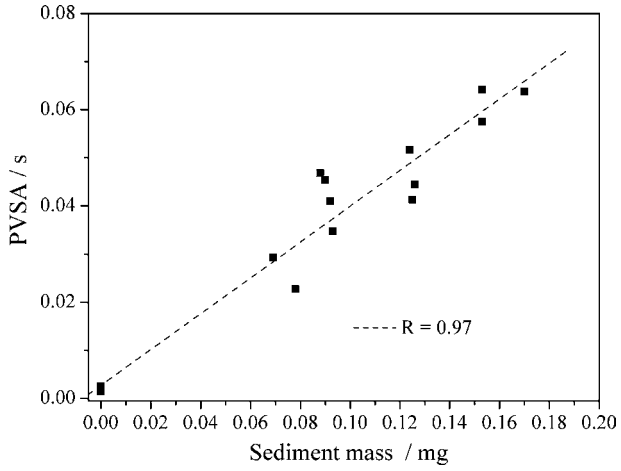


Fig. 8. Correlation between the sediment mass (NIST SRM 8704, Buffalo River Sediment) introduced into the graphite furnace and the PVSA ($A_{\Sigma 3,int}$); T_{pyr} = 1100 °C; T_{at} = 2100 °C; Ir as permanent modifier.

In essence only the analyte signal and the atomic absorption due to Fe are visible under these conditions.

3.3. Figures of merit

The limit of detection (LOD) has been calculated as three times the standard deviation of 10 measurements of a blank divided by the slope of the calibration curve; in SS-GF AAS the blank measurements are usually carried out according to the "zero mass response" technique [35], introducing repeatedly an SS platform containing only the modifier and running a full atomization cycle. The limit of quantification (LOQ) is based on the same measurements, using 10 times the standard deviation of the blank readings. The LOD and LOQ were determined as 0.02 and 0.07 μg g^{-1} Sb, respectively, based on a sample mass of 0.2 mg introduced into the furnace. A larger sample mass could obviously be introduced, resulting in even lower LOD and LOQ; however this was not found necessary for the present investigation. The characteristic mass (m_0), defined as the mass of the analyte that produces a PVSA of 0.0044 s, has been determined as m_0 = 28 pg Sb. There is no literature data available for the characteristic mass for the secondary Sb line at 231.147 nm used in this work. The characteristic mass at the main resonance line for Sb at 217.58 nm using line source AAS is around m_0 = 20 pg, and the secondary line used in this work is about a factor of 2.4 less sensitive than the primary resonance line [24], which would result in a characteristic mass of about 48 pg; it is quite typical for HR-CS AAS that the sensitivity obtained with PVSA is better than that obtained with line source AAS. A calibration curve established using a blank and six calibration solutions in the concentration range 5–50 μg L^{-1} Sb (mass range: 100–1000 pg Sb) in 0.007 mol L^{-1} HNO_3, using the conditions described in Section 2 gave the linear relationship:

$$A_{\Sigma 3,int} = 1.55 \times 10^{-4} m + 0.00002 \quad (R = 0.9998),$$

where $A_{\Sigma 3,int}$ is the PVSA, i.e., the integrated absorbance summated over three pixels, and m is the analyte mass.

3.4. Accuracy, precision and analytical application

The correlation between the sediment mass introduced into the graphite furnace and the integrated absorbance (PVSA, $A_{\Sigma 3,int}$) for NIST SRM 8704 is shown in Fig. 8. The sample mass has been varied in the range from 0.069 ± 0.001 to 0.170 ± 0.001 mg; each measurement point corresponds to an individual sample weighing and measurement, and is hence an indication for the precision of the entire procedure, which will be discussed in some more detail later. The good linear correlation shows that at least up to about 0.2 mg of sediment sample can be introduced and measured with the proposed procedure.

Six sediment CRM (one river, one estuarine and four marine sediments) have been analyzed; each concentration value was obtained as the mean of five individual weighings and measurements, using a calibration curve established with aqueous standards for quantification. The results are shown in Table 4 together with the calculated recovery and uncertainty (95% confidence interval). There is no statistically significant difference between the results obtained with the proposed method and the certified or informed values based on a Student's t-test ($t_{calculated}$ = 0.93; t_{value} = 2.57, n = 6). These results show that the determination of antimony in sediment using SS-HR-CS GF AAS can be carried out with calibration against aqueous standards.

The precision, expressed as relative standard deviation (% RSD), ranged between 7% and 17%, which are typical values for the direct analysis of solid samples. Although these values should not be over-interpreted, it might be interesting to note that the highest imprecision has been obtained for the sample with the highest antimony content, and the best precision for a sample with about an order of magnitude lower antimony content. As smaller sample masses are usually introduced into the furnace for samples with high analyte content, this difference in precision might be

Table 4
Results obtained for the determination of antimony in sediment samples using SS-HR-CS GF AAS and calibration against aqueous standards; T_{pyr} = 1100 °C; T_{at} = 2100 °C; Ir as permanent modifier.

CRM	Certified value (μg g^{-1})	Found value (μg g^{-1})[a]	Recovery (%)[b]
NIST SRM 8704	3.07 ± 0.32	2.96 ± 0.29	96 ± 9
PACS-2	11.6 ± 2.6	12.6 ± 2.0	109 ± 17
MESS-3	1.02 ± 0.9	0.98 ± 0.07	96 ± 7
NIST SRM 2703	5.62 ± 0.26	5.80 ± 0.67	103 ± 12
NIST SRM 2702	5.60 ± 0.24	5.49 ± 0.68	98 ± 12
NIST SRM 1646a[c]	0.40	0.45 ± 0.05	113 ± 13

[a] Average of five determinations ± confidence interval (at the 95% level).
[b] Recovery factor = (found value/certified value) × 100 ± confidence interval.
[c] Informed value, not certified.

directly related to the sample mass and the natural inhomogeneity of samples such as sediments. Another interesting comparison is that between NIST SRM 2702 and 2703, which are actually the same CRM, with the only difference that the latter one is ground to smaller particle size. The fact that the same imprecision has been obtained for both CRM might suggest that particle size is not of decisive importance for SS-GF AAS, as was proposed by others previously [36].

4. Conclusion

A simple, fast and reliable method for the determination of antimony in sediment has been developed using direct solid sampling HR-CS GF AAS and calibration against aqueous standards, i.e., without interference. As the spectral environment of the analytical line becomes visible at high resolution with this technique, it is possible to draw some conclusion about the performance of conventional line source AAS in the analysis of these samples. Spectrometers with deuterium or similar continuum source background correction are unable to cope with this background, which appears in time together with the analyte signal; as this kind of correction system makes an average of the background over the spectral band pass, background correction errors are inevitable. The same is true for Smith–Hieftje background correction, which measures the background on both sides of the analytical line, which is in this case obviously not the same as on the analytical line. To which extent Zeeman-effect background correction could deal with this spectral situation is difficult to predict; however, it is known that the narrow rotational lines of various diatomic molecules also exhibit Zeeman splitting. This would mean that the background measured with magnetic field is not identical to that without magnetic field, which would result in a correction error. The extent of this error could obviously only be determined by experiment. Nevertheless, the background correction systems available with HR-CS AAS are far superior to those available for line source AAS, and it might be expected that a variety of other trace elements could be determined in sediment and similar materials without interference using this technique. In addition, with modern equipment, in contrast to the prototype used in this work, full automation of direct solid sampling analysis is possible, which is obviously of importance for routine analysis.

Acknowledgements

The authors are grateful to Conselho Nacional de Desenvolvimento Científico and Tecnológico (CNPq) for financial support. R.G.O.A., B.W. and F.V. have research scholarships from CNPq. The authors are also grateful to Analytik Jena for financial support and donation of the prototype high-resolution continuum source atomic absorption spectrometer.

References

[1] J.L.G. Ariza, E. Morales, D. Sanchez-Rodas, I. Giraldez, Trends Anal. Chem. 19 (2000) 200.
[2] K. Müller, B. Daus, P. Morgenstern, R. Wennrich, Water Air Soil Poll. 183 (2007) 427.
[3] W. Shotyk, M. Krachler, B. Chen, in: A. Sigel, H. Sigel, R.K.O. Sigel (Eds.), Metal Ions in Biological Systems, vol. 44, M. Dekker, New York, 2005, p. 172.
[4] P. Smichowski, Talanta 75 (2008) 2.
[5] J.M. Carlosena, M.L. Andrade, S. Martínez, P.L. Muniategui, D. Prada, M.J. Cal-Prietro, Water Air Soil Poll. 129 (2001) 333.
[6] Toxicological Profile for Antimony, U.S. Department of Health and Human Services, Public Health Service, Agency for Toxic Substances and Disease Registry, Atlanta, GA, USA, 1992.
[7] E.V. Bogdanov, V.V. Vladimirov, V.N. Gorshkov, Solid State Comm. 46 (1983) 193.
[8] United Nations Environment Programme, International Labour Organization, World health Organization, Environmental Health Criteria 192, Flame Retardants: A General Introduction. http://www.inchem.org/documents/ehc/ehc/ehc192.htm (accessed July 2009).
[9] Antimony and Compounds Fact Sheet, Australian Government. http://www.npi.gov.au/database/substance-info/profiles/10.html#npi-rank (accessed July 2009).
[10] P.J. Potts, Handbook of Silicate Rocks Analysis, Blackie & Sons, Glasgow, 1987.
[11] E.A.H. Carballo, J.R. Domínguez, J. Alvarado, Atom. Spectrosc. 21 (2000) 132.
[12] D.C. Bartenfelder, A.D. Karathanasis, Commun. Soil. Sci. Plant 19 (1988) 471.
[13] M. Bettinelli, Anal. Chim. Acta 148 (1983) 193.
[14] A.A. Verbeek, M.C. Mitchell, A.M. Ure, Anal. Chim. Acta 135 (1982) 215.
[15] H. Agemian, E. Bedek, Anal. Chim. Acta 119 (1980) 323.
[16] P. Woitke, A. Thiesies, G. Henrion, G. Steppuhn, Z. Chem. 29 (1989) 180.
[17] J.B.B. da Silva, M.A.M. da Silva, A.J. Curtius, B. Welz, J. Anal. At. Spectrom. 14 (1999) 1737.
[18] M. Chen, L.Q. Ma, Soil Sci. Soc. Am. J. 65 (2001) 491.
[19] M.G.R. Vale, N. Oleszczuk, W.N.L. dos Santos, Appl. Spectrosc. Rev. 41 (2006) 377.
[20] W. Slavin, D.C. Manning, G.R. Carnrick, Atom. Spectrosc. 2 (1981) 137.
[21] M.G.R. Vale, B. Welz, Spectrochim. Acta Part B 57 (2002) 1821.
[22] B. Welz, H. Becker-Ross, S. Florek, U. Heitmann, High-resolution Continuum Source AAS—The Better Way to Do Atomic Absorption Spectrometry, Wiley–VCH, Weinheim, 2005.
[23] B. Welz, M.G.R. Vale, D.L.G. Borges, U. Heitmann, Anal. Bioanal. Chem. 389 (2007) 2085.
[24] B. Welz, M. Sperling, Atomic Absorption Spectrometry, 3rd edn, Wiley–VCH, Weinheim, 1999.
[25] M.G.R. Vale, M.M. Silva, B. Welz, E.C. Lima, Spectrochim. Acta Part B 56 (2001) 1859.
[26] M.G.R. Vale, M.M. Silva, B. Welz, R. Nowka, J. Anal. At. Spectrom. 17 (2002) 38.
[27] A.F. Silva, B. Welz, A.J. Curtius, Spectrochim. Acta Part B 57 (2002) 2031.
[28] A.F. Silva, D.L.G. Borges, F.G. Lepri, B. Welz, A.J. Curtius, U. Heitmann, Anal. Bioanal. Chem. 382 (2005) 1835.
[29] D.L.G. Borges, A.F. Silva, B. Welz, A.J. Curtius, U. Heitmann, J. Anal. At. Spectrom. 21 (2006) 763.
[30] O.A. Güell, J.A. Holcombe, J. Anal. At. Spectrom. 7 (1992) 135.
[31] U. Heitmann, M. Schütz, H. Becker-Ross, S. Florek, Spectrochim. Acta Part B 51 (1996) 1095.
[32] B. Welz, D.L.G. Borges, F.G. Lepri, M.G.R. Vale, U. Heitmann, Spectrochim. Acta Part B 62 (2007) 873.
[33] U. Heitmann, B. Welz, D.L.G. Borges, F.G. Lepri, Spectrochim. Acta Part B 62 (2007) 1222.
[34] A.F. da Silva, D.L.G. Borges, F.G. Lepri, B. Welz, A.J. Curtius, U. Heitmann, Anal. Bioanal. Chem. 382 (2005) 1835.
[35] U. Kurfürst, in: U. Kurfürst (Ed.), Solid Sample Analysis, Springer, Heidelberg, 1998, p. 21.
[36] M.A. Belarra, M. Resano, J.R. Castillo, J. Anal. At. Spectrom. 13 (1998) 489.

Talanta 80 (2009) 853–857

Contents lists available at ScienceDirect

Talanta

journal homepage: www.elsevier.com/locate/talanta

Optical fiber biosensor coupled to chromatographic separation for screening of dopamine, norepinephrine and epinephrine in human urine and plasma

Lurdes I.B. Silva[a,*], Filipe D.P. Ferreira[a,b], Ana C. Freitas[a], Teresa A.P. Rocha-Santos[a], A.C. Duarte[b]

[a] ISEIT/Viseu - Instituto Piaget, Estrada do Alto do Gaio, Galifonge, 3515-776 Lordosa, Viseu, Portugal
[b] CESAM & Department of Chemistry, University of Aveiro, 3810-193 Aveiro, Portugal

ARTICLE INFO

Article history:
Received 17 June 2009
Received in revised form 31 July 2009
Accepted 5 August 2009
Available online 13 August 2009

Keywords:
Biosensor
Optical fiber
Laccase
Catecholamines
Urine
Plasma

ABSTRACT

An optical fiber biosensor has been developed for the determination of catecholamines (dopamine, norepinephrine and epinephrine) based on the recognition capacity of the enzyme laccase. In this study, a glass tube constituted by a fused silica fiber coated with a film of polystyrene/divinylbenzene resin (PS/DVB) was used for catecholamines separation. Firstly, the analyzer was tested for calibration and its analytical performance for catecholamines detection was compared with a classical analytical method, namely high performance liquid chromatography-electrochemical detector (HPLC-ED). The developed analytical device shows a high potential for catecholamines quantification with a detection limit of 2.1, 2.6 and 3.4 pg mL^{-1} for dopamine, norepinephrine and epinephrine, respectively. The analytical sensitivity, inferred from the slope of the calibration curves established for a range of concentrations between 5 and 125 pg mL^{-1}, was found to be 0.344, 0.252 and 0.140 dB/pg mL^{-1} for dopamine, norepinephrine and epinephrine, respectively. Furthermore, catecholamines speciation with the PS/DVB fiber was completely achieved in 3 min. The analytical performance of the reported sensor was also evaluated and found adequate for catecholamines determination in human urine and plasma samples.

© 2009 Elsevier B.V. All rights reserved.

1. Introduction

Biosensors constitute an expanding field of analytical devices for the detection of analytes and other parameters of biological interest, which usually combines a biological component with a physic-chemical transducer.

Optical fiber (OF) biosensors are analytical devices in which the OF serves as a transduction element, showing several analytical advantages due to their high analytical sensitivity, fast response, large geometrical versatility, possibility of continuous monitoring of many chemical parameters, low cost, lightweight associated to small size, and high degree of miniaturization. These advantages make them an excellent alternative to laboratory-scale analytical methods and highly competitive in non-invasive clinical applications.

The use of the enzyme laccase as recognition element towards the development of biosensors for catecholamines determination has received a great deal of attention from several research groups [1–7]. Although some analytical devices have been reported for catecholamines determination which combines the enzymatic recognition with the OF technology, such as for example, an OF biosensor for epinephrine determination based on immobilized laccase catalysis and fluorescence quenching [7], they have not shown yet an adequate analytical selectivity and sensitivity.

Catecholamines, namely dopamine, norepinephrine and epinephrine, play an important role in the central nervous system as neurotransmitters or hormones, and they also affect the regulation of blood pressure, heart rate and lipolysis [4,8]. The determination of catecholamines in different human fluids, such as plasma and urine, is of great interest in medical diagnostics, especially for patients suffering from Parkinson's disease or Phaeochromocytoma and stress. An early and accurate determination of the catecholamines concentration in urine and plasma could prevent unnecessary drug treatment.

This work aimed at the development of an optical fiber biosensor for screening of catecholamines (dopamine, norepinephrine and epinephrine) based on a sensitive cladding of laccase. The OF biosensor, named LacOF biosensor, is composed of a miniaturized column for catecholamines separation, a biocomponent enzymatic cladding of laccase, and an OF component with associated electronics. The results obtained by applying the LacOF biosensor to the analysis of human urine and plasma were compared to those

* Corresponding author. Tel.: +351 232 910 100; fax: +351 232 910 183.
E-mail address: lsilva@viseu.ipiaget.org (L.I.B. Silva).

0039-9140/$ – see front matter © 2009 Elsevier B.V. All rights reserved.
doi:10.1016/j.talanta.2009.08.003

obtained by a methodology based on high performance liquid chromatography coupled to an electrochemical detector (HPLC-ED).

2. Experimental

2.1. Development of the LacOF biosensor

2.1.1. Preparation of the optical fiber (OF) and deposition of the enzymatic cladding

A directional 50:50 Y optical coupler was prepared from a single-mode optical fiber (OF) with core and cladding diameters of 9 and 125 μm, respectively. The OF was mechanically uncladded, immersed in dichloromethane in order to remove the protective cladding, and cleaved in a length of 15 mm with a Cleaver V6 (Future Instrument, Spain) precision fiber cleaver. The sensitive coating (enzymatic cladding) was deposited onto the cleaved ended surface of the fiber following the dip-coating technique. The uncladded OF section was dipped into an alginate/enzyme suspension, followed by the immersion into a 0.2 M calcium chloride ($CaCl_2$) solution. The suspension of alginate and laccase of *Trametes versicolor* a white-rot fungus (E.C.1.10.3.2) (22.4 U mg^{-1}), was prepared mixing 400 U mL^{-1} of laccase, with a 3% (w/v) alginic acid solution salt from brown algae and kept stored at 4 °C.

2.1.2. Assemblage of the optical fiber biosensor and the underlying analytical principles

Fig. 1 shows the schematics of the whole LacOF biosensor detection system, including enzymatic cladding at the OF surface which provides the analytical principle underlying this biosensor.

The developed biosensor is constituted by two main components. The first analytical component aiming at the separation of the three catecholamines, includes a pump, a mobile phase, an injection cell (IC), and a glass tube (GT) which contains a fused silica fiber coated with a polystyrene/divinylbenzene resin (50–100 mesh particles size). The second component aiming at the detection of the catecholamines is constituted by an analytical tube (AT) containing the sensitized OF section, an optical coupler (OC), a photodetector (OZ Optics, Spain) and a laser diode (OZ Optics, working in the infrared region (λ = 1550 nm)). The connections between the following system elements: IC-GT; GT-AT and AT-OF, were made of Teflon. The various components of the sensor, excluding the mobile phase, the pump and the laptop were appropriately located inside a home-made aluminum box (height: 14.0 cm, width: 17.7 cm and length: 25.1 cm), providing the analytical system with a very compact design.

The catecholamines standards and samples are injected with a micro-syringe (Hamilton) at the top of a glass cell (injection cell) which are then carried by a constant flow (0.75 mL min^{-1}) of mobile phase to the glass tube and finally reach the analytical tube. The mobile phase consisted of 5% acetronitrile, 0.025 M sodium phosphate, 0.025 M citric acid, 0.001 M heptane and sulphonic acid pH 2.85, being its flow rate controlled by a mass flowmeter (Supelco, Spain).

Fig. 1b shows a schematic design of the OF surface coated with an enzymatic cladding and the oxidation of the catecholamine (epinephrine) by the enzyme (laccase) to the respective aminoquinone (adrenoquinone). The linkage of catecholamines to the enzyme changes the refractive index of the sensitive cladding (laccase incorporated in an alginate matrix) causing changes of the reflected optical power, which are independent of the produced quinone. The optical power changes are measured as the analytical signal by the photodetector and data acquisition and processing performed by a computer (PC) with home-made software.

2.2. Application of a HPLC-ED methodology

The HPLC-ED methodology was carried out in an Aliance 2695 HPLC system (Waters, USA) with a PLRP-S 100 Å 5 μm, 150 mm × 4.6 mm I.D. reversed-phase analytical column (from Polymer Laboratories Inc., USA). The detection of catecholamines was attained by a Waters 2465 electrochemical detector with a glassy working electrode set at 750 mV to a salt-bridge Ag/AgCl reference electrode. The mobile phase at a constant flow rate of 0.75 mL min^{-1} consisted of 5% acetonitrile, 0.025 M sodium phosphate, 0.025 M citric acid, 0.001 M heptane and sulphonic acid pH 2.85, as in the case of the OF system.

2.3. Preparation of standards mixtures of catecholamines

The standard solutions of mixtures of the three catecholamines were prepared in phosphate-citrate buffer pH 5.5 and used for calibration studies, performing five replicates of the various standard concentrations (5, 35, 65, 95 and 125 pg mL^{-1}) of each catecholamine. All reagents used were analytical grade from Sigma–Aldrich and used without further purification.

2.4. Preparation and analysis of human urine and plasma samples

Urine and blood samples were obtained from healthy volunteers in a certificated laboratory of clinical analysis. Blood samples were stored in glass tubes containing EDTA as the anticoagulant, and then

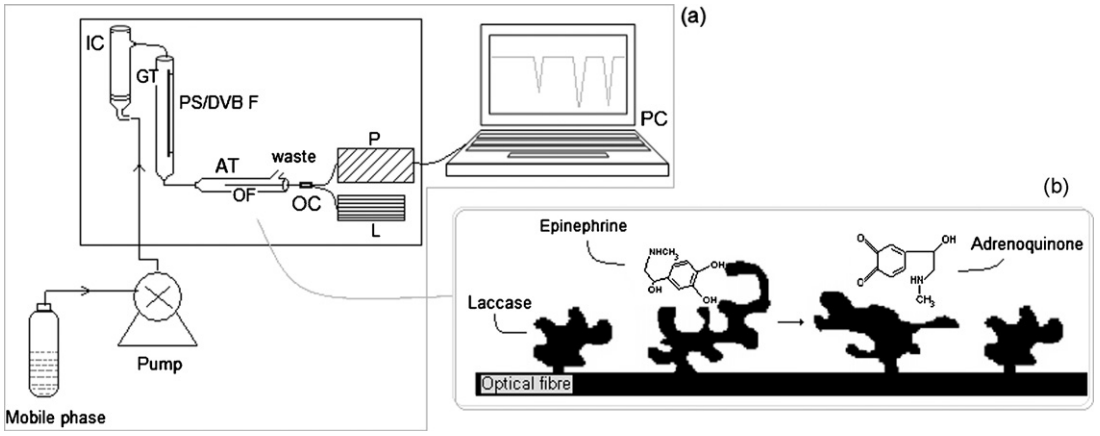


Fig. 1. (a) Schematic configuration of the experimental layout (AT – analytical tube; GT – glass tube; IC – injection cell; L – laser; OC – optical coupler; OF – optical fiber; P – photodetector; PC – laptop for data acquisition and processing; PS/DVB F – styrene/divinylbenzene fiber) and (b) schematics of the enzymatic reaction occurring at the OF surface coated with laccase.

centrifuged at 1400 × *g* for 15 min; the supernatant, i.e. plasma, was then transferred to polypropylene test tubes. Urine and plasma samples were stored at −18 °C until further processing for each of the analytical methodologies implemented in this work (LacOF biosensor and HPLC-ED). The preparation of the samples of urine (2.4.1) and plasma (2.4.2) was carried out by solid phase extraction (SPE) and performed according to Janichy-Deverts et al. [9] and Mercolini et al. [10] procedures, respectively. After the extraction procedure, the obtained solutions were analyzed by LacOF biosensor and HPLC-ED; quantification of the catecholamines in urine and plasma samples was attained by linear regression of the calibration data, performing five repeated measurements for each sample analyzed, exactly in the same way as in the calibration studies. The samples were numbered from 1 to 5 and the same number in urine and plasma analysis means that the sample has the same subject as source.

2.4.1. *Preparation of urine samples*

Prior to extraction by SPE the thawed samples were centrifuged at 10,000 × *g* for 3 min and diluted with ultra-pure water (SG Water, Germany). Aliquots of 3 mL of the diluted sample were mixed with 5 mL of dilution reagent (30 mM ammonium acetate, 2.7 mM EDTA; pH 7.5) and 100 μL of 0.5 M NaOH. Each prepared sample was adjusted to a pH value of approximately 6.5 with 0.5 M of NaOH. The extraction of catecholamines of urine samples was performed by SPE column filled with Bio-Rex 70 cation exchange resin (50–100 mesh) previously washed with dilution reagent and ultra-pure water. Elution of the analytes was achieved by 6 mL of 3.6 mM ammonium pentaborate following a procedure developed by Janichy-Deverts et al. [9].

2.4.2. *Preparation of plasma samples*

The plasma samples were extracted by SPE on Waters (Milford, Mass., USA) Oasis MAX cartridges (30 mg, 1 mL). The SPE cartridges were preconditioned and activated with 2× 1 mL of carbonate buffer (200 mM Na_2CO_3, pH 9.0) and 2× 1 mL of methanol prior to loading with plasma sample. After that, the cartridges were then washed with 2× 1 mL of carbonate buffer and vacuum dried. Elution of the analytes was achieved with 1 mL of 5% acetic acid in methanol. The eluate was dried using a rotary evaporator and the residue was re-dissolved in 150 μL of mobile phase for analysis.

3. Results and discussion

Fig. 2 shows the optical power changes obtained during the process of preparation of the LacOF biosensor for determination of different amounts of catecholamines. Fig. 2a shows the sensor response for 35 and 95 pg mL^{-1} of dopamine, norepinephrine and epinephrine and Fig. 2b reports the calibration curves obtained for the three catecholamines tested, with estimates of slope and intercept with their respective standard deviation.

The maximum amplitude of the optical power variation recorded before the injection of dopamine, norepinephrine and epinephrine (baseline) was approximately 0.01 dB, which was about 1% of the minimum analytical signal obtained during the lower concentration of catecholamines tested (0.9 dB for 5 pg mL^{-1} of epinephrine).

The total analytical time was found to be around 3 min for the three completely separated catecholamines detected as shown in Fig. 3a.

This analytical system shows a high statistical degree of linearity for the calibration model used, as it can be inferred from the r^2 and respective *p* values also shown in Fig. 2b. The intensity and therefore the sensitivity (measured as the slope of the calibration curve) of the analytical signal obtained for dopamine was higher than the ones obtained for norepinephrine and even for epinephrine.

The results obtained during the calibration process also revealed that the detection capacity of the developed sensor system reaches

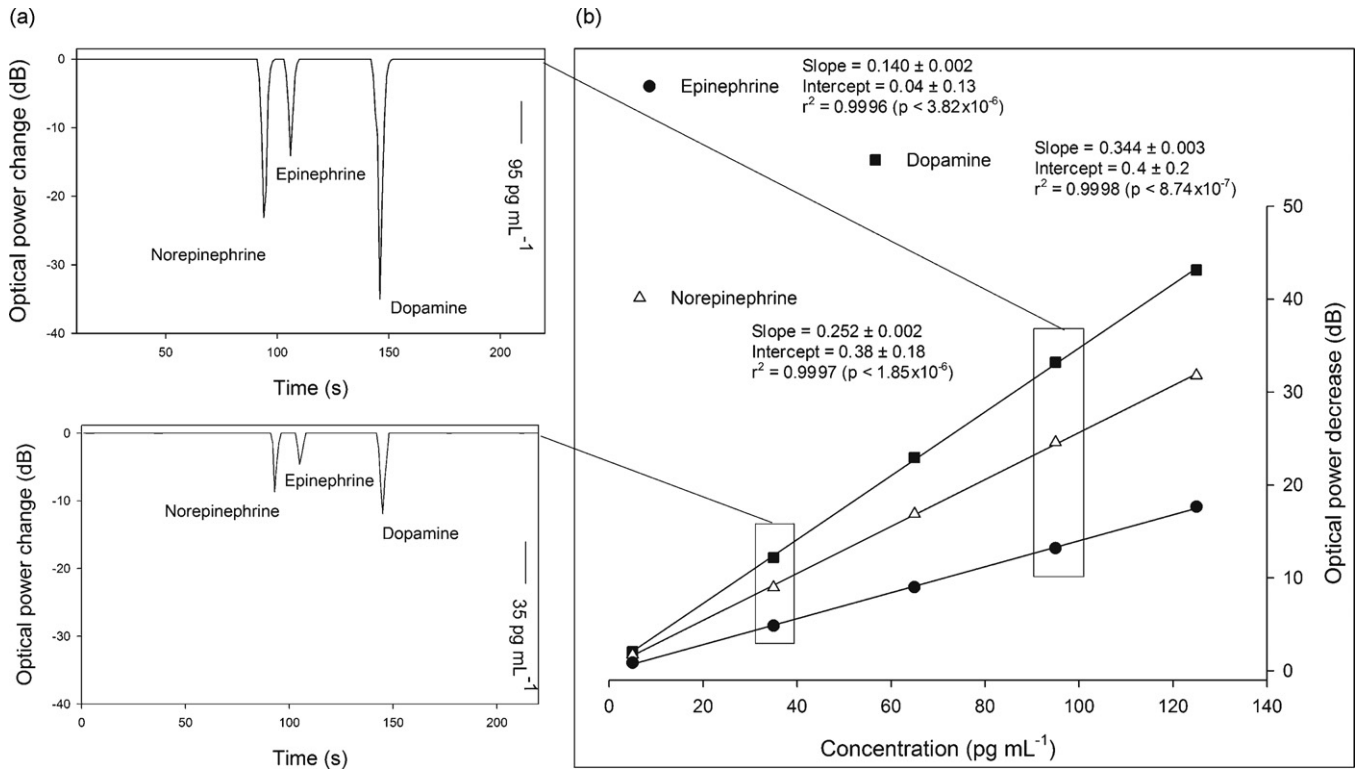


Fig. 2. LacOF biosensor response for different amounts of catecholamines, namely, dopamine, norepinephrine, and epinephrine: (a) example of the biosensor profile obtained for 35 and 95 pg mL^{-1} of catecholamines; (b) calibration of the LacOF biosensor with amounts of catecholamine in a range between 5 and 125 pg mL^{-1}.

Table 1
Results obtained for catecholamines analysis by the LacOF biosensor and the HPLC-ED method.

Standards ($pg\,mL^{-1}$)	Dopamine		Norepinephrine		Epinephrine	
	LacOF biosensor ($pg\,mL^{-1}$)	HPLC-ED ($pg\,mL^{-1}$)	LacOF biosensor ($pg\,mL^{-1}$)	HPLC-ED ($pg\,mL^{-1}$)	LacOF biosensor ($pg\,mL^{-1}$)	HPLC-ED ($pg\,mL^{-1}$)
10	10.1 ± 0.4	10.4 ± 0.6	10.2 ± 0.3	10.6 ± 0.7	10.4 ± 0.2	10.4 ± 0.8
20	20.3 ± 0.3	20.2 ± 1.2	20.1 ± 0.4	20.1 ± 0.5	20.2 ± 0.6	20.2 ± 0.8
30	30.1 ± 0.3	30.0 ± 1.0	30.0 ± 0.3	30.1 ± 0.7	30.1 ± 0.6	30.1 ± 1.8
40	40.1 ± 0.4	39.9 ± 2.4	40.0 ± 0.3	40.0 ± 1.8	40.0 ± 0.5	39.6 ± 3.1
50	50.0 ± 0.6	49.8 ± 3.0	50.1 ± 0.2	50.1 ± 1.8	50.2 ± 0.4	50.1 ± 3.7
60	59.8 ± 0.5	59.3 ± 2.8	60.0 ± 0.3	60.0 ± 1.8	60.2 ± 0.5	60.1 ± 3.1
70	70.1 ± 0.7	69.6 ± 3.3	69.8 ± 0.3	69.7 ± 2.5	69.6 ± 0.6	69.4 ± 3.1
80	79.9 ± 0.2	79.6 ± 4.1	79.9 ± 0.3	79.9 ± 2.5	79.8 ± 0.7	79.7 ± 3.7
90	90.1 ± 0.2	89.4 ± 5.8	90.1 ± 0.3	90.1 ± 2.8	90.2 ± 0.5	90.1 ± 3.5
100	99.9 ± 0.4	99.5 ± 5.8	100 ± 0.6	100.3 ± 6.9	99.9 ± 1.1	99.7 ± 7.5

a plateau in terms of maximum capacity of detection for concentrations of catecholamines higher than about 130 $pg\,mL^{-1}$, with a decrease of the analytical performance of the LacOF biosensor for concentrations above that value.

Since the linkage of the catecholamine to the enzyme is the most relevant factor for the analytical signal generation, the differences in the analytical sensitivities obtained with the developed LacOF sensor are mainly due to the differences in the affinity of laccase to each of the catecholamines under study. Therefore, the highest analytical sensitivity obtained for dopamine could be attributed to the high affinity of the enzyme to this catecholamine, with consequent increase of the optical power change amplitude.

The detection limits obtained for the three catecholamines analyzed, based on three times the residual standard deviation [11] for both LacOF biosensor and HPLC-ED method were, respectively, 2.1 and 5.1 $pg\,mL^{-1}$ for dopamine, 2.6 and 4.5 $pg\,mL^{-1}$ for norepinephrine and 3.4 and 4.5 $pg\,mL^{-1}$ for epinephrine. These values show that the detection limits for both analytical methodologies have the same order of magnitude.

A set of experiments has been carried out for the assessment of the sensor system stability; thus five repeated measurements of catecholamines (35 $pg\,mL^{-1}$) have been performed during different weeks of 2 months of operation with the same system. The developed biosensor showed a relative standard deviation of the performed measurements of less than 5%, suggesting an adequate degree of stability of the analytical system. However, additional studies regarding the monitoring of the LacOF device behavior for periods of operation longer than 2 months showed a slightly analytical signal degradation after the 13th week of the device operation. This observation was not find to be of special concern, since the sensors head (OF section coated with the enzymatic matrix) can be easily replaced, after 12 weeks, avoiding any losses of the analytical signal or decrease of performance caused by extensive utilization for longer periods of the developed LacOF based biosensor.

The analytical performance of the LacOF biosensor was also compared with HPLC-ED method: 10 different concentrations (10, 20, 30, 40, 50, 60, 70, 80, 90 and 100 $pg\,mL^{-1}$) of a standard mixture of catecholamines were injected, five times each, using both methods in order to test the performance of the developed sensor against the HPLC-ED method. The obtained results are displayed in Table 1.

The ANOVA of the results shows that there is no statistically significant difference ($p = 0.431$, 0.832 and 0.704, for dopamine, norepinephrine and epinephrine, respectively) for the effects of differences in the two methods. However, and as expected, there is a significant statistic difference ($p < 0.001$) between the different levels of the concentrations.

The analytical error, measured as the residual standard deviation of both LacOF biosensor and HPLC-ED, varied between 1.9 and 2.5 $pg\,mL^{-1}$.

The ANOVA can also be confirmed with a regression analysis of the results obtained with the two analytical systems during the determination of different amounts of catecholamines ranging from 10 to 100 $pg\,mL^{-1}$. Assuming the null hypothesis (same sensitivity, i.e. slope equals 1 and no systematic errors, i.e. intercept equals to 0) for the results obtained with both methods the slope, the intercept, r^2 and p of the regression line, of each of the data sets were calculated and included in Table 2.

For all the three catecholamines analyzed the regression line has an intercept not significantly different of zero and a slope not significantly different of 1. The values above mentioned and a correlation coefficient of approximately 1, allows concluding that the results obtained with the two analytical systems cannot be statistically differentiated, as already inferred from the ANOVA.

Both analytical methodologies were also applied to samples of human urine and plasma, for assessing comparatively the concentrations of catecholamines. Figs. 3 and 4 depict the results obtained in the analysis of five samples of human urine and plasma, respec-

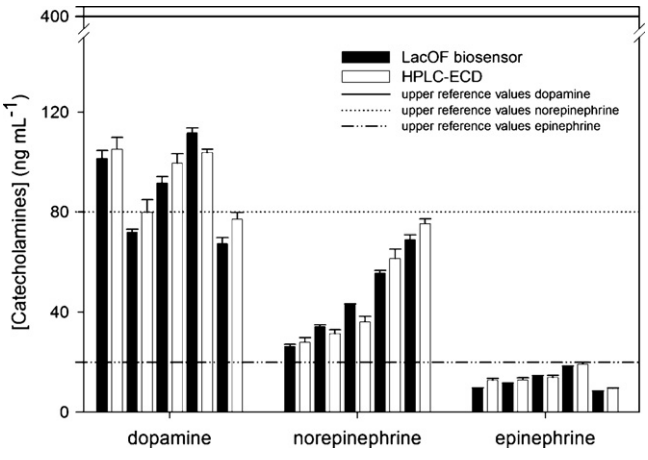


Fig. 3. Results obtained for catecholamines determination of five actual samples of human urine by LacOF biosensor and HPLC-ED methods.

Table 2
Analytical parameters obtained for the comparison of the results obtained with the LacOF biosensor and HPLC-ED method for determination of catecholamines.

	Intercept	Slope	Coefficient of determination (r^2)
Dopamine	0.0 ± 0.1	1.0 ± 0.1	0.99997 ($p < 3.48 \times 10^{-17}$)
Norepinephrine	0.1 ± 0.1	0.998 ± 0.002	0.99998 ($p < 1.15 \times 10^{-17}$)
Epinephrine	0.1 ± 0.1	1.001 ± 0.002	0.99997 ($p < 2.88 \times 10^{-17}$)

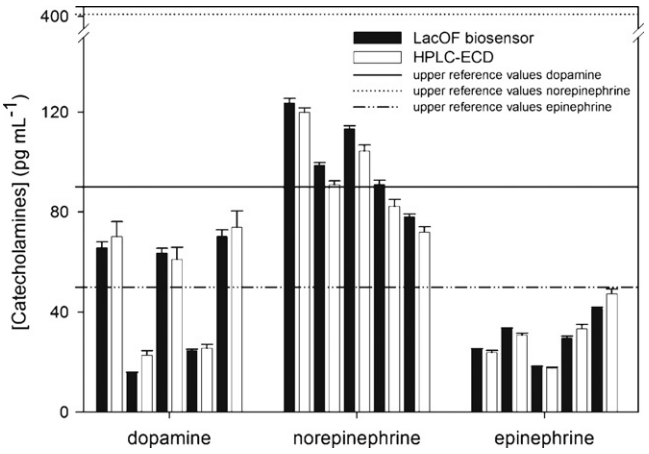


Fig. 4. Results obtained of catecholamines determination for five actual samples of human plasma with five replicates by LacOF biosensor and HPLC-ED methods.

tively by both the LacOF biosensor and the HPLC-ED method for dopamine, norepinephrine and epinephrine.

The levels of catecholamines found in the urine samples analyzed do not exceed the values accepted as normal for these compounds, according to Moyer et al. [12] studies: <400 μg 24 h^{-1} for dopamine; <80 μg 24 h^{-1} for norepinephrine; and <20 μg 24 h^{-1} for epinephrine.

The concentration obtained for dopamine, norepinephrine and epinephrine in plasma are also below the normal values, according to Peaston and Weinkove [13] studies: 0.01–0.475 nmol L^{-1} for dopamine; 0.71–4.02 nmol L^{-1} for norepinephrine; and 0.01–0.328 nmol L^{-1} for epinephrine.

The comparison of the means of the five samples analyzed by the biosensor and the HPLC-ED method, showed that there is no statistically significant difference between the results obtained by the two analytical systems in both urine ($p = 0.460$, 0.868 and 0.848 for dopamine, norepinephrine and epinephrine, respectively) and plasma ($p = 0.970$, 0.995 and 0.889 for dopamine, norepinephrine and epinephrine, respectively).

In order to test the developed biosensor for interferences that could be present in the biological matrices (urine and plasma), the effects of normetanephrine and metanephrine used as example of interferences compounds, on the analytical signal were also evaluated. Each compound tested produces a peak, but in a different analytical time window of the compounds of interest, therefore none of the above mentioned compounds exhibit any interference in the analytical signal. The obtained results allow concluding that the adjustment of the time window could be used for avoiding other potential interferences, as a consequence it is also possible to infer that the developed biosensor could be also applied to determine of a large variety of analytes.

4. Conclusions

An optical fiber biosensor has been successfully developed for determining the concentration of dopamine, norepinephrine and epinephrine. The reported analytical system showed a high analytical signal and a linear response between 5 and 125 pg mL^{-1}, allowing the determination of catecholamines with detection limit less than 3.4 pg mL^{-1}. In addition, the new and compact design of the developed LacOF analytical system has obvious analytical advantages, constituting an excellent alternative to the more classical methods for catecholamines detection.

Acknowledgments

This work has been developed under the scope of the FCT (Portugal) funded research project PTDC/QUI/70970/2006: "Development of a new Optical Fiber Biosensor for Determination of Catecholamines (CATSENSOR)". A Ph.D. grant (SFRH/BD/44175/2008) awarded to Filipe D.P. Ferreira is also gratefully acknowledged.

References

[1] F.F. Bier, E. Ehrentreich-Forster, F.W. Scheller, A. Makower, A. Eremenko, U. Wollenberger, C.G. Bauer, D. Pfeiffer, N. Michael, Sens. Actuators B 33 (1996) 5–12.
[2] Y. Ferry, D. Leech, Electroanalysis 17 (2005) 113–119.
[3] A.L. Ghindilis, A. Makower, C.G. Bauer, F.F. Bier, F.W. Scheller, Anal. Chim. Acta 304 (1995) 25–31.
[4] O.D. Leite, K.O. Lupetti, O. Fatibello-Filho, I.C. Vieira, A.M. Barbosa, Talanta 59 (2003) 889–896.
[5] F. Lisdat, U. Wollenberger, A. Makower, H. Hörtnagl, D. Pfeiffer, F.W. Scheller, Biosens. Bioelectron. 12 (1997) 1199–1211.
[6] J. Szeponik, B. Möller, D. Pfeiffer, F. Lisdat, U. Wollenberger, A. Makower, F.W. Scheller, Biosens. Bioelectron. 12 (1997) 947–952.
[7] J. Huang, H. Fan, H. Liu, E. Gu, D. Jiang, Anal. Lett. 41 (2008) 1430–1442.
[8] M. Tsunoda, Anal. Bioanal. Chem. 386 (2006) 506–514.
[9] D. Janichy-Deverts, K. Zilles, S. Cohen, A. Baum, J. Appl. Biobehav. Res. 11 (2006) 69–78.
[10] L. Mercolini, G. Gerra, M. Consorti, L. Somaini, M.A. Raggi, Talanta 78 (2009) 150–155.
[11] J.N. Miller, J.C. Miller, Statistic and Chemometrics for Analytical Chemistry, 5th ed., Pearson Prentice Hall, New York, 2005.
[12] T.P. Moyer, N. Jiang, G.M. Tyce, S.G. Sheps, Clin. Chem. 25/2 (1979) 256–263.
[13] R.T. Peaston, C. Weinkove, Ann. Clin. Biochem. 41 (2004) 17–38.

Talanta 80 (2009) 858–863

Contents lists available at ScienceDirect

Talanta

journal homepage: www.elsevier.com/locate/talanta

The petentiometric determination of peroxide hydrogen and glucose on the glassy electrode modified by the calix[4]arene

Gendi Jin, Shi Du, Xiaoya Hu*

College of Chemistry and Engineering, Yangzhou University, 88 South University Avenue, Yangzhou 225002, China

ARTICLE INFO

Article history:
Received 16 April 2009
Received in revised form 3 August 2009
Accepted 5 August 2009
Available online 13 August 2009

Keywords:
Calix[4]arene
Glassy carbon electrode
Peroxide hydrogen
Glucose
Petentiometric determination

ABSTRACT

A new petentiometric method to determine peroxide hydrogen and glucose had been studied. This method had been applied on the petentiometric determination of peroxide hydrogen and glucose in the total ionic strength adjustment buffer (TISAB) (pH 7.5) solution with the glassy electrode modified by the calix[4]arene. The glassy carbon electrode covered with the calix[4]arene depended on the H_2O_2 concentration in the range of log[H_2O_2] from −3.3 to −1.2 in the solution of TISAB (pH 7.5) with nearly Nernstian slope of about 65.6 ± 3 mV and the detection limit of peroxide hydrogen was 4.0×10^{-5} mol L^{-1}. The glassy carbon electrode covered with the calix[4]arene depended on the glucose concentration in the range of log[glucose] from −3.6 to −2.8 in the solution of TISAB (pH 7.5) with nearly Nernstian slope of about 50.2 ± 2 mV and the detection limit of glucose was 2.0×10^{-5} mol L^{-1}. The electrode had the good selectivity, sensitivity, stability and repeatability.

© 2009 Elsevier B.V. All rights reserved.

1. Introduction

Chemically modified electrodes [1,2] as useful analytical tools have been widely used in different research fields since more analytical possibilities [3–5] have been offered by electrode manufacture. However, only a few analytical applications have employed chemically modified electrodes as potentiometric sensors [6–8], and the preparation of these potentiometric sensors often suffer from the complicated preparation process of the based electrodes and are time-consuming.

Recent years have witnessed a wide application of electroconducting polymers in the solid state ion-selective electrodes [9,10]. The incorporation of conducting polymer into the surface coating of the ion-selective sensor simplifies its manufacture. The thickness, conductivity and charge of the surface layer obtained in electropolymerization are easily controlled by the electrolysis parameters and reaction media content. This makes it possible to change the operational characteristics and analytical performance of the sensors in accordance with the particular tasks of their application. Due to these advantages, the application of electroconductive polymers offers broad opportunities for developing ion-selective electrodes, which is of great importance in chemical, environmental and clinical analysis.

Generally, the electropolymerized polymer is used either as a solid redox mediator between the transducer and ion-exchangeable component or as an immobilization matrix entrapping the components with intrinsic ionic/electron conductivity. In accordance with this, the sensor potential changes either with the redox potential of the electroconductive polymer or with the number of charged complexes formed by a neutral carrier and guest species on the surface.

Neutral carriers on the calix[4]arene platform are intensively investigated to obtain selective and sensitive recognition response toward various analytes. Simple and cost-effective synthesis, variety of substitutes introduced into the lower and upper rims as well as complication abilities toward inorganic [11–13] and organic [14,15] ions have made calix[4]arenes promising components of ion-selective membranes and solid-contact sensors. Most calix[4]arene-based sensors have been developed for selective detection of alkali and alkali-earth metals.

Hydrogen peroxide (H_2O_2) is a very important intermediate in environmental and biological reactions. The monitoring of H_2O_2 with a reliable, rapid and economical method is of great significance for numerous processes. Several analytical techniques have been employed for its determination [16,17], including the manganese dioxide-modified CPE amperometric sensor [18], but most suffer from interference, complex instrumentation and expensive reagents [19–21]. The potentiometric analytical method has turned out to be more suitable for the determination of many analytes since it possesses advantages such as rapid, simple instrumentation and a widely linear range. But until now, to the best of our knowledge, a potentiometric method for the determination of H_2O_2 has been not reported except Xingwang Zheng and Zhihui Guo had detected H_2O_2 with

* Corresponding author. Tel.: +86 514 87971818; fax: +86 514 87311374.
E-mail address: xyhu@yzu.edu.cn (X.-Y. Hu).

0039-9140/$ – see front matter © 2009 Elsevier B.V. All rights reserved.
doi:10.1016/j.talanta.2009.08.005

the potentiometric method by MnO_2-doped carbon paste electrode [22].

In this paper, a new GCE-based electrode was prepared by electrodepositing the calix[4]arene on the glassy carbon electrode and it was found that this GCE-based electrode presented the Nernstian response for H_2O_2. Based on this observation, a new potentiometric sensor for the determination of H_2O_2 was proposed and the pH of the support solution together with some factors which affected the analytical performance of this sensor such as the thickness of the film was studied. At the same time, the possible response mechanism of the sensor was discussed. This sensor had been used to detect H_2O_2 in antisepsis water samples and it had manifested some advantages such as simple instrumentation, simple preparation procedures, good stability and reproducibility.

2. Experimental

2.1. Apparatus

The potentials were measured with a PXD-2 ION-meter (JiangShu Jiangfen Electroanalytical Instrument Ltd., China). The reference electrode was a saturated calomel electrode (SCE) and the total ionic strength adjustment buffer (TISAB) solution was stirred with a Teflon-coated magnetic bar during measurement on the JB-1 magnetic force stirrer (Shanghai Leici Instrument Plant, China). The electrochemical cell used can be represented by the calix[4]arene film-modified glassy carbon electrode/sample solution (pH 7.5, TISAB solution)/SCE.

Electrochemical measurements were performed on a CHI 660A Electrochemical Workstation (CH Instruments, USA). A conventional three-electrode system was used throughout the experiments. The working electrode was a GCE (3.0 mm in diameter); the auxiliary electrode was a platinum wire and a saturated calomel electrode was used as the reference. All potentials in this paper refer to this reference electrode. Cyclic voltammetric experiments were carried out with a scan rate of 100 mV s^{-1}, unless otherwise stated.

Atomic force microscopy (AFM) images of the films were collected on a multimode Nanoscope III scanning probe microscopy (Veeco Company, USA) in the tapping mode. A microfabricated silicon cantilever with a bending spring constant of 20–80 N m^{-1} and a resonance frequency of 229–287 kHz was used to collect the images at a scan rate of 1.0 Hz in air.

Electrochemical impedance spectroscopy (EIS) was performed in 1.0×10^{-3} mol L^{-1} $K_3Fe(CN)_6/K_4Fe(CN)_6$ (1/1) mixture with 0.10 mol L^{-1} KCl as supporting electrolyte, using an alternating current voltage of 5 mV within the frequency range of 0.1–1E6(1,000,000) Hz by Autolab Electrochemistry Instruments (Autolab, Eco Chemie, The Netherlands). Prior to modification of the calix[4]arene, a bare GCE was polished successively with 0.3 μm and 0.05 μm Al_2O_3 slurry on silk. Then, it was rinsed with double-distilled water and sonicated subsequently in a 1:1 aqueous HNO_3 solution (volume ratio of water to HNO_3 = 1:1), acetone, and doubly distilled water. After being cleaned, the electrode was immersed in 0.5 mol L^{-1} H_2SO_4 and was activated by cyclic potential scanning from 0.5 V to 1.6 V at 100 mV s^{-1} until the stable cyclic voltammograms were obtained in order to increase the concentration of the electroactive points. Electrochemical modification of the activated GCE was performed by cyclic voltammetry in 0.1 mol L^{-1} tetrabutylammonium perchlorate containing 7.0×10^{-4} mol L^{-1} calix[4]arenein with a potential range of −0.2 V to +0.8 V at a scan rate of 100 mV s^{-1} for 20 cyclic times. After the electropolymerization, the modified electrode was rinsed thoroughly with distilled water for further application.

2.2. Reagents

All reagents (such as $K_3Fe(CN)_6$, $K_4Fe(CN)_6$, KCl, acetone, citrate sodium, NaH_2PO_4, Na_2HPO_4, H_3PO_4, $NaNO_3$, and NaOH) were of analytical-reagent grade or better and water doubly distilled in a fused-silica apparatus was used throughout the experiment. A stock solution of H_2O_2 (0.100 mol L^{-1}) was prepared by diluting 5.5 mL of 30% (v/v) H_2O_2 (Shanghai Chemical Reagents Plant) to 500 mL with water. The solution was standardized by titration with potassium permanganate. Test standard solutions were prepared daily by appropriate dilution of the stock solution. A TISAB solution ($I \approx 1.23$) was prepared by dissolving 58.3 g of citrate sodium and 85 g $NaNO_3$ in 1 L water.

Tetrabutylammonium perchlorate (TBAP) was purchased from BeiJing Ouhe Technology Co. Ltd. And the stock solution of 0.1 mol L^{-1} tetrabutylammonium perchlorate was prepared by directly dissolving it in double-distilled water and then stored in a refrigerator at 4 °C. The calix[4]arene was synthesized by literature [23] (methyl resorcin calix[4]arene azobenzol sulfonate sodium) and the structure of it was shown in Fig. 1 and the stock solution of 0.01 mol L^{-1} calix[4]arene was prepared by directly solving it in doubly distilled water and then stored in a refrigerator at 4 °C.

Glucose oxidase (from Aspergillus niger, EC 1.1.3.4, 210 U/mg) and b-D-(II)-glucose were obtained from Sigma.

2.3. Construction of the sensor

Voltammograms of 7.0×10^{-4} mol L^{-1} calix[4]arene in 0.1 mol L^{-1} TBAP on the GCE was shown in Fig. 2. With a continuous increase of the number of cycles, anodic peaks appeared at potentials about +0.3 V and trended to be stable after 20 cycles, reflecting the continuous growth of the polymer film and the saturation of polymerization. These facts implied that calix[4]arene membrane was deposited on the surface of GCE by electropolymerization. After electropolymerization, the modified electrode was carefully rinsed with doubly distilled water and then kept at room temperature. The GCE modified by calix[4]arene was immerged in the solution of 0.1% glutaraldehyde for 40 min and then dipped in 0.1 g L^{-1} of the glucose oxidase (GOD) for 2 h. Finally, the modified electrode was carefully rinsed with doubly distilled water and then stored in a refrigerator at 4 °C. Thus the electrode used to determine the glucose was prepared.

Before using the modified GCE for potentiometric measurements, the electrode was preconditioned in TISAB solution for 2 h until a steady potential response was obtained.

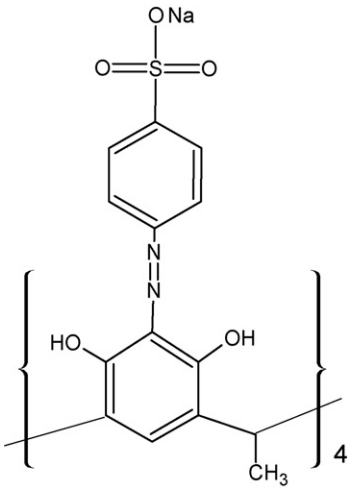


Fig. 1. The structure of the calix[4]arene.

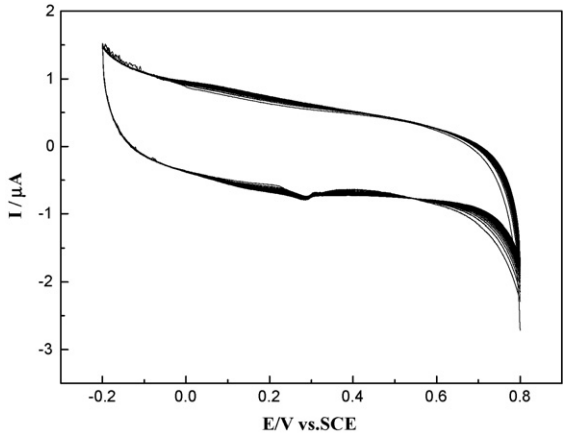


Fig. 2. Cyclic voltammograms of polymerization of calix[4]arene (7.0×10^{-4} mol L^{-1}) on a bare glassy carbon electrode in the potential range from −0.2 V to 0.8 V at a scan rate of 100 mV s^{-1}.

2.4. EMF measurement and selectivity

The electrode potential was measured in 10 mL TISAB solution by adding sample or standard hydrogen peroxide solutions continually with stirring at room temperature, and potentiometric measurement of the steady-state response was carried out in the usual manner. After each measurement, the H_2O_2 sensor was washed free of residual H_2O_2 and pH buffer solution with water until a stable blank potential was obtained. The glucose determination was carried through by the same method mentioned above. The selectivity coefficients of the electrode for H_2O_2 and the glucose with respect to other ions were quantified by the mixed solution method.

3. Results and discussion

3.1. Impedance characterization of the calix[4]arene film-modified GCE

The bare GCE and the calix[4]arene modified GCE was characterized by EIS (shown in Fig. 3). From Fig. 3a–e, we could see that the redox process of the $[Fe(CN)_6]^{3-}/[Fe(CN)_6]^{4-}$ ions showed a lower electron transfer resistance at a bare GCE(Fig. 3, curve a) than that at the calix[4]arene modified GCE. When a bare GCE was electropolymerized with calix[4]arene for different cyclic times, the

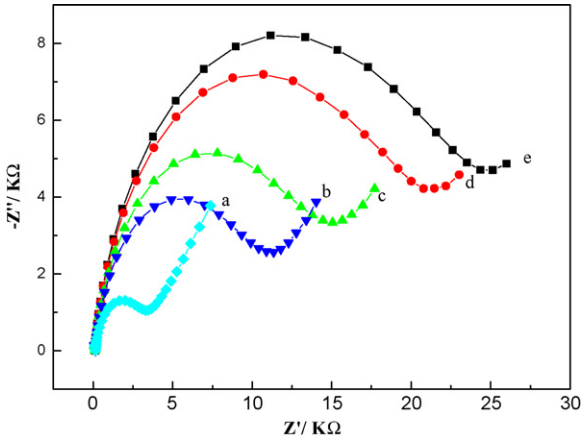


Fig. 3. Nyquist plots in impedance measurements of electrodes: (a) a bare GCE; (b–e) the calix[4]arene film-modified GCEs with different electropolymerization cyclic times. Cyclic times: (b) 10; (c) 20; (d) 30; (e) 40.

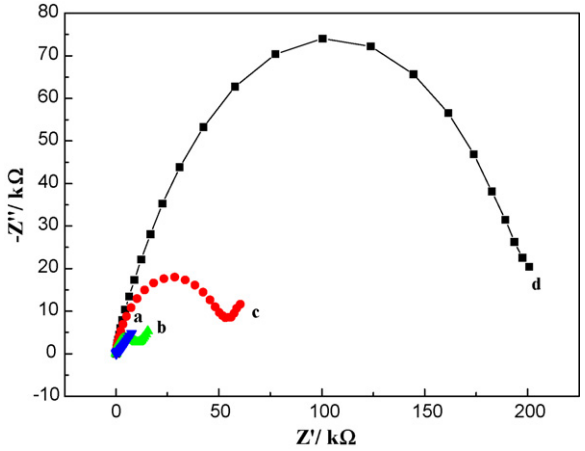


Fig. 4. Nyquist plots in impedance measurements of electrodes: (a) a bare GCE; (b) the calix[4]arene film-modified GCE; (c) the calix[4]arene film-modified GCE modified by glutaraldehyde again; (d) the calix[4]arene film-modified GCE modified by GOD again.

electron transfer resistance increased significantly along with the increasing scan cycles. Fig. 4 showed the impedance characterization of different conditions of the same GCE. Curves a–d respectively represented the impedance of the bare GCE, this GCE modified by calix[4]arene, this modified GCE after immersing in glutaraldehyde and this GCE then dipped in the glucose oxidase. It indicated that the glutaraldehyde and the glucose oxidase were modified on the GCE successfully.

3.2. The AFM characteristic of the modified GCE

The formation and morphology of the calix[4]arene modified GCE were characterized by AFM in air (shown in Fig. 5). The AFM images showed that the bare GCE surface was relatively smoother. After modification with the calix[4]arene, the surface morphology became very rough. This result demonstrated that the calix[4]arene film with mesoporous morphology was deposited on the GCE surface.

3.3. Effect of the thickness on the property of the modified GCE

The different thickness modified GCE were obtained by scanning different cycles and then the modified GCE was applied on the potentiometric detection of H_2O_2. The results (shown in Table 1) showed that the GCE modified 20 cycles enjoyed such superiorities as the wide range of potentiometric response, the good linear relation, the low detection limit and the response slope was 65.6 mV/log[H_2O_2], which was close to Nernstian response.

3.4. Effect of pH on the response

The potentiometric determination was performed in the TISAB of the different pH. The results showed that while the pH changed in the range of 3.0–11.0, the potential response slope descended, the response range increased and the detection limit increased with the rise of pH. These results might be related to the response of calix[4]arene modified GCE to the pH variation in this range and the results could be seen in Table 2. Simultaneity, the potentiometric response of H_2O_2 (10^{-2} mol L^{-1}) and the glucose (10^{-3} mol L^{-1}) were tested in buffer solution of different pH. The results were shown in Figs. 6 and 7. From Fig. 6 we could see that the potential response decreased with the increased of pH. Fig. 7 showed that the potential response of glucose was similar with the poten-

Table 1
Effect of the thickness on the property of the modified GCE.

Modified cycles	Linear range, mol L^{-1}	Response slope, mV/log[H_2O_2]	Correlation coefficient	Detection limit, mol L^{-1}	Stability, d	Response, time/s
10	5.5×10^{-4} to 1.2×10^{-2}	79.2	0.978	3.5×10^{-5}	7	180
20	5.5×10^{-4} to 6.3×10^{-2}	65.6	0.998	4.0×10^{-5}	60	240
30	5.5×10^{-4} to 3.7×10^{-2}	47.1	0.988	4.2×10^{-5}	30	420
40	1.8×10^{-3} to 2.5×10^{-2}	64.1	0.994	2.0×10^{-4}	30	600

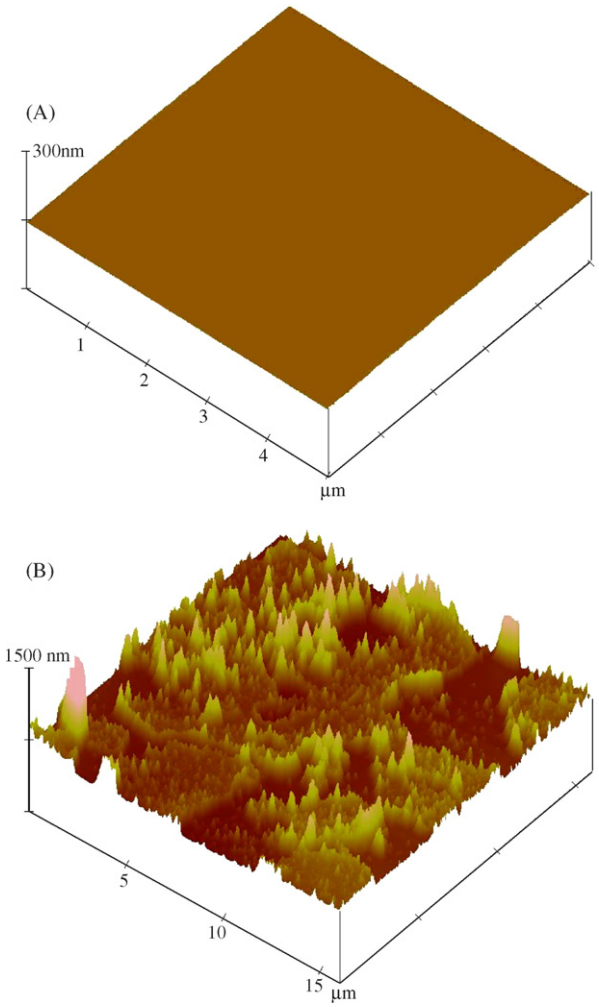


Fig. 5. AFM images of a bare GCE (A) and calix[4]arene film-modified GCE with 30 cyclic times surface (B).

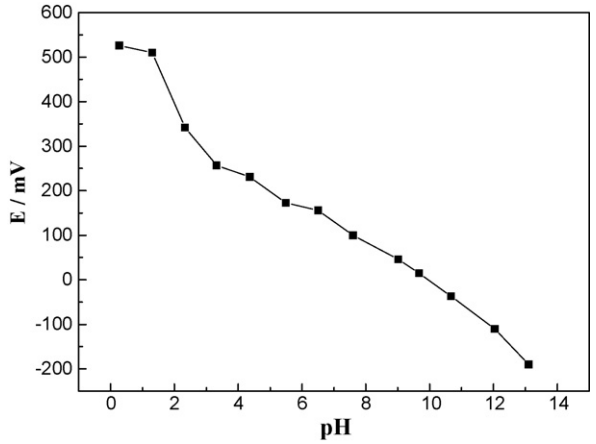


Fig. 6. The potentiometric response of 10^{-2} mol L^{-1} H_2O_2 in buffer solution of different pH.

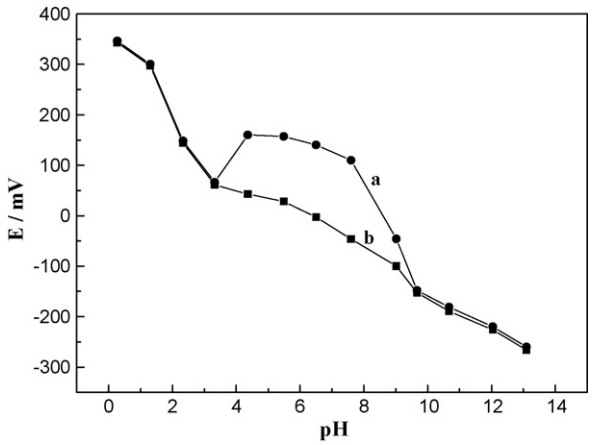


Fig. 7. The potentiometric response of 10^{-3} mol L^{-1} glucose in the buffer solution of different pH (a) and the potentiometric response of different pH (b).

tial response of pH when pH >9.5 or pH <3. For pH values in the range 4–8, the potential response of glucose was almost constant. The results might be related to that the glucose oxidase was inactive in alkali and strong acid solution. Considering different factors, TISAB (pH 7.5) solution was selected for the further experiments in detection of H_2O_2 and glucose.

3.5. Electrode response

A typical calibration curve of the electrode response for 2.2×10^{-4} to 0.32 mol L^{-1} H_2O_2 (shown in Fig. 8a) showed that the linear range of electrode response was 5.5×10^{-4} to 6.3×10^{-2} mol L^{-1} H_2O_2 and the electrode gave near-Nernstian response of 65.6 mV/log[H_2O_2] and a detection limit of 4.0×10^{-5} mol L^{-1} H_2O_2. In addition, the calibration curve of the electrode response to glucose showed that the linear range of electrode response was 2.5×10^{-4} to 1.6×10^{-3} mol L^{-1} and the electrode gave a near-Nernstian response of 50.2 mV/log[glucose] (shown in Fig. 8b) and the detection limit of 2.0×10^{-5} mol L^{-1} glucose.

3.6. Selectivity of the electrode

The selectivity of the sensor was evaluated by the mixed solution method. The results were presented in Table 3 and showed that the sensor offered a good selectivity for H_2O_2 and the glucose, and of many potentially interfering ionic species, only SCN^- interfered in the determination of H_2O_2 and the glucose.

Table 2
Effect of pH on the response.

pH	Linear range, mol L^{-1}	response slope, mV/log[H_2O_2]	detection limit, mol L^{-1}
3	3.2×10^{-3} to 3.6×10^{-2}	72.5	8.0×10^{-5}
5	1.5×10^{-3} to 4.5×10^{-2}	70.8	1.0×10^{-4}
7	5.5×10^{-4} to 6.3×10^{-2}	65.6	4.2×10^{-5}
9	6.5×10^{-4} to 5.2×10^{-2}	49.0	2.0×10^{-4}
11	6.0×10^{-4} to 5.5×10^{-2}	40.5	3.5×10^{-4}

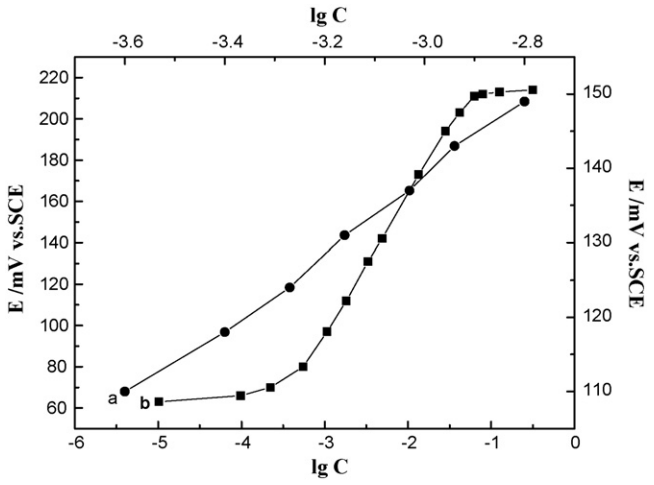


Fig. 8. The potentiometric response of H_2O_2 (a) and the glucose (b) at the GCE modified by the calix[4]arene.

Table 3
Values of selectivity coefficient for modified electrode.

Interfering ions	K (H_2O_2, j)	K (glucose, j)
Sb^{3+} (0.1 mol L^{-1})	2.9×10^{-3}	1.8×10^{-3}
Bi^{3+} (0.1 mol L^{-1})	1.8×10^{-3}	2.3×10^{-3}
Ca^{2+}(0.1 mol L^{-1})	1.2×10^{-4}	2.1×10^{-4}
Mg^{2+} (0.1 mol L^{-1})	5.4×10^{-4}	3.6×10^{-4}
K^{+}(0.1 mol L^{-1})	1.0×10^{-4}	2.1×10^{-4}
Hg^{2+}(0.02 mol L^{-1})	1.6×10^{-3}	4.2×10^{-3}
Pb^{2+} (0.02 mol L^{-1})	1.0×10^{-2}	3.0×10^{-2}
Cu^{2+}(0.1 mol L^{-1})	3.0×10^{-3}	6.1×10^{-3}
$C_2O_4^{2-}$ (0.1 mol L^{-1})	9.2×10^{-2}	7.8×10^{-2}
SO_4^{2-} (0.1 mol L^{-1})	4.1×10^{-3}	1.7×10^{-3}
Cl^{-} (0.2 mol L^{-1})	1.0×10^{-4}	2.0×10^{-4}
Br^{-} (0.1 mol L^{-1})	4.0×10^{-3}	5.0×10^{-3}
SCN^{-} (0.1 mol L^{-1})	1	1.5
Dopamine (0.01 mol L^{-1})	6.6×10^{-2}	2.6×10^{-2}
Ascorbic acid (0.01 mol L^{-1})	8.2×10^{-2}	2.4×10^{-2}
Citric acid ion (0.1 mol L^{-1})	5.0×10^{-4}	4.1×10^{-4}
Uric acid (0.1 mol L^{-1})	3.6×10^{-3}	2.2×10^{-3}

3.7. The performance of the sensor

3.7.1. The response time

When the hydrogen peroxide concentration was above 2.0×10^{-3} mol L^{-1}, the response time was shorter than 3 min; when the H_2O_2 concentration was lower than 2.0×10^{-3} mol L^{-1}, the response time turned to be 5 min. The response time of glucose detection was 5 min.

3.7.2. The repeatability of the sensor

The repeatability of the sensor was examined using the reference method [24]. The results are shown in Table 4 and reveal that the sensor had a good repeatability for the determination of H_2O_2 and glucose.

Table 4
Results of examination of the sensors reproducibility.

Number of repeats for determination of H_2O_2/glucose	6.0×10^{-4} mol L^{-1} H_2O_2/glucose	1.0×10^{-3} mol L^{-1} H_2O_2/glucose
1	84/128 (mV)	96/139 (mV)
2	83/129 (mV)	98/138 (mV)
3	84/131 (mV)	99/136 (mV)
4	81/128 (mV)	97/137 (mV)
Average value	83/129 (mV)	97.5/137.5 (mV)
RSD (%)	1.7/1.1	1.3/0.9

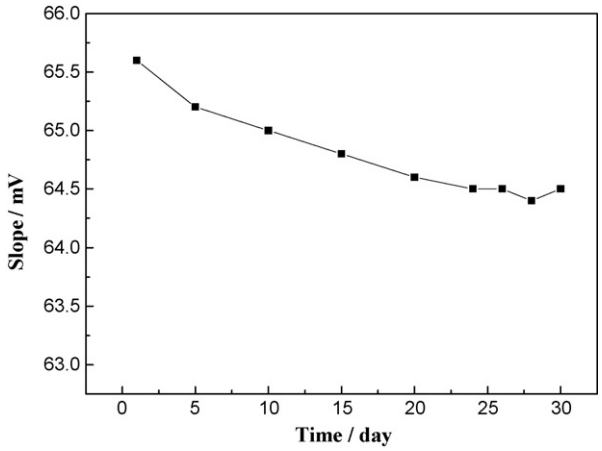


Fig. 9. Effect of the usage time of the sensor.

3.7.3. The life time of the sensor

After the new sensor had been conditioned for a given time, it showed a stable response for H_2O_2 when it was used continually for 30 days; the response slope and linear range of the sensor for H_2O_2 kept from any obvious varieties (shown in Fig. 9). The sensor appeared the poor stability and long response time after it was continually used over such a long time as 40 days; at the same time, the response linear range of the sensor for H_2O_2 was also poor.

3.8. Discussion on the possible response mechanism of the sensor

When the sensor was conditioned in 0.10 mol L^{-1} TISAB solution, the electromotive force (EMF) increased with time at first and then gave a constant response over a long time. While a few of H_2O_2 presented in the testing buffer solution, the response of this sensor was faster than that in blank testing buffer solution. Based on those experimental phenomena and the literature of the calix[4]arene petentiometric response mechanism to some molecule such as methanol [25], dopamine [26], p-methylphenol [27], sugars [28], carbon dioxide [29] and ions such as Ag^{+} [30], we proposed the possible response mechanism was that the calix[4]arene formed the host–guest complex with H_2O_2 by the hydrogen bond between H_2O_2 and hydroxybenzene of the calix[4]arene. Since the content of calix[4]arene modified on the electrode was limited, when the concentration of H_2O_2 increased to a certain value, all calix[4]arene on the electrode surface formed the complex with H_2O_2, and consequently, the potential became a constant(shown in Fig. 8a). However, the sensor regained its EMF response after it was washed by distilled water and measurement solution (TISAB) and used again.

3.9. The sample analysis and recovery test

By using standard addition method, the recoveries of ten H_2O_2 samples with concentrations from 5.5×10^{-4} mol L^{-1} to 4.9×10^{-2} mol L^{-1} were obtained. The recovery was satisfactory in the range of 96.2–103.5% and average recovery was 97.8% (RSD = 4%, n = 7).

The utility of this sensor was checked by using it for the quantitative determination of H_2O_2 in antisepsis water sample and compared the result (3.2%) with that of the titration with potassium permanganate (3.5%). The result clearly showed that the proposed method performed exceptionally well in the determination of H_2O_2 in samples.

Similarly, the recoveries of ten glucose samples with concentrations from 1.6×10^{-4} mol L^{-1} to 1.2×10^{-3} mol L^{-1} were achieved

Table 5
Results of the analysis of the blood samples with different glucose concentrations.

Blood samples	Clinical assay result, mol L^{-1}	Test result, mol L^{-1}	Deviation, mol L^{-1}
Sample1	8.7×10^{-3}	8.4×10^{-3}	-0.3×10^{-3}
Sample2	8.9×10^{-3}	8.8×10^{-3}	-0.1×10^{-3}
Sample3	9.0×10^{-3}	8.8×10^{-3}	-0.2×10^{-3}

by using standard addition method. The recovery was also satisfactory in the range of 97.2–102.5% and average recovery was 96.8% (RSD = 3.6%, $n = 7$). The sensor was used to quantify glucose on blood sample collected from diabetic patients of Affiliated Hospital of Yangzhou University by the standard addition method and the results shown in Table 5. The results obtained with sensor are in good agreement with reference values obtained with a yellow springs blood sugar analyzer (YSI Model 2300).

4. Conclusion

A novel peroxide hydrogen and glucose sensor with good sensitivity, selectivity, stability and reproducibility and anti-interferent ability was constructed by an electrochemical deposition method. Glucose oxidase was immobilized on the modified glassy carbon electrodes by dipping in the solution of the glucose oxidase (GOD) after immerged in the solution of glutaraldehyde. The method is simple and easy to control. The interference of ascorbic and uric acid could be avoided. The presence of the calix[4]arene film increased the stability of the sensor.

Acknowledgement

This project was financially supported by the National Natural Science Foundation (no. 20675071, no. 20875081) of China.

References

[1] R.A. Durst, A.J. Baumner, R.W. Murray, R.P. Buck, C.P. Andrieux, Pure Appl. Chem. 69 (1997) 1317.
[2] J.A. Cox, M.E. Tess, T.E. Cummings, Rev. Anal. Chem. 15 (1996) 173.
[3] I.G. Casella, M.R. Guascito, A.M. Salvi, E. Desimoni, Anal. Chim. Acta 354 (1997) 333.
[4] J. Liu, W. Zhoui, T. You, F. Li, E. Wang, S. Dong, Anal. Chem. 68 (1996) 3350.
[5] M.E.G. Lyons, Analyst 119 (1994) 805.
[6] J. Kankare, L.A. Vinokurov, Anal. Chem. 69 (1997) 2337.
[7] J.M. Teresa, A. Lewenstam, Anal. Chim. Acta 322 (1996) 141.
[8] R.K. Meruva, M.E. Meyerhoff, Anal. Chim. Acta 341 (1997) 187.
[9] J. Bobacka, A. Ivaska, A. Lewenstam, Electroanalysis 15 (2003) 366.
[10] R. Buck, Ion Selective Electrodes in Analytical Chemistry, Plenum Press, New York, 1980.
[11] T. Katsua, K. Ido, K. Takaishi, H. Yokosu, Sens. Actuators B 87 (2002) 331.
[12] A.K. Jaina, V.K. Gupta, L.P. Singh, P. Srivastava, J.R. Raisoni, Talanta 65 (2005) 716.
[13] L. Chen, J. Zhang, W. Zhao, X. He, Y. Liu, J. Electroanal. Chem. 589 (2006) 106.
[14] N. Ramamurthy, R.B. Brown, R. Hower, M.E. Meyerhoff, Fresenius J. Anal. Chem. 364 (1999) 41.
[15] J. Radecki, H. Radecka, T. Piotrowski, S. Depraetere, W. Dehaen, J. Plavec, Electroanalysis 16 (2004) 2073.
[16] A.A. Karyakin, O.V. Gitelmacher, E.E. Karyakina, Anal. Chem. 67 (1995) 2419.
[17] Q. Chin, S. Dong, Anal. Chim. Acta 310 (1995) 429.
[18] K. Schachl, H. Alemu, K. Kalcher, J. Jezkova, Analyst 122 (1997) 985.
[19] A.L. Vogel, Textbook of Inorganic Analysis, 4th ed., Longman, New York, 1981.
[20] C. Matsubura, N. Kawamoto, K. Takamura, Analyst 117 (1992) 1781.
[21] W. Oungpipat, P. Alexander, P. Southwell-Kelly, Anal. Chim. Acta 309 (1995) 35.
[22] Z. Xingwang, G. Zhihui, Talanta 50 (2000) 1157.
[23] A.K. Mine Sulak, Hasslettin Deligoz, J. Incl. Phenom. Macrocycl. Chem. 59 (2007) 115.
[24] P.D. Hong, Z.P. Sheng, G.L. Wu, The Application and Principle of ISE, New Time Press, Beijing, 1982, p. 64.
[25] C.Y.Shi, J.Q. Cao, P. Fan, Liaoning Daxue Xuebao, Ziran Kexueban 30 (2003), 82.
[26] S. Ryosuke, T. Saori, M. Hiroyuki, S. Naohiro, I. Shin-ichi, O. Kazunori, Bioorg. Med. Chem. Lett. 17 (2007) 767.
[27] G. Wei, J. Zhihua, Huaxue Gongye Yu Gongcheng Jishu 25 (2004) 25.
[28] T. Haino, M. Nakamura, Y. Fukazawa, Heterocycles 68 (2006) 2477.
[29] B.F. Graham, J.M. Harrowfield, R.D. Tengrove, A.F. Lagalante, R.D. Bruno, J. Incl. Phenom. Macrocycl. Chem. 43 (2002) 179.
[30] G.A. Evtugyn, I.I. Stoikov, S.V. Beljyakova, et al., Talanta 71 (2007) 1720.

Talanta 80 (2009) 864–869

Contents lists available at ScienceDirect

Talanta

journal homepage: www.elsevier.com/locate/talanta

Ultrasonic nebulization extraction coupled with on-line gas chromatography for determination of *trans*-anethole in spices

Lu Wang, Yue Liang, Ziming Wang, Chenling Qu, Dan Li, Yuhua Shi, Hanqi Zhang*

College of Chemistry, Jilin University, Changchun 130012, PR China

ARTICLE INFO

Article history:
Received 31 May 2009
Received in revised form 4 August 2009
Accepted 5 August 2009
Available online 13 August 2009

Keywords:
On-line detection
Illicium verum Hook. f.
Foeniculum vulgare Mill.
Trans-anethole
Ultrasonic nebulization extraction
Gas chromatography (GC)

ABSTRACT

Ultrasonic nebulization extraction (UNE) coupled with on-line gas chromatography (GC) was proposed for the determination of *trans*-anethole in fruits of *Illicium verum* Hook. f. and *Foeniculum vulgare* Mill. The extraction was performed in a common self-made extraction system. In the UNE the analyte was transferred and enriched from the solid sample to gas phase. The sample gas containing analyte obtained by UNE was introduced into the sampling loop with the purging gas (N_2). And then the sample gas in the sampling loop was introduced into the GC column. Several experimental parameters of on-line UNE-GC, including sampling time, flow rate of purging gas, standstill time and temperature of tubing, were optimized. The calibration curve ranging from 0.05 to 1.5 mg g^{-1} for determining the *trans*-anethole was obtained. The recoveries for determining *trans*-anethole are between 99.2% and 111.2% and RSDs are less than 8.3% when the UNE was applied. The analytes can rapidly be extracted and transferred from the solid sample to gas phase. The analytes in the gas phase are easier to be introduced into GC system than those in the solid and liquid phase. Compared with off-line systems, the proposed on-line system is more suitable to detect volatile compounds.

© 2009 Elsevier B.V. All rights reserved.

1. Introduction

Fruits of *Illicium verum* Hook. f. and *Foeniculum vulgare* Mill. are widely used as cooking spices and medicinal materials. The essential oils are the active components in fruits of the two kinds of plants. Many investigations about their antimicrobial and insecticidal behaviors have been reported [1–4]. In the essential oils, *trans*-anethole is the major component. The *trans*-anethole is one of the common rough materials and reaction solvent in the chemical industry. For example, alkylanisole derivatives producing from *trans*-anethole are valuable intermediates for the manufacture of pharmaceuticals, antioxidant, etc. [5]. Anisaldehyde producing from *trans*-anethole is an important chemical and chemical intermediate in the pharmaceutical, perfumery and agrichemical industry [6].

Several methods, such as hydrodistillation (HD) which is the state standard method of China [1,7,8], ultrasonic-assisted extraction (UAE) [9,10] and microwave-assisted extraction (MAE) [11–13], were usually applied to the extraction of the volatile compounds from spices. Recently, these methods coupled with some enrichment techniques, e.g. solid-phase extraction (SPE) [14,15], solid-phase microextraction (SPME) [16,17], and single-drop microextraction (SDME) [18,19], were applied to the extraction and determination of the volatile and semivolatile compounds on-line.

The ultrasonic nebulization extraction (UNE) was first studied by our group in the extraction of quercetin from *Rhizoma Alpiniae Officina-rum* [20] and Anthraquinones from *Rheum palmatum* L. [21]. These experiments confirmed that the UNE is a feasible and alternative method for extraction of effective constituents from plant samples. But the UNE was not applied to the extraction of volatile compounds. It can be seen from literature [21] that the high frequency ultrasonic wave (1.7 MHz) can result in "ultrasonic fountain" and aerosol at the same time. In the UNE process, the volatile compounds in the spices were transferred from the spices to the extraction solvent and then to gas phase. Namely, the UNE method is different from other conventional extraction methods, analyses can rapidly be extracted, transferred and enriched from the solid sample to gas phase.

The purge and trap (P&T) method [22–26] is used to transfer the volatile compounds from a liquid or solid matrix to gas phase by an inert gas flow and has been applied to the analysis of water [22], soil [23], body fluids [24], and so on [25,26]. It is a simple and fast method to detect the volatile and semivolatile compounds in liquid. But for the solid sample, it needed pre-extraction off-line, which made operation steps increase.

In this paper, a novel on-line analytical method combined the UNE and purge technique was used to detect *trans*-anethole in

* Corresponding author. Fax: +86 431 85112355.
E-mail address: analchem@jlu.edu.cn (H. Zhang).

0039-9140/$ – see front matter © 2009 Elsevier B.V. All rights reserved.
doi:10.1016/j.talanta.2009.08.006

fruits of *I. verum* Hook. f. and *F. vulgare* Mill. It has both advantages of UNE and on-line analysis. Compared with off-line systems, the on-line UNE coupled with GC technique has several advantages: (1) minimal sample contamination, (2) ideal method for the labile samples, (3) reduction of manual operation, (4) more inexpensive settings-up, (5) reduction of analyzing time, (6) the possibility for a totally automated analytical system. In addition, compared with P&T, the proposed method is suitable to analyze solid sample. And the UNE coupled with many enrichment techniques (SPE, SPME, SDME and so on) can improve the sensitivity.

2. Experimental

2.1. Chemicals and sample preparation

Three kinds of fruits of *I. verum* Hook. f. (named as Sample 1, 2 and 3) and three kinds of fruits of *F. vulgare* Mill. (named as Sample 4, 5 and 6) were purchased from Changchun, Jilin Province, China. The fruits of *I. verum* Hook. f. and *F. vulgare* Mill. were crushed by high-speed disintegrator (FW-100 Test Instrument Co., Ltd., Tianjin, China) at 24,000 rpm, and the powders obtained were passed through 80 mesh sieve and stored in the desiccators.

The standard of *trans*-anethole was purchased from Acros Company (NJ, USA). The naphthalene was used as internal standard and purchased from Beijing Chemical Factory (Beijing, China). Both analyte and internal standard were dissolved in n-hexane to obtain stock solution. These solutions were stored in the dark glass bottles at 4 °C. Pure water was obtained by using Milli-Q water purification system (Millipore Co., USA). The other reagents purchased from Beijing Chemical Factory (Beijing, China) are all of analytical grade.

2.2. Instruments and apparatus

The on-line UNE-GC system was assembled in our laboratory. A schematic diagram of the system is shown in Fig. 1. An ultrasonic humidifier (Beijing Branson Ultrasound Co. Ltd., China) working at 1.7 MHz with maximum output power of 35 W was employed as the ultrasonic source. A self-made glass flask (100 mL, ID 10 cm) was used as extraction vessel. There were three ports on this vessel. One of the ports on the bottom of the vessel has the same size as the piezocrystal and was sealed by PVC film. Other accessories, such as an injection valve (Nanda Analysis Instrument Graduate School, Nanjing, China), a sampling loop (1 mL) and a few stainless steel tubes, were used to fabricate the on-line system. A filtering column consisting of a stainless steel cylinder (2 cm × 3 mm i.d.) packed with glass wool was closed by screws at either end. A thermocouple sensor (XMTD-2001 Xinghua AOTE temperature Instrument Co., Xinghua, China) connected with a heating tape was used to measure the temperature. In addition, an ultrasonic generator (KQ2200E Kunshan Ultrasonic Instrument Co. Ltd., Kunshan, China) with 150 W of output power and 40 kHz of frequency was used in UAE.

The extract was analyzed by GC (Hewlett Packard computerized system comprising a 4890 gas chromatograph) with a HP-1 column (30.0 m × 250 μm × 0.32 μm film thickness). Nitrogen was used as the carrier gas at a flow rate of 4 mL min^{-1}.

2.3. Extraction procedures

2.3.1. On-line UNE-GC

In sequence 1 (Fig. 1a), the mixture of 0.1 g of sample and 15 mL of n-hexane, which was referred to as the extract, was put into extraction vessel and the nebulizer was switched in. During this

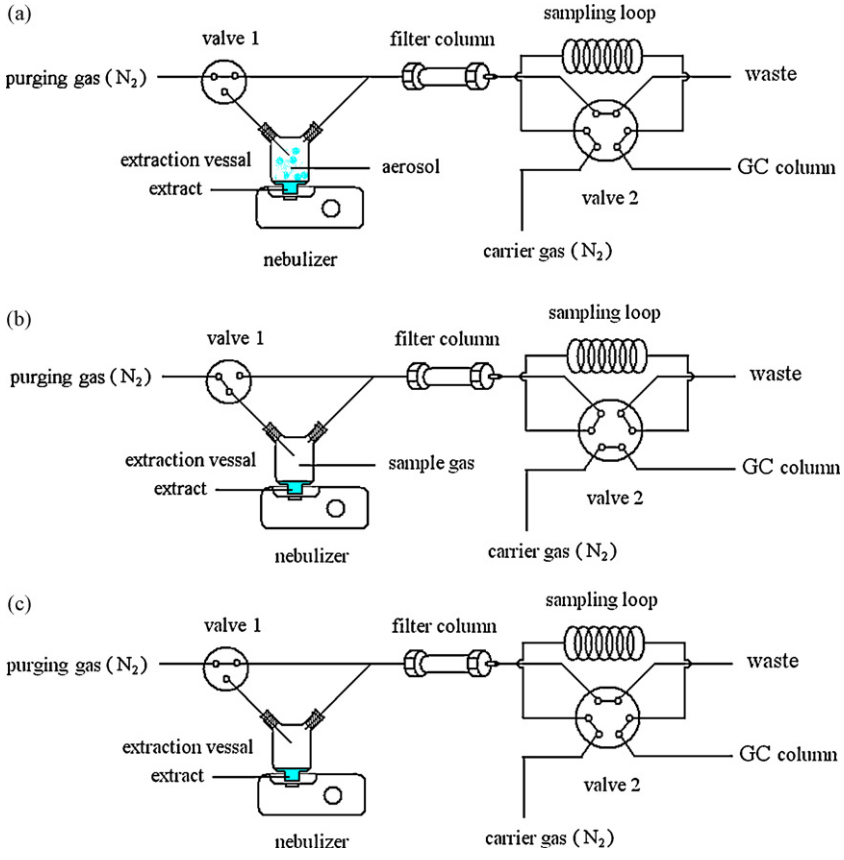


Fig. 1. On-line UNE system. (a) Extraction, (b) sampling and (c) injection.

sequence, the extraction vessel was full of aerosol. The valve 1 was in extraction position and valve 2 in sampling position. 5 min later, the nebulizer was switched off. The nebulizer was at a standstill for a certain standstill time. The aerosol in the headspace of extraction vessel will drop into the extract located in the bottom of extraction vessel. In sequence 2 (Fig. 1b), the valve 1 was in injection position, and valve 2 was also in sampling position. The purging gas (N_2) (270 mL min^{-1}) was passed through the extraction vessel for a certain purging time and the sampling loop was fill with the sample gas containing analyte. In sequence 3 (Fig. 1c), the valve 1 was in extraction position and valve 2 was in injection position. The sample gas in sampling loop was introduced into GC column and analyzed. The tubing in the UNE system was wrapped by a heating tape except the extraction vessel, and the temperature of heating tape was controlled at 80 °C.

In the method, the volatile compounds in the spices were transferred from solid phase (spices) to liquid phase (extraction solvent) because of the UNE extraction, and then transferred from liquid phase to gas phase due to the gas–liquid equilibrium. The focused energy of UNE makes the extraction solvent and sample powders spurt from the bottom of the extraction vessel, which looks like a fountain. Thank to the "ultrasonic fountain", the sample powders can be spurted from the bottom of the extraction vessel and suspended in the headspace in the aerosol and then dropped into the bottom of the extraction vessel. In this process, because the collision between extraction solvent and sample powder occurred frequently and the extraction solvent around the sample powder was renewed rapidly, the extraction efficiency of the analytes was enhanced. In the other hand, a lot of aerosols, which are small in size, were produced in UNE. The transfer the analytes from the aerosols into the gas phase is easy because the surface area of aerosols is large [27] and the interface between gas and liquid is frequently renewed. The gas–liquid distribution equilibrium of analytes was rapidly reached. So the total amount of the volatile compounds in gas phase increased at a certain time.

2.3.2. Off-line UNE

0.10 g of sample powder and 15 mL of n-hexane were added into the extraction vessel. The optimized UNE conditions were as follows: extraction solvent was 15 mL of n-hexane; ultrasonic power was 35 W; extraction time was 5 min. The extract was filtered with 0.45 μm micropore filter membrane and then analyzed by GC.

2.3.3. UAE

The comparison between conventional UAE with on-line UNE was carried out to evaluate the extraction efficiencies of different methods. 0.10 g of sample powders and 15 mL of n-hexane were added into the extraction vessel. After UAE for 5 min, the resulting suspension was filtered through a 0.45 μm micropore filter membrane. And 0.3 μL extract was injected into the GC system for analysis.

2.3.4. HD

According to Chinese Pharmacopoeia [1], 20 g of sample and 300 mL of water were put into a 500 mL flask and heated by heating jacket at 100 °C for 4 h. The essential oil was collected, dried with anhydrous sodium sulphate and then stored at 4 °C until analyzed.

2.3.5. Gas chromatography

The operating conditions were as follows: nitrogen carrier gas flow rate 4.0 mL min^{-1}; split ratio 1:10; injection and detection temperature 260 °C; oven temperature progress from 60 °C (holding for 3 min) to 240 °C at the rate of 5 °C min^{-1}. The injection volume is 0.3 μL in off-line methods. The flame ionization detector was used and its temperature was 260 °C.

3. Results and discussion

3.1. Optimization of on-line UNE-GC

Some parameters can affect the performances of on-line UNE-GC, such as purging time, flow rate of purging gas, standstill time and temperature of tubing. When one parameter was changed, other parameters were fixed at their optimal values.

3.1.1. Effect of purging time

The effect of purging time on peak area of *trans*-anethole is shown in Fig. 2. It can be seen that the peak area increases with the increase of purging time from 10 s to 20 s, does not significantly changes from 20 s to 60 s and slightly decreases from 60 s to 120 s. When purging time was shorter than 20 s, the analyte concentration in the sample gas in the extraction vessel and the sampling loop was not identical, and concentration of analyte in sampling loop was lower than that in the extraction vessel. On the contrary, the concentration of analyte in extraction vessel was diluted when purging time was longer than 60 s. Remarkably, the precision was not satisfactory when the purge time was 10 s. So 20 s was chosen finally to be purging time in this work.

3.1.2. Effect of flow rate of purging gas

The effect of flow rate of purging gas ranging from 70 to 630 mL min^{-1} on the peak areas was examined, and the result is shown in Fig. 3. It can be seen that the peak area of *trans*-anethole increases at first, but then decreases when the flow rate of purging gas is higher than 270 mL min^{-1}. The flow rate of purging gas was measured by soap film flowmeter in waste vent. At low flow rate, small amount of analyte was introduced into the sampling loop. On the contrary, the overhigh flow rate will dilute the sample gas in extraction vessel. So, the flow rate of purging gas was chosen finally to be 270 mL min^{-1}.

3.1.3. Effect of standstill time

In the UNE extraction process, the sample powders of small diameter will spurt from extract, suspend in the headspace and exist in the aerosol. Under the gravitational effect those powders fall into the extract after a period of time. This circulating process is beneficial to the renewal of the solvent on the surface of sample powders and the extraction efficiency can be enhanced. If the nebulization stopped, the sample powders would gradually drop into the

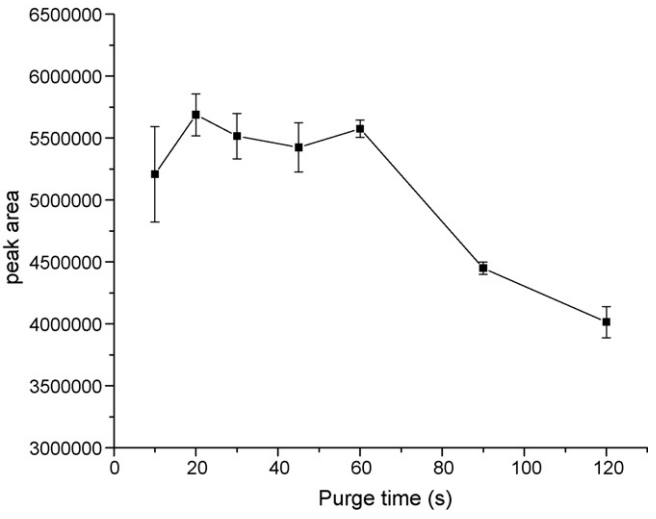


Fig. 2. Influence of the purging time. Flow rate of purging gas, 270 mL min^{-1}; standstill time, 5 min; temperature of tubing, 80 °C.

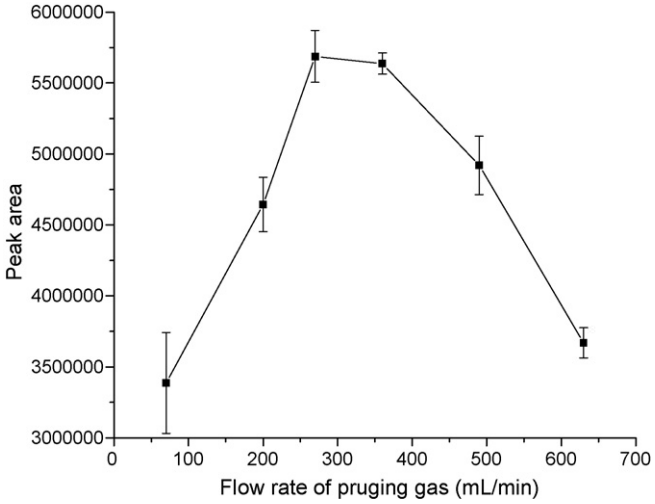


Fig. 3. Influence of the flow rate of purging gas. Purging time, 20 s; standstill time, 5 min; temperature of tubing, 80 °C.

extract along with the aerosol. The concentration of volatile compounds was highest in the headspace of extraction vessel when the nebulization stopped. If the sampling was performed immediately, a large quantity of aerosol was introduced into the sampling loop in which the solution droplet can form and block the tubing. So, the sampling was performed after a period of standstill. The effect of standstill time of 0, 1, 3, 5, 8 and 10 min was tested, respectively. When the standstill time was longer than 5 min, a large quantity of aerosol containing sample powders would drop into the extract, which was observed by the naked eye. The results are shown in Fig. 4. It can be seen that the extraction yield of *trans*-anethole decreases with the increase of the standstill time. If the standstill time is too long, the *trans*-anethole in gas phase would loss, which results in the decrease of concentration of *trans*-anethole in sample gas. So the standstill time of 5 min was selected in the work.

3.1.4. Effect of temperature of tubing

The effect of tubing temperature from 20 to 120 °C on the peak area was evaluated, and the result is shown in Fig. 5. It can be seen that the peak area increases obviously along with the increase

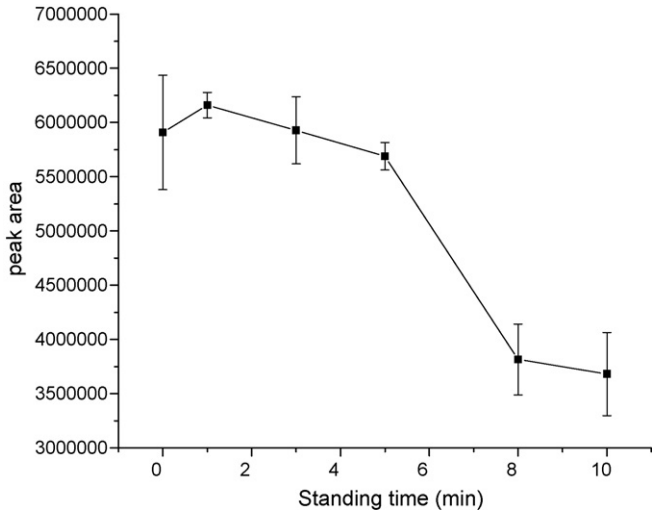


Fig. 4. Influence of the standstill time. Purging time, 20 s; flow rate of purging gas, 270 mL min^{-1}; temperature of tubing, 80 °C.

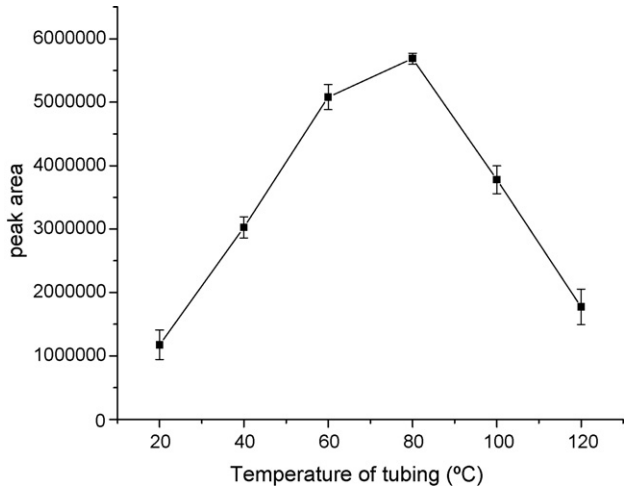


Fig. 5. Influence of the temperature of tubing. Purging time, 20 s; flow rate of purging gas, 270 mL min^{-1}; standstill time, 5 min.

of temperature from 20 to 80 °C, whereas it decreases when the temperature is higher than 80 °C. Before the sample gas was introduced into GC column the main component in the gas phase and the aerosol was n-hexane whose boiling point was 68.7 °C. At the 270 mL min^{-1} of flow rate, small amount of aerosol in sampling gas was introduced into the sampling loop. When the temperature is lower than 68.7 °C, n-hexane can precipitate on the wall of tubing. Therefore, the analyte transferred to the sampling loop lost. If the temperature was too high the small amount of aerosol which was transferred to the sampling loop will vaporize and then the volume of sample gas was expanded and the concentration of analyte in sample gas decreases. Finally, the temperature of tubing was chosen to be 80 °C in this work.

3.2. Evaluation of the method

3.2.1. Standard curve and limit of quantification

In the work, *trans*-anethole was determined by on-line and off-line UNE-GC. The working standard solutions of *trans*-anethole at the concentrations ranging from 0.05 to 1.5 mg mL^{-1} were prepared. The linear equations for on-line and off-line UNE-GC are $A = 0.01574 + 4.05186C$ and $A = -0.3107 + 2.50664C$ and limits of quantification (LOQs) are 0.020 and 0.017 mg g^{-1}, respectively. The LOQs were determined as the lowest concentration that yielded a signal-to-noise (S/N) ratio of 10.

3.2.2. Enrichment effect of UNE

In the UNE process, the frequency of acoustic vibration is about 1.7 MHz. When the vibration was transmitted through the solvent, "ultrasonic fountain" and aerosol would occur. If the analyte has good volatility, its concentration in gas phase obtained by UNE is higher than that obtained by stirring extraction. The reasons may be that compared with the stirring extraction, the transfer rate of volatile compounds from liquid to gas phase is more rapid and gas–liquid equilibrium is more rapidly reached when the UNE is applied. Compared with the conventional stirring extraction, the UNE process also can be viewed as an enrichment step. In order to evaluate the enrichment effect of UNE, the stirring method without nebulization was applied. In the two experiments, the standard solution at concentration of 0.2 mg mL^{-1} was added into the 15 mL n-hexane in extraction vessel. In the UNE, both the nebulization and the standstill time was 5 min; while in the stirring method, the stirring time was 10 min. The resulting sample gas in extraction vessel was introduced into GC for analysis. The results indicted that the concentration of the analyte obtained by the UNE was 5 times

Table 1
Contents of *trans*-anethole in fruits of *Illicium verum* Hook. f. and *Foeniculum vulgare* Mill. obtained from different cultivated areas.

Sample	Method	Content (mg g^{-1})	RSD (%) (n = 3–5)	Added (mg g^{-1})	Found (mg g^{-1})	Recovery (%)	RSD (%)
1	On-line	109.1 ± 4.6	4.2	120.0	228.1	99.2	8.3
	Off-line	108.9 ± 2.2	2.0	120.0	229.0	100.1	7.7
2	On-line	65.6 ± 2.0	3.3	60.0	125.9	100.5	4.8
	Off-line	65.3 ± 0.9	1.4	60.0	126.1	101.4	5.4
3	On-line	118.6 ± 5.8	4.9	120.0	252.0	111.2	3.2
	Off-line	115.1 ± 2.6	2.3	120.0	252.7	114.7	5.4
4	On-line	11.6 ± 0.5	4.6	24.0	35.7	100.4	3.5
	Off-line	13.8 ± 0.3	2.5	24.0	36.5	94.6	3.1
5	On-line	22.8 ± 0.8	3.5	24.0	46.6	99.2	6.7
	Off-line	23.1 ± 0.8	3.6	24.0	46.6	98.0	2.3
6	On-line	30.2 ± 2.1	7.0	24.0	54.7	102.1	3.6
	Off-line	29.9 ± 0.6	2.2	24.0	53.8	99.5	1.6

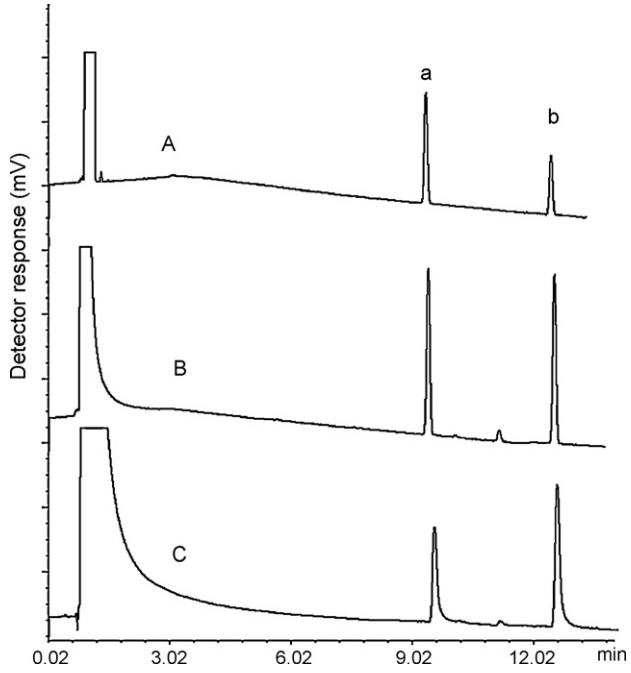


Fig. 6. Chromatograms of standard solution (A) and extracts obtained by off-line UNE-GC (B), and on-line UNE-GC (C). a, naphthalene; b, *trans*-anethole.

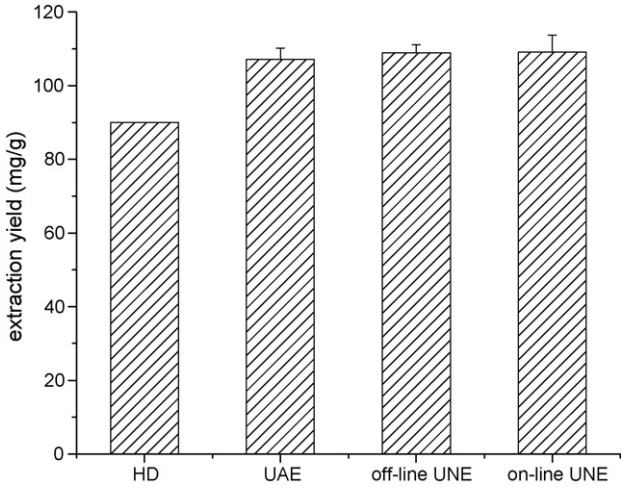


Fig. 7. Comparison of different extraction methods.

higher than that obtained by stirring method. It was obvious that enrichment effect of UNE was significant.

3.2.3. Sample analysis

The *trans*-anethole in fruits of *I. verum* Hook. f. and *F. vulgare* Mill. obtained from different cultivated areas was determined by on-line and off-line UNE-GC, respectively. The chromatograms of standard solution and extracts obtained by on-line UNE-GC and off-line UNE-GC are shown in Fig. 6. The contents of *trans*-anethole obtained by on-line and off-line UNE-GC are shown in Table 1. From Table 1, it can be seen that the contents of *trans*-anethole in fruits of *I. verum* Hook. f. and *F. vulgare* Mill. obtained by on-line are very similar. The results demonstrate proposed method can be applied to the real sample analysis with good accuracy. But, it was worth to notice that there were significant differences in the contents of *trans*-anethole belong to different samples, which was perhaps due to the different cultivated areas and picking periods. The contents of *trans*-anethole in the samples collected from different areas were compared applying of variance. For this purpose, the Student's t test was applied. The statistical analysis indicated that there are significant differences among contents of *trans*-anethole in the samples collected from different area. The difference between sample 5 and 6 was significant ($P < 0.01$) and the differences between the other samples were very significant ($P < 0.001$). In addition, the RSDs and recoveries obtained by on-line UNE-GC are 3.3–7.0% and 99.2–111.2%, respectively. The results also indicate the on-line UNE-GC can be applied to the determination of *trans*-anethole in fruits of *I. verum* Hook. f. and *F. vulgare* Mill. with good precision and accuracy.

3.3. Comparison of HD, UAE, off-line UNE and on-line UNE

In order to evaluate the extraction efficiency of proposed method, HD and UAE were applied to extract *trans*-anethole from sample 1. The extraction yields obtained by different methods are shown in Fig. 7. Correspondingly, the extraction yield obtained by HD is the lowest. So, compared with HD, the extraction yield obtained by on-line UNE-GC is higher, but shorter extraction time was required and lower energy was consumed. Furthermore, the extraction yield obtained by proposed method is in agreement with those obtained by UAE and off-line UNE-GC, which indicates that on-line UNE-GC is a feasible method for extracting volatile compounds from spices. In addition, it is worth to notice that on-line UNE-GC is also a gentle and enjoyable method without any noise.

4. Conclusion

In this study, UNE coupled with on-line GC detection was applied to determining *trans*-anethole in fruits of *I. verum* Hook. f. and *F. vulgare* Mill. The experimental conditions for on-line UNE-GC were examined and optimized. On-line UNE-GC was then compared with HD, UNE and off-line UNE-GC. The extraction yield obtained by on-line UNE-GC was obviously higher than those obtained by conventional HD, and RSD and recovery obtained by

the proposed method are also satisfactory. Therefore, it can be concluded that on-line UNE-GC is a simple, labor saving, sensitive, novel and feasible method for extracting and determining the constituents in essential oil from spices. If the UNE coupled with many enrichment techniques (SPE, SPME, SDME and so on), the sensitivity of the proposed method would be improved.

References

[1] The State Pharmacopoeia Commission of P.R. China, The Pharmacopoeia of People's Republic of China 2005, Chemical Industry Publishing House, Beijing, 2005.
[2] B.G. Sun, J. He, Introduction of Essence—Spice, Modification, Application, Chemical Industry Publishing house, Beijing, 1999 (in Chinese).
[3] A. Padmashree, N. Roopa, A.D. Semwal, G.K. Sharma, G. Agathian, et al., Food Chem. 104 (1) (2007) 59.
[4] M. Faudale, F. Viladomat, J. Bastida, F. Poli, C. Codina, J. Agric. Food Chem. 56 (6) (2008) 1912.
[5] Q.X. Guo, L.S. Li, L.W. Chen, Y.Q. Wang, S.Y. Ren, B.J. Shen, Energy Fuel 23 (2009) 51.
[6] Y. Xiao, H.M. Huang, D.L. Yin, D. Guo, L.Q. Mao, Z.H. Fu, Catal. Commun. 10 (2008) 29.
[7] M.T. Golmakani, K. Rezaei, Food Chem. 109 (2008) 925.
[8] M. El Hattab, G. Culioli, L. Piovetti, S.E. Chitour, R. Valls, J. Chromatogr. A 1143 (2007) 1.
[9] R. Chizzola, H. Michitsch, C. Franz, J. Agric. Food Chem. 56 (16) (2008) 6897.
[10] E.S. Giray, S. Kirici, D.A. Kaya, M. Türk, Ö. Sönmez, M. İnan, Talanta 74 (2008) 930.
[11] Z.M. Wang, L. Ding, T.C. Li, X. Zhou, L. Wang, H.Q. Zhang, J. Chromatogr. A 1102 (2006) 11.
[12] M.E. Lucchesi, F. Chemat, J. Smadja, J. Chromatogr. A 1073 (2004) 323.
[13] Z.M. Wang, L. Wang, T.C. Li, X. Zhou, L. Ding, Y. Yu, A.M. Yu, H.Q. Zhang, Anal. Bioanal. Chem. 386 (2006) 1863.
[14] K. Ridgway, S.P.D. Lalljie, R.M. Smith, J. Chromatogr. A 1153 (2007) 36.
[15] V. Radulescu, S. Chiliment, E. Oprea, J. Chromatogr. A 1027 (2004) 121.
[16] L.H. Ribeiro, A.M.C. Freitas, M.D.R.G. da Silva, Talanta 77 (2008) 110.
[17] E. Klimánková, K. Riddellová, J. Hajšlová, J. Poustka, J. Kolářová, V. Kocourek, Talanta 75 (4) (2008) 1082.
[18] M. Adam, P. Dobias, A. Eisner, K. Ventura, J. Sep. Sci. 31 (2) (2008) 356.
[19] C.H. Deng, X.H. Yang, X.M. Zhang, Talanta 68 (1) (2005) 6.
[20] X. Zhou, L. Ding, Z.M. Wang, L.F. Bai, J. Zheng, et al., J. Jilin Univ. (Science edition) 43 (2) (2005) 228.
[21] L. Wang, D. Li, L. Ch. Bao, J.Y. You, Z.M. Wang, et al., Ultrason. Sonochem. 15 (5) (2008) 738.
[22] A. Lara-Gonzalo, J.E. Sanchez-Uria, E. Segovia-Garcia, A. Sanz-Medel, Talanta 74 (5) (2008) 1455.
[23] N. Campillo, P. Viñas, I. López-García, N. Aguinaga, M. Hernández-Córdoba, Talanta 64 (2004) 584.
[24] L. Dunemann, H. Hajimiragha, Anal. Chim. Acta 283 (1993) 199.
[25] N. Campillo, P. Viñas, I. López-García, N. Aguinaga, M. Hernández-Córdoba, J. Chromatogr. A 1035 (2004) 1.
[26] L. Zoccolillo, L. Amendola, C. Cafaro, S. Insogna, J. Chromatogr. A 1077 (2005) 181.
[27] X.C. Fu, W.X. Shen, T.X. Yao, Physical Chemistry, Higher Education Press, Beijing, 1990, B896.

Talanta 80 (2009) 870–874

Contents lists available at ScienceDirect

Talanta

journal homepage: www.elsevier.com/locate/talanta

$[Ru(bpy)_3]^{2+}$ nanocomposites containing heteropolyacids: Simple preparation and stable solid-state electrochemiluminescence detection application

Yali Li[a,b], Hui Zhu[a,b], Xiurong Yang[a,b,*]

[a] State Key Laboratory of Electroanalytical Chemistry, Changchun Institute of Applied Chemistry, Chinese Academy of Sciences, Renmin Street, Changchun, Jilin 130022, China
[b] Graduate School of the Chinese Academy of Sciences, Beijing 100039, China

ARTICLE INFO

Article history:
Received 10 May 2009
Received in revised form 6 August 2009
Accepted 8 August 2009
Available online 18 August 2009

Keywords:
Heteropolyacid
Nanocomposite
$[Ru(bpy)_3]^{2+}$
Solid-state electrochemiluminescene

ABSTRACT

In order to solidify the electrochemiluminescence (ECL) luminophor tris(2,2′-bipyridyl) ruthenium(II) ($[Ru(bpy)_3]^{2+}$) onto the electrode surfaces robustly, the negative charged heteropolyacids (HPAs) moieties were utilized to attract and bond cations $[Ru(bpy)_3]^{2+}$ via an adsorption method. The compositions and microstructures of the hybrid complexes were characterized by elemental analysis (EDS), spectroscopic techniques (UV–vis, FTIR) and field-emission scanning electron microscopy (FE-SEM). The electrochemical and ECL behaviors of the $[Ru(bpy)_3]^{2+}/[PW_{12}O_{40}]^{3-}$ hybrid complex contained in the solid film of the nanocomposites formed on the electrode surfaces were also studied. It was found that the corresponding solid membranes exhibited a diffusion-controlled voltammetric feature and excellent electrochemiluminescence behaviors. Hence potential prospects as new electrochemiluminescent materials for application in electroanalytical detection are envisioned.

© 2009 Elsevier B.V. All rights reserved.

1. Introduction

Nowadays, electrogenerated chemiluminescence (ECL) has been paid considerable attention due to its inherent advantages such as low background signal, simple optical setup, and versatility [1–3]. Among various ECL reagents, $[Ru(bpy)_3]^{2+}$ is selected and studied most extensively because of its superior properties including excellent stability, and good efficiency in aqueous solution [4]. Compared with those solution-phase ECL procedures, the immobilization of $[Ru(bpy)_3]^{2+}$ on electrode surfaces can provide several advantages such as reducing the consumption of expensive reagents, enhancing ECL signal, and simplifying experimental design [5–7]. Thus increasing attention has been paid to immobilize $[Ru(bpy)_3]^{2+}$ on electrode surfaces [8–12]. Some of the above-mentioned methods possess a fast response and good stability, but the synthesis processes are complicated and arduous. Therefore, developing a simple method to stably and sensitively modify the electrodes is quite urgent. Recently, Wang et al. prepared a series of ion conductors via adsorption between cationic $[Ru(bpy)_3]^{2+}$ and anionic $PtCl_6^{2-}$, $AuCl_6^{2-}$ or citric-capped AuNPs [13–15]. The prepared ion conductors have been utilized in ECL detection and exhibited good stability. The method proposed by Wang et al. is relatively simple and the generated sensors exhibit fast responses and excellent ECL behaviors. However, the high prices of the precursors have hindered their potential practical utilizations. Therefore, developing an economical and simple method to solidify $[Ru(bpy)_3]^{2+}$ on the electrodes becomes an urgent task.

Heteropolyacids (HPAs) of Keggion structure is a family of complexes with the general formula $[X_yM_zO_m]^{n-}$ (where M represents Mo, W, V, etc. and X represents P, Si, As, etc.), presenting excellent properties such as stability and availability depending on the counter-ion, quite small size and very high electronic density [16]. Most importantly, they have good ability to form very stable membranes [17,18]. Thus, they are usually used as the charged anionic moieties to attract and bond multiply cations in assembled films [19,20]. Although a few reports about multilayer films such as $[Os(bpy)_3]^{2+}/[P_2Mo_{18}O_{62}]^{6-}$ and $[Ru(bpy)_3]^{2+}/[Si_2Mo_{18}O_{62}]^{4-}$ have been reported [21–23], these studies mainly focused on the properties of transition metal ions and their electrochemistry. Few studies reported the synthesis of $[Ru(bpy)_3]^{2+}/[X_yM_zO_m]^{n-}$ via a precipitation reaction followed by a simple mixing method and their corresponding ECL properties.

In this research, a direct mixing method was introduced to construct a series of $[Ru(bpy)_3]^{2+}/[X_yM_zO_m]^{n-}$ hybrid films, which is simple and economical. To our knowledge, it is the first attempt to prepare robust $[Ru(bpy)_3]^{2+}$ nanocomposites containing HPAs via a precipitation reaction by adsorption. In addition, electrochemical and ECL behaviors of the $[Ru(bpy)_3]^{2+}$ hybrid membranes on ITO electrodes are investigated. Good stability and high sensitivity in solid-state ECL detection are observed. All the merits above of

* Corresponding author at: State Key Laboratory of Electroanalytical Chemistry, Changchun Institute of Applied Chemistry, Chinese Academy of Sciences, Renmin Street, Changchun, Jilin 130022, China. Tel.: +86 431 85262056; fax: +86 431 85689278.
E-mail address: xryang@ciac.jl.cn (X. Yang).

0039-9140/$ – see front matter © 2009 Elsevier B.V. All rights reserved.
doi:10.1016/j.talanta.2009.08.008

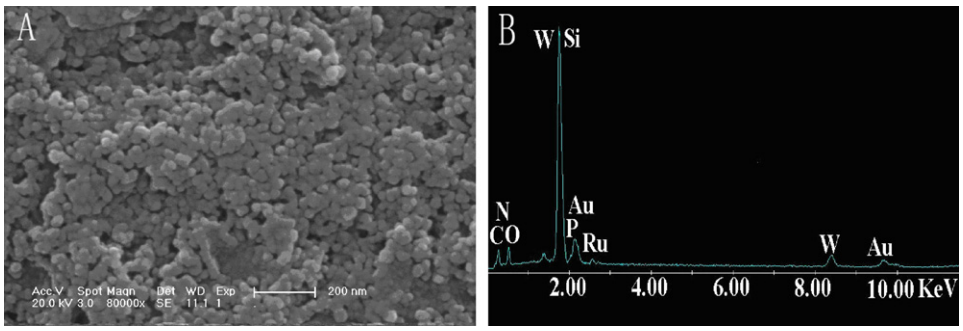


Fig. 1. The FE-SEM image of the aggregates and (B) the corresponding EDS of 100 μL 0.20 mM PTA and 1 mL 0.030 mM $[Ru(bpy)_3]^{2+}$ solution.

the $[Ru(bpy)_3]^{2+}/[X_yM_zO_m]^{n-}$ hybrid films indicate great potential applications in electroanalysis.

2. Experimental

2.1. Reagents

PTA ($H_3PW_{12}O_{40}\cdot nH_2O$) was purchased from Fluka. $Ru(bpy)_3Cl_2\cdot 6H_2O$ and 2-(dibutylamino)ethanol (DBAE) were obtained from Aldrich. $Na_2H_9PW_{12}O_{42}$, $H_4SiW_{12}O_{40}\cdot nH_2O$, and other chemicals and reagents were of analytical grade, and all the reagents were used as received without further purification.

2.2. Instruments and characterizations

The field-emission scanning electron microscopy (FE-SEM) measurements were carried out on a PHILIPS XL-30 ESEM with an accelerating voltage of 20 kV. The silicon slides were used as substrates for the FE-SEM experiments. Energy-dispersed spectrum (EDS) analysis was performed using an EDAX system. UV–visible (UV–vis) absorption spectra were detected from a Cary 50 UV-vis spectrometer (Varian, USA). Fourier transform infrared (FTIR) spectra were recorded on a FTIR spectrometer (Nicolet 520, USA) using the KBr wafer technique. Electrochemical experiments were carried out with a CHI 832 (Shanghai, China). In our three-electrode system, the ITO or nanocomposite-coated ITO electrodes were selected as working electrodes. Ag/AgCl (saturated KCl) was chosen as a reference electrode, and a platinum foil was employed as a counter electrode. The ECL signals were recorded by an MPI-A chemiluminescence analyzer (Xi'An Remax Science & Technology Company, Xi'An, China). The photomultiplier tube was biased at 800 V. It was worthwhile mentioning that all the work electrodes used in our experiment were set at a fixed area by carrying out in the place of the reservoir with a defined area (Ø, 3 mm).

2.3. Procedures

2.3.1. $[Ru(bpy)_3]^{2+}$ nanocomposites containing HPAs preparation

In a typical experiment, 100 μL of 0.2 mM $[PW_{12}O_{40}]^{3-}$ was diluted to 1 mL aqueous solution first, and then 1 mL of 0.03 mM $[Ru(bpy)_3]^{2+}$ aqueous solution (3:2 molar ratio of $[Ru(bpy)_3]^{2+}$ to $[PW_{12}O_{40}]^{3-}$) was added into the resulting solution under vigorous stirring to mix them uniformly. After the addition, the stirring was stopped and the resulting solution was kept at room temperature. Several minutes later, a large amount of precipitates were produced. The resulting precipitates were collected by centrifugation, washed several times with water, and then suspended in water for the further experiments and characterizations.

2.3.2. Sensors fabrication

Sensors were fabricated by sonicating and rinsing indium tin oxide (ITO) electrodes clearly, and then a 10 μL aliquot of as-prepared suspension was coated on the ITO electrode and allowed to dry at room temperature. Finally some completely dry brown $[Ru(bpy)_3]^{2+}/[X_yM_zO_m]^{n-}$ composite films on ITO electrodes were obtained. When not in use, the films were kept under in dry state at room temperature.

3. Results and discussion

3.1. SEM characterizations

Fig. 1A showed the typical SEM of the resulting precipitates of sample $[Ru(bpy)_3]^{2+}/[PW_{12}O_{40}]^{3-}$. It was clear that the precipitates consisted of a large quantity of spherical shape nanocomposites in a relative uniform size range. It was worthwhile to mention that the formed structure was robust enough to undergo an ultrasonication for about 15 min using a sonifier with 100 W. The chemical composition of the precipitates was further determined by the EDS. As shown in Fig. 1B, the peaks of Ru, P, W, C, O, and N elements were observed (other peaks such as Si and Au elements originated from the substrate), demonstrating the precipitates formed by the proposed method consist of $[Ru(bpy)_3]^{2+}$ and $[PW_{12}O_{40}]^{3-}$. The quantitative elemental analysis was conducted to determine the stoichiometry. It was observed that the atom number ratio of Ru and W in the as-formed nanocomposites was 10.19:79.27, which was consistent with the 3:2 reaction molar ratio of $[Ru(bpy)_3]^{2+}$ to $[PW_{12}O_{40}]^{3-}$. Based on these observations, it was concluded that these structures were produced via the interaction between $[PW_{12}O_{40}]^{3-}$ and $[Ru(bpy)_3]^{2+}$. Control experiments by mixing $[Ru(bpy)_3]^{2+}$ and other negative charged polyoxometalates ($Na_2H_9P(W_2O_7)_6$ or HPAs ($H_4SiW_{12}O_{40}\cdot nH_2O$) were also investigated, and the similar hybrids were obtained (Supporting Information, Fig. S1). In comparison, $[Ru(bpy)_3]^{2+}$ with other anions (SO_4^{2-}, PO_4^{3-}) were also mixed. It was found that the solution was still clear and none of any precipitates occurred. Considering the positive charge of $[Ru(bpy)_3]^{2+}$ ions and the negative charge of $[X_yM_zO_m]^{n-}$ groups, the electrostatic attractions between these two complexes may impulse these hybrid composites formation, and the unique properties of HPAs such as counter-ion, small size and very high electronic density might play an important role in the hybrids fabrication.

The effects of the reactant molar ratio on the morphologies and stoichiometry compositions of these hybrid complexes were examined. If the concentration of $[Ru(bpy)_3]^{2+}$ and $[PW_{12}O_{40}]^{3-}$ were set, the quantity of the precipitates increased with the quantity of $[Ru(bpy)_3]^{2+}$ and $[PW_{12}O_{40}]^{3-}$. However, similar morphologies and same stoichiometry compositions were obtained for them, and similar results were obtained for $Na_2H_9P(W_2O_7)_6$ and

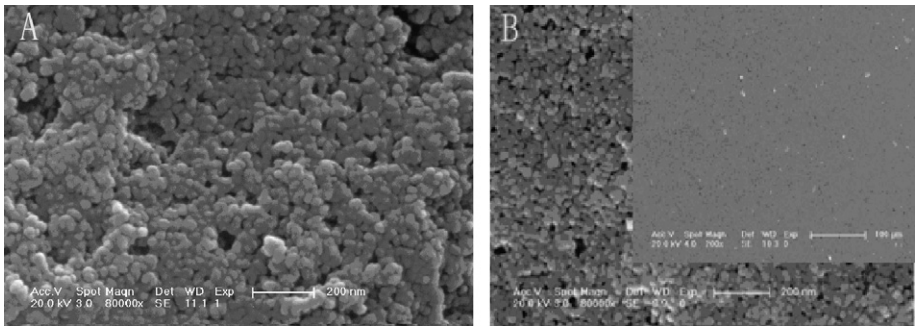


Fig. 2. SEM images of the precipitates were obtained at (A) fivefold, (B) one-fifth the concentration of Fig. 1 sample and (inset of (B)) SEM image of the resulting aggregates $[Ru(bpy)_3]^{2+}/[PW_{12}O_{40}]^{3-}$ formed film on an ITO substrate.

$H_4SiW_{12}O_{40}{\cdot}nH_2O$ (data not shown here). The results showed that the original molar ratios had no significant effects on the morphologies and stoichiometry compositions of the hybrid complexes. Fig. 2 showed typical SEM images of other two samples obtained at different concentrations of reactants under the otherwise identical conditions. When the concentrations of both $[Ru(bpy)_3]^{2+}$ and $[PW_{12}O_{40}]^{3-}$ were increased to fivefold, the size of precipitates slightly increased (Fig. 2A). When the concentrations of both $[Ru(bpy)_3]^{2+}$ and $[PW_{12}O_{40}]^{3-}$ were decreased to one-fifth, the resulting precipitates exhibited more uniform spherical morphologies in a narrower size distribution of about 20 nm (Fig. 2B). Their small sizes and uniform distributions may favor the membrane fabrication on various substrates. Hence, the one-fifth concentration of the sample was utilized to do the next experiment. The inset of Fig. 2B showed a SEM image of the aggregates formed film on an ITO substrate, indicating that the aggregates formed a fairly smooth and quite uniform film on the substrate. No cracks were observed. This suggested that the PTA had good ability to form films [19,20]. The thickness of the composite films was also determined by FE-SEM, and the mean thickness was 800 nm.

3.2. Spectra study of the $[Ru(bpy)_3]^{2+}/[PW_{12}O_{40}]^{3-}$ hybrid nanocomposites

As the $[Ru(bpy)_3]^{2+}$ ions had characteristic absorption in the UV–vis region, the UV–vis absorption spectra of the $[Ru(bpy)_3]^{2+}$ aqueous solution and their hybrid complexes were collected and compared. For free $[Ru(bpy)_3]^{2+}$ solution, two obvious peaks appeared at about 286.0 and 454.0 nm (Fig. 3A, curve a), which were assigned to ligand-centered transitions and metal-to-ligand charge transfer (MLCT), respectively [2]. For the $[Ru(bpy)_3]^{2+}/[PW_{12}O_{40}]^{3-}$ hybrid complexes, the similar absorption peaks were found except an red-shift phenomena from 286.0, 454.0 to 293.0 and 465.0 nm respectively (curve b). The red shift of 7–9 nm for every absorption peak further demonstrated the strong electrostatic interaction between $[Ru(bpy)_3]^{2+}$ and negatively charged $[PW_{12}O_{40}]^{3-}$ [2,4]. UV–vis spectroscopy of other hybrids $[Ru(bpy)_3]^{2+}/[H_9P(W_2O_7)_6]^{2-}$ and $[Ru(bpy)_3]^{2+}/[SiW_{12}O_{40}]^{4-}$ were also obtained (Supporting Information, Fig. S2). These curves also exhibited red-shift phenomena compared with that of free $Ru(bpy)_3Cl_2$.

The FTIR spectra were shown in Fig. 3B, and the results were listed in Table 1. Free $[Ru(bpy)_3]^{2+}$ (curve b) and $[Ru(bpy)_3]^{2+}/[PW_{12}O_{40}]^{3-}$ (curve c) exhibited several absorption peaks located in the range of 1400–1650 cm^{-1} corresponding to the characteristic of 2,2′-bpy [24]. The peaks at 1081 and 1012 cm^{-1} might be attributed to the P–O stretches and the W=O stretches respectively. The bands at 879 and 792 cm^{-1} were assigned to the edge shared (W–Ob–W) and corner-shared octahedral of Keggin unit (W–Oc–W) compared to the pure PTA (curve a). The

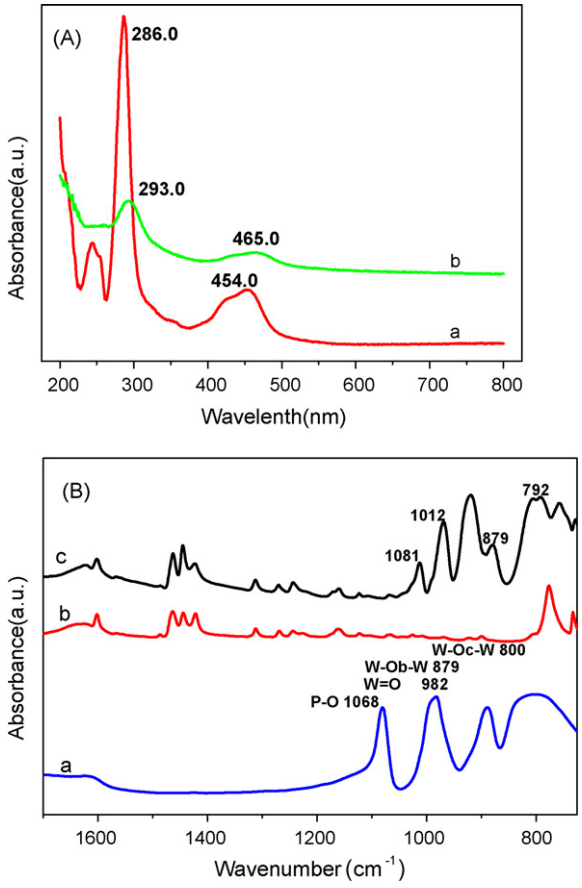


Fig. 3. (A) UV–vis absorbance spectra of (curve a) free $[Ru(bpy)_3]^{2+}$ and (curve b) $[Ru(bpy)_3]^{2+}/[PW_{12}O_{40}]^{3-}$ in aqueous solution, (B) FTIR spectra of (curve a) pure PTA, (curve b) $[Ru(bpy)_3]^{2+}$ and (curve c) $[Ru(bpy)_3]^{2+}/[PW_{12}O_{40}]^{3-}$.

Table 1
Predominant modes and vibrational frequencies of $[PW_{12}O_{40}]^{3-}$, $[Ru(bpy)_3]^{2+}$ and $[Ru(bpy)_3]^{2+}/[PW_{12}O_{40}]^{3-}$ determined from FT-IR spectroscopy.

$[PW_{12}O_{40}]^{3-}$ and $[Ru(bpy)_3]^{2+}$		$[Ru(bpy)_3]^{2+}/[PW_{12}O_{40}]^{3-}$	
Predominant modes	Frequency (cm^{-1})	Predominant mode	Frequency (cm^{-1})
W–Oc–W	800	W–Oc–W	792
W–Ob–W	879	W–Ob–W	879
W=O_d	982	W=O_d	1012
P–O_a	1068	P–O_a	1081
2,2′-bpy	1400–1650	2,2′-bpy	1400–1650

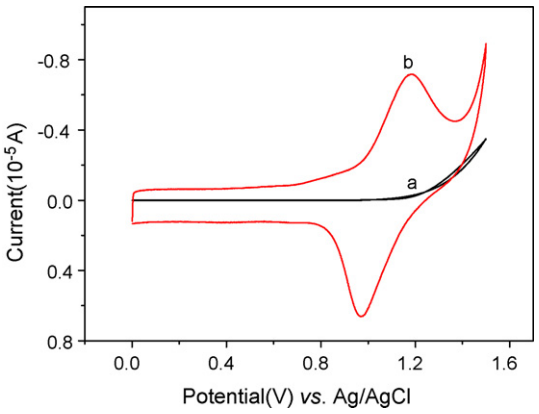


Fig. 4. CVs of (curve a) bare and (curve b) $[Ru(bpy)_3]^{2+}/[PW_{12}O_{40}]^{3-}$-coated ITO electrodes in 100 mM PBS at scan rate of 100 mV s^{-1}.

P–O and the W=O band stretches appeared at higher wavenumbers indicating an interaction of PTA with $[Ru(bpy)_3]^{2+}$ to form the hybrids robustly [25,26]. The FTIR results for the precipitates of $[Ru(bpy)_3]^{2+}$ between $[H_9P(W_2O_7)_6]^{2-}$ and $[SiW_{12}O_{40}]^{4-}$ were also confirmed the formation of $[Ru(bpy)_3]^{2+}/[H_9P(W_2O_7)_6]^{2-}$ and $[Ru(bpy)_3]^{2+}/[SiW_{12}O_{40}]^{4-}$ hybrids (Supporting Information, Fig. S3). These spectra indicated that $[Ru(bpy)_3]^{2+}$ were successfully immobilized in the hybrids via the electrostatic interaction using the simple mixing method.

3.3. Electrochemistry investigation of the $[Ru(bpy)_3]^{2+}/[PW_{12}O_{40}]^{3-}$ hybrid nanocomposites

Cyclic voltammograms (CVs) of the hybrid nanocomposite $[Ru(bpy)_3]^{2+}/[PW_{12}O_{40}]^{3-}$ suspension on ITO electrodes were recorded. Fig. 4 showed a pair of redox waves appeared at 1.18 V, which was attributed to the one-electron redox reaction of $[Ru(bpy)_3]^{2+}$ [15]. Furthermore, it was found that the anode peak currents were proportional to the square roots of scan rates ($V^{1/2}$) in the range of 100–500 mV s^{-1} (data not shown here), indicating that the $[Ru(bpy)_3]^{2+}$ components contained in the nanocomposite film on the electrode surfaces underwent a diffusion-controlled process [15]. Therefore, it may be expected that the resulting hybrid material is an ion conductor with redox-active sites. The effects of pH on the electrode responses and the formal redox potential were studied. It was found that the shifts of the anodic and the cathodic peaks towards negative potentials with the increase of the solution pH (from 4 to 10), but the separation between oxidation and reduction peaks remains constant during the displacement.

3.4. ECL behaviors and linear range

The effect of the quantity of hybrid complexes $[Ru(bpy)_3]^{2+}/[PW_{12}O_{40}]^{3-}$ on the DBAE ECL responses was investigated. It was found that the concentration and amount of $[Ru(bpy)_3]^{2+}/[PW_{12}O_{40}]^{3-}$ on the ITO surfaces determine the thickness of the film, and hence influence the ECL responses of DBAE. The responses increased gradually with the increase of the film thickness. However, the film becomes too thick, and blocks electron transfer when the original concentration of $[Ru(bpy)_3]^{2+}$ exceeds 0.06 mM and the amount of $[Ru(bpy)_3]^{2+}/[PW_{12}O_{40}]^{3-}$ dispersion exceeds 10 μL. Therefore, the 0.06 mM $[Ru(bpy)_3]^{2+}$ and 10 μL dispersion were chosen in our experiment. Fig. 5A showed the ECL intensity-potential curve of the hybrid nanocomposite $[Ru(bpy)_3]^{2+}/[PW_{12}O_{40}]^{3-}$ suspension-coated ITO containing 4.0×10^{-5} M DBAE. The highest ECL occurred near 1.18 V, which was consistent with the oxidation of the $[Ru(bpy)_3]^{2+}$ [15]. The wide

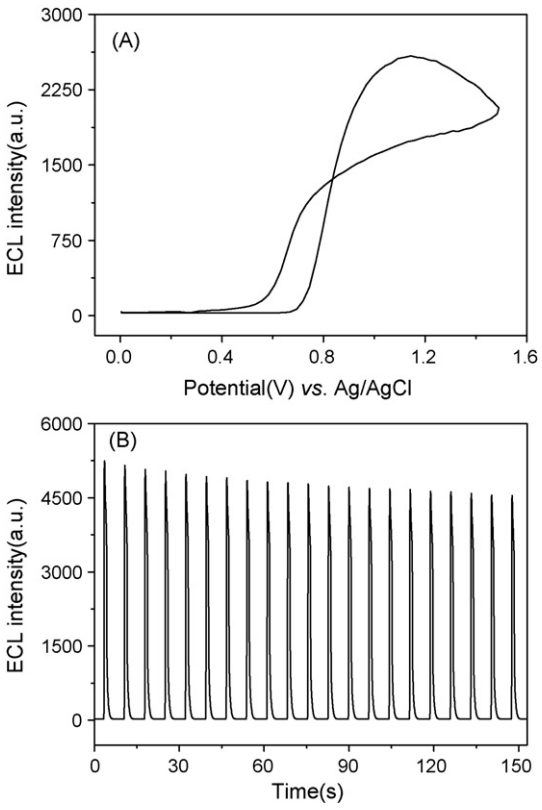


Fig. 5. (A) ECL intensity–potential curve and (B) ECL intensity–time curve of $[Ru(bpy)_3]^{2+}/[PW_{12}O_{40}]^{3-}$-coated ITO containing 4.0×10^{-5} M DBAE under continuous cyclic voltammetry for 21 cycles in PBS with the scan rate of 500 mV s^{-1}.

linear range for DBAE detection from 6.0×10^{-9} to 8.0×10^{-3} M ($R = 0.98$) with the detection limit of 1.33×10^{-10} M (S/N = 3) was obtained. The $[Ru(bpy)_3]^{2+}/[PW_{12}O_{40}]^{3-}$ nanocomposite-coated ITO electrodes also showed excellent reproducibility and stability towards DBAE detection. Fig. 5B showed the ECL intensity–time curve with 4.0×10^{-5} M DBAE under continuous potential scanning for 21 cycles, and the relative average deviation was 4.38%. The reduced ECL intensity in a span is possibly because of the fact that partial of the structure of $[Ru(bpy)_3]^{2+}/[PW_{12}O_{40}]^{3-}$ became loose and the $Ru(bpy)_3{}^{2+}$ began to leach out of the hybrid film. However, in previous report using the AuNPs to immobilize $Ru(bpy)_3{}^{2+}$, the relative average deviation of the biosensor was 2.77% only after continuous potential scanning for five cycles [13]. Most importantly, there was no additional formed film materials added in our experiments. The electrode had good ECL stability and kept over 85% its initial intensity within 2 weeks. The results indicated that the $[Ru(bpy)_3]^{2+}$ components contained HPAs nanocomposite films on the electrode surfaces were very stable. Note that the other two samples, $[Ru(bpy)_3]^{2+}/[H_9P(W_2O_7)_6]^{2-}$ and $[Ru(bpy)_3]^{2+}/[SiW_{12}O_{40}]^{4-}$, also exhibited good ECL behaviors (Supporting Information in Fig. S4).

4. Conclusions

In summary, the nanocomposites containing $[Ru(bpy)_3]^{2+}$ and HPAs have been successfully synthesized via a simple directly mixing method. Because of the good ability to form membranes of HPAs, the $[Ru(bpy)_3]^{2+}/[X_yM_zO_m]^{n-}$ nanocomposites have been robustly formed on the ITO electrode surfaces. The nanocomposite-coated ITO electrodes exhibited excellent and stable ECL behaviors. Due to their simpleness, universalness and low price, potential

applications for solid-state ECL detection in capillary electrophoresis (CE) or a CE microchip could be envisioned.

Acknowledgements

This work was supported by the National Natural Science Foundation of China (No. 90713022), the National Key Basic Research Development Project of China (No. 2007CB714500) and the Project of Chinese Academy of Sciences (Nos. KJCX2.YW.H09 and KJCX2.YW.H11).

Appendix A. Supplementary data

Supplementary data associated with this article can be found, in the online version, at doi:10.1016/j.talanta.2009.08.008.

References

[1] X. Lin, F. Li, Y. Pang, H. Cui, Anal. Bioanal. Chem. 378 (2004) 2028–2033.
[2] L. Qian, X. Yang, Adv. Funct. Mater. 17 (2007) 1353–1358.
[3] R. Pyati, M. MarkRichter, Annu. Rep. Prog. Chem. Sect. C 103 (2007) 12–78.
[4] K. Honda, M. Yoshimura, T.N. Rao, A. Fujishima, J. Phys. Chem. B 107 (2003) 1653–1663.
[5] H.S. White, A.J. Bard, J. Am. Chem. Soc. 104 (1982) 6891.
[6] B.A. Gorman, P.S. Francis, N.W. Barnett, Analyst 131 (2006) 616–639.
[7] H. Wei, E. Wang, Trends Anal. Chem. 27 (2008) 447–459.
[8] H.N. Choi, S.H. Cho, W.Y. Lee, Anal. Chem. 75 (2003) 4250–4256.
[9] J.K. Lee, S.H. Lee, M. Kim, H. Kim, D.H. Kim, W.Y. Lee, Chem. Commun. 13 (2003) 1602–1603.
[10] G.M. Greenway, A. Greenwood, P. Watts, C. Wiles, Chem. Commun. 1 (2006) 85–87.
[11] L. Armelao, R. Bertoncello, S. Gross, D. Badocco, P. Pastore, Electroanalysis 15 (2003) 803.
[12] M.M. Collinson, B. Novak, S.A. Martin, J.S. Taussig, Anal. Chem. 72 (2000) 2914.
[13] X. Sun, Y. Du, S. Dong, E. Wang, Anal. Chem. 77 (2005) 8166–8169.
[14] X. Sun, Y. Du, L. Zhang, S. Dong, E. Wang, Anal. Chem. 78 (2006) 6674–6677.
[15] X. Sun, Y. Du, L. Zhang, S. Dong, E. Wang, Anal. Chem. 79 (2007) 2588–2592.
[16] N. Fay, E. Dempsey, T. McCormac, Electrochim. Acta 51 (2005) 281–288.
[17] W. Feng, T. Zhang, Y. Liu, R. Lu, C. Guan, Y. Zhao, J. Yao, Mater. Chem. Phys. 77 (2002) 294–298.
[18] M.N. Timofeeva, Appl. Catal. A 256 (2003) 19–35.
[19] S.O. Liu, D.G. Kurth, H. Mohwald, D. Volkmer, Adv. Mater. 14 (2002) 225.
[20] S. Gao, X. Li, C. Yang, T. Li, R. Cao, J. Solid State Chem. 179 (2006) 1407–1414.
[21] A. Kuhn, F.C. Anson, Langmuir 12 (1996) 5481.
[22] V.M. Hultgren, A.M. Bond, A.G. Weld, J. Chem. Soc. Dalton Trans. (2001) 1076.
[23] L. Qian, X. Yang, Electrochem. Commun. 7 (2005) 547–551.
[24] Z. Han, E. Wang, G. Luan, Y. Li, C. Hu, P. Wang, N. Hu, H. Jia, Inorg. Chem. Commun. 4 (2001) 427.
[25] M. Aparicio, J. Mosa, M. Etienne, A. Dur'an, J. Power Sources 145 (2005) 231–236.
[26] J. Mosa, G. Larramona, A. Dur'an, M. Aparicio, J. Membr. Sci. 307 (2008) 21–27.

Talanta 80 (2009) 875–879

Contents lists available at ScienceDirect

Talanta

journal homepage: www.elsevier.com/locate/talanta

Ligandless dispersive liquid–liquid microextraction for the separation of trace amounts of silver ions in water samples and flame atomic absorption spectrometry determination

Sayed Zia Mohammadi [a,*], Daryoush Afzali [b], Mohammad Ali Taher [c], Yar Mohammad Baghelani [a]

[a] Department of Chemistry, Payame Noor University (PNU), 22 Bahman Blv., Kerman, Iran
[b] Environment Department, Research Institute of Environmental Sciences, International Center for Science, High Technology & Environmental Sciences, Kerman, Iran
[c] Department of Chemistry, Shahid Bahonar University, Kerman, Iran

ARTICLE INFO

Article history:
Received 22 June 2009
Received in revised form 7 August 2009
Accepted 9 August 2009
Available online 18 August 2009

Keywords:
Dispersive liquid–liquid microextraction
Silver determination
Preconcentration
Ligandless

ABSTRACT

In this article, a new ligandless dispersive liquid–liquid microextraction method has been developed for preconcentration of trace quantities of silver as a prior step to its determination by flame atomic absorption spectrometry. In the proposed approach, carbon tetrachloride and ethanol were used as extraction and dispersive solvents. Several factors that may be affected on the extraction process, like, extraction solvent, disperser solvent, the volume of extraction and disperser solvent, pH of the aqueous solution and extraction time were optimized. Under the optimal conditions, the calibration curve was linear in the range of 5.0 ng mL^{-1} to 2.0 μg mL^{-1} of silver with $R^2 = 0.9995$ ($n = 9$) and detection limit based on three times the standard deviation of the blank ($3S_b$) was 1.2 ng mL^{-1} in original solution. The relative standard deviation for eight replicate determination of 0.5 μg mL^{-1} silver was ±1.5%. The high efficiency of dispersive liquid–liquid microextraction to carry out the determination of silver in complex matrices was demonstrated. The proposed method has been applied for determination of trace amount of silver in standard and water samples with satisfactory results.

© 2009 Elsevier B.V. All rights reserved.

1. Introduction

The widespread use of silver compounds and silver-containing procedures in industry, medicine, jewellery, cloud seeding and in the disinfection of drinking water has resulted in an increasing silver content of environmental samples. Silver impregnated filters are used in water disinfection, while silver concentrations up to 200 μg L^{-1} is permitted for antimicrobial activities for human health [1]. Silver often presented as an impurity in Cu, Zn, As and Sb ores and thus it is possible to be entered into the environment from industrial wastes [2,3]. Bowen [4] suggested that silver may pose a potential risk as a water pollutant, because of the lack of recycling of mined silver. Also, recent information about the interaction of silver with essential nutrients, especially selenium, copper and vitamins E and B_{12}, has focused attention on its potential toxicity [1]. Consequently, determination of trace amounts of silver is important for many areas of chemical analysis.

Several atomic spectrometric techniques such as flame and electrothermal atomic absorption spectrometry (FAAS and ETAAS) [5–8], inductively coupled plasma atomic emission spectrometry (ICP-AES) [9] and inductively coupled plasma mass spectrometry (ICP-MS) [10–13] have been proposed for the determination of silver in different environmental samples. However, aforementioned methods except to FAAS involve a greater cost and increased instrumentation complexity, limiting its widespread application to routine analytical works. FAAS is still being used because it combines a fast analysis time, a relative simplicity and a cheaper cost. All of these features have been responsible for its broad utilization in the determination of trace elements in different samples. Although the development of modern analytical instruments provides a great enhancement in analysis, in many cases the available analytical instrumentation does not demonstrate enough sensitivity for the analysis of natural samples [14]. Nevertheless, the detection of metal trace elements in aqueous samples is difficult due to various factors, particularly their low concentration and the matrix effects [15]. Several methods have been reported for the separation and preconcentration of metal ions, such as coprecipitation [16,17], liquid–liquid extraction (LLE) [18,19], solid-phase extraction (SPE) [20–22] and cloud point extraction (CPE) [23–25], but the disadvantages such as time-consuming, unsatisfactory enrichment factors, large organic solvents and secondary wastes, limit their applications. In recent years, liquid-phase microextraction (LPME) has been developed as a solvent-minimized sample pretreatment procedure because it is inexpensive and has a minimal exposure to toxic organic solvents [26]. However, LPME method suffers from some disadvantages such as the fast stirring would

* Corresponding author. Tel.: +98 3413342466; fax: +98 3413321492.
E-mail address: szmohammadi@yahoo.com (S.Z. Mohammadi).

0039-9140/$ – see front matter © 2009 Elsevier B.V. All rights reserved.
doi:10.1016/j.talanta.2009.08.009

tend to format air bubble [27], time-consuming and equilibrium could not be attained after a long time in most cases [28]. In order to overcome the problems, a novel modality of LPME termed as dispersive liquid–liquid microextraction (DLLME), was proposed recently [29].

DLLME is based on a ternary component solvent system like homogeneous liquid–liquid extraction and cloud point extraction. In this method, the appropriate mixture of extraction solvent and dispersive solvent is injected into an aqueous sample rapidly by a syringe, and a cloudy solution is formed. The analyte in the sample is extracted into the fine droplets of extraction solvent. After extraction, phase separation is performed by centrifugation. The advantages of the DLLME method are simplicity of operation, rapidity, low cost, high recovery, and enrichment factors. This method has been applied for the determination of trace organic pollutants and metal ions in the environmental samples [30–35].

The aim of this work is at combining DLLME with FAAS and proposes a new method for separation, preconcentration and determination trace amounts of silver in water and standard samples. In this work, DLLME as separation method and FAAS as analytical method were selected for preconcentration and determination of silver.

2. Experimental

2.1. Instrumentation

A SensAA GBC atomic absorption spectrometer equipped with deuterium background correction and silver hollow cathode lamp was used for absorbance measurements at wavelength of 328.1 nm according to instrument instruction. The instrumental parameters were adjusted according to the manufacturer's recommendations. A Metrohm 692 pH meter was used for pH measurements.

2.2. Reagents and solutions

All chemicals were of analytical-reagent grade and all solutions were prepared with deionized water. The laboratory glassware was kept overnight in a 1.4 mol L^{-1} HNO_3 solution. Before using, all of the glassware were washed with deionized water and dried. A stock solution of silver at a concentration of 1000.0 μg mL^{-1} was prepared by dissolving appropriate amounts of $AgNO_3$ (Merck, Darmstadt, Germany) in deionized water containing 1 mL concentrated nitric acid (Merck) and stored in the dark. The working reference solutions were obtained daily by stepwise dilution from stock solution with deionized water. A solution of 1% NaCl (Merck) was prepared by dissolving of 1 g of NaCl in 100 mL of deionized water. The solutions of alkali metal salts (1%) and various metal salts (0.1%) were used to study the interference of anions and cations, respectively.

2.3. Dispersive liquid–liquid microextraction procedure

An aliquot of 8.0 mL water samples or standard solutions were placed in a screw cap glass test tube with conic bottom and 1 mL of 0.1 mol L^{-1} phosphate buffer (pH 5.0) and 1 mL of NaCl 1% (w/v) were sequentially added to it. Then, 0.5 mL of ethanol (disperser solvent) containing 15.0 μL of carbon tetrachloride (extraction solvent) was injected rapidly into the sample solution. Then, the solution was centrifuged at 4000 rpm for 5 min, and the dispersed fine droplets of CCl_4 were deposited at the bottom of conical test tube. The sediment phase was removed and 0.50 mL of dimethylformamid (DMF) was added to it. The final solution was aspirated directly into the flame of AAS against the blank prepared in the same manner without the addition of metal ions.

2.4. Sample preparation

Tow certified reference material furnished by the Nippon Keikinzoku Kogyo (NKK) No. 916 and No. 920 Aluminum Alloy has been analyzed. Approximately 0.10 g of these materials were weighed accurately into a Teflon cup and dissolved in concentrated nitric acid (~10 mL) with heating on a water bath. The solutions were cooled, and pH was adjusted to 5 by NaOH and was diluted to 100.0 mL with deionized water in a calibrated flask. Then, 8.0 mL of the sample solution was taken individually and silver ion was determined by the general procedure.

X-ray photographic films were washed with distilled water and were cut into small pieces after drying in an oven at 40 °C for 20 min. Then, 5 mL of aqueous nitric acid (4 mol L^{-1}) was added to 0.01 g of film. The mixture was filtered and solution was diluted to 100.0 mL and pH adjusted to 5 by NaOH. An aliquot of the sample solution was taken and silver ion was determined by the general procedure.

Water samples were collected in acid leached polyethylene bottles. The only pretreatment was acidification to pH 2 with nitric acid, which was performed immediately after collection, in order to prevent adsorption of the metal ions on the flask walls. The samples were filtered before analyses through a cellulose membrane of 0.45 μm pore size (Millipore).

3. Results and discussion

In this study, combination of DLLME with FAAS was developed for determination trace amounts of silver. It is based on microextraction of silver chloride with using of ethanol as dispersive solvent and carbon tetrachloride as extraction solvent. At first, phosphate buffer and NaCl solution were added to silver solution. In this step, silver reacted with chloride ion for AgCl formation, then the aqueous, dispersive and extraction solvents were mixed and a cloudy solution was formed. After formation of cloudy solution, AgCl diffuses into the extraction solvent quickly, because of the infinitely large surface area between extraction solvent and the aqueous phase. Then, the solution was centrifuged and the dispersed fine droplets of CCl_4 were deposited at the bottom of conical test tube. The sediment phase was removed and DMF was added to it. The final solution was aspirated directly into the flame of AAS.

3.1. Selection of disperser solvent

The disperser solvent must be miscible in extraction solvent (organic phase) and also sample solution (aqueous phase). Therefore, acetone, methanol, ethanol and tetrahydrofuran were tested. The effect of these solvents on the extraction efficiency of DLLME was investigated using 1.0 mL of each solvent containing 15.0 μL of CCl_4 as the extraction solvent. The maximum extraction efficiency of DLLME was obtained by using ethanol as a disperser solvent. That is due to the high compatibility of ethanol with aqueous solution than other solvents. Therefore, ethanol was selected for further experiments.

3.2. Effect of the disperser solvent volume

The volume of the disperser solvent is one of the important factors to be considered in DLLME. At lower volumes of the disperser, tiny droplet formation may not be effective. Additionally, the lack of ethanol availability for partitioning into CCl_4 phase may occur. Both phenomena will decrease the extraction efficiency. When the volume of the dispersive solvent is an increased, two competitive processes may occur. One is the increase in the solubility of the analytes in the aqueous phase leading to diminished partition of the polar compounds into CCl_4 droplets. On the contrary, an increased volume of the partitioned ethanol phase into CCl_4 phase leads to

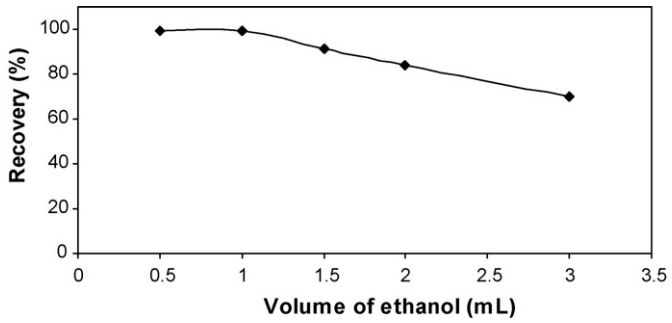


Fig. 1. Effect of the disperser solvent volume (ethanol) on the ligandless DLLME extraction. *Conditions*: Ag(I), 5.0 μg; buffer, 1 mL; NaCl 1% (w/v), 1 mL; and CCl_4, 15.0 μL.

increase in the extraction efficiency. Hence it was necessary to evaluate the volume effect of dispersive solvent. For this, a fixed amount of organic extractant (15.0 μL CCl_4) was dissolved in an increasing volume of the disperser ranging 0.5–3.0 mL. The results are presented in Fig. 1. It was observed that the extraction efficiency was constant up to 1.0 mL and then extraction efficiency was decreased for increasing volume of ethanol (1.0–3.0 mL). Finally, 0.5 mL ethanol was chosen as the optimum volume.

3.3. Selection of the extraction solvent

Choosing the most suitable extraction solvent is of primary importance to achieve good selectivity of the target compounds. This solvent must be immiscible with water and the solubility of analytes in this solvent in organic phase should be higher than the donor phase to promote the extraction of the analytes and in the case of DLLME, the density of the extraction organic solvent must be higher than water [36,37]. Dichloromethane (CH_2Cl_2), chloroform ($CHCl_3$), 1,2-dicholorobenzene (1,2-DCB) and carbon tetrachloride (CCl_4) were studied as extraction solvent. A series of sample solution were studied by using 0.5 mL of ethanol and 15.0 μL of different kind of extraction solvents. Three replicate tests were performed for each of these solvents under the same conditions. The results showed that, extraction efficiency of CCl_4 is higher than CH_2Cl_2, $CHCl_3$ and 1, 2-DCB. Therefore, CCl_4 was selected as extraction solvent for subsequent experiments.

3.4. Effect of the organic extraction volume

To study the effect of volume the extraction solvent, a series of solutions containing increasing volumes of CCl_4 (15.0–90.0 μL) dissolved in a fixed volume of ethanol were subjected to DLLME. The results are shown in Fig. 2. It was observed that the extraction efficiency was constant up to 30.0 μL and then extraction efficiency was decreased for increasing volume of CCl_4 (30.0–90.0 μL). A small

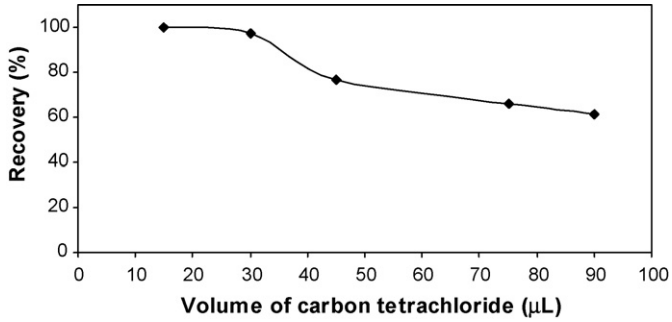


Fig. 2. Effect of the extraction solvent volume (CCl_4) on the ligandless DLLME extraction. Conditions were the same as Fig. 1.

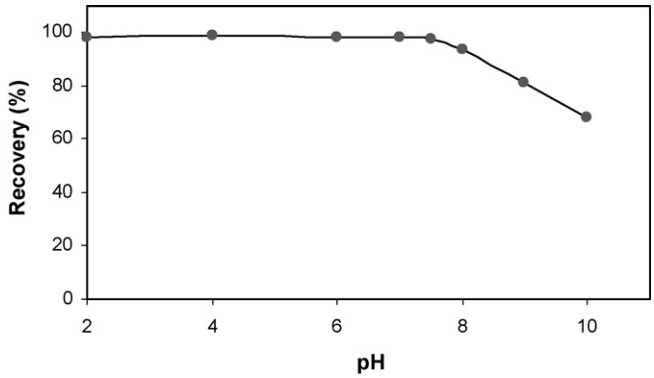


Fig. 3. Effect the pH of sample solution on the ligandless DLLME extraction of silver. Conditions were the same as Fig. 1.

decrease in efficiency was observed above 30.0 μL probably due to the decrease in the ratio between the dispersive and the extractant solvent. The decreased ratio lowers the number of droplets formation available for extraction thereby lowering the extraction efficiency. Based on these observations, 15.0 μL CCl_4 was used for further experiments.

3.5. Effect of pH

The effect of pH to the extraction systems was investigated in the range of 2–10 and keeping other variable constant. The results demonstrated in Fig. 3 reveals that the recovery is nearly constant in the pH range of 2.0–7.5. Accordingly, a pH approximately of 5 was selected for further experiments.

3.6. Effect of chloride concentration

The influence of the chloride concentration on the recovery of silver ion was studied in the range of 0.05–1% (w/v). The results are shown in Fig. 4. The recovery was increased by increasing the chloride concentration up to 0.3%. A further excess of 0.3% would cause a decrease in extraction. Therefore, the chloride concentration of 0.1% was selected for further experiments.

3.7. Effect of the extraction time

In DLLME, the extraction time is defined as interval time between the injection of the disperser and extraction solvents and the starting of centrifuge. The effect of extraction time was examined in the range of 10 s to 30 min with the constant experimental conditions. The obtained results showed that the extraction time was no significant influence on the signal of silver. Therefore, the DLLME method was time-independent, which was the most

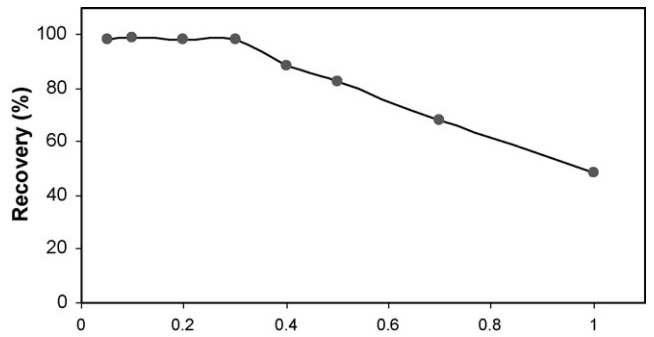


Fig. 4. Effect of chloride amount on the ligandless DLLME extraction of silver. Conditions were the same as Fig. 1.

Table 1
Tolerance limit of foreign ions.

Foreign ions	Interference/Ag(I) ratio	Recovery (%)
PO_4^{3-}, $H_2PO_4^-$, HPO_4^{2-}	4000	95
CH_3COO^-	3000	96
Ca^{2+}, Mg^{2+}	2000	97
Co^{2+}, Cu^{2+}, Mn^{2+}	1000	105
Fe^{2+}	1000	95
Ni^{2+}, Zn^{2+}	800	103
Al^{3+}	1000	95
As^{3+}	600	98
Fe^{3+}	200	96
Cd^{2+}	400	95

Conditions were the same as Fig. 1.

important advantage of this technique. In this method, the most time-consuming step was the centrifuging of sample solution in the extraction procedure. The process took about 5 min.

3.8. Effect of foreign ions

In view of the high selectivity provided by flame atomic absorption spectrometry, the only interference may be attributed to the separation step. Interferences studied were those related to the separation step, cations that may react with chloride or species that may react with analytes and decrease the extraction efficiency. To perform this study, interference ions in different interference-to-analyte ratios were added to a solution containing 5.0 μg of Ag(I) and were subjected to the recommended procedure. Table 1 shows the tolerance limits of the interference ions (error ±5%). The results demonstrate that the presence of large amounts of species commonly present in water samples have no significant effect on the DLLME of silver.

3.9. Calibration, precision and detection limit

Repeatability, linearity, correlation coefficient and detection limit were investigated under the optimized experimental conditions. For a sample volume of 8.0 mL, the calibration graph exhibited linearity over the range of 5.0 ng mL^{-1} to 2.0 μg mL^{-1} with a correlation coefficient of 0.9995 ($A = 0.46C + 0.007$). Eight replicate determination of 0.5 μg mL^{-1} silver gave a mean absorbance of 0.236 with relative standard deviation ±1.5%. Detection limit was 1.2 ng mL^{-1} for Ag(I) based on three times of blank standard deviation.

3.10. Accuracy of the method

The accuracy of the proposed method has been studied by adding silver ion in Nippon Keikinzoku Kogyo (NKK) No. 916 and No. 920 Aluminum Alloy. Results are given in Table 2 and were shown good recovery for silver ion. Therefore, the proposed method was shown good accuracy.

3.11. Analysis of water samples

The proposed procedure has been applied to the determination of silver content in different water samples. The results are given in Table 3.

The recovery of silver from water samples spiked with Ag(I) were also studied. The results were tabulated in Table 3. According this table, the added silver ion can be quantitatively recovered from the water samples by the proposed procedure.

These results demonstrate the applicability of the procedure for silver determination in water samples. The recovery of silver

Table 2
Recovery of Ag(I) ion from standard alloy.

Sample	Composition (%)	Added Ag^+ (μg)	Found[a] (μg)	Recovery (%)
NKK No. 916 Aluminum Alloy	Si, 0.41; Fe, 0.54; Mg, 0.10; Cr, 0.05; Zn, 0.30; Ti, 0.10; Sn, 0.05; Pb, 0.04; Sb, 0.01; B, 0.0006; Zr, 0.05; Bi, 0.03; Co, 0.03; Mn, 0.11; Ni, 0.06; V, 0.02	10.0	9.9 ± 0.5	99
NKK No. 920 Aluminum Alloy	Si, 0.78; Fe, 0.72; Mg, 0.46 Cr, 0.27; Zn, 0.80; Ti, 0.15; Sn, 0.20; Pb, 0.10; Sb, 0.10; Bi, 0.06; Ga, 0.05; Ca, 0.03; Co, 0.10; Mn, 0.20; Ni, 0.29; V, 0.15	10.0	10.2 ± 0.6	102

[a] Mean ± standard deviation ($n = 4$).

Table 3
Determination of silver in water samples.

Sample	Silver amount (ng mL^{-1})[a]		Recovery (%)
	Added	Found	
Wastewater (Copper factory, Sarchashmeh, Rafsanjan)	0.0	6.2 ± 0.4	–
	10.0	16.0 ± 1.0	98
Tap water (Sarchashmeh, Rafsanjan)	0.0	BLR[b]	–
	10.0	10.6 ± 0.5	106
Springer water (Sarchashmeh, Rafsanjan)	0.0	BLR	–
	10.0	10.1	101

[a] Mean ± standard deviation ($n = 4$).
[b] Below of linear range.

Table 4
Comparison of the proposed method with other reported methods for preconcentration of silver.

System	Analysis method	Sample volume (mL)	Sample preparation time (min)	Enrichment factor	RSD (%)	Linear range (ng mL^{-1})	LOD (ng mL^{-1})	Ref.
CPE	FAAS	10	25	43	2.14	3.0–200.0	0.56	[38]
CPE	ETAAS	15	10	60	4.2	5.0–100.0	1.2	[39]
CPE	FAAS	15	36	42	2.1	–	1.4	[40]
Ligandless DLLME	FAAS	8	5	16	1.5	5.0–2000.0	1.2	Present work

added to the samples demonstrates the efficiency of the proposed method.

4. Conclusion

This work has been demonstrated combination of ligandless DLLME with flame atomic absorption spectrometry provides a novel route for trace determination of silver in water samples. The main benefits of the ligandless DLLME methodology were: minimum use of toxic organic solvent, simplicity, low cost, enhancement of sensitivity, and rapid analysis time.

A comparison of the represented method with the other reported methods [38–40] was shown in Table 4. As shown in Table 4, the detection limit of the proposed method is comparable to those in reported methods.

References

[1] Environment Protection Agency (EPA), Ambient Water Quality Criteria for Silver, EPA 4405-80-071, Office of Water Regulations, Washington, DC, 1980.
[2] R. Soager, Metallic Raw Materials Dictionary, Bank Tobel, Zurich, 1984.
[3] M.M. Gomez, M.M.H. Garsia, M.A.P. Corvillo, Analyst 120 (1995) 1911.
[4] H.J.M. Bowen, Trace Element Biochemistry, Academic Press, London, 1996.
[5] J. Sramkova, S. Kotrly, P. Jakoubkova, Anal. Chim. Acta 408 (2000) 183.
[6] P. Bermejo-Barrera, J. Moreda-Pineiro, A. Moreda-Pineiro, A. Bermejo-Barrera, J. Anal. At. Spectrom. 13 (1998) 777.
[7] M.G. Baron, R.T. Herrin, D.E. Armstrong, Analyst 25 (2000) 123.
[8] I. Lopez-Garcıa, N. Campillo, I. Arnau-Jerez, M. Hernandez-Cordoba, Spectrochim. Acta Part B 58 (2003) 1715.
[9] R.P. Singh, E.R. Pambid, Analyst 115 (1990) 301.
[10] K. Ndungu, M.A. Ranville, R.P. Franks, A.R. Flegal, Mar. Chem. 98 (2006) 109.
[11] L. Yang, R.E. Ralph, J. Anal. At. Spectrom. 17 (2002) 88.
[12] J. Hu, Z. Liu, H. Wang, Anal. Chim. Acta 451 (2002) 329.
[13] C.C. Chang, H.T. Liu, S.J. Jiang, Anal. Chim. Acta 493 (2003) 213.
[14] E. Carasek, J.W. Tonjes, M. Scharf, Talanta 56 (2002) 185.
[15] J. Chena, S. Xiao, X. Wu, K. Fang, W. Liu, Talanta 67 (2005) 992.
[16] Y. Wang, M.L. Chen, J.H. Wang, J. Anal. Atom. Spectrom. 21 (2006) 535.
[17] M. Soylak, M. Tuzen, J. Hazard. Mater. 152 (2008) 656.
[18] A.N. Anthemidis, D.G. Themelis, J.A. Stratis, Talanta 54 (2001) 37.
[19] L. Pan, Y.C. Qin, B. Hu, Z.C. Jiang, Chem. Res. Chin. Univ. 23 (2007) 399.
[20] S.Z. Mohammadi Mobarakeh, M.A. Taher, A. Mostafavi, Can. J. Anal. Sci. Spect. 50 (2005) 7.
[21] D. Afzali, M.A. Taher, A. Mostafavi, S.Z. Mohammadi Mobarakeh, Talanta 65 (2005) 476.
[22] M.A. Taher, B.K. Puri, R.K. Bansal, Microchem. J. 58 (1998) 21.
[23] A. Shokrollahi, M. Ghaedi, O. Hossaini, N. Khanjari, M. Soylak, J. Hazard. Mater. 160 (2008) 435.
[24] S. Candir, I. Narin, M. Soylak, Talanta 77 (2008) 289.
[25] F. Shemirani, R. Rahnama Kozani, Y. Assadi, Microchim. Acta 157 (2007) 81–85.
[26] E. Psillakis, N. Kalogerakis, Trends Anal. Chem. 22 (2003) 565.
[27] G. Shen, H.K. Lee, Anal. Chem. 74 (2002) 648.
[28] F. Ahmadi, Y. Assadi, M.R.M. Hosseini, M. Rezaee, J. Chromatogr. A 1101 (2006) 307.
[29] M. Rezaee, Y. Assadi, M.R. Milani Hosseini, E. Aghaee, F. Ahmadi, S. Berijani, J. Chromatogr. A 1116 (2006) 1.
[30] N. Fatahi, S. Samadi, Y. Assadi, M.R. Milani Hosseini, J. Chromatogr. A 1169 (2007) 63.
[31] F. Rezaei, A. Bidari, A. Pajand Birjandi, M.R. Milani Hosseini, Y. Assadi, J. Hazard. Mater. 158 (2008) 621–627.
[32] E. Zeini Jahromi, A. Bidari, Y. Assadi, M.R. Milani Hosseini, M.R. Jamali, Anal. Chim. Acta 585 (2007) 305.
[33] M.T. Naseri, M.R. Milani Hosseini, Y. Assadi, A. Kiani, Talanta 75 (2008) 56.
[34] P. Liang, H. Sang, Anal. Biochem. 380 (2008) 21.
[35] A. Bidari, E. Zeini Jahromi, Y. Assadi, M.R. Milani Hosseini, Microchem. J. 87 (2007) 6.
[36] D.K. Dubey, D. Pardasani, J. Chromatogr. A 1107 (2006) 29.
[37] S. Berijani, Y. Assadi, M. Anbia, M. Milani Hosseini, E. Aghaee, J. Chromatogr. A 1123 (2006) 1.
[38] J.L. Maanzoori, G. Karim Nezhad, Anal. Chim. Acta 484 (2003) 155.
[39] J.L. Maanzoori, H. Abdolmohammad Zadeh, M. Amjadi, J. Hazard. Mater. 144 (2007) 458.
[40] M. Ghaedi, A. Shokrollahi, K. Niknam, E. Niknam, A. Najibi, M. Soylak, J. Hazard. Mater. 168 (2009) 1022.

Talanta 80 (2009) 880–888

Contents lists available at ScienceDirect

Talanta

journal homepage: www.elsevier.com/locate/talanta

Simultaneous determination of sulpiride and its alkaline degradation product by second derivative synchronous fluorescence spectroscopy

Amina Abdelal, Nahed El-Enany*, Fathalla Belal

Department of Pharmaceutical Analytical Chemistry, Faculty of Pharmacy, University of Mansoura, 35516 Mansoura, Egypt

ARTICLE INFO

Article history:
Received 24 April 2009
Received in revised form 6 August 2009
Accepted 9 August 2009
Available online 15 August 2009

Keywords:
Sulpiride
Synchronous fluorimetry
Second derivative synchronous fluorimetry
Real plasma
Kinetics
Stability study

ABSTRACT

Simple and sensitive synchronous fluorimetric, and second derivative synchronous fluorometric methods were developed for the validated and simultaneous determination of sulpiride (SLP) and its alkaline degradation product (DSLP). The method is based on measuring the synchronous fluorescence of both the drug and its degradation product in borate buffer of pH 8 at $\Delta\lambda$ of 45 nm. The peak amplitude (^{2}D) was measured at 295.5 and 342 nm for SLP and DSLP, respectively. The different experimental parameters affecting the synchronous fluorescence intensity of both compounds were studied and optimized. The fluorescence–concentration plots were rectilinear over the range of 0.05–1.0 and 2–10 μg mL^{-1} for SLP and DSLP, respectively. The limits of detection (LOD) were 0.02 and 0.4 μg mL^{-1} and quantification limits (LOQs) were 0.05 and 1.2 μg mL^{-1} for SLP and DSLP, respectively. The proposed methods were successfully applied to commercial capsules and tablets. Statistical comparison of the results with those of the official method revealed good agreement and proved that there were no significant difference in the accuracy and precision between the two methods, respectively. The method was utilized to study the kinetics of the alkaline induced degradation of the drug. The application was further extended to include the *in vivo* and *in vitro* determination of sulpiride. The mean % recoveries (n = 3) were 100.22 ± 2.04 and 92.00 ± 3.00 for spiked and real human plasma, respectively.

© 2009 Elsevier B.V. All rights reserved.

1. Introduction

Sulpiride (SLP); 2-methoxy-*N*-((1-propylpyrrolidin-2-yl) methyl)-5-sulphamoyl benzamide (Fig. 1) is the most widely prescribed anti-psychotic drug. It is a selective dopamine D2 antagonist with antidepressant activities [1]. It has found widespread clinical applications for the treatment of acute and chronic schizophrenia as well as similar mental disorders such as hallucination [1].

The British Pharmacopoeia (BP) recommended non-aqueous titration method for the determination of SLP in its pure form, using perchloric acid as a titrant and glacial acetic acid as a solvent. For its dosage forms, the BP recommended a spectrophotometric method based on measuring its absorbance in 0.1 M NaOH at 291 nm [2]. Several methods have been reported for the determination of SLP in pharmaceutical preparations and biological fluids. These methods include: spectrophotometry [3], HPLC [4–8], capillary electrophoresis [9,10] and adsorptive stripping voltammetry [11].

A spectrofluorimetric method was reported for the determination of SLP in spiked human urine. It involved the incorporation of excitation–emission matrix (EEM) fluorescence and second-order calibration methodologies based on the alternating fitting residue (AFR) and self-weighted alternating trilinear decomposition (SWATLD) algorithms [12].

To the best of our knowledge, nothing has been reported concerning determination of SLP in presence of its alkaline degradation product (DSLP). For this reason our target was to study the application of second derivative synchronous fluorescence spectroscopic (SDSFS) technique for the simultaneous determination of SLP and DSLP. The present study describes a novel spectrofluorimetric method with enhanced sensitivity, specificity and good separation for the simultaneous determination of SLP and DSLP without prior separation step.

The proposed spectrofluorimetric method is more simple and more sensitive than the reported method [12].

Synchronous fluorescence spectroscopy (SFS) provided narrow and sharp spectrum contrast to broad fluorescence emission/excitation spectra obtained in conventional fluorescence measurement [13].

Synchronous fluorescence spectroscopy (SFS) can further be classified according to scanning modes of monochromators into constant-wavelength, variety-angle and constant-energy. At present study, constant-wavelength method, that is to maintain a constant difference between the emission and excitation wavelengths, is used.

* Corresponding author. Fax: +20 502247496.
E-mail address: nelenany1@yahoo.com (N. El-Enany).

0039-9140/$ – see front matter © 2009 Elsevier B.V. All rights reserved.
doi:10.1016/j.talanta.2009.08.007

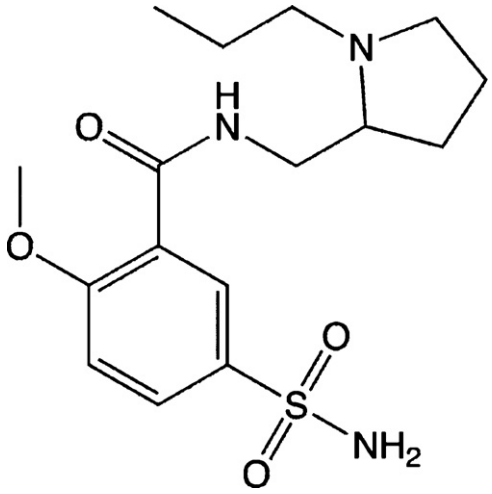


Fig. 1. Chemical structure of sulpiride.

The combination of SFS and derivatives is more advantageous than differentiation of the conventional emission spectrum in terms of sensitivity, because the amplitude of the derivative signal is inversely proportional to the bandwidth of the original spectrum [14]. Derivative synchronous fluorometric (DSF) technique is the most widely used in pharmaceutical analysis of several mixtures in their co-formulated dosage forms and biological fluids such as metoclopramide/pyridoxine [15], cinnarzine/nicergoline and cinnarzine/domperidone [16,17].

2. Experimental

2.1. Apparatus

The fluorescence spectra and measurements were recorded using a PerkinElmer model LS 45 luminescence spectrometer, equipped with a 150 W Xenon arc lamp, grating excitation and emission monochromators and a PerkinElmer recorder. Slit widths for both monochromators were set at 10 nm. A 1-cm quartz cell was used. Derivative spectra were evaluated using Fluorescence Data Manger (FLDM) software. FL WINLAB, Version 4.00.02, copyright 2001, PerkinElmer, Inc., UK. $\Delta\lambda$ of 45 nm was chosen as it resulted in two distinct peaks with good regular shapes and reduced the spectral interference caused by each compound in the mixture.

A pH meter (Model pHS-3C, Shanghai Leici Instruments, China) was used for pH adjustment.

2.2. Materials and reagents

All reagents and solvents were of Analytical Reagent grade.

Sulpiride pure sample was obtained from Sigma (St. Louis, Mo, USA) and used as received. Dogmatil® capsules each containing 50 mg SLP, batch # 3051022 (product of Memphis Chemical Co. For Pharmaceutical and Chemical Industries, Cairo, Egypt. Topmode® capsules each containing 50 mg SLP, batch # 14296 and Topmode® tablets each labelled to contain 200 mg SLP, batch # 61089 (products of Delta Pharm for Pharmaceutical Industries, Cairo, Egypt). All were obtained from local Pharmacy. Methanol (Merck, Darmstadt, Germany). Borate buffer (0.2 mol L^{-1}, pH 6–11). Acetate buffer (0.2 mol L^{-1}, pH 3.6–5.6). Sodium hydroxide and hydrochloric acid (BDH, UK), 2 mol L^{-1} aqueous solutions. Plasma samples were obtained from Mansoura University Hospital, Blood Bank, Mansoura, Egypt, and were kept frozen until use after gentle thawing.

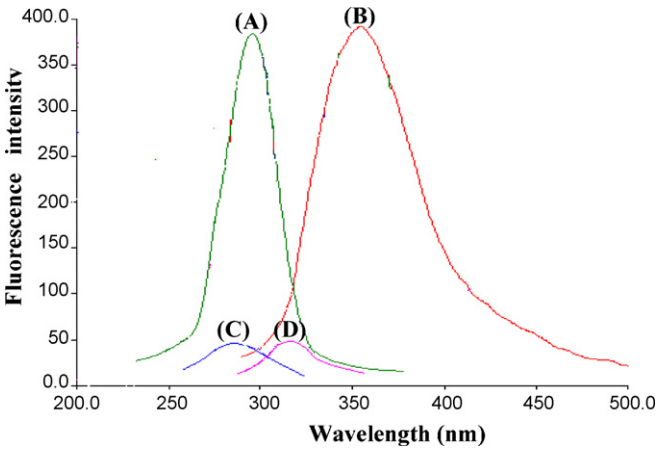


Fig. 2. Excitation and emission fluorescence spectra of: (A and B) SLP (1.0 μg mL^{-1}) and (C and D) DSLP (1.0 μg mL^{-1}).

2.3. Preparation of standard solution

2.3.1. Preparation of stock standard solution

Stock solution of SLP was prepared by dissolving 20.0 mg in 100 mL of methanol and was further diluted with the same solvent as appropriate. The standard solutions were stable for 10 days when kept in the refrigerator.

2.3.2. Preparation of alkaline degradation product

Methanolic SLP solution containing 400 μg mL^{-1} was mixed with 20 mL of 2 mol L^{-1} NaOH in a small flask, heated under refluxed in a boiling water bath for 2 h. The solution was cooled, neutralized with 2 mol L^{-1} HCl and transferred to 50 mL volumetric flask and diluted to the mark with methanol. This solution was further diluted with the same solvent as appropriate to obtain the working standard solutions.

2.4. Construction of calibration graph

Aliquots of SLP and DSLP standard solutions covering the working concentration ranges were transferred into a series of 10 mL volumetric flasks. Two milliliters of borate buffer (pH 8.0) were added, and the solution was completed to the volume with distilled water. The synchronous fluorescence spectra of the solutions were recorded by scanning both monochromators at a constant-wavelength difference, $\Delta\lambda$ of 45 nm and scan rate of 600 nm min^{-1} using 10 nm excitation and emission windows. The second derivative fluorescence spectra of SLP and DSLP were derived from the normal synchronous spectra using FLDM software. For best resolution and smoothing, the number of points used were 99 for deriving the second derivative spectra. The fluorescence intensities of the second derivative spectra were estimated at 295.5 and 342 nm for SLP and DSLP, respectively. A blank experiment was carried out simultaneously. The peak amplitude of the second derivative technique was plotted *versus* final concentration (μg mL^{-1}) to get the calibration graphs. Alternatively, the corresponding regression equations were derived.

2.5. Procedure for the synthetic mixture

Aliquots of SLP with DSLP standard solutions in different ratios were transferred into a series of 10 mL volumetric flasks. Two milliliters of borate buffer (pH 8.0) were added, and completed to the volume with distilled water and mixed well. The procedure described under Section 2.4 was performed.

2.6. Procedure for commercial capsules and tablets

The contents of 10 capsules were emptied and mixed well. For tablets, 20 tablets were weighed and pulverized well. A weighed quantity of the powdered capsules or tablets equivalent to 20.0 mg of SLP was transferred into a small conical flask and extracted with 3 × 30 mL of methanol. The extract was filtered into a 100 mL volumetric flask. The conical flask was washed with few mLs of methanol. The washings were passed into the same volumetric flask and completed to the volume with the same solvent. Aliquots covering the working concentration range were transferred into a series of 10 mL volumetric flasks. The procedure described under Section 2.4 was applied. The nominal content of the capsules or tablets was determined either from the previously plotted calibration graph or using the corresponding regression equation.

2.7. Procedure for spiked human plasma

One ml aliquots of plasma were transferred into a series of centrifuge tubes. Aliquots of sulpiride working solution were added so that their final concentration is in the range of 0.05-0.15 μg mL^{-1}. 0.1 mL of 1 mol L^{-1} NaOH was added. The samples were mixed well using a vortex mixer, then extracted with 3 × 3 mL of ethylacetate/dichloromethane (5:1, v/v) by centrifugation for 5 min at 3500 rpm. The organic layer was transferred into an evaporating dish and evaporated till dryness. The residue was reconstituted in 3 mL of methanol. The procedure described under Section 2.4 was followed. The nominal content of the drug was determined from the previously plotted calibration graph or using the corresponding regression equation.

2.8. Procedure for real human plasma

Sulpiride (50 mg/capsule) was orally administered to a healthy fasting volunteer (male, 40 years old). Five milliliters of blood sample was withdrawn after 4 h, 4 mL of citrate solution was added, and centrifuged at 3500 rpm for 15 min to get about 3 mL of plasma. The "procedure for spiked human plasma" was applied. The nominal content of SLP in plasma was determined adopting the following equation [18]:

$$\text{Recovery}_{\text{“}in\ vivo\text{”}} = \text{Delivery}_{\text{“}in\ vivo\text{”}} \times \text{Recovery}_{\text{“}in\ vitro\text{”}}/\text{Delivery}_{\text{“}in\ vitro\text{”}}$$

$$\text{The \% recovery for sulpiride in real human plasma} = \frac{\text{concentration of the drug in real plasma} \times \text{\% recovery in spiked plasma}}{\text{concentration of the drug in spiked plasma}}$$

3. Results and discussion

Both sulpiride and its alkaline degradation product exhibit native fluorescence at 350 and 317 nm, after excitation at 295 and 288 nm, respectively, as shown in Fig. 2.

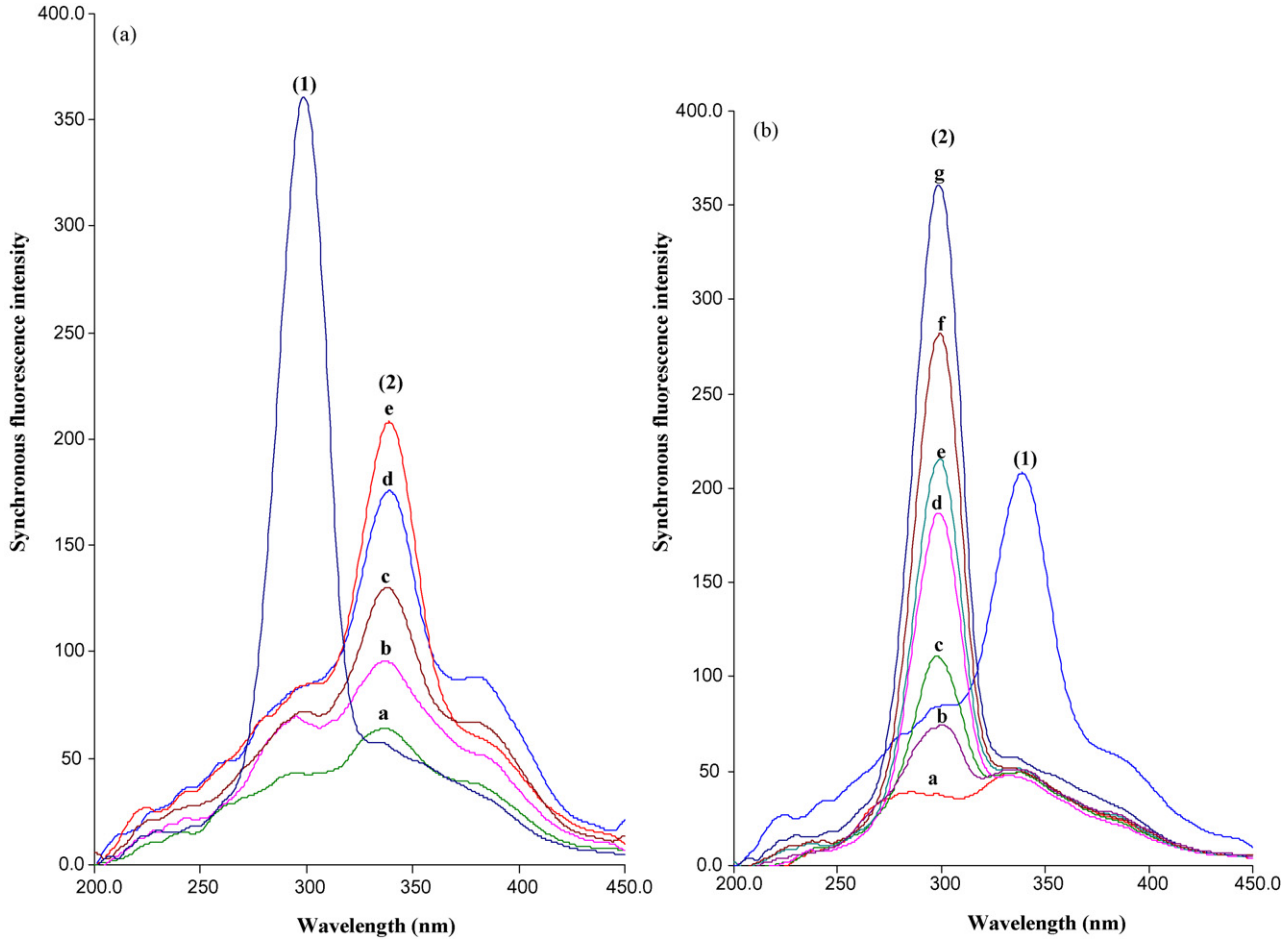


Fig. 3. (a) Synchronous fluorescence spectra of: (1) SLP (1 μg mL^{-1}) at 299 nm and (2) (a–e) of DSLP (2, 4, 6, 8 and 10 μg mL^{-1}) at 336 nm. (b) Synchronous fluorescence spectra of: (1) DSLP (10 μg mL^{-1}) at 336 nm and (2) (a–g) of SLP (0.1, 0.2, 0.3, 0.5, 0.6, 0.7 and 1 μg mL^{-1}) at 299 nm.

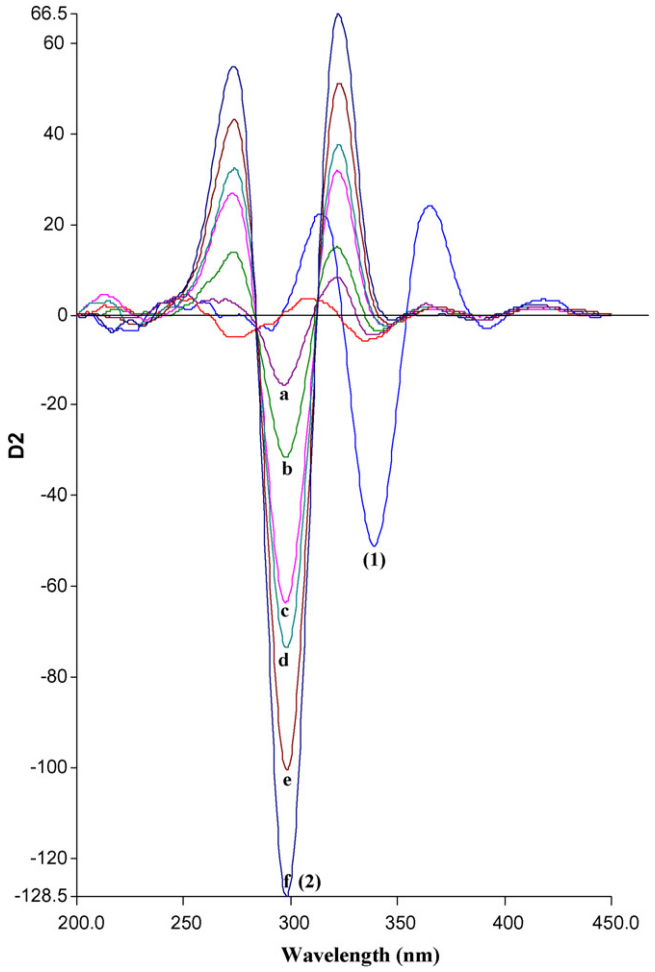


Fig. 4. Second derivative synchronous fluorescence spectra of: (1) DSLP (10 μg mL^{-1}) at 342 nm and (2) (a–f) of SLP (0. 1, 0.2, 0.5, 0.6, 0.8 and 1 μg mL^{-1}) at 295.5 nm.

Fig. 3(a) and (b) shows the synchronous fluorescence spectra of SLP at 299 and different concentrations of DSLP at 336 nm and SF spectra of different concentrations of SLP at 299 nm and DSLP at 336 nm, respectively. It is clear that, there is strong overlapping between the two spectra. This led us to adopt second derivative synchronous fluorescence spectroscopy (SDSFS) technique for the simultaneous determination of the two compounds. The fluorescence spectra of SLP and DSLP were well separated with a zero-crossing point for each compound. Under the described experimental conditions, the two peaks appeared at 295.5 for SLP (Fig. 4) and 342 nm for DSLP (Fig. 5).

The different experimental parameters affecting the fluorescence of the studied compounds were carefully studied and optimized. Such factors were changed individually while others were kept constant. These factors included $\Delta\lambda$ selection, pH, type of diluting solvent and stability time.

3.1. Effect of pH

The influence of pH on the synchronous fluorescence intensity of the studied compound and its degradation product was studied. Different salts were used to prepare the various kinds of buffers covering the whole pH range, such as 0.1 M HCl of pH 1.0, acetate buffer, borate buffer and 0.1 M NaOH. The results showed that, the synchronous fluorescence intensity of SLP increased with the increase of pH up to 7.8, then remained constant up to pH 8.2, after which the fluorescence intensity decreased gradually.

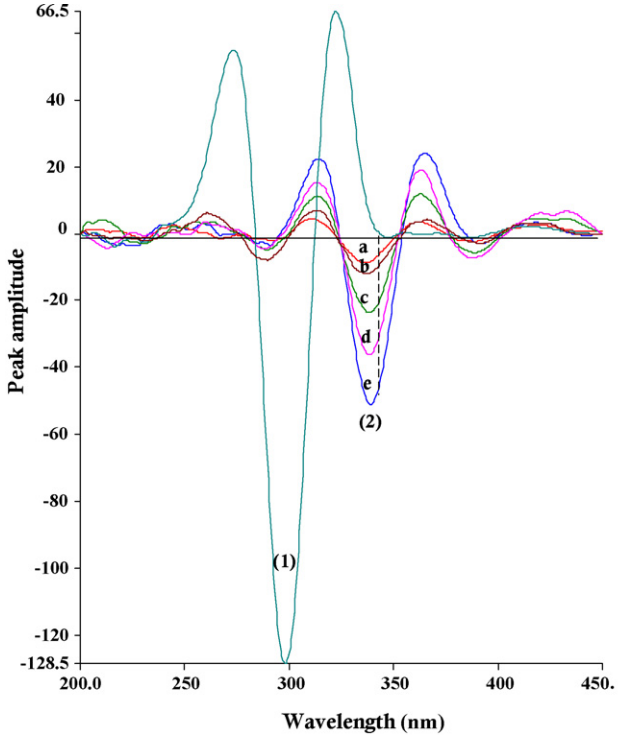


Fig. 5. Second derivative synchronous fluorescence spectra of (1) SLP (1 μg mL^{-1}) at 295.5 nm and (2) (a–f) of DSLP (2, 4, 6, 8 and 10 μg mL^{-1}) at 342 nm.

3.2. Effect of diluting solvent

Dilution with different solvents such as water, methanol, isopropanol, dimethyl sulphoxide (DMSO), tetrahydrofurane (THF) and dimethyl formamide (DMF) was attempted. Each of DMSO, THF and DMF decreased the fluorescence intensities of SLP, since they initiated intersystem crossing process (similar to heavy atom effect) [19]. On the other hand, the fluorescence intensities of SLP and DSLP were higher in water compared to other solvents. Moreover, its use adds another advantage of the method. The results are summarized in Table 1. In water, the fluorescence readings were stable for up to 2 h as revealed in Table 1.

Table 1
Effect of solvents and time on the synchronous fluorescence intensity of sulpiride (1 μg mL^{-1}).

Parameter	Synchronous fluorescence intensity
1: Effect of solvents	
Water	377
Methanol	360
Dimethyl sulphoxide	−78
Dimethyl formamide	−13
Tetrahydrofuran	155
2: Effect of time (min)	
Immediate	377
10	377
20	376
40	376
60	375
90	373
120	371

Table 2
Performance data of the proposed method.

Parameter	SLP	DSLP
Concentration range ($\mu g\,mL^{-1}$)	0.05–1.0	2–10
Correlation coefficient	0.9999	0.9994
Slope	121.9	4.1
Intercept	0.017	−0.13
Limit of detection (LOD) ($\mu g\,mL^{-1}$)	0.02	0.4
Limit of quantification (LOQ) ($\mu g\,mL^{-1}$)	0.05	1.2
$S_{y/x}$: standard deviation of the residuals	0.26	0.53
S_a: standard deviation of the intercept	0.64	0.49
S_b: standard deviation of the slope	0.280	0.074
% RSD = relative standard deviation	1.24	1.93
% Error = % RSD/$\sqrt{n}$	0.47	0.86

3.3. Analytical performance

The fluorescence–concentration plots for the studied compounds by SDSFS were linear over the concentration ranges of 0.05–1.0 and 2–10 $\mu g\,mL^{-1}$ for SLP and DSLP, respectively (Table 2). Linear regression analysis of the data gave the following equations:

For SLP:. . .. . .

$$^2D = 0.017 + 121.9C \quad (r = 0.9999)$$

For DSLP:. . .. . .

$$^2D = -0.13 + 4.1C \quad (r = 0.9994)$$

where ^2D is the peak amplitude in the second derivative synchronous fluorescence mode, C is the concentration of the drug ($\mu g\,mL^{-1}$).

LOQ and LOD were calculated according to ICH Q2B recommendations [20]. The values of LOD and LOQ for SLP and DSLP by SDSFS method are abridged in Table 2.LOQ and LOD were calculated according to the following equation [20]:

$$LOQ = 10\sigma/S$$

$$LOD = 3.3\sigma/S$$

S is the slope and σ is the standard deviation of the intercept of regression line of the calibration curve.

The proposed method was evaluated by studying the accuracy as percent relative error and precision as percent relative standard deviation. The results are abridged in Table 2.

Statistical analysis of the results obtained by the proposed and the official methods [2] using Student's t-test and variance ratio F-test [21] shows no significant difference between the performance of the two methods regarding the accuracy and precision, respectively as shown in Table 3.

3.4. Analysis of mixture of SLP and DSLP

The proposed method was applied to the simultaneous determination of SLP and DSLP in synthetic mixtures containing different concentrations of both compounds in different ratios (Table 4). The concentrations of both compounds in the synthetic mixture were calculated according to the linear regression equation. The results indicate the accuracy of the proposed method as shown in Table 4.

3.5. Validation of the method

The proposed method was tested for linearity, specificity, accuracy and precision. Linear regression equations using the proposed method were obtained. The regression plots showed a linear dependence of peak amplitudes on drug concentration over the range

Table 3
Application of the second derivative synchronous fluorimetry to the determination of sulpiride in pure form and dosage forms.

Sample	Concentration taken ($\mu g\,mL^{-1}$)	Concentration found ($\mu g\,mL^{-1}$)	Recovery (%)	Official method
1: Raw material	0.05	0.049	98.00	101.05
	0.10	0.101	101.00	99.69
	0.20	0.202	101.00	100.57
	0.40	0.403	100.75	
	0.60	0.591	98.50	
	0.80	0.797	99.63	
	1.0	1.006	100.60	
$x' \pm SD$			99.93 ± 1.24	100.44 ± 0.69
t-test			0.65 (2.26)	
F-test			3.23 (5.14)	
2: Dogmatil® capsule (50 mg SLP/capsule), Batch # 3051022	0.20	0.196	98.15	97.45
	0.40	0.406	101.45	97.72
	0.60	0.599	99.75	101.67
$x' \pm SD$			99.78 ± 1.65	98.95 ± 2.36
t-test			0.50 (2.76)	
F-test			2.05 (19.0)	
3: Topmode®capsule (50 mg SLP/capsule), Batch # 14296	0.20	0.199	99.55	99.09
	0.40	0.393	98.25	97.95
	0.60	0.605	100.83	98.63
$x' \pm SD$			99.54 ± 1.29	98.56 ± 0.57
t-test			1.02 (2.76)	
F-test			5.12 (19.0)	
4: Topmode® tablets (200 mg SLP/tablet), Batch # 61089	0.20	0.204	102.05	102.27
	0.40	0.401	100.25	100.45
	0.60	0.592	98.67	98.33
$x' \pm SD$			100.32 ± 1.70	100.35 ± 1.97
t-test			0.02 (2.76)	
F-test			1.36 (19.0)	

N.B.: Values between parenthesis are the tabulated t and F values, respectively, at $p = 0.05$ [21].

Table 4
Application of second derivative synchronous fluorimetry for the determination of sulpiride in presence of its degradation product.

Sample	Concentration taken ($\mu g\,mL^{-1}$)		Concentration found ($\mu g\,mL^{-1}$)	Recovery (%)
	SLP	DSLP	SLP	SLP
	0.4	2.0	0.406	101.50
		4.0	0.409	102.25
		6.0	0.395	98.75
		10.0	0.399	99.75
X'				100.56
±SD				1.6
% RSD				1.6
% Error				0.792
	0.6	2.0	0.615	102.25
		4.0	0.605	100.83
		6.0	0.591	98.50
		10.0	0.595	99.17
X'				100.19
±SD				1.69
% RSD				1.69
% Error				0.845
	1.0	2.0	1.029	102.90
		4.0	1.019	101.80
		6.0	0.983	98.30
		10.0	0.986	98.60
X'				100.31
±SD				1.88
% RSD				1.88
% Error				0.935

N.B.: Each result is the average of three separate determinations.

cited in Table 2. Statistical evaluation of the regression lines for SLP and DSLP, respectively, regarding standard deviation of the residual ($S_{y/x}$), standard deviation of the intercept (S_a) and standard deviation of the slope (S_b) is given in Table 2. The small value of the figures point out to low scattering of the points around the calibration curve and thus indicating the high accuracy and high precision of the method.

3.5.1. Precision

The intra-day precision was evaluated through replicate analysis of different concentrations of SLP (0.2–0.6 $\mu g\,mL^{-1}$) both in raw material and in dosage forms. Each sample was analyzed three successive times. The precision expressed by % RSD values were fairly acceptable. The results are summarized in Table 5.

Similarly, the inter-day precision was evaluated through replicate analysis of the same samples on three successive days. The results obtained are abridged in Table 5.

3.5.2. Accuracy

The accuracy of the proposed method was evaluated by analyzing standard solutions of the studied drug and the results were favorably compared with those obtained using the British Pharmacopoeia method [2].

The robustness of the proposed method is demonstrated by the constancy of the fluorescence intensity with the deliberated changes in the experimental parameters such as pH, 8.0 ± 0.2. This minor change that may take place during the experimental operation did not greatly affect the fluorescence intensity SLP and DSLP, respectively.

3.6. Validation of the method as applied to pharmaceutical preparations

The proposed method was applied to the determination of the studied drug in its commercial tablets and capsules. The selectivity of the method was investigated by observing any interference encountered from the common excipients, such as starch, lactose, magnesium stearate and avisil. These excipients did not interfere with the proposed method. The results were compared with those obtained using the BP method [2]. Statistical analysis of the results [21] obtained using Student's *t*-test and variance ratio *F*-test revealed no significant difference between the performance of the two methods regarding the accuracy and precision, respectively (Table 3).

3.7. Application to plasma samples

The high sensitivity of the proposed method allowed the determination of SLP in biological fluids by SDSFS technique. Sulpiride is absorbed from gastro-intestinal tract. Following oral ingestion of a single oral dose of 50 mg of SLP, a peak plasma concentration of 0.03–0.60 $mg\,L^{-1}$ (mean 0.18 $mg\,L^{-1}$) is attained in about 4–7 h [22]. This value lies within the working concentration range of the proposed method. The method involved extraction with ethylacetate/dichloromethane (5: 1, v/v). The extraction procedure described by Huang et al. [23] was adopted. The proposed method applied to spiked human plasma was tested for linearity, specificity, accuracy and precision, respectively.

The second derivative signal of SLP–concentration plot in spiked human plasma was applied over the working concentration. Linear regression analysis of the results gave the following equation:

$$^2D = -0.203 + 98.70C \quad (r = 0.999) \quad \text{for SLP}$$

Second derivative synchronous fluorescence spectroscopy (SDSFS) is specific for the determination of SLP at 295.5 nm. The proposed method was applied to human plasma by studying the accuracy as percent relative error and precision as percent relative standard deviation. The results are abridged in Table 6.

Intra-day precision was evaluated through replicate analysis of plasma samples spiked with different concentrations of the drug (0.05–0.15 $\mu g\,mL^{-1}$). The mean percentage recoveries based on the average of three separate determinations were 100.22 ± 2.04 and 92.00 ± 3.00 for spiked and real human plasma, respectively (Table 6).

Table 5
Validation of the proposed method to the determination of sulpiride using SDSF mode.

Concentration added ($\mu g\,mL^{-1}$)	% Recovery	% RSD	% Error
SLP			
Intra-day			
0.2	99.44 ± 1.68	1.68	0.98
0.4	99.84 ± 1.42	1.42	0.82
0.6	100.29 ± 1.36	1.36	0.79
Inter-day			
0.2	100.27 ± 1.50	1.50	0.87
0.4	100.50 ± 1.40	1.40	0.81
0.6	99.56 ± 1.29	1.29	1.04
Dogmatil® capsules		0.24	0.14
(50 mgSLP/capsule)		0.53	0.31
Intra-day			
0.2	100.00 ± 1.32	1.32	0.76
0.4	99.19 ± 0.94	0.94	0.55
0.6	99.96 ± 1.39	1.39	0.80
Inter-day			
0.20	100.88 ± 1.11	1.11	0.64
0.40	99.81 ± 1.16	1.16	0.67
0.60	99.33 ± 0.84	0.84	0.49
Topmode® capsules (50 mg SLP/capsule)			
Intra-day			
0.2	99.13 ± 1.11	1.11	0.65
0.4	99.25 ± 1.31	1.31	0.76
0.6	99.83 ± 1.27	1.27	0.73
Inter-day			
0.20	99.17 ± 1.26	1.26	0.73
0.40	99.00 ± 0.25	0.25	0.14
0.60	100.33 ± 1.48	1.48	0.85
Topmode® tablets (200 mg SLP/tablet)			
Intra-day			
0.20	99.00 ± 1.08	1.08	0.63
0.40	100.69 ± 1.39	1.39	0.80
0.60	100.08 ± 1.45	1.45	0.84
Inter-day			
0.20	101.00 ± 1.58	1.58	0.90
0.40	99.50 ± 1.65	1.65	0.96
0.60	100.09 ± 1.73	1.73	0.75

Inter-day precision was performed through replicate analysis of plasma samples spiked with 0.10 $\mu g\,mL^{-1}$ SLP on three successive days and the results are abridged in Table 6.

3.8. Degradation kinetics Study

The alkaline treatment of sulpiride with 2 mol L^{-1} NaOH was accompanied by a gradual decrease in the synchronous fluorescence intensity. Upon heating in a boiling water bath for 2 h complete degradation of the drug occurred as revealed by complete disappearance of the synchronous fluorescence spectrum of the drug at 299 nm and the appearance of a new fluorescence spectrum peak at 336 nm. The degradation was found to be temperature dependent (Fig. 6). The apparent first order degradation rate constant and half-life time at each temperature were calculated (Table 7). By plotting log K_{obs} values *versus* $1/T$, Arrhenius plot was obtained. The activation energy E_a was calculated and was found to be 7.57 K Cal mol^{-1} (Table 7).

3.8.1. Pathway of degradation

Upon heating sulpiride in alkaline medium, it undergoes complete degradation. Being an amide, SLP is proposed to be decomposed to the corresponding carboxylic acid (sodium salt) (A) and the primary amine (B). Also, the sulphonamide group is probably hydrolysed to the corresponding sulphonic acid (sodium salt) (A) and ammonia. Compound B is non-fluorescent as it is devoid of conjugation and chromophores. So the entire study is devoted to compound (A). The proposal of the alkaline degradation pathway is postulated in the following Scheme 1.

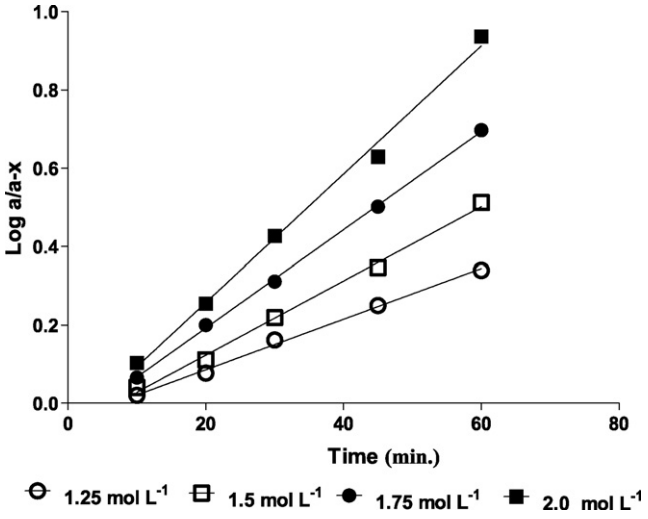
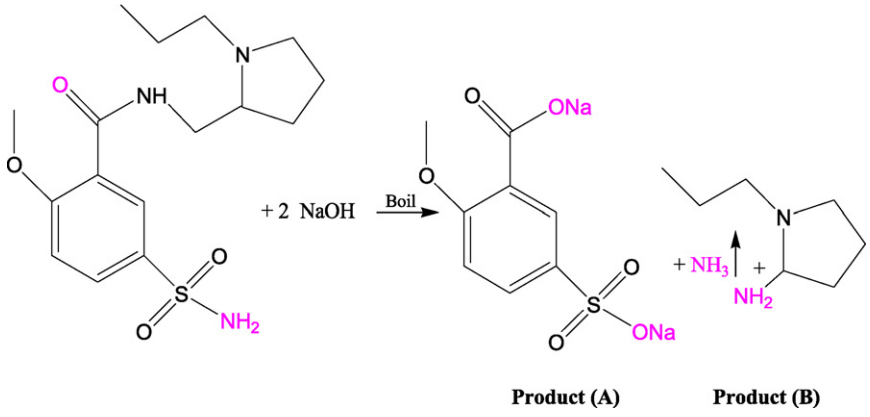


Fig. 6. Semilogarithmic plot of sulpiride (20 $\mu g\,mL^{-1}$) *versus* different heating times using different molarities of NaOH: 1.25 mol L^{-1} NaOH, 1.5 mol L^{-1} NaOH, 1.75 mol L^{-1} NaOH and 2 mol L^{-1} NaOH.

Table 6
Application of the proposed method for the determination of sulpiride in spiked and real human plasma.

Sample	Amount added ($\mu g\,mL^{-1}$)	Amount found ($\mu g\,mL^{-1}$)	Recovery (%)
1 – Spiked plasma sample			
a – Intra-day precision			
	0.05	0.051	102.00
	0.10	0.098	98.00
	0.15	0.151	100.67
Mean found, X'			100.22
±SD			±2.04
% RSD			2.04
% Error			1.18
b – Inter-day precision			
	0.10	0.096	96.00
	0.10	0.098	98.00
	0.10	0.102	102.00
Mean found, X'			98.67
±SD			±3.06
% RSD			3.10
% Error			1.79
2 – Real plasma sample			
	0.10	0.095	95.00
	0.10	0.092	92.00
	0.10	0.089	89.00
Mean found, X'			92.00
±SD			±3.00
% RSD			3.26
% Error			1.88

N.B.: Each result is the average of three separate determinations.



Scheme 1. Proposal of pathway of alkaline degradation of sulpiride.

Table 7
Effect of temperature on the kinetic parameters of the degradation of sulpiride.

Temperature (°C)	K (min^{-1})	$t_{1/2}$ (min)	E_a (K Cal. mol L^{-1} K)
70	0.016	45	6.55
80	0.021	34	6.99
90	0.027	26	9.16
100	0.038	18	X' = 7.57

4. Conclusion

The present study described a fully validated and novel second derivative synchronous spectrofluorimetric method for the simultaneous determination of sulpiride and its degradation product with enhanced sensitivity and specificity. The proposed method do not require elaborate treatment for the sample or tedious procedure for the extraction. As well as, the method is sensitive enough for the analysis of lower concentration of sulpiride as low as 0.05 $\mu g\,mL^{-1}$. Furthermore, the proposed method is a good analytical tool for the determination and monitoring of sulpiride in spiked and real human plasma.

References

[1] J.F. Liu, W.D. Cao, H.B. Qiu, X.H. Sun, X.R. Yang, E. Wang, Clin. Chem. 48 (2002) 1049.
[2] The British Pharmacopoeia, The Stationary Office, London, 2007 (electronic version).
[3] S.I. Zayed, Anal. Sci. 21 (2005) 985.
[4] Y. Sato, E. Yamamoto, S. Takakuwa, T. Kato, N. Asakawa, J. Chromatogr. A 1190 (2008) 8.
[5] N. Bergemann, F. Abu-Tair, K.R. Kress, P. Parzer, J. Kopitz, J. Clin. Psychopharmacol. 27 (2007) 546.
[6] R. Skibiński, Ł. Komsta, H. Hopkała, I. Suchodolska, Anal. Chim. Acta 590 (2007) 195.
[7] H. Kirchherr, W.N. Kühn-Velten, J. Chromatogr. B 843 (2006) 100.
[8] A. Maślanka, J. Krzek, J. AOAC Int. 88 (2005) 70.
[9] A. Musenga, R. Mandrioli, E. Morganti, S. Fanali, M.A. Raggi, J. Pharm. Biomed. Anal. 46 (2008) 966.
[10] J. Li, F. Zhao, H. Ju, J. Chromatogr. B 835 (2006) 84.
[11] O.A. Farghaly, J. Pharm. Biomed. Anal. 23 (2000) 783.
[12] J.F. Nie, H.L. Wu, A.L. Xia, S.H. Zhu, Y.C. Bian, S.F. Li, R.Q. Yu, Anal. Sci. 23 (2007) 1377.
[13] D. Patra, A.K. Mishra, Trends Anal. Chem. 21 (2002) 787.
[14] P. John, I. Soutar, Anal. Chem. 48 (1976) 520.
[15] N. El-Enany, J. AOAC. Int. 91 (2008) 542.
[16] M.I. Walash, F. Belal, N. El-Enany, A.A. Abdelal, J. AOAC Int. 91 (2008) 349.
[17] M.I. Walash, F. Belal, N. El-Enany, A.A. Abdelal, J. Fluoresc. 18 (2008) 61.

[18] Y. Sun, M.N. Nakashima, M. Takahashi, N. Kuroda, K. Nakashima, Biomed. Chromatogr. 16 (2002) 319.
[19] D.A. Skoog, F.J. Holler, S.R. Crouch, Principles of Instrumental Analysis, 6th ed., Thomson, Belmont, USA, 2007, p. 406.
[20] Guidance for Industry, Q2B of Analytical Procedures: Methodology, in: International Conference on Hormonization (ICH), November 1996, http://www.fda.gov/eder/guidance/1320fnl.pdf (accessed September 1, 2004).
[21] J.C. Miller, J.N. Miller, Statistics and Chemometrics for Analytical Chemistry, 5th ed., Pearson Prentice Hall, England, 2005, p. 256.
[22] A.C. Moffat, M.D. Osselton, B. Widdop, Clark's Analysis of Drugs and Poisons in Pharmaceuticals. Body Fluids and Postmortem Material, 3rd ed., The Pharmaceutical Press, London, 2004, p. 1594.
[23] M.C. Huang, H.O. Ho, G.C. Yeh, W.T. Ke, L.C. Lin, T.M. Hsu, C.C. Kao, M.T. Sheu, J. Chromatogr. B: Biomed. Sci. Appl. 763 (2001) 157.

Talanta 80 (2009) 889–894

Contents lists available at ScienceDirect

Talanta

journal homepage: www.elsevier.com/locate/talanta

Biomimetic fabrication of hydroxyapatite-coated zirconia–magnesia composite and its application in the separation of proteins

Ting Li, Yu-Qi Feng*

Key Laboratory of Analytical Chemistry for Biology and Medicine (Ministry of Education), Department of Chemistry, Wuhan University, Wuhan 430072, China

ARTICLE INFO

Article history:
Received 11 June 2009
Received in revised form 9 August 2009
Accepted 10 August 2009
Available online 18 August 2009

Keywords:
Biomimetic technique
Hydroxyapatite
Zirconia–magnesia composite
Stationary phase
Protein separation

ABSTRACT

In this work, biomimetic technique was proposed for the first time to prepare chromatographic packings (2HAp-ZM) for protein separation. By mimicking the mineralization procedures in vivo, this type of matrix with hydroxyapatite (HAp) coating and zirconia–magnesia (ZM) composite core was fabricated. Systematic characterizations, including scanning electron microscopy (SEM), X-ray photoelectron spectroscopy (XPS), X-ray diffraction (XRD) and specific surface area analysis, were carried out to investigate the properties of the material. Results showed that the surface of 2HAp-ZM was composed of bead-like, amorphous or nanocrystalline HAp. The specific surface area, total pore volume, and average pore diameter of the resultant material were 25 m^2/g, 0.09 cm^3/g, and 14 nm, respectively. Furthermore, 2HAp-ZM exhibited good mechanical stability through repeated testing and its application as stationary phases for protein separation was then studied. Five model proteins (bovine serum albumin, trypsin, lysozyme, ribonuclease A, and cytochrome *c*) were successfully separated on 2HAp-ZM. Finally, the mass recovery of protein and the dynamic loading capacity were studied; the results were calculated to be no less than 93% and 80 μg/mL of blank column volume, respectively.

© 2009 Elsevier B.V. All rights reserved.

1. Introduction

Protein separation has been attracting increasing interests with the development of biology and physiology in recent years. High-performance liquid chromatography (HPLC) is by far the most widely utilized technique in this field; its performance is mainly based on the packing materials [1]. In this case, some common criteria have been proposed to dictate the selection of chromatographic media for protein separation in a previous review [2], which are summarized as: (a) chemically and physically stable to withstand regeneration and cleaning procedures; (b) good mechanical strength to allow high flows; (c) not containing groups that bind proteins non-specifically; (d) easy to be derived to allow the introduction of functional groups for interactive chromatography applications; (e) good control of particle size and pore size; (f) high selectivity and loading capacity; (g) low cost. However, it is often not possible to reconcile all the criteria, and therefore compromises have to be searched and further development of the stationary phases is required for their application to protein separation.

During the past decades, continuous efforts have been devoted to improve the stationary phases for protein chromatography by the employment of new packing materials. Zirconia (ZrO_2) was introduced as a competitive alternative to the traditional silica with enhanced chemical, thermal or mechanical stability [3]. This advantage made it can be cleaned and sterilized using hot acids and bases to remove irreversibly adsorbed proteins [4–6]. Furthermore, this oxide showed ligand-exchange behavior due to the presence of Lewis acid sites at its surface, which could interact with Lewis bases, such as fluoride, phosphate ions or carboxylic acids, and also with the carboxyl groups of proteins. Hence, protein separation was able to be achieved using a mobile phase containing strong Lewis base at well defined concentrations [7,8] or on a strong Lewis base-modified ZrO_2 [9–14]. Unfortunately, its selectivity and loading capacity were relatively limited, owing to the single modal mechanism of separation and lower surface area, respectively [9,10].

Hydroxyapatite [HAp: $Ca_{10}(PO_4)_6(OH)_2$] was another promising medium for protein separation. It had unique bioaffinity and biocompatibility, which could adsorb and desorb biomolecules such as proteins and nucleic acids without denaturation [15–17]. Its underlying mechanism of separation was multimodal [1,18–23]: cation exchange took place at PO_4^{3-} (P) sites; anion exchange as well as ligand exchange took place at Ca^{2+} (C) sites. Nevertheless, the original crystalline HAp was too fragile to withstand high packing pressure and flow rates [2]. One way to solve this problem was the preparation of ceramic HAp, which was sintered into a spherical particle with large pores [24]. The other was the fabrication of HAp-based composites. Majumder and Ramesh [25] suspended phosphorylated silica in 2 M $CaCl_2$ solution and then in 1 M phosphate buffer to obtain a HAp substitute, which could be employed for open column LC as well as for HPLC purpose. Though it was

* Corresponding author. Tel.: +86 27 68755595; fax: +86 27 68755595.
E-mail address: yqfeng@whu.edu.cn (Y.-Q. Feng).

0039-9140/$ – see front matter © 2009 Elsevier B.V. All rights reserved.
doi:10.1016/j.talanta.2009.08.012

successfully used in the purification of topoisomerase I and II from wheat germ, no detailed information on its morphological features or stability were reported. Later on, Honda et al. [26,27] reported two kinds of HAp-coated composite particles, which were made of orthodox fragile HAp (or cattle bone powder) and polyethylene beads by the dry impact blending method. Irreversible adsorption of proteins onto the columns was observed during the chromatographic running.

Considering the inherent properties of the packing materials listed above, we aimed at preparing a type of matrix that consisted of a HAp surface and a ZrO_2-based core for protein chromatography. Through integrating unique bioaffinity and biocompatibility, and excellent thermal and mechanical stability as a whole, this stationary phase was expected to provide better separation efficiency and larger application scale. Thus, it is of great importance to select an appropriate method to achieve this objective.

Biological systems are a rich source of ideas for individuals concerned with the synthesis of new materials and processes [28], from which the biomimetic technique was derived and developed. The biomimetic technique was a low-cost and facile process to coat implants (usually used in orthopedic surgery) with calcium phosphate [29–34]. It was performed by soaking substrates under mild pH and temperature conditions into simulated body fluid (SBF) solutions that have a similar inorganic content as human blood plasma [35]. Once the apatite nuclei formed on the surface of the substrate, they could spontaneously grow by consuming the calcium and phosphate ions from the fluid [36]. It was worthwhile to point out that the functional groups on the surface of the substrate were important to induce the nucleation of apatite [37]. Wen et al. [38] reported that HAp could deposit and grow on oxide layers of titanium in a modified SBF solution (supersaturated calcification solution, SCS), indicating TiO_2 were favorable to induce apatite formation in the body environment. Fortunately, ZrO_2 possessed the similar surface chemical properties as TiO_2 [39], which inspired us that biomimetic technique would be a feasible pathway to prepare HAp-coated zirconia–magnesia (a ZrO_2-based composite) as stationary phase for protein chromatography.

In the present work, HAp-coated zirconia–magnesia (ZM) microspheres were prepared via biomimetic technique by incubating the substrates in SCS and applied to the separation of proteins with HPLC. This was, to the best of our knowledge, the first demonstration of using biomimetic technique to fabricate chromatographic packings for biological analysis. Five proteins, i.e. bovine serum albumin, trypsin, lysozyme, ribonuclease A, and cytochrome *c*, were employed as model analytes to evaluate the separation performance of the resultant materials. Enhanced separation efficiency and dynamic loading capacity, as well as improved mechanical stability, were observed when compared with unmodified ZM and HAp, respectively.

2. Experimental

2.1. Chemicals and materials

ZM microspheres (8–10 μm) were synthesized by sol–gel method in our laboratory [40]. Tiselius type HAp, NaCl, KCl, anhydrous Na_2HPO_4 (NaP), $CaCl_2$, HCl, trihydroxymethylaminomethane (Tris), anhydrous K_2HPO_4 (KP) and H_3PO_4 were purchased from Shanghai General Chemical Reagent Factory (Shanghai, China). Lysozyme was purchased from Shanghai Bio Life Science & Technology (Shanghai, China). Trypsin was purchased from Amresco (Solon, OH, USA). Bovine serum albumin (BSA), ribonuclease A (RNase A), cytochrome *c* (Cyt *c*), ovalbumin and α_1-acid glycoprotein (AGP) were purchased from Sigma (St. Louis, MO, USA). Double-distilled water was used for all experiments.

2.2. Preparation of SCS

The SCS was prepared according to the method described by Kokubo et al. [41] with a little modification. NaCl, KCl, anhydrous NaP and $CaCl_2$ were dissolved one by one in distilled water, the concentrations of each ion were listed as follows: $[Na^+] = 136.8$ mM, $[K^+] = 3.71$ mM, $[Cl^-] = 144.5$ mM, $[Ca^{2+}] = 3.10$ mM, and $[HPO_4^{2-}] = 1.86$ mM. The SCS was buffered at pH 7.4 with HCl and Tris at 36.5 °C. After preparation, it was preserved at 5–10 °C in a refrigerator, and was used within 30 days.

2.3. Preparation of the HAp-coated ZM microspheres

The preparation of HAp-coated ZM was composed of four successive steps: activation, pre-calcification, incubation, and calcination.

ZM microspheres were firstly dispersed in 1 M NaOH at room temperature overnight, then washed to neutral and dried at 160 °C for 8 h. Pre-calcification treatment was then performed by immersing the activated ZM in 0.5 M NaP solution at 100 °C for 12 h, followed by suspending them in freshly prepared saturated $Ca(OH)_2$ solution for 2 h. The particles were thoroughly rinsed with distilled water and dried at 120 °C. Afterwards, the pretreated ZM were soaked in SCS in a 36.5 °C water bath to produce HAp coatings on their surfaces. The SCS was replaced every 2 days. In this study, all the HAp-coated ZM were denoted as HAp-ZM, ZM obtained after one incubation in SCS were denoted as 1HAp-ZM, after two incubations in SCS were denoted as 2HAp-ZM, and so forth. Finally, the calcination procedure was carried out by heating at a rate of 0.5 °C/min to 600 °C and holding for 2 h to age the HAp coating.

2.4. Instrumentation

Surface morphology of the particles was displayed by a QUANTA-200 scanning electron microscopy (SEM) system (FEI, Eindhoven, the Netherlands). Ca/P ratios of the HAp coatings were determined by an XSAM800 X-ray photoelectron spectroscopy (XPS) system (Kratos, Manchester, UK), with Mg Kα radiation as the exciting source. Crystal structure of HAp-ZM was determined with an XRD-6000 X-ray diffraction (XRD) system (Shimadzu, Kyoto, Japan) using Cu Kα radiation and a rotating anode operating at 40 kV and 30 mA. Specific surface area, pore volume, and pore size were measured by nitrogen sorption at 77 K using a SA3100 Plus surface area analyzer (Beckman, Fullerton, CA, USA).

2.5. Chromatographic conditions

Unmodified ZM and 2HAp-ZM were both slurry-packed into 150 mm × 4.6 mm I.D. stainless steel columns with 0.3 M sodium phosphate buffer (pH 6.8) at 6000 psi.

All chromatographic measurements were carried out at room temperature on an Agilent 1100 HPLC system (Agilent Technologies, Palo Alto, CA, USA) including a Rheodyne Model 7125 injector with a 20 μL loop, a quaternary pump, a micro-vacuum degasser and a diode array detector (DAD). Separation of proteins was performed at a flow rate of 1 mL/min. The gradient elution was firstly water for 3 min, and then transferred to 300 mM, pH 6.8 NaP buffer in 1 min, delayed for 12 min, at last transferred to 500 mM, pH 6.8 KP buffer in 1 min, and delayed for 18 min. The eluent was monitored at 220 nm. When investigating the dynamic loading capacity of the 2HAp-ZM stationary phase, 1 mL injection loop was used.

2.6. Protein recovery studies

The protein mass recovery was measured according to a previously reported method [9,10], by comparing the amount of protein

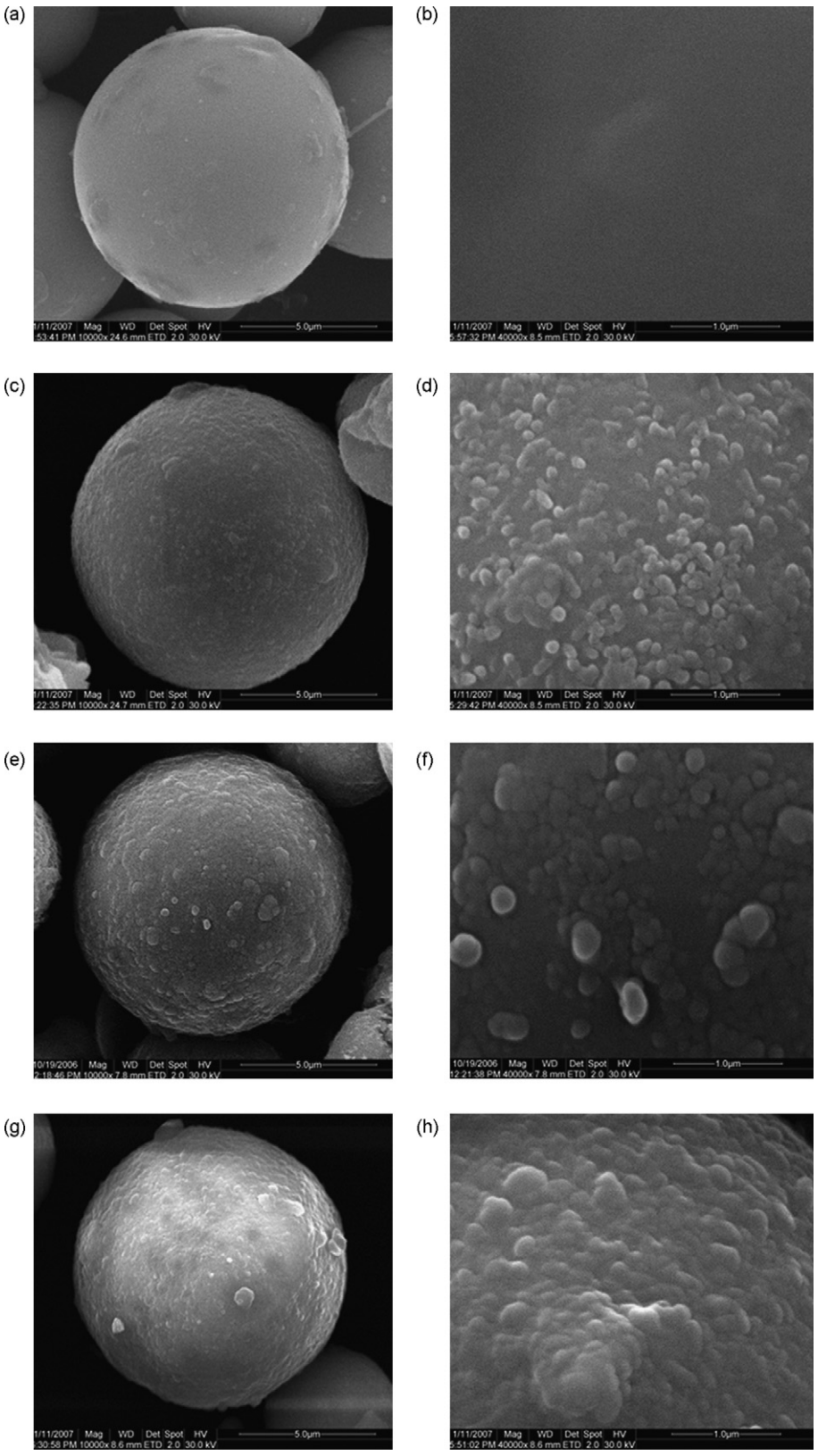


Fig. 1. Typical SEM photographs of unmodified ZM and HAp-ZM: (a), (b) unmodified ZM; (c), (d) pre-calcified ZM; (e), (f) 2HAp-ZM; (g), (h) 10HAp-ZM.

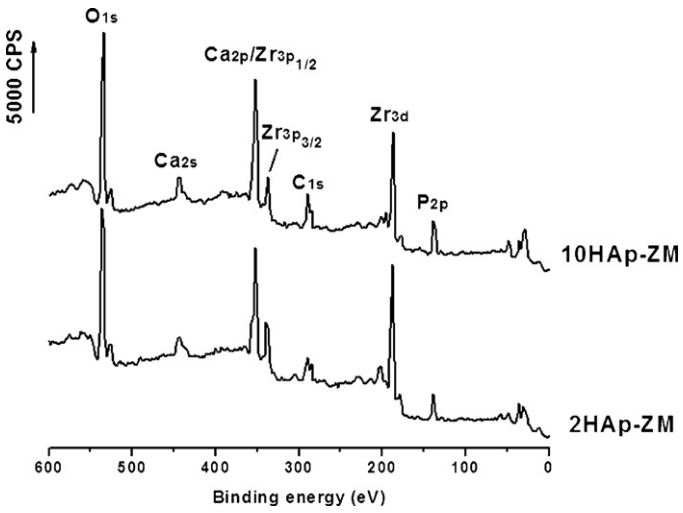


Fig. 2. XPS spectrums of HAp-ZM.

collected in a control experiment in which the column was replaced with a zero dead volume pipe to that obtained with the column in place. The mass recovery was calculated as follows:

$$\text{mass recovery\%} = \frac{\text{area (column)}}{\text{area (pipe)}} \times 100\%$$

The proteins were eluted isocratically, and the analysis was repeated three times for each protein.

3. Results and discussion

By definition, biomimetic technique for HAp deposition is the mimic formation of inorganic compounds in vivo (biomineralization). Its mechanism is complicated and the process is time-consuming. Hence, pre-calcification was proposed to accelerate the precipitation rate of HAp [38]. In this procedure, phosphate anions and calcium cation were adsorbed onto ZM surface one after the other; and a nonstoichiometric calcium phosphate was formed. When the pre-calcified ZM were immersed in SCS, some components are released from the material into the fluid and, thereby, increase the ionic activity product of the apatite, which can accelerate apatite formation. Additionally, SCS rather than SBF was utilized in this study because the former one provided higher concentration of phosphate and calcium ions, which could consequently speed up the deposition rate of apatite [42].

3.1. Characterization of the HAp-ZM

Direct observation of the surface morphology of unmodified ZM and HAp-ZM is provided by the SEM micrographs illustrated in Fig. 1. Fig. 1b shows a smooth surface of unmodified ZM, and Fig. 1d, f and h shows the modified surfaces of ZM after pre-calcification, 2 and 10 repetitions of incubation in SCS, respectively. It can be seen that rod-like nanoparticles are formed on the substrate after pre-calcification (Fig. 1d), which is speculated to be composed of nonstoichiometric calcium phosphate. After repeating the immersion in SCS, the rod-like nanoparticles grow more and bigger (bead-like, Fig. 1f) gradually, and finally a dense and uniform HAp coating emerged via attraction and attachment of the nanoparticles (Fig. 1h).

The composition of HAp coating on the surfaces of ZM was characterized by XPS. Results are shown in Fig. 2. It can be found that considerable amount of Ca and P elements has existed on ZM after 4 days immersing in SCS. Increasing the immersion time, tiny differences in peak area of Ca, P and Zr are observed between 2HAp-ZM and 10HAp-ZM. This means that a HAp coating was basically formed at the stage of 2HAp-ZM; long immersion time was avoided because of the introduction of pre-calcification treatment, which stimulates the apatite nucleation and accelerates the growth rate of the HAp layer. Furthermore, the Ca/P ratio of the resultant coating is calculated to be 1.59, close to the Ca/P ratio of HAp 1.66. Therefore, we considered that this coating was mainly composed of HAp and 2HAp-ZM was selected for the following experiments.

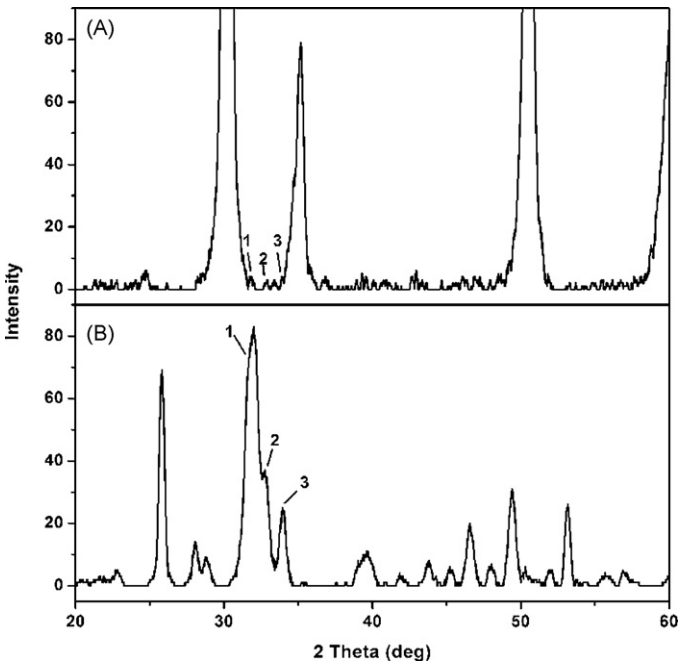


Fig. 3. XRD patterns of (A) HAp and (B) 10HAp-ZM. Peaks (1–3) around 32–34° were ascribed to the diffraction of 2 1 1, 3 0 0 and 2 0 2 planes of HAp crystal. The strong peaks in (B) were engendered by the ZM matrix.

The X-ray diffraction patterns of 2HAp-ZM were displayed in Fig. 3 in comparison with that of Tiselius type HAp. Only small typical peaks (around 32° and 34°), which are ascribed to the diffraction of 2 1 1, 3 0 0 and 2 0 2 planes of HAp crystal, are observed, suggesting the poor crystallinity of the HAp on 2HAp-ZM. Combined with the SEM photos, we can suppose that the coating is composed of an amorphous or nanocrystalline apatite. This phenomenon is consistent with the previously reported results [36,43].

The specific surface area, total pore volume, and average pore diameter of 2HAp-ZM are 25 m^2/g, 0.09 cm^3/g, and 14 nm, respectively, calculated using the standard BET method.

3.2. Chromatography of proteins

The feasibility of the HAp-coated ZM used as HPLC stationary phase for protein chromatography was evaluated using BSA, trypsin, lysozyme, RNase A and Cyt *c* as model analytes. The physical and chemical properties of these proteins are listed in Table 1.

It is reported that there are two types of interaction site on HAp. An acidic protein, such as BSA, mainly interacts with the C sites, while a basic protein, such as lysozyme, mainly interacts with the P sites [27]. Hence, both acidic and basic proteins were able to be resolved within a single run of HPLC on the basis of multimodal mechanism of separation [49]. In this study, five proteins were successfully separated on the 2HAp-ZM stationary phases in gradient elution mode using pH 6.8 phosphate buffer as mobile phase, as shown in Fig. 4. Compared to the unmodified ZM, on which lysozyme and RNase A were eluted in one peak without sufficient resolution, it can be concluded that the HAp coating is

Table 1
Properties of proteins investigated in this study.

Protein	Source	MW	pI[a]	R_s[b] (nm)
BSA	Bovine serum	66 000	4.7	3.39[c]
Trypsin	Bovine pancreas	23 300	10.1	2.40[d]
Lysozyme	Chicken egg white	14 700	11.0	1.95[e]
RNase A	Bovine pancreas	13 700	9.6	1.93[c]
Cyt *c*	Horse heart	12 384	9.8	1.70[c]
Ovalbumin	Chicken white	44 287	4.7	3.02[c]
AGP	Bovine serum	41 000	2.7	3.64[f]

[a] Isoelectric point.
[b] The Stokes radii (R_s) values of proteins whose intrinsic viscosity ([η]) is known from literature were calculated using the relationship proposed by Tanford [44]: $[\eta] = (2.5\,Na/MW)(4/3\pi R_s^3)$, where Na is Avogadro's number and MW is the protein molecular weight.
[c] Ref. [45].
[d] Ref. [46].
[e] Ref. [47].
[f] Ref. [48].

effective to improve the selectivity of 2HAp-ZM, mainly resulting from its unique bioaffinity toward biomolecules. Compared to a commercial HAp packing [27], although the retention of basic proteins on 2HAp-ZM is comparable, the retention of acidic proteins varies. BSA as well as other acidic proteins (ovalbumin and α_1-acid glycoprotein) has been tested on this column under different chromatographic conditions. Unfortunately, they were all hardly retained even eluted with pure water as mobile phase. Comparing the Stocks radii of acidic and basic proteins in our study (Table 1), the relatively small pore size of the stationary phases may be one possible explanation. Another explanation may be the electrostatic repulsion between the negatively charged Zr–OH on the uncoated matrices and the acidic proteins, which were also negatively charged at pH 6.8.

The dependence of protein retention on pH values was also investigated on 2HAp-ZM. Three pH values (pH 6.0, 6.8 and 7.8) were employed; lower or higher pH was avoided in view of its chemical instability at acidic conditions and lack of selectivity at basic conditions. Results are shown in Fig. 5. Retention increases with decreasing pH for all proteins except BSA, implying that cation exchange provides significant contributions to the retention of basic proteins. Higher pH of the mobile phase may deprotonate the proteins. Accordingly, basic proteins, which were less positively charged at higher pH, are less retained on 2HAp-ZM via weaker cation exchange interaction.

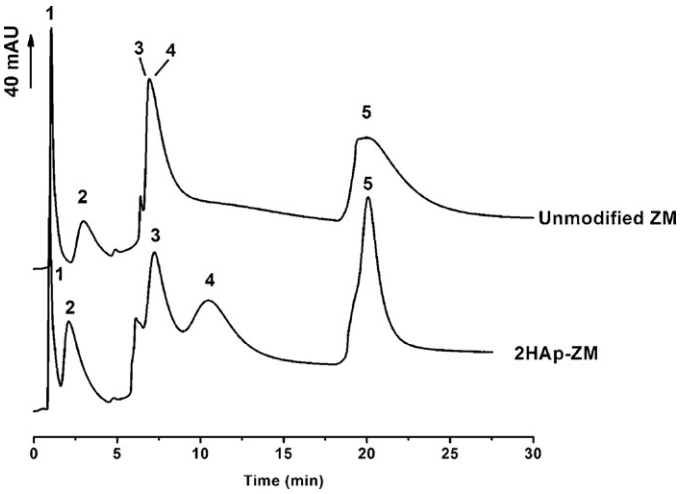


Fig. 4. Separation of five model proteins on unmodified ZM and 2HAp-ZM. Chromatographic conditions: NaP–KP buffer at pH 6.8, 1 mL/min, the gradient of mobile phase was outlined in Section 2.5; detection at 220 nm. Peaks: 1 = BSA; 2 = trypsin; 3 = RNase A; 4 = lysozyme; 5 = Cyt *c*.

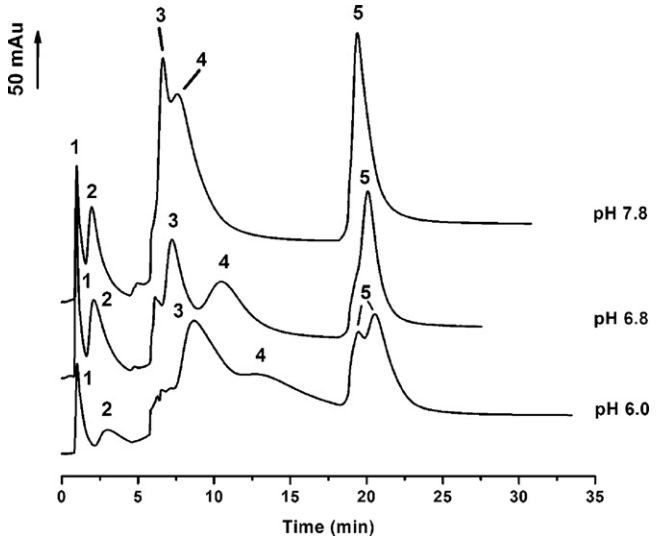


Fig. 5. Separation of five model proteins at three pH values on 2HAp-ZM column. Other conditions were the same as those in Fig. 4. Two forms of Cyt *c* (oxidized and reduced) were separated on at pH 6.0.

3.3. Stability

Mechanical stability is a crucial criterion for stationary phase of HPLC, and also the primary objective for us to prepare the HAp-coated ZM. The backpressure as well as the separation performance was thus monitored on 2HAp-ZM throughout the whole experiment. It was demonstrated that this particle could withstand the packing pressure (approximately 6000 psi) and allow the use of high flow rate of mobile phase (1 mL/min). Moreover, during the 3-month experiment, the backpressure of 2HAp-ZM column remained stable; and the separation performance was also preserved, as shown in Fig. 6.

3.4. Protein recovery and loading capacity

The goal of this work was to synthesize a viable support for protein chromatography. To be well suited for this application,

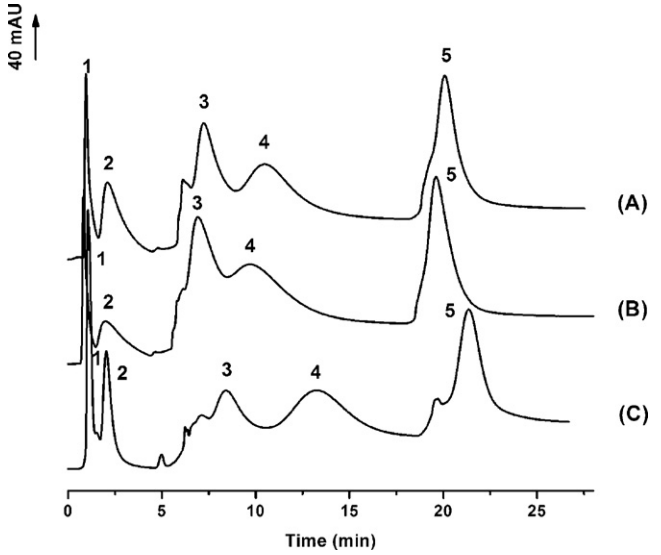


Fig. 6. Chromatograms of proteins on 2HAp-ZM column at different times: (A) once in the experiment; (B) 3 months later (approximately 100 injections had been operated within this period); (C) 6 months later (stored in refrigerator at about 4 °C). Other conditions were the same as those in Fig. 4.

Table 2
Protein recovery study on 2HAp-ZM column.

Protein	Mobile phase	% Recovery ($n = 3$)
BSA	5 mM NaP buffer, pH 6.0	99.7 ± 3.1
Trypsin	5 mM NaP buffer, pH 6.8	93.3 ± 3.5
Lysozyme	150 mM NaP buffer, pH 6.8	102.6 ± 0.9
RNase A	300 mM NaP buffer, pH 7.8	97.0 ± 3.7
Cyt *c*	500 mM KP buffer, pH 6.8	100.2 ± 1.1

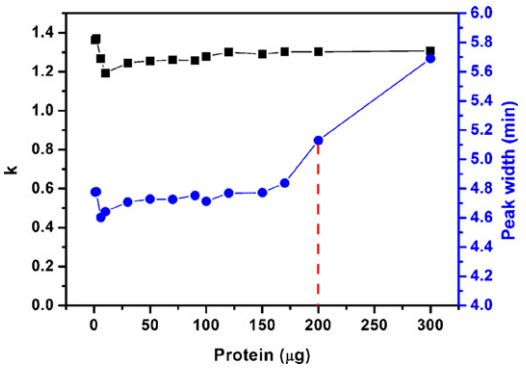


Fig. 7. Study of loading capacity of the 2HAp-ZM column. Experimental conditions: isocratic elution with 150 mM NaP mobile phase at pH 6.8; 1 mL/min; detection at 220 nm. Symbols: (■) capacity factor; (●) peak width.

very high recoveries are essential. Therefore, protein recovery was studied on 2HAp-ZM with results listed in Table 2. In order to ensure accurate peak integration, mobile phases were deliberately selected to obtain reasonable retention time and suitable peak width [6]. It can be found that the 2HAp-ZM column gave good recovery for all tested proteins, with the average recovery higher than 93%, indicating little irreversible adsorption of proteins.

The dynamic loading capacity of the 2HAp-ZM column was investigated by monitoring the column performance with increasing sample quantity. It is reported that the retention time and peak width will remain constant when the sample quantities are below the loading capacity of the column, while overloading will cause a decrease in retention time and an increase in peak width [9]. Lysozyme was chosen as a tested sample, and the results are shown in Fig. 7. The peak width is somewhat more sensitive to sample loading than the capacity factor. The dynamic loading capacity of the 2HAp-ZM-600 column was estimated to be about 80 μg/mL of blank column volume, based on the amount of sample which caused a 10% increase in peak width. This is higher than those reported for fluoride- and phosphate-modified zirconia (60 μg/mL) [9,10], but lower than that of a particular high-performance hydroxyapatite support (120 μg/mL) [50].

4. Conclusions

In this paper, biomimetic technique was demonstrated to be a low-cost and facile approach to prepare biocompatible and stable column packings (2HAp-ZM) for protein chromatography. Systematic characterization showed that bead-like HAp was successfully deposited on the surface of zirconia–magnesia microspheres after pre-calcification and 4 days incubation in SCS. Using this material as stationary phase, improved separation efficiency, resulting from the unique selectivity of HAp coating, was confirmed by the separation of lysozyme and RNase A (their physical and chemical properties were similar) in comparison with an unmodified ZM column. And following experiments also indicated that 2HAp-ZM exhibited good mechanical stability, relatively high recovery, and acceptable dynamic loading capacity, which made it a promising HPLC support in the separation of proteins or other biomolecules, but there remained much to be understood and optimized before routine use.

Acknowledgments

This work was partly supported by the National Science Fund for Distinguished Young Scholars (No. 20625516), the Science Fund for Creative Research Groups (No. 20621502), NSFC, and the National 973 project of China (2007CB914200).

References

[1] A. Jungbauer, J. Chromatogr. A 1065 (2005) 3.
[2] M. Leonard, J. Chromatogr. B 699 (1997) 3.
[3] J. Nawrocki, C.J. Dunlap, P.W. Carr, J.A. Blackwell, Biotechnol. Prog. 10 (1994) 561.
[4] C. McNeff, P.W. Carr, Anal. Chem. 67 (1995) 2350.
[5] L. Sun, P.W. Carr, Anal. Chem. 67 (1995) 2517.
[6] Y. Hu, P.W. Carr, Anal. Chem. 70 (1998) 1934.
[7] J. Nawrocki, M.P. Rigney, A. McCormick, P.W. Carr, J. Chromatogr. A 657 (1993) 229.
[8] J.A. Blackwell, P.W. Carr, J. Chromatogr. 596 (1992) 27.
[9] J.A. Blackwell, P.W. Carr, J. Chromatogr. 549 (1991) 59.
[10] W.A. Schafer, P.W. Carr, J. Chromatogr. 587 (1991) 149.
[11] A.M. Clausen, P.W. Carr, Anal. Chem. 70 (1998) 378.
[12] A.M. Clausen, A. Subramanian, P.W. Carr, J. Chromatogr. A 831 (1999) 63.
[13] A. Subramanian, P.W. Carr, C.V. McNeff, J. Chromatogr. A 890 (2000) 15.
[14] A. Subramanian, S. Sarkar, J. Chromatogr. A 944 (2002) 179.
[15] V. Sabine, R. Freitag, J. Chromatogr. A 760 (1997) 125.
[16] T. Akazawa, M. Kobayashi, M. Yoshida, K. Matsushima, H. Minoshima, H. Sugimura, T. Kanno, J. Horiuchi, J. Chromatogr. A 862 (1999) 217.
[17] R.-B. Suen, S.-C. Lin, W.-H. Hsu, J. Chromatogr. A 1048 (2004) 31.
[18] T. Kawasaki, M. Niikura, Y. Kobayashi, J. Chromatogr. 515 (1990) 125.
[19] T. Kawasaki, S. Takahashi, K. Ikeda, Eur. J. Biochem. 152 (1985) 361.
[20] T. Kawasaki, J. Chromatogr. 544 (1991) 147.
[21] M.J. Gorbunoff, Anal. Biochem. 136 (1984) 425.
[22] M.J. Gorbunoff, Anal. Biochem. 136 (1984) 433.
[23] M.J. Gorbunoff, Anal. Biochem. 136 (1984) 440.
[24] T. Kadoya, T. Isobe, M. Ebihara, T. Ogawa, M. Sumita, H. Kuwahara, A. Kobayashi, T. Ishikawa, T. Okuyama, J. Liq. Chromatogr. 9 (1986) 3543.
[25] K. Majumder, N. Ramesh, Chromatographia 24 (1987) 400.
[26] F. Honda, H. Honda, M. Koishi, J. Chromatogr. A 696 (1995) 19.
[27] F. Honda, H. Honda, M. Koishi, T. Matsuno, J. Chromatogr. A 813 (1998) 21.
[28] S. Mann, Nature 365 (1993) 499.
[29] N. Costa, P.M. Maquis, Med. Eng. Phys. 20 (1998) 602.
[30] C.B. Mao, H.D. Li, F.Z. Cui, Q.L. Feng, H.C. Wang, L. Ma, J. Mater. Sci. Lett. 17 (1998) 1479.
[31] J.F. Shackelford, Mater. Sci. Forum 293 (1999) 99.
[32] S. Sobieszczyk, A. Zieliński, Adv. Mater. Sci. 8 (2008) 35.
[33] E.L. Zhang, C.M. Zou, S.Y. Zeng, Surf. Coat. Technol. 203 (2009) 1075.
[34] A.K.A.R. Wijenayaka, C.B. Colby, G.J. Atkins, P. Majewski, J. Mater. Sci.: Mater. Med. 20 (2009) 1467.
[35] T. Kokubo, H. Kushitani, S. Sakka, T. Kitsugi, T. Yamamuro, J. Biomed. Mater. Res. 24 (1990) 721.
[36] M. Uchida, H.M. Kim, T. Kokubo, F. Miyaji, T. Nakamura, J. Am. Ceram. Soc. 84 (2001) 2041.
[37] C.B. Mao, H.D. Li, F.Z. Cui, Q.L. Feng, H. Wang, C.L. Ma, J. Mater. Chem. 8 (1998) 2795.
[38] H.B. Wen, J.G.C. Wolke, J.R. de Wijn, Q. Liu, F.Z. Cui, K. de Groot, Biomaterials 18 (1997) 1471.
[39] J. Nawrocki, C. Dunlap, A. McCormick, P.W. Carr, J. Chromatogr. A 1028 (2004) 1.
[40] Q.H. Zhang, Y.Q. Feng, S.L. Da, Chromatographia 50 (1999) 654.
[41] T. Kokubo, H. Takadama, Biomaterials 27 (2006) 2907.
[42] H.B. Wen, J.R. de Wijn, F.Z. Cui, K. de Groot, J. Biomed. Mater. Res. 41 (1998) 227.
[43] F. Barrere, C.A. van Blitterswijk, K. de Groot, P. Layrolle, Biomaterials 23 (2002) 1921.
[44] C. Tanford, Adv. Protein Chem. 24 (1970) 1.
[45] V.N. Uversky, Biochemistry 32 (1993) 13288.
[46] G. Bohne, E. Richter, H. Woehlecke, R. Ehwald, Ann. Bot. 92 (2003) 289.
[47] V.N. Uversky, O.B. Ptitsyn, Biochemistry 33 (1994) 2782.
[48] J.K. Armstrong, R.B. Wenby, H.J. Meiselman, T.C. Fisher, Biophys. J. 87 (2004) 4259.
[49] T. Kawasaki, M. Niikura, Y. Kobayashi, J. Chromatogr. 515 (1990) 91.
[50] T. Kadoya, T. Isobe, M. Ebihara, T. Ogawa, M. Sumita, H. Kuwahara, A. Kobayashi, T. Ishikawa, T. Okuyawa, J. Liq. Chromatogr. 9 (1986) 3543.

Talanta 80 (2009) 895–902

Contents lists available at ScienceDirect

Talanta

journal homepage: www.elsevier.com/locate/talanta

Tailoring noise frequency spectrum to improve NIR determinations

Shaofei Xie [a], Bingren Xiang [a,*], Liyan Yu [a], Haishan Deng [b]

[a] Center for Instrumental Analysis, China Pharmaceutical University (Key Laboratory of Drug Quality Control and Pharmacovigilance, Ministry of Education), Nanjing, 210009, China
[b] Jiangsu Key Laboratory for TCM Formulae Research, College of Pharmacy, Nanjing University of Chinese Medicine, Xianlin Avenue 138,Nanjing 210046, China

ARTICLE INFO

Article history:
Received 30 April 2009
Received in revised form 10 August 2009
Accepted 10 August 2009
Available online 18 August 2009

Keywords:
NIR
Savitzky–Golay filter
PLS
Noise frequency spectrum

ABSTRACT

Near infrared spectroscopy (NIR) contains excessive background noise and weak analytical signals caused by near infrared overtones and combinations. That makes it difficult to achieve quantitative determinations of low concentration samples by NIR. A simple chemometric approach has been established to modify the noise frequency spectrum to improve NIR determinations. The proposed method is to multiply one Savitzky–Golay filtered NIR spectrum with another reference spectrum added with thermal noises before the other Savitzky–Golay filter. Since Savitzky–Golay filter is a kind of low-pass filter and cannot eliminate low frequency components of NIR spectrum, using one step or two consecutive Savitzky–Golay filter procedures cannot improve the determination of NIR greatly. Meanwhile, significant improvement is achieved via the Savitzky–Golay filtered NIR spectrum processed with the multiplication alteration before the other Savitzky–Golay filter. The frequency range of the modified noise spectrum shifts toward higher frequency regime via multiplication operation. So the second Savitzky–Golay filter is able to provide better filtering efficiency to obtain satisfied result. The improvement of NIR determination with tailoring noise frequency spectrum technique was demonstrated by both simulated dataset and two measured NIR spectral datasets. It is expected that noise frequency spectrum technique will be adopted mostly in applications where quantitative determination of low concentration sample is crucial.

© 2009 Elsevier B.V. All rights reserved.

1. Introduction

Near-infrared (NIR) spectroscopy is a powerful analytical technique used in various industrial sectors, e.g. the agricultural [1–3], petrochemical [4,5], textile [6,7], medical diagnostics and pharmaceutical [8–10]. Due to its fast, accurate and non-destructive analytical characters, NIR spectroscopy is considered as a replacement of the traditional chemical analysis in some sense. NIR spectra consist of near infrared overtones and combinations thereof, making interpretation of the results complicated. Thus, multivariate analysis (MVA) such as principal-component regression (PCR) and partial least-squares regression (PLS) come to be crucial in translating the large amount of spectral data into useful information, mainly for predictive purposes [11]. The performance of above methods was affected by spectral interferences, including background and noise. The interference of background and noise not only worsen the precision of prediction, but also complicate the multivariate models, which usually leads to over fitting of the calibration [12,13]. Therefore, usually the first step of a multivariate calibration based on NIR spectra data is to preprocess the data for the purpose of removing interference. However, the diverse sources of background and noise make it a hard task to eliminate them completely. There are several methods presented for eliminating varying background and noise of data [14–22], but they usually require more sophisticated software procedures and sometimes tedious trials in their computational procedures.

Recently, the applications of noise frequency spectrum modification to eliminate the noise have been used in analytical technologies to improve the LC-MS/MS determinations [23,24]. This simple chemometric technique multiplies one match-filtered or low-pass filtered chromatogram with another artificial chromatogram of similar peak features containing only thermal noises. The noise on the modified chromatogram can be more efficiently removed with the second filtering procedure via the multiplication procedures which can smear the bandwidth-limited noise frequency spectrum of a filtered chromatogram to a wider range [23]. However, you will find it is difficult to perform the cross-correlation of a NIR spectrum with a simulated spectrum during the matched filtering if you are trying to use this method to remove the noise on NIR spectral signal, because the weak signal of NIR always submerged in a wide background.

In this paper, we develop an improved noise frequency spectrum modification to remove the noise of NIR spectra. This simple chemometric technique is to multiply one Savitzky–Golay filtered NIR spectrum with another Savitzky–Golay filtered NIR spectrum of reference substance added with thermal noise before the other

* Corresponding author. Tel.: +86 25 83271180.
E-mail address: cpuxiang@yahoo.com (B. Xiang).

0039-9140/$ – see front matter © 2009 Elsevier B.V. All rights reserved.
doi:10.1016/j.talanta.2009.08.010

Savitzky–Golay filter. For illustration, we use simulated spectra that exemplify how noise frequency spectrum modification technique eliminates the background noise and improves the NIR determinations. We also used the spectra of water samples and plasma samples to validate the presented method.

2. Theory and algorithm

2.1. Savitzky–Golay filter

The Savitzky–Golay (SG) filter is a type of low-pass digital filter that was proposed in 1960s [25] as a good smoothing and differentiating technique for spectral use [26–30]. Their simple smoother has become an almost universal method to improve the signal-to-noise ratio of any kind of signal [31,32]. Since the algorithm is well-known, it will not be explained in detail in this paper. More information can be found in the literatures [25,33,34].

2.2. Multiplication

The signal process using multiplication method is originated from the sequential paired covariance (SPC) [35] and applied to improve signal-to-noise ratio of liquid chromatography-tandem mass spectrometry peaks using noise frequency spectrum modification between two consecutive matched-filtering procedures [23,24]. The simulated NIR spectrum $sp(\lambda)$ is the summation of a smooth peak $s(\lambda)$ and noise $n(\lambda)$. The features of $s(\lambda)$ are estimated from those of Savitzky–Golay filtered NIR spectrum $SGf(\lambda)$. When the Savitzky–Golay filtered NIR spectrum $SGf(\lambda)$ is multiplied by $sp(\lambda)$, the expansion can be expressed as Eq. (2) [23],

$$SGf(\lambda)sp(\lambda) = SGf(\lambda)s(\lambda) + SGf(\lambda)n(\lambda) \quad (2)$$

The first term $SGf(\lambda)s(\lambda)$ maintains the NIR signal peak because the features of $SGf(\lambda)$ are similar to these of $s(\lambda)$. Therefore, the tailored noise spectrum of the above multiplication product is mainly contributed by the second term $SGf(\lambda)n(\lambda)$. The Fourier transform of the product $SGf(\lambda)n(\lambda)$ to frequency domain is proportional to the convolution of two spectra $SGF(\nu)$ and $N(\nu)$, which are the Fourier transforms of $SGf(\lambda)$ and $n(\lambda)$, respectively [23,36],

$$F\left\{SGf(\lambda)n(\lambda)\right\} = \int [SGf(\lambda)n(\lambda)]\, e^{-i\omega\lambda} d\lambda = \frac{1}{2\pi} \int SGF(\nu)N(\omega-\nu)d\nu \quad (3)$$

The Fourier transform of a Savitzky–Golay filtered spectrum $SGF(\nu)$ only contains low-frequency components due to Savitzky–Golay filter works as a low-pass filter. $SGF(\nu)$ is estimated as an exponential-decay profile in Fig. 1A. The profile of $N(\nu)$, the Fourier transform of random noises $n(\lambda)$, is a flat line in Fig. 1B. As shown in Fig. 1C, although $SGF(\nu)$ falls to zero quickly as the frequency gets higher, the convolution of $SGF(\nu)$ with a flat line $N(\nu)$ results in a wider frequency spectrum. Therefore, on the modified spectrum, its noise spectrum is shifted toward higher frequency regime. Since the noise spectrum is no longer squeezed at the low-frequency regime, therefore the second Savitzky–Golay filter efficiently removes more noises to obtain higher signal-to-noise ratio spectrum. The baseline of the final NIR spectrum was therefore not fluctuated or shifted due to the low-frequency components on the noise spectrum of the conditioned spectrum remain suppressed.

2.3. Signal processing procedures

NIR spectra of sample and reference substance are firstly processed with Savitzky–Golay filter procedure. As illustrated in Eq. (4), the Savitzky–Golay filter of the sample NIR spectrum of total length k points Sample(Λ_i) is calculated.

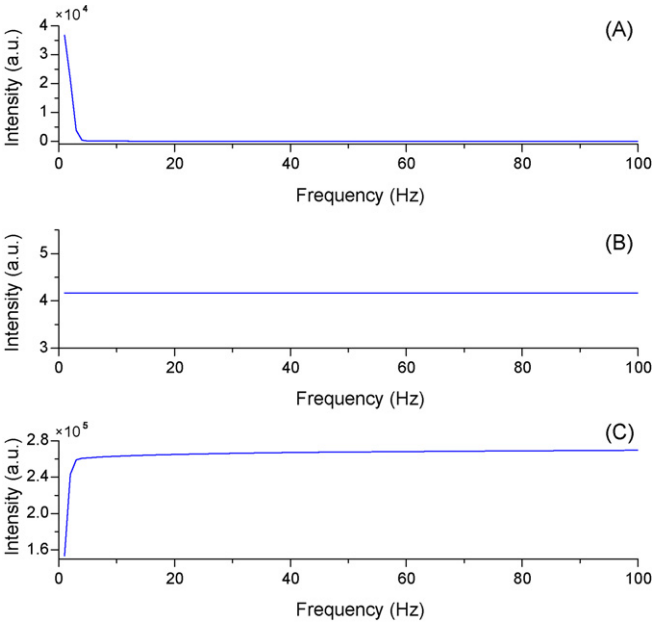


Fig. 1. (A) The simulated frequency spectrum of one Savitzky–Golay filtered NIR spectrum. (B) The simulated frequency spectrum of the thermal noise. (C) The convolution results of the spectra in parts A and B.

$$SGF_1(\Lambda_i) = \frac{1}{N}\sum_{j=-m}^{m} w_j \mathrm{Sample}(\Lambda_{i+j}); \quad i = 0,\ 1,\ 2,\ \ldots,\ k \quad (4)$$

Where N is the number of convoluting integers and m is the number of neighboring points. $SGF_1(\Lambda_i)$ represents Savitzky–Golay filtered spectrum of sample NIR spectrum and (Λ_i) is the ith wavenumber points.

The Savitzky–Golay filter of the reference substance NIR spectrum of total length k points $ref(\Lambda_i)$ is also calculated.

$$SGref(\Lambda_i) = \frac{1}{N}\sum_{j=-m}^{m} w_j ref(\Lambda_{i+j}); \quad i = 0, 1, 2, \ldots, k \quad (5)$$

Where $SGref(\Lambda_i)$ represents Savitzky–Golay filtered spectrum of the reference substance NIR spectrum.

The multiplication product result of the filtered sample spectrum with another reference spectrum, which contains the one Savitzky–Golay filtered reference substance spectrum added with additional thermal noises, is obtained.

$$MP(\Lambda_i) = SGF_1(\Lambda_i)[SGref(\Lambda_i) + N(\Lambda_i)] \quad (6)$$

Where the term $MP(\Lambda_i)$ represents the multiplication operation result. The term $N(\Lambda_i)$ represents the random noises added on the Savitzky–Golay filtered reference substance spectrum $SGref(\Lambda_i)$. The noises $N(\Lambda_i)$ are generated with a random number generator of normal distribution function with zero mean. The variance of this distribution function is estimated by the root mean square (RMS) of noise in sample NIR spectrum. As illustrated in Eq. (6), the modified spectrum $MP(\Lambda_i)$ will no longer contain only low-frequency noise when the Savitzky–Golay filtered spectrum $SGF_1(\Lambda_i)$ with only low-frequency noises is multiplied with a reference spectrum containing random noise $N(\Lambda_i)$. The noise frequency spectrum range of $MP(\Lambda_i)$ becomes wider via this modification.

Eq. (7) shows that each point on the modified spectrum $MP(\lambda)$ is then divided by the summation of its corresponding point on the Savitzky–Golay filtered reference substance spectrum $SGref(\lambda)$ and

Table 1
The parameters of the simulated NIR spectra dataset.

Parameters	Background	Analytical signal
Sample spectra		
x_0	925	1601
σ	371	14
A	Random	Proportional to concentrations
Reference spectrum		
x_0	925	1601
σ	371	14
A	3	3

the average intensity of noises $\langle N \rangle$ to adjust the exaggerated peak intensity.

$$AMP(\Lambda_i) = \frac{MP(\Lambda_i)}{SGref(\Lambda_i) + \langle N \rangle} \quad (7)$$

Where $AMP(\Lambda_i)$ indicates the adjusted result. The noise frequency range of $AMP(\Lambda_i)$ should be similar to that of $MP(\Lambda_i)$ because Eq. (7) only results in intensity adjustment.

The adjusted spectrum is processed with the second Savitzky–Golay filter procedures to obtain the final results.

$$SGF_2(\Lambda_i) = \frac{1}{N}\sum_{j=-m}^{m} w_j AMP(\Lambda_{i+j}); \quad i = 0, 1, 2, \ldots, k \quad (8)$$

Where $AMP(\Lambda_i)$ is the adjusted result of $MP(\Lambda_i)$. Because $AMP(\Lambda_i)$ also contains high frequency noises, the second Savitzky–Golay filter is able to accomplish efficient noise reduction.

When the sample signal spectrum Sample(Λ_i) in Eq. (4) is multiplied by a factor k, the same multiplication k will appear in the final results $SGF_2(\Lambda_i)$ in Eq. (8). So these filtering procedures are able to maintain the signal intensity linearity.

3. Experimental section

3.1. Simulated dataset

The simulated data mimicked common NIR spectral data with excessive background. A simulated sample spectrum was obtained by adding a background (a broader Gaussian peak), an analytical signal (a narrower Gaussian peak), and normal distributed noise. The Gaussian peaks were generated by

$$x_i = A \exp\left[-\frac{(x_i - x_0)^2}{2\sigma^2}\right] \quad (9)$$

Where A is the height at the centre, x_0 is the position of the centre and σ is the standard deviation of the Gaussian peak, and 4σ is the peak width.

A simulated dataset with 42 samples were used in this paper. In total, there are about 2203 points in each simulated NIR spectrum. The parameters x_0, σ and A of background and analytical signal in simulated sample spectra and reference substance spectrum are shown in Table 1. The peak heights A of simulated sample spectra are proportional to concentrations for analytical signal, whereas the peak heights for background are random. The simulated sample spectra and reference substance spectrum are shown in Fig. 2 and Fig. 3(B), respectively.

3.2. Measured dataset

3.2.1. Water samples

Fifty samples of chlorpyrifos in drinking water with concentration range from 1 to 125 ng/ml were prepared. All samples were measured using a multipurpose Fourier transform NIR (FT-NIR) spectrometer (MPA, Bruker Optics, Inc., Ettlingen, Germany)

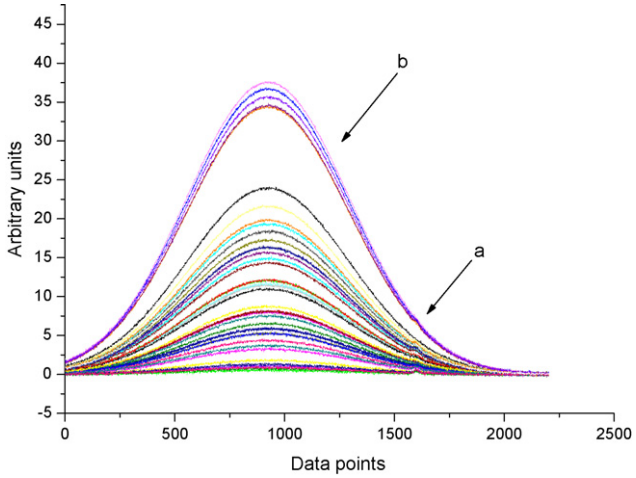


Fig. 2. The simulated NIR spectra. (a) The simulated analytical signal; (b) The simulated background.

equipped with a PbS detector and a fiber optic probe. OPUS/IDENT (version 5.0) multivariate statistical qualitative analysis software (Bruker Optics, Inc.) was used for spectral data collection and transformation. Each spectrum represented the average of 64 scans at a resolution of 16 cm^{-1}, over the wave number of 12,500 to 4000 cm^{-1}. Each sample was scanned three times. The average spectrum of each sample was used for further analysis.

3.2.2. Plasma samples

Plasma samples were from 19 healthy Chinese male volunteers received an oral dosage of 300 mg acyclovir capsule [37]. The sample set was split randomly into separate training and test sets that spanned nearly identical concentration ranges, containing 60 and 20 samples, respectively.

High performance liquid chromatography based procedures were employed to determinate the concentration of samples used for PLS model. The flow-rate was set at 1.0 ml/min and the effluent was monitored by UV detector at 254 nm. The mobile phase was acetonitrile–water containing 5 mmol/l perchloric acid, (pH 2.0; 4:96, v/v). All the analyses were performed at an ambient temperature.

Forty microliters H_3PO_4 solution (20%, v/v) was added to 500 μl plasma. Vortex mixed for 1 min, and then added 400 μl perchloric acid to the mixture. After vortex mixing for 3 min, the last mixture was then centrifuged for 10 min at 16000 rpm. After centrifugation, 20 μl of the clear supernatant was injected into the LC system. The area values of the chromatographic peaks were used to calculate the concentrations of samples from standard curve.

An appropriate amount of sample was transferred to quartz cell with a 1 mm optical path (NIR).The FT-NIR spectrum was recorded from 12500 to 4000 cm^{-1} using a nominal resolution of 8 cm^{-1}, accumulating 64 scans per spectrum and air was used as reference (empty sample holder). Each sample was scanned in triplicate (repack) and the spectra were averaged for chemometric analysis.

3.3. Computation

The algorithm described in this paper was implemented in Matlab (The Mathworks, Inc., Natick, MA, USA). PLS calibrations were derived using the PLS algorithm included in OPUS (Version 5.0, Bruker Optics, Inc.).

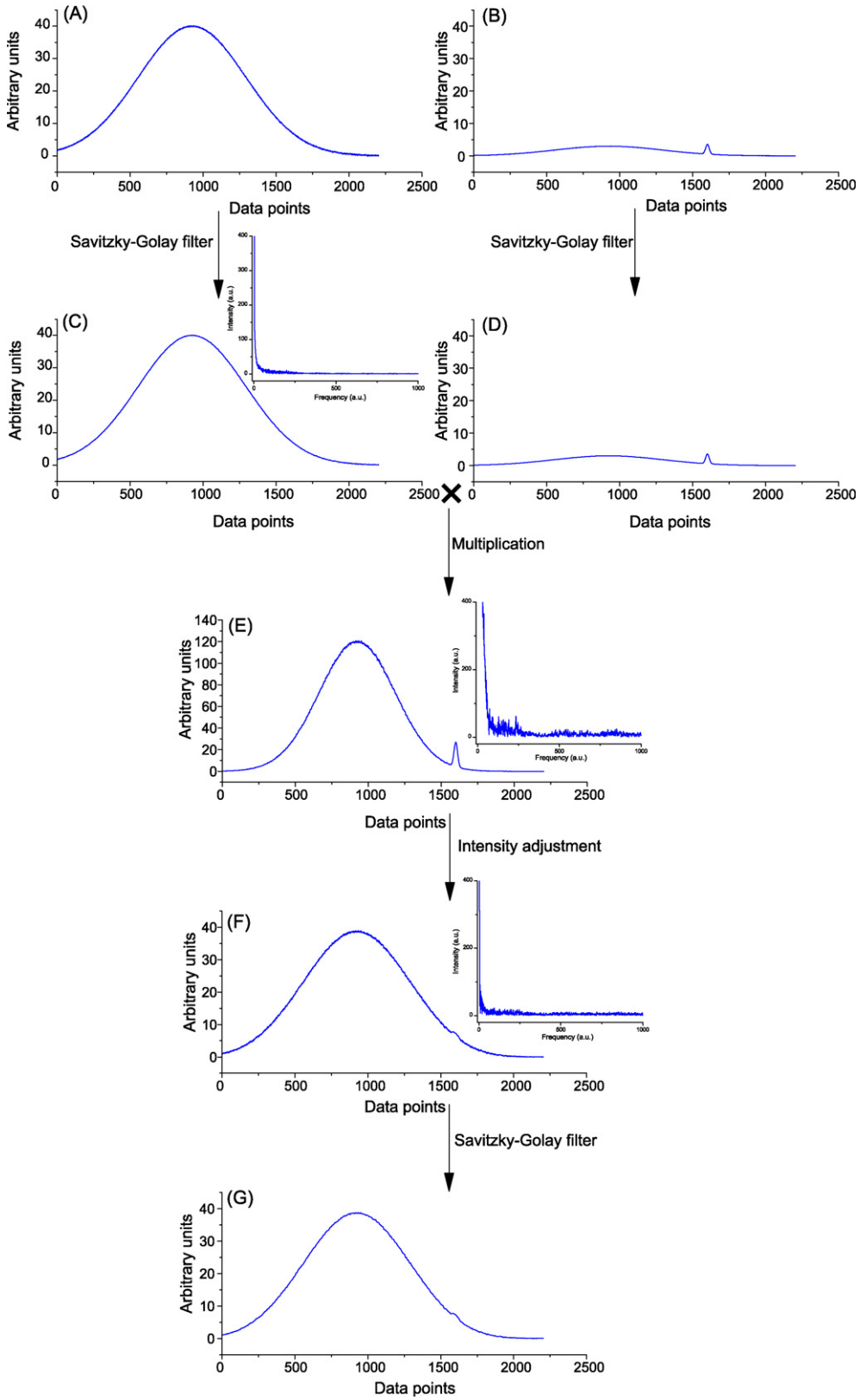


Fig. 3. The flow chart shows the filtering procedures using the noise modification steps between two consecutive Savitzky–Golay filters. (A) The simulated NIR spectrum. (B) The simulated reference substance spectrum. (C) The NIR spectrum of (A) processed with Savitzky–Golay filter. The imbedded graph shows the frequency spectrum of spectrum (C). (D) The NIR spectrum of (B) processed with Savitzky–Golay filter. (E) The NIR spectrum via performing the multiplication using spectrum (C) with reference spectrum (D) added with certain intensity thermal noise. The imbedded graph shows the frequency spectrum of spectrum (E). (F) The intensity-adjusted spectrum of (E). The imbedded graph shows the frequency spectrum of spectrum (F). (G) The final NIR spectrum via processing (F) with second Savitzky–Golay filter.

Table 2
The results of the PLS model of the simulated NIR spectra dataset processed with different preprocess methods.

Process method	Calibration set		Validation set	
	RMSECV	R^2	RMSEP	R^2
No process	0.165	92.61	0.139	94.74
Constant offset elimination	0.202	88.89	0.203	88.68
Straight line subtraction	0.214	87.44	0.201	88.99
Vector normalization	0.51	29.03	0.551	17.06
Min-max normalization	0.446	45.75	0.4	56.23
Multiplicative scattering correction	0.648	14.82	0.591	4.436
First derivative	0.171	91.98	0.164	92.67
Second derivative	0.231	86.4	0.472	39.03
Multiplication modification between two Savitzky–Golay filters	0.0578	99.09	0.0931	97.63

4. Results and discussion

4.1. Analysis of simulated dataset

The simulated data mimicked typical NIR spectral data with excessive background and weak analytical signal. The peak heights and widths of the background are obviously larger than those of the analytical signals (Fig. 2). Forty-two samples were randomly divided into two datasets, 28 in calibration set and the others in validation set. All spectra were preprocessed by proposed noise frequency spectrum modification between two consecutive filtering procedures as described in the flowchart of Fig. 3. Fig. 3(A) shows one simulated NIR spectrum obtained by adding a background (a broader Gaussian peak, $A = 40$), an analytical signal (a narrower Gaussian peak, $A = 0.01$), and normal distributed noise. The analytical signal was embedded completely in excessive background noise. Fig. 3(B) shows the simulated reference substance spectra obtained by adding a small background ($A = 3$), an analytical signal of certain intensity ($A = 3$) and some tiny normal distributed noise. Fig. 3(C) and(D) were Savitzky–Golay filtered spectra of simulated sample spectrum Fig. 3(A) and reference spectra Fig. 3(B), respectively. As mentioned above, Savitzky–Golay filter works as a low-pass filter. The frequency spectrum imbedded in Fig. 3(C) shows almost no high frequency components. The remaining low-frequency noises cannot be eliminated with the second Savitzky–Golay filter or any other types of low-pass filter. Fig. 3(E) shows the results of the multiplication product of sample spectrum in Fig. 3(C) with reference substance spectrum in Fig. 3(D) added with certain intensity thermal noise. Fig. 3(F) shows the intensity-adjusted results of spectra in Fig. 3(E). The appearance of noises in Fig. 3(F) shows more high frequency components and is significantly different from that in Fig. 3 (C). The multiplication of two spectra at the signal space is in equivalence to the convolution between the two frequency spaces of these spectra. When the remaining low-frequency noises on the Savitzky–Golay filtered spectrum are multiplied by the random noises on the simulated spectra, the noise spectrum of this multiplication product no longer contains only low-frequency components. The range of noise spectrum becomes wider. The imbedded graphs in Fig. 3(E) and (F) show the frequency spectra of these two spectra, respectively. Like the previous discussion, when the noise spectrum of conditioned spectra is shifted toward the higher frequency range, the second Savitzky–Golay filter procedures are able to eliminate noise more efficiently. Fig. 3(G) shows the final result of the second Savitzky–Golay filter product of spectrum in Fig. 3(F).

After all NIR spectra being preprocessed by noise spectrum modification technique, a PLS model of analytical signals was built. The results are shown in Table 2. Table 2 shows the R^2 of the calibration set, the root mean square error of cross validation (RMSECV), the R^2 of the validation set and the root mean square error of prediction (RMSEP) were obtained in each preprocess method of simulated NIR spectra. Without preprocess method of noise frequency spectrum modification between two consecutive Savitzky–Golay filtering procedures, the RMSEP was 0.139 and the R^2 of the validation set was only 94.74. The results showed that the RMSEP was decreased to 0.0931 and R^2 of validation set was increased to 97.63. The prediction of PLS model should be improved. But after correcting with conventional preprocess method provided by OPUS software, such as constant offset elimination, straight line subtraction, vector normalization, min-max

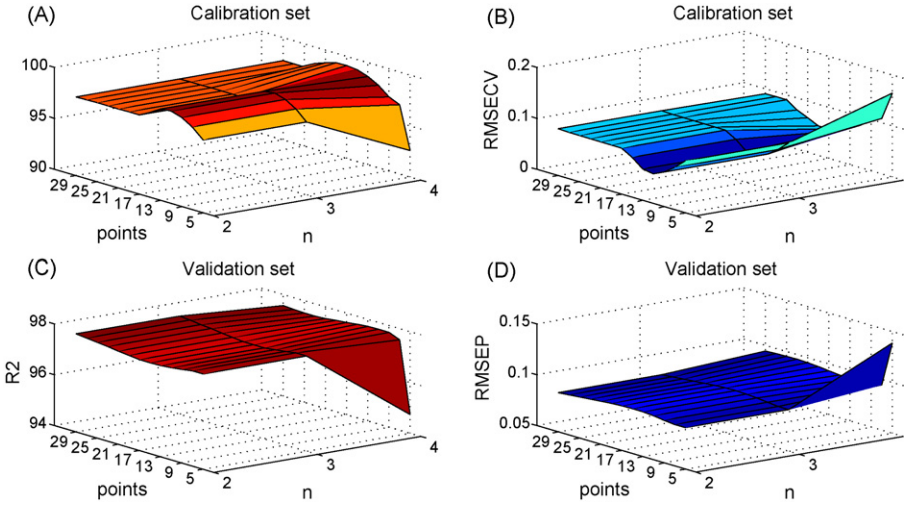


Fig. 4. The results of PLS model with different parameters of Savitzky–Golay filter. (A) The R^2 of calibration set in different parameters of filter. (B) The RMSECV in different parameters of filter. (C) The R^2 of validation set in different parameter of filter. (D) The RMSEP in different parameters of filter.

normalization, multiplicative scattering correction, first derivative and second derivative, poor results were obtained. It was clear that the proposed noise frequency spectrum modification technique can be used to eliminate excessive background and spectra noise for improve NIR determination.

The final result of spectrum processed by noise spectrum modification technique can be affected by the parameters of Savitzky–Golay filter. The commonly used setup of Savitzky–Golay filter consists of an interleaving polynomial function of length of about 5–29 data points and polynomial degree *n*. The effectiveness of the various functions was tested in this study. The tested length of the interleaving function varied from 5 to 29 data points and a polynomial degree from 3 to 7. Fig. 4 shows the results of PLS model with different parameters of Savitzky–Golay filter. The result shows the optimum value of RMSECV and RMSEP were obtained simultaneously with polynomial degree *n* was 4 and data points of interleaving function was 17.

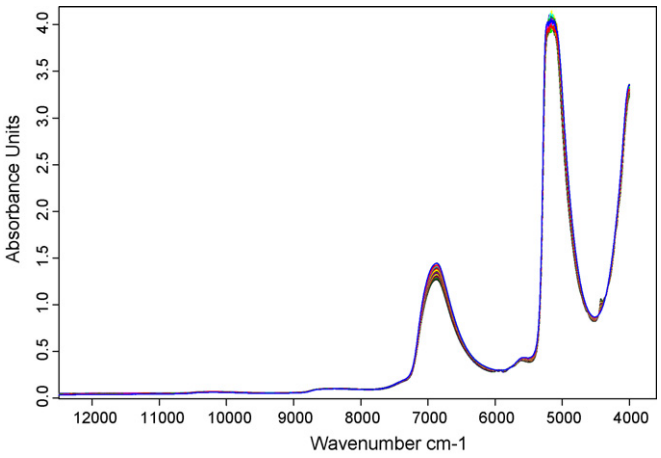


Fig. 5. The NIR spectra of chlorpyrifos water samples.

4.2. Analysis of measured datasets

4.2.1. Water samples

In order to test the efficiency of noise frequency spectrum modification technique in practice, the method was tested by measured NIR spectral data on chlorpyrifos water solution. Half of the samples were used in the calibration set and the others in the validation set. Fig. 5 shows that the absorbance peaks of the O–H bond at 6944 and 5155 cm^{-1} are very large, which peaks are mainly attributed to water. While the absorbance of the low concentration of chlorpyri-

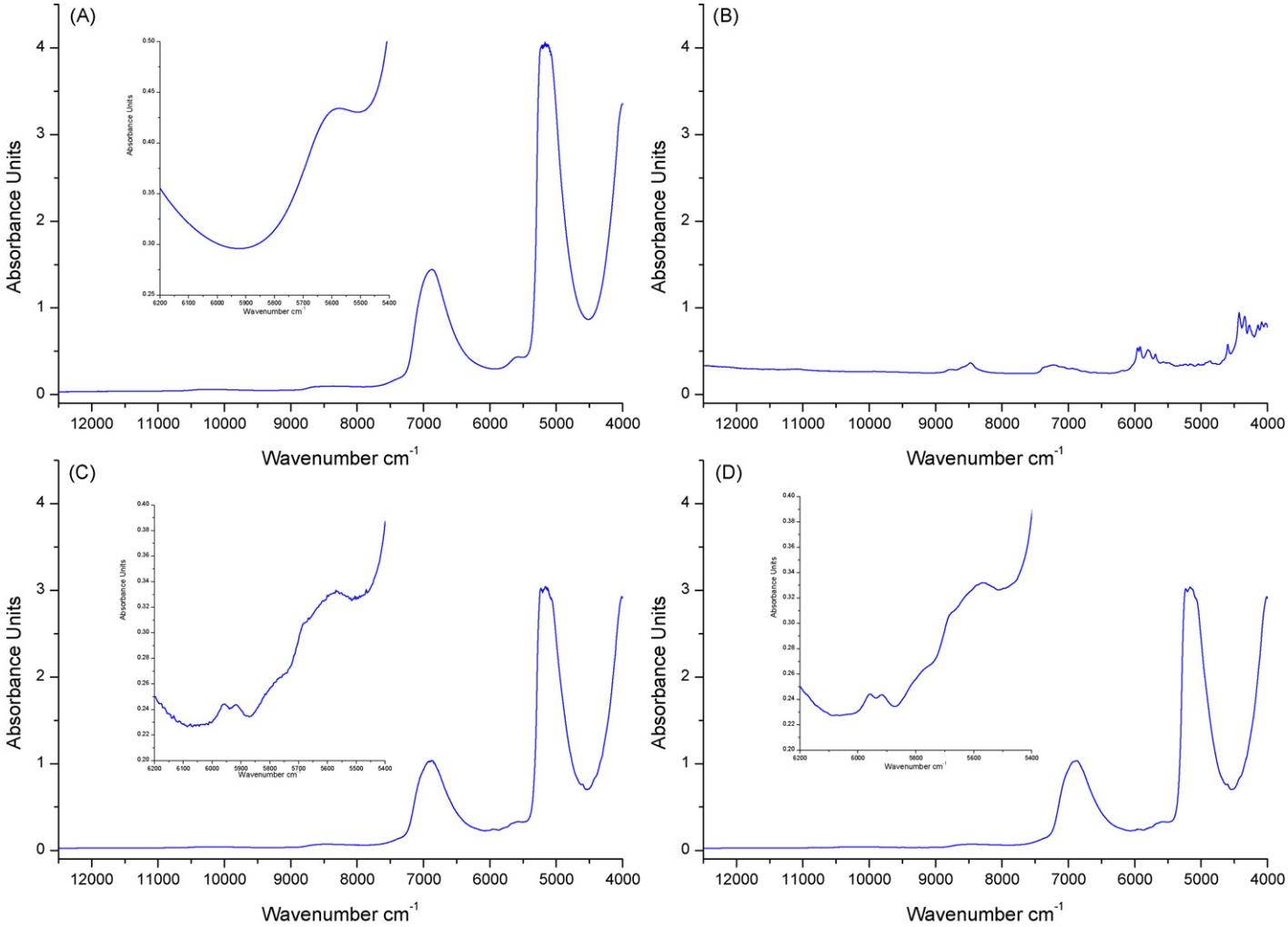


Fig. 6. (A) The NIR spectrum of chlorpyrifos water sample at concentration 1 ng/ml. The imbedded graph shows the special enlarged spectrum at region 6102–5446 cm^{-1}. (B) The NIR spectrum of chlorpyrifos powder (reference substance). (C) The intensity-adjusted spectrum via performing the multiplication using Savitzky–Golay filtered spectrum of (A) with the same processed spectrum of (B) added with thermal noises. The imbedded graph shows the special enlarged spectrum of (C) at region 6102–5446 cm^{-1}. (D) The final NIR spectrum via processing (C) with second Savitzky–Golay filter. The imbedded graph shows the special enlarged spectrum of (D) at region 6102–5446 cm^{-1}.

Table 3
The results of the PLS model the chlorpyrifos water sample NIR spectra dataset processed with different preprocess methods.

Process method	Calibration set		Validation set	
	RMSECV	R2	RMSEP	R2
No process	3.06	99.29	3.49	99
Constant offset elimination	2.76	99.42	3.09	99.21
Straight line subtraction	2.71	99.45	3.06	99.23
Vector normalization	3.15	99.25	3.1	99.21
Min-max normalization	3.14	99.26	2.7	99.4
Multiplicative scattering correction	2.94	99.35	2.96	99.28
First derivative	2.91	99.36	3.37	99.07
Second derivative	2.97	99.33	3.2	99.16
Multiplication modification between two Savitzky–Golay filters	1.69	99.78	2.37	99.54

Table 4
The results of the PLS model of chlorpyrifos water sample NIR spectra processed with one or two consecutive Savitzky–Golay fitlers and conditioned with multiplication modification between two Savitzky–Golay filters.

Process method	Calibration set		Validation set	
	RMSECV	R2	RMSEP	R2
No process	3.06	99.29	3.49	99
One Savitzky–Golay filter	2.77	99.42	3	99.26
Two consecutive Savitzky–Golay filters	3.21	99.22	2.64	99.43
Multiplication modification between two Savitzky–Golay filters	1.69	99.78	2.37	99.54

fos was so weak that no clear absorbance peaks can be found in the spectra. Building a PLS model of chlorpyrifos would be a challenging work.

Fig. 6(A) shows the representative NIR spectrum of chlorpyrifos water solution. The signal-to-noise ratio of the spectrum was 19.49 (estimated by OPUS software). The absorbance peaks of chlorpyrifos were submerged in excessive background of H_2O. Fig. 6(B) shows the NIR spectrum of chlorpyrifos powder (reference substance). The representative absorbance peaks of chlorpyrifos were at regions 6102–5446 cm^{-1} and 4600–4000 cm^{-1}. The intensity-adjusted result of the multiplication product of Savitzky–Golay filtered sample spectrum with Savitzky–Golay filtered reference spectrum was showed in Fig. 6(C). The embedded graph in Fig. 6(C) shows the enlarged spectrum at with region 6102–5446 cm^{-1}. This region in Fig. 6(C) is significantly different from Fig. 6(A). The high frequency noise shifted from low frequency using noise frequency spectrum modification technique can be eliminated with the second Savitzky–Golay filter to obtain better improvement of spectral characteristics. The final processed spectrum of chlorpyrifos water solution was shown in Fig. 6(D). The signal-to-noise ratio of the processed spectrum was improved to 24.96.

A PLS model of chlorpyrifos was built after all spectra being preprocessed by noise frequency spectrum modification technique. The results were shown in Table 3. The results suggested that without data preprocess, poor results were obtained. Slightly better or even worse results were obtained by the classical data preprocess methods provided by OPUS software, such as constant offset elimination, straight line subtraction, vector normalization, min-max normalization, multiplicative scattering correction, first derivative and second derivative. The best results were obtained by the proposed noise frequency spectrum modification technique, as shown in the simulated datasets. Table 4 illustrates the results of chlorpyrifos water solution NIR spectra processed by one or two consecutive Savitzky–Golay filter procedures with and without performing additional multiplication modification steps before the second Savitzky–Golay filtering computation. Compared to original PLS without spectra preprocess, RMSECV and RMSEP of PLS model with noise frequency spectrum modification steps decreased from 3.06 and 3.49 to 1.69 and 2.37, respectively, and the corresponding R^2 of calibration set and validation set increased from 99.29 and 99 to 99.78 and 99.54, respectively.

The parameters of Savitzky–Golay filter were also optimized by the same way as in the simulated datasets. The optimum value of RMSECV and RMSEP were obtained simultaneously with polynomial degree n was 3 and data points of interleaving function was 9.

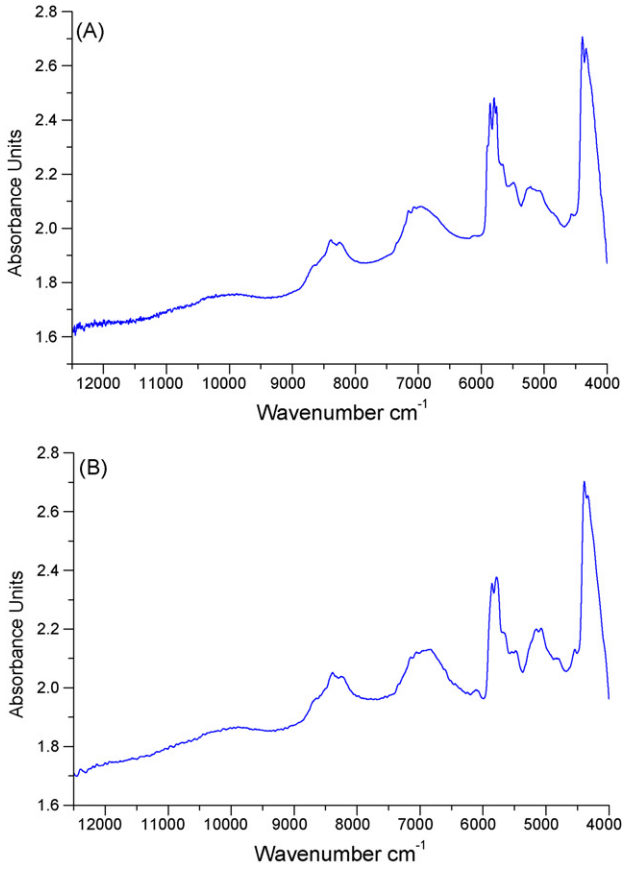


Fig. 7. (A) The NIR spectrum of acyclovir plasma sample at concentration 1.92 μg/ml.
(B) The final NIR spectrum via processing (A) with noise frequency spectrum modification technique.

Table 5
The results of the PLS model of the acyclovir plasma sample NIR spectra dataset processed with different preprocess methods.

Process method	Calibration set		Validation set	
	RMSECV	R^2	RMSEP	R^2
No process	0.283	78.01	0.848	74.63
Constant offset elimination	0.202	88.73	0.422	85.51
Straight line subtraction	0.381	74.72	1.24	69.44
Vector normalization	0.161	91.68	0.25	90.29
Min-max normalization	0.217	87.04	0.329	86.85
Multiplicative scattering correction	0.241	84.06	0.233	84.82
First derivative	0.257	82.45	0.513	80.38
Second derivative	0.159	92.19	0.301	91.87
Multiplication modification between two Savitzky–Golay filters	0.13	94.77	0.213	94.16

4.2.2. Plasma samples

The proposed method was also validated by treating plasma samples. Fig. 7(A) shows a representative NIR spectrum of acyclovir plasma sample and the signal-to-noise ratio of the spectrum was 19.35. All spectra of plasma samples were preprocessed by noise frequency spectrum modification technique. The optimized polynomial degree n and data points of interleaving function were 3 and 17, respectively. Fig. 7(B) shows the final processed spectrum of acyclovir plasma sample and the signal-to-noise ratio of the processed spectrum was improved to 22.91. A PLS model of acyclovir was built after all spectra being preprocessed by the proposed method. The results were shown in Table 5. The optimum value of RMSECV and RMSEP were 0.13 and 0.213, respectively, and the corresponding R^2 of calibration set and validation set were 94.77 and 94.16, respectively. It was obvious that the best results were obtained by the proposed noise frequency spectrum modification technique.

5. Conclusion

Within non-destructive analytical technology, NIR spectroscopy has been found to be an effective technique for the determination of solid, semisolid, fluid, and vapor sample. However, NIR spectra consist of excessive background, weaker analytical signal and thermal noise making interpretation of the analysis and modeling results complicated. On both simulated and measured NIR case studies, we have shown that the recent tailoring noise frequency spectrum technique provides an intrinsic improvement for the interpretation of NIR data. This is achieved through multiplying one Savitzky–Golay filtered NIR spectrum containing only low-frequency noises with another reference spectrum containing thermal noises. The conditioned spectrum is processed with the second Savitzky–Golay filter to obtain much better RMSECV and RMSEP than the corresponding value using two Savitzky–Golay filters without noise conditioning. This noise-tailoring technique can shift the low-frequency noise spectrum of Savitzky–Golay filtered spectrum toward the higher frequency range. As a result, the noises on the conditioned spectrum can be removed more efficiently using the second Savitzky–Golay filter. Our study proves that this noise-modification technique is able to improve PLS model using Savitzky–Golay filter to process NIR spectrum, which typically contain many background. Furthermore, it is simple to develop software works to implement this noise tailoring technique. Potentially, this noise-modification technique can be also used between any two low-pass filters to eliminate low-frequency noises to improve NIR determination.

References

[1] C.J. Clark, V.A. McGlone, R.B. Jordan, Postharvest Biol. Technol. 28 (2005) 65.
[2] V.A. McGlone, R.B. Jordan, R. Seelye, P.J. Martinsen, Postharvest Biol. Technol. 26 (2002) 191.
[3] J. Moros, M.J. Martinez-Sánchez, C. Pérez-Sirvent, S. Garrigues, M. de la Guardia, Talanta 78 (2009) 388.
[4] R.M. Balabin, R.Z. Safieva, Fuel 87 (2008) 1096.
[5] H.L. Fernandes, I.M.R. Jr., C. Pasquini, J.J.R. Rohwedder, Talanta 75 (2008) 804.
[6] A. Durand, O. Devos, C. Ruckebusch, J.P. Huvenne, Anal. Chim. Acta 595 (2007) 72.
[7] Y. Langeron, M. Doussot, D.J. Hewson, J. Duchene, Eng. Appl. Artif. Intell. 20 (2007) 415.
[8] Y. Dou, Y. Sun, Y.Q. Ren, P. Ju, Y.L. Ren, J. Pharm. Biomed. Anal. 37 (2005) 543.
[9] E.W. Ciurczak, Am. Pharm. Rev. 5 (2002) 68.
[10] J. Luypaert, D.L. Massart, Y. Vander Heyden, Talanta 72 (2007) 865.
[11] H. Stenlund, E. Johansson, J. Gottfries, J. Trygg, Anal. Chem. 81 (2009) 203.
[12] S.C. Rutan, O.E. De Noord, R.R. Andréa, Anal. Chem. 70 (1998) 3198.
[13] D. Chen, X.G. Shao, B. Hu, Q.D. Su, Anal. Chim. Acta 511 (2004) 37.
[14] C.R. Mittermayr, H.W. Tan, S.D. Brown, Appl. Spectrosc. 55 (2001) 827.
[15] H.W. Tan, S.D. Brown, J. Chemometr. 16 (2002) 228.
[16] T.V. Karstang, O.M. Kvalheim, Chemometr. Intell. Lab. Syst. 12 (1991) 147.
[17] P.J. Gemperline, J.H. Cho, B. Archer, J. Chemometr. 13 (1999) 153.
[18] R.P. Raradkar, R.P. Williams, Appl. Spectrosc. 51 (1997) 92.
[19] J.G. Sun, Appl. Spectrosc. 11 (1997) 525.
[20] W. Windig, J.M. Phalp, A.W. Payne, Anal. Chem. 68 (1996) 3602.
[21] A.M. Woodward, B.K. Alsberg, D.B. Kell, Chemometr. Intell. Lab. Syst. 40 (1998) 101.
[22] Y. Li, X. Shao, W. Cai, Talanta 72 (2007) 217.
[23] S.C. Wang, C.J. Lin, S.M. Chiang, S.N. Yu, Anal. Chem. 80 (2008) 2097.
[24] S.C. Wang, C.M. Huang, S.M. Chiang, J. Chromatogr., A 1161 (2007) 192.
[25] A. Savitzky, M.J.E. Golay, Anal. Chem. 36 (1964) 1627.
[26] S.T. Sum, S.D. Brown, Appl. Spectrosc. 52 (1998) 869.
[27] B.B. Ivanova, D.L. Tsalev, M.G. Arnaudov, Talanta 69 (2006) 822.
[28] M. Člupek, P. Matějka, K. Volka, J. Raman Spectrosc. 38 (2007) 1174.
[29] C. Gendrin, Y. Roggo, C. Collet, Talanta 73 (2007) 733.
[30] G. Mcleod, K. Clelland, H. Tapp, E.K. Kemsley, R.H. Wilson, G. Poulter, D. Coombs, C.J. Hewitt, J. Food Eng. 90 (2009) 300.
[31] P. Jonsson, L. Eklundh, Comput. Geosci. 30 (2004) 833.
[32] R.C. Schneider, K.A. Kovar, Forensic Sci. Int. 134 (2003) 187.
[33] B.C.H. Turton, Meas. Sci. Technol. 3 (1992) 858.
[34] G. Vivó-Truyols, J.R. Torres-Lapasió, A.M. van Nederkassel, Y. Vander Heyden, D.L. Massart, J. Chromatogr. A 1096 (2005) 133.
[35] C.M. Fleminga, B.R. Kowalskia, A. Apffelb, W.S.J. Hancockb, Chromatogr. A 849 (1999) 71.
[36] T.K. Nadler, S.T. McDaniel, M.O. Westerhaus, J.S. Shenk, Appl. Spectrosc. 43 (1989) 1354.
[37] L.Y. Yu, B.R. Xiang, Y. Zhan, Arzneim-Forsch Drug Res. 58 (2008) 199.

Talanta 80 (2009) 903–908

Contents lists available at ScienceDirect

Talanta

journal homepage: www.elsevier.com/locate/talanta

Process sampling module coupled with purge and trap–GC–FID for in situ auto-monitoring of volatile organic compounds in wastewater

Hsin-Wang Liu [a], Yung-Tsun Liu [a], Bei-Zen Wu [a], Hung-Chi Nian [a], Hsing-Jung Chen [b], Kong-Hwa Chiu [c,*], Jiunn-Guang Lo [a,**]

[a] Department of Biomedical Engineering and Environmental Science, National Tsing-Hua University, Hsinchu 310, Taiwan, ROC
[b] Department of Chemistry, National Chung Hsing University, Taichung 402, Taiwan, ROC
[c] Department of Applied Science, National DongHwa University, 123, Hua-his Rd., Hualian 970, Taiwan, ROC

ARTICLE INFO

Article history:
Received 14 May 2009
Received in revised form 7 August 2009
Accepted 10 August 2009
Available online 18 August 2009

Keywords:
Process sampling module
P&T–GC–FID
In situ auto-monitoring
VOCs
Water

ABSTRACT

An automatic sampling device, i.e., process sampling module (PSM), connected with a purge and trap–GC–FID system has been developed for real-time monitoring of VOCs in wastewater. The system was designed to simultaneously monitor 17 compounds, including one polar compound, i.e., acetone, and 16 non-polar compounds. The trapping tube is packed with two adsorbents, Carbopack B and Carbosieve III, to trap target compounds. For the purpose of in situ monitoring, the flush valve of the sampling tube is composed of two two-way valves and a time controller to prevent absorption interference of the residue. The optimal conditions for the analytical system include a 12 min purge time at a temperature of 60 °C, and 4 min of desorption time with a desorption temperature of 260 °C. Good chromatograms have been obtained with the analytical system even if a cryogenic device and de-misting were not used. The relative standards deviation (RSD) of the system is between 2% and 13.4%, and accuracies between 0.3 and 23.5% have been achieved. The detection limits of the method range from 0.32 to 2.39 ppb. In this system, the four parts, i.e., PSM, P&T, GC, and FID, were simple, reliable and rugged. Also, the interface of these four parts was simple and dependable.

© 2009 Elsevier B.V. All rights reserved.

1. Introduction

Volatile organic compounds (VOCs) are persistent, toxic, and carcinogenic or mutagenic, and they have adverse effects on human health, even at very low concentrations [1–3]. At industrial or accidental spill sites, VOCs can accumulate in ground water up to concentrations of several hundred mg L^{-1} [1], and VOCs in indoor environments are as worrisome as those in the outdoors [4]. For example, many consumer products found around the house, such as cleaning solvents, paints, and wood preservatives in certain furniture all emit VOC compounds, which may contribute to sick building syndrome [5,6]. Consequently, the spread of VOCs in our surroundings is a serious environmental concern, and monitoring of VOCs is critical. VOCs occur in numerous products including fuels, solvents, paints, adhesives and deodorants. Other sources include combustion exhaust and electronic manufacture processes. VOCs may also exist in the air due to the evaporation of organic solvents in water or soil [7]. Due to low concentrations of VOCs in water, and their volatility, they are not often found in concentrations above a few μg L^{-1} in surface water; hence, their quantification is a big challenge. Therefore, measurement of VOCs usually requires preconcentration prior to detection in order to get reliable and satisfactory results. It is widely known that VOCs may be lost during sampling, preservation, shipping, and storage greatly affecting the resulting data. Therefore, in situ and automatic sampling/sample preparation techniques are quite important for their quantification.

For the determination of VOCs in waste water, static headspace (HS) techniques [8], dynamic HS [9–11], liquid–liquid extraction [2], membrane [12,13], solid-phase extraction, and solid-phase micro-extraction (SPME) [14–20] and many other methods [21] are used as sample preparation techniques. Purge and trap extraction (PTE) has been successfully applied in the separation and preconcentration of a variety of VOCs from different matrices [22,23]. By coupling with various detection modes, PTE has been widely used to quantify the amount of VOCs in drinking water, seawater [24], industrial wastewater [22], rainwater, blood, urine, mud [25], food [26–28] and beverages [29]. Recently, PTE has been adopted for the long-term monitoring of VOC content in surface water [30,31]. In addition, Chen and Her [32] proposed applying the purge and trap system for continuous analysis of flowing samples, e.g., halocarbons can be measured effectively in the low-flow samples.

* Corresponding author. Tel.: +886 3 8235175; fax: +886 3 8833635.
** Corresponding author. Tel.: +886 0939038798.
E-mail addresses: ckh@mail.ndhu.edu.tw (K.-H. Chiu), jglo@mx.nthu.edu.tw (J.-G. Lo).

0039-9140/$ – see front matter © 2009 Elsevier B.V. All rights reserved.
doi:10.1016/j.talanta.2009.08.011

Table 1
QA and QC of the automated system.

VOC	Precision (%)	Accuracy (%)	MDL (ppb)	*R*-square
1,1-Dichloroethylene	13.35	19.37	2.39	0.996
Acetone	4.82	4.57	9.07	0.993
Methylenechlorin	13.1	9.49	2.15	0.999
Chloroform	9.49	23.54	1.76	0.994
Benzene	8.33	7.34	1.34	0.998
Trichloroethylene	8.64	9.07	1.41	0.999
Bromodichloromethane	9.44	0.32	1.41	0.996
Toluene	8.97	9.99	1.48	0.999
Tetrachloroethylene	9.43	12.03	1.58	0.999
Dibromochloromethane	5.93	0.27	0.89	0.998
m,p-Xylene	9.64	12.20	1.66	0.998
Bromoform	3.73	0.42	0.56	0.998
1,2,4-Trimethylbenzene	3.05	13.69	0.39	0.997
1,3-Dichlorobenzene	3.83	12.51	0.50	0.998
1,4-Dichlorobenzene	2.78	11.49	0.37	0.999
1,2,4-Trichloro benzene	4.67	7.72	0.67	0.996
Naphthalene	1.99	7.86	0.32	0.998

HsinChu High Technology Park (HTP) is located in a populated area. The factories inside this park produce large amounts of organic substances due to their unique and necessary processes. Although these organic substances have been treated before released by a wastewater treatment plant, their concentrations need to be closely monitored, using a simple, fast, instantaneous and automatic method. The process sampling module (PSM) is an appropriate apparatus; sampling times for PSM are programmable through the GC's timed events control. By collecting a fixed volume sample of a sample stream upon command from the analytical system, the PSM eliminates the need for labor intensive, repeated manual sampling. The collected sample is subsequently transferred to the purge and trap apparatus for concentration and then is analyzed by the appropriate analytical systems, e.g., GC, GC/MS, etc.

The objectives of this work were twofold: first, simplification of the sampling apparatus and second, determination of the relationship between the concentration of VOCs and their time variations. One way to simplify would be to omit the SPME which is expensive and complicated when coupled with GC. To that end the design and applicability of PSM combined with P&T followed by GC–FID was investigated in the analysis of 17 VOCs, e.g., chloroform, toluene, naphthalene, methylene chloride, trichloroethylene, bromodichloromethane, tetrachloroethylene and acetone (Table 1), in waste water taken from the effluent released by the waste water treatment plant in HTP.

2. Experimental

2.1. Chemicals

All chemicals and reagents used in this study (the standard solutions were 5000 $\mu g\,L^{-1}$ in concentration) were obtained from Supelco (Supelco Individual Calibration Standards).

2.2. Apparatus and procedure

2.2.1. Automatic sampling system and procedure

The process sampling module (PSM) (an automatic sampling device) was commercially available (OI Analytical, College Station, TX) and was composed of a signal-receiving circuit board, a six-way valve, and a Teflon tube with volume of 5 mL and a caliber of 1/8″ in connected with a set of time controllers for sampling time control. The pushing gas was high-purity nitrogen. When the pre-set sampling time was completed, the time controllers delivered a signal to the circuit board, hence, the six-way valve return to its original place as that in the status of rinsing, and was ready for the next task. In this study, the sampling time was set at 8 min. If the sampling time is not long enough, the amount of water sample in the 5-ml Teflon tube cannot completely reach the purge and trap device, resulting in sample loss.

2.2.2. Purge and trap system and procedure

An O.I. analytical purge and trap concentrator (model 4560), GC (model 6890, Hewlett-Packard, Avondale, MA, USA) with fused-silica column (OV-624, 75 m × 0.25 mm i.d.) equipped with a flame ionization detector (FID) was used for the measurement of VOCs. Helium (99.9995%) was used as it carries gas at constant head column pressure. Temperature programming of the GC and data acquisition were begun simultaneously. Chromatographic separations were carried out using a temperature program, i.e., the temperature was held constant at 36 °C for 14 min, then linearly increased to 180 °C at 8 °C/min for 2 min, and finally increased to 210 °C at 15 °C/min for 2 min. Flow rate of the helium was set at 0.9 mL min^{-1}.

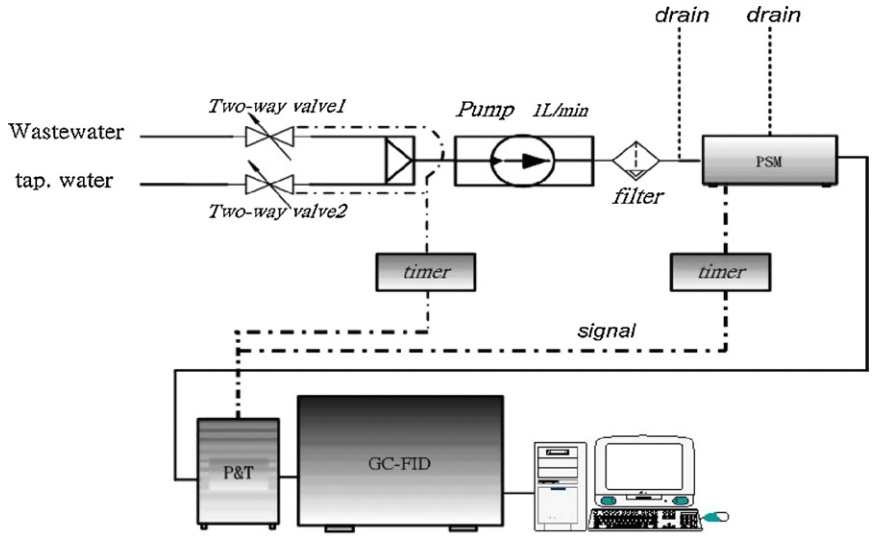


Fig. 1. Schematic diagram of the PSM–P&T–GC–FID system.

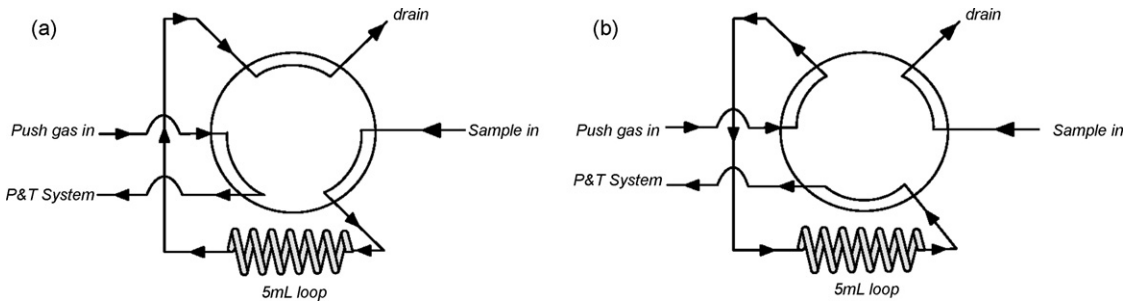


Fig. 2. Flow direction diagram of the PSM when (a) rinsing and (b) sampling.

2.2.3. Sampling tube and flush system

In this study, time controllers, a medium flux piston pump, silicosteel tube and two sets of two-way valves were assembled to form the sampling tube and tube flush system. Fig. 1 presents the schematic diagram of the complete automated PSM–P&T–GC–FID system. The inlet of the piston pump was connected via a three-way tie-in, and the outlet, working as the water sample flow port and the PSM sampling port, was also connected via a three-way tie-in. The water-in (flushing) tube was connected with a common PE tube. Fig. 2 describes the flow direction of PSM.

2.2.4. Trap tube

The stainless steel desorption tube used in this setup consisted of 0.25 g Carbopack B and 0.05 g Carbosieve III (Supelco Ltd.) separated by glass wool. The two head portions of the tube were also filled with glass wool and sealed by Swagelok fittings. The filled trap tube was formed into a U-shape for conditioning in the P&T system.

2.3. Calibration curve

The calibration curve for VOCs was established with seven different concentrations, i.e., 5, 10, 15, 20, 25, 30, 35 $\mu g\,L^{-1}$, and for acetone, the concentrations were 60, 100, 120, 160, 180, 220, and 240 $\mu g\,L^{-1}$.

3. Results and discussion

3.1. Automatic sampling (PSM) and flush systems

3.1.1. Feasibility of PSM

In this work, to verify the performance of this system, the response evaluation of the PSM was compared with that of the Archon auto-sampler (Varian). The Archon auto-sampler was specially designed for lab use, and it consisted of 51 sample trays to accept water or soil samples, providing easy loading and refrigeration. Water samples containing 5 ppb of benzene, toluene or m,p-xylene, individually, were used separately in both the PSM and the Archon auto-sampler to investigate the feasibility of PSM. As can be seen in Fig. 3, the response from the PSM system was excellent, i.e., over 90% of those of the Archon auto-sampler.

3.1.2. Stability of the flushing system

To understand the stability of the in situ operation, i.e., why the pollutants did not accumulate or remain in the tube as sewage samples continuously passed through the tube, the tube flush system was installed for continuous monitoring. Before sample collection, the container was rinsed with a real water sample. When the rinse time was longer than 30 s, the peak area remained stable with a fluctuation of only $\pm 3\sigma$ (Fig. 4). The rinse time before sampling was set at more than 5 min to ensure that the sampling tube was fully rinsed by the real water sample. Fig. 5 shows the effects of flushing

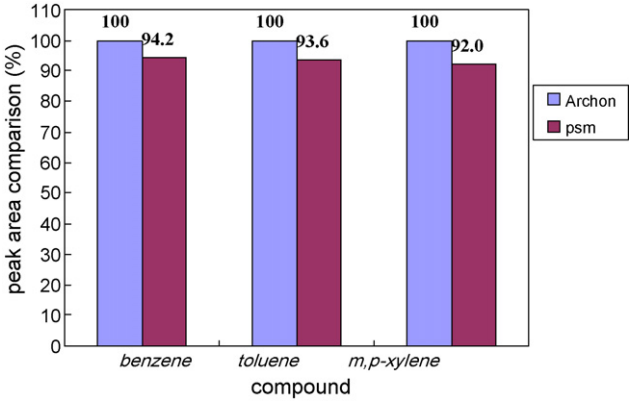


Fig. 3. Comparison of the response from PSM system and from Archon auto-sampler.

a 35 ppb BTX standard and blank sample. After flushing for 20 min, no residual sample remained to influence the next analytical result.

3.1.3. Accuracy, precision and detection limit

Results in Table 1 show the performance of the system that we developed. The data show that the *r*-squared (r^2) values of the calibration curve for all target compounds were greater than 0.990. Among them, methylene chloride, trichloroethylene, toluene, and tetrachloroethylene yielded values of 0.999; acetone and chloroform values were 0.993 and 0.994, respectively. The data show that this method is feasible for analyzing these 17 compounds. The method detection limit (MDL) of the polar compound acetone was 9.07 ppb, and the MDLs for the other target compounds ranged from 0.32 to 2.39 ppb. The accuracy value is defined as the difference between the numerical value of the concentration and the known theoretical concentration divided by the theoretical value, and is written as a percentage.

For our system, we used a calibration curve of the lowest concentration to test the accuracy. The results indicate that only

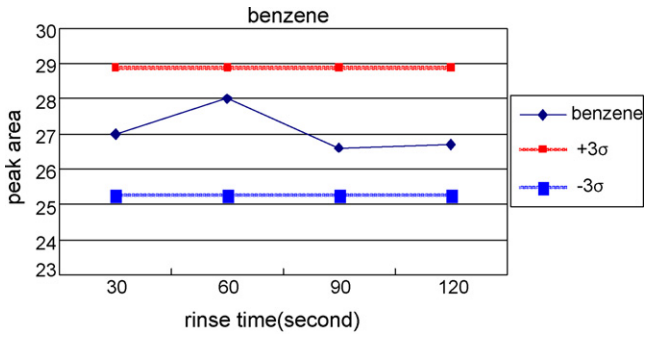


Fig. 4. Relationship between the rinse time and peak area (benzene, 5 ppb).

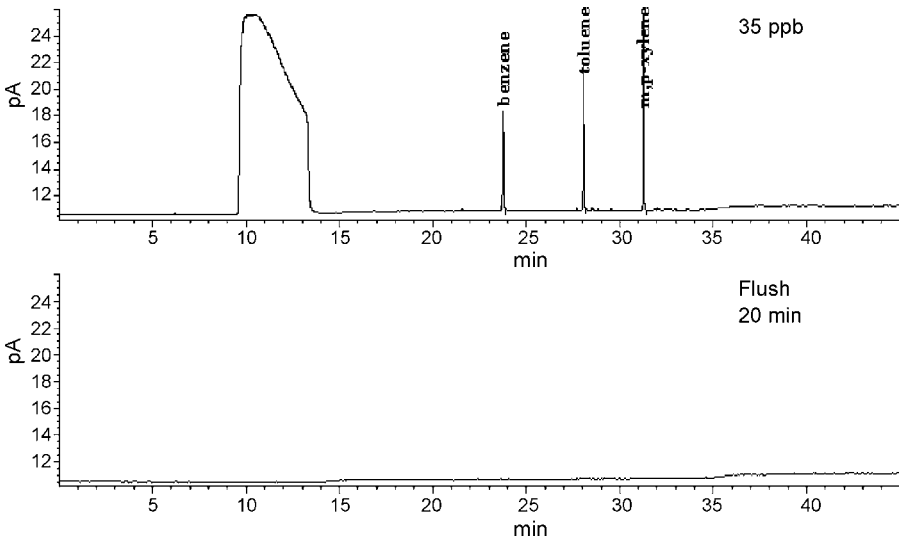


Fig. 5. Diagram of the flushing effect.

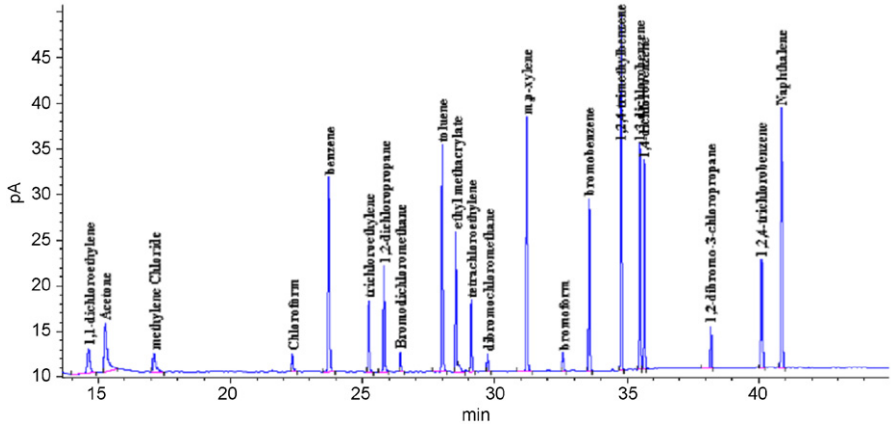


Fig. 6. Chromatogram of standards as measured by laboratory-made automated system.

chloroform reached an accuracy of 23.5%, which was close to the theoretical limit of 30%. The accuracies of the other compounds were all lower than 20%. The average accuracy value was 9.6%, and all 17 VOCs were completely separated in 41 min (Fig. 6). Based on the results of continual analysis of seven calibration curves of the compounds with the lowest concentration at 5 ppb (acetone = 60 ppb), the standard deviation was calculated. The precision of 1,1-dichloroethylene and methylene chloride was around 13%, and the rest of the compounds were within 10%. The average precision value was 7%. The above mentioned results suggest that this method is consistent in repetition.

3.2. *In situ application to environmental wastewater samples*

Once the validity of the proposed method was determined, real wastewaters were collected for long-term in situ VOCs analysis to estimate the capability of this system. A continuous 36 h test was carried out near the wastewater treatment plant. Water samples were collected every 2 or 3 h from a sampling site near the sewage treatment plant in high-tech industry park. A graph of the concentration tendency of acetone is shown in Fig. 7. The graph shows that from 9:30 p.m. of day 1 to 11:00 a.m. of day 3, the highest concentration peak was 1270.42 ppb. From 7:00 to 10:00 p.m. of

Table 2
VOC concentration analysis between laboratory-made automated system and Archon auto-sampler.

Compounds	Sampling time							
	01:50 a.m.		09:14 a.m.		03:37 p.m.		10:54 a.m.	
	Laboratory-made system (ppb)	Archon system (ppb)	Laboratory-made system (ppb)	Archon system (ppb)	Laboratory-made system (ppb)	Archon system (ppb)	Laboratory-made system (ppb)	Archon system (ppb)
Acetone	523.26	543.71	609.06	620.98	472.7	483.23	248.94	254.14
Chloroform	3.27	3.69	4.95	5.23	7.25	8.48	3.45	4.3
Trichloroethylene	2.93	3.17	4.16	4.52	2.86	3.38	5.37	5.71
Toluene	–	–	–	1.58	–	1.68	–	1.51
1,4-Dichlorobenzene	–	–	–	–	–	–	–	0.39
Naphthalene	1.68	1.58	1.59	1.54	1.56	1.54	1.68	1.69
Total VOCs	521.14	552.15	611.34	632.27	484.37	498.32	239.43	267.74

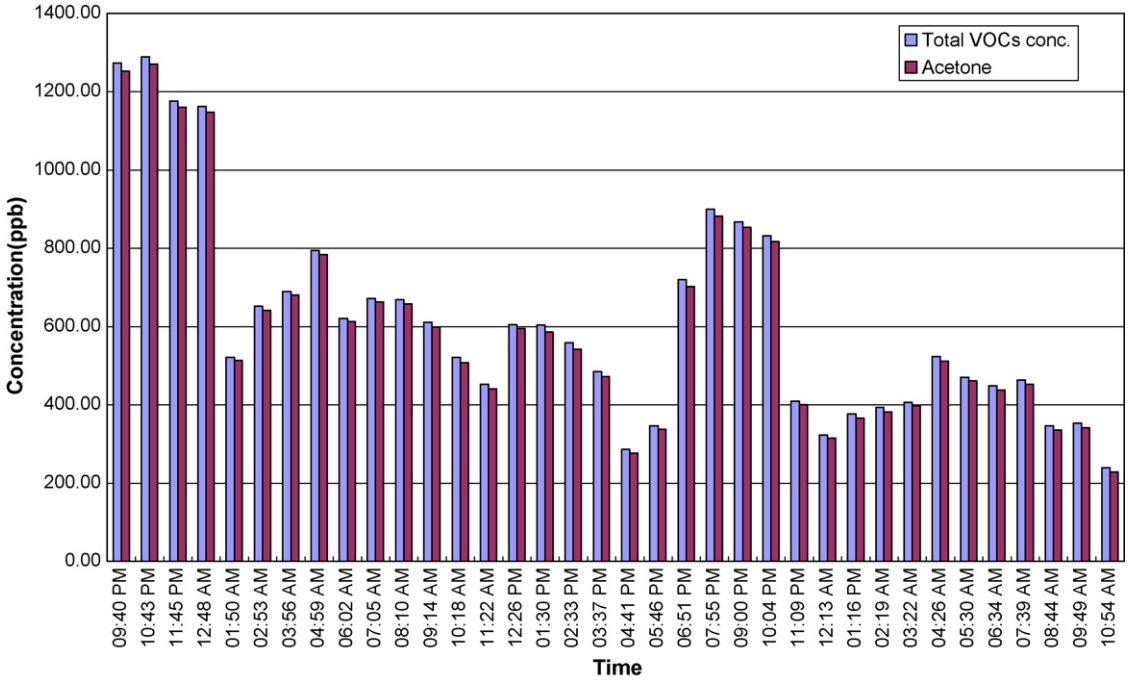


Fig. 7. Hourly concentration variations of acetone and total VOC determined by the laboratory-made automated system. The period of in situ monitoring was 36 h.

the second day, the highest concentration peak was 882.14 ppb. This second concentration peak was considerably lower than the first one. Except for these two relatively high peaks, the concentrations in the other time periods showed a tendency to decline. The average concentration was 601 ppb. In situ monitoring continued for 54 h (from 12:30 a.m. of day 1 to 4:05 p.m. of day 3) in the same location after a 36 h in situ experiment (as shown in Fig. 8). The peaks with higher VOC concentrations (526, 532 and 390 ppb) appeared individually at 5:55 a.m., 1:45 p.m. and 5:00 a.m. of day 1, respectively. In day 2, another peak reflecting a concentration of 308.29 ppb appeared at 10:45 p.m. During the entire period of in situ monitoring, a total of six different VOCs were detected: acetone, chloroform, trichloroethylene, toluene, 1,4-dichlorobenzene and naphthalene. The average concentration for the total VOCs was 220 ppb. In both in situ monitoring results, the concentration of acetone was higher than the concentrations of other VOCs in the chromatograms.

3.3. Comparison between this system and Archon system

To compare the results between the laboratory-made system and the commercial Archon system, wastewater samples were col-

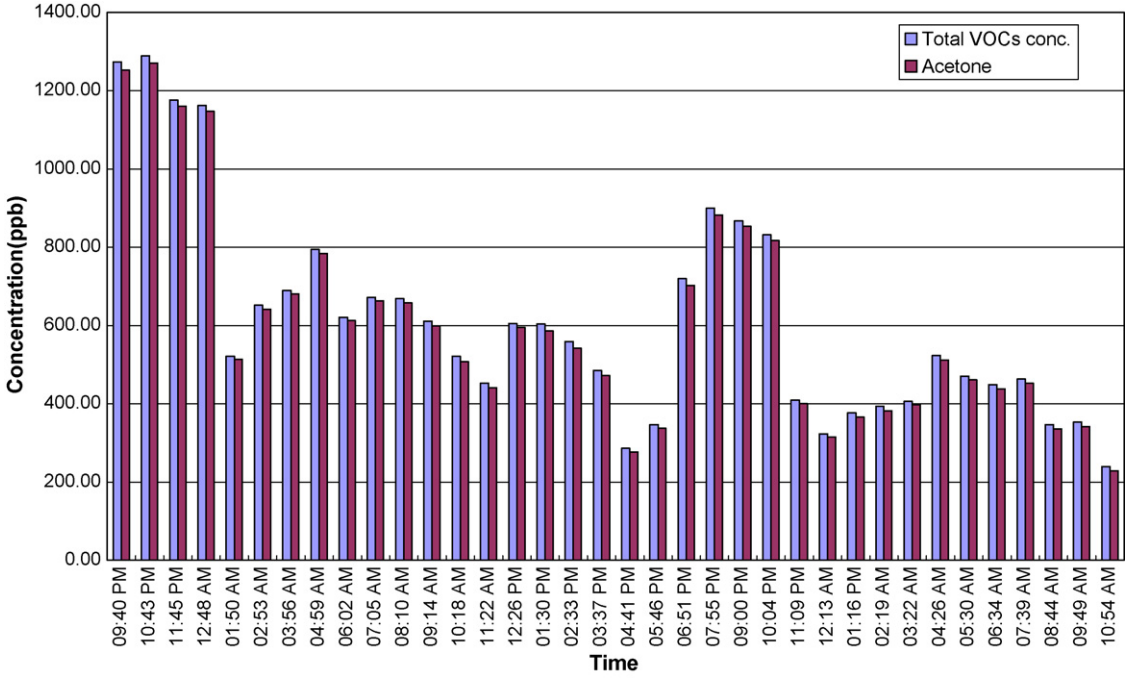


Fig. 8. Hourly concentration variations of acetone and total VOC determined by the laboratory-made automated system. The period of in situ monitoring was 54 h.

lected for advanced study by both systems. The sampling sites were the same, and the sampling times were at 1:50, 9:40, 10:52 a.m., and 3:37 p.m. during a 36 h in situ monitoring experiment. The VOCs under study were acetone, chloroform, trichloroethylene, toluene, 1,4-dichlorobenzene, and naphthalene. The wastewater samples were analyzed immediately by both systems, and the results are presented in Table 2. As can be seen in Table 2, there are very slight differences between these two systems in the four different sampling times, and all the differences are less than 4%. Because acetone was the major organic solvent used for cleaning electronic parts, its extremely high concentration in the effluent measured by both systems is reasonable.

4. Conclusion

This study demonstrates the feasibility of this laboratory-made in situ continual PSM–purge and trap–GC–FID system when using real water samples. The cycle time can be reduced to an hour (including the tube washing time), resulting in a maximum frequency of 24 samples day^{-1}. Detection limits of 17 VOCs were at ppb levels, and the suitability of the system for on-line monitoring of VOCs in wastewater was proven excellent after extended continuous in situ monitoring of wastewater from the treatment plant. The RSDs of the system were between 2 and 13.4%, and accuracies between 0.3 and 23.5% were achieved. The detection limits of the method ranged from 0.32 to 2.39 ppb. In this system, the four parts, i.e., PSM, P&T, GC, and FID, were simple, reliable and rugged. Also, the interface of these four parts was simple and dependable. In the future, it can be applied in instant monitoring of environmental pollution. Based on these data, we are able to measure pollutant activity immediately in order to reduce damage to our environment.

Acknowledgement

Financial support from National Science Council of the Republic of China is acknowledged

References

[1] WHO, Guidelines for Drinking Water Quality, World Health Organization, Geneva, 2004.
[2] S.K. Golfinopoulos, T.D. Lekkas, A.D. Nikolaou, Chemosphere 45 (2001) 275–284.
[3] V.I. Safarova, S.V. Sapelnikova, E.V. Djazhenko, G.I. Teplova, G.F. Shajdulina, F.Kh. Kudasheva, J. Chromatogr. B 800 (2004) 325–330.
[4] J.A. Bernstein, N. Alexis, H. Bacchus, I.L. Bernstein, P. Fritz, E. Horner, J. Allergy Clin. Immunol. 121 (2008) 585–591.
[5] R. Dales, L. Liu, A.J. Wheeler, N.L. Gilbert, Can. Med. Assoc. J. 179 (2008) 147–152.
[6] P. Irigaray, J.A. Newby, R. Clapp, L. Hardell, V. Howard, L. Montagnier, Biomed. Pharm. 61 (2007) 640–658.
[7] A.M. Vega, V.A. Lancaster, M.H. Roulier, Environ. Sci. Technol. 38 (2004) 6790–6794.
[8] S. Hashimoto, T. Tanaka, N. Yamashita, T. Maeda, J. Sep. Sci. 24 (2001) 97–103.
[9] T. Hino, S. Nakanishi, T. Maeda, T. Hobo, J. Chromatogr. A 10 (1998) 141–147.
[10] D. Nikolaou, S.K. Golfinopoulos, M.N. Kostopoulou, G.A. Kolokythas, T.D. Lekkas, Water Res. 36 (2002) 2883–2890.
[11] J.L. Wang, W.L. Chen, J. Chromatogr. A 927 (2001) 143–154.
[12] C. Bloch, J. Simon, L.N. Moskvin, O.V. Rodinkov, Talanta 52 (2000) 123–128.
[13] M.A. Mendes, R. Sparran, M.N. Eberlin, Anal. Chem. 72 (2000) 2166–2170.
[14] J. Yang, S.S. Tsai, Anal. Chim. Acta 436 (2001) 31–40.
[15] M.A. Stack, G. Fitzgerald, S. O'Connel, K.J. James, Chemosphere 41 (2000) 1821–1826.
[16] Ó. Ezquerro, B. Pons, M.T. Tena, J. Chromatogr. A 999 (2003) 155–164.
[17] G. Luna, R. Aparicio, D.L. García-González, Food Chem. 97 (2006) 621–630.
[18] A. Gierak, M. Seredych, A. Bartnicki, Talanta 69 (2006) 1079–1087.
[19] N. Kayali, F.G. Tamayo, L.M. Polo-Díez, Talanta 69 (2006) 1095–1099.
[20] L. Mateo-Vivaracho, V. Ferreira, J. Cacho, J. Chromatogr. A 1121 (2006) 1–9.
[21] A. Lara-Gonzalo, J.E. S'anchez-Ur'ıa, E. Segovia-Garc'ıa, A. Sanz-Medel, Talanta 74 (2008) 1455–1462.
[22] D.L. Vassilaros, T.J. Bzik, Environ. Sci. Technol. 25 (1991) 843–878.
[23] O. Ilkka, P. Katja, V. Erkki, J. Anal. Toxicol. 22 (1998) 290–295.
[24] A.S. Allonier, M. Khalanski, A. Bermond, V. Camel, Talanta 51 (2000) 467–477.
[25] O. Zuloaga, N. Etxebarria, L.A. Fernandez, J.M. Madariaga, Anal. Chim. Acta 416 (2000) 43–53.
[26] C. Gerbersmann, R. Lobinski, C. Adams, Anal. Chim. Acta 316 (1995) 93–104.
[27] P. Milena, C. Giovanna, J. Chromatogr. A 985 (2003) 117–125.
[28] J.M. Jesús, P. Torre, Food Chem. 70 (2000) 409–417.
[29] F. Fabietti, M. Delise, A.P. Bocca, Food Control 12 (2001) 505–509.
[30] M.N. Kostopoulou, S.K. Golfinopoulos, A.D. Nikolaou, N.K. Xilourgidis, T.D. Lekkas, Chemosphere 40 (2000) 527–532.
[31] A.D. Nikolaou, S.K. Golfinopoulos, M.N. Kostopoulou, G.A. Kolokythas, T.D. Lekkas, Water Res. 36 (2002) 2883–2890.
[32] T.C. Chen, G.R. Her, J. Chromatogr. A 927 (2001) 229–235.

Talanta 80 (2009) 909–915

Contents lists available at ScienceDirect

Talanta

journal homepage: www.elsevier.com/locate/talanta

Wireless biosensor system for real-time cholesterol monitoring in fish "Nile tilapia"

Yohei Yoneyama[a], Yuki Yonemori[a], Masataka Murata[b], Hitoshi Ohnuki[c], Kyoko Hibi[a], Tetsuhito Hayashi[a], Huifeng Ren[a], Hideaki Endo[a,*]

[a] Department of Ocean Sciences, Faculty of Marine Science, Tokyo University of Marine Science and Technology, Konan, Minato, Tokyo 108-8477, Japan
[b] Hokkaido Industrial Technology Center, Hakodate, Hokkaido 041-0801, Japan
[c] Department of Marine Electronics and Mechanical Engineering, Faculty of Marine Technology, Tokyo University of Marine Science and Technology, Etchujima, Koto-ku, Tokyo 135-8533, Japan

ARTICLE INFO

Article history:
Received 6 June 2009
Received in revised form 11 August 2009
Accepted 12 August 2009
Available online 19 August 2009

Keywords:
Biosensor
Enzyme sensor
Total cholesterol
Interstitial fluid
Fish
Monitoring
Wireless

ABSTRACT

The rapidly increasing demand for cultured fish as a food resource requires simple, effective methods for controlling fish health in culture conditions. Plasma total cholesterol levels are significantly related to fish mortality following bacterial challenge, and are thus a good indicator of the general health of fish. We developed a wireless biosensor system to continuously monitor the total cholesterol concentration in fish (Nile tilapia, *Oreochromis niloticus*). The biosensor was constructed with Pt–Ir wire (φ0.178 mm) as the working electrode and Ag/AgCl paste as the reference electrode. Cholesterol oxidase and cholesterol esterase were immobilized on the working electrode using glutaraldehyde. The sensor output was linear and strongly correlated with the cholesterol level ($R = 0.9970$) in the range of 2.65–403 mg dl^{-1}. This range covers the range of total cholesterol levels in fish. To avoid blood coagulation and proteins coalescing on the sensor, we implanted the sensor in the fluid under the scleral surface of the eyeball (EISF). The EISF is presumed to reflect the levels of most blood components and does not include the substances contained in blood that inhibit sensor measurement. Total cholesterol concentrations in blood and EISF were strongly correlated ($R = 0.8818$, $n = 72$) in the blood total cholesterol range of 74–480 mg dl^{-1}. Therefore, we used EISF as an alternative to blood and performed continuous *in vivo*-monitoring of the total cholesterol concentration in fish. We also investigated the application of the calibration method and wireless monitoring system. These applications enabled us to securely monitor total cholesterol levels in free-swimming fish in an aquarium for over 40 h. Thus, our newly developed sensor provided a rapid and convenient method for real-time monitoring of total cholesterol concentrations in free-swimming fish.

© 2009 Elsevier B.V. All rights reserved.

1. Introduction

There is growing concern that many resources, such as food and energy, are in limited supply and may eventually run out. Fisheries are also at a crisis point because of increased worldwide consumption, over-fishing, and regulatory demands. The demand for fishery products will eventually exceed supply. The development of aquaculture is expected to resolve this problem, providing society with a sustainable food supply. Aquaculture, however, must still overcome many issues before it can be regarded as a mainstream method of fish production. In particular, aquafarms are plagued by fish disease. Due to overcrowded farming conditions, the diseases quickly spread through the water to other fish. Dead or diseased fish have no value as food and aquafarmers thus sustain considerable financial hardship. Although antibiotics are effective, their use affects the risk of exposing the consumer to residual drug. Therefore, a method to maintain fish health without using drugs is in high demand. Several blood tests have been developed for monitoring fish health [1]. For example, plasma total cholesterol concentration is significantly related to fish mortality following bacterial and viral challenge, and unhealthy fish have below normal plasma total cholesterol concentrations [2]. Therefore, plasma total cholesterol concentration is a good indicator of the general health of fish. Currently, in aquaculture, plasma total cholesterol concentration is measured using a colorimetric determination method. This method, however, is complicated, costly, and time-consuming. Therefore, a simple, cost-effective, and convenient system for monitoring fish health is needed.

Electrochemical technology, especially biosensor technology, is potentially useful for solving this problem. Many types of

* Corresponding author. Tel.: +81 3 5463 0616; fax: +81 3 5463 0616.
E-mail address: endo@kaiyodai.ac.jp (H. Endo).

0039-9140/$ – see front matter © 2009 Elsevier B.V. All rights reserved.
doi:10.1016/j.talanta.2009.08.014

biosensors for measuring blood components, such as glucose [3], cholesterol [4,5], and lactic acid [6] have been developed. In 1982, Karube et al. [7] developed a sensor system comprising an immobilized enzyme and an oxygen electrode. Since then, various sensors have been developed based on the same principle and that implemented innovations such as the use of a hydrogen peroxide electrode [8], quartz crystal [9], silicate sol–gel [10], and Langmuir–Blodgett films [11]. Sensors for measuring total cholesterol concentration in the blood have also been developed [12,13], but these sensor systems do not provide continuous measurement.

We have developed enzyme sensor systems for measuring total cholesterol and glucose concentration in fish blood. These sensor systems are based on flow injection analysis [14], which allows for rapid and convenient measurement of total cholesterol and glucose, but separate procedures are required for collecting the blood samples for testing. Moreover, the flow injection analysis system is large and complicated compared with a batch-type measurement system. To miniaturize and simplify the sensor system for measuring blood components in fish, we developed a needle-type enzyme sensor comprising a needle-type hollow container, an immobilized enzyme membrane, and a fiber optic probe coated with ruthenium complexes [15]. In this system, direct insertion of the sensor into the caudal vein allows for rapid and convenient measurements of blood glucose concentrations, but continuous long-term measuring is difficult because the sensor output is decreased by blood coagulation and coalescing protein (e.g., albumin, γ-globulin) deposits on the sensor. Methods for continuous *in vivo*-monitoring of glucose concentrations in human and other mammals have been studied, focusing on measurements of glucose in interstitial fluid (ISF) [16,17]. ISF is the biologic fluid present between the blood vessels and cells. The reason for selecting ISF for the sampling site is that ISF is presumed to reflect the concentration of most blood components and does not include the substances in blood that hamper sensor measurement. We focused on the fluid under the scleral surface of the eyeball (EISF) in fish as a site for collecting ISF and developed a needle-type enzyme sensor to wirelessly monitor fish glucose levels [18]. The sensor system was constructed using a platinum–iridium (Pt–Ir) Ag/AgCl electrode, controlled potentiostat, electric wave sensor, and personal computer. The sensor was inserted into the external layer of the fish (Nile tilapia, *Oreochromis niloticus*) eyeball. Real-time glucose monitoring was performed using the sensor system. Glucose concentrations reflecting those in fish blood could be monitored in free-swimming fish.

The present paper describes the development of a rapid and convenient method for real-time monitoring of cholesterol concentrations in fish, as follows; (1) investigating the relationship between EISF and blood total cholesterol levels in fish, (2) determining the characteristics of the needle-type cholesterol biosensor, (3) developing a wireless system for monitoring total cholesterol levels under free-swimming conditions in an aquarium.

2. Experimental

2.1. Reagents

Cholesterol esterase (EC 232-808-6, 2.8 U mg^{-1}), cholesterol oxidase (EC 232-842-1, 2.4 U mg^{-1}), and nonaethylene glycol monododecyl ether were purchased from Sigma–Aldrich (St. Louis, MO). Bovine serum albumin, cholesterol oleate, 2-phenoxy ethanol, and 5% nafion dispersion solution were purchased from Wako Pure Chemical Industries (Tokyo, Japan). Standard solutions of cholesterol ester were prepared by first dissolving cholesterol oleate in nonaethylene glycol monododecyl ether and then in 0.1 M phosphate buffered saline (PBS). Approximately 3 g of nonaethylene glycol monododecyl ether was added to 100 mg cholesterol oleate. The solution was then stirred until it became clear and colorless at 60 °C and 600 rpm. PBS (pH 8.0) was added to bring the solution to the desired volume, and the solution was stirred again until it became clear and colorless. A fresh standard solution was prepared for each experiment.

2.2. Total cholesterol analysis for evaluating the relationship between total cholesterol concentration in blood and EISF

2.2.1. Collection and analysis of the sample

We used Nile tilapia (*O. niloticus*) as the test fish, cultured at Tokyo University of Marine Science & Technology. Total cholesterol concentrations between blood and EISF were measured. Each fish (body weight; ca. 100–300 g, body length; ca. 15–25 cm) was netted from the preserve and anesthetized with 400 ppm 2-phenoxy ethanol by bath exposure. Blood samples were collected from the caudal vein along the backbone by inserting a heparinized syringe fitted with a 23G needle (0.65 mm × 25 mm) into the basal anal fin. The blood samples (100–200 μl) were then centrifuged (550 × *g*) for 10 min to separate the plasma. EISF samples were collected by inserting a syringe fitted with a 27G needle (0.40 mm × 19 mm) into the sclera of the eyeball. To minimize measurement error, the collection procedure never lasted more than 10 min per fish. Each collected sample was transferred to a test tube and stored at −80 °C until analysis.

Total cholesterol concentrations were determined by an enzymatic colorimetric method (E-test, Wako Pure Chemical Industries, Tokyo, Japan). Each sample (20 μl) was mixed with 3 ml buffer solution (pH 6.1) containing enzymes (cholesterol esterase, cholesterol oxidase, horseradish peroxidase) and a color-producing reagent. Total cholesterol was hydrolyzed and then oxidized to produce 4-cholesten-3-one and hydrogen peroxide. The hydrogen peroxide reacted with 4-aminoantipyrine and D-amino acid oxidases to produce a blue color (600 nm). Total cholesterol concentrations were measured using a UV/Vis spectrophotometer (JASCO Co., Tokyo, Japan).

2.2.2. Temporal change of total cholesterol concentration between blood and EISF in individual fish over days

We evaluated whether the temporal changes in total cholesterol concentrations in the blood were reflected by changes in the total cholesterol concentration in EISF in individual fish. The testing system comprised a 45-L plastic tank (50 cm × 30 cm × 30 cm). During the test, the water temperature was maintained at 30 °C with continuous aeration and recirculation through a biologic filter. The photoperiod, provided by a fluorescent light, was set to be on from 10:00 to 20:00. Blood and EISF samples were collected at 12:00 daily, as described above. The testing period spanned 30 days and the fish were fed on days 7 and 15.

2.2.3. Correlation of total cholesterol concentration between blood and EISF in randomly selected fish

We evaluated whether there were differences in the relationship between total cholesterol concentration in the blood and EISF in individual fish. Our stock population consisted of 72 adults Nile tilapia (ca. 100–300 g). The fish were randomly selected, netted from the tank, and blood and EISF were collected by the methods described above.

2.3. Needle-type total cholesterol sensor

2.3.1. Preparation of hydrogen peroxide electrode

The sensor was constructed using a 15-mm Teflon-coated platinum/iridium (Pt–Ir) wire (φ0.178 mm), 10-mm copper wire (φ0.1 mm), Ag/AgCl coating paste (BAS, Tokyo, Japan), and two copper lead wires (Fig. 1). The sensor was composed by two electrodes (working electrode and reference electrode/counter

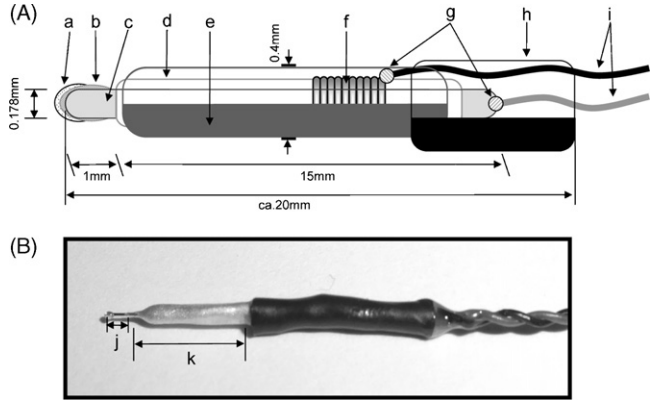


Fig. 1. Diagram (A) and photograph (B) of needle-type total cholesterol sensor. (A): (a) enzyme membrane, (b) nafion, (c) platinum/iridium, (d) Teflon-coat, (e) Ag/AgCl paste, (f) copper wire, (g) connection, (h) heat-shrink tubing, (i) lead wire, (B): (j) working electrode (Pt–Ir) and (k) reference electrode/counter electrode (Ag/AgCl).

electrode) because of less invasive for biological body. Thus, a material electric potential of which is relatively stable was used as reference electrode/counter electrode. The Teflon-coated Pt–Ir wire was stripped of 1.0-mm Teflon to expose the Pt–Ir wire as a sensing cavity (working electrode). The copper wire was wound around the Teflon-coated surface as extended line of lead wire. Then, the copper wire was coated with the Ag/AgCl paste and used as a reference electrode/counter electrode. After soldering each lead wire to either the Pt–Ir or the copper wire, each connection was covered with heat-shrink tubing and epoxy adhesive.

2.3.2. Enzyme immobilization on the working electrode

First, a 5% nafion dispersion solution (10 μl) was applied to the working electrode to prevent noise induced by oxidized substances in the EISF. Then, the enzyme membrane was immobilized on the tip of the working electrode. An enzyme solution containing cholesterol oxidase (8.4×10^{-4} units), cholesterol esterase (3.36×10^{-4} units), and 20 mg bovine serum albumin dissolved in 1.0 ml of 0.1 M PBS (pH 7.8) was applied to the tip of the working electrode and the enzymes were immobilized by a cross-linking reaction using 25% glutaraldehyde (20 μl) for 6 h. This immobilization method was repeated 2 times per electrode.

2.4. Amperometric total cholesterol measurement

The enzyme sensor was connected to a multichannel potentiostat (Pinnacle Technology Inc, Lawrence, KS) attached to a personal computer (DELL Dimension 4700C, Round Rock, TX) via either a USB 2.0 or RS232C port. Then, a 650-mV potential (vs. Ag/AgCl) was applied to the Pt–Ir working electrode using the potentiostat. Amperometric total cholesterol measurement was then performed based on the following 3 reactions that occurred on the surface of the working electrode.

$$\text{Cholesterolesters---(cholesterolesterase)} \rightarrow \text{cholesterol} + \text{fattyacid} \quad (1)$$

$$\text{Cholesterol} + O_2\text{--(cholesteroloxidase)} \rightarrow \text{4-cholesten-3-one} + H_2O_2 \quad (2)$$

$$H_2O_2\text{--(electrocatalyticoxidation)} \rightarrow O_2 + 2H^+ + 2e^- \quad (3)$$

Reaction (3) produced an electric output current that was recorded via the computer-controlled data acquisition software (Pinnacle Acquisition Laboratory).The sensor was placed in 50 ml of 0.1 M PBS (pH 8.0). After the output current stabilized, a 1.0-ml aliquot of the 1000 mg dl^{-1} cholesterol oleate standard solution was added to the 0.1 M PBS. After the output current again stabilized, another 1.0-ml aliquot of the cholesterol standard solution was added. This procedure was repeated until 20 aliquots had been added. The sensor output current was measured after each addition of cholesterol and the background current was subtracted from the response current. Because cholesterol generally exists as a cholesterol ester, cholesterol oleate was used for the cholesterol standard.

2.5. Total cholesterol monitoring in fish

2.5.1. Wired sensor system for continuous total cholesterol monitoring

Sensor implantation and fixation were performed after anaesthetizing fish with 400 ppm 2-phenoxy ethanol. A small hole was created in the sclera using a 20G catheter (φ1.10 mm) consisting of an outer Teflon layer and inner puncture needle (22G, 23 mm, Serflow™ Terumo, Tokyo, Japan). The inner puncture needle was then removed, and the excess exposed catheter on the skin was trimmed off. The sensor was then inserted into the scleral ISF, immersing the working and reference electrodes of the sensor in the EISF. The sensor was then fixed in place using a biomedical adhesive (Aronalpha-A Sankyo, Toagosei, Tokyo, Japan). The adhesive was applied around the insertion point to fill the hole and the sensor was stapled to the fish's body. After implantation and fixation, the sensor was connected to a multichannel potentiostat. Monitoring of total cholesterol was performed after the background current of the sensor became stable. During monitoring, EISF from the contralateral eyeball was collected periodically using a syringe fitted with a 27G needle (0.40 mm × 19 mm) to compare the obtained sensor response to the actual total cholesterol concentration. To prevent the fish from moving while collecting the EISF sample, the fish was transferred to a 7.5-L water tank containing 200 ppm of 2-phenoxy ethanol as a light-anesthetic agent. The fish was held in place using a string to simplify the EISF sample collection process.

2.5.2. In vivo calibration

Continuous estimation of total cholesterol in EISF was performed using one-point or two-point *in vivo* calibration methods [19–21]. The one-point calibration method is represented by the following formula:

$$\text{TC}(t) = \frac{I(t)}{S}$$

The sensor sensitivity (S), expressed in nA/(mg dl^{-1}), was determined from a single total cholesterol measurement in EISF as the ratio between the concomitant sensor output current (I; expressed in nA) and the total cholesterol (TC) concentration. Subsequently, the TC concentration was estimated based on the sensor output current (I).

First, the sensor output current was measured until it stabilized after the sensor was implanted into the sclera. An EISF sample was obtained from the other sclera using a syringe fitted with a 27G needle. TC concentration in EISF was determined by an enzymatic colorimetric method. These parameters (I, TC) were used as the calibration reference.

The two-point calibration method is represented by the following formula:

$$\text{TC}(t) = \frac{I(t) - I_0}{S}.$$

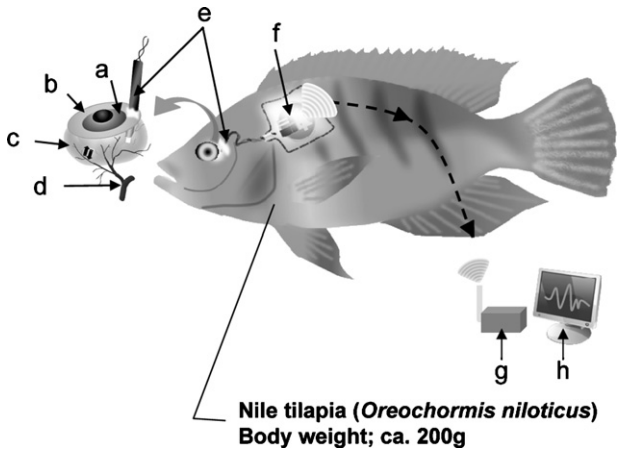


Fig. 2. Schematic diagram of the wireless monitoring system for fish (Nile tilapia). (a) Eyeball, (b) sclera, (c) EISF, (d) blood vessel, (e) needle-type total cholesterol sensor, (f) wireless potentiostat, (g) receiver and (h) personal computer.

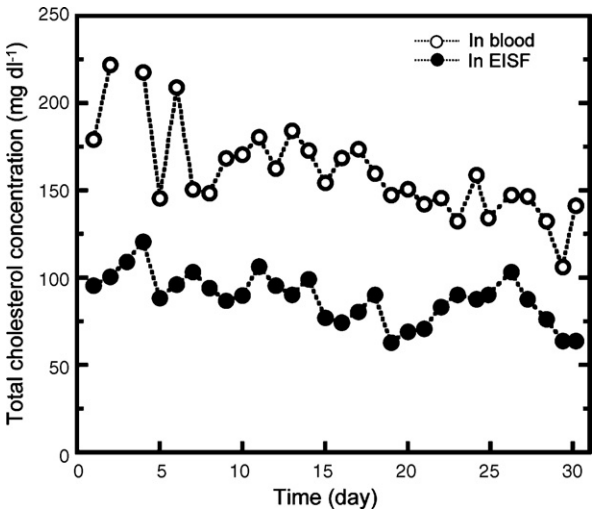


Fig. 3. Representative plot of total cholesterol concentration in the blood and EISF in an individual fish over 30 days. Total cholesterol concentration in blood was plotted as white circles and that in EISF was plotted as a black circles.

The formula consists of the sensor sensitivity (S) and the intercept I_0 of the sensor output. Parameters (S) and (I_0) were calculated from the change of total cholesterol concentration in EISF from TC_1 to TC_2, the change in the sensor current I from I_1 to I_2: $S = (I_2 - I_1)/(TC_2 - TC_1)$, followed by calculation of I_0 using the following formula: $I_0 = I_1 - (S \times TC_1)$.

2.5.3. *Wireless sensor system for total cholesterol monitoring under free-swimming conditions*

A schematic diagram of the wireless monitoring system is shown in Fig. 2. Sensor implantation and fixation were performed according to the same method used for the wired monitoring. The sensor was connected to a wireless potentiostat (3102BP, Pinnacle Technology, Inc) and covered with a waterproof polypropylene sheet. The waterproofed wireless potentiostat was attached to the dorsal and pectoral fins of the fish using nylon thread. The signal of the sensor output current signal was sent to a receiver (3100RX, Pinnacle Technology Inc) using a radio wavelength of 916.5 MHz. The fish were then transferred to a water tank (40 cm × 24 cm × 50 cm). During the monitoring, EISF samples from the contralateral eyeball were collected periodically from fish anesthetized with 400 ppm 2-phenoxy ethanol to prevent noise signals due to fish movement. After collecting the EISF, the water dissolved 2-phenoxy ethanol in tank was changed with new one. During the experiment, the water was maintained at 30 °C, aerated, and filtered. Continuous monitoring of total cholesterol was performed after the sensor output current became stable.

3. Results and discussion

3.1. *Comparison of total cholesterol between blood and EISF*

It is difficult to perform continuous monitoring of blood components using a biosensor because the sensor output decreases over time due to blood coagulation and protein coalescing on the sensor. We investigated the correlation between total cholesterol concentrations in blood and EISF. Changes in cholesterol levels in individual fish over time were measured to assess whether fluctuations of cholesterol concentrations in the blood were reflected by changes in cholesterol concentrations in the EISF. We examined the correlation between total cholesterol concentration in blood and in EISF over 30 days in a fish. The temporal changes in total cholesterol concentration in a single representative fish are shown in Fig. 3. The fluctuations of the total cholesterol concentrations in the blood and EISF over 30 days were significantly correlated. Additionally, two specific properties of EISF were discovered by comparing the two temporal cholesterol concentration profiles. First, total cholesterol concentration in EISF was approximately half that in blood. Second, the kinetics of the changes in EISF cholesterol concentrations were dependent on the valence of the change; increases in the blood concentration were slowly reflected by increases in the EISF concentration, whereas decreases in blood concentration were rapidly reflected by decreases in the EISF concentration. This difference in kinetics likely reflects the fact that the EISF cholesterol concentration is a product of cholesterol moving into the EISF along a concentration gradient and cholesterol being removed from the EISF by the cells, which depends on the requirements of the cells for cholesterol. An increase in cholesterol availability can lead to a rapid increase in cell demand. In addition, the amount demanded by the cell has an established minimum. Thus, total cholesterol concentration in EISF was reflected by blood concentrations, especially when the total cholesterol concentration in the blood decreased.

We next examined interindividual variations in the relationship between blood and EISF cholesterol concentrations at a single time point. The tilapia were captured randomly from the water tank ($n = 72$), and both blood and EISF samples were obtained. Total cholesterol concentration in EISF was strongly correlated ($R = 0.8818$) with blood total cholesterol in the range of 74–480 mg dl^{-1} (Fig. 4), thus indicating that the EISF is a useful alternative to blood collection for measuring total cholesterol. In general, in the aquafarm setting, blood tests are performed once a day. Although there is a small time-lag between total cholesterol concentration in the blood and that in the EISF, total cholesterol concentration in the EISF generally reflects the total cholesterol concentration in the blood. Thus, sampling the EISF to determine total cholesterol levels should be a good indicator of fish health.

3.2. *Characteristics of the needle-type total cholesterol biosensor*

Fig. 5 shows a relationship between output current and cholesterol oleate concentration. Cholesterol oleate, which is a kind of esterified cholesterol, was prepared as standard sample of total cholesterol. Good linearity was observed in the concentration range of 2.65–403 mg dl^{-1} (correlation coefficient: 0.9970). The mean total cholesterol concentration in the blood of Nile tilapia is 140.35 mg dl^{-1} [22] and the concentration in the EISF is usually lower than that in blood (Fig. 3). Thus, the physiologic cholesterol

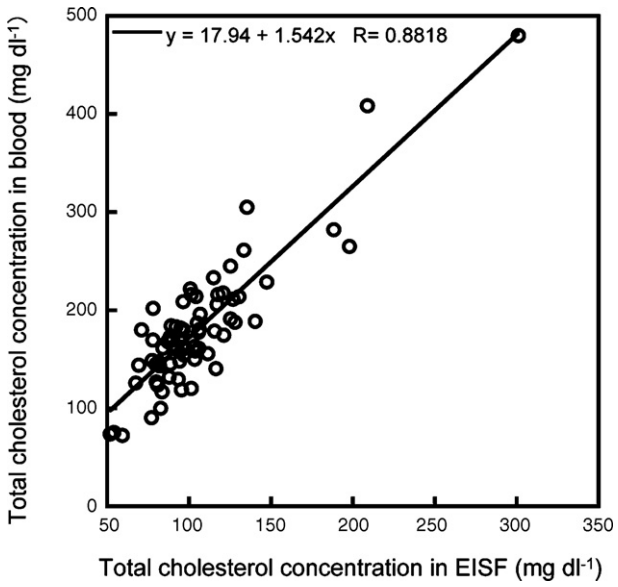


Fig. 4. Correlation of total cholesterol concentration in blood and EISF in randomly selected fish ($n = 72$, 74–480 mg dl^{-1}).

concentrations in EISF are well within the linear range of the sensor.

As the sensor comprises a biologic catalyst (enzyme), the response can vary depending on the pH and temperature of the solutions in which the immobilized enzyme is placed. The effects of pH and temperature on the sensor induced current for a 100 mg dl^{-1} standard solution are shown in Fig. 6. The sensor current gradually increased in the range of pH 5.5–6.5 and rapidly decreased at pH greater than 6.5 (Fig. 6 A). The EISF pH in Nile tilapia is 8.0 [23]. Although pH affects enzyme activity, even at pH 8.0 the sensor induced enough current to detect changes in the total cholesterol concentration. Temperature also has important effects on enzyme activity. For temperatures ranging from 10 to 40 °C, the sensor current increased rapidly up to 30 °C and then became nearly constant (Fig. 6 B). Above 40 °C, the current

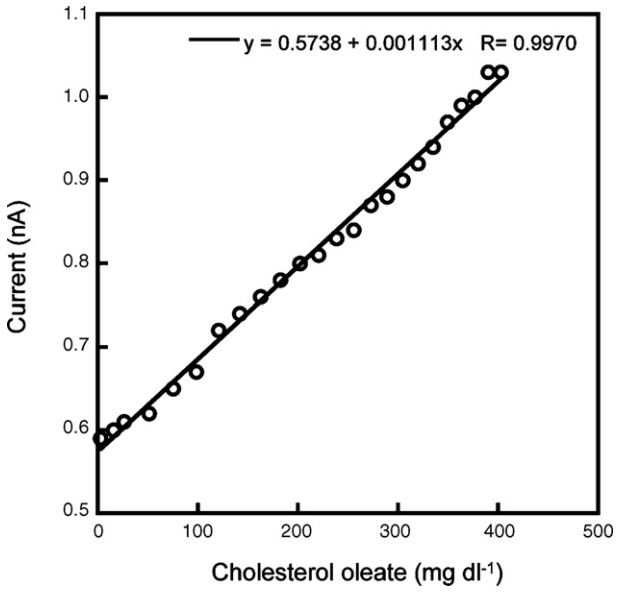


Fig. 5. Relationship between sensor output current and cholesterol oleate concentration (range of cholesterol oleate concentration 2.65–403 mg dl^{-1}). The measurement was performed by sequential addition of 100 mg dl^{-1} cholesterol oleate standard solution in pH 8.0, 30 °C PBS under a +650 mV potential (vs. Ag/AgCl).

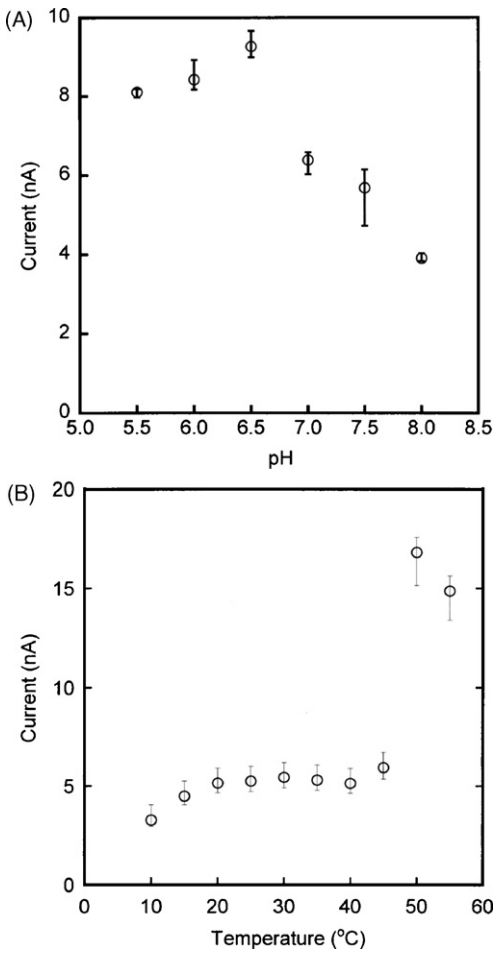


Fig. 6. Typical effects of pH (A) and temperature (B) on the total cholesterol sensor response in PBS. In (A) the temperature was 30 °C, in (B) the pH was 8.0. The measurements were performed using 100 mg dl^{-1} cholesterol oleate standard solution under a +650 mV potential (vs. Ag/AgCl).

increased rapidly again and reached the maximum output. At temperatures above 40 °C, however, the signal was very noisy and the output current was not stable. EISF is assumed to be at the same temperature as the environmental water temperature since the internal body fluid temperature of fish is influenced by its environment. The water temperature used for rearing Nile tilapia is in the range of 15–30 °C. Thus, the sensor induces sufficient output current under typical EISF temperature conditions and can be applied to *in vivo*-measurements.

The reproducibility of sensor measurements is shown in Table 1. The reproducibility of the measurements was demonstrated by immersing a single sensor in 100 mg dl^{-1} standard solution (30 °C).

Table 1
Reproducibility of total cholesterol measurements using the cholesterol biosensor ($n = 20$).

Electrode no.	Relative standard deviation (RSD %)
1	4.02
2	2.40
3	2.68
4	9.37
5	4.45
Mean ± SD	4.58 ± 2.52

The measurement was performed using 100 mg dl^{-1} cholesterol oleate in PBS, pH 8.0, 30 °C under a +650 mV potential (vs. Ag/AgCl).
Absolute response value for five sensors: 2.97–6.49 nA.

Each of five enzyme sensors was tested 20 times. The relative standard deviation (RSD %) was used to evaluate the reproducibility because of lot-dependent variability in the sensor output current. The RSD was 4.58 ± 2.52% in the absolute response values for five sensors was from 2.97 to 6.49 nA. The low RSD values indicated that the sensor can be used to determine total cholesterol concentrations with satisfactory precision. Therefore, the sensors have excellent reproducibility for measuring total cholesterol, and can be applied to continuous measurement of total cholesterol concentration *in vivo* with stable and accurate results.

3.3. Continuous cholesterol monitoring using the wired enzyme sensor system

We performed continuous total cholesterol monitoring in Nile tilapia using a wired sensor system. The fish were immobilized in the water tank to minimize experimental error while collecting the EISF samples. After sensor implantation in the EISF, the fish were not touched until the output current became stable (approximately 240 min). The total cholesterol concentration was then continuously monitored for 230 min. The time course of the total cholesterol concentration in EISF and the sensor output current were similar. In fact, the correlation coefficient between the actual total cholesterol concentration and sensor output current was 0.8961 ($n = 6$), confirming the corresponding relationship between them.

Sensor-calibrated cholesterol concentrations were estimated using either a one-point or two-point calibration method. The one-point calibration method used the calibration value (TC_1, I_1) in which TC_1 was the total cholesterol concentration in EISF (165 mg dl^{-1}) and I_1 was the subsequently obtained sensor output current (5.05 nA). The two-point calibration method used the first parameter (I_1; 5.05 nA, TC_1; 165 mg dl^{-1}) and the total cholesterol concentration in EISF and sensor output current obtained 90 min after sensor implantation (I_2; 4.53 nA, TC_2; 157 mg dl^{-1}). The relationship between the actual concentration and calibrated curve of the sensor is shown in Fig. 7. The two-point calibration method appeared to be more accurate than the one-point calibration method for determining the actual cholesterol concentration.

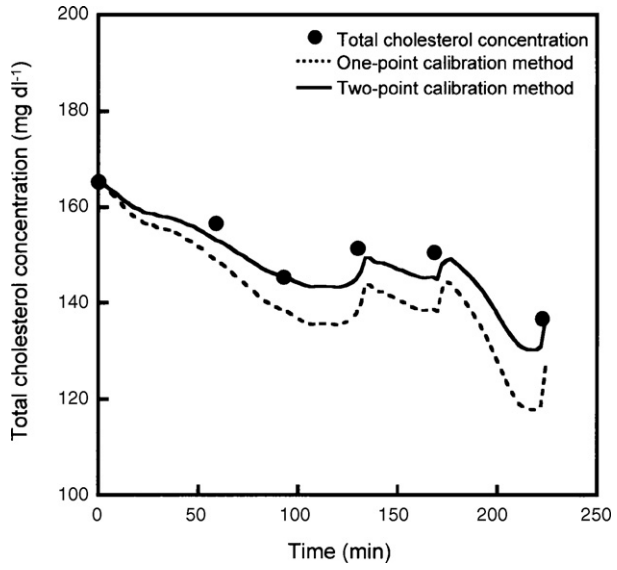


Fig. 7. The relationship between total cholesterol concentration in EISF and the calibrated sensor response. Total cholesterol concentrations were plotted as black circles, the calibrated response using the one-point calibration was plotted as the broken line, and the calibrated response using the two-point calibration was plotted as the solid line.

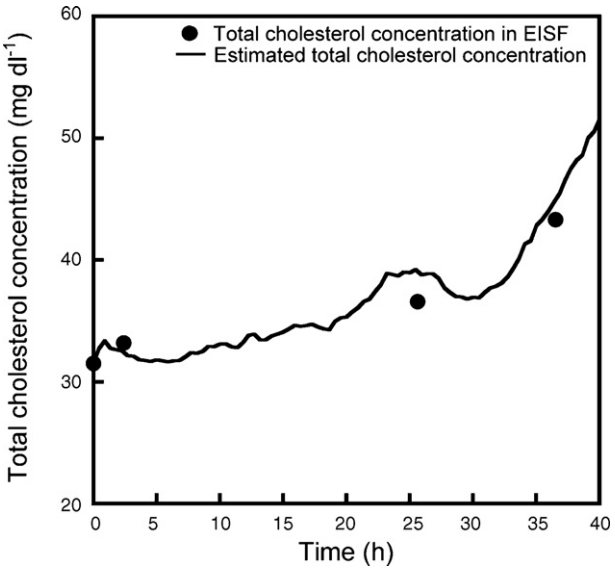


Fig. 8. The change in estimated total cholesterol concentrations in the wireless monitoring system. Total cholesterol concentrations in EISF at 0 and 90 (min), plotted as black circles, were used in the two-point calibration method.

To judge this relationship objectively, we compared the range of error between the actual and estimated cholesterol concentration values. The range of error was calculated as the mean value of the difference between the estimated value and the actual value for all 6 time points. The results indicated that the error for the two-point calibration method was lower (−1.18 mg dl^{-1}) than that for the one-point calibration method (−13.11 mg dl^{-1}). Therefore, the two-point calibration method should be used to measure total cholesterol concentration in fish. These findings confirm that the needle-type sensor monitoring system can be used for real-time measuring of total cholesterol concentration in fish.

3.4. Total cholesterol monitoring using the wireless enzyme sensor system under free-swimming conditions

We applied the sensor system to wirelessly monitor total cholesterol concentrations in free-swimming fish in an aquarium. Nile tilapia was anesthetized with 400 ppm 2-phenoxy ethanol, and then the wireless sensor system was attached. The fish were transferred to a 50-L fish water tank containing no anesthetic. The time courses of the output current of the sensor and sensor-calibrated total cholesterol levels are shown in Fig. 8. The two-point calibration method was adopted using the first measurement (I_1; 3.65 nA, TC_1; 31.5 mg dl^{-1}) and a second measurement obtained 90 min later (I_2; 3.79 nA, TC_2; 3.32 mg dl^{-1}). Wireless monitoring was continued for over 40 h and the results indicated that this system can be used for short-term measurement of total cholesterol in free-swimming fish. Actually, the calibration curve showed actual concentration of total cholesterol in EISF well. The estimated total cholesterol levels that were monitored for 40 h were within the range of standard values for Nile tilapia. The point of notice is that periodical calibration will be essential for practical chronic monitoring, which range for several weeks or a month, of total cholesterol levels. The results of wireless monitoring showed potential of the sensor as ubiquitous tool for aqua farm.

4. Conclusion

The present findings confirm that a needle-type enzyme biosensor-based monitoring system can be used to continuously

measure total cholesterol concentrations in fish. We used EISF as an alternative to blood and investigated the relationship between total cholesterol concentration in the blood and EISF. The total cholesterol concentration in EISF strongly correlated with that in blood. We prepared a needle-type enzyme sensor for measuring total cholesterol in fish. The sensor size was ca. 0.4 mm width × 20 mm length and provided a rapid response, good linearity, and good reproducibility. Continuous *in vivo*-monitoring was performed when the sensor was implanted under the scleral surface of the fish eyeball. The changes in the cholesterol concentrations in EISF and those in the sensor output current were similar. We investigated two steps for practical application; (1) establishing an accurate calibration method and (2) application of a wireless monitoring system. The two-point calibration method was more effective than the one-point calibration method for calculating the actual cholesterol concentration. Additionally, the wireless monitoring system enabled us to securely monitor total cholesterol levels in free-swimming fish in an aquarium. The wireless monitoring system detected changes in total cholesterol concentration and thus the ability of the fish to fight disease. Several issues, however, remain. One is determining how to protect the sensor output response from changes in the *in-vivo* environment of the fish, such as those due to changes in temperature and dissolved oxygen in EISF. Another is that the monitoring space must be enlarged so that the free-swimming fish can be placed in larger tanks that are typically used for aquaculture. Future improvements should address these issues. This system will contribute to monitoring fish health in aquaculture.

Acknowledgments

This research was supported in part by a Grant-in-Aid for Scientific Research (B) from "The Ministry of Education, Culture, Sports, Science and Technology", and Grant-in-Aid of "Faculty of Marine Science, Tokyo University of Marine Science and Technology". We wish to thank Prof. Koji Sode and Dr. Wakako Tsugawa of Tokyo University of Agriculture and Technology for their helpful discussion.

References

[1] M. Maita, K. Shiomitsu, Y. Ikeda, Fish. Sci. 50 (1984) 1991–1998.
[2] Y. Fukuda, M. Maita, K. Satoh, N. Okamoto, Fish. Pathol. 32 (1997) 129–130.
[3] R. Kurita, H. Tabei, Y. Iwasaki, K. Hayashi, K. Sunagawa, O. Niwa, Biosens. Bioelectron. 20 (2004) 518.
[4] L. Charpentier, N. El Murr, Anal. Chim. Acta 318 (1995) 89–93.
[5] E. Salinas, V. Rivero, A.A. Torriero, D. Benuzzi, M.I. Sanz, J. Raba, Talanta 70 (2006) 244–250.
[6] S. Suman, Rahul Singhal, Amit L. Sharma, B.D. Malthotra, C.S. Pundir, Sens. Actuators B: Chem. 107 (2005) 768–772.
[7] I. Karube, K. Hara, H. Matsuoka, S. Suzuki, Anal. Chem. Acta 139 (1982) 127–132.
[8] S. Singh, A. Chaubey, B.D. Malhotra, Anal. Chim. Acta 502 (2004) 229–234.
[9] S.P. Martin, D.J. Lamb, J.M. Lynch, S.M. Reddy, Anal. Chim. Acta 487 (2003) 91–100.
[10] A. Kumar, R. Malhotra, B.D. Malhotra, S.K. Grover, Anal. Chim. Acta 414 (2000) 43–50.
[11] Z. Matharu, G. Sumana, S.K. Arya, S.P. Singh, V. Gupta, B.D. Malhotra, Langmuir 23 (2007) 13188–13192.
[12] S. Aravamudhan, A. Kumar, S. Mohapatra, S. Bhansali, Biosens. Bioelectron. 22 (2007) 2289–2294.
[13] W.C. Shin, M.C. Yang, M.S. Lin, Biosens. Bioelectron. 24 (2009) 1679–1684.
[14] H. Endo, M. Maita, M. Takikawa, H. Ren, T. Hayashi, N. Urano, K. Mitsubayashi, Fish. Sci. 69 (2003) 1194–1199.
[15] H. Endo, Y. Yonemori, K. Musiya, M. Maita, T. Shibuya, H. Ren, K. Mitsubayashi, Anal. Chim. Acta 573–574 (2006) 117–124.
[16] J.J. Mastrototaro, Diab. Technol. Ther. 2 (2000) 13–18.
[17] S. Woderer, N. Henninger, C.D. Garthe, H.M. Hajnsek, U. Kamecke, N. Gretz, B. Kraenzlin, J. Pill, Anal. Chim. Acta 581 (2007) 7–12.
[18] H. Endo, Y. Yonemori, K. Hibi, H. Ren, T. Hayashi, W. Tsugawa, K. Sode, Biosens Bioelectron. 24 (2009) 1417–1423.
[19] C. Choleau, J.C. Klein, G. Reach, B. Aussedat, V. Demaria-Pesce, G.S. Wilson, R. Gifford, W.K. Ward, Biosens. Bioelectron. 17 (2002) 641–646.
[20] C. Choleau, J.C. Klein, G. Reach, B. Aussedat, V. Demaria-Pesce, G.S. Wilson, R. Gifford, W.K. Ward, Biosens. Bioelectron. 17 (2002) 647–654.
[21] E. Csöregi, C.P. Quinn, D.W. Schmidtke, S.E. Lindquist, M.V. Pishko, L. Ye, I. Katakis, J.A. Hubbell, A. Heiier, Anal. Chem. 66 (1994) 3131–3138.
[22] M.A.A. Metwally, World J. Fish. Mar. Sci. 1 (2009) 56–64.
[23] Y. Yonemori, E. Takahashi, H. Ren, T. Hayashi, H. Endo, Anal. Chim. Acta 633 (2009) 90–96.

Talanta 80 (2009) 916–923

Contents lists available at ScienceDirect

Talanta

journal homepage: www.elsevier.com/locate/talanta

Determination of pyrrolizidine alkaloids in comfrey by liquid chromatography–electrospray ionization mass spectrometry

Feng Liu[a], Sow Yin Wan[a], Zhangjian Jiang[a], Sam Fong Yau Li[a,*], Eng Shi Ong[b,**], Jhon Carlos Castaño Osorio[c,d]

[a] Department of Chemistry, National University of Singapore, 3 Science Drive 3, Singapore, Republic of Singapore 117543
[b] Department of Epidemiology and Public Health, National University of Singapore, MD3, 16 Medical Drive, Singapore, Republic of Singapore 117543
[c] Centro de Investigaciones Biomedicas, Facultad de Medicina, Universidad del Quindío, Carrera 14 Calle 12 Norte, Armenia, Quindío, Colombia
[d] Productos Naturales Aral-Thel Km 2 via Armenia. Calarca, Alto del Rio, Quindio, Colombia

ARTICLE INFO

Article history:
Received 30 May 2009
Received in revised form 13 August 2009
Accepted 14 August 2009
Available online 20 August 2009

Keywords:
Symphytum officinale L.
Pressurized hot water extraction
Lycopsamine
Orbitrap MS
Liquid chromatography–electrospray ionization mass spectrometry

ABSTRACT

Symphytum officinale L. (comfrey) is a medicinal plant commonly used in decoctions and aliments. Besides therapeutic bioactive compounds present in the herb, it is found to contain hepatotoxic pyrrolizidine alkaloids (PAs), such as lycopsamine and others. In the present study, PAs such as lycopsamine, echimidine and lasiocarpine were determined using electrospray liquid chromatography–mass spectrometry (LC–MS) with the method precision (relative standard deviation, RSD) <10%. Detection of lycopsamine, symviridine and their N-oxides could be confirmed with a newly developed method based on HPLC ion-trap and orbitrap MS with electrospray ionization interface. With LC–MS, quantitative analysis of lycopsamine in the botanical extract was carried out. The effect of extraction solvent was optimized by sonication and methanol: H_2O (50:50) was selected. Then a rapid method based on pressurized hot water extraction (PHWE) was employed for the extraction of lycopsamine from comfrey followed by the comparison with heating under reflux with the RSD ranging from 2.49% to 19.32%. Our results showed a higher extraction efficiency for heating under reflux compared with PHWE. It was proposed that the lower extraction efficiency for PHWE was attributable to dissolved nitrogen from air which caused the reduction in the solubility of lycopsamine in the compressed hot solvent. In this study, quantitative analysis of PAs in comfrey was demonstrated. In addition, it was found that the use of subcritical water for extractions depended on the physical properties of the dissolved solutes and their tendency to degrade under the chosen extraction conditions.

© 2009 Elsevier B.V. All rights reserved.

1. Introduction

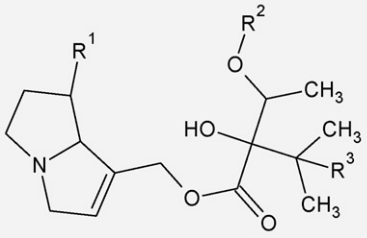
Symphytum officinale L. (comfrey) is a well-known herb that has been used extensively to treat a wide variety of aliments such as arthritis, varicose ulcers and sprains. In addition, it is also consumed in tea form or as part of dietary supplements. Unfortunately, this herb is also potentially toxic and has been mentioned in monographs on poison plants. The toxins in comfrey include pyrrolizidine alkaloids (PAs), such as lycopsamine, echimidine and lasiocarpine (Table 1), and their N-oxides [1]. PAs are of special interest currently because several of them have been shown to cause toxic reactions in humans, primarily veno-occlusive liver disease, when ingested as food or herbal medicines. For this reason, it is necessary to monitor the concentration of toxic PAs and researchers have highlighted essential analytical requirements for confident assessment of pyrrolizidine alkaloid-related safety of food and herbal products [2]. As their occurrence is widely distributed, it is important to develop rapid methods for their qualitative and quantitative analyses in plant samples or food products.

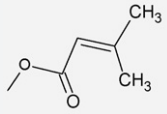
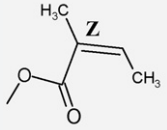
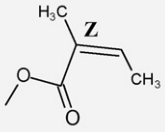
For the chemical standardization of botanicals and herbal preparations, the extraction of bioactive components or marker compounds is an important step. The methods found in the monographs of Pharmacopeias and other reports [3,4] often use extraction methods that require significant volume of organic solvents and are rather tedious. In previous PAs extraction studies, the use of methanol at temperature 50–60 °C for 12 h was often recommended [5]. The best result of extraction of PAs from comfrey was obtained using 1% methanolic solution of tartaric acid and electric basket technique at the temperature 100 ± 5 °C for 2 h [6]. Recently, simpler and more environmental friendly extraction methods have been developed. These include supercritical fluid extraction (SFE), microwave-assisted extraction (MAE), pressurized fluid extraction (PFE) [7,8]. Pressurized hot water extraction (PHWE) is another

* Corresponding author. Tel.: +65 6516 2681.
** Corresponding author. Tel.: +65 6779 1489.
E-mail addresses: chmlifys@nus.edu.sg (S.F.Y. Li), ephoes@nus.edu.sg (E.S. Ong).

0039-9140/$ – see front matter © 2009 Elsevier B.V. All rights reserved.
doi:10.1016/j.talanta.2009.08.020

Table 1
Some pyrrolizidine alkaloids in *Symphytum officinale L.*



Pyrrolizidine alkaloids	Molecular formula	R^1	R^2	R^3	Molecular weight ($g\,mol^{-1}$)
Lycopsamine	$C_{15}H_{25}NO_5$		H	H	299.173273
Symviridine	$C_{20}H_{31}NO_6$		H	H	381.215138
Echimidine	$C_{20}H_{31}NO_7$		H		397.210052
Lasiocarpine	$C_{21}H_{33}NO_7$				411.225702

new extraction technique which can be applied for the isolation of bioactive or marker compounds from botanicals and medicinal plants [9]. It is effective for a wide range of analytes and matrices because the physico-chemical properties of water are readily altered through changes in temperature and pressure. The applied temperature is generally the main parameter affecting extraction efficiency and selectivity in PHWE [9]. Pressure is usually applied to maintain water in the liquid phase, and its effect on the extraction efficiency is usually not significant. To our best knowledge, the application of PHWE on comfrey is limited.

Methods based on GC–MS and LC–MS have been reported for the detection of PAs due to their sensitivity and specificity [10–16]. However, GC–MS is not very suitable for the analysis of PA N-oxides due to their thermal instability. A pre-reduction of the N-oxides followed by derivatization is required if analysis is to be done by GC–MS. For these reasons, LC–MS is the preferred method in our study. LC–MS analysis of macrocyclic PAs in *Senecio* spp. using thermospray interface was previously reported [17,18]. Lin et al. [11], analysed various types of macrocyclic PAs with both in-source (collision induced dissociation in the collision cell) and out-source HPLC/MS or HPLC/MS/MS using electrospray interface. Mroczek et al., performed structure characterization of PAs in various plant species by RP-HPLC ion trap MS method with atmospheric pressure chemical ionization (APCI) interface [19] and gradient HPLC with diode array (DAD) and thermabeam electron impact (EI) MS [20]. Till now, HPLC ion-trap and orbitrap MS with electrospray ionization interface has not been used in the determination of PAs in comfrey.

The recent success with the use of LC–ESI–MS for the analysis of constituents in complex botanical extracts suggests that this technique can be effective for both the qualitative and quantitative determination of pyrrolizidine alkaloids in botanical extracts. Hence, one of the aims of the current work is to develop a new method based on HPLC ion trap and orbitrap MS with electrospray ionization interface for the qualitative analysis of hepatotoxic PAs such as lycopsamine present in *S. officinale L.* Another aim of the present study is to perform quantitative determination of lycopsamine present in comfrey. For this purpose, proper sample preparation is of utmost importance. Therefore, comparative studies on different extraction methods, including sonication, pressurized hot water extraction (PHWE) and heating under reflux were performed prior to quantitative analysis by LC–MS.

2. Experimental

2.1. Chemicals and reagents

All reagents were of HPLC grade. Methanol was the product of Merck (Nordic European center, Singapore). Ethanol, chloroform, isopropyl alcohol were purchased from Fisher scientific (Loughborough, Leicestershire LE11 5RG UK). Acetonitrile was the product of Tedia (Fairfield, OH45014, USA). Formic acid was obtained from Fluka (Sigma–Aldrich Pte Ltd, Science Park II, Singapore). Lycopsamine was purchased from Planta Analytica (USA), echimidine and lasiocarpine were purchased from Phyto Lab (Germany). Sand (white quartz, 50–70 mesh) was purchased from Sigma (St. Louis, MO, USA). Ultra-pure water was obtained using an Omega NANOpure ultrapure water system (Barnsteas Int., Dubuque, IA, USA). The plant comfrey of *S. officinale* L. was kindly provided by University of Quindío, Colombia.

2.2. Preparation of reference standards

Stock solutions of lycopsamine, echimidine and lasiocarpine at 200 ppm were prepared in methanol. For all analysis, the working solutions of lycopsamine, echimidine and lasiocarpine were prepared in the range of 0.05–2 ppm in methanol and their linearity was determined. For the quantitation of marker compounds, a four-point calibration based on the linearity established were used.

2.3. Preparation of medicinal plants

To prepare a homogenous sample, the real sample comfrey was ground using an IKA MF10 microfine grinder (Staufen, Germany) with sieve insert of hole size 0.5 mm. For PHWE, 1 g of the comfrey sample was weighed directly into a glass tube and mixed thoroughly with a high proportion of sand. The sand and plant material mixture were transferred into the extraction cell for PHWE as mentioned below. The extraction cell was finally filled with sand to avoid any voids.

2.4. Extraction

2.4.1. Sonication extraction

Briefly, 1 g of ground comfrey sample was extracted with 50 mL of solvent (methanol/water (50:50), methanol/chloroform (15:85), methanol, and ethanol) at room temperature for 10 min and filtered. The extracts were obtained, then excess solvent was evaporated with the rotary evaporator and the residues were transferred into a 10 mL volumetric flask.

2.4.2. Extraction by heating under reflux

Weigh 1 g comfrey into a round bottom flask, then add in 60 mL methanol/water (50:50) and gently reflux the mixture at 65 °C for 1 h in an electromantle before centrifuge at 2000 rpm for 10 min to isolate the extract. Excess solvent was evaporated on the hotplate and the residues were transferred into a 50 mL volumetric flask.

2.4.3. Pressurized hot water extraction (PHWE) system

For the instrumentation used for PHWE, the stainless steel tubings were 1/16 in. OD and 0.18 mm ID. The extraction cells from Phenomenex were of stainless steel with 10 mm ID × 1/2 in. OD × 250 mm (approx. 17 ml). The extraction cell was heated in a HP5890, gas chromatograph oven (Hewlett Packard, USA). The pump used was a Shimadzu LC-10AT HPLC pump (Kyoto, Japan). The pump flow was set at 1.5 mL/min and the oven temperature from 60 to 120 °C was studied. The pressure in the system indicated by the HPLC pump was between 20 and 30 bar. The extraction cell was pre-filled with methanol/water (50:50) to check for possible leakage before setting the temperature of the oven to the required value. Extraction with methanol/water (50:50) was carried out for a period of 40 min and 60–70 ml of liquid was collected. In between runs, the system was washed with methanol/water (50:50) for 5 min. The excess liquid was evaporated with the rotary evaporator under vacuum or by heating on a hotplate to 20–25 ml, and the residues were transferred into a 50 ml volumetric flask.

2.5. LC/MS analysis

Before HPLC analysis, all the real samples were filtered using the Acrodisc 32 mm Syringe filters with 0.2 μm Supor membrane (Pall Newquay, Cornwall, UK). For quantitative analysis, the LC/ESI–MS system comprised an Agilent 1100 series (Waldbronn, Germany) binary gradient pump, autosampler, column oven, diode-array detector and a LCQ-Duo ion trap mass spectrometer (Thermo Finnigan, San Jose, CA, USA). The column used for the separation was a Luna C18 (2), 100 × 2.0 mm, 3 μ (Phenomenex, USA). The gradient elution consisted of mobile phase of (A) water with 0.1% formic acid and (B) acetonitrile with 0.1% formic acid. The initial condition was set at 5% of (B), gradient up to 100% in 15 min and returning to the initial condition for 10 min. Oven temperature was set at 40 °C and flow rate was set at 0.2 mL/min. For all experiments, 5 μL of standards and sample extracts were injected. ESI–MS was performed in the positive mode. The LCQ mass spectrometer was operated with the capillary temperature at 270 °C, sheath gas at 80 (arbitrary units) and auxiliary gas at 20 (arbitrary units). The target was fixed at 2×10^7 ions and the automatic gain control was turned on. The electrospray voltage was set at 4.5 kV, the capillary voltage at 10 V and lens tube offset at 0 V. Mass spectra were recorded from m/z 100–600.

2.6. LC–MS^n analysis

For qualitative analysis of PAs and N-oxides, LC–MS^n experiments were performed using a Thermo Finnigan (San Jose, CA, USA) LTQ Orbitrap hybrid mass spectrometer coupled to a Thermo Finnigan Surveyor micro autosampler and liquid chromatography system. The extract was injected onto a Waters Symmetry 300 C18 column (3.5 μm, 2.1 × 50 mm ID). The mobile phase consisted of (A) 10 mM ammonium acetate and (B) acetonitrile. The gradient for elution was as follows: 0–5 min: 5% B; 5–15 min: 5–40% B; 15–30 min: 95% B; 30–45 min: 5% B. Flowrate was 0.2 mL/min.

The mass spectrometer was equipped with an electrospray interface as ionization source, an ion trap and an orbitrap for MS^n experiments and high mass accuracy determination. The mass spectrometer was operated in the positive mode with the following conditions: sheath gas N_2 with flow of 45 L/min; auxiliary gas at 5 L/min; sweep gas at 3 L/min; spray voltage, 4 kV; source current, 100 μA; capillary temperature, 400 °C; capillary voltage, 50 V; tube lens, 120 V. Full-scan mass spectra (50–500 amu) were recorded every 50 ms.

For MS/MS experiments, the conditions were: isolation width, 1 amu; normalized collision energy, 25%; activation time, 30 ms. The protonated parent ion $[M+H]^+$ of the PAs and N-oxides were chosen as precursor ions for isolation and fragmentation.

For MS^3 experiments, the conditions were: isolation width 1 amu; activation time, 30 ms; normalized collision energy, 25–35%. The most intense product ions with m/z greater than 150 (excluding parent ions) were chosen as precursor ion for isolation and fragmentation.

3. Results and discussions

3.1. Separation and determination of PAs in comfrey extracts

In other reports [12], one of the problems encountered in the development of a method to characterize the PAs in *S. officinale L.* was the lack of commercial standards. Using the HPLC conditions stated above, the three standards of lycopsamine, echimidine and lasiocarpine were separated well and their retention times were 2.82, 9.10 and 9.63 min, respectively. In positive ion ESI experiments, lycopsamine, echimidine and lasiocarpine form $[M+H]^+$ at 300.2, 398.2 and 412.0, respectively. Fig. 1 showed the selected ion chromatogram of lycopsamine, echimidine and lasiocarpine in their standard mixture solution (Fig. 1a) and comfrey extracts (Fig. 1b), respectively. As lycopsamine could be clearly identified from comfrey extracts, it will be quantitated in the following extraction study. Linearity was established from 0.05 to 2 ppm, and their

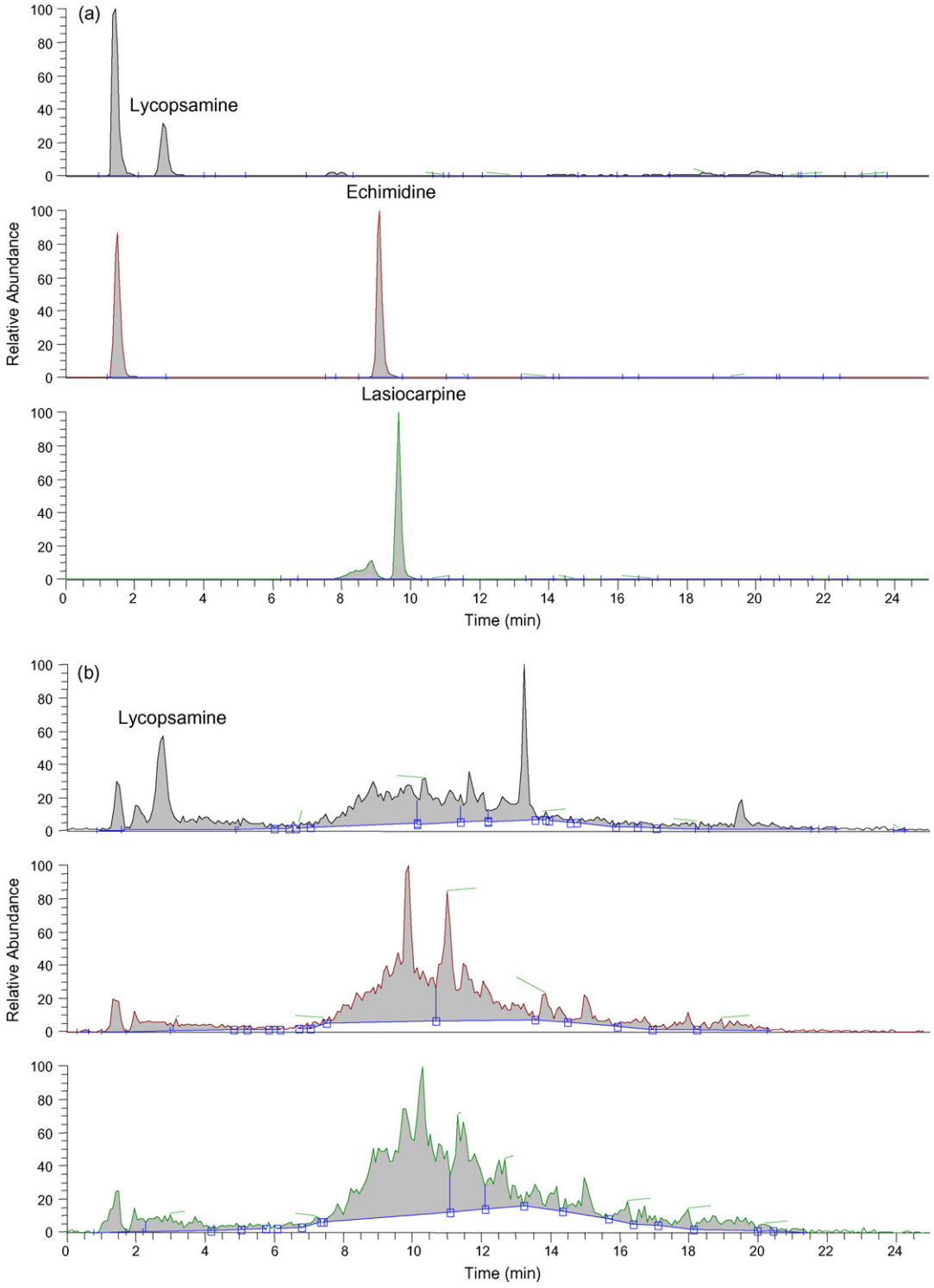


Fig. 1. Spectra under SRM of lycopsamine, echimidine and lasiocarpine in their standard mixture solution (a) and comfrey extracts (b); peak identification of (a): t_R = 2.82 min (lycopsamine); t_R = 9.10 min (echimidine); t_R = 9.63 min (lasiocarpine); peak identification of (b): t_R = 2.80 min (lycopsamine).

linear correlation coefficients r^2 all equaled to 0.999. The system precision (RSD) for the analysis of lycopsamine, echimidine and lasiocarpine by this method was determined at the concentration level 0.1, 1, 2 ppm and the results showed in Table 2 were found to vary between 2.06% and 9.21%.

3.2. LC–MS^n analysis of PAs

LC combined with MS^n detection can provide mass-based resolution of the PAs based on the specific product ions or fragments that arise from the MS^n. LC–MS^n with its low detection limit also allows the detection of trace amounts of PAs present. The results of the MS^n experiments for lycosamine, echimidine and lasiocarpine standards were summarized in Table 3 (mass spectrum not shown). All the three PAs contain the fragment, m/z 120, which is a characteristic of the retronecine moiety, the basic structure which they are derived from [21]. In comfrey extracts, lycopsamine was detected and its MS^2 spectrum was showed in Fig. 2a. As can be seen from the fragmentation pathway, lycopsamine showed characteristic frag-

Table 2
RSD ($n = 6$) values of LC–MS method for determination of lycopsamine, echimidine and lasiocarpine.

Compounds	Concentration (ppm)	RSD (%)
Lycopsamine	2.0	4.25
	1.0	2.06
	0.1	9.21
Echimidine	2.0	3.45
	1.0	5.29
	0.1	2.32
Lasiocarpine	2.0	5.24
	1.0	8.00
	0.1	5.29

ment ions at m/z 120.0806 and 138.0912, which were characteristic fragmentation ions of retronecine-type alkaloids [21]. In addition, mass spectral analysis has revealed some common fragmentation pathways that are shared by the PAs based on some of the product ions that they gave rise to. One of the fragmentation pathways that occur commonly among PAs is the McLafferty rearrangement [12,15], and the fragment ion at m/z 256.1546 was presumed as the product of this rearrangement.

In the analysis of $[M+H]^+$ at 398.22, two compounds share the same protonated molecular weight, the N-oxides of symviridine and the PAs of echimidine. Both share similar structure except that the R^3 of echimidine is a hydroxyl group instead of a hydrogen atom (Table 1). MS^2 of the echimidine standard produced fragments of m/z 120, 220, 336, and 380 with m/z 220 being the most intense. The fragment m/z 336 was derived from McLafferty rearrangement with the loss of an acetylaldehyde molecule and a water molecule ($[M+H]^+ - 44 - 18$). However, by comparing the MS^2 and MS^3 spectra that arise from m/z 398.22 (Fig. 2b and c) with that of the echimidine standard, it was found that the MS^n data did not match with that of the standard. By prediction, MS^2 of the N-oxides of symviridine via McLafferty rearrangement would give rise to the product ion m/z 354 (no water molecule is lost due to R^3 being hydrogen instead of hydroxyl) which was what was detected in the spectrum. A further confirmation was determined by performing a selected reaction monitoring (SRM) experiment on the parent/daughter ion pair of m/z 398.22/336 to determine the presence of echimidine. The result obtained suggested that echimidine was absent in *S. officinale L.* extract and the mass spectra in Fig. 2b and c were attributed entirely to the N-oxides of symviridine. Additionally, the PAs of symviridine were also detected in comfrey extracts and the MS^2 spectrum was shown in Fig. 2d. In the analysis of $[M+H]^+$ at 412.23, the absence of lasiocarpine was also confirmed. Thus, only lycopsamine of the PAs standards was detected in comfrey extracts, so in the following quantitative work, lycopsamine analysis would be focused on.

3.3. Extraction of comfrey

3.3.1. Sonication extraction of comfrey

Solvent has a significant effect on the extraction efficiency of PAs in comfrey [22,23] and the main aim of sonication extraction in this work is to choose the most appropriate solvent for lycopsamine extraction from comfrey. Hence, the effect of solvent was evaluated by using methanol/water (50:50), methanol/chloroform (15:85), methanol and ethanol and the results were showed in Fig. 3a. It is obvious that higher amount of lycopsamine could be obtained while using methanol/water (50:50) compared to the other solvent. Hence, methanol/water (50:50) was selected as the optimum solvent for subsequent studies. The effect of solvent pH was next investigated. Hydrochloric acid was added for the preparation of acidified solvent methanol/water (50:50) (HCl, pH 2.51). Fig. 3b showed that comparable amounts of lycopsamine were extracted using both the acidified and non-acidified solvent. Hence, there was no need to use the acidified solvent in the extraction of PAs from comfrey.

3.3.2. Pressurized hot water extraction (PHWE) of comfrey

To further improve the extraction efficiency and to reduce the extraction time, a new and rapid technique for the extraction of target compounds from comfrey based on PHWE was investigated. The key parameter that would have a significant effect on the extraction efficiency of PHWE was the applied temperature [24–26]. Hence, the effects of temperature from 60 to 120 °C on the extraction efficiency of lycopsamine in comfrey were studied and the results (Fig. 4a) showed that the amount of lycopsamine extracted decreased with increasing temperature. It was proposed that the presence of dissolved gases in the subcritical solvent could have caused the oxidation of lycopsamine in comfey at a higher applied temperature. Therefore, 60 °C was selected as the optimum temperature since the highest amount of lycopsamine was extracted out. The time for extraction was set at 40 min as it was observed that a significant amount of target analytes would be extracted in the first 30 min [27,28].

Table 3
MS^2 & MS^3 results of the pyrrolizidine alkaloids standards.

Compounds	Theoretical $[M+H]^+$	Retention time (min)	Experimental $[M+H]^+$	RSD (ppm)	Fragments derived from MS^2 (m/z)	Fragments derived from MS^3 (m/z)
Lycopsamine	300.181213	2.78	300.1806	2.0421	94, 120, 138[a], 156	–
Echimidine	398.217992	11.66	398.2169	2.7422	120, 220[a], 336, 380	220 → 120
Lasiocarpine	412.233642	12.91	412.2325	2.7703	120, 220, 238, 336[a], 394	336 → 120, 220, 238, 254

[a] Major fragment.

Table 4
Comparison of amount of lycopsamine extracted from comfrey by PHWE and reflux.

Concentration of lycopsamine (mg/kg)	Comparison 1		Comparison 2		Comparison 3	
	PHWE (60 °C) Day 1 ($n = 6$)	Reflux ($n = 3$)	PHWE (60 °C) Day 2 ($n = 6$)	Reflux ($n = 3$)	PHWE (80 °C) ($n = 6$)	Reflux ($n = 3$)
Mean ± S.D.	13.88 ± 2.68	31.73 ± 1.70	13.59 ± 1.30	30.87 ± 4.08	9.72 ± 1.25	29.15 ± 0.73
RSD (%)	19.32	5.36	9.57	13.22	12.87	2.49

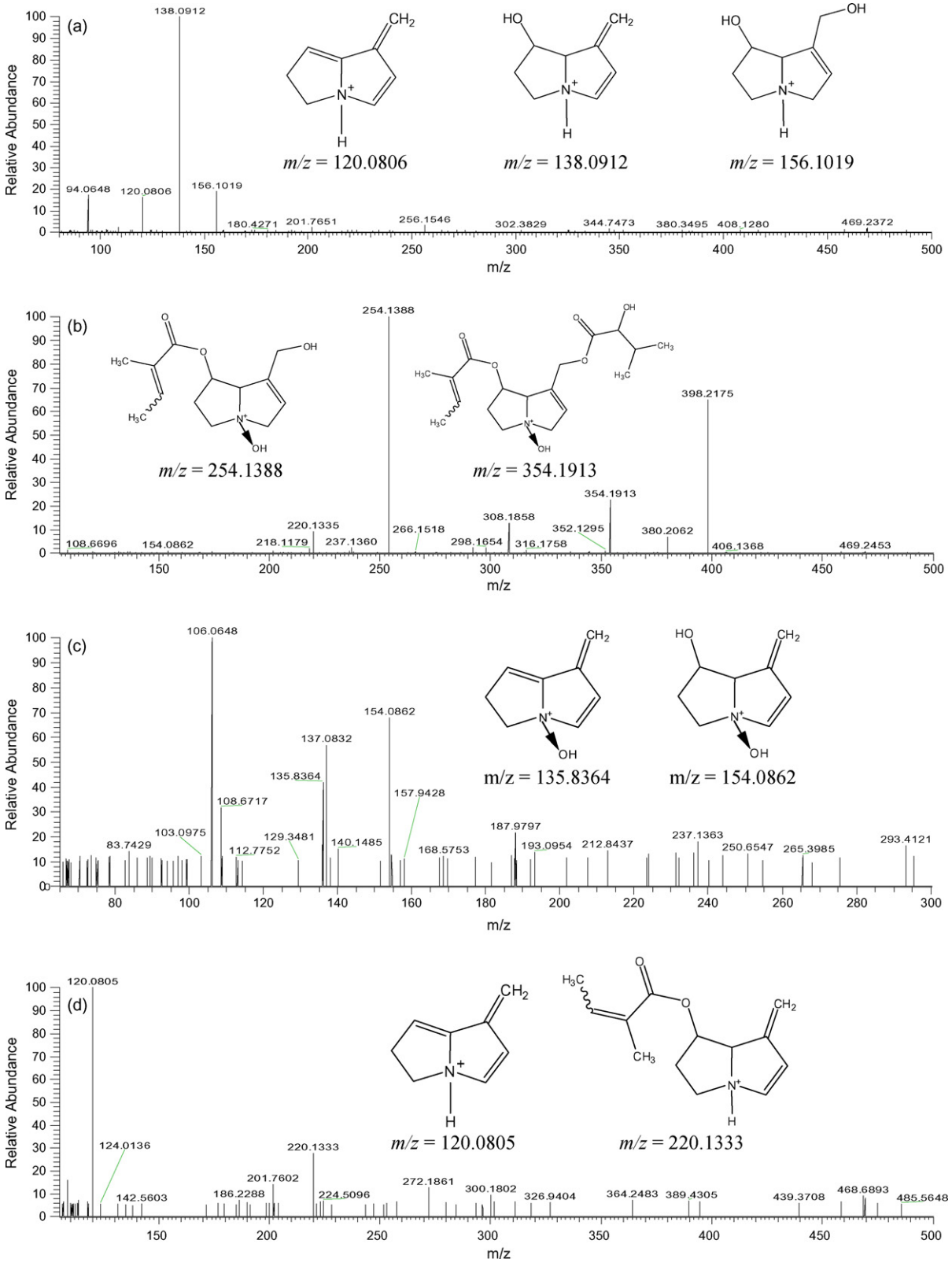


Fig. 2. (a) Positive MS^2 spectrum of lycopsamine extracted from *Symphytum officinale L.*, product ion of $[M+H]^+$ at *m/z* 300.18 and fragmentation pattern of lycopsamine; MS^n with *m/z* 398.22 extracted from *Symphytum officinale L.* (b) MS^2 of $[M+H]^+$ 398.22, (c) MS^3 of *m/z* 254.10; and MS^2 of PAs with *m/z* 382.22 extracted from *Symphytum officinale L.*; and (d) MS^2 with *m/z* 382.22 extracted from *Symphytum officinale L.*

3.3.3. *Extraction of comfrey by heating under reflux*

Due to the intrinsic property of plant extraction by PHWE, its extraction efficiency could be evaluated by comparing with other methods such as Soxhlet extraction, heating under reflux and others [27,29,30]. In this study, a comparison of PHWE with heating under reflux was carried out and the results obtained are showed in Fig. 4b–d and Table 4. For PHWE at 60 °C and 80 °C, the amount of lycopsamine was comparably lower than that obtained for heating

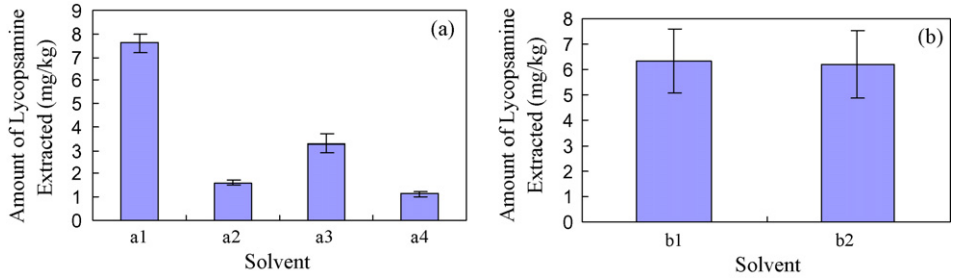


Fig. 3. (a) Effects of solvent on the amount of lycopsamine extracted from comfrey by sonication. Extraction solvent: a1-methanol/water (50:50), a2-methanol/chloroform (15:85), a3-methanol, a4-ethanol ($n = 3$); (b) pH Effects of solvent on the amount of pyrrolizidine alkaloids extracted from comfrey by sonication. Extraction solvent: b1-methanol/water (50:50), b2-methanol/water (50:50) (HCl, pH 2.51) ($n = 3$). Other sonication extraction conditions: time, 10 min; temperature, 25 °C.

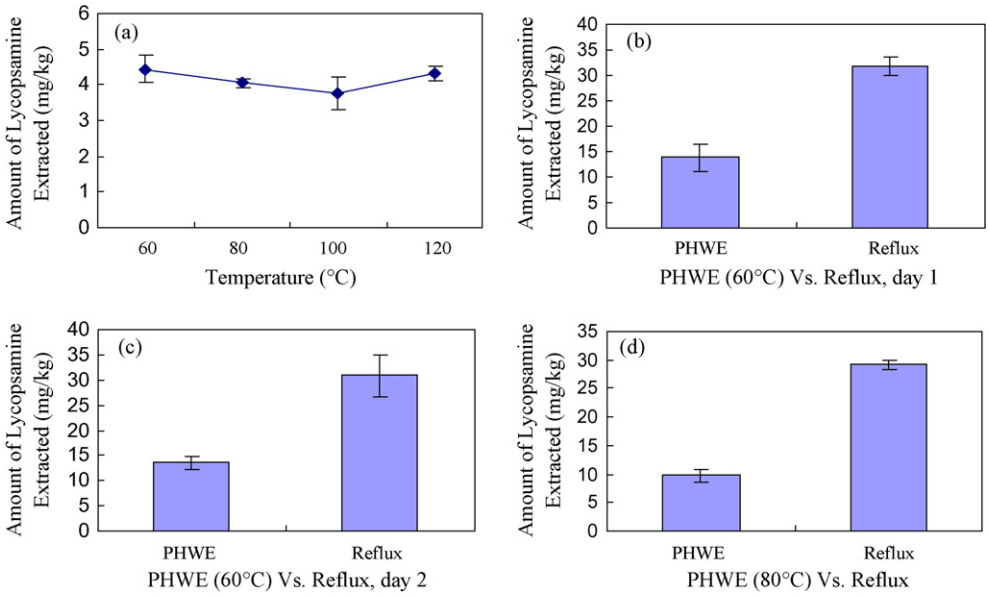


Fig. 4. (a) Effects of temperature on the amount of lycopsamine extracted from comfrey by PHWE ($n = 3$); and comparison of amount of lycopsamine extracted from comfrey by PHWE and heating under reflux ($n = 6$): (b) PHWE (60 °C) vs. Reflux, day 1. PHWE conditions, (c) PHWE (60 °C) vs. Reflux, day 2 and (d) PHWE (80 °C) vs. Reflux. PHWE conditions. PHWE conditions: solvent, methanol/water (50:50); flow rate, 1.5 ml/min; time for extraction, 40 min.

under reflux. The reason for the lower extraction efficiency of PHWE was presumably due to the reduction in solubility of lycopsamine in the pressurized hot solvent caused by the dissolved nitrogen of air [31,32]. The results observed in the current work was consistent with our earlier work [29] where certain naturally occurring compounds in medicinal plants was observed to be degraded in hot pressurized water rather than hot water due to the high reactivity of hot pressurized water [33].

However, in one of our other studies on the extraction of senkirkine and senecionine from *Tussilago farfara* by PHWE, a comparable extraction efficiency was obtained [34]. Although senkirkine, senecionine and lycopsamine all belong to hepatotoxic pyrrolizidine alkaloids, their extraction efficiencies by PHWE vary significantly. It proves that PHWE is not a universalizable technique and the use of subcritical water for extractions depends on the physical properties of the dissolved solutes and their tendency to degrade under the chosen extraction conditions [31]. Concurrently, the method precision (RSD) of both the two methods was found to be varied from 2.49% to 19.32% (Table 4), respectively. The proposed reason of the relatively high RSD may be that lycopsamine is not stable enough under pressurized hot water conditions, its solubility may be affected by dissolved gases, and its content in comfrey is quite low. As a result, though PHWE is a more rapid method, heating under reflux was found to be more appropriate for the extraction of lycopsamine from comfrey in quantitative analysis considering its higher extraction efficiency.

4. Conclusions

The combination of HPLC with orbitrap mass spectrometry allows for the rapid and accurate determination of pyrrolizidine alkaloids such as lycopsamine in botanical extracts. At the same time, the MS^n spectra gave characteristic ions that are useful for the identification of PAs in unknown samples. Subsequently, quantitative analysis of lycopsamine in comfrey was carried out, which has seldom been reported previously. The extraction of lycopsamine from comfrey was studied by evaluating different methods, including sonication extraction, pressurized hot water extraction and heating under reflux. The results obtained showed that LC–ESI–obitrap MS provide a powerful method for the identification and determination of hepatotoxic pyrrolizidine alkaloids in botanicals and dietary supplements. In addition our results provide new insights into the understanding and practical application of PHWE.

Acknowledgements

The authors would like to acknowledgement support from A-STAR (SERC 052 101 0044) and MOE (R–143-000-293-112).

References

[1] J.A. Pfister, R.J. Molyneux, D.C. Baker, J. Range Manage. 45 (1992) 254.

[2] Y. Cao, S.M. Colegate, J.A. Edgar, Phytochem. Anal. 19 (2008) 526.
[3] F. Li, S. Sun, J. Wang, D. Wang, Biomed. Chromatogr. 12 (1998) 78.
[4] H.J. Issaq, Electrophoresis 20 (1999) 3190.
[5] E. Roeder, K. Liu, R. Mütterlein, Fresenius J. Anal. Chem. 343 (1992) 621.
[6] T. Mroczek, J. Widelski, K. Glowniak, Chem. Anal. (Warsaw) 51 (2006) 567.
[7] V. Camel, Analyst 126 (2001) 1182.
[8] B. Kaufmann, P. Christen, Phytochem. Anal. 13 (2002) 105.
[9] E.S. Ong, J.S.H. Cheong, D. Goh, J. Chromatogr. A 1112 (2006) 92.
[10] Y. Jiang, P.P. Fu, G. Lin, Asian J. Pharmacodyn. Pharmacokinet. 6 (2006) 187.
[11] G. Lin, K.Y. Zhou, X.G. Zhao, Z.T. Wang, P.P.H. But, Rapid Commun. Mass Spectrom 12 (1998) 1445.
[12] J.C.A. Wuilloud, S.R. Gratz, B.M. Gamble, K.A. Wolnik, Analyst 129 (2004) 150.
[13] D.E. Gray, A. Porter, T. O'Neill, R.K. Harris, G.E. Rottinghaus, J. AOAC Int. 87 (2004) 1049.
[14] J. Brauchli, J. Luthy, U. Zweifel, C. Schlatter, Experientia 38 (1982) 1085.
[15] T. Mroczek, K. Ndjoko-Ioset, K. Glowniak, A. Mietkiewicz-Capala, K. Hostettmann, Anal. Chim. Acta 566 (2006) 157.
[16] S.M. Colegate, J.A. Edgar, A.M. Knill, S.T. Lee, Phytochem. Anal. 16 (2005) 108.
[17] C.E. Parker, S. Verma, K.B. Tomer, R.L. Reed, D.R. Buhler, Biomed. Environ. Mass Spectrom. 19 (1990) 1.
[18] K. Ndjoko, J.L. Wolfender, E. Roeder, K. Hostettmann, Planta Med. 65 (1999) 562.
[19] T. Mroczek, K. Ndjoko, K. Głowniak, K. Hostettmann, J. Chromatogr. A 1056 (2004) 91.
[20] T. Mroczek, S. Baj, A. Chrobok, K. Glowniak, Biomed. Chromatogr. 18 (2004) 745.
[21] S.L. Li, G. Lin, P.P. Fu, C.L. Chan, M. Li, Z.H. Jiang, Z.Z. Zhao, Rapid Commun. Mass Spectrom 22 (2008) 591.
[22] M.M. Mossoba, H.S. Lin, D. Andrzejewski, J.A. Sphon, J.M. Betz, L.J. Miller, R.M. Eppley, M.W. Trucksess, S.W. Page, J. AOAC Int. 77 (1994) 1167.
[23] J.C. Altamirano, S.R. Gratz, K.A. Wolnik, J. AOAC Int. 88 (2005) 406.
[24] S.B. Hawthorne, Y. Yang, D.J. Miller, Anal. Chem. 66 (1994) 2912.
[25] D.J. Miller, S.B. Hawthorne, Anal. Chem. 70 (1998) 1618.
[26] B. van Bavel, K. Hartonen, C. Rappe, M.J. Riekkola, Analyst 124 (1999) 1351.
[27] E.S. Ong, S.M. Len, Anal. Chim. Acta 482 (2003) 81.
[28] S. Morales-Munoz, J.L. Luque-Garcia, M.D. Luque de Castro, Anal. Chem. 74 (2002) 4213.
[29] E.S. Ong, S.M. Len, J. Sep. Sci. 26 (2003) 1533.
[30] C. Nerín, J. Salafranca, M. Aznar, R. Batlle, Anal. Bioanal. Chem. 393 (2009) 809.
[31] J.W. King, K. Srinivas, J. Supercrit. Fluids 47 (2009) 598.
[32] H.J. Gahrs, Ber. Bunsenges. Phys. Chem. 88 (1984) 894.
[33] G. Brunner, J. Supercrit. Fluids 47 (2009) 373.
[34] Z. Jiang, F. Liu, J.J.L. Goh, L. Yu, S.F.Y. Li, E.S. Ong, C.N. Ong, Talanta 79 (2009) 539.

Talanta 80 (2009) 924–934

Contents lists available at ScienceDirect

Talanta

journal homepage: www.elsevier.com/locate/talanta

Multi-component analysis (sterols, tocopherols and triterpenic dialcohols) of the unsaponifiable fraction of vegetable oils by liquid chromatography–atmospheric pressure chemical ionization–ion trap mass spectrometry

Wissem Zarrouk[a], Alegría Carrasco-Pancorbo[b], Mokhtar Zarrouk[a], Antonio Segura-Carretero[b,*], Alberto Fernández-Gutiérrez[b]

[a] Laboratoire Caractérisation et Qualité de l'Huile d'Olive, Centre de Biotechnologie de Borj Cedria, BP 901, 2050 Hammam-Lif, Tunisia
[b] Department of Analytical Chemistry, University of Granada, 19071 Granada, Spain

ARTICLE INFO

Article history:
Received 4 February 2009
Received in revised form 6 August 2009
Accepted 17 August 2009
Available online 25 August 2009

Keywords:
Sterols
Tocopherols
Trierpenic dialcohols
Oils
Liquid chromatography
Mass spectrometry
Atmospheric pressure chemical ionization
Ion trap

ABSTRACT

A simple and sensitive method for the analysis of sterols, tocopherols and triterpenic dialcohols from the unsaponifiable fraction from oil samples in a single analytical run using liquid chromatography coupled to mass spectrometry was developed. With this method, the compounds could be detected directly after dissolving the unsaponifiable fraction in acetonitrile without necessity of time-consuming sample pretreatment or derivatization. Separation of the analytes was carried out at room temperature, by using a C18 column (5 μm i.d. 3.0 mm × 250 mm) with a linear gradient of acetonitrile/water (0.01% acetic acid) at a flow rate of 1.5 mL/min. The full scan mass spectra of the investigated compounds were measured by an ion trap mass spectrometer equipped with an APCI ion source. The optimized methodology was suitable for the identification of 23 compounds belonging to different families present in olive oil and other kinds of oils, as well as for the quantification of 15 analytes (vs. their commercial standards).
© 2009 Elsevier B.V. All rights reserved.

1. Introduction

Vegetable oils are mainly composed of triacylglycerols (95–98%) and complex mixtures of minor compounds (2–5%) of a wide-ranging chemical nature [1]. Among these minor compounds, tocopherols and phytosterols can be found; their beneficial health effects have sparked great interest in the past few years. Phytosterols have been receiving particular attention because of their capability to lower serum cholesterol levels in human resulting in significant reduction in the risk of cardiovascular disease [2]. They have also been described as a kind of natural product with anti-inflammatory [3], anti-bacterial [4], anti-oxidation [5] and anti-cancer properties [6,7]. On the other hand, tocopherols have also antioxidant properties, since they can act as scavengers of free radicals and prevent the propagation of lipid peroxidation in food and biological systems [3,8]. Thus, they protect body tissues against oxidative damage and play important roles in the prevention of cancer, cardiovascular and neurological diseases.

Phytosterols and tocopherols are bioactive components occurring in all vegetable foods, and make up the greatest proportion of the non-saponificable fraction of lipids [9], so it is mandatory to develop tools able to generate accurate quantitative data of these nutritionally important compounds. Tocopherols and sterols are mostly determined separately in oils and fats by using different techniques or different methods when the same technique is used. Capillary gas chromatography with flame ionization detection (GC–FID) is most frequently applied in plant sterol analysis [10,11]. The method mainly used for the analysis of sterolic fraction of edible oils involve several steps, namely, the saponification of the oil to remove triglycerides, the fractionation of the unsaponifiable matter into several classes of compounds by thin layer chromatography (TLC), and their subsequent analysis by gas chromatography as trimethylsilyl (TMS) derivatives in non-polar capillary gas chromatography columns [12]. This method is described in different regulations [13,14], and although is an useful tool, it is widely recognized that this conventional method is tedious, time-consuming, may involve the loss of analytes and is suitable only for a limited number of compounds. In the past few years, normal-phase (NP) and reversed-phase (RP) liquid chromatography (HPLC) have been widely used for the analysis of some classes of lipid and sterols from various sample matrices. In general, RP-HPLC has been more

* Corresponding author. Tel.: +34 958243296; fax: +34 679933455.
E-mail address: ansegura@ugr.es (A. Segura-Carretero).

0039-9140/$ – see front matter © 2009 Elsevier B.V. All rights reserved.
doi:10.1016/j.talanta.2009.08.022

widely used than NP-HPLC for the separation of individual sterols [15]. Sterol detection has been carried out by UV (200–210 nm), photodiode array detection (DAD), refractive index (RI) detection, evaporative light scattering detection (ELSD), nuclear magnetic resonance (NMR) detection and mass spectrometry (MS) [9]. Because sterols are highly lipophilic with few polar functional groups, they are difficult to ionize through conventional electrospray (ESI) methods [16]. Recently, atmospheric pressure chemical ionization (APCI) with liquid chromatography mass spectrometry (LC–MS) was found to be suitable for sterol analyses in different samples matrices. LC–APCI–MS has been used to identify sterols in soybean oil [17], to characterize phytosterols in spelt [15], to determine ergosterol levels in bulrush [18] and to measure cholesterol oxides in different food supplies [19]. The direct infusion approach in MS has recently been used to classify vegetable oils according to their botanical origin, based on direct injection of sterol extracts into a mass spectrometer with either an ESI ionization or an atmospheric pressure photoionization source (APPI) [20].

For tocopherols determination two possible ways of elution using liquid chromatography have been used, normal and reversed phase. For routine analyses most of researchers still use high HPLC with UV–vis or fluorescent detection [21]. When a separation of carotenes or sterols from tocopherols is needed, the reversed-phased elution is advisable [22,23]. This type of elution is claimed to be more reproducible and sensitive than normal-phased elution for tocopherol analysis [24,25].

Our objective in this study was to develop a simple method for simultaneous analysis of different families from vegetable oils (tocopherols, triterpenic dialcohols and phytosterols) by RP-HPLC–APCI–Ion Trap MS. To the best of our knowledge, this is the first time that components of three different families from the unsaponifiable fraction of oils have been analysed by HPLC–APCI–MS in a single run. Analysing two different categories of phytosterols (4-desmethyl sterols and 4,4-dimethyl sterols), tocopherols and triterpenic dialcohols simultaneously reduce significantly the time, cost and effort needed. The method we describe here is robust and reliable and permits to identify 23 compounds (fifteen 4-desmethyl sterols, two 4,4-dimethyl sterols, two triterpenic dialcohols and four tocopherols). The analytical characteristics of the method were checked (linearity, detection limit, calibration range, absence of ion suppression phenomena) and all the MS and MS^n patterns observed were explained. When the standards were commercially available, we quantified them as well. The use of ion trap (IT) as MS analyzer provides an accurate identification of the compounds under study, since this analyzer is able to carry out MS/MS analyses.

2. Experimental

2.1. Samples, reagents and chemicals

Commercially available edible oils were acquired in a local supermarket: sunflower blended with soybean oil, corn oil, refined sunflower oil, olive oil, olive pomace oil, soy "plus omega 3" oil and walnut oil. Cholesterol was acquired from Riedel-de Haën (Germany), β-sitosterol and erythrodiol were from Fluka (Buchs, Switzerland). Sitostanol, uvaol, Δ5-avenasterol, stigmasterol, campesterol, brassicasterol were from Sigma–Aldrich (St. Louis, MO). The two 4,4-desmetyhl sterols under study were from Sigma–Aldrich as well. α-, β-, γ-, and δ-tocopherols were purchased as an isomer kit from Merck (Darmstadt, Germany).

Stock solution (0.1 mg/mL) was prepared by dissolving all standards in acetonitrile (ACN) and stored in dark at −20 °C over a maximum period of one month. Working standard solutions were prepared daily by dilution of this concentrated solution in acetonitrile. All reagents used were of analytical grade. HPLC grade acetonitrile, methanol, diethyl ether and ethyl acetate were purchased from Panreac (Barcelona, Spain). Potassium hydroxide and sodium sulphate anhydrous were from Sigma. Milli-Q water of 18.2 MΩ cm^{-1} resistivity was used throughout (Millipore, Billerica, MA, USA).

2.2. Instrumentation

Analyses were carried out at room temperature on a System Gold HPLC (Beckman Couter, Fullerton, CA, USA), including a 126 solvent module, a 168 diode array detector module and a manual sample valve injector with a 20 μl loop (Rheodyne, Cotati, CA, USA). The HPLC column used was a Phenomenex C18 (5 μm, 3.0 mm × 250 mm) fitted with a Phenomenex C-18 guard column (Phenomenex, Torrance, CA). The mass spectrometer used was a Bruker Esquire 3000 ion trap purchased from Bruker Daltonics (Bremen, Germany) equipped with an APCI interface.

Solvents were filtered using a Solvent Filtration Apparatus 58061 (Supelco, Bellefonte, PA, USA) prior to degassification by ultrasonication.

A model MicropH 2002 meter from Crison (Barcelona, Spain) was used to adjust the pH of the mobile phase with a precision of 0.01 pH unit. A Heidolph VV rotary evaporator (Schwabach, Germany) coupled to a Büchi B-169 Vacuum System (Flawill, Switzerland) was used to concentrate the sample extracts.

2.3. Sample preparation

The sample (5 g oil) was saponified by refluxing with 50 mL of ethanolic solution of KOH 2 M for 30 min. After cooling at room temperature, 100 mL of distilled water were added. After phase separation in a separation funnel, the aqueous phase was washed three times with diethyl ether. The diethyl ether fractions were collected and washed three times with distilled water and with ethanolic solution of KOH 0.5N successively. Finally, the ether extracts were washed with distilled water until the wash water gave a neutral reaction and dried with anhydrous sodium sulphate. They were then filtered and evaporated to dryness using a rotary evaporator at reduced pressure and the residue was dissolved in acetonitrile. Samples extracts were filtred through a membrane filter (0.45 μm) before being analysed by HPLC–APCI–IT MS.

2.4. LC–APCI–IT MS method

Compounds in the non-saponificable fractions of the oil samples were analysed by LC–APCI–IT MS. The compounds were separated with a gradient of acetonitrile/water (0.01% acetic acid) at a flow rate of 1.5 mL/min. The mobile phase were acetonitrile (Phase A) and water (acetic acid 0.01%) (Phase B) and the solvent gradient changed according to the following conditions: from 0 to 60 min, 90% A:10% B to 92% A:8% B. From 60 to 63 min, 92% A:8% B to 100% A:0% B; from 63 to 65 min, 100% A:0% B to 90% A:10% B. The column temperature was set to 30 °C during the whole run and the injection volume was 20 μl. The monitoring of the examined compounds was performed at 280/240 nm.

The HPLC system was coupled to an IT mass spectrometer equipped with an APCI interface operating in positive ion mode using the following parameters: optimized temperature and flow rate of the dry gas (nitrogen) were 350 °C and 5 L/min, respectively, and the APCI interface temperature was 450 °C. The pressure of the nebulizer gas (nitrogen) was set to 50 psi, and the voltage of the corona discharge needle was +3500 V. Capillary voltage was set at −3000 V and the end-plate offset, at -500 V. The IT MS scanned in the m/z range from 50 to 800. Source and transfer parameters were optimized by direct infusion experiments with solutions contain-

ing all the compounds under study which we had as commercially available standards looking for the best conditions regarding peak intensity and resolution. We confirmed that the MS compromise solutions found were the most appropriate for every compounds making direct infusion experiments with individual solutions as well.

Identification of analytes was based on the comparison of their retention times and mass spectra with those of authentic reference compounds. Peak identification was also done with spiked samples at different concentration levels.

2.5. Analytical parameters of the method

2.5.1. Method validation

Linearity of the MS detector response was verified with standard solutions at different concentration levels over the calibration range. To calculate the regression model, standard solutions at six different concentrations (10, 20, 33, 50, 100 and 200 mg/L) were used to define the calibration curves for all the reference compounds under study. In addition to that, some more points between 200 and 2000 mg/L were analyzed in the case of the β-sitosterol. Three independent injections were performed for each concentration of standard compound. Calibration curves were obtained for each standard with good linearity ($r^2 > 0.97$) by plotting the standard concentration as a function of the peak area obtained from HPLC–APCI–IT MS analyses. For this purpose, the stock solution (1000 mg/L) of the standards was diluted with ACN to have different concentrations. The analysis of variance (ANOVA) with a lack-of-fit test (LOF) at a confidence interval of 95% was performed to validate the regression data using the SPSS 13.0 for windows (SPSS Inc., 2004).

The limits of detection and quantification of the individual analytes in standard solutions were calculated according to the IUPAC method [26] when MS detection was carried out. The sensitivity of the method in that case was studied by defining the limit of detection (LOD) and limit of quantification (LOQ) for individual compounds in standard solutions. The limit of detection was considered S/N = 3, whilst the limit of quantification was S/N = 10).

The precision of the method described was measured as repeatability, it was assessed for each standard compound at two concentration levels (20 and 100 ppm).

2.5.2. Ion suppression

The ion suppression effect may be caused by a number of factors such as the matrix or interference co-eluting compounds. We used a strategy described by Nelson and Dolan [27] for systematic investigation of ion suppression in HPLC–MS analysis. So, we produced a continuous flow of analyte solution resulting in a constant but elevated baseline in MS detection. This flow was then continuously mixed with eluate from an LC-separated blank sample. Consequently, ion-suppressing components will be detectable as a drop in the baseline over the complete LC run. Such investigations enable optimization of HPLC conditions to prevent coelution of analyte and interfering substances.

3. Results and discussion

3.1. Extraction and isolation of sterols, tocopherols and triterpenic dialcohols from oil samples

We analyzed sterols, tocopherols and triterpenic dialcohols compounds from different kind of oils by HPLC–APCI–IT MS after saponification of the lipid matrix. The direct saponification method is employed frequently for the sample preparation of phytosterols in order to remove triacyglycerols from oils. It is usually performed at 60–85 °C [10,28] and sometimes at room temperature [16,29]. Both procedures were tested with comparable results. As cold saponification is time consuming (all overnight at room temperature and in the dark), we avoid this procedure of sample preparation although it seems more convenient in term of stability of the extracted compounds. So, we studied the saponification time effect at 80 °C on the profile of the extract analysed by LC–MS, since tocopherols and phytosterols are exposed to thermal degradation in the process of saponification at hot temperature. After the preliminary studies, we decided that the optimum time of saponification was 30 min at 80 °C. Also, in order to minimize risk of thermal degradation, we reduced the time in which the extract was exposed to vaccum. Several extraction solvents were used for extracting unsaponifiables, including petroleum ether, hexane, ether acetate and diethyl ether [30,31]. Diethyl ether is the most commonly used extraction solvent for unsaponifiable fraction of oils and, thus, diethyl ether was chosen as an extraction solvent in this study. Furthermore, we increased the amount of diethyl ether until 100 mL and also the extraction time of unsaponifiables as it increases the recovery rates of tocopherols [32].

So, taking into consideration the previous experience of other researches [31,33], we succeeded finally to reduce the time needed to isolate sterols in comparison to the official method. We simplified the official method, since we avoid the separation by TLC, and we offer the opportunity to enlarge the number of families from the unsaponifiable fraction of oils suitable to be analyzed by the described method. As a final step, the solvent was evaporated and the extract was redissolved in acetonitrile.

3.2. Chromatography separation

The experimental conditions that were established enabled the simultaneous analysis of three classes of compounds (sterols, tocopherols and the triterpene dialcohols, erythrodiol and uvaol). The high lipophilicity of tocopherols and sterols can make sample processing and chromatography difficult. In this respect, reversed phase C18 column was chosen for the elution of analytes. After realizing that water (with 0.01% acetic acid) (as phase A) and acetonitrile (as phase B) were the most appropriate mobile phases for achieving our aim, we found that with a C18 stationary phase and the following gradient between 90% acetonitrile: 10% water + 0.01% acetic acid and 92% acetonitrile: 8% water + 0.01% acetic acid from 0 to 60 min on column temperature of 30 °C gave the best separation. Several different flow rates were assessed to optimize the resolution among all the analytes and also the peak intensity. A flow rate of 1 mL/min offered the highest peak intensity but the separation of all the compounds was achieved over 60 min; we decided to choose 1.5 mL/min as the optimum flow rate for the analysis, as the resolution was still good enough and the analysis time was shorter. For the choice of an appropriate reversed-phase C18, we tested two different columns: Atlantis d C18 150 mm × 2.1 mm i.d., 5 μm (Waters) and Phenomenex C18 3.0 mm × 250 mm i.d., 5 μm. To compare column performances, we used a mixture of standards of all the compounds concerned in our aim. We found that longer reversed-phase column with MS detection was more appropriate for the separation of the standard mix we were working with. As seen in Fig. 1, brassicasterol was separated from β- and γ-tocopherols, cholesterol and Δ-5-avenasterol peaks in the longer reversed-phase column, whereas all of them were overlapped in the same peak when the separation was made with the shorter column. Also, a higher resolution between peaks of campesterol and β-amyrin, and between stigmasterol and α-tocopherol was obtained using longer reversed-phase column. Separation of analytes was achieved in 34.4 min using short column, whilst 39.0 min were necessary to do the same where the longer column was used. Although the baseline resolution of all the compounds was not achieved, the study of the analytical parameters (in particular linearity and ion

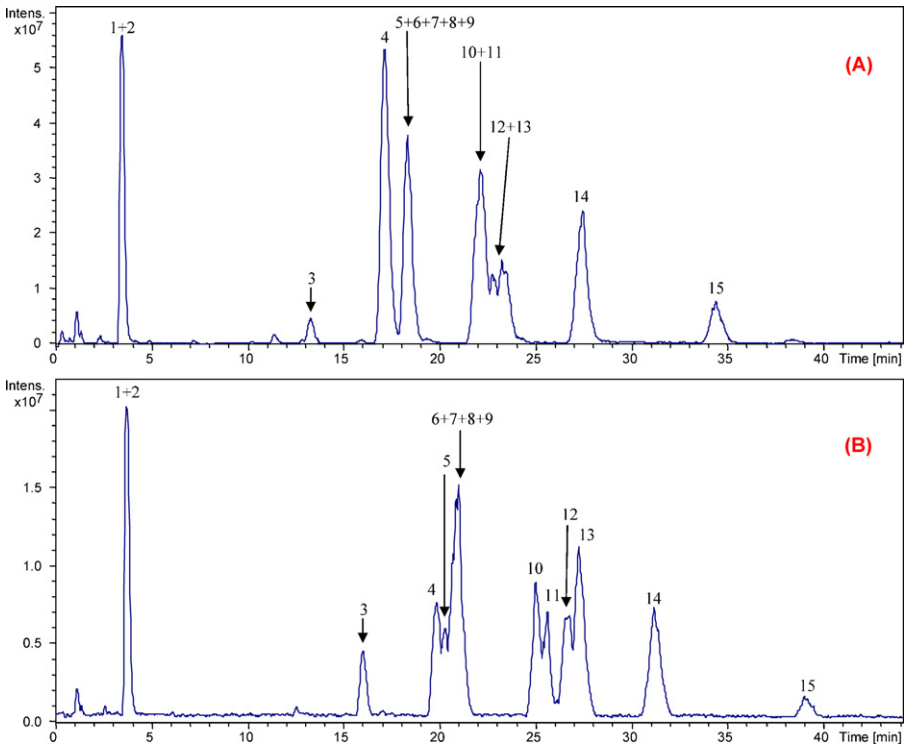


Fig. 1. HPLC–APCI–IT MS chromatograms of a standard mixture of sterols, tocopherols and triterpenic dialcohols using different columns, (A) C18 150 mm × 2.1 mm i.d., 5 μm; (B) Phenomenex C18 3.0 mm × 250 mm i.d., 5 μm, eluent flow rate1.5 mL/min. Gradient from 90% acetonitrile: 10% water + 0.01% acetic acid to 92% acetonitrile: 8% water + 0.01% acetic acid from 0 to 60 min. (1) erythrodiol, (2) Uvaol, (3) γ-tocopherol, (4) lupeol, (5) brassicasterol, (6) β-tocopherol, (7) γ-tocopherol, (8) cholesterol, (9) Δ-5-avenasterol, (10) campesterol, (11) β-amyrin, (12) stigmasterol, (13) α-tocopherol, (14) β-sitosterol and (15) sitostanol.

suppression studies) assured the reliability of our method, which could be able to determine some interesting compounds in a very reasonable time. Indeed, in HPLC–MS baseline separation of peaks is not always mandatory due to high specificity and selectivity of the detection method. The optimum chromatogram (Base peak chromatogram (BPC)) and extracted ion chomatograms (EIC) of all the compounds under study sorted by families can be observed in Fig. 2. As lupeol and β-amyrin have the same molecular weight and both of them are ionized giving $[M+H-H_2O]^+$, we injected separately these compounds to make sure about the identify of each one. In the same way, we proceed to confirm the order of stigmasterol and (-5-avenasterol, which showed the same main fragment ion at 395 *m*/*z*. In both cases to bear in mind the chemical structure of the compounds and the previous reports already published was helpful.

3.3. APCI–IT MS fragmentation of sterols, tocopherols and triterpenic dialcohols

Atmospheric pressure chemical ionization is considered to be a soft ionization technique and should be therefore a suitable procedure for labile compounds. The effect of the following parameters was investigated: corona current, capillary voltage, end plate offset voltage, nebulizer, dry gas, dry temperature and vaporizer temperature. Optimized values are referred in Section 2. The IT MS scanned in the *m*/*z* range from 50 to 800. Source and transfer parameters were optimized by direct infusion experiments with solutions containing all the compounds under study which we had as commercially available standards looking for the best conditions regarding peak intensity and resolution.

On the current study, vaporizer temperature was one of the parameter which had more influence in the intensity and quality of the spectra. In general, most of the researches working with APCI claim that the increase of the vaporizing temperature leads to an improvement in desolvation and evaporation of the compounds and provides better ionization efficiency. However, the fact that the high temperatures can decompose the labile analytes has to be considered as well. The vaporizer temperature was varied between 250 and 450 °C in positive APCI. We found a compromise value for as high as possible signal for all the compounds in the mixture at 450 °C. Signal intensity for tocopherols was quite sensitive to changes in APCI interface temperature.

In APCI, the capillary voltage was varied between 2.0 and 4.5 kV (negative values). The response of sterols, tocopherols and triterpenic dialcohols was higher in the range between 2.8 and 3.2 kV. As the differences in this range varied depending on the family of analytes observed, we took as optimum value 3.0 kV.

In the current study, the drying gas flow rate was varied from 2 to 9 L/min. For APCI in positive polarity-that we chose after comparing the analytical performance with APCI in negative polarity-the optimum flow rate was found at 5 L/min. By using higher values than 5 L/min, the signal intensity for some compounds was even higher but the stability of the signal and also the currents was much lower.

Finally, the temperature of dry gas and the nebulizing pressure were checked; concluding that 350 °C was the optimum dry temperature and 50 psi was the most appropriate value for nebulizing pressure.

The positive mass spectra of analytes are shown in Fig. 3. Intense fragment ions at *m*/*z* 409.2 (for lupeol and β-amyrin), 381.2 (for brassicasterol), 369.2 (for cholesterol), 395.2 (for (-5-avenasterol and stigmasterol), 383.2 (for campesterol), 397.2 (for β-sitosterol) and 399.2 (for sitostanol) were observed, indicating the loss of water $[M+H-H_2O]^+$ (see Table 1). This seems to be characteristic for sterols as dehydration was observed in earlier reports with cholesterol oxides [34], phytosterols [16,17], and ergosterol [18]. For the tocopherols, we consistently observed that APCI generated major fragments ions at *m*/*z* 402.2 (for δ-tocopherol), 416.2 (for β and γ-tocopherols) and 430.2 (for α-tocopherol). However APCI

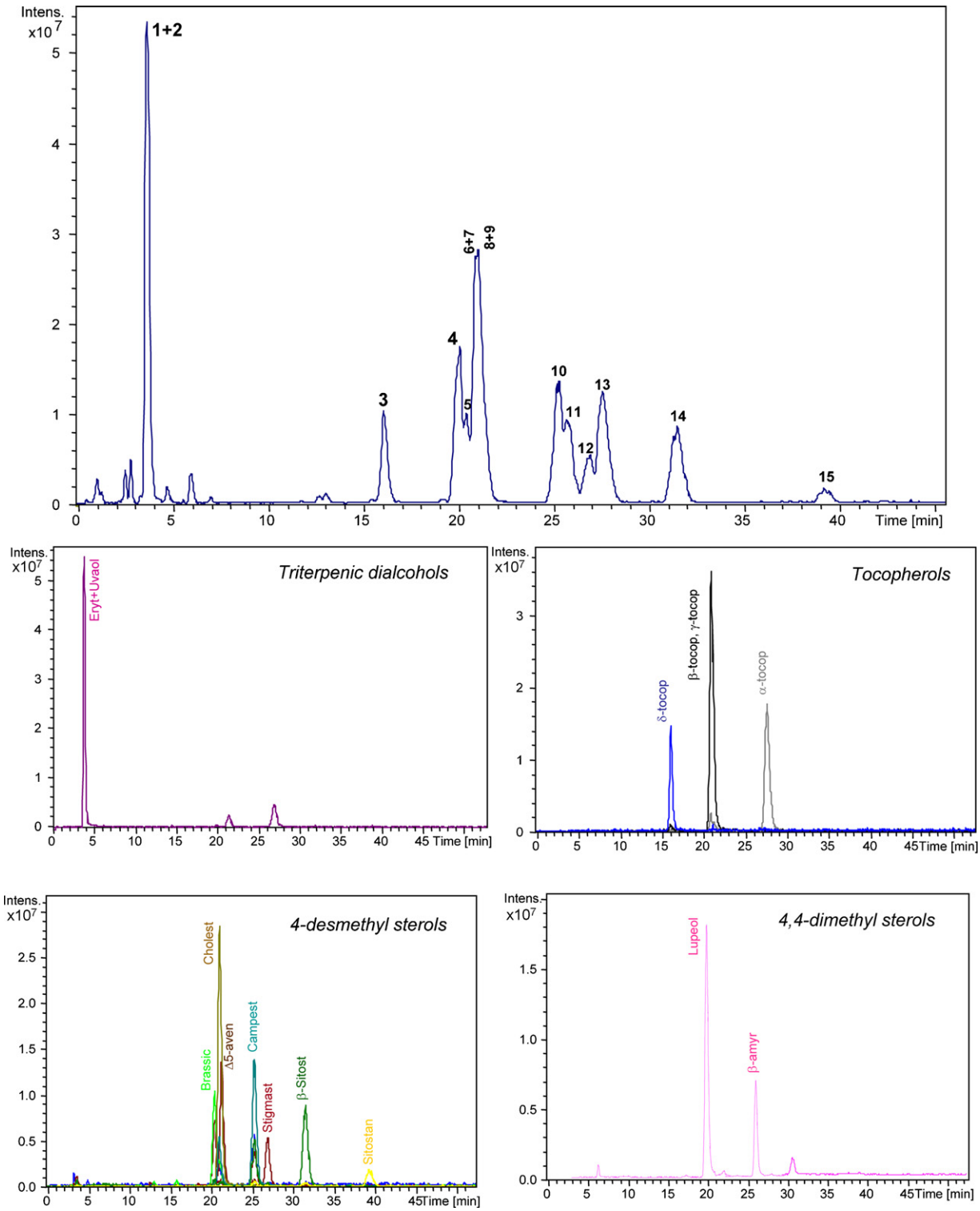


Fig. 2. Base peak chromatogram (BPC) of the standard mix containing sterols, tocopherols and triterpenic dialcohols analyzed at optima conditions and extract ion chromatograms of the compounds sortened by families. Peaks number as in Fig. 1.

typically produces protonated molecular ions $[M+H]^+$, which for tocopherols compounds would be expected at *m*/*z* 403, 417 and 431. The formation of the observed ions from tocopherols could be explained by the facile one-electron oxidation of tocopherol by the corona discharge in the APCI source [35,36]. Both the molecular ion $[M]^{\bullet+}$ and the protonated molecule $[M+H]^+$ in a constant ratio were observed for the tocopherols under study, although as said before the major ion in the mass spectra was $M^{\bullet+}$ for the four tocopherols. We can say that tocopherols (like most of non-polar compounds with systems conjugated π-bonds and donor substitutents) in positive ion mode, ionization proceeds via two competitive mechanisms: target pseudo-molecular ion $[M+H]^+$ formation via protonation of analyte and molecular ion $[M]^{\bullet+}$ formation via one-electron oxidation inside the MS interface.

The main ions in the mass spectra of erythrodiol and uvaol were *m*/*z* 407.2 $[M+H-2H_2O]^+$ and 427.2 $[M+H-H_2O]^+$.

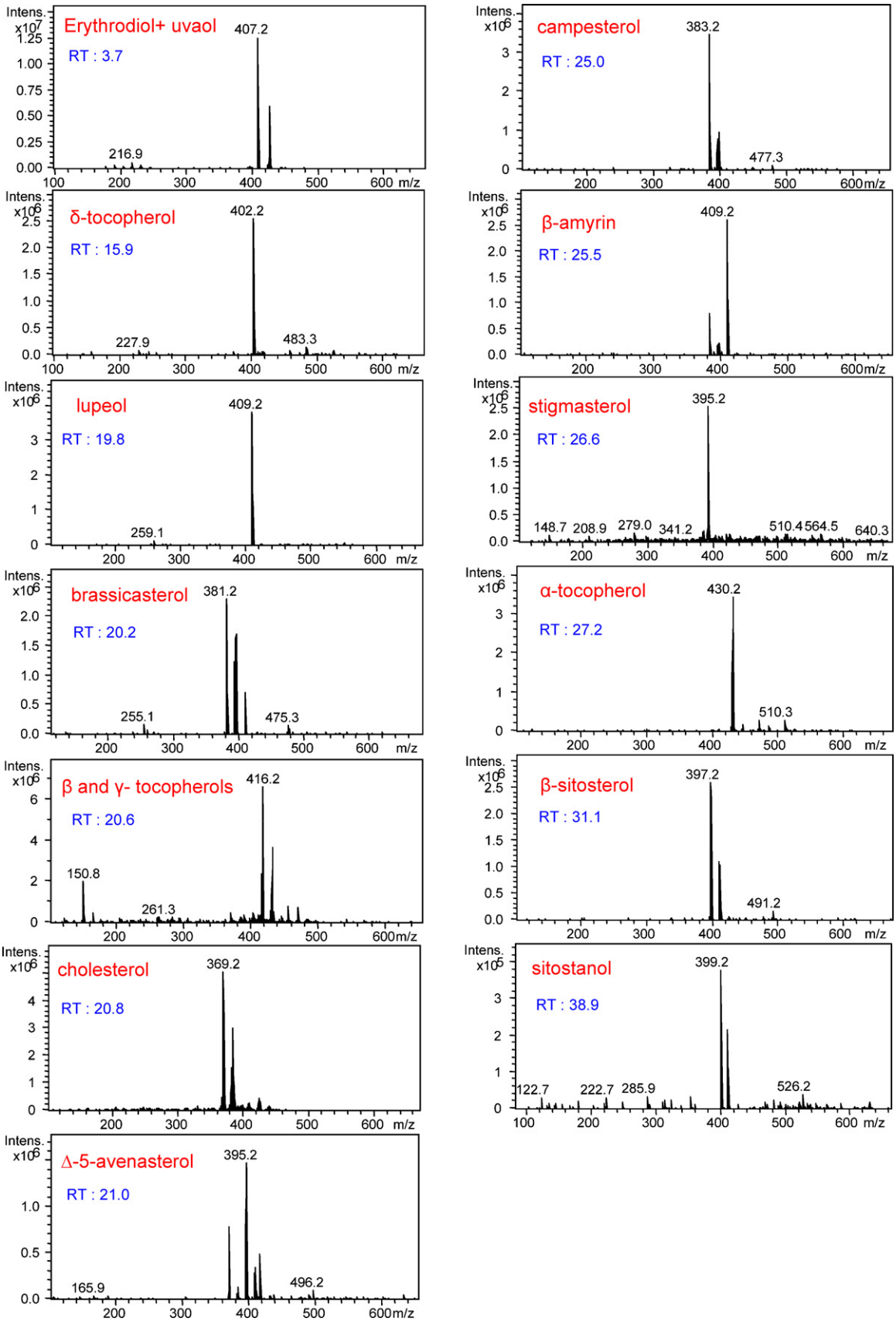


Fig. 3. APCI–IT MS spectra of sterols, tocopherols, erythrodiol and uvaol standards.

Table 1
Ions observed in the APCI mass spectra of sterols, tocopherols and triterpenic dialcohols in positive mode and their retention time.

Analytes	Molecular mass	$[M+H-H_2O]^+$	$[M+H-2H_2O]^+$	$[M]^{\bullet+}$	Retention time
Erythrodiol	442	425.2	407.2		3.7
Uvaol	442	425.2	407.2		3.7
δ-Tocopherol	402			402.2	15.9
Lupeol	426	409.2			19.8
Brassicasterol	398	381.2			20.2
β- and γ-Tocopherols	416			416.2	20.6
Cholesterol	386	369.2			20.8
(-5-Avenasterol	412	395.2			21.0
Campesterol	400	383.2			25.0
β-Amyrin	426	409.2			25.5
Stigmasterol	412	395.2			26.6
α-Tocopherol	430			430.2	27.2
β-Sitosterol	414	397.2			31.1
Sitostanol	416	399.2			38.9

We carried out MS/MS analyses. IT provides a better understanding of the fragmentation pathways, as is able to make MS^n experiments. The use of tandem mass spectrometry can assure the identity of the compounds under study improves the selectivity and therefore diminishes matrix interference which is always critical in food analysis. The MS^n product-ion spectra were produced by collision-induced dissociation (CID) of the main detected ion for all the analytes at their respective HPLC retention times.

4-desmethyl sterols share a common fragmentation pattern during tandem mass spectrometry. The statistically dominant breaking sites of the molecule are situated in the sterol ring system between the carbon atoms with numbers 11–12, 12–13, and 8–14 according to IUPAC nomenclature. For the asymmetric structure of the sterol carbon skeleton it is possible to identify the fragmentation points of the molecule as shown in Fig. 4, taking as example cholesterol (MS/MS spectra for all the 4-desmethyl sterols are not shown to contain the size of the paper). Two main fragments of the sterol molecule are formed: one with *m*/*z* 178 (or 178-H_2O) and one with *m*/*z* 95 or 81.

It is possible to assume the first step during the fragmentation process is disconnection of the aliphatic side chain and the sterol ring system which would result in two primary fragments with *m*/*z* 113 and 273. Because the conditions in the collision cell are rather rough further fragmentations occur. The incidence of these processes is so high that the side chain fragment and the main sterol fragment are hardly detectable. The side chain fragment appears to further break into very small parts that are below the detected mass range. It is the sterol ring fragment that causes the typical MS/MS spectra found.

MS/MS spectra of lupeol and β-amyrin obtained after ion trap collision induced dissociation of the precursor ion at *m*/*z* 409 showed at our scanning conditions similar and characteristic fragmentation patterns. Fragment ion peaks appeared at *m*/*z* 259.0, 270.9, 285.1, 313.1, 340.2, etc. (Fig. 4); although significant differences in relative intensities of fragment ions allow to distinguish between the two compounds easily.

The full-scan spectrum of tocopherols displays a predominant cluster of ions at *m*/*z* $[M]^{\bullet+}$, as commented before. When we carried out MS/MS experiments, we found as shown in Fig. 4 (considering α-tocopherol as example) one main fragment with *m*/*z* 164.8, which is attributed to the loss of the phytyl chain. The same fragmentation pattern was observed for the other tocopherols; for example the main fragment for γ- and β-tocopherol was *m*/*z* 150.8 (observing 190.8 as well); for δ-tocopherol was *m*/*z* 136.8 (observing 176.8 too). To distinguish between γ- and β-tocopherol we changed the fragmentation conditions and by using other weaker conditions (width 4; CutOff 115 and Ampl 0.65), we observed a peak in the mass spectra of γ-tocopherol which was not present in β-tocopherol (*m*/*z* 276.0).

MS/MS spectra of erythrodiol and uvaol obtained after ion trap collision induced dissociation of the precursor ions at *m*/*z* 425.2 and 407.2 showed, at our scanning conditions, the characteristic fragmentation patterns included in Fig. 4.

3.4. Analytical parameters

Calibrations curves were constructed with standard solutions containing all the commercially available analytes. There were obtained by plotting the standard concentration as a function of the peak area obtained from HPLC–APCI–IT MS analyses. In order to calculate the regression equations and LODs we considered the extracted ion chromatogram (EIC) of the most intense or base peak in the mass spectrum for each compound, although it is important to bear in mind that for carrying out the identification of these compounds in real samples, we should consider all the detected ion fragments in the MS spectra, as well as their relative abundance.

Each point of the calibration plot was repeated three times in an independent solution prepared in the same way. The obtained calibration curves showed acceptable linear response between peak areas and analytes concentrations, since the regression coefficients (r^2) were higher than 0.97 for all the compounds quantified. The results of lack-of-fit test (LOF) obtained in the calibration range were estimated. For all the reference compounds, the probability of the *F* test statistic (*p*) was greater than the alpha level of significance of 0.05 and linear regression models were thus adequate for the obtained data at a confidence level of 95%, as we have seen from Table 2. The parameters of the regression equations, LOD, LOQ and calibration range are summarized in the mentioned table.

The limits of detections (LOD, based on signal-to-noise ratio of 3) achieved using these experimental conditions were within the range from 0.12 and 1.05 mg/kg for sitostanol and δ-tocopherol, respectively.

Repeatability was assessed for each standard compound at two concentration levels (20 and 100 ppm). The two solutions containing all the analytes were prepared and analyzed on the same day (intraday precision, $n=6$) and on 3 consecutive days (interday precision, $n=18$). The relative standard deviations of peak areas and the relative standard deviations of migration times were determined for each analyte at the two mentioned concentrations. The intraday repeatability of the migration time (expressed as relative standard deviation) was 1.32% and 1.93% for 20 and 100 ppm, respectively, whereas the interday repeatability of the migration time was within 1.89% and 2.24% for 20 and 100 ppm, respectively. The intraday repeatability of the total peak area (expressed as relative standard deviation) was 4.75% and 5.23% for the 20 and 100 ppm, respectively, while the interday repeatability of the total peak area was 7.34% and 7.89% for 20 and

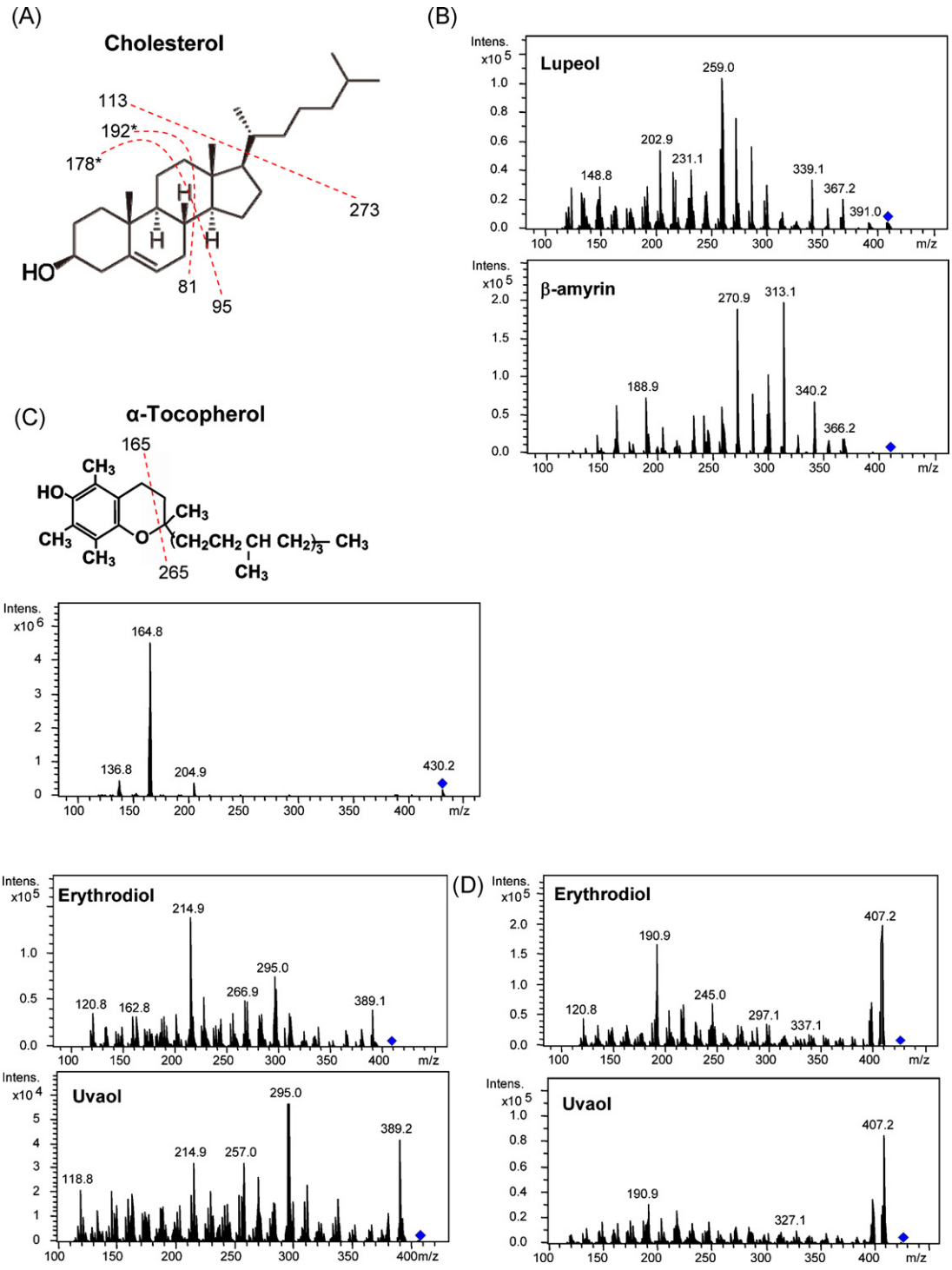


Fig. 4. MS/MS fragmentation patterns of the different families of compounds included in the current study ((A) 4-desmethyl sterols, (B) 4,4-dimethyl sterols, (C) tocopherols and (D) triterpenic dialcohols).

100 ppm, respectively. Although the interday precision was worse than the intraday precision, good overall repeatability was still obtained.

Concerning ionization suppression phenomena, the results obtained while a continuous flow of analyte solution (resulting in a constant but elevated baseline in MS detection) was continuously mixed with the eluate from an HPLC-separated blank sample did not show any drop in the baseline over the complete chromatographic run; that means the ion suppressions from co-eluting compounds were negligible.

3.5. Application and quantification to real samples

Using the described extraction protocol and the HPLC–APCI–MS method, we analyzed seven different oil samples (sunflower blended with soybean oil, corn oil, refined sunflower oil, olive oil, olive pomace oil, soy "plus omega 3" oil and walnut oil). Sample preparations of all oils were made as described in Section 3.1. The analyses were carried out under the optimum conditions described in Section 3.2 and compounds were identified by comparison of their retention times and mass spectra (MS

Table 2
Analytical parameters of the developed method for the analysis of sterols, tocopherols and triterpenic dialcohols.

Analytes	Detection limit (mg kg^{-1})	Quantitation limit (mg kg^{-1})	Calibration range (mg kg^{-1})	Calibration equations	r^2	F_{LOF}	p (α = 0.05)
Erythrodiol + uvaol	0.13	0.43	LOQ-200	$y = 3465494.15x + 20023091.71$	0.993	1.155	0.398
δ-Tocopherol	1.05	3.50	LOQ-200	$y = 2304882.41x + 49613335.23$	0.997	1.318	0.342
Lupeol	0.46	1.53	LOQ-200	$y = 1972748.062x + 117814952.42$	0.967	2.396	0.136
Brassicasterol	0.24	0.80	LOQ-200	$y = 1031316.36x + 492596.28$	0.997	0.888	0.513
β- and γ-Tocopherols	0.23	0.77	LOQ-200	$y = 12617515.14x - 33555806.01$	0.981	0.128	0.968
Cholesterol	0.31	1.03	LOQ-200	$y = 3350273.73x - 369104.67$	0.981	0.033	0.997
(-5-Avenasterol	0.33	1.10	LOQ-200	$y = 453881.29x + 34181761.92$	0.983	1.818	0.219
Campesterol	0.41	1.37	LOQ-200	$y = 533072.79x + 40492329.98$	0.985	0.617	0.663
β-Amyrin	1.03	3.43	LOQ-200	$y = 1572605.20x + 58190925.76$	0.981	1.334	0.337
Stigmasterol	1.01	3.37	LOQ-200	$y = 159908.01x + 24682944.08$	0.977	1.338	0.336
α-Tocopherol	0.59	1.97	LOQ-200	$y = 3578457.62x + 122518057.67$	0.967	0.008	1.000
β-Sitosterol	1.03	3.43	LOQ-2000	$y = 437936.53x + 62036519.49$	0.987	0.441	0.811
Sitostanol	0.12	0.77	LOQ-200	$y = 792922.14x - 195643.01$	0.967	3.489	0.062

and MS/MS) with those of standards. Peak identification was also done with spiked real samples at different concentration levels. For the identification of the other sterols that can be analyzed by the official GC-FID method but are not available as commercial standard, we took into account the analyses carried out by GC-FID on each of the oil samples in question. These results helped us to identify them in the samples analyzed by HPLC. In other words, when we use the official method (GC-FID), we know the sterols are eluted in the following order: cholesterol, brassicasterol, 24-methylene cholesterol, campesterol, campestanol, stigmasterol, Δ-7-campesterol, Δ-5,23-stigmastadienol, chlerosterol, β-sistosterol, sitostanol, Δ-5-avenasterol, Δ-5,24-stigmastadienol, Δ-7-stigmasterol, Δ-7-avenasterol. That means we can identify and quantify all the mentioned compounds by GC-FID. After doing that, we could use these results and the relative concentrations of the different compounds to iden-

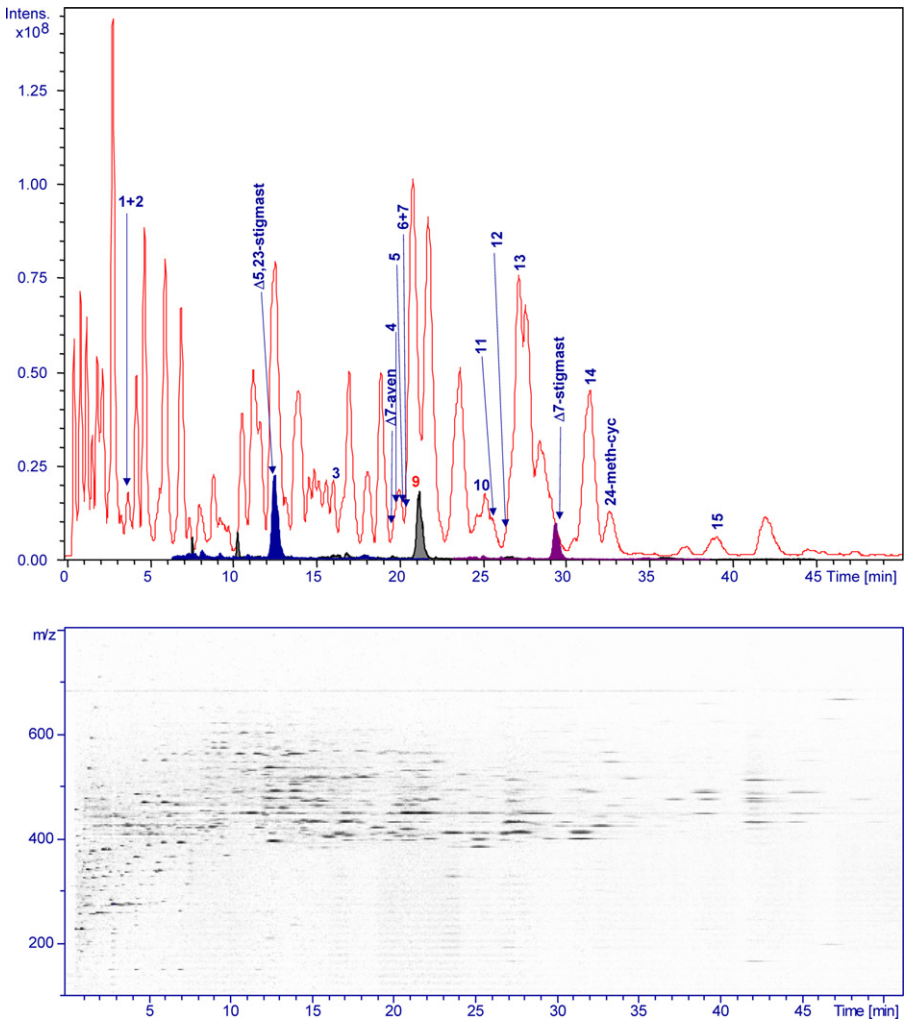


Fig. 5. BPC of sunflower blended with soybean oil identifying with numbers (as in Fig. 1) the compounds we had as standards. Some other compounds could be identified taking into consideration the GC data (using the official method) and their relative intensity. On the bottom of the figure, the 2D plot is shown to give to the reader an idea about the complexity of the sample analyzed and the potential of the method.

Table 3
Sterols, tocopherols and triterpenic dialcohols contents (mg kg^{-1}) of the different kinds of oils analyzed by HPLC–APCI–MS method.

Analytes	Different oils						
	Sunflower + soybean	Corn	Refined sunflower	Olive	Olive pomace	Soy "plus omega 3"	Walnut
Erythrodiol + uvaol	4.58	nd	3.52	15.65	420.08	0.55	nd
Lupeol	12.85	4.16	8.18	nd	nq	7.00	nd
Brassicasterol	nq	nd	nd	nd	nd	nq	nd
Cholesterol	nd	1.23	nd	nq	nd	1.71	nq
(-5-Avenasterol	54.98	359.74	46.02	124.58	22.68	26.03	212.15
Campesterol	111.86	386.62	35.05	18.66	11.65	90.48	84.07
β-Amyrin	9.22	nq	nq	5.19	8.61	10.28	nd
Stigmasterol	58.63	90.24	nq	nq	nq	43.61	nd
β-Sitosterol	1115.53	2004.54	542.50	707.19	1616.05	503.56	1628.48
Sitostanol	nq	4.28	nd	nq	nq	nq	nd
δ-Tocopherol	37.67	8.07	nd	nd	nd	132.97	25.89
β- and γ-Tocopherols	99.92	13.77	33.96	11.99	9.90	376.78	229.94
α-Tocopherol	329.33	129.40	454.50	199.41	190.77	94.66	78.70

nd: non detectable. nq: non quantifiable.

tify those analytes in the HPLC profiles when they will be present.

In Fig. 5, we can observe the BPC of the extract of sunflower blended with soybean oil analyzed at optima conditions. We were able to identify all the compounds we had as standards and also some more sterols based on the GC-FID data previously achieved. In the bottom of the figure, we include a bidimensional plot of the same analysis to try to show the great potential of the developed method, since can generate information about a high number of molecules.

Quantification of the analytes was carried out using the extracted ion chromatogram at 369, 381, 383, 395, 397, 399, 402, 407, 409, 416 and 430 *m*/*z*. δ-tocopherol, brassicasterol, cholesterol, (-5-avenasterol, campesterol, stigmasterol, α-tocopherol, β-sitosterol and sitostanol were quantified individually in mg/kg (Table 3), whilst erythrodiol and uvaol, β- and γ-tocopherols were quantified together because they appeared at the same time (with the same retention time) and provided the same *m*/*z* in MS. The chromatograms of seven samples of different oils are shown in Fig. 6. All the compounds were eluted within the retention time range between 3.7 and 39 min and with an ascending order of: erythrodiol and uvaol, δ-tocopherol, brassicasterol, β- and γ-tocopherols, cholesterol, Δ-5-avenasterol, campesterol, stigmasterol, α-tocopherol, β-sitosterol and sitostanol. The peak

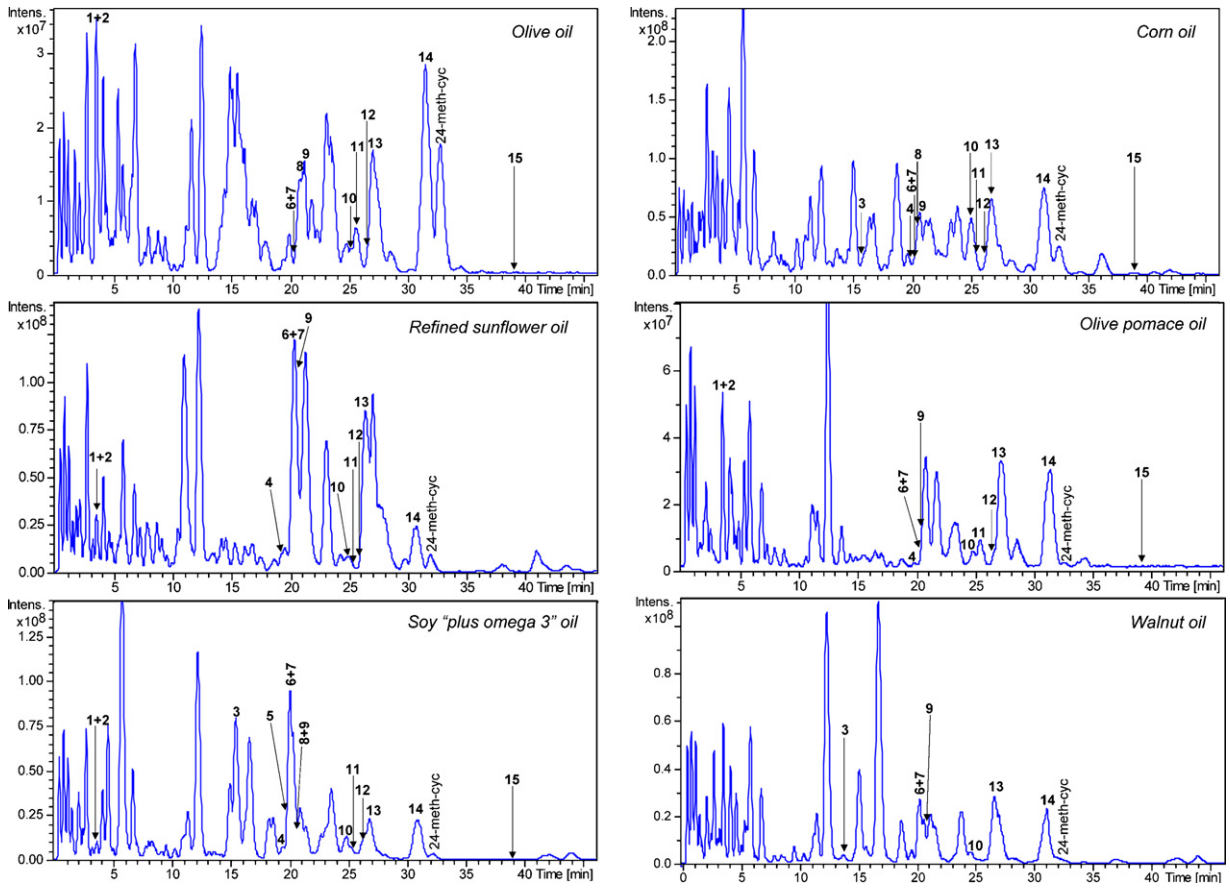


Fig. 6. BPCs of seven different kinds of oil samples (olive oil, corn oil, refined sunflower oil, olive pomace oil, soy "plus omega 3" oil and walnut oil). Peaks number as in Fig. 1. Note that we include in this figure only the most intense peaks detected; when the intensity of a peak was not remarkable, we did not add its identity in the profile.

which eluted directly after β-sitosterol is tentatively identified as 24-methylene cycloartanol based on MS data of the literature, the higher apolarity due to the additional methyl group in the molecular structure of this compound, and also with taking into account the huge quantity of this compound found in olive oils as reported by Azadmard and Dutta [37]. APCI fragmentation of this compound showed an intense fragment ion at m/z 423 $[M+H-H_2O]^+$. As seen in Table 3, β-sitosterol, (-5-avenasterol and campesterol are the predominant sterols in all the oils. Corn oil was distinguishable for its higher level of sitostanol in comparison the other oils. Concerning tocopherols compounds, a huge quantity of δ-tocopherol was recorded in soy "plus omega 3" oil. Erythrodiol and uvaol, as belong to triterpenic dialcohols family, were not detected only in corn and walnut oils.

4. Conclusions

In the present paper we report a rapid and effective HPLC–APCI–IT MS procedure to carry out a quantitative muticomponent analysis (sterols, tocopherols and triterpenic dialcohols) in vegetable oils. One of the main advantages of this new HPLC–MS method is its ability to simultaneously detect and quantify a great number compounds belong to three families of the unsaponifiable fraction of oils, taking into account the simplicity and the cheaper process of sample preparation. This new analytical method proved to be suitable for the sensitive quantitation of 15 compounds present in oil samples extracts and has the potential to identify 23 analytes. Furthermore, this study confirms that the liquid chromatography method coupled to APCI–IT MS can be applied in the direct analysis of lipophilic compounds such as sterols, which are typically processed and derivatized prior to gas chromatographic analysis.

The information that the analyst gets after applying this method is quite abundant and we will consider as future direction the identification of as many compounds as possible in the profiles by using MS^n data.

References

[1] D. Boskou, Olive Oil: Chemistry and Technology, AOCS Press, Champaign, IL (USA), 1996, pp. 52–83.
[2] M.D. Patel, P.D. Thompson, Atherosclerosis 186 (2006) 12.
[3] P.J.D. Bouic, Drug Disc., Today 7 (2002) 775.
[4] C.C. Zhao, J.H. Shao, X. Li, J. Xu, P. Zhang, Arch. Pharmacal Res. 28 (2005) 1147.
[5] S.J. Van Rensburg, W.M. Daniels, J.M. Van Zyl, J.J. Taljaard, Metab. Brain Dis. 15 (2000) 257.
[6] A.B. Awad, A. Downie, C.S. Fink, U. Kim, Anticancer Res. 20 (2000) 821.
[7] F.B. Gregg, U.S. Patent 6, 319, 524 (2001).
[8] P. Laakso, Eur. J. Lipid Sci. Technol. 107 (2005) 402.
[9] M.J. Lagarda, G. GarcaLlatas, R. Farre, J. Pharm. Biomed. Anal. 41 (2006) 1486.
[10] P.C. Dutta, L. Normén, J. Chromatogr. A 816 (1998) 177.
[11] J. Toivo, K. Phillips, A.M. Lampi, V. Piironen, J. Food Compos. Anal. 14 (2001) 631.
[12] G. Lercker, M.T. Rodriguez-Estrada, J. Chromatogr. A 881 (2000) 105.
[13] Codex Alimentarius Commission Fats, Oils and Derivatives, vol. 8, Joint FAO/WHO Food Standards Program, Rome, 1993, pp 41–46.
[14] COI/T.15/NC no. 2/Rev. 9, Trade Standard Applying to Olive Oil and Olive-Pomace Oil, International Olive Oil Council, Madrid, Spain (10 June 1999).
[15] S.L. Abidi, J. Chromatogr. A 935 (2001) 173.
[16] R. Rozenberg, N.L. Ruibal-Mendieta, G. Petitjean, P. Cani, D.L. Delacroix, N.M. Delzenne, M. Meurens, J. Quetin-Leclercq, J.L. Habib-Jiwan, J. Cereal Sci. 38 (2003) 189.
[17] M. Careri, L. Elviri, A. Mangia, J. Chromatogr. A 935 (2001) 249.
[18] J. Headley, K. Peru, B. Verna, R. Roberts, J. Chromatogr. A 958 (2002) 149.
[19] E. Razzazi-Fazeli, S. Kleineisen, W. Luf, J. Chromatogr. A 896 (2000) 149.
[20] M.J. Lerma-García, G. Ramis-Ramos, J. Guillermo, M. Herrero-Martínez, E.F. Simó-Alfonso, Rapad Commun. Mass Spectrom. 22 (2008) 973.
[21] S.L. Abidi, J. Chromatogr. A 881 (2000) 197.
[22] J.C. Bada, M.L. Camacho, M. Prieto, L. Alonso, Eur. J. Lipid Sci. Technol. 106 (2004) 294.
[23] F.J. Ruperez, D. Martín, E. Herrera, C. Barbas, J. Chromatogr. A 935 (2001) 45.
[24] B. Rodas, S. Morema, A.I. Castellote, M.C. López Sabater, J. Chromatogr. A 1018 (2003) 197.
[25] F.J. Ruperez, C. Barbas, M. Castro, E. Herrera, J. Chromatogr. A 839 (1999) 93.
[26] L.A. Curie, Pure Appl. Chem. 67 (1995) 1699.
[27] M.D. Nelson, J.W. Dolan, LCGC Eur. 15 (2002) 73.
[28] J. Toivo, A.M. Lampi, S. Aalto, V. Piironen, Food Chem. 68 (2000) 239.
[29] R.G. Dyer, C.S. Hetherington, K.G.M.M. Alberti, M.F. Laker, J. Chromatogr. B 663 (1995) 1.
[30] A.J. King, P. Paniangvait, A.D. Jones, J.B. German, J. Food Sci. 63 (1998) 382.
[31] B. Cañabate-Díaz, A. Segura-Carretero, A. Fernández-Gutiérrez, A. Belmonte Vega, A. Garrido Frenich, J.L. Martínez Vidal, J. Duran Martos, Food Chem. 102 (2007) 593.
[32] M. Du, D.U. Ahn, J. Food Sci. 67 (2002) 1696.
[33] J.L. Martinez-Vidal, A. Garrido-Frenich, M.A. Escobar-Garcia, R. Romero-Gonzalez, Chromatographia 65 (2007) 695.
[34] E. Razzazi-Fazeli, S. Kleineisen, W. Luf, J. Chromatogr. A 896 (2000) 321.
[35] G.J. Van Berkel, J.M. Quirke, R.A. Tigani, A.S. Dilley, T.R. Covey, Anal. Chem. 70 (1998) 1544.
[36] C. Lauridesen, S.W. Leonard, D.A. Griffin, T. McLure, D. Liebler, M.G. Traber, Anal. Biochem. 289 (2001) 89.
[37] S. Azadmard-Damirchi, P.C. Dutta, J. Chromatogr. A 1108 (2006) 183.

Talanta 80 (2009) 935–941

Contents lists available at ScienceDirect

Talanta

journal homepage: www.elsevier.com/locate/talanta

N-way modelling of sediment monitoring data from Mar Menor lagoon, Spain

Stefan Tsakovski[a], Błażej Kudłak[b,*], Vasil Simeonov[c], Lidia Wolska[b,f], Gregorio Garcia[d], Manos Dassenakis[e], Jacek Namieśnik[b]

[a] *Department of Physical Chemistry, Faculty of Chemistry, University of Sofia "St. Kl. Okhridski", 1, J. Bourchier Blvd., 1164 Sofia, Bulgaria*
[b] *Department of Analytical Chemistry, Chemical Faculty, Gdansk University of Technology, 11/12 Naturowicza, 80-233 Gdansk, Poland*
[c] *Department of Analytical Chemistry, Faculty of Chemistry, University of Sofia "St. Kl. Okhridski", 1, J. Bourchier Blvd., 1164 Sofia, Bulgaria*
[d] *Soil Science and Agriculture Chemistry Unit, Agriculture Science and Technology Department, Technical University of Cartagena (UPCT), Paseo de Alfonso XIII, 48, 30203 Cartagena, Spain*
[e] *University of Athens, Department of Chemistry, Laboratory of Environmental Chemistry, Panepistimiopolis, 15771 Athens, Greece*
[f] *Medical University of Gdańsk, Inter-Faculty Institute of Maritime and Tropical Medicine, Department of Environmental Toxicology, Powstania Styczniowego Str. 9b, 81-519 Gdynia, Poland*

ARTICLE INFO

Article history:
Received 2 April 2009
Received in revised form 11 August 2009
Accepted 17 August 2009
Available online 22 August 2009

Keywords:
Heavy metals
Sediments
Mar Menor coastal lagoon
Pollution fate
Environmental modelling
Tucker3 model

ABSTRACT

The present paper deals with the application of Tucker3 modelling to a sediment monitoring data set from the area of Mar Menor coastal lagoon (Spain). The aim of the study is to model and interpret the fractionation of heavy metals in the suspended particulate matter and sediment fractions resulting by sedimentation processes. Since the lagoon is seriously influenced by anthropogenic activities the modelling aims an assessment of the environmental hazard, too. After application of various scaling and centering procedures and estimation of the model dimensionality, an optimal (3, 3, 3) Tucker3 model was chosen for data interpretation. Using the model output (factor loadings connected to the four main core elements) it could be concluded that the heavy metal concentrations in the suspended particulate matter and sediment fractions increase in order Cu > Mn > Zn ≈ Pb > Cd and could be examined as estimation of basic levels for all heavy metals caused by different sedimentation processes. The second important core element summarizes the anthropogenic influence of the mining activity in the region. The third important core element shows the different mobility of the heavy metals. The fourth important core element should be related to the specific sediment formation at one of the sampling location.
© 2009 Elsevier B.V. All rights reserved.

1. Introduction

The Sierra of Cartagena-La Unión (Murcia, South-East Spain) has been subjected to mining for more than 2500 years. Regarding this, although all mining activities ceased in 1991, the opencast mining practised in this area in the second half of the 20th century has resulted in a highly altered and degraded landscape. As a result of it, huge amounts of wastes are present in the mining district Cartagena-La Unión (Murcia, South-East Spain). These mining wastes from the Sierra de Cartagena have been acting for centuries as a source of heavy metal pollution for all the surrounding areas. Therefore, these activities that have been developed historically in the mountains in the south basin of the Mar Menor coastal lagoon have caused the metal pollution of the marine sediments of this small sea.

Mar Menor is the largest lagoon of the Spanish Mediterranean coast with a high ecological, fishing and tourism value. Furthermore, it has been included in several international conservation agreements, like the Ramsar List of Wetlands of International Importance, Specially Protected Area under the EU Wild Birds Directive (SPA), Site of Community Importance (SCI) to be integrated in the Nature 2000 Network (EU Habitats Directive), and besides is a Special Protected Area of Mediterranean Interest (SPAMI). Although during the last three decades has been an increase in the inputs into the lagoon as a consequence of changes in agricultural practices [20], there is a remarkable lack of knowledge concerning the influence of metal inputs coming from the close mining areas [21]. Any case, the lagoon ecosystem is being affected to a degree that depends on the phase in which the metals are carried, since the bioavailability and toxicity of the metals are influenced by the distribution of trace metals in particulate, sediments or dissolved phases [21].

Learning about the phenomena occurring in the environment (especially in sea ecosystems which are multiphase ones) requires applying numerous tools including intelligent data mining at the last stages of data interpretation.

Scientists and policy makers are interested in pollutants environmental fate, transport, accumulation in different fractions and

* Corresponding author. Tel.: +48 58 3471356.
E-mail address: blaizek@gmail.com (B. Kudłak).

0039-9140/$ – see front matter © 2009 Elsevier B.V. All rights reserved.
doi:10.1016/j.talanta.2009.08.015

compartments in order to learn about routes and remediation strategies for specific distribution of pollutants of interest. Recently, some efforts have been made to interpret sequential extraction procedures for sediment monitoring data by the use of chemometrics [1,2]. Additional studies have been performed to examine the relationship between the distributions of elements in different compartments of a river catchment [3] and to predict the concentration of elements in river sediments from monitoring data [4]. Both studies use the PLS multiway models. No studies have been detected for advanced data treatment aiming to understand the fractionation due to sedimentation processes.

The aim of the present study is to model and interpret the fractionation of heavy metals in suspended particulate matter and sediment fractions resulting by sedimentation processes in Mar Menor coastal lagoon, South-East Spain. Since the lagoon is seriously influenced by anthropogenic activities, the modelling also aims an assessment of the environmental hazard.

2. Materials and methods

2.1. Study area

Mar Menor coastal lagoon is placed in the SE of the Iberian Peninsula, Spain. This ecosystem is one of the largest coastal lagoons of the Mediterranean (135 km^2 area, average depth 4 m, maximum 6.5 m), that is isolated from the Mediterranean Sea by a 24 km long sandy bar called "La Manga", that is crossed by five channels. La Manga is limited by "Cabo de Palos" to the South and "Punta del Mojón", to the North, with a width that oscillates between 900 and 100 m. It was formed over volcanic blooming and miocenic chalconsandstone. Through these channels there is an active water exchange that makes that the average water residence time being 0.79 years [22]. The lagoon is hyperhaline, with salinity levels (42–47 g/l) greater than the adjacent Mediterranean Sea because of low precipitation (around 300 mm per year) and high evaporation rates (mean annual temperature 18 °C).

From the geological origin of the Menor Sea, sediments from the watercourses flowing into the lagoon have filled it. However, in the last centuries deforestation, mining activities, agricultural practices and other human activities have accelerated the fill up [5].

Although there are no permanent superficial watercourses in the area, several ephemeral watercourses called "*ramblas*" of wide beds and planes form a surface hydrologic system that flow into the Mar Menor. These *ramblas* carry water from the rain during the episodes of torrential storms and some of their beds disappear before arriving to the lagoon. In the last decades, the flows of some *ramblas* have been increased due to the contributions of waters coming from the surpluses of the irrigated zones [6], in some cases loaded with fertilizers and pesticides, what could generate some environmental problems.

Since the lagoon is hyper saline during the whole year, it is unlikely to observe seasonal fluctuations of metal fractionation in sediments, at least concerning a time period of 1 year, as the sampling took place.

The expansion of intensive agriculture is linked to an increase in the use of water and fertilizers. The modern irrigation systems are designed to optimise water and nutrients inputs into the soils. However, the necessity to increase production according to social–economical causes, sometimes lead to large water and fertilizer applications. The latter can create a surplus of water enriched in nutrients that could generate some environmental problems. For these reasons, several technical solutions are being considered. One of this is the desalinisation plants.

In the mining areas, the soils of these places are strongly altered by human activity for over a thousand of years. Both the mining industry already initiated in times of the Phoenicians and continued until our days, and the intensive agriculture and, more recently, the industrial activities have exercised a strong disturbance of the natural soils of this zone that have been replaced in important proportions by soils derived from the human action.

Along mining area it can be found the remains of the mining exploitations: wells, dumps, sterile pools, opencast extractions, etc. The strong slopes and the scanty but intense rains typical of the Mediterranean climate have provoked an intense erosion of the soils which thinner materials have been dragged up to places very remote from its origin across the temporary riverbeds (*rambla*): Ramblas of Beal, Albujón, etc. Thus, sediments with heavy metals (Pb and Zn especially, but also Cu, Cd, Mn, etc.) high content are distributed by wide zones and even coming to the sea, both the Mediterranean Sea and the Mar Menor. Occasionally, as result of the uncontrolled exploitation of the mining resources and the spillage of enormous quantities of sterile to the sea, the depth of some marine zones has decreased. This process has driven to the filling and landfill of natural marine spaces as Portman Bay, whose recovery waiting a suitable plan. There are numerous mining wastes placed in southern part of the lagoon that have been dragged into the Mar Menor by temporary streams (*wadis*) through more than 2000 years.

2.2. Experimental

2.2.1. Sampling stations

The sampling work took place during May 2007 and included tracing points of interest concerning or affecting pollution conditions in the area (from farmlands or from a mining area). For this reason, in order to create a complete picture about the pollution in Mar Menor up to 10 different sampling points have been distributed among the three main seawater flows that seems to be in this coastal lagoon (Fig. 1). In this way, there are 10 sampling points, 9 inside the lagoon and 1 outside (Fig. 2). From each sampling 1l water samples and 1 surface sediment sample were collected (with a grab). *In situ* measurements of abiotic parameters in surface and

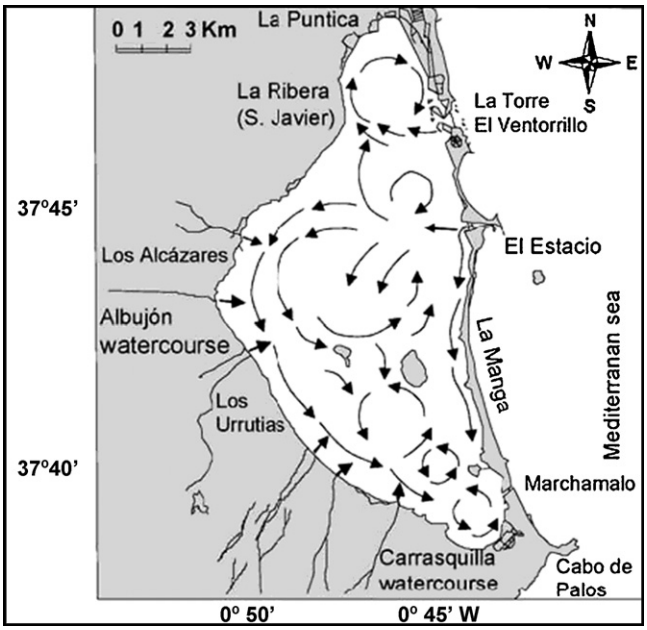


Fig. 1. Mar Menor lagoon seawater dynamics according to Perez-Ruzafa [22]. Water inputs from the Mediterranean sea and from inland by Rambla de Miranda, Rambla del Albujón and Rambla de los Alcázares (west part of the coastal lagoon), Rambla del Beal, Rambla de Ponce and Rambla de la Carrasquilla (south part of the coastal lagoon). Seawater flows inside the Mar Menor.



Fig. 2. Sampling stations in Mar Manor coastal lagoon.

subsurface waters and sampling of water and sediment cores also took place.

2.3. Chemical analysis

The chemical analysis aimed at estimating concentration levels of metals in the water column (total, dissolved and suspended) and in the sediments.

The water samples were filtered by Millipore nitrocellulose filters. Dissolved metals were preconcentrated with the resin Chelex 100 and measured with FAAS and GFAAS (flame and graphite furnace atomic absorption spectrometry). Suspended metals were determined by GFAAS and FAAS after digestion of the filters with concentrated nitric acid [7].

The sediment samples were wet sieved and dried. Not lattice held metals were extracted with dilute hydrochloric acid and total metals with condensed nitric and hydrofluoric acid. The acid extracts were analyzed for trace metals with FAAS [8].

2.4. Statistical analysis

A three-way modelling was chosen as a modelling technique since it directly takes into account the three-way structure of the data, allowing correct and easier interpretation of the results. In this study, a three-way factor analysis using Tucker3 model was applied to a three-dimensional data set, which represents concentrations of 5 heavy metals (Zn, Cu, Mn, Pb, Cd), measured at 10 sampling locations, for 5 different heavy metal distributions in water, 2 suspended particulate fractions and 2 sediment fractions (DISS, PM 0.45, PM 8, SED < 63, SED > 63). The dimensions of the three ways (i.e., the heavy metals, the sampling locations, the heavy metal distributions) are 5, 10 and 5, respectively, for a total of 250 results. The measurements below the respective heavy metal limit of detection (LOD) were replaced by the half of detection limit value – LOD/2. This simple substitution method is used as the detection frequency is higher than 90% [9]. In this way the major statistical parameters of the data set (means, standard deviations) are practically unaffected.

Two pre-processing procedures were tested to the three-way data structure. The first procedure includes scaling within and centering across the first mode (heavy metals) while the second one includes only scaling within the first mode. The first procedure was recommended as an appropriate way for removing the difference among variables arising from their different variations and magnitude, while retaining the differences within the other two modes (sampling locations and heavy metal distribution in the different phases) [10]. Preserving of the data structure is the reason for excluding of centering from the second procedure [11]. Here, only the results for scaling within the first mode are presented. The Tucker3 models obtained after implementation of both preprocessing procedures are discussed farther in Section 3.

Table 1
Convex hull method results for Tucker3 models obtained from scaling within first mode data array.

Model	Sum of components	Explained variance (%)	st-value
(2, 1, 2)	5	79.70	1.40
(3, 3, 3)	9	94.13	2.04
(4, 3, 3)	10	95.90	1.30
(4, 4, 3)	11	97.26	2.94

The Tucker3 model decomposes the three-way data array X (I, J, K) into three loading matrices, **A** ($I \times P$), **B** ($J \times Q$), **C** ($K \times R$) and a core matrix as indicated bellow:

$$X_{ijk} = \sum_{p=1}^{P}\sum_{q=1}^{Q}\sum_{r=1}^{R} a_{ip} b_{jq} c_{kr} g_{pqr} + e_{ijk}$$

where a_{ip}, b_{jq}, and c_{kr} are the elements of the loadings matrices **A**, **B** and **C**; g_{pqr} denotes the element (p, q, r) of the core array **G** ($P \times Q \times R$), and e_{ijk} denotes the error term for element x_{ijk} and is an element of the error matrix **E** ($I \times J \times K$). The number of factors extracted from modes A, B and C are P, Q and R, respectively. The squared element of (g^2_{pqr}) of the core array reflects the variance explained by the interaction between the three modes (A, B, C). More detailed descriptions of Tucker3 model could be found elsewhere [12–15].

Selection of the optimal model was done by numerical convex-hull method proposed by Ceulemans and Kiers [16]. Instead of free parameters estimation used in the original work [16], the sum of the components in each mode was accepted since only Tucker3 models were investigated in the present study. In addition, instead of term "goodness-of-fit", in the present study the expression "explained variation" was adopted since it is more widespread in multi way applications in chemistry.

3. Results and discussion

The first step in Tucker3 analysis is the estimation of the model dimensionality. All possible Tucker3 models with different number of components in each mode ($P = 1, \ldots, 4$; $Q = 1, \ldots, 4$; $R = 1, \ldots, 4$) were evaluated. All the solutions for each complexity ($P + Q + R$) were sorted according to the explained data variance. The six models lying on the upper convex hull boundary are shown in Fig. 4. Following strictly the convex-hull method the model (4, 4, 3) with the highest st-value should be selected (Table 1). However, the more relaxed way of modelling [16] suggests that not only the model with the highest st-value but also the models with high enough (not maximal) st-values could be considered as important alternative models. Some substantive considerations concerning interpretability of the model should also be taken into account. From the st-values presented in Table 1 one could see that the models (3, 3, 3) and (4, 4, 3) have high st-values. The explained variance difference between two models is only 3.13%. The increasing of components in the first mode seems to be not so important since the model (4, 3, 3) has the lowest st-value. On the other side, the increasing of the components in the second mode (sampling locations) does not correspond to the sampling plan (Fig. 1) where the sampling stations are arranged in three groups along north–south

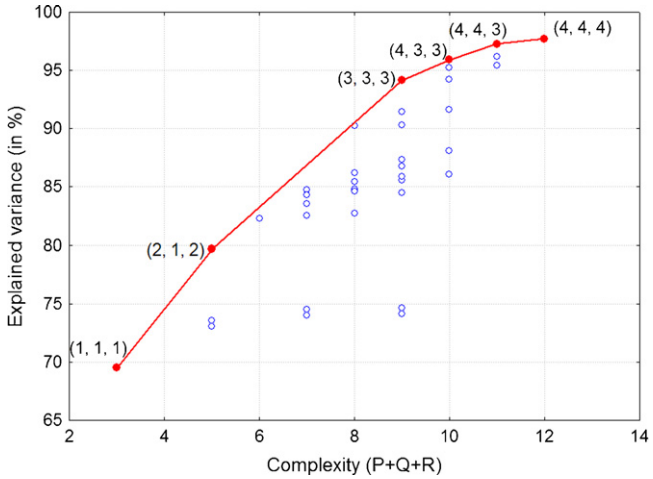


Fig. 3. Higher boundary of the convex hull graph.

direction. Thus, the model (3, 3, 3) was chosen as more interpretative for the investigated data array (Fig. 3).

The same convex hull method selection was performed for Tucker3 models obtained from scaling within and centering across first mode data array. The similar results were obtained and again the model (3, 3, 3) was chosen as more appropriate for further consideration. Comparison between the two (3, 3, 3) models obtained by different pre-processing procedures is shown in Table 2.

The explained variance for both models is quite good for an environmental data set possessing inherent variation caused by different natural and anthropogenic factors [10,17]. However, the core structure of the model obtained from scaling within first mode data array is simpler with smaller number of core elements representing significant interactions. Thus, the Tucker3 model obtained from scaling only pre-processed data was taken for further interpretation.

Two rotation procedures to selected core array (3, 3, 3), related to optimal diagonality and maximizing variance of squares, were performed. In both cases the reduction of the number of significant core elements was not achieved. That is why the unrotated core array will be discussed farther. The goodness of fit and stability of the selected Tucker3 model (3, 3, 3) was assessed employing the split-half method [2]. A mean difference of *1.37* among the elements of two cores suggested that the selected Tucker3 model is sufficiently stable.

The possible explanation for such a relatively "complex" core array could be found in the nature of sediment formation, which is affected by many natural and anthropogenic processes. The four of the most important core elements explaining 86.96% of the core variance and 81.86% of the data variance will be taken into consideration (Table 3).

In Fig. 4, the loading plots connected with the four main core elements are presented. These plots reveal similarities and dissimilarities between the elements in each mode. The similar loadings values of Zn and Pb separate them from the other heavy metals (Fig. 4a and b). This fact could be easily explained with the mining activity in the region, being the main emitter of these heavy metals [18] well documented since Phoenicians and Cartagenian times. The first mode loadings of Cd reflect the different behaviour of this element, which is indicated by the high positive A2 and A3 loadings. Probably, the reason for this particular situation could be found in the specific processes controlling the sedimentation of Cd. All sampling stations have negative loadings for the first factor in the second mode (Fig. 4c). The positive high loading of locations 4 for B2 is an indication for particular sediment formation at this site. All factor loading plots of the third mode (Fig. 4d and e) show that the dissolved and suspended particulate matter fraction below 0.45 μm distributions of the heavy metals posses loadings close to 0 and prove the uniform distribution of the heavy metals fractionalization for all sampling locations. These plots also reveal that the formation of both sediment fractions (higher and lower than 63 μm) is controlled by different processes.

Table 2
Explained variance and explained core variance by four main core elements.

Preprocessing	Explained variance (in %)	Explained core variance by first four core elements (in %)
Scaling and centering	89.57	75.97
Scaling	94.13	86.96

Table 3
Four most important core elements of a Tucker3 model of complexity (3, 3, 3).

Core element	Explained core variance (in %)	Core element value
(1, 1, 1)	73.58%	15.55
(2, 1, 2)	7.85%	−5.08
(3, 1, 3)	3.02%	−3.15
(1, 2, 2)	2.51%	−2.88

The detailed explanation of the loading plots and the relationships between the modes could be performed if they are interpreted parallel to the most important elements of core array [12,19].

The most prominent core element (1, 1, 1) explains 73.58% of the core variation and reflects the interaction between the first factors in each node (A1, B1, C1). Taking into account the positive loadings of all heavy metals along A1 (+), negative loadings of all sampling stations along B1 (−), negative loadings of all heavy metals distributions along C1 (−) and the sign of g_{111} (−), one can find that the sign of the product is "+". Thus, the heavy metal concentrations in the suspended particulate matter and sediment fractions increase in order Cu > Mn > Zn ≈ Pb > Cd. This sequence is observed for all sampling locations, most seriously pronounced for sampling locations 4 and 5, and for sediment fraction below 63 μm. This interaction represents the main order of concentrations of heavy metals in all fractions and could be examined as estimation of basic levels for all heavy metals caused by different sedimentation processes.

The second important core element (2, 1, 2) explains 7.85% of the core variation. It summarizes the interaction between the second factor in first mode (A2), the first factor in the second mode (B1) and the second factor in the third mode (C2). The negative loadings of Zn and Pb along A2 (−), the negative loadings of all sampling stations along B1 (−), the negative loading of SED < 63 along C2 (−), and the sign of respective core element (−) give a positive product. This interaction accounts for the anthropogenic influence of the mining activity in the region as was discussed above and is related to the accumulation of Zn and Pb in the sediment fraction below 63 μm. Another evidence supporting this hypothesis is the southern disposition of the most affected sampling sites 4 and 5 where the mining wastes are reaching the lagoon Mar Menor by Rambla del Beal, Rambla de Ponce and Rambla de la Carrasquilla. It is important to perform one more calculation for this core element related to Cd and Cu. The positive loadings of Cd and Cu along A2 (+), the negative loadings of all sampling stations along B1 (−), the positive loadings of SED > 63 and PM 8 along C2 (+), and the sign of g_{212} (−) give also a positive product, which is an evidence for the accumulation of Cd and Cu in the suspended particulate matter below 8 μm and coarse sediment fraction. The reason for this accumulation could be found in the agricultural activity in the region since the presence of Cu and Cd in some fertilizers is a well

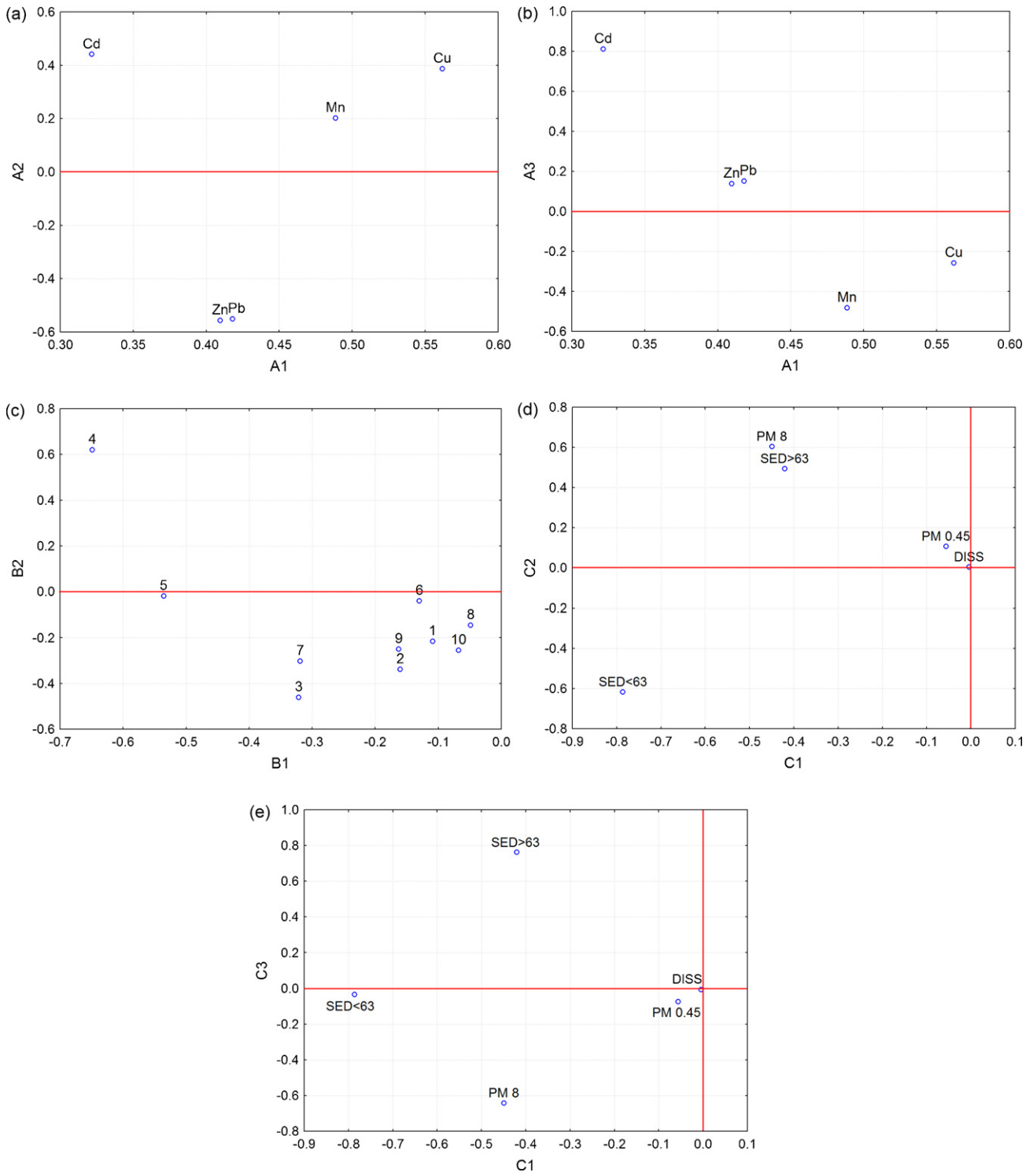


Fig. 4. Loading plots of the Tucker3 (3, 3, 3) model: (a) projection of heavy metals according to A1 and A2; (b) projection of heavy metals according to A1 and A3; (c) projection of sampling locations according to B1 and B2; (d) projection of heavy metal distributions according to C1 and C2; (e) projection of heavy metal distributions according to C1 and C3.

known fact and supports the farming impact, while Cd seems to be more related to mining activities due to the presence of this metal associated to sphalerite ores. It means that the second important core element has anthropogenic origin and represents mining and agricultural pollution influences on the heavy metal distributions.

The third important core element (3, 1, 3) explains 3.02% of the core variation. It shows the interaction between the third factor in the first mode (A3), the first factor in the second mode (B1) and the third factor in the third mode (C3). The interpretation of this core element should be related to the different mobility of heavy metals. The positive loadings of Cd, Pb and Zn along A3 (+), the negative loadings of all sampling locations along B1 (−), the negative loading of PM 8 along C3 (−) and the sign of the respective core element (−) give a positive product, which gives an explanation for the higher concentration of Cd, Pb and Zn in the suspended particulate matter fraction below 8 μm. This accumulation is more pronounced for Cd than for Pb and Zn. If one substitutes in the previous calculation the loadings of Cd, Pb and Zn with the loadings of Mn and Cu and the

loading of PM 8 with the loading of SED > 63, again positive product will be derived. The second calculation represents the accumulation of Mn and Cu in the coarse sediment fraction. It seems that this interaction represents redistribution processes in water column and sediment fractions. The more mobile heavy metals like Cd, Pb and Zn are accumulated in suspended particulate matter fraction below 8 μm while less mobile like Mn and Cu are accumulated in coarse sediment fraction.

The fourth important core element (1, 2, 2) explains 2.52% of the core variation. It reflects the interaction between the first factor in the first mode (A1), the second factor in the second mode (B2) and the second factor in the third mode (C2). The interpretation of this core element despite the low level of explanation of the core variance is important since it is related to the specific position of sampling location 4. The positive loadings of all heavy metals along A1 (+), the positive loading of the sampling location 4 along B2 (+), the negative loading of SED < 63 along C2 (−) and the sign of g_{122} (−) produce a positive product, which corresponds to increased concentrations of all heavy metals in the sediment fraction below 63 μm. This accumulation in the fine sediment fraction at sampling location 4 could be explained by its location in the southern mining affecting part of the lagoon. It seems that when mining wastes carried by the southern inlets and water flows in the lagoon reach sampling location 4 the initial accumulation in sediment fraction below 63 μm is observed.

Obviously, the first factor in sampling locations mode (B1) is involved in interactions related to the three most important core elements: g_{111}, g_{212} and g_{313}. These three core elements explain 84.45% of the core variation and 79.49% of the whole data set variation. The interactions represent the general heavy metal distributions for all sampling sites and reasons for its formation – anthropogenic influences and redistribution processes. In this sense B1 loadings could be taken as an indicator of the environmental risk for heavy metal distributions in the suspended particulate matter and the sediment fractions of lagoon Mar Menor. The potential environmental impact of the different sampling locations decreases with increasing of their negative B1 loadings in the order 4 > 5 > 3 ≈ 7 > 9 ≈ 2 > 6 > 1 > 10 > 8. The environmental hazard ranking of the sampling locations and the contour plot of B1 loadings as a function of the UTM coordinates (Fig. 5) shows that one region with the highest potential environmental hazard can be observed in south-eastern part of the lagoon. This fact is mainly connected with mining wastes reaching this part of Mar Menor coastal lagoon.

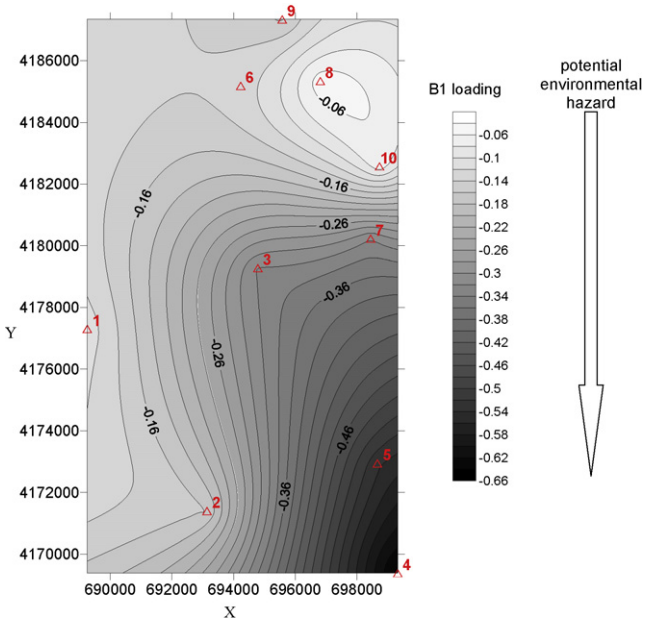


Fig. 5. Environmental hazard ranking of the sampling locations and the contour plot of B1 loadings as a function of the UTM coordinates.

4. Conclusions

The sediment monitoring data interpretation using multivariate statistics (Tucker3 modelling) has revealed some specific patterns of the fractionation of heavy metals in the suspended particulate matter and sediment fractions resulting by sedimentation processes as follows:

- Specific distribution of Cd as compared to the distribution of all other heavy metals in the sediment fractions.
- Increase of the heavy metal concentrations in the suspended particulate matter and sediment fractions in the following order: Cu > Mn > Zn ≈ Pb > Cd for all sampling locations, most seriously pronounced for sampling locations 4 and 5, and for sediment fraction below 63 μm; this could be accepted as an estimation of the basic levels for all heavy metals caused by different sedimentation processes.
- Assessing the anthropogenic influence of the mining activity in the region and relating it to the accumulation of Zn and Pb in the sediment fraction below 63 μm.
- The more mobile heavy metals like Cd, Pb and Zn are accumulated in the suspended particulate matter fraction below 8 μm while less mobile like Mn and Cu are accumulated in the coarse sediment fraction.
- Specific pattern of behaviour of sampling site 4 explained by the specific metallic mining source in the vicinity of the site.

Acknowledgements

The study has been performed in the framework of a project of the Spanish National Research Programme (ref. CGL2007-66861-C04-04/HID), entitled "Mobility and redistribution of metals along unsaturated zone and their effects on groundwater quality changes".

Special thanks for partial financial support of the Bulgarian co-authors are due to the National Fund of Scientific Research, Bulgarian Ministry of Education and Science (Project VUH 206/06 – 2472 and Project VUH 02/05 – 2437).

This research was supported by the European Union within the European Social Fund in the framework of the project "InnoDoktorant – Scholarships for PhD students, I edition".

References

[1] R. Pardo, B.A. Helena, C. Cazurro, C. Guerra, L. Deban, C.M. Guerra, M. Vega, Anal. Chim. Acta 523 (2004) 125.
[2] K.P. Singh, A. Malik, N. Basant, V.K. Singh, A. Basant, Chemom. Intell. Lab. Syst. 87 (2007) 185.
[3] J.W. Einax, A. Aulinger, W.V. Tümpling, A. Prange, Fresenius J. Anal. Chem. 363 (1999) 655.
[4] A. Aulinger, J.W. Einax, A. Prange, Chemom. Intell. Lab. Syst. 72 (2004) 35.
[5] F. López, F, Calvo, A. Morales, Geografía de la Región de Murcia, Ketres Barcelona, 1986, p. 267. ISBN 84-85256-55-7.
[6] J. Martínez Fernández, M.A. Esteve, Mediterránea. Ser. Estudios Biol. (2000).
[7] Scoullos, M. Dassenakis, Proceeding of the 1st Symposium on Oceanography and Fisheries, 1984, pp. 302–309.
[8] M. Dassenakis, H. Andrianos, G. Depiazi, A. Konstantas, M. Karabela, A. Sakellari, M. Scoullos, Greece Appl. Geochem. 18 (2003) 781.
[9] R.D. Gibbons, D.E. Coleman, Statistical Methods for Detection and Quantification of Environmental Contamination, John Willey & Sons, NY, 2001, p. 139.
[10] K.P. Singh, A. Malik, S. Sinha, D. Mohan, V.D. Singh, Anal. Chim. Acta 596 (2007) 171.
[11] I. Stanimirova, V. Simeonov, Chemom. Intell. Lab. Syst. 77 (2005) 115.
[12] R. Henrion, Chemom. Intell. Lab. Syst. 25 (1994) 1.

[13] P. Geladi, Chemom. Intell. Lab. Syst. 7 (1989) 11.
[14] C.A. Andersson, R. Bro, Chemom. Intell. Lab. Syst. 42 (1998) 93.
[15] R. Bro, Crit. Rev. Anal. Chem. 36 (2006) 279.
[16] E. Ceulemans, H.K.L. Kiers, Br. J. Math. Stat. Psychol. 56 (2006) 133.
[17] P. Barbieri, G. Adami, S. Piseli, F. Gemiti, E. Reisenhofer, Chemom. Intell. Lab. Syst. 62 (2002) 89.
[18] A. Maria-Cervantes, F.J. Jimenez-Carceles, J. Alvarez-Rogel, Water Air Soil Pollut. 200 (2009) 289.
[19] A. Astel, S. Malek, J. Chemom. 22 (2008) 738.
[20] A. Pérez-Ruzafa, S. Navarro, A. Barba, C. Marcos, M.A. Cámara, F. Salas, Mar. Pollut. Bull. 40 (2000) 140–151.
[21] L. Marín-Guirao, J. Lloret, A. Marín, G. García, A.J.G. Fernández, Chem. Ecol. 23 (3) (2007) 217–231.
[22] A. Pérez-Ruzafa, Estudio ecológico y bionómico de los poblamientos bentónicos del Mar Menor (Murcia, SE de España), Ph.D. Thesis, University of Murcia, Spain, 1989.

Talanta 80 (2009) 942–946

Contents lists available at ScienceDirect

Talanta

journal homepage: www.elsevier.com/locate/talanta

Characterization of the gold-catalyzed deposition of silver on graphite screen-printed electrodes and their application to the development of impedimetric immunosensors

Attila Vig[a,b], Xavier Muñoz-Berbel[b,*], Antonio Radoi[b], Montserrat Cortina-Puig[b], Jean-Louis Marty[b]

[a] Department of Biochemistry, College of Károly Eszterházy, Eger, Leányka u. 6, 3300, Hungary
[b] IMAGES EA 4218 Université de Perpignan Via Domitia, 52 avenue Paul Alduy, 66860 Perpignan Cedex, France

ARTICLE INFO

Article history:
Received 16 April 2009
Received in revised form 15 August 2009
Accepted 17 August 2009
Available online 22 August 2009

Keywords:
Impedance spectroscopy
Immunosensor
Colloidal gold nanoparticles
Silver deposition
Screen-printed electrodes
Toxins

ABSTRACT

This paper describes the characterization of the gold-catalyzed deposition of silver on graphite screen-printed electrodes (SPEs) using electrochemical impedance spectroscopy (EIS) and the application of this approach to the development of impedimetric immunosensors. After applying −0.1 V for 45 s, the amount of electrodeposited silver quantitatively changes the magnitude of two elements of the electrical equivalent circuit: the interface capacitance, *Ci*, and the charge-transfer resistance, R_{CT}. Better correlations have been found when considering the R_{CT} since this parameter is almost exclusively dependent on the amount of deposited silver under these experimental conditions. This approach has been successfully applied to the development of an impedimetric immunosensor for aflatoxin M_1. The R_{CT} magnitude shows good correlation with the amount of gold immobilized on the electrode surface after a competitive assay and thus, with the toxin concentration. This approach has been found sensitive in a wide range of concentrations, from 15 to 1000 free-AFM_1 ppt with a limit of detection of 12 ppt.

© 2009 Elsevier B.V. All rights reserved.

1. Introduction

Aflatoxins are toxic fungal metabolites produced by *Aspergillus flavis* and *Aspergillus parasiticus* with an important carcinogenic effect that can contaminate certain agricultural commodities and animal foodstuff [1,2]. For instance, aflatoxin M_1 (AFM_1, (6aR-cis)-2,3,6a,9a-tetrahydro-9a-hydroxy-4-methoxycyclopenta[c] furo[3′,2′:4,5]furo[2,3-h] [1]benzopyran-1,11-dione, CAS Number: 6795-23-9), the hydroxylated form of the aflatoxin B1 (AFB_1), can be found in milk or milk-derived products (cheese, yogurt, cream, etc.) from mammals that ingest AFB_1 infected feed [3]. The presence of these toxins cannot always be correlated to visible fungal infection and many efforts have been focused on the development of analytical methods for their quantitative determination [4–6]. Thin layer chromatography (TLC) [7], enzyme-linked immunosorbent assay (ELISA) [8] and especially the high performance liquid chromatography analysis with fluorimetric detection (HPLC-FD) coupled with a clean-up treatment by immunoaffinity columns (IC) [9], the method of reference for detection of aflatoxins in milk, have been developed and widely used last years. These methods show good sensitivity and high efficiency, although they are very tedious and time-consuming, especially the chromatographic methods that require an initial extraction step with organic solvents [10]. Electrochemical immunosensors, principally those based on the use of enzymatic labels, have been extensively applied to the detection of toxins for being rapid, simple and low cost methods [11–13]. Special attention has been given to the development of impedimetric immunosensors. In terms of aflatoxins, several strategies have been used, mainly based on changes in the charge-transfer resistance when redox couples are present in the medium [14]. Recently, the application of nanostructures in biosensing has also shown a remarkable interest. One of the most popular strategies is focused on the use of gold nanoparticles labels and silver enhancement [15]. This approach, initially used in chemical and biological analyses to improve microscopic visualization or to increase the sensitivity [16,17], has been successfully applied to the development of electrochemical immunosensors and genosensors by directly measuring the oxidation current response of the deposited silver [18,19].

This paper describes the characterization of the gold-catalyzed deposition of silver on graphite screen-printed electrodes (SPEs) using electrochemical impedance spectroscopy (EIS) and the application of this approach to the development of impedimetric immunosensors for toxins. The changes produced in the electrode-solution interface by the catalytic deposition of silver were monitored using impedance spectroscopy by following the mag-

* Corresponding author. Tel.: +33 468662253; fax: +33 468662223.
E-mail address: fxmber@gmail.com (X. Muñoz-Berbel).

0039-9140/$ – see front matter © 2009 Elsevier B.V. All rights reserved.
doi:10.1016/j.talanta.2009.08.016

nitude of the charge-transfer resistance, R_{CT}, and the interface constant phase element, CPE_i. These elements of the equivalent circuit showed good correlation with the amount of silver deposited on the electrode and thus, with the concentration of toxin in a wide range of concentrations. Better correlations were found when considering the R_{CT} since this parameter is almost exclusively dependent on the amount of deposited silver under these experimental conditions.

2. Materials and methods

2.1. Reagents and chemicals

Bovine serum albumin (BSA), bovine serum albumin-aflatoxin M_1 conjugate (BSA-AFM_1) and 20 nm colloidal gold suspensions were purchased from Sigma. The polyclonal anti-aflatoxin M_1 antibody (anti-AFM_1) from mouse was kindly supplied by C.E.A. (Paris, France). Silver nitrate (Fluka), ammonium nitrate (Prolabo), sodium chloride (Sigma), potassium chloride (Sigma–Aldrich), Tween 20 (Aldrich), dibasic sodium phosphate (Sigma), monobasic potassium phosphate (Sigma) and 3-[(1,1-dimethyl-2-hydroxiethyl) amino] 2-hydroxypropanesulfonic acid (AMPSO) (Sigma) were used as received without further purification. All solutions were prepared with distilled water.

2.2. Preparation of colloidal gold antibody conjugate

The antibody-colloidal gold conjugate was prepared following the protocol previously detailed in the literature [20]. Briefly, 25 μL of 0.9 mg mL^{-1} anti-AFM_1 prepared in 15 mM phosphate buffered saline (PBS, pH 7.4) and 100 μL of 20 mM AMPSO (pH 9.01) were added to 1 mL of a 20 nm colloidal gold suspension. After fixing the pH at 8, the solution was agitated for 30 min at room temperature. Next, 100 μL of 1% (w/v) BSA prepared in AMPSO buffer were added and the solution was centrifuged at 6000 rpm (Eppendorf Minispin centrifuge) for 30 min at 4 °C. The supernatant was removed and the pellet was re-suspended in 1 mL of 0.1% (w/v) BSA in AMPSO buffer. The centrifugation step was then repeated. The final pellet was re-suspended in 100 μL of 15 mM PBS, pH 7.4 and stored at 4 °C until needed.

2.3. Electrodes fabrication and preconditioning

The electrodes production was carried out in-house at the University of Perpignan (France) using a DEK 248 screen-printing system (Weymouth, UK). The fabrication process followed the protocol detailed in previous papers of the group [21,22]. Geometrically, these screen-printed electrodes (SPEs) contained a graphite working electrode disc of 0.12 cm^2 surrounded by a graphite counter electrode of bigger size area integrated on clear plastic sheets with a Ag|AgCl electrode, used as pseudo-reference.

Before measurement, SPEs were treated by successive cycling in 0.5 M H_2SO_4 between −0.5 V to 1.1 V versus Ag|AgCl to remove impurities (10 cycles; scan rate 100 mV s^{-1}, step potential 10 mV).

2.4. Immunosensor preparation protocol

In the impedimetric detection of AFM_1, an indirect competitive protocol was followed. A volume of 20 μL (15 μg mL^{-1} BSA-AFM_1 conjugate in 15 mM PBS, pH 7.4) was inoculated on the working electrode area and incubated overnight at 4 °C in a humid chamber to avoid drying. The un-adsorbed conjugate was removed by washing with 15 mM PBS + 0.5% (v/v) Tween 20 (pH 7.4). The non-reacted surface was blocked with 1% (w/v) BSA in 15 mM PBS (pH 7.4) for 1 h at room temperature. After washing with the PBS-Tween 20 solution, the competition assay was performed. During com-

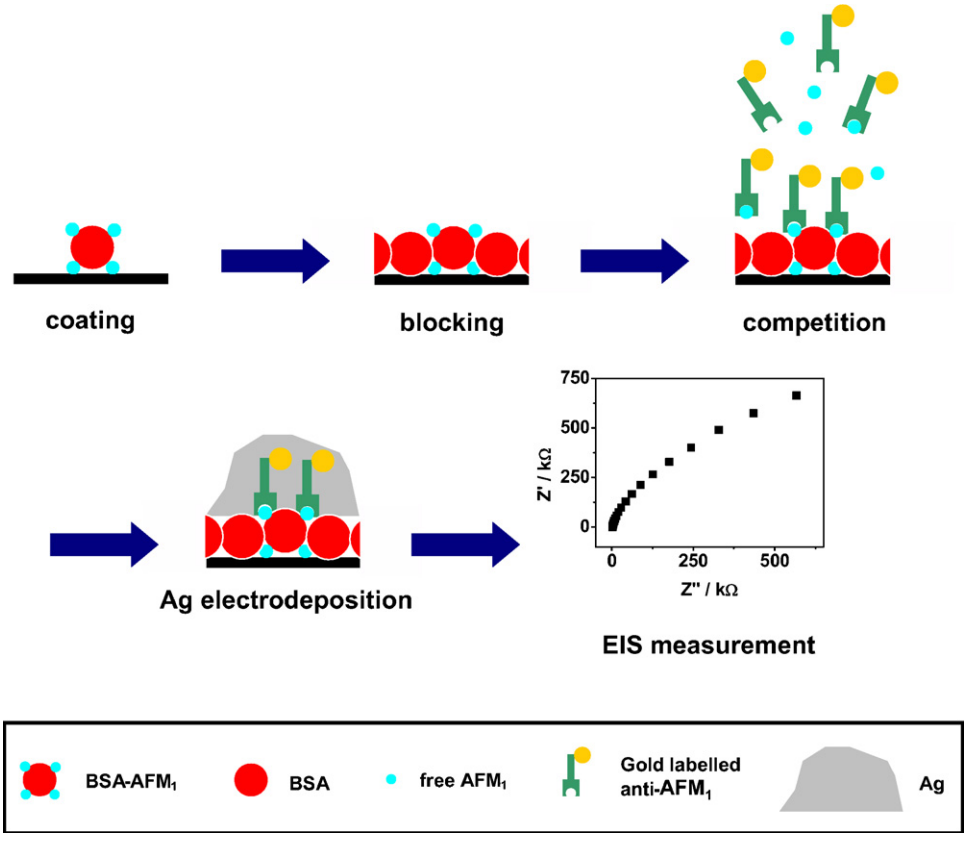


Fig. 1. Schematic illustration of gold-labelled antibody recognition and signal amplification with silver enhancement.

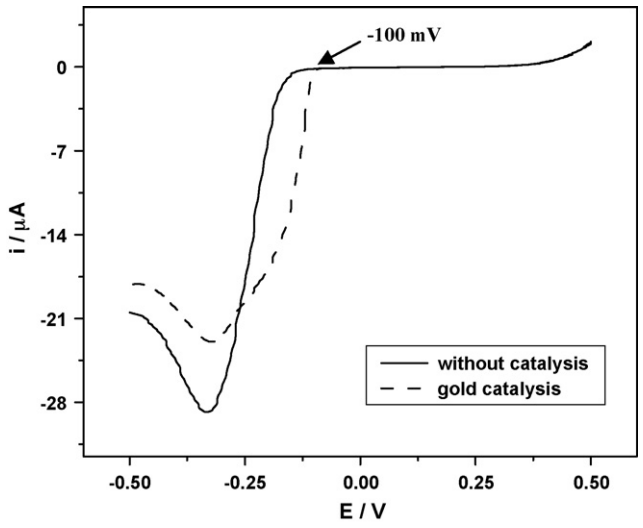


Fig. 2. Representation of the reduction peak of silver with and without the catalytic effect of 20 nm colloidal gold nanoparticles (scan rate: 100 mV s^{-1}).

petition, equal volumes (50 μL) of free-AFM_1 (from 15.625 ng L^{-1} to 2500 ng L^{-1} prepared in 15 mM PBS + 0.5% (v/v) Tween 20, pH 7.4) and 1/250 gold-labelled antibodies were allowed to compete for 1 h, at room temperature. The optimal concentration of gold-labelled antibodies was obtained from previous works [23]. Finally, SPEs were washed as before and stored in 0.1 M NH_4NO_3 at room temperature until measurement. The immunosensor preparation is illustrated in Fig. 1.

2.5. Silver enhanced impedimetric measurements

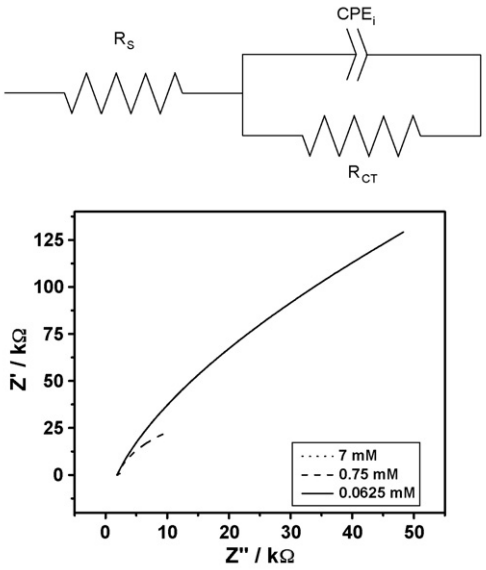
All measurements were carried out in 0.1 M NH_4NO_3 to avoid silver precipitation as silver chloride. Before impedance measurements, SPEs were additionally washed with distilled water to remove chloride traces. Silver was electrodeposited using the catalytic effect of the gold nanoparticles immobilized on the electrode surface. A 1 mM $AgNO_3$ in 0.1 M NH_4NO_3 solution was electrodeposited on the working electrode surface by applying −0.1 V for 45 s. At this potential, the catalytic effect of gold was the responsible of the metallic silver deposition (see Fig. 2). Finally, electrodes were washed with distilled water and measured in 0.1 M NH_4NO_3 at room temperature following the protocol detailed above. It is important to note that the silver deposition and the measurement should be done in a free-Cl^- media to avoid undesirable AgCl precipitation.

Impedance measurements were performed with an AUTOLAB PGSTAT 12 (EcoChemie, BV, The Netherlands) containing a FRA-2 module controlled by the AUTOLAB FRA-2 software (EcoChemie, BV, The Netherlands). Spectra were recorded at −20 mV over a frequency range from 1 kHz to 0.1 Hz, using a sinusoidal AC potential perturbation of 10 mV. The measurement time was around 120 s after registering 10 points per frequency decade. Impedance measurements were made in the dark to avoid the oxidation of the electrodeposited silver. All measurements given in this work are in relation to the Ag|AgCl reference electrode.

3. Results and discussion

3.1. Fitting and interpretation of impedance data

Z-View software was used to fit impedance data to the equivalent circuit shown in Fig. 3, which included the solution resistance, R_S, the double layer capacitance, which appears as the interface



[$AgNO_3$] mM	R_S Ω	R_S (% error)	CPE_i Ω $s^{-\beta}$	CPE_i (% error)	R_{CT} Ω	R_{CT} (% error)
7	1969	0.04	3.07E-4	1.56	4706	7.58
0.75	1837	0.33	7.54E-6	1.14	194340	8.77
0.0625	1879	0.36	1.28E-6	0.70	744630	4.18

Fig. 3. Impedance complex plane plot for 7, 0.75 and 0.0625 mM $AgNO_3$ solutions. The impedance spectra were fitted to the equivalent circuit shown inset, which contains the solution resistance (R_S), the interface constant phase element (CPE_i) and the charge-tranfer resistance (R_{CT}). The magnitude and error percentage from the fitting for each silver concentration are also included.

constant phase element, CPE_i, and the charge-transfer resistance, R_{CT}.

The use of the CPE_i instead of a conventional double layer capacitance was discussed in previous works [24,25]. Briefly, the double layer impedance of most solid electrodes behaves as a non-pure capacitance with a phase angle always smaller than 90°. Although being still controversial, a roughness factor appears to be one important cause of this [26]. Consequently, the double layer capacitance is frequently fitted using a constant phase element. Following the protocol exposed in Sections 2.4 and 2.5, toxins, antibodies, gold and silver become part of the interfacial region, thus, modifying the dielectric properties of the electrode. Hence, the CPE contains more parameters than simply the surface roughness or the charge separation, such as gold concentration or the deposited silver. For this reason, Fig. 3 shows a CPE labelled CPE_i as a generic element that accounts for many complex processes which cannot, themselves, be deconvoluted.

Fig. 3 shows impedance measurements for 7, 0.75 and 0.0625 mM $AgNO_3$ solutions after 45 s of deposition at −0.1 V. The change in the magnitude of the impedance (Z) with the concentration of silver nitrate can be clearly seen.

3.2. Impedimetric characterization of the immunosensor

Impedance spectroscopy is a powerful electrochemical technique for the investigation of the electrode-solution interface. In this work, impedance spectroscopy was used for the characterization of the process of fabrication of the immunosensors. Electrodes were prepared following the protocol detailed in Section 2.4 and impedance spectra were recorded under the conditions specified in Section 2.5. The Nyquist plot illustrating the real and the imaginary components of the impedance in the range of frequencies under study after each modification step of the fabrication protocol are presented in Fig. 4.

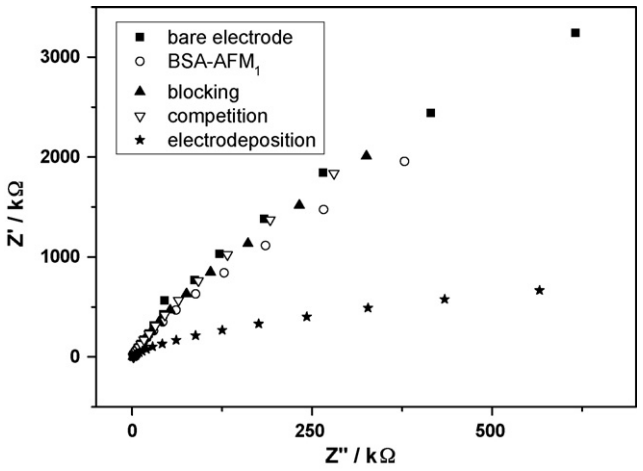


Fig. 4. Representation of the impedance complex plane plot for each stage of the immunosensor fabrication protocol.

Results show that the magnitude of the imaginary component of the impedance at low frequencies decreased with the modification of the electrode surface, which may be due to the isolating properties of the molecules covering the surface of the electrode [27]. For the suitable fitting of impedance data after the gold-mediated catalytic electrodeposition of silver, an extra element should be included in the equivalent circuit: the charge-transfer resistance, R_{CT}. Thus, the metallic silver layer was the responsible of the electron exchange with the electrode under the experimental conditions here described and the R_{CT} magnitude could be directly related to it.

3.3. Impedimetric characterization of the catalytic deposition of silver

For the characterization of the catalytic deposition of silver, SPEs were prepared as described in Section 2.4 and were measured following the protocol detailed in Section 2.5 using different concentrations of $AgNO_3$ (ranging from 7 mM to 0.0625 mM $AgNO_3$). In Fig. 5, the magnitude of both CPE_i and R_{CT} is represented versus the concentration of $AgNO_3$.

Fig. 5 shows that the CPE_i value increased with the amount of deposited silver whereas the magnitude of the R_{CT} decreased. As previously detailed, the CPE_i is an electrical element consisting in a group of parallel or branched resistive-capacitive transmission lines commonly used for adjusting deviations from the pure-capacitive behaviour of the interface capacitance, C_i, originating in surface heterogeneities [27]. The increase in the capacitance magnitude may be understood by considering how the deposition of silver modified the electrode-solution interface. Several factors (the increase of the bare electrode area, probably due to the roughness of the silver layer, or the compacting of the electrode double layer) might be thought to cause the increase of the C_i, since:

$$C_i = \frac{\varepsilon_0 \varepsilon_i A}{d} \quad (1)$$

where ε_0 is the permittivity of the vacuum, ε_i is the permittivity of the interface, A is the area of the bare electrode and d is the distance between layers in the electrolytic double layer. However, the change in the C_i could not be directly related to a single factor. Besides, the complex structure of the electrode-solution interface, a biometallic matrix containing immobilized biomolecules, gold and electrodeposited silver, suggested that the experimental results may be caused by a combination of factors that could not be deconvoluted. Hence, the huge number of parameters involved in the change of the CPE_i magnitude, some of them probably not directly related to the amount of silver electrodeposited on the electrode surface, did not recommend the use of this electrical element in the development of quantitative immunosensors.

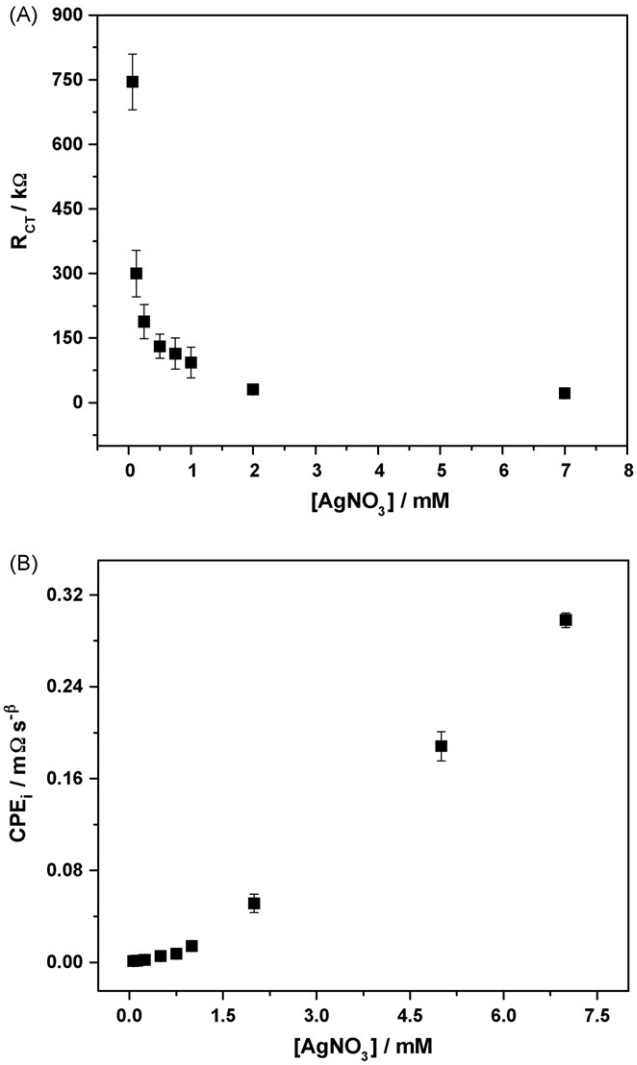


Fig. 5. Representation of the variation of the magnitude of the R_{CT} (A) and the CPE_i (B) with the concentration of $AgNO_3$. Individual points represent means from the measurement of two different electrodes and error bars are estimates of the relative standard deviation (R.S.D.).

On the other hand, the theoretical expression describing the behaviour of the R_{CT} magnitude is illustrated in Eq. (2).

$$R_{CT} = \frac{RT}{nFi_0} \quad (2)$$

where R is the constant of the ideal gases, F is the Faraday constant, T is the temperature, n is the number of electrons exchanged in the reaction and i_0 is the exchanged current density. Thus, the R_{CT} may be considered to be mainly dependent on a single parameter, the exchanged current density and consequently on the amount of redox species in the bulk or on the electrode surface. In this case, as the R_{CT} was only present in the equivalent electrical circuit when a silver layer was electrodeposited on the electrode surface, the R_{CT} magnitude could be directly correlated to the amount of silver deposited: the increasing amount of deposited silver increased the current density, decreasing the R_{CT} value. Hence, the R_{CT} is highly recommended in the development of silver enhanced impedimetric immunosensons.

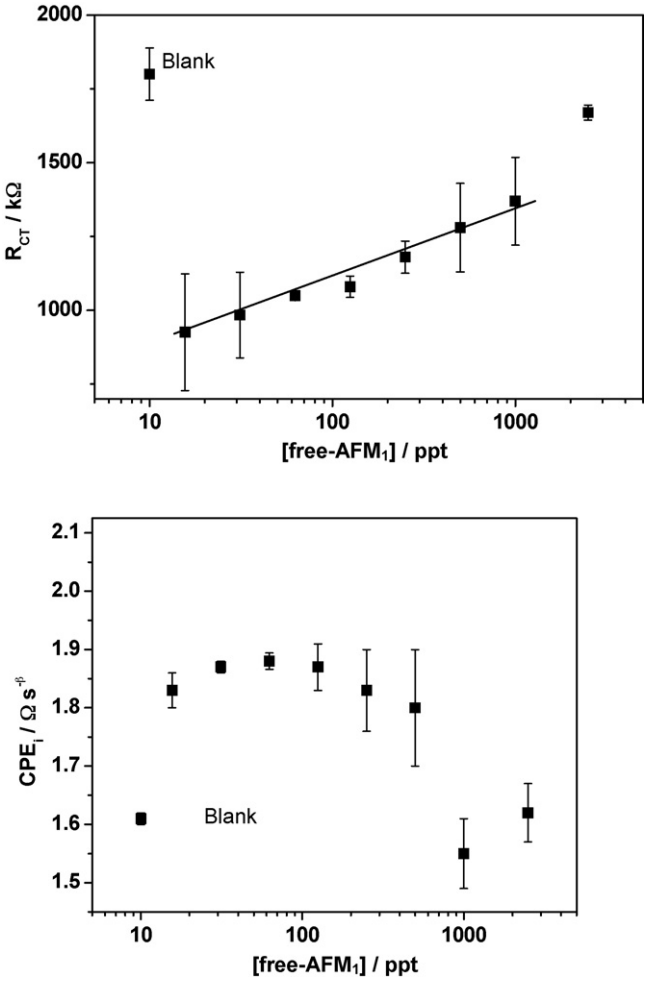


Fig. 6. Representation of the variation of the magnitude of the R_{CT} (A) and the CPE_i (B) with the concentration of free-AFM_1. The blank (samples containing AFM_1 antibody without colloidal gold nanoparticles) has been also included as control. Individual points represent means from the measurement of two different electrodes and error bars are estimates of the relative standard deviation (R.S.D.).

3.4. Immunoimpedimetric competitive assay

Finally, the sensors previously described were used in an immunoimpedimetric competitive assay. SPEs were prepared following the protocol described in Section 2.4 and measured as detailed in Section 2.5. The results are shown in Fig. 6, which illustrates the variation of the CPE_i and the R_{CT} with the concentration of free-AFM_1.

As expected, the R_{CT} magnitude tended to increase and the CPE_i to decrease when increasing the free-AFM_1 concentration. This should be caused by the decreasing amount of colloidal gold immobilized on the electrode surface after the competitive assay (when increasing the free-toxin concentration), which reduced the catalytic deposition of silver. It has to be pointed out that the charge-transfer resistance showed a better correlation with the toxin concentration than the interface capacitance. As previously discussed, this might suggest that, apart from the silver deposition, several factors not linked with that process could change the electrode-solution interface magnitude introducing a huge error in the measurement. In the case of the R_{CT}, an evident correlation was found between 15 and 1000 free-AFM_1 ppt with a limit of detection of 12 ppt. The limit of detection was calculated according to the $3 \times Sb/m$ criteria, where m is the slope of the linear calibration plot and Sb was estimated as the standard deviation ($n = 3$) of the impedimetric signals obtained in absence of colloidal gold.

4. Conclusions

We have impedimetrically charactarized the catalyzed electrodeposition of silver using graphite SPEs. We have demostrated that impedance spectroscopy, and particularly the charge-transfer resistance, can be used to quantitatively determine the amount of electrodeposited silver. This approach has been successfully applied to the development of an impedimetric immunosensor for toxins. Good correlations have been found between the logarithm of the toxin concentration and the magnitude of the charge tranfer resistance between 15 and 1000 free-AFM_1 ppt, with a limit of detection of 12 ppt.

Acknowledgements

Attila Vig acknowlegdes the support of Eötvös Hungarian State Fellowship. This work was supported by a financial contribution from EraSME Food for Better Human Health (project FASTDETECT). Especial thanks to University of Perpignan for ensuring research background and to Eötvös Hungarian State Fellowship for funding the research project.

References

[1] P.M. Scott, Food Addit. Contam. 12 (1995) 395.
[2] M. Miraglia, in: M. Miraglia, et al. (Eds.), Proceedings of the International IUPAC Symposium on Mycotoxin and Phycotoxin, Alaken Inc., Fort Collins, CO, USA, 1998.
[3] H.P. Van Egmond, Mycotoxins in Dairy Products, Elsevier Applied Science, Amsterdam, The Netherlands, 1989.
[4] R.J. Cole, Modern Methods in the Analysis and Structural Elucidation of Mycotoxins, Academic Press Inc., Orlando, USA, 1986.
[5] E.W. Sydenham, G.S. Shephard, in: J. Gilbert (Ed.), Progress in Food Contaminant Analysis, Blackie Academic and Professional, London, UK, 1996.
[6] N.W. Turner, S. Subrahmanyam, S.A. Piletsky, Anal. Chim. Acta 632 (2009) 168.
[7] M. Holcomb, D.M. Wilson, M.W. Trucksess, H.C. Thompson, J. Chromatogr. A 624 (1992) 341.
[8] L. Decastelli, J. Lai, M. Gramaglia, A. Monaco, C. Nachtmann, F. Oldano, M. Ruffier, A. Sezian, C. Bandirola, Food Control 18 (2007) 1263.
[9] S. Dragacci, F. Grosso, J. Gilbert, J. Assoc. Off. Anal. Chem. Int. 84 (2001) 437.
[10] H.H. Oruc, R. Cibik, E. Yilmaz, O. Kalkanli, Food Addit. Contam. A 23 (2006) 190.
[11] L. Micheli, R. Grecco, M. Badea, D. Moscone, G. Palleschi, Biosens. Bioelectron. 21 (2005) 588.
[12] R.M. Pemberton, R. Pittson, N. Biddle, G.A. Drago, J.P. Hart, Anal. Lett. 39 (2006) 1573.
[13] Y. Liu, Z. Qin, X. Wu, H. Jiang, Biochem. Eng. J. 32 (2006) 211.
[14] J. Owino, A. Ignaszak, A. Al-Ahmed, P. Baker, H. Alemu, J. Ngila, E. Iwuoha, Anal. Bioanal. Chem. 388 (2007) 1069.
[15] X. Chu, Z.-F. Xiang, X. Fu, S.-P. Wang, G.-L. Shen, R.-Q. Yu, J. Immunol. Methods 301 (2005) 77.
[16] Y.W. Xu, in: Y.W. Xu (Ed.), Detection Techniques in Immunology, Science Press, Beijing, China, 1997.
[17] Y.C. Cao, R. Jin, C.A. Mirkin, Science 297 (2002) 1536.
[18] T.M.H. Lee, L.L. Li, I.M. Hsing, Langmuir 19 (2003) 4338.
[19] H. Cai, Y. Wang, P. He, Y. Fang, Anal. Chim. Acta 469 (2002) 165.
[20] A. Fan, C. Lau, J. Lu, Anal. Chem. 77 (2005) 3238.
[21] S. Andreescu, L. Barthelmebs, J.-L. Marty, Anal. Chim. Acta 464 (2002) 171.
[22] B. Prieto-Simón, M. Campàs, J.-L. Marty, T. Noguer, Biosens. Bioelectron. 23 (2008) 995.
[23] A. Vig, A. Radoi, X. Muñoz-Berbel, G. Gyemant, J.-L. Marty, Sens. Actuators B 138 (2009) 214.
[24] X. Muñoz-Berbel, N. Vigués, J. Mas, A.T.A. Jenkins, F.J. Muñoz, Electrochem. Commun. 9 (2007) 2654.
[25] X. Muñoz-Berbel, N. Vigués, A.T.A. Jenkins, J. Mas, F.J. Muñoz, Biosens. Bioelectron. 23 (2008) 1540.
[26] W.H. Mulder, J.H. Sluyters, T. Pajkossy, L. Nyikos, J. Electroanal. Chem. 285 (1990) 103.
[27] M.I. Prodromidis, Electrochim. Acta, in press (corrected proof).

Talanta 80 (2009) 947–953

Contents lists available at ScienceDirect

Talanta

journal homepage: www.elsevier.com/locate/talanta

Optimization of multiple reaction monitoring mode for the trace analysis of veterinary sulfonamides by LC–MS/MS

Anna Białk-Bielińska[a], Jolanta Kumirska[a], Richard Palavinskas[b], Piotr Stepnowski[a,*]

[a] Department of Environmental Analysis, Faculty of Chemistry, University of Gdańsk, ul. Sobieskiego 18, 80-952 Gdańsk, Poland
[b] Federal Institute for Risk Assessment BfR, Thielallee 88-92, 14195 Berlin, Germany

ARTICLE INFO

Article history:
Received 19 April 2009
Received in revised form 14 August 2009
Accepted 17 August 2009
Available online 22 August 2009

Keywords:
Veterinary drugs
Sulfonamides
Environment
LC–MS/MS analysis
MRM
Soil

ABSTRACT

One of the oldest groups of veterinary chemotherapeutic agents, sulfonamides have been widely used for more than 50 years, thanks to their low cost and their broad spectrum of activity in preventing or treating bacterial infections. Nowadays, those compounds are regularly detected in a wide variety of environmental samples, including natural waters, sediments and soils. Since the environmental concentrations of sulfonamides are usually very low and their occurrence multicomponental, their determination in these matrices still pose significant analytical problems. The present paper describes the optimization of ESI-MS/MS parameters and the chromatographic separation of 12 sulfonamides commonly used in veterinary medicine. The methodology developed in this study, unlike many others, satisfied the requirements of EU Commission Decision 2002/657/EC, which defines the criteria for both screening and confirmatory methods with respect to drug residues on the basis of identification points. Each MRM transition was tested not only for the qualitative but also for the quantitative analysis of sulfonamides. The method was validated for its analytical performance parameters and applied to the determination of those compounds in soil samples.

© 2009 Elsevier B.V. All rights reserved.

1. Introduction

Scientists have devoted much attention to the occurrence of pharmaceuticals in the environment. Consequently, large numbers of reports have been published on traces of drugs detected in many different environmental samples, e.g., fresh-, sea-, and wastewaters, soils, sediments and biota [1]. Because of their polar nature, however, a number of drugs are not significantly adsorbed onto soils and therefore easily reach groundwater, the usual source of drinking water [2]. At present, some 3000 different active substances are used in human and veterinary medicine [3]. Drugs commonly detected in the environment include antibiotics, non-steroidal anti-inflammatory drugs, beta-blockers, anti-epileptics, blood-lipid lowering agents, antidepressants, hormones and anti-histamines [1–5]. Antibiotics are of particular concern: continuous exposure to them, even to low concentrations, can induce bacterial resistance. This constitutes pose a serious threat to public health, as fewer and fewer infections can be treated with the existing suite of antibiotics [5]. The term "antibiotic" is normally reserved for a diverse range of compounds, both natural and semi-synthetic, that possess antibacterial activity [6]. In addition to the treatment of human diseases, those drugs are used extensively in veterinary medicine as growth promoters and to improve feed efficiency [7]. Playing a crucial role in modern agriculture and the livestock industry, their use has been on the rise in many developing countries [4].

As antibiotics do not undergo complete metabolism in animal organisms [4–5], a large proportion of them is excreted in unchanged form in feces and urine. Both antibiotics and their metabolites are released either directly into the environment by grazing animals or indirectly during the application of manure/slurry as fertilizer. Contaminated manure is considered to be the main source from which antibiotics and their corresponding resistant genes enter different environmental compartments, food and plants [8]. Moreover, once in the aquatic environment, antibiotics have been found to break through classical wastewater treatment facilities, thereby presenting a threat to surface and groundwater [9–10]. It has also been found that the conventional drinking water treatment processes of coagulation, flocculation and sedimentation do not completely remove these compounds, so they are detected in finished drinking waters in various concentrations [11–15].

Pharmaceuticals enter the environment in low or very low concentrations; this, together with their diverse physico-chemical properties and the complexity of environmental matrices, makes their determination difficult. It is therefore necessary to develop sensitive, selective and easily reproducible methods for tracing these chemicals in different environmental materials. Since in most

* Corresponding author. Tel.: +48 58 5235448; fax: +48 58 5235 454.
E-mail address: sox@chem.univ.gda.pl (P. Stepnowski).

0039-9140/$ – see front matter © 2009 Elsevier B.V. All rights reserved.
doi:10.1016/j.talanta.2009.08.023

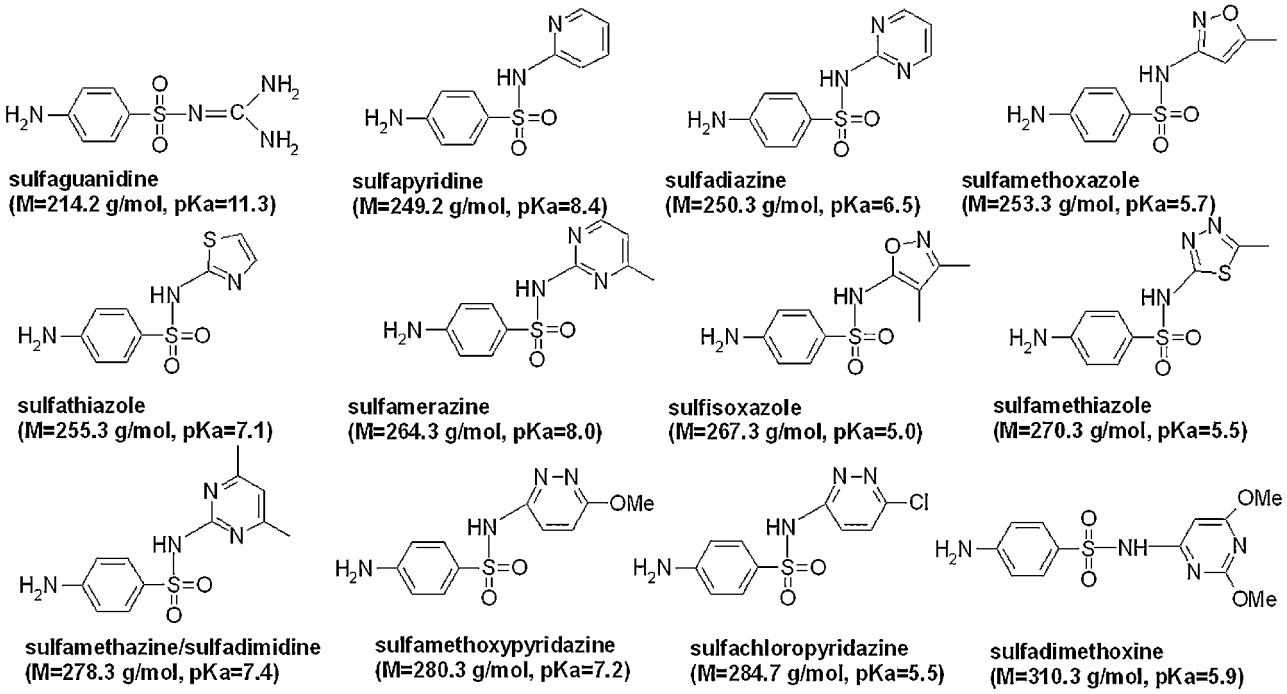


Fig. 1. The chemical structures of the sulfonamides under investigation [32,44].

cases we are dealing with complex mixtures of several chemicals from one or several groups of pharmaceuticals, chromatographic techniques need to be applied prior to their final determination. Their relatively high polarity and low thermal stability precludes gas chromatography (GC), so liquid chromatography (LC) coupled to mass spectrometry (MS), fluorescence, ultraviolet or radioimmunoassay [16] detection is used; among these latter techniques, LC coupled to MS, especially in tandem with MS, has made impressive progress in the analysis of residual pharmaceuticals [17–18]. The vast majority of studies have focused on the optimization of mobile phase composition, instrumental conditions and validation parameters (including limit of detection (LOD) and limit of quantification (LOQ)) in order to obtain favorable analytical protocols for the pharmaceuticals of interest. However, rather more methods have been described for the determination of antibiotics in different water compartments than in soil; the latter is more challenging owing to the complexity of soil matrices, interferences, and the longer sample preparation requirements (clean-up procedure). For these reasons, only a few papers have been published on the quantification of antibiotics in solid matrices (e.g. [19]). Likewise, sulfonamides as veterinary chemotherapeutics have usually been analyzed in water samples like wastewater [20–26], drinking water [13], surface/groundwater [27–28] or liquid manure [29–31] rather than in solid samples [32–37].

However, since there are no official guidelines for the trace analysis of pharmaceuticals in environmental samples, most of the reported methodologies suffer from a lack of confirmatory methods with respect to MS.

Reports on the qualitative and quantitative analysis of many different pharmaceuticals (including sulfonamides) in environmental samples using HPLC systems with UV-detection are still being published [23,25,30,36,38] this method cannot be used as a confirmatory technique, because identification of a compound in complex materials based solely on retention time is not sufficient. According to the EU Commission Decision of August 12, 2002 (2002/657/EC), also referred to as SANCO 1085/2002, determination of an analyte using LC with UV/VIS detection (single wavelength) is not suitable on its own for use as a confirmatory method.

The aim of this study was therefore to optimize MS/MS parameters using ion-trap mass spectrometry with electrospray ionization for the analysis of sulfonamides – the most common veterinary chemotherapeutics – and to select characteristic fragmentation ions of these compounds in order to work in multiple reaction monitoring (MRM) mode. The experiments were performed in accordance with the above-mentioned Commission Decision, which defines the criteria for both screening and confirmatory methods with respect to drug residues on the basis of identification points. A precursor ion and a minimum of two product ions were selected for every compound, which yields four identification points and enables confirmation of the compounds analyzed. The chromatographic separation of these compounds was optimized, and also validated using parameters such as selectivity, linearity, sensitivity, limits of detection and quantification, precision (intra-day and inter-day precision) and accuracy (recovery). Finally, the method was applied to the analysis of selected sulfonamides in soil samples.

2. Materials and methods

2.1. Chemicals

Standards of sulfaguanidine, sulfathiazole, sulfadiazine, sulfamethiazole, sulfamerazine, sulfamethoxypyridazine, sulfachloropyridazine, sulfisoxazole, sulfamethoxazole, sulfadimethoxine were purchased from Sigma–Aldrich (Steinheim, Germany), those of sulfadimidine and sulfapyridine from Serva (Heidelberg, Germany) (Fig. 1). Methanol (MeOH) and acetonitrile (ACN) (HPLC grade), used for the mobile phases and for the dissolution of standards, were obtained from POCH S.A. (Gliwice, Poland); the acetonitrile (LC–MS Chromasolv®) used for the LC–MS/MS analysis was purchased from Sigma–Aldrich (Steinheim, Germany). Deionized water was produced by the HYDROLAB System (Gdańsk, Poland). Ammonium acetate (NH_4Ac) and acetic acid (both of ana-

lytical reagent grade) were purchased from Chempur (Piekary Śląskie, Poland).

Standard stock solutions were prepared by dissolving each compound in methanol at a concentration of 500 μg ml^{-1} and stored at −18 °C in the dark. Working solutions (1 μg ml^{-1}) of sulfonamides were prepared by diluting the stock solutions in a mixture of ACN:H_2O (50:50, v/v) or in acetic buffer at pH 3.5 (acetic acid was added to the mixture of ACN:H_2O, 10:90, v/v, containing 1 mM NH_4Ac until pH 3.5 was reached), depending on the purpose, and stored at 4 °C. During the experiments pH was measured using a CP-411 laboratory pH-meter (Elmetron-Zabrze, Poland). The pH of the solution for the analysis of selected antibiotics ensured their stability and the appropriate conditions for the electrospray ionization and chromatographic separation. Strata-X Polymeric Reversed Phase (SPE-Phenomenex Inc., Torrance, CA) cartridges with 200 mg of packing material and a 3 ml reservoir were used for sample preparation.

2.2. Soil samples

Soils (fluvial meadow soil) were sampled from the region of Pomerania in northern Poland. The soil was air-dried, ground in a mortar and passed through a 2 mm sieve, then re-ground in a mortar with a small rubber pestle. Their organic carbon content was determined by loss-on-ignition. The pH of the soil (measured in 1 M KCl) was 5.3, the clay content (>0.01 mm fraction) was 94% and the organic content was 21.5%.

2.3. Optimization

2.3.1. Liquid chromatography conditions

Agilent 1200 Series LC system (Agilent Technologies, Inc., Santa Clara, USA) and ChemStation for LC systems software were used for the chromatographic separation of the sulfonamides. For the LC–MS/MS analysis Brucker Daltonics Data Analysis software was utilized. The separation was performed on Gemini C_{18} and Gemini C_6 columns (both 150 mm × 4.6 mm, 5 μm pore size) (Phenomenex Inc., Torrance, CA) with the direct infusion of the eluent from the LC to the mass spectrometer. To optimize the chromatographic separation, a serial of preliminary experiments were performed to test different mobile phases. Both acetonitrile and methanol mixed with water were tested as mobile phases. Additionally the flow rate of the eluent, injection volume and the column temperature as well as the pH of a mobile phase consisting of ammonium acetate and acetic acid was also optimized.

2.3.2. ESI-MS/MS parameters

All mass spectrometric measurements were performed on an HCT Ultra ion trap mass spectrometer (Brucker Daltonics, Bremen, Germany) equipped with an electrospray ionization (ESI) source. All the compounds were tested in both positive and negative ion modes. MS–MS parameters were optimized in continuous flow mode using an integrated syringe pump at a flow rate of 5 μl min^{-1} of standard solutions. EsquireControl software was employed to optimize spectrometric conditions such as the nebulizer gas and dry gas flow rates and the dry gas temperature. The nebulizer gas and dry gas was nitrogen, and helium (99.999%) was used as the collision gas in the ion trap. The parameters were optimized manually, separately for each compound. After the best conditions for isolating the precursor ion (proton adduct of the analyte) had been determined, full scan MS/MS mode was used to record product ions from the standard solution of chemotherapeutics. For each compound, the fragmentation amplitude and isolation width were also optimized manually to increase the sensitivity and selectivity of the method and to select three of the most intensive and characteristic fragmentation ions for qualitative analysis and one of the highest intensity for quantitative analysis.

2.4. Extraction method

Soil samples (1 g) were spiked with the solution (2.5 ml) of 12 sulfonamides of known concentrations (250 μg sulfonamide kg^{-1} soil) and then left to dry in the dark at room temperature for three days. Next, the analytes were extracted from the dry soil with 5 ml MeOH, placed in an ultrasonic bath (Polsonic, Warsaw, Poland) for 1 h, and finally shaken for another 1 h (RS 10 Control, IKA, Germany). The samples were then centrifuged (10 min, 4000 rpm; MPW-250 Centrifuge, Warsaw, Poland) and the supernatant transferred to a 10 ml flask, after which the procedure was repeated. The resulting extract was concentrated to a volume of about 1 ml. Two alternative procedures were applied in the next step. In the first one, the residual extract was transferred to a plastic tube, evaporated to dryness under a stream of nitrogen, after which 1 ml of mobile phase A was added. The sample was centrifuged (15 min, 5500 rpm; MPW-250 Centrifuge, Warsaw, Poland), transferred to an amber vial and analyzed by LC–MS/MS. In the second procedure, 250 ml water was added to the residual extract and the whole cleaned up on a Strata-X Polymeric Reversed Phase SPE-column (3 ml, 200 mg, Phenomenex Inc.). The cartridges were rinsed with 3 ml MeOH and conditioned with 6 ml H_2O:MeOH (95:5, v/v); after sample loading the cartridge was dried and then rinsed with 3 ml H_2O:ACN (95:5, v/v) to remove interferences. Sulfonamides were eluted with 6 ml of a mixture of MeOH:ACN (50:50, v/v) and allowed to dry under a stream of nitrogen. The dried extract was reconstituted in 1 ml mobile phase A and analyzed by LC–MS/MS.

3. Results and discussion

3.1. Optimization of the LC–MS/MS method

According to EU Commission Decision 2002/657/EC, the presence of the residues of veterinary drugs is confirmed so long as the drug is identified both chromatographically and spectrally. If these criteria are not satisfied, a new method or a better procedure should be developed for extracting and/or separating the analytes from interferences. Nowadays, LC–MS/MS in multiple reaction monitoring (MRM) mode is the 'state-of-art'. It is the technique of the highest sensitivity and selectivity, which for these reasons has been used in these experiments.

Comparison of positive and negative ion modes shows that working in the former mode causes more high-intensity product ions to be formed. During the optimization of sulfonamides in full scan MS, the most intensive ions were $[M+H]^+$; ions like $[M+Na]^+$ or $[M+NH_4]^+$ were also detected but were of lower intensity. All the MS/MS parameters were selected to obtain the most intensive precursor ions for every compound $[M+H]^+$. The most relevant parameters were: nebulizer gas (30 psi), dry gas (10 L min^{-1}), dry temperature (300 °C), maximum accumulation time (200 ms), average (3 scans), smart target (50,000), target mass (m/z = 250), capillary exit (109.8 V) and skimmer (40.0 V); ultra scan was used as the mass range mode. Moreover, for every compound a precursor ion and a minimum of two product ions were selected, earning, according to Commission Decision 2002/657/EC, four identification points for the confirmation of the compound. According to Council Directive 96/23/EC, veterinary drugs such as antibacterial agents, including sulfonamides and quinolones belong to Group B in Annex I of this Directive, and for those compounds a minimum of three identification points are required [39]. The value of a low-resolution MS precursor ion is 1.0 identification points and that of each low-

Table 1
Precursor ion and product ion masses selected during optimization for the MRM detection of sulfonamides.

Substance	Precursor ion	Isolation width	Product ions	Fragmentation amplitude (V)
Sulfaguanidine	215 $[M+H]^+$	2.0	156	0.55
			173	0.50
			122	0.55
Sulfapyridine	250 $[M+H]^+$	0.9	156	0.50
			184	0.60
			108	0.55
Sulfadiazine	251 $[M+H]^+$	0.8	156	0.75
			174	0.55
			108	0.75
Sulfamethoxazole	254 $[M+H]^+$	2.0	156	0.65
			188	0.65
			147	0.50
Sulfathiazole	256 $[M+H]^+$	2.0	156	0.55
			108	0.60
			92	0.65
Sulfamerazine	265 $[M+H]^+$	2.0	190	0.65
			174	0.60
			156	0.55
Sulfisoxazole	268 $[M+H]^+$	2.0	156	0.70
			113	0.65
			108	0.65
Sulfamethiazole	271 $[M+H]^+$	2.0	156	0.60
			108	0.70
			92	0.60
Sulfamethazine	279 $[M+H]^+$	1.9	204	0.60
			124	0.55
			156	0.55
Sulfamethoxypyridazine	281 $[M+H]^+$	1.9	156	0.45
			126	0.55
			188	0.50
Sulfachloropyridazine	285 $[M+H]^+$	2.0	156	0.75
			108	0.60
			92	0.75
Sulfadimethoxine	311 $[M+H]^+$	2.0	156	0.60
			245	0.60
			218	0.65

resolution MS product ion is 1.5 IPs. For these reasons, a minimum of two product ions in low-resolution MS must be monitored for the minimum number of identification points to be acquired. Note, that working in SIM or MRM mode with only one product ion in low-resolution MS does not fulfill the minimum IP requirement. Table 1 presents the results together with selected values of the optimized fragmentation amplitude for each of the transitions and the isolation width for every product ion. The fragmentation of sulfonamides has already been described [40]. For sulfonamides, the most characteristic ions described in the literature, such as m/z 156, 108 and 92, corresponding to $[M-RNH_2]^+$, $[M-RNH_2-SO_2]^+$, and $[M-RNH_2-SO]^+$, respectively, were also observed in this experiment. Additionally, fragmentation of some of those compounds produced such ions as 124, 186 and 204, which correspond to $[RNH_2+2H]^+$, $[RNH_2+SO_2]^+$ and $[RNH_2+SO_2+H_2O]^+$.

Although complete separation is not necessary for selective MS–MS detection, it much improves detectability and reduces the ion suppression effect; this was one of the main reasons for performing the experiments [18]. Therefore, the influence of different parameters on retention time was optimized. The separation was done by reversed-phase chromatography on two types of column—C_6 and C_{18}. The C-phenyl column was excluded from the later experiments because of the very strong hydrophobic and $\pi\cdots\pi$ interactions between the phenyl groups on the stationary phases and the specific groups in the sulfonamide structures. Retention times were therefore longer and peaks were broader. Both acetonitrile and methanol were tested as mobile phases, as were the pH and different salt contents. It was demonstrated that acetonitrile and water were preferable for sulfonamide separation. Moreover, it was necessary to work under acidic conditions for two reasons: first, to achieve better separation, and second, to improve ionization in the mass spectrometer. In the HPLC system, trifluoroacetic acid is usually used for this purpose; but it causes ion suppression so is not recommended for LC–MS/MS analysis. This was why an acetic buffer of different pH was tested. Generally, it was found that the lower the pH, the higher the retention time and the better the separation. This is because most veterinary sulfonamides have at least two nitrogen-containing functional groups (Fig. 1). The amine attached to the aromatic ring-referred to as N^4 – is protonated at pH < 2.5, whereas the one attached to the sulfur-referred as N^1 – is deprotonated at pH > 5.5–7.0. Hence, most of these compounds are positively charged under acidic conditions, negatively charged under alkaline conditions, and neutral between pH 2.5–6.0 [32]. Additionally, very weakly basic or acidic sites may also be present in the side R-group, which can also play a crucial role in retention on the stationary phase. As observed by Botsoglou et al. [41], the retention time of the investigated sulfonamides increased slightly in the pH range 2.5–3.5, the greatest retention being obtained for sulfonamides bearing an additional methyl group on the R-side-chain. This suggests that the R-side-chain plays a crucial role in the hydrophobic interactions of the compounds with the stationary phase [41], which was also observed in the

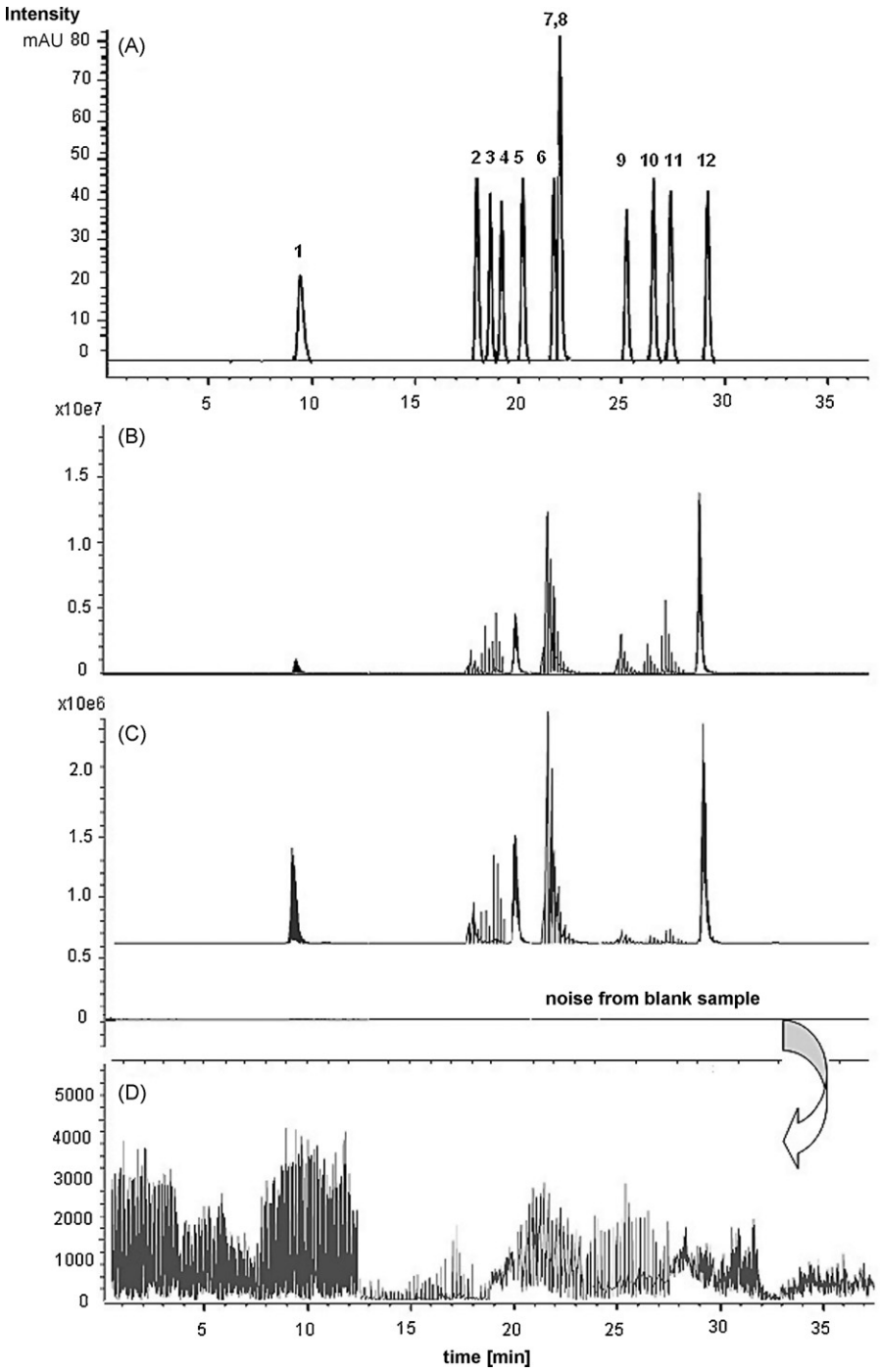


Fig. 2. Chromatograms of the optimized method: (A) (HPLC–UV) and (B) (MRM-LC–MS/MS) chromatograms of the standard mixture (1 μg ml^{-1}) of 12 sulfonamides: 1, sulfaguanidine; 2, sulfadiazine; 3, sulfathiazole; 4, sulfapyridine; 5, sulfamerazine; 6, sulfadimidine; 7, sulfamethiazole; 8, sulfamethoxypyridazine; 9, sulfachloropyridazine; 10, sulfamethoxazole; 11, sulfisoxazole; 12, sulfadimethoxine; C_{18}-column, detection wavelength 270 nm, 300 μl min^{-1}, injection volume 50 μl, mobile phase A – H_2O:ACN (90:10, v/v, 1 mM NH_4Ac, HAc at pH 3.5), mobile phase B – 100% ACN; gradient program: 0–64% B for 32 min, temperature 25 °C); (C) (MRM-LC–MS/MS) chromatogram of sulfonamides extracted from soil (procedure 1 – without any clean-up) spiked with the standard solution (250 μg kg^{-1}); (D) blank sample of soil.

present experiments. The selection of pH 3.5 for the mobile phase and the solution of the standard compounds was based on the pK_a of the sulfonamides (Fig. 1). Since it was below the lowest value of pK_a, a pH of 3.5 ensured that the sulfonamides were in their neutral form, their retention time increased and the baseline separation was better; all these observations were confirmed by Haller et al. [32]. Moreover, mobile phase A consisted of 1 mM ammonium acetate, which is the right concentration for ionization, because the higher the salt content, the greater the loss of MS sensitivity during measurements. Additionally, the flow rate in the 150–300 μl min^{-1} range as well as the injection volume in the range 10–50 μl and the temperature in the 25–45 °C range were also optimized. Increasing the temperature did not significantly improve sulfonamide separation but did diminish the intensity of chromatographic peaks. A temperature of 25 °C was therefore the best option. In summary, the antibiotics were separated on a C_{18}-column at a temperature of 25 °C, a wavelength of 270 nm, an injection volume of 50 μl, and a flow rate of 300 μl min^{-1}. Mobile phase A was a mixture of

Table 2
Validation parameters of the optimized method (n is the number of replicates).

Transitions	LOD ($\mu g\,L^{-1}$), $n=10$	LOQ ($\mu g\,L^{-1}$), $n=10$	Intra-day precision RSD (%), $n=6$	Inter-day precision RSD (%), $n=3$	Accuracy (%), $n=6$
215 > 156	1.05	2.10	3.61–9.87	14.27–14.74	80.07–113.89
250 > 156	2.08	4.16	2.46–12.89	14.78–17.54	97.13–119.77
251 > 156	2.63	5.26	5.28–13.54	2.95–17.73	98.07–115.98
254 > 156	2.74	5.48	3.47–12.01	4.76–8.52	96.75–113.19
256 > 156	0.94	1.88	2.22–5.91	8.16–14.13	87.98–108.41
265 > 156	0.52	1.03	2.27–7.68	6.99–9.92	82.19–109.93
268 > 156	1.26	2.52	11.97–12.59	8.03–14.34	80.18–90.02
271 > 156	1.49	2.99	1.87–5.56	18.24–28.00	113.08–125.59
279 > 204	0.70	1.40	3.71–6.37	9.14–13.88	85.16–113.79
281 > 156	0.44	0.88	2.81–8.21	6.60–8.78	76.18–100.73
285 > 156	2.61	5.22	1.86–12.67	1.84–11.91	101.20–108.51
311 > 156	0.31	0.62	1.30–4.92	5.24–8.74	86.33–115.80

H_2O:ACN (90:10, v/v, 1 mM NH_4Ac/AcH, pH 3.5) and mobile phase B was 100% ACN; both were selected in the gradient program. Elution began with 100% of mobile phase A, which was reduced to 36% within 32 min. Complete separation of 10 of the 12 sulfonamides was possible within less than 30 min (Fig. 2A and B), which is a satisfactory result compared to the methods described in the literature [23,25,27,30], where, for example, five sulfonamides were separated in 16 min or eight in 35 min.

3.2. Validation of the analytical method

3.2.1. Linearity

Linearity is a measure of the method's sensitivity: the greater the slope of the calibration curve, the more sensitive the method [42]. To determine the linearity of the method a minimum of five different concentrations were analyzed with six replicates each. The calibration curves obtained for both the quantification and the confirmation MRMs were linear for all compounds over a wide range of concentrations from 2.5 to 1000 $\mu g\,L^{-1}$ with a correlation coefficient (R^2) > 0.99. However, after taking into consideration the expected concentration of sulfonamides in environmental samples, and to improve the accuracy of the method, it was decided to work with the lowest concentrations. Only one MRM transition for the fragmentation ion of the highest intensity was selected for the quantification (Table 2), which resulted in lower LODs and LOQs. All calibration curves displayed good linearity with R^2 from 0.9984 to 1.000.

3.2.2. Limits of detection and quantification

The limits of detection (LODs) of the analytical methods developed in this study for all sulfonamides were evaluated by the measurement of 10 independent blank water samples fortified at the lowest acceptable concentration: LODs were equal to three times standard deviation of the measured signals [43]. The limits of quantification (LOQ) were calculated as twice the LOD values. The limits of detection (LODs) ranged from 0.31 to 2.74 $\mu g\,L^{-1}$ (Table 2). The method thus enables sulfonamides to be determined at very low levels.

3.2.3. Precision and accuracy

The precision of the method (expressed as RSD values) was determined in the intra-day and inter-day tests. The intra-day precision of the method was determined by calculating the relative standard deviation (RSD) for the repeated measurements ($n=6$). The accuracy of the method was determined by assessing the agreement between the measured and known concentration of analysed samples. All the results are presented in the Table 2. To determine the inter-day precision of the method, three selected concentrations (5, 10 and 50 $\mu g\,L^{-1}$), with the exception of sulfadiazine, sulfathiazole and sulfisoxazole (10, 50 and 500 $\mu g\,L^{-1}$) were analyzed by the same person under the same conditions on six consecutive days with three replicates on each day. Instrumental repeatability, expressed as RSD, was in general <20%. According to the U.S. EPA recommendations, the method is considered precise when RSD is less than or equal to 20% (Table 2).

3.2.4. Selectivity

Selectivity is the degree to which a method can quantify the analyte accurately in the presence of interferents. It is particularly important to check interferents that are likely, on chemical principles, to respond to the test [42]. To determine the selectivity of the method the blank sample of the soil extract was analyzed (Fig. 2C and D). None of the analyzed compounds was detected. Therefore, presented method is characterized by good selectivity.

3.3. Applicability of the method

The method's applicability was assessed by an analysis of 12 sulfonamides in soil samples. A very quick, simple and cost-effective method without any sample clean-up was implemented for this analysis using LC–MS/MS in MRM mode. The great advantage of this mode is its high selectivity and sensitivity when working with very complex matrices, which was also demonstrated in this experiment. Two different procedures in three replicates were performed to compare the results: one without any sample preparation and the other with sample clean-up using Solid Phase Extraction (see Section 2.4). The recoveries of the 12 sulfonamides from the spiked soil samples were calculated for both methods: they ranged from $8.78 \pm 0.79\%$ (sulfisoxazole) to $96.66 \pm 3.55\%$ (sulfadiazine) for the first procedure (six compounds had the recovery level over 50%, three between 20–50% and three lower than 20%), and from $5.59 \pm 0.47\%$ (sulfisoxazole) to $61.39 \pm 5.59\%$ (sulfadiazine) for the second procedure (three compounds had the recovery level over 50%, three between 20–50% and six lower than 20%) (the uncertainty is expressed as the standard deviation). The only matrix effect to be observed in the samples prepared without any clean-up was with sulfaguanidine, the recovery values of which were extremely high ($293.65 \pm 27.72\%$); however, after the extract had been cleaned up on an SPE-column, the recovery was $7.43 \pm 0.75\%$. Generally, the recovery results show that there is no significant difference between the two different sample preparation steps, from which it may be inferred that this methodology can be used to determine sulfonamides in soil samples without prior clean-up. These experiments are still at a preliminary stage, however, so further investigations into the extraction procedure are necessary to improve recoveries from soil samples and to validate this analytical procedure.

In summary, the optimized method for determining veterinary sulfonamides with LC–MS/MS in MRM mode, unlike many other methods, satisfied both the criteria laid down in the Commission Decision of August 12, 2002 (2002/657/EC) and the validation requirements. In the literature, many different meth-

ods are described for determining these compounds, which usually use LC–MS/MS full scan mode, SIM mode or only one MRM transition [26,27,31–33,35]. According to the Commission Decision, this is not sufficient to confirm the presence of these compounds. The methodology developed in the present work is characterized by good validation parameters, low LODs and LOQs, as well as good precision, repeatability and applicability to real samples. The fact that no preconcentration step was necessary is also worthy of note.

4. Conclusion

The optimized chromatographic separation and MS/MS parameters for the analysis of common veterinary sulfonamide antibiotics by LC–MS/MS was done in order to deliver a systematic analytical methodology for their determination in both environmental and biological samples. The experiments were performed using ion trap mass spectrometry with electrospray ionization in order to work in multiple reaction monitoring (MRM) mode. Four identification points for every compound (a precursor ion and a minimum of two daughter ions) were selected according to the existing criteria for both screening and confirmatory methods for drug residues based on the identification points proposed by EU Commission Decision 2002/657/EC. Each MRM transition was tested not only for the qualitative but also for quantitative analysis of sulfonamides, which is a huge advantage due to the fact, that the quantification of the sulfonamides in a very complex matrices can be done not only based on one-selected transition. If there are some interferences, it is always possible to use another transition for the quantification purposes. Unlike other methodologies, this one satisfied these criteria and is applicable to the qualitative and quantitative analysis of sulfonamide residues in environmental and biological matrices.

Acknowledgement

Financial support was provided by the Polish Ministry of Research and Higher Education under grants DS 8200-4-0085-9 and BW 8000-5-0357-9.

References

[1] A. Nikolaou, S. Meric, D. Fatta, Anal. Bioanal. Chem. 387 (2007) 1225–1234.
[2] S.K. Khetan, T.J. Collins, Chem. Rev. 107 (2007) 2319–2364.
[3] S.D. Richardson, Anal. Chem. 78 (2006) 4021–4046.
[4] A.K. Sarmah, M.T. Meyer, A.B.A. Boxall, Chemosphere 65 (2006) 725–759.
[5] N. Kemper, Ecol. Indicat. 8 (2008) 1–13.
[6] I. Kanfer, M.F. Skinner, R.B. Walker, J. Chromatogr. A 812 (1998) 255–286.
[7] J.B. Addison, Residue Rev. 92 (1984) 1–28.
[8] M. Grote, C. Schwake-Anduschus, R. Michel, H. Stevens, W. Heyser, G. Langenkämper, T. Betsche, M. Freitag, Landbauforschung Völkenrode 1 (2007) 25–32.
[9] C.S. McArdell, E. Molnar, M.J.F. Suter, W. Giger, Environ. Sci. Technol. 37 (2003) 5479–5486.
[10] M.S. Díaz-Cruz, D. Barceló, Anal. Bioanal. Chem. 386 (2006) 973–985.
[11] T. Heberer, J. Hydrol. 266 (2002) 175–189.
[12] W.C. Lin, H.C. Chen, W.H. Ding, J. Chromatogr. A 1065 (2005) 279–285.
[13] Z. Ye, H.S. Weinberg, M.T. Meyer, Anal. Chem. 79 (2007) 1135–1144.
[14] A.J. Watkinson, E.J. Murby, S.D. Costanzo, Water Res. 41 (2007) 4164–4176.
[15] A. Gulkowska, H.W. Leung, M.K. So, S. Taniyasu, N. Yamashita, L.W.Y. Yeug, B.J. Richardson, A.P. Lei, J.P. Giesy, P.K.S. Lam, Water Res. 42 (2008) 395–403.
[16] W.L. Shelver, N.W. Shappell, M. Franek, F.R. Rubio, J. Agric. Food Chem. 56 (2008) 6609–6615.
[17] F. Hernández, J.V. Sancho, M. Ibáñez, C. Guerrero, Trends Anal. Chem. 26 (2007) 466–485.
[18] S.D. Richardson, Anal. Chem. 80 (2008) 4373–4402.
[19] S.C. Kim, K. Carlson, Analysis of antibiotics in solid samples, in: M. Petrović, D. Barceló (Eds.), Comprehensive Analytical Chemistry, vol. 50, 2007, pp. 95–131.
[20] C. Hartig, T. Storm, M. Jekel, J. Chromatogr. A 854 (1999) 163–173.
[21] S. Yang, J. Cha, K. Carlson, J. Chromatogr. A 1097 (2005) 40–53.
[22] V.K. Balakrishnan, K.A. Terry, J. Toito, J. Chromatogr. A 1131 (2006) 1–10.
[23] J.D. Li, Y.Q. Cai, Y.L. Shi, S.F. Mou, G.B. Jiang, J. Chromatogr. A 1139 (2007) 178–184.
[24] E.L. McClure, C.S. Wong, J. Chromatogr. A 1169 (2007) 53–62.
[25] C. Lin, S. Huang, Anal. Chim. Acta 612 (2008) 37–43.
[26] C. Hong, H. JianYing, W. LeZheng, S. Bing, Chin. Sci. Bull. 53 (2008) 514–520.
[27] M.E. Lindsey, M. Meyer, E.M. Thurman, Anal. Chem. 73 (2001) 4640–4646.
[28] A.L. Batt, D.S. Aga, Anal. Chem. 77 (2005) 2940–2947.
[29] A.M. Jacobsen, B. Halling-Sørensen, Anal. Bioanal. Chem. 384 (2006) 1164–1174.
[30] N.T. Malintan, M.A. Mohd, J. Chromatogr. A 1127 (2006) 154–160.
[31] W. Ben, Z. Qiang, C. Adams, H. Zhang, L. Chen, J. Chromatogr. A 1202 (2008) 173–180.
[32] M.Y. Haller, S.R. Müller, C.S. McArdell, A.C. Alder, M.J.F. Suter, J. Chromatogr. A 952 (2002) 111–120.
[33] A.M. Jacobsen, B. Halling-Sørensen, F. Ingerslev, S.H. Hansen, J. Chromatogr. A 1038 (2004) 157–170.
[34] A. Göbel, A. Thomsen, C.S. McArdell, A.C. Alder, W. Giger, N. Theiβ, D. Löffler, T.A. Ternes, J. Chromatogr. A 1085 (2005) 179–189.
[35] E. Martínez-Carballo, C. González Barreiro, S. Scharf, O. Gans, Environ. Pollut. 148 (2007) 570–579.
[36] M. de Liguoro, C. Poltronieri, F. Capolongo, C. Montesissa, Chemosphere 68 (2007) 671–676.
[37] A. Nieto, F. Borrull, R.M. Marcé, E. Pocurull, J. Chromatogr. A 1174 (2007) 125–131.
[38] J.J. Berzas Nevado, G. Castañeda Peñalvo, F.J. Guzmán Bernard, Anal. Chim. Acta 442 (2001) 241–248.
[39] G. Balizs, A. Hewitt, Anal. Chim. Acta 492 (2003) 105–131.
[40] A. Gentili, D. Perret, S. Marchese, Trends Anal. Chem. 24 (2005) 704–733.
[41] N.A. Botsoglou, D.J. Fletouris, E.J. Simeonidou, I.E. Psomas, Chromatographia 46 (1997) 477–482.
[42] M. Thompson, S. Ellison, R. Wood, Pure Appl. Chem. 74 (2002) 835–855.
[43] I. Taverniers, M. de Loose, E.V. Bockstaele, Trends Anal. Chem. 23 (2004) 535–551.
[44] W.M.A. Niessen, J. Chromatogr. A 812 (1998) 53–75.

Talanta 80 (2009) 954–958

Contents lists available at ScienceDirect

Talanta

journal homepage: www.elsevier.com/locate/talanta

Antibodies conjugated with new highly luminescent Eu^{3+} and Tb^{3+} chelates as markers for time resolved immunoassays. Application to simultaneous determination of clenbuterol and free cortisol in horse urine

M.A. Bacigalupo[a,*], G. Meroni[a], F. Secundo[a], C. Scalera[b], S. Quici[b]

[a] Istituto di Chimica del Riconoscimento Molecolare, CNR, Via M. Bianco 9, Milan 20131, Italy
[b] Istituto di Scienze e Tecnologie Molecolari, CNR, Via Golgi 19, Milan 20133, Italy

ARTICLE INFO

Article history:
Received 5 May 2009
Received in revised form 4 August 2009
Accepted 17 August 2009
Available online 22 August 2009

Keywords:
Clenbuterol
Hydrocortisone
Immunoassay
Lanthanide chelates
Time-resolved fluorescence
Horse urine

ABSTRACT

Highly luminescent Eu^{3+} and Tb^{3+} complexes of 10-[4-(3-isothiocyanatopropoxy)benzoylmethyl]-1,4,7,10-tetraazacyclododecane-1,4,7 triacetic acid $Eu^{3+} \subset \mathbf{1}$ and $Tb^{3+} \subset \mathbf{1}$ were conjugated with a goat anti-rabbit IgG and a rabbit anti-mouse IgG, respectively, and applied as markers in a time resolved immunoassay for simultaneous quantitative determination of anabolic compounds clenbuterol (CL) and hydrocortisone (HC). The assay was performed in horse urine, using a monoclonal antibody specific to CL and a rabbit polyclonal antibody specific to the free HC. These lanthanide chelates are very stable and highly luminescent in aqueous solution and allowed to reach 10 $\mu g\,L^{-1}$ and 40 $\mu g\,L^{-1}$ sensitivities for CL and for HC, respectively. Application to the horse urine, that is a very complex matrix, has a considerable interest in the control of illegal use of these compounds.

© 2009 Elsevier B.V. All rights reserved.

1. Introduction

Clenbuterol (4-amino-α-(t-butlaminomethyl)-3,5-dichloro-benzyl alcohol)(CL) and hydrocortisone (11β,17α,21-trihydroxy-pregn-4-ene-3,20-dione) (HC) are anabolic compounds used in veterinary field.

CL is a bronchodilatator used in non-infectious respiratory diseases or a supportive medication in infectious diseases [1,2]. Sometime CL is used for illegal purposes: it may be used as anabolic drug because it accelerates animals' growth developing of muscle mass and decreasing fat deposition. In this case CL presents a potential health problem in the consumption of food products from treated animals [3]. CL operates in any tissue with β_2-receptors; for protection of consumers, illegal treatment with CL is usually controlled by analysis in different tissues. In addition it may have a positive effect on the performance of racing horses. Furthermore its presence in urine in post race animals may lead to sanctions fixed by international racing authorities. In fact regulations regarding CL in race horses give zero tolerance. Therefore, several analytical approaches such as liquid-chromatography or gas-chromatography and mass-spectrometry [4–6], and immunoassay [7,8] have been described for detection of this compound.

Many natural or synthetic corticosteroids possess anti-inflammatory characteristics and also HC is used in veterinary medicine as anti-inflammatory drug [9]. Because its anabolic properties HC can be used for illegal purposes, as above reported for the CL. High urinary concentrations of HC in post race horses can be index of administration of this compound as doping substance for performance amelioration of the animals [10]. Considering the presence of endogenous hormone, the International Federation of Horseracing Authorities has fixed a threshold value of free HC in equine urine at 1 $\mu g\,mL^{-1}$. Many analytical methods, as above mentioned for CL, are used to control the presence of this compound [11–16].

Analysis of urine with conventional methods consist in separative techniques to isolate the target compound from other more concentrated compounds so that internal standard controls are necessary to monitor the recovery. For these techniques interferent peaks in the chromatograms and noisy base line must be removed to allow sensitivity. Therefore in conventional approach, the samples must be singly processed, that is laborious and time-consuming; furthermore the screening of many samples becomes very expensive. Moreover, each step of an analytical process introduces errors into the final result. Immunological methods appear to be a more convenient approach for these controls. These methods cover a wide concentration range and do not require pre-treatment

* Corresponding author. Tel.: +39 02 28500023; fax: +39 02 28901239.
E-mail address: mariangela.bacigalupo@icrm.cnr.it (M.A. Bacigalupo).

0039-9140/$ – see front matter © 2009 Elsevier B.V. All rights reserved.
doi:10.1016/j.talanta.2009.08.019

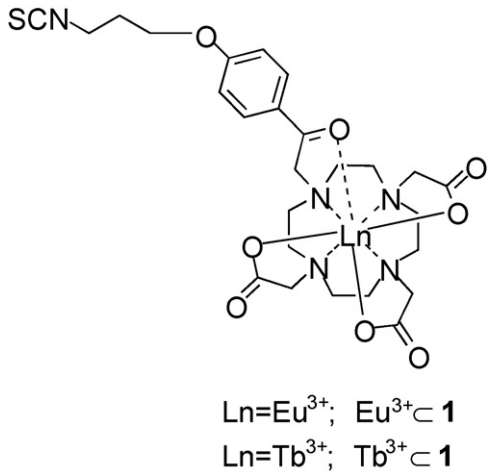


Fig. 1. Structural formula of $Eu^{3+} \subset \mathbf{1}$ and $Tb^{3+} \subset \mathbf{1}$ chelates.

of samples. They are simple, rapid, sensitive, and specific. Furthermore many samples can be analysed simultaneously in a short incubation time.

The use of lanthanide chelates as fluorescent labels in a time-resolved immunoassay results in the background elimination. In addition the high stability of complexes used in assay reported below allows the simultaneous determination of two different analytes, by reading the fluorescence at emission wavelengths specific for terbium or europium, respectively.

In this paper we report the preparation of goat anti-rabbit IgG and rabbit anti-mouse IgG conjugates with luminescent lanthanide chelates $Eu^{3+} \subset \mathbf{1}$ and $Tb^{3+} \subset \mathbf{1}$ (Fig. 1) and their use as markers in a time-resolved fluoroimmunoassay (TR-FIA) for simultaneous quantitative determination of anabolic compounds clenbuterol (CL) and hydrocortisone (HC). Application to the horse urine analysis, that is a very complex matrix (it contains a large excess of metabolites and conjugates that can interfere with assay), has a considerable interest to control the illegal use of these substances.

2. Materials and methods

2.1. Materials

Standard CL and the chemical related cross-reacting compounds (salbutamol, terbutaline, epinephrine, norepinephrine, fenoterol, ambroxol, phenylbutazone), standard HC and the chemical related compounds (prednisolone, cortisone, dexamethasone, betamethasone, flumethasone, beclomethasone,), hydrocortisone-3-(O-carboximethyl)oxime (HC-3CMO), hydrocortisone-21-hemisuccinate (HC-21HS) and all of the other chemicals, including bovine serum albumin (BSA), chicken egg albumin (OVA), rabbit anti-mouse IgG and goat anti-rabbit IgG, were obtained from Sigma–Aldrich (Milan, Italy). Complexes $Eu^{3+} \subset \mathbf{1}$ and $Tb^{3+} \subset \mathbf{1}$ were synthesized through a multi-step procedure [17].

2.2. Apparatus

A single-photon-counting time-resolved fluorometer (1232 DELFIA Fluorometer; Wallac, Turku, Finland) was used to measure fluorescence.

2.3. Specimen collection

Horse urine from five healthy animals were pooled, filtered in a glass vials, fractionated and stored at −20 °C until use.

2.4. Syntheses

2.4.1. CL-OVA and HC-BSA

The synthesis of CL-diazo-ovalbumin (CL-OVA) was performed according to [18].

HC-BSA was synthesized and used as immunogen and as solid phase on polystyrene microwells. Briefly 6.5 mg of HC-3CMO were dissolved in 0.2 mL of anhydrous dimethylformamide and cooled to 4 °C with 5 μL of tri-*n*-butylamine. After 5 min 5 μL of isobutylchloroformate were added and the solution was left for 30 min at 4 °C. This mixture was added to 19 mg of BSA dissolved in 0.5 mL 40% dimethylformamide in water and then 50 μL 1N NaOH was added. Reaction mixture was stirred at 4 °C for 1 h while the pH was kept at 8.5–9 by repeatedly adding 5 μL 1N NaOH, and then left at 4 °C overnight. The conjugate was purified by gel filtration on Sephadex G-50 column with 0.05 M NH_4HCO_3 and lyophilized.

2.4.2. IgG-($Tb^{3+} \subset \mathbf{1}$) and IgG-($Eu^{3+} \subset \mathbf{1}$)

$Tb^{3+} \subset \mathbf{1}$ was conjugated with a rabbit anti-mouse IgG and $Eu^{3+} \subset \mathbf{1}$ was conjugated with a goat anti-rabbit IgG, respectively. The conjugates were prepared using 2 mg of affinity purified IgG dissolved in 2 mL of 0.1 mol L^{-1} sodium carbonate buffer (pH 9). A solution of 500 μg of each chelates in 100 μL of ethanol was then added and the mixture was incubated for 30 min at room temperature. The labelled IgG was separated on Sephadex G-50 column, eluting with 0.05 mol L^{-1} Tris–HCl buffer (pH 7.5).

2.5. Antibody preparation

Monoclonal antibody specific for CL was obtained as described in [18].

Polyclonal antibody is specific for free HC and was obtained using as immunogen HC-3CMO-BSA. Antiserum was produced in New Zealand white rabbits with 100 μg of conjugate for each immunization. The rabbits were subcutaneously injected monthly with the conjugate suspended in 1 mL of saline solution and Freund's complete adjuvant. The antisera were characterized by immuno-enzymometric assay with anti rabbit IgG antibody conjugated with horseradish peroxidase. Antiserum with satisfactory characteristics was obtained 3–4 months after the first immunization. The anti-BSA present was eliminated by precipitation by adding 0.2% BSA to the rabbit serum. The affinity determined according to [19] was 1.6×10^9 L mol^{-1}. The antiserum was fractioned and stored at −20 °C in phosphate buffered saline 0.15 mol L^{-1} pH 7.4 containing 0.02% timerosal as preservative.

2.6. Antibody titre evaluation

The antibodies were assayed separately by incubation in wells coated with OVA-CL and BSA-HC respectively: 100 μL of serial dilutions of ascites or antiserum in 0.05 M Tris–HCl buffer pH 7.5 containing 0.9% NaCl (1:250, 1:2500 and 1:25 000) were applied to the coated wells, and the antibody bound to the solid phase was detected by means of rabbit anti-mouse IgG conjugated to $Tb^{3+} \subset \mathbf{1}$, or goat anti-rabbit IgG conjugated to $Eu^{3+} \subset \mathbf{1}$. After washing 100 μL of dissociation solution containing 4 mol L^{-1} urea and 1% sodium dodecylsulfate in water were added to each well. Fluorescence was measured after 10 min with the time-resolved fluorometer with Xenon lamp as source at 545 nm the delay time being 500 μs for Tb^{3+}chelate, and at 615 nm with delay time 400 μs for Eu^{3+} chelate. The dilution giving 70% of fluorescence intensity in comparison

with 100% of saturate solid phase fluorescence was chosen as working titre.

2.7. Solid phase

Polystyrene micro-titre wells were coated overnight at 27 °C with 200 μL of 0.1 M carbonate buffer, pH 9.0, containing 15 μg/mL of OVA-CL conjugate and 15 μg/mL of BSA-HC conjugate. The micro-titre wells were washed with carbonate buffer and a second coat was made with 250 μL of 2% BSA solution in the same buffer for 4 h at 27 °C. The wells were washed five times with 0.05 M Tris–HCl buffer pH 7.5 containing 0.9% NaCl and 0.05% NaN_3 and stored dry at 4 °C until use.

2.8. TR-FIA

TR-FIA was performed with the CL and HC standards dissolved in Tris–HCl buffer pH 7.5 containing 0.9% NaCl, and 0.25% BSA: the presence of BSA in solution avoids possible non specific adsorption. The use of chicken egg albumin, both in the second coating and in assay buffer does not change the results (not reported data).

Serial dilutions between 50 pg and 100 ng of the two standards were transferred in duplicate (20 μL + 20 μL) into polystyrene micro-wells coated with OVA-CL and BSA-HC conjugates. Specific antibodies were diluted at a working titre 1:1200 for anti-CL and 1:2500 for anti-HC; 50 μL of each dilution were added to all of the wells other than that used for the blank evaluation, to which the same volume of buffer was added. The volume in each well was adjusted to 200 μL with buffer. Assay was performed directly in urine by applying 20 μL of samples in duplicate instead of the standards. Validation of the method was performed by assaying recovery and matrix effect in urine samples spiked with 100, 1000 and 10 000 pg of standard CL and the same quantities of HC. The wells were washed and 100 μL of buffer containing an excess (0.3 nmol) of rabbit anti-mouse IgG-($Tb^{3+} \subset \mathbf{1}$) and 100 μL (0.3 nmol) of goat anti-rabbit IgG-($Eu^{3+} \subset \mathbf{1}$) complex were added and incubated for 30 min. After washing 200 μL of dissociation solution were added to each well and fluorescence was measured as described in antibody titre evaluation section.

3. Results and discussion

3.1. Antibody specificity

Specificity of the monoclonal antibody was evaluated by assaying the cross-reactions of CL related compounds, calculated at 50% of fluorescent signal reduction against the 100% of standard CL according to the formula:

$$\frac{IC_{50}(\mu g\,L^{-1})\ \text{of CL}}{IC_{50}(\mu g\,L^{-1})\ \text{of competitor}}\%$$

All assayed compounds did not significantly interfere in the assay, as shown in Table 1.

Specificity of polyclonal antibody was assayed in the same way, with HC related compounds.

Values are listed in Table 1.

3.2. Assay performances

In order to evaluate possible interferences between the reagents we previously set up the standard curves separately for each analyte. Each curve resulted superimposed to the corresponding curve obtained in the simultaneous determination: that may be ascribed to the lower affinity of anti-rabbit IgG-($Eu^{3+} \subset \mathbf{1}$) for anti-mouse conjugated with Tb^{3+} chelates in comparison with its affinity for non conjugated specific antibody.

Table 1
(A) Percentage of cross reactivity of CL-related compounds with CL specific antibody calculated at 50% of fluorescence signal reduction. (B) Percentage of cross reactivity of HC-related compounds with HC specific antibody calculated at 50% of fluorescence signal reduction.

A		B	
Compounds	%CR	Compounds	%CR
Clenbuterol	100	Hydrocortisone	100
Salbutamol	1.6	Prednisolone	5.5
Terbutaline	0.4	Cortisone	5.3
Epinephrine	<0.1	Dexamethazone	<0.1%
Norepinephrine	<0.1	Betamethasone	<0.1%
Fenoterol	<0.1	Flumethasone	<0.1%
Ambroxol	<0.1	Beclomethasone	<0.1%
Phenylbutazone	<0.1		

3.2.1. Sensitivity

The antibody dilution giving 70% of fluorescence intensity in comparison with 100% of saturate solid phase fluorescence was chosen as working titre. Dose–response curves for CL and HC were obtained by averaging eight individual curves normalized by reporting fluorescence values as $\%F/F_0$ where F was the mean of cps for each standard and F_0 was the mean of cps for zero CL or HC concentration; blank values (2100 ± 218 cps for IgG-Eu^{3+}chelate and 3650 ± 355 cps for IgG-Tb^{3+}chelate) were subtracted. The high slope of calibration graphs allows accurate and precise determinations. Sensitivity, defined by detection limit of the method, was determined by calculating the minimum amount of standards that could be significantly distinguished from zero (mean binding at zero dose at three times the SD). This value, calculated from three curves prepared in duplicate was 10 $\mu g\,L^{-1}$ for CL and 40 $\mu g\,L^{-1}$ for HC. These detection limits allow direct determination in horse urine using 20 μL of sample.

3.2.2. Recovery evaluation

Accuracy was assayed by evaluation of standard recovery: we compared the calibration graph with the graph obtained by spiking urine samples with 10, 100, 1000 and 10 000 pg of CL and HC. Results were shown in Fig. 2 for CL and in Fig. 3 for HC analysis. As shown in Fig. 2 the curve resulted superimposed to the standard curve obtained in buffer. In Fig. 3 HC determination was carried out as reported for CL: the curve resulted parallel to the standard curve obtained in buffer, with the difference due to the endogenous free HC, evaluated as 1.5 ng/well. Reproducibility and precision profile are reported in Figs. 1 and 2. The stability of two conjugated antibodies stored at −20 °C was evaluated by measuring the maximum binding capacity and was at least eight months. The coated plates are very stable if stored dry at +4 °C.

3.2.3. Matrix effect

TR-FIA was also validated by determining the matrix effect as recovery of CL and HC in different volumes of urine spiked with CL (500 ng/100 mL) and HC (500 ng/100 mL). Results are reported in Table 2.

The values obtained by TR-FIA show a good recovery for all sample dilutions.

HC recovery takes in account the presence of endogenous concentration of analyte.

This study combines advantages of immunological methods, sensitivity of time-resolved fluorescent revelation, and high stability constants of the new chelates. The detectability of labels is one of the most critical factors that limit sensitivity of immunoassay. The development of fluorescent labels provides an important

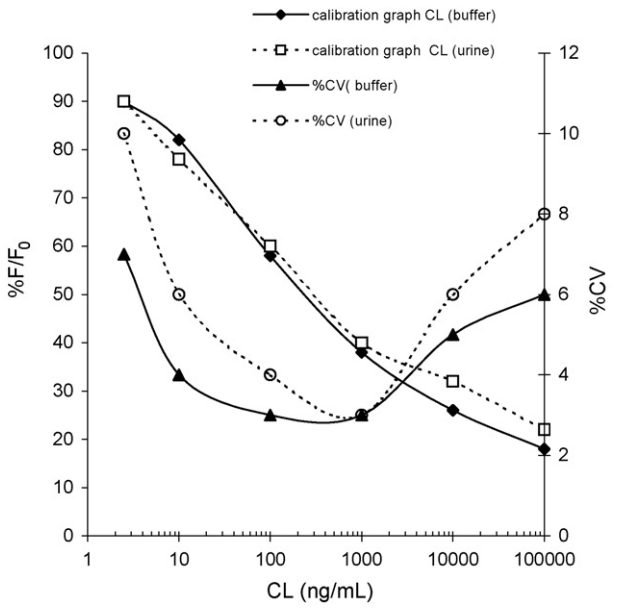


Fig. 2. Dose–response curve and precision profile (percent coefficient of variation) for TR-FIA of CL in buffer and in pooled horse urine. *F* and F_0 are expressed as cps. Each point represents the mean of eight determinations in duplicate.

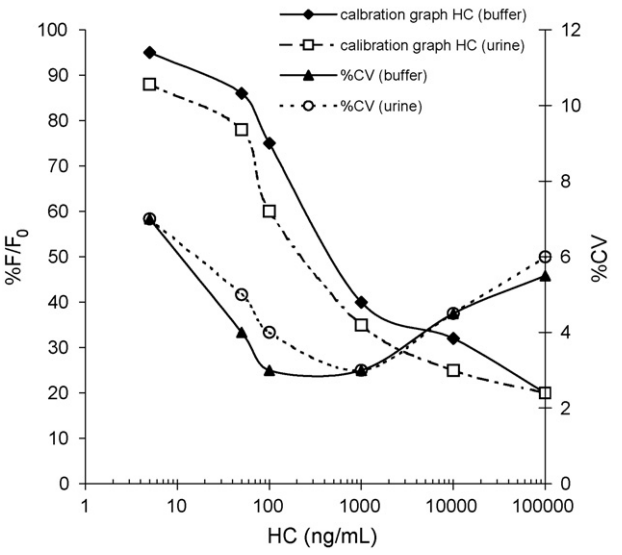


Fig. 3. Dose–response curve and precision profile (percent coefficient of variation) for TR-FIA of HC in buffer and in pooled horse urine. *F* and F_0 are expressed as cps. Each point represents the mean of eight determinations in duplicate.

simplification of immunological procedures. Their usefulness has, however, been limited by the high background fluorescence always present in the measurements, which seriously limits the sensitivity of the assay. Chemiluminescent signals also present similar problems.

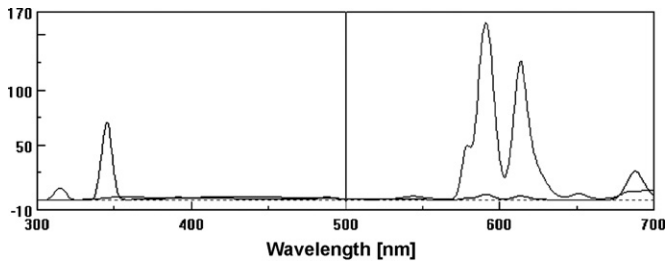


Fig. 4. Emission spectra of $Eu^{3+} \subset \mathbf{1}$ complex at 315 nm (grey) and 325 nm (black) excitation wavelength.

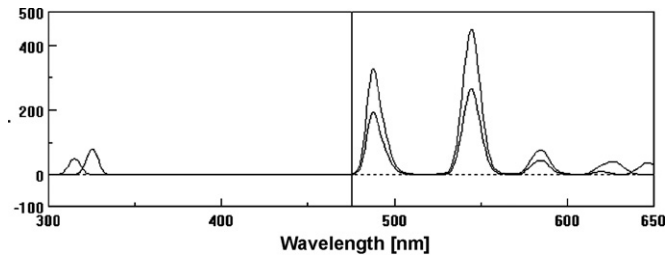


Fig. 5. Emission spectra of $Tb^{3+} \subset \mathbf{1}$ complex at 315 nm (grey) and 325 nm (black) excitation wavelength.

Lanthanide chelates show narrow and strong emission bands around 600 nm and an exceptionally long decay time (up to a millisecond instead nanoseconds of most molecules), which allow the elimination of the high background of the fluorescent labels.

Florescence spectra of $Eu^{3+} \subset \mathbf{1}$ and $Tb^{3+} \subset \mathbf{1}$ chelates are reported in Figs. 4 and 5.

Excitation by Xenon lamp without filter is useful for both derivatives.

Simultaneous dual label TR-FIA using Eu^{3+} and Tb^{3+} chelates are already reported [20,21]. In comparison with markers used in these assays, the Eu^{3+} and Tb^{3+} complexes described in this paper have an important advantage, because they are fluorescent in aqueous solution. Tanks to this characteristic, the addition of enhancement solution used to transfer lanthanide ions to β-diketone complexes can be avoided. This allows obtaining higher signal stability and cost reduction.

In addition the $Eu^{3+} \subset \mathbf{1}$ and $Tb^{3+} \subset \mathbf{1}$ complexes have high stability constants similar to those of the lanthanide complexes reported in [22], so we can directly determine the fluorescence, for two analytes simultaneously and with a good sensitivity. Fluorescent intensity of chelates decreases dramatically when they are bound to the antibodies, as already reported for same ter-pyridyne derivatives [23]. It decreases up to the 10% of value obtained with the same concentration of free chelates in Tris–HCl buffer. Nevertheless the fluorescent signals are still sufficient for application in time-resolved immunoassay with good sensitivity. The reagents can be easily obtained and moreover their use does not need expert technicians. This assay should thus provide a useful alternative to the conventional methods to control illegal use of CL and CH: in fact many samples can be analysed simultaneously in a short incubation time and with a low cost. In case a sample should result

Table 2
Matrix effect evaluation in urine spiked with standard CL (500 ng/100 mL) and standard HC (500 ng/100 mL).

Spiked urine (μL)	CL			HC		
	Expected (ng)	Found (ng, ±SD)	Recovery (%)	Expected (ng)	Found (ng, ±SD)	Recovery (%)
5	0.025	0.026 ± 0.007	104	0.400	0.405 ± 0.037	101.2
10	0.050	0.049 ± 0.005	98	0.800	0.785 ± 0.080	98.3
20	0.100	0.99 ± 0.008	99	1.600	1.589 ± 0.098	98.5

positive, a confirmatory assay with a chromatographic method is always recommended.

References

[1] J.D. Harkins, N.E. Robinson, W.E. Woods, A.F. Lehner, M.D. Smith, R.S. Gates, M. Fisher, T. Tobin, J. Vet. Pharmacol. Ther. 23 (2000) 251.
[2] L.R. Soma, C.E. Uboh, F. Guan, Y. Luo, D. Teleis, L. Runbo, E.K. Birks, D.S. Tsang, P. Habecker, J. Vet. Pharmacol. Ther. 27 (2004) 91.
[3] C.F. Kearns, K.H. McKeever. Vet. J., 2008.
[4] P. Van Eenoo, F.T. Delbeke, P. Deprez, Biomed. Chromatogr. 16 (2002) 475.
[5] F. Guan, C.E. Uboh, L.R. Soma, Y. Luo, R. Li, E.K. Birks, D. Teleis, J.A. Rudy, D.S. Tsang, Rapid Commun. Mass Spectrom. 16 (2002) 1642.
[6] M. Thevis, G. Opfermann, W. Schänzer, J. Mass Spectrom. 38 (2003) 1197.
[7] M.A. Bacigalupo, A. Ius, G. Meroni, M. Dovis, E. Petruzzelli, Analyst 120 (1995) 2269.
[8] J.D. Harkins, W.E. Woods, A.F. Lehner, M. Fisher, T. Tobin, J. Vet. Pharmacol. Ther. 24 (2001) 7.
[9] J.P. Antignac, B. Le Bizec, F. Monteau, F. André, Steroids 67 (2002) 873.
[10] L.M. Ribeiro Neto, M.C. Salvatori, H.S. Spinosa, Vet. Res. Commun. 24 (2000) 239.
[11] P.W. Tang, W.C. Law, T.S. Wan, J. Chromatogr. B Biomed. Sci. Appl. 754 (2001) 229.
[12] J.E. Wear, L.J. Owen, K. Duxbury, B.G. Keevil, J. Chromatogr. B Analyt Technol. Biomed. Life Sci. 858 (2007) 27.
[13] J.H. Andersen, L.G. Hansen, M. Pedersen, Anal. Chim. Acta 617 (2008) 216.
[14] A. Vonaparti, E. Lyris, I. Panderi, M. Koupparis, C. Georgakopoulos, J. Mass Spectrom. 43 (2008) 1255.
[15] H. Horie, T. Kidowaki, Y. Koyama, T. Endo, K. Homma, A. Kambegawa, N. Aoki, Clin. Chim. Acta 378 (2007) 66.
[16] L. Wood, D.H. Ducroq, H.L. Fraser, S. Gillingwater, C.L. Evans, A.J. Pickett, D.W. Rees, R. John, A. Turkes, Ann. Clin. Biochem. 45 (2008) 380.
[17] C. Scalera, Doctoral Thesis, Faculty of Mathematical, Physical and Natural Sciences, University of Milan, 2008.
[18] E. Petruzzelli, A. Ius, S. Berta, M. Dovis, A. Albertini, Food Agric. Immunol. 8 (1996) 3.
[19] B. Friguet, A.F. Chaffotte, L. Djavadi-Ohaniance, M.E. Goldberg, J. Immunol. Methods 77 (1985) 305.
[20] S. Eriksson, M. Vehniäinen, T. Jansén, V. Meretoja, P. Saviranta, K. Pettersson, T. Lövgren, Clin. Chem. 46 (2000) 658.
[21] M. Ankelo, A. Westerlund, K. Blomberg, M. Knip, J. Ilonen, A.E. Hinkkanen, Clin. Chem. 53 (2007) 472.
[22] S. Quici, M. Cavazzini, M.C. Raffo, M. Botta, G.B. Giovenzana, B. Ventura, G. Accorsi, F. Barigelletti, Inorg. Chim. Acta 360 (2007) 2549.
[23] V.M. Mukkala, M. Helenius, I. Hemmilä, J. Kankare, H. Taralo, Helv. Chim. Acta 76 (1993) 1361.

Talanta 80 (2009) 959–966

Contents lists available at ScienceDirect

Talanta

journal homepage: www.elsevier.com/locate/talanta

Simultaneous determination of CFC-11, CFC-12 and CFC-113 in seawater samples using a purge and trap gas-chromatographic system

Serena Massolo*, Paola Rivaro, Roberto Frache

Department of Chemistry and Industrial Chemistry, University of Genoa, via Dodecaneso 31, 16146 Genoa, Italy

ARTICLE INFO

Article history:
Received 5 June 2009
Received in revised form 7 August 2009
Accepted 17 August 2009
Available online 21 August 2009

Keywords:
Chlorofluorocarbons
Gas-chromatography
Purge and trap technique
Seawater analysis
Environmental analysis

ABSTRACT

We have optimized the analytical parameters of a homemade instrument for the simultaneous measurement of the chlorofluorocarbons CCl_2F_2 (CFC-12), CCl_3F (CFC-11) and $C_2Cl_3F_3$ (CFC-113) in seawater. Seawater samples are flame sealed into 60 ml glass ampoules avoiding any contact with the atmosphere and stored in cold, dark condition until analysis. In the laboratory, after cracking the ampoule in an enclosed chamber filled with ultra-pure nitrogen, the seawater sample is transferred to a stripping chamber, where ultra-pure nitrogen is used to purge the dissolved CFCs from the seawater. The extracted gases are then cryogenically trapped, subsequently the trap is isolated and heated and the CFCs are transferred by a carrier gas stream into a precolumn and then are separated on a gaschromatographic packed column. To separate adequately CFC-12 from N_2O, during the early part of the chromatographic run, the gas stream passes through a molecular sieve, which is then isolated and backflushed. The CFCs are detected on an electron capture detector (^{63}Ni ECD). After a careful choice of the experimental conditions, the performances of the system were evaluated. The detection limits for seawater samples are: 0.0081 pmol kg^{-1} for CFC-12, 0.0073 pmol kg^{-1} for CFC-11 and 0.0043 pmol kg^{-1} for CFC-113. The reproducibility of replicate samples lies within 5% for the three CFCs. The system has been successfully employed for CFC measurements in seawater samples collected in the Ross Sea (Antarctica) in the framework of the Italian Antarctic research project.

© 2009 Elsevier B.V. All rights reserved.

1. Introduction

Several chemical compounds have been widely used as tracers of ocean circulation and mixing processes. They include nutrients and dissolved oxygen, which have a natural background level and a quasi-steady state distribution in the deep ocean, radiocarbon and tritium, which have background levels significantly altered by human activities and anthropic compounds such as chlorofluorocarbons (CFCs).

Production and release of CCl_2F_2 (CFC-12) and CCl_3F (CFC-11) in the atmosphere began in the 1930s and increased rapidly during the following five decades. Differently, the atmospheric concentration of $C_2Cl_3F_3$ (CFC-113) increased rapidly during the 1980s. CFCs are volatile, chemically stable and characterized by rapid mixing rates within the lower atmosphere, so their tropospheric concentrations are relatively uniform. The CFC concentrations in the atmosphere can be reconstructed as functions of location and time [1]. Atmospheric CFCs cross the air-sea interface and dissolve in surface seawater; their equilibrium concentrations can be calculated as a function of seawater temperature and salinity and atmospheric gas concentration [2]. Indeed, CFCs have a time-dependent oceanic input. Although the degradation of CFCs in marine environment under reducing conditions (such as fjords) was reported [3], in well-oxygenated waters (such as oceanic waters) they are chemically stable. Thus, they can serve as transient tracers of the ocean circulation.

Oceanic CFC measurements have been widely used to evaluate the variability of water mass formation and rates of ocean ventilation [4–7], to assess ocean circulation and climate models [8–13] and to quantify the ocean uptake of anthropogenic CO_2 [14–17]. CFCs are often used to calculate the "age" of a water sample, commonly defined as the time elapsed since the water parcels contained in the water sample lost direct contact with the atmosphere [18].

Volatile and semi-volatile organic compounds account for a large part of chemicals of environmental interest, which are analyzed by gas chromatographic (GC) methods. Several compounds, including CFCs, have low concentration levels in aqueous samples and the most used GC detectors are not able to detect them. For this reason, the sample preparation becomes essential. Further,

* Corresponding author. Tel.: +39 010 3536178; fax: +39 010 3536190.
E-mail addresses: massolo@chimica.unige.it (S. Massolo), rivaro@chimica.unige.it (P. Rivaro), frache@chimica.unige.it (R. Frache).

0039-9140/$ – see front matter © 2009 Elsevier B.V. All rights reserved.
doi:10.1016/j.talanta.2009.08.021

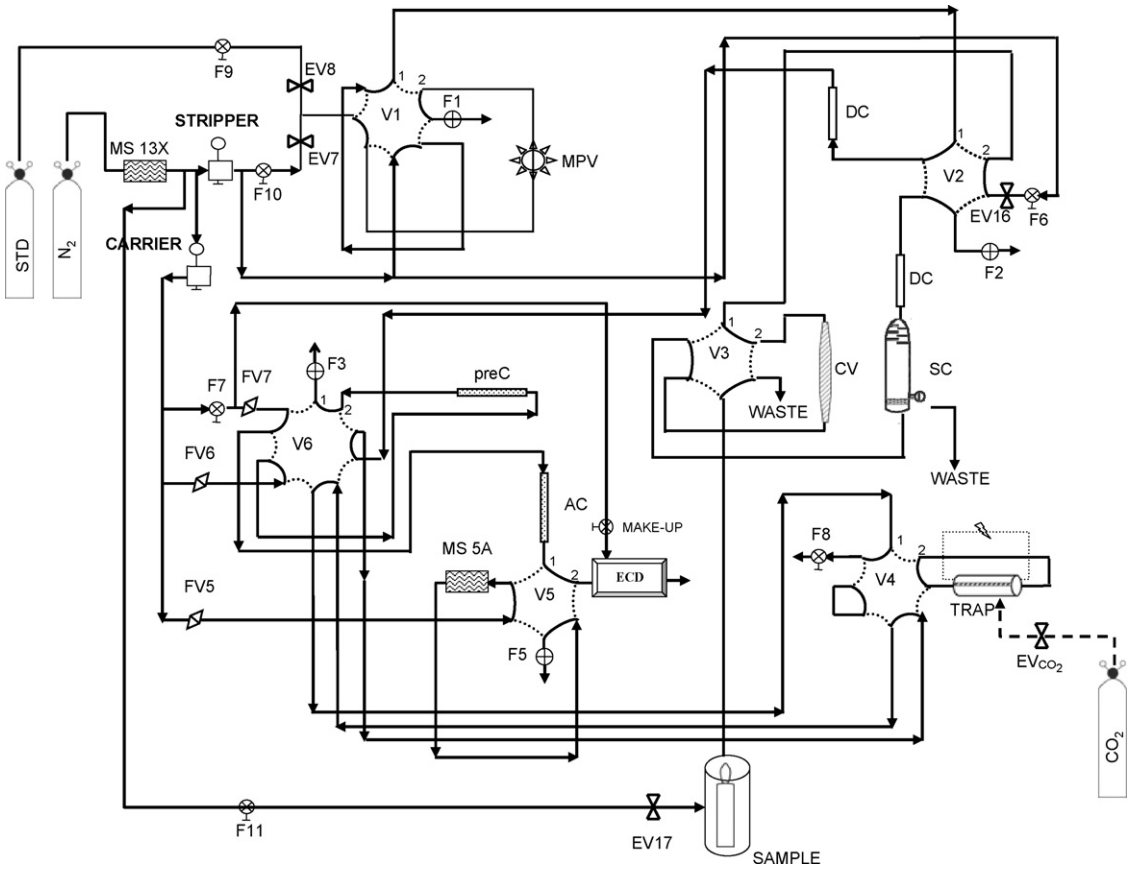


Fig. 1. Schematic flow scheme of the CFC extraction and analytical system in "stand by" mode. Tubing connecting all the components are stainless steel (SS). All the valves are electrically actuated under program control. For abbreviations see Table 1.

the number of operations and processes involved in the sample preparation stage should be kept to a minimum.

The CFC-11 and CFC-12 analysis in seawater was introduced by Bullister and Weiss [19] and it has been widely used in the succeeding years. The introduction of the CFC-113 measure, the necessity to improve the data quality and to reduce the sample contamination, the aim to shorten the analysis time and to eliminate most of the manual procedures encourage several laboratories to develop ocean tracer methods and measurements [8,20–22].

This paper describes the optimization of the main instrumental parameters of a purge and trap-gaschromatographic system for the simultaneous determination of CFC-11, CFC-12 and CFC-113 in seawater samples. Particularly, a thorough study of the CFC stripping from the seawater samples was carried out. The purge and trap system was built in our laboratories following the design provided by W. Smethie and E. Gorman (LDEO, Columbia University, New York, USA). Some design modifications have been made. They mainly concerned the ampoule housing, the nitrogen flow regulation and the trap heating system. These modifications are described in Sections 2.1 and 2.4. The optimized analytical system has been used to analyze seawater samples collected in the Ross Sea (Antarctica) during the austral summer 2002–03 Italian Antarctic Expedition.

2. Experimental

2.1. Apparatus

The apparatus consists of a purge-and-trap system interfaced to a gas chromatographer (GC) equipped with an electron capture detector (ECD). The purge and trap system and the interfacing devices were built in our laboratories following, and partially modifying, the instrumental schemes provided by W. Smethie and E. Gorman (LDEO, Columbia University, New York, USA). A part of the apparatus is devoted to gas analysis and it is used for calibration with standard gas mixture, while another part is devoted to CFC extraction from water samples.

The flow scheme is shown in Fig. 1, while Table 1 lists the main components of the analytical system.

Ultra-high purity nitrogen (N_2) is used as both stripping and carrier gas. Pressure from the gas cylinder is reduced to approximately 7 bar using a high purity pressure regulator. To remove CFC impurities present in the nitrogen supply, N_2 flows through a trap (molecular sieve MS 13X 60/80 mesh) held at room temperature. The trap is reconditioned by heating to 200 °C and by purging with a reverse N_2 flow of several hundred ml min^{-1} for about 4 h. The MS 13X reconditioning is required when the baseline increases during the analysis of system blanks due to a gradual CFC release from the trap. The nitrogen, downstream from MS 13X, is divided into three pathways: carrier gas, stripper gas and make up gas straight directed to the ECD. The upstream pressure of the stripper gas and of the carrier gas is adjusted to 2.0 bar and to 3.0 bar respectively, using two pressure regulators. We modified the Smethie's design by adding a needle valve for the fine adjustment of the carrier gas flow rate (approximately 30 ml min^{-1} as measured at the ECD inlet) (cf. F7 in Fig. 1). In addition, we split the carrier gas stream into three ways, each of them provided with an on/off valve (cf. FV5, FV6, FV7 in Fig. 1). This adjustment helped us in the leak procedure test and allowed a separate cleaning of the analytical column and the molecular sieve 5 Å, improving the control of the system contamination. The standard gas inlet is connected to a cylinder of a compressed calibration standard gas mixture, which is injected into the analytical system through an electro-valve (EV8). The sam-

Table 1
List of the components of the analytical system.

MS 13X	Molecular Sieve 13X columns are used for removing contaminants from the ultra high purity supply. Pressure from the nitrogen cylinder to the MS 13X is set at 7 bar using a SS pressure regulator (Air Liquide). MS 13X column consists of 1.5 m length of MS 13X 60/80 mesh, packed in 1/4 in. OD stainless steel (SS) tubing and is activated by heating at 300 °C for 12 h.
Pressure regulator	Air Liquide high precision SS pressure regulator is used to set upstream pressure of the nitrogen stream.
Flowmeter (F1- F5, F8)	Flowmeters used for checking the purged gas stream.
Metering valves (F6- F7, F9-F11)	Swagelok SS needle valves for regulating flow rate of the nitrogen stream.
Tubing	The SS tube diameters of the analytical system are 1/8 in. (Swagelok fittings).
Stripping chamber (SC)	Seawater sparging chamber with volume of about 75 cm^3, fitted with a fine pore glass frit at the lower end is used to extract the dissolved CFCs from the seawater sample. At the upper end glass flats orthogonally to the gas flow are attached to the chamber walls to reduce spray generated from bursting bubbles during the sparging process from being carried out the stripping chamber and through valve V2.
V1	An eight port Valco valve for directing flow from the MPV to valve V2.
V2	A six port Valco valve for connecting/isolating the stripping chamber from the rest of system.
V3	A six port Valco valve for directing water sample/stripper gas from calibrated volume to stripping chamber and for connecting ampoule in the cracking chamber with the analytical system.
V4	An eight port Valco valve for switching the trap in/off line with valve V6.
V5	A six port Valco valve for directing flow from MS 5A to ECD and from analytical column to ECD.
V6	A 10 port Valco valve for directing flow through pre-column and analytical column and for connecting V4 to V5.
EV	Electro-Valves automatically actuated via software input to enable/prevent gas stream.
MPV	A 10 port multi-position Valco valve with the calibrated gas loop.
FV(5-7)	On/off ball valve used to alternatively isolate a part of the gas analytical track.
Trap	A 1/16 in. OD SS tube 25 cm long packed in the central part with 10 cm of 80/100 mesh Unibeads 2S (Superchrom).
MS 5A	A 1/8 in. OD SS tube packed with 10 cm of Molecular Sieve 5Å (Superchrom) kept at 50 °C.
Precolumn (PreC)	A 1/8 in. OD SS tube packed with 1 m of 80/100 mesh Porasil B (Superchrom) kept at 140 °C in the GC oven.
Column (AC)	A 1/8 in. OD SS tube packed with 1.5 m of 60/80 mesh Carbopack B (Superchrom) held in the GC oven at 140 °C.
ECD	Electron Capture Detector with ^{63}Ni source held at 300 °C in a Varian 3400 gas chromatograph.
Calibrated Volume (CV)	A glass graduate burette with volume of about 34 cm^3 used to sub sample a known volume of seawater sample from the ampoule.
Drying Column (DC)	A 17 cm long 3/8 in. diameter glass tube packed with desiccant magnesium perchlorate ($Mg(ClO_4)_2$) held in place with glass wool.

ple gas passes through a short glass tube filled with magnesium perchlorate ($Mg(ClO_4)_2$), which acts as a drying agent preventing from the analytical column contamination. Then the sample flows through the trap to hold CFC-11, CFC-12 and CFC-113. The trap consists of 1/16 in. OD tubing packed with Unibeads 2S 80/100 mesh, cooled at -78 °C by directing a flow of compressed CO_2 in an enclosure around the trap. After 270 s, the trap is isolated by switching the valve V4, then it is rapidly heated to 100 °C by passing a high amperage current through the wall of the 1/8 in. SS tube that holds the trap. The trap temperature is controlled by a thermocouple welded to SS wall of the trap. The trap temperature maintenance was improved with respect to the Smethie's design by adding a further thermostatic cover outside the trap. After 120 s of heating, the valves V4, V5 and V6 are switched and the sample gases held in the trap are flushed onto the precolumn (80/100 mesh Porasil B packed in a 1/8 in. OD SS tube and held in the GC oven at 140 °C) for the elution of the higher molecular weight compounds and the initial separation of CFCs. During the trapping of the next sample, the precolumn and the main column are backflushed to purge the late-eluting compounds.

The separation of CFC-11, CFC-12 and CFC-113 occurs on the GC main column (80/100 mesh Carbopack B held in the GC oven at 140 °C). To adequately separate CFC-12 from N_2O, the gas stream passes through a Molecular Sieve 5 Å (MS 5A) kept at 50 °C, during the early part of the chromatographic run. After 130 s since the run beginning, the MS 5A is isolated by switching V5 and backflushed to allow any gases remaining in the MS 5A to be vented. The timing for the V5 valve switching was determined empirically to limit the baseline noise during the elution of the CFCs.

The GC is equipped with a ^{63}Ni ECD held at 300 °C. The frequency signal from the ECD is converted by a Varian Star 800 Module Interface to an output and sent to the Varian Star Workstation for data acquisition, plotting and integration of the peak areas.

All the procedures (loop selection, trap cooling/heating, etc.) and the valve switching are controlled by a personal computer equipped with multifunction cards (National Instruments PCI-6013 and PCI-6503) using a software exclusively written for this system by OMEGA s.r.l. (Genoa, Italy) utilizing a commercially available software library (National Instruments-LabVIEW 7 Express).

2.2. Standards and calibration

The CFC-11, CFC-12 and CFC-113 working standard mixture is obtained by diluting in ultra high–pure N_2 a concentrated standard mixture prepared and certified by SIAD S.p.A. (Bergamo, Italy).

As the three CFCs have different solubility in seawater [2,23], their amounts and ratios in seawater do not match the atmospheric ones. Thus, the working standard gas mixture matches the concentrations and the ratios of the CFCs extracted from samples of surface seawater. CFC concentrations in the working standard mixture were accurately measured and certified by the Lamont Doherty Earth Observatory tracer group (LDEO, Columbia University, New York, USA) against Scripps Institution of Oceanography (SIO, San Diego, USA) primary standard.

An example of the chromatogram obtained for a working standard CFC mixture injection is shown in Fig. 2.

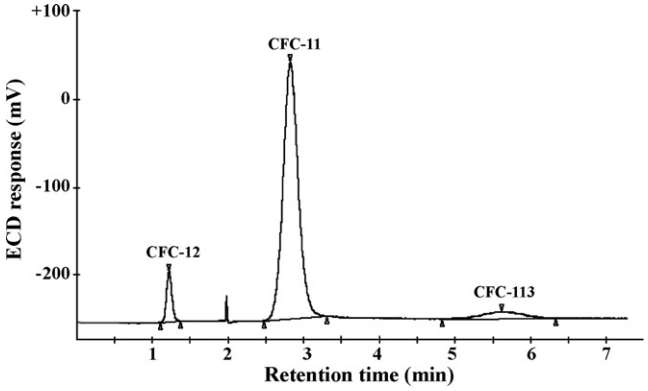


Fig. 2. Chromatogram of a working CFC standard gas mixture injection. The discontinuity of the baseline after the CFC-12 elution depends on a change of the carrier gas flow due to valve V5 switching.

The analytical system is calibrated by multiple injections of the working standard mixture in ten loops of different volumes (from few microlitres to few millilitres). The range of the volumes allows the system to be calibrated over a relatively wide range of seawater sample concentrations. The volume of the loops has been determined gravimetrically, by filling with distilled water, with a precision of approximately 0.5%.

Room temperature and pressure are recorded during each set of analyses to calculate the injected gas moles. A whole calibration curve is carried out before measuring each set of seawater samples; moreover measurements of a selected loop are daily carried out during and after the sample analyses to account for short-term system fluctuations depending on the variability of room temperature and pressure. Detector responses for the three CFCs are non-linear in the range of our measurements.

The CFC peak areas are converted into moles using polynomial expressions obtained by a non-linear least squares fit of the calibration data using a specially written software. System blank peak areas are subtracted from the peak areas of all the standard gas samples, while stripper blank areas are subtracted from seawater samples peak areas.

2.3. Water sampling

Seawater samples for CFC analysis are collected in 12 l Niskin oceanographic sampling bottles. To limit the possible sample contamination due to lubricants, greases and silicones employed on plastic devices, all the bottles and the stopcock O-rings were substituted with Buna-N O-rings previously treated in a vacuum oven set at 100 °C for 48 h. Following Bullister and Weiss [19], all rubber bottle closure systems were replaced with epoxy-coated stainless steel spring. To avoid the contact with air, the seawater samples for CFC analysis are drawn directly from the stopcocks of the Niskin bottles into 60 ml glass ampoules through dedicated 3-way sampling systems, following the optimized standard procedures [21,24,25]. The ampoules are flame-sealed meanwhile clean N_2 flows (at about 10 ml min^{-1}), avoiding any contact with atmosphere. This procedure leaves a gas space in the ampoules, which is necessary to allow thermal expansion of the seawater during the storage period. Corrections for CFC loss from the seawater into the ampoule headspace are therefore required. Seawater samples in flame sealed ampoules are stored under cold and dark condition until the analysis. CFCs in seawater samples in flame-sealed ampoules stored in these conditions remain stable for years [26].

2.4. Water sample analysis

The ampoule containing the seawater sample is positioned into the chamber containing the cracking device, which is connected through an electro-valve (EV17) to the ultra high pure N_2 cylinder. The N_2 flowing into the chamber is purified by passing through the MS 13X trap. The chamber has glass wall instead of tygon wall and a different cracking device system respect to the Smethie's design. After breaking the neck of the ampoule by a hand-moved rod with a chisel-shaped end, a 1/8 in. SS tube is inserted into the ampoule and the seawater transfer is started by purging the ampoule with the stripper gas. The seawater sample is transferred to a 34 ml calibrated volume (CV) until overflow through the V3 waste system. The exact volume of the CV was evaluated gravimetrically. The tubings connecting V3 to the cracking chamber are then purged by flushing of the carrier gas. Switching EV17, V2 and V3, the calibrated volume of the sample is then transferred to the stripping chamber by purging the calibrated volume with the stripper gas.

In the inert gas-stripping method an inert gas (N_2) is used to sparge an organic solute (CFCs) from an aqueous solution (seawater sample). Thus, in order to extract the CFCs from the seawater sample, the transfer gas stream is directed into the stripping chamber via V3 valve. The gas stream enters the bottom of the glass stripping chamber, where a fine frit element disperses the stripping N_2 into fine bubbles, thus enhancing the extraction efficiency for the dissolved CFCs. It is particularly relevant that the bubbles generated are small, because that leads to a high surface area to volume ratio. The extraction procedure is conducted at an upstream stripper gas pressure of 2.0 bar for 330 s. The extracted gases pass through V2, a dessicant column containing $Mg(ClO_4)_2$, V6 and V4, then they follow the same pathway as described for the gaseous samples (cf. Section 2.1 and Fig. 1).

The trap is cooled at −78 °C before transferring the seawater sample to the stripping chamber. At the end of the stripping process the trap is kept cool for an additional time (15 s) to allow all the extracted CFCs to be trapped. After the trapping, the trap is isolated by switching the valves V2 and V4 and it is rapidly heated to 100 °C. The injection and the gas chromatographic run take place as described for gaseous samples (Section 2.1).

In order to evaluate the stripping efficiency and the recovery of the procedure, the same seawater sample is subsequently extracted several times. If the stripper efficiency is not 100%, corrections are made accordingly to the number of moles.

The final CFC concentrations are calculated by dividing the moles of the gases by the net weight of the sample and they are expressed in pmol kg^{-1}. The analyzed water volume (ml) is converted to mass (kg), through the seawater sample density. An additional correction is made to take into account the CFC loss from the water sample to the overlying headspace during sample storage in ampoules.

3. Results

3.1. Performance optimization

An optimization of the operating conditions was required to improve the performances of the analytical method. In particular, the carrier gas flow rate, the filling and the rinsing loop time, the trap performances, the temperature of the analytical column and of the ECD detector, the efficiency of the CFC stripping from seawater samples were evaluated.

The carrier gas flow must satisfy some important requirements, such as an adequate current signal recorded by the detector, a good chromatographic peak resolution, an adequate analyte dilution and a satisfactory system sensitivity. Since literature studies reported that an optimal carrier gas flow at the detector entrance is 33 ml min^{-1} [18,22], we studied a range of carrier gas inflow pressures able to produce a comparable flow. We evaluated the system response setting the carrier gas pressure at 2.8 bar (equivalent to 29 ml min^{-1}), 3.0 bar (equivalent to 30 ml min^{-1}) and 3.4 bar (equivalent to 32 ml min^{-1}); higher carrier gas flows produce a drop in the detector signal to values lower than the minimum acquirable voltage. With this aim, repeated CFC measurements of a fixed standard gas aliquot were made at different carrier gas flows evaluating the column efficiency (i.e. the retention time versus the peak width ratio). In Fig. 3 the column efficiency values obtained for each carrier gas flow condition are reported.

The column efficiency for CFC-11 and CFC-12 does not differ varying the carrier gas pressure between 3.0 bar and 3.4 bar, whereas it significantly decreases when the carrier gas pressure is 2.8 bar. Differently, column efficiency does not vary for CFC-113 in the full range of the tested carrier gas pressures. Therefore, the carrier gas inflow pressure was set at 3.0 bar (corresponding to an ECD gas inflow of 30 ml min^{-1}), because increasing further the pressure the normalized peak areas decreased due to an enhanced dilution of the analytes.

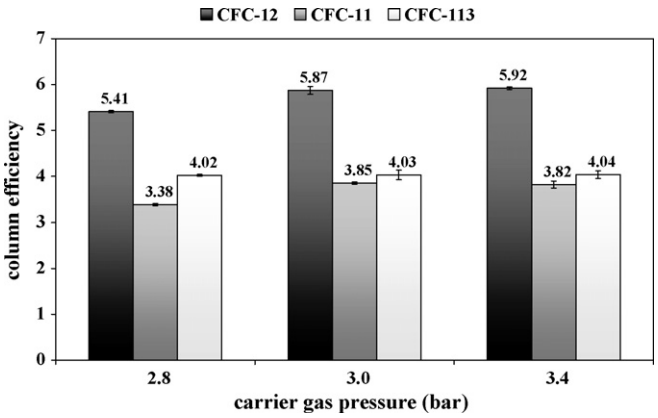


Fig. 3. Column efficiency (i.e. the analyte retention time versus the peak width ratio) calculated for CFC-12, CFC-11 and CFC-113 at different carrier gas upstream pressures. (mean value ± standard deviations; $n = 6$).

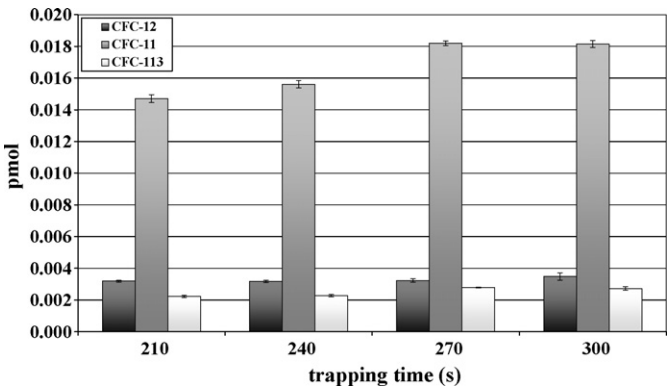


Fig. 5. CFC-12, CFC-11 and CFC-113 picomoles (mean value ± standard deviations; $n = 5$) pre-concentrated in the trap at −78 °C versus the trapping time. The gas flow rate was set at 30 ml min^{-1} throughout all the measurements.

Regarding the standard gas analysis, the time required for the loop filling and rinsing was evaluated. The optimal filling loop time corresponds to the time necessary to fill six times the loop volume. Different filling times between 60 s and 100 s (on the basis of the flow rate) were experienced employing the loop with the largest volume. Fig. 4 reports the detected picomoles against the loop filling time; the time at which the curve is plateau-shape (80 s) was chosen.

Secondly, the time necessary for rinsing the system with the carrier gas was analyzed in order to provide an efficient cleaning of the system between consecutive sample analyses. System blanks analyzed before and after a gas sample were compared for different rinsing times. The rinsing time at which the system blank analyzed before and after the standard gas sample did not significantly differ (equal or less than the system precision) was chosen (120 s).

Peak separation and resolution were optimized by testing different analytical column temperatures between 110° and 150 °C. A column temperature of 150 °C was at once discarded, because it causes a significant increase in the baseline noise. The 110 °C column temperature causes an increase in the retention times (and as a consequence in the analysis time), tailed peaks and a decrease in sensitivity. In addition, a column temperature at 110 °C could induce analyte condensation since the temperature of desorption from the trap is 100 °C. The best compromise between a low background, high sensitivity and peak resolution and short retention times is obtained for all the analytes when column is held at 140 °C.

Since electron capture detector response is temperature dependent, the temperature effect on the ECD sensitivity was considered. In particular, ECD responses at 250°, 300° and 350 °C were compared. CFCs display a wide range of thermal electron attachment coefficients and consequently large differences in relative ECD response. As already observed [27], highly responsive compounds such as CFC-11 have a decreasing signal to noise ratio (hence, sensitivity) when the ECD temperature increases, while more weakly electron capturing species, such as CFC-12, exhibit a small sensitivity increase. The 350 °C ECD temperature was at once rejected, because it caused an increased baseline, hence a decreased sensitivity. An ECD temperature of 300 °C was selected as the best compromise in overall sensitivity.

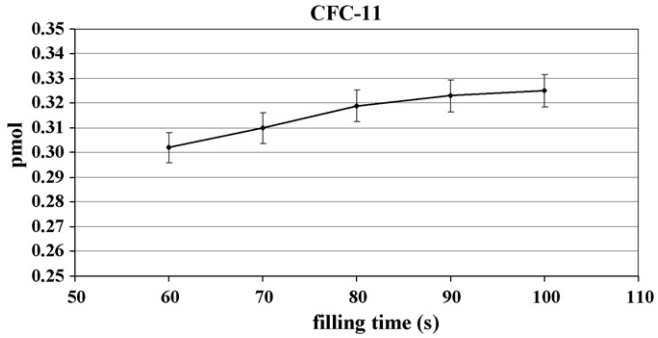


Fig. 4. CFC-11 picomoles (mean value ± standard deviations; $n = 5$) detected as a function of the filling loop time.

Since the concentration range of CFCs in aqueous samples is in ng l^{-1} range, generally too low for the direct GC analysis, a preconcentration step is required prior to the sample injection. The use of the trap allows larger volume to be analyzed for trace measurements. The trapping time was studied to obtain the best efficiency in the pre-concentration process. The Unibeads 2S consists of spherical porous silica beads as adsorbent and preconcentrator. The sorbent traps the CFCs as the carrier gas passes through it while the carrier gas and most of the other components pass through the cold trap. The retained analytes can be rapidly desorbed by resistive heating using a pulse of electric current. Fast desorption is essential for generating a narrow injection band so that a high resolution separation can be achieved.

The breakthrough volume (or sample capacity) and the desorption efficiency are important parameters of a trap. The traps, usually, are packed with small amount of sorbent and are designed to retain the analytes only for a few minutes. Since it is desirable to adsorb as much sample as possible to increase the sensitivity, the sample capacity of the employed trap has to be calculated. In fact, if a component breaks through, only a fraction of this analyte is desorbed during the injection in the GC column, generating a low signal. In other words, the trapping time and the trapped analyte amount are not necessarily in direct proportion.

At a given flow rate, the breakthrough volume can be evaluated considering the trapping time.

Following literature indications [18], the study was focused on a limited range of trapping time (210–300 s). At each trapping time five replicates of standard gas were injected in a calibrated loop and the procedure was repeated in three loops of different volume. Varying the loop volume no differences were noticed. The results (mean value ± standard deviation) obtained for a loop with an intermediate volume are reported in Fig. 5.

The trapped CFC picomoles rose significantly by increasing the trapping time from 240 s to 270 s, while a less significant increase was observed from 270 s to 300 s. Considering the standard deviation of the mean values, the best efficiency of the trapping process was achieved at 270 s, particularly for CFC-11.

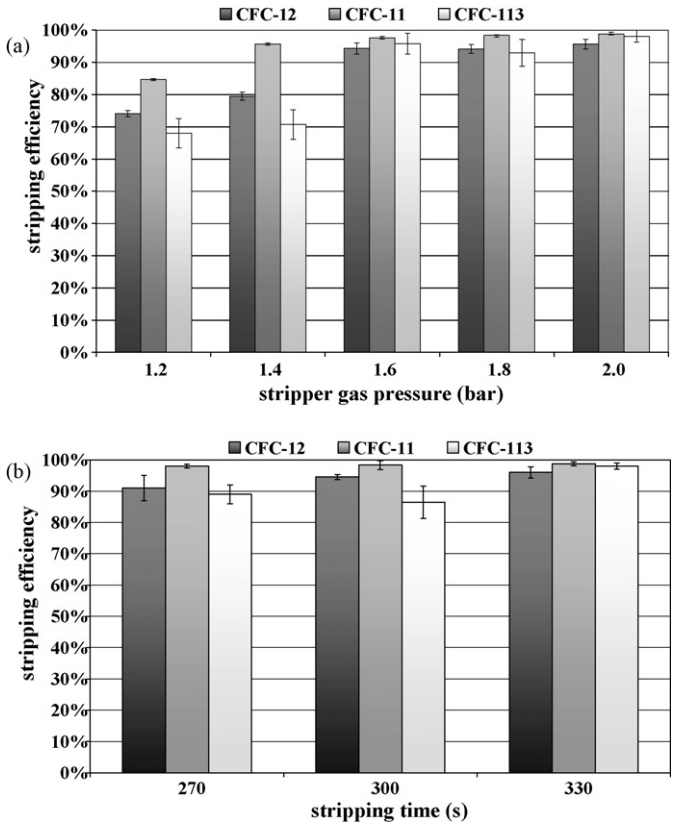


Fig. 6. CFC-12, CFC-11 and CFC-113 stripping efficiency (mean value ± standard deviations; $n = 5$) varying (a) the stripper gas pressure (stripping time set at 330 s) and (b) the stripping time (stripper gas set at 2.0 bar).

As already described in Section 2.4, during seawater analysis the CFC trapping phase is preceded by the analyte stripping from the seawater sample using a stripper gas stream.

The dispersion of the gas into the stripping chamber is a critical aspect determining the performance of the gas–liquid system.

In first instance the stripper gas flow was considered. Stripper gas flows corresponding to a stripper upstream pressure varying between 1.2 and 2.0 bar were tested. The stripping process efficiency was estimated by stripping, trapping and analyzing four times the same water sample. We calculated the stripping process efficiency dividing the area obtained from the first extraction by the sum of the areas obtained from the four carried out extractions. The stripping efficiency was assessed by analyzing several surface seawater samples characterized by relatively high CFC concentrations. In Fig. 6a the mean efficiencies obtained for the three CFCs with different stripper gas pressures using a 330 s stripping time are shown.

The efficiency significantly improves for CFC-12 and CFC-113, increasing the gas stripper upstream pressure from 1.4 bar to 1.6 bar, whereas for CFC-11 the best efficiency improvement is obtained varying stripper gas pressure from 1.2 bar to 1.4 bar. A further increase of the stripper gas pressure to 1.6 bar, 1.8 bar and 2.0 bar did not increase the efficiency of the CFC-11 and CFC-12 stripping. On the contrary, a significant improvement in the CFC-113 stripping efficiency was observed when the stripper gas pressure was set at 2.0 bar. Since the extraction is simultaneous for the three CFCs, the stripper gas upstream pressure was set at 2.0 bar.

Fixed the stripper gas pressure at 2.0 bar, the stripping time was considered. In particular, the stripping efficiency was studied for stripping times ranging between 270 s and 330 s. As shown in Fig. 6b, long lasting stripping times improve particularly CFC-12 and CFC-113 efficiency, while CFC-11 efficiency does not vary significantly in the studied time range. The increase of the stripping time improved the reproducibility of the stripping efficiency (evaluated as the standard deviation) for all the three CFCs. The best efficiency is obtained with a 330 s stripping time.

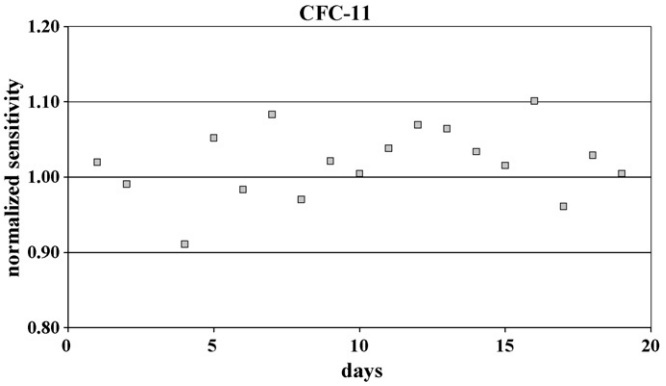


Fig. 7. CFC-11 normalized sensitivity control chart versus time throughout a 20 day analysis period.

Several surface seawater samples (70) were re-stripped. The results showed that on average 96% of CFC-12, 99% of CFC-11 and 98% of CFC-113 are stripped after 330 s of stripping at the lab temperature. In many cases the efficiency was about 100%, being the restripped sample peak areas of the same order of magnitude of stripper blanks. These efficiencies are comparable with the values obtained by Vollmer and Weiss [18] with a stripper gas-flow of 35 ml min^{-1} for 5 min (98% for CFC-12, 91% for CFC-11 and 95% for CFC-113).

Temporal changes in the CFC analysis sensitivity (peak area per amount of compound) are represented in Fig. 7, showing the repeated CFC-11 measurements of a fixed standard gas aliquot in the same loop for a period of daily sample analysis. The sensitivity was normalized respect to the mean value calculated for the whole period of analysis and respect to the measured laboratory pressure and temperature. The shape are quite stable in time; the sensitivity variations are mainly due to changes in the detector sensitivity. Comparable results were obtained for CFC-12 and CFC-113. The linear dependence of sensitivity on laboratory atmospheric pressure already observed [28] is confirmed.

3.2. Figures of merit

The analytical system blank was evaluated by trapping the carrier gas flushing the purge and trap system in the same way as during the standard gas analysis. System blank concentrations resulted 0.0003 ± 0.0001 pmol for CFC-12, 0.0005 ± 0.0001 pmol for CFC-11 and 0.0003 ± 0.0001 pmol for CFC-113.

The blank resulting from the seawater sample stripping and trapping procedure (stripper blank) was evaluated by passing the stripper gas through the empty stripping chamber for the same time adopted for the seawater. The stripper blank resulted 0.0004 ± 0.0001 pmol for CFC-12, 0.0005 ± 0.0001 pmol for CFC-11 and 0.0003 ± 0.0007 pmol for CFC-113.

The precision of an analytical procedure expresses the closeness of agreement between a series of measurements obtained from the same homogeneous sample under the prescribed conditions. It can be considered at different levels, in particular, the repeatability expresses the precision under the same operating conditions over a short interval of time.

Precision for the measurements (as repeatability) of each CFC in the standard gas was determined by the ratio of each standard to the mean of the considered measurements of standard gas in

Table 2
Mean retention time, limit of detection, precision and signal to noise for CFC-12, CFC-11 and CFC-113 in gas and seawater samples.

	CFC-12	CFC-11	CFC-113
Mean retention time (min)	1.26	2.84	5.49
D.L Gas Sample (pmol)	0.0002	0.0003	0.0002
D.L Water Sample (pmol kg^{-1})	0.0081	0.0073	0.0043
Precision (RSD%)	5.9	4.2	5.8
Signal to noise	481	1027	395

the same loop and expressed through relative standard deviation (RSD), as suggested by [29].

We calculated two different detection limits: one for the standard gas injection and one for the seawater samples. The detection limit of the analytical system is based on the analysis of 20 system blank replicates: we considered the detection limit as three times the standard deviation of this set of analyses. We define the minimal detectable CFC concentration in seawater as two standard deviations ($n = 18$) of the stripper blank concentrations divided by the stripper efficiencies, according to [18]. The limits of detection for the CFCs in seawater using this approach yield to a signal-to-noise higher than 400 (higher than 1000 in CFC-11 case), which allows the measurement of these compounds in the polar oceans (see Table 2). An increase in this ratio may be possible by changing GC conditions or by improving stripping and trapping techniques.

Precision and detection limits resulted comparable with the last applications [20,22] and are reported in Table 2 together with the mean retention time of the three CFCs obtained in the chosen analytical conditions.

Since a Certified Reference standard is not commercially available, checking the accuracy of the procedure was difficult. To the purpose an intercalibration exercise was carried out with LDEO (Lamont Doherty Earth Laboratory-Columbia University, NY, USA) on seawater samples collected during the XVIII Italian Antarctica Expedition. Considering LDEO data as the indicative reference values, our recovery was 89% for CFC-11, 93% for CFC-12 and 110% for CFC-113. Nevertheless, it has to be considered that these values refer to few samples only.

3.3. Applications

The purge and trap-GC-ECD system and the optimized method were used to determine CFC concentrations in seawater samples from the Ross Sea (Antarctica). Seawater samples were collected in the austral summer (January–February) 2003 aboard the RV *Italica*, in the framework of the CLIMA (Climatic Long-term Interactions for the Mass Balance) Project cruise as part of the PNRA (National Program for Research in Antarctica) activities. The samples were analyzed at Department of Chemistry and Industrial Chemistry, University of Genoa (Italy). The measurements carried out with our instrument allowed us to describe the distribution of CFCs in the main water masses of the Ross Sea and the storage of the anthropogenic CO_2 in the deep ocean [16,30,31].

Surface CFC concentrations cover a wide range of values in relation to the seawater temperature and salinity, which influence their solubility. The typical highest CFC-11, CFC-12 and CFC-113 concentrations calculated on the basis of the SIO scale 2004 [32], considering mean Antarctic seawater surface salinity and temperature, are roughly 7.8, 4.0 and 1.8 pmol kg^{-1}, respectively. These values are similar to those measured in surface samples. The surface CFC saturation percentage was calculated with respect to the southern hemisphere background [32] using the solubility functions [2,23]. The saturation values range between 80% and 90% in the Ross Sea areas free from pack-ice for a large part of the year.

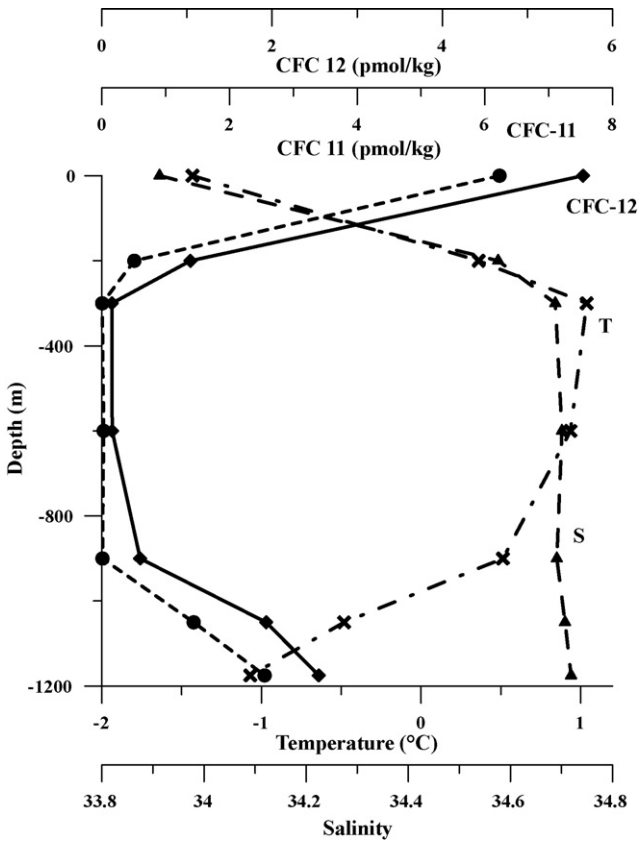


Fig. 8. Vertical profiles for CFC-11 (● dots), CFC-12 (♦ squares), Temperature (× crosses) and salinity (▲ triangles) at the CLIMA Project cast AN03091 in the northwestern Ross Sea (71°53.619' S; 172°13.150' E) on February 08, 2003.

On the other hand, the lowest CFC concentrations, close to the detection limit, are found in correspondence with the warmest temperature, identifying the Circumpolar Deep Water. Such low CFC levels proved the long time segregation at mid depths of this water mass. Beneath this layer CFC concentrations increase, indicating that the bottom layer is occupied by a recently ventilated water mass.

As an example, in Fig. 8 are shown temperature, salinity and CFC vertical profiles concerning a station located in the northwestern Ross Sea.

4. Conclusions

An automated purge and trap–GC-ECD system for the analysis of CFCs in seawater samples consisting of both hardware and software was manufactured with cheap cost in our laboratories.

This method resulted sensitive, reproducible and the sample contamination was negligible, as demonstrated by system and stripper blanks. The precision was always better than 6%. The stripping efficiencies and the limits of detection for CFCs in seawater were improved respect to previous methods and yield a signal to noise ratio higher than 1000 for CFC-11 and close to 400 for CFC-12 and CFC-113.

The method was successfully applied to the determination of chlorofluorocarbons in seawater samples collected in the Ross Sea (Antarctica).

We will study further improvements to increase the sensitivity of CFC-113 measurements and to extend the analytical method to the measurements of other compounds used as ocean tracer, such as SF_6.

Acknowledgements

This study was performed as part of the Italian "National Program for Research in Antarctica" (PNRA) and was financially supported by ENEA through a joint research programme.

Thanks are due to Dr. W. M. Smethie Jr and Mr. E. Gorman for their contributions during instrument start up and chemical analysis. We are grateful to Mr. S. Chiarugi and to OMEGA s.r.l. for their continuous and punctual technical support. We thank Mr. A. Scianca for his assistance with the CFC measurements. We are grateful to Prof. G. Gragnani (Department of Biophysical and Electronic Engineering-DiBE – University of Genoa) for writing the software used to obtain polynomial expressions from calibration empirical data. CTD data were kindly provided from Prof. G. Spezie and the CLIMA project physical oceanography group. We thank the two anonymous reviewers for providing helpful comments on the manuscript.

References

[1] S.J. Walker, R.F. Weiss, P.K. Salameh, J. Geophys. Res. 105 (2000) 14285.
[2] M.J. Warner, R.F. Weiss, Deep-Sea Res. 32 (1985) 1485.
[3] S.D. Shapiro, P. Schlosser, W.M. Smethie, M. Stute, Mar. Chem. 59 (1997) 141.
[4] S.C. Doney, J.L. Bullister, Deep-Sea Res. 39 (1992) 1857.
[5] A.H. Orsi, G.C. Johnson, J.L. Bullister, Prog. Oceanogr. 43 (1999) 55.
[6] S.C. Doney, M.W. Hecht, J. Phys. Oceanogr. 32 (2002) 1642.
[7] C. Andrié, M. Rhein, S. Freudenthal, O. Plahn, Deep-Sea Res. I 49 (2002) 281.
[8] S.E. Trumbore, S.S. Jacobs, W.M. Smethie, Deep-Sea Res. 38 (1991) 845.
[9] R.E. Sonnerup, P.D. Quay, J.L. Bullister, Deep-Sea Res. I 46 (1999) 777.
[10] M.H. England, E. Maier-Reimer, Rev. Geophys. 39 (2001) 29.
[11] J.C. Dutay, J.L. Bullister, S.C. Dooney, J.C. Orr, R. Najjar, K. Caldeira, J.M. Campin, H. Drange, M. Follows, Y. Gao, N. Gruber, M.W. Hecht, A. Ishida, F. Joos, K. Lindsay, G. Madec, E. Maier-Reimer, J.C. Marshall, R.J. Matear, P. Monfray, A. Mouchet, G.K. Plattner, J. Sarmiento, R. Schlitzer, R. Slater, I.J. Totterdell, M.F. Weiring, Y. Yamanaka, A. Yool, Ocean Model 4 (2002) 89.
[12] W.M. Smethie, S.S. Jacobs, Deep-Sea Res. I 52 (2005) 958.
[13] C.B. Rodehacke, H.H. Hellmer, A. Beckmann, W. Roether, J. Geophys. Res. 112 -C9 (2007) C09001.
[14] C.L. Sabine, R.M. Key, K.M. Johnson, F.J. Millero, A. Poisson, J.L. Sarmiento, D.W.R. Wallace, C.D. Winn, Glob. Biogeochem. Cycle 13 (1999) 179.
[15] B.I. McNeil, R.J. Matear, R.M. Key, J.L. Bullister, J.L. Sarmiento, Science 299 (2003) 235.
[16] S. Sandrini, N. Ait-Ameur, P. Rivaro, S. Massolo, F. Touratier, L. Tositti, C. Goyet, Ant. Sci. 19 (2007) 395.
[17] S. Jutterström, E. Jeansson, L.G. Anderson, R. Bellerby, E.P. Jones, W.M. Smethie, J.H. Swift, Prog. Oceanogr. 78 (2008) 78.
[18] M.K. Vollmer, R.F. Weiss, Mar. Chem. 78 (2002) 137.
[19] J.L. Bullister, R.F. Weiss, Deep-Sea Res. 35 (1988) 839.
[20] M. Hofer, M. Imboden, Anal. Chem. 70 (1998) 724.
[21] M. Mensch, W.M. Smethie Jr., P. Schlosser, R. Weppernig, R. Bayer, Antarctic Res. Series 75 (1998) 241.
[22] J.L. Bullister, D.P. Wisegarver, Deep-Sea Res. 55 (2008) 1063.
[23] X. Bu, M.J. Warner, Deep-Sea Res. 42 (1995) 1151.
[24] E. Busenberg, L.N. Plummer, Water Resour. Res. 28 (1992) 2257.
[25] W.M. Smethie, P. Schlosser, T.S. Hopkins, G. Boenisch, J. Geophys. Res. 105 (2000) 1105.
[26] E. Busenberg, L.N. Plummer, P.G. Cook, D.K. Solomon, L.F. Han, M. Gröning, H. Oster, in: I.A.E.A. (Ed.), Use of Chlorofluorocarbons in Hydrology: A Guidebook, IAEA, Vienna, 2006, pp. 199–220.
[27] M.R. Bassford, P.G. Simmonds, G. Nickless, Anal. Chem. 70 (1998) 958.
[28] K. Bulsiewicz, R. Henning, O. Klatt, A. Putzka, W. Roether, J. Geophys. Res. 103 (1998) 15959.
[29] R.G. Prinn, J. Geophys. Res. 105 (2000) 17751.
[30] S. Massolo, P. Rivaro, G. Budillon, III International Conference on the Oceanography of the Ross Sea Antarctica, Venice, Italy, October 10–14, 2005.
[31] S. Massolo, PhD Thesis, 2006. http://www.mna.it/italiano/Didattica/dott_polare/Tesi_abstract/Massolo_XVIII_2006.pdf.
[32] Appendix II, in: I.A.E.A. (Ed.), Use of Chlorofluorocarbons in Hydrology: a Guidebook, Printed by the IAEA, Vienna, 2006, pp. 222–227.

Talanta 80 (2009) 967–973

Contents lists available at ScienceDirect

Talanta

journal homepage: www.elsevier.com/locate/talanta

Direct visual detection of DNA based on the light scattering of silica nanoparticles on a human papillomavirus DNA chip

Jing Yu Piao[a], Eun Hee Park[a], Kihwan Choi[a], Bo Quan[a], Dong Ho Kang[b], Pan Yun Park[c], Dai Sik Kim[b], Doo Soo Chung[a,*]

[a] Department of Chemistry, Seoul National University, Kwanak-gu, Seoul 151-747, Republic of Korea
[b] School of Physics and Astronomy, Seoul National University, Seoul 151-747, Republic of Korea
[c] Biomedlab Co., Seoul 143-805, Republic of Korea

ARTICLE INFO

Article history:
Received 16 June 2009
Received in revised form 17 August 2009
Accepted 19 August 2009
Available online 26 August 2009

Keywords:
Plain silica nanoparticle
Light scattering
Aggregation
Visual detection

ABSTRACT

A detection system for a human papillomavirus (HPV) DNA chip based on the light scattering of aggregated silica nanoparticle probes is presented. In the assay, a target HPV DNA is sandwiched between the capture DNA immobilized on the chip and the probe DNA immobilized on the plain silica nanoparticle. The spot where the sandwich reaction occurs appears bright white and is readily distinguishable to the naked eye. Scanning electron microscopy images clearly show the aggregation of the silica nanoparticle probes. When three different sized (55 nm, 137 nm, 286 nm) plain silica nanoparticles were compared, probes of the larger silica nanoparticles showed a higher scattering intensity. Using 286-nm silica nanoparticles, the spots obtained with 200 pM of target DNA were visually detectable. The demonstrated capability to detect a disease related target DNA with direct visualization without using a complex detection instrument provides the prerequisite for the development of portable testing kits for genotyping.

© 2009 Elsevier B.V. All rights reserved.

1. Introduction

To perform highly sensitive but low-cost analysis of nucleic acids, a great deal of progress has been made to develop signal amplification and detection methodologies. Various types of fluorescent nanomaterials, such as quantum dots [1], fluorophore-doped silica nanoparticles [2–5], and metal nanoparticles [6–10], have been extensively explored for ultrasensitive DNA detection, both in homogeneous reactions and on microarrays. Other detection methods based on absorbance, scattering, or conductivity have also been employed. Recently, gold nanoparticles [11,12] and silver-amplified gold nanoparticles [13] have been used to perform highly selective and sensitive detection of DNA, utilizing the enhanced light scattering of nanoparticle probes. The advantages of light scattering [14] are that (a) high intensity signals can be obtained by using intense light sources without photodecomposing the light scattering probes, (b) there is negligible quenching by the substances normally used in biological studies, and (c) more importantly, the signal can be detected by relatively simple instruments, including the naked eye.

Silica nanoparticles and microspheres have been widely used in bioanalysis due to their easy synthesis and surface modification, biocompatibility, and high chemical and thermal stability. In addition, silica nanoparticles can load a large quantity of fluorescent dye molecules and serve as signaling probes of amplified sensitivity for cell imaging, DNA detection, and amino acid sensing [15]. However, plain silica particles, having neither dye molecules doped inside silica matrix nor a specific resonance light scattering band like gold or silver particles, have not been used as signaling tags for DNA detections.

Human papillomavirus (HPV) is the major etiological agent of cervical cancer which is the second most common form of cancer among women with a mortality rate of almost 300,000 per year worldwide [16]. Among more than 20 distinct HPV types which are associated with cervical carcinoma, the HPV-16 type is the most prevalent one in patients with cervical intraepithelial neoplasia and cervical carcinoma. Currently, a hybrid capture (HC) system [17,18], which has been approved by the U.S. Food and Drug Administration, and a PCR-based HPV test [19] are used for the detection of high-risk HPV subtypes in a cervical sample obtained with a Pap test. While the HC system is a ready-to-use test for routine diagnosis of the disease, low selectivity and sensitivity still limit its wide application in a clinical setting. Although the PCR-based HPV test has shown improved sensitivity, its low reproducibility, demanding work, and complex instrumentation hinder its use in point-of-care clinical diagnostics.

In this report, we outline our exploration of the potential of plain silica particles as signal tags for a HPV DNA chip. The detection is

* Corresponding author. Tel.: +82 2 880 8130; fax: +82 2 872 3231.
E-mail address: dschung@snu.ac.kr (D.S. Chung).

0039-9140/$ – see front matter © 2009 Elsevier B.V. All rights reserved.
doi:10.1016/j.talanta.2009.08.024

Table 1
DNA sequences used for silica particle probes formation and hybridization experiments.

Name	Sequence	Description
Prm1	5′-TTTKTTACHGTKGTDGATACYAC-3′ K; G/T, H; T/A/C, D; A/T/G, Y; T/C	Primers used in PCR amplification of HPV DNA
Prm2	5′-GAAAHATAAAYTGYAADTCATAYTC-3′ K; G/T, H; T/A/C, D; A/T/G, Y; T/C	Reversed primers used in PCR amplification of HPV DNA
T1	5′-ACAGGTTCCTACCCTAAGGACCTTTATGTAGTTTCTGAAGTAGATATGGCAGCACATAT-3′	Target DNA (for HPV-16) complementary to the capture DNA on a DNA chip and P1
NT	5′-AAGAGAATTGACTTATATGTACCTTCCTTAGTTACTTCAGTG-3′	DNA non-complementary to the capture DNA on a DNA chip and P1
P1	5′-AAGGTCCTTAGGGTAGGAACCTGT-biotin-3′	Probe DNA immobilized on SP1
P2	5′-biotin-TAACTTAGTTCAACGAAGCTCGCC-3′	Probe DNA immobilized on SP2
L	5′-CCTAAGGACCTTGGCGAGCTTCGT-3′	Linker DNA complementary to P1 and P2

based on the light scattering of silica particle probes aggregated on a glass slide chip through DNA hybridization. The spots where DNA hybridization occurred appeared brightly white and were directly visible to the naked eye or by a simple flatbed scanner. To our knowledge, this is the first time that plain silica particles have been used as signal tags for a DNA chip. The detection system is quite simple and inexpensive and thus represents a promising step toward the development of portable testing kits for genotyping.

2. Experimental

2.1. Materials

All the oligonucleotides (see Table 1) used were purchased from Bioneer (Seoul, Korea). The HPV DNA chips with the capture DNA array spots of 120 μm diameter were obtained from Biomedlab (Seoul, Korea). The HPV DNA chip (25 mm × 75 mm) has four silicon-separated reaction chambers (20 mm × 5 mm × 1 mm) and each chamber has two 5 × 3 DNA array blocks composed of 10 probe spots to capture HPV-16, and -5 control spots to capture HPV-18. Tetraethyl orthosilicate (TEOS), 29 wt% aqueous ammonia solution, 3-(aminopropyl)trimethoxysilane (APTMS), 25 wt% aqueous solution of glutaraldehyde, sodium dodecyl sulfate (SDS), phosphate buffered saline (PBS, pH 7.4), anhydrous ethanol, and avidin were from Sigma–Aldrich (St. Louis, MO, USA). 3-(Trihydroxysilyl)-propylmethylphosphonate (THPMP) was from Gelest (Tullytown, PA, USA). Deionized water was prepared with a NANOpure II purification system (Barnstead, Dubuque, IA, USA).

2.2. Synthesis and surface modification of silica particles

2.2.1. Plain silica nanoparticles

Plain silica particles of 55 nm, 137 nm, and 286 nm in diameter were used. The plain silica particles of 137 nm and 286 nm were purchased from Bangs Laboratories (Fishers, IN, USA) and the 55-nm plain silica particles were synthesized using the Stöber method [20] with some modification. Briefly, to a mixture of 875 μL ammonia solution and 12.5 mL ethanol, 1 mL of TEOS was added and the resultant mixture was stirred at room temperature overnight. The reaction mixture was then centrifuged for 20 min at 4000 × *g* and washed with ethanol three times and PBS once, and then suspended in PBS for future use. All three kinds of plain silica particles were processed with the same surface modification procedures below.

2.2.2. Amine-modification

10 mg of plain silica nanoparticles were suspended in 4 mL of PBS with sonication. 50 μL of APTMS and 50 μL of THPMP were added to the suspension and the mixture was stirred for 4 h in a sealed glass vessel at room temperature [21]. The amine-modified particles were separated by centrifugation at 4000 × *g* for 15 min, washed three times with PBS, then dispersed in 2 mL of PBS, and stored at 4 °C until use.

2.2.3. Avidin-modification [22]

0.5 mL of the amine-modified silica particle suspension in PBS (5 mg/mL) was mixed with 0.9 mL of PBS for better dispersion of the silica particles. After adding 1.6 mL of glutaraldehyde solution, the mixture was sonicated for 10 min and then stirred for 1.5 h at room temperature. The silica particles were separated by centrifugation at 4000 × *g* for 15 min, washed with PBS and separated by centrifugation twice, and then dispersed in 3 mL of PBS, to which 1 mg of avidin in 1 mL of PBS was added. The mixture was stirred for 3.5 h at room temperature. To block any unreacted amine groups on the silica surface, 50 μL of 1 M glycine was added to the mixture which was then stirred for a further 30 min. The avidin-modified particles were separated by centrifugation at 4000 × *g* for 15 min, washed three times with PBS, dispersed in 2 mL of PBS, and stored at 4 °C until use.

2.2.4. Oligonucleotide-modification

Two kinds of silica particle probes were prepared from the avidin-modified silica particles through the avidin–biotin interaction with P1 DNA and P2 DNA, respectively. P1 DNA-modified plain silica nanoparticles (SP1) were used in both sandwich hybridization and three-step hybridization, while P2 DNA-modified plain silica nanoparticles (SP2) were only used in the three-step hybridization. To 0.5 mL of the avidin-modified plain silica particle suspension, 6 μL of 100 μM P1 DNA was added and the mixture was stirred at room temperature for 1 h. The resulting SP1 were separated by centrifugation at 4000 × *g* for 20 min and washed with PBS three times. The successful immobilization of probe DNA on the surface of the silica particles was confirmed by the absorbance at 260 nm. Then, the resulting SP1 were suspended in 0.5 mL of PBS and stored at 4 °C for future use. SP2 were prepared similarly using P2 DNA.

In order to estimate the number of DNA probe molecules immobilized on the surface of a silica particle, a double-labeled (5′-fluorescein and 3′-biotin) oligonucleotide with the same sequence as the P1 DNA was conjugated with the avidin-modified silica particle. By comparing the fluorescence intensities of the fluorescein-oligonucleotide-modified silica particles with free double-labeled oligonucleotides, the numbers of probe DNA molecules on a single silica particle were estimated to be about 42, 190, and 1100 for the silica particles of 55 nm, 137 nm, and 286 nm diameter, respectively.

2.3. Sandwich (two-step) and three-step DNA hybridization

2.3.1. Sandwich DNA hybridization

(1) Synthetic HPV-16 target (T1). Each 10 μL aliquot of HPV-16 DNA (T1) of various concentrations in water was mixed with 90 μL of PBS, containing 0.2 wt% SDS, and then injected into the reaction chambers of a HPV DNA chip. The hybridization was performed for 2 h at 40 °C with shaking. (2) PCR-amplified HPV-16 DNA target from the SiHa cell line (Korean Cell Line Bank, Seoul, Korea). The

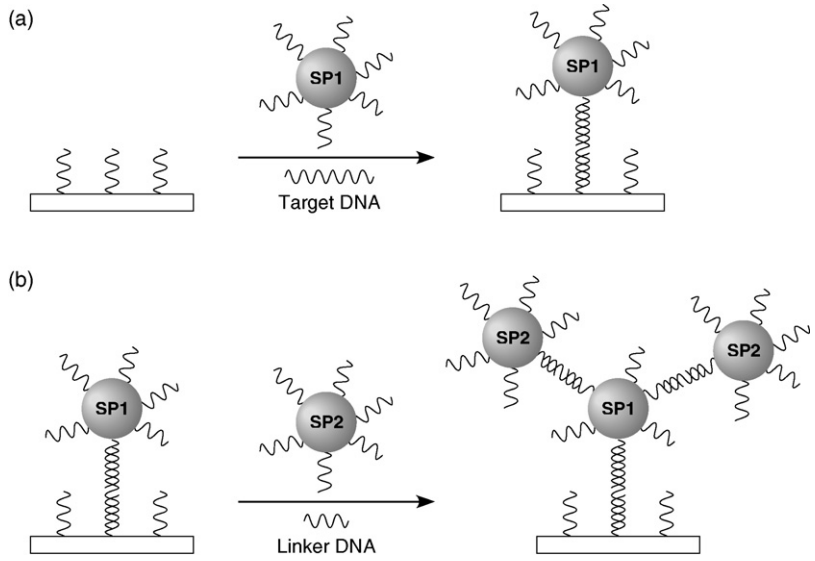


Fig. 1. Schematics of (a) sandwich or two-step DNA assay on a HPV DNA chip using SP1 and (b) the third step DNA hybridization reaction using SP2 to form dendrimer-like silica particle networks in a probe spot.

target DNA was extracted from the HPV-16 positive SiHa cell line using a DNA extraction kit (Intron Biotech, Seoul, Korea), and the L1 region of the HPV DNA was amplified with primers (Prm1/Prm2) using a thermocycler (Biometra, Goettingen, Germany) without dye labeling. The PCR-amplified HPV-16 DNA in PBS, containing 0.2 wt% SDS, was denatured at 95 °C for 5 min and chilled on ice for 3 min, then injected into the reaction chamber to perform the hybridization reaction as in (1). After hybridization, the silicon chamber with its cover was detached from the DNA chip. Then the opened DNA chip was washed with PBS in a dish at 40 °C for 2 min, to remove unbound DNA molecules, and dried in air. For the next step, a clean silicon chamber with a cover was attached to the DNA chip. Then, the second hybridization was performed by adding a mixture of 10 μL of 100 ppm SP1 suspension and 90 μL of PBS containing 0.2 wt% SDS to the reaction chamber and incubating for 2 h at 40 °C with shaking. Then, the hybridized DNA chip was washed with PBS in a dish at 40 °C and dried in air. Fig. 1 shows the schematics of this procedure.

2.3.2. Three-step DNA hybridization

The first two hybridization procedures were the same as those of the sandwich DNA hybridization. As shown in Fig. 1, after the second hybridization, a mixture of 10 μL of 100 nM linker DNA (L) in water, 10 μL of 100 ppm SP2 suspension, and 80 μL of PBS containing 0.2 wt% SDS was injected into the reaction chamber and incubated for 2 h at 40 °C with shaking. After hybridization, the silicon chamber was detached from the DNA chip first. Then the DNA chip was washed with PBS in a dish at 40 °C for 2 min and dried in air.

2.4. Instruments

A transmission electronic microscope (H-7600, Hitachi, Tokyo, Japan) was used to check the size and dispersion state of the silica particles. The hydrodynamic diameters of the silica particles were estimated using a light scattering system (BI-200SM, Brookhaven, New York, NY, USA) with a He–Ne laser (632.8 nm) light source. A silica particle sample for measurement was first diluted by water to 2.0 vol.%, filtered through a 0.45 μm filter (Whatman, Maidstone, England), and then transferred to a sample cell kept at 20 °C. The morphology of the silica particles in a probe spot was assessed with a field emission-scanning electron microscope (S-4000, Hitachi, Tokyo, Japan). Fluorescence measurements were conducted with a fluorescence spectrophotometer (Eclipse, Palo Alto, CA, USA). The UV–visible absorbance of silica particles was measured with a spectrophotometer (S-3100, Scinco, Seoul, Korea). The concentration of PCR-amplified DNA was determined by a NanoDrop Spectrophotometer (Thermo Fisher Scientific, Wilmington, DE, USA). A flatbed scanner (HP Scanjet 7400c, Palo Alto, CA, USA) was used to show the entire image of hybridized spots in each chamber. The scattered light from probe spots can also be observed with the naked eye by holding the chip toward a daylight lamp. A microscope illumination system was arranged for detecting the scattered light from the silica particles, as shown in Fig. 2, following the method in Ref. [24]. A light beam from a 20 mW argon-ion laser (Melles Griot, CA, USA) was focused onto a probe spot of an HPV DNA chip placed on the slide holder of a microscope (IX71, Olympus, Tokyo, Japan). The laser beam was incident from below the DNA chip at an angle of 35° for maximum contrast between the dark background and the bright scatter of the spots. Images collected by a 20× objective lens were recorded with an iXon CCD camera (Andor, Belfast, UK) and analyzed using a public domain software Image J (NIH, Bethesda, MD, USA). A photomultiplier tube (PMT) (Hamamatsu, Bridgewater, NJ, USA) was also used for monitoring light intensities.

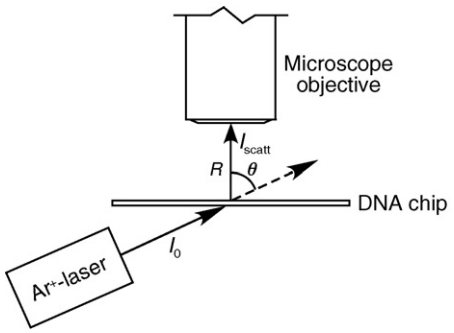


Fig. 2. Microscope illumination arrangements for detecting light scattering from silica particle probes hybridized on a DNA chip. θ is the angle between the incident light and the detector and R is the distance from the DNA chip to the detector.

3. Results and discussion

3.1. Characterization of the silica particle probes

Changes in the hydrodynamic diameters of the silica particles before and after the probe DNA immobilization were monitored by dynamic light scattering. The hydrodynamic diameters were estimated from the diffusion constants of silica particles obtained from the cumulant fit to the autocorrelation functions of scattering signals [23,24]. After the probe DNA immobilization, the hydrodynamic diameters of all three sizes of silica particles were increased from 67 ± 9 nm, 161 ± 1 nm, and 317 ± 2 nm to 93 ± 5 nm, 199 ± 1 nm, and 353 ± 2 nm, while the diameters from TEM remained at 55 ± 5 nm, 137 ± 10 nm, and 286 ± 11 nm, respectively. The discrepancies between the diameters were due to the water molecules and the probe DNA attached to silica particles in solution not being observable by TEM of a dried sample because of their low electron densities [25]. In the UV spectra of SP1 or SP2 around 260 nm, the characteristic peak of DNA was observed, which further confirmed the successful immobilization of the probe DNA on the silica particle surface. The increases of ~32 nm in the hydrodynamic diameters of the silica particles after series of modifications correspond reasonably well to the sizes of avidin and DNA moieties, as reported in the literature [26,27].

3.2. Light scattering from two-step hybridization

3.2.1. Detection with the naked eye

SP1 prepared from the plain silica particles of three sizes were two-step hybridized in different reaction chambers of a HPV DNA chip. The concentration of T1 in each reaction chamber was kept at 10 nM. The concentrations of SP1 for the silica particles of each size were also kept at 100 ppm, which corresponds to 640 fM, 47 fM, and 6.0 fM of 55-nm, 137-nm, and 286-nm silica particles, respectively and 26 pM, 12 pM, and 6 pM of probe DNA molecules, respectively. The fourth chamber was used as a control chamber to check non-specific interactions with similar hybridization reactions with a non-complementary DNA sequence (NT) instead of T1. The concentration of 100 ppm for SP1 was chosen as optimal for a sufficient hybridization reaction between SP1 and the target DNA but also low interferences from the nonspecific binding of SP1 to the chip surface (data not shown). When observed by the naked eye, the hybridized spots obtained with larger SP1 were brighter and larger than those with smaller SP1. The *S*/*N* ratios of the hybridized spots in the scanned image for SP1 of 55 nm, 137 nm and 286 nm diameter were 7.6, 8.3 and 10.6, respectively, which agreed with the trend observed by the naked eye (Fig. 3a–c). Using SP1 of 55 nm, 137 nm and 286 nm, probe spots of down to 1 nM, 500 pM, 200 pM of T1 were detectable by the naked eye, respectively. It is quite surprising that the DNA hybridization results can be observed with the naked eye, since, unlike gold or silver particles, both the plain silica particles and surface modified silica particles have negligible absorbance and no resonance light scattering bands in the visible range.

3.2.2. Aggregation of silica particles

SEM images of hybridized probe spots revealed the aggregation of SP1 immobilized onto the chip surface by hybridization (Fig. 3d–i). The whole region of a spot was neither regularly nor completely covered by SP1. In some regions of a probe spot, silica particles aggregated to form large particle complexes with sizes from several hundred nanometers to several micrometers. However, in some regions, only a few single silica particles were present. The 286-nm SP1 were likely to be bound in one layer, while the 137-nm and 55-nm SP1 often aggregated heterogeneously to show multilayer morphology in some regions. Inside the spots of the control chamber and the control spots of the T1 hybridized chambers, no silica particle probes were found. Decreasing the T1 concentration from 10 nM to 100 pM, the fraction of areas with 137-nm SP1 aggregation decreased roughly from 18% to 3%. When the T1 concentration was lower than 100 pM, it was difficult to find aggregated or single silica particles in a probe spot. We suppose the SP1 aggregation was through non-cross-linking mechanism [28], since no cross-linking DNA connecting two silica particles together was present. More investigation is needed to understand the aggregation mechanism of silica particle probes during the sandwich DNA hybridization on a DNA chip.

3.2.3. Laser light scattering

Using the microscope illumination system, the relationship between light scattering performance of silica particle probes and their sizes were investigated. In Rayleigh scattering by a small spherical particle of radius r much smaller than the wavelength of light λ in a particular medium ($r < \lambda/20$), the scattered light intensity is proportional to r^6. However, when the particle becomes larger, the intensity of scattered light is described by Mie theory [29]. Following the numerical method of Yguerabide and Yguerabide [14,30], the intensities of the scattered light, I_{scatt}, can be calculated as a function the particle radius. When linearly polarized light of intensity I_0 is scattered by a spherical particle of radius r and detected by a detector in the plane parallel to the polarization direction and at a distance R from the particle and an angle θ from the direction of incident light, the intensity is given as

$$I_{scatt} = I_0 \frac{\lambda^2 |S_2|^2}{4\pi^2 R^2} \tag{1}$$

where

$$S_2 = \sum_{n=1} \frac{(2n+1)(a_n \tau_n + b_n \pi_n)}{n(n+1)} \tag{2}$$

is a function that depends on the size parameter $x = 2\pi r/\lambda$ and the angle θ. The coefficients a_n and b_n are defined as

$$a_n = \frac{[(D_n(mx)/m) + (n/x)]\Psi_n(x) - \Psi_{n-1}(x)}{[(D_n(mx)/m) + (n/x)]\xi_n(x) - \xi_{n-1}(x)} \tag{3}$$

$$b_n = \frac{[mD_n(mx) + (n/x)]\Psi_n(x) - \Psi_{n-1}(x)}{[mD_n(mx) + (n/x)]\xi_n(x) - \xi_{n-1}(x)} \tag{4}$$

with

$$D_n(mx) = \frac{d \ln \Psi_n(mx)}{d(mx)} \tag{5}$$

where m is the relative index of the bulk particle material. The coefficients π_n and τ_n depend on θ and are evaluated by the recurrence relations

$$\pi_n = \frac{(2n-1)\cos\theta}{n-1}\pi_{n-1} - \frac{n}{n-1}\pi_{n-2} \tag{6}$$

$$\tau_n = (n \cos\theta)\pi_n - (n+1)\pi_{n-1} \tag{7}$$

starting with $\pi_0 = 0$ and $\pi_1 = 1$. Refer to Ref. [29] for the definitions of $\Psi_n(x)$ and $\xi_n(x)$ and detailed description of the numerical evaluations.

Fig. 4 shows the dependence of the scattering intensity on the silica particle radius. The solid line represents the theoretical ratio I_{scatt}/I_0 calculated from Eq. (1) using Mathematica (Wolfram, Champaign, IL, USA) with the values $m = 1.37$, $\lambda = 488.0$ nm, $\theta = 55^\circ$, and $R = 1$ cm. Instead of estimating the values of I_{scatt}/I_0 by measuring both I_{scatt} and I_0, we compared the relative changes in the light scattering intensity per particle with respect to the one by one SP1 of 55-nm diameter. The number of SP1 in a probe spot (N; 7×10^6, 5×10^5 and 7×10^4 for SP1 of 55 nm, 137 nm and 286 nm, respectively) was estimated by multiplying the fraction of SP1-covered

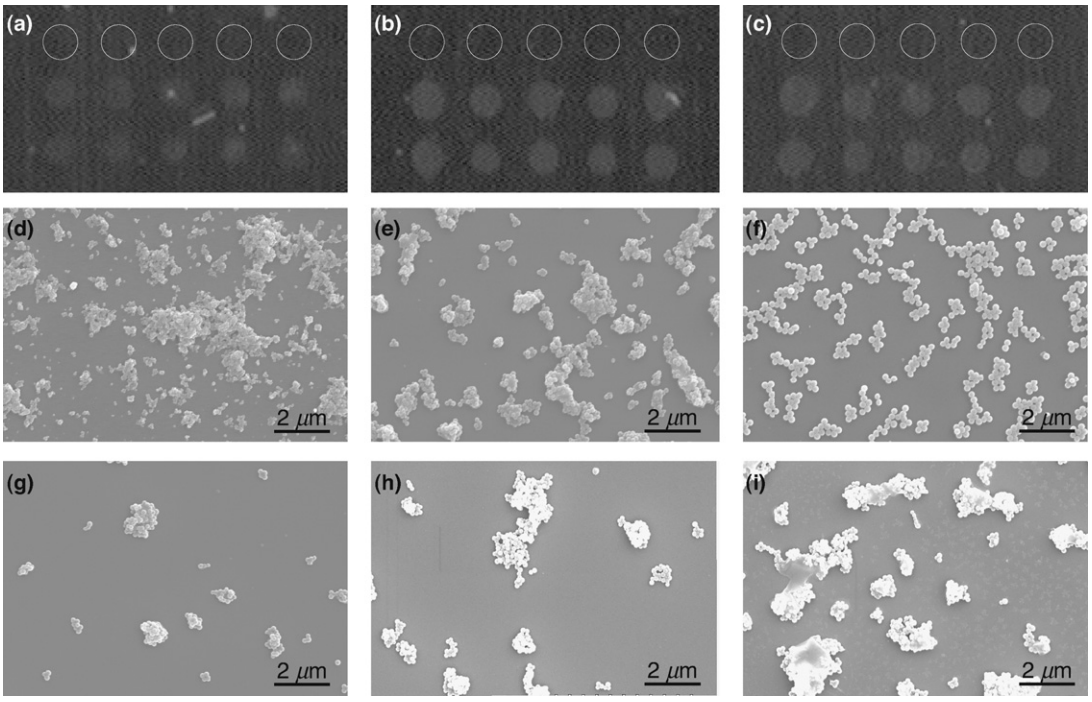


Fig. 3. (a–c) Images of DNA (both probe and control) arrays after sandwich hybridization using the SP1 of 55 nm, 137 nm and 286 nm, respectively, scanned by a flatbed scanner. The white circles highlight the region where control spots were present; (d–f) SEM images of one region of probe spots where three silica particle probes with diameters of 55 nm, 137 nm and 286 nm, respectively, hybridized with 10 nM target DNA in a two-step hybridization; (g–i) SEM images of one region of probe spots where silica particle probes with diameter of 137 nm hybridized with target DNA concentration of 100 pM, 1 nM, 10 nM, respectively, in a two-step hybridization. The spots are about 120 μm in diameter.

areas (21%, 18%, and 22% for SP1s of 55 nm, 137 nm and 286 nm, respectively obtained using Image J) and the average number of layers of the aggregated SP1s (4, 2, and 1 for SP1s of 55 nm, 137 nm and 286 nm, respectively, by visual inspection of SEM images) with the number of SP1s needed to cover the spot with a close-packed SP1 monolayer (8.6×10^6, 1.4×10^6 and 3.2×10^5 for SP1 of 55 nm, 137 nm, and 286 nm, respectively). Note that the obtained SP1 numbers were rough approximations only due to the randomly aggregated states of the SP1s and these numbers were used only for rough comparisons. The general trends of the light scattering intensity per particle with respect to the particle size — the larger the size of a particle, the stronger the light scattering intensity — showed a good agreement between theory and experimental data. However, the rate of increase in the observed scattering intensity (Fig. 4, solid circles) was

$$I_{\text{scatt}} \sim r^{3.4} \tag{8}$$

which is smaller than that expected by Mie theory (Fig. 4, solid line) for the SP1 used,

$$I_{\text{scatt}} \sim r^{5.8} \tag{9}$$

This is supposedly due to the different degrees of aggregation of the three kinds of SP1 particles as shown in Fig. 3d–i. If z particles aggregate together acting as one big particle, the number of aggregates and their radii are respectively given as $N_{\text{agg}} \sim N/z$ and $r_{\text{agg}} \sim z^{1/3} r$. If we assume the exponent f for the dependence of I_{scatt} on r does not change much in the range of particle sizes we are considering, the scattered intensity of the aggregates is given by

$$I_{\text{scatt}} \propto N_{\text{agg}} r_{\text{agg}}^f \sim \frac{N}{z}(z^{1/3} r)^f = N z^{(f/3-1)} r^f \tag{10}$$

Therefore, as long as $f > 3$, the aggregation of particles will give a scattering intensity higher than the scattering from unaggregated particles,

$$I_{\text{scatt}} \propto N r^f \tag{11}$$

In addition, from the visual inspection of the SEM images, it was clear that the smaller the particles, the larger the degrees of aggregation (z). Then the apparent increase in the scattering intensity with respect to the SP1 diameter should be slower than expected by Mie theory, as shown in Fig. 4.

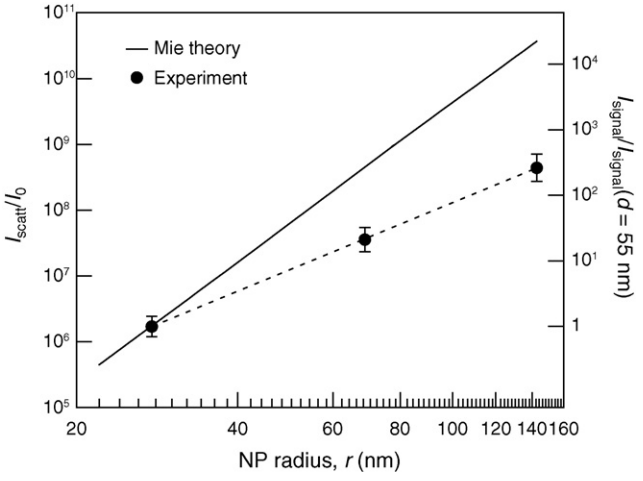


Fig. 4. Scattered light intensity *vs.* the radius of silica nanoparticles. The solid line represents I_{scatt}/I_0 calculated from Eq. (1) and circles are experimentally measured light intensity scattered by one silica nanoparticle normalized to the intensity scattered by one 55-nm SP1.

3.3. Enhanced light scattering from three-step hybridization

According to the above observation of aggregated silica particle probes, it was reasonable to expect that additional aggregation

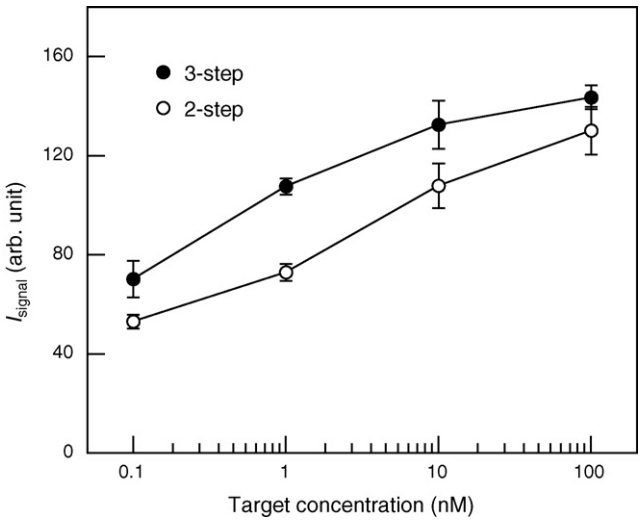


Fig. 5. Comparison of the scattering signals of probe spots between two-step and three-step DNA hybridization ($n \geq 10$). Target DNA concentration range: 100 pM, 1 nM, 10 nM, 100 nM. 286 nm diameter silica particle probes were used. The spots are about 120 μm in diameter. The solid lines are guides to the eye.

could improve DNA detection sensitivity. Formation of dendrimer-like silica particle networks may increase the aggregation degree of silica particle probes, as in Fig. 1b. As a proof-of-concept experiment, after the sandwich hybridization of SP1 of 286 nm, a second generation of silica particle probe (SP2) and a linker DNA was introduced into the reaction chamber. As expected, the light scattering signal from a probe spot, measured using the microscope set up, increased more by the three-step hybridization than by the two-step hybridization (Fig. 5). The improvement after the third step hybridization was also easily observed with the naked eye as much brighter spots. The SEM image in Fig. 6 shows a highly aggregated state of silica particle probes. After three-step hybridization, the probe spots for the target concentration down to 50 pM were discernable using the microscope system, while the probe spots for the target concentration down to 100 pM were discernable in the two-step hybridization.

3.4. Real HPV DNA assay using plain silica particle probes

The signal detection strategy based on the light scattering from silica particles can be applied to DNA genotyping to get yes-or-no answers, important in clinical HPV genotyping. The DNA sample extracted from the HPV-16 positive SiHa cell line was PCR amplified and then directly used to perform the two-step hybridization. The concentration of the amplified DNA was 350 μg/mL. When the

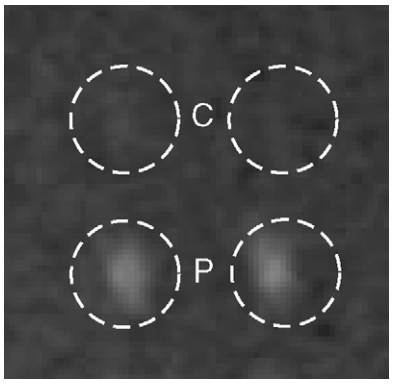


Fig. 7. Photograph of real HPV DNA detection with a sandwich hybridization reaction. The probe spots (P) show discernible patterns, while the control spots (C) remain unchanged as background. PCR-amplified HPV DNA concentration: 350 μg/mL. The dotted circles are guides to the eye.

hybridization reaction was finished, the probe spots were readily visible to the naked eye, while within the control spots no discernible patterns could be recognized (Fig. 7). The total time used for the two-step hybridization analysis, including the sample preparation and PCR, was 5–6 h, which is comparable to that required by the fluorescent dye-based test using a commercial HPV DNA chip (Biomedlab). Although the sensitivity of our system capable of detecting subnanomolar target DNA is relatively lower than those of both an HPV DNA chip test (LOD of low pM) and a fluorescent dye-doped silica nanoparticle based system (LOD of 1 pM) [3], our system offers the advantage of using a simple detection system such as a flatbed scanner or even the naked eye without requiring an expensive and complicated fluorescence detection system. Therefore, our detection system provides the possibility of developing portable clinical devices for diagnosing a disease related DNA of low to high nM concentrations after PCR.

4. Conclusions

We have described a novel and simple method for detection of specific DNA sequences based on light scattering from aggregated silica particles on a HPV DNA chip. The light scattering performance of the silica particles was analyzed by Mie theory, to account for the enhanced light scattering in terms of the increased effective sizes through aggregation. The scattering signal intensities were further enhanced after three-step hybridization compared with that after two-step hybridization due to the increased aggregation state of the silica particle probes. It was the first time that the scattering from plain silica particles was used for a DNA detection system. The detection method provides the possibility for the development of

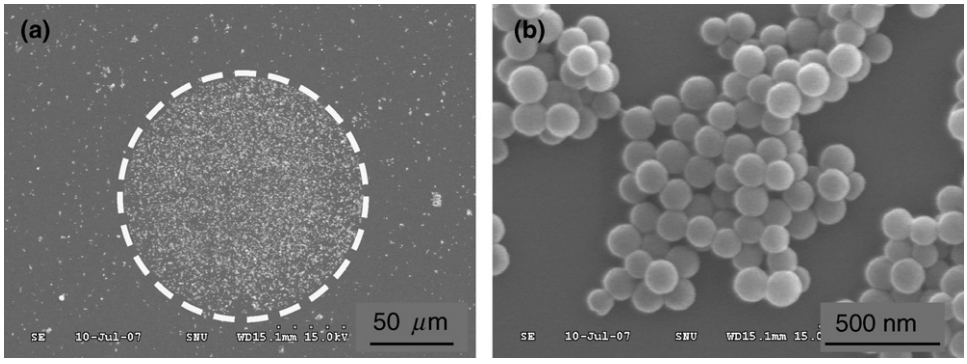


Fig. 6. SEM images of (a) a probe spot (guided by the dotted circle) and (b) one region of the spot after a three-step hybridization. 137 nm sized SP1 and SP2 were used and the target DNA concentration was 10 nM.

rapid, easy, and economic genetic diagnosis due to the advantages of using (1) a low cost light scattering detector systems such as a flatbed scanner or even the naked eye and (2) plain silica particles either commercially available or easily synthesized by the Stöber method. Even with only two-step hybridization, the limit of detections were about 100 pM with a simple microscope illumination system or 200 pM to 1 nM by the naked eye and a flatbed scanner, respectively, sufficient for most real DNA samples (usually in the nanomolar concentration range) obtained from a standard PCR protocol.

Acknowledgement

This work was supported by the Ministry of Education, Science and Technology in Korea.

References

[1] C.Y. Zhang, H.C. Yeh, M.T. Kuroki, T.H. Wang, Nat. Mater. 4 (2005) 826.
[2] X. Zhao, R. Tapec-Dytioco, W. Tan, J. Am. Chem. Soc. 125 (2003) 11474.
[3] X. Zhou, J. Zhou, Anal. Chem. 76 (2004) 5302.
[4] X.X. He, K. Wang, W. Tan, B. Liu, X. Lin, C. He, D. Li, S. Huang, J. Li, J. Am. Chem. Soc. 125 (2003) 7168.
[5] L. Wang, K.M. Wang, S. Santra, X.J. Zhao, L.R. Hilliard, J.E. Smith, J.R. Wu, W.H. Tan, Anal. Chem. 78 (2006) 646.
[6] T.A. Taton, C.A. Mirkin, R.L. Letsinger, Science 289 (2000) 1757.
[7] W. Fritzsche, T.A. Taton, Nanotechnology 14 (2003) R63.
[8] Y.W.C. Cao, R. Jin, C.A. Mirkin, Science 297 (2002) 1536.
[9] R. Elghanian, J.J. Storhoff, R.C. Mucic, R.L. Letsinger, C.A. Mirkin, Science 277 (1997) 1078.
[10] J.M. Nam, S.I. Stoeva, C.A. Mirkin, J. Am. Chem. Soc. 126 (2004) 5932.
[11] T.A. Taton, G. Lu, C.A. Mirkin, J. Am. Chem. Soc. 123 (2001) 5164.
[12] P. Bao, A.G. Frutos, C. Greef, J. Lahiri, U. Muller, T.C. Peterson, L. Warden, X. Xie, Anal. Chem. 74 (2002) 1792.
[13] X. Xu, D.G. Georganopoulou, H.D. Hill, C.A. Mirkin, Anal. Chem. 79 (2007) 6650.
[14] J. Yguerabide, E.E. Yguerabide, Anal. Biochem. 262 (1998) 137.
[15] M. Qhobosheane, S. Santra, P. Zhang, W. Tan, Analyst 126 (2001) 1274.
[16] J. Li, J.Y. Lee, E.S. Yeung, Anal. Chem. 78 (2006) 6490.
[17] C.L. Peyton, M. Schiffman, A.T. Lorincz, W.C. Hunt, I. Mielzynska, C. Bratti, S. Eaton, A. Hildesheim, L.A. Morera, A.C. Rodriguez, R. Herrero, M.E. Sherman, C.M. Wheeler, J. Clin. Microbiol. 36 (1998) 3248.
[18] M.T. Sandri, P. Lentati, E. Benini, P. Dell'Orto, L. Zorzino, F.M. Carozzi, P. Maisonneuve, R. Passerini, M. Salvatici, C. Casadio, S. Boveri, M. Sideri, J. Clin. Microbiol. 44 (2006) 2141.
[19] L. Rozendaal, J. Westerga, J.C. van der Linden, J.M.M. Walboomers, F.J. Voorhorst, E.K.J. Risse, M.E. Boon, C.J.L.M. Meijer, J. Clin. Pathol. 53 (2000) 606.
[20] L.M. Rossi, L. Shi, F.H. Quina, Z. Rosenzweig, Langmuir 21 (2005) 4277.
[21] R.P. Bagwe, L.R. Hilliard, W. Tan, Langmuir 22 (2006) 4357.
[22] TechNote 205, Bangs Laboratories Inc., Fishers, IN 46038-2886, USA, 2008.
[23] D.E. Koppel, J. Chem. Phys. 57 (1972) 4814.
[24] B.J. Frisken, Appl. Opt. 40 (2001) 4087.
[25] Y. Kaneko, K. Nitta, K. Nagayama, Plasma Fusion Res. 2 (2007) S1007.
[26] F. Huo, A.K.R. Lytton-Jean, C.A. Mirkin, Adv. Mater. 18 (2006) 2304.
[27] X. Xu, N.L. Rosi, Y. Wang, F. Huo, C.A. Mirkin, J. Am. Chem. Soc. 128 (2006) 9286.
[28] K. Sato, K. Hosokawa, M. Maeda, J. Am. Chem. Soc. 125 (2003) 8102.
[29] C.F. Bohren, D.R. Huffman, Absorption and Scattering of Light by Small Particles, Wiley-VCH, Weinheim, 2004.
[30] J. Yguerabide, E.E. Yguerabide, Anal. Biochem. 262 (1998) 157.

Talanta 80 (2009) 974–979

Contents lists available at ScienceDirect

Talanta

journal homepage: www.elsevier.com/locate/talanta

Determination of total arsenic and arsenic (III) in phosphate fertilizers and phosphate rocks by HG-AAS after multivariate optimization based on Box-Behnken design

Samuel M. Macedo[a,b], Raildo M. de Jesus[a,b,c], Karina S. Garcia[d], Vanessa Hatje[a,b], Antonio F. de S. Queiroz[d], Sergio L.C. Ferreira[a,b,*]

[a] Instituto de Química, Universidade Federal da Bahia, CEP 40170-270, Salvador-BA, Brazil
[b] Instituto Nacional de Ciência e Tecnologia, INCT, de Energia e Ambiente, Universidade Federal da Bahia, 40170-290 Salvador-BA, Brazil
[c] Universidade Estadual de Santa Cruz, Departamento de Ciências Exatas e Tecnológicas, CEP 45650-000, Ilhéus-BA, Brazil
[d] Universidade Federal da Bahia, Instituto de Geociências, Núcleo de Estudos Ambientais, Brazil

ARTICLE INFO

Article history:
Received 21 July 2009
Received in revised form 19 August 2009
Accepted 20 August 2009
Available online 28 August 2009

Keywords:
Multivariate optimization
Slurry sampling
Phosphate rocks
Phosphate fertilizers
Arsenic
Hydride generation
Atomic absorption spectrometry

ABSTRACT

In the present paper, a procedure for the determination of total arsenic and arsenic (III) in phosphate fertilizers and phosphate rocks by slurry sampling (SS) with hydride generation atomic absorption spectrometry (HG-AAS) is proposed. Arsenic (III) is determinated directly and total arsenic is determinated after reduction reaction. The procedure was optimized for the flow rate of $NaBH_4$, $NaBH_4$ and hydrochloric acid concentrations using a full two-level factorial and also a Box-Behnken design. Slurry preparation with hydrochloric acid in an ultrasonic bath allowed the determination of arsenic (III) with limits of detection and quantification of 0.1 and 0.3 $\mu g\,L^{-1}$, respectively. The precision of results, expressed as relative standard deviation (RSD), was always lower than 3%. The accuracy of this method was confirmed by analysis of certified sediment reference materials, while the procedure also allows for calibration using aqueous external standards. This method (SS/HG-AAS) was used to determine total arsenic and arsenic (III) in two phosphate rock samples and two phosphate fertilizer samples. In these samples, total arsenic concentrations varied from 5.2 to 20.0 $mg\,kg^{-1}$, while As (III) concentrations varied from 2.1 to 5.5 $mg\,kg^{-1}$, in agreement with published values. All samples were also analyzed using acid digestion/HG-AAS. Both, a paired *t*-test and a linear regression model demonstrated no significant difference (95% CL) between the results obtained using these two sample preparation procedures.

© 2009 Elsevier B.V. All rights reserved.

1. Introduction

Arsenic is a highly toxic element, and arsenic exposure is a serious concern worldwide. Several studies have shown that the widespread use of phosphate rock in fertilizers is a significant source of arsenic contamination and exposure [1,2]. A study of 196 fertilizer samples from 12 European countries concluded that these fertilizers and the phosphate rock used to produce them were significant sources of arsenic, chromium, cadmium and lead [3]. Chen et al. [4], evaluated arsenic and cadmium exposure from the application of phosphate fertilizers to agricultural soils, while another study demonstrated adverse impacts from arsenic, antimony and lead in phosphorus-based fertilizers [5,6], and Mirlean and Roisenberg found significant arsenic and cadmium contamination of rainwater, groundwater, and soil in the area surrounding a phosphate fertilizer factory [7]. These studies underscore the importance of measuring and controlling arsenic inputs to soil from fertilizers prepared with phosphate rocks.

The toxicity of arsenic compounds is highly dependent on their speciation and valence state. Trivalent (As III) forms are more toxic than pentavalent (As V) forms, while inorganic arsenic species tend to be more toxic than organic forms [8,9]. Considering the high prevalence of As in phosphate rocks and fertilizers, as well as the role of chemical speciation in determining arsenic toxicity, optimizing rapid, low-cost analytical procedures for determining the concentration and speciation of arsenic in phosphate fertilizers and rocks is of great importance. In this work, a rapid method for the inorganic speciation of arsenic in phosphate fertilizers and phosphate rocks using slurry sampling is presented. Currently, several analytical techniques exist for determining arsenic concentration and speciation with adequate selectivity, accuracy, precision and sensitivity. These techniques include hydride generation atomic

* Corresponding author at: Instituto de Química, Universidade Federal da Bahia, CEP 40170-270, Salvador-BA, Brazil. Fax: +55 71 32355166.
E-mail addresses: slcf@ufba.br, sergio1057@hotmail.com (S.L.C. Ferreira).

0039-9140/$ – see front matter © 2009 Elsevier B.V. All rights reserved.
doi:10.1016/j.talanta.2009.08.025

absorption spectrometry (HG-AAS) [10–12], electrothermal atomization atomic absorption spectrometry (ET AAS) [13,14], hydride generation atomic fluorescence spectrometry (HG-AFS) [15,16], and inductively coupled plasma mass spectrometry (ICP-MS) [17–19]. However, sample preparation and decomposition can present significant problems, particularly for solid sample matrices [20]. This step is further complicated by the volatility of arsenic, which requires that all acid digestion procedures be performed in closed systems to reduce losses. Several efficient sample pre-treatment methods already exist for the determination of arsenic, including closed-vessel microwave-assisted digestion [21,22], in-line digestion systems [23,24] and others. Currently, solid sampling is the preferred technique for arsenic determination in solid matrices, due to the complete elimination of the sample pre-treatment step [25]. However, this technique requires specialized instrumentation that is not always available. Procedures involving this technique have been proposed for the determination of arsenic in barites [26] and sediments [27] employing electrothermal atomic absorption spectrometry (ET AAS) as a detection technique. When the required instrumentation for the above techniques is not available, slurry sampling [28,29] presents an excellent alternative, eliminating the need of sample pre-treatment and reducing the risk of analyte loss or contamination. Methods for As speciation analysis using slurry sampling have been reported [30]. Considering the advantages of the slurry sampling technique, several methods have been proposed for the determination of arsenic in solid matrices. Table 1 shows some of these methods published [30–42].

In this paper it has been proposed a procedure for quantification of total arsenic and arsenic (III) in phosphate fertilizers and phosphate rocks employing slurry sampling (SS) and hydride generation atomic absorption spectrometry (HG-AAS). Arsenic (III) is determinated directly and total arsenic is determinated after reduction reaction.

2. Experimental

2.1. Instrumentation

Arsenic concentrations were measured using a Varian model SpectrAA 220 (Mulgrave, Victoria, Australia) flame atomic absorption spectrometer with an arsenic hollow cathode lamp. The absorption wavelength was set at 193.7 nm, and measurements were made using a lamp current of 10 mA and slit width of 0.5 nm. A deuterium lamp was used for background correction. The flame composition was acetylene (2.0 L min^{-1}) and air (13.5 L min^{-1}). An Alitea C-6 XV peristaltic pump (Stockholm, Sweden) fitted with Tygon tubing was used to propel all solutions. High purity (99.99%) argon was used as a purge gas, with a flow rate of 100 mL min^{-1}. For arsenic determinations, a quartz T-tube cell with a path-length of 165 mm and a diameter of 12 mm was heated to approximately 900 °C. Sample slurries were sonicated at room temperature using a VWR model 75D ultrasonic bath.

2.2. Reagents

All reagents used were of analytical grade, and all solutions were prepared using Milli-Q water (18.2 MΩ cm^{-1}). A standard stock solution of 1000 mg L^{-1} As (III) was prepared by dissolving 0.1320 g of As_2O_3 in 25 mL of 1 mol L^{-1} KOH solution. This solution was neutralized with 2 mol L^{-1} H_2SO_4 and diluted to 100 mL with deionized water. The stock solution was stored at 4 °C. Working solutions of arsenic (0.3–5.0 μg L^{-1}) were prepared daily by diluting aliquots of the stock solution with deionized water. A solution of hydrochloric acid (6 mol L^{-1}) was prepared from concentrated HCl (37%, v/v, Merck). Aqueous solutions of 2% (w/v) sodium tetrahydroborate were prepared freshly daily by dissolving solid $NaBH_4$ in 0.5% (w/v) NaOH before 0.45 μm membrane filtration. Pre-reducing solutions containing 10% (w/v) potassium iodide and 2.0% (w/v) ascorbic acid

Table 1
Methods proposed for the determination of arsenic using slurry sampling.

Sample	Detection technique	Calibration	Slurry preparation	Precision (%)	Reference
Sediments	HG-AAS	DCAS CRM	Aqua regia + HF	<13	31
Coal	ET AAS			<8.9	32
Environmental and biological	ET AAS	TSA CRM	HCl + ozone	<7.8	33
Soil	HG AFS	DCAS CRM	HCl	<4.5	34
Sediment	ETV-ICP-MS	SRM	HNO_3 + HF	<8	35
Sediment and soil	ET AAS	DCAS CRM		<3.8	36
Soil	HG-AAS	TSA	HCl	<5	37
Fish	ETV-ICP-MS	DCAS CRM		<11	38
Sediment	HG-AAS	DCAS CRM	HNO_3 + triton X-100	<8.5	39
Cigarette tobaccos	HG-AAS	DCAS CRM	HNO_3	<7.6	40
Soil and sediment	ET AAS	TSA DCAS CRM	HF	<5.5	41
Soil and sediment	ETV–ICP OES	TSA DCAS CRM		<5.1	42

TSA, technique of standard additions; DCAS, direct calibration against aqueous standards; CRM, certified reference materials.

were prepared freshly daily in distilled water. A citric acid/sodium citrate buffer (0.5/0.5 mol L^{-1}, pH 7.1) was prepared freshly daily in water. Two marine sediment reference materials for trace metals, MESS-2 and MESS-3 (National Research Council of Canada, Ottawa, Canada) were used for method calibration and validation.

2.3. Samples

Two commercial phosphate fertilizer samples (Superphosphate Simple) and two phosphate rocks (from Algeria and Brazil) were analyzed as described below.

2.4. Slurry preparation

Slurries were prepared by combining 0.1 g of dry, granular sample material (particle size range: 20–100 μm) with 3.0 mL of 6.0 mol L^{-1} hydrochloric acid in a 25 mL flask and immersing this mixture in an ultrasonic bath for 30 min before diluting to 25 mL with Milli-Q water. All reagent blanks were prepared in exactly the same way as sample slurries. Aqueous standards were used to generate standard calibration curves.

2.5. Sample preparation using a digester block

In order to evaluate the accuracy of the slurry sampling method, triplicate samples were also prepared via temperature-controlled acid digestion. Briefly, 2 mL of concentrated nitric acid and 1 mL of 30% (v/v) hydrogen peroxide were sequentially added to 0.1 g of each sample in a digester tube. Each tube was then fitted with a cold finger and heated at 100–110 °C for 4 h in a digester block [43]. The resultant solution was diluted to 25 mL with Milli-Q water.

2.6. Analytical procedure

2.6.1. Total arsenic

For determination of total arsenic, 3.33 mL of a 6 mol L^{-1} hydrochloric acid solution, 1 mL of pre-reducing solution (KI 10% + ascorbic acid 2%) and aliquots of the sample slurries were added to reaction flasks. After 30 min, these resultant solutions were diluted to 10 mL with Milli-Q water. Sodium tetrahydroborate was introduced into the closed system at a rate of 2.70 mL min^{-1} using a peristaltic pump, and the arsine vapor generated was transported to the AAS spectrometer using argon as carrier, with a flow rate of 100 mL min^{-1}. Calibration curves were generated by processing aqueous As (III) standards (0.3–5.0 μg L^{-1}) using the same procedure.

For analysis of the digested samples aliquots of the sample solutions were substituted by sample slurries.

2.6.2. Arsenic (III)

For the determination of arsenic (III), aliquots of the samples slurries were transferred to reaction flasks containing 2 mL of citric acid/sodium citrate buffer solution and diluted to a final volume of 10 mL with Milli-Q water. Sodium tetrahydroborate was introduced into the closed system at a rate of 2.70 mL min^{-1} using a peristaltic pump, and the arsine vapor generated was transported to the AAS spectrometer using argon as carrier, with a flow rate of 100 mL min^{-1}.

For analysis of the digested samples aliquots of the sample solutions were substituted by sample slurries.

3. Results and discussion

3.1. Optimization of the procedure for hydride generation

Optimization was conducted using 10.0 mL of 3.0 μg L^{-1} As (III) solution and experiments were carried out in random order. Variables involved in the hydride generation step, including flow rate of $NaBH_4$ (FRB), $NaBH_4$ concentration [BH_4^-] and hydrochloric acid concentration [HCl], were optimized using a two-level factorial multivariate design. Experimental domains for each factor were defined based upon literature data. Coded and real values, as well as analytical signals (integrated absorbance), are shown in Table 2. The concentrations of sodium hydroxide (0.5% w/v), pre-reducing solution (potassium iodide and ascorbic acid) and the flow rate of argon (100 mL min^{-1}) were selected based on literature values.

Effect coefficients calculated for each factor [44] were: (+0.1109 ± 0.0237), (+0.0672 ± 0.0237) and (+0.0016 ± 0.0237) for [BH4], FRB and [HCl], respectively. The evaluation of these data demonstrated that [BH4] and FRB were significant factors, while [HCl] was not. The positive sign of the significant coefficients indicated that integrated absorbance increased with increasing borohydride concentration and flow rate as experimental domains established for each factor. However, an Analysis of Variance (ANOVA) indicated a poor fit of these data to a linear model ($p = 0.086$). A curvature test [45] was also applied, in which the curvature was calculated using the equation: curvature = c, where RFD is the average of the responses obtained from experiments specified by the factorial design, and RCP is the average of the responses obtained for the central point. An analysis of the results, RFD = (0.1812) and RCP = (0.2392), suggests negative curvature, and thus a maximum analytical signal in the region of the central point. On the basis of these results, a Box-Behnken design [46,47] was performed in order to fit a quadratic model to the data and identify the optimal conditions for the SS/HG-AAS procedure (Table 3).

This approach yielded the quadratic model:

$R = 0.2390 + 0.0469[BH_4^-] - 0.0571[BH_4^-]^2 + 0.0632FRB - 0.0413\ FRB^2 - 0.0301[HCl]$, which resulted in an improved fit ($p = 0.1346$). This model obtained has its maximum response for the following experimental conditions: ([BH_4^-] = 0.3178 and

Table 2
Full two-level factorial design—optimization of the procedure for HG.

Experiment	[BH_4^-] concentration % (w/v)	FRB (mL min^{-1})	[HCl] concentration (mol L^{-1})	Integrated absorbance
1	1.50 (−)	1.00 (−)	1.00 (−)	0.0683
2	2.50 (+)	1.00 (−)	1.00 (−)	0.1679
3	1.50 (−)	3.00 (+)	1.00 (−)	0.2032
4	2.50 (+)	3.00 (+)	1.00 (−)	0.2016
5	1.50 (−)	1.00 (−)	3.00 (+)	0.0142
6	2.50 (+)	1.00 (−)	3.00 (+)	0.1655
7	1.50 (−)	3.00 (+)	3.00 (+)	0.2177
8	2.50 (+)	3.00 (+)	3.00 (+)	0.2371
9	2.00 (0)	2.00 (0)	2.00 (0)	0.2462
10	2.00 (0)	2.00 (0)	2.00 (0)	0.2308
11	2.00 (0)	2.00 (0)	2.00 (0)	0.2407

Results found using 10 mL of a 3.0 μg L^{-1} of arsenic (III) solution; FRB = flow rate of $NaBH_4$.

Table 3
Box-Behnken design—optimization of the procedure for HG.

Experiment	$[BH_4^-]$ concentration % (w/v)	FRB (mL min^{-1})	HCl concentration (mol L^{-1})	Absorbance
1	1.50 (−)	1.00 (−)	2.00 (0)	0.0164
2	2.50 (+)	1.00 (−)	2.00 (0)	0.1265
3	1.50 (−)	3.00 (+)	2.00 (0)	0.1854
4	2.50 (+)	3.00 (+)	2.00 (0)	0.2340
5	1.50 (−)	2.00 (0)	1.00 (−)	0.0822
6	2.50 (+)	2.00 (0)	1.00 (−)	0.2085
7	1.50 (−)	2.00 (0)	3.00 (+)	0.1130
8	2.50 (+)	2.00 (0)	3.00 (+)	0.2032
9	2.00 (0)	1.00 (−)	1.00 (−)	0.1256
10	2.00 (0)	3.00 (+)	1.00 (−)	0.2303
11	2.00 (0)	1.00 (−)	3.00 (+)	0.0949
12	2.00 (0)	3.00 (+)	3.00 (+)	0.2192
13	2.00 (0)	2.00 (0)	2.00 (0)	0.2392
14	2.00 (0)	2.00 (0)	2.00 (0)	0.2309
15	2.00 (0)	2.00 (0)	2.00 (0)	0.2469

Results found using 10 mL of a 3.0 μg L^{-1} of arsenic (III) solution.

2.15%), (FRB = 0.7040 and 2.70 mL min^{-1}) and ([HCl] = −0.0241 and 1.97 mol L^{-1}) (coded and real values, respectively). Critical points were calculated as described previously [48]. The optimal delay time for analytical measurements was found to be 15 s.

3.2. Optimization of the procedure for speciation of arsenic

Effect of the addition of citric acid/sodium citrate buffer (0.5/0.5 mol L^{-1}) to standard solutions of As (III) and As (V) were studied with concentrations on the order of μg L^{-1}. In the absence of buffer, As (V) signal was observed (Fig. 1A), while the addition of from 2 mL of buffer masked the As (V) signal and hindered hydride formation.

Optimal [HCl] for arsenic extraction was found to be 6 mol L^{-1} for the extraction procedure described above, as illustrated by a plot of absorbance vs. [HCl] (Fig. 2). At this concentration, recovery was between 100 and 108%.

3.3. Method validation

The SS/HG-AAS method described above was validated according to IUPAC protocols [49]. HG-AAS signal was found

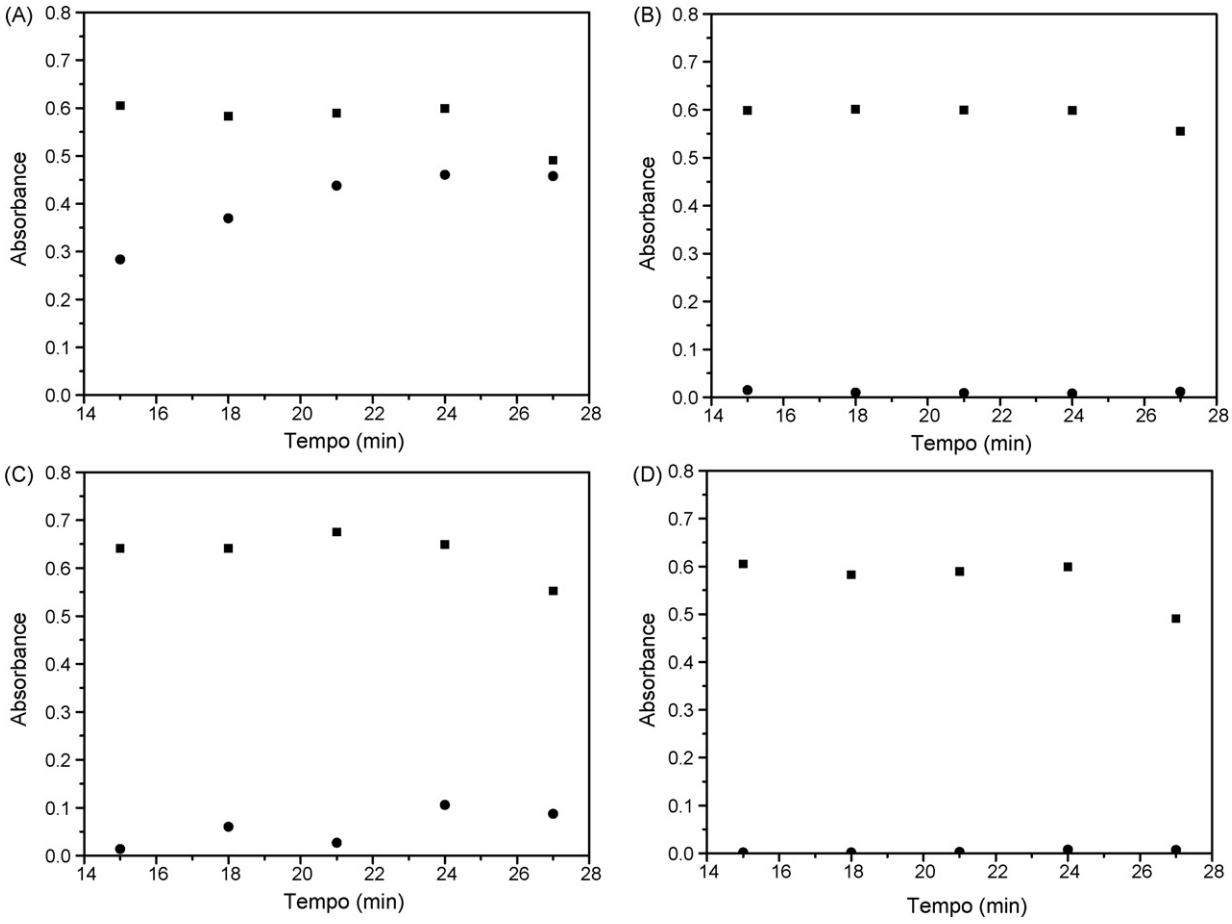


Fig. 1. Measure of the absorbance of ■ As (V) and ● As (III) in function of the time of analysis. 1A – without addition of buffer in the solution of As (V). 1B, 1C and 1D – with addition of 1, 2 and 3 mL of the buffer, respectively.

Table 4
Results of the determination of total arsenic after acid digestion and of total arsenic and As (III) in Marine Sediment Certificated Reference Material after slurry sampling and acid digestion ($n = 3$).

CRM	Certified values As total	Acid digestion As total		Slurry sampling As total		Slurry sampling As (III)	
	($mg\,kg^{-1}$)	($mg\,kg^{-1}$)	RSD%	($mg\,kg^{-1}$)	RSD%	($mg\,kg^{-1}$)	RSD%
MESS-2	20.7 ± 0.8	20.9 ± 0.9	1.7	20.5 ± 1.2	2.4	5.4 ± 0.4	3.0
MESS-3	21.2 ± 1.1	21.6 ± 0.9	0.1	20.2 ± 0.6	1.0	8.7 ± 0.1	0.3

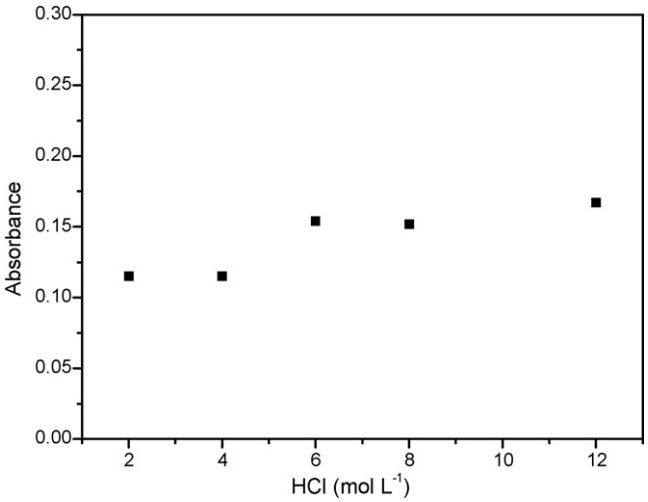


Fig. 2. Measure of the absorbance in function of the concentration of HCl.

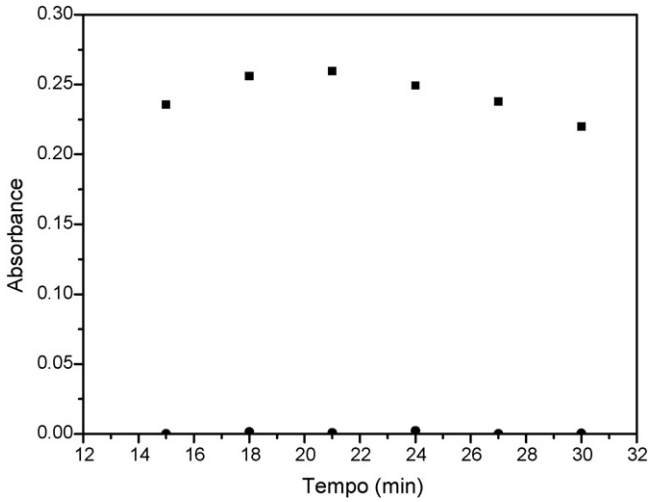


Fig. 3. Measure of analytical signal of ● As (III) and ■ As (V) in function of the time after taken to a bath of ultrasound for 30 min.

to vary with arsenic concentration according to the equation: $Abs = (0.0812 \pm 0.0024)CAs(mL\,\mu g^{-1}) + (0.0193 \pm 0.0042)$, $r2 = 0.9993$ within the linear range of 0.3–5.0 $\mu g\,L^{-1}$. The limits of detection ($3\sigma b/S$) and quantification ($10\sigma b/S$) were calculated as recommended by IUPAC [50], and were found to be 0.1 and 0.3 $\mu g\,L^{-1}$, respectively. These data are in good agreement with the literature values [37,31,51,52].

Standards of As (III) and As (V) were taken to a bath of ultasound for 30 min under the same conditions of samples. There was no significant change in the oxidation state of species after addition of 2 mL buffer (Fig. 3).

The precision (expressed as relative standard deviation) was evaluated during analysis of the four samples, and was found to be less than 8% in each case (Table 4).

The slope of the standard curve for arsenic concentration was found to be $(0.0816 \pm 0.0029)\ C_{As}$ and is quite comparable with the slope obtained by the external calibration technique, $(0.0812 \pm 0.0024)\ C_{As}$. These results demonstrate that the quantification of arsenic in phosphate matrices by slurry sampling can be performed using the external calibration technique with aqueous standard solutions.

The accuracy of the method was evaluated by analyzing marine sediment reference materials: MESS-2 and MESS-3. The certified total arsenic concentrations and the results obtained for As by SS/HG-AAS are presented in Table 4. Measured total arsenic concentrations were in good agreement with certified values.

3.4. Applications

The SS/HG-AAS method was applied for the determination of total arsenic and As (III) in two phosphate fertilizers and two phosphate rock samples. In these samples, total arsenic concentrations varied from 5.2 to 20.0 $mg\,kg^{-1}$ and As (III) concentrations varied from 2.1 to 5.5 $mg\,kg^{-1}$. Measured total arsenic concentrations were in good agreement with the literature values [53,54]. These results, expressed as 95% confidence intervals, are presented in Table 5. As a comparison to the SS-HG/AAS method, triplicate samples were digested with hydrochloric acid and hydrogen peroxide in a closed system prior to total arsenic determination by HG-AAS (Table 5). A statistical comparison using a paired *t*-test [55] (95% confidence level) showed no significant difference between the results obtained by both methods. A linear regression of the results obtained with the two methods followed the equation [slurry sampling] = 0.959 ± 0.046 [digestion method] + 0.259 ± 0.727, $r = 0.9982$.

These results demonstrate that the calculated slope and intercept do not differ significantly from the "ideal" values of 1 and 0, respectively, and that there is no evidence for a systematic difference between the results obtained employing either procedure for the determination of arsenic in the samples under study.

Table 5
Results of the determination of total arsenic and As (III) in phosphate fertilizers and phosphate rocks samples ($n = 3$).

Sample	Acid digestion As total		Slurry sampling As total		Slurry sampling As (III)	
	($mg\,kg^{-1}$)	RSD%	($mg\,kg^{-1}$)	RSD%	($mg\,kg^{-1}$)	RSD%
SSP1	20.4 ± 1.3	1.2	19.5 ± 0.6	2.6	5.5 ± 0.5	1.0
SSP2	13.0 ± 2.9	8.0	12.6 ± 2.5	9.0	7.5 ± 1.0	5.2
PR1	5.1 ± 0.2	1.8	5.2 ± 0.2	1.8	3.9 ± 0.2	2.5
PR2	20.2 ± 1.5	1.3	20.0 ± 0.6	3.0	2.1 ± 0.2	4.6

SSP = phosphate fertilizer (superphosphate simple) and PR = phosphate rocks.

4. Conclusions

The SS/HG-AAS method demonstrated appropriate precision, accuracy, and detection limits for the determination of arsenic in phosphate rocks and phosphate fertilizer. In this work, slurry sampling was found to be a useful extraction technique, particularly given the volatility of arsenic species and the low solubility of phosphate matrices in acid media. Arsenic concentrations found in the four samples analyzed agreed with the literature values for phosphate rocks and commercial phosphate fertilizers.

Acknowledgements

The authors would like to acknowledge the support of Fundação de Amparo a Pesquisa do Estado da Bahia (FAPESB), Conselho Nacional de Desenvolvimento Científico e Tecnológico (CNPq) and Coordenação de Aperfeiçoamento de Pessoal de Nível Superior (CAPES).

References

[1] Yu, A. Potatueva, V.G. Ignatov, E.A. Karpova, Agrokhimiya (1) (2007) 31.
[2] C. Beni, G. Diana, S. Marconi, Agrochimica 52 (2008) 99.
[3] G. Nziguheba, E. Smolders, Sci. Total Environ. 390 (2008) 53.
[4] W.P. Chen, A.C. Chang, L.S. Wu, Ecotox. Environ. Safe. 67 (2007) 48.
[5] D.W. Kilgour, R.B. Moseley, M.O. Barnett, K.S. Savage, P.M. Jardine, J. Environ. Quality 37 (2008) 1733.
[6] Z. Chen, K.F. Akter, M.M.R. Rahman, R. Naidu, Microchem. J. 89 (2008) 20.
[7] N. Mirlean, A. Roisenberg, Environ. Pollut. 143 (2006) 335.
[8] M. Burguera, J.L. Burguera, Talanta 44 (1997) 1581.
[9] X. Yan, X. Yin, X. He, Y. Jiang, Anal. Chem. 74 (2002).
[10] A.N. Anthemidis, E.K. Martavaltzoglou, Anal. Chim. Acta 573 (2006) 413.
[11] M. Tuzen, D. Citak, D. Mendil, M. Soylak, Talanta 78 (2009) 52.
[12] X. Li, J. Jia, Z.H. Wang, Anal. Chim. Acta 560 (2006) 153.
[13] L. Zhang, Y. Morita, A. Sakuragawa, A. Isozaki, Talanta 72 (2007) 723.
[14] P. Bermejo-Barrera, M.C. Barciela-Alonso, M. Ferrón-Novais, A. Bermejo-Barrera, J. Anal. Atom Spectrom. 10 (1995) 247.
[15] H. Matusiewicz, Appl. Spectrosc. Rev. 38 (2003) 263.
[16] R. Liu, P. Wu, M. Xi, K. Xu, Y. Lv, Talanta 78 (2009) 885.
[17] Y.L. Feng, H.Y. Chen, L.C. Tian, H. Narasaki, Anal. Chim. Acta 375 (1998) 167.
[18] J.L. Ellis, S.D. Conklin, C.M. Gallawa, K.M. Kubachka, A.R. Young, P.A. Creed, J.A. Caruso, J.T. Creed, Anal. Bioanal. Chem. 390 (2008) 1731.
[19] C. Wolf, N. Wenda, A. Richter, A. Kyriakopoulos, Anal. Bioanal. Chem. 389 (2007) 799.
[20] J. Sneddon, C. Hardaway, K.K. Bobbadi, A.K. Reddy, Appl. Spectrosc. Rev. 41 (2006) 1.
[21] M. Kosanovic, A. Adem, M. Jokanovic, Y.M. Abdulrazzaq, Anal. Lett. 41 (2008) 406.
[22] K.C. Chan, Y.C. Yip, H.S. Chu, W.C. Sham, J. AOAC Int. 89 (2006) 469.
[23] M. Burguera, J.L. Burguera, Talanta 366 (1998) 63.
[24] V. Dufailly, T. Guerin, L. Noel, J.M. Fremy, D. Deauchemin, J. Anal. Atom Spectrom. 23 (2008) 1263.
[25] M.G.R. Vale, N. Oleszczuk, W.N.L. dos Santos, Appl. Spectrosc. Rev. 41 (2006) 377.
[26] R. Nowka, I.L. Marr, T.M. Ansari, H. Muller, Fresen. J. Anal. Chem. 364 (1999) 533.
[27] A. Sahuquillo, G. Rauret, A. Rehnert, H. Muntau, Anal. Chim. Acta 476 (2003) 15.
[28] M.J. Cal-Prieto, M. Felipe-Sotelo, A. Carlosena, J.M. Andrade, P. Lopez-Mahia, S. Muniategui, D. Prada, Talanta 56 (2002) 1.
[29] M.C. Santos, J.A. Nóbrega, Appl. Spectrosc. Rev. 41 (2006) 427.
[30] H. Matusiewicz, M. Mroczkowska, J. Anal. Atom Spectrom. 18 (2003) 751.
[31] D.P. Torres, M.A. Weira, A.S. Ribeiro, A.J. Curtius, J. Braz. Chem. Soc. 18 (2007) 728.
[32] S.Z. Chen, Spectrosc. Spect. Anal. 24 (2004) 1267.
[33] A. Caballo-Lopez, M.D.L. de Castro, Anal. Chem. 75 (2003) 2011.
[34] L.F. Dias, T.D. Saint'Pierre, S.M. Maia, M.A.M. da Silva, V.L.A. Frescura, B. Welz, A.J. Curtius, Spectrochim. Acta Part B 57 (2002) 2003.
[35] F. Barbosa, E.C. Lima, F.J. Krug, Analyst 125 (2000) 2079.
[36] H. Gurleyuk, J.F. Tyson, P.C. Uden, Spectrochim. Acta Part B 55 (2000) 935.
[37] S.F. Chen, S.J. Jiang, J. Anal. Atom Spectrom. 13 (1998) 673.
[38] J. Mierzwa, R. Dobrowolski, Spectrochim. Acta Part B 53 (1998) 117.
[39] J. Mierzwa, S.B. Adeloju, H.S. Dhindsa, Analyst 122 (1997) 539.
[40] I. Lopez Garcia, M. Sanchez Merlos, M. Hernandez Cordoba, Spectrochim. Acta Part B 52 (1997) 437.
[41] G. Zaray, T. Kantor, Spectrochim. Acta Part B 50 (1995) 489.
[42] P. Bermejo-barrera, M.J. Lorenzoalonso, M. Aboalsomoza, A. Bermejobarrera, Mikrochim. Acta 117 (1994) 49.
[43] E.V. Silva-Filho, S.M. Sella, E.C. Spinola, I.R. Santos, I.R.W. Machado, L.D. Lacerda, Microchim. J. 82 (2006) 196.
[44] R.E. Bruns, I.S. Scarminio, B.B. Neto, Statistical Design—Chemometrics, Elsevier, Amsterdam, 2006.
[45] D.L. Massart, B.G.M. Vandeginste, L.M.C. Buydens, S. de Jong, P.J. Lewi, J. Smeyers-Verbeke, Handbook of Chemometrics and Qualimetrics: Part A, Elsevier, Amsterdam, 1997.
[46] S.L.C. Ferreira, R.E. Bruns, H.S. Ferreira, G.D. Matos, J.M. David, G.C. Brandão, E.G.P. da Silva, L.A. Portugal, P.S. dos Reis, A.S. Souza, W.N.L. dos Santos, Anal. Chem. Acta 597 (2007) 179.
[47] S.L.C. Ferreira, M.D.G.A. Korn, H.S. Ferreira, E.G.P. da Silva, R.G.O. Araujo, A.S. Souza, S.M. Macedo, D.D.C. Lima, R.M. de Jesus, F.A.C. Amorim, M.D.G.A. Korn, Appl. Spectrosc. Rev. 42 (2007) 475.
[48] S.L.C. Ferreira, M.A. Bezerra, W.N.L. dos Santos, B.B. Neto, Talanta 61 (2003) 295.
[49] IUPAC, Pure Appl. Chem. 74 (2002) 835.
[50] Analytical Methods Commitee, Analyst 119 (1994) 2363.
[51] A.R. Kumar, P. Riyazuddin, Int. J. Environ. Anal. Chem. 88 (2008) 255.
[52] Y.L. Zhang, S.B. Adeloju, Talanta 76 (2008) 724.
[53] F.A. Nicholson, S.R. Smith, B.J. Alloway, C. Carlton-Smith, B.J. Chambers, Sci. Total Environ. 311 (2003) 205.
[54] W. Chen, A.C. Chang, L. Wu, Ecotox. Environ. Safe. 67 (2007) 48.
[55] G.D. Christian, Analytical Chemistry, 5th ed., EUA, 1994.

Talanta 80 (2009) 980–984

Contents lists available at ScienceDirect

Talanta

journal homepage: www.elsevier.com/locate/talanta

Ultrasound-assisted emulsification–microextraction combined with flame atomic absorption spectrometry for determination of trace cadmium in water samples

Jing Jun Ma, Xin Du, Jing Wen Zhang, Jing Ci Li*, Lian Zeng Wang

Hebei Key Laboratory of Bioinorganic Chemistry, College of Sciences, Agricultural University of Hebei, Hebei, Baoding 071001, China

ARTICLE INFO

Article history:
Received 23 May 2009
Received in revised form 18 August 2009
Accepted 21 August 2009
Available online 28 August 2009

Keywords:
Ultrasound-assisted
emulsification–microextraction
Pre-concentration
Atomic absorption spectrometry
Cadmium

ABSTRACT

The process of ultrasound-assisted emulsification–microextraction (USAEME) was successfully applied for the first time for the extraction and pre-concentration of trace cadmium from water samples, followed by flame atomic absorption spectrometry (FAAS). In the proposed approach, sodium diethyldithiocarbamate trihydrate solution ($NaDDTC{\cdot}3H_2O$) was used as a chelating agent and carbon tetrachloride was selected as extraction solvent. Some effective parameters on the microextraction and the complex formation were selected and optimized. These parameters included extraction solvent type as well as extraction volume, time, temperature, and pH, the amount of the chelating agent, and salt effect. Under optimum conditions, an enrichment factor of 95 was obtained from only 5.0 mL of water sample. The calibration graph was linear in the range of 10–600 $\mu g\,L^{-1}$ with a detection limit of 0.91 $\mu g\,L^{-1}$. The relative standard deviation (R.S.D) for ten replicate measurements of 50 and 500 $\mu g\,L^{-1}$ of cadmium were 2.56 and 1.62%. This proposed method was successfully applied in the analysis of four real environmental water samples and good spiked recoveries over the range of 96.5–101.7% were obtained.

© 2009 Elsevier B.V. All rights reserved.

1. Introduction

Cadmium is known to be highly toxic for animals, plants and humans even at low concentrations and can be accumulated in several organs [1]. Long-term consumption of drinking water containing cadmium at levels higher than 0.005 $mg\,L^{-1}$ can cause nausea, salivation, diarrhea, muscular cramps, renal degradation, lung insufficiency, bone lesions and hypertension in humans [2]. Experimental and epidemiological studies have provided substantial evidence that low levels of long-term exposure to cadmium can attribute to an increased risk of cancer [3]. In light of this, trace determinations of Cd in environmental and in biological samples have become of increasing interest.

Flame atomic absorption spectrometry (FAAS) has been widely used for the determination of trace metal ions because of the relatively simple and inexpensive equipment required. However, direct determination of metal ions at trace levels by FAAS is limited not only due to insufficient sensitivity, but also to matrix interference. Under these circumstances, in order to determine trace levels of Cd, a separation and enrichment step prior to their determinations may be beneficial. Several methods have been proposed for separation and pre-concentration of trace Cd including: Liquid–liquid extraction (LLE) [4–7], coprecipitation [8,9], solid phase extraction (SPE) [10,11], and cloud point extraction (CPE) [12,13]. However, liquid–liquid extraction (LLE), as the oldest preconcentration and separation technique in analytical chemistry [14], is time-consuming and requires large amounts of organic solvents [15]. Compared with LLE, SPE offers simpler operation, a higher enrichment factor, and ease of automation, but the amounts of elution solvents are still relative large [16,17]. CPE is a comparatively simple, cheap and less toxic method [18,19], but it too has several limitations associated with it. For instance, because of the viscosity of the surfactant-rich phase, samples prepared this way cannot be injected directly into conventional analytical instruments. As well, the surfactants bear chromophores, which interfere with the UV detection by overlapping with the analyte signal [17].

Modern trends in analytical chemistry lean towards the simplification and miniaturization of sample preparation, as well as the minimization of the organic solvent used. Jeannot and Cantwell developed a liquid-phase microextraction (LPME) technique in 1996, which is based on analyte partition between a drop of organic solvent (extraction phase) and the aqueous sample bulk [20]. Several different types of LPME have been developed, including single drop microextraction (SDME) [21–23], hollow fiber LPME [24,25] and homogeneous liquid–liquid extraction (HLLE) [26,27]. Microextraction techniques are fast, simple, inexpensive,

* Corresponding author.
E-mail address: jingcili63@yahoo.com.cn (J.C. Li).

0039-9140/$ – see front matter © 2009 Elsevier B.V. All rights reserved.
doi:10.1016/j.talanta.2009.08.029

environmentally friendly and compatible with many analytical instruments. Nevertheless some drawbacks, such as instability of the droplet and relatively low precision are often reported [28].

Recently, Assadi and co-workers developed a novel microextraction technique, termed dispersive liquid–liquid microextraction (DLLME) [29]. This technique is based on the formation of tiny droplets of the extractant in the sample solution using a water-immiscible organic solvent (extractant) dissolved in a water-miscible organic dispersive solvent [30–32]. The advantages of the DLLME method are rapidity, low cost, and high enrichment factors. Its main drawback is the necessity of using a third component (disperser solvent), which usually decreases the partition coefficient of analytes into the extraction solvent [33].

Ultrasonic energy, when applied to solutions, causes acoustic cavitation: That is, bubble formation and implosion. The collapse of bubbles formed by ultrasonic energy results in the generation of extremely high temperatures and pressures at the interface of the collapsing bubble and another phase, leading to enhanced chemical reactivity [34]. The combination of microextracting systems and ultrasound radiation provides an efficient pre-concentration technique, named ultrasound-assisted emulsification–microextraction (USAEME). USAEME is based on the implosion bubbles generated by the cavitation phenomenon, which produces intensive shock waves in the surrounding liquid and high-velocity liquid jets. Such microjets can cause droplet disruption in the vicinity of collapsing bubbles and thus, improve emulsification by generating a smaller droplet size of the dispersed phase right after disruption. Submicron droplet size leads to significant enlargement of the contact surface between both immiscible liquids, improving the mass-transfer between the phases [35]. In USAEME, the appropriate extraction solvent is rapidly injected by syringe into aqueous samples containing analytes. After sonication, a cloudy solution forms. Then, this cloudy solution is centrifuged and the fine droplets sediment at the bottom of the conical test tube. The determination of analytes in the sedimented phase can be performed by instrumental analysis. In fact, this pre-concentration technique has been developed by Regueiro et al. [33] for the determination of synthetic musk fragrances, phthalate esters and lindane in aqueous samples. They demonstrated that USAEME is an efficient, simple, and nonexpensive extraction procedure for GC analysis. Up to now, it has been also used for the pre-concentration of polybrominated diphenyl ethers and polychlorinated biphenyls from water samples [32,35]. We extend its application to inorganic analysis, and have obtained the consistent conclusion.

This paper describes the first application of ultrasound-assisted emulsification–microextraction for the determination of trace cadmium in water samples without the addition of the dispersive solvent, thereby overcoming DLLME disadvantages. In order to obtain a high enrichment factor, the effect of different parameters affecting the complex formation and extraction conditions (such as type and volume of the extraction solvent, pH, the chelating agent amount, extraction time, extraction temperature and ionic strength) were tested. USAEME can be employed as a simple and efficient extraction and pre-concentration procedure for heavy metals in aqueous samples with satisfactory results.

2. Experimental

2.1. Apparatus

The experiments were performed with a Hitachi Z-5000 atomic absorption spectrometer (Japan) equipped with Zeeman background correction. A cadmium hollow cathode lamp operating at 228.8 nm was utilized as the radiation source. The instrumental parameters were adjusted according to the manufacturer's recommendations. All pH measurements were carried out using a pH_3-3C digital pH meter equipped with a combined glass-calomel electrode (Hangzhou Dongxing Instrument Factory, Hangzhou, P.R.China). A Model LD5-2A centrifuge (Beijing Jingli Instrument Factory, Beijing, P.R.China) was used to accelerate the phase separation. A 59 kHz, 200 W ultrasonic bath with temperature control (Shanghai Kudos Ultrasonic instrument Co, Ltd., Shanghai, P.R.China) was used to assist the emulsification process of the microextraction technique.

2.2. Reagents and solutions

A stock standard solution of cadmium at a concentration of 1000 $\mu g\,mL^{-1}$ was purchased from the National Institute of Standards (Beijing, China). Working standard solutions were prepared by serial dilutions of the stock solution with deionized water immediately prior to analysis. The chelating agent, 0.5 $g\,L^{-1}$ sodium diethyldithiocarbamate trihydrate solution ($NaDDTC{\cdot}3H_2O$), was prepared by dissolving the appropriate amount of $NaDDTC{\cdot}3H_2O$ (Beijing Chemistry Reagent Company, Beijing, China) in water. The NaCl solution was prepared by dissolving the appropriate amount of NaCl in deionized water. Carbon tetrachloride, chloroform and dichloromethane as extraction solvent were obtained from Tianjin Tianda Chemicals Reagent Company (Tianjin, China).

Nitric acid (0.1 $mol\,L^{-1}$) was used to adjust the pH 2–3, ammonium acetate buffers (0.2 $mol\,L^{-1}$) were prepared by adding an appropriate amount of acetic acid to ammonium acetate solutions resulting in solutions of pH 4–6. For pH 7–8, a phosphate (0.2 $mol\,L^{-1}$) buffer solution was prepared by adding an appropriate amount of disodium hydrogen phosphate to sodium dihydrogen phosphate. Ammonium chloride buffer solutions (0.2 $mol\,L^{-1}$) were prepared by adding an appropriate amount of ammonia to ammonium chloride solutions, resulting in solutions of pH 9–10.

All reagents used were of analytical reagent grade. Deionized water was used in the preparation of all solutions. The laboratory glassware was kept in 10% nitric acid for at least 24 h and subsequently washed four times with deionized water.

Tap, sea, river and waste water samples used for development of the method were collected in polytetrafluoroethylene (PTFE) containers from Hebei province, filtered using a 0.45 μm pore size membrane filter to remove suspended particulate matter, and stored in a refrigerator in the dark.

2.3. Ultrasound-assisted emulsification–microextraction procedure

A 5.0 mL sample of standard solution containing 500 $\mu g\,L^{-1}$ of cadmium was poured in a test tube with a conical bottom. 1.0 mL acetate buffer and 2.0 mL $NaDDTC{\cdot}3H_2O$ (0.5 $g\,L^{-1}$) solution were added. Then, 100 μL of carbon tetrachloride (extraction solvent) was injected rapidly into the sample solution using a syringe. The tube was immersed into an ultrasonic bath for 20 min at 50 °C. As a result, oil-in-water (O/W) emulsions of carbon tetrachloride (dispersed phase) in water (continuous phase) were formed. Emulsions were then disrupted by centrifugation at 4600 rpm for 5 min, which resulted in the organic phase sedimenting at the bottom of the conical tube. The sedimented phase was quantitatively transferred to another test tube and the solvent was allowed to evaporate at room temperature. Finally, the residue was dissolved in 0.5 mL 0.1 $mol\,L^{-1}$ nitric acid and the cadmium concentration was determined by flame atomic absorption spectrometry. Fig. 1 shows a scheme of the USAEME procedure.

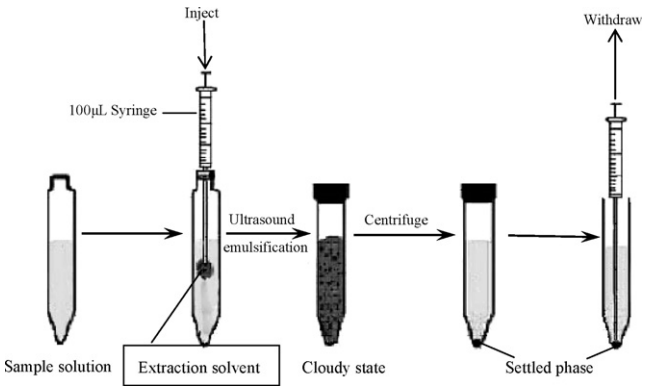


Fig. 1. Ultrasound-assisted emulsification–microextraction procedure.

3. Results and discussion

3.1. Effect of type and volume of the extraction solvent

Extraction solvent should have special characteristics: it should have a higher density than water, high extraction capability of the interested compounds and low solubility in water. Chloroform ($CHCl_3$), carbon tetrachloride (CCl_4) and dichloromethane (CH_2Cl_2) were examined in the extraction of cadmium.

The compatibility of these solvents with the USAEME technique was studied by adding 100 μL of each of the solvents mentioned above to a 5.0 mL aqueous solution containing 500 $\mu g\,L^{-1}$ of cadmium. Dichloromethane was completely dissolved in the ultrasonic process. Therefore, this solvent was ruled out for further optimization. Chloroform and carbon tetrachloride as extraction solvents resulted in enrichment factors of 50 and 95, respectively. Conversely, in comparison of these two extraction solvents, carbon tetrachloride forms a well stable cloudy solution; the sedimented phase can easily be removed by sampler and has less consumption volume to obtain the 80 μL sedimented phase. Therefore, Carbon tetrachloride was selected as the extraction solvent for further studies.

In order to obtain the highest extraction efficiency of the USAEME procedure, the extraction solvent volume was optimized. For this purpose, different volumes of carbon tetrachloride in the range of 50–130 μL were examined in the extraction procedure. It was found that by increasing the volume of CCl_4, the analytical signal increases, reaching the maximum value at 100 μL, after which, remained constant. Therefore, in the subsequent studies, 100 μL carbon tetrachloride was used as the optimum volume of the extraction solvent.

3.2. Influence of pH

The separation of metal ions by USAEME involves prior formation of a complex with sufficient hydrophobicity to be extracted into the small volume of the sedimented phase, whereby the desired pre-concentration is obtained. pH plays a unique role on metal-chelate formation and subsequent extraction. The effect of pH on the complex formation and extraction of cadmium from water samples was studied in the range of 2.0–10.0 by using nitric acid, ammonium acetate, phosphate and ammonium chloride. As can be seen in Fig. 2, the highest signal intensity of Cd was obtained at pH 6.0. Therefore, pH 6.0 was selected for further study.

3.3. Influence of the amount of NaDDTC·3H$_2$O

The effect of the amount of NaDDTC·3H_2O (0.5 $g\,L^{-1}$) on the absorption was studied using various volumes of the reagent ranging from 0.5 mL to 3.0 mL. The results showed that the signal of Cd was increased with the increase of NaDDTC·3H_2O volume up to 1.6 mL, and then remained constant. Hence, 2.0 mL of 0.5 $g\,L^{-1}$ NaDDTC·3H_2O solution was chosen to account for other extractable species that might potentially interfere with the assaying of cadmium.

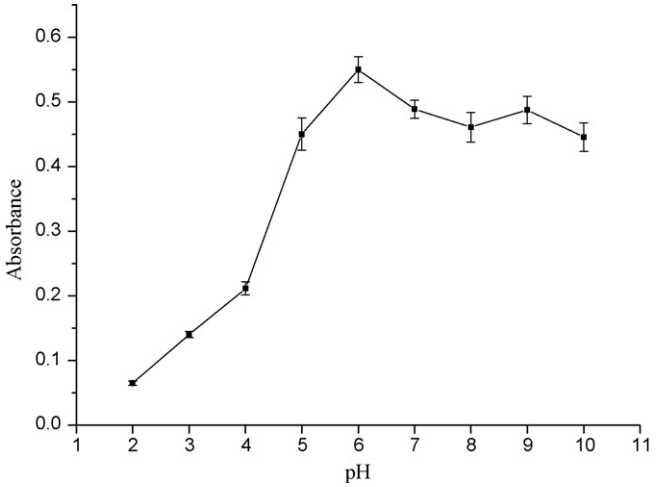


Fig. 2. Effect of pH on the absorbance of Cd obtained from USAEME. Extraction conditions: water sample volume, 5.0 mL; DDTC volume, 2.0 mL; extraction solvent (CCl_4) volume, 100 μL; concentration of Cd, 500 $\mu g\,L^{-1}$; extraction time, 20 min; extraction temperature, 50 °C.

3.4. Effect of the extraction time

Time plays an important role in the emulsification and mass-transfer phenomena. In USAEME, extraction time is defined as the time between injection of extraction solvent and the end of the sonication stage. The effect of extraction time was examined in the range of 5–35 min under constant experimental conditions. It was found that by increasing the extraction time, the absorbance increases reaching a plateau at 20 min, which is considered as 100% extraction. Therefore, 20 min extraction time was chosen as the working condition for further studies.

3.5. Effect of extraction temperature

Temperature affects organic solvent solubility in water as well as the emulsification phenomenon. Thus, this affects the mass-transfer process and the extraction efficiency. To determine the influence of the extraction temperature, 5.0 mL aqueous solution containing 500 $\mu g\,L^{-1}$ of cadmium was extracted at different temperatures ranging from 20 °C to 70 °C. At temperatures lower than 40 °C, it was difficult to get a homogeneous emulsion resulting in a prompt phase separation. Therefore, the mass-transfer process was limited to a short amount of time, leading to poor extraction efficiency, and consequently low absorbance. In the 40–60 °C temperature range, the emulsification was easily achieved and the highest absorbance obtained at 50 °C. At a temperature higher than 60 °C, carbon tetrachloride was partially dissolved into the aqueous bulk, leading to the reduction of the analytical signal. Hence, 50 °C is recommended for further studies.

3.6. Effect of salt

For investigating the influence of ionic strength on performance of USAEME, various experiments were performed by adding varying NaCl amounts from 0% to 5% (w/v). Other experimental conditions were kept constant. By increasing the NaCl from 0% to

Table 1
Effect of interferents on the recovery of 500 μg L^{-1} Cd^{2+} in water sample using USAEME–FAAS.

Interferent	Concentration (μg L^{-1})	Interferent/Cd^{2+} ratio	Recovery (%)
Na^+	50,000	100	98.1
K^+	50,000	100	95.6
Ag^+	5,000	10	96.3
Ba (II)	25,000	50	97.3
Mn (II)	5,000	10	96.8
Co (II)	5,000	10	97.5
Cu (II)	5,000	10	100.2
Ni (II)	5,000	10	95.6
Zn (II)	25,000	50	96.7
Pb (II)	25,000	50	96.2
Fe (II)	20,000	40	98.4
Ca (II)	15,000	30	97.3
Mg (II)	15,000	30	98.7
Hg (II)	2,500	5	95.7
Bi (III)	15,000	30	95.4
Cr (III)	10,000	20	94.5
Al (III)	25,000	50	100.7
Fe (III)	50,000	100	98.2
As (III)	10,000	20	96.5
As (V)	25,000	50	97.6
Sn (IV)	25,000	50	96.5
Cl^-	50,000	100	100.2
NO_3^-	50,000	100	101.6
I^-	50,000	100	99.5
CH_3COO^-	50,000	100	98.3
SO_4^{2-}	50,000	100	95.4
$Cr_2O_7^{2-}$	50,000	100	97.2
PO_4^{3-}	50,000	100	94.8

5%, the volume of the sedimented phase increases slightly from 80 μL to 83 μL. The results showed that salt addition has no significant effect on the enrichment factor, perhaps because of the two opposite effects of salt addition in USAEME of cadmium: one involves increasing the volume of the sedimented phase, which decreases the enrichment factor, and the other is the salting-out effect that increases the enrichment factor [36,37]. Therefore, the enrichment factor is nearly constant by increasing the amount of sodium chloride, and the extraction experiments were carried out without adding salt.

3.7. Effect of coexisting ions

The effects of common coexisting ions in natural water samples on the recovery of cadmium were studied. In these experiments, 5.0 mL solutions containing 500 μg L^{-1} of cadmium and various amounts of interfering ions were treated according to the recommended procedure. A given species was considered to interfere if it resulted in a ± 5% variation of the absorbance signal. The results obtained are given in Table 1.

3.8. Analytical figures of merit

In the optimum conditions, a calibration graph was obtained by preconcentrating a series of the solutions according to procedure under experiment. Table 2 shows the analytical characteristics of this method. The calibration graph was linear in the range of 10–600 μg L^{-1} of cadmium. The equation of the calibration curve after the pre-concentration procedure was given as $A = 1.75 \times 10^{-3}C + 0.0202$ with a correlation coefficient of 0.9954 ($n = 10$), where A is the atomic absorbance for cadmium in the rich phase at 228.8 nm and C is the concentration of cadmium in the sample solution in μg L^{-1}. The limit of detection, defined as $C_L = 3S_B/m$ (where C_L, S_B and m are the limit of detection, standard deviation of the blank and slope of the calibration graph, respectively), was 0.91 μg L^{-1}. The relative standard deviation (R.S.D) for ten replicate measurements of 50 and 500 μg L^{-1} of cadmium were 2.56 and 1.62%. Table 2 also shows the calibration obtained with standard solutions of Cd not subjected to the USAEME preconcentration step. Phase volume ratio, calculated as the ratio between the volume of the aqueous phase (8.0 mL) and the final injection volume (0.5 mL nitric acid containing the analyte), was 16 times.

Table 2
Analytical characteristics of the method.

Analytical parameters	Without USAEME preconcentration	With USAEME preconcentration
Linear range (μg L^{-1})	100–6000	10–600
Slope	1.31×10^{-4}	1.75×10^{-3}
Intercept	0.0155	0.0202
Correlation coefficient	0.9972	0.9954
Detection limit (μg L^{-1})	13.78	0.91
Relative standard deviation (R.S.D%) ($n = 10$)	3.62 (200 μg L^{-1})	2.56 (50 μg L^{-1})
	3.20 (500 μg L^{-1})	1.62 (500 μg L^{-1})
Phase volume ratio	–	16
The enrichment factor[a]	–	95
The enrichment factor[b]	–	15.3
The enhancement factor[c]	–	13.4

[a] The enrichment factor is the ratio of the cadmium concentration in the organic-rich phase(80 μL) to that in the bulk phase initially.
[b] The enrichment factor is the ratio of the cadmium concentration in 0.5 mL 0.1 mol L^{-1} nitric acid to that in the bulk phase initially.
[c] The enhancement factor is the slope ratio of calibration graph after and before extraction.

The enrichment factor (EF) [3,38] is defined as the ratios of the cadmium concentration in the organic-rich phase to that in the bulk phase, initially. Eq. (1) was used for calculation of the enrichment factor:

$$EF = \frac{C_{sed}}{C_0} \quad (1)$$

where C_{sed} is cadmium concentration (μg L^{-1}) in the organic-rich phase after phase separation (80 μL organic-rich phase) and C_0 is the initial concentration of cadmium (μg L^{-1}). The enrichment factor was obtained as 95 ($n = 3$).

As for the determination of the absorbance for cadmium in the organic-rich phase, the extraction solvent (80 μL) was evaporated at room temperature, Finally, the residue was dissolved into 0.5 mL 0.1 mol L^{-1} nitric acid; the enrichment factor for the proposed method is 15.3.

The enhancement factor [39,40], defined as the ratio of the slope of the calibration graph for the USAEME method, to that of the calibration graph in water phase without pre-concentration, was 13.4.

3.9. Analysis of natural waters

The proposed method was used for the determination of cadmium in several water samples and the results along with the recovery for the spiked samples were given in Table 3. The recoveries for the addition of different concentrations of cadmium to water samples were in the range 96.5–101.7%. To verify the accuracy of the proposed procedure, the method was then used for the determination of the content of Cd in National Standard Reference Material for Environment Water (GSBZ50009-88 and GSB07-1185-2000) after the appropriate dilution. These results are presented in Table 3. A good agreement between the determined values and the certified values was obtained.

Table 3
Analytical results of cadmium determination (dissolved fraction) in certified reference materials and spiked natural water samples with the USAEME–FAAS method ($n = 3$).

Sample	Certified	Added	Found[a]	Recovery (%)
GSBZ50009-88 ($\mu g L^{-1}$)	15.0 ± 0.6	–	14.13 ± 0.66	94.2
	22.5 ± 0.9	–	21.26 ± 0.75	94.5
	37.5 ± 1.5	–	35.96 ± 1.53	95.9
GSB07-1185-2000 ($\mu g L^{-1}$)	16.26 ± 1.2	–	15.04 ± 0.75	92.5
	20.325 ± 1.5	–	19.31 ± 1.0	95.0
	40.65 ± 3.0	–	39.31 ± 2.1	96.7
Tap water ($\mu g L^{-1}$)		0.0	<LOD	–
		10.0	9.92 ± 0.42	99.2
		15.0	14.84 ± 0.42	98.9
Sea water ($\mu g L^{-1}$)		0.0	7.85 ± 0.64	–
		5.0	12.81 ± 0.53	99.2
		10.0	18.02 ± 0.36	101.7
River water ($\mu g L^{-1}$)		0.0	<LOD	–
		10.0	9.84 ± 0.53	98.4
		15.0	14.48 ± 0.49	96.5
Waste water ($\mu g L^{-1}$)		0.0	14.2 ± 0.36	–
		10.0	24.02 ± 0.55	98.2
		15.0	29.37 ± 0.42	101.1

LOD: limit of detection.
[a] Mean of three experiments ± standard deviation.

4. Conclusions

USAEME combined with the flame atomic absorption spectrometry (FAAS) was evaluated for the pre-concentration and the determination of the trace amounts of cadmium (at $\mu g L^{-1}$ level) from water samples. USAEME is a sensitive, efficient, and simple method for pre-concentration and separation of trace metals with the use of low sample volumes. A high enrichment factor was easily obtained using this method. In addition, it is important to point out that USAEME is a low organic solvent consuming extraction technique, which turns it into a low cost and also an environmentally friendly technique [29]. In this method, the consumption of the toxic organic solvent (at μL level) was minimized without affecting the method sensitivity. Although the obtained results of this research were related to the cadmium determination, the system could be readily applied to the determination of other metals with the help of various chelating agents, extractable by other organic solvents.

Acknowledgements

This project was sponsored both by Development Foundation of the Department of Education of Hebei Province, P R China (2007121), and the Research Development Foundation of the Agricultural University of Hebei.

References

[1] K. Robards, P. Worsfold, Analyst 116 (1991) 549.
[2] D. Mohan, K.P. Singh, Water. Res. 36 (2002) 2304.
[3] A. Afkhami, T. Madrakian, H. Siampour, J. Hazard. Mater. 138 (2006) 269.
[4] A. Oliva, A. Molinari, F. Zuniga, P. Ponce, Microchim. Acta 140 (2002) 201.
[5] R.A. Vanderpool, W.T. Buckley, Anal. Chem. 71 (1999) 652.
[6] A.N. Anthemidis, G.A. Zachariadis, C.G. Farastelis, J.A. Stratis, Talanta 62 (2004) 437.
[7] A.N. Anthemidis, G.A. Zachariadis, J.A. Stratis, J. Anal. At. Spectrom. 18 (2003) 1400.
[8] M. Soylak, A. Kars, I. Narin, J. Hazard. Mater. 159 (2008) 435.
[9] T. Oymak, S. Tokalioglu, V. Yilmaz, S. Kartal, D. Aydin, Food Chem. 113 (2009) 1314.
[10] F.Z. Xie, X.C. Lin, X.P. Wu, Z.H. Xie, Talanta 74 (2008) 836.
[11] E.J.D. Santos, A.B. Herrmann, A.S. Ribeiro, A.J. Curtius, Talanta 65 (2005) 593.
[12] J.L. Manzoori, H. Abdolmohammad-Zadeh, M. Amjadi, Talanta 71 (2007) 582.
[13] L.M. Coelho, M.A.Z. Arruda, Spectrochim. Acta Part B 60 (2005) 743.
[14] H.H. Liu, P.K. Dasgupta, Anal. Chem. 68 (1996) 1817.
[15] F. Pena-Pereira, I. Lavilla, C. Bendicho, Spectrochim. Acta Part B 64 (2009) 1.
[16] E. Melek, M. Tuzen, M. Soylak, Anal. Chim. Acta 578 (2006) 213.
[17] H.M. Jiang, Y.C. Qin, B. Hu, Talanta 74 (2008) 1160.
[18] C.D. Stalikas, Trends. Anal. Chem. 21 (2002) 343.
[19] R. Carabias-Martinez, E. Rodriguez-Gonzalo, B. Moreno-Cordero, J.L. Perez-Pavon, C. Garcia-Pinto, E. Fernandez-Laespada, J. Chromatogr. A 902 (2000) 251.
[20] M.A. Jeannot, F.F. Cantwell, Anal. Chem. 68 (1996) 2236.
[21] S. Fragueiro, I. Lavilla, C. Bendicho, Talanta 68 (2006) 1096.
[22] H.M. Jiang, B. Hu, Microchim. Acta 161 (2008) 101.
[23] A.N. Anthemidis, I.S.I. Adam, Anal. Chim. Acta 632 (2009) 216.
[24] J.S. Carletto, R.M. Luciano, G.C. Bedendo, E. Carasek, Anal. Chim. Acta 638 (2009) 45.
[25] L.B. Xia, Y.L. Wu, B. Hu, J. Mass Spectrom. 42 (2007) 803.
[26] M.A. Farajzadeh, M. Bahram, S. Zorita, B.G. Mehr, J. Hazard. Mater. 161 (2009) 1535.
[27] M.R. Jamali, Y. Assadi, F. Shemirani, Sep. Sci. Technol. 42 (2007) 3503.
[28] L. Xu, C. Basheer, H.K. Lee, J. Chromatogr. A 1152 (2007) 184.
[29] M. Rezaee, Y. Assadi, M.R.M. Hosseini, E. Aghaee, F. Ahmadi, S. Berijani, J. Chromatogr. A 1116 (2006) 1.
[30] P. Liang, H.B. Sang, Anal. Biochem. 380 (2008) 21.
[31] A.N. Anthemidis, K.I.G. Ioannou, Talanta 79 (2009) 86.
[32] S. Ozcan, A. Tor, M.E. Aydin, Anal. Chim. Acta 647 (2009) 182.
[33] J. Regueiro, M. Llompart, C. Garcia-Jares, J.C. Garcia-Monteagudo, R. Cela, J. Chromatogr. A 1190 (2008) 27.
[34] K. Ashley, Trends. Anal. Chem. 17 (1998) 366.
[35] A.R. Fontana, R.G. Wuilloud, L.D. Martinez, J.C. Altamirano, J. Chromatogr. A 1216 (2009) 147.
[36] E.Z. Jahromi, A. Bidari, Y. Assadi, M.R.M. Hosseini, M.R. Jamali, Anal. Chim. Acta 585 (2007) 305.
[37] A. Bidari, E. Zeini Jahromi, Y. Assadi, M.R.M. Hosseini, Microchem. J. 87 (2007) 6.
[38] A. Moghimi, J. Chin. Chem. Soc. 55 (2008) 369.
[39] F. Shemirani, R.R. Kozani, Y. Assadi, Microchim. Acta 157 (2007) 81.
[40] Z.F. Fan, Microchim. Acta 152 (2005) 29.

Talanta 80 (2009) 985–990

Contents lists available at ScienceDirect

Talanta

journal homepage: www.elsevier.com/locate/talanta

An aptameric molecular beacon-based "Signal-on" approach for rapid determination of rHuEPO-α

Zhaoyang Zhang[a,b], Lei Guo[a], Jijun Tang[a], Xingjie Guo[b], Jianwei Xie[a,*]

[a] Beijing Institute of Pharmacology and Toxicology, No. 27 Tai Ping Road, Hai Dian District, Beijing 100850, China
[b] School of Pharmacy, Shenyang Pharmaceutical University, No. 103 Wen Hua Road, Shen He District, Shenyang 110016, China

ARTICLE INFO

Article history:
Received 14 June 2009
Received in revised form 19 August 2009
Accepted 21 August 2009
Available online 28 August 2009

Keywords:
DNA aptamer
Erythropoietin
Molecular beacon
Binding
Fluorescence

ABSTRACT

The aim of this work is to describe the first example of aptameric molecular beacon (MB)-based probe for the detection of recombinant human erythropoietin (rHuEPO-α) in physiological buffer, using a novel 35 nt ssDNA aptamer (807–35 nt) originally isolated by Systematic Evolution of Ligands by Exponential enrichment (SELEX) technique in our laboratory. Both "Signal-on" and "Signal-off" MB modes were developed, respectively, in which the conformational alteration of aptamer before and after binding to rHuEPO-α can be demonstrated in terms of the correspondingly fluorescent changes. Comparing with "Signal-off" mode, "Signal-on" mode provided higher sensitivity, while with the addition of target rHuEPO-α, quenching between fluorescent 807–35 nt aptamer (F-Apt) and a short quencher-labeled complementary sequence (QDNA) was disturbed by the specific binding between rHuEPO-α and F-Apt. QDNA was thus loosened and released from F-Apt, leading to a consequently full fluorescent restoration. Systematic optimization of parameters in "Signal-on" mode were carried out, the choice of QDNA length, the hybridization site of a small supplementary DNA (SDNA) stabilizer, and the existence of Mg^{2+} cation played essential roles for the performance characterization. A convenient and sensitive determination of rHuEPO-α with a LOD of 0.4 nM was achieved.

© 2009 Elsevier B.V. All rights reserved.

1. Introduction

Erythropoietin is an endogenously hematopoietic growth factor, which can regulate erythropoiesis production by promoting the proliferation and differentiation of erythroid progenitor cells and maintains the red blood cell mass at an optimum level [1]. Recent development of biological recombinant techniques has allowed large scale production of biologically active erythropoietin called recombinant human EPO (rHuEPO) as pharmaceuticals for anaemia treatment in clinic. Meanwhile, rHuEPO was a kind of famous doping hormone which was strictly prohibited by International Olympics Committee [2,3], due that it can enhance the performance of athletes in endurance competition sports by stimulating more production of new red blood cells and boosting delivery of oxygen to the tissues. Immunological assays have the main applications in monitoring this widespread recombinant glycoprotein drug [4–6], but how to overcome the interference and narrow the specificity of anti-rHuEPO antibodies is still a challenge. For example, anti-rHuEPO monoantibody (mAb) AE7A5 was widely adopted in the assays as the capturing or probing molecules, but it has a broad cross-reactivity with eukaryotic or bacterial proteins, even human urothelium tissue [7]. In comparison with antibody, aptamers, known as "chemical antibodies", have a number of advantages such as higher specificity and affinity, non-immunogenic, stable, robust against denaturation, ease of chemical modification and ease of being synthesized, which would offer an alternative and novel way for the detection of rHuEPO-α in the analytical field.

Aptamers are the artificial single-stranded (ss) DNA or RNA sequences generated by an *in vitro* selection technique known as SELEX from an oligonucleotide pool with immense combinatorial random sequences [8–11]. They have attracted much attention as biosensors for many important biomedical targets, such as metal ions, peptides, proteins and even intact cell [12,13]. The oligonucleotide aptamers are one kind of excellent recognition module, they exert specific binding capability for the targets by the shape fit, *i.e.*, by forming special three-dimensional structures. These spatial structures are the natural result of their complicated secondary structures including partial Watson-Crick, Hoogsteen hydrogen bonds, hairpins, loops and bulges, *etc.* Particularly, aptameric MB sensors attract great concern in the diagnostics area in recent years, because the recognition events can be easily reflected by the Signal changes of an oligonucleotide ssDNA aptamer, and the fast, simple and cost-effective determination of targets can thus be achieved [14]. It is reported that MB are DNA sequences composed of one target recognition region of about 30 bases flanked by two short complementary stem sequences, which force the entire

* Corresponding author. Fax: +86 10 68225893.
E-mail addresses: xiejw@nic.bmi.ac.cn, ammslta@gmail.com (J. Xie).

0039-9140/$ – see front matter © 2009 Elsevier B.V. All rights reserved.
doi:10.1016/j.talanta.2009.08.028

Table 1
Sequences of constructed oligonucleotides.

ssDNA	Sequence (5′ → 3′)
FQ-Apt1 (807-39 nt)	5′-FAM-GATTGAAAGGTCTGTTTTTGGGGTTGGTTTGGGTCAATA-DABCYL-3′
FQ-Apt2 (807-35 nt)	5′-FAM-TTGAAAGGTCTGTTTTTGGGGTTGGTTTGGGTCAA-DABCYL-3′
FQ-Apt3 (807-33 nt)	5′-FAM-TGAAAGGTCTGTTTTTGGGGTTGGTTTGGGTCA-DABCYL-3′
F-Apt (807-35 nt)	5′-TTGAAAGGTCTGTTTTTGGGGTTGGTTTGGGTCAA-FAM-3′
QDNA1 (7 nt)	5′-DABCYL-TTGACCC-3′
QDNA2 (8 nt)	5′-DABCYL-TTGACCCA-3′
QDNA3 (10 nt)	5′-DABCYL-TTGACCCAAA-3′
QDNA4 (12 nt)	5′-DABCYL-TTGACCCAAACC-3′
SDNA1 (8 nt)	5′-GACCTTTC-3′
SDNA2 (5 nt)	5′-AAAAA-3′
SDNA3 (7 nt)	5′-AAACCAA-3′

sequence to form a stem-loop structure in the absence of a target [15].

In our recent work, we have firstly *in vitro* isolated a series of anti-rHuEPO-α ssDNA aptamers, in which aptamer 807 is a prevalent sequence (55% in 42 clones) [16]. The binding capacity of random sequence 807-39 nt was almost identical with the full sequence 807 (Fig. S1). The secondary hairpin structure of 807-39 nt meets the prerequisite of MB probe quite well, its loop would function as a recognition site, and its stem as a support. That makes aptamer 807-39 nt as an ideal framework to build signal transduction module. Therefore, a convenient aptameric MB approach was constructed in this paper, both "Signal-off" and "Signal-on" MB modes were investigated. Fluorescent conformational changes could be observed when the specific binding between aptamer and rHuEPO-α occurred. Systematic optimization on conditions in the case of "Signal-on" MB mode were undertaken by examining the quencher-labeled DNA (QDNA) length and concentration, the hybridization site of a short supplementary DNA (SDNA), the role of metal ions, and the concentration of glycerol as a fluorescence stabilizer. Finally a LOD of 0.4 nM for rHuEPO-α was achieved.

2. Experimental

2.1. Chemical and reagents

rHuEPO-α (3.89 mg/mL, purity higher than 98.5%) was donated by SCIPROGEN Bio-pharmaceutical Company (Shenzhen, China). Fluorophore and quencher dual end-labeled MB, fluorophore single end-labeled MB, QDNA and SDNA were synthesized in Shanghai Sangon Biological Engineering Technology & Services Company (Shanghai, China) (Table 1). In the dual end-labeled MB (FQ-Apt) and single end-labeled MB (F-Apt/QDNA) sequences, 6-carboxyfluorescein (6-FAM) and 4-(4′-dimethylaminophenylazo) benzoic acid (DABCYL) are used as the fluorophore and quencher groups, respectively. HSA, hemoglobin and cytochrome C were obtained from Sigma-Aldrich (St. Louis, Mo, USA). BSA and lysozyme were purchased from Shanghai Sangon Biological Engineering Technology & Services. Ig G was purchased from Tianlai Bioengineering Company (Beijing, China). Globin was purified by our laboratory. All other reagents were of analytical purity and obtained from Beijing Chemical Company (Beijing, China). The physiological buffer as well as the selection buffer consisted of 20 mM Tris, 140 mM NaCl, 5 mM $MgCl_2$ and 5 mM KCl (pH 7.4). Deionized, distilled water was purified from a Milli-Q water purification system (Millipore, France).

2.2. Measurements

All fluorescence experiments were performed on a HITACHI F4010 spectrofluorometer, using a 0.5 mL quartz cuvette as the sample cell. The fluorescence emission spectra of the aptameric MB were obtained from 510 nm to 600 nm with an excitation wavelength fixed at 494 nm ("Signal-on" mode) or 488 nm ("Signal-off" mode), respectively. The slit widths of excitation and emission were set at (5 nm and 10 nm) and (10 nm and 10 nm) for "Signal-on" and "Signal-off" modes, respectively. The concentrations of F-Apt and FQ-Apt in all samples were 10 nM. Prior to the fluorescent determination, the aptameric MB was denatured at 94 °C for 5 min and annealed at the optimum condition, then mixed with rHuEPO-α in selection buffer and incubated at room temperature for 1 h. The titration curves were ploted as quenching percentage ($y = (\bar{F}_0 - F)/\bar{F}_0$) or as $\Delta F(y = F - \bar{F}_0)$ versus increasing concentration of rHuEPO-α (x) for "Signal-off" and "Signal-on" mode, respectively. To examine the specificity of the aptameric molecular beacon for "Signal-on", other proteins were used, including HSA, BSA, IgG, hemoglobin, globin, lysozyme and cytochrome C.

2.3. Gel electrophoresis

Electrophoretic gel mobility shift assay was used to confirm the binding between rHuEPO-α and the MB. Aptamer 807–35 nt, FQ-Apt2 and F-Apt (1 μM) were incubated with rHuEPO-α (1 μM) in physiological buffer for 1 h at room temperature, respectively. Electrophoresis was performed on 12% non-denatured polyacrylamide gel electrophoresis at 22 V/cm for 1 h at 4 °C. The gel was stained in ethidium bromide and analyzed by UVP VisionWorks™LS Image System.

2.4. Determination of K_d and T_m

To calculate the K_d values, the changes of fluorescence intensity or the quenching percentage versus increasing rHuEPO-α concentrations (x) was plotted, and the data points were fitted by the non-linear regression analysis based on one-site direct binding model with the following equation using Originpro 7.5 software (OriginLab, USA):

$$y = \frac{B_{max} \cdot x}{K_d + x} \quad (1)$$

where B_{max} is the degree of saturation, and K_d is the dissociation constant.

T_m values for short probe (<15 nt) were determined by the Wallace rule [17]:

$$T_m = 2\,^\circ\mathrm{C}(A + T) + 4\,^\circ\mathrm{C}(C + G) \quad (2)$$

where T_m = temperature (°C) at which 50% of the oligonucleotides are annealed to its complementary sequence. The number of each particular nucleotide in the sequence is inserted into the equation in place of the letters. When the sequence is free in solution, add 7–8 °C to T_m.

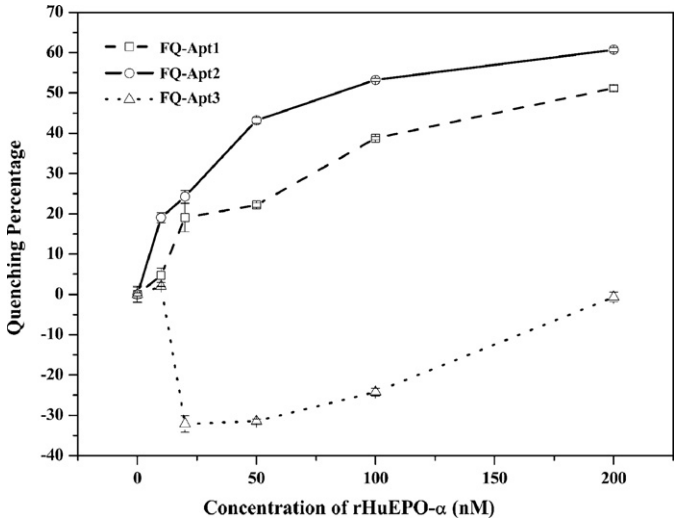


Fig. 1. The titration curves of the "Signal-off" aptameric MB mode. FQ-Apt (10 nM) of different stem length was titrated with increasing concentration of rHuEPO-α from 0 nM to 200 nM in the physiological buffer (20 mM Tris, 140 mM NaCl, 5 mM $MgCl_2$, 5 mM KCl; pH 7.4). Data are reported as mean ± SD values with RSD < 5.0% ($n = 3$).

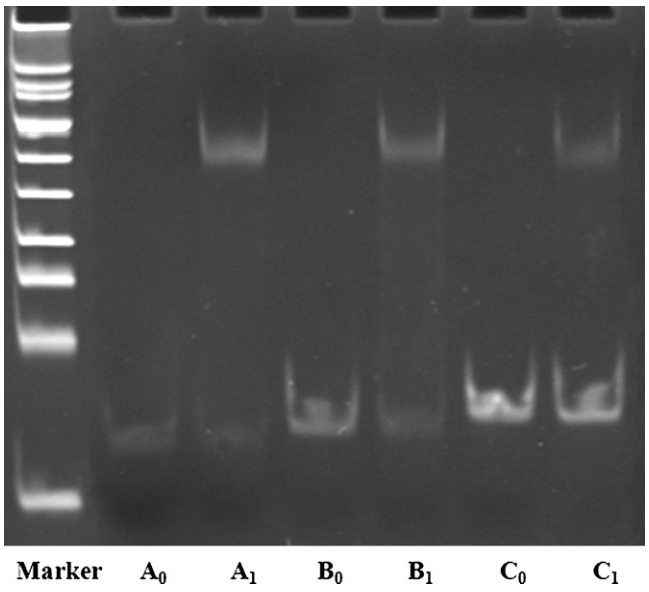


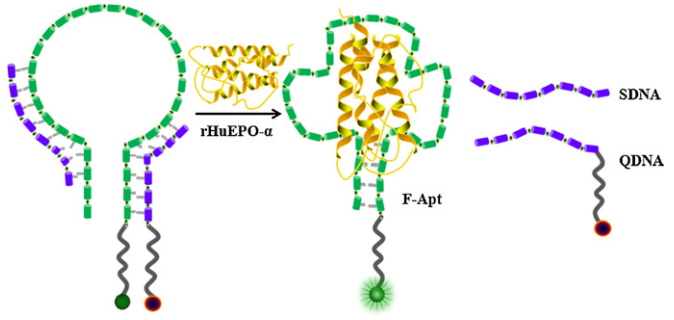
Fig. 2. Binding experiments of aptamer 807–35 nt with or without labeling group and rHuEPO-α in PAGE. Lanes X_0 and X_1 represent aptamer alone and aptamer with the addition of rHuEPO-α (1 μM). *X* represents A, B and C. A: 807–35 nt (1 μM); B: FQ-Apt2 (1 μM); C: F-Apt (1 μM), QDNA1 (10 μM).

3. Results and discussion

3.1. Design of "Signal-off" and "Signal-on" aptameric MB

Based on the simulated secondary stem-loop structure of our selected aptamer 807-39 nt by M-fold [18] (Fig. S2), a dual end-labeled design was chosen as a readily start to test the possibility in formation of MB alike structure [19]. Binding of dual end-labeled MB with rHuEPO-α target brought the fluorophore and quencher in close proximity, resulted in the decrease of fluorescence. The stems with 3 bp (FQ-Apt3)/4 bp (FQ-Apt2)/5 bp (FQ-Apt1) in the dual end-labeled MB form were investigated, respectively (sequences shown in Table 1), and 4 bp (FQ-Apt2) in the stem was found to be the minimum length to achieve the specific recognition. FQ-Apt2 (807–35 nt) was then considered as the shortest motif for binding with rHuEPO-α. The addition of rHuEPO-α mainly facilitates the forming and stabilizing of stem-loop structure of FQ-Apt2, drawing the distance closer between fluorophore and quencher. Because the fluorescent change is limited to the close proximate extent of fluorophore and quencher groups, a detection concentration of 10 nM rHuEPO-α was merely obtained by "Signal-off" mode (Fig. 1).

Another single-labeled "Signal-on" mode was followed on the fully utilization of the stem and loop binding ability of 807–35 nt aptamer for the target protein, it can further increase the detection sensitivity as expected (Scheme 1). In this "Signal-on" design, toward a single 3′ end-labeled F-Apt, a short 5′-end quencher-labeled complementary QDNA sequence was employed and the fluorescence background became "darken". When the "Signal-on" system was exposed to rHuEPO-α, QDNA was departed from F-Apt and the fluorescent signal was restored. This kind of structural-switching approach is obviously leading to an increase of a fluorescent signal.



Scheme 1. Illustration of "Signal-on" mode using 807–35 nt aptamer.

The fluorescent signal change either in "Signal-off" or "Signal-on" mode was indeed induced by the aptamer-target complexation by using binding experiments in gel electrophoresis. As shown in Fig. 2, aptameric MBs both adopted in "Signal-off" and "Signal-on" modes still maintain the binding ability with rHuEPO-α. The complex of MB with rHuEPO-α shifted slowly than free MB, and the binding capacity is not weaken by the labeling in comparison with the non-labeled aptamer 807–35 nt. Furthermore, since the degree of fluorescence recovery is depended on the binding ability of aptamer for rHuEPO-α, which is a reflection of the aptamer's spatial structure. Several factors that can affect the folding and binding efficiency of aptamer should be optimized firstly.

3.2. Systematic optimization on "Signal-on" mode

To achieve the most sensitivity of this aptameric MB-based fluorescent "Signal-on" mode, how to eliminate the background fluorescence and how to fully regenerate the inherent fluorescence of F-Apt in the presence of rHuEPO-α are both the key considerations. Such parameters as length and concentration of QDNA, the hybridization site of a short SDNA stabilizer, the role of metal ions, and the concentration of glycerol as a fluorescence stabilizer are systematically investigated.

3.2.1. The length and concentration of QDNA

QDNA adopted here should meet two points. One point is to hybridize with the 3′-end stem of F-Apt so as to compose a fluorescent quenching resonance energy transfer, and the other is to be a displaceable element when the rHuEPO-α as a competitor added. Only the suitable length of QDNA can offer both low background fluorescence in the absence of the target and a possibility for fast structural switching when the target is present [20]. In a series of

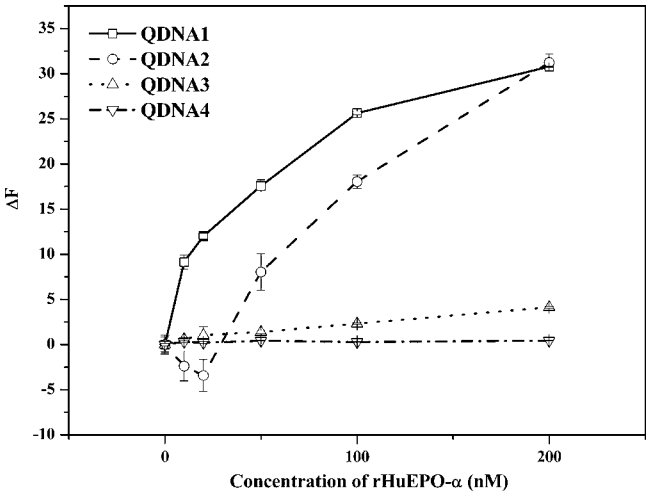


Fig. 3. Effects of QDNA length on the "Signal-on" aptameric MB mode. F-Apt (10 nM) and QDNA (100 nM) with different length were titrated with increasing concentration of rHuEPO-α from 0 to 200 nM in the physiological buffer. Data are reported as mean ± SD values with RSD < 7.0% (n = 3).

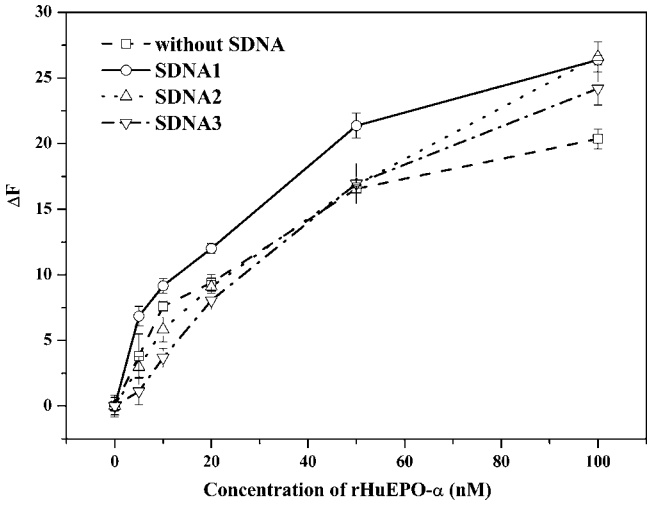


Fig. 5. Effects of the hybridization site of SDNA on the "Signal-on" aptameric MB mode. Concentrations of F-Apt, QDNA1 and SDNA were 10 nM, 100 nM and 100 nM, respectively. The MB solution was titrated against increasing concentration of rHuEPO-α (0–100 nM) in physiological buffer. Data are reported as mean ± SD values with RSD < 4.0% (n = 3).

QDNAs with different lengths, QDNA1 (7 nt), QDNA2 (8 nt), QDNA3 (10 nt) and QDNA4 (12 nt), QDNA1 shows the best signal response. The background of fluorescence was more decreased when QDNA with excess length (QDNA2-4) was added, but the specific competition ability of F-Apt was obviously weaken in some extent (Fig. 3). A possible explanation is QDNAs with excess complementary bases would produce a more tight duplex structure in MB, which induce the partially hybridized F-Apt is hardly to effectively bind with rHuEPO-α.

The fluorescent intensities of system background and the signal restoration with target addition were also influenced by the concentration of QDNA. The results showed that addition of 50 nM or 100 nM QDNA1 had the almost same contribution to the recovery of fluorescence, and lower background was obtained with 100 nM QDNA1. Although background of fluorescence is decreased by the higher concentration of QDNA1 (150 nM), the addition of excess QDNA1 would lead to fluorescence self-quenching, which affected the restoration of fluorescence (Fig. 4).

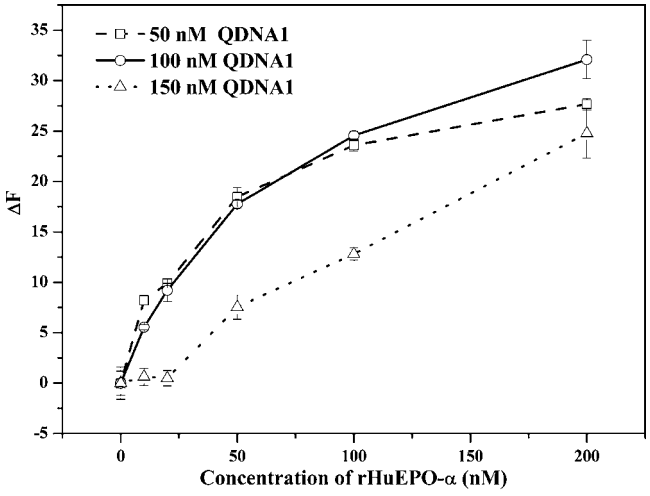


Fig. 4. Effects of QDNA1 concentration on the "Signal-on" aptameric MB mode. F-Apt (10 nM) and various concentration of QDNA1 (50 nM, 100 nM and 150 nM) were titrated with increasing concentration of rHuEPO-α from 0 to 200 nM in the physiological buffer. Data are reported as mean ± SD values with RSD < 5.0% (n = 3).

3.2.2. The hybridization site of SDNA

An aptamer with a hairpin motif, the loop part is generally considered as the key motif for recognizing rHuEPO-α [15]. In the "Signal-on" mode, F-Apt was partially hybridized with QDNA1 in a 7 bp from its 3′-end, other 28 nt sequence would remain a free coiling status. A short supplemental sequence which form a complementary duplex with the 5′-end stem of F-Apt is expected to aid the other 28 nt sequence in an order status and expose full recognition sites of loop for target rHuEPO-α. Different SDNA sequences with different binding sites of F-Apt were synthesized to confirm this presumption. SDNA2 and SDNA3, which were partly hybridized with the loop part in F-Apt, might interfere the binding between rHuEPO-α and F-Apt, so less QDNA1 was departed, and the fluorescent change was lower than the case of SDNA1. Only SDNA1 with 8 nt sequences participated in the 5′-end stem hybridization can achieve the most signal change by stabilizing the "Signal-on" mode and exposing the loop with possible recognition site (Fig. 5). Another possible reason is that the higher T_m value of SDNA1 (32 °C) than that of SDNA2 (18 °C) and SDNA3 (26 °C), which could make the aptameric MB system more stabilizer [21].

3.2.3. Concentration of metal ions

It is known that the presence of alkali and alkaline-earth metal ions has important effect on the aptamer–target interaction. For example, it is reported that the cations K^+ and Mg^{2+} can directly induce a dominant structural formation of nucleotides through a size-selective coordination mechanism in free solution [22]. In this work, the maximum fluorescence signal can be kept well in the range of 0–10 mM K^+, while the specific binding between aptamer and rHuEPO-α lowered when K^+ cation was higher than 10 mM (Fig. 6). It is assumed that under higher concentration of K^+, formation of complex was reduced by the possible distortion of aptamer spatial structures [23].

The concentration of divalent Mg^{2+} cation was also investigated. In the range of 0–50 mM Mg^{2+}, the fluorescent signal recovery was steadily increased at first and then significantly decreased at the concentration higher than 10 mM (Fig. 6), indicating that the formation ability of aptamer–target complex was greatly enhanced at lower Mg^{2+} concentration [24,25]. However, at the higher Mg^{2+} level, the fluorescence was quenched in some extent [26]. Since the existence of Mg^{2+} is reported to be helpful to form and stabilize the duplex of oligonucleotide [22], it is assumed that the spatial

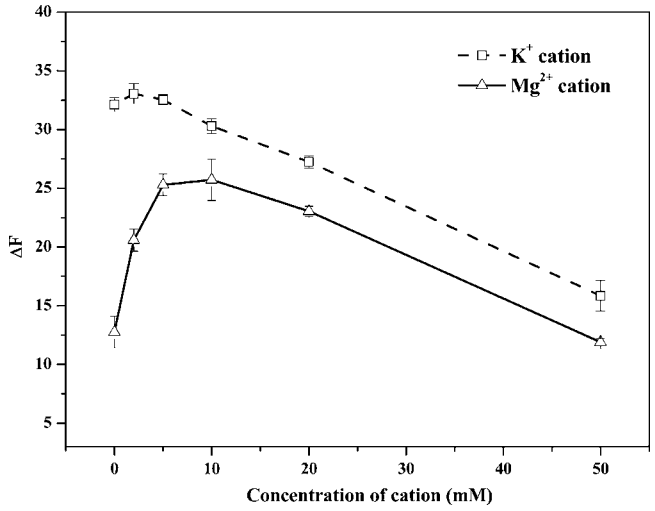


Fig. 6. Effects of cation concentration on the "Signal-on" aptameric MB. Concentrations of F-Apt, QDNA1 and SDNA1 were 10 nM, 100 nM and 100 nM, respectively. The MB solution was titrated with 100 nM rHuEPO-α in the physiological buffer contained various concentration of metal ion. Data are reported as mean ± SD values with RSD < 3.0% (n = 3).

recognition of F-Apt and rHuEPO-α was also benefited from the addition of Mg^{2+}. As shown in Fig. 7, specific recognition between F-Apt and target protein was deteriorated without Mg^{2+}. This behavior is in accord with other Mg^{2+}-dependent aptamer–ATP or OTA target binding [27,28]. Moreover, for such a negatively charged rHuEPO-α and the likelihood negatively charged aptamers, it is supposed that proper concentration of Mg^{2+} cation could shield the negative charges of DNA and act as the electrostatic attractive cation bridge, which probably facilitate the approaching of the negatively charged rHuEPO-α to the surface of the oligonucleotide [29]. Since higher Mg^{2+} concentration is disadvantageous for fluorescence intensity, the Mg^{2+} concentration kept at 5 mM was selected in the "Signal-on" mode.

3.2.4. Other parameters have effect on hybridization and complex formation

The hybridization of oligonucleotides complementary sequences is following a slow kinetics process, which requires a relative long annealing period [30]. Since the extent of quenching efficiency is directly depending on the Förster distance in such a fluorescent resonance energy transfer format, the tighter base-pairing of oligonucleotides, the more decreased background of fluorescence, and the best result was achieved in an annealing condition of 4 °C overnight. The background of fluorescence under other conditions such as room temperature 30 min, room temperature overnight and ice bath for 10 min are higher 27%, 15% and 30% than that under the condition of 4 °C overnight, respectively.

As a kind of additives with high viscosity and good biological compatibility, glycerol was tested to increase the viscosity of solution and stabilize the formation of F-Apt–QDNA hybridization or F-Apt–target protein complex. Although 0, 0.5%, 1.5% and 3% (v/v) glycerol have no significant effect on the change of fluorescence, addition of 0, 0.5% and 3% glycerol made the increasing extent of fluorescence lower 26%, 29% and 13% than addition of 1.5% glycerol, respectively, at a low concentration of rHuEPO-α (50 nM). So 1.5% glycerol was chosen to facilitate the improvement of sensitivity by stabilizing the MB system when low concentration of rHuEPO-α was added.

3.3. Determination of rHuEPO-α in "Signal-on" mode

Best performance of our "Signal-on" mode was found in the psychological buffer of 140 mM NaCl, 5 mM $MgCl_2$, 5 mM KCl, and with 1.5% glycerol added. Titration experiment was then performed with increasing concentration of rHuEPO-α from 0 to 600 nM under above optimized conditions. The fluorescence signal was first rapidly increased with an increased rHuEPO-α concentration from 0 to 50 nM, indicating that the added rHuEPO-α was largely bound to the F-Apt, and then steadily increased when the concentration of rHuEPO-α was beyond 50 nM. In the presence of 600 nM rHuEPO-α, full fluorescence was recovered. Using the "Signal-on" mode, 1 nM of rHuEPO-α could be detected without any pre-treated procedure in the physiological buffer. The linear range was 1–10 nM ($y = 1.976 + 1.229x$, $r = 0.9905$) (Fig. 7), and a LOD could be calculated according to the equation of $LOD = 3SD_{blank}/k$ (where k represents the slope of linear curve, the repeated number of blank is 11), so the LOD is 0.4 nM. The RSD values of high and middle concentration in the linear curve are determined as 3.3% and 4.2%, respectively. Also the dissociation constant ($K_d = 50 \pm 7$ nM) was

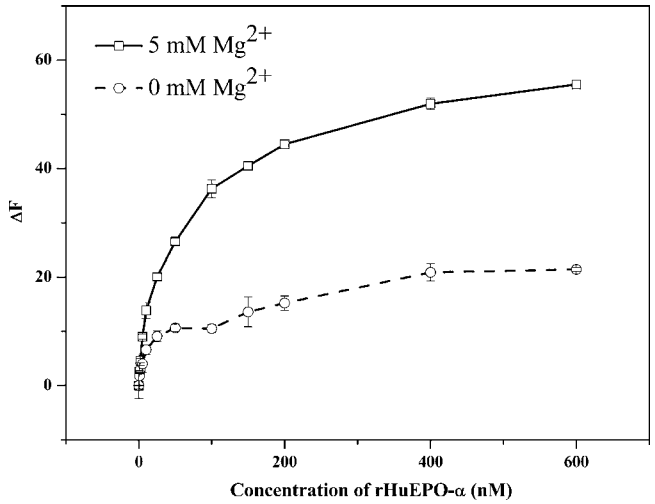


Fig. 7. The titration curves of the "Signal-on" aptameric MB against the increasing concentration of rHuEPO-α (0–600 nM) in physiological buffer contained 1.5% (v/v) glycerol with or without 5 mM Mg^{2+}. Data are reported as mean ± SD values with RSD < 5.0% (n = 3). Other conditions are same as in Fig. 6.

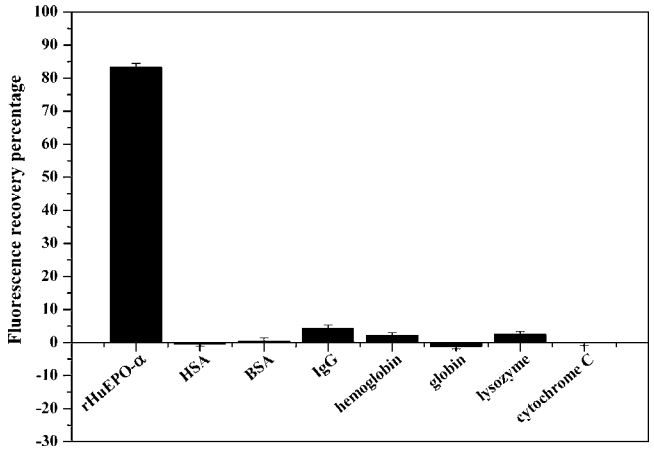


Fig. 8. Binding specificity of the "Signal-on" aptameric MB. Different proteins HSA, BSA, IgG, hemoglobin, globin, lysozyme and cytochrome C were compared with rHuEPO-α in their capability to bind with F-Apt in physiological buffer contained 5 mM Mg^{2+} and 0.5 μM BSA. Other conditions are same as in Fig. 7. The concentration of rHuEPO-α is 200 nM, other proteins is fivefold of rHuEPO-α. Data are reported as mean ± SD values with RSD < 2.0% (n = 3).

determined by the titration curve of "Signal-on" based on one-site direct binding model (Fig. S4), which is in agreement with the dissociation constant (K_d = 33 ± 4 nM) determined by "Signal-off" mode (Fig. S3).

3.4. Binding specificity of "Signal-on" MB

The specificity of the "Signal-on" MB mode was demonstrated in the physiological buffer containing 0.5 μM BSA as fluorescence sensitized stabilizer. Here the full recovery of 100% was defined as the fluorescence intensity reached the value of FDNA alone, when equivalent amount of F-Apt–QDNA (combined with SDNA) was considered as the background in the "Signal-on" mode. rHuEPO-α brought about 80% of fluorescence recovery, while fivefold of HSA, BSA, IgG, hemoglobin, globin, lysozyme and cytochrome C showed no cross binding toward the F-Apt. It is indicated that this "Signal-on" MB probe has good selectivity when compared with other interfering proteins (Fig. 8).

4. Conclusion

Here we reported an aptameric MB-based probe for direct determination of rHuEPO-α in homogeneous physiological buffer for the first time. The structural switchable "Signal-on" strategy demonstrated here using 807–35 nt aptamer as a proof of principle, the effective signal transduction module showed a potential practical utility of our new selected ssDNA aptamer for rHuEPO-α detection with a LOD of 0.4 nM. Improved sensitivity can be achieved when coupling preconcentration procedures and signal amplification strategies in the further work. Aptamer 807–35 nt was also expected to be a powerful biosensor probe or a potential clinic diagnosis element to facilitate new methodological developments for rHuEPO-α, including *in vitro* diagnostics, or high-throughput screening of abused samples in doping control area.

Acknowledgement

We thank the National Natural Science Foundation of China (Nos. 20575078 and 20705039) for their financial support.

Appendix A. Supplementary data

Supplementary data associated with this article can be found, in the online version, at doi:10.1016/j.talanta.2009.08.028.

References

[1] D. Choi, M. Kim, J. Park, J. Chromatogr. B 687 (1996) 189–199.
[2] F.R. Khuri, N. Engl. J. Med. 356 (2007) 2445–2448.
[3] R. Parissotto, M. Wu, M.J. Ashenden, K.R. Emslie, C.J. Gore, C. Howe, R. Kazlauskas, K. Sharpe, G.J. Trout, M.H. Xie, A.G. Hahn, Haematologica 86 (2001) 128–137.
[4] R. Abellan, R. Ventura, S. Pichini, A.F. Remacha, J.A. Pascual, R. Pacifici, R.D. Giovannandrea, P. Zuccaro, J. Segura, J. Pharm. Biomed. Anal. 35 (2004) 1169–1177.
[5] B. Yu, H.L. Cong, H.W. Liu, Y.Z. Li, F. Liu, J. Sep. Sci. 28 (2005) 2390–2400.
[6] F.Y. Guan, C.E. Uboh, L.R. Soma, E. Birks, J.W. Chen, J. Mitchell, Y.W. You, J. Rudy, F. Xu, X.Q. Li, G. Mbuy, Anal. Chem. 79 (2007) 4627–4635.
[7] W.W. Franke, H. Heid, Clin. Chim. Acta 373 (2006) 189–190.
[8] A.D. Ellington, J.W. Szostak, Nature 346 (1990) 818–822.
[9] C. Tuerk, L. Gold, Science 249 (1990) 505–510.
[10] S.E. Osborne, A.D. Ellington, Chem. Rev. 97 (1997) 349–370.
[11] C.V. Forst, J. Biotechnol. 64 (1998) 101–118.
[12] S. Tombelli, M. Minunni, M. Mascini, Biomol. Eng. 24 (2007) 191–200.
[13] L. Cerchia, P.H. Giangrande, J.O. McNamara, V. de Franciscis, Methods Mol. Biol. 535 (2009) 59–78.
[14] X.H. Fang, Y. Mi, J.J. Li, T. Beck, S. Schuster, W.H. Tan, Cell Biochem. Biophys. 37 (2002) 71–81.
[15] K.M. Wang, Z.W. Tang, C.J. Yang, Y.M. Kim, X.H. Fang, W. Li, Y.R. Wu, C.D. Medley, Z.H. Cao, J. Li, P. Colon, H. Lin, W.H. Tan, Angew. Chem. Int. Ed. 47 (2008) 2–17.
[16] Z.Z. Zhang, L. Guo, J.J. Tang, X.J. Guo, J.W. Xie, Proceedings of 2nd National Conference on Analytical Chemistry for Life Sciences, 2008, 454 pp.
[17] S.V. Suggs, T. Hirose, E.H. Miyake, M.J. Kawashima, K.I. Johnson, R.B. Wallace, Using Purified Genes, Academic Press, New York, 1981, 683 pp.
[18] M. Zuker, Nucleic Acids Res. 31 (2003) 3406–3415.
[19] R. Nutiu, Y.F. Li, Chem. Eur. J. 10 (2004) 1868–1876.
[20] R. Nutiu, S. Mei, Z.J. Liu, Y.F. Li, Pure Appl. Chem. 76 (2004) 1547–1561.
[21] V.V. Didenko, Fluorescent Energy Transfer Nucleic Acid Probes, Human Press, New Jersey, 2006, 41 pp.
[22] J.T. Davis, Angew. Chem. Int. Ed. 43 (2004) 668–698.
[23] S.D. Lefebvre, S.W. Morrical, J. Mol. Biol. 272 (1997) 312–326.
[24] G. Gokulrangan, J.R. Unruh, D.F. Holub, B. Ingram, C.K. Johnson, G.S. Wilson, Anal. Chem. 77 (2005) 1963–1970.
[25] C. André, A. Xicluna, Y.-C. Guillaume, Electrophoresis 26 (2005) 3247–3255.
[26] N. Rupcich, W. Chiuman, R. Nutiu, S. Mei, K.K. Flora, Y.F. Li, J.D. Brennan, J. Am. Chem. Soc. 128 (2006) 780–790.
[27] P.L. Sazani, R. Larralde, J.W. Szostak, J. Am. Chem. Soc. 126 (2004) 8370–8371.
[28] J.A. Cruz-Aguado, G. Penner, J. Agric. Food Chem. 56 (2008) 10456–10461.
[29] Y.L. Lyubchenko, L.S. Shlyakhtenko, Proc. Natl. Acad. Sci. U.S.A. 94 (1997) 496–501.
[30] R.F. Weaver, Molecular Biology, second ed., Mc Graw-Hill Companies, Inc., 2002, pp. 30–31.

Talanta 80 (2009) 991–995

Contents lists available at ScienceDirect

Talanta

journal homepage: www.elsevier.com/locate/talanta

Time-resolved fluorescence based DNA detection using novel europium ternary complex doped silica nanoparticles

Pin-Zhu Qin[a,b,c], Cheng-Gang Niu[a,b,c,*], Guang-Ming Zeng[a,b,c], Min Ruan[a,b,c], Lin Tang[a,b,c], Ji-Lai Gong[a,b,c]

[a] College of Environmental Science and Engineering, Hunan University, Changsha 410082, China
[b] Key Laboratory of Environmental Biology and Pollution Control, Hunan University, Ministry of Education, Changsha 410082, China
[c] State Key Laboratory of Powder Metallurgy, Central South University, Changsha 410083, China

ARTICLE INFO

Article history:
Received 16 June 2009
Received in revised form 18 August 2009
Accepted 21 August 2009
Available online 28 August 2009

Keywords:
DNA detection
Time-resolved fluorescence
Eu(TTA)$_3$(5-NH$_2$-phen)
Nanoparticles

ABSTRACT

A two-probe tandem DNA hybridization assay including capture DNA$_1$, probe DNA$_2$, and target DNA$_3$ was prepared. The long-lived luminescent europium complex doped nanoparticles (NPs) were used as the biomarker. The complex included in the particle was Eu(TTA)$_3$(5-NH$_2$-phen)-IgG (ETN-IgG), the europium complex Eu(TTA)$_3$(5-NH$_2$-phen) linking an IgG molecule. Silica NPs containing ETN-IgG were prepared by the reverse microemulsion method, and were easy to label oligonucleotide for time-resolved fluorescence assays. The luminophores were well-protected from the environmental interference when they were doped inside the silica network. The sequences of *Staphylococcus aureus* and *Escherichia coli* genes were designed using software Primer Premier 5.0. Amino-modified capture DNA$_1$ was covalently immobilized on the common glass slides surface. The detection was done by monitoring the fluorescence intensity from the glass surface after the hybridization reaction with the NPs labeled probe DNA$_2$ and complementary target DNA$_3$. The sensing system presented short hybridization time, satisfactory stability, sensitivity, and selectivity. This approach was successfully employed for preliminary application in the detection of pure cultured *E. coli*, it might be an effective tool for pathogen DNA monitoring.

© 2009 Elsevier B.V. All rights reserved.

1. Introduction

Among many detection techniques of microbial pathogens, DNA hybridization method has been popularly developed for its accurate specificity and high selectivity [1–3]. Compared to the well developed electrochemical biosensors [4–6], there is increasing interest in the investigation of optical sensing systems. Fluorescence based detection, such as polymerase chain reaction (PCR) [7], fluorescence in situ hybridization (FISH) [8], and DNA chip technology [9] have become the standard techniques for quantifying extents of hybridization between surface-immobilized probes and fluorophore-labeled analytic targets in DNA microarrays.

A fluorescent dye is usually utilized to signal the hybridization. Many fluorescent dyes are well known as markers for nucleic acids, such as fluorescein [10], rhodamine [11] and cyanine [12] dyes. However, there is a main problem of how to eliminate background noises caused by autofluorescence from biological samples, the scattering light from solid substrates, and the luminescence from the optical components. For this purpose, more and more attention has been paid on the time-resolved fluorescent technique using lanthanide complexes as the fluorescence labels [13–15]. However, most reported time-resolved fluorescence DNA hybridization assay was based on fluorescence resonance energy transfer technology (FRET) [16–18]. It only occurs under very exacting conditions of overlapping of the emission peak of the donor and the excitation peak of the acceptor, the distance between the donor fluorophore and acceptor fluorophore, and the position of the fluorophores within the biomolecules, etc. It is difficult to find a suitable donor–acceptor system.

On the other hand, the demand of ultratrace gene analysis has driven nanomaterials toward biomedical fields and biotechnology. Recently, dye-doped silica NPs were extensively used in bioimaging and biochemical analysis due to its advantages like signal enhancement, photostability and surface modification for the immobilization of biomolecules [19–21]. To the best of the authors' knowledge, there are only a limited number of reports on the use of lanthanide complex doped NPs as biolabels [22–29]. Dye leakage can efficiently be reduced through covalent binding, and a special functional ligand is usually necessary. However, the synthesis of the chlorosulfonylated β-diketones such as 5-(4″-chlorosulfo-1′,1″-diphenyl-4′-yl)-1,1,1,2,2,3,3-heptafluoro-4,6-hexanedione

* Corresponding author at: College of Environmental Science and Engineering, Hunan University, Changsha 410082, China. Tel.: +86 731 8882 3820; fax: +86 731 8882 2829.
E-mail address: cgniu@hnu.cn (C.-G. Niu).

0039-9140/$ – see front matter © 2009 Elsevier B.V. All rights reserved.
doi:10.1016/j.talanta.2009.08.027

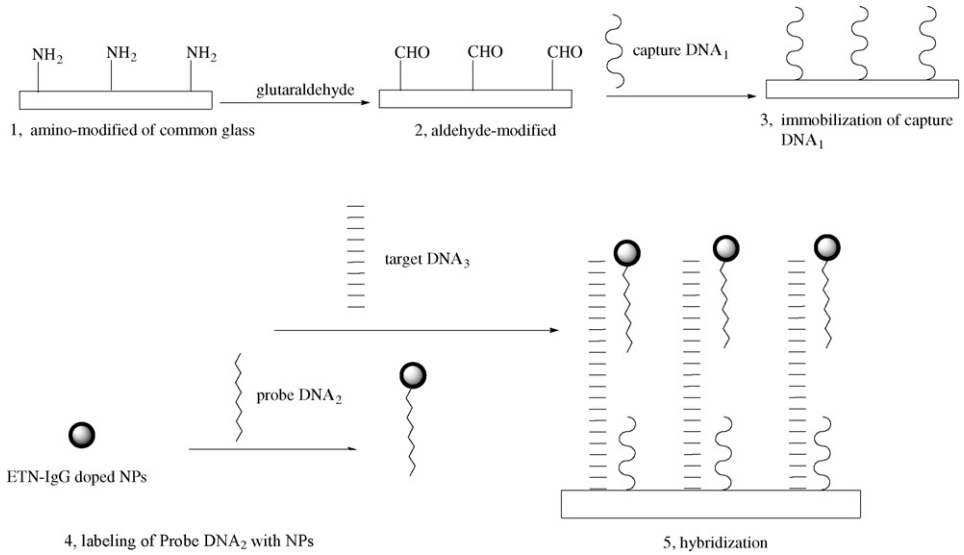


Fig. 1. The two-probe tandem DNA hybridization assay.

(CDHH), 4,4′-bis(1″,1″,1″,2″,2″,3″,3″-heptafluoro-4″,6″-hexanedion-6″-yl)chlorosulfo-*o*-terphenyl (BHHCT), and 4,4′-bis(1″,1″,1″-trifluoro-2″,4″-butanedion-4″-yl)chlorosulfo-*o*-terphenyl (BTBCT) was somewhat difficult. Furthermore, a number of reported biological detection systems were based on confocal fluorescence imaging technology to improve sensitivity [20,23,25,26,29–31]. The drawback is that confocal microscopes are expensive and require very precise mechanical alignment that can be difficult to maintain. DNA detection based on the measurement of time-resolved fluorescence intensity of a suitable labelling of lanthanide complex doped NPs is still an exciting area of research.

In this work, the authors synthesized a europium complex $Eu(TTA)_3(5\text{-}NH_2\text{-phen})$ with long fluorescence lifetime of 0.657 ms and intense time-resolved fluorescence intensity in simple steps. The amino substituent in the phenyl ring in phenanthroline allowed for facile conjugation to IgG. The ETN-IgG doped amino-modified silica NPs were prepared and allowed for facile conjugation to DNA. The DNA hybridization assay [20] was shown in Fig. 1. The combined sequences of capture DNA_1 and probe DNA_2 are complementary to that of the target DNA_3. The sequences of these DNA strands were designed using software Primer Premier 5.0, and commercially synthesized. The detection system showed satisfactory sensitivity, the detection limits could be as low as 4×10^{-10} mol l^{-1}. Additional applications will be used for detection in real samples of microbial pathogens.

2. Experimental

2.1. Instrumentation

All fluorescence measurements were conducted on a Perkin-Elmer LS-55 spectrofluorimeter with both excitation and emission slits set at 10 nm and controlled by a personal computer data processing unit. A modified home-made poly(tetrafluoroethylene) detection-cell and two arms of the bifurcated optical fiber were fixed in the detecting chamber of the spectrofluorimeter to carry the excitation and emission light. The excitation light was carried outside the spectrofluorimeter to the sensor fixed in the detection-cell through one arm of the fiber and the emission light was collected inside the spectrofluorimeter through the other. A foursquare glass plate (side length 12 mm, thickness 1.5 mm) covered with the hybrid of capture DNA_1, NPs labeled probe DNA_2, and target DNA_3 was fixed on the top of the flow chamber by the mounting screw nut. All measurements were performed at room temperature and atmospheric pressure.

2.2. Materials and reagents

Europium oxide was purchased from Sinopharm Chemical Reagent Co. (Shanghai, China). 2-Thenoyltrifluoroacetone (TTA), a ligand reagent, was obtained from J&K Chemical Ltd. Human IgG was purchased from Beijing Solarbio Science & Technology Co., Ltd (Beijing, China). Tetraethyl orthosilicate (TEOS), Triton X-100, 3-aminopropyltrimethoxysilane (APTES), 2-(*N*-morpholino)ethanesulfonic acid (MES), *N*-hydroxysuccinimide (NHS), and 1-ethyl-3-(3-dimethylaminopropyl) carbodiimide hydrochloride (EDC) were purchased from Acros organics. The oligonucleotides were synthesized by Shanghai Sangon Biological Engineering Technology & Services Co. Ltd (Shanghai, China). All other chemicals of analytical reagent grade were commercially obtained. PBS buffer (pH 7.2) was used during the oligonucleotide label and immobilization. Double-distilled water was used for the preparation of all aqueous solutions.

2.3. Synthesis of europium ternary complexes

The europium ternary complex $Eu(TTA)_3(5\text{-}NH_2\text{-phen})$ (ETN) using thenoyltrifluoroacetone (TTA) and 5-amino-1,10-phenanthroline ($5\text{-}NH_2$-phen) as the ligands was synthesized, the formula of the complex was shown in Fig. 2. The synthesis of $5\text{-}NH_2$-phen was according to the literature [32].

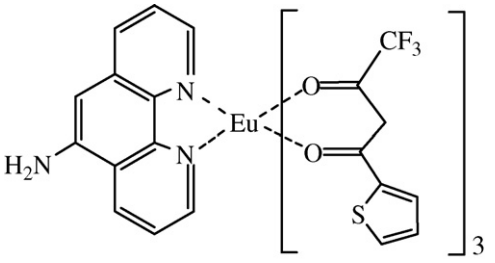


Fig. 2. Formula of complex $Eu(TTA)_3(5\text{-}NH_2\text{-phen})$.

The ternary europium complex was prepared by stirring an ethanol solution of the $EuCl_3$ (europium oxide was dissolved in hydrochloric acid to form europium chloride), TTA, and was adjusted to pH 6 by adding a sodium hydroxide solution, and the mixture was reacted for 40 min. Subsequently, another ethanol solution of 5-NH_2-phen was added, and the mixture was stirred for 5 h at 55–60 °C. A yellow precipitate formed upon cooling was filtered and recrystallized from a mixed solvent of methanol and chloroform (1:1, v/v), MS *m/z* 1032 (M^++H_2O). ^{1}H NMR (acetone) δ (ppm): 2.83 (6H, –CO–CH_2–), 6.02–7.28 (9H, -thiophene), 7.40 (2H, –NH_2), 8.01–11.11 (7H, -phenanthrene). The ternary complex was further characterized through IR and elemental analysis. The $\nu_{(C=O)}$ stretching vibration in the infrared spectrum at 1637 cm^{-1} of TTA shifts to 1626 cm^{-1} in the spectrum of ETN, and the $\nu_{(C=N)}$ stretching vibration at 1564 cm^{-1} of 5-NH_2-phen shifts to 1550 cm^{-1} of ETN. Elemental analysis: $EuC_{36}H_{24}N_3F_9S_3O_6$ (1013.66), Calcd. C, 42.62; H, 2.37; N, 4.14. Found C, 42.58; H, 2.31; N, 4.19.

2.4. Preparation of functional nanoparticles

It is reported that biomacromolecule conjugated organic dyes as the core material for the preparation of core–shell structure NPs can effectively improve the efficiency of dye-embedded and hydrophilicity [20]. The authors converted ETN to hydrophilic molecule by linking an IgG molecule to the ETN. The ETN-IgG doped NPs were successfully synthesized by the reverse microemulsion method [33]. A certain aqueous ETN-IgG solution was added in a microemulsion of 1.77 ml Triton X-100, 7.5 ml cyclohexane, 1.8 ml n-hexanol, and 340 μl water. The final luminophore concentration in the mixture was 1.2×10^{-3} mol l^{-1}. After stirring the microemulsion for 20 min, 0.1 ml of TEOS was added, the polymerization of TEOS was initiated by adding 0.06 ml of ammonium hydroxide. The reaction was allowed to continue for 24 h. Then 0.1 ml of silanization reagent APTES was introduced to the mixture, the reaction was allowed to continue for another 2 h. To release the NPs from the microemulsion and remove surfactant molecules, acetone and ethanol were used to break microemulsion and wash the NPs. After washing with ethanol and double-distilled water several times, the amino-modified ETN-IgG doped silica NPs were obtained and dried in a desiccator prior to modification.

2.5. Designing of oligonucleotide sequences

All the sequences were designed using Primer Premier 5.0 software, on the basis of the published specific nucleotide sequences of *Staphylococcus aureus* and *Escherichia coli* genes [34]. The sequences of these oligonucleotides and the hybridization conditions set for respective genes are shown in Table 1.

2.6. Glass slides surface modification with capture DNA_1

The glass slides surface was modified as described in the literature [35]. The glass slides were immersed in 25.0% ammonium hydroxide overnight then washed with double-distilled water. A solution of 2.0% APTES in 95% ethanol was prepared and adjusted to the desired pH of 4.5 with glacial acetic acid. The glass slides were soaked in this solution for 30 min then ultrasonically washed by ethanol and double-distilled water. Reactive amino groups were then introduced at the glass surface. The amine-modified glass slides were then immersed in the solution of 2.5% glutaraldehyde in PBS buffer stirring for 3 h, and washed with PBS buffer and double-distilled water (1 min/time), respectively, then dried at normal temperature.

The solution of capture DNA_1 was dropped onto the glutaraldehyde-treated glass slides, and was kept at room temperature overnight. The capture DNA_1 was then covalently immobilized on the glass surface. The DNA_1 modified glass slides were then soaked in a sodium cyanoborohydride solution for 30 min to block any remaining glutaraldehyde groups, and the carbon–nitrogen double bond was reduced. The final glass was dried at room temperature after washing with 0.2% SDS solution (sodium dodecyl sulfate) and double-distilled water.

2.7. Surface modification of NPs with probe DNA_2

Certain amine-modified silica NPs were suspended in PBS buffer by ultrasonication. Some 10% succinic anhydride DMF solution was added, the mixture was stirred for 3 h under the condition of nitrogen atmosphere. After centrifuging and washing with ethanol and double-distilled water, the NPs were dispersed in 0.1 mol l^{-1} MES buffer (pH 6.0). A certain probe DNA_2 dissolved in double-distilled water, EDC and NHS was added to the solution, and the reaction was continued for 3 h. The NPs were removed from the solution by centrifugal precipitation and then treated with 0.02 mol l^{-1} glycine solution for 1 h to remove the unreacted carboxyl groups. The final DNA_2 modified NPs were washed, and resuspended in PBS buffer for future usage.

2.8. Hybridization with target DNA_3

The target DNA_3 was first diluted in double-distilled water. The DNA_2 immobilized NPs and target DNA_3 were then added on the capture DNA_1 modified glass slides surface for hybridization under the condition of hybridization solution containing 5.0× SSC (NaCl, sodium citrate) and 0.1% SDS. Following hybridization, the glass slides were washed with 1× SSC + 0.03% SDS, 0.2× SSC, 0.05× SSC, and double-distilled water at room temperature in order to remove non-hybridized oligonucleotides. The detection of the DNA_3 was done by monitoring fluorescence signals of the DNA_2 labeled NP conjugates left on the glass slides surface with proper excitation.

3. Results and discussion

3.1. Nanoparticles characterization

ETN-IgG doped NPs were characterized by scanning electron microscopy (SEM), transmission electron microscopy (TEM), and fluorescence spectroscopy. As shown in Fig. 3, the average diameter of the NPs is about 55–65 nm. Europium ternary complex particles are visible as dark dots embedded inside the silica sphere as a result

Table 1
Sequences used to hybridizing.

Name	Sequence (5′–3′)	Length (bp)	Hybridizing temperature
Staphylococcus aureus	DNA_1: CACTT TTTCT TAAAT GTTGT TC $(A)_{10}$-NH_2	22	38.3 °C
	DNA_2: NH_2-$(A)_{10}$ATTTT CTCTT TTTTC GCTT	19	
	DNA_3: GAACA ACATT TAAGA AAAAG TGAAG CACAA GCGAA AAAAG AGAAA AT	47	
E. coli	DNA_1: ACATT GACGC AGGTG ATCGG ACG$(A)_{10}$-NH_2	23	29.4 °C
	DNA_2: NH_2-$(A)_{10}$GTATC GGTGT GAGCG TCGCA GAA	23	
	DNA_3: CGTCC GATCA CCTGC GTCAA TGTAA TGTTC TGCGA CGCTC ACACC GATAC	50	

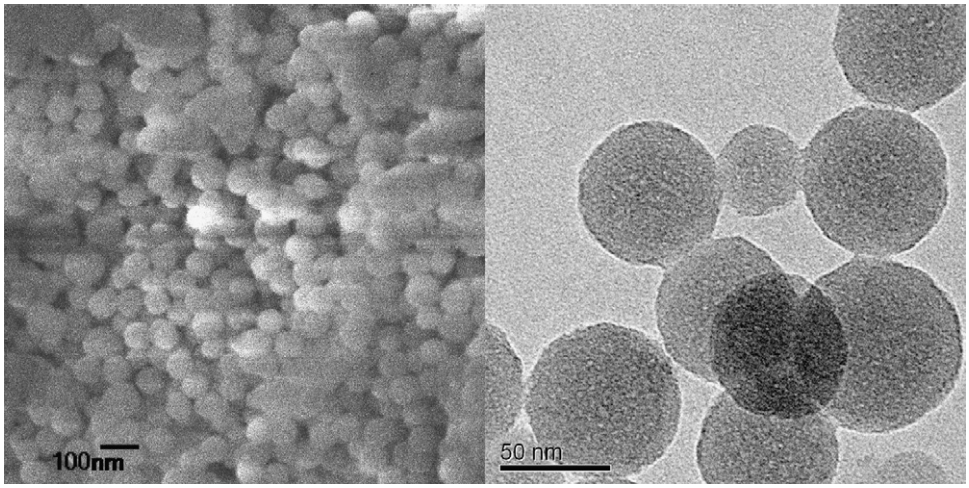


Fig. 3. SEM and TEM images of ETP-IgG NPs.

of the presence of the heavy metal europium atom from the TEM image. The time-resolved fluorescence spectra of the europium complex and its NPs were investigated (Fig. 4). Results showed that the bandwidth of excitation spectrum was compressed and the emission spectral maxima position shifts by 4 nm (from 615 to 611 nm) toward the shorter wavelength when compared to the complex ETN. This clearly confirmed that silica cell generally has no effect on the luminescence performance of europium complex.

The lifetime of ETN-IgG doped NPs was easily calculated with the spectrofluorimeter. As shown in Fig. 5, there is satisfactory linearity between the logarithm of the fluorescence intensity and delay time, and the lifetime is the negative reciprocal of the slope of 0.657 ms. The NPs gave an intense and long-lived signal which enables efficient elimination of background signal, and all measurements were carried out at a delay time of 0.1 ms.

3.2. DNA hybridization detection

It is desirable to use time-resolved fluorometry of lanthanide chelates-doped NPs in the area of nucleic acid hybridization assays as a means of improving the signal-to-noise ratio by increasing the signal intensity and decreasing the background associated with conventional fluorescence measurements. Time-resolved fluorescence intensity of different concentrations of target DNA_3 of *S. aureus* detected from glass surfaces was recorded at $\lambda_{ex} = 375$ nm, $\lambda_{em} = 611$ nm. As shown in Fig. 6, the time-resolved fluorescence intensity was increased with the increasing concentration of DNA_3 (from 11.55 of blank to 96.75 of 4×10^{-7} mol l^{-1}). The ETN-IgG doped NPs could be a super excellent labelling reagent for DNA detection with high sensitivity. The fitting spectra of *E. coli* detection were similar to that of *S. aureus*. The detection limit for *S. aureus* and *E. coli* was about 4×10^{-10} mol l^{-1}.

3.3. Dye leaching and stability experiment

In order to investigate the dye leakage from the NPs, appropriate NPs were ultrasonically exposed to an aqueous environment. The time-resolved fluorescence intensity at emission wavelength 611 nm was recorded after washing for 10 times. A mean value of 105.3 ($n = 10$) and a relative standard deviation of 3.18% were obtained. The ETP-IgG NPs displayed little dye leaching. Furthermore, the time-resolved fluorescence intensity has little decrease (from 125 to 121) under continuous lighting for 5 h.

3.4. Capability and selectivity of the prepared detection system

The experiments were carried out by recording the time-resolved fluorescence intensity of hybridization with different

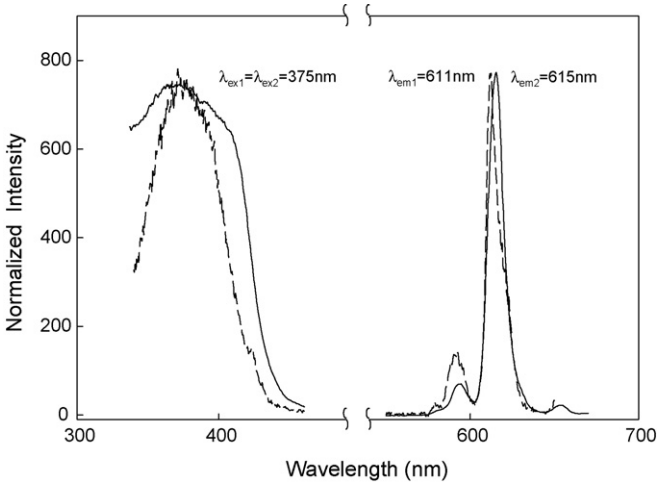


Fig. 4. Time-resolved fluorescence spectra for the ETN (—) and ETN-IgG doped NPs (- - -). For time-resolved spectra: delay time, 0.1 ms, gate time, 1.0 ms.

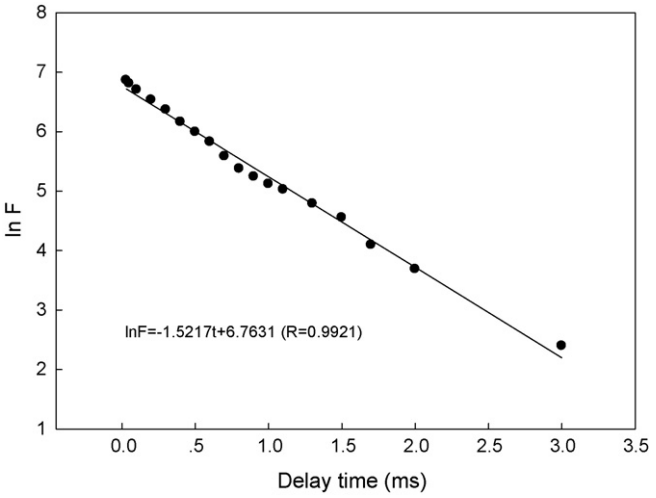


Fig. 5. The natural log of the intensity, ln *F*, as a function of the delay time.

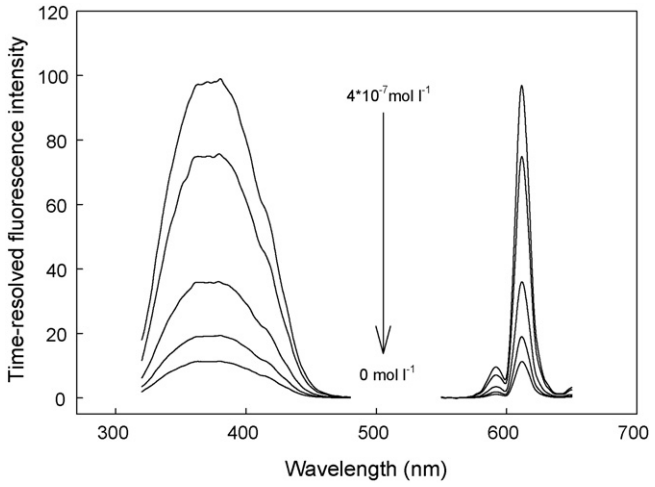


Fig. 6. Time-resolved fluorescence spectra for different concentrations of target DNA_3 of *Staphylococcus aureus* (from top to bottom: 4×10^{-7} mol l^{-1}, 4×10^{-8} mol l^{-1}, 4×10^{-9} mol l^{-1}, 4×10^{-10} mol l^{-1}, 0 mol l^{-1}), for time-resolved spectra: λ_{ex} = 375 nm, λ_{em} = 611 nm, delay time, 0.1 ms, gate time, 1.0 ms.

sequences of target DNA_3 and a mixture sample with other DNA species existed. Take *S. aureus* for example. In order to investigate the availability of this assay, the authors employed three random target sequences: s_1, 5′GAA GAA CAT TTA AGA AAA AGT GAA GCA CAA GCG AAA AAA GAG AAA AT3′; s_2, 5′AAG CCA TGA AGC GGC TTA TGA TTC TTA CCG CCC ACT TGA CGA AAG CG3′; s_3, 5′AAG GGA CGA TGA AAG CCG ATG AAG CCT CCT TTA CCT GGA CCG ATA AC3′. Five samples of different target DNA in same concentration including s_0 (the pure target DNA_3 of *S. aureus*), s_1, s_2, s_3, and a mixture sample of s_0, s_1, s_2, s_3 (same concentration of s_0 with first sample) were prepared. The results showed that fluorescence intensities of the five samples were 75.88, 15.22, 14.93, 19.92 and 80.67, showing little non-specific binding of random DNA sequences.

3.5. Optimal hybridization time

The optimal hybridization time for this assay was also investigated. The result showed that, in the initial stage of hybridization time less than 2.5 h, the hybridization signal increased, and then reached a steady state at a hybridization time longer than 2.5 h. On the basis of this, all the experiments were carried out for the hybridization time of 2.5 h.

3.6. Preliminary analytical application

Detections of DNA extracted from pure cultured *S. aureus* and *E. coli* were studied with the proposed hybridization assay. Strains of *S. aureus* and *E. coli* purchased from Guangdong Institute of Microbiology were cultured, and the double-stranded DNA was extracted using Genomic DNA extraction Kit (Generay Biotech Co., Ltd., Shanghai, China). The double-stranded DNA fragments were denatured to single-stranded DNA by heating at 90 °C for 15 min before use. Targets DNA of *S. aureus* and *E. coli* in a same concentration of about 2×10^{-7} mol l^{-1} were prepared. Satisfactory fluorescence intensities of 56.43 and 48.71 obtained showed that the method might have potential values for pathogen detection.

4. Conclusion

This work reported an approach of DNA detection using a lanthanide europium complex ETN-IgG doped NPs based two-probe tandem DNA hybridization assay. The oligonucleotide sequences of *S. aureus* and *E. coli* genes were designed. The NPs exhibited extremely long lifetime and excellent signaling ability of a trace amount of target DNA. The selectivity and capability of the prepared detection system were also investigated. The authors believe the method has enormous promise for applications to pathogen detection.

Acknowledgements

This work was financially supported by the National 863 High Technology Research Foundation of China (2006AA06Z407), the Hunan Provincial Natural Science Foundation of China (06JJ20062), the National Natural Science Foundation of China (50808070, 50608029) and the Changjiang Scholars and Innovative Research Team in University (PCSIRT).

References

[1] P.A.E. Piunno, U.J. Krull, R.H.E. Hudson, M.J. Damha, H. Cohen, Anal. Chem. 67 (1995) 2635–2643.
[2] A.R. Jilbert, Methods Mol. Biol. 123 (2000) 177–193.
[3] C.Z. Huang, Q.G. Liao, Y.F. Li, Talanta 75 (2008) 163–166.
[4] L.J. Wang, Q.J. Liu, Z.Y. Hu, Y.F. Zhang, C.S. Wu, M. Yang, P. Wang, Talanta 78 (2009) 647–652.
[5] G.J. Li, X.L. Li, J. Wan, S.S. Zhang, Biosens. Bioelectron. 24 (2009) 3281–3287.
[6] S.R. Nugen, P.J. Asiello, J.T. Connelly, A.J. Baeumner, Biosens. Bioelectron. 24 (2009) 2428–2433.
[7] S. Toze, Water Res. 33 (1999) 3545–3556.
[8] J. Bertaux, U. Gloger, M. Schmid, A. Hartmann, S. Scheu, Microbiol. Methods 69 (2007) 451–460.
[9] B. Lemieux, A. Aharoni, M. Schena, Mol. Breed. 4 (1998) 277–289.
[10] D.J. Maxwell, J.R. Taylor, S.M. Nie, J. Am. Chem. Soc. 124 (2002) 9606–9612.
[11] A. Castro, J.G.K. Williams, Anal. Chem. 69 (1997) 3915–3920.
[12] R.B. Mujumdar, L.A. Ernst, S.R. Mujumdar, C.J. Lewis, A.S. Waggoner, Bioconjug. Chem. 4 (1993) 105–111.
[13] A.K. Saha, K. Kross, E.D. Kloszewski, D.A. Upson, J.L. Toner, R.A. Snow, C.D.V. Black, V.C. Desai, J. Am. Chem. Soc. 115 (1993) 11032–11033.
[14] E. Waddell, Y. Wang, W. Stryjewski, S. McWhorter, A.C. Henry, D. Evans, R.L. McCarley, S.A. Soper, Anal. Chem. 72 (2000) 5907–5917.
[15] J.L. Yuan, G.L. Wang, J. Fluoresc. 15 (2005) 559–568.
[16] S. Sueda, J.L. Yuan, K. Matsumoto, Bioconjug. Chem. 11 (2000) 827–831.
[17] M. Gabourdes, V. Bourgine, G. Mathis, H. Bazin, B. Alpha-Bazin, Anal. Biochem. 333 (2004) 105–113.
[18] E.B. Getz, R. Cooke, P.R. Selvin, Biophys. J. 74 (1998) 2451–2458.
[19] D. Knopp, D. Tang, R. Niessner, Anal. Chim. Acta 647 (2009) 14–30.
[20] X.J. Zhao, R. Tapec-Dytioco, W.H. Tan, J. Am. Chem. Soc. 125 (2003) 11474–11475.
[21] C.H. Song, Z.Q. Ye, G.L. Wang, D.Y. Jin, J.L. Yuan, Y.F. Guan, J. Piper, Talanta 79 (2009) 103–108.
[22] H. Härmä, T. Soukka, T. Lövgren, Clin. Chem. 47 (2001) 561–568.
[23] Y. Chen, Y.M. Chi, H.M. Wen, Z.H. Lu, Anal. Chem. 79 (2007) 960–965.
[24] J. Wu, G.L. Wang, D.Y. Jin, J.L. Yuan, Y.F. Guan, J. Piper, Chem. Commun. 3 (2008) 365–367.
[25] Z.Q. Ye, M.Q. Tan, G.L. Wang, J.L. Yuan, J. Mater. Chem. 14 (2004) 851–856.
[26] M.Q. Tan, G.L. Wang, X.D. Hai, Z.Q. Ye, J.L. Yuan, J. Mater. Chem. 14 (2004) 2896–2901.
[27] J. Wu, Z.Q. Ye, G.L. Wang, J.L. Yuan, Talanta 72 (2007) 1693–1697.
[28] Z.Q. Ye, M.Q. Tan, G.L. Wang, J.L. Yuan, Anal. Chem. 76 (2004) 513–518.
[29] Y. Chen, Z.H. Lu, Anal. Chim. Acta 587 (2007) 180–186.
[30] H.T. Li, L.M. Ying, J.J. Green, S. Balasubramanian, D. Klenerman, Anal. Chem. 75 (2003) 1664–1670.
[31] A. Dorfman, N. Kumar, J. Hahm, Langmuir 22 (2006) 4890–4895.
[32] S. Kemp, N.J. Wheate, D.P. Buck, M. Nikac, J.G. Collins, J.R. Aldrich-Wright, J. Inorg. Biochem. 101 (2007) 1049–1058.
[33] S. Santra, P. Zhang, K.M. Wang, R. Tapec, W.H. Tan, Anal. Chem. 73 (2001) 4988–4993.
[34] Z.J. Yao, Y. Yu, J.T. Pang, L.R. Ma, Z.C. Zhen, P. Zhou, Gene chips, preparation methods and Kits for detection of many common bacterial pathogens, China Patent CN 101,045,945 A, 2007.
[35] J.R. Falsey, M. Renil, S. Park, S.J. Li, K.S. Lam, Bioconjug. Chem. 12 (2001) 346–353.

Talanta 80 (2009) 996–1000

Contents lists available at ScienceDirect

Talanta

journal homepage: www.elsevier.com/locate/talanta

A novel fluorescent and chromogenic probe for cyanide detection in water based on the nucleophilic addition of cyanide to imine group

Yue Sun, Yunlong Liu, Maliang Chen, Wei Guo*

School of Chemistry and Chemical Engineering, Shanxi University, Wucheng Road, Taiyuan 030006, China

ARTICLE INFO

Article history:
Received 17 June 2009
Received in revised form 16 August 2009
Accepted 21 August 2009
Available online 28 August 2009

Keywords:
Chemosensor
Cyanide sensing
Hydrazone functionality
2-Hydroxy-1-naphthaldehyde
4-(*N*,*N*-Dimethylamino)benzoylhydrazine

ABSTRACT

A fluorescent and colorimetric probe bearing salicylaldehyde hydrazone functionality has been prepared for cyanide sensing. The detection of cyanide was performed via the nucleophilic attack of cyanide anion on the imine group of the probe with a 1:1 binding stoichiometry, which could be confirmed by ^{1}H NMR and MS studies. The specific reaction results in a prominent fluorescence enhancement and a color change from colorless to yellow.

© 2009 Elsevier B.V. All rights reserved.

1. Introduction

Anion recognition is an area of growing interest in supramolecular chemistry due to its important role in a wide range of environmental, clinical, chemical, and biological applications, and considerable attention has been focused on the design of artificial receptors that are able to selectively recognize and sense anion species [1,2]. Among various anions, cyanide is one of the most concerned anions because it is being widely used in synthetic fibers, resins, herbicide, and the gold-extraction process [3]. Unfortunately, cyanide anion is extremely detrimental, and could be absorbed through lungs, gastrointestinal track and skin, leading to vomiting, convulsion, loss of consciousness, and eventual death [4–6]. Thus, there is a need for an efficient sensing system for cyanide to monitor cyanide concentration from contaminant sources.

Many of the cyanide anion receptors reported to date have relied on hydrogen-bonding motifs and, as a consequence, have generally displayed poor selectivity relative to other anions [7–9]. To overcome this limitation, reaction-based receptors, rationally designed cyanide anion indicators, have been developed recently [10–21]. This reaction-based recognition mode takes advantage of the particular feature of the cyanide ion: its nucleophilic character, and enables the recognition system with some characteristic features such as analyte-specific response and little competition from the aqueous media, which are highly desirable features for an efficient recognition and detection system. Based on this idea, nucleophilic addition of cyanide to oxazine [10,11], pyrylium [12], squarane [13], trifluoroacetophenone [14,15], acyltrazene [16], acridinium [17], salicylaldehyde [18,19] and carboxamide [20,21] has been reported in the past few years, in which the interference by other anions, such F^- and AcO^-, can be efficiently minimized.

Recently, we have developed a series of nitroaniline-based benzamide compounds for the 'naked-eye' detection of cyanide in aqueous environment with high selectivity [22]. These compounds react with CN^- in a 1:1 stoichiometric manner, a process which induces a large enhancement in absorption intensity and a marked color changes from colorless to yellow in DMSO–H_2O (1:1, v/v) at room temperature. In continuation of our work, in this paper, we wish to report a new type of probe molecule (**1**) bearing hydrazone functionality for highly selective cyanide detection in water (Scheme 1). **1** was designed on the basis of 4-(*N*,*N*-dimethylamino)benzamide fluorophore [22] and 2-naphthol fluorophore, which were connected by a rigid hydrazone functionality. Cyanide is expected to be detectable by nucleophilic attack toward an imine functional group of **1**, which is activated by an intramolecular hydrogen bond, and fast proton transfer of the phenol hydrogen to the developing nitrogen anion would then bring about a spectroscopic change (Scheme 1).

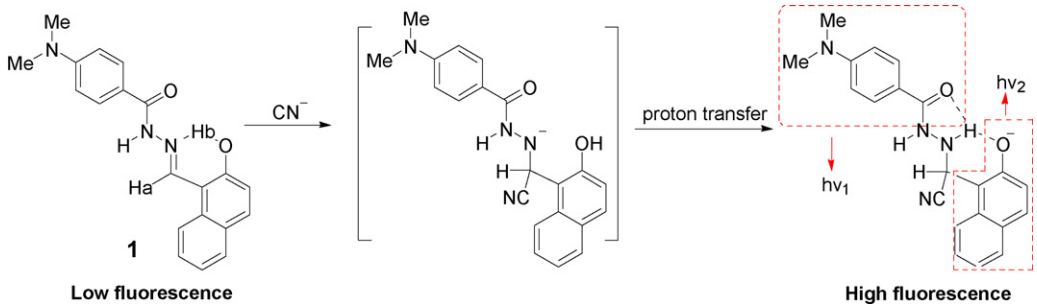
2. Experimental

2.1. Materials and apparatus

Commercially available compounds were used without further purification. Solvents were dried according to standard proce-

* Corresponding author. Tel.: +86 351 7011600.
E-mail address: guowsxu@yahoo.com.cn (W. Guo).

0039-9140/$ – see front matter © 2009 Elsevier B.V. All rights reserved.
doi:10.1016/j.talanta.2009.08.026



Scheme 1. Proposed cyanide-sensing mechanism of **1**.

dures. All reactions were magnetically stirred and monitored by thin-layer chromatography (TLC) using Huanghai GF_{254} silica gel coated plates. The fluorescence spectra were carried out on Varian Cary Edipse fluorescence spectrometer. The absorbance spectra were recorded with Agilent 8453 UV–vis spectrophotometer. NMR spectra were recorded on a Bruker Avance DRX300 MHz nuclear magnetic resonance spectrometer with tetramethylsilane (TMS) as internal standards. ESIMS were taken on Fourier transform ion cyclotron resonance mass spectrometry (Varian 7.0T).

2.2. Preparation of probe molecule *1*

A solution of 4-(*N*,*N*-dimethylamino)benzoylhydrazine (89 mg, 0.5 mmol) and 2-hydroxy-1-naphthaldehyde (86 mg, 0.5 mmol) in ethanol (20 mL) was heated under reflux for 1 h. After left to cool, the precipitated crystals were filtered and washed with ethanol to give pure **1** as yellow solid (160 mg, 95%). ^{1}H NMR (300 MHz, DMSO-d_6) δ 12.99 (s, 1H), 11.91 (s, 1H), 9.46 (s, 1H), 8.16 (d, 1H), 7.86 (m, 4H), 7.61 (s, 1H), 7.40 (s, 1H), 7.23 (d, 1H), 6.80 (d, 2H), 3.02 (s, 6H); ^{13}C NMR (75 MHz, DMSO-d_6) δ 168.1, 163.7, 158.3, 150.8, 137.8, 137.4, 134.8, 133.5, 133.1, 129.0, 125.8, 124.8, 124.4, 116.5, 114.3, 84.6, 84.2; HRMS (ESI): 356.1368 $(M+Na)^+$.

2.3. Titration experiment of *1*

Deionized water and a spectroscopic grade of DMSO were used as the solvent for titration experiment. The titrations were carried out in 10-mm quartz cuvettes at 25 °C. **1** was dissolved in DMSO to afford a concentration of 20 mM stock solution, which was diluted with DMSO–H_2O (1:1, v/v) up to 20 μM. The sodium cyanide stock solution of 1.0×10^{-1} M was diluted to 1.0×10^{-2} M with deionized water. The absorbance was measured from 250 to 550 nm, against a blank DMSO–H_2O (1:1, v/v) solution, and different cyanide solutions were added to the 20 μM host solution (2 mL) in portions (total volume: 4, 8, 12, 16, 20, 24, 32, 40, 48, 60 μL, of 1.0×10^{-2} M, and 62, 64, 66, 70, 74, 78, 82 μL, of 1.0×10^{-1} M). The emission was measured from 400 to 600 nm, and different cyanide solutions were added to the 20 μM host solution (2 mL) in portions (total volume: 4, 8, 12, 16, 20, 28, 36, 44, 52, 60 μL, of 1.0×10^{-2} M, and 62, 64, 66, 68, 70, 74, 78, 82, 86, 94, 102 μL, of 1.0×10^{-1} M). The resulting solution was shaken well and the absorption and emission spectra were recorded immediately. For detection limit measurements, 1.0×10^{-4} and 1.0×10^{-3} M solutions of sodium cyanide were used. Unless otherwise noted, for all measurements, the excitation wavelength was at 334 nm, and both the excitation and emission slit widths were 5 nm.

3. Results and discussion

3.1. Absorption and fluorescence spectral characteristics of *1*

The ability of **1** to complex with anions was explored with UV–vis absorption and fluorescence spectrometry. Among the eleven anions tested in solution (DMSO–H_2O, 1:1, v/v), namely, CN^-, F^-, Cl^-, Br^-, I^-, AcO^-, ClO_4^-, NO_3^-, $H_2PO_4^-$, N_3^-, and HSO_4^- as their sodium salts, **1** responded to only CN^- resulting in a color change from colorless to yellow and a bright green fluorescence (Fig. 1), indicating that probe **1** can serve as a "naked-eye" indicator

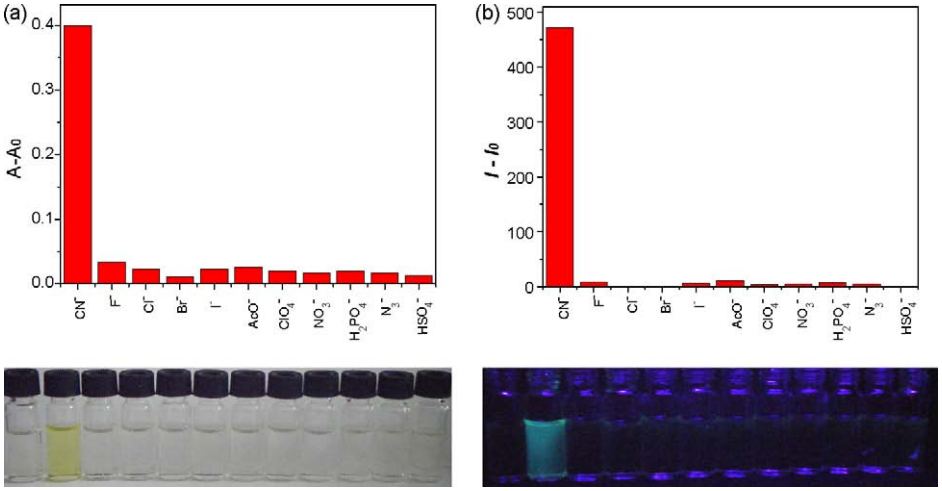


Fig. 1. (a) Absorbance changes, (b) fluorescence changes and the corresponding color changes of **1** (20 μM, 25 °C) in DMSO–H_2O (1:1, v/v) upon addition of 50 equiv. of various anions (vials from the left: only **1**, CN^-, F^-, Cl^-, Br^-, I^-, AcO^-, ClO_4^-, NO_3^-, $H_2PO_4^-$, N_3^- and HSO_4^-). The excitation wavelength for the complex was 334 nm, and the splits were 5.0 nm.

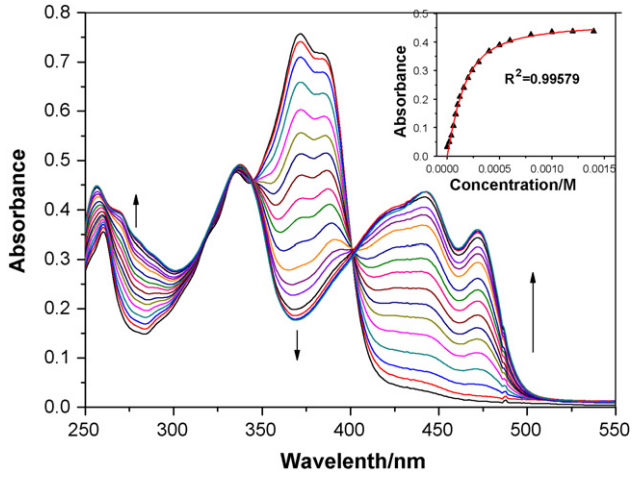


Fig. 2. Absorption spectra of **1** (20 μM) in DMSO–H_2O (1:1, v/v) upon addition of cyanide anion (0–70 equiv.). (Inset) Plots of absorption 443 nm vs. the cyanide concentration.

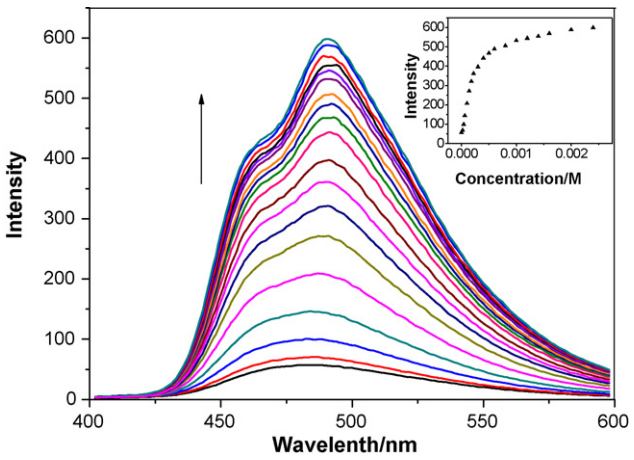


Fig. 3. Fluorescence spectra of **1** (20 μM) in DMSO–H_2O (1:1, v/v) upon addition of cyanide anions (0–120 equiv.). The excitation wavelength for the complex was 334 nm, and the splits were 5 nm. (Inset) Plots of emission at 495 nm vs. the cyanide concentration.

for CN^- in DMSO aqueous media. The absorption and fluorescence profiles of the sensor showed a remarkably higher selectivity for cyanide over the other anions in water.

The nucleophilicity of cyanide in water seems to be the major contributor to the high selectivity of **1** for cyanide. In 1:1 DMSO–H_2O (v/v), anion such as F^- and AcO^- should interact with the aqueous medium through H-bonding, and this solvation leads to a decrease in their basicity, thus, resulting in the poor deprotonation reaction. In contrast, cyanide has much weaker H-bonding ability in comparison with F^- and AcO^- but has stronger carbonyl carbon affinity, which results in the addition reaction of CN^- to imine group (Scheme 1). However, in DMSO, not only the nucleophilicity but also the basicity of anions (F^- and AcO^-) may cause large changes in the UV–vis spectra of **1** and therefore result in less selectivity for cyanide.

Fig. 2 illustrates the absorption spectral changes for **1** upon addition of CN^- in DMSO–H_2O (1:1, v/v). **1** shows an absorption band at 371 nm and two shoulders at 336 and 386 nm. The band at 336 nm can be assigned to 4-(*N*,*N*-dimethylamino)benzamide group of **1**, and the band at 371 nm and a shoulder at 386 nm can be assigned to 2-naphthol group. Upon addition of CN^-, the band at 336 nm kept almost unchanged; however, the bands at 371 and 386 nm were attenuated while two new bands appeared at 443 and 473 nm, which is similar to the observation on the deprotonation of 2-naphthol by anions where the new absorption was assigned to the naphtholate anion. Two isosbestic points at 344 and 403 nm were observed throughout the titration process. The variation of the absorbance at 443 nm was used to evaluate the binding constants of **1** with CN^- by assuming a 1:1 binding stoichiometry. Nonlinear least-squares regression analysis [23–26] of these changes gave a binding constant of $1.17 \times 10^5\ M^{-1}$. Nice fittings supported the 1:1 binding stoichiometry.

Fluorescence monitoring of the cyanide addition reaction was also performed by using a 20-μM solution of **1** in 1:1 of DMSO–H_2O at room temperature (Fig. 3). **1** shows a weak emission. Upon addition of CN^-, the fluorescence emission intensity of **1** was increased and was saturated at 2.4 mM cyanide (120 equiv.). It is noteworthy that the cyanide adducts display dual luminescence with two emission bands, 460 and 495 nm, in the visible region. Titration of **1** with CN^- ions gave a simultaneous increase in the intensity of two bands. The former can be assigned to the excited-state CT for the parent CT fluorophore 4-(*N*,*N*-dimethylamino)benzamide [27–29], and the latter can be assigned to the naphtholate anion [30–32]. The resultant Job plot indicated a 1:1 receptor–cyanide binding stoichiometry (Fig. 4).

Several factors can be proposed for rationalizing the observed emission enhancement of **1** upon the addition of the cyanide anion. Molecules with lowest excited singlet states of the $n\pi^*$ type are typically nonemissive in fluid solution [33]. In the presence of CN^-, as shown in Scheme 1, an intramolecular hydrogen-bond network will be created by nucleophilic attack of CN^- at the imine group, and followed by fast proton transfer of the phenol hydrogen to the developing nitrogen anion. With such an intramolecular hydrogen-bond network that interacts with the lone pair of the carbonyl oxygen of 4-(*N*,*N*-dimethylamino)benzamide group, the energy of the $n\pi^*$ state of this group would be raised so that the emission from the π–π^* transition of the fluorophore would be restored, leading to a substantial fluorescence enhancement [33]. There was no change in the UV absorption band at 336 nm on cyanide anion binding, which suggests that the fluorescence enhancement may also be a consequence of a restriction in the conformational flexibility of 4-(*N*,*N*-dimethylamino)benzamide fluorophore due to the intramolecular hydrogen-bond network that would otherwise lead to nonradiative decay through rotatory motion of the amide group [34–36]. In addition, the proton transfer of the phenol hydrogen to the developing nitrogen anion upon cyanide attack can also lead to the opening of another fluorescence emission channel relative to naphtholate anion, resulting in the emission enhancement [37].

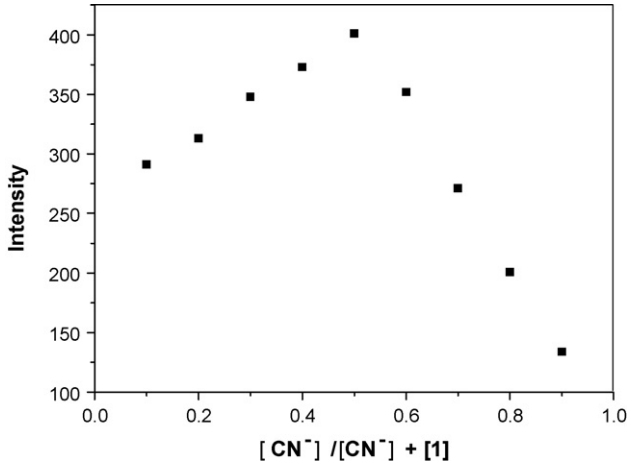


Fig. 4. Job's plot between **1** and cyanide anion in DMSO–H_2O (1:1, v/v) at 25 °C.

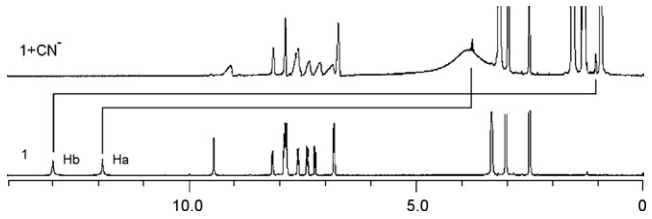


Fig. 5. ^{1}H NMR spectral change of **1** in DMSO-d_6 upon addition of cyanide anions: **1** only (bottom) and **1** and 20 equiv. of Bu_4NCN (top). *Note*: the broad peak at 3.8 is water.

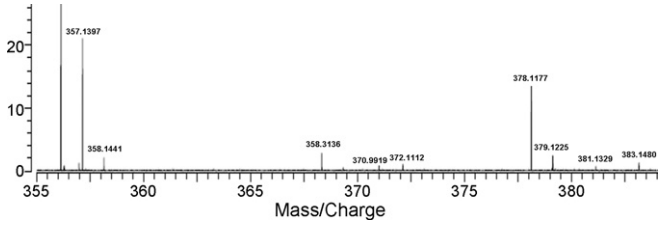


Fig. 6. The ESIMS for the cyanide adduct of **1** [(**1**+NaCN+H$^+$): 383.1478].

The detailed mechanism, however, remains to be further clarified. Detailed work is now underway in this laboratory.

3.2. ^{1}H NMR and ESIMS investigation

An analysis on the ^{1}H NMR spectra of **1** before and after the cyanide addition proved informative (Fig. 5). The imine proton of **1** (H_a) and the phenol proton (H_b) at around δ 11.9 and 13.0 ppm was dramatically shifted upfield to δ 3.7 and 1.1 ppm, respectively, upon cyanide addition at room temperature, indicating that the cyanide anion functions as a nucleophile in water. The formation of cyanide adduct was further confirmed by mass spectrometry. The electrospray ionization mass spectrum of the cyanide adducts for **1** showed a molecular mass of 383.1, which correspond to the formula of [**1**+NaCN+H$^+$] (Fig. 6).

3.3. Fast response

As known, chemosensors always have a problem of long response time. In our case, the binding process of CN^- to **1** was found to be very fast (Fig. 7). After adding the sodium cyanide, two new absorbance bands at 443 and 473 nm appeared and reached

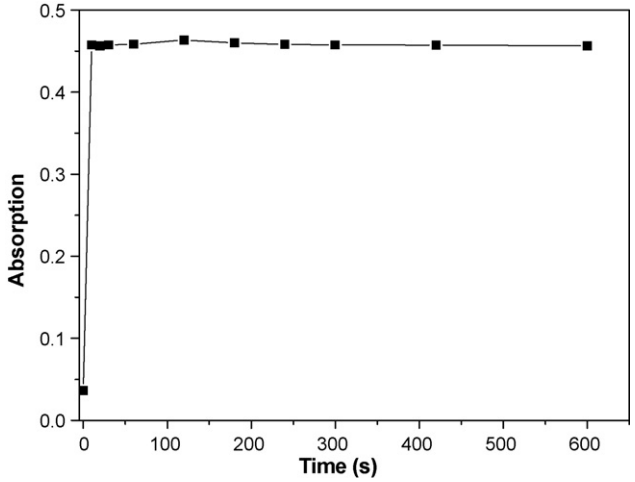


Fig. 7. Absorbance changes at 443 nm for **1** (20 μM, 25 °C) in a mixture of DMSO–H_2O (1:1, v/v) after addition of NaCN (1 mM).

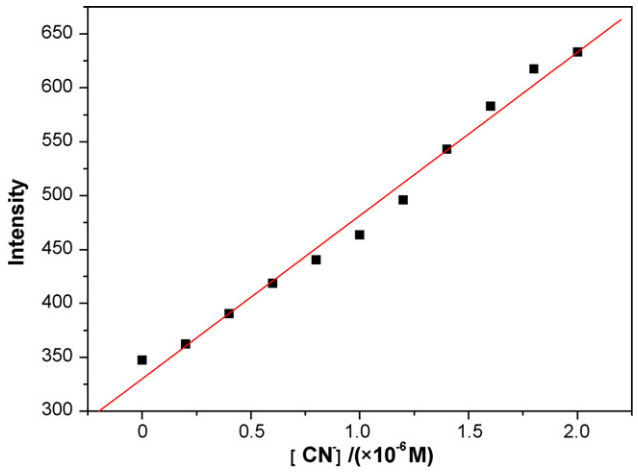


Fig. 8. Fluorescence intensity change at 495 nm for **1** (20 μM) in DMSO–H_2O (1:1, v/v) as a function of the concentration of cyanide anions. The excitation wavelength for the complex was 334 nm, and the splits were 10 nm.

the plateau region less than 2–3 s, and remains quite stable from 3 s to 10 min, suggesting that the addition reaction of CN^- to imine group of **1** might be completed instantly and the chemosensor has rapid detection ability for cyanide anion.

3.4. Detection limits

The detection limit was calculated based on the fluorescence titration. To determine the S/N ratio, the emission intensity of **1** without cyanide anion was measured by 10 times and the standard deviation of blank measurements was determined. Under the present conditions, a good linear relationship between the fluorescence intensity and the cyanide concentration could be obtained in the 2×10^{-7} to 2×10^{-6} M ($R^2 = 0.9935$), as shown in Fig. 8. The detection limit is then calculated with the equation: detection limit = $3\sigma_{bi}/m$, where σ_{bi} is the standard deviation of blank measurements, m is the slope between intensity versus sample concentration. The detection limit was measured to be 7.4×10^{-8} M. According to the World Health Organization (WHO), cyanide concentrations lower than 1.9 μM are acceptable in drinking water. This means that our proposed fluorescent method based on probe molecule **1** is sensitive enough to monitor cyanide concentrations in drinking water.

3.5. Applications

In order to assess the utility of the proposed method, it was applied to the quantitative determination of cyanide anion in drinking water sample (drinking water from commence). The water sample was found to be free from cyanide and so the sample was prepared by adding known amounts of cyanide to sample. The applications were performed using 2 mL of sample volume, and after addition of cyanide with the concentration of 1.9×10^{-6} M, which was within the linear calibration range, the sample was injected in triplicate. The average content of cyanide anion was found to be 1.88×10^{-6} M for drinking water. Then, the recovery percentage performed well with relative standard deviation lower than 2%.

4. Conclusion

In summary, an anion probe bearing 2-hydroxy-1-naphthaldehyde hydrazone moiety for cyanide anion recognition

was synthesized, and its absorption and fluorescence properties in the presence of anions were evaluated. The probe displayed an obvious color change from colorless to yellow and a dramatic change in fluorescence intensity selectively for cyanide anions over other anions in aqueous solution. Such selectivity results from the nucleophilicity of the cyanide anion and the imine activation by the neighboring phenol proton through an intramolecular hydrogen bond. The cyanide detection method described here should have potential application as a new family of probes for detecting cyanide in aqueous solution.

Acknowledgements

We would like to thank the Natural Science Foundation of China (NSFC no. 20772073) and the Natural Science Foundation of Shanxi Province (2008011015) for financial support.

References

[1] P.D. Beer, P.A. Gale, Angew. Chem., Int. Ed. 40 (2001) 486.
[2] V. Amendola, D. Esteban-Gómez, L. Fabbrizzi, M. Licchelli, Acc. Chem. Res. 39 (2006) 343.
[3] G.C. Miller, C.A. Pritsos, Proc. Symp. Annu. Meet., TMS, 2001, pp. 73–81.
[4] K.W. Kulig, Cyanide Toxicity, U.S. Department of Health and Human Services, Atlanta, GA, 1991.
[5] S.L. Baskin, T.G. Brewer, in: F.R. Sidell, E.T. Takafuji, D.R. Franz (Eds.), Medical Aspects of Chemical and Biological Warfare, TMM Publications, Washington, DC, 1997, pp. 271–286.
[6] C. Baird, M. Cann, Environmental Chemistry, Freeman, New York, 2005.
[7] P. Anzenbacher Jr., D.S. Tyson, K. Jursíková, F.N. Castellano, J. Am. Chem. Soc. 124 (2002) 6232.
[8] S.S. Sun, A.J. Lees, Chem. Commun. 17 (2000) 1687.
[9] H. Miyaji, J.L. Sessler, Angew. Chem., Int. Ed. 40 (2001) 154.
[10] M. Tomasulo, F.M. Raymo, Org. Lett. 7 (2005) 4633.
[11] M. Tomasulo, S. Sortino, A.J.P. White, F.M. Raymo, J. Org. Chem. 71 (2006) 744.
[12] F. García, J.M. García, B. García-Acosta, R. Martínez-Máñez, F. Sancenón, J. Soto, Chem. Commun. 22 (2005) 2790.
[13] J.V. Ros-Lis, R. Martínez-Máñez, J. Soto, Chem. Commun. 19 (2002) 2248.
[14] H. Lee, Y.M. Chung, K.H. Ahn, Tetrahedron Lett. 49 (2008) 5544.
[15] H. Miyaji, D.-S. Kim, B.-Y. Chang, E. Park, S.-M. Park, K.H. Ahn, Chem. Commun. 6 (2008) 753.
[16] Y. Chung, H. Lee, K.H. Ahn, J. Org. Chem. 71 (2006) 9470.
[17] Y.-K. Yang, J. Tae, Org. Lett. 8 (2006) 5721.
[18] K.-S. Lee, J.T. Lee, J.-I. Hong, H.-J. Kim, Chem. Lett. 36 (2007) 816.
[19] K.-S. Lee, H.-J. Kim, G.-H. Kim, I. Shin, J.-I. Hong, Org. Lett. 10 (2008) 49.
[20] C.-L. Chen, Y.-H. Chen, C.-Y. Chen, S.-S. Sun, Org. Lett. 8 (2006) 5053.
[21] H.-T. Niu, X. Jiang, J. He, J.-P. Cheng, Tetrahedron Lett. 49 (2008) 6521.
[22] Y. Sun, G. Wang, W. Guo, Tetrahedron 65 (2009) 3480.
[23] B. Valeur, J. Pouget, J. Bouson, M. Kaschke, N.P. Ernsting, J. Phys. Chem. 96 (1992) 6545.
[24] J. Bouson, J. Pouget, B. Valeur, J. Phys. Chem. 97 (1993) 4552.
[25] A. Tsuda, C. Fukumoto, T. Oshima, J. Am. Chem. Soc. 125 (2003) 5811.
[26] R.-H. Yang, K.-A. Li, K.-M. Wang, F.-L. Zhao, N. Li, F. Liu, Anal. Chem. 75 (2003) 612.
[27] D. Braun, W. Rettig, S. Delmond, J.F. Létard, R. Lapouyade, J. Phys. Chem. A 101 (1997) 6836.
[28] F.-Y. Wu, Y.-B. Jiang, Chem. Phys. Lett. 355 (2002) 438.
[29] Z.-C. Wen, R. Yang, H. He, Y.-B. Jiang, Chem. Commun. 2 (2006) 106.
[30] L.M. Tolbert, S.M. Nesselroth, Phys. Chem. 95 (1991) 10331.
[31] M. Lawrence, C.J. Marzzacco, C. Morton, C. Schwab, A.M. Halpern, J. Phys. Chem. 95 (1991) 10294.
[32] K.M. Solntsev, D. Huppert, J. Phys. Chem. A 102 (1998) 9599.
[33] A. Prasanna de Silva, H.Q. Nimal Gunaratne, T. Gunniaugsson, A.J.M. Huxiey, C.P. McCoy, J.T. Rademacher, T.E. Rice, Chem. Rev. 97 (1997) 1515.
[34] K. Rechthaler, G. Köhler, Chem. Phys. 189 (1994) 99.
[35] G. Jones II, W.R. Jackson, C. Choi, W.R. Bergmark, J. Phys. Chem. 89 (1985) 294.
[36] W. Rettig, A. Klock, Can. J. Chem. 63 (1985) 1649.
[37] X. Zhang, L. Guo, F.-Y. Wu, Y.-B. Jiang, Org. Lett. 5 (2003) 2667.

Talanta 80 (2009) 1001–1006

Contents lists available at ScienceDirect

Talanta

journal homepage: www.elsevier.com/locate/talanta

Quantitation of atorvastatin in human plasma using directly suspended acceptor droplet in liquid–liquid–liquid microextraction and high-performance liquid chromatography-ultraviolet detection

Hadi Farahani [a], Parviz Norouzi [b,c], Abolghasem Beheshti [b], Hamid Reza Sobhi [d], Rasoul Dinarvand [e], Mohammad Reza Ganjali [b,c,*]

[a] Industrial and Environmental Protection Division, Research Institute of Petroleum Industry (RIPI), Tehran, Iran
[b] Center of Excellence in Electrochemistry, Faculty of Chemistry, University of Tehran, P.O. Box 14155-6455, Tehran, Iran
[c] Endocrinology & Metabolism Research Center, Medical Science/University of Tehran, Tehran, Iran
[d] Department of Chemistry, Payame - Noor University, Tehran Branch, Tehran, Iran
[e] Medical Nanotechnology Research Center, Medical Sciences/University of Tehran, P.O. Box 14155-6451, Tehran, Iran

ARTICLE INFO

Article history:
Received 20 May 2009
Received in revised form 5 August 2009
Accepted 22 August 2009
Available online 31 August 2009

Keywords:
Liquid–liquid–liquid microextraction
High-performance liquid chromatography-ultraviolet detection
Atorvastatin
Human plasma

ABSTRACT

A simple and sensitive methodology based on liquid–liquid–liquid microextraction (LLLME) followed by high-performance liquid chromatography-ultraviolet detection (HPLC-UV) has been successfully developed for the determination of atorvastatin (AT) in human plasma. AT was first extracted from 4.5 mL acidic aqueous sample (diluted plasma, donor phase, pH 1) at temperature 45 °C through 400 μL 1-octanol for 4.5 min, while being agitated by a stirring bar at 1250 rpm. Then, a 5.5 μL free suspended basic aqueous droplet (acceptor phase, pH 10) was delivered to the top-center position of the organic membrane. The mixture was stirred at 650 rpm for 7.5 min and the analyte was back-extracted into the droplet. Finally, the acceptor phase was taken into a microsyringe and injected directly into the HPLC. An enrichment factor of 187 along with substantial sample clean up was obtained under the optimized conditions. The calibration curve showed linearity in the range of 1–500 ng mL^{-1} with regression coefficient corresponding to 0.996. Limits of detection (S/N = 3) and quantification (S/N = 10) were 0.4 and 1 ng mL^{-1}, respectively. A reasonable relative recovery (91%) and satisfactory intra-assay (4.4–7.0%, $n = 6$) and inter-assay (4.9–7.7%, $n = 8$) precision illustrated good performance of the analytical procedure. This technique was eventually applied for the determination of AT in human plasma after oral administration of 40 mg single dose of drug. The protocol proved to be highly cost-effective and reliable for the screening purpose.

© 2009 Elsevier B.V. All rights reserved.

1. Introduction

Sample preparation is a tedious and yet unavoidable procedure in analytical chemistry [1]. The objective of this challenging and critical step is to transfer the analyte into a form that is pre-purified, concentrated and compatible with the analytical system [2,3]. The extracted and enriched analytes of interest from the sample matrix are often accomplished by procedures such as liquid–liquid extraction (LLE) [4,5] and solid-phase extraction (SPE) [6,7]. The invention of solid-phase microextraction (SPME) by Pawliszyn and co-worker [8] basically initiated the interest for microextraction techniques in analytical chemistry. SPME satisfies most of the requirements of a good sample preparation technique, including simplicity of use, automation, and low consumption of materials [9]. Thus, it has been applied to determine a broad range of organic compounds in numerous types of samples [10].

An alternative solvent-minimized sample preparation approach to complement SPME appeared in the middle-to-late 1990s [11–13]; liquid-phase microextraction (LPME) utilizes only a small amount of solvent (low microliter range) for concentrating analytes from aqueous samples. It is simply a miniaturized format of LLE and overcomes many of its disadvantages as well as some of those of SPME (e.g. non-dependence on a commercial supplier and sample carryover). LPME is simple to implement and use, generally fast, and is characterized by its affordability and reliance on widely available apparatus or materials [14]. The applications of LPME in environmental and biological analysis have been described in several papers [15–17].

LPME can be classified as two- and three-phase categories. In two-phase LPME, the target analytes are extracted from the aqueous sample matrix into the organic receiving phase [13,18,19]. Three-phase LPME (liquid–liquid–liquid microextraction, LLLME) is

* Corresponding author at: Center of Excellence in Electrochemistry, Faculty of Chemistry, University of Tehran, P.O. Box 14155-6455, Tehran, Iran.
Tel.: +98 21 61112788; fax: +98 21 66405141.
E-mail address: ganjali@khayam.ut.ac.ir (M.R. Ganjali).

0039-9140/$ – see front matter © 2009 Elsevier B.V. All rights reserved.
doi:10.1016/j.talanta.2009.08.033

performed as hollow fiber or droplet based mode [20–24]. In hollow fiber LLLME, the analytes are first extracted from an aqueous sample matrix into the thin layer of the organic phase inside the wall pores of a hollow fiber, and then back-extracted into the acceptor phase located inside the hollow fiber [25]. In the other mode, the receiving phase is a microdrop of aqueous phase suspended from the tip of a microsyringe and located inside the organic phase [20,21,26]. Today, LLLME has been successfully utilized for the clean up and pre-concentration of ionizable analytes from a variety of matrixes [27–29], owing to its advantages.

Recently, Sarafraz-Yazdi et al. have developed a simple, efficient and novel LLLME that initially applied for the determination of diclofenac in environmental water samples [30]. The method was simplified droplet based LLLME using larger volumes of organic solvent to eliminate the use of microsyringe which is employed for suspending the acceptor drop at the tip of the needle. This quantitative LLLME is an efficient and satisfactory analytical procedure, because excellent accuracy and precision are demonstrated.

Atorvastatin ([R-(R*,R*)]-2-(4-fluorophenyl)-b, d-dihydroxy-5-(1-methylethyl)-3-phenyl-4 [(phenylamino) carbonyl] 1H-pyrrole-1-heptanoic acid, AT, $pK_a = 4.46$, $\log P_{ow} = 6.36$) is a potent inhibitor of HMG-CoA reductase, the rate limiting enzyme in cholesterol biosynthesis and has been demonstrated to be effective in reducing both cholesterol and triglyceride [31–33]. Also, AT is indicated to diminish the risk of myocardial infarction [34,35], stroke [36] which decreases the risk for revascularization procedures [37] and angina [38]. AT is rapidly absorbed after oral administration, however, due to pre-systematic clearance in the gastro-intestinal mucosa and metabolism in the liver, its absolute bioavailability is approximately 12%, and low plasma concentration is followed after taking the drug [39,40].

According to literature survey there have been several reports for the determination of AT in biological samples. Existing analytical methods for AT included an enzyme immunoassay [41], gas chromatography–mass spectrometry (GC/MS) [42] and also high-performance liquid chromatography equipped with mass spectrometry detection (HPLC-MS) [43,44]. GC–MS and HPLC–MS methods are sensitive and specific, but these devices may not be available in many pharmaceutical laboratories and need highly trained persons. In addition extraction and pre-concentration techniques, which are commonly applied to monitor the drug, are liquid–liquid extraction (LLE) [45,46] and solid-phase extraction (SPE) [47,48]. However, these sample pretreatment methods are considered expensive, time-consuming and labor-intensive, which often result in high blank values [49].

The aim of the present study is to assess the LLLME technique suitability for the determination of AT in human plasma. The factors affecting the microextraction efficiency were studied in detail and the optimal conditions were established. The resulting method was validated for quantitative purposes and applied to volunteer's plasma for sample analysis after oral administration of the drug in combination with high-performance liquid chromatography-ultraviolet detection (HPLC-UV).

2. Experimental

2.1. Materials and reagents

AT (purity 99%) and diclofenac sodium (DS, purity 99%), as internal standard (I.S.), were kindly supplied from Darou-Pakhsh Pharmaceutical Company (Tehran, Iran). All of organic solvents, sodium chloride, sodium hydrogen phosphate and hydrochloride acid were of analytical grade and purchased from Merck (Darmstadt, Germany). Trichloroacetic acid (TCAA) was obtained from Fluka (Buchs, Switzerland).

2.2. Instrument and apparatus

Separation, identification and quantification were performed with a Younglin HPLC system (ACME 9000, Korea), consisted of a Rheodyne 7725 injector (Cotati, CA, USA) equipped with a 5 μL sample loop. The separation was accomplished using a 150 mm × 4.6 mm i.d. × 5 μm particle size ODS-3 C_{18} analytical column (MZ, Germany) at room temperature (25 ± 0.5 °C). Isocratic mobile phase consisted of acetonitrile:0.1% acetic acid (70:30) was run through the column at flow rate of 1 mL min^{-1}. UV detection was performed at 246 nm and data were collected and processed with Autochrom 2000 software (Younglin, Korea). The temperature-controlling centrifuge (model: 2-16KC, Sigma, Germany) was used for centrifugation. The used water was purified with a Milli-Q water purification system (Millipore, Bedford, MA, USA). A 10 μL HPLC microsyringe (Bondaduz, Switzerland) was applied to introduce the acceptor phase and act as an injection syringe.

2.3. Preparation of standard solutions and plasma samples

Frozen, drug-free human plasma was obtained from the research center of Darou-Pakhsh pharmaceutical company (Tehran, Iran) and thawed at room temperature (25 ± 0.5 °C) before use. The plasma samples were obtained from healthy male volunteers. Stock solutions of AT (1 mg mL^{-1}) and I.S. (100 mg mL^{-1}) were prepared by dissolving proper amounts of pure substances in methanol, stored at 4 °C. Working solutions were prepared by diluting the stock solution with water. Spiked plasma samples were generated by adding 20 μL working solutions with different concentrations to 1 mL drug-free matrixes to yield final desired concentrations.

2.4. Directly suspended droplet LLLME procedure and deproteinization of plasma

The experimental microextraction setup is illustrated in Fig. 1. A water bath was placed on a magnetic stirring plate (IKA-Werke, Staufen, Germany) and the temperature (in the range of 25–55 °C) was controlled. 4.5 mL of the acidic aqueous sample (diluted plasma) was transferred in a 5 mL commercially available glass vial. A stirring bar (7 mm × 3 mm) was used to facilitate the mass transfer process. 400 μL of an organic phase was added to the sample solution by a 500 μL syringe (Hamilton, Reno, NV, USA) and stirred at 1250 rpm. After extraction for a prescribed time, the acceptor phase (5.5 μL, adjusted to pH 11 with 0.1 M Na_2HPO_4) was delivered to the top-center position of the organic membrane. The mixture was agitated at 600 rpm for a specified time and back-extraction was performed. Subsequently, the 5 μL of microdrop was taken into a microsyringe and injected into the HPLC system.

AT is extensively bounded to plasma proteins (98%) [50], and should be librated prior to extraction. Plasma sample (1 mL) was spiked with particular level of the drug and vortexed for 3 min. The mixture was acidified with 75 μL hydrochloric acid (37%) to disturb the drug protein binding. Then, 100 μL TCAA (100%, w/v) was added to denature the proteins. These processes eventually led to the precipitation of proteins. Subsequently, the sample was centrifuged at 10,000 rpm for 5 min. A volume of 0.75 mL of the supernatant was transferred to the sample vial, mixed with proper amounts of I.S (45 μL of the stock solution added to sample vial to achieve final concentration of 1 mg mL^{-1}) and then, diluted with water to 4.5 mL. The pH was adjusted to 1 with 0.1 mol L^{-1} HCl. To adjust the pH to desired value, a micropipette was used for the addition of appropriate amount of concentrated HCl.

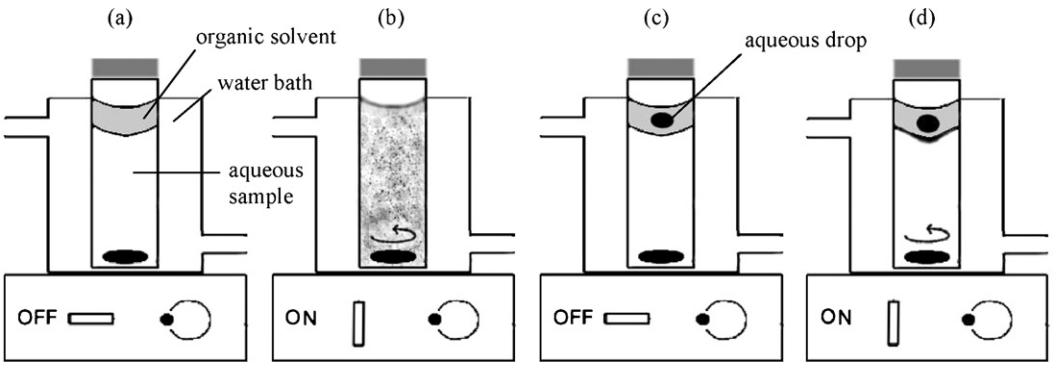


Fig. 1. Directly suspended droplet LLLME setup.

3. Results and discussion

The important aims of LLLME are to separate and clean up the analytes from the complex matrixes and to provide an efficient pre-concentration prior to HPLC or capillary electrophoresis (CE) determination. It involves the extraction of ionizable compounds from the aqueous sample (donor phase) at suitable pH into the organic layer (as membrane), followed by back-extraction into the receiving aqueous phase (acceptor phase) by adjusting the pH on the desired value. This back-extraction step introduces extra selectivity since neutral compounds will preferably stay in the organic phase. Extraction was induced by the pH difference inside and outside an organic membrane located at the interface [25,51,52].

3.1. Optimization of the LLLME process

A univariate approach was employed to optimize the influential factors in this method. The optimization was executed using 1 mL plasma containing 250 ng AT. In order to improve the precision and accuracy of the procedure in all of the experiments, DS with the concentration of 100 ng mL^{-1} was used as the I.S. and was added into the donor phase. Quantifications were performed by calculating peak areas relative to the I.S. from the average of 3 replicate measurements.

3.1.1. Selection of the organic solvent

The selection of appropriate organic solvent is of great importance in LLLME, in order to achieve satisfactory analyte pre-concentration [53,54]. Several organic solvents with different polarities were used to study their effects on extraction efficiency. The solvents including isooctane, 2-octanone, 1-octanol and hexyl acetate were examined. Fig. 2 depicts that 1-octanol presented the maximum extraction efficiency and thus was selected as the most suitable solvent.

3.1.2. Phase volume ratios

In three-phase LPME higher enrichment factors can be resulted by decreasing the volume ratio of acceptor to donor phase. However, in many cases optimization of the enrichment factor is not the primary goal, but rather optimization of recovery (R), defined by IUPAC as the ratio of the moles extracted (nA) and the number of moles initially present in the sample (nD):

$$R = \frac{nA}{nD}$$

At equilibrium the maximum recovery will be limited by the distribution coefficient and the volume ratio between the sample and acceptor phases [25,52]. To enhance recovery the acceptor volume must therefore be increased.

The phase ratio was varied by changing the volume of the microdrop in the range 3.0–6.0 μL, while the donor solution volume was kept constant (4.5 mL). It was found that the signal intensity of the analyte increased with the amplification of drop volumes. However, from a practical point of view, the drop greater than 5.5 μL was unstable especially with a high stirring speed. Accordingly, the following investigations were carried out with the drop volume of 5.5 μL to get higher extraction efficiency.

Due to the design of our extraction device, the volume of the organic phase was also important and needed to be optimized. The best volume of the organic solvent was found to be 400 μL. A smaller volume of organic solvent tended to cause instability of the aqueous drop during agitation, whereas the extraction efficiency is reduced if a larger volume of organic phase is used. Hence, a 400 μL volume of organic solvent was selected as the optimum on the basis of these observations.

3.1.3. The donor phase and acceptor drop pHs

The pH difference between donor and acceptor phases can promote the transfer analyte from the former to the latter [55]. To get a high distribution coefficient result leading to a high preconcentration, the donor solution should be sufficiently acidic to keep the drug in molecular form, and consequently reduce their solubility within this phase. The acceptor phase should be basic in order to promote dissolution of the acidic analyte.

The experiments were conducted to optimize the composition (leading to variation of pH) of both donor and acceptor solutions. First, the effect of the donor phase's pH on extraction efficiency was investigated. Solutions with different acidic pHs (0.5–3.5) were prepared by addition of appropriate amounts of HCl, while pH of the

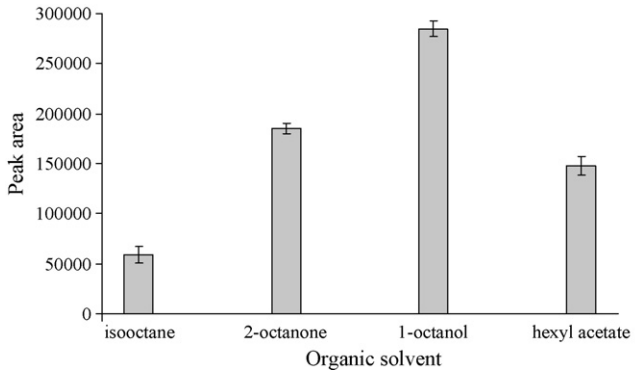


Fig. 2. Extraction efficiencies obtained for different organic solvents. Conditions: 4.5 mL aqueous sample (pH 1) at room temperature (25 ± 0.5 °C); organic phase volume: 400 μL; acceptor phase: 5.5 μL aqueous drop adjusted to pH 11 with 0.1 mol L^{-1} Na_2HPO_4; extraction and back-extraction time: 6.0 and 9.0 min, respectively; stirring rate for extraction and back-extraction: 1250 and 600 rpm, respectively.

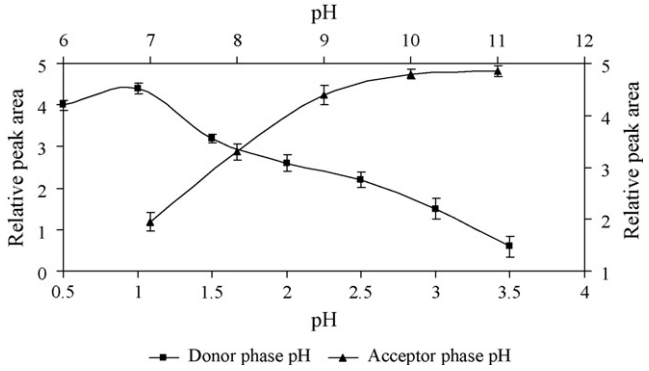


Fig. 3. Effect of the donor and acceptor phases' pH on the extraction of AT. Conditions: as with Fig. 2, organic solvent: 1-octanol.

acceptor phase was adjusted to 11.0 using 0.1 mol L^{-1} Na_2HPO_4. Since pH 1 provided the highest extraction efficiency (Fig. 3), it thus was selected for subsequent experiments. Secondly, the acceptor phase's pH, which was adjusted by 0.1 mol L^{-1} Na_2HPO_4 in the range of 7–11, was examined. The results, also shown in Fig. 3, indicate that the receiving phase with pH 10 could ionize the analyte more conveniently to prevent re-entering into the organic phase. Also, in order to investigate the effect of concentration of phosphate buffer on the extraction efficiency, aqueous solutions with various concentrations of Na_2HPO_4 (0.01, 0.05, 0.1 and 0.5 mol L^{-1}) were prepared and the extraction procedure was conducted. The results show that the best extraction efficiency was obtained at: 0.05 mol L^{-1} of Na_2HPO_4. Therefore, further experiments were done using the aqueous acceptor solutions containing 0.05 mol L^{-1} Na_2HPO_4 with pH 10.

3.1.4. Effect of the temperature

The temperature of extraction can influence the mass transfer rate and the partition coefficient of the analyte. So, it affects extraction kinetics and the time required to reach equilibrium diminishes [53,55]. The effect of sample solution temperature was studied in the range of 25–55 °C. An increase in analytical signal was observed up to 45 °C during this study (Fig. 4). After this point, some practical difficulties such as instability of the microdrop and reduction of its volume due to its higher solubility in the organic phase could occur. Thus, the sample temperature was held at 45 °C for the rest of the experiments as it gave a higher efficiency.

3.1.5. Effect of the ionic strength

The addition of salt to an analytical sample can potentially cause the formation of hydration spheres, which reduce the amount of water available to dissolve the analyte in water. This effect resulted in an increase in analyte recovery in microextraction procedures [56–58]. The NaCl concentration effect (0–20%, w/v) was investigated and the extraction efficiency was monitored. Based on the obtained results (Fig. 4), addition of salt did not improve the extraction efficiency. While the extraction efficiency was highest without the addition of sodium chloride, it subsequently decreased as more salt was added. This may be related to the formation of a physical barrier across donor phase and organic solvent interface, which could prevent the mass transfer of analyte into the organic phase. Hence, no salt was added in the subsequent experiments.

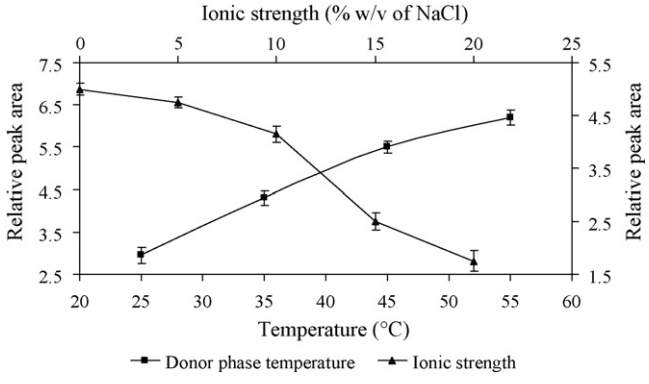


Fig. 4. Influence of the temperature and salt on the extraction efficiencies. Conditions: as with Fig. 3, donor and acceptor phases' pH 1 and 10, respectively.

3.1.6. Effect of the stirring rate

Magnetic stirring facilitates the mass transfer process and reduces the time required to reach thermodynamic equilibrium. So, it has been used universally to improve microextraction efficiency [59]. In this work, extraction was performed at the maximum magnetic stirrer performance, 1250 rpm. After utilizing the acceptor phase for back-extraction, this effect was studied at three different stirring rates: 0 (static case), 400 and 650 rpm. Faster stirring speeds were avoided due to the production of vortex flow in the membrane phase that could reduce stability of the microdrop. In this step, agitation of donor phase induces convection in the organic membrane. The obtained results show that the agitation improves the extraction efficiency of the target analyte significantly. Thus, a stirring rate of 650 rpm was used in the subsequent studies.

3.1.7. Extraction and back-extraction time profiles

LLLME system is an equilibrium based process that involves mass transfer from donor phase to organic layer and subsequently from organic layer to acceptor phase. The main objective in microextraction techniques is to achieve sufficiently high extraction efficiency within a relatively short period of time [60].

For the first equilibrium, extraction time was studied in the range of 0.5–6.5 min, while the time for back-extraction process was kept constant for 9.0 min. As shown in Fig. 5, the relative peak area was enhanced with the increase in exposure time up to 4.5 min and remained constant afterwards. An extraction time of 4.5 min therefore, was selected as the optimum.

The time of back-extraction was also investigated in the range of 3.0–12.0 min. As demonstrated in Fig. 5, the analytical signal increases quickly with sampling time of 7.5 min and after that the rate of increase slows down. It can be seen when the extraction time was set at 7.5 min, satisfactory extraction efficiency was achieved while equilibrium in the extraction of the analyte was not reached even at 12.0 min. Since it is not considered practicable for exposure time to be excessively long to allow equilibrium to occur, it

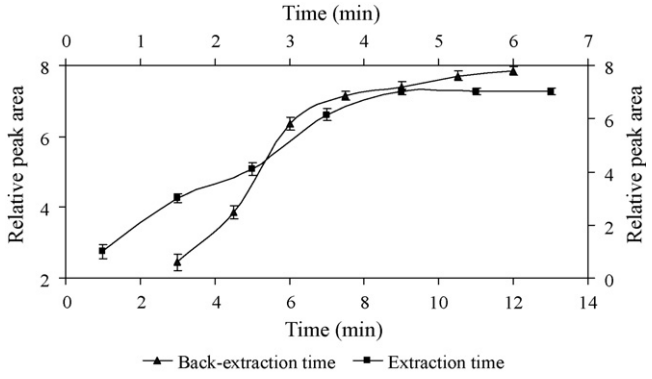


Fig. 5. Effect of the extraction and back-extraction time profiles on the LLLME efficiency. Conditions as with Fig. 4, stirring rate of back-extraction: 650 rpm and sample solution temperature: 45 °C.

Table 1
Quantitative data obtained after the LLLME–HPLC-UV determination of AT in human plasma.

Parameter	Analytical feature
Limit of detection (LOD based on S/N = 3, ng mL^{-1})	0.4
Limit of quantification (LOQ based on S/N = 10, ng mL^{-1})	1
Linear range (LR, ng mL^{-1})	1–500
Regression coefficient (r^2)	0.996
Enrichment factor (EF, at concentration level of 50 ng mL^{-1})	187
Extraction recovery (%) (ER)	22.9

should be just long enough for the extraction rate to have slowed to improve precision [12,61,62]. Furthermore, droplet lifetime cannot be too long due to drop dissolution or loss. Hence, a back-extraction time of 7.5 min appeared to be an appropriate value.

3.2. Evaluation of the method performance

To access the practical applicability of the LLLME method, the optimized conditions were adopted in the evaluation of linear range (LR), correlation coefficient (r^2), limit of detection (LOD, S/N = 3), limit of quantification (LOQ, S/N = 10), enrichment factor (EF) and also extraction recovery % (ER). An external calibration curve was plotted using plasma samples spiked with known concentrations of AT. For each level, three replicate extractions were performed. The results are summarized in Table 1. As shown, the LR is enough to cover the possible concentration of AT in various real samples. LOD and LOQ values imply a high sensitivity of the developed method.

For the EF calculation, three replicate extractions were performed from the aqueous solution containing 50 ng mL^{-1} of the analyte. EF was calculated as the ratio of the final analyte concentration in the acceptor phase and its concentration in the original solution. The AT standard solutions were prepared in acceptor phase and a calibration curve was drawn in the concentration ranges of 0.5–25 μg mL^{-1} with three replicate direct injections. The actual concentration of AT in acceptor phase was calculated from the non-extractive calibration curve and the EF value was determined.

ER% was calculated based on the following equation:

$$ER\% = (C_{acceptor} \times V_{acceptor}/C_{donor} \times V_{donor}) \times 100$$
$$= EF \times (V_{acceptor}/V_{donor}) \times 100$$

where $C_{acceptor}$ and C_{donor} are the analyte concentration in acceptor and donor phase, respectively. Moreover, $V_{acceptor}$ and V_{donor} are the volume of the acceptor and donor phase, respectively.

The results of the intra-day and inter-day precision at three different concentration levels are presented in Table 2. As it is illustrated, the intra-assay RSD measured at 6 runs a day of a sample was relatively low (4.4–7.0%). Also, the inter-assay precision evaluated on different days with a total of 8 runs provided RSD values in the range of 4.9–7.7%.

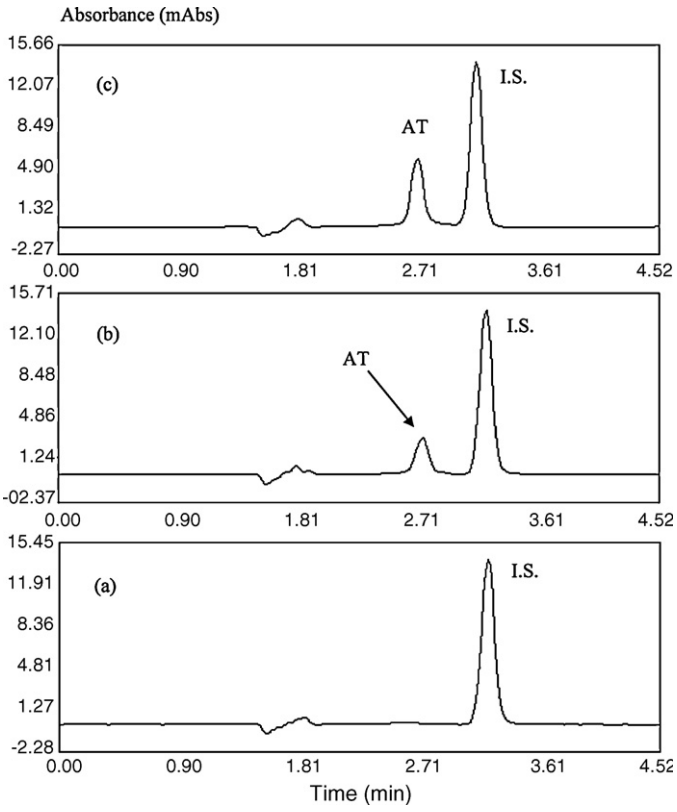


Fig. 6. HPLC-UV chromatograms obtained using developed method after oral administration of 40 mg single dose of AT at time (a) 0 h, (b) 2 h and (c) spiked sample.

Table 2
The intra-assay and inter-assay reproducibility of the method and instrument on plasma sample.

AT concentration (ng mL^{-1})	RSD (%)	
	Intra-day (n = 6)	Inter-day (n = 8)
5	7.0	7.7
50	5.8	6.4
250	4.4	4.9

As shown in Table 3, comparing LLLME–HPLC-UV with other analytical methods applied for the determination of AT in plasma samples, this technique along with its simplicity provided wider LR, lower LOD and an acceptable reproducibility.

3.3. Application

The developed protocol at optimal conditions was used to determine AT concentration in human plasma. Oral administration of a 40 mg single dose was performed to a healthy male volunteer. The concentration of AT 2 h after it was administrated was

Table 3
Comparison of different analytical methods applied for the determination of AT in plasma.

Analytical technique	LR[a] (ng mL^{-1})	LOD[b] (ng mL^{-1})	RSD[c] (%)	Reference
LLE–HPTLC[d]-UV	101–353.5[e]	30.3[e]	1.7–3.4	[63]
LLE–HPLC-UV	4–256	1	≤11.7	[45]
LLLME–HPLC-UV	1–500	0.4	4.4–7.7	Represented method

[a] Linear range.
[b] Limit of detection for S/N = 3.
[c] Relative standard deviation.
[d] High-performance thin layer chromatography.
[e] ng zone^{-1}.

found to be 12.3 ng mL^{-1}. This sample was spiked with AT standard (C_{added} = 10.0 ng mL^{-1}) to assess the matrix effects. LLLME is a non-exhaustive extraction procedure and the relative recovery (determined as the ratio of concentrations found in real sample and reagent water sample, spiked with the same amount of analyte), instead of the absolute recovery (used in exhaustive extraction procedures), was employed. The relative recovery value of 91% (C_{found} = 21.4 ng mL^{-1} with RSD% = 7.2, n = 6) was achieved, which indicated that the real matrix in our present context had little effects on the LLLME. Fig. 6 shows the HPLC-UV chromatograms at 0 and 2 h after administration, and also the spiked sample. The obtained chromatograms reveal that in spite of the complex matrix of the sample, due to the high sample clean up performance, almost no other components than the target analyte were recovered in the acceptor solution.

4. Conclusion

The results from this work show that the LLLME technique in combination with HPLC-UV is a valid means of enrichment and quantification of AT at trace level in human plasma. The established protocol demonstrates good sample clean up with high sensitivity and reproducibility. Moreover, the entire analytical process presents an economical and rapid way for the screening purpose. Simplicity of operation and significant increase in acceptor phase volume (which causes major enhancement in the extraction recovery), are the important advantages of the method over conventional droplet based LLLME. Excellent extraction efficiency is achieved almost independent of the matrix in the actual application. Putting all the benefits together, it possesses great potential to be employed in bio-analytical and pharmacokinetic studies.

Acknowledgements

This work has been supported by grants from the University of Tehran Research Council, which is hereby gratefully acknowledged. Also, the research center of Darou-Pakhsh pharmaceutical company is appreciated for supplying plasma samples.

References

[1] L. Xu, H.K. Lee, J. Chromatogr. A 1192 (2008) 203.
[2] S. Ulrich, J. Chromatogr. A 902 (2000) 167.
[3] M.B. Melwanki, M.-R. Fuh, J. Chromatogr. A 1198–1199 (2008) 1.
[4] K.B. Borges, E.F. Freire, I. Martins, M.E.P.B.D. Siqueira, Talanta 78 (2009) 233.
[5] Y.M. Park, H. Pyo, S.J. Park, S.K. Park, Anal. Chim. Acta 548 (2005) 109.
[6] A.L. Saber, Talanta 78 (2009) 295.
[7] C.-E. Bānos, M. Silva, Talanta 77 (2009) 1597.
[8] C.L. Arthur, J. Pawliszyn, Anal. Chem. 62 (1990) 2145.
[9] J. Pawliszyn, Solid Phase Microextraction: Theory and Practice, Wiley-VCH Inc., New York, 1997.
[10] J. Pawliszyn, Applications of Solid Phase Microextraction, Royal Society of Chemistry, UK, 1999.
[11] H. Liu, P.K. Dasgupta, Anal. Chem. 68 (1996) 1817.
[12] F.F. Cantwell, M.A. Jeannot, Anal. Chem. 68 (1996) 2236.
[13] Y. He, H.K. Lee, Anal. Chem. 69 (1997) 4634.
[14] L. Xu, C. Basheer, H.K. Lee, J. Chromatogr. A 1152 (2007) 184.
[15] L.-W. Chung, M.-R. Lee, Talanta 76 (2008) 154.
[16] Y. Wu, L. Xia, R. Chen, B. Hu, Talanta 74 (2008) 480.
[17] K. Reddy-Noone, A. Jain, K.K. Verma, Talanta 73 (2007) 684.
[18] A.L. Theis, J.W. Waldack, S.M. Hansen, M.A. Jeannot, Anal. Chem. 73 (2001) 5651.
[19] L. Zhao, H.K. Lee, Anal. Chem. 74 (2002) 2486.
[20] M.H. Ma, F.F. Cantwell, Anal. Chem. 70 (1998) 3912.
[21] M.H. Ma, F.F. Cantwell, Anal. Chem. 71 (1999) 388.
[23] T.G. Halvorsen, S. Pedersen-Bjergaard, K.E. Rasmussen, J. Chromatogr. B 760 (2001) 219.
[24] M.B. Melwanki, S.-D. Huanga, M.-R. Fuh, Talanta 72 (2007) 373.
[25] S. Pedersen-Bjergaard, K.E. Rasmussen, J. Chromatogr. A 1184 (2008) 132.
[26] Z. Fan, X. Liu, J. Chromatogr. A 1180 (2008) 187.
[27] J. Lee, H.K. Lee, K.E. Rasmussen, S. Pedersen-Bjergaard, Anal. Chim. Acta 624 (2008) 253.
[28] H. Bagheri, F. Khalilian, E. Babanezhad, A. Es-haghi, M.-R. Rouini, Anal. Chim. Acta 610 (2008) 211.
[29] H. Ebrahimzadeh, Y. Yamini, A. Gholizade, A. Sedighi, S. Kasraee, Anal. Chim. Acta 626 (2008) 193.
[30] A. Sarafraz-Yazdi, F. Mofazzeli, Z. Es'haghi, Chromatographia 67 (2008) 49.
[31] D.M. Black, R.G. Bakker-Arkema, J.W. Nawrocki, Arch. Intern. Med. 158 (1998) 577.
[32] G.C. Ness, C.M. Chambers, D. Lopez, J. Lipid Res. 39 (1998) 75.
[33] A.M. Turner, N.I. Jowett, Nurs. Times 102 (2006) 25.
[34] Y. Kodama, Y. Kitta, T. Nakamura, H. Takano, K. Umetani, D. Fujioka, Y. Saito, K. Kawabata, J. Obata, A. Mende, T. Kobayashi, K. Kugiyama, JACC 48 (2006) 43.
[35] X. Cheng, Y.H. Liao, J. Zhang, B. Li, H. Ge, J. Yuan, M. Wang, B. Lu, Y. Liu, Y. Cheng, Eur. J. Heart Fail. 7 (2005) 1099.
[36] P.S. Sever, N.R. Poulter, B. Dahlöf, H. Wedel, AJC 96 (2005) 39.
[37] C. Newman, J. Tsai, M. Szarek, D. Luo, E. Gibson, AJC 97 (2006) 61.
[38] D. Tousoulis, C. Antoniades, V. Katsi, E. Bosinakou, M. Kotsopoulou, C. Tsioufis, C. Stefanadis, Int. J. Cardiol. 109 (2006) 48.
[39] R.G. Bakker-Arkema, M.H. Davidson, R.J. Goldstein, R.J. Isaacsohn, S.L. Davignon, S.R. Weiss, L.M. Keilson, W.V. Brown, V.T. Miller, L.J. Shurzinske, J. Am. Med. Assoc. 275 (1996) 128.
[40] J.W. Nawrocki, S.R. Weiss, M.H. Davidson, D.L. Sprecher, S.L. Schwartz, P.-J. Lupien, P.H. Jones, H.E. Haber, D.M. Black, Arterioscler. Thromb. Vasc. Biol. 15 (1995) 678.
[41] Y.Y. Shum, H. Huang, G.A. Walter, A.E. Black, C.S. Sekerke, R. Homan, R.S. Newton, G.S. Nordblom, D.S. Wright, T. Chang, L.R. Whitfield, Pharm. Res. 10 (Suppl.) (1993) S415 (abstract PPDM 8467).
[42] R. Hayes, D. Minser, J.A. Jersey, B.E. Lilley, Pharm. Res. 13 (Suppl.) (1996) S47 (Abstract APQ 1180).
[43] W.W. Bullen, R.A. Miller, R.N. Hayes, J. Am. Soc. Mass Spectrom. 10 (1999) 55.
[44] M. Jemal, Z. Ouyang, B.C. Chen, D. Teitz, Rapid Commun. Mass Spectrom. 13 (11) (1999) 1003.
[45] G. Bahrami, B. Mohammadi, A. Mirzaeei, A. Kiani, J. Chromatogr. B 826 (2005) 41.
[46] R.V.S. Nigori, V.N. Kandikere, M. Shukla, K. Mudigonda, S. Maurya, R. Boosi, Y. Anjaneyulu, Biomed. Chromatogr. 20 (2006) 924.
[47] M. Hermann, H. Christensen, J.L.E. Reubsaet, Anal. Bioanal. Chem. 382 (2005) 1242.
[48] C.K. Van Pelt, T.N. Corso, G.A. Schultz, S. Lowes, J. Henion, Anal. Chem. 73 (2001) 582.
[49] G. Prokupkova, K. Holadova, J. Poustka, J. Hajslova, Anal. Chim. Acta 457 (2002) 211.
[50] A.C. Moffat, Clarke's Analysis of Drugs and Poisons in Pharmaceuticals, Body Fluids and Post Mortem Material, 3rd edition, 2004, London.
[51] X. Jiang, S. Yin Oh, H.K. Lee, Anal. Chem. 77 (2005) 1689.
[52] K.E. Rasmussen, S. Pedersen-Bjergaard, Trends Anal. Chem. 23 (2004) 1.
[53] Y. He, Y.J. Kang, J. Chromatogr. A 1133 (2006) 35.
[54] A. Sarafraz-Yazdi, D. Beiknejad, Z. Es'haghi, Chromatographia 62 (2005) 49.
[55] L. Hou, H.K. Lee, Anal. Chem. 75 (2003) 2784.
[56] E. Martendal, D. Budziak, E. Carasek, J. Chromatogr. A 1148 (2007) 131.
[57] A. Penalver, E. Pocurull, F. Borrull, R.M. Marce, J. Chromatogr. A 872 (2000) 191.
[58] M.N. Sarrion, J.F. Santos, M.T. Galceran, J. Chromatogr. A 947 (2002) 155.
[59] Z. Zhang, M. Yang, J. Pawliszyn, Anal. Chem. 66 (1994) 844.
[60] S. Shariati, Y. Yamini, M. Darabi, M. Amini, J. Chromatogr. B 855 (2007) 228.
[61] E. Psillakis, N. Kalogerakis, J. Chromatogr. A 907 (2001) 211.
[62] F.J.P. Pereira, C. Bendicho, N. Kalogerakis, E. Psillakis, Talanta 74 (2007) 47.
[63] A. Jamshidi, A.R. Nateghi, Chromatographia 65 (2007) 763.

Talanta 80 (2009) 1007–1011

Contents lists available at ScienceDirect

Talanta

journal homepage: www.elsevier.com/locate/talanta

Amperometric detection of dopamine based on tyrosinase–SWNTs–Ppy composite electrode

Kyoungseon Min, Young Je Yoo*

School of Chemical and Biological Engineering, Seoul National University, Seoul 151-744, Republic of Korea

ARTICLE INFO

Article history:
Received 31 July 2009
Accepted 24 August 2009
Available online 29 August 2009

Keywords:
3-Dimensional composite electrode
Tyrosinase
Chemically polymerized polypyrrole
Single wall carbon nanotube
Dopamine sensor
Ascorbic acid

ABSTRACT

A novel 3-dimensional single wall carbon nanotubes (SWNTs)–polypyrrole (Ppy) composite was prepared as an electrode by chemically polymerizing polypyrrole onto SWNTs using a $LiClO_4$ oxidant. This composite electrode was characterized by scanning electron microscopy (SEM) and cyclic voltammetry with 1 mM $[Fe(CN)_6]^{-3}/[Fe(CN)_6]^{-4}$. The SWNTs were thickly coated with chemically polymerized polypyrrole and the composite had many surface pores and crevices which could enhance mass transfer. The SWNTs–Ppy composite electrode showed a large specific surface area (30 m^2/g) and a good reproducible current response, at about 100 times the peak current of a glassy carbon electrode (GCE). The diffusion coefficient was calculated to be 4.81×10^{-6} cm^2/s. As a biosensor application, tyrosinase was immobilized on the functionalized SWNTs and tyrosinase–SWNTs–Ppy composite was prepared in the same manner. This tyrosinase–SWNT–Ppy composite electrode was used for amperometric detection of dopamine in the presence of ascorbic acid and showed high sensitivity (467 mA/M cm^2) and lower detection limit (5 μM) compared to previous reports.

© 2009 Elsevier B.V. All rights reserved.

1. Introduction

Recently, the combination of nanoscale materials and biomolecules has been of great interest in the field of biotechnology, especially in bioelectronics [1–4]. Among several currently available nanoscale materials such as carbon nanotubes (CNTs), nanoporous silica, and gold nanodots, CNTs have drawn the highest interest since their discovery by Iijima in 1991 because of their extraordinary physical properties [5]. CNTs have been used as nanoscale conductors, catalyst carriers, and electrode materials [6–8]. In electrochemistry, CNTs have been widely used as a modified material in the preparation of electrodes because CNTs have advantages such as a large surface area, a good electrical conductivity, and easy surface functionalization that can enhance the performance of the electrodes. In previous studies, carbon nanotube modified electrodes (CNT-MEs) have been prepared by (1) filling a bare electrode with a mixture of the CNTs and mineral oil, (2) embedding or mixing carbon nanotubes into a graphite or a glassy carbon electrode and (3) coating directly onto the electrode surface [9–11]. However, the previous CNT-MEs have made a limited use of the advantages of CNTs, the large specific surface area and the good electrical conductivity. In the case of the CNT-MEs constructed by embedding or coating of the substrate electrode, which have a small, specific surface area, the large surface area of CNTs could not be used to the full effect. Also, chemical functionalization, such as an acidic treatment for the immobilization of proteins, can affect defeat sites, which are the broken parts of the bond network, and consequently affect the electrical properties of the CNT-MEs. In this paper, a single walled carbon nanotubes (SWNTs)–polypyrrole (Ppy) composite electrode was prepared to make the best use of the large surface area and the good electrical conductivity of CNTs. Although substrate such as glassy carbon electrodes or metal which can play a role as a current collector in the composite electrodes have been required in previous methods, a SWNTs–Ppy composite can be applied to the electrode itself without any substrate. For the electrode preparation, the conducting polymer polypyrrole was electrically polymerized as a thin film on the surface of the substrate electrode in general. However in this research, polypyrrole was chemically polymerized using $LiClO_4$ as an oxidant that played the role of a cross-linker for connecting the SWNTs and forming the thick 3-dimensional SWNT–Ppy composite, not an electrically deposited thin film.

Tyrosinase (E.C.1.14.18.1) is a multifunctional copper containing oxidoreductase widely distributed in nature. Tyrosinase has two catalytic activities in the presence of oxygen; hydroxylation of monophenols by a cresolase activity and oxidation of diphenols to quinine by a catecholase activity. Tyrosinase has a broad substrate specificity for various phenolic compounds such as phenol, catechol, cresol, dopamine and ephinephirine, which can be

* Corresponding author. Tel.: +82 2 880 7411; fax: +82 2 887 1659.
E-mail address: yjyoo@snu.ac.kr (Y.J. Yoo).

0039-9140/$ – see front matter © 2009 Elsevier B.V. All rights reserved.
doi:10.1016/j.talanta.2009.08.032

applied for the determination of phenolic compounds in food, environment and clinical diagnosis [12–14]. Dopamine, which can be a substrate of tyrosinase, is one of the most important neurotransmitter which affects the brain function. Deficiency of dopamine in the brain tissue causes Parkinson's disease, a neurological disorder which many elderly people have suffered from. Development of a tool for dopamine measurement in tissues can make a great contribution to diagnose Parkinson's disease. An electrochemical method has been widely used as a direct measurement for dopamine and has several advantages such as a small dimension, an easy operation, a fast response, and a high accuracy. However, the major problem of the electrochemical detection of dopamine in a real tissue is the co-existence of many interfering compounds. Among the interfering compounds, ascorbic acid is particularly important because both ascorbic acid and dopamine can be oxidized at similar potentials and these results in an overlap of the voltammetric response [15–17]. Therefore it is important to develop a method for the selective determination of dopamine with a high sensitivity and a low detection limit. For the biosensor application, tyrosinase was immobilized on the functionalized SWNTs and the prepared tyrosinase–SWNTs–Ppy composite was tested for determination of dopamine in the presence of ascorbic acid.

The goals of this study were (1) the characterization and the calibration of a 3-dimensional SWNTs–Ppy composite as an electrode and (2) the applications of the tyrosinase-immobilized SWNTs–Ppy composite to detect dopamine selectively in the presence of ascorbic acid.

2. Material and methods

2.1. Materials

SWNTs were purchased from IlJin NanoTech (Seoul, Korea). Tyrosinase (E.C. 1.14.18.1), monomer pyrrole, $LiClO_4$, $K_3Fe(CN)_6$, $K_4Fe(CN)_6$ and all other reagents were obtained from Sigma–Aldrich at the highest grade available and were used without a further purification.

2.2. Apparatus

Electrochemical measurements were performed with an AUTOLAB potentiostat at ambient temperature with a conventional 3-electrode system: working electrode, the SWNT–Ppy composite; counter electrode, coiled Pt wire; reference electrode, Ag/AgCl. Scanning electron microscope images were photographed out using a JEOL JSM-5210 to characterize the SWNT–Ppy composite electrode.

2.3. Tyrosinase immobilization

Before immobilization, 1 mg SWNTs were functionalized by 1.5 ml 1-pyrenebutyric acid (0.1 M in dimethylformaldehyde) for non-covalently introducing carboxyl groups on the surface, shaking at 200 rpm for 1 h. After washing the functionalized SWNTs with methanol and distilled water, respectively, tyrosinase was covalently attached onto the functionalized SWNTs by 100 mM EDC (1-ethyl-3-(3-dimethylaminopropyl)carbodiimide), in 50 mM phosphate buffer (pH 6.5),with an activation time of 30 min [18].

2.4. Preparation of 3D SWNTs–Ppy composite electrodes

The SWNTs–Ppy composite was prepared by chemical polymerization of monomer pyrrole by mixing the monomer pyrrole and 0.1 M $LiClO_4$ in a phosphate buffer (50 mM, pH 6.5) in a 2:1 volume ratio. SWNTs with/without tyrosinase were added rapidly to the mixture, which was then cast in an electrode holder and hardened overnight at the ambient temperature.

3. Results and discussion

3.1. Characterization of the composite electrode

3.1.1. SEM of the SWNTs–Ppy composite

Fig. 1 shows the SEM images of the SWNTs–Ppy composite electrode. As shown in Fig. 1(a), the SWNT was thickly coated by chemically polymerized polypyrrole. The SWNTs–Ppy composite had many pores on the surface which could prevent mass

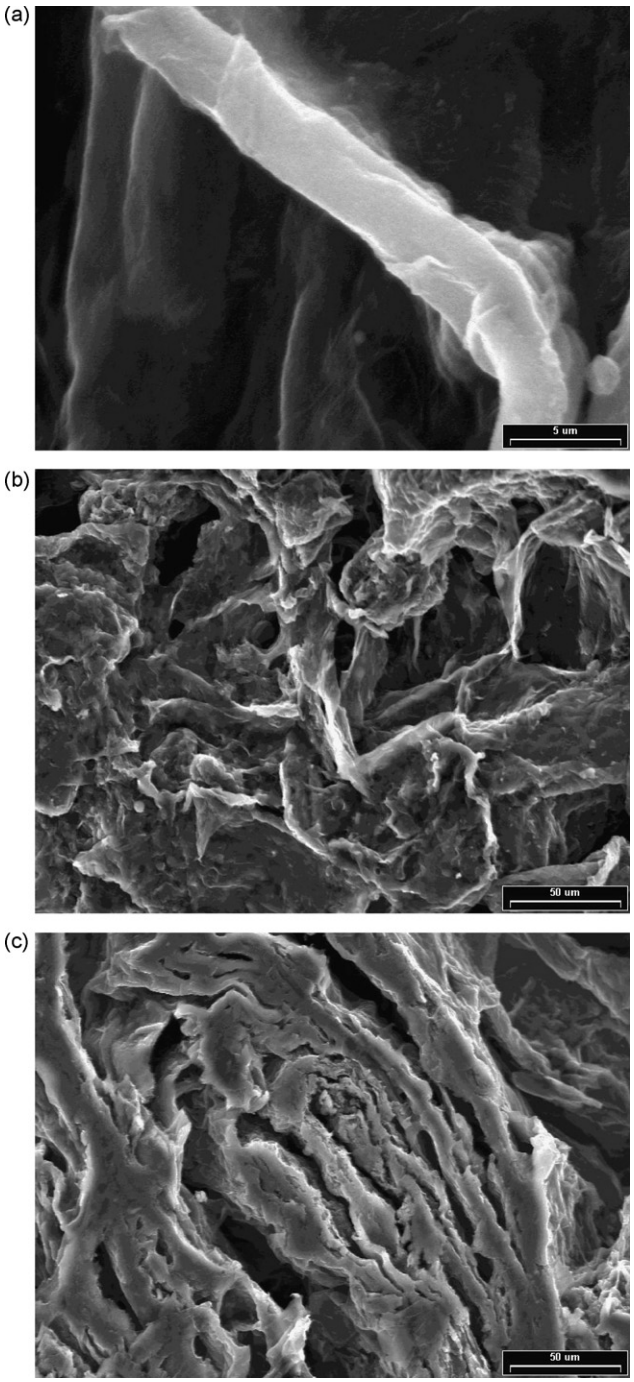


Fig. 1. SEM image of SWNT–Ppy composite (a) Ppy coated SWNT, (b) surface of SWNT–Ppy composite and (c) cross-section image of SWNT–Ppy composite.

transfer limitation as shown in Fig. 1(b). Fig. 1(c) reveals that the SWNTs–Ppy composite electrode had several layers and many crevices in the cross-section, which could also reduce mass transfer limitation. The composite surface was non-uniform and had some partially excessive polymerized surface. To prevent the excessive polymerization, the ratio of the oxidant $LiClO_4$ and monomer pyrrole was optimized. As a result, the excessive polymerization was minimized by using a 2:1 ratio mixture of the reactants (v/v, monomer pyrrole to 0.1 M $LiClO_4$) and 10 μl of the mixture was enough to produce 1 mg SWNT.

3.1.2. Cyclic voltammogram of the SWNTs–Ppy composite

Fig. 2 shows the cyclic voltammograms for a glassy carbon electrode(GCE) and the SWNTs–Ppy composite in 0.1 M $[Fe(CN)_6]^{-3}/[Fe(CN)_6]^{-4}$ solution in 10% H_2SO_4 (v/v%) with a scanning rate of 20 mV/s. From Fig. 2, the current response of the SWNTs–Ppy composite electrode was about 100 times larger than that of the GCE under the same testing conditions. As shown in Table 1, compared to other papers previously reported, the current response of the SWNTs–Ppy composite electrode was higher although the system was in low $K_3Fe(CN)_6$ concentration and with a slow scan rate. The difference between the GCE and SWNTs–Ppy composite also indicated that the SWNTs–Ppy composite had a larger capacitance than the GCE. This enhanced that the current response could be attributed to the much larger specific surface area of the composite (30 m^2/g, from BET result, data not shown) effectively increasing the electron transfer and consequently increasing the current response. The large specific surface area of the SWNTs–Ppy composite provides a high probability of contacts between electrons and the electrode surface and causes the increase in the current response, consequently. The larger current response of SWNTs–Ppy composite electrode was also the result of the increased numbers of defeat sites on the electrode surface.

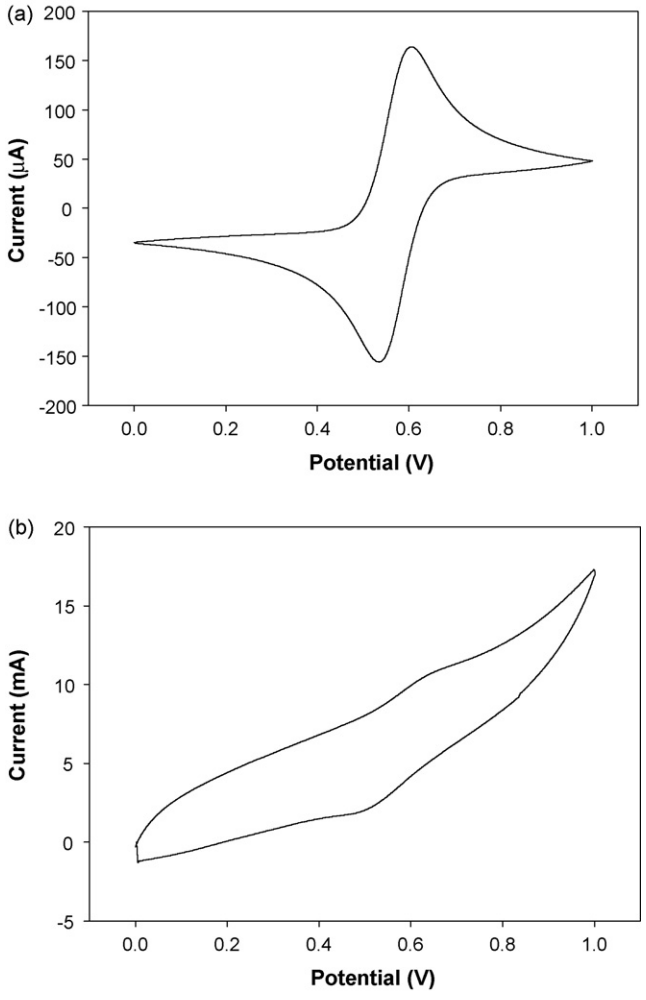


Fig. 2. Cyclic voltammogram of (a) glassy carbon electrode and (b) SWNT–Ppy composite with 0.1 M $[Fe(CN)_6]^{-3}/[Fe(CN)_6]^{-4}$ solution in 10% H_2SO_4 (v/v%) with a scanning rate 20 mV/s.

Table 1
Current responses for the different carbon based composite.

Electrode	I_p (A)	Ref.
Carbon–castor oil polyurethane composite	5.0×10^{-5} [a]	[23]
Carbon nanotube–epoxy composite	1.6×10^{-3} [b]	[24]
Graphite–silicon rubber composite	7.9×10^{-6} [c]	[25]
Graphite–poly(methylmethacrylate) composite	2.2×10^{-5} [d]	[26]
SWNT–Ppy composite	1.0×10^{-2} [e]	This study

[a] 5 mM $K_3Fe(CN)_6$, scan rate 100 mV/s.
[b] 10 mM $K_3Fe(CN)_6$, scan rate 100 mV/s.
[c] 5 mM $K_3Fe(CN)_6$, scan rate 50 mV/s.
[d] 5 mM $K_3Fe(CN)_6$, scan rate 200 mV/s.
[e] 1 mM $K_3Fe(CN)_6$, scan rate 20 mV/s.

The SWNTs–Ppy composite electrode, which showed the large current response and had the high effective surface area, may contribute to develop a biosensor system with a high sensitivity. Recently, amperometric enzyme-based biosensors have been developed for chemical and biomedical analysis [19–21]. However, the sensitivity of these biosensors is low without a mediator because the active sites of the enzymes are deeply buried and the electron transfer efficiency is not good in the absence of mediator. This SWNTs–Ppy composite with a high current response can be a potential candidate for the development of mediator-less enzyme-based biosensors. This SWNTs–Ppy composite can also provide a large surface, which is for a large amount of enzyme loading and for frequent contacts with electrons generated from the enzyme catalysis, and additionally enhance the current response.

In this study, a 3-dimensional SWNTs–Ppy composite electrode was prepared without a substrate electrode as a current collector. It was unknown whether the prepared 3-dimensional composite electrode could exhibit accuracy without a current collector, so the accuracy of the prepared composite as an electrode was also examined by the $[Fe(CN)_6]^{-3}/[Fe(CN)_6]^{-4}$ pair solution. As shown in Fig. 2, in the case of the GCE, the oxidation peak voltage and the reduction peak voltage were 603 and 535 mV, respectively. In the case of the SWNTs–Ppy composite, the oxidation peak voltage and the reduction peak voltage were 600 and 469 mV, respectively. The difference between the oxidation peak voltage and the reduction peak voltage was small, because the system was reversible. The high regression coefficient of the relationship between the oxidation peak current and the square root of the scanning rate also indicated the accuracy of the prepared SWNTs–Ppy composite electrode. Fig. 3 indicates that the $[Fe(CN)_6]^{-3}/[Fe(CN)_6]^{-4}$ system with the prepared SWNTs–Ppy composite electrode was a reversible system. In fact, the $[Fe(CN)_6]^{-3}/[Fe(CN)_6]^{-4}$ was a reversible oxidation–reduction pair. Consequently, the prepared SWNTs–Ppy composite electrode-incorporated system appeared reliable.

3.1.3. Diffusion coefficient

In the composite electrode, the accessibility of the reactant to the inner part of the electrode has been one of the most important factors. Although the SWNTs–Ppy composite electrode had enough pores and crevices detectable in SEM images to decrease mass transfer limitation, the question remains whether the reactant can actually access the SWNT through the thickly polymerized

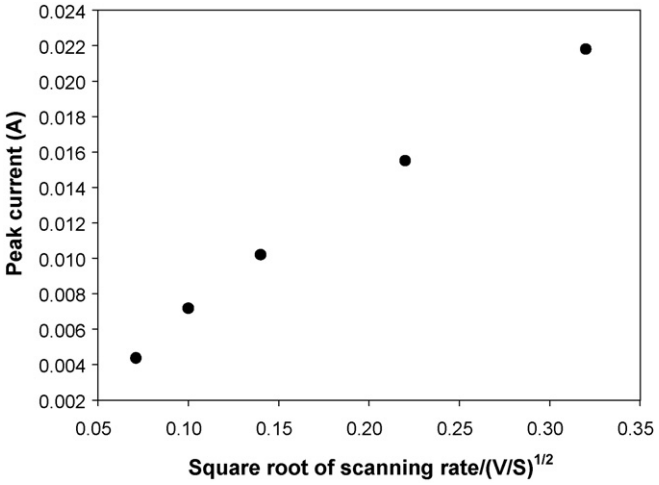


Fig. 3. Relationship between the square root of scanning rates and the peak currents of the SWNT–Ppy composite in the $[Fe(CN)_6]^{-3}/[Fe(CN)_6]^{-4}$ solution.

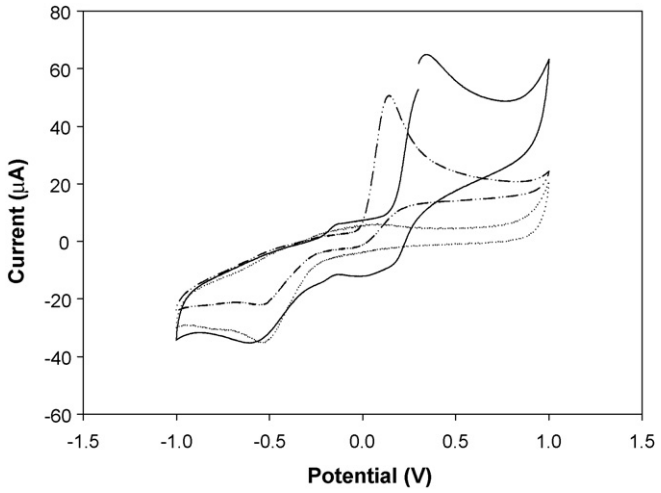


Fig. 4. Cyclic voltammogram of 1 mM dopamine (—), 1 mM ascorbic acid (— - - —), and phosphate buffer (- - - -) using 20 unit free tyrosinase and glassy carbon electrode, scanning rate 50 mV/s.

polypyrrole layer. To validate the accessibility of the reactants to the SWNTs–Ppy composite electrode, the diffusion coefficient was determined from cyclic voltammetry at different scanning rates operating with the $[Fe(CN)_6]^{-3}/[Fe(CN)_6]^{-4}$ solution. The relationship between the oxidation peak current and the square root of the scanning rate was studied as shown in Fig. 3, which yielded a linear relationship with a high regression coefficient ($R^2 = 0.996$). The slope is proportional to the diffusion coefficient of $Fe(CN)_6$ within the SWNT–Ppy composite and the diffusion coefficient was calculated from the following equation, shown in Table 2 [22].

$$I_p = 2.69 \times 10^5 \times n^{3/2} \times S \times C \times V^{1/2} \times D^{1/2} \quad (1)$$

where I_p, peak current (A); n, charge transfer number ($n = 1$); S, surface area of electrode (cm^2); D, diffusion coefficient (cm^2/s); V, scanning rate (V/s).

Based on the diffusion coefficient, we believe that this 3-dimensional composite electrode will solve the problem of mass transfer limitation in enzyme-based biosensors.

3.2. Application for dopamine sensor in the presence of ascorbic acid

3.2.1. Determination of working potential for dopamine detection

Fig. 4 shows the cyclic voltammograms of the 200 mM phosphate buffer (pH 6.5), 1 mM dopamine and 1 mM ascorbic acid with a glassy carbon electrode and 20 unit free tyrosinase at the scan rate 50 mV/s. In the absence of dopamine, there is no peak in the cyclic voltammogram. In the presence of 1 mM dopamine, the cyclic voltammogram had a definite oxidation peak at 346 mV, which was due to the oxidation of the dopamine by the enzyme catalysis on the electrode surface. As shown in Fig. 4, ascorbic acid is also oxidized at 143 mV. Therefore, the potential of 346 mV was determined as a working potential for the amperometric measurement of dopamine.

Table 2
Diffusion coefficients for the different electrodes.

Electrode	Diffusion coefficient (cm^2/s)	Ref.
SWNT–epoxy composite	6.32×10^{-6} [a]	[24]
Polycarbonate membrane	4×10^{-6} [b]	[27]
SWNT–Ppy composite	4.81×10^{-6} [c]	This study

[a] 10 mM $K_3Fe(CN)_6$.
[b] 1 mM $K_3Fe(CN)_6$.
[c] 1 mM $K_3Fe(CN)_6$.

3.2.2. Amperometric response of the tyrosinase–SWNTs–Ppy composite electrode for dopamine detection in the presence of ascorbic acid

Dopamine was detected by the tyrosinase–SWNTs–Ppy composite electrode in 50 mM phosphate buffer (pH 6.5) at a working potential of 346 mV (vs. Ag/AgCl) under constant stirring. The amperometric responses to the addition of various concentration of dopamine are indicated in Fig. 5. A well-defined oxidation current was observed in proportion to the concentration of dopamine. A major problem of the electrochemical detection of dopamine in real tissues is the co-existence of many interfering compounds. Among the interfering compounds, ascorbic acid is particularly important because both ascorbic acid and dopamine can be oxidized at similar potentials and this results in an overlap of the voltammetric responses. As shown in Fig. 5, only ascorbic acid solution with no dopamine did not show any amperometric response although the ascorbic acid concentration (40 μM) was 8 times higher than the initial concentration of dopamine (5 μM). The selective determination of dopamine in the presence of ascorbic acid is feasible

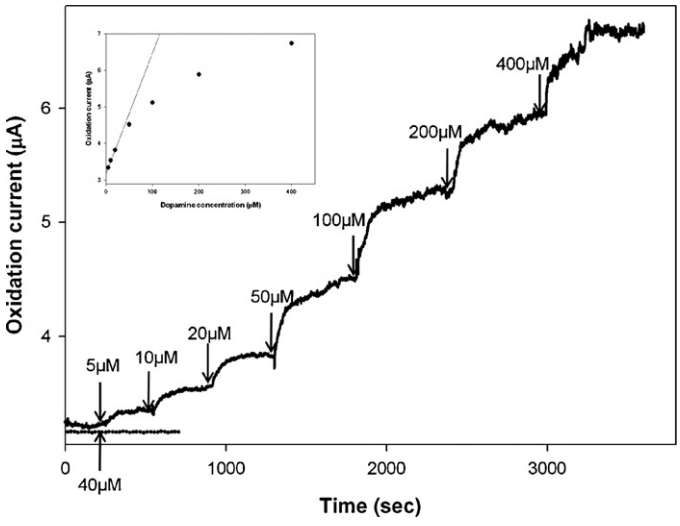


Fig. 5. Amperometric response of the tyrosinase-immobilized carbon nanoparticle polypyrrole composite electrode (- - - - -) ascorbic acid (—) dopamine in an air-saturated blank buffer (50 mM phosphate buffer, pH 6.5) under stirring. Inset: calibration plots of the electrode to dopamine.

Table 3
Performances of the tyrosinase-immobilized dopamine sensors.

Sensitivity (mA/M cm^2)	Linear range (μM)	R^2[a]	Detection limit (μM)	Response time (s)	Reference
1.66	120–360	0.995	39.6	438	[28]
12	5–23	0.998	0.52	<20	[29]
10.6	50–250	0.972	25		[30]
68.6	5–120	0.999		<10	[31]
467	5–50	0.998	5	<5	This study

[a] R represented as correlation coefficients of the linear ranges.

using the tyrosinase–SWNT–Ppy composite electrode. This electrode also shows a rapid response within 5 s when dopamine was added to the system. Inset of Fig. 5 shows the dependence of the steady state current on the concentration of dopamine. Linearity was observed within the range 5–50 μM and the sensitivity corresponding to the linear range for dopamine was 467 mA/M cm^2. The characteristics of the tyrosinase-immobilized electrode for dopamine detection was summarized in Table 3, where the tyrosinase–SWNTs–Ppy composite electrode shows the highest sensitivity and a low detection limit compared with the previously reported tyrosinase-immobilized biosensor for dopamine detection. The tyrosinase–SWNTs–Ppy composite electrode showed a good reproducibility. The relative standard deviation estimated by 5 measurements of 20 μM dopamine at 346 mV (vs. Ag/AgCl) was about 2.5%.

4. Conclusions

The 3-dimensional SWNTs–Ppy composite was prepared with chemically polymerized polypyrrole using $LiClO_4$ as an oxidant without any substrate such as GCE or metal plate. The prepared SWNTs–Ppy composite electrode showed a much larger current response than the GCE, due to the large specific surface area that increased the frequency of contacts between the electrode surface and electrons and enhanced the electron transfer rate. This system has a great potential for applications in the amperometric enzyme-based biosensor for high sensitivity because the amount of enzyme loading could be increased considering the large specific surface area of the SWNTs–Ppy composite leading to a large current response. Considering the diffusion coefficient determined with the $[Fe(CN)_6]^{-3}/[Fe(CN)_6]^{-4}$ solution, mass transfer could not be a problem in the amperometric enzyme-based biosensors. The tyrosinase–SWNTs–Ppy composite was developed for the determination of dopamine. This composite electrode showed a high sensitivity and a low detection limit and could make a contribution to the diagnosis of neurological disorders.

References

[1] P. Wang, Current Opinion in Biotechnology 17 (6) (2006) 574–579.
[2] T. Konno, J. Watanabe, K. Ishihara, Biomacromolecules 5 (2) (2004) 342–347.
[3] S.G. Penn, L. He, M.J. Natan, Current Opinion in Chemical Biology 7 (5) (2003) 609–615.
[4] A. Star, et al., Nano Letters 3 (4) (2003) 459–463.
[5] S. Ijima, Nature 354 (1991) 56–58.
[6] H. Peng, Journal of the American Chemical Society 130 (1) (2008) 42–43.
[7] C.M.L. Philip Kim, Science 286 (1999) 2148–2150.
[8] N.W. Shi Kam, et al., Journal of the American Chemical Society 126 (22) (2004) 6850–6851.
[9] S.H. Chough, A. Mulchandani, P. Mulchandani, W. Chen, J. Wang, K.R. Rogers, Electroanalysis 14 (4) (2002) 273–276.
[10] D.R.S. Jeykumari, S.S. Narayanan, Biosensors and Bioelectronics 23 (11) (2008) 1686–1693.
[11] J. Tkac, T. Ruzgas, Electrochemistry Communications 8 (5) (2006) 899–903.
[12] Z. Liu, et al., Analytica Chimica Acta 533 (1) (2005) 3–9.
[13] S. Wang, et al., Biosensors and Bioelectronics 23 (12) (2008) 1781–1787.
[14] J. Zhao, D. Wu, J. Zhi, Bioelectrochemistry 75 (1) (2009) 44–49.
[15] C. Deng, et al., Biosensors and Bioelectronics 24 (7) (2009) 2091–2094.
[16] J. Chou, et al., Journal of Electroanalytical Chemistry 632 (1–2) (2009) 97–101.
[17] M. Zhang, et al., Biosensors and Bioelectronics 20 (7) (2005) 1270–1276.
[18] W. Huang, et al., Nano Letters 2 (4) (2002) 311–314.
[19] K. Yamamoto, et al., Talanta 66 (5) (2005) 1175–1180.
[20] A.K. Upadhyay, T.-W. Ting, S.-M. Chen, Talanta 79 (1) (2009) 38–45.
[21] K.I. Ozoemena, T. Nyokong, Electrochimica Acta 51 (24) (2006) 5131–5136.
[22] M. Zhou, et al., Electrochemistry Communications 10 (6) (2008) 859–863.
[23] R.K. Mendes, S. Claro-Neto, E.T.G. Cavalheiro, Talanta 57 (5) (2002) 909–917.
[24] M. Pacios, et al., Journal of Electroanalytical Chemistry 619–620 (2008) 117–124.
[25] A.C. de Oliveira, S.X. dos Santos, e.T.G. Cavalheiro, Talanta 74 (4) (2008) 1043–1049.
[26] H. Dai, et al., Electrochemistry Communications 11 (2) (2009) 343–346.
[27] M. Strawski, M. Szklarczyk, Journal of Electroanalytical Chemistry 624 (1–2) (2008) 39–44.
[28] J.P. Herv? P?ez, et al., Biosensors and Bioelectronics 22 (3) (2006) 429–439.
[29] Y.-C. Tsai, C.-C. Chiu, Sensors and Actuators B: Chemical 125 (1) (2007) 10–16.
[30] S. Tembe, et al., Analytica Chimica Acta 612 (2) (2008) 212–217.
[31] Y.L. Zhou, R.H. Tian, J.F. Zhi, Biosensors and Bioelectronics 22 (6) (2007) 822–828.

Talanta 80 (2009) 1012–1015

Contents lists available at ScienceDirect

Talanta

journal homepage: www.elsevier.com/locate/talanta

Short communication

Heat-induced solution mixing in thermo-responsive polymer-coated microchannels for the fluorometric determination of polyamines in saliva

Tohru Saitoh*, Norio Suzuki, Takehiro Furuse, Masataka Hiraide

Department of Molecular Design and Engineering, Graduate School of Engineering, Nagoya University, Furo, Chikusa-ku, Nagoya 464-8603, Japan

ARTICLE INFO

Article history:
Received 25 May 2009
Received in revised form 1 July 2009
Accepted 1 July 2009
Available online 9 July 2009

Keywords:
Microchannel
Fluid manipulation
Thermo-responsive polymer
Weattability
Fluorometric analysis
Polyamines

ABSTRACT

We developed a simple and easy method for solution mixing based on the heat-induced regulation of capillary action in thermo-responsive polymer-coated microchannels. The channels having two T-junctions were fabricated on a glass plate by a sand-blast technique and then coated with a poly(*N*-isopropylacrylamide) film. The polymer-coating was performed by the modification with allyltrimethoxysilane and the subsequent radical polymerization of *N*-isopropylacrylamide and *N*,*N*′-methylenebisacrylamide. When the channel was warmed by a Peltier device, a capillarity-based solution flow completely stopped because of the water-repellency of channel surfaces. On the other hand, the cooling of the channels allowed the restart of the solution flow through hydrophilic channels. Solution mixing downstream a T-junction was readily conducted by a Peltier device that had placed at the junction. The technique was applied to the fluorometric analysis of polyamines in saliva. The saliva sample was mixed with nickel(II) chloride solution at the first junction to mask amino acids and then mixed with *o*-phthalaldehyde solution at the second junction to form the fluorometric derivatives of polyamines. Blue fluorescence was observed downstream the second junction. Linear correlation was obtained between the emission intensity and the spermine concentration in the range of 20–100 μM. No mechanical pump or valve was required for the fluid manipulation.

© 2009 Elsevier B.V. All rights reserved.

1. Introduction

Fluid manipulation has been an important research topic increasing interest in the microfluidic analytical systems. Highly precise micro-pumps or high-voltage power supplies have extensively been used for driving solution flows. Physically driven valves or electric fields have widely been utilized for regulating fluids. Various techniques have been examined and adopted to the fluid manipulation inside microchannels [1–8]. However, these techniques tend to require expensive instruments and delicate operations. Highly precise techniques are also necessary for fabricating channels including micro-valves, ators, or micro-patterns. The development of simple and easy methods for fluid manipulation helps the practical use of microfluidic systems in wide areas.

We have designed a novel fluid control technique based on the heat-induced wettability change on thermo-responsive polymer-coated microchannels [9–11]. The mechanism is explained by the significant decrease of the capillary action inside narrow glass channels coated with poly(*N*-isopropylacrylamide) [PNIPAAm] above the lower critical solution temperature (LCST, ca. 32 °C [12]). The surface of PNIPAAm-coated glass is hydrophilic below LCST, while it turned to be hydrophobic above LCST. Indeed, the water-contact angle was 32° at 30 °C, while it was 68° at 35 °C [9]. Discontinuous air/water flow generated by micro-syringe pumping was switched by warming the branch of PNIPAAm-coated capillary channel [9]. Another example is heat-induced actuation of a water plug inside a PNIPAAm-coated fused silica capillary. When a point of the capillary close to a water plug was warmed, the water plug was moved toward opposite direction of the warmed position [10].

More recently, heat-induced water-repellency was achieved when PNIPAAm-coated frost glass having sub-micrometer levels of surface roughness was used. The contrast of temperature dependent water-contact angles was remarkably extended (24° at 30 °C, while 104° at 35 °C) [11]. Switching of liquid flow downstream a junction of a PNIPAAm-coated microchannel was successfully demonstrated. In the present study, we examined the usefulness of the heat-induced fluid manipulation for a simple method for solution mixing. The applicability of the proposed technique to the fluorometric determination of polyamines in saliva was investigated.

2. Experimental

2.1. Materials and reagents

A microchannel (depth and width; 200 ± 5 μm, surface roughness; R_a = 0.3–0.7 μm) having three reservoirs and two T-

* Corresponding author. Tel.: +81 52 789 3579; fax: +81 52 789 3241.
E-mail address: saitoh@numse.nagoya-u.ac.jp (T. Saitoh).

0039-9140/$ – see front matter © 2009 Elsevier B.V. All rights reserved.
doi:10.1016/j.talanta.2009.07.001

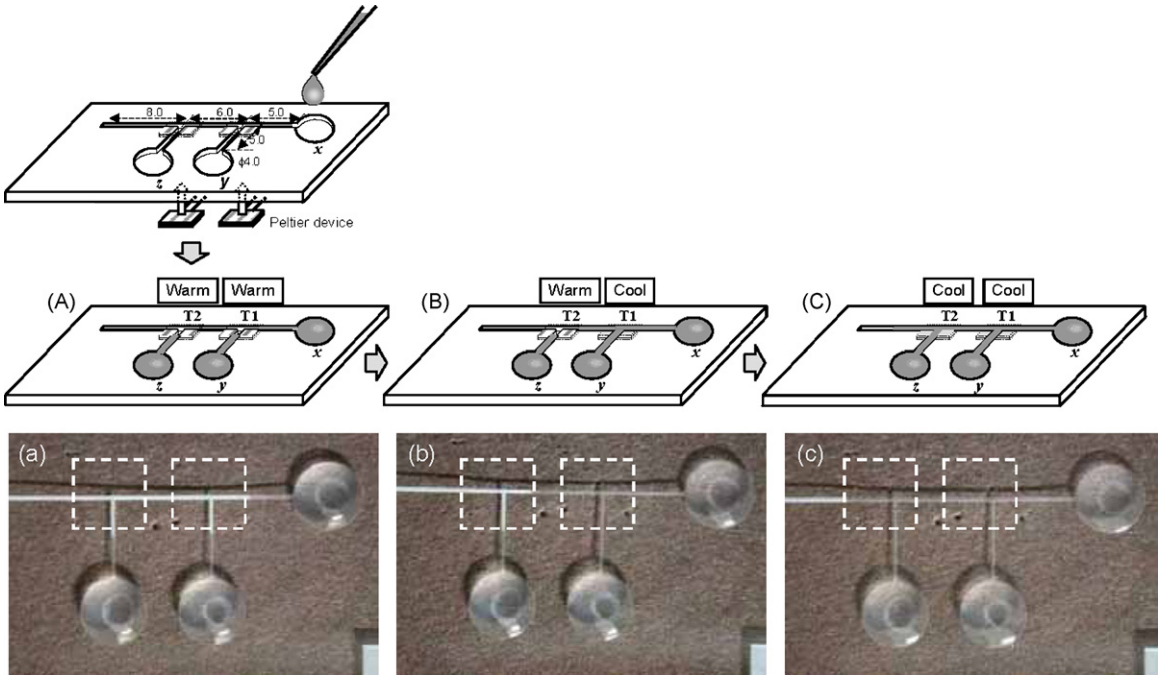


Fig. 1. Features of heat-induced solution mixing on a PNIPAAm-coated microchannel. The reservoirs *x*, *y*, and *z* are for sample solution, nickel (II) chloride solution, and OPA agent solution. Dashed lines in photographs indicate the position of Peltier device.

junctions (Fig. 1) was fabricated on a glass plate (borosilicate, 21 mm × 36 mm, 1.0–1.2 mm thickness, Matsunami Glass, Kishiwada, Japan) by a sand-blast technique (Fuji Manufactory, Tokyo, Japan). The polymer-coating on the surfaces of microchannels was performed by the similar manner to previously reported [11]. It included the modification with allyltriethoxysilane instead of Bind-Silane™ and the subsequent radical polymerization to form a PNIPAAm film. The modification was performed by immersing the microchannel plate in toluene solution of 10% allyltriethoxysilane (Tokyo Chemical Industries, Tokyo, Japan) for 48 h at 25 °C. After washing with ethanol and subsequently with water, the plate was placed into 25 ml of 10 mM phosphate (pH 7) containing 1.7 g *N*-isopropylacrylamide and 0.11 mg methylene bisacrylamide. The solution was precedently passed through a Sep-Pak C_{18} solid-phase extraction cartridge (for environmental analysis, Waters, Milford, MA, USA) for removing polymerization inhibitors. Under nitrogen atmosphere, 0.5 ml aqueous solution of 0.05 g ammonium persulfate and 25 μl of *N*,*N*,*N*′,*N*′-tetramethyethylenediamine were added to start radical polymerization. Four hours later, the plate taken out from the solution was washed with water and then dried by blowing air in a clean bench. The polymer-coating was evaluated from the ATR-IR spectrum (ν_{N-H} 3300 cm^{-1}, ν_{C-H} 2960 cm^{-1}, and $\nu_{C=O}$ 1640 cm^{-1}).

Spermine tetrahydrochloride (for molecular biology) was obtained from Sigma (St. Louis, MO, USA). A 0.5-ml aliquot of methanol [containing 20 mg of *o*-phthalaldehyde (OPA) and 20 μl of 2-mercaptoethanol] was mixed with 4.48 ml of 1 mM borate buffer (pH 9). The solution was 60-fold diluted with the borate buffer to prepare 0.5 mM OPA solution. A 0.5 mM nickel(II) chloride solution was used for masking amino acids.

2.2. Measurement of water-contact angle

The static water-contact angle was measured with a Kyowa Kaimen (Asaka, Japan) CA-D contact angle meter having a thermostatic module. After setting temperature, one drop (10 μl) of water was deposited on a surface of the PNIPAAm-coated glass plate. The water-contact angle was observed microscopically.

2.3. Observation of fluid in microchannels

One drop (ca. 10 μl) each of sample or reagent solution was placed into the respective reservoir of a PNIPAAm-coated microchannel. Two T-junctions were precedently warmed to 37 °C with attaching Peltier devices (Telecom grade thermo-module KSML007, 4.4 mm × 4.4 mm, Komatsu Electronics, Hiratsuka, Japan) below the glass plate of the channel. The electric current and voltage applied to the device were 0.45 A and 0.5 V, respectively. The fluid in the channel was photographed with a Nikon COOLPIX 4500 digital camera (4.0 mega pixels, Tokyo, Japan) to obtain JPEG images. In the fluorometric analysis, the channel plate was illuminated with a UV lamp SLUV-6 (365 nm, 9 W, AS ONE, Osaka, Japan). The experiment was performed in a dark room.

3. Results and discussion

3.1. Water-contact angle of PNIPAAm-coated glass surfaces

Hydrophilic or hydrophobic properties of PNIPAAm-coated glass surfaces were evaluated on the basis of static water-contact angle. As reported previously, the contact angle on the PNIPAAm-coated glass surfaces dramatically changed across the LCST of PNIPAAm [11]. However, the contrast of hydrophilic–hydrophobic property gradually decreased by soaking the PNIPAAm-coated glass plate in weakly alkaline media (pH 9) probably due to the hydrolysis of ester moiety of Bind-Silan™ or 3-(methacryloyloxy)propyltrimethoxysilane. Indeed, the water-contact angle (104°) above the LCST decreased to <90° after soaking the glass plate for 2 h. This problem was solved by using allyltrimethoxysilane having no ester moiety and by adjusting the solution pH to 7 (10 mM phosphate) during radical polymerization. Reversible and reproducible change of hydrophilic–hydrophobic properties on the surfaces was achieved. The water-contact angle was 106 ± 6° at 37 °C, while it was 24 ± 4° at 25 °C (n = 50). They were stable in the aqueous buffer solution of 10 mM of borate (pH 9) at least for 15 min.

3.2. Heat-induced solution mixing in a PNIPAAm-coated microchannel

Solution mixing on a PNIPAAm-coated microchannel was illustrated in Fig. 1. Firstly, both T-junctions (T1 and T2) of the channel were warmed to 37 °C with Peltier devices. Here, Milli-Q water was used instead of sample or reagent solution. Water placed in the respective reservoirs (*x*, *y*, and *z*) flowed through narrow channels and stopped at the edge of Peltier devices (Fig. 1A). The photograph for the situation of Fig. 1A is shown in Fig. 1a. The portion of channel filled with water is blackish, while the unfilled channel is bright due to the light scattering on the frost glass surfaces. A black paper was laid behind the glass plate in order to minimize reflection light. Capillarity-based flow was not further introduced into water-repellent portions of the channels.

When the electric current to the Peltier device at T1-junction was turned off, the solution flow soon restarted. This is ascribable to the rapid recovery of the wettability inside the channels. The solutions from reservoirs *x* and *y* joined at T1-junction and further flowed downstream the junction. Solution mixing was conducted only by the warming and the subsequent cooling of the junction. The position for brief solution stop was important to adjust the meeting of two fluids at the junction. The fluid stopped again at the edge of another Peltier device (Fig. 1B and b). Finally, the electric current to the Peltier devise at T2-junction was turned off. The solution from reservoir *z* joined to that from T1-junction and then further moved downstream T2-junction (Fig. 1C and c). The sequential mixing of fluids was conducted just by turning on and off the electric current to Peltier devices.

The width or depth of channels, orientation of junctions, and conditions of channel walls may affect the mixing ratio and accuracy of solution mixing. These factors would also be available to control flow rate or mixing ratio. For example, Y-junctions seem to be more suitable for the accurate and equi-volume solution mixing. In the present study, T-junctions were adopted because of the easiness in the disposition of Peltier devices and their manipulation.

3.3. Application to polyamine analysis

Aliphatic polyamines such as spermine, spermidine, putrescine, and cadaverine play important roles in DNA, RNA, and protein synthesis as well as in varieties of metabolic systems [13–15]. Therefore, the determination of polyamines is important for evaluating cell growth or cancer progress [16–18]. They can be fluorometrically determined by the *o*-phathaldehyde (OPA) method in the basis of the formation of fluorometric derivatives with OPA in the presence of 2-mercaptoethanol [19]. However, amino acids in saliva also react with OPA to form their fluorescent derivatives and, hence, give positive error to the determination of polyamines. Nickel(II) ions have been found to be a good masking agent for amino acids, because they form stable complexes with amino acids in weakly alkaline conditions [20]. Therefore, the sample solutions have to be mixed with nickel(II) solution before mixing with the OPA solution. The determination was started by depositing one drop (ca. 10 μl) each of sample solution, 0.5 mM nickel(II) chloride solution, and 0.5 mM OPA solution into reservoirs *x*, *y*, and *z*, respectively. The heat-induced solution mixing was conducted as described above. After two-step solution mixing, bright blue fluorescence was observed downstream T2-junction. The intensity became maximum and constant ca. 1 cm downstream the junction, indicating effective diffusion in the narrow channels.

The calibration curves of spermine are shown in Fig. 2, in which the fluorescence intensities are represented by 256-scale intensities of blue, green, and red color elements. The color images downstream T2-junction on the digital photographs were analyzed by the color evaluation method using Adobe Photoshop Elements® [21].

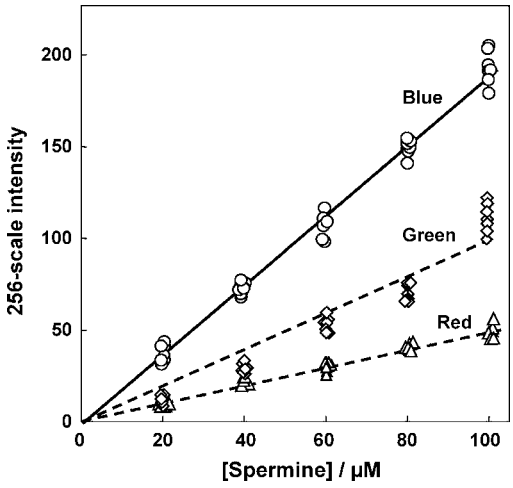


Fig. 2. Calibration curve of spermine based on 256-scale intensities of blue, green, and red color elements.

The angle between camera lens axis and light source axis was optimized to 60° for obtaining reproducible results with minimizing diffuse reflection. The net intensities were calculated by subtracting blank intensities. When blue color was used, linear calibration curves were obtained in the concentration range of 20–100 μM. Standard deviation in the determination of 40 μM spermine was ca. 10%. The determination using green or red color element was less sensitive.

The fluorescence intensities for four major polyamines (spermine, spermidine, putrescine, and cadaverine) reached constant after 1 min of the solution mixing. Venza et al. [19] reported that the fluorescence intensities were dependent on the kind of polyamine and rapidly decreased in the aqueous solution due to the low stability of the OPA derivatives. However, the fluorescence intensities of the derivatives of these polyamines were almost independent of the kind of polyamine and stable for 5 min in the present experimental conditions (ca. 0.25 mM OPA). Therefore, the calibration curve for spermine was used for estimating approximate concentration of total polyamines.

Next, the interference of amino acids was studied, because saliva contains sub-mM levels of total amino acids [22–24]. Table 1 shows the determination of 40 μM spermine in the presence of several amounts of glycine. Negligible interference was observed in the concentration of glycine up to 50 μM. However, the presence of more than 60 μM of glycine gave remarkable positive error. As described below, this problem was solved by diluting samples with a buffer solution.

Sample introduction was performed just by dripping one drop of saliva sample on a reservoir. However, saliva was so viscous for the smooth flow through narrow channels. Additionally, the con-

Table 1
Prevention of interference of an amino acid.

[Spermine] (μM)	[Glycine] (μM)	Intensity of blue color	
		Without masking	With masking
0	0	0	0
	20	215 ± 7	3 ± 2
	50	232 ± 4	4 ± 2
40	0	73 ± 7	72 ± 6
	20	–	71 ± 6
	50	–	72 ± 7
	60	–	142 ± 8
	80	–	171 ± 12

Average of 6 experiments.

Table 2
Time course of polyamine concentration in saliva.

Sampling	[Polyamines][a] (mM)
Wake up	1.1 ± 0.1
After brushing	0.9 ± 0.1
After lunch	2.5 ± 0.2
After brushing	1.1 ± 0.1
Evening	1.2 ± 0.2
Midnight	0.9 ± 0.1

Average of 6 experiments.
[a] Estimated by spermine.

centration of polyamines was remarkably greater than the upper limit of the calibration. Therefore, saliva was precedently 20-fold diluted with 10 mM borate (pH 9). The resulting solution smoothly flowed through microchannels. The dilution was also favorable for the determination of polyamines in the range of the calibration. Furthermore, amino acids were also diluted to lower concentration than the tolerance limit. Small amounts of proteins in saliva negligibly interfered with the determination of polyamines.

Table 2 shows the determination of total polyamines in saliva samples taken at different times. The values are in the range of 0.9–2.5 mM and dependent on time or daily activity. The concentrations of the respective polyamines reported in literatures are in the range from several to hundred μM levels [19,25–27]. The evaluation in the present study seems reasonable. Fairly good reproducibility (ca. 10%) is admirable for such simple method using no mechanical flow control system.

4. Conclusion

A simple method for fluid manipulation in microchannels was developed. Solution mixing was readily conducted just by warming and subsequently cooling at the junctions of the thermo-responsive polymer-coated microchannel with Peltier devices. The method was successfully applied for the quantitative analysis of polyamines with fluorometric detection. Because of the needless of mechanical pumps, high-voltage power supplies, or mechanical valves, the use of the heat-induced solution mixing can significantly simplify the fluid manipulation in microchannels. The application to varieties analytical reaction would be fruitful for designing simple and easy microchannel-based analytical methods.

Acknowledgement

This study was supported by a Grants-in-Aid for Exploratory Research of Japan (16655028).

References

[1] D.J. Beebe, G.A. Mensing, G.M. Walker, Annu. Rev. Biomed. Eng. 4 (2002) 261.
[2] K. Sato, A. Hibara, N. Tokeshi, H. Hisamoto, T. Kitamori, Adv. Drug Deliv. Rev. 55 (2003) 379.
[3] K. Huikko, R. Kostiainen, T. Kotiaho, Eur. J. Pharm. Sci. 20 (2003) 149.
[4] K.W. Oh, C.H. Ahn, J. Micromech. Microeng. 16 (2006) R13.
[5] G.T. Roman, R.T. Kennedy, J. Chromatogr. A 1168 (2007) 170.
[6] C.C. Chang, R.J. Yang, Microfluid. Nanofluid. 3 (2007) 501.
[7] B.D. Iverson, S.V. Garimella, Microfluid. Nanofluid. 5 (2008) 145.
[8] L. Chen, S. Lee, J. Choo, E.K. Lee, J. Micromech. Microeng. 18 (2008) 013001.
[9] T. Saitoh, Y. Suzuki, M. Hiraide, Anal. Sci. 18 (2002) 203.
[10] T. Saitoh, A. Sekino, M. Hiraide, Chem. Lett. 33 (2004) 912.
[11] T. Saitoh, A. Sekino, M. Hiraide, Anal. Chim. Acta 536 (2005) 179.
[12] H.G. Schild, D.A. Tirrell, J. Phys. Chem. 94 (1990) 4352.
[13] C.W. Tabor, H. Tabor, Annu. Rev. Biochem. 53 (1984) 749.
[14] U. Bachrach, Amino Acids 26 (2004) 307.
[15] R. Montañez, F. Sánchez-Jiménez, J.F. Aldana-Montes, M.Á. Medina, Amino Acids 33 (2007) 283.
[16] J.P. Moulinoux, V. Quemener, N.A. Khan, Cell. Mol. Biol. 37 (1991) 773.
[17] M.Y. Khuhawar, G.A. Qureshi, J. Chromatogr. B 764 (2001) 385.
[18] D. Teti, M. Visalli, H. McNair, J. Chromatogr. B 781 (2002) 107.
[19] M. Venza, M. Visalli, D. Cicciu, D. Teti, J. Chromatogr. B 757 (2001) 111.
[20] M. Kai, T. Ogata, K. Haraguchi, Y. Ohkura, J. Chromatogr. 163 (1979) 151.
[21] K.L. Yam, S.E. Papadakis, J. Food Eng. 61 (2004) 137.
[22] G.C. Battiston, G.W. Burnett, Arch. Oral Biol. 3 (1961) 161.
[23] J. Rotgans, R. Wodarz, W. Schoknecht, K. Drysch, Arch. Oral Biol. 28 (1983) 1121.
[24] S.M. Syrjänen, L. Alakuijala, P. Alakuijala, S.O. Markkanen, H. Markkanen, Arch. Oral Biol. 35 (1990) 189.
[25] R. Gopalakrishna, B. Nagarajan, Biochem. Int. 1 (1980) 605.
[26] S. Goldberg, A. Kozlovsky, D. Gordon, I. Gelernter, A. Sintov, M. Rosenberg, J. Dental Res. 73 (1994) 1168.
[27] M. Cooke, N. Leeves, C. White, Arch. Oral Biol. 48 (2003) 323.

Talanta 80 (2009) 1016–1019

Contents lists available at ScienceDirect

Talanta

journal homepage: www.elsevier.com/locate/talanta

Short communication

Analysis of polyhexamethylene biguanide in multipurpose contact lens solutions☆

Anne D. Lucas*, Edward A. Gordon, Melvin E. Stratmeyer

U.S. Food and Drug Administration, Center for Devices and Radiological Health, OSEL/DB, 10903 New Hampshire Ave, Bldg 64 Room 4011, Silver Spring, MD 20993, USA

ARTICLE INFO

Article history:
Received 8 June 2009
Received in revised form 15 July 2009
Accepted 16 July 2009
Available online 23 July 2009

Keywords:
Contact lens
Polyhexamethylene biguanide
Liquid chromatography

ABSTRACT

The objective of this study was to establish a reasonably simple and reliable method to measure very low concentrations of polyhexamethylene biguanide (PHMB) in multipurpose contact lens solutions (MPSs). By using a weak cation exchange solid phase extraction cartridge to extract the PHMB from MPS, followed by HPLC analysis using an evaporative light scattering detector, low levels (0.1 ppm) of PHMB were detected. Application of this method to a series of off-the-shelf MPS with PHMB as the active ingredient demonstrated these solutions contain 1 ppm. The contact lens solution with hydrogen peroxide as the active ingredient gave no peak where the PHMB peak eluted. The Polyquad® contact lens solution generated a peak close to the retention time of PHMB. Recovery of PHMB from fortified hydrogen peroxide contact lens solution was good at 0.25 ppm and above; 105% with a RSD of 17% or less. The repeatability of the HPLC system ranged from 4 to 11% RSD; the reproducibility of the entire method was less than 17.5% RSD. Storage and stability studies indicated that storage of MPS with PHMB for chemical analysis are not temperature dependent, but are affected by the composition of the container in which the contact lens solution is stored.

Published by Elsevier B.V.

1. Introduction

PHMB[1] (polyhexamethylene biguanide) is a chemical germicide used in a variety of applications: as a preservative in wet wipe, to prevent microbial contamination in wound irrigation and sterile dressings, and to disinfect medical/dental utensils and trays. PHMB is also used as an active ingredient for recreational water treatment, in cosmetics, personal care products, fabric softeners, contact lens solutions, and hand washes [1]. This widely used biocide has been reviewed by EPA and noted, with the exception of occupational handlers, as having very low aggregate risk of adverse health effects to the public or environment [2].

This compound is a challenge to quantitate at low levels because it is a mixture of polymers with no distinctive chromophores [3] and is a polyelectrolyte with a mix of end groups [4]. Dye-binding assays [5–7] have limits of detection around 5 ppm and greater; the concentration of PHMB in some contact lens solutions is 1 ppm. High pressure liquid chromatographic (HPLC) using photodiode array detectors also are not sensitive enough because UV absorption of PHMB is too weak [7–9]. The mix of different end groups of the PHMB polymer prevents the possibility of quantitative derivitization. A capillary electrophoresis (CE) method [10] for determination of PHMB in eye drops was described with a limit of detection of 4 ppm. Other means of PHMB analysis include titrimetric methods [11] that do not have adequate levels of sensitivity or potentiometric titration methods that involve custom synthesis [12]. There appears to be no established method for measuring PHMB in contact lens solution or at sub-ppm levels.

In this paper, a method to reliably measure PHMB at sub-ppm levels in MPS[2] (multipurpose contact lens solution) is detailed. This was accomplished by developing a solid phase extraction method followed by HPLC analysis using an evaporative light scattering detector.

2. Materials and methods

2.1. Reagents and solutions

Several commercially available brands of MPS were purchased from local stores; six different brands contained PHMB as the active ingredient, two contained hydrogen peroxide, and the last one contained Polyquad® as the chemical disinfectant. Methanol and acetonitrile were obtained from Fisher Scientific (Waltham, MA, USA), and triethylamine (TEA), trifluoroacetic acid (TFA), and formic acid (FA) were from Sigma–Aldrich (St. Louis, MO, USA). Deionized water was produced with a Barnstead NANOpure Diamond water

☆ The mention of commercial products, their sources, or their use in connection with material reported herein is not to be construed as either an actual or implied endorsement of such products by the Department of Health and Human Services.

* Corresponding author. Tel.: +1 301 796 0283; fax: +1 301 796 9826.
E-mail address: anne.lucas@fda.hhs.gov (A.D. Lucas).

[1] Polyhexamethylene biguanide.

[2] Multipurpose contact lens solution.

0039-9140/$ – see front matter. Published by Elsevier B.V.
doi:10.1016/j.talanta.2009.07.031

purification unit. The PHMB, trade name Cosmocil CQ (a 20% solution in water), was graciously donated by Arch Chemical Company (Norwalk, CT, USA).

2.2. HPLC method

Samples were analyzed using a Waters HPLC system, equipped with 515 pumps, a 717 plus autoinjector, a 996 photodiode array detector and an evaporative light scattering detector (PL-ELS2100, Polymer Laboratories) with Waters Empower chromatographic software. Settings for the evaporative light scattering detector were: evaporator 111 °C, nebulizer 80 °C, zero-grade nitrogen at 1.6 SLM (standard liters per minute). The photodiode array detector was set at 254 nm, but was not used for quantitation. Separation was performed on a Supelco Supelcosil™ LC-8 column (5 cm × 4.6 mm, 5 μm). The mobile phase component was 100% deionized water held isocratically for 4 min, then an immediate change to 50:50 water: a solution composed of acetonitrile (76%), water (9.5%), triethylamine (5%), and formic acid (9.5%), pH adjusted to 3.1 with formic acid for the next 2 min, then a linear gradient back to 100% water at 10 min. The flow rate was 2 ml/min and the injection volume was 0.25 ml.

2.3. Extraction of contact lens solutions

Extraction and concentration of PHMB from MPS were performed with weak cation exchange solid phase extraction cartridge from Waters (WCX Oasis 1 cc, 30 mg). Cartridges were first pre-washed with two column volumes of 50:50 acetonitrile:distilled deionized water with 0.25% TFA, then two column volumes of acetonitrile, followed by two column volumes of distilled deionized water. Five ml of sample were then loaded onto the cartridge followed by washing with two column volumes of water, then with 0.5 ml of 50:50 acetonitrile:water with 0.02% TFA. PHMB was eluted with 0.5 ml of 50:50 water:acetonitrile with 0.25% TFA directly into 8 mm × 40 mm HPLC vials. Injection volume for the HPLC was usually 0.25 ml. HPLC vials were pre-washed with 50:50 water:acetonitrile with 0.25% TFA, then acetonitrile and left to air dry prior to use.

2.4. Storage stability studies

MPS brand A was used to examine the storage and stability of PHMB at three different temperatures (25 °C, 4 °C, and −20 °C). Using aseptic technique, approximately 20 ml of the MPS was placed in each of 12 separate 50 ml polypropylene test tubes. Four of these test tubes were left at room temperature (25 °C); four were placed in the refrigerator (4 °C), and four in a standard freezer (−20 °C). Over time, one test tube from each different temperature locale was removed and triplicate aliquots of 5 ml were extracted as previously described. In addition, the stability of PHMB in glass vials compared to polypropylene test tubes was examined by aseptically placing 20 ml of MPS brand A in glass or polypropylene containers and leaving them overnight at room temperature. The following day, triplicate extracts of the MPS brand A stored in glass vials was compared to triplicate extracts stored in polypropylene test tubes.

3. Results and discussion

3.1. Evaluation of dye binding methods

Initially, the colorimetric methods were explored because of the potential for high throughput and low cost. The method described by Rowhani and Lagalante [7] was tested first. However, the absorbance from a MPS with PHMB was roughly 100 times higher than the PHMB standard concentration. Other compounds in the MPS were probably exerting a large positive influence in this assay. The second colorimetric assay evaluated was detailed by Rosenthal et al. [5]. Again, the MPS overestimated the amount of PHMB, but only by a factor of four. The third colorimetric assay [6] overestimated the PHMB concentration in MPS by a factor of five. In addition, none of these assays were very sensitive; all the colorimetric methods had limits of detection around 5 ppm or greater. Because MPS labels state a concentration of 1 ppm of PHMB, a more sensitive and selective method was needed.

3.2. Solid phase extraction

A series of solid phase extraction cartridges were evaluated in sample extraction. Although PHMB is a cation, an anion exchange column and a lipophilic column were examined to see if they would trap interfering substances while permitting PHMB to pass through. However, significant interfering substances eluted with the PHMB from both the lipophilic and strong anion exchange columns. The weak and strong cation exchange columns were used to trap the PHMB while allowing most interfering substances to elute. Because it was possible to elute PHMB from the weak cation exchange column using less caustic conditions, this was the cartridge chosen. Coupling the solid phase extraction method to the colorimetric assays did not work as the strong acid needed to elute the PHMB occupied the binding sites for the dyes.

3.3. Detector performance

Although the reproducibility of the evaporative light scattering detector (ELSD) has been noted to be worse than UV [13] and the use of a gradient increases the variability of the analyte signal [14], this is a more sensitive detector for compounds without chromophores. The light scattering by the solute after removal of the eluent is measured [13]; detection is dependent on the amount of solute. Fig. 1 illustrates the difference between using an ELS detector (Fig. 1A) and a UV detector (Fig. 1B) in detecting PHMB extracted from contact lens solution brand A. The Refractive Index detector is useful for detecting compounds that do not absorb UV, it is not useful for gradient elution [15]. Attempts to generate a useful ion for mass spectroscopy with electrospray or atmospheric pressure ionization were not fruitful.

3.4. Recovery

MPS contain salts, surfactants, and other additives, as well as the active biocide; although not all brands are identical chemically or in quantity. Because the hydrogen peroxide contact lens solution gave no peak near the retention time of PHMB, it was used in the recovery studies as the best available approximation of a blank MPS. Recovery of hydrogen peroxide MPS fortified with 0, 0.125, 0.25, 0.5, and 1.0 ppm PHMB are depicted in Fig. 2. The recovery was determined from triplicate experiments each with triplicate samples. Recoveries were good, 107%, at the 0.25 ppm level and above (RSD 17% or less), but the error at the 0.125 ppm level was quite large (RSD 66%). The bias towards high recovery at low levels is likely due to intergration errors because of the steep gradient used and the increasing background and error of the detector over time (Section 3.6 Table 1).

3.5. Evaluation of commercially available contact lens solutions

Six different MPSs with PHMB as the active ingredient were purchased at local stores and analyzed. Fig. 3 details the PHMB levels found in these six different MPS with PHMB; the data represent triplicate experiments with each contact lens solution run in triplicate. The PHMB concentration in all the MPS was 1 ppm with RSD of 17.5% or less; this supported the utility of the method. The contact

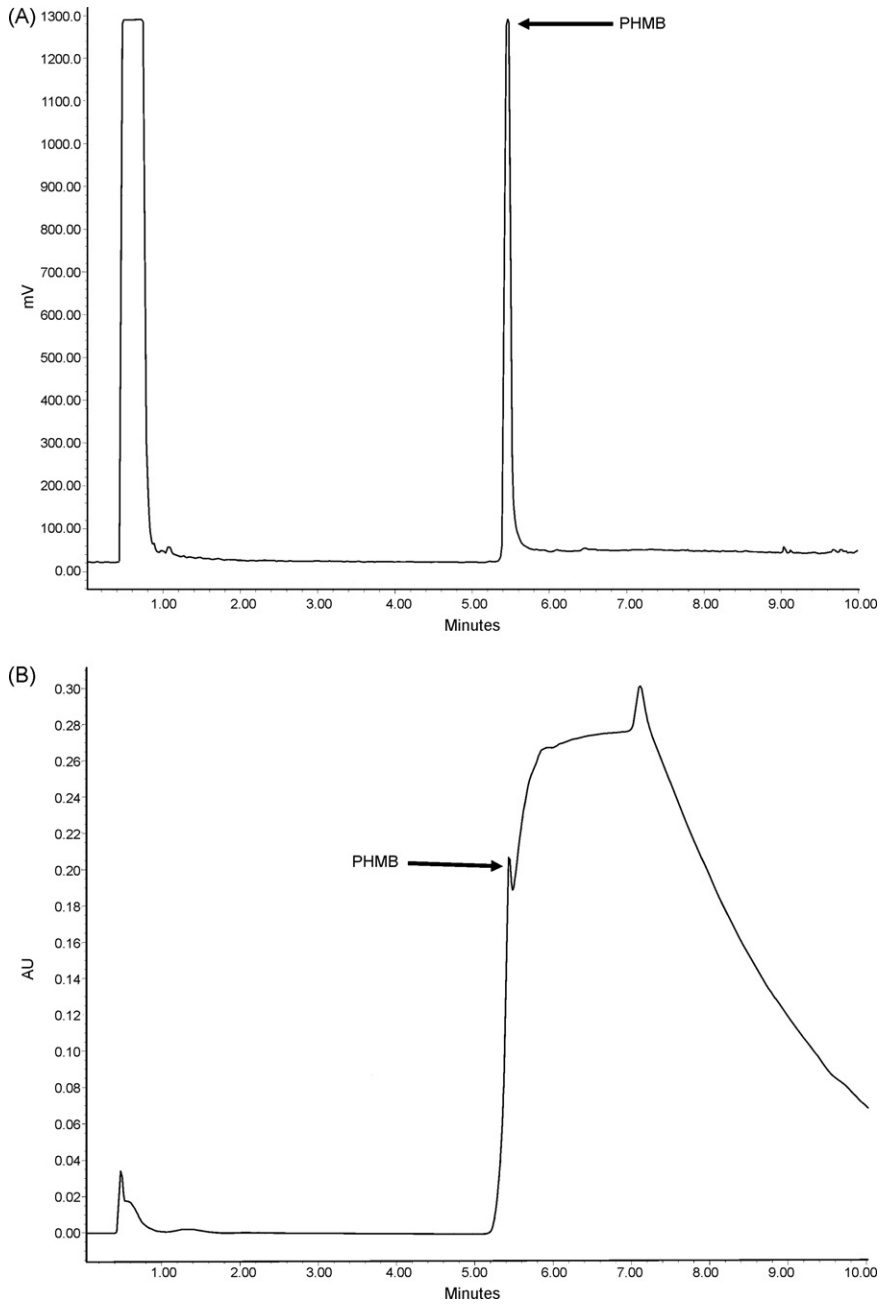


Fig. 1. The difference in the sensitivity of the ELSD detector (A) and the UV detector (B) for PHMB analysis of contact lens solution brand A.

lens solution with hydrogen peroxide as an active ingredient generated no peak in the PHMB area. The MPS containing Polyquad® generated a large peak that appeared 0.05 min ahead of the PHMB peak (data not shown). It can be possible to confuse this peak with PHMB based on the close retention times; however the Polyquad® peak area was three times larger than that of the PHMB. It might be possible to tease the Polyquad® peak away from the PHMB by using a gentler gradient. The purpose of using an immediate change in pH and mobile phase composition in this study was to generate one peak for PHMB [16]. Other investigators reported the need to integrate multiple peaks to quantitate PHMB [7]. The purpose of this study was to develop a sensitive reliable method for PHMB in contact lens solutions. The baseline separation of the Polyquad® from the PHMB peak was not considered to be necessary as, at present, both chemical disinfectants are not found together in commercially available MPS.

Table 1
The repeatability of the system as a function of peak area for a 10 ppm PHMB standard.

Peak area			
Number	Average	Std	cv%
6	1,311,365	135,376.7	10.3
5	1,423,358	159,430.7	11.2
10	3,171,998	145,270.5	4.6
8	4,170,078	318,143.5	7.6
8	4,412,432	172,020	3.9

3.6. HPLC system repeatability

The error of the system was evaluated by making a large volume of a 10 ppm PHMB in the elution solution (50:50 water:acetonitrile

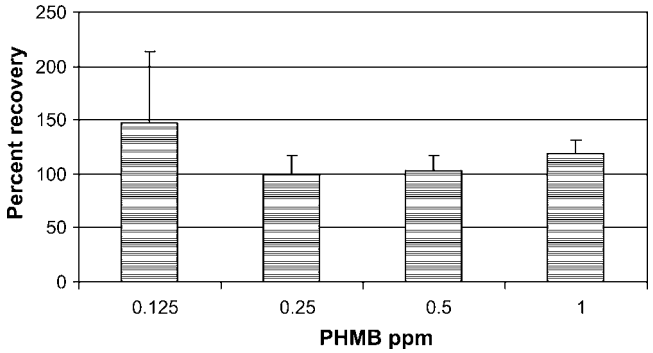


Fig. 2. Recovery of PHMB fortified with 0, 0.125, 0.25, 0.5, and 1.0 ppm into hydrogen peroxide contact lens solution. Recoveries were good, 107%, at the 0.25 ppm level and above (RSD 17% or less), but the error at the 0.125 ppm level was quite large (RSD 66%).

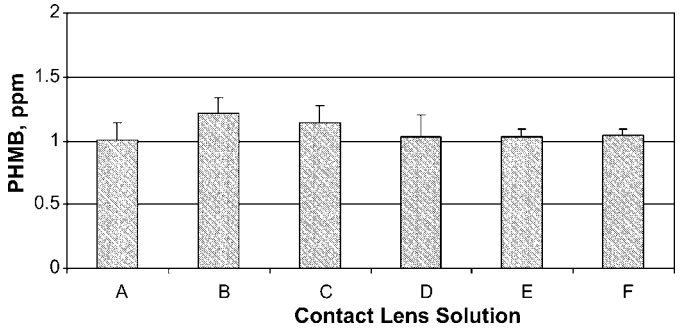


Fig. 3. The average concentration of PHMB in six different commercially available MPSs.

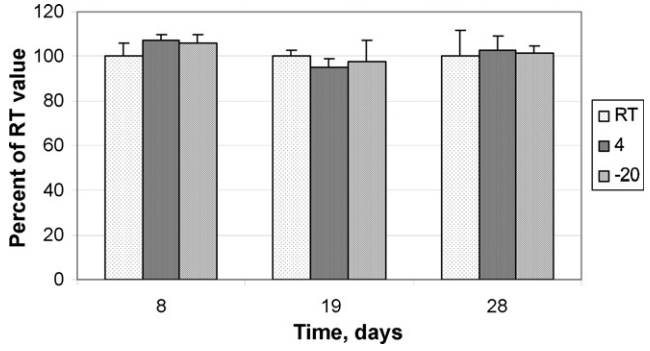


Fig. 4. The effect of temperature on the storage of PHMB, MPS brand A was used for this study.

with 0.25% TFA) and placing it into a series of HPLC vials. Single injections were made for each set of standards; the number of the 10 ppm standards prepared varied over time (Table 1). The variability of the peak area for the same concentration of PHMB was due to the need to 'steam clean' the ELSD every 40 h of use. Standards were run over a period of two months at various time points before and after the detector cleaning. Just after steam cleaning the detector, the peak area was largest and peak shape was sharpest. Table 1 summarizes the data; that increasing peak area shows decreasing error expressed as RSD%.

3.7. Storage and stability studies

Storage of MPS brand A was evaluated at room temperature, 4 °C, or −20 °C for up to a four week period. No significant difference in total PHMB concentration was seen. Fig. 4 illustrates the temperature stability of MPS brand A; the RSD for this data set was less than 10%. When MPS brand A was placed overnight at room temperature in a glass container and its peak area was compared to the same MPS stored in a polypropylene container at the same temperature, a 50% decrease in signal was observed (data not shown). This is likely due to the negative charge of the glass [17] binding the cation PHMB.

4. Conclusion

A reasonably simple method for the determination of PHMB in MPS was developed. Recovery from fortified solutions and commercially available MPS containing PHMB were around 100% at the relevant 1 ppm PHMB level, with a limit of detection at around 0.2 ppm. All commercially available MPS containing PHMB that were tested had concentrations around the labeled 1 ppm level. The storage stability studies conducted demonstrated that the temperature (25 °C to −20 °C) did not negatively impact the chemical analysis of PHMB from contact lens solutions over 28 days. In comparing glass and polypropylene containers for contact lens solution storage, polypropylene is superior to glass for maintaining the concentration of PHMB in MPSs. However, with out analyte-free MPS, the true accuracy cannot be unequivocally established. Still, the circumstantial evidence would support this method as a reasonable means for determining PHMB in MPS.

Acknowledgements

The authors wish to thank Mr Peart, Arch Chemical Co, for donating PHMB, Gail Matson for her editorial expertise, Ann Koustenis for laboratory support, and Dr. Seungil Cho and Dr. Victoria Hitchins for the technical review.

References

[1] http://www.archchemicals.com/Fed/Corporate/Docs/ACC/ARCH_CHEMICALS-PHMB.pdf.
[2] http://www.epa.gov/oppsrrd1/REDs/phmb_red.pdf.
[3] P. Gilbert, D. Pemberton, D.E. Wilkinson, J. Appl. Bacteriol. 69 (1990) 593.
[4] L.P. O'Malley, A.N. Collins, G.F. White, J. Ind. Microbiol. Biotechnol. 33 (2006) 677.
[5] I. Rosenthal, B.J. Juven, E. Ben-Hur, J. Food Saf. 4 (1982) 191.
[6] M.W. Dawson, T.J. Brown, D.G. Till, NZ J. Mar. Freshwater Res. 17 (1983) 305.
[7] T. Rowhani, A.F. Lagalante, Talanta 21 (2007) 946.
[8] C. Yiping, D. Xiaojing, Z. Shan, L. Pengyan, CJI 7 (2005) 55, http://www.chemistrymag.org/cji/2005/078055ne.htm.
[9] R.H. Moman, M. Al-sagher, P. Gilbert, Microbiol. Hyg. Alim. 19 (2007) 20.
[10] E.M. Abad-Villar, S.F. Etter, M.A. Thiel, P.C. Hauser, Anal. Chim. Acta. 561 (2006) 133.
[11] T. Hattori, Y. Nakata, R. Kato, Anal. Sci. 19 (2003) 1525.
[12] T. Masadome, Y. Yamagishi, M. Takano, Anal. Sci. 24 (2008) 415.
[13] R. Schultz, H. Engelhardt, Chromatographia 29 (1990) 517.
[14] H.E. Fries, C.A. Evans, K.W. Ward, J. Chromatogr. B 819 (2005) 339–344.
[15] R.P.W. Scott, Liquid Chromatography Detectors, http://www.chromatography-online.org/5/contents.html.
[16] N. Lendero, J. Vidic, P. Brne, V. Frankovic, A. Strancar, A. Podgornik, J. Chromatogr. A 1185 (2008) 59.
[17] S.H. Behrens, D.G. Grier, J. Chem. Phys. 115 (2001) 6716, DOI:10.1063/1.1404988.

Talanta 80 (2009) 1020–1024

Contents lists available at ScienceDirect

Talanta

journal homepage: www.elsevier.com/locate/talanta

Short communication

Measurement of anions in ambient particulate matter by ion chromatography: A novel sample preparation technique and development of a generic uncertainty budget

Richard J.C. Brown [a,*], Peter R. Edwards [b]

[a] Analytical Science Team, National Physical Laboratory, Hampton Road, Teddington, Middlesex, TW11 0LW, UK
[b] School of Chemistry, University of Southampton, Southampton SO17 1BJ, UK

ARTICLE INFO

Article history:
Received 11 May 2009
Received in revised form 3 July 2009
Accepted 20 July 2009
Available online 28 July 2009

Keywords:
Anions
Air quality
Particulate matter
Extraction
Uncertainty

ABSTRACT

A novel sample preparation technique for the measurement of anions in particulate matter by ion chromatography is presented. The technique uses the eluant from the ion chromatography analysis stage to perform the extraction of the anions from the particulate matter. The demonstrated advantages of the new technique are manifold: faster sample throughput, minimised sample preparation, and a matrixed-matched sample for analysis. The repeatability of the technique has been tested using nominally identical ambient particulate matter samples (sub-sampled from one large filter) and the uncertainty of the technique has been estimated. The uncertainty estimate is transferable to other similar methods used to measure ions in particulate matter. Real data obtained using the new method are also presented.

© 2009 Elsevier B.V. All rights reserved.

1. Introduction

The chemical composition of ambient aerosols continues to be a subject of great interest to the environmental and atmospheric chemistry communities [1]. The determination of the anionic content of particulate matter (PM) is of increasing interest in this context because of the requirement to work toward mass closure in PM studies, and also because the presence of many anions in PM arise as a result of conversion from primary air pollutants such as CO, SO_2 and NO_x [2]. Moreover anions in PM can be precursors for acid rain formation [3]. Therefore there is a need to perform accurate and traceable measurements of the mass concentration of anions in ambient air, and the mass fraction of anions in PM, in order to provide reliable data sets to: measure the exposure of the general population to these compounds; assess compliance with legislative limits or similar target values; and inform policy development and assess the effectiveness of abatement strategies. To this end the anion mass concentration in ambient air is currently measured daily at three sites in the UK as part of the UK Airborne Particulate Concentrations and Numbers Network [4]. Moreover the requirement to perform these measurements (together with measurements of cations) will soon be mandated in the European Union [5] – and as a result of this requirement a standard method for the measurement of anions and cations in PM will be prepared by the European Committee for Standardisation Technical Committee 264 Working Group 34.

In this paper we present a novel method to extract the anions from PM more efficiently than current standard methods [6–9]. Repeatability data for this technique is presented, together with a proposed uncertainty budget for the measurement. The extraction technique described is not transferable to the measurement of cations because of the large sodium concentration following extraction, but the uncertainty budget presented is applicable to all similar measurements of the ionic content of PM. Whilst other techniques have been proposed for the measurement of anions in PM, ion chromatography remains by far the most popular [10,11]. Although some standard methods for anions in PM already exist, these use deionised water [6–8] or an ethanol–water mix [9,12] for extraction and none are accompanied by a rigorous uncertainty budget. Recent research work in this area has focussed on the development of techniques to examine an increased number of PM species in an individual scan [13], and also the use of surfactants to improve extraction efficiency [14]. However to the best of the authors' knowledge no study has examined the use of the ion chromatography eluant itself as the extraction medium, or has estimated the likely uncertainty due to the measurement.

* Corresponding author. Tel.: +44 20 8943 6409; fax: +44 20 8614 0423.
E-mail address: richard.brown@npl.co.uk (R.J.C. Brown).

0039-9140/$ – see front matter © 2009 Elsevier B.V. All rights reserved.
doi:10.1016/j.talanta.2009.07.042

2. Materials and methods

2.1. Chemicals and reagent preparation

All solutions were prepared in fully cleaned and dried (in a nitrogen flow (oxygen free nitrogen, BOC)) polypropylene labwear (Fisher) using deionised water (18.2 MΩ cm, Milli-Q system, Millipore). All chemicals were of high purity (99.9+%, Fisher) and were prepared according to the supplier's guidelines (drying at elevated temperatures for the inorganic salts). All solutions were prepared gravimetrically. Calibration solutions were prepared such that the solutions requiring measurement were approximately located towards the centroid of the calibration curve wherever possible, and usually constituted of at least four solutions of different concentration plus a blank solution. The eluent used for the IC analysis and for extraction of the anions from the filters was an aqueous solution of 11 mM Na_2CO_3 and 2 mM $NaHCO_3$.

2.2. Sample collection

In order to test the proposed method, samples of ambient particulate were taken onto quartz fibre filters (Whatman QM-A) using a Thermo GMW PM_{10} high volume air sampler at a flow rate of 68 $m^3\ h^{-1}$. To demonstrate measurements made using the final procedure, real samples were taken onto quartz fibre filters (Whatman QM-A) using Thermo Partisol 2000 PM_{10} low volume air samplers at a flow rate of 1 $m^3\ h^{-1}$. Samples were taken for one day periods. The use of the high volume air sampler is crucial to the development of the measurement method and to the assessment of the uncertainty of the method. Whilst having the same face velocity as the low volume sampler – therefore collecting approximately the same mass of particulate matter per unit area per unit time, the larger filter area means that several nominally identical sub-samples may be taken for the same large filter and used for studies to examine the repeatability of the extraction procedure. Up to twelve sub-samples may be taken from each high volume sample.

2.3. Sample preparation

Sampled filters were sub-sampled using a circular wad-punch with a 20 mm diameter (Fisher, UK). In order to ensure these sub-samples are as equal as possible, the centre of each was coincident with the centre of one of the nozzles within the sampler that delivers sampled material onto the filter. These sub-samples were then sonicated in an ultrasonic bath (37 kHz, 80 W RMS power, Ultrasonics Ltd.) in a weighed amount (approximately 10 g) of the IC eluent. Solutions were then filtered through 0.45 mm PPE filters (Whatman) as they were introduced into the ion chromatograph.

2.4. Analysis using ion chromatography

Analysis for chloride, sulphate and nitrate was performed with a Dionex DX-120 ion chromatograph (IC), with a G14 guard column, AS14 anion separation column, ASRS – Ultra II self-regenerating suppressor unit and a DS4 conductivity detector. A flow rate of 1.0 mL min^{-1} was used throughout. The volume of the sample injection loop was nominally 25 μL (although larger sample loops were used during method development to improve repeatability). Quantification was performed with NPL's XLGenline software [15], using the peak areas provided by the proprietary software (Peak Net Software, Dionex).

All experimentation, except for the sample collection, was conducted in a temperature-controlled laboratory at 20 ± 2 °C.

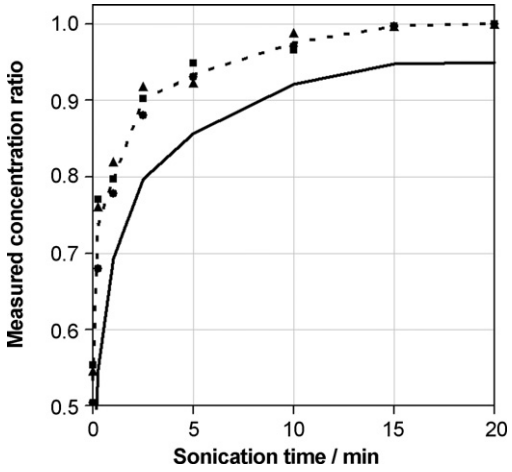


Fig. 1. Measured concentration of chloride (●), nitrate (▲) and sulphate (■) ratioed to the maximum measured concentrations over different sonication times and the average trend of these three species (dotted line). The average trend for the same investigation using just deionised water as the extraction eluant is shown as a solid line.

3. Results and discussion

3.1. Eluant extraction technique

The IC eluent has been used as a novel extraction media for the collected particulate matter in the results presented here. The advantages of this technique over the usual extraction media of deionised water or ethanol–deionised water mixtures are manifold, as will be demonstrated in the results below, but in summary: the use of this extraction medium wets the filter more quickly, speeds up the extraction process, results in a more complete extraction of anions within the particulate matter, and provides a sample which is already matrix matched to the IC eluent, thereby requiring no further sample preparation to eliminate the water dip which can obscure some anion species. A comparison of anion extraction using the IC eluant as compared to using deionised water is shown in Fig. 1, which shows that the IC eluant speeds up the extraction procedure, achieving full extraction after approximately 10–15 min compared to between 15 and 20 min for deionised water alone. Use of the eluant solution showed on average a 5% higher extraction than using only water as an extraction medium. One explanation for this higher extraction may be owing to the exchange of sodium ions from the extraction solution with the native cations in the particulates, leading to increased solubility. Moreover, for the use of both eluant and deionised water, extraction of anions from the particulate matter occurs more quickly than the time periods specified for the extraction procedure in most standard methods, which usually recommend an extraction time of 1 h [9]. However, it is best to err on the side of longer extraction times in all cases (assuming sample throughput is not adversely affected) since extraction conditions such as ultrasonic powers and frequencies are rarely standardised and may vary considerably, and in any event no sample is expected to be lost by using longer extraction times. The effect of elevated temperatures on extraction rate was also tested but did not give a significant enough improvement to warrant the extra complication of heating the samples in the sonic bath and the loss of extraction solution via evaporation that this might cause. However, as the elevated temperature did not extract significantly more anions we can conclude that the conditions routinely being used (room temperature sonication) are sufficient to extract fully the anions from the PM.

Fig. 2 shows the mass of chloride, nitrate and sulphate, measured on twelve filter cuts taken from a high volume filter sample

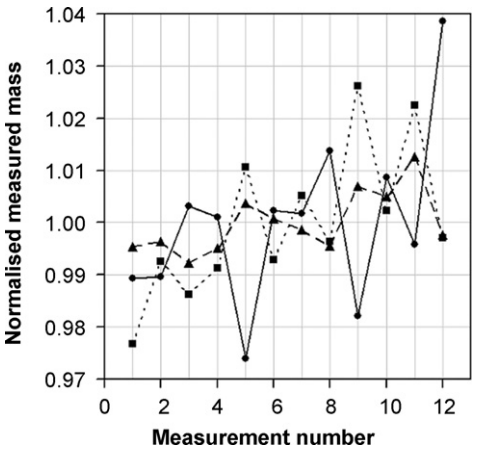


Fig. 2. The mass of chloride (●), nitrate (▲) and sulphate (■), measured on twelve filter cuts taken from a high volume filter sample. These results have been normalised to the average value for each anion and displayed in order of the average normalised mass of the three anions, from lowest to highest.

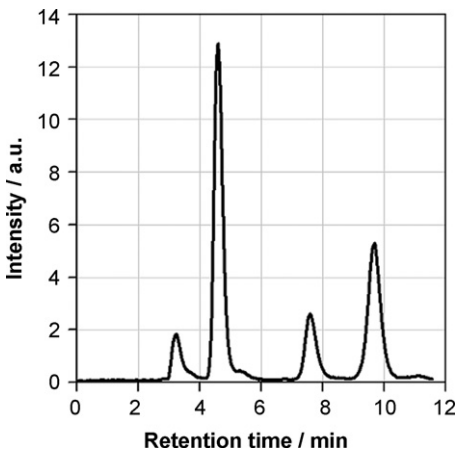


Fig. 3. Ion chromatogram from a sampled filter, extracted using the ion chromatography eluant itself, showing complete absence of a water dip (expected after approximately 2 min) with four anions clearly visible: fluoride at 3.25 min, chloride at 4.5 min (possibly with a nitrite shoulder), nitrate at 7.5 min and sulphate at 9.5 min.

– all nominally with identical mass loadings. These results have been normalised to the average value for each anion and displayed in order of the average normalised mass of the three anions on each filter, from lowest to highest. Each sub-sample extract was measured ten times and the use of a previously described [16] drift correction procedure was applied in order to minimise the contribution of instrument repeatability to the variability of the measurement. In addition a larger sample loop (100 μL) was used for these measurements to increase the amount of sample introduced, and therefore decrease further the relative repeatability of the instrument. The standard deviations of these measurements for chloride, nitrate and sulphate were, 2.0%, 0.8% and 1.8% respectively, showing that the extraction technique is highly repeatable. Following this extraction procedure an example of the ion chromatogram produced from a real sample, with no further sample preparation, is displayed in Fig. 3. In particular, it is important to note the flat baseline, showing the absence of any water dip, making elucidation of the peaks with low retention times simple, without any further sample preparation.

3.2. Uncertainty budget

The measurement of anions in particulate matter can be described by a simple set of equations given below:

$$\gamma_{amb} = \frac{m_{ion}}{V_{amb}\eta_{sam}} \quad (1)$$

$$m_{ion} = \frac{m_{ext}x_{ext}}{\eta_{ext}r} \quad (2)$$

$$x_{ext} = \frac{I_{ext}}{\dot{V}_{cal}} \quad (3)$$

where γ_{amb} is the mass concentration of anions in ambient air, in μg/m^3; V_{amb} is the volume of ambient air sampled, in m^3; η_{sam} is the sampling efficiency, in g/g; m_{ion} is the mass of anion on the filter, in μg; x_{ext} is the mass fraction of anion in the PM extract, in μg/g; m_{ext} is the mass of extraction solution, in g; η_{ext} is the extraction efficiency of anions from the PM, in g/g; r is the ratio of sub-sampled filter area to the total filter area, in m^2/m^2; I_{ext} is the blank corrected instrument response at the measured concentration; $\dot{V}_{cal}$ is the gradient of calibration curve, in g/μg.

Substituting Eq. (3) into Eq. (2), and Eq. (2) into Eq. (1) yields:

$$\gamma_{amb} = \frac{m_{ext}I_{ext}}{V_{amb}\eta_{sam}\eta_{ext}r\dot{V}_{cal}} \quad (4)$$

This allows a simple 'Guide to the expression of uncertainty in measurement' (GUM) [17] uncertainty treatment to be performed, which yields the exemplar uncertainty budget shown in Table 1. This estimates a relative standard uncertainty of approximately 6% at the anion mass concentrations expected in ambient air, yielding an expanded measurement uncertainty of approximately 12% at the 95% confidence level (assuming a coverage factor of $k = 2$). The contribution of individual parameters to this standard uncertainty,

Table 1
Exemplar uncertainty budget for the measurement of the mass concentration of anions in ambient air.

Symbol	Quantity	Units	Estimate	Sensitivity coefficient	Uncertainty	Probability distribution	Divisor	Contribution to standard uncertainty
Eq (4): Uncertainty in the mass concentration of anions in ambient air								
V_{amb}	Volume of ambient air sampled	m^3	24.00	−0.14	1.20	Rectangular	$\sqrt{3}$	−0.096
η_{sam}	Sampling efficiency	g/g	1.00	3.33	0.00	Rectangular	$\sqrt{3}$	0.000
m_{ext}	Mass of extraction solution	g	10.00	0.33	0.01	Normal	1	0.003
η_{ext}	Extraction efficiency of anions from the PM	g/g	1.00	−3.33	0.02	Normal	1	−0.067
r	Ratio of the sub-sampled filter area to the total filter area	m^2/m^2	0.25	−13.33	0.01	Rectangular	$\sqrt{3}$	−0.077
I_{ext}	Filter blank corrected instrument response at the measured concentration	1	20.00	0.17	0.50	Normal	1	0.083
$\dot{V}_{cal}$	Gradient of calibration curve	g/μg	10.00	−0.33	0.28	Normal	1	−0.094
γ_{amb}	Mass concentration of anions in ambient air	μg/m^3	3.33	–	–	–	–	0.19

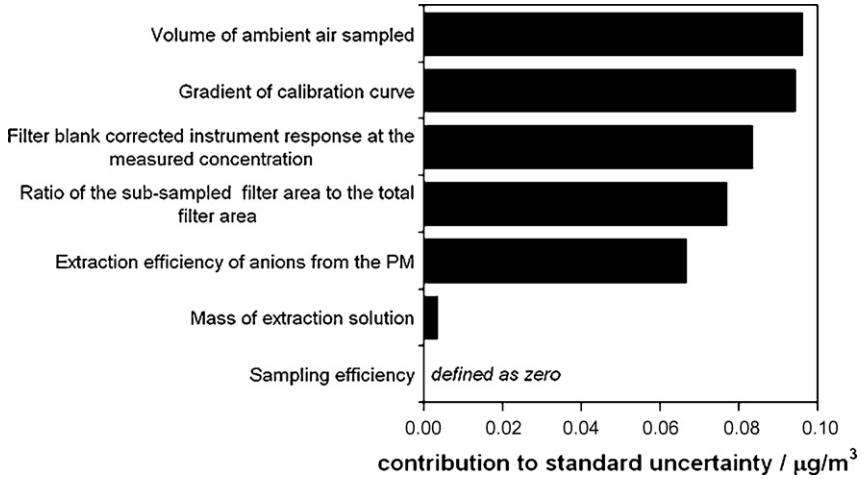


Fig. 4. Contribution of individual sources to the combined standard uncertainty of the measurement of anion mass concentration in ambient air as determined in Table 1.

as obtained during the work presented here, is given in Fig. 4. A brief discussion of the standard uncertainty $u(x)$ in the individual parameters x is given below.

- $u(m_{ext})$ can be estimated from the uncertainty of repeat weighing, and the calibration of the analytical balance.
- $u(\eta_{sam})$ is defined as zero, with η_{sam} defined as 1, because it is assumed that the sample is measured as received, following sampling according to EN12341 [18], and any losses of material during the sampling process are not considered (although it has been known for some time that some losses of volatile components may occur [19]).
- $u(V_{amb})$is defined in EN12341 [18] as a maximum of $5/\sqrt{3}$% (including flow rate calibration, drift in sampling flow rate during measurement, etc.).
- $u(\eta_{ext})$ may be estimated from the experimental data obtained from extraction of multiple nominally identical samples, as displayed in Fig. 2. A symmetrical distribution centred on 100% extraction has been considered for ease of calculation – although in reality this distribution is certainly asymmetrical and centred below 100% [20].
- $u(r)$ is a measure of the uncertainty in the ratio of the area of the sub-sample (if taken) to the area of the sampled filter. This may also include a component of uncertainty to recognise that a sub-sample may not be representative of the filter as a whole [21].
- $u(\dot{V}_{cal})$ may be estimated by regression software such as XLGenline [15], but will be approximately equal to the repeatability of the instrument response at the centre of the calibration range added in quadrature to the uncertainty in the composition of the calibration standards at this concentration (including consideration of the uncertainty of gravimetric preparation and the purity of the salts used).
- $u(I_{ext})$ can be estimated from the repeatability of measurements using the ion chromatograph. This has been gauged for representative concentrations of chloride, nitrate and sulphate solutions by performing repeat measurement of the same solution over the period of 1 h, and is shown in Fig. 5. The relative standard deviation of the repeat measurements for chloride, nitrate and sulphate were 1.8%, 0.6% and 1.4% respectively. Consideration of this parameter should also include drift of the measurement between calibrations. However, Fig. 5 shows that drift over the measurement period is negligible compared with the repeatability. As I_{ext} is the filter blank corrected intensity, $u(I_{ext})$ needs additionally to include a contribution to recognise the uncertainty in the anion content of the blank filter. Usually the anion content of the blank filter is very low (<2% of the anion content in a daily PM sample). However, it may be quite variable, and this needs to be gauged by repeat measurements of a series of filter blanks using Eqs. (2) and (3). As with all filter-based air quality measurements using destructive analysis it is unfortunately not possible to determine the blank levels of the filters being used for sampling – which would be the preferred measure of subtracting blank values.

The relative uncertainties of the individual components of the uncertainty budget would not be expected to change significantly with ambient mass concentration. The exception to this is I_{ext} which would be expected to show a dependence on anion mass fraction in solution, especially at very low mass fractions when the contribution of the blank becomes significant, and the uncertainty in I_{ext} would need to be reassessed.

Real data obtained using this proposed method on the NPL site, in Teddington, during a 19-day period in October 2006 is shown in Fig. 6, with the expanded measurement uncertainties estimated using the proposed budget also shown. The concentrations measured during this period were broadly consistent with those observed at the UK air quality monitoring network sites measuring chloride, sulphate and nitrate [4]. In general, the chloride concentrations recorded were lower than both the sulphate and nitrate concentrations, except in few cases. As expected, the chloride, usually from primary sources, showed little correlation

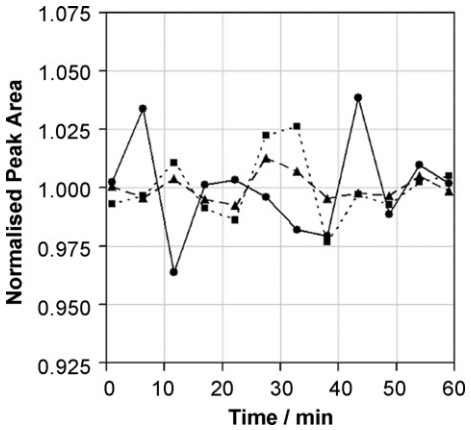


Fig. 5. Repeatability of chloride (●), nitrate (▲) and sulphate (■) measurements using the ion chromatograph, at concentrations relevant to those seen from real samples, over a 1 h period.

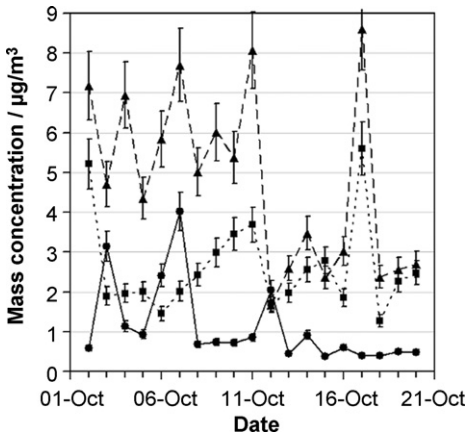


Fig. 6. The chloride (●), nitrate (▲) and sulphate (■) mass concentrations in the PM_{10} phase of ambient air, measured on the NPL site, in Teddington, during October 2006 using the method described in the text. The error bars represent the overall expanded measurement uncertainty at the 95% confidence level (assuming a coverage factor of $k = 2$).

with the sulphate and nitrate, usually from secondary sources. Conversely, the sulphate and nitrate values showed quite strong correlation, especially towards the end of the measurement period, as they originate from similar secondary sources. In general, the measured nitrate concentrations were higher than the sulphate concentrations.

In summary, a new method for the extraction of anions from particulate matter has been proposed, which uses the ion chromatography eluant as the extraction media. Data has been presented for the repeatability of this extraction technique and its comparability against the use of deionised water (as specified in other standard methods). It has been shown that the use of eluant as the extraction medium can speed up the extraction process as compared with deionised water also yielding a greater extraction efficiency. This method has the additional advantages of reducing the quantity of sample preparation required, and yielding a matrix-matched sample without further manipulation, thereby allowing a more accurate assessment of anionic species with low retention times. The drawback of this method is that it is not suitable for the measurement of cationic species by ion chromatography owing to the large sodium content in the extracted sample. However a similar technique could be applied for cationic species via the use of a suitable eluant (for instance sulphuric acid) as the extraction medium. In addition, the carbonate/hydrogen carbonate eluant used would interfere with the measurement of CO derived species, although these are not currently measured by the UK Airborne Particulate Concentrations and Numbers Network.

An uncertainty budget for the method has also been presented which has considered all factors contributing to the uncertainty of the measurements. This budget is generic and is extendable to the measurement of any ionic species in particulate matter by most measurement techniques that first rely on an extractive step. It has been assumed that the sampling of the PM is made according to EN 12341 and thus any volatile material lost during sampling, prior to analysis, is not considered in the uncertainty budget. That notwithstanding there are no particularly dominant contributions to the expanded measurement uncertainty, assuming a coverage factor of $k = 2$ at the 95% confidence interval, which was determined to be approximately 12% for these measurements.

4. Conclusions

This study has presented a new method to extract the anionic content of ambient particulate matter using the chromatography eluant as the extraction medium. This method has led to increases in extraction efficiencies of approximately 5% over the use of deionised water alone, and has shown reproducibilities of 2% or better, as gauged by extraction of nominally identical samples.

The relative expanded uncertainty of the overall method has been calculated to be approximately 12% assuming a coverage factor of $k = 2$ at the 95% confidence interval.

Real data obtained during a test sampling period has demonstrated the use of this method in practice. The method described in this work is now used on the UK Airborne Particulate Concentrations and Numbers Network to make daily measurements of anion mass concentration.

Acknowledgements

The UK Department for Innovation, University and Skills' funding of the National Measurement System Chemical & Biological Metrology Programme, and the UK Department for Environment, Food and Rural Affairs' funding of NPL's operation and management of the UK Airborne Particulate Concentrations and Numbers Network, are both gratefully acknowledged.

References

[1] C.I. Davidson, R.F. Phalen, P.A. Solomon, Aerosol Sci. Technol. 39 (2005) 737–749.
[2] Y.C. Lin, M.T. Cheng, Atmos. Environ. 41 (2007) 1903–1910.
[3] C. Anatolaki, R. Tsitouridou, Atmos. Res. 92 (2009) 100–113.
[4] NPL Report AS 25, CPEA 28: Airborne Particulate Concentrations and Numbers in the United Kingdom (phase 2), Annual Report. NPL, Teddington, 2008.
[5] Directive 2008/50/EC of the European Parliament and of the Council of 21 May 2008 on ambient air quality and cleaner air for Europe, Official Journal of the European Union L152 1–44, 2008.
[6] SOP MLD064: Standard Operating Procedure for the Analysis of Anions and Cations in PM2.5 Speciation Samples by Ion Chromatography, California Environmental Protection Agency Air Resources Board, California, 2002.
[7] No. 153: Aerosol Measurement Procedures Guidelines and Recommendations, World Meteorological Organisation Global Atmosphere Watch, Geneva, 2003.
[8] EMEP Manual for sampling and chemical analysis, Norwegian Institute for Air Research, Oslo, 2001.
[9] VDI 3497 Part 3: Analysis of Chloride, Nitrate and Sulphate by Ion Chromatography Using Suppressor Technique After Aerosol Sampling on PTFE Filters, VDI, Berlin, 1988.
[10] M. Fosco, M. Schmeling, Environ. Monit. Assess. 130 (2007) 187–199.
[11] J.S. Fritz, D.T. Gjerde, Ion Chromatography, Wiley-VCH, Weinheim, 2009.
[12] R.J.C. Brown, P.R. Edwards, J. Sep. Sci. 29 (2006) 2072–2077.
[13] S. Karthikeyan, S.W. See, R. Balasubramanian, Anal. Lett. 40 (2007) 793–804.
[14] S.M. Talebi, M. Abedi, J. Chromatogr. A 1094 (2005) 118–121.
[15] I. M. Smith, F. O. Onakunle, XLGENLINE Version 1.0, Document CMSC/M/06/657, NPL, Teddington, 2007.
[16] R.J.C. Brown, A.S. Brown, Analyst 133 (2008) 1611–1618.
[17] ISO/IEC Guide 98: 1995, Guide to the expression of uncertainty in measurement (GUM), ISO, Geneva, 1995.
[18] EN 12341: 1999, Air quality: determination of the PM10 fraction of suspended particulate matter. Reference method and field test procedure to demonstrate reference equivalence of measurement methods, CEN, Brussels, 1999.
[19] C.J. Tsai, S.N. Perng, Atmos. Environ. 32 (1998) 1605–1613.
[20] S. Cowen, S.L.R. Ellison, Analyst 131 (2006) 710–717.
[21] G. Steinhoff, O. Haupt, W. Dannecker, Fres. J. Anal. Chem. 366 (2000) 174–177.

Talanta 80 (2009) 1025–1028

Contents lists available at ScienceDirect

Talanta

journal homepage: www.elsevier.com/locate/talanta

Short communication

Determination of low-molecular-weight dicarboxylic acids in atmospheric aerosols by injection-port derivatization and gas chromatography–mass spectrometry

Ching-Lin Hsu, Wang-Hsien Ding*

Department of Chemistry, National Central University, 300 Jungda Rd., Chung-Li 320, Taiwan

ARTICLE INFO

Article history:
Received 8 June 2009
Received in revised form 22 July 2009
Accepted 22 July 2009
Available online 30 July 2009

Keywords:
Low-molecular weight dicarboxylic acids
Injection-port derivatization
Gas chromatography–mass spectrometry
Aerosol

ABSTRACT

A rapid and environmental-friendly injection-port derivatization with gas chromatography–mass spectrometry (GC–MS) method was developed to determine selected low-molecular weight (LMW) dicarboxylic acids (from C2 to C10) in atmospheric aerosol samples. The parameters related to the derivatization process (i.e., type of ion-pair reagent, injection-port temperature and concentration of ion-pair reagent) were optimized. Tetrabutylammonium hydroxide (TBA-OH) 20 mM in methanol gave excellent yield for di-butyl ester dicarboxylate derivatives at injection-port temperature at 300 °C. Solid-phase extraction (SPE) method instead of rotary evaporation was used to concentrate analytes from filter extracts. The recovery from filter extracts ranged from 78 to 95% with relative standard deviation (RSD) less than 12%. Limits of quantitation (LOQs) ranged from 25 to 250 pg/m^3. The concentrations of di-carboxylated C2–C5 and total C6–C10 in particles of atmospheric aerosols ranged from 91.9 to 240, 11.3 to 56.7, 9.2 to 49.2, 8.7 to 35.3 and n.d. to 37.8 ng/m^3, respectively. Oxalic acid (C2) was the dominant LMW-dicarboxylic acids detected in aerosol samples. The quantitative results were comparable to the results obtained by the off-line derivatization.

© 2009 Elsevier B.V. All rights reserved.

1. Introduction

Currently, the investigations on aerosol water-soluble organic compounds (WSOCs) formed by vehicular exhaust emission and burning biomass have become increasingly concerned with the role of these compounds in atmospheric research owing to their effect on climate and human health. Low-molecular weight (LMW) dicarboxylic acids (from C2 to C10) have attracted the most interest because they are ubiquitous components in tropospheric aerosols, and have been detected in various ambient environments ranging from continental to remote Arctic atmospheres [1–6]. Reliable quantification of these LMW-dicarboxylic acids can help us to evaluate the importance of the secondary photochemical reactions.

Routinely, diazomethane or BF_3 with alcohol (i.e., propanol, n-butanol) method has been used to derivatize LMW-dicarboxylic acids for GC–MS analysis [1,3–6]. However, the procedure was time-consuming and the reagent was costly and toxic. Large-volume injection-port derivatization with various ion-pair reagent (i.e., tetrapropylammonium salts or tetrabutylammonium salts) has been successfully developed in our laboratory and widely used to determine various surfactants and their degradation products, acidic herbicides, naphthalenesulfonic acids and pharmaceutical residues in water samples [7–11]. Currently, this procedure has also been applied to determine long-chain fatty acids, perfluorooctane sulfonate isomers and phenolic herbicides because of its reducing solvent waste, simplifying sample preparation, and avoiding the use of hazardous reagents [12–16]. This convenient procedure has been successfully employed to the analytes with mono-carboxylate and sulfonate groups. However, the derivatization to the analytes with LMW-dicarboxylic acids has not been reported so far. For the molecules with dicarboxylated groups, the procedure may be initiated by reacting dicarboxylic acid with tetrabutylammonium hydroxide ($N(Bu)_4^+HO^-$), for example, to form dicarboxylate ion pairs [$^+N(Bu)_4{}^-OOCRCOO^-N(Bu)_4{}^+$] in methanol. Upon introduction to a high temperature (i.e., above 280 °C) in GC injection-port, the dicarboxylic acid groups were transformed to their corresponding volatile di-butyl esters [BuOOCRCOOBu] and then they were directly separated and determined by GC–MS.

This work presents the preliminary results of a modified method to rapidly and quantitatively determine the selected LMW-dicarboxylic acids in aerosol samples. The various tetraalkylammonium salts (TAA salts), its concentration and injection-port

* Corresponding author. Tel.: +886 3 4227151x65905; fax: +886 3 4227664.
E-mail addresses: wding@cc.ncu.edu.tw, wanghsiending@gmail.com (W.-H. Ding).

0039-9140/$ – see front matter © 2009 Elsevier B.V. All rights reserved.
doi:10.1016/j.talanta.2009.07.047

temperatures were investigated and optimized. The off-line BF_3/n-butanol derivatization method was employed for comparison.

2. Experimental

2.1. Chemicals and reagents

Unless noted otherwise all high purity chemicals and solvents were purchased from Aldrich (Milwaukee, USA) and Merck (Darmstadt, Germany), and were used without further purification. Internal standards 1-phenyldodecane was purchased from Merck. Standards of LMW-dicarboxylic acids: oxalic acid (C2), malonic acid (C3), maleic acid (cis-C4), fumaric acid (trans-C4), succinic acid (C4), glutaric acid (C5), adipic acid (C6), pimelic acid (C7), suberic acid (C8), azelaic acid (C9), and sebacic acid (C10) were purchased from AccuStandard (New Haven, USA). Deionized water was further purified with a Mill-Q Plus water purification device (Millipore, Bedford, USA). Reagent-grade tetraalkylammonium salts (TAA salts): tetramethylammonium hydroxide (TMA-OH), tetraethylammonium hydroxide (TEA-OH), tetrabutylammonium hydroxide (TBA-OH) and tetrabutylammonium tetrafluoroborate (TBA-BF_4) were purchased from Acros Organics (Morris Plains, USA).

2.2. Sampling collection and preparation

Samples of atmospheric aerosols were collected by aerosol sampler (10 l/min) at the roof of the Graduate Institute of Environmental Engineering Center in National Central University (Chung-Li, Taiwan). Sampling time was 12 h. The aerosol sampler and sampling procedures acquired to determine selected LMW-dicarboxylic acids have been described elsewhere [17,18]. Particles and aerosol samples were collected on Pallflex quartz fiber filters (o.d. 102 mm).

The procedure used to extract selected LMW-dicarboxylic acids from the aerosol samples under ultrasonic agitation and solid-phase extraction (SPE) has been described by Limbeck et al. [5], and was used with minor modifications. The filter was extracted for 30 min using 50 ml of deionized water under ultrasonic agitation. The aqueous extract was then preconcentrated using Oasis HLB-SPE cartridges (3 ml, 60 mg; Waters, Milford, USA). After conditioning steps, the extract passed through the HLB-SPE cartridge at a flow rate of about 2–3 ml/min with the aid of a vacuum. The analytes were eluted from the cartridge with 3 ml of methanol/methyl-t-butyl ether (1:9, v/v) eluent. Then, the eluent was completely evaporated to dryness by a stream of nitrogen, and the residue was redissolved in 100 μl of methanol with 20 mM TBA-OH (optimized, see Section 3) containing 5 ng/μl of 1-phenyldodecane (as an internal standard), and made ready for GC–MS analysis.

2.3. GC–MS analysis

A Varian 3800CP gas chromatograph directly connected to a Saturn 2000 ion-trap mass spectrometry (Walnut Creek, USA) was used in the analysis of the sample extracts. A ChromatoProbe and a temperature-programmed injector (Varian) with a 3.4 mm i.d. liner, was used to introduce a large-volume sample (10 μl) for injection-port derivatization, as described elsewhere [10,11]. A DB-5 MS capillary column (30 m × 0.25 mm i.d., 0.25 μm film, J&W, USA) was used. After the injector temperature had reached 300 °C, the following GC temperature program was used: 80 °C for 5 min; following by a temperature ramp of 10 °C/min up to 300 °C; and then holding this temperature for 5 min. The transfer line was set at 280 °C. Full scan EI data was acquired under the following conditions: mass range 45–350 *m*/*z*, scan time 1 s, manifold temperature 160 °C, emission current 10 μA, automatic gain control (AGC) target 20,000 (represents as the target total ion current value).

3. Results and discussion

3.1. Optimization of injection-port derivatization

The precision of the injector-port derivatization with the GC–MS analysis, as determined from the relative standard deviation (RSD) of over 30 injections of LMW-dicarboxylic acids, ranged from 2.4 to 10%. No retention effect either for TBA-OH or analytes was observed since the disposable micro-vial was used for sample introduction.

The derivatization efficiencies were optimized with respect to three parameters: the type of TAA salt, the injection-port temperature and the concentration of TAA salt co-injected with the sample. Tetraalkylammonium hydroxides have been reported as the most common used ion-pair reagents for ion-pair formation in methanol [11,16,19]. Furthermore, according to our previous report [11] indicates that methanol was used as the final solvent increasing the solubilities of di-carboxylated analytes and ion-pair reagents, so enhanced their reaction efficiency. Therefore, three TAA-OH salts: TMA-OH, TEA-OH and TBA-OH, and TBA-BF_4 were evaluated according to the previous experimental conditions: injection-port temperature at 300 °C and 20 mM of TAA salt in methanol. The derivatization efficiency was obtained from the related abundance of the GC–MS peak area of the di-alkylated derivatives to the internal standard from four different TAA salts. Fig. 1 shows that related abundance increased with the long alkyl groups of TAA salts, both TBA salts gave highest yield of derivatives than those of TME-OH and TEA-OH. In here, TBA salt reagents produced the highest average peak areas and stable quantitative results in the extracted ion chromatograms of di-butylated derivatives. However, TAA salts with longer alkyl groups (i.e., tetraheptyl ammonium hydroxide (THA-OH)) cannot be employed as an ion-pair reagent because of their poor solubility in the methanol (data not shown). Due to the relatively higher peak abundances of di-butyl ester of C4 and C5 derivatives, higher related abundances were observed in this study. The effects of the injection temperature and the concentration of TBA-OH co-injected with the sample were also evaluated. The average peak areas ($16.3 \pm 5 \times 10^5$) for the di-butylated derivatives were not significantly different at the injection temperatures 280, 300 or 320 °C, and at the TBA-OH concentrations 10, 20 or 30 mM, respectively (data not shown). A detailed study was not made of the decrease in yield at a lower temperature since 280–320 °C represents a temperature range appropriate for most practical purposes. Since TBA-OH is the more commonly used ion-pair reagent, 20 mM of TBA-OH at the injection temperature at 300 °C were employed in this study.

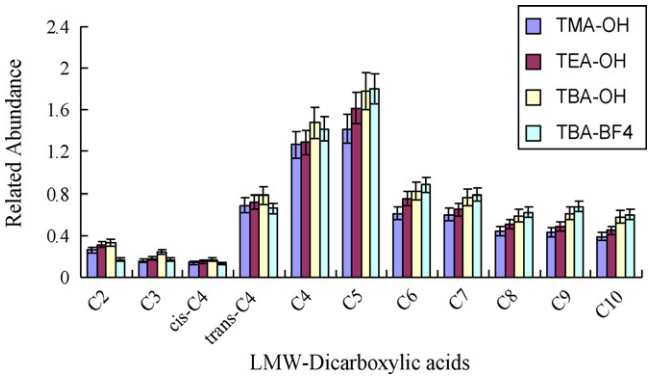


Fig. 1. Related abundance of injection-port derivatization with four ion-pair reagents. The derivatizations were performed on three replicates, standard deviation is reported as an error bar. "Related abundance" in *y*-axis was defined that the peak areas of analytes were normalized to the peak area of the internal standard obtained in each set of the experimental condition.

Table 1
Detection characteristics, linear range, linearity, limits of quantitation and spiked recoveries.

Compound	Retention time (min)	Quantitation ions (m/z)[a]	Linear range (μg/ml)	r^2	LOQ (pg/m^3)[b]	Spiked recovery (%)
C2	12.98	202 ([M]$^+$), 101 ([M−101]$^+$)	0.05–5.00	0.995	100	81[c] (9)[d]
C3	14.66	216 ([M]$^+$), 143 ([M−73]$^+$)	0.05–5.00	0.994	250	78 (10)
cis-C4	15.22	228 ([M]$^+$), 155 ([M−73]$^+$)	0.05–5.00	0.994	250	80 (12)
trans-C4	15.65	228 ([M]$^+$), 155 ([M−73]$^+$)	0.05–5.00	0.997	50	80 (6)
C4	15.34	230 ([M]$^+$), 101 ([M−129]$^+$)	0.01–1.00	0.999	25	92 (6)
C5	16.51	244 ([M]$^+$), 171 ([M−73]$^+$), 115 ([M−129]$^+$)	0.01–1.00	0.999	25	95 (6)
C6	17.59	258 ([M]$^+$), 185 ([M−73]$^+$), 111 ([M−147]$^+$)	0.01–1.00	0.999	50	93 (7)
C7	18.76	272 ([M]$^+$), 199 ([M−73]$^+$), 125 ([M−147]$^+$)	0.01–1.00	0.998	50	90 (8)
C8	19.75	286 ([M]$^+$), 157 ([M−129]$^+$)	0.025–1.50	0.996	75	88 (7)
C9	20.77	300 ([M]$^+$), 227 ([M−73]$^+$)	0.025–1.50	0.995	75	87 (9)
C10	21.70	314 ([M]$^+$), 241 ([M−73]$^+$), 185 ([M−129]$^+$)	0.025–1.50	0.996	50	85 (8)

[a] Underlined ions correspond to the base peaks.
[b] A nominal volume of 7.2 m^3 for a typical 12 h sample period.
[c] Mean spiked recovery (%, $n = 3$) from the filter extracts of the aerosol sample 1 via SPE, and the spiked concentration for each analyte in extracts was 0.5 μg/ml.
[d] Relative standard deviation (%RSD) of recovery is given in parentheses ($n = 3$).

3.2. Mass spectra of derivatives

Table 1 presents an overview of the retention times and the major ions using as the quantitation ions for GC–MS analysis. These di-butylated derivatives showed some common fragmentation pathways. The molecular ions of di-butylated LMW-dicarboxylic acids were all detected with 10–40% intensities to their corresponding base peaks, furthermore, the base peaks of trans-C4 and C9 were their molecular ions. Two most intensive ions, [M−73]$^+$ and [M−129]$^+$, were observed and were tentatively attributed to the loss of OC_4H_9 and further loss of butene (m/z 56) from another side of the butyl ester end, respectively. This double-hydrogen rearrangement mechanism resulting in elimination of an alkene is common for propyl or higher esters [20]. For C2, the base peak m/z 101 may correspond to homolytic cleavage of carbobutoxy group ([$COOC_4H_9$]$^+$, m/z 101) at the α-position. The characteristic ion of [M−147]$^+$, m/z 111 for C6 and m/z 125 for C7 (as a base peak), was detected and was tentatively attributed to the loss of two OC_4H_9 from the molecular ion. These two or three characteristic ions as listed in Table 1 were used as the quantitation ions to obtain maximum detection sensitivity and specificity.

3.3. Method performance and applications

The analytical characteristics of the method, such as linear response range, reproducibility and quantitation limits, were investigated to evaluate the efficiency of the method and the possibility of the method application to atmospheric aerosol samples. Table 1 also presents the linear response range, linearity and limits of quantation (LOQ) for these derivatives. The quantitation of these derivatives was calculated from the five-level calibration curve (or average response factor) covering the range as shown in Table 1, each divided by the fixed concentration of internal standard (1-phenyldodecane). The calibration curves were linear with coefficients of determination $r^2 > 0.994$. The curve covered a range equivalent to the concentration of the analytes in aerosol samples after the extract was concentrated to 100 μl. The limits of quantitation (LOQs) ranged from 25 to 250 pg/m^3, at a nominal volume of 7.2 m^3 for a typical 12 h sample period (Table 1). Solid-phase extraction (SPE) method was used to concentrate analytes from filter extracts and the recoveries from filter extracts of the aerosol sample 1 ranged from 78 to 95% with relative standard deviation (RSD) less than 12%.

Table 2 lists the concentrations of selected LMW-dicarboxylic acids detected in atmospheric aerosols. The BF_3/n-butanol derivatization procedure [3,6] was also applied to the same aerosol samples (samples 1–3) to compare the results of on-line and off-line derivatization techniques. Student's t-test procedure was employed to compare individual differences [21], the two methods for analytes determination were evaluated. In this test, injection-port derivatization (on-line) and BF_3/n-butanol derivatization (off-line) methods were used to make single measurements on three samples, in this case, such that no measurement was duplicated. The t-test was to determine whether the two methods yielded the same results "within experimental error", or was one systematically different from the other in certain confidence level. The t-calculated

Table 2
Concentrations (ng/m^3) of LMW-dicarboxylic acids detected in atmospheric aerosols and comparison the results from on-line and off-line derivatization.

Sample	LMW-dicarboxylic acids											t_{calcu}[a]
	C2	C3	cis-C4	trans-C4	C4	C5	C6	C7	C8	C9	C10	
1 (on-line)	91.9	31.2	11.2	n.d.	14.2	8.7	n.d.	n.d.	n.d.	n.d.	n.d.	0.070
1 (off-line)	93.5	24.6	17.3	n.d.	9.2	13.5	n.d.	n.d.	n.d.	n.d.	n.d.	
				n.d.								
2 (on-line)	101	25.7	17.4	n.d.	35.7	13.2	n.d.	n.d.	n.d.	n.d.	n.d.	0.425
2 (off-line)	97.0	31.5	11.1	n.d.	30.2	17.8	n.d.	n.d.	n.d.	n.d.	n.d.	
				n.d.								
3 (on-line)	156	48.1	30.2	n.d.	32.2	28.5	9.6	n.d.	n.d.	8.2	n.d.	0.287
3 (off-line)	138	31.2	33.2	n.d.	38.0	31.0	15.2	n.d.	n.d.	17.6	n.d.	
4	110	11.3	20.1	n.d.	15.6	9.3	n.d.	6.3	n.d.	10.2	n.d.	
5	126	32.2	14.6	15.3	33.4	10.8	n.d.	n.d.	n.d.	n.d.	n.d.	
6	202	25.7	36.5	n.d.	49.2	21.8	10.5	8.5	n.d.	15.4	n.d.	
7	98.6	33.9	20.8	14.7	12.6	8.2	n.d.	n.d.	n.d.	n.d.	n.d.	
8	240	56.7	28.6	23.5	41.5	35.3	12.4	8.0	n.d.	17.4	n.d.	
9	173	34.2	22.3	13.9	28.4	33.4	8.2	6.2	n.d.	n.d.	n.d.	

n.d. not detected at limits of quantitation (LOQ), as listed in Table 1.
[a] Calculation from the equations in Ref [21], Eqs. (4-10) and (4-11).

values (in Table 2) were less than the *t*-table list values: 2.776 for samples 1 and 2; 2.447 for sample 3, in 95% confidence level with four and six degree of freedom, respectively. Therefore, these two methods are not significantly different at the 95% confidence level. Moreover, the percent differences of the total concentrations (from C2 to C10) obtained from these two methods were less than 2.8%. A comparison of the two methods reveals that, for off-line derivatization, the derivatization time and reagent consumption were 30 min (at 100 °C) and 250 μl per each sample, respectively [4], however, for on-line method, no derivatization time at high temperature was necessary and only 100 μl of methanol with 20 mM TBA-OH was used.

The concentrations of dicarboxylated C2–C5 and total C6–C10 in atmospheric aerosols ranged from 91.9 to 240, 11.3 to 56.7, 9.2 to 49.2, 8.7 to 35.3 and n.d. to 37.8 ng/m^3, respectively. The concentrations of maleic acid (cis-C4) and fumaric acid (trans-C4) ranged from 11.1 to 36.5 and n.d. to 23.5 ng/m^3, respectively. Oxalic acid (C2) was the dominant selected LMW-dicarboxylic acids detected in these aerosol samples, followed by malonic acid (C3) and succinic acid (C4). These values are similar to those measured in suburban southern Taiwan [22]. The profiles of these dicarboxylic acids in atmospheric aerosol samples are also similar to the profiles present in Hong Kong [6], urban Tokyo area [23], and urban and rural sites in Germany [24]. However, considerably lower concentrations have been detected in the atmospheres of the Arctic [2] and the savanna biome in South Africa [5]. Moreover, the different profiles in summer and winter times have been observed in urban and rural sites in Germany [25].

4. Conclusion

The improved large-volume injection-port derivatization with TBA-OH ion-pair reagent is a simple, rapid and accurate method for the determination of trace levels of selected LMW-dicarboxylic acids in atmospheric aerosol samples. Injection-port derivatization method completely avoided the open derivatization with hazardous reagents. This developed method could be adopted as an alternative rapid screen tool to obtain detailed information in understanding the transport and photochemical production of selected LMW-dicarboxylic acids in the atmosphere; it is a effective and environmental-friendly analytical method.

Acknowledgement

This research was supported by a grant from the National Science Council of Taiwan, contract No. NSC 94-2113-M-008-013.

References

[1] D. Grosjean, K. Van Cauwenberghe, J.P. Schmid, P.E. Kelley, J.N. Pitts Jr., Environ. Sci. Technol. 12 (1978) 313.
[2] V.M. Kerminen, K. Teinilä, R. Hillamo, T. Mäkelä, Atmos. Environ. 33 (1999) 2089.
[3] K. Kawamura, I.R. Kaplan, Environ. Sci. Technol. 21 (1978) 105.
[4] K. Kawamura, H. Kasukabe, L.A. Barrie, Atmos. Environ. 30 (1996) 1709.
[5] A. Limbeck, H. Puxbaum, L. Otter, M.C. Scholes, Atmos. Environ. 35 (2001) 1853.
[6] H. Wang, K. Kawamura, K.F. Ho, S.C. Lee, Environ. Sci. Technol. 40 (2006) 6255.
[7] W.H. Ding, C.T. Chen, J. Chromatogr. A 862 (1999) 113.
[8] W.H. Ding, C.H. Liu, S.P. Yeh, J. Chromatogr. A 896 (2000) 111.
[9] C.H. Liu, W.H. Ding, J. Chromatogr. A 929 (2001) 341.
[10] W.C. Lin, H.C. Chen, W.H. Ding, J. Chromatogr. A 1065 (2005) 279.
[11] C.Y. Cheng, W.H. Ding, Rapid Commum. Mass Spectrom. 21 (2007) 1687.
[12] J.M. Wu, H.K. Lee, J. Chromatogr. A 1133 (2006) 13.
[13] J.M. Wu, H.K. Lee, Anal. Chem. 78 (2006) 7292.
[14] C. Diez, E. Barrado, P. Marinero, J. Atienza, J. Chromatogr. A 1125 (2006) 244.
[15] M. Rompa, E. Kremer, B. Zygmunt, Pol. J. Environ. Stud. 14 (2005) 81.
[16] S.G. Chu, R. Letcher, Anal. Chem. 81 (2009) 4256.
[17] C.T. Chang, C.J. Tsai, C.T. Lee, S.Y. Chang, M.T. Cheng, H.M. Chein, Atmos. Environ. 35 (2001) 5741.
[18] C.Y. Lin, S.C. Liu, C.C.K. Chou, T.H. Liu, C.T. Lee, C.S. Yuan, C.J. Shiu, C.Y. Young, Terrest. Atmos. Ocean. Sci. 15 (2004) 839.
[19] M. Rompa, E. Kremer, B. Zygmunt, Anal. Bioanal. Chem. 377 (2003) 590.
[20] F.W. McLafferty, Interpretation of Mass Spectra, 3rd ed. University Science Books, Mill Valley, pp. 203–205.
[21] D. Harris, Quantitative Chemical Analysis, 7th ed., W.H. Freeman and Co., New York, 2007, pp. 58–63.
[22] L.Y. Hsieh, C.L. Chen, M.W. Wan, C.H. Tsai, Y.I. Tsai, Atmos. Environ. 42 (2008) 6836.
[23] K. Kawamura, K. Ikushima, Environ. Sci. Technol. 27 (1993) 2227.
[24] A. Röhrl, G. Lammel, Environ. Sci. Technol. 35 (2001) 95.
[25] A. Röhrl, G. Lammel, Chemosphere 46 (2002) 1195.

Talanta 80 (2009) 1029–1033

Contents lists available at ScienceDirect

Talanta

journal homepage: www.elsevier.com/locate/talanta

Short communication

A novel nonenzymatic hydrogen peroxide sensor based on multi-wall carbon nanotube/silver nanoparticle nanohybrids modified gold electrode

Wei Zhao[a], Huicai Wang[a], Xia Qin[a], Xinsheng Wang[a], Zixia Zhao[b], Zhiying Miao[a], Lili Chen[a], Miaomiao Shan[a], Yuxin Fang[a], Qiang Chen[a,*]

[a] The Key Laboratory of Bioactive Materials, Ministry of Education, College of Life Science, Nankai University, Tianjin 300071, China
[b] The Center for Applied Aquatic Genomics Chinese Academy of Fishery Sciences, China

ARTICLE INFO

Article history:
Received 19 June 2009
Received in revised form 22 July 2009
Accepted 27 July 2009
Available online 5 August 2009

Keywords:
Sensor
Silver nanoparticles
Multi-wall carbon nanotubes
Hydrogen peroxide

ABSTRACT

A novel strategy to fabricate hydrogen peroxide (H_2O_2) sensor was developed based on multi-wall carbon nanotube/silver nanoparticle nanohybrids (MWCNT/Ag nanohybrids) modified gold electrode. The process to synthesize MWCNT/Ag nanohybrids was facile and efficient. In the presence of carboxyl groups functionalized multi-wall carbon nanotubes (MWCNTs), silver nanoparticles (Ag NPs) were *in situ* generated from $AgNO_3$ aqueous solution and readily attached to the MWCNTs convex surfaces at room temperature, without any additional reducing reagent or irradiation treatment. The formation of MWCNT/Ag nanohybrids product was observed by transmission electron microscope (TEM), and the electrochemical properties of MWCNT/Ag nanohybrids modified gold electrode were characterized by electrochemical measurements. The results showed that this sensor had a favorable catalytic ability for the reduction of H_2O_2. The resulted sensor could detect H_2O_2 in a linear range of 0.05–17 mM with a detection limit of 5×10^{-7} M at a signal-to-noise ratio of 3. The sensitivity was calculated as 1.42 μA/mM at a potential of −0.2 V. Additionally, it exhibited good reproducibility, long-term stability and negligible interference of ascorbic acid (AA), uric acid (UA), and acetaminophen (AP).

Crown Copyright © 2009 Published by Elsevier B.V. All rights reserved.

1. Introduction

In recent years, there has been a considerable interest in the accurate determination of hydrogen peroxide (H_2O_2) because it is an essential mediator in food, pharmaceutical, clinical and environmental analyses [1,2]. Also many enzymatic reactions create H_2O_2 as an end product, so its concentration may be used as an indicator of the progress of a reaction [3–6]. Many techniques have been employed in the determination of H_2O_2, including spectrophotometry [7], chemiluminescence [8], and electrochemistry [9–11]. Among these methods, electrochemistry technique based on a simple and low cost electrode has been extensively applied for accurate determination of H_2O_2. For most electrochemistry sensors, the detection of H_2O_2 was achieved at a relatively high potential around 0.6 V. However, at this relatively high potential, there may be interferences from other oxidable species such as ascorbic acid (AA), uric acid (UA), and acetaminophen (AAP). Thus, it becomes significant to construct a sensor to detect H_2O_2 at a lower potential.

Recent studies indicated that Ag nanoparticles (Ag NPs) exhibited catalytic activity for the reduction of H_2O_2 [12,13]. Electrochemical results showed that the presence of Ag NPs was responsible for sensor response, in terms of cathodic current increment, regarding the reduction of H_2O_2 [14]. Welch et al. proved that the reduction of H_2O_2 could be facilitated by the modification of the glassy-carbon surface with nanosized silver assemblies [12]. In order to synthesize Ag NPs, many kinds of methods have been used. Several materials have been used to control the growth of Ag NPs, such as DNA [13], polyacrylonitrile [15], microemulsions [16], DNA–lipid thin films [17], polyelectrolytes [18] and mesoporous materials [19]. Additionally, type I collagen network was used as a template to fabricate Ag NPs because of its porous structure [20]. Reducing metallic ions were also taken in use to prepare Ag NPs [21].

Carbon nanotubes (CNTs) were discovered by Iijima [22] and have enormous potentials as components of nanoscale electronic devices and biosensors, as a result of their ability to promote electron transfer reactions and high thermal capacity [23–25]. Both single-wall carbon nanotubes (SWCNTs) and multi-wall carbon nanotubes (MWCNTs) have been utilized in the detection of various kinds of biological reagents [26]. CNTs [27,28] and Ag NPs [12–14] have been employed for detecting H_2O_2 respectively. In order to take full advantage of the two kinds of nanomaterials, it is desirable to create novel CNT/Ag nanohybrids, so that the unique properties of each material can be integrated, and the interactions between the two components may bring out novel properties.

To fabricate Ag NPs coated MWCNTs, electrochemical, chemical and physical methods have been employed [29]. Several kinds

* Corresponding author. Tel.: +86 22 23506173; fax: +86 22 23506122.
E-mail address: qiangchen@nankai.edu.cn (Q. Chen).

0039-9140/$ – see front matter. Crown Copyright © 2009 Published by Elsevier B.V. All rights reserved.
doi:10.1016/j.talanta.2009.07.055

of chemical reagents, irradiations and temples were used in the synthesis of MWCNT/Ag nanohybrids. For instance, in the study of Wu et al., gamma-ray irradiation was taken in use to functionalize MWCNTs. MWCNT/polymer/Ag hybrids were synthesized relying on covalently bonded polymers [30]. The report of Bale et al. proved that proteins/polypeptides, including bovine serum albumin (BSA) and poly-L-lysine (PLL), mediated the formation of Ag NPs as bio-inspired template when adsorbed onto CNTs [31]. Lin et al. used trisodium citrate as reducing reagent and synthesized Ag NPs/CNTs/chitosan film by chemical plating method [32]. Electrodeposition of Ag NPs on MWCNTs was also carried out in some previous researches [33]. However, most of the methods in the synthesis of MWCNTs/Ag nanohybrids are verbose and complex, requiring different kinds of chemicals and templates.

In this article, by combining the advantages of carbon nanotubes and Ag NPs, MWCNT/Ag nanohybrids were designed and synthesized for the detection of H_2O_2. In our work, no additional chemical as reducing reagent or irradiation was employed, indicating the fundamental difference and extraordinary advantage of our approach over other reports. Utilizing the inherent properties of MWCNTs, the Ag NPs were reduced onto the MWCNTs surfaces. The resulted nanomaterials were characterized by transmission electron microscopy (TEM), and the properties of the modified electrode were investigated by amperometric measurements. The Ag NPs with good reduction catalysis for H_2O_2 would promote the ability of the electrode to eliminate the interferences from other electroactive biomolecules. The study can provide a promising platform for fabricating nonenzymatic electrodes, affinity matrix and detecting other biochemistry reagent.

2. Materials and methods

2.1. Materials

Multi-wall carbon nanotubes (30–50 nm diameter and 15 μm length), with >95% purity, and carboxylic acid groups 0.73 wt% were obtained from Institute of Organic Chemistry, Chinese Academy of Sciences (ChengDu, China). Hydrogen peroxide (30%, v/v aqueous solution), was obtained from Tianjin Eastern Chemical Reagent Company. Uric acid, ascorbic acid and acetaminophen were obtained from Tianjin Damao Chemical Reagent Co. (China). Sliver nitrate ($AgNO_3$) were purchased from Tianjin Yingda Rare Chemical Reagent Company. All other reagents were of analytical grade and used without further purification. All aqueous solutions were prepared with doubly distilled water. Phosphate-buffered saline (PBS) buffer: dissolve 6.8 g of KH_2PO_4 in 25 ml of doubly distilled water, adjust to pH 7.0 with 0.1 M NaOH and dilute to 100 ml with double distilled water. All experiments were performed in PBS at room temperature, approximately 25 °C.

2.2. Apparatus and electrochemical measurements

The MWCNT/Ag nanohybrids were characterized with transmission electron microscopy (TEM, Philips EM400ST microscopy). Electrochemical measurements were carried out in a conventional three-electrode electroanalysis system. The MWCNT/Ag nanohybrids modified gold electrodes (3 mm diameter) were used as a working electrode, and a platinum spiral wire (1 mm diameter) as a counter electrode, an Ag/AgCl electrode (saturated with KCl) as a reference electrode. Amperometric measurements were performed by using Potentiostat–Galvanostat (EG&G PARC Model 283 with a software M270) (USA).

2.3. Preparation of the biosensor

2.3.1. Modification of multi-wall carbon nanotubes

Pristine MWCNTs were dissolved in the mixture of concentrated H_2SO_4 and HNO_3 (3:1, v/v), and then dispersed in ultrasonic bath for about 4 h. The resulted MWCNTs were separated and washed with distilled water by centrifugation (10,000 rpm) until the pH of the resulted MWCNTs solution became neutral.

2.3.2. Synthesis of MWCNT/Ag nanohybrids

Synthesis of carbon nanotube/silver nanoparticle nanohybrids was carried out according to the previously reported method [34].

MWCNTs (1 mg/ml) were dispersed in an ultrasonic bath (40 kHz) for about 3 min, and then placed in a flask on magnetic stirrer. While stirring at room temperature, $AgNO_3$ (0.01 M) was added dropwise into the flask. After 20 h, the solid product (MWCNT/Ag nanohybrids) was collected by centrifuging.

In control experiment, the same protocol was employed to prepare the sample of MWCNT/Ag nanohybrids use the MWCNTs without carboxylic acid groups.

2.3.3. Electrode surface preparation and modification with MWCNT/Ag nanohybrids

Gold electrode was polished before each experiment with chamois leather containing 0.05 μm alumina powders, rinsed thoroughly with doubly distilled water, ultrasonically cleaned in ethanol and doubly distilled water, and dried at room temperature.

MWCNT/Ag nanohybrid solutions (5 μl, 1 mg/ml) were droped on the surface of polished gold electrode. In this way, the MWCNT/Ag nanohybrids were deposited on the electrode by absorption. After drying, the modified electrode was washed and used as an amperometric sensor in phosphate buffer (pH 7.0).

3. Results and discussion

3.1. Microscopic studies on the formation of MWCNT/Ag nanohybrids

The morphology of resulted nanohybrids was shown in Fig. 1. The observations of a transmission electron microscope (TEM) showed clearly that nanoparticles with a uniform size of about 8–12 nm were deposited onto the MWCNTs surfaces (Fig. 1(a)). By comparison, no such morphology of nanoparticles was observed on the surfaces of the neat MWCNTs (Fig. 1(b)). Fig. 1(c) shows the selected area electron diffraction (ED) image of the nanoparticles, indicating the phase structures of silver single nanoparticles [35–37]. After stored at 4 °C for a month, although the spherical structure of Ag NPs decomposed to some degree, the main structure could still be observed on MWCNTs (Fig. 1(d)), and the Ag NPs were binding well on the MWCNTs, proving the adsorption stability of the Ag NPs on the MWCNTs.

The inherent properties of MWCNTs such as rich-electron and strong absorption in a wide range of wavelength might be responsible for the synthesis of Ag NPs. The numerous carboxylic acid groups the MWCNTs possessed could play the roles of catalyst, silver 'catcher' and supporter. In this case, Ag NPs were *in situ* generated from the $AgNO_3$ aqueous solution at room temperature and attached to the convex surfaces of MWCNTs, forming the MWCNT/Ag nanohybrids [34]. MWCNTs without carboxylic acid groups were also used to compose MWCNT/Ag nanohybrids, but the result showed no Ag NPs appeared on the surface of the MWCNTs, which indicated that the reduction of Ag on the surface of MWCNTs depended on the assistance of carboxylic acid groups. In the report of Gao, either MWCNTs or SWCNTs could be utilized as the material for the synthesis of Ag NPs. The Ag NPs produced by the SWCNTs were much bigger than those produced by the MWCNTs, indicating that SWCNTs have a higher Ag productivity than MWCNTs, which was likely due to the higher special surface area or greater absorbance in water [34]. However, the nanoparticles which are smaller in size were considered to have better nano-effects. Thus, we chose the MWCNTs as the material in our research.

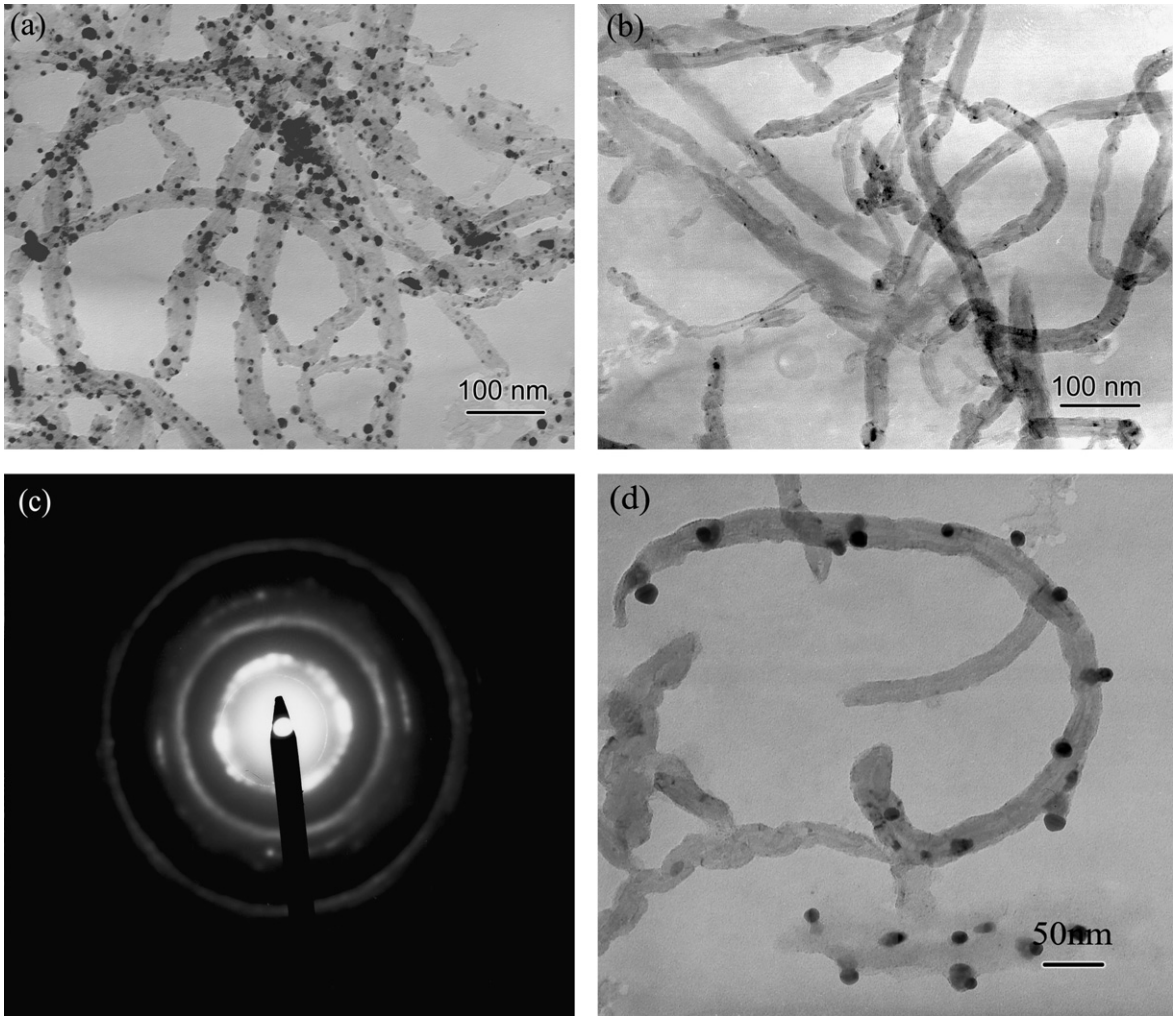


Fig. 1. TEM images of the MWCNT/Ag nanohybrids (a), MWCNTs (b), electron diffraction of Ag NPs (c), MWCNT/Ag nanohybrids stored at 4 °C for a month (d).

3.2. *Electrochemical response to hydrogen peroxide on MWCNT/Ag nanohybrids*

Cyclic voltammograms of the sensors were illustrated in Fig. 2. As shown in Fig. 2(a), in cyclic voltammograms of bare gold electrode there was no apparently redox process. After modified with MWCNTs (Fig. 2(b)), the diffused current increased clearly, because MWCNTs had a catalytically active surface, and they can increase the active surface area of the modified electrode. Two peaks at the potential of 0.2 V and 0.45 V were observed in MWCNT/Ag nanohybrids modified electrode (Fig. 2(d) and (e)). They were attributed to the reduction and oxidation of Ag, and could prove the existence of Ag NPs. The diffused current of MWCNT/Ag nanohybrids modified electrode (Fig. 2(d)) increased much more than that of MWCNTs modified electrode, due to the synergistic effect of MWCNTs and Ag NPs.

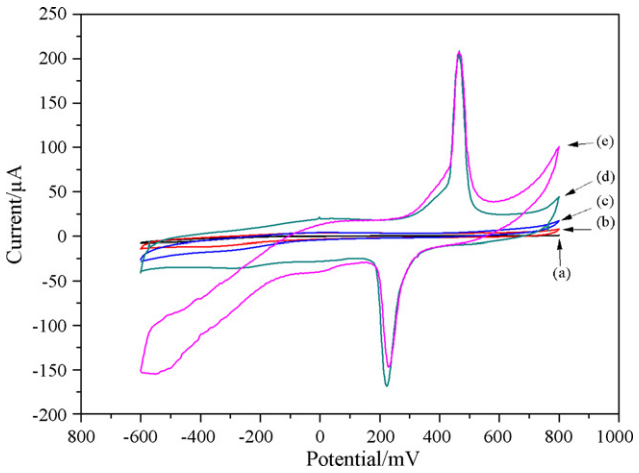


Fig. 2. Cyclic voltammograms of bare gold electrode (a), MWCNTs modified gold electrode (b and c), and MWCNT/Ag nanohybrids modified gold electrode (d and e) in PBS with (c and e) and without H_2O_2 (a, b and d).

When H_2O_2 was added into the PBS solution, it can be observed (Fig. 2(c) and (e)) that response current at the potential range of −0.15 V to −0.6 V indicated the reduction of H_2O_2, and the peak current appeared at the potential of −0.45 V. As it was shown, the reduction current in MWCNT/Ag nanohybrids modified electrode was markedly larger than that of MWCNTs modified electrode with the presence of H_2O_2. The difference was probably engendered by the synergistic amplification effect of MWCNTs and Ag NPs as well as the electrocatalysis reduction effect of Ag toward H_2O_2.

In the solution of PBS, the H_2O_2 was reduced via the mechanism shown below:

$$H_2O_2 + e^- \rightleftharpoons OH_{(ads)} + OH^-$$

$$OH_{(ads)} + e^- \rightleftharpoons OH^-$$

$$2OH^- + 2H^+ \rightleftharpoons 2H_2O$$

When the Ag NPs were deposited on the electrode, the reduction of H_2O_2 becomes more irreversible, as shown below [38]:

$$H_2O_2 \xrightarrow{Ag} \frac{1}{2}O_2 + H_2O$$

$$O_2 + 2e^- + 2H^+ \xrightarrow{electrode} H_2O_2$$

Then the O_2 generated in the action above would turn into the detection signal on electrode. It has been proposed [39] that the electro-reduction of oxygen on electrode occurs via the mechanism shown below [40]:

$$O_2 + e^- \rightleftharpoons [O_2^{\bullet -}]_{(ads)}$$

$$[O_2^{\bullet -}]_{(ads)} + H_2O \rightleftharpoons HO_2^{\bullet}{}_{(ads)} + OH^-$$

Then

$$HO_2^{\bullet}{}_{(ads)} + O_2^{\bullet -} \rightleftharpoons HO_2^{-}{}_{(aq)} + O_2$$

Or

$$HO_2^{\bullet}{}_{(ads)} + e^- \rightleftharpoons HO_2^{-}{}_{(aq)}$$

For most electrochemistry sensors, the detection of H_2O_2 was achieved at a relatively high potential around 0.6 V, which made it liable to interferences from electroactive compounds. In our work, we employed Ag NPs which had proved to exhibit catalytic activity for the reduction of H_2O_2 at lower potential to solve this problem. In contrast with Ag NPs modified GC electrode which showed a reduction peak current at −0.85 V [12], the wave that appeared at −0.45 V (Fig. 2(e)) on the MWCNT/Ag nanohybrids modified electrode due to the reduction of H_2O_2 means the smaller overpotentials of reduction of H_2O_2. At the same time, the cathodic current of the reduction of H_2O_2 on the MWCNT/Ag nanohybrids modified electrode is larger than that on the MWCNTs modified electrode. This may be due to that the Ag NPs on the MWCNTs could facilitate the reduction of H_2O_2 [12]. Although it exhibited the biggest response current at the electric potential of −0.45 V, we chose the potential of −0.2 V as work potential in consideration of anti-interference. At such a low applied potential, the background current decreased, the response of common interference species can be minimized, and the oxygen reduction current can be limited.

The amperometric responses of the electrodes modified with different nanomaterials were studied in Fig. 3, at the applied potential of −0.2 V. In order to check the catalytic performance of the two kinds of nanomaterials to H_2O_2, we compared the MWCNTs (a) and MWCNT/Ag nanohybrids (b) modified electrodes with the same amount of H_2O_2. For MWCNTs modified electrodes, small response currents can be observed. Whereas, the response current of MWCNT/Ag nanohybrids modified electrode was much larger, which could due to the excellent catalytic property of Ag NPs as well as synergistic amplification action of the MWCNT/Ag nanohybrids.

The insert (lower left) of Fig. 3 shows the steady-state calibration curve of the MWCNTs modified electrode (Fig. 3(a)) and MWCNT/Ag nanohybrids modified electrode (Fig. 3(b)). The experimental result showed that the two kinds of electrodes both gave a linear response to H_2O_2. In comparison with the sensitivity of 0.059 μA/mM in MWCNTs modified electrode, the MWCNT/Ag nanohybrids modified electrode had a sensitivity of 1.42 μA/mM, in the concentration range of 0.05–17 mM, and possessed a detection limit of 5×10^{-7} M at the signal-to-noise ratio of 3, and a fast current response time (within 5 s). The great sensitivity of MWCNT/Ag nanohybrids modified electrode could be attributed to the large catalytically electroactive surface area, the synergistic amplification effect of the two kinds of nanomaterials and the excellent catalysis reduction to H_2O_2 of Ag NPs.

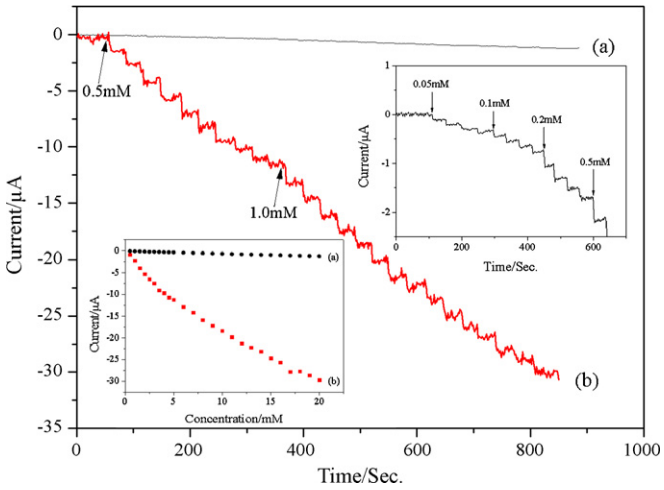


Fig. 3. Current–time recording obtained at the MWCNTs modified gold electrode (a) and MWCNT/Ag nanohybrids modified gold electrode (b) upon increasing the concentration of H_2O_2 in steps of 0.5 mM and 1.0 mM at −0.2 V. The insert (lower left) was the calibration curve of MWCNTs modified gold electrode (a) and MWCNT/Ag nanohybrids modified gold electrode (b) at −0.2 V in the concentration range of 0.5–20 mM of H_2O_2. The insert (upper right) was the current–time recording obtained at MWCNT/Ag nanohybrids modified gold electrode upon increasing the concentration of H_2O_2 in steps of 0.05 mM, 0.1 mM, 0.2 mM and 0.5 mM at −0.2 V.

3.3. Anti-interference experiment of hydrogen peroxide sensor

In real samples, some co-existing electroactive species might affect the sensor response, for example, ascorbic acid (AA), uric acid (UA), acetaminophen (AP), etc. The selectivity and anti-interference advantages were shown in Fig. 4, demonstrated by comparing the amperometric responses of three relevant electroactive species (UA, AA, AP, 0.1 mM, respectively) and H_2O_2 (1.0 mM) on a modified gold electrode at a working potential of −0.2 V. The successive addition of each interfering species brought out hardly discernible current response, and a well-defined H_2O_2 response was obtained. The good ability of anti-interference was largely attributed to the low working potential of −0.2 V used in the determination of H_2O_2.

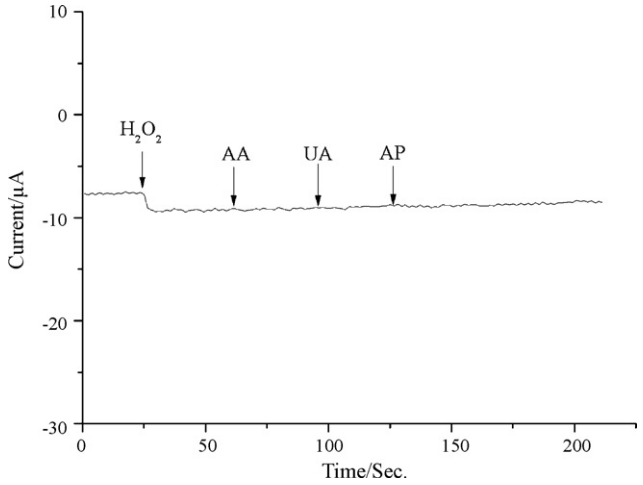


Fig. 4. Current–time curves for the MWCNT/Ag nanohybrids modified gold electrode exposed to AA, UA, AP, 0.1 mM each.

3.4. Reproducibility and long-term stability of the hydrogen peroxide sensor

To examine the reproducibility, repeatability and long-term stability of the sensor system, it was stored in phosphate buffer (pH 7) at 4 °C after several successive chronoamperometric experiments.

The reproducibility was estimated from the response to 5 mM H_2O_2 at five different H_2O_2 biosensors. A mean current response of −7.5 μA was acquired with a R.S.D. of 3.3%. It remained 90% of its initial current response for H_2O_2 after intermitting use over a month.

4. Conclusions

The main feature of this work was to propose a new nonenzymatic H_2O_2 sensor based on MWCNT/Ag nanohybrids, which was realized in a very fast and simple method.

In particular, experimental results indicated that Ag NPs were able to electrocatalyse the electro-reduction of H_2O_2. When they were used to modify MWCNTs, the two kinds of nanomaterials had a synergistic amplification effect, which could enhance the electrocatalytic properties of the sensor. There was an obvious difference in response current between the electrode modified with MWCNT/Ag nanohybrids and the one modified with MWCNTs at the potential of −0.2 V. When the two kinds of nanomaterials were used at one time the sensitivity enhanced 24 times than the MWCNTs modified electrode. Data collected from amperometric experiments showed that the performance of this kind of sensor made it suitable for the quantitative determination of H_2O_2. The resulted sensor exhibited good ability of anti-interference to electroactive biomolecules, which was attributed to the relatively lower potential at −0.2 V. The study may provide a feasible approach to develop new kinds of nonenzymatic amperometric sensors.

Acknowledgements

The financial supports from National Natural Science Foundation of China (Grant Nos. 30772746 and 30870665), and Natural Science Foundation of Tianjin (Grant No. 08JCZDJC20600) are well acknowledged.

References

[1] P.N. Bartlett, P.R. Birkin, J.H. Wang, F. Palmisano, G.D. Benedetto, Anal. Chim. Acta 70 (1998) 3685–3694.
[2] R.M. Sellers, Analyst 105 (1980) 950–954.
[3] G.G. Guilbault, Handbook of Enzymic Methods of Analysis, Dekker, New York, 1976.
[4] M. Darder, K. Takada, F. Pariente, E. Lorenzo, H.D. Abruna, Anal. Chim. Acta 71 (1999) 5530–5537.
[5] M. Masullo, G. Raimo, A. Dello Russo, V. Bocchini, J.V. Bannister, Biotechnol. Appl. Biochem. 23 (1996) 47–54.
[6] Y. Jiang, P.W. Miles, Phytochemistry 33 (1993) 29–34.
[7] C. Matsubara, N. Kawamoto, K. Takamura, Analyst 117 (1992) 1781–1784.
[8] S. Hanaoka, J.M. Lin, M. Yamada, Anal. Chim. Acta 426 (2001) 57–64.
[9] J. Li, S.N. Tan, H.L. Ge, Anal. Chim. Acta 335 (1996) 137–145.
[10] M.G. Garguilo, N. Huynh, A. Proctor, A.C. Michael, Anal. Chem. 65 (1993) 523–528.
[11] Y. Xiao, H.X. Ju, H.Y. Chen, Anal. Chim. Acta 391 (1999) 299–306.
[12] C.M. Welch, C.E. Banks, A.O. Simm, R.G. Compton, Anal. Bioanal. Chem. 382 (2005) 12–21.
[13] K. Cui, Y. Song, Y. Yao, Z. Huang, L. Wang, Electrochem. Commun. 10 (2008) 663–667.
[14] G. Flätgen, S. Wasle, M. Lübke, C. Eickes, G. Radhakrishnan, K. Doblhofer, G. Ertl, Electrochim. Acta 44 (1999) 4499–4506.
[15] H.Ng. Kwok, H. Liu, R.M. Penner, Langmuir 16 (2000) 4016–4023; Z. Zhang, M. Han, J. Mater. Chem. 13 (2003) 641–643.
[16] M. Andersson, J. Pedersen, A. Palmqvist, Langmuir 21 (2005) 11387–11396.
[17] A. Kumar, V. Ramakrishnan, R. Gonnade, K. Ganesh, M. Sastry, Nanotechnology 13 (2002) 597–600.
[18] L. Shang, S. Dong, Chem. Commun. 9 (2008) 1088–1090.
[19] D.H. Lin, Y.X. Jiang, Y. Wang, S.G. Sun, J. Nanomater. 1 (2008) 1–10.
[20] Y. Song, K. Cui, L. Wang, S. Chen, Nanotechnology 20 (2009) 105501–105508.
[21] C. Ren, Y. Song, Z. Li, G. Zhu, Anal. Bioanal. Chem. 381 (2005) 1179–1185.
[22] Iijima, Nature 354 (1991) 56–58.
[23] M.J. Moghaddam, S. Taylor, M. Gao, S. Huang, L. Dai, M.J. McCall, Nano Lett. 4 (2004) 89–93.
[24] J. Wang, M. Li, Z.J. Shi, N. Li, Z. Gu, Anal. Chem. 74 (2002) 1993–1997.
[25] G. Liu, Y. Lin, Electrochem. Commun. 8 (2006) 251–256.
[26] G.A. Rivas, M.D. Rubianes, M.C. Rodríguez, N.F. Ferreyra, G.L. Luque, M.L. Pedano, S.A. Miscoria, C. Parrado, Talanta 74 (2007) 291–307.
[27] P.A. Prakash, U. Yogeswaran, S.M. Chen, Talanta 78 (2009) 1414–1421.
[28] J.W. Shie, U. Yogeswaran, S.M. Chen, Talanta 78 (2009) 896–902.
[29] G.G. Wildgoose, C.E. Banks, R.G. Compton, Meth. Appl. Small 2 (2006) 182–193.
[30] B.Y. Wu, S.H. Houb, F. Yin, Z.X. Zhao, Y.Y. Wang, X.S. Wang, Q. Chen, Biosens. Bioelectron. 22 (2007) 2854–2860.
[31] S.S. Bale, P. Asuri, S.S. Karajanagi, J.S. Dordick, R.S. Kane, Adv. Mater. 19 (2007) 3167–3170.
[32] J. Lin, C. He, Y. Zhao, S.S. Zhang, Sens. Actuators B 137 (2009) 768–773.
[33] Y.C. Tsai, P.C. Hsu, Y.W. Lin, T.M. Wu, Electrochem. Commun. 11 (2009) 542–545.
[34] C. Gao, W. Li, Y.Z. Jin, H. Kong, Nanotechnology 17 (2006) 2882–2890.
[35] S.H. Im, Y.T. Lee, B. Wiley, Y.N. Xia, Angew. Chem. Int. Edn. 44 (2005) 2154–2161.
[36] Y.N. Xia, P.D. Yang, Y.G. Sun, Y.Y. Wu, B. Mayers, B. Gates, Y.D. Yin, F. Kim, Y.Q. Yan, Adv. Mater. 15 (2003) 353–389.
[37] Y. Liu, Y. Chu, L. Yang, D. Han, Z. Lu, Mater. Res. Bull. 40 (2005) 1796–1801.
[38] M. Honda, T. Kodera, H. Kita, Electrochim. Acta 31 (1986) 377–383.
[39] J. Xu, W. Huang, R.L. McCreery, J. Electroanal. Chem. 410 (1996) 235–242.
[40] B. Sljukic, C.E. Banks, R.G. Compton, Iran. J. Chem. 2 (2004) 1–25.

Talanta 80 (2009) 1034–1038

Contents lists available at ScienceDirect

Talanta

journal homepage: www.elsevier.com/locate/talanta

Short communication

An accurate model for the determination of the kinetic coefficients of the copper-catalyzed oxidation of iodide by oxygen in an aqueous acidic medium

Anouk de Brauwere[a,b,*], Willy Baeyens[a], Fjo De Ridder[c], Marc Elskens[a]

[a] Vrije Universiteit Brussel, Analytical and Environmental Chemistry, Pleinlaan 2, B-1050 Brussels, Belgium
[b] Université Catholique de Louvain, Centre for Systems Engineering and Applied Mechanics (CESAME), 4 Avenue G. Lemaître, B-1348 Louvain-la-Neuve, Belgium
[c] Vlaamse Instelling voor Technologisch Onderzoek (VITO), Boeretang 200, B-2400 Mol, Belgium

ARTICLE INFO

Article history:
Received 14 April 2009
Received in revised form 29 July 2009
Accepted 3 August 2009
Available online 28 August 2009

Dedicated to the work of Sigalla and Herbo (1958).

Keywords:
Reaction rate
Model
Parameter estimation
Measurement uncertainties
Cost function
Weighted least squares

ABSTRACT

The reaction rate of the copper-catalyzed oxidation of iodide by oxygen in an aqueous acidic medium is first order in copper and oxygen concentrations, Michaelis–Menten in pH and a complex, asymmetrical bell shaped function in iodide concentrations. A theoretical, multivariate reaction rate equation was proposed which enabled to optimise the various kinetic coefficients. During the parameter optimisation, the experiments were weighted taking into account all measurement uncertainties, i.e. both on the reaction rate (output) and on the reactants' concentrations (inputs). This has two important advantages: (1) the model can be statistically checked to be acceptable for the description of the available measurements, and (2) the parameter uncertainties can be estimated accurately. In this case study, the model was indeed validated to be acceptable and the kinetic parameters could be estimated with a standard deviation between 5% (minimum) and 16% (maximum). As an application of this model, copper concentrations can be determined.

© 2009 Elsevier B.V. All rights reserved.

1. Introduction

This short note aims to model the copper-catalyzed oxidation of iodide by oxygen and to determine the various kinetic coefficients included in the rate equation. This study is based on the experimental work of Sigalla and Herbo [1] (hereafter abbreviated as SH58), more than half a century after their original study. They observed the remarkable kinetics of the oxidation of iodide by dissolved molecular oxygen, in an aqueous acid medium and in the presence of copper as a catalyst. They also proposed an incomplete reaction rate equation to account for these observations but did not take all factors into account. Hence they were not able to estimate all necessary kinetic constants and to further validate their suggestion.

The current study starts from their observations and their original model proposition to formulate a multivariate model describing the reaction rate as a function of the identified major reactant concentrations. Subsequently, this model is fitted on the observations and the optimal model is assessed statistically to verify its quality. This procedure results in a mathematical model for the reaction rate with all model parameters being quantified, such that the reaction rate can be predicted for any experimental conditions. Or, alternatively, one of the reactants' concentration can be predicted from the reaction rate, which is measured, and the remaining reactant concentrations, which are known. The presented parameter estimation and model validation procedure are very generic although not widely used, and may therefore be of interest to a wide audience.

The following reaction scheme of the copper-catalyzed oxidation of iodide by oxygen was proposed by SH58 (with their numbering):

$$2Cu^{2+} + 2I^- \leftrightarrows 2Cu^+ + I_2 \quad \text{(III0)}$$

$$O_2 + H^+ + Cu^+ \leftrightarrows O_2H + Cu^{2+} \quad \text{(III1)}$$

$$O_2H + H^+ + 2I^- \leftrightarrows H_2O_2 + I_2^- \quad \text{(III2)}$$

$$Cu^{2+} + I_2^- \leftrightarrows Cu^+ + I_2 \quad \text{(III3)}$$

$$H_2O_2 + H^+ + I^- \leftrightarrows H_2O + IOH \quad \text{(III4)}$$

$$IOH + H^+ + I^- \leftrightarrows H_2O + I_2 \quad \text{(III5)}$$

* Corresponding author at: Vrije Universiteit Brussel, Analytical and Environmental Chemistry, Pleinlaan 2, B-1050 Brussels, Belgium. Tel.: +32 2 629 32 64; fax: +32 2 629 32 74.
E-mail address: adebrauw@vub.ac.be (A. de Brauwere).

0039-9140/$ – see front matter © 2009 Elsevier B.V. All rights reserved.
doi:10.1016/j.talanta.2009.08.030

Table 1
Summary of optimisation results. Initial values are arbitrary, except for K_1 and K_2 for which the values proposed by SH58 were taken.

	Initial	Optimised	Standard deviation
k ($M^{-1}\,s^{-1}$)	100,000	40,211	2,000
K_S (M)	0.35	0.370	0.05
K_1 (M^{-6})	390	61,900	10,000
K_2 (M^{-3})	1,700	493	30
V_{WLS}	2,310	42.3	8.1 (assuming $\chi^2_{df=33}$)

The first step of this complex process, (III0), describes a rapidly established equilibrium which strongly favors the right hand side of the reaction. As such, the (very small) amount of copper introduced in solution, [Cu], will quasi-completely be under the form of Cu^+ species. The first step of the actual reaction, (III1), is the rate determining step. In addition, the following trends influencing the catalyzed reaction rate were observed:

(a) The presence of Cl^- ions and the ionic strength of the solution do not influence the reaction rate.
(b) The reaction is first order with respect to [Cu^+] (or [Cu] according to the above discussion of equilibrium (III0), and as it will be denoted from now on).
(c) When [I^-] increases, and all other concentrations are kept constant, the reaction rate first increases rapidly, then reaches a maximum and decreases almost as rapidly.
(d) The reaction order with respect to [H^+] changes from 1 to 0, as [H^+] increases.
(e) The reaction order is 1 with respect to [O_2].

Combining these observations, SH58 proposed the following overall kinetic equation:

$$v_c = k_c[O_2][Cu]f_1([I^-])f_2([H^+]) \quad (1)$$

In an appendix, they derive, from mechanistic assumptions, a possible expression for $f_1([I^-])$:

$$f_1([I^-]) = \frac{K_1^{1/2}[I^-]^{7/2}}{[I_3^-]^{1/2} + K_1^{1/2}[I^-]^{7/2} + K_1^{1/2}K_2[I^-]^{13/2}} \quad (2)$$

K_1 and K_2 are equilibrium constants associated with the following reactions, representing the actual nature of the copper complexes present in the equilibrium (III0):

$$2CuI^+ + 7I^- \leftrightarrows 2CuI_3^{2-} + I_3^- \qquad \text{(equilibrium constant } K_1\text{)}$$

$$CuI_3^{2-} + 3I^- \leftrightarrows 2CuI_6^{5-} \qquad \text{(equilibrium constant } K_2\text{)}$$

and SH58 even proposed values for K_1 and K_2 (see Section 3 and Table 1). Baeyens [2] studied the same reaction but with an auto-analyzer (AutoAnalyser Technicon) which allowed him to vary more easily and reproducibly one variable keeping the others constant. He observed similar trends in the reaction rate with changing reagent concentrations. However, his intention was not to decipher the mechanisms but to investigate the potential of this copper-catalyzed method as an analytical tool to quantify small concentrations of copper. Therefore, no further attempt was made to propose a model for the kinetics.

Kimura et al. [3], apparently unaware of the previous work of SH58 (which is not surprising as SH58 is written in French), performed a similar study on the kinetics and mechanisms copper-catalyzed oxidation of the iodide ion. Again, their observations concerning the influence of the different species on the reaction rate were essentially identical to those of SH58. In particular, they confirm the remarkable feature of this reaction, i.e. that v "*has a maximum around* 0.075–0.1 M *of* I^-" [for all other conditions kept constant]. Finally, they also propose an expression for the reaction rate:

$$v_c = \frac{k_5K_4[Cu^{2+}]_{added}[I^-]^2}{K_4[I^-] + 1} \quad (3)$$

However, they reported that the observed maximum rate relative to [I^-] might deviate from the one resulting from this equation. Consequently, this mathematical function expressing the rate dependence of [I^-], is probably not the most appropriate. It is also curious that the concentrations of [O_2] and [H^+] do not appear in Eq. (3). Therefore, we will not further consider this equation but continue on the proposition of SH58 (1)–(2).

2. Methods

2.1. Experimental data of SH58

In our search for a suitable model and its subsequent calibration and validation, we use the original data from SH58. The measurements of reaction rate and reactant concentrations are unavoidably associated with errors or uncertainties. These should all be taken into account in order to accurately estimate model parameters, and certainly their uncertainties. Most importantly, they must all be considered when assessing the goodness of fit of the final model. Indeed, a good model should fit the data "within their uncertainties". Quantitative statistical criteria exist to evaluate how acceptable the fit is, but these depend on a reliable incorporation of the measurement uncertainties. In particular, the uncertainties of the "input" or "independent" variables (in this case the concentrations of [O_2], [Cu], [H^+] and [I^-]) are often neglected, although they are more often than not highly significant. As we use the data from SH58 (number of experiments, $N = 37$) where any mention of the associated uncertainties lack, we estimated them as follows (s stands for the standard deviation estimate):

- $s(v_c)$ is estimated from the standard deviation of three replicate experiments (>2 replicates), resulting in a relative value of 3.58%, which seems reasonable;
- s(input concentrations) for concentrations > limit of detection: estimated to be equal to 2.5% of the measured concentration;
- s(input concentrations) for concentrations > limit of detection: an uncertainty was assumed equal to 2.5% of the limit of detection, i.e. a constant value [4].

2.2. Model

Combining the equations (1)–(2), the observations (a)–(e) and visual inspection of the data, we propose the following multivariate model to describe and predict the rate of the catalyzed reaction:

$$v_c([O_2], [Cu], [H^+], [I^-]) = k[O_2][Cu]\frac{[H^+]}{K_S + [H^+]} \times \frac{K_1^{1/2}[I^-]^{7/2}}{[I_3^-]^{1/2} + K_1^{1/2}[I^-]^{7/2} + K_1^{1/2}K_2[I^-]^{13/2}} \quad (4)$$

The overall reaction rate is represented as a product of the univariate reaction rate functions (i.e. the rate as a function of only one concentration). These univariate reaction rate functions are simply linear for [O_2] and [Cu], Michaelis–Menten-type with respect to [H^+] and a more complex kinetic function for [I^-]. Note that data for [I_3^-] were available only for a fraction of the dataset. Within these experiments it did not vary much [1], therefore we fixed its value to an average of 2.1×10^5 M. This model contains four parameters ($p = [k, K_S, K_1, K_2]$; $n_p = 4$), which are to be estimated by fitting the model on the available data. The advantage of this model equation

is that all unknown parameters can be interpreted kinetically. Note that as we are only concerned with the catalyzed reaction, we will from now on drop the subscript "*c*".

2.3. Parameter and uncertainty estimation

The unknown parameters were estimated by fitting model (4) on measurements of reaction rates y_i ($i = 1, \ldots, N$). The optimal fit was found by varying the values of the parameters p until the weighted least squares (WLS) cost function:

$$V_{\mathrm{WLS}} = \sum_{i=1}^{N} \frac{[y_i - v_i]^2}{s_i^2} \tag{5}$$

was minimal. v_i represents the reaction rate as computed using (4) and the input concentrations ($[O_2]_i$, $[Cu]_i$, $[H^+]_i$, $[I^-]_i$) associated with experiment *i*. The inverse weights s_i^2 are usually defined as the variance associated with experiment *i*. In a classical WLS approach s_i^2 is defined as the variance of measurement y_i, i.e. only the output uncertainty is used to weigh the pointwise misfit. Here, we use a refined approach where the input uncertainties are taken into account as well [5]:

$$s_i^2 = s_{y,i}^2 + \sum_{m=1}^{4} \left| \frac{\partial v_i}{\partial C_m} \right|^2 s_{C,m}^2 \tag{6}$$

In the above equation C_m ($m = 1, \ldots, n_C$) represents either of the n_C (4 in this case) input concentrations. All s_i^2 are inverted to form the weights and stored on the diagonal of a weighting matrix W.

As model (4) is nonlinear with respect to the parameters, there is no analytical expression for the optimal solution (i.e. the minimal V_{WLS}); instead a numerical optimisation procedure must be employed. Here, we used a Levenberg–Marquardt optimisation. This procedure requires knowledge of the Jacobian matrix J, containing the derivatives of the model output v_i ($i = 1, \ldots, N$) with respect to the parameters p_j ($j = 1, \ldots, n_p$):

$$J(i,j) = \frac{\partial v_i}{\partial p_j} \tag{7}$$

Once the optimal parameter values $\hat{p}$ are found, their associated covariance matrix is calculated by the following linear approximation:

$$Cov_{\hat{p}} = (J^T W J)^{-1} \tag{8}$$

where J and W are both dependent on the parameter values, and hence should be recomputed with the final, optimal parameter values before calculating $Cov_{\hat{p}}$. This linear approximation of the parameter covariance matrix is only exact in the case that the model is linear in the parameters. In the nonlinear case, (8) is only asymptotically valid, i.e. for the sample size tending to infinity [6]. Nevertheless, it has been demonstrated to be a satisfactory estimation in several cases [5,7]—although this is obviously only the case if all measurement uncertainties are taken into account (in W). Therefore, the inclusion of the input uncertainties (Eq. (6)) is essential.

Another advantage of such an overall weighting is that the final, minimal value of V_{WLS} can be interpreted statistically, or more precisely: its "acceptability" can be assessed. Indeed, assuming that

(i) the model (equation) is correct or appropriate for the observations under study, and
(ii) the measurement errors are independent, normally distributed with known variances:

$$(s_{y,i}^2 \text{ and } s_{C,m}^2 \text{ for all } i = 1, \ldots, N \text{ and } m = 1, \ldots, n_C)$$

the minimal V_{WLS} is a sample from a χ^2 distribution with $N–n_p$ degrees of freedom [8,9] (n_p = number of parameters, N = number of output measurements). Knowing this, the minimal V_{WLS} value can be compared to the percentiles of the relevant distribution, enabling an estimation of the probability to obtain this value. In practice, if the minimal V_{WLS} value is too high, this means that the remaining difference between model and measurements is too large to be attributable to only noise with the assumed properties. Consequently, either the noise variances are not estimated correctly (and are actually larger), or the model is not adequate. As a third possible cause the measurements could contain an error (e.g. an outlier), but these errors are usually removed in a preprocessing stage. The minimal V_{WLS} value can also be too low, which could indicate that the data are overmodelled (i.e. a too complex model is used) or that the measurement errors are overestimated.

To summarise, we are concerned here with a model, proposed to describe some (kinetic) measurements, but still containing some parameters that need to be estimated based on these measurements. In this case it is strongly advised to take into account all measurement uncertainties in the parameter estimation procedure (Eq. (6)). This has two main advantages: (1) the residual cost function can be interpreted statistically to assess whether the proposed model does an acceptable job in describing the measurements; (2) the parameter uncertainties can be estimated (more) accurately.

3. Results and discussion

The results obtained when fitting model (4) on the data from SH58 with the procedure outlined above are shown in Fig. 1 and Table 1. Both visually and statistically the fit is acceptable. The statistical evaluation was based on a comparison between the minimal V_{WLS} value (42.3) and the theoretical $\chi^2_{\mathrm{df}=33}$ distribution from which it should be a sample. The theoretical distribution has expected value $E\left\{\chi^2_{\mathrm{df}=33}\right\} = 33$ and standard deviation $\sqrt{\mathrm{Var}\left\{\chi^2_{\mathrm{df}=33}\right\}} = 8.1$. Hence, the minimal V_{WLS} value falls well within its expected value and ±2 standard deviations (95% probability interval) and cannot be rejected.

The results shown in Fig. 1 correspond to an optimisation starting from the values given in Table 1. These are not completely arbitrary as the initial values of K_1 and K_2 were the ones suggested by SH58, however, without giving details about the way they were estimated. A sensitivity study was performed to assess the robustness of the optimised results when starting from different initial parameter values. The optimal parameter values seem to be relatively well constrained: for initial parameter values ranging from 0 to 10 times the previously found optimal parameters (Table 1), the optimal parameter values (except diverged values) vary with a relative standard deviation of maximum 2.6% (for K_S).

In an attempt to further validate the model and the calculated parameter values, independent measurements of reaction rates at 25 °C were made using an automated Technicon system. Combining the experimental reaction rate, the concentrations of H^+, I^- and O_2 and the optimal parameter values from Table 1 into Eq. (4), we can predict the copper concentrations according to the proposed, calibrated model. These values compare well to the experimental copper concentrations (Table 2), especially considering the fact that the experiments are conducted with a completely different method, many years after the original measurements made by SH58.

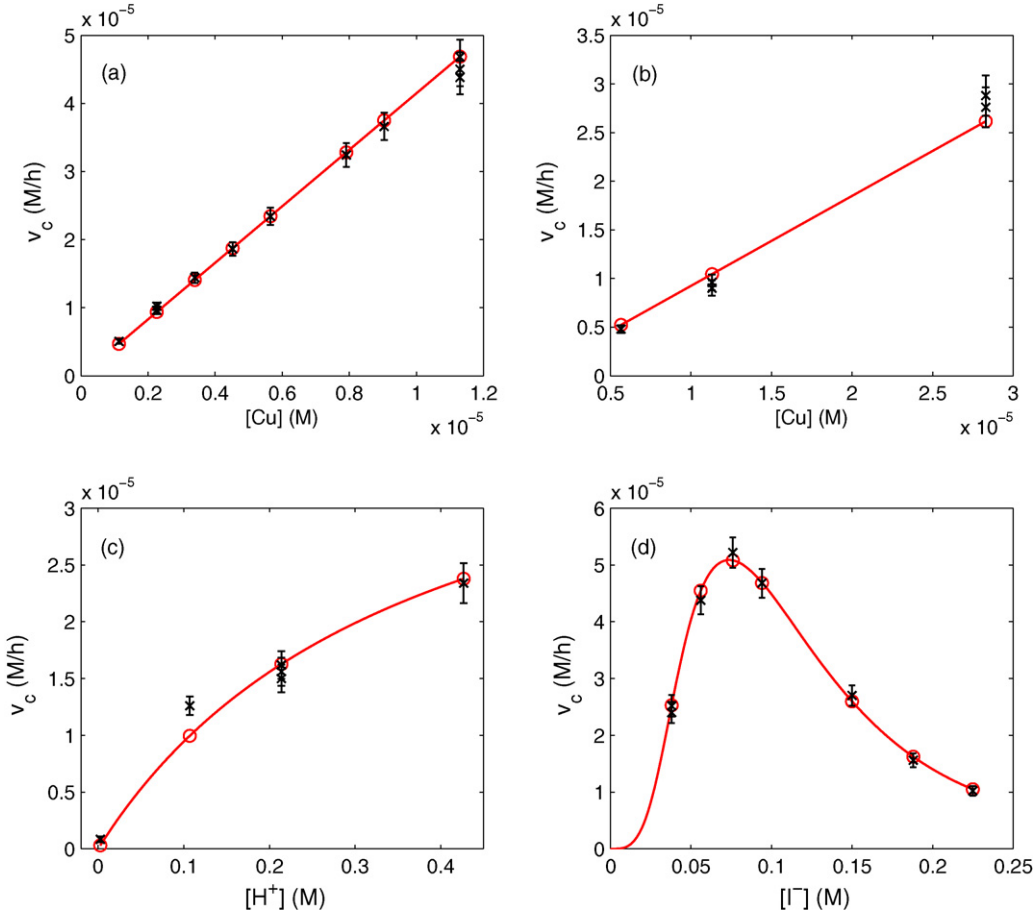


Fig. 1. Visual comparison between measurements (black crosses with error bars representing ±1 standard deviation s_i, as computed from Eq. (6)) and optimised model (red circles and line). Experimental conditions are: (a) $[H^+] = 0.488$ M, $[I^-] = 0.094$ M; (b) $[H^+] = 0.214$ M, $[I^-] = 0.188$ M; (c) $[Cu] = 1.13 \times 10^{-5}$ M, $[I^-] = 0.038$ M; (d) $[H^+] = 0.49$ M; $[Cu] = 1.13 \times 10^{-5}$ M. All experiments were conducted at 25 °C. All experiments were conducted at 25 °C and with saturated oxygen concentrations (2.69×10^{-4} M). (For interpretation of the references to color in this figure legend, the reader is referred to the web version of the article.)

Table 2
Comparison between measured and modelled copper concentrations for independent measurements. Concentrations are given in M, reaction rates in M/h.

	Measured v	$[H^+]$	$[I^-]$	$[O_2]$	Exper. [Cu]	Modelled [Cu]
Experiment 1	1.43×10^{-4}	1.25	0.050	2.69×10^{-4}	2.39×10^{-5}	1.92×10^{-5}
Experiment 2	2.66×10^{-4}	1.25	0.11	2.69×10^{-4}	2.39×10^{-5}	1.24×10^{-5}

4. Conclusions

This study continued the work of SH58 and added the following steps to the description of the copper-catalyzed oxidation of iodide by oxygen in an aqueous acidic medium:

(i) a multivariate model was proposed for the reaction rate as a function of the reactants' concentrations;
(ii) this model was fitted on the observations to estimate each of the kinetic coefficients;
(iii) the four coefficients were optimised simultaneously – not in a sequential procedure where one coefficient is optimised after the other – which gives more guarantee that the obtained values are truly optimal;
(iv) during the parameter optimisation, the experiments were weighted taking into account all measurement uncertainties, i.e. both on the reaction rate (output) and on the reactants' concentrations (inputs);
(v) this procedure allows a statistical analysis to assess the probability of the outcome; in this case accepting the optimisation results and hence the proposed model. This can be viewed as an internal validation of the model, which can be applied even if relatively few data are available (and thus cross-validation is not an option). On the other hand, information on the measurement uncertainties is essential.

Points (ii)–(v) are very generic and can be applied to any (chemical) dataset, as long as an appropriate model can be formulated for the reaction under study (i.e. point (i)). This step is indeed application-specific. Formulating an accurate model may not be so straightforward, especially if the underlying mechanism is only poorly understood. However, note that if the interest lies in prediction rather in the parameter interpretation, any functional expression can be used as a model, as long as it is able to satisfactorily describe the observations. For instance, we were able to find another effective expression for the rate dependence on $[I^-]$, giving the following multivariate model for the reaction rate:

$$v_c([O_2], [Cu], [H^+], [I^-]) = k[O_2][Cu]\frac{[H^+]}{K_S + [H^+]}\frac{[I^-]^3}{Ae^{B[I^-]} - 1}$$

This model was derived from the expression proposed by Max Planck to account for the black body radiation! Only based on the

statistics of the minimal cost function, this model was as acceptable as model (4). Furthermore, both models have the same number of parameters, so no considerations on parsimony can be used to discriminate between them. However, model (4) was preferred because it has the advantage of being derived from kinetic principles and the model parameters are chemically interpretable.

In short, this modelling work delivered a calibrated and internally validated model which enables the prediction of the catalyzed reaction rate under given experimental conditions (i.e. input concentrations), at 25 °C. In addition, the calibrated model parameters can be interpreted as kinetic/equilibrium constants and therefore also have some interest of their own.

Finally, the model has a potential added value for analytical applications. Indeed, on the basis of this model it is possible to estimate copper concentrations in a sample by measuring the formation of I_2 or I_3^- at optimal values of dissolved oxygen, pH and iodide concentration and after a fixed reaction time. A good agreement between our experimental and theoretical results was observed. Furthermore, the availability of a model permits advanced experimental design: future experiments can be designed to deliver maximal information. Although here the focus was on a specific kinetic reaction, the procedure could be used for other reactions, which may offer more application possibilities, e.g. the Fenton reaction.

Acknowledgement

Anouk de Brauwere is a postdoctoral researcher at the Research Foundation Flanders (FWO-Vlaanderen) and was honoured by a postdoctoral intercommunity fellowship from the Francqui Foundation.

References

[1] J. Sigalla, C. Herbo, J. Chim. Phys. 55 (1958) 407 (in French).
[2] W. Baeyens, M.Sc. Thesis, Vrije Universiteit Brussel, 1971 (in Dutch).
[3] M. Kimura, M. Tokuda, K. Tsukahara, Bull. Chem. Soc. Jpn. 67 (1994) 2731.
[4] S.L.R. Ellison, M. Rosslein, A. Williams (Eds.), EURACHEM/CITAC Guide, Quantifying Uncertainty in Analytical Measurement., Second edition, 2000, ISBN 0 948926 15 5.
[5] A. de Brauwere, F. De Ridder, M. Elskens, J. Schoukens, R. Pintelon, W. Baeyens, J. Mar. Syst. 55 (2005) 205.
[6] R. Pintelon, J. Schoukens, System Identification: A Frequency Domain Approach, IEEE, New York, 2001.
[7] J.R. Donaldson, R.B. Schnabel, Technometrics 29 (1987) 67.
[8] M.J. Box, Technometrics 12 (1970) 219.
[9] V. Rod, V. Hancil, Comput. Chem. Eng. 4 (1980) 33.

Talanta 80 (2009) 1039–1043

Contents lists available at ScienceDirect

Talanta

journal homepage: www.elsevier.com/locate/talanta

Short communication

Sensitivity improvement in ICP MS analysis of fuels and light petroleum matrices using a microflow nebulizer and heated spray chamber sample introduction

Guilhem Caumette[a,b], Charles-Philippe Lienemann[b], Isabelle Merdrignac[b], Hugues Paucot[c], Brice Bouyssiere[a,*], Ryszard Lobinski[a,d]

[a] CNRS-UPPA, UMR 5254, LCABIE, Hélioparc, 2 av. Pr. Angot, 64053 Pau, France
[b] Physics and Analysis Division, Refining-Petrochemicals Technology Business Unit, IFP-Lyon, F-69360 Solaize, France
[c] ADERA-UT2A, Hélioparc, 2 av. Pr. Angot, 64053 Pau, France
[d] Department of Analytical Chemistry, Warsaw University of Technology, ul. Noakowskiego 3, 00-664 Warszawa, Poland

ARTICLE INFO

Article history:
Received 20 April 2009
Received in revised form 7 August 2009
Accepted 17 August 2009
Available online 22 August 2009

Keywords:
ICP-MS
Fuel analysis
Direct injection
Heated spray chamber

ABSTRACT

Reasons for signal suppression during the analysis of light petroleum matrices by inductively coupled plasma mass spectrometry (ICP MS) were examined. A decrease of the ionization efficiency of the plasma was found to be the principal factor responsible for this loss of sensitivity. Consequently, an interface based on a total consumption micronebulizer and a heated spray chamber was constructed to alleviate this problem. A method based on flow-injection ICP MS using this interface was developed for the direct multielement analysis of undiluted fuels (gasoline, kerosene) and gas condensates offering an increase in sensitivity by at least a factor of 3–4 in comparison with the existing setups.

© 2009 Elsevier B.V. All rights reserved.

1. Introduction

Light petroleum matrices and refining products, such as gas condensates and fuels (gasoline or kerosene) contain several metals, including mercury [1–4], arsenic [5,6] or lead [7,8] present in the $\mu g\,kg^{-1}$ range. Their analysis is important in the different sectors of economy from refining to environmental risk assessment. Mercury or arsenic, identified as the major metals present in natural gas and gas condensates, are responsible for catalyst poisoning, fouling and corrosion of refining installations. Lead and manganese have been of interest because of their use in additives to improve the antiknock properties of gasoline [7–9].

A number of techniques have been developed for the metal determination in fuels and related petroleum samples [10,11]. They include graphite-furnace atomic absorption spectrometry (GF-AAS) [12–14], inductively coupled plasma atomic emission spectrometry (ICP-AES) [10,15], and, more recently, ICP-MS [10,16–18]. The latter is particularly attractive because of its capacity of the simultaneous multielemental analysis and the sub-$\mu g\,kg^{-1}$ limits of detection (LOD) theoretically allowing the direct analysis. However, the introduction of organic, especially oxygen-free, solvents in ICP-MS is known to be affected by plasma quenching and matrix effects [19]. Therefore, petroleum matrices were usually analysed after digestion [20] or considerable dilution [17,20].

Recent advances in ICP MS analysis of organic solvents were based on the reduction of the amount of solvent arriving at the plasma by lowering the uptake rate and desolvation as well as on operating the plasma at higher power levels. The use of conventional micronebulizers (100–300 $\mu l\,min^{-1}$) equipped with a low-volume spray chamber limits the risk of memory effects and allows an increase in sample throughput [21]. The use of conventional (double-pass Scott) spray chamber results in a low fraction of sample introduced into the plasma and can cause analyte fractionation. An interesting alternative is the use of direct injection nebulizers, such as the DIN (not commercially available anymore) and the DIHEN (direct injection high efficiency nebulizer) [18,22,23] because of a low internal dead volume, rapid response time, reduced memory effects, absence of analyte loss and the elimination of the problem of fractionation in the spray chamber. However, routine analyses of petroleum matrices with DIHEN have not been demonstrated, likely because of plasma perturbation, clogging and instability in time.

In our former works [4,21] an interface was developed, based on a total consumption micronebulizer for the introduction of xylene solutions into ICP MS. The increase in the nebulizer capillary diameter and the elimination of the internal connections has limited the problem of clogging, pressure instability and memory effects [24].

* Corresponding author. Tel.: +33 0 559407752; fax: +33 0 559407781.
E-mail address: brice.bouyssiere@univ-pau.fr (B. Bouyssiere).

0039-9140/$ – see front matter © 2009 Elsevier B.V. All rights reserved.
doi:10.1016/j.talanta.2009.08.017

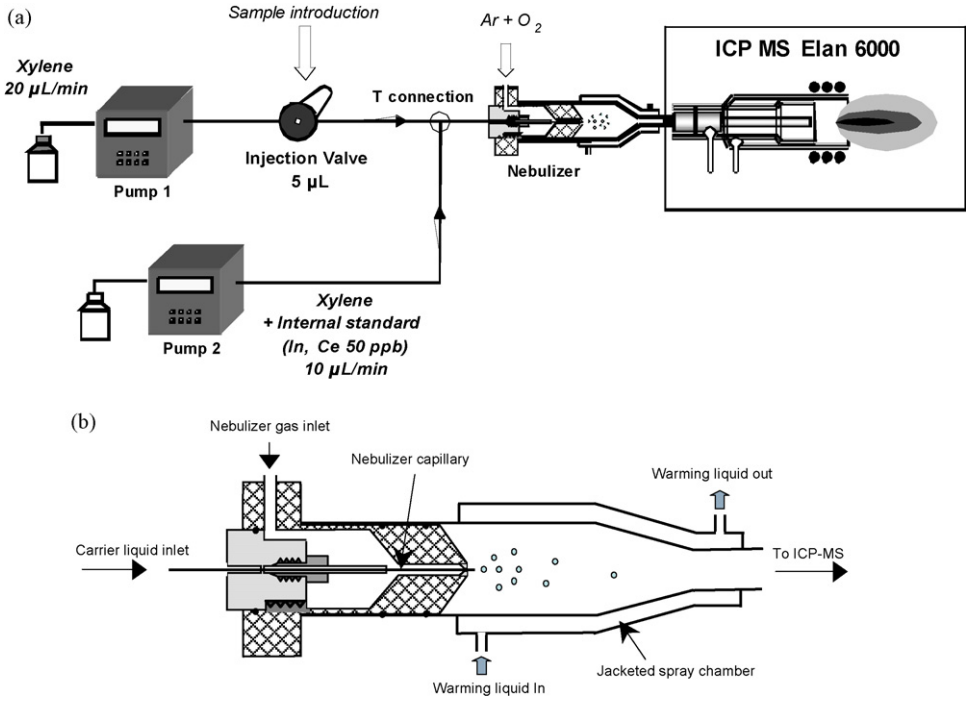


Fig. 1. (a) Scheme of the analytical setup used. (b) Blowup of the sample introduction system.

However, the introduction of light petroleum fractions (gasoline, naphta) using this interface resulted in a significant plasma perturbation and, consequently, required dilution of the sample. This negatively affected the detection limits and was unsuitable for the analysis of trace elements (<0.1 mg kg^{-1}).

The purpose of this study was to examine the reasons for this loss of sensitivity and to propose sample nebulization into a heated drain-free spray chamber to reduce the perturbation of plasma and to increase the sensitivity of the analysis. This setup is the origin of an analytical method allowing the multielement analysis of fuels without dilution resulting in the detection limits at the 1 µg kg^{-1} level (gain of a factor 3–4).

2. Experimental

2.1. Apparatus

The ICP MS instrument used was a PerkinElmer Elan 6000 (PE-SCIEX, ON, Canada). The ICP AES was a Spectro Arcos (Kleeve, Germany) with radial viewing. The analytical setup is shown in Fig. 1a. A dual syringe pump (Model 140C, Applied Biosystems, Foster City, CA, USA) was used to assure a stable delivery of xylene into the ICP at a flow rate of 20 µl min^{-1} without the use of a splitter to limit the solvent consumption. Another pump (Smartline Pump 1000, Knauer, Berlin, Germany) was used to deliver internal standard (In, Ce) in xylene to the nebulizer to control the stability of the instrument. Injections were made using a low port-to-port dead volume micro-injection valve (8125i, Rheodyne, Rohnert Park, CA, USA) fitted with a 5 µl sample loop. The fused silica capillary used was 180 µm i.d. (375 µm o.d.). The sample introduction system was based on a microflow total consumption nebulizer described elsewhere [21]. The spray chamber was jacketed to allow the thermostating at a desired temperature (Fig. 1b). The heating liquid (glycol/water) was circulated through a Neslab RTE–111 (Thermo Fisher Scientific, Waltham, MA) thermostat. For ICP MS analysis, oxygen gas flow, controlled by a mass flow controller, was mixed with the carrier argon nebulizer gas via a T-connection prior to nebulization, to prevent carbon deposition on the sampler and skimmer cones of the instrument. Oxygen was not needed for ICP AES analysis.

2.2. Samples and solutions

Alkanes (pentane, hexane, heptane, octane, decane, dodecane and hexadecane) were purchased from Acros (Acros Organics, NJ) and xylene (ACS grade) was purchased from Baker (Phillipsburg, NJ). Conostans monoelemental standards in oil (1000 mg kg^{-1}) and multielemental S-21 oil standard (100 mg kg^{-1}) were purchased from SCP Science (Baie D'Urfé, Canada). The standard reference material (CRM) crude oil 1634c was purchased from NIST (Gaithersburg, MD). Petroleum samples with different boiling range were provided by the French Institute of Petroleum (IFP-Lyon, France). They were kerosene (IBP = 162 °C and FBP = 252 °C), gasoline (IBP = 0 °C and FBP = 197 °C) and full range gas condensate (IBP = −25° and FBP = 470 °C) (IBP – initial boiling point; FBP – final boiling point).

2.3. Procedure

The ICP MS conditions were optimized daily using a solution of 50 µg kg^{-1} indium and cerium in xylene. The typical settings are RF power 1300 W, Ar nebulizer gas 0.8 l min^{-1}, and auxiliary O_2 flow 45 ml min^{-1}. The sample (5 µl) was injected into the carrier xylene at 20 µL min^{-1} and was mixed before the nebulizer with another xylene flow of 10 µl min^{-1} containing 50 µg kg^{-1} indium and cerium (internal standards) (Fig. 1a). Molybdenum was added at 50 µg kg^{-1} in each matrix analyzed to monitor the ionization efficiency. The isotopes measured in light petroleum matrices were ^{48}Ti, ^{51}V, ^{57}Fe, ^{107}Ag, ^{112}Cd, ^{114}Cd, ^{202}Hg, ^{208}Pb, and ^{53}Cr. ^{98}Mo was measured as a spiked analyte, ^{114}In as the internal standard and ^{58}Ni was measured in the CRM 1634c. The integration time per isotope was 20 ms, three readings were made per analysis, and each injection was made in triplicate. Quantification was made by the method of standard additions using the

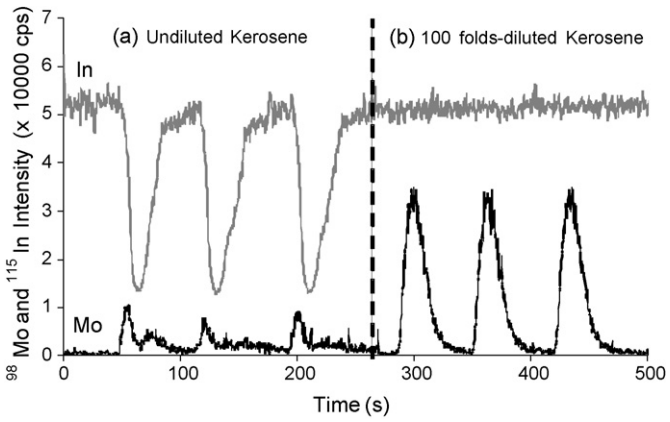


Fig. 2. Effect of light petroleum matrix injection on the signal intensity. μFIA-ICP MS. (a) Three injections of undiluted kerosene sample and (b) Three injections of kerosene 100-folds diluted with xylene. Indium (50 μg kg^{-1}) was added post-injection on-line as internal standard and molybdenum (50 μg kg^{-1}) was spiked in each sample.

multielement S21 standard at concentrations of 10, 25, 50, 100, 150 and 200 μg kg^{-1}.

3. Results and discussions

3.1. Signal intensity suppression by petroleum matrices

Direct injection of petroleum and automotive fuel matrices into an ICP leads to plasma quenching and loss of signal intensity. Fig. 2 shows the effect of μFIA-ICP MS injection of a kerosene sample on the sensitivity and on the internal standard intensity in operational conditions optimized in the previous work [21]. Molybdenum added to the samples was measured as an analyte. In addition, indium and cerium were continuously introduced into the plasma. The addition of these elements directly in the nebulizer allows the control of the plasma stability all along the analysis, before and during the injection of the petroleum sample. Therefore, the impact of the injection of the petroleum sample on the ionization efficiency of the plasma could be observed.

A significant effect can be seen on the intensity of both the analyte signal (^{98}Mo) added to the sample, and of the internal standard indium added to the carrier liquid at the moment of arrival of the injected sample to the plasma (Fig. 2a). The perturbation of the plasma results in a reduction of the flow-injection peak of the analyte. This effect can be avoided by a large dilution of the sample with xylene (Fig. 2b) which, however, results in an increase of the detection limits when referred to the metals concentration in the sample.

Two hypotheses can be put forward to explain this drop in sensitivity:

(i) The volatility of the injected sample creates an expansion of the plasma which disperses the ions formed in the central channel of the plasma; consequently, fewer ions arrive at the detector resulting in the decrease of the signal intensity.
(ii) The injected sample matrix is responsible for the decrease in ionization power of the plasma which results in fewer ions formed and, consequently, a decrease of sensitivity.

In order to validate one of these hypotheses, the signal intensity of the same elements molybdenum and indium was investigated during injection of series of alkanes with increasing boiling points *n*-pentane (36 °C), *n*-heptane (98 °C), *n*-octane (125 °C), *n*-decane (174 °C), *n*-dodecane (216 °C), and *n*-hexadecane (287 °C). These alkanes were chosen to simulate different petroleum matrices with different boiling points. Indeed, classical automotive fuels contain molecules with fewer than 14 carbons, and their boiling point is generally below 250 °C. The analyses were carried out using the same sample introduction system but with ICP AES as detector which allows an independent measurement of intensity at the atomic and ionic lines. During ICP AES analysis, the atomic and ionic lines of carbon were measured to monitor the stability of the plasma. Indeed, the carbon is the major element in petroleum matrix, with a high ionization potential. The impact on ionization and atomisation efficiency of the plasma during injection of organic matrices was reported to be reflected by this element [25].

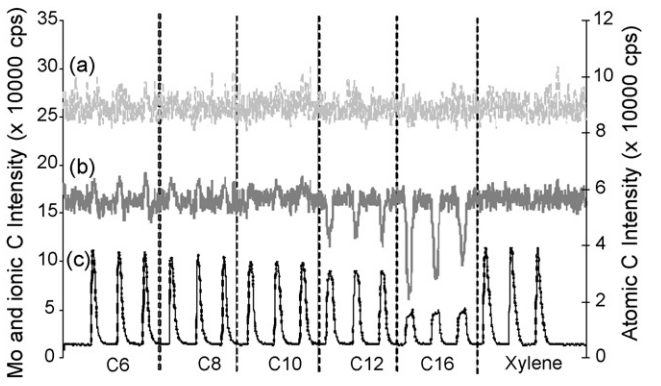


Fig. 3. Effect of boiling point of the matrix on the ionization efficiency. μFIA-ICP AES analysis of alkanes from C6 to C16. (a) Atomic carbon line intensity (λ = 146.334 nm); (b) ionic carbon line (λ = 133.571 nm); (c) molybdenum added at 50 μg kg^{-1} in each sample (λ = 281.615 nm).

The results (Fig. 3) show that the intensity of the carbon atomic line is stable along the analysis, which indicates that

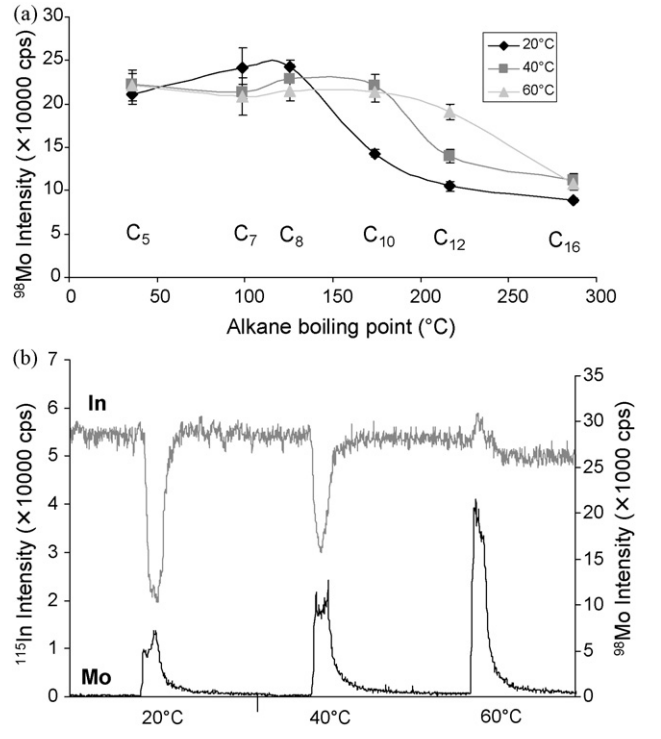


Fig. 4. Effect of temperature on the samples analysed. (a) Ionization efficiency as a function of the matrix boiling point, for the μFIA-ICP MS analyse of molybdenum 50 μg kg^{-1} in Alkanes from C5 to C16. (b) Analyte intensity (50 μg kg^{-1} Mo) and post-injection internal standard intensity (50 μg kg^{-1} In) during μFIA-ICP MS analysis of kerosene.

Table 1
Results of the multielement analysis of light petroleum matrices and figures of merit.

	^{48}Ti	^{51}V	^{53}Cr	^{57}Fe	^{107}Ag	^{112}Cd	^{120}Sn	^{202}Hg	^{208}Pb
Kerosene									
Concentration ($\mu g\,kg^{-1}$)	1 ± 4	<0.8	9 ± 4	12 ± 4	<0.1	124 ± 27	826 ± 40	36 ± 2	179 ± 13
Added, $\mu g\,kg^{-1}$, Found, $\mu g\,kg^{-1}$									
13	13 ± 3	13 ± 4	12 ± 4	12 ± 4	12 ± 4	14 ± 7	–	13 ± 2	20 ± 7
32	31 ± 3	30 ± 4	31 ± 4	–	30 ± 4	26 ± 10	–	32 ± 2	31 ± 7
60	61 ± 3	58 ± 4	62 ± 4	62 ± 4	64 ± 4	52 ± 15	–	61 ± 2	54 ± 7
126	123 ± 4	121 ± 5	121 ± 4	140 ± 5	125 ± 4	131 ± 17	128 ± 7	128 ± 2	113 ± 7
184	181 ± 4	184 ± 4	180 ± 5	183 ± 4	183 ± 5	176 ± 23	180 ± 8	180 ± 4	177 ± 8
251	254 ± 5	254 ± 6	252 ± 7	260 ± 6	251 ± 6	272 ± 38	252 ± 9	257 ± 7	257 ± 11
$Y = ax + b$									
LOD ($\mu g\,kg^{-1}$)	0.9	0.8	6	9	0.1	0.8	0.5	1.6	0.7
R^2	0.9991	0.9992	0.9996	0.9996	0.9996	0.9796	0.9982	0.9995	0.9961
a ($\times 10^3$)	0.9	12	1.5	0.5	17	4.3	22	1.9	12
b ($\times 10^3$)	14	30	14	2.4	0.085	530	18115	74	2199
Gasoline									
Concentration ($\mu g\,kg^{-1}$)	1 ± 1	1.5 ± 3	4 ± 2	< 7	2 ± 1	8 ± 3	200 ± 10	30 ± 10	33 ± 3
Added, $\mu g\,kg^{-1}$, Found, $\mu g\,kg^{-1}$									
12	11 ± 1	12 ± 4	11 ± 2	10 ± 5	12 ± 2	11 ± 4	9 ± 4	11 ± 6	11 ± 3
28	27 ± 1	26 ± 4	22 ± 3	27 ± 5	28 ± 2	26 ± 4	27 ± 5	20 ± 8	27 ± 3
59	59 ± 2	57 ± 3	59 ± 2	60 ± 5	56 ± 2	57 ± 4	57 ± 5	62 ± 8	54 ± 3
112	115 ± 4	117 ± 4	120 ± 5	120 ± 5	115 ± 2	109 ± 4	115 ± 6	–	111 ± 3
162	158 ± 5	163 ± 4	157 ± 6	165 ± 6	162 ± 2	159 ± 5	159 ± 6	–	163 ± 4
237	238 ± 7	240 ± 5	240 ± 7	235 ± 7	237 ± 3	239 ± 6	238 ± 7	–	238 ± 5
$Y = ax + b$									
LOD ($\mu g\,kg^{-1}$)	0.8	0.1	5	7	0.04	0.3	0.2	1	0.1
R^2	0.9995	0.9994	0.9993	0.9994	0.9998	0.9997	0.9995	0.96	0.9997
a ($\times 10^3$)	13	21	2.5	0.8	34	15	30	0.7	48
b ($\times 10^3$)	14	32	10	−0.5	77	121	6023	20	1611
Gas condensate									
Concentration ($\mu g\,kg^{-1}$)	8 ± 2	69 ± 3	45 ± 4	90 ± 30	2 ± 1	3 ± 1	3 ± 2	400 ± 50	4 ± 2
Added, $\mu g\,kg^{-1}$, Found, $\mu g\,kg^{-1}$									
14	14 ± 2	13 ± 3	–	10 ± 6	13 ± 1	13 ± 1	15 ± 3	–	15 ± 2
35	35 ± 2	37 ± 3	33 ± 3	–	35 ± 2	33 ± 2	33 ± 3	27 ± 10	32 ± 2
67	63 ± 3	65 ± 3	69 ± 3	51 ± 10	67 ± 2	68 ± 2	66 ± 3	67 ± 13	62 ± ± 3
135	136 ± 2	137 ± 3	–	–	135 ± 4	135 ± 3	134 ± 3	–	133 ± 4
172	169 ± 3	174 ± 3	174 ± 4	173 ± 17	168 ± 4	166 ± 4	168 ± 4	160 ± 14	165 ± 5
258	259 ± 4	263 ± 4	257 ± 4	261 ± 23	260 ± 5	263 ± 7	261 ± 6	254 ± 26	260 ± 7
$Y = ax + b$									
LOD ($\mu g\,kg^{-1}$)	3	1	10	20	0.4	1	0.5	2	0.2
R^2	0.9998	0.9997	0.9998	0.9905	0.9993	0.9988	0.9992	0.994	0.9994
a ($\times 10^3$)	9	13	1.4	0.8	21	9.3	22	1.6	32
b ($\times 10^3$)	73	891	66	77	40	23	46	622	118

the atomisation of the sample is effective, regardless the matrix injected (Fig. 3a). In contrast to that, the intensity of the carbon ionic line drops significantly when high-boiling point alkanes (C12 and C16) are injected (Fig. 3b). This perturbation of the signal measured using the ionic line indicates that the ionization step is not complete for the injection of heavy alkanes. Moreover, Fig. 3c shows a decreasing intensity of the analyte (molybdenum) signal with the increasing number of carbons of the alkane.

These conclusions correlate with the fact that the energy needed for vaporization, atomization and ionization steps increases with the number of carbons of the alkane. The vaporization and atomization of heavy alkanes in the plasma require more energy which is then not available for ionisation.

Hence, the loss of signal intensity is not due to an expansion of the plasma, as no expansion or perturbation of the plasma could be observed visually during the alkanes injections, but to a decrease of ionisation of the analyte elements in a plasma becoming not energetic enough. Following this conclusion we attempted to improve the ionization efficiency by pre-heating the aerosol in the spray chamber.

3.2. Effect of the spray chamber temperature on the signal intensity

A jacketed spray chamber was designed to heat the aerosol prior to introduction into ICP MS. Fig. 4a shows the effect of the spray chamber temperature on the molybdenum signal intensity for the different alkanes. The alkane solutions were injected at a spray chamber temperature of 20, 40 and 60 °C, respectively. No effect of the temperature observed for low boiling matrices (40–120 °C) confirms the observation made in Fig. 3 that the ionization is not perturbed at these conditions. However, for matrices with boiling points in the range between 150 and 250 °C (typical for fuels) a significant increase in sensitivity is observed with the spray chamber temperature of 60 °C. A possible explanation is that pre-vaporization of the organic solvent occurs in the heated spray chamber. Then, the introduction of the pre-heated solvent requires less energy from the plasma for vaporization and atomisation so more energy is left for efficient ionization.

Fig. 4b shows the effect of the spray chamber temperature on the analysis of undiluted kerosene. The heating of the spray

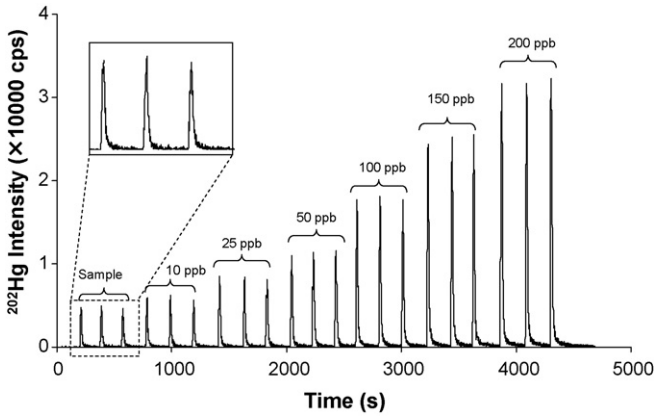


Fig. 5. μFIA-ICP-MS analysis of ^{202}Hg in a kerosene sample by the method of standard additions (each determination was carried out in triplicate). The added concentrations are 10, 25, 50, 100, 150 and 200 μg kg^{-1}, respectively.

chamber to 60 °C results in a decrease of the perturbation of the internal standard indium and in a 3–4-fold increase in signal intensity of the analyte measured. As the background does not change at different temperatures, the detection limits are reduced by a factor 3–4 when the spray chamber temperature increases. By heating the spray, the sample is probably partly vaporized in the chamber, which facilitates the atomization step in the plasma, and the sensitivity of the instrument increases.

3.3. Multielement μFIA-ICP MS analysis of metals in fuels and gas condensates

The interface developed was used for the multielement analysis of samples of kerosene, gasoline and gas condensate. Each petroleum sample was injected without dilution, and the spray chamber was heated to 60 °C. The analysis was done in triplicate followed by standard additions on 6 levels, each in triplicate in order to verify the repeatability of the method. A typical graphic recording of data acquisition for ^{202}Hg is shown in Fig. 5. Table 1 shows the figures of merit and demonstrates that the calibration curves were linear in the range 1–250 μg kg^{-1}. The limits of detection were from 0.04 μg kg^{-1} for Ag in gasoline, to 1 μg kg^{-1} for other elements in all the matrices, except iron and chromium where values up to 20 μg kg^{-1} were measured. The precision calculated according to the Student's *t*-test at 95% was in the 2–5% range. The table shows that heavy metals at concentrations at the μg kg^{-1} level can be successfully determined in light petroleum matrices and fuels by μFIA-ICP MS with spray chamber heated up to 60 °C. However, even if the measured concentrations were precise, the "*a*"-coefficient values show that a matrix effect still remains. The expectation would be the same "*a*" values for a given metal, regardless of the matrix.

The method was validated by the analysis of certified reference material (CRM) residual oil 1634c. This is a heavy oil so it was diluted 1000 times in xylene, in order to obtain metal concentrations in the appropriate range for analysis. Note that a light petroleum reference material was, to our knowledge, not available. The certified concentrations given are 28.2 ± 0.4 mg kg^{-1} vanadium and 17.5 ± 0.2 mg kg^{-1} nickel. The concentrations found on this work were 28.7 ± 0.9 mg kg^{-1} vanadium and 18.4 ± 0.7 mg kg^{-1} nickel respectively.

4. Conclusion

The direct flow-injection analysis of light petroleum matrices (kerosene, gasoline, gas condensate) results in a serious quenching of the plasma leading to the signal intensity suppression. An insight into the mechanism of this sensitivity decrease showed that it was not due to the expansion of the plasma following the introduction of a volatile solvent but to the insufficient energy of the plasma to assure effective ionization of the determined elements. Heating the spray chamber in the μflow-injection setup allows the alleviation of this effect, and a rapid simultaneous multielement analysis of petroleum-related samples with detection limits below 1 μg kg^{-1}.

Acknowledgments

The authors want to thank the company AMETEK SPECTRO for the loan of the ICP-AES Arcos.

References

[1] N.S. Bloom, Fresenius J. Anal. Chem. 366 (2000) 438–443.
[2] B. Bouyssiere, F. Baco, L. Savary, R. Lobinski, J. Chromatogr. A 976 (2002) 431–439.
[3] B. Bouyssiere, F. Baco, L. Savary, R. Lobinski, Oil Gas Sci. Technol. 55 (2000) 639–648.
[4] B. Bouyssiere, Y.N. Ordonez, C.P. Lienemann, D. Schaumlöffel, R. Lobinski, Spectrochim. Acta, Part B 61 (2006) 1063–1068.
[5] B. Bouyssiere, F. Baco, L. Savary, H. Garraud, D.L. Gallup, R. Lobinski, J. Anal. At. Spectrom. 16 (2001) 1329–1332.
[6] E.M. Krupp, C. Johnson, C. Rechsteiner, M. Moir, D. Leong, J. Feldmann, Spectrochim. Acta, Part B 62 (2007) 970–977.
[7] A.W. Kim, M.E. Foulkes, L. Ebdon, S.J. Hill, R.L. Patience, A.G. Barwise, S.J. Rowland, J. Anal. At. Spectrom. 7 (1992) 1147–1149.
[8] I. Rodriguez, S. Mounicou, R. Lobinski, V. Sidelnikov, Y. Patrushev, M. Yamanaka, Anal. Chem. 71 (1999) 4534–4543.
[9] H.B. Swan, Environ. Contam. Toxicol. 63 (1999) 491–498.
[10] C. Duyck, N. Miekeley, C.L. Porto da Silveira, R.Q. Aucelio, R.C. Campos, P. Grinberg, G.P. Brandao, Spectrochim. Acta, Part B 62 (2007) 939–951.
[11] G. Caumette, C.P. Lienemann, I. Merdrignac, B. Bouyssiere, R. Lobinski, J. Anal. At. Spectrom. 24 (2009) 263–276.
[12] J.A. De Azerêdo Amaro, S.L.C. Ferreira, J. Anal. At. Spectrom. 19 (2004) 246–249.
[13] M.G.R. Vale, I.C.F. Damin, A. Klassen, M.M. Silva, B. Welz, A.F. Silva, F.G. Lepri, D.L.G. Borges, U. Heitmann, Microchem. J. 77 (2004) 131–140.
[14] G.P. Brandão, R.C. de Campos, E.V.R. de Castro, H.C. de Jesus, Spectrochim. Acta, Part B 63 (2008) 880–884.
[15] W.A.J. De Waal, C.C.H.M. Kuiper, F.J.M.J. Maessen, J.C. Kraak, R. Wijnands, R.J. Jonker, J. Chromatogr. A 462 (1989) 115–135.
[16] C. Duyck, N. Miekeley, C.L. Porto da Silveira, P. Szatmari, Spectrochim. Acta, Part B 57 (2002) 1979–1990.
[17] S. Dreyfus, C. Pecheyran, C. Magnier, A. Prinzhofer, C.P. Lienemann, O.F.X. Donard, J. ASTM Int. 2 (2005) 51–58.
[18] K. Kahen, A. Strubinger, J.R. Chirinos, A. Montaser, Spectrochim. Acta, Part B 58 (2003) 397–413.
[19] S. Liu, D. Beauchemin, Spectrochim. Acta, Part B 61 (2006) 319–325.
[20] D. Hausler, C. Rosemary, Spectrochim. Acta 14 (1991) 125–140.
[21] P. Giusti, Y. Nuevo Ordonez, C.P. Lienemann, D. Schaumlöffel, B. Bouyssiere, R. Lobinski, J. Anal. At. Spectrom. 22 (2007) 88–92.
[22] E. Björn, W. Frech, Anal. Bioanal. Chem. 376 (2003) 274–278.
[23] J. Heilmann, S.F. Boulyga, K.G. Heumann, Anal. Bioanal. Chem. 380 (2004) 190–197.
[24] P. Giusti, R. Lobinski, J. Szpunar, D. Schaumlöffel, Anal. Chem. 78 (2006) 965–971.
[25] R.I. Botto, Spectrochim. Acta, Part B 42 (1987) 181–199.

Talanta 80 (2010) 1045–1051

Contents lists available at ScienceDirect

Talanta

journal homepage: www.elsevier.com/locate/talanta

Review

A review of chromatographic methods for determination of synthetic food dyes

Marta Kucharska [a,*], Jan Grabka [b,1]

[a] Institute for Engineering of Polymer Materials and Dyes, Department of Dyes and Organic Products in Zgierz, 2/4 Chemików Street, 95-100 Zgierz, Poland
[b] Faculty of Biotechnology and Food Sciences, Technical University of Lodz, 171/173 Wólczańska Street, 90-924 Lodz, Poland

ARTICLE INFO

Article history:
Received 22 May 2009
Received in revised form 7 September 2009
Accepted 18 September 2009
Available online 24 September 2009

Keywords:
Synthetic food dyes
TLC
HPTLC
HPLC
Analysis

ABSTRACT

The purpose of this work was to present a chromatographic methods to analyse synthetic food dyes. The following techniques has been described: thin-layer liquid chromatography (TLC), high performance thin-layer chromatography (HPTLC), traditional column chromatography, high performance liquid chromatography (HPLC), include: ion-pair chromatography (HPLC IP), reversed phase chromatography (RP HPLC) and high performance ion chromatography.

© 2009 Elsevier B.V. All rights reserved.

Contents

1. Introduction 1045
2. Sample preparation 1047
3. Thin layer chromatography (TLC) 1047
4. Traditional column chromatography 1047
5. High performance liquid chromatography (HPLC) 1049
6. Conclusions 1050
Acknowledgements 1050
References 1050

1. Introduction

Food dyes are the most interesting group of food additives. Frequently color of a product determinates its attractiveness for consumer. Incentive hue associates with freshness and good taste value of nutrition. However natural dyes are unstable and easily undergo degradation during the food processing. That is why synthetic food dyes are so widely use according to Directive no 94/36/WE including its later changes. In European Union it is aloud to use following synthetic food dyes (SFD): tartrazine (E102); Quinoline Yellow (E104); Sunset Yellow (E110); Carmoisine (E122); Amaranth (E123); Ponceau 4R (E124); Erythrozine (E127); Allura Red (E129); Patent Blue (E131); Indigo Carmine (E132); Brilliant Blue FCF (E133); Brown HT (E155) [1].

SFD guarantees intensive and permanent color of food products. The costs of production process are much lower in comparison with production of natural dyes [2]. These advantages encourage producers to use them, in spite of many resources which confirm their negative influence on human organism. For instance azodyes are decomposing by natural intestinal flora to aromatic amines [3], which are the cause of frequent headaches in adults while children often become distractible and hyperactive [4]. That is why there is a necessity to control the content of the synthetic dyes in food. For that purpose many analytical methods has been used, such as: thin-layer chromatography; spectrometry [5], derivative spectrometry and other spectrophotometric methods correlated with chemometrics [6,7], for instance hybrid linear analysis a calibration method proposed by Goicoechea and Olivieri (HLA\GO) [8]; adsorptive voltammetry; differential pulse polarography [9,10]; capillary electrophoresis [11,12]; high performance liquid chromatography (HPLC) and ion chromatography.

* Corresponding author. Tel.: +48 42 716 46 61; fax: +48 42 716 13 19.
E-mail addresses: marta.kucharska@impib.pl (M. Kucharska), grabka@snack.p.lodz.pl (J. Grabka).
[1] Tel.: +48 42 631 34 50/48 602 379413.

0039-9140/$ – see front matter © 2009 Elsevier B.V. All rights reserved.
doi:10.1016/j.talanta.2009.09.032

Table 1
Examples of chromatographic conditions for TLC technique.

Matrix	Sample preparation	Stationary phase	Mobile phase	References position
0.1% aqueous solution of dyes standards	–	Kieselgel G (250 um) previously activated at 105 °C (2 h), cellulose CC4l previously dried overnight	Isopropyl alcohol/concentrated aqueous NH3 (4:1) isobutyl alcohol/water/ethanol/concentrated aqueous NH_3 (25:25:50:2)	[13]
Ethanolic solution of dyes standards	–	Kieselgel G (250 um) heated at 100 °C for 30 min, purified with ethanol and heated again before use	Ethanol/butanol/water (9:2:1)	[14]
Dyes standards	–	Glass plates coated with magnesia (250 um) activated for 1 h at 130 °C	15% sodium citrate/methanol (4:1)	[15]
Indian country liquors	Sample evaporated to dryness, residue dissolved in 40% ethanol.	KieselgelG (250 um)	Butanol/anhydrous acetic acid/ethanol/water (20:4:1:10)	[16]
Soft drinks, juices, Jello®	Acetic acid solutions of the samples boiled with white wool (first purified by boiling in dilute NaOH, then in water), washed the wool with cold water, then stripped the dye from it by boiling the wool with dilute ammonia. Extract evaporated to near dryness, then chromatographed.	Kieselgel G (250 um)	Butanol/ethanol/water/NH_4OH (50:25:25:10)	[17]
Gelatin- containing sweets	Sweets dissolved in warm pH 4,0 phosphate buffer, shook solution with polyamide powder, centrifuged the mixture, then removed the supernatant liquid. Polyamide powder washed by shaking with hot water, then centrifuged the mixture and removed the water layer. Extracted dyes adsorbed on the polyamide by shaking with methanol–aqueous NH_3 (19:1). Evaporated the extract to dryness, dissolved the residue in phosphate buffer pH 5,5. Then extracted colorants into Tri-n-octylamine in $CHCl_3$.	Cellulose plate	Ethyl acetate/propanol/ammonia/water (35:35:20:20)	[18]
Mustard and related products	Samples were treated with NH_3, then dyes were extracted with light petroleum and cleaned up by passing the extracts through a column of polyamide.	Cellulose plate	Ethanol/butanol/pyridine/water (1:7:6:6)	[19]
Drinks, solid foods	Acidify drinks applied to a C_{18} Sep-Pak cartridge then eluted color with ethanol, made alkaline with aqueous NH3. Foods macerated with ethanol or 50% acetone made alkaline with $Na_2B_4O_7$ solution and Celite 545, filtered, evaporated solvent, acidified residue with HCl and added it to a Sep-Pak as above.	Kieselgel 60 F_{254}	Ammonia/isopropanol (1:3), propanol/water/acetic acid (3:1:1), (propan-2-ol/ethanol/water/ammonium acetate (12:6:2:1), 2-methylopropanol/water/ethanol (3:2:2)	[20]
Aqueous solution of dyes standards	–	DC Plastikfolien Kieselgel 60[1]	Propanol/butyl acetate/water/pyridine (25:15:10:5)	[39]
Flavoured sugar, jelly, sugar candy	Sample solutions were prepared in 70% ethanol.	Silicagel 60	Isopropanol/amonnia/water (10:1:1)	[44]

Sample preparing is also very important problem in analysis of food dyes. Extracting them from different kinds of matrices is not an easy task. Substances contained in food samples can make colors determination impossible. That is why pretreatment stage is necessary for receiving satisfactory results. In this article chromatographic techniques and methods of sample preparing has been described.

2. Sample preparation

First stage of SFD analysis is extracting them from food sample, which sometimes can be difficult. Everything depends on the kind of matrices and substances which it contains. Pretreatment method is also strictly connected with analytical technique that will be using to determinate the food dyes. In many cases this stage is more complicated then instrumental analysis itself.

For TLC analysis, extracts must be purified from sugars, fats and other substances that can make dyes separation impossible. The most effective method is boiling acetic acid solutions of the samples with white wool. Then the wool is washed with water to remove impurities. The dyes are stripping from fabric by boiling with dilute ammonia. Next evaporated to near dryness extract is chromatographed [17]. In publications many modification of this method can be found, for instance replacing the wool with polyamide fiber or powder [18]. The last one may be use as a column filling [19]. That kind of pretreatment is using for candies, jams and greasy foods. Juices or alcoholic beverages in most cases do not need that complicated methods for extracting SFD, especially when determinate on HPLC. Dyes can be extracted from food with water, ethanol or methanol. Extracts usually are filtering through 0.45 μm filter [32,33] or centrifuging [38]. If analyzed beverage is carbonated it need to be degassed by ultrasonication [35] or heated to boiling.

Sample preparation is fundamental stage of analysis. It has large influence on interpretation of results. For instance in TLC technique partial removal of sugars or fats causes the blurring of spots. That is why careful realization of this stage of analysis allows to save time, it prevents of doing again the same analysis.

3. Thin layer chromatography (TLC)

The easiest chromatographic technique is thin layer chromatography (TLC), because it not needs expensive, complicated apparatus. The only one difficulty is choosing appropriate mobile phase and stationary phase, on which dyes are applied. In appropriate conditions it is possible to separate mixture few dyes and identify them as a result of comparison: migration coefficient R_f, spots shape and its color with standards spots.

Examples of chromatographic conditions (eluent and stationary phase) which have been used to qualitative analysis of dyes are listed in Table 1.

Organic solvents are the most popular in chromatographic techniques. Unfortunately usually they have intensive disagreeable smell and cancerogenic activity. To replace them water-methanol solution of β-cyclodextrine was proposed as mobile phase and polyamide sorbent as stationary phase. This chromatographic system assured satisfactory separation of following dyes: Eosin, Erythrosine and Rhodamine 6G [21].

Derivative of thin layer chromatography is high performance thin-layer chromatography (HPTLC). This method based on utilization of appropriate plates, which ensures better separation of analyze compounds and gives satisfactory result on shorter developing distance. The TLC and HPTLC differ with a kind of adsorbent. In first technique the size of stationary phase particles is 4–25 μm, while in second about 4–9 μm. This way of analysis had been used to assay synthetic dyes in alcoholic beverages. Separation was done on Whatman LHP-K, Analtech HETLC and Analtech HERPS using following mobile phases: butanol/2-butanol/actonitrile/tatrahydrofuran/ethylo-methylo ketone/NaCl 0.5% water solution/ammonia in ratio of 10:10:25:15:20:18:2 or propanol/actonitrile/tatrahydrofuran/ethylo-methylo ketone/ethyl acetate/NaCl 0.5% water solution/ammonia in ratio of (20:15:25:10:10:18:2) [22]. As a stationary phase porous silica gel with 3-aminepropyl functional groups connected with the matrix was used. As an eluent mixture of isopropanol/diethyl ether/ammonia in ratio of 2:2:1 was used [23].

HPTLC technique ensures better separation of chromatographed substances, the spots are less blurry and more clear.

TLC method has many advantages. First of all it does not require laborious preparation of the sample. Slight amount of impurities does not have greater impact on analysis process. Then, this is a rapid and cheap method which enables simultaneous assay of several dozen samples and breaking examination when results are satisfactory [24].

This is the best way for qualitative determination of analyzed mixture, because in relatively short time good separation results can be obtain.

However quantitative determination brings more difficulty, which connects with getting out separated components from the stationary phase. For example it can be done by scratching spots and extracting dye with appropriate solvent and then measure the absorbance of the solution on the spectrophotometer. Nevertheless this is very laborious, the color intensity of extracted dye might be weak and does not guarantee high precision.

Much better results can be received by utilizing digital processing of images. Chromatograms are scanned on flatbed scanner and processed using appropriate software [23], for instance the Adobe Photoshop [42] or ColorDens [43]. The intensity of the spots is measured in the RGB color mode (red, green and blue color channels), length and width are determined using ruler in the instrument bar and finally calculated in arbitrary units by appropriate equation.

This is a simple, rapid and precise method for quantitative determination of SFD. The difference between determined and initial concentration are shown on an example of tartrazine, it amounts 0.7% [44]. Which is better then results obtained by using extraction method.

Quantitative determination of food dyes by TLC technique is much easier when use of digital processing of images. It allows to assay concentration of SFD rapidly and precisely without using complicated apparatus.

4. Traditional column chromatography

Next separation technique is traditional column chromatography. Glassy columns filled with various sorts of adsorbents (e.g. aluminium oxide, polyamide) are using in this method. Subsequently with the help of appropriate eluent particular ingredients of analyze mixture are leaching. In case of food dyes stationary phase can be polyamide powder, while mobile phase is mixture of: 70% aqueous solution of methanol/25% aqueous solution of ammonia (49:1) heated to 55 °C [25]. As an eluent mixture acetone/ammonia/water (40:1:9) [26] or ammonia/methanol/water (5:15:80) can be used [27]. In order to remove of natural alkaline dyes, which are also adsorbing on polyamide carboxymethylcellulose can be used [28].

Currently this method is used very rarely with regard for long analysis time, which can last even a few hours. Additionally it does not ensure high separation of assaying components and it is eluent consuming.

Table 2
Examples of chromatographic systems for HPLC technique.

Column	Mobile phase	Flow rate (ml/min)/time of analysis (min)	Detector	Ref.
C_{18} (25 cm–4.6 mm, 5 μm)	(A) Tetrabutylammonium dihydrogen phosphate in Na_2HPO_3 (B) A/methanol (1:4) (gradient elution 45–100%A)	1/35	UV-DAD	[29]
Kromasil C_{18} (25 cm–4.6 mm, 5 μm) (Fig. 1)	(A) 10 mM tetrabutylammonium dihydrogen phosphate buffer (pH 4.2) (B) Acetonitrile (isocratic elution 45:55%)	1/25	Spectroflow	[30]
Kromasil C_{18} (25 cm–4.6 mm, 5 μm)	(A) Acetonitrile (B) 10 mM phosphate buffer (pH 4.2) (isocratic elution 20:80%)		575	
Tracer Analitica ODS (15 cm–4 mm, 5 μm)	(A) Methanol (B) Ammonium acetate 40 mM (pH 5), (gradient elution 10–75% A)	1/20	UV–vis (Uvicon 923)	[31]
C_{18} (25 cm–4.6 mm, 5 μm) (Fig. 2)	(A) Acetonitrile:methanol (20:80) (B) 1% Ammonium acetate buffer (pH 7.5), (gradient elution 100–47.5% A)	1.5/31	UV-DAD	[32]
ODS Zorbax (25 cm–4.6 mm, 5 μm)	I. (A) Methanol/(B) ammonium acetate (0.08 mol/L) II. (A) Methanol/(B) EDTA* (5×10^{-3} mol/L) + sodium acetate (3×10^{-2} mol/L), (pH 3.5) (I and II 45:55% isocratic elution)	1/5	UV-DAD	[33]
C_{18} (25 cm–4.6 mm, 5 μm)	0.25% Tryton X-100 water solution + phosphate buffer (pH 7) (50 mM/L)	1/8	UV-DAD	[34]
Zorbax Eclipse XDB-C_{18} Rapid resolution (50–4.6 mm, 1.8 μm)	(A) 0.1 mol/l water solution ammonium acetate (pH 6.7) (B) Acetonitrile/methanol (50:50 v/v)	1.5/19	UV-DAD	[35]
Cosmosil C_{18} (125–2 mm, 5 μm)	(A) Triethylamine + acetic acid (pH 6.2) (B) Methanol (gradient elution 95–30% A – 35 min, 30–95% – 5 min)	0.2/40	UV-DAD, ES-MS	[38]
C_{18} (25 cm–4.6 mm, 5 μm)	(A) 0.02 M ammonium acetate (B) Methanol (gradient elution – 20–100–20% B)	1/35	UV-DAD	[40]
Lichrospher 100 RP-18 (250–4 mm, 5 μm)	(A) Methanol (B) Triethylamine 5.00 mM and acetic acid 5.00 mM aqueous solution (pH 6.5), (45/55 (v/v)	0.3/19	UV-DAD	[41]
BDSHypersilC_{18} (250–4.6 mm, 5 μm)	(A) Methanol (B) Tetrabutyl ammonium hydrogenosulfate (0.005 M, pH 3.5) (gradient 25%, – 100% methanol)	0.8/16	UV-DAD	[45]
ODS-2 spherisorb phase Separations (250–4.6 mm, 5 μm)	(A) Water (B) Acetonitryl 5 mM octylamine (pH 4.6) (gradient elution – 70:30 v/v A:B)	1/30	UV–vis	[46]

*Sodium salt of ethylenediaminetetraacetic acid.

5. High performance liquid chromatography (HPLC)

Other method used for separation, qualitative and quantitative determination of synthetic food dyes is high performance liquid chromatography. This technique ensures separation of any mixtures to component substances whereas appropriate detector allow to identification and quantitative determination of them. Examining substances also can be identified by any other detector by comparison with their standard. The basis of separation is differences of affinity components to two phases, stationary phase and mobile phase. Dyes have different adsorption affinity to stationary phase. That appears from differences of their mass, structural space and presence of functional groups in each dye's molecule.

The most popular kind of HPLC technique is reversed phase high performance liquid chromatography (RP HPLC) and ion-pair high performance liquid chromatography (HPLC IP).

In reversed phase system, stationary phase is slightly polar or non-polar, while mobile phase has stronger polarity (e.g. tetrahydrofuran, acetonitrile, methanol, water) [24]. Application of the appropriate conditions allows analyzing most of the food dyes. Ionized samples must have possibility to form neutral molecules. The most important characteristics that must be taken into consideration during selection of analysis conditions are hydrophobic properties of assaying dyes and presence in theirs molecules acidic groups. Hydrophobicity of azodyes is larger then others. It is similar in case of dyes with naphthalene ring in comparison to dyes with benzene ring. In purpose to improvement of separation and shorten time of analysis inorganic electrolyte is added to mobile phase. That kind of modificator often is ammonium acetate buffer in optimal concentration above 0.1 mol/l. Larger concentration causes increasing of retention times. Probably the reason of this is "salting-out" effect. Testing substance precipitated on the surface of stationary phase. The limit of detectability amounts from about 2 μg/l for Tartrazine to 22 μg/l for Ponceau 4*R* [32].

HPLC IP consists in adding hydrophobic ionic substance to mobile phase. It could be quaternary ammonium cation (e.g. ammonium acetate buffer), alkilo- or arylsulfonium anion (e.g. $C_7H_{15}SO_3$). As a result of the reaction between sample and eluent neutral ionic pairs are formed and separated chromatographically in reversed phase system. Another way is preparing of sample which enables the conducting of analysis on ionic exchanger or modification of mobile phase which provides to obtainment of ion-exchanger [24].

In case of absence of ionic compound elution of many dyes (e.g. E102, E124, E132) from column occurs really fast, near dead volume. Addition of ionic substance significantly increases retention time of compounds containing acidic groups in their molecules. It ensures simultaneous separation of many dyes [30]. In this aim tetrabutylammonium phosphate (TBA) is used [28–30]. It promises the best separation of synthetic dyes in presence of natural dyes. It also extends usefulness time of chromatographic column. Ionic pairs create in mobile phase and retention is controlled by interaction with sorbent surface. When the concentration of TBA increases a part of dyes molecules, which occur in the form of ionic pairs also increases which provides to better separation. Significant role in determination of dyes by this method has pH. For column filled with silica gel optimal pH should be in the range of 4–6, what results from low hydrolytic stability of gel. Next important parameter is proportion of organic phase to buffer. In order to prevent overlapping of peaks it is necessary to increase concentration of organic solvent [30].

In most of liquid chromatography methods organic solvents are used. This substances negatively influences on environment and human health. That is why it is justifiable to use green methods. One of them is using a surfactant solution 4-(1,1,3,3-tetramethylbutyl)-phenyl-polyethylene glycol (Tryton X-100) as a mobile phase. This compound is changing the polarity of water and characteristic of a C_{18} column. In its presence column becomes more polar while charges of a dyes molecules are stabilized. Using these method three dyes had been analyzed: Brilliant Blue FCF, Sunset Yellow and Tartrazine. Optimal concentration of surfactant should be in the range of 0.25–1%. Too low concentration of Tryton X-100 makes correct preparation of a column impossible, while too high concentration causes inaccurate separation and quantitative determination of each mixture compounds. Essential role plays here pH as well. It should be equal to 7. Below of this value disappearance of peaks has been observed. The addition of the phosphate buffer was necessary. The charges of buffer components balance the charges of dyes molecules. This method allows getting satisfactory result in 8 min using 15 mg surfactant and 38.8 mg buffer. This is cheap and fast way of analysis of dyes. However if the differences in concentration of separating substances are considerable it could be difficulties in its application [34].

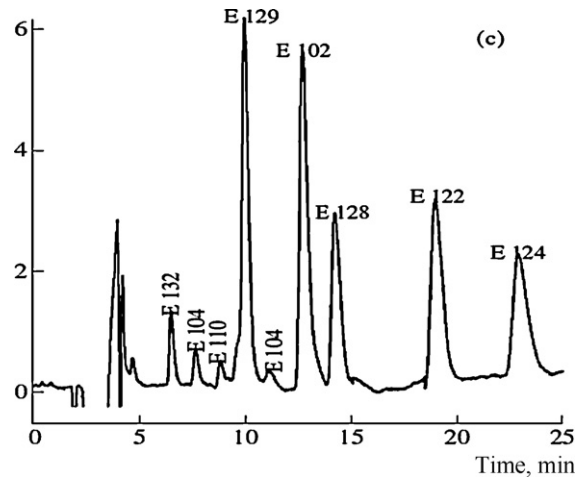


Fig. 1. Chromatogram of nine synthetic food dyes – the conditions of separation are listed in Table 2 [30].

Examples of chromatographic conditions for HPLC technique (eluent, stationary phase, flow rate and time of analysis) which have been used to determination of dyes are listed in Table 2. Figs. 1 and 2 are examples of chromatograms, which presents food dyes separation.

For analysis of the food dyes high performance ion chromatography (HPIC) is used. It consists in using of special column filed in resins with functional groups with constant charge bounded ions. In a direct surrounding of the core there are specified counterions, which ensure inertness of the system. Ions of the sample

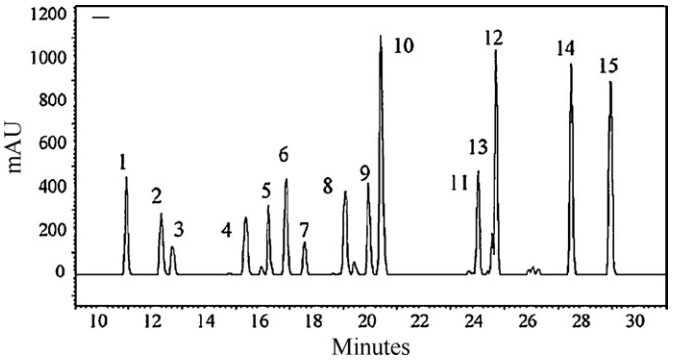


Fig. 2. Chromatogram of 13 food dyes, conditions of separation are listed in Table 2. (1) Tartrazine, (2) Amaranth, (3) Indigo Carmine, (4) Quinoline Yellow I, (5) Ponceau 4R, (6) Sunset Yellow, (7) Quinoline Yellow II, (8) Allura Red, (9) Red 2 G, (10) Green S, (11) Carmoisine, (12) Brilliant Blue, (13) Quinoline Yellow III, (14) Patent Blue, (15) Erythrozine [32].

Table 3
Chromatographic system for determination of dyes mixture by HPIC technique [37].

Time (min)	0.0	6.0	9.5	9.6	12.0	20.0	20.1	23.0	35.0	35.1
HCl (%)	10	10	10	2.5	2.5	2.5	10	10	10	10
Acetonitrile (%)	50	50	50	95	95	95	90	90	90	50
Water (%)	40	40	40	2.5	2.5	2.5	0	0	0	40
λ (nm)	625	430	430	480	480	480	480	525	525	625

are exchanging counter-ions and bonds with stationary phase for specific time. This time is dependent on ions affinity for core. On this ground the separation of the mixture can be done [36]. Theoretically HPIC should not be used for organic, multivalent, hydrophobic ions, because they are bound with stationary phase very strong result in a very long elution times. However using an anion exchange column with slight hydrophobic properties and strongly acidic eluent endures ionization, satisfactory separation can be obtained. It has been proved with eight dyes, among them: E102, E110, E123, E129, E132, and E133. Dione IonPac AS11 was used. It is stable in the range of pH value from 0 to 14. Mobile phase was mixture of 2 mol/l HCl/acetonitrile/water, gradient elution was applied, the chromatographic system is shown in Table 3. Hydrochloric acid was chosen for the sake of its better solubility in acetonitrile, but this last one guarantees better separation then methanol.

In the first succession dyes without azo-baond that is Brilliant blue and Indigo Carmine, then Tartrazine and monoazodyes were eluted. This sequence is connected with hydrophobic properties of the compounds. All assaying dyes had linear dependence between the concentrations and peak area. The detection limits were from 0.03 μg/ml for Brilliant blue to 2 μg/ml for Allura Red and Tartrazine.

This method is reliable and guarantees repeatability of results and the process preparation of the sample is not complicated [37].

6. Conclusions

Each of the described methods can be used to analyze synthetic food dyes successfully. It is necessary to take into consideration that none of them is ideal. To qualitative determination of dyes mixture TLC method is the best solution. It enables obtaining satisfactory results in short time. Quantitative determination in this case might be labour-consuming. For this kind of assays one of HPLC techniques will be better. Deciding for chromatography in reversed phase or ion pair we must be conscious that buffer negatively affects on chromatographic system.

In the future there will be a tendency to use more sophisticated apparatus. Already it can be adduce a few examples of publication about using in HPLC technique various kinds of detectors, like DAD-ESI-MS [38,41].

However using of expensive equipment connects with bearing high costs of amortization. Also the identification of dyes is more complicated then in TLC technique. Natural and synthetic dyes could have the same absorption maximum and similar R_f coefficient which can present a difficulties. TLC technique guaranties the correct interpretation of results of analysis because we take into the consideration a few elements: shape and color of spots, the R_f coefficient and light resistance (natural dyes expose to the light fades in the course of time). Additionally digital processing of images allowed to quantitative determination with high precision. TLC technique seems to be a little forgotten and underestimated method but in authors opinion it is worth to discover it anew.

Choose of analytical technique is also dependent to the method of sample preparation. For TLC and HPTLC chromatographed sample must be carefully purified, that assures satisfactory separation. For that purpose the most appropriate method is boiling acetic acid solutions of the samples with white wool and then stripping dyes from it by boiling with dilute ammonia. It allows to remove substances which may be a reason of problems with separation chromatographed dyes. That kind of sample pretreatment is also useful for other chromatographic techniques.

Acknowledgements

The authors whish to thank to Krzysztof Krach and Ilona Kijewska from Institute for Engineering of Polymer Materials and Dyes, Department in Zgierz for valuable remarks and advices.

References

[1] European Parliament and Council Directive 94/36/EC of 30 June 1994 on colours for use in foodstuffs.
[2] J. Walford, Developments in Food Colours – 1, Applied Science Publishers LTD, London, 1980.
[3] F. Rafii, J.D. Hall, E.D. Cerniglia, Food Chem. Toxicol. 35 (1997) 897–901.
[4] C. Hawley, R.E. Buckley, J Orthomol. Psych. 5 (2) (1976) 129–137.
[5] J. Grabka, A. Sztekmiller-Szymańska, Listy Cukrov. Repar. 124 (2008) 27–31.
[6] K. Hofer, D. Jenewein, Z. Lebensm, Z Lebensm Unters Forsch A 204 (1997) 32–38.
[7] X. Ni, Y. Gong, Anal. Chim. Acta. 354 (1997) 163–171.
[8] Y.S. Al-Degs, Food Chem. 117 (2009) 485–490.
[9] S. Combeau, M. Chatelut, O. Vittori, Talanta 56 (2002) 115–122.
[10] S. Chanlon, L. Joly-Pottuz, M. Chatelut, O. Vittori, J.L. Creticr, J. Food Compos. Anal. 18 (2005) 503–515.
[11] N. Doss, R. Tonido, A. Pizzariello, S. Susmel, J. Electroanal. Chem. 601 (2007) 1–7.
[12] M. Ryvolova, P. Taborsky, P. Vrabel, P. Krasensky, J. Preisler, J. Chrom. A. 1141 (2007) 206–211.
[13] W.B. Chapman, D.J. Oakland, J. Assoc. Publ. Analysts. 6 (1968) 124–128.
[14] S.J. Lyle, M.S. Tehrani, J. Chromat. 175 (1979) 163–168.
[15] J. Masłowska, J. Chromatog. 20 (1985) 99–101.
[16] K.A. Ambade, P.V. Vaidya, S.K. Meghal, J. Food Sci. Technol. 14 (1977) 60–63.
[17] H.T. McKone, G.J. Nelson, J. Chem. Ed. 53 (1976) 722.
[18] M. Puttemans, L. Dryon, D. Massart, Jaoac 66 (1983) 1039–1044.
[19] C. Corradi, G. Michaeli, Boll. Chim. Unione Ital. Lab Prov. Parte Sci. 5 (1979) 651–661.
[20] J. Love, N.Z. J. Sci. 27 (1984) 113–116.
[21] V.Z. Atayan, E.G. Sumina, S.N. Shtykov, J. Anal. Chem. 58 (2003) 7.
[22] J.A. Steele, Jaoac 58 (1984) 540–541.
[23] F. Soponar, A.C. Mot, C. Sarbu, J. Chrom. A 1188 (2008) 295–300.
[24] Z. Witkiewicz, Basics of Chromatography, WNT, Warsaw, 2000.
[25] E. Andrzejewska, Rocz Państw. Zak. Hig. 31 (1980) 277–281.
[26] R.A. Gilhooley, R.A. Hoodless, K.G. Pitman, J. Thomson, J. Chrom. A. 72 (1972) 325–331.
[27] J. Davidek, E. Davidkova, J. Chromatog. 26 (1967) 519–521.
[28] G. Lehmann, P. Collet, H. Hahn, M. Ashworth, Jaoac 53 (1970) 1182–1189.
[29] K.M. Wever, E.J. Neale, J. Chrom. A. 354 (1986) 486–489.
[30] M.G. Kiseleva, V.V. Pimenova, K.I. Eller, J. Anal. Chem. 58 (2003) 685–690.
[31] M.S. García-Falcón, J. Simal-Gándara, Food Control 16 (2005) 293–297.
[32] K.S. Minioti, C.F. Sakellariou, N.S. Thomaidis, Anal. Chim. Acta. 583 (2007) 103–110.
[33] S. Pereira Alves, D. Mares Brum, E. Castello Branco de Andrade, A. Duarte Pereira Netto, Food Chem. 107 (2008) 489–496.
[34] E.C. Vidotti, W.F. Costa, C.C. Oliveira, Talanta 68 (2006) 516–521.
[35] N. Yoshioka, K. Ichihashi, Talanta 74 (2008) 1408–1413.
[36] J. Siepak, Application of Ionic Chromatography in Water Analysis, Publication of Adam Mickiewicz University, Poznań, 1999.
[37] Q. Chen, S. Mou, X. Hou, J.M. Riviello, Z. Ni, J. Chrom. A. 827 (1998) 73–81.
[38] M.R. Fuh, K.J. Chia, Talanta 56 (2002) 663–671.
[39] Materials obtained from Institute for Engineering of Polimer Materials and Dyes Department of Dyes and Organic Products in Zgierz, Poland.
[40] M. Ma, X. Luo, B. Chen, S. Su, S. Yao, J. Chrom. A 1103 (2006) 170–176.

[41] F. Gosetti, V. Gianotti, S. Angioi, S. Polati, E. Marengo, M.C. Gennaro, J. Chrom. A. 1054 (2004) 379–387.
[42] A.V. Gerasimov, J. Anal. Chem. 58 (2003) 209–210.
[43] A.V. Gerasimov, J. Anal. Chem. 59 (2004) 348–353.
[44] S. Sayar, Y. Ozdemir, Food Chem. 61 (1993) 367–372.
[45] M. Poul, G. Jarry, M. Ould Elhkim, J. Poul, Food Chem. Toxicol. 47 (2009) 443–448.
[46] M.C. Gennaro, E. Gioannini, S. Angelino, R. Aigotti, D. Giacosa, J. Chrom. A. 767 (1997) 87–92.

Talanta 80 (2010) 1052–1067

Contents lists available at ScienceDirect

Talanta

journal homepage: www.elsevier.com/locate/talanta

Review

Application of chemometric methods to environmental analysis of organic pollutants: A review

Sílvia Mas[a], Anna de Juan[b], Romà Tauler[a,*], Alejandro C. Olivieri[c], Graciela M. Escandar[c,**]

[a] Department of Environmental Chemistry, IDAEA-CSIC, Jordi Girona 18, 08034 Barcelona, Spain
[b] Chemometrics Group, Department of Analytical Chemistry, University of Barcelona, Diagonal 647, 08028 Barcelona, Catalonia, Spain
[c] Department of Analytical Chemistry, Faculty of Biochemical and Pharmaceutical Sciences, National University of Rosario and Chemical Institute of Rosario (IQUIR-CONICET), Suipacha 531, Rosario S2002LRK, Argentina

ARTICLE INFO

Article history:
Received 28 July 2009
Received in revised form
22 September 2009
Accepted 24 September 2009
Available online 2 October 2009

Keywords:
Chemometric methods
Organic pollutants
Pesticides
Polycyclic aromatic hydrocarbons
Environment

ABSTRACT

Organic pollutants include a very wide variety of chemical compounds with different structures, properties, functions and origins, which may produce diverse damages to the ecosystem and the human beings. This review presents the recent progress on the use of chemometrics to evaluate the occurrence of these substances in the environment. The main topics addressed are: (a) the problems related to the interpretation of the analytical measurements used in the determination of organic pollutants (*quantitative analytical determinations section*), (b) the profiling of the related environmental pollution sources through their compositional, geographical and temporal distribution patterns (*environmental exploratory studies section*) and (c) the prediction of the toxicological activity of these substances through models based on the use of structural or physical/chemical descriptors (*toxicity studies section*). Each section includes selected works related to pesticides, polycyclic aromatic hydrocarbons and other organic pollutants.
© 2009 Elsevier B.V. All rights reserved.

Contents

1. Introduction 1053
2. Quantitative analytical determinations 1056
   2.1. Pesticides 1056
   2.2. Polycyclic aromatic hydrocarbons 1057
   2.3. Other pollutants 1058
3. Environmental exploratory studies 1060
   3.1. Pesticides 1060
   3.2. Polycyclic aromatic hydrocarbons 1061
   3.3. Other pollutants 1063
4. Toxicity studies 1065
   4.1. Pesticides 1065
   4.2. Polycyclic aromatic hydrocarbons 1065
   4.3. Other pollutants 1066
   Acknowledgements 1066
   References 1066

* Corresponding author.
** Corresponding author. Tel.: +54 341 4372704; fax: +54 341 4372704.
E-mail addresses: escandar@iquir-conicet.gov.ar, gmescandar@hotmail.com (G.M. Escandar).

0039-9140/$ – see front matter © 2009 Elsevier B.V. All rights reserved.
doi:10.1016/j.talanta.2009.09.044

1. Introduction

In recent years, there has been a growing concern about the increasing environmental occurrence of persistent organic pollutants (POPs) [including polycyclic aromatic hydrocarbons (PAHs) and organochlorine pesticides] and emerging organic pollutants [e.g., brominated flame retardants (BFRs)] and the proven toxic potential of these compounds on human health and wildlife [1]. The existence of these harmful substances has disrupted the natural cycles and processes and, therefore, there is a need to obtain better and deeper knowledge on the organic pollutant discharge and the related environmental impact.

The increasing use of Chemometrics in environmental studies over the last two decades responds to the intensive research devoted to test and prove the power of data processing techniques in this field and to the availability of appropriate software. Three main areas of interest can be distinguished in chemometric environmental studies: quantitative chemical analysis, monitoring for environmental quality assessment and modeling and prediction of toxicological effects.

Difficulties on the quantitative chemical analysis of organic pollutants in environmental samples are linked to both the inherent complexity of these natural matrices and the low analyte levels to be quantified. The determination of organic pollutants in environmental samples is largely carried out using chromatographic techniques combined with specific detection schemes [2,3]. However, these methodologies are relatively expensive, time consuming and often require laborious sample treatment before analysis. Other authors have also proposed alternative strategies based on phosphorimetric and fluorimetric detection [4], which are suitable for the analysis of very low concentrations. Nevertheless, the spectroscopic measurement lacks the required selectivity, particularly when similar chemical compounds must be analyzed in complex samples. The lack of selectivity or the presence of interfering species linked to natural samples calls for the application of chemometric methods based on multivariate calibration techniques, in order to overcome these limitations and to complement these analytical methodologies.

Multivariate calibration methods focus on the establishment and application of mathematical models that relate multivariate instrumental signals with analyte concentrations or sample properties [5]. While in univariate calibration a single numerical value (scalar, zero-order data) per sample is recorded and analyzed, multivariate calibration works with increasingly complex data arrays per sample and allows analytical quantitative estimations in multicomponent systems lacking selectivity [6]. In first-order calibration methods, the response analyzed is a vector of numerical values (first-order data, e.g., spectra, voltammograms, time profiles) per each sample. The use of this information provides the so-called first-order advantage, i.e., the possibility to quantify an analyte in the presence of interferences, as long as the interfering compounds are present in the calibration samples during the establishment of the calibration model [7]. In second-order calibration methods, the instrumental response analyzed is a data matrix per sample (second-order data, e.g., an HPLC-DAD chromatogram or an excitation–emission fluorescence measurement). The so-called second-order advantage is achieved, which implies that the analyte contribution can be appropriately modelled, quantitatively estimated and resolved in the presence of unknown interferences, absent in the calibration samples [7]. Higher-order data sets and their related calibration strategies (higher-order tensors and higher-order calibration methods) are possible and improve resolution power and quantitative estimations.

The possibility to use very diverse instrumental responses to predict analyte concentrations explains why multivariate calibration methods have become very powerful analytical tools. Although the first publications in this research area appeared about 30 years ago, a significant growth of applications of second- and third-order instrumental data to different areas of analytical chemistry has taken place in the last decade [8]. Second- and third-order multivariate calibration algorithms and applications have been reviewed and discussed [9]. Apart from second-order calibration algorithms, such as multivariate curve resolution-alternating least-squares (MCR-ALS) [10,11] and parallel factor analysis (PARAFAC) [12], other techniques have been proposed based on flexible data modelling, such as partial least-squares (PLS) with residual bilinearization (RBL), as recently discussed [8] and applied to environmental analysis [13–16].

Environmental monitoring studies result in huge amounts of physical parameters and chemical concentrations, collected in different geographical sites, time periods and/or different environmental compartments (i.e., air, water, sediments and biota). In order to reveal relevant patterns and sources of variation in these large environmental data sets, chemometric approaches based on statistical multivariate data analysis and factor analysis have been proposed in the last decades. The basic assumption of these methods is that the variation of each of the parameters or chemical concentrations measured in a particular sample can be mostly explained by a reduced number of different contributions coming from independent environmental sources [17]. In this way, point and diffuse pollution sources can be compositionally characterized and attributed to a particular origin (natural, anthropogenic, industrial, agricultural) and their relative apportionment can help to reveal geographical, temporal or compartmental patterns [18]. In this context, the application of chemometrics to environmental pollution research is often referred to as source apportionment, receptor modelling and/or mixture analysis discipline [19,20].

Principal component analysis (PCA) is a multivariate statistical method frequently used in exploratory data analysis [21]. This method extracts the main orthogonal contributions (principal components) which explain most of the variance of the data matrix. The abstract principal components may be rotated to increase interpretability. In some approaches, the rotated profiles can be quantitatively interpreted as possible sources, such as in absolute principal component analysis [22]. Sometimes, the interpretability of PCA is enhanced by the so-called varimax rotation [23], a change of coordinates that maximizes the sum of the variance of the loading vectors. However, these methods suffer from several drawbacks: individual factors (components) can be seldom attributed to a single specific source, fully satisfactory rotation techniques have not been found [24] and most of them cannot properly handle missing values or data below the detection limit, often encountered in environmental measurements. To solve the limitations of PCA-based methods, several factor analysis-based approaches have been developed over the past decade, such as UNMIX [25], positive matrix factorization (PMF) [26] and, more recently, MCR-ALS [10,11]. Both UNMIX and PMF have been adopted by the US Environmental Protection Agency (EPA) as robust methods (i.e., accurate for different operating conditions) for air quality management and can be freely downloaded from its web page (http://www.epa.gov). MCR-ALS was initially developed to investigate evolving processes of multicomponent systems by means of spectroscopic methods. However, its application was satisfactorily introduced in the study of environmental pollution data from sediment [27], water [28] and, more recently, for air quality management [29].

Assessment of environmental pollution in different geographical sampling sites requires consequent and constant monitoring of carefully selected parameters as a function of time, compartment or other environmental variables of interest. This usually results in data with multi-way structure, i.e., data cubes or hypercubes, which contain in each of the directions the conditions identify-

Table 1
Classification of the different chemometric methods employed in the works reviewed in this paper, according to the different data structures and goals of the study.[a].

First-order calibration
- Artificial neural networks (ANNs)
  - (i) Back-propagation neural network (BNN)
  - (ii) Radial basis function-artificial neural networks (RBF-ANNs)
  - (iii) Wavelet neural networks (WNNs)
- Multiple linear regression (MLR)
- Partial least-squares
  - (i) Partial least-squares (PLS)
  - (ii) Partial least-squares-1 (PLS-1)
- Principal component regression (PCR)
- Projection pursuit regression (PPR)

Second- and higher-order calibration and resolution methods
- Absolute principal component analysis (APCA)
- Bilinear least-squares (BLLS)
- Factor analysis (FA)
- Generalized rank annihilation method (GRAM)
- Multivariate curve resolution-alternating least-squares (MCR-ALS)
- Parallel factor analysis
  - (i) Parallel factor analysis (PARAFAC)
  - (ii) Weighted parallel factor analysis (WPARAFAC)
- Partial least-squares
  - (i) N-way partial least-squares (N-PLS)
  - (ii) N-way partial least-squares with residual bilinearization (N-PLS/RBL)
  - (iii) Unfolded partial least-squares (U-PLS)
  - (iv) Unfolded partial least-squares with residual bilinearization (U-PLS/RBL)
- Positive matrix factorization (PMF)
- Trilinear decomposition (TLD)
- Unfolded principal component analysis (U-PCA)
- UNMIX

Unsupervised pattern recognition methods
- Artificial neural networks (ANN)
- Chemical mass balance (CMB)
- Cluster analysis (CA)
  - (i) Fuzzy
  - (ii) Hierachical (HCA)
- Concentration weighted trajectory (CWT)
- Multi-dimensional scaling (MDS)
- Principal component analysis (PCA)
- Polytopic vector analysis (PVA)
- Potential source contribution function (PSCF)
- Residence time weighted concentration (RTWC)
  - (i) Radial basis function-artificial neural networks (RBF-ANNs)
  - (ii) Self-organizing maps (SOM)
- Support vector machines (SVM)

Supervised pattern recognition methods
- Artificial neural networks (ANN)
  - (i) Adaptive fuzzy partitions (AFP)
  - (ii) Adaptive neural network-based fuzzy inference system (ANFIS)
  - (iii) Back-propagation neural network (BNN)
  - (iv) Counterpropagation artificial neural network (CP-ANN)
  - (v) Multilayer perceptron (MLP)
- Classification and regression tree (CART)
- Discriminant analysis (DA)
  - (i) Linear discriminant analysis (LDA)
  - (ii) Non-linear discriminant analysis (NLDA)
  - (iii) Partial least-squares discriminant analysis (PLS-DA)
  - (iv) Quadratic discriminant analysis (QDA)
  - (v) Regularized discriminant analysis (RDA)
  - (vi) Sparse linear discriminant analysis (SLDA)
- K-nearest neighbours (KNN)
- Nearest mean classifier (NMC)
- Soft independent modelling of class analogy (SIMCA)

[a] The theory behind the chemometric methods mentioned in this table can be found in books [5,43], reviews [8,9], and in the references cited in the presently reviewed application works.

Table 2
Analytical determinations.

Analyte	Multivariate method[a]	Sample and technique	References
Pesticides			
Captan, captafol, folpet	PLS, PCR, ANNs	River water by DC and DPP	[44]
Carbaryl, phoxim	PLS, PCR, RBF-ANNs	Tap, lake and pond water samples by kinetic/UV–visible	[45]
Chlordecone	PLS	Soil by NIRS	[46]
Carbaryl	PLS, PCR, BNN	Vegetables and water samples	[47]
Oxamyl, methomyl, resorcinol phenol, 4-nitrophenol, 2,4-dinitrophenol	GRAM, PARAFAC, MCR-ALS	River and waste water by HPLC-DAD	[48]
Methomyl, deethylsimazine, deethylatrazine, carbendazim, carbofuran, simazine, atrazine, alachlor, chlorpyrifos-oxon, terbutryn, chlorfenvinphos, pirimiphos methyl, chlorpyrifos	MCR-ALS	Wastewater and sediment by HPLC-DAD	[49]
Methomyl, deethylsimazine, deethylatrazine, carbendazim, carbofuran, simazine, atrazine, alachlor, chlorpyrifos-oxon, terbutryn, chlorfenvinphos, pirimiphos methyl, chlorpyrifos	MCR-ALS	Wastewater and sediment by HPLC-MS	[50]
Alachlor, atrazine, carbendazim, carbofuran, chlorfenvinphos, chlorpyrifos, chlorpyrifos-oxon, deethylatrazine, deethylsimazine, methomyl, pirimiphos methyl, simazine, terbutryn	MCR-ALS	Wastewater and sediments by HPLC-DAD-MS	[51]
Alachlor, atrazine, chlorfenvinphos, pirimiphos methyl, terbutryn	MCR-ALS and calibration methods	Mussels by HPLC-MS in scan and SIM mode	[52]
Bifenthrin, tetramethrin	MCR-ALS, PARAFAC	Synthetic samples by GC-MS	[53]
Metsulfuron methyl and hydrolysis products	MCR-ALS	Synthetic samples by kinetic/NMR	[54]
Triphenyltin	MCR-ALS	Sea water by EEFMs	[55]
Carbendazim, fuberidazole, thiabendazole	PARAFAC	Synthetic samples by EEFMs	[56]
Carbendazim, fuberidazole, thiabendazole	GRAM, TLD	Water by EEFMs	[57]
Carbendazim, thiabendazole	PLS/RBL, PARAFAC	Water by EEFMs in solid-phase	[13]
Fenvalerate, lufenuron, deltamethrin diflubenzuron	Three- and four-way PARAFAC	Synthetic samples by PI-EEKF	[58]
Carbaryl	PARAFAC	Water effluents by EEFMs	[59]
Fenitrothion, fenitrooxon 3-methyl-4-nitrophenol	PARAFAC, U-PLS, N-PLS, U-PLS/RBL, N-PLS/RBL	River water by Ad-SSWV	[60]
Polycyclic aromatic hydrocarbons			
Benzo[*a*]pyrene, fluoranthene, benzo[*k*]fluoranthene, benzo[*ghi*]perylene, benzo[*b*]fluoranthene, indeno[1,2,3-*cd*]pyrene	PLS	Artificial drinking water by fluorescence	[61]
Sixteen EPA-regulated PAHs	PLS	Submerged freshwater sediments by LIF system and PFE-GC-MS	[62]
PAHs	PARAFAC	Synthetic samples by EEFMs	[63]
Benz[*a*]anthracene, benzo[*k*]fluoranthene, dibenz[*a,h*]anthracene,	Three- and four-way PARAFAC	Synthetic samples by photocatalytic degradation EEFMs	[64]
PAHs	GRAM	Marine sediments samples by HPLC-DAD	[65]
Anthracene, pyrene, fluoranthene, 1-methylpyrene, 2,3-benzofluorene	TLD	Light gas oil sample by GC-MS	[66]
Dibenz[*a,h*]anthracene, benz[*a*]anthracene, benz[*a*]pyrene, benz[*k*]fluorantene	PARAFAC, MCR-ALS	Aqueous medium by photodegradation EEFMs	[67]
Pyrene, benzo[*a*]pyrene	PARAFAC, PLS/RBL	Artificial and real water samples by RT-EEPMs	[15]
Benzo[*a*]pyrene, dibenz[*a,h*]anthracene	PARAFAC, PLS/RBL	Artificial and real water samples by EEFMs	[16]
Ten EPA-regulated PAHs	MCR-ALS, PARAFAC2	Artificial and real water samples by HPLC-FSFS	[68]
Other organic pollutants			
Different organic compounds	PLS	Ambient aerosols by ATR-FTIR	[69]
Phenol, catechol, 4-acetamidophenol	WNNs	Synthetic water samples by voltammetry	[70]
Methoxy-2-propyl acetate, chlorobenzene	TLD and PARAFAC	Environmental sample containing fuel components, pesticides and natural products by GC × GC/TOFMS	[71]
2,3,7,8-Tetrachloro dibenzo-*p*-dioxin	Four-way PARAFAC	Water samples by Shpol'skii spectroscopy	[72]
Tetracycline, chlortetracycline, oxytetracycline	N-PLS, PARAFAC, BLLS	Water samples using photochemical-induced EEFMs	[73]
Antibiotics	MCR-ALS, U-PLS/RBL	Effluent wastewater by HPLC-DAD	[74]
Pyridine	N-PLS, PARAFAC	River water and field wastewater samples by pH-modulated UV data	[75]
1- and 2-Naphthylamines	U-PLS, RBL, PLS-1, N-PLS	Drinking waters by MIP-fluorescence optosensing system	[76]
Decabromo diphenyl ether	HS-MCR	Elucidation of the mechanism, resolution of kinetic profiles and pure spectra and evaluation of the rate constants	[77]

[a] See acronyms in Table 1. Ad-SSWV, adsorptive stripping square-wave voltammetry; ATR-FTIR, attenuated total reflectance-Fourier transform infrared; DAD, diode-array detector; DC, direct current; DPP, differential pulse polarography, DPV, differential pulse voltammetry; EEFMs, excitation–emission fluorescence matrices; FSFS, fast scanning fluorescence spectroscopy; GC, gas chromatography; HPLC, high performance liquid chromatography; LIF, laser-induced fluorescence; MIP, molecularly imprinted polymer; MS, mass spectroscopy; NIRS, near infrared spectroscopy; NMR, nuclear magnetic resonance; PFE-GC-MS, pressurized fluid extraction-gas chromatography-mass spectroscopy; PI-EEKF, photochemically induced excitation–emission kinetic fluorescence; RT-EEPMs, room-temperature excitation–emission phosphorescence matrices; SIM, selected ion monitoring; TOFMS time-of-flight mass spectrometry; UV–visible, ultraviolet–visible spectrophotometry.

ing the measurement (time, site, compartment, etc.). In certain cases, these data have been analyzed by unfolding them in large data tables, 'matricizing' them and employing bilinear models [28]. Alternatively, methods based on trilinear and multilinear models have been proposed for three- and multi-way data arrangements in the investigation of environmental problems, such as PARAFAC [12], TUCKER-3 [30] and multilinear engine (ME) [31]. More details and comparison of these methods can be found in the literature [29,32,33]. The use of multivariate factor analysis methods like those mentioned above has also been discussed in different books [5,18,20].

Organic pollutants often produce toxic effects. There are several in vivo and in vitro methods to test the toxicity of chemicals, which can provide reliable quantitative and qualitative indicators about the interaction of a given compound with a biological system. However, the direct estimation of the toxicological activity for a certain compound is expensive and time consuming and this explains the lack of available indicators for many compounds. Thus, the development of quantitative structure–activity relationships (QSAR) data analysis tools that allow for an indirect toxicity evaluation is of great importance for the purpose of pollutant risk assessment. QSAR models describe a mathematical relationship between the structural properties of a set of chemicals and the particular activity (toxicological or other), associated with them.

Several chemometric methods have been applied to develop valid and reliable QSAR models [34]. In a first phase, efficient methods are employed to select the most relevant parameters (descriptors) associated with the ranges of toxicity levels. Several selection strategies, based on methods, such as stepwise regression [35], PCA and genetic algorithms (GA) [36] have been proposed in the literature. The latter are probably the most powerful tools, since they are able to thoroughly explore the molecular descriptor hyperspace. The next step consists of using a chemometric method to develop robust predictive models. QSAR modelling techniques are based on: (1) linear regression, such as multiple linear regression (MLR) and PLS, (2) non-linear techniques, such as artificial neural networks (ANN) [37] and support vector machines (SVM) [37] and (3) classification methods [38]. In the present review, emphasis is directed to recently published QSAR models developed using chemometric methods beyond classical MLR.

Table 1 summarizes the different chemometric methods employed in the reviewed works, according to the different data structures and goals of the study. Detailed explanations about these methods can be found in previous works [39,40]. Data preprocessing techniques are not reviewed for brevity, in spite of their importance in the quality and interpretability of the results obtained.

The present paper reviews chemometric applications for the study of organic pollutants in the environment since 2000. Following the above discussion, we have organized the material in three sections: (1) quantitative analytical determinations, (2) environmental exploratory studies and (3) toxicity studies. In each section, rather than performing an exhaustive review, we critically selected some representative works, with the main purpose of showing the evolution of chemometric strategies and being representative of the different kinds of studied data sets. Attention is focused on families of compounds, such as pesticides, PAHs and other organic pollutants. Pesticides heavily influence water and soil pollution and they are defined as chemicals used to repel or destroy pests of any sort [41]. They include fungicides, insecticides and herbicides. PAHs, on the other hand, arise from the incomplete combustion of hydrocarbons. They consist of fused aromatic rings with no heteroatoms or substituents and they are toxic to aquatic life and suspected to be human carcinogens [42]. Other organic compounds can disperse in various environmental media, due their water solubility, vapour pressure or partition coefficient between organic matter (in soil or sediment) and water, inducing potential hazardous problems in the ecosystem and in humans.

2. Quantitative analytical determinations

2.1. Pesticides

A summary of selected works devoted to analytical determination of pesticides is shown in Table 2 [44–77]. Most determinations were carried out in water samples because the main pathway of ecological impact is water contamination by pesticide runoff, which may easily reach both surface and ground waters. Despite the known analytical advantages of higher-order methods, many of the pesticide systems were analyzed using first-order algorithms [44–47] (Table 2). However, there are some examples of use of second-order calibration methods, such as MCR-ALS or PARAFAC to process high performance liquid chromatography (HPLC) or molecular fluorescence data.

In [48], three second-order calibration algorithms, GRAM, PARAFAC and MCR-ALS, were compared for the determination of mixtures of pesticides and phenolic compounds at trace levels in river and wastewater samples. The authors showed that techniques that do not require the fulfilment of trilinearity, such as MCR-ALS, provide better results than methods based on trilinear models, such as PARAFAC or GRAM, when drift and baseline problems occur. This is due to the fact that MCR-ALS only requires that one of the two measurement dimensions (usually the spectral one) matches between the different data matrices and, therefore, variations among drifts and baselines coming from different runs are allowed.

MCR-ALS was used to resolve and quantify 13 different biocides in sediment and wastewater samples by HPLC coupled to diode-array detection (HPLC-DAD) [49] and by HPLC coupled to mass spectrometry detection (HPLC-MS) [50]. Despite the very strong coelutions and matrix interferences, the analyzed biocides were properly resolved and their quantitation could be performed satisfactorily by external calibration. The difficulties encountered in practice for optimal reproducible quantitative determinations by HPLC-MS come from the combination of complex environmental matrices, embedded peaks, strong coelutions and ion suppression effects. Interestingly, the fusion of DAD and MS detector signals improved the results and provided more reliable estimations compared to those obtained using only one of the two detection systems, as was demonstrated in [51].

To cope with sensitivity changes and matrix effects encountered in the HPLC-MS analysis of complex natural environmental samples, as those mentioned in [52], different analytical calibration approaches, such as external calibration, standard addition and the use of an internal standard, were evaluated for the quantification of coeluting biocides in mussel samples. HPLC-MS data coming from the scan mode detection were processed using MCR-ALS [52]. The authors showed that the combination of the multivariate extension of standard addition and internal standard methods together with MCR-ALS was the best calibration strategy for the optimal analyte quantification. Similar quantitative results to those obtained by HPLC-MS in the selected ion monitoring (SIM) mode were achieved. Moreover, the scan mode MCR-ALS results provided analyte confirmation *via* its resolved pure mass spectrum, complete information about the whole chromatographic process and allowed for the simultaneous determination of multiple analytes in the same chromatographic run using the same experimental and instrumental conditions. An intermediate situation among the classical univariate SIM mode and the scan mode can be found in a work, where GC-MS data built with several SIM mode detection channels were

analyzed by PARAFAC and MCR-ALS to quantify two insecticides (bifenthrin and tetramethrin) in synthetic samples [53].

MCR-ALS was also applied in kinetic–spectroscopic studies of degradation or hydrolysis of pollutants to provide quantitative and qualitative information about these processes. The objective is then the identification of by-products and end products in the process and the postulation of the underlying reaction model with the related kinetic parameters. Along this line, Bezemer and Rutan have shown the applicability of MCR to resolve overlapped nuclear magnetic resonance signals using a kinetic reaction constraint in the determination of metsulfuron methyl and its hydrolysis products [54]. The use of the kinetic constraint applied during the iterations resulted in the direct estimation of the reaction rate constants. This avoids the need for subsequent fitting of the kinetic profiles, reducing the analysis time and complexity, with the possibility of modelling a particular process in the presence of interferences.

Excitation–emission fluorescence matrices (EEFMs) are the best examples of trilinear data sets and, therefore, all the available second-order methods are potentially applicable to them. However, phenomena such as Rayleigh and Raman scatterings and diffraction harmonics are not trilinear and should be avoided by selecting a suitable wavelength range or modelled with a specific algorithm, e.g., weighted PARAFAC (WPARAFAC) [9].

In [55], the application of MCR-ALS allowed the resolution and quantitative determination of triphenyltin in sea water samples using EEFM measurements and a single synthetic analyte standard. The method was successfully applied to the determination of the analyte at very low concentrations (part per trillion levels), with overall prediction errors around 12%. Ordinary PARAFAC, GRAM, MCR-ALS, trilinear decomposition (TLD) and the combination of PLS with RBL, all achieving the second-order advantage [9], were used to determine carbamate pesticides using fluorescence data [13,56,57]. In cases of trilinearity losses due to inner filter effects or sample-to-sample spectral variations (because analyte–background interactions may vary between samples), methods taking into account deviations from trilinearity (MCR-ALS or PLS/RBL) were preferable.

A problem which hinders a wider application of fluorescence spectroscopy in environmental monitoring is the intrinsic lack of selectivity in excitation and emission fluorescence measurements. Data sets obtained from kinetic experiments may help to increase the selectivity of spectroscopic determinations in the calibration models. Indeed, time-dependent measurements introduce an additional dimension to the classical EEFM three-way data sets (excitation × emission × sample), leading to four-way data sets (excitation × emission × sample × time), which allow for a potential increase in the predictive ability of the models. Booksh and co-workers [58] extended EEFM determinations to four non-fluorescent pesticides after their photochemical degradation to fluorescent species. Three-way PARAFAC was employed to resolve the pure fluorescent spectra of the overlapping photolysis products. The time profiles yielded a fourth dimension (four-way data) that led to an increase in sensitivity and selectivity. The four-way PARAFAC models were then used to predict original pesticide concentrations. An analogous four-way PARAFAC model with kinetic information was successfully applied for the determination of carbaryl in effluent samples in the presence of an uncalibrated fluorescent background [59].

The adaptation of three-way stripping square-wave voltammetry (Ad-SSWV) to a second-order calibration strategy is described in [60] for the simultaneous determination of fenitrothion and its metabolites in environmental samples. To obtain the three-way data set, the Ad-SSWV profiles recorded at different accumulation times on the hanging mercury electrode were used as the third mode of the calibration data. In this way, the sensitivity of the electroanalytical signals was enhanced and the selectivity was improved from the differences in shape in the kinetic species profiles originated by adsorption processes.

2.2. Polycyclic aromatic hydrocarbons

The main difficulties linked to the determination of PAHs in environmental samples (Table 2) arise from the complexity of the sample natural background and the low analyte concentrations to be detected. However, the combination of different analytical methods with multivariate calibration has allowed for the successful determination of these pollutants. The luminescent properties of PAHs are useful for their direct analysis at very low concentration levels and have been widely exploited for PAH determination. Usually, fluorimetric methods involve recording synchronous fluorescence scanning EEFMs data, which are afterwards treated with suitable chemometric tools.

As can be seen in Table 2, many PAHs have been determined by coupling EEFMs with PLS and PARAFAC. In [61], PAHs were analyzed in synthetic drinking water by synchronous fluorescence spectroscopy and PLS. The use of a Plackett–Burman (PB) experimental design for the creation of the sample calibration data set is described and compared with a collinear analogue. External validation shows that the sample collinear data set is inappropriate to quantify PAHs in real samples, whereas the PB sample calibration data set affords optimal results.

Grundl et al. described a method for real-time *in situ* characterization of PAHs in freshwater sediments [62]. A cone penetrometer-type apparatus was designed for probe penetration and a field-portable laser-induced fluorescence (LIF) system was used for *in situ* measurements, in which the output of a pulsed exciter laser was transmitted by an optical fiber to a sapphire window in the probe wall. Fluorescent emission was collected by a separate optical fiber for transmission to the spectrometer on deck. Four wavelengths were selected via optical delay lines and multiple-wavelength waveforms were created. These waveforms contain information on the fluorescence frequency, intensity and emission decay rate. Field testing was conducted at ten different sites in the Milwaukee Harbor. The core samples were analyzed by gas chromatography-mass spectrometry and a PLS model was created based on laboratory LIF measurements and pressurized fluid extraction gas chromatography-mass spectrometry (PFE-GC-MS) of the core samples. The N-PLS model was applied then to the *in situ* field test data and 13 of the 16 EPA-regulated PAHs were quantified with a relative overall error lower than 30% (the remaining three PAHs were present under the quantification level).

A field-portable single-exposure excitation–emission matrix fluorometer was used together with PARAFAC for sub-ppb PAH determinations in the presence of spectral interferences [63]. It was found that reducing eight-sample PAH calibration sets to two or three calibration standards significantly decreased the computation intensity, yet generating adequate predictions. It was also found that spectral resolution can be decreased to reach an optimal compromise between calibration accuracy and analysis speed, while minimizing instrumental requirements.

The application of photocatalytic degradation EEFMs in combination with PARAFAC has been proposed to determine benz[*a*]anthracene, benzo[*k*]fluoranthene and dibenz[*a,h*]anthracene. Three- and four-way PARAFAC analyses were employed to extract the fluorescent species spectra from overlapping EEFMs [64]. The additional time dimension increased the selectivity for each PAH determination.

In [65], PAHs in marine sediment samples were determined by a method based on solvent extraction followed by chromatographic separation with diode-array detection. Second-order calibration with GRAM was used for quantification because interfering substances coeluted with the compounds studied. For calibration, a

spiked sample was used instead of a standard solution to cope with the complexity of the samples and the presence of matrix effects. With this method, the compounds do not need to be chemically separated from the interferences and quantification can be carried out with only one spiked sample for calibration. The ability of the method to quantify the studied compounds was comparable to the results with those of a univariate standard addition calibration, with the additional advantage of avoiding the previous isolation of the analytes.

Three-component (anthracene, pyrene, 1-methylpyrene) and four-component (fluoranthene, anthracene, pyrene, 2,3-benzofluorene) synthetic mixtures were resolved by TLD of third-order tensors formed by EEFM data modulated by the concentration of the fluorescence quencher nitromethane [66]. The addition of a quencher to PAH mixtures selectively reduces the fluorescence intensity according to the Stern–Volmer equation. TLD allows the three-way array to be decomposed to provide unique solutions for the excitation spectrum, emission spectrum and quenching profile for each component. TLD was applied to a real sample from a chromatographic cut from the analysis of a light gas oil and the TLD extracted spectra and quenching constants suggested the presence of three classes of PAHs, consistent with data from an independent GC-MS analysis.

PARAFAC and MCR-ALS were used to process EEFMs in order to obtain semi-quantitative information related to the concentrations of dibenz[*a,h*]anthracene, benz[*a*]anthracene, benz[*a*]pyrene and benz[*k*]fluoranthene stemming from a photodegradation process in an aqueous medium [67]. The results obtained showed no statistical differences with data obtained using an HPLC reference methodology and suggested the EEFM approach as a time saving and more ecological alternative.

Room-temperature excitation–emission phosphorescence matrices combined with second-order chemometric calibration were applied to the determination of pyrene and benzo[*a*]pyrene in both synthetic and real water samples [15]. The study was used to test the applicability of PARAFAC and PLS/RBL. The superior capability of PLS/RBL to model the profiles of potential interferences from other PAHs was demonstrated.

The simultaneous ultra-trace determination of benzo[*a*]pyrene and dibenzo[*a,h*]anthracene in the presence of the remaining fourteen US-EPA PAHs at total concentrations ranging from 1400 and 14,000 ng L^{-1} was reported [16]. The approach consisted of measuring EEFMs on a nylon-membrane surface, combining the ability of this membrane to retain and concentrate PAHs on its surface, the sensitivity of molecular fluorescence and the selectivity of second-order chemometric algorithms [PARAFAC and unfolded PLS/RBL (U-PLS/RBL)]. The superiority of U-PLS/RBL to quantify benzo[*a*]pyrene and dibenzo[*a,h*]anthracene at concentrations below 10 ng L^{-1} in tap, underground, mineral and river water samples was demonstrated.

PARAFAC2 and MCR-ALS coupled to HPLC-fast scanning fluorescence spectroscopy were employed for the analysis of ten selected PAHs (six of them heavy PAHs) in the presence of real interferences [68]. Analytical recoveries from different types of water and olive oil samples were analysed and the superiority of MCR-ALS to successfully resolve these clear non-trilinear complex systems was demonstrated.

2.3. Other pollutants

Table 2 collects analytical works on other organic pollutants. Coury and Dillner developed an ATR-FTIR spectroscopic method to quantify functional groups of organic compounds and ammonium sulphate and ammonium nitrate in size-segregated ambient aerosol samples for particles smaller than 1 μm in diameter [69]. The ATR-FTIR instrumentation and multivariate calibration improved sensitivity and accuracy of quantification over more commonly used transmission FTIR and univariate calibration.

Multivariate calibration was used to quantify four carbonyl functional groups (aldehydes/ketones, carboxylic acids, esters/lactones and acid anhydrides), nine additional functional groups associated with organic molecules (methyl, methylene, aliphatic and aromatic CH, alkene, carbohydrate ether and hydroxyl, amino acids and amine groups) and two inorganic compounds, ammonium sulphate and ammonium nitrate. Comparison of the sum of the mass predicted by the ATR-FTIR technique and the gravimetric mass indicated that this method can quantify on average 91% of the aerosol mass. This method bridged the gap between individual compound identification with GC-MS and total organic carbon (TOC) obtained by thermal/optical methods and provided a nearly complete characterization of size-fractionated submicrometer aerosol mass. The method characterized the organic fraction in a potentially useful way for climate modelling, source region identification and physicochemical investigation of the properties of this large and complicated part of atmospheric aerosols.

Three phenolic compounds (phenol, catechol and 4-acetamidophenol) were simultaneously determined by voltammetric monitoring of their oxidation reaction at the surface of an epoxy-graphite transducer [70]. Because of strong signal overlapping, wavelet neural networks were used in the data treatment, in a nice combination of chemometrics and electrochemical sensors, already known as the electronic tongue concept.

The determination of methoxy-2-propyl acetate and chlorobenzene in an environmental sample containing fuel components, pesticides and natural products was carried out by GC × GC/TOFMS and TLD and PARAFAC [71]. It was found that PARAFAC initialized by TLD performed a better resolution than TLD. After resolution, mass spectral profiles were matched to library spectra for identification. Quantification by TLD-initialized PARAFAC using the standard addition method for one of the resolved analytes was proposed to avoid retention time alignment between sample and standard data sets.

The analysis of 2,3,7,8-tetrachloro dibenzo-*p*-dioxin in water samples was carried out using solid–liquid extraction laser-excited time-resolved Shpol'skii spectroscopy. The measurement obtained provided four-way data that were processed by PARAFAC [72]. The work reported the first application of PARAFAC to high-order instrumental data generated from Shpol'skii matrixes at liquid helium temperature. Moreover, the authors demonstrated the feasibility to directly determine parts per trillion of the target compound in heavily contaminated samples of unknown composition.

The antibiotics tetracycline, chlorotetracycline and oxytetracycline were determined in surface water samples using photochemical-induced EEFMs and three-way analysis [73]. Aqueous basic solutions of the antibiotics were irradiated with UV light and the generated photoproducts after solid-phase extraction were fluorometrically determined. According to the obtained results, while N-PLS and PARAFAC were not able to handle the extreme collinearities found, especially in the presence of uncalibrated interferences, bilinear least-squares (BLLS) rendered the best results. The authors presented BLLS as a promising technique for processing this kind of data, yielding analyte profiles and concentrations in samples where both a strong overlapping and background signal occur. In [74], U-PLS/RBL was applied for the first time to second-order LC-DAD data and compared with MCR-ALS for the simultaneous determination of eight tetracyclines in wastewaters. The results showed that the eight analytes could be successfully determined in wastewaters and the drawbacks due to matrix interferences could be adequately handled and overcome by using U-PSL/RBL. The use of a latent variable structure could cope with complex LC-DAD data, which do not follow a trilinear structure and provided comparable predictive results with MCR-ALS. One of

Table 3
Monitoring studies.

Compounds	Multivariate method[a]	Aim of the multivariate method in the study	References
Pesticides			
Pesticides and PAHs	PCA	Exploration of the main pollution sources and their geographical and temporal distribution in river sediments	[79]
Twenty-two pesticides	CA, LDA, PCA	Elucidation of the impact of pesticides used in soils. Spatial and temporal trends	[80]
Hexachlorobenzene, hexachlorobutadiene, hexachlorocyclohexane, dichlorodiphenyldichloro ethane and metabolites, polychlorinated biphenyls	PCA with orthogonal varimax rotation	Exploration of main pollution sources, their geographical distribution and their accumulation effects in river sediments and fishes	[23]
Fifteen herbicides and derivatives	PCA and MCR-ALS with unfolding scores	Identification of the pollution sources, determination of their composition, their temporal and geographical contributions in outflows of reservoirs	[28]
Nineteen pesticides	PCA and MCR-ALS with unfolded scores, TUCKER-3, PARAFAC	Exploration of the main pollution sources, their geographical and temporal distribution in surface waters	[81]
Seventeen pesticides	PCA with unfolded scores and geographical information systems	Geographical and temporal variation in sediments	[82]
Hexachlorocyclohexane, dichlorodiphenyltrichloro ethane, chlordane	PCA/MLR	Identification of main pollution sources and their contributions in soils	[83]
Pesticides	ANN models (BNN, RBF-ANNs, ANFIS)	Prediction of pesticide occurrence in rural domestic wells	[84]
Hexachlorobenzene, hexachlorocyclohexane, polychlorinated biphenyls, dichlorodiphenyldichloro ethane	PCA, PLS	Assessment of the dependence of pollution pattern on geographical and physiological parameters	[85]
Polybrominated diphenyl ethers, hexabromocyclo dodecane, polychlorinated biphenyls, dichlorodiphenyltrichloro ethane	PCA, SIMCA, PLS, PLS-DA	Correlations between biological characteristics and pollutant concentrations in eggs and muscle of birds	[86]
Organophosphorus compounds and polycyclic aromatic hydrocarbons	PCA, PLS	Measured contaminant levels and general physicochemical parameters with biological responses	[87]
Polycyclic aromatic hydrocarbons			
Sixteen PAHs	CA, PCA with varimax rotation	Classification of the general distribution patterns or similarities of individual pollutants occurring in soil	[88]
Thirteen PAHs	PCA with orthogonal varimax rotation	Analysis of the emissions profile in a rural area identifying and quantifying the main sources in airborne particles	[89]
PAHs	PCA	Ecological risk assessment and source diagnostics	[90]
Twenty-three PAHs	PCA	Contamination of surface sediments and oysters	[91]
Fifteen PAHs	CMB	Apportionment of the pollution sources in lake sediments	[92]
Fifteen PAHs	FA, FA with non-negative constraints (rotation)	Apportionment of the pollution sources in lake sediments and comparison of results obtained in [92]	[93]
Fifteen PAHs	PCA, PCA/APCA	Identification and apportionment of the main pollution sources in urban atmosphere	[94]
Sixteen PAHs	Linear mixing model	Apportionment of pollution sources in soil taking into account the pattern of all 16 pollutants as a whole	[95]
PAHs	PMF, PCA/MLR	Identification and apportionment of pollution sources in soils	[96]
PAHs	PCA/MLR, PMF, UNMIX	Comparison of the methods of apportionment of pollution sources	[97]
Eight PAHs	PCA, ANN (SOM, MLP)	Identification of any patterns in air pollution occurring during heating and non-heating seasons	[98]
One hundred and thirty-six PAHs and biomarkers	PLS	Source allocation of oil spill	[99]
Twenty-four PAHs	PLS	Evaluation of the influence of physicochemical parameters and soil characteristics on the degradation patterns	[100]
Other organic pollutants			
Phthalate esters	PCA	Distribution patterns in urban soils	[101]
VOCs	CMB	Evaluation of source contributions to organic gases in ambient	[102]
Non-methane hydrocarbons	CMB, UNMIX	Estimation of pollution source profiles and their contributions in urban atmosphere	[103]
VOCs	CMB, NNLS	Relationships between VOCs and transient high ozone formation in the Houston area	[104]

Table 3 (*Continued*)

Compounds	Multivariate method[a]	Aim of the multivariate method in the study	References
Forty-eight non-methane hydrocarbons	PMF, UNMIX	Estimation of pollution source profiles and their contributions in urban atmosphere	[105]
Twenty VOCs	PCA/APCA, UNMIX, PMF, CMB	Estimation of pollution source profiles and their contributions in indoor exposure	[106]
VOCs	PCA	Source identification of personal exposure to fine particulate matter using organic tracers	[107]
VOCs	ME (missing/no missing mass)	Source identification and comparison of receptors models	[108]
VOCs	Non-parametric regression	Relationship of the concentration of VOCs to wind direction	[109]
Polychlorinated biphenyls	PVA	Identification and characterization of sources, dechlorination patterns and lateral and vertical distribution in soils	[110]
Polychlorinated biphenyls	PMF/PSCF	Identification and apportionment of pollution sources and their geographical and temporal distribution in atmosphere	[111]
Polychlorinated biphenyls	PSCF, CWT, RTWC	Locating sources contributing to the atmospheric concentrations in urban area	[112]
Eighteen endocrine disruptor chemical compounds	PCA, MCR-ALS	Exploration of the main pollution sources and their geographical distribution in coastal and harbour waters and sediments	[113]

[a] See acronyms in Table 1. VOCs, volatile organic compounds.

the most important advantages of MCR-ALS is the physical meaning of the results obtained, absent in the U-PLS/RBL algorithm. However, U-PLS/RBL showed good analytical performance and ease and speed of program operation.

Pyridine, considered by US-EPA as a priority pollutant [1], was quantified in a concentration range of 0.67–51.7 $\mu g\,mL^{-1}$ in river water and field wastewater samples, coupling pH-modulated UV-spectrophotometry with PARAFAC and N-PLS [75]. Both methods yielded satisfactory results.

Very recently, a chemometric-assisted molecularly imprinted polymer (MIP)-fluorescence optosensing system was developed for determining the contaminants 1- and 2-naphthylamine in drinking waters [76]. In this work, fluorescence emission spectra coupled to PLS-1 and EEFMs combined with N- and U-PLS were applied. The combinations of both N- and U-PLS with RBL allowed the achievement of the second-order advantage and satisfactory results were obtained in the presence of a potential interference (1-naphthalenemethylamine).

Decabromodiphenyl ether is the only polybrominated diphenyl ether (PBDE) of worldwide accepted use. However, it can degrade by the action of light into lower banned congeners in the environment. The photochemical degradation process of decabromodiphenyl ether was investigated by UV-spectrophotometric monitoring [77]. A novel hybrid data analysis approach, based on the combination of hard- and soft-multivariate curve resolution (HS-MCR), was applied to elucidate the mechanism of the degradation process, to resolve kinetic profiles and pure spectra of the photodegradation products and to evaluate the rate constants [78]. This method combines the qualities of deterministic (rate law) hard-modelling and of soft-modelling methods (no physicochemical model is assumed), allowing the simultaneous treatment of several experiments performed in different conditions with different kinetic models and rate constants in the presence of interferences.

3. Environmental exploratory studies

3.1. Pesticides

As seen in Table 3, PCA [21], PARAFAC [12], TUCKER-3 [30] and MCR-ALS [10,11] are the most commonly applied chemometric methods in environmental monitoring studies of pesticides. All these methods decompose an environmental data array into separate linear contributions or components describing the main sources of data variance, which are related to the main contamination sources or patterns. The differences among these approaches lie in the specific assumptions and type of data structure and decomposition.

PCA has been extensively applied as an exploratory tool to characterize pesticide sources and/or to evaluate their geographical and/or temporal distributions in environmental monitoring programs. For example, in [79], PCA was applied to historical data from 1996 to 2003 concerning the concentration of different organochlorine pesticides and PAHs in sediment samples from different sampling sites of the Ebro River basin. Three major contamination sources were identified and their composition and distribution profiles were resolved. The first contamination source was mostly loaded by PAHs, the second contamination source was loaded by some organochlorine compounds and the third contamination source was more specifically loaded by naphthalene. Samples from the different geographical regions of the Ebro River basin were grouped according to the contamination described by these three major sources.

The use of unsupervised exploratory techniques, such as cluster analysis (CA) and PCA and a supervised classification technique, linear discriminant analysis (LDA) led to the successful elucidation of the impact of pesticides (Directive 91/676/EEC) on the intensive horticulture performed in a particular vulnerable geographical zone located in Portugal [80]. CA was used as an unsupervised exploratory technique to discover unanticipated natural affinities within the data, considering associations of both pesticides and samples. Clusters of samples were further examined with the assistance of LDA in order to check the discriminant capacity of the measured variables. Finally, PCA was applied to reveal the main sources of data variance, thus allowing the interpretation of eventual relationships between the pesticide abundance and typology and the environmental mechanisms or agrochemical procedures.

PCA results from analysis of environmental data can be further improved for interpretation after the so-called varimax rotation [23]. As an example, PCA and varimax orthogonal rotation were applied and compared to investigate the main pollution sources in the Catalonia rivers basin [23]. The goal of this study was the evaluation of the geographical distribution and accumulation effects of these pollution sources in sediment and fish samples. A clear correspondence was found between different pollution sources in fish and in sediments, dominated by pesticides and by PCBs, respec-

tively. The geographical distribution, including hot pollution spots and the temporal evolution of these sources was also described.

A multivariate study of environmental data requires the integrated application of different multivariate methods to reciprocally validate the models obtained. In [28], multivariate correlations among the concentrations of selected herbicides and their derivatives in outflows from selected reservoirs in US Midwest were investigated by PCA and MCR. Whereas PCA allowed the identification and qualitative interpretation of the main contamination sources, MCR-ALS resolved their composition, geographical and temporal distribution profiles. In this work, a preliminary method for averaging PCA and MCR-ALS geographical profiles over time was proposed as an efficient and useful way to enhance either hidden geographical or temporal information of contamination sources. Additionally, the averaged source profiles obtained by MCR-ALS could be easily compared with the source profiles obtained using three-way methods, such as PARAFAC or TUCKER-3. In [81], several chemometric methods, such as PCA, MCR-ALS, PARAFAC and TUCKER-3, were compared to resolve and model the main contamination sources of pesticides in surface waters of Portugal.

An interesting adaptation of the MCR bilinear algorithm to perform the data set decomposition following PARAFAC and TUCKER-3 models has shown the flexibility of the former method to handle different data structures and to set different constraint schemes [33]. When MCR-ALS is applied to three-way data *via* matricization or matrix augmentation, trilinearity constraints may be implemented in a very flexible way using an algorithm previously developed [114]. A variant was developed to implement TUCKER-3 models using new component interaction constraints. The results obtained in this way could be easily compared to those obtained by classical PARAFAC or TUCKER-3 decompositions. TUCKER-3 models offer the advantage of defining a different number of components for each mode in the three-way data decomposition. This is of environmental significance, since it describes the real scenario of sources with different contamination patterns that may display a similar geographical or temporal distribution. A reduction of the number of components in the similar mode allows for an improved and more compact environmental description of the different contamination patterns.

Results of chemometric modelling and multivariate data analysis of large monitoring multivariate data sets may be coupled with geographical information systems (GIS) and mapping tools to facilitate the description of environmental patterns and to improve environmental knowledge and risk assessment. In [82], the environmental quality of the Ebro River delta (Catalonia, NE Spain) was assessed and the spatial and temporal distribution of pesticide pollution in the irrigation and drainage channels coming from the river during the rice-growing season were investigated in detail.

Receptor-based source apportionment of various potential pollution sources is also important in regional environmental management. Receptor models identify and quantify the sources of ambient air pollution and their effects at a site (receptor), primarily on the basis of concentration measurements at the receptor site and generally without the need of emission inventories and meteorological data studies [18]. PCA followed by varimax rotation, absolute scores recalculation and multilinear regression analysis (PCA/APCA, a popular receptor model [22]) have been used to apportion the different sources of contaminants (mostly inorganic particulate matter), especially in air pollution. The number of studies is smaller, however, in the case of organic pollutants. In [83], PCA with MLR analysis was used to distinguish the relative contribution of historic residues from current illegal usage of technical DDT and dicofol-type DDT in the Pearl River area (China).

Other non-linear chemometric methods have been applied to investigate pesticide contamination sources. Among them, three ANN models [a feed-forward back-propagation (BNN), a radial basis function (RBF) and an adaptive neural network-based fuzzy inference system (ANFIS)] [38] were employed [84]. The BNN neural network was found to be superior to the RBF and to the ANFIS types of ANN in the detection of pesticide occurrences in wells.

In other similar studies, PCA and related techniques have also been used to determine correlations between pesticide contamination and particular environmental properties. For example, the relationship of the concentration of some pesticides and organochlorine compounds with geographical and physical parameters, such as altitude, longitude, latitude or temperature and with physiological or biological parameters, such as lipid content, age, weight and size in fish was investigated by PCA and PLS in [85]. The results confirmed that temperature and altitude were the main factors influencing the accumulation of most investigated compounds in the lipids of fish muscle and liver tissues.

PCA, PLS, soft independent modelling of class analogy (SIMCA) and PLS discriminant analysis (PLS-DA) were used [86] to investigate the correlation between biological characteristics and pollutant concentration in eggs and muscle of birds. In this work, PLS was applied to investigate the relationship between the biological variables of guillemot eggs and the residue levels of OCs and BFRs and to investigate whether concentrations of OCs and BFRs in guillemot egg covaried. SIMCA classification was used to investigate whether the contaminant pattern in the two matrices, egg and muscle, differed significantly from each other. SIMCA performs a classification model using PCA on selected observations (e.g., contaminant concentrations in the eggs) and then determines class membership by calculating the distance between a new observation (e.g., the contaminant concentrations in an individual muscle or in an egg) and the PCA model. PLS discriminant analysis (PLS-DA) was used to identify the discriminating variables that contributed the most to the class separation between egg and muscle contamination. A PLS-DA model showed that some of the contaminants had significantly higher concentrations in egg than in muscle, although 7 of the 14 contaminants showed no difference in concentrations between the two matrices. The concentrations of lower chlorinated biphenyls were higher in egg than in muscle. This might be due to absence/low activity of metabolizing enzymes in the egg and/or differences in lipid composition between the two matrices.

Multivariate techniques can also be used to relate measured contaminant levels and general physicochemical parameters to biological responses and to eventually find causality behind the emergence of the responses. In a recent work [87], environmental factors of industrialized and urbanized Llobregat river (NE Spain) affecting aquatic invertebrate communities were assessed using *Daphnia magna in situ* bioassays and biological indices based on community assemblages of benthic macroinvertebrates. To explore causal relationships between the studied environmental variables and parameters and the biological responses, PCA and PLS methods were used. The authors showed that environmental variables, such as habitat degradation, suspended solids, nitrogenous and conductivity related parameters affected macroinvertebrate assemblages. On the other hand, river levels of organophosphorus pesticides and PAHs were high enough to trigger the responses of *Daphnia magna in situ* bioassays.

3.2. Polycyclic aromatic hydrocarbons

The high variability of PAHs concentrations according to the sampling site and to the environment (urban, rural, coastal and remote) requires a very careful evaluation and interpretation. Multivariate statistical approaches deliver substantial information on links among sampling sites and pollutant concentrations through latent factors responsible for the data set structure and pollutant sources allocated. Among these approaches, PCA and PCA with varimax rotation were the most used techniques.

As an example, Golobocanin et al. proved PCA and cluster analysis to be a very effective tool in finding patterns to explain PAH occurrence in surface soil. They found PAHs distributed in three groups, mainly according to the number of rings in their structure, for grossly contaminated areas [88].

PCA with varimax rotation has been used to identify contributing sources of particle-phase PAHs in rural areas of Candiota region, Rio Grande do Sul, Brazil [89]. The data analysis separated the compounds studied in 3 factors, grouping emissions from the combustion of coal and wood, vehicle emissions from the combustion of diesel oil and gasoline and emissions from unburned diesel oil and gasoline. This study also demonstrated the influence of weather parameters, such as rainfall and concentration of particulate matter, on the different PAHs present in the area under study; hence, physicochemical characteristics, such as size of particles and water solubility, are determinant to the distribution of these compounds in the atmosphere.

Distribution characteristics, probabilistic risk assessment and identification of possible sources of PAHs were investigated in the Yellow River delta (China) [90]. For PAH source identification, both diagnostic tools based on ratios of selected PAHs and principal component analysis (PCA) with multiple linear regression (MLR) analysis were studied, suggesting mixed sources of pyrogenic and petrogenic derived PAHs in this river.

23 PAHs were analyzed in surface sediments and oyster samples from the intertidal areas of Dar es Salaam (Tanzania) by GC-MS. Diagnostic indices and PCA were used to identify possible contamination sources. Interestingly, no correlation between sediment and oyster PAHs concentrations measured in the same sites was found. This conclusion was supported by completely different contamination patterns, suggesting different sources or accumulation mechanisms for both environmental compartments [91].

Different receptor models, such as chemical mass balance (CMB) [92], factor analysis (FA) with non-negativity constraints, PCA/APCA, UNMIX and positive matrix factorization (PMF) were used to determine the profiles and relative contributions of PAH sources in different environmental media.

CMB and FA with non-negativity constraints were the most used receptor models to apportion sources of PAHs. CMB uses historical emission source profiles that are assumed to be known and weighted regression methods to apportion their related mass. In CMB, the output does not include the source profiles because they are required inputs and are used to build the receptor models. Li et al. used CMB to apportion the major sources of PAHs found in the sediments of Lake Calumet and surrounding wetlands in southeast Chicago [92]. The results indicated the feasibility of applying CMB to pollutants found in aquatic sediments. To establish the fingerprints of PAH sources, 28 source profiles were collected from the literature. The profiles under the same source category were averaged and the fingerprints of six sources were established, including coke oven, residential coal burning, coal combustion in power generation, gasoline engine exhaust, diesel engine exhaust and traffic tunnel air. The results indicated that coke ovens and traffic are the two major sources of PAHs in the area. The average contribution from coke oven emissions ranged from 21% to 53% and that from traffic ranged from 27% to 63%. The pattern of source contributions also showed spatial and temporal variations. Bzdusek and Christensen used an FA model with non-negative constraints, which supported the results of the work mentioned above [93]. In addition, FA provided new insights, since wood burning and secondary coke oven profiles were not recognized in the CMB model studied by Li et al. [92]. This was the first application of an FA model for source apportionment of PAHs in sediments. This methodology does not require input of source profiles and provides factor loading and factor score plots, which can be interpreted as PAH source profiles and PAH source contributions, respectively.

A PCA/APCA receptor modelling approach has been proposed for the estimation of source contributions of PAHs in particulate depositions on near highway vegetation foliage in the urban environment of Lucknow City (India) [94]. PCA identified three major sources of PAHs, *viz*. combustion, vehicle emissions and diesel-based activities. Whereas APCA was used to quantify the contributions of all sources to each measured PAH, a subsequent MLR step related the sample mass concentration to the APCA-estimated mass concentration of each source. Finally, the PCA/APCA receptor modelling approach revealed that the combustion sources (natural gas, wood, coal/coke, biomass) contributed 19–97% to the total measured PAHs, vehicular emissions 0–70%, diesel-based sources 0–81% and other miscellaneous sources 0–20%. The chemically meaningful PCA/APCA receptor model enables their validation by comparison of estimated source profiles with literature data.

A linear mixing model using FA was proposed to identify site parameters that may influence the PAH concentrations in Swiss background soil and to assess whether it was possible to identify sources of PAH in background soils [95]. The application of the receptor model was performed taking into account the pattern of all 16 EPA-regulated PAHs sources. The comparison of three soil profiles identified with a linear mixing model from the pattern of 16 PAH with more than 300 PAH emission profiles from the literature suggested urban dust, wood combustion and binders from asphalt as main PAH sources.

In [96], two receptor modelling methods (PCA with MLR and PMF) were compared to determine the profiles and relative contributions of the sources of PAHs and sulphur heterocycles in the sediments of Hamilton Harbour (Ontario, Canada) and surrounding harbour creeks. Both methods identified four factors and gave excellent correlation coefficients between predicted and measured levels of pollutant compounds and they assigned similar contributions from coal and tar/coal combustion sources to the harbour (19 and 26%, respectively). One PCA factor was identified as contributions from vehicular emissions (61%). PMF was able to differentiate vehicular emissions into two factors, one attributed to gasoline emissions sources (28%) and the other to diesel emissions sources (24%). Overall, PMF afforded better source identification than PCA with MLR. In PMF, an explicit least-squares approach is considered, which individually weights measured values by its estimated uncertainty [26]. This individual data point weighting in PMF has been stated to outperform eigenbased analysis methods, such as PCA, since it deals better with values below the detection limit (DL) and with missing data and takes into consideration the real uneven uncertainty associated with the analyzed values [115]. Other weighted least-squares-based approaches (MCR) have also been recently proposed for the same purposes [29].

In another study [97], two eigenbased source apportionment methods (PCA with MLR and UNMIX [25]) and one non-eigenbased source apportionment method were applied and compared to determine the sources of PAHs in ambient air in Baltimore, MD (USA). Overall source contributions compare well among methods. Vehicles, both diesel and gasoline, contribute 16–26%, coal 28–36%, oil 15–23% and wood/other having the greatest disparity, 23–35% of the total (gas plus particle-phase) PAHs. Seasonal trends were found for both coal and oil. Coal was the PAH dominating source during the summer, while oil dominated during the winter. The information obtained from the different techniques is complementary and allows for a deeper and more reliable interpretation of the resulting source profiles. PMF was the only method to separate diesel from gasoline sources.

An ANN approach to the analysis of seasonal air pollution (e.g., PAHs) within the area of the city of Gdansk was introduced by Wesolowski et al. [98]. They applied two different types of ANN: multilayer perceptron (MLP) and SOM. MLP was used as a tool to predict the season in which a certain sample was collected and

SOM was applied for sample mapping to recognize similarities. This study also presented the comparison between two projection methods, linear (PCA) and non-linear (SOM), to extract valuable information from multi-dimensional environmental data.

Burns et al. used PLS to reassess the percentage contribution of coal, seep oil, shales and rivers to the total hydrocarbon loading in Prince William Sound (PWS) and the Gulf of Alaska (GoA) [99]. Data provided from NOAA and Exxon were analyzed using selected sites as sources in order to develop signatures. These signatures were based on 40 and 136 compounds, respectively and included PAH and terpane/sterane biomarkers in the case of the Exxon data. The authors used PCA to identify how many different sources could exist and to expand the number of PLS signatures to encompass all possible sources. These were then combined to determine the relative contribution from each source and to quantify the overlap among similar signatures. Using the Exxon data, a mixed combination of coal, seep oil, eroding shales and two different river sources described 13%, 18%, 24%, 26% and 20%, respectively, of the variance in PWS and GoA data. The first river signature was very similar to that of coal, while the second one was more similar to the eroding shales. With the NOAA data, the authors observed a considerable overlap in the signatures.

In [100], the influence of soil characteristics and PAH physicochemical properties in the chemical degradability of PAHs contained in aged soil samples from several contaminated sites was investigated using PLS. The PAH-contaminated soil samples were characterised and subjected to relatively mild, slurry-phase Fenton's reaction conditions. In general, low molecular weight PAHs were more degraded than large, highly hydrophobic variants. The presence of organic matter and the specific surface area of the soil were negatively correlated with the degradation of bi- and tri-cyclic PAHs, whereas the amount of degraded organic matter correlated positively with the degradation of PAHs with five or six fused rings. This was explained because larger PAHs were released from the organic matter as it degraded.

3.3. Other pollutants

Phthalate esters were investigated in surface soils from 37 sampling sites including roadsides, parks and residential areas of Guangzhou (China) [101]. These compounds were detected in all surface soils analyzed as ubiquitous environmental contaminants. PCA was applied to reveal their distribution patterns.

Because volatile organic compounds (VOCs) play an important role in the formation of photochemical O_3 and other oxidants in the troposphere, it is crucial the characterization of their sources and distribution in the atmosphere. Different multivariate techniques such as PCA/APCA, CMB, PMF and UNMIX were applied in order to identify and to apportion the VOCs sources in rural and urban sites.

In [102], the CMB receptor model has apportioned VOCs in more than 20 urban areas, mostly in the USA. The models in these areas differ in terms of the total fraction apportioned, the calculation method, the chemical compounds used in the calculation, the apportionment units and the source profiles applied. Nevertheless, they show similar results for VOC fractions contributed by different sources. Gasoline vehicle exhaust, liquid gasoline and gasoline evaporation contribute up to 50% or more of the ambient VOCs in many of these studies. In another study, a CMB receptor model and a multivariate receptor model (UNMIX) were used for the determination of the contributions of different non-methane hydrocarbon sources in Helsinki [103]. Source contributions were estimated for different seasons of the year and weekly and diurnal variations were examined using the CMB mode. UNMIX was used to confirm that the major sources were included in the CMB calculations. According to the CMB analysis, major sources of C2–C10 hydrocarbons were traffic and emissions from distant sources. For C6–C10 hydrocarbons, the major sources in both CMB and UNMIX analyses were gasoline exhaust.

Relationships between VOCs and transient high ozone formation in the Houston area were evaluated by Gan and Hopke [104]. Based on CMB analysis, a linear model was established between the subset of the VOCs data and the positive ozone transition. Non-negative least-squares were used to calculate the regression coefficient of the VOCs that have the most significant direct relationship to the positive ozone transition. The results show that more attention should be paid to additional non-considered VOCs, which can have significant relationship to the transient high ozone formation.

UNMIX and PMF were used to analyze ambient VOCs measured in a spring campaign in 1996 at Santiago de Chile. Two sites were sampled: a downtown site, close to major traffic emissions and a residential site, downwind of major industrial sources and highways [105]. It was found that the number of factors given by the UNMIX model was a good starting point to refine the solution using PMF. Both models showed good performance at discriminating between source profiles that had similar compositions in subsets of common species, but PMF was able to find better and cleaner source profiles than UNMIX.

Four receptor models (CMB, PCA/APCA, PMF and UNMIX) were used to describe personal exposure measurements to toxic VOCs. The measurements were from the total exposure assessment studies conducted from 1980 to 1984 in New Jersey and California and from the 1987 to 1990 California Indoor Exposure study [106]. From the four receptor models compared, PMF and UNMIX showed the closest agreement, extracting six similar factors from the New Jersey personal exposure data and four similar factors from the California data. Between the two methods, PMF has the advantage of reporting more complete information on model performance than the current version of UNMIX. The lack of a non-negativity constraint is a significant limitation of both PCA/APCA and CMB. Nevertheless, results from CMB were useful to help in the interpretation of factors extracted by the other models.

In [107], the effectiveness of using trace organic speciation data to identify sources influencing fine particulate matter (PM2.5) exposure concentrations was investigated. PM2.5 samples, with organic carbon as dominant constituent, were obtained from seven different individuals in and around Boulder, CO (USA). The data set was analyzed by PCA to determine the factors that account for the largest variance. Eight significant factors were identified and each of them was matched to a potential source according to the marker species that mostly loaded the factor. Meat cooking was an important source of variability and its associated factor was highly correlated to organic carbon concentration. The exposure time while developing an activity was generally not well correlated to the PCA factor scores because exposure time is not directly related to emissions intensity. The PCA results demonstrated that organic tracers can aid in identifying factors that influence personal exposures to PM2.5.

In [108], PM2.5 and VOCs data collected at Beacon Hill in Seattle between 2000 and 2004 were analyzed with the Multilinear Engine method [31] in order to quantify source contributions to the mixture of hazardous air pollutants (HAPs). ME solves a positively constrained bilinear mass balance model using an explicit least-squares equation. The required input data include the mass concentrations and uncertainties of each measured species. ME is an evolution of the different PMF methods towards an improved generalized multilinear modelling tool. The authors tested the performance of the model with and without the addition of VOCs data. They also used the 'missing mass', defined as the concentration of the measured total particle mass minus the sum of all analyzed species, as an additional variable and implemented an auxiliary equation to constrain the sum of all species mass fractions to be

Table 4
QSAR studies.

Compounds	Multivariate method[a]	Aim of the multivariate method in the study	References
Pesticides			
Pesticides	BNN	Prediction of the toxicity to *Lepomis macrochirus* under varying experimental conditions	[116]
Thiazoline derivatives	PCA, GA-MLR, LS-SVM, PPR	Fungicidal activities of thiazoline derivatives against rice blast. PCA was used to built a validate training set	[117]
One hundred and sixteen pesticides	PCA, GA, SVM, LDA, KNN	Prediction of the avian oral toxicity. GA for variable selection in PCA	[118]
Pesticides	MLR, GA, SOM, AFP	Prediction of toxicity against fathead minnow. SOM (selection training)	[119]
Two hundred and thirty-five pesticides	NMC, LDA, QDA, RDA, SIMCA, KNN, CART	Critical analysis of the different models and descriptors in order to predict ecotoxicity	[120]
Phenylureas and triazines	MDS, GA (for variable selection)-MDS	Selection of congeneric compounds with a similar toxicological mode of action	[121]
Polycyclic aromatic hydrocarbons			
PHAs	PLS	QSAR model to predict the phototoxicity .	[122]
Sixty-seven PAHs	GA (variable selection) KNN, CART, SOM (external validation)	QSAR model to predict mutagenicity in human cells of the pollutants	[123]
Other organic pollutants			
One hundred and twenty-five organic compounds	GA (for variable selection), PCA (*a priori* classification), KNN, CART, LDA, SLDA, RDA	Qsar models to predict toxicity on algae, *Daphnia*, and fish	[124]
Two hundred and fifty organic compounds	HCA (*a priori* classification), KNN, CART, CP-ANN	QSAR model to screen and rank POPs with regard to their tendency towards atmospheric persistence and mobility	[125]
One hundred and ninety-one organic compounds	RBF-ANNs, LDA, NLDA and SVM	Comparison of the QSAR models to predict aquatic toxicity	[126]
15 PBDEs	PLS/LOO-CV (variable selection), SVM and RBF-ANNs	QSAR models to predict the Aryl hydrocarbon Receptor Relative Binding Affinities (RBA) of pollutants	[127]

[a] See acronyms in Table 1. PBDEs, polybrominated diphenyl ethers.

100%. Using only PM2.5 data, the model distinguished two diesel sources with the 100% constraint, but identified only one diesel source without the constraint. When both PM2.5 and VOCs data were used, an additional feature was identified as the major contributor to total VOC mass. Adding VOCs data to the speciated PM2.5 data in source apportionment modelling resulted in more accurate source contribution estimates for combustion related sources, as evidenced by the less 'missing mass' percentage in PM2.5. Using the source contribution estimates, the authors did also evaluate the validity of using black carbon as a surrogate for diesel exhaust during different seasons.

Non-parametric regression is also a powerful technique that has many potential uses in air quality studies and atmospheric sciences. In [109], the relationship between the concentration of cyclohexane and other VOCs with wind direction was determined at two sites near a heavy industrial region in Houston (USA), by non-parametric regression using a Gaussian kernel. The results were smooth curves with error bars that allowed for the accurate determination of the wind direction where the concentration peaks and thus, the location of nearby sources. Cyclohexane was chosen to test the method because 70% of the industrial emissions in the region are known to be from this single source. Thus, the intersection of two lines drawn from each site in the direction of the largest concentration peak should be the location of this source. The success of the method can be judged by how closely the predicted position of the source corresponds to the known location. The non-parametric regression correctly identified the direction of this source from each site and the predicted location of the source was less than 500 m away from that given in the inventory.

Among the persistent organic pollutants targeted for monitoring, control and virtual elimination by international research projects and agreements (UNEP, 2001), polychlorinated biphenyls (PCBs) are ubiquitous contaminants in the environment. Polytopic vector analysis (PVA) has been used for the characterization of sources and alteration patterns of PCBs in complex environmental settings. As an example, in [110] the authors discussed PCB dechlorination processes measured in Lake Hartwell sediments using a PVA receptor model. The GC-MS resolution of 107 PCB congeners provided insight into PCB sources and the degree of PCB weathering in the sediments. Modifications in congener concentrations and typology were characterized by comparing surface sediment congener distributions with the distributions in buried sediments and were matched with literature-reported dechlorination patterns from other sites. PVA results were used to determine PCB sources and dechlorination end member (EM) patterns and their distributions in each of the cores. The authors showed the advantage of such an approach to identify fingerprints (EMs) with minimal assumption of contributing source patterns and/or alteration mechanisms.

The usefulness of the combination of the probabilistic model called potential source contribution function (PSCF) with PMF was proposed as a tool to identify atmospheric PCB sources regions in Philadelphia [111]. PSCF can only reveal the potential source location, but cannot give a quantitative indication of the source strength. Thus, the combination with PMF can provide an effective tool for identification of atmosphere source and apportionment.

Results of three hybrid receptor models, PSCF, concentration weighted trajectory (CWT) and residence time weighted concentration (RTWC), were compared for locating PCB sources contributing to the atmospheric concentrations in Chicago [112]. All three trajectories ensemble models consistently indicated similar PCB source locations. Each approach was found to have some advantages com-

pared to the others. Thus, when used together, they provide better information on source areas than the obtained by using only one of them.

Chemometric assessment of multivariate data sets generated in monitoring studies of other pollutant compounds, such as PBDEs, non-ionic surfactants and linear alkylbenzene sulfonates have also been done. As an example, identification, resolution and distribution of main microcontaminant sources of endocrine disruptors in Spanish harbours, coastal waters and sediments were investigated using PCA and MCR-ALS [113]. In this study, the authors interpreted the main environmental contamination sources of these endocrine disruptor compounds according to their chemical composition and to their resolved geographical distribution profiles. Whereas PCA allowed the qualitative interpretation of the major contamination sources, MCR-ALS confirmed these results and allowed a semi-quantitative view of contamination sources allowing their apportionment. Although 'hot spots' with point sources of municipal and industrial discharges were identified, it could be concluded that the investigated compounds were widespread contaminants in the marine environment of the Mediterranean Spanish coasts and harbours. Large accumulation effects of most of these contaminants were observed for sediment samples collected near discharges of domestic or industrial wastewaters in the studied harbour areas, as compared with less contaminated sea water samples.

4. Toxicity studies

4.1. Pesticides

As can be seen in Table 4, many pesticide toxicity studies have been conducted using ANN, which is appropriate in cases of highly non-linear relationships between the input and output variables. Several QSAR models have been developed to predict the aquatic toxicity of pesticides using ANNs. An example of these QSAR studies can be found in [116], where the estimation of the acute toxicity of pesticides against *Lepomis macrochirus* (freshwater fish) under different experimental and biological conditions (e.g., fish weight, exposure time, temperature, pH and water hardness) was done using a three-layer feed-forward neural network trained by the back-propagation algorithm.

However, ANNs may tend to overfit the training data set unless very careful external validation strategies are applied that will ensure reliable prediction models. Alternatively, genetic algorithm-multilinear regression (GA-MLR), least-squares support vector machine (LS-SVM, which performs classification tasks by constructing hyperplanes in a multi-dimensional space to separate cases of different class labels) and projection pursuit regression (PPR, which involves finding the most 'interesting' projections in multi-dimensional data, i.e., those which deviate more from a normal distribution) have been proposed to model the fungicidal activity of thiazoline against rice blast [117]. The GA-MLR method was used to select the most appropriate molecular descriptors from the large original set to develop a linear quantitative structure–activity relationship (QSAR) model. On the basis of the selected descriptors, two more accurate models (LS-SVM and PPR) were built. Both the linear and non-linear models gave satisfactory prediction results, but the non-linear models provided better prediction ability, which means that LS-SVM and PPR methods could simulate more adequately the real relationship between the structural descriptors and the fungicidal activity.

Mazzatorta et al. also demonstrated the ability of SVM combined with GA for feature selection and prediction of the avian oral toxicity of 116 pesticides [118]. A comparison with several other classification methods was performed.

A QSAR model to predict the toxicity of pesticides against fathead minnow (freshwater fish) was built by Pintore et al. [119]. In their work, the authors combined genetic algorithms and stepwise regression methods in order to select the best descriptors for the model. GA is very effective for exploratory search, applicable to problems where little information is available, but it is less appropriate for a local search. Then, a stepwise approach was combined with GA (GA/SW) in order to reach local convergence. The selection of the training set was performed by SOM, which provided a 2D-space representation of molecular descriptors obtained from the original multi-dimensional space. Finally, a QSAR model was built by the adaptive fuzzy partition (AFP) method. This consists of modelling the relationship between molecular descriptors and biological activities of pesticides by dynamically dividing the molecular descriptor hyperspace into new fuzzy subspaces. Several models were attempted for the study, classification and prediction of toxicities of 253 pesticides. Seven classification algorithms were used and compared in detail and the performance of the different models was assessed [120]. The methods used were nearest mean classifier (NMC), LDA, quadratic discriminant analysis (QDA), regularized discriminant analysis (RDA), SIMCA, KNN and classification and regression tree (CART). The first four are parametric statistical systems based on Fisher's discriminant analysis, the fifth and sixth are non-parametric statistical methods and the last is a classification tree. CART and RDA appeared to be the classification algorithms which best described the biological activities of the pesticides considered. RDA had a further advantage: because of the definition of RDA, the classification is easier to understand. The regularization was used to overcome the problems of linear and quadratic discriminant analysis.

Gramatica et al. proposed a new approach for the selection of chemicals with similar mode of action, based on the analysis of structural similarities by means of QSAR and chemometric methods (PCA, multi-dimensional scaling (MDS) and GA) [121]. PCA and MDS were used for data exploration. MDS gave the best two-dimensional projection able to approximate the whole set of the Euclidean distances among the compounds. GA was used as variable selection method. The proposed approach seems to be a very promising tool, even if the available information is too scarce to fully understand the precise role of the different molecular descriptors in explaining the toxicological behaviour of the investigated pesticides.

4.2. Polycyclic aromatic hydrocarbons

The increasing concern about the input of PAHs in the environment has stimulated the investigation of their properties and biological activities, mainly because of their carcinogenic and toxic potential. PAHs containing four or more condensed rings are particularly hazardous because most of them are carcinogenic, mutagenic and extremely resistant to enzymatic degradation. Recent research has demonstrated that the toxic effect of chemicals can be induced or enhanced by visible or UV radiation. The photocytotoxicity and mutagenic and carcinogenic activity have been studied in a number of aquatic organisms. However, these QSAR models were usually developed using MLR, which will not be reviewed in this paper.

Alves de Lima Ribeiro et al. proposed a QSAR model to predict the phototoxicity of PAHs using electronic descriptors and PLS [122]. The relationship between these molecular descriptors and the photoinduced toxicity is non-linear and Gaussian type functions were used to linearize them. Once the model was validated, the phototoxicity was predicted for a set of molecules in which experimental measurements were unknown. Among them, pentaphene, benzo[*b*]chrysene and dibenz[*a*,*j*]anthracene are the compounds potentially phototoxic as predicted by the model.

In [123], experimental data of a mutagenicity test on human B-lymphoblastoid cells (alternative to the Ames bacterial test) for a

set of 70 oxo-, nitro- and unsubstituted PAHs detected in particulate matter (PM), were modelled by QSAR classification methods (KNN and CART) based on different theoretical molecular descriptors selected by genetic algorithms. The best models were internally and externally validated for prediction. For external validation, SOM was applied to split the original data set. The best models, developed on the training set alone, also showed good predictive performance on the prediction set of chemicals. The classification of PAHs according to their mutagenicity, based only on a few theoretical molecular descriptors, allowed a preliminary assessment of the human health risk and the prioritization of these compounds.

4.3. Other pollutants

As previously stated, there is a need for predictive tools capable to perform a preliminary hazard ranking for the very large number of existing chemicals discharged into the environment and for which experimental data are insufficient. In [124], QSAR models were developed in order to produce additional toxicological data for unmeasured compounds. The QSAR models to predict aquatic toxicity (algae, *Daphnia* and fish) of 125 organic compounds were performed based on: (1) the use of a large set of traditional and non-traditional molecular descriptors, (2) the selection of molecular descriptors by a genetic algorithm and (3) the production of models by ordinary least-squares regression. This approach was proven to be suitable to build models with satisfactory predictive capability, even on a largely heterogeneous data set. Afterwards, the data set was analyzed by PCA to rank chemicals as a function of their toxicity on different representative aquatic organisms and to help in the definition of *a priori* classes of toxicity. Finally, several classification methods (CART, KNN, RDA and LDA) were applied in order to classify the hazard of chemicals for the aquatic environment as a function of their molecular structure. The authors emphasized that different classification models may produce, in some cases, different evaluations. Thus, the best way to obtain reliable results is the combined use of several classification models, taking as starting point the *a priori* classes suggested by the PCA results of toxicity data.

In [125], a quantitative structure–property relationship (QSPR) study for the prediction of the environmental persistence of a set of 250 heterogeneous organic compounds was presented. Three *a priori* defined classes of environmental persistence were suggested by HCA, from the analysis of half-life data in air, water, soil and sediment and three interpretable theoretical molecular descriptors for all the studied compounds. QSPR classification models were successfully developed using different techniques, such as KNN, CART and counter propagation-ANN (CP-ANN), which is an adaptation of the Kohonen network to solve supervised problems. The models obtained for the prediction of potential persistence of heterogeneous organic compounds could be potentially useful as preliminary tools for the identification and prioritization of new potential POPs among already existing chemicals. A step forward would be their use as 'screening prior to synthesis' procedures to prevent the production and consequent release into the environment of potential POPs. Among the three presented strategies, the CP-ANN model gave the best results and was robust and accurate in the classification task for the three classes of persistence level. The CART model gave the most unbalanced results among the three classes, but they were still satisfactory. However, the simplicity of this approach is a good point when CART is compared with the other classification techniques presented in this study.

The performance and predictive capability of SVM and RBF-ANNs for classification problems in QSAR/QSPR were investigated and compared with several other classification methods, such as LDA and non-linear DA (NLDA). In [126], two different data sets are evaluated. The first one involves the classification of four action modes of 221 phenols and the second deals with the classification of three narcosis mechanisms of aquatic toxicity for 194 organic compounds. In both cases, the predictive ability of the SVM model is comparable or better than those obtained by LDA, NLDA and RBF-ANNs. The results obtained indicate that the SVM model with the RBF kernel function can be used as an alternative tool for classification problems in QSAR/QSPR. In another study [127], PLS was used to extract the seven best descriptors from more than 80 quantum descriptors in order to predict the aryl hydrocarbon receptor relative binding affinities of PBDEs. The extracted seven descriptors were correlated with the relative binding affinities of 15 PBDE congeners using SVM and RBF-ANNs. SVM models were proven to be of more general applicability than the RBF-ANNs models.

Acknowledgements

The authors gratefully acknowledge Agencia Española de Cooperación Internacional (AECI), Project A/8964/07, Universidad Nacional de Rosario, Agencia Nacional de Promoción Científica y Tecnológica (Project PAE 22204) and Consejo Nacional de Investigaciones Científicas y Técnicas (CONICET, Argentina, Project PIP No. 1950), for financial support of this work.

References

[1] http://www.epa.gov/ebtpages/pollutants.html.
[2] S.P.J. van Leeuwen, J. de Boer, J. Chromatogr. A 1186 (2008) 161.
[3] M. Gros, M. Petrović, D. Barceló, Talanta 70 (2006) 678.
[4] A. Salinas Castillo, A. Segura Carretero, J.M. Costa, Anal. Chim. Acta 516 (2004) 213.
[5] D.L. Massart, B.G.M. Vandeginste, L.M.C. Buydens, S. de Jong, P.J. Lewi, J.S. Verbeke, Handbook of Chemometrics and Qualimetrics, Elsevier, Amsterdam, The Netherlands, 1997, Parts A and B.
[6] R. Bro, Anal. Chim. Acta 500 (2003) 185.
[7] K.S. Booksh, B.R. Kowalski, Anal. Chem. 66 (1994) 782A.
[8] A.C. Olivieri, Anal. Chem. 80 (2008) 5713.
[9] G.M. Escandar, N.M. Faber, H.C. Goicoechea, A. Muñoz de la Peña, A.C. Olivieri, R.J. Poppi, Trends Anal. Chem. 26 (2007) 752.
[10] R. Tauler, A. Smilde, B.R. Kowalski, J. Chemometrics 9 (1995) 31.
[11] A. de Juan, E. Casassas, R. Tauler, in: R.A. Myers (Ed.), Encyclopedia of Analytical Chemistry, vol. 11, Wiley, Chichester, West Sussex, UK, 2002, pp. 9800–9837.
[12] R. Bro, Chemom. Intell. Lab. Syst. 38 (1997) 149.
[13] D. BohoyoGil, A. Muñoz de la Peña, J.A. Arancibia, G.M. Escandar, A.C. Olivieri, Anal. Chem. 78 (2006) 8051.
[14] G.N. Piccirilli, G.M. Escandar, Analyst 131 (2006) 1012.
[15] J.A. Arancibia, G.M. Escandar, Anal. Chim. Acta 584 (2007) 287.
[16] S.A. Bortolato, J.A. Arancibia, G.M. Escandar, Anal. Chem. 80 (2008) 8276.
[17] P.K. Hopke, J. Chemometrics 17 (2003) 225.
[18] R.C. Henry, C.W. Lewis, P.K. Hopke, H.J. Williamson, Atmos. Environ. 18 (1984) 1507.
[19] P.K. Hopke, Receptor Modeling in Environmental Chemistry, Wiley, New York, 1985.
[20] J. Einax, H. Zwanziger, S. Geiss (Eds.), Chemometrics in Environmental Analysis, VCH, Weinheim, Germany, 1997.
[21] I.T. Joliffe, Principal Component Analysis, Springer, New York, USA, 1986.
[22] G.D. Thurston, D. Spengler, Atmos. Environ. 19 (1985) 9.
[23] E. Peré-Trepat, L. Olivella, A. Ginebreda, J. Caixach, R. Tauler, Sci. Total Environ. 371 (2006) 223.
[24] P. Paatero, P.K. Hopke, X.-H. Song, Z. Ramadan, Chemom. Intell. Lab. Syst. 60 (2002) 253.
[25] R.C. Henry, Chemom. Intell. Lab. Syst. 65 (2003) 179.
[26] P. Paatero, U. Tapper, Environmetrics 5 (1994) 111.
[27] J.S. Salau, R. Tauler, J.M. Bayona, I. Tolosa, Environ. Sci. Technol. 31 (1997) 3482.
[28] R. Tauler, D. Barcelo, E.M. Thurman, Environ. Sci. Technol. 34 (2000) 3307.
[29] R. Tauler, M. Viana, X. Querol, A. Alastueya, R.M. Flight, P.D. Wentzell, P.K. Hopke, Atmos. Environ 43 (2009) 3989.
[30] L.R. Tucker, Psychometrika 31 (1966) 279.
[31] P. Paatero, J. Comput. Graph. Stat. 8 (1999) 854.
[32] A. de Juan, R. Tauler, J. Chemometrics 15 (2001) 749.
[33] E. Peré-Trepat, A. Ginebreda, R. Tauler, Chemom. Intell. Lab. Syst. 88 (2007) 69.
[34] L. Eriksson, J. Jaworska, A.P. Worth, M.T.D. Cronin, R.M. McDowell, P. Gramatica, Chemom. Intell. Lab. Syst. 34 (1996) 1.
[35] S. Weisberg, Applied Linear Regression, John Wiley & Sons, New York, USA, 1985.

[36] D.E. Goldberg, Genetic Algorithms in Search, Optimization and Machine Learning, Addison-Wesley, New York, USA, 1989.
[37] S. Haykin, Neural Networks. A Comprehensive Foundation, 2nd ed., Prentice-Hall, Upper Saddle River, NJ, USA, 1999.
[38] R. Schalkoff, Pattern Recognition Statistical, Structural and Neural Approaches, John Wiley & Sons, New York, USA, 1992.
[39] I.M. Fharnham, A.K. Singh, K.J. Stetzenbach, K.H. Lohannesson, Chemom. Intell. Lab. Syst. 60 (2002) 265.
[40] M. Daszykowski, B. Walczak, Trends Anal. Chem. 25 (2006) 1081.
[41] G.T. Miller, Sustaining the Earth, 6th ed., Thompson Learning Inc. Pacific Grove, California, USA, 2004, Ch 9, pp. 211–216.
[42] T. Wenzl, R. Simon, J. Kleiner, E. Anklam, Trends Anal. Chem. 25 (2006) 716.
[43] A. Smilde, R. Bro, P. Geladi, Multi-way Analysis with Applications in the Chemical Sciences, Wiley, Chichester, UK, 2004.
[44] A. Guiberteau-Cabanillas, T. Galeano-Díaz, N. Mora, F. Salinas, J.M. Ortíz, J.C. Viré, Comp. Chem. 25 (2001) 459.
[45] Y. Ni, D. Cao, S. Kokot, Anal. Chim. Acta 588 (2007) 131.
[46] D. Brunet, T. Woignier, M. Lesueur-Jannoyer, R. Achard, L. Rangon, B.G. Barthès, Environ. Pollut. 157 (2009) 3120.
[47] Y. Ni, W. Xiao, S. Kokot, J. Hazard. Mater. 168 (2009) 1239.
[48] E. Comas, R.A. Gimeno, J. Ferré, R.M. Marcé, F. Borrull, F.X. Rius, J. Chromatogr. A 1035 (2004) 195.
[49] E. Peré-Trepat, A. Hildebrandt, D. Barceló, S. Lacorte, R. Tauler, Chemom. Intell. Lab. Syst. 74 (2004) 293.
[50] E. Peré-Trepat, S. Lacorte, R. Tauler, J. Chromatogr. A 1096 (2005) 111.
[51] E. Peré-Trepat, R. Tauler, J. Chromatogr. A 1131 (2006) 85.
[52] E. Peré-Trepat, S. Lacorte, R. Tauler, Anal. Chim. Acta 595 (2007) 228.
[53] T. Khayamian, G.H. Tan, A. Sirhan, Y.F. Siew, S.M. Sajjadi, Chemom. Intell. Lab. Syst. 96 (2009) 149.
[54] E. Bezemer, S. Rutan, Anal. Chim. Acta 459 (2002) 277.
[55] J. Saurina, C. Leal, R. Compañó, M. Granados, R. Tauler, M.D. Prat, Anal. Chim. Acta 409 (2000) 237.
[56] M.J. Rodríguez Cuesta, R. Boqué, F.X. Rius, D. Picón Zamora, M. Martínez Galera, A. Garrido Frenich, Anal. Chim. Acta 491 (2003) 47.
[57] A. GarridoFrenich, D. PicónZamora, M. MartínezGalera, J.L. MartínezVidal, Anal. Bioanal. Chem. 375 (2003) 974.
[58] M.L. Nahorniak, G.A. Cooper, Y.C. Kim, K.S. Booksh, Analyst 130 (2005) 85.
[59] S.H. Zhu, H.L. Wu, A.L. Xia, J.F. Nie, Y.C. Bian, C.B. Cai, R.Q. Yu, Talanta 77 (2009) 1640.
[60] T. Galeano-Díaz, A. Guiberteau-Cabanillas, A. Espinosa-Mansilla, M.D. López-Soto, Anal. Chim. Acta 618 (2008) 131.
[61] O. Devos, B. Fanget, A.I. Saber, L. Paturel, E. Naffrechoux, J. Jarosz, Anal. Chem. 74 (2002) 678.
[62] T.J. Grundl, J.H. Aldstadt, J.G. Harb, R.W. St. Germain, R.C. Schweitzer, Environ. Sci. Technol. 37 (2003) 1189.
[63] M.L. Nahorniak, K.S. Booksh, J. Chemometrics 17 (2003) 608.
[64] Y.C. Kim, J.A. Jordan, M.L. Nahorniak, K.S. Booksh, Anal. Chem. 77 (2005) 7679.
[65] R.A. Gimeno, E. Comas, R.M. Marcé, J. Ferré, F.X. Rius, F. Borrull, Anal. Chim. Acta 498 (2003) 47.
[66] P.D. Wentzell, S.S. Nair, R.D. Guy, Anal. Chem. 73 (2001) 1408.
[67] M.V. Bosco, M.S. Larrechi, Talanta 71 (2007) 1703.
[68] S.A. Bortolato, J.A. Arancibia, G.M. Escandar, Anal. Chem. 81 (2009) 8074.
[69] Ch. Coury, A.M. Dillner, Atmos. Environ. 42 (2008) 5923.
[70] J.M. Gutiérrez, A. Gutés, F. Céspedes, M. del Valle, R. Muñoz, Talanta 76 (2008) 373.
[71] A.E. Sinha, C.G. Fraga, B.J. Prazen, R.E. Synovec, J. Chromatogr. A 1027 (2004) 269.
[72] H.C. Goicoechea, S. Yu, A.C. Olivieri, A.D. Campiglia, Anal. Chem. 77 (2005) 2608.
[73] R. SantiagoValverde, M.D. GilGarcía, M. MartínezGalera, H.C. Goicoechea, Talanta 70 (2006) 774.
[74] M.M. de Zan, M.D. GilGarcía, M.J. Culzoni, R.G. Siano, H.C. Goicoechea, M. MartínezGalera, J. Chromatogr. A 1179 (2008) 115.
[75] K.P. Singh, N. Basant, A. Malik, V.K. Singh, D. Mohan, Anal. Chim. Acta 630 (2008) 10.
[76] A. ValeroNavarro, P.C. Damiani, J.F. FernándezSánchez, A. SeguraCarretero, A. FernándezGutiérrez, Talanta 78 (2009) 57.
[77] S. Mas, A. de Juan, S. Lacorte, R. Tauler, Anal. Chim. Acta 618 (2008) 18.
[78] A. de Juan, M. Maeder, M. Martínez, R. Tauler, Chemom. Intell. Lab. Syst. 54 (2000) 123.
[79] A. Navarro, R. Tauler, S. Lacorte, D. Barceló, Anal. Bioanal. Chem. 385 (2006) 1020.
[80] C.M. Gonçalves, J.C.G. Esteves da Silva, M.F. Alpendurada, J. Agric. Food Chem. 55 (2007) 6227.
[81] R. Tauler, S. Lacorte, M. Guillamón, R. Cespedes, P. Viana, D. Barceló, Environ. Toxicol. Chem. 23 (2004) 565.
[82] M. Terrado, M. Kuster, D. Raldúa, M. Lopez de Alda, D. Barceló, R. Tauler, Anal. Bioanal. Chem. 387 (2007) 1479.
[83] J. Li, G. Zhang, S. Qi, X. Li, X. Peng, Sci. Total Environ. 372 (2006) 215.
[84] G.B. Sahoo, C. Ray, H.F. Wade, Ecol. Modell. 183 (2005) 29.
[85] M. Felipe-Sotelo, R. Tauler, I. Vives, J.O. Grimalt, Sci. Total Environ. 404 (2008) 148.
[86] K. Lundstedt-Enkel, L. Asplund, K. Nylund, A. Bignert, M. Tysklind, M. Olsson, J. Örberg, Chemosphere 65 (2006) 1591.
[87] J. Damásio, R. Tauler, E. Teixidó, M. Rieradevall, N. Prat, M.C. Riva, A. Soarese, C. Barata, Aquat. Toxicol. 87 (2008) 310.
[88] D.D. Golobocanin, B.D. Skrbic, N.R. Miljevic, Chemom. Intell. Lab. Syst. 72 (2004) 219.
[89] J. Braga Dallarosa, E. Calesso Teixeira, M. Pires, J. Fachel, Atmos. Environ. 39 (2005) 6587.
[90] L. Wang, Z. Yang, J. Niu, J. Wang, J. Hazard. Mater. 169 (2009) 460.
[91] L. Gaspare, J.F. Machiwa, S.J.M. Mdachi, G. Streck, W. Brack, Environ. Pollut. 157 (2009) 24.
[92] A. Li, J.K. Jang, P.A. Scheff, Environ. Sci. Technol. 37 (2003) 2958.
[93] P. Bzdusek, E. Christensen, Environ. Sci. Technol. 38 (2004) 97.
[94] K.P. Singh, A. Malik, R. Kumar, P. Saxena, S. Sinha, Environ. Monit. Assess. 136 (2008) 183.
[95] R.C. Brändli, T.D. Bucheli, S. Ammann, A. Desaules, A. Keller, F. Blum, W.A. Stahel, J. Environ. Monit. 10 (2008) 1278.
[96] U. Sofowotw, B. McCarry, C. Marvin, Environ. Sci. Technol. 42 (2008) 6007.
[97] R.K. Larsen, J.E. Baker, Environ. Sci. Technol. 37 (2003) 1873.
[98] M. Wesolowski, B. Suchacz, J. Halkiewicz, Anal. Bioanal. Chem. 384 (2006) 458.
[99] W.A. Burns, S.M. Mudge, A.E. Bence, P.D. Boehm, J.S. Brown, D.S. Page, K.R. Parker, Environ. Sci. Technol. 40 (2006) 6561.
[100] S. Jonsson, Y. Persson, S. Frankki, B. van Bavel, S. Lundstedt, P. Haglund, M. Tysklind, J. Hazard. Mater. 149 (2007) 86.
[101] F. Zeng, K. Cui, Z. Xie, L. Wu, D. Luo, L. Chen, Y. Lin, M. Liu, G. Sun, J. Hazard. Mater. 164 (2009) 1171.
[102] J.G. Watson, J.C. Chow, E.M. Fujita, Atmos. Environ. 35 (2001) 1567.
[103] H. Hellén, H. Hakola, T. Laurila, Atmos. Environ. 37 (2003) 1413.
[104] F. Gan, P.K. Hopke, Anal. Chim. Acta 490 (2003) 153.
[105] H. Jorquera, B. Rappenglück, Atmos. Environ. 38 (2004) 4243.
[106] M.J. Anderson, E.P. Daly, S.L. Miller, J.B. Milford, Atmos. Environ. 36 (2002) 3643.
[107] G.L. Brinkman, J.B. Milford, J.J. Schauer, M.M. Shafer, M.P. Hannigan, Atmos. Environ. 43 (2009) 1972.
[108] C.F. Wu, T.V. Larson, S. Wu, J. Williamson, H.H. Westberg, L.-J.S. Liu, Sci. Total Environ. 386 (2007) 42.
[109] R.C. Henry, Y.S. Chang, C.H. Spiegelman, Atmos. Environ. 36 (2002) 2237.
[110] V.S. Magar, G.W. Johnson, R.C. Brenner, J.F. Quensen, E.A. Foote, G. Durell, J.A. Ickes, C. Peven-McCarthy, Environ. Sci. Technol. 39 (2005) 3538.
[111] S. Du, L.A. Rodenburg, Atmos. Environ. 41 (2007) 8596.
[112] Y.-K. Hsua, T.M. Holsena, P.K. Hopke, Atmos. Environ. 37 (2003) 545.
[113] E. Peré-Trepat, M. Petrovic, D. Barcelo, R. Tauler, Anal. Bioanal. Chem. 378 (2004) 642.
[114] R. Tauler, I. Marques, E. Casassas, J. Chemometrics 12 (1998) 55.
[115] P.K. Hopke, A guide to positive matrix factorisation, 2009, http://www.epa.gov/ttn/amtic/files/ambient/pm25/workshop/laymen.pdf.
[116] J. Devillers, SAR QSAR Environ. Res. 11 (2001) 397.
[117] H. Du, J. Wang, Z. Hu, X. Yao, X. Zhang, J. Agric. Food Chem. 56 (2008) 10785.
[118] P. Mazzatorta, M.T.D. Cronin, E. Benfenati, QSAR Comb. Sci. 25 (2006) 616.
[119] M. Pintore, N. Piclin, E. Benfenati, G. Gini, J.R. Chrétien, QSAR Comb. Sci. 22 (2003) 210.
[120] P. Mazzatorta, E. Benfenati, P. Lorenzini, M. Vighi, J. Chem. Inform. Comput. Sci. 44 (2004) 105.
[121] P. Gramatica, M. Vighi, F. Consolaro, R. Todeschini, A. Finizio, M. Faust, Chemosphere 42 (2001) 873.
[122] F. Alves de Lima Ribeiro, M.C. Ferreira, J. Mol. Struct. THEOCHEM 719 (2005) 191.
[123] E. Papa, P. Pilutti, P. Gramatica, SAR QSAR Environ. Res. 19 (2008) 115.
[124] M. Vighi, P. Gramatica, F. Consolaro, R. Todeschini, Ecotox. Environ. Safety 49 (2001) 206.
[125] E. Papa, P. Gramatica, J. Mol. Graph. Model. 27 (2008) 59.
[126] X.J. Yao, A. Panaye, J.P. Doucet, H.F. Chen, R.S. Zhang, B.T. Fan, M.C. Liu, Z.D. Hu, Anal. Chim. Acta 535 (2005) 259.
[127] G. Zheng, M. Xiao, X. Lu, QSAR Comb. Sci. 26 (2007) 536.

Talanta 80 (2010) 1068–1072

Contents lists available at ScienceDirect

Talanta

journal homepage: www.elsevier.com/locate/talanta

The electrochemical determination of phenolic derivates using multiple pulsed amperometry with graphite based electrodes

Adriana Bebeselea[a,*], Florica Manea[a], Georgeta Burtica[a], Livia Nagy[b], Geza Nagy[b]

[a] "Politehnica" University of Timisoara, P-ta Victoriei no. 2, 300006 Timisoara, Romania
[b] Department for General and Physical Chemistry, University of Pecs, Ifjusag u.6, H-7624 Hungary

ARTICLE INFO

Article history:
Received 13 March 2009
Received in revised form 17 July 2009
Accepted 20 July 2009
Available online 25 July 2009

Keywords:
Carbon-based electrodes
4-Chlorophenol
4-Nitrophenol
Electrochemical detection
Pulsed amperometry

ABSTRACT

The electrochemical determinations of 4-chlorophenol (4-CP) and 4-nitrophenol (4-NP) by chronoamperometry (CA) and multiple pulsed amperometry (MPA) using expanded graphite-epoxy composite (EG-Epoxy) and rotating spectral graphite disc (SG) electrodes are reported. The electrochemical behaviours of both electrodes in the presence of organics informed about oxidation peak potential and the electrode fouling with organics concentration increasing. Setting up the oxidation peak potential as detection potential, only SG gave good electroanalytical performance using CA. However, by MPA applying both electrodes exhibited the capability to assess electrochemically and quantitatively the pollutants from aqueous solutions. UV spectrometric method detecting 4-CP and 4-NP at $\lambda = 280$ nm and $\lambda = 398$ nm wavelength, respectively was used for validation and parallel determinations.

© 2009 Elsevier B.V. All rights reserved.

1. Introduction

Priority phenols consist of a number of substituted phenolic compounds including halogenated and nitrated phenols, e.g., chlorophenols (CPs) and respective, nitrophenols (NPs). Priority phenols are used/produced in several industrial processes, being commonly used as preservatives, disinfectants, in pulp processing, in pesticides and their intermediars manufacturing. Many priority phenols are known for their toxicity, carcinogenetic and environmental persistence character [1–3]. They are common pollutants found in water, sediments and soil. Due to their toxicity, stability and bioaccumulation, the European Union has set the "black list" of the dangerous substances that should be monitored in waters [4]. The phenols were included in that list that was later accepted in Water Framework Directive [5]. The severe toxicity of 4-chlorophenol (4-CP) and 4-nitrophenol (4-NP) requires the development of simple, sensitive and reliable determination method. Various methods have been employed for the measurement of phenol derivates, e.g., method using HPLC [6,7], gas chromatography [8,9], biosensors [10,11]. However, these methods require expensive and most often laboratory locked complicated instruments. The specific cost of analysis can be high, and the methods are not suitable for in situ measurements.

Electrochemical methods present a growing interest because of high sensitivity, good selectivity, rapid response, and the instruments are relatively simple with the possibility of miniaturization for in situ measurement. Successful application of chemically modified electrodes [12–15] and boron-doped diamond electrodes in combination with different electrochemical methods [16–18] was reported for the determination of phenol derivates. Recently carbon-based materials such as graphite, carbon fibers, etc. have been used most often as the conductive phase in preparing composite working electrodes [19–22].

Although phenol derivates in general, can be oxidized at many electrode materials, the oxidation at carbon-based solid electrodes produces phenoxy radicals which couple to form an insulating polymeric film fouling the surfaces of the electrodes. A simple method of renewing the electrode surface is based on the anodic treatment. This relies on adjusting the working electrode potential high enough to oxidize the insulating film and making it water soluble without damaging the electrode.

In different working programs applied in practice of the well-known pulsed amperometric detection (PAD) the measurement potential is kept for a short time (measurement pulse) after the electrode cleaning pulse and conditioning potential pulse. Among presently used electroanalytical techniques, multiple pulsed amperometry (MPA) has proved to be extremely sensitive for the detection of organic molecules because of the advantage of

* Corresponding author. Tel.: +40 256 403069.
E-mail addresses: adriana.bebeselea@chim.upt.ro (A. Bebeselea), florica.manea@chim.upt.ro (F. Manea), georgeta.burtica@chim.upt.ro (G. Burtica), lnagy@ttk.pte.hu (L. Nagy), g-nagy@ttk.pte.hu (G. Nagy).

0039-9140/$ – see front matter © 2009 Elsevier B.V. All rights reserved.
doi:10.1016/j.talanta.2009.07.036

in situ cleaning and reactivating the electrode surface during the electroanalytical detection [23].

The purpose of this work is to evaluate comparatively the application of the multiple pulsed amperometry (MPA) technique for determination of 4-chlorophenol and 4-nitrophenol in water samples. The performances of the rotating spectral graphite disc (SG) and expanded graphite-epoxy composite (EG-Epoxy) electrodes were compared. The development and optimization of a MPA method for the determination of 4-CP and 4-NP in aqueous solution using both graphite based electrodes are described. Finally, the proposed method applied to determine either 4-CP or 4-NP in drinking water using EG-Epoxy electrode was found advantageous.

2. Materials and methods

All measurements were carried out using an Autolab potentiostat/galvanostat PGSTAT 12 (Eco Chemie, The Netherlands) controlled with GPES 4.9005 software and a three-electrode cell, with a Ag/AgCl reference electrode and a platinum counter electrode. In the study of the detection properties ED/101 disc electrode (Radiometer Analytical S.A., France) was applied. The spectral graphite and EG-Epoxy composite electrodes were used as working electrodes. The spectral graphite (SG) was an OD 3 mm disc electrode (ED), purchased from Electrocarbon Topol'cany (Bratislava, Slovakia).

The EG-Epoxy composite electrode was prepared from two-component epoxy resin (LY5052, Araldite) mixed with conductive expanded graphite (EG) fillers powder (Conductograph, SGL Carbon). To prepare EG-Epoxy composite electrode, the two parts of the epoxy were mixed together and the full amount of the EG was added in steps forming a thick paste. Then the epoxy was cured in a hot press at 80 °C for 40 min. Simultaneously the material was shaped in a plate of 1 mm thickness. The plate was slowly cooled down (for about 12 h) to the room temperature without removing the applied pressure. The prepared carbon-based composite showed good mechanical strength and low electrical resistance [22].

Prior to use, the working electrode with the surface area of 4 cm^2 was gradually cleaned, first polished with abrasive paper and then on a felt-polishing pad by using 0.6 and 0.3 μm alumina powder (Metrohm, Switzerland) in distilled water for 5 min and rinsing with distilled water. The electrode was sonicated to clean from the alumina powder.

0.1 mol L^{-1} stock solutions of 4-chlorophenol (4-CP) and 4-nitrophenol (4-NP) were prepared using distilled water. The supporting electrolyte was 0.1 M sodium sulphate freshly prepared with distilled water. All reagents were analytical grade. Analytical curves were obtained by the standard addition method.

3. Results and discussion

Examples of cyclic voltammetric curves of different concentrations of 4-CP at EG-Epoxy and SG electrodes recorded at scan rate of 0.1 V s^{-1} are shown in Figs. 1 and 2. From such curves it is determined the peak potential, e.g., *ca.* +0.8 V vs. Ag/AgCl for EG-Epoxy and *ca.* +0.9 V vs. Ag/AgCl for SG electrode. The different curves were obtained using standard addition method, without electrode cleaning between additions. For both electrodes 4-CP concentration increasing led to the electrode fouling, because of the complex oxidation process on graphite electrodes. The oxidation process of phenols involves both the adsorption of reactant/intermediate or phenols oxidation products and the formation of passive, nonconductive layer of oligomer products of oxidation process on their surface by electropolymerization [24]. The electropolymerization process is proven by changing the shape of the voltammogram

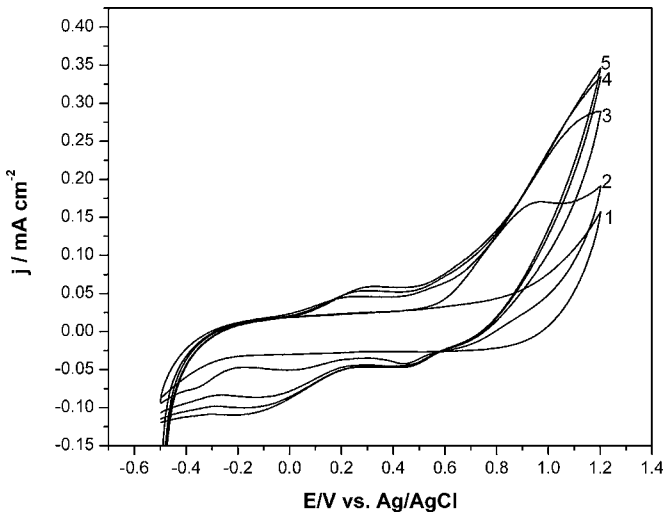


Fig. 1. Cyclic voltammograms recorded at EG-Epoxy electrode in 0.1 M Na_2SO_4 supporting electrolyte (curve 1) and in the presence of different concentrations of 4-CP: 2-0.2 mM; 3-0.4 mM; 4-0.6 mM; 5-0.8 mM; starting potential: 0 V vs. Ag/AgCl; potential range: −0.5 V → +1.25 V → −0.5 V vs. Ag/AgCl; scan rate: 0.1 V s^{-1}.

after the first scanning in the presence of 4-CP (curves 3–5 from Figs. 1 and 2). Compared with EG-Epoxy electrode behaviour, the rotating SG electrode exhibited the higher background current, and 4-CP concentration increasing did not lead to significant electrode fouling. This aspect could be attributed to the avoidance of the adsorption effect by rotating.

The similar results regarding the behaviours of the electrodes in the presence of 4-NP subjected to the electrode fouling were found (the results are not shown here). Based on these results, the chronoamperometry as the easiest electrochemical technique used for detection was applied for two detection potential values for each using the standard addition method. The two detection potential values were chosen based on the different considerations, the first was in line with the cyclic voltammetry, *i.e.*, +0.8 V vs. Ag/AgCl for EG-Epoxy electrode and +0.9 V vs. Ag/AgCl for SG electrode, and the second one had to be higher even under oxygen evolution process to assure a faster oxidation rate (+1.1 V vs. Ag/AgCl). As example,

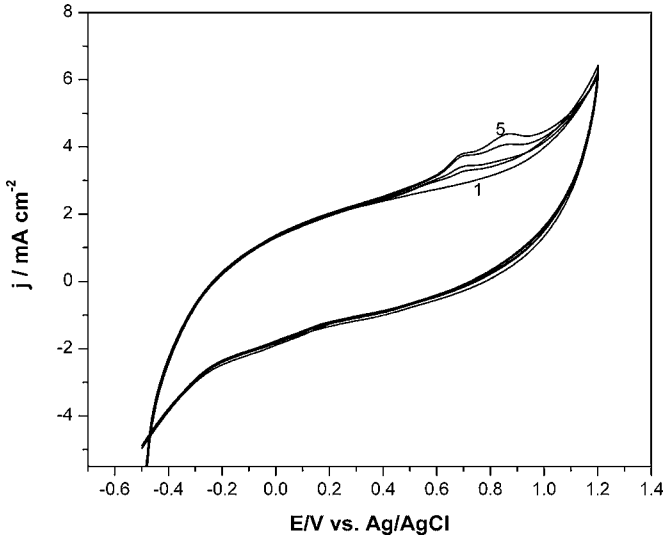


Fig. 2. Cyclic voltammograms recorded at SG electrode in 0.1 M Na_2SO_4 supporting electrolyte (curve 1) and in the presence of different concentrations of 4-CP: 2-0.2 mM; 3-0.4 mM; 4-0.6 mM; 5-0.8 mM; starting potential: 0 V vs. Ag/AgCl; potential range: −0.5 V → +1.25 V → −0.5 V vs. Ag/AgCl; scan rate: 0.1 V s^{-1}.

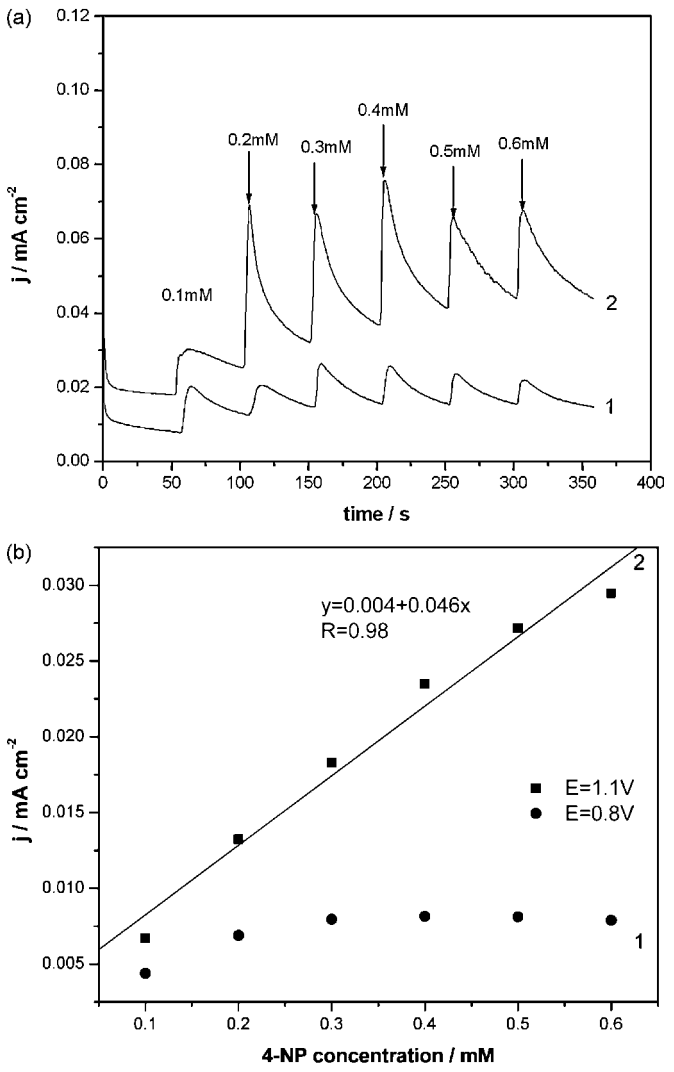


Fig. 3. (a) Chronoamperograms (CAs) recorded at EG-Epoxy electrode in 0.1 M Na_2SO_4 supporting electrolyte and in the presence of different 4-NP concentrations recorded at $E = 0.8$ V vs. Ag/AgCl (curve 1) and $E = 1.1$ V vs. Ag/AgCl (curve 2). (b) The calibration plots of the densities of the currents vs. 4-NP concentrations of the chronoamperograms recorded at $E = 0.8$ V vs. Ag/AgCl and $E = 1.1$ V vs. Ag/AgCl.

Fig. 3a shows the results obtained for EG-Epoxy electrode used for 4-NP detection using chronoamprometry technique.

Based on the two continuous chronoamperograms recorded at the two detection potential values, the calibration plots of current vs. 4-NP concentration was linear for the detection potential value of +1.1 V vs. Ag/AgCl, while for the detection potential value of +0.8 V vs. Ag/AgCl the amperometric current did not depend linear on the 4-NP concentrations, over the concentration range of 0.1–0.6 mM (Fig. 3b). Under the detection potential of +1.1 V vs. Ag/AgCl, the electrode sensitivity for 4-NP detection was 0.046 mA mM^{-1}, with the correlation coefficient of 0.98.

In Fig. 4a are presented the results of MPA applying to test the detection of 4-NP at the two detection potential at which CA was applied. For both situations, potential value for cleaning was +1.4 V vs. Ag/AgCl.

It can be concluded that MPA applying allowed the detection of 4-NP on EG-Epoxy electrode at the detection potential of +0.8 V vs. Ag/AgCl, which corresponds only to 4-NP oxidation, without oxygen evolution involving. For both detection potential, the linear relationships between amperometric current and 4-NP concentrations were obtained, with better electrode sensitivity at +1.1 V vs. Ag/AgCl (0.22 mA mM^{-1} vs. 0.14 mA mM^{-1} obtained at +0.8 V vs. Ag/AgCl), and the correlation coefficient higher than 0.99 (Fig. 4b).

In Fig. 5 is presented a typical batch chronoamperometry obtained by CA and adding 4-CP to 0.1 M Na_2SO_4 using rotating disc spectral graphite electrode. The applied potential was set at +1.1 V vs. Ag/AgCl and the response time was about 50 s. The calibration plots of current vs. 4-CP concentration was linear over the concentration range of 0.1–0.5 mM, with the electrode sensitivity of 0.12 mA mM^{-1}, and correlation coefficient higher than 0.99. The similar multiple pulsed amperograms in the presence of different concentrations of 4-CP on rotating disc spectral graphite for the same concentration range at the potential value and the cleaning potential value of 1.4 V vs. Ag/AgCl are presented in Fig. 6. The amperograms recorded at the cleaning potential value is also shown. Under these last conditions, a better electrode sensitivity was obtained as 0.25 mA mM^{-1}. Even the relationships between current recorded at +1.4 V vs. Ag/AgCl and 4-CP concentration is linear, the abundant oxygen evolution occurred and this aspect is undesired for electroanalysis.

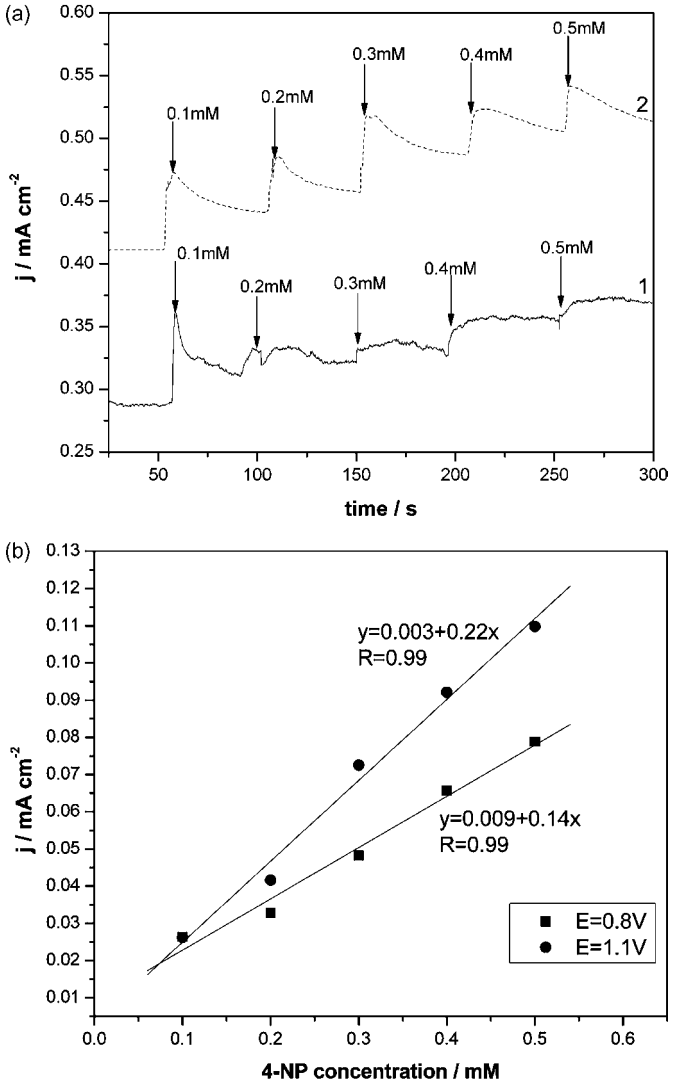


Fig. 4. (a) Multiple pulsed amperograms (MPAs) recorded at EG-Epoxy electrode in 0.1 M Na_2SO_4 supporting electrolyte and in the presence of different 4-NP concentrations; E_{det} was +0.8 V (curve 1), respective +1.1 V (curve 2) and E_{clean} was +1.4 V vs. Ag/AgCl; t_{det} was 0.05 s and t_{clean} was 0.15 s. (b) The calibration plots of the currents densities vs. 4-NP concentrations of the multiple pulsed amperograms recorded at the detection potential: $E_{det} = +0.8$ V, respective $E_{det} = +1.1$ V vs. Ag/AgCl; t_{det} was 0.05 s.

Table 1
Electroanalytical detection performance of EG-Epoxy and rotating SG disc electrode for the detection of 4-NP and 4-CP using CA and MPA.

Electrode	Pollutant	Technique		Sensitivity ($mA\,mM^{-1}$)	
		CA parameters	MPA parameters	CA	MPA
EG-Epoxy electrode	4-NP	E_{det} = +1.1 V	E_{det} = +1.1 V; t_{det} = 0.05 s E_{clean} = +1.4; t_{clean} = 0.15 s	0.046	0.22
		E_{det} = +0.8 V	E_{det} = +0.8 V; t_{det} = 0.05 s E_{clean} = +1.4; t_{clean} = 0.15 s	–	0.14
	4-CP	E_{det} = +1.1 V	E_{det} = +1.1 V; t_{det} = 0.05 s E_{clean} = +1.4; t_{clean} = 0.15 s	0.042	0.24
Rotating SG disc electrode	4-NP	E_{det} = +1.1 V	E_{det} = +1.1 V; t_{det} = 0.05 s E_{clean} = +1.4; t_{clean} = 0.15 s	0.17	0.28
	4-CP	E_{det} = +1.1 V	E_{det} = +1.1 V; t_{det} = 0.05 s E_{clean} = +1.4; t_{clean} = 0.15 s	0.12	0.25

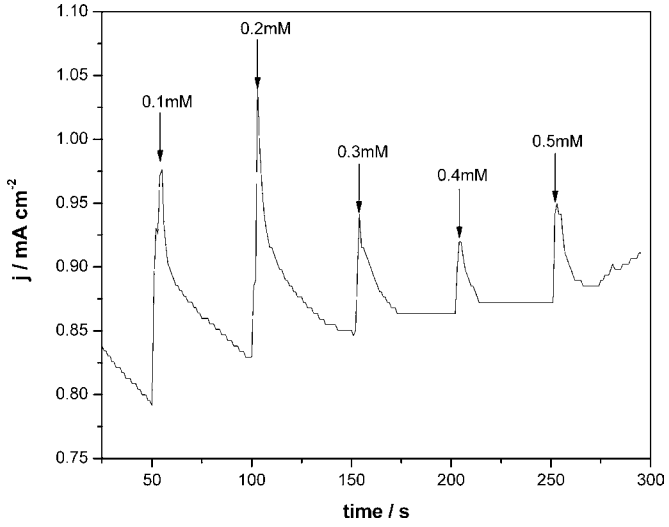


Fig. 5. Chronoamerogram (CA) recorded at the rotating disc SG electrode in 0.1 M Na_2SO_4 supporting electrolyte and in the presence of different 4-CP concentrations recorded at E = +1.1 V vs. Ag/AgCl.

The performance of both electrodes for the detection of 4-NP and 4-CP is summarized in Table 1. It can be concluded that rotating SG disc electrode showed a better sensitivity for the detection of both organic pollutants due to the adsorption effect was diminished by rotating. MPA applying improved significantly the detection performance of the electrode, owing the electrode cleaning during the detection experiments. Under the conditions of MPA applying (E_{det} = + 1.1 V, t_{det} = 0.05 s and E_{clean} = + 1.4 V, t_{clean} = 0.15 s), the detection limits of 0.01 mM for both organics were determined using a 3σ/slope ratio [14], where σ is the standard deviation of the mean value for three MPAs of the blank. The repeatability expressed as the relative standard deviation (R.S.D.) was 2.8% for 4-CP and 3.1% for 4-NP at three replicates.

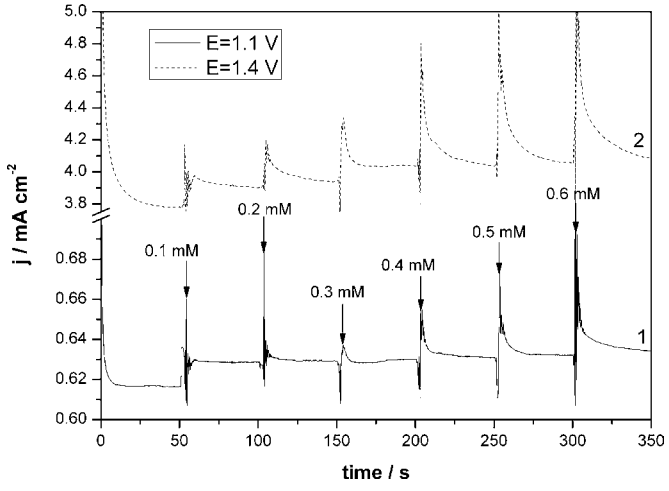


Fig. 6. Multiple pulsed amperogram (MPA) recorded at the rotating SG disc electrode in 0.1 M Na_2SO_4 supporting electrolyte and in the presence of different 4-CP concentrations; E_{det} was +1.1 V (curve 1) and E_{clean} was +1.4 V vs. Ag/AgCl (curve 2); t_{det} was 0.05 s and t_{clean} was 0.15 s.

Table 2
Recoveries of 4-CP and 4-NP in drinking water samples using continuous MPA method at EG-Epoxy electrode.

Spiked ($mg\,L^{-1}$)	Recovery, % (n = 3)	
	4-CP	4-NP
40	96.0	94.6
120	93.5	92.4

The electroanalytical performance for the detection of 4-CP and 4-NP using EG-Epoxy electrode and MPA technique exhibited the advantage of a simple and fast method with the results comparable to those published by us [25,26], which require the electrode renewing after each measurement and the use of specific voltammetric techniques.

A recovery test was also performed by analyzing three parallel tap water samples for two spiked levels of each pollutant. This test was run in 0.1 M Na_2SO_4 solution as supporting electrolyte and the results are summarized in Table 2. Finally, the results obtained by this method were compared with that obtained by means of a conventional UV spectrometric determination method at two certain wavelengths (λ = 280 nm for 4-CP and λ = 398 nm for 4-NP). By comparison the results in order to evaluate the precision of this electrochemical method using EG-Epoxy electrode by continuous application MPA, it can be concluded that the results obtained by the two methods are very closely and the accuracy of the proposed amperometric method is good.

4. Conclusions

In this paper the oxidation of 4-CP and 4-NP at the EG-Epoxy and the rotating SG electrodes studied by CV showed the loss of the electrode activity because of the electrode fouling effect. This phenomenon did not allow the application of CA, the easiest electrochemical technique for the detection of phenol derivates. The use of MPA technique improved the electroanalytical performance for the detection of 4-CP and 4-NP. The optimization of the experimental condition for MPA applying yielded to the detection results comparable to those obtained under the conditions of the electrode renewal and voltammetric techniques.

The good recovery degrees for both organic pollutants from drinking water suggested that this proposed method has good accuracy.

Acknowledgements

Funding for this project was provided by the Romanian Excellence Research for Young Researcher CEEX-ET Program: *Smart sensors for waste water quality monitoring*, and Romanian National Research of Excellence Program – CEEX, Grant 62/03.10.2005 – Advanced Treatment Technologies for Recycling Industrial Wastewater/RIWATECH.

References

[1] A. Penalver, E. Pocurull, F. Borrull, R.M. Marce, J. Chromatogr. A 953 (2002) 79.
[2] B. Nasr, G. Abdellatif, J. Electrochem. Soc. 152 (2005) D113.
[3] Y. Cong, Z. Wu, Q. Ye, T. Tan, J. Zhejiang, Science 5 (2004) 180.
[4] 76/464/EEC concerning pollution caused by dangerous substances discharged into the aquatic environment, 1976.
[5] 2000/60/EC Directive of the European Parlament and of the Council of 23 October 2000 establishing a framework of Community action in the field of water policy, 2000.
[6] A. Brega, P. Prandini, C. Amaglio, E. Pafuni, J. Chromatogr. A 535 (1990) 311.
[7] R. Wissiak, E. Rosenberg, J. Chromatogr. A 963 (2002) 149.
[8] H. Kontsas, C. Rosenberg, P. Jappinen, M.I. Riekkola, J. Chromatogr. A 636 (1993) 255.
[9] H. Kontsas, C. Rosenberg, P. Pfaeffli, P. Jappinen, Analyst 120 (1995) 1745.
[10] M.L. Antonelli, L. Campanella, P. Ercole, Anal. Bioanal. Chem. 381 (2005) 1041.
[11] A.K.M. Kafi, A. Chen, Talanta 79 (2009) 97.
[12] D. Sun, H. Zhang, Water Res. 40 (2006) 3069.
[13] C. Li, J. Appl. Polym. Sci. 103 (2006) 3271.
[14] R.C.S. Luz, F.S. Damos, A.B. de Oliveira, J. Beck, L. Tatsuo, Talanta 64 (2004) 935.
[15] S. Hu, C. Xu, G. Wang, D. Cui, Talanta 54 (2001) 115.
[16] A.J. Saterlay, J.S. Foord, R.G. Compton, Electroanalysis 13 (2001) 1065.
[17] G.S. Garbellini, G.R. Salazar-Banda, L.A. Avanca, J. Braz. Chem. Soc. 18 (2007) 1095.
[18] V.A. Pedrosa, L. Codognoto, L.A. Avaca, J. Braz. Chem. Soc. 14 (2003) 530.
[19] J. Wang, In Analytical Electrochemistry, VCH Publishers, New York, 2000, p. 131.
[20] B. Ballarin, M.M. Cordero-Rando, E. Blanco, J.L. Hidalgo-Hidalgo De Cisneros, R. Seeber, D. Tonelli, Collect. Czech. Chem. Commun. 68 (2003) 1420.
[21] S. Ramirez-Garcia, S. Alegret, F. Cespedes, R.J. Forster, Analyst 127 (2002) 1512.
[22] I. Corb, F. Manea, C. Radovan, A. Pop, G. Burtica, P. Malchev, S. Picken, J. Schoonman, Sensors 7 (2007) 2626.
[23] T. Charoenraks, S. Chuanuwatanakul, K. Honda, Y. Yamaguchi, O. Chailapakul, Anal. Sci. 21 (2005) 241.
[24] M.S. Ureta-Zanartu, P. Bustos, C. Berrios, M.C. Diez, M.L. Mora, C. Gutierrez, Electrochim. Acta 47 (2002) 2399.
[25] A. Pop, F. Manea, C. Radovan, I. Corb, G. Burtică, P. Malchev, S. Picken, J. Schoonman, Rev. Chim. 53 (2008) 623.
[26] A. Pop, F. Manea, C. Radovan, P. Malchev, A. Bebeşelea, C. Proca, G. Burtică, S. Picken, J. Schoonman, Electroanalysis 20 (2008) 2460.

Talanta 80 (2010) 1073–1080

Contents lists available at ScienceDirect

Talanta

journal homepage: www.elsevier.com/locate/talanta

Modelling of acid–base equilibria in binary-solvent systems: A comparative study

Bogusław Pilarski [a], Agnieszka Dobkowska [a], Henryk Foks [b], Tadeusz Michałowski [c,*]

[a] P.P.H.U. Cerko s.c., 80 299 Gdańsk, Afrodyty 9, Poland
[b] Medical University of Gdańsk, Department of Organic Chemistry, 80-416 Gdańsk, Poland
[c] Faculty of Chemical Engineering and Technology, Cracow University of Technology, 31-155 Kraków, Poland

ARTICLE INFO

Article history:
Received 22 May 2009
Received in revised form 14 July 2009
Accepted 20 July 2009
Available online 25 July 2009

Keywords:
Binary systems
Excess functions
pH titration
Curve fitting
Monoprotic acids

ABSTRACT

A new approach to modelling of some binary (hydro-organic, HL/H_2O + B) acid–base systems with organic co-solvent B fully miscible with water, is suggested and applied for the determination of acidity parameters pK for some weak acids HL. The models are designed to get the pK = p$K(x)$ relationships (x—mole fraction of B in H_2O + B) from results of pH titrations made in such systems and for the determination of pK_B = p$K(1)$ for HL in pure B. The Redlich–Kister equation, together with its asymmetric extensions, and the Legendre functions with orthogonal polynomials, appeared to be suitable for such purposes.

© 2009 Elsevier B.V. All rights reserved.

1. Introduction

Composition of mobile phase strongly affects chromatographic retention and electrophoretic migration of substances appearing acid–base behaviour [1]. The satisfactory knowledge of an effect of mobile phase composition on acid–base properties of solutes is therefore essential for analytical procedures applied in optimizing of the separation techniques. It enables to predict and optimize the influence of pH on selectivity and retention in reversed-phase liquid chromatography (RP-HPLC), especially in the gradient elution technique applied for the separation of ionizable compounds.

We focus our attention on binary-solvent hydro-organic systems, whose composition is expressed by the mole fraction $x = x_B$ of organic co-solvent B. Denoting the numbers of moles of A = H_2O and B in a solvent system by n_A and n_B, we have:

$$x = \frac{n_B}{n_A + n_B} \quad (1)$$

Acid–base properties of a weak monoprotic acid HL in aqueous solutions is expressed by its dissociation constant K, usually represented by pK = −log K value. In binary-solvent media, the pK value depends on x-value, pK = p$K(x)$, and changes when the solvent composition is varied, e.g. during the gradient elution. For this purpose, pK is termed as the acidity parameter [2] or as apparent acid dissociation constant [3] for HL. In further parts of the paper, pK will be referred to K expressed in terms of concentrations, i.e. $K = [H^+][L^-]/[HL] = [H^+]^2/(C - [H^+])$ for C mol L^{-1} HL.

pH measurements made for HL solutions in pure B and in close vicinity of $x = 1$ are not repeatable, and then the pK = pK_B value, calculated from the formula

$$pK = 2pH + \log(C - 10^{-pH}) \quad (2)$$

on the basis of a single pH measurement is doubtful. On the other hand, the results obtained for lower x assume firm values. Application of a regression equation that fits very well within the predominant part of experimental points obtained from pH titration, provides repeatable results for pK_B = p$K(1)$, also when the doubtful points (V_j, pH$_j$) from the immediate vicinity of $x = 1$ are included in the set of points taken for calculations, realised according to the least squares method. In other words, the approximating function firmly fastened in the predominant part of experimental points withstands the perturbations of the part of doubtful points; this approach has been assumed in this paper. The HL/A+B system, with HL introduced into binary-solvent system A+B, can be obtained by mixing two solutions of HL in pure solvents; the solutions will be denoted later as HL/A and HL/B, respectively. The mixing will be made according to potentiometric titration mode, with pH registration. In order to cover the whole x interval [0, 1], the initial solutions should be titrated mutually: HL/A → HL/B and HL/B → HL/A. The two titrations will be denoted briefly as HL/A ⇔ HL/B titration.

Except potentiometry and absorption spectrophotometry, as the well-established currently applied methods for pK determination

* Corresponding author. Tel.: +48 12 628 21 77.
E-mail addresses: michalot@o2.pl, michalot@chemia.pk.edu.pl (T. Michałowski).

0039-9140/$ – see front matter © 2009 Elsevier B.V. All rights reserved.
doi:10.1016/j.talanta.2009.07.033

Nomenclature

Nomenclature

A = H_2O, B	organic co-solvent
C	concentration [mol L^{-1}] of HL in T and D
D	titrand (solution titrated)
HL	weak acid (solute)
HL/B	solution of HL in B
HL/A	aqueous solution of HL
LOP	Legendre function with orthogonal polynomials
M–S	Myers–Scott equation
pK	–log K acidity parameter
R–K	Redlich–Kister equation
T	titrant
V	volume [mL] of T
V_0	volume [mL] of D
x	mole fraction of B in the binary-solvent system A + B

[4–6], other techniques such as cyclic voltammetry [7], coulometry [8], NMR [9], HPLC [10] and capillary electrophoresis [11–13], appeared to be also applicable for such purposes.

For modelling purposes, designed to get the pK = p$K(x)$ relationships and pK_B values (pK_A = p$K(0)$ is determined incidentally), the principle of excess functions is applied.

2. Excess functions and their implications

Non-ideal behaviour of real solutions, formed of two miscible solvents: A = H_2O and organic co-solvent B, whose content is defined by x-value (Eq. (1)), can be expressed in terms of functions $y^E = y^E(x)$, referred to different excess variables [14], of physicochemical or physical nature: excess molar volume ($V^E = V^E(x)$) [15,16], excess molar enthalpy ($\Delta H^E = \Delta H^E(x)$) [17], excess molar free enthalpy ($\Delta G^E = \Delta G^E(x)$) [18] and many other excess properties, referred to surface tension, viscosity, speed of sound, refractive index, etc. The excess molar free enthalpy

$$\Delta G^E = \Delta G - \Delta G_{id} \tag{3}$$

expresses the deviation of the standard (s) free enthalpy (Gibbs function), $\Delta G = \Delta G^s$, from its ideal value:

$$\Delta G_{id} = \Delta G_{id}(x) = (1-x)\Delta G_A + x\Delta G_B \tag{4}$$

In other words, ΔG^E reflects the joint effect of solute–solute, solute–solvent, and solvent–solvent interactions [19–21]. The ΔG interrelates with pK in the relation:

$$\Delta G = b\,\mathrm{p}K, \text{ i.e. } \Delta G(x) = b\,\mathrm{p}K(x) \tag{5}$$

where

$$b = RT\ln 10 \tag{6}$$

Then we get:

$$\begin{aligned} \Delta G(0) &= \Delta G_A = b\,\mathrm{p}K(0) = b\,\mathrm{p}K_A \text{ and } \Delta G(1) = \Delta G_B \\ &= b\,\mathrm{p}K(1) = b\,\mathrm{p}K_B \\ \Delta G^E(0) &= \Delta G(0) - \Delta G_{id}(0) = b(\mathrm{p}K(0) - \mathrm{p}K_{id}(0)) = 0 \\ \Delta G^E(1) &= \Delta G(1) - \Delta G_{id}(1) = b(\mathrm{p}K(1) - \mathrm{p}K_{id}(1)) = 0 \end{aligned} \tag{7}$$

$$\mathrm{p}K(x) = (1-x)\mathrm{p}K_A + x\mathrm{p}K_B + \frac{1}{b}\Delta G^E(x) \tag{8}$$

In this paper, some approximating functions for $\Delta G^E(x)$ are applied for modelling the pK = p$K(x)$ relationships referred to different acid–base HL/A+B systems, tested experimentally according to pH titration, made in thermostated systems (isothermal titration). The functions applied here are as follows: (a) the function derived [22] from the empirical Redlich–Kister (R–K) [23,24] equation, together with its asymmetric versions, suggested by (b) Myers and Scott [25] (M–S) and (c) Michałowski and co-workers [22], where a hyperbolic transformation of x is applied. Moreover, (d) the Legendre function with orthogonal polynomials is applied; the latter function has been used hitherto only for modelling the V^E vs. x relationship, $V^E = V^E(x)$ [26,27]. In this paper, however, a growth in C value during the titration, $C = C(x)$, occurred as a result of contraction of mixed solutions, is neglected when compared with an error resulting from uncertainty ΔpH = 0.02 in common pH titrations [22]. In other words, $C(x) = C$ = const is assumed in HL/H_2O + B systems thus formed. At C = 0.01 mol L^{-1} HL, the inequality $x_{HL} \ll x_{H_2O} + x_B$, referred to mole fractions of HL, H_2O and B respectively, is valid. This way, one can assume that the densities of the solutions HL/A and HL/B are equal to densities ρ_A and ρ_B [g/mL] of the corresponding solvents A and B.

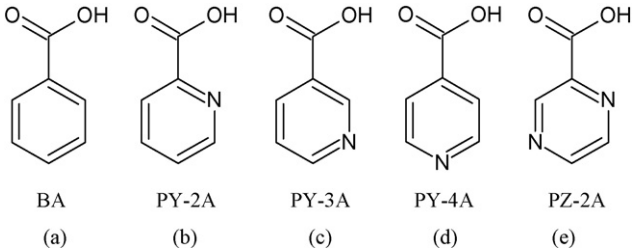


Fig. 1. The acids (HL) tested: (a) BA, (b), PY-2CA, (c) PY-3CA, (d) PY-4CA, and (e) PZ-2CA.

In this paper, the experimental data $\{(V_j, \mathrm{pH}_j)\,|j = 1, \ldots, N\}$, were obtained from pH titration HL/B ⇔ HL/H_2O, with C mol L^{-1} HL in both solutions: HL/H_2O and HL/B, i.e. $C(0) = C(1) = C$.

Benzoic acid (abbr. BA) and a series of heterocyclic compounds: pyridine-2-carboxylic acid (picolinic acid, PY-2A), pyridine-3-carboxylic acid (nicotinic acid, niacin, vitamin B_3, PY-3A), pyridine-4-carboxylic acid (isonicotinic acid, PY-4A), and pyrazine-2-carboxylic acid (PZ-2A) (Fig. 1) as weak acids (HL) in different hydro-organic media: H_2O + MeOH, H_2O + Me_2SO (Me≡CH_3) are applied in the titration, where V mL of titrant (T) was added dropwise into V_0 mL of titrand (D)

To recalculate V and V_0 on x-values, the formulae:

$$(1^\circ)\; x = \frac{V}{\chi V_0 + V} \text{ valid for titration HL/B} \rightarrow \text{HL/A, or}$$

$$(2^\circ)\; x = \frac{V_0}{\chi V + V_0} \text{ valid for titration HL/A} \rightarrow \text{HL/B}$$

are applied, where A = H_2O, $\chi = (\rho_A/\rho_B)\cdot(M_B/M_A)$; M_A, M_B—molar masses [g/mol] of A and B. Particularly, χ = 2.2431 for H_2O + CH_3OH system, and χ = 3.9293 for H_2O + $(CH_3)_2SO$ system of solvents [22].

3. Modelling the functions pK = p$K(x)$

3.1. Some earlier approaches

An effect of the solvent composition on pK value was considered in numerous papers issued recently, e.g. [28–31]. In all instances, acid–base titrations in mixed-solvent media were performed in the titrand (D) and titrant (T) systems (D + T systems), containing the same proportion of the solvent components (A and B), sometimes in the presence of a basal (background) salt securing approximately constant ionic strength value [30]. The linear relationship p$K = a_0 + a_1 x$ has been reported in a majority of earlier papers, e.g. [32–34], related to the determination of pK in binary-solvent systems. However, some reports [35,36] testify on account of non-linear relationships between the related variables.

Bosch et al. [36] determined p$K(x)$ values from results of pH titrations made in D + T systems, composed of two solutions, D and T, characterized by the same $x = x_i$-value of B (methanol, ethanol, 2-propanol); HL in D was titrated with tetrabutylammonium hydroxide in T. It was stated, however, that the hyperbolic approximating function $pK = pK_A + ax/(1 + bx)$ is satisfactory only for $x < 0.2$, $pK_A = pK(0)$. An inadequacy of the hyperbolic approximation for higher x was explained by stronger A ↔ B interactions, expressed through a kind of stability constant formulated for associates AB. The resulting expression for p$K(x)$ was acknowledged as a more adequate for modelling purposes.

Another approach was provided by the Jouyban–Acree (J–A) model [3,37], that is very similar to one derivable from R–K function [23] and Eq. (8) but involves the volume fraction (f) put for the mole fraction x of the co-solvent B [37,38]; however, contrary to x, f depends on the contraction/expansion and temperature effects. One should also notice that J–A model was derived in an unnecessarily complicated manner.

3.2. The approximating functions applied

The approach applied for derivation of the functions $pK = pK(x)$ is based on Eq. (8), where pK is expressed by Eq. (2), and pK_A and pK_B refer to the acidity parameter pK in pure solvents A and B, respectively, see Eq. (7). The expression for $\Delta G^E = \Delta G^E(x)$ in Eq. (8), when referred to x-interval [0, 1], can be written in terms of the R–K function:

$$\Delta G^E(x) = x(1-x)\sum_{i=0}^{n} a_i(1-2x)^i \tag{9}$$

or in terms of the shifted Legendre orthogonal polynomials, $s_i(x)$ [22]:

$$\Delta G^E(x) = x(1-x)\sum_{i=0}^{n} b_i s_i(x) \tag{10}$$

Putting (9) and (10) into (8) and denoting:

$$z = 1 - 2x \tag{11}$$

We get the functions:

$$pK = \varphi_0 + \varphi_1 z + (1-z^2)\sum_{i=0}^{n} \alpha_i z^i \tag{12}$$

$$pK = \varphi_0 + \varphi_1 z + (1-z^2)\sum_{i=0}^{n} \beta_i l_i(z) \tag{13}$$

Referred to the 'normal' Legendre orthogonal polynomials (LOP), $z \in [-1, 1]$, where

$$\varphi_0 = \frac{pK_A + pK_B}{2} \tag{14}$$

$$\varphi_1 = \frac{pK_A - pK_B}{2} \tag{15}$$

$$\alpha_i = \frac{0.25 a_i}{b} \tag{16}$$

$$\beta_i = \frac{0.25 b_i}{b} \tag{17}$$

Equations (12) and (13), expressed in terms of variable z (Eq. (11)), are related to LOP, where $z \in [-1, 1]$ in $l_i(z)$ [22]. The first five orthogonal polynomials, $l_i(z)$, in Eq. (13) are as follows:

$$l_0(z) = 1,\ l_1(z) = z,\ l_2(z) = 3z^2 - 1,\ l_3(z) = 5z^3 - 3z$$
$$l_4(z) = 35z^4 - 30z^2 + 3 \tag{18}$$

The numbers: 0.5 and 0.125 in expressions for $l_2(z)$, $l_3(z)$ and $l_4(z)$, cited in [39], enter the coefficients β_2, β_3 and β_4 in Eq. (13) as factors and then are omitted in (18). Note that the expressions for φ_0 and φ_1 are the same in (12) and (13). Then from (14) and (15) we have:

$$pK_A = \varphi_1 + \varphi_2 \text{ and } pK_B = \varphi_1 - \varphi_2 \tag{19}$$

In Eq. (2), the value $\gamma = 1$ [40] for activity coefficient γ of hydrogen ions in mixed-solvent system is assumed during the titration.

Other (asymmetric) modifications of R–K function were also considered for approximating purposes, namely the Myers and Scott (M–S) function:

$$pK = \varphi_0 + \varphi_1 z + \frac{1-z^2}{1-\varepsilon z}\sum_{i=0}^{n} \alpha_i z^i \tag{20}$$

and the function with hyperbolic transformation of variable z

$$pK = \varphi_0 + \varphi_1 z + (1-z^2)\sum_{i=0}^{n} \alpha_i \left(\frac{z}{1-\varepsilon z}\right)^i \tag{21}$$

proposed by Michałowski [22]; Eqs. (20) and (21) involve the assymetry parameter ε.

The parameters: $\varphi_0, \varphi_1, \alpha_0, \alpha_1, \ldots, \alpha_n$ in Eqs. (12), (20) and (21), or the parameters: $\varphi_0, \varphi_1, \beta_0, \beta_1, \ldots, \beta_n$ in Eq. (13) can be determined according to least squares (LS) method. Application of LS method in Eqs. (20) and (21) is possible after preliminary assignation for ε-value. The LS method is applied to results $\{(V_j, pH_j)\,|j = 1, \ldots, N\}$ obtained from pH metric titrations HL/B ⇔ HL/H_2O. Eq. (12) will be considered later as the modified R–K function, and Eq. (13) as the function with LOP, all used to formulate the $pK = pK(x)$ function. The number $n + 3$ of parameters on the right side of Eqs. (12) and (13) is equal to the number of parameters σ_i in the equation

$$pK = \sum_{i=0}^{n+2} \sigma_i z^i \tag{22}$$

to which (12) and (13) can be transformed. It means that the columns of a matrix obtained from (12) or (13) are linearly independent and the problem of singularity of the matrix does not occur. The latter case is closely related to the non-singular properties of the Vandermonde matrix [41].

The fit of the approximating function $pK = pK(x)$ to the data $\{(x_j, pK_j)\,|j = 1, \ldots, N\}$ obtained, by recalculations, from N experimental points $\{(V_j, pH_j)\,|j = 1, \ldots, N\}$ is expressed by the variance (s^2) value:

$$s^2 = s^2(n) = \frac{\sum_{j=1}^{N}(pK_j - pK(x_j, n))^2}{N - n - 3} \tag{23}$$

where n is the upper number in the sum on the right side of Eqs. (12) or (13); $pK(x_j, n)$ is the pK value calculated at $x = x_j$ from the model with $n + 1$ components in the sum involved in these equations; $N - n - 3$ is the number of degrees of freedom.

4. Experimental

4.1. Apparatus and reagents

The pH titrations: HL/H_2O ⇔ HL/B were performed in 30 mL thermostated (20.0 ± 0.2 °C) cell using Cerko Lab System microtitration unit fitted with pH electrode (Hydromet – ERH-13-6 type) and Ag/AgCl reference electrode and a self-made measuring cell equipped with magnetic stirrer and PT 1000 system. The temperature was controlled in the Huber thermostat system. The electrode was conditioned in the organic solvent B (MeOH and Me_2SO for 15–30 min and calibrated before each titration in HL/H_2O + B system, with the use of buffer solutions: potassium hydrogen phthalate (pH 4.00), citric acid/Na_2HPO_4 (pH 7.00) and boric acid/KCl/NaOH

(pH 10.00) from Eurochem BGD Company. The electrode was stored in water or KCl standard solution when not in use. The potentiometric microtitrator was automatically controlled by PC system.

Benzoic acid (extra pure, >99.5%), pyridine-2-carboxylic acid, pyridine-3-carboxylic acid, pyridine-4-carboxylic acid, were purchased from Sigma–Aldrich Laborchemikalian GmbH. The pyridine carboxylic acids were purified by recrystallization before preparing solutions for titration. Pyrazine-2-carboxylic acid was synthesized by hydrolysis of pyrazine amide and recrystallized from water (m.p. 225–226 °C).

Doubly distilled water with conductivity approx. 0.18 μS/cm was freshly produced in order to avoid carbon dioxide absorption; it was used throughout for preparation of aqueous solutions of organic acids under study. Other solvents: methanol (MeOH, analytical grade, 99.8%) and dimetylsulphoxide (Me_2SO, HPLC grade, 99.5%) were supplied by POCH S.A.

4.2. Procedures

The pH titrations $HL/H_2O \Leftrightarrow HL/B$, with HL = BA, PY-2CA, PY-3CA, PY-4CA, and PZ-2CA; B = $(CH_3)_2SO$ or CH_3OH), were performed with the use of a Cerko Lab System equipped with a syringe pump. In all titrations, $C = 0.01\ mol\ L^{-1}$ and titrand volume $V_0 = 3.000$ mL were applied. The titrations were performed at least two times for each $HL/H_2O + B$ system tested. The stability of indication of the measuring system was also tested. The titration parameters were: $\Delta V = 0.0100$ mL and pause 10–20 s. The pK values were obtained on the basis of Eq. (2) from the experimental points $\{(V_j, pH_j)\ |j = 1, \ldots, N\}$ and the resulting set of points $\{(x_j, pK_j)\ |j = 1, \ldots, N\}$ was modelled with use of the approximating functions specified in Section 3.2. Then $pK_A = pK(0)$ and $pK_B = pK(1)$ were calculated from Eq. (19), with use of self-prepared computer program, based on application of the least-squares (LS) method in its classical version.

5. Results and discussion

Examples of titration curves in binary-solvent systems $HL/H_2O + B$ are presented in Fig. 2 (HL = PY-3CA, B = MeOH) and Fig. 3 (HL = PY-4CA, B = Me_2SO). The related pairs of curves intersect at $V_{int} = 2.94$ mL (Fig. 2) and $V_{int} = 3.07$ mL (Fig. 3), near to the expected value $V = V_0 = 3.00$ mL. It should be noted that the point of intersection in Fig. 3 lies in the x-region of relatively flat course of the curves, see Fig. 3. The coincidence $V_{int} \approx 3$ mL testifies very well about reversibility of processes occurred during the titrations.

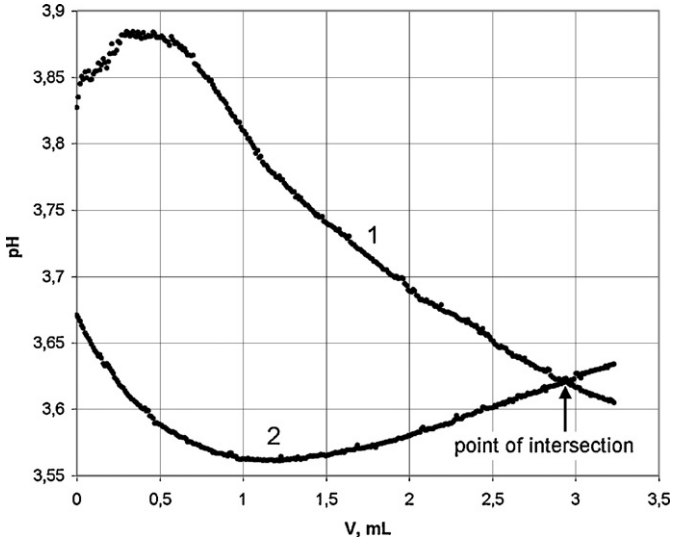


Fig. 2. The titration curves pH = pH(V) obtained for titrations: (1) $HL/H_2O \rightarrow HL/MeOH$ and (2) $HL/MeOH \rightarrow HL/H_2O$, where HL = PY-3CA.

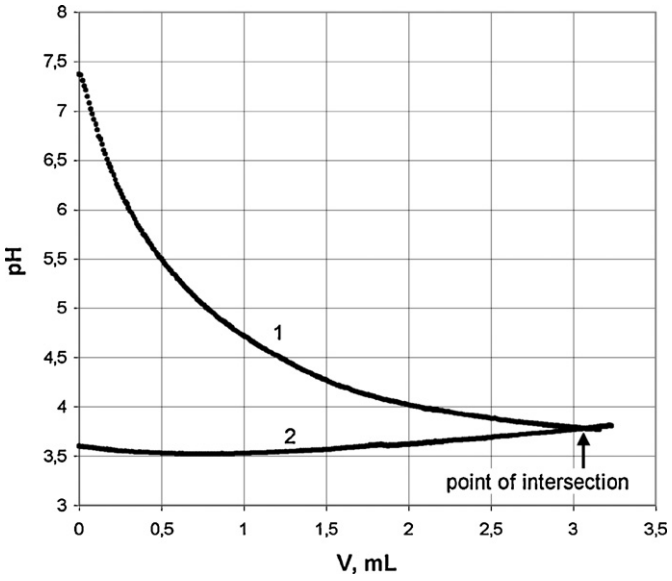


Fig. 3. The titration curves pH = pH(V) obtained for titrations: (1) $HL/H_2O \rightarrow HL/Me_2SO$ and (2) $HL/Me_2SO \rightarrow HL/H_2O$, where HL = PY-4CA.

Generally, the shape of the pH = pH(V) curve depends mainly on the co-solvent B used in the $HL/H_2O + B$ system. Particularly, the plot of pH-curves pH = pH(V) pass through extreme values for different acids HL applied in the titrations $HL/H_2O \Leftrightarrow HL/MeOH$ (Fig. 2) whereas the plots of the pH-curves in $HL/H_2O \Leftrightarrow HL/Me_2SO$ systems are monotonic [22] (Fig. 3), as a rule. The pH values, obtained at the start for titration $HL/H_2O \rightarrow HL/B$, i.e. at x-values close to 1 (see e.g. Fig. 2), are less repeatable than ones in the reverse titration $HL/B \rightarrow HL/H_2O$ and then the $pK_B = pK(1)$ values obtained from Eq. (2) for HL/B solution are doubtful.

The results $\{(V_j, pH_j)\ |j = 1, \ldots, N\}$ of titrations made in the system HL/H_2O + MeOH with HL = PY-2CA, PY-3CA, PY-4CA, were modelled with use of Eq. (12). The coefficients φ_0, φ_1, α_0, α_1, α_2, α_3, α_4 are specified in Tables 1–3, together with pK_A and pK_B values. As we see, the results obtained for $pK_B = pK(1)$ and $pK_A = pK(0)$ are repeatable within each series of titrations, at relatively low standard deviation (s) values stated at $n = 4, 3, 2$. The values obtained for pK_B and pK_A for defined system HL/H_2O + MeOH at $n = 4$ and 3 are similar, as a rule. It testifies in favour of the opinion that the R–E function with $n = 3$ appears to be sufficient for approximation purposes. The fit of the related curves $pK = pK(x) = pK(x, n)$ to the points $\{(V_j, pH_j)\ |j = 1, \ldots, N\}$, exemplified in Fig. 4 is excellent for $n = 4$ (and $n = 3$, as well). The values for $pK_A = pK(0)$ found for HL = PY-2-CA in titrations made in HL/H_2O + MeOH system (Table 1) are comparable with those found in $HL/H_2O + Me_2SO$ system (Table 2), when the results with the same n-values are compared. It testifies also about the repeatability of results obtained in different systems, where other values for the coefficients φ_i ($i = 0, 1$), α_j ($j = 0, \ldots, n$) are involved. At $n = 1$, the pK_B and pK_A assume lower values and s^2 values are relatively high. It is also confirmed by pK_B and pK_A values presented in Table 4, obtained with use of LOP function (Eq. (13)).

It can be stated (Figs. 5 and 6 a and b) that the asymmetry parameter ε in Eqs. (20) and (21) equalizes, to some degree, the effect resulting from lower n-value applied in approximating functions and the related curves cover nearly the same interval for pK_B and pK_A values.

Critical $F_c(f, f, \alpha)$ Snedecor's F-values at equal number of degrees of freedom, $f_1 = f_2 = f$, where $f = N - n - 3$ (see Eq. (23)) are equal to: 1.139 for $f = 640$ and 1.138 for $f = 650$, at confi-

Table 1
The parameters of R–K function for the pyridine carboxylic acids (HL) in HL/H_2O + MeOH systems, at different *n*-values in Eq. (12).

n	*N*	PY-2CA in HL/H_2O + CH_3OH system, R–K model								
		φ_0	φ_1	α_0	α_1	α_2	α_3	α_4	$pK_A \pm s$	$pK_B \pm s$
4	653	6.1361	−0.5057	−0.2830	−0.1249	0.0015	0.2390	−0.7481	5.63 ± 0.03	6.64 ± 0.03
	631	6.1319	−0.4613	−0.2299	−0.1866	−0.1791	0.1589	−0.5735	5.67 ± 0.02	6.59 ± 0.02
3	653	6.0760	−0.4856	−0.2110	−0.0944	−0.2229	0.0502		5.59 ± 0.03	6.56 ± 0.03
	631	6.0860	−0.4462	−0.1750	−0.1644	−0.3522	0.01781		5.64 ± 0.02	6.53 ± 0.02
2	653	6.0735	−0.4780	−0.2098	−0.0927	−0.2108			5.60 ± 0.03	6.55 ± 0.03
	631	6.0851	−0.4435	−0.1745	−0.1637	−0.3479			5.64 ± 0.02	6.53 ± 0.02
1	653	6.0166	−0.4590	−0.1656	−0.1428				5.56 ± 0.04	6.48 ± 0.04
	631	5.9913	−0.4122	−0.1016	−0.2461				5.58 ± 0.03	6.40 ± 0.03
n	*N*	PY-3CA in HL/H_2O + CH_3OH system, R–K model								
		φ_0	φ_1	α_0	α_1	α_2	α_3	α_4	$pK_A \pm s$	$pK_B \pm s$
4	650	5.5226	−0.1831	0.0026	−0.5374	−0.2371	−0.0074	−0.2578	5.33 ± 0.005	5.71 ± 0.005
	650	5.4810	−0.1366	0.0283	−0.5544	−0.2976	0.0202	−0.2985	5.34 ± 0.005	5.62 ± 0.005
3	650	5.5019	−0.1762	0.0274	−0.5271	−0.3148	−0.0718		5.33 ± 0.01	5.68 ± 0.01
	650	5.4571	−0.1286	0.0570	−0.5424	−0.3875	−0.0544		5.33 ± 0.01	5.59 ± 0.01
2	650	5.5055	−0.1872	0.0257	−0.5295	−0.3323			5.32 ± 0.01	5.69 ± 0.01
	650	5.4598	−0.1369	0.0557	−0.5443	−0.4007			5.32 ± 0.01	5.60 ± 0.01
1	650	5.4158	−0.1574	0.0955	−0.6078				5.25 ± 0.02	5.57 ± 0.02
	650	5.3517	−0.1010	0.1399	−0.6387				5.24 ± 0.02	5.45 ± 0.02
n	*N*	PY-4CA in HL/H_2O + CH_3OH system, R–K model								
		φ_0	φ_1	α_0	α_1	α_2	α_3	α_4	$pK_A \pm s$	$pK_B \pm s$
4	456	5.1740	0.0319	0.0325	−0.4713	−0.3059	0.1259	0.1259	5.21 ± 0.005	5.14 ± 0.005
	646	5.1722	0.0541	0.0404	−0.5103	−0.2571	0.1101	−0.3863	5.23 ± 0.005	5.12 ± 0.005
3	456	5.1554	0.0390	0.0557	−0.4678	−0.4021	0.0680		5.19 ± 0.005	5.12 ± 0.005
	646	5.1413	0.0644	0.0775	−0.4960	−0.3736	0.0139		5.20 ± 0.01	5.10 ± 0.01
2	456	5.1522	0.0489	0.0571	−0.4642	−0.3864			5.20 ± 0.005	5.10 ± 0.005
	646	5.1406	0.0665	0.0778	−0.4946	−0.3702			5.21 ± 0.01	5.07 ± 0.01
1	456	5.0554	0.0742	0.1324	−0.5152				5.13 ± 0.03	4.97 ± 0.03
	656	5.0407	0.0997	0.1556	−0.5818				5.14 ± 0.03	4.94 ± 0.03

Table 2
The parameters of R–K function for HL = PY-4CA in HL/H_2O + Me_2SO system at different *n*-values in Eq. (12).

n	*N*	φ_0	φ_1	α_0	α_1	α_2	α_3	α_4	$pK_A \pm s$	$pK_B \pm s$
4	650	9.0166	−3.8239	−2.2408	−0.1533	−0.3549	0.2352	−0.2184	5.19 ± 0.02	12.84 ± 0.02
	650	9.0055	−3.8185	−2.2229	−0.1581	−0.5019	0.1060	−0.0471	5.19 ± 0.03	12.82 ± 0.03
	643	9.0412	−3.8589	−2.2516	0.2137	−0.4411	0.2520	−0.1507	5.18 ± 0.03	12.90 ± 0.03
	643	9.0527	−3.8641	−2.2698	−0.2079	−0.2908	0.3788	−0.3294	5.19 ± 0.02	12.92 ± 0.02
3	650	8.9991	−3.8181	−2.2198	−0.1446	−0.4206	0.1806		5.18 ± 0.02	12.82 ± 0.02
	650	9.0017	−3.8172	−2.2184	−0.1562	−0.5160	0.0942		5.18 ± 0.03	12.82 ± 0.03
	643	9.0292	−3.8549	−2.2371	−0.2078	−0.4866	0.2147		5.17 ± 0.04	12.88 ± 0.04
	643	9.0264	−3.8554	−2.2382	−0.1949	−0.3901	0.2971		5.17 ± 0.03	12.98 ± 0.03
2	650	8.9901	−3.7905	−2.2155	−0.1386	−0.3767			5.20 ± 0.03	12.78 ± 0.03
	650	8.9970	−3.8029	−2.2162	−0.1531	−0.4931			5.19 ± 0.04	12.80 ± 0.04
	643	9.0185	−3.8222	−2.2320	−0.2003	−0.4343			5.20 ± 0.04	12.84 ± 0.04
	643	9.0116	−3.8102	−2.2311	−0.1846	−0.3179			5.20 ± 0.03	12.82 ± 0.03
1	650	8.8885	−3.7567	−2.1364	−0.2273				5.13 ± 0.04	12.65 ± 0.04
	650	8.8639	−3.7586	−2.1126	−0.2693				5.10 ± 0.05	12.62 ± 0.05
	643	8.9013	−3.7832	−2.1407	−0.3027				5.12 ± 0.07	12.68 ± 0.07
	643	8.9258	−3.7817	−2.1643	−0.2595				5.14 ± 0.06	12.70 ± 0.06

dence level $\alpha = 95\%$. On this basis we have stated that application of Eq. (21) makes, as a rule, a significant improvement in variance (Eq. (23)) when compared with the M–S function (Eq. (20)). For example, the variances obtained at $N = 650$, $n = 4$, $\varepsilon = -0.4$ are: $1.0235/(650-7) = 15.92 \times 10^{-4}$ for Eq. (20) and $0.6116/(650-7) = 9.51 \times 10^{-4}$ for Eq. (21); then $F(643, 643, 0.95) = 1.674 > 1.139$.

The p*K* vs. *x* relationships for different acids are plotted for HL/H_2O + MeOH (Fig. 7a) and HL/H_2O + Me_2SO (Fig. 7b) systems; the enumeration of the curves is identical with those applied in Fig. 1. Nearly closely overlapped plots obtained on the basis of the related titration curves, exemplified in Figs. 2 and 3, are another proof of reversible behaviour of the indicator electrode applied in pH titrations.

Table 3
The parameters of R–K function for HL = PZ-4CA in HL/H_2O + Me_2SO obtained at different n in Eq. (12).

n	N	φ_0	φ_0	α_0	α_1	α_2	α_3	α_4	$pK_A \pm s$	$pK_B \pm s$
4	650	7.5526	−4.7384	0.0635	−0.0778	0.0396	−0.8551	−0.4539	2.81 ± 0.02	12.29 ± 0.02
	650	7.5810	−4.7800	−0.0319	0.0098	−0.1060	−0.5964	−0.4199	2.80 ± 0.02	12.36 ± 0.02
3	650	7.5167	−4.7207	0.1063	−0.0492	−0.0936	−1.0280		2.80 ± 0.02	12.24 ± 0.02
	650	7.5478	−4.7637	0.0076	0.0362	−0.2292	−0.7564		2.78 ± 0.02	12.31 ± 0.02
2	650	7.5945	−4.8730	0.0655	−0.0941	−0.4799			2.72 ± 0.04	12.47 ± 0.04
	650	7.6050	−4.8758	−0.0223	0.0032	−0.5135			2.73 ± 0.03	12.48 ± 0.03
1	650	7.4622	−4.8014	0.1691	−0.2893				2.66 ± 0.05	12.26 ± 0.05
	650	7.4635	−4.7991	0.0885	−0.2057				2.66 ± 0.04	12.26 ± 0.04

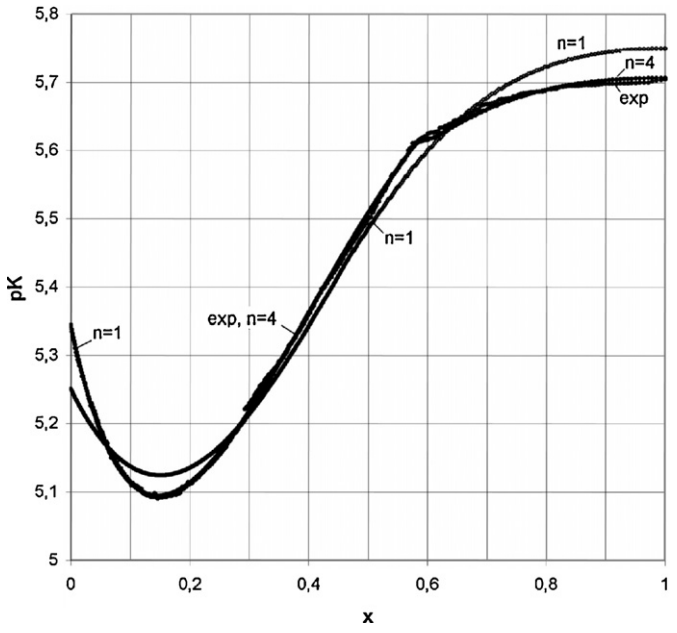


Fig. 4. The fit of R–K functions for PY-3CA/H_2O + MeOH system at $n = 1$ and at $n = 4$.

Table 4
pK_A and pK_B values for HL = PY-4CA in HL/H_2O + Me_2SO system, found from Eq. (14) at different n-values.

n	pK_A	pK_B
4	5.228	12.766
3	5.225	12.844
2	5.220	12.848
1	5.007	12.494

The pK_A and pK_B values referred to different acids HL in (a) HL/H_2O + MeOH and (b) HL/H_2O + Me_2SO system are presented in Table 5.

The literature data for pK_A of the acids considered in this paper are scarce and incomplete. The pK_B values are unknown or not attainable in literature. The results obtained for pK_A are in satisfactory accordance with literature data. For example, the pK_A values for PZ-2CA in Table 1 are close to the value 2.79 [42]. The pK_A = 4.19 value [22] found for BA (Table 5) is close to 4.17 [43], 4.18 [44], 4.19 [45], 4.20 [46], 4.206 [47], 4.21 [48]. The pK_A values for PY-2CA (Table 1) are by ca. 0.1 higher than 5.47 [44] or 5.52 [49,50]. For PY-3CA, the values for pK_A (Table 1) differ significantly from 4.87 [44] and 4.90 [51]. The pK_A values for PY-4CA in Table 1 are somewhat higher than 4.96 [51].

Table 5
The pK_A and pK_B values obtained from Eq. (12) and referred to different acids HL (see Fig. 1) considered in HL/H_2O + MeOH and HL/H_2O + Me_2SO systems.

System		HL/H_2O + MeOH		HL/H_2O + Me_2SO	
No.	Acid, HL	pK_A	pK_B	pK_A	pK_B
a	Benzoic	4.19	8.59	4.19	15.52
b	Pyridine-2-carboxylic	5.65	6.62	5.64	16.08
c	Pyridine-3-carboxylic	5.33	5.66	5.16	13.85
d	Pyridine-4-carboxylic	5.22	5.13	5.19	12.87
e	Pyrazine-2-carboxylic	3.00	3.14	2.81	12.33

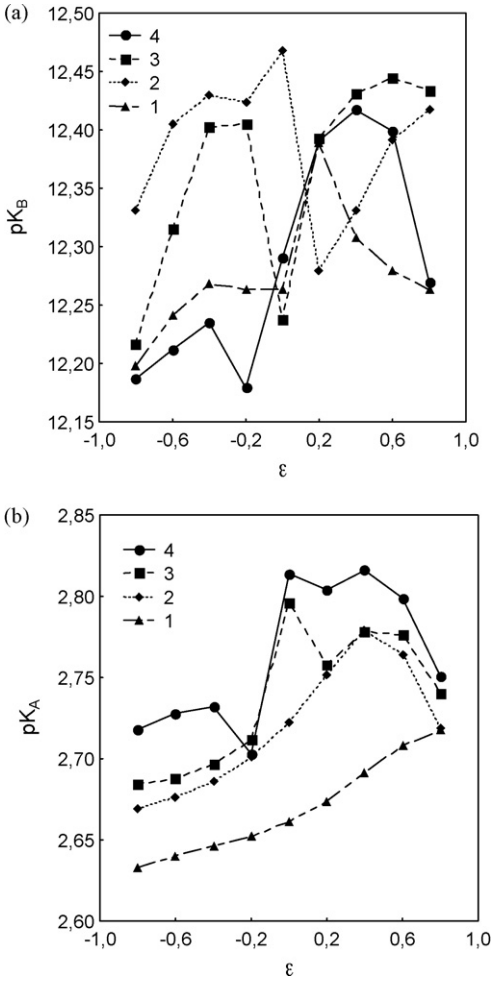


Fig. 5. The plots of (a) pK_A vs. ε and (b) pK_B vs. ε relationships for HL = PZ-2CA in HL/H_2O + Me_2SO system on the basis of Eq. (20) for $n = 4, 3, 2, 1$.

6. Final remarks

The paper provides a new approach to modelling the systems with mixed solvents: H_2O + B, where B = MeOH or Me_2SO is the organic solvent, wholly mixed with water. The modelling aimed principally to get accurate $pK_B = pK(1)$ values for acids HL consid-

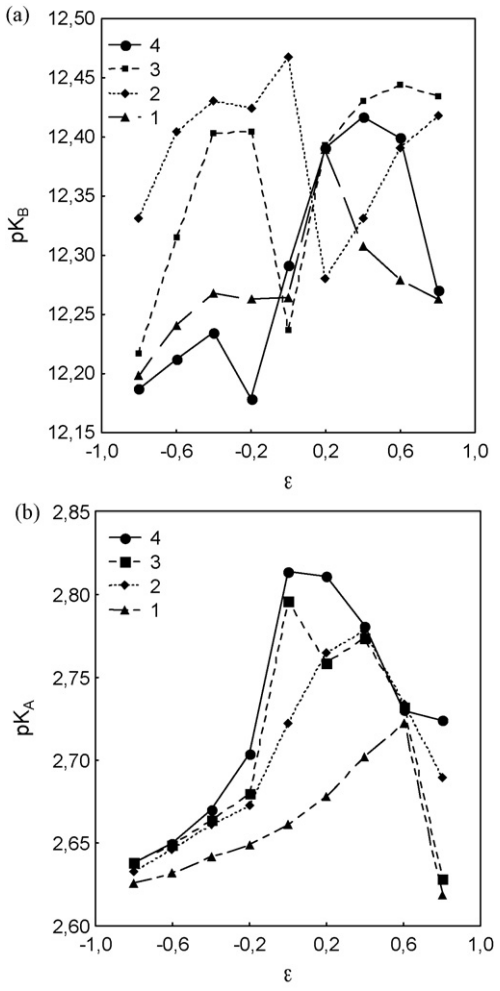


Fig. 6. The plots of (a) pK_A vs. ε and (b) pK_B vs. ε relationships for HL = PZ-2CA in HL/H_2O + Me_2SO system on the basis of Eq. (21) for n = 4, 3, 2, 1.

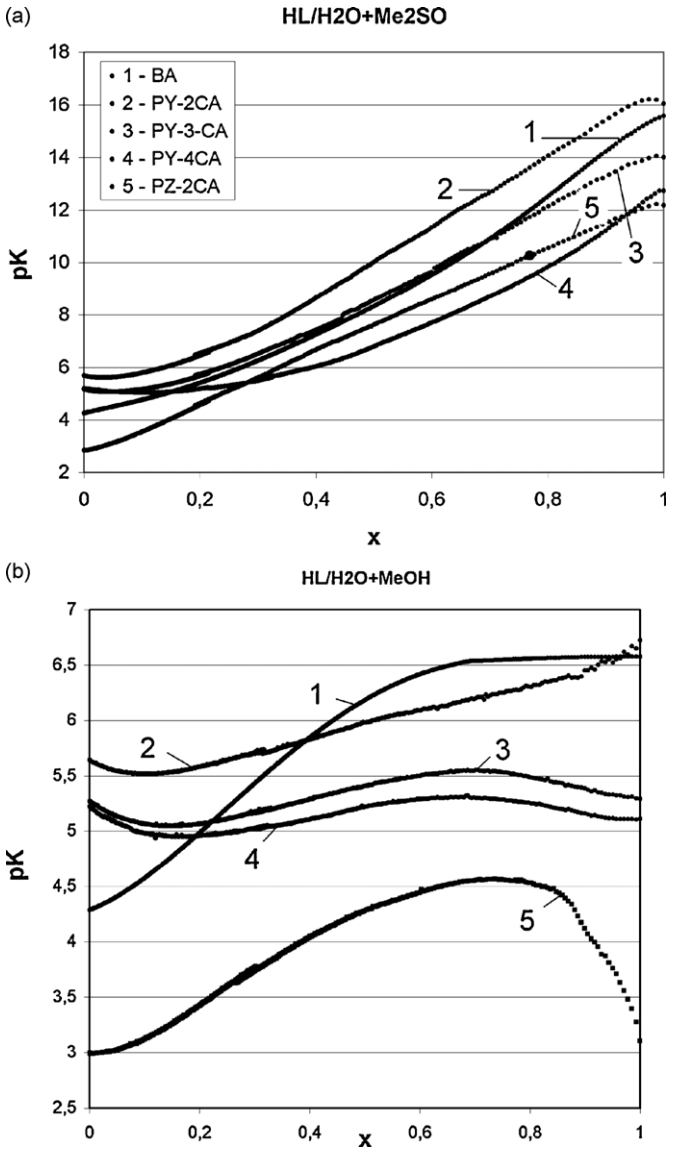


Fig. 7. The converted points referred to different acids HL in (a) HL/H_2O + MeOH and (b) HL/H_2O + Me_2SO system. Enumeration of the acids as in Fig. 1.

ered in pure organic solvent (B). An exact evaluation of pK_B is not an easy task from direct pH measurement in HL/B solution. The new approach is based on results obtained from mutual mixing two solutions, HL/H_2O and HL/B, of the same acids HL of the same molar concentration C, but dissolved in different solvents: H_2O and organic co-solvent B, respectively. The mixing is made according to titrimetric mode, with pH registration. This way, the entire x-range is covered by experimental points. The primary experimental points (V_j, pH$_j$) are recalculated in terms of the mole fraction (x) on the abscissa and pK on the ordinate and the (x_j, pK_j) points are obtained; some of the points can cover a common part of the x-range in both titrations: HL/H_2O → HL/B. The curves pK = pK(x) applied fit perfectly the experimental/transformed (Eq. (2)) results of titration, at n = 3 and 4 applied in the related functions: (12), (13), (20) or (21). The great advantage of this approach is the fact that the dispersed (in repeated titrations) points at x close to 1 do not affect substantially the pK_B = pK(1) value. Other advantage is the fact that pK_B and pK_A are calculated from the same formulae (Eq. (19)), irrespectively of the approximating function applied. The pK values for this system are obtained from Eq. (2), under assumption that pH = $-\log[H^+]$, i.e. at the activity coefficient of hydrogen ions equal to unity (γ = 1), see also [40].

All the remarks testify on account of the opinion that all approximating functions applied in this paper are applicable for modelling purposes. The results for pK_B are repeatable in the series of successive measurements. The pK_A values, referred to aqueous systems, are comparable with ones found in the literature.

References

[1] J. Schneede, P.M. Ueland, Analytical Chemistry 64 (1992) 315.
[2] S. Nigam, A. de Juan, R.J. Stubbs, S.C. Rutan, Analytical Chemistry 72 (2000) 1956.
[3] A. Jouyban, H.-K. Chan, B.J. Clark, W.E. Acree, International Journal of Pharmaceutics 246 (2002) 135.
[4] G. Völgyi, R. Ruiz, K. Box, J. Comer, E. Bosch, K. Takács-Novák, Analytica Chimica Acta 583 (2007) 418.
[5] A. Argemí, J. Saurina, Journal of Pharmaceutical and Biomedical Analysis 44 (2007) 859.
[6] M. Meloun, S. Bordovská, L. Galla, Journal of Pharmaceutical and Biomedical Analysis 45 (2007) 552.
[7] S.S. Kurek, B.J. Laskowska, A. Stokłosa, Electrochimica Acta 51 (2006) 2306.
[8] R. Mihajlović, Z. Sonić, Lj. Mihajlović, Vukićević, Talanta 43 (1996) 2131.
[9] A.F. McDonagh, A. Phimister, S.E. Boiadijev, D.A. Lightner, Tetrahedron Letters 40 (1999) 8515.
[10] X. Subirats, E. Bosch, M. Rosés, Journal of Chromatography A 1121 (2006) 170.
[11] E. Örnskov, A. Linusson, S. Folestad, Journal of Pharmaceutical and Biomedical Analysis 33 (2003) 379.
[12] V. de Nogales, R. Ruiz, M. Rosés, C. Ràfols, E. Bosch, Journal of Chromatography A 1123 (2006) 113.
[13] E. Fuguet, C. Ràfols, E. Bosch, M. Rosés, Journal of Chromatography A 1216 (2009) 3646.

[14] G. Scatchard, C.L. Raymond, Journal of the American Chemical Society 60 (1938) 1278.
[15] A. Valtz, Ch. Coquelet, C. Nikitine, D. Richon, Thermochimica Acta 443 (2006) 251.
[16] L. Xu, G. Lin, X. Wang, R. Lin, Journal of Molecular Liquids 123 (2006) 130.
[17] S. Didaoui-Nemouchi, A.A. Kaci, Journal of Thermal Analysis and Calorimetry 69 (2002) 669.
[18] R. Francesconi, F. Comelli, Thermochimica Acta 258 (1995) 49.
[19] H. Wang, Y. Wu, Journal of Solution Chemistry 34 (2005) 1067.
[20] B. Löwen, S. Schulz, Thermochimica Acta 262 (1995) 69.
[21] H.A. Zarei, Journal of Molecular Liquids 130 (2007) 74.
[22] B. Pilarski, T. Michałowski, A. Dobkowska, H. Foks, K. Kupiec, Analytica Chimica Acta, in press.
[23] O. Redlich, A.T. Kister, Industrial and Engineering Chemistry Research 40 (1948) 341.
[24] J.D.G. de Oliveira, J.C.R. Reis, Thermochimica Acta 468 (2008) 119.
[25] D.M. Myers, R.L. Scott, Industrial and Engineering Chemistry 55 (1963) 43.
[26] J. Wisniak, R.D. Peralta, R. Infante, G. Cortez, Journal of Chemical Thermodynamics 37 (2005) 729.
[27] J. Wisniak, G. Cortez, R.D. Peralta, R. Infante, L.E. Elizalde, T.A. Amaro, O. Garcia, H. Soto, Journal of Chemical Thermodynamics 40 (2008) 1671.
[28] J. Fan, X. Shen, J. Wang, Analytica Chimica Acta 364 (1998) 275.
[29] J. Fan, J. Wang, C. Ye, Talanta 46 (1998) 1285.
[30] J. Fan, X. Shen, J. Wang, Talanta 49 (1999) 843.
[31] J. Ghasemi, A. Niazi, M. Kubista, Analytica Chimica Acta 455 (2002) 335.
[32] N.M. Ballach, E.B. Robertson, M.D. Sokołowska, Journal of the Chemical Society, Faraday Transactions I 66 (1970) 2622.
[33] R.G. Bates, Z. Pawlak, Journal of Solution Chemistry 5 (1976) 213.
[34] C.H. Rochester, D.N. Wilson, Journal of the Chemical Society, Faraday Transactions I 72 (1976) 2930.
[35] B. Leśniewski, Z. Pawlak, B. Przybyszewski, Journal of the Chemical Society, Faraday Transactions I 80 (1984) 1769.
[36] E. Bosch, C. Ràfols, M. Rosés, Analytica Chimica Acta 302 (1995) 109.
[37] A. Jouyban, S. Soltani, H.-K. Chan, W.E. Acree Jr., Thermochimica Acta 428 (2005) 119.
[38] A. Jouyban, W.E. Acree Jr., Journal of Pharmacy & Pharmaceutical Sciences 9 (2006) 262.
[39] http://www.en.wikipedia.org/wiki/Legendre_polynomials.
[40] F. Rived, I. Canals, E. Bosch, M. Rosés, Analytica Chimica Acta 439 (2001) 315.
[41] http://www.en.wikipedia.org/wiki/Vandermonde_matrix.
[42] M. Sak-Bosnar, K. Kovar, Analytical and Bioanalytical Chemistry 383 (2005) 539.
[43] M.R. Wright, An Introduction to Aqueous Electrolyte Solutions, Wiley, 2007.
[44] M.S.K. Niazi, J. Mollin, S. Ghosh, Bulletin of the Chemical Society of Japan 60 (1987) 2605.
[45] J.I. Partanen, P.M. Juusola, P.O. Minkkinen, Journal of Solution Chemistry 30 (2001) 443.
[46] K. Kashiwagi, R. Sugise, T. Shimakawa, T. Matuura, M. Shirai, Journal of Molecular Catalysis A: Chemical 264 (2007) 9.
[47] R.M. Kettler, D.J. Wesolowski, D.A. Palmer, Journal of Solution Chemistry 24 (1995) 385.
[48] K. Sarmini, E. Kenndler, Journal of Biochemical and Biophysical Methods 38 (1999) 123.
[49] K.K.S. Gupta, B. Pal, N. Bhattacharjee, S. Ghosh, Bulletin of the Chemical Society of Japan 72 (1999) 1769.
[50] K.K.S. Gupta, N. Bhattacharjee, B. Pal, S. Ghosh, Transition Metals Chemistry 24 (1999) 268.
[51] J.-C. Hallé, J. Lelievre, F. Terrier, Canadian Journal of Chemistry 74 (1996) 613.

Talanta 80 (2010) 1081–1087

Contents lists available at ScienceDirect

Talanta

journal homepage: www.elsevier.com/locate/talanta

Developing automated analytical methods for scientific environments using LabVIEW

Christoph Wagner, Sergio Armenta, Bernhard Lendl*

Institute of Chemical Technologies and Analytics, Vienna University of Technology, Getreidemarkt 9/164 AC, A-1060 Vienna, Austria

ARTICLE INFO

Article history:
Received 15 May 2009
Received in revised form 4 August 2009
Accepted 17 August 2009
Available online 22 August 2009

Keywords:
Capillary electrophoresis
Infrared spectroscopy
Sequential injection analysis
LabVIEW programming
Automated analytical methods
Enzyme inhibition

ABSTRACT

The development of new analytical techniques often requires the building of specially designed devices, each requiring its own dedicated control software. Especially in the research and development phase, LabVIEW has proven to be one highly useful tool for developing this software. Yet, it is still common practice to develop individual solutions for different instruments. In contrast to this, we present here a single LabVIEW-based program that can be directly applied to various analytical tasks without having to change the program code. Driven by a set of simple script commands, it can control a whole range of instruments, from valves and pumps to full-scale spectrometers. Fluid sample (pre-)treatment and separation procedures can thus be flexibly coupled to a wide range of analytical detection methods. Here, the capabilities of the program have been demonstrated by using it for the control of both a sequential injection analysis - capillary electrophoresis (SIA-CE) system with UV detection, and an analytical setup for studying the inhibition of enzymatic reactions using a SIA system with FTIR detection.

© 2009 Elsevier B.V. All rights reserved.

1. Introduction

Current trends in analytical chemistry clearly aim at developing fully automated, integrated analytical solutions, comprising necessary sample (pre-)treatment, the actual analyte detection, and data processing. Hence, nowadays, practically all newly developed analytical methods involve computers for system control and/or data recording. Yet, in research and development the configurations of the experimental set-ups change frequently, making it necessary to adapt not only the analytical system itself, but also very often the software. In this context, the possibility of flexible control software for the automation of an experimental set-up and the corresponding data analysis would be of great practical value. Such a software platform would allow quick adaptation of experimental set-ups to new findings and ideas, thus focusing on the evaluation of new approaches and characterisation of their analytical performance, rather than re-writing software.

LabVIEW, by National Instruments, is widely used as a control software development tool in both academic and industrial R&D. This software allows programming of virtual instruments (VIs), combining electronics with computer resources to control instruments and collect sets of data [1–3]. In contrast to C++ or Visual Basic for example, LabVIEW is a graphical programming language enabling the creation of high quality programs within short time periods. Typically, different (sub-)VIs, each fulfilling its own specific duties, are placed on a programming diagram and wired together. These virtual wires directly visualise the program and all data flows while writing the program, making it easier to interpret programs compiled by someone else and adjust them to specific needs. Furthermore, it also helps by keeping a sustainable knowledge base, allowing the handing over of software responsibility from one employee/student to another. Using controls and indicators from a large set of predefined elements, a user-friendly graphical user interface (GUI, called a panel) can easily be designed [4]. A final practical advantage of LabVIEW is that a parallelisation of code execution can easily be achieved, something that can be of great advantage, e.g. for decoupling data acquisition and data processing and evaluation.

A variety of previously published papers describe such LabVIEW-based programs aiming towards the automation of specific analytical systems fulfilling a particular task, including developing a new flow injection analysis (FIA) method by replacing the mixing coil with a continuously variable volume reactor [5], measuring picomolar concentrations of silver in seawater [6], monitoring particle/water interactions [7], determining morphine by a sequential injection analysis (SIA) system [8] or coupling such a system to a combined electro-generated chemiluminescence and amperometric detection [9]. Altogether, applications range from automating sample pre-treatment using a FIA system over autosampling devices to the possibility of combining versatile liquid handling with different kinds of detectors, like SIA with capillary

* Corresponding author.
E-mail address: blendl@mail.tuwien.ac.at (B. Lendl).
URL: http://www.cta.tuwien.ac.at/cavs (B. Lendl).

0039-9140/$ – see front matter © 2009 Elsevier B.V. All rights reserved.
doi:10.1016/j.talanta.2009.08.018

electrophoreses (CE) separation [10,11]. Irrespective of the actual analytical detection principle, a common denominator of these and many other analytical systems is the need to precisely handle fluids, very often different types of liquids. Still, each of these VIs is highly specialized and not very well suited to rapid adaptation for new systems and requirements.

This circumstance was the motivation behind the development described here. The goal was to develop a VI that allows the experimentalist to flexibly combine different laboratory equipment into new setups, without having to rewrite the control software. As outlined above, this requires combining fluid handling systems based, for example, on one of the various embodiments of flow injection, with different types of analytical detectors, and eventually some sort of analyte separation. A detailed analysis of these methods show that, while diverse and complex in overall operation, the active hardware core elements are essentially just a few pumps and valves. The resulting solution thus focused on designing a system that can flexibly control different such devices, irrespective of their specific combination or function in the analytical set-up. These functions are supplemented by a number of interfaces to optical detectors and auxiliary instruments, such as high-voltage supplies for CE separation.

The possibilities of the resulting control platform are demonstrated by successfully applying the identical control software to two widely different analytical devices, (i) a fully automated SIA-CE-UV system and (ii) label-free inhibition monitoring of an enzyme using a second SIA system coupled to an FTIR spectrometer. While the first analytical set-up includes capillary conditioning, sample preparation and analyte detection using a UV detector, the second example application requires rapid mixing of an enzyme solution with an inhibitor/substrate solution, transfer of the mixture into an IR measurement cell before the reaction of the enzyme with the substrate starts, and monitoring of minute spectral features changes over time.

2. Experimental

2.1. System components

In its present form, the program supports Vici's selection- and injection valves (Vici AG, Switzerland), Cavro's XP3000 and XL3000 syringe pumps and Smart Valves XL (Cavro Scientific Instruments, Sunnyvale, CA, USA), the kDS200 syringe pump (KD Scientific, Holliston, MA, USA) and Gilson's Miniplus peristaltic pump series (Gilson Inc., Middleton, WI, USA). For data acquisition, interfaces to both a UV detector (Dionex, Sunnyvale, CA, USA) and Bruker's FT-IR spectrometers (Bruker Optics GmbH, Ettlingen, Germany) have been implemented, together with a control device for a Spellman CZE 1000R high voltage power supply (Spellman, NY, USA).

The valves, the syringe pumps and the UV detector were interfaced to the PC running the LabVIEW VI using standard RS232 data connections, both for sending commands and receiving confirmation or error responses, which in turn allow the program to react to such events immediately. It is worth noting here that one RS232 interface can control up to nine different Vici valves.

The Gilson pump and the high voltage supply were connected via a cDAQ system from National Instruments using application specific protocols. For the Gilson pump this comprised two TTL signals, switching between the ON/OFF state and selecting the rotation direction, respectively, and a speed control in form of a continuously variable 0–5 V signal, corresponding to 0–100% of the maximum speed, as manually entered on the pump's control panel. The high voltage power supply was similarly controlled by a continuously variable 0–10 V input voltage signal, here corresponding to 0–30 kV output voltage.

Table 1
Typical example commands for sequence programming.

Command	Effect
PP*n*	Pick up *n* steps with the Cavro pump and do not wait to finish
PDW*n*	Dispense *n* steps with the Cavro pump and stay further program execution until it finishes
GO*n*|*k*	Switch the Vici valve with ID *n* to port *k*, choosing the fastest way (clockwise or counter-clockwise)
OS*n*|*k*	Start an IR measurement, where *n* is the number of spectra to be recorded and *k* the time between two spectra acquisitions in seconds
UV*n*|*k*	Start an UV measurement, where *n* is the sampling rate in microseconds and *k* the total measurement time in minutes
HV*n*|*k*	Apply *n* Volts in *k* seconds, using the Spellman high voltage power supply
SM	Stop running UV or IR measurements as soon as the Cavro syringe pump stops moving
WA*n*	Wait for *n* milliseconds
LOOP*n* END LOOP	Repeat the sequence between LOOP and END LOOP for *n* times

The Bruker spectrometers were controlled over a network connection through interaction with an OPC (OLE for Process Control) server, which is part of the "Process" package of the OPUS software. Due to the complexity of an IR measurement and to limitations in the OPC software itself, in its present development state the LabVIEW program is only capable of starting background and sample data acquisition; all setup parameters, such as optical resolution, number of scans as well as data post processing, have to be defined in a process control script in OPUS. Another restriction to the IR measurements is the fact that the "Process" package does not support rapid scanning or step-scan measurements yet.

Altogether, a large number of different system components can be integrated and controlled by the VI developed here, allowing the realisation of practically any relevant liquid sample pre-treatment. Furthermore, the modular approach of LabVIEW allows easy incorporation of sub-VIs for almost any other hardware component that can be controlled by LabVIEW.

2.2. The program

Since the program has been designed to control a variety of different hardware modules at once, and to keep the graphical user interface (GUI) as simple as possible (Fig. 1), all the commands controlling the hardware are entered in a text box (refer to Table 1 for command code examples out of more than 40 available commands). Every command is written on a separate line. This list of commands is then taken by the program code and executed from top to bottom. This approach keeps the graphical user interface simple and each of the sequences can be stored as plain text files for archiving. While running a sequence, all upcoming commands are displayed in a second text box in order to see the actual execution state of the sequence. The hardware setup parameters, including COM ports, channel numbers for the analogue outputs or the hostname of the computer running OPUS, can be entered in a separate setup area. The outputs of the UV detector and/or the IR spectrometer are displayed in two different tabs to save room on the GUI. A third tab holds all the error displays.

The internal design of the program code consists mainly of five parallel loops. The first loop, the master loop, executes the sequence entered by the user. When a command to move the plunger of the Cavro syringe pump is executed, a second loop is triggered by the master-loop, sending a notifier message to monitor the plunger movement. This can be done in parallel to the script execution, enabling data acquisition in the meantime, or the sequence can wait for the pump to finish its movement, which can be useful e.g.

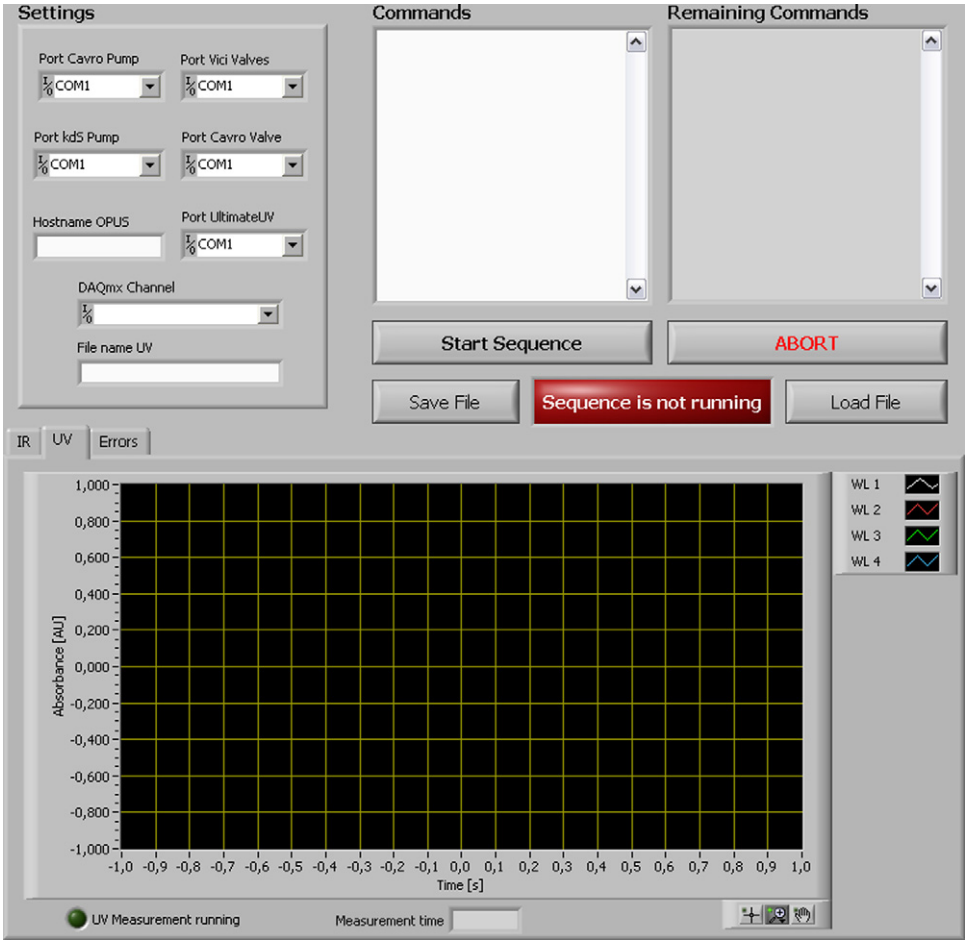


Fig. 1. Graphical user interface showing three different sections: in the upper row on the left is the communication port selector, on the right the interfaces for entering commands and surveying the sequence execution; in the lower row, a display with three tabs displays the data output of the UV and the IR detectors, and error messages, respectively.

during cleaning steps. The third loop polls an Abort button, so the user can terminate the script execution if an error occurs that is not recognized by the program itself. As soon as an error occurs or the Abort button is pressed, the program tries to shutdown any attached pump and the high voltage power supply. In addition, it switches to the error tab and displays a comprehensive error message. The two remaining loops handle IR and UV data acquisition. These two measurement loops are also triggered by the master-loop by a notifier message. The measurement loops will send back a notifier message to the main loop as soon as the measurement begins. This approach ensures that the entered sequence is kept in the event of any delay.

3. Results and discussion

3.1. Application I: sequential injection analysis – capillary electrophoresis with UV detection

Sequential injection analysis (SIA) is a viable tool to automate sample pre-treatment steps like pre-concentration and/or purification, applying chemical reactions and diluting samples. Capillary electrophoresis (CE) is a highly effective separation technique separating molecules by their charge to size ratio. Coupling SIA with CE has been successfully demonstrated in literature combining the advantages of both techniques making it even easier to apply conditioning or cleaning steps to the separation capillary. However, the main problem associated with this coupling arises from the discontinuous sample introduction mode of CE, where the system needs to be decoupled and coupled before and after the application of the separation voltage. This usually requires specially designed interfaces [11]. One of the first coupling systems by Arce et al. used a programmable arm to connect a FIA system to an at-line commercial CE analyzer [12]. Zacharis et al. used a special micro valve with a very low port-to-port volume and a CE capillary as a kind of injection loop [13] to couple the SIA system to the CE separation part. Wu et al. utilized a Lab-on-Valve approach for this purpose [14]. Both ways share the need for special equipment for the coupling process and the introduction of the electrodes needed to apply the separation voltage. Another approach by Kulka et al. used T-connection pieces connecting the capillary and the electrodes to the SIA system [10]. This manifold suffers from the fact that using capillaries with bigger inner diameters than 50 μm, as used by Kulka et al., can be problematic as the valve used to close the system for cleaning purposes creates some backpressure, even in the opened position. This results in the sample already being injected into the capillary while pumping it through the T-piece.

In the presented work the capillary is connected directly to an inexpensive valve, making special valves unnecessary, and overcoming pressure problems with capillaries.

3.1.1. Material and methods

3.1.1.1. Instrumentation. The manifold shown in Fig. 2 used a Cavro XP 3000 (Cavro Scientific Instruments, Sunnyvale, CA, USA) pump equipped with a 2500 μl syringe, a Valco (Valco Instruments Co.

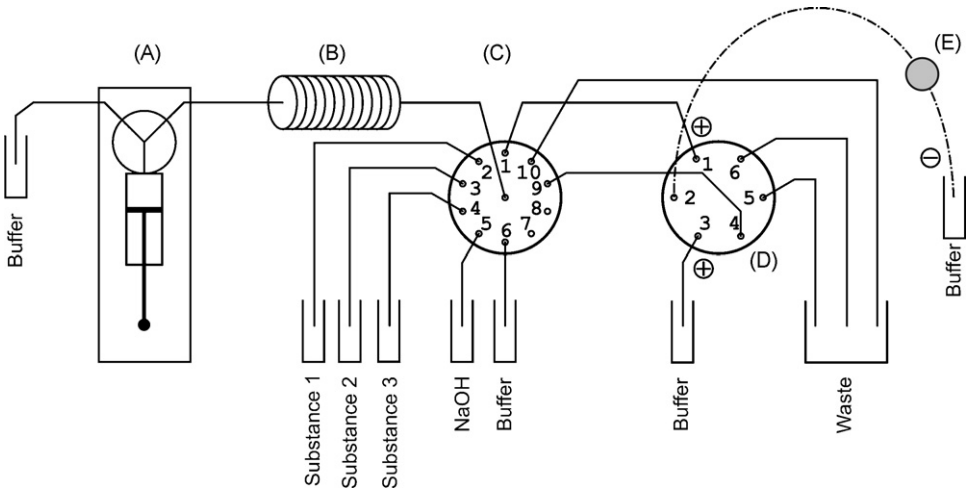


Fig. 2. Schematic view of the SIA-CE-UV manifold. (A) Cavro syringe pump; (B) 500 μl Teflon holding coil; (C) Vici selection valve; (D) Vici injection valve; (E) Capillary (100 μm ID) with UV detection window (not shown): Spellman high voltage power supply to apply 15 kV between the buffer reservoir and either Port 1 or Port 3.

Inc, Houston, TX, USA) six-port injection valve and a Valco ten-port selection valve. The HV system was a Spellman CZE 1000R (Spellman, New York, USA), capable of delivering up to 30 kV and 300 μA. Two metal tubings, each of the length of 2 cm, were connected to ports 1 and 3 of the injection valve and served as connections for the ground electrodes. The negative potential was applied by using a platinum wire (0.5 mm OD, ÖGUSSA, Austria) placed inside a glass vial. The capillary (Polymicro Technologies LLC, Phoenix, AZ, USA) had an ID of 100 μm, an OD of 350 μm, a total length of 60 cm and was covered by a Teflon tubing (1.588 mm OD) on the end connected to the injection valve. UV detection was achieved with a fiber optic Ultimate UV–Vis detector (Dionex, Sunnyvale, CA, USA) at 50 cm capillary length.

3.1.1.2. Procedure. A new capillary was first initialized by flushing it with 0.10 M sodium hydroxide and BGE buffer solutions using an automated sequence. By placing the injection valve in position B (ports 1–2, 3–4 and 5–6 connected), the syringe pump pressurized the whole SIA-CE system, forcing the solutions to flow through the capillary. Before each separation run the capillary was flushed, applying the same procedure with BGE buffer only. As the electrophoresis process alters the running buffer pH by electrolysis and subsequently changes the electro-osmotic flow (EOF), the separation buffer was renewed before every run by pumping buffer through port 9 of the selection valve.

The separation background electrolyte consisted of 100 mM phosphate buffer at pH 6.8. The UV detector was set to 241, 270 and 294 nm, corresponding to the absorption maxima of the three analytes, the applied voltage used for electrophoretic separation was 15 kV and samples were introduced into the capillary in the electrokinetic injection mode. The samples were prepared on the fly by aspiring small volumes of pyridine-2-aldoxime methochloride, thiamine and 1,10-phenantroline (3500 mg L^{-1} each) in a sequential order, repeating the sequence 10 times, into the holding coil. By varying the aspirated volume of each of the substances, different sample concentrations could be produced. In the electrokinetic injection mode, the sample flowed from the selection valve to port 1 of the injection valve, which was in position A (ports 1–6, 2–3 and 4–5 connected). Then, the injection valve changed to position B following counter clockwise rotation and the high voltage power supply applied a constant potential of 15 kV for 10 s. Finally, the 2-way valve switched back to position A by clockwise rotation connecting the capillary with the buffer reservoir at position 3 of the valve and the electrophoretic separation was initiated by applying 15 kV.

3.1.2. Results

The analytical performance of the SIA-CE-UV automated system was evaluated by considering the linearity, linear range, limit of detection (LOD), limit of quantification (LOQ) and precision expressed as relative standard deviation (RSD).

An electropherogram obtained is shown in Fig. 3. The linear relationships deduced between absorbance and drug concentration are summarized in Table 2. The LOD and LOQ were calculated as 3 and 10 times, respectively, the standard deviation of the intercept of the calibration line divided by the slope of the curve. The intra-day precision of the method was evaluated using the results obtained for five independent runs of 500 mg L^{-1} pyridine-2-aldoxime methochloride, 1000 mg L^{-1} thiamine and 500 mg L^{-1} 1,10-phenantroline standards mixture and the results were expressed as RSD. The linearity was tested using a pure error lack of fit test with simple regression, which was not significant at the 5% level.

3.2. Application II: SIA-FTIR coupling for enzymatic reaction monitoring

To demonstrate the suitability of the developed LabVIEW program for the automated control of analytical instrumentation in process monitoring and analysis of evolving systems, an enzy-

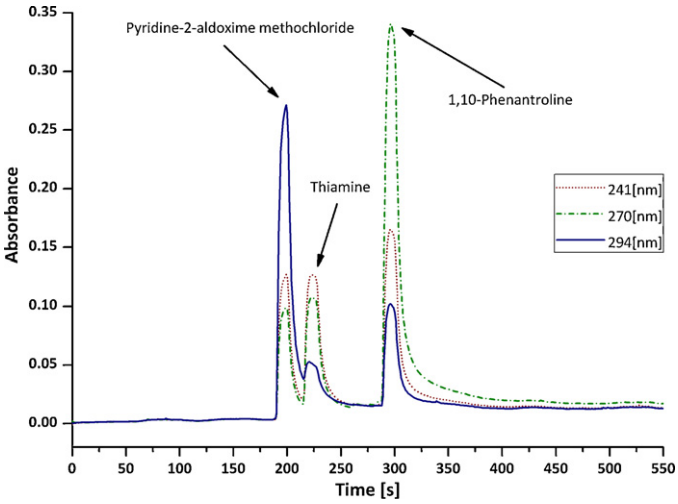


Fig. 3. Electrophoretic separation of pyridine-2-aldoxime methochloride, thiamine and 1,10-phenantroline using a capillary with an internal diameter of 100 μm by applying 15 kV potential. See the text for further details.

Table 2
Analytical features of the SIA-CE-UV automated procedure for the determination of pyridine-2-aldoxime methochloride, thiamine and 1,10-phenantroline.

	Pyridine-2-aldoxime methochloride	Thiamine	1,10-Phenantroline
Wavelength (nm)	294	241	270
Migration time (s)	201	227	303
Regression equation			
Slope	0.00628 ± 0.00016	0.00261 ± 0.00005	0.0175 ± 0.0006
Intercept	-0.12 ± 0.11	-0.10 ± 0.08	-0.4 ± 0.4
Linearity (R^2)	0.997	0.998	0.996
Linear range (mg L^{-1})	52–1273	90–2722	66–1273
LOD (mg L^{-1})[a]	52	90	66
LOQ (mg L^{-1})	174	299	220
RSD area (%)[b]	5.0	5.1	4.2
RSD migration time (%)	3.4	3.3	4.5

[a] LOD and LOQ established as 3 and 10 times, respectively, the standard deviation of the intercept of the calibration curve divided by the slope of the calibration line.
[b] Relative standard deviation value of five independent runs of 500 mg L^{-1} pyridine-2-aldoxime methochloride, 1000 mg L^{-1} thiamine and 500 mg L^{-1} 1,10-phenantroline standards mixture.

matic reaction, the dephosphorylation of fructose 1,6-bisphosphate (F16BP) to fructose 6-phosphate (F6P) and inorganic phosphate in the presence of divalent cations, such as Mg^{2+}, and its inhibition by adenosine 5′-monophosphate (AMP) was selected as a case study. In this way, the use of infrared spectroscopy allows the direct monitoring of enzymatic activity because of the specific absorption bands in the middle infrared spectral range providing molecular specific information on the substrate and reaction products.

The most critical step of reaction process monitoring, especially of enzymatic systems, is the accurate control of the process starting point. It is absolutely necessary to use of a fully automated system to define the starting point of the reaction, thus avoiding human error and thereby increasing the quality of the obtained analytical data. This problem has been overcome by using a SIA system coupled to a FTIR spectrometer both controlled by the developed LabVIEW program.

3.2.1. Material and methods

3.2.1.1. Instrumentation. Enzymatic experiments were carried out on an Equinox 55 FTIR spectrometer (Bruker Optics GmbH., Karlsruhe, Germany) equipped with a narrow band mercury cadmium telluride (MCT) detector. Spectra were recorded by co-adding 128 scans at a resolution of 4 cm^{-1} and a scanner velocity of 100 kHz HeNe frequency.

The IR cell consisted of a temperature-controlled aluminium flow cell [15] with CaF_2 windows (thickness 2 mm) separated by a polyethylene spacer of 25 μm, thus establishing a constant IR path length.

The SI manifold (Fig. 4) was set up with a Cavro XP 3000 syringe pump (Cavro Scientific Instruments, Sunnyvale, CA, USA; syringe size 5000 μL) and a Valco (Valco Instruments Co. Inc, Houston, TX, USA) 10 port selection valve. A 1.5 mL safe-lock Eppendorf tube placed in a TTS2 minishaker (IKA Works Inc., Wilmington, NC, USA) was used as a mixing chamber to ensure a complete and homogeneous mixing prior to measurement.

3.2.1.2. Procedure. Different and accurately measured volumes of F16BP, AMP and working buffer were aspirated sequentially into the holding coil, and delivered into the mixing chamber obtaining a final volume of 250 μL. After that, FBPase solution was added and homogenized by shaking. The mixture was injected into the carrier stream and the flow was stopped at a fixed time, with the bulk of sample in the flow cell. FTIR spectra were recorded for 15 min at equal time intervals of 30 s to monitor the course of the reaction taking place using the spectrum of the cell filled with working buffer as background.

Using FTIR difference spectroscopy enabled the monitoring of the progress of the enzyme catalyzed reaction even though enor-

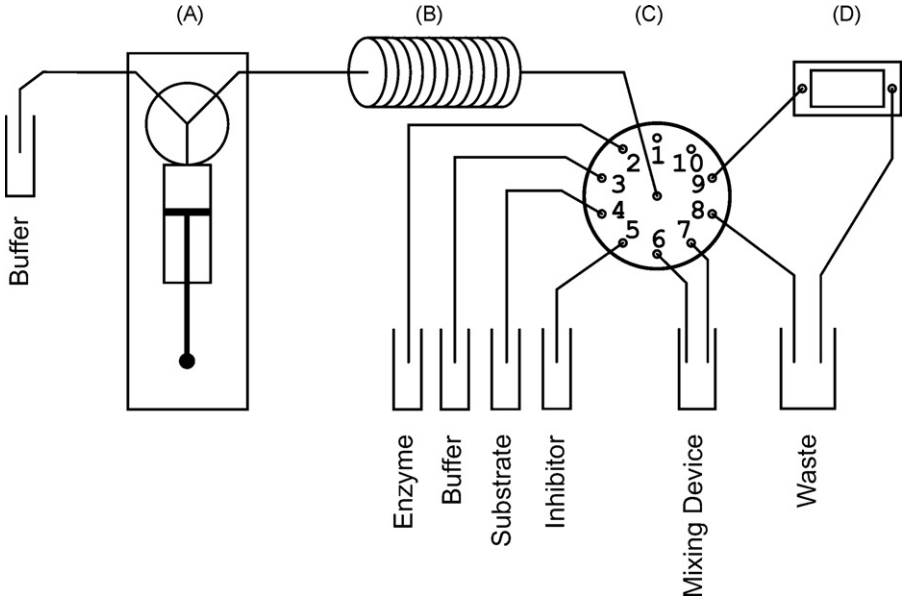


Fig. 4. Schematic view of the SIA-IR manifold for measuring enzymatic reactions. (A) Cavro syringe pump; (B) Teflon holding coil (500 μl); (C) Vici selection valve; (D) IR flow cell 25 μm path length.

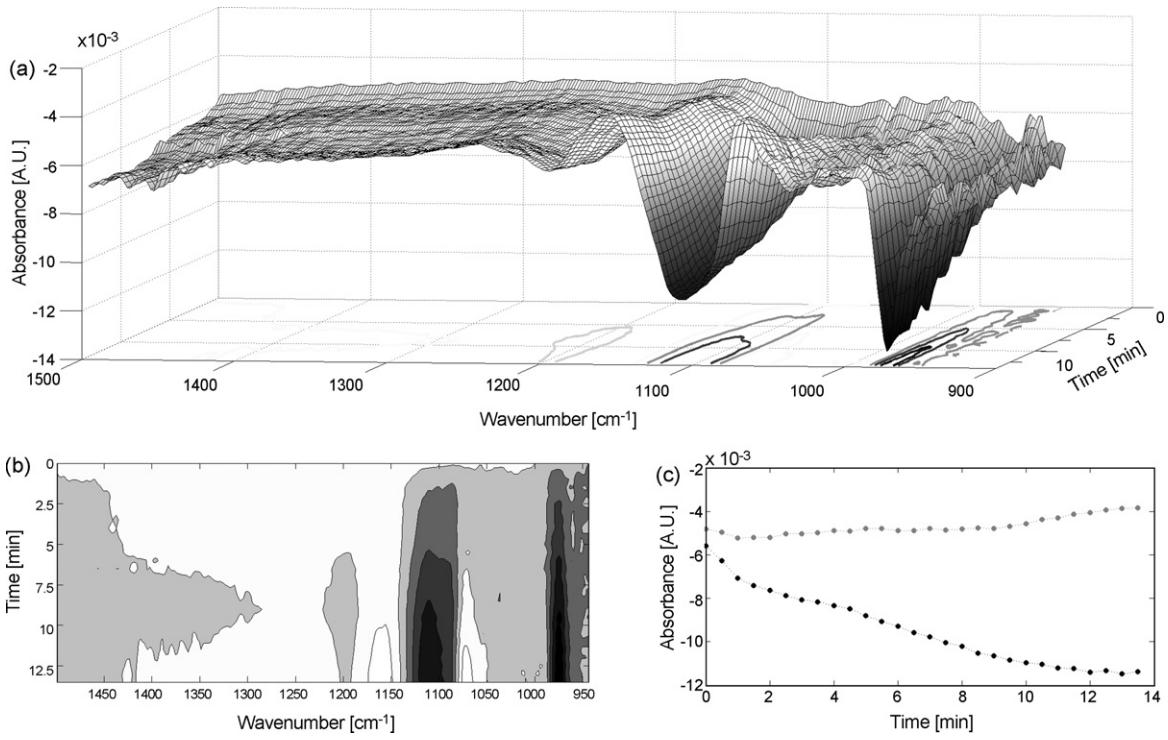


Fig. 5. FTIR difference spectra of the dephosphorylation of F16BP to F6P and phosphate in the presence of FBPase (a) three dimensional view, (b) projection on the space defined by the time and wavenumbers and (c) absorbance values of the selected wavenumbers (1109 and 1156 cm^{-1}) in the difference spectrum used for data evaluation.

mous similarities between the products and the substrate infrared spectra exist. Difference spectra, containing the spectral fingerprint of the reaction under investigation, were obtained by subtracting the first spectrum from the whole dataset, as it can be seen in Fig. 5. The absorbance difference between two selected wavenumbers (1109 and 1156 cm^{-1}), a maximum and a minimum, in the difference spectrum were used for data evaluation. The concentration of hydrolyzed F16BP was obtained by interpolation of those difference values in a calibration curve obtained from synthetic mixtures of substrate and products with the same data treatment.

3.2.2. Results

FTIR spectroscopy has been demonstrated to be an appropriate technique for the rapid investigation of enzymatic reactions [16,17] as the recording of a spectrum takes only a few seconds and is able to monitor the reaction of interest directly, in real-time. The starting point of the reaction can be accurately controlled and reproduced by using the automated SIA system for sample preparation and introduction into the FTIR cell. Thus, from the mixing of the enzyme with the substrate and buffer into the mixing chamber to the recording of the first spectrum only a few seconds (15 s approximately) passed, obtaining a highly reproducible starting point.

The Michaelis–Menten constant (K_M) can be determined in conditions of zero order kinetics with respect to the substrate. The K_M value was calculated from the Lineweaver-Burk graph, plotting the reciprocal of initial velocity against the reciprocal of substrate concentration. K_M was found to be 14.1 g L^{-1}.

Moreover, the inhibitor activity of AMP on the enzymatic dephosphorylation of F16BP at different inhibitor concentrations was evaluated. Kinetic studies demonstrate the capability of the methodology for label free monitoring of enzyme inhibition. The presence of increasing concentrations of the inhibitor AMP (0, 7.5 and 15 μM) reduces the maximum rate of the reaction without changing the apparent binding affinity of the catalyst for the substrate (Michaelis–Menten constant K_M^{App}). The obtained K_M^{App} values were determined to be 12.5 and 12.2 g L^{-1}, for 7.5 and 15 μM AMP, respectively. The results obtained were published in detail separately [18].

4. Conclusion and outlook

The developed LabVIEW program has been shown to be suitable for controlling various different liquid handling systems and coupling them to different analytical measurement techniques. The next steps will focus on expanding the program to work with other hardware, such as quantum cascade lasers or oscilloscopes. In essence, any hardware with LabVIEW drivers, or defined control interfaces reacting to specific input signals, could be incorporated into the program. Setting up an archive of relevant sub-VIs representing different hardware functionalities is another future step of this development. These VIs can be directly placed and wired in the program's case structure, executing corresponding hardware functionalities triggered by a command in a scripted sequence. This makes it easy even for inexperienced programmers to add new functionalities to the LabVIEW program.

If you are interested in using this program please do not hesitate to contact the authors by email.

Acknowledgement

C. Wagner gratefully acknowledges the financial support by Carinthian Tech Research AG and the COMET Competence Centre Programme of the Austrian Government.

S. Armenta acknowledges the financial support provided by the Ministerio de Educación y Ciencia (Ref. EX2007-1257).

References

[1] R.A. Aspey, I.S. McDermid, T. Leblanc, J.W. Howe, T.D. Walsh, Rev. Sci. Instrum. 79 (2008) 094502.
[2] J. Fernandez de Canete, P. Del Saz Orozco, S. Gonzalez-Perez, Int. J. Comput. Inf. Syst. Sci. Eng. 4 (2007) 222–225.

[3] Z. Stevic, Z. Andjelkovic, D. Antic, Sensors 8 (2008) 1819–1831.
[4] A. Krauss, U. Weimar, W. Gopel, Trends Analyt Chem. 18 (1999) 312–318.
[5] L.L. Lipe, S.M. Purinton, E. Mederios, C.C. Harrell, C. Efta, M. Murray, M. Wood, R.B. Portier, S.J. Chalkt, Anal. Chim. Acta. 455 (2002) 287–304.
[6] J.L. Barriada, J.B. Truscott, E.P. Achterberg, J. Autom. Methods Manag. Chem. 25 (2003) 93–100.
[7] M.J.M. Séguret, S.J. Ussher, P.J. Worsfold, M. Nimmo, J.W. Wood, Instrum. Sci. Technol. 36 (2008) 18–31.
[8] C.E. Lenehan, N.W. Barnett, S.W. Lewis, J. Autom. Methods Manag. Chem. 24 (2002) 99–103.
[9] A. Economou, M. Nika, J. Autom. Methods Manag. Chem. (2006) 1–9.
[10] S. Kulka, G. Quintás, B. Lendl, Analyst 131 (2006) 739–744.
[11] G.A. Theodoridis, C.K. Zacharis, A.N. Voulgaropoulos, J. Biochem. Biophys. Methods 70 (2007) 243–252.
[12] L. Arce, A. Rios, M. Valcárcel, Fresenius, J. Anal. Chem. 360 (1998) 697–701.
[13] C.K. Zacharis, F.W.A. Tempels, G.A. Theodoridis, A.N. Voulgaropoulos, W.J.M. Underberg, G.W. Somsen, G.J. de Jong, J. Chromatogr. A 1132 (2006) 297–303.
[14] C. Wu, L. Scampavia, J. Ruzicka, Analyst 128 (2003) 1123–1130.
[15] S. Armenta, W. Tomischko, B. Lendl, Appl. Spectrosc. 62 (2008) 1322–1325.
[16] M. Haberkorn, P. Hinsmann, B. Lendl, Analyst 127 (2002) 109–113.
[17] R. Pacheco, M.L.M. Serralheiro, A. Karmali, P.I. Haris, Anal. Biochem. 322 (2003) 208–214.
[18] M. López-Sánchez, M. Ayora-Cañada, A. Molina-Díaz, M. Siam, W. Huber, G. Quintás, S. Armenta, B. Lendl, Anal. Bioanal. Chem. 394 (2009) 2137–2144.

Talanta 80 (2010) 1088–1093

Contents lists available at ScienceDirect

Talanta

journal homepage: www.elsevier.com/locate/talanta

An osmotic micro-pump integrated on a microfluidic chip for perfusion cell culture

Zhang-Run Xu[a], Chun-Guang Yang[a], Cui-Hong Liu[a], Zhe Zhou[b], Jin Fang[b], Jian-Hua Wang[a,*]

[a] Research Center for Analytical Sciences, Box 332, Northeastern University, Shenyang 110004, China
[b] Department of Cell Biology, Key Lab of Cell Biology of Ministry Public Health, China Medical University, Shenyang, 110001, China

ARTICLE INFO

Article history:
Received 18 July 2009
Received in revised form 21 August 2009
Accepted 24 August 2009
Available online 29 August 2009

Keywords:
Osmotic micro-pump
Microfluidic chip
Cell culture

ABSTRACT

A novel microfluidic chip integrating an osmosis-based micro-pump was developed and used for perfusion cell culture. The micro-pump includes two sealed chambers, i.e., the inner osmotic reagent chamber and the outer water chamber, sandwiching a semi-permeable membrane. The water in the outer chamber was forced to flow through the membrane into the inner chamber via osmosis, facilitating continuous flow of fluidic zone in the channel. An average flow rate of 0.33 μL min^{-1} was obtained within 50 h along with a precision of 4.3% RSD (n = 51) by using a 100 mg mL^{-1} polyvinylpyrrolidone (PVP) solution as the osmotic driving reagent and a flow passage area of 0.98 cm^2 of the semi-permeable membrane. The power-free micro-pump has been demonstrated to be pulse-free offering stable flow rates during long-term operation. The present microfluidic chip has been successfully applied for the perfusion culture of human colorectal carcinoma cell by continuously refreshing the culture medium with the osmotic micro-pump. In addition, in situ cell immunostaining was also performed on the microchip by driving all the reagent zones with the integrated micro-pump.

© 2009 Elsevier B.V. All rights reserved.

1. Introduction

Fluidic driving device is a key component for the transportation and distribution of liquid in a microfluidic system. An ideal driving device for this purpose should be featured by precision and stability in fluidic flow rate in addition to small scale. Since the application of electro-osmosis to microfluidic chip-based capillary electrophoresis [1], various micro-pumps have been exploited for microfluidic transportation [2], with diverse actuation mechanisms, e.g., piezoelectric [3], pneumatic [4], peristaltic [5], electrostatic [6], centrifugal [7], ultrasonic [8], electro-osmotic [9] or magneto-hydrodynamic effects [10]. For these approaches, however, external power supply is required. Power-free pumping methods have attracted considerable interests, including fluidic driving by gravitational approach [11]. Surface tension [12] or the combination of gravity and surface tension as the pumping force facilitates further miniaturization of the pumps, but it provides only short-term reliability [13]. Micro-pumps based on capillary and/or evaporation effects have also been used in microchip systems [14,15]. Recently, filter paper plug was reported as an on-chip integrated pump device [16], while the close dependence of flow rate on the ambient temperature and humidity limits its application.

The osmotic effect provides a potential power-free pumping approach. Osmosis plays an important role in fluidic transport in living organisms. The plant root hair cells entail the passage of water from a region of high water chemical potential to a region of low potential through a semi-permeable membrane (cell membrane), which allows small molecules to pass through but blocks larger molecules [17]. The driving force derives from osmotic pressure of the solute, and it has been used in microfluidics [18–20]. An osmotic microactuator was proposed and used for drug delivery in a microfluidic system [19,20]. Three different osmotic dispense pumps were reported to supply flow rate at 1 μL h^{-1} for a period of one year [21]. Another osmotic pump by simulating phloem loading in plant leaves with a hollow fiber as the permeable membrane and saturated salt solution as the driving reagent provided constant and pulse-free flow for 26 days [22]. Although these two types of pumps are durable, it is very difficult to integrate them into microchips owing to their complex structures.

Microfluidic chip provides ideal platforms for the study of cells. The scale of the microchannels is well suited to the size of cells, and the microfluidic flow feature mimics the in vivo cellular microenvironments. Continuously perfusion cell culture allows long-term cell cultivation owing to the constant supply of nutrients. Thus a variety of microfluidic perfusion culture strategies have been developed [23], and syringe/peristaltic pumps were usually used to deliver the culture media [24–26]. Gravity-driven pumping schemes were used for this purpose by providing steady pulse-free

* Corresponding author. Tel.: +86 24 83688944; fax: +86 24 83676698.
E-mail address: jianhuajrz@mail.neu.edu.cn (J.-H. Wang).

0039-9140/$ – see front matter © 2009 Elsevier B.V. All rights reserved.
doi:10.1016/j.talanta.2009.08.031

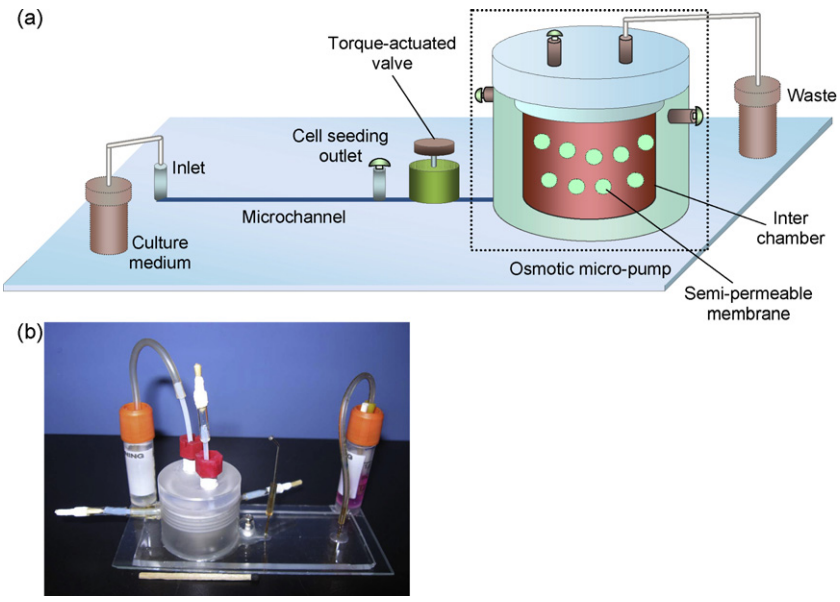


Fig. 1. Schematic diagram (a) and photograph (b) of the microfluidic chip integrating an osmotic micro-pump for perfusion cell culture.

flow [27]. Microfluidic perfusion culture lasting for two weeks was achieved [28]. However, the dead volume of the connecting tubes and off-chip valves brought long response time and large solution consumption. Therefore, some chip integrated micro-pumps were developed for cell culture. A computer controlled microfluidic perfusion cell culture platform was developed using integrated pumps and valves to precisely control fluidic flow [29], and a handheld recirculation perfusion platform was developed similarly [30]. An automated cell culture platform created arbitrary culture media formulations in 96 independent culture chambers and maintained cell viability for weeks using pneumatically actuated valves and pumps [31]. A similar cell culture platform with integrated pneumatic micro-pumps was used for high throughput drug testing [32]. Recently, electro-osmotic pumps were designed for cell culture in a microfluidic platform [33], but external energy sources and off-chip peripheral components were required, which is inconvenient when putting the devices into a CO_2 incubator or on the microscope platform. An osmosis-driven pump without bulky peripheral devices was developed for generating a concentration gradient of fetal bovine serum in the culture of human mesenchymal stem cells [34]. However, the osmotic pump, consisting of a PDMS chamber and a big vessel containing osmotic reagent solution, was connected to the chip by a tube instead of being integrated on the chip.

We have previously reported an off-chip osmosis-based pump for driving fluid [35]. In the present work, the osmotic pump was integrated on a microfluidic chip for perfusion cell culture and immunofluorescence staining. The micro-pump was positioned above the outlet of the microchannel, which provides pulse-free flow for the delivery of cell culture media.

2. Experimental

2.1. Fabrication of the device

The entire microfluidic chip integrating an osmotic pump is illustrated in Fig. 1. The chip (64 mm × 45 mm) is composed of two permanently plasma-bonded layers, i.e., the bottom glass substrate and the upper PDMS layer with microchannels of 500 μm (wide) × 80 μm (height) × 5 cm (length). There are two outlet holes located on the downstream channel, one serving as cell seeding outlet and the other connecting to the osmotic micro-pump (hidden under the osmotic micro-pump and not shown). A torque-actuated valve was integrated between the two holes for the control of opening/closing of the microchannel and the micro-pump. The valve was formed by fixing a small plastic block with a screw on the chip, and the opening/closing of the channel is facilitated by turning the screw to push down the PDMS layer [36].

The micro-pump was located at the end of the channel. It consists of a cup-shaped inner chamber and a cylindrical outer chamber. The inner chamber (1.5 cm in diameter and 1.6 cm in height) was used as the osmotic reagent reservoir (ca. 2.8 mL), and the outer chamber (2.4 cm in diameter and 1.4 cm in height) as the water reservoir (ca. 2.8 mL). An inlet and an outlet on the wall of the outer chamber were fabricated for the introduction of water. A semi-permeable membrane, i.e., a dialysis membrane (regenerated cellulose fiber, 16 mm i.d., Union Carbide, USA) with molecular weight cutoffs (MWCO) of 3500, was clamped tightly around the outside of the inner chamber wall using a flexible plastic pipe. Dozens of holes (2 mm in diameter) were drilled on the wall and plastic pipe, and total area of the holes serves as the effective osmotic area of the membrane. The inner chamber with membrane was assembled together with a plastic cap possessing an inlet and an outlet for the introduction of osmotic reagent. Then, the cap was screwed on the top of the outer chamber. A water-soluble polymer, polyvinylpyrrolidone (PVP, M = 30,000, Boai New Kaiyuan Pharmacy Co. Ltd, Henan, China), was used as the osmotic reagent.

2.2. Measurement of flow rate of the micro-pump

The flow rates of the micro-pump were measured with an electronic balance (Model BP211D, Beijing Sartorius Balance Co., China) by weighing the water driven out by the micro-pump within a defined period of time [15,16]. The waste outlet of the chip was blocked, and the inlet was connected with a plastic conduit addressing the water in a vessel which was positioned on the weighing pan of the balance. The water was covered by silicon oil to avoid evaporation during the operation. The micro-pump was placed in a sealed container of constant temperature. The temperature in the sealed container was controlled with a halogen lamp and a PID digital temperature controller (Model NE-6412–2, Shanghai Yatai Instruments, China).

2.3. Cell culture

The human colorectal carcinoma cell line CCL-187 was kindly donated by the Key Lab of Cell Biology of Ministry of Public Health, China Medical University. The CCL-187 cells were routinely maintained in Dulbecco's modified Eagle's medium (DMEM, Invitrogen, USA) supplemented with 10% fetal bovine serum (FBS), 100 U mL^{-1} penicillin (Amresco, USA) and 100 mg mL^{-1} streptomycin (Amresco, USA). The cells were cultured in a glass culture flask, which was placed in a CO_2 incubator at 37 °C with 5% CO_2. The CCL-187 cells were detached from the culture flask using 0.25% trypsin in a 1.0 mM EDTA solution when they have grown to approximately 80% confluence. The cells were centrifuged in a centrifugal tube at 1000 rpm for 5 min and then suspended in the culture medium at a cellular density of ca. 5×10^5 cells mL^{-1}.

2.4. Cell culture in the microfluidic chip

The microfluidic device was entirely sterilized by autoclaving at 120 °C for 20 min. Afterwards, the semi-membrane was immersed in deionized water to avoid degradation. Deionized water and the phosphate buffer solution (PBS) were autoclaved at 120 °C for 20 min, and the PVP solution at 115 °C for 15 min.

The torque-actuated valve kept closed in the following operations. The channel for cell culture was pre-coated at 37 °C first with poly-L-lysine (PLL, Sigma, USA) for 0.5 h, and then with 0.01% sterile rat-tail collagen for another 0.5 h. The coated channel was rinsed for 10 min with sterile water driven by a syringe pump (Model MD-1001, Bioanalytical Systems, Inc., USA) at a flow rate of 20 μL min^{-1}. It was thereafter washed with PBS for 10 min, and then filled with culture medium. After the cell suspension was introduced into the microfluidic channel using a syringe pump at a flow rate of 5 μL min^{-1}, the microfluidic device was put into the incubator for 6 h to ensure attachment of the cells onto the channel. Subsequently, water was introduced into the outer chamber, and osmotic driving reagent into the inner chamber. The channel inlet was connected to a vessel containing the culture medium, and the inner chamber outlet was connected to a waste bottle. Then the torque-actuated valve was opened, and the osmosis pump began working and continuously delivering the culture medium for the perfusion cell culture. Thereafter, the microfluidic device was placed again into the incubator. The osmotic driving reagent was refreshed every two days in order to keep long-term stability of the flow rate during the cell culture process. The osmotic driving reagent was completely refreshed to avoid any potential variation of its concentration. In addition, the connection between the microchannel and the osmotic pump was controlled by using torque-actuated valve in order to minimize the introduction of air bubbles into the system. All these procedures were carried out under sterile conditions.

2.5. Immunostaining on the microchip

The CCL-187 cells were cultured in the osmotic micro-pump integrated microchip for 24 h in the incubator, and identified by means of in situ indirect immunofluorescence staining. The osmotic micro-pump was employed for driving fluids in the following process. First, PBS was continuously driven into the microchannel for 5 min followed by introducing 1% bovine serum albumin (BSA, Sigma, USA) for 30 min to block the cells. Afterwards, the chip was placed in the incubator, and the first antibody, i.e., the murine monoclonal antibody ND-1 (diluted 1:100, provided by the China Medical University), was successively loaded for 1 h, and then the channel was washed with PBS for 10 min. The second antibody, i.e., the fluorescein-conjugated AffiniPure goat anti-mouse IgG (diluted 1:100, Zhongshan Goldenbridge Biotechnology Co. Ltd., Beijing, China), was used to incubate cells in the incubator for 1 h. The PBS solution was delivered once again for 10 min to wash away the free antibody, and the chip was right away placed on the platform of a fluorescence microscope (NMIL, Leica Co., USA) to obtain the fluorescent images of the cells excited by blue light.

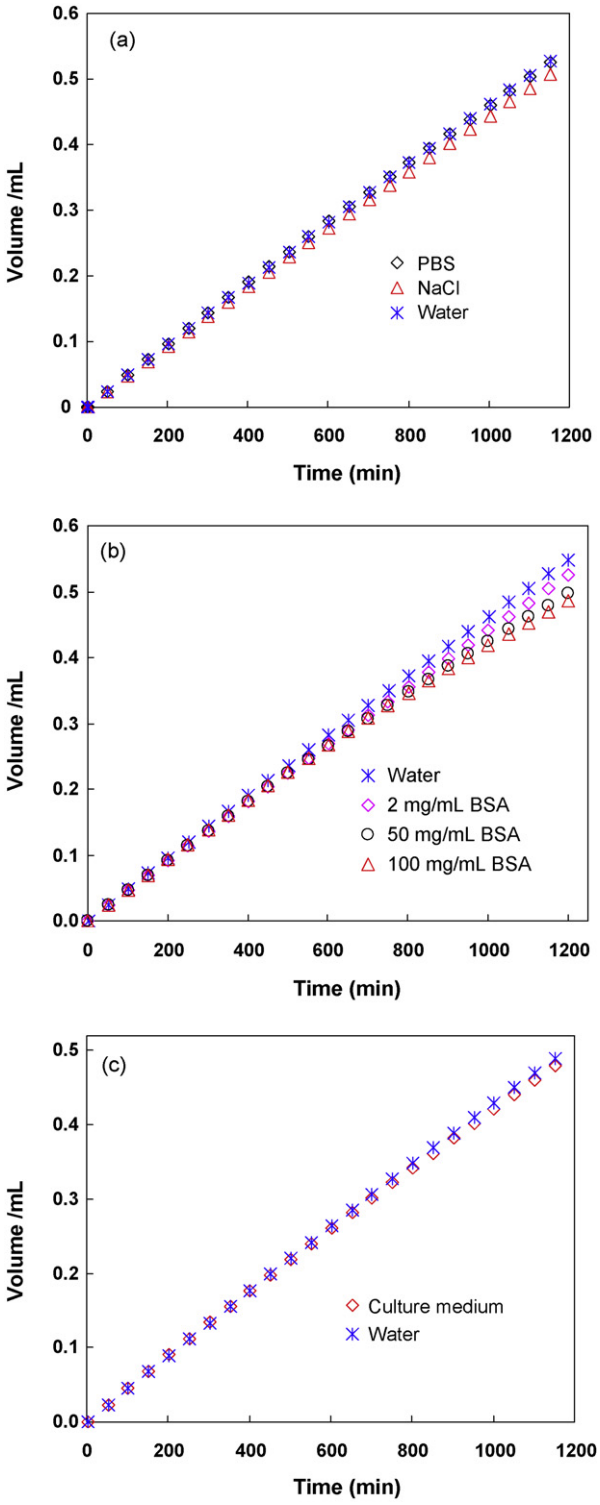


Fig. 2. Effects of the solutes on the flow rate. (a) The flow rates of 1.0 mol L^{-1} NaCl solution, 0.1 mol L^{-1} PBS and water; (b) the flow rates of 2 mg mL^{-1}, 50 mg mL^{-1} and 100 mg mL^{-1} BSA solutions; (c) the flow rates of culture medium and water. Osmotic area: 1.96 cm^2; PVP solution: 50 mg mL^{-1}; temperature: 25 ± 1 °C.

Table 1
Effects of the temperature on the flow rate of water at a PVP concentration of 50 mg mL^{-1} and an osmotic area (evaporation area) of 1.47 cm^2.

Temperature (°C)	22	27	32	37	42
Average flow rate (μL min^{-1})	0.36 ± 0.02	0.36 ± 0.01	0.38 ± 0.01	0.38 ± 0.01	0.39 ± 0.02
RSD (n = 15)	5.7%	3.8%	2.1%	1.9%	3.8%

Table 2
Effects of osmotic area (evaporation area) on the flow rate of water at 25 ± 1 °C with 50 mg mL^{-1} PVP as the osmotic reagent.

Evaporation area (cm^2)	0.49	0.98	1.47	1.96
Average flow rate (μL min^{-1})	0.13 ± 0.01	0.25 ± 0.01	0.36 ± 0.02	0.48 ± 0.01
RSD (n = 30)	1.1%	1.8%	4.4%	2.3%

3. Results and discussion

3.1. Considerations in the design of the osmotic micro-pump

Osmosis is a passive transport mechanism of fluids for achieving concentration balance in living organisms. Osmotic pressure π is expressed by van't Hoff's law [37]:

$$\pi = CRT \quad (1)$$

where C is the mole concentration of the solute, R the gas constant and T the absolute temperature. The volumetric flow rate of water across the membrane is thus given as [38]:

$$J = K \cdot A \cdot (\sigma \Delta\pi - \Delta P) \quad (2)$$

where J is the volumetric flow rate, K the water permeability of the membrane, A the effective area, $\Delta\pi$ the difference in osmotic pressure across the membrane, ΔP the difference in hydrostatic pressure, and σ the osmotic reflection coefficient of the membrane, which depends only on the characteristics of the membrane and the type of solute. When pure water is used as the driven fluid, $\Delta\pi$ is equal to the osmotic pressure of the solute. By neglecting the hydrostatic pressure difference between the two sides of the membrane, Eq. (2) can be simplified as

$$J = K \cdot A \cdot \sigma CRT \quad (3)$$

Eqs. (1) and (3) respectively indicated the dependence of the osmotic pressure on the concentration of the osmotic reagent and the dependence of flow rate on the concentration of the osmotic reagent. An ideal membrane, which is selectively permeable to water molecules but not to the osmotic driving reagent, should have an unity value of σ [38]. Thus the volumetric flow rate J will depend on the temperature, the concentration of the driving reagent and the characteristics of the semi-permeable membrane, e.g., area and permeability. In the present work, the water in the outer chamber moved across the semi-permeable membrane into the inner chamber containing osmotic reagent, resulting in a decrease of the pressure in the outer chamber, which actuated the flow of the fluid through the channel towards the micro-pump.

In a previous work, we reported a simple osmotic micro-pump consists of two reservoirs sandwiching a semi-permeable membrane [35], where an external tube was necessary to connect the micro-pump and the driven fluid. In the present work, the osmotic micro-pump was integrated on the chip without any additional tube, which reduced significantly the dead volume of the system and increased the reliability of the micro-pump.

According to the osmosis theory, the area of the semi-permeable membrane is one of the main factors affecting the flow rate. The chambers were designed into cylinder shape in order to obtain a larger membrane area for a micro-pump of limited dimension. The semi-permeable membrane is clamped around the outside of the inner chamber wall by plastic pipe. The effective area of the membrane can be adjusted by the number of holes drilled on the wall and the pipe, and the flow rate can be easily regulated by controlling the number of holes on the inner chambers.

The opening and closing of the micro-pump was facilitated by controlling a torque-actuated valve integrated on the chip. The valve was closed during the process of channel pretreatment and cell perfusion in order to avoid contamination of the water in the outer chamber.

3.2. Effects of various factors on the flow rate

The flow rates of the integrated osmotic micro-pump were investigated by varying the temperature, the osmotic reagent PVP concentration and the effective osmotic area. Table 1 illustrated a virtually constant flow rate within a temperature range of 22–42 °C, by fixing an osmotic area of 1.47 cm^2 and a PVP concentration of 50 mg mL^{-1}. It is obvious that only a slight variation of 0.03 μL min^{-1} was observed with a 20 °C increase of temperature, this well indicated the suitability of the integrated osmotic micro-pump for routine laboratories operated at ambient temperature.

Table 2 showed a linear dependence of the flow rate of water in the microchannel on the osmotic area, which is in accordance with that indicated in Eq. (3). This observation provides a convenient approach for the regulation of the flow rate by simply adjusting the effective area of the osmotic micro-pump.

PVP was chosen as the osmotic reagent because of its favorable biocompatibility and selective molecular weight. In the present work, PVP with molecular weight of 30,000 was used and the effect of its concentration within a range of 20–200 mg mL^{-1} on the flow rate of water was summarized in Table 3. A gradual increase of the flow rate was recorded with the increase of the PVP concentration. This phenomenon offers a further scheme for the control of the fluidic flow rate in the microchannel by varying the concentration of the PVP solution.

In practice, different fluids are drawn via the microchannel into the outer chamber. Consequently, various solutes dissolved in the fluid might cause fluctuation of the flow rate. The effect of the solutes on the flow rate was thus investigated by driving fluids containing solutes with different molecular weights,

Table 3
Effects of PVP concentration on the flow rate of water at 25 ± 1 °C and an osmotic area (evaporation area) of 1.47 cm^2.

PVP concentration (mg mL^{-1})	20	50	100	150	200
Average flow rate (μL min^{-1})	0.16 ± 0.01	0.36 ± 0.02	0.52 ± 0.02	0.66 ± 0.05	0.78 ± 0.03
RSD (n = 30)	2.9%	4.4%	3.1%	6.8%	4.0%

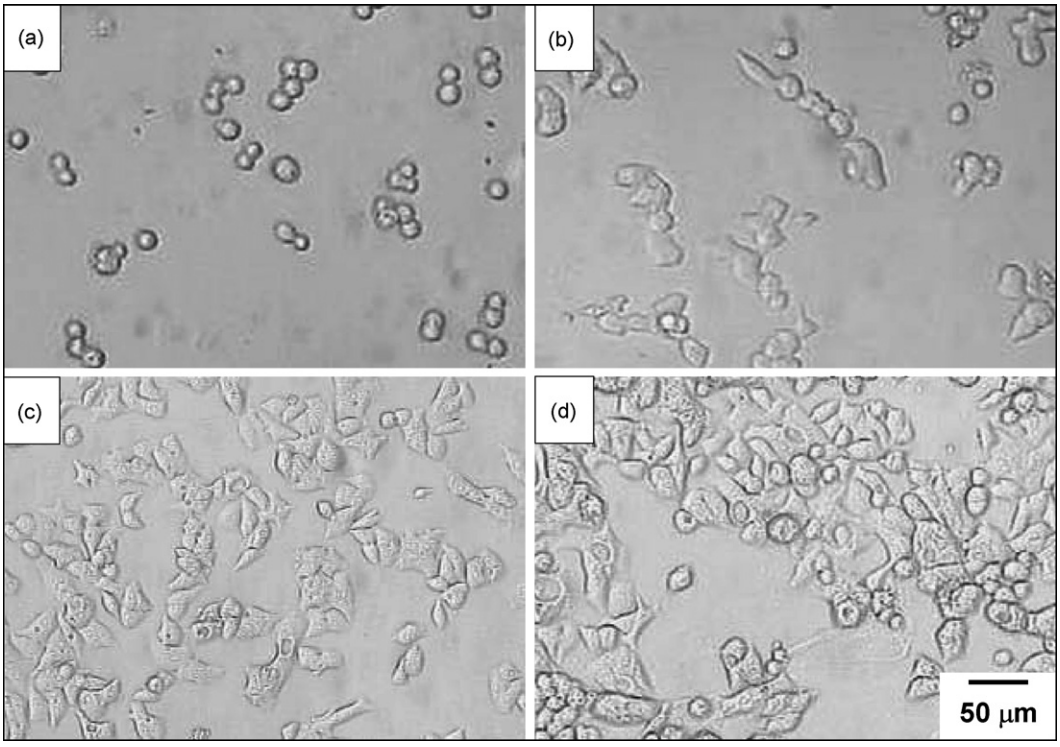


Fig. 3. Microscope images of CCL-187 cells cultured in the microfluidic chip. (a) 0 h; (b) 48 h; (c) 72 h; (d) 96 h.

e.g., sodium chloride, PBS and bovine serum albumin (BSA). The flow rates of 1.0 mol L^{-1} NaCl solution and 0.1 mol L^{-1} PBS were 0.44 μL min^{-1} and 0.46 μL min^{-1}, respectively by using an osmotic area of 1.96 cm^2, a PVP solution of 50 mg mL^{-1} and a temperature of 25 ± 1 °C. These flow rates are almost identical with that of water, i.e., 0.48 μL min^{-1} (Fig. 2a). This might be because that the diameters of inorganic ions are much smaller than the pore size of the membrane (MWCO 3500 of the dialysis membrane), and thus facilitates their free traveling through the membrane. Fig. 2b illustrated that the flow rate of BSA solution at 2 mg mL^{-1} was virtually constant in comparison with that of water. However, the increase of BSA concentration results in a gradual decline of the flow rate, and an obvious decrease was encountered after running the micro-pump for 10 h by continuously driving BSA solution of 50 mg mL^{-1} or 100 mg mL^{-1}. In fact, the molecular weight of BSA is larger than the MWCO of the membrane. As a result, the BSA molecules were blocked and accumulated outside the membrane, and thus a reverse osmotic pressure was generated, leading to a decline of the flow rate. The reverse osmotic pressure is negligible at a lower BSA concentration, while it becomes much stronger at higher BSA concentration and the drop of the flow rate has to be carefully considered in such a case. In the following cell culture experiment, the culture medium containing a total protein of 3.8 mg mL^{-1} was driven by the osmotic micro-pump. Similar trends of flow rate variation of the culture medium and water were observed within 20 h (Fig. 2c).

It is demonstrated that the osmotic micro-pump was capable of providing pulse-free flow in the absence of external power supply. When using a 100 mg mL^{-1} PVP solution as driving reagent, an osmotic area of ca. 0.98 cm^2 and a temperature of 25 ± 1 °C, an average flow rate of 0.33 μL min^{-1} was obtained within 50 h, with a precision of 4.3% RSD (n = 51). A maximum output pressure of 11.1 kPa for the micro-pump was achieved by using a measurement procedure reported previously [15]. The micro-pump can thus be operated for a long period by regularly replacing the osmotic reagent in the inner chamber.

3.3. Continuous perfusion cell culture

Microfluidic perfusion culture provides an opportunity to keep the culture environment more stable compared with traditional static culture mode. Continuous nutrition supply and waste removal were realized by means of the flow of fluids. In the present work, the microfluidic chip integrated with an osmotic micropump was used for cell perfusion culture. It is convenient to put the entire microfluidic system into the incubator. Considering that the PDMS cover layer has favorable gas permeability, it thus provides sufficient oxygen for keeping the cells in good condition during the culture process. The culture channel was pre-coated with poly-L-lysine and rat-tail collagen for enhancing the cell attachment on the channel surface.

The flow rate of the culture medium drawn into the culture channel by the osmotic micro-pump has obvious effect on the culture of cells, and its effect was investigated within a range of 0.2–0.9 μL min^{-1}. The results indicated that at a lower flow rate of 0.2 μL min^{-1}, very tiny bubbles were observed in the microchannel after 24 h. Owing to the gas-permeable property of PDMS and lower air pressure in the fluid, air bubbles might occur and grow until they occlude the microchannel and impede the flow as described in the literature [39]. In this respect, the bubbles would exert stress on the cells. Therefore, the elimination of bubbles is required. In our system, the bubbles can be readily carried away by the continuous flow of the culture medium at a flow rate of higher than 0.4 μL min^{-1}, while a large part of the cells cultured on the channel wall will be flushed away by increasing the flow rate up to 0.9 μL min^{-1}. Therefore, a flow rate of 0.4 μL min^{-1} for the culture medium was employed in the practice. This corresponds to a fluid shear stress of 0.37 dyn cm^{-2} on the cells attached on the channel [25,39]. This shear stress is significantly lower than those acceptable for common mammal cells [23].

The system was used successfully for continuous perfusion culture of CCL-187 cells. Fig. 3(a–d) showed the cell growth in the microchannel during a culture period of four days, indicating the

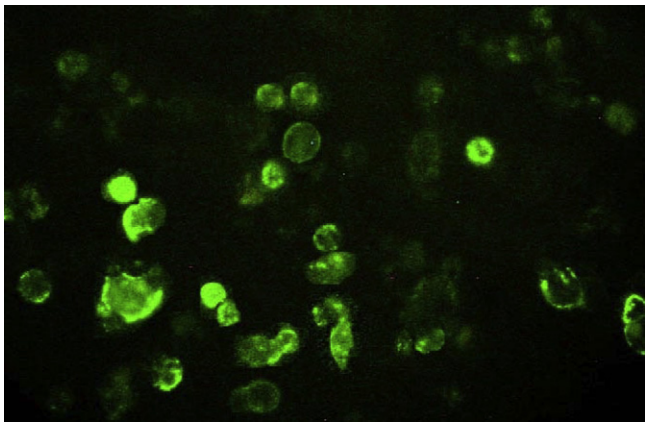


Fig. 4. Immunofluorescence micrograph of the CCL-187 cells labeled by ND-1.

attachment of the CCL-187 cells onto the channel wall followed by their elongation and gradual proliferation. The normal morphology and 95% viability of the cells cultured for four days were demonstrated by a Trypan Blue exclusion test. Further experiments illustrated that after seven days, the cells cultured began to aggregate with the increase of the number of cells in a limited channel space.

3.4. In situ cell immunostaining

An in situ indirect immunofluorescent staining was carried out to demonstrate the characteristics of CCL-187 cells cultured in the microfluidic device. The murine monoclonal antibody ND-1 has specific binding activity to the tumor-associated antigen LEA expressed in human colorectal carcinoma, which has high selectivity on well identifying colon carcinoma [40]. Fluorescein-conjugated affinipure goat anti-mouse IgG used as the second antibody has a maximal absorption at 492 nm. As shown in Fig. 4, the irradiated cells emitted green fluorescence via blue light excitation, showing a clear evidence for the remaining of the characteristics of the cultured CCL-187 cells. In the immunostaining experiment, the integrated osmotic micro-pump was desirable to deliver all the solutions by taking the advantages of less reagent consumption and minimized potential contamination.

4. Conclusions

A novel microfluidic chip integrating an osmosis-based micro-pump was developed.

The distinct features of the osmotic micro-pump include its simple structure by consisting of only two sealed chambers and a semi-permeable membrane, and the flow rate could be readily regulated by controlling the osmotic area of the membrane or the concentration of the osmotic reagent. In addition, the micro-pump is characterized by low fabrication cost, small dimensions and free operations without the need of external power supply. In comparison with the micro-pump based on evaporation effect, the osmotic micro-pump is independent on the humidity, and it is suitable for long-term operation at a steady flow rate by regularly refresh the osmotic reagent.

The feature of the osmotic micro-pump integrated microfluidic chip was illustrated by on-chip perfusion culture of the human colorectal carcinoma cell line CCL-187 with the osmotic micro-pump as fluidic driving device. The present osmotic micro-pump also has the potential in other applications, e.g., microfluidic flow injection system and fluid driving in parallel channels.

Acknowledgements

Financial supports from the Natural Science Foundation of China (Nos. 20675012, 20805004, key project No. 20635010, National Science Fund for Distinguished Young Scholars No. 20725517 and Major International Joint Research Project 20821120292) and the 973 program (2007CB714503) are highly appreciated.

References

[1] D.J. Harrison, A. Manz, Z.H. Fan, H. Luedi, H.M. Widmer, Anal. Chem. 64 (1992) 1926.
[2] A. Nisar, N. Afzulpurkar, B. Mahaisavariya, A. Tuantranont, Sens. Actuators B 130 (2008) 917.
[3] M. Koch, N. Harris, A.G.R. Evans, N.M. White, A. Brunnschweiler, Sens. Actuators A 70 (1998) 98.
[4] M.A. Unger, H.P. Chou, T. Thorsen, A. Scherer, S.R. Quake, Science 288 (2000) 113.
[5] T. Thorsen, S.J. Maerkl, S.R. Quake, Science 298 (2002) 580.
[6] R. Zengerle, J. Ulrich, S. Kluge, M. Richter, A. Richter, Sens. Actuators A 50 (1995) 81.
[7] D.C. Duffy, H.L. Gillis, J. Lin, N.F. Sheppard, G.J. Kellogg, Anal. Chem. 71 (1999) 4669.
[8] M. Wiklund, C. Gunther, R. Lemor, M. Jager, G. Fuhr, H.M. Hertz, Lab Chip 6 (2006) 1537.
[9] I.M. Lazar, B.L. Karger, Anal. Chem. 74 (2002) 6259.
[10] A.V. Lemoff, A.P. Lee, Sens. Actuators B 63 (2000) 178.
[11] W.B. Du, Q. Fang, Q.H. He, Z.L. Fang, Anal. Chem. 77 (2005) 1330.
[12] R. Khnouf, D.J. Beebe, Z.H. Fan, Lab Chip 9 (2009) 56.
[13] B.S. Cho, T.G. Schuster, X.Y. Zhu, D. Chang, G.D. Smith, S. Takayama, Anal. Chem. 75 (2003) 1671.
[14] D. Juncker, H. Schmid, U. Drechsler, H. Wolf, M. Wolf, B. Michel, N. de Rooij, E. Delamarche, Anal. Chem. 74 (2002) 6139.
[15] Y.X. Guan, Z.R. Xu, J. Dai, Z.L. Fang, Talanta 68 (2006) 1384.
[16] Z.R. Xu, C.H. Zhong, Y.X. Guan, X.W. Chen, J.H. Wang, Z.L. Fang, Lab Chip 8 (2008) 1658.
[17] T.Y. Cath, A.E. Childress, M. Elimelech, J. Membr. Sci. 281 (2006) 70.
[18] G.C. Randall, P.S. Doyle, Proc. Natl. Acad. Sci. U.S.A. 102 (2005) 10813.
[19] Y.C. Su, L.W. Lin, A.P. Pisano, J. Microelectromech. S. 11 (2002) 736.
[20] Y.C. Su, L.W. Lin, J. Microelectromech. S. 13 (2004) 75.
[21] T. Deem, P.M. Ligrani, D. Tower, J. Connelly, Sens. Actuators A 136 (2007) 742.
[22] M. Ehwald, H. Adleff, P. Geggier, R. Ehwald, Biotechnol. Bioeng. 94 (2006) 37.
[23] L. Kim, Y.C. Toh, J. Voldman, H. Yu, Lab Chip 7 (2007) 681.
[24] S.M. Ong, C. Zhang, Y.C. Toh, S.H. Kim, H.L. Foo, C.H. Tan, D. van Noort, S. Park, H. Yu, Biomaterials 29 (2008) 3237.
[25] L. Kim, M.D. Vahey, H.Y. Lee, J. Voldman, Lab Chip 6 (2006) 394.
[26] E. Leclerc, B. David, L. Griscom, B. Lepioufle, T. Fujii, P. Layrolle, C. Legallaisa, Biomaterials 27 (2006) 586.
[27] X.Y. Zhu, L.Y. Chu, B.H. Chueh, M.W. Shen, B. Hazarika, N. Phadke, S. Takayama, Analyst 129 (2004) 1026.
[28] A. Tourovskaia, X. Figueroa-Masot, A. Folch, Lab Chip 5 (2005) 14.
[29] W. Gu, X.Y. Zhu, N. Futai, B.S. Cho, S. Takayama, Proc. Natl. Acad. Sci. U.S.A. 101 (2004) 15861.
[30] N. Futai, W. Gu, J.W. Song, S. Takayama, Lab Chip 6 (2006) 149.
[31] R. Gomez-Sjoberg, A.A. Leyrat, D.M. Pirone, C.S. Chen, S.R. Quake, Anal. Chem. 79 (2007) 8557.
[32] M.H. Wu, S.B. Huang, Z.F. Cui, Z. Cui, G.B. Lee, Sens. Actuators B 129 (2008) 231.
[33] T. Glawdel, C.L. Ren, Mech. Res. Commun. 36 (2009) 75.
[34] J.Y. Park, C.M. Hwang, S.H. Lee, S.H. Lee, Lab Chip 7 (2007) 1673.
[35] C.G. Yang, Z.R. Xu, Proceedings of the 1st Shenyang International Colloquium on Microfluidics, Shenyang, China, 2007, p. 92.
[36] D.B. Weibel, M. Kruithof, S. Potenta, S.K. Sia, A. Lee, G.M. Whitesides, Anal. Chem. 77 (2005) 4726.
[37] J.J. Feher, G.D. Ford, Advan. Physiol. Educ. 268 (1995) 10.
[38] F. Theeuwes, S.I. Yum, Ann. Biomed. Eng. 4 (1976) 343.
[39] G.M. Walker, H.C. Zeringue, D.J. Beebe, Lab Chip 4 (2004) 91.
[40] R. Bleday, J. Song, E.S. Walker, B.F. Salcedo, P. Thomas, R.E. Wilson, L.B. Chen, G. Steele Jr., Cancer 57 (1986) 433.

Talanta 80 (2010) 1094–1101

Contents lists available at ScienceDirect

Talanta

journal homepage: www.elsevier.com/locate/talanta

Poly(malachite green) at nafion doped multi-walled carbon nanotube composite film for simple aliphatic alcohols sensor

Yogeswaran Umasankar, Arun Prakash Periasamy, Shen-Ming Chen*

Department of Chemical Engineering and Biotechnology, National Taipei University of Technology, No. 1, Section 3, Chung-Hsiao East Road, Taipei 106, Taiwan, ROC

ARTICLE INFO

Article history:
Received 20 May 2009
Received in revised form 15 August 2009
Accepted 24 August 2009
Available online 31 August 2009

Keywords:
Multiwall carbon nanotubes
Malachite green
Composite film
Modified electrodes
Electrocatalysis
Methanol
Ethanol
Propanol

ABSTRACT

Conductive composite film which contains nafion (NF) doped multi-walled carbon nanotubes (MWCNTs) along with the incorporation of poly(malachite green) (PMG) has been synthesized on glassy carbon electrode (GCE), gold and indium tin oxide (ITO) electrodes by potentiostatic methods. The presence of MWCNTs in the composite film (MWCNTs–NF–PMG) enhances surface coverage concentration (Γ) of PMG to ≈396%, and increases the electron transfer rate constant (k_s) to ≈305%. Similarly, electrochemical quartz crystal microbalance study reveals the enhancement in the deposition of PMG at MWCNTs-NF film. The surface morphology of the composite film deposited on ITO electrode has been studied using scanning electron microscopy (SEM) and scanning tunneling microscopy (STM). These two techniques reveal that the PMG incorporated on MWCNTs–NF film. The MWCNTs–NF–PMG composite film also exhibits promising enhanced electrocatalytic activity towards the simple aliphatic alcohols such as methanol, ethanol and propanol. The electroanalytical responses of analytes at NF–PMG and MWCNTs–NF–PMG films were measured using both cyclic voltammetry (CV) and differential pulse voltammetry (DPV). From electroanalytical studies, well defined voltammetric peaks have been obtained at MWCNTs–NF–PMG composite film for methanol, ethanol and propanol at Epa = 609, 614 and 602 mV respectively. The sensitivity of MWCNTs–NF–PMG composite film towards methanol, ethanol and propanol in CV technique are 0.59, 0.36 and 0.92 $\mu A\,mM^{-1}\,cm^{-2}$ respectively, which are higher than NF–PMG film. Further, the sensitivity values obtained using DPV are higher than the values obtained using CV technique.

© 2009 Elsevier B.V. All rights reserved.

1. Introduction

Electropolymerization is a simple but powerful method in targeting selective modification of different type electrodes with desired matrices. However, the materials on the matrices do not possess peculiar properties when compared with those materials which are chemically synthesized by traditional methods. The electroactive polymers and carbon nanotubes (CNTs) matrices have received considerable attraction in recent years. Numerous conjugated polymers have been electrochemically synthesized for their application in the fabrication of chemical and biochemical sensor devices [1–3]. These conjugated polymers for sensor devices exhibit interesting enhancement in the electrocatalytic activity towards the oxidation or reduction of several biochemical and inorganic compounds [4] where, some of the functional groups in polymers will act as catalyst [5–7]. In this article, the word "enhanced electrocatalytic activity" could be explained as both; increase in peak current and lower overpotential [8]. The wide variety of applications of matrices made of CNTs for the detection of inorganic and bioorganic compounds such as IO_3^-, ascorbic acid, etc., have already been reported in the literature [9–12].

Even though the electrocatalytic activity of conjugated polymers and CNTs matrices individually shows good results; some properties like mechanical stability, sensitivity for different techniques, and electrocatalysis for multiple compound detections are found to be poor. To overcome this difficulty, new studies have been developed in the past decade for the preparation of composite films composed of both CNTs and conjugated polymers. The rolled-up graphene sheets of carbon exhibit π-conjugative structure with highly hydrophobic surface. This unique property of the CNTs allows them to interact with organic aromatic compounds through π–π electronic and hydrophobic interactions to form new structures [13,14]. There were past attempts in the preparation of composite and sandwiched films made of polymer adsorbed on CNTs, and used them for electrocatalytic studies such as, selective detection of dopamine in the presence of ascorbic acid [15]. The sandwiched films were also been used in the designing of nanodevices with the help of noncovalent adsorption, electrodeposition, etc. [16].

Among these conjugated polymers, a group of them representing azines such as phenazines, phenothiazines, phenoxazines, etc., have a wide use in bioelectrochemistry as redox indica-

* Corresponding author. Tel.: +886 2270 17147; fax: +886 2270 25238.
E-mail address: smchen78@ms15.hinet.net (S.-M. Chen).

0039-9140/$ – see front matter © 2009 Elsevier B.V. All rights reserved.
doi:10.1016/j.talanta.2009.08.034

tors and mediators [17]. The electropolymerization of azine group compounds are usually performed by anodic oxidation in acidic medium [18,19]. Similar to these azine dyes, malachite green (MG) is also a dye compound which has an open but ionized structure, and hence the resulting polymer is promising in exhibiting interesting features like fast rate of charge transfer and ion transport and nice catalytic ability towards small bio-molecules [20]. Previous studies reported poly(malachite green) (PMG) can be synthesized by electrochemical polymerization of malachite green. These studies also reported the growth mechanism of PMG along with the electrochemical, FT-IR and UV–vis studies [20,21]. The chemical structures of MG and PMG are given in Scheme 1.

The oxidation of simple aliphatic alcohols to the corresponding products is an important transformation in organic synthesis. Recently, from the environmental point of view, various catalytic methods using oxidants have been reported [22–25]. Among these, methanol has been widely used in the direct methanol fuel cells at lower temperatures, where the methanol oxidation was done with the help of metal oxide catalysts [26,27]. Similarly, ethanol is the most common substance consumed by humans and it is frequently a contributory factor in a variety of accidents. Further, the determination of ethanol is very important to control the fermentation processes in some industrial fields, which includes the pulp, food and beverage industries. The measurement of ethanol is particularly needed for quality control of beer, wines and spirits [28–30]. The oxidation of propanol is also an important transformation in laboratory and industrial synthetic chemistry, which could be used as important intermediate for the synthesis of chemicals [31]. Various methods have been reported for the determination of simple aliphatic alcohols with the help of different techniques [28,32]. Within these several methods of determination, the electrochemical methods have more advantages over the others in sensing the analytes [33–35].

The literature survey reveals that there were no previous attempts made for the synthesis of composite film composed of CNTs, nafion (NF) and PMG for the use in sensor application. In this article, we report a novel composite film made of multi-walled carbon nanotubes (MWCNTs) which have been dispersed in NF, and incorporated with PMG. MWCNTs–NF–PMG composite film's characterization, enhancement in functional properties, peak current and electrocatalytic activity have also been reported along with its application in the determination of methanol, ethanol and propanol. The film formation processing involves the modification of electrodes with uniformly well dispersed MWCNTs–NF, and which is then modified with PMG.

2. Experimental

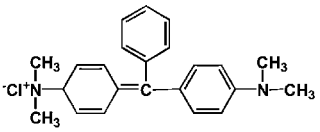
2.1. Materials

PMG, NF, MWCNTs (OD = 10–20 nm, ID = 2–10 nm and length = 0.5–200 μm), methanol, ethanol and propanol obtained from Aldrich and Sigma–Aldrich were used as received. All other chemicals used were of analytical grade. The preparation of aqueous solution was done with twice distilled deionized water. Solutions were deoxygenated by purging with pre-purified nitrogen gas. The pH 1.0 aqueous solution was prepared from H_2SO_4. The pH 4.0 aqueous solution was prepared from 0.01 M potassium hydrogen phthalate (KHP) solution, which was then added to 0.1 M Na_2SO_4 solution (1:1).

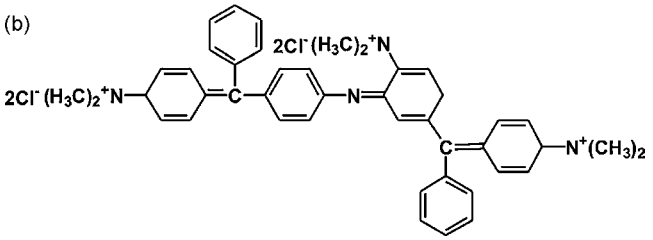
2.2. Apparatus

Cyclic voltammetry (CV), electrochemical quartz crystal microbalance (EQCM) and differential pulse voltammetry (DPV) were performed using analytical system models CHI-405, CHI-400 and CHI-750 potentiostats respectively. A conventional three-electrode cell assembly consisting of an Ag/AgCl reference electrode and a Pt wire counter electrode were used for the electrochemical measurements. The working electrode was glassy carbon electrode (GCE) modified with PMG, NF, NF–PMG or MWCNT–NF–PMG composite films. In these experiments, all the potentials are reported vs. Ag/AgCl reference electrode. The working electrode for EQCM measurements was an 8 MHz AT-cut quartz crystal coated with a gold electrode. The diameter of the quartz crystal is 13.7 mm; the gold electrode diameter is 5 mm. The morphological characterizations of the films were examined by means of scanning electron microscopy (SEM) (Hitachi S-3000H) and scanning tunneling microscopy (STM) (Being Nano-Instruments CSPM4000). All the measurements were carried out at 25 ± 2 °C.

(a)



(b)



Scheme 1. Chemical structure of MG and PMG.

2.3. Preparation of MWCNT–NF–PMG composite electrodes

The important challenge in the preparation of MWCNTs was the difficulty in dispersing them in to a homogeneous solution. Generally, the dispersion of CNTs has been carried out by physical (milling) and chemical methods (covalent and noncovalent functionalization). These methods cause damage to CNTs and add impurities to it [36,37]. To overcome these drawbacks, hydrophobic interaction between NF and MWCNTs has been used for our experiments [38,39]. Briefly, 5% NF prepared by adding 2 ml of NF in 10 ml water, which was used to disperse 10 mg of MWCNTs. The uniform dispersion of MWCNTs was obtained by 6 h ultrasonication of MWCNTs–NF mixture.

Before starting each experiment, GCEs were polished by BAS polishing kit with 0.05 μm alumina slurry, then rinsed and then ultrasonicated in double distilled deionized water. The GCEs studied were uniformly coated with 10 μl of MWCNTs–NF mixture (0.13 mg cm^{-2} of MWCNTs) and dried at room temperature. Then, MG (0.5 mM) was electropolymerized on the MWCNT–NF modified GCE, which was present in pH 4 KHP aqueous solution. The electropolymerization was performed by consecutive CVs over a suitable potential range of −0.3 to 1.4 V. Then, the modified MWCNT–NF–PMG electrode was carefully washed with double distilled deionized water. The concentrations of homogeneously dispersed MWCNTs–NF were exactly measured using micro-syringe.

3. Results and discussions

3.1. Electropolymerization of PMG at MWCNTs–NF composite film

The electropolymerization of MG (0.5 mM) using electrochemical oxidation on unmodified, MWCNT–NF modified, and only

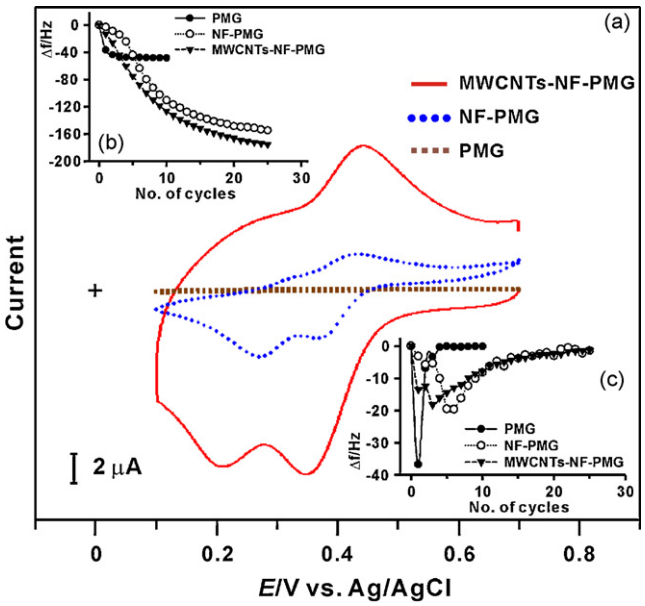


Fig. 1. (a) CVs of GCE modified from PMG, NF–PMG and MWCNTs–NF–PMG films in KHP solution, scan rate at 20 mV s^{-1}. EQCM frequency change responses recorded together with consecutive CVs (PMG formation on NF, MWCNTs–NF modified and unmodified gold electrodes, potential between −0.2 and 1.4 V; scan rate: 100 mV s^{-1}), where (b) shows the gross change in the frequency shift vs. scan cycles, whereas (c) shows the change between each consecutive scans.

NF modified GCEs have been performed for the preparation and comparative studies of PMG, NF–PMG and MWCNT–NF–PMG composite films. On subsequent cycles, the redox peaks corresponding to PMG have found growing in all these films (figures not shown). This above result indicates that during the cycles, deposition of PMG takes place on the electrode surface. However, there are no peaks representing PMG appears at bare GCE. The optimized number of cycles for the deposition of PMG at MWCNTs–NF modified GCE using CV technique is 25. This optimization is done by observing the monomer oxidation current at Epa = 0.99 V, where the Ipa decreases during cycling and the oxidation peak disappears after 25 cycles. These above prepared three films (PMG, NF–PMG and MWCNT–NF–PMG) have been characterized using various electrochemical techniques in pH 4.0 KHP or pH 1.0 aqueous solution. Before transferring the films in to aqueous solution for other electrochemical characterizations, the prepared films have been washed carefully in deionized water to remove the loosely attached non-polymerized MG monomer on the modified GCE. Fig. 1(a) shows the reversible and irreversible redox couples of PMG, NF–PMG and MWCNT–NF–PMG modified GCEs. The corresponding CVs have been measured at 20 mV s^{-1} scan rate in the potential range of 0.7–0.1 V. Among these three films, the $E^{0\prime}$ values of both redox couples for MWCNT–NF–PMG composite film are at 395 mV (Redox-I) and 210 mV (Redox-II) vs. Ag/AgCl in KHP aqueous solution. Among these two redox couples, the $E^{0\prime}$ at 395 mV is the redox reaction of PMG and $E^{0\prime}$ at 395 mV could be the redox reaction of MG's dimer. The Epa, Epc and Ipc values of PMG at various film modified electrodes are given in Table 1. Interestingly the values in Table 1 reveal, MWCNT-NF modified GCE has higher polymerizing current for PMG than at other modified or unmodified GCEs. Further, the presence of MWCNTs in the MWCNT–NF–PMG composite film increases the overall back ground current. These above results represent more deposition of PMG on MWCNT-NF modified GCE than on other GCEs.

Table 2
Surface coverage concentration (Γ) of various species present in PMG at different modified electrodes obtained using CV studies.

Modified electrode	Type of film	Γ (pmol cm^{-2})	
		Redox-I	Redox-II
GCE	[a]-PMG	490	145
	[b]-PMG	2430	177
Gold	[a]-PMG	139	20.5
	[b]-PMG	229	115
ITO	[b]-PMG	675	–

[a] PMG electropolymerized on NF modified electrode.
[b] PMG electropolymerized on MWCNTs–NF modified electrode.

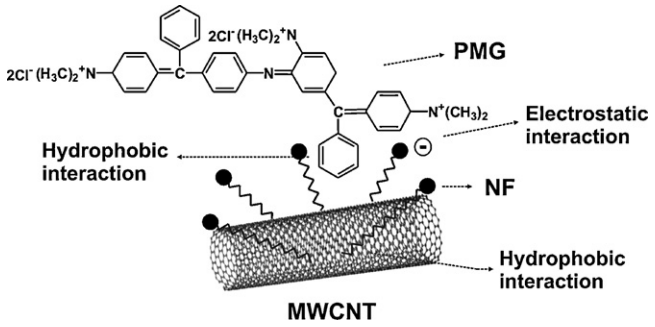
The increase in deposition of PMG in the presence of MWCNTs is evident with the active surface coverage concentration (Γ) given in Table 2 where, Γ of both species (Redox-I and -II) of PMG enhances at MWCNTs-NF film modified GCE when comparing at only NF and bare GCE. The calculated values from the same table shows that, MWCNTs enhances Γ of PMG by 15 pmol cm^{-2} μg^{-1}; and the overall increase in percentage of PMG Γ at MWCNTs film is 396%. In these Γ calculations, the number of electrons involved in PMG redox reactions is assumed as two. The comparison of PMG, NF–PMG and MWCNT–NF–PMG films on gold and indium tin oxide (ITO) electrodes are given in supplementary materials, which show that MWCNTs catalyze the PMG electropolymerization similar in that of GCE. However, the comparison of Epa and Epc values in Table 1 shows that the Redox-I of MWCNT–NF–PMG composite film at GCE and gold electrode is highly reversible than at ITO electrode, where ΔE at GCE and gold electrode is 93.2 mV and ITO electrode is 198 mV vs. Ag/AgCl. In these above experiments too, MWCNT-NF modified electrodes show higher polymerizing current for PMG than at other modified or unmodified electrodes, which are consistent with the Ipc and Γ values given in Tables 1 and 2, respectively. The possible interactions between MWCNTs, NF and PMG present in the composite film are given in Scheme 2, where the interaction between MWCNTs and NF is hydrophobic, and the interaction between NF and PMG is both hydrophobic and electrostatic interactions.

The MG electropolymerization is further confirmed using EQCM experiments, which have been carried out by modifying the gold in electrochemical quartz crystal with uniformly coated MWCNTs-NF or NF and then dried at 40 °C. The increase in voltammetric peak

Table 1
Epa, Epc and Ipc values of redox reactions of PMG at various modified electrodes present in pH 4.0 KHP aqueous solution.

Modified Electrodes		Epa (mV)	Epc (mV)		Ipc (μA)	
Electrodes	Films	Redox-I	Redox-I	Redox-II	Redox-I	Redox-II
GCE	[a]-PMG	434.5	366.9	270.8	−3.33	−1.41
	[b]-PMG	441.4	348.2	210.0	−10.42	−1.53
Gold	[a]-PMG	453.1	332.6	234.5	−0.53	−0.09
	[b]-PMG	441.4	348.2	214.9	−2.83	−0.33
ITO	[b]-PMG	433.5	235.5	–	−11.64	–

[a] PMG electropolymerized on NF modified electrode.
[b] PMG electropolymerized on MWCNTs–NF modified electrode.



Scheme 2. Possible interactions between MWCNTs, NF and PMG present in MWCNTs–NF–PMG composite film.

current of PMG redox couple and the frequency decrease (or mass increase) are found to be consistent with the growth of PMG film on MWCNTs-NF or NF modified gold electrode (figures not shown). These results too show that the obvious deposition potential has started between −0.2 and 1.4 V. From the frequency change, the change in the mass of composite film at the quartz crystal can be calculated by the Sauerbrey equation (1), however 1 Hz frequency change is equivalent to 1.4 ng cm^{-2} of mass change [40,41]. The mass change during PMG incorporation on MWCNTs-NF modified, NF modified and unmodified gold electrodes for total cycles are 246, 217 and 68 ng cm^{-2} respectively.

$$\text{Mass change } (\Delta m) = -\tfrac{1}{2}(f_0^{-2})(\Delta f)A(K\rho)^{1/2} \quad (1)$$

where f_0 is the oscillation frequency of the crystal; Δf is the frequency change; A, the area of gold disk; K, the shear modulus of the crystal; ρ, the density of the crystal. Fig. 1(b) indicates the variation of frequency with increase of scan cycles for PMG at bare gold electrode, NF modified and MWCNTs–NF modified gold electrodes. Fig. 1(c) indicates every cycle of frequency with the increase of scan cycles for PMG at bare gold electrode, NF modified and MWCNTs–NF modified gold electrodes. These EQCM results prove that the deposition of PMG on the MWCNTs-NF film is more stabilized and more homogeneous than on the NF modified or bare gold electrodes.

3.2. Surface morphological studies of MWCNTs–NF, NF–PMG and MWCNTs–NF–PMG composite films

Three different films MWCNTs–NF, NF–PMG and MWCNTs–NF–PMG have been prepared on ITO electrodes with similar conditions and similar potential as that of GCE, and were characterized using SEM. Comparison of Fig. 2(a–c) reveals significant morphological difference between all the three films. The top views of nanostructures in Fig. 2(a) on the ITO electrode surface show uniformly deposited homogeneously dispersed MWCNTs in NF. The NF–PMG film in Fig. 2(b) shows elongated beads of NF and PMG deposited over ITO electrode surface. However, there are no bead formations if only NF coated over ITO, instead a porous NF film is formed (image not shown). Similarly, a uniform thin film with no morphology is formed for only PMG deposited over ITO electrode surface. The MWCNTs–NF–PMG composite film in Fig. 2(c) shows that plateaus of PMG formed over MWCNTs–NF film. Further, in Fig. 2(c) MWCNTs are not obviously visible as in Fig. 2(a), because PMG deposition covered over MWCNTs. These results in Fig. 2(c) could be explained as the increase in deposition of PMG over MWCNTs–NF, which creates plateaus instead of beads and covers over MWCNTs. The same three film modified ITO electrodes have been used to measure STM topography images shown in Fig. 3(a–c). The higher magnification (7 μm × 7 μm) of STM images than that of SEM images reveals that in Fig. 3(a)

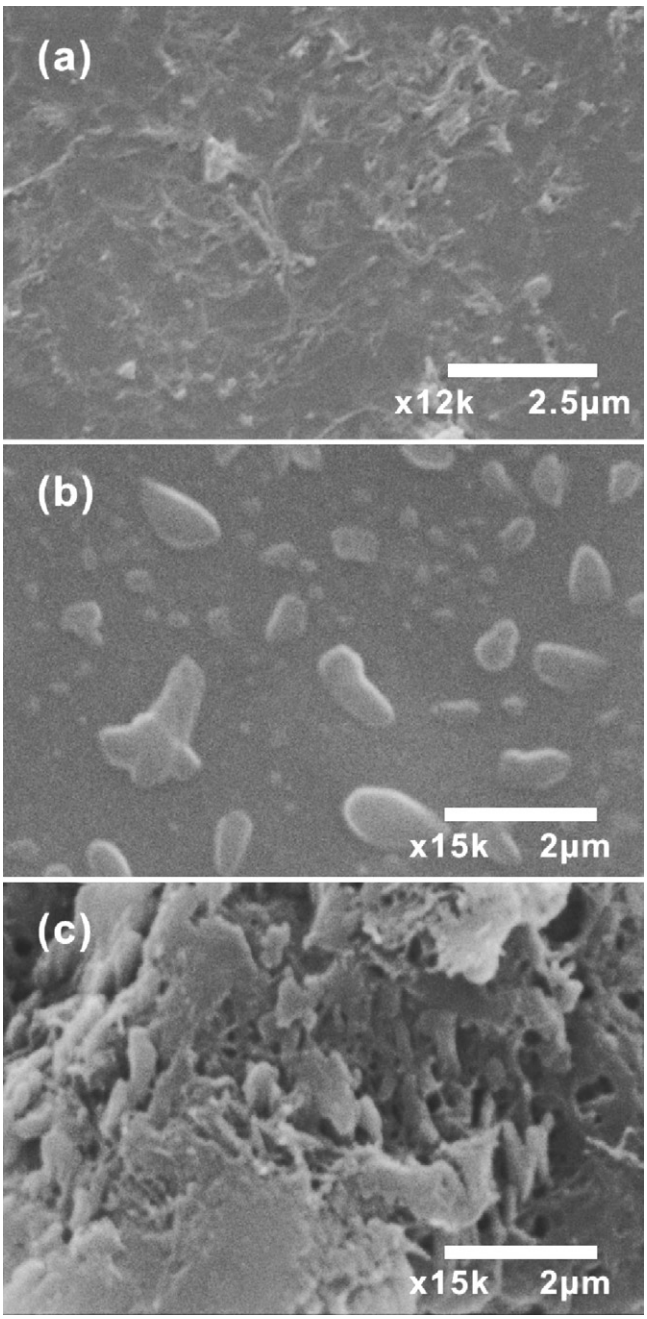


Fig. 2. SEM images of (a) MWCNTs–NF, (b) NF–PMG and (c) MWCNTs–NF–PMG films.

well dispersed MWCNTs in NF coated over ITO electrode. Similarly in Fig. 3(b), formation of nanometer sized grains in between PMG beads and in Fig. 3(c) more deposition of PMG over MWCNTs. These above details are not clearly visible in SEM images. Comparison of Fig. 3(a) with Fig. 3(c) also reveals that higher concentration of PMG deposited on MWCNTs modified ITO electrode, which is consistent with the Γ values shown in Table 2. Further, the thicknesses of MWCNTs–NF, NF–PMG and MWCNTs–NF–PMG obtained using STM results are 120, 70 and 180 nm respectively. These values too show MWCNTs–NF–PMG has higher thickness than the other two films, which is due to the presence of MWCNTs–NF covered under PMG film. These SEM and STM results reveal the coexistence of MWCNTs–NF and PMG in the composite film.

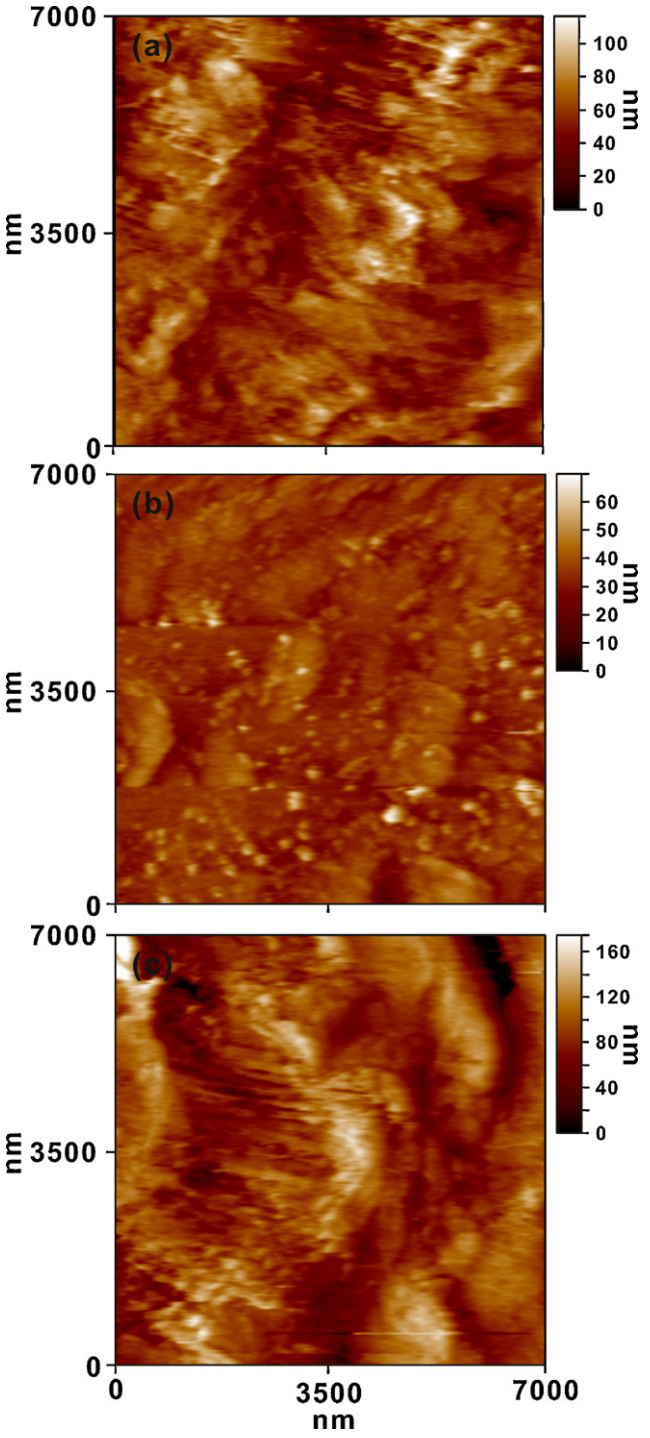


Fig. 3. STM images of (a) MWCNTs–NF, (b) NF–PMG and (c) MWCNTs–NF–PMG films.

3.3. Electrochemical and stability studies of MWCNTs–NF–PMG composite film

The CVs of NF–PMG and MWCNTs–NF–PMG composite films on GCE in pH 4.0 KHP aqueous solution at different scan rates show that the anodic and cathodic peak currents of the composite film's redox couple, which increases linearly with the increase of scan rates (figure not shown). The ratio of Ipa/Ipc for both the film demonstrates that the redox process is not controlled by diffusion. However, the ΔEp of each scan rate reveals that the peak separation of both film's redox couple increases as the scan rate increase. From the slope values of ΔE vs. log scan rate, by assuming the value of $\alpha \approx 0.5$, number of electrons involved as two, the electron transfer rate constant (k_s) has been calculated using Eq. (2) based on Laviron theory [42].

$$\log k_s = \alpha \log(1-\alpha) + (1-\alpha)\log \alpha - \log\left(\frac{RT}{nF\upsilon}\right) - \alpha(1-\alpha)nF\frac{\Delta E}{2.3RT} \quad (2)$$

In Eq. (2), the scan rate and ΔE values are in unit volts. The k_s values obtained are 0.12 and 0.49 s^{-1} for NF–PMG and MWCNTs–NF–PMG modified GCEs respectively. From these k_s values, the increase in ability of electron transfer between the electrode surface and PMG in presence of MWCNTs is ≈305%. The reproducibility of the obtained k_s values for both NF–PMG and MWCNTs–NF–PMG films have also been studied, where the relative standard deviation (RSD) values obtained are 5% ($n = 7$) for NF–PMG and 7% ($n = 7$) for MWCNTs–NF–PMG films. These results show the enhancement in functional property of MWCNTs–NF–PMG composite film in the presence of MWCNTs.

Fig. 4(a) shows the CVs of MWCNTs–NF–PMG on GCE obtained in pH 4.0 KHP aqueous solution, then washed with deionized water, and was transferred to various pH aqueous buffer solutions without the presence of MG. The results show that the film is highly stable in the pH range between 1 and 13. The values of Epa and Epc depend on the pH value of buffer solution. The inset in Fig. 4(a) shows the formal potential of MWCNTs–NF–PMG plotted over the pH range from 1 to 13. The response shows a slope of −65 mV pH^{-1}, which is close to that given by Nernstian equation for equal number of electrons and protons transfer. All these above results show the enhancement in functional properties of MWCNTs–NF–PMG composite film due to the presence of both PMG and MWCNTs.

The enhancement in stability of PMG in the presence of MWCNTs has been studied, and the percentage of degradation of MWCNTs–NF–PMG and NF–PMG calculated using an equation given in the previous literature [43]. The experimental results in Fig. 4(b) indicates the successive 280 min cycling (scan rate 20 mV s^{-1}) applied over a potential range of 0.1–0.7 V on MWCNTs–NF–PMG and NF–PMG in pH 4.0 KHP aqueous solution. The CVs have been recorded at the interval of 30 min each; from which the values of Ipc were noted and plotted against time. From these results it is clear that after 220 min the response of MWCNTs–NF–PMG becomes constant with time and cycling, indicating it is a stable film. However, the NF–PMG continues to degrade upon cycling. The amount of degradation after 280 min cycling for MWCNTs–NF–PMG and NF–PMG are 29% and 63% respectively. From this above result, the percentage of decrease in degradation of PMG in presence of MWCNTs is about 34% for 280 min cycling. Similar enhancements in CNTs with polymer composite properties when comparing CNT or polymer alone were already reported in the literature [44]. Repeatability of the stability studies have also been carried out at 280 min cycling for MWCNTs–NF–PMG film, where the RSD value obtained is 6% ($n = 3$).

3.4. Electroanalytical responses of methanol, ethanol and propanol at MWCNTs–NF–PMG composite film

The MWCNTs–NF–PMG composite film has been synthesized on GCE at similar conditions as given in Section 2. Then the composite film modified electrode has been washed carefully in deionized water and transferred to pH 1 aqueous solution for the electrocatalysis studies of methanol, ethanol and propanol. All the CVs have been recorded at the constant time interval of 1 min with nitrogen purging before the start of each experiments. Fig. 5(a–c) shows the electrocatalytic oxidation of methanol, ethanol and propanol

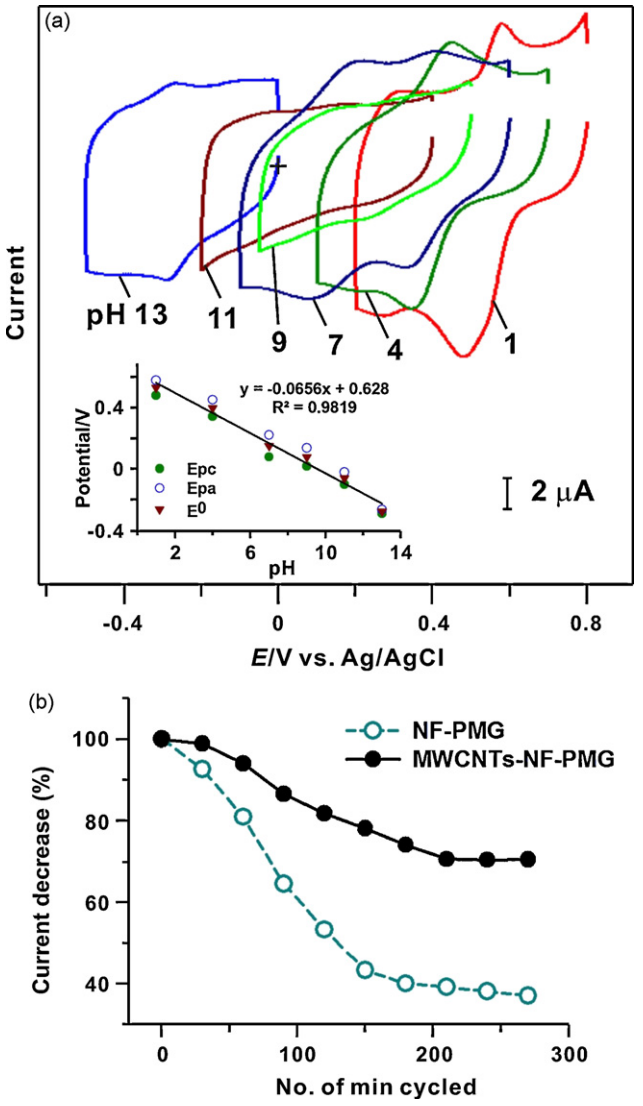


Fig. 4. (a) CVs of the MWCNTs–NF–PMG film synthesized using pH 4.0 KHP solution on GCE and transferred to various pH solutions. The insets shows Epa, Epc and the formal potential vs. pH from 1 to 13 (slope = −65 mV/pH), where the slope is almost nearer to Nernstian equation for equal number of electrons and protons transfer. (b) Number of minutes cycled vs. current decrease in (%) for NF–PMG and MWCNTs–NF–PMG films, which shows that MWCNTs–NF–PMG is highly stable when comparing with NF–PMG.

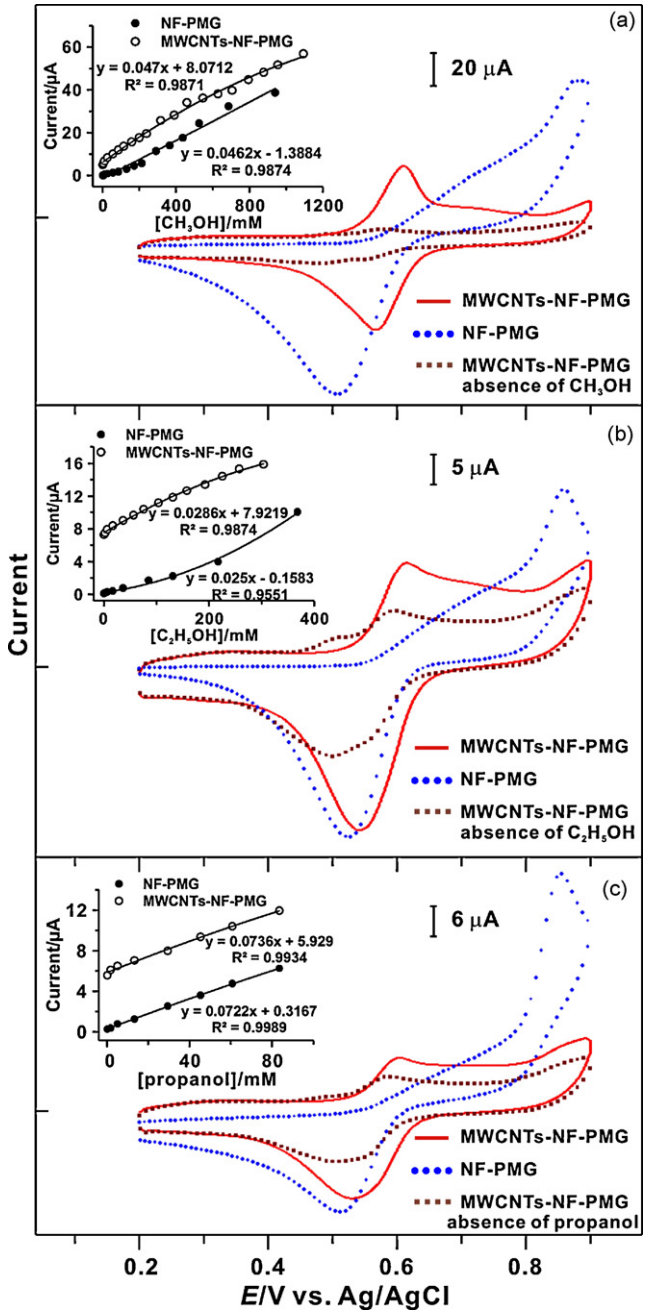


Fig. 5. The CVs in (a) is the comparison of 0 and 0.96 M of methanol at MWCNTs–NF–PMG with that of 0.96 M of methanol at NF–PMG in pH 1 aqueous solution; (b) is the comparison of 0 and 0.3 M of ethanol at MWCNTs–NF–PMG with that of 0.3 M of ethanol at NF–PMG at similar conditions and (c) is the comparison of 0 and 0.08 M of propanol at MWCNTs–NF–PMG with that of 0.08 M of propanol at NF–PMG at similar conditions. The insets in (a–c) show the plot of current vs. different concentration of methanol, ethanol and propanol respectively at MWCNTs–NF–PMG and NF–PMG. In these results, the analytes show higher electrocatalytic activity at MWCNTs–NF–PMG film.

at NF–PMG and MWCNTs–NF–PMG composite films respectively; scan rate 20 mV s^{-1}. In all the sections of Fig. 5, electrocatalytic activity at MWCNTs–NF–PMG composite films are shown with (higher concentration) and without the presence of analytes. However for NF–PMG film, only higher concentrations of analytes are shown, where the highest concentration of analytes are 0.96 M for methanol, 0.3 M for ethanol and 0.08 M for propanol. The CVs for MWCNTs–NF–PMG exhibits respective redox couples as discussed in Section 3.1 in the absence of analytes, and upon addition of analytes, new growth in the oxidation peak of respective analytes appears at Epa = 609, 614 and 602 mV for methanol, ethanol and propanol respectively. These peak currents show that electrocatalytic oxidation of all three analytes takes place at PMG redox couple. The methanol, ethanol and propanol oxidation at MWCNTs–NF–PMG composite film could be given by the following equations.

$$CH_3OH \rightarrow CO_{ads} + 4H^+ + e^- \quad (3)$$

$$C_2H_5OH \rightarrow CH_4 + CO_{ads} + 2H^+ + (1/2)e^- \quad (4)$$

$$(CH_3)_2CHOH \rightarrow C_2H_4 + CO_{ads} + 4H^+ + e^- \quad (5)$$

$$CO_{ads} + H_2O \rightarrow CO_2 + 2H^+ + 2e^- \quad (6)$$

In these above electrocatalysis experiments, an increase in concentration of methanol (3.12 mM) to (1.1 M), ethanol (2.06 mM) to (0.3 M) and propanol (1.65 mM) to (83.4 mM) simultaneously produces a linear increase in the oxidation peak currents of the respective analytes with good film stability at NF–PMG and

MWCNTs–NF–PMG films. The anodic peak currents are linear with the concentration of analytes. It is obvious that MWCNTs–NF–PMG shows higher electrocatalytic activity for the analytes. More specifically, the enhanced electrocatalytic activity of MWCNTs–NF–PMG can be defined in terms of both the lower in overpotential and higher peak current than that of NF–PMG film. These results can be observed from the Ipa and Epa values of various analytes, which are given in supplementary materials. Where, the increase in peak current and decrease in over potential; both are considered as the electrocatalytic activity [8]. The calculated limit of detections (LOD) at NF–PMG is 10.7 mM for methanol, 8 mM for ethanol and 1.8 mM for propanol. Similarly, the LOD at MWCNTs–NF–PMG is 8.3 mM for methanol, 5.1 mM for ethanol and 0.6 mM for propanol.

From the slopes of linear calibration curves, the sensitivities of NF–PMG and MWCNTs–NF–PMG composite film modified GCEs have been calculated. The sensitivity values of NF–PMG are 0.58 $\mu A\,mM^{-1}\,cm^{-2}$ for methanol, 0.31 $\mu A\,mM^{-1}\,cm^{-2}$ for ethanol and 0.90 $\mu A\,mM^{-1}\,cm^{-2}$ for propanol. Similarly, the sensitivity values of MWCNTs–NF–PMG are 0.59 $\mu A\,mM^{-1}\,cm^{-2}$ for methanol, 0.36 $\mu A\,mM^{-1}\,cm^{-2}$ for ethanol and 0.92 $\mu A\,mM^{-1}\,cm^{-2}$ for propanol. The correlation coefficients of linear calibration curves at NF–PMG are 0.9874, 0.9551 and 0.9989 for methanol, ethanol and propanol respectively. Similarly, correlation coefficients obtained at MWCNTs–NF–PMG are 0.9871, 0.9874 and 0.9934 for methanol, ethanol and propanol respectively. It is obvious that the sensitivity of MWCNTs–NF–PMG film is higher for all the three analytes when compared with NF–PMG film. The reproducibility of NF–PMG and MWCNTs–NF–PMG films on GCE has also been studied for all the three analytes using CV technique (36 h; $n = 4$). The results show that there is an enhancement in reproducibility for all the three analytes in presence of MWCNTs at the film. The values are 38% enhancement for methanol, 47% enhancement for ethanol and 62% enhancement for propanol in presence of MWCNTs. The overall view of these results, clearly reveal that MWCNTs–NF–PMG composite film is efficient than NF–PMG film for methanol, ethanol and propanol detection.

3.5. DPV studies of methanol, ethanol and propanol at MWCNTs–NF–PMG composite film

Fig. 6(a–c) shows the DPVs which have been obtained for methanol, ethanol and propanol at MWCNTs–NF–PMG composite film respectively. The DPVs have been recorded at a constant time interval of 1 min with nitrogen purging before the start of each experiment. They demonstrate that the calibration curves for the three analytes are linear for a wide range of concentrations; for methanol from 1.55 to 95.44 mM, ethanol from 3.09 to 72.48 mM and for propanol from 6.12 to 48.98 mM. The calculated LODs are 0.6 mM for methanol, 0.1 mM for ethanol and 6.9 mM for propanol. Similarly, the limit of quantifications (LOQ) is 2 mM for methanol, 0.4 mM for ethanol and 21.1 mM for propanol. From the slopes of linear calibration curves, the sensitivity of MWCNTs–NF–PMG composite film modified GCE towards all three analytes have been calculated. The sensitivity values are 19.62 $\mu A\,mM^{-1}\,cm^{-2}$ for methanol, 3.75 $\mu A\,mM^{-1}\,cm^{-2}$ for ethanol and 4.06 $\mu A\,mM^{-1}\,cm^{-2}$ for propanol. The correlation coefficients of linear calibration curves are 0.9786, 0.9933 and 0.9988 for methanol, ethanol and propanol respectively. When comparing these sensitivity values with the values obtained in CV studies reveals that DPV technique possess higher sensitivity than CV technique. These results show that DPV technique is more efficient than CV technique for methanol, ethanol and propanol detection at MWCNTs–NF–PMG composite film.

The interference of ascorbic acid (AA) and uric acid (UA) during methanol determination has been studied using DPV technique. In these experiments, methanol concentration has been kept constant

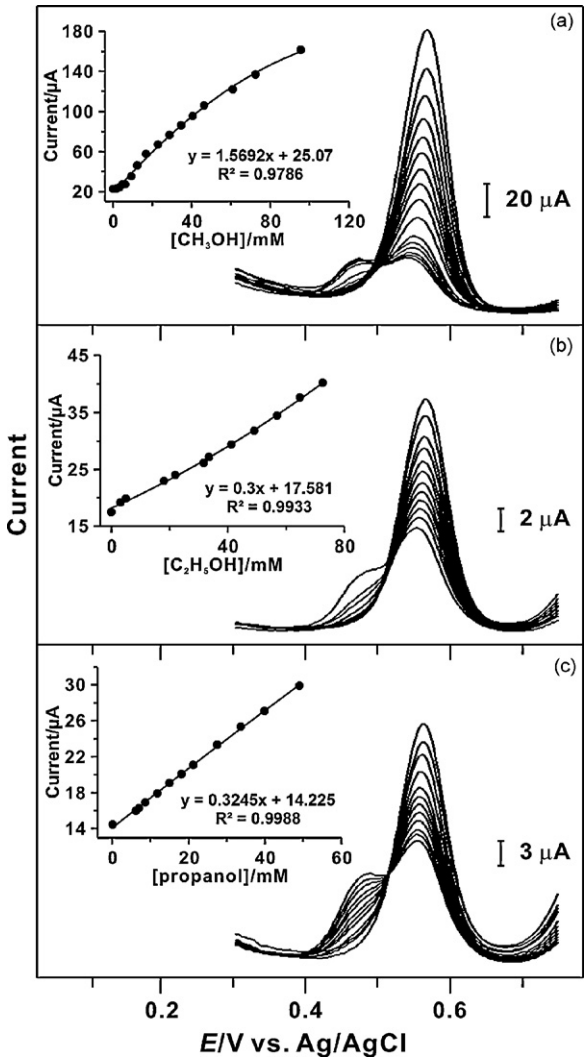


Fig. 6. DPVs of MWCNTs–NF–PMG film shown in (a) various concentrations of methanol (0.0; 1.55–95.44 mM); (b) various concentrations of ethanol (0.0; 3.09–72.48 mM) and (c) various concentrations of propanol (0.0; 6.12–48.98 mM) in pH 1 aqueous solution. The insets in (a–c) show the plot of current vs. different concentration of methanol, ethanol and propanol at MWCNTs–NF–PMG film respectively.

(2.3 mM) and the concentrations of AA and UA have been increased from 24.9 μM to 0.9 mM. The results reveal that there is no obvious change in the methanols' peak current during the addition of AA and UA. The change in peak current of methanol during the addition of AA is 2% with RSD = 1% ($n = 6$), whereas for UA it is 5% with RSD <1% ($n = 6$). Similarly, the interference of glycerin during ethanol determination has also been studied, where the ethanol concentration kept at 2.6 mM, and the concentration change of glycerin is from 1.3 to 87.2 mM. Results show that the change in ethanol peak current during the addition of glycerin is 9% with RSD = 2% ($n = 6$). The above data reveal that MWCNTs–NF–PMG composite film could be used for the efficient determination of simple aliphatic alcohols.

3.6. Analysis of methanol, ethanol and propanol containing real samples

The performance of MWCNTs–NF–PMG composite film modified GCE has been tested by applying it to the determination of the analytes present in real samples. The technique used for the determination was DPV. In these experiments, the real sample of methanol is green (scar removal and ache treatment agent),

Table 3
Electroanalytical results of simple aliphatic alcohol determination present in real samples using DPV in pH 1.0 aqueous solution at MWCNTs–NF–PMG composite film modified GCE.

Sample	Added (mM)	Found (mM)	Recovery (%)	RSD (%)	LOQ (mM)
Methanol (scar removal and ache treatment agent)	3.10	2.94	94.5	3	8.6
	4.64	4.74	102.1		
	9.23	9.00	97.4		
Ethanol (white wine)	0.56	0.58	97.0	2	8.3
	9.73	9.55	101.8		
	10.77	10.70	100.6		
Propanol (protan tablets)	16.02	15.98	100.2	2	3.5
	24.97	25.05	99.7		
	33.85	32.73	103.3		

ethanol is white wine, and propanol is protan tablets. The scar removal and ache treatment agent's labeled composition is triclosan, hyaluronic acid, collagen, glycerine, catechins, etc., along with methanol as solvent. Similarly, the white wine's labeled composition is 13% ethanol, and the protan tablet's labeled composition is 70% propanol. The scar removal and ache treatment agent was obtained from Stylecosmo International, France. The white wine is the product of Domaine de Pourthce, France, and the protan tablets were obtained from Protan, USA. In these experiments, the concentration added, concentration found, recovery, RSD and LOQ are given in Table 3. These above results show that MWCNTs–NF–PMG composite film is efficient for methanol, ethanol and propanol detection.

4. Conclusions

We developed a novel composite material using MWCNTs, NF and PMG at GCE, gold and ITO electrodes, which are more stable in pH 1–4 aqueous solutions. The developed MWCNTs–NF–PMG composite film for the electrocatalysis combines the advantages of ease of fabrication, high reproducibility and sufficient long-term stability. The EQCM results confirmed the incorporation of PMG on MWCNTs–NF modified gold electrode. The SEM and STM results have shown the difference between MWCNTs–NF, NF–PMG and MWCNTs–NF–PMG composite films morphology. Further, it has been found that MWCNTs–NF–PMG composite film has excellent functional properties along with good electrocatalytic activity towards methanol, ethanol and propanol. The experimental methods of CV and DPV with MWCNTs–NF–PMG composite film sensor integrated into the GCE which is presented in this article provide an opportunity for qualitative and quantitative characterization. Therefore, this work establishes and illustrates in principle and potential, a simple and novel approach for the development of a voltammetric sensor which is based on modified GCE.

Acknowledgements

This work was supported by the National Science Council and the Ministry of Education of Taiwan (Republic of China).

Appendix A. Supplementary data

Supplementary data associated with this article can be found, in the online version, at doi:10.1016/j.talanta.2009.08.034.

References

[1] C.P. McMahon, G. Rocchitta, S.M. Kirwan, S.J. Killoran, P.A. Serra, J.P. Lowry, R.D. O'Neill, Biosens. Bioelectron. 22 (2007) 1466.
[2] H.A. Al Attar, A.P. Monkman, J. Phys. Chem. B 111 (2007) 12418.
[3] K. Pu, B. Liu, Biosens. Bioelectron. 24 (2009) 1067.
[4] I. Becerik, F. Kadirgan, Synth. Met. 124 (2001) 379.
[5] T. Selvaraju, R.R. Ramaraj, J. Electroanal. Chem. 585 (2005) 290.
[6] M. Mao, D. Zhang, T. Sotomura, K. Nakatsu, N. Koshiba, T. Ohsaka, Electrochim. Acta 48 (2003) 1015.
[7] M. Yasuzawa, A. Kunugi, Electrochem. Commun. 1 (1999) 459.
[8] C.P. Andrieux, O. Haas, J.M. SavGant, J. Am. Chem. Soc. 108 (1986) 8175.
[9] J. Wang, M. Musameh, Anal. Chim. Acta 511 (2004) 33.
[10] H. Cai, X. Cao, Y. Jiang, P. He, Y. Fang, Anal. Bioanal. Chem. 375 (2003) 287.
[11] A. Erdem, P. Papakonstantinou, H. Murphy, Anal. Chem. 78 (2006) 6656.
[12] H. Beitollahi, M.M. Ardakani, H. Naeimi, B. Ganjipour, J. Solid State Electrochem. 13 (2009) 353.
[13] Q. Li, J. Zhang, H. Yan, M. He, Z. Liu, Carbon 42 (2004) 287.
[14] J. Zhang, J.K. Lee, Y. Wu, R.W. Murray, Nano Lett. 3 (2003) 403.
[15] C. Deng, J. Chen, M. Wang, C. Xiao, Z. Nie, S. Yao, Biosens. Bioelectron. 24 (2009) 2091.
[16] R.J. Chen, Y. Zhang, D. Wang, H. Dai, J. Am. Chem. Soc. 123 (2001) 3838.
[17] A.A. Karyakin, E.E. Karyakina, H.L. Schmidt, Electroanalysis 11 (1999) 149.
[18] A.G. MacDiarmid, J.C. Chiang, A.G. Richter, A. Epstein, Synth. Met. 18 (1987) 285.
[19] R. Mazeikiene, G. Niaura, O. Eicher-Lorka, A. Malinauskas, Vib. Spectrosc. 47 (2008) 105.
[20] Q. Wan, X. Wang, X. Wang, N. Yang, Polymer 47 (2006) 7684.
[21] X. Wang, N. Yang, Q. Wan, X. Wang, Sens. Actuators B 128 (2007) 83.
[22] H. Zhao, S. Bennici, J. Shen, A. Auroux, J. Mol. Catal. A: Chem. 309 (2009) 28.
[23] R. Irie, T. Katsuki, Chem. Rec. 4 (2004) 96.
[24] T. Mallat, A. Baiker, Chem. Rev. 104 (2004) 3037.
[25] M.J. Schultz, M.S. Sigman, Tetrahedron 62 (2006) 8227.
[26] A. Bauer, E.L. Gyenge, C.W. Oloman, J. Power Sources 167 (2007) 281.
[27] L.M. Huang, T.C. Wen, J. Power Sources 182 (2008) 32.
[28] S. Engelhard, H.G. Lohmannsroben, F. Schael, Appl. Spectrosc. 58 (2004) 1205.
[29] M. Rocchia, A.M. Rossi, G. Zeppa, Sens. Actuators B 123 (2007) 89.
[30] N.G. Patel, S. Meier, K. Cammann, G.C. Cheminitius, Sens. Actuators B: Chem. 75 (2001) 101.
[31] S.S. Stahl, Angew. Chem. Int. Ed. 43 (2004) 3400.
[32] E. Segal, R. Tchoudakov, M. Narkis, A. Siegmann, Y. Wei, Sens. Actuators B 104 (2005) 140.
[33] E. Akyilmaz, E. Dinckaya, Talanta 53 (2000) 505.
[34] M. Revenga-Parra, T. Garcia, E. Lorenzo, F. Pariente, Sens. Actuators B 130 (2008) 730.
[35] A.G.V. de Prada, N. Pena, C. Parrado, A.J. Reviejo, J.M. Pingarron, Talanta 62 (2004) 896.
[36] N. Darsono, D. Yoon, J. Kim, Appl. Surf. Sci. 254 (2008) 3412.
[37] J. Chen, A.M. Rao, S. Lyuksyutov, M.E. Itkis, R.E. Smalley, R.C. Haddon, J. Phys. Chem. B 105 (2001) 2525.
[38] Y.C. Tsai, S.C. Li, J.M. Chen, Langmuir 21 (2005) 3653.
[39] G.A. Rivas, S.A. Miscoria, J. Desbrieres, G.D. Barrera, Talanta 71 (2007) 270.
[40] S.M. Chen, M.I. Liu, Electrochim. Acta 51 (2006) 4744.
[41] S.M. Chen, C.J. Liao, V.S. Vasantha, J. Electroanal. Chem. 589 (2006) 15.
[42] E. Laviron, J. Electroanal. Chem. 101 (1979) 19.
[43] A. Mohadesi, M.A. Taher, Sens. Actuators B: Chem. 123 (2007) 733.
[44] J. Wang, T. Dai, Yarlagadda, Langmuir 21 (2005) 9.

Talanta 80 (2010) 1102–1109

Contents lists available at ScienceDirect

Talanta

journal homepage: www.elsevier.com/locate/talanta

Comparison between ordinary least squares regression and weighted least squares regression in the calibration of metals present in human milk determined by ICP-OES

Rosilene S. Nascimento[a], Roberta E.S. Froes[b], Nilton O.C. e Silva[b], Rita L.P. Naveira[b], Denise B.C. Mendes[c], Waldomiro B. Neto[a], José Bento B. Silva[a,*]

[a] Departamento de Química, Universidade Federal de Minas Gerais, Belo Horizonte 31270-901, MG, Brazil
[b] Fundação Ezequiel Diaz, FUNED, Belo Horizonte, MG, Brazil
[c] Maternidade Odete Valadares, Belo Horizonte, MG, Brazil

ARTICLE INFO

Article history:
Received 28 April 2009
Received in revised form 13 August 2009
Accepted 25 August 2009
Available online 12 September 2009

Keywords:
Ordinary Least squares regression
Weighted least squares regression
Heteroscedasticity
Atomic spectroscopy
Human milk

ABSTRACT

In this study we compared the use of ordinary least squares and weighted least squares in the calibration of the method for analyzing essential and toxic metals present in human milk by ICP-OES, in order to avoid systematic errors in the measurements used. Human milk samples were provided by maternity clinic Odete Valadares and digested by means of a high-performance microwave (MW) oven. Evaluation of plasma short and long-term stability was made using a solution of digested milk (1:50) with 2.0 mg L^{-1} Mg in HNO_3 2% (v/v). The detection power resulted to be at or below the μg L^{-1} level, whilst the precision expressed as relative standard deviation R.S.D. was almost always equal to or better than 3.3%. Certified reference material Infant Formula (NIST SRM 1846) was used to assess the accuracy of the proposed method, which proved to be accurate and precise. Recovery rates were in the range of 83–117%. Aqueous calibration was carried out for each element under study.

© 2009 Elsevier B.V. All rights reserved.

1. Introduction

When validating quantitative analysis methods, it is essential to know a function of the instrumental response, i.e., the relationship between response (the measured signal) and the concentration or quantity of analyte in the sample within an application range. This relationship is obtained by means of a simple linear regression, whose parameters (slope and intercept) are estimated through the least squares [1]. In instrumental chemical analysis, linear regression is used to perform the calibration of the measurement method, generally using the analyte concentration as the independent variable. The most commonly used linear regression method is the least squares (LS). There are two basic types of LS:

- OLS—ordinary least squares (data having constant uncertainty (σ^2)) and
- WLS—weighted least squares (data having varying uncertainty)

We obviously do not know the values of σ^2 or $\sigma^2(y_i)$ and, therefore, saying that they are known values means that we have a very safe estimate. According to ISO GUM [2], it is possible to use the square of the experimental uncertainties obtained from a systematic accounting of the contributions of all uncertainty sources as safe estimates of such variances. It is true that most of reports in the literature refer to OLS, however, this method can only be used if the following conditions are fulfilled: (1) linearity between y and x variables is available; (2) x is error-free or less than one-tenth of the error in y; (3) errors in y are normally distributed; (4) error in y is homoscedastic (constant variance across the entire response range); and (5) errors associated with different observations are independent [3,4]. Several in atomic spectroscopy researchers have been using OLS to calibrate the analytical method, without considering the behavior of the data obtained, such as instrumental responses to certain analyte concentration ranges. The inappropriate use of a method for performing linear regression and neglect of heteroscedasticity in calibration by using unweighted or "ordinary" least squares (OLS) instead of weighted least squares (WLS) can lead to significant loss of precision, especially in the low signal limit, which is often important for quantifying substances present at trace levels. It can also contribute to systematic measurement errors. Both OLS and WLS assume that all uncertainty resides in the dependent variable, y [5]. Several methods suggest the use of WLS in the case of heteroscedastic data, i.e., when there is varying uncertainty within the concentration range to be calibrated [6,7]. In this study, we compared the use of OLS and WLS to calibrate the analysis method for essential and toxic metals present in

* Corresponding author. Tel.: +55 31 3409 5708; fax: +55 31 3409 5700.
E-mail address: bentojb@terra.com.br (J.B.B. Silva).

0039-9140/$ – see front matter © 2009 Elsevier B.V. All rights reserved.
doi:10.1016/j.talanta.2009.08.043

milk by inductively coupled plasma optical emission spectrometry (ICP-OES).

2. The least squares method

In this section, we present the general least squares theory, mainly in matrix notation. Even though the mathematical explanation on the different linear regression construction methods (OLS and WLS) is a bit long, it is necessary to better understand how such methods are composed and the factors considered by them, such as heteroscedasticity instrumental responses. Another reason for keeping the explanations is that the data matrices shown have been constructed using Microsoft Excel® spreadsheets, and not programs integrated in Excel®. That is, the data matrices and respective multiplications have been "manually" constructed in the spreadsheets, and not performed by the software. Furthermore, most of the programs that construct linear regressions, including programs integrated in analysis tools, only consider OLS and do not take into account other linear regression methods, such as weighted least squares.

Consider that mensurand y depends on mensurand x and on parameters p_i, so that the observational equations may be expressed as:

$$y_1 = a_{11}p_1 + a_{12}p_2 + \cdots + a_{1m}p_m + e_1,$$
$$y_2 = a_{21}p_1 + a_{22}p_2 + \cdots + a_{2m}p_m + e_2,$$
$$\cdots$$
$$y_n = a_{n1}p_1 + a_{n2}p_2 + \cdots + a_{nm}p_m + e_n$$

These equations can be expressed in matrix notation [7]:

$$Y_{n,1} = J_{n,m}P_{m,1} + E_{n,1} \tag{1}$$

Matrix J is frequently called the design matrix and depends on the values of x_i:

$$J = \begin{bmatrix} a_{11} & a_{12} & \cdots & a_{1n} \\ a_{21} & a_{22} & \cdots & a_{2n} \\ \vdots & \vdots & a_{ii} & \vdots \\ a_{n1} & a_{n2} & \cdots & a_{nn} \end{bmatrix} = \begin{bmatrix} \frac{\partial y_1}{\partial p_1} & \frac{\partial y_1}{\partial p_2} & \cdots & \frac{\partial y_1}{\partial p_n} \\ \frac{\partial y_2}{\partial p_1} & \frac{\partial y_2}{\partial p_2} & \cdots & \frac{\partial y_2}{\partial p_n} \\ \vdots & \vdots & \frac{\partial y_i}{\partial p_i} & \vdots \\ \frac{\partial y_n}{\partial p_1} & \frac{\partial y_n}{\partial p_2} & \cdots & \frac{\partial y_n}{\partial p_n} \end{bmatrix} \tag{2}$$

The e_i errors of matrix E have zero mean and finite variances. Our problem is to find the best estimator $\hat{P}$ for the P parameters. We will start assuming that the variances (uncertainty $u(y_i) = \sigma_i$) and covariances of all instrumental response values y_i are given by the variance–covariance matrix, V_y:

$$V_y = \begin{bmatrix} \mathrm{var}(y_i) & \mathrm{cov}(y_1, y_2) & \cdots & \mathrm{cov}(y_1, y_n) \\ \mathrm{cov}(y_2, y_1) & \mathrm{var}(y_2) & \cdots & \mathrm{cov}(y_2, y_n) \\ \vdots & \vdots & \mathrm{var}(y_i) & \vdots \\ \mathrm{cov}(y_n, y_1) & \mathrm{cov}(y_n, y_2) & \cdots & \mathrm{var}(y_n) \end{bmatrix} \tag{3}$$

The least squares method proposed by Gauss for the case of equal variances (OLS) consisted of minimizing the sum of the squares of deviations d_i (residuals), between the calculated experimental values, y_i, and the estimated values, $\hat{y}_i$:

$$SQ = \sum_{i=1}^{n} d_i^2 = \sum_{i=1}^{n} (y_i - \hat{y}_i)^2 \tag{4}$$

where

$$\hat{Y} = J\hat{P} \tag{5}$$

which is the same as minimizing:

$$SQ = \frac{1}{\sigma^2}\sum_{i=1}^{n} d_i^2 = \sum_{i=1}^{n} \frac{(y_i - \hat{y}_i)^2}{\sigma^2} \tag{6}$$

Defining the matrix of residuals:

$$D_{n,1} = Y - \hat{Y} = Y - J\hat{P} \tag{7}$$

Thus, minimizing SQ is the same as minimizing the quadratic form:

$$SQ = \sigma^{-2} D^t I D \tag{8}$$

When variances are not constant, i.e., in the case of the WLS, it is also necessary to minimize the quadratic form:

$$SQ = D^t V_y^{-1} D = (Y - J\hat{P})^t V_y^{-1} (Y - J\hat{P}) \tag{9}$$

Thus, we have:

$$\begin{aligned} D^t V_y^{-1} D = (Y - J\hat{P})^t V_y^{-1} (Y - J\hat{P}) &= Y^t V_y^{-1} Y + \hat{P}^t J^t V_y^{-1} J\hat{P} \\ &\quad - Y^t V_y^{-1} J\hat{P} - \hat{P}^t J^t V_y^{-1} Y \\ &= Y^t V_y^{-1} Y + (J\hat{P})^t V_y^{-1} J\hat{P} - 2\hat{P}^t J^t V_y^{-1} Y \end{aligned}$$

Deriving SQ in relation to the parameters to adjust, p_i, and equating to zero:

$$\frac{\partial SQ}{\partial \hat{P}^t} = \frac{\partial (D^t V_y^{-1} D)}{\partial \hat{P}^t} = 2(J^t V_y^{-1} J\hat{P} - J^t V_y^{-1} Y) = 0 \tag{10}$$

We obtain the so-called normal equations:

$$(J^t V_y^{-1} J)\hat{P} = J^t V_y^{-1} Y \tag{11}$$

The matrix of the normal equations, B, is defined by the equation:

$$B \equiv J^t V_y^{-1} J \tag{12}$$

Using Eq. (12), Eq. (11) can be rewritten:

$$\begin{aligned} B\hat{P} &= J^t V_y^{-1} Y \\ \hat{P} &= B^{-1} J^t V_y^{-1} Y \end{aligned} \tag{13}$$

The LS estimator of P, given by Eq. (13), is a minimum-variance and also minimizes the variance of the estimate of any linear function of the parameters. This is one of the reasons for the importance of the least squares estimates [7]. In particular, using the uncertainties of the adjusted parameters, it is possible to obtain the uncertainty of the interpolation of a given x_0 value from the experimentally measured instrumental response y_0.

The covariance matrix of the adjusted parameters is defined by:

$$V_p = B^{-1} = \sigma^2 (J^t W J)^{-1} \tag{14}$$

In order to obtain the uncertainties of the adjusted parameters, it is necessary to know the value of σ^2. Moreover, we can estimate the uncertainties in the adjusted parameters by replacing σ^2 in Eq. (14) by its unbiased estimator s^2:

$$\hat{V}_p = s^2 (J^t W J)^{-1} \tag{15}$$

So we must obtain s^2 from the experimental data. The moment method provides a unitary-weight unbiased estimator for variance σ^2 of the observation:

$$s^2 = \hat{\sigma}^2 = \frac{D^t W D}{n - m} \tag{16}$$

where n is the number of experimental points in the calibration and m is the number of adjusted parameters of B. s^2 is sort of a weighted variance of the adjustment. Finally, introducing Eq. (16)

into Eq. (14) or (15) gives an unbiased estimator for the covariance matrix for the parameters:

$$\hat{V}_p = s^2 B^{-1} = \frac{D^t W D}{n-m}\left(J^t W J\right)^{-1} \quad (17)$$

Or simply the inverse of the normal-equations matrix multiplied by the estimate of σ^2.

In the context of OLS, if the value of the common variance σ^2 is known, it is used in Eq. (14) to obtain the variances of the parameters on the diagonal of V_p and the covariances between them outside the diagonal. If σ^2 is unknown, we estimate σ^2 through Eq. (16) and obtain V_p through Eq. (15), where we calculate V_p using Eq. (17). In both cases we use $W = I$.

3. Experimental

3.1. Instrumentation

The experiments for this study were performed using the PerkinElmer® Model Optima™ 2000 DV inductively coupled plasma optical emission spectrometer (Dual View ICP-OES) with axial (AX-ICP-OES) and radial configurations (RD-ICP-OES) (PerkinElmer Life and Analytical Sciences, Shelton, CT, USA). The instrument was equipped with a radio frequency source of 40 MHz providing 0.75–1.5 kW power. It utilizes an Echelle grating (79 lines nm^{-1}), a solid-state detector, a plasma torch with a 2.0-mm internal diameter injection and a cross-flow nebulizer coupled with a double-pass Scott-type spray chamber. The equipment is also provided with an interface (shear gas) that introduces high air perpendicularly to the torch, in order to remove the low temperature extremity of the plasma. The sample introduction system was automated with a PerkinElmer Model 90 Plus autosampler. The operational parameters are listed in Table 1. The wavelengths used for the elements to be determined avoid any spectral interferences as described in the literature (Table 2). Human milk samples were mineralized by means of a closed-pressurized, high-performance microwave (MW) digestion oven (MLS 1200 MEGA, Milestone, Bergamo, Italy) equipped with 10 Teflon® vessels, capable of withstanding pressures of up to 30 bar.

3.2. Reagents and solutions

A standard multi-element 1000 mg L^{-1} solution (Std. 3 PerkinElmer Pure Plus) containing all the elements studied was used. Nitric acid (65%, v/v) and hydrogen peroxide (30%, v/v) were obtained from Merck. All working standard solutions were prepared daily from the stock solutions by simple dilution with Milli-Q ultrapure water. Ultrapure water was obtained with a Millipore (Millipore, Milford, MA, USA) Milli-Q water purification system. Certified reference material Infant Formula (NIST SRM 1846) was obtained from the National Institute of Standards and Technology (Gaithersburg, MD, EUA).

Table 1
ICP-OES operating conditions.

Parameters	
Applied power	1.3 kW
Nebulization gas flow	0.6 L min^{-1}
Sample flow	1.0 mL min^{-1}
Auxiliary gas flow	0.2 L min^{-1}
Plasma gas flow	15 L min^{-1}
Pumping flow	1.0 mL min^{-1}
Injector tube diameter	2.0 mm
Radially viewed height	14 mm
Interface	Shear gas

Table 2
Wavelength (λ) and ionization energy (*E*) of the elements determined.

Element	Line	λ (nm)	*E* (eV)
K	I	766.49	5.96
Na	I	589.59	7.24
Ba	II	455.403	7.93
Al	I	396.153	9.13
Cu	I	324.75	11.55
Mg	I	285.213	11.99
Mn	II	257.61	12.25
Cr	II	267.716	12.95
Fe	II	238.204	13.07
Ca	I	317.933	13.15
Ni	II	221.65	13.67
Co	II	228.62	13.7
Cd	II	214.44	14.77
Pb	II	220.35	14.79
Zn	II	213.86	15.19
Li	I	670.784	7.24
V	II	270.094	11.37

I = atomic line; II = ionic line.

3.3. Samples

Human milk samples were provided by maternity clinic Odete Valadares, Belo Horizonte, Minas Gerais, Brazil. The method proposed was applied to 17 mature-milk and 12 colostrum-milk samples of approximately 10 mL each. Samples were kept frozen at −18 °C until the moment of analysis.

3.4. Sample preparation

In order to determine the concentration of the elements studied, human milk aliquots of 1.0 mL were transferred into Teflon® vessels, added with 2.0 mL HNO_3 and 0.5 mL H_2O_2 (Suprapur, Merck, Darmstadt, Germany) and digested by means of a high-performance microwave (MW) oven (MLS 1200 MEGA, Milestone, Bergamo, Italy) with power steps increasing from 250 to 600 W. After cooling the digest vials in water bath (30 min), the completely clear, colorless and homogeneous digests obtained were diluted 1:50 (v/v) with deionized water. The heating program for digesting human milk samples in microwave oven is summarized in Table 3.

The certified reference material Infant Formula (NIST SRM 1846) was digested in a microwave oven with 0.05 g SRM for 2 mL nitric acid, 0.5 mL H_2O_2 and 1 mL deionized water, into a final volume of 25 mL. A certified material solution was prepared in independent triplicates and read in random triplicates. The heating program for digesting samples of certified materials in microwave oven is summarized in Table 4.

3.5. Procedure

Evaluation of plasma short and long-term stability was made using a solution of digested milk (1:50, v/v) containing 2.0 mg L^{-1} Mg in HNO_3 2% (v/v). For short-term stability, 15 consecutive measurements of the intensity of the Mg II line of 280.265 nm were made with subsequent analysis of the relative standard devia-

Table 3
Heating program for human milk samples in microwave oven.

Step	*T* (min)	Power (W)
1	5	250
2	5	400
3	5	500
4	1	600
Vent	10	–

Table 4
Heating program for certified reference material in microwave oven.

Step	T (min)	Power (W)
1	1	250
2	1	0
3	6	250
4	6	400
5	4.5	600
6	1.5	250
Vent	10	–

tion. In order to test long-term stability, the emission line of Mg was monitored for 2 h and 8 measures were performed at 15-min intervals. Both tests were performed using the AX-ICP-OES with nebulization gas flow rate of 0.6 L min^{-1} and 1.3 kW power applied, as suggested by the literature [8].

The equipment was adjusted using a nebulization gas flow rate ranging from 0.3 to 1.1 L min^{-1} and power ranging from 1.1 to 1.5 kW. Plasma robustness as such parameters were changed was evaluated using the ratio Mg II/Mg I as diagnosis. Plasma is considered robust when the Mg II/Mg I ratio ≥ 8 [9].

The linearity range studied was between 2.0 and 70.0 μg L^{-1} for Al, Cr, Mn, Fe, Ni, Cu, Zn, Cd, Pb, Ba, V, Co and Li; 10.0 to 600.0 mg L^{-1} for Ca; 5.0 to 80.0 mg L^{-1} for Mg and 15.0 to 900.0 mg L^{-1} for K and Na. The linearity curve was plotted with standard aqueous solutions ($n = 3$) and digested milk ($n = 3$). The curve slopes for each analyte (angular coefficients) in water and digested milk were compared to assess the presence of significant matrix effect using Student's t test. The counts per second (CPS) for each concentration were measured three times and the average values were used to plot the linearity curves.

The choice of an internal standard was made by evaluating the profile of the analytical signals of Al, Pb and the elements tested as internal standards (Li, Co, Ni, and Y), using the same experimental conditions. To evaluate the internal standard performance, 2.0 mg L^{-1} of each analyte solution and 1.0 mg L^{-1} of the internal standard were added to the samples equivalent to each point of the calibration curve.

4. Results and discussion

4.1. Figures of merit

4.1.1. Evaluation of internal standard

The elements tested as internal standard and their analytical lines were Co 228.61 nm (13.7 eV), Li 670.78 nm (3.87 eV), Ni 231.60 nm (14.03 eV) and Y 371.03 nm (9.9 eV). It was not necessary to use an internal standard, since no significant differences were detected between the analytical signals of solutions with and without an internal standard.

4.1.2. Plasma stability

Plasma stability was assessed by short and long-term stability tests. Both tests were performed using the AX-ICP-OES, a nebulization gas flow of 0.6 L min^{-1} and an applied power of 1.3 kW. The precision obtained for the short-term and long-term measurements were 0.84% and 1.08%, respectively, which is consistent with the results obtained by Silva et al. [8]. The adequate R.S.D. values obtained allow continuous analysis with significant precision.

4.1.3. Calibration by OLS and WLS

In order to perform calibration by OLS and WLS, we started by multiplying various data matrices [7]. This procedure offers several advantages, including calibration line parameters and their uncertainties, residuals for evaluating the quality of the adjustment, uncertainties in x and y, confidence limit and prevision curves for the adjustment and others.

In order to construct the calibration by both linear regression methods we need:

- the Jacobian matrix or design matrix J (Eq. (2)), which depends on the values of x_i;
- the matrix Y (Eq. (1)), which corresponds to the average of the instrumental responses;
- the matrix $s_{\bar{y}}$, which corresponds to the mean standard deviation;
- the matrix V_y (Eq. (3)), which consists of the variance and covariance matrix for the instrumental responses; and
- matrices J and V_y, from which we obtain the transpose and inverse matrices.

The problem in this case is finding the best estimator $\hat{P}$ for parameters P of the calibration line. Therefore, to adjust the calibration for OLS, we must simply multiply matrix B^{-1} (the matrix of the inverse normal equations, obtained by multiplying matrix J by matrix J^t) by matrices J^t and Y:

$$P = B^{-1}J^tY \tag{18}$$

On the other hand, to adjust the calibration using WLS, we must only add the inverse variance and covariance matrix of the instrumental responses (V_y^{-1}) to the matrix multiplication used for the adjustment by OLS, which will weight the values according to the heteroscedastic behavior of the instrumental response variances:

$$\hat{P} = B^{-1}J^tYV_y^{-1} \tag{13}$$

With the covariance matrix for the adjusted parameters, V_p (Eq. (17)), we obtain the uncertainties s_a and s_b for the parameters adjusted. In this work, comparison was carried out only between the OLS and WLS methods, since we know the variances of the data and their behavior (whether they present equal or different variances).

4.1.4. Comparison between OLS and WLS regressions

Previous to performing calibration, an evaluation was carried out to choose the best linear regression method (OLS or WLS) to be used. The software used for the data matrices and respective calculations was Microsoft Office Excel 2003®, a simple and affordable tool.

It is known that the inappropriate use of a method for performing linear regression results in a systematic measurement error and precision loss. Thus, to avoid such errors, we verified whether the instrumental response variance of the analytes studied presented a homoscedastic (constant uncertainty) or heteroscedastic (varying uncertainty) behavior. Elements Ca, K, Mg, Na, Ba, Cd, Cr, Cu, Mn, Fe, Li, Ni, Co, Zn and Pb presented varying uncertainty and should therefore be calibrated by WLS. Elements V and Al showed constant variance and thus should be calibrated by OLS. Fig. 1 shows the heteroscedastic behavior of the data related to Ca and the homoscedastic behavior of the data related to V. Evaluation was performed whether these methods are statistically similar or different for calibrating the same analyte, bearing in mind that WLS is a more laborious method than OLS.

To assess the statistical similarity of the OLS and WLS methods, we applied the paired Student's t test to compare the angular coefficients of both aqueous curves (OLS and WLS) for all elements studied. Table 5 presents the equations corresponding to the linear regressions performed by OLS and WLS, along with the Student's t_c. The value of $t_{95\%,2}$ is 4.303, which indicates that the methods were statistically different for elements Cu, Cd, Zn, Al, Ca, Mg, Na, K and Fe. Therefore, calibration must be performed for these elements using

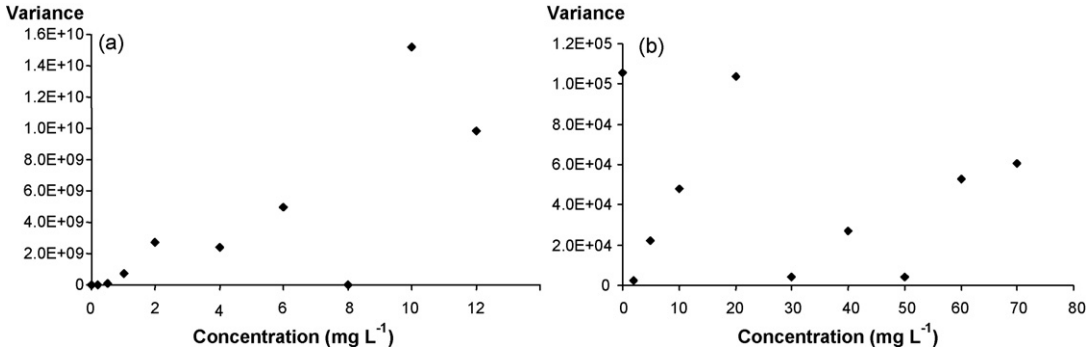


Fig. 1. (a) Heteroscedastic behavior of the Ca-related data. (b) Homoscedastic behavior the V-related data.

Table 5
Comparison between the OLS and WLS for ICP-OES analysis.

Analyte	Equation adjusted for OLS	Equation adjusted for WLS	Student's t_c[c]
Ba	$y = 23{,}527\ (\pm 33)^{a}\ x - 11{,}052\ (\pm 42)^{b}$	$y = 23{,}171.8\ (\pm 234.3)^{a}\ x + 9599.9\ (\pm 142.5)^{b}$	2.600
V	$y = 220.7\ (\pm 2.7)\ x + 405.0\ (\pm 3.0)$	$y = 230.4\ (\pm 2.8)\ x + 25{,}163.7\ (\pm 104.5)$	4.185
Cr	$y = 172.6\ (\pm 0.4)\ x - 12.8\ (\pm 0.1)$	$y = 173.4\ (\pm 2.5)\ x + 1157.8\ (\pm 9.4)$	0.562
Ni	$y = 26.4\ (\pm 0.1)\ x + 28.3\ (\pm 1.8)$	$y = 27.0\ (\pm 1.1)\ x + 68.6\ (\pm 2.4)$	0.893
Mn	$y = 1307.6\ (\pm 1.0)\ x - 70.3\ (\pm 0.9)$	$y = 1308.7\ (\pm 3.2)\ x + 2372.5\ (\pm 9.7)$	0.584
Pb	$y = 6.4\ (\pm 0.1)\ x + 7.2\ (\pm 0.1)$	$y = 6.3\ (\pm 0.2)\ x + 194.0\ (\pm 4.0)$	0.614
Cu	$y = 220.4\ (\pm 3.1)\ x + 1713.0\ (\pm 24.9)$	$y = 211.5\ (\pm 1.1)\ x + 150.3\ (\pm 1.4)$	4.627
Co	$y = 58.8\ (\pm 0.1)\ x - 68.8\ (\pm 0.5)$	$y = 59.0\ (\pm 0.1)\ x + 30.9\ (\pm 0.3)$	1.732
Cd	$y = 72.0\ (\pm 0.2)\ x - 192.4\ (\pm 1.2)$	$y = 74.7\ (\pm 0.2)\ x - 227.3\ (\pm 1.7)$	13.231
Zn	$y = 63.8\ (\pm 0.4)\ x - 86.4\ (\pm 2.0)$	$y = 66.7\ (\pm 0.1)\ x - 79.9\ (\pm 1.5)$	10.356
Al	$y = 183.6\ (\pm 3.6)\ x + 361.5\ (\pm 2.4)$	$y = 151.9\ (\pm 0.4)\ x + 5984.3\ (\pm 6.4)$	14.867
Li	$y = 29{,}541\ (\pm 1151)\ x - 27{,}109\ (\pm 114)$	$y = 26{,}743\ (\pm 1261)\ x + 41{,}528\ (\pm 118)$	2.837
Ca	$y = 1.14 \times 10^{6}\ (\pm 29{,}211)\ x + 2{,}430{,}964\ (\pm 9842)$	$y = 1.0 \times 10^{6}\ (\pm 28{,}143)\ x - 123{,}707\ (\pm 8211)$	5.971
Mg	$y = 4.5 \times 10^{6}\ (\pm 24{,}753)\ x + 2.1 \times 10^{6}\ (\pm 7147)$	$y = 5.0 \times 10^{6}\ (\pm 26{,}845)\ x - 2.0 \times 10^{6}\ (\pm 8286)$	23.717
Na	$y = 1.3 \times 10^{6}\ (\pm 31{,}128)\ x + 2.2 \times 10^{6}\ (\pm 2478)$	$y = 1.0 \times 10^{6}\ (\pm 31{,}657)\ x - 20{,}203\ (\pm 1101)$	11.703
K	$y = 5.06 \times 10^{5}\ (\pm 2642)\ x + 5.84 \times 10^{5}\ (\pm 121)$	$y = 480{,}815\ (\pm 2401)\ x - 85{,}804\ (\pm 140)$	12.217
Fe	$y = 163.4\ (\pm 1.3)\ x + 2388.9\ (\pm 6.3)$	$y = 172.1\ (\pm 0.2)\ x + 1447.7\ (\pm 5.4)$	11.193

[a] Standard deviation of the regression-line coefficient a: $y = a\ (s_a)\ x + b\ (s_b)$.
[b] Standard deviation of the regression-line coefficient b: $y = a\ (s_a)\ x + b\ (s_b)$.
[c] $t_{95\%,2} = 4.303$.

WLS (and not OLS, as in several atomic absorption studies). As for Al, calibration should necessarily be performed using OLS. The methods employed were not statistically different for the other elements (V, Ba, Cr, Mn, Li, Ni, Co and Pb) and so performing calibration using OLS or WLS does not significantly affect the final results in the case of such analytes for the sample of interest. Thus, we prefer using OLS, since it is a simpler method that can be performed by various programs, including the one used by the equipment.

Table 5 shows that all macrominerals present in human milk (Ca, Mg, Na and K), as well as microminerals Fe, Cu and Zn (with higher concentrations than those of other microminerals), presented significant differences in the comparison between the OLS and WLS methods at a 95% confidence level. This draws attention to the behavior of these elements.

Fig. 2(a) shows the comparison between OLS and WLS for K and Fig. 2(b) presents the comparison for Zn. The figures indicate that the inappropriate choice of the linear regression method directly affects the concentration of the analyte of interest, causing precision loss. In some cases (Fig. 2(b)), sensitivity loss of the analytical method can occur due to a simple systematic error when choosing the linear regression method. This work aims at awakening this concern, which is forgotten by several authors that study atomic absorption.

4.1.5. Matrix effect

The method presented linear response to the concentrations within the ranges tested for all analytes, both in aqueous and in digested milk curves. When verifying the presence of matrix effect,

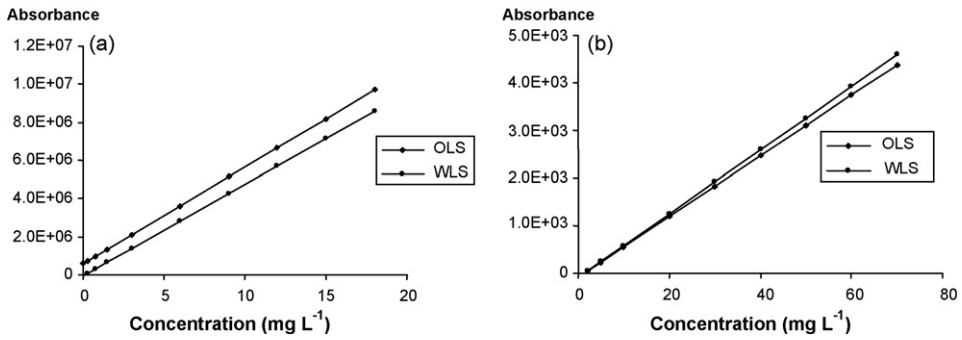


Fig. 2. (a) Comparison between OLS and WLS for K. (b) Comparison between OLS and WLS for metal Zn.

Table 6
Correlation coefficients and calibration equations for the analytes ($n = 3$) along with the limits of detection and quantification.

Analyte	Correlation coefficient	Calibration equation	LOD[c]	LOQ[c]
Ba	0.9980	$y = 23{,}527\ (\pm 33)^{a}\ x - 11{,}052\ (\pm 42)^{b}$	0.01	0.03
V	0.9995	$y = 220.7\ (\pm 2.7)\ x + 405.0\ (\pm 3.0)$	2.8	9.3
Cr	0.9999	$y = 172.6\ (\pm 0.4)\ x - 12.8\ (\pm 0.1)$	0.3	0.9
Ni	0.9992	$y = 26.4\ (\pm 0.1)\ x + 28.3\ (\pm 1.8)$	0.5	1.6
Mn	0.9999	$y = 1307.6\ (\pm 1.0)\ x - 70.3\ (\pm 0.9)$	0.05	0.2
Pb	0.9979	$y = 6.4\ (\pm 0.1)\ x + 7.2\ (\pm 0.1)$	0.6	1.8
Cu	0.9998	$y = 211.5\ (\pm 1.1)\ x + 150.3\ (\pm 1.4)$	0.4	1.4
Co	0.9992	$y = 58.8\ (\pm 0.1)\ x - 68.8\ (\pm 0.5)$	0.05	0.2
Cd	0.9981	$y = 74.7\ (\pm 0.2)\ x - 227.3\ (\pm 1.7)$	0.1	0.4
Zn	0.9992	$y = 66.7\ (\pm 0.1)\ x - 79.9\ (\pm 1.5)$	0.1	0.4
Al	0.9993	$y = 183.6\ (\pm 3.6)\ x + 361.5\ (\pm 2.4)$	0.1	0.2
Li	0.9990	$y = 29{,}541\ (\pm 1151)\ x - 27{,}109\ (\pm 114)$	0.03	0.1
Ca	0.9990	$y = 1.0 \times 10^{6}\ (\pm 28{,}143)\ x - 123{,}707\ (\pm 8211)$	0.06	0.2
Mg	0.9973	$y = 5.0 \times 10^{6}\ (\pm 26{,}845)\ x - 2.0 \times 10^{6}\ (\pm 8286)$	0.01	0.03
Na	0.9985	$y = 1.0 \times 10^{6}\ (\pm 31{,}657)\ x - 20{,}203\ (\pm 1101)$	0.07	0.2
K	0.9973	$y = 480{,}815\ (\pm 2401)\ x - 85{,}804\ (\pm 140)$	0.01	0.04
Fe	0.9978	$y = 172.1\ (\pm 0.2)\ x + 1447.7\ (\pm 5.4)$	0.2	0.7

[a] Standard deviation of the regression-line coefficient a: $y = a\ (s_a)\ x + b\ (s_b)$.
[b] Standard deviation of the regression-line coefficient b: $y = a\ (s_a)\ x + b\ (s_b)$.
[c] LOD and LOQ in mg L^{-1} to Ca, Na, Mg and K; and to the others analytes in μg L^{-1}.

the angular coefficients of the analytical curves presented no significant difference at a 95% confidence interval for the concentration ranges tested. This indicates the absence of matrix interference on the measurements. Thus, aqueous calibration was used to determine all the elements analyzed by ICP-OES.

4.1.6. Limits of detection and quantification

The limits of detection for each element under study, based on three times the standard deviation of the average of 10 individually prepared blank solutions, as well as the limits of quantification, based on 10 times the standard deviation of the average of 10 individually prepared blank solutions, are listed in Table 6.

4.1.7. Precision of the measurements

Method precision was evaluated by calculating the R.S.D. (%) of 10 independent samples, taken in random triplicates, for the following concentrations: 10.0 μg L^{-1} for Li, Ba, V, Cr, Ni, Mn, Pb, Cu, Co, Cd, and Al; 15.0 μg L^{-1} for Fe and Zn; 200.0 mg L^{-1} for Ca; 300.0 mg L^{-1} for K and 30.0 mg L^{-1} for Mg and Na. The detection power resulted to be at or below the μg L^{-1} level, whilst the precision expressed as relative standard deviation R.S.D. was almost always equal to or better than 3.3% (see Table 7), indicating repeatability.

4.1.8. Accuracy of the measurements

Method accuracy was evaluated by quantification of samples of certified reference material Infant Formula (NIST SRM 1846) and also by recovery tests using spiked samples. The reason why we make use of milk infant formula certified reference material to evaluate method accuracy is that there is no human milk certified reference material commercially available. Therefore, considering that the matrix of infant formula is very similar to that of human

Table 7
ICP-OES analytical performance in the quantification of elements in human milk.

Analyte	LOQ[a]	Repeatability[b] R.S.D. (%)	Accuracy[c]		
			Certified[d] (μg g^{-1})	Found[d] (μg g^{-1})	Student's t_c[e]
Ba	0.03	1.8	nc[f]	–	–
V	9.3	2.2	nc	–	–
Cr	0.9	1.7	nc	–	–
Ni	1.6	1.1	nc	–	–
Mn	0.2	2.3	ic	–	–
Pb	1.8	2.8	nc	–	–
Cu	1.4	3.1	nc	–	–
Co	0.2	0.9	nc	–	–
Cd	0.4	1.6	nc	–	–
Zn	0.4	2.0	122.2 ± 1.1	116.8 ± 3.0	2.944
Al	0.2	1.2	nc	–	–
Li	0.1	1.8	nc	–	–
Ca	0.2	2.7	7.4 ± 0.2	7.2 ± 0.5	0.678
Mg	0.03	1.5	1.08 ± 0.02	1.1 ± 0.1	0.020
Na	0.2	3.3	4.8 ± 0.4	5.6 ± 0.5	2.134
K	0.04	2.8	14.4 ± 0.5	14.4 ± 0.8	0.093
Fe	0.7	2.4	127.0 ± 1.9	119.5 ± 3.1	3.533

[a] LOQ in mg L^{-1} to Ca, Na, Mg and K; and to the others analytes in μg L^{-1}.
[b] Calculated on 10 independent samples at the following concentrations: 10.0 μg L^{-1} to Li, Ba, V, Cr, Ni, Mn, Pb, Cu, Co, Cd, and Al; 15.0 μg L^{-1} to Fe and Zn; 200.0 mg L^{-1} to Ca; 300.0 mg L^{-1} to K and 30.0 mg L^{-1} to Mg and Na.
[c] Performed on the NIST SRM 1846 Infant Formula.
[d] Mean ± S.D.
[e] $t_{95\%,2} = 4.303$
[f] nc: not certified and ic: informed concentration.

Table 8
Metal recoveries in human milk ($n = 3$).

Analyte	Recovery (%)		
	Level 1	Level 2	Level 3
Ba	107.4 ± 4.3	94.6 ± 0.4	90.0 ± 0.3
V	107.9 ± 10.8	84.8 ± 2.3	74.5 ± 2.2
Cr	107.8 ± 8.6	96.5 ± 3.0	91.9 ± 0.3
Ni	93.3 ± 1.7	89.0 ± 2.9	86.8 ± 0.8
Mn	100.9 ± 6.5	94.2 ± 1.9	91.0 ± 0.8
Pb	103.4 ± 9.4	100.1 ± 10.2	83.2 ± 1.0
Cu	134.1 ± 2.3	100.4 ± 1.0	97.2 ± 1.2
Co	106.6 ± 5.5	97.5 ± 1.4	90.3 ± 0.7
Cd	100.3 ± 2.2	90.9 ± 1.2	86.4 ± 0.5
Zn	161.8 ± 3.0	105.8 ± 4.3	117.3 ± 2.8
Al	101.8 ± 13.6	91.8 ± 5.5	72.7 ± 1.9
Li	115.5 ± 5.5	97.9 ± 1.9	95.8 ± 1.3
Ca	168.7 ± 3.6	113.6 ± 5.9	109.9 ± 1.8
Mg	104.5 ± 4.3	91.4 ± 0.8	114.2 ± 1.6
Na	184.5 ± 3.4	115.6 ± 3.4	114.3 ± 6.4
K	218.1 ± 2.7	113.8 ± 5.7	110.8 ± 1.1
Fe	43.2 ± 3.3	95.7 ± 3.3	83.1 ± 2.5

Level 1: 50.0 mg L^{-1} to Ca; 75.0 mg L^{-1} to K; 20.0 mg L^{-1} to Mg and Na; and 5.0 μg L^{-1} to the other metals.
Level 2: 200.0 mg L^{-1} to Ca; 300.0 mg L^{-1} to K; 40.0 mg L^{-1} to Mg and Na; and 20.0 μg L^{-1} to the other metals.
Level 3: 400.0 mg L^{-1} to Ca; 600.0 mg L^{-1} to K; 60.0 mg L^{-1} to Mg and Na; and 40.0 μg L^{-1} to the other metals.
Underlined values are values which showed recovery below or above of the recommended values.

milk (both contain the same concomitant elements and potential interference materials), it was used in order to get as close as possible to the real condition whilst studying method accuracy. The accuracy of the method, using reference material was evaluated by Student's *t* test. Milk reference materials were reconstituted as recommended by the supplier and the resulting solution was digested (as described, under microwave digestion procedures). In general terms, adequate equivalence levels were found between obtained and recommended values. Table 7 reports the analytical performance of ICP-OES in terms of LOQs, precision and accuracy.

Recovery assays were carried out to verify the presence of the interference effects on the developed method. Adequate amounts of the elements were added to milk before digesting of the sample. For the recovery tests, the digested milk solutions were spiked and prepared at three concentration levels: 5.0, 20.0 and 40.0 μg L^{-1} for analytes Al, Cr, Mn, Fe, Ni, Cu, Zn, Cd, Pb, Ba, V, Co, Li; 50.0, 200.0 and 400.0 mg L^{-1} for Ca; 20.0, 40.0 and 60.0 mg L^{-1} for Mg and Na; and 75.0, 300.0 and 600.0 mg L^{-1} for K, prepared in triplicate and measured under robust operation conditions. Recovery rates were in the range 83–117%, as listed in Table 8. It was not possible to recover elements Fe, Cu, Zn, Ca, Na and K at the first level, due to their low concentration levels at this level, considering the great amounts of these metals in human milk. It was also not possible to recover Al and V at the third level, possibly due to interferences occurred during the measurements.

Aqueous calibration was carried out for each element under study. Our method offers advantages such as simplicity and reduced time (<2 h), as well as reduced volume required (1 mL), when compared with other techniques [10–13]. The dilution level used in the assay, 1 mL of human milk to 50 mL of solution, is adequate for measuring the usual contents of the elements studied. However, microwave digestion has certain limitations. For instance, the number of samples that can be simultaneously digested is restricted to the number of slots (10) for digestion vessels in the microwave oven. Moreover, precautions must be adopted to prevent alterations on the inner surface of the digestion vessels, which may cause adsorption of the elements, leading to aggressive conditions, such as large concentrations of acid, high temperatures or prolonged times.

4.2. Quantification

Table 9 presents the results obtained for each element present in mature and colostrum milk, in terms of means and standard deviations (S.D.). In general, the data do not indicate the presence of potentially toxic metals beyond the national recommended values. Concentrations are also comparable to the values referred to in the literature, especially to those of an international collaborative WHO IAEA survey on the contents of trace elements in milk worldwide [14,15]. No values were found in the literature indicating the concentrations of analyte V in milk. The concentration ranges of the elements considered in this study in human milk were in satisfactory agreement with those reported in the literature. As indicated

Table 9
Concentrations of trace elements in 17 mature human milk samples and 12 colostrum human milk samples and reference ranges for human milk.

Analyte	Concentration[a]		
	Colostrum (mean ± S.D.)	Mature (mean ± S.D.)	Literature range
Ba	14.4 ± 14.1	7.9 ± 3.4	0.9–47
V	107.0 ± 81.9	89.8 ± 76.7	–
Cr	43.4 ± 15.3	31.0 ± 15.8	0.2–0.8
Ni	35.6 ± 34.9	43.8 ± 38.5[b]	0.5–10
Mn	29.5 ± 23.2	18.5 ± 13.5	3–40
Pb	70.9 ± 61.3	48.1 ± 39.9	2–30
Cu	587.4 ± 290.7	431.7 ± 233.5	180–751
Co	1.2 ± 0.6	0.9 ± 0.8	0.1–2.0
Cd	nd	nd	0.7–4.6
Zn	5310.3 ± 2569.8	2676.2 ± 2018.5	700–4000
Al	159.4 ± 78.2[c]	217.3 ± 35.8[d]	3–125
Li	4.2 ± 2.3[e]	4.4 ± 0.9[d]	0.08–1.3
Ca	275.0 ± 65.2	272.2 ± 71.1	180–300
Mg	23.1 ± 4.2	24.2 ± 5.4	10–63
Na	604.8 ± 311.6	491.5 ± 401.0	76–506
K	686.4 ± 90.3	571.7 ± 139.3	351–741
Fe	422.4 ± 319.7	433.4 ± 331.8	200–800

[a] Concentration in mg L^{-1} to Ca, Na, Mg and K, and μg L^{-1}, to the other analytes.
[b] Value with exception of 6 samples which has values less than LOQ.
[c] Value with exception of 7 samples which has values less than LOQ.
[d] Value with exception of 5 samples which has values less than LOQ.
[e] Value with exception of 12 samples which has values less than LOQ.

by the standard deviations of the samples analyzed, all metal concentrations vary widely from mother to mother. This suggests that diet, as well as the use of hair chemicals, cosmetics and others, may have a great influence on the concentrations of such metals in milk.

It was also observed that the concentration levels of most of the metals studied in colostrum milk were higher, on average, than those of metals present in mature human milk. This is because colostrum milk has a larger amount of nutrients (particularly metals) than mature milk.

5. Conclusions

Selecting the most adequate linear regression model (OLS or WLS) to be used for calibrating the analytical method in atomic spectroscopy, has proven extremely useful and necessary to reduce systematic errors embedded in the measurement results (in this case, the concentration of the analyte of interest in the sample). It also helps avoiding loss in the analytical method precision. Quantification of essential and toxic elements in human milk by ICP-OES offers several advantages, such as simple sample preparation, reduced time (<2 h) and a small volume of sample required (1 mL), comparing to other techniques.

Acknowledgments

The authors are thankful to Conselho Nacional de Pesquisa e Desenvolvimento Tecnológico (CNPq), Fundação de Amparo à Pesquisa do Estado de Minas Gerais (FAPEMIG) and Maternidade Odete Valadares. W.B. Neto has scholarships granted by CNPq and FAPEMIG. J.B.B. Silva is grateful to CNPq for the research grants.

References

[1] J.O. De Beer, T.R. De Beer, L. Goeyens, Anal. Chim. Acta 584 (2007) 57.
[2] ISO, Guide to the Expression of Uncertainty in Measurement, 1st edition, 1993.
[3] J.N. Miller, J.C. Miller, Statistics and Chemometrics for Analytical Chemistry, 4th edition, Prentice Hall, Edinburgh, 2000.
[4] K. Baumann, H. Watzig, Proc. Control. Qual. 10 (1997) 59.
[5] J. Tellinghuisen, Analyst 132 (2007) 536.
[6] P.C. Meier, R.E. Zünd, Statistical Methods in Analytical Chemistry, 2nd edition, John Wiley & Sons, New York, 2000.
[7] W.C. Hamilton, Statistics in Physical Science: Estimation, Hypothesis Testing and Least Squares, The Ronald Press Company, New York, 1964.
[8] F.V. Silva, C.L. Trevisan, C.S. Silva, A.R. Nogueira, J.A. Nóbrega, Spectrochim. Acta B 57 (2002) 1905.
[9] I.B.A. Brenner, A.T. Zander, Spectrochim. Acta B 55 (2000) 1195.
[10] N.F. Krebs, M. Hambidge, M.A. Jacobs, S. Myler, J. Pediatr, Gastroenterol. Nutr. 4 (1985) 227.
[11] M.F. Picciano, Ph.D. Guthrie, Am. J. Clin. Nutr. 29 (1976) 242.
[12] E. Vuori, P. Kuitunen, Acta Pediatr. Scand. 68 (1979) 33.
[13] L.A. Vaughan, C.W. Weber, S.R. Kemberling, Am. J. Clin. Nutr. 32 (1979) 2301.
[14] WHO, Report of a Joint World Health Organization International Atomic Energy Agency Collaborative Study. Minor and Trace Elements in Breast Milk, 1989, Geneva.
[15] E. Coni, S. Caroli, D. Ianni, A. Bocca, Food Chem. 50 (1994) 203.

Talanta 80 (2010) 1110–1115

Contents lists available at ScienceDirect

Talanta

journal homepage: www.elsevier.com/locate/talanta

A liquid chromatography-electrospray ionization-tandem mass spectrometry study of ethanolamines in high salinity industrial wastewaters

Pablo Campo [a], Makram T. Suidan [a,*], Yunzhou Chai [b], John Davis [b]

[a] Civil and Environmental Engineering Department, University of Cincinnati, Cincinnati, OH 45221, USA
[b] Toxicology and Environmental Research and Consulting, The Dow Chemical Company, Midland, MI 48674, USA

ARTICLE INFO

Article history:
Received 5 June 2009
Received in revised form 24 August 2009
Accepted 25 August 2009
Available online 1 September 2009

Keywords:
Ethanolamines
Hypersaline wastewater
Sodium interference
Electrospray
Matrix-matched calibration

ABSTRACT

The detection and quantitation of four ethanolamines, tris(2-hydroxyethyl)amine (triethanolamine, TEA), *N*,*N*-bis(2-hydroxyethyl)methylamine (methyldiethanolamine, MDEA), *N*-(2-aminoethyl)ethanolamine (AEA), and *N*,*N*-diethylethanolamine (DEA), were achieved in wastewaters from two aerobic activated sludge bioreactors located in an industrial wastewater treatment plant. The streams had salt concentrations of approximately 3% and 7% by weight in Reactor 1 and Reactor 2, respectively. The use of liquid chromatography-electrospray ionization-tandem mass spectrometry avoided the need for some sample preparation steps such as extraction, concentration, and derivatization. Ion suppression in the electrospray, attributable to the presence of sodium clusters, was attenuated by a 10-fold dilution of the wastewaters with acetonitrile. A matrix-matched calibration model averted other potential interferences. For the compounds analyzed in selected reaction monitoring mode (TEA, MDEA, and DEA), the calibration curves presented linearity in a range of 10–1000 μg/L with corresponding detection limits ranging from 2 to 11 μg/L, depending upon the specific analyte and aqueous matrix. AEA was calibrated in selected ion monitoring mode (100–1000 μg/L), with corresponding detection limits in the two wastewaters of 74.6 and 85.3 μg/L, respectively. Overall good precision (<10%) and accuracy (97–110%) were achieved for both matrices, which fell within-laboratory reproducibility. Finally, the amines were introduced into six mixed liquor samples from both reactors and quantified following the reported protocol. Again, recoveries were close to 100% with a relative standard deviation of less than 10% in all cases.

© 2009 Elsevier B.V. All rights reserved.

1. Introduction

β-Hydroxylamines are generally synthesized through the reaction of epoxies and nitrogen reagents [1]. Common to all these synthesis reactions is the combination of ethylene oxide and aqueous ammonia, which represents the main pathway for the formation of ethanolamines [2]. These organic compounds are raw materials or synthetic precursors in the manufacture of herbicides, surfactants, textile fabrics, and metal cutting fluids. Furthermore, these amines are extensively used in gas plants and oil refineries as active components in aqueous scrubbing solutions during sweetening, that is, the removal of hydrogen sulfide and carbon dioxide from natural gas [3–5]. In the USA alone 1345 million pounds of ethanolamines were produced in 2004 [6].

This broad range of applications for these compounds is due to their chemical structure: an alkane backbone that combines the presence of both hydroxy- and aminofunctional groups. Hence, in aqueous solution, this combination gives a weakly-to-moderately basic behavior and complete solubility in polar solvents such as water, acetone, or methanol. Normally, these aliphatic amines have low vapor pressures (below 1 mm Hg at 20 °C), with boiling points ranging from 96 to 208 °C, and exhibit varying degrees of decomposition at temperatures above 200 °C [7]. Owing to the widespread use, the amines may be found in wastewaters, ground water, and soils located at industrial sites associated with the natural gas production [8,9].

Analytical methods for the identification and quantification of this group of amines have been developed in earnest since they are known degradation byproducts of nitrogen mustards [10]. The most commonly utilized technique involves the use of gas chromatography mass spectrometry because the protocols were developed for monitoring the parent compounds mainly [11]. Nevertheless, ethanolamines are problematic candidates for gas chromatography on account of their high polarity, basic nature, and low volatility. In fact, their identification in aqueous phases requires extensive sample preparation involving extraction, concentration, and derivatization. These preparatory steps can introduce analytical errors as manifested by poor extraction efficiency, low derivatization yields, and thermal destruction of the analytes [12].

* Corresponding author. Tel.: +1 513 556 3695; fax: +1 513 556 2599.
E-mail address: Makram.Suidan@uc.edu (M.T. Suidan).

0039-9140/$ – see front matter © 2009 Elsevier B.V. All rights reserved.
doi:10.1016/j.talanta.2009.08.035

The development of electrospray tandem mass spectrometry (ESI-MS/MS) has led to marked improvements in the detection of polar compounds in water samples. In fact, this technique facilitates the measurement of trace concentrations without the need for the derivatization or intensive sample preparation [13,14]. It presents an alternative to the time-consuming classical approaches and research effort has been expended to adapt these methods to the detection of ethanolamines [15–17]. Nevertheless, to the best of our knowledge, no ESI-MS/MS analytical methods have been reported for these compounds in high saline wastewaters (over 3% (w/v) of total dissolved solids). These industrial streams are commonly generated during the manufacture of chemicals, textiles, and oil and gas recovery operations, which involve the use of ethanolamines. Hence, the objective of the present study was to develop and validate analytical protocols for measuring tris(2-hydroxyethyl)amine (triethanolamine, TEA) *N*,*N*-bis(2-hydroxyethyl)methylamine (methyldiethanolamine, MDEA), *N*-(2-aminoethyl)ethanolamine (AEA), and *N*,*N*-diethylethanolamine (DEA) in hypersaline effluents by ESI-MS/MS as a previous step for the study of the biodegradation of the compounds in highly saline industrial wastewaters. For this purpose, wastewater streams from two aerobic activated sludge bioreactors (denoted as Reactor 1 and Reactor 2) in an industrial wastewater treatment plant were used in this study. On a routine basis, these two reactors generate wastewaters whose saline content average 3% and 7% by weight in Reactor 1 and Reactor 2, respectively. These high salt concentrations represent a challenge to the application of ESI for detection of the analytes.

2. Experimental

2.1. Chemicals and reagents

Reagent grade triethanolamine was purchased from Sigma (St. Louis, MO, USA), while methyldiethanolamine, N-(2-aminoethyl)ethanolamine, and *N*,*N*-diethylethanolamine were obtained from Aldrich (Milwaukee, WI, USA). The organic solvents, acetonitrile (ACN) and methanol (MeOH), were HPLC quality and were purchased from Tedia (Fairfield, OH, USA). Deionized ultra-filtered water and ammonium formate were obtained from Fisher Scientific (Pittsburg, PA, USA). All chemicals and solvents were analytical reagent grade with a minimum purity of 98%.

2.2. Samples and standards

Stock solutions of the analytes (20 mg/L) were prepared in SuperQ water, using Class A volumetric glassware and then stored at 4 °C. Supernatants from Reactor 1 and Reactor 2 were used as aqueous matrices for the preparation of working standards. Matrix samples were prepared by combining biomass and supernatants from each reactor so that each sample contained 500 mL of mixed liquor with 1000 mg/L of total suspended solids with the final pH adjusted to 7.5 using concentrated HCl. Both bioreactors receive streams from various processes ranging from basic to performance chemicals. The typical salinities of the wastewaters were around 3% and 7% for Reactor 1 and Reactor 2, respectively. Prior to sample injection in the instrument, samples and standards were filtered through 0.2 μm membrane filters.

2.3. Instrumentation

Chromatographic separation of the amines was performed on a 1200 Series rapid resolution liquid chromatograph (LC) from Agilent (Palo Alto, CA, USA) with an Inertsil ODS-3 (2.1 mm × 150 mm, 5 μm) column (Alltech, Deerfield, IL, USA). The target compounds were identified and quantified on a 6410A triple quadrupole mass spectrometer equipped with an electrospray ionization source (ESI) by (Agilent, Palo Alto, CA, USA). Nitrogen was the gas used in both the nebulizer and the collision cell.

The equipment was tuned following the manufacturer's specifications, using an ESI calibrant mix from Agilent (Palo Alto, CA, USA). The software for the control of the LC–MS/MS, the data acquisition, and the qualitative and quantitative analysis was Agilent MassHunter Workstation.

The conditions for the flow injection analysis (FIA) were gas temperature, 300 °C; gas flow, 10 L/min; nebulizer, 50 psi; and capillary voltage, 3000 V. The eluent composition was water and MeOH (1:1, v/v) with 5 mM of ammonium formate, and the flow was 0.4 mL/min. The MS was operated in full scan between 50 and 300 *m*/*z*.

3. Results and discussion

3.1. Method development

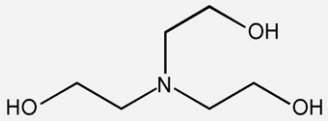
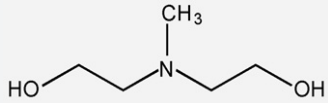
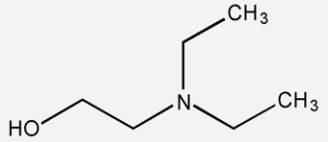
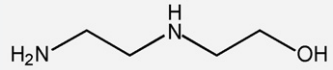
3.1.1. Ionization and MS/MS conditions

In order to establish the precursor ions of the ethanolamines, FIA was individually performed on the analytes. Standards were prepared in water (20 mg/L) and 1 μL was injected. As expected, owing to the basic nature of the aminogroup, the target compounds presented strong protonated molecules $[M+H]^+$ in the positive ionization mode. Once the precursors were determined, product ion scans were conducted to identify the reaction products of each analyte. The ethanolamines presented typical cleavages of water with the subsequent loss of the vinyl groups. In selected reaction monitoring (SRM) the most abundant product ion was preferred for quantitative purposes and a second ion was also monitored for confirmation (see Table 1). Because of the poor fragmentation yield of AEA, detection was performed in selected ion monitoring (SIM) mode monitoring the precursor ion. After that, the electrospray parameters were optimized to achieve the maximum sensitivity when the instrument was operated in either SRM or SIM. For TEA and MDEA the conditions were as follows: gas temperature, 350 °C; gas flow, 12 L/min; nebulizer, 35 psi; and capillary voltage, 3500 V. The source parameters for DEA were gas temperature, 250 °C; gas flow, 10 L/min; nebulizer, 50 psi; and capillary voltage, 3000 V. Finally, for AEA, the ionization conditions were gas temperature, 350 °C; gas flow, 12 L/min; nebulizer, 35 psi; and capillary voltage, 4000 V. The dwell time for all the amines was 300 ms.

3.1.2. Background interferences

High salt concentrations imply an appreciable increase in background signal in the electrospray [18]. Actually, sodium may form clusters with analytes and solvents that, in the low mass region, entirely suppress the analyte response [19]. For this reason, working standards prepared with a sodium chloride solution (7% by weight) were analyzed. First, the standards were run in scan mode and adduct formation was ruled out; then the FIA conditions were re-tested. As Fig. 1(A) and (B) shows sodium chloride dramatically masked the TEA signal (20 μg/L). So 10-fold dilutions of the standards were carried out with different combinations of solvents (MeOH and ACN) as a way of reducing the impact of the clusters. When the 7% NaCl standard was diluted in water (Fig. 1C) or MeOH/water (Fig. 1D), TEA was detected, but the signal was, at best, 40% of the original standard in water alone. When water was substituted with a combination of ACN and MeOH or ACN alone (Fig. 1E and F), the dilution of the 7% NaCl standard further improved the sensitivity with the signal strength. In fact, the dilution in neat ACN reached approximately 60% of the original standard in water alone. It is speculated that such an increment in the signal was due to a combination of the dilution effect (i.e. less NaCl competing in the

Table 1
Mass spectrometry parameters for target analytes. Frag, fragmentor voltage; CE, collision energy. NA, no applicable.

Compound	CAS number	Structure	Precursor ion, *m/z*	Fragment ion, *m/z*	Confirmation ion, *m/z*	Frag, V	CE, V
TEA	102-71-6		150 $C_6H_{16}NO_3^+$	70 $C_4H_8N^+$	88 $C_4H_{10}NO^+$	100	17
MDEA	105-59-9		120 $C_5H_{14}NO_2^+$	58 $C_3H_8N^+$	45 $C_2H_5O^+$	100	15
DEA	100-37-8		118 $C_6H_{16}NO^+$	100 $C_6H_{14}N^+$	72 $C_4H_{10}N^+$	130	13
AEA	114-41-1		105 $C_4H_{13}N_2O^+$	NA	NA	80	NA

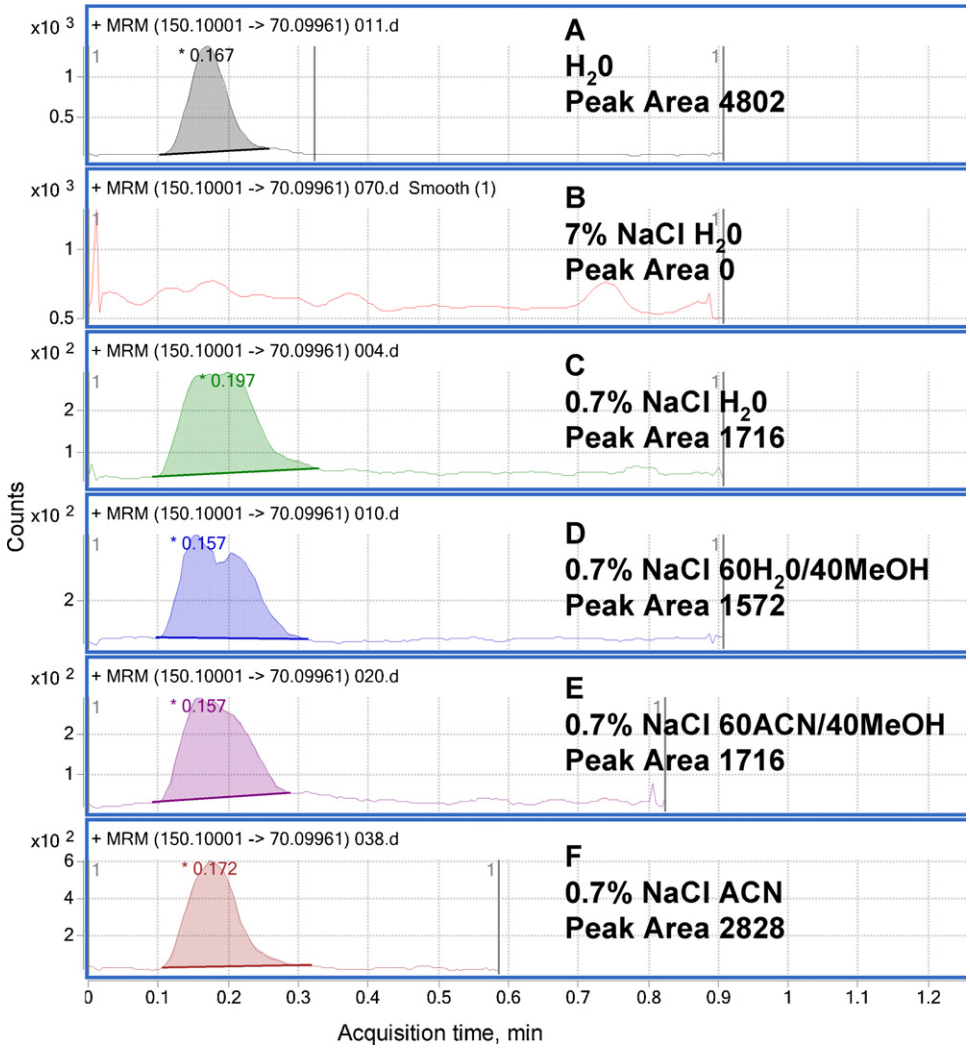


Fig. 1. TEA signal suppression by sodium chloride background in different solvents. TEA concentration 20 μg/L.

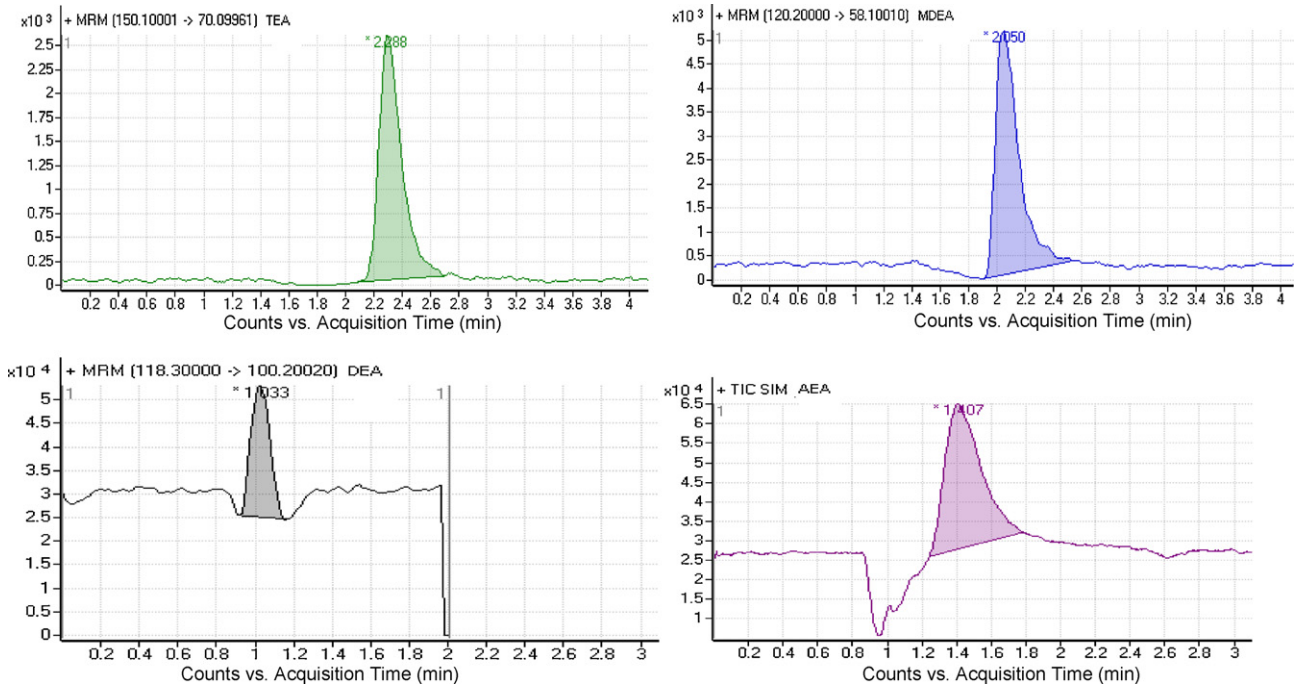


Fig. 2. SRM chromatograms for 10 g/L of TEA, MDEA, and DEA 1 in supernatant from Reactor 2 (7% NaCl). SIM chromatogram for 100 g/L of AEA in supernatant from Reactor 2 (7% NaCl).

ionization process) and the presence of ACN, an aprotic organic modifier. In fact, this solvent barely interacts with sodium chloride and, therefore, solvation is weak [20]. Hence, this lack of ion stabilization leads to a minimal presence of clusters. Similar results were observed with the remaining amines (data not shown).

3.1.3. Liquid chromatography

The final step dealt with the behavior of the amines in the LC. The objective was to achieve the best transfer of analytes in the electrospray as well as adequate resolution of the peaks. Hence, matrix-matched standards (i.e. supernatants fortified with the amines and diluted 1:10 in ACN) were separated by reversed-phase chromatography. After testing different combinations of eluents and flows, the optimal LC parameters were as follows: in the case of TEA and MDEA, the composition of the mobile phase was water (98%)/ACN (2%). The flow was 0.2 mL/min and the run time was 5 min at 50 °C. A mix of water and MeOH (1:1) was used as eluent for AEA, with ammonium formate (5 mM) added as a buffer. The flow was 0.4 mL/min and the run time was 5 min as well and the temperature 40 °C. The DEA composition of the mobile phase was water (30%) and MeOH (70%) with ammonium formate (5 mM) added as a buffer in both eluents. The flow was 0.4 mL/min and the run time was 2 min and the temperature 40 °C. One micro-liter of either calibration standards or samples was injected for TEA, MDEA, and AEA, whereas the injection volume for DAE was 10 μL. The retention times for the compounds were TEA, 2.53 min; MDEA, 1.94 min; AEA, 1.50 min; and DEA, 1.01 min. A chromatogram for a 10 μg/L standard of TEA, MDEA, and DEA as well as for 100 μg/L of AEA is shown in Fig. 2.

3.2. Calibration experiments and validation

Besides sodium chloride, other species could be present in the wastewaters and compete with the amines in the ionization process. For this reason, a matrix-matched calibration approach was used in order to neutralize disruptions of instrument signal. The advantage of this technique resides in the preparation of calibration standards with the sample matrix instead of a pure solvent. Hence, both translational and rotational effects are prevented during the analysis (i.e. signal modifications are just due to the detector's responses toward different concentrations of analyte) [21,22]. Under these circumstances, however, the cause of the background interferences remains unsolved; thus the impact on the signal may change depending upon the test material (e.g. the

Table 2
Calibration curves for the WWTP matrices. For each analyte the first line corresponds to Reactor 1 (3% NaCl) and the second for Reactor 2 (7% NaCl); LD, limit of detection; *t*, values for the *t*-test comparison of the regression slopes.

Compound	Slope	Intercept	r^2	LD (μg/L)	t^a
TEA	3004.3	496.3	0.998	7.4	11.08
	2224.9	679.0	0.999	4.3	
MDEA	5360.9	−1160.3	0.999	4.2	11.06
	3864.5	28037.6	0.995	11.2	
DEA	25971.4	−155671.0	0.999	2.7	15.14
	30273.5	−105398.0	0.999	2.2	
AEA	1155.9	37875.4	0.999	74.6	16.53
	728.87	20530.2	0.999	85.3	

[a] Values for the *t*-test comparison of the regression slopes. Critical *t*-value for TEA, MDEA, and AEA $t_{0.025;12} = 2.18$; for AEA $t_{0.025;8} = 2.31$.

Table 3
Precision, accuracy, and fortified sample recovery. For each analyte, the left column corresponds to Reactor 1 (3% NaCl) and the right column to Reactor 2 (7% NaCl); SD, standard deviation; RSD, relative standard deviation.

	TEA		MDEA		DEA		AEA	
Within-run[a]								
Mean ± SD (μg/L)	248.8 ± 4.5	247.8 ± 21.0	248.1 ±10.6	251.7 ± 15.7	248.8 ± 25.9	256.4 ± 24.9	513.3 ± 16.0	506.8 ± 6.9
Precision (RSD)	1.8	8.5	4.3	6.3	9.7	6.7	3.1	1.4
Accuracy (%)[a]	99.5	99.1	99.2	100.7	102.5	99.8	102.7	103.3
Between-run[b]								
Mean ± SD (μg/L)	523.4 ± 34.6	507.9 ± 26.1	548.7 ± 27.4	500.2 ± 21.5	485.0 ± 43.8	502.9 ± 14.8	502.7 ± 17.6	495.6 ± 20.0
Precision (RSD)[b]	6.6	5.1	5.0	4.3	9.0	2.9	3.5	4.0
Accuracy (%)[b]	104.7	101.6	109.7	100.0	97.0	100.6	100.5	99.1
Recovery[c]								
Mean ± SD (%)	103.8 ± 6.3	101.8 ± 7.6	103.2 ± 6.7	105.1 ± 5.3	104.1 ± 2.3	97.1 ± 2.2	102.5 ± 5.8	103.3 ± 7.4
Precision (RSD)	6.0	7.4	6.5	5.0	2.2	2.3	5.7	7.1

[a] Precision calculated as the RSD of 5 replicates. Accuracy calculated as the percentage ratio between measured and theoretical concentrations. Concentration for TEA, MDEA, DEA 250 μg/L and for AEA 500 μg/L.
[b] Precision calculated as the RSD of one standard (500 μg/L) run on five days. Accuracy calculated as the percentage ratio between measured and theoretical concentrations.
[c] Recovery target concentration for all the compounds 500 μg/L. Precision calculated as the RSD of 6 replicates.

two saline wastewaters herein studied). Additionally, only blank matrices are suitable for this calibration method since the presence of endogenous analytes in the sample would require standard additions. Regardless of the ad hoc character defined by these two limitations, a matrix-matched calibration, when suitable, is a valid solution dealing with strong matrix problems as in the present case.

With this objective, the supernatants from Reactor 1 (3% NaCl) and Reactor 2 (7% NaCl), which were amine-free upon analysis, became the solvents used in the stock solutions of the analytes. Subsequently, the preparation of the calibration standards consisted in sequential 1:10 dilutions of the stocks with ACN. In this fashion, TEA, MDEA, and DEA presented linear calibration curves for both matrices in a concentration range of 10–1000 μg/L, with seven levels injected in duplicate; as to AEA, for the two salinities linearity was achieved between 100 and 1000 μg/L with five levels run in duplicate (see Table 2 and Fig. 3). For all the compounds, the two regression lines manifested the contrast between sensitivities as a consequence of the salt contents; this difference is significant after comparing the slopes by means of a *t*-test as described by Massart et al. [23]. The Student's test corroborated signal dependence on sample composition and the need for using the specific matrix in each calibration. The detection limits were calculated through the calibration curve method [24] and the obtained values were

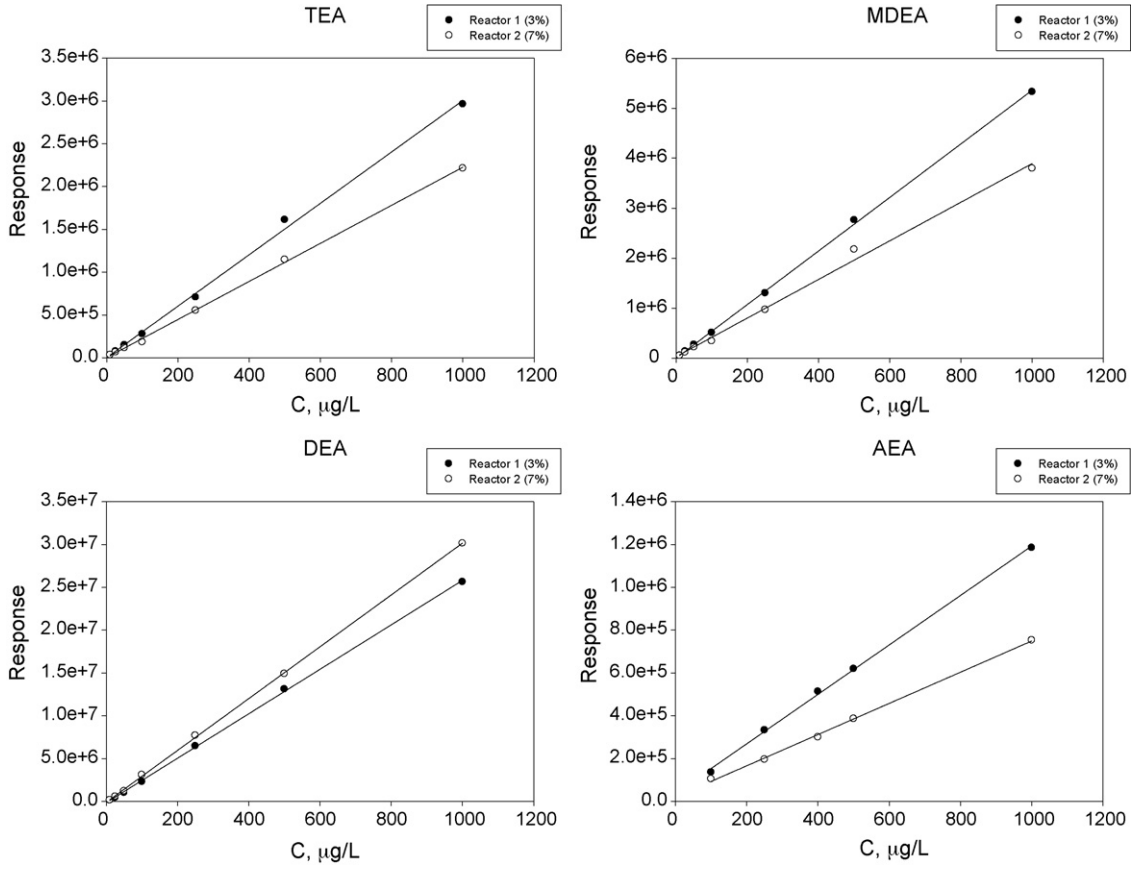


Fig. 3. Calibration curves for the target analytes in both Reactor 1 (3% NaCl) and Reactor 2 (7% NaCl) wastewaters.

comparable to other reported instrumental detection limits in less complex matrices [16,25].

For both salinities, an assay of the within-laboratory reproducibility was conducted and the results are listed in Table 3. In order to ascertain the precision, the relative standard deviation (RSD) of replicates was calculated, where the percentage of actual to expected concentration of the standards determined the accuracy. The study of the within-run repeatability consisted of the concurrent analysis of five standards (500 μg/L for AEA; 250 μg/L for TEA, MDEA, and DEA) and supernatant samples. With this objective, a standard was injected at the beginning of the run and after every ten samples. In all cases, the RSD values were under 10% and the accuracy values close to 100%. A second test was designed for determining the between-run variation. For five days, a standard (500 μg/L for all the amines) was injected and, each time, quantified with a fresh calibration curve. The precision values ranged between 3% and 9% and the accuracy varied from 97% to 108%. The validation of the protocol was completed with a recovery experiment. In this case, the ethanolamines (5 mg/L) were spiked in six mix liquor samples (500 mL) from each bioreactor and mixed for 30 min. Subsequently, aliquots (2 mL) were withdrawn and, after filtration and dilution in ACN, the measured concentration should be 500 μg/L. Again, good precision and accuracy were achieved: RSD values were smaller than 10% and the amines were recovered quantitatively.

4. Conclusions

An analytical protocol for the determination of ethanolamines is provided for its application to industrial saline wastewaters. Trace levels (10–1000 μg/L) were measured by LC–ESI-MS/MS without extraction, pre-concentration, or derivatization. Dissolution of hypersaline wastewaters in acetonitrile minimized the ion suppression attributable to sodium clusters. Other errors due to potential unknown interferences were compensated by the application of a matrix-match calibration model. The pertinent requirements for precision and accuracy were achieved in the analysis of working standards and fortified samples prepared with both mixed liquors from the industrial treatment plant.

References

[1] M.B. Smith, J. March, March's Advanced Organic Chemistry, sixth ed., John Wiley& Sons, Inc., Hoboken, 2007.
[2] K. Weissermel, H.-J. Arpe, Industrial Organic Chemistry, fourth ed., Wiley-VCH, Weinheim, 2003.
[3] J.S. Connors, C.L. Perkins, F.E.V. Vandaveer, in: C.G. Segeler (Ed.), Gas Engineers Handbook, Industrial Press Inc., New York, 1974.
[4] S.-Y. Horng, M.-H. Li, Ind. Eng. Chem. Res. 41 (2002) 257–266.
[5] S.H. Ali, Int. J. Chem. Kinet. 37 (2005) 391–405.
[6] C. Edser, Focus Surfactants 2004 (2004) 2.
[7] The Dow Chemical Company, Ethanolamines, The Dow Chemical Company, Midland, MI, USA, 2003.
[8] M. Furhacker, A. Pressl, R. Allabashi, Chemosphere 52 (2003) 1743–1748.
[9] S.B. Hawthorne, A. Kubatoba, J.R. Gallagher, J.A. Sorensen, D.J. Miller, Environ. Sci. Technol. 39 (2005) 3639–3645.
[10] Mesilaakso, in: R.A. Meyers (Ed.), Encyclopedia of Analytical Chemistry, Wiley, Chichester, 2000, p. 899.
[11] E.R.J. Wils, in: R.A. Meyers (Ed.), Encyclopedia of Analytical Chemistry, Wiley, Chichester, 2000, p. 979.
[12] R.M. Black, B. Muir, J. Chromatogr. A 1000 (2003) 253–281.
[13] S.D. Richardson, Anal. Chem. 79 (2007) 4295–4324.
[14] S.D. Richardson, Anal. Chem. 80 (2008) 4373–4402.
[15] R.M. Black, R.W. Read, J. Chromatogr. A 759 (1997) 79–92.
[16] J.V. Headley, K.M. Peru, L.C. Dickson, Rapid Commun. Mass Spectrosc. 13 (1999) 730–736.
[17] H.C. Chua, H.S. Lee, M.T. Sng, J. Chromatogr. A 1102 (2006) 214–223.
[18] C. Liu, Q. Wu, A.C. Harms, R.D. Smtih, Anal. Chem. 68 (1996) 3295–3299.
[19] N.B. Cech, C.G. Enke, Mass Spectrom. Rev. 20 (2001).
[20] H.A. Laitinen, W.E. Harris, Chemical Analysis: An Advanced Text and Reference, 2nd, McGraw-Hill, New York, 1975.
[21] L. Cuadros-Rodriguez, M.G. Bagur-Gonzalez, M. Sanchez-Viñas, A.M. Gomez-Saez, J. Chromatogr. A 1158 (2007) 33–46.
[22] M. Thompson, S.L.R. Ellison, Accred. Qual. Assur. 10 (2005) 82–97.
[23] D.L. Massart, B.M.G. Vandeginste, L.M.C. Buydens, S. De Jong, P.J. Lewi, J. Smeyers-Verbeke, Handbook of Chemometrics and Qualimetrics: Part A, Elsevier, Amsterdam, The Netherlands, 1997.
[24] P. Campo, G.A. Sorial, M.T. Suidan, A.D. Venosa, Talanta 68 (2006) 888–894.
[25] I. Ohsawa, Y. Seto, J. Chromatogr. A 1122 (2006) 242–248.

Talanta 80 (2010) 1116–1120

Contents lists available at ScienceDirect

Talanta

journal homepage: www.elsevier.com/locate/talanta

Supercritical fluid extraction of polybrominated diphenyl ethers (PBDEs) from house dust with supercritical 1,1,1,2-tetrafluoroethane (R134a)☆

Frank C. Calvosa, Anthony F. Lagalante*

Villanova University, Department of Chemistry, 800 Lancaster Avenue, Villanova, PA 19085, USA

ARTICLE INFO

Article history:
Received 26 May 2009
Received in revised form 25 August 2009
Accepted 26 August 2009
Available online 2 September 2009

Keywords:
Supercritical fluid extraction
Polybrominated diphenyl ethers
R134a
Dust

ABSTRACT

The extraction of polybrominated diphenyl ethers (PBDEs) from SRM 2585 (Organic Contaminants in House Dust) was investigated using supercritical fluid R134a as an extraction solvent. Three methods of dust extraction were studied: (1) extraction of dry dust, (2) extraction of dry dust dispersed on Ottawa sand and (3) extraction of dust wet with dichloromethane. For each of the three sample preparation methods, extracts at three temperatures (110, 150, and 200 °C) above the critical temperature of R134a were performed. Eight PBDE congeners (BDE-28, -47, -99, 100, -153, -154, -183, and -209) in the SFE extracts were analyzed by liquid chromatography negative-ion atmospheric pressure photoionization tandem mass spectrometry (LC/NI-APPI/MS/MS). The optimum extraction of PBDEs from house dust using supercritical R134a is obtained when the dust is pre-wet with dichloromethane prior to extraction to swell the dust. For all sample preparation methods, higher temperatures afforded higher percent recoveries of the eight PBDE congeners. Only a combination of high-temperature (200 °C) and pre-wetting the dust with dichloromethane produced high recovery of the environmentally important, fully brominated PBDE congener, BDE-209.

© 2009 Elsevier B.V. All rights reserved.

1. Introduction

In comparison to liquid phase solvents, supercritical (sc) solvents possess the ability to manipulate the solvent strength based upon the fluid temperature and pressure. This can have a dramatic effect on the solvency properties of the fluid that can be advantageously selected to permit good-solvency at high fluid density and poor-solvency at low fluid density. This solvent strength manipulation is most readily accomplished by adjusting the fluid pressure of a gaseous solvent. At high-pressure, the dense, liquid-like solvent can selectively extract target analytes and then by rapidly reducing the pressure through expansion through a valve or restrictor the solvent is instantaneously transformed into a low-density gas with poor solvent strength. The dissolved analyte rapidly nucleates from the solvent and the target analyte can be collected and concentrated by directing the gas onto a solid support or by bubbling through a liquid solvent. The primary advantages of a supercritical fluid extraction (SFE) over liquid based extractions are the rapid extraction kinetics due to the high-diffusivity of the dense gas solvent, copious amounts of solvent are not utilized during the extraction, and that time and energy intensive solvent reduction steps are not necessary post collection. Despite these advantages, supercritical fluid extraction has not gained widespread use over conventional liquid based extractions or pressurized liquid extraction (PLE) due to the safety issues associated with high-temperature, high-pressure gases, the lack of commercial automated SFE instrumentation, and the lack of suitable solvents with reasonable critical points. The most widely used supercritical solvent is carbon dioxide which possesses a low critical temperature (T_c = 32 °C) yet has a relatively high critical pressure (P_c = 72 atm). The lack of a permanent dipole moment relegates $scCO_2$ extractions to applications where non-polar analytes need be extracted. While the use of small percentages of fluid modifiers in $scCO_2$ will increase the polarity range of the analytes that can potentially be extracted, other gaseous fluids are commercially available that do possess permanent dipole moments which may be better exploited for SFE.

One class of compounds that has a long history of use as vapor phase solvents are the chlorofluorocarbons (CFCs) and more recently the hydrochlorofluorocarbons (HCFCs). However, countries ratifying the 1987 *Montreal Protocol on Substances that Deplete the Ozone Layer* have agreed to phase-out CFCs and HCFCs. Consequently, industry has turned to hydrofluorocarbon (HFC) replacements for CFCs and HCFCs across a broad spectrum of applications. Studies concluded that best replacement for R12 (dichlorodifluoromethane) was R134a (1,1,1,2-tetrafluoroethane).

☆ The research described in this paper has been funded in part by the United States Environmental Protection Agency (EPA) under the Greater Research Opportunities (GRO) Undergraduate Program. EPA has not officially endorsed this publication and the views expressed herein may not reflect the views of the EPA.

* Corresponding author. Tel.: +1 610 519 5409.
E-mail address: anthony.lagalante@villanova.edu (A.F. Lagalante).

0039-9140/$ – see front matter © 2009 Elsevier B.V. All rights reserved.
doi:10.1016/j.talanta.2009.08.038

This increase in commercial availability and resultant lowered cost of R134a in combination with a permanent dipole moment (2.05 D) and reasonable critical properties (101.1 °C, 40.6 atm) led to evaluation of its use as an alternative to $scCO_2$ for the extraction of more polar analytes [1]. One group of semi-volatile analytes that has emerged as a ubiquitous contaminant in recent years are the brominated flame retardants (BFRs).

Flame retardant chemicals are required by law to be added to consumer products and have undeniably reduced the loss of property and human lives to fires [2]. The BFRs are currently the largest market group of flame retardants due to their low-cost and high-performance efficiency. The five major BFRs are tetrabromobisphenol A (TBBPA), hexabromocyclododecane (HBCD), and three commercial polybrominated diphenyl ether (PBDE) mixtures (pentaBDE, octaBDE, and decaBDE). Unlike the other two PBDE mixtures, decaBDE is almost exclusively BDE-209. Of the 209 unique PBDE congeners, BDE-28, BDE-47, BDE-99, BDE-100, BDE-153, BDE-154, BDE-183, and BDE-209 are the most prevalent in the environment due to their presence in these commercial mixtures. While the main producer of PBDEs in the U.S. voluntarily discontinued production of pentaBDE and octaBDE mixtures in 2004 [3] and Maine and Washington have recently banned the use of decaBDE; BDE-209 remains the most widely used PBDE globally (56,100 tons in 2001) with equal use in North America and Asia [4]. As of July 2008, the European Court of Justice has overturned a prior exemption for the use of DecaBDE in electronics and electrical applications [5]. Even with a cease on production and use of PBDEs, long-term monitoring of PBDEs will be necessary for an indefinite future time.

Since emergence the late 1970s, PBDE levels have increased in human blood and breast milk [6–11]. In addition to PBDE dietary intake [12–14], recent studies have found that the inhalation, ingestion, or dermal contact of house dust is the predominant route of human exposure [15–23]. The extraction, chromatographic separation, and detection of PBDEs have recently been reviewed [24,25]. While pure polyaromatic hydrocarbons (PAHs) and polychlorinated biphenyls (PCBs) exhibit high solubilities in supercritical fluids, when present in real-world matrices (e.g. dust), SFE is unpredictable due to the presence of organic co-contaminants, the matrix porosity, and analyte chemisorption [26–30]. Select applications for $scCO_2$, such as extraction of PBDEs from waste plastics [31] or for sample cleanup prior to analysis [32] have been reported. While di-brominated PBDEs show exhaustive extraction in $scCO_2$ from sediment samples [33], it is expected that the higher brominated congeners will not be highly soluble in $scCO_2$ similar to results found for higher molecular weight PAHs [26]. Though studies are limited, the use of scR134a in place of $scCO_2$ results in higher extraction efficiencies polar analytes from environmental matrices [34,35].

The scope of the current work is to evaluate R134a for the SFE of PBDEs from NIST SRM 2585 (Organic Contaminants in House Dust). Supercritical dust extracts will be quantified on a recently validated liquid chromatography with negative-ion atmospheric pressure photoionization tandem mass spectrometry (LC/NI-APPI/MS/MS) method [36] for the determination of the eight PBDE congeners of primary interest in dust.

2. Experimental

2.1. Chemicals

HPLC grade methanol (99.93%, Sigma–Aldrich, St. Louis, MO) and distilled–deionized water (>20 MΩ cm) from a Millipore Direct-Q water purification system (Billerica, MA) were used as LC mobile phase solvents. HRGC/HPLC-trace grade toluene (Pharmco, Brookfield, CT) was purified on an MBraun MB-SPS solvent purification system (Stratham, NH). HPLC grade dichloromethane (>99.9%) was purchased from Sigma–Aldrich (St. Louis, MO). SFE dispersants included diatomaceous earth (J.T. Baker, Phillipsburg, NJ), 40–63 μm silica (EM Science, Gibbstown, NJ), and Ottawa ignition sand (EMD Chemicals, Gibbstown, NJ). SRM 2585 (Organic Contaminants in House Dust) was obtained from NIST (Gaithersburg, MD). Individual PBDE standards prepared at 50 μg mL^{-1} in isooctane:toluene (9:1) of BDE-28 (99.3% purity), BDE-47 (100%), BDE-99 (100%), BDE-100 (100%), BDE-153 (99.3%), BDE-154 (100%), and BDE-183 (100%) were purchased from AccuStandard (New Haven, CT). Certified purity was determined by the vendor by GC/MS. Solid BDE-209 (98%) was purchased from Aldrich (St. Louis, MO).

2.2. Supercritical fluid extraction

A SFE instrument was constructed in-house. R134a is filled from the low-pressure side of an ISCO 260D syringe pump (Lincoln, NE). A Brinkmann circulating refrigeration bath (Westbury, NY) was used to cool the syringe pump to 5 °C and provided a liquid R134a fill. The high-pressure side of the syringe pump was connected to a temperature controlled (±0.1 °C) extraction cell. The extraction cell is comprised of a stainless-steel cell and a removable polyetheretherketone (PEEK) sample holder (Upchurch Scientific, part numbers C1000 and C-1035) with 0.5 μm stainless-steel frits at the entrance and exit of the sample holder. The extraction cell is capable of holding approximately 0.5 g of dust and has an internal volume of approximately 0.8 mL when empty. The extraction cell is placed in a heated aluminum block and controlled using the injection port heating control from a Hewlett-Packard 5890 gas chromatograph (Wilmington, DE). The aluminum block is large enough to accommodate a coiled section of tubing to preheat the R134a. Within the chromatographic oven, a 5 cm piece of 150 μm o.d., 75 μm i.d., fused silica capillary tubing (Polymicro Technologies, Phoenix, AZ) restricted the SFE cell exit flow out and maintained fluid backpressure when the ISCO 260D was operated in constant pressure mode.

Three methods of dust extraction were studied: (1) extraction of dry dust, (2) extraction of dry dust dispersed on Ottawa sand and (3) extraction of dust wet with dichloromethane. For the extraction of dry dust, approximately 0.25 g of NIST SRM 2585 was quantitatively transferred into an empty PEEK extraction cell. For the extraction of dry dust dispersed on Ottawa sand, approximately 0.25 g of NIST SRM 2585 and approximately 0.5 g of Ottawa sand were mixed and added to an empty PEEK extraction cell. For the extraction of dust wet with dichloromethane, approximately 0.25 g of NIST SRM 2585 was quantitatively transferred into an empty PEEK extraction cell and loaded into the stainless-steel extraction vessel. Dichloromethane was added to the dust in a 3:2 dichloromethane to dust ratio by mass. Once the PEEK cell was prepared it was placed into the stainless-steel extraction vessel. Immediately thereafter, 20 mL of liquid R134a (monitored at the syringe pump) was passed through the extraction vessel at a pressure of 204 atm, the valve at the syringe pump exit was closed and the cell was allowed to depressurize through the restrictor. Upon expansion out of the restrictor, gaseous R134a and the extracted solutes were bubbled through approximately 3 mL of dichloromethane in a 5 mL collection vial that resided on the inside of the GC oven. The GC oven was maintained at 40 °C to warm the expanding refrigerant and prevent restrictor freezing and plugging. Extraction efficiencies were evaluated at 110, 150 and 200 °C to investigate kinetics and solubility of the PBDEs.

REFPROP (Version 7.1, NIST 2006) was used to calculate the fluid densities from equations of state explicit in Helmholtz energy, the modified Benedict–Webb–Rubin equation of state, and an extended corresponding states model. At 204 atm, the R134a densities were calculated to be 1.04, 0.91, and 0.73 g mL^{-1} for 110, 150, and 200 °C, respectively.

Table 1
Values of the mean PBDE concentrations ± standard deviation (ng g^{-1}) after SFE of SRM 2585 for three extraction temperatures with NIST certified values for comparison.

Dry	110 °C (n = 2)	150 °C (n = 3)	200 °C (n = 2)	SRM 2585
BDE-28	25.8 ± 14.2	<LOD	24.0 ± 32.1	46.9 ± 4.4
BDE-47	271 ± 322	355 ± 99	270 ± 317	497 ± 46
BDE-99	415 ± 549	666 ± 135	429 ± 463	892 ± 53
BDE-100	77.1 ± 90.3	122 ± 28	68.7 ± 83.9	145 ± 11
BDE-153	60.3 ± 69.2	62.3 ± 15.4	50.8 ± 58.5	119 ± 1
BDE-154	46.7 ± 42.8	43.6 ± 7.9	34.4 ± 22.5	83.5 ± 2.0
BDE-183	26.4 ± 22.3	<LOD	16.5 ± 21.6	43.0 ± 3.5
BDE-209	19.7 ± 22.6	156 ± 21	174 ± 180	2510 ± 190
Dispersed on Ottawa sand	110 °C (n = 3)	150 °C (n = 3)	200 °C (n = 2)	SRM 2585
BDE-28	35.8 ± 15.7	33.9 ± 9.3	46.7 ± 1.3	46.9 ± 4.4
BDE-47	499 ± 43	469 ± 50	494 ± 45	497 ± 46
BDE-99	803 ± 27	743 ± 70	757 ± 102	892 ± 53
BDE-100	141 ± 13	117 ± 13	128 ± 9	145 ± 11
BDE-153	109 ± 11	90.6 ± 8.3	92.2 ± 9.4	119 ± 1
BDE-154	76.9 ± 16.4	39.7 ± 13.0	50.3 ± 18.5	83.5 ± 2.0
BDE-183	42.2 ± 10.6	24.3 ± 2.9	31.8 ± 1.2	43.0 ± 3.5
BDE-209	35.6 ± 3.7	255 ± 101	301 ± 47	2510 ± 190
Wet with dichloromethane	110 °C (n = 4)	150 °C (n = 3)	200 °C (n = 4)	SRM 2585
BDE-28	71.4 ± 8.3	47.6 ± 16.9	49.7 ± 16.9	46.9 ± 4.4
BDE-47	444 ± 59	497 ± 73	575 ± 98	497 ± 46
BDE-99	639 ± 141	719 ± 151	909 ± 166	892 ± 53
BDE-100	108 ± 21	133 ± 36	142 ± 27	145 ± 11
BDE-153	71.9 ± 17.5	79.8 ± 19.6	112 ± 9	119 ± 1
BDE-154	56.7 ± 0.9	54.4 ± 5.0	83.4 ± 8.1	83.5 ± 2.0
BDE-183	32.6 ± 8.0	36.0 ± 18.2	68.7 ± 14.9	43.0 ± 3.5
BDE-209	35.6 ± 3.7	369 ± 24	2171 ± 152	2510 ± 190

2.3. Analysis of supercritical fluid extracts

BDE-28, BDE-47, BDE-99, BDE-100, BDE-153, BDE-154, BDE-183, and BDE-209 were quantified in the SFE extracts by LC/NI-APPI/MS/MS that is particularly well-suited for the analysis of the problematic BDE-209 [36]. Field blanks (n = 3) were obtained by SFE extraction of Ottawa ignition sand and analysis by LC/NI-APPI/MS/MS. Levels of tri- to hepta-BDE congeners in field blanks were below the detection limit and thus data were not blank corrected.

3. Results and discussion

3.1. SRM 2585 sample preparation

The levels of the eight PBDEs in SRM 2585 extracted with scR134a and quantified by LC/NI-APPI/MS/MS along with the certified NIST values for the PBDE congeners are presented in Table 1. The effects of wetting, not wetting, and dispersing SRM 2585 on an inert media on SFE recoveries and precision for the eight PBDE congeners were investigated. As a baseline to compare subsequent wetting and dispersant effects on SFE recoveries, a temperature study was performed on non-wet (dry) SRM 2585. At all temperatures studied, recoveries were approximately 50% for the tri- to hexa-PBDE congeners while recoveries were dramatically lower for the higher brominated congeners. Dispersing the dry dust onto an Ottawa ignition sand matrix was explored for its ability to evenly distribute the dust and permit a more uniform pathway for scR134a and increase the efficiency of R134a extraction by increasing the fluids access to dust particles. Dispersing SRM 2585 resulted in less restrictor plugging than without a matrix dispersant. Additionally, the micro-pores of the dust may become more accessible to the low viscosity, supercritical R134a which would increase the kinetics of extraction and recoveries over dry dust. For isothermal extractions, while neither SFE on dry dust nor SFE on the dry dust dispersed on Ottawa sand produced exhaustive extraction for the highly brominated congeners, an increased extraction of the higher molecular weight PBDE congeners was observed in the dust dispersed on Ottawa sand. The percent average relative standard deviation (%ARSD) for dry dust samples dispersed on Ottawa sand was 19.0%, while the %ARSD for the dry samples with no dispersant present was 29.1%, indicating that a higher precision was achieved by dispersing the dust on the Ottawa sand. Visually, it was observed that dry SFE changed the dust from a fluffy texture with a grey hue, to a compact, brick-like texture with a tan hue during extraction. When the R134a is flushed through a dry, compact dust sample, dust would entrain and block the stainless-steel frit on the SFE cell exit. The restricted R134a remains statically pressurized in the dust cell and the flow of R134a will either cease, or intermittently release from the restrictor giving irreproducible SFE flow and poor precision.

Benner studied the SFE of PAHs and PCBs from SRM 1649a Urban Dust standards and concluded that when the dust matrix is swollen with water or dichloromethane extraction efficiency is increased [26]. This increase in recovery over SFE on non-wet dust is hypothesized to be due to matrix sites interacting with high molecular weight PAHs which are not easily disrupted by fluid modified carbon dioxide [26]. Increased temperatures and water swelling have a greater effect than fluid modifiers such as dichloromethane for soil matrices, but dust matrices are an even more challenging matrix from which to extract large molecules. In our study, we also found severe restrictor plugging with SFE on dust wet with water. The use of an automated ISCO 3560 is recommended in such cases; however, as this instrument is no longer commercially produced and one was not available for our use, wetting of the dust matrix with dichloromethane was explored for its ability to swell the dust and increase the permeability of the matrix so that PBDE desorption is facilitated. Our dichloromethane wet dust samples were amenable to SFE using our in-house extraction unit. Additionally, less restrictor plugging was observed in the dichloromethane wet SFE experiments, allowing for greater extraction efficiencies at higher temperatures. When the SFE extraction cell was examined post-extraction it was noted that the dust retained its fluffy texture throughout the extraction and did not compact or change color.

Swelling of the dust matrix can potentially disrupt the strong matrix–analyte interactions and reduce the energy necessary to desorb and solvate the analyte from the matrix. Thus, lower extraction temperatures may be required for lower molecular weight analytes with wetting. As the micro-pores of the dust swell open, the low viscosity, supercritical R134a can more readily permeate the dust and increase the extraction kinetics. In comparing the isothermal extraction of dry and dichloromethane wet dust, an increased extraction of the higher molecular weight PBDE congeners was observed in the dichloromethane wet samples of Table 1. The ARSD for the dichloromethane wet samples was 23.6% while the ARSD for the dry samples was 29.1%, indicating that in addition to higher recoveries, a higher precision was achieved by wetting the dust. Although the recoveries are improved for the lower congeners with dichloromethane wetting, it is only by wetting the dust with dichloromethane at 200 °C that a high recovery (86.5 ± 6.1%) for BDE-209 was realized.

While it can be argued that in the dichloromethane wet R134a extracts the R134a fluid was modified with dichloromethane, this was not done in the traditional fashion of adding the fluid modifier to the high-pressure pump and delivering the fluid in a constant percentage of the modifier. In these experiments SRM 2585 was wet with dichloromethane primarily to swell the dust matrix and affect the extraction efficiency. Various models such as the Hildebrand solubility parameter, Hansen solubility parameters, and Kamlet–Taft solvatochromic parameters will afford the comparison of solvent properties between

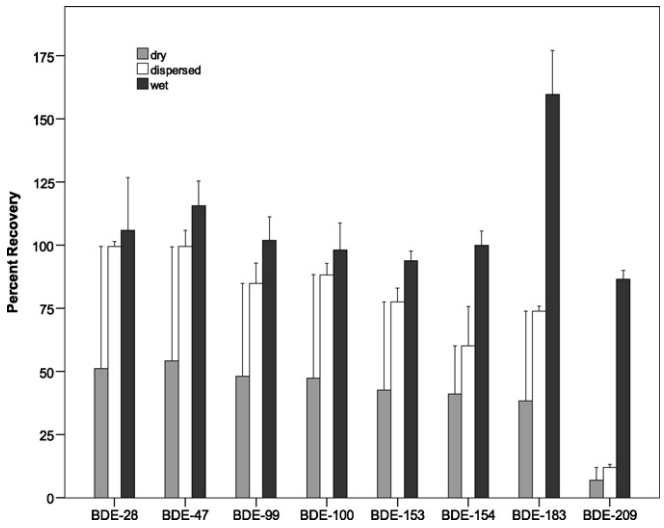


Fig. 1. Comparison of percent recoveries at 200 °C for SRM 2585 using the three SFE sample preparation techniques. Error bars represent ±1.0 standard error of the mean.

supercritical and liquid solvents [34,37–39]. Though the dipole moment of dichloromethane (1.55 D) and dielectric constant are slightly less than R134a, both the Hildebrand and Hansen parameters for dichloromethane suggest that the dispersion parameter can be enhanced by using dichloromethane modified mixtures. Kamlet–Taft solvatochromic parameters ascribe little to no acidity or basicity to both fluids but the dipolarity/polarizability parameter for dichloromethane ($\pi^* = 0.82$) is greater than that of scR134a (π^* is adjustable between 0 and 0.4 with fluid density above the critical point).

3.2. SFE temperature

For each SRM 2585 sample preparation method, SFE temperatures of 110, 150 and 200 °C were investigated. The thermodynamic relationship for the mole fraction solubility, y_2, of a solid in a supercritical fluid at equilibrium is given by

$$y_2 = \frac{P_2^{sat}[V_2^o(P - P_2^{sat})/RT]}{\phi_2} \approx \frac{P_2^{sat}[V_2^o P/RT]}{\phi_2} \quad (1)$$

where P_2^{sat} is the saturated vapor pressure of the solid, ϕ_2 is the fugacity coefficient, V_2^o is the solid molar volume, and P and T are the system pressure and temperature, respectively. Solid solubility in supercritical fluids can be envisioned as the enhancement over ideal solubility based upon vapor pressure alone. This enhancement scales with fluid pressure (density) and at pressures about the critical point the enhancement is more pronounced due to a microscopic phenomenon known as "clustering" where solvent molecules cluster about a solute and the local solvent density approaches 2.5 times the bulk fluid density. As solvent–solute clustering usually occurs at ~0.6 the critical density of the solvent (R134a $\rho_c = 0.51\ g\ mL^{-1}$), this effect will not be relevant to the liquid-like densities studied herein.

However, with elevated fluid temperatures, P_2^{sat} is increased and the solubility of higher brominated congeners with high enthalpies of vaporization and lower vapor pressures will benefit. The vapor pressures of the PBDEs range from 0.12 Pa for mono-brominated PBDEs to 58 μPa for the hepta-brominated congeners [40]. A drawback to an increased extraction temperature is decreased supercritical fluid density which will reduce fluid density, π^* values, and consequently solvent strength.

PBDEs can exist adsorbed to the surface of the dust particle and trapped in the bulk of the particle as the particle continues to grow. If PBDEs are simply adsorbed to the surface of the dust particle, the dry and dispersed SF experiments will produce similar recoveries. This should be dictated mainly by extraction kinetics exhibiting increased extractions at higher temperatures as is observed in Table 1. The effect of lowered fluid density at higher temperatures does not decrease recoveries indicating that the temperature effect on vapor pressure or overcoming the matrix interaction dominates the extraction efficiency. Fig. 1 compares SF extractions at high temperatures using the three sample preparation techniques investigated. When the dust is swollen with dichloromethane, (1) potentially the inner PBDEs trapped in the bulk dust particle become accessible to the fluid or (2) the fluid modifier effect is pronounced, or a combination of both. Regardless, enhanced recoveries are observed for the highly brominated PBDEs that cannot be achieved by the other two extraction techniques.

4. Conclusions

The optimum extraction of PBDEs from house dust using supercritical R134a is obtained when the dust is pre-wet with dichloromethane prior to extraction to swell the dust. An increase in fluid temperature is more important than maintaining high fluid densities at lower temperatures to increase extraction efficiencies and extraction at 200 °C. Only a combination of high temperatures and pre-wetting the dust with dichloromethane produced high recovery of the environmentally important, fully brominated PBDE congener, BDE-209.

Acknowledgments

We are grateful to Michelle Schantz at NIST for providing SRM 2585. This material is based upon work supported by the National Science Foundation under grant number CHE-0718530. F.C.C. acknowledges the support of the EPA GRO Program.

References

[1] S. Corr, J. Fluorine Chem. 118 (2002) 55–67.
[2] M.J. Karter, Fire Loss in the United States during 2006, NFPA, Fire Analysis and Research Division, Quincy, MA, 2007, p. 34.
[3] R. Renner, Environ. Sci. Technol. 38 (2004) 14A.
[4] B.S.E.F., Major Brominated Flame Retardants Volume Estimates, Bromine Science and Environmental Forum, Brussels, 2003.
[5] European Court of Justice, Directive 2002/95/EC – Electrical and Electronic Equipment – Restriction of Use of Certain Hazardous Substances – Decabromodiphenyl Ether ('DecaBDE') – Commission Decision 2005/717/EC – Exemption of DecaBDE from the Prohibition on Use, 2008.
[6] D. Meironyte, K. Noren, A. Bergman, J. Toxicol. Environ. Health 58 (1999) 329–341.
[7] R.A. Hites, Environ. Sci. Technol. 38 (2004) 945–956.
[8] A. Schecter, M. Pavuk, O. Päpke, J.J. Ryan, L. Birnbaum, R. Rosen, Environ. Health Perspect. 111 (2003) 1723–1729.
[9] A. Sjödin, D.G. Patterson, A. Bergman, Environ. Sci. Technol. 35 (2001) 3830–3833.
[10] A. Sjödin, L. Wong, R.S. Jones, A. Park, Y. Zhang, C. Hodge, E. Dipietro, C. McClure, W. Turner, L.L. Needham, D.G. Patterson, Environ. Sci. Technol. 42 (2008) 1377–1384.
[11] M. Lorber, J. Expos. Sci. Environ. Epidemiol. 18 (2008) 2–19.
[12] A. Bocio, J.M. Llobet, J.L. Domingo, J. Corbella, A. Teixidó, C. Casas, J. Agric. Food Chem. 51 (2003) 3191–3195.
[13] A.N. Schecter, O. Päpke, R.T. Harris, K.C. Tung, A. Musumba, J. Olson, L. Birnbaum, Environ. Health Perspect. 114 (2006) 1515–1520.
[14] A. Schecter, O. Päpke, K. Tung, D. Staskal, L. Birnbaum, Environ. Sci. Technol. 38 (2004) 5306–5311.
[15] J.G. Allen, M.D. McClean, H.M. Stapleton, J.W. Nelson, T.F. Webster, Environ. Sci. Technol. 41 (2007) 4574–4579.
[16] H.M. Stapleton, N.G. Dodder, J.H. Offenberg, M.M. Schantz, S.A. Wise, Environ. Sci. Technol. 39 (2005) 925–931.
[17] H.A. Jones-Otazo, J.P. Clarke, M.L. Diamond, J.A. Archbold, G. Ferguson, T. Harner, G.M. Richardson, J.J. Ryan, B. Wilford, Environ. Sci. Technol. 39 (2005) 5121–5530.
[18] H.M. Stapleton, T. Harner, M. Shoeib, J.M. Keller, M.M. Schantz, S.D. Leigh, S.A. Wise, Anal. Bioanal. Chem. 384 (2006) 791–800.

[19] S. Harrad, S. Hazrati, C. Ibarra, Environ. Sci. Technol. 40 (2006) 4633–4638.
[20] J. Tan, S.M. Cheng, A. Loganath, Y.S. Chong, J.P. Obbard, Chemosphere 66 (2007) 985–992.
[21] M. Karlsson, A. Julander, B. van Bavel, L. Hardel, Environ. Int. 33 (2007) 62–69.
[22] N. Wu, T. Herrmann, O. Paepke, J. Tickner, R. Hale, E. Harvey, M.J. La Guardia, M.D. McClean, T.F. Webster, Environ. Sci. Technol. 41 (2007) 1584–1589.
[23] A. Schecter, O. Päpke, J.E. Joseph, K. Tung, J. Toxicol. Environ. Health 68 (2005) 501–513.
[24] A. Covaci, S. Voorspoels, L. Ramos, H. Neels, R. Blust, J. Chromatogr. A 1153 (2007) 145–171.
[25] H.M. Stapleton, Anal. Bioanal. Chem. 386 (2006) 807–817.
[26] B.A. Benner, Anal. Chem. 70 (1998) 4594–4601.
[27] M.D. Burford, S.B. Hawthorne, D.J. Miller, Anal. Chem. 65 (1993) 1497–1505.
[28] S.B. Hawthorne, D.J. Miller, Anal. Chem. 58 (1987) 1705–1708.
[29] J.J. Langenfeld, S.B. Hawthorne, D.J. Miller, J. Pawliszyn, Anal. Chem. 67 (1996) 1727–1736.
[30] J.J. Langenfeld, S.B. Hawthorne, D.J. Miller, J. Pawliszyn, Anal. Chem. 65 (1993) 338–344.
[31] A. Altwaiq, M. Wolf, R. van Eldik, Anal. Chim. Acta 491 (2003) 111–123.
[32] R. Rodil, A.M. Carro, R.A. Lorenzo, R.C. Torrijos, Anal. Chem. 77 (2005) 2259–2265.
[33] K. Hartonen, S. Bøwadt, S.B. hawthorne, M. Riekkola, J. Chromatogr. A 774 (1997) 229–242.
[34] A.P. Abbott, C.A. Eardley, J. Phys. Chem. B 102 (1998) 8574–8578.
[35] A.F. Lagalante, A.M. Clarke, T.J. Bruno, J. Phys. Chem. B 102 (1998) 8889–8892.
[36] A.F. Lagalante, T.D. Oswald, Anal. Bioanal. Chem. 391 (2008) 2249–2256.
[37] A.P. Abbott, S. Corrs, N.E. Durling, E.G. Hope, J. Phys. Chem. B 107 (2003) 10628–10633.
[38] A.P. Abbott, C.A. Eardley, J.E. Scheirer, Phys. Chem. Chem. Phys. 3 (2001) 3722–3726.
[39] A.F. Lagalante, R.L. Hall, T.J. Bruno, J. Phys. Chem. B 102 (1998) 6601–6604.
[40] A. Wong, Y.D. Lei, M. Alaee, F. Wania, J. Chem. Eng. Data 46 (2001) 239–242.

Talanta 80 (2010) 1121–1128

Contents lists available at ScienceDirect

Talanta

journal homepage: www.elsevier.com/locate/talanta

Assessment uncertainty associated to the analysis of organic compounds linked to particulate matter of atmospheric aerosols

Oscar Pindado Jiménez*, Rosa Mª Pérez Pastor, Susana García Alonso

Chemistry Division, CIEMAT, Av. Complutense 22, 28040 Madrid, Spain

ARTICLE INFO

Article history:
Received 17 April 2009
Received in revised form 20 August 2009
Accepted 27 August 2009
Available online 2 September 2009

Keywords:
Assessment uncertainty
Atmospheric aerosol
Gas chromatography–mass spectrometry (GC–MS)
Organic compounds
Validation

ABSTRACT

Current work has evaluated uncertainty associated to quantification of several organic compounds present in particulate matter of atmospheric aerosols, setting out the stages of analytical procedure that contribute most to the global uncertainty. Several sources of uncertainty have been identified, which were clustered into five main contributions: sampling, extraction, clean-up, derivatization and analysis. A discussion of the main contributions to the overall uncertainty is reported, allowing authors to locate the largest ones and plan future improvements. Combined uncertainties ranged between 10–18% (alkanes), 12–16% (PAHs), 10–18% (alcohols) and 9–21% (acids). The analytical procedure was validated by analysing a standard reference material (SRM1649a, urban dust). Also, the proposed method was applied to the analysis of four samples of particulate matter.

© 2009 Elsevier B.V. All rights reserved.

1. Introduction

Nowadays, there is a growing concern about atmospheric aerosols due to two main causes: their hazardous effects on human health as far as its role in climate change [1]. Particulate matter can induce chronic respiratory illness, cancer and premature dead; so many studies related to aerosols have been published recently [2–4]. Also, aerosols influence the global climate, directly by scattering and absorbing solar radiation, and indirectly by modifying cloud optical properties due to their ability to act as cloud condensation nuclei [5]. Thanks to increased awareness of the scientific community and the suppression almost all analytical difficulties, number of published works related to atmospheric aerosols have increased considerably [6–13]. Particulate matter is comprised for thousand of organic components. Many studies have summarized into aliphatic hydrocarbons, PAHs and polar species (acids and alcohols). Despite so many published studies, nowadays it is not known the accurate composition of atmospheric aerosols; simply it is known only a part of the organic fraction of the atmospheric aerosol [14].

Sample preparation for quantifying organic compounds involves several steps: firstly extraction procedures, in second place a clean-up step, followed by a derivatization reaction when necessary, and eventually quantification by chromatographic techniques [6]. Almost all these stages can produce losses or contamination and therefore generate uncertainty. Published studies have focused on quantifying the maximum number of species associated with particles and are not published data on their associated uncertainty.

Studying organic composition of atmospheric aerosol will allow understand and reduce dangerous effects that aerosols could produce. In order to make decisions it is important to have data with high quality. In analytical chemistry, quality can be demonstrated by calculating the uncertainty associated with the outcomes [15]. Specifically, uncertainty is defined as "*A parameter associated with the result of a measurement that characterises the dispersion of the values that could reasonably be attributed to the measure*' [16]. For this purpose, the expanded uncertainty might be used because provides an interval within which the results measured are believed to lie with higher level of confidence. This uncertainty is obtained by multiplying the combined standard uncertainty by a coverage factor, which is function on the level of confidence desired [17].

This work presents an analytical method for the identification and quantification of some constituents linked to particulate matter of atmospheric aerosols, including *n*-alkanes, PAHs, alcohols and carboxylic acids. In light of the above, purposes of this work were to assess uncertainty associated to quantification of organic compounds presents in particulate matter of aerosol, and to study each uncertainty source to determine critical stages of the analytical method in order to reduce them. Validation of methodology has been performed by analysing a standard reference material. Also, this methodology has been implemented to samples of particulate matter collected in a rural area of Madrid (Spain).

* Corresponding author. Tel.: +34 913 466 523; fax: +34 913 466 121.
E-mail address: oscar.pindado@ciemat.es (O.P. Jiménez).

0039-9140/$ – see front matter © 2009 Elsevier B.V. All rights reserved.
doi:10.1016/j.talanta.2009.08.036

2. Experimental

2.1. Chemicals

The analytical standards of *n*-alkanes and fatty acids were purchased to Sigma–Aldrich. Solution composed of alkanes from C_8 to C_{40}, was dissolved in hexane at 500 μg mL^{-1}. PAHs mixture (100 μg mL^{-1}) was obtained from Dr. Ehrenstorfer, GMBH. The analytical standard of alcohols (C_{12} to C_{24}) was acquired to Accustandart. Also, linoleic and oleic acids with purity higher than 99% were purchased from Fluka, meanwhile pinic, pinonic and norpinonic acids were obtained from Aldrich. Hexane, dichloromethane, acetonitrile, acetone, isooctane, ethyl acetate and methanol of GC grade were acquired to SDS. Other compounds, such as BSTFA, deuterated palmitic acid and 1–chlorododecane were supplied by Aldrich and Supelco.

All standards prepared from stock solutions were placed in sealed flasks and refrigerated at −4 °C until their analysis.

2.2. Materials and instruments

A high volume sampler with size cut <2.5 μm (CAV-A/HF, MCV España) was employed to collect aerosol particulate matter. Flow rate was 30.4 m^3 h^{-1}, sampling time was 24 h, collecting 730 m^3 of air. This volume of air generated 1.5 g of particulate matter.

Extraction was performed with an automatic Soxhlet device (Büchi B-811), being extracts concentrated using rotary evaporator (Büchi R-200). Clean-up step was carried out with silica gel column.

For gas chromatography, an Agilent 6890 chromatograph with automatic sampler and coupled to an Agilent 5975 mass spectrometer, was employed. For PAHs analysis, an Agilent series 1100 HPLC system with fluorescence detector was used.

2.3. Analytical procedure

Sample deposited on filters were Soxhlet extracted with 150 mL dichloromethane/acetone (4:1) for 8 h. The extracts were concentrated with a rotary evaporator to 1 mL and later with a slight stream of nitrogen to 100 μL. This extract was cleaned-up via sequential elution through a silica gel column using solvents of increasing polarity to provide four fractions to separate chromatographic analysis of: (1) alkanes; (2) PAHs; (3) alcohols; and (4) acids. Polar fractions were derivatized by reaction with N,O-bis-(trimethylsilyl)-trifluoroacetamide (BSTFA) to convert alcohols and acids to the trimethylsilyl ethers before GC/MS analyses.

Extracts with alkanes, alcohols and acids were analyzed using GC/MS. Operating conditions were as follows: initial oven temperature 50 °C, increased at a rate of 100 °C min^{-1} to 90 °C, held 5 min, then increased at rate of 5 °C min^{-1} to 200 °C and finally increased at rate of 10 °C min^{-1} to 300 °C and held for 23 min; PTV injector had a initial temperature of 60 °C, held for 0.5 min, then increased at a rate of 350 °C min^{-1} to 350 °C; operation mode: splitless with multiple injection; carrier gas: He; capillary column HP-5MS (30 m × 0.25 mm i.d. film thickness 0.25 μm) with flow-rate: 1 mL min^{-1}; detector operated in electronic impact mode (70 eV). For alcohols and acids temperature program changed slightly: initial temperature 50 °C, increased at a rate of 100 °C min^{-1} to 90 °C, held 1 min, then increased at rate of 10 °C min^{-1} to 150 °C and finally increased at rate of 5 °C min^{-1} to 290 °C and held for 5 min. PAHs were submitted to HPLC device according to an analytical procedure previously published [18].

Chromatographic peaks were identified by coinjection with authentic standard compounds, also compounds were identified by GC–MS analysis. Ions monitored were: alkanes (m/z = 51, 77, 85), alcohols (m/z = 75, 103) and acids (m/z = 75, 117).

3. Results and discussion

3.1. Validation of the analytical methodology

Validation can involve evaluating up to 14 parameters [19], without include uncertainty. In this paper, in addition to uncertainty, were determined the following parameters: precision, linearity and selectivity. For this purpose, calibration curves were obtained for all studied species.

Standard solution were analyzed in the range from 0.1 to 10 mg L^{-1} (alkanes), 5 to 500 μg L^{-1} (PAHs), 0.1–50 mg L^{-1} (alcohols) and 0.1–25 mg L^{-1} (acids) with good linearity (correlation coefficient > 0.996, >0.996, >0.990, >0.992 for alkanes, PAHs, alcohols and acids). Calculation of a seven-point linear plot with three replicates, based on linear regression and squared correlation coefficient were performed.

For an analytical system where the validation range does not include or approach it, the detection limit does not need to be part of a validation [19].

Sensitivity can be defined as the slope of calibration curve. For alkanes sensitivity ranged from 0.6 to 2.1 L mg^{-1}, for PAHs ranged from 0.2 to 5.7 L μg^{-1}, meanwhile ranged from 0.07 to 0.09 L mg^{-1} and from 0.04 to 0.08 L mg^{-1} for alcohols and acids, respectively.

Taking into account the lack of a certified reference material with all compounds involved in this work, traceability cannot be demonstrated for all ones. Just the reference material SRM1649a of urban dust certifies some PAHs. So, it has been employed to evaluate traceability of the analytical procedure described in this work for PAHs. Results are showed in Table 1.

3.2. Estimation of uncertainty

Uncertainty estimation associated with a result involves four main steps: (a) specify measure and; (b) identify uncertainty sources; (c) quantify uncertainty components; and (d) calculate combined uncertainty.

The expression to calculate the concentration of an analyte into atmospheric aerosol, expressed in ng m^{-3}, is shown in Eq. (1). This equation specifies measured in function of different variables:

$$\text{concentration} = \left(\frac{C_{\text{cal}} \times A \times V_{\text{s}}}{V_{\text{A}}}\right) \quad (1)$$

where C_{cal} is the analyte concentration obtained from calibration (in mg L^{-1}); A is the area of filter analyzed; V_{s} is the final diluted volume (0.5 mL for PAHs and 1 mL for the rest of compounds); V_{A} is the volume of air sampled (730 m^3). Area of filter affects final concentration because in this study we do not analyze the entire filter, half of the filter was used for inorganic analysis.

All parameters in Eq. (1) are main sources of uncertainty. However, they are not the only ones because each step of the analytical procedure can be an uncertainty source. The three schemes of the

Table 1
Results for analyze of certified material SRM1649a.

Analyte	Concentration certified SRM1649a (mg kg^{-1})	Concentration measured (mg kg^{-1})
An	0.432 ± 0.082	0.43 ± 0.05
Fl	6.45 ± 0.18	5.4 ± 0.8
Py	5.29 ± 0.25	5.4 ± 0.9
BaA	2.208 ± 0.073	1.9 ± 0.3
Chr	3.049 ± 0.060	2.5 ± 0.5
BbF	6.45 ± 0.64	4.9 ± 0.9
BkF	1.913 ± 0.031	1.5 ± 0.3
BaP	2.509 ± 0.087	2.0 ± 0.3
In(123cd)Py	3.18 ± 0.72	2.8 ± 0.5

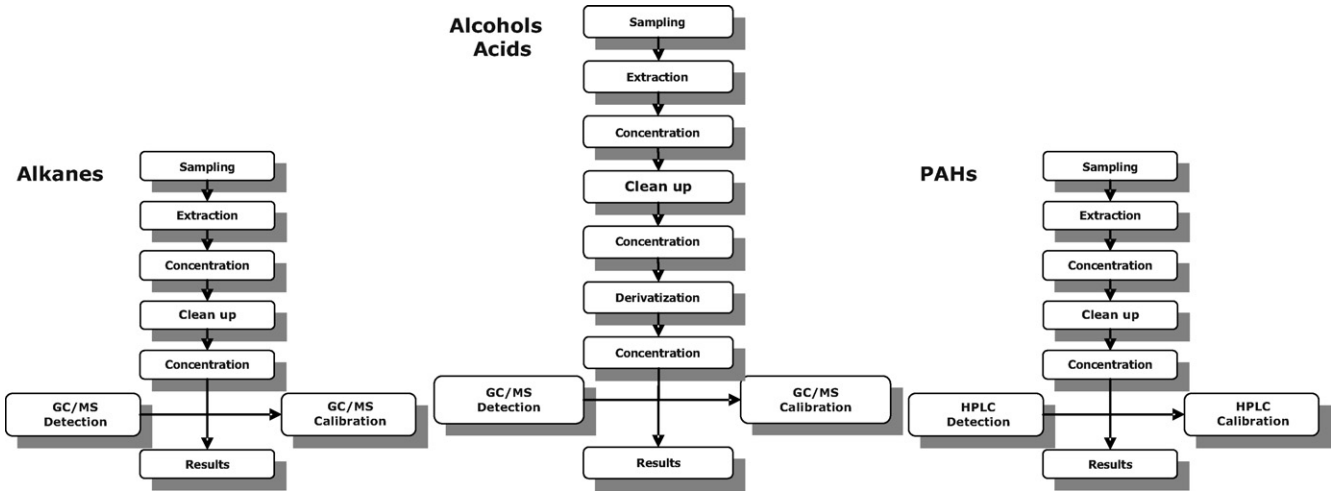


Fig. 1. Diagrams of analytical procedures to determinate concentrations of alkanes, PAHs, alcohols and acids associated to particulate matter of atmospheric aerosol.

analytical procedures to determinate the concentrations of alkanes, PAHs, alcohols and acids are presented in Fig. 1.

According to these schemes, the air concentrations of organic compounds were mainly affected by the following sources: sampling; extraction; clean-up; derivatization; chromatographic analysis.

The combined uncertainty (in terms of relative uncertainty) can be calculated using Eq. (2):

$$U_r(\text{Total}) = \sqrt{U_r^2(\text{Conc}) + U_r^2(\text{Samp}) + U_r^2(\text{Ext}) + U_r^2(\text{Clean}) + U_r^2(\text{Deriv})} \quad (2)$$

To calculate all variables present in Eq. (2), called sources of uncertainty, and resolve it, there are two alternatives: (a) evaluating uncertainty arising from each individual source and then combining them or (b) determining directly the combined contribution to the uncertainty on the result from some or all of the sources using method performance data [15]. In practice, a combination of both alternatives is usually necessary and convenient.

3.2.1. Estimation of the uncertainty derived from chromatographic analysis

This uncertainty is a combination of the uncertainties associated with chromatographic analysis. It includes uncertainty coming from sample volume, air volume, filter area and analyte concentration.

3.2.2. Sample volume

Uncertainty derived from volume of sample, $U(V_{\text{sample}})$, is calculated from three different sources: (a) the tolerance of volumetric material, through a triangular distribution within 0.01 mL as minimal division ($U_{\text{Vs1}} = 0.0041$ mL), (b) the volumetric repeatability is described by the standard uncertainty obtained from the weighing (four times) each volumetric material full of solvents ($U_{\text{Vs2}} = 0.0004$ mL) and (c) the temperature effect, that was negligible. The uncertainty from the volume of sample, $U(V_{\text{sample}})$, was 0.0041 mL for all compounds evaluated.

3.2.3. Air volume

This uncertainty is calculated in section 3.2.2.

3.2.4. Filter area

Uncertainty derived from filter area is calculated through a triangular distribution within 0.1 cm ($U_{\text{F}} = 0.041$ cm).

3.2.5. Analyte concentration

Uncertainty associated with analyte concentration (U_{AC}) is a combination of three sources which in turn are combination of several uncertainties. The three main sources are (a) analytical standards employed [U_{AS}], (b) chromatographic calibrate involve uncertainty from linear least squares calibration [U_{cal}] and (c) repeatability [U_{rep}].

In order to estimate uncertainty associated with analytical standards (U_{AS}) there were considered three main contributions: the first one was uncertainty of initial concentrations (U_{AS1}) according to certificates, the second one was uncertainty of dilution procedure along all analytical process (U_{AS2}) and the third one was uncertainty of weighty of each analytical standard ($U_w = 1.9\,\text{exp}^{-5}\,g$). Contribution to uncertainty of initial concentration was estimated from certificate values supplied by the manufacturer, 0.5% for alkanes and 1% for PAHs. Thus U_{AS1} was 0.1 mg L^{-1} for PAHs and ranged from 2.45 to 2.51 mg L^{-1} for alkanes. On the other hand, contribution to uncertainty of dilution procedure was 0.01 mL for alkanes and PAHs, and 0.02 mL for alcohols and acids. To calculate these uncertainties were considered contributions of temperature, repeatability and certified uncertainty in volumetric material. There is no information available about dilution procedure and 100% of the compound dissolves.

Uncertainty from linear least squares calibration [U_{cal}] is mainly due to variability in responses showed by the instrument. According with expression of linear regression, to calculate uncertainty of calibration, the subsequent expression is employed:

$$U^2_{C_{\text{calibration}}} = \frac{U^2_{\text{signal}}}{(\text{signal-intercept})^2} + \frac{U^2_{\text{intercept}}}{(\text{signal-intercept})^2} + \frac{U^2_{\text{slope}}}{(\text{slope})^2} \quad (3)$$

The first term have to be calculated by a repetition test. However, the second and third terms can be estimated from information given by software used to derive calibration. Table 2 includes the uncertainties associated with calibration of all compounds.

The last contribution to uncertainty of analyte concentration is repeatability [U_{rep}]. It was calculated by the standard uncertainty obtained from the repetition (four times) of the chromatographic measurement. Table 3 summarized these uncertainties.

As result, uncertainty associated with analyte concentration is shown in Table 4. In order to calculate this uncertainty, the subsequent expression is employed:

$$U^2_{\text{conc}} = U^2_{\text{AS}} + U^2_{\text{cal}} + U^2_{\text{rep}} \quad (4)$$

Table 2
Uncertainties associated with calibration parameters.

Analyte	U^2_{signal}/(signal-intercept)^2	$U^2_{intercept}$/(signal-intercept)^2	U^2_{slope}/(slope)^2	Analyte	U^2_{signal}/(signal-intercept)^2	$U^2_{intercept}$/(signal-intercept)^2	U^2_{slope}/(slope)^2
Heneicosane	0.00045	2.38×10^{-06}	1.51×10^{-06}	Dodecanol	0.00217	1.79×10^{-03}	4.71×10^{-06}
Docosane	0.00055	2.58×10^{-06}	3.28×10^{-06}	Tridecanol	0.00015	8.97×10^{-04}	3.21×10^{-06}
Tricosane	0.00050	2.58×10^{-06}	3.27×10^{-06}	Tetradecanol	0.00005	3.32×10^{-04}	1.37×10^{-06}
Tetracosane	0.00064	1.78×10^{-06}	2.70×10^{-07}	Pentadecanol	0.00010	4.42×10^{-04}	1.89×10^{-06}
Pentacosane	0.00062	1.48×10^{-06}	2.44×10^{-06}	Hexadecanol	0.00024	4.63×10^{-04}	1.84×10^{-06}
Hexacosane	0.00035	1.83×10^{-06}	2.51×10^{-06}	Octadecanol	0.00006	3.57×10^{-04}	1.25×10^{-06}
Heptacosane	0.00058	1.29×10^{-06}	2.84×10^{-06}	Eicosanol	0.00012	2.76×10^{-04}	8.80×10^{-07}
Octacosane	0.00044	1.53×10^{-06}	2.51×10^{-06}	Docosanol	0.00009	3.84×10^{-04}	1.36×10^{-06}
Nonacosane	0.00048	1.16×10^{-06}	2.81×10^{-06}	Dodecosanoic	0.00012	7.11×10^{-06}	2.80×10^{-06}
Triacontane	0.00050	1.10×10^{-06}	2.68×10^{-06}	Tridecanoic	0.00026	7.18×10^{-06}	3.62×10^{-06}
Hentriacontane	0.00049	1.07×10^{-06}	2.25×10^{-06}	Tetradecanoic	0.00350	9.55×10^{-06}	4.36×10^{-06}
Dotriacontane	0.00077	9.73×10^{-07}	2.63×10^{-06}	Pentadecanoic	0.00084	8.91×10^{-06}	4.14×10^{-06}
Tritriacontane	0.00060	8.99×10^{-07}	2.08×10^{-06}	Hexadecanoic	0.00015	8.49×10^{-06}	4.12×10^{-06}
Ph[a]	0.00020	3.98×10^{-09}	8.13×10^{-10}	Heptadecanoic	0.00008	1.14×10^{-05}	4.15×10^{-06}
An	0.00078	1.09×10^{-09}	2.07×10^{-10}	Octadecanoic	0.00016	1.11×10^{-05}	4.17×10^{-08}
Fl	0.00021	8.58×10^{-10}	1.76×10^{-10}	Nonadecanoic	0.00008	1.30×10^{-05}	3.72×10^{-06}
Py	0.00144	2.83×10^{-09}	6.04×10^{-10}	Eicosanoic	0.00013	1.70×10^{-05}	4.49×10^{-06}
BaA	0.00039	1.54×10^{-09}	2.92×10^{-10}	Heneicosanoic	0.00016	2.06×10^{-05}	4.05×10^{-06}
Chr	0.00027	1.64×10^{-11}	1.21×10^{-11}	Docosanoic	0.00002	2.31×10^{-05}	4.11×10^{-06}
BbF	0.00039	8.09×10^{-10}	1.95×10^{-10}	Tricosanoic	0.00021	3.76×10^{-05}	4.98×10^{-06}
BkF	0.00032	6.36×10^{-12}	3.41×10^{-10}	Tetracosanoic	0.00072	6.16×10^{-05}	4.87×10^{-06}
BaP	0.00031	1.30×10^{-09}	9.63×10^{-10}	Pinic	0.00012	1.77×10^{-03}	8.82×10^{-06}
DBA	0.00040	1.48×10^{-09}	3.45×10^{-10}	Pinonic	0.00047	3.37×10^{-04}	3.00×10^{-05}
BghiPe	0.00096	1.96×10^{-09}	4.28×10^{-10}	Norpinonic	0.00144	7.65×10^{-04}	8.98×10^{-05}
				Oleic	0.00018	1.25×10^{-03}	2.25×10^{-05}
				Linoleic	0.00008	1.02×10^{-02}	1.57×10^{-05}

[a] PAHs: Ph, Phenanthrene; An, Anthracene; Fl, Fluoranthene; Py, Pyrene; BaA, Benzo[a]anthracene; Chr, Chrysene; BbF, Benzo[b]fluoranthene; BkF, Benzo[k]fluoranthene; BaP, Benzo[a]pyrene; DBA, Dibenzo[ah]anthracene; BghiPe, Benzo[ghi]perilene.

Table 3
Uncertainties associated with repeatability of chromatographic measure.

Analyte	U_{Rep} (mg L^{-1})[a]	U_{Rep} standard	Analyte	U_{Rep} (mg L^{-1})[a]	U_{Rep} standard	Analyte	U_{Rep} (mg L^{-1})	U_{Rep} standard
Heneicosane	0.0732	0.0146	BaA	1.9422	0.0202	Tetradecanoic	1.1000	0.0022
Docosane	0.0671	0.0134	Chr	1.7337	0.0177	Pentadecanoic	1.0600	0.0022
Tricosane	0.0828	0.0166	BbF	1.9987	0.0206	Hexadecanoic	1.2200	0.0027
Tetracosane	0.0779	0.0156	BkF	1.8476	0.0187	Heptadecanoic	1.2400	0.0028
Pentacosane	0.0653	0.0131	BaP	1.8325	0.0178	Octadecanoic	1.3100	0.0028
Hexacosane	0.0724	0.0145	DBA	1.9985	0.0205	Nonadecanoic	0.9700	0.0023
Heptacosane	0.0781	0.0156	BghiPe	3.0384	0.0320	Eicosanoic	1.2500	0.0029
Octacosane	0.0796	0.0159	Dodecanol	1.3400	0.0019	Heneicosanoic	0.7400	0.0025
Nonacosane	0.0899	0.0180	Tridecanol	1.5100	0.0024	Docosanoic	0.8700	0.0026
Triacontane	0.0833	0.0167	Tetradecanol	1.6800	0.0017	Tricosanoic	0.8500	0.0027
Hentriaconta.	0.1136	0.0227	Pentadecanol	1.3300	0.0020	Tetracosanoic	0.6500	0.0019
Dotriacontan.	0.0934	0.0187	Hexadecanol	1.4200	0.0023	Pinic	0.1640	0.0212
Tritriacontane	0.1089	0.0218	Octadecanol	1.4700	0.0025	Pinonic	0.2241	0.0274
Ph	1.4769	0.0159	Eicosanol	1.7700	0.0028	Norpinonic	0.3357	0.0357
An	2.7887	0.0288	Docosanol	1.8800	0.0028	Oleic	0.1713	0.0274
Fl	1.4066	0.0152	Dodecosanoic	1.0200	0.0024	Linoleic	0.1324	0.0204
Py	3.9174	0.0397	Tridecanoic	0.3300	0.0006			

[a] PAHs: U_{Rep} (μg L^{-1}).

Table 4
Uncertainties associated with concentration.

Analyte	U^2_{conc}	Analyte	U^2_{conc}	Analyte	U^2_{conc}
Heneicosane	0.000443	BaA	0.000412	Tetradecanoic	0.000088
Docosane	0.000405	Chr	0.000317	Pentadecanoic	0.000076
Tricosane	0.000501	BbF	0.000428	Hexadecanoic	0.000078
Tetracosane	0.000605	BkF	0.000354	Heptadecanoic	0.000078
Pentacosane	0.000397	BaP	0.000321	Octadecanoic	0.000078
Hexacosane	0.000433	DBA	0.000424	Nonadecanoic	0.000076
Heptacosane	0.000469	BghiPe	0.001029	Eicosanoic	0.000079
Octacosane	0.000478	Dodecanol	0.000090	Heneicosanoic	0.000077
Nonacosane	0.000550	Tridecanol	0.000077	Docosanoic	0.000077
Triacontane	0.000504	Tetradecanol	0.000074	Tricosanoic	0.000078
Hentriaconta.	0.000741	Pentadecanol	0.000075	Tetracosanoic	0.000075
Dotriacontan.	0.000576	Hexadecanol	0.000076	Pinic	0.000524
Tritriacontane	0.000701	Octadecanol	0.000077	Pinonic	0.000822
Ph	0.000257	Eicosanol	0.000079	Norpinonic	0.001350
An	0.000834	Docosanol	0.000079	Oleic	0.000823
Fl	0.000235	Dodecosanoic	0.000076	Linoleic	0.000594
Py	0.001582	Tridecanoic	0.000071		

In order to estimate the uncertainty derived from chromatographic analyses, all contributions were expressed as standards uncertainties. For models involving only a product or quotient, for instance expression (1), the combined standard uncertainty is given by

$$U_{\text{chromatography analysis}} = \sqrt{\left(\frac{U_{V_{\text{sample}}}}{V_{\text{sample}}}\right)^2 + \left(\frac{U_F}{A_{\text{filter}}}\right)^2 + \left(\frac{U_{\text{concentration}}}{\text{concentration}}\right)^2} \quad (5)$$

In order to calculate combined standard uncertainty we chose the procedure that considers there is not covariance between each source of uncertainty. Thus, Table 5 shows the uncertainties derived from chromatographic analysis for each compounds.

3.2.6. Estimation of the uncertainty derived from sampling

High volume samplers do not maintain constant flow rate so can generate bias in caudal of sampling air. However, this bias is hardly ever published, only there is studies have compared different methods for sampling of atmospheric aerosol [20,21]. For this reason, uncertainty related to sampling is difficult to evaluate and thus to minimize.

This uncertainty is calculated considering two contributions: (a) temperature effect, produced by variation of temperature during sampling, through a rectangular distribution within ±15 °C (U_{S1} = 2.32 m^3) and (b) precision of samplers, in this case we assumed an error of 5% in the air volume collected by the samplers (U_{S2} = 36.50 m^3). The combination of these contributions, considering both independents, generate a final value for $U(V_{\text{sampling}})$ of 36.57 m^3. The high volume sampler used in this work, collected a total air volume of 730 m^3, so standard uncertainty $U^2_{(\text{sampling})}$ was 0.00251.

3.2.7. Estimation of the uncertainty derived from Soxhlet extraction

As part of the in-house evaluation of the method, an extraction experiment was planned to evaluate repeatability and recovery. It was performed four replicates. Filters, which are similar those employed to collect samples, were spiked with analytes at similar concentration to those of air samples (the standard solution range chosen (0.5 and 1 mg L^{-1}) was selected in order to averaging the entire compounds studied). The standard solution range chosen was selected in order to averaging the entire range of compounds studied. Uncertainties were calculated as uncertainties type A. However, uncertainties associated to this experiment actually included contributions from extraction process, chromatographic analysis and derivatization process when be necessary. Hence, to know the contributions from Soxhlet extraction, uncertainty value must be calculated as follows:

$$u^2_{\text{extraction}} = u^2_{\text{ext.exp}} - (u^2\text{chrom analysis} + u^2\text{derivatization}) \quad (6)$$

Table 6 summarizes the contribution of the extraction to uncertainty for each analyte.

3.2.8. Estimation of the uncertainty derived from clean-up step

It has been designed a method with performance data of the clean-up stage in order to evaluate its uncertainty. It was performed four replicates. As same as uncertainty derived from extraction, uncertainty calculated experimentally for clean-up included contributions from chromatographic analysis and derivatization procedure, so the uncertainty value is calculated as follows:

$$u^2_{\text{clean-up}} = u^2_{\text{clean-up exp.}} - (u^2\text{chrom analysis} + u^2\text{derivatization}) \quad (7)$$

Table 6 recapitulates results for this contribution.

3.2.9. Estimation of the uncertainty derived from derivatization

This source of uncertainty is only associated with polar compounds. To evaluate its contribution four derivatization experiments were performed. Uncertainty experimental includes the contribution from chromatographic analysis so it was necessary subtract it. Table 6 shows results obtained.

3.2.10. Calculating the combined uncertainty

Before combine the components of uncertainty, they must be expressed as standard uncertainties. The relationship between the combined standard uncertainty of a value y, $U_c(y)$, and the uncertainty of independent parameters $x_1, x_2, \ldots, x_n$ on which depends is shown in Eq. (3):

$$U_c(y(x_1, x_2, \ldots)) = \sqrt{\sum U(x, y_i)^2} \quad (8)$$

Standard uncertainties of each source are shown in Fig. 2. It has been shown that contributions derived of extraction are the most significant for several compounds. On the other hand, uncertainties derived of clean-up and derivatization are the lowest contribution for most compounds.

The final stage is to multiply the combined standard uncertainty by the chosen coverage factor k in order to obtain an expanded uncertainty (k = 2; coverage probability of 95%). Table 7 shows

Table 5
Uncertainties associated with analytical measure.

Analyte	$U^2_{\text{chrom anal}}$	Analyte	$U^2_{\text{chrom anal}}$	Analyte	$U^2_{\text{chrom anal}}$
Heneicosane	0.00680	BaA	0.00882	Tetradecanoic	0.00564
Docosane	0.00671	Chr	0.00882	Pentadecanoic	0.00558
Tricosane	0.00694	BbF	0.00882	Hexadecanoic	0.00559
Tetracosane	0.00716	BkF	0.00882	Heptadecanoic	0.00559
Pentacosane	0.00670	BaP	0.00882	Octadecanoic	0.00559
Hexacosane	0.00678	DBA	0.00882	Nonadecanoic	0.00557
Heptacosane	0.00687	BghiPe	0.00884	Eicosanoic	0.00559
Octacosane	0.00689	Dodecanol	0.00565	Heneicosanoic	0.00558
Nonacosane	0.00705	Tridecanol	0.00558	Docosanoic	0.00558
Triacontane	0.00695	Tetradecanol	0.00556	Tricosanoic	0.00559
Hentriaconta.	0.00742	Pentadecanol	0.00557	Tetracosanoic	0.00557
Dotriacontan.	0.00710	Hexadecanol	0.00558	Pinic	0.00699
Tritriacontane	0.00735	Octadecanol	0.00558	Pinonic	0.00757
Ph	0.00882	Eicosanol	0.00559	Norpinonic	0.00838
An	0.00883	Docosanol	0.00559	Oleic	0.00757
Fl	0.00882	Dodecosanoic	0.00558	Linoleic	0.00714
Py	0.00884	Tridecanoic	0.00555		

Table 6
Uncertainties associated with Soxhlet extraction, clean-up stage and derivatization procedure.

Analyte	$U^2_{(Soxhlet)}$	$U^2_{(clean\text{-}up)}$	$U^2_{Derivat}$	Analyte	$U^2_{(Soxhlet)}$	$U^2_{(clean\text{-}up)}$	$U^2_{Derivat}$
Heneicosane	0.0056	0.0008	–	Dodecanol	0.0006	0.0002	0.00143
Docosane	0.0071	0.0004	–	Tridecanol	0.0013	0.00001	0.00126
Tricosane	0.0032	0.0025	–	Tetradecanol	0.0056	0.0002	0.00013
Tetracosane	0.0046	0.0002	–	Pentadecanol	0.0035	0.00001	0.00090
Pentacosane	0.0002	0.0020	–	Hexadecanol	0.0072	0.0001	0.00087
Hexacosane	0.0018	0.00004	–	Octadecanol	0.0160	0.0003	0.00018
Heptacosane	0.0011	0.0032	–	Eicosanol	0.0179	0.0001	0.00030
Octacosane	0.0001	0.0003	–	Docosanol	0.0170	0.00004	0.00032
Nonacosane	0.0005	0.0026	–	Dodecosanoic	0.0012	0.0002	0.00004
Triacontane	0.0089	0.0002	–	Tridecanoic	0.0006	0.0001	0.00011
Hentriaconta.	0.0209	0.0003	–	Tetradecanoic	0.0029	0.0002	0.00007
Dotriacontan.	0.0056	0.00004	–	Pentadecanoic	0.0012	0.00001	0.000001
Tritriacontane	0.0001	0.0002	–	Hexadecanoic	0.0001	0.0001	0.00002
Ph	0.0071	0.0056	–	Heptadecanoic	0.0032	0.00001	0.00004
An	0.0024	0.0094	–	Octadecanoic	0.0029	0.000002	0.00004
Fl	0.0027	0.0003	–	Nonadecanoic	0.0039	0.0001	0.00014
Py	0.0024	0.0008	–	Eicosanoic	0.0016	0.0001	0.00030
BaA	0.0023	0.0001	–	Heneicosanoic	0.0007	0.00003	0.00008
Chr	0.0076	0.0006	–	Docosanoic	0.0008	0.0001	0.00021
BbF	0.0051	0.0002	–	Tricosanoic	0.0007	0.0027	0.00064
BkF	0.0060	0.0002	–	Tetracosanoic	0.0009	0.0048	0.00084
BaP	0.0040	0.0007	–	Pinic	0.0024	0.0001	0.00015
DBA	0.0035	0.0008	–	Pinonic	0.0154	0.0002	0.00002
BghiPe	0.0039	0.0001	–	Norpinonic	0.0131	0.0008	0.00034
				Oleic	0.0019	0.0004	0.00013
				Linoleic	0.0354	0.0001	0.00005

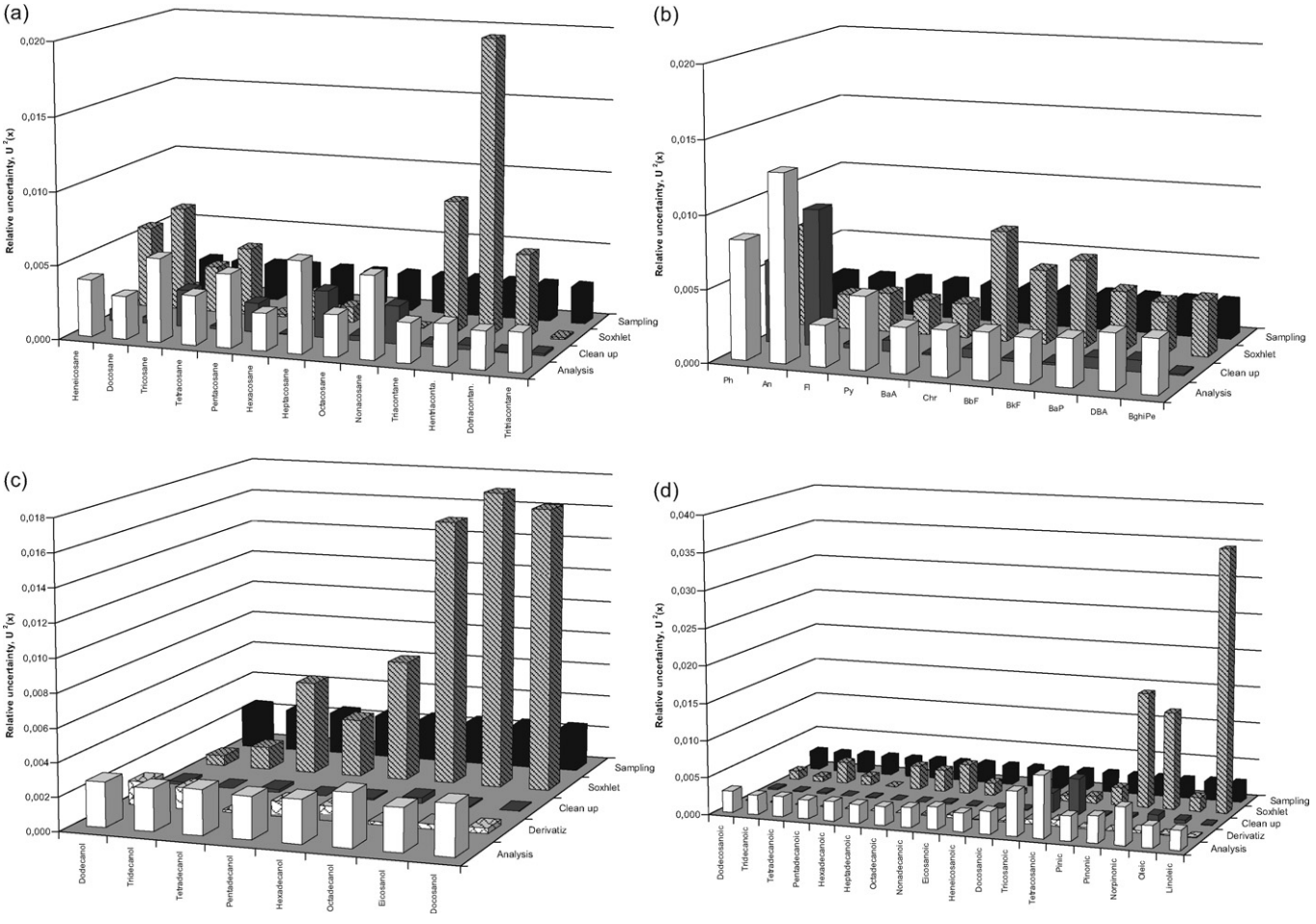


Fig. 2. Diagram of standard uncertainty of each contribution for (a) alkanes, (b) PAHs, (c) alcohols and (d) acids.

Table 7
Combined uncertainty and expanded uncertainty from several components presents in atmospheric aerosols.

Analyte	U_{combin} (%)	U_{expand} (%)	Analyte	U_{combin} (%)	U_{expand} (%)	Analyte	U_{combin} (%)	U_{expand} (%)
Heneicosane	13	25	BaA	12	23	Tetradecanoic	11	21
Docosane	13	26	Chr	14	28	Pentadecanoic	10	19
Tricosane	12	25	BbF	13	26	Hexadecanoic	9	18
Tetracosane	12	24	BkF	13	26	Heptadecanoic	11	21
Pentacosane	11	21	BaP	13	25	Octadecanoic	11	21
Hexacosane	11	21	DBA	13	25	Nonadecanoic	11	22
Heptacosane	12	23	BghiPe	12	25	Eicosanoic	10	20
Octacosane	10	20	Dodecanol	10	20	Heneicosanoic	9	19
Nonacosane	11	23	Tridecanol	10	21	Docosanoic	10	19
Triacontane	14	27	Tetradecanol	12	24	Tricosanoic	11	22
Hentriaconta.	18	35	Pentadecanol	11	22	Tetracosanoic	12	24
Dotriacontan.	12	25	Hexadecanol	13	26	Pinic	11	22
Tritriacontane	10	20	Octadecanol	16	31	Pinonic	16	32
Ph	16	31	Eicosanol	16	32	Norpinonic	16	32
An	15	30	Docosanol	16	32	Oleic	11	22
Fl	12	24	Dodecosanoic	10	20	Linoleic	21	43
Py	12	24	Tridecanoic	9	19			

Table 8
Concentrations and expanded uncertainties of several compounds.

Analyte	8/11 ($ng\,m^{-3}$)[a]	8/19 ($ng\,m^{-3}$)[a]	8/27 ($ng\,m^{-3}$)[a]	9/4 ($ng\,m^{-3}$)[a]	Analyte	8/11 ($ng\,m^{-3}$)	8/19 ($ng\,m^{-3}$)	8/27 ($ng\,m^{-3}$)	9/4 ($ng\,m^{-3}$)
Heneicosane	0.7 (0.1)	1.0 (0.2)	1.1 (0.2)	0.8 (0.2)	Dodecanol	64 (9)	56 (8)	56 (8)	50 (7)
Docosane	0.8 (0.2)	1.1 (0.2)	1.3 (0.3)	1.1 (0.2)	Tridecanol	11 (2)	9 (1)	9 (1)	9 (1)
Tricosane	0.8 (0.2)	1.0 (0.2)	1.6 (0.3)	1.3 (0.3)	Tetradecanol	63 (12)	36 (7)	36 (7)	43 (8)
Tetracosane	0.4 (0.1)	0.6 (0.1)	1.4 (0.2)	1.1 (0.2)	Pentadecanol	9 (2)	8 (1)	8 (1)	8 (1)
Pentacosane	0.5 (0.1)	0.6 (0.1)	1.8 (0.3)	1.3 (0.2)	Hexadecanol	12 (3)	10 (2)	9 (2)	12 (2)
Hexacosane	0.24 (0.03)	0.31 (0.04)	1.2 (0.2)	0.9 (0.1)	Octadecanol	9 (3)	7 (2)	7 (2)	11 (3)
Heptacosane	0.4 (0.1)	0.4 (0.1)	1.2 (0.2)	0.9 (0.2)	Eicosanol	–	–	15 (4)	18 (5)
Octacosane	0.26 (0.04)	0.26 (0.04)	0.8 (0.1)	0.7 (0.1)	Docosanol	–	–	–	–
Nonacosane	0.5 (0.1)	0.5 (0.1)	1.1 (0.2)	1.0 (0.1)	Dodecosanoic	19 (3)	17 (2)	16 (2)	18 (2)
Triacontane	0.3 (0.1)	0.3 (0.1)	0.6 (0.1)	0.5 (0.1)	Tridecanoic	6.0 (0.7)	5.0 (0.6)	6.1 (0.7)	5.1 (0.6)
Hentriaconta.	0.3 (0.1)	0.3 (0.1)	0.8 (0.2)	0.8 (0.2)	Tetradecanoic	24 (4)	22 (3)	23 (4)	23 (4)
Dotriacontan.	–	–	0.3 (0.1)	0.18 (0.04)	Pentadecanoic	11 (1)	11 (1)	14 (2)	12 (2)
Tritriacontane	–	–	0.18 (0.02)	0.13 (0.01)	Hexadecanoic	66 (7)	68 (7)	7.4 (0.8)	95 (10)
Ph	50 (12)	55 (14)	56 (14)	85 (21)	Heptadecanoic	7 (1)	6 (1)	0.6 (0.1)	7 (1)
An	3.0 (0.7)	1.0 (0.2)	2.0 (0.5)	2.0 (0.5)	Octadecanoic	39 (6)	35 (5)	48 (7)	49 (4)
Fl	75 (11)	94 (14)	104 (16)	86 (13)	Nonadecanoic	0.6 (0.1)	–	0.8 (0.1)	0.6 (0.1)
Py	235 (40)	420 (72)	480 (83)	352 (60)	Eicosanoic	2.1 (0.3)	–	4.3 (0.6)	2.7 (0.4)
BaA	19 (3)	24 (4)	30 (4)	28 (4)	Heneicosanoic	–	–	–	–
Chr	68 (14)	118 (25)	156 (33)	125 (26)	Docosanoic	3.8 (0.5)	–	5.2 (0.6)	4.0 (0.5)
BbF	28 (5)	40 (7)	68 (12)	56 (10)	Tricosanoic	1.6 (0.3)	–	1.8 (0.3)	2.0 (0.3)
BkF	7 (1)	9 (2)	16 (3)	14 (3)	Tetracosanoic	4.4 (0.8)	5 (1)	7 (1)	6 (1)
BaP	6 (1)	9 (2)	9 (2)	12 (2)	Pinic	7 (1)	7 (1)	17 (3)	17 (3)
DBA	–	–	–	–	Pinonic	29 (8)	21 (6)	27 (8)	28 (8)
BghiPe	26 (5)	48 (8)	–	56 (10)	Norpinonic	–	–	–	25 (7)
					Oleic	2.5 (0.4)	3.0 (0.5)	3.1 (0.5)	3.3 (0.5)
					Linoleic	0.6 (0.2)	–	–	–

[a] PAHs: ($pg\,m^{-3}$).

uncertainties combined and uncertainties expanded for all compounds analyzed.

3.3. Application to real samples

The developed method was applied to the analysis of four particulate matter samples of atmospheric aerosol collected in a rural area of Madrid (Spain) during summer of 2004. The data results of these samples are summarized in Table 8.

4. Conclusions

Some figures of merit, such as accuracy, linearity and selectivity for the simultaneous determination of alkanes, PAHs, alcohols and acids linked to atmospheric aerosol particles have been determined. Validation of methodology has been accomplished by analysing standard reference material SRM1649a of urban dust.

This work aimed at identifying the main sources of uncertainty associated to determination of organic components of atmospheric aerosols, being the expanded uncertainty also calculated. From the analysis of each step of our analytical procedure, we could identify those steps of the method carrying the highest contributions to the overall uncertainty. It may be concluded from this study that the extraction stage generates more uncertainty, mainly for unsaturated acids and alcohols with high molecular weight. Thanks this assessment uncertainty we can try to plan specific improvements able to enhance accuracy of this procedure. Soxhlet is a conventional extraction procedure so it will be difficult to improve their results, however microwave extraction and accelerate solvent extraction (ASE), which are worldwide used and are accepted in EPA methods, can be an adequate alternative to reduce uncertainty associated to extraction.

Acknowledgements

The authors would like to thanks the old “Ministerio de Ciencia y Educación” for finance this work under the project REN2003-08603-C04-02. In addition, “Comunidad de Madrid” for their sampling support is acknowledged.

References

[1] IPCC, Intergovernmental Panel on Climate Change, Third Assessment Report, Cambridge University Press, Cambridge, 2001.
[2] B.D. Ostro, S. Hurley, M.J. Lipsett, Environ. Res. 81 (1999) 231.
[3] C. Arden Pope III, R.T. Burnett, M.J. Thun, E.E. Calle, D. Krewski, K. Ito, G.D. Thurston, J. Med. Assoc. 287 (March 6) (2002).
[4] G. Wang, H. Wang, Y. Yu, S. Gao, J. Feng, S. Gao, L. Wang, Atmos. Environ. 37 (2003) 2893.
[5] O.L. Mayol-Bracero, O. Rosario, C.E. Corrigan, R. Morales, I. Torres, V. Pérez, Atmos. Environ. 35 (2001) 1735.
[6] A.I. Gogou, M. Apostolaki, E.G. Stephanou, J. Chromatogr. A 799 (1998) 215.
[7] I.G. Kavouras, N. Mihalopoulos, E.G. Stephanou, Environ. Sci. Technol. 33 (1999) 1028.
[8] C. Pio, C. Alves, A. Duarte, Atmos. Environ. 35 (2001) 389.
[9] Z.G. Guo, J.L. Feng, M. Fang, H.Y. Chen, K.H. Lau, Atmos. Environ. 37 (2004) 909.
[10] Y. Cheng, S.M. Li, A. Leithead, P.C. Brickell, W.R. Leaitch, Atmos. Environ. 38 (2004) 5789.
[11] X. Bi, G. Sheng, P. Peng, Y. Chen, J. Fu, Atmos. Environ. 39 (2005) 477.
[12] H. Yang, J. Zhen Yu, S. Sai Hang Ho, J. Xu, W.S. Wu, C. Hong Wan, W. Xiaodong, W. Xiaorong, W. Liansheng, Atmos. Environ. 39 (2005) 3735.
[13] J. Feng, C.K. Chan, M. Fang, M. Hu, L. He, X. Tang, Chemosphere 61 (2005) 623.
[14] C.A. Pio, C.A. Alves, A.C. Duarte, Atmos. Environ. 35 (2001) 1365.
[15] Quantifying Uncertainty in Analytical Measurement, Second edition, EURACHE/CITAC Guide CG 4, 2000.
[16] International Vocabulary of Basis and General Terms in Metrology, ISO, Geneve, 1993.
[17] S. Yenisoy-Karakaş, Anal. Chim. Acta 571 (2006) 298.
[18] S. García, R.M. Pérez, M.L. Sevillano, O. Escolano, F.J. García Frutos, Polycycl. Aromat. Compd. 28 (2008) 67.
[19] M. Thompson, S.L.R. Ellison, R. Wood, Pure Appl. Chem. 74 (2002) 835.
[20] S.V. Hering, B.R. Appel, W. Cheng, F. Salameh, S.H. Cadle, P.A. Mulawa, T.A. Cahill, R.A. Eldred, M. Surovik, D. Fitz, J.E. Howes, K.T. Knapp, L. Stockburger, B.J. Turpin, J.J. Huntzicker, X.Q. Zhang, P.H. McMurry, Aerosol Sci. Technol. 12 (1990) 200–213.
[21] B.T. Mader, J.J. Schauer, J.H. Seinfeld, R.C. Flagan, J.Z. Yu, H. Yang, H. Lim, B.J. Turpin, J.T. Deminter, G. Heidemann, M.S. Bae, P. Quinn, T. Bates, D.J. Eatough, B.J. Huebert, T. Bertram, S. Howell, Atmos. Environ. 37 (2003) 1435–1449.

Talanta 80 (2010) 1129–1132

Contents lists available at ScienceDirect

Talanta

journal homepage: www.elsevier.com/locate/talanta

Preparation of a new solid state fluoride ion selective electrode and application

Güler Somer*, Şükrü Kalaycı, İbrahim Başak

Gazi University, Department of Chemistry, 06500 Ankara, Turkey

ARTICLE INFO

Article history:
Received 29 June 2009
Received in revised form 21 August 2009
Accepted 27 August 2009
Available online 2 September 2009

Keywords:
Fluoride electrode
Determination of fluoride
Solid state
Fluoride in water

ABSTRACT

A new solid state fluoride ion selective electrode composed of 70% Ag_2S, 10% Cu_2S and 20% CaF_2 has been developed. An analytically useful potential change occurred, from 1×10^{-6} to 1×10^{-1} M fluoride ion. The slope of the linear portion (1×10^{-1}–1×10^{-5} M) was about 26 ± 2 mV/10-fold concentration changes in fluoride. It was found that pH change between 1 and 8 had no effect on the potential of the electrode. There was no interference of most common cations such as K^{+}, Na^{+}, Ca^{2+} and Mg^{2+} and anions such as Cl^{-}, NO_3^{-}, SO_4^{2-} and PO_4^{3-}. The lifetime of the electrode was more than 2 years, when used at least 4–5 times a day, and the response time was about 60 s.

The measurements were made at constant ionic strength (0.1 M $NaNO_3$) and at room temperature. This electrode has been used for the determination of fluoride ion in Ankara city tap water and in bottled spring water using standard addition method. The validation of the electrode has been made with a commercial fluoride ion selective electrode (Orion) and high consistency was obtained.

© 2009 Elsevier B.V. All rights reserved.

1. Introduction

The first investigations relating to the ion selective electrodes were done at the beginning of 1900. Increasing number of investigations about ion selective electrodes are being continuing as they have certain advantages such as they have good selectivity and give specific and sensitive results in short time. These electrodes are being used in clinical analysis and in routine control analysis of some ions and some biological species, because of their ease in use and selectivity characters [1,2]. They can be prepared rapidly, they can simply be produced with a very low cost and above all they allow us to analyze the solution without pre-treatments. Silver salts of spare solubility are used mostly for their preparation. It was found that solid state electrodes prepared from silver halogenides were sensitive to halogenides, however these electrodes could also be used for the determination of some cations such as mercury [3–5] indirectly. Pungor and Hollos [6] could determine iodide ion in the presence of chloride ion using an electrode prepared from silver iodide and paraffin. It was found that the electrodes made from two sulfide salts such as Ag_2S–PbS and Ag_2S–CdS were sensitive to lead and cadmium ions respectively [7]. A solid state ion selective electrode was prepared using Ag_2Se and Cu_2S which was selective to selenite [8].

Some of the ion selective electrodes are in solid state such as lead and cadmium [7], selenite [8], and hydroxide electrodes [9], some of them are prepared using PVC or silicon rubber membrane such as halide and sulfide [10], selenite [11], ferric ion [12], iodide [5] and glucose electrodes [1].

Small amounts of fluorine are vital for the human body, although larger quantities are toxic.

For two reasons the production of fluoride ion selective electrode is necessary.

(1) Fluoride is important in commerce and technology.
(2) Determining fluoride by previous techniques is difficult.

Some feeling for importance of a rapid and reliable method for monitoring fluoride can be gained by considering a list of materials in which fluoride occurs: (a) consumer products (toothpaste), (b) biological materials (present in tooth enamel, and bone), (c) pharmaceuticals (e.g. vitamins), (d) public water supplies (fluoridation), (e) water and air (pollution by discharge of industrial wastes), (f) electroplating and pickling baths (continuous monitoring for fluoride level regulation) and (g) manufactured materials (e.g. fertilizers, pesticides, glass, etc.).

For fluoride ion detection, LaF_3 membrane electrode [13] has been developed which is probably the most widely applied fluoride ion selective electrode for practical measurements. Thorium, calcium and the rare earth fluorides were also used for study as being suitably insoluble [14]. However, detailed investigation of precipitation procedures was necessary since normal precipitates of these fluorides tend to be gelatinous. In a recent study [15] a fluoride selective electrode with LaF_3 membrane and stainless steel internal contact has been prepared.

From the literature survey it maybe seen that there are very few electrodes for the determination of fluoride. The aim of this work

* Corresponding author. Tel.: +90 312 202 1150; fax: +90 312 2122279.
E-mail address: gsomer@gazi.edu.tr (G. Somer).

0039-9140/$ – see front matter © 2009 Elsevier B.V. All rights reserved.
doi:10.1016/j.talanta.2009.08.037

was to fulfill this gap and to prepare an electrode selective for fluoride ion which is easy to prepare, easy to handle and has long lifetime. The present work describes the preparation and application of a new potentiometric fluoride selective electrode, which fulfills the above given futures.

2. Materials and methods

2.1. Apparatus and reagents

A JENWAY 3040 Ion Analyzer has been used for potential measurements and 924036 double junction Ag/AgCl reference electrode was used as the outer reference electrode. Chiltern H531 magnetic stirrer was used.

Reagent grade chemicals were used without further purification. Stock solutions were prepared with doubly distilled water and kept in dark. In order to keep the ionic strength constant, 0.1 M $NaNO_3$ was used. Measurements were made at room temperature 22 ± 2 °C and under nitrogen atmosphere.

2.2. Preparation of solid state crystal electrodes

For this purpose Ag_2S, Cu_2S and CaF_2 were mixed in various ratios so that the total weight was changing between 0.1 and 0.3 g.

Cu_2S was prepared by the addition of Na_2S to CuCl solution. To protect CuCl from air oxidation, this reaction was made under nitrogen atmosphere. About 2 g of CuCl were dissolved in 100 mL de-aerated water. By slowly addition of 0.1 M Na_2S and passing nitrogen, Cu_2S was precipitated. It was left waiting for about 30 min at 60 °C. Then it was filtered and washed until no precipitate formation was observed with silver nitrate. It was dried in an oven at about 110 °C and left waiting in a desiccator.

Ag_2S was prepared as given above for Cu_2S, except there was no need to protect from air oxidation but Ag_2S had to be kept in dark.

For the preparation of CaF_2, 4 g of $Ca(OH)_2$ was dissolved in 100 mL water with 1–2 drops of HCl and then 0.1 M NaF was added. CaF_2 precipitate was filtered and dried.

A certain amount of the salt or salt mixture of Ag_2S, Cu_2S and CaF_2 (10–15 mg) was taken and pellets were made by holding first under a pressure of 1940 atm for 1 min, then pressure was increased to 7760 atm by adding each time 1940 atm for 1 min. The pellets of 7 mm diameter were sealed with epoxy resin (0.7 g epoxy and 0.9 g hardener). To obtain a good sealing the epoxy resin on the edge of the tubing had to wait for about 10 min and then the pellet was sealed. One day after the pellet was sealed a silver wire is connected. For this purpose the inside of the glass tube was filled to about 1 cm with a mixture of 0.5 g graphite powder and epoxy resin. The electrode prepared had to wait for about 2 days so that the resin can get dry. The surface of the electrode is washed and then polished with a soft paper. These electrodes should be kept in air and in a dark place when they are not in use. The lifetime of these electrodes was more than 2 years, when used at least 4–5 times a day.

3. Results and discussion

3.1. Effect of electrode composition

Membrane composition has a great effect over the sensitivity, selectivity and stability of the ion selective membrane electrodes. In this study, electrodes in four different compositions were prepared to identify its effect. The measurements were made in 20 mL 0.1 M $NaNO_3$ solution, in order to keep the ionic strength of medium constant. The response of each electrode was measured after the additions of 0.2 mL NaF solutions so that fluoride ion concentrations changed from 0.1 to 1×10^{-6} M.

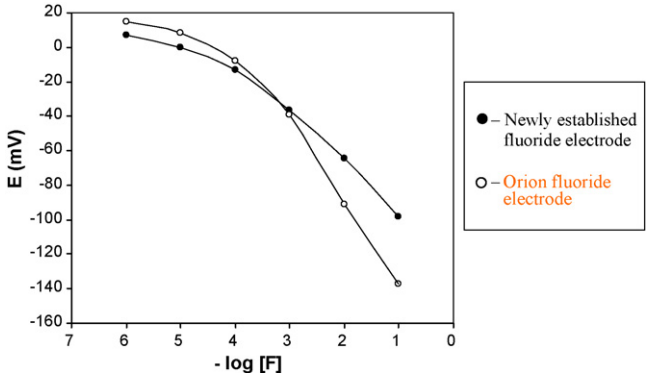


Fig. 1. Calibration curves for the new fluoride selective electrode (70% Ag_2S, 10% Cu_2S, 20% CaF_2) and for the commercial Orion electrode.

To obtain the calibration graph the potential readings were plotted against −log of fluoride ion concentration. For each composition four electrodes were prepared and their responses were measured. The Ag_2S percentage varied from 60% to 80% and CaF_2 from 5% to 30%.

The average slope of the curve in 1×10^{-4}–1×0.1 M concentration range was 5.6 mV ($R^2 = 0.9795$) for the electrode having 80% Ag_2S, 10% Cu_2S and 10% CaF_2 composition. The slope became very small at fluoride concentrations lower than 10^{-4} M. For the electrode having 75% Ag_2S, 25% Cu_2S and 5% CaF_2 composition the slope was about 12 mV for 1×10^{-4}–0.1 M concentration range. But no response was observed at concentrations lower than 10^{-4} M. The highest slope was obtained for the electrode having 70% Ag_2S, 10% Cu_2S and 20% CaF_2 composition. The slope was 26 ± 2 mV ($R^2 = 0.9923$) in 1×10^{-5}–1×0.1 M fluoride concentration range. The calibration curve for this electrode is shown in Fig. 1, together with the calibration curve obtained for the commercial Orion electrode. For the electrode having 60% Ag_2S, 20% Cu_2S and 20% CaF_2 composition, the slope was about 12 mV for 1×10^{-3}–0.1 M concentration range. The electrode with 30% CaF_2 could not be used since it was easily breakable.

The calibration curves for electrodes in different compositions are shown in Fig. 2. As can be seen the highest slope was obtained with the electrode in 70% Ag_2S, 10% Cu_2S and 20% CaF_2 composition.

3.2. The effect of pressure on the electrode sensitivity

The pressure applied on the electrode during preparation was changed from 4850, 7760, 9700 atm. The electrode with highest

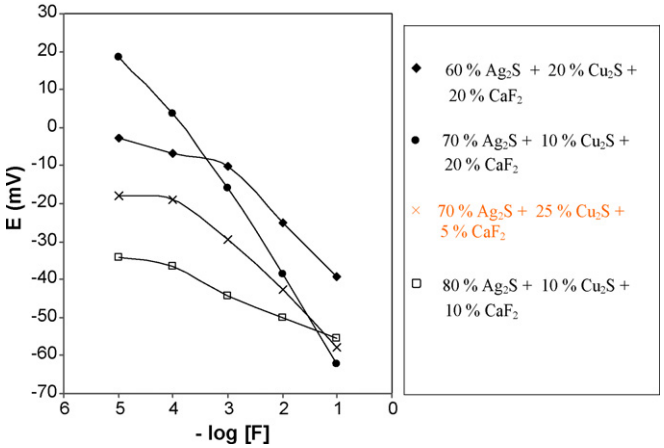


Fig. 2. Calibration curves for fluoride electrodes in different compositions.

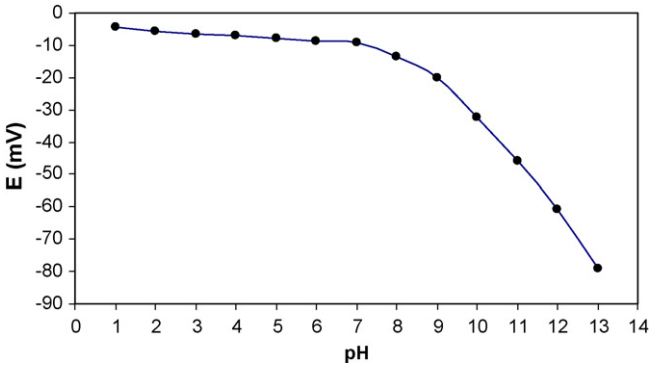


Fig. 3. pH dependence of (70% Ag_2S, 10% Cu_2S, 20% CaF_2) fluoride electrode.

slope was used for all pressures which had the composition of 70% Ag_2S, 10% Cu_2S and 20% CaF_2. It was found that the highest slope was obtained when 7760 atm was applied.

3.3. Effect of pH

Effect of pH on the potential readings at various fluoride concentrations, were investigated. For this purpose to 20 mL 0.1 M $NaNO_3$ solutions 0.02 mL aliquots of 1 M HCl was added and the potentials after each addition was measured. The same procedure was applied for the NaOH additions. The electrode with the highest slope (70% Ag_2S) was used during the measurements. The change in potential with pH was only 1–2 mV for each pH unit change from pH 1 to 8. At pH values larger than 8, the change in potential with pH was about 15 mV for each pH unit. As can be seen from Fig. 3, this electrode can be used between pH 1–8 safely.

3.4. The response time of the electrode

The response time of the electrode depends to the concentration change. The electrode with the highest slope was used throughout the measurements. The potential values were measured for each concentration change after 30, 60, 90, 120 and 150 s. When fluoride concentration was changed from 1×10^{-5} to 1×10^{-4}, 1×10^{-4} to 1×10^{-3}, 1×10^{-3} to 1×10^{-2}, and 1×10^{-2} to 1×10^{-1} M, the response of the electrode was about 60 s, which is a short period and it is an advantage. For this reason, this electrode can easily be used for routine analyses.

The responses of electrode obtained for various concentration changes are shown in Fig. 4. All these measurements were made at constant temperature.

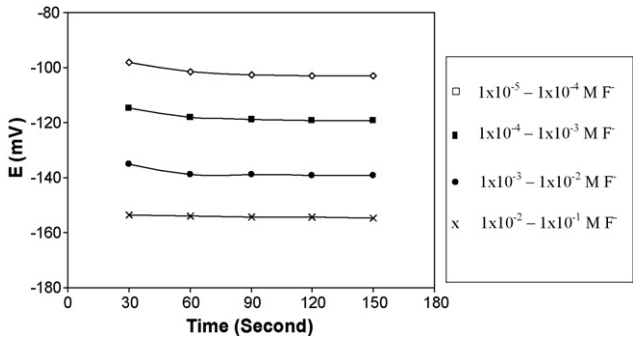


Fig. 4. The dependence of response time on the change of concentration.

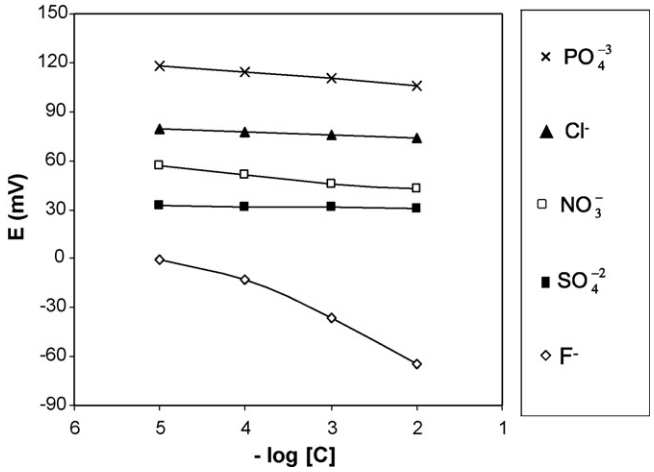


Fig. 5. The response of electrode against some anions in the presence of 10^{-3} M fluoride (70% Ag_2S, 10% Cu_2S, 20% CaF_2).

3.5. Conditioning of the electrode and lifetime

In order to identify the conditioning medium, electrodes having the same composition were kept in air (dark) and in distilled water and in 1×10^{-2} M $NaNO_3$ solution under same duration of time and their responses to fluoride ion were measured. Their performances were found out to be close to each other. In further studies the electrodes were kept in air (in dark) while not in use. The lifetime of this electrode was more than 2 years when it was used at least 4–5 times per day.

3.6. Interference effects of various cations and anions

It usually is not possible to obtain an ISE which is only specific for one ion. Thus, in order to achieve correct and sensitive results in analysis it is important to know the effects of all other ions in the medium. These effects are identified through selectivity coefficient. In this study mixed solutions method was used to determine selectivity coefficient, $k^{pot}_{A,B}$ [16], as it usually corresponds more closely to the situation in samples. Selectivity coefficient values were calculated via making use of the below given equation:

$$k^{pot}_{A,B} a_B{}^{n_A/n_B} = a_A\{\text{antilog}[(E_1 - E_2)/S]\} - a_A$$

Here, $S = 2.303RT/n_AF$ (the slope of fluoride electrode), a_A is the activity of the primary ion, a_B the activity of the interfering ion, E_1 the potential measured when only A is present, E_2 the potential responsive to the primary ion in the presence of interfering ion, $k_{A,B}$ the selectivity coefficient and n_A, n_B are the charges of A and B. In this method, solutions were prepared with a constant activity of the main ion (fluoride) and varying activity of interfering ion. For this purpose, interfering ion was added to 10^{-3} M fluoride solution (in 0.1 M $NaNO_3$) so that its concentration was 10^{-2}–10^{-5} M and after each addition, the change of potential was measured. The potentials obtained at different concentrations of interfering ions are plotted against concentrations as shown in Fig. 5 for anions and in Fig. 6 for cations. For comparison the curve obtained for fluoride electrode is also given in the same figure.

As can be seen nearly no interference was observed for chloride, nitrate, sulfate and phosphate ions. While no interference was observed for sodium, potassium, calcium and magnesium, slight interference was observed for silver ions.

For the determination of the selectivity coefficients, the $a_B{}^{n_A/n_B}$ values are plotted against the right hand side of the above given equation and the slope will be equal to the selectivity coefficient of

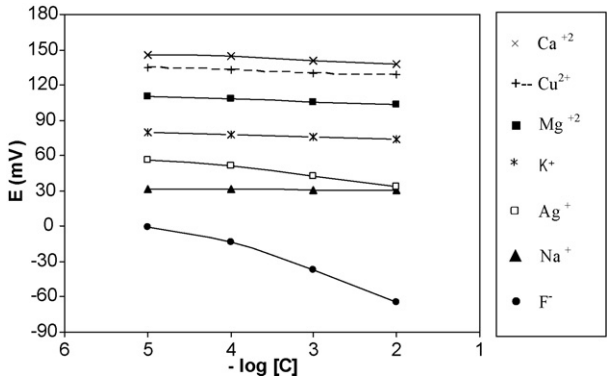


Fig. 6. The response of electrode against some cations, in the presence of 10^{-3} M fluoride (70% Ag_2S, 10% Cu_2S, 20% CaF_2).

Table 1
Selectivity coefficients ($k^{pot}_{A,B}$) for the fluoride electrode in mixed solutions (in the presence of 10^{-3} M fluoride) (B: interfering ion; A: fluoride ion).

Ions	$k^{pot}_{A,B}$
Cl^-	3×10^{-3}
NO_3^-	8×10^{-3}
SO_4^{2-}	6×10^{-4}
PO_4^{3-}	3×10^{-4}
K^+	3×10^{-3}
Na^+	8×10^{-3}
Ag^+	1×10^{-2}
Ca^{2+}	1×10^{-4}
Cu^{2+}	2×10^{-4}
Mg^{2+}	5×10^{-3}

the interfering ion. The selectivity coefficients obtained for mentioned anions and cations are given in Table 1. As can be seen the present fluoride ion selective electrode displayed very good selectivity for fluoride ion with respect to sodium, potassium, calcium and magnesium cations and to chloride, nitrate, sulfate and phosphate anions.

3.7. Determination of fluoride in spring and tap water

The aim of the sample study was to test the accuracy of the results achieved by the analyses done with the fluoride sensitive electrode prepared in our laboratory. A sample of spring water (bottled) was analyzed with the newly established electrode. For this purpose first the potential of 20 mL 0.1 M $NaNO_3$ is measured using fluoride ion selective electrode. Then 0.2 mL spring water sample was added and once more potential was measured. The fluoride content of this water was determined by standard addi-

Table 2
Determination of fluoride in spring and tap water ($N = 4$).

	Newly established fluoride electrode (mg/L)	Orion fluoride electrode (mg/L)
Spring water	0.25 ± 0.01	0.29 ± 0.01
Tap water	2.87 ± 0.03	3.21 ± 0.02

tions. Same procedure was applied four times and the result found was 0.25 ± 0.01 mg/L. The same water sample was analyzed with the commercial Orion fluoride electrodes and the result found was 0.29 ± 0.01 mg/L. The fluoride content in bottled drinking water was given (on tag) as 0.20 mg/L. As can be seen there is about 12% difference in results between these two electrodes. The slope of Orion electrode is smaller at low concentrations, but then suddenly increases at higher concentrations Fig. 1. This large change in slope may be the cause of this difference.

The same procedure was applied to tap water of Ankara city. The fluoride content found with the new electrode was 2.87 ± 0.03 mg/L ($N = 4$), with Orion electrode it was 3.21 ± 0.02 mg/L. The results for two different kinds of water are given in Table 2.

4. Conclusions

This electrode enables the determination of fluoride ion in 1×10^{-6}–1×10^{-1} M concentration range in the presence of most common ions. The slope of the linear portion (1×10^{-1}–1×10^{-5} M) was 26 ± 2 mV per decade change in fluoride ion. The present fluoride ion selective electrode displayed very good selectivity for fluoride ion with respect to sodium, potassium, calcium, magnesium, copper, chloride, nitrate, sulfate and phosphate ions. It was possible to determine fluoride ion quantity in spring and tap water. The preparation of the electrode is simple, it displays very good performance in regard to reproducibility, sensitivity and long lifetime.

References

[1] Ş. Kalaycı, G. Somer, G. Ekmekci, Talanta 65 (2005) 87–91.
[2] M. Mascini, G.G. Guilbault, Biosensors 2 (1986) 147.
[3] R.F. Overman, Anal. Chem. 43 (1971) 616–617.
[4] G. Somer, Anal. Chem. 53 (1981) 2143–2145.
[5] G. Somer, Ş. Kalaycı, G. Ekmekci, Sens. Actuators B 81 (2001) 122–127.
[6] E. Pungor, R. Hollos, Acta Chim. Acad. Sci. Hung. 27 (1961) 63.
[7] G.A. Rechnitz, Z.F. Lin, S.B. Zamochnick, Anal. Lett. 1 (1967) 29.
[8] G. Ekmekci, G. Somer, Talanta 49 (1999) 91–98.
[9] G. Ekmekci, Ş. Kalaycı, G. Somer, Sens. Actuators B 101 (2004) 260–264.
[10] E. Pungor, Anal. Chem. 39 (1967) 28A.
[11] G. Ekmekçi, G. Somer, Talanta 49 (1999) 83–89.
[12] G. Ekmekci, D. Uzun, G. Somer, S. Kalaycı, J. Membr. Sci. 288 (2007) 36–40.
[13] M.S. Frant, J.W. Ross, Science 154 (1966) 1553.
[14] A.M.U. Macdonald, K. Toth, Anal. Chim. Acta 41 (1968) 99–106.
[15] M. Bralic, N. Radic, S. Brinic, E. Generalic, Talanta 55 (2001) 581–586.
[16] K. Srinivasan, G.A. Rechnitz, Anal. Chem. 41 (1969) 1203–1208.

Talanta 80 (2010) 1133–1138

Contents lists available at ScienceDirect

Talanta

journal homepage: www.elsevier.com/locate/talanta

Determination of cadmium in alcohol fuel using *Moringa oleifera* seeds as a biosorbent in an on-line system coupled to FAAS

Vanessa Nunes Alves[a], Rafael Mosquetta[a], Nívia Maria Melo Coelho[a], Joyce Nunes Bianchin[b], Kalya Cravo Di Pietro Roux[b], Edmar Martendal[b], Eduardo Carasek[b,*]

[a] *Instituto de Química, Universidade Federal de Uberlândia, Uberlândia 38400-902, MG, Brazil*
[b] *Departamento de Química, Universidade Federal de Santa Catarina, Florianópolis 88040900, SC, Brazil*

ARTICLE INFO

Article history:
Received 17 June 2009
Received in revised form 26 August 2009
Accepted 27 August 2009
Available online 4 September 2009

Keywords:
Cadmium
Fuel alcohol
Moringa oleifera seeds
Solid phase extraction
On-line preconcentration
Multivariate design

ABSTRACT

In this study a new method for determination of cadmium in alcohol fuel using *Moringa oleifera* seeds as a biosorbent in an on-line preconcentration system coupled to flame atomic absorption spectrometry (FAAS) was developed. Flow and chemical variables of the proposed system were optimized through multivariate designs. The limit of detection for cadmium was 5.50 $\mu g\,L^{-1}$ and the precision was below 2.3% (35.0 $\mu g\,L^{-1}$, $n = 9$). The analytical curve was linear from 5 to 150 $\mu g\,L^{-1}$, with a correlation coefficient of 0.9993. The developed method was successfully applied to spiked alcohol fuel, and accuracy was assessed through recovery tests, with recovery ranging from 97.50 to 100%.

© 2009 Elsevier B.V. All rights reserved.

1. Introduction

In Brazil, the oil crisis in the 1970s contributed to the implementation of a government program called Proálcool (National Alcohol Program) in 1975 to stimulate the production of ethanol from sugar cane [1,2]. Ethanol is a renewable fuel that contributes significantly to the energy independence of Brazil, attracting interest from several countries. However, for Brazilian ethanol to be introduced successfully in the international market it is extremely important to develop methods of analysis to ensure its quality. During the processes of production, transport and storage of alcohol fuel, several sources of contamination are present, including by metal ions. The presence of metal ions, even at low concentrations can adversely affect the performance of the engine [3,4], intensify the corrosive properties of ethanol and increase the emission levels of pollutants generated and the consequent environmental pollution [5–7].

Flame atomic absorption spectrometry (FAAS) has been extensively used for the determination of several metal species [8–11]. However, detection limits in the order of mg L^{-1} prevent the use of this technique in the analysis of samples containing low concentrations of analytes, requiring preconcentration steps to improve the sensitivity [12–16].

Among the existing preconcentration techniques, solid phase extraction has some advantages such as simplicity, high analytical frequency and enrichment factors, besides reducing the matrix effects [16–18].

Many studies involving metal preconcentration have been reported, mostly with the use of commercially available sorbents. However, other materials known as 'natural adsorbents' have recently been successfully employed in metal adsorption processes [19–21]. The term 'natural adsorbent' is assigned to any material that is not synthetically produced and has adsorptive properties in terms of chemical species of inorganic and organic origins.

The use of natural adsorbents in procedures for solid phase extraction becomes more attractive when coupled on-line with the detection system and when using an adsorbent with high adsorptive capacity, such as the seeds of *Moringa oleifera*. Table 1 lists various biosorbents and their applications in solid phase extraction procedures as well as their limits of detection.

M. oleifera is the best known species of the Moringaceae family. It is a plant native to northwest India but has spread all over the world, mainly in tropical countries. *M. oleifera* seeds have been used for the treatment of turbid water due to their flocculation properties. A flocculating protein from the seeds of *M. oleifera* Lam. was isolated by Gassenschmidt et al. [29] and its molecular mass was found to be around 6.5 kDa and the isoelectric point was above pH 10. Flocculation activity could be explained by the charge-patch mechanism due to low molecular weight and high charge den-

* Corresponding author. Fax: +55 48 3721 6850.
E-mail address: carasek@qmc.ufsc.br (E. Carasek).

0039-9140/$ – see front matter © 2009 Elsevier B.V. All rights reserved.
doi:10.1016/j.talanta.2009.08.040

Table 1
Use of bioadsorbents in solid phase extraction systems.

Bioadsorbent	Sample	Detection	LOD	Ref
Agrobacterium tumefaciens immobilized in Amberlite XAD-4	Water, baby food and certified samples	FAAS	3.6 ng mL^{-1} Fe(III) 3.0 ng mL^{-1} Co(II) 2.8 ng mL^{-1} Mn(II) 3.6 ng mL^{-1} Cr(III)	[22]
Pilayella littoralis immobilized in silica	Drinking water	ICP-OES	0.6 ng mL^{-1} Cu(II) 11 ng mL^{-1} Fe(III) 8 ng mL^{-1} Al(III) 0.4 ng mL^{-1} Co(II)	[23]
Penicillium italicum immobilized in Sepabeads SP 70	Natural waters	FAAS	0.41 μg L^{-1} Cd (II) 1.60 μg L^{-1} FeIII	[24]
Pseudomonas aeruginosa immobilized in Chromosorb 106	Natural waters and food	GFAAS	30 ng L^{-1}	[25]
Bacillus sphaericus immobilized in Diaion SP-850	Certified water samples and foods.	FAAS	Water samples: 0.20 μg L^{-1} Cu(II) 0.75 μg L^{-1} (PbII) 0.25 μg L^{-1} Fe(III) 0.30 μg L^{-1} Co(II) Solid samples: 2.5 ng L^{-1} Cu(II) 9.4 ng L^{-1} Pb(II) 3.1 ng L^{-1} Fe(III) 3.8 ng L^{-1} Co(II)	[26]
Saccharomyces cerevisiae	River water	ICP-OES	0.1 μg L^{-1} Cd(II)	[27]
Bacillus subtilis immobilized in Amberlite XAD-4	Certified water samples and foods.	FAAS	0.0297 mmol L^{-1} Cu(II) 0.035 mmol L^{-1} Cd(II)	[28]

sity. The amino acids detected were mostly glutamic acid, proline, methionine and arginine. However, the mechanism of coagulation by polypeptides is still unknown. The shelled and non-shelled seeds contain approximately 37 and 27% of protein, respectively. Studies involving the use of natural adsorbents for the treatment of industrial effluents in terms of the removal of heavy metals have been published [30–32]. However, the use of this material in the preconcentration of metals in alcohol fuel has not been reported in the literature.

Thus, due to the possible sources of contamination by metal ions, such as cadmium, during the production of alcohol, the objective of this study was to develop a methodology for an on-line preconcentration system, using *M. oleifera* seeds as a biosorbent, coupled to flame atomic absorption spectrometry, for the determination of cadmium in alcohol fuel.

2. Experimental

2.1. Instrumentation

A Varian SpectrAA 50 (Victória, Australia) flame atomic absorption spectrometer (FAAS), equipped with a cadmium hollow cathode lamp and a deuterium lamp for background correction, was used for the detection of cadmium. The instrument was operated under the conditions recommended by the manufacturer, as shown in Table 2.

The pH value of the point of zero charge of the proposed biosorbent was measured over the pH range of 3–12 using a Microelectrophoresis Apparatus Mk II (Cambridge, UK).

Table 2
Operating parameters employed in Cd(II) determination by FAAS.

Parameters	
Wavelength (nm)	228.8
Lamp current (mA)	4
Burner height (mm)	17
Acetylene flow rate (L min^{-1})	1
Air flow rate (L min^{-1})	10
Aspiration flow rate (mL min^{-1})	5

A Fourier Transform Infrared (FT-IR) spectrometer (Shimadzu, IRPrestige-21, Tokyo, Japan) and a thermogravimetric analyzer (TA Instruments TGA 2950, New Castle, USA) were used to characterize the *M. oleifera* biosorbent.

A Mettler Toledo 320 pH meter was used to adjust the pH of the samples and working solutions. An Ismatec-IPC (Zurich, Switzerland) peristaltic pump equipped with eight channels and Tygon® and polyethylene tubes were used to pump the solutions through the mini-column (60 mm × 0.2 mm) in the elution and preconcentration steps. The mini-column was filled with 200 mg of seeds in the size range of 140–850 μm.

2.2. Reagents and solutions

All working solutions were prepared with ultrapure water obtained from a Milli-Q system (Millipore, Bedford, MA, USA). All reagents were analytical grade. All laboratory glassware was washed with a neutral detergent and then kept overnight in 10% nitric acid aqueous solution, followed by ultra-sonification for 1 h and finally rinsed with deionized water.

Working solutions were prepared daily through dilution of a 2000 mg L^{-1} stock solution of cadmium in a hydro-alcoholic solution containing 80% (v/v) of alcohol fuel and 20% (v/v) of water with a tris(hydroxymethyl)aminomethane buffer.

The nitric acid solution used as the eluent was prepared through dilution in water of concentrated nitric acid obtained from Merck (Darmstadt, Germany).

The 10^{-3} mol L^{-1} potassium chloride solution was adjusted within a pH range of 3–12 for the determination of the point of zero charge of the *M. oleifera* biosorbent.

2.3. Preparation of the biosorbent

The Moringa seeds used to construct the mini-column were obtained from trees cultivated in the city of Uberlândia (Minas Gerais, Brazil) and collected during September–November 2007. The seeds were separated from the pods, washed with deionized water and dried at 25 °C. After drying, the seeds were crushed in a blender (Black & Decker, São Paulo, Brazil) and passed through 850 μm sieves.

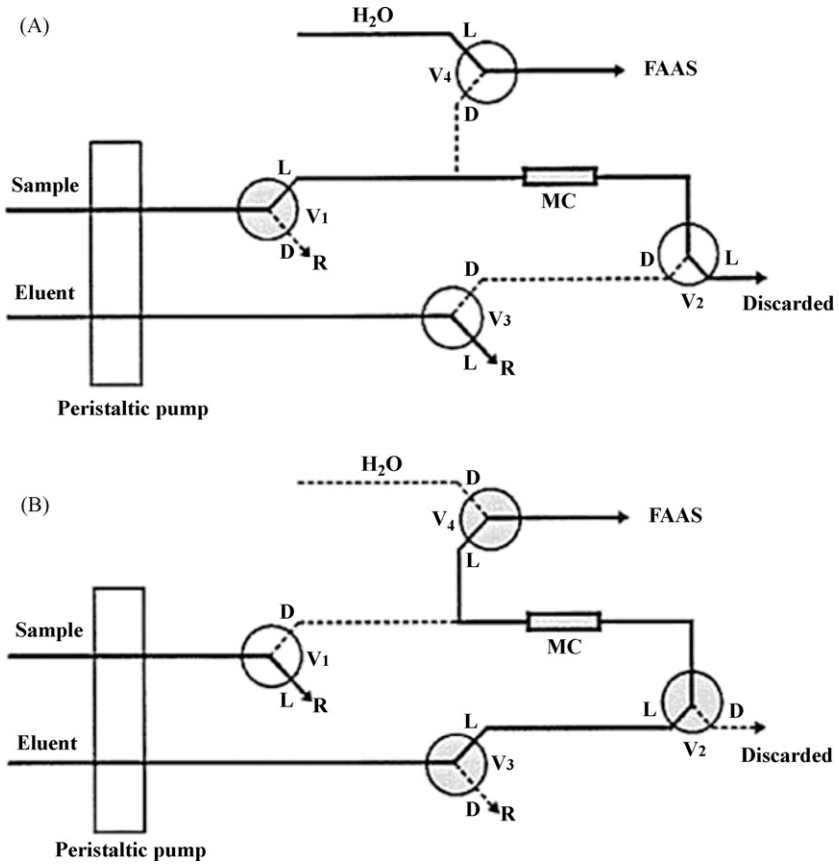


Fig. 1. Diagram of the on-line preconcentration system used in this study. (A) Adsorption process and (B) desorption process. V, valve; L, open; D, closed; MC, mini-column containing adsorbent; R, sample or eluent back stream; hatched circle, valve on; white circle, valve off.

The functional groups of the *M. oleifera* were characterized by FT-IR in the spectral range of 4000–500 cm^{-1}, with twenty-eight scans and a resolution of 4 cm^{-1}. TGA curves were obtained using 10 mg of seeds heated up to 950 °C in an oxidant atmosphere at rate of 20 °C min^{-1}.

2.4. On-line preconcentration system

The on-line flow system used for the development of the proposed method is shown in Fig. 1. The flow system consists of a peristaltic pump equipped with Tygon® tubes, four three-way solenoid valves and a mini-column filled with *M. oleifera* seeds. The system was coupled to the FAAS. During the preconcentration step (Fig. 1A), valve 1 is open and the other valves remain closed, the samples or working solutions are pumped through the mini-column and the effluent is discharged. In the elution step (Fig. 1B), valve 1 is closed and valves 2, 3 and 4 are open. Thus, the eluent percolates through the mini-column in the opposite direction to that of the preconcentration step. The eluate is carried directly to the nebulization system of the FAAS.

2.5. Optimization system

The optimization of the parameters affecting the sorption of Cd by the *M. oleifera* seeds was performed using a two-level full factorial experimental design involving four factors and a final optimization using a Doehlert matrix design. All experiments were carried out in duplicate, using 10.0 mL of 50 μg L^{-1} Cd solution. The variables studied were sample pH, buffer concentration, eluent concentration and sample flow rate.

3. Results

3.1. Characterization of biosorbent

The FT-IR technique was used to study the main functional groups of the Moringa seeds and Fig. 2 shows the FT-IR spectrum obtained.

The spectrum presents a broad band centered at 3420 cm^{-1} assigned to O–H stretching. This functional group appears predom-

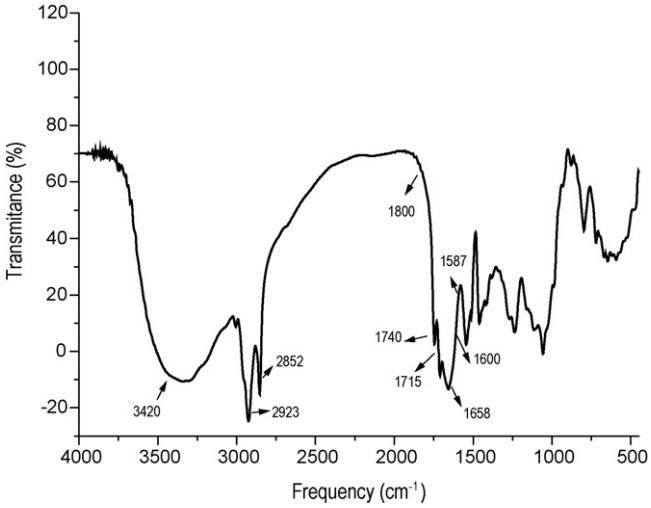


Fig. 2. FT-IR spectrum of *Moringa oleifera* seeds.

Table 3
Conditions for Cd(II) preconcentration and the analytical response for the multivariate optimization study using SPE with the *Moringa oleifera* column and detection by FAAS.

Run	Sample pH	Buffer (mol L^{-1})	Eluent (mol L^{-1})	Sample flow rate (mL min^{-1})	Integrated absorbance
1	7.3	0.01	0.5	3.0	0.6104
2	7.3	0.01	0.5	6.0	0.5543
3	7.3	0.01	1.5	3.0	0.4362
4	7.3	0.01	1.5	6.0	0.3954
5	7.3	0.05	0.5	3.0	0.4585
6	7.3	0.05	0.5	6.0	0.4490
7	7.3	0.05	1.5	3.0	0.4894
8	7.3	0.05	1.5	6.0	0.3780
9	9.3	0.01	0.5	3.0	0.6196
10	9.3	0.01	0.5	6.0	0.6356
11	9.3	0.01	1.5	3.0	0.6173
12	9.3	0.01	1.5	6.0	0.5706
13	9.3	0.05	0.5	3.0	0.7176
14	9.3	0.05	0.5	6.0	0.7131
15	9.3	0.05	1.5	3.0	0.7208
16	9.3	0.05	1.5	6.0	0.6699
17	8.3	0.03	1.0	4.5	0.5669
18	8.3	0.03	1.0	4.5	0.5996
19	8.3	0.03	1.0	4.5	0.5869
20	8.3	0.03	1.0	4.5	0.5291

inantly in protein and fatty acid structures of the Moringa seeds. Due to the high content of protein in the seeds there is also a contribution in this region from the N–H stretching of amide groups. The peaks at 2923 and 2852 cm^{-1} are assigned to symmetrical and asymmetrical C–H stretching of the CH_2 group present in fatty acids. In the region between 1800 and 1600 cm^{-1} there are three intense bands assigned to C=O bond stretching. The carbonyl group is present in the fatty acid and protein structures. In this case, the spectrum shows two bands at 1740 and 1715 cm^{-1} associated with fatty acids and a band at 1658 cm^{-1} associated with the amide group of the protein. The peak at 1587 cm^{-1} can be assigned to C–N stretching and/or N–H deformation. The presence of this band confirms the protein structure of the Moringa seeds.

The appearance of the curve obtained from the thermogravimetric analysis confirms the heterogeneity of the sample. Fig. 3 shows the mass loss curve for the Moringa samples. This curve can be divided into three phases. From 30 °C to 128 °C a mass loss of the order of 8% can be observed, associated with the dehydration of the seed. In the second phase, there was a 32% mass loss in the temperature range of 128–268 °C, due to the decomposition of organic matter. The third stage occurs from 268 °C to 541 °C, with decomposition of most components of the seed. At a temperature of 950 °C there was around 14.6% of residue, due to the presence of ash and probably inorganic oxides.

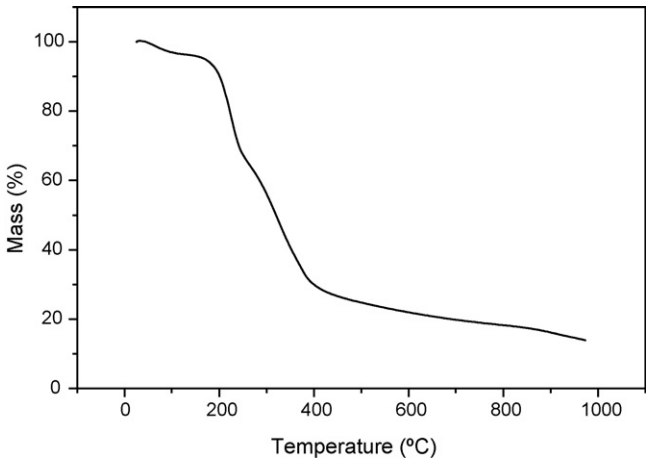


Fig. 3. Thermogravimetric curves of *Moringa oleifera* seeds.

The pH value of the point of zero charge for the proposed adsorbent was within the range of 6–7. Thus, above this pH range the surface of the sorbent will be negatively charged and will adsorb positively charged species.

3.2. Optimization

Preliminary tests were performed to investigate which factors exert significant influence on the adsorption of Cd (II) by the *M. oleifera* seeds. The factors selected were: eluent concentration, pH, buffer concentration and sample flow rate. The type of eluent and the mass of the mini-column were set as HNO_3 and 200 mg, respectively.

Table 3 shows the response for each factorial design experiment. The analytical response was taken as the integrated absorbance and the sample volume used for the preconcentration was 10 mL spiked at 50 μg Cd L^{-1}.

From the results reported in Table 3, a Pareto chart (Fig. 4) was plotted to check the influence of the factors and their interactions in the system. An effect was considered significant when it was above the standard error at the 95% confidence level ($p > 0.05$), which is denoted by the vertical line on the graph.

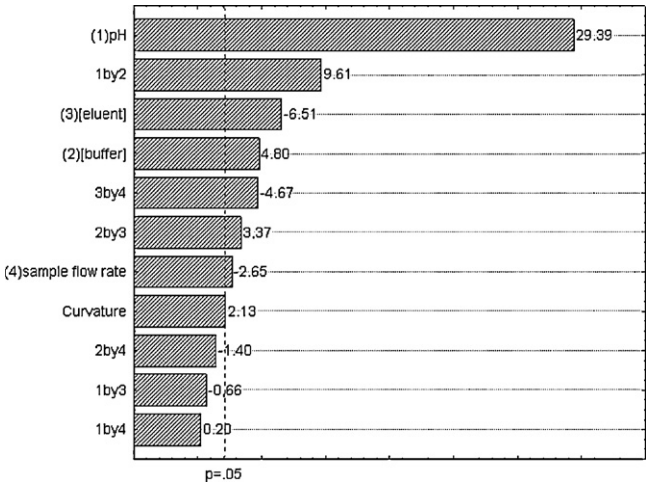


Fig. 4. Pareto chart obtained from the optimization study of the variables, with their significance, for the preconcentration of Cd(II) using *Moringa oleifera* seeds as the sorbent and FAAS.

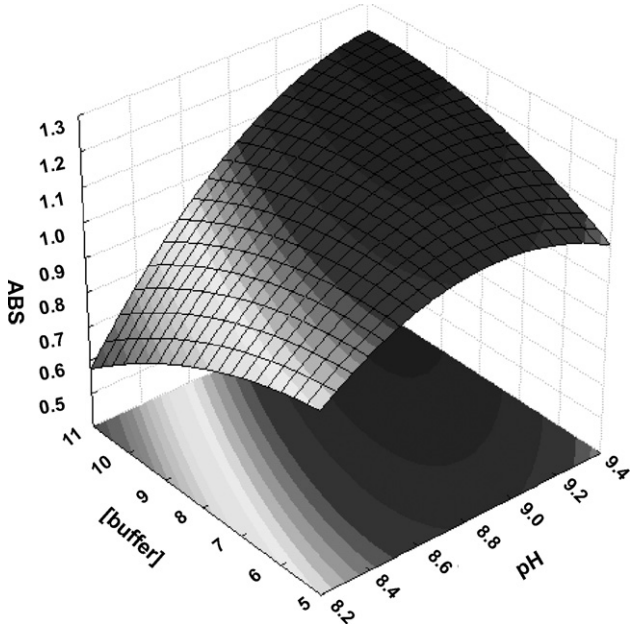


Fig. 5. Response surface for optimization of pH and buffer concentration: sample volume, 10.0 mL; sample concentration, 50 $\mu g\,L^{-1}$; sorbent mass, 200 mg; eluent concentration, 0.5 mol L^{-1}.

The sample pH, eluent concentration and buffer concentration, as well as the interaction between the sample pH and the buffer concentration, were the factors that had significant influence on the extraction efficiency.

The sample pH is one of the most important parameters for the adsorption process, since the capture of metal ions by functional groups of the biomass is highly dependent on pH. Thus, according to the Pareto chart, in the range studied, pH 9.3 leads to better results than pH 7.3. The eluent concentration showed low significance in relation to the interaction between sample pH and buffer concentration. Thus, an eluent concentration of 0.5 mol L^{-1} was chosen to increase the lifetime of the adsorbent material and reduce the consumption of reagents. The sample flow rate was fixed at 6.0 mL min^{-1} to ensure an adequate time for interaction between the sample and the mini-column, in spite of reducing the analytical frequency. The curvature parameter was not significant, indicating that the response is roughly linear between the minimum and maximum levels selected for each variable.

The most significant variables indicated by the factorial design (sample pH and buffer concentration) were then optimized using a Doehlert matrix. In this case, seven experiments were performed as shown in Table 4. The results were used to construct the surface response shown in Fig. 5.

As can be seen in Fig. 5, higher buffer concentrations combined with high pH will lead to stronger analytical signals. The literature shows that to ensure the interaction between the metal ion and the surface of the adsorbent, the pH must be such that Mn^{+} is the most abundant metal ion species [21] and the sorbent surface is negatively charged, that is, above its point of zero charge. The *M. oleifera* seeds have several functional groups, mainly amino groups. Most of these amino groups have isoelectric points between pH 4.0 and 8.0, which is in agreement with the pH range obtained for the isoelectric point in our study (6–7). Above this pH, the sorbent surface is negatively charged and the most abundant species of cadmium is Cd^{2+}. Thus, the interaction between the negative surface of the sorbent and the positive metal ion leads to the retention of the cadmium in the proposed preconcentration system [32].

Table 4
Doehlert matrix for the final optimization of pH and buffer concentration.

Experiment	Sample pH	Buffer (mol L^{-1})	Integrated absorbance
1	8.3	0.04	0.8972
2	8.6	0.03	1.0642
3	8.6	0.05	0.9546
4	8.8	0.04	1.1378
5	9.1	0.03	1.1552
6	9.1	0.05	1.2017
7	9.3	0.04	1.1630

Table 5
Analytical features for the determination of cadmium in alcohol fuel using the proposed method.

Linear range[a] ($\mu g\,L^{-1}$)	5–150
Correlation coefficient (R)	0.9993
R.S.D.% (35.0 $\mu g\,L^{-1}$, $n=9$)	2.3
Limit of detection ($\mu g\,L^{-1}$)	5.50

[a] Linear range studied.

Table 6
Relative recovery for the samples used to evaluate the proposed method.

Sample	Recovery (%)	R.S.D. (%)
Sample 1	99.10	3.2
Sample 2	97.50	4.5
Sample 3	100	5.4

On analyzing the results of the optimization procedures, the following working conditions were selected: tris(hydroxymethylaminomethane) buffer 0.05, 0.5 mol L^{-1} HNO_3 as the eluent, pH 9.1 and sample flow rate 6.0 mL min^{-1}.

3.3. Analytical features

With the optimized system, the method was evaluated through the main analytical features shown in Table 5. The results obtained were compared with those previously published by our research group [21], where preconcentration of Cd(II) in samples of alcohol fuel was carried out using vermicompost as the biosorbent. A good correlation coefficient was obtained (0.9993) between the analytical signal predicted by the linear function and the analytical signal observed experimentally in the linear range of 5–150 $\mu g\,L^{-1}$.

The repeatability of the proposed method was assessed by performing seven consecutive extractions at a concentration level of 35 $\mu g\,L^{-1}$, and expressing the result in terms of the relative standard deviation. A value of 2.3% was obtained demonstrating an excellent repeatability.

3.4. Application of the method and recovery tests

The proposed method was applied to three alcohol fuel samples. In all samples the analyte concentration was below the limit of detection of the method. Thus, in order to assess the analyte recovery, all the samples were spiked at concentration levels from 0 to 50 $\mu g\,L^{-1}$, and analytical curves were constructed in order to compare the slopes. The results obtained are shown in Table 6, where it can be seen that there is no difference between the recovery values for the three samples, indicating that the analyte is quantitatively retained in all of the samples evaluated.

4. Conclusions

The seeds of *M. oleifera* were shown to be an efficient adsorbent material of natural origin for the preconcentration of cadmium present in alcoholic matrices, thereby contributing to the development of low cost analytical methodologies which fall within the current concept of clean chemistry.

The method showed satisfactory limits of detection and good accuracy. The results are in agreement with a method previously developed by our research group, based on the adsorption of cadmium present in samples of alcohol fuel using vermicompost as the adsorbent material [21].

Acknowledgments

The authors are grateful for financial support from Conselho Nacional de Desenvolvimento Científico e Tecnológico (CNPq), Fundação de Amparo à Pesquisa do Estado de Minas Gerais (FAPEMIG) and Coordenação de Aperfeiçoamento de Pessoal de Nível Superior (CAPES).

References

[1] T. Saint'Pierre, R.Q. Aucélio, A.J. Curtis, Microchem. J. 75 (2003) 59.
[2] R.M. Takeuchi, A.L. Santos, P.M. Padilha, N.R. Stradiotto, Anal. Chim. Acta 295 (2007) 584.
[3] M.F. Bergamini, S.I. Vital, A.L. Santos, N.R. Stradiotto, Ecl. Quím. 31 (2006) 45.
[4] D.B. Taylor, R.E. Synovec, Talanta 40 (1993) 495.
[5] T. Saint'Pierre, T.A. Maranhão, V.L.A. Frescura, A.J. Curtis, Spectrchim. Acta Part B 60 (2005) 605.
[6] R.C.C. Pereira, V.M.D. Pasa, Energy Fuels 19 (2005) 426.
[7] E.L. Silva, D. Budziak, E. Carasek, Anal. Lett. 37 (2004) 1.
[8] J.W. Robinson, Atomic Spectroscopy, 2nd edition, Marcel Dekker, Inc., New York, 1996, p. 391.
[9] M.G. Pereira, M.A.Z. Arruda, Microchim. Acta 141 (2003) 115.
[10] G. Tao, Z. Fang, J. Baasner, B. Welz, Anal. Chim. Acta 481 (2003) 273.
[11] V.A. Lemos, R.E. Santelli, M.S. de Carvalho, S.L.C. Ferreira, Spectrochim. Acta B 55 (1998) 1497.
[12] K. Pyrznsk, M. Trojanowicz, Crit. Rev. Anal. Chem. 29 (1999) 313.
[13] A. Goswami, A.K. Singh, Anal. Chim. Acta 454 (2002) 229.
[14] H.F. Maltez, E. Carasek, Talanta 65 (2005) 537.
[15] R.L. Dutra, H.F. Maltez, E. Carasek, Talanta 69 (2006) 488.
[16] E.L. da Silva, A.O. Martins, A. Valentini, V.T. de Fávere, E. Carasek, Talanta 64 (2004) 181.
[17] E.H. Hansen, J. Wang, Anal. Chim. Acta 467 (2002) 3.
[18] K. Benkhedda, H.G. Infante, F.C. Adams, Anal. Chim. Acta 506 (2004) 137.
[19] B. Godlewska-Zylkiewicz, Crit. Rev. Anal. Chem. 31 (2001) 175.
[20] F. Veglio, F. Beolchini, Hydrometallurgy 44 (1997) 301.
[21] J.N. Bianchin, E. Martendal, R. Mior, V.N. Alves, C.S.T. Araújo, N.M.M. Coelho, E. Carasek, Talanta 78 (2009) 333.
[22] S. Baytak, A.R. Turker, Talanta 65 (2005) 938.
[23] E.N.V.M. Carrilho, J.A. Nóbrega, T.R. Gilbert, Talanta 60 (2003) 1131.
[24] D. Mendil, M. Tuzen, M. Soylak, J. Hazard. Mater. 152 (2008) 1171.
[25] M. Tuzen, M. Soylak, J. Hazard. Mater. 154 (2008) 519.
[26] M. Tuzen, O.D. Uluozlu, C. Usta, M. Soylak, Anal. Chim. Acta 581 (2007) 241.
[27] P.A. Biscaro, A.A. Menegário, P.S. Tonello, R. Caldorin, Quím. Nova 30 (2007) 323.
[28] M. Dogru, R. Gul-Guven, S. Erdogan, J. Hazard. Mater. 149 (2007) 166.
[29] U. Gassenschmidt, K.D. Jany, B. Tauscher, H. Niebergall, Biochim. Biophys. Acta 1243 (1995) 477.
[30] C.R.T. Tarley, M.A.Z. Arruda, Analytica 4 (2003) 25.
[31] M. Voss, R.W.S.P. Thomas, Cienc. Rural 31 (2001) 947.
[32] H.N. Bhatti, B. Mumtaz, M.A. Hanif, R. Nadeem, Process Biochem. 42 (2007) 547.

Talanta 80 (2010) 1139–1144

Contents lists available at ScienceDirect

Talanta

journal homepage: www.elsevier.com/locate/talanta

A green and sensitive method to determine phenols in water and wastewater samples using an aqueous two-phase system

Guilherme Dias Rodrigues[a], Leandro Rodrigues de Lemos[a], Luis Henrique Mendes da Silva[a], Maria do Carmo Hespanhol da Silva[a,*], Luis Antonio Minim[b], Jane Sélia dos Reis Coimbra[b]

[a] Grupo de Química Verde Coloidal e Macromolecular, Departamento de Química, Centro de Ciências Exatas e Tecnológicas, Universidade Federal de Viçosa, Av. P.H. Rolfs s/n, Viçosa, MG 36560-000, Brazil
[b] Departamento de Tecnologia de Alimentos, Universidade Federal de Viçosa, Viçosa, MG, Brazil

ARTICLE INFO

Article history:
Received 26 May 2009
Received in revised form 3 July 2009
Accepted 30 August 2009
Available online 4 September 2009

Keywords:
Aqueous two-phase system
Green chemistry
Phenols determination
Water
Wastewater

ABSTRACT

A greener and more sensitive spectrophotometric procedure has been developed for the determination of phenol and *o*-cresol that exploits an aqueous two-phase system (ATPS) using a liquid–liquid extraction technique. An ATPS is formed mostly by water and does not require organic solvent. Other ATPS components used in this study were the polymer, polyethylene oxide, and some salts (i.e., Li_2SO_4, Na_2SO_4 or K_2HPO_4 + KOH). The method is based on the reaction between phenol, sodium nitroprusside (NPS) and hydroxylamine hydrochloride (HL) in an alkaline medium (pH 12.0), producing the complex anion $[Fe_2(CN)_{10}]^{10-}$ that spontaneously concentrates in the top phase of the system. The linear range was 1.50–500 μg kg^{-1} ($R \geq 0.9997$; $n = 8$) with coefficients of variation equal to 0.38% for phenol and 0.30% for *o*-cresol ($n = 5$). The method yielded limits of detection (LODs) of 1.27 and 1.88 μg kg^{-1} and limits of quantification (LOQs) of 4.22 and 6.28 μg kg^{-1} for phenol and *o*-cresol, respectively. Recoveries between 95.7% and 107% were obtained for the determination of phenol in natural water and wastewater samples. In addition, excellent agreement was observed between this new ATPS method and the standard 4-aminoantipyrine (4-AAP) method.

© 2009 Elsevier B.V. All rights reserved.

1. Introduction

The restricted availability of unpolluted freshwater sources coupled with the high costs of obtaining potable water has caused increasing awareness about the use of water sources. Thus, there is a constant search for inexpensive and greener analytical methods that can provide reliable results for monitoring water pollutants such as phenolic compounds.

Phenol and its derivatives (e.g., cresol) are extremely harmful to the environment and human health [1,2] due to their high toxicity. As a result, they have been included on lists of high priority pollutants in several countries [2,3]. American and Brazilian environmental legislation established limits of 10.0 μg L^{-1} of total phenols permitted in bodies of water [4,5].

Several analytical procedures with different systems of detection were developed to determine phenolic compounds, including gas chromatography (GC) [6–9], liquid chromatography (LC) [10–13], capillary electrophoresis (CE) [14–16], voltammetry [17–19] and amperometric analysis [20–22]. However, these methods do not allow *in situ* continuous monitoring, are costly to implement, demand skilled operators and require derivatization of analytes. Spectrophotometric analysis is applied in the determination of phenols [23,24], exploiting mainly UV–vis detection [25–27].

The most commonly used analytical methods (e.g., those described in the Standard Methods for the Examination of Water and Wastewater [28]) are spectrophotometric methods based on the oxidative coupling of phenols with 4-aminoantipyrine (4-AAP). However, this procedure has many disadvantages, including (i) employment of large amounts of reagents, especially chloroform, which is toxic and carcinogenic [29]; (ii) difficulty in finding suitable buffers, due to the reactive sensitivity to pH variations; and (iii) tedious operations such as a distillation step required for some sample analysis.

An interesting spectrophotometric method for the determination of phenolic compounds has been reported by Nagaraj et al. [30] and improved by Kang et al. [31]. It is based on the reaction between phenol, sodium nitroprusside (NPS) and hydroxylamine hydrochloride (HL) in an alkaline medium, producing the blue-colored complex anion $[Fe_2(CN)_{10}]^{10-}$. However, this procedure is not yet suitable for the determination of phenols at concentrations lower than 50.0 μg L^{-1} and for analyses in the presence of elec-

* Corresponding author. Tel.: +55 31 38992175; fax: +55 31 38993065.
E-mail address: mariacarmo@ufv.br (M.d.C.H. da Silva).

0039-9140/$ – see front matter © 2009 Elsevier B.V. All rights reserved.
doi:10.1016/j.talanta.2009.08.039

trolytes such as phosphates and sulfates, which promote serious errors. Moreover, a previous distillation step for sample preparation is required.

A convenient approach to address these limitations is to promote the complex formation reaction at the interface between the bottom and top phase of an aqueous two-phase system (ATPS). This reaction avoids salt interference and the posterior transfer of the complex to a small volume of the ATPS top phase. Within this context, ATPS is a strategic liquid–liquid extraction technique for phenol determination. Under specific thermodynamic conditions, an ATPS can be formed by the mixtures of aqueous solutions of (i) certain inorganic salts and a polymer [32], (ii) two types of water-soluble polymers [33] or (iii) two types of salts [34]. The resulting systems are two immiscible liquid phases with a polymer-enriched top phase (or enriched with a salt) and a salt-enriched bottom phase (or enriched with the second polymer or salt). Moreover, water is the major component of both phases, thus providing an extraction technology that eliminates the use of hazardous solvents. Finally, ease of use, low costs, shorter times for phase splitting and recycling of the system components are advantages of the technique [35]. ATPS methodologies have already been applied successfully in the separation of different ions [35–38].

The aim of this work was to develop a novel, greener and more sensitive procedure for determining phenol and *o*-cresol compounds. The proposed method is based on the reaction between phenolic compounds, NPS and HL in ATPSs composed of polyethylene oxide 1500 (PEO1500) + salt (Li_2SO_4, Na_2SO_4 or K_2HPO_4 + KOH) + water, exploiting spectrophotometric detection of reaction products. Parameters, such as ATPS electrolyte nature, pH, reagent concentrations, sample stirring time and tie-line length (TLL) were also optimized for the method.

2. Experimental

2.1. Apparatus

Spectrophotometric measurements were performed with a UV-visible (UV/vis) spectrophotometer (Shimadzu UV-2550) with quartz microcells with a 1.00-cm optical path length and total capacity of 450 μL. The slit width was kept at 2.0 nm. The software used for system control and data acquisition was UVProbe. The pH measurements were collected with a combined glass electrode using a digital pH meter (Digimed model DM-20, Digicron Analítica Ltda, São Paulo, Brazil).

2.2. Chemicals

All reagents were of analytical grade quality and used as received without further purification. Distilled water was used throughout the experiments. The polymer was polyethylene oxide (Synth, Diadema, São Paulo, Brazil) with an average molar mass (M_m) of 1500 g mol^{-1} (denoted as PEO1500). The chemicals in the proposed method, Li_2SO_4, Na_2SO_4, K_2HPO_4, KOH, NaOH, NPS and HL, were obtained from Vetec (Duque de Caxias, Rio de Janeiro, Brazil). The reagents used in the 4-AAP procedure [28] were 4-aminoantipyrine, NH_4OH, $K_3[Fe(CN)_6]$ (Merck, Darmstadt, Germany), K_2HPO_4 and KH_2PO_4 (Vetec). Phenol and *o*-cresol were purchased from Sigma–Aldrich (Milwaukee, WI, USA).

2.3. ATPS composition, solutions and standards

The three types of ATPS applied in the development of the procedure were PEO1500 + Li_2SO_4 + water; PEO1500 + Na_2SO_4 + water [32] and PEO1500 + (K_2HPO_4 + KOH) + water. For each system at least three different compositions were studied to verify the effect of the TLL in the partitioning behavior of the $[Fe_2(CN)_{10}]^{10-}$ complex (Table 1). Moreover, global compositions shown in Table 1 are relative to an ATPS composed of 2.00 g of top phase and 10.0 g of bottom phase, which were used in most assays.

All solutions were prepared with distilled water. In the ATPS method, the pH of the water was adjusted to 12.0 with NaOH because this pH is more favorable to the complete reaction of NPS with phenol compounds. For systems composed of the salts K_2HPO_4 + KOH, correction was not necessary because the pH was 12. Stock solutions of top and bottom phases were prepared in distilled water (pH 12.0). PEO1500 and salt concentrations in the phase stock solutions are provided in Table 1. These solutions were used as solvent to prepare all solutions of phenols, NPS and HL. Working standard solutions of phenol within 5.00 and 2000 μg kg^{-1} were prepared daily by using the bottom phase as a solvent and the appropriate dilution of a 1.00 g kg^{-1} stock solution. HL working stock solutions (518 mg kg^{-1}) were prepared by weighing the appropriate quantity of hydroxylamine hydrochloride in the bottom phase using an analytical balance (Shimadzu, AY 220) with an uncertainty of ±0.0001 g. NPS working stock solutions (1992 mg kg^{-1}) were obtained by dissolving the appropriate amount of salt in the top phase. In the 4-AAP method, the solutions and standards were prepared as described in the literature [28].

2.4. Procedure

Liquid–liquid equilibrium cells were used to prepare the ATPSs. Working stock solutions of 5.000 g of phenol, 2.000 g of NPS and 5.000 g of HL were weighed. In spectroscopic measurement reference cell were carried out with the top or bottom phase stock solutions containing NPS and HL, respectively. Thus, a final composition of phenol within 2.50 and 1000 μg kg^{-1} in the bottom phase was obtained, and the global concentrations of NPS and HL were 332.0 and 216 mg kg^{-1}, respectively. The final concentrations of PEO1500 and salt in the ATPS were depended on the TLL studied (Table 1). Subsequently, the biphasic systems were manually stirred for 3 min and allowed to settle for 20 min at 25.0 ± 0.1 °C in a temperature-controlled bath (Microquímica, MQBTC 99-20). Finally, aliquots of the top phase were collected with a syringe and diluted by a factor of 1.50. UV/vis spectrophotometric measurements were carried out at 722.0 nm for phenol and 717.5 nm for *o*-cresol.

2.5. Partitioning experiments

To determine the $[Fe_2(CN)_{10}]^{10-}$ complex partition coefficient $\left(K_{[Fe_2(CN)_{10}]^{10-}}\right)$ between the two phases, the types of ATPS studied were kept for 24 h in a temperature-controlled bath to reach thermodynamic equilibrium. Subsequently, aliquots of top and bottom phases were collected. The parameter $K_{[Fe_2(CN)_{10}]^{10-}}$ can therefore be defined as

$$K_{[Fe_2(CN)_{10}]^{10-}} = \frac{A_T}{A_B} \quad (1)$$

where A_T and A_B are the absorbance (at 722.0 or 717.5 nm) of the $[Fe_2(CN)_{10}]^{10-}$ complex in the top and bottom phases, respectively.

The influence of TLLs in the partitioning behavior of the complex anion was studied by determining *K* as a function of the two different TLL values for each ATPS.

2.6. Environmental samples

A distilled sample of furnace coke effluent was used to determine the applicability of the method in environmental samples. To determine the concentration of phenol in these samples, without

Table 1
Percent composition (w/w) for PEO1500 (w_P), salt (w_S) and water aqueous two-phase system (ATPS) at 25.0 °C.

Tie-line length (TLL)	Global		Top phase		Bottom phase	
	w_P	w_S	w_P	w_S	w_P	w_S
PEO1500 + Li_2SO_4 + water						
29.43	11.4	13.83	34.44	5.30	6.85	15.54
34.97	12.0	14.73	39.18	4.15	6.60	16.85
41.71	12.3	16.64	44.40	3.25	5.91	19.32
46.36	12.8	17.62	48.38	2.58	5.68	20.63
51.67	13.5	18.79	53.26	2.15	5.60	22.12
PEO1500 + (K_2HPO_4 + KOH) + water						
16.61	9.31	14.83	20.60	6.82	7.05	16.43
27.06	9.01	18.09	27.36	4.99	5.34	20.71
30.09	9.75	18.79	30.35	4.50	5.63	21.65
37.05	8.87	21.15	34.32	3.68	3.78	24.65
42.80	8.66	23.31	38.13	3.23	2.76	27.33
PEO1500 + Na_2SO_4 + water						
32.51	7.45	13.50	32.36	2.84	2.47	15.63
35.96	7.52	15.17	34.51	2.16	2.12	17.77
40.10	7.87	16.53	37.94	1.95	1.86	19.45

matrix effects, the Standard Addition Method was performed by adding 0.250 g of sample to each ATPS standard. The recovery rate provided by the proposed method was also determined in samples such as natural river water, industrial water, distilled water and samples from wastewater treatment plants (WWTPs). In these cases, samples without the distillation step were used as the bottom phase of the ATPS, to which appropriate amounts of phenol were added. The 4-AAP method [28] was also applied to the same samples for comparison and to check the accuracy of the proposed method.

3. Results and discussion

3.1. Chemical aspects

The procedure is based on an aromatic electrophilic reaction, which is represented by Eq. (2). In strongly alkaline mediums, phenol is converted to phenolate. Thus, the electrophilic reaction can take place more easily because the benzene ring becomes very active due to the presence of the negative oxygen (O^-). According to theoretical calculations, the sites that the nitroso group (^+NO) of the NPS attacks the phenolate molecule at *para*- or *ortho*-positions. The electrophilic or electrophobic properties of the substituents in the benzene ring affect the reaction extension, and consequently the sensitivity of the method [31]. Fig. 1 shows the absorption spectra of the reaction product ($[Fe_2(CN)_{10}]^{10-}$) obtained in the ATPS top phase. The complex chemical structure was determined by Kang et al. [31]. The maximum absorbance is at 722.0 nm for phenol and 717.5 nm for *o*-cresol. Blank signals are insignificant in the wavelength chosen for taking measurements. Moreover, the spectra show (Fig. 1) that the procedure is more sensitive for phenol than *o*-cresol, which confirms that substituents present on the benzene ring affect the properties of the compounds and the formation of the $[Fe_2(CN)_{10}]^{10-}$ complex.

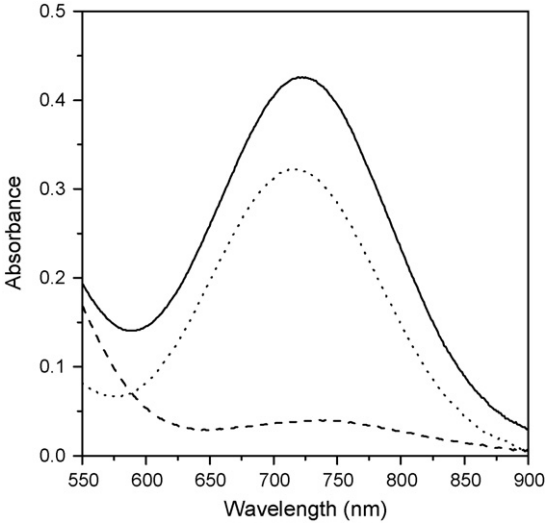
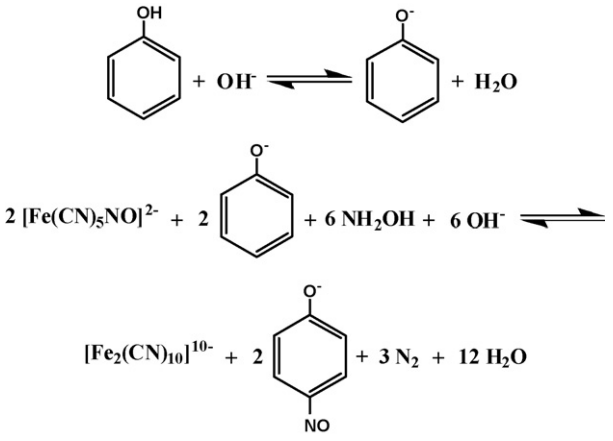


Fig. 1. Absorption spectra of the $[Fe_2(CN)_{10}]^{10-}$ anion formed by the reaction system between NPS, HL and (—) phenol or (···) *o*-cresol, and (---) blank assay spectrum in the PEO1500/Li_2SO_4 aqueous two-phase system (ATPS) with a tie-line length (TLL) = 41.71% (w/w).



(2)

3.2. Optimization of method

Method optimization was done to improve the sensitivity for low phenol concentrations. An experiment was carried out using Central Composite Rotatable Design (CCRD) in Response Surface Methodology (RSM) to evaluate the significance level of the factors. Five factors were investigated: system pH; NPS concentration; HL concentration; sample stirring time and phase splitting time. After exposure to conditions determined by the CCRD, analytical responses were evaluated by spectrophotometric measurements. Only significant coefficients at 5% probability were considered in the model using a Student's *t*-test. Table 2 shows the evaluated range and the optimum values for each variable.

Table 2
System optimization for the proposed aqueous two-phase system (ATPS) method using a standard of 600 μg kg^{-1} phenol in the bottom phase.

Parameter	Evaluated range	Selected value
pH	8.00–12.0	12.0
NPS concentration (mg kg^{-1})	140.0–670.0	332.0
HL concentration (mg kg^{-1})	110.0–385.0	216.0
Stirring time (min)	1–5	3
Phase splitting time (min)	20–60	20

NPS = sodium nitroprusside; HL = hydroxylamine hydrochloride.

3.3. Stability of the $[Fe_2(CN)_{10}]^{10-}$ anion in ATPS

In general, cyan complexes are photosensitive, so experiments were performed in the absence of light to avoid complex decomposition. Fig. 2 shows the stability of the $[Fe_2(CN)_{10}]^{10-}$ anion complex. Stability was studied through UV/vis absorption spectra of the top phase. After a period of 75 h, no change in the UV/vis spectra was observed, and the absorbance at 722.0 nm for phenol or 717.5 nm for *o*-cresol remained constant over 75 h.

3.4. Partition coefficients and effects of the tie-line length (TLL)

The TLL is a thermodynamic parameter that expresses the difference in intensive thermodynamic functions between the top and bottom phases at a constant pressure and temperature [39]. The TLL is expressed by the difference between polymer and salt concentrations present in the different phases. Generally, this parameter is a determinant in the partitioning process of some solutes and is calculated with the following equation:

$$\mathrm{TLL} = [(C_P^T - C_P^B)^2 + (C_S^T - C_S^B)^2]^{1/2} \quad (3)$$

where C_P^T and C_P^B are the polymer concentrations in the top and bottom phases, respectively, and C_S^T and C_S^B are applied in the same way to the salt.

Table 3 shows the values of $K_{[Fe_2(CN)_{10}]^{10-}}$ for two different TLL values for all ATPSs studied. Similar values of TLL were chosen to determine the influence of electrolytes in the partitioning behavior of the complex. The $[Fe_2(CN)_{10}]^{10-}$ anion shows a preferential concentration in the polymer-rich phase, reaching $K_{[Fe_2(CN)_{10}]^{10-}}$ values as high as 66.2 for a TLL of 41.71% (w/w) of the ATPS PEO1500 + Li_2SO_4 + water, which shows the best responses for both phenol and *o*-cresol. Moreover, the value of $K_{[Fe_2(CN)_{10}]^{10-}}$ increases as the TLL increases because more variable intensive thermodynamic difference between top and bottom phases properties (i.e., salt and polymer compositions) is associated with increasing TLL values [40]. As a consequence, higher concentrations of $[Fe_2(CN)_{10}]^{10-}$ anion are observed in the top phase [41].

Table 3
Partition coefficient values of the $[Fe_2(CN)_{10}]^{10-}$ anion complex for different aqueous two-phase system (ATPS) with different tie-line lengths (TLLs).

ATPS	TLL (% (w/w))	$K_{[Fe_2(CN)_{10}]^{10-}}$	
		Phenol	*o*-Cresol
PEO1500 + Li_2SO_4	29.43	17.8	56.6
	41.71	66.2	60.2
PEO1500 + (K_2HPO_4 + KOH)	30.09	13.7	27.3
	42.80	32.4	36.6
PEO1500 + Na_2SO_4	32.51	3.86	6.30
	40.10	7.52	8.88

Figs. 3 and 4 show the influence of the TLL on the sensitivity of the method for phenol and *o*-cresol determination for the three kinds of ATPS. These data were obtained by plotting analytical curves for all the TLLs of the ATPSs and then comparing the absorbance values of the same phenol standard (600 μg kg^{-1}). ATPS PEO1500/Na_2SO_4 studies in TLLs >40.10% (w/w) were not practical due to the precipitation of sulfate. Absorbance increases as the TLL increases, but for higher TLL values the signal becomes constant or even decreases. A possible reason for this behavior is that the increase in TLL also induces an ATPS salt concentration increase (Table 1), which interferes with the formation of $[Fe_2(CN)_{10}]^{10-}$ anion, as described by Kang et al. [31]. Thus, the sensitivity of the method depends on the competition between forming $[Fe_2(CN)_{10}]^{10-}$ anions and its concentration in the top phase, which in turn depends on the TLL. Since the reaction process occurs at interfaces using an ATPS method, it is interesting to note that the interference of ions, such as sulfate and phosphate, is insignificant compared to reports by Nagaraj et al. [30] and Kang et al. [31], indicating that the tolerance limit for sulfate and phosphate is lower than 25,000 and 5000 mg L^{-1}, respectively.

The effects of electrolytes on the determination of phenol are also shown in Figs. 3 and 4. A TLL value of 41.71% (w/w) using

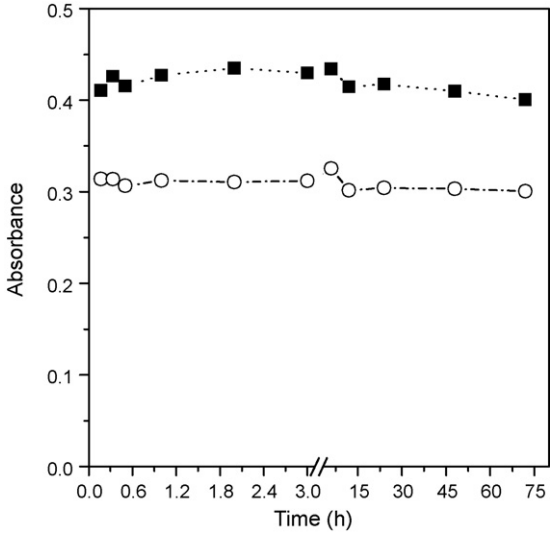


Fig. 2. Stability of the anion $[Fe_2(CN)_{10}]^{10-}$ formed by the reaction between NPS, HL and (■) phenol or (○) *o*-cresol in the PEO1500/Li_2SO_4 aqueous two-phase system (ATPS) with a tie-line length (TLL) = 41.71% (w/w).

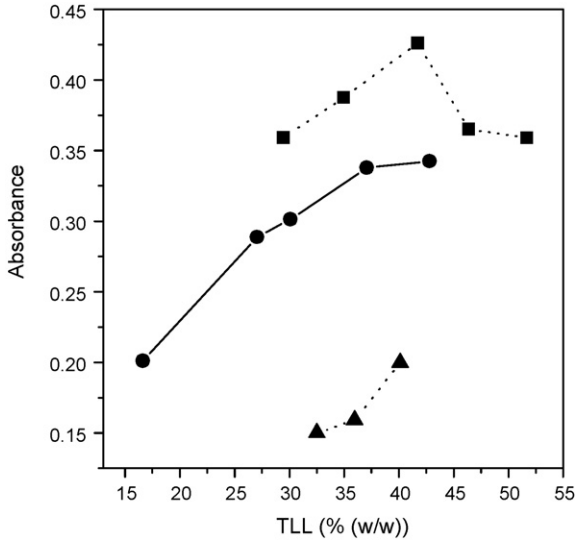


Fig. 3. Effect of tie-line length (TLL) and electrolytes on the phenol determination in an aqueous two-phase system (ATPS) composed of PEO1500, salt and water: (■) Li_2SO_4, (○) K_2HPO_4 + KOH and (▲) Na_2SO_4.

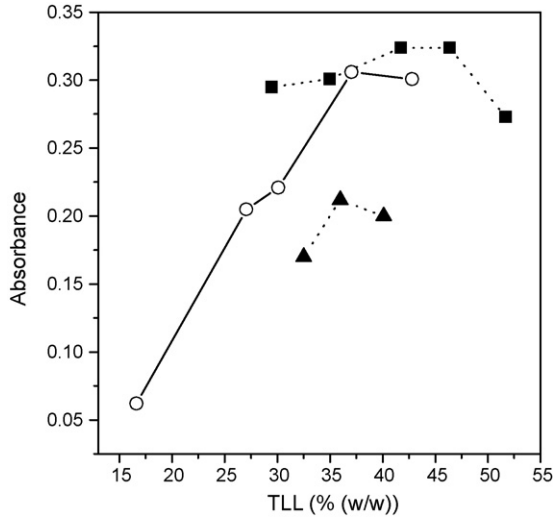


Fig. 4. Effect of tie-line length (TLL) and electrolyte on the *o*-cresol determination in an aqueous two-phase system (ATPS) composed of PEO1500, salt and water: (■) Li_2SO_4, (○) K_2HPO_4 + KOH and (▲) Na_2SO_4.

PEO1500/Li_2SO_4 ATPS presented the highest response among all the systems studied. This behavior may be explained by the model proposed by da Silva and Loh [42]. Through calorimetric measurements, it was suggested that the trend in the effectiveness of a salt to induce ATPS formation is associated with cation–polymer interactions. According to this model, when salts and polymers are mixed, cations of the salt interact with the ethylene oxide PEO groups, releasing water molecules that solvate the polymer in a process driven by an entropy increase. This cation binding continues as more electrolytes are added until saturation is reached and after which no further gain in entropy is possible, and phase splitting becomes more favorable. In da Silva and Loh's study [42], it was proposed that a higher amount of the Li^+ cation is necessary to energetically saturate the polymer chain compared to K^+ and Na^+ cations. Thus, in the ATPS composed of Li_2SO_4, the macromolecule of PEO is more positively charged than the systems composed of K_2HPO_4 + KOH or Na_2SO_4, which enables a stronger electrostatic interaction between the PEO segments and the $[Fe_2(CN)_{10}]^{10-}$ complex. Consequently, higher partitioning of the complex anion to the PEO-rich phase occurs. Therefore, the PEO1500/Li_2SO_4 ATPS system is more suitable for applying the proposed method in the determination of trace concentrations of phenols in environmental samples.

3.5. Analytical figures of merit

Under optimum experimental conditions (Table 2), additional experiments were performed to establish the analytical features of the procedure. The PEO1500/Li_2SO_4 ATPS system was used in these studies due to its higher sensitivity (Figs. 3 and 4).

Table 4 shows the main characteristics of the proposed method compared to the standard method [28] and described by Kang et al. [31]. To increase the limits of detection (LOD) and limits of quantification (LOQ), ATPS with 1.0000 g of top phase and 23.0000 g of bottom phase were used, offering a higher concentration factor of $[Fe_2(CN)_{10}]^{10-}$ anion and consequently a reduction in the range of the analytical curve. The linear responses ($R \geq 0.9997$) were within 1.00–500 μg kg^{-1} phenol, which is suitable for the determination of phenols in water samples according to the limits established by the American and Brazilian legislation [4,5]. The method achieves LODs of 1.27 and 1.88 μg kg^{-1}, and LOQs of 4.22 and 6.28 μg kg^{-1} for phenol and *o*-cresol, respectively. These values are lower than those obtained using the 4-AAP method [28] or the reaction between phenol, NPS and HL [31] without extraction. However, it is also notable that spectrometric UV/vis methods that provide the lowest LOD involve the use of an optical path length of 100 cm [27] or three consecutive extractions with chloroform [28]. Nevertheless, the employment of chloroform is harmful to the environment and human health.

The coefficients of variation (CV) were 0.38% for phenol and 0.30% for *o*-cresol. The proposed method offers a significant reduction in the volume of waste compared to the reference method. Hence, the new procedures are a suitable and environmentally friendly alternative to methods available in the literature that employ hazardous solvents, such as chloroform, or generate large amounts of waste. Furthermore, these results support the feasibility of applying the proposed method to the determination of phenol in environmental samples.

3.6. Analysis of environmental samples

Table 5 shows the results of recovery studies on water samples. The ATPS method was compared with the standard 4-AAP method [28] to check the accuracy and reliability of the proposed procedures. Studies were carried out using natural river water, industrial water, distilled water and samples from WWTPs. Recovery rates between 95.7% and 107% were obtained, and the results

Table 5
Recoveries of phenol and *o*-cresol in water samples ($n = 3$).

Sample	ATPS method recovery (%)		4-AAP method recovery (%)	
	Phenol	*o*-Cresol	Phenol	*o*-Cresol
Distilled water	97.6 ± 1.6	99.4 ± 1.5	97.8 ± 0.1	98.6 ± 0.2
River water	107 ± 0	108 ± 0.1	104 ± 1	105 ± 1
Industrial water	98.0 ± 1.5	100 ± 3	95.8 ± 0.3	95.8 ± 0.3
WWTP water 1	100 ± 2	98.5 ± 1.0	101 ± 0	96.2 ± 0.2
WWTP water 2	95.7 ± 0.5	96.4 ± 0.3	99.2 ± 0.6	99.2 ± 0.6

ATPS = aqueous two-phase system; 4-AAP = 4-aminoantipyrine; WWTP = wastewater treatment plant.

Table 4
Analytical features of different UV/vis spectrophotometric procedures for phenol determinations.

Parameter	Proposed method		4-AAP method [28] (without extraction)	Literature method [31]
	Phenol	*o*-Cresol		
Linear range	1.50–500 μg kg^{-1}		1000–5000 μg L^{-1}	50–5000 μg L^{-1}
R ($n = 8$)	0.9999	0.9997	0.9998	0.9998
Cell optical path	1.00 cm		1.00 cm	2.00 cm
LOD (μg kg^{-1})	1.27	1.88	100	50
LOQ (μg kg^{-1})	4.22	6.28	NA	NA
CV (%) ($n = 5$)	0.38	0.30	0.35	1.3
Waste volume (mL)[a]	24.0	24.0	100	50.0

NA = mean not available; LOD = limit of detection; LOQ = limit of quantification; CV = coefficients of variation.
[a] Estimated per determination.

had excellent agreement with the standard method [28] at the 95% confidence level according to a paired *t*-test [43]. Moreover, concentrations of total phenols in furnace coke effluent without spiked phenol were determined. This sample was previously distilled and diluted according to the linear range of the method. The concentration values of total phenols found in the sample with the ATPS and 4-AAP methods were 815.7 and 781.7 mg kg^{-1}, respectively, which correspond to a relative error of 4.35% between both methods.

4. Conclusions

The analytical utility of an ATPS method for determining trace phenols in water and wastewater was demonstrated for the first time by exploiting the reaction between phenol, NPS and HL. This reaction produced the $[Fe_2(CN)_{10}]^{10-}$ anion complex, which concentrated in the top phase of the ATPSs studied. The proposed method offers clearly advantageous analytical features in comparison to procedures involving the same reaction [31] or with a standard method [28], including an enhanced sensitivity and linear range as well as reduced waste volumes and no organic solvents. Pre-concentrations of analyte in the polymer-rich phase of the system allow the method to reach LOD and LOQ values that are suitable for determining total phenols in natural water and wastewater with high accuracy and in compliance with the regulatory requirements of environmental health agencies.

Acknowledgements

The authors acknowledge Fundação de Amparo a Pesquisa do Estado de Minas Gerais (FAPEMIG) and Conselho Nacional de Pesquisa e Desenvolvimento Tecnológico (CNPq) for their financial support. G.D.R. and L.R.L. thank CNPq for research fellowships.

References

[1] K.P. Kringtad, E. Lindstrom, Sci. Technol. 18 (1984) 236A.
[2] http://www.epa.gov (accessed in May 2009).
[3] D. Puig, D. Barceló, Trends Anal. Chem. 15 (1996) 362.
[4] J. Švitel, S. Miertuš, Environ. Sci. Technol. 32 (1998) 828.
[5] http://www.mma.gov.br (accessed in May 2009).
[6] S. Vichi, A. Romero, J. Tous, E.L. Tamames, S. Buxaderas, J. Chromatogr. A 1211 (2008) 1.
[7] X. Chen, T. Zhang, P. Liang, Y. Li, Microchim. Acta 155 (2006) 415.
[8] B.N. Estevinho, I. Martins, N. Ratola, A. Alves, L. Santos, J. Hazard. Mater. 143 (2007) 535–540.
[9] J. Rolfes, J.T. Andersson, Anal. Chem. 73 (2001) 3073.
[10] B. Bennett, B.F.J. Bowler, S.R. Larter, Anal. Chem. 68 (1996) 3697.
[11] H.M. Oliveira, M.A. Segundo, J.L.F.C. Lima, V. Cerdà, Talanta 77 (2009) 1466.
[12] J. Meyer, A. Liesener, S. Gtz, H. Hayen, U. Karst, Anal. Chem. 75 (2003) 922.
[13] C. Terashima, T.N. Rao, B.V. Sarada, D.A. Tryk, A. Fujishima, Anal. Chem. 74 (2002) 895.
[14] W. Wei, X.B. Yin, X.W. He, J. Chromatogr. A 1202 (2008) 212.
[15] Y. Ding, C.D. Garcia, Analyst 131 (2006) 208.
[16] K. Tsukagoshi, T. Kameda, M. Yamamoto, R. Nakajima, J. Chromatogr. A 978 (2002) 213.
[17] J.M. Gutiérrez, A. Gutés, F. Céspedes, M. del Valle, R. Muñoz, Talanta 76 (2008) 373.
[18] K.S. Khachatryan, S.V. Smirnova, I.I. Torocheshnikova, N.V. Shvedene, A.A. Formanovsky, I.V. Pletnev, Anal. Bioanal. Chem. 381 (2005) 464.
[19] M.A. El Mhammedi, M. Achak, M. Bakasse, A. Chtaini, J. Hazard. Mater. 163 (2009) 323.
[20] S. Korkut, B. Keskinler, E. Erhan, Talanta 76 (2008) 1147.
[21] J. Kochana, A. Gala, A. Parczewski, J. Adamski, Anal. Bioanal. Chem. 391 (2008) 1275.
[22] W.J.R. Santos, P.R. Lima, C.R.T. Tarley, L.T. Kubota, Anal. Bioanal. Chem. 389 (2007) 1919.
[23] M. Shaghaghi, J.L. Manzoori, A. Jouyban, Food Chem. 108 (2008) 695.
[24] W. Cao, X. Mu, J. Yang, W. Shi, Y. Zheng, Spectrochim. Acta A 66 (2007) 58.
[25] J. Vuković, S. Matsuoka, K. Yoshimura, V. Grdinić, R.J. Grubešić, Microchim. Acta 159 (2007) 277.
[26] M. Manera, M. Miró, J.M. Estela, V. Cerdà, Anal. Chim. Acta 582 (2007) 41.
[27] K.O. Lupetti, F.R.P. Rocha, O. Fatibello-Filho, Talanta 62 (2004) 463.
[28] L.S. Clesceri, A.E. Greenberg, A.D. Eaton, Standard Methods for the Examination of Water and Wastewater, twentieth ed., American Public Health Association, Washington, DC, 1999.
[29] M.C.H. da Silva, L.H.M. da Silva, F.J. Paggioli, Anal. Sci. 21 (2005) 933.
[30] P. Nagaraj, J.M. Bhandari, B.N. Achar, Indian. J. Chem. 32A (1993) 641.
[31] C. Kang, Y. Wang, R. Li, Y. Du, J. Li, B. Zhang, L. Zhou, Y. Du, Microchem. J. 64 (2000) 161.
[32] J.P. Martins, P.C. Carvalho, L.H.M. da Silva, J.S.R. Coimbra, M.C.H. da Silva, G.D. Rodrigues, L.A. Minim, J. Chem. Eng. Data 53 (2008) 238.
[33] X. Zeng, K. Osseo-Asare, Colloids Surf. A: Physicochem. Eng. Aspects 226 (2003) 45.
[34] N.J. Bridges, K.E. Gutowski, R.D. Rogers, Green Chem. 9 (2007) 177.
[35] G.D. Rodrigues, M.D.H. da Silva, L.H.M. da Silva, F.J. Paggiolli, L.A. Minim, J.S.R. Coimbra, Sep. Purif. Technol. 62 (2008) 687.
[36] L.H.M. da Silva, M.C.H. da Silva, J.A. Júnior, J.P. Martins, J.S.R. Coimbra, L.A. Minim, Sep. Purif. Technol. 60 (2008) 103.
[37] A.E. Visser, S.T. Griffin, D.H. Hartman, R.D. Rogers, J. Chromatogr. B 743 (2000) 107.
[38] L. Bulgariu, D. Bulgariub, J. Chromatogr. A 1196 (2008) 117.
[39] L. Capezio, D. Romanini, G.A. Pico, B. Nerli, J. Chromatogr. B 819 (2005) 25.
[40] L.H.M. da Silva, M.C.H. da Silva, R.A.N. de Aquino, K.R. Francisco, M.V.C. Cardoso, L.A. Minim, J.S.R. Coimbra, J. Phys. Chem. B 110 (2006) 23540.
[41] L.H.M. da Silva, M.C.H. da Silva, K.R. Francisco, M.V.C. Cardoso, L.A. Minim, J.S.R. Coimbra, J. Phys. Chem. B 112 (2008) 11669.
[42] L.H.M. da Silva, W. Loh, J. Phys. Chem. B 104 (2000) 10069.
[43] J.C. Miller, J.N. Miller, Statistics for Analytical Chemistry, fourth ed., Prentice Hall, 2000.

Talanta 80 (2010) 1145–1151

Contents lists available at ScienceDirect

Talanta

journal homepage: www.elsevier.com/locate/talanta

A novel molecularly imprinted polymer thin film as biosensor for uric acid

Po-Yen Chen[a], R. Vittal[a], Po-Chin Nien[a], Guey-Sheng Liou[b], Kuo-Chuan Ho[a,b,*]

[a] Department of Chemical Engineering, National Taiwan University, Taipei 10617, Taiwan
[b] Institute of Polymer Science and Engineering, National Taiwan University, Taipei 10617, Taiwan

ARTICLE INFO

Article history:
Received 11 June 2009
Received in revised form 30 August 2009
Accepted 31 August 2009
Available online 6 September 2009

Keywords:
Ascorbic acid
Biosensor
Imprinting efficiency
Molecularly imprinted polymer
Poly(PD–BCD)
Uric acid determination

ABSTRACT

A novel amine–imide type conducting polymer, denoted as poly(PD–BCD), was molecularly imprinted on an indium–tin oxide (ITO) glass, with uric acid (UA) as the template and without any functional monomer. Intending to improve the imprinting efficiency, the polymer content was varied from 0.3 to 0.9 wt% during the preparation of the molecularly imprinted polymer (MIP), thereby varying the thickness of the polymer film; the content of UA as the template was maintained to be the same for all the films. The sensitivities of the thus prepared MIP electrodes were calculated to be more than 3-fold, compared to those of the corresponding non-MIP (NMIP) electrodes, which were obtained through the same method, however, without adding UA during their preparation. A polymer content of 0.6 wt% rendered the best performing MIP electrode, as judged by the imprinting efficiency and sensitivity of the electrode for UA. A linear relationship between steady-state currents and UA concentrations from 0 to 1.125 mM was obtained for both types of the sensors. The sensitivities of the MIP and the NMIP electrodes made with 0.6 wt% of polymer were calculated to be 24.72 and 6.63 $\mu A\,mM^{-1}\,cm^{-2}$, respectively. The limit of detection (LOD) for this MIP was found to be 0.3 μM at a signal to noise ratio (S/N) of 3. This MIP electrode was used as a biosensor for the detection of UA in the presence of ascorbic acid (AA) in a sample containing these species in the same concentrations as those in a human serum. The selectivity of MIP electrode is higher than that of NMIP electrode, and the values are 28.76 and 8.85, respectively. The results are substantiated by using cyclic voltammetry (CV), linear sweep voltammetry, amperometry, and scanning electron microscopy.
© 2009 Elsevier B.V. All rights reserved.

1. Introduction

There has been a very active research in this decade on molecular imprinting owing to its importance in a broad range of applications [1–3]. Molecularly imprinted polymer (MIP) is usually obtained by imprinting the polymer on a substrate through a template molecule. This template molecule is the analyte, which produces cavities specific to its detection in a bulk solution. After the extraction of the template molecule, the polymer matrix becomes complementary to the molecule and can rebind it with very high affinity and specificity.

During the last decade, molecularly imprinting technique has been developed as an analytical tool for the estimation of various electroactive species [4,5]. Efforts have been made to use MIPs for the detection of biomolecules [4–9]. MIP sensors can be substituted for enzyme-based sensors, because MIPs are enzyme mimics and can play the role of enzymes for catalyzing the reactions. In addition, they can be made at low cost and have higher thermal and chemical stability than that of enzymes [10,11]. There have been a number of reports on sensors based on molecularly imprinted conducting polymers, e.g., polyphenol [12], polypyrrole [13,14] and poly(phenylenediamines) [15]; in these reports, electrochemical methods, such as those with amperometry, impedance spectroscopy, and electrical capacitance were adopted. Malitesta et al. [16] reported the first successful application of electropolymerization for the preparation of MIPs. Ulyanova et al. [17] employed potentiodynamic electropolymerization technique to form a polyazine conducting polymer which was molecularly imprinted for the detection of theophyline. Benzimidazole compounds were determined in water samples by using MIPs [18] and performing the measurements in an HPLC system. Suedee et al. developed an MIP conductometric sensor for on-line sensing of haloacetic acids [19].

Uric acid (UA) is the principle final product of urine metabolism in human body [20] and is related to the occurrence of many disorders such as gout, hyperuricemia and Lesch–Nyhan syndrome [21]. Besides, UA is also one of the most important kidney calculus indices in human plasma. Thus, monitoring of the concentration of UA in human blood and urine is important for the prevention of the mentioned and other similar diseases. As mentioned above, electrochemical methods are very often used both at the stages of preparing and using the MIPs to detect the analytes. The common and well-developed electrochemical method for the detection of UA is based on the enzymatic approach. Uricase enzyme is

* Corresponding author. Tel.: +886 2 2366 0739; fax: +886 2 2362 3040.
E-mail address: kcho@ntu.edu.tw (K.-C. Ho).

0039-9140/$ – see front matter © 2009 Elsevier B.V. All rights reserved.
doi:10.1016/j.talanta.2009.08.041

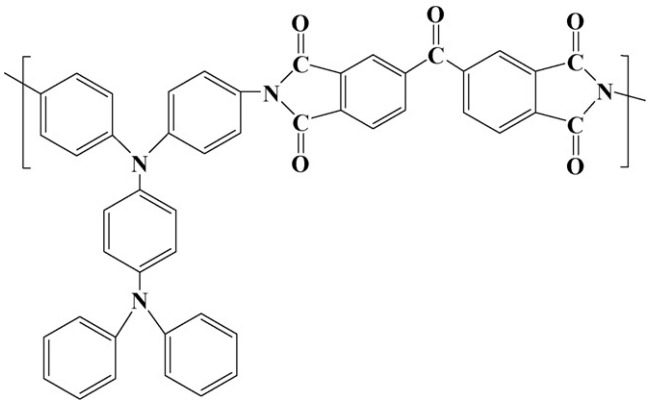
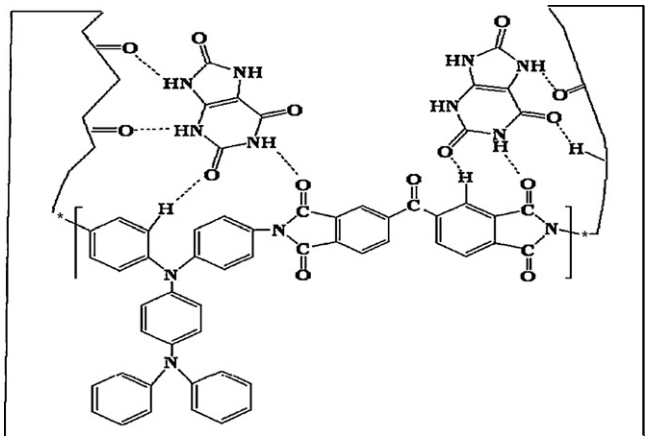


Fig. 1. Structure of poly(PD–BCD).

allowed to react with UA and the corresponding hydrogen peroxide is detected electrochemically. However, this method inherits some problems, such as high cost and low stability of enzymes; in addition the detection is indirect (detection of the reaction products). Several studies based on non-enzymatic methods have also been made to detect UA. These include the usage of carbon paste or activated glassy carbon electrodes [22,23], modified electrodes containing multi-wall carbon nanotubes (MWCNTs) [24] or a redox mediator [25].

The present study reports an electrochemical sensor for UA which is based on a novel molecularly imprinted amine–imide type conducting polymer. This is the first report using the polymer, denoted as poly(PD–BCD), as the MIP for sensing UA, in which the polymer was synthesized with N,N-bis(4-aminophenyl)-N′,N′-diphenyl-1,4-phenylenediamine (PD) and 3,3′,4,4′-benzophenonetetra carboxylic dianhydride (BCD). To the best of our knowledge, this is also the first quantitative study with regard to the content of any polymer to be used for optimizing the sensor for UA determination. Fig. 1 shows the structure of this polymer. Unlike the common approach of using a functional monomer and cross linker for the preparation of MIP, we directly applied for its preparation a sample of the polymer synthesized by us previously [26]. Incorporation of the analyte (UA) is purely a van der Waals interaction between the analyte and the sensor layer (polymer) (Scheme 1). The scheme shows formation of possible hydrogen bonds between the poly(PD–BCD) and the UA. Amine groups of UA can form hydrogen bonds with the ketone groups of poly(PD–BCD). In the same way, ketone groups of UA can also form hydrogen bonds with hydrogen atoms of benzene rings of the polymer. Such constitution can provide very strong adsorption force between UA and poly(PD–BCD). We studied the effects of varying the concentration of the novel polymer on its performance for the detection of UA. The optimum concentration of this polymer was evaluated in terms of the sensitivity of the MIP sensor for the detection of UA and in terms of the imprinting efficiency. This MIP electrode was also tested for the estimation of UA in the presence of ascorbic acid (AA) in a sample containing these species in the same concentrations as those of a human serum.



Scheme 1. Schematic representation of the formation of possible hydrogen bonds for the incorporation of UA in poly(PD–BCD).

2. Experimental

2.1. Chemicals and apparatus

The conducting polymer used for molecular imprinting was synthesized from N,N-bis(4-aminophenyl)-N′,N′-diphenyl-1,4-phenylenediamine and 3,3′,4,4′-benzo-phenone-tetracarboxylic dianhydride, and the synthesis steps were reported previously [26]. Uric acid (98%), ascorbic acid (99%), phosphate buffer saline tablet (PBS) and potassium chloride (KCl) were purchased from Aldrich (USA). 1-Methyl-2-pyrrolidinone (NMP, 99%) was purchased from Sigma (USA). Deionized water (>18 MΩ) was produced by Purelab Maximum (ELGA, UK). Indium–tin oxide (ITO, 10 Ω/□) glass was supplied by RiTdisplay Corporation (Hsinchu Industrial Park, Taiwan). All chemicals were used as received.

Amperometric measurements were carried out using potentiostat/galvanostat model CHI 440 (CH Instruments) and its compatible software. All electrochemical experiments were carried out at room temperature with a three-electrode system, containing a 50 mL glass cell with Ag/AgCl/saturated KCl reference electrode, platinum plate counter electrode and MIP or non-molecularly imprinted polymer (NMIP) working electrode.

2.2. Preparation of MIP and NMIP electrodes

The ITO glass was ultrasonically cleaned in a 0.1 M HCl for 5 min before using. The substrate was rinsed with deionized water and dried in air. After cleaning, epoxy tapes were fixed at the edges of the ITO-surface to restrict the active surface area to be 1.0 cm × 1.0 cm. For preparing the MIP electrodes, poly(PD–BCD) was mixed at various concentrations from 0.3 to 0.9 wt% with 1.5 mM UA dissolved in 1-methyl-2-pyrrolidinone, NMP, and the thus obtained solutions were drop-coated onto the ITO glass electrodes. The ITO electrodes were put into a vacuum oven and were subjected to a programmed temperature variation to remove the solvent from the electrodes. Then the temperature was kept at 60 °C for 4 h and raised to 80 °C for 2 h; finally the temperature was increased to 180 °C for 2 h. Such programmed temperature during the solvent removal is necessary to obtain uniform MIP films, and thereby higher detection currents in the amperometric analysis. After removing the solvent, Cu tape (3 M Company) was pasted at one edge of the conductive surface of the electrodes as a bus bar. Each electrode was then washed with deionized water to extract the UA template out of the polymer matrix, and then dried under nitrogen gas blow. The extracted MIP films were subjected to CV experiments within a potential window of 0.1–0.9 V (vs. Ag/AgCl/saturated KCl) for confirming the removal of the template. Disappearance of oxidation peak of the UA indicates its removal from the polymer. NMIP electrodes were also prepared in the same way, except that there was no addition of UA during their preparation.

2.3. Electrochemical measurements

Cyclic voltammetry (CV) was used to ascertain the complete removal of the template from the polymer film after the extrac-

tion with deionized water; the potential of the polymer electrode was swept from 0.1 to 0.9 V at a scan rate of 0.1 V s^{-1}. Furthermore, the charge capacities of MIP and NMIP electrodes were checked by comparing the areas under the pertinent CVs.

Linear sweep voltammetry (LSV) was performed to obtain the detecting potential of UA. The detection potential was determined by sweeping the potential of the MIP electrode (0.6 wt% of the polymer) in a window of potentials between 0.5 and 1.0 V. The corresponding background current was recorded in a 0.02 M phosphate buffer saline (PBS, pH 7.4), containing 0.1 M KCl as the supporting electrolyte, and the total current was recorded in a solution containing 1.5 mM UA. The net current was obtained by subtracting the background current from the total current. A proper operating potential was determined from the plateau part of the net current of the LSV curve. This way of estimating the operating potential was based on the fact that the plateau part corresponds to the diffusion control region of UA oxidation reaction and the sensing potential set at this region can obtain a current proportional to the concentration of UA.

UA was detected by the MIP and NMIP electrodes using an amperometric method. For this, steady-state current densities were obtained for MIP and NMIP electrodes at various concentrations of UA from 0 to 1.125 mM and the corresponding calibration curves were made with these values; the sensitivity and the detection limit were estimated from the calibration curve. Steady-state currents were also obtained by the amperometric method for the detection of 0.4 mM UA in the presence of 0.04 mM AA, which are their usual concentrations in a human serum; these experiments were simulated experiments intended to determine the selectivity of the MIP biosensor for UA in the presence of AA in a human serum. We mention here that the interference study of this work was restricted to AA and further study is envisaged with respect to other impurities such as dopamine and thiols.

We make here a simple comparison between amperometric and other electrochemical detection methods, to rationalize our preference of the former. Amperometric sensor has relatively short response time and can be designed easily as a portable sensor. Other special detection methods were used by several workers. Chou and Liu have used impedance detection method for sensing cholesterol with a thick film-MIP sensor. In this method a current decrease could be noticed when the analyte was attached to the MIP thick film [27]. A pulsed amperometric detection (PAD) method interprets the difference in currents obtained due to different bias potentials for dedoping and redoping as the analytical signal [28]; this method provides an accurate way for detecting the recombination of the target on the MIP electrode [29,30]. Potentiodynamic methods are usually suitable for sensing non-electroactive compounds, such as caffeine, protein and cholesterols. Both potentiodynamic and amperometric methods entail interferences, which disturb the current signal. This problem can be solved by modifying the electrodes with special materials such as Nafion® and mediators [31].

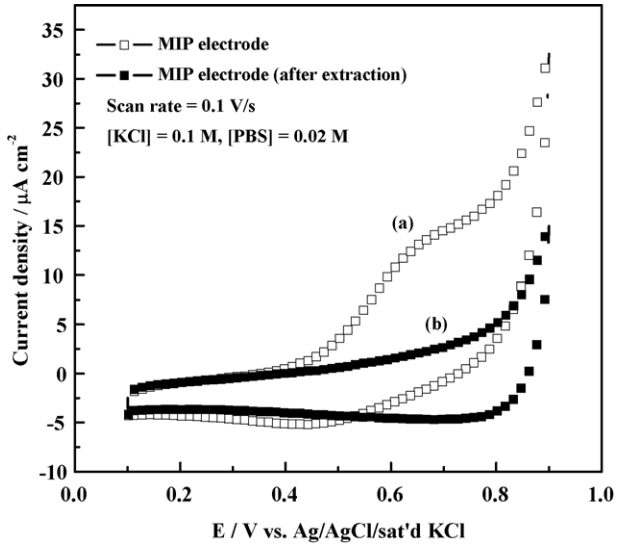


Fig. 2. CVs of the MIP electrode with 0.6 wt% of the polymer, in 0.1 M KCl + 0.02 M PBS (pH 7.4) at the scan rate of 0.1 V s^{-1}: (□) before extraction of UA and (■) after its extraction.

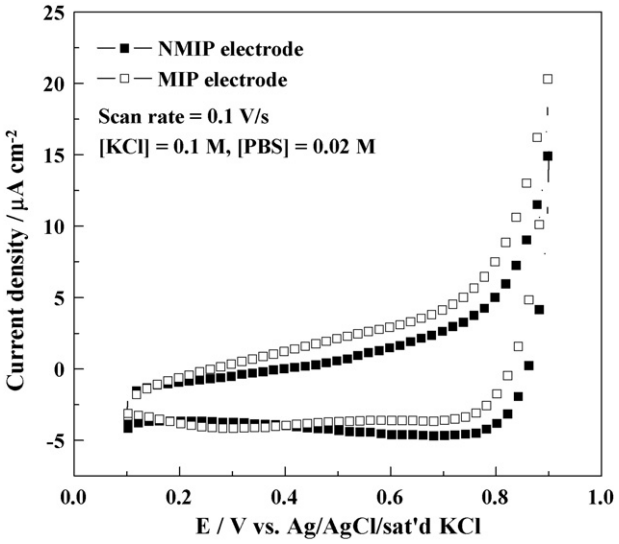


Fig. 3. Charge capacities of MIP electrode (□) and NMIP electrode (■) after the extraction of UA, both CVs being obtained in 0.1 M KCl + 0.02 M PBS (pH 7.4) at the scan rate of 0.1 V s^{-1}.

2.4. Morphological characterization

Scanning electron microscopy (SEM) images were obtained by Hitachi S-800 Field Emission SEM. For this purpose, the MIP and NMIP electrodes were sputtered with a layer of gold and the images were observed under a voltage of 20 kV.

3. Results and discussion

3.1. Performance evaluation of the MIP sensor

For evaluating the performance of a sensor, most important factors are sensitivity and selectivity. Fig. 2a shows the CV of the MIP electrode prepared with 0.6 wt% of the polymer in 0.1 M KCl and 0.02 M PBS. Fig. 2b shows the CV of the same electrode after the extraction of UA. The oxidation peak of UA can be clearly seen in Fig. 2a; after the extraction of UA its oxidation peak is absent in Fig. 2b, as desired and expected. This implies that UA molecules of the MIP electrode were removed after the extraction process. Further discussion will render evidence through SEM images that the extraction has removed only surface bound UA. In order to ensure that the same amount of poly(PD–BCD) remained after the extraction, the charge capacities of the MIP and NMIP electrodes were calculated using the CVs, as shown in Fig. 3. Calculation on the charge capacities was based on the integrated areas of the CVs. The charge capacities of the MIP and NMIP electrodes were found to be 4.812 and 4.475 μC, respectively, which clearly indicate that only UA was removed and not the polymer after the extraction process.

Before amperometric detection, the detection potential for UA was determined, using polarization curves of the MIP electrode in pure electrolyte and in electrolyte containing UA. Fig. 4 shows

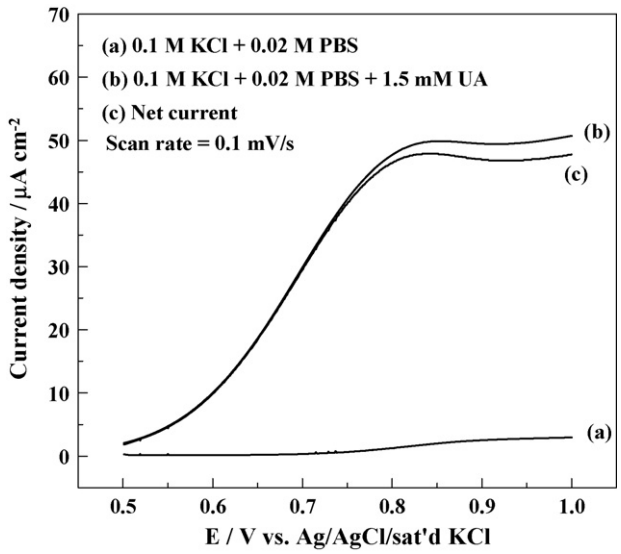


Fig. 4. Liner sweep voltammograms of MIP electrode in (a) 0.1 M KCl + 0.02 M PBS, and (b) 0.1 M KCl + 0.02 M PBS + 1.5 mM UA, at the scan rate of 0.1 V s^{-1}. This figure also shows the net current (c).

the LSVs of the electrode with 0.6 wt% of the polymer at a sweep rate of 0.1 mV s^{-1}. A plateau region between 0.8 and 1.0 V is the limiting current zone. Within this limiting current zone the current density is proportional to the concentration of an electroactive species. From these LSVs, the sensing potential was set at 0.85 V for obtaining amperometric steady-state current responses of UA. The mechanism is electro-oxidation of UA on the imprinted site of MIP modified electrode. At the limiting current region, diffusion of UA would control the whole system. The surface concentration of UA would be zero in this case and the current would depend on the bulk concentration of UA.

Amperometric experiments were carried out to examine the current responses of UA with the MIP and NMIP modified electrodes. The UA concentration was increased stepwise from 0 to 1.125 mM and the potential was fixed at 0.85 V. Fig. 5 shows the calibration curves of MIP and NMIP electrodes, both with a polymer content of 0.6 wt%. Both MIP and NMIP electrodes show good linear relationship between the current density and the concentration of UA for the entire concentration range of UA, with the correlation coefficients greater than 0.995 for both the electrodes. The calibration curves give the sensitivities of MIP and NMIP electrodes to be 24.72 and 6.63 μA mM^{-1} cm^{-2}, respectively. The current density responses of the MIP electrode are higher than those of the NMIP electrode at all the concentrations. The consistently enhanced current densities with MIP electrode reveal that imprinted sites were formed, most likely at the surface of the MIP electrode and they enabled the MIP electrode to recognize more UA molecules, than were recognized by the corresponding NMIP electrode. Indeed these sites or pores can be clearly seen in the corresponding SEM images in further discussions. When the template molecules were removed, a geometrically adopted polymer skeleton with fitting cavities and diffusion pathways for UA was left behind. The imprinting efficiency, defined as the ratio of the sensitivity of the MIP electrode to that of the NMIP electrode, is a property of an MIP electrode used for evaluating the recognition grade of the electrode. For the MIP electrode made by 0.6 wt% of the polymer, the imprinting efficiency is about 3.7, the highest in this study (Table 1). The limit of detection (LOD) for the MIP electrode was calculated to be 0.3 μM on the basis of signal to noise ratio (S/N) of 3. In real applications, the MIP electrode acts as the sensing electrode and the NMIP electrode as the reference one; this will be explained in further discussions.

3.2. Optimization of the polymer content for the MIP electrode

In our preliminary investigations we intended to study the effects of changing the polymer film thickness of the MIP electrode on the sensing performance of the electrode for UA. For this 0.3, 0.5, 0.6, 0.7, and 0.9 wt% of the polymer was mixed with 1.5 mM of UA for preparing the electrodes with different thicknesses of the polymer. Amperometric experiments were carried out with each of the thus fabricated electrodes, and the corresponding calibration curves were obtained. From these calibration curves sensitivities of the electrodes for UA detection were obtained. Sensitivities were also obtained for the corresponding NMIP electrodes. From the values of the sensitivities of the MIP electrodes and NMIP electrodes imprinting efficiencies of the MIP electrodes for various polymer concentrations were calculated. The performance parameters of the sensors with different polymer contents are listed in Table 1. Up to a polymer content of 0.6 wt%, the sensitivity of the MIP electrode shows an increase and reaches a maximum value of 24.72 μA mM^{-1} cm^{-2}. However, the sensitivity shows a decrease with higher polymer contents up to 0.9 wt%. This can be attributed to the inhibition to the electron conductivity in thick polymer films due to the presence of UA. It is known that electron conductivity cannot be sustained in a disproportionately thick conducting film

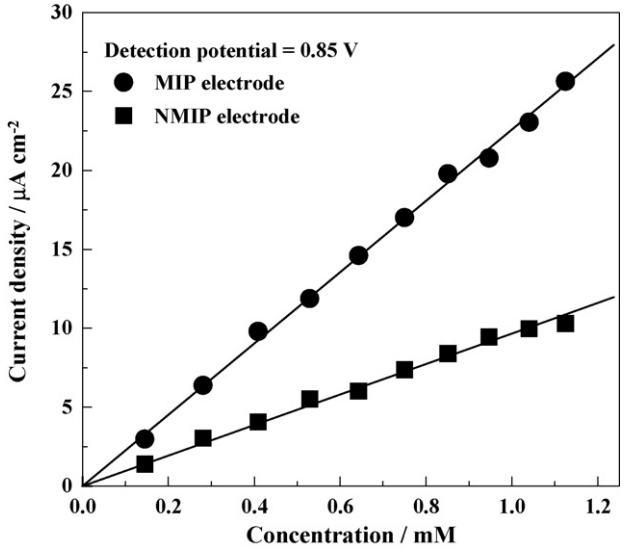


Fig. 5. Calibration curves of MIP (solid spheres) and NMIP (solid squares) electrodes with 0.6 wt% of the polymer in each case.

Table 1
Sensitivities of the MIP and NMIP electrodes and the corresponding imprinting efficiencies with different polymer contents of the electrodes.

Polymer content (wt%)	Sensitivity of MIP electrode (mA mM^{-1} cm^{-2})	Sensitivity of NMIP electrode (mA mM^{-1} cm^{-2})	Imprinting efficiency
0.3	22.59	9.67	2.34
0.5	22.94	6.53	3.51
0.6	24.72	6.63	3.73
0.7	17.43	7.16	2.43
0.9	0.03	8.54	0.0035

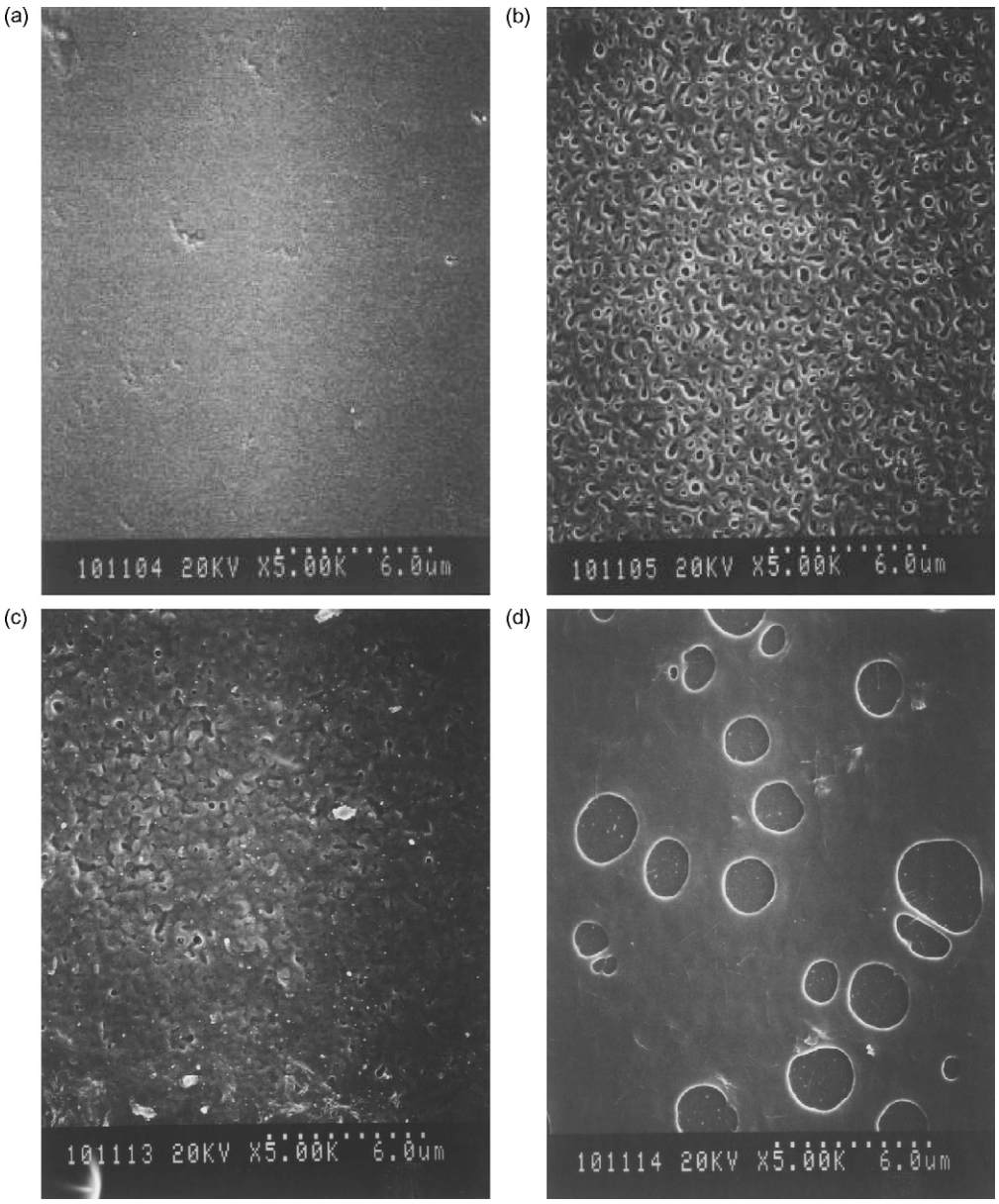


Fig. 6. SEM images of (a) NMIP electrode with 0.6 wt% of the polymer, (b) MIP electrode with 0.6 wt% of the polymer, (c) MIP electrode with 0.9 wt% of the polymer, and (d) MIP electrode with 0.3 wt% of the polymer.

on a substrate. In the case of high polymer contents, UA molecules are likely buried deep within the polymer film and the recognition sites are therefore much fewer on the surface of the polymer. As the imprint molecules are buried inside the polymer membrane, the effective electron diffusion coefficient within the membrane decreases, thereby decreasing the sensitivity of the pertinent electrode for UA detection. In order to verify the presence of these recognition sites, SEM was used to observe the surface morphol-

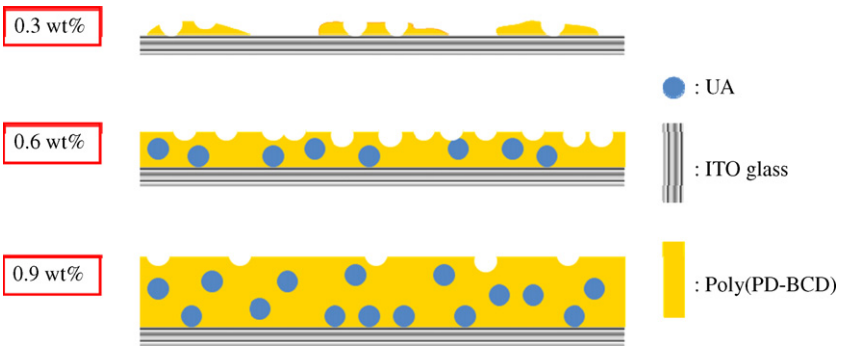


Fig. 7. Schematics representation of imprints of UA with different contents of the polymer.

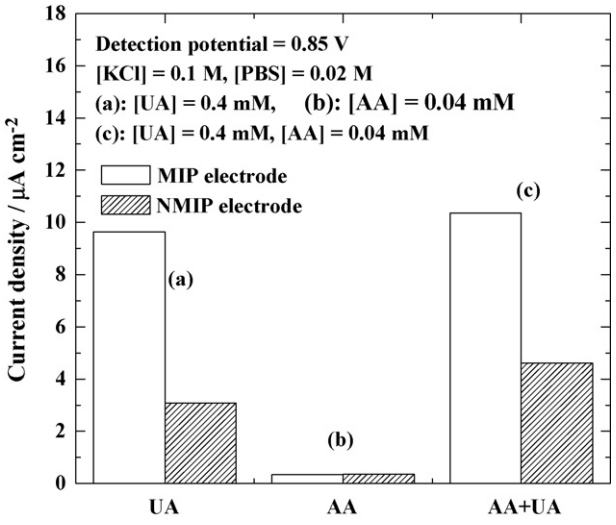


Fig. 8. Current density responses of the MIP and NMIP electrodes with 0.6 wt% of the polymer for (a) 0.4 mM of UA, (b) 0.04 mM of AA, and (c) 0.4 mM of UA + 0.04 mM of AA.

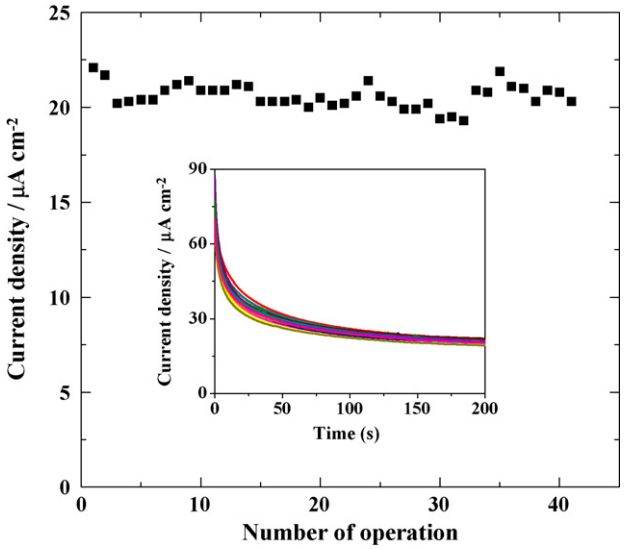


Fig. 9. Reusability of the MIP electrode with 0.6 wt% of the polymer for 40 operations.

ogy of MIP and NMIP electrodes. Fig. 6a and b is the SEM photos of NMIP and MIP electrodes, respectively, with 0.6 wt% of the polymer. The NMIP surface displays a relatively smooth surface. The MIP electrode shows disordered but mostly circular cavities with scattered large irregular pores, all obviously due to the templating process of the polymer with UA. These are the recognition sites of the MIP film for UA. When the polymer content is increased to 0.9 wt%, the MIP electrode shows insignificant number of pores and buried pores (Fig. 6c) with reference to those with 0.6 wt% of the polymer (Fig. 6b). Since the quantity of the template, i.e., UA used for each film is the same, the recognition sites created by the template should depend on the polymer content. Again, as the content of UA is the same in both the cases of MIPs with 0.6 and 0.9 wt% of the polymer, same extent of pores should have appeared in Fig. 6c (with 0.9 wt% of polymer) as that in Fig. 6b (with 0.6 wt% of polymer), if all the UA was bound to the surface of the electrode. As the surface pores are obviously not the same in both the figures, it implies that most of the UA molecules were buried in the thicker polymer film with 0.9 wt% of polymer and the subsequent recognition sites for UA in this case were much fewer than those of the film with 0.6 wt% of polymer. We believe that the MIP electrode with 0.9 wt% of polymer with buried UA has lost its usual polymer conductivity due to the damage of conductive paths for electron transfer, caused by the irregular burial of UA in the matrix of the polymer film. We attribute this non-conductivity behavior for the insignificant sensitivity of this MIP electrode for UA. With slightly higher content of the polymer, i.e., with 0.7 wt%, the MIP electrode showed lesser sensitivity of 17.43 $\mu A\,mM^{-1}\,cm^{-2}$, compared to that of the MIP electrode with 0.6 wt% of the polymer, for which the sensitivity was 24.72 $\mu A\,mM^{-1}\,cm^{-2}$. The damage caused for this MIP electrode with 0.7 wt% of the polymer was obviously less, as this content of the polymer was only slightly higher than that of the MIP electrode (0.6 wt%). Thus now it is clear from the results, that the optimum content of this polymer is 0.6 wt% for achieving the highest imprinting efficiency, and thereby sensitivity.

Table 1 also shows that the highest sensitivity of an NMIP electrode is with 0.3 wt% of the polymer. With 0.3 wt% of the polymer the electrode is virtually an ITO film because the polymer coverage is negligible. This is evidenced from SEM image in Fig. 6d. The figure provides solid evidence that the coverage of the ITO substrate with the polymer is little and polymer islands are indeed formed. The templating possibilities of UA with the films with 0.3, 0.6, and 0.9 wt% of the polymer are schematically represented in Fig. 7. The NMIP electrode with 0.5 wt% of the polymer is a "polymer modified" electrode and is different from the one with 0.3 wt% of polymer which has only islands of polymer, and otherwise is virtually an ITO bare electrode. Thus the trend of the sensitivity of NMIP electrode should be considered beginning from the NMIP electrode with 0.5 wt% of polymer. Increase in the polymer content has rendered a consistent increase in the sensitivity of the NIMP sensor, which can be attributed to the intrinsic nature of the conducting polymer. The optimum thickness of the polymer film for the NMIP electrode has apparently not reached and we have not used higher contents of polymer to investigate this, as the focus of our study is with MIP, for which the optimum thickness of this particular film is with 0.6 wt% of the polymer, as judged from its imprinting efficiency and sensitivity for UA. In absence of UA, the NMIP electrode with 0.9 wt% of polymer was apparently not damaged and the thickness can be probably increased for this type of NMIP electrode.

3.3. Selectivity of the MIP electrode for UA in the presence of AA

Intending to verify the sensitivity of this MIP sensor for the bioanalysis of human serum, a preliminary amperometric analysis was made for its specificity for UA in the presence of AA, which is the most important interference in electrochemical routine analysis of UA in a human serum. The normal concentration of AA in a human serum is about $45.8 \pm 16.2\ \mu M$ and is less influenced by dietary or smoke behavior [32]. In this study, the interference test was carried out with AA concentration set at 0.04 mM. Fig. 8 shows the individual and the coexistence current density responses of the MIP and NMIP electrode (0.6 wt% of polymer) for 0.4 mM of UA and 0.04 mM of AA. The figure indicates that the MIP electrode detects negligible current densities for AA. The current response of 0.04 mM AA is less than 7% of the total current obtained with 0.4 mM of UA and 0.04 mM of AA. The selectivity is defined as the sensitivity of UA divided by the sensitivity of AA using the same electrode. Higher selectivity implies better performance in sensing UA against AA. The selectivity of MIP electrode is about 28.76, this result shows that AA has low interference on the sensing of UA by the MIP electrode. Fig. 8 also shows the current density responses of the corresponding NMIP electrode for UA, AA and UA + AA. From this result, the selectivity of NMIP electrode is about 8.85. Compared to the case of

the MIP electrode, the current density response of the NMIP electrode is far lesser for UA, though it is the same for AA. Measured with the NMIP electrode, the current response for 0.4 mM of UA and 0.04 mM of AA is about 48% higher than that for 0.4 mM of UA. These results clearly demonstrate that the interference due to AA is higher in the case of the NMIP electrode with reference to the MIP electrode and thus the selectivity for UA with MIP electrode is far better than that with NMIP electrode. As mentioned already, in real applications, the MIP electrode can act as the sensing electrode and the NMIP electrode as the reference electrode. This may be rationalized as follows. Since the MIP electrode offers specific recognition sites for UA detection, the difference in sensitivities for the optimized MIP electrode (with 0.6 wt% of polymer) and its corresponding NMIP electrode is essentially to be attributed to the UA. Contribution to the sensitivity from the polymer film is eliminated in this way. Therefore the difference in sensitivities between the MIP electrode and its corresponding NMIP electrode is a better measure for the estimation of UA. The 7% interference due to AA in the estimation of UA in human serum would thus be further reduced. The reusability of the MIP electrode is shown in Fig. 9. The figure shows the steady-state current densities of the MIP electrode obtained for 40 different operations. The values were extracted from the steady-state currents of the MIP electrode versus time (shown as inset). The reusability was tested in a solution containing 0.02 M PBS, 0.1 M KCl and 1 mM of UA. After forty operations, an average current density was calculated to be $20.6 \pm 0.6\ \mu A\ cm^{-2}$. The error range of these results indicates that the MIP electrode is reusable for at least 40 operations, without a significant reduction in its sensitivity.

4. Conclusions

The novel polymer, denoted as poly(PD–BCD) was used to prepare a molecularly imprinted polymer (MIP) electrode using the template UA for its sensing. This MIP electrode was directly made from the polymer without a functional monomer and cross linker. As expected the MIP electrode showed about 3-fold higher sensitivity for UA than its counterpart, i.e., a non-molecularly imprinted (NMIP) electrode. The limit of detection (LOD) for this MIP sensor was found to be 0.3 μM at a signal to noise ratio (S/N) of 3. It is well established that the sensitivity of the MIP sensor depends on the thickness of the polymer, and the optimum thickness of the polymer is with 0.6 wt% of it, for obtaining the best sensitivity, and thereby imprinting efficiency. SEM photographs show clearly that the polymer at a concentration of more than 7 wt% had buried the UA in it, causing an adverse effect with respect to imprinting efficiency and thereby sensitivity of the pertinent MIP sensor. The porous structure caused by the UA in the polymer determines the sensitivity of the sensor. The MIP electrode can be used for a human serum as the biosensor with high selectivity for the estimation of UA in the presence of AA as the major impurity. The MIP-sensor was observed to be highly stable for at least forty times of operation.

Acknowledgments

This work was supported by the National Research Council of the Republic of China (Taiwan) under grant numbers NSC 96-2220-E-006-015 and NSC 97-2220-E-006-008.

References

[1] W. Li, S.J. Li, Adv. Polym. Sci. 206 (2007) 191.
[2] X. Hu, Q. An, G. Li, S. Tao, J. Liu, Angew. Chem. Int. Ed. 45 (2006) 8145.
[3] H.J. Wang, W.H. Zhou, X.F. Yin, Z.X. Zhuang, H.H. Yang, X.R. Wang, J. Am. Chem. Soc. 128 (2006) 15954.
[4] K. Haupt, K. Mosbach, Chem. Rev. 100 (2000) 2495.
[5] P.K. Owens, L. Karlsson, E.S.M. Lutz, L.I. Andersson, Trac-Trends Anal. Chem. 18 (1999) 146.
[6] T.R. Ling, Y.Z. Syu, Y.C. Tasi, T.C. Chou, C.C. Liu, Biosens. Bioelectron. 21 (2005) 901.
[7] Y. Lu, C.L. Yan, S.Y. Gao, Appl. Surf. Sci. 255 (2009) 6061.
[8] W.X. Su, J. Rick, T.C. Chou, Microchem. J. 92 (2009) 123.
[9] A. Bossi, S.A. Piletsky, E.V. Piletska, P.G. Righetti, A.P.F. Turner, Anal. Chem. 73 (2001) 5281.
[10] G. Wulff, Chem. Rev. 102 (2002) 1.
[11] G. Wulff, T. Gross, R. Schonfeld, Angew. Chem. Int. Ed. 36 (1997) 1962.
[12] K.C. Ho, W.M. Yeh, T.S. Tung, J.Y. Liao, Anal. Chim. Acta 542 (2005) 90.
[13] A. Namvar, Biosens. Bioelectron. 22 (2007) 2018.
[14] A. Ramanavisius, A. Ramanaviciene, Electrochim. Acta 51 (2006) 6025.
[15] T.L. Panasyuk, V.M. Mirsky, S.A. Piletsky, O.S. Wolfbeis, Anal. Chem. 71 (1999) 4609.
[16] C. Malitesta, I. Losito, P.G. Zambonin, Anal. Chem. 71 (1999) 1366.
[17] Y.V. Ulyanova, A.E. Blackwell, S.D. Minteer, Analyst 131 (2006) 257.
[18] C. Cacho, E. Turiel, C. Pérez-Conde, Talanta 78 (2009) 1029.
[19] R. Suedee, W. Intakong, F.L. Dickert, Anal. Chim. Acta 569 (2006) 66.
[20] V.V.S. Eswara Dutt, H.A. Mottola, Anal. Chem. 46 (1974) 1777.
[21] H. Yamanaka, R. Togashi, M. Hakoda, C. Terai, S. Kashiwazaki, T. Dan, N. Kamatani, Adv. Exp. Med. Biol. 431 (1998) 13.
[22] X.H. Cai, K. Kalcher, C. Neuhold, B. Ogorevc, Talanta 41 (1994) 407.
[23] K. Shi, K.K. Shiu, Electroanalysis 13 (2001) 1319.
[24] Y.Y. Sun, J.J. Fei, K.B. Wu, S.S. Hu, Anal. Bioanal. Chem. 375 (2003) 544.
[25] S.B. Khoo, F. Chen, Anal. Chem. 74 (2002) 5734.
[26] S.H. Cheng, S.H. Hsaio, T.H. Su, G.S. Liou, Macromolecules 38 (2005) 307.
[27] L.C.S. Chou, C.C. Liu, Sens. Actuator B: Chem. 110 (2005) 204.
[28] A. Ramanaviciene, A. Ramanavisius, Anal. Bioanal. Chem. 379 (2004) 287.
[29] A. Ramanaviciene, A. Ramanavisius, Biosens. Bioelectron. 20 (2004) 1076.
[30] A. Ramanaviciene, A. Finkelsteinas, A. Ramanavisius, J. Chem. Educ. 83 (2006) 1212.
[31] P.Y. Chen, R. Vittal, P.C. Nien, K.C. Ho, Biosens. Bioelectron. 24 (2009) 3504.
[32] J. Lykkesfeldt, M. Viscovich, H.E. Poulsen, Free Radic. Biol. Med. 35 (2003) 1439.

Talanta 80 (2010) 1152–1157

Contents lists available at ScienceDirect

Talanta

journal homepage: www.elsevier.com/locate/talanta

Determination of non-steroidal anti-inflammatory drugs in wastewaters by magnetic matrix solid phase dispersion–HPLC

K. Aguilar-Arteaga [a], J.A. Rodriguez [a,*], J.M. Miranda [a,b], J. Medina [c], E. Barrado [c]

[a] Centro de Investigaciones Químicas, Universidad Autónoma del Estado de Hidalgo, Carr. Pachuca Tulancingo Km 4.5, 42074, Pachuca, Hgo, Mexico
[b] Departamento de Química Analítica, Nutrición y Bromatología, Facultad de Veterinaria, Universidad de Santiago de Compostela, 27002 Lugo, Spain
[c] QUIANE, Departamento de Química Analítica, Universidad de Valladolid, Prado de la Magdalena s/n, 47005 Valladolid, Spain

ARTICLE INFO

Article history:
Received 12 June 2009
Received in revised form 28 August 2009
Accepted 31 August 2009
Available online 6 September 2009

Keywords:
Magnetic-MSPD
NSAIDs
HPLC
Magnetic separation

ABSTRACT

A series of supports functionalized with different alkyl chains and covered with magnetite were synthesized, characterized and applied in the sample pre-concentration of four non-steroidal anti-inflammatory drugs (acetaminophen, naproxen, diclofenac and ibuprofen) contained in wastewater samples. The general methodology involved magnetic solid phase dispersion followed by the analysis by high-performance liquid chromatography with ultraviolet detection. The magnetic supports were initially dispersed in the samples with the aid of Triton X-100, then supports were magnetically isolated and the analytes were eluted with methanol. Finally the extract was injected into the HPLC system. The highest recovery percentage (>90%) was obtained with the support containing octyl chains (C8) at pH 3. The lowest limits of detection achieved ranged within 1–2 $\mu g\,L^{-1}$ with repeatability (expressed as RSD) below 5% in all cases. The method was applied in the analysis of wastewater samples.

© 2009 Elsevier B.V. All rights reserved.

1. Introduction

The determination of non-steroidal anti-inflammatory drugs (NSAIDs) residues in the environment is a field of special interest due to the risks to human health and aquatic environment [1]. In these reports the critical point during the experimental part is the right selection of the quantification method. There has been a continuous increase on the improvement for the isolation of NSAIDs from environmental matrices in order to generate efficient and economical methodologies with a high sampling rate.

In most of the cases, the NSAIDs determination involves a pre-concentration step followed by the separation and quantification generally performed by liquid chromatographic methods [2–6]. The main disadvantages of the reported method are the time required for the pre-concentration of large sample volumes to minimize the interferences and the limits of detection [7]. The sample pre-treatment includes strategies such as liquid–liquid extraction [8], solid phase extraction (SPE) [9] and the use of molecularly imprinted polymers [10]. Recently the matrix solid phase dispersion (MSPD) [11] has been applied successfully in the isolation and analysis of estrogens, pesticides and natural components from complex samples matrices and animal tissues. In some cases the results obtained are equivalent or better than the classic methodologies like SPE. The MSPD is an extraction process based on the dispersion of solid adsorbent in the sample. The MSPD use solids with similar polarity than stationary phases used in liquid chromatography allowing the selective extraction of present compounds of interest in the sample in smaller time than the SPE.

Magnetic separation technology has received considerable attention in recent years due to their potential application in cell isolation, enzyme immobilization, protein separation and pre-concentration of organic compounds from large volume environmental water samples. A unique and attractive property of this technology is that magnetic supports can be isolated from sample solutions by the application of an external magnetic field. Therefore suspended magnetic particles tagged with the analytes can be removed from large volume samples by a magnet [12]. To achieve selective and easy isolation of NSAIDs, silica supports functionalized with organic chains of different polarities were synthesized and absorbed onto magnetite as solid phase.

In this paper, a method for routine determination of four anti-inflammatory drugs (acetaminophen, naproxen, diclofenac and ibuprofen) in wastewater effluents is proposed. Environmentally relevant pharmaceuticals were chosen according to human consumption in Mexico. The method involves sample pre-treatment by magnetic-MSPD and analytical determination by HPLC with ultraviolet (UV) detection.

* Corresponding author.
E-mail address: josear@uaeh.edu.mx (J.A. Rodriguez).

0039-9140/$ – see front matter © 2009 Elsevier B.V. All rights reserved.
doi:10.1016/j.talanta.2009.08.042

2. Experimental

2.1. Starting materials and general information

Ferrous sulfate heptahydrate ($FeSO_4{\cdot}7H_2O$), ammonium solution (NH_3 25%, w/w), sodium hydroxide and hydrochloric acid were purchased from J.T. Baker (Phillipsburg, NJ, USA). Triton X-100, cetyltrimethylammonium bromide (CTAB), tetramethoxysilane (TMOS), phenyltrimethoxysilane (PTMS), octyltriethoxysilane (C_8-TEOS), octadecyltrimethoxysilane (C_{18}-TMOS), chlorotrimethylsilane (CTMS), 4-acetamidophenol (acetaminophen) 98%, (S)-(+)-6-metoxy-a-methyl-2-naphthaleneacetic acid (naproxen) 98%, 2-[(2,6-dichlorophenyl)amino]benzeneacetic acid sodium salt (diclofenac) 98%, α-methyl-4-(isobutyl)phenylacetic acid sodium salt (ibuprofen) 98% and methanol HPLC grade were obtained from Sigma (St. Louis, MO, USA).

Stock solutions of the NSAIDs were prepared at a concentration of 1 mg mL^{-1} by dissolving the pure substances in 0.001 M sodium hydroxide. These solutions were protected from light and stored under refrigeration (4 °C) until use to avoid possible decomposition. Calibration standards were prepared at concentrations of 20–1000 μg L^{-1} by mixing adequate volumes of each standard solution.

2.2. Synthesis of magnetic supports

The magnetic solids were synthesized by emulsion polymerization using a modification of the methodology of synthesis reported by Zhu et al. [13]. Magnetite particles Fe_3O_4 were synthesized by co-precipitation method reported by Barrado et al. [14,15]. The magnetite obtained was washed three times with 50.0 mL portions of deionized water and added to the flask containing the precursors indicated in Table 1. The silica precursors were previously solubilized in 24 mL of a solution that contained: Triton X-100 (2.0%, w/v), CTAB (0.20%, w/v), methanol (12.5%, v/v) and 200.0 μL of catalyst (NH_3 28%, v/v). The mixture was heated and refluxed at 120 °C for 12 h with stirring.

In order to block superficial silanol groups (–Si–OH), the solids obtained in the previous process were derivatized using a mixture of 0.9 g of clorotrimethylsilane (CTMS), and 1.0 mL of pyridine per each gram of support in 50.0 mL of toluene. The pyridine was added to neutralize the HCl produced during the derivatization. The supports were washed with 20.0 mL portions of each of the following solvents: toluene, ethanol and deionized water. The sequence was repeated until the washing liquid was colorless. The obtained magnetic particles were dried at 60 °C for 24 h.

2.3. Sampling and sample treatment

Two liter polypropylene bottles were conditioned by filling with 2% (v/v) H_2SO_4 for at least three days. Once at the sampling site, the bottles were rinsed several times with the water to be collected. Wastewaters were collected in October 2008 from three municipal waste effluents in Pachuca, Mexico. The samples were filtered through 0.45 μm cellulose acetate filters in a glass filtration device connected to a hand-operated vacuum pump into the prewashed sample bottles. Bottles were completely filled with the sample, wrapped in hermetic plastic bags and transported to the laboratory in iceboxes. Once in the laboratory, samples were stored not longer than five days at 4 °C prior analysis.

The magnetic-MSPD procedure using SiO_2–Fe_3O_4 of different polarities allowed rapid separation by a simple magnetic extraction. First 1.0 mL of Triton X-100 (2.0%, w/v) and 0.1 g of the magnetic support was added into an adequate volume of wastewater sample (0.2, 0.5 or 1.0 L), the pH was adjusted to 3 with HCl 1.0 M and the mixture was dispersed in an ultrasonic bath for 10 min. Subsequently, a magnet was placed on the bottom of the beaker and the magnetic support containing the analytes was isolated from the solution. After the retention process, the solid was flushed twice with 10 mL of deionized water. Finally, the analytes were eluted with 1.0 mL of methanol and the extract obtained was filtered through a 0.45 μm cellulose acetate filter and injected into HPLC system for their separation and analysis.

The SPE procedure was performed following the method reported by Santos et al. [9]. The SPE cartridges (60 mg, Oasis HLB from Waters, Milford, MA, USA) were conditioned using 3 mL of ethyl acetate, 3 mL of methanol and 3 mL of deionized water at a flow-rate of about 3 mL min^{-1}. Samples (1.0 L) were transferred to the SPE. The loaded cartridges were rinsed with 3 mL of methanol:water (5:95, v/v) and 3 mL of n-hexane at a flow-rate of about 1 mL min^{-1}. The elution was performed with three aliquots (1 mL) of ethyl acetate at a flow-rate of about 1 mL min^{-1}. The combined aliquots were evaporated to dryness by a gentle stream of nitrogen. The residues were dissolved in 1.0 mL of methanol and injected into the HPLC system.

Chromatographic separation was achieved with a Microsorb 100-C18 column (5 μm; 150 mm × 4.6 mm i.d.) (Varian, Palo Alto, CA, USA). The mobile phase was methanol–phosphate buffer (2:1, v/v), pH 2.5, 0.01 mol L^{-1}. A flow-rate of 1.0 mL min^{-1} was established at 25 °C.

2.4. Equipment

The structures of the products obtained were examined by X-ray diffraction (XRD) patterns using a PHILIPS PW1710 instrument equipped with a Cu anode, automatic divergence slit and a graphite monochrometer under the following experimental conditions: CuK_α radiation, 1.54 Å; generator tension, 40 kV; generator current, 30 mA; intensity ratio (α_2/α_1), 0.500; divergence slit, 1°; receiving slit, 0.1; start angle (°2θ), 5; end angle (°2θ), 70.

The solid products were characterized using a Fourier transform infrared (FTIR) spectrophotometer (PerkinElmer, model IRDM). Dry samples were prepared in the form of KBr tablets (1:100, w/w).

The morphological analysis of the products was performed using a JEOL JSM-820 scanning electron microscope (SEM).

Table 1
Synthesis conditions for magnetic supports, via emulsion polymerization using TMOS like co-monomer.

Support	Functionalized monomer (g)	Seed monomer TMOS (g)	Fe_3O_4 (g)	Calculated ratio SiO_2/Fe_3O_4 (w/w)
Polar 1 (P1)	5.949 TMOS	–	1.5	1:1
Polar 2 (P2)	5.949 TMOS	–	3.0	1:2
C_8 1 (C8-1)	5.910 C_8-TEOS	1.182	1.5	1:1
C_8 2 (C8-2)	5.910 C_8-TEOS	1.182	3.0	1:2
Phenyl 1 (PH1)	5.560 PTMS	1.182	1.5	1:1
Phenyl 2 (PH2)	5.560 PTMS	1.182	3.0	1:2
C_{18} 1 (C18-1)	5.910 C_{18}-TEOS	1.182	1.5	1:1
C_{18} 2 (C18-2)	5.910 C_{18}-TEOS	1.182	3.0	1:2

TMOS: tetramethoxysilane; PTMS: phenyltrimethoxysilane; C_8-TEOS: octyltriethoxysilane; C_{18}-TEOS: octadecyltrimethoxysilane.

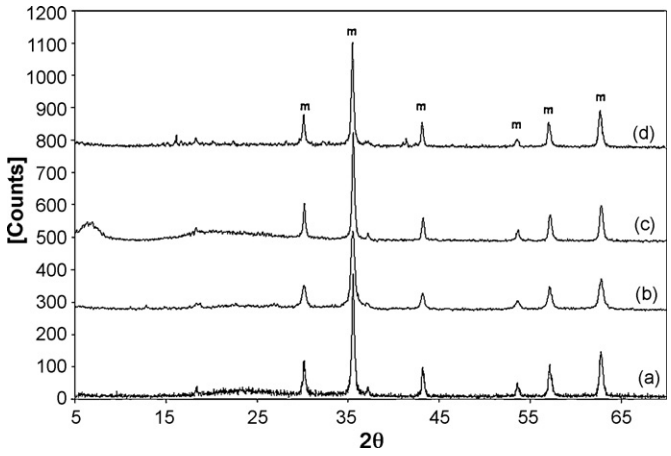


Fig. 1. Diffraction patterns for the magnetic supports (m: diffraction lines for magnetite). Solids synthesized from: (a) TMOS monomer, (b) C_8-TEOS, (c) PTMS and (d) C_{18}-TEOS.

All chromatography experiments were done using reverse phase HPLC (RP-HPLC), the standard technique used in pharmaceutical analysis [16]. The apparatus used was a PerkinElmer Series 200 liquid chromatograph (PerkinElmer, MA, USA) equipped with a UV–vis detector at 220 nm and a manual injector connected to a 20 μL external loop.

3. Results and discussion

3.1. Characterization of solids used as absorbent

The diffraction patterns for the magnetic supports show the reflections corresponding to magnetite ("m" in Fig. 1). Also, the presence of a wide band at 2θ angles from 10° to 40° is consistent with the amorphous phase of the silica gel [15].

Fig. 2 shows FTIR spectra for the magnetic supports. Magnetite has an inverse spinal type structure with a characteristic vibration M_T–O–M_O at ≈600–550 cm^{-1}, where M_T and M_O correspond to the metal occupying tetrahedral and octahedral positions, respectively [15]. On the other hand, the spectra showed a band of intense stretching at ≈3450 cm^{-1}, attributable to the vibration of the silanol group (SiOH). A group of signals above 3000 cm^{-1} are assigned to the vibration of–C=C–H and are observed only for the PH1 solid. The peaks below 3000 cm^{-1} corresponds to the vibration of $-CH_2-$ and they are observed in the solid obtained by polymerization of P1, C8-1 and C18-1. The bending band at ∼1630 cm^{-1} corresponds to H_2O occluded in the support. The flexion vibration band at ∼1400 cm^{-1} represents the C–H bond of the alkyl groups joined to the silicon. The stretching band at 1100–1000 cm^{-1} is assigned to the Si–O–Si bond and the deformation band at ∼888 cm^{-1} belongs to Si–OH bonds. The aromatic character of phenyl support (PH1) was corroborated by the vibrations at 1600, 1430, 740 and 690 cm^{-1}. The polarity of the solids decreases with the use of longer alkyl chains as confirmed with the decrease of the Si–OH and H_2O vibration signals.

SEM analysis of the morphology of the magnetic supports indicated differences between the compounds. Thus, according to the synthetic procedure, we expected solids with spherical morphology. However, as shown in Fig. 3a, irregular granules of mean size up to 5 μm were obtained with the TMOS monomer. This result indicates that the monomer TMOS presents an enhanced reactivity in comparison to that of the less polar monomers favouring polymerization at higher reaction rates and creating a hydrophilic tridimensional network. The supports obtained with less reactive monomers present a spherical morphology (Fig. 3b–d). In the case of the C8 solids two types of particles were observed. The first one was spherical with a particle size around 3 μm and the second one displayed a solid gelatinous appearance and they correspond to silica gel and magnetite, respectively. The phenyl solid is a homogenous solid with spherical morphology and with a particle size around 3 μm. The C18 solid is a homogenous porous solid with a particle size around 10 μm. The magnetite particles partly cover the surface of the silica gel particles, then the magnetic moments are randomly oriented such that when an external magnetic field is applied these moments become aligned parallel to the field providing to the magnetic support properties similar to those of pure magnetite. This feature makes the solids suitable for their use as supports in magnetic-MSPD pre-concentration.

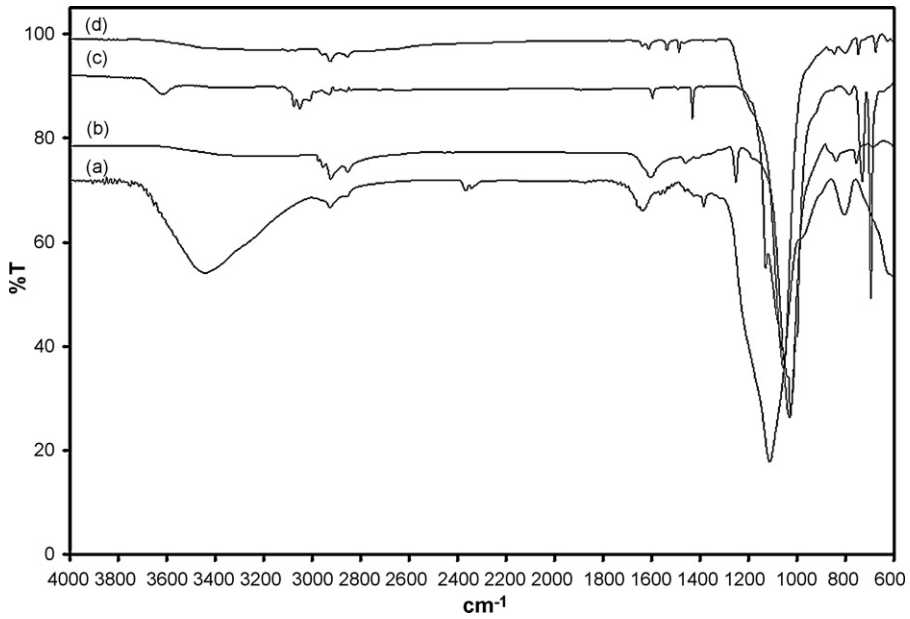


Fig. 2. FTIR spectra for magnetic supports. Solids synthesized from: (a) TMOS monomer, (b) C_8-TEOS, (c) PTMS and (d) C_{18}-TEOS.

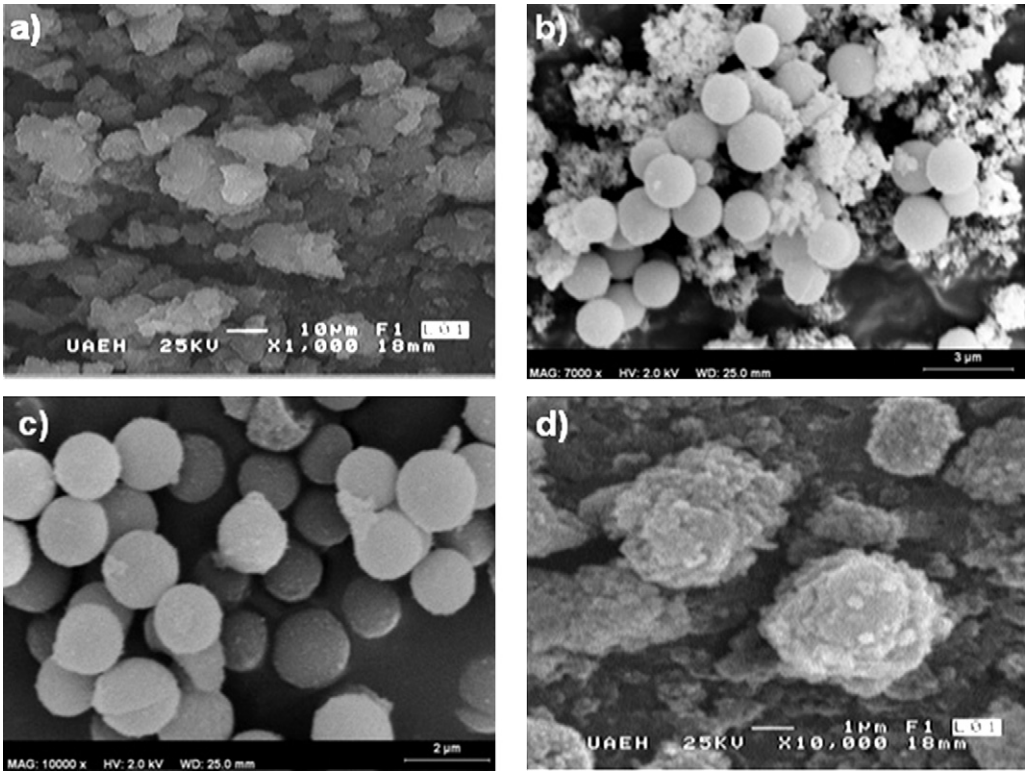


Fig. 3. Scanning electron micrograph of porous magnetic silicamicrospheres. Solids synthesized from: (a) TMOS monomer, (b) C_8-TEOS, (c) PTMS and (d) C_{18}-TEOS.

3.2. Anti-inflammatory extractions by magnetic-MSPD

Fig. 4 shows the recovery percentages using spiked wastewater samples. The extraction of the NSAIDs depends on pH value and kind of support. It is possible to observe that as the value of pH increases the extraction percentage diminishes. Low recovery values were obtained (<2%) at pH values of 9 and 11, thus the results are omitted in Fig. 4. From the observed results it is possible to deduce that the species adsorbed on the solids are in their neutral form. If the pH value is higher than the anti-inflammatory pK_a value, ionization takes place, thus its adsorption in solids is affected in a negative way. Acetaminophen has a pK_a value of 9.38, remaining neutral in almost all the pH interval, then its extraction is higher with respect to the more acidic analytes with pK_a values around 4.0–5.0 [17,18].

The polarity of the support is also an important parameter in the recovery percentage. The polar solids P1 and P2, was not shown to be a good adsorbents in most of the anti-inflammatory results. Nevertheless, according to their polar characteristics, these solids could be used as stationary phases in normal phase for magneto-chromatography [19]. On the other hand, with the supports synthesized from the C18 monomer the recovery percentages were below 50%. It is possible that the highly hydrophobic character of these supports avoid the correct dispersion of the solid matrix in aqua samples even in presence of Triton X-100. The anti-inflammatory elution from the solid was carried out with methanol; this solvent is commonly reported in the pre-concentration sample of NSAIDs by solid phase extraction [9]. We found for the retention process using magnetic supports that NSAIDs were well-retained onto the solid and not eluted during the washing step. Thus, we studied the optimum dispersion time using 1, 5, 10, 15 and 20 min. Our results showed that recovery with 10 min was significantly higher than the experiments done with 1 and 5 min, while no improvement was observed at higher times. Therefore, we chose 10 min as the optimum value.

According to the results depicted in Fig. 4, the best conditions to make the extraction and quantification involve the use of the C8-2 support and a pH value of 3. Under the latter conditions, recovery percentages of 100% acetaminophen, 94% naproxen, and 96% for diclofenac and ibuprofen were obtained. The analytical parameters of the method and the quantification of the analytes in the wastewater samples were evaluated using the conditions mentioned above.

3.3. Analytical parameters of the method

In the selected conditions, the analytical parameters were evaluated using different volumes of spiked wastewater (0.2, 0.5 and 1.0 L) with an interval concentration of 50–700 $\mu g\,L^{-1}$. The results obtained are listed in Table 2. The limits of detection (LODs) was calculated for a signal/noise relation equal to (S/N = 3). The LOQ was determined using a signal/noise relation equal to 10 (S/N = 10). The calibration curves were constructed from the area versus concentration $\mu g\,L^{-1}$.

According to the results from Table 2, it is possible to observe that the LODs decrease when higher initial sample volumes are used. The lower limits of detection reached were between 1 and 2 $\mu g\,L^{-1}$ using 1 L of initial sample. LOD and LOQ obtained by the method are comparable to those reported by other methods. Despite that lower LOD can be achieved with SPE–HPLC–UV [9], the reduction in sample time treatment is the main advantage of the method proposed. This improvement makes the proposed method a viable alternative to be implemented as a routine in the analysis of NSAIDs, without the necessity of expensive or difficult access equipment.

3.4. Analysis of wastewater samples

Once the capacity of extraction of the absorbents was evaluated, C8-2 was used for the analysis of wastewater samples. The devel-

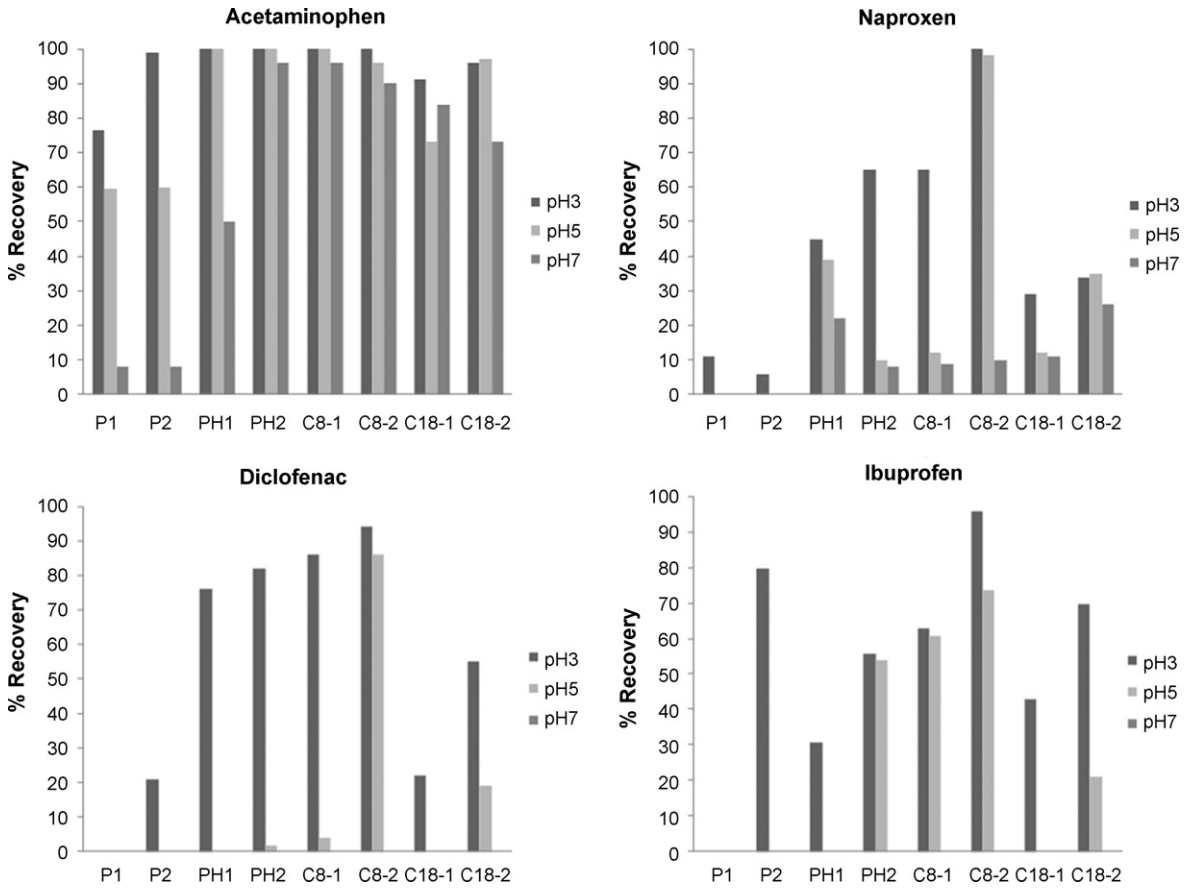


Fig. 4. Effect of polarity and pH value on the NSAIDs recoveries in spiked wastewater.

oped pre-concentration method was applied for the determination of the NSAIDs in wastewater samples. Five replicate determinations of the analytes were carried out on each sample. The samples were also analyzed by SPE–HPLC for comparison. Results are displayed in Table 3 and Fig. 5. For each sample, average of each analyte (determined by both methods) was compared by means of a *t*-test of comparison of means, assuming comparable variances (verified by a *F*-test). Calculated *t* values were compared with the tabulated *t* value for 8 degrees of freedom and a significance level of $p = 0.05$ ($t = 2.30$). In the case of diclofenac and naproxen, the tabulated *t*

Table 2
Analytical parameters for different sample volumes.

Initial volume (L)	Analyte	Limit of detection ($\mu g\,L^{-1}$)	Limit of quantification ($\mu g\,L^{-1}$)	Repeatability (%RSD)		Reproducibility (%RSD)	
				50 $\mu g\,L^{-1}$	100 $\mu g\,L^{-1}$	50 $\mu g\,L^{-1}$	100 $\mu g\,L^{-1}$
0.2	Acetaminophen	8	24	1.10	2.02	2.02	1.34
	Naproxen	10	30	2.01	3.15	4.01	3.02
	Diclofenac	7	21	2.06	2.02	1.03	2.07
	Ibuprofen	8	24	1.22	4.03	2.04	3.09
0.5	Acetaminophen	2	7	2.02	1.04	2.01	2.02
	Naproxen	4	11	1.01	2.02	1.02	2.05
	Diclofenac	3	8	4.30	3.31	3.03	3.07
	Ibuprofen	3	9	3.16	1.05	1.05	3.09
1.0	Acetaminophen	1	3	2.04	1.10	1.40	3.60
	Naproxen	2	5	2.15	3.04	1.05	2.10
	Diclofenac	1	4	1.01	3.02	2.01	4.03
	Ibuprofen	1	4	1.03	2.06	1.04	3.07

Table 3
NSAIDs concentrations (mean and RSD, $n = 5$) in wastewater samples. Unit concentration $\mu g\,L^{-1}$.

Sample	Acetaminophen		Naproxen		Diclofenac		Ibuprofen	
	M-MSPD	SPE	M-MSPD	SPE	M-MSPD	SPE	M-MSPD	SPE
1	194(1.11)	ND	47(2.30)	49(2.61)	51(1.13)	50(1.51)	ND	ND
2	119(2.07)	ND	19(1.02)	18(1.10)	70(2.02)	68(1.70)	ND	ND
3	203(1.49)	ND	20(3.36)	19(4.41)	58(2.94)	59(2.78)	ND	ND

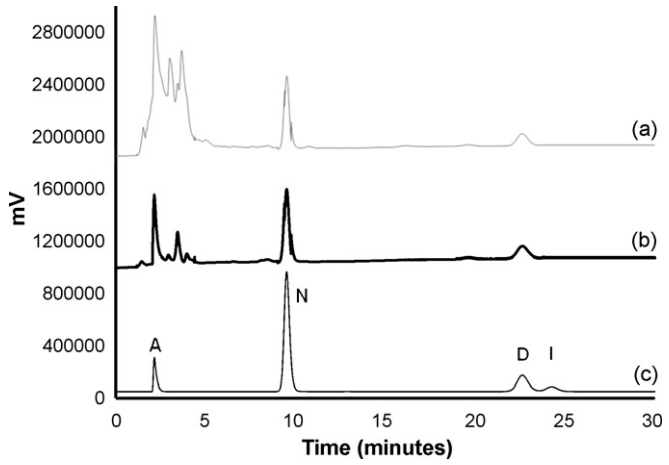


Fig. 5. Chromatograms obtained at the optimized conditions: (a) wastewater sample obtained by SPE pre-concentration method, (b) wastewater sample obtained by magnetic-MSPD pre-concentration method and (c) NSAIDs standard solution 100 $\mu g\,L^{-1}$. A: acetaminophen; N: naproxen; D: diclofenac; I: ibuprofen.

value exceeded the calculated one, thus allowing us to accept the null hypothesis that there are no significant differences between the results provided by both methods. In any sample ibuprofen was detected.

Acetaminophen cannot be quantified in samples, using the evaluated SPE method due to the clean-up process in this case did not eliminate the interferences present in the analytical matrix.

The obtained results are related to the medication prescribed in Mexico, where most of the population consumes the anti-inflammatory drugs found in greater amount.

4. Conclusions

A novel method for routine analysis of four non-steroidal anti-inflammatory drugs of frequent use in wastewater samples has been proposed. This method proposes the pre-concentration of the analytes by magnetic-MSPD, followed by its quantification by HPLC with UV detection. Different solids as adsorbent were tested, concluding that the solid C8-2 is adequate in the pre-concentration of NSAIDs. This solid is functionalized with organic chains C8, and covered with magnetite, characteristic that confers it paramagnetic properties. The sample pre-concentration time is around 30 min. This time is less than that required by other methodologies like SPE or even to that required by conventional MSPD. It has been demonstrated that pH is a determining condition in the adsorption process of the anti-inflammatory onto the solid, being pH 3 the best for the NSAIDs chosen for the analysis. In addition, the polarity of the supports also plays a determining role in the pre-concentration process. In the conditions proposed, the recovery percentages for all the NSAIDs are greater than 90% with adequate precision in terms of repeatability and reproducibility. The method proposed is faster and allows the NSAIDs determination, including acetaminophen. Then this technique is a novel alternative for the analysis of acetaminophen, naproxen, diclofenac and ibuprofen in wastewater samples.

Acknowledgements

The authors wish to thank the CONACyT (project 61310), PROMEP (SIATA-Project), Consejería de Educación y Cultura de la *Junta de Castilla y León* (project VA029A07) and Dirección Xeral de Investigación, Desenvolvemento e Innovación (Xunta de Galicia) for their financial support.

References

[1] B.I. Escher, N. Bramaz, R.I.L. Eggen, M. Richter, Environ. Sci. Technol. 39 (2005) 3090.
[2] S.D. Richardson, Anal. Chem. 79 (2007) 4295.
[3] M. Clara, B. Strenn, O. Gans, E. Martinez, N. Kreuzinger, H. Kroiss, Water Res. 39 (2005) 4797.
[4] C. Basheer, H.G. Chong, T.M. Hii, H.K. Lee, Anal. Chem. 79 (2007) 6845.
[5] J. Siemens, G. Huschek, C. Siebe, M. Kaupenjohann, Water Res. 42 (2008) 2124.
[6] N. Nakada, H. Shinohara, A. Murata, K. Kiri, S. Managaki, N. Sato, H. Takada, Water Res. 41 (2007) 4373.
[7] Ma.J. Martínez-Bueno, A. Agüera, Ma.J. Gómez, Ma.D. Hernando, J.F. García-Reyes, A.R. Fernández-Alba, Anal. Chem. 79 (2007) 9372.
[8] X. Wen, C. Tu, H.K. Lee, Anal. Chem. 76 (2004) 228.
[9] J.L. Santos, I. Aparicio, E. Alonso, M. Callejón, Anal. Chim. Acta 550 (2005) 116.
[10] S. Zorita, B. Boyd, S. Jönsson, E. Yilmaz, C. Svensson, L. Mathiasson, S. Bergström, Anal. Chim. Acta 626 (2008) 147.
[11] Y. Liu, L. Jia, Microchem. J. 89 (2008) 72.
[12] P. Campíns-Falcó, J. Verdú-Andrés, A. Sevillano-Cabeza, C. Molins-Legua, R. Herráez-Hernández, J. Chromatogr. A 1211 (2008) 13.
[13] G.R. Zhu, Q.H. Yang, D.M. Jiang, J. Yang, L. Zhang, Y. Li, C. Li, J. Chromatogr. A 1103 (2006) 257.
[14] E. Barrado, F. Prieto, M. Vega, F. Fdez-Polanco, Water Res. 32 (1998) 3055.
[15] E. Barrado, J.A. Rodríguez, F. Prieto, J. Medina, J. Non-Cryst. Solids 351 (2005) 906.
[16] Real Farmacopea Española, 3ª edición, Ministerio de Sanidad y Consumo, Madrid, 2005.
[17] A.C. Hari, R.A. Paruchuri, D.A. Sabatini, T.C.G. Kibbey, Environ. Sci. Technol. 39 (2005) 2592.
[18] N. Lindqvist, T. Tuhkanen, L. Kronberg, Water Res. 39 (2005) 2219.
[19] E. Barrado, J.A. Rodríguez, J. Chromatogr. A 1128 (2006) 189.

Talanta 80 (2010) 1158–1163

Contents lists available at ScienceDirect

Talanta

journal homepage: www.elsevier.com/locate/talanta

Methylmercury and inorganic mercury determination in blood by using liquid chromatography with inductively coupled plasma mass spectrometry and a fast sample preparation procedure

Jairo L. Rodrigues, Samuel S. de Souza, Vanessa C. de Oliveira Souza, Fernando Barbosa Jr.*

Laboratório de Toxicologia e Essencialidade de Metais, Faculdade de Ciências Farmacêuticas de Ribeirão Preto, Universidade de São Paulo, Ribeirão Preto, SP, Brazil

ARTICLE INFO

Article history:
Received 16 July 2009
Received in revised form 31 August 2009
Accepted 1 September 2009
Available online 9 September 2009

Keywords:
ICP-MS
Speciation
Blood samples
Mercury
Sample preparation
Methylmercury
Thimerosal
Liquid chromatography

ABSTRACT

Despite the necessity to differentiate chemical species of mercury in clinical specimens, there are a limited number of methods for this purpose. Then, this paper describes a simple method for the determination of methylmercury and inorganic mercury in blood by using liquid chromatography with inductively coupled mass spectrometry (LC–ICP-MS) and a fast sample preparation procedure. Prior to analysis, blood (250 μL) is accurately weighed into 15-mL conical tubes. Then, an extractant solution containing mercaptoethanol, L-cysteine and HCl was added to the samples following sonication for 15 min. Quantitative mercury extraction was achieved with the proposed procedure. Separation of mercury species was accomplished in less than 5 min on a C18 reverse-phase column with a mobile phase containing 0.05% (v/v) mercaptoethanol, 0.4% (m/v) L-cysteine, 0.06 mol L^{-1} ammonium acetate and 5% (v/v) methanol. The method detection limits were found to be 0.25 μg L^{-1} and 0.1 μg L^{-1} for inorganic mercury and methylmercury, respectively. Method accuracy is traceable to Standard Reference Material (SRM) 966 Toxic Metals in Bovine Blood from the National Institute of Standards and Technology (NIST). The proposed method was also applied to the speciation of mercury in blood samples collected from fish-eating communities and from rats exposed to thimerosal. With the proposed method there is a considerable reduction of the time of sample preparation prior to speciation of Hg by LC–ICP-MS. Finally, after the application of the proposed method, we demonstrated an interesting *in vivo* ethylmercury conversion to inorganic mercury.

© 2009 Elsevier B.V. All rights reserved.

1. Introduction

Speciation analysis of clinical samples is gradually becoming more widely accepted for nutritional and/or toxicological purposes. According to International Union of Pure and Applied Chemistry (IUPAC), speciation analysis is defined as the analytical process of identifying and/or measuring quantities of one or more individual chemical forms in a sample, and speciation of an element is defined as the distribution of an element among defined chemical species in a system [1,2].

Mercury (Hg) is one of the most hazardous pollutants in the environment. It exists in three basic forms: elemental mercury (Hg^0) known as metallic mercury, inorganic mercury compounds (Ino-Hg), primarily mercuric chloride, and organic mercury, primarily methylmercury (Met-Hg) [3,4]. Organic forms are more toxic than inorganic [4].

The main sources of human exposure to organic mercurials, mainly in the form of methylmercury (Met-Hg) or ethylmercury (Et-Hg), are the consumption of fish [4] and vaccines containing thimerosal, respectively [5]. On the other hand, the most common forms of exposure to inorganic forms are by inhalation of Hg vapor released from dental amalgams or from gold mining activities [4].

Measurements of Hg in both blood and hair are used to determine whether adverse health effects are likely to occur. The contents of mercury species in blood may represent a cumulative exposure from the daily diet and/or occupational environment exposure. However, despite the difference in toxicity related to the form of mercury, total mercury concentration (THg) in blood is usually used to estimate the clinical outcomes after mercury exposure. Moreover, the proportion between chemical forms of mercury in blood may vary among individuals. This makes it essential to have analytical methods, based on speciation analysis, which can differentiate between chemical forms in blood to diagnose risks of toxicity.

The most effective instrumental-based techniques for chemical speciation analysis rely on the use of chromatography (mainly gas chromatography (GC) [6–9] or liquid chromatography (LC)) [10–12] coupled to a specific and sensitive detector, such as inductively coupled plasma mass spectrometry (ICP-MS). Compared with GC, LC is

* Corresponding author. Tel.: +55 16 36024701.
E-mail address: fbarbosa@fcfrp.usp.br (F. Barbosa Jr.).

0039-9140/$ – see front matter © 2009 Elsevier B.V. All rights reserved.
doi:10.1016/j.talanta.2009.09.001

the preferred separation technique used for mercury speciation, because the mercury species do not need to be derived to volatile compounds before HPLC separation.

Although several methods have been developed for measuring mercury in blood samples [13–17], there is merely a few proposing speciation analysis [18,19]. Moreover, all of them suggested very tedious and time-consuming sample preparation procedures. Moreover, artifact formation during the sample preparation step is a potential source of error [20,21]. On the other hand, clinical laboratories must cope with an increasing demand for trace element analysis in body fluids and tissues in response to increasing concern for occupational and environmental exposure to mercury. Thus, fast sample preparation procedures with minimal handling are extremely desirable in routine analysis.

The aim of this paper was therefore to evaluate a simple method for methylmercury and inorganic mercury determination in blood by high-performance liquid chromatography (HPLC) coupled to inductively coupled plasma mass spectrometry (ICP-MS) with a fast sample preparation procedure prior to analysis. The method was then applied for speciation of mercury in blood samples collected from a Brazilian riparians, living in the Amazon region, exposed to mercury from fish consumption. It was also demonstrated for the first time that ethylmercury is *in vivo* converted to inorganic mercury, making the determination of the inorganic form of mercury in blood relevant for thimerosal exposed populations.

2. Material and methods

2.1. Instruments and apparatus

All measurements were made with an ICP-MS (Elan DRC II PerkinElmer, Norwalk, CT) for total mercury determination and for speciation.

2.2. Measuring of mercury species

A PerkinElmer model L-200 LC pump, six-port injector (Rheodyne 9725) with a reverse-phase column (C18, 5 μm, 150 mm × 4 mm, Brownlee Columns PerkinElmer, USA) and a pre-column (guard column) RP18 (7 μm, 15 mm × 3.2 mm, Brownlee Columns PerkinElmer, USA) comprised the LC system. Samples were loaded with a syringe into a 100-μL sample loop. All separations were performed at room temperature under isocratic conditions. The isocratic mobile phase was 0.05% (v/v) mercaptoethanol, 0.4% (m/v) L-cysteine, 0.06 mol L^{-1} ammonium acetate and 5% (v/v) methanol. The flow rate was 1.0 mL min^{-1}. The effluent from the LC column was directly connected to the nebulizer with PEEK tubing (1.59 mm o.d.) and a low dead volume PEEK connector. Data evaluation was performed using Chromera® software supplied with the instrument, and quantification was based on peak high by external calibration.

The optimum experimental conditions for both ICP-MS and LC are given in Table 1.

2.3. Measurements of total mercury in blood

The method used for the determination of total mercury in blood samples was based on a previous publication described by Palmer et al. [13]. Briefly, blood specimens were diluted 1 + 49 into a 15-mL polypropylene Falcon® tube (Blue Max™ Jr., Becton Dickinson) with a diluent solution containing 0.5% (v/v) double-distilled HNO_3, 25 μg L^{-1} Rh as internal standard, 1 mg L^{-1} Au to control Hg memory effects in the spray-chamber, and 0.005% (v/v) Triton® X-100 and analyzed by ICP-MS.

Table 1
Liquid chromatography and ICP-MS operating conditions for Hg speciation in blood samples.

LC conditions	
Column	C18 (5 μm, 150 mm × 4 mm)
Pre-column (Guard column)	RP18 (7 μm, 15 mm × 3.2 mm)
Mobile phase	0.05% (v/v) mercaptoethanol 0.4% (m/v) L-cysteine 0.06 mol L^{-1} ammonium acetate 5% (v/v) methanol
Mobile phase flow rate	1 mL min^{-1}
Sample loop	100 μL
Measurement	Peak high
ICP-MS experimental conditions	
Radio frequency power (W)	1200
Scan mode	Peak hopping
Nebulizer gas flow (L min^{-1})	0.58
Resolution (amu)	0.7
Replicates	3
Isotopes	^{202}Hg

2.4. Reagents

All reagents used were of analytical grade and the solutions were prepared using high-purity water with a resistivity of 18.2 MΩ cm, obtained from a Milli-Q Plus water purification system (Millipore, Bedford, MA, USA). Nitric acid (Merck, Darmstadt, Germany), was doubly distilled in a quartz sub-boiling apparatus (Kürner Analysentechnik, Rosenheim, Germany).

A clean laboratory and laminar-flow hood capable of producing class 100 were used for preparing solutions and samples. All solutions were stored in high-density polyethylene bottles. Plastic bottles and glassware materials were cleaned by soaking in 10% (v/v) HNO_3 for 24 h, rinsed five times with Milli-Q water and dried in a class 100 laminar-flow hood before use. All operations were performed on a clean bench.

A 10-mg L^{-1} standard solution of inorganic mercury was obtained from PerkinElmer (PerkinElmer, Norwalk, CT). A 1000-mg L^{-1} standard solution of methylmercury chloride (CH_3HgCl) and 1000-mg L^{-1} standard solution of ethylmercury chloride (CH_3CH_2HgCl) in water were obtained from Alfa Aesar. Analytical calibration standards of mercury species were prepared daily over the range of 0.0–20.0 μgL^{-1} for the LC–ICP-MS method by suitable serial dilutions of the stock solution in the mobile phase.

Additional chemicals for the speciation studies were HPLC grade methanol (99.9%, v/v) and mercaptoethanol (Sigma–Aldrich, USA), L-cysteine (Fluka, Japan). Ammonium acetate (99.99%) was obtained from Aldrich Chemical Company (Milwaukee, USA).

For the ICP-MS method for total mercury determination, Rh and Au were each diluted from 1000 mg L^{-1} stock standards (Assurance grade; Spex Certiprep®). Triton® X-100 was obtained from the Sigma–Aldrich Co. (Sigma Ultra Grade, Sigma–Aldrich Co., St. Louis, MO, USA) and was diluted to 10% (v/v) with double-deionized water. A rinse solution consisting of 0.005% (v/v) Triton X-100® and 1 mg L^{-1} Au in 2% (v/v) nitric acid was prepared before each run.

2.5. Sample preparation for speciation analysis

Blood samples (250 μL) were placed in 15 mL polypropylene test tubes with 4.75 mL of a solution containing 0.10% (v/v) HCl + 0.05% (m/v) L-cysteine + 0.10% (v/v) 2-mercaptoethanol and then sonicated for 15 min in an ultrasonic bath 1400 A (UNIQUE, Brazil). The resulting solution was centrifuged and then filtered through 0.20 μm Nylon® filters (Millipore, USA). Sample extraction was performed in triplicate and extraction blanks were prepared in the same manner.

2.6. Standard reference materials and ordinary blood specimens

Standard Reference Material (SRM) 966 Toxic Metals in Bovine Blood was purchased from the National Institute of Standards and Technology (NIST, Gaithersburg, MD). For additional validation purposes, human blood specimens ($n = 10$) collected as part of another research study involving Hg exposure in the Brazilian Amazon region were available for method comparison purposes with identifiers removed [22,23]. These specimens had been obtained with informed consent from human subjects in accordance with procedures approved by our Institutional Review Board.

2.7. Blood specimen collection

Venous blood was collected into pre-screened, 3-mL draw lavender-capped BD Vacutainer® blood collection tubes containing K2EDTA anticoagulant (Becton Dickinson, Franklin Lakes, NJ, USA; part no. 367856). These tubes were used with BD Vacutainer® Eclipse™ 22 gauge, 1–1.25 in. blood collection needles (Becton Dickinson; part no. 368608). After blood was drawn into the Vacutainer®, the tube was inverted several times to mix blood with K2EDTA. Prior to freezing (−80 °C), an aliquot of blood was transferred under a Class II Biosafety cabinet into a 2-mL Nalgene® cryovial (sterile, bulk-packed part no. 5012-0020, or similar) for storage until analysis.

3. Results and discussion

3.1. Preliminary experiments

Different procedures have been proposed for the extraction of mercury species in biological samples for speciation purposes based on HPLC–ICP-MS [10,11] or GC–ICP-MS [18,19]. In general, protocols are based on acid [9,10] or basic extractions [18] mediums. However, most of these methodologies have several disadvantages when coupling with HPLC–ICP-MS. Moreover, as far as we know there are no papers dealing with mercury speciation in blood by using HPLC–ICP-MS.

Firstly, as far as a compatible pH value for the reverse-phase column is concerned, a laborious procedure usually has to be adopted to adjust appropriate pH of the extracted solution prior to injection into the HPLC. Secondly, Hg species transformation might occur during sample preparation [20,21].

In order to avoid the aforementioned limitations, alternative extraction procedures have been suggested with reagents containing thiol ligands, such as mercaptoethanol [10], L-cysteine [10] or thiorea [24]. These procedures are associated with the use of microwave energy [25]. Alternatively, quantitative mercury extractions from hair samples have been demonstrated even in low acid conditions when associated with ultrasound energy [26].

The method of extraction evaluated here is based in part on a previous method described by Chiou et al. [10] for Hg speciation in fish samples. In that method, the authors have suggested the use of an extraction solution containing L-cysteine and 2-mercaptoethanol in combination with microwave radiation. Thus, our preliminary experiments were carried out to explore the efficiency of using mercaptoethanol and L-cysteine for quantitative mercury extraction from hair samples with two basic differences from the method proposed by Chiou et al. [10] Firstly, we used ultrasound energy instead of microwave energy. Secondly, we also evaluated the use of a dilute solution of HCl (0.10%, v/v) in the extractant to accelerate the ultrasound extraction without a major change in the pH. The use of an ultrasound bath simplifies the method, since this system is much simpler and less expensive than commercial microwave systems.

3.2. Evaluation of the time of ultrasound extraction

For this experiment, it has been evaluated the extractor solution containing 0.10% (v/v) HCl + 0.05% (m/v) L-cysteine + 0.10% (v/v) 2-mercaptoethanol and different times of ultrasound energy (from 0 to 30 min). Different aliquots (250 μL) of the SRM NIST 966 were used for the experiment. Quantitative extraction of Hg (>95%) was observed for the NIST 966 blood by using the proposed extraction solution and 15 min of ultrasound energy. Then, for the subsequent experiments, mercury species were extracted from the blood samples by using the solution containing 0.10% (v/v) HCl + 0.05% (m/v) L-cysteine + 0.10% (v/v) 2-mercaptoethanol and 15 min of ultrasound energy.

3.3. Optimization of LC operating conditions

After the optimization of mercury extraction from blood samples, we optimized the mobile phase composition. Different combinations of reagents in the mobile phase are usually recommended for the speciation of Hg in biological samples by HPLC–ICP-MS. Some authors recommend the use of L-cysteine and mercaptoethanol [10] while others recommend methanol, mercaptoethanol and ammonium acetate [11] or a mixture of L-cysteine, pyridine and methanol [27]. Our preliminary experiments demonstrated more promising results (time of separation, resolution, selectivity and sensitivity) for the mixture of mercaptoethanol, L-cysteine, ammonium acetate and methanol. According to Chiou et al. [10] the retention time of mercury species increases with the increase in mercaptoethanol concentration in the mobile phase. We have observed the same results (data not shown). Thus, we fixed mercaptoethanol concentration at 0.05% (v/v) as a compromise between selectivity and time of analysis. Ammonium acetate was also fixed at 0.06 mol L^{-1}. This concentration is able to maintain a favorable pH at 6.7. On the other hand, different concentrations of methanol in the mobile phase were evaluated. For this study the concentrations of ammonium acetate, L-cysteine and mercaptoethanol were fixed at 0.06 mol L^{-1}, 0.05% (m/v) and 0.05% (v/v), respectively and the concentration of methanol was varied from 0.0% to 5% (v/v). A considerable increase in Hg sensitivity was observed with the increase in methanol concentration. Three mechanisms have been put forward to explain the above enhancement effect on signal intensities: (1) charge transfer reaction from C+ species to analyte atoms, (2) improvement in the nebulization transport of the sample, and (3) shift of the zone of maximum ion density [28]. Concentrations of methanol higher than 5% (v/v) were not evaluated, since they lead to plasma instability and an increase in carbon residues on cones. Thus the methanol concentration in the mobile phase was fixed at 5% (v/v) for further studies.

Subsequent experiments were carried out to optimize the concentration of L-cysteine in the mobile phase. Separation of mercury species can take place based on the cysteine–mercury complexes on the polymeric-based C18 reverse-phase column. Concentrations of L-cysteine between 0.05% and 0.4% (m/v) were evaluated with the concentration of mercaptoethanol, ammonium acetate and methanol fixed at 0.05% (v/v), 0.06 mol L^{-1} and 5% (v/v), respectively. It has been observed that the higher the concentration of L-cysteine, the lower the retention time of the three mercury species and the higher the sensitivity for all mercury species. The separation of the three mercury species is achieved in less than 8 min with L-cysteine concentration fixed in 0.4% (m/v) compared to 35 min when 0.05% (m/v) L-cysteine is used in the mobile phase. Concentrations of L-cysteine higher than 0.4% (m/v) do not provide a complete separation between Met-Hg and Ino-Hg peaks. As a result, a solution containing 0.4% (m/v) L-cysteine, 0.05% (v/v) mercaptoethanol, 0.06 mol L^{-1} ammonium acetate and 5% (v/v) methanol was used as the mobile phase.

Table 2
Speciation of mercury in the NIST 966 blood reference material. Found values are denoted as mean (SD), $n = 3$.

Sample	Target values		LC–ICP-MS method		
SRM	Ino-Hg concentration ($\mu g L^{-1}$)	Total concentration ($\mu g L^{-1}$)	Ino-Hg concentration ($\mu g L^{-1}$)	Met-Hg concentration ($\mu g L^{-1}$)	Total concentration ($\mu g L^{-1}$)
NIST 966	14.87 ± 0.93	31.4 ± 1.7	14.8 (0.4)	16.5 (0.5)	31.3

Table 3
Mercury speciation in blood samples collected from riparians living in the Brazilian Amazon exposed to Met-Hg from fish consumption (values are denoted as mean (SD), $n = 3$). ND = not detected.

Sample	Ino-Hg ($\mu g L^{-1}$)	Met-Hg ($\mu g L^{-1}$)	Et-Hg ($\mu g L^{-1}$)	Total Hg Proposed method ($\mu g L^{-1}$)	Total Hg [ICP-MS] [13] ($\mu g L^{-1}$)
1	6.4 (1.1)	70.7 (1.6)	ND	77.1	76.8 (1.9)
2	5.0 (0.2)	47.3(0.1)	ND	52.4	52.9 (1.7)
3	5.0 (0.3)	59.1 (0.2)	ND	64.1	66 (1.8)
4	6.7 (1.1)	85.1 (0.7)	ND	91.8	103.3 (2)
5	4.8 (0.6)	83.1 (0.2)	ND	88	86 (1)
6	5.8 (0.8)	33.2 (1.4)	ND	39.0	39.8 (1.6)
7	5.8(1.1)	53.1 (1.7)	ND	59	58.8 (1.8)
8	4.2 (0.2)	24.5 (0.6)	ND	28.7	28.2 (0.5)
9	2.0 (0.1)	20.3 (0.4)	ND	22.3	22 (0.2)
10	2.3 (0.1)	23.2 (1.4)	ND	25.5	24.1 (1.4)

3.4. Validation studies

Validation of the proposed method was accomplished using NIST SRM 966 Bovine Blood. For additional validation, it was also analyzed 10 human blood specimens. Data obtained with the proposed method were compared to the results obtained using direct sample introduction for total mercury determination by ICP-MS. Results for NIST SRM 966 are shown in Table 2. Values found using the proposed method are in good agreement with established target values for the SRM 966. Moreover, no statistical differences were observed between the sum of the Hg species concentration (proposed method) and the total Hg values found by an alternative method at 95% level on applying the *t*-test for the analysis of the 10 human blood samples (Table 3). Typical calibration graphics for methylmercury, ethylmercury and inorganic mercury are shown in Fig. 1 with a very good linearity.

3.5. Analytical parameters

The LC–ICP-MS proposed method detection limit (3 SD) was 0.1 $\mu g L^{-1}$ and 0.25 $\mu g L^{-1}$ for methylmercury and inorganic mercury, respectively. Typical within-day precision was always lower

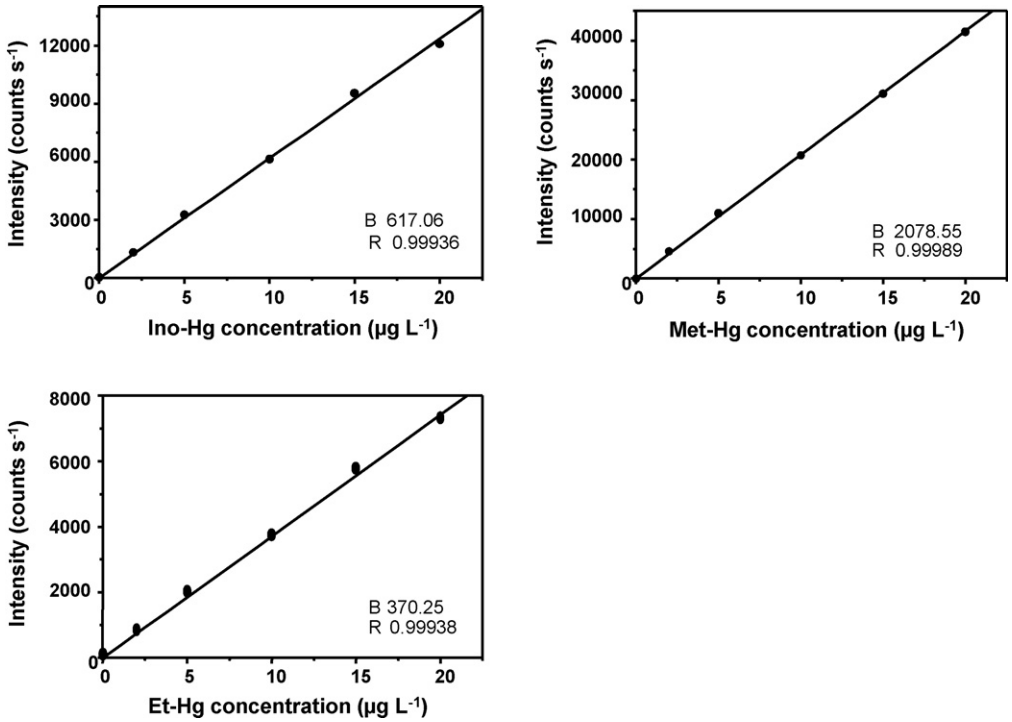


Fig. 1. Calibration curves for different mercury species by applying the proposed LC–ICP-MS method. Standards of each mercury form were prepared from 0.0 $\mu g L^{-1}$ to 20 $\mu g L^{-1}$. Mobile phase consisting of 0.4% (m/v) L-cysteine, 0.05% (v/v) mercaptoethanol, 0.06 mol L^{-1} ammonium acetate and 5% (v/v) methanol. For other conditions see Table 1.

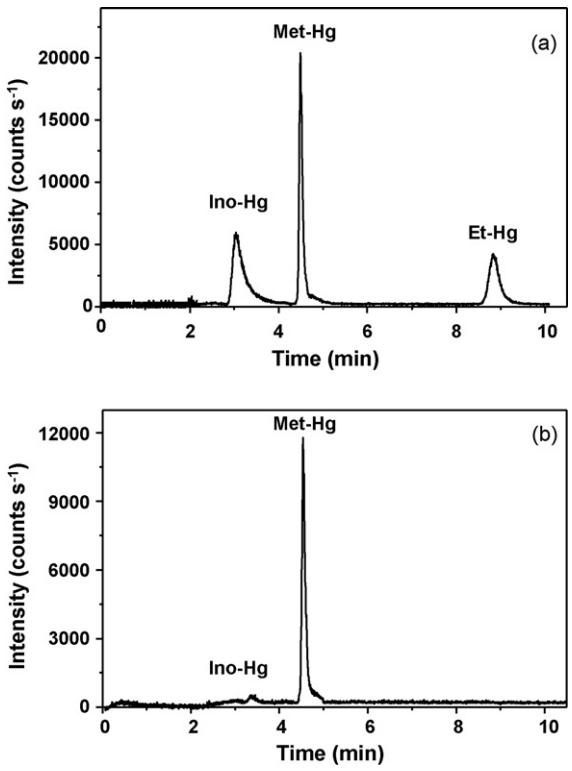


Fig. 2. Chromatograms showing the separation of mercury species in: (a) standards containing 10 μg L^{-1} of each mercury compound and (b) human blood (volunteer from fish-eating communities of the Amazon region). Mobile phase consisting of 0.4% (m/v) cysteine, 0.05% (v/v) mercaptoethanol, 0.06 mol L^{-1} ammonium acetate and 5% (v/v) methanol. For other conditions see Table 1.

than 7.0% (NIST SRM 966), while between-day precision was <12.0% RSD (NIST SRM 966) for both methylmercury and inorganic mercury determinations.

3.6. Method application for the speciation of mercury in blood samples collected from fish-eating communities

Human blood specimens were collected from 10 volunteers living in the Brazilian Amazon and exposed to high levels of methylmercury from fish consumption. Results are shown in Table 3. Only methylmercury and inorganic mercury were identified in these samples (Fig. 2). Moreover, total mercury levels found with the proposed method as a sum of inorganic and methylmercury are in good agreement with Hg values found by ICP-MS.

3.7. Stability of blood samples after collection for mercury speciation

After the speciation analysis of blood samples collected from fish-eating communities, they were left at −80 °C during 6 months to check the long-term stability of samples after collection. After this period, samples were re-analyzed by the proposed procedure. There were no statistical differences between the values in the two periods of analysis, demonstrating that samples are stable after collection at least 6 months at −80 °C.

3.8. Stability of mercury species after extraction

To verify the stability of the mercury species after extraction, a time study of sample storage at room temperature was carried out. For this experiment the SRM NIST 966 reference material was divided into four different fractions of 250 μL. From each fraction, mercury was extracted according to the proposed procedure and left at room temperature until analysis. Then, samples were analyzed after the first hour (T0), 3 h later (T1), 8 h later (T2), 24 h later (T3) and 4 days later (T4). Our results demonstrated that mercury species present in this certified material (methylmercury and inorganic mercury) can be extracted and left at room temperature up to 4 days before analysis. Since this blood reference material does not contain ethylmercury, additional experiment was carried out with an ordinary blood (human blood), divided in four fractions of 250 μL and each fraction spiked with ethylmercury to contain 10 μg L^{-1}. The proposed method of extraction was then applied and the resulted extracted solutions were left at room temperature at the same time of the previous experiment with the NIST 966. Contrary to methylmercury and inorganic mercury recovery of ethylmercury was lower than 30% even when the speciation analysis was performed just after the blood was spiked. Moreover, this loss was proportional to an increase on the amount of inorganic mercury. Since ethylmercury is stable in the standards (at room temperature and after 15 min of ultrasound energy application), it means that ethylmercury is converted to inorganic mercury in blood for some blood component with a mechanism not yet known.

3.9. In vivo conversion of ethylmercury to inorganic mercury

Based on the preliminary results with ethylmercury in blood, we did a further experiment with exposed rats. Two male Wistar rats weighting 200 g each were treated by gavage with ethylmercury solution during 3 days (100 μg kg^{-1} day^{-1}) and the blood was collected from the animals before the treatment (blank) and in the fourth day after the beginning of the treatment. Then, the determination of three mercury species (inorganic, methylmer-

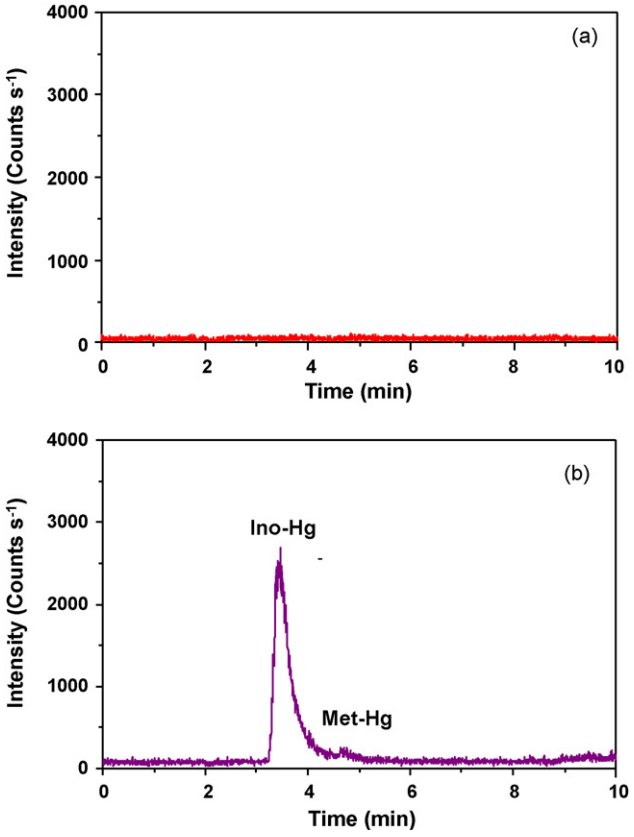


Fig. 3. Chromatograms showing the separation of mercury species in blood of: (a) rat before ethylmercury exposure (control) and (b) exposed to 100 μg kg^{-1} day^{-1} of ethylmercury during 3 days. For experimental conditions see Table 1.

cury and ethylmercury) was carried out by applying the proposed method. Fig. 3 shows the chromatogram of one of the rat's blood before (Fig. 3a) and after ethylmercury exposure (Fig. 3b). As can be observed two peaks were obtained in the blood of the exposed animal, one predominant of inorganic mercury and a very small peak of methylmercury. It demonstrates the *in vivo* conversion of ethylmercury largely to inorganic mercury and to much less extent to methylmercury. This finding is extremely relevant in the evaluation of thimerosal exposed populations, since, thimerosal, a preservative in many currently marketed vaccines throughout the world, releases ethyl mercury radical as the active species.

4. Conclusion

A simple method has been developed for mercury speciation in blood samples based on LC–ICP-MS. Sample preparation procedure is very fast and simple with a quantitative extraction of mercury in 15 min. In addition, the number of handling steps, sample preparation and analysis time, as well as potential sources of analytical errors, is reduced. The method was successfully applied for the speciation of mercury in blood samples collected from volunteers exposed to methylmercury by fish consumption. Finally, it was demonstrated the ethylmercury is practically fully converted *in vivo* to inorganic mercury and in much lees extend to methylmercury and then the inorganic form. It brings new insights to the toxicological aspects and mechanisms of thimerosal containing vaccines.

Acknowledgments

The authors are grateful to Fundação de Amparo à Pesquisa do Estado de São Paulo (FAPESP) and Conselho Nacional de Desenvolvimento Científico e Tecnológico (CNPq) for financial support and fellowships.

References

[1] D.M. Templeton, F. Ariese, R. Cornelis, L.G. Danielsson, H. Muntau, H.P. Van Leeuwen, R. Lobinski, Pure Appl. Chem. 72 (2000) 1453.
[2] P.J. Parsons, F. Barbosa, Spectrochim. Acta 62 (2007) 992.
[3] D.E. Nixon, G.V. Mussmann, T.P. Moyer, J. Anal. Toxicol. 20 (1996) 17.
[4] Toxicological Profile for Mercury (Update), Agency for Toxic Substances and Disease Registry (ATSDR), U.S. Department of Health and Human Services, Atlanta, GA, 1999, 617 pp.
[5] R.C. Marques, J.G. Dorea, M.F. Fonseca, W.R. Bastos, O. Malm, Eur. J. Pediatr. 166 (2007) 935.
[6] Y.X. Mao, G.L. Liu, G. Meichel, Y. Cai, G.B. Jiang, Anal. Chem. 80 (2008) 7163.
[7] D. Yan, L.M. Yang, Q.Q. Wang, Anal. Chem. 80 (2008) 6104.
[8] V.N. Epov, P. Rodriguez-Gonzalez, J.E. Sonke, E. Tessier, D. Amouroux, L.M. Bourgoin, O.F.X. Donard, Anal. Chem. 80 (2008) 3530.
[9] G.M.M. Rahman, T. Fahrenholz, H.M.S. Kingston, J. Anal. Atom. Spectrom. 24 (2009) 83.
[10] C.S. Chiou, S.J. Jiang, K.S.K. Danadurai, Spectrochim. Acta 56 (2001) 1133.
[11] J. Morton, V.A. Carolan, J.P.H.E. Gardiner, J. Anal. Atom. Spectrom. 17 (2002) 377.
[12] W. Meng, F. Weiyue, S. Junwen, Z. Fang, W. Bing, Z. Motao, L. Bai, Z. Yuliang, C. Zhifang, Talanta 71 (2007) 2034.
[13] C.D. Palmer, M.E. Lewis, C.M. Geraghty, F. Barbosa, P.J. Parsons, Spectrochim. Acta: B 61 (2006) 980.
[14] F. Barbosa, C.D. Palmer, F.J. Krug, P.J. Parsons, J. Anal. Atom. Spectrom. 19 (2004) 1000.
[15] T.Z. Guo, J. Baasner, Talanta 40 (1993) 1927.
[16] J.A. Moreton, H.T. Delves, J. Anal. Atom. Spectrom. 13 (1998) 659.
[17] W.J. McShane, R.S. Pappas, V. Wilson-McElprang, D. Paschal, Spectrochim. Acta 63 (2008) 638.
[18] D. Gibicar, M. Logar, N. Horvat, A. Marn-Pernat, R. Ponikvar, M. Horvat, Anal. Bioanal. Chem. 388 (2007) 329.
[19] D.C. Baxter, I. Rodushkin, E. Engstrom, H. Waara, Clin. Chem. 53 (2007) 111.
[20] L. Liang, S. Lazoff, Talanta 48 (1999) 231.
[21] J. Qvarnstrom, W. Frech, J. Anal. Atom. Spectrom. 17 (2002) 1486.
[22] J.L. Rodrigues, B.L. Batista, M. Fillion, C.J.S. Passos, D. Mergler, F. Barbosa, Sci. Total Environ. 407 (2009) 4168.
[23] F. Barbosa, M. Fillion, M. Lemire, C.J.S. Passos, J.L. Rodrigues, A. Philibert, J.R. Guimaraes, M. Mergler, Environ. Res. 109 (2009) 594.
[24] M.V.B. krishna, M. Ranjit, D. Karunasagar, J. Arunachalam, Talanta 67 (2005) 70.
[25] D. Point, W.C. Davis, J.I.G. Alonso, M. Monperrus, S.J. Christopher, O.F.X. Donard, P.R. Becker, S.A. Wise, Anal. Bioanal. Chem. 389 (2007) 787.
[26] S. Rio-Segade, C. Bendicho, J. Anal. Atom. Spectrom. 14 (1999) 263.
[27] B. Vallant, R. kadnar, W. Goessler, J. Anal. Atom. Spectrom. 22 (2007) 322.
[28] Z.C. Hu, S.H. Hu, S. Gao, Y.S. Liu, S.L. Lin, Spectrochim. Acta 59 (2004) 1463.

Talanta 80 (2010) 1164–1169

Contents lists available at ScienceDirect

Talanta

journal homepage: www.elsevier.com/locate/talanta

Multi-wall carbon nanotubes (MWCNTs)-doped polypyrrole DNA biosensor for label-free detection of genetically modified organisms by QCM and EIS

Truong Thi Ngoc Lien [a], Tran Dai Lam [b,*], Vu Thi Hong An [a], Tran Vinh Hoang [a], Duong Tuan Quang [c,1], Dinh Quang Khieu [c], Toshifumi Tsukahara [d], Young Hoon Lee [e], Jong Seung Kim [e,**]

[a] Hanoi University of Technology, Hanoi 8404, Viet Nam
[b] Institute of Materials Science, Vietnamese Academy of Science and Technology, Hanoi 8404, Viet Nam
[c] Hue University, Hue 84054, Viet Nam
[d] Center for Nano Materials and Technology, Japan Advanced Institute of Science and Technology, Ishikawa 923-1292, Japan
[e] Department of Chemistry, Korea University, Anam dong 5-1, Seongbuk gu, Seoul 136-701, Republic of Korea

ARTICLE INFO

Article history:
Received 30 July 2009
Accepted 2 September 2009
Available online 9 September 2009

Keywords:
MWCNTs-doped polypyrrole
Electrochemical DNA biosensor
Quartz crystal microbalance
Electrochemical impedance spectroscopy

ABSTRACT

In this paper, we describe DNA electrochemical detection for genetically modified organism (GMO) based on multi-wall carbon nanotubes (MWCNTs)-doped polypyrrole (PPy). DNA hybridization is studied by quartz crystal microbalance (QCM) and electrochemical impedance spectroscopy (EIS). An increase in DNA complementary target concentration results in a decrease in the faradic charge transfer resistance (R_{ct}) and signifying "signal-on" behavior of MWCNTs-PPy-DNA system. QCM and EIS data indicated that the electroanalytical MWCNTs-PPy films were highly sensitive (as low as 4 pM of target can be detected with QCM technique). In principle, this system can be suitable not only for DNA but also for protein biosensor construction.

© 2009 Elsevier B.V. All rights reserved.

1. Introduction

In recent years, there has been considerable interest in the development of DNA sensors thanks to their numerous applications such as the analysis of unknown or mutant genes, diagnosis of infectious agents in various environments and detection of analytes (drugs, pollutants, etc.). Traditional methods for DNA detection, based on the radioisotopic and fluorescent detection, are labor and time consuming, and are, thus, not well suited for routine and rapid medical analyses, particularly for point-of-care tasks. Among some new approaches to DNA detection, electrochemical detection has many advantages such as the reduction of the assay time, simple protocol and therefore can be used for on-site monitoring. In this context, oligonucleotides (ODN, a short fragment of DNA) immobilization at an electrode surface has been used in the most studies [1–4].

Among known conducting polymers, polypyrrole (PPy) is most frequently used in the commercial applications due to the high conductivity, long-term stability of its conductivity and the possibility of forming homopolymers or composites with optimal mechanical properties. PPy offers potential applications in the domain of composite materials, tissue engineering, actuators, supercapacitors, electronic and electro optic devices [5–9]. Especially, functionalized PPy polymers have attracted great attention in label-free detection because of their surface functionality and electron transduction [10]. On the other hand, carbon nanotubes (CNTs) have attracted considerable studies since their discovery [11]. They display high electrical conductivity, good mechanical strength and excellent chemical stability. The ability of CNTs-modified electrodes to promote electron-transfer reactions has been reported in connection with many important biomolecules [12,13].

Therefore, the combination of conducting polymer with CNTs was a good idea and in reality it was proven to have enhanced charge density, electrical conductivity and electrocatalytic activity compared with each pure component [14–16].

Recently, agricultural enterprises in the world have developed new plant varieties by adopting modern biotechnology, including genetic transformation. In the US, more than 40% of the corn, 50% of the cotton and >45% of soybean acres planted in 1999 have been genetically modified; at least 60% of food production US supermarkets contain genetically modified organisms (GMOs) [17]. A GMO is referred to as a living organism whose genome has been modified by the introduction of an exogenous gene able to express an additional protein that confers new characteristics, i.e. herbicide tolerance [18–20].

* Corresponding author. Tel.: +84 439948160; fax: +84 437564996.
** Corresponding author. Tel.: +82 2 32903143; fax: +82 2 32903121.
E-mail addresses: lamtd@ims.vast.ac.vn (T.D. Lam), jongskim@korea.ac.kr (J.S. Kim).
[1] Tel.: +84 543826359; fax: +84 543825824.

0039-9140/$ – see front matter © 2009 Elsevier B.V. All rights reserved.
doi:10.1016/j.talanta.2009.09.002

The exogenous DNA that has been integrated into a crop consists of a promoter (P), a structural gene ('encoding region') and a transcription terminator (T). Two particular sequences are inserted in most of the available transgenic products: the promoter of the subunit 35S of ribosomal RNA of *Cauliflower mosaic virus* (35S) and the Terminator of nopaline synthase (NOS) gene from *Agrobacterium tumefaciens*. In particular, they are widely used for the production of many transgenic vegetables commercially available, as Roundup Ready soy, MaisGard maize and the Flavr Savr tomato. Thus, the 35S and NOS sequences are the most frequently used targets for GMO screening in DNA detection approach (this approach is more often used than the second one of protein detection because DNA stability is much higher than that of proteins and therefore DNA detection can be used for both raw and processed materials while protein detection is suitable only for raw materials).

On the need of fast and sensitive analytical methods for GMO screening, in this study, we described the setup of a novel DNA label-free electrochemical biosensor for GMO (soybean) detection, based on MWCNT-doped PPy matrices for ODN immobilization and hybridization.

2. Experimental

2.1. Chemicals

Pyrrole (Py) 99% were purchased from Sigma–Aldrich. It was distilled under reduced pressure before use. Other reagents used were of analytical grade or the highest commercially available purity and used as supplied without further purification. The multi-wall carbon nanotubes (MWCNT, ~95% purity), prepared by the Chemical vapor deposition method, were obtained from Nanolab (China). The diameter of MWCNT is in the range of 40–60 nm and with a length of 1–2 μm. All aqueous solutions were prepared using Milli-Q water (18 MΩ cm).

2.2. Functionalization of MWCNT with carboxylic groups

The functionalization of CNTs has been achieved by an oxidation process, which involves extensive ultrasonic treatment in a mixture of concentrated H_2SO_4/HNO_3. The ends and sidewalls of the treated CNTs are mainly decorated with carboxyl groups. CNTs functionalized in this manner obtain good solubility in water and retain their primary electronic and mechanical properties [21].

A calculated amount of MWNTs was added into 3:1 H_2SO_4/HNO_3 mixture, then ultrasonicated in a water bath for several hours at 40 °C. The resulting suspension was diluted with deionized (DI) water and was centrifuged. The pretreated MWNTs (functionalized cMWCNT) were then washed with DI water for several times, treated with 0.1 M NaOH (to reach pH of 7), filtered, and dried at 60 °C overnight. The desired amount of the cMWCNTs (3 mg ml^{-1}) was added in DI water and ultrasonicated for about 15 min to form a uniform cMWCNTs black solution.

2.3. ODN sequences

In this study the herbicide-resistance RR soybean (product of Monsanto Inc.) has been chosen as a model. In this genome, promoter sequence is found as the CaMV 35S, which is extracted from *Cauliflower mosaic virus*. The synthesized ODN probe-pyrrole, non-complementary and complementary targets were purchased from Invitrogen. Their sequences were listed in Table 1. The PCR amplification of ODN 35S probe and its complementary target were presented in Fig. 1.

Table 1
Composition of PBS buffer and sequences of used ODN probe and targets (complementary and non-complementary strands).

Materials	Composition/sequence
PBS buffer	0.14 M NaCl; 2.7 mM KCl; 10 mM Na_3PO_4; 1.7 mM K_3PO_4; pH 7.4
ODN probe (P35S)	5′ GGCCATC **G**TTGAAG**A**TGCCTCTGCC 3′
ODN target CaMV 35S promoter (complementary target)	5′ GGCAGAGGCA**T**CTTCAA**C**GATGGCC 3′
2-Base non-complementary target (NC target)	5′ GGCAGAGGCA**A**CTTCAA**G**GATGGCC 3′

2.4. Electrosynthesis of films

Pure PPy film (denoted as PPy) was electrochemically deposited on the Au microelectrode either at a constant potential and time (+0.7 V vs. Ag/AgCl for 30 min or by voltammetric cycling from 0 to 0.9 V vs. Ag/AgCl for 30 scans, with the scan rate of 20 mV s^{-1}) from electrolytic solution containing PBS buffer, Py (0.3 M).

Probe immobilized PPy films (PPy-ODN) and probe immobilized CNT-doped PPy (C-PPy-ODN) films were obtained with the same procedure as described above with addition of ODN probe (1 μl ml^{-1}) and mixture of ODN probe (1 μl ml^{-1}) and cMWCNTs (3 mg ml^{-1}), respectively, followed by the action of ultrasonication.

2.5. ODN hybridization

For hybridization experiments, a set of ODN targets (1 μl ml^{-1}) was used: CaMV 35S as complementary target, and 2-base muted sequence, non-complementary (NC) target as a control. The hybridization experiments were performed in PBS buffer (pH 7.4) containing target strand for 30 min or 1 h at room temperature followed by an adequate rinse with the same buffer solution.

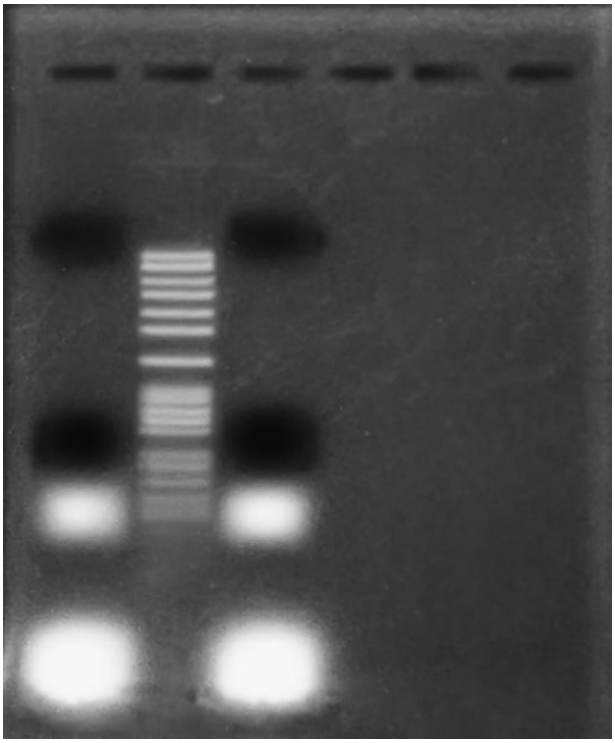


Fig. 1. The amplicon obtained by the PCR of ODN probe (P35S, left band) and its complementary target (right band).

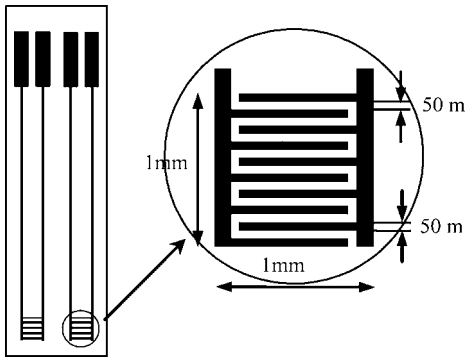


Fig. 2. Schematic representation of working interdigitated microelectrode.

2.6. Quartz crystal microbalance (QCM)

The quartz crystals employed in this study were sputtered AT-cut type (13.67 mm diameter) with Au electrodes (5.1 mm in diameter), nominal frequency (5 MHz) with Stanford QCM 200 frequency analyzer. Frequency variations are related to mass change following the Sauerbrey equation: $\Delta f = -(2/\rho\nu)f_0^2(\Delta m/S)$. The sensitivity is an experimental value determined by the constructor. ρ is the quartz density and ν its frequency coefficient. QCM measurements enable the detection of the variation of attached mass through the modification of the quartz crystal frequency to occur. Under the condition of linear behavior, occurred when the mass variation Δm is lower than some $\mu g\,cm^{-2}$, the mass uptake is directly proportional to minus the frequency variation Δf through an experimental factor determined by the following calibration equation: $\Delta m/\Delta f = -1.1 \times 10^{-9}\,g\,Hz^{-1}$. Regarding the aforementioned sensitivity, the QCM offers the ability to detect the hybridization of the immobilized ODN probes with the ODN targets (Table 2).

2.7. Electrochemical measurements

All electrochemical experiments in this work were performed using Autolab PGSTAT 12 system (EcoChemie B.V., Utrecht, The Netherlands). A conventional three-electrode cell was employed. Working electrode (WE) was either Au or Pt comb-type microelectrodes (Fig. 2) (in electrochemical experiments) or quartz (in QCM experiments). Pt foil was employed as the counter electrode (CE) and Ag/AgCl 3 M KCl was used as a reference electrode (RE). The electrolyte and the monomer (pyrrole) were mixed together to form a solution and then the solution was purged with nitrogen for 10 min to remove oxygen from the solution.

Electrochemical impedance spectroscopy (EIS) measurements were performed in the frequency range 200 kHz to 100 MHz using 5 mV alternating voltage superimposed on DC potential. Before each measurement, the same constant was imposed as a pretreatment for 120 s (Table 3).

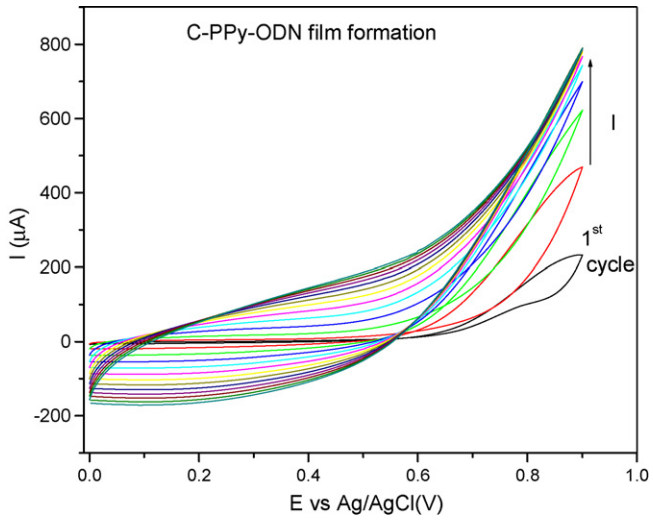


Fig. 3. Cyclic voltammograms during electropolymerization of C-PPy-ODN film.

3. Results and discussion

3.1. Film formation and morphology

Normally, sensitivity and reproductibility of DNA sensors are determined by the surface chemistry of the recognition interface, therefore immobilization of DNA probe on solid surfaces is the primary issue for DNA sensor construction. In our case, ODN probe immobilization was carried out via copolymerization of pure Py monomer with ODN modified Py moieties (Py-ODN) according to the following reaction:

$$\underbrace{\text{Py} + \text{Py-ODN}}_{\text{monomer}} \xrightarrow{\text{electro-copolymerization}} \underbrace{(\text{PPy-ODN})}_{\text{polymer}}$$

The cyclic voltammograms during film formation were presented in Fig. 3. The WE consists of two electrode pairs, called measuring and reference one, made of Pt thin film, sputtered on a silicon wafer of which the surface was oxidized. The thickness of the metal electrode is about 150 nm. The use of this couple of electrodes is aimed at eliminating the change of charges in solution allowing the improvement of the signal to noise (S/N) ratio of WE. Morphologies of pure PPy, PPy before and after hybridization with ODN were presented in Fig. 4: from left to right are SEM images of pure PPy, PPy-ODN and C-PPy-ODN, respectively.

3.2. Label-free detection of CaMV 35S complementary target by QCM measurements

The hybridization events with complementary and muted targets were detected by QCM and EIS. QCM is known to provide

Table 2
Frequency variation on C-PPy-ODN films vs. CaMV 35S concention during hybridization experiments.

CaMV 35S concentration (pM)	Frequency (kHz)	CaMV 35S concentration (pM)	Frequency (kHz)	CaMV 35S concentration (pM)	Frequency (kHz)
0	2803.620	39	2728.606	81	2671.772
4	2798.995	43	2711.519	96	2668.262
9	2794.660	46	2706.566	117	2663.669
13	2790.531	49	2699.414	134	2659.030
17	2787.518	52	2693.783	164	2654.393
21	2784.145	56	2687.886	195	2646.078
25	2780.431	59	2683.734	224	2640.364
28	2776.974	62	2681.768	251	2636.650
32	2771.526	65	2678.836	296	2634.700
36	2746.940	70	2676.459		

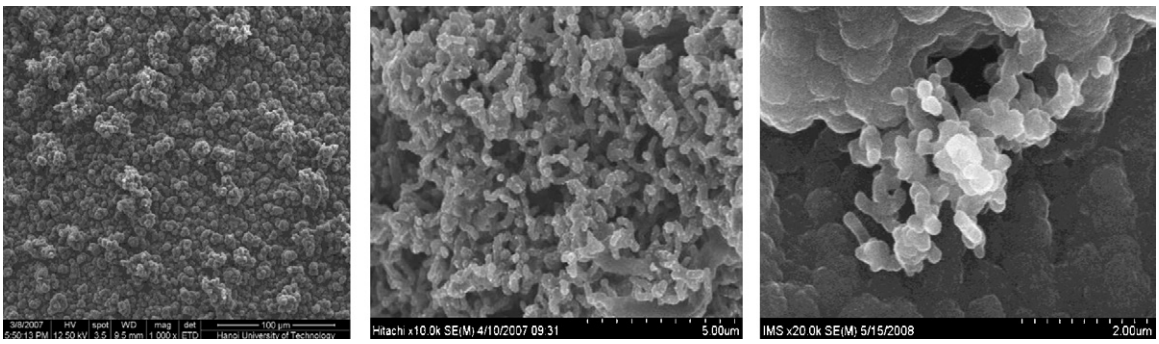


Fig. 4. SEM images of PPy (left), C-PPy (middle) and C-PPy-ODN (right).

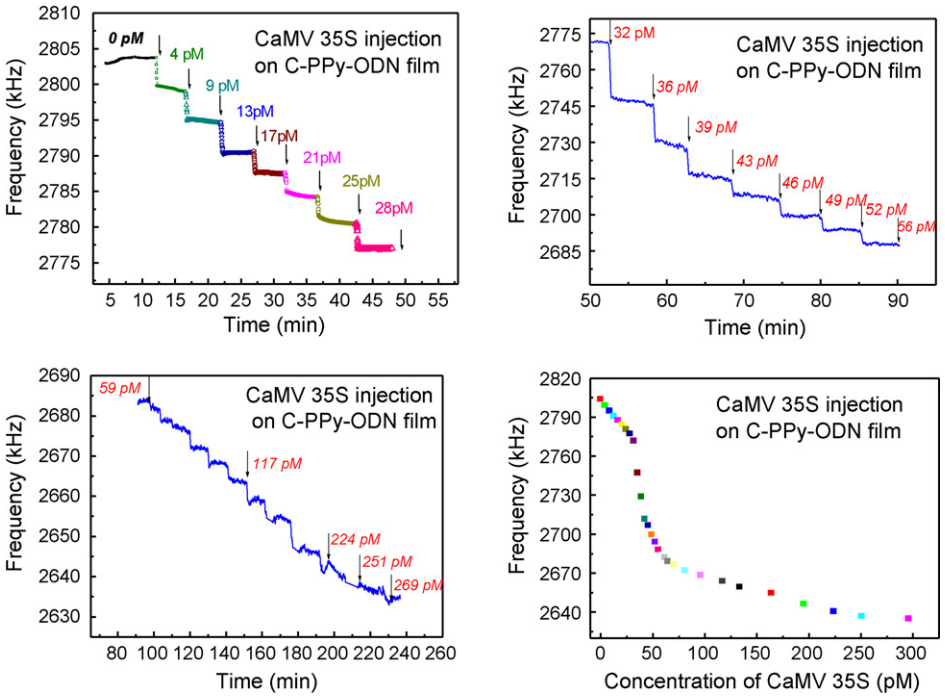


Fig. 5. QCM graph of frequency vs. time during CaMV 35S (complementary target) injection on C-PPy-ODN electrode surface. ODN target concentration varies from 1 up to 300 pM.

extremely sensitive mass variation because of its resonance frequency decrease upon the increase of a given mass on the quartz crystal. Therefore, QCM is a direct and sensitive tool to assess the immobilization of biomolecules and to evaluate their affinity to react with complementary ones in certain specific biochemical reactions [22]. Fig. 5 shows the resonance frequency variation of a quartz electrode modified with C-PPy-ODN during the hybridization with CaMV 35S complementary strand. It can be seen from these graphs that ODN hybridization did occur at as low as 4 pM of target concentration, corresponding of mass variation of *ca.*

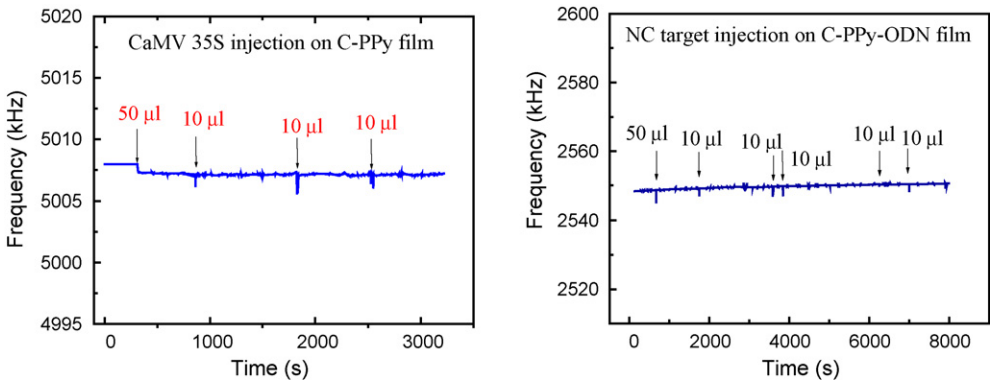


Fig. 6. QCM graph of frequency vs. time during CaMV 35S injection on ODN probe-free C-PPy film (left) and NC target (non-complementary) injection on C-PPy-ODN electrode surface (right) (blank experiments).

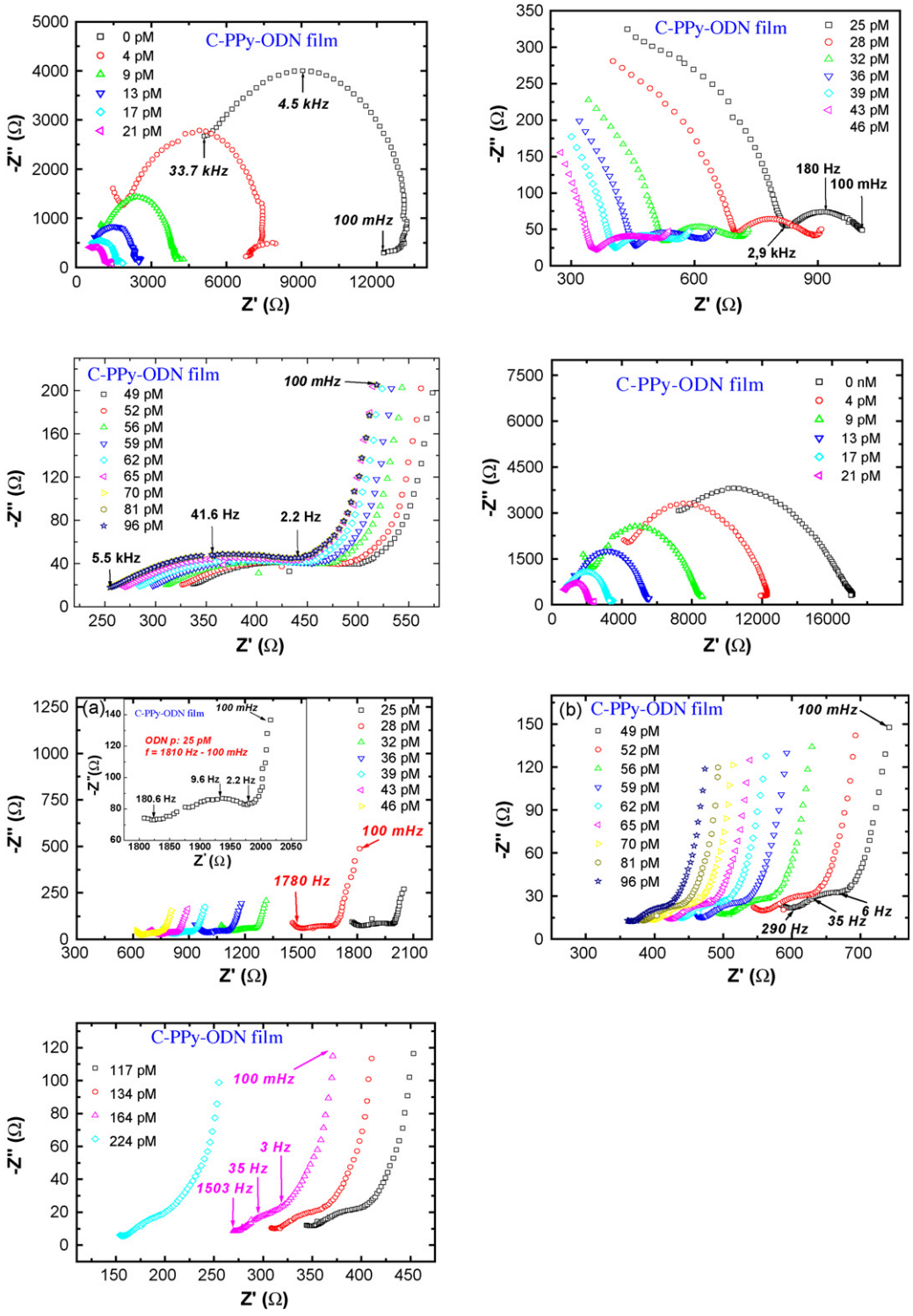


Fig. 7. EIS spectra of C-PPy-ODN films during hybridization with CaMV 35S sequence. Frequency range: 200 kHz to 100 mHz, E_{AC} = 5 mV, E_{DC} = 0.32 V vs. Ag/AgCl.

100 μg cm^{-2}. The frequency continued to fall with increasing injection volume of target. The saturation can be reached at concentration of 300 pM of target. In order to validate the transduction effect the first blank experiment with the injection of two-base mutative non-complementary (NC) target on C-PPy-ODN film and the other control of injection of complementary CaMV 35S on C-PPy film (without ODN probe!) have been carried out. In these two control experiments, the injection did not induce any frequency variation but only a slight destabilization of the quartz. It clearly demonstrated that the resonance frequency variation in case of CaMV 35S sequence injection on C-PPy-ODN film was uniquely due to hybridization (Fig. 6).

3.3. *Direct detection of CaMV 35S complementary target by EIS measurements*

EIS spectra were obtained at open circuit potential. For each set of experiment (each electrode) tree spectra were recorded

Table 3
Kinetic parameters, fitted with Randles model.

CaMV 35S concentration (pM)	R_s[a] (Ω cm^2)	R_{ct} (Ω cm^2)	CPE (μF cm^{-2})	N	χ^2 ($\times 10^{-4}$)
0	500	2525.0	0.2	0.85	2.6
25	500	1717.5	0.35	0.88	3.5
28	500	767.5	0.76	0.95	2.6
32	500	457.5	0.63	0.94	3.2
36	500	347.5	0.5	0.85	2.2
39	500	119.5	2.4	0.66	2.0
42	500	95.7	3.14	0.65	3.1
46	500	71.2	3.00	0.61	2.6
49	500	71.2	1.10	0.54	2.8
52	500	70.0	1.64	0.51	2.4
56	500	67.0	1.54	0.49	3.6
59	500	61.2	1.53	0.47	3.2
62	500	60.0	1.43	0.44	2.8
65	500	69.5	0.82	0.48	4.1
70	500	75.0	0.56	0.54	4.6
81	500	75.0	0.60	0.34	5.6

[a] R_s was fixed at 500 Ω cm^2.

corresponding to pre-ODN probe immobilization, the post-ODN probe immobilization and post-hybridization with ODN targets events, respectively. EIS Nyquist plot spectra were shown in Fig. 7. Simulated values of kinetic parameters were derived from EIS experimental data by fitting an equivalent circuit model based on Randles model [23]. This equivalent circuit includes a solution resistance (R_s); a constant phase element (CPE); and the charge transfer resistance (R_{ct}). The CPE reflects inhomogeneities of the surface layer and the substitution of the double layer capacitance with a CPE improved the adequateness of fitting. The parameter n determines the extent of the deviation from the Randles model. When $n = 1$, 0 and 0.5 the CPE represents an ideal capacitor, pure resistor and Warburg element, respectively. The values of the fitted parameters were given in Table 3. Small values of χ^2 in the range of low CaMV 35S target concentration (from 25 to 80 pM) suggest that this Randles model fit the experimental data quite well in this low range of concentration. Furthermore, the value of $1/R_{ct}$ is linearly proportional to the target concentration according to the following equation: $1/R_{ct}\ (\Omega^{-1}) = 0.32 \times 10^{-4} \times C - 0.3 \times 10^{-3}$ (pM). In the higher (than 81 pM) concentration data the fitting with Randles model encountered big error, related to the diffusion element of Redox probe (n approaches 0.5). For this reason Vorotyntsev's model [24] was considered to be used for a high range of concentration (96–296 pM) (Fig. 8). Previously, this model was successfully applied for quinone-containing conducting polymers [25] Vorotyntsev's model choice for our C-PPy-ODN system was rationalized on the similar "signal-on" behavior (i.e. decrease of R_{ct} during hybridization, firstly reported by Pham's group [26,27]) of this C-PPy-ODN system to the quinone one. "Signal-on" effect means that DNA hybridization at the vicinity of the polymer/solution interface increases the switching rate of electronically conducting polymer. According to the studies of this group, two main explanations can be envisaged: the electrostatic effect and/or the steric effect due to the polyelectrolyte character of ODN strands. Both could modify the ionic transport to and across the polymer/solution interface [26–28]. However, the variation tendency of obtained kinetic parameters for C-PPy-ODN system was not fully interpreted and it will be subjected for the further study and discussion.

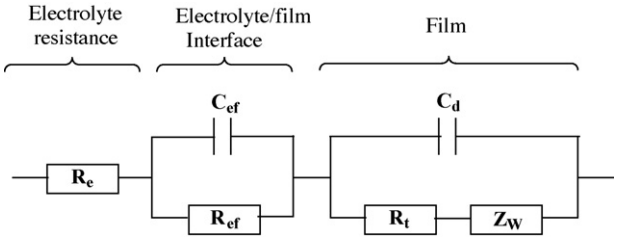


Fig. 8. Equivalent circuit of Vorotyntsev's model.

4. Conclusions

Electrochemical DNA detection is advantageous because of its fast performance and simple instrumentation. In this study, the free-label DNA detection (applied for GMO) is demonstrated based on C-PPy-ODN system. A quite low detection limit can be reached thanks to enhanced performance of C-PPy-ODN composite material. EIS data were well fitted with Randles model (in the low range of DNA concentration). In the higher range of DNA concentration, the other model, taking into account the diffusion of redox couple is needed to simulate the experimental data. Furthermore, complementary studies are necessary to interpreting all EIS values as well as understanding the signal-on mechanism of C-PPy-ODN system.

Acknowledgements

T.T.N. Lien wishes to thank the receipt of a grant from the Flemish Interuniversity Council for University Development cooperation (VLIR UOS), V.T.H. An would like to acknowledge HUT university grant T2008-01. J.S. Kim is grateful for grant of Creative Research Initiative program supported by MEST.

References

[1] Rajesh, T. Ahuja, D. Kumar, Sens. Actuat. B: Chem. 136 (2009) 275–286.
[2] F. Garnier, H. Korri-Youssoufi, P. Srivastava, B. Mandrand, T. Delair, Synth. Met. 100 (1999) 89–94.
[3] E. Palecek, M. Fojta, F. Jelen, Bioelectrochemistry 56 (2002) 85–90.
[4] E. Palecek, M. Fojta, Talanta 74 (2007) 276–290.
[5] M. Sun, S. Zhang, T. Jiang, L. Zhang, J. Yu, Electrochem. Commun. 10, 12 (2008) 1819–1822.
[6] R.A. Green, N.H. Lovell, G.G. Wallace, L.A. Poole-Warren, Biomaterials 29 (2008) 3393–3399.
[7] J. Oh, M.E. Kozlov, B.G. Kim, H.K. Kim, R.H. Baughman, Y.H. Hwang, Synth. Met. 158 (2008) 638–641.
[8] S. Skaarup, L. Bay, K. West, Synth. Met. 157 (2007) 323–326.
[9] T. Livache, A. Roget, E. Dejean, C. Barthet, G. Bidan, R. Teoule, Nucl. Acids Res. 22 (1994) 2915–2921.
[10] N. Lassalle, P. Mailley, E. Vieil, T. Livache, A. Roget, J.P. Correia, L.M. Abrantes, J. Electroanal. Chem. 509 (2001) 48–57.
[11] S. Iijima, Nature 354 (1991) 56–58.
[12] V. Raffa, G. Ciofani, S. Nitodas, T. Karachalios, D. D'Alessandro, M. Masini, A. Cuschieri, Carbon 46 (2008) 1600–1610.
[13] R.K. Gupta, V. Saraf, Curr. Appl. Phys. 9 (Suppl. 1) (2009) S149–S152.
[14] C. Peng, J. Jin, G.Z. Chen, Electrochim. Acta 53 (2007) 525–537.
[15] J.Y. Kim, K.H. Kim, K.B. Kim, J. Power Sources 176 (2008) 396–402.
[16] J.C.C. Yu, E.P.C. Lai, React. Funct. Polym. 66 (2006) 702–711.
[17] R.N. Beachy, Science 285 (5426) (1999) 335.
[18] S. Vollenhofer, K. Burg, J. Schmidt, H. Kroath, J. Agric. Food Chem. 47 (1999) 5038–5043.
[19] F.E. Ahmed, Trends Biotechnol. 20 (2002) 215–223.
[20] E. Mariotti, M. Minunni, M. Mascini, Anal. Chim. Acta 453 (2002) 165–172.
[21] J. Zhang, H. Zou, Q. Qing, Y. Yang, Q. Li, Z. Liu, X. Guo, Z. Du, J. Phys. Chem. B 107 (2003) 3712–3718.
[22] D.A. Buttry, M.D. Ward, Chem. Rev. 92 (1992) 1355–1379.
[23] J.E.B. Randles, Discuss. Faraday Soc. 1 (1947) 11.
[24] M.A. Vorotyntsev, C. Deslouis, M.M. Musiani, B. Tribollet, K. Aoki, Electrochim. Acta 44 (1999) 2105–2115.
[25] T.D. Lam, A novel functionalized conducting polymer based DNA biosensor. Direct electrochemical detection of hybridization, PhD thesis of Univ. Paris VII, 2003.
[26] S. Reisberg, B. Piro, V. Noël, M.C. Pham, Anal. Chem. 77 (2005) 3351–3356.
[27] S. Reisberg, L.A. Dang, Q.A. Nguyen, B. Piro, V. Noël, P.E. Nielsen, L.A. Le, M.C. Pham, Talanta 76 (2008) 206–210.
[28] S. Reisberg, B. Piro, V. Noël, T.D. Nguyen, P.E. Nielsen, M.C. Pham, Electrochim. Acta 54 (2008) 346–351.

Talanta 80 (2010) 1170–1176

Contents lists available at ScienceDirect

Talanta

journal homepage: www.elsevier.com/locate/talanta

Solid-phase extraction of organic compounds in atmospheric aerosol particles collected with the particle-into-liquid sampler and analysis by liquid chromatography–mass spectrometry

Jevgeni Parshintsev[a], Tuulia Hyötyläinen[a,1], Kari Hartonen[a], Markku Kulmala[b], Marja-Liisa Riekkola[a,*]

[a] Laboratory of Analytical Chemistry, Department of Chemistry, P.O. Box 55, FI-00014, University of Helsinki, Finland
[b] Division of Atmospheric Sciences, Department of Physical Sciences, P.O. Box 64, FI-00014, University of Helsinki, Finland

ARTICLE INFO

Article history:
Received 18 May 2009
Received in revised form 27 August 2009
Accepted 3 September 2009
Available online 9 September 2009

Keywords:
Particle-into-liquid sampler
Aerosol
cis/*trans*-Pinonic acid
Solid-phase extraction
HPLC–MS
β-Caryophyllene
Ozonolysis

ABSTRACT

Atmospheric aerosol particles, collected with the particle-into-liquid sampler at SMEARII station in Finland in mid-August 2007, were analysed for biogenic acids. The sample pretreatment method, comprising solid-phase extraction with anion exchange and hydrophilic–lipophilic balance materials, was optimized. Extraction efficiencies of solid-phase extraction from 10 and 20 ml samples were about 100%, with average relative standard deviation of 8.9%, in concentration range from 12.5 to 50 ng/ml of the acid. Extraction of aldehydes was less successful, with efficiencies from 69 to 163% and average 10% deviation. Pretreated samples were analysed by reversed phase high performance liquid chromatography with ion trap mass spectrometric detection. Limits of detection achieved for organic acids with the analytical procedure developed ranged from 9 to 27 μg/l of extracted sample, while limits of quantitation were from 31 to 90 μg/l. Oxidation with ozone was used for the preparation of the acid of β-caryophyllene (β-caryophyllinic acid), which was also studied in aerosol samples. MS^2 experiments were used to confirm the identification of *trans*-pinic, *trans*-pinonic and β-caryophyllinic acids. Azelaic, hexadecanoic, *cis*-pinonic, and *cis*- and *trans*-pinic acids were quantitated in the samples with use of authentic standards, while the concentrations of *trans*-pinonic and β-caryophyllinic acids were determined with *cis*-pinonic acid as surrogate. Also, the contribution of β-caryophyllene oxidation products to aerosol organic carbon was evaluated. Aldehydes could not be analysed in real samples due to the insufficient extraction. The particle-into-liquid sampler proved to be suitable for the collection of aerosol particles for the elucidation of daily and diurnal variation of selected species. The optimized sample pretreatment, together with the analysis method, offer a promising approach for the study of aerosol chemical composition, where artifact formation is minimal and time resolution is good.

© 2009 Elsevier B.V. All rights reserved.

1. Introduction

The significance of atmospheric aerosol particles for climate and air quality is well recognized [1–3]. The effects of atmospheric aerosols are strongly dependent on their chemical composition, and numerous studies dealing with this topic have been published during recent years. Because the chemical composition of aerosols varies significantly with time and place, the research is challenging.

At present, the collection of aerosol particles is the most difficult step of the analytical cycle. Atmospheric aerosols are usually collected on a filter or an impactor plate and analysed either off-line with various techniques or directly with an aerosol mass-spectrometer [4,5]. The particle-into-liquid sampler (PILS), invented by Weber et al. [6] in 2001, has recently been recognized as a useful device for the collection of aerosols. It has also been modified for ground and airborne measurements of water-soluble aerosol composition [7]. The PILS combines two conventional techniques in aerosol measurements: particle growth in supersaturated water vapor and impaction of the particles on a quartz plate. Elsewhere, the device has been used for the determination of ion composition in atmospheric aerosols by on-line coupling it with an ion chromatograph [6,7] and for the determination of water-soluble organic carbon [8]. In our most recent work, we used PILS for the collection of aerosol samples for the determination of α-pinene and its oxidation products [9].

Typically, organic compounds in aerosols are investigated by gas chromatographic (GC) or liquid chromatographic methods with mass spectrometric detection (MS) [9–11]. Several methods have been developed for the sample preparation of aerosol particles. The sampling technique strongly determines the method selected. The

* Corresponding author. Tel.: +358 9 191 50 268; fax: +358 9 191 50 253.
E-mail address: marja-liisa.riekkola@helsinki.fi (M.-L. Riekkola).
[1] Current address: VTT Technical Research Centre of Finland, Quantitative Biology and Bioinformatics, P.O. Box 1000, FI-02044 VTT, Finland.

0039-9140/$ – see front matter © 2009 Elsevier B.V. All rights reserved.
doi:10.1016/j.talanta.2009.09.004

most common method for extracting aerosol particles collected on filters is simple solid–liquid extraction (SLE), but other methods, such as sonication-assisted extraction (SAE), have also been utilized [10,11]. Liquid–liquid extraction (LLE) has been used for PILS samples [9]. Solid-phase extraction (SPE) has also been applied but, mainly for fractionation and concentration of samples extracted by SLE or SAE [12,13].

Our aim was to develop an easy and reliable analytical method for acids and aldehydes in aerosol samples collected by PILS. In our previous study, GC–MS was applied with LLE used for the sample preparation [9]. Although the results were promising, LLE proved to be laborious and time consuming. Furthermore, the analytical procedure was not sufficient in terms of selectivity, especially in the case of *cis*-pinonic acid. In this study, SPE was used in sample pretreatment, with hydrophilic–lipophilic balance (HLB) and anion exchange absorbents evaluated as the trapping material. After solid-phase extraction, the biogenic acids were separated by reversed phase liquid chromatography and detected by ion trap mass spectrometry (RPLC–ITP-MS). Use of RPLC–ITP-MS, instead of GC as earlier, makes MS^n experiments possible. In the determination of acidic compounds, special attention was paid to hexadecanoic and azelaic acids and β-caryophyllinic acid because of their presumed importance in aerosol chemistry [14–16]. Azelaic acid was recently identified as a marker compound in aerosol transport [17] and found to have cloud condensation nuclei properties [18]. Despite its importance, azelaic acid has rarely been analysed in aerosol particles [19,20]. The relevance of oxidation products of sesquiterpenes, especially β-caryophyllene, to aerosol growth has also been noted [21]. The presence of β-nocaryophyllone aldehyde in atmospheric aerosols has been demonstrated with the use of authentic standard, while β-caryophyllinic acid has been identified tentatively [22,23]. A part of our research was dedicated to the synthesis of β-caryophyllinic acid via ozonolysis of β-caryophyllene and to its determination in PILS samples.

2. Experimental

2.1. Chemicals

Azelaic acid (>99%) and stearic acid (≥99.5%) were purchased from Fluka Chemie GmbH (Buchs, Switzerland). Pinic acid (library of rare chemicals, no purity available), cis-pinonic acid (98%), palmitic acid (99%), 2,4-dichlorobenzoic acid (98%, used as internal standard), decafluorobenzophenon (98%, internal standard in GC) and bis(trimethylsilyl)trifluoroacetamide (BSTFA, 99%) used as a derivatization agent were obtained from Sigma–Aldrich Chemie GmbH (Steinheim, Germany). Methanol and pyridine were purchased from J.T. Baker (Deventer, The Netherlands), while ethyl acetate and dichloromethane were from LabScan (99.8%, Dublin, Ireland). Acetonitrile for the HPLC analysis (HPLC Far UV, Lab Scan, Analytical Sciences, Poland), and water (DirectQ-UV, Millipore Corp., Billerica, USA) with formic acid (98–100%, Merck, Darmstadt, Germany) were used. Pinonaldehyde was synthesised in the laboratory by oxidation of (1S,2S,3R,5S)-(+)-pinanediol (Aldrich, Steinheim, Germany) with periodic acid (Merck, Darmstadt, Germany) as described by Glasius et al. [24]. β-Nocaryophyllene aldehyde was synthesised as described by Parshintsev et al. [22]. Heptanal (98.5%), octanal (100%), nonanal (96%), undecanal (97%) and benzaldehyde (98.5%) were purchased from Accu Standard Inc. (New Haven, USA).

For the denuder coating, phosphoric acid (85%) and potassium iodide were purchased from Merck (Darmstadt, Germany); glycerol was obtained from Sigma–Aldrich (Steinheim, Germany), and XAD-2 resin (polystyrene-divinylbenzene) from EGA-Chemie (Steinheim, Germany).

2.2. Aerosol sampling

Samples were collected with the PILS during August 2007 at the Station for Measuring Forest Ecosystem Atmosphere Relations (SMEAR II) at Hyytiälä (61°51′N, 24°17′E, 180 m above sea level), which is 230 km north of Helsinki. The forest consists of Scots pines (*Pinus sylvestris* L.) 30–40 years old, homogeneously spread through 200 m in all directions from the measurement site. A more detailed description of SMEAR II is presented by Kulmala et al. [25].

A fuller description of the aerosol sampling with PILS can be found elsewhere [9]. Briefly, the sampling system consists of an ADI2081 particle-into-liquid sampler (Applikon Analytical, Schiedam, The Netherlands) coupled with an eight-channel peristaltic pump (Watson Marlow 205S, Wilmington, USA). DirectQ-UV water was used as a working liquid and for transport flow. To remove gas phase compounds, three channel annular denuders (242 mm length, Teflon coated, stainless steel sheath, URG, Chapel Hill, USA) with different coatings (XAD, phosphoric acid, potassium iodide) were added to the sampling line. Aerosols were size separated before the denuder line with a cyclone (PM2.5, URG, Chapel Hill, USA).

Two-hour samples were collected into screw-capped vials and stored in a refrigerator until sample pretreatment. The volume of samples varied from 20 to 40 ml. One half of each sample was used for the analysis, while the other half was stored for future need.

2.3. Solid-phase extraction

For the optimization of solid-phase extraction (SPE), standard mixtures of the studied acids and aldehydes were prepared in water, extracted and analysed. Acid standards with concentrations of 5, 10, 12.5, 25, 50 and 100 μg/l were prepared from methanol stock solutions (10 mg/l) in water, so amount of methanol could not affect the SPE. Both 10 and 20 ml of standard solutions were extracted with solid-phase materials to obtain the efficiency in the volume range of real PILS samples. Possible break through was also determined.

Two types of SPE materials were used in this research. At first, a hydrophilic–lipophilic balance sorbent (HLB, 3 ml, 30 mg of poly(N-vinylpyrrolidone)-divinylibenzene, StrataX, Phenomenex, USA) was tested with the following procedure: activation (5 ml of methanol), equilibrium (5 ml of water), addition of sample (10 or 20 ml), drying (20 min in reduced pressure) and elution with 1 ml of ethyl acetate. The second material was anion exchange OasisMAX (1 cm^3, 30 mg, Waters Corp., Milford, USA), which is basically HLB that has been chemically modified with quaternary amine group. The sample pretreatment procedure included the following steps: activation (2 ml of methanol), equilibrium (2 ml of water), sample addition (10 or 20 ml) and elution with 1 ml of 2% formic acid in methanol.

Water solutions of aldehyde mixture with concentrations of 125, 250, 500 and 1000 μg/l were prepared and extracted with HLB as explained above.

In all extractions, gravitational force was used without additional vacuum. Each concentration and volume were extracted three times. PILS samples from 12 to 20 ml (depending on original amount of sample) were extracted with OasisMAX material only.

2.4. Liquid chromatographic–mass spectrometric analysis

Analysis was performed with a Hewlett-Packard Series 1100 liquid chromatograph (Palo Alto, USA) coupled with an Esquire 3000 plus ion trap mass-spectrometer (Bruker Daltonics, USA). Electrospray ionization (ESI) in negative ion mode was used. The combination of eluents, gradient, injection volume, flow rate and ionization parameters was optimized. Final parameters for

the liquid chromatography were XBridge Shield column (RP-18, 2.1 mm × 150 mm, 5 μm, Waters Corp, USA), linear gradient from 10 to 100% of B (ACN; A: 0.1% formic acid in water) in 30 min with following 15 min of 100% B, flow 0.3 ml/min, and injection volume 3 μl for the standards and 15 μl for the samples. Parameters for the ESI-MS were capillary voltage +4000 V, end plate offset −500 V, nebulizer pressure 2.76 bar (nitrogen), 8 l/min of drying gas (nitrogen) and drying temperature of 300 °C. Mass range of 50–370 amu was recorded. For quantitation of the target compounds, extracted ion chromatograms were used with the masses 185 amu (*cis*-/*trans*-pinic acid), 183 amu (*cis*-/*trans*-pinonic acid), 187 amu (azelaic acid), 255 amu (hexadecanoic acid), 283 amu (octadecanoic acid), 189 amu (internal standard).

2.5. Gas chromatographic–mass spectrometric analysis

Standard solutions of aldehydes and HLB extracted samples were analysed by GC–MS. Before each analysis, 10 μl of quantitation standard, decafluorobenzophenone, was added to the vials. A gas chromatograph (Agilent 6890N, Santa Clara, USA) equipped with a mass selective detector (Agilent 5973N, USA) was used. The GC column was an HP-5 (28 m × 0.25 mm × 0.25 μm, Hewlett-Packard, USA) coupled with a 2-m deactivated retention gap (i.d. 0.53 mm, Agilent, USA) via a press-fit connector (0.30–0.75 mm OD, deactivated; BGB Analytik, Switzerland). The GC oven temperature was programmed as follows: initial temperature 60 °C (2 min), temperature gradient 8 °C/min with final temperature 300 °C (5 min). 1 μl of sample was injected by on-column injection. The injector temperature program was in oven tracking mode. Helium was used as carrier gas with a constant flow of 1 ml/min. The interface between the GC and the MS was maintained at 300 °C, while the ionization source was kept at 230 °C and the quadrupole temperature was 150 °C. Electron impact ionization (EI) was used at 70 eV. Selected ion monitoring (SIM) was employed. Two ions were monitored for each aldehyde: quantitative and qualitative ions. The GC–MS data was analysed with Enhanced ChemStation D.00.01.27 software (Agilent, USA), and the compounds of interest were identified by their retention times and selected ions.

2.6. Synthesis and purification of β-caryophyllinic acid

β-Caryophyllene (*trans*-(1R,9S)-8-methylene-4,11,11-trimethylbicyclo[7.2.0]undec-4-ene, 80+ %, GC, sum of enantiomers, Sigma–Aldrich Chemie, Steinheim, Germany) solution (10%, v/v) was prepared in dichloromethane (HPLC grade, Labscan Ltd., Dublin, Ireland). Aliquots of 10 ml were used for ozonolysis. A test-tube containing the sesquiterpene solution was placed in a beaker filled with cooled ethanol. Pieces of dry carbon dioxide (−78 °C) were added to the ethanol to reduce the temperature to at least −68 °C. Dried, purified and ozonolysed air was bubbled through the solution at a flow rate of 10 l/h (500 M corona discharge ozone generator, Fisher, UK). Temperature was controlled throughout the experiment. Reaction times were 15, 30 and 45 min.

The reaction mixture was extracted twice with 10 ml of 5% ammonia solution in water. Then aqueous fractions were combined and extracted by solid-phase extraction with MAX material as described in Section 2.3. The obtained sample was analysed by HPLC–MS as explained in Section 2.4. Ion 253 was used for the MS^2 experiments.

To obtain an EI spectrum for β-caryophyllinic acid, ten fractions of HPLC effluent containing target compound were collected to the vial and dried under nitrogen. Then 30 μl of derivatization reagent (BSTFA) was added together with 10 μl of pyridine and the mixture was held at 70 °C for three hours. For GC–MS analysis, the mixture was dried and redissolved in 100 μl of hexane. The parameters for the GC–MS analysis were the same as those given in Section 2.5 except that mass range from 50 to 550 amu was used in scan mode.

3. Results and discussion

The PILS sampling for the determination of oxidation products of α-pinene and acids was optimized in our previous study [9]. In this study, sample preparation based on SPE and analysis, mainly with RPLC–MS, were developed and applied to the study of selected compounds in aerosol samples.

3.1. PILS sampling

The volume of PILS samples varied significantly from sample to sample. The tubing used in the peristaltic pump did not provide a constant flow due to the deformation that takes place over time. Also, humidity and temperature of the sampled air may have affected the volume of samples. The inventors of PILS added lithium fluoride to the sample flow to correct for differences in sample volume during the on-line analysis [6,7]. In the present study, the addition of calibrant was unnecessary because the analysis was carried out off-line, and the final sample volume could be measured. Note that only half of the sample collected for two hours and representing 2 m^3 of sampled air was used, so that each analysed sample represented 1 m^3 of sampled air. This simplified the calculations.

3.2. Solid-phase extraction of acids

Two materials were tested for SPE of acids: HLB and anion exchange (MAX) materials. Two different sample volumes were employed. To guarantee sufficient retention of acids in the HLB material, the pH of the sample should have been optimized for all compounds. However, to avoid alteration of the sample this was not done. As a result, only azelaic acid was retained in the HLB material. Owing to the insufficient extraction, HLB was not used for the extraction of acids in PILS samples.

Fortunately, and as expected, anion exchange material worked well for acids because pH of the standards and samples was always about two units higher than pK_a values of the studied acids, so that the acids were deprotonated. Two sample volumes (10 and 20 ml) were tested because in PILS the volumes of the samples typically range from 10 to 20 ml per hour. Table 1 shows the extraction efficiencies for all studied acids, with different sample volumes, in all

Table 1
Extraction efficiencies obtained with OasisMAX SPE material (% ± RSD%, $n = 9$).

Conc, μg/l	*cis*-Pinic acid, 10 ml	*cis*-Pinic acid, 20 ml	*trans*-Pinic acid, 10 ml	*trans*-Pinic acid, 20 ml	*cis*-Pinonic acid, 10 ml	*cis*-Pinonic acid, 20 ml	Azelaic acid, 10 ml	Azelaic acid, 20 ml
5	64 ± 17	80 ± 19	148 ± 10	115 ± 18	96 ± 15	95 ± 6	107 ± 10	100 ± 8
10	75 ± 8	77 ± 9	104 ± 18	71 ± 48	96 ± 4	94 ± 7	116 ± 12	77 ± 30
12.5	90 ± 2	93 ± 1	111 ± 8	97 ± 2	100 ± 8	98 ± 5	100 ± 3	90 ± 1
25	88 ± 7	91 ± 15	89 ± 5	89 ± 7	99 ± 3	100 ± 6	97 ± 7	93 ± 6
50	93 ± 6	99 ± 1	83 ± 5	91 ± 12	96 ± 6	100 ± 2	91 ± 5	93 ± 2
100	110 ± 6	110 ± 8	94 ± 5	100 ± 10	108 ± 5	112 ± 8	95 ± 4	93 ± 9

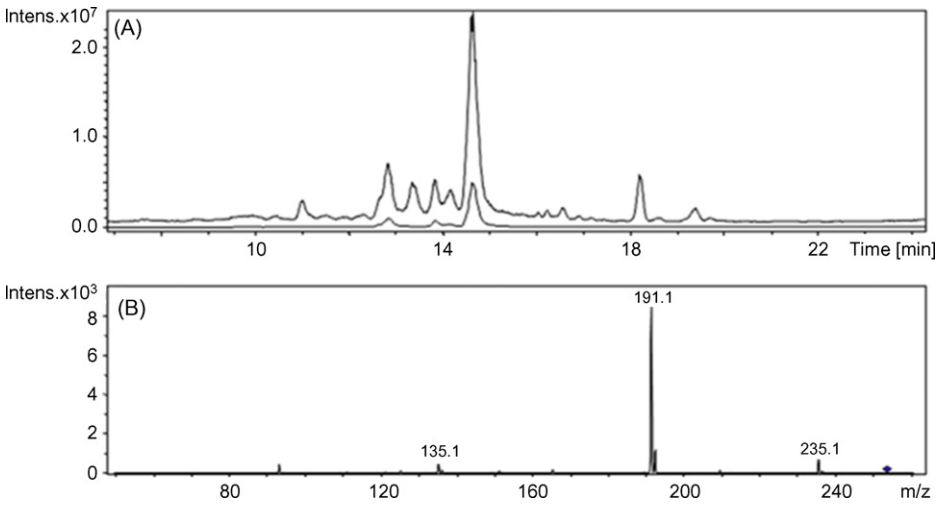


Fig. 1. HPLC–MS (TIC), MS^2 (from ion 253) chromatograms (A) and MS^2 spectrum (B) of MAX extracted β-caryophyllene oxidation products. Retention time of β-caryophyllinic acid is 14.8 min.

concentrations. As can be seen from Table 1, almost 100% recoveries (within the standard deviation) were obtained in concentration range from 12.5 to 100 ppb with both sample volumes. Evidently, compounds were retained and eluted well, and the retention was not affected by the volume of the sample.

The sample pretreatment procedure developed here was faster and easier than the liquid–liquid extraction employed in our previous research [9]. Reduced pressure, which is usually applied in SPE to make the flow faster and more stable, was not needed because the flow obtained simply by gravitation was sufficient (about 1 ml/min).

3.3. Solid-phase extraction of aldehydes

The results for the extraction of aldehydes with HLB material are summarized in Table 2. As can be seen, extraction efficiencies were not acceptable. Poor results were obtained even for high concentrations, such as 125 μg/l. Also, the limits of detection ranged from 50 ng/ml for pinonaldehyde and β-nocaryophyllene aldehyde to 250 ng/ml for undecanal. Since the concentrations of aldehydes in real atmospheric aerosol samples are much lower than the concentrations for which moderate extraction efficiencies could be achieved, our method is not suitable for the analysis of aldehydes in real samples. The sensitivity could be increased by concentrating the samples or by increasing the sample air flow during the sampling. However, because the repeatability of the extraction was not satisfactory, the HLB material was not used in the extraction of real PILS samples and aldehydes were not analysed.

3.4. Chromatographic analysis

HPLC–MS was used as the analytical technique for the analysis of acids because it is simple and fast, and has frequently been employed for the analysis of organic acids in atmospheric aerosols [11,26–28]. In our previous study [9], we analysed PILS samples for *cis*-pinonic and pinic acids by GC after sample derivatization. However, the amount of *cis*-pinonic acid was overestimated owing to its co-elution with other compounds, such as *trans*-pinonic acid [9,28].

Acetic acid and formic acid were tested as modifiers of the HPLC eluent. Formic acid gave better separation of the analytes than did acetic acid and it was chosen for further studies. The ionization of the studied acids in ESI suffers from low pH, but in this case a compromise was made between good separation and ionization. The limits of detection (LOD) and quantitation (LOQ) in μg/l obtained by HPLC–MS for the acids were as follows: *cis*-pinic 16/55; *trans*-pinic 12/40; *cis*-pinonic 27/90; azelaic 9/31; hexadecanoic 12/38. LOD and LOQ values were calculated from peak heights as three and ten times the background noise of the blank samples. The quantitation of target compounds was done from peak areas because of slightly better repeatability.

3.5. Ozonolysis of β-caryophyllene

In our previous study, β-caryophyllinic acid was only tentatively identified in aerosol samples. Since a commercial standard for β-caryophyllinic acid was not available, we synthesised this compounds by ozonolysis of β-caryophyllene and purified it by SPE, as described in Section 2.6. Fig. 1 presents the HPLC–MS and MS^2 (ion 253) chromatograms for the ozonolysed sample (30 min). From the anion exchange step it is clear that ozonolysis produces several acids of β-caryophyllene. Tandem mass spectrometric analysis showed the molecular mass of a few of them to be 254, with identical loss of water (M-18) and carbon dioxide (M-44), as is typical for the acids. For conformation of the identification of the synthesised β-caryophyllinic acid, GC–MS analyses were conducted after derivatization with BSTFA. Fig. 2 presents the EI spectrum obtained for the trimethylsilyl derivative of β-caryophyllinic acid. For more reliable identification, by nuclear magnetic resonance spectroscopy (NMR), a greater amount of β-caryophyllinic acid must be prepared and purified.

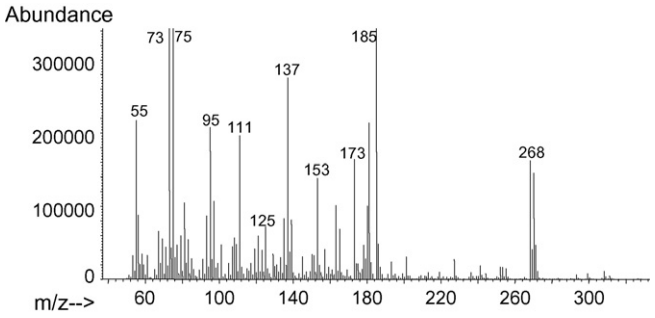


Fig. 2. MS (EI) spectrum of β-caryophyllinic acid trimethylsilyl derivative.

Table 2
Extraction efficiencies for aldehydes obtained with HLB SPE material (% ± RSD%, $n = 9$).

Sample	β-Nocaryophyllene aldehyde	Pinene aldehyde	Heptanal	Benzaldehyde	Octanal	Nonanal	Undecanal
125 μg/l, 10 ml	–	151 ± 3	134 ± 12	88 ± 4	89 ± 3	–	–
125 μg/l, 20 ml	–	156 ± 2	141 ± 3	93 ± 6	98 ± 5	–	–
250 μg/l, 10 ml	107 ± 19	87 ± 5	99 ± 13	73 ± 9	66 ± 17	–	–
250 μg/l, 20 ml	–	112 ± 6	122 ± 4	107 ± 7	103 ± 8	–	–
500 μg/l, 10 ml	103 ± 26	58 ± 3	111 ± 5	111 ± 3	92 ± 4	98 ± 20	84 ± 1
500 μg/l, 20 ml	105 ± 13	69 ± 5	95 ± 3	90 ± 8	76 ± 4	127 ± 23	89 ± 9
1000 μg/l, 10 ml	137 ± 13	93 ± 6	71 ± 9	82 ± 10	70 ± 8	97 ± 12	73 ± 8
1000 μg/l, 20 ml	163 ± 13	113 ± 10	74 ± 9	83 ± 8	80 ± 4	159 ± 21	96 ± 10

3.6. Analysis of aerosol samples

In the analysis of PILS samples by the LC method developed in this study, two peaks with mass of 183 amu, corresponding to [M−1] of *cis*-pinonic acid, eluted near each other. The reference *cis*-pinonic acid gave only one peak, with retention time matching that of the first of the two peaks. The results obtained from an MS/MS experiment (cleavage of water and carbon dioxide molecules in both peaks) showed the fragmentation patterns of the two peaks to be almost identical. Thus, the peak eluting slightly after that of *cis*-pinonic acid most probably is that of *trans*-pinonic acid (Fig. 3). The quantitation of *trans*-pinonic acid was done with use of *cis*-pinonic acid as a surrogate. The same situation was observed for pinic acid, which gave two peaks even from the reference material. The same logic was applied here since exact information about the standard was not available (library of rare chemicals). A tandem mass spectrometry experiment showed the two peaks to give the same MS/MS spectra. Most probably then, the first eluting peak was *cis*- and the second *trans*-pinic acid. Comparison of the peak areas obtained from the standard solution showed the ratio 75:25 for these acids, and this was taken into account in the quantitation.

The two-hour and overnight PILS samples collected between 13 August 2007 (10 am–12 am) and 16 August 2007 (4 pm–6 pm) were extracted with OasisMAX and analysed by HPLC–MS. Results of the quantitation are presented in Table 3 and plotted in Fig. 4. As can be seen, *trans*-pinic acid was not found in these samples, and octadecanoic acid was not quantitated due to problems with the zero samples. Long chain acids were well retained in the LC column causing a memory effect. Blank samples were run with pure methanol between the PILS samples, but they did not eliminate the problem. Subtracting the peak areas of zero samples lead to increasing in uncertainty and this is why it was decided to exclude the compound from the quantitation.

The concentrations of *cis*- and *trans*-pinonic acids were closely similar, probably because of the similar formation mechanism without a dominant formation route. This discovery is important because it means that, in our previous study, the amount of oxidation products of α-pinene in aerosols was underestimated. Unfortunately, the number of sampling days was too few to allow statistically reliable conclusions on the influence of *trans*-pinonic acid on the growth of aerosol particles.

The surprisingly high amount of azelaic acid in all studied samples can be considered as important and relevant for aerosol

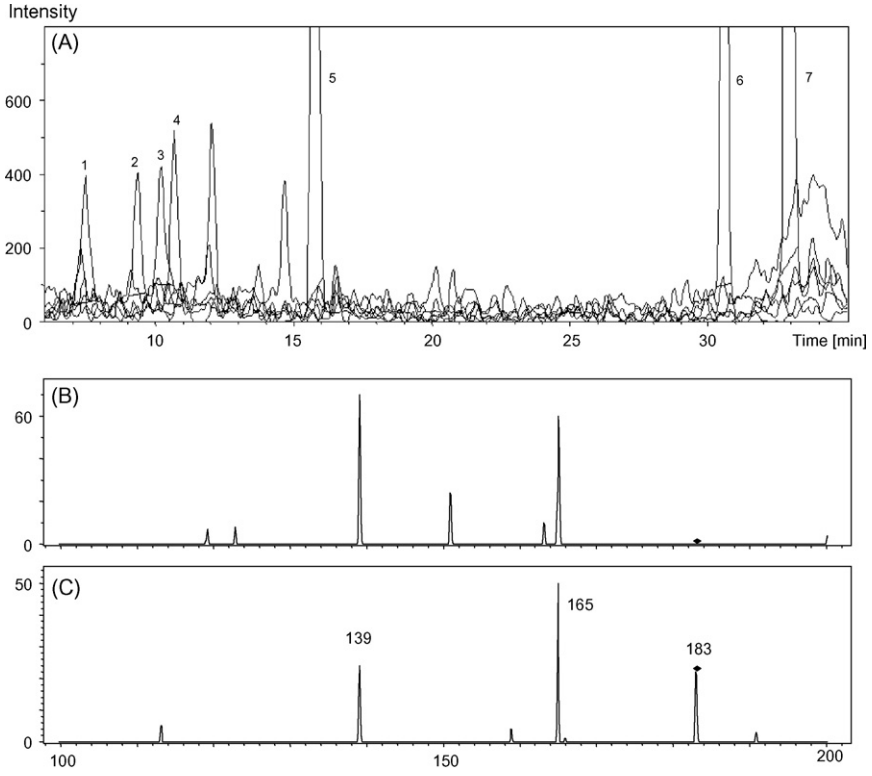


Fig. 3. (A) HPLC–MS extracted ion chromatogram of aerosol sample collected 13 August 2007 from 10 am to 12 am. Peaks: (1) *cis*-pinic acid (185 amu); (2) *cis*-pinonic acid (183 amu); (3) *trans*-pinonic acid (183 amu), (4) azelaic acid (187 amu), (5) ISTD (2,4-dichlorobenzoic acid, 189 amu), (6) palmitic acid (255 amu), (7) stearic acid (283 amu). (B) MS^2 spectrum of *cis*-pinonic acid and (C) MS^2 spectrum of *trans*-pinonic acid (cleavage of water at 165 amu and carbon dioxide at 139 amu).

Table 3
Concentrations of acids studied in aerosols in ng/m^3 ± RSD% (n = 3) of sampled air.

Sample	*cis*-Pinic acid	*cis*-Pinonic acid	*trans*-Pinonic acid	Azelaic acid	β-Caryophyllinic acid	Hexadecanoic acid
13 August 10 am–12 am	7 ± 15	28 ± 36	27 ± 19	8 ± 7	nd	40 ± 10
13 August 12 am–2 pm	–	22 ± 28	19 ± 27	8 ± 6		27 ± 14
13 August 2 pm–4 pm	–	21 ± 19	23 ± 11	8 ± 33		17 ± 15
13 August 4 pm–6 pm	–	16 ± 13	20 ± 31	7 ± 10		43 ± 14
13–14 August 6 pm–08 am	1 ± 9	18 ± 31	18 ± 24	20 ± 6		17 ± 21
14 August 08 am–10 am	–	17 ± 2	14	8 ± 19		14 ± 5
14 August 10 am–12 am	–	18 ± 21	17 ± 18	8 ± 12	56 ± 8	16 ± 2
14 August 12 am–2 pm	–	13 ± 14	13 ± 36	8 ± 19		33 ± 6
14 August 2 pm–4 pm	–	13 ± 27	14 ± 14	6 ± 38		13 ± 17
14 August 4 pm–6 pm	–	13 ± 32	12 ± 51	7 ± 8		12 ± 8
14–15 August 6 pm–08 am	–	–	–	6 ± 1		10 ± 1
15 August 08 am–10 am	–	–	–	12 ± 11		–
15 August 10 am–12 am	–	–	–	13 ± 9	42 ± 5	14 ± 40
15 August 12 am–2 pm	–	–	–	7 ± 24		23 ± 16
15 August 2 pm–4 pm	–	11 ± 24	11 ± 18	5 ± 16		14 ± 31
15 August 4 pm–6 pm	–	–	–	20 ± 5		17 ± 72
15–16 August 6 pm–08 am	–	11 ± 13	11 ± 24	5 ± 25		10 ± 42
16 August 08 am–10 am	–	–	–	7 ± 9		17 ± 41
16 August 10 am–12 am	–	–	–	7 ± 19	102 ± 10	–
16 August 12 am–2 pm	–	–	–	9 ± 16		15 ± 12
16 August 2 pm–4 pm	–	21 ± 34	15 ± 1	12 ± 13		17 ± 22
16 August 4 pm–6 pm	–	18 ± 1	–	9 ± 23		19 ± 25

chemistry. Aerosol samples have nevertheless rarely been analysed for azelaic acid. Reynolds et al. [29] have elucidated its formation from oleic acid, and also its potential to form large oligomeric structures (over 1000 Da), which are important in aerosol growth. Correlations between azelaic acid and oxidative species such as NOx, NO and ozone were not noticed here, and although a slight correlation was seen between global radiation and azelaic acid, it was not statistically significant. Clearly, more studies are needed before azelaic acid can be regarded as an important biogenic aerosol component. Although correlations between the studied compounds, aerosol growth properties and atmospheric conditions, including gas phase oxidants, were not clearly shown, the method we have developed for the collection and analysis of aerosol particles provides a valuable tool for the study of these relationships in the future.

The MS^2 analysis of PILS samples revealed the presence of one acid corresponding to the main peak in the chromatogram obtained from the ozonolysed sample of β-caryophyllene. The acid was identified as β-caryophyllinic acid. This identification is in agreement with previous work of Jaoui et al. [23]. The peaks found in two-hour PILS samples were too small to allow their integration, and thus six-hour samples were prepared by combining three samples (from 10 am to 4 pm) and evaporating them to a volume of 500 μl.

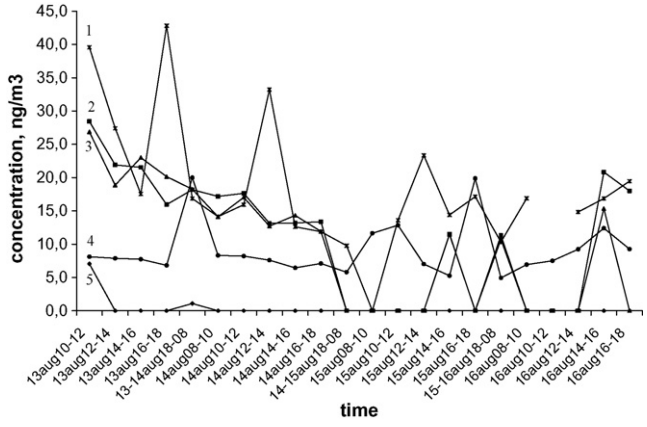


Fig. 4. Concentration trends of the studied acids in ng/m^3 of sampled air. (1) Stearic acid, (2) *cis*-pinonic acid, (3) *trans*-pinonic acid, (4) azelaic acid, and (5) *cis*-pinic acid.

Relative peak areas and the calibration curve of *cis*-pinonic acid were used for the quantitation (Table 3). Although the quantitation error, estimated with azelaic acid as reference, was about 50%, the concentration of β-caryophyllinic acid was still very high relative to the concentrations of α-pinene acids, and also the values of Jaoui et al. [23]. The reason for the disparity may be the stability of β-caryophyllinic acid, in contrast to α-pinene acids, which react to form more complex compounds after their formation. The stability of β-caryophyllinic acid was apparent in our study of various ozonolysis times in out synthesis of the acid. The ozonolysis time did not significantly affect the chromatographic profiles (HPLC–MS^2) of the samples, showing that the compound did not react further once the ozonolysis was complete. The relatively high concentrations of β-caryophyllinic acid in aerosol samples show that it is a relevant compound in atmospheric aerosol formation in boreal forest, and more detailed studies are desirable. The high concentration of the acid of sesquiterpene is not surprising in view of the results of Tarvainen et al. [30], who showed that the emission rate of β-caryophyllene may be as much as 40% of the emission rates of monoterpenes in northern Finland.

4. Conclusions

A particle-into-liquid sampler was used for the collection of atmospheric aerosols from Finnish coniferous forest. The sample pretreatment procedure with SPE for the extraction and concentration of selected organic acids was optimized, and extraction efficiencies were determined. Unfortunately, aldehydes were not successfully extracted and could not be quantified in the PILS samples. The analytical procedure, HPLC–MS, was optimized for the determination of acids. The amounts of the studied acids in atmospheric aerosol samples ranged from 1 to 40 ng/m^3 and are in the agreement with previous results. The oxidation product of β-caryophyllene, β-caryophyllinic acid was synthesised and determined in PILS samples by HPLC–MS^2. The amount of β-caryophyllinic acid ranged from 41.6 to 102.1 ng/m^3 with estimated error of 50%. Reliability of the method was moderate, and the limits of detection and quantitation were good. Our study confirmed that PILS is a highly promising collection device for aerosol samples and it, together with well-optimized sample pretreatment and analysis, can be successfully applied for the determination of acids in atmospheric aerosol particles.

Acknowledgements

This research was supported by the Academy of Finland Centre of Excellence program (project number 1118615). We are grateful to Hanna Brusin, Päivi Pöhö and Joonas Nurmi for helping in the laboratory and to Pasi Aalto from the Department of Physics for the instrument arrangements at the SMEARII station. Ilkka Kilpeläinen is thanked for his help with oxidation reaction mechanisms and Heikki Junninen for providing the meteorological data.

References

[1] M. Kulmala, I. Riipinen, M. Sipilä, H.E. Manninen, T. Petäjä, H. Junninen, M. Dal Maso, G. Mordas, A. Mirme, M. Vana, A. Hirsikko, L. Laakso, R.M. Harrison, I. Hanson, C. Leung, K.E.J. Lehtinen, V.-M. Kerminen, Science 318 (5847) (2007) 89–92.
[2] T.X.-P. Zhao, H. Yu, I. Laszlo, M. Chin, W.C. Conant, J. Quant. Spectrosc. Radiat. Transf. 109 (7) (2008) 1162–1186.
[3] U. Lohmann, J. Feichter, Atmos. Chem. Phys. 5 (2005) 717–737.
[4] J.L. Jimenez, J. Jayne, Q. Shi, C.E. Kolb, D.R. Worsnop, I. Yourshaw, J.H. Seinfeld, R.C. Flagan, X. Zhang, K.A. Smith, J.W. Morris, P. Davidovits, J. Geophys. Res. 108 (2003) 8425–8438.
[5] F. Drewnick, S. Hings, P. DeCarlo, J. Jayne, M. Gonin, K. Fuhrer, S. Weimer, J. Jimenez, K. Demerjian, S. Borrmann, D. Worsnop, Aerosol Sci. Technol. 39 (2005) 637–658.
[6] R.J. Weber, D. Orsini, Y. Daun, Y.-N. Lee, P.J. Klotz, F. Brechtel, Aerosol Sci. Technol. 35 (3) (2001) 718–727.
[7] D.A. Orsini, Y. Ma, A. Sullivan, B. Sierau, K. Baumann, R.J. Weber, Atmos. Environ. 37 (9/10) (2003) 1243–1259.
[8] A.P. Sullivan, R.J. Weber, A.L. Clements, J.R. Turner, M.S. Bae, J.J. Schauer, Geophys. Res. Lett. 31 (2004) L13105, doi:10.1029/2004GL019681.
[9] J. Parshintsev, R. Räsänen, K. Hartonen, M. Kulmala, M.-L. Riekkola, Bor. Environ. Res. 14 (2009) 630–640.
[10] T. Rissanen, T. Hyötyläinen, M. Kallio, J. Kronholm, M. Kulmala, M.-L. Riekkola, Chemosphere 64 (7) (2006) 1185–1195.
[11] P. Anttila, T. Hyötyläinen, A. Heikkilä, M. Jussila, J. Finell, M. Kulmala, M.-L. Riekkola, J. Sep. Sci. 28 (2005) 337–346.
[12] M. Kallio, T. Hyötyläinen, M. Lehtonen, M. Jussila, K. Hartonen, M. Shimmo, M.-L. Riekkola, J. Chromatogr. A 1019 (1/2) (2003) 251–260.
[13] A. Asa-Awuku, A.P. Sullivan, C.J. Hennigan, R.J. Weber, A. Nenes, Atmos. Chem. Phys. 8 (2008) 799–812.
[14] K. Kawamura, H. Kasukabe, Atmos. Environ. 30 (1996) 1709–1722.
[15] T. Moise, Y. Rudich, J. Phys. Chem. 106 (2002) 6469–6476.
[16] P.J. Ziemann, Faraday Discuss. 130 (2005) 469–490.
[17] O. Hellmuth, Atmos. Chem. Phys. 6 (2006) 4253–4274.
[18] K.E. Huff Hartz, J.E. Tischuk, M.N. Chan, C.K. Chan, N.M. Donahue, S.N. Pandis, Atmos. Environ. 40 (2006) 605–617.
[19] A. Kubatova, R. Vermeylen, M. Claeys, J. Cafmeyer, W. Maenhaut, G. Roberts, P. Artaxo, Atmos. Environ. 34 (2000) 5037–5051.
[20] G. Wang, S. Niu, C. Liu, L. Wang, Atmos. Environ. 36 (2002) 1941–1950.
[21] A. Asa-Awuku, G.J. Engelhart, B.H. Lee, S.N. Pandis, A. Nenes, Atmos. Chem. Phys. 9 (2009) 795–812.
[22] J. Parshintsev, J. Nurmi, I. Kilpeläinen, K. Hartonen, M. Kulmala, M.-L. Riekkola, Anal. Bioanal. Chem. 390 (2008) 913–919.
[23] M. Jaoui, M. Lewandowski, T.E. Kleindienst, J.H. Offenberg, E.O. Edney, Geophys. Res. Lett. 34 (2007) L05816, doi:10.1029/2006GL028827.
[24] M. Glasius, A. Calogirou, N.R. Jensen, J. Hjorth, C.J. Nielsen, Int. J. Chem. Kinet. 29 (1997) 527–533.
[25] M. Kulmala, K. Hämeri, P.P. Aalto, J. Mäkelä, L. Pirjola, E.D. Nilsson, G. Buzorius, U. Rannik, M. Dal Maso, W. Seidl, T. Hoffmann, R. Janson, H.-C. Hansson, Y. Viisanen, A. Laaksonen, C. O'Dowd, Tellus 53B (2001) 324–343.
[26] M.-C. Reinnig, L. Müller, J. Warnke, T. Hoffmann, Anal. Bioanal. Chem. 391 (2008) 171–182.
[27] A. Römpp, R. Winterhalter, G.K. Moortgat, Atmos. Environ. 40 (2006) 6846–6862.
[28] J. Warnke, R. Bandur, T. Hoffmann, Anal. Bioanal. Chem. 385 (2006) 34–45.
[29] J.C. Reynolds, D.J. Last, M. McGillen, A. Nijs, A.B. Horn, C. Percival, L.J. Carpenter, A.C. Lewis, Environ. Sci. Technol. 40 (2006) 6674–6681.
[30] V. Tarvainen, H. Hakola, H. Hellén, J. Bäck, P. Hari, M. Kulmala, Atmos. Chem. Phys. 5 (2005) 989–998.

Talanta 80 (2010) 1177–1182

Contents lists available at ScienceDirect

Talanta

journal homepage: www.elsevier.com/locate/talanta

Task-specific ionic liquid trioctylmethylammonium salicylate as extraction solvent for transition metal ions

Vladimir M. Egorov, Dmitry I. Djigailo, Dmitry S. Momotenko, Denis V. Chernyshov, Irina I. Torocheshnikova, Svetlana V. Smirnova, Igor V. Pletnev*

Department of Chemistry, M.V. Lomonosov Moscow State University, 1/3 Leninskiye gory, 119992 Moscow, Russia

ARTICLE INFO

Article history:
Received 22 June 2009
Received in revised form 30 August 2009
Accepted 3 September 2009
Available online 9 September 2009

Keywords:
Ionic liquids
Solvent extraction
Transition metals
Voltammetric analysis

ABSTRACT

A quaternary ammonium-based room temperature ionic liquid trioctylmethylammonium salicylate (TOMAS) has been studied as an extractant of transition metal ions (Fe^{3+}, Cu^{2+}, Ni^{2+}, Mn^{2+}) in aqueous solutions. The effect of pH value on the recovery of metal ions has been investigated. The mechanism of extraction into the ionic liquid has been proposed. The possibility of stripping voltammetric determination of transition metals in aqueous solutions using TOMAS-modified electrodes has been demonstrated.

© 2009 Elsevier B.V. All rights reserved.

1. Introduction

Ionic liquids (ILs, low-melting organic salts) have been widely employed in liquid–liquid extraction for about a decade, since the first report by Rogers and co-workers [1]. Ionic liquids are growingly popular because of a combination of unique properties [2]. Though their widely declared environmentally friendliness may be over-estimated [3,4], a promising possibility of tuning of solvent properties by modification of IL cation or anion is beyond any doubt [5,6]. Such tuning may enable to find not only ILs with desirable physicochemical properties (density, viscosity, mutual miscibility with other solvents) but also ILs adjusted for particular applications (task-specific ionic liquids).

It has been reported that ionic liquids can be used in solvent extraction of metal ions. There exist two different approaches in the field. The first approach is using ILs as inert diluents for reagent-assisted extraction, while the second one implies that IL serves as a complexing reagent itself due to a presence of appropriate functionalities in either cationic or anionic component. Crown ether assisted extraction of alkali and alkaline earth metal ions [7–11] is a typical example of the former approach. The use of other IL/complexing reagents for heavy metals extraction has also been reported [12–20]. Several task-specific ILs (TSILs) incorporating complexing functionality have been reportedly used for extraction of metal ions representing the second approach [21–26].

Typically, TSILs bear complexing groups in cationic (imidazolium-based) part that makes them relatively expensive and difficult to synthesize. An attractive alternative may be ILs, which contain complexing anions, in particular, tetraalkylammonium carboxylates. Many carboxylates are known to strongly bind metal ions. Several tetraalkylammonium-based ILs (including carboxylates) obtained from commercially available Aliquat® 336 have been reported (see, e.g. [27]). Noteworthy is mentioning that an Aliquat-based thiosalicylate IL has been previously reported [28] as an extractant for metal ions. However, no detailed study of extraction has been published to the best of our knowledge.

Herein, we report on the study of extraction of transition metal ions into newly obtained task-specific IL trioctylmethylammonium salicylate (TOMAS). It is important that both starting substances used for TOMAS synthesis are readily available and inexpensive, and the procedure of synthesis is quite easy.

2. Experimental

2.1. Reagents and solutions

Aliquat® 336 (Aldrich; 2:1 mol/mol mixture of methyltrioctyl- and methyltridecylammonium chloride), sodium salicylate (Panreac, USP), chloroform (Ekros, Russia), ethanol, tetrahydrofurane (analytical reagent grade) were used as received. Transition metal salt solutions, $Fe_2(SO_4)_3$, $Cu(NO_3)_2$, $NiCl_2$, $Cr_2(SO_4)_3$, $CoSO_4$, $ZnSO_4$,

* Corresponding author. Tel.: +7 495 939 5464; fax: +7 495 939 4675.
E-mail address: pletnev@analyt.chem.msu.ru (I.V. Pletnev).

0039-9140/$ – see front matter © 2009 Elsevier B.V. All rights reserved.
doi:10.1016/j.talanta.2009.09.003

and $MnCl_2$, were prepared by dissolving a weighted amount of a salt in distilled water. All transition metal salts were of analytical reagent grade. Aqueous ammonia, sulfosalicylic acid, 4-(2-pyridylazo)resorcinol, murexide, borate buffer (all of analytical reagent grade) were used for spectrophotometrical determination of metal ions. For adjusting pH values of aqueous phase, 0.05–3 M H_2SO_4 (analytical reagent grade) was used. Potassium hydroxide and chloride were of analytical reagent grade.

2.2. Synthesis of TOMAS

Aliquat® 336 (~0.2 mol) was mixed with 30% excess amount of sodium salicylate in 200 mL of chloroform. The mixture was shaken for 4 h and then rinsed with large amount of distilled water 20 times. After that solvent was evaporated in rotary evaporator and remained liquid was heated up to 100 °C under reduced pressure for 5 h. After cooling to room temperature white solid was obtained. ^{1}H NMR ($CDCl_3$, δ/ppm relative to TMS): 0.88 (t; 9 H), 1.24 (m; 30 H), 1.59 (m; 6 H), 3.19 (s; 3 H), 3.27 (m; 6 H), 6.70 (t; 1 H), 6.81 (d; 1 H), 7.20 (t; 1 H), 7.92 (d; 1 H). ^{13}C NMR (126 MHz, DMSO-d6, δ/ppm relative to TMS): 13.80 (C^*H_3C); 21.93 ($C^*H_2CH_3$); 21.25, 25.68, 28.27, 28.32, 31.04 (various CH_2CH_2); 47.41 (CH_3N); 60.50 (CH_2N); 115.35, 115.62, 120.73, 129.73, 130.88 (aromatic C); 163.17 (COH); 171.00 (COO). Density 0.943 g cm^{-3}. $T_m = (32.8 \pm 0.4)$ °C, $T_f = (14 \pm 2)$ °C. ^{1}H and ^{13}C NMR data were recorded with NMR spectrometer DRX500 (Bruker, Germany). After being equilibrated with water the compound becomes slightly yellowish viscous liquid with density 0.942 g mL^{-1} that does not freeze at least to −18 °C. Found water content is ca. 0.18 wt.% (0.09 M) and 4.83 wt.% (2.52 M) (Karl Fisher titration) for solid and equilibrated with water liquid compound, respectively.

2.3. Extraction procedure

Extraction experiments were performed by adding 0.5 mL of water-equilibrated TOMAS to 2.5 mL of aqueous solutions of transition metal salt (in the case of extraction of Mn^{2+}, 1.0 mL to 1.0 mL, respectively). The two-phase systems were shaken for the time necessary to reach the extraction equilibrium (15 min for Fe^{3+}, 25 min for Cu^{2+} and Mn^{2+}, 30 min for Ni^{2+}). After centrifugation for 30 min the necessary volume of aqueous phase was taken, and pH value was measured (pH-meter pH-410; combined glass microelectrode ESLK-13.7, Akvilon, Russia). Aqueous phase was diluted if necessary. The recovery (R, %) and the distribution ratio (D) of a metal ion were calculated using the Eqs. (1) and (2):

$$R(\%) = \left(1 - \frac{C_w}{C_w^0}\right) \times 100\%, \quad (1)$$

$$D = \frac{C_0}{C_w} = \frac{R}{100 - R} \times \frac{V_w}{V_0}, \quad (2)$$

where C_w^0 and C_w are the initial and equilibrium concentrations of the metal ion in aqueous phase, respectively, V_w and V_0 denote the volumes of aqueous and organic phases, respectively (mL). Metal ion concentrations were measured in aqueous phase using spectrophotometric techniques [29–31]. For determination of Fe^{3+}, aqueous solution of sulfosalicylic acid (0.6 mL, 5 wt.%) was added to 1.0 mL of aqueous phase; then aqueous ammonia (5 wt.%) and water were added to the total volume 3.0 mL (pH ~10). Absorbance was measured after 15 min at 423 nm. Determination of Mn^{2+} was performed by adding 2.4 mL of borate buffer (pH = 9.18), 0.3 mL of 4-(2-pyridylazo)resorcinol solution (0.05 wt.%) to 0.3 mL of aqueous phase; absorbance was measured at 500 nm after 10 min. Nickel (II) was determined by addition of 1.6 mL of murexide, 0.4 mL of aqueous ammonia (2%) to 0.3 mL of aqueous phase. Absorbance was measured after 24 h at 450 nm. Spectrophotometric measurements were performed with U-2900 UV–vis Recording Spectrophotometer (Hitachi, Japan), 1 cm quartz cells, after 30 min centrifugation of samples. The content of copper ions Cu^{2+} in aqueous phases was determined with atomic absorption spectrometer AAS Kvant-2A (Kortek, Russia).

2.4. The processing of Fe(III) loaded systems

These experiments were conducted by adding 4 mL of water-saturated TOMAS to 20 mL of aqueous solutions of $Fe_2(SO_4)_3$ (with $C_0(Fe) = 1 \times 10^{-1}$ and 2×10^{-1} M) and shaking of the systems for 15 min. After centrifugation (1 h) the phases were separated; two portions of aqueous phase (15 and 3 mL) were collected. The 3 mL portions were used for measuring pH, for determination of residual metal concentrations, and for spectral measurements. The 15 mL ones were placed into preliminary weighted round-bottom flasks and water was evaporated. After cooling down to room temperature in desiccators, the solid residues were weighed. The nitrogen content was determined by Kjeldahl's method.

A small sample was taken from each extract to determine nitrogen and sulphur by means of element organic analysis (Kjeldahl's method for nitrogen and gravimetric in the form of $BaSO_4$ for sulphur).

The acidity of extract was determined directly by potentiometric titration. The extracts were diluted by $CHCl_3$ to total volumes equal to 25 mL, rinsed 5 times by 50 mL of distilled water to remove possible admixtures of H_2SO_4, then aliquots (0.5 mL) of obtained solutions were dissolved in 30 mL of ethanol and titrated by 0.01 M aqueous KOH (pH-meter pH-410; combined glass microelectrode ESLK-13.7, Akvilon, Russia).

2.5. The study on separation of Fe(III) in synthetic samples

Two synthetic samples (10 mL) containing 1×10^{-3} M Fe^{3+} and equal molar concentrations of Ni^{2+}, Cr^{3+}, Co^{2+}, Zn^{2+}, Mn^{2+} (1×10^{-3} and 1×10^{-2} M) were shaken with 2 mL of water-saturated TOMAS for 2 h. After centrifugation (30 min), the residual concentrations of metals were determined with ICP-MS instrument Agilent 7500 (Agilent Technologies, USA).

2.6. Electrochemical apparatus and measurements

Screen-printed electrodes (SPE) were purchased form "RuSens" (Moscow, Russia). Three electrodes (work, counter and reference) were printed on the polyester substrate. Work and counter electrodes were fabricated using graphite paste (graphite powder dispersed in polymeric matrix); Ag/AgCl paste was used as reference electrode.

Electrochemical measurements were performed using "Intelligent Potentiostatic Control" IPC-Compact version 8.60× (Cronas Ltd., Russia).

For preparation of SPE-modifying compositions, weighed quantities of spectral pure (99.999%) high dispersion (<100 μm) graphite powder and TOMAS in a ratio 1:1 by weight were mixed intensively in tetrahydrofurane (THF); after full evaporation of THF the viscous composition was obtained. Actual amount of modifier was determined gravimetrically; average total mass of modifying composition was 0.5 mg.

For preparation of supporting electrolyte, potassium chloride was utilized as component for reference electrode potential stabilization while sulphuric acid was applied to regulate pH. Aqueous Fe(III) solutions were prepared by dissolving a weighed amounts of $Fe_2(SO_4)_3$ in supporting electrolyte.

Pre-concentration of Fe(III) in modifying layer of TOMAS-based graphite paste was performed under open circuit during 10 min of mechanical mixing of examined solutions. For performing the

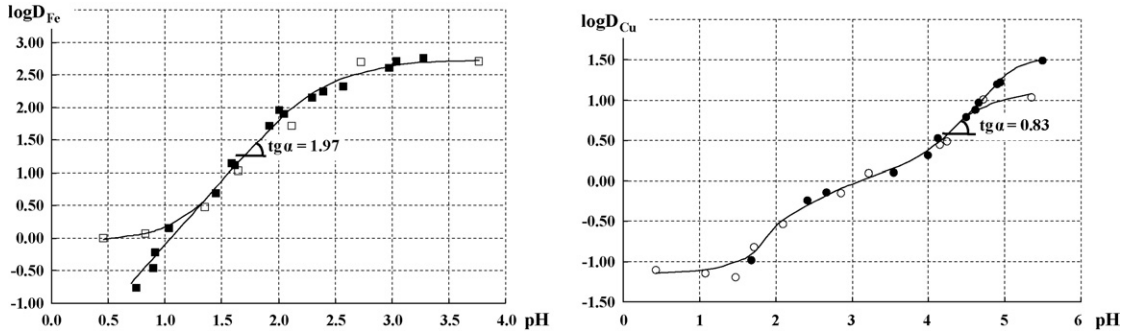


Fig. 1. The effect of pH on distribution ratio of Fe^{3+} and Cu^{2+} (■, Fe^{3+} 1×10^{-3} M; □, Fe^{3+} 1×10^{-4} M; ●, Cu^{2+} 1×10^{-3} M; ○, Cu^{2+} 1×10^{-4} M).

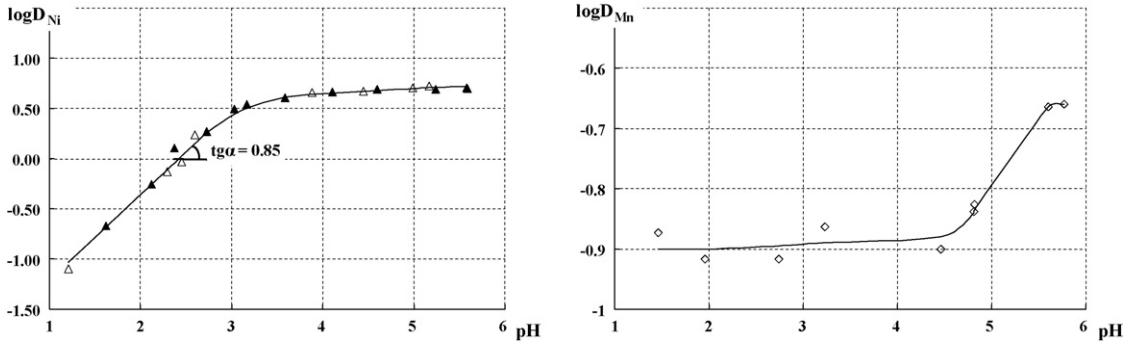


Fig. 2. The effect of pH on distribution ratio of Ni^{2+} and Mn^{2+} (△, Ni^{2+} 1×10^{-4} M; ▲, Ni^{2+} 1×10^{-3} M; ◊, Mn^{2+} 1×10^{-4} M).

stripping voltammetry, pre-reduction potential of −1.0 V during 1 min was applied. The potential scan was from −1.0 V to +1.0 V with scan rate of 100 mV/s.

3. Results and discussion

Iron(III) and copper(II) represent the most straightforward choice of metal ions for efficient recovery by TOMAS, because they are known to form stable salicylate complexes. In contrast, Ni^{2+} and Mn^{2+} form much less stable complexes, hence they were chosen to illustrate the effect of complex stability on the extraction.

The dependencies of distribution ratios for copper(II) and iron(III) on pH of aqueous solution are presented in Fig. 1.

As can be seen, in the absence of any additional reagents TOMAS effectively extracts Fe^{3+} and Cu^{2+} (99% and 89% for 1×10^{-3} M, respectively; note that the recovery values are given for phase volume ratio $V_{IL}:V_W = 1:5$). The pH-profiles of extraction have the characteristic shape with sharp decrease in log D at acidic media. The decrease may be explained by dissociation of salicylate complexes due to protonation of salicylate. In alkaline media the extraction has not been studied by reason of the precipitation of metal hydroxides.

The maximal distribution ratio of Fe^{3+} (log D = 2.70, pH 3.0, 1×10^{-3} M) into TOMAS is considerably higher than that of Cu^{2+} (1.49, pH 5.5, 1×10^{-3} M). Also, pH_{50} value of Fe^{3+} (1.45) is significantly lower than that of Cu^{2+} (4.36). This is in agreement with the fact that stability constants for mono- and disalicylate complexes of Fe^{3+} are higher than those of Cu^{2+} [32,33].

The pH-dependences of Ni^{2+} recovery have the shape similar to that found for Fe^{3+} and Cu^{2+} (Fig. 2). A rather different profile is observed for Mn^{2+} recovery, which may be explained by an instability of manganese salicylates.

As can be seen, the extraction efficiency ($\log D_{max}$, pH_{50}) is in good agreement with the stability constants of salicylate complexes with corresponding metal ions (Tables 1 and 2).

Table 1
Maximal distribution ratios, pH_{50} values, slopes of $\log D = f(pH)$ dependencies and stability constants [32] of salicylate complexes for the studied metal ions.

Metal ion	C_{Me} (M)	$\log D_{max}$	pH_{50}	Slope	$\log \beta_1$	$\log \beta_2$	$\log \beta_3$
Fe^{3+}	1×10^{-4} 1×10^{-3}	2.70	1.45	1.97	15.35	27.20	36.27
Cu^{2+}	1×10^{-4} 1×10^{-3}	1.03 1.49	4.36	0.83	12.02	20.70	–
Ni^{2+}	1×10^{-4} 1×10^{-3}	0.70	4.99	0.85	6.95	11.75	–
Mn^{2+}	1×10^{-4} 1×10^{-3}	−0.17 −0.49	–	–	5.90	9.80	–

We studied the mechanism of extraction of Fe^{3+} into TOMAS in details. The information about the composition of iron complex in the IL and aqueous phases was obtained from UV–vis spectra of corresponding phases. Organic samples were diluted with ethanol before measurements. As was reported by Babko [34], Fe^{3+} forms three types of complexes with salicylic acid in aqueous solutions (here and below the following notation is used: H_2Sal = *o*-$C_6H_4(OH)COOH$, $HSal^-$ = *o*-$C_6H_4(OH)COO^-$,

Table 2
The characteristics of salicylate complexes of iron(III) in aqueous solution [34].

Specie	Color	λ_{max} (nm)	ε_{max} (L/(mol cm))	Range of pH of complex formation
$[FeSal]^+$	Violet	510	900	<5
$[FeSal_2]^-$	Red	470	1800	2.5–8
$[FeSal_3]^{3-}$	Yellow	–	–	>8

$Sal^{2-} = o\text{-}C_6H_4(O^-)COO^-$):

$$Fe^{3+} + H_2Sal \Leftrightarrow [FeSal]^+ + 2H^+;$$

$$[FeSal]^+ + HSal^- \Leftrightarrow [FeSal_2]^- + H^+ \quad \text{or}$$
$$[FeSal]^+ + Sal^{2-} \Leftrightarrow [FeSal_2]^-;$$

$$[FeSal_2]^- + Sal^{2-} \Leftrightarrow [FeSal_3]^{3-}.$$

The other authors [33,35,36] reported on the formation of only monosalicylate complex $[FeSal]^+$. In all the cases, the value of $\lambda_{max} = 530$ nm is attributed to the monosalicylate complex.

In our extraction system, absorbance spectra of aqueous phases after extraction have maxima at 298 and 530 nm, which correspond to salicylate ion and monosalicylate complex of iron $[FeSal]^+$, respectively. Interestingly, the maximum absorbance decreases during 15 min of phase contact and then remains constant. Maximum of absorbance of IL phase spectrum is observed at 465 nm, suggesting a presence of iron bisalicylate complex in the extract.

Thus, the proposed mechanism of Fe^{3+} extraction into TOMAS includes the following steps:

a) Partial dissolution of TOMAS in aqueous phase:

$$TOMA^+HSal^-_{(O)} \Leftrightarrow TOMA^+_{(W)} + HSal^-_{(W)}$$

(as it was previously [37] established, the solubility of TOMAS in water is 2×10^{-4} mol L^{-1});

b) Formation of complex:

$$Fe^{3+}_{(W)} + HSal^-_{(W)} \Leftrightarrow FeSal^+_{(W)} + H^+_{(W)};$$

c) Extraction of ion pair:

$$FeSal^+_{(W)} + HSO^-_{4(W)} \Leftrightarrow [FeSal^+HSO^-_4]_{(O)}$$

(hydrosulfate comes from source Fe^{3+} salt);

d) Addition of the second salicylate in IL phase:

$$[FeSal^+HSO^-_4]_{(O)} + HSal^-_{(O)} \Leftrightarrow FeSal^-_{2(O)} + HSO^-_{4(O)} + H^+_{(W)}.$$

The total extraction equilibrium may be represented as follows:

$$Fe^{3+}_{(W)} + 2TOMA^+HSal^-_{(O)} + HSO^-_{4(W)}$$
$$\Leftrightarrow TOMA^+[FeSal_2]^-_{(O)} + TOMA^+HSO^-_{4(O)} + 2H^+_{(W)}. \quad (3)$$

This equation assumes the release of two protons that is in good agreement with the observed slope of pH-profile of Fe^{3+} extraction (≈2, Fig. 1).

As it is seen from Fig. 1, pH-profiles of Fe^{3+} extraction for $C_0(Fe) = 1 \times 10^{-4}$ and 1×10^{-3} M match each other, except strong-acidic medium (pH < 1.5). In wide range of initial concentrations of Fe^{3+} (1×10^{-4}–1×10^{-1} M) the metal ion (Fe^{3+}) is recovered almost quantitatively (at $V_{IL}:V_W = 1:5$, pH = 2.5–3.0) with average value of $\log D_{Fe}$ being equal to 2.7 (Fig. 3).

However, in the case of $C_0(Fe) = 2 \times 10^{-1}$ M, the recovery of iron drops to 81%. This fact may be attributed to the limited extraction capacity of TOMAS. Indeed, according to Eq. (3) 1 mL of TOMAS may extract 8.40×10^{-4} mol of Fe^{3+}, which corresponds to recovery of 84% (from 2×10^{-1} M Fe^{3+} solution), in a nice agreement with the experiment.

The Fe^{3+} extracts and aqueous phases (for $C_0(Fe) = 1 \times 10^{-1}$ and 2×10^{-1} M) were analyzed (elemental composition, titratable acidity, Fe and $TOMA^+$ content) to further verify the proposed mechanism of extraction (Table 3).

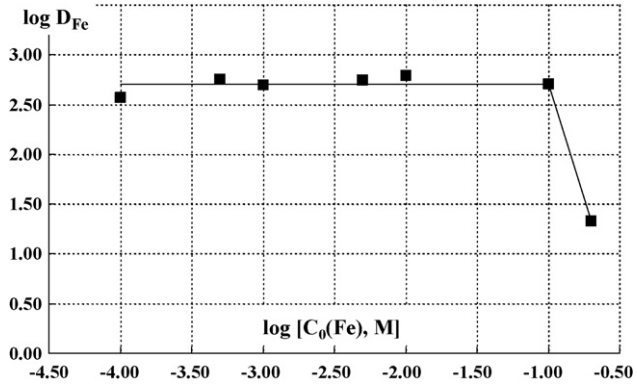


Fig. 3. The dependence of distribution ratio of Fe^{3+} on its initial concentration in aqueous phase.

One can see that the acidic protons found in extracts do belong to HSO_4^-, since they are in equimolar amount to sulphur determined *ibidem*. Calculated by Eq. (3) and actually found in extracts molar S/N-ratios are also in excellent agreement.

As to the extraction of divalent metal ions, the general two-phase equilibrium may be represented as follows:

$$Me^{2+}_{(W)} + TOMA^+HSal^-_{(O)} + HSO^-_{4(W)}$$
$$\Leftrightarrow MeSal_{(O)} + TOMA^+HSO^-_{4(O)} + H^+_{(W)}, \quad (4)$$

where Me^{2+} is Cu^{2+}, Ni^{2+}, and Mn^{2+}. The slopes of the dependencies $\log D_{Cu} - pH$ and $\log D_{Ni} - pH$, both close to 1, which is indicative of mode (4). As to the dependency $\log D_{Mn} - pH$ (0.25), it may be difficult to identify a characteristic slope because of low Mn^{2+} recovery.

We studied the selectivity of iron extraction in our TOMAS-based system. We have determined the separation factors of Fe^{3+} (1×10^{-3} M) with respect to the commonly coexisting metal ions (Cr^{3+}, Ni^{2+}, Mn^{2+}, Zn^{2+}, and Co^{2+}) at different ratios Fe: interfering ions. For equal concentrations of Fe^{3+} and other ions the separation factors are as follow: Fe/Mn 490, Fe/Co 387, Fe/Zn 382, Fe/Ni 370, Fe/Cr 62 (pH 2.60). For the ten fold excess of foreign metal ions, the factors are: Fe/Mn 142, Fe/Co 108, Fe/Zn 105, Fe/Ni 90, Fe/Cr 13 (pH 2.35). As is seen, the separation factors are rather high (with the exception of Fe/Cr pair; still, this separation factor is quite significant).

Noteworthy is mentioning that Papp and Inczédy [38] 35 years ago actually used TOMAS in a trichloromethane solution (that is, solely as a complexing reagent rather than solvent) for the recovery

Table 3
The composition of aqueous and organic phases after extraction as calculated according to Eq. (3) and found experimentally ($V_{IL} = 4$ mL; $V_W = 20$ mL).

	C_0(Fe)	
	1×10^{-1} M	2×10^{-1} M
Fe content, mol, calc.	2.00×10^{-3}	3.36×10^{-3}
Fe content, mol, found	1.98×10^{-3}	3.24×10^{-3}
$C(TOMA^+_W)$, M, found	$<3 \times 10^{-4}$ [a]	5.6×10^{-3}
$n(TOMA^+HSO^-_{4(O)})$, mol, calc.	1.98×10^{-3}	3.24×10^{-3}
n (acidic H in extract), mol, found	$(2.12 \pm 0.08) \times 10^{-3}$, $S_r = 0.1$, $n = 4$, $P = 0.95$	$(3.7 \pm 0.4) \times 10^{-3}$, $S_r = 0.3$, $n = 3$, $P = 0.95$
S/N-ratio in extract, calc.	1:3.39	1:2.07
S/N-ratio in extract, found	1:3.18	1:1.88
n (S in extract), mol, found	2.11×10^{-3}	3.57×10^{-3}

[a] The limit of determination of nitrogen by means of element organic analysis (by Kjeldahl's method) was 0.2 wt.%, which corresponds in this case to 3×10^{-4} M of $TOMA^+$ in aqueous phase.

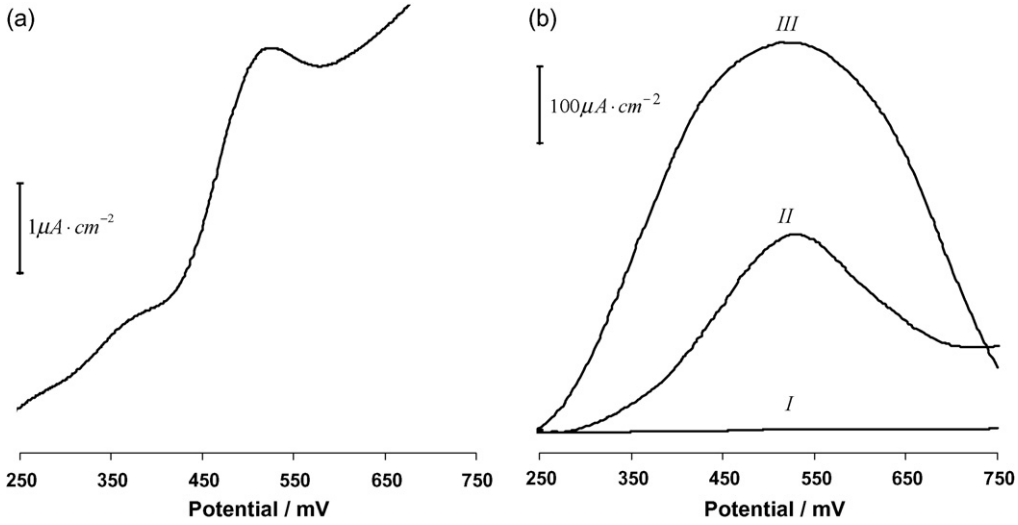


Fig. 4. Linear scan stripping voltammograms in aqueous solutions of 1×10^{-7} M Fe(III) at bare SPE (a and b, curve I); 1×10^{-7} M Fe(III) and 1×10^{-5} M Fe(III) (b, curves II and III, respectively) at TOMAS-modified SPE. Supporting electrolyte: 0.01 M H_2SO_4, 0.01 M KCl. Pre-concentration under an open circuit during 10 min under mixing. Pre-reduction potential is −1.0 V, the time is 1 min. The potential scanned from −1.0 V to +1.0 V, scan rate 100 mV/s.

of copper from aqueous solution in the presence of salicylate. The maximal $\log D_{Cu}$ they reported was 1.5 (at $C(NaHSal)_{W,0} = 0.10$ M and pH = 6), which is very close to our data (at the same values of pH and $C_0(Cu)$). However, our IL-based extraction system does not require any addition of salicylate to aqueous solution prior extraction and does not require the use of molecular solvent, $CHCl_3$.

Extraction of iron and copper with TOMAS may be favorably compared to other reported conventional solvent extraction systems, which use the reagents related to TOMAS constituents—amine/ammonium-based ion exchangers or salicylic acid.

For example, the authors of [39] described the extraction of copper(II) with Amberlite® LA-2 (a mixture of long-chain secondary amines) in thiocyanate form dissolved in isobutyl methyl ketone. However, there were serious problems associated with the necessity of ammonium thiocyanate addition to the aqueous solutions before extraction (to adjust its concentration equal to 0.06 M), emission of volatile and hazardous secondary amines (besides ketone), and, finally, low selectivity of extraction (especially, with respect to zinc). Methyldioctylamine, methyltrioctylammonium chloride, Amberlite® LA-1, Amberlite® LA-2, and trioctylamine were used for copper(II) recovery from hydrohalogenic media into benzene and xylene [40] and 1,2-dichloroethane [41]. Methyldioctylamine-based system demonstrated insufficient recovery of Cu^{2+}, while systems based on methyltrioctylammonium chloride, Amberlite® LA-1, and Amberlite® LA-2 showed a very low selectivity with respect to the common coexisting metal ions. The drawbacks also include a volatility of amine-based reagents themselves and the fact that a high recovery is achieved only in strongly acidic media. The last is also true for the iron(III) extraction into benzene with Aliquat® 336 (additionally, the problems with selectivity were also reported) [42].

Aggett et al. [43] investigated iron(III) recovery from aqueous solutions into tributylphosphate in the presence of salicylic acid. The maximum achieved $\log D_{Fe}$ was less than 1.0, which is almost two orders of magnitude lower than in the case of TOMAS. Moreover, the registered pH-profiles demonstrate very narrow range of optimal extraction (less than 0.5 pH units). The same disadvantage was also noted by Sonawale et al. [44] who studied the extraction of copper(II) from aqueous solutions into solutions of tributylphosphine oxide (TBPO) in toluene in the presence of sodium salicylate. The quantitative recovery of copper was reached only in the very narrow pH range, 2.9–3.1.

Finally, compared to all above described cases (and to other cases involving recovery of copper and iron with effective and/or selective complexing reagents, e.g. [45,46]), extraction with TOMAS looks advantageous as it totally eliminates the need in organic solvent.

As many other extraction reagents, TOMAS may be employed in various other analytical applications besides the separation and pre-concentration. One of the most obvious options is electrochemical determination of (efficiently extracted) metal ions with TOMAS-modified electrodes.

We found that combining TOMAS with conductive matrix (carbon-based materials; similar approach was described in [47]) in an appropriate proportion yields a viscous composition suitable for modification of the work-electrode surface and further electrochemical detection of appropriate metals.

In a model experiment, we compared the efficiency of analytical signal (current density) increase for bare and chemically modified screen-printed electrodes (SPE) in Fe(III) aqueous solutions in a chosen support electrolyte; linear scan stripping voltammetry was used (see Fig. 4). As is seen, in both cases the well-defined peaks of oxidative current have been obtained at approx 0.55 V (vs. Ag/AgCl reference electrode) which is well-known as characteristic redox-potential for Fe(II)/Fe(III) couple [32]. Nevertheless, in the case of TOMAS-modified SPE the absolute value of current density for the same 1×10^{-7} M concentration of Fe(III) (5.6 ppb) is much higher and, naturally, the signal increases with increase of analyte concentration (cf. Fig. 4a and b). Such an improvement of sensitivity cannot be associated solely with the enlargement of effective work-electrode surface because only a very negligible amount of graphite paste was used for modification. Evidently, the combination of highly efficient pre-concentration under an open circuit with further pre-reduction takes place. The principal possibility of the electrochemical determination of transition metals in aqueous solutions at TOMAS-modified electrodes has been clearly demonstrated.

4. Conclusion

In conclusion, a novel tetraalkylammonium-based ionic liquid TOMAS has been found to be a highly efficient extraction solvent for

recovery of some transition metal ions from aqueous solutions (99% for Fe^{3+} and 89% for Cu^{2+}, $V_{IL}:V_w = 1:5$, $C_w^0 = 1 \times 10^{-3}$ M). From the results obtained in the present work, it is seen that TOMAS extracts metal ions in the form of salicylate complexes. The extraction efficiency is directly related to the stability constants of corresponding salicylate complexes (this may be used for the separation of transition metal ions based on the different stability of salicylate complexes). The pre-concentration of Fe^{3+} or Cu^{2+} in voltammetric analysis may also be achieved with the use of TOMAS. The principal possibility of a sensitive electrochemical determination of Fe^{3+} in aqueous solutions at TOMAS-modified electrodes has been demonstrated.

Acknowledgements

The authors are grateful to Prof. S.I. Petrov for Karl Fischer titration and to Prof. S.M. Leschev (Belarussian State University, Minsk, Republic of Belarus) for valuable discussions. This work was partially funded by the Russian Foundation for Basic Research (grant no. 08-03-91319), and INTAS (grant no. 05-1000008-8020).

References

[1] J.G. Huddleston, H.D. Willauer, R.P. Swatloski, A.E. Visser, R.D. Rogers, Chem. Commun. (1998) 1765.
[2] I.V. Pletnev, S.V. Smirnova, K.S. Khachatryan, V.V. Zernov, Russ. Chem. J. 58 (2004) 51.
[3] R.P. Swatloski, J.D. Holbrey, S.B. Memon, G.A. Caldwell, K.A. Caldwell, R.D. Rogers, Chem. Commun. (2004) 668.
[4] R.P. Swatloski, J.D. Holbrey, R.D. Rogers, Green Chem. 5 (2003) 361.
[5] A.E. Visser, R.P. Swatloski, R.D. Rogers, Green Chem. 3 (2001) 156.
[6] J.D. Holbrey, K.R. Seddon, J. Chem. Soc., Dalton Trans. (1999) 2133.
[7] S. Dai, Y.H. Ju, C.E. Barnes, J. Chem. Soc., Dalton Trans. (1999) 1201.
[8] M.L. Dietz, J.A. Dzielawa, I. Laszak, B.A. Young, M.P. Jensen, Green Chem. 5 (2003) 682.
[9] M.L. Dietz, D.C. Stepinski, Green Chem. 7 (2005) 747.
[10] H. Heitzman, B.A. Young, D.J. Rausch, P. Rickert, D.C. Stepinski, M.L. Dietz, Talanta 69 (2006) 527.
[11] M.L. Dietz, S. Jakab, K. Yamato, R.A. Bartsch, Green Chem. 10 (2008) 174.
[12] G.-T. Wei, Z. Yang, C.-J. Chen, Anal. Chim. Acta 488 (2003) 183.
[13] S.C.N. Hsu, C.-J. Su, F.-L. Yu, W.-J. Chen, D.-X. Zhuang, M.-J. Deng, I.-W. Sun, P.-Y. Chen, Electrochim. Acta 54 (2009) 1744.
[14] K. Kidani, N. Hirayama, H. Imura, Anal. Sci. 24 (2008) 1251.
[15] N. Hirayama, Bunseki Kagaku 57 (2008) 949.
[16] U. Domańska, A. Ręka wek, J. Solut. Chem. 38 (2009) 739.
[17] J.S. Wang, C.N. Sheaff, B. Yoon, R.S. Addleman, C.M. Wai, Chem. A Eur. J. 15 (2009) 4458.
[18] E.M. Martinis, R.A. Olsina, J.C. Altamirano, R.G. Wuilloud, Talanta 78 (2009) 857.
[19] P. Berton, E.M. Martinis, L.D. Martinez, R.G. Wuilloud, Anal. Chim. Acta 640 (2009) 40.
[20] F. Pena-Pereira, I. Lavilla, C. Bendicho, L. Vidal, A. Canals, Talanta 78 (2009) 537.
[21] A.E. Visser, R.P. Swatloski, W.M. Reichert, J.H. Davis Jr., R.D. Rogers, R. Mayton, S. Sheff, A. Wierzbicki, Chem. Commun. (2001) 135.
[22] P. Nockemann, B. Thijs, T.N. Parac-Vogt, K.V. Hecke, L.V. Meervelt, B. Tinant, I. Hartenbach, T. Schleid, V.T. Ngan, M.T. Nguyen, K. Binnemans, Inorg. Chem. 47 (2008) 9987.
[23] S.H. Park, D. Demberelnyamba, S.H. Jang, M.W. Byun, Chem. Lett. 35 (2006) 1024.
[24] H. Liu, H.-Z. Wang, G.-H. Tao, Y. Kou, Chem. Lett. 34 (2005) 1184.
[25] J.R. Harjani, T. Friščić, L.R. MacGillivray, R.D. Singer, Dalton Trans. (2008) 4595.
[26] P. Nockemann, B. Thijs, S. Pittois, J. Thoen, C. Glorieux, K.V. Hecke, L.V. Meervelt, B. Kirchner, K. Binnemans, J. Phys. Chem. B 110 (2006) 20978.
[27] J.-P. Mikkola, P. Virtanen, R. Sjöholm, Green Chem. 8 (2006) 250.
[28] R.S. Kalb, M.J. Kotschan, Aldrich ChemFiles 5 No. (2005) 17.
[29] C. Paipa, E. Poblete, M.I. Toral, Miner. Eng. 19 (2006) 1465.
[30] H.A.D. Filho, Ê.S.O.N. de Souza, V. Visani, S.R.R.C. de Barros, T.C.B. Saldanha, M.C.U. Araújo, R.K.H. Galvão, J. Braz. Chem. Soc. 16 (2005) 58.
[31] M.Ya. Shapiro, Zh. Analit. Khim. (Russ. J. Anal. Chem.) 14 (1959) 365.
[32] Yu.Yu. Lurie, The Handbook on Analytical Chemistry, Khimia, 1971, p. 276 (in Russian).
[33] W.A.E. McBryde, J.L. Rohr, J.S. Penciner, J.A. Page, Can. J. Chem. 48 (1970) 2574.
[34] A.K. Babko, Zh. Obshch. Khim. (Russ. J. Gen. Chem.) 15 (1945) 745.
[35] J.D. Chanley, E. Feageson, J. Am. Chem. Soc. 78 (1956) 2237.
[36] Z.L. Ernst, J. Menashi, Trans. Faraday Soc. 59 (1963) 1794.
[37] V.M. Egorov, S.V. Smirnova, I.V. Pletnev, Sep. Purif. Technol. 63 (2008) 710.
[38] E. Papp, J. Inczédy, J. Chromatogr. 102 (1974) 225.
[39] D.A. Tinsley, A. Iddon, Talanta 21 (1974) 633.
[40] P.S. Patil, V.M. Shinde, Microchim. Acta 68 (1977) 207.
[41] W. Zaborska, M. Leszko, A. Krzymowska-Hachuła, Talanta 36 (1989) 1295.
[42] A.M. El-Wakil, A.B. Farag, A.Kh. Ez-Eldin, Fresenius Z. Anal. Chem. 311 (1982) 522.
[43] J. Aggett, P. Crossley, R. Hancock, J. Inorg. Nucl. Chem. 31 (1969) 3241.
[44] S.B. Sonawale, Y.V. Ghalsasi, A.P. Argekar, Anal. Sci. 17 (2001) 285.
[45] J. Jayachandran, P.M. Dhadke, Talanta 44 (1997) 1285.
[46] M.H. Youcef, T. Benabdallah, H. Ilikti, H. Reffas, Solv. Extr. Ion Exch. 26 (2008) 534.
[47] D.V. Chernyshov, N.V. Shvedene, E.R. Antipova, I.V. Pletnev, Anal. Chim. Acta 621 (2008) 178.

Talanta 80 (2010) 1183–1190

Contents lists available at ScienceDirect

Talanta

journal homepage: www.elsevier.com/locate/talanta

Extraction of biogenic amines using sorbent materials containing immobilized crown ethers

Mardiana Saaid[a,b], Bahruddin Saad[a,*], Ismail Ab Rahman[c], Abdussalam Salhin Mohamed Ali[a], Muhammad Idiris Saleh[a]

[a] School of Chemical Sciences, Universiti Sains Malaysia, 11800 Minden, Penang, Malaysia
[b] Faculty of Applied Sciences, Universiti Teknologi MARA, 40450 Shah Alam, Selangor, Malaysia
[c] School of Dental Sciences, Universiti Sains Malaysia, 16150 Kubang Kerian, Kelantan, Malaysia

ARTICLE INFO

Article history:
Received 26 May 2009
Received in revised form 3 September 2009
Accepted 4 September 2009
Available online 2 October 2009

Keywords:
Biogenic amines
Spermidine
Crown ethers
Batch sorption method
Food
HPLC

ABSTRACT

Three sorbent materials (A18C6-MS, DA18C6-MS and AB18C6-MS) based on the crown ether ligands, 1-aza-18-crown-6, 1,4,10,13-tetraoxa-7,16-diazacyclo octadecane and 4′-aminobenzo-18-crown-6, respectively, were prepared by the chemical immobilization of the ligand onto mesoporous silica support. The sorbents were characterized by FT-IR, scanning electron microscopy-energy dispersive X-ray microanalysis, elemental analysis and nitrogen adsorption–desorption test. The applicability of the sorbents for the extraction of biogenic amines by the batch sorption method was extensively studied and evaluated as a function of pH, biogenic amines concentration, contact time and reusability. Under the optimized conditions, all the sorbents exhibited highest selectivity toward spermidine (SPD) compared to other biogenic amines (tryptamine, putrescine, histamine and tyramine). Among the sorbents, AB18C6-MS offer the highest capacity and best selectivity towards SPD in the presence of other biogenic amines. The AB18C6-MS sorbent can be repeatedly used three times as there was no significant degradation in the extraction of the biogenic amines (%E > 85). The optimized procedure was successfully applied for the separation of SPD in food samples prior to the reversed-phase high performance liquid chromatography separation.

© 2009 Elsevier B.V. All rights reserved.

1. Introduction

Biogenic amines (Table 1) are extensively studied because of their potential toxicity to humans and their usage as food quality markers [1,2]. They can be found in a wide range of food products of both animal and plant origin, as well as in beverages and fermented foods. They are mainly generated by microbial decarboxylation of amino acids [3,4]. The presence of high levels of biogenic amines in food constitutes a potential public concern due to their physiological and toxicological effects. Some of the effects of these amines are well known, e.g., headache, nausea, hypo- or hypertension, migraine, skin allergy and digestive problems. Moreover, they are precursors of carcinogenic nitrosamines and are not reduced by high-temperature treatment [3,5].

Many analytical methods for the separation and quantification of biogenic amines in various kinds of food have been developed, including thin layer chromatography [6], gas chromatography [3], liquid chromatography [4,7] and capillary electrophoresis [1,8]. As biogenic amines do not exhibit strong fluorescence characteristics, a suitable derivatization technique is frequently used to increase the method sensitivity.

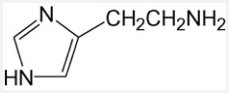
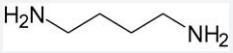
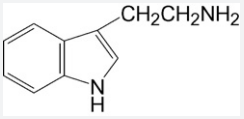
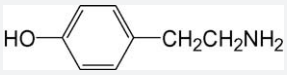
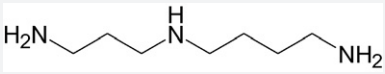
The determination of biogenic amines in food is problematic not only due to their low concentration levels but also due to the complexity of the matrix. Thus, sample clean-up plays an important role for the isolation and enrichment of the biogenic amines prior to the analytical determination. Liquid–liquid extraction (LLE) [9–11], solid phase extraction (SPE) [12–15] and more recently, solid phase microextraction (SPME) [3] have been described.

LLE technique is not recommended because it involves long extraction procedures and often uses harmful organic solvents. Moreover, low recoveries for some amines is sometimes found [10,16]. SPE represents a good alternative to the LLE technique, especially by virtue of the wide commercial availability of sorbent materials and also due to the fact that the need to dispose organic solvents is to a large extent minimized [17]. Using sorbent materials based on anionic [13] and cationic [14] exchangers or non-polar functional groups (e.g., octadecylsilane groups (C18)) [12,15] often show better extraction efficiencies than the LLE counterpart. These kinds of sorbents, however, lack selectivity as constituents of similar polarities are also co-extracted [18]. On-line SPE has also been reported to increase the throughput [12].

* Corresponding author. Tel.: +60 4 6534049; fax: +60 4 6574854.
E-mail address: bahrud@usm.my (B. Saad).

0039-9140/$ – see front matter © 2009 Elsevier B.V. All rights reserved.
doi:10.1016/j.talanta.2009.09.006

Table 1
Structures and chemical properties of the biogenic amines studied [1,2].

Name	Abbreviation	Structure	Molecular weight	p*K*
Histamine	HIS		111.1	$pK_1 = 9.8$ $pK_2 = 6.0$
Putrescine	PUT		88.2	$pK_1 = 10.8$ $pK_2 = 9.4$
Tryptamine	TYP		160.2	$pK = 10.2$
Tyramine	TYR		137.2	$pK = 9.6$
Spermidine	SPD		145.3	$pK_1 = 9.5 pK_2 = 10.8 pK_3 = 11.6$

More recently, SPME and liquid-phase microextraction (LPME) represent interesting developments in extraction as solvent consumption is considerably minimized [19]. The drawbacks with SPME are the relatively high cost of the fiber, its fragility, limited lifetime and carryover effects between analysis [20].

Despite the various developments, the SPE technique still remains a practical approach in sample preparation. The lack of selectivity can be improved by incorporating molecular recognition compounds onto a suitable support [21]. A SPE method for the extraction of catecholamines (norepinephrine, epinephrine and dopamine) based on a chemically modified polymeric resin (Amberlite XAD-4) with 4′-carboxybenzo-18-crown-6 has been described [22]. Satisfactory recoveries (79.1–95.1%) were obtained. Thus, it was the aim of this work to develop selective extraction method for the determination of biogenic amines. This was realized by the immobilization of three crown ethers, namely 1-aza-18-crown-6 (A18C6), 1,4,10,13-tetraoxa-7,16-diazacyclo octadecane (DA18C6) and 4′-aminobenzo-18-crown-6 (AB18C6) within the mesoporous silica as support. The ability of crown ethers to form selective host–guest complexes with alkali, alkaline-earth, amines and amino acids have been documented [23]. The selectivity feature is due to the inclusion complex-formation ability of crown ether with the protonated cations that was made possible by the hydrogen bonding and electrostatic interactions between the cations and the unshared pair of electrons from oxygen, sulfur or nitrogen donor atoms [24]. These ligands have found wide applications such as ion carriers in LLE and ion transport, as well as in the preparation of sensors [25]. The preparation of a mesoporous π-complexing sorbent by covalently immobilizing ionic liquids onto SBA-15-supported ionic liquid compounds containing silver salts was described by Li et al. [26].

2. Experimental

2.1. Chemicals and reagents

All chemicals and solvents used were of analytical and chromatographic grades, respectively. They were used as received. 18 mΩ ultrapure water (Nanopure Diamond, Barnstead, USA) was used throughout. Standard amine hydrochlorides namely spermidine (SPD), putrescine (PUT), histamine (HIS) and tryptamine (TRP), maleic acid, ethanol, toluene and trichloroacetic acid were purchased from Sigma–Aldrich (Steinheim, Germany). Tyramine hydrochloride (TYR), dansyl chloride, A18C6, DA18C6, AB18C6, 3-chloropropyltrimethoxysilane and tetraethoxysilane (TEOS) were from Fluka (Buchs, Switzerland). HPLC grade acetonitrile was purchased from Fisher Scientific (Leicestershire, UK). Glutamic acid monosodium monohydrate, sodium hydroxide, diethyl ether and hydrochloric acid (Acros Organics, New Jersey, USA), sodium hydrogen carbonate (BDH Chemicals, Poole, England) and potassium dihydrogen orthophosphate (Merck, Darmstadt, Germany) were also used. Tomato ketchup, soy sauce, cheese, fish sauce and canned tuna were purchased from a local supermarket in Penang, Malaysia.

2.2. Apparatus

FT-IR spectrum (4000.0–400.0 cm^{-1}) were recorded using a PerkinElmer 2000 FT-IR system. LEO Supra 50vp field emission scanning electron microscope (SEM) equipped with Oxford INCA 400 energy dispersive X-ray microanalysis system (EDX) was used to study the surface morphology and semi-quantitative analysis of the sorbent surface. The samples were sputtered with a thin layer of gold using a Polaron (Fisons) SC515 sputter coater. Elemental analysis was carried out using a CHNS/O Analyzer (PerkinElmer, Series II 2400). The surface area, pore volume, pore diameter and pore size distribution were measured by nitrogen adsorption–desorption isotherms at 77 K on an Aurusorb Automated Gas Sorption analyzer (Quantachrome Corporation) using Brunauer–Emmett–Teller (BET) and Barrett–Joyner–Halenda (BJH) desorption methods. An Orion ion analyzer in conjunction with a glass pH electrode was used for pH measurements. An ultrasonic bath was used for the sonication during the preparation of mesoporous silica. A mechanical shaker (Stuart Scientific) was used for the extraction studies.

2.3. HPLC analysis

Quantitative analysis of biogenic amines was carried out using a Jasco HPLC system that consisted of a pump (Jasco PU-1580), a quarternary gradient unit (Jasco LG-1580-04), a UV–VIS detector (Jasco UV-1570 UV/VIS), an injector (Jasco model 7725) and a 20 μL sample loop. Separation was achieved using a 250 mm × 4.5 mm, Waters Spherisorb 5 μm ODS2 column. The HPLC was operated under isocratic elution (mobile phase of acetonitrile:water (67:33, v/v)) at a flow rate of 1.2 mL min^{-1}. 20 μL of sample was injected and was monitored at 254 nm. The mixture was filtered using 0.45 μm nylon membrane filter from Whatman and was degassed by an ultrasonic bath for 15 min prior to use.

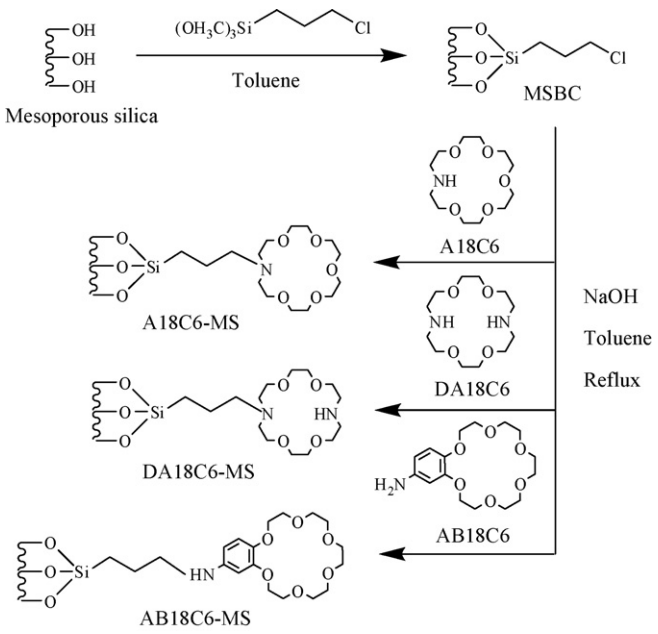


Fig. 1. Reaction for the immobilization of ligands on mesoporous silica.

2.4. Preparation of mesoporous silica

The preparation of mesoporous silica was adapted from procedure as described in the literature [27]. The silica was prepared using a sol–gel process where ethanol (24 mL) was first mixed with distilled water (3.2 mL) for 30 min to homogenize the reaction medium. This was followed by drop-wise addition of TEOS (9.6 mL) into the medium. The reaction was carried out for 1 h, followed by the addition of 0.1 M HCl (40 mL) as catalyst. The mixture was next sonicated for 5 h. Upon cooling to room temperature, the solution of 0.45 g mL^{-1} maleic acid solution (5 mL) was added drop-wise under stirring. The gel was aged at room temperature for 15 h, followed by drying in the oven (7 h) at 70 °C and finally the hard transparent solids were obtained. In order to remove the maleic acid template, the solid was ground into powder and was extracted with ethanol in a soxhlet apparatus (40 h), followed by drying in an oven until constant mass.

2.5. Preparation of sorbents

Mesoporous silica (10 g) was mixed with toluene (100 mL) and 3-chloropropyltrimethoxysilane (10 mL) in a round bottom flask and was refluxed with stirring for 24 h. The phase was left to cool, filtered, washed with toluene, ethanol and diethyl ether and the product (mesoporous silica immobilized with 3-chloropropyltrimethoxysilane (MSBC)) was dried in an oven (70 °C) for 7 h. Sorbents were prepared by mixing MSBC (0.25 g) with 0.5 g of A18C6, DA18C6 and AB18C6 ligand, respectively, in toluene (30 mL) in the presence of NaOH (0.16 g) as a catalyst. The mixture was refluxed for 24 h, left to cool, filtered, washed with toluene, ethanol and diethyl ether and dried (70 °C) for 7 h. The sorbents prepared (A18C6-MS, DA18C6-MS and AB18C6-MS) were stored in a vacuum desiccator. The preparation pathway is outlined in Fig. 1.

2.6. Preparation of standard solutions

Stock solution (1000 mg L^{-1}) of a mixture of TRP (61.4 mg), PUT (91.5 mg), HIS (82.8 mg), TYR (63.2 mg) and SPD (87.7 mg) was prepared in 0.1 M HCl in a volumetric flask (50 mL). The solution was stored at 4 °C and protected from light. Working solutions were prepared by appropriate dilution from this stock solution and was used to obtain the calibration curves.

2.7. Derivatization procedure of standards and sample extracts

The derivatization procedure was adapted from the studies of Mah et al. [28]. 1 mL of standard or sample extract was mixed with a saturated solution of $NaHCO_3$ (200 μL), 2 M NaOH (20 μL) and 2 mL of dansyl chloride (10 mg of dansyl chloride in 1 mL acetone). The mixture was heated in a water bath (70 °C) for 10 min. After the reaction, the unbound dansyl chloride was removed by adding 1 mL of glutamic acid (50 mg of glutamic acid in 1 mL water). After 1 h, the mixture was adjusted to 5 mL with acetonitrile. The solution

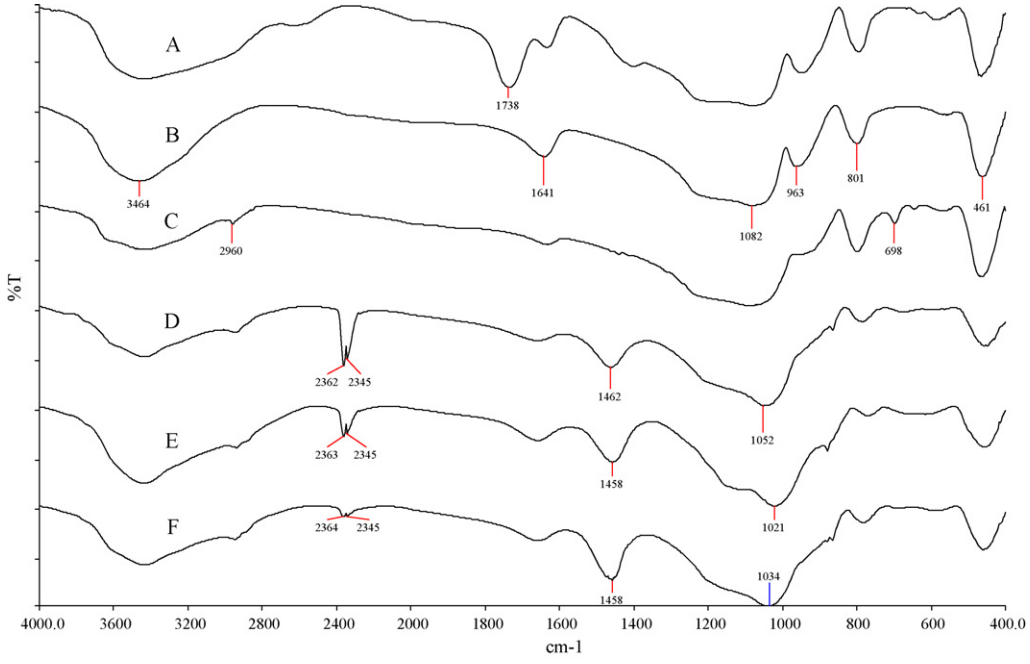


Fig. 2. FT-IR spectra of mesoporous silica (A) before, (B) after the removal of maleic acid, (C) MSBC, (D) A18C6-MS, (E) DA18C6-MS and (F) AB18C6-MS sorbents.

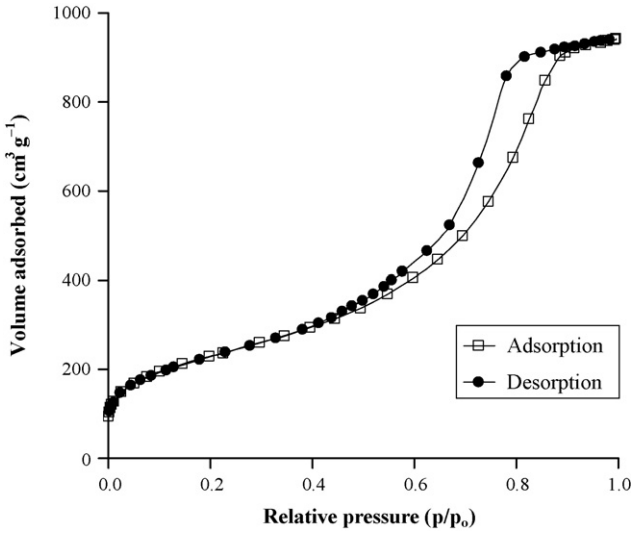


Fig. 3. N_2 adsorption–desorption isotherms of the mesoporous silica.

was filtered through a 0.45 μm nylon membrane filter and injected into the HPLC column.

2.8. Batch sorption method

Sorbent material (10 mg) was equilibrated with 5 mL of 1 mg L^{-1} mixture of standard biogenic amine solution (TRP, PUT, HIS, TYR and SPD) in a sample vial. The mixture was shaken mechanically at room temperature for 1 h. After equilibration, the mixture was briefly centrifuged and 1 mL of the mixture was derivatized. The amount of the biogenic amines left in the solution was analyzed by HPLC.

The sorbent was regenerated by shaking with of 0.1 M NaOH (5 mL) for 30 min, followed by rinsing several times with water. The sorbent was dried in an oven (60 °C) before the next extraction cycle was conducted.

2.9. Determination of SPD in food samples

Different preparation procedures were used according to the type of sample. TCA (5%) was used for the extraction of fish sauce and canned tuna while HCl (0.1 M) was used for the extraction of cheese, tomato ketchup and soy sauce samples. Each sample (5 g) was extracted twice with the respective acid (15 mL) and was homogenized using a vortex mixer (3 min). The homogenates were centrifuged (3000 rpm) for 15 min. For cheese and canned tuna samples, the homogenates were stored at 4 °C to allow the precipitation of fats [29]. The supernatant were combined, adjusted to pH 6 and made up to the 50 mL mark and filtered through a filter paper (Whatman no. 42). Some samples were spiked with SPD to give a final concentration of 1 and 5 mg L^{-1}. The sample (5 mL) was shaken in the presence of 10 and 30 mg of AB18C6-MS sorbent (15 min). The unextracted SPD was derivatized and determined by HPLC to determine the percentage removal of SPD.

3. Results and discussion

Mesoporous silica was prepared as they offer the possibility of producing sorbent materials of different physical properties (e.g., surface area, porosities, controllable and narrowly distributed pore sizes and ordered pore arrangements).

3.1. FT-IR analysis

FT-IR spectra of the prepared sorbents are shown in Fig. 2. For the mesoporous silica, the characteristic absorption band at 1738 cm^{-1} corresponding to the C=O stretching vibration of maleic acid molecule disappeared completely after the extraction with ethanol, indicating the complete removal of the template compound from the mesoporous silica (Fig. 2A and B) [27]. The peak at 1641 cm^{-1} and the broad absorption band at 3464 cm^{-1} are due to the absorbed water. The band at 1082, 801 and 461 cm^{-1} represent the fundamental vibration bands corresponding to Si–O–Si asymmetric stretching, symmetric stretching and bending vibrations for the mesoporous silica [30]. The absorption peaks at 963 cm^{-1} is due to the stretching vibrations of the silanol group (Si–OH) (Fig. 2B) [31,32]. The small absorption band at 2960 cm^{-1} is due to the stretching and bending of C–H bond of 3-chloropropyltrimethoxysilane (Fig. 2C) [31]. Moreover, the spectrum of MSBC shows evidence that the chloride group was attached to silica support because the characteristic C-Cl stretching band at 698 cm^{-1} was observed.

The spectra of the A18C6-MS and DA18C6-MS sorbents show characteristic absorption band at 1462 and 1458 cm^{-1}, respectively, due to CH_2–N–CH_2 stretching, while the NH–CH_2 stretching bands for AB18C6-MS appear at 1458 cm^{-1} (Fig. 2D–F). The CH_2–O–CH_2 linkage of six membered rings for crown ether that absorbs in ~1070 cm^{-1} due to the asymmetric stretching vibrations was not detected as it overlapped with the strong and broad Si–O–Si vibration. The Si–OH stretching frequency in mesoporous silica at 3464 cm^{-1} overlapped with the N–H stretching frequency in immobilized crown ether at ~3450 cm^{-1}. The N–H stretching bands at 1462, 1458 and 1458 cm^{-1} for A18C6-MS, DA18C6-MS and AB18C6-MS (Fig. 2D–F), respectively, indicate the presence of amine groups in the sorbents prepared. The characteristic stretching band at ~2340 and ~2360 cm^{-1} in the three sorbents is further evidence of the presence of a crown ether ligand in the structure. Hence, these spectra suggest that the A18C6, DA18C6 and AB18C6 ligands were incorporated into the mesoporous silica prepared.

3.2. SEM, EDX and elemental analysis

SEM reveals that the mesopores can be described as through pores, which preferentially determine the permeability properties. A high surface area is anticipated to provide a large stationary phase loading. The mesoporous structures are located on the silica skele-

Table 2
Analytical characteristics of the HPLC method.

Biogenic amine	Linear range (mg L^{-1})	R^2	LOD (μg L^{-1})	LOQ (μg L^{-1})	Intraday (%RSD) (n = 3)		Interday (%RSD) (n = 3)	
					t_R	Area	t_R	Area
TYP	0.1–250	0.9989	5.36	17.88	0.71	0.42	0.34	2.38
PUT	0.1–100	0.9999	4.43	14.76	0.49	0.86	0.39	2.47
HIS	0.1–130	0.9993	5.11	17.04	0.34	0.18	0.47	3.09
TYR	0.1–200	0.9995	7.34	24.45	0.14	2.07	0.48	2.72
SPD	0.1–130	0.9979	6.96	23.19	0.09	2.12	0.44	2.69

R^2, square of regression coefficient; t_R, retention time; LOD, limit of detection; LOQ, limit of quantification; RSD, relative standard deviation.

ton and are the ones which provide the surface area needed for the extraction. Numerous interconnected wormhole-like framework pore structures can be observed, which are relatively regular in diameter but largely disordered in the channel arrangements [27].

The EDX results indicate the absence of nitrogen in the mesoporous silica. Analysis on A18C6-MS, DA18C6-MS and AB18C6-MS sorbents showed that nitrogen, ranging from 1.14–1.78% was detected, indicating the presence of crown ethers in the mesoporous silica matrix. This was further supported by the elemental analysis where nitrogen ranging from 0.42 to 1.00% was found for immobilized sorbents. Based on the elemental analysis results, the loading amount of A18C6, DA18C6 and AB18C6 are 0.71, 0.30 and 0.36 mmol g^{-1}, respectively.

3.3. Nitrogen adsorption–desorption test

BET surface area and pore volume were 796 $m^2 g^{-1}$ and 1.31 $cm^3 g^{-1}$, respectively, suggesting that the prepared materials have large surface areas and pore volumes. The isotherms of the mesoporous silica prepared can be classified as type IV with a type A hysterisis loop that is typical of mesoporous material according to the IUPAC nomenclature [33] (Fig. 3). The adsorption isotherm exhibited a large increase in p/p_0 range from 0.6 to 0.8, a characteristic of capillary condensation within the uniform mesoporous. The p/p_0 position of the inflection points is clearly related to the diameter in the mesoporous range and the step indicates the mesoporous size distribution [34]. A narrow pore size distribution with a mean pore size of 6.3 nm is obtained from the BJH desorption method.

3.4. Analytical characteristics of the HPLC method

The HPLC was evaluated for the linear range, limit of detection (LOD) and quantification (LOQ), precision and recovery. Results are summarized in Table 2. The linearity of the calibration curves was investigated by injecting five concentrations of standard mixtures (0.1–250 mg L^{-1}). All the analytes showed good linearity with squared regression coefficient (R^2) ranging from 0.9979 to 0.9999. LOD and LOQ based on signal-to-noise ratio (S/N) of 3 and 10, were in the range of 4.43–7.34 and 14.76–24.45 μg L^{-1}, respectively. These values were comparable to those reported in the literature [35,36]. To evaluate the precision of the method, the repeatability and reproducibility was investigated by injecting five times each of the five standard mixtures on the same day (intraday) and over 7 days (interday), respectively. Good reproducibility of both peak areas (RSD ≤ 3.09%) and retention times (RSD ≤ 0.71%) were found. Recovery studies were carried out by spiking three concentrations (1, 5 and 10 mg L^{-1}) of a mixture of amine standards to fish, cheese, soy bean and tomato ketchup samples studied. Satisfactory recoveries for all amines were obtained (90.7–106.3%) (Table 3).

3.5. Extraction of biogenic amines

The potential application of the sorbents prepared for the extraction of biogenic amines is studied by the batch sorption method. The extraction was optimized for key parameters such as pH, biogenic amines concentration, contact time and reusability. Extraction of a mixture of the five biogenic amines (TRP, PUT, HIS, TYR and SPD) using the sorbents were studied using reversed-phase HPLC. Biogenic amines ranging from 1 to 20% were extracted when blank mesoporous silica (without any crown ether ligand) were used.

3.5.1. Effect of pH

The extraction of the biogenic amines at various pH (2–9) were studied. It was found that SPD was the main analyte extracted for all sorbents (Fig. 4), the optimum extraction was at pH 6. SPD was 98%

Table 3
Recoveries and RSD of biogenic amines when spiked to different food samples.

Biogenic amine	% Recovery											
	1 mg L^{-1}				5 mg L^{-1}				10 mg L^{-1}			
	Fish	Cheese	Soy bean	Tomato ketchup	Fish	Cheese	Soy bean	Tomato ketchup	Fish	Cheese	Soy bean	Tomato ketchup
TYP	96.9 (0.6)	96.3 (1.4)	96.2 (4.7)	96.8 (4.7)	100.0 (2.7)	100.2 (0.6)	97.4 (4.1)	96.7 (1.6)	103.7 (0.6)	102.5 (7.5)	97.4 (1.4)	94.7 (0.8)
PUT	97.3 (0.9)	94.1 (1.0)	96.7 (1.9)	98.7 (4.3)	104.9 (1.4)	105.5 (3.2)	103.7 (4.7)	106.3 (0.2)	103.9 (2.5)	100.7 (2.2)	99.4 (0.4)	99.2 (0.8)
HIS	94.0 (4.7)	93.6 (0.3)	100.8 (2.4)	98.5 (2.9)	99.6 (1.0)	96.8 (2.3)	97.3 (4.2)	99.6 (3.1)	104.1 (1.2)	95.1 (8.0)	99.1 (1.1)	102.4 (2.0)
TYR	98.8 (3.1)	90.7 (2.0)	95.4 (4.9)	94.3 (4.5)	101.7 (3.1)	103.5 (3.4)	102.6 (2.8)	102.4 (0.7)	98.4 (0.8)	101.8 (0.1)	102.7 (0.1)	102.9 (2.2)
SPD	90.9 (5.3)	97.4 (2.9)	95.4 (4.9)	93.9 (1.2)	99.9 (0.2)	101.5 (0.1)	98.9 (4.9)	103.7 (1.2)	96.6 (0.7)	98.1 (2.2)	96.5 (1.9)	97.1 (2.2)

Values in brackets denote relative standard deviation (RSD) ($n = 3$).

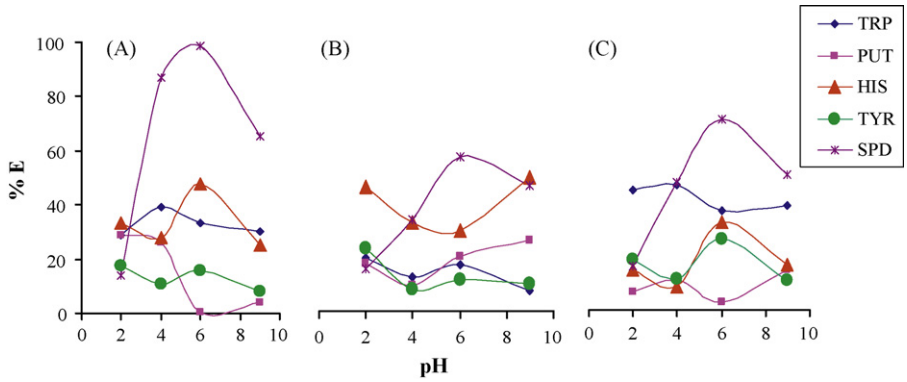


Fig. 4. Effect of pH on the extraction of biogenic amines with AB18C6-MS (A), DA18C6-MS (B) and A18C6-MS (C) sorbents. Mixture contained 1 mg L^{-1} of each biogenic amine. Contact time, 60 min.

extracted when AB18C6-MS sorbent was used compared to A18C6-MS and DA18C6-MS (70 and 60% extracted, respectively). The other amines were less than 50% extracted. Lower extraction at pH other than 6 is probably due to the fact that the amino group of the crown ether is protonated at low pH values while the amino group of the biogenic amine is unprotonated at higher pH values. These two conflicting factors lead to an optimum extraction at pH 6 as shown in Fig. 4. For the recognition of amines, crown ethers have been shown to coordinate with the primary ammonium ion by anchoring the R-NH_3^+ group into their cavity via three H-bonds (N–H···O) [37]. The good selectivity toward SPD is probably due to the ability of the aliphatic amine to fit into the host compared to the aromatic and heterocyclic amines (TRP, HIS and TYR). The good selectivity of SPD towards AB18C6-MS sorbent due to host–guest interaction is further supported by the lower loading of the ligand on the silica support (0.36 mmol g^{-1}) compared to A18C6 (0.71 mmol g^{-1}). The AB18C6-MS sorbent was further used due to its good extraction characteristics.

3.5.2. Effect of biogenic amines concentration

Four different concentrations (0.5–10 mg L^{-1}) of a mixture of biogenic amine were used to study the extraction efficiency (Fig. 5). It was observed that SPD was quantitively extracted up to 10 mg L^{-1} by the AB18C6-MS sorbent. The percentages of extraction for other biogenic amines were low (<50%) at any concentrations. Therefore, 1 mg L^{-1} of biogenic amines was chosen for subsequent experiments.

3.5.3. Effect of contact time

Fig. 6 shows the effect of contact time (5–120 min) on the biogenic amines extraction. It is evident that SPD is the efficiently extracted and within 15 min of contact time, the percentage of extraction was 98%. Therefore, 15 min of contact time was chosen for the subsequent studies.

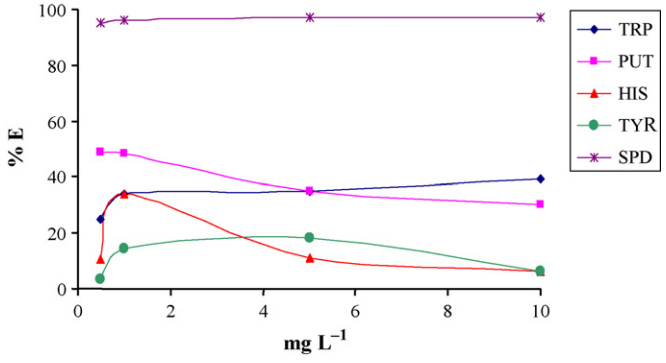


Fig. 5. Effect of biogenic amines concentrations on the extraction. Contact time, 60 min; pH 6; sorbent, AB18C6-MS.

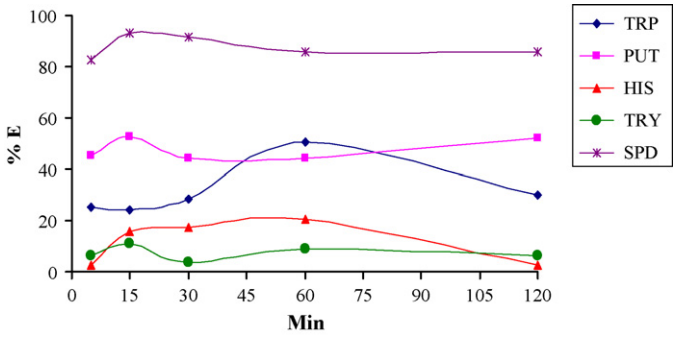


Fig. 6. Effect of contact time on the extraction of the biogenic amines. Mixture containing 1 mg L^{-1} of each biogenic amine; pH 6; sorbent; AB18C6-MS.

3.5.4. Reusability of sorbent materials

To test the reusability of the AB18C6-MS sorbent, it was used to extract biogenic amines through three extraction cycles. The stripping reagent used was 0.1 M NaOH (5 mL). The sorbent still maintained their extraction ability towards SPD through three extraction cycles. No major degradation of the performance was observed, and the sorption capacity was reduced by 9%. The loss of reactivity of the sorbent is probably due to the strong complexation of the crown ether with biogenic amines in the pores. It seems that the remaining biogenic amines in the pores do not affect the sorbent performance in the subsequent extraction cycle.

3.5.5. Adopted extraction conditions

The adopted conditions for the batch extraction were: AB18C6-MS mass, 10 mg; phosphate buffer (0.1 M), pH 6; contact time, 15 min; biogenic amines concentration, 1 mg L^{-1} (5 mL).

Table 4
Recoveries (%) of SPD from spiked food samples using AB18C6-MS sorbent ($n = 3$).

	AB18C6-MS mass		
	10 mg		30 mg
	Spiked concentration (mg L^{-1})		
	1	5	5
Fish sauce	99.8 ± 5.1	93.1 ± 0.3	97.6 ± 2.6
Soy sauce	98.4 ± 2.8	83.7 ± 1.5	96.6 ± 0.9
Tomato ketchup	98.8 ± 5.9	80.1 ± 0.8	93.4 ± 1.6
Canned tuna	99.6 ± 3.4	78.4 ± 1.0	98.9 ± 2.2
Cheese	88.9 ± 1.3	71.2 ± 0.5	92.9 ± 0.7

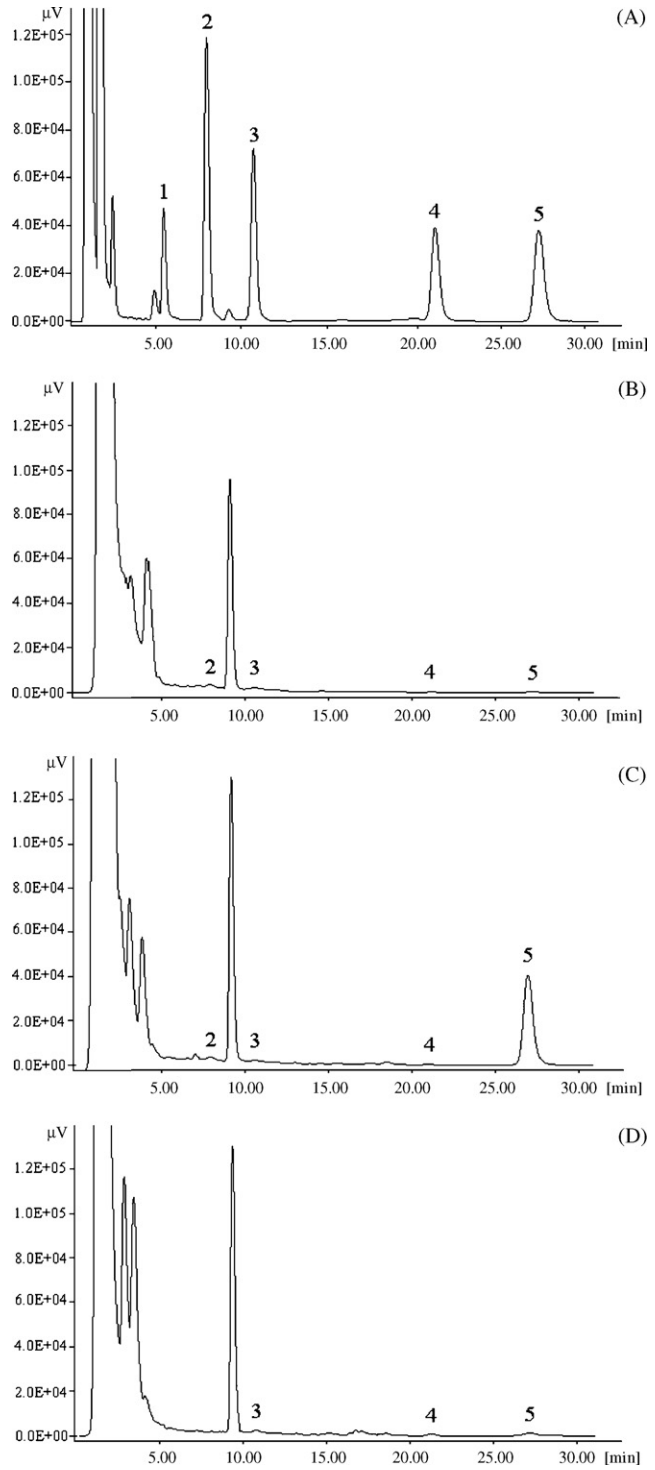


Fig. 7. HPLC chromatogram of (A) biogenic amines standard solution (5 mg L^{-1} each); (B) tomato ketchup; tomato ketchup spike with SPD at 5 mg L^{-1} level before (C) and after (D) extraction with AB18C6-MS sorbent. Peak identity: TRP (1), PUT (2), HIS (3), TYR (4), SPD (5).

3.5.6. Selectivity of the sorbent

Under the optimized conditions, the extraction of SPD is always higher than other biogenic amines. Therefore, based on the amount of biogenic amines remaining in the effluent solution, the distribution coefficient (K_d) and selectivity coefficient (k) was calculated [38]. From the K_d value, the selectivity coefficient of SPD over other biogenic amines can be calculated. The selectivity coefficients (k) of SPD over TRP, PUT, HIS and TYR when extracted using the AB18C6-MS sorbent were 48.6, 26.3, 48.6 and 150, respectively.

3.5.7. Capacity of sorbent

The capacity of the sorbents can be defined as the mmol of M^{n+} extracted/g of sorbent. As the concentration of SPD increases, the capacity also increases. The value of the capacity was found to depend on the initial concentration of SPD in solution, i.e., 1.6, 3.3, 16.7 and 33.4×10^{-3} mmol g^{-1} for 0.5, 1, 5 and 10 mg L^{-1}, respectively. The capacity of this sorbent is higher than those of the sorbents based on immobilized thia crown ethers ($3.8–26.8 \times 10^{-5}$ mmol g^{-1}) [39], but lower for some other researchers (e.g., 0.1–3.1 mmol g^{-1}) [31,40].

3.5.8. Extraction of SPD from food samples

In order to investigate the viability of the AB18C6-MS sorbent, five samples, namely tomato ketchup, soy sauce, cheese, fish sauce and canned tuna were used. To assess the matrix effect, two concentrations of SPD (1 and 5 mg L^{-1}) were spiked to the samples, and its concentration was later determined by the batch sorption method using AB18C6-MS sorbent. The results of the recoveries are shown in Table 4 while representative chromatograms of the standard solution and tomato ketchup samples are shown in Fig. 7. Over 88% of 1 mg L^{-1} spiked SPD was extracted using 10 mg of the sorbent (for cheese sample). However, as the amount of the spiked SPD increased to 5 mg L^{-1}, the percentage of extraction decreased to 71%. Thus, 30 mg of AB18C6-MS sorbent was further used to extract 5 mg L^{-1} of the spiked SPD. The high recoveries of SPD from the food matrices are good indicators that this method could be applied successfully for the determination of SPD in foods. Matrix components were effectively eliminated and only some of the interferences caused by by-products of derivatization reaction with dansyl chloride remained in the final extract. However, these peaks do not interfere with the analyte peaks.

The LOD and LOQ of the method were found to be 15.1 and 35.5 μg L^{-1}. This was carried out by subjecting standard SPD to the AB18C6-MS sorbent and the HPLC determination.

4. Conclusion

Three sorbent materials, namely A18C6-MS, DA18C6-MS and AB18C6-MS have been prepared by the chemical immobilization of the crown ether ligands onto mesoporous silica support. The sorbents have been evaluated for the extraction of five biogenic amines (TRP, PUT, HIS, TYR and SPD). Results obtained showed that all the sorbents exhibit highest selectively towards SPD. Among the sorbents, AB18C6-MS offers the higher extraction of SPD in the presence of other biogenic amines.

The applicability of the proposed method for the selective extraction of SPD was demonstrated by the reasonable recoveries attained (71.2–99.8%) when different food matrices were used. The sorbent also offer distinct advantages over the LLE technique as it does not require organic solvent during the extraction process. The studies further demonstrate that selective extractions can be realized by capitalizing on the host–guest interactions.

Acknowledgements

Leave of absence by the UiTM to M. Saaid is much appreciated. This work was financed by the Universiti Sains Malaysia Research University Grant Scheme.

References

[1] F. Kvasnička, M. Voldřich, J. Chromatogr. A 1103 (2006) 145.
[2] A. Gugliucci, Clin. Chim. Acta 344 (2004) 23.

[3] M.A. Awan, I. Fleet, C.L.P. Thomas, Food Chem. 111 (2008) 462.
[4] H. Yongjin, X. Wenshui, L. Xiaoyong, Food Chem. 104 (2007) 188.
[5] E. Chiacchierini, D. Restuccia, G. Vinci, Talanta 69 (2006) 548.
[6] J. Lapa-Guimarães, J. Pickova, J. Chromatogr. A 1045 (2004) 223.
[7] V. Gianotti, U. Chiuminatta, E. Mazzucco, F. Gosetti, M. Battaro, P. Frascarolo, M.C. Gennaro, J. Chromatogr. A 1185 (2008) 296.
[8] C. Simó, M.V. Moreno-Arribas, A. Cifuentes, J. Chromatogr. A 1195 (2008) 150.
[9] J.O. Fernandez, M.A. Ferreira, J. Chromatogr. A 886 (2000) 183.
[10] N. García-Villar, J. Saurina, S. Hernández-Cassou, Anal. Chim. Acta 575 (2006) 97.
[11] N. Innocente, M. Biasutti, M. Padovese, S. Moret, Food Chem. 101 (2007) 1285.
[12] E.K. Paleologos, M.G. Kontominas, Anal. Chem. 76 (2004) 1289.
[13] O. Busto, M. Miracle, J. Guasch, F. Borrull, J. Chromatogr. A 757 (1997) 311.
[14] S. Köse, G. Hall, Food Res. Int. 33 (2000) 839.
[15] J. Hernandez-Borges, G. D'Orazio, Z. Aturki, S. Fanali, J. Chromatogr. A 1147 (2007) 192.
[16] C. Molins-Legua, P. Campins-Falcó, Anal. Chim. Acta 546 (2005) 206.
[17] C. Basheer, A.A. Alnedhary, B.S.M. Rao, H.K. Lee, Anal. Chim. Acta 605 (2006) 147.
[18] H. Chen, H. Chen, J. Ying, J. Huang, L. Liao, Anal. Chim. Acta 632 (2009) 80.
[19] S. Pedersen-Bjergaard, K.E. Rasmussen, J. Chromatogr. A 1184 (2007) 132.
[20] P. Varanusupakul, N. Vora-adisak, B. Pulpoka, Anal. Chim. Acta 598 (2007) 82.
[21] M.E. Mahmoud, G.A. Gohar, Talanta 51 (2000) 77.
[22] M. Lee, S.Y. Oh, T.S. Pathak, I.R. Paeng, B.-Y. Cho, K.-I. Paeng, J. Chromatogr. A 1160 (2007) 340.
[23] N. Demiral, Y. Bulut, Tetrahedron: Asymmetry 14 (2003) 2633.
[24] T. Iványi, K. Pál, I. Lázár, D.C. Massart, Y.V. Heyden, J. Chromatogr. A 1028 (2004) 325.
[25] F. Chekin, M. Bordbar, Y. Fathollahi, N. Alizadeh, Spectrochim. Acta A 63 (2006) 370.
[26] M. Li, P.J. Pham, C.U. Pittman Jr., T. Li, Micropor. Mesopor. Mater. 117 (2009) 436.
[27] J.B. Pang, K.Y. Qiu, Y. Wei, J. Non-Cryst. Solids 283 (2001) 101.
[28] J.H. Mah, H.K. Han, Y.J. Oh, M.G. Kim, H.J. Hwang, Food Chem. 79 (2002) 239.
[29] G. Saccani, E. Tanzi, P. Pastore, S. Cavalli, M. Rey, J. Chromatogr. A 1082 (2005) 43.
[30] H.S. Mansur, W.L. Vasconcelos, R.F.S. Lenza, R.L. Oréfice, E.F. Reis, Z.P. Lobato, J. Non-Cryst. Solids 273 (2000) 109.
[31] Y.K. Lu, X.P. Yan, Anal. Chem. 76 (2004) 453.
[32] A.V. Rao, M.M. Kulkarni, Mater. Res. Bull. 37 (2002) 1667.
[33] K. Schumacher, M. Grün, K.K. Unger, Micropor. Mesopor. Mater. 27 (1999) 201.
[34] Z. Yuan, W. Zhou, Chem. Phys. Lett. 333 (2001) 427.
[35] F. Gosetti, E. Mazzucco, V. Gianotti, S. Polati, M.C. Gennaro, J. Chromatogr. A 1149 (2007) 151.
[36] R.J. Shakila, T.S. Vasundhara, K.V. Kumudavally, Food Chem. 75 (2001) 255.
[37] J.H. Jung, H.Y. Lee, S.H. Jung, S.J. Lee, Y. Sakata, T. Kaneda, Tetrahedron 64 (2008) 6705.
[38] T.L. Yost, J.B.C. Fagan, L.R. Allain, C.E. Barnes, S. Dai, M.J. Sepaniak, Z. Xue, Anal. Chem. 72 (2000) 5516.
[39] B. Saad, C.C. Chong, A.S.M. Ali, M.F. Bari, I.A. Rahman, N. Mohamad, M.I. Saleh, Anal. Chim. Acta 555 (2006) 146.
[40] E.M. Soliman, M.B. Saleh, S.A. Ahmed, Anal. Chim. Acta 523 (2004) 133.

Talanta 80 (2010) 1191–1197

Contents lists available at ScienceDirect

Talanta

journal homepage: www.elsevier.com/locate/talanta

Simultaneous spectrophotometric determination of trace amounts of uranium, thorium, and zirconium using the partial least squares method after their preconcentration by α-benzoin oxime modified Amberlite XAD-2000 resin

Jahan B. Ghasemi*, E. Zolfonoun

Department of Chemistry, Faculty of Sciences, K.N. Toosi University of Technology, Tehran 16617, Iran

ARTICLE INFO

Article history:
Received 13 July 2009
Received in revised form 5 September 2009
Accepted 7 September 2009
Available online 15 September 2009

Keywords:
Uranium
Thorium
Zirconium
Solid phase extraction
Partial least squares
Spectrophotometric determination

ABSTRACT

A new solid phase extraction method for separation and preconcentration of trace amounts of uranium, thorium, and zirconium in water samples is proposed. The procedure is based on the adsorption of U(VI), Th(IV) and Zr(IV) ions on a column of Amberlite XAD-2000 resin loaded with α-benzoin oxime prior to their simultaneous spectrophotometric determination with Arsenazo III using orthogonal signal correction partial least squares method. The enrichment factor for preconcentration of uranium, thorium, and zirconium was found to be 100. The detection limits for U(VI), Th(IV) and Zr(IV) were 0.50, 0.54, and 0.48 μg L^{-1}, respectively. The precision of the method, evaluated as the relative standard deviation obtained by analyzing a series of 10 replicates, was below 4% for all elements. The practical applicability of the developed sorbent was examined using synthetic seawater, natural waters and ceramic samples.
© 2009 Elsevier B.V. All rights reserved.

1. Introduction

Uranium and thorium find extensive application as nuclear fuel in power plants and their main sources are soil, rocks, plants, sand and water [1,2]. Uranium and thorium are known to cause acute toxicological effects for human and their compounds are potential occupational carcinogens [3]. These elements and compounds are highly toxic which cause progressive or irreversible renal injury. Zirconium is used in the nuclear industry as a fuel rod cladding, as a catalyst in organic reactions and, additionally, in the manufacture of water repellent textiles, in metal alloys and in dye pigments and ceramics [4,5]. Thus, there is a need for specific and precise determination of uranium, thorium, and zirconium traces in environmental and biological samples [6]. Flame atomic absorption spectrometry is an unfavorable method because of the difficult atomization of these elements [7]. The use of inductively coupled plasma atomic emission spectrometry and inductively coupled plasma mass spectrometry improve sensitivity but these methods are time-consuming and generally involve expensive instrumentation which is not available at all laboratories [8].

Spectrophotometric methods are most commonly used for the determination of uranium, thorium, and zirconium [9]. However, the simultaneous determination of uranium, thorium, and zirconium by traditional spectrophotometric techniques is difficult because, generally, the absorption spectra overlap in a bright region and the superimposed curves are not suitable for quantitative evaluation [10,11].

Under computer-controlled instrumentation, derivative techniques and multivariate calibration methods play a very important role in the multicomponent analysis of mixtures by ultraviolet (UV)/visible, molecular absorption spectrophotometry [12–14]. The application of quantitative chemometrics, particularly partial least squares (PLS), to multivariate chemical data is becoming more widespread owing to the availability of digitized spectroscopic data and commercial software for laboratory computers.

The theory and application of PLS in spectrometry have been discussed by several authors [15–21]. Several multicomponent determination of inorganic substances based on the application of these methods to spectrophotometric data has also been reported [22–30]. A particularly detailed study of multivariate calibration by PLS was carried out for the spectrophotometric determination of metals [31]. Orthogonal signal correction (OSC) was introduced by Wold et al. [32] to remove systematic variation from the response matrix (**X**) that is unrelated, or orthogonal, to the properly matrix (**Y**). Therefore, one can be certain that important information regarding the analyte is retained. Recently, multicomponent determinations based on the application of OSC-PLS method to spectrophotometric and voltammetric data have been published [29,33].

* Corresponding author. Tel.: +98 21 22850266; fax: +98 21 22853650.
E-mail address: Jahan.ghasemi@gmail.com (J.B. Ghasemi).

0039-9140/$ – see front matter © 2009 Elsevier B.V. All rights reserved.
doi:10.1016/j.talanta.2009.09.007

Solid phase extraction (SPE) for the analysis of trace concentrations of metal ions in various samples has received much attention in recent years. This technique reduces solvent usage and exposure, disposal costs, and extraction time. Various adsorbents, such as octadecyl functional groups bonded on silica gel, C_{18} [34], glycerol–silica gel [35], chelating adsorbents [36], Amberlite XAD resins [37], Chromosorb resins [38] and other sorbents [39,40] have been used for adsorption of metal chelates in the preconcentration and separation of metal ions.

Amberlite XAD resins have physically or chemically been loaded with the various ligands to prepare new chelating resins and explored extensively for metal enrichment. Their attractive features are easy regeneration for multiple sorption–desorption cycles, good mechanical stability and reproducible sorption characteristics. The impregnation of polymer matrices with common chelating ligands is an easy way to design chelating collectors. Amberlite XAD-2 [41], Amberlite XAD-4 [42], Amberlite XAD-7 [43], Amberlite XAD-16 [44] and Amberlite IRC-718 [45] have been used as a support for such preparations.

In this paper we introduce a procedure for the separation and preconcentration of trace amounts of uranium, thorium and zirconium ions using Amberlite XAD-2000 resin impregnated with α-benzoin oxime, prior to their simultaneous spectrophotometric determination by Arsenazo III as a chromogenic reagent using multivariate calibration techniques (partial least squares) with preprocessing by orthogonal signal correction.

2. Experimental

2.1. Reagents

All reagents were of analytical grade, purchased from the Merck Company. Standard stock solutions (1000 μg mL^{-1}) of thorium(IV) and uranium(VI) and zirconium(IV) were prepared by dissolving appropriate amounts of $UO_2(NO_3)_2{\cdot}6H_2O$, $Th(NO_3)_4{\cdot}5H_2O$ and $ZrOCl_2{\cdot}8H_2O$, in water, respectively. Stock solutions of diverse elements were prepared from the high purity salts of the cations (all from Merck, Germany). Amberlite XAD-2000 (styrenedivinylbenzene copolymer, surface area: 620 $m^2\,g^{-1}$, pore diameter: 4.2 nm and bead size 20–60 mesh) was supplied by Sigma.

2.2. Instrumentation and software

A Perkin Elmer (Lambda 25) spectrophotometer with 10 mm quartz cells was used for UV–vis spectra acquisition. A Metrohm model 744 digital pH meter, equipped with a combined glass-calomel electrode, was employed for the pH adjustments.

The data were processed on a Toshiba computer with Pentium IV as central processing unit (2 Gb RAM) using MATLAB software, version 7.6. PLS and other calculations were carried out using PLS-Toolbox, version 4.0 (Eigenvectors Company).

2.3. Preparation of chelating resin

Amberlite XAD-2000 resin obtained from the supplier contained organic and inorganic impurities. To remove the contaminants, it was washed successively with methanol, water, 1.0 mol L^{-1} HNO_3, water, 1.0 mol L^{-1} NaOH and water. For the impregnation of the resin, 1.0 g of clean and dry XAD-2000 resin beads were added to the solution of α-benzoin oxime in methanol (10 mL of 0.01 mol L^{-1}) and equilibrated with constant stirring for 1 h. The ligand penetrated into the resin bed and was held up strongly. The treated beads were loaded in a glass column (10 cm long and 1 cm i.d.) and washed with deionized water.

2.4. Recommended procedure for solid phase extraction

The general procedure for the extraction of U(VI), Th(IV) and Zr(IV) ions on the impregnated resin was as follows. The column containing 1.0 g of modified resin was first washed with 25 mL water. This step pre-wets the surface of the resin prior to ion extraction. Then 50 mL of the sample solution containing 10.0 μg U(VI), Th(IV) and Zr(IV) (pH = 3), was passed through the column (flow rate = 10 mL min^{-1}). The extracted U(VI), Th(IV) and Zr(IV) were then stripped from the column using 5.0 mL of a 1 mol L^{-1} solution of hydrochloric acid (flow rate = 5 mL min^{-1}) into a 10.0 mL volumetric flask. The uranium, thorium and zirconium concentrations were then determined spectrophotometrically using Arsenazo III as a metallochromic indicator.

2.5. Recommended procedure for spectrophotometric determination

A solution containing no more than 35.0 μg of U(VI), 35.0 μg of Th(IV) and 22.0 μg of Zr(IV) was transferred into a 10.0 mL volumetric flask and 1.0 mL of 0.1% Arsenazo III solution was added. The concentration of hydrochloric acid was adjusted to 0.1 mol L^{-1} by using appropriate volumes of either NaOH or HCl solution. The volume was made up to the mark with distilled water and the solution was mixed. After 15 min, the absorption spectra were recorded between 600 and 700 nm against a reagent blank in a 10 mm cell.

2.6. Analysis of the real samples

A 250 mL of tap water, well water, and seawater samples were filtered through 0.45 μm membrane filter, adjusted to the optimum pH and subjected to the recommended column procedure for the preconcentration and determination of metal ions. To 1.0 g of ceramic samples in a platinum crucible, 10 mL of HF, 1 mL of H_2SO_4, and 1 mL of $HClO_4$ were added and heated to 150 °C on a hot plate. The process was repeated three times. The residue was cooled and dissolved in 50 ml of 0.1 mol L^{-1} HCl and diluted up to 100 mL. Suitable aliquots were taken and subjected to preconcentration and determination by the procedure described above.

3. Results and discussion

In the preliminary experiments, the effect of chemical medium on the reaction between U(VI), Th(IV), and Zr(IV) ions and Arsenazo III was studied. For this purpose, absorption spectra of the U(VI), Th(IV) and Zr(IV) ions in the range of 600–700 nm, in the different concentrations of hydrochloric acid and also different pH values (adjusted by hydrochloric acid and sodium hydroxide) were examined. 0.1 mol L^{-1} hydrochloric acid was found to be optimum medium for this analytical work, to compromise the sensitivity and selectivity of all three metal ions.

Fig. 1 shows the absorption spectra in aqueous solution of the individual uranium, thorium, and zirconium complexes and Arsenazo III at 0.1 mol L^{-1} HCl. As this figure shows, there is a clear overlapping of the three spectra. This prevents the simultaneous determination of the uranium, thorium, and zirconium by direct UV–vis absorbance measurements. To overcome this problem a suitable and simple technique, which presents a good recovery, is PLS regression. Spectra of mixtures of uranium and thorium solutions between 600 and 700 nm wavelengths by 1 nm intervals were recorded, and then the data were digitized and stored for late treatment.

3.1. Individual calibration

Individual calibration curves were constructed with several points as absorbance versus uranium, thorium, and zirconium ions concentration. For constructing the individual calibration lines the absorbances were measured at 650, 620 and 630 nm against a blank for uranium, thorium, and zirconium, respectively. The linear regression equation for the calibration graph for uranium for the concentration range of 0.2–3.5 μg mL^{-1} was $A = 0.0937C + 0.0304$ ($r^2 = 0.9991$, $n = 10$), for thorium for the concentration range of 0.2–3.5 μg mL^{-1} was $A = 0.0933C + 0.0125$ ($r^2 = 0.9989$, $n = 10$) and for zirconium for the concentration range of 0.2–2.2 μg mL^{-1} was $A = 0.0993C + 0.113$ ($r^2 = 0.9988$, $n = 10$).

3.2. Multivariate calibration

The determination of the uranium, thorium and zirconium in mixtures by spectrophotometry using multivariate calibration involves constructing calibration and prediction sets. An experimental design was used to maximize statistically the information content in the spectra. A training set of 36 samples was taken (Table 1). The concentrations of uranium, thorium, and zirconium were 0–3.5, 0–3.5, and 0–2.1 μg mL^{-1}, respectively. For the prediction set, 6 mixtures were prepared (see Table 3). The chemometrics calibrations were computed with the PLS and OSC-PLS algorithms, using the correlation for the training set concentration and its current data.

Fig. 2 shows the score plot for when the PLS and OSC-PLS are used. The score plots are shown for comparison of the results obtained from PLS and OSC-PLS. The results show that score plots have better results when OSC-PLS is used. Score plots reveal the geometrical placement of the solutions in principal components space. The experimental noise can destroy this relation but by removing the noise using OSC filtering, the OSC-PLS score plots depicted in a more clear way the location of the solutions in the scores map which are the same as triangular experimental design was used in preparation of calibration and prediction solution sets.

For the evaluation of the predictive ability of multivariate calibration models, the root mean square error of prediction (RMSEP) and relative error of prediction (REP) can be used (Table 2):

$$\mathrm{RMSEP} = \left[\frac{1}{n}\sum_{i=1}^{n}(y_i - \hat{y}_i)^2\right]^{0.5}$$

$$\mathrm{REP\%} = \frac{100}{\bar{y}}\left[\frac{1}{n}\sum_{i=1}^{n}(yi - \hat{y}i)^2\right]^{0.5}$$

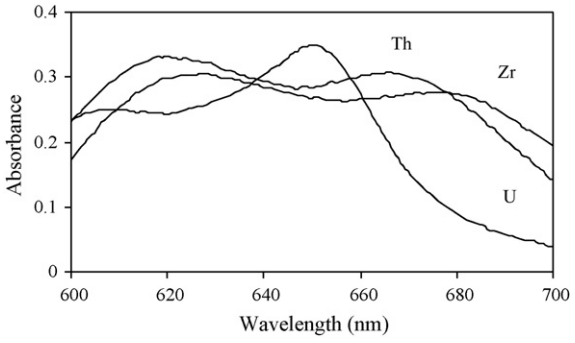


Fig. 1. Absorption spectra of metal–Arsenazo III solution. Curves for 3.5 μg mL^{-1} of U(VI), 3.5 μg mL^{-1} of Th(IV) and 2.1 μg mL^{-1} of Zr(IV).

Table 1
Concentration data of the different mixtures used in the calibration set for the determination of U(VI), Th(IV), and Zr(IV).

Solution number	Concentration (μg mL^{-1})		
	UO_2^{2+}	Th^{4+}	Zr^{4+}
1	0	0	2.1
2	0.5	0	1.8
3	1	0	1.5
4	1.5	0	1.2
5	2	0	0.9
6	2.5	0	0.6
7	3	0	0.3
8	3.5	0	0
9	3	0.5	0
10	2.5	1	0
11	2	1.5	0
12	1.5	2	0
13	1	2.5	0
14	0.5	3	0
15	0	3.5	0
16	0	3	0.3
17	0	2.5	0.6
18	0	2	0.9
19	0	1.5	1.2
20	0	1	1.5
21	0	0.5	1.8
22	0.5	0.5	1.5
23	1	0.5	1.2
24	1.5	0.5	0.9
25	2	0.5	0.6
26	2.5	0.5	0.3
27	0.5	1	1.2
28	1	1	0.9
29	1.5	1	0.6
30	2	1	0.3
31	0.5	1.5	0.9
32	1	1.5	0.6
33	1.5	1.5	0.3
34	0.5	2	0.6
35	1	2	0.3
36	0.5	2.5	0.3

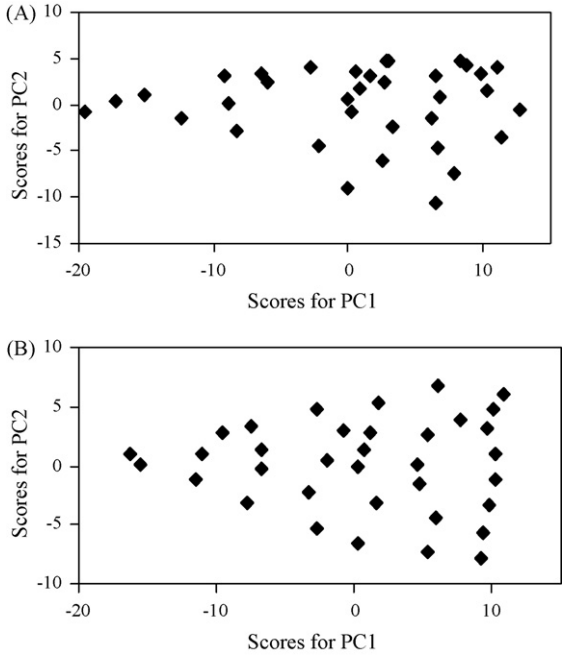


Fig. 2. Score plots: (A) PLS and (B) OSC-PLS.

Table 2
Statistical parameters obtained by applying the OSC-PLS methods to the synthetic mixtures.

Cations	NPC[a]	RMSEP	REP (%)	R^2
UO_2^{2+}	4	0.0897	7.66	0.992
Th^{4+}	6	0.0541	4.63	0.997
Zr^{4+}	5	0.0427	6.11	0.995

[a] Number of principal component.

3.3. Selection of optimum number of factors

The optimum number of factors (latent variables) to be included in the calibration model was determined by computing the prediction error sum of squares (PRESS) for cross-validated models using a high number of factors (half the number of total standard + 1), which is defined as follows:

$$\text{PRESS} = \sum (yi - \hat{y}i)^2 \quad (1)$$

where y_i is the reference concentration for the ith sample and $\hat{y}_i$ represents the estimated concentration. A cross-validation method was employed to eliminate only one sample at a time and then OSC-PLS algorithm models the remaining **Y** matrix and corresponding **X** matrix. By using the established calibration model the concentration of the sample, left out was predicted. This process was repeated until each standard had been out once. A plot of the PRESS against the number of factors for each individual component indicates a minimum value for optimal number of factors. For finding the fewest number of factors the *F*-statistics was used to carry out the significance determination [46]. Fig. 3 shows the PRESS obtained by optimizing the calibration matrix of the spectrophotometric data with PLS and OSC-PLS.

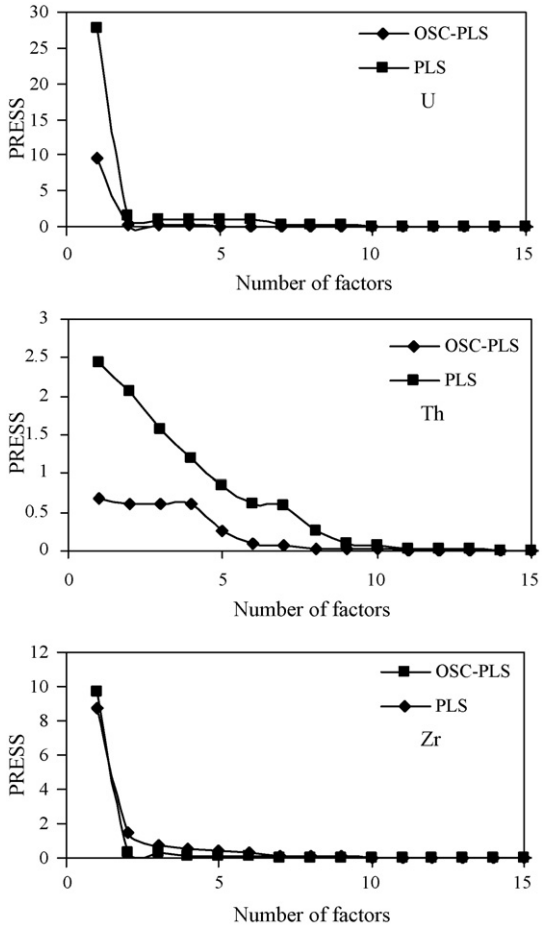


Fig. 3. PRESS versus number of principal components.

3.4. Determination of uranium, thorium, and zirconium in synthetic mixtures

The predictive ability and validation of the calibration model were assessed using six three-component of U(VI), Th(IV), and Zr(IV) mixtures. The results obtained by applying OSC-PLS based calibration model to five synthetic samples are listed in Table 3.

3.5. Optimum conditions for solid phase extraction

3.5.1. Effect of pH

The pH of the sample solution is a very important factor in the separation of metal ions by chelation, and determines the values of the conditional stability constants of the metal complexes on the surface of the sorbent. Thus, the effect of pH on the extraction of uranium, thorium, and zirconium ions was studied. To do this, the pH of 50 mL aqueous samples containing 10 μg U(VI), Th(IV), and Zr(IV) was varied from 2.0 to 6.0. The pH was adjusted by using 0.1 mol L^{-1} of nitric acid and sodium hydroxide solutions. The resulting percent recovery-pH plots are shown in Fig. 4, which indicate that sorption

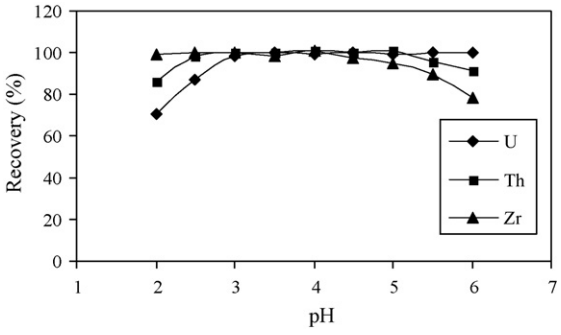


Fig. 4. Effect of pH of sample solution on extraction efficiency of U(VI), Th(IV), and Zr(IV) ions. Conditions: sample volume, 50 mL; amount of metal ions, 10 μg; amount of resin, 1 g; eluent, 5 mL of 1 mol L^{-1} HCl; sample flow rate, 10 mL min^{-1}; eluent flow rate, 5 mL min^{-1}.

Table 3
Added and found results of synthetic mixtures of U(VI), Th(IV), and Zr(IV) (μg mL^{-1}).

Uranium			Thorium			Zirconium		
Added	Found	Recovery (%)	Added	Found	Recovery (%)	Added	Found	Recovery (%)
0.50	0.65	130.0	3.00	2.94	98.0	1.00	0.99	99.0
1.00	0.97	97.0	1.5	1.42	95.0	2.00	1.95	98.0
2.00	2.00	100.0	1.00	1.22	122.0	0.50	0.42	84.0
2.50	2.44	98.0	1.00	1.00	100.0	0.30	0.24	80.0
3.00	2.87	96.0	0.50	0.59	118.0	–	–	–
–	–	–	2.50	2.66	106.0	1.00	0.94	94.0

Table 4
Percent recovery of uranium, thorium, and zirconium from the modified Amberlite XAD-2000 using different stripping acid solutions.

Stripping acid	Recovery (%)								
	0.1 mol L^{-1}			0.5 mol L^{-1}			1.0 mol L^{-1}		
	UO_2^{2+}	Th^{4+}	Zr^{4+}	UO_2^{2+}	Th^{4+}	Zr^{4+}	UO_2^{2+}	Th^{4+}	Zr^{4+}
HNO_3	77.3	79.8	36.8	91.0	88.3	81.3	97.8	98.3	94.6
HCl	82.6	80.9	42.6	93.5	96.8	87.9	99.5	99.8	100.0
H_2SO_4	86.7	84.1	64.2	98.4	99.6	99.1	100.1	99.6	99.1

is maximum and quantitative in the pH range of 3.0–6.0 for uranium, 2.5–5.0 for thorium and 2.0–4.0 for zirconium. Consequently, a solution pH of 3.0 was used in further experiments.

3.5.2. Choice of eluent

In order to choose a proper eluent for the retained U(VI), Th(IV) and Zr(IV) ions after extraction of 10 μg of uranium, thorium, and zirconium in a 50 mL solution by the impregnated resin, the uranium, thorium, and zirconium ions were stripped with 5.0 mL of varying concentrations of different mineral acids, and the results are listed in Table 4. The results revealed that a 5.0 mL of 1 mol L^{-1} concentration of hydrochloric acid and sulfuric acid could afford the quantitative elution of U(VI), Th(IV), and Zr(IV) from the column. However, the use of sulfuric acid as elutant was avoided due to its interfering effect in the spectrophotometric determination of uranium, thorium, and zirconium using Arsenazo III. Subsequent elutions of U(VI), Th(IV), and Zr(IV) were carried out with 1 mol L^{-1} HCl solution.

3.5.3. Effect of flow rate

The effect of flow rates of the sample and stripping solutions through the Amberlite XAD-2000-α-benzoin oxime column on the retention and recovery of uranium, thorium, and zirconium ions was investigated. It was found that, in the range of 0.5–10.0 mL min^{-1}, the retention of uranium, thorium, and zirconium by the impregnated resin is not affected by the sample solution flow rate. On the other hand, quantitative stripping of U(VI), Th(IV), and Zr(IV) ions from the column was achieved in a flow rate range of 0.5–5.0 mL min^{-1}, using 5 mL of 1 mol L^{-1} hydrochloric acid. At higher flow rates, larger volumes of 1 mol L^{-1} HCl were necessary for quantitative stripping of uranium, thorium, and zirconium.

3.5.4. Effect of the amount of resin

The effect of sorbent amount on the retention and the recovery was studied for U(VI), Th(IV) and Zr(IV) ions and the results are shown in Fig. 5. As it is seen from Fig. 5, the recovery yields increased with increasing amounts of impregnated resin up to 0.8 g and remained almost constant in the range of 0.8–1.8 g. However, a further increase in the amount of sorbent resulted in some decreased recovery of the metal ions, most probably because the retained metals cannot be completely eluted with 5 mL of eluent (1 mol L^{-1} HCl). According to these results, the optimum amount of resin for the column was found to be 0.8–1.8 g using 5 mL of eluent.

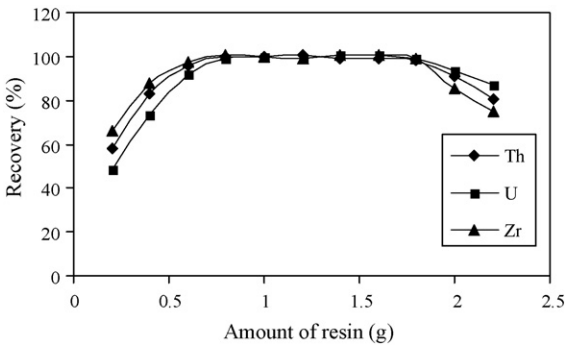


Fig. 5. Effect of amount of resin on extraction efficiency of U(VI), Th(IV), and Zr(IV) ions. Conditions: sample volume, 50 mL; pH, 3; amount of metal ions, 10 μg; eluent, 5 mL of 1 mol L^{-1} HCl; sample flow rate, 10 mL min^{-1}; eluent flow rate, 5 mL min^{-1}.

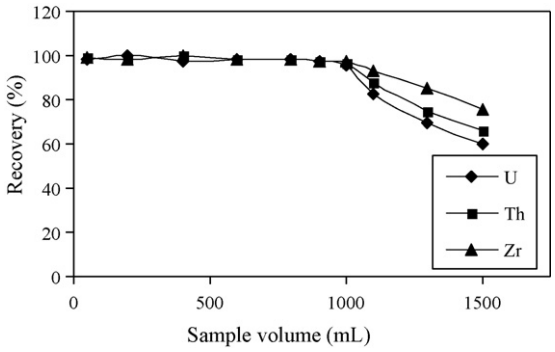


Fig. 6. Effect of sample volume on extraction efficiency of U(VI), Th(IV), and Zr(IV) ions. Conditions: pH, 3; amount of resin, 1 g; amount of metal ions, 10 μg; eluent, 5 mL of 1 mol L^{-1} HCl; sample flow rate, 10 mL min^{-1}; eluent flow rate, 5 mL min^{-1}.

3.5.5. Effect of sample volume

In order to deal with real samples, especially water samples containing very low concentrations of the metal ions, the maximum applicable sample volume must be determined. The recoveries of 10 μg of U(VI), Th(IV), and Zr(IV) ions from different volumes of aqueous solutions are shown in Fig. 6. As seen, the recoveries were found to be quantitative until a sample volume of 1000 mL is reached; hence, 1000 mL was chosen as the largest sample volume to work. Consequently, since the final solution volume to be measured by spectrophotometric method was 10 mL, the preconcentration factors for uranium, thorium, and zirconium ions were evaluated as 100.

3.5.6. Total sorption capacity

The total sorption capacity of modified Amberlite XAD-2000 was determined for each of U(VI), Th(IV), and Zr(IV) ions by the batch method [38]. Here, 0.2 g of the chelating resin was equilibrated with each metal ion solution (50 mL, 50 μg mL^{-1}) for 3 h at the optimum pH. Then, the metal ions were stripped off from the resin with 10 mL of 1 mol L^{-1} HCl and their concentrations were determined with

Table 5
Tolerance limits of some cations and anions on the sorption and determination of uranium, thorium, and zirconium.

Ion	Tolerance limit (μg mL^{-1})
Li^+, Na^+, K^+, Cl^-, NO_3^-	>2000
Ca^{2+}, Mg^{2+}, Ba^{2+}	1000
Ag^+, Hg^{2+}, Zn^{2+}, SO_4^-	100
Ni^{2+}, Co^{2+}, Cr^{3+}, Mn^{2+}	50
Cu^{2+}, Fe^{3+}, Pb^{2+}	10

Conditions: sample volume, 50 mL; amount of metal ions, 10 μg; pH, 3; amount of resin, 1 g; eluent, 5 mL of 1 mol L^{-1} HCl; flow rate, 10 mL min^{-1}.

Table 6
Recovery of uranium, thorium, and zirconium from water samples ($n = 3$, sample volume: 250 mL).

Sample	Uranium amount (μg)			Thorium amount (μg)			Zirconium amount (μg)		
	Added	Found	Recovery (%)	Added	Found	Recovery (%)	Added	Found	Recovery (%)
Tap water	0.0	BDL	–	0.0	BDL	–	0.0	BDL	–
	5.0	4.8 ± 0.25[a]	96	5.0	5.2 ± 0.35	104	5.0	5.0 ± 0.15	100
	10.0	11.3 ± 1.05	113	10.0	10.6 ± 0.30	106	10.0	10.3 ± 0.26	103
Well water	0.0	BDL	–	0.0	BDL	–	0.0	BDL	–
	5	5.5 ± 0.45	110	5.0	4.7 ± 0.47	94	5.0	5.1 ± 0.35	102
	10	9.6 ± 0.20	96	10.0	11.1 ± 0.40	111	10.0	9.5 ± 0.40	95
Seawater	0.0	BDL	–	0.0	BDL	–	0.0	BDL	–
	5.0	4.9 ± 0.55	98	5.0	5.1 ± 0.15	102	5.0	4.6 ± 0.23	92
	10.0	9.7 ± 0.37	97	10.0	9.4 ± 0.65	94	10.0	9.4 ± 0.30	94

BDL: below the detection limit.
[a] Standard deviation.

Table 7
Determination of uranium, thorium, and zirconium in the ceramic samples ($n = 3$).

Sample	Uranium found (μg g^{-1})		Thorium found (μg g^{-1})		Zirconium found (mg g^{-1})	
	Proposed method	ICP-OES	Proposed method	ICP-OES	Proposed method	ICP-OES
1	BDL	BDL	BDL	BDL	0.40 ± 0.11	0.49
2	14.7 ± 0.60[a]	16.1	7.1 ± 0.45	8.5	1.18 ± 0.18	1.14

BDL: below the detection limit.
[a] Standard deviation.

spectrophotometric method. The sorption capacities calculated for uranium, thorium, and zirconium ions were found to be 3.6, 3.3, and 2.6 mg g^{-1}, respectively.

3.6. Effect of diverse ions on the recovery

In order to assess the possible analytical applications of the recommended procedure, the effect of foreign ions on the separation and preconcentration of uranium, thorium, and zirconium ions was studied. A fixed amount of analytes was taken with different amounts of foreign ions and the recommended procedure was followed. Tolerable limit was defined as the highest amount of foreign ions that produced an error not exceeding ±5% in the determination of investigated analyte ions by the combination of the column solid phase extraction and the spectrophotometric method determination methods. The results are summarized in Table 5. As it is seen, large numbers of ions used have no considerable effect on the determination of uranium, thorium, and zirconium ions.

3.7. Precision studies and limit of detection

The limit of detection (LOD) of the proposed method for the determination of uranium, thorium, and zirconium was studied under the optimal experimental conditions. The LOD, defined as three times the standard deviation of 10 measurements of the blank solution divided by the slope of the calibration curve and the enrichment factor, was evaluated as 0.50, 0.54, and 0.48 μg L^{-1} for uranium, thorium, and zirconium, respectively. The reproducibility of the proposed method for extraction and determination of 10 μg uranium, thorium, and zirconium from 100 mL water ($n = 10$) was also studied. The relative standard deviations (R.S.D.) of these determinations were 3.3% for uranium, 3.7% for thorium, and 3.9% for zirconium.

3.8. Applications

The accuracy of the proposed method was tested by separation and determination of U(VI), Th(IV) and Zr(IV) ions in tap water, well water and synthetic seawater samples. In order to validate the method, analytes were determined in spiked real samples. The results obtained are shown in Table 6. As is evident, the uranium, thorium, and zirconium ions added can be quantitatively recovered from the water matrices. Also this method was applied to the determination of uranium, thorium, and zirconium in ceramic materials. Since in ceramic materials the concentration of zirconium is higher than uranium and thorium, determination of uranium and thorium was carried out after addition of fluoride ion (1×10^{-3} mol L^{-1}) as a masking agent for zirconium. The results are given in Table 7. As seen, there is good agreement between the results obtained by proposed method and ICP-OES method.

4. Conclusions

A new method for the preconcentration and simultaneous spectrophotometric determination of uranium, thorium, and zirconium using solid phase extraction and orthogonal signal correction partial least squares method is proposed. The results demonstrate that α-benzoin oxime loaded Amberlite XAD-2000 is an effective sorbent for trace amounts of U(VI), Th(IV) and Zr(IV) ions that can be used for their preconcentration or removal from their dilute sample solutions. The simultaneous determination of uranium, thorium, and zirconium using Arsenazo III as a metallochromic indicator is very difficult due to the high spectral overlap observed in the absorption spectra of these components. To overcome the drawback of spectral interferences, PLS multivariate calibration approaches are applied. The proposed preconcentration and determination method gives a low limit of detection and good R.S.D. values. The developed SPE method possesses a high potential for the separation of uranium, thorium, and zirconium ions from host of coexisting alkali, alkaline earth, transition and heavy metal ions. The method can be successfully applied to the separation and determination of uranium, thorium, and zirconium in real samples.

References

[1] C. Nuccetlli, M. Grandolfo, S. Risica, Microchem. J. 79 (2005) 331.
[2] V.K. Jain, R.A. Pandya, S.G. Pillai, P.S. Shrivastav, Talanta 70 (2006) 257.
[3] Agency for Toxic Substances and Disease Registry, U.S. Public Health Service, Chapman and Hall, New York, 2000.

[4] A. Abbaspour, L. Baramakeh, Anal. Sci. 18 (2002) 1127.
[5] CRC Handbook of Chemistry and Physics, 87th ed., 2006.
[6] G. Tamborini, Microchim. Acta 145 (2004) 237.
[7] B. Welz, M. Sperling, Atomic Absorption Spectrometry, Wiley-VCH, New York, 1999.
[8] J.R. Dean, Atomic Absorption and Plasma Spectroscopy, Wiley & Sons, London, 1997.
[9] Lutfullah, M.N. Alam, N. Rahman, S.N.H. Azmi, J. Hazard. Mater. 155 (2008) 261.
[10] Z. Marczenko, M. Balcerzak, Separation, Preconcentration and Spectrophotometry in Inorganic Analysis, Elsevier, Amsterdam, 2000.
[11] H. Perkampus, UV–Vis Spectroscopy and its Applications, Springer-Verlag, Berlin, 1992, 33.
[12] T.C.O. Haver, G.L. Green, Anal. Chem. 48 (1976) 312.
[13] T.C.O. Haver, Anal. Chem. 51 (1979) 91.
[14] P. Geladi, B.R. Kowalski, Anal. Chim. Acta 185 (1986) 1.
[15] H. Martens, T. Naes, Multivariate Calibration, John Wiley, New York, 1991.
[16] A. Lorber, L.E. Wagnon, B.R. Kowalski, J. Chemometr. 1 (1987) 19.
[17] R. Marbach, H.M. Heise, Chemometr. Intell. Lab. Syst. 9 (1990) 45.
[18] J.H. Kalivas, J. Chemometr. 13 (1999) 111.
[19] J.H. Kalivas, Chemometr. Intell. Lab. Syst. 45 (1999) 215.
[20] A. Hoskuldsson, J. Chemometr. 2 (1988) 211.
[21] J.H. Kalivas, Anal. Chim. Acta 428 (2001) 31.
[22] J. Ghasemi, A. Niazi, Microchem. J. 68 (2001) 1.
[23] J. Ghasemi, A. Niazi, A. Safavi, Anal. Lett. 34 (2001) 1389.
[24] J. Ghasemi, R. Amini, A. Niazi, Anal. Lett. 35 (2002) 533.
[25] J. Ghasemi, D.E. Mohammadi, Microchem. J. 71 (2002) 1.
[26] J. Ghasemi, A. Niazi, R. Leardi, Talanta 59 (2003) 311.
[27] J. Ghasemi, N. Shahabadi, H.R. Seraji, Anal. Chim. Acta 510 (2004) 121.
[28] J. Ghasemi, S. Saaidpour, A.A. Ensafi, Anal. Chim. Acta 508 (2004) 119.
[29] J. Ghasemi, A. Niazi, Talanta 65 (2005) 1168.
[30] J. Ghasemi, A. Niazi, Anal. Chim. Acta 533 (2005) 169.
[31] M. Otto, W. Wegscheider, Anal. Chem. 61 (1989) 1847.
[32] S. Wold, H. Antti, F. Lindgren, J. Öhman, Chemometr. Int. Lab. Syst. 44 (1998) 175.
[33] A. Rouhollahi, R. Rajabzadeh, J. Ghasemi, Microchim. Acta 157 (2007) 139.
[34] M. Karve, R.V. Rajgor, J. Hazard. Mater. 141 (2007) 607.
[35] A. Safavi, N. Iranpoor, N. Saghir, S. Momeni, Anal. Chim. Acta 569 (2006) 139.
[36] K. Suvardhan, K.S. Kumar, D. Rekha, B. Jayaraj, G.K. Naidu, P. Chiranjeevi, Talanta 68 (2006) 735.
[37] V.N. Bulut, A. Gundogdu, C. Duran, H.B. Senturk, M. Soylak, L. Elci, M. Tufekci, J. Hazard. Mater. 146 (2007) 155.
[38] M. Tuzen, M. Suylak, L. Elci, Anal. Chim. Acta 548 (2005) 101.
[39] S. Baytak, A.R. Turker, J. Anal. Chem. 61 (2006) 483.
[40] F. Gode, E. Pehlivan, Bioresour. Technol. 98 (2007) 904.
[41] S.L.C. Ferreira, W.N.L. dos Santos, V.A. Lemos, Anal. Chim. Acta 445 (2001) 145.
[42] B.N. Singh, B. Maiti, Talanta 69 (2006) 393.
[43] H. Matsumiya, S. Yasuno, N. Iki, S. Miyano, J. Chromatogr. A 1090 (2005) 197.
[44] C. Gok, S. Seyhan, M. Merdivan, M. Yurdakoc, Microchim. Acta 157 (2007) 13.
[45] A.A. Zogorodni, M. Muhammed, Sep. Sci. Technol. 34 (1999) 2013.
[46] D.M. Haaland, E.V. Thomas, Anal. Chem. 62 (1990) 1091.

Talanta 80 (2010) 1198–1204

Contents lists available at ScienceDirect

Talanta

journal homepage: www.elsevier.com/locate/talanta

Langmuir–Blodgett film of *p-tert*-butylthiacalix[4]arene modified glassy carbon electrode as voltammetric sensor for the determination of Hg(II)

Fei Wang[a,b], Xiaohan Wei[a], Chenbin Wang[a], Shusheng Zhang[a], Baoxian Ye[a,*]

[a] *Department of Chemistry, Zhengzhou University, Da xue Road, Zhengzhou 450001, PR China*
[b] *Department of Material and Chemistry Engineering, Henan Institute of Engineering, Zhengzhou 450007, PR China*

ARTICLE INFO

Article history:
Received 19 June 2009
Received in revised form 26 August 2009
Accepted 8 September 2009
Available online 13 September 2009

Keywords:
Langmuir–Blodgett film
p-tert-Butylthiacalix[4]arene
Anodic stripping voltammetry
Mercury(II) ion

ABSTRACT

The π–A isotherms and UV–vis spectra of the transferred films suggested that the monolayer of *p-tert*-butylthiacalix[4]arene can coordinate with Hg^{2+} at the air–water surface. From these observations, a glassy carbon electrode coated with Langmuir–Blodgett film of *p-tert*-butylthiacalix[4] arene as a new voltammetric sensor is designed for the determination of trace amounts of Hg^{2+}. Compared with bare glassy carbon electrode and modified glassy carbon electrode using direct coating method, the Langmuir–Blodgett film-modified electrode can greatly improve the measuring sensitivity of Hg^{2+}. Under the selected conditions, the Langmuir–Blodgett film-modified electrode in 0.1 mol L^{-1} H_2SO_4 + 0.01 mol L^{-1} KCl solution shows a linear voltammetric response for Hg^{2+} in the range of 5.0×10^{-10} to 1.5×10^{-7} mol L^{-1}, with a detection limit of 2.0×10^{-10} mol L^{-1}. The proposed method was also applied to determine Hg^{2+} in water samples (tap, lake and river water). In addition, the fabricated electrode exhibited a distinct advantage of simple preparation, non-toxicity, good reproducibility and good stability.

© 2009 Elsevier B.V. All rights reserved.

1. Introduction

Mercury is one of the most toxic elements in environment, because of its high reactivity, its extreme volatility and its relative solubility in water and living tissues. It can have several effects on human health even at very low concentrations, especially organo-mercury compounds. Therefore, the determination of mercury is necessary and urgent, particularly at trace levels [1]. Some analytical techniques have been employed in mercury analysis, such as atomic absorption spectrometry (AAS) [2], atomic fluorescence spectrometry (AFS) [3,4], X-ray fluorescence [5] and UV spectrophotometry [6]. These techniques, commonly used for trace measurement of mercury(II) ion in the laboratory, are not suitable for the task of in situ testing and monitoring. Electrochemical methods, in particular differential pulse anodic stripping voltammetry (DPASV), are the most favourable techniques for the determination of metal ions because of its low cost, high sensitivity, easy operation and the ability for carry out speciation analysis.

Chemically modified electrodes (CMEs) have received increasing attentions in the past decades, which enhance the sensitivity and selectivity of electrochemical analysis techniques [7]. A number of articles discussed the determination of mercury(II) ion by CMEs. The modifiers used include organic chelating groups [8–10], polymer [11–14], sol–gel [15,1,16] and nanoparticles [17]. However, most of these procedures have difficulties achieving the sensitivity required for the determination of low levels of mercury(II) ion in some real samples. In recent years, a great deal of keen interest has been devoted to the Langmuir–Blodgett (LB) films. This is due to the fact that the LB technique is a useful way of forming sequential layers of ultrathin organic films [18] and can precisely control the thickness and order of a film at the molecular scale [19].

Calixarenes, cyclic oligomers of phenol–formaldehyde condensates, have received a lot of attention as a basis for molecular and ionic recognition because of their conformational and structural flexibility [20]. A number of calixarenes derivations have been successfully employed in ion selective electrodes (ISEs) [21,22]. Thiacalixarenes have recently emerged as new members of the calixarene family. The presence of four sulfur atoms (which possess lone pairs and vacant 3d orbitals) in the place of methylene groups imparts many novel features and properties compared with conventional calixarenes. The specific metal-binding property should be one of the most noticeable features of these thiacalix class ligands [23]. Xiaojun Hu and co-workers [24] investigated the molecular recognition of thiacalixarenes to Cu^{2+}, Zn^{2+}, Cd^{2+}, Pb^{2+} and Ag^{+} by UV spectroscopy and solvent extraction. C. Dridi et al. [25] reported that *p-tert*-butylthiacalix[4]arene with amide moiety was used as a receptor material for Hg^{2+} detection by impedance measurements. We recently reported that GCE modified with a LB film of *p-tert*-butylthiacalix[4]arene (TCA) was used

* Corresponding author. Tel.: +86 371 67781757; fax: +86 371 67763654.
E-mail address: yebx@zzu.edu.cn (B. Ye).

0039-9140/$ – see front matter © 2009 Elsevier B.V. All rights reserved.
doi:10.1016/j.talanta.2009.09.008

for determination for Cu^{2+}, Cd^{2+} and Pb^{2+} [26,27]. In this approach, a glassy carbon electrode (GCE) modified with LB film of TCA is designed for the determination of trace amounts of Hg^{2+}. Compared with bare GCE and modified GCE using direct coating method, the LB film-modified electrode can greatly improve the measuring sensitivity of Hg^{2+}. The UV–vis spectra and surface pressure–area isotherms suggested that TCA has effective molecular recognition to Hg^{2+}. The fabricated electrode of LB film exhibited excellent sensitivity and reproducibility for preconcentration and stripping analysis of Hg^{2+} ion in water.

2. Experimental

2.1. Apparatus and reagents

All electrochemical techniques were carried out on the CHI 650 Electrochemical analyzer (CH Instruments Company, USA). A traditional three-electrode system consisting of a saturated calomel reference electrode (SCE), a platinum wire auxiliary electrode, and a LB film of TCA (LB TCA) modified GC working electrode (the geometric diameter of GCE is 3 mm), were employed. The electrochemical cell consists of a 10 mL vessel supplied with an electrical spiral stirrer. LB films were formed and deposited on GCE by using JML-04 LB trough (Shanghai Zhongchen Company, China). UV–vis spectra were measured by Model UV-2102 spectrophotometer (UNICO Company, Shanghai, China). A model AFS-9800 atomic fluorescence spectrometry (Beijing Kechuang haiguang Instruments Co. Ltd., Beijing, China) was employed.

All reagents were analytical grade and were used without any further purification. The aqueous solutions were prepared with redistilled water. TCA was purchased from Tokyo Kasei Kogyo Company (Japan) and its structure is shown in Fig. 1. Stock solutions (1.0×10^{-3} and 1.0×10^{-6} mol L^{-1} of $Hg(NO_3)_2$) were prepared by dissolving $Hg(NO_3)_2$ solid reagent into 0.1 mol L^{-1} HNO_3 and stored darkly. The working standard solutions, for optimization studies, were prepared daily by suitable dilution of above stock solution. High grade nitrogen was used for deoxygenated of samples and solvents during analysis.

2.2. Preparation of modified electrode

Before immobilization, the GCE was polished with 0.1 μm aluminum slurry, rinsed thoroughly with redistilled water and sonicated successively in ethanol and redistilled water, respectively, each for 3 min. The electrodes were pretreated with electrochemical method by cycle scan between ±1 V in 0.5 mol L^{-1} H_2SO_4. A sample of TCA chloroform solution (3.0×10^{-4} mol L^{-1}) was spread on pure water subphase surface at about 25 °C. A Wilhelmy balance was used as the surface pressure sensor and situated in the middle of the trough. After evaporation of the chloroform solvent for 30 min, the monolayer of TCA was compressed with a rate of 10 mm min^{-1} and then transferred onto the GCE (vertical dipping) with rate of 2.5 mm min^{-1} under a surface pressure of 30 mN m^{-1}. This modified electrode was named LB-TCA/GCE. The multilayer films were assembled by sequential monolayer transfer. For comparability, a direct modified GCE of TCA was prepared by direct drop smearing of some TCA solution on GCE surface. After drying for 30 min, a direct coating TCA-GCE was obtained.

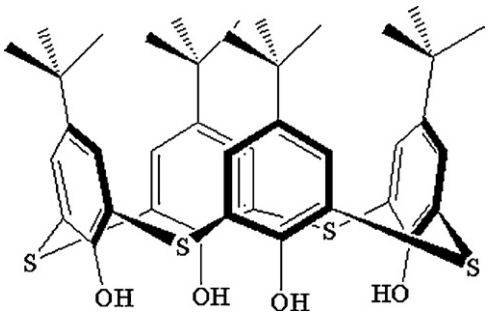


Fig. 1. The chemical structure of *p-tert*-butylthiacalix[4]arene (TCA).

For UV–vis measurement, the LB film of TCA must be transferred on quartz slice. The quartz slices were cleaned in sulfuric acid containing potassium dichromate and rinsed with deionized water before use. LB films of TCA anchored on quartz slices were performed with a vertical dipping method at 30 mN m^{-1} (during the up- and downward, the dipping speed was 2.5 mm min^{-1}). The transfer ratio was almost unity during the upward and downward cycles. Therefore, the transformations of monolayer were Z-type.

2.3. Analytical procedure

Analytical determination of Hg^{2+} was performed by differential pulse anodic stripping voltammetry. The accumulation step was carried out under potential of −0.6 V for a certain period of time while stirring solution. After resting solution for 30 s, the differential pulse voltammograms were recorded from −0.2 to +0.6 V. After each determination, the LB-TCA/GCE was held at 0.6 V for at least 1 min, and then dipped into 0.02 mol L^{-1} EDTA solution of 5 min for renovating it. All measurements were carried out at room temperature (25 ± 1 °C).

3. Results and discussion

3.1. π–A isotherm

The π–A isotherm of TCA on the pure water surface is presented in Fig. 2(curve a). At a relatively high area per molecule, the surface pressure is low, and further compression shows a continuous rise of isotherms. During the compression process of the apparently condensed phase, a sharp rise curve at the air–water interface was displayed. The collapse pressure was 58 mN m^{-1} and the limiting area of per molecule in condensed state was 0.18 nm^2 obtained by extrapolating the linear part of the isotherm to π = 0. Obviously, this result means that TCA can form a stable monolayer on the water surface. On the other hand, if the subphase aqueous solution contained 1.0×10^{-4} mol L^{-1} Hg^{2+}, an absolute change isotherm was observed (Fig. 2, curve b). This different isotherm implied that TCA molecule can coordinate to Hg^{2+} ion and forms a monolayer at the air–water interface.

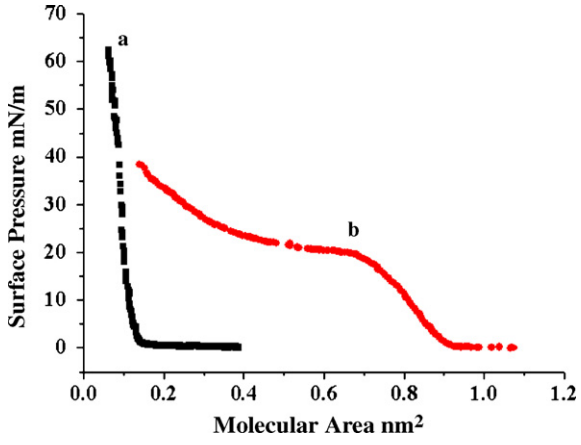


Fig. 2. π–A isotherms of TCA on (a) pure water, (b) aqueous subphase containing 1.0×10^{-4} mol L^{-1} Hg^{2+}.

Shi and co-workers [28] reported that the isotherm of TCA was influenced dramatically owing to the electrostatic repulsion among bound metal cations, when the metal ions were added into the subphase and there was the coordination between TCA and metal ions. On the other hand, from π–A isotherm, we can deduce that the Hg^{2+} ion was not situated inside the TCA cavities (if that is so, mercury ions in the subphase would not significantly affect the limiting area of TCA monolayer [29]). Thus, we may deduce that the TCA molecule coordinates with Hg^{2+} ion, through bridging-sulfur atom and its neighboring phenolic oxygen atoms, and forms a monolayer at the air–water interface.

3.2. UV–vis spectra of LB-TCA films

In order to confirm the above results, UV–vis spectra of monolayer transferred to quartz slices were measured. The UV spectra of TCA in chloroform solution were also studied. Compared to *p-tert*-butylcalix[4]arene, whose absorption bands at 280.0 and 288.0 nm are characteristic adsorption of the phenyl moiety [30], TCA shows the absorption bands at 292.0 and 302.0 nm which are mainly due to the sulfur atoms induced into TCA molecule. In the case of transferred films, a red shift of the absorption peaks was observed as compared with solution spectrum (from 292.0 to 297.0 nm and 302.0 to 307.0 nm, respectively). Such behavior was due to the formation of J-aggregates [31].

Fig. 3 shows the UV–vis spectra of the films transferred from the monolayer of TCA on aqueous Hg^{2+} ion (1.0×10^{-4} mol L^{-1}) solution (Fig. 3, curve b) in comparison with those on deionized water (Fig. 3, curve a). In the spectrum of the transferred film prepared from the subphase containing Hg^{2+} ion, the bands at 298.0 and 307.0 nm of ligand (TCA) LB film were disappeared and a strong band at 311.5 nm was observed. These spectral changes indicate that coordination of TCA, through sulfur and phenoxo anion, to Hg^{2+} ion exits. Of course, this phenomenon can be explained by hard soft acid and base (HSAB) principle. In this principle, hard acids are preferably coordinated to hard bases, and soft acids to soft bases. Accordingly, Hg^{2+} is soft acids, and sulfur atom and phenoxo group are soft bases. Thus, it can be understood easily why TCA molecule can coordinates to Hg^{2+} ion, and Hg^{2+} can change remarkably the monolayer isotherm of TCA.

3.3. Electrochemical impedance spectroscopy and cyclic voltammetry characterization of the LB-TCA/GCE

It is well known that electrochemical impedance spectroscopy (EIS) is an effective tool for studying the interface properties

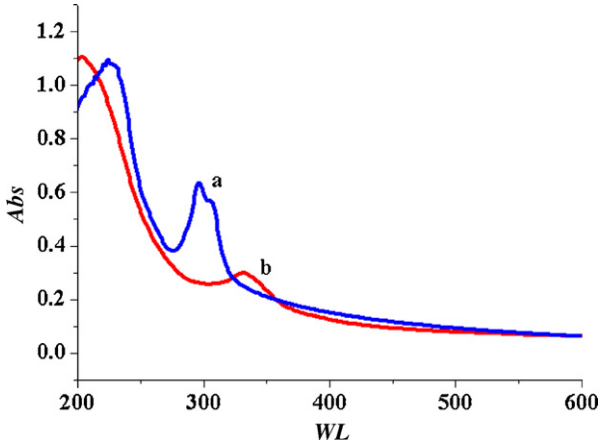


Fig. 3. The UV–vis spectra of 15-layer LB films of TCA transferred from pure water subphase (a) and from a 1.0×10^{-4} mol L^{-1} Hg^{2+} subphase (b).

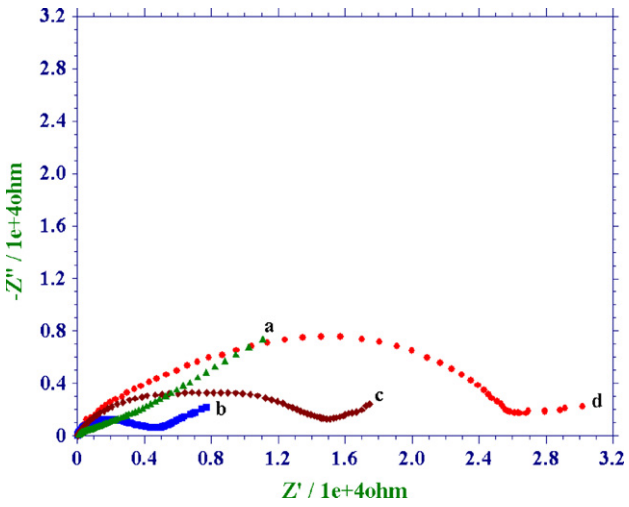


Fig. 4. Electrochemical impedance spectroscopy (EIS) of a clean, freshly polished bare GCE (a) and different layers modified GCE (b–d) in 1×10^{-3} mol L^{-1} $Fe(CN)_6^{4-/3-}$ and 0.1 mol L^{-1} KCl solution; (b) 1 layer, (c) 2 layers, (d) 3 layers. The frequency range is from 1 MHz to 0.01 Hz, and the perturbation signal is 5 mV.

of surface-modified electrodes. R_{et}, the semicircle diameter at higher frequencies in Nyquist plot of EIS can be used to describe the interface properties of the electrode, because it controls the electron transfer rate of the redox probe at the liquid/solid (solution/electrode) interface. Its value varies when different substances are adsorbed on the electrode surface [32]. Fig. 4 shows the results of ac impedance spectroscopy on bare GCE and different layers of LB-TCA/GCE in the solution of equimolar 1.0×10^{-3} mol L^{-1} $Fe(CN)_6^{3-/4-}$ ions, respectively. As the result, the Nyquist plot exhibits an almost straight line at bare GCE (Fig. 4, curve a), that is the characteristic of a diffusing limiting step of the electrochemical process. At the LB-TCA/GCE, the Nyquist plots are composing from a semicircle portion and a linear part (Fig. 4, curves b–d). The semicircle portions are observed at higher frequencies, which correspond to the electron transfer limited process, and the linear parts are observed at lower frequencies, which attribute to a diffusing limited electron transfer. It can also be seen that the diameter of the semicircle at the high frequency increases along with the increasing layer numbers of TCA film modified on the electrode surface. The respective semicircle diameter corresponds to the electron transfer resistance (R_{et}) at the electrode surface [33]. After fitting suitable

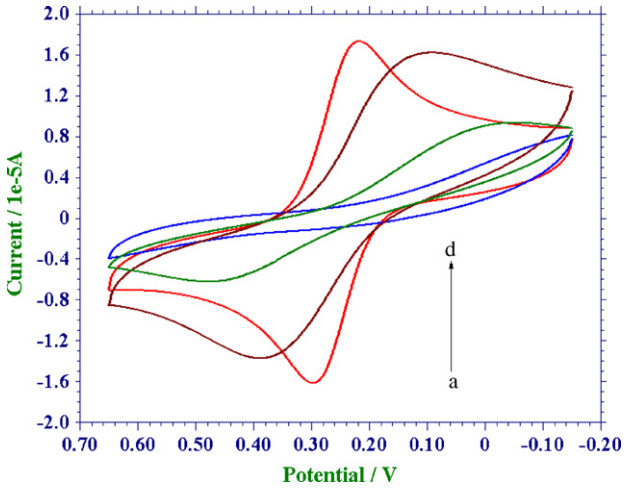


Fig. 5. Cyclic voltammograms of 1×10^{-3} mol L^{-1} $Fe(CN)_6^{3-}$ and 0.1 mol L^{-1} KCl solution at a clean, freshly polished bare GCE (a), and different layers modified GCE (b–d) with scan rate $\nu = 0.10$ V s^{-1}; (b) 1 layers, (c) 2 layers, (d) 3 layers.

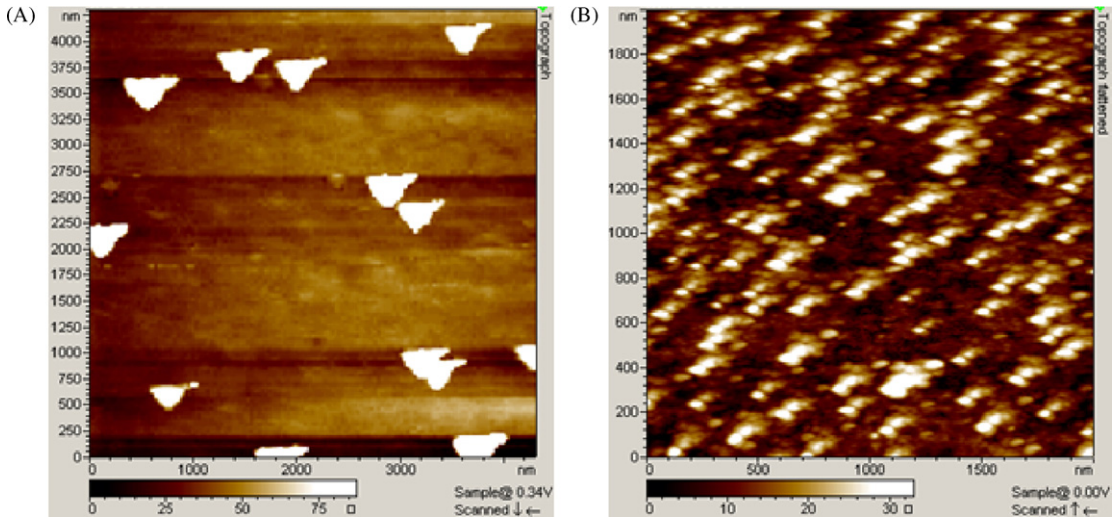


Fig. 6. AFM 2D topography images of bare silicon surface (A, scan area: 4 μm × 4 μm) and the silicon covered with a layer of TCA LB film (B, scan area: 2 μm × 2 μm).

circuit and calculation, R_{et} obtained is about 4, 12.7 and 24 kΩ for 1 layer, 2 layers and 3 layers (Fig. 4, curves b–d) TCA film, respectively. This result suggests that TCA acts as a blocking layer for electron and mass transfer that hinders the diffusion of ferricyanide toward the electrode surface, which obviously also prove that TCA film is successfully immobilized on the GCE surface.

The cyclic voltammetry of ferricyanide is also a valuable and convenient tool to monitor the barrier of the modified electrode. Therefore, it was chosen as a marker to investigate the change of the electrode behavior after each layer modifier. The experiment further confirmed that the TCA was successfully assembled on GCE surface. Fig. 5 shows cyclic voltammograms (CVs) of TCA modified electrodes with different layers in the solution of 1.0×10^{-3} mol L^{-1} $K_3Fe(CN)_6$. Well-defined CV, characteristic of a diffusion-limited redox process, was observed at the bare GCE (Fig. 5, curve a). After modifying the electrode, the redox peak currents decreased and the peak potential separation increased remarkably by increasing the modified layer (Fig. 5, curves b–d). The redox peak of $K_3Fe(CN)_6$ disappeared at 3 layers TCA film-modified GCE. For reason is that the LB-TCA can act as a bulwark for blocking the electron and mass transfer, and it hinders the diffusion of ferricyanide toward to the electrode surface. On the basis of the EIS and CV results, we can conclude that TCA is successfully immobilized on the GCE surface as LB film form.

3.4. Atomic force microscopy of LB-TCA films

Atomic force microscope (AFM) was employed to observe the structure of TCA LB films. Silicon was used as substrates to substitute GCEs. Silicon substrates were sonicated successively in ethanol and redistilled water, respectively, each for 10 min. Then the substrates were dipped in piranha solution (1:3 mixtures of H_2O_2 and H_2SO_4) for 20 min. Later, they were again ultrasonic cleaned in redistilled water for 5 min. Finally, the pretreated silicon was kept in redistilled water for further using. Fig. 6 shows typical contact mode AFM images of the bare silicon surface and the silicon covered with a layer of TCA LB film that was transferred from air–water interface to silicon surface under the surface pressure of 30 mN m^{-1}. The bare silicon has no impurity on its surface and shows very even surface (Fig. 6A). The compact and well-ordered structure of TCA LB film was observed (Fig. 6B) which is formed by aggregates of TCA molecules during compressing process, which also indicate successfully immobilization of TCA molecules on the substrate surface.

3.5. Electrochemical behavior of Hg^{2+} on the LB-TCA/GCE

The ability of the LB-TCA/GCE for recognition and preconcentration of Hg^{2+} was studied. Fig. 7 shows the DPVs of 1×10^{-8} mol L^{-1} Hg^{2+} in 0.1 mol L^{-1} H_2SO_4 + 0.01 mol L^{-1} KCl solutions at bare GCE (curve a) and GCE modified of TCA by direct coating method (curve b). At bare GCE and GCE modified using direct coating method case, a small anodic peak could be discerned at about +0.10 and +0.11 V, indicating some adsorption of Hg^{2+} could have occurred at the electrode surface. However, this miniscule peak provided evidence for the absence of significant preconcentration of Hg^{2+} at these two kind electrodes. In contrast, when LB-TCA/GCE was applied, a well-defined anodic stripping peak with peak potential of +0.12 V appeared after accumulation at negative potential (curve c). Under the same operating condition, the peak current was 6 times comparing to that of direct coating TCA/GCE and 20 times comparing to that of bare GCE. And there was no electrochemical response of LB-TCA/GCE itself in this medium (Fig. 8, curve a). So this peak was due to the oxidation of Hg^0 to Hg^{2+}, and Hg^0 was produced by the reduction of Hg^{2+} at the accumulation step under negative potentials. If the cyclic scan was performed after precon-

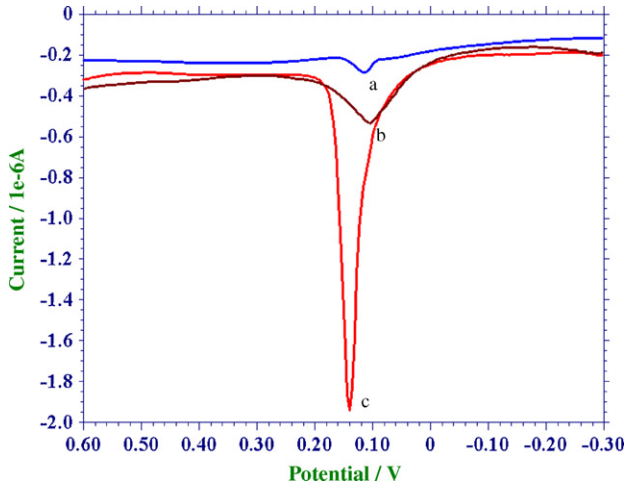


Fig. 7. Differential pulse anodic stripping voltammograms of 1.0×10^{-8} mol L^{-1} Hg^{2+} in 0.1 mol L^{-1} H_2SO_4 + 0.01 mol L^{-1} KCl at different glassy carbon electrodes: (a) bare GCE, (b) modified GCE using direct coating method, (c) LB-TCA/GCE (2 layers). Accumulation time: 90 s; accumulation potential: −0.6 V.

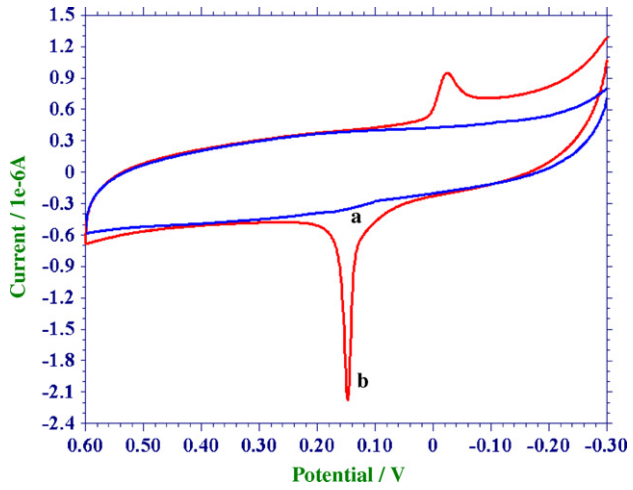


Fig. 8. Cyclic voltammograms of blank solutions (a) and 1.0×10^{-8} mol L^{-1} Hg^{2+} (b) at LB-TCA/GCE (2 layers); other experimental conditions are the same as those described in Fig. 7.

centration, a small reduction peak at −0.1 V was appearance (Fig. 8, curve b) during the reverse scan. It implied that majority of Hg^{2+} was stripped out from the surface of electrode and diffused into solution. Because the oxidation peak current was more sensitive to reduction peak current, the anodic peak of Hg^{2+} was systematically studied by differential pulse anodic stripping voltammetry for analytical applications.

3.6. Mechanism of the method

To investigate the mechanism of the method, the preconcentration step was performed under open-circuit condition. Subsequently, the electrode was removed from the accumulation cell, rinsed thoroughly with water, and placed in quiescent blank electrolyte solution. Then, an initial potential of −0.6 V (versus SCE) was applied to the working electrode for 20 s, and the differential pulse anodic stripping voltammograms (DPASV) were recorded. A distinct anodic peak could be discerned at about +0.11 V, due to the oxidation of Hg^0 to Hg^{2+}. Thus, the possible mechanism of electrode reaction can be described as follows:

Accumulation step:

$$\text{LB-TCA/GCE (surface)} + Hg^{2+}\text{ (solution)} \rightarrow \text{LB-TCA/GCE} - Hg^{2+}\text{ (surface)}$$

Reduction step:

$$\text{LB-TCA/GCE} - Hg^{2+}\text{ (surface)} + 2e \rightarrow \text{LB-TCA/GCE} - Hg^{0}\text{ (surface)}$$

Stripping step:

$$\text{LB-TCA/GCE} - Hg^{0}\text{ (surface)} \rightarrow \text{LB-TCA/GCE (surface)} + Hg^{2+}\text{ (solution)} + 2e$$

Table 2
Influence of other metal ions on the peak current of 5×10^{-8} mol L^{-1} Hg^{2+}.

Interferent	Concentration	Signal change (%)
Fe^{3+}	1×10^{-6} mol L^{-1}	2.0
Mn^{2+}	1×10^{-6} mol L^{-1}	2.4
Co^{2+}	1×10^{-6} mol L^{-1}	1.5
Ni^{2+}	1×10^{-5} mol L^{-1}	2.6
Zn^{2+}	1×10^{-6} mol L^{-1}	2.3
Cr^{3+}	1×10^{-5} mol L^{-1}	−1.8
Cd^{2+}	1×10^{-6} mol L^{-1}	−3.4
Ti^{4+}	1×10^{-5} mol L^{-1}	−1.2
Ag^{+}	1×10^{-7} mol L^{-1}	4.2
Pb^{2+}	1×10^{-6} mol L^{-1}	−4.3
Al^{3+}	1×10^{-6} mol L^{-1}	−1.4
Cu^{2+}	1×10^{-6} mol L^{-1}	−2.3

In real operation procedure, the accumulation step and reduction step were performed simultaneously under potential of −0.6 V.

3.7. Analytical applications and methods validation

3.7.1. Optimum condition of determination

The influences of supporting electrolytes were investigated in $HClO_4$, H_2SO_4, HNO_3, HAc-NaAc, phosphate buffer solution and B-R buffer solution, respectively. The results showed that voltammetric peaks were observed in all these electrolyte solutions, but the electrochemical responses in 0.1 mol L^{-1} H_2SO_4 + 0.01 mol L^{-1} KCl solutions were the best shape and largest stripping peak current among these solutions. Therefore, this supporting electrolyte was employed in following experiments.

Accumulation potential (E_{acc}) and accumulation time (t_{acc}) are very important parameters for stripping techniques and have non-negligible influence on the efficiency of preconcentration and the sensitivity of determination. E_{acc} between −1.4 and −0.4 V were investigated in a solution of 1.0×10^{-8} mol L^{-1} Hg^{2+} for accumulation of 90 s under every potential. Then DPV was performed with the same operation parameters. The results shown that the anodic peak currents were higher in E_{acc} interval of between −0.6 and −0.8 V. At more positive potentials a decrease of the anodic peak current was caused by the inefficient reduction of Hg^{2+} to Hg^0 at the electrode surface. Thus −0.6 V was chosen as the E_{acc} in all experiments. The anodic peak currents were linearly increscent as the t_{acc} increases, and start to reach a plateau around 210 s with the mercury concentration of 1.0×10^{-8} mol L^{-1}. For all we know, the longer accumulation time, the higher sensitivity is gotten in stripping voltammetry, but narrow detect range is emerged. In this detection system containing 1.0×10^{-8} mol L^{-1} Hg^{2+}, accumulating saturation was reached by preconcentration of 210 s. Considering the detect limit and linear range, t_{acc} 90 s was chosen in following study. The peak currents were linearly relationship with Hg^{2+} concentrations in nearly three quantitative orders under 90 s preconcentration time.

The relationship between peak currents and the modified layers of LB-TCA was also investigated. 1-Layer of LB-TCA/GC had a low efficiency of preconcentration and a low peak current. When the layers of LB-TCA were ≥3, the peak currents were decreased grad-

Table 1
Characteristic parameters for determination of Hg^{2+} with macrocyclic modified electrochemical sensors from published methods.

Modifier	Linear concentration range (mol L^{-1})	Detection limit (mol L^{-1})	Reference
Evaporated thin films of thiacalix[4]arene amide modified gold electrode	3.2×10^{-3} to 1.0×10^{-4}	1.0×10^{-4}	[25]
Novel calix[4]arene modified GCE	5.0×10^{-8} to 5.0×10^{-5}	1.5×10^{-8}	[34]
$CPE_{\alpha\text{-CD}}$, $CPE_{\beta\text{-CD}}$ modified GCE	$CPE_{\alpha\text{-CD}}$: 2.6×10^{-8} to 1.41×10^{-5} $CPE_{\beta\text{-CD}}$: 1.7×10^{-8} to 3.77×10^{-5}	5.0×10^{-8} 9.0×10^{-8}	[9]
PVC membrane of ehexathiacyclooctadecane and chromoionophore V	2.1×10^{-7} to 1.2×10^{-4}	2.0×10^{-7}	[35]
Langmuir–Blodgett film *p*-allylcalix[4] arene modified GCE	3.5×10^{-10} to 2.0×10^{-7}	2.0×10^{-10}	[36]
Langmuir–Blodgett film *p-tert*-butylthiacalix[4]arene modified GCE	5.0×10^{-10} to 1.5×10^{-7}	2.0×10^{-10}	This work

Table 3
Determination of Hg^{2+} in water samples by DPV at fabricated electrode and AFS.

Sample	DPV ($n=3$)					AFS ($n=3$)	
	Original found (1.0×10^{-8} mol L^{-1})	Added (1.0×10^{-8} mol L^{-1})	Total found (1.0×10^{-8} mol L^{-1})	R.S.D. (%)	Recovery (%)	Total found (1.0×10^{-8} mol L^{-1})	R.S.D. (%)
Tap water	BD[a]	4.00	4.12	2.3	103.0	4.03	1.9
Lake water	BD[a]	4.00	4.38	3.4	109.5	4.20	3.7
River water	0.8	4.00	4.99	2.7	104.8	4.79	2.2

[a] BD: below the detection limit.

ually by increasing the LB-TCA layer. This phenomenon was due to their high resistance which blocked electron transfer between Hg and electrode. The best response was obtained when 2-layer LB-TCA was used, which was employed in following experiment.

3.7.2. Calibration curve, detection limit, reproducibility and stability

Series concentrations of standard solutions of Hg^{2+} were detected under the optimized working conditions described above. A linear relationship could be established between i_{pa} and the concentration of Hg^{2+} in the range of 5.0×10^{-10} to 1.5×10^{-7} mol L^{-1}. The linear regression equation and correlation coefficient are:i_{pa} (μA) $= 0.665 + 1.028\times10^{8}c$ ($r = 0.998$)where i_{pa} was the oxidation peak current in μA and c was the concentration of Hg^{2+} in mol L^{-1}. Based on the signal-to-noise ratio of 3 (S/N), the detection limit was obtained as 2.0×10^{-10} mol L^{-1}. These values confirmed the sensitivity of the proposed method for the determination of Hg^{2+}. To estimate the reproducibility of the proposed electrode, the R.S.D. of five times successful measurement the peak current of 1×10^{-8} mol L^{-1} Hg^{2+} was calculated to be 3.9%, which demonstrated the good reproducibility of the proposed electrode. The stability of the electrode was examined by repetitive scanning in 1×10^{-8} mol L^{-1} Hg^{2+} solution. 108.4% of the initial response was remained after continuous scanning for 30 potential cycles. The LB-TCA/GCE can be stored about 4 weeks and the decrease of the response was got as 3.96%, which indicated that LB-TCA/GCE had good stability.

The proposed LB-TCA/GCE for Hg^{2+} determination was compared with other macrocyclic kinds of modified electrode and the results were listed in Table 1. Among macrocyclic modified electrodes [25,34,9,35,36], most of their detection limits were between 1.0×10^{-8} and 1.0×10^{-7} mol L^{-1}. The higher sensitive detect limit of 2.0×10^{-10} mol L^{-1} was achieved by use of a LB film *p*-allylcalix[4]arene modified GCE [36]. This research suggests that designed and modified electrode with LB techniques as voltammetric sensors might be a very promising direction in trace analysis of electrochemistry.

3.7.3. Interference studies

For analytical application of the proposed method, possible interference by coexisting metal ions were evaluated by analyzing sample solutions containing a fixed amount of Hg^{2+} (5.0×10^{-8} mol L^{-1}) spiked with various excess amount of species under the same experimental conditions. The results showed that no interference was observed in the presence of 1.0×10^{-5} mol L^{-1} alkaline metal ions and earth metal ions. Table 2 lists the interference data of Fe^{3+}, Mn^{2+}, Co^{2+}, Ni^{2+}, Zn^{2+}, Cr^{3+}, Cd^{2+} Ti^{4+}, Ag^{+}, Pb^{2+}, Al^{3+} and Cu^{2+} for determination of 5.0×10^{-8} mol L^{-1} Hg^{2+}. Most of these coexisting ions bring the detection signal deviation below 5% under sufferable coexisting amount. The only trouble may be from Ag^{+}. It bring 4.2% signal increase when $[Ag^{+}]/[Hg^{2+}] = 2$ is present.

3.7.4. Analysis of real samples

To evaluate the practical applicability of the proposed method, it was employed to the detection of Hg^{2+} in tap water, lake water and river water samples. No distinct signal of Hg^{2+} was observed when the tap water and lake water samples were analyzed. Thus, the proposed method was applied to detect water samples spiked with Hg^{2+} standard solution at a certain concentration. The determination of Hg^{2+} concentration was performed by the calibration curve method. The mean recovery of 4.00×10^{-8} mol L^{-1} Hg^{2+} was 105.77%. In addition, the results were compared with those obtained by AFS and were shown in Table 3. At 95% confidence level, no difference between results from the proposed and AFS methods had been established. Therefore, this proposed method could be applied to the determination of a trace level of Hg^{2+} in real samples.

4. Conclusions

In the present work, a new voltammetric sensor for the detection of trace amounts of Hg^{2+} based on a calixarene derivative LB film-modified GCE was designed. The recognition mechanism of this electrode for Hg^{2+} in aqueous solution was discussed and some experimental parameters were optimized. By using this LB film-modified electrode, trace amounts of Hg^{2+} could be detected with LOD of 2.0×10^{-10} mol L^{-1} by differential pulse anodic stripping voltammetry with accumulation of 90 s under −0.6 V. This research suggest also that designed and modified electrode with LB techniques might be a very promising basis for analytical sensing.

Acknowledgements

The authors gratefully acknowledge the financial support of the National Natural Science Foundation of China (nos. 20775073, 20875083).

References

[1] N.L. Dias Filho, D.R. do Carmo, L. Caetano, A.H. Rosa, Anal. Sci. 21 (2005) 1359.
[2] J.L. Capelo, I. Lavilla, C. Bendicho, Anal. Chem. 72 (2000) 4979.
[3] A. Morales-Rubio, M.L. Mena, C.W. McLeod, Anal. Chim. Acta 308 (1995) 364.
[4] L. Rahman, W.T. Corns, D.W. Bryce, P.B. Stockwell, Talanta 52 (2000) 833.
[5] E.K. Pavlos, G.K.K. Nikolaos, Anal. Chem. 76 (2004) 4315.
[6] M.-S. Jeoung, H.-S. Choi, Bull. Korean Chem. Soc. 25 (2004) 1877.
[7] M.A. Rahman, M.S. Won, Y.B. Shim, Anal. Chem. 75 (2003) 1123.
[8] H.M.J. Luiz, C.J. Bruno, C.L. Bruna, F.F. Orlando, Anal. Lett. 40 (2007) 3119.
[9] G. Roa-Morales, M.T. Ramírez-Silva, R.L. González, L. Galicia, M. Romero-Romo, Electroanalysis 17 (2005) 694.
[10] W. Huang, S. Zhang, Anal. Sci. 18 (2002) 187.
[11] U. Tamer, T. Oymak, N. Ertas, Electroanalysis 19 (2007) 2565.
[12] H. Zejli, P. Sharrock, J.L. Hidalgo-Hidalgo de Cisneros, I. Naranjo-Rodriguez, K.R. Temsamani, Talanta 68 (2005) 79.
[13] A.A. Khan, Inamuddin, T. Akhtar, Anal. Sci. 24 (2008) 881.
[14] K.C. Cheng, P.Y. Chen, Electroanalysis 20 (2008) 207.
[15] G. Cabello-Carramolino, M.D. Petit-Dominguez, Anal. Chim. Acta 614 (2008) 103.
[16] A. Doménech, Ma.T. Doménech-Carbó, E. García-España, Ma.D. Soriano, Analyst 124 (1999) 1661.
[17] O. Abollino, A. Giacomino, M. Malandrino, G. Piscionieri, E. Mentasti, Electroanalysis 20 (2008) 75.
[18] G.E. Fanucci, R. Backov, R. Fu, D.R. Talham, Langmuir 17 (2001) 1660.
[19] Z. Wu, S. Wu, Y. Liang, Langmuir 17 (2001) 7267.
[20] A. Ikeda, S. Shinkai, Chem. Rev. 97 (1997) 1713.
[21] R.K. Mahajan, I. Kaur, M. Kumar, Sens. Actuat. B 91 (2003) 26.

[22] M. Giannetto, G. Mori, A. Notti, S. Pappalardo, M.F. Parisi, Chem. Eur. J. 7 (2001) 3354.
[23] H. Akdas, E. Graf, M.W. Hosseini, A.D. Cian, J.M. Harrowfield, Chem. Commun. 22 (2000) 2219.
[24] X.J. Hu, Zh.G. Pan, L. Wang, X.F. Shi, Spectrochim. Acta, Part A 59 (2003) 2419.
[25] C. Dridi, M. Ben Ali, F. Vocanson, J. Davenas, S. Ben Maamar, F. Meganem, R. Lamartine, N. Jaffrezic-Renault, Mater. Sci. Eng. C 28 (2008) 765.
[26] H. Zheng, Zh.N. Yan, H.M. Dong, B.X. Ye, Sens. Actuat. B 120 (2007) 603.
[27] H. Zheng, H.M. Dong, Zh.N. Yan, L.Y. Wen, Sh. Zhang, B.X. Ye, Electroanalysis 18 (2006) 2115.
[28] Z.F. Ye, S.F. Pang, W.J. He, X.F. Shi, Z.J. Guo, L.G. Zhu, Spectrochim. Acta, Part A 57 (2001) 1443.
[29] J.P. Santos, M.E.D. Zaniquelli, P.J. Dutton, Colloids Surf. A 198–200 (2002) 605.
[30] H. Kämmerer, G. Happel, B. Mathiasch, Die Makromol. Chem. 182 (1981) 1685.
[31] A.H. Herz, Adv. Colloid Interface Sci. 8 (1977) 237.
[32] Y.J. Liu, F. Yin, Y.M. Long, Z.H. Zhang, S.Z. Yao, J. Colloid Interface Sci. 258 (2003) 75.
[33] R.J. Pei, Z.L. Cheng, E.K. Wang, X.R. Yang, Biosens. Bioelectron. 16 (2001) 355.
[34] J.Q. Lu, X.W. He, X.S. Zeng, Q.J. Wan, Zh.Zh. Zhang, Talanta 59 (2003) 553.
[35] A.A. Ensafi, M. Fouladgar, Sens. Actuat. B 136 (2009) 326.
[36] H.M. Dong, L. Lin, H. Zheng, G.X. Zhao, B.X. Ye, Electroanalysis 18 (2006) 1202.

Talanta 80 (2010) 1205–1209

Contents lists available at ScienceDirect

Talanta

journal homepage: www.elsevier.com/locate/talanta

Silica gel modified with 1-(2-aminoethyl)-3-phenylurea for selective solid-phase extraction and preconcentration of Sc(III) from environmental samples

Zhifeng Tu, Zheng Hu, Xijun Chang*, Lijun Zhang, Qun He, Jianping Shi, Ru Gao

Department of Chemistry, Lanzhou University, Tianshui Road 222, Lanzhou, Gansu 730000, PR China

ARTICLE INFO

Article history:
Received 19 June 2009
Received in revised form 25 August 2009
Accepted 8 September 2009
Available online 17 September 2009

Keywords:
Silica gel
1-(2-Aminoethyl)-3-phenylurea
Sc(III)
Solid-phase extractant
Inductively coupled plasma atomic emission spectrometry

ABSTRACT

A new method that utilizes 1-(2-aminoethyl)-3-phenylurea-modified silica gel as a solid-phase extractant has been developed for preconcentration of trace Sc(III) prior to the measurement by inductively coupled plasma atomic emission spectrometry (ICP-AES). Experimental conditions for effective adsorption of trace level of Sc(III) were optimized using batch and column procedures in detail. The optimum pH value for the separation of Sc(III) on the new sorbent was 4 and complete elution of Sc(III) from the sorbent surface was carried out using 1.0 mL of 0.1 mol L^{-1} HCl. Common coexisting ions did not interfere with the separation and determination of the analyte. The maximum static adsorption capacity of the sorbent at optimum conditions was found to be 32.5 mg g^{-1} while the time of 95% adsorption was less than 2 min. The detection limit of present method was found to be 0.091 μg g^{-1}, and the relative standard deviation (RSD) was lower than 3.0% (n = 8). The method was successfully applied for the preconcentration of trace Sc(III) in the environmental samples with satisfactory results.

© 2009 Elsevier B.V. All rights reserved.

1. Introduction

The rare earth elements (REEs) are a particularly useful suite of trace elements. With the development of new materials, REEs were applied in many industrial fields, such as superconducting materials, permanent magnets, fluorescent materials, and solid-state laser areas and so on. So, the industrial usage of REEs is growing rapidly [1]. Scandium belongs to the rare element group which possesses special physical and chemical features, especially surface activity. Compared to other rare earth elements, scandium is the first element with lowest density. And it is forecasted as "Boron-like" element in Mendeleev elements' period table [2]. For the research of lanthanide and Y, scandium is believed to be important for a reference element. Furthermore, scandium could be a surrogate for Al in estimating global dust fluxes to the oceans [3]. It also has emerged as an element of technological promise especially in the fields of laser research, radio and illuminations engineering and also in space applications as scandium-based alloys with Ti, Ce, W and Cr [4]. So, the research of scandium becomes very important. However, it often happens that the trace scandium remains unseparated from REEs, which makes a fatal defect for the determination. Therefore, the preconcentration and determination of scandium from samples need to be paid more attention [5].

A number of instrumental methods are now available for accurate determination of scandium such as neutron activation analysis (NAA) [3,6], inductively coupled plasma-mass spectrometry (ICP-MS) [7,8], atomic absorption spectrometry (AAS) [9] and inductively coupled plasma atomic emission spectrometry (ICP-AES) [10,11]. In comparison, ICP-AES is a timesaving, simple, and well-available technique and has now been established as a powerful analytical technique for the determination of scandium in real samples [5,10]. However, its detection capability is usually insufficient due to the matrix interferences and the very low content of scandium. Therefore, a separation/preconcentration step is required.

Nowadays, solid-phase extraction (SPE) becomes the most common technique for environmental sample pretreatment because of its advantages of high recovery, short extraction time, high enrichment factor, low cost, and low consumption of organic solvents over liquid–liquid extraction [12,13].

In SPE procedure, the choice of appropriate sorbent is a critical factor to obtain full recovery and high enrichment factor. Among the many types of solid phase used in SPE, silica gel immobilized with various organic compounds such as a metal chelating agent for metal ions' removal, extraction, separation and preconcentration from different matrices, has received great attention for its good mechanical and thermal stability and its less susceptibility to swelling, shrinking and microbial and radiation decay [14]. The modified silica gel are used in the fields of normal or selective solid-phase extraction of the target species [15–17]. Such variations in the behavior of the modified solid sorbents are mainly dependent

* Corresponding author. Tel.: +86 931 891 2422; fax: +86 931 891 2582.
E-mail address: tuzhf07@lzu.cn (X. Chang).

0039-9140/$ – see front matter © 2009 Elsevier B.V. All rights reserved.
doi:10.1016/j.talanta.2009.09.009

on the presence of some active donor atoms or groups such as O, N, S and P into the incorporated organic modifier [18].

In our work, 1-(2-aminoethyl)-3-phenylurea chemically modified silica gel (SG-AEP) was synthesized and characterized. The new sorbent showed great affinity, relatively high adsorption capacity, less equilibrium time and easy elution for Sc(III). Parameters that affect the sorption and elution efficiency of the metal ions were also studied. Then, the method was applied to preconcentrate trace Sc(III) from environmental samples with satisfactory results.

2. Experimental

2.1. Chemicals and reagents

Unless otherwise stated, all water is double distilled water and all reagents used were of analytical and spectral purity. Standard labware and glassware used were repeatedly cleaned with HNO_3 and rinsed with double distilled water, according to a published procedure [19].

All single element REE, Y, Sc (as oxides) of 1.0 mg mL^{-1} standard stock solutions were made by dissolving rare earth oxides in hydrochloric acid with the exception of CeO_2 that was dissolved in a mixture of HNO_3 and H_2O_2 and later converted to HCl medium. Single element working standards were prepared by dilution of the stock solution with 0.5 mol L^{-1} HCl according to a published procedure [10]. Silica gel (100–200 mesh, Mouping Kangbinuo Chemical Factory, Yantai, China), ethylenediamine (EDA) (The First Reagent Factory, Shanghai, China), isopropyl isocyanate (Weiwei Reagent Factory, Shanghai, China) were used in this work. *N*,*N*′-Dicyclohexylcarbodiimide (DCC) was purchased from Sinopharm Chemical Reagent Co. Ltd. (Shanghai, China) and 3-chloropropyltrimethoxysilane was purchased from Wuhan University Chemical factory (Wuhan, China).

2.2. Instruments and apparatus

An IRIS Advantage ER/S inductively coupled plasma emission spectrometer (Thermo Jarrel Ash, Franklin, MA, USA) was used for all metal ions determination. The instrumental parameters were those recommended by the manufacturer. The wavelength of scandium selected is 363.074 nm [20]. A pHs-3C digital pH meter (Shanghai Lei Ci Device Works, Shanghai, China) was used for the pH adjustments. Infrared spectra (4000–400 cm^{-1}) in KBr were recorded on a Nicolet NEXUS 670 FT-IR spectrometer (Nicolet, Madison, WI, USA). Thermogravimetric analysis (TG) was carried out on a STA 449 C (Netzsch, Germany). An YL-110 peristaltic pump (General Research Institute for Non-ferrous Metals, Beijing, China) was used in the column process. A PTFE (polytetrafluoroethylene) column (45 mm × 3.0 mm i.d, Tianjin Jinteng Instrument Factory, Tianjin, China) was used.

2.3. Sample preparation

The reference materials (GBW08302, Tibet soil and GBW07602, shrubbery leaves) were purchased from National Research Center for Certified Reference Materials (Beijing, China). Orange leaves were obtained from Anning village, Lanzhou, China. Fish was purchased from Hualian market, Lanzhou, China. Fish and orange leaves were dried in an oven at 80 °C to constant weight. A 1.0 g fish or orange leaves sample was weighted and transferred into a digestion tube, and then 5 mL of concentrated HNO_3 was added into it. The tube was left at room temperature for one night. Then it was placed in a digester block and heated slowly until the temperature was up to 165 °C. This temperature was maintained until ceasing the evolution of brown fumes. After the tube was cooled down, 1.3 mL perchloric acid was added into it. Then the temperature was raised to 210 °C until evolution of white fumes began. The volume was adjusted to 100 mL with double distilled water after the tube was cooled down [21].

Kaolin ore was obtained from Beijing Chemical Factory (Beijing, China). The sample (0.2 g) was weighed into a PTFE beaker, and 5 mL of 70% $HClO_4$ and 10 mL of 48% HF were added. Following the directions found in the literature [5], the beaker was heated on a sand bath to incipient dryness. The mixed acid ($HClO_4$ + HF) was repeated three times to complete digestion of the silicate matrix. Finally, the sample was transferred into flasks and diluted to 50 mL with 0.2% HCl.

2.4. Preparation of new sorbent

2.4.1. Preparation of SG-AEP

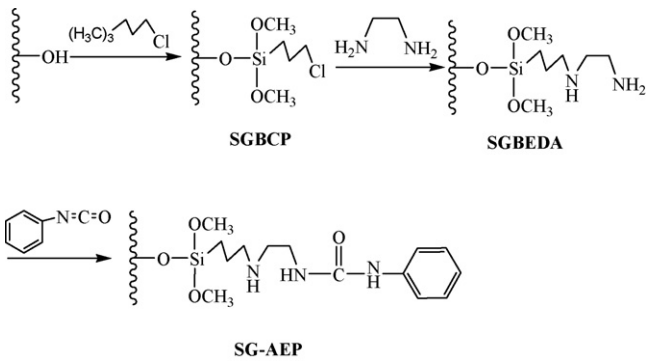
Activation of silica gel surface was first accomplished by refluxing in a concentrated hydrochloric acid for 4 h to remove any adsorbed metal ions, then filtered and repeatedly washed with water until the filtrate is neutral and dried in an oven at 160 °C for 8 h to remove surface-adsorbed water. Then 10.0 g of dry activated silica gel was suspended in 150 mL dry toluene containing 10 mL of 3-chloropropyltrimethoxysilane and refluxed overnight. The product silica gel phase was filtered off, washed with toluene, ethanol and diethyl ether and dried in an oven at 60 °C for 6 h. The product was silica gel-bound 3-chloropropyl phase (SGBCP). For the synthesis of silica gel-bound amines phase, a 10.0 g amount of SGBCP was suspended in 75 mL of dry toluene and 10 mL of ethylenediamine were added to the suspension and refluxed for 12 h. The product (SGBEDA) was filtered off, washed with toluene, ethanol and diethyl ether and dried in an oven at 60 °C for 6 h.

Chemically immobilized silica gel with 1-(2-aminoethyl)-3-phenylurea was synthesized according to the following procedure. A 5.0 g amount of SGBEDA and 2.0 mL phenyl isothiocyanate were suspended in 30 mL of ether under N_2 atmosphere and stirred for 40 h at room temperature. The product SG-AEP was filtered off, washed with ethanol and dried under vacuum at 80 °C for 8 h. The synthetic route of SG-AEP is illustrated in Scheme 1.

2.4.2. Characterization of SG-AEP

The modified silica gel was confirmed by IR analysis as shown in Fig. 1. Comparison of the IR spectrum of SG-AEP with that of SGBCP, many new peaks appeared in the spectrum. According to the literature [22,23], the new peaks can be assigned as follows: the peak at 1639.10 cm^{-1} is due to $\nu_{C=O}$, the peaks at 754.71 cm^{-1} are caused by δ_{N-H}. The bands around 3420.75 cm^{-1} can be assigned to ν_{N-H}. The peaks at 1447.41, 1501.48, 1555.25 and 1603.21 cm^{-1} are due to the benzene ring characteristic vibrations in the SG-AEP.

Thermogravimetry (TG) curves of SGBCP and SG-AEP were presented in Fig. 2(a) and (b), respectively. As seen in Fig. 2, the starting temperature of weight loss for SG-AEP occurred at 171.4 °C, which



Scheme 1. Synthetic route of the SG-AEP.

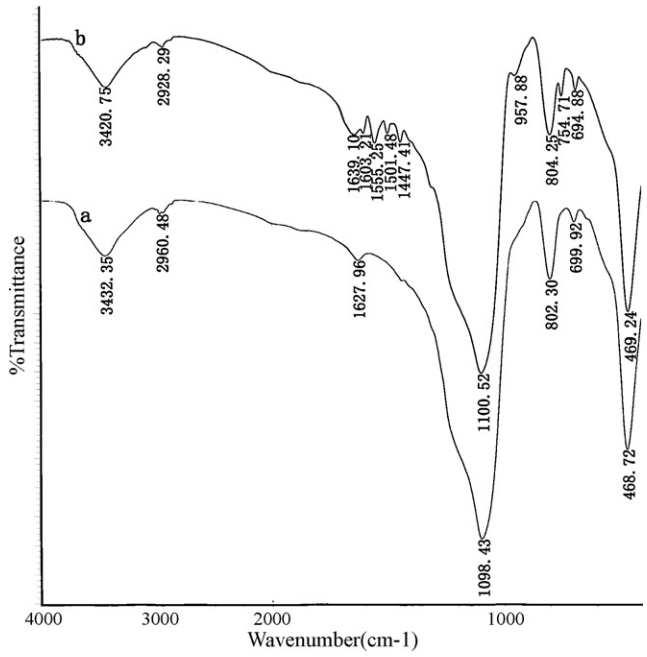


Fig. 1. IR spectra of SGBCP (a) and SG-AEP (b).

is lower than SGBCP (319.8 °C). The TG curves indicated that the weight loss of SG-AEP is step by step from 171.4 to 800 °C, and the rate of the fastest weight loss for SG-AEP is higher than SGBCP. At 800 °C the weight losses of SGBCP and SG-AEP are 7.50% and 13.02%, respectively. All of the results confirmed that 1-(2-aminoethyl)-3-phenylurea is chemically bonded to activated silica gel.

Consequently, the above experimental results suggest that activated silica gel is successfully modified by 1-(2-aminoethyl)-3-phenylurea.

2.5. Procedures

2.5.1. Batch method

The data are given on the simple mean of three replicates, whereas those of the applications were repeated eight times from which the statistical evaluation is pertained.

A portion of standard or sample solution containing Sc(III) was transferred into a 25 mL beaker, and the pH value was adjusted to the desired value with 0.1 mol L^{-1} HNO_3 and 0.1 mol L^{-1} $NH_3{\cdot}H_2O$. Then the volume was adjusted to 10 mL with double distilled water. 40 mg of SG-AEP was added, and the mixture was shaken vigorously for 30 min to facilitate adsorption of the metal ions onto the sorbents. The concentrations of the metal ions in the solution were directly determined by ICP-AES. The adsorbent was then eluted with HCl at optimum concentration and volume. Then the desorbed metal ions were measured by ICP-AES.

2.5.2. Column SPE procedure

A total 50 mg of SG-AEP was packed in the PTFE column plugged with a small portion of glass wool at both ends. Before use, 0.5 mol L^{-1} HCl and double distilled water were successively passed through the microcolumn in order to equilibrate, clean and neutralize it. A suitable aliquot of the sample solution containing 1.0 μg mL^{-1} Sc(III) in a volume of 10 mL was passed through the column after adjusting its pH to 4, at a flow rate of 2.0 mL min^{-1} controlled with a peristaltic pump. The bound metal ions were stripped off from the gel column with 0.1 mol L^{-1} HCl. The analytes in the eluate were determined by ICP-AES.

3. Results and discussion

3.1. Effect of pH

The pH value plays an important role with respect to the adsorption of different ions on oxide surfaces. Therefore, solution pH value is the first parameter to be optimized. According to the recommended procedure (batch method), several metal ions, viz. Sc(III), La(III), Er(III), Ce(III), Ho(III), Nd(III), Sm(III), Ir(IV) and Y(III) were tested and determined at different pH value, namely pH 1, 2, 3, 4, 5 and 6. Aliquots of 10 mL of the solutions were tested by equilibrating 40 mg sorbent. The results showed that the SG-AEP had excellent adsorptive selectivity towards Sc(III) from pH 4–6 than any other ions. It could be seen in Fig. 3 that the optimum pH for quantitative extraction (>95%) of Sc(III) occurred at pH ≥ 4. In order to avoid hydrolyzing at higher pH, pH 4 was selected as the enrichment acidity for further study. In addition, Ce(III) and Ir(IV) were not enriched by SG-AEP at pH 4; La(III), Er(III), Ho(III), Nd(III), Sm(III) and Y(III) could be adsorbed by SG-AEP about 20–50% at pH 4, but they do not interfere with enrichment and determination of Sc(III).

3.2. Effect of shaking time

Modification of silica gel surface with organic complexing agents results in producing metal ion extractors that need only a few minutes to complete the metal ion extraction processes in comparison with other organic adsorbents [24], and this is another

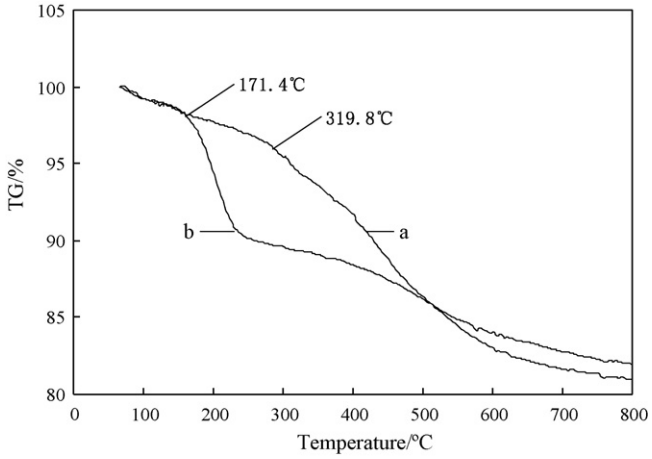


Fig. 2. TG curves of SGBCP (a) and SG-AEP (b).

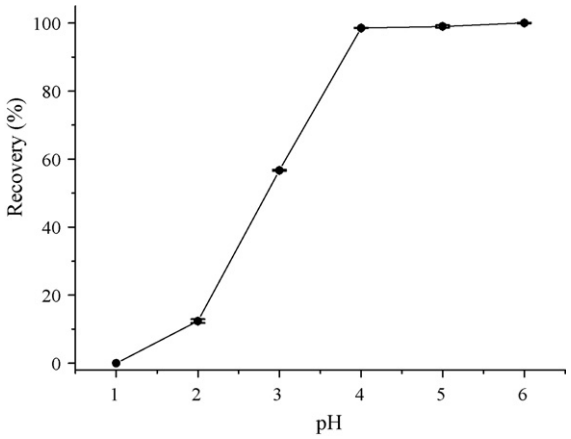


Fig. 3. Effect of pH on adsorption of 1.0 μg mL^{-1} Sc(III) on SG-AEP. Other conditions: shaking time 30 min, temperature 25 °C.

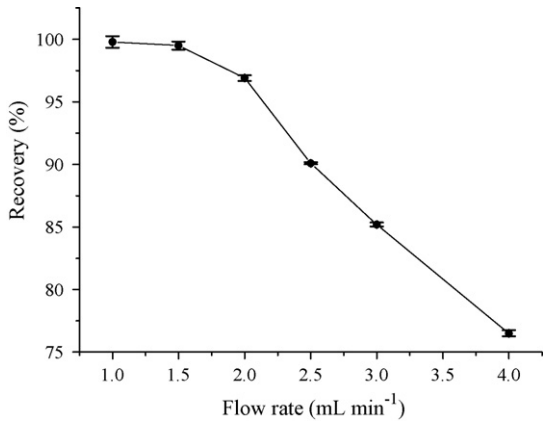


Fig. 4. Effect of solution flow rates on adsorption of 1.0 μg mL^{-1} Sc(III) on SG-AEP. Other conditions: 50 mg of SG-AEP, volume 10 mL, pH 4, temperature 25 °C.

advantage of using silica gel as inorganic solid support for immobilization of chelating compounds.

In this work, different shaking time (ranged from 2 to 30 min) was studied for the percentage extraction of Sc(III) by SG-AEP. The results showed that the adsorption of Sc(III) was over 95% sorption during the first 2 min, which indicated that kinetics of adsorption equilibrium was very fast.

3.3. Effect of flow rate

The flow rate of the sample solution affects the retention of cations on the adsorbent and the duration of complete analysis. Therefore, the effect of the flow rate of sample solution was examined under the optimum conditions by passing 10 mL of sample solution through the microcolumn with a peristaltic pump. The flow rates were adjusted in range of 1.0–4.0 mL min^{-1}. As shown in Fig. 4, it was found that the retention of the studied ion was practically not changed up to 2.0 mL min^{-1} flow rate. The recovery of the analyte decreases slightly when the flow rate is over 2.0 mL min^{-1}. Thus, a flow rate of 2.0 mL min^{-1} is employed in this work.

3.4. Maximum sample volume, enrichment factor and elution condition

In order to explore the possibility of enriching low concentration of the analyte from large volume of solution, the effect of sample volume on the retention of metal ion was also investigated. For this purpose, 50, 100, 150, 200, 250 and 300 mL of sample solutions containing 1.0 μg Sc(III) were passed through the microcolumn at the optimum flow rate. Quantitative recovery (>95%) was obtained for the sample volume of 150 mL for Sc(III), and at greater volume percent of recovery decreased.

The elution condition was studied by using various concentrations and volumes of HCl solution for the desorption of retained Sc(III). The obtained results were shown in Table 1. It was found that 1.0 mL of 0.1 mol L^{-1} HCl was sufficient for complete elution for Sc(III) (recovery >95%). Therefore, 1.0 mL of 0.1 mol L^{-1} HCl solution was used as eluent in further experiments. Thus, the high enrichment factor of 150 was obtained.

Table 1
Eluent data (%) for Sc(III) adsorbed on SG-AEP.

	Concentration (mol L^{-1})[a]					
	0.01	0.05	0.1	0.5	1	2
Recovery (%)						
HCl	75.2	90.1	98.6	99.2	100	100
Eluent volume (mL)[b]	0.5	1.0	1.5	2.0	2.5	3.0
	75.6	96.3	97.5	99.1	99.8	100

[a] 2 mL.
[b] 0.1 mol L^{-1} HCl.

3.5. Adsorption capacities

The capacity of the adsorbent is an important factor because it determines how much adsorbent is required to quantitatively remove a specific amount of metal ions from the solutions. The adsorption capacity was tested following the batch procedure. 20 mg of sorbent was equilibrated with 10 mL of various concentrations of Sc(III) for 1 h. In order to reach the "saturation", the concentration of Sc(III) was increased till the plateau value (adsorption capacity value) obtained. The maximum adsorption capacity has been found to be 32.5 mg g^{-1} for Sc(III).

3.6. Stability tests

To test the stability, the sorbent material was subjected to several loading and elution bath operations. The sorption conditions are referenced according to the above experiments. The elution operations were carried out by shaking the adsorbent with 20 mL of 0.1 mol L^{-1} HCl for 1 h in order to ensure complete equilibration. Then the adsorbent was treated with doubly distilled water until neutral equilibration was reached. The operating capacity was calculated from the loading and elution tests. The results from three tests yielded <5% error up to 12 cycles of repeated experiments. The adsorbent showed better reusability and stability towards Sc(III).

3.7. Effects of coexisting ions

The effects of common coexisting ions on the adsorption of Sc(III) on SG-AEP were investigated. In these experiments, solutions of 1.0 μg mL^{-1} of Sc(III) containing the added interfering ions were treated according to the recommended procedure. The tolerance limit was set as the amount of ions causing recoveries of the examined element to be less than 95%. The results showed that 100-fold Ce(III), Ir(IV), 30-fold La(III), Er(III), Ho(III), Nd(III), Sm(III), Y(III), 1500-fold K(I), Na(I), Cl^-,1000-fold Ca(II), Mg(II), SO_4^{2-} and 50-fold Co(II), Ni(II), Zn(II), Cd(II) ions did not interfere with the separation and determination of the analyte. The results showed that SG-AEP had a high selectivity towards Sc(III) and have a potential to be applied to analyze real sample.

3.8. Analytical precision and detection limits

Under the selected conditions, eight portions of standard solutions were enriched and analyzed simultaneously following the general procedure. In accordance with the definition of IUPAC, the detection limit of the method was calculated based on three times the standard deviation of eight runs of the blank solution [25], the

Table 2
Analytical results for the determination of Sc(III) in certified reference materials.

Sample	Concentration of Sc(III) (μg g^{-1})	
	Found by the proposed method[a] (μg g^{-1})	Certified value (μg g^{-1})
GBW07602 (shrubbery leaves)	0.31 ± 0.03	0.29 ± 0.06
GBW08302 (Tibet soil)	10.81 ± 0.80	10.69 ± 0.41

[a] The value following "±" is the standard deviation (n = 8).

Table 3
Analytical results for the determination of Sc(III) in environmental samples.

Sample	Concentration of Sc(III) ($\mu g\,g^{-1}$)				
	Added	Found[a] by ICP-AES	Recovery (%)	Found[a] by ET-AAS	Recovery (%)
Fish	0	0.18 ± 0.04		0.17 ± 0.10	
	0.5	0.65 ± 0.11	96.5	0.65 ± 0.17	97.0
	1.0	1.16 ± 0.13	98.3	1.15 ± 0.33	98.3
Orange leaves	0	–		–	
	0.5	0.48 ± 0.02	96.0	0.48 ± 0.11	96.0
	1.0	1.01 ± 0.08	101.0	0.98 ± 0.32	98.0
Soil sample	0	0.20 ± 0.03		0.19 ± 0.26	
	0.5	0.69 ± 0.16	98.6	0.67 ± 0.44	97.1
	1.0	1.18 ± 0.22	98.3	1.16 ± 0.23	97.5

–: not detected.
[a] The value following "±" is the standard deviation ($n = 8$).

detection limit of this method was found to be 0.091 $\mu g\,g^{-1}$ for Sc(III). The relative standard deviation (RSD) of the eight replicate determinations was lower than 3.0%, which indicated that the method had good precision for the analysis of trace Sc(III) in solution samples.

3.9. Application of the method

In order to ascertain the accuracy of the suggested procedure, the method was applied to the determinations of trace Sc(III) in the certified reference materials (GBW08302, Tibet soil and GBW07602, shrubbery leaves), fish, orange leaves and kaolin ore sample. The results were listed in Tables 2 and 3. The analytical results for the standard materials were in good agreement with the certified values. The analytical results for fish, orange leaves and kaolin ore were in agreement with the electrothermal atomic absorption spectrometry (ET-AAS) method. The results indicate that the proposed method is reliable.

3.10. Comparison with other methods

Several methods have been reported for the determination of scandium in various types of samples including geological materials such as solvent extraction, extraction chromatography, ion exchange, chemical precipitation, flotation, electrophoresis, and liquid membrane separation [4,11,26–30] as well as their combined techniques [20]. However, these methods are complicated, time-consuming and/or reagent-consuming, sensitivity lowly, costs highly and the scandium yield of those methods is low [5,30]. In compared with those methods mentioned above, the present method possessed the advantages of excellent adsorptive selectivity, short analysis time, high enrichment factor, low consumption of organic solvents and low costs. Though it takes relatively long time for preparation of the material than the reported literature [5], it shows more mild reaction conditions. In addition, the synthetic method of the adsorbent is very simple. It also shows better or comparable capacity value to other solid support used for enrichment of Sc(III) mentioned above.

4. Conclusions

In this study, a simple, rapid, sensitive and reliable method was established for determination of trace level of Sc(III) in environmental samples based on silica gel modified with 1-(2-aminoethyl)-3-phenylurea as a solid-phase extractant. The most important characteristics of 1-(2-aminoethyl)-3-phenylurea-modified silica gel are its faster sorption and easy elution for Sc(III), and excellent adsorptive selectivity towards Sc(III) over other ions. Moreover, the synthetic method is very simple. This new developed method has been successfully applied to the analysis of trace Sc(III) in environmental samples. The precision and accuracy of the method are satisfactory. In summary, we have demonstrated that the new sorbent has high analytical potential for analysis of trace scandium from environmental samples.

References

[1] Z.G. Wei, M. Yin, X. Zhang, F.S. Hong, B. Li, Y. Tao, G.W. Zhao, C.H. Yan, Environ. Pollut. 114 (2001) 345.
[2] Y. Xie, J.T. Guo, Y.C. Liang, L.Z. Zhou, H.Q. Ye, Intermetallics 17 (2009) 400.
[3] M. Nomura, M. Sato, H. Amakawa, Y. Oura, M. Ebihara, Anal. Chim. Acta 553 (2005) 58.
[4] K. Satyanarayana, S. Durani, G.V. Ramanaiah, Anal. Chim. Acta 376 (1998) 273.
[5] L.J. Zhang, X.J. Chang, Y.H. Zhai, Q. He, X.P. Huang, Z. Hu, N. Jiang, Anal. Chim. Acta 629 (2008) 84.
[6] B.J.B. Nyarko, E.H.K. Akaho, J.J. Fletcher, A. Chatt, Appl. Radiat. Isotopes 66 (2008) 1067.
[7] W.R. Pedreira, C.A. Queiroz, A. Abrao, S.M. Rocha, M.E. de Vasconcellos, G.R. Boaventura, M.M. Pimentel, J. Alloys Compd. 418 (2006) 247.
[8] P. Robinson, A.T. Townsend, Z. Yu, C. Munker, Geostand. Geoanal. Res. 23 (1999) 31.
[9] J.G.S. Gupta, Talanta 31 (1984) 1045.
[10] G.V. Ramanaiah, Talanta 46 (1998) 533.
[11] P.J. Watkins, J. Nolan, Chem. Geol. 95 (1992) 131.
[12] Z.H. Li, X.J. Chang, X.J. Zou, X.B. Zhu, R. Nie, Z. Hu, R.J. Li, Anal. Chim. Acta 632 (2009) 272.
[13] Q. He, X.J. Chang, Q. Wu, X.P. Huang, Z. Hu, Y.H. Zhai, Anal. Chim. Acta 605 (2007) 192.
[14] Y.M. Cui, X.J. Chang, X.B. Zhu, H.X. Luo, Z. Hu, X.J. Zou, Q. He, Microchem. J. 87 (2007) 20.
[15] M.E. Mahmoud, Anal. Chim. Acta 398 (1999) 297.
[16] M.E. Mahmoud, G.A. Gohar, Talanta 51 (2000) 77.
[17] P.K. Jal, S. Patel, B.K. Mishra, Talanta 62 (2004) 1005.
[18] M.E. Mahmoud, M.S.M. Al Saadi, Anal. Chim. Acta 450 (2001) 239.
[19] D.P.H. Laxen, R.M. Harrison, Anal. Chem. 53 (1981) 345.
[20] M. Ochsenkühn-Petropulu, T. Lyberopulu, G. Parissakis, Anal. Chim. Acta 315 (1995) 231.
[21] X.B. Zhu, X.J. Chang, Y.M. Cui, X.J. Zou, D. Yang, Z. Hu, Microchem. J. 86 (2007) 189.
[22] H.T. Tang, Organic Compound Spectra Determination, Publishing House of Beijing University, Beijing, 1992, pp. 124–159.
[23] Q.N. Dong, IR Spectrum Method, Publishing House of the Chemical Industry, Beijing, 1979, pp. 104–168.
[24] M.E. Mahmoud, E.M. Soliman, A. El-Dissouky, Anal. Sci. 13 (1997) 765.
[25] G.L. Long, J.D. Winefordner, Anal. Chem. 52 (1980) 2242.
[26] M.H. Chhatre, V.M. Shinde, Talanta 47 (1998) 413.
[27] G. Guo, Y. Chen, Hydrometallurgy 23 (1990) 333.
[28] Z. Hubicki, Hydrometallurgy 23 (1990) 319.
[29] S. Himeno, E. Kitano, M. Kanaya, M. Takamoto, Talanta 71 (2007) 822.
[30] X.J. Yang, Z.M. Gu, D.X. Wang, J. Membr. Sci. 106 (1995) 131.

Talanta 80 (2010) 1210–1215

Contents lists available at ScienceDirect

Talanta

journal homepage: www.elsevier.com/locate/talanta

New MSPQC-PLS method for the early clinic identification of commonly encountered *Candida* species

Fengjiao He*, Ming Zhong

College of Chemistry and Chemical Engineering, State Key Laboratory of Chemo/Biosensing and Chemometrics, Hunan University, Changsha 410082, China

ARTICLE INFO

Article history:
Received 4 May 2009
Received in revised form 4 September 2009
Accepted 8 September 2009
Available online 17 September 2009

Keywords:
Candida species
PLS
Early identification
MSPQC

ABSTRACT

The early clinic identification of commonly encountered *Candida* species became more important with the increasing human candidiasis. In this paper, a new MSPQC-PLS (multi-channel series piezoelectric quartz crystal biosensor combined with partial least square) method was proposed for early identification of the most frequent *Candida* species encountered in human pathology. This method was based on these fact that (1) MSPQC method is a real-time monitoring method based on the sensitive frequency response to the change of electric parameters of the culture media caused by the growth of microorganisms; (2) various *Candida* species produce significantly different types of frequency curves in 1 or 2 days' culture period; (3) this difference can be identified by the partial least square technique. Using the proposed method, three species (*Candida albicans*, *Candida glabrata*, and *Candida tropicalis*) from a collection of 53 clinical strains of *Candida*, isolated from hospitalized patients, were identified with a classification rate of 98.1%. New proposed MSPQC-PLS method is simple, rapid and convenient to perform. It can identify clinical *Candida* species directly without passing through pure culture process. This will save identification time greatly. It could be popularized in clinical microbiology laboratories.

© 2009 Elsevier B.V. All rights reserved.

1. Introduction

Nosocomial candidiasis has become an important cause of morbidity and mortality [1–3]. Invasive candidiasis is the predominant fungal infection in the intensive care unit setting, neutropenic patients and post-surgery units [4–6]. *Candida* species Account for 70–80% of invasive bloodstream fungal infections, and they represent the fourth most common nosocomial bloodstream infection [7–9]. Among the *Candida* species causing invasive infections, *Candida albicans* is by far the species most commonly isolated, causing up to two-thirds of all cases of invasive candidiasis. *C. albicans*, *Candida tropicalis*, and *Candida glabrata* account for about 80% of fungal isolates encountered in the clinical laboratory [1,10]. Hence early identification of these commonly encountered *Candida* species is very important for doctor to do optimal antifungal therapy and patient management.

Commercially available identification systems used in routine were automatic identification system, such as ID32C of VITEK2, manual identification system like API *Candida*. These identification system were based on the identification of physiological and nutritional (sugar assimilation and/or fermentation, enzymatic tests) characteristics of pure yeast colonies which isolated from the raw clinical samples. So it usually need up to 5 days between the receipt of patient material and presentation of identification results to the clinician [11]. It is more serious for blood samples, because several days will be taken for positive reporting.

Some novel approaches for the rapid identification of clinically relevant microorganisms, including genotypic techniques base on PCR and spectroscopic techniques combined with chemometrics, were also performed on isolated pure colonies [12–17]. These techniques especially genotypic techniques showed some serious drawbacks, such as sensitivity to contamination and mutations, complicated protocol, reagent costs, etc., and are not up to now applied in routine.

MSPQC is a bioelectrochemical device based on the series piezoelectric quartz crystal (SPQC) sensor [18,19]. It attracted the attention of many analysts because of its sensitive response, low cost and easy operation. MSPQC system, which composed of eight single channels SPQC system, has been proposed to detect pathogens in clinical samples, to test susceptibility of clinical *Escherichia coli* isolates against ampicillin [20,21].

Chemometrics is the technique for extracting useful information from detected data. In this paper, MSPQC combined with PLS method was proposed for early identification of *Candida* species without preisolation of pure colonies from raw clinical species. This method was based on the fact that fingerprints response curve of *Candida* species while growing in our self-prepared culture media can be detected by MSPQC system, and these curves can be differentiated by the partial least square (PLS) technique effectively. For the reasonable explanation of those special frequency curves, the

* Corresponding author.
E-mail address: fengjiao863@hotmail.com (F. He).

0039-9140/$ – see front matter © 2009 Elsevier B.V. All rights reserved.
doi:10.1016/j.talanta.2009.09.011

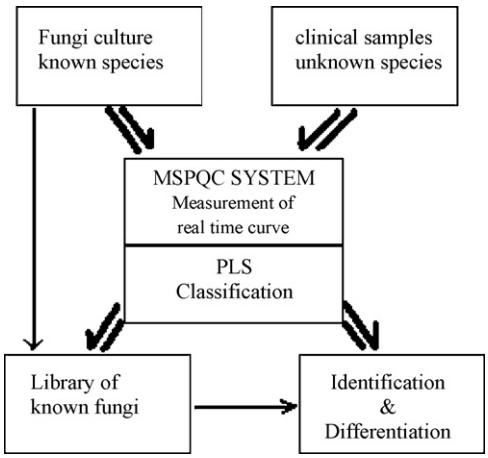


Fig. 1. Schematic representation of the MSPQC-PLS concept.

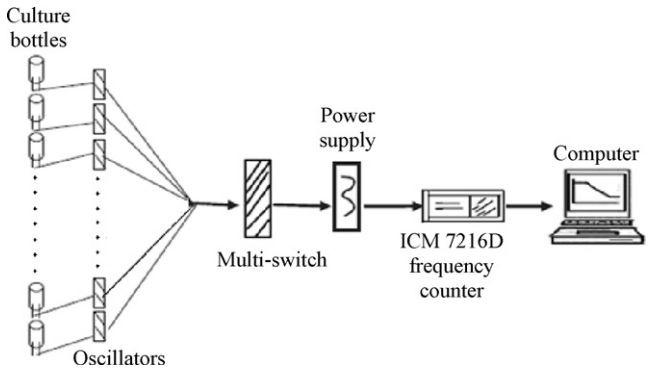


Fig. 2. Diagram of MSPQC system.

impedance characters of the three types of *Candida* species were studied by impedance analyzer.

The concept of the MSPQC-PLS system is shown in Fig. 1. First, real-time frequency curve of known clinical *Candida* species was detected by MSPQC system. These species and curves are made up of our library of known fungi. Then, the library was connected to a data processing and classification module via a specifically designed PLS algorithm. The PLS trained the data library to got a regression coefficient matrix which possess the ability of pattern recognition. The matrix was called "prediction machine". For an unknown clinical species, importing the data of frequent curve record by MSPQC system to the PLS system, the prediction machine will recognize the curve belong to which species' curve pattern, and give out the early identification result of *Candida* species.

2. Materials and methods

2.1. Strains

Fifty-three *Candida* strains provided by Xiangya Hospital of Central South University, Changsha, China, were isolated from different hospitalized patients and identified by standard identification system API20C.AUX (bioMerieux, France). Prior to use for identification, isolated strains were stored at room temperature in Sabouraud dextrose broth. For long preservation, these strains were frozen at −20 °C in distilled water.

2.2. Culture media

All the culture media used in our experiment were prepared by ourselves.

YC broth: beef extract, 2 g; yeast extract, 1 g; glucose, 40 g; YC nutrient fluid, 16 ml; ionized water, 1000 ml; pH 7.0–7.2.

Sabouraud dextrose broth: peptone 10 g, dextrose 40 g, distilled water 1000 ml; pH 5.4.

2.3. MSPQC system

The diagram of MSPQC is shown in Fig. 2. It is composed of 32 detection cells and 32 oscillator circuits. For single detection cell and oscillator circuit, an AT-cut 9 MHz piezoelectric quartz crystal coated with 0.5 mm silver disc at two sides was connected to the self-made TTL oscillated circuit and a pair of conductive stainless steel electrodes. The temperature of culture bottle was maintained at 37 ± 0.2 °C. 32 oscillator circuits share universal frequency counter, computer, and temperature controller system. The frequency outputs were switched alternately by multi-switches. Using the MSPQC, 32 samples can be tested at the same time. The on-line curves of frequency shift vs. culture time could be seen in screen by using self-developed software, so the growth of microorganism could be observed in real time. All frequencies and corresponding test times were autosaved by computer with TXT format.

2.4. MSPQC method for recording the frequency curve

Fungi were grown on Sabouraud dextrose agar plates at 37 °C overnight. The next day, the cells were harvested and suspended in 10 mL sterile water, the concentration were adjusted to 9.0×10^8 cfu/mL and 1.0×10^2 cfu/mL, respectively. 1 mL fungi suspension was transferred into culture bottles which contained 9 mL YC broth. Culture bottles were placed into MSPQC system and incubated at 37 ± 0.2 °C for a period of 1–3 days. At the same time, the on-line curves of frequency shift vs. culture time was recorded by using self-developed software. To avoid contamination, all glassware, culture media and equipment were sterilized. For comparison, the capacitance and resistance curves of fungi (9.0×10^8 cfu/mL) growth were recorded by HP-4192A LF impedance analyzer (Hewlett Packard) at 37 ± 0.2 °C.

2.5. Method for building the library of known fungi and creating the prediction machine

Each fungus sample can be represented by frequency shift data vector, $x = (x_1, x_2, x_3, \ldots, x_n)$, where x_n was the frequency shift measured by MSPQC system after frequency detect time(FDT). The FDT was defined as the time at which oscillating frequency shift of MSPQC changed rapidly [22]. If frequency shift was recorded at a interval of 10 min by MSPQC system, then x_1 was the frequency shift measured at 10 min after the FDT and x_2 was the frequency shift measured at 20 min after the FDT, x_n is the frequency shift measured at $n \times 10$ min after the FDT. Frequency shift data vector of total clinical collected fungi detected by MSPQC formed a data matrix. This data matrix is the library of known fungi. Every row of the data matrix represented one clinical sample. Then PLS was used to train the library. 70% of the total samples in library were selected randomly as the training set. Through the training, the characteristic of data vectors of each species was extracted by the PLS algorithm respectively and a $n \times 3$ regression coefficient matrix Y was construct (see Eq. (1)). Each column of the matrix Y denoted the characteristic of one type of species. So the number of fungi species need to be differentiated was equal to the column number of Y. The rest of 30% of the total samples were selected as the testing

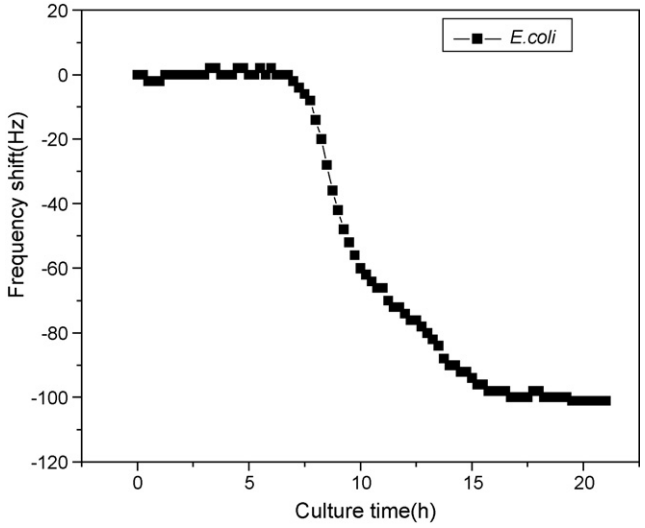


Fig. 3. Typical frequency curve of *E. coli*.

set to confirm the validity of the Y

$$\begin{bmatrix} x_{11}, x_{12}, \ldots, x_{1n} \\ x_{21}, x_{22}, \ldots, x_{2n} \\ \vdots \quad \ddots \quad \vdots \\ x_{m1}, x_{m2}, \ldots, x_{mn} \end{bmatrix}_{m\times n} \xrightarrow{PLStrainning} \begin{bmatrix} Y_{11}, Y_{12}, Y_{13} \\ Y_{21}, Y_{22}, Y_{23} \\ \vdots \quad \ddots \quad \vdots \\ Y_{n1}, Y_{n2}, Y_{n3} \end{bmatrix}_{n\times 3} \tag{1}$$

For an unknown sample X, a 1×3 vector Z was obtained by $X \times Y$ (see Eq. (2)). Sample X was regarded as the same species which show maximal value in vector Z. The regression coefficient matrix Y was called as "prediction machine".

$$\begin{bmatrix} X_1, & X_2, & \ldots, & X_n \end{bmatrix}_{1\times n} \times \begin{bmatrix} Y_{11}, Y_{12}, Y_{13} \\ Y_{21}, Y_{22}, Y_{23} \\ \vdots \quad \ddots \quad \vdots \\ Y_{n1}, Y_{n2}, Y_{n3} \end{bmatrix}_{n\times 3} = \begin{bmatrix} Z_1, & Z_2, & Z_3 \end{bmatrix}_{1\times 3} \tag{2}$$

2.6. Early identification of Candida species

The simulating clinical blood sample was prepared by adding 1 mL of 1.0×10^2 cfu/mL known *Candida* species to 1 mL human fresh blood. They were added individually to MSPQC bottle which contained 8 mL culture media. These culture bottles then were placed into MSPQC system and incubated at $37 \pm 0.2\,^{\circ}C$ for a period of 1–3 days. Then the real-time frequency shift curve was transformed to a data vector X and the simulating sample was identified by PLS system.

3. Results and discussion

3.1. Theory

MSPQC system is based on the monitoring electric parameter change of the culture media caused by the growth of microorganism. The theory basis for the SPQC can be represented by the following

$$\Delta F = \frac{\pi F_0^2 C_m (4\pi F_0 G_0 C_d + 4\pi^2 F_0^2 C_d^2 tg\theta - G_0^2 tg\theta)}{[G_0^2 - 2\pi F_0 C_0 G_0 tg\theta + 4\pi^2 F_0^2 C_d (C_0 + C_d)]^2} \Delta G \tag{3}$$

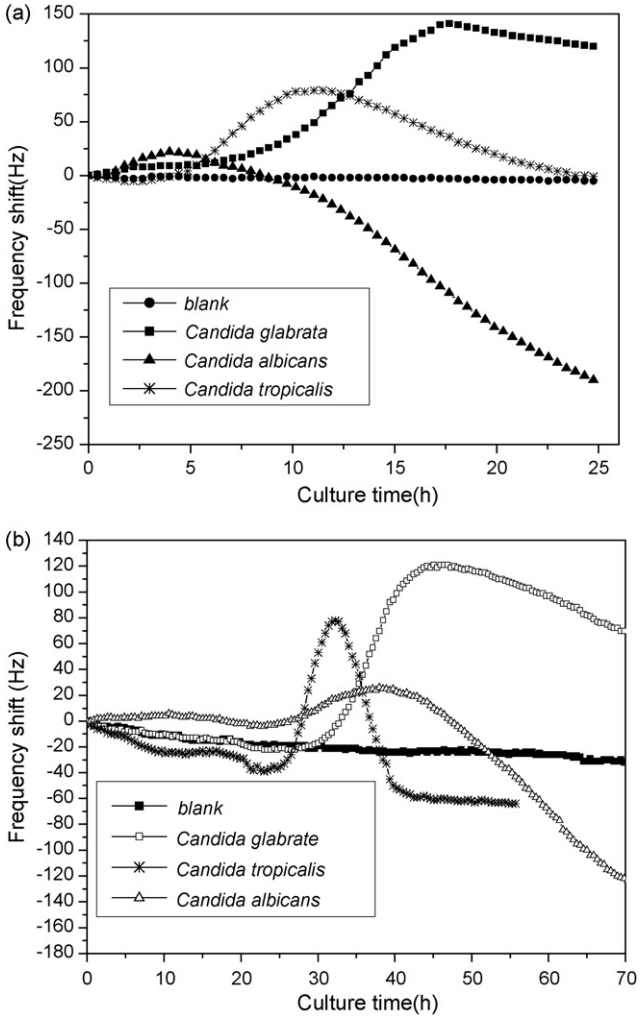


Fig. 4. Typical frequency curve of three species of *Candida* cultured in YC broth with the initial concentration: (A) 9.0×10^7 cfu/ml; (B) 1.0×10^1 cfu/ml.

where F_0 is the resonant frequency of the crystal, C_m and C_0 are the dynamic capacitance and static capacitance of the crystal respectively, C_d is the capacitance of solution which mostly based on the solution permittivity and parasitic capacitance between the leading wires of the electrode. G_0 is the solution conductance, θ is the phase shift. $\Delta F = F_i - F_0$, F_i is the oscillating frequency of crystal. From Eq. (3), the change of F is mainly dependent on solution conductivity and permittivity if other above-mentioned parameters are kept as constant. So the conductivity and permittivity change of the culture media caused by the growth of microorganism can be represented by the sensor frequency change. The typical frequency curve of *E. coli* detected by SPQC is shown in Fig. 3.

This curve was related to the metabolism of *E. coli*: at the first stage, oscillating frequency varied slowly because bacterium adjusted itself to new culture. After a few hours, bacterium came into an exponential growth stage and oscillating frequency started to decrease rapidly. Finally, when the growth of bacterium reached saturation, frequency arrived at the second flat stage. For the fungi, different species shows different way of metabolism. Further more, the same species in different culture medium, or at different stages of growth may also show different morphology and different ways of metabolism. These led to more specific diversity of MSPQC response in the grown process. These specific diversity were the basis of identification of fungi species.

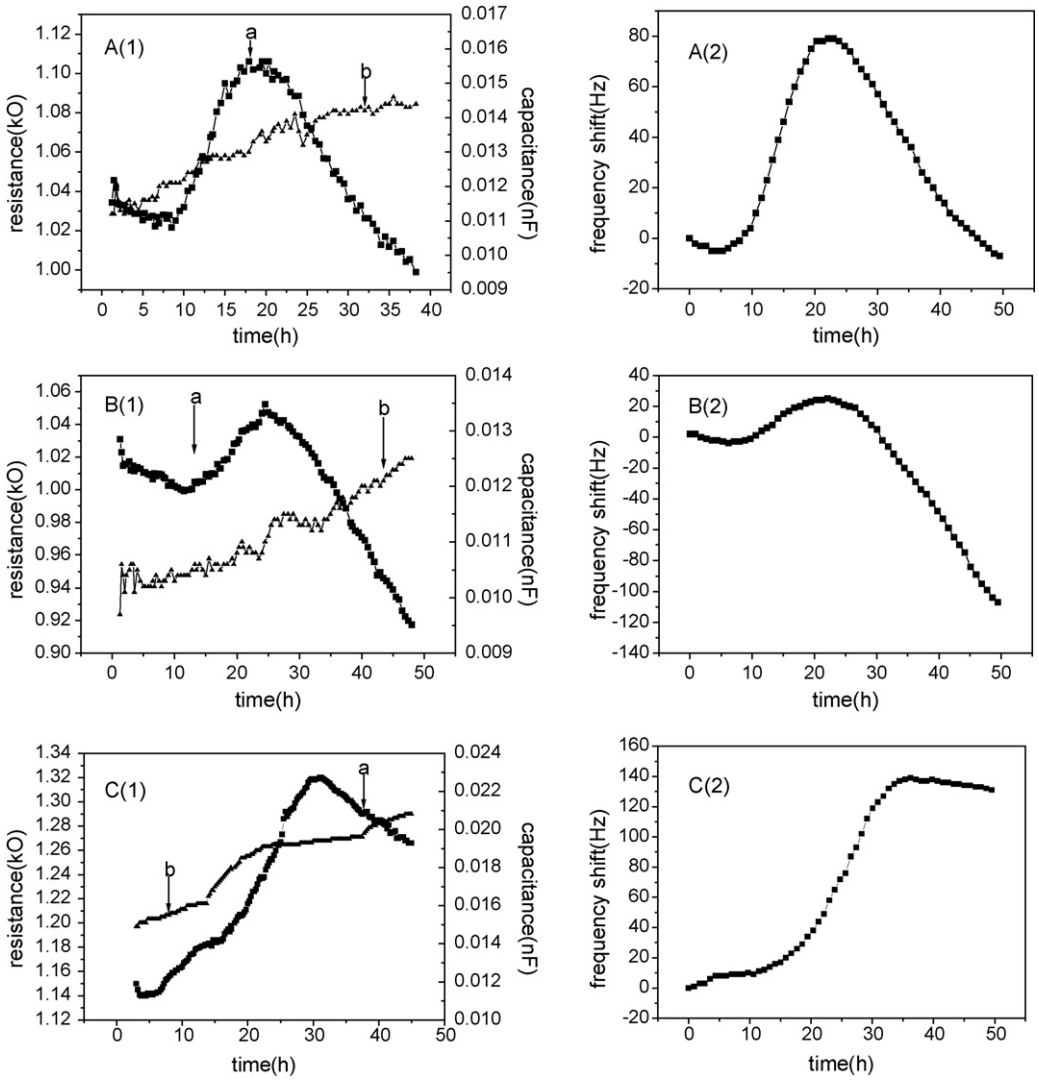


Fig. 5. The resistance curves[A(1)a, B(1)a, C(1)a], capacitance curves [A(1)b, B(1)b, C(1)b] and frequency shift curves [A(2), B(2), C(2)] between the two electrodes caused by the growth of three *Candida* species. A for *C. tropicalis*; B for *Candida albicans*; C for *C. glabrata*.

3.2. Typical frequency curve of three species of Candida

Typical frequency curves of three species of *Candida* (*C. albicans*, *C. glabrata*, *C. tropicalis*) in YC broth with high initial concentration are shown in Fig. 4(A). It showed clearly that three *Candida* species produced significant different type of frequency curve in 1 days' culture. For *C. tropicalis*, it showed a clear upward at first and then downward trend; *C. glabrata*, showed a clear upward trend; *C. albicans*, showed a clear downward trend after a unconspicuous upward trend. And from Fig. 4(B), it can be seen that *Candida* species gave out the same pattern of frequency curve no matter cultured with high initial concentration or low initial concentration. The only difference between the curve of high and low initial concentration was the FDT. For high initial concentration, the FDT of each *Candida* species was about 3–5 h (see Fig. 4(A)). For low initial concentration, the FDT of each *Candida* species was about 25–30 h (see Fig. 4(B)). Anyway, the three different species of *Candida* showed different pattern of frequency curve. Those diversity was easily recognized by PLS system.

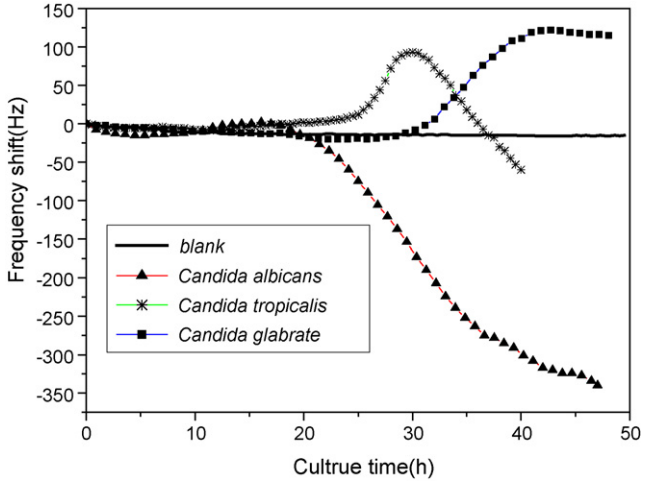


Fig. 6. Typical frequency curve of three species of *Candida* in simulating blood sample.

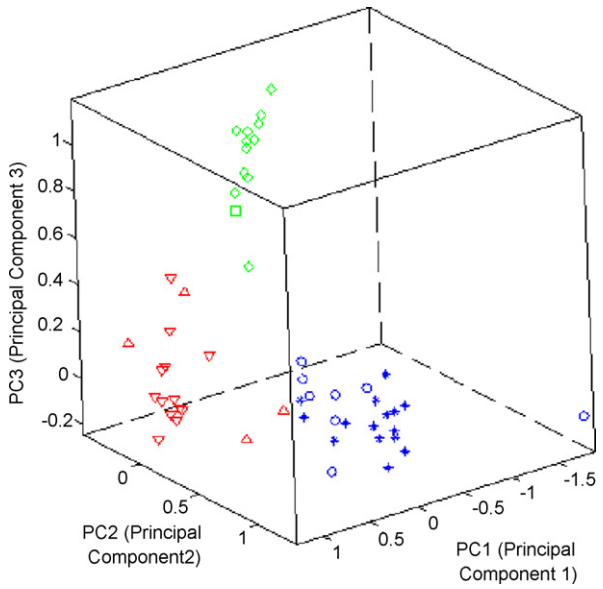


Fig. 7. Three-dimensional PLS plot showing discrimination of 53 samples. (▽) Training samples of *C. glabrata*. (△) Testing samples of *C. glabrata*. (○) Training samples of *C. albicans*. (✱) Testing samples of *C. albicans*. (◇) Training samples of *C. tropicalis*. (□) Testing samples of *C. tropicalis*.

3.3. Impedance changing curve of three species of Candida

Fig. 5 shows the resistance and capacitance change between the two electrodes of culture bottle while *Candida* species were growing in YC broth.

From Fig. 5, it can be seen that the capacitance between the two electrodes changed about 0.003–0.005 nF during the growing period of these *Candida* species. It means that there is no significant change in capacitance. But for the resistance between the two electrodes changed about 100 Ω and the pattern of the resistance changing curve is the same as the pattern of frequency shift curve produced by *Candida* species in comparative experiment. It clearly showed that the reason of producing those typical frequency curve was mainly related to the resistance changed by the growth of *Candida* species.

3.4. Typical frequency curves of three Candida species in simulating blood sample

As pathogens in raw clinical materials are always in low concentration, frequency curve of *Candida* species in simulating blood sample with low initial concentration were determined. From Fig. 6, it can be seen that the pattern of frequency curve was not affected by human blood. There is no significant difference in frequency curve between the simulating experiment and the low initial concentration experiment. This result means that raw clinical samples can be identified by proposed method directly without passing through pure culture process.

3.5. Construction of the prediction machine

A total of 53 clinical fungi were used to construct the prediction machine. All the fungi used here were pure culture species. Three types of frequency curve were identified. They were produced by *C. albicans*, which showed a clear downward trend after a unconspicuous upward trend, by *C. glabrata*, which showed a clear upward trend curve, by *C. tropicalis*, a clear upward and downward trend, respectively. Fig. 7 is a three-dimensional plot differentiated by PLS classification which was based on 53 samples of the three types of frequency curve caused by three species of *Candida*. Seventy percent of the 53 samples were used as the training set and the rest 30% were used as the testing set. From Fig. 7, it can be seen clearly that frequency curve produced by three types of fungi were successfully classified into three types by the PLS program.

Table 1
Identification result for 53 *Candida* species.

Candida species	Number of sample	Classification rate
C. albicans	23	100%
C. tropicalis	13	100%
C. glabrata	17	94.1%

Table 2
Identification result of early identification in simulating clinical blood samples.

Candida species	Number of sample	Prediction accuracy	Average identification time (h)
C. albicans	6	100%	46.5
C. tropicalis	6	83.3%	52.3
C. parapsilosis	5	100%	49.6

Table 1 shows very satisfying result. Only one *C. glabrata* sample was misclassified. The total classification rate of the 53 clinical samples was 98.1%. So the three types of clinically commonly encountered *Candida* species can be identified by proposed method in about 1 day.

3.6. Early identification of Candida species in simulating clinical blood samples

Simulating clinical blood sample were prepared by adding 1.0×10^2 cfu/mL dilutions of known *Candida* species to human fresh blood. A total of six *C. albicans*, five *C. glabrata*, six *C. tropicalis* were identified from the simulating blood samples. The PLS prediction machine which trained from 53 known fungi of the four *Candida* species was used to predict simulating clinic blood samples, the results are shown in Table 2. Only one *C. tropicalis* sample was misclassified. The average identification time of each *Candida* species was about 50 h. This is much shorter than the time needed in clinical routine. It means that several days can be saved using the new proposed method.

4. Conclusion

A MSPQC-PLS system was constructed to identify the most frequent *Candida* species encountered in human pathology with a single measurement. A "fingerprint frequency curve" of the sample measured by MSPQC can be recognized and classified by PLS. Pure cultures of clinical fungi can be identified by proposed method in about 1 day, with the classification rate of 98.1%. The identification of *Candida* species in simulating clinic blood samples showed that the proposed method has a potential capacity to identify *Candida* species directly without pure culture process. Proposed method enables early classification and differentiation of fungi at species level.

Acknowledgements

This research work was supported by the National Natural Science Foundation of China (No. 20875026). We are also grateful to Hunan Yingcai Keji Ltd and Xiangya Hospital of Central South University.

References

[1] M.A. Pfaller, Clin. Infect. Dis. 22 (1996) S89–S94.

[2] D. Abi-Said, E. Anaissie, O. Uzun, I. Raad, H. Pinzcowski, S. Vartivarian, Clin. Infect. Dis. 24 (1997) 1122–1228.
[3] A. Lupetti, A. Tavanti, P. Davini, E. Ghelardi, V. Corsini, I. Merusi, A. Boldrini, M. Campa, S. Senesi, J. Clin. Microbiol. 40 (2002) 2363–2369.
[4] J. Bross, G.H. Talbot, G. Maislin, S. Hurwitz, B.L. Strom, Am. J. Med. 87 (1989) 614–620.
[5] S.B. Wey, M. Motomi, M.A. Pfaller, R.F. Wolsen, R.P. Wenzel, Arch. Intern. Med. 149 (1989) 2249–2253.
[6] J.A. Vazquez, L.M. Dembry, V. Sanchez, M.A. Vazquez, J.D. Sobel, C. Dmuchowski, M.J. Zervos, J. Clin. Microbiol. 36 (1998) 421–426.
[7] C. Beck-Sague, W.R. Jarvis, J. Infect. Dis. 167 (1993) 1247–1251.
[8] S.K. Fridkin, W.R. Jarvis, Clin. Microbiol. Rev. 9 (1996) 499–511.
[9] W.E. Trick, S.K. Fridkin, J.R. Edwards, R.A. Hajjeh, R.P. Gaynes, Clin. Infect. Dis. 35 (2002) 627–630.
[10] M.A. Pfaller, D.J. Diekema, R.N. Jones, H.S. Sader, A.C. Fluit, R.J. Hollis, S.A. Messer, J. Clin. Microbiol. 39 (2001) 3254–3259.
[11] J.M. Miller, C.M. O'Hara, in: P.R. Murray, E.J. Baron, M.A. Pfaller, F.C. Tenover, R.H. Yolken (Eds.), Manual of Clinical Microbiology, 7th ed., ASM Press, Washington, DC, 1999, pp. 193–201.
[12] S.A. Sakallah, Biotechnol. Annu. Rev. 6 (2000) 141–161.
[13] K.J. Albert, D.R. Walt, Anal. Chem. 75 (2003) 4161–4167.
[14] P.C. Jurs, G.A. Bakken, H.E. McClelland, Chem. Rev. 100 (2000) 2649–2678.
[15] B. Lavine, J.J. Workman, Anal. Chem. 76 (2004) 3365–3372.
[16] E.C. Lopez-Diez, R. Goodacre, Anal. Chem. 76 (2004) 585–591.
[17] M. Essendoubi, D. Toubasb, M. Bouzaggou, J.M. Pinon, M. Manfaita, G.D. Sockalingum, Biochim. Biophys. Acta 1724 (2005) 239–247.
[18] D.Z. Shen, Z.Y. Li, L.H. Nie, S.Z. Yao, Anal. Chim. Acta 280 (1993) 209–216.
[19] D.Z. Shen, W.H. Zhu, L.H. Nie, S.Z. Yao, Anal. Chim. Acta 276 (1993) 87–97.
[20] F.J. He, X.Q. Zhang, J.D. Zhou, Z.H. Liu, J. Microbiol. Methods 66 (2006) 56–62.
[21] F.J. He, J. Zhou, J. Microbiol. Methods 68 (2007) 563–567.
[22] F.J. He, W. Zhu, Q. Geng, L.H. Nie, S.Z. Yao, Anal. Lett. 27 (1994) 655–669.

Talanta 80 (2010) 1216–1221

Contents lists available at ScienceDirect

Talanta

journal homepage: www.elsevier.com/locate/talanta

Magnetic bead-based approach to monitoring of cigarette smoke-induced DNA oxidation damage and screening of natural protective compounds

Hongjun Chen[a], Guohai Chu[b], Zhijuan Cao[a], Jianying Liang[a], Jianzhong Lu[a,*], Guojun Zhou[b,*]

[a] School of Pharmacy, Fudan University, 826 Zhangheng Road, Shanghai 201203, China
[b] Technology Center, China Tobacco Zhejiang Industrial Co. Ltd., 77 South Zhongshan Road, Hangzhou 310008, China

ARTICLE INFO

Article history:
Received 30 May 2009
Received in revised form 1 September 2009
Accepted 8 September 2009
Available online 13 September 2009

Keywords:
Cigarette smoke
Chemiluminescence monitoring
DNA oxidative damage
Protectant screening
Natural products

ABSTRACT

Cigarette smoking can damage DNA and induce spontaneous mutagenesis or carcinogenesis. Here, we describe a novel strategy for in situ monitoring of cigarette smoke-induced DNA oxidation damage and offer a method for screening natural compounds that protect DNA against tobacco smoke. The present protocol takes advantage of a fast and simple magnetic separation/mixing method and a highly sensitive chemiluminescence (CL) ELISA. The DNA immobilized on the magnetic beads was oxidized by the smoke in the absence or presence of natural compounds, and then oxidative DNA was conveniently held by magnetic force, whereas the complex tobacco smoke matrix and any remaining compounds were completely eliminated by extensive washing, and possible interferences were thus removed and oxidative damage was then sensitively monitored by CL ELISA. A library of 32 natural products was then screened and three were found to protect DNA from oxidative damage and thus may be promising compounds for the development of new drugs. Moreover, the protection effect of these three natural compounds against DNA oxidation damage was successfully classified by directly spiking them in the reference cigarettes. In addition, the potential to screen a mixture in a complex sample matrix, such as crude extracts, was also demonstrated, and hence the proposed technique can screen compounds within a complex matrix and enhance the screening throughput.

© 2009 Elsevier B.V. All rights reserved.

1. Introduction

Cigarette smoke is a complex mixture of literally thousands of compounds, of which more than 60 are known carcinogens, mutagens, and cocarcinogens. Tobacco smoke contains high levels of tumor promoter and reactive oxygen species (ROS) [1–5], which includes superoxide, hydroxyl and peroxyl radicals, and is capable of causing oxidative damage to cellular DNA involving base oxidation and DNA strand structure changes such as strand breaks, interstrand/intrastrand cross-links, and DNA-protein cross-links [6,7]. DNA oxidation damages appear to be prominent in the etiology and progression of numerous cancers as well as coronary, carotid atherosclerosis and autoimmune diseases [8,9]. In addition, the role of natural products in life science is of great interest both to the general public and to experts in different disciplines including medicine, nutrition, health, and food science [10]. Therefore, it is important to study the damaging effects of cigarette smoke on DNA and screen natural protective compounds against such damages.

8-Hydroxy-2′-deoxyguanosine (8-OHdG) (Fig. 1) is one of such important oxidative DNA lesions formed by the oxidation of the C-8 position of 2′-deoxyguanosine, which has often been used as a biomarker of oxidative DNA damage [11,12]. Current evidence suggests that 8-OHdG lesions are present in DNA during cellular replication and carcinogenesis [13–18], and its level have been shown to increase in Alzheimer's disease or on exposure to tobacco smoke [19–21]. Thus it can be regarded as a sensitive and stable biomarker of DNA oxidative damage to estimate the toxicity of internal and external factors. Hence, here we used 8-OHdG as the biomarker for DNA oxidative damage induced by cigarette smoke.

Many powerful analytical techniques have been developed to determine 8-OHdG. HPLC coupled with electrochemical and radioactive detectors, post-labeling assays [22,23] and GC/MS with selected ion monitoring [24,25] after DNA digestion are the most commonly used techniques for 8-OHdG detection. All of these detection methods are sensitive, but they are bulky, expensive and often require specialized and cumbersome technical processing. The application of various immunological approaches has made a seminal contribution to the quantitative assessment of bulky as well as subtle structural alterations produced in damaged DNA [26–29]. High affinity polyclonal and monoclonal antibodies able to specifically recognize the 8-OHdG lesion in DNA hydrolysates have been developed and utilized for several biomonitoring studies [30]. To avoid cumbersome DNA degradation or the use of expensive equipment, Musarrat et al. developed an immunoslot blot assay

* Corresponding authors. Tel.: +86 21 51980058; fax: +86 21 51980058.
E-mail addresses: jzlu@shmu.edu.cn (J. Lu), guojun_zhou@163.com (G. Zhou).

0039-9140/$ – see front matter © 2009 Elsevier B.V. All rights reserved.
doi:10.1016/j.talanta.2009.09.012

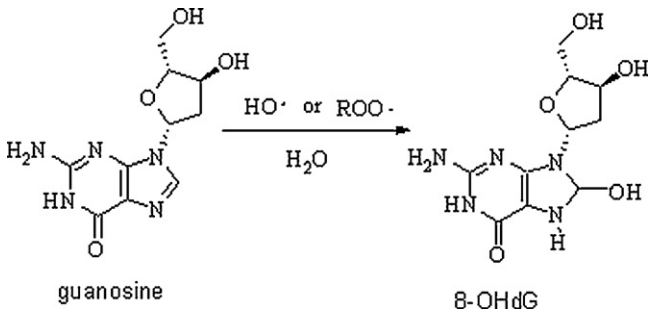


Fig. 1. Mechanism of formation of 8-OHdG after G attacked by ROS.

to detect DNA lesions oxidized by methylene blue plus light and H_2O_2, where polyclonal antibodies specific for the 8-OHdG moiety in oxidized DNA were used for sensitive detection and quantitation of this biomarker of oxidative damage to unhydrolyzed DNA [31]. Yarborough et al. reported an ELISA procedure for the detection of 8-OHdG in single cells, and found that the amount of 8-OHdG in oral cells of smokers was 1.6-fold higher than in nonsmokers [32].

In this article, we demonstrate a novel strategy for in situ monitoring of cigarette smoke-induced DNA oxidative damage and describe a method for screening natural compounds that protect DNA against tobacco smoke. Magnetic beads (MB) and chemiluminescence (CL) detection, which offers unique advantages including simple instrumentation, high sensitivity, low detection limit, wide linear ranges and feasibility for apparatus miniaturization in analytical tests [33–38], were used to establish this sensitive and simple 8-OHdG detection method and the screening platform for natural protective compounds. A library of 32 natural products was then screened and three were found to protect DNA from oxidative damage and thus may be promising compounds for the development of new drugs.

2. Experimental

2.1. Materials

2.1.1. Chemicals

All chemicals were of analytical reagent grade and were used as received. Goat anti-8-OHdG polyclonal antibody and HRP-labeled donkey anti-goat IgG (1 mg/mL) were bought from AbD Serotec. HRP CL substrate was obtained from Milipore Co. Carboxyl BioMag®Plus magnetic beads (MB, 1.5 μm, 20 mg/mL) were obtained from Polyscience, Inc. BSA was bought from Sino-American Biotechnology Co. N-3-Dimethylaminopropyl-N′-ethylcarbodiimide hydrochloride (EDC) was purchased from Alfa Aesar. Research cigarettes (Liqun) were obtained from China Tobacco ZheJiang Industrial Co. Ltd. Before smoking, cigarettes were conditioned for 24 h in an environmental chamber that was maintained at a temperature of 20 °C and 60% relative humidity. The DNA (5′-NH_2-AAAAAAAAAAATGGTGGAGAGTGTGTGGA-3′) was acquired from Shanghai Invitrogen Biotechnology Co. Ltd. Natural products were from Shanghai U-sea Biotech Co. Ltd. and other chemical reagents were obtained from Sinopharm Chemical Reagent Co. Ltd.

2.1.2. Buffers

The water was prepared using Milli-XQ equipment. The buffer for immobilization of DNA on MB was 0.1 M imidazole buffer, pH 6.0. Reaction buffer for antigen–antibody immunoreactions was phosphate buffer solution (PBS), consisting of 9-g sodium chloride, 6-g disodium phosphate and 0.4-g sodium dihydrogen phosphate in 1-L buffer, pH 7.4 and PBS (K+) consisting of 6.8-g potassium dihydrogen phosphate, 0.944-g sodium hydrate in 1-L buffer, pH 6.8. Wash buffer (WB) was PBS with the addition of 0.1% Tween 20 (TW). Blocking buffer was PBS consisted of 0.02% BSA for blocking the residual reactive sites on the capture antibody and reducing the nonspecific absorption effects.

2.1.3. Apparatus

Cigarette smoke was generated by an automated smoker (Borgwaldt Technik Co.) that was operated according to the standard of Federal Trade Commission (FTC) protocol. CL measurements were performed with a computerized Fluoroskan Ascent (Thermo Electron Corporation).

2.2. Online DNA oxidation with smoke ROS and DNA protectant screening procedure

120-μg MB was first washed 3 times and then added to 100 μL of imidazole buffer (pH 6.0) containing 2-mg N-3-dimethylaminopropyl-N′-ethylcarbodiimide hydrochloride (EDC). The solution was continuously shaken for 30 min to ensure the activation of the carboxyl groups, and then reacted with 80-pmol DNA for 1 h at 37 °C. The conjugates were washed three times with WB by a magnetic separation/mixing process and then stored in PBS–0.5% TW buffer at 4 °C until use. Each cigarette was smoked according to the FTC protocol. The protocol specifies that the cigarette should be puffed in such a way that one puff would last 2 s with puff volume of 35 mL and frequency of 1 puff/min. The puff volume was calibrated using a bubble calibrator matched with the automated smoker. The smoke was passed through a gas dispersion tube connected to a frit disk to the trapping solvent containing the DNA–MB conjugates. For screening, the compounds were first mixed with the DNA–MB conjugates in the trapping solution, or the compound solution was spiked into the cigarette by a syringe. After smoking, the interaction between DNA and the smoke was kept at 37 °C for 80 min, and the DNA–MB conjugates were then separated from the smoke solution by magnetic force and washed in PBS–0.1% TW buffer for four times. The obtained DNA–MB conjugates were blocked and then stored at 4 °C for use. All reactions were run in triplicate at least.

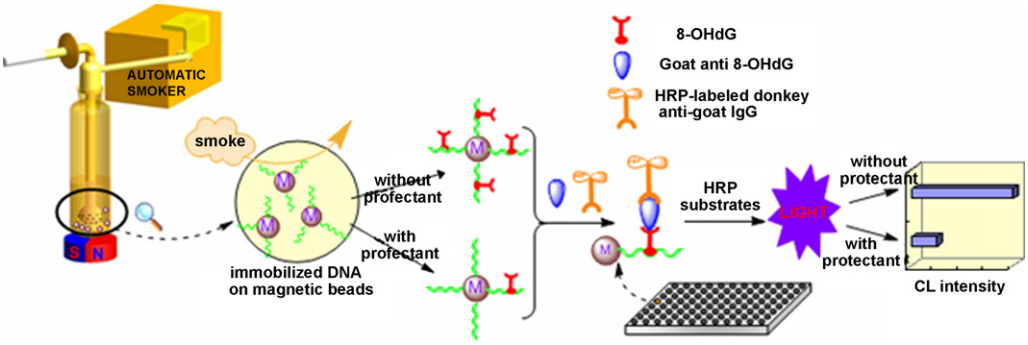
2.3. CL ELISA procedure

In a typical experiment, after the elimination of the blocking buffer, goat anti-8-OHdG diluted with blocking buffer was added and reacted with the oxidized DNA obtained as described above at 37 °C for 1 h. Then, the HRP-labeled donkey anti-goat IgG diluted with blocking buffer was added and reacted for another 1 h and the resultant MB was washed with WB for three times, the CL signals on the surface of MB were detected with 100 μL of CL HRP substrate.

3. Results and discussion

3.1. The principle

The method consists of the following four steps: (1) DNA oxidative damage: DNA is immobilized on the surface of MB by covalent binding, online DNA oxidation is carried out with tobacco smoke and natural products are screened for the protection of DNA against oxidative damage; (2) impurity elimination and 8-OHdG purification: oxidative DNA is conveniently held by a magnetic force, whereas the complex tobacco smoke matrix and any remaining compounds are completely eliminated, and possible interferences are thus removed; (3) 8-OHdG-antibody immunoreaction: anti-8-OHdG antibody is added, which reacts with 8-OHdG induced by oxidative DNA damage. A HRP-labeled secondary antibody is then added; (4) CL detection: the CL signal on the surface of mag-



Scheme 1. Schematic representation of the magnetic bead-based immunoassay to monitor cigarette smoke-induced oxidative DNA damage and screening of potential compounds for DNA protection.

netic beads is directly determined with CL HRP substrate. The principle of in situ monitoring of cigarette smoke-induced DNA oxidation damage and screening of natural products for DNA protection is depicted in Scheme 1. Since ROS produced by cigarette smoke is often of transient species, we combined a gas–liquid reactor with an automatic smoker, and the radical intermediates in the combustion were simultaneously and effectively captured by the DNA in the gas–liquid reactor as the smoking cigarette was 'puffed'. Oxidation of DNA by cigarette smoke was done without using the Cambridge filter, therefore, the smoke was considered as whole smoke containing both the particulate phase and the gas phase.

3.2. Choice of reaction media

Several factors were taken into account when we choose the solvent mixture to trap the ROS of cigarette smoke. First, the solvent should have good solubility and allow adequate dispersion of the smoke. Second, the contact time between the smoke and the solvent should be as long as possible to ensure there is sufficient time for the ROS in the smoke to dissolve into the liquid phase. Third, the surfactant could disperse the smoke into tiny bubbles and greatly facilitate the interaction of smoke with the liquid phase, with larger contact area between the smoke and liquid [3]. Taking these factors into consideration, we tested water and some other buffers containing the non-ionic surfactant Tween-20 (TW), which does not affect DNA, and were used to collect the cigarette smoke. After the oxidized DNA was collected in these smoke-trapping solutions, the CL signals of 8-OHdG were detected using an enhanced CL assay kit. As shown in Fig. 2, we found that, when using PBS–0.5% TW as the smoke-trapping buffer, the CL signals reached maximum. Thus PBS–0.5% TW was used in the subsequent experiments.

3.3. Optimization of assay conditions

Several parameters were investigated systematically in order to establish optimal conditions for in situ monitoring of cigarette smoke-induced DNA oxidation damage using CL ELISA, including the amounts of DNA and the dilution coefficient of the antibody. First, as the concentration of DNA increased, CL intensity increased and then almost leveled off above 80 pmol for 120 μg MB (Fig. 3), possibly due to that 80 pmol DNA has saturated ROS produced by cigarette smoke. Hence, subsequent work employed 80 pmol DNA for 120 μg MB.

Goat anti-8-OHdG polyclonal antibody from AbD Serotec has been tested in both a competitive ELISA and paraffin sections and shown to have high specificity towards 8-hydroxydeoxyguanosine and 8-hydroxyguanosine nucleotides. Partial cross-reactivity was also observed for this antibody with 8-mercaptoguanosine and 8-bromoguanosine whereas 2-deoxyadenosine, 7-methylguanosine, guanosine monophosphate and guanosine showed no reactivity. In our methodology, this polyclonal antibody was employed to recognize the formation of 8-OHdG moiety on the DNA backbone after

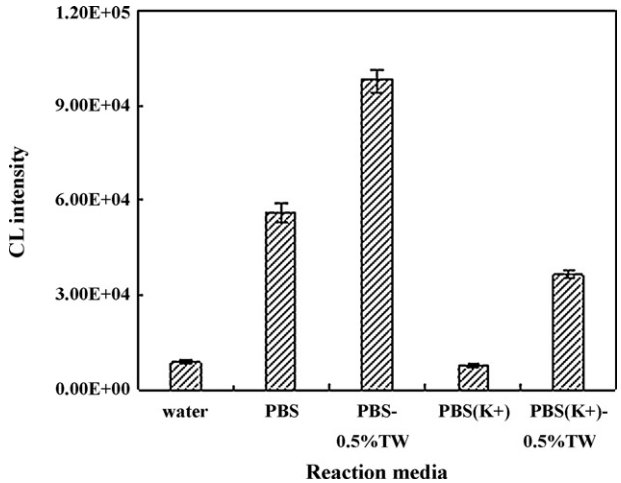


Fig. 2. CL signal versus different cigarette smoke-trapping solutions. Experimental conditions: 3 mL reaction solution containing 120 μg MB and 80 pmol DNA, four puffs of cigarette smoke, 80-min contact time between DNA and smoke, 10,000-fold-diluted primary antibody and 1000-fold-diluted secondary antibody.

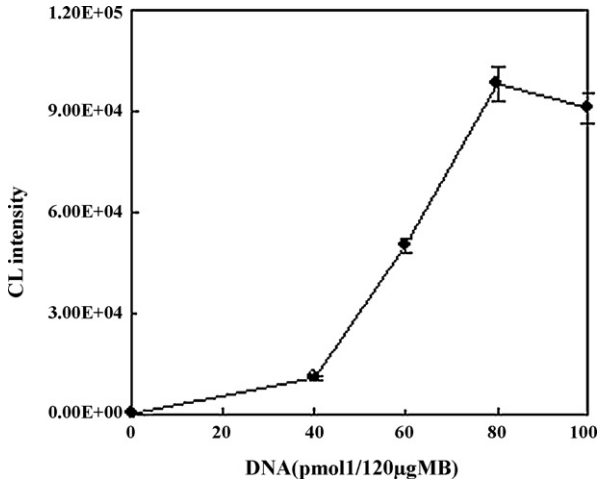


Fig. 3. CL intensity versus the concentration of DNA immobilized on MB. Experimental conditions: 3 mL reaction solution containing 120 μg MB, four puffs of cigarette smoke, 80-min contact time between DNA and smoke, 10,000-fold-diluted primary antibody and 1000-fold-diluted secondary antibody.

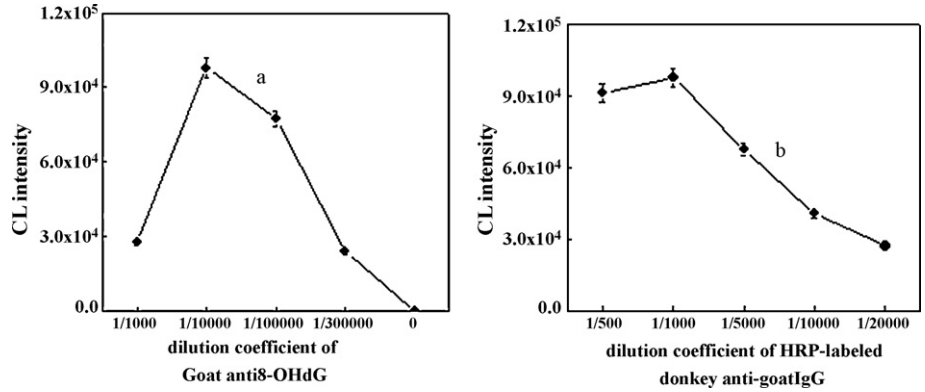


Fig. 4. CL intensity versus the dilution coefficient of the antibody. Experimental conditions: 3 mL reaction solution containing 120 μg MB, 80 pmol DNA, 1000-fold-diluted HRP-labeled secondary antibody (a) and 10,000-fold-diluted primary antibody (b), four puffs of cigarette smoke and 80-min contact time between DNA and smoke.

oxidation by the smoke. In CL ELISA procedure, CL intensity could be affected by the dilution coefficient of the antibody. Fig. 4 illustrated the CL intensity versus different dilution coefficients of primary and secondary antibodies, respectively. As the amount of antibodies increased, CL signal increased and reached maximum at 1/10,000 for primary antibody (a) and 1/1000 for second antibody (b). Thus, 10,000-fold-diluted goat anti-8-OHdG and 1000-fold-diluted HRP-labeled donkey anti-goat IgG were selected for use in subsequent studies.

3.4. Monitoring of cigarette smoke-induced DNA oxidation damage

The CL signal produced from 8-OHdG, which represent DNA oxidation damage arising from cigarette smoke here, can be also greatly affected by the amount of cigarette smoke and oxidation time. First, as shown in Fig. 5, the CL intensity increased when the amount of smoke was increased from one to four puffs and then maintained at almost the same level with four to five puffs of cigarette smoke. After that, the level decreased gradually, possibly an excess of ROS resulted in the formation of secondary oxidation products such as oxazolone, spiroiminodihydantoin, and guanidinohydantoin [39–41]. Thus four puffs of cigarette smoke were used in subsequent experiments. Furthermore, Fig. 5 also indicates that the CL intensity was almost constant after 4-h reaction of DNA with four puffs of cigarette smoke at 37 °C. We chose 80-min contact time between DNA and smoke to screen natural products because it is sufficient to observe intense CL and could greatly shorten the screening time.

3.5. Screening of natural compounds for protection against DNA oxidation damage

It is well known that some compounds play an important role in eliminating ROS and protecting DNA from oxidative damage. For example, flavonoids are the most widely studied with respect to their antioxidant and biological activities. They have powerful antioxidant activities in vitro, being able to scavenge a wide range of ROS, such as superoxide, hydroxyl and peroxyl radicals [42–47]. Kanazawa et al. [48] investigated bioavailable flavonoids to suppress the formation of 8-OHdG in HepG2 cells. Moreover, Traber et al. [49] reported that antioxidant micronutrient supplementation could inhibit DNA damage induced by cigarette smoke. Lee et al. [50] found that β-carotene and red ginseng could inhibit the formation of 8-OHdG in smokers. Thus a small natural compound library listed in Table 1 was used to evaluate our technique for screening of compounds providing effective protection of DNA against cigarette smoke. The library contained 32 natural compounds. As shown in Fig. 6, we found that three compounds, quercetin, sodium danshensu and baicalein, completely inhibited the formation of 8-OHdG (relative to the Control group) with a very low CL emission. Six natural compounds including scutellarin, notoginsenoside R1, puerarin, naringenin, rhein and panaxsaponin Rg1 partially protected DNA from oxidative damage caused by cigarette smoke. The other 23 natural compounds exhibited no obvious protection of DNA against oxidative damage.

To investigate the dose of each compound required to inhibit the formation of 8-OHdG and protect DNA from oxidative damage, a scavenging activity (SA) of the natural compounds was defined as

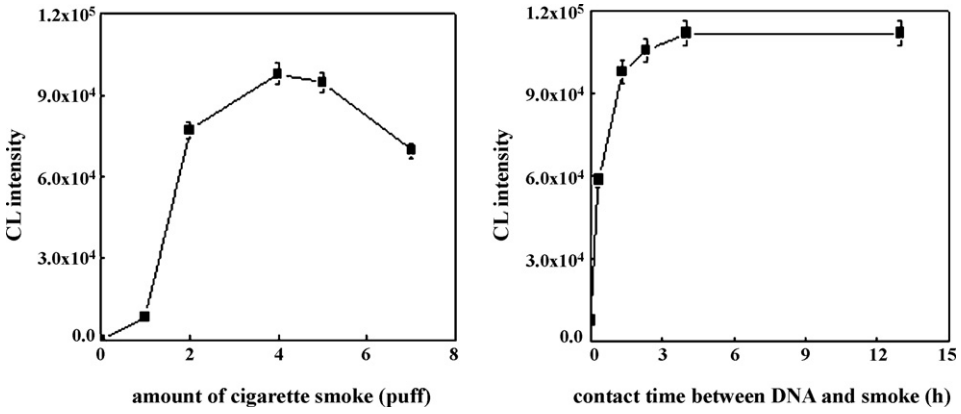


Fig. 5. CL intensity versus the amount of cigarette smoke and the contact time between DNA and smoke. Experimental conditions: 3 mL reaction solution containing 120 μg MB and 80 pmol DNA, 10,000-fold-diluted primary antibody and 1000-fold-diluted secondary antibody.

Table 1
Natural compound library used for screening of DNA protectant against tobacco smoke. 10^{-4}-M natural compounds, other conditions were the same as described in the caption of Fig. 2. Each result represents the mean value of triplicate measurements.

Natural compound	%SA	Natural compound	%SA
Quercetin	100	Isofraxidin	0
Sodium Danshensu	100	Ephedrine Hydrochloride	0
Baicalein	100	Berberine Hydrochloride	0
Scutellarin	22	Silibinin	0
Notoginsenoside R1	16	Gardenoside	0
Puerarin	23	Emodin	0
Naringenin	26	Ascorbic Acid	0
Rhein	15.4	Ginsenoside Rb1	0
Panaxsaponin Rg1	12.9	Aloe-emodin	0
Scopoletin	3.7	Ferulic acid	0
Icariin	3	Chlorogenic acid	0
Wogonin	0	Rutin	0
Isorhamnetin	0	Baicalin	0
Tanshinone II A	0	Astragaloside	0
Tanshinone I	0	Aloin	0
Cryptotanshinone	0	Oleanolic acid	0

follows:

$$SA = \frac{CL_{control} - CL_{natural\ product}}{CL_{control}} \times 100\%$$

where $CL_{control}$ is the chemiluminescence of the control group and $CL_{natural\ product}$ is the chemiluminescence of natural product added. The SA plots for several natural compounds are shown in Fig. 7. This figure shows a similar dose dependence of SA for the three most effective compounds (quercetin, sodium danshensu and baicalein) in addition to naringenin and scopoletin. When their concentration was low, the SA was also very low. Concentrations of 10^{-4} M, or higher, of quercetin, sodium danshensu and baicalein completely inhibited DNA oxidation in our experiments. However, for naringenin, even at a concentration of 0.5 mM, the SA was only 36% while for scopoletin, SA was not dose dependent. Thus their protection against DNA damage was very weak.

The potential to screen a mixture in a complex sample matrix, such as crude extracts, is another feature of the present method. Because of the combination of magnetic force separation and highly sensitive CL ELISA, our technique avoids effects of the sample and oxidation byproducts on the assay. To demonstrate the potential

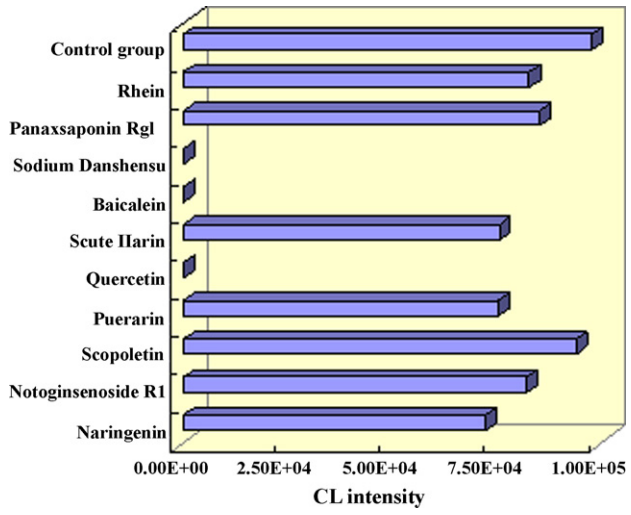


Fig. 6. Screening of natural compounds for the protection against DNA oxidation damage. Experimental conditions: 10^{-4} M of the natural compound, 3 mL reaction solution containing 120 μg MB and 80 pmol DNA, four puffs of cigarette smoke, 80-min contact time between DNA and smoke, 10,000-fold-diluted primary antibody and 1000-fold-diluted secondary antibody. Each result represents the mean value of triplicate measurements.

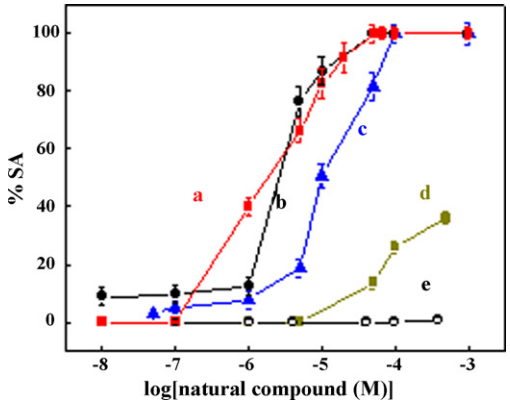


Fig. 7. SA plots for sodium danshensu (a), baicalein (b), quercetin (c), naringenin (d) and scopoletin (e). Experimental conditions: 3 mL reaction solution containing 120 μg MB and 80 pmol DNA, four puffs of cigarette smoke, 80-min contact time between DNA and smoke, 10,000-fold-diluted primary antibody and 1000-fold-diluted secondary antibody.

of the present method for screening a complex mixture, three crude extracts, baicalein-rich fractions, sodium danshensu-rich fractions and quercetin-rich fractions (their contents were 60, 40 and 95%, respectively, quantified by HPLC–UV) were assayed, and they yielded 87.6, 72.3 and 57.2% SA, respectively. As shown in Fig. 8, although with a relatively low concentration, they show prominent protection of DNA. When the amount of baicalein in the crude extract was the same as the corresponding natural compound (pure baicalein), their SA was nearly equivalent. The other two crude extracts had the similar results. These results show that the presence of a DNA protectant in a complex sample matrix can be clearly identified. This finding confirms that our new technique can screen compounds within a complex matrix and enhance the screening throughput.

3.6. Evaluation of natural compounds for protection against DNA oxidation damage in research cigarettes

To demonstrate the protection effect of natural compounds against DNA oxidation, 1 mg of baicalein, sodium danshensu, quercetin, naringenin and scopoletin in 20% ethanol were directly spiked into one cigarette tobacco, respectively, and a cigarette containing the same volume of 20% ethanol was used as control sample. After the solvent evaporation, the above cigarettes were smoked, and their influences on DNA were assayed by CL ELISA (Fig. 9). Compared with control cigarette without any natural compound, the signal of 8-OHdG was intensively inhibited in

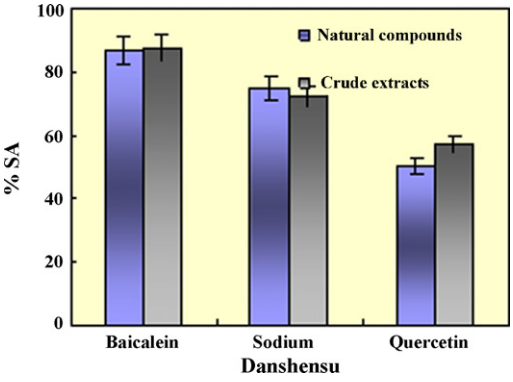


Fig. 8. SA comparison between the crude extracts and natural compounds. Experimental conditions: the amount of them is the same, 2.7 μg/mL for baicalein, 2.0 μg/mL for sodium danshensu, and 3 μg/mL for quercetin, other conditions were the same as described in the caption of Fig. 2.

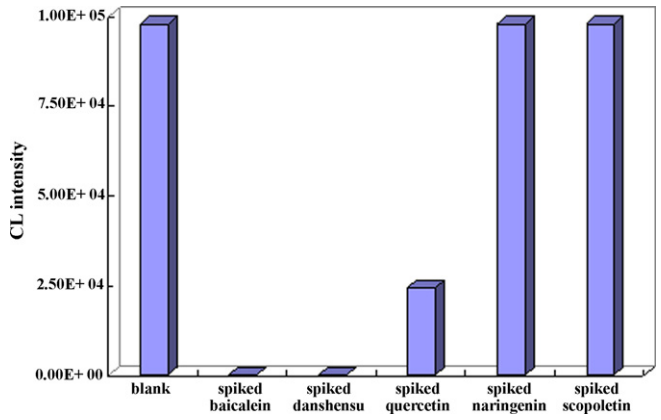


Fig. 9. CL intensity versus cigarette spiked with different natural compounds. Experimental conditions: the content of natural compounds was 1 mg/cigarette, and other conditions were the same as described in the caption of Fig. 2. Each result represents the mean value of triplicate measurements.

the cigarettes spiked with either baicalein, danshensu or quercetin while cigarettes spiked with naringenin and scopoletin have no obvious protection of DNA. These data indicate that our natural compounds indeed exert protection effects against smoke-induced DNA oxidative damage even in the real cigarette samples. The reasons may be: (1) ROS was partly consumed at the burning site by the natural compounds when the cigarette was 'smoked' and thus reduced the harm to DNA; (2) partial natural compounds, which were not so near to the burning site and thus had not been destroyed at a high temperature, volatilized together with the smoke into the trap solution and protected the DNA from the destruction.

4. Conclusions

In conclusion, we have developed a novel strategy for in situ monitoring of cigarette smoke-induced DNA oxidation damage and offer a method for screening natural compounds that protect DNA against tobacco smoke. The present protocol couples a fast and simple magnetic separation/mixing method with a highly sensitive CL ELISA, and thus oxidative DNA is conveniently maintained in situ by magnetic force and sensitively monitored. Moreover, a gas–liquid reactor and an automatic smoker are combined to ensure that transient ROS was simultaneously and effectively captured by the DNA on the MB surface, i.e. DNA was online oxidized as the smoking cigarette is 'puffed'. In addition, the potential to screen a mixture in a complex sample matrix, such as crude extracts, was also demonstrated and provides a key advantage of the present method as compared to other screening methods. Our results indicate that three natural compounds, quercetin, sodium danshensu and baicalein, can greatly protect DNA from oxidative damage caused by cigarette smoke and further successfully evaluated in the spiked cigarettes and thus these natural products may be promising compounds for the development of new drugs and the preparation of low-harm cigarettes. The search for more effective products for the protection of DNA against oxidative damage induced by other oxidants is underway in our group.

Acknowledgments

We acknowledge financial support from Shanghai Key Basic Research Program (08JC1402600) and Shanghai TCM Research Program (08DZ1971201).

References

[1] M.J. Lyons, J.F. Gibson, D.J.E. Ingram, Nature 181 (1958) 1003.
[2] Y.F. Hu, Z.J. Zhang, C.Y. Yang, Anal. Chim. Acta 601 (2007) 95.
[3] B.X. Ou, D.J. Huang, Anal. Chem. 78 (2006) 3097.
[4] G.M. Polzin, R.E. Kosa-Maines, D.L. Ashley, C.H. Watson, Environ. Sci. Technol. 41 (2007) 1297.
[5] J. Wu, P. Joza, M. Sharifi, W.S. Rickert, J.H. Lauterbach, Anal. Chem. 80 (2008) 1341.
[6] E.C. Friedberg, R. Wagner, M. Radman, Science 296 (2002) 1627.
[7] B. White, M.R. Smyth, J.D. Stuart, J.F. Rusling, J. Am. Chem. Soc. 125 (2003) 6604.
[8] M.D. Evans, M.S. Cooke, BioEssays 26 (2004) 533.
[9] M. Hashimoto, M.M. Greenberg, Y.W. Kow, J.T. Hwang, R.P. Cunningham, J. Am. Chem. Soc. 123 (2001) 3161.
[10] B. Tang, L. Zhang, Y. Geng, Talanta 65 (2005) 769.
[11] S. Toyokuni, K.K. Okamoto, J.J. Yodoi, H. Hiai, FEBS Lett. 358 (1995) 1.
[12] R.R. Singh, R.J. Sram, B. Binkova, I. Kalina, T.A. Popov, T. Georgieva, S. Garte, E. Taioli, P.B. Farmer, Mutat. Res. 620 (2007) 83.
[13] B. Halliwell, Free Radic. Biol. Med. 32 (2002) 968.
[14] K.C. Cheng, D.S. Cahill, H. Kasai, S. Nishimura, L.A.J. Loeb, Biol. Chem. 267 (1992) 166.
[15] S. Shibutani, M. Takeshita, A.P. Grollman, Nature 349 (1991) 431.
[16] M.L. Wood, M. Dizdaroglu, E. Gajewski, J.M. Essigmann, Biochemistry 29 (1990) 7024.
[17] C.M. Gedik, S.P. Boyle, S.G. Wood, N.J. Vaughan, A.R. Collins, Carcinogenesis 23 (2002) 1441.
[18] CDC, Annual smoking-attributable mortality, years of potential life lost, and economic costs—United States, 1995–1999, MMWR Wkly. 51 (2002) 300.
[19] H. Kiyosawa, M. Suko, H. Okudaira, K. Murata, T. Miyamoto, M.H. Chung, H. Kasai, S. Nishimura, Free Radic. Res. Commun. 11 (1990) 23.
[20] S. Asami, T. Hirano, R. Yamaguchi, Y. Tomioka, H. Itoh, H. Kasai, Cancer Res. 56 (1996) 2546.
[21] J. Wang, S. Xiong, C. Xie, W.R. Markesbery, M.A. Lovell, J. Neurochem. 93 (2005) 953.
[22] B. Halliwell, O.L. Aruoma, FEBS Lett. 281 (1991) 9.
[23] K. Frenkel, Pharmacol. Ther. 53 (1992) 127.
[24] Z. Djuric, D.A. Luongo, D.A. Harper, Chem. Res. Toxicol. 4 (1991) 687.
[25] M. Dizdaroglu, FEBS Lett. 315 (1993) 1.
[26] M.C. Poirier, Mutat. Res. Fundam. Mol. Mech. Mulagen. 288 (1993) 31.
[27] R.M. Santella, Mutat. Res. 205 (1988) 271.
[28] A.A. Wani, S.M. D'Ambrosio, Carcinogenesis 8 (1987) 1137.
[29] A.A. Wani, J.K.J. Sullivan, J. Lebowitz, Nucleic Acids Res. 17 (1989) 9957.
[30] P. Degan, M.K. Shigenaga, E.M. Park, P.E. Alperin, B.N. Ames, Carcinogenesis 12 (1991) 865.
[31] J. Musarrat, A.A. Wani, Carcinogenesis 15 (1994) 2037.
[32] A. Yarborough, Y.J. Zhang, T.M. Hsu, Cancer Res. 56 (1996) 683.
[33] A.M. Powe, K.A. Fletcher, N.N. St Luce, M. Lowry, S. Neal, M.E. McCarroll, P.B. Oldham, L.B. McGown, I.M. Warner, Anal. Chem. 76 (2004) 4614.
[34] A.M. Garcia-Campana, W.R.G. Baeyens, Chemiluminescence in Analytical Chemistry, Marcel Dekker, New York, 2001.
[35] R.A. Agbaria, P.B. Oldham, M. McCarroll, L.B. McGown, I.M. Warner, Anal. Chem. 74 (2002) 3952.
[36] A. Roda, M. Guardigli, E. Michelini, M. Mirasoli, P. Pasini, Anal. Chem. 75 (2003) 463A.
[37] X.H. Li, G.X. Zhang, H.M. Ma, D.Q. Zhang, J. Li, D.B. Zhu, J. Am. Chem. Soc. 126 (2004) 11543.
[38] A.P. Fan, C.W. Lau, J.Z. Lu, Anal. Chem. 77 (2005) 3238.
[39] N.Y. Tretyakova, J.C. Niles, S. Burney, J.S. Wishnok, S.R. Tannenbaum, Chem. Res. Toxicol. 12 (1999) 459.
[40] P.G. Slade, M.K. Hailer, B.D. Martin, K.D. Sugden, Chem. Res. Toxicol. 18 (2005) 1140.
[41] H.B. Yu, L. Venkatarangan, J.S. Wishnok, S.R. Tannenbaum, Chem. Res. Toxicol. 18 (2005) 1849.
[42] L. Mira, M.T. Fernandez, M. Santos, R. Rocha, M.H. Florencio, K.R. Jennings, Free Radic. Res. 36 (2002) 1199.
[43] D. Ozyurt, B. Demirata, R. Apakb, Talanta 71 (2007) 1155.
[44] S. Martinez-Florez, B. Gutierrez-Fernandez, S. Sanchez-Campos, J. Gonzalez-Gallego, M.J.J. Tunon, J. Nutr. 135 (2005) 1359.
[45] L. Magnani, E.M. Gaydou, J.C. Hubaud, Anal. Chim. Acta 411 (2000) 209.
[46] M.G. Hertog, P.C. Hollman, M.B. Katan, D. Kromhout, Nutr. Cancer 20 (1993) 21.
[47] S.O. Keli, M.G. Hertog, E.J. Feskens, D. Kromhout, Arch. Intern. Med. 156 (1996) 637.
[48] K. Kanazawa, M. Uehara, H. Yanagitani, T. Hashimoto, Arch. Biochem. Biophys. 455 (2006) 197.
[49] M.G. Traber, A.V. Vliet, A.Z. Reznick, C.E. Cross, Clin. Chest Med. 21 (2000) 173.
[50] B.M. Lee, S.K. Lee, H.S. Kim, Cancer Lett. 132 (1998) 219.

Talanta 80 (2010) 1222–1227

Contents lists available at ScienceDirect

Talanta

journal homepage: www.elsevier.com/locate/talanta

Development of an on-line isotope dilution laser ablation inductively coupled plasma mass spectrometry (LA–ICP-MS) method for determination of boron in silicon wafers

Chao-Kai Yang[a,b], Po-Hsiang Chi[c], Yong-Chine Lin[a], Yuh-Chang Sun[c,*], Mo-Hsiung Yang[c]

[a] Department of Chemistry, National Tsing-Hua University, Hsinchu, Taiwan
[b] Forensic Science Center, Taipei City Police Department, Taipei, Taiwan
[c] Department of Biomedical Engineering and Environmental Sciences, National Tsing-Hua University, Hsinchu, Taiwan

ARTICLE INFO

Article history:
Received 9 June 2009
Received in revised form 1 September 2009
Accepted 8 September 2009
Available online 24 September 2009

Keywords:
Silicon wafer
LA–ICP-MS
On-line isotope dilution

ABSTRACT

A method has been developed based on an on-line isotope dilution technique couple with laser ablation/inductively coupled plasma mass spectrometry (LA–ICP-MS), for the determination of boron in p-type silicon wafers. The laser-ablated sample aerosol was mixed on-line with an enriched boron aerosol supplied continuously using a conventional nebulization system. Upon mixing the two aerosol streams, the isotope ratio of boron changed rapidly and was then recorded by the ICP-MS system for subsequent quantification based on the isotope dilution principle. As an on-line solid analysis method, this system accurately quantifies boron concentrations in silicon wafers without the need for an internal or external solid reference standard material. Using this on-line isotope dilution technique, the limit of detection for boron in silicon wafers is 2.8×10^{15} atoms cm^{-3}. The analytical results obtained using this on-line methodology agree well with those obtained using wet chemical digestion methods for the analysis of p-type silicon wafers containing boron concentrations ranging from 1.0×10^{16} to 9.6×10^{18} atoms cm^{-3}.
© 2009 Elsevier B.V. All rights reserved.

1. Introduction

In general, direct analyses of solid samples are preferable to conventional wet analytical methods because of their chemical-, labor-, and time-saving features. As non-destructive methods, although X-ray fluorescence (XRF) and neutron activation analysis (NAA) have been used with varying degrees of success for direct solid elemental analyses, but the poor sensitivity for light elements provided by XRF and the inconvenience of handling radioactive materials and the dependence on large irradiation facilities required for NAA make them unsuitable for routine determinations. Several destructive systems—with prior excitation followed by instrumental determination—have been developed as more practical approaches for direct solid sample analyses. Among them, spark source optical emission spectrometry (spark source-OES), spark source mass spectrometry (SSMS), glow discharge mass spectrometry (GD-OES), glow discharge mass spectrometry (GD-MS), laser microprobe mass spectrometry (LAMMA), and secondary ion mass spectrometry (SIMS) are widely known techniques employing single excitation sources. Because both sampling and excitation processes are generally performed simultaneously, single-excitation-source instruments sometimes provide poor analytical sensitivity and poor spatio-temporal resolving power [1,2]. To decouple the sampling and excitation processes, instruments featuring dual excitation sources have been developed to improve the analytical performance. Thus, sparks [3–12], arcs [13,14] and laser beams [15–19] have all been applied to generate aerosols that are then transported to an inductively coupled plasma mass/optical spectrometer (ICP-MS/OES) using a stream of inert gas. Among such instruments, LA–ICP-MS is the most commonly used analytical technique that has received the most attention in recent years.

Although the potential of LA–ICP-MS has been recognized in various scientific fields, this technique also suffers from severe matrix effects—as do all solid mass spectrometric techniques—as a result of the varying ablation yields associated with differences in the material properties between the solid standards and the samples. To overcome the matrix and calibration problems, various approaches have been used to develop effective calibration methods for quantification. For conventional quantification techniques, a matrix-matched standard is typically required to calibrate the laser ablation processes and the ICP response. Because of the limited availability of standards, matrix-matched synthetic laboratory standards are always needed to produce calibration curves for quantification purposes [20,21]. As noted by Becker et al. [22], however, the preparation of synthetic laboratory standards is often the most time-consuming step in solid state mass spectrometry, it is

* Corresponding author. Tel.: +886 3 5715131x35596; fax: +886 3 5723883.
E-mail address: ycsun@mx.nthu.edu.tw (Y.-C. Sun).

0039-9140/$ – see front matter © 2009 Elsevier B.V. All rights reserved.
doi:10.1016/j.talanta.2009.09.013

not feasible for all types of samples, and it can lead to homogeneity problems.

To overcome the difficulties resulting from conventional quantification techniques, on-line solution-based calibration methods have been developed as simple, rapid quantification procedures for LA–ICP-MS analyses. Indeed, Günther and coworkers [23–25] and Chenery and coworkers [26,27] developed dual-gas introduction systems to perform the solid/liquid calibration. They suggested that the concentration of at least one element in the sample should be determined by another independent analytical technique to obtain the relative sensitivity factor (RSF), which is defined as the certified concentration of the internal standard element in the standard divided by the measured concentration of the internal standard element in the sample [28,29]. Simultaneous solution nebulization and laser ablation sample introduction have also been developed as techniques to overcome mass discrimination effects in LA–ICP-MS, due to the occurrence of space charge effects, which are major sources of uncertainty when measuring isotope ratios [30]. However, according to Horn et al. [31], the balance between the gas flows of the liquid nebulizer and laser ablation systems can cause inferior transport efficiencies in both introduction systems. To overcome this problem, a single gas sample introduction system has also been developed to optimize the gas flow rates for both sample introduction systems [29].

To compensate for the matrix effects observed in LA–ICP-MS, standard addition methods [22,32] have also been developed for the determination of trace elements in various sample matrices, where neither matrix-matched standard reference materials nor high-purity blank targets were available. This calibration strategy consists of on-line mixing the dried aerosol containing known amounts of the analyte(s) from the nebulizing system to the ablated aerosol from the LA cell. Becker [32] found that, when using the standard addition method, the advantages of solid/liquid calibration are introduced without sacrificing the rapid, sensitive, and spatially specific characteristics of the LA–ICP-MS measurement. In view of the transient nature of the LA–ICP-MS signal, however, it is almost impossible to correct the signal drift—resulting from instrument instability and fluctuations in the laser firing and transport processes—when using the standard addition mode. In addition, the restricted amount of sample available for the number of measurements required is another limiting factor affecting the use of the standard addition method for quantification. To overcome these problems, an effective solution-based quantitative strategy—on-line isotope dilution analysis (IDA) in LA–ICP-MS (on-line LA–ID-ICP-MS)—has been used for the successful determination of trace elements in environmental and minute solid samples [33–35].

Isotope dilution mass spectrometry (IDMS) is one of the few methods capable of achieving analytical results that are not affected by signal drifts, matrix effects, or analyte losses. Therefore, according to Fernández et al. [34], the incorporation of isotope dilution into LA–ICP-MS can eliminate some common fractionation and matrix effects that cannot be addressed using other calibration procedures. Although isotope dilution techniques have been applied widely as calibration methods for various solid state mass spectrometers (e.g., SIMS [36], SSMS [37], and LA–ICP-MS [38–40]), the isotope-diluted powders still must be prepared using time-consuming and laborious procedures in which they are mixed with an internal standard solution or enriched isotope standard, dried, homogenized in a ball-mixer/mill, and pressed into the form of a pellet. As a result, the merits of the LA–ICP-MS and IDMS approach might be deteriorated because of the need for the pelletization procedure and the uncertainty of the total isotopic exchange between the sample and the spiking isotope during the mixing step. To eliminate the inconvenience of preparing the pellet sample, Becker et al. [33,35] developed a new analysis procedure to determine trace elements in solid samples: on-line isotope dilution in LA–ICP-MS equipped with a single gas sample introduction system.

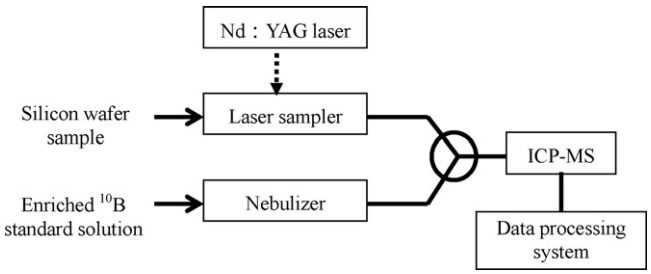


Fig. 1. Experimental setup for on-line isotope dilution LA–ICP-MS.

In view of the high demand for the determination of trace impurities, particularly in high-purity solid materials for the microelectronics industry, in this study we developed an on-line LA–ID-ICP-MS method for the determination of boron in silicon wafers. Although internal standards are usually used in solid state mass spectrometry, Ramendik [41] noted that the relative systematic errors can be as high as 30–50% which is unsatisfactory for routine analysis, when we ignore the dependence of the RSF on the sample matrix and the experimental conditions. Pisonero et al. [42] observed a range of 15–30% for the differences between the concentrations of boron obtained using a wet chemical method and LA–ICP-MS, individually, when they used NIST SRM 610 (silicate sample) and Si as the external calibration material and internal standard element, respectively, for quantitative analysis of metallurgical-grade Si. Because on-line solution-based isotope dilution in laser ablation ICP-MS is a simple, accurate, and precise quantification procedure, our aim in this study was to establish a new calibration method—combining IDA and LA–ICP-MS without the use of solid standard reference materials or internal standard element—and to verify the extent to which this technique could be applied to the accurate and precise determination of boron in high-purity silicon wafers.

2. Experimental

2.1. Instrumentation

A PerkinElmer Sciex laser sampler model 320 was used for ablation of the silicon wafer samples. The laser system, which contained a neodymium-doped yttrium aluminum garnet (Nd–YAG) laser with a fundamental wavelength of 1064 nm, could be operated under either a Q-switched or free-running mode and either a single-shot mode or at a repetition rates of up to 10 Hz. The wafer was secured by a sample holder in a quartz cell mounted on a programmable *xyz*-translation stage operated via computer control. A Teflon disk was inserted between the wafer and the sample holder to adjust the defocus distance from the laser; the desired area of the silicon wafer sample was then subjected to the laser shot. During laser ablation, the sample surface was monitored using a CCD camera and displayed on a TV screen.

After laser ablation, the sample was transported through Tygon plastic tubing (I.D.: 10 mm; length: 1.0 m) to be on-line mixed with the sample aerosol from a cross-flow nebulizer equipped with a Scott-type spray chamber (PerkinElmer Sciex). Subsequently, the mixed sample aerosol was introduced into the ICP-MS system (PerkinElmer Sciex Elan 5000, Thornhill, Ontario, Canada) for detection of the signal intensity of the boron isotopes. Fig. 1 provides a schematic representation of the LA–ICP-MS and solution nebulization system. Table 1 summarizes the instrumental parameters and operating conditions of the laser ablation and solution nebulization system coupled to ICP-MS.

Table 1
Instrumentation and parameters.

Laser ablation system	
Model	PE Sciex Laser Sampler 320
Type	Solid state Nd:YAG
Wavelength	1064 nm
Operating mode	Q-switched
Ablation time	30 s
Laser beam energy	330 mJ
Pulse width	10 ns
Q-switched delay	240 μs
Focusing position	On sample surface
Spot diameter	40 μm
ICP-MS	
Model	PE Sciex Elan 5000
RF power	1250 W
Plasma gas flow rate	15 L min^{-1}
Auxiliary gas flow rate	0.8 L min^{-1}
Acquisition mode	Peak hopping
Sampler cone	Platinum
Skimmer cone	Platinum
Dwell time	10 ms
Sweeps/reading	20
Readings/replicate	150
Replicate	1
Points per peak	1
Mass resolution	Normal
Nebulizer	Cross-flow
Spray chamber	Scott-type

2.2. Materials and reagents

PTFE vessels and polyethylene containers were used throughout to avoid boron contamination. One side polished silicon (1 0 0) p-type wafers (diameter: 20 cm; thickness: 725 μm; Taisil Electronic Materials Corp., Taiwan) were sliced into 2 cm × 2 cm pieces prior to use. All reagents, of analytical or higher grade, were obtained from E. Merck. Nitric acid (Tracepure grade) was further treated in-house by sub-boiling. High-purity water that had been deionized using a Milli-Q system (Millipore, Bedford, MA, USA) was subsequently purified through sub-boiling distillation and passage through a boron-selective anion-exchange resin (Amberlite IRA-742, Rohm and Haas, France) to remove trace amounts of boron. The boron isotope standard SRM 951 (^{10}B/^{11}B ratio = 0.2473; ^{10}B = 19.827%; ^{11}B = 80.173%) and the enriched isotope ^{10}B standard SRM 952 (^{10}B/^{11}B ratio = 18.798; ^{10}B = 94.949%; ^{11}B = 5.051%) were purchased from the National Institute of Standards and Technology (NIST, USA).

2.3. Experimental procedure

Upon connecting the laser ablation system and the nebulization system through a Y-shaped connector, the enriched boron standard was introduced continuously into the ICP-MS system to measure the enriched boron isotopic signal. The spot position and focusing position of the laser ablation system were aligned to provide the maximum and consistent signal with reasonable stability. Once a steady boron isotope signal from the nebulization system was established, the laser was switched on. After a suitable sampling time, the laser ablation system was switched off. This process yielded a signal profile with respect to the elapsed time. For example, in Fig. 2(a) the incipient region represents the continuous signal of the enriched boron standard solution obtained from the nebulization system; the plateau represents the steady-state signal arising from the mixing of the sample aerosol from the nebulization and laser ablation systems. The transient intensities of the boron isotopes measured by the ICP-MS system were further transformed into time-dependent ratios [$R(t) = {}^{10}B/{}^{11}B$; Fig. 2(b)] and corresponding boron mass flow profiles [Fig. 2(c)]. Table 2 sum-

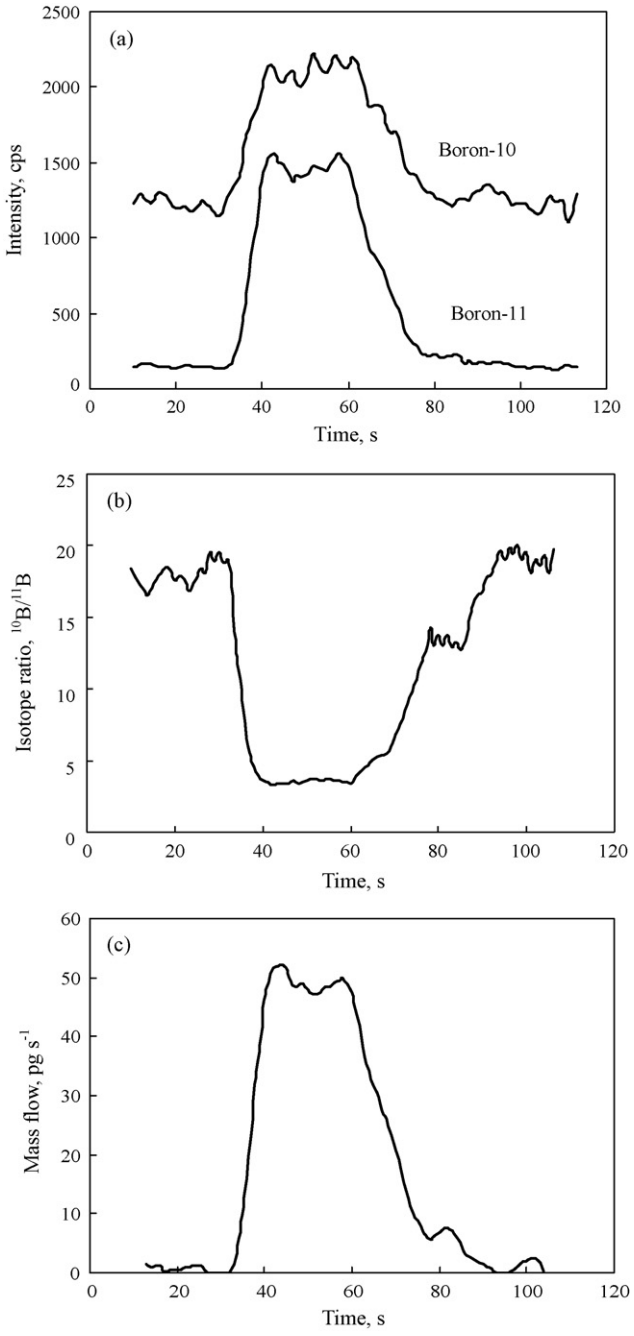


Fig. 2. (a) Plot of the boron isotopic signal profile with respect to time. (b) Plot of the time-dependent isotope ratio ^{10}B/^{11}B. (c) Corresponding mass flow profile of boron.

Table 2
Typical operating conditions for on-line isotope dilution analysis.

Spike standard (NIST SRM 952)	^{10}B/^{11}B = 18.80
^{10}B abundance	94.949%
^{11}B abundance	5.051%
Measured enriched ^{10}B/^{11}B ratio	12.09
Mass discrimination factor	1.56
Carrier gas flow rate (laser sampler)	0.5 L min^{-1}
Weight of sample ablated in a laser firing	0.032 mg
Nebulizer gas flow rate	0.5 L min^{-1}
Enriched spike concentration	24.7, 397 ng g^{-1}
Enriched spike delivery rate	0.026, 0.41 mg s^{-1}

marizes the typical operating conditions for the isotope dilution analyses.

3. Result and discussion

3.1. Calibration and data processing of on-line dilution analysis

The principle of IDMS involves altering the natural ratio between two isotopes in a sample, by adding an accurately known quantity of an isotope spike, and then measuring the isotope ratio in the mixture. The concentration (C) of the analyte in the sample can be deduced using the equation

$$C = \frac{W_{sp} \times K}{W_s} \times \left(\frac{h_{sp}^2 - R \times h_{sp}^1}{R \times h_s^1 - h_s^2} \right) \quad (1)$$

where W_{sp} is the mass of the spike; K is the ratio of the natural atomic weight and the atomic weight of the enriched material; W_s is the mass of the sample; h_s^1 and h_s^2 are the isotope abundances of isotopes 1 and 2 in the sample, respectively; and h_{sp}^1 and h_{sp}^2 are the isotope abundances of isotopes 1 and 2 in the spike, respectively.

Fig. 1 displays a schematic representation of the on-line-LA–ICP-IDMS system. In essence, the data manipulation was performed according to the procedure described previously by Rottmann and Heumann [43]. Fig. 2(a) presents the transient signals of the boron isotopes measured by the ICP-MS system, plotted as the ^{10}B and ^{11}B signal profiles over time. After correcting the background levels of the measured boron isotopes, each data point of the time-dependent isotope ratio [$R(t)$] was calculated based on the net signal intensities of the measured isotopes; Fig. 2(b) displays the results for boron in a silicon wafer with respect to the measured isotope ratio ^{10}B:^{11}B. When no boron was ablated from the wafer, we measured the ^{10}B:^{11}B ratio of the spike solution (ca. 18.8). An aerosol containing boron from the sample shifted the isotope ratio in the direction of the natural isotopic composition, as is evident in the significant negative band obtained during the laser ablation process. Subsequently, we converted the isotope ratio curve in Fig. 2(b) into a mass flow diagram [$M_s(t)$] of boron by using the equation [44]

$$M_s(t) = M_{sp} \times \left(\frac{h_{sp}^{10} - R(t) \times h_{sp}^{11}}{R(t) \times h_s^{11} - h_s^{10}} \right) \quad (2)$$

where M_{sp} is the mass flow of the enriched boron spiked into the system and $h_s^{isotope}$ and $h_{sp}^{isotope}$ are the abundances of the respective boron isotopes in the sample and in the spike. Because M_{sp} is determined by the nebulization (transport) efficiency of the boron-enriched standard solution, at a given nebulizer gas flow rate, it can be obtained from the difference between the mass of the standard solution consumed and the mass of the drain solution of the nebulization system during the measurement process.

Although we could readily obtain the absolute boron mass from the area under the band in the mass flow diagram, obtaining the concentration of boron in the silicon wafer required us to determine the weight of the sample ablated in each laser firing at a constant laser power. We determined the weight of the sample ablated by using a fixed volume of an HF/HNO_3 mixture as an absorbing solution to grab and dissolve the ablated aerosol after the laser firing. Because the silicon wafer used in this study comprised over 99.9% pure silicon, we calculated the weight of the sample ablated simply from the silicon concentration in the absorbing solution. In this study, the average weight of sample ablated, obtained from 25 measurements, was 0.032 mg; the relative standard deviation of all of the individual determinations was less than 14%.

3.2. Optimization of dual sample introduction system

To ensure the best conditions for the LA–ICP-IDMS-based determination of boron in the silicon wafers, we evaluated several parameters that could influence the performance of the dual sample introduction system with a sliced p-type silicon wafer. In general, silicon wafers feature both polished and rough sides. To avoid reflection loss of the laser beam energy, in this study we chose the rough side to be the test side. Günther et al. [44] found that improved sensitivity and lower background levels could be achieved by optimizing the gas flows, mixing behavior, and tuning parameters for a system involving simultaneous introduction of a solution aerosol and a laser-induced aerosol. They also reported that the total flow rate for the transport of laser-ablated material into the ICP system was inappropriately high when they optimized each individual system (laser ablation and liquid nebulization) separately. Accordingly, to maintain the stability and excitation capability of the plasma, improve the transport efficiency, and minimize excessive dilution of the ablated material, we investigated the optimal gas flow rates for the laser ablation and solution nebulization systems under a total flow rate of 1.0 L min^{-1}, which provided the most favorable conditions for good detection sensitivity for the determination of boron.

To characterize our dual introduction system, we optimized each individual system separately. Fig. S1 displays the effect of two different gas flow rates (total flow rate: 1.0 L min^{-1}) on the signal intensity of boron obtained when using the dual sample introduction system. The signal intensities in Fig. S1 were obtained by introducing Ar gas at a flow rate of X L min^{-1} through the nebulization system and $(1.0 - X)$ L min^{-1} through the laser ablation system. The signal intensities increased upon increasing the nebulizer gas flow rate from 0.2 to 0.5 L min^{-1}, with an abrupt increase in the signal intensity occurring when the gas flow rate ratio increased from 0.6/0.4 to 0.5/0.5 (laser sampler/nebulizer). Curve "b" presents the variation in the signal intensities obtained when introducing X L min^{-1} of the blank solution aerosol from the nebulization system and $(1.0 - X)$ L min^{-1} of the ablated sample aerosols from the laser ablation system. The signal intensities increased upon decreasing the gas flow rate of the laser sampler system from 0.8 to 0.6 L min^{-1}, reaching a maximum when the gas flow rate ratio was 0.6/0.4 (laser sampler/nebulizer). A compromise gas flow rate ratio of 0.5/0.5 for the laser ablation and solution nebulization systems was chosen to be optimal for all subsequent experiments. Table 2 summarizes the optimized parameters for the on-line isotope dilution analysis process.

3.3. Optimization of on-line isotope dilution analysis

Mass discrimination relies on discrepancies between the natural isotope ratio and the measured isotope ratio. According to Diemer et al. [45], the repeatability of the correction for mass discrimination is one of the dominating sources of instrumental uncertainty during ICP-IDMS measurement. Because of the intrinsic mass difference of 10% between ^{10}B and ^{11}B, measurement of the boron isotope ratio might suffer from a severe mass discrimination effect [46]. To correct this mass discrimination effect, we measured the isotope ratio of the boron standard solution (NIST SRM 952) and obtained a mass discrimination factor by dividing the certified isotope ratio by the measured isotope ratio. The isotope ratio measured in the sample analysis could then be corrected by multiplying by the mass discrimination factor [47]. Based on the results presented in Fig. 2(b), we obtained a mass discrimination factor of 1.56 and, in turn, used the corrected isotope ratio and Eq. (2) to calculate the mass flow of boron.

To minimize the error resulting from the uncertainty of the concentration of the ^{10}B-enriched spiked boron solution, in this study

Table 3
Boron concentrations in Si wafers.

Method	Concentration, 1×10^{16} atoms cm^{-3}		
	Wafer 1	Wafer 2	Wafer 3
LA–ICP-MS (this study)[a]	1.25 ± 0.29	669 ± 58	1360 ± 110
Wet chemical[b] [49]	1.32 ± 0.057	693 ± 3.6	1470 ± 51
Four-point probe [50]	0.931	433	953

[a] $n = 3$; seven sites per sample.
[b] $n = 3$.

we also determined the concentration of boron in the enriched spike solution and the resulting boron isotopic ratio of the spiked sample. The concentration of enriched spike solution was determined using the reversed-ID technique and a certified standard (NIST SRM 951). Because the optimal performance of the ID technique is achieved by controlling the resulting isotope ratio of the analyte within a range from 0.1 to 10 after mixing with the enriched spike solution [48], we estimated the approximate concentration of boron in a silicon wafer based on the relationship between the resistivity and boron dopant concentration provided by Taisil Electronic Materials Corp. After determining the approximate concentration of the analyte, two appropriate amounts of the enriched spike solutions (24.7 and 397 ng g^{-1}) was intentionally added to maintain the isotopic ratio within the favorable range from 0.1 to 10 during the on-line isotope dilution analysis. As indicated in Table 2, we set the calculated enriched spike delivery rates to 0.026 and 0.41 mg s^{-1} for the determination of boron in silicon wafer.

3.4. Analytical features and applicability

To demonstrate the applicability of this on-line system, we determined the concentrations of boron in several silicon wafers. Because no certified values for the analyte's contents in the silicon wafers were available, we validated the accuracy of our on-line methodology through inter-method comparative analysis with wet chemical digestion and electrical four-point probe measurements. Table 3 reveals that the results obtained using our on-line method to analyze three different silicon wafers agreed well with the values obtained using the wet chemical method (the difference being less than 10%), but were significantly different (25–35%) from those obtained using the four-point probe method, presumably because only the levels of electroactive boron in the silicon crystal can be determined through electrical measurement. In contrast, both the electroactive and -inactive fractions of boron in the silicon wafers were measured using both our newly developed method and the wet chemical method.

We estimated the detection limit of our developed analytical method from seven individual measurements after on-line introducing enriched boron standard solution into the system. Each enriched boron isotope ratio was calculated using the same procedure described above. The limit of detection of this method, based on three times the standard deviation (3σ) of the calculated results, was 2.8×10^{15} atoms cm^{-2}. We also tested the precision of this method through the analyses of three replicate silicon wafer samples; the average coefficient of variation was ca. 8% for higher-concentration samples. Overall, the high performance of our proposed analytical method—evaluated in terms of the detection limit, accuracy, and precision—indicates that on-line-LA–ICP-IDMS hyphenated systems are suitable for use for the determination of trace boron in silicon wafers.

4. Conclusion

Similar to SIMS, LA–ICP-MS exhibits excellent multi-elemental and isotopic performance in bulk analysis, microanalysis, and depth profile analysis, but accurate determination of trace elements in solid samples, such as silicon wafer, remains a difficult task for either technique. To overcome the difficulties encountered in the quantitative determination of trace boron in silicon wafers, we combined on-line IDMS with LA–ICP-MS to establish an on-line-LA–ICP-IDMS system incorporating a reliable solid/liquid calibration method. A distinct feature of this on-line-LA–ICP-MS technique is that neither an internal standard nor a matrix-matched standard is required for the quantitative analysis of silicon wafers. In future studies, we will focus on the applicability of this on-line LA–ICP-IDMS quantification concept to the determination of trace analytes in various other matrices for which the on-line sample weight measurement apparatus is available.

Acknowledgements

We thank the National Science Council of Taiwan for supporting this study financially (NSC-89-3011-M-007-005-NU and NSC-90-3011-E-007-005-NU).

Appendix A. Supplementary data

Supplementary data associated with this article can be found, in the online version, at doi:10.1016/j.talanta.2009.09.013.

References

[1] J.P. Walters, Science 198 (1977) 787.
[2] A. Scheeline, D.M. Coleman, Anal. Chem. 59 (1987) 1185A.
[3] R. Maibusch, H.M. Kuss, A.G. Coedo, T. Dorado, I. Padilla, J. Anal. Atom. Spectrom. 14 (1999) 1155.
[4] K.A. Ivanovic, D.M. Coleman, F.W. Kunz, D. Schuetzle, Appl. Spectrosc. 46 (1992) 894.
[5] A.G. Coedo, T.P. Lopez, I.G. Cobo, E.E. Baquero, J. Anal. Atom. Spectrom. 7 (1992) 247.
[6] A.G. Coedo, T. Dorado, C.J. Rivero, I.G. Cobo, J. Anal. Atom. Spectrom. 8 (1993) 1023.
[7] A.G. Coedo, T.P. Lopez, I.G. Cobo, J. Anal. Atom. Spectrom. 9 (1994) 223.
[8] A.G. Coedo, T.P. Lopez, I.G. Cobo, B.J. Fernandez, J. Anal. Atom. Spectrom. 9 (1995) 223.
[9] A. Lemarchand, G. Labarraque, P. Masson, J.A.C. Broekaert, J. Anal. Atom. Spectrom. 2 (1987) 481.
[10] R.L.V. Hoven, S.H. Nam, A. Montaser, M.W. Doughten, A.F. Dorrzapf Jr., Spectrochim. Acta 50B (1995) 549.
[11] M. Gagean, J.M. Mermet, J. Anal. Atom. Spectrom. 12 (1997) 189.
[12] N. Jakubowski, I. Feldmann, D. Stuewer, Spectrochim. Acta 50B (1995) 639.
[13] S.J. Jiang, R.S. Houk, Anal. Chem. 58 (1986) 1739.
[14] S.J. Jiang, R.S. Houk, Spectrochim. Acta 42B (1987) 93.
[15] R.E. Russo, Appl. Spectrosc. 49 (1995) 14A.
[16] S.F. Durrant, J. Anal. Atom. Spectrom. 14 (1999) 1385.
[17] E. Hoffmann, C. Ludke, J. Skole, H. Stephanowitz, J. Wollbrandt, W. Becker, Spectrochim. Acta 57B (2002) 1535.
[18] D. Günther, Anal. Bioanal. Chem. 372 (2002) 31.
[19] B. Hattendorf, C. Latkoczy, D. Günther, Anal. Chem. 75 (2003) 341A.
[20] A.A. Heuzen, Spectrochim. Acta 46B (1991) 1803.
[21] A.A. Heuzen, J.B.J. Morsink, Spectrochim. Acta 46B (1991) 1819.
[22] J.S. Becker, C. Pickhardt, H.J. Dietze, J. Anal. Atom. Spectrom. 16 (2001) 603.
[23] L. Moenke-Blankenburg, M. Gackle, D. Günther, J. Kammel, in: K.E. Jarvis, A.L. Gray, J.G. Williams (Eds.), Plasma Source Mass Spectrometry, Royal Society of Chemistry, Cambridge, UK, 1990.
[24] L. Moenke-Blankenburg, D. Günther, Chem. Geol. 95 (1992) 85.
[25] L. Moenke-Blankenburg, T. Schumann, D. Günther, H.M. Kuss, M. Paul, J. Anal. Atom. Spectrom. 7 (1992) 251.
[26] M. Thompson, S. Chenery, L. Brett, J. Anal. Atom. Spectrom. 4 (1989) 11.
[27] S. Chenery, J.M. Cook, J. Anal. Atom. Spectrom. 8 (1993) 299.
[28] C. Pickhardt, J.S. Becker, Fresen. J. Anal. Chem. 370 (2001) 534.
[29] C. Pickhardt, J.S. Becker, H.J. Dietze, Fresen. J. Anal. Chem. 368 (2000) 173.
[30] C. Pickhardt, H.J. Dietze, J.S. Becker, Int. J. Mass Spectrom. 242 (2005) 273.
[31] I. Horn, R.L. Rudnick, W.F. McDonough, Chem. Geol. 164 (2000) 281.
[32] J.S. Becker, Spectrochim. Acta 57B (2002) 1805.
[33] J.S. Becker, C. Pickhardt, W. Pompe, Int. J. Mass Spectrom. 237 (2004) 13.
[34] B. Fernández, F. Claverie, C.e. Pécheyran, O.F.X. Donard, J. Anal. Atom. Spectrom. 23 (2008) 367.
[35] C. Pickhardt, A.V. Izmer, M.V. Zoriy, D. Schaumlöffel, J.S. Becker, Int. J. Mass Spectrom. 248 (2006) 136.
[36] A.G. Adriaens, J.D. Fassett, W.R. Kelly, D.S. Simons, F.C. Adams, Anal. Chem. 64 (1992) 2945.
[37] K.P. Jochum, M. Seufert, S. Best, Fresen. J. Anal. Chem. 309 (1981) 308.

[38] H. Scholze, E. Hoffmann, C. Ludke, A. Platalla, Fresen. J. Anal. Chem. 355 (1996) 892.
[39] Y.L. Lee, C.C. Chang, S.J. Jiang, Spectrochim. Acta 58B (2003) 523.
[40] M. Tibi, K.G. Heumann, J. Anal. Atom. Spectrom. 18 (2003) 1076.
[41] G.I. Ramendik, Int. J. Mass Spectrom. 172 (1998) 221.
[42] J. Pisonero, I. Kroslakova, D. Günther, C. Latkoczy, Anal. Bioanal. Chem. 386 (2006) 12.
[43] L. Rottmann, K.G. Heumann, Fresen. J. Anal. Chem. 350 (1994) 221.
[44] D. Günther, H. Cousin, B. Magyar, I. Leopold, J. Anal. Atom. Spectrom. 12 (1997) 165.
[45] J. Diemer, C.R. Quétel, P.D.P. Taylor, J. Anal. Atom. Spectrom. 17 (2002) 1137.
[46] D.C. Gregoire, J. Anal. Atom. Spectrom. 5 (1990) 623.
[47] A.G. Coedo, T. Dorado, B.J. Fernandez, F.J. Alguacil, Anal. Chem. 68 (1996) 991.
[48] M. Thomson, J.N. Walsh, Handbook of Inductively Coupled Plasma Spectrometry, Blackie, Chapman and Hall, New York, 1989.
[49] P.P. Mahoney, G. Li, G. Hieftje, J. Anal. Atom. Spectrom. 11 (1999) 401.
[50] C. Latkoczy, D. Günther, J. Anal. Atom. Spectrom. 17 (2002) 1264.

Talanta 80 (2010) 1228–1233

Contents lists available at ScienceDirect

Talanta

journal homepage: www.elsevier.com/locate/talanta

Study the damage of DNA molecules induced by three kinds of aqueous nanoparticles

Chao Wang, Xue Gao, Xingguang Su*

Department of Analytical Chemistry, College of Chemistry, Jilin University, Changchun, 130012, China

ARTICLE INFO

Article history:
Received 11 June 2009
Received in revised form 1 September 2009
Accepted 8 September 2009
Available online 22 September 2009

Keywords:
DNA damage
Quantum dots
Mn:ZnSe d-dots
Aqueous phase
Biocompatible materials

ABSTRACT

In this paper, the interaction of DNA molecules with aqueous CdTe quantum dots (CdTe QDs), CdTe/SiO_2 composite nanoparticles (CdTe/SiO_2 NPs), and Mn-doped ZnSe quantum dots (Mn:ZnSe d-dots) was studied with ethidium bromide as a probe. The purpose of this work was to study the damage of DNA molecules induced by these three kinds of water-soluble nanoparticles. It was found that ionic strength, pH value and UV irradiation influenced the PL emission properties of CdTe QDs, CdTe/SiO_2 NPs and Mn:ZnSe d-dots, and also influenced the interaction of DNA molecules with them. Among the three kinds of nanoparticles, DNA molecules were most easily damaged by CdTe QDs whether in the dark or under UV irradiation. The CdTe/SiO_2 NPs led to much less DNA damage when compared with CdTe QDs, as a silica overcoating layer could isolate the QDs from the external environment. Mn:ZnSe d-dots as a new class of non-cadmium doped QDs demonstrated almost no damage for DNA molecules, which have great potentials as fluorescent labels in the applications of biomedical assays, imaging of cells and tissues, even in vivo investigations.

© 2009 Elsevier B.V. All rights reserved.

1. Introduction

Semiconductor nanocrystals, also named quantum dots (QDs), have attracted a lot of attentions in the past few decades due to their unique optical properties and applications, which endow them as ideal optical probes used in biomedicine and biotechnology [1,2]. Their photoluminescence (PL) can be tuned by simply controlling particle size and the varied PL emitted from QDs with different size can be simultaneously excited with a single excitation light source. Simultaneously, QDs possess high surface-to-volume ratios and their sizes can be well controlled during the synthesis process, making them good candidates for interfacing with biological systems. Furthermore, fluorescence of QDs is intrinsic, bright, and prolonged, endowing QDs with "*in situ*" imaging functionality which surpasses the sensitivity and resolution capability of organic dyes and proteins.

QDs can be synthesized by two kinds of chemical methods, which are organometallic synthesis and aqueous synthesis, respectively. Contrast to organometallic method, aqueous synthesis is more reproducible, cheaper and less toxic, and the prepared QDs have high stability and biological compatibility, which are more suitable for biomedical applications. Although the popularity of QD labeling soars, whether QDs synthesized by aqueous synthesis or organometallic synthesis, they are still facing an unsolved problem, which is the toxicity of these cadmium-containing nanoparticles induced by heavy metal ions used in the process of synthesis released upon oxidative and/or photolytic degradation [3].

In 2006, Hardman reviewed the toxicity of QDs depending on physicochemical and environmental factors [4]. It is suggested that QD size, charge, concentration, outer coating bioactivity (capping material, functional groups), and oxidative, photolytic, and mechanical stability have each been shown to be determining factors in QDs toxicity. Several researches about cytotoxicity of QDs have been published [5–13]. Besides cytotoxicity of QDs, QDs can also damage DNA molecules. Green and Howman [14] reported the observation of DNA damage in plasmid nicking assays with water-soluble CdSe/ZnS QDs. They attributed the effect of QDs to free radicals both photogenerated and surface oxide generated, which suggested that there may be serious issues to address concerning the use of such materials in DNA based assays or in in vivo applications, as well as highlighting potential toxicological and environmental implications. Han and co-workers [15] investigated the calf thymus DNA (ctDNA) damaged induced by water-soluble CdSe QDs using nucleic acid molecular "light switches" as probes. It was found that the ctDNA damage caused by CdSe QDs was not due to photo-induced liberation of Cd^{2+}, but due to the production of free radicals and reactive oxygen species. More recently, Biju and co-workers [16] investigated the strand breakages and nucleobase damages in plasmid DNA by CdSe-ZnS QDs under different conditions of photoactivation. The results confirmed that the production of reactive oxygen intermediates by QDs induced the breakage and damage of DNA molecules, which

* Corresponding author. Tel.: +86 431 85168352.
E-mail address: suxg@jlu.edu.cn (X. Su).

0039-9140/$ – see front matter © 2009 Elsevier B.V. All rights reserved.
doi:10.1016/j.talanta.2009.09.014

showed possibilities of QDs in nucleus-targeted photodynamic therapy.

The effects of QDs on biomolecules have been an important issue to obstruct the development of QD biomedical applications. Depositing a silica layer with the capability of impeding surface ruin of QDs and inhibiting the release of heavy metal ions is an effective way to solve the problem. In addition, a new class of potential non-cadmium fluorescence emitters – transition metal ion-doped quantum dots (d-dots) – can also overcome the toxicity of QDs induced by heavy metal ions [17,18].

In this paper, we explored another fluorescent method for systematically investigated the DNA damage induced by a series of water-soluble nanoparticles, including CdTe QDs, CdTe/SiO_2 composite nanoparticles (CdTe/SiO_2 NPs), and Mn-doped ZnSe QDs (Mn:ZnSe d-dots). Ethidium bromide (EB) is a fluorescent compound, which is normally used to probe DNA structure in drug–DNA and protein–DNA interactions by its intercalating in the DNA double helix to enhance its fluorescence [19]. Once the double helix structure of DNA molecules is destroyed, the fluorescence of EB will be quenched. The previous reports [14,16] had demonstrated that the double helix structure of DNA molecules were damaged by QDs via gel electrophoreses analyses method. In this paper, we applied the fluorescent method and chose EB as the probe to study the damage of DNA molecules, which is very simple, and rapid. The experimental results showed that Mn:ZnSe d-dots led to the least damage of DNA molecules among the three kinds of nanoparticles mentioned above, which can be used as biocompatible fluorescence labels in in vitro and in vivo biomedical applications.

2. Experimental

2.1. Materials

All chemicals used are of analytical reagent grade without further purification. Mercaptosuccinic acid (MSA) (99%), and poly(dimethyldiallyl ammonium chloride) (PDDA, Mw = 70,000 g/mol) were purchased from J&K Chemical Co. Tellurium powder (~200 mesh, 99.8%), $CdCl_2{\cdot}2.5H_2O$ (99%), $NaBH_4$ (99%), mercaptopropionic acid (MPA) (99%), ethidium bromide (EB) (>95%), Herring Sperm DNA (DNA), cyclohexane, Triton X-100, n-hexanol, tetraethoxysilane (TEOS), 3-aminopropyltrimethoxysilane (APS), 3-(trihydroxysilyl)-propylmethylphosphonate (THPMP), selenium powder (~200 mesh, 99.9%), $Zn(NO_3)_2{\cdot}6H_2O$ (99.9%), $MnCl_2{\cdot}4H_2O$ (99.9%) were purchased from Sigma–Aldrich Chemical Co. The water used in all experiments has a resistivity higher than 18 MΩ/cm.

2.2. Instrument

Fluorescence measurements were performed on a ShimadzuRF-5301 PC spectro fluorophotometer. The photobleaching experiments were also performed on the spectrofluorometer. In both experiments, a 1 cm path-length quartz cuvette was used. The transmission electron microscope (TEM) images of nanoparticles were obtained with JEOL-2010 electron microscope operating at 200 kV and JEOL-3010 electron microscope operating at 300 kV. For TEM, the samples were prepared by dropping the aqueous nanoparticles solution onto carbon-coated copper grids with the excess solvent evaporated.

2.3. Preparation of CdTe QDs, CdTe/SiO_2 NPs, and Mn:ZnSe d-dots

The aqueous phase synthesis of CdTe QDs was based on our previous report [20]. Briefly, the precursor solution of CdTe QDs was formed in water by adding fresh NaHTe solution to 10 mM N_2-saturated $CdCl_2$ solution at pH 11.2 in the presence of MSA as the stabilizing agent. The molar ratio of Cd^{2+}/MSA/HTe^- was set at 1:1.5:0.2. The CdTe precursor solution was subjected to reflux at 100 °C under open-air conditions with condenser attached. CdTe QDs with PL emission wavelength at 547 nm were obtained. The synthesis of CdTe QDs with MSA as stabilizer was less time consuming and the obtained QDs had high quantum yield. According to the calculation method in Ref. [20], the concentration of CdTe QDs is 2.0×10^{-6} mol/L.

CdTe/SiO_2 NPs were synthesized by reverse microemulsion method based on our previous report [21]. Briefly, we mixed 7.5 mL cyclohexane, 1.77 mL Triton X-100, 1.8 mL n-hexanol, 400 μL aqueous solution of as-prepared CdTe QDs, 40 μL PDDA solution (0.075%, v/v) and 60 μL NH_4OH to form microemulsion. Then adding 100 μL TEOS to the microemulsion system to initiate the hydrolysis, the reaction progressed in the dark for 24 h of stirring. Then adding 50 μL TEOS to the reaction system, after stirring for 30 min, 10 μL APS and 40 μL THPMP were injected into the reaction system. The reaction system was then kept under stirring for one more day. The microemulsion was broken by adding 20 mL of acetone to the reaction system and the resultant precipitate was amine-funcationalized CdTe/SiO_2 composite nanoparticles which were washed in sequence with iso-propyl alcohol, ethanol and water. Ultimately, CdTe/SiO_2 composite nanoparticles were dispersed in 1 mL water, obtaining 1 mL CdTe/SiO_2 NPs aqueous solution.

In this research, Mn:ZnSe d-dots were prepared in aqueous solution by nucleation doping method based on our recent report [22]. Generally, we prepared Mn:ZnSe d-dots by nucleation doping method and the synthesis procedure of Mn:ZnSe d-dots is operated as follows: in a typical experiment, 0.2 mL $MnCl_2$ solution (1.25×10^{-2} M) and 90 mL H_2O were loaded into a 250 mL three neck flask and degassed for 30 min by bubbling with nitrogen. Fresh NaHSe solution was added to N_2-saturated $MnCl_2$ solution at pH 11.2 in the presence of MPA as stabilizing agent. The reaction was then switched from nitrogen bubbling to nitrogen flow and subjected to a reflux at 100 °C for 40 min. 10 mL of the stock solution of $Zn(NO_3)_2$ (1.25×10^{-2} M) was injected and the reaction was refluxed for 5 h. The precursor concentration of Zn^{2+} is 1.25 mM, and precursor ratios of Mn-to-Se-to-Zn and Zn-to-MPA are 1:35:50 and 1:33, respectively. The freshly produced CdTe QDs and Mn:ZnSe d-dots were dialyzed with pH 11.2 PBS buffer solution (2 mM) just before the experiments to avoid the influence of residual reagents in solution.

2.4. Damage assays of DNA molecules

DNA and EB aqueous solution were prepared using pH 7.4 PBS buffer solution (2 mM), and the concentrations were 2.8×10^{-4} M and 5.39×10^{-5} M, respectively. With the aim of keeping the initial concentration of QDs consistent for each experiment, 20 μL CdTe QDs, 50 μL CdTe/SiO_2 NPs, and 160 μL Mn:ZnSe d-dots were taken and diluted to 2 mL with water, and used as stock solution. For a typical DNA damage experiment, 400 μL DNA solution, 100 μL EB solution, and 100 μL nanoparticles were added to cuvettes and diluted to 3 mL with PBS buffer solution (2 mM) for 16 h incubation. For UV irradiation experiment, nanoparticles were irradiated firstly with 150 W xenon lamp for 60 min continuous intensive excitation at 280 nm and then added to the reaction system.

3. Results and discussion

3.1. Characteristics of CdTe QDs, CdTe/SiO_2 NPs and Mn:ZnSe d-dots

PL emission spectra of the three kinds of nanoparticles used in this study were shown in Fig. 1. From Fig. 1, it can be seen that PL emission wavelength of CdTe QDs is at 547 nm. The TEM

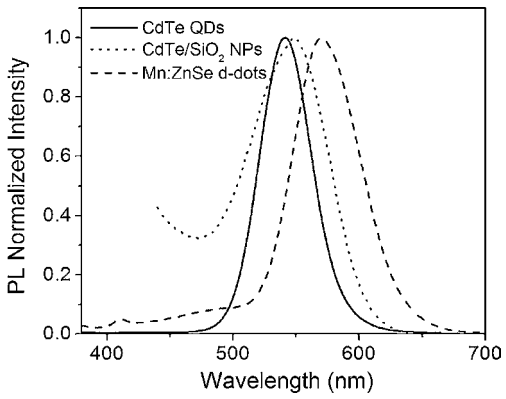


Fig. 1. The PL spectra of CdTe QDs, CdTe/SiO_2 NPs, and Mn:ZnSe d-dots.

image of CdTe QDs (Fig. 2A) shows the diameter of CdTe QDs is 2.5 nm. CdTe/SiO_2 NPs prepared by using above CdTe QDs have similar PL emission spectrum with maximum PL emission wavelength at 549 nm. The average diameter of CdTe/SiO_2 NPs was 40 nm determined by TEM image (Fig. 2B). The PL emission spectrum of Mn:ZnSe d-dots exhibited three distinct emission bands. These bands center at 410 nm, 480 nm, and 570 nm, which can be assigned to ZnSe band edge, trap state, and Mn^{2+} $^4T_1 \rightarrow {}^6A_1$ emission, respectively. Also from the TEM image (Fig. 2C), it can be seen that the diameter of Mn:ZnSe d-dots was 3.8 nm.

3.2. The PL emission properties of CdTe QDs, CdTe/SiO_2 NPs and Mn:ZnSe d-dots

PL emission properties of nanoparticles are related with the surface structure properties of nanoparticles. Once the surface structure of nanoparticles is destroyed, the PL emission intensity of nanoparticles will decrease greatly. So before evaluating the DNA damage induced by CdTe QDs, CdTe/SiO_2 NPs and Mn:ZnSe d-dots, it is necessary to study the factors that affect the PL emission properties of the three kinds of nanoparticles.

Fig. S1 shows the effect of ionic strength and pH value on PL emission properties of CdTe QDs, CdTe/SiO_2 NPs, and Mn:ZnSe d-dots. It can be seen that the effect of different ionic strength on the PL emission intensity of CdTe QDs, CdTe/SiO_2 NPs has the similar trend, but CdTe/SiO_2 NPs are more insusceptible than the naked CdTe QDs. When the concentration of NaCl was up to 50 mM, the PL emission intensity of CdTe/SiO_2 NPs was still preserved 90% and there was not any precipitation in the CdTe/SiO_2 NPs solution. In the same ionic strength solution, the PL emission intensity of CdTe QDs was preserved 80%, which was lower than that of CdTe/SiO_2 NPs. As to the Mn:ZnSe d-dots, the effect of ionic strength on PL emission of Mn^{2+} $^4T_1 \rightarrow {}^6A_1$ has a different trend compared with that of CdTe QDs, and CdTe/SiO_2 NPs. When the concentration of NaCl was 5 mM, the PL emission of Mn^{2+} $^4T_1 \rightarrow {}^6A_1$ reached the maximum, and the PL emission of Mn^{2+} $^4T_1 \rightarrow {}^6A_1$ was preserved above 80% whether Mn:ZnSe d-dots dispersed in lower or higher ionic strength solution. As compared with the effect of ionic strength, pH value can influence the PL emission properties of the three kinds of nanoparticles greatly. From the results shown in Fig. S1, it can be seen that the nanoparticles dispersed in higher pH buffer solution, exhibit higher PL emission intensity. When the pH value declined down to 4.24, the PL emission intensity of CdTe/SiO_2 NPs was 60% as compared with that in alkalescent solution (pH 11). However, in the same pH buffer solution, the PL emission intensity of CdTe QDs nearly decreased to zero and the flocculates began to appear. For Mn:ZnSe d-dots in pH 4.24 PBS buffer solution, the PL emission intensity of Mn^{2+} $^4T_1 \rightarrow {}^6A_1$ was about 40% compared with that in alkalescent solution (pH 11). In acidic solution (pH < 6), the surface structure of CdTe QDs is not as perfect as that in alkalescent solution, which is caused by incomplete ionization of stabilizers. CdTe/SiO_2 NPs have a layer of silica overcoating, which can protect the surface structure of CdTe QDs to weaken the effect of pH value. Mn:ZnSe d-dots investigated in this study were prepared by nucleation method which had the doped nuclei covered by the host shell. The ZnSe host shell can also impair the effect of pH value on the Mn^{2+} $4T_1 \rightarrow 6A_1$ emission.

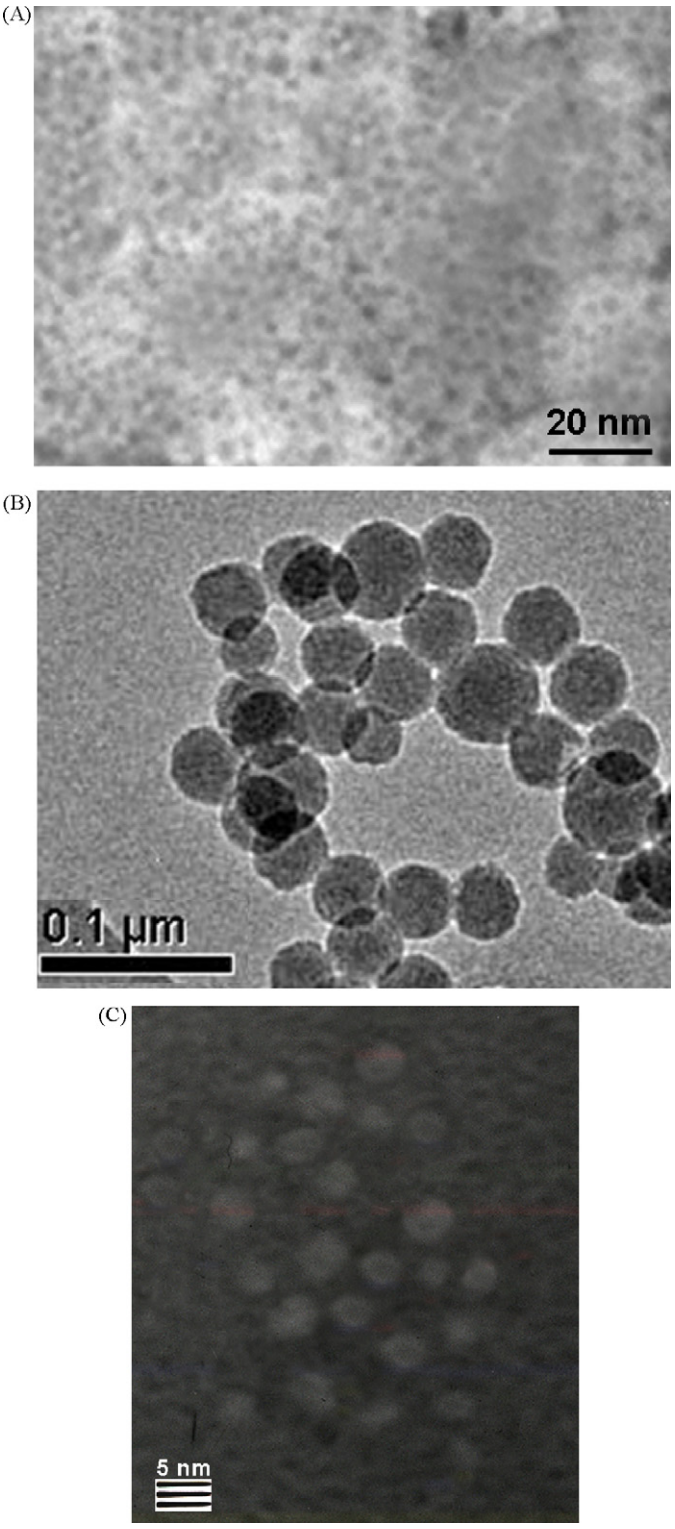


Fig. 2. The TEM images of CdTe QDs (A), CdTe/SiO_2 NPs (B), and Mn:ZnSe d-dots (C).

Besides the chemical stability, the photostability of nanoparticles is also a key issue for fluorescent labels. The photostability of CdTe QDs, CdTe/SiO_2 NPs and Mn:ZnSe d-dots was studied by using a 150 W xenon lamp for continuous intensive excitation at 280 nm and the results were shown in Fig. S2. With the UV irradiation, the PL emission intensity of CdTe QDs decreased gradually. After 60 min UV irradiation, the PL emission intensity of CdTe QDs was preserved only 20% compared with that of CdTe QDs before UV irradiation and some flocculates appeared in the aqueous solution, which implied that CdTe QDs began to aggregate and the surface structure of CdTe QDs had been destroyed. Different from CdTe QDs, CdTe/SiO_2 NPs have much better photostability. During 1 h UV irradiation, the PL emission intensity of CdTe/SiO_2 NPs retained constantly, which indicated that the silica network structure can well protect CdTe QDs embedded in silica nanoparticles. With regard to Mn:ZnSe d-dots, the PL emission intensity of Mn^{2+} $^4T_1 \rightarrow {}^6A_1$ were also kept constantly during the whole 1 h UV irradiation process, which is 90% as compared with Mn:ZnSe d-dots before UV irradiation. The extraordinary photostability of Mn:ZnSe d-dots is also due to the unique structure of d-dots. Mn:ZnSe d-dots prepared by nucleation doping method have a ZnSe host overcoating layer to protect the nuclei with the dopant Mn^{2+} ions, which avoids the photobleaching of Mn^{2+} $^4T_1 \rightarrow {}^6A_1$ emission induced by UV irradiation.

3.3. The interaction of DNA with CdTe QDs, CdTe/SiO_2 NPs and Mn:ZnSe d-dots

In this study, the assay system contains EB, DNA and nanoparticles. The fluorescence spectra of EB, EB incubated with CdTe QDs, EB incubated with DNA, and EB incubated with DNA and CdTe QDs for overnight were shown in Fig. 3. It can be seen that the fluorescence intensity of EB molecules was low and it was not influenced by CdTe QDs. The fluorescence intensity of EB was enhanced greatly in the presence of DNA, because the strong binding of EB to DNA results in the intercalation of the planar phenanthridinium ring between adjacent base pairs on the double helix [23]. However, the fluorescence intensity of EB and DNA system was weakened by adding CdTe QDs, which could be attributed to the interaction between DNA molecules and CdTe QDs-the strand breakages and nucleobase damages of DNA molecules inducing by QDs [14–16]. So the quenching of the fluorescence of EB is due to the damage of double helix structure of DNA molecules, which can be used to probe the damage of DNA molecules by nanoparticles. The optimal ratio of DNA interacting with EB in solution was determined by the fluorescence method. 100 μL EB (5.39×10^{-5} M) and different volumes of DNA (2.8×10^{-4} M) was mixed and diluted to 3 mL with PBS buffer solution (pH 7.4). The fluorescence signals of the mixed solution

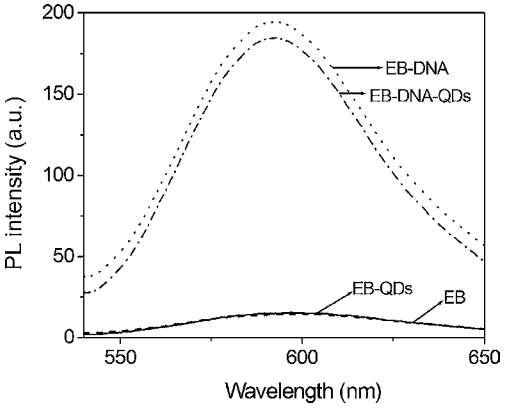


Fig. 3. The PL spectra of EB, EB-CdTe QDs, EB-DNA, EB-DNA incubated with CdTe QDs.

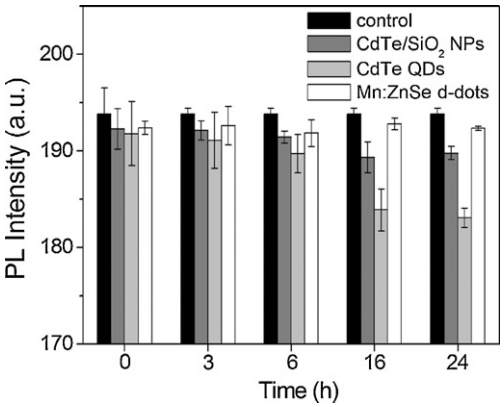


Fig. 4. The effect of incubate time on fluorescence quenching of EB-DNA induced by CdTe/SiO_2 NPs, CdTe QDs and Mn:ZnSe d-dots. The fluorescence intensity was the average value of three times.

increased with the increase of DNA volume (Fig. S3). When DNA volume increased to higher than 400 μL, the fluorescence intensity tended to be constant. Based on this result, the DNA volume was fixed at 400 μL in further experiments.

The emission wavelength of the three kinds of nanoparticles used in this study is at or shorter than 570 nm, which will not overlap with the fluorescence of EB in the presence of DNA molecules (EB-DNA). Furthermore, the PL emission of the three kinds of nanoparticles in experimental system is very weak due to the dilution before used. So the PL emission of the three kinds of nanoparticles will not interfere with the fluorescence of EB-DNA for the determination of DNA damage.

Incubation time is an important factor for studying the DNA damage caused by nanoparticles. Fig. 4 shows the results of the DNA damage caused by the three kinds of nanoparticles with the increase of incubation time. Within 6 h incubation time, both EB-DNA fluorescence quenching and the difference of the quenching by the three nanoparticles did not exhibit clearly, which indicated that DNA molecules had not been damaged obviously by the three kinds of nanoparticles during 6 h incubation. But after an overnight incubation (16 h), the fluorescence of EB-DNA was quenched evidently by CdTe QDs, indicating that quite amounts of DNA molecules were damaged by CdTe QDs. Under the same condition, CdTe/SiO_2 NPs performed less effect to DNA molecules than CdTe QDs, which due to the overcoating of a silica layer. Mn:ZnSe d-dots almost exhibited no damage of DNA molecules, which did not quenched the fluorescence of EB-DNA considerably even after 24 h incubation time. Thus, the incubation time was fixed 16 h in the following experiments to study the DNA damage induced by the three kinds of nanoparticles.

Based on the study above, ionic strength can affect the PL emission properties of the three kinds of nanoparticles, which can also affect the DNA damage caused by them. The results (Fig. 5) showed that with the increase of ionic strength, the fluorescence of EB-DNA decreased. In the same ionic strength solution, the fluorescence quenching of EB-DNA by CdTe QDs was the most among the three kinds of nanoparticles. While NaCl concentration of assay system was up to 50 mmol/L, the high ionic strength interfered the fluorescence of EB-DNA and the interaction of EB and DNA, so DNA damage cannot be well shown. Compared with CdTe QDs, CdTe/SiO_2 NPs and Mn:ZnSe d-dots did not quench the fluorescence of EB-DNA greatly, especially Mn:ZnSe d-dots, which hardly quenched the fluorescence of EB-DNA in varied ionic strength solution.

Besides the effect of ionic strength, pH value also influences the DNA damage induced by CdTe QDs, CdTe/SiO_2 NPs and Mn:ZnSe d-dots. The effect of pH value on EB-DNA fluorescence with the three kinds of nanoparticles was shown in Fig. 6. The phenomenon of flu-

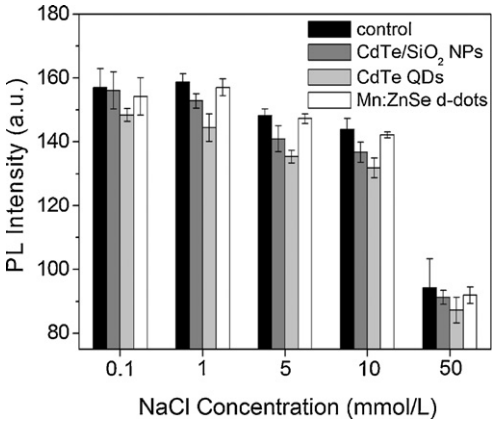


Fig. 5. The effect of different ionic strength on fluorescence quenching of EB-DNA induced by $CdTe/SiO_2$ NPs, CdTe QDs and Mn:ZnSe d-dots. The fluorescence intensity was the average value of three times.

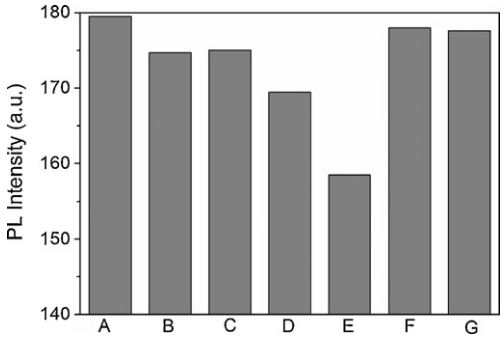


Fig. 7. The effect of UV irradiation on fluorescence quenching of EB-DNA induced by $CdTe/SiO_2$ NPs, CdTe QDs and Mn:ZnSe d-dots. (A) Control (EB-DNA), (B) $CdTe/SiO_2$ NPs incubated with EB-DNA for overnight, (C) $CdTe/SiO_2$ NPs after 1 h UV irradiation incubated with EB-DNA for overnight, (D) CdTe QDs incubated with EB-DNA for overnight, (E) CdTe QDs after 1 h UV irradiation incubated with EB-DNA for overnight, (F) Mn:ZnSe d-dots incubated with EB-DNA for overnight, and (G) Mn:ZnSe d-dots after 1 h UV irradiation incubated with EB-DNA for overnight.

orescence quenching of EB-DNA by the three kinds of nanoparticles in different pH buffer solutions was analogous with that in different ionic strength solutions. CdTe QDs showed the most fluorescence quenching effect among the three kinds of nanoparticles. Simultaneously, when the assay system was in acidic buffer solution (pH < 6), the fluorescence quenching of EB-DNA induced by CdTe QDs was more than that of EB-DNA in alkalescent buffer solution, which suggested that DNA damage in acidic buffer solution was more than that in alkalescent buffer solution. This phenomenon could be attributed to the detachment of the stabilizers from the QD surface and release of Cd^{2+} and free radicals generated by Cd^{2+} [16]. Because the silica overcoating layer can protect the CdTe QDs, $CdTe/SiO_2$ NPs have more resistance than CdTe QDs to pH effect (Fig. S1), which leads to less fluorescence quenching of EB-DNA by $CdTe/SiO_2$ NPs. Although the surface property of Mn:ZnSe d-dots is also influenced by pH value, doped ions of d-dots can hold charge carriers in the internal structure of the d-dots [14], which will not damage the DNA molecules, so the fluorescence of EB-DNA is almost constant. Remarkably, when $CdTe/SiO_2$ NPs and Mn:ZnSe d-dots were added to the assay system with pH 4.22, the fluorescence of EB-DNA was enhanced instead of quenching. As mentioned in Section 2, the pH value of Mn:ZnSe d-dots solution was 11.2. While d-dot solution was added to the assay system with pH 4.22, the pH value of assay system was increased to about 5 and there was no damage for DNA molecules in the assay system. Therefore, the assay system exhibited higher fluorescence of EB-DNA.

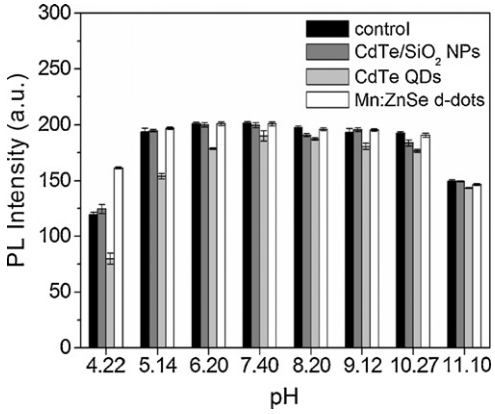


Fig. 6. The effect of different pH value on fluorescence quenching of EB-DNA induced by $CdTe/SiO_2$ NPs, CdTe QDs and Mn:ZnSe d-dots. The fluorescence intensity was the average value of three times.

Though the experimental system was stored in the dark, CdTe QDs also result in DNA damage, which could be due to the free radicals generated by the slow oxidation and gradual desorption of surface oxide into solution, that is consistent with the results published previously [14–16]. $CdTe/SiO_2$ NPs have a silica overcoating to isolate CdTe QDs from the external environment, thus $CdTe/SiO_2$ NPs lead to less DNA damage. As for Mn:ZnSe d-dots, the doped ions Mn^{2+} could hold the charge carriers in the internal structure which avoids the generation of free radical, so the damage of DNA caused by Mn:ZnSe d-dots is neglectable.

The ionic strength and pH value are both environmental factors influencing the DNA damage induced by three kinds of nanoparticles. Besides that, UV irradiation also plays a critical role in studying DNA damage by three kinds of nanoparticles. For studying the effect of UV irradiation, CdTe QDs, $CdTe/SiO_2$ NPs, and Mn:ZnSe d-dots were irradiated firstly with 150 W xenon lamp for 60 min continuous intensive excitation at 280 nm. We compared the fluorescence of EB-DNA incubated with the three kinds of nanoparticles before and after UV irradiation, and the results were shown in Fig. 7. From Fig. 7, it can be seen that the column E represented the fluorescence intensity of EB-DNA incubated with CdTe QDs without UV irradiation, and column F represented the fluorescence intensity of EB-DNA incubated with CdTe QDs surviving from 1 h UV irradiation. The fluorescence quenching of column E was lower than that of column F, which suggested that CdTe QDs after 1 h UV irradiation provoked a statistically significant DNA damage compared with that without UV irradiation. During the UV irradiation, reactive oxygen species (ROS) produced by resonance energy transfer from excited QDs to surrounding oxygen molecules, which should take the main responsibility for the DNA damage [15,24–26]. As for $CdTe/SiO_2$ NPs, the fluorescence intensity of EB-DNA had no difference between adding $CdTe/SiO_2$ NPs with and without UV irradiation (column B and column C). That may be due to the protection of silica network which can prevent the photobleaching of CdTe QDs by UV irradiation (Fig. S2) and inhibit the resonance energy transfer from excited QDs to oxygen molecules, thus $CdTe/SiO_2$ NPs after UV irradiation do not result in more DNA damage than $CdTe/SiO_2$ NPs before UV irradiation. Similarly, fluorescence quenching of EB-DNA by Mn:ZnSe d-dots was subtle essentially, which is less than that induced by $CdTe/SiO_2$ NPs, and furthermore the difference of fluorescence quenching induced by d-dots before and after UV irradiation was also neglectable. For Mn:ZnSe d-dots, luminescence results from recombination of the exciton as well as from energy transfer to Mn^{2+} d–d levels [27], and doped ions Mn^{2+} could hold the charge carriers in the internal structure [14], simultaneously, the excited Mn^{2+} ions coated by

host ZnSe layer, which all inhibited the excited Mn^{2+} ions reacting with the surrounding oxygen molecules. So the PL emission intensity of Mn^{2+} $^4T_1 \rightarrow {}^6A_1$ were not influenced by UV irradiation and the Mn:ZnSe d-dots with 1 h UV irradiation do not lead to DNA damage either.

All results show that the Mn:ZnSe d-dots are highly biocompatible, possibly because the d-dots were synthesized without cadmium ions and the coated ZnSe outlayer is a type of non-toxic, chemically stable wide band gap semiconductor. On the other hand, the Mn:ZnSe d-dots used are directly synthesized in aqueous solution, which do not carry residual organic molecules. The low DNA damaged by Mn:ZnSe d-dots may bring some potential applications, for example, as a new gene delivery agent [28]. With these excellent properties and biocompatibility in mind, this kind of water dispersed Mn:ZnSe d-dots might be a highly promising probe for biological applications.

4. Conclusions

In this work, the DNA damage induced by water-soluble CdTe QDs, CdTe/SiO_2 NPs and Mn:ZnSe d-dots was systematically studied for the first time with EB as the probe. It was found that the ionic strength, pH value, and UV irradiation influenced PL emission properties of the three kinds of nanoparticles, which also influenced the DNA damage caused by the three kinds of nanoparticles. The results indicated that CdTe QDs led to more DNA damage than CdTe/SiO_2 NPs and Mn:ZnSe d-dots, which was due to the free radicals generated by the slow oxidation and gradual desorption of surface oxide into solution. When CdTe QDs were irradiated by UV source for 1 h, the more DNA damage by CdTe QDs should be attributed to the photo oxidation of QDs companied with the generation of reactive oxygen species, which can be avoided by CdTe/SiO_2 NPs and Mn:ZnSe d-dots. All results clearly demonstrated that Mn:ZnSe d-dots resulted in the least DNA damage among the three kinds of nanoparticles, which can be used in various biomedical applications as highly biocompatible fluorescent labels.

Acknowledgements

This work was financially supported by the National Natural Science Foundation of China (No. 20475020, No. 20075009, No. 20875036) and the Development Program of the Ministry of Science and Technology of Jilin Province, China (No. 20080544).

Appendix A. Supplementary data

Supplementary data associated with this article can be found, in the online version, at doi:10.1016/j.talanta.2009.09.014.

References

[1] M. Bruchez Jr., M. Moronne, P. Gin, S. Weiss, A.P. Alivisatos, Science 281 (1998) 2013.
[2] W.C. Chan, S. Nie, Science 281 (1998) 2016.
[3] Y. Yang, L. Jing, X. Yu, D. Yan, M. Gao, Chem. Mater. 19 (2007) 4123.
[4] R. Hardman, Environ. Health Persp. 114 (2006) 165.
[5] A.M. Derfus, W.C.W. Chan, S.N. Bhatia, Nano. Lett. 4 (2004) 11.
[6] A. Hoshino, K. Fujioka, T. Oku, M. Suga, Y.F. Sasaki, T. Ohta, M. Yasuhara, K. Suzuki, K. Yamamoto, Nano. Lett. 4 (2004) 2163.
[7] C. Kirchner, T. Liedl, S. Kudera, T. Pellegrino, J.A. Munoz, H.E. Gaub, Nano. Lett. 5 (2005) 331.
[8] J. Lovric, H.S. Bazzi, Y. Cuie, G.R.A. Fortin, F.M. Winnik, D. Maysinger, J. Mol. Med. 83 (2005) 377.
[9] C. Kirchner, A.M. Javier, A.S. Susha, A.L. Rogach, O. Kreft, G.B. Sukhorukov, Talanta 67 (2005) 486.
[10] K.B. Male, B. Lachance, S. Hrapovic, G. Sunahara, J.H.T. Luong, Anal. Chem. 80 (2008) 5487.
[11] Y. Su, Y. He, H. Lu, L. Sai, Q. Li, W. Li, L. Wang, P. Shen, Q. Huang, C. Fan, Biomaterials 30 (2009) 19.
[12] E. Chang, N. Thekkek, W.W. Yu, V.L. Colvin, R. Drezek, Small 2 (2006) 1412.
[13] N. Lewinski, V. Colvin, R. Drezek, Small 4 (2008) 26.
[14] M. Green, E. Howman, Chem. Commun. (2005) 121.
[15] J. Liang, Z. He, S. Zhang, S. Huang, X. Ai, H. Yang, H. Han, Talanta 71 (2007) 1675.
[16] A. Anas, A. Hidetaka, H. Harashima, T. Itoh, M. Ishikawa, V. Biju, J. Phys. Chem. B 112 (2008) 10005.
[17] N. Pradhan, X. Peng, J. Am. Chem. Soc. 129 (2007) 3339.
[18] N. Pradhan, D.M. Battaglia, Y. Liu, X. Peng, Nano. Lett. 7 (2007) 312.
[19] Y. Sun, S. Bi, D. Song, C. Qiao, D. Mu, H. Zhang, Sens. Actuators B: Chem. 129 (2008) 799.
[20] C. Wang, Q. Ma, X. Su, J. Nanosci. Nanotechnol. 8 (2008) 4408.
[21] C. Wang, Q. Ma, W. Dou, S. Kanwal, G. Wang, P. Yuan, X. Su, Talanta 77 (2009) 1358.
[22] C. Wang, X. Gao, Q. Ma, X. Su, J. Mater. Chem. 19 (2009) 7016.
[23] S. Bi, H. Zhang, C. Qiao, Y. Sun, C. Liu, Spectrochim. Acta Part A 69 (2008) 123–129.
[24] J. Ma, J.Y. Chen, Y. Zhang, P.N. Wang, J. Guo, W.L. Yang, C.C. Wang, J. Phys. Chem. B 111 (2007) 12012.
[25] A.C.S. Samia, X.B. Chen, C. Burda, J. Am. Chem. Soc. 25 (2003) 15736.
[26] A.C.S. Samia, S. Dayal, C. Burda, Photochem. Photobiol. 2 (2006) 617.
[27] S. Mahamuni, A.D. Lad, S. Patole, J. Phys. Chem. C 112 (2008) 2271.
[28] D. Li, G.P. Li, W.W. Guo, P.C. Li, E.K. Wang, J. Wang, Biomaterials 29 (2008) 2776.

Talanta 80 (2010) 1234–1238

Contents lists available at ScienceDirect

Talanta

journal homepage: www.elsevier.com/locate/talanta

Determination of trace iodide in iodised table salt on silver sulfate-modified carbon paste electrode by differential pulse voltammetry with electrochemical solid phase nano-extraction

Yongchun Zhu*, Jingjing Guan, Lu Cao, Jie Hao

Key University Laboratory on Separation and Analysis in Complex Systems of Liaoning Province, Chemistry Department, College of Chemistry and Life Science, Shenyang Normal University, Shenyang, Liaoning 110034, PR China

ARTICLE INFO

Article history:
Received 13 June 2009
Received in revised form 25 August 2009
Accepted 8 September 2009
Available online 17 September 2009

Keywords:
Electrochemical solid phase
nano-extraction
Iodide
Differential pulse voltammetry
Cyclic voltammetry
Table salt

ABSTRACT

Electrochemical solid phase nano-extraction, a novel sample preparation technique, was used for the determination of trace iodide in iodised table salt based on the silver sulfate nanoparticle-modified carbon paste electrode. Electrochemical solid phase nano-extraction was realized in the exchange between the sulfate anion in nanoparticles and an iodide anion from aqueous solution. The released silver cation serves as the electrochemical probe for the determination of iodide. The extraction follows a Freundlich adsorption isotherm, and can be used in the detection of iodide in the concentration range 5.0×10^{-12}–4.0×10^{-9} M. The amount of iodide in iodised table salt was determined as 0.875 ± 0.002 μg/g, which is about 2.5% of the addition amount of iodate with a relative deviation of 5.92% and a standard addition recovery of 90–110%. The large amounts of chloride and iodate did not interfere with the detection.

© 2009 Elsevier B.V. All rights reserved.

1. Introduction

Solid phase micro-extraction (SPME) was developed by Pawliszyn and co-workers as a solvent-free green sample preparation method [1–3], and have been widely used in many areas [4–6]. If the adsorbent consists of nanoparticles, the method is called solid phase nano-extraction (SPNE) [7,8]. The SPNE method retains all the advantages of SPME, and has some new characteristics, such as a larger specific adsorption area, multiple active sites for recognitions of the analyte(s), controllable surface states, and modificative solid nanoparticle surface. The combination of electrochemistry with SPNE (ESPNE) is a new technique for sample preparation. In ESPNE, electrochemistry offers a way to control the redox states of extractants and analytes, and the un-uniformed electric field on nanoparticle-modified electrode surface offers a dielectric force for the separations. Some examples have shown the possibility for integration of analysis with separation [9–12]. The carbon paste electrode (CPE), composed of a flexable mixture of solid and liquid phase, offers a renewable electrode surface for the solid and liquid extractants, and very suitable for ESPNE [13].

Iodine is one of the biologically important elements, an adult human requires 100–150 μg/day, and it has been suggested that potassium iodate or potassium iodide should be added to table salt called iodised table salt [14]. In practice, however, long-term storage of iodised table salt under adverse conditions results in some loss of iodine due to the inverse disproportional reaction [15]. The trace iodine detection methods, such as UV–visible spectrophotometry [16], catalysis [17], chromatography [18], ion-selective electrode [19], cyclic voltammetry (CV) [20], and ICP-AES [21] with chemical oxidation and liquid–liquid extraction techniques cannot be used directly, and they all suffer from interference by chloride [22] and iodate. Therefore, it is important to develop a method that can determine iodide directly and without interference by the large amounts of chloride and iodate.

We modified the surface of graphite powder in a CPE with Ag_2SO_4 colloidal nanoparticles (ssn-CPE) and used it to extract iodide from aqueous solution. The amount of iodide extracted was determined directly by anodic stripping of silver with differential pulse voltammetry (DPV). This method was investigated for the detection of iodide in iodised table salt without interference by iodate or chloride, and the results are reported here.

2. Experimental

2.1. Instrument and reagents

Electrochemical experiments were carried out on a CHI electrochemical system (CHI620B, CHI Co., USA) with three electrodes;

* Corresponding author. Tel.: +86 024 86593298; fax: +86 024 86594825.
E-mail address: yongchunzhu@126.com (Y. Zhu).

0039-9140/$ – see front matter © 2009 Elsevier B.V. All rights reserved.
doi:10.1016/j.talanta.2009.09.015

a piece of platinum wire as the auxiliary electrode, an in-house built silver sulfate-modified CPE as the working electrode and a KCl-saturated calomel electrode as the reference electrode. All potentials reported here are with respect to this reference electrode.

Graphite powder (200 #, spectrophotometrically pure), epoxy resin, polyacetamide resin, castor oil (chemically pure), ethyl benzoic acid, potassium sulfate, silver nitrate, citric acid, sodium hydrogen phosphate, sodium iodide, sodium nitrate, and other chemicals were all analytical grade. All solutions were prepared with ultra-pure MilliQ-treated water (18.2 MΩ from MilliQ A-10). All the electrolyte solutions were de-oxygenated by sparging with high-purity nitrogen gas for 20 min before use. All experiments were done at room temperature (~20 °C).

The iodised table salt used in this work was purchased from a supermarket, which composed of sodium chloride (>97%) and potassium iodate (35 ± 15 mg/kg) followed the national standard of table salt.

2.2. Preparation of the working electrode

The basic electrode was prepared as follows. Graphite powder, epoxy resin and polyacetamide resin were mixed into a paste with a weight ratio of 8:3:2, pressed tightly into a clean glass tube (inner diameter ~ 4 mm) with a copper wire at the other end as an electrode, and left to solidify in air for 72 h. Then, the upper end of the electrode was scraped out to produce an ~1 mm cavity to accept the carbon paste. This solid graphite–epoxy composite electrode (GECE) with a small cavity was used as the basis of the Ag_2SO_4-modified electrode (ssn-GECE).

K_2SO_4 solution (5.0 mL of 5.0 mmol/L) was mixed with 10.0 mL of 10 mmol/L $AgNO_3$ in an ultrasonic bath, and a colloidal solution was obtained. A 1.0 g sample of graphite powder was added to the colloidal solution, stirred with a glass rod and heated at 110 °C to evaporate water, leaving the Ag_2SO_4-modified graphite powder.

This powder was mixed with castor oil in a weight ratio of 1:1 to give a uniform paste, which was used to fill the cavity in the prepared basic GECE, polished on glass-paper, and used as the working electrode. The paste in the working electrode cavity can be renewed for the new measurement after usage. The prepared carbon paste can be stored in air for several months without loss of its activity.

3. Results and discussion

3.1. The electrochemical behaviour of iodide at the modified electrode

The different electrodes in 0.5 M $NaNO_3$ electrolyte solution (pH 3.2) including 0.5 mM NaI, gave the CV curves shown in Fig. 1.

The iodide on the bare CPE (with castor oil and ethyl benzoate) shows only one irreversible oxidation peak at 0.559 V (Fig. 1, curve 2) without the reduction peak due to the extraction of iodine into the organic phase. Iodide at the ssn-CPE had a CV with cathodic peaks at 0.400 V and at 0.192 V, and anodic peaks at 0.233 V and at 0.570 V (Fig. 1, curve 1). The ssn-CPE in the electrolyte solution without iodide had a CV with anodic peaks at 0.320 V and 0.530 V, and cathodic peaks at 0.306 V and 0.040 V (Fig. 1, curve 3). Comparison of curve 1 with curves 2 and 3 reveals that the first oxidation peak, at 0.233 V, belongs to the oxidation of a silver atom deposited at the initial potential, which is 0.087 V negative shifts compared than oxidation peak (at 0.320 V in curve 3) of silver at silver sulfate nanoparticles. The sharp oxidation peak at 0.570 V belongs to the oxidation of iodide, and was sensitized by silver sulfate (at

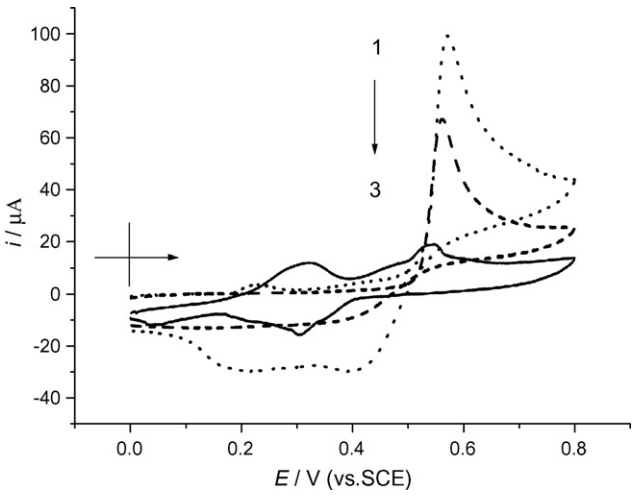
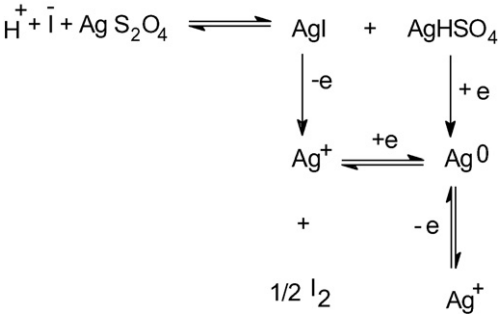


Fig. 1. The CVs of silver sulfate-modified CPE (ssn-CPE) with (1, dot line) and without (3, solid line) iodide and bared CPE with iodide (2, dash line). In 0.5 M $NaNO_3$ electrolyte solution (pH 3.2) including 0.5 mM NaI. Scan rate, 100 mV/s, quiet time, 12 s.

0.530 V). The corresponding reduction peak at 0.400 V belongs to the reduction of iodine. The reduction peak at 0.200 V belongs to the reduction of silver in the sulfate precipitate. Without iodide, the free silver gives reduction peaks at 0.306 V and 0.040 V, and oxidation peaks at 0.320 V and 0.530 V, which will sensitise the oxidation of iodide. In the iodide solution, there is an exchange reaction between iodide and sulfate, and silver hydrosulfate is released. The whole process can be described as



(1)

Eq. (1) offers two methods for the determination of iodide. If the concentration of iodide in aqueous solution is very large, all released silver cations are combined with iodide ions, and the oxidation of iodide in silver iodide can be used for its detection. If the concentration of iodide is very low, one of the silver cations combines with iodide and another is released as silver hydrosulfate, which serves as a sensitive electrochemical probe for the measurement of iodide and this is the method chosen for the ultra-trace iodide analysis described here.

The first anodic peak at 0.233 V is proportional to the square-root of the scan rate and the regression equation is:

$$i_{pa}(\mu A) = -3.891 + 12.31\nu^{1/2} \quad (2)$$

R is 0.9995, SD is 2.12.

This relationship indicates that the oxidation is a diffusion-controlled process. The silver cation released is not adsorbed on the electrode surface or on the surface of the silver sulfate precipitate but diffuses to the bulk solution. This is one piece of evidence that supports the suggested mechanism in Eq. (1).

3.2. The effects on the ESPNE

3.2.1. The influence of the amount of modifier (Ag_2SO_4)

The loading amount of modifier, colloidal Ag_2SO_4, influences the extraction of iodide directly. Different volumes of Ag_2SO_4 colloidal solution at a given concentration were used in the modification of the CPE. The modified CPE was used in the CV experiments under the same experimental conditions. The anodic peak current was plotted against the volume of the colloidal solution/g of graphite powder; there was a sharp peak with a maximum at 20 mL, as shown in Fig. 2. The anodic peak current increased linearly with the volume of colloidal solution in the range 2–20 mL/g. The regression equation is:

$$i_{pa}(\mu A) = 9.053 + 0.353V \quad (3)$$

R is 0.9996, SD is 0.103.

The anodic peak current reached a maximum at 20 mL/g and then decreased exponentially with the increase of the volume/g of colloidal solution with the regression equation:

$$i_{pa}(\mu A) = 12.71 + 3.4654e^{((V-20)/19.43)}, \quad (4)$$

$\chi^2 = 0.00954$.

As described above, the extraction is an anion-exchange process between iodide and sulfate, the anodic peak current is dependent on the amount of exchange, the exchange ratio, the exchange time and the coverage of the electrode surface at a fixed concentration of iodide. The coverage of the graphite powder surface was lower with a lower volume of colloidal solution, and all the sulfate anions in the silver sulfate modified at the surface were exchanged with iodide 100% at a given exchange time. So, the peak current is directly proportional to the coverage of the surface and to the volume of the colloidal solution. With an increase of the volume of the colloidal solution, the extraction timescale limited the amount of iodide in the contacting solution that diffused to the electrode surface. The extraction reached a maximum at about 20 mL. After this, the coverage was increased with the volume of colloidal solution/g of graphite, but the exchange ratio decreased exponentially due to the limited amount of iodide anion available to diffuse to the electrode surface at a given time and a given concentration.

3.2.2. The influence of extraction time

The extraction time, t_e, is the length of time between the electrode contacting the sample solution for the ion exchange and the beginning of the CV experiments. The anodic peak current plotted

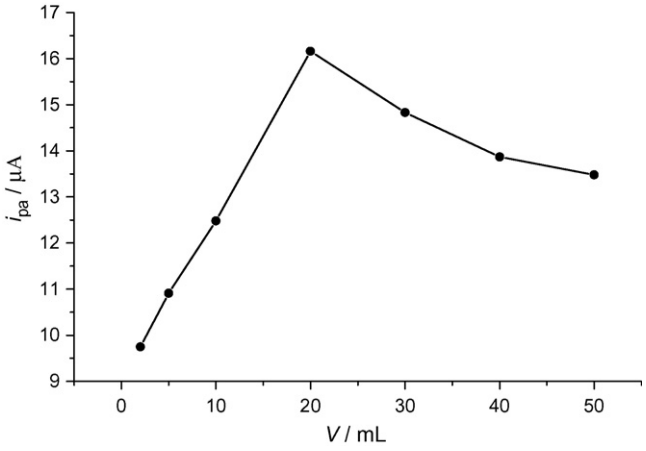


Fig. 2. The relation between anodic peak current and volume of colloidal solution for the CPE modification. The experimental conditions were the same as those in Fig. 1.

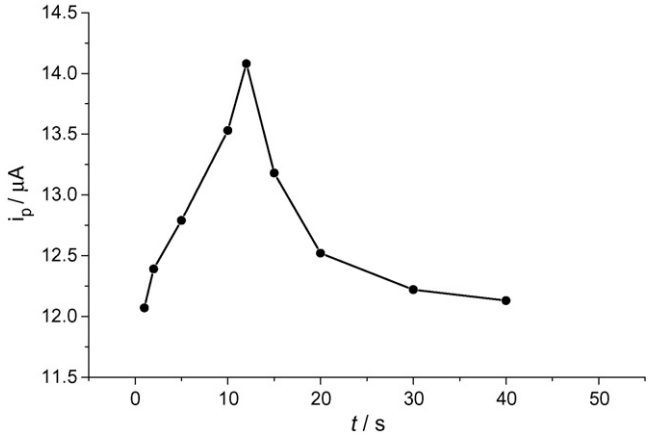


Fig. 3. The relation of anodic peak current with extraction time. The other experimental conditions were the same as those in Fig. 1.

versus extraction time is shown in Fig. 3. The anodic peak current increased linearly with extraction time in the range 2–20 s with the regression equation:

$$i_{pa}(\mu A) = 69.364 + 0.5541t_e, \quad (5)$$

R is 0.9973, SD is 0.325.

This result indicates that the extraction follows the linear adsorption process as described above. After 20 s, the anodic peak current is not changed greatly with extraction time; i.e. 20 s is the saturated extraction time for a given concentration of iodide.

3.2.3. The influence of quiet time

The extraction process is the exchange between iodide and sulfate anions. The amount of silver released was determined by the oxidation peak current of silver deposited on the electrode surface at the negative potential. The quiet time, t_q, is the length of time from the start-point of the applied potential of −0.400 V at the electrode for the electrochemical deposition of the released silver cation to the potential scanning or CV experiment. So, t_q is very important for the evaluation of the extraction. The anodic peak current plotted *versus* t_q is shown in Fig. 4.

The anodic peak current increased linearly with t_q in the range 2–12 s with the regression equation:

$$i_{pa}(\mu A) = 11.97 + 0.1692t_q \quad (6)$$

R is 0.9936, SD is 0.108.due to the electrochemical deposition of a silver cation and the linear extraction as described above. With increased $t_q > 12$ s, the anodic peak current decreased exponentially with the regression equation:

$$i_{pa}(\mu A) = 12.15 + 1.93e^{-((t_q-12)/4.854)} \quad (7)$$

R is 0.9786, SD is 0.193.

With increased t_q of the extraction at a higher concentration of iodide, the reduction of silver in the nanoparticles may be reduced to a silver atom, and extracted into the organic phase without taking part in the extraction and oxidation process. This reduction process has an apparent first-order rate constant of 0.206 s^{-1}. The optimal t_q was chosen as 12 s in the following experiments.

3.2.4. The influence of solution pH

The solution pH is another important factor that influences the extraction, because hydrosulfate is a weak acid with an acid dissociation constant k_{a2} of 1.21×10^{-2}. The CV experiments were done at a scan rate of 100 mV/s, extraction time 20 s, quiet time 12 s in solutions of different pH controlled with a phosphate buffer system. The anodic peak current plotted *versus* the solution pH is shown in

Fig. 5A. The anodic peak current does not change greatly with solution pH in the range 2–4; the maximum point is located at pH 3.2, and then decreased sharply at pH ≥ 4.2, which may be due to the formation of silver hydroxide.

The anodic peak potential was not changed with solution pH in the range 2.2–4.2, but increased linearly at pH > 4.2 with the regression equation:

$$E_{pa}(\mathrm{V}) = 0.506 + 0.0143\mathrm{pH} \quad (8)$$

R is 0.9979, SD is 0.0015.

This is evidence for the formation of silver hydroxide.

3.2.5. The influence of the concentration of iodide

The concentration of iodide is the most important factor for the extraction. Under the optimal Freundlich adsorption isotherm with the adsorption constant K_F, the differential pulse voltammetric experiments were done with 0.5 M $NaNO_3$ electrolyte solution (pH 3.2) including different concentrations of iodide, with extraction time 20 s and quiet time 12 s. The anodic peak current obtained from the experiments plotted *versus* the concentration of iodide is a curve. According to the Freundlich adsorption theory [23], the plot of the logarithm of the anodic peak current *versus* the logarithm of the concentration of iodide in aqueous solution was a straight line with the regression equation:

$$\log(i_{pa}) = 1.5887 + 0.498\log(c, M) \quad (9)$$

R is 0.9966, SD is 0.0512.

This result indicates that the SPNE of iodide follows the Freundlich adsorption isotherm with an adsorption equilibrium constant of $K_F = 38.79$ and $n = 2.008$, which means two iodides can be extracted with Ag_2SO_4.

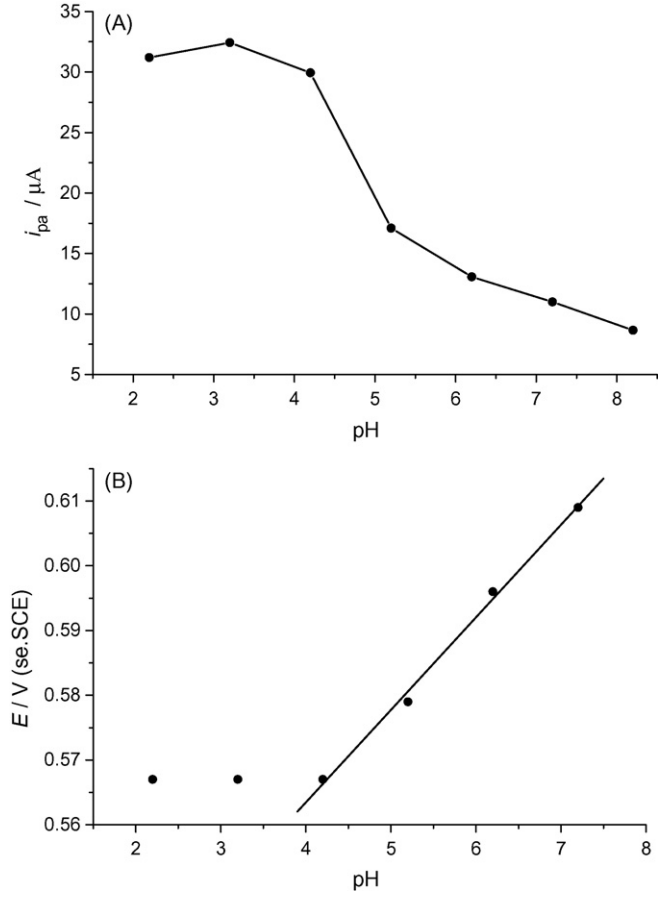


Fig. 4. The relation of anodic peak current with quiet time. The other experimental conditions were the same as those in Fig. 1.

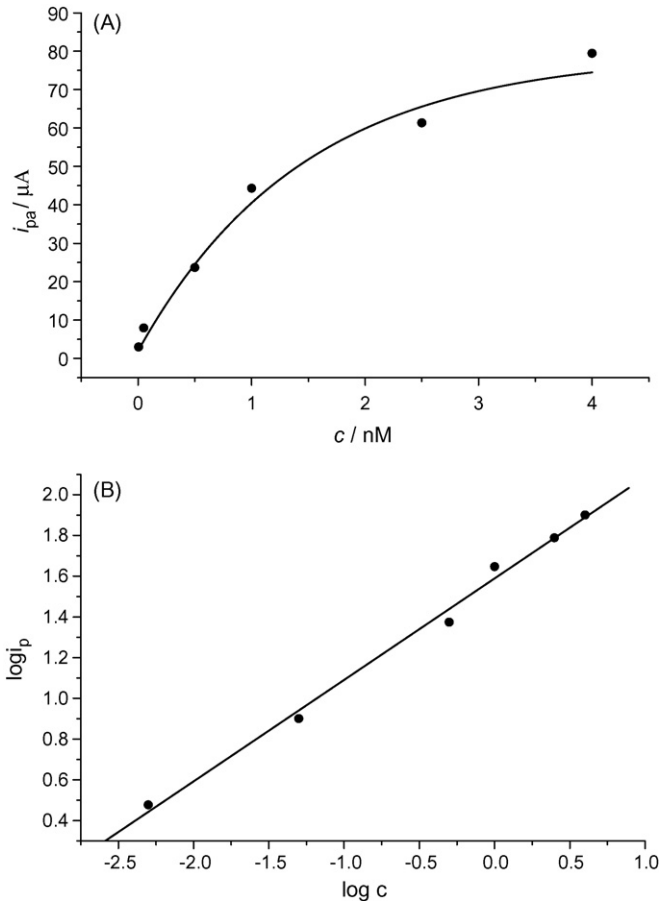


Fig. 5. The relations of anodic peak current (A) and peak potential (B) with solution pH. The other experimental conditions were the same as those in Fig. 1.

3.3. Determination of iodide

3.3.1. The standard working curve

The relationship between anodic peak current and concentration of iodide is a non-linear curve with a saturation growth-rate function as:

$$i_{pa}(\mu\mathrm{A}) = \frac{113.1c}{1.828 + c} \quad (10)$$

R is 0.9921, SD is 3.92.

The saturation growth-rate function is commonly used to describe a population growth model in terms of the nutrient concentration. In our case, the amount of iodide extracted depended directly on the concentration of iodide in solution, with a maximum rate of 113.1, and a half-saturation growth constant of 1.828.

The non-linear relationship can be further linearised by replacement of concentration *c* with: $x = 113.1c/(1.828 + c)$.

The plot of anodic peak current *versus* *x* is a straight line with the regression equation:

$$i_{pa}(\mu\mathrm{A}) = 1.394 + 0.9746x \quad (11)$$

R is 0.9928, SD is 3.76.

The linear range of the detection is in the concentration range of 0.005–4.0 nM with correlation coefficient of 0.9928. The limit of detection (LOD) is 5.0 pM, and the standard deviation is 3.76 pM.

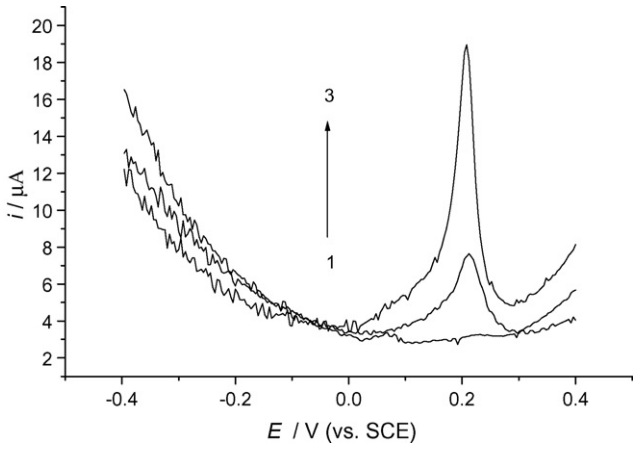


Fig. 6. The DPV curves of iodide in table salt sample solution (2), after standard addition of standard solution (3) and electrolyte solution (1), quiet time = 12 s, pH 3.2.

3.3.2. The determination of iodide in iodised table salt

Sodium iodate is suggested for addition to table salt to make iodised table salt. The analytical methods used in the determination of total iodine, do not consider the residue of iodide in iodised table salt. There is no suitable method in the literature to determine iodide directly in iodised table salt. The principle of the method developed in this work may be suitable for this target, because the exchange reaction is specific for iodide, not iodate.

The sample solution was 1.0 g of iodised table salt dissolved in 50 mL of water and 5.0 mL of this was added to 15 mL of the KNO_3 electrolyte and buffer solution. The DPV experiments were done 10 times under optimal conditions. The average anodic peak current was 4.34 ± 0.26 μA. The concentration of iodide was calculated as 0.050 ± 0.003 nM. The amount of iodide in the table salt was calculated as 0.875 ± 0.002 μg/g. The national standard for iodine in iodised table salt is 35 μg/g. So, about 2.5% of iodide was present in the table salt sample. Iodide is a very active species, and may be responsible for the deterioration of iodised table salt during long-term storage due to the disproportionate reaction of iodide and iodate. This result proved that the method is highly selective for iodide rather than iodate or chloride.

Typical DPV curves of the sample solution and the standard addition solution are shown in Fig. 6. In the electrolyte solution, there is no any anodic peak (Fig. 6, curve 1). After addition of 5.0 mL table salt solution into the 15.0 mL electrolyte solution, the resulted solution includes 0.0825 M NaCl and 1.44 mM KIO_3, the solution gives out an anodic peak with 4.34 μA peak current, calculated as 0.05 nM, After addition of fivefold standard iodide, the peak current increases to 15.89 μA, and concentration of iodide was calculated as 0.275 nM. This experiment results indicate that the anodic peak is related to the iodide, and more than 10^{5-8} times of chloride and iodate do not interference the detection of iodide. From these experiments, the standard addition coverages were obtained in the range of 90–110%.

4. Conclusions

This paper describes the solid phase nano-extraction of iodide from iodised table salt on graphite powder surface modified with silver sulfate nanoparticles in a carbon paste electrode. Some important points are summarized as follows.

(1) The extraction mechanism is the exchange reaction between a sulfate anion in a nanoparticle of silver sulfate precipitate and iodide from aqueous solution, depending on the extraction time, solution pH, and the concentration of iodide
(2) The extraction isotherm follows a Freundlich adsorption isotherm.
(3) The extraction can be used directly in the electrochemical determination of iodide with an electrochemical probe of silver without interference by large amounts of chloride or iodate.
(4) The electrochemical method is a powerful tool in the sensitive, selective and rapid detection of iodide in iodised table salt and in the study of solid phase nano-extraction processes.

Acknowledgements

The authors acknowledge financial support by the Chinese National Science Foundation (20875063), the Liaoning Education Minister (2004-22) and the national key. Laboratory of Electroanalytical Chemistry (2006-06), Shenyang Sciences and the Technology Bureau Foundation (2007-GX-32).

References

[1] J. Pawliszyn, Solid Phase Microextraction. Theory and Practice, Wiley, New York, 1997.
[2] R.C. Sparrenberger, C.K. Cross, E.D. Conte, Anal. Chem. 76 (2004) 6156–6159.
[3] Z. Zhang, M. Yang, J. Pawliszyn, Anal. Chem. 66 (1994) 844A–853A.
[4] K.R. Reid, L.J. Kennedy, E.W. Crick, E.D. Conte, J. Chromatogr. A 975 (2002) 135–143.
[5] U. Ceglarek, J. Efer, A. Schreiber, E. Zwanziger, W. Engewald, Fresenius J. Anal. Chem. 365 (1999) 674–681.
[6] S. Reverté, F. Borrull, E. Pocurull, R.M. Marcé, J. Chromatogr. A 1010 (2003) 225–232.
[7] A.J. Bystol, J.L. Whitcomb, A.D. Campiglia, Environ. Sci. Technol. 35 (2001) 2566–2571.
[8] J. Li, X. Zhao, Y. Shi, Y. Cai, S. Mou, G. Jiang, J. Chromatogr. A 1180 (2008) 24–31.
[9] C. Pan, S. Xu, H. Zou, Z. Guo, Y. Zhang, B. Guo, J. Am. Soc. Mass Spectrom. 16 (2005) 263–270.
[10] J. Wu, W.M. Mullett, J. Pawliszyn, Anal. Chem. 74 (2002) 4855–4859.
[11] D.L. Luscombe, A.M. Bond, D.E. Davey, J.W. Bixler, Anal. Chem. 62 (1990) 27–31.
[12] M. Valcárcel, S. Cárdenas, B.M. Simonet, Anal. Chem. 79 (2007) 4788–4797.
[13] I. Svancara, K. Vytras, K. Kalcher, A. Walcarius, J. Wang, Electroanalysis 21 (2009) 7–28.
[14] M.M. Murry, E.E. Pochin, J. Physiol. Lond. 114 (1951) 6p–7p.
[15] P. Dasgupta, Y. Liu, J. Dyke, Environ. Sci. Technol. 42 (2008) 1315–1323.
[16] V.W. Truesdale, Mar. Chem. 6 (1978) 253–273.
[17] O.P. Skadauskinen, J.S. Skadauskas, J. Anal. Chem. 56 (2001) 170–172.
[18] S. Chandramouleeswaran, B. Vijayalakshmi, S. Kartihkeyan, T.P. Rao, C.S.P. Iyer, Microchim. Acta 128 (1998) 75–77.
[19] J.E. O'Reilly, J. Chem. Educ. 56 (1979) 279.
[20] G.W. Luther, C.B. Swartz, W.J. Ullman, Anal. Chem. 60 (1988) 1721–1724.
[21] I. Varga, Microchem. J. 85 (2007) 127–131.
[22] S. Rastegarzadeh, N. Pourreza, I. Saeedi, Talanta 77 (2009) 1032–1036.
[23] N.L. Dias Filho, D.R. do Carmo, Talanta 68 (2006) 919–927.

Talanta 80 (2010) 1239–1244

Contents lists available at ScienceDirect

Talanta

journal homepage: www.elsevier.com/locate/talanta

UV-induced carbonyl generation with formic acid for sensitive determination of nickel by atomic fluorescence spectrometry

Liwei Liu [a], Hao Deng [a], Li Wu [b], Chengbin Zheng [a], Xiandeng Hou [a,b,*]

[a] College of Chemistry, Sichuan University, Chengdu, Sichuan 610064, China
[b] Analytical & Testing Center, Sichuan University, Chengdu, Sichuan 610064, China

ARTICLE INFO

Article history:
Received 17 June 2009
Received in revised form 27 August 2009
Accepted 8 September 2009
Available online 13 September 2009

Keywords:
Carbonyl generation
Sample introduction
Atomic fluorescence spectrometry

ABSTRACT

UV-induced carbonyl generation with formic acid is used for gaseous sample introduction into an atomic fluorescence spectrometer for the determination of ultra-trace nickel. Compared with conventional carbonyl generation, no toxic gas CO is involved in this work, and volatile $Ni(CO)_4$ is generated with a single reagent formic acid under the irradiation of UV light (253.7 nm, 15 W). The reaction conditions, including reaction medium, UV irradiation time and reaction temperature, are optimized for the best signal. Under the optimized conditions, a limit of detection of 10 ng L^{-1} for nickel is obtained without any analyte-preconcentration, which is comparable to that using in situ trapping technique. Interferences from common transition metal ions, noble metal ions and mineral acids are also investigated. The proposed method is applied to the analysis of three certified reference materials and two organic acid samples for trace nickel, with analytical results in good agreement with certified values or those obtained by electrothermal atomic absorption spectrometry. This is a simple, fairly green and highly sensitive method for ultra-trace nickel determination.

© 2009 Elsevier B.V. All rights reserved.

1. Introduction

Determination of nickel is of great importance due to its both essentialness in low concentration and toxicity in high concentration to living organism [1,2]. The most popular analytical methods for the determination of metal elements are analytical atomic spectrometry, including flame atomic absorption spectrometry (FAAS), electrothermal atomic absorption spectrometry (ET-AAS), inductively coupled plasma-optical emission spectrometry (ICP-OES) and inductively coupled plasma mass spectrometry (ICP-MS). Unfortunately, the far low concentration level of nickel in many environmental or clinical samples (usually ng mL^{-1} or sub-ng mL^{-1}) makes it difficult to directly determine nickel without pre-concentration. Therefore, numerous pre-concentration techniques are usually applied prior to nickel measurement, such as liquid–liquid extraction [3], ion exchange [4], cloud point extraction [5], solid phase extraction [6], and membrane filtration [7]. Indeed, these enrichment methods offer advantages of both enhancement of the nickel concentration before spectrometric detection and preliminary separation of nickel from a complex sample matrix, and thus successfully conquer the difficulty of nickel determination in the ng mL^{-1} or sub-ng mL^{-1} concentration level. However, such methods are very vulnerable to analyte contamination and loss as a consequence of tedious manipulation steps and many reagents involved during the pre-concentration process. Moreover, these enrichment steps are often labor- and time-consuming. Therefore, a simple and sensitive analytical method for nickel determination is demanded for the analysis of many real samples.

Nickel can rapidly react with carbon monoxide to form a stable gaseous tetracarbonyl at ambient temperature and pressure. This was first used by Vijan in 1980 [8] for nickel determination. Generally, nickel chemical vapor generation (CVG) consists of three different types: $NaBH_4$–CO system [9–12], electrochemical reduction–CO system [13] and $NaBH_4$–HCl system [14–16]. As far as the $NaBH_4$–CO system concerned, the main principle is that dissolved nickel ion is reduced by $NaBH_4$ to nickel free atoms which subsequently combine carbon monoxide to form gaseous $Ni(CO)_4$, with a detection limit achievable as low as 4 ng L^{-1} [10]. Since nickel is ubiquitous naturally, this system is often bothered by the high blank problem resulted from the nickel impurity in $NaBH_4$ and CO, and a purification of reagents is usually required. Therefore, Johansson et al. [13] developed electrochemical reduction of nickel ion as an alternative to $NaBH_4$ reductant, but this technique was not generally applicable to the analysis of real samples because of heavy memory effect and the uncontrollable change in the electrode. The third type, $NaBH_4$–HCl system, is virtually the scope expansion of the traditional hydride generation (HG). Guo and Huang found that

* Corresponding author at: College of Chemistry, Sichuan University, Chengdu, Sichuan 610064, China. Fax: +86 28 8541 2798.
E-mail addresses: houxd@scu.edu.cn, houxiandeng@yahoo.com.cn, houxiandeng@yahoo.com.cn (X.D. Hou).

0039-9140/$ – see front matter © 2009 Elsevier B.V. All rights reserved.
doi:10.1016/j.talanta.2009.09.016

volatile nickel species could be generated by reaction in an aqueous solution with sodium or potassium borohydide at room temperature without using poisonous carbon monoxide [14]. Later, several studies by Sturgeon and coworkers [17] and other chemists [15,16] made this system feasible to real sample analysis for trace nickel, even though such a system intrinsically had the defect of unstable nickel volatile species, which resulted in low transportation efficiency.

Photochemical vapor generation (photo-CVG) is a newly emerging research field in analytical chemistry, providing a significant alternative to traditional CVG. Due to its unique features such as simple reaction and instrumentation, greener analytical methods in most cases, less interference especially from transition metals, and cost-effectiveness [18], many efforts have been made to apply it in analytical atomic spectrometry. In 2004, Sturgeon and coworkers [19] made a broad study in the UV photo-CVG as a sample introduction tool and expanded its scope to 20 elements including nickel, and this interested many chemists to further investigate its analytical application [20,21]. Additionally, Sturgeon developed this method to synthesize $Ni(CO)_4$ [22] and organic species of selenium [23], providing a novel means of synthesizing organic metal compounds with high yield. It is worthwhile to further explore its application for the determination of trace nickel concentration. Therefore, this work aims to develop an atomic fluorescence spectrometric method to determine ultra-trace nickel without any pre-concentration, by using UV-induced carbonyl generation for sample introduction with a single reagent formic acid.

2. Experimental

2.1. Apparatus

As illustrated in Fig. 1, the experimental set-up mainly consists of two parts: a laboratory-constructed flow-through photochemical reactor and a commercial atomic fluorescence spectrometer (AFS-2202E, Beijing Haiguang Instrument Co., Beijing, China). A quartz tube (4/6 mm, i.d/o.d.) coiled around a UV lamp (253.7 nm, 15 W, Philip, Holland) is used as the photochemical reactor. The quartz tube has 26 turns with 25 mm in diameter suiting the size of the UV lamp in order to maximize the UV irradiation onto the reactor. The whole photochemical reactor is mounted in a black box to prevent the UV light from leaking. A hot plate is used for heating the flow-through photochemical reactor, and a thermometer is inserted into the black box near the photochemical reactor to monitor the reaction temperature. Because the photochemical reaction for the production of nickel carbonyl is temperature-dependent, the cooling water used in our previous work [21] is eliminated to increase the temperature. Polytetrafluoroethylene tubing is used to deliver the solutions. A nickel hollow cathode lamp (Hebei Ningqiang Lighting Co., Ltd, China) is specially designed for the AFS measurement. More detailed information about the AFS instrument can be found in a previous publication [21], but its working parameters are summarized in Table 1.

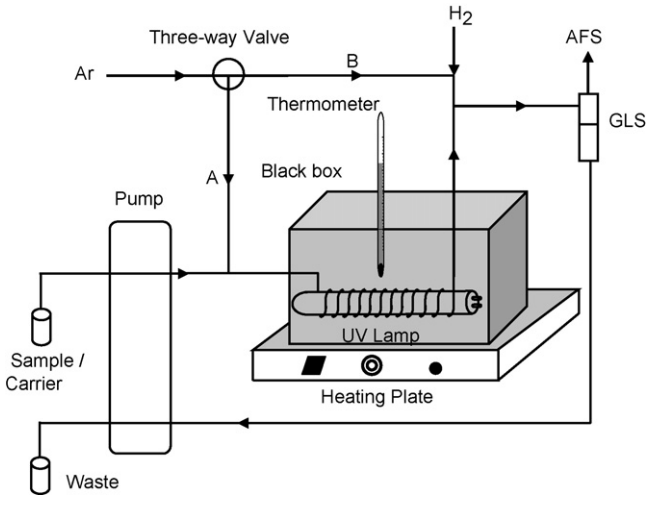


Fig. 1. Schematic diagram of the instrumentation.

Table 1
AFS instrumental parameters.

Parameter	Setting
Lamp current (mA)	80
Voltage of PMT (V)	−300
Atomizer height (mm)	10
Carrier gas flow rate (Ar, mL min^{-1})	300
Shied gas flow rate (mL min^{-1})	1200

For comparison of the analytical results, a SpectrAA 220Z polarized Zeeman electrothermal atomic absorption spectrometer (Varian, USA) is used for the determination of Ni in formic and acetic acid samples. Pyrolysis and atomization temperature of 800 °C and 2600 °C, respectively, are used.

2.2. Reagents

All reagents used in this work are at least of analytical grade. Doubly distilled water (DDW) is used throughout the whole work. 1000 mg L^{-1} Ni(II) standard stock solution is prepared by dissolving 0.1273 g spectropure NiO in 2 mL concentrated nitric acid and subsequently diluting with DDW to 100 mL. After step diluting the standard stock solution, the final working standard solutions are prepared in formic acid with proper concentrations. Chemicals HCOOH, HCl, H_2SO_4, HNO_3 and $HClO_4$ are all purchased from Kelong Chemical Reagents Factory (Chengdu, China.). Formic acid is distilled at 100.8 °C (formic acid boiling point) for its purification prior to use. All vessels used in the experiments are soaked in 1% (v/v) nitric acid overnight and cleaned sequentially with tap water and DDW before use.

2.3. Procedures

For the computer-programmable operation procedure, the nickel and formic acid mixed solution is sucked (Ar flow set to path A) for 40 s into the photochemical reactor in the first step (to fulfill the reaction coil). In the second step, the three-way valve is immediately switched to path B to prevent the Ar flow from purging the sample solution out of the flow-through photochemical reactor, and the peristaltic pump pauses for 120 s; meanwhile the sample channel is shifted from the sample solution to the carrier solution, 20% (v/v) formic acid. During this 120 s interval, sample solution is subject to UV irradiation to generate nickel carbonyl. In the third step (14 s), the peristaltic pump is activated again and the Ar flow is turned back to path A to propel the reaction solution into the gas–liquid separator (GLS). The resultant nickel carbonyl is subsequently introduced into AFS for the peak area measurement of the atomic fluorescence signal. In the fourth step, the peristaltic pump pauses for 6 s to make ready for the next measurement. In the first and the third step, the pump is set at 100 and 120 rpm, respectively.

Caution: UV exposure. Besides, $Ni(CO)_4$ is extremely toxic, and proper ventilation is highly recommended.

3. Results and discussion

3.1. Nickel carbonyl generation

The possible mechanism of photochemical vapor generation remains largely in a state of "discussion", due to the complicated nature of the photoreactions. It is believed that under the UV irradiation, formic acid may follow either of two following anaerobic photolytic decomposition pathways [22]:

$$H - COOH \xrightarrow{UV} H^{\bullet} + {}^{\bullet}COOH \rightarrow H_2 + CO_2 \quad (1)$$

$$H - COOH \xrightarrow{UV} HCO^{\bullet} + {}^{\bullet}OH \rightarrow CO + H_2O \quad (2)$$

Guo and Huang reported that the reaction product of nickel salt with tetrahydroborate might be nickel hydride [14], for the generated nickel volatile species was highly unstable. Only one Ni-containing volatile species naturally exists, namely $Ni(CO)_4$. So the possible pathway for generation of $Ni(CO)_4$ in this work is most probably based on the fact that the photo-generated radicals could behave as a precursor for the reducing species, which plays a role in the reduction of Ni^{2+} to Ni^0. Although Khriachtchev et al. [24] and Langford et al. [25] reported that for formic acid decomposition, Eq. (1) occurred 6-fold more frequently than Eq. (2), the reaction of Ni with CO is known to occur very quickly (Mond process), resulting in rapid consumption of photo-generated CO, and this may substantially accelerate the reaction of Eq. (2). Therefore, the generation of $Ni(CO)_4$ in this work may be followed as:

$$Ni(II) + \text{reducing species (radicals)} \rightarrow Ni(0)_{sol} \quad (3)$$

$$Ni(0)_{sol} + 4CO \rightarrow Ni(CO)_4 \quad (4)$$

In fact, Guo and Sturgeon used GC–MS to identify the volatile species generated in the UV irradiation of nickel salt and formic acid mixture [22]. The resultant fragmentation patterns were in fair agreement with the previously reported mass spectrum of $Ni(CO)_4$.

3.2. Effect of reaction medium

It is structurally evident that only low molecular weight organic acids can photo-generate $CO^{\bullet}$ radical, which accounts for the generation of $Ni(CO)_4$. So in this work, five aliphatic organic acids, namely formic acid, acetic acid, propionic acid, oxalic acid, and malonic acid, are initially tested for $Ni(CO)_4$ generation. These organic acids have similar structures, and are prone to be decomposed under UV light irradiation. Within 4 min UV irradiation, no obvious nickel signal is detected in the medium of oxalic acid (from 0.025 mol L^{-1} to 0.5 mol L^{-1}) and malonic acid (from 0.05 mol L^{-1} to 0.1 mol L^{-1}). The other three acids can be used to photo-generate volatile Ni-containing species (Fig. 2) among which formic acid is the best choice. In our previous work for Hg cold vapor generation under UV irradiation, it was found that the simpler the organic structures, the higher the generation efficiency [26]. Considering the structures of the five acids studied, formic acid is the simplest one, thus the best performance for volatile Ni-containing species generation. Besides, Guo and Sturgeon underlined that oxalic and malonic acid may firstly proceed in a CO_2 lost pathway [27], which would further make it difficult for the generation of $CO^{\bullet}$ radical, thus $Ni(CO)_4$ was hardly generated.

The effect of formic acid concentration on the atomic fluorescence signal of Ni is shown in Fig. 2. When the formic acid concentration is below 20% (v/v), the nickel carbonyl generation efficiency increases almost linearly with formic acid concentration. However, further increase of formic acid concentration cannot lead to a signal plateau, but a decrease of nickel signal. With high concentration of formic acid, more active radicals are generated and they

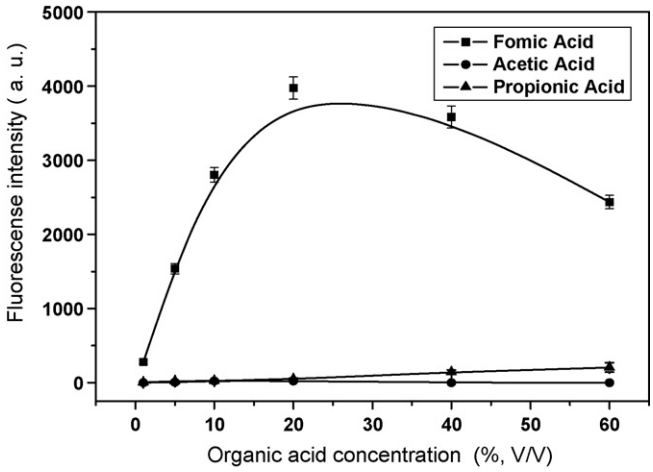


Fig. 2. Effect of the different organic acids on the nickel carbonyl generation. Analyte concentration: 10 μg L^{-1} Ni^{2+}.

are prone to recombine with each other, leading to lower reducing ability. On one hand, excess CO might be produced with high concentration formic acid, and this would lower the atomization efficiency; on the other hand, high concentration of H^+ is likely to capture the Ni precursor generated [9], resulting in inferior generation efficiency. Therefore, 20% (v/v) formic acid concentration is used in this work.

3.3. Reaction coil materials

Three types of materials, glass, PTFE and quartz, are selected to construct the reaction coil. It is known that UV light can be blocked by the glass material, so no appreciable nickel signal can be obtained with a glass coil. In several previous work of photo-induced CVG, PTFE tubes were used [27,28]. It was found that the nickel carbonyl generation efficiency in PTFE was half in a quartz coil, so a quartz reaction coil (4/6 mm, i.d/o.d.) is chosen for use in this work.

3.4. Reaction temperature

It is well-known that $Ni(CO)_4$ will decompose into Ni and CO in liquid phase at 60 °C. As shown in Fig. 3, when the temperature is below 333 K (60 °C), the release of nickel carbonyl from liquid phase increases linearly with the temperature. Further increase of the

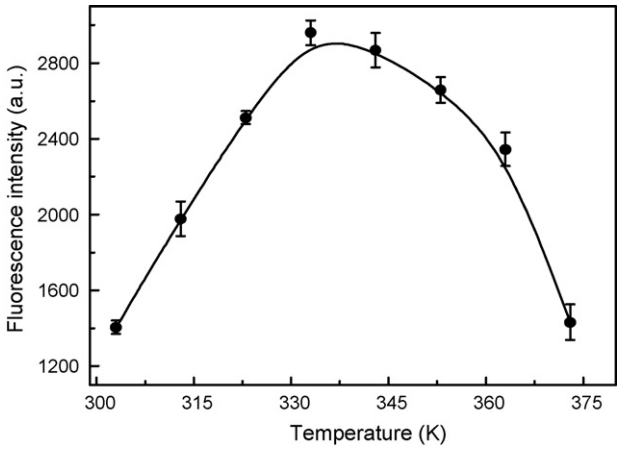


Fig. 3. Effect of temperature on the nickel carbonyl generation. Analyte concentration: 5 μg L^{-1} Ni^{2+}.

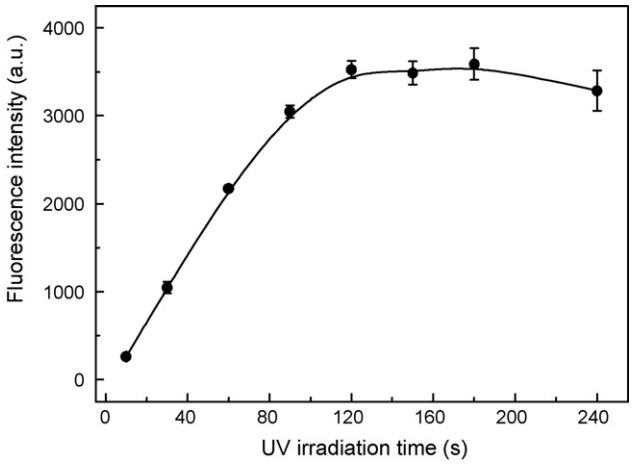


Fig. 4. Effect of UV irradiation time on the nickel carbonyl generation. Analyte concentration: 5 μg L^{-1} Ni^{2+}.

reaction temperature leads to a sharp decrease of analyte signals. When the reaction temperature is below the critical decomposition temperature of $Ni(CO)_4$ in liquid phase, increasing the temperature accelerates the UV-induced nickel carbonyl generation, leading to rapid release of volatile $Ni(CO)_4$ and high transport efficiency. In order to obtain the best signal, reaction temperature of 333 K (60 °C) was used in the following work.

3.5. UV irradiation time

As reported previously, the photo-induced CO• generation is more difficult than the generation of "H•" [24,25]. Also in our previous work for mercury photo-CVG, 5 s UV light irradiation time was enough [20,26]. In this work, the nickel carbonyl generation efficiency is largely associated with the irradiation time, probably partially because of the use of a difference type of UV lamp. A high pressure mercury lamp and a low pressure mercury lamp were tested and the CVG efficiencies are compared. It is found that the low pressure mercury lamp leads to a better signal-to-noise ratio, and thus it is used throughout this work. The intense UV radiation from the high pressure mercury lamp may decompose the carbonyl products. As illustrated in Fig. 4, 120 s irradiation is needed to reach the signal plateau, which is much longer than that needed for the case of mercury [20,26] using a high pressure mercury lamp. In Guo and Sturgeon's work for photosynthesis of nickel carbonyl [22], they also found that longer irradiation time could increase the generation efficiency.

It was initially believed that if prolonged UV irradiation time would lead to higher generation efficiency, increasing the number of the UV lamps might also promote the generation process and accordingly decrease the irradiation time. However, the case is totally different from what was expected. Simply increasing the number of the UV lamps (at fixed temperature, 60 °C) has no obvious effect on nickel carbonyl generation. The reason for such phenomenon remained unclear at the present stage.

3.6. Hydrogen gas flow rate

In order to atomize the photo-generated nickel carbonyl, additional energy must be provided. Without an Ar–H_2 flame for atomization, nickel atomic fluorescence signal cannot be observed. However, excess amount of H_2 would sharply decrease the signal, which was similar to the situation for Se [21]. Hydrogen flow rate at 20 mL min^{-1} is enough for $Ni(CO)_4$ atomization. The temperature of the Ar–H_2 flame at 20 mL min^{-1} H_2 is about 800 °C, much higher than the decomposition temperature needed for $Ni(CO)_4$ in gas phase.

Table 2
Interference of common ions with nickel determination.

Coexisting ion	[M] (μg L^{-1})	[M]/[Ni(II)]	Recovery (%)
Cl^-	50,000[a]	10,000	96
NO_3^-	50,000[a]	10,000	97
SO_4^{2-}	50,000[a]	10,000	104
ClO_4^-	50,000[a]	10,000	98
K^+	50,000[a]	10,000	101
Na^+	50,000[a]	10,000	98
Ca^{2+}	50,000[a]	10,000	99
Mg^{2+}	50,000[a]	10,000	96
As^{3+}	250	50	90
Sb^{3+}	10,000	2,000	98
Bi^{3+}	20,000	4,000	95
Ge^{2+}	25,000	5,000	95
Sn^{2+}	10,000	2,000	96
Pb^{2+}	2,500	500	95
Zn^{2+}	10,000	2,000	92
Cd^{2+}	500	100	90
Te^{4+}	500	100	90
Co^{2+}	5,000	1,000	90
Fe^{3+}	5,000	1,000	90
Cu^{2+}	2,500	500	97
Mn^{2+}	25,000	5,000	90
Au^{3+}	1,000	200	96
Ag^+	5,000	1,000	95

[a] Maximum concentration studied.

3.7. Effect of concomitants

To evaluate the analytical applicability of the proposed method, the effect of some concomitants (several alkaline and alkaline earth salts as well as some transition and heavy metals) was studied (Table 2), with Ni(II) concentration fixed at 5 μg L^{-1}. Four mineral acids typically used for solid sample treatment, namely nitric acid, hydrochloric acid, perchloric acid and sulfuric acid, were investigated in the interference study (Fig. 5). All these acids depress signals sharply. In order to identify which ion is responsible for the signal depression (H^+ or acid anion), four corresponding salts containing the same anion with each acid, were studied, and the results are also illustrated in Fig. 5. It can be concluded that both H^+ and acid anions contributed to the signal depression.

3.8. Analytical figures of merit and sample analysis

Under the optimal conditions, the analytical performance of the proposed method for the determination of nickel was evaluated (Table 3). The LOD (3σ) of the proposed method is 10 ng L^{-1}, without any analyte enrichment step. Compared with other analytical atomic spectrometric techniques, such as GF-AAS [29], ICP-OES [29], ETV-ICP-MS [30] and in situ trapping GF-AAS [10] (Table 4), this approach represents one of the most sensitive yet simplest ones for ultra-trace nickel determination.

Table 3
Analytical characteristics of the proposed method.

Details	Value
Sample volume (mL)	4
Calibration equation (C in μg L^{-1})	$I_f = 1267.7C - 19.4$
Upper linear range (μg L^{-1})	8
Correlation coefficient (R)	0.9994
Limit of detection (ng L^{-1})	10
Precision at 5 μg L^{-1} (RSD, $n = 11$)	3.2%

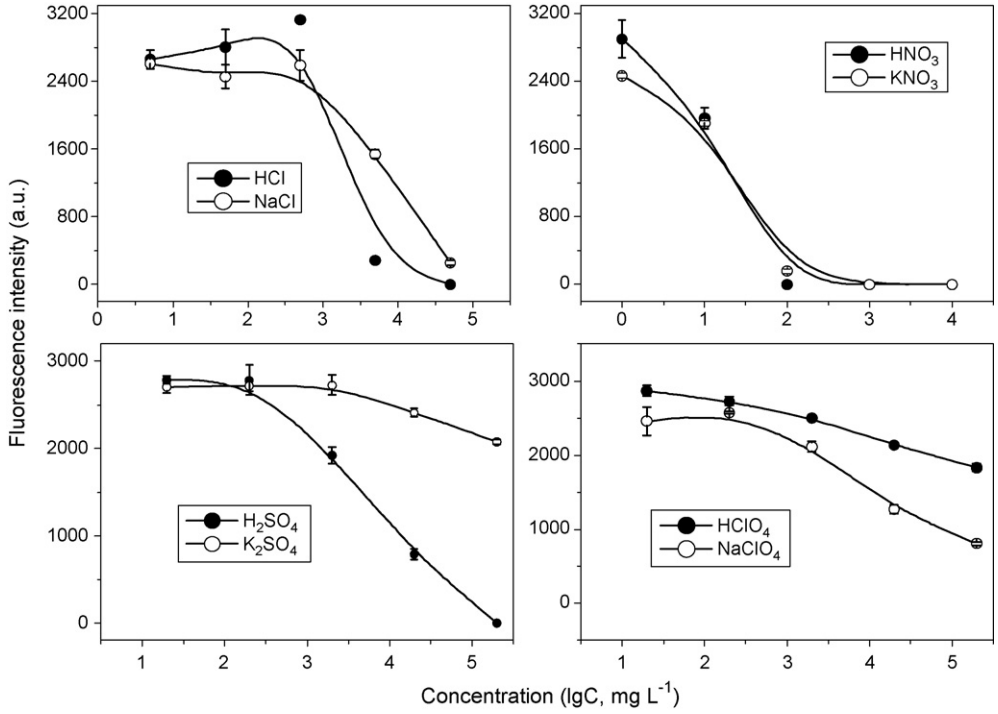


Fig. 5. Interference of common mineral acids and their corresponding salts on the nickel carbonyl generation. Analyte concentration: 5 μg L^{-1} Ni^{2+}.

Table 4
Comparison of LODs with other analytical atomic spectrometric techniques.

Techniques	LOD (ng L^{-1})	Pre-concentration	Ref.
GF-AAS	70	No	[29]
GF-AAS	4	Yes, in situ trapping	[10]
ETV-ICP-MS	3	No	[30]
ICP-MS	0.4	No	[29]
ICP-OES	500	No	[29]
CVG-ICP-OES	1800	No	[15]
CVG-AFS	10	No	This work

To validate the accuracy of the proposed method, three certified reference materials (GBW 08607 water, GBW 09101 human hair and GBW 07605 tea) were analyzed (Table 5) for nickel. Water samples were diluted directly for analysis. For solid samples, firstly they were digested with 1 mL nitric acid, heated to dryness, and dissolved and diluted with DDW. Before analysis, the samples were further diluted with 20% (v/v) formic acid. The total dilution factor was 1000. The *t*-test concludes that analytical results (Table 5) agree very well with the certified values, at the confidence level of 95%.

This method is further applied to nickel analysis in formic and acetic acid samples. The analytical scheme of formic acid sample is based on our previously reported sample matrix-assisted chemical vapor generation [31]. For comparison, these samples were further analyzed by electrothermal atomic absorption spectrometry, and the analytical results of the two methods also agree with each other very well (Table 5).

Table 5
Analytical results of real samples.

Samples	This work (μg g^{-1})[a]	Certified (μg g^{-1})	GF-AAS (μg g^{-1})[a]
GBW 08607 water	0.520 ± 0.050	0.517 ± 0.006	–
GBW 09101 human hair	3.15 ± 0.20	3.17 ± 0.40	–
GBW 07605 tea	4.5 ± 0.4	4.6 ± 0.5	–
Formic acid[b]	50.5 ± 0.6	–	50.1 ± 0.9
Acetic acid[b]	41.5 ± 0.7	–	41.3 ± 0.3

[a] Average ± one standard deviation of three trials.
[b] μg L^{-1}.

4. Conclusions

UV-induced carbonyl generation for the atomic fluorescence spectrometric determination of ultra-trace nickel enjoys many advantages over conventional nickel determination technologies. Firstly, only formic acid is required for the analysis of liquid samples, so the contamination from reagents can be largely minimized; secondly, the use of toxic CO is eliminated; thirdly, the products of the method are CO_2 and H_2O, so it represents a greener analytical methodology [32,33] for nickel determination; and fourthly, it is highly sensitive. UV-induced carbonyl generation can be possibly extended to determine other carbonyl-forming elements, such as Fe, Co, W and Mo [34,35]. Besides, the proposed carbonyl generation can serve as a sample introduction method for nickel determination by other atomic spectrometric techniques, such as GF-AAS and ICP-MS/OES.

Acknowledgements

We gratefully acknowledge the financial support for this project from the National Natural Science Foundation of China (No. 20775051 and No. 20835003). Thanks given to Mr. Peng Wu and Mr. Guanglei Cheng of Analytical & Testing Center of Sichuan University for their kind help with the comparison test.

References

[1] K. Salnikow, K.S. Kasprzak, Environ. Health Perspect. 113 (2005) 577.
[2] K. Salnikow, T. Davidson, M. Costa, Environ. Health Perspect. 110 (2002) 831.
[3] I. Komjarova, R. Blust, Anal. Chim. Acta 576 (2006) 221.
[4] J.H. Wang, E.H. Hansen, Anal. Chim. Acta 424 (2000) 223.
[5] J.R. Chen, K.C. Teo, Anal. Chim. Acta 434 (2001) 325.
[6] F.Z. Xie, X.C. Lin, X.P. Wu, Z.H. Xie, Talanta 74 (2008) 836.
[7] U. Divrikli, A.A. Kartal, M. Soylak, L. Elci, J. Hazard. Mater. 145 (2007) 459.
[8] P.N. Vijan, At. Spectrosc. 1 (1980) 143.

[9] D.S. Lee, Anal. Chem. 54 (1982) 1182.
[10] R.E. Sturgeon, S.N. Willie, S.S. Berman, J. Anal. At. Spectrom. 4 (1989) 443.
[11] C.J. Park, S.A. Yim, J. Anal. At. Spectrom. 14 (1999) 1061.
[12] B. Docekal, P. Marek, M. Vobecky, J. Anal. At. Spectrom. 15 (2000) 131.
[13] M. Johansson, R. Hansson, J. Snell, W. Frech, Analyst 123 (1998) 1223.
[14] X.M. Guo, B.L. Huang, Z.H. Sun, R.Q. Ke, Q.Q. Wang, Z.B. Gong, Spectrochim. Acta Part B 55 (2000) 943.
[15] J. Marrero, P. Smichowski, Anal. Bioanal. Chem. 374 (2002) 196.
[16] S. Cerutti, S. Moyano, J. Marrero, P. Smichowski, L.D. Martinez, J. Anal. At. Spectrom. 20 (2005) 559.
[17] Y.L. Feng, R.E. Sturgeon, J.W. Lam, J. Anal. At. Spectrom. 18 (2003) 1435.
[18] Y.H. He, X.D. Hou, C.B. Zheng, R.E. Sturgeon, Anal. Bioanal. Chem. 388 (2007) 769.
[19] X.M. Guo, R.E. Sturgeon, Z. Mester, G.J. Gardner, Anal. Chem. 76 (2004) 2401.
[20] C.B. Zheng, Y. Li, Y.H. He, Q. Ma, X.D. Hou, J. Anal. At. Spectrom. 20 (2005) 746.
[21] C.B. Zheng, L. Wu, Q. Ma, Y. Lv, X.D. Hou, J. Anal. At. Spectrom. 23 (2008) 514.
[22] X.M. Guo, R.E. Sturgeon, Z. Mester, G.J. Gardner, Appl. Organometal. Chem. 18 (2004) 205.
[23] X.M. Guo, R.E. Sturgeon, Z. Mester, G.J. Gardner, Appl. Organometal. Chem. 17 (2003) 575.
[24] L. Khriachtchev, E. Macoas, M. Pettersson, M. Rasanen, J. Am. Chem. Soc. 124 (2002) 10994.
[25] S.R. Langford, A.D. Batten, M. Kono, M.N.R. AShfold, J. Chem. Soc., Faraday Trans. 93 (1997) 3757.
[26] C.F. Han, C.B. Zheng, J. Wang, G.L. Cheng, Y. Lv, X.D. Hou, Anal. Bioanal. Chem. 388 (2007) 825.
[27] X.M. Guo, R.E. Sturgeon, Z. Mester, G.J. Gardner, Anal. Chem. 75 (2003) 2092.
[28] Q.Q. Wang, J. Liang, J.H. Qiu, B.L. Huang, J. Anal. At. Spectrom. 19 (2004) 715.
[29] The Guide to Techniques and Applications of Atomic Spectroscopy, The Perkin Elmer Corporation, Norwalk, CT, USA, 2003, p. 7.
[30] S. Laly, K. Nakagawa, T. Arimura, T. Kimijima, Spectrochim. Acta Part B 51 (1996) 1393.
[31] Y. Li, C.B. Zheng, Q. Ma, L. Wu, C.W. Hu, X.D. Hou, J. Anal. At. Spectrom. 21 (2006) 82.
[32] L.H. Keith, L.U. Gron, J.L. Young, Chem. Rev. 107 (2007) 2695.
[33] Y.H. He, L. Tang, X. Wu, X.D. Hou, Y.I. Lee, Appl. Spectrosc. Rev. 42 (2007) 119.
[34] P. Grinberg, Z. Mester, R.E. Sturgeon, A. Ferretti, J. Anal. At. Spectrom. 23 (2008) 583.
[35] J. Feldmann, J. Environ. Monit. 1 (1999) 33.

Talanta 80 (2010) 1245–1250

Contents lists available at ScienceDirect

Talanta

journal homepage: www.elsevier.com/locate/talanta

Discrimination of *Ephedra* plants with diffuse reflectance FT-NIRS and multivariate analysis

Qi Fan[a,b], Yuanliang Wang[a,*], Peng Sun[b], Sha Liu[b], Yang Li[b]

[a] *Bioengineering College, Chongqing University, Chongqing 400030, People's Republic of China*
[b] *School of Pharmacy, Chongqing Medical University, Chongqing 400016, People's Republic of China*

ARTICLE INFO

Article history:
Received 18 July 2009
Received in revised form 26 August 2009
Accepted 8 September 2009
Available online 17 September 2009

Keywords:
Fourier transform near infrared spectroscopy
Multivariate analysis
Species
Habitat
Picking time
Ephedra plant

ABSTRACT

The secondary metabolites of different *Ephedra* plants are various. Therefore, the discrimination of different *Ephedra* plants is significant. An objective, easy-to-use, rapid and pollution-free approach is proposed for discriminating *Ephedra* plants of different species, habitats and picking times on the basis of diffuse reflectance Fourier transform near infrared spectroscopy (FT-NIRS) measurements and multivariate analysis. The Fourier transform near infrared diffuse reflectance spectra (NIRDRS) were acquired from 37 pulverized samples of *Ephedra* plants put in glass vials in the near infrared (NIR) region between 10 000 and 4000 cm^{-1}, averaging 64 scans per spectrum at a resolution of 4 cm^{-1}. After spectra processing and data pre-processing, spectral data were analyzed respectively with three multivariate analysis techniques: discriminant analysis (DA), self-organizing map (SOM) and back-propagation artificial neural network (BP-ANN). The proposed method could distinguish not only the *Ephedra* plants of three species and two habitats but also the plants picked at different times of day without special sample treatment and the use of chemical reagents. The performance indexes of the DA model were 84.2–91.9% and the prediction accuracies of both the SOM and the BP-ANN models reached 93.3–100.0%.

© 2009 Elsevier B.V. All rights reserved.

1. Introduction

Ephedra plants (Ephedraceae) are widely distributed in the world. Among them, *Ephedra sinica* (*E. sinica*), *Ephedra intermedia* (*E. intermedia*) and *Ephedra equisetina* (*E. equisetina*) are dominant and economically important species in China and their main habitats are in Inner Mongolia, Xinjiang, Shanxi, Gansu and so on. The secondary metabolites contained in *Ephedra* plants mainly include alkaloids, essential oils, tannins, flavonoids and organic acids [1–3]. They are very important for the plants' survivals because they play a significant role in defending against herbivores, microbes, viruses or competing plants [4–6]. The levels and types of plant secondary metabolites represent adaptive characters that have been subject to natural selection during evolution, that is, plant secondary metabolites are primarily decided by the plant species and habitats [2,4,6–8]. In addition, the levels of plant secondary metabolites change with the plants' phenophases and metabolic rhythms [9]. On the other hand, plant secondary metabolites are unique sources for pharmaceuticals, food additives, flavors, and other industrial materials [10,11]. The secondary metabolites of *Ephedra* plants of different species, habitats and picking times are various so that the applications of these plants are divergent [2,12]. For example, *E. sinica* is usually used for extracting (−)-ephedrine and *E. intermedia* for (+)-pseudoephedrine; *E. sinica*, *E. intermedia* and *E. equisetina* have been authorized to be used as herbs in China and Japan [13,14]. Hence, the identification of *Ephedra* plants of different species, habitats and picking times could help the research of phytoecology of *Ephedra* and the utilization of *Ephedra* plants.

The regular approaches to the authentication of *Ephedra* plants of different species and habitats are made with morphological and histological methods [13,14]. However, the application of these methods is seriously limited to practitioners' experience due to the subjectivity and complexity of the methods. Analytical methods such as chemical analysis [13], chromatographic analysis [12–14], and DNA sequence analysis [7] have also been used for these purposes with the disadvantages that are time-consuming and polluting. The discrimination between the plants picked at different times of day is meaningful because it can demonstrate whether the chemical components (especially volatile components, e.g. 4-vinylanisole, a marker compound for *E. sinica*) of the plants are divergent [9,12]. To our knowledge, however, there have not so far been any publications focused on the identification of *Ephedra* plants of different species and habitats with FT-NIRS, and of different times of day.

Near infrared spectroscopy (NIRS) has been proved to be a powerful analytical tool. The chemical and physical information about a sample can be extracted simultaneously from its NIR data by multivariate analysis techniques [15,16]. Compared with the meth-

* Corresponding author. Tel.: +86 23 6510 2509; fax: +86 23 6848 5161.
E-mail address: wyl@cqu.edu.cn (Y. Wang).

0039-9140/$ – see front matter © 2009 Elsevier B.V. All rights reserved.
doi:10.1016/j.talanta.2009.09.018

Table 1
37 samples of *Ephedra* plants from four Chinese habitats.

Species	Habitat	Picking time	Number of samples
E. sinica	Shanxi	10:00–11:30 am	10
	Shanxi	4:30–5:00 pm	6
	Shanxi	Unknown	10
	Inner Mongolia	Unknown	6
E. intermedia	Xinjiang	Unknown	2
	Gansu	Unknown	1
	Inner Mongolia	Unknown	1
E. equisetina	Xinjiang	Unknown	1

ods described above [7,12–14], NIRS possesses many advantages. NIR results are obtained from the measured data, and not from the experience; the operation of NIR analyzer is very easy: the lengthy skill training is unnecessary; the sample preparation is minimal; the analysis time is inherently rapid: the measurement of a spectrum is accomplished within seconds; and chemicals are not used in the analytic process. Moreover, multiple NIR modes mainly including diffuse reflection [17], reflection [18] and transmission [19] have been developed to satisfy various requirements; the remote NIR analysis [20] and in situ NIR analysis [21] have been implemented with optical fiber probes. Particularly, diffuse reflectance NIRS is suitable for the analysis of powders and solids. At present, NIRS technique is widely used in various fields, such as foods [22,23], pharmaceuticals [24], and chemicals [25].

In this contribution, the feasibility of the discrimination of *Ephedra* plants of different species, habitats and picking times is evaluated with diffuse reflectance FT-NIRS. The optimization of the spectral measurement conditions, spectra processing approaches, data pre-processing methods, and data analysis techniques is also discussed.

2. Experimental

2.1. Samples

Whole plants were collected for each sample. A total of 37 samples consisting of *E. sinica*, *E. intermedia* and *E. equisetina* were obtained from four main Chinese habitats Inner Mongolia, Xinjiang, Shanxi and Gansu. Thereinto, 16 samples of *E. sinica* from Shanxi were picked by us between 10:00 and 11:30 am and between 4:30 and 5:00 pm. The details of the sample collection are shown in Table 1.

The samples of *E. sinica*, *E. intermedia* and *E. equisetina* were respectively divided into the calibration and validation samples for the identification of *Ephedra* plants of different species. However, it was unfortunate that there was no sample of *E. equisetina* in the validation samples. The samples of *E. sinica* from Shanxi and Inner Mongolia and the samples of *E. sinica* from Shanxi picked in the morning and afternoon were divided respectively in the same way for the discrimination of *Ephedra* plants of different habitats and picking time sections. The details of the sample utilization are presented in Table 2.

All samples were discriminated with reference to morphological characters. After that, they were put in open vessels and stored at $22 \pm 1\,^{\circ}C$ and $55 \pm 5\%$ RH for a long time until their moisture contents became uniform. The herbaceous stems [13] of each sample were pulverized and separated by a series of sieves into six different portions with the size ranges 20–40 mesh, 40–60 mesh, 60–80 mesh, 80–100 mesh, 100–200 mesh, and 200–300 mesh.

2.2. Near infrared instrument and measurement

The NIRDRS were measured with Antaris II FT-NIR analyzer (Thermo Fisher Scientific, USA), furnished with an indium gallium arsenide (InGaAs) detector and an integrating sphere attachment. The instrument was controlled with RESULT 3.0, a software package accompanying this analyzer.

The pulverized samples of equal size range were poured severally into circular glass vials of the same diameter up to a certain thickness and weight to maintain a uniform bulk density. Subsequently, each circular vial was placed on the circular detection window of the integrating sphere module and the position of the vial was adjusted to keep the bottom of the vial concentric with the detection window.

All the NIRDRS were acquired under the same measurement conditions, i.e. scan region: 10 000–4000 cm^{-1}; number of scans: 64; resolution: 4 cm^{-1}; and sample thickness: 20 mm. The room conditions for the spectral measurement were identical with those for the sample store. The measurement background, the gold-plated inner wall of the integrating sphere, was measured to deduct the interference of water vapor and CO_2 in the air. Each pulverized sample was loaded and was measured five times [26].

2.3. Spectra processing and data pre-processing

Spectral noise is generally reduced by smoothing techniques [15]. Baseline offset and drift can be corrected respectively with the first and second derivatives [15]. In the diffuse reflectance measurement, the light travels various distances because the distribution of sample particles is uneven and the particle sizes are different.

Table 2
Utilization of the samples of *Ephedra* plants.

Discrimination	*Ephedra* plant	Number of calibration samples	Number of validation samples
Species	*E. sinica*	9	3
	E. intermedia	3	1
	E. equisetina	1	0
Habitat	*E. sinica* from Shanxi	21	5
	E. sinica from Inner Mongolia	5	1
Picking time	*E. sinica* from Shanxi picked between 10:00 and 11:30 am	8	2
	E. sinica from Shanxi picked between 4:30 and 5:00 pm	5	1

The scattering effects can be eliminated with multiplicative signal correction (MSC) [27]. Accordingly, six techniques of spectra processing, consisting of absorbance, Savitzky–Golay smoothing, Norris smoothing, first derivative, second derivative, and MSC, were explored for the optimal prediction performance of individual calibration models [28]. Additionally, the segment size taken into account during the smoothing process is an important parameter. The measurement sensitivity is low for the large segment size and the noise is high for the small segment size. Hence, the size was chosen case by case.

The NIRDRS data over the spectral range were used in the analysis. The data sets reached 3112 dimensions. The high dimensional datasets possessed collinearity because some spectral variables had a high correlation with the other ones. To avoid the overfitting problem caused by the collinearity, the data containing redundant information were compressed by dimension reduction before modeling to improve the modeling speed and the model stability.

The spectra processing and data pre-processing were finished in TQ Analyst 8.0 (Thermo Fisher Scientific, USA), a chemometric analysis software.

2.4. Data analysis

The prevailing modeling method for discrimination is DA, which can classify a group of analytes into predefined subgroups based on a set of linear functions of input variables [29]. ANN, involving several non-linear data analysis and modeling tools that can model complex relationships between inputs and outputs, is also used in qualitative analysis. SOM, a type of ANN, is trained by unsupervised learning to map a low-dimensional, typically two-dimensional, representation of the calibration and validation samples. BP-ANN, one of the most popular ANN, minimizes the global error of the system by modifying node weights in the supervised learning procedure [15].

In this investigation, the data analysis was performed respectively with the linear DA and the non-linear ANN, including the SOM trained by unsupervised learning and the BP-ANN trained by supervised learning, to compare prediction performances of the models obtained by various data analysis methods. The two- and three-dimensional maps of the DA can visualize the analytical results of the calibration samples. The ANN of the same architecture was used in the discrimination of *Ephedra* plants of different species, habitats and picking time sections. The two-dimensional distribution maps in the output layer of the SOM (10×10) visually displayed the outcomes of the calibration and validation of the models. The three layer BP-ANN was composed of one input layer with 10 neurons, 1 hidden layer with 10 neurons, and 1 output layer with 1 neuron.

The data analysis was performed using the chemometric analysis software TQ Analyst 8.0 (Thermo Fisher Scientific, USA) for the DA and the mathematical modeling software Matlab 6.5 (The MathWorks, USA) for both the SOM and the BP-ANN.

3. Results and discussion

3.1. Conditions for spectral measurement

The resolution and number of scans are important parameters of NIRDRS measurement. In high-resolution spectral measurement, the data are large, but the noise is high; in low-resolution spectral measurement, the situation is opposite. The resolution of 4 cm^{-1} was adopted for the qualitative analysis after attempting the resolution of 2 cm^{-1}, 4 cm^{-1}, 8 cm^{-1}, 16 cm^{-1}, and 32 cm^{-1}. When the number of scans is increased, the consuming time in the spectral measurement is extended while the noise is counteracted greatly; when the number of scans is decreased, the situation is reversed.

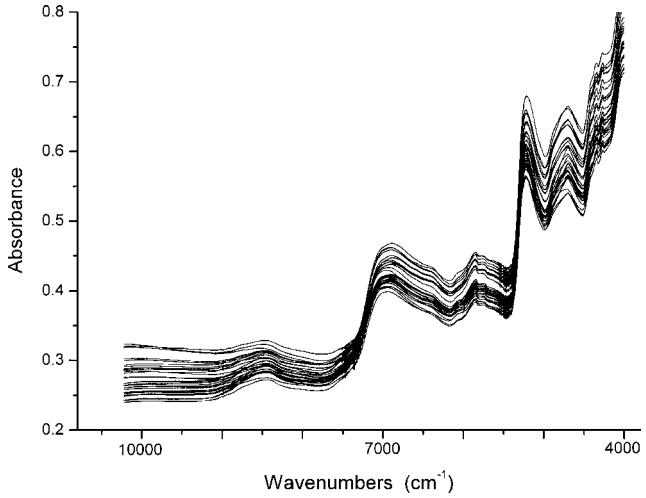


Fig. 1. Raw NIRDRS of 37 samples of *Ephedra* plants.

It was found that the optimal number of scans was 64 from the intercomparison of the numbers 16, 32, 64, and 128.

The sample thickness is one factor influencing NIRDRS. It was noted that the sample absorbance was large and steady once the sample thickness was more than 8 mm by comparing the NIRDRS measured respectively with the thickness of 1 mm, 2 mm, 4 mm, 8 mm, 16 mm, and 20 mm. Finally, the sample thickness of 20 mm was used in the measurement because there was a sign at 20 mm high on the outside surface of the sample vial.

For the same pulverized samples of *Ephedra* plants with different particle sizes, their physical characters are various and their chemical characters may be diverse. It was demonstrated that the optimal size range for the identification was 100–200 mesh based on the prediction performances of the models established respectively by the pulverized samples with different size ranges.

Fig. 1 indicates the raw NIRDRS of 37 samples of *Ephedra* plants.

3.2. Discrimination of Ephedra plants of different species

The NIRDRS of *Ephedra* plants of different species were processed first with smoothing techniques. The five-point Norris smoothing was used in the DA and the seven-point Savitzky–Golay smoothing in the ANN. The methods for subsequent processing were first derivative and MSC. The dimensions of the spectral data were reduced to 9 principle components (PCs) for the DA and to 10 PCs for the ANN. The cumulative contribution rates of 9 and 10 PCs were 98.7% and 99.9% in sequence.

Ephedra plants of different species could be discriminated respectively with the DA, SOM and BP-ANN.

The performance index of the DA model was 84.2%. In Fig. 2, the calibration samples of *Ephedra* plants of three species are logically distributed with the DA in three corresponding spaces, not only two-dimensionally but also three-dimensionally.

The prediction accuracy of the SOM model was 95.0%. Fig. 3 displays the outcomes of the calibration and validation of the SOM model. *E. sinica*, *E. intermedia* and *E. equisetina* are successfully classified in three areas painted with light gray, gray and dark gray. The calibration and validation samples of *Ephedra* plants of three species are expressed by the capitals (A, B and C) and the lowercases (a, b and c), respectively. Although one "b", presenting one validation sample of *E. intermedia*, is located in one light gray block (8,8) describing *E. sinica*, the light gray block is adjacent to two gray blocks (7,8 and 8,9) describing *E. intermedia*.

This small discrimination error can be attributed to the operation error of the NIRDRS measurement and the different sizes of the

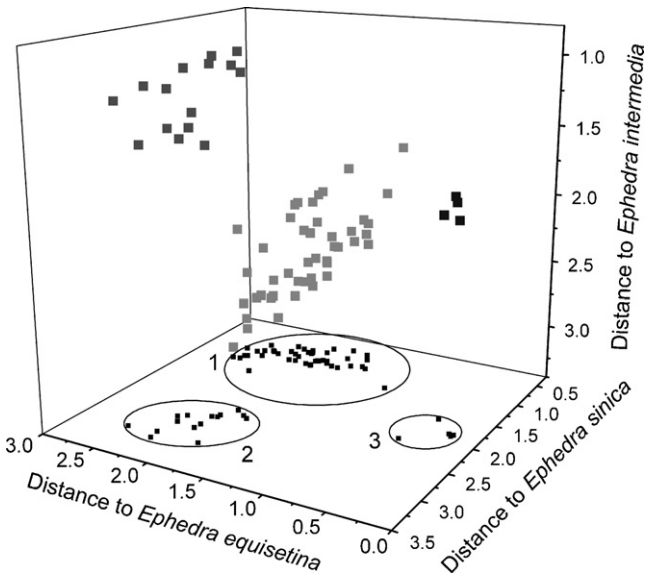


Fig. 2. Projection maps of the DA of the calibration samples of *Ephedra* plants of three species. *E. sinica*, *E. intermedia* and *E. equisetina* are respectively labeled by (1), (2) and (3) in the two-dimensional map, and represented with light gray, gray and dark gray spots in the three-dimensional map.

calibration sample sets of three subgroups, *E. sinica*, *E. intermedia* and *E. equisetina*.

In the NIRDRS measurement, the operations were mostly composed of the loading of the pulverized sample and the laying of the sample vial. The operation error should be taken into account in modeling to avoid erroneous discrimination. In this study, each pulverized sample was loaded and measured five times; all the five spectra were used in the analysis. When the operation error exceeded some scope, however, one out of the five spectra of one calibration sample would be identified mistakenly as one spectrum of another calibration sample in the same subgroup in the modeling. In the analysis of the validation and unknown samples, not only the same discrimination error as described above was existent, but also the spectrum would be identified mistakenly as a spectrum of a sample in another subgroup when the operation error exceeded the scope permitted in the analysis of the calibration samples in the same subgroup.

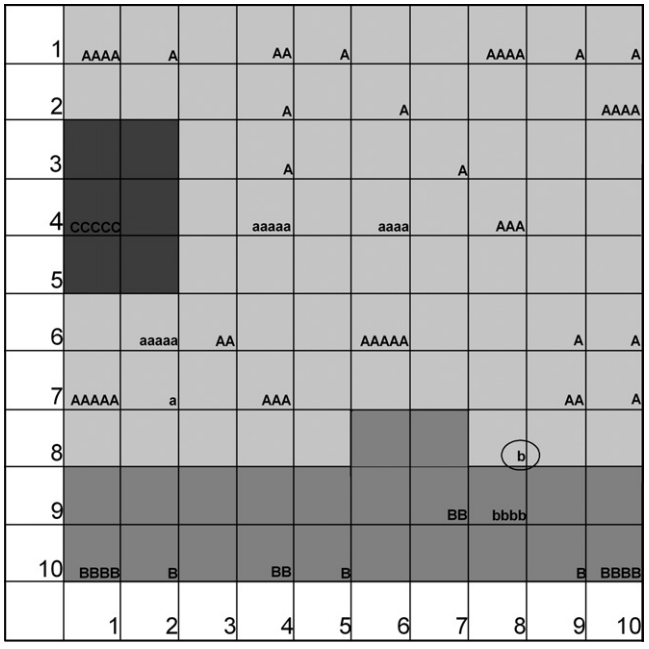


Fig. 3. Two-dimensional distribution map of *Ephedra* plants of three species in the output layer of the SOM (10 × 10): light gray blocks for *E. sinica* (A, a), gray for *E. intermedia* (B, b), and dark gray for *E. equisetina* (C, c); capitals (A, B, C) for calibration samples, and lowercases (a, b, c) for validation samples.

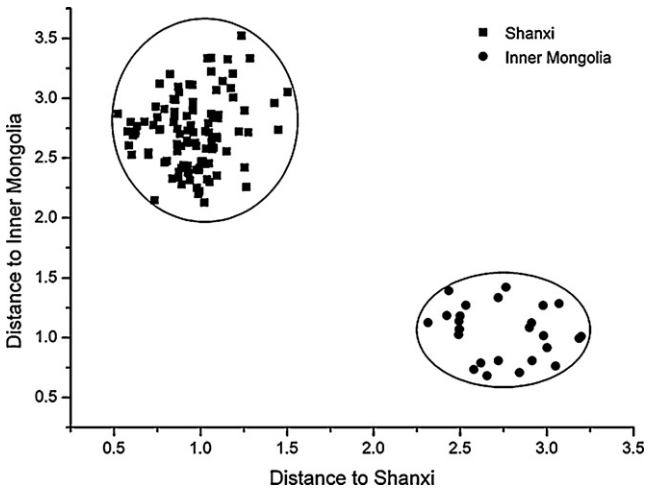


Fig. 4. Two-dimensional projection map of the DA of the calibration samples of *E. sinica* from Shanxi and Inner Mongolia.

Furthermore, the calibration sample set of *E. sinica* was the largest in the three subgroups, that is, the calibration sample set of *E. sinica* had the most diversity. Thus, one sample unused in the modeling would be identified as *E. sinica* most easily.

For the two reasons above, in Fig. 3, there are same letters of different numbers in only one block. The number is small when the variances among the samples and the operation errors are large. There is also one "b" in a light gray block.

The prediction accuracy of the BP-ANN model for the discrimination was 95.0% when the goal error between the training network output and the ideal output was defined as 10^{-5}.

3.3. Discrimination of E. sinica from different habitats

The NIRDRS of the samples of *E. sinica* from different habitats were processed by the five-point Savitzky–Golay smoothing technique and MSC. The dimensions of the spectral data were reduced to 10 PCs and the cumulative contribution rate was 99.8% for the three data analysis methods used.

E. sinica from different habitats could be identified respectively with the DA, SOM and BP-ANN.

The performance index of the DA model was 91.9%. Fig. 4 demonstrates that the DA assigns the calibration samples of *E. sinica* from Shanxi and Inner Mongolia into two separate two-dimensional zones.

The prediction accuracy of the SOM model was 100.0%. In the SOM distribution map (Fig. 5), the calibration and validation samples of *E. sinica* from two habitats are completely separated into two areas, marked respectively by light gray and gray, without any errors.

The prediction accuracy of the BP-ANN model was 100.0% when the goal error between the training network output and the ideal output was defined as 10^{-5}.

3.4. Discrimination of E. sinica from Shanxi picked at different times of day

The techniques of spectra processing and data pre-processing for this task were the same as those used in Section 3.3. Neverthe-

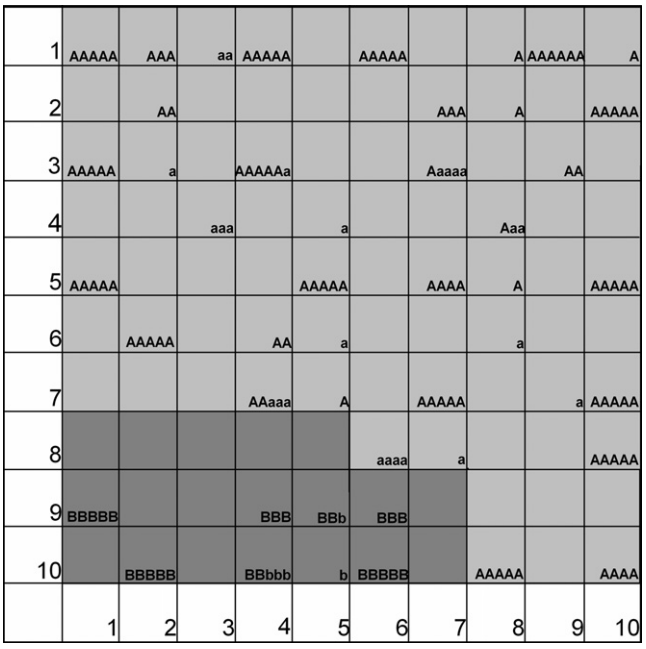


Fig. 5. Two-dimensional distribution map of *E. sinica* from two habitats in the output layer of the SOM (10 × 10): light gray blocks for Shanxi (A, a), and gray for Inner Mongolia (B, b); capitals (A, B) for calibration samples, and lowercases (a, b) for validation samples.

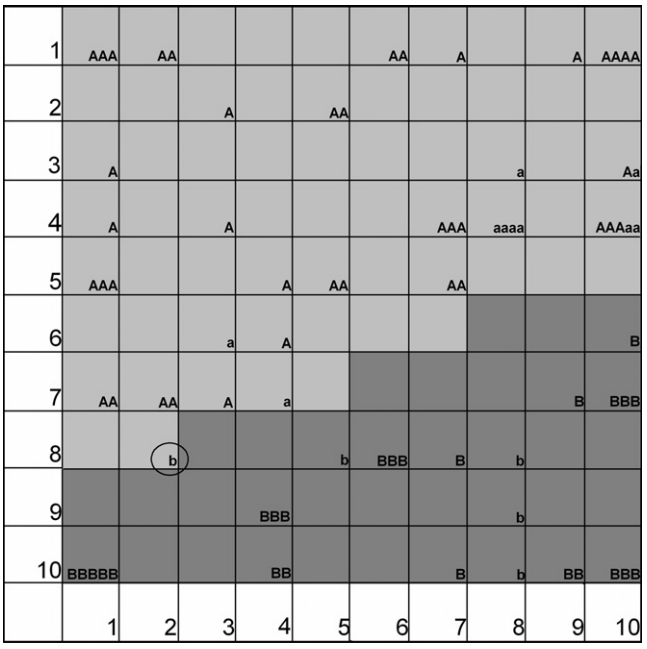


Fig. 7. Two-dimensional distribution map of *E. sinica* from Shanxi picked during two time sections in the output layer of the SOM (10 × 10): light gray blocks for 10:00–11:30 am (A, a), and gray for 4:30–5:00 pm (B, b); capitals (A, B) for calibration samples, and lowercases (a, b) for validation samples.

less, the cumulative contribution rate of 10 PCs was 99.7% for the three data analysis methods.

E. sinica from Shanxi picked at different times of day could be distinguished respectively with the DA, SOM and BP-ANN.

The performance index of the DA model was 88.1%. Fig. 6 describes that the DA reasonably divides the calibration samples of *E. sinica* from Shanxi picked in the morning and afternoon into two separate two-dimensional regions.

The prediction accuracy of the SOM model was 93.3%. The results of the calibration and validation of the SOM model are shown in Fig. 7. *E. sinica* from Shanxi picked during two time sections are readily separated into two areas painted with light gray and gray. The calibration and validation samples picked between 10:00 and 11:30 am and between 4:30 and 5:00 pm are indicated by the capitals (A and B) and the lowercases (a and b), respectively. In despite

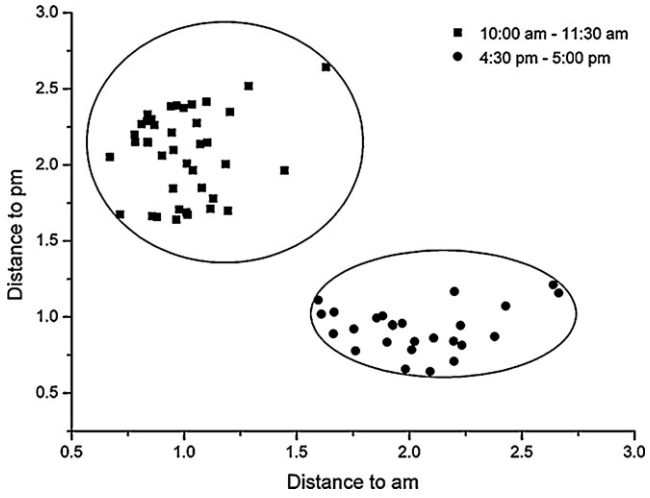


Fig. 6. Two-dimensional projection map of the DA of the calibration samples of *E. sinica* from Shanxi picked between 10:00 and 11:30 am and between 4:30 and 5:00 pm.

of the position of one "b", which describes one validation sample picked in the afternoon, is fixed in one light gray block (2,8) representing the sample picked in the morning, the light gray block is surrounded with two gray blocks (2,9 and 3,8) representing the samples picked in the afternoon. The reasons for the small discrimination error are similar to those in Fig. 3.

The prediction accuracy of the BP-ANN model for this task was 93.3% when the goal error between the training network output and the ideal output was defined as 10^{-5}.

The results obtained in this task suggest that there is significant difference between *E. sinica* picked in the morning and afternoon. This fact implies that the chemical components of *E. sinica* are modulated by time of day.

In all the three tasks, the prediction performances of the three models of the DA, SOM and BP-ANN for the discrimination of *E. sinica* from different habitats are the best. It can be explained by the following reasons. *E. sinica* from two habitats are distinguished more easily than *Ephedra* plants of three species because the exact probability of the discrimination of one sample in a group is larger between few subgroups than many subgroups. *E. sinica* from Shanxi and Inner Mongolia are also distinguished more easily than those from Shanxi picked during two time sections for the difference between the former is larger than the later.

The three multivariate analysis techniques adopted in the investigation are all valid. The best prediction performance and visualization function is achieved with the SOM.

4. Conclusions

The relationships between *Ephedra* plants and the NIRDRS have been established. The experiment has proved that *Ephedra* plants of different species, habitats and picking times can be reliably discriminated by diffuse reflectance FT-NIRS combined with multivariate analysis techniques without special sample treatment and the use of chemicals. The approach established is a useful tool for the research of phytoecology of *Ephedra* and the utilization of *Ephedra* plants. The discrimination between the plants picked in the morn-

ing and afternoon is the most notable because it infers that the chemical components of *E. sinica* are modulated by time of day. The prediction performance and visualization function of the SOM model are the best among the DA, SOM and BP-ANN.

In this experiment, each pulverized sample was loaded and measured repeatedly. All the spectra obtained from the calibration samples were used in the modeling. This strategy can reduce the impacts of the operation error on the identification and improve the prediction performances of the models established because it increases the representative spectra used in the modeling.

Acknowledgements

We are grateful for the support of the Municipal Science and Technology Committee of Chongqing through a grant from the "*Natural Science*" program (2006BB5303).

References

[1] S. Caveney, D.A. Charlet, H. Freitag, M. Maier-Stolte, A.N. Starratt, Am. J. Bot. 88 (2001) 1199–1208.
[2] Q. Wang, Y. Yang, X. Zhao, B. Zhu, P. Nan, J. Zhao, L. Wang, F. Chen, Z. Liu, Y. Zhong, Food Chem. 98 (1) (2006) 52–58.
[3] N. Kondo, M. Mikage, K. Idaka, Nat. Med. 54 (5) (2000) 241–246.
[4] M. Wink, Phytochemistry 64 (1) (2003) 3–19.
[5] W.J. Foley, B.D. Moore, Curr. Opin. Plant Biol. 8 (4) (2005) 430–435.
[6] R. Mithen, A.F. Raybould, A. Giamoustaris, Heredity 75 (1995) 472–484.
[7] J.L. Huang, D.E. Giannasi, R.A. Price, Mol. Phylogenet. Evol. 35 (2005) 48–59.
[8] J. Zhao, L.C. Davis, R. Verpoorte, Biotechnol. Adv. 23 (4) (2005) 283–333.
[9] L. Poll, M.B. Petersen, G.S. Nielsen, Eur. Food Res. Technol. 216 (2003) 212–216.
[10] A. Gurib-Fakim, Mol. Aspects Med. 27 (1) (2006) 1–93.
[11] I. Raskin, D.M. Ribnicky, S. Komarnytsky, N. Ilic, A. Poulev, N. Borisjuk, A. Brinker, D.A. Moreno, C. Ripoll, N. Yakoby, J.M. O'Neal, T. Cornwell, I. Pastor, B. Fridlender, Trends Biotechnol. 20 (12) (2002) 522–531.
[12] M.R. Tellez, I.A. Khan, B.T. Schaneberg, S.L. Crockett, A.M. Rimando, M. Kobaisy, J. Chromatogr. A 1025 (1) (2004) 51–56.
[13] Chinese Pharmacopoeia Commission, Pharmacopoeia of the People's Republic of China, vol. I, Chemical Industry Press, Beijing, 2005, pp. 223–224.
[14] The Society of Japanese Pharmacopoeia, Japanese Pharmacopoeia, vol. II, fourteenth ed., Labour and Welfare of Japan, Tokyo, 2001, p. 914.
[15] M. Otto, Chemometrics, Science Press, Beijing, 2003.
[16] J. Gasteiger, T. Engel, Chemoinformatics, Chemical Industry Press, Beijing, 2005.
[17] J. Moros, M.J. Martínez-Sánchez, C. Pérez-Sirvent, S. Garrigues, M. de la Guardia, Talanta 78 (2) (2009) 388–398.
[18] E.D. Teles Moreira, M.J. Coelho Pontes, R.K. Harrop Galvão, M.C. Ugulino Araújo, Talanta 79 (5) (2009) 1260–1264.
[19] D. Christensen, M. Allesø, I. Rosenkrands, J. Rantanen, C. Foged, E.M. Agger, P. Andersen, H.M. Nielsen, Eur. J. Pharm. Biopharm. 70 (3) (2008) 914–920.
[20] I. González-Martín, C. González-Pérez, J.M. Hernández-Hierro, J.M. González-Cabrera, Talanta 75 (2) (2008) 351–355.
[21] L.O. Rodrigues, L. Vieira, J.P. Cardoso, J.C. Menezes, Talanta 75 (5) (2008) 1356–1361.
[22] M.T. Sánchez, D. Pérez-Marín, K. Flores-Rojas, J.E. Guerrero, A. Garrido-Varo, Talanta 78 (2) (2009) 530–536.
[23] Y.N. Shao, Y. He, Y.Y. Wang, Eur. Food Res. Technol. 224 (2007) 591–596.
[24] S.S. Rosa, P.A. Barata, J.M. Martins, J.C. Menezes, Talanta 75 (3) (2008) 725–733.
[25] P. Baptista, P. Felizardo, J.C. Menezes, M.J. Neiva Correia, Talanta 77 (1) (2008) 144–151.
[26] H. Yang, J. Irudayaraj, J. Am. Oil. Chem. Soc. 78 (9) (2001) 889–895.
[27] M. Watari, Y.P. Du, Y. Ozaki, Appl. Spectrosc. 61 (4) (2007) 397–405.
[28] L. Xu, Y.P. Zhou, L.J. Tang, H.L. Wu, J.H. Jiang, G.L. Shen, R.Q. Yu, Anal. Chim. Acta 616 (2008) 138–143.
[29] P.A. Lachenbruch, M. Goldstein, Biometrics 35 (1979) 69–85.

Talanta 80 (2010) 1251–1256

Contents lists available at ScienceDirect

Talanta

journal homepage: www.elsevier.com/locate/talanta

A highly sensitive HPLC method with automated on-line sample pre-treatment and fluorescence detection for determination of reboxetine in human plasma

Nasr Y. Khalil*

Department of Pharmaceutical Chemistry, College of Pharmacy, King Saud University, P.O. Box 2457, Riyadh 11451, Saudi Arabia

ARTICLE INFO

Article history:
Received 2 May 2009
Received in revised form 8 September 2009
Accepted 10 September 2009
Available online 13 September 2009

Keywords:
Reboxetine
NBD-F
HPLC
Co-sense
Fluorescence detection
Plasma

ABSTRACT

A fully automated, rapid and highly sensitive HPLC method with automated sample pre-treatment by column-switching system and fluorescence detection has been developed for the trace quantitative determination of the new antidepressant reboxetine (RBX) in human plasma. A simple pre-column derivatization procedure with 7-flouro-4-nitrobenzo-2-oxa-1,3-diazole (NBD-F) reagent was employed. Paroxetine (PXT) was used as an internal standard. Plasma samples containing both RBX and PXT, after filtration, were derivatized by heating with NBD-F in borate buffer of pH 8 at 70 °C for 30 min. The derivatized plasma samples were injected into the HPLC system where an on-line sample clean up was achieved on the pre-treatment column (Co-sense Shim-pack MAYI-ODS) with a washing mobile phase (acetonitrile:2% acetic acid; 40:60, v/v) at a flow rate of 5 mL min^{-1} for 1 min. After an automated on-line column switching to the analytical Hypersil phenyl 120A column (250 mm × 4.6 mm, 5 μm), the separation of the derivatized RBX and PXT was performed using a mobile phase consisting of sodium acetate buffer (pH 3.5):tetrahydrofuran:acetonitrile (55:35:10, v/v/v) at a flow rate of 2.0 mL min^{-1}. The eluted derivatives were monitored by a fluorescence detector set at an excitation wavelength of 470 nm and an emission wavelength of 530 nm. Under the optimum chromatographic conditions, a linear relationship with good correlation coefficient ($r = 0.9995$, $n = 5$) was found between the peak area ratio of RBX to PXT and RBX concentration in the range of 2–500 ng mL^{-1}, with limits of detection and quantification of 0.5 and 1.7 ng mL^{-1}, respectively. The intra- and inter-day precisions were satisfactory; the relative standard deviations were 2.25 and 3.01% for the intra- and inter-day precisions, respectively. The accuracy of the method proved as the mean recovery values were 100.11 ± 2.24% and 100.99 ± 2.98% for the intra- and inter-day assay runs, respectively. The proposed method involved simple and minimum sample preparation procedure and short run-time (<12 min) and therefore it can be applied to the routine therapeutic monitoring and pharmacokinetic studies of RBX.

© 2009 Elsevier B.V. All rights reserved.

1. Introduction

Reboxetine (RBX); (RS)-2-[(RS)-α-(2-ethoxyphenoxy) benzyl-morpholine methane sulphonate, was first introduced in 1997 as the first drug of the new selective noradrenalin reuptake inhibitor (SNRI) antidepressant class [1]. It has similar therapeutic potency to tricyclic antidepressants [2,3]. The drug does not affect dopamine or serotonin reuptake, and it has low affinity for adrenergic, cholinergic, histaminergic, dopaminergic and serotonergic receptors [4]. RBX provides an alternative rational for patients resistant to the conventional antidepressants therapy with an advantage of significantly improved adverse effects profile [5,6]. In contrast to certain serotonergic drugs, there is no evidence of any withdrawal syndrome upon sudden discontinuation or tapering of RBX therapy [7]. RBX is also prescribed in the treatment of narcolepsy [8], panic disorders [9], and Parkinson's disease [10]. RBX is rapidly and extensively absorbed following oral administration. The maximum plasma concentration is achieved within 2–2.5 h after a 4 mg oral dose; and it is highly bound (~98%) to plasma proteins mainly α1-acid glycoprotein [11]. It is eliminated mainly via urine with a relatively short elimination half-life (~13 h), therefore it is given twice daily [12].

Most psychiatric patients are usually subjected to simultaneous poly-pharmacotherapy to achieve successful control of the symptoms. Therefore, careful monitoring and subsequent optimization of dosing regimen of potent drugs, such as RBX, in the plasma of the patients are extremely necessary. Because of the small doses of RBX, its concentrations in plasma samples are expected to be quite low [11]. For these reasons, a sensitive, selective, and accessible method is required for quantitative determination of RBX in plasma. Considerable efforts have been made to provide competent analytical techniques for the determination of RBX in plasma.

* Tel.: +966 14679841; fax: +966 14676220.
E-mail address: nasrykhalil@hotmail.com.

0039-9140/$ – see front matter © 2009 Elsevier B.V. All rights reserved.
doi:10.1016/j.talanta.2009.09.010

These techniques include two related gas chromatography with mass detector [13,14], and several HPLC methods with UV or fluorescence [15–21], mass [22,23] and tandem mass [24] detectors. All these methods involved lengthy liquid–liquid or solid-phase extraction for RBX from the plasma samples prior to their analysis. Indeed, these pre-treatment procedures are cumbersome and time-consuming. They will also lead to large amount of errors in the recovery of RBX. Accordingly, these methods do not meet the needs of pharmacokinetic studies, which require an accurate and rapid feedback for the analytical information of pre-clinical and clinical specimens. Moreover, the cost and complexity of the instrumentation of HPLC–MS limited its applications in clinical laboratories.

The present work describes, for the first time, the development of a new automated highly sensitive and accurate HPLC method with fluorescence detection for the determination of RBX in plasma. The method involved a pre-column derivatization with 7-fluoro-4-nitrobenzo-2-oxa-1,3-dizole (NBD-F), and an automated highly efficient on-line pre-treatment procedure by using a bio-sample analysis column-switching system (co-sense for BA) equipped with a Shim-pack MAYI-ODS bio-sample pre-treatment column. The method was successfully applied to the determination of RBX in spiked human plasma samples.

2. Experimental

2.1. Chemicals and materials

Reboxetine (RBX) and 7-flouro-4-nitrobenzo-2-oxa-1,3-diazole (NBD-F) were purchased from Sigma Chemical Co. (St. Louis, MO, USA). Paroxetine (PXT) was obtained from SmithKline Beecham Pharmaceuticals (Brentford, England). Human plasma samples were collected from normal healthy volunteers at King Khaled University Hospital (Riyadh, Saudi Arabia), and they were kept frozen at −20 °C until analysis. Acetonitrile, tetrahydrofuran and all the other solvents were of HPLC grade (Merck, Darmstadt, Germany). All other materials were of analytical grade.

2.2. Preparation of stock solutions

2.2.1. Reboxetine (RBX) and paroxetine (PXT) standard solutions

An accurately weighed amount (10 mg) of each of RBX and PXT was quantitatively transferred into a 10-mL volumetric flask, dissolved in distilled water, and completed to volume with the same solvent to produce stock solutions of 1 mg mL^{-1}. The stock solutions were further diluted with water to obtain working standard solutions containing 2000 ng mL^{-1} and 400 ng mL^{-1} for RBX and PXT, respectively.

2.2.2. 7-Fluoro-4-nitrobenzo-2-oxa-1,3-diazole (NBD-F) derivatizing reagent

An accurately weighed amount (5 mg) of NBD-F was transferred into a 10-mL volumetric flask, dissolved in 10 mL acetonitrile, completed to volume with the same solvent to produce a stock solution of 0.05% (w/v). The solution was freshly prepared and protected from light during use.

2.2.3. Borate buffer solution

Weighed amounts of boric acid (0.62 g) and potassium chloride (0.75 g) were dissolved in 100 mL distilled water. A volume of 4.0 mL of 0.2 mol L^{-1} NaOH and 40 mL of ethanol were added and the mixture was diluted to 200 mL with distilled water. The pH of the solution was adjusted to 8 ± 0.1 by a calibrated pH-meter (Microprocessor pH meter BT-500, Boeco, Germany).

2.3. Chromatographic system

HPLC apparatus consisted of a Shimadzu system (Shimadzu Corporation, Kyoto, Japan) equipped with two solvent delivery systems (LC-20AD VP) with FCV-12AH high-pressure flow channel changeover valve, DGU-20AS on-line degasser, SIL-20A auto-sampler, co-sense BA LC system, CTO-20A column oven, SPD-20A UV–vis detector, SPD-M20A photodiode-array detector, RF-10A XL fluorescence detector, and CBM-20A system controller. The pre-treatment column was a Shim-pack MAY1-ODS (10 mm length × 4.6 mm i.d., 12 nm pore diameter, and 50 μm particle diameter). The chromatographic separations were performed on an analytical column Hypersil 120A (250 mm length × 4.6 mm i.d., 5 μm particle diameter) manufactured by Phenomenex (USA). The column temperature was kept constant at 25 ± 2 °C. Separations were performed in isocratic mode. The pre-treatment mobile phase consisted of acetonitrile:2% acetic acid (40:60, v/v) pumped for 1 min at a flow rate of 5 mL min^{-1}. The analytical mobile phase used for the separation consisted of 10 mmol L^{-1} sodium acetate buffer (pH 3.5):tetrahydrofuran:acetonitrile (55:35:10, v/v/v) pumped at flow rate of 2.0 mL min^{-1}. The mobile phases were filtered by a Millipore vacuum filteration system equipped with a 0.45 μm pore size filter, degassed by ultrasonication, and further by passing through the DGU-20AS on-line degasser. The samples (50 μL each) were injected by the aid of the auto-sampler. The fluorescence detector was set at 470 nm as an excitation wavelength and 530 nm as an emission wavelength. The system control and data acquisition were performed by Shimadzu "LC solution" software (Shimadzu Corporation, Kyoto, Japan). The ratio of peak area of RBX to that of the internal standard (paroxetine; PXT) was used for the quantitation.

2.4. Sample preparation, derivatization and quantitation

The stock solutions of RBX and PXT were brought to room temperature, and working stock solutions of RBX (2000 ng mL^{-1}) and PXT (400 ng mL^{-1}) were prepared. The calibration standard samples were prepared by spiking blank human plasma with RBX to yield concentrations of 0, 2, 5, 10, 20, 50, 100, and 500 ng mL^{-1}. The spiked plasma sample was filtered through a 0.45 μm pore size Millipore filter or mixed with an equal volume of acetonitrile, vortexed for 30 s, and centrifuged for 20 min at 13,000 rpm by Biofuge Pico centrifuge (Heraeus Instruments, Germany). A 500 μL of the filterate (or the supernatant solution) was transferred into a screw-capped reaction tube using a micropipette followed by 200 μL of the working solutions of the internal standard (PXT), 1000 μL of the borate buffer solution, and 200 μL of the NBD-F solution. The tube was capped, swirled, and left to stand in a thermostatically controlled water-bath (MLW type, Memmert GmbH, Co. Schwa Bach, Germany) at 70 °C for 30 min. After cooling the tube rapidly to room temperature, a volume of 100 μL of HCl was added, mixed, and 50 μL of the resulting solution was injected into the HPLC system with the aid of the auto-sampler. The calibration curve was constructed by plotting the peak area ratio of RBX to PXT versus the concentration of RBX. The data were analyzed by least square regression and the intercept, slope, and correlation coefficient were calculated. The linear regression equation was used for calculating the concentrations of RBX in the spiked plasma samples based on their peak area ratios.

3. Results and discussion

3.1. Design and strategy for the method development

Reboxetine molecule contains weak chromophoric activity, and does not have a native fluorescence, therefore the determination

of its low concentrations in plasma by HPLC using UV or fluorescence detectors was not possible without pre-derivatization. The previously reported HPLC methods for the determination of RBX after its pre-derivatization suffered from inadequate sensitivity, and the multiple tedious liquid–liquid or solid-phase extraction procedures. The use of MS and/or MS–MS detectors overcome the sensitivity problem, however no doubt the sensitivity achieved by these expensive detectors did not compensate their high cost, and instrumental complexity. For these reasons, the present work was directed towards the development of a new highly sensitive HPLC method employing a non-extractive automated pre-treatment procedure with column-switching system.

In our previous studies [25,26], we described non-extractive pre-treatment procedures prior to HPLC analysis of some therapeutic amines in plasma samples after pre-column derivatization with the 7-chloro-4-nitrobenzo-2-oxa-1,3-diazole (NBD-Cl), the chloro analogue of NBD-F. The methods offered adequate sensitivity, however the rapid elution of massive amounts of derivatized polar biogenic amines was problematic, as special care was necessary to achieve good resolution between the peaks of the analytes and those of the derivatized plasma endogenous amines. Therefore, the present study was devoted to overcome such problems by using a special configuration setup composed of a co-sense system equipped with a pre-treatment Shim-pack MAYI-ODS column. The Shim-pack MAYI-ODS column is an inner surface type reversed-phase packing material [27–30]. As well, it has the ability to trap the low molecular weight compounds like most of the drugs while allowing the high molecular size plasma proteins to be washed out to the waste by size exclusion mechanism.

RBX doses are small, thus its concentrations in plasma are expected to be very low, and consequently highly fluorogenic derivatizing reagent was required prior to its fluorescence-based HPLC analysis. RBX contains a piprazinyl NH group, which was proved to react with NBD-Cl giving a fluorescent aduct [26]. However, NBD-F is known to be several times more reactive than NBD-Cl. Therefore, the present study was devoted to investigate NBD-F as a derivatizing reagent for RBX. The preliminary investigations in this study revealed the high reactivity of RBX with NBD-F, and the produced RBX-NBD derivative was found to be highly fluorescent, and exhibited its highest fluorescence intensity at 530 nm after excitation at 470 nm. For these reasons, it is anticipated that the employment of NBD-F as a derivatizing reagent for RBX (for the first time in this study) would lead to the development of highly sensitive assay. Fig. 1 presents the scheme of the reaction of both RBX and PXT (internal standard) with NBD-F.

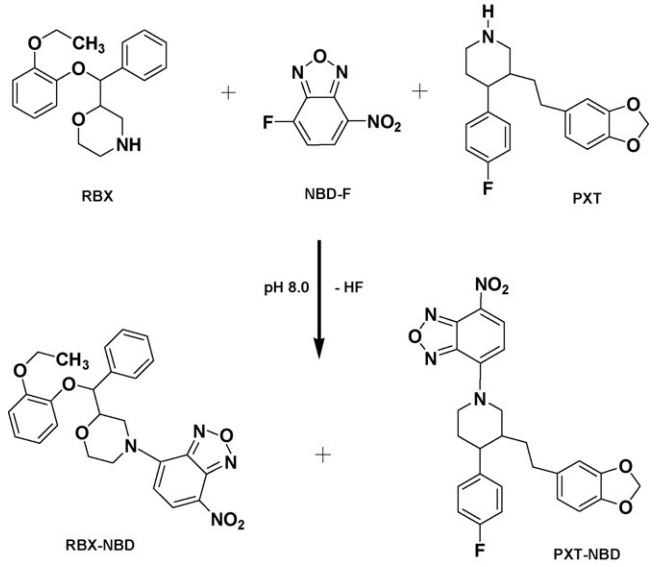


Fig. 1. A scheme for the reaction of RBX and PXT with NBD-F.

3.2. Optimization of the derivatization reaction conditions

The different experimental conditions (concentration of NBD-F, pH of the reaction medium, reaction time, and temperature) affecting the derivatization reaction were thoroughly investigated. The experiments were initiated with studying the effect of the NBD-F reagent concentration. Owing to the presence of labile fluoride in the chemical structure of NBD-F, a daily fresh solution is recommended. In order to select the optimum NBD-F concentration, the reaction was carried out using varying concentrations (0.01–1%, w/v) of NBD-F reagent. The maximum detector signal was obtained when the concentration of NBD-F reagent was 0.05% (w/v), therefore this concentration was used in all the subsequent experiments. The reaction was found to proceed satisfactorily in 0.1 mol L^{-1} borate buffer of pH 8.0 ± 0.1. The reaction was found to go to completion by heating the solution for 30 min in a water-bath at 70 °C. Under these conditions, significantly high background fluorescence was observed. This was attributed to the hydrolysis of NBD-F to the corresponding hydroxy derivative namely, 7-hydroxy-4-nitrobenzo-2-oxa-1,3-diazole (NBD-OH). This background fluorescence of NBD-OH was fortunately found to be quenched by decreasing the pH of the reaction medium to less than one [31]. Therefore, acidification of the reaction mixture by adding 100 μL of HCl prior to the injection into the HPLC system was necessary. This remarkably decreased the background signal without affecting the reaction product, thus increased the sensitivity. The stability of the derivatized RBX was investigated by repeated injections from the same reaction mixtures at different time intervals over a period of forty-eight hrs. No significant variation in the peak area values was observed, indicating the stability of RBX-NBD for at least 2 days at room temperature.

3.3. Optimization of chromatographic system

3.3.1. Pre-treatment phase

The outer surface of the packing material (silica gel) of the pre-treatment column (Shim-pack MAYI-ODS) is coated with a water-soluble polymer. The inner surfaces of the silica pores are chemically bonded with octadecylsilane (ODS) groups. Therefore, the column is an internal reversed-phase with a hydrophilic polymer coating, constructed as shown in Fig. 2A. Proteins and other macromolecules are blocked by the hydrophilic polymer coating and cannot enter the micropores. Instead, they pass out of the pre-treatment column through the particles and directly to the waste. On the other hand, the small RBX molecules penetrate into the micropores, where they are trapped in the stationary phase. Consequently, the column selectively excludes macromolecules such as proteins. In the conventional HPLC procedures, such proteins are eliminated before the analysis by adding a protein-precipitating reagent (e.g., organic solvent or acid) followed by the separation of the proteins by centrifugation. As well, solid-phase or liquid–liquid extraction procedures for small analytes may also be necessary. This manual process complicates the operations and may lower the analysis accuracy, therefore an automatic deproteinization process is desirable. In the system described herein, the pre-filtered derivatized plasma was directly injected into the system, transported by the pre-treatment mobile phase to the Shim-pack MAYI-ODS pre-treatment column where the free or derivatized endogenous plasma proteins are washed out. In general, the pre-treatment process usually increases the overall analysis time depending on the length of time selected for washing. In the present study, washing time of 2 min at a flow rate of 2.5 mL min^{-1} or 1 min at a

flow rate of 5 mL min^{-1} was similarly adequate, and accordingly the later settings were selected before the column-switching to the analytical column. The 50-μm silica gel based particles keep the maximum operating pressure inside the pre-treatment column as low as 20 MPa, ensuring high durability. This is advantageous against pressure fluctuations due to flow-path switching or gradient analysis. In the present study, the pressure was approximately 8 MPa when the flow rate of the pre-treatment mobile phase was 5 mL min^{-1}.

3.3.2. Analytical phase

After the pre-selected period of washing, the high-pressure flow channel selection valve is rearranged in a way that the analytical mobile phase passes through the pre-treatment column in the reverse direction thus pushing the derivatized RBX, trapped in the Shim-pack MAYI-ODS column, into the analytical column for separation and subsequent detection. This is shown in Fig. 2B. The isocratic separation of RBX and PTX (IS) was investigated by changing the composition of the mobile phase. Several experiments have shown that the employment of an appropriate ratio of sodium acetate buffer solution in organic solvent (acetonitrile) improved the shape and the resolution of the chromatographic peaks. Different ratios of sodium acetate and organic solvents in the mobile phase were tested. Good separation was achieved when the ratio of aqueous sodium acetate:acetonitrile was 55:45% (v/v). Better separations were achieved when acetonitrile was gradually replaced by tetrahydrofuran, and the best separation was achieved when the mobile phase composed of sodium acetate:tetrahydrofuran:acetonitrile (55:35:10, v/v/v), and the flow rate was 2 mL min^{-1}. It was found that the shape and symmetry of the chromatographic peaks of both RBX and PXT were affected by the concentration and pH of the sodium acetate buffer, and the best results were obtained when the concentration was 10 mmol L^{-1}, adjusted to pH 3.5 with acetic acid. Different analytical columns were tested; these columns were reversed-phase C18, amino-, cyano-, and phenyl-columns. The best results were achieved when phenyl column (with the specifications given in Section 2) was used. The obtained chromatographic parameters and performance data for RBX and PXT are presented in Table 1. Experiments conducted without pre-treatment (i.e., using non-co-sense mode) resulted in poor quality chromatograms with high background signal from the derivatizing reagent. More important finding is the appearance of interfering peaks from plasma endogenous amines just prior to and after the RBX peak (Fig. 3A). Under the same chromatographic conditions, the use of co-sense mode resulted in symmetrical and well-resolved peaks (Fig. 3B). The run-time was less than 12 min, with retention times of 7.6 and 9.4 min for RBX and PXT, respectively. The small increase noticed in the retention times in the later case is of course due the pre-selected washing time.

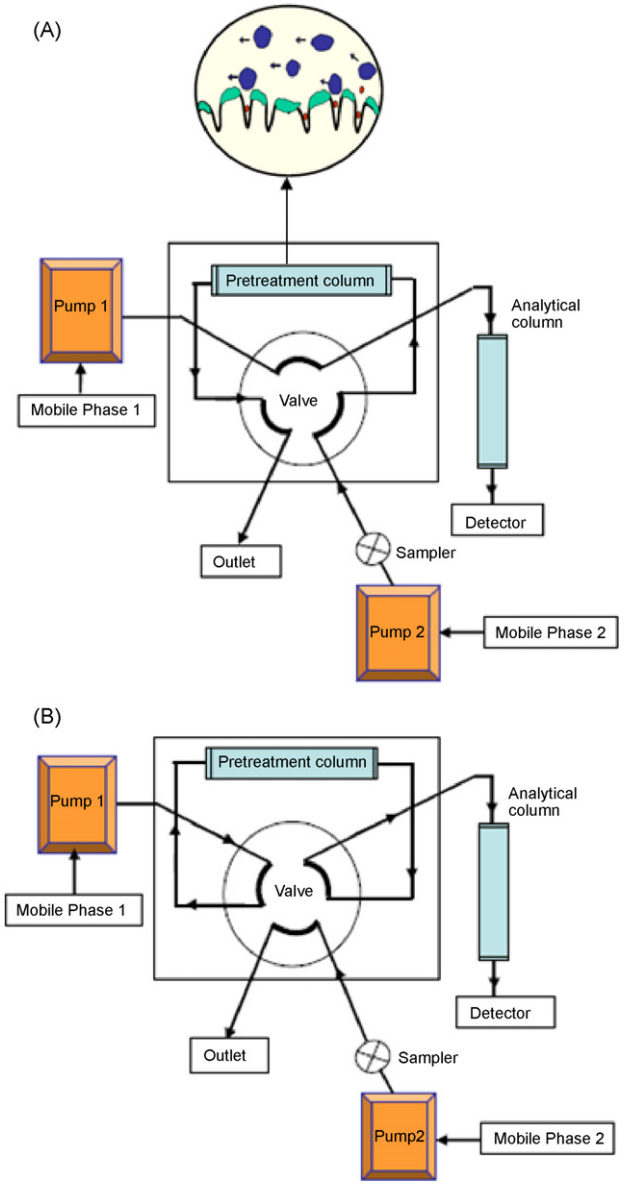


Fig. 2. Washing (A) and analytical (B) phases of the proposed HPLC method. Panel (A) shows a flow diagram for the co-sense system before column switching; pathways of the analytical and washing mobile phases are separated. The washing mobile phase takes the sample from the auto-sampler through the pre-treatment column to the waste. Panel (B) shows a flow diagram for the system after column switching; the analytical mobile phase takes the trapped drugs from the pre-treatment column, in the reverse direction, to the analytical column. Mobile phase 1 is the analytical mobile phase, while mobile phase 2 is the washing mobile phase: ( ) protein; ( ) drug; ( ) water-soluble polymer; ( ) ODS layer.

Table 1
Chromatographic parameters and performance data of the proposed HPLC method for determination of RBX in plasma.

Parameter	Value
Retention time for RBX (min)	7.6
Retention time for PXT (min)	9.4
Capacity factor (k') for RBX	3.44
Resolution between RBX and PXT peaks	3.16
RBX peak asymmetry factor at 10% peak height	1.28
Number of theoretical plates (N)	2602
Height equivalent to theoretical plate (μm)	96
Correlation coefficient	0.9995
Slope (b)±SD	0.0264 ± 0.0003
Intercept (a)±SD	0.0044 ± 0.007
Linearity range (ng mL^{-1})	2–500
LOD (ng mL^{-1})	0.5
LOQ (ng mL^{-1})	1.7

3.4. Validation of the method

3.4.1. Selectivity, linearity, and sensitivity

The selectivity of the method was evaluated by conducting the experiments using batches of blank human plasma to identify the peaks due to the unreacted reagent and the derivatized biogenic plasma components. The typical chromatograms obtained from using the blank plasma spiked with 8 ng mL^{-1} of internal standard (PXT) and plasma spiked with the same concentration of PXT together with RBX (2 and 20 ng mL^{-1}) analyzed without pre-treatment by the co-sense system are given in Fig. 3A. The same

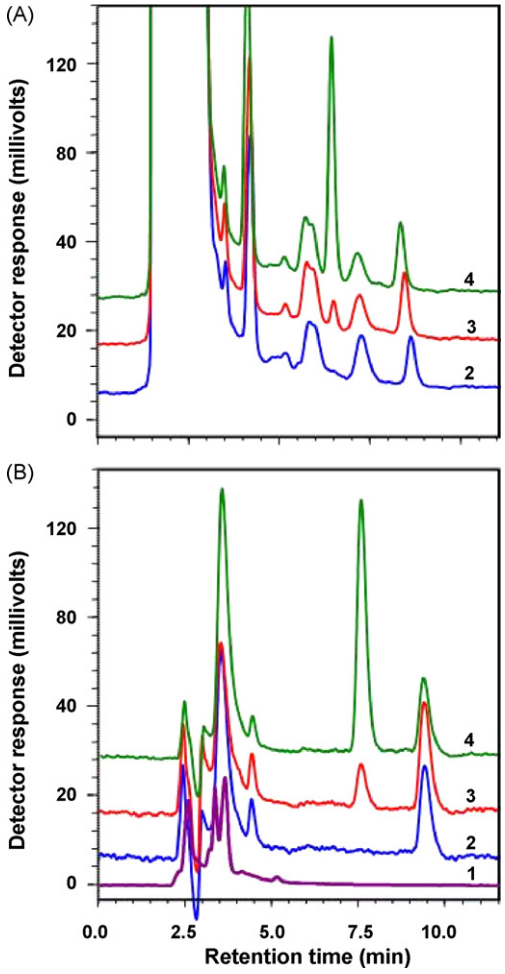


Fig. 3. Typical chromatograms obtained without the use of co-sense mode (A), and those obtained using the co-sense mode (B). Chromtaograms of unspiked blank plasma (chromatogram 1); chromtaograms of plasma spiked with the internal standard PXT, 8 ng mL^{-1} (chromatogram 2); plasma sample spiked with PXT, 8 ng mL^{-1} and RBX, 2 ng mL^{-1} (chromatogram 3) and plasma sample spiked with PXT, 8 ng mL^{-1} and RBX, 20 ng mL^{-1} (chromatogram 4).

experiments in addition to an unspiked blank plasma sample were repeated using the proposed method with employment of the on-line pre-treatment co-sense system; the chromatograms are given in Fig. 3B. Obviously, with employment of the co-sense system in the second case, complete separation of RBX and PXT peaks from those due to the reagent and endogenous plasma constituents was achieved. These results confirm the efficiency of the co-sense system in the pre-treatment of plasma samples.

Under the optimized conditions, linear relationship with good correlation coefficient ($r = 0.9995$, $n = 5$) was found between the peak area ratio of RBX to PXT versus RBX concentration in the range of 2–500 ng mL^{-1}. The regression equation of the calibration curve obtained was $Y = 0.0044 \pm 0.007 + 0.0264 \pm 0.0003X$; where X and Y are the RBX concentration and detector signal, respectively. The limit of detection (LOD) and limit of quantification (LOQ) were calculated according to the ICH guidelines for the validation of analytical procedure [32]. The calculation was based on the standard deviation of the intercept and the slope of the calibration curve using the formula: LOD or LOQ = $\kappa\sigma/S$, where $\kappa = 3.3$ for LOD and 10 for LOQ, σ is the standard deviation of the intercept, and S is the slope of the calibration curve. LOD and LOQ were found to be 0.5 and 1.7 ng mL^{-1}, respectively. These small values of LOD and LOQ confirmed the high sensitivity of the proposed method.

3.4.2. Precision and accuracy

Intra-day precisions were studied at three concentration levels (2, 50, and 100 ng mL^{-1}) of RBX and 40 ng mL^{-1} of PXT (IS). Repeated aliquots were prepared for each concentration level. The spiked plasma samples were derivatized according to the general procedure and analyzed by the proposed method. The mean recovery value was found to be 99.76% with RSD of 0.45%. The inter-day precision was carried out on three RBX concentration levels (5, 100 and 500 ng mL^{-1}) and 40 ng mL^{-1} of PXT on 4 different days. The mean recovery value was found to be 98.36% with RSD of 1.44%. Obviously, the small values of RSD confirmed the high precision of the proposed method.

Similarly, the accuracy of the proposed method was determined by the recovery studies of RBX from plasma samples spiked with different concentrations of RBX covering the linear range of the method; all samples were spiked with 40 ng mL^{-1} of PXT (IS). The samples were subjected to the analysis by the proposed method within a single day (intra-day) and on 4 different days (inter-day). The ratios of RBX peak area to PXT peak area versus the concentration of RBX were then interpolated from the linear regression equation. The recovery values (presented as percentages) were calculated using the formula: calculated experimental concentration/nominal concentration $\times$ 100. The mean recovery values were found to be $100.11 \pm 2.24\%$ and $100.99 \pm 2.98\%$ from intra-day and inter-day analysis, respectively, indicating the accuracy of the proposed method (Table 2).

3.4.3. Robustness and ruggedness

In order to measure the extent of the method robustness, some of the critical reaction conditions as well as the chromatographic parameters were changed while keeping the other parameters unchanged. The changes made were within the range of 1–10% of the optimum recommended conditions. The studied parameters included the pH of the reaction medium, the temperature and time of the derivatization reaction, the composition of the mobile phase, percentage of tetrahydrofuran and acetonitrile, concentration and pH of sodium acetate buffer. The chromatographic profile including capacity factor (k'), retention time (Rt), peak symmetry, resolution and column efficiency was calculated and compared to those of the system suitability (Table 1). The results revealed that the method was robust for these small changes and the results were not significantly different.

The ruggedness of the method was evaluated by applying the recommended analytical procedures on the same HPLC system (independently on different days) on the analysis of series of spiked plasma samples. The results obtained were comparable indicating the ruggedness of the method.

3.4.4. Sample carry-over

Sample carry-over is a major problem, which may significantly affect the accuracy and precision of different HPLC methods for bioanalysis. It is usually caused by the residual analyte from a sample analyzed earlier in the analysis run. It does not necessarily involve only the next sample in the sequence but it can affect several samples analyzed later on a sequence. Carry-over from analyte residues can occur via dislodgment from a sample's flow-path (including injection loops, auto-sampler needles and seals, switching valves, connection tubings, and columns) through a chromatographic system. Adsorption of basic and hydrophobic compounds to the sampling needles and rotor seals of the auto-samplers may also be another cause of carry-over problems. The effect is more likely to be in the systems involving pre-treatment for the sample and subsequent column-switching. In such systems, the mobile phase used to flush the sample from the sample loop into the pre-treatment column is usually polar and poor in organic solvent. This is necessary to help washing out the plasma constituents while the drug

Table 2
Intra-day and inter-day recovery of RBX from spiked human plasma.

Intra-day			Inter-day		
Added conc. (ng mL^{-1})	Measured conc. (ng mL^{-1})	Recovery (%)	Added conc. (ng mL^{-1})	Measured conc. (ng mL^{-1})	Recovery (%)
2	2.08	104.14	2	2.08	104.14
5	4.86	97.23	5	4.86	97.23
10	10.02	100.2	20	21.10	105.50
50	49.57	99.14	50	50.60	101.20
100	100.01	100.01	100	97.5	97.50
			500	501.8	100.36
	Mean ± SD	100.11 ± 2.25		Mean ± SD	100.99 ± 3.01

molecules are retained in the pre-treatment column. When the column switching occurs, the retained compounds are flushed into the analytical column by the aid of the analytical mobile phase. The problem arises because such pre-treatment mobile phases, poor in organic solvents, are not suitable enough to completely wash the whole quantity of many compounds, specially the hydrophobic ones, into the pre-treatment column. Consequently, some significant amounts may remain adsorbed onto different parts of the sample flow-path.

In the present study, this carry-over problem was satisfactorily solved in two ways. First, the auto-sampler used during the analysis was of type Sil-20A (Shimadzu, Japan), which includes a specially treated outer needle surface with improved needle seal composition which prevents adsorption of the samples to the auto-sampler parts [33]. Secondly, the mobile phase used for the pre-treatment was very rich in organic solvent (composed of 40% (v/v) of acetonitrile in 2% acetic acid). It was necessary to use such mobile phase composition in order to ensure the washing out of the relatively nonpolar derivatives formed between the excess NBD-F reagent and the plasma constituents during the derivatization reaction. This shortened the time required for the pre-treatment phase to only 1 min at a flow rate of 5 mL min^{-1}. At the same time, it positively added to the degree of elimination of the carry-over problems, which was practically observed during this study.

4. Conclusion

A highly sensitive HPLC method with fluorescence detection has been developed for the determination of RBX in plasma samples. The method employed non-extractive automated "co-sense" for sample pre-treatment, and mild derivatization conditions for RBX with the highly reactive fluorogenic reagent NBD-F. The outstanding feature of using such system is the no need for the extraction of RBX from the plasma and no need to use a guard column to protect the analytical column against the huge amount of plasma proteins. As well, the run-time was short (<12 min). These qualities added the property of the high throughput to the method. The analytical results demonstrated that the proposed method is suitable for the accurate quantification of RBX in human plasma. The performance of the method makes it valuable for the combined pharmacokinetic studies and bioavailability evaluation of RBX in human subjects after oral administration of the therapeutic doses.

References

[1] E. Brenner, R.M. Baldwin, G. Tamagnan, Org. Lett. 7 (2005) 937.
[2] J.M. Kent, Lancet 355 (2000) 911.
[3] G. Sacchetti, M. Bernini, A. Bianchetti, S. Parini, R.W. Invernizzi, R. Samanin, Br. J. Pharmacol. 128 (1999) 1332.
[4] S.A. Montgomery, J. Clin. Psychiatry 59 (Suppl. 14) (1998) 26.
[5] E.H.F. Wong, M.S. Sonders, S.G. Amara, P.M. Tinholt, M.F.P. Piercey, W.P. Hoffmann, D.K. Hyslop, S. Franklin, R.D. Porsolt, A. Bonsignori, Biol. Psychiatry 47 (2000) 818.
[6] H. Berzewski, M. Van Moffaert, C.A. Gagiano, Eur. Neuro-psychopharmacol. 7 (1997) S37.
[7] L. Tanum, Acta Psychiatry Scand. 402 (2000) 37.
[8] O. Larrosa, Y. de la Llave, S. Bario, J.J. Granizo, D. Garcia-Borreguero, Sleep 24 (2001) 282.
[9] P.N. Dannon, I. Iancu, L. Grunhaus, Hum. Psychopharmacol. 17 (2002) 329.
[10] M.R. Lemke, J. Clin. Psychiatry 63 (2002) 300.
[11] J.K. Holm, C.M. Spencer, CNS Drugs 12 (1999) 65.
[12] P. Dostert, M.S. Benedetti, I. Poggesi Eur, Neuropsychopharmacology 7 (1997) S23.
[13] S.M.R. Wille, K.E. Maudens, C.H. Van Peteghem, W.E.E. Lambert, J. Chromatogr. A 1098 (2005) 19.
[14] S.M.R. Wille, P. Van Hee, H.M. Neels, C.H. Van Peteghem, W.E. Lambert, J. Chromatogr. A 1176 (2007) 236.
[15] D. Ohman, B. Norlander, C. Peterson, F. Bengtsson, Ther. Drug Monit. 23 (2001) 27.
[16] C. Frahnert, M.L. Rao, K. Grasmader, J. Chromatogr. B 794 (2003) 35.
[17] S. Hartter, H. Weigmann, C. Hiemke, J. Chromatogr. B 740 (2000) 135.
[18] M.A. Raggi, R. Mandrioli, G. Casamenti, V. Volterra, S. Pinzauti, J. Chromatogr. A 949 (2002) 23.
[19] A. Onal, A.O. Sagirli, S.M. Cetin, S. Toker, Chromatographia 66 (2007) S103.
[20] D. Ohman, B. Norlander, C. Peterson, F. Bengtsson, J. Chromatogr. A 947 (2002) 247.
[21] G. Cannazza, D. Braghiroli, M.M. Carrozzo, C. Parenti, C. Sabbioni, R. Mandrioli, S. Fanali, M.A. Raggi, J. Pharm. Biomed. Anal. 48 (2008) 991.
[22] D. Oehman, M.D. Cherma, B. Norlander, F. Bengtsson, Ther. Drug Monit. 25 (2003) 174.
[23] P. Turnpenny, D. Fraier, J. Pharm. Biomed. Anal. 49 (2009) 133.
[24] H. Kirchherr, W.N. Kühn-Velten, J. Chromatogr. B 843 (2006) 100.
[25] I.A. Darwish, A.M. Mahmoud, N.Y. Khalil, J. AOAC Int. 91 (2008) 1037.
[26] I.A. Darwish, A.A. Al-Majed, A.M. Mahmoud, N.Y. Khalil. J. AOAC. Int. (2009). In press.
[27] X. Zhao, W. Zang, X. Zhao, S. Wang, X. Zheng, J. Zheng, Chromatographia 65 (2007) 149.
[28] N. Saori, S. Riho, Y. Reiko, K. Yoko, M. Shoko, K. Hikaru, S. Sadahiko, O. Shin, Y. Susumu, Chem. Pharm. Bull. 56 (2008) 328.
[29] S. Sundd, J. Manish, S. Hiten, G. Sapna, T. Purav, S. Ruchy, L. Bhushan, J. Chromatogr. B 81 (2004) 247.
[30] H. Hattori, K. Ito, M. Iwai, T. Arinobu, Y. Mizutani, T. Kumazawa, A. Ishii, O. Suzuki, H. Seno, Forensic Toxicol. 25 (2007) 100.
[31] K. Imai, T. Toyo Oka, H. Miyano, Analyst 109 (1984) 1365.
[32] ICH Guideline, Q2 (R1): Validation of Analytical Procedure: Text and Methodology, London, 2005.
[33] HPLC Application Report No. 23: Direct Analysis of Drugs in Blood Plasma Using "Co-sense for BA" Bio-samples Pretreatment System, Shimadzu Corporation, Kyoto, Japan.

Talanta 80 (2010) 1257–1263

Contents lists available at ScienceDirect

Talanta

journal homepage: www.elsevier.com/locate/talanta

A modified acid digestion procedure for extraction of tungsten from soil

A.J. Bednar[a,*], W.T. Jones[a], M.A. Chappell[a], D.R. Johnson[a], D.B. Ringelberg[b]

[a] U.S. Army Engineer Research and Development Center, Environmental Laboratory, 3909 Halls Ferry Rd., Vicksburg, MS 39180, United States
[b] U.S. Army Engineer Research and Development Center, Cold Regions Research and Engineering Laboratory, 72 Lyme Rd., Hanover, NH 03755, United States

ARTICLE INFO

Article history:
Received 10 July 2009
Received in revised form 9 September 2009
Accepted 10 September 2009
Available online 12 September 2009

Keywords:
Tungsten
Acid digestion
Extraction procedures

ABSTRACT

Interest in tungsten occurrence and geochemistry is increasing due to increased use of tungsten compounds and its unknown biochemical effects. Tungsten has a complex geochemistry, existing in most environmental matrices as the soluble and mobile tungstate anion, as well as poly- and heteropolytungstates. Because the geochemistry of tungsten is substantially different than most trace metals, including the formation of insoluble species under acidic conditions, it is not extracted from soil matrices using standard acid digestion procedures. Therefore, the current work describes a modification to a commonly used acid digestion procedure to facilitate quantification of tungsten in soil matrices. Traditional soil digestion procedures, using nitric and hydrochloric acids with hydrogen peroxide yield <1 up to 50% recovery on soil matrix spike samples, whereas the modified method reported here, which includes the addition of phosphoric acid, yields spike recoveries in the 76–98% range. Comparison of the standard and modified digestion procedures on National Institute of Standards and Technology Standard Reference Materials yielded significantly improved tungsten recoveries for the phosphoric acid modified method. The modified method also produces comparable results for other acid extractable metals as the standard methods, and therefore can be used simultaneously for tungsten and other metals of interest.

Published by Elsevier B.V.

1. Introduction

Recently, interest in tungsten geochemistry and occurrence in groundwater has increased due to specific human toxicological events, related to local natural deposits of tungsten ore [1–3]. Additionally, industrial (e.g. tungsten carbide tools), mining, civilian recreational (e.g. lead shotshell replacement), and military (e.g. kinetic penetrators and small arms ammunition) activities are potential sources of tungsten in the environment [2–4]. Tungsten metal is not found in nature, but oxyanion species of tungsten are found in a variety of minerals, which can dissolve to yield the thermodynamically stable tungstate in most environmental matrices [2–4]. The chemistry of tungstate is not limited to the soluble monomeric species, as polymerization with other common oxyanions, such as molybdate, phosphate, and silicate, can yield a plethora of ill-defined poly-species with variable biogeochemical properties [3,5–7]. Because of the complex speciation of tungsten, particularly the anionic nature, it does not behave as traditional cationic metals in soils [3,6]. Tungsten sorption to soil has been studied, and tungsten species have been shown to be more mobile under alkaline conditions, similar to other anionic compounds, such as arsenic [8–11].

One of the most fundamental pieces of information needed to investigate geochemistry of metals in the environment is quantitation of the amount of the metal present, or at least the fraction of that metal that could become 'environmentally relevant' [12]. However, due to the complex chemistry of tungsten, traditional acid digestion techniques do not extract tungsten from soil that could become mobile under normal environmental conditions, primarily due to the precipitation of insoluble tungstates or the polymerization of tungstates onto soil particles [6,11,13].

Traditional acid digestion techniques often use nitric and hydrochloric acids, usually with hydrogen peroxide, to solubilize metals for analysis by inductively coupled plasma atomic emission spectroscopy or inductively coupled plasma mass spectrometry (ICP-AES and ICP-MS) [12]. Due to the precipitation of insoluble species, low extraction efficiencies and matrix spike recoveries are observed for tungsten using these procedures [13]. Total dissolution procedures are also reported which can dissolve the entire sample matrix, yet usually involve hydrofluoric acid or other complex and potentially hazardous acid cocktails, and require specialized digestion and analytical equipment (e.g. fluoropolymer vessels and sample introduction systems) [14–16].

Some researchers have also investigated the use of alkaline extractions, however, these procedures often do not extract all tungsten species with equal effectiveness, and do not work well for simultaneous extraction of other metals, necessitating at least two digestions/analyses be performed for a complete metals characterization [13,14,17]. Furthermore, alkaline digestion is more

* Corresponding author. Tel.: +1 601 634 3652.
E-mail address: Anthony.J.Bednar@usace.army.mil (A.J. Bednar).

0039-9140/$ – see front matter. Published by Elsevier B.V.
doi:10.1016/j.talanta.2009.09.017

effective with sodium versus ammonium hydroxide, which can lead to plasma instabilities and interferences necessitating sample dilution which raises analyte reporting limits [14,17].

The modified procedure described in the current work capitalizes on tungsten's ability to polymerize with oxyanion acids, particularly phosphoric acid, to yield acid soluble tungsten species for measurement by ICP-AES or ICP-MS, while simultaneously allowing determination of other metals extracted during the digestion procedure. The modification involves the addition of phosphoric acid to a standard nitric acid and hydrogen peroxide digestion procedure to promote tungsten solublization [12–14]. The phosphoric acid modified procedure was tested on standard reference materials and test field soils. Results were compared for tungsten and other metals routinely measured by ICP-AES following acid digestion. Tungsten recoveries are greatly improved using the modified procedure, with only minor differences observed for some metals between the modified and standard digestion procedures.

2. Experimental

2.1. Reagents

All chemicals used were of trace metal grade purity and used without further purification; the deionized (DI) water used had a resistivity of 18.3 MΩ cm. Trace metal grade nitric acid, hydrochloric acid, phosphoric acid, and hydrogen peroxide were purchased from Fisher Scientific (Pittsburg, PA) and used as received. Single element and mixed analyte standards for tungsten and other metals were purchased from SPEX CertiPrep (Metuchen, NJ) and CPI (Santa Rosa, CA).

2.2. Soil sample preparation

Standard reference soil materials (SRM 2709 and 2710) were purchased from the National Institute of Standards and Technology (NIST), and used as received. A tungsten-spiked soil was formed by mixing a Grenada Loring soil (GL) with metallic tungsten (<1 μm particles). The soil was aged approximately 3 years to oxidize the metallic tungsten. The silty loam soil of the Grenada Loring series (Alfilsols order) was collected from the Brown Loam Experimental Station, Learned, MS. The use of this soil in other geochemical investigations of tungsten has been previously described [10,11,18]. Finally, field soil 1 (FS-1), and field soil 2 (FS-2) were collected from training ranges where tungsten munitions have been previously used [19]. The soils were collected in bulk, mixed, and sieved (<1 cm) to remove plant debris and rocks. FS-1 is an iron-rich clay and FS-2 is a sandy soil. The three test soils were air-dried, ground with a mortar and pestle, and sieved through a #40 ASTM sieve to improve sample homogeneity similar to the NIST reference soils [20].

2.3. Digestion procedures

Three digestion procedures were compared for the present work, two published versions of US EPA method 3050B [12], and a third modified from the standard procedures by adding phosphoric acid to the acid cocktail, as described below and outlined in Table 1. All acid digestions were conducted on a DigiPrep hotblock digestion system (SCP Science, Champlain, NY), using fluoropolymer digestion vessels to prevent tungsten polymerization onto borosilicate glass vessel walls. Each digestion batch included a matrix blank, blank spike, and NIST standard reference soils, as well as the three test soils (GL, FS-1, FS-2), digested in triplicate.

2.3.1. Nitric acid digestion

The first procedure follows the US EPA method 3050B nitric acid and hydrogen peroxide digestion protocol [12]. Briefly, one half gram of dried, ground, and sieved soil was placed in a fluoropolymer digestion vessel, to which 5 mL of 1:1 nitric acid:DI water was added and the mixture heated at 95 °C for 30 min. Then, 4 sequential additions of 2.5 mL of concentrated nitric acid were added, with 30 min of heating between each acid addition. After the final nitric acid addition, the mixture was heated for 2 h. The samples were allowed to cool to room temperature before 3 mL of 30% hydrogen peroxide was added, followed by heating for 15 min. Finally, 2 mL of hydrogen peroxide were added, and the mixture heated for an additional 2 h. Five milliliters of hydrogen peroxide was generally sufficient for complete reaction with the samples tested, although more can be added as needed for other soil matrices. The digestate was then cooled to room temperature and filtered through a Whatman #40 filter and diluted to 50 mL with 1% nitric acid.

2.3.2. Nitric and hydrochloric acids digestion

The second digestion procedure also follows USEPA 3050B where hydrochloric acid is added to increase the solubility of certain elements for ICP-AES determination [12]. A second 0.5 g aliquot of each of the solid samples was weighed into fluoropolymer vessels and digested following the above described procedure, except that after the second 2 h heating period, 5 mL of concentrated hydrochloric acid was added to the digestion vessel with a final 15 min of heating. After cooling, the digestates were filtered and diluted to volume as described above.

Table 1
Procedures for the three acid digestions compared in the current work.

	Nitric acid	Nitric–hydrochloric acids	Phosphoric–nitric acids
Sample mass and digestion vessel	0.5 g in PTFE vessels	0.5 g in PTFE vessels	0.5 g in PTFE vessels
1st acid addition	5 mL of 1:1 nitric acid	5 mL of 1:1 nitric acid	5 mL 1:1 nitric acid + 1 mL concentrated phosphoric acid
Heating	30 min at 95 °C	30 min at 95 °C	30 min at 95 °C
Acid additions	4–2.5 mL concentrated nitric acid each with 30 min heating	4–2.5 mL concentrated nitric acid each with 30 min heating	4–2.5 mL concentrated nitric acid each with 30 min heating
Heating	120 min at 95 °C	120 min at 95 °C	120 min at 95 °C
1st hydrogen peroxide addition	3 mL 30% hydrogen peroxide	3 mL 30% hydrogen peroxide	3 mL 30% hydrogen peroxide
Heating	15 min at 95 °C	15 min at 95 °C	15 min at 95 °C
2nd hydrogen peroxide addition	2 mL 30% hydrogen peroxide	2 mL 30% hydrogen peroxide	2 mL 30% hydrogen peroxide
Heating	120 min at 95 °C	120 min at 95 °C	120 min at 95 °C
Hydrochloric acid addition		5 mL concentrated hydrochloric acid	
Heating		15 min at 95 °C	
Dilution to volume	Filter and dilute to 50 mL with 1% nitric acid	Filter and dilute to 50 mL with 1% nitric acid	Filter and dilute to 50 mL with 1% nitric acid

2.3.3. Phosphoric and nitric acids digestion

The third digestion procedure was developed specifically to increase tungsten extraction. A third 0.5 g aliquot of each of the solid samples was weighed into fluoropolymer vessels and digested following the above described nitric acid procedure, with the modification of adding 1 mL of concentrated phosphoric acid with the initial 5 mL of 1:1 nitric acid:deionized water. The digestate was then filtered and diluted as described above.

Aliquots of the 50 mL digestate solutions were further diluted with 1% nitric acid prior to analysis as needed such that analyte concentrations were within the calibration range of the analytical instrumentation (generally 1:4 dilution).

2.4. Instrumentation

Metal concentrations in the diluted digestates, including tungsten, were determined by Inductively Coupled Plasma Atomic Emission Spectroscopy (ICP–AES, following modifications of EPA Method 6010C [21]), using a PerkinElmer (Wellesley, MA) Optima 5300DV equipped with a MiraMist nebulizer and cyclonic spray chamber. The plasma was operated at 1400 W and nebulizer gas flow rate of 0.65 mL/min. Tungsten was quantified using the 207.912 nm emission line with analyte confirmation at 224.876 nm using axial plasma viewing. Due to the low concentration of tungsten in the standard reference soil 2709, tungsten was also measured by Inductively Coupled Plasma Mass Spectrometry (ICP-MS following modifications of EPA Method 6020A [21]), using a PerkinElmer Elan DRC-II equipped with a MiraMist nebulizer and Scott spray chamber. The ICP-MS plasma was operated at 1250 W and nebulizer gas flow of 0.85 mL/min. Tungsten was quantified at m/z 182 with confirmation using m/z 184 after correction for ^{184}Os.

2.5. Calibration and quality control

The ICP-AES was calibrated using NIST-traceable calibration standards. Scandium, added on-line using a mixing-T, was used as an internal standard to correct for instrumental drift during analysis. Calcium, magnesium, sodium, potassium, aluminum, and iron were calibrated using mixed analyte standards containing 0, 0.100, 1.000, 10.00, and 100.0 mg/L of each analyte. All other analytes, including tungsten, were calibrated using mixed analyte standards containing 0, 0.100, 1.000, and 10.00 mg/L of each element. The ICP-MS was calibrated using standards containing 0, 0.001, 0.010, and 0.100 mg/L tungsten, and used holmium as the internal standard.

All calibration responses were linear and had correlation coefficients of at least 0.9999. A second source calibration verification standard was analyzed immediately after calibration following standard US EPA Method 6010C procedures [21]; analyte recoveries were within ±10% of the nominal value (4.000 and 0.040 mg/L for ICP-AES and ICP-MS, respectively). Continuing calibration verification standards and blanks were analyzed periodically throughout the analytical batch, with recoveries within ±10% of the nominal value (5.000 and 0.050 mg/L for ICP-AES and ICP-MS, respectively) and subsequent blanks below the instrument reporting limits (<0.020 and <0.001 mg/L for ICP-AES and ICP-MS, respectively).

3. Results and discussion

3.1. Tungsten

The tungsten concentrations measured in the two standard reference materials, using the three digestion procedures, and associated quality control samples are listed in Table 2. The digestion blanks for all three procedures were below the instrument reporting limit (<0.040 mg/L including dilution factor), indicating that contamination was not present in the acids or vessels used. However, the blank spike sample, consisting of aqueous 10 mg/L tungsten from a NIST-traceable standard shows a marked difference among the three digestion procedures. The nitric acid method yielded a blank spike recovery of 39%, while the nitric–hydrochloric acid procedure recovery was 43%, both were well below the phosphoric–nitric procedure recovery of 98%. The nitric and nitric–hydrochloric procedures produced a yellow precipitate consisting of insoluble tungstic and polytungstic acids that was captured by the filtration process resulting in poor

Table 2
Comparison of the modified digestion procedure to two standard methods for extraction of tungsten from two standard reference materials and three test soils. Concentrations are in mg/kg ± standard deviation of triplicate digestions for soils and mg/L for liquid quality control samples determined by ICP-AES, values in parentheses were determined by ICP-MS.

	Tungsten concentration (mg/kg)	Tungsten concentration (mg/L)	Reported value recovery (%)	Matrix spike recovery (%)
Sample	Nitric acid			
Digestion blank		<0.04		
Digestion blank spike (10 mg/L)		3.9		39
SRM 2709 (2 mg/kg)	<4 (<0.1)		NA (NA)	
SRM 2710 (93 mg/kg)	27.4		29	
Grenada Loring	210 ± 30			39
Field soil 1	90.2 ± 11			0.4
Field soil 2	440 ± 28			47
Sample	Nitric–hydrochloric acids			
Digestion blank		<0.04		
Digestion blank spike (10 mg/L)		4.3		43
SRM 2709 (2 mg/kg)	<4 (0.2)		NA (10)	
SRM 2710 (93 mg/kg)	50.0		54	
Grenada Loring	221 ± 25			56
Field Soil 1	190 ± 22			3.7
Field Soil 2	737 ± 145			25
Sample	Phosphoric–nitric acids			
Digestion blank		<0.04		
Digestion blank spike (10 mg/L)		9.8		98
SRM 2709 (2 mg/kg)	<4 (0.5)		NA (25)	
SRM 2710 (93 mg/kg)	79.9		86	
Grenada Loring	762 ± 44			98
Field soil 1	483 ± 191			76
Field soil 2	1695 ± 203			79

NA—concentration measured is below instrument reporting limit.

spike recovery [6,22]; the phosphoric–nitric digestion produced no precipitate, and therefore the soluble phosphotungstates formed during the modified phosphoric–nitric digestion procedure were not removed by filtration. Improved recoveries for the nitric and nitric–hydrochloric acid procedures were not obtained by rinsing the filtrate with 2% phosphoric acid, indicating that the precipitates are stable once formed.

The NIST standard reference soil material results listed in Table 2 show a similar trend as the blank spike samples. The reference soil 2709 has a total tungsten concentration determined by Neutron Activation Analysis reported by NIST of 2 mg/kg, which is below the ICP-AES reporting limit for the current study, although, this demonstrates that matrix interferences are not present, which could yield a false positive. However, ICP-MS analysis indicated that increased tungsten recoveries in reference soil 2709 were obtained using the phosphoric–nitric digestion procedure compared to the standard techniques. The phosphoric–nitric procedure yielded 0.5 mg/kg tungsten, which is approximately 25% of the reported value, however, this is a higher recovery than either the nitric or nitric–hydrochloric digestions.

The reference soil 2710 has a total tungsten concentration determined by Neutron Activation Analysis reported by NIST of 93 mg/kg. The nitric acid digestion procedure yielded a concentration of 27.4 mg/kg, whereas the nitric–hydrochloric acid digestion yielded 50 mg/kg, which represent 29 and 54% recovery, respectively. The phosphoric–nitric acid procedure yielded a concentration of approximately 80 mg/kg, or 86% recovery. These recoveries are in line with values reported by others when standard acid digestion procedures are used for tungsten determinations [13,17].

It should be noted that all three acid digestion procedures tested are not intended to be total dissolutions, but rather are strong extractions, therefore, 86% tungsten recovery for the reference soil 2710 by the phosphoric–nitric method compared to Neutron Activation Analysis is considered acceptable. Furthermore, some of the tungsten may be present in these samples in silicate phases, which would normally only be extracted by a total dissolution technique (e.g. hydrofluoric acid, [15,16]), or a solid phase analysis technique, such as Neutron Activation or X-ray Fluorescence Spectroscopy. This likely explains the low recovery observed in the reference soil 2709, even with the phosphoric–nitric digestion procedure. However, in light of the two standard acid digestion procedures extracting less tungsten in all matrices, the phosphoric–nitric acid procedure performs well. Additionally, the tungsten concentrations reported by NIST are not certified values, but presented for 'information purposes only', and therefore may have some inherent error associated with them. A total dissolution procedure using a four acid cocktail, including hydrofluoric acid [16], was performed on the reference soils 2709 and 2710 to verify the NIST reported concentrations. Reference soil 2709 yielded a tungsten concentration of 2.2 ± 0.05 mg/kg determined by ICP-MS, while reference soil 2710 yielded a tungsten concentration of 97.8 ± 0.4 mg/kg determined by ICP-AES. These values are 110 and 105% of the NIST reported concentrations, respectively.

The three digestion procedures are also compared in Table 2 on the three test soils, with similar trends in tungsten extraction and matrix spike recovery observed. The nitric acid procedure yielded tungsten concentrations of 210 ± 30, 90.2 ± 11, and 440 ± 28 mg/kg for the GL, FS-1, and FS-2 samples, respectively. Tungsten concentrations in the nitric–hydrochloric digestion procedure samples were approximately the same for the GL soil (220 ± 25 mg/kg) as the nitric acid procedure, although the concentrations measured for the FS-1 and FS-2 samples were about a factor of two higher than those measured with the nitric acid procedure. The phosphoric–nitric procedure yielded the highest tungsten concentrations, 762 ± 44, 483 ± 191, and 1695 ± 203 mg/kg for the GL, FS-1, and FS-2 soils, respectively, further suggesting that the two standard methods have a low bias for tungsten extraction.

The lower concentrations determined by the standard methods explains the poor matrix spike recovery values listed in Table 2. The nitric acid digestion yielded a spike recovery of 39% for the GL soil, but less than 1% for FS-1, and 47% for the FS-2 sample. The nitric–hydrochloric acid procedure yielded slightly higher tungsten recoveries than the nitric acid procedure, with the GL spike recovery being 56%, but only 4 and 25% for the FS-1 and FS-2 samples, respectively. Finally, the matrix spike recoveries for the phosphoric–nitric procedure were 98, 76, and 79% for the GL, FS-1, and FS-2 samples, respectively, substantially higher than the standard methods. FS-1 contains a high amount of iron, and therefore it is possible that an iron–tungstate phase is causing exceptionally low extraction of tungsten, even lowering the phosphoric–nitric digestion, which was 76%. The FS-2 sample is a sandy soil, which could facilitate the formation of polytungstates on the silicon dioxide particles, resulting in low tungsten recovery, although the phosphoric–nitric procedure yielded 79% recovery. These experiments demonstrate that the phosphoric–nitric modified procedure greatly improves tungsten extraction from soils compared to the unmodified standard procedures.

3.2. Other metals

In addition to tungsten, other metal analyses in soils may also be required simultaneously, therefore, the digestate solutions were analyzed for 20 other metals to determine the comparability of the three procedures for determination of other metals. The addition of phosphoric acid could potentially lower recoveries of metals that form insoluble phosphate salts, such as lead, aluminum, iron, nickel, and cobalt, therefore, extraction efficiencies and matrix spike recoveries were tested and compared.

The digestion blanks listed in Table 3 show only 2 analyte detections, 0.081 mg/L iron in the phosphoric–nitric digestion solution, and 0.104 mg/L calcium in the nitric–hydrochloric acid digestion solution. However, these major cations are present at several orders of magnitude higher concentrations in soil matrices, suggesting these blank levels are acceptable. The blank spike recoveries listed in Table 3 for all elements measured from the three digestion procedures are within ±10% of the nominal spike concentration indicating no bias among the three digestion procedures for the elements determined.

Table 3 lists other metal concentrations for the two NIST standard reference soils determined using the three digestion procedures. The acid leachable metals concentrations reported by NIST are not certified values (only the total metals concentrations are certified by NIST), but are listed for 'information purposes only'. However, the recoveries listed generally agree among the three procedures, indicating that low recoveries are not an issue for these soil matrices and that the phosphoric–nitric procedure can be used for simultaneous determination of other metals. For example, Co determined by the nitric acid procedure yielded 90 and 101% recovery for the standard reference soils 2709 and 2710, respectively, in agreement with recoveries obtained for the nitric–hydrochloric procedures (93 and 100%, respectively). In comparison, the phosphoric–nitric procedure produced cobalt recoveries of 105 and 102% for the reference materials 2709 and 2710, respectively, indicating similar extraction efficiencies for the three digestion procedures. Similar agreement is observed for other analytes listed in Table 3 (e.g. arsenic, barium, calcium, cadmium, lead, strontium, and zinc). Elements such as chromium, copper, iron, potassium, magnesium, molybdenum, and nickel appear to have a slightly higher extraction efficiency by the phosphoric–nitric procedure, compared to the standard digestion procedures, although the difference is generally less than a 10% increase.

Table 3
Comparison of the modified digestion procedure to standard methods for extraction of other metals from two standard reference materials.

Elements	2709 reported[a] (mg/kg)	2710 reported[a] (mg/kg)	Nitric acid				Nitric–hydrochloric acids				Phosphoric–nitric acids			
			Digestion blank (mg/L)	Digestion blank spike[b] (% recovery)	2709 (% recovery)	2710 (% recovery)	Digestion blank (mg/L)	Digestion blank spike[b] (% recovery)	2709 (% recovery)	2710 (% recovery)	Digestion blank (mg/L)	Digestion blank spike[b] (% Recovery)	2709 (% recovery)	2710 (% recovery)
Al	26000	18000	<0.08	90	70	80	<0.08	90	71	78	<0.08	92	116	109
As	<20	590	<0.08	91	NA	89	<0.08	93	NA	85	<0.08	98	NA	94
Ba	398	360	<0.08	98	86	81	<0.08	98	86	78	<0.08	99	94	82
Ca	15000	4100	<0.08	NS	83	86	0.104	NS	83	81	<0.08	NS	85	80
Cd	<1	20	<0.08	101	NA	71	<0.08	99	NA	68	<0.08	96	NA	76
Co	12	8.2	<0.08	100	90	101	<0.08	99	93	100	<0.08	100	105	102
Cr	79	19	<0.08	102	75	81	<0.08	101	77	80	<0.08	105	100	106
Cu	32	2700	<0.08	96	75	91	<0.08	97	83	92	<0.08	103	89	99
Fe	30000	27000	<0.08	100	86	87	<0.08	99	86	86	0.081	103	98	100
K	3200	4500	<0.08	NS	97	99	<0.08	NS	101	95	<0.08	NS	147	120
Mg	14000	5700	<0.08	NS	75	79	<0.08	NS	78	75	<0.08	NS	88	93
Mn	470	7700	<0.08	98	88	92	<0.08	97	89	87	<0.08	99	93	94
Mo	<2	20	<0.08	NS	NA	57	<0.08	NS	NA	63	<0.08	NS	NA	73
Na	680	540	<0.08	NS	85	87	<0.08	NS	88	83	<0.08	NS	86	78
Ni	78	10.1	<0.08	100	83	97	<0.08	100	83	95	<0.08	100	91	117
Pb	13	5100	<0.08	94	NA	90	<0.08	95	NA	86	<0.08	92	NA	87
Sr	101	100	<0.08	NS	90	91	<0.08	NS	90	87	<0.08	NS	89	81
Ti	380	1000	<0.08	NS	58	74	<0.08	NS	65	77	<0.08	NS	155	45
V	62	43	<0.08	95	84	87	<0.08	95	87	89	<0.08	97	126	110
Zn	100	5900	<0.08	98	83	85	<0.08	97	86	80	<0.08	100	91	87

NA—concentration measured by one of the digestion procedures is below instrument reporting limit. NS—matrix spike solution did not contain this analyte.

[a] Acid leachable metal concentrations are reported by NIST for information purposes only, they are not certified values.

[b] Spike levels (mg/L): Al = 10, As = 0.5, Ba = 2.5, Cd = 0.25, Co = 1, Cr = 1, Cu = 1, Fe = 5, Mn = 1, Ni = 1, Pb = 0.5, V = 1, Zn = 2.5.

Table 4
Metal concentrations and matrix spike recoveries in the three test soils obtained using the modified phosphoric–nitric acids digestion procedure.

Element	Grenada Loring soil metals concentration (mg/kg) ± standard deviation	Matrix spike recovery (%)	% of nitric acid digestion	% of nitric–hydrochloric digestion	Field soil 1 metals concentration (mg/kg) ± standard deviation	Matrix spike recovery (%)	% of nitric acid digestion	% of nitric–hydrochloric digestion	Field soil 2 metals concentration (mg/kg) ± standard deviation	Matrix spike recovery (%)	% of nitric acid digestion	% of nitric–hydrochloric digestion
Al	15369 ± 350	233	173	182	10852 ± 1620	615	231	227	4742 ± 42	108	128	128
As	12 ± 1.1	86	160	NA	13 ± 4.4	81	NA	NA	<10	83	NA	NA
Ba	94 ± 5.9	94	89	143	23 ± 1.5	91	144	146	13 ± 0.2	91	120	139
Ca	852 ± 11	NS	101	105	91 ± 3.1	NS	105	99	9438 ± 69	NS	101	102
Cd	<10	92	NA	NA	<10	91	NA	NA	<10	91	NA	NA
Co	8 ± 0.2	91	75	NA	<10	92	NA	NA	<10	90	NA	NA
Cr	19 ± 0.6	96	151	163	114 ± 1.1	105	95	95	10 ± 0.2	93	NA	124
Cu	12 ± 5.2	94	158	145	415 ± 92	268	111	107	337 ± 75	40	85	89
Fe	15446 ± 705	18	102	117	13409 ± 351	294	125	105	6481 ± 222	-67	134	113
K	1651 ± 37	NS	261	263	305 ± 50	NS	267	261	583 ± 6.9	NS	177	172
Mg	1589 ± 29	NS	149	154	199 ± 13.1	NS	190	189	689 ± 2.7	NS	115	115
Mn	628 ± 65	50	47	109	45 ± 1.1	94	105	105	47 ± 0.6	91	113	107
Mo	<10	NS	NA	NA	<10	NS	NA	NA	<10	NS	NA	NA
Na	81 ± 1.3	NS	123	131	26 ± 4.3	NS	146	123	40 ± 0.1	NS	121	117
Ni	14 ± 0.2	91	135	143	<10	92	NA	NA	<10	90	NA	NA
Pb	<10	83	NA	NA	8023 ± 1250	-4667	96	95	996 ± 339	-207	130	107
Sr	10 ± 0.2	NS	NA	NA	21 ± 1.4	NS	111	111	11 ± 0.2	NS	111	113
Ti	388 ± 4.9	NS	446	408	135 ± 29.7	NS	385	282	197 ± 5.9	NS	168	147
V	35 ± 1.0	92	145	162	24 ± 1.0	94	131	114	11 ± 0.8	88	145	125
Zn	29 ± 0.5	95	110	114	56 ± 10.0	615	111	106	43 ± 5.5	91	83	94

NA—concentration measured by one of the digestion procedures is below instrument reporting limit.
NS—matrix spike solution did not contain this analyte.

There appears to be a significant increase in extraction efficiency for titanium and vanadium in standard reference soil 2709 when using the phosphoric–nitric procedure. A similar trend is also observed for reference soil 2710, which has increased titanium extraction by the phosphoric–nitric procedure. These results suggest that reference material 2709, in particular, may possess a refractory vanadium and titanium phase that is sensitive to the presence of phosphoric acid.

Listed in Table 4 are the additional metals concentrations in the three test soils determined using the three digestion procedures. Because there are no reference values for the concentrations of metals in these soils, as there is with the NIST standard reference materials, the values obtained for the standard nitric and nitric–hydrochloric acid procedures are used as the reference values. The concentrations determined by the phosphoric–nitric procedure are listed in Table 4, and the relative recovery of each analyte compared to the standard digestion procedures.

The matrix spike recoveries for the Grenada Loring soil are all within ±20% of the nominal value except for aluminum, iron, and manganese, primarily due to the spike concentrations being less than 10% of the sample concentration for aluminum and iron, and less than 20% of the manganese concentration in the samples. Similarly, the matrix spike recoveries for most elements in the FS1 and 2 samples are acceptable (±20%) except where the spike concentration was small relative to the amount of metal present in the sample (e.g. aluminum, iron, copper, lead, and zinc in FS-1, and copper, iron, and lead in FS-2).

Aluminum, chromium, copper, potassium, magnesium, sodium, nickel, titanium, and vanadium tend to have higher extraction efficiencies by the phosphoric–nitric procedure in at least one of the test soil matrices compared to the nitric or nitric–hydrochloric digestion procedures. However, chromium, copper, and nickel are only elevated in the GL soil, which has relatively low concentrations of these elements (<20 mg/kg), suggesting that this could be a matrix anomaly, or an effect of being near the instrument reporting limit. For example, the agreement between the three digestion procedures is excellent for copper in the field soils 1 and 2 that have much higher concentrations.

It is also possible that the phosphoric acid improves extraction efficiency of anionic species, such as vanadium, due to surface complexation competition. The major cations (aluminum, potassium, magnesium, and sodium) could also be elevated due to the presence of additional acid (phosphoric) in the digestion cocktail, although a similar trend would be expected for the nitric–hydrochloric procedure compared to the nitric acid only procedure, which is not observed. However, the anomalies observed with the major cations only indicate a potential increased efficiency extraction, toward the recoveries of a total dissolution method, and therefore are not necessarily a negative effect, the comparability of the modified phosphoric–nitric procedure for the determination of metals still demonstrates its utility.

4. Conclusions

An acid digestion method modified from standard procedures is described for the quantitative recovery of tungsten from soil matrices. The modified method involves the addition of phosphoric acid to the acid cocktail to form stable polymeric phosphotungstate species for the acid solubilization of tungsten from soils. The method was tested on NIST standard reference soils and three test soils and shown to improve tungsten solubilization and yield acceptable matrix spike recoveries. Additionally, other common metals were determined in the digestate solutions with similar recoveries obtained to the standard methods, although some anomalies were observed. However, the modified procedure generally performed similarly to the standard digestion

procedures and can be used for tungsten and other metals simultaneously.

Acknowledgments

The use of trade, product, or firm names in this report is for descriptive purposes only and does not imply endorsement by the U.S. Government. The tests described and the resulting data presented herein, unless otherwise noted, were obtained from research conducted under the Environmental Quality Technology Program of the United States Army Corps of Engineers by the USAERDC. Permission was granted by the Chief of Engineers to publish this information. The findings of this report are not to be construed as an official Department of the Army position unless so designated by other authorized documents. The authors also thank Jennifer Seiter and Frances Hill of the USACE for their editorial comments.

References

[1] R.L. Seiler, K.G. Stollenwerk, J.R. Garbarino, Appl. Geochem. 20 (2005) 423.
[2] P.R. Sheppard, G. Ridenour, R.J. Speakman, M.L. Whitten, Appl. Geochem. 21 (2006) 152.
[3] A. Koutsospyros, W. Braida, C. Christodoulatos, D. Dermatas, N. Strigul, J. Hazard. Mater. 136 (2006) 1.
[4] N. Strigul, A. Koutsospyros, P. Arienti, C. Christodoulatos, D. Dermatas, W. Braida, Chemosphere 61 (2005) 248.
[5] F. Feigl, Spot Tests in Inorganic Chemistry, Elsevier Publishing Co., Amsterdam, 1958, 600p.
[6] S.R. Kraynov, The effect of acidity-alkalinity of ground waters on the concentration and migration of rare elements, Geochemistry International (1971) 828.
[7] A.J. Bednar, R.A. Kirgan, D.R. Johnson, A.L. Russell, C.A. Hayes, C.J. McGrath, Land Contam. Reclam. 17 (2009) 129.
[8] J.P. Gustafsson, Chem. Geol. 200 (2003) 105.
[9] M.J. Vissenberg, L.J.M. Joosten, M.M.E.H. Heffels, A.J. van Welsenes, V.H.J. de Beer, R.A. van Santen, J.A.R. van Veen, J. Phys. Chem. B 104 (2000) 8456.
[10] A.J. Bednar, W.T. Jones, R.E. Boyd, D.B. Ringelberg, S.L. Larson, J. Environ. Qual. 37 (2008) 229.
[11] A.J. Bednar, R.E. Boyd, W.T. Jones, C.J. McGrath, D.R. Johnson, M.A. Chappell, D.B. Ringelberg, Chemosphere 75 (2009) 1049.
[12] U.S. Environmental Protection Agency, SW-846 Test Methods for Evaluating Solid Waste, Method 3050B, U.S. Environmental Protection Agency, 1996.
[13] C. Griggs, S. Larson, C. Nestler, M. Thompson, Land Contam. Reclam. 17 (2009) 121.
[14] US Occupational Safety Health Administration, Tungsten and Cobalt in workplace atmospheres (ICP-AES Analysis), Method ID-213, US Occupational Safety and Health Administration, 2004.
[15] US Environmental Protection Agency, SW-846 SW-846 Test Methods for Evaluating Solid Waste, Method 3052B, U.S. Environmental Protection Agency, 1996.
[16] P.H. Briggs and A.L. Meier, The determination of forty-two elements in geological materials by inductively coupled plasma-mass spectrometry: in Taggart, J.E., ed., Analytical methods for chemical analysis of geologic and other materials, U.S. Geological Survey Open-File Report 02-223, 2002, Chapter I, 14 p.
[17] C.S. Griggs, Evaluation of alkaline digestion for the determination of total tungsten in soil by ICP-OES, Poster Presentation, DoD Environmental Monitoring and Data Quality Workshop, 30 March–1 April, San Antonio, TX, 2009.
[18] L.S. Inouye, R.P. Jones, A.J. Bednar, Environ. Toxicol. Chem. 25 (2006) 763.
[19] J. Clausen, S. Taylor, S. Larson, A. Bednar, M. Ketterer, C. Griggs, D. Lambert, A. Hewitt, C. Ramsey, S. Bigl, R. Bailey, N. Perron, ERDC-CRREL TR-07-5, US Army Engineer Research and Development Center, 2007.
[20] D.R. Felt, A.J. Bednar, T. Georgian, Talanta 77 (2008) 380.
[21] US Environmental Protection Agency, SW-846 SW-846 Test Methods for Evaluating Solid Waste. Method 6010C and Method 6020A, U.S. Environmental Protection Agency, 2007.
[22] M.V. Regnault, Elements of Chemistry for the use of Colleges, Academies, and Schools, vol. 2, 2nd ed., Clarke and Hesser, Philadelphia, 1853, pp. P230–232.

Talanta 80 (2010) 1264–1268

Contents lists available at ScienceDirect

Talanta

journal homepage: www.elsevier.com/locate/talanta

Fluorescence aptasensor based on competitive-binding for human neutrophil elastase detection

Jing-Lin He, Zai-Sheng Wu, Song-Bai Zhang, Guo-Li Shen, Ru-Qin Yu*

State Key Laboratory for Chemo/Biosensing and Chemometrics, College of Chemistry and Chemical Engineering, Hunan University, Changsha 410082, PR China

ARTICLE INFO

Article history:
Received 6 June 2009
Received in revised form 8 September 2009
Accepted 13 September 2009
Available online 19 September 2009

Keywords:
Aptasensor
Competitive-binding reaction
Human neutrophil elastase
Molecular beacon
Fluorescence

ABSTRACT

To our knowledge, we report the first fluorescence aptasensor for detecting human neutrophil elastase (HNE) in homogeneous solution. The biosensor contains a short DNA scrambled sequence strand (SS) complementary to part of the aptamer sequence or the loop of molecular beacon (MB). The aptamer-HNE recognition event involves competition between the molecular beacon and loose HNE aptamer for the binding the short DNA strand. The new biosensor can detect as little as 0.34 nM of HNE, and the response is linear in the tested concentration range of 0.34–68 nM with the detection limit of 47 pM.

© 2009 Elsevier B.V. All rights reserved.

1. Introduction

Neutrophil granulocytes are primary antimicrobial effector cells of the innate immune system and contribute to the first line of defence against infectious agents or nonself substances that penetrate the body's physical barriers [1]. The human neutrophil elastase (HNE), a serine proteinase, is the principal enzyme released from neutrophils [2]. It is capable of solubilising fibrous elastin, cartilage proteoglycans, several collagens and fibronectin, hence facilitating the migration of cells to inflammatory regions. HNE is thought to physiologically participate in disease resistance by facilitating the degradation and phagocytosis of pathogenic bacteria [3]. Uncontrolled activity of HNE has been shown to contribute to the pathogenesis of rheumatoid arthritis [4], chronic obstructive pulmonary disease [5], adult respiratory distress syndrome [6], glomerulonephritis [7], and chronic and burn wounds [8,9].

Lin et al. [10] identified a specific high-affinity DNA ligand targeted to HNE using an in vitro selection technique (SELEX). The DNA ligand folds into a G-quartet structure with duplex ends. According to Davis's work [11], the fluoresceinated DNA ligand equally effective as an anti-HNE antibody in detecting HNE can be useful in diagnostic applications based on flow cytometry. Charlton et al. [12] applied the DNA aptamer ligand to the field of diagnostic imaging.

Fluorescence spectroscopic methods offer high sensitivity and selectivity and applicability in nonseparation detection and in situ monitoring [13–16]. Nutiu and Li [17], for example, described aptamer-based fluorescent reporters for detecting for thrombin over the range of 10 nM–1.0 μM that a structural switch releases a dabcyl-labeled nucleotide strand from the fluorophore-labeled aptamer. Li et al. [18], on the other hand, prepared a molecular aptamer beacon (MAB) for recognizing the thrombin producing significant fluorescent signal change, which is attributed to a significant conformational change at low concentration (112 pM). Lerga and O'Sullivan [19] developed thrombin MAB labeling fluorescein and coumarin to selectively detect Ca^{2+} and Mg^{2+} with detection limit (40 μM) for determination of total water hardness in tap and bottle water. Heyduk and Heyduk [20] introduced a fluorescent assay involving thrombin-induced coassociation of two aptamers with analyte resulted in bringing the two short fluorophore-labeled oligonucleotides into proximity. Change of fluorescence resonance energy transfer was even at the lowest thrombin concentration tested (50 pM).

In our research, we proposed a sensitive method for HNE analysis in homogeneous solution. The molecular beacon was designed by appending fluorescein to 5′-ends and dabcyl quencher to 3′-ends. The HNE aptamer was free-labeled in order to retain the bioactivity. The short DNA scrambled sequence was complementary to the binding sites of the HNE aptamer or the loop of molecular beacon. Our biosensor involves aptamer-HNE recognition, competition between the molecular beacon and loose HNE aptamer for binding the short DNA strand, and monitoring the extent of

* Corresponding author. Fax: +86 731 8822782.
E-mail address: rqyu@hnu.cn (R.-Q. Yu).

0039-9140/$ – see front matter © 2009 Elsevier B.V. All rights reserved.
doi:10.1016/j.talanta.2009.09.019

competition through highly sensitive fluorescence detection of the captured HNE.

2. Experimental

2.1. Materials and reagents

HNE from human plasma (SERVA Electrophoresis GmbH, Heidelberg, Germany) was dissolved in a storage buffer (50 mM Tris–HCl, 50 mM NaCl, 3.0 mM KCl, 1.0 mM $MgCl_2$, pH 7.5) to yield 3.39 μM solutions. This standard was divided into 100 μL aliquots and stored at −20 °C. Immediately before use, each aliquot was warmed to 4 °C and diluted with a storage buffer solution to the required concentration. HNE concentration mentioned in our work was the molarity of HNE storage solution before fluorescence measurements.

Oligonucleotides used in the study were customer-designed and synthesized by Sangon Biotechnology Co. Ltd. (Shanghai, China) as follows.

The HNE aptamer: 5′-TAGC GATA CTGC GTGG GTTG GGGC GGGT AGGG CCAG CAGT CTCGT,
The molecular beacon (MB): 5′-fluorescein-CCTA GCGC GTGG GTTG GGGC TAGG-Dabcyl,
Four scrambled sequence (SS):
S12: 5′-CCCA ACCC ACGC; S14: 5′-GC CCCA ACCC ACGC; S16: 5′-CCGC CCCA ACCC ACGC; S19: 5′-TAC CCGC CCCA ACCC ACGC.

Ultrapure water used to prepare all of the solutions was obtained through a Nanopure Infinity Ultrapure water system (Barnstead/Thermolyne Corp., Dubuque, IA) with an electrical resistance larger than 18.3 MΩ. All buffer solutions and ultrapure water were sterilized and used throughout experiments. Sodium chloride, potassium chloride, human serum albumin (HSA), magnesium chloride and Tris–HCl were purchased from China National Medicines Co. Ltd. (Beijing, China).

2.2. Fluorescence measurements

If not otherwise specified, the following concentrations of oligonucleotides were used for fluorescence measurements: 40 nM for aptamers, 40 nM for the SS and 40 nM for the MB. MB was dissolved in storage buffer to form hairpin duplex, while HNE aptamer and SS were dissolved in ultrapure water to keep flexible structure. The binding buffer (pH 7.5) consisted of 100 mM Tris–HCl, 850 mM NaCl, 16 mM KCl, 5.0 mM $MgCl_2$ and 0.12% HSA (wt.%).

To perform the fluorescence experiments, 50 μL HNE solution of a specific concentration and 100 μL binding buffer were incubated with 50 μL HNE aptamer for 45 min. After the addition of 50 μL of a SS solution, the mixture was incubated for 10 min at 10 °C and then added 50 μL MB solution.

All fluorescence measurements were performed in 50 mM Tris–HCl (pH 7.5), 300 mM NaCl, 6.0 mM KCl, 2.0 mM $MgCl_2$ and 0.02% HSA (wt.%). All fluorescence spectra were recorded on a Hitachi F-4500 fluorescence spectrometer (Hitachi Ltd., Japan) controlled by FL Solution software to fit a curve and determine the peak height. A quartz fluorescence cell with an optical path length of 1.0 cm was used. The excitation was made at 495 nm with a recording emission range of 500–600 nm. All excitation and emission slits were set at 5 nm. The fluorescence spectrum of all mixtures was recorded at 10 ± 2 °C.

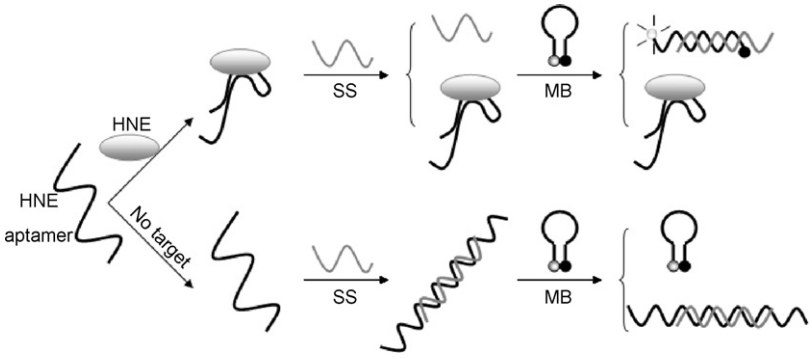
3. Results and discussion

3.1. Experimental principle

Scheme 1 illustrates the concept of the competitive-binding process coupled with fluorescence increase in this design. Before the addition of target, HNE aptamer (the long black coil) kept flexible structure in the blank experiment. SS (the short grey coil) was introduced in this homogeneous solution, and naturally binds to the aptamer. When MB (the short coil with two rotundities) was introduced, the hybridization of SS with MB would not take place immediately, which kept the fluorescence off. In the presence of HNE (the ellipse), the flexible structure of aptamer was transformed into a HNE-aptamer duplex assembly with G-quartet structure. Upon addition of SS and MB, the corresponding complementary sections of SS would hybridize with MB producing a strong concentration-dependent fluorescent signal.

3.2. Fluorescence increase of HNE binding

Fig. 1 demonstrates fluorescence spectra of MB solutions, a mixture of aptamer/SS/MB, an assembly of aptamer/HNE/SS/MB and a duplex of SS/MB. The sample containing MB only (Fig. 1, curve a) shows rather low fluorescence intensity for its hairpin structure keeping the fluorophore and the quencher into proximity. A slight fluorescence increase was observed when the MB was added into solution containing aptamer and SS (curve b). It can be interpreted as that a small quantity of MB captured SS dissociated from aptamer/SS. In the presence of HNE (17 nM, curve c), a significant fluorescence intensity increase (102%) was recorded at the emission peak around 518 nm. Binding of target proteins forces the aptamers to undergo a conformational change, while MB opens its hairpin structure leading to an increase in fluorescent signal. When



Scheme 1. Schematic representation of the aptamer-based HNE sensor. HNE: the ellipse; unmodified aptamer: the long coil; DNA scrambled sequence (SS): the short coil; DNA molecular beacon (MB): the short coil with two rotundities.

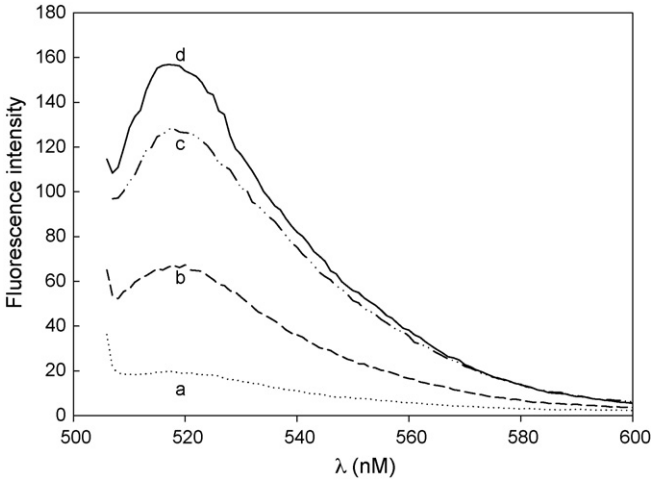


Fig. 1. Fluorescence spectra of solutions containing MB (a), a mixture of aptamer, SS and MB (b), a mixture of aptamer/HNE, SS and MB (c), and a complex of SS/MB (d). The relative standard deviations obtained by five repeated measurements were not more than 5%.

binding buffer contains SS and MB without addition of aptamer (curve d), the fluorescence intensity recorded was the maximum fluorescence intensity obtainable corresponding to the complete hybridization of MB with SS. This observation shows that SS could hybridize really with MB inducing fluorescence increase and HNE could be detected using the proposed method.

3.3. Experimental conditions of target detection

The efficiency of the competitive-binding process depends on the amount of SS released from aptamer and the ability of SS to force the MB stem apart. To investigate the effect of SS strand length on the performance of this method, the aptamer and aptamer/HNE assembly were hybridized with specific SS with a 12-, 14-, 16- or 19-nucleotide segment. As shown in Fig. 2, S12 provides the lowest fluorescent signal in the presence of HNE (curve a′) and also the least background (curve a). S12 has the least number of complementary oligonucleotides, which are too short to promote efficient hybridization with MB. The number of adjacent nucleotides on aptamer-SS binding region was 14 in the assay with S14, S16 or S19. The extra –CG sequence was designed to hybridize with the stem region of MB. The extra sequence might be beneficial to increase the ability of the corresponding SS to force the MB stem apart and restore the fluorescence. When the number of nucleotides rose from 14, 16 to 19, the decreasing background fluorescence in absence of HNE (curves b, c and d) seemed due to the ever increasing hybridizing force between the aptamer and the corresponding SS strand. In presence of HNE (curve b′, c′ and d′), a longer SS strand would induce higher fluorescence increase. In particular, S19 provides the best signal increase for HNE sensing. The extra length of the S19 strand (5′-TAC sequence) might loose the inner molecular interaction between the MB stem sections, which probably lead to fluorescence signal increase. Therefore, S19 was used as optimum SS in the experiment.

We also investigated the effects of pH on the response of the proposed sensor to HNE over the pH range from 7.0 to 9.0 and

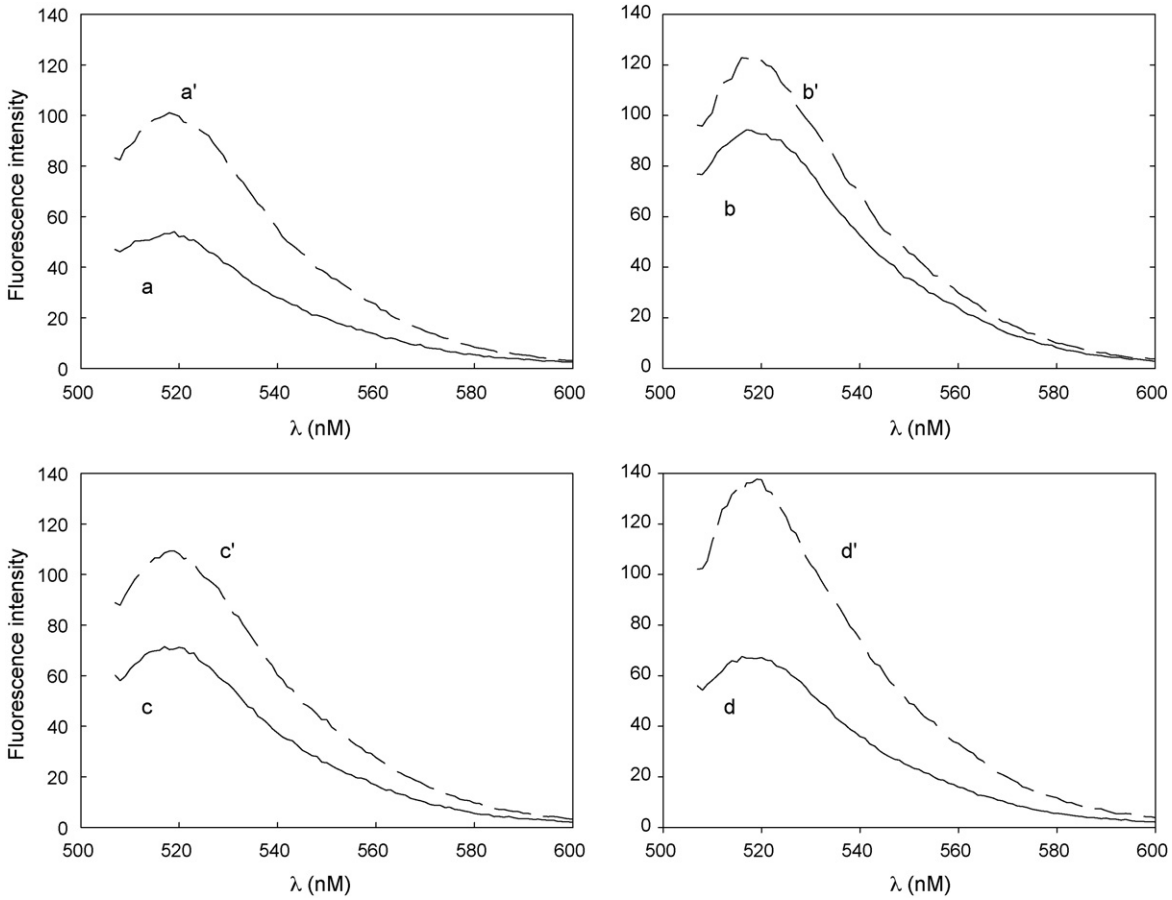


Fig. 2. Fluorescence spectra of the sensor using S12 (a and a′), S14 (b and b′), S16 (c and c′) and S19 (d and d′) with and without HNE respectively. The relative standard deviations obtained by five repeated measurements were not more than 5%. S12: 5′-CCCA ACCC ACGC; S14: 5′-GCCC CAAC CCAC GC; S16: 5′-CCGC CCCA ACCC ACGC; S19: 5′-TACC CGCC CCAA CCCA CGC.

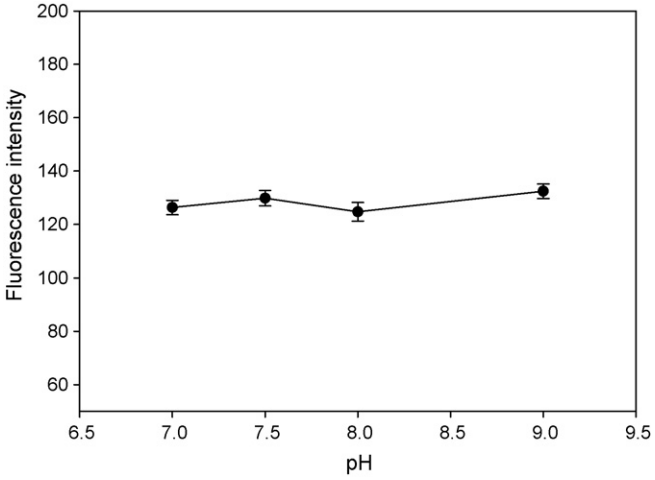


Fig. 3. The effect of pH of the incubating solution on the activity of the sensor containing HNE (17 nM). The standard deviations obtained by five repeated measurements were shown as the error bars.

the results are shown in Fig. 3. As can be seen, the sensor can be carried out in this pH range. There is no obvious change in the fluorescence of the assay when the pH of the buffer increases from 7.0 to 9.0. This indicates that competitive-binding reaction can occur over a wide pH range. An ideal pH of 7.5 was chosen for the sensor experiments, which is also a general pH value in immunology.

Thermal denaturation experiments were performed (Fig. 4) to investigate the relationship between fluorescence signal and incubation temperature. For this purpose, we increased the incubation temperature from 10 to 24, 37 or 45 °C. The binding event of aptamer/S19 is less efficient at high temperatures in the absence of HNE (Fig. 4, closed circles), resulting in the increase in fluorescence background. The low fluorescence intensity at 45 °C in absence or presence of HNE was possible due to the thermal quenching of the fluorescence. After introducing the analyte (Fig. 4, open circles), a high incubation temperature might lead to the HNE protein denaturalization. As a result, more aptamer dissociated from aptamer/HNE conjugate and hybridized with S19, bringing fluorescence intensity to decrease. This phenomenon indicated that the optimum incubation temperature was 10 °C.

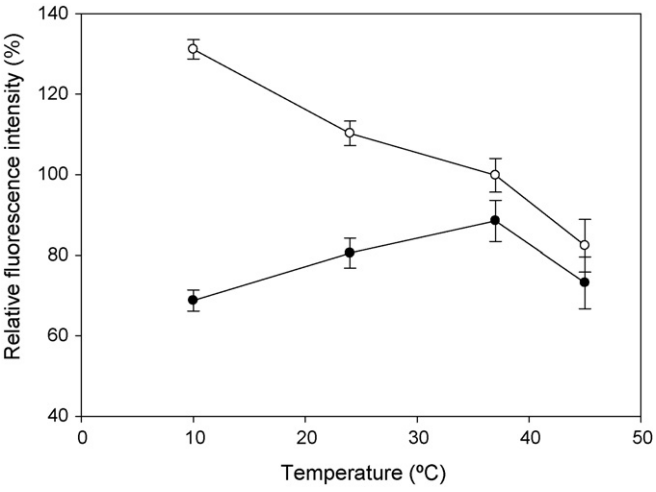


Fig. 4. The DNA aptamer mixture was incubated at 10, 24, 37 and 45 °C with (open circles) and without (closed circles) 17 nM HNE. The standard deviations obtained by five repeated measurements were shown as the error bars.

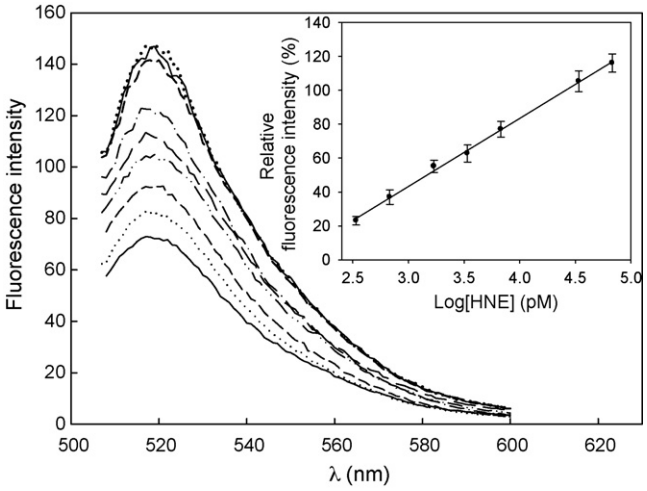


Fig. 5. Fluorescence spectra of sensors in the presence of HNE at different concentrations (from bottom to top): (1) 0.067 nM; (2) 0.34 nM; (3) 0.68 nM; (4) 1.7 nM; (5) 3.4 nM; (6) 6.8 nM; (7) 34 nM; (8) 68 nM; (9) 110 nM. Inset shows the linear fluorescence responses to the logarithm of HNE concentration in the range of 0.34–68 nM. The illustrated error bars represent the standard deviation of three measurements obtained at each HNE concentration.

3.4. Analytical performance of the aptamer-based sensor

Fig. 5 shows the change in fluorescence signal as a function of the HNE concentration. With the increased amount of HNE, the fluorescence intensity of the aptamer probe is increased. The relative fluorescence intensity R (%) was calculated from the equation $R(\%) = ((F_{\text{target}} - F_{\text{no target}})/F_{\text{no target}}) \times 100\%$, where F is the fluorescence intensity, and the subscripts "target" and "no target" refer to the case in the presence and absence of HNE respectively. Significantly, the aptamer-based sensor exhibited a high degree of sensitivity for HNE (Fig. 5, inset). And the response is linear in the tested concentration range of 0.34–68 nM ($r = 0.9980$). The linear regression equation was expressed as

$$\text{Relative fluorescence intensity}\,(\%) = 40.12\ \log[\text{HNE}] - 77.09$$

The detection limit (at S/N = 3) calculated from the slope of the calibration curve in the lowest concentration range was 47 pM.

3.5. Specificity of the HNE fluorescence sensor

Due to the inherent specificity of the aptamer toward its target protein, the fluorescence change of the HNE biosensor is highly

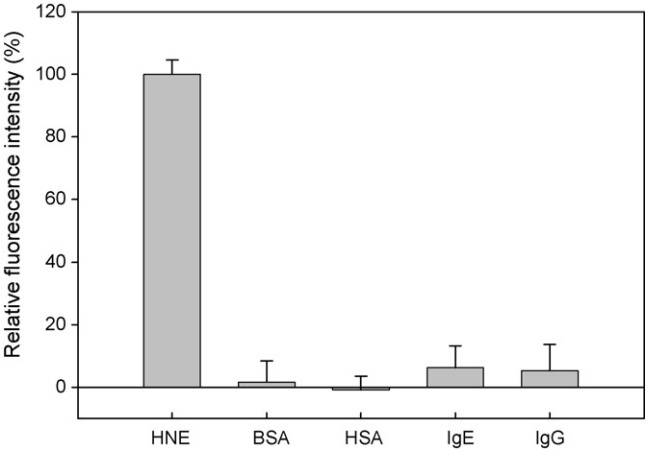


Fig. 6. Selectivity for the proposed sensor of five proteins. The sensor was exposed to HNE (17 nM) or other four proteins (BSA, HSA, IgE and IgG, 85 nM) respectively. Error bars were estimated from at least three independent measurements.

selective. Aliquots of the aptamer was incubated with either HNE (17 nM) or some other proteins commonly present in serum such as bovine serum albumin (BSA), human serum albumin, immunoglobulin E (IgE) and immunoglobulin G (IgG). The relative responses to fluorescence changes of the interfering protein, even at 5-fold higher concentrations (85 nM) than those used for HNE, are negligible in comparison to those from HNE (seen in Fig. 6). Hence the developed biosensor could exhibit a high degree of selectivity for the HNE detection, as expected.

4. Conclusion

We have developed a fluorescence aptasensor for the detection of protein HNE in homogeneous solution using MB. The proposed sensor was designed to observe its fluorescence intensity increase, which was attributed to the difference in structure-switching between the free aptamer and its HNE binding complex. The proposed strategy has been proved applicable in HNE aptasensing. This is of paramount importance for a new selective and highly sensitive method of HNE detection.

Acknowledgements

This research was supported by the National Natural Science Foundation of China (Grants No. 20675028 and 20775023), the "973" National Basic Research Program of China (No. 2007CB310500) and the Science Commission of Hunan Province.

References

[1] C. Nathan, Nat. Rev. Immunol. 6 (2006) 173.
[2] N.D. Burg, M.H. Pillinger, Clin. Immunol. 99 (2001) 7.
[3] P. Birrer, Agents Actions Suppl. 40 (1993) 3.
[4] L. Ekerot, K. Ohlsson, Adv. Exp. Med. Biol. 167 (1984) 335.
[5] S.D. Shapiro, Biochem. Soc. Trans. 30 (2002) 98.
[6] C. Jaffray, J. Yang, G. Carter, C. Mendez, J. Norman, Surgery 128 (2000) 225.
[7] T. Oda, O. Hotta, Y. Taguma, H. Kitamura, K. Sudo, I. Horigome, S. Chiba, N. Yoshizawa, H. Nagura, Hum. Pathol. 28 (1997) 720.
[8] D.R. Yager, S.M. Chen, S.I. Ward, O.O. Olutoye, R.F. Diegelmann, I.K. Cohen, Wound Repair Regen. 5 (1997) 23.
[9] F. Grinell, M. Zhu, J. Invest. Dermatol. 103 (1994) 155.
[10] Y. Lin, A. Padmapriya, K.M. Morden, S.D. Jayasena, Proc. Natl. Acad. Sci. 92 (1995) 11044.
[11] K.A. Davis, B. Abrams, Y. Lin, S.D. Jayasena, Nucleic Acids Res. 24 (1996) 702.
[12] J. Charlton, J. Sennello, D. Smith, Chem. Biol. 4 (1997) 809.
[13] M.U. Kumke, G. Li, C.P. Linn, G.T. Walker, L.B. McGown, Anal. Chem. 67 (1995) 3945.
[14] X. Fang, J.J. Li, W. Tan, Anal. Chem. 72 (2000) 3280.
[15] C.J. Yang, H. Lin, W. Tan, J. Am. Chem. Soc. 127 (2005) 12772.
[16] L. Wang, C.J. Yang, C.D. Medley, S.A. Benner, W. Tan, J. Am. Chem. Soc. 127 (2005) 15664.
[17] R. Nutiu, Y. Li, J. Am. Chem. Soc. 125 (2003) 4771.
[18] J.J. Li, X. Fang, W. Tan, Biochem. Biophys. Res. Commun. 292 (2002) 31.
[19] T.M. Lerga, C.K. O'Sullivan, Anal. Chim. Acta 610 (2008) 105.
[20] E. Heyduk, T. Heyduk, Anal. Chem. 77 (2005) 1147.

Talanta 80 (2010) 1269–1276

Contents lists available at ScienceDirect

Talanta

journal homepage: www.elsevier.com/locate/talanta

The influence of indoxyl sulfate and ammonium on the autofluorescence of human urine

Sandeep Menon Perinchery[a], Unnikrishnan Kuzhiumparambil[b], Subramanyam Vemulpad[c], Ewa M. Goldys[a,d,*]

[a] Department of Physics and Engineering, Macquarie University, Sydney 2109, NSW, Australia
[b] Department of Chemistry and Biomolecular Sciences, Macquarie University, Sydney 2109, NSW, Australia
[c] Faculty of Science, Macquarie University, Sydney 2109, NSW, Australia
[d] ARC/NHMRC Network "Fluorescence Applications in Biotechnology and Life Sciences", Macquarie University, Sydney 2109, NSW, Australia

ARTICLE INFO

Article history:
Received 25 August 2009
Received in revised form
11 September 2009
Accepted 13 September 2009
Available online 18 September 2009

Keywords:
Autofluorescence
Human urine
Indoxyl sulfate
Inner filter effect
Quenching

ABSTRACT

Despite biological variability the spectral characteristics of undiluted human urine show relatively low autofluorescence at short UV (250–300 nm) excitation. However with dilution the fluorescence intensity remarkably increases. This paper examines the mechanisms behind this effect, by using excitation–emission matrices. Corrections for the inner filter effect were made for improved understanding of the spectral patterns. We focused on three major fluorophores (tryptophan, indoxyl sulfate and 5-hydroxyindole-3-acetate) that are excited at these wavelengths, and whose content in urine is strongly linked with various health conditions. Their fluorescence was studied both individually and in combinations. We also examined the effect of ammonium on the fluorescence of these major fluorophores individually and in combinations. Through these studies we have identified the leading effects that reduce the UV fluorescence, namely higher concentration of indoxyl sulfate producing the inner filter effect and concentration quenching and quenching of fluorophores by ammonium. This result will assist in broader utilisation of UV fluorescence in medical diagnostics.

© 2009 Elsevier B.V. All rights reserved.

1. Introduction

Human urine is a complex biological fluid containing a range of chemical compounds produced by the body, some of which are fluorescent [1–3]. The concentration of fluorophores in urine is influenced by many factors including body metabolism, dietary intake, age and disease [1,2]. Thus the measurement of autofluorescence of urine is, in principle, able to provide an indication of a number of health conditions, including urinary tract infection, proteinuria, renal disorder, nephrotic syndrome, hepatopathy, and neuronal ceroid lipofuscinosis [3–6]. However, despite the simplicity and speed of the fluorescence measurement, urine fluorescence is underutilised in medical diagnostics. One of the key impediments is the observed high inter- and intra-individual variability of the fluorescence properties. Moreover, the broad spectral features of individual fluorophores tend to overlap, making the data interpretation quite complex and the identification of chemical constituents extremely difficult. Upon closer inspection, the spectral characteristics of urine fluorescence are somewhat less variable at short UV excitation wavelengths (250–300 nm), corresponding to the region where the key, most abundant indole fluorophores, tryptophan and its metabolites can be excited (Supplemental material, Table 1) [7]. These fluorophores are directly linked to cellular metabolism and, indirectly, to various health conditions. However, they are practically difficult to observe in undiluted healthy human urine that shows very weak fluorescence with short UV excitation [5]. Thus the majority of earlier studies have focused on analyzing diluted urine [7]. The dilution greatly enhances the fluorescence of tryptophan and its metabolites, but it tends to compromise the fluorescence from less abundant components observable in other spectral regions, possibly reducing the diagnostic potential of such measurement. Moreover, it would be preferable to be able to use undiluted urine for diagnostics due to simpler procedures.

Our work is aimed at a better understanding of urine fluorescence by identifying and quantifying the factors responsible for low intensity of fluorescence when excited at 250–300 nm. The principles governing the observed fluorescence intensity of fluorophores are well established; they include the value of fluorophore quantum yield, the possibility of fluorescence quenching occurring at higher concentrations, and the reduced intensity of exciting light (or emitted light or both) known as the inner filter effect [8,9].

* Corresponding author at: Department of Physics and Engineering, Faculty of Science, Macquarie University, Sydney 2109, NSW, Australia. Tel.: +61 2 98508902; fax: +61 2 98508115.
E-mail address: goldys@ics.mq.edu.au (E.M. Goldys).

0039-9140/$ – see front matter © 2009 Elsevier B.V. All rights reserved.
doi:10.1016/j.talanta.2009.09.020

As urine is a multicomponent liquid, there is an additional possibility of energy transfer [5]. However, no detailed investigations of these factors have been reported. We focused on studying the three most abundant, high quantum yield fluorophores excited at 250–300 nm, indoxyl sulfate, tryptophan and 5-hydroxyindole-3-acetate and the abundant non-fluorescent ammonium known for its quenching properties. A clearer understanding of the interactions between the key fluorophores and other components in urine is essential to broaden the potential of fluorescence as a diagnostic tool.

2. Experimental methodology

2.1. Urine samples

Urine samples were collected from a local pathology laboratory where they were analyzed for pH, protein, glucose, bilirubin, nitrate, specific gravity, blood, ketones, urobilinogen and leukocyte esterase. The presence of red blood cells, white blood cells, casts, epithelial cells and crystals was also tested for these samples (using iQ200 Sprint, IRIS Diagnostics Division, Chatsworth, CA). Semi-quantitative culture on chromogenic agar plates was also carried out to test for the presence of bacteria. A total of 46 human urine samples were used in this study, including samples from 35 males (age 2–90 years) and 11 females (age 5–90 years). These samples showed no abnormal laboratory findings, *i.e.*, they were culture-negative as well as negative for other abnormal findings such as protein, glucose, bilirubin, nitrate, specific gravity, blood, ketones, urobilinogen, leukocyte esterase and they had pH within the range of 5–7. They are referred to as healthy human samples. The urine samples were stored in a refrigerator (4 °C) and examined within 48 h after collection.

2.2. Other materials and reagents

L-Tryptophan, indoxyl sulfate and 5-hydroxyindole-3-acetate were obtained from Sigma–Aldrich (Sydney, Australia). Stock solutions of 300 μmol indoxyl sulfate, 50 μmol of L-tryptophan and 24 μmol of 5-hydroxyindole-3-acetate were prepared in deionised water. The required dilutions of ammonia (Unilab, Sydney, 28%, v/v) were made in milli-Q water. We also used 'simulated urine' that consisted of a mixture of 300 μmol indoxyl sulfate, 50 μmol of L-tryptophan and 24 μmol of 5-hydroxyindole-3-acetate (at approximately physiological concentrations) with a pH of 5.1.

2.3. Measurement of autofluorescence

The fluorescence was measured using a Fluorolog Tau3 system (JY Horiba, Edison, NJ) in 10 mm quartz cuvettes at room temperature. The fluorescence emission spectra after excitation at various wavelengths as well as the excitation/emission matrices (EEMs) were obtained. These three-dimensional plots of fluorescence intensity as a function of excitation and emission wavelengths represent the complete fluorescence characteristics of the sample. In order to cover the broad spectral region of relevance in the most time-efficient way, four separate smaller EEMs were obtained and digitally integrated into a single one using MATLAB. In EEM measurements the spectral band passes were 5 nm in both excitation and emission. The spectra were corrected for optical system response.

2.4. Measurement of absorption

The absorption was measured using double beam CARY absorption spectrometer system (Varian Inc., USA) in 10 mm quartz cuvettes at room temperature.

2.5. Liquid chromatography–mass spectrometry (LC–MS) analysis

The mass spectrum was obtained on a Shimadzu LCMS 2010 EV system with an SIL 20 AL autosampler. The mobile phase was water–acetonitrile (9:1, v/v) in the isocratic mode, with a flow rate of 0.2 mL/min. The analysis was performed with the Electron Spray Ionisation (ESI) probe.

3. Results and discussion

3.1. Spectral characteristics of undiluted healthy human urine

The literature on urine fluorescence is surprisingly scarce in spite of its easy availability [5,7] and it is therefore worthwhile to present some examples of urine spectral characteristics. Fluorescence characteristics of urine are variable and strongly sample-dependent. Two examples of excitation/emission matrices of undiluted healthy samples with different spectral features are shown in Fig. 1a and b. The observed differences are due to variations in the relative composition of fluorophores in the urine. The fluorescence is observed mainly at 300–450 nm excitation wavelength range and we note that one of the samples (Fig. 1a) shows similar characteristics to that reported by Kusnir and Leskova [5]. The identification of the fluorescence features is difficult due to the similarities in the spectral properties of the component fluorophores and large spectral widths; however, the spreading of the spectral features in a two-dimensional EEM makes the task easier. The major fluorophores which are likely to contribute to urine fluorescence at 300–450 nm excitation are 4-pyridoxic acid, pterins, flavins and porphyrins [4,7].

It is apparent from Fig. 1a and b that autofluorescence of urine excited in 250–300 nm range is very weak when compared to longer UV (300–450 nm) excitation. This property was consistently observed in all samples examined in this study and in our earlier work [6]. In order to establish the level of individual variability at the short UV excitation wavelengths we used a larger set of 40 samples taken from a mixed age/gender population (Fig. 1c). The fluorescence spectra when excited at 290 nm for all these samples have a similar spectral pattern with some intensity variations. The peak fluorescence was observed at 420 ± 15 nm and the peak intensity varied by ±50%. We were unable to identify any sub-classes in these spectra based on gender or age, by using the Principal Component Analysis.

Thus, we have established that the key fluorescence features of undiluted healthy human urine are observed at 300–450 nm excitation and are highly variable, while shorter UV excitation produces only very weak fluorescence that is much more consistent. This finding is in agreement with the earlier literature that introduced the terms "group A" and "group B" fluorophores excited at 250–300 nm, and 300–450 nm, respectively [5,7]. Accordingly, the EEM in Fig. 1a and b shows very prominent but less abundant group B fluorophores, some of which are of direct dietary origin and highly variable, while the group A fluorophores, which are more abundant, are barely observed. This low intensity of group A fluorophores is generally attributed to fluorescence quenching [5,7].

3.2. Spectral characteristics of diluted healthy human urine

The dilution of the urine profoundly affects the excitation/emission matrices. This is shown in Fig. 2 where we compared the EEMs for healthy human urine at various dilutions (1:30, 1:300 and 1:1000). In undiluted urine we observed features at 365 nm/470 nm (where 365 nm refers to peak excitation wavelength and 470 nm to peak emission wavelength), 380 nm/520 nm

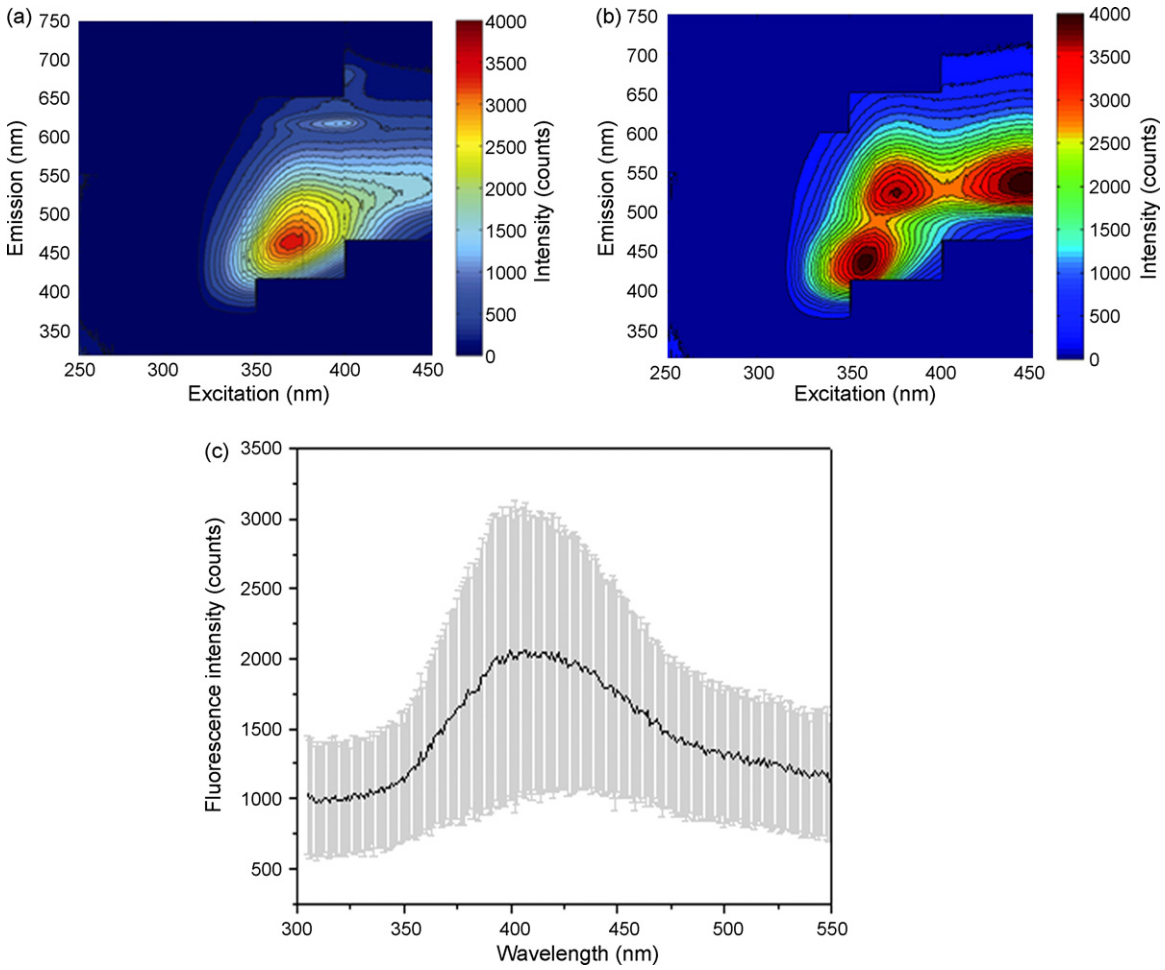


Fig. 1. (a and b) Excitation/emission matrices of two representative undiluted healthy human urine samples. (c) The mean emission spectrum for 40 undiluted healthy human urine samples at 290 nm excitation (black line). The error bars represent standard deviation.

and at 400 nm/625 nm (attributable to group B fluorophores). These disappear at 1:30 dilution, and a moderately intense emission peak at 325 nm/425 nm emerges (tentatively attributed to 4-pyridoxic acid [7]) and a very weak 290 nm/350 nm feature attributable to one of group A fluorophores. At 1:300 dilution, the peak at 325 nm/425 nm practically disappears but the 290 nm/350 nm peak becomes more intense. With 1:1000 dilution, this peak dominates the spectrum. This result shows that by adjusting the dilution, especially in the range from 1:30 to 1:1000 it is possible to enhance emission of various fluorophores that are not observable without dilution. This is because the undesired absorption of excitation light at lower dilutions that underpins the inner filter effect is reduced or eliminated at higher dilutions [8]. Thus, high dilution expands the spectral window available for fluorescence observation. Consequently, high dilution makes it possible to start observing the group A fluorophores (Fig. 2b and c). As the dilution is increased, at some point, the quenching starts to be reduced as well, and this additionally enhances the fluorescence from group A fluorophores (Fig. 2d). We now discuss the details of these two effects and the influence they have on the EEMs of urine.

3.3. The inner filter effect

The recorded fluorescence intensity may not be proportional to the fluorophore concentration due to a well known phenomenon known as the inner filter effect [10]. This can be due to high absorption of excitation light by the sample (primary inner filter effect) and by reabsorption of emitted light (secondary inner filter effect) [10]. Both can be completely accounted for and the spectra can be corrected. The correction for the primary inner filter effect can be done using the following equation [10,11],

$$\beta_i = \frac{\alpha_i L_i}{1 - \exp(-\alpha_i L_i)} \quad (1)$$

where β_i is the inner filter correction factor by which the spectra need to be multiplied, α_i is the optical density for the sample at the excitation wavelength and L_i is the cuvette dimension. In deriving this equation, two assumptions are made that the optical density for the emitted light is negligible and the fluorescence is collected from the full length of the cuvette. This correction requires the knowledge of the absorption spectra that are presented in Fig. 3. The absorption spectrum of human urine (Fig. 3a) indicates that the absorbance, especially in the region 250–350 nm, is quite high (note that the absorption spectra in Fig. 3 were taken at 1:10 dilution as compared to physiological conditions). It is well known that in order to avoid the inner filter effect, the optical density of the sample for fluorescence measurement should be less than 0.05 [8,9,12]. Thus, Fig. 3a indicates that the primary inner filter correction factors are significant in the range below 300 nm, especially for undiluted urine. At the same time, the absorbance in 300–500 nm range is negligible; hence, the secondary inner filter correction (equation not shown) is not required. On these grounds our EEMs and the underlying spectra have been corrected by using Eq. (1) so that the issue of quenching can be addressed.

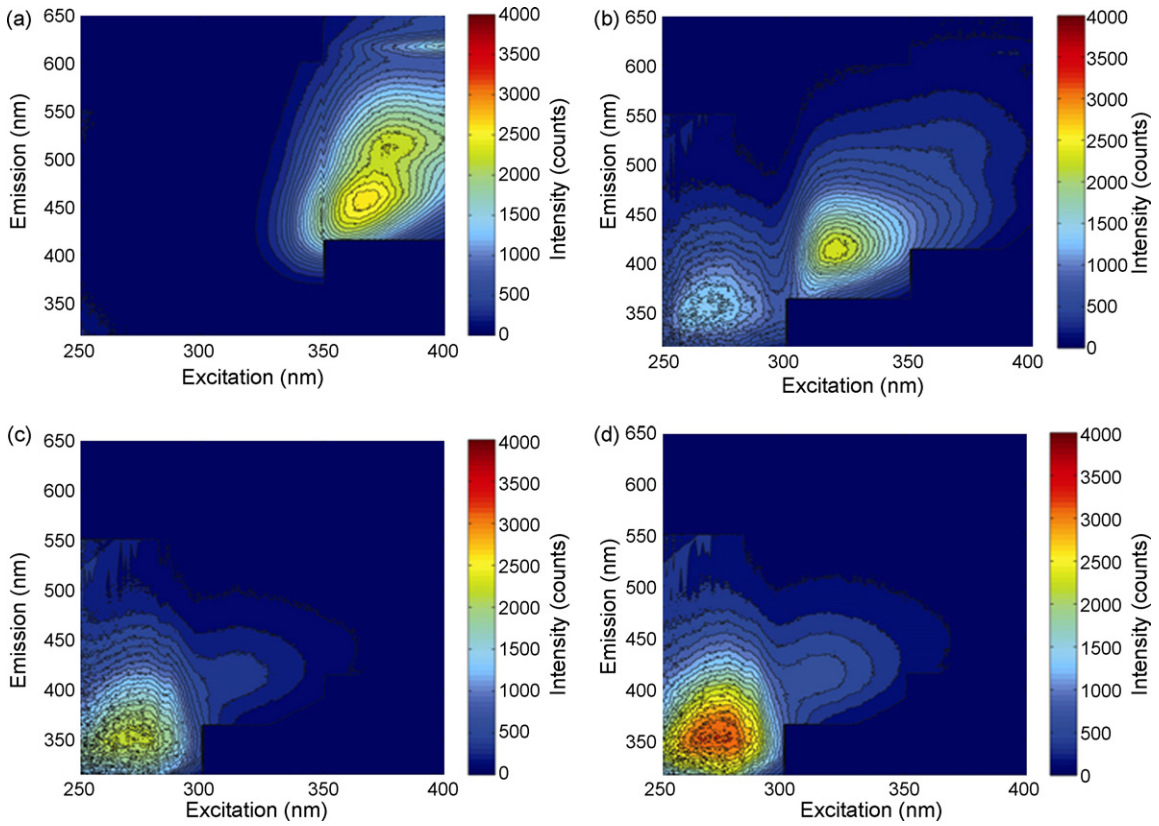


Fig. 2. Excitation/emission matrices of healthy urine sample. (a) Undiluted urine and (b–d) diluted 1:30, 1:300 and 1:1000, respectively.

It is illustrative to see the influence of the inner filter effect in the EEM matrices of a selected component of urine, indoxyl sulfate (Fig. 4a–c), which produces dramatically varying spectral features as the dilution is varied. The EEM of indoxyl sulfate at physiological concentration of 300 μmol shows a peak at 300 nm/380 nm. At 1:10 and 1:1000 dilutions, the peak excitation changes to 280 nm but the emission maximum remains the same, *i.e.*, 380 (±10) nm.

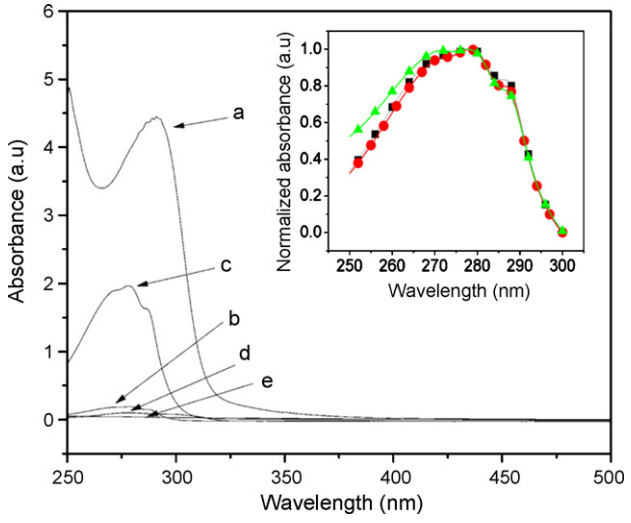


Fig. 3. Comparison of optical absorption spectra. (a) Healthy human urine, (b) tryptophan (50 μmol), (c) indoxyl sulfate (300 μmol), (d) 5-hydroxyindole-3-acetate (24 μmol), which were all diluted 1:10 in double distilled water and (e) 19 mmol of ammonium in distilled water. The inset shows the absorption spectra of 300 μmol of indoxyl sulfate at various dilutions. (-■-) undiluted, (-●-) diluted 1:1, (-▲-) diluted 1:30.

This result shows that interpreting peaks in emission spectra or excitation/emission matrices needs to be done with a great deal of caution, as major shifts and spectral shape changes can be observed at higher fluorophore concentration, when the inner filter effect is operational. Indeed, Fig. 3c indicates that indoxyl sulfate at physiological concentration contributes significantly to the total absorption of undiluted urine (OD = 17 at peak) and that the fluorescence data for indoxyl sulfate must be corrected for the inner filter effect. However, these matrices can be corrected, by using the inner filter correction (Eq. (1)), provided the inner filter effect does not reduce fluorescence to unobservable levels. Fig. 4d shows an EEM corrected for the inner filter effect, and we note that the corrected EEM shows a close similarity with the EEM for a highly diluted fluorophore (Fig. 4c).

3.4. Fluorescence quenching in urine

With the inner filter effect fully accounted for, we are able to establish the extent of fluorescence quenching in this complex fluid. In order to capture the key features of all quenching processes, we focused on the most abundant group A fluorophores, indoxyl sulfate, tryptophan and 5-hydroxyindole-3-acetate [7]. The fluorescence of these three fluorophores was studied in isolation as well as in mixtures, including a representative 'simulated urine' with selected urine components (indoxyl sulfate, tryptophan and 5-hydroxyindole-3-acetate) at typical physiological concentrations of 300, 50 and 24 μmol, respectively. In order to establish the significance of the inner filter effect we also measured the absorbance of these three fluorophores (see Fig. 3 where a 1:10 dilution was used to obtain measurable values). As indicated earlier, the absorbance of indoxyl sulfate at physiological concentration is high, and the other two fluorophores did not show significant absorption in the examined region.

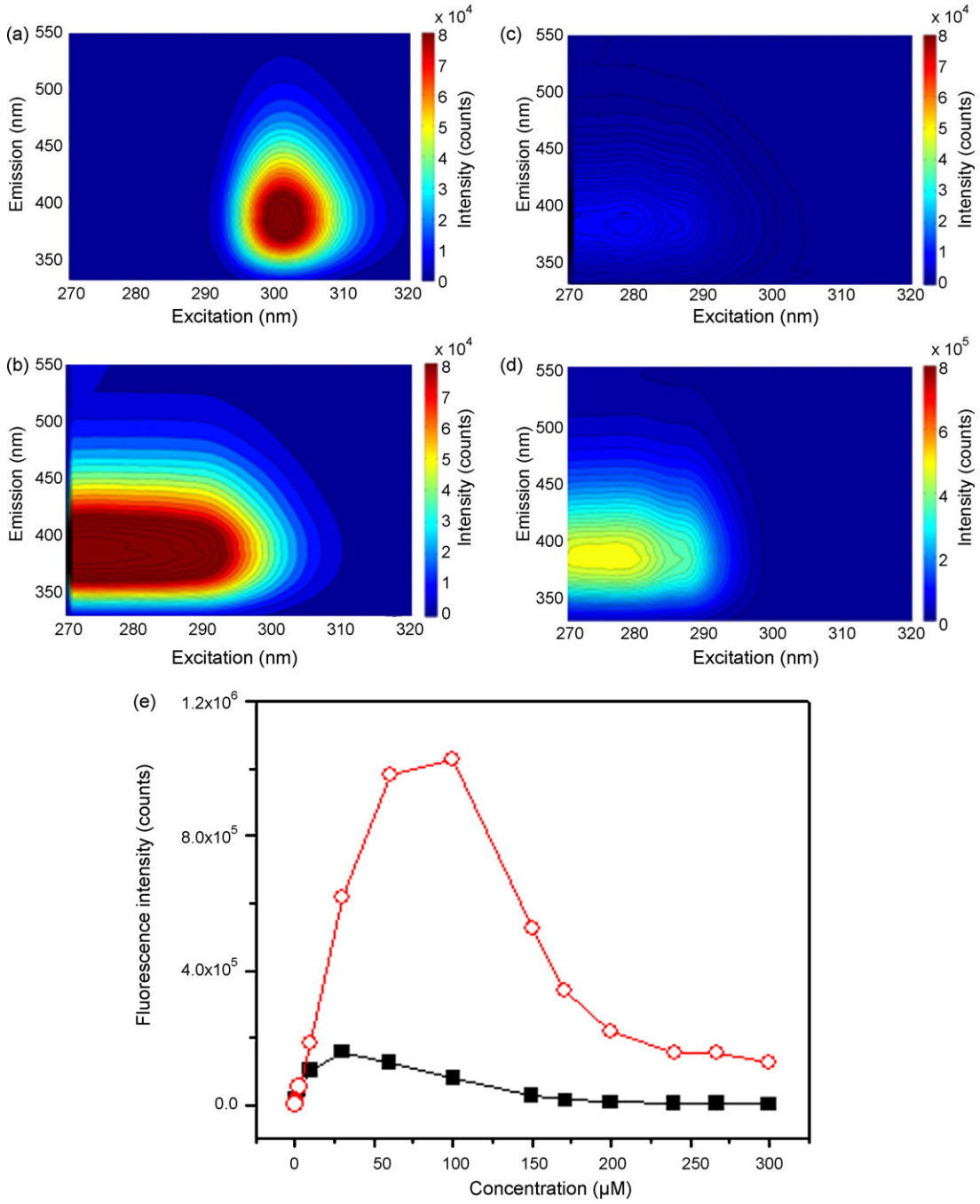


Fig. 4. Excitation/emission matrices of indoxyl sulfate. (a) Indoxyl sulfate at a concentration of 300 μmol, (b) diluted 1:1000 in double distilled water, (c) diluted 1:10 in double distilled water, (d) 1:10 dilution corrected for the inner filter effect and (e) fluorescence intensity at 280 nm/380 nm *versus* concentration of indoxyl sulfate; (-■-) uncorrected data; (-○-) data corrected for the inner filter effect; note the different colour scale in (d).

We measured the fluorescence of indoxyl sulfate as a function of dilution. Fig. 4e shows the peak fluorescence intensity at 280 nm/380 nm, of indoxyl sulfate at various concentrations, before and after correcting for the inner filter effect. It shows that the fluorescence intensity at 300 μmol concentration after correcting for the inner filter effect is lower than that of the 30 μmol concentration, confirming that at physiological concentration (300 μmol), indoxyl sulfate exhibits concentration quenching. Consequently, indoxyl sulfate in undiluted healthy human urine must also be subject to concentration quenching (self-quenching). We examined the other two fluorophores, tryptophan and 5-hydroxyindole-3-acetate below and at physiological concentrations. These did not show the self-quenching effect (data not presented).

Common mechanisms behind concentration quenching include collisional quenching and dimer formation. The dimers are known to show a relatively weak fluorescence compared with fluorescent monomers [13]. In order to test this possibility, we used liquid chromatography/mass spectrometry (LCMS) to detect the presence of indoxyl sulfate dimers at physiological concentration. The peak at 463 (mass/charge) in the LCMS (Supplemental material, Fig. 2) indicates that dimers are indeed formed, but at a low relative concentration of 10% compared with the monomers. Also, aggregate formation if significant, could change the shape and shift the maxima of absorption bands [14]. The absorption spectra of urine as well as its key fluorescent component at varying dilutions, do not suggest much influence of aggregate formation, as seen by the

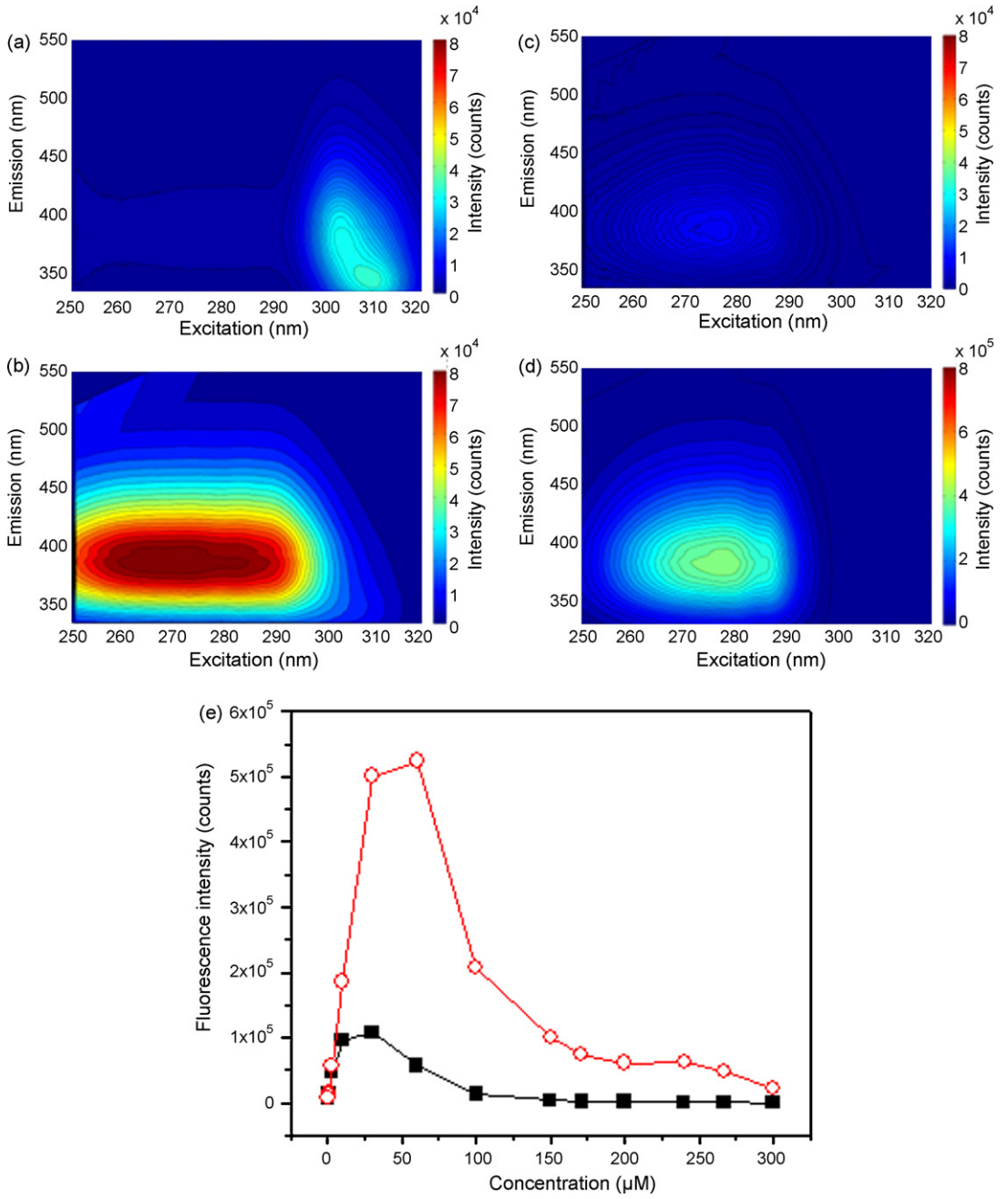


Fig. 5. Excitation/emission matrices of 'simulated urine' containing indoxyl sulfate (300 μmol), tryptophan (50 μmol) and 5-hydroxyindole-3-acetate (24 μmol). (a) Undiluted; (b) diluted 1:1000; (c) diluted 1:10; (d) diluted 1:10, with spectra corrected for inner filter effect. Note the different colour scale in (d). All dilutions were made in double distilled water. (e) Fluorescence intensity at 280 nm/380 nm of 'simulated urine' as a function of indoxyl sulfate concentration. (-■-) uncorrected data; (-○-) data corrected for the inner filter effect.

almost identical absorption of indoxyl sulfate at physiological concentration and at two dilutions (Fig. 3, inset). Thus we infer that the fluorescence reduction due to dimer or aggregate formation is very minimal. We therefore propose collisional quenching as the major mechanism of concentration quenching by indoxyl sulfate at physiological concentrations.

We also studied the mutual interactions between the three key group A fluorophores (tryptophan, 5-hydroxyindole-3-acetate and indoxyl sulfate) at physiological concentrations and at various dilutions. In the presence of indoxyl sulfate, the fluorescence of tryptophan as well as 5-hydroxyindole-3-acetate showed reduced fluorescence (data not shown). The fluorescence intensity of the 'simulated urine' (a combination of these three fluorophores) was also very weak, with a peak at 310 nm/340 nm (Fig. 5a–c). This is consistent with the spectral position for the 5-hydroxyindole-3-acetate peak (Supplemental material, Table 1), although in light of a very strong inner filter effect, an unambiguous assignment is not possible. Overall, the trend observed in Fig. 5 with dilution is similar to that in Fig. 4, *i.e.*, a deformed peak at 1:10 dilution which, after correction for the inner filter effect, reveals a pure indoxyl sulfate feature, more clearly observed at 1:1000 dilution. This is an indication that indoxyl sulfate reduces the fluorescence of tryptophan and 5-hydroxyindole-3-acetate when these are in combination. Moreover, the maximum fluorescence intensity at physiological concentration of the 'simulated urine' (Fig. 5a) is significantly lower than that of indoxyl sulfate alone

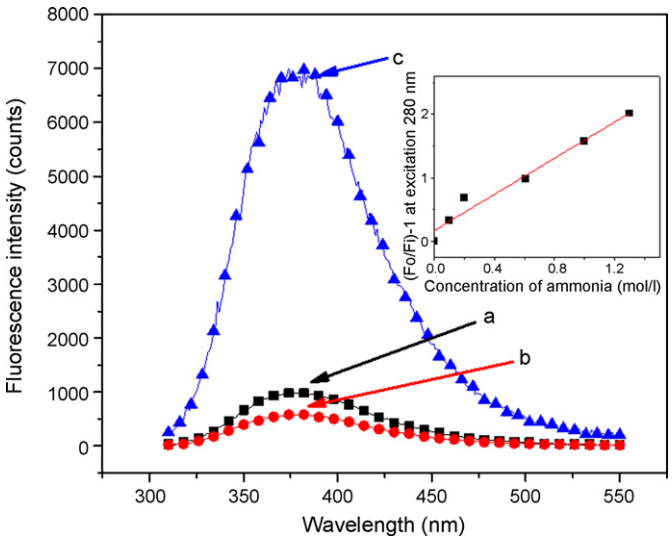


Fig. 6. Effect of the addition of varying amounts of ammonium on the fluorescence spectra of 'simulated urine' containing tryptophan (50 μmol), indoxyl sulfate (300 μmol) and 5-hydroxyindole-3-acetate (24 μmol), at 280 nm excitation. (a) 'Simulated urine', without any ammonium, (b) 'simulated urine' with 19 mmol of ammonium and (c) 'simulated urine' with 19 mmol of ammonium, diluted 1:10 with double distilled water. The inset shows the Stern–Volmer plot representing the fluorescence quenching of the 'simulated urine' by ammonium (fluorescence intensity at 380 nm for excitation at 280 nm as a function of ammonium concentration).

(Fig. 4a), confirming energy transfer between these fluorophores and indoxyl sulfate. Similar to the case of pure indoxyl sulfate, the concentration quenching was confirmed by observing the concentration trends in peak fluorescence intensity of the 'simulated urine' before and after correcting for inner filter effect (Fig. 5e).

Finally, we explored the effect of other non-fluorescent components in urine, on its fluorescence. As previously, we focused on the key group A fluorophores, indoxyl sulfate, tryptophan and 5-hydroxyindole-3-acetate and their interaction with a major non-fluorescent component ammonium. Ammonium was selected because it is reported to be an efficient quencher of indole fluorophores [15], and this behaviour is confirmed in our study. Moreover, its physiological concentration tends to be high, and a 24 h sample of normal human urine contains 19 mmol (0.7 g) of ammonium, derived from protein metabolism and from glutamine in kidneys. The concentration of ammonium varies depending on blood and tissue fluid acidity [16]. Fig. 6 shows that the addition of a physiological amount of ammonium lowers the fluorescence of the 'simulated urine' by a factor of two. To understand the quenching effect in detail, the Stern–Volmer quenching constant was calculated using the following equation [12]:

$$\frac{F_0}{F} = 1 + K[Q] \quad (2)$$

where F_0 and F are the fluorescence intensities in the absence and presence of quencher (ammonium), [Q] is the concentration of quencher and K is the Stern–Volmer constant. The K value was calculated to be approximately 1.4 L/mol. The Stern–Volmer plot is shown in Fig. 6(inset).

Our additional quenching studies, with each of the three fluorophores independently, showed that ammonium quenched the fluorescence of all the three examined fluorophores, tryptophan, indoxyl sulfate and 5-hydroxyindole-3-acetate (data not presented). Fig. 6 also shows that dilution reduces the quenching of 'simulated urine' by ammonium, as expected. However, the fact that in Fig. 6 the emission peak of 'simulated urine' does not change with dilution indicates that the concentration quenching is not due to reabsorption. This result is consistent with the increased intensity observed for the human urine at shorter UV region with dilution (Fig. 2). Separately, we observed that ammonium also reduced the fluorescence of each of the three examined fluorophores in a concentration dependent way (data not shown). The overall conclusion from this study is that the key indole fluorophores in healthy human urine are quenched by the presence of ammonium. The mechanism behind this quenching is the sensitivity of indole fluorophores to the local environment [12,17–19]. The electron transfer from excited fluorophores to ammonium has been reported to be the cause of this quenching [15].

A survey of the literature indicates that the fluorescence properties of human urine are also affected by factors other than those examined here. For example, the pH can rebalance the fluorescence intensities of component fluorophores in favour of certain components such as, pterin and 4-pyridoxic acid [7,20,21]. Undiluted healthy human urine has a pH between 5 and 7.5. As the pH is increased from 8 to 10, the quantum yield and mean life time of the indole fluorophores increases three-fold as compared with that at pH between 3 and 7.5 [12]. This means that the quantum yield of indole fluorophores in normal urine is suboptimal. Pterin and 4-pyridoxic acid contribute significantly to the fluorescence of undiluted healthy human urine at 300–450 nm excitation. The 4-pyridoxic acid and pterins have high fluorescence intensity in an acidic medium (pH 4–7) as compared to a basic medium [22,23]. These fluorophores therefore exhibit optimal fluorescence at the pH of undiluted normal human urine. This is in contrast to the indole fluorophores whose quantum yield is not at their peak in healthy human urine. The overall picture of fluorescence quenching in urine is also more complex. In addition to ammonium, urine contains other known quenchers. A 24 h sample of human urine contains hippuric acid, whose carboxyl group is able to quench the indole fluorophores in urine. All these effects additionally contribute to the main quenching mechanisms discussed here, *i.e.*, the autoquenching of indoxyl sulfate, quenching of tryptophan and 5-hydroxyindole-3-acetate by indoxyl sulfate and the quenching of indole fluorophores by ammonium.

4. Summary

Despite high concentration of UV excitable (250–300 nm) fluorophores, the fluorescence of undiluted healthy human urine is weak. However, with dilution, the fluorescence intensity increases substantially. Although this is generally attributed to fluorescence quenching and/or inner filter effect, the existing literature does not provide any explanation concerning the factors contributing to the relatively low UV fluorescence of undiluted healthy human urine. A detailed understanding of the factors influencing UV fluorescence of human urine could contribute to harnessing fluorescence as a diagnostic tool.

In this work, we analyzed the fluorescence of undiluted healthy human urine samples as well as three major UV-excitable fluorophores in urine: tryptophan, indoxyl sulfate and 5-hydroxyindole-3-acetate, in order to understand the key fluorescence features in this complex biological fluid. Both undiluted (physiological concentration) as well as various dilutions were studied. We also established the effect of physiological concentration of another major component of urine, ammonium, on the fluorescence of key urine fluorophores and their mixtures.

Our findings indicate that the key factors contributing to the reduction of fluorescence observed in the undiluted healthy human urine samples excited in the shorter UV wavelength include high concentration of indoxyl sulfate contributing to the inner filter effect and the concentration quenching of fluorophores by ammonium. This work fills a gap in the existing literature concerning the factors influencing UV fluorescence of human urine.

Acknowledgments

The authors acknowledge the staff of Douglass Hanly Moir Pathology laboratories (DHM), Sydney, for providing the urine samples. SMP and UK are supported by Macquarie University Research Scholarships.

Appendix A. Supplementary data

Supplementary data associated with this article can be found, in the online version, at doi:10.1016/j.talanta.2009.09.020.

References

[1] E. Saude, D. Adamko, B. Rowe, T. Marrie, B. Sykes, Metabolomics 3 (2007) 439–451.
[2] S.G. Guminetsky, O.R. Gayka, G.I. Kokoschuk, P.M. Grigorishin, N.L. Kirsh, SPIE (1999) 579–589.
[3] T. Ohashi, Y. Kanamoto, S. Yamaguchi, Y. Eto, K. Maekawa, Tohoku J. Exp. Med. 148 (1986) 335–339.
[4] K. Dubayova, J. Kusnir, L. Podracka, J. Biochem. Biophys. Methods 55 (2003) 111–119.
[5] J. Kusnir, L. Leskova, Anal. Lett. 38 (2005) 1559–1567.
[6] A.G. Anwer, P.M. Sandeep, E.M. Goldys, S. Vemulpad, Clin. Chim. Acta 401 (2009) 73–75.
[7] M.J.P. Leiner, M.R. Hubmann, O.S. Wolfbeis, Anal. Chim. Acta 198 (1987) 13–23.
[8] M. Kubista, Analyst (London) 119 (1994).
[9] M.G.J. Allesia, Manual of Fluorometric and Spectrophotometric Experiments, Gordon and Breech Science Publishers, SA, 1985.
[10] M.M. Puchalski, M.J. Morra, R. Wandruszka, Fresenius J. Anal. Chem. 340 (1991) 341–344.
[11] B. Valeur, Molecular Fluorescence Principles and Applications, WILEY-VCH, Weinheim, Federal Republic of Germany, 2002.
[12] J.R. Lakowicz, Principles of Fluorescence Spectroscopy, second ed., Kluwer Academic Plenum Publishers, New York, 1999.
[13] J. Georges, Spectrochim. Acta A Mol. Biomol. Spectrosc. 51 (1995) 985–994.
[14] K.Y. Burshtein, A.A. Bargatur'yants, M.V. Alfimov, Chem. Phys. Lett. 239 (1995) 195–200.
[15] E.A. Permyakov, Luminescent Spectroscopy of Proteins, CRC Press, 1992.
[16] S.K. Strasinger, Urinalysis and Body Fluids, The Taber's Publisher, 2001.
[17] E.P. Kirby, R.F. Steiner, J. Phys. Chem. 74 (1970) 4480–4490.
[18] J. Lipinski, H. Chojnacki, Spectrochim. Acta A Mol. Biomol. Spectrosc. 51 (1995) 381–386.
[19] R.K.I. Tatischeff, Photochem. Photobiol. 22 (1975) 221–229.
[20] W.B. De Lauder, P. Wahl, Biochim. Biophys. Acta 243 (1971) 153–163.
[21] J. Leonard, L.S.F. Andrews, Photochem. Photobiol. 19 (1974) 353–360.
[22] C. Bueno, J. Guerrero, M.V. Encinas, Helv. Chim. Acta 87 (2004) 940–948.
[23] A.H. Thomas, C. Lorente, A.L. Capparelli, M.R. Pokhrel, A.M. Braun, E. Oliveros, Photochem. Photobiol. Sci. 1 (2002) 421–426.

Talanta 80 (2010) 1277–1281

Contents lists available at ScienceDirect

Talanta

journal homepage: www.elsevier.com/locate/talanta

Electrocatalytic oxidation of phytohormone salicylic acid at copper nanoparticles-modified gold electrode and its detection in oilseed rape infected with fungal pathogen *Sclerotinia sclerotiorum*

Zhan Wang[a], Fang Wei[b], Sheng-Yi Liu[b], Qiao Xu[a], Jun-Yan Huang[b], Xu-Yan Dong[b], Jiu-Hong Yu[a], Qin Yang[a], Yuan-Di Zhao[a,*], Hong Chen[b,**]

[a] *Wuhan National Laboratory for Optoelectronics, Hubei Bioinformatics and Molecular Imaging Key Laboratory, College of Life Science and Technology, Huazhong University of Science and Technology, Wuhan, Hubei 430074, PR China*

[b] *Oil Crops Research Institute, Chinese Academy of Agricultural Sciences-Key Laboratory for Genetic Improvement of Oil Crops, Ministry of Agriculture, Wuhan, Hubei 430062,PR China*

ARTICLE INFO

Article history:
Received 27 May 2009
Received in revised form 8 September 2009
Accepted 13 September 2009
Available online 19 September 2009

Keywords:
Salicylic acid
Electrocatalytic oxidation
Copper nanoparticles
Phytohormone

ABSTRACT

Salicylic acid (SA) is a biological substance that acts as a phytohormone and plays an important role in signal transduction in plants. It is important to accurately and sensitively detect SA levels. A gold electrode modified with copper nanoparticles was used to assay the electrocatalytic oxidation of salicylic acid. It was found that the electrochemical behavior of salicylic acid was greatly improved at copper nanoparticles, indicating that anodic oxidation could be catalyzed at copper nanoparticles. And the pH had remarkable effect on the electrochemical process, a very well-defined oxidation peak appeared at pH 13.3 (0.2 M NaOH). The kinetics parameters of this process were calculated and the heterogeneous electron transfer rate constant (k) was determined to be 1.34×10^{-3} cm s^{-1}, and $(1-\alpha)n_\alpha$ was 1.22. The gold electrode modified with copper nanoparticles could detect SA at a higher sensitivity than common electrodes. The electrode was used to detect the SA levels in oilseed rape infected with the fungal pathogen *Sclerotinia sclerotiorum*. The results showed that the SA concentration reached a maximum during the 10th–25th hours after infection. This result was very similar to that determined by HPLC, indicating that the gold electrodes modified with copper nanoparticles could be used as salicylic acid sensors.

© 2009 Elsevier B.V. All rights reserved.

1. Introduction

Over the past three decades, the use of oilseed rape (*Brassica napus* L.) as an source of plant oil and protein in human and animal nutrition has increaseed. The fungal pathogen *Sclerotinia sclerotiorum* affects plant development and has a strong negative impact on the quality and production of oilseed rape. In China, the pathogen causes heavy losses in yield of oilseed rape [1]. However, no immune or highly resistant cultivars of oilseed rape are currently available to breeders, and genetic sources of resistance to the pathogen are also limited [2].

Plants routinely respond to insect feeding, pathogen infection, or environmental stress by an array of defense mechanisms. These responses confer protection at the damaged site, as well as throughout the plant, by the systemic accumulation of defense-related proteins in healthy tissues, distant to the damaged site. The induction of systemic defense responses is thought to be regulated by low-molecular-weight plant hormones, such as jasmonic acid, methyl jasmonate and salicylic acid (SA) [3]. A sensitive and reliable quantification method for these hormones in plant extracts is essential because of the significance of these compounds as putative signaling molecules. The determination of the levels of these hormones in oilseed rape tissues will help in the study of the disease resistance mechanism and will aid in the genetic engineering of cultivars of oilseed rape with increased resistance.

Among these plant hormones, SA plays an important role in signal transduction in plants [4]. Many methods have been used to detect SA, for example, UV spectrophotometery [5], fluorescence [6] and chromatography [7].

Electrochemistry is a sensitive and convenient method for the determinations of many molecules. Unfortunately, using ordinary electrodes (Pt, Au, carbon paste, and graphite), the electrochemical behavior of SA is poor; no stable electrochemical responses could be

* Corresponding author at: Wuhan National Laboratory for Optoelectronics, Hubei Bioinformatics and Molecular Imaging Key Laboratory, College of Life Science and Technology, Huazhong University of Science and Technology, Wuhan, Hubei 430074, PR China. Tel.: +86 27 87792235; fax: +86 27 87792202.

** Corresponding author at: Oil Crops Research Institute, Chinese Academy of Agricultural Sciences, Wuhan, Hubei 430062, PR China. Tel.: +86 27 86711669; fax: +86 27 86816451.

E-mail addresses: zydi@mail.hust.edu.cn (Y.-D. Zhao), chenhong@oilcrops.cn (H. Chen).

0039-9140/$ – see front matter © 2009 Elsevier B.V. All rights reserved.
doi:10.1016/j.talanta.2009.09.023

observed [8], or high potential was needed [9]. Then it was difficult to study its real electrochemical behavior using ordinary electrodes.

For molecules with poor electrochemical behavior, modified electrodes have given good results [10]. Many kinds of materials have been used to modify electrodes, such as polymers [11], thiols self-assembling monolayers [12], inorganic polynuclear transition metal hexacyanometallate films [13], polyacid films [14] and metal particles [15]. Due to their favorable properties, such as simple operation, good repeatability and rapid response, noble metals have been used to prepare particles-modified electrodes, such as gold [16], silver [17] and platinum [18]. However, such noble metals exhibited severe electrode poisoning in the detection of carbohydrates and amino acids [19], it was important to adopt other materials to modify electrode to carry out those researches. Copper nanoparticles have also been used to modify electrodes because they can cause unique catalysis in some systems [20]. For example, Zen et al. have used copper nanoparticle-modified electrode to detect glucose [21] and *o*-dihydrophenolic compounds [22]. In this paper, the anodic oxidation of SA at a copper nanoparticles-modified gold electrode was studied. The results showed that the electrochemical behavior of SA at this kind of modified electrode could be greatly improved. The electrode was used to detect the SA levels in oilseed rape infected with the fungal pathogen, *Sclerotinia sclerotiorum*, and the results were very similar to those obtained by HPLC, indicating that the copper nanoparticles-modified gold electrode has a potential application in the detection of SA.

2. Materials and methods

2.1. Reagents and instrumentation

Salicylic acid (SA) was obtained from Sigma. The SA stock solution (2.5 mmol L^{-1}) was prepared by dissolving the required amounts of SA in 0.2 mol L^{-1} sodium hydroxide solution. Other reagents were of analytical grade. All solutions were prepared with double distilled water.

A DL-180A ultrasonic cleaning device (Shanghai ZX equipment Ltd., China) was used to clean the electrodes. Cyclic voltammetry (CV) experiments were carried out in oxygen-free water under nitrogen using a CHI660A electrochemical workstation (CH Instruments, China) coupled to a conventional three-electrode cell. The electrodes for Scanning Electron Microscopy (SEM, S-3000N, Hitachi, Japan) studies were dried at room temperature before each test.

2.2. Detection of salicylic acid by using high performance liquid chromatography

Isolation and measurement of salicylic acid in plant materials was carried out by a high performance liquid chromatography (HPLC) system equipped with UV detector (Shimadzu, Japan). Separation was achieved on a Kromasil ODS column (200 mm × 4.6 mm, I.D.; 5 μm; Bohus, Sweden). The mobile phase was methanol: 5% acetate (50:50, v/v) and the flow rate was maintained at 0.7 mL min^{-1}. UV detection was set at 278 nm for salicylic acid detection.

2.3. Preparation of the modified electrode

The gold electrode was prepared by inserting a gold fiber (0.2 mm diameter) into a glass tube and then the tube was heated to seal the gold fiber. The tube was then polished to expose the gold, thus forming the gold electrode. Prior to each experiment, the electrode was polished with 0.05 μm alumina slurry, sonicated in acetone and twice distilled water for 3–5 min, respectively. The copper nanoparticles-modified gold electrode (nano-Cu/Au) was constructed by applying −0.3 V for 25 s in a 0.2 M acetate buffer solution (pH 4.0) containing 5.0 mM $CuCl_2$ according to a previously published protocol [20].

2.4. Electrochemistry measurement

The working electrodes were glassy carbon electrode (GC), Pt, Au or nano-Cu/Au electrodes, the auxiliary electrode was a platinum wire, and the reference electrode was a saturated calomel electrode (SCE). All the potentials given in this paper were calculated against the SCE. The cathodic current was assigned to be negative, and the anodic current was assigned to be positive. Each measurement was repeated at least three times and was conducted at 25 °C.

2.5. Treatment of plant materials

The oilseed rape samples were grown in a plant growth room at 15–21 °C up to the four-true-leaf stage, and then the leaves were excised for study. *S. sclerotiorum* mycelial discs (2 mm thick and 3 mm in diameter) were excised from the colony edge of 5-day-old culture and put on the upper sides of detached leaves. The inoculated leaves were incubated at 22 °C under conditions of above 95% relative humidity. Non-wounded control leaves were collected at 0 h. The infected leaves were collected at 5, 10, 20, 30 and 35 h after inoculation. Collected leaves were immediately flash-frozen in liquid nitrogen to terminate any metabolic activity and stored at −80 °C until they could be analyzed.

Samples (0.1 g fresh weight) of frozen leaves were homogenised in 0.5 mL cold water (4 °C) and stirred overnight. The extract was subjected to ultrasonication in KQ-500DB ultrasound cleaning bath (Ultrasound instrument Co., Ltd., Kunshan, China) for 60 min, the working frequency and power were 40 kHz and 500 W, respectively. After that, the extract was centrifuged at 12,000 rpm for 10 min. Before the electrochemical measurement, the solutions of extracts were adjusted with NaOH to obtain a 0.2 M NaOH final concentration.

3. Results and discussion

As was found by other research groups [8,9], using an Au electrode, the electrochemical responses of SA were poor and no well-defined peak of its oxidation could be seen (Fig. 1, curve c), compared with a blank solution (curve a in Fig. 1). However, a very well-defined oxidation peak appeared when using the nano-Cu/Au (Fig. 1, curve d) in the same solution. This peak was not observed in

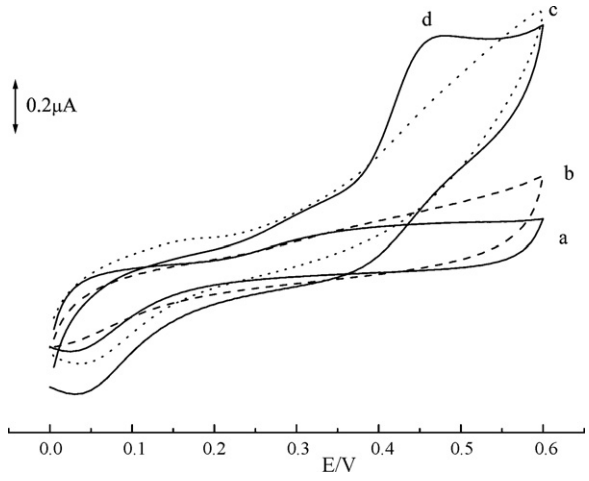


Fig. 1. The CV curves at Au (a and c) and nano-Cu/Au (b and d) electrodes in 0.2 M NaOH with (c and d) or without (a and b) 2.5 mM SA at a scan rate of 100 mV s^{-1}.

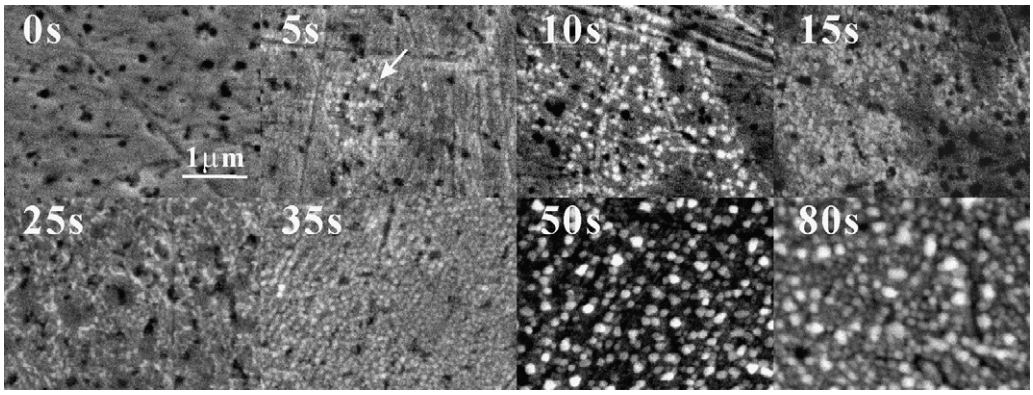


Fig. 2. SEM images of a copper nanoparticles-modified gold electrode with different deposition times.

the blank solution at the same electrode, indicating that the electro-oxidation of SA was greatly improved using a nano-Cu/Au, and that copper nanoparticles could catalyze its anodic process. And the peak at copper nanoparticles-modified gold electrode was very stable, after one cycle, the anodic current decreased from 0.576 μA to 0.482 μA, after that, the current became to steady, no evident decrease was observed after 25 cycles (0.479 μA), indicating that the electro-oxidation of SA at Cu electrode was stable enough to study the electrochemical behavior of SA.

The experiments were also carried out at GC and Pt electrodes. Just as we have known, the electrochemical behavior of SA was poor at ordinary GC electrode [8,9]. But an oxidation peak appeared at *ca.* 0.55 V in the same solution at Pt electrode (figures are not given), indicating that the electro-oxidation of SA could be obtained at Pt electrode, but this electrochemical behavior was not stable, the peak decreased rapidly along with continued CV scan, after 25 cycles, no well-defined peak could be found. This indicated that, although the oxidation of SA could be obtained at Pt electrode, it still could not be used to study its electrochemical behaviour disappointedly.

The response for different pH values had been studied; it was found that the pH had remarkable effect on the electrochemical process. NaOH was adopted to adjust the pH of solution. It was found that if pH was under 12, no well-defined peak of SA oxidation could be seen. When pH was 12.6, there was a flat peak appearing at 0.55 V, and the current was 0.225 μA. The peak current rose with increasing pH value from that pH. There was a very well-defined oxidation peak appeared at 0.468 V when pH reached 13.3 (0.2 M NaOH), and the current was increased to 0.479 μA. Then, the experiment was carried out in 0.2 M NaOH.

The surface morphology of the modified electrodes was observed using scanning electron microscopy (SEM) after their preparation (Fig. 2). The results showed that the bare Au electrode was clean, and had some holes of about 100–200 nm on its surface. After the beginning of copper deposition, a few of particles (<50 nm) appeared on the surface. With continued deposited time, the particles began to appear (less than 100 nm) and had spread over the surface after 25 s, however, the 100–200 nm holes are remained. Eventually, the copper nanoparticles began to stack on the surface, and the holes disappeared. After 80 s, the layer of copper nanoparticles became to about 300 nm thick. And this result is similar to Pan' experiment [20], in which 200 nm Cu particles with spherical shape were obtained by applying 0.0 V for 180 s in the same kind of solution. The electrochemical responses of SA using these modified electrodes with different deposition times were assayed, as shown in Table 1. It was found that the peak rose with increasing deposited time. After 25 s, the peak began to stable. Then 25 s was found to be the optimum deposition time. In subsequent experiments, 25 s was used to deposit the copper nanoparticles.

Table 1
The peak potentials and currents for different copper deposited times.

Deposited time/s	5	10	15	20	25	35
Peak potential/V	0.495	0.479	0.475	0.471	0.468	0.467
Peak current/μA	0.395	0.44	0.465	0.471	0.479	0.483

The CV curves for the anodic oxidation of SA at the nano-Cu/Au electrode at various scan rates are shown in Fig. 3. It can be found that the peak potentials shifted positively with the rising scan rate, while the peak current increased. As expected for a diffusion-controlled reaction, the I_{pa} of SA oxidation increased linearly with $\upsilon^{1/2}$ (figures are not given). The slope of the straight line ($r = 0.995$) of I_{pa} versus $\upsilon^{1/2}$ is $(1.16 \pm 0.03) \times 10^{-6}$ A V$^{-1/2}$ s$^{1/2}$. The plot of peak potential (E_{pa}) versus the logarithm of the scan rate is a straight line ($r = 0.991$) (figures are not given). From the straight line, the slope and the intercept determined as 0.0242 and 0.494, respectively. For an irreversible process, the peak potential (E_{pa}) could be represented by the equation [23]:

$$Ep = K + \frac{2.3RT}{2(1-\alpha)n_\alpha F}\log\upsilon$$

$$K = E^{\circ\prime} + \frac{RT}{(1-\alpha)n_\alpha F}\left(0.78 + \frac{2.3}{2}\log\left(\frac{(1-\alpha)n_\alpha FD}{k^2RT}\right)\right)$$

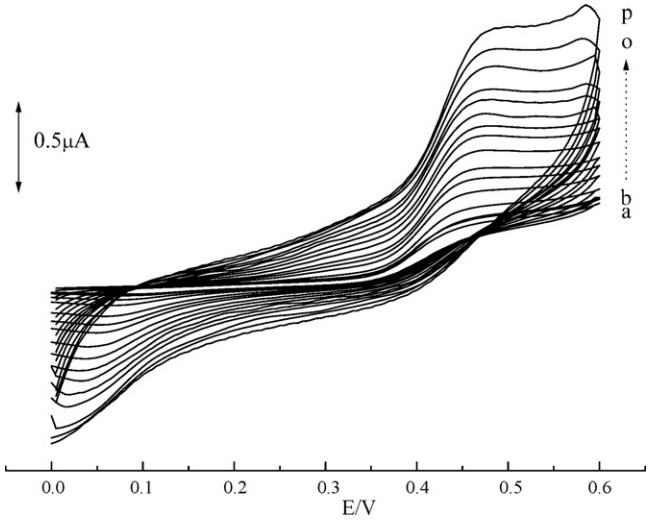


Fig. 3. The CV curves for 2.5 mM SA at a nano-Cu/Au electrode at various scan rates (mV s^{-1}): (a) 2; (b) 3; (c) 5; (d) 10; (e) 20; (f) 30; (g) 40; (h) 60; (i) 80; (j) 100; (k) 120; (l) 150; (m) 180; (n) 240; (o) 300 and (p) 400. The other conditions are as in Fig. 1.

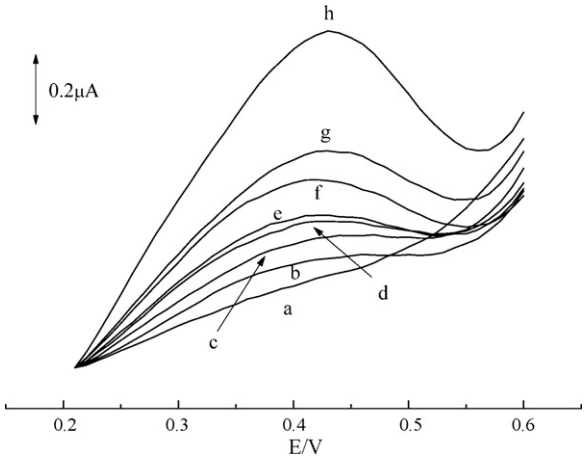


Fig. 4. DPVs of the nano-Cu/Au electrode for different concentrations of SA. (a) 0 μM; (b) 1 μM; (c) 2 μM; (d) 10 μM; (e) 20 μM; (f) 50 μM; (g) 0.2 mM and (h) 1 mM.

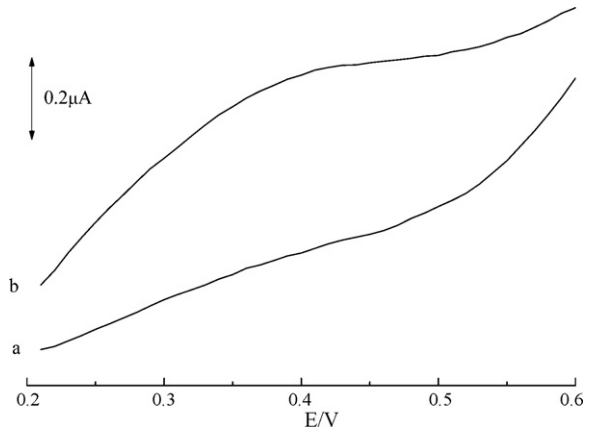


Fig. 5. DPVs of the nano-Cu/Au electrode in buffer (a) and extract of oilseed rape leaves after inoculating with fungal pathogen *Sclerotinia sclerotiorum* for 30 h (b). The other conditions are as in Fig. 4.

where υ is the scan rate, $E^{\circ\prime}$ is the standard electrode potential, k is the heterogeneous electron transfer rate constant, and D is the diffusion coefficient (for SA, it is 1.11×10^{-5} cm^2 s^{-1} [24]). Therefore, the $(1-\alpha)n_\alpha$ was calculated as 1.22, and k was 1.34×10^{-3} cm s^{-1}. For the bare Au electrode, these parameters could not be calculated at all because of the lack of a well-defined peak.

The electrochemical responses of the nano-Cu/Au electrode in various concentrations of SA solution were studied. Differential pulse amperometry (DPV) was chosen to test these responses. We found a DPV peak appearing at 0.4 V (Fig. 4), and the logarithm of the current and SA concentration had a good linear relationship down to 0.8 μM ($\log I = -5.38 + 0.264 \log C$), with a correlation coefficient of 0.992, and a detection limit of 0.1 μM, which is higher than that obtained at carbon paste electrode (12.3 μM) [8] and glassy carbon electrode by voltammetry (3.6 mM) [25], and is similar to that obtained at glassy carbon electrode by DPV (0.65 μM) [9].

The interference experiments were carried out. It is well known that, ascorbic acid is a major interferent existing in life widely. Its concentration in oilseed rape is 26.33 mg per 100 g fresh weight [26]. It was found that seven times the usual concentration of ascorbic acid could not interfere with the detection of SA. Then the nano-Cu/Au electrode has a good anti-interference effect for ascorbic acid.

The nano-Cu/Au electrode was used to detect SA in oilseed rape leaves infected by *Sclerotinia sclerotiorum*. It was found that after inoculating with the fungal pathogen *Sclerotinia sclerotiorum* for 30 h, a peak appeared at 0.4 V compared with a blank solution (Fig. 5). The concentration was calculated as 8.58 μM confirmed by the linear equation, which is close to the result obtained by HPLC-UV (9.42 μM), indicating that the nano-Cu/Au electrode has a high sensitivity for SA; it could be used as an SA sensor after further research.

The interferent in biosystem was also considered in the study. It is known that salicylic acid is changed to 2, 5-dihydroxybenzoic acid by an enzymatic hydroxylation pathway through the cytochrome P-450 microsomal system [27]. And that compound could be also oxidized at electrode [28], and then in this experiment, when copper particles-modified electrode was adopted to detect SA in real sample, 2, 5-dihydroxybenzoic acid maybe would interfere with the detection, which was an avoidless factor in the real plant sample.

The electrode was then used to monitor the change in SA level during infection with *Sclerotinia sclerotiorum* (Fig. 6). It was found that the SA level rose rapidly after inoculation with *Sclerotinia sclerotiorum* and reach a plateau after 10 h, at which point the SA concentration in oilseed rape leaves was four times that of the original, non-inoculated leaves. This SA level persisted until 20 h after inoculation, thereafter the SA concentration began to decline, and after 35 h the SA level returned to the initial value. For different parallel samples, there is little difference in the absolute intensities of peaks, but the trends are all the same basically. We think the difference maybe is resulted from several factors, such as the diversity of leaves, the avoidless difference in infection with the fungal pathogen *Sclerotinia sclerotiorum*.

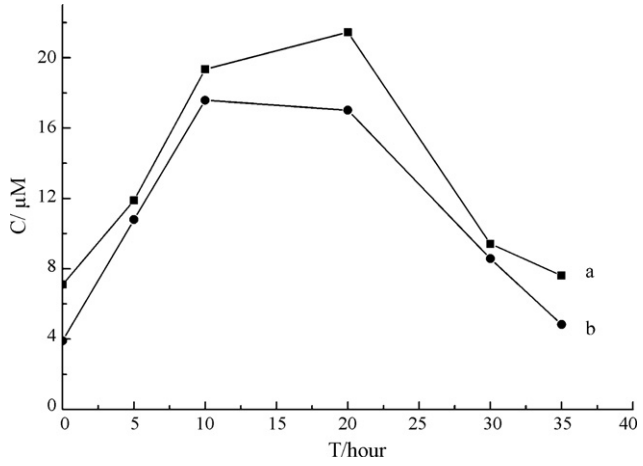


Fig. 6. The change of SA level in oilseed rape leaves after inoculating with fungal pathogen *Sclerotinia sclerotiorum* for different times as determined by HPLC (a) and the nano-Cu/Au electrode (b). The other conditions are as in Fig. 4.

SA plays an important role as a signaling molecule in the plant defense responses. Our results showed a sharp increase in the levels of SA in the leaves infected by *Sclerotinia sclerotiorum* 10 h after inoculation. The high levels of SA in the leaves might be due to stimulation of the octadecanoid pathway and signal transduction. Due to scavenging mechanisms, the SA concentration in cells returns to low levels to avoid potential toxic effects. These results indicate that SA signaling has an important role in the response to infection by *Sclerotinia sclerotiorum*.

4. Conclusions

Salicylic acid is considered to act as a phytohormone and plays an important role in signal transduction in plants. Its poor electrochemical behaviour at ordinary electrodes limits detection of its concentration. Here we report the anodic oxidation of SA at a copper nanoparticles-modified gold electrode. We found that the

electrochemical behavior of SA at this kind of modified electrode was greatly improved. The electrode was used to detect the SA levels in oilseed rape infected with the fungal pathogen *Sclerotinia sclerotiorum*. The electrode showed results is very similar to those obtained by HPLC, indicating that the electrode could be used as a sensor for SA detection.

Acknowledgements

This work was supported by the National Natural Science Foundation of China (Grant No. 90717101, 30670553). Dr. Hong Chen is grateful to Director Foundation of Institute of Oil Crops Research, Chinese Academy of Agricultural Sciences. We also thank Analytical and Testing Center (Huazhong University of Science and Technology) for the help in SEM measurement.

References

[1] S. Liu, H. Wang, J. Zhang, B.D.L. Fitt, Z. Xu, N. Evans, Y. Liu, W. Yang, X. Guo, Plant Cell Rep. 24 (2005) 133.
[2] X. Dong, R. Ji, X. Guo, S.J. Foster, H. Chen, C. Dong, Y. Liu, Q. Hu, S. Liu, Planta 228 (2008) 331.
[3] D.F. Klessig, J. Durner, R. Noad, D.A. Navarre, D. Wendehenne, D. Kumar, J.M. Zhou, J. Shah, S. Zhang, P. Kachroo, Y. Trifa, D. Pontier, E. Lam, H. Silva, Proc. Natl. Acad. Sci. USA 97 (2000) 8849.
[4] P. Meuwly, W. Molders, A. Buchala, J.P. Metraux, Plant Physiol. 109 (1995) 1107.
[5] I.M. Scott, H. Yamamoto, Phytochemistry 37 (1994) 335.
[6] A.R. Medina, M.L. Fernández de Córdoba, A.M. Díaz, Fresen. J. Anal. Chem. 365 (1999) 619.
[7] S.M. Wilbert, L.H. Ericsson, M.P. Gordon, Anal. Biochem. 257 (1998) 186.
[8] J. Petrek, L. Havel, J. Petrlova, V. Adam, D. Potesil, P. Babula, R. Kizek, Russ. J. Plant Physiol. 54 (2007) 553.
[9] A.A.J. Torriero, J.M. Luco, L. Sereno, J. Raba, Talanta 62 (2004) 247.
[10] Y.D. Zhao, W.D. Zhang, Q.M. Luo, S.F.Y. Li, Microchem. J. 75 (2003) 189.
[11] T. Lindfor, A. Ivaska, J. Electroanal. Chem. 531 (2002) 43.
[12] Y.D. Zhao, D.W. Pang, M. Zhang, J.K. Cheng, H.P. Dai, Chem. J. Chin. Univ. 22 (2001) 744.
[13] T.R.L.C. Paixao, M. Bertotti, Electroanalysis 20 (2008) 1671.
[14] M.I. Prodromidis, P.G. Veltsistas, C.E. Efstathiou, M.I. Karayannis, Electroanalysis 13 (2001) 960.
[15] M.W. Christine, G.C. Richard, Anal. Bioanal. Chem. 384 (2006) 601.
[16] M.C. Tsai, P.Y. Chen, Talanta 76 (2008) 533.
[17] O.D. Renedo, M.J.A. Martinez, Electrochem. Commun. 9 (2007) 820.
[18] J.H. Yoon, G. Muthuraman, S.B. Yoon-Bo, M.S. Won, Electroanalysis 19 (2007) 1160.
[19] K.B. Male, S. Hrapovic, Y. Liu, D. Wang, J.H.T. Luong, Anal. Chim. Acta 516 (2004) 35.
[20] D. Pan, J. Chen, S. Yao, L. Nie, J. Xia, W. Tao, Sensor Actuat. B 104 (2005) 68.
[21] A.S. Kumar, J.M. Zen, Electroanalysis 14 (2002) 671.
[22] J.M. Zen, H.H. Chung, A.S. Kumar, Anal. Chem. 74 (2002) 1202.
[23] A.J. Bard, L.R. Faulkner, Electrochemical Methods, Fundamentals and Application, Wiley, New York, 1980, p 222–223.
[24] J.M.P.Q. Delgado, J. Phase Equilib. Diff. 28 (2007) 427.
[25] Y.S. Fung, S.F. Luk, Analyst 114 (1989) 943.
[26] Y. Li, X. Guo, Z. Fang, B. Di, Chin. Agr. Sci. Bull. 23 (2007) 98.
[27] M. Ingelman-Sundberg, H. Kaur, Y. Terelius, J.O. Person, B. Halliwell, Biochem. J. 276 (1991) 753.
[28] S. Ai, Q. Wang, H. Li, L. Jin, J. Electroanal. Chem. 578 (2005) 223.

Talanta 80 (2010) 1282–1286

Contents lists available at ScienceDirect

Talanta

journal homepage: www.elsevier.com/locate/talanta

Determination of sodium, potassium, calcium, magnesium, zinc, and iron in emulsified egg samples by flame atomic absorption spectrometry

C.V.S. Ieggli[a], D. Bohrer[a,*], P.C. do Nascimento[a], L.M. de Carvalho[a], S.C. Garcia[b]

[a] Departamento de Química, Avenida Roraima 1000, Universidade Federal de Santa Maria, 97110-970 Santa Maria, RS, Brazil
[b] Toxicology Laboratory, Av. Ipiranga 2752, Universidade Federal do Rio Grande do Sul, 90610-000 Porto Alegre, RS, Brazil

ARTICLE INFO

Article history:
Received 19 June 2009
Received in revised form
11 September 2009
Accepted 13 September 2009
Available online 22 September 2009

Keywords:
Emulsion
Egg
Metal
Flame atomic absorption spectrometry

ABSTRACT

In this study, oil-in-water formulations were optimized to determine sodium, potassium, calcium, magnesium, zinc, and iron in emulsified egg samples by flame atomic absorption spectrometry (FAAS). This method is simpler and requires fewer reagents when compared with other sample pre-treatment procedures and allows the calibration to be carried out using aqueous standards. Different oily phases such as corn oil, decyl oleate and octyl stearate were tested, as well as Tween 80, Triton X-100 and Triton 114 were analyzed as surfactants. The optimum type and proportion of formulations were determined and their use depended on the element studied. The emulsion preparation was performed by a conventional method that involves mixing both phases at 60 °C by magnetic stirring and phase inversion to change the water-to-oil ratio by increasing the volume of the surfactant–water external phase and correspondingly decreasing the volume of internal phase. The accuracy of the method was further confirmed by determining the metals in a whole egg powder CRM and recoveries ranged from 97.5% for Mg to 102.2% for Na, with relative standard deviations lower than 2.3%. The precision of the procedures was determined through repeatability (intra-day precision) and intermediate precision (inter-day). The repeatability presented RSD values lower than 4.2%. The intermediate precision was evaluated using the RSD and *F*-test. The RSD values to intermediate precision was lower than 5.3% and the computed *F*-values were lower than tabulated *F*-values, indicating no significant difference between the results obtained on different days. The proposed method including, sample emulsification for subsequent metal determination for FAAS, has proved to be sensitive, reproducible, simple and economical.

© 2009 Elsevier B.V. All rights reserved.

1. Introduction

Knowledge of the mineral composition of hen eggs is increasingly required for different purposes; these include the estimation of accumulation of toxic species from the hen egg and the role of egg composition in human nutrition [1].

The egg is a system naturally emulsified by components such as phospholipids, lipoproteins and proteins [2]. Eggs are included in several food products exercising various functions. As emulsifier (e.g. mayonnaise) it forms a strong and cohesive film around oil droplets which stabilizes them against coalescence and interacts to form network structures which gives viscoelasticity to products, with unique sensory and textural characteristics [3].

The quality of food products has received great attention due to its influence on human nutrition and health. In this context, the determination of trace metals in foods has become an important field in food analysis [4–6]. However, the accurate determination of trace metals in hen eggs is still an analytical challenge, due to their low concentration level and the difficulties that arise from matrix characteristics. Flame atomic absorption spectrometry (FAAS) is a powerful detection technique for determining trace elements. The advantages of FAAS include well-known interferences, low operator skill required for operation, and comparatively low cost of instrumentation and maintenance [7]. One disadvantage, however, is the sample pre-treatment which is a necessary step for determining trace elements in complex matrices such as egg. Due to its high viscosity and content of organic matter, direct egg analysis is particularly difficult.

Methods for egg sample treatment involving digestion with acids and peroxides reported in the literature [1,8,9], have attempted to improve digestion by combining the use of these reagents with ultraviolet [10] or microwave radiation [2,11–13]. All these procedures result in additional steps, which may lead to inconveniences such as sampling errors, contamination and losses during handling [10].

Direct emulsification with surfactants provides a rapid procedure for sample preparation since this approach does not require any destruction of the organic matrix [14]. It simply reduces the

* Corresponding author. Fax: +55 55 3220 8870.
E-mail address: ndenise@quimica.ufsm.br (D. Bohrer).

0039-9140/$ – see front matter © 2009 Elsevier B.V. All rights reserved.
doi:10.1016/j.talanta.2009.09.024

Table 1
Instrumental parameters for metal determination in emulsified egg samples.

Metal	Wavelength (nm)	Slit width (nm)	*I* (mA)	Integration time (s)	Flame
Na	589.0	0.8	3.0	3.0	C_2H_2–air
K	766.5	0.8	4.0	3.0	C_2H_2–air
Ca	422.7	1.2	4.0	3.0	N_2O–C_2H_2
Mg	285.2	1.2	2.0	3.0	C_2H_2–air
Zn	213.9	0.5	6.0	3.0	C_2H_2–air
Fe	248.3	0.2	8.0	3.0	N_2O–C_2H_2

viscosity and the organic content of the sample, making the properties of the egg emulsion close to those capable of being analyzed by FAAS, while maintaining the system's homogeneity and stability. In an earlier study, emulsification of egg samples was satisfactorily used for the determination of Se in whole hen eggs by graphite furnace atomic absorption spectrometry (GFAAS). The oil-in-water emulsion stabilized the sample, maintaining the system's homogeneity, and reduced the viscosity and the organic content of the sample, thus allowing egg sample analysis by GFAAS [15].

The goal of this study was to investigate the use of emulsions as sample preparation for a routine determination of Na, K, Ca, Mg, Zn and Fe in whole chicken eggs by FAAS. The expected advantages of this procedure are the higher stability and easy handling of sample emulsions, allowing the use of aqueous standards for calibration. The reliability of the procedure was checked by analyzing standard reference material.

2. Experimental

2.1. Instrumentation/procedure

All measurements were carried out using an ANALYTIK Jena AG (Jena, Germany) model novAA 300 atomic absorption spectrometer equipped with SpectrAA (Varian, Australia) hollow cathode lamps as the radiation source. An acetylene–air or acetylene–nitrous oxide flame was used; the gas flow rates and the burner height were adjusted in order to obtain the maximum absorbance signal for each element. Other instrumental parameters were set to the values shown in Table 1.

2.2. Reagents

All reagents were of analytical grade, and all emulsions were prepared with distilled and deionized water that was further purified by a Milli-Q high purity water device (electrical resistivity of 18.0 MΩ cm) (Millipore, USA). Laboratory glassware was kept overnight in 10% (v/v) HNO_3 in ethanol solution and shortly before use was washed with water and dried in a dust free environment. Concentrated nitric acid used in this study was supplied by Merck (Germany). Na, K, Ca, Mg, Zn and Fe standard solutions (1000 mg L^{-1}) were obtained from the National Institute of Standards and Technology (NIST, USA) and diluted as necessary to obtain working standards. The non-ionic surfactants Triton X-100 (Fluka, Switzerland), Triton 114 (Sigma–Aldrich, USA) and Tween 80 (Fluka) were tested for emulsion preparation. Commercial corn oil, decyl oleate (DEG, Brazil) and octyl stearate (Galena, Brazil) were tested as the oily phase. The certified reference material (CRM) RM 8415 whole egg powder (NIST) was used to check the accuracy of the proposed method.

2.3. Emulsion preparation

Oil-in-water emulsions were prepared using a specific sequence in order to guarantee their stability. Aliquots of surfactant, oil and egg sample or reference material were weighed and placed in an 80 mL beaker, and then water at 60 °C was added with continuous agitation until the required volume was reached. Magnetic stirring (3000 rpm) was maintained during 15 min at room temperature (22 °C). The total volume of the system was 50 mL, which was attained by increasing the volume of the surfactant–water external phase and correspondingly decreasing the volume of internal phase. A blank emulsion was prepared in the same way without sample addition.

Table 2
Variables and levels of 2^3 factorial design for preparation of emulsions.

Factor	Level		
	Low (−1)	Medium (0)	High (+1)
Emulsifier (%, w/v)	1.0	2.0	4.0
Oil (%, w/v)	1.0	2.0	4.0

2.4. Experimental design

A preliminary factorial design was applied to investigate the influence of oil and emulsifier amounts on emulsion stability. Since the egg is itself an emulsified system the oil added to the sample was already stabilized, therefore in order to establish the best formulation only oil and emulsifier quantities were regarded as factors. Their influence on the emulsion stability was evaluated using a 2^3 full factorial design (Table 2). The design required a total of 9 experiments per oil/emulsifier combination.

2.5. Determination of creaming behaviour

Stability of optimized emulsion was monitored by measuring the extent of gravitational phase separation. The best formulations from experimental planning, showed in Table 3, were monitored by this creaming test. For the measurement of physical stability, 10 mL of each prepared egg emulsion were poured into graduated tubes and kept at room temperature (25 °C). The volume of the separated cream layer in each tube was recorded after 1, 2, 7 14 and 21 days of storage. The emulsion stability index (ESI) was calculated as percentage: ESI (%) = (remaining emulsion height/initial emulsion height) × 100. The ESI was calculated to show the stability of the emulsions since the larger the ESI value the higher emulsion stability.

2.6. Application to real samples

Fresh eggs from domestic hens (*Gallus gallus*) commercially available were purchased from commercial establishments, including supermarkets in Santa Maria city as well as directly from small-scale farms. A total of six different samples were analyzed, consisting of pooled samples from the same carton of six eggs each.

2.7. Sample preparation regarding individual metal determination

Although there is general procedure described for the preparation of the emulsions, in this study it was necessary to consider that

Table 3
Optimized formulation compositions and determinable metals for each.

Formulation	Oily phase (%)		Emulsifier (%)		Metal
1	Corn oil	4.0	Triton 114	2.0	K
2	Octyl stearate	4.0	Tween 80	4.0	K, Ca, Mg, Zn
3	Decyl oleate	2.0	Triton 114	1.0	K, Mg
4	Octyl stearate	2.0	Triton 114	1.0	K, Ca, Mg, Fe
5	Octyl stearate	4.0	Triton X-100	4.0	Na

the metals were present in different concentrations in egg samples and, therefore, appropriate sample amounts that make the concentration of the element fall within analytical curve must be used. Sample amounts varied between 0.6 and 4.0% (w/v) according to the expected amount of the analyte in the sample. For components present in larger concentrations, such as sodium and potassium, the emulsion should be prepared with a maximum sample amount of 0.6%. For calcium amounts between 0.6 and 1.0% can be used and for magnesium, between 0.6 and 2.0%. Finally, for zinc and iron amounts between 2.0 and 4.0% must be used.

3. Results and discussion

Four criteria were used to choose the components and their relative quantity in the emulsion: (i) the emulsion should contain only the components necessary to stabilize the sample, in other words, sample, surfactant, water and an oily component; (ii) the emulsion should be stable for a reasonable period and not produce coalescence or creaming; (iii) the emulsion should present low viscosity to allow correct sample aspiration; and (iv) all components should present low background during the FAAS measurement and low metal contamination.

3.1. Formulation studies

The oil-in-water emulsion was chosen mainly due to its characteristics of long-term stability and low viscosity [16]. After choosing the type of appropriate emulsion, the next step was to select the emulsifier, since the optimum tensoactive characteristics for each oil–water system are determined by the hydrophilic–lipophilic balance (HLB). Surfactants with HLB values between 9.6 and 16.7 are considered hydrophilic (water-soluble), and tend to form oil-in-water emulsions [17]. Triton 114, Triton X-100 and Tween 80 have HLB values of 12.4, 13.5 and 15.0 respectively. It should also be taken into account that it is better to use emulsifiers without foaming properties in order to avoid heterogeneous distribution of the oil drops in the final emulsion. Furthermore, for analytical purposes, other factors should be considered such as surfactant solubility and low background during the FAAS measurement [14,18]. Non-ionic emulsifiers such as Tween 80, Triton X-100 and Triton 114 satisfy all these requirements and are inexpensive and readily available in most analytical laboratories. Corn oil, decyl oleate, and octyl stearate were chosen due to their low cost and easy obtainment.

The oil/surfactant ratio was determined by experimental planning. In all of the experiments in which the amount of oil was smaller than the amount of emulsifier, the separation of phases took place immediately after preparation. This shows that an excess of emulsifier in relation to oily phase favors the emulsion instability. The diverse combinations presented different behaviors of stability and the best formulations are presented in Table 3. Table 3 also present the metals possible of being determined in each formulation. The selection criteria are discussed in Section 3.3.

In spite of formulations stability and metal determination possibility, it was necessary to determine the level of contamination by the metals studied in the oils and surfactants investigated. The surfactant metal content was determined after its dilution in water. However, oil was measured after stabilization with an emulsifier, which was used as a blank. Table 4 presents the metal contents of oils and surfactants selected for this study. Triton 114 and Tween 80 presented high content of sodium and Triton X-100 high potassium and calcium content. The oily components presented low contamination, with exception of corn oil, which contains Ca in some level. Contamination limited the choice of surfactant and oil.

Table 4
Concentration levels of metals (mg kg^{-1}) in oils and surfactants used in this study.

	Na	K	Ca	Mg	Zn	Fe
Corn oil	0.1	1.3	26.4	0.9	<LOD	9.2
Octyl stearate	14.4	1.4	6.6	<LOD	0.7	0.7
Decyl oleate	0.6	0.7	1.7	0.3	<LOD	12.4
Triton 114	367	3.8	8.7	0.4	1.5	8.8
Tween 80	82	<LOD	<LOD	<LOD	0.6	10.2
Triton X-100	1.3	342	32.1	<LOD	0.2	3.5

LOD = limit of detection.

Table 5
Calibration curves and regression parameters for metal determination in emulsified egg sample.

Metal	Range (mg L^{-1})	Regression equation[a]	R^2	C_0 (mg L^{-1})	LOD (mg L^{-1})
Na	1.0–8.0	$A = (0.0032 + 0.2038\,C)/(1 + 0.0728\,C)$	0.9999	0.0263	0.02
K	1.0–10.0	$A = -0.003549 + 0.104891\,C$	1.0000	0.0426	0.04
Ca	0.5–8.0	$A = 0.001232 + 0.110905\,C$	0.9996	0.0395	0.11
Mg	0.5–4.0	$A = (0.0147 + 0.4702\,C)/(1 + 0.2392\,C)$	0.9944	0.0139	0.01
Zn	0.05–0.4	$A = 0.001455 + 0.13473\,C$	0.9923	0.0357	0.03
Fe	0.1–2.0	$A = -0.001426 + 0.02232\,C$	0.9979	0.2412	0.07

C (mg L^{-1}) = concentration of element in standard solution.
[a] Absorbance.

Table 6
Precision of the proposed method for the selected metals and accuracy evaluated using a certified reference material (egg powder, NIST RM 8415).

Metal	Formulation[a]	Concentrations (μg g^{-1})		Recovery (%)	t_{exp}[c]	Precision (%)	
		Certified value	Found[b]			Intra-day (RSD)	Inter-day (RSD/F_{exp}[d])
Na	5	3770 ± 34	3854 ± 25	102.2	1.46	0.8	0.6/2.25
K	4	3190 ± 37	3241 ± 99	101.6	0.25	2.4	2.3/3.27
Ca	4	2480 ± 19	2419 ± 75	97.6	2.30	3.0	3.3/3.99
Mg	2	305 ± 27	297 ± 12	97.5	0.67	1.1	1.9/3.34
Zn	2	67.5 ± 8	68.6 ± 2.7	101.6	0.94	4.2	3.3/3.98
Fe	4	112 ± 16	110.9 ± 3.7	99.0	1.62	3.5	5.3/3.06

RSD = relative standard deviation.
[a] From Table 3.
[b] Mean value ± standard deviation.
[c] $t_{tab} = 2.31$ (p 0.05).
[d] $F_{tab} = 4.26$ (p 0.05).

Table 7
Concentration levels of metals ($\mu g\,g^{-1}$) ± SD, ($n = 6$) in egg samples.

Egg samples	Na	K	Ca	Mg	Zn	Fe
1	1410.3 ± 5.1	1185.8 ± 28.8	525.2 ± 14.6	154.3 ± 1.7	12.2 ± 0.8	37.4 ± 2.5
2	1492.5 ± 12.1	1259.4 ± 39.7	486.5 ± 15.9	132.8 ± 3.6	7.4 ± 0.5	24.5 ± 1.0
3	1477.6 ± 11.0	1167.4 ± 52.6	509.2 ± 8.3	137.1 ± 0.8	10.4 ± 0.7	36.6 ± 3.1
4	1444.1 ± 22.6	1222.1 ± 29.0	567.4 ± 23.4	148.6 ± 1.9	11.3 ± 0.4	44.2 ± 1.7
5	1617.8 ± 23.9	1205.2 ± 75.0	425.7 ± 7.5	161.1 ± 1.1	11.0 ± 0.7	35.3 ± 2.8
6	1595.5 ± 13.2	1157.4 ± 64.8	494.0 ± 14.3	143.5 ± 0.9	11.1 ± 0.5	38.5 ± 4.7

3.2. Formation and stabilization of the emulsion

The spontaneous formation of emulsion rarely occurs, but rather this process requires a sequence of steps: (i) formation of droplets of the internal phase and (ii) stabilization of these droplets in the external phase. Moreover the application of energy in the form of heat and mechanical stirring is necessary [19].

The increase of the temperature reduces the interfacial tension, however the heat can favor the separation of the phases due to the increased kinetic energy of the droplets. Usually emulsions are prepared at temperatures between 70 and 80 °C, and the aqueous phase is heated up 5 °C more than the oily phase. However, the maximum temperature used in this work was 60 °C due to the presence of proteins in the egg matrix, but was high enough to stabilize the emulsion.

Since the behavior of stable systems depends on the preparation conditions, care was taken to assure that the procedure was carried out in exactly the same way for all experiments [20]. Providing a finely dispersed oil-in-water emulsion with long-term stability is phase inversion to change the water-to-oil ratio by increasing the surfactant–water external phase volume and correspondingly decreasing the internal phase volume [19]. In the initial period of stirring the droplets necessary for the emulsification are formed. If the stirring exceeds the necessary period for ideal stability, adhesion can take place due to collision among the droplets. This period of time is usually determined empirically. In this study, the stipulated time was 2 min of manual mechanical stirring to reach emulsification, followed by magnetic stirring at 3000 rpm for 15 min at room temperature for complete stabilization of the system.

Creaming test may also be used to determine emulsion stability [21,22]. The final appearance of all emulsions was milky white and all egg emulsions presented relatively high values of ESI, since emulsion composition was previously optimized by experimental planning. The octyl stearate/Tween 80/egg sample combination presented highest values of ESI ($ESI_{1\ day} = 100\%$ to $ESI_{21\ days} = 97.5\%$). The octyl stearate/Triton X-100/egg sample combination presented lower values of ESI ($ESI_{1\ day} = 97.6\%$ to $ESI_{21\ days} = 93.9\%$). Emulsions containing CRM presented a precipitate after 24 h. The precipitate was probably formed from the solid content that was not stabilized by the micelles due to the lyophilization process, however homogeneity was re-established by shaking the mixture.

3.3. Analytic applicability study and validation

Ideally, a single emulsion should be used for determination of all elements, however this was not possible mainly due to: (1) the presence of the analytes as contaminants in both surfactants and oil components (Table 4) and (2) different metal contents in the samples. Based on these criteria, the metals that could be analyzed in the same emulsion are showed in Table 3.

The characteristics of an analytical method are defined by the figures of merit, which should be determined experimentally. The proposed method was validated for six metals (Na, K, Ca, Mg, Zn and Fe). Figures of merit presented were linearity of the analytical curves, accuracy and precision. In addition, sensitivity was determined by characteristic concentration (C_0).

The advantages of the emulsification procedure for fatty samples have been described in the literature. When properly stabilized, the emulsified sample is compatible with most analytical instrumentation, allowing the use of simple calibration procedures due to the minimization of interferences [14]. In this study, calibration with aqueous standards was possible and the linearity ranges were selected to span the metal concentrations expected in real samples. Analytical curves were constructed by evaluating the relation between response (peak height and absorbance) and concentration by linear regression analysis yielding the results shown in Table 5. In all instances, a linear fit was found to be adequate for the purpose. Table 5 also presents the values found for characteristic concentration and limit of detection (LOD) for all elements.

The accuracy of the method was further confirmed by determining the metals in a whole egg powder CRM. The results are shown in Table 6. Statistical comparison by means of the *t*-test showed that there was no significant difference between the values obtained with the proposed method and the certified values.

The precision of the procedures was determined through repeatability (intra-day precision). Six egg emulsions were assayed during the same day, under the same experimental conditions. Intermediate precision (inter-day) was evaluated by assaying freshly prepared emulsions on three different days ($n = 3$). The repeatability presented good RSD values for all metals. The intermediate precision was evaluated using the RSD and *F*-test. The computed *F*-values were lower than tabulated *F*-values, indicating no significant difference between the results obtained on different days. All precision data are shown in Table 6.

3.4. Real samples analysis

The proposed method was applied to the determination of Na, K, Ca, Mg, Zn and Fe in fresh egg samples. We aimed to provide a baseline of these elements in eggs from six different suppliers (commercial and farm eggs). Six determinations were made for each element and the results are listed in Table 7. There was no significant difference among the content of the major components (Na, K, Ca and Mg) in the eggs from different suppliers. The largest variations were in the minor component contents, Zn and Fe, which ranged from 7.4 to 12.2 $\mu g\,g^{-1}$ and from 24.5 to 44.2 $\mu g\,g^{-1}$, respectively.

Information on egg metal composition is being sought [1,8–12,23], despite the interest, data are still limited. Ca, Mg, Zn and Fe levels obtained in this study were similar to those reported by Shang and Hong [23]. There are no literature reports for Na and K levels. The proposed method could be of interest in poultry and nutriology research and can be recommended for routine analyses. It can also be applied for metal determination in eggs from other bird species.

4. Conclusion

Ideally a single emulsion should be used for the determination of all selected elements, however, this was not possible due to the sur-

factant metal content and the different levels of each metal in egg samples. The main advantages of the proposed method over traditional digestion methods are that it does not require a long sample treatment or large amounts of organic solvents or inorganic acids and it is simple and shows good accuracy and reproducibility. As the challenges and main requirements for emulsion application in atomic spectrometry involve the attainment of stable emulsions with low viscosity, the proposed method including emulsification and subsequent metal determination for FAAS fulfilled these requisites and proved to be sensitive, reproducible, simple, and economical.

Acknowledgements

The authors thank CNPq (Conselho Nacional de Desenvolvimento Científico e Tecnológico, Brazil) for scholarships and to DAAD (Deutscher Akademischer Austausch Dienst, Germany) for financial support (project no. PKZ P/06/00902).

References

[1] A.C. Pappas, F. Karadas, P.F. Surai, N.A.R. Wood, P. Cassey, G.R. Bortolotti, B.K. Speake, J. Trace Elem. Med. Biol. 20 (2006) 155.
[2] Y. Mine, Food Hydrocolloids 12 (1998) 409.
[3] V. Kiosseoglou, Curr. Opin. Colloid Interface Sci. 8 (2003) 365.
[4] M.N.M. Reyes, R.C. Campos, Talanta 70 (2006) 929.
[5] M. Tuzen, M. Soylak, Food Chem. 102 (2007) 1089.
[6] S. Demirel, M. Tuzen, S. Saracoglu, M. Soylak, J. Hazard. Mater. 152 (2008) 1020.
[7] B. Welz, M. Sperling, Atomic Absorption Spectrometry, 3rd ed., Wiley–VCH, Weinheim, 1999.
[8] C. Pan, K. Huang, Y. Zhao, S. Qin, F. Chen, Q. Hu, J. Agric. Food Chem. 55 (2007) 1027.
[9] Z. Kiliç, O. Acar, M. Ulasan, M. Ilim, Food Chem. 76 (2002) 107.
[10] R. Manjusha, K. Dash, D. Karunasagar, Food Chem. 105 (2007) 260.
[11] A. Bargellini, I. Marchesia, L. Rizzi, L. Cauteruccio, R. Masironi, M. Simioli, P. Borella, J. Trace Elem. Med. Biol. 22 (2008) 234.
[12] J. Burger, M. Gochfeld, Sci. Total Environ. 311 (2003) 91.
[13] O.D Uluozlu, M. Tuzen, D. Mendil, M. Soylak, J. Hazard. Mater. 163 (2009) 982.
[14] A. Sanz-Medel, M.R.F. de la Campa, E.B. Gonzalez, M.L. Fernandez-Sanchez, Spectrochim. Acta Part B 54 (1999) 251.
[15] D. Bohrer, C.V.S. Ieggli, S. Noremberg, P.C. do Nascimento, L.M. de Carvalho, S.L. Vieira, R.N. Reis, Spectrochim. Acta Part B 64 (2009) 605.
[16] N. Prista, A.C. Alves, R. Morgado, J.S. Lobo, Tecnologia Farmacêutica, vol. 1, 6th ed., Editora Fundação Calouste Guebenkian, Lisboa, 2003.
[17] Remington Farmacia, Tomo 1, 19th ed., Editorial Médica Panamericana, Buenos Aires, 1998.
[18] A. Sanz-Medel, M.R.F. de La Campa, M.C. Valdez-Hevia y Temprano, B.A. Fernandez, Y.M. Liu, Talanta 40 (1993) 1759.
[19] T. Engels, T. Förster, W. von Rybinski, Colloids Surf. A 99 (1995) 141.
[20] L. Lachman, H.A. Lieberman, J.L. Kanig, Teoria e Prática na Indústria Farmacêutica, vol. 2, Editora Fundação Calouste Guebenkian, Lisboa, 2001, Chap. 17.
[21] H. Mirhosseini, C.P. Tan, N.S.A. Hamid, S. Yusof, B.H. Chern, Food Hydrocolloids 23 (2009) 271.
[22] X. Huang, Y. Kakuda, W. Cui, Food Hydrocolloids 15 (2001) 533.
[23] S. Shang, W. Hong, Talanta 44 (1997) 269.

Talanta 80 (2010) 1287–1291

Contents lists available at ScienceDirect

Talanta

journal homepage: www.elsevier.com/locate/talanta

A highly selective nanogold-aptamer catalytic resonance scattering spectral assay for trace Hg^{2+} using $HAuCl_4$-ascorbic acid as indicator reaction

Zhiliang Jiang*, Guiqing Wen, Yanyan Fan, Caina Jiang, Qingye Liu, Zhi Huang, Aihui Liang

Guangxi Key Laboratory of Environmental Engineering, Protection and Assessment, School of Environment and Resource, Guangxi Normal University, Guilin 541004, China

ARTICLE INFO

Article history:
Received 20 June 2009
Received in revised form 9 September 2009
Accepted 13 September 2009
Available online 19 September 2009

Keywords:
Hg^{2+}
Nanogold-aptamer catalysis
$HAuCl_4$
Ascorbic acid
Resonance scattering spectral assay

ABSTRACT

Single strand DNA (ssDNA) was used to modify nanogold to obtain a nanogold-aptamer resonance scattering (RS) probe (NGssDNA) for Hg^{2+}, based on the formation of stable thymine-Hg^{2+}-thymine (T-Hg^{2+}-T) mismatches and aggregation of the released nanogold particles. After removing the aggregated particles by filtrate membrane, the excess NGssDNA in the filtration solution exhibit catalytic effect on the gold particle reaction between $HAuCl_4$ and ascorbic acid (AA) that appear as RS peak at 596 nm. When Hg^{2+} concentration increased, the RS intensity at 596 nm decreased. The decreased intensity is linear to Hg^{2+} concentration in the range of 0.00008–0.888 ng/mL Hg^{2+}, with detection limit of 0.000034 ng/mL. The nanogold-aptamer catalytic RS assay was applied to determination of Hg^{2+} in water with satisfactory results.

© 2009 Elsevier B.V. All rights reserved.

1. Introduction

Application of new analytical reaction and novel material is a good way to obtain good analytical method. Aptamers are short single stranded oligonucleotides, which is selected from synthetic and random sequence library in vitro via a combinatorial chemistry technique known as SELEX. It can bind specifically to a wide range of target molecules, such as proteins, polypeptideor, some other organic compounds or metal ions with very small dissociation constants. Due to their high affinity, easy and quick preparation in vitro and functionalized, more and more aptamers are used to study the specific functions and interactions of protein [1,2], and applied in bioassays with naked-eye, spectrophotometric, fluorescence, electrochemical and surface plasmon resonance (SPR) detections [3–5]. Nanogold is one of the best nanoparticles in nanoanalytical chemistry. Being unique optical and electrical properties, high catalytic activity and good biocompatibility, it is widely applied in nanocatalytic, bioanalysis and other fields [6]. Recently, nanogold has been utilized to aptamer assay to develop visual colorimetric, fluorescence, SPR, electrochemical aptamer methods [7,8]. However, there is no report about nanogold catalytic reaction of Au(IV)-AA-cetyltrimethyl ammonium bromide and the aptamer-nanogold catalytic resonance scattering (RS) assay. RS is simple, rapid and sensitive, and has been applied to the analysis of proteins, nucleic acids, inorganic ion, based on the simple molecular interaction between analyte and small molecules such as dye. However, the selectivity for most RS methods remains to be improved. Recently, some highly selective reactions such as immunoreaction, and enzyme-catalyzed reaction have been utilized to develop some highly selective sensitive RS assays for protein antigen and enzyme [9–11]. However, highly selective and sensitive RS assays for metal ions have not been reported yet. In this paper, a novel aptamer-nanogold catalytic RS assays was proposed to detect environmental endocrine disrupting chemicals Hg^{2+} [12], based on T-Hg^{2+}-T mismatches, nanogold aggregation, aptamer-nanogold catalytic reactions and RS effect of gold particles.

2. Experimental

2.1. Apparatus

A model of Cary Eclipse fluorescence spectrophotometer (Varian Company, Palo Alto, CA) was used to record the RS intensity, with the excited and emission slit of 2.5 nm, and PMT voltage of 500 V, emission filter of 1%T attenuator. A model of RF 540 fluorescence spectrophotometer (Shimadzu, Japan) was also used to record the RS intensity. A model of F732-V cold atomic absorption apparatus (Shanghai Huaguang Instrument Factory, China) was used for the determination of mercury, using $SnCl_2$ reduced procedure and an absorption line of 253.7 nm. A model of 79-1 magnetic heat agitator (Zhongda Instrumental Plant, Jiangsu, China), a model of SK8200LH ultrasonic reactor (Kedao Ultrasonic Instrument Limited Company, Shanghai, China) and a model of H-600

* Corresponding author.
E-mail address: zljiang@mailbox.gxnu.edu.cn (Z. Jiang).

0039-9140/$ – see front matter © 2009 Elsevier B.V. All rights reserved.
doi:10.1016/j.talanta.2009.09.026

transmission electron microscope (TEM) (Electronic Stock Limited Company, Japan) were used.

2.2. Reagents

Single strand DNA used in this paper was purchased from Sanbo Yuanzhi Biotechnology Limited Company, Beijing, China. The aptamer for Hg^{2+} is reference to the articles of Yang's research group [13]. Its sequence is 5′-TTTCTTCTTTCTTCCCCCCTTGTTTGTTGTTT-3′, and a random DNA sequence is 5′-AAACGGCAAACATCCCCCCAAGTAAGAAGAAA-3′. 1.0% $HAuCl_4{\cdot}4H_2O$ (National Pharmaceutical Group Chemical Reagents Company, China) was used to prepare nanogold. 0.20 mol/L Na_2HPO_4 and 0.20 mol/L NaH_2PO_4 solutions were used to prepare different pH phosphate buffer solution according to a certain volume ratio. 2.00×10^4 ng/mL Hg^{2+} standard solution, 1.0% tri-sodium citrate (Shanghai Chemical Reagent Plant, Shanghai, China), 2 mol/L NaCl solution, 0.05 mol/L cetyltrimethyl ammonium bromide (CTAMB), 0.05 mol/L tetradecyl pyridinium bromide (TPB), 0.05 mol/L stearyl dimethyl benzyl ammonium chloride (SDBAC) were prepared. Nanogolds were prepared by citrate reduction of $HAuCl_4$ according to the procedure described in the reference [11]. All reagents were of analytical grade and the water was doubly distilled.

2.3. Preparation of the aptamer-nanogold probe

A different amount of ssDNA, a 400 μL pH 7.0 Na_2HPO_4–NaH_2PO_4 buffer solution, a 375 μL 58.0 μg/mL nanogold solution were added into a 5 mL marked tube in turn, mixed well, and holding for 5 min at room temperature. Then added 22.5 μL 2 mol/L NaCl solution, and diluted to 1.5 mL. Another 5 mL marked tube without ssDNA was used as contrast tube. The RS intensity at 540 nm ($I_{540\,nm}$) was measured. Results indicated that 2.04 nmol (18.0 μL) ssDNA is the minimum amount interacting with 375 μL nanogold to form aptamer-nanogold probe.

A 1.8 mL 0.17 μmol/L ssDNA and 37.5 mL 58.0 μg/mL nanogold solution were added into a 50 mL conical bottle, mixed well, and holding for 5 min at room temperature, in order that ssDNA interact with nanogold fully to form aptamer-nanogold probe (NGssDNA). Its concentration, calculated as Au, is 55.3 μg/mL NGssDNA.

2.4. Procedure

A 400 μL pH 7.0 Na_2HPO_4–NaH_2PO_4 buffer solutions, a 393 μL 55.3 μg/mL NGssDNA and a certain amount of Hg^{2+} solution were added into a 5 mL marked tube in turn, mixed well. Then a 22.5 μL 2 mol/L NaCl solution was added, diluted to 1.5 mL with doubly distilled water, mixed well. The reaction solution was filtered by 0.15 μm filtrate membrane and the filtrate solution was obtained for use.

A 10 μL 9.69×10^{-3} mol/L $HAuCl_4$ solution, 140 μL 0.1 mol/L HCl solution, 80 μL the filtrate solution (diluted 10 times) and 400 μL 0.05 mol/L CTMAB solution were added into a 5 mL marked tube in turn, diluted to 2.5 mL with water. Then 7.5 μL 0.057 mol/L AA solution was added, diluted to 3.0 mL with water. The mixing solution was placed in 60 °C water for 15 min, and then rapid cooled to room temperature. The RS spectra were recorded by means of synchronous scanning excited wavelength λ_{ex} and emission wavelength λ_{em} ($\lambda_{ex} - \lambda_{em} = \Delta\lambda = 0$) on fluorescence spectrophotometer. The RS intensity at 596 nm ($I_{596\,nm}$) and the blank solutions without Hg^{2+} $(I_{596\,nm})_b$ were recorded. The value of $\Delta I_{596\,nm} = [(I_{596\,nm})_b - I_{596\,nm}]$ was calculated.

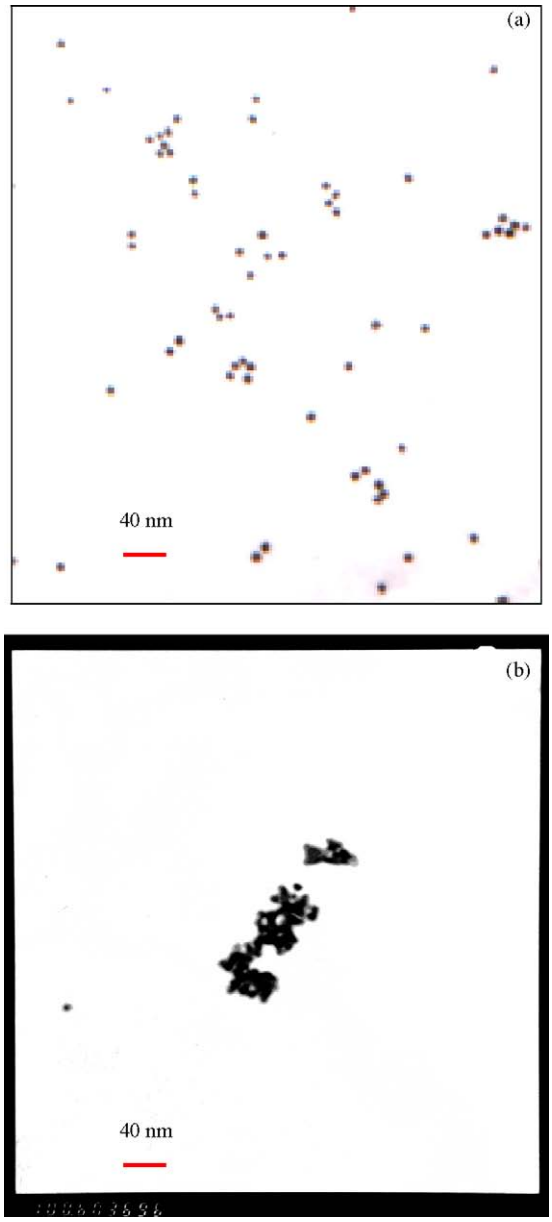


Fig. 1. Transmission electron microscope of NGssDNA-Hg^{2+} system. (a) 14.5 μg/mL NGssDNA; (b) 14.5 μg/mL NGssDNA-600 nmol/L Hg^{2+}-0.03 mol/L NaCl-pH 7.0, amplified 100,000 times.

3. Results and discussion

3.1. Transmission electron microscope

Transmission electron microscope (TEM) showed that the 10 nm nanogold particles are spherical and evenly distributed. ssDNA were found to interact with nanogold to form stable aptamer-nanogold complex. The NGssDNA is dispersed and the size of nanogold is unchanged (Fig. 1a). If Hg^{2+} was added, stable T-T mismatches of T-Hg^{2+}-T were formed, and the nanogolds released from the NGssDNA. In the presence of high concentration of salt, the nanogolds aggregated to form large clusters as in Fig. 1b.

3.2. Circular dichroism

One way to study the nucleic acid structure change is by investigating the circular dichroism (CD) properties, which arise from the chirality of the individual molecule. CD is able to provide infor-

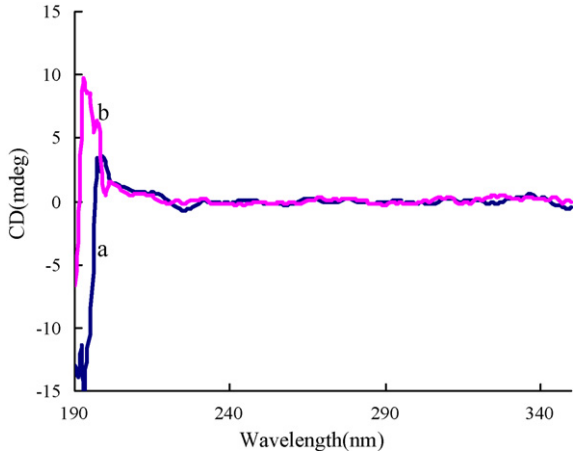


Fig. 2. CD spectra of Hg^{2+}-NGssDNA system. (a) 14.5 μg/mL NGssDNA-0.03 mol/L NaCl-pH 7.0; (b) a-40.0 ng/mL Hg^{2+}.

mation on the secondary structure by measuring the difference in left and right absorbance of the macromolecule ($\Delta\varepsilon=\varepsilon_L-\varepsilon_R$). Fig. 2 showed that, at wavelength of 195 nm, the absorption of the NGssDNA-Hg^{2+} system was stronger than the NGssDNA system, because the absorption of double strand DNA was stronger than the ssDNA [14]. This indicated that there is double strand DNA in the system.

3.3. Absorption spectra

ssDNA were found to interact with nanogold to form stable aptamer-nanogold complex (NGssDNA) in the presence of pH 7.0 Na_2HPO_4–NaH_2PO_4 buffer solution and 0.03 mol/L NaCl solution. The NGssDNA system exhibited one max absorption peak at about 516 nm as shown in Fig. 3a. This indicated that the nanoglod size did not change after coated ssDNA. Upon addition of Hg^{2+}, it combined with ssDNA to form more stable and double strand T-Hg^{2+}-T complex by T-T mismatches. This enables the ssDNA cannot interact with nanogolds. That is, the NG was released from the NGssDNA. Thus, the nanogolds aggregated to form bigger clusters in the presence of 0.03 mol/L NaCl, that exhibit a new and unobvious absorption peak at long wavelength as in Fig. 3c, and the color changes from red to blue which lead the peak absorption value

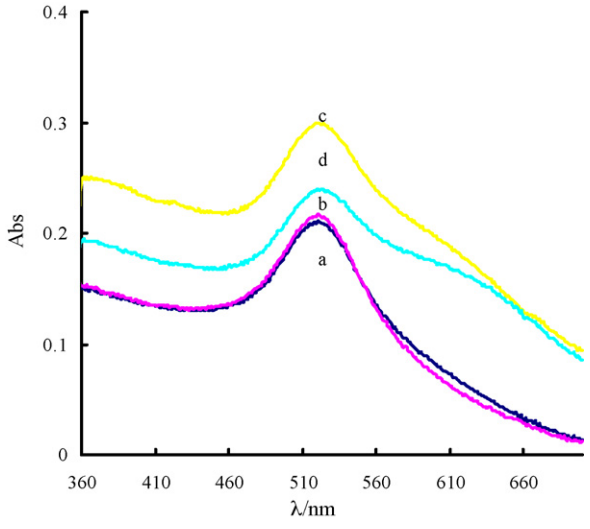


Fig. 3. Absorption spectra of NGssDNA-Hg^{2+}. (a) 14.5 μg/mL NGssDNA-0.03 mol/L NaCl-pH 7.0; (b) a-0.133 nmol/L Hg^{2+}; (c) a-40.0 ng/mL Hg^{2+}; (d) a-66.7 ng/mL Hg^{2+}.

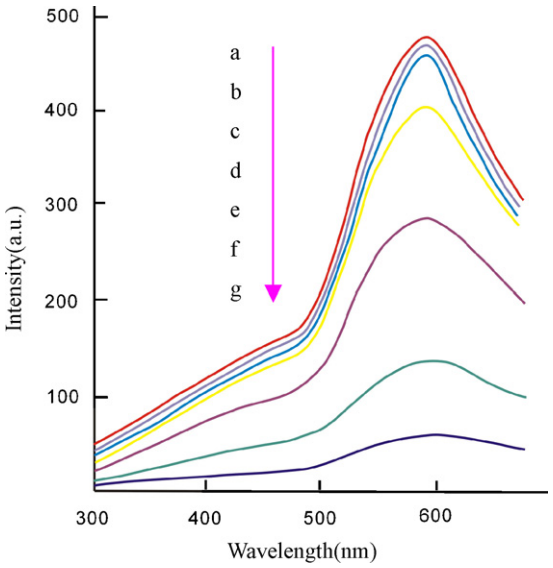


Fig. 4. RS spectra of Hg^{2+}-NGssDNA-$HAuCl_4$-AA catalytic system. (a) 3.23×10^{-5} mol/L $HAuCl_4$-5 mmol/L HCl-6.7 mmol/L CTMAB-0.14 mmol/L AA-NGssDNA filtrate solution; (b) a-0.0107 ng/mL Hg^{2+}; (c) a-0.0424 ng/mL Hg^{2+}; (d) a-0.107 ng/mL Hg^{2+}; (e) a-0.356 ng/mL Hg^{2+}; (f) a-0.712 ng/mL Hg^{2+}; (g) a-0.888 ng/mL Hg^{2+}.

increased at low concentration of Hg^{2+}. With further increasing of the Hg^{2+} concentration, the absorbance at 516 nm decreased considerably and the new peak was more obvious because the nanogolds aggregated into the larger particles. This can lead to false analytical results. In addition, other bivalent cations interfere with the spectrophotometric determination of Hg. This indicated that the aptamer spectrophotometric assay for Hg^{2+} was not good.

The absorption spectra of NGssDNA nanocatalytic system indicated that in the absence of Hg^{2+}, the amount of NGssDNA in the filtrate solution is the most and the catalytic reaction product of gold particles is the most, so the absorption value is maximum. The concentration of NGssDNA in the filtrate solution decreased with the Hg^{2+} concentration increased. Thus, the absorption values decreased linearly. However, the catalytic spectrophotometric assay was not sensitive, so it was not good for detection of Hg^{2+}.

3.4. RS spectra

The 10 nm nanogold particles exhibited weak RS signal at about 540 nm. After it was coated by ssDNA to form NGssDNA in the presence of pH 7.0 Na_2HPO_4–NaH_2PO_4 buffer solutions and 0.03 mol/L NaCl solution, its signal is also weak. Upon addition of Hg^{2+}, the RS intensity at 540 nm increased linearly. Thus, 0.0266–333.4 ng/mL Hg^{2+} can be detected rapidly and simply by the aptamer-nanogold RS probe. However, its sensitivity is not high. Hg^{2+}-NGssDNA-$HAuCl_4$-ascorbic acid catalytic system has a strong RS peaks at 596 nm. In the absence of Hg^{2+}, the concentration of NGssDNA in the filtrate solution and the RS intensity are the highest . The concentration of NGssDNA in the filtrate decreased as the Hg^{2+} concentration increased. Thus, the catalytic capacity decreased, which leaded the RS intensity weaken linearly at 596 nm as in Fig. 4.

3.5. Catalytic effect of nanogold on the reaction of $HAuCl_4$-AA

In the presence of CS such as CTMAB, yellow Au^{3+} exhibited an absorption peak at 396 nm. It was reduced quickly to colorless Au^{+} by ascorbic acid, that was observed in the process of preparing nanogold rod [15]. With addition of AA, the absorption peak decreased, and there is no scattering signal. This indicated that

Table 1
Analytical features for the nanogold catalytic systems.

Nanogold size (nm)	CS	Linear range (ng/mL)	Regress equation	Coefficient	Detection limit (ng/mL)
10	CTMAB	0.480–96.0	$\Delta I = 8.56C + 1.5$	0.9972	0.06
	TPB	0.480–48.0	$\Delta I = 8.39C + 3.7$	0.9709	0.06
	SDBAC	0.480–38.4	$\Delta I = 7.41C + 2.1$	0.9748	0.07
30	CTMAB	0.960–96.0	$\Delta I = 5.99C + 8.0$	0.9983	0.2
	TPB	2.40–48.0	$\Delta I = 8.05C + 2.4$	0.9841	0.3
	SDBAC	4.80–38.4	$\Delta I = 7.41C + 2.1$	0.9516	0.7
50	CTMAB	0.96–192	$\Delta I = 3.39C + 3.5$	0.9991	0.3
	TPB	4.80–48.0	$\Delta I = 4.02C + 1.3$	0.9762	1.2
	SDBAC	9.60–38.4	$\Delta I = 3.29C + 7.3$	0.9868	3

the AA reduction of Au^+ to Au was very slow in the absence of nanogold particles. Upon addition of gold nanoparticles as catalyst, the big gold particles form considerably, and the RS peak intensity at 596 nm increase linearly. In the absence of CS, $AuCl_4^-$ would be reduced quickly to gold particles by AA, although nanogold particles were not added. The effect of nanogold catalyst concentration on the increased RS intensity at 596 nm (ΔI) was showed in Table 1. For the 10, 30, and 50 nm nanogold catalytic systems, the regress equation slope for the 10 nm nanogold catalytic system is bigger than the correspondence other systems. In them, the 10 nm nanogold exhibited strongest catalytic effect in the presence of CTMAB, and was chosen for the assay. In the nanocatalytic system, CTMAB was the best stabilizer and disperser for gold particles, because it forms stable micelle in cationic charges that interact with $AuCl_4^-$. When $AuCl_4^-$ was reduced catalytically by AA to atom Au coated on nanogold in big size that was also enwrapped by CTMAB to an electric double layer on the surface of gold particle, this avoids gold particle aggregations [14].

3.6. Optimization of conditions for Hg^{2+}-NGssDNA

The system of NGssDNA has been reported for Hg^{2+} assay with naked-eye, and spectrophotometry, based on forming stable double strand mismatches of T-Hg^{2+}-T. The naked-eye assay is a qualitative one, and the absorption peak wavelength varied with Hg^{2+}concentration. Our work showed that the RS assay for Hg^{2+} was better than the above two assays, and its analytical conditions were optimized. The effect of pH 5.3–8.0 Na_2HPO_4–NaH_2PO_4 buffer solution on the $\Delta I_{540\,nm}$ was tested. When pH is 7.0, the system has the maximum of $\Delta I_{540\,nm}$. Because phosphate is an electrolyte, the effect of Na_2HPO_4–NaH_2PO_4 buffer solution concentration on the $\Delta I_{540\,nm}$ was also tested. When the concentration of Na_2HPO_4–NaH_2PO_4 is 53.3 mmol/L, the system has the maximum of $\Delta I_{540\,nm}$. So the 53.3 mmol/L pH 7.0 Na_2HPO_4–NaH_2PO_4 buffer solution was chosen. The effect of NGssDNA concentration on $\Delta I_{540\,nm}$ was considered, $\Delta I_{540\,nm}$ attained the maximum when the concentration is 14.5 μg/mL. Accordingly, a 14.5 μg/mL NGssDNA was chosen. NaCl can disturb the surface charge balance of nanogold particles to lead the aggregation that is a good aggregation reagent for nanogold particles, and was chosen for use. The results demonstrated that $\Delta I_{540\,nm}$ attained the maximum when the NaCl concentration is 0.03 mol/L. Thus, a 0.03 mol/L NaCl was chosen.

3.7. Separation of NGssDNA and aggregation nanogold

Commonly, centrifugation is used to separate nanogold. However, the operation time is long and precious centrifugation apparatus should be purchased. Membrane separation is fast and low-cost, and was chosen for use. The influence of 150, 250 and 500 nm filtrate membrane on the separating NGssDNA and the aggregated nanogold was tested. The results showed that the 150 nm filtrate membrane attained the maximum sensitivity, and was selected for use. The influence of volume of the filtrate solution on $\Delta I_{596\,nm}$ was shown in Fig. 5. The $\Delta I_{596\,nm}$ increased as the volume increased within 0–80 μL. $\Delta I_{596\,nm}$ attained the maximum when the filtrate amount is 80 μL. Accordingly, 80 μL the diluted filtrate solution was chosen.

3.8. Optimization of conditions for NGssDNA catalytic system

Catalytic reactions, including inorganic catalytic reaction and enzyme catalytic reaction, have been utilized to amplify analytical signal in analytical chemistry [15–18]. The above two catalytic reactions were also applied in RS analysis with good results. Nanocatalytic reaction is a new, sensitive and important way to amplify analytical signal. It is well known that gold particles were more stable than the silver, copper particles. Thus, a stable and convenient nanogold catalytic-gold particle system is necessary to explore. Study showed that NGssDNA has a strong catalytic effect on $HAuCl_4$-AA-CTMAB reaction to form stable gold particle. It was convenient and was chosen for use. The effect of HCl, $HAuCl_4$, AA and CTMAB concentration, reaction time and temperature on $\Delta I_{596\,nm}$ were studied separately. The results showed that 10 μL 9.69×10^{-3}mol/L $HAuCl_4$, 140 μL 0.1 mol/L HCl solution, 400 μL 0.05 mol/L CTMAB, 7.5 μL 0.057 mol/L ascorbic acid, in 60 °C water for 15 min, giving max $\Delta I_{596\,nm}$, and were chosen for use.

3.9. Effect of foreign substances

According to the procedure, the influence of foreign substances on the determination of 0.133 ng/mL Hg^{2+} was tested, with a relative error of ±10%. Table 2 showed that 50 times Pb^{2+}, 40 times Zn^{2+}, 250 times Cd^{2+}, etc., did not interfere with the determina-

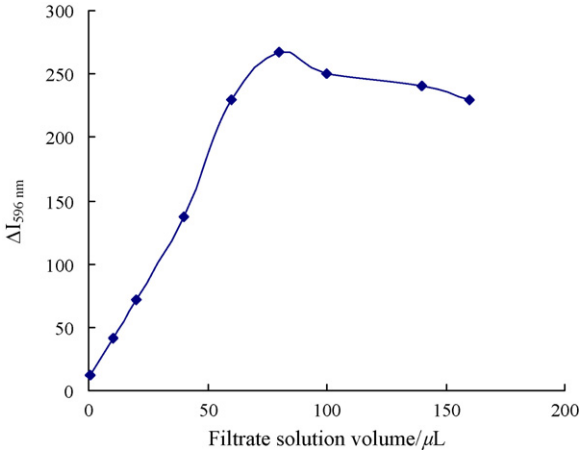


Fig. 5. Effect of the filtrate solution volume, 3.23×10^{-5} mol/L $HAuCl_4$-5 mmol/L HCl-6.7 mmol/L CTMAB-0.14 mmol/L AA.

Table 2
Effect of foreign substances.

Coexistent substance	Tolerance limit [M]/[Hg^{2+}]	Relative error (%)	Coexistent substance	Tolerance limit [M]/[Hg^{2+}]	Relative error (%)
Ni^{2+}	40	4.8	Fe^{3+}	40	6.7
Fe^{2+}	120	5.9	Ba^{2+}	50	−4.2
Mg^{2+}	80	−4.2	Mn^{2+}	40	7.2
Pb^{2+}	50	−6.0	Mo^{6+}	40	8.7
Co^{2+}	50	−8.4	Ca^{2+}	50	5.1
Zn^{2+}	40	−7.5	Al^{3+}	40	−9.0
Pd^{2+}	30	3.5	Cd^{2+}	250	−6.5

Table 3
Analytical results for Hg^{2+} in waste water samples.

Sample	Average (ng/mL, $n=5$)	RSD (%)	Added Hg^{2+} (ng/mL)	Found Hg^{2+} (ng/mL)	Recovery (%)	CV-AAS (ng/mL)
No. 1	24.9 ± 0.6	2.5	20.0	18.9	94.5	25.8
No. 2	18.0 ± 0.3	1.6	20.0	19.6	98.0	18.3
No. 3	23.1 ± 0.5	2.2	20.0	19.7	98.5	23.8
NESS 1490113[a]	9.02 ± 0.50	5.5	20.0	19.8	99.0	9.22
NESS 1400114	21.1 ± 0.7	3.3	20	19.7	98.5	20.9

[a] Certified values for NESS1490113 and 1400114 are 9.66 ± 1.09 ng/mL Hg and 20.2 ± 1.6 ng/mL Hg, respectively.

tion, which indicated that this method had good selectivity. This is owing to the specificity of aptamer reaction.

3.10. Working curve

According to the procedure, the working curve between Hg^{2+} concentration ($C_{Hg^{2+}}$) and their corresponding $\Delta I_{596\,nm}$ was drawn. The linear range was 0.00008–0.888 ng/mL. The regression equation was $\Delta I_{596\,nm} = 414.0C + 0.1$, with a correlation coefficient of 0.9965, and a 0.000034 ng/mL of detection limit. Compared with the reported methods [19–22], this aptamer-nanogold catalytic RS method is one of the most sensitive, and the cost is lower. Compared with the reported RS method for Hg [23], this RS assay is more sensitive, and the gold particles are stable than the Cu_2O particles.

3.11. Analysis of Hg^{2+} in wastewater

Wastewater samples were digested by aqua regia after centrifugation [23]. A 25 mL wastewater sample was pipetted to a 50 mL tested tube, and 3 mL aqua regia solution were added. Then the sample was digested in a boiling water bath for about 1 h to convert all species Hg to Hg^{2+}, and the sample solution was diluted to 25 mL with water. Finally, a certain volume of the digested solution was used to detect Hg^{2+} content according to the procedure. The results were agreement with that of the cold vapor atomic absorption spectrophotometry (CV-AAS). In the sample solution, a-20.0 ng/mL Hg^{2+} was added, then the Hg^{2+} content was also measured according to the procedure, and the recovery was obtained as in Table 3, the recovery was in the range of 94.5–99.0%, and relative standard deviation was in the range of 1.6–5.5%. This showed that this RS assay is precision and accuracy. Moreover, two national environmental standard sample (NESS) for mercury were determined by the nanogold-aptamer catalytic RS assay and CV-AAS, respectively. Both results were all agreement with the certified values. This results indicated that this RS assay is accuracy.

4. Conclusions

Hg^{2+} interact with the ssDNA to form stabile T-Hg^{2+}-T mismatches that cannot combine with nanogold particles. When the NGssDNA probe interacted with Hg^{2+} to form T-Hg^{2+}-T mismatches, and the released nanogolds cause aggregation under high concentration of NaCl. Coupled this feature with membrane filtration technique and nanogold catalytic reaction, a novel aptamer-nanogold catalytic RS assay, using Hg^{2+} as a model, has been established. The new RS method was applied to determine Hg^{2+} in wastewater, with high sensitivity and selectivity, rapidity and simplicity.

Acknowledgements

This work was supported by the Natural Science Foundation of Guangxi (Nos. 0832260, 0991021Z) and the Research Funds of Guangxi Key Laboratory of Environmental Engineering, Protection and Assessment (Nos. 0701Z022, 0701k008).

References

[1] C.C. Huang, Z. Cao, H.T. Chang, W. Tan, Anal. Chem. 76 (2004) 6973.
[2] J. Hwang, S. Nishikawa, J. Biomol. Screen. 11 (2006) 599.
[3] S. Centi, S. Tombelli, M. Minunni, M. Mascini, Anal. Chem. 79 (2007) 1466.
[4] A. Wochner, M. Menger, D. Orgel, B. Cech, M. Rimmele, V.A. Erdmann, J. Glökler, Anal. Biochem. 373 (2008) 34.
[5] K. Min, M. Cho, S.Y. Han, Y.B. Shim, J. Ku, C. Ban, Biosens. Bioelectron. 23 (2008) 1819.
[6] X.C. Sheng, X.W. He, H. Liang, Anal. Chem. 31 (2003) 880.
[7] W.J. Wang, C.L. Chen, M.X. Qian, X.S. Zhao, Anal. Biochem. 373 (2008) 213.
[8] S. Chen, Y.F. Huang, C.C. Huang, K.H. Lee, Z.H. Lin, H.T. Chang, Biosens. Bioelectron. 23 (2008) 1749.
[9] B.A. Du, Z.P. Li, C.H. Liu, Angew. Chem. Int. Ed. 45 (2006) 8022.
[10] Y.F. Long, C.Z. Huang, Y.F. Li, J. Phys. Chem. B 111 (2007) 4535.
[11] Z.L. Jiang, W.X. Huang, A.H. Liang, B. Chen, Talanta 73 (2007) 926.
[12] H.H. Harris, I.J. Pickering, G.N. George, Science 301 (2003) 1203.
[13] H. Wang, Y.X. Wang, J.Y. Jin, R.H. Yang, Anal. Chem. 80 (2008) 9021.
[14] Y.Z. Li, W.B. Chang, Biochemical Analysis, Higher Education Press, Beijing, 2003, p. 159.
[15] J.X. Gao, C.M. Bender, C.J. Murphy, Langmuir 19 (2003) 9065.
[16] Z.L. Jiang, S.P. Liu, Q.Y. Liu, Talanta 58 (2002) 635.
[17] A.H. Liang, N.N. Zhang, Z.L. Jiang, S.M. Wang, J. Fluoresc. 18 (2008) 1035.
[18] Z.L. Jiang, X.J. Liao, A.P. Deng, A.H. Liang, J.S. Li, H.C. Pan, J.F. Li, S.M. Wang, Y.J. Huang, Anal. Chem. 80 (2008) 8681.
[19] R. Sheng, P. Wang, W. Liu, X. Wu, S. Wu, Sens. Actuators B 128 (2008) 507.
[20] J. Chen, A.F. Zheng, A.H. Chen, Y. Gao, C. He, X. Kai, G. Wu, Y. Chen, Anal. Chim. Acta 599 (2007) 134.
[21] X. Xu, T.G. Thundat, G.M. Brown, H.F. Ji, Anal. Chem. 74 (2002) 3611.
[22] X. Xue, F. Wang, X. Liu, J. Am. Chem. Soc. 130 (2008) 3244.
[23] Z.L. Jiang, Y.Y. Fan, M.L. Chen, A.H. Liang, X.J. Liao, G.Q. Wen, X.C. Shen, X.C. He, H.C. Pan, H.S. Jiang, Anal. Chem. 81 (2009) 5439.

Talanta 80 (2010) 1292–1297

Contents lists available at ScienceDirect

Talanta

journal homepage: www.elsevier.com/locate/talanta

Application of ionic liquids based microwave-assisted extraction of three alkaloids *N*-nornuciferine, *O*-nornuciferine, and nuciferine from lotus leaf

Wenyan Ma[a], Yanbin Lu[b], Ruilin Hu[a], Jihang Chen[a], Zizhang Zhang[a], Yuanjiang Pan[a,*]

[a] *Department of Chemistry, Zhejiang University, Hangzhou 310027, China*
[b] *College of Food Science and Biological Engineering, Zhejiang Gongshang University, Hangzhou 310035, China*

ARTICLE INFO

Article history:
Received 25 June 2009
Received in revised form 9 September 2009
Accepted 13 September 2009
Available online 19 September 2009

Keywords:
Ionic liquids
Microwave-assisted extraction
Alkaloids
Lotus leaf

ABSTRACT

The application of ionic liquids based microwave-assisted extraction (ILMAE) was successfully developed for extracting three alkaloids *N*-nornuciferine, *O*-nornuciferine, and nuciferine from lotus leaf. Seven kinds of 1-alkyl-3-methylimidazolium with different cations and anions were investigated in this work and 1.0 M 1-hexyl-3-methylimidazolium bromide ([C_6MIM]Br) solution was selected as solvent. In addition, the microwave parameters including irradiation power, extraction time and solid–liquid ratio were optimized. Compared with the regular MAE and conventional heat-reflux extraction (HRE), the proposed approach exhibited higher efficiency (0.9–43.7% enhanced) and shorter extraction time (from 2 h to 2 min), which indicated ILMAE was an efficient, rapid and simple sample preparation technique. Moreover, the proposed method was validated by the linearity, reproducibility, and recovery experiments. Good linearity was observed with the regression coefficients (r^2) between 0.9998 and 0.9999. The recoveries of all methods were in the range of 94.6% and 105.5% with RSD lower than 6.6%, which indicated that the proposed method was credible.

© 2009 Elsevier B.V. All rights reserved.

1. Introduction

Medicinal plants have served as an important source of drugs for treating diseases since ancient times. In modern pharmaceutical industries, despite the remarkable progress in synthetic organic chemistry of the twentieth century, over 25% of prescribed medicines in industrialized countries derive directly or indirectly from plants. This percentage can reach 50% when the over-the-counter (OTC) market is taken into consideration [1,2]. In recent years, the validated analytical methods (μHPLC, CE, CEC, LC/MS^n, LC/NMR, LC/SPE/NMR, etc.) [3–6] are developing rapidly to guarantee the safety and efficacy of medicinal products. However, the importance of sample preparation has always been ignored. The metabolites extraction from solid plant samples is usually achieved by using well-established methods such as heat-reflux extraction (HRE) and Soxhlet extraction, which have some drawbacks including time-consuming, laborious, and using of a large amount of toxic and hazardous organic solvents. To overcome the above-mentioned problems, microwave-assisted extraction (MAE) has attracted broad interest as an alternative extraction technique with unique advantages of rapidness, high efficiency and low cost [7,8].

Ionic liquids (ILs), also known as molten salts, are a new class of nonmolecular ionic solvents with a melting point fixed at or below 100 °C. The potential of ILs in both academic and industrial fields is related to their unique properties of negligible vapor pressure, high thermal stability, low or virtually no volatility and ease of handling. ILs are therefore regarded as an attractive alternative or replacement to conventional volatile organic solvents (VOS) [9–12]. Over the past few years, ILs have attracted extensive attention in modern chemistry. The initial research interests are focused on organic synthesis [13], catalysis [14], and the process of green chemistry [15]. Recently, application of ILs has also extended into areas of analytical chemistry including electrochemistry, separation science, mass spectrometry, and spectroscopy. Due to the distinct features compared to conventional volatile organic solvents, sample pretreatment techniques using ILs have been successfully applied in liquid–liquid extraction, liquid-phase microextraction, solid-phase microextraction and aqueous two-phase systems extraction [16–20]. It has been found that ILs as solvents and co-solvents can efficiently absorb microwave energy [21]. Therefore, ILs as solvent is of promising potential in the application of the preparation of various useful substances from solid samples such as trans-resveratrol from *Rhizma Polygoni* Cuspidati [22], three phenolic alkaloids liensinine, isoliensinine, and neferine from traditional Chinese herbal medicine "Lien Tze Hsin" [23], and polyphenolic compounds from medicinal plants [24].

* Corresponding author. Tel.: +86 571 87951629; fax: +86 571 87951629.
E-mail address: panyuanjiang@zju.edu.cn (Y. Pan).

0039-9140/$ – see front matter © 2009 Elsevier B.V. All rights reserved.
doi:10.1016/j.talanta.2009.09.027

Lotus leaf is the leaves of *Nelumbo nucifera* Gaertn. It is a traditional Chinese medicine for losing weight and has been commonly used for clearing heat, removing heatstroke, cooling blood, and stanching blood [25]. The major phytochemicals present in lotus leaf are three aporphine alkaloids, *N*-nornuciferine, *O*-nornuciferine, and nuciferine (Fig. 1). Total alkaloids have been found with biological functions of lowering hyperlipemia [26] and level of cholesterol [27], resisting karyokinesis as well as antimicrobial activity [28]. Recently, nuciferine is newly reported to show anti-HIV activity [29]. Presently, the alkaloids from this medicinal plant are mainly extracted by HRE, which is time-consuming and laborious [30–32]. The aim of this work was to develop a rapid, effective, validated and environmental friendly ionic liquids based microwave-assisted approach for extraction of three alkaloids from this herbal medicine, and compare the results with the conventional reference methods. Herein we systematically investigated the performance of various ILs with different cations and anions as well as the microwave parameters which demonstrated that the proposed ILMAE approach has great potential for the ease of quality assessment of medicinal plants by providing the rapid and facile alkaloids extraction.

2. Experimental

2.1. Chemicals

All chemical solvents in this study were at least of analytical reagent grade, while reverse osmosis Milli-Q water (18 MΩ, Millipore, Bedford, MA, USA) was used throughout. Acetonitrile used for HPLC analysis was of chromatographic grade and purchased from Merck, Darmstadt, Germany.

Three alkaloids *N*-nornuciferine, *O*-nornuciferine, and nuciferine used for HPLC-UV determinations were isolated from lotus leaf and were confirmed by comparing their ^{1}H NMR, ^{13}C NMR, MS and MS^{2} with those given in the references [33–35]. All ionic liquids were gained from Chemer, Hangzhou, China, and used as received.

Lotus leaf was purchased from a local drug store, Hangzhou, China. All samples were dried, milled, passed through a stainless steel sieve and stored in closed desiccators at 4 °C until use. The same batch of sample was used through this study to be representative of variable hardness and density.

2.2. Apparatus

A domestic microwave-assisted extraction unit (Glanz, Shunde, China) with a 2450 MHz magnetron was used. It was modified in our laboratory with the addition of a water condenser. The whole system was run at atmospheric pressure and could be employed at the maximum power of 700 W.

An Agilent 1100 liquid chromatography equipped with a G1311A QuatPump, a G1322 Degasser, a G1314A variable wavelength detector (VWD), a model 7725i injection valve with a 20 μL loop was used for HPLC analysis, and an Agilent ChemStation for data treatment. An Agilent Zorbax Extend C18 (150 mm × 4.6 mm i.d., 5 μm, 120 Å) was used as the LC analytical column. Preparative HPLC was performed using a Varian Prepstar pump equipped with a Varian 210 UV detector (Varian Co., USA). A reversed-phase Shim-pack PRC ODS column (250 mm × 20 mm, 10 μm) was used for preparation. MS and MS^{2} figure were obtained from a Bruker Esquire 3000 mass spectrometer. ^{1}H and ^{13}C NMR spectra were performed in a Bruker Advance 500 NMR spectrometer.

2.3. Ionic liquids based microwave-assisted extraction

Ionic liquid-based microwave-assisted extraction was performed in microwave unit. 0.5 g of dried sample was mixed with 10 mL of different ILs solutions and then the suspension was extracted by MAE. The optimum anion, cation, concentration of selected IL, microwave power, irradiation time, and solid–liquid ratio were systematically studied in this work. After irradiation, the extracts obtained were cooled down to the room temperature, then diluted to 50 mL with deionized water, and filtrated through a 0.45 μm filter prior to HPLC analysis.

2.4. Conventional reference extraction method

Two HRE methods including acid extraction and organic solvent extraction were selected following the reference methods for extraction of the three alkaloids from lotus leaf [30–32].

The process of acid extraction: 0.5 g sample was mixed with 15 mL hydrochloric acid aqueous solution (pH 2) in a round-bottom flask (100 mL) and the suspensions were boiled at 100 °C for 2 h in an open system.

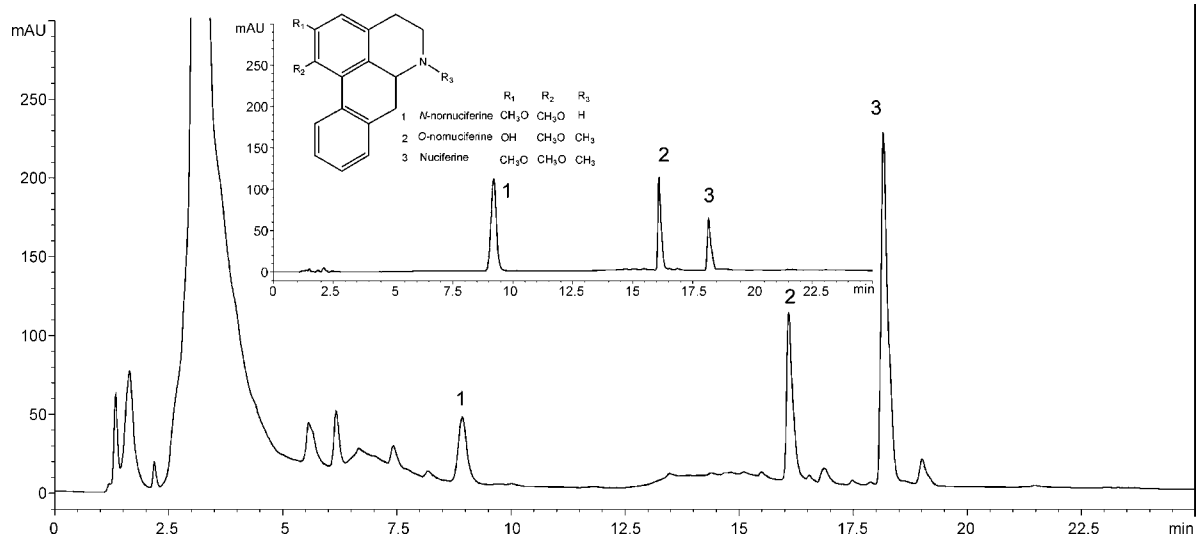


Fig. 1. HPLC chromatogram of three alkaloids in the [C_6MIM]Br extract. Inset: HPLC chromatogram of mixture of three standard alkaloids.

The process of organic solvent extraction: 0.5 g sample was mixed with 15 mL 95% ethanol in a round-bottom flask (100 mL) and the suspensions were boiled at 80 °C for 2 h in an open system.

After extraction, the obtained extracts were cooled down to the room temperature, then diluted to 50 mL with identical solvent, and filtrated through a 0.45 μm filter prior to HPLC analysis.

2.5. HPLC analysis and quantification

The diluted extracts were directly injected into the liquid chromatography. The mobile phase composed of solvent A (0.1% triethylamine aqueous solution) and solvent B (CH_3CN) was delivered at a flow rate of 0.8 mL min^{-1}. The gradient elution was programmed as follows: 0–5 min, 20–30% B; 5–10 min, 30% B; 10–13 min, 30–60% B; 13–20 min, 60–80% B. The UV detection wavelengths were 280 nm. Each injection volume was 20 μL and the column temperature was ambient. Under these conditions, the three alkaloids were baseline separated. *N*-nornuciferine, *O*-nornuciferine, and nuciferine were identified by comparing their retention time with corresponding peaks in the standard solution. A comparison of the chromatograms of the three alkaloids obtained from standard solutions with those contained in ILs extract is shown in Fig. 1.

2.6. Purification of standards of three alkaloids

Dried and powdered lotus leaf (1 kg) was extracted with 16 L of 95% ethanol for 2 h and repeated with three times. Then, the extract solutions were combined and evaporated under reduced pressure and 40 °C to about 200 mL. The concentrated solution was dissolved in 2 L 1.0% hydrochloric acid aqueous solution. The supernatant after centrifugation was adjusted to pH 10 with ammonia, and then extracted with chloroform (three times). The crude alkaloids which were obtained after solvent evaporation were dissolved in the mobile phase solvent, and then were injected into preparative HPLC. Methanol–0.2% ammonia aqueous solution was used as eluent solvents at 6 mL min^{-1} flow rate under 280 nm. Volume ratios of eluent solvents were 60:40, 65:35, 70:30, for *N*-nornuciferine, *O*-nornuciferine, and nuciferine, respectively.

3. Results and discussion

3.1. Screening of the ILs

The structure of ILs has significant influence on its physicochemical properties, which might greatly affect the extraction efficiency of target analytes [23]. The effects of changing the anion and the alkyl chain length of the cation of 1-alkyl-3-methylimidazolium-

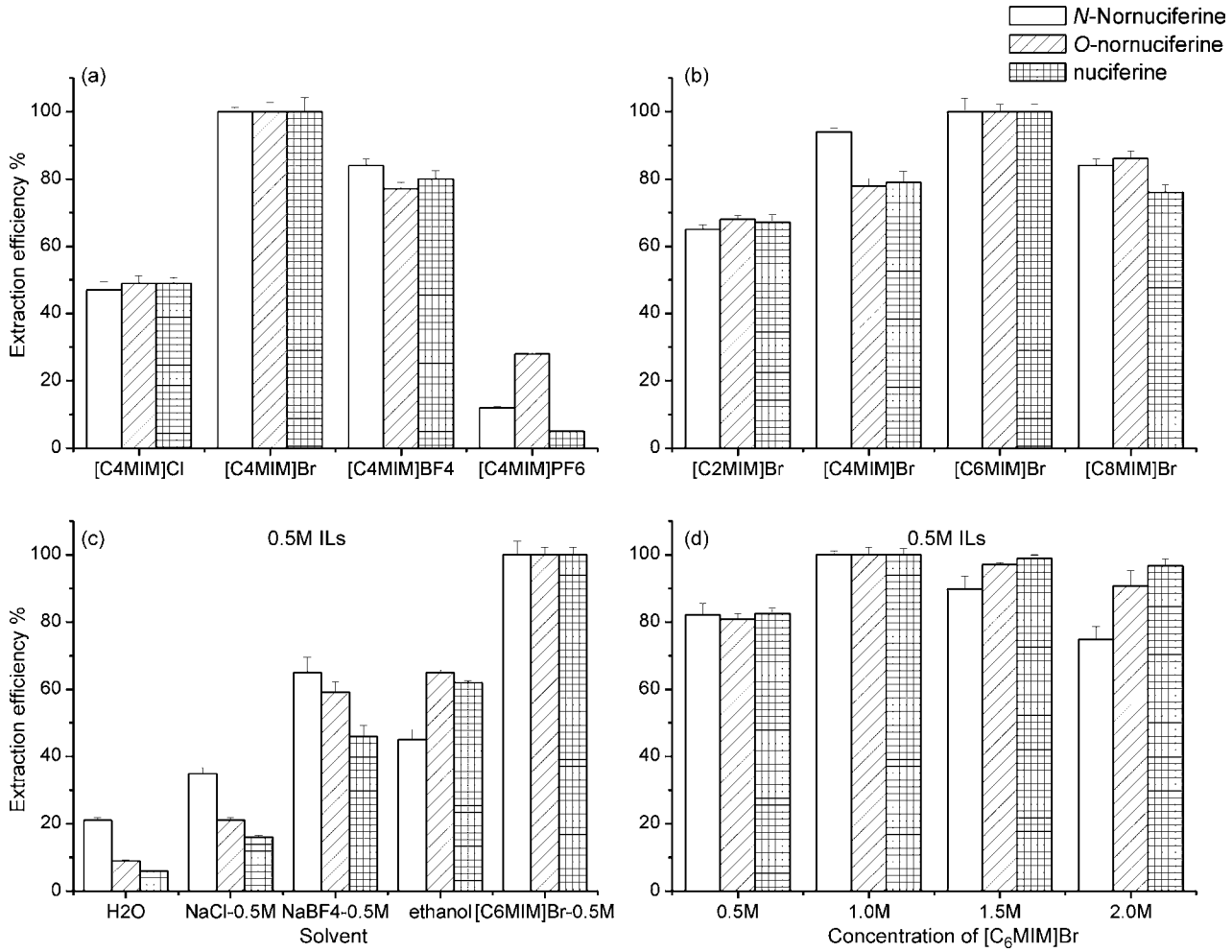


Fig. 2. Effect of ILs anions (a), ILs cations (b), compared [C_6MIM]Br with other solvents (c) and [C_6MIM]Br concentrations (d) on the extraction efficiency of target analytes. Sample: 0.5 g, extractant volume: 10 mL; irradiation power: 280 W; extraction time: 2 min. The extraction efficiency is expressed as the observed values of target analytes and the maximum amount in each curve was taken to be 100%.

Table 1
Some physicochemical properties of the studied ILs.

Cation	Anion	MW	Form (25 °C)	Solubility in H_2O (g/100 mL)
[C_2MIM]Br	Br^-	191	Solid	Totally miscible[a]
[C_4MIM]Cl	Cl^-	174.5	Solid	Totally miscible[a] [10]
[C_4MIM]Br	Br^-	219	Solid	Totally miscible[a]
[C_4MIM]BF_4	BF_4^-	225.8	Liquid	Totally miscible[a] [10]
[C_4MIM]PF_6	PF_6^-	284	Liquid	1.17[a] [10]
[C_6MIM]Br	Br^-	247	Liquid	Miscible[a]
[C_8MIM]Br	Br^-	275	Liquid	Miscible[a]

[a] Refers to the chemer home page on ionic liquid properties (www.chemer.com).

type ILs (see Table 1) on the extraction efficiency were studied in this work.

3.1.1. Anion effect

The anion identity is considered to be fore mostly important and has the most dramatic effect on the properties [10]. It is readily apparent from Table 1 that in the series of ILs studied here, the identity of the anion greatly influences the water miscibility. Therefore, the 1-butyl-3-methylimidazolium ILs with four different anions (Cl^-, Br^-, BF_4^-, PF_6^-) were studied. Among them, the former three ILs are hydrophilic and could miscible in any proportion with water, however, [C_4MIM][PF_6] is relatively hydrophobic and is only sparingly water soluble. The results obtained were given in Fig. 2a. Fig. 2a shows that Br^- is more efficient than others. This result indicated the extraction efficiency of alkaloids was mainly anion-dependent, which was similar to the previous studies [24,36]. It probably because [C_4MIM]Br solution had stronger multi-interactions including π–π, ionic/charge–charge and hydrogen bonding with alkaloids [22]. Besides, [C_4MIM]Br solution had slightly higher acidity, which might facilitate the extraction of target alkaloids from lotus leaf [30–32]. By contrast, the extraction efficiency of [C_4MIM][PF_6] is the lowest possibly due to its hydrophobicity.

3.1.2. Effect of the alkyl chain length

With the same anion of Br^-, a series of 1-alkyl-3-methylimidazolium cations including C_2mim^+, C_4mim^+, C_6mim^+, and C_8mim^+ were evaluated. The results were shown in Fig. 2b. It showed that extraction efficiency increased significantly when the alkyl chain length was increased from ethyl to hexyl. However, increasing alkyl chain length from hexyl to octyl dramatically decreased the extraction efficiency. The length of the alkyl chain is related with the water miscibility of the Br^- IL [10], and this property may be related with the extraction efficiency.

Considering the effect of both anion and cation, [C_6MIM]Br was selected for the subsequent evaluation (Fig. 2c).

3.1.3. Concentration effect

It has been proven that, polar molecule could strongly absorb the microwave energy [37,38], and therefore water is always selected as the co-solvent in various MAE process. To find out the optimum IL concentration for microwave-assisted extraction of three alka-

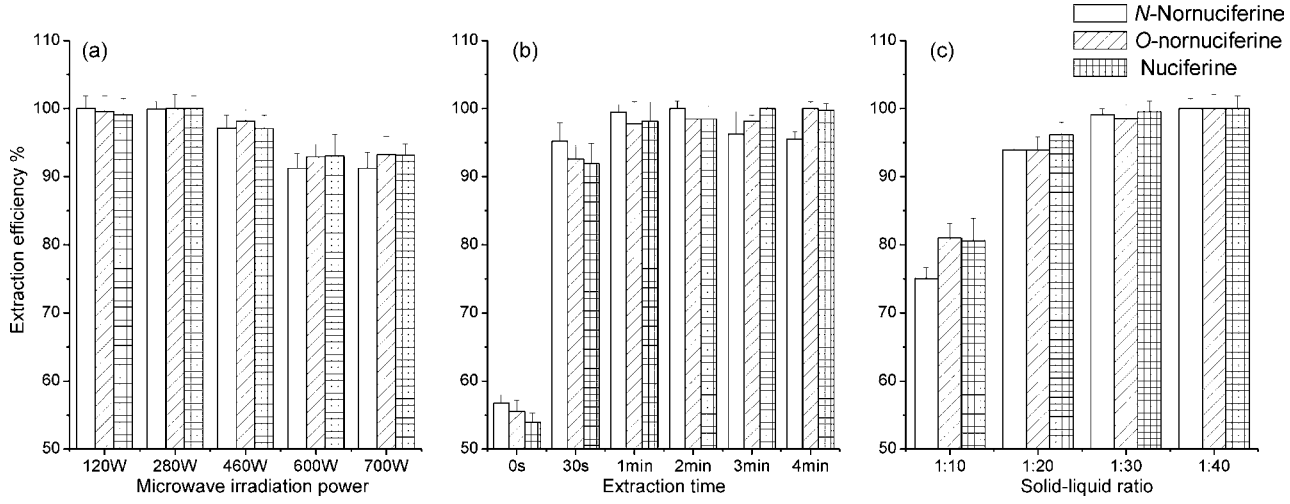


Fig. 3. Effect of microwave irradiation power (a), extraction time (b), and solid–liquid ratio (c) on the extraction efficiency of target analytes with 1.0 M [C_6MIM]Br. Sample: 0.5 g. The extraction efficiency is expressed as the observed values of target analytes and the maximum amount in each curve was taken to be 100%.

Table 2
Comparison of extraction efficiencies under different extraction methods.

Analytes	MAE methods								HRE method							
	IL MAE [C_6MIM]Br (n = 3)[a]				MAE 80% EtOH (n = 3)[b]				HRE 95% EtOH (n = 3)[c]				HRE HCl solution (n = 3)[c]			
	Observed values (mg/g)		Recovery yields (%)		Observed values (mg/g)		Recovery yields (%)		Observed values (mg/g)		Recovery yields (%)		Observed values (mg/g)		Recovery yields (%)	
	Mean	SD	Mean	SD	Mean	SD	Mean	SD	Mean	SD	Mean	SD	Mean	SD	Mean	SD
N-nornuciferine	0.973	0.0086	97.3	0.60	0.772	0.0184	95.2	1.48	0.825	0.0292	98.1	3.38	0.677	0.0285	102.3	4.63
O-nornuciferine	1.701	0.0341	98.9	1.74	1.506	0.0554	99.6	2.90	1.686	0.0573	102.5	1.17	1.590	0.1027	105.5	3.03
Nuciferine	5.945	0.0928	99.2	1.86	5.264	0.1693	95.1	2.14	5.765	0.1247	94.6	0.84	4.763	0.1650	99.5	6.66

[a] Operation under optimized conditions.
[b] The same operation conditions except the extracting phase.
[c] See experimental section for operation conditions. The total extraction time is 2 h.

loids, extraction was carried out in IL water solution of different concentrations (from 0.5 to 2 M). Based on the results in Fig. 2d, the extraction efficiency increased when the IL concentration over the range of 0.5–1.0 M. When it further increased, however, slight decrease was observed. Finally, 1.0 M of [C_6MIM]Br was selected in the following experiments.

3.2. Optimization of the MAE parameters

The univariate method was used in all instances to optimize the three parameters: irradiation power, extraction time and solid–liquid ratio.

3.2.1. Irradiation power

The irradiation power effect of this method has been examined as it has been claimed to influence interactions and equilibrium rates and controls partition of analytes between sample and extracting phase. To examine the effect of the microwave power on the extraction efficiency, extractions were carried out at 120, 280, 460, 600, and 700 W, respectively, with a constant irradiation time of 2 min. From Fig. 3a, irradiation power did not significantly influence the extraction efficiency. Irradiation power of 280 W (40% of the maximum value) could reach a little higher efficiency of three alkaloids than others.

3.2.2. Extraction time

To optimize extraction time, extractions were carried out at 280 W when microwave irradiation was changed within 4 min. As shown in Fig. 3b, when the extraction time increased from 0 to 1 min, the extraction efficiency of the three alkaloids increased dramatically. When the variable was changed from 1 min to 4 min, slight improvements were observed. Therefore, 2 min was selected for further experiments.

3.2.3. Solid–liquid ratio

The solid–liquid ratio is a crucial factor that should be studied to increase the extraction efficiency of three alkaloids. Larger solvent volumes could make procedure complex and unnecessary waste while smaller ones would make the targets extraction incomplete. A series of extractions were carried out with different solid–liquid ratios (1:10, 1:20, 1:30, and 1:40 g mL^{-1}) to evaluate the effect of the solid–liquid ratio. Fig. 3c indicated that the extraction efficiency increased obviously with the increase of the solvent volume before the solid–liquid ratio reached 1:30, and then the efficiency was not significantly improved with the further increase of the solvent amount. Thus, a solid–liquid ratio of 1:30 was used in the present study.

Based on the above experiment, the optimum MAE conditions were found to be: 1.0 M [C_6MIM]Br as extraction solvent, microwave irradiation power of 280 W, extraction time of 2 min, solid–liquid ratio of 1:30 (g mL^{-1}).

3.3. Comparison of the proposed ILMAE approach with the conventional methods

For the comparison of the extraction efficiency of ILMAE with other conventional extraction techniques, HRE including acid extraction, organic solvent extraction and regular MAE extraction were carried out to extract three alkaloids from lotus leaf (Table 2). From Table 2, the proposed approach not only obviously increased the extraction efficiency (0.9–43.7% enhanced), but also dramatically reduced the total extraction time (from 2 h to 2 min).

In order to further demonstrate the use of ILs, the regular MAE process was used to compare with the proposed ILMAE approach. All experiments were carried out under the same MAE conditions except the extractant. 80% ethanol which was optimized as the best

Table 3
Calibration graphs of the proposed method.

Analytes	Linearities	Correlation coefficients	Calibration range (mg/L)	LOD (μg/L)	LOQ (μg/L)
N-nornuciferine	$y = 49864x + 28.324$	$R^2 = 0.9999$	0.412–165.0	13.6	45.3
O-nornuciferine	$y = 41646x + 36.714$	$R^2 = 0.9998$	0.500–160.0	6.01	20.1
Nuciferine	$y = 31173x + 12.888$	$R^2 = 0.9999$	1.075–344.0	23.6	78.9

The linearity plotting at 280 nm and x was analytes concentration as g mL^{-1} and y was the peak area.

solvent was used in the regular MAE. Results shown in Table 2 indicated that the extraction efficiency of ILMAE was slightly higher than that of organic solvent (95% EtOH) HRE method, and much higher than that of regular MAE and acid HRE methods. This showed that, compared with HRE and regular MAE technique, the proposed approach used only small amount of ILs could obtain higher extraction efficiency (0.9–43.7% enhanced) in shorter extraction time (from 2 h to 2 min), which indicated that the aqueous ILs solutions were excellent extractant and ILMAE was a more rapid and effective sample preparation method. Even though ILs are more expensive than most organic solvents and water, the ILMAE method is still economical considered the saved time and potential recycle of ILs. On the other hand, although wastes have been left after extraction in our method as happened in traditional techniques, it is a much safer and greener process since no waste have been vented to the air during the extraction.

3.4. Analytical performance of the proposed method

To evaluate the proposed IL-based MAE approach, some parameters such as linearity, reproducibility, and recovery were determined under the above optimized conditions. The results were summarized in Table 3. Calibration graphs plots in the form of peak area versus standard concentration of each compound were run for all analytes. Good linearity was observed with the regression coefficients (r^2) between 0.9998 and 0.9999. The limits of detection (LODs) and the limits of quantification (LOQs) of the analytes were ranged from 6.01 μg L^{-1} to 23.6 μg L^{-1} and from 20.1 μg L^{-1} to 78.9 μg L^{-1}, respectively. The reproducibility study was carried out on three repeated extraction with all MAE and HRE methods. From Table 2, all methods had good reproducibilities (RSD obtained was between 0.9% and 6.5%). Moreover, the extracts were spiked with known quantities of standards. The recoveries of the four methods were in the range of 94.6% and 105.5% with RSD lower than 6.6%. The method validation studies indicated that the proposed method was credible.

4. Conclusions

An efficient ILMAE method has been developed for extraction and quantification of three alkaloids *N*-nornuciferine, *O*-nornuciferine, and nuciferine from lotus leaf. The optimum MAE conditions were studied. Compared with regular MAE and conventional HRE methods, the present approach obtained higher extraction efficiency (0.9–43.7% enhanced) and obviously reduced extraction time (from 2 h to 2 min), which demonstrated that the aqueous ILs solutions were excellent extractant and ILMAE was a simple, rapid, effective extraction method. Moreover, considering the unique properties of ILs, the ILMAE method proposed will have a broad potentiality as an environmental friendly technique in sample preparation.

Acknowledgements

Authors thank the National Natural Science Foundation of China for Grant 20775069, Ministry of Education of China for Grant NCET-06-0520 and Natural Science Foundation of Zhejiang Province for Grant Z206510.

References

[1] G.A. Cordell, Phytochem. Rev. 1 (2002) 261–273.
[2] K. Hostettmann, A. Marston, Phytochem. Rev. 1 (2002) 275–285.
[3] Y.S. Fung, H.S. Tung, Electrophoresis 22 (2001) 2242–2250.
[4] C. Seger, M. Godejohann, L.H. Tseng, M. Spraul, A. Girtler, S. Sturm, H. Stuppner, Anal. Chem. 77 (2005) 878–885.
[5] L.A. McDonald, L.R. Barbieri, G.T. Carter, G. Kruppa, X. Feng, J.A. Lotvin, M.M. Siegel, Anal. Chem. 75 (2003) 2730–2739.
[6] P.A. Cremin, L. Zeng, Anal. Chem. 74 (2002) 5492–5500.
[7] C.P. Eskilsson, E. Bjorklund, J. Chromatogr. A 902 (2000) 227–250.
[8] M. Letellier, H. Budzinski, Analusis 27 (1999) 259–271.
[9] T. Welton, Chem. Rev. 99 (1999) 2071–2083.
[10] J.G. Huddleston, A.E. Visser, W.M. Reichert, H.D. Willauer, G.A. Broker, R.D. Rogers, Green Chem. 3 (2001) 156–164.
[11] C.F. Poole, J. Chromatogr. A 1037 (2004) 49–82.
[12] J.L. Anderson, R. Ding, A. Ellern, D.W. Armstrong, J. Am. Chem. Soc. 127 (2005) 593–604.
[13] C.E. Song, E.J. Roh, Chem. Commun. 10 (2000) 837–838.
[14] A.J. Carmichael, D.M. Haddleton, S.A.F. Bon, K.R. Seddon, Chem. Commun. 14 (2000) 1237–1238.
[15] R.A. Sheldon, R.M. Lau, M.J. Sorgedrager, R.F. Van, Green Chem. 4 (2002) 147–151.
[16] J.G. Huddleston, H.D. Willauer, R.P. Swatloski, A.E. Visser, R.D. Rogers, Chem. Commun. 16 (1998) 1765–1766.
[17] J.H. Wang, D.H. Cheng, X.W. Chen, Z. Du, Z.L. Fang, Anal. Chem. 79 (2007) 620–625.
[18] J.F. Liu, G.B. Jiang, Y.G. Chi, Y.Q. Cai, J.T. Hu, Q.X. Zhou, Anal. Chem. 75 (2003) 5870–5876.
[19] J. Liu, N. Li, G. Jiang, J. Liu, J.A. Jonsson, M.J. Wen, J. Chromatogr. A 1066 (2005) 27–32.
[20] Z. Du, Y.L. Yu, J.H. Wang, Chem. Eur. J. 13 (2007) 2130–2137.
[21] J. Hoffmann, M. Nüchter, B. Ondruschka, P. Wasserscheid, Green Chem. 5 (2003) 296–299.
[22] F.Y. Du, X.H. Xiao, G.K. Li, J. Chromatogr. A 1140 (2007) 56–62.
[23] Y.B. Lu, W.Y. Ma, R.L. Hu, X.J. Dai, Y.J. Pan, J. Chromatogr. A 1208 (2008) 42–46.
[24] F.Y. Du, X.H. Xiao, X.J. Luo, G.K. Li, Talanta 78 (2009) 1177–1184.
[25] Pharmacopoeia Committee of P.R. China (Ed.), Chinese Pharmacopoeia, Chemical Industry Publishing House, Beijing, 2000.
[26] C.C. Tu, X.Y. Li, J.P. Yang, L. Zhou, J. Jianxi College Tradit. Chin. Med. 13 (2001) 120–121.
[27] L.J. Du, H. Sun, M. Li, W. Jin, L.Z. Xu, Zhongcaoyao 31 (2000) 526–528.
[28] L.P. Ji, Food Sci. 20 (1999) 64–66.
[29] A. Aoshima, Y. Ikeshiro, Y.P. Chen, H. Furukawa, M. Itoigawa, T. Fujioka, K. Mihashi, M. Cosentino, S.L. Morris-Natschke, K.H. Lee, Bioorgan. Med. Chem. 13 (2005) 443–448.
[30] J. Zhao, H.Z. Wang, X.H. Ji, M.Y. Gao, Z. Gao, Zhongcaoyao 34 (2003) 916–917.
[31] Y.H. Jiang, J. Zhejiang Univ. (Agric. & Life Sci.) 30 (2004) 519–523.
[32] H.G. Chen, Q.X. Zeng, Food Ferment. Ind. 27 (2001) 34–38.
[33] M. Tomita, Y. Watanable, M. Tomita, H. Furukawa, Yakugaku Zasshi 81 (1961) 469–473.
[34] J. Kunitomo, Y. Nagai, Y. Okamoto, H. Furukawa, Yakugaku Zasshi 90 (1970) 1165–1169.
[35] X.B. Luo, B. Chen, J.J. Liu, S.Z. Yao, Anal. Chim. Acta 538 (2005) 129–133.
[36] Z. Guo, B.M. Lue, K. Thomasen, A.S. Meyer, X.B. Xu, Green Chem. 9 (2007) 1362–1373.
[37] G.F. Barbero, M. Palma, C.G. Barroso, Anal. Chim. Acta 578 (2006) 227–233.
[38] M.A. Rostagno, M. Palma, C.G. Barroso, Anal. Chim. Acta 588 (2007) 274–282.

Talanta 80 (2010) 1298–1304

Contents lists available at ScienceDirect

Talanta

journal homepage: www.elsevier.com/locate/talanta

Immobilization of enzyme on detonation nanodiamond for highly efficient proteolysis

Liming Wei, Wei Zhang, Haojie Lu*, Pengyuan Yang*

Department of Chemistry & Institutes of Biomedical Sciences, Fudan University, Shanghai 200032, China

ARTICLE INFO

Article history:
Received 19 May 2009
Received in revised form 8 September 2009
Accepted 13 September 2009
Available online 19 September 2009

Keywords:
Detonation nanodiamond (dND)
Immobilized enzyme
Proteolysis
Glycosidase

ABSTRACT

Immobilization of enzyme on detonation nanodiamond (dND, 3–10 nm) and its application for efficient proteolysis have been demonstrated. By evaluation of the Michaelis constant (K_m) and maximum velocity (V_{max}) of immobilized enzyme, its activity was not impaired significantly by immobilization. And enzyme immobilized on dNDs exhibited much better thermal and chemical stabilities than its free counterpart and maintained high activity even after 10 times reuse. The efficient proteolysis by trypsin immobilized on dNDs (dND-trypsin) is demonstrated with the digestion of myoglobin (or other model protein) in a short time (5 min). Large numbers of identified peptides obtained by dNDs-trypsin enable a higher degree of sequence coverage and more positive identification of proteins than those obtained by in-solution digestion and the commercial immobilized trypsin beads, respectively. Moreover, immobilization of peptide-*N*-glycosidase F (PNGase F) on dNDs was realized and resulted in faster sequential glycosidase digestion of glycopeptides in less than 10 min.

Crown Copyright © 2009 Published by Elsevier B.V. All rights reserved.

1. Introduction

The rapid progress in genomics and proteomics has resulted in an increasing demand to identify and characterize proteins as efficiently and rapidly as possible [1]. Proteolysis is the key step for positive sequencing in proteomics research integrated with mass spectrometry (MS) analysis. Digestion with protease is generally performed in solution, which presents a number of drawbacks limiting the progress in high-throughput protein identification. To reduce the appearance of interfering autolysis peptides, the concentration of enzyme is always kept very low (1:20 to 1:100) and thus results in current enzymatic proteolysis ranging from several hours to overnight. If a high concentration of free enzyme is used, the digestion proceeds quicker but enzyme autolysis products become more abundant. Meanwhile, the use of long incubation times inevitably leads to more digestion artifacts like transpeptidation, non-specific cleavage, deamidation, and oxidation [2,3]. To solve these problems, the immobilized enzyme has been developed for characterization of proteins with the advantage of reducing autolysis product formation, allowing the use of higher enzyme concentrations that yield shorter digestion times, and reducing the interference of enzyme fragments on MS results [4]. Meanwhile, immobilized enzymes have the possible reusability and easy removal from the digestion medium.

Several reports have demonstrated the feasibility and performance of proteolysis using enzyme immobilized on various supports, such as poroszyme beads [5], porous glass beads [6], porous silicon matrix [7], zeolite nanocrystals [8], sol–gel supports [9], membrane [10], magnetic beads [11], polymer [12], and porous monolithic materials [13]. However, the poor biocompatibility properties of the most supports mentioned above are not advantageous for the immobilization of enzymes directly. The surface of these supports needs some intricate modification to satisfy with bio-analysis. Meanwhile, numerous enzyme immobilization methods have been developed [14,15]. In brief, enzymes could be physically adsorbed, trapped, or covalently bonded onto different supports. The physical adsorption method has been proposed for its simplicity and low cost, but its major disadvantage is that enzyme is easily desorbed from support [16]. Enzyme could also be trapped within matrix directly by some entrapment methods, such as sol-gel technique etc. [17]. However, due to the slow diffusion to achieve the mass transfer of both substrate and product, the digestion proceed was slow. In comparison, the covalence method is a little more complicated, but the stability of enzyme toward chemical denaturants and organic solvent can be enhanced when enzyme is firmly immobilized on support [18].

Nanodiamond, a carbon derivative nanomaterial, has a great potential for biological applications, due to its chemical stability, biological compatibility, non-toxicity and the unbleachable fluorescence from nitrogen vacancy centers [19–21]. The surface of nanodiamond provides a unique platform for conjugation of

* Corresponding authors at: Department of Chemistry & Institutes of Biomedical Sciences, Fudan University, Box 145, 138 Yi Xueyuan Road, Shanghai 200032, China. Tel.: +86 21 54237961; fax: +86 21 54237961.
E-mail addresses: weiliming@fudan.edu.cn (L. Wei), luhaojie@fudan.edu.cn (H. Lu), pyyang@fudan.edu.cn (P. Yang).

0039-9140/$ – see front matter. Crown Copyright © 2009 Published by Elsevier B.V. All rights reserved.
doi:10.1016/j.talanta.2009.09.029

biological molecules. It has been reported that the modified surface of nanodiamond can be conjugated with bio-molecules such as DNA [22], antigen [23], cytochrome *c* [24] and hormone [25]. Recently, nanodiamond prepared by detonation (dND) came into focus as a potential useful material for bio-applications due to its unique properties, such as small size of diamond nucleus, chemically active surface area, stability towards corrosive media, etc. [26,27]. Because the surface of dND is covered with a variety of functional groups including carboxyl, lactone, ketone, hydroxy, and some alkyl groups, which may be easily activated for conjugation of biological molecules. Also, the small particle size makes less effect to the activity of immobilized enzyme.

In this study, we report the covalent immobilization of enzyme on dNDs, which realized by the diimide-activated amidation of dND-bound carboxylic acids under the experimental conditions designed to avoid denaturing of bonded enzyme. As the core of immobilized enzyme, dNDs can provide a high binding rate of enzyme and good dispersibility in aqueous solution. The trypsin immobilized on dND particles (dND-trypsin) was successfully applied for proteolysis of model proteins. High efficient proteolysis was demonstrated with peptide mapping analysis of myoglobin and bovine serum albumin by MALDI-TOF MS. Meanwhile, peptide-*N*-4-(*N*-acetyl-beta-D-glucosaminyl) asparagine amidase F (PNGase F) was immobilized onto dNDs, and it could complete the glycosidase digestion of glycopeptides in less than 10 min.

2. Experimental

2.1. Materials and chemicals

Detonation nanodiamond was purchased from Gansu Lingyun Nanomaterial Corp. (Lanzhou, China). Chemical reagents, 1-ethyl-3-(3-dimethylaminopropyl)-carbodiimide hydrochloride (EDC) and *N*-hydroxysuccinimide (NHS) were purchased form Alfa Aesar (Ward Hill, MA, USA). Bovine serum albumin (BSA), horse heart myoglobin (Myo), fetuin, peptide-*N*-4-(*N*-acetyl-beta-D-glucosaminyl) asparagine amidase F (PNGase F), casein, α-cyano-4-hydroxycinnamic acid (CHCA), 2-(*N*-morpholino)ethanesulfonic acid (MES) and NH_4HCO_3 were from Sigma–Aldrich (Mississauga, ON, Canada). 2,5-Dihydroxybenzoic acid (DHB) was obtained from LaserBio Labs (Sophia-Antipolis, France). Porcine trypsin (sequence grade) was purchased from Promega (Madison, WI, USA). Poroszyme bulk immobilized trypsin was purchased from Applied Biosystems (Foster, CA, USA, Part # 2-3127-00; http://www.appliedbiosystems.com/). Analytical grade acetonitrile (ACN) and trifluoroacetic acid (TFA) were from Merck (Darmstadt, Germany). Water used for all experiments was purified using a Milli-Q Plus system (Millipore, Bedford, MA, USA), with resistance ≥18.2 MΩ/cm.

2.2. Preparation of enzyme immobilized dNDs

dNDs were further carboxylated and oxidized with strong oxidative acid treatments following the procedure of Huang and Chang [24]. Carboxylic acid groups on the surface of carboxylated and oxidized dND particles were activated by carbodiimide and subsequently reacted with NHS to provide a reactive site for covalent attachment to enzyme, as previously described [28,29]. dNDs (1 mg) and 7 mg of NHS were prepared in a 50 mM MES buffer solution (pH 6.1). Under the assistant by ultrasonic, 8 mg of EDC was added quickly, and the mixture was continually stirred at room temperature for 1 h. The suspension was then centrifuged and rinsed thoroughly with MES buffer solution to remove excess EDC, NHS and byproduct urea. The precipitate of the estered dNDs was redispersed in 1 mL of MES buffer solution. Then enzyme (2 mg) was added and stirred at 4 °C for 6 h. After immobilization, the pellet was washed with MES buffer solution, and then with 1 mL of glycine solution (1 M) to block unreacted epoxy groups. Finally, the pellet was washed with water in consecutive washing/centrifugation cycles to yield a light gray powder after drying in vacuum. And the supernatant solution was collected to measure the immobilized amount of enzyme. The amount of enzyme immobilized onto dNDs (μg/mg) was determined from changes in enzyme solution before and after the estered dNDs redispersed using the Bradford assay [30]. Two kinds of enzymes, trypsin and PNGase F, were immobilized onto dNDs in this study, respectively.

2.3. Characterization of enzyme immobilized on dNDs

dNDs, trypsin powder, and dND-trypsin particles were characterized by using Fourier transform infrared (FT-IR), respectively. FT-IR spectra were collected using a Nexus 470 FT-IR spectrometer (Nicolet, Madison, WI, USA). All samples were dehydrated before analysis. Absorbance spectra were acquired using 32 scans and an instrumental resolution of 4 cm^{-1}. The size and morphology of dNDs and dND-trypsin particles were observed using a JEOL model JEM-2011 (HR) transmission electron microscope, TEM, (Tokyo, Japan) at 200 kV, respectively.

2.4. Properties of enzyme immobilized on dNDs

The activity of enzyme against casein was determined by Keay's method [31]. Here, one unit (U) of enzyme activity is the quantity of enzyme that releases 1.0 μg tyrosine (Tyr)/min at pH 8.0 and 37 °C. The relationship between the initial rate of the reaction and the casein concentration (*S*) (0.25–4.0%) in PBS buffer solution (pH 8.0) at 37 °C was measured. The Michaelis–Menten kinetic parameters (i.e., Michaelis constant, K_m, and maximum effective velocity, V_{max}) were calculated from Lineweaver–Burk double reciprocal plots.

Thermal stability of enzyme was determined by measuring the residual activity of enzyme after it exposed to 60 °C for several hours with a given time interval. pH stability of enzyme was investigated by measuring the residual activity of enzyme after pre-incubated in PBS buffer with different pH. Ethanol solution was chosen as denaturant for enzyme. Enzyme was treated by ethanol solution with volume percentage ranged from 10% to 60% (v/v) at 37 °C for 30 min, and then the residual activity of enzyme was determined. To investigate the operational stability of dND-trypsin particles, it was repeatedly used to hydrolyze casein at the same conditions mentioned above. After the proteolysis of casein, the dND-trypsin particles were collected and washed five times with PBS buffer solution (pH 8.0) to start a new run. The supernatant was saved for quantitative analysis. These results were expressed in a normalized form with the highest value of each set assigned to 100% activity.

2.5. Protein digestion

Model proteins, myoglobin (Myo), bovine serum albumin (BSA) and fetuin were dissolved in 25 mM NH_4HCO_3 buffer solution separately, denatured at 95 °C for 15 min and digested with modified trypsin (enzyme-to-protein ratio of 1:50 (w/w)) overnight at 37 °C. To stop the digestion, the activity of trypsin was denatured by boiling at 95 °C for 10 min at last.

For tryptic digestion of protein by porozyme bulk immobilized trypsin beads, model proteins were dissolved in 25 mM NH_4HCO_3 buffer solution, and digested with trypsin beads (Applied Biosystems) (beads-to-protein ratio of 12:1 (v/w)) for 5 min at 37 °C with vortex. After centrifugation, beads and insoluble material were removed, and tryptic peptides were analyzed by MALDI-TOF MS.

dND-enzyme particles (1 mg) were suspended in 100 μL of 25 mM NH_4HCO_3 buffer solution. 10 μL of dND-trypsin particles

solution was added into each model protein solution. After incubation at 37 °C for 5 min, dND-enzyme particles were retained by centrifugation at 16,000 rpm for 5 min, and the supernatant was transferred to MS analysis.

2.6. MALDI-TOF MS analysis

A 4700 proteomics analyzer (Applied Biosystems, Framingham, MA, USA) performed in positive ion mode was applied for the measurement of peptide fragments. 1 μL of sample solution was dropped on a MALDI plate. After the solvent evaporated, 1 μL of matrix solution (4 mg/mL CHCA dissolved in 50% aqueous acetonitrile containing 0.1% TFA) was dropped on the sample layer. The MS instrument was operated at an accelerating voltage of 20 kV. A Nd:YAG laser with 200 Hz pulse at 355 nm was used. GPS Explorer software obtained from Applied Biosystems with Mascot (Matrix Sciences, London, UK) as a search engine and NCBI as a database were used to identify proteins by peptide fingerprint mass spectra.

The mass spectra of tryptic glycopeptides from fetuin were analyzed by an Axima MALDI-QIT-TOF MS instrument (Shimadzu Corp., Kyoto, Japan) with the nitrogen pulsed laser (337 nm). For QIT measurements, the matrix system was 10 mg/mL DHB dissolved in a 0.1% (v/v) TFA and 50% (v/v) acetonitrile solution. The measurements were carried out in positive ion mode.

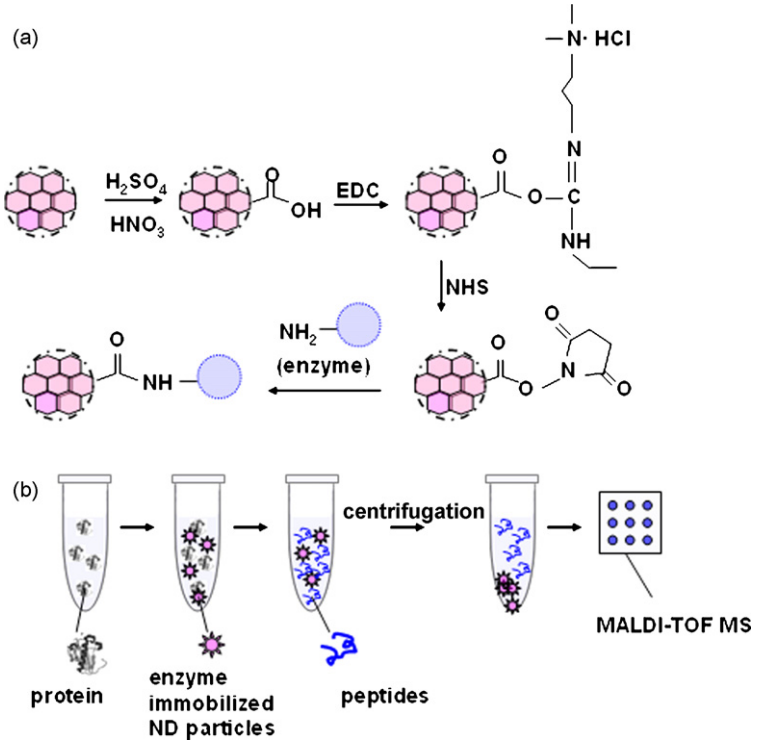
3. Result and discussion

3.1. Preparation and characterization of dND-enzyme

dNDs was chosen for enzyme immobilization due to its important characteristics, such as consistency, stability, easy handling and good biological compatibility. Moreover dNDs have some other advantages, including (1) high surface/mass ratio and the existence of large amount of stabilizer (i.e., carboxylic acid groups) on their surface which can provide a higher binding rate of enzyme; (2) high dispersibility in liquid media due to the oxidized, hydrophilic surface. Remarkably, the carboxylic acid groups on their surface can readily bio-conjugate with enzyme using a mild coupling agents carbodiimide, which cut short the complicated and time-consuming procedures of surface modification for enzyme immobilization.

The chemical functionlization of dNDs is shown in Scheme 1a. Enzyme was covalently immobilized on the particles surface by coupling it to the carboxyl groups of dNDs. FT-IR was used to evaluate the surface functional groups in the immobilized procedure. Fig. 1 shows the FT-IR spectra of dNDs, trypsin powder, and dND-trypsin particles. In the spectrum of dNDs (Fig. 1(a)), bands in the region 1123.2–1205.4 and 1682.2 cm^{-1} can be assigned to the C–O–C stretching vibration and the C=O stretching vibration, respectively. After enzyme immobilized on dNDs, these functional groups were disappeared. But the functional groups of trypsin, such as amide I (R–CONHR', C=O stretching) at 1651.4 cm^{-1} and the amide II (R–NHR', NH deformation, N–H bending and C–N stretching) at 3320.3 cm^{-1} and 1538.7 cm^{-1} (Fig. 1(b)) were emerged in the spectrum of dND-trypsin particles (Fig. 1(c)). These results illustrated that enzyme was successful covalent bonded on dNDs surfaces.

Fig. 2 presents the TEM images obtained from dNDs before and after enzyme immobilized. dND particles had a spherical shape with an average diameter of 3–10 nm (Fig. 2(a)). After the enzyme immobilization of dNDs, a blurry and loose layer was generated on dNDs surface, and increased the particles size by more than 0.5–1 nm (Fig. 2(b)). Although the enzyme immobilized dNDs was sonicated in isopropyl alcohol before TEM measurements, the immobilization was not destroyed. The immobilization ability of dNDs for enzyme was evaluated by measuring the UV absorption value of supernatant enzyme solution after immobilization procedure. The amount of enzyme immobilized on dNDs was calculated about 223 ± 30 μg/mg, which increased more than about seven times compared with the magnetic nanoparticles (~200 nm) prepared in Lin's work (32 μg/mg) [32].



Scheme 1. Schematic illustrating (a) the immobilization of enzyme onto dNDs *via* a process of diimide-actived amidation, (b) the procedure for protein digestion using enzyme immobilized dNDs.

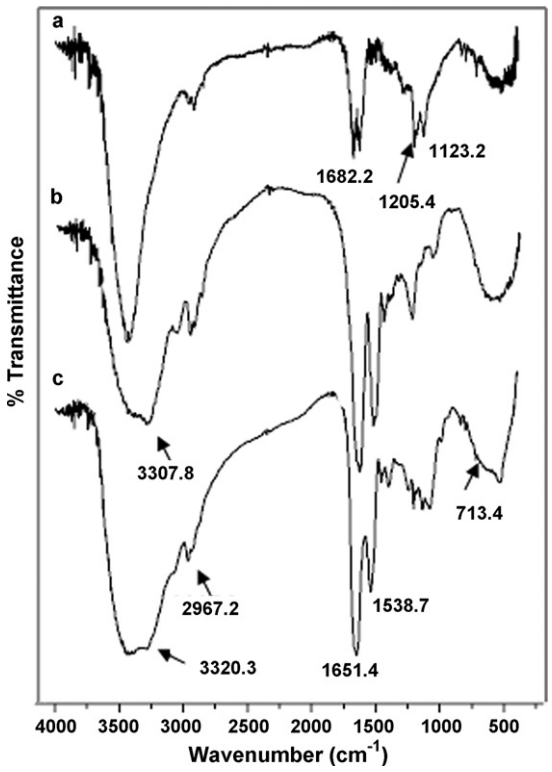


Fig. 1. FT-IR spectra of (a) dND particles, (b) trypsin, and (c) dND-trypsin particles.

3.2. Properties of enzyme immobilized on dNDs

One of the most important characteristics of an enzyme is its affinity for the substrate, usually assessed by the values of Michaelis constant (K_m) and maximum effective velocity (V_{max}). The most commonly used transformation is the double reciprocal or Lineweaver–Burke plot. The Lineweaver–Burke equation is

$$\frac{1}{V} = \frac{1}{V_{max}} + \left[\frac{K_m}{V_{max}}\right]\frac{1}{S}$$

in which the value of $1/V$ are plotted against $1/S$. From the slope and intercept of the plot of $1/V$ versus $1/S$ (Supporting Information, Figure S1), the K_m values of dND-trypsin and free trypsin were found to be 127.7 and 67.9 mg/mL, and V_{max} to be 353.5 and 1303.8 μg/min, respectively. In the experiment, the increase in K_m and the decrease in V_{max}, generally observed in the literature for enzyme immobilization, and is results from the combination of numerous effects such as chemical modification of enzyme during the immobilization reaction, chemical environment in the proximity of the reactive site, and diffusion effects. For example, trypsin immobilized on Sepharose beads was rather sluggishly exhibiting K_m value 2 orders of magnitude higher than free enzyme [33]. However, the values of free trypsin and dND-trypsin were of the same order of magnitude. This means that the catalytic function of trypsin was not impaired significantly by its immobilization. The initial activities of free trypsin and dND-trypsin in the hydrolysis of casein (1 mg/mL) were about 61.0×10^3 U/mg free enzyme and 14.0×10^3 U/mg immobilized enzyme (or 3.13×10^3 U/mg dried particles), respectively, which were better than other method for immobilizing enzyme [34,35].

Properties of the immobilized enzyme and free enzyme were compared in order to study the real stabilization of immobilized enzyme under various conditions. Trypsin as a model enzyme was employed for investigation. These results showed that the inactivity rate of immobilized trypsin was much lower than that of free form (Fig. 3). In Fig. 3(a), at 60 °C, the dND-trypsin retained 82% of its initial activity after 3 h incubation, and still retained its activity at 50%, even after 7 h incubation. However, free trypsin only retained about 76% and 14% of its initial activity after 1 and 3 h incubation, respectively. Therefore, the thermal stability of trypsin immobilized on dNDs shows remarkably higher durability than its free form, which may be attributed to the stabilization of weak intermolecular forces and the prevention of enzyme autolysis [36]. Meanwhile, since trypsin is firmly connected to the surface of dNDs by covalent bonds, pH stability and denaturant stability of dND-trypsin were also increased than its free form (Fig. 3(b) and (c)). Furthermore, the operational stability of dND-trypsin was evaluated by successive batch processes. As demonstrated in Fig. 3(d), the relative activity of dND-trypsin decreased slowly as the cycle number increased. But at least 70% of its initial activity was still reserved after reusing 10 times, which is much better than previous report [37]. These results demonstrate that the immobilization of enzyme on dNDs has benefit to enhance its stability.

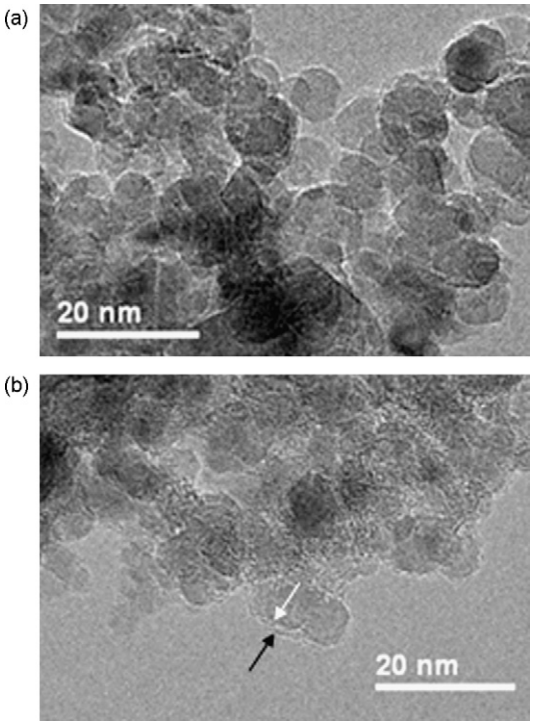


Fig. 2. TEM image of (a) dNDs and (b) enzyme immobilzed dNDs.

3.3. Performance of different digestion approaches for protein identification

Generally, the immobilized enzyme has been developed for characterization of proteins with the advantage of reducing autolysis product formation, allowing the use of high enzyme concentrations for short digestion times. The feasibility and performance of dND-trypsin were demonstrated by the tryptic digestion of model proteins, Myo (MW 16.9 kDa) and BSA (MW 66.0 kDa). The digestion procedure using dND-trypsin is illustrated in Scheme 1b. For control experiment, the digestion of these model proteins was also performed by free trypsin in-solution (for 5 min or 12 h) and poroszyme immobilized trypsin beads (for 5 min), respectively.

Fig. 4(a) displays peptide mass fingerprinting (PMF) spectra of the tryptic fragments of Myo and BSA (40 ng/μL) obtained by dND-trypsin in a short time (5 min) and peaks marked with asterisk correspond to peptides derived from model protein. Table S1 (Supporting Information) presents the identified peptide

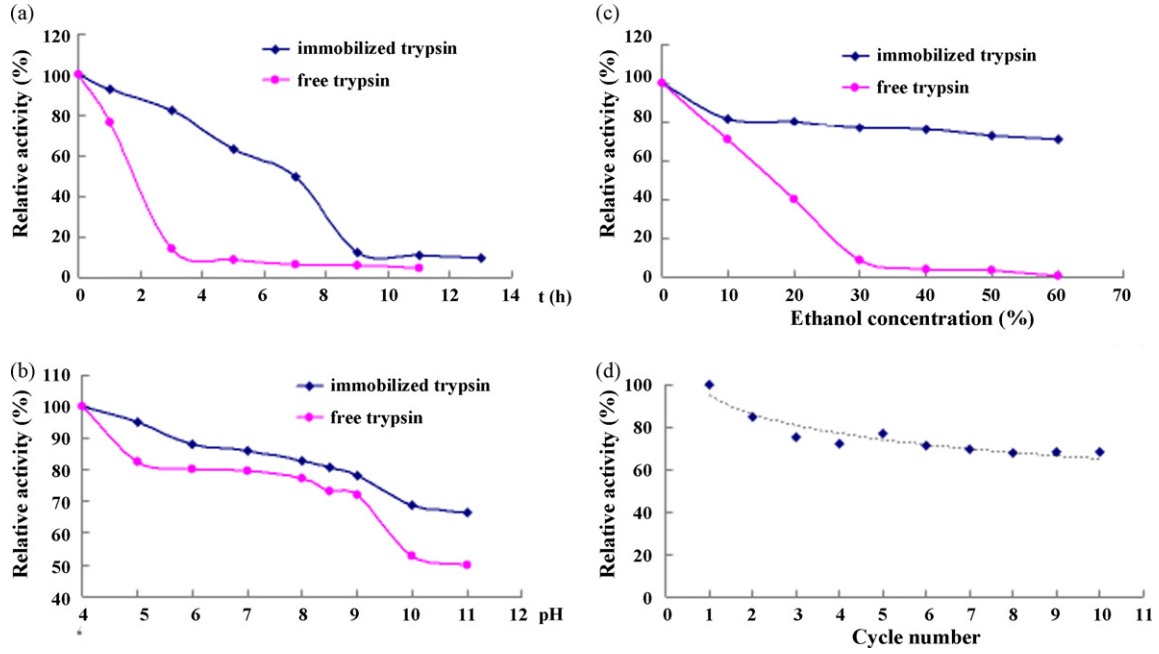


Fig. 3. Properties of enzyme under various conditions (a) thermal stability of free and the immobilized trypsin at 60 °C, (b) pH stability of free and the immobilized trypsin at 25 °C (free trypsin for 24 h, immobilized trypsin for 72 h), (c) denaturalized stability of free and the immobilized trypsin (37 °C, 30 min), (d) operational stability of dND-trypsin.

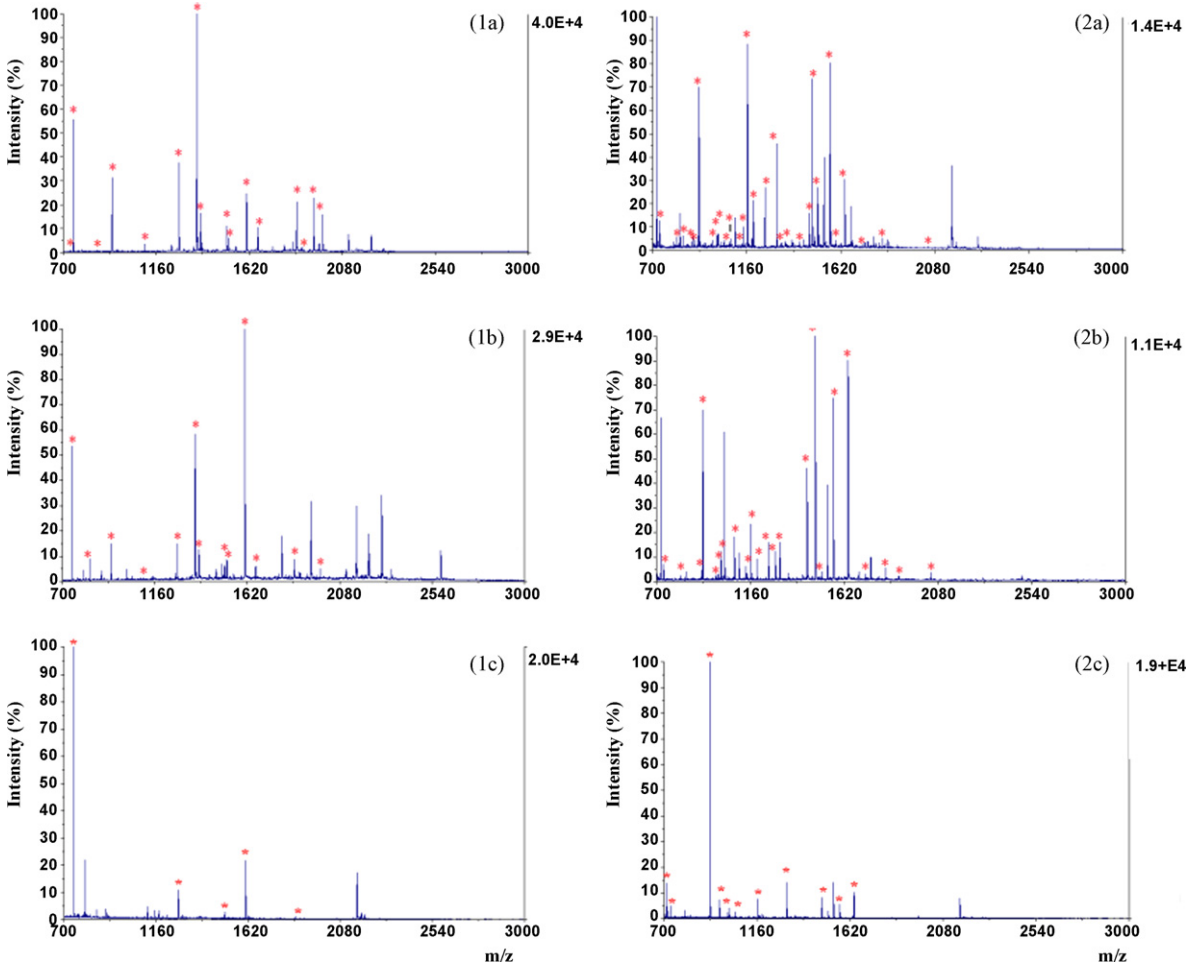


Fig. 4. MALDI-TOF mass spectra of the tryptic fragments of (1) Myo and (2) BSA (40 ng/μL) obtained from (a) 5-min digestion using dND-trypsin particles, (b) in-solution digestion for 12 h, and (c) 5-min digestion using poroszyme immobilized trypsin beads, respectively. All matched peptides were marked with asterisk.

Table 1
Summary of MALDI-TOF MS results obtained from 5-min digestion using dND-trypsin particles compared with in-solution digestion for 12-h and 5-min digestion using poroszyme immobilized trypsin beads (Applied Biosystems).

Protein	Myo			BSA		
Digestion approach	dND-trypsin	In-solution	Poroszyme	dND-trypsin	in-solution	Poroszyme
Sequence coverage (%)	83	73	41	35	32	27
Peptides matched	16	13	5	29	23	19
Protein scores	166	149	66	220	194	159

residues obtained from 5 min digestion using dND-trypsin particles. A total of 16 and 29 tryptic peptides from Myo and BSA were identified with the corresponding amino-acid sequence coverage of 83% and 35%, respectively. However, model proteins could not be digested and positively identified by free trypsin in-solution digestion in 5 min (data not show), which might be attributed to the low concentration of enzyme to reduce the appearance of interfering autolysis peptides. After it incubated for 12 h with free trypsin in solution, model proteins were fully digested and given good quality of mass spectra (Fig. 4(b)). As can be clearly seen from the comparison of these spectra, dND-trypsin digestion approach is comparable or better than in-solution digestion (for 12 h). It indicates protein can be digested totally in 5 min by dND-trypsin.

In Fig. 4(c), tryptic peptides obtained using poroszyme immobilized trypsin beads (for 5 min, Applied Biosystems) show lower response than that obtained by dND-trypsin. And there are a few tryptic peptides assigned to model protein. For example, in Fig. 4 1(c), only five peptides from Myo were assigned with the corresponding amino-acid sequence coverage of 41%. All mentioned above may be attributed to the lower enzyme binding rate and bigger size of poroszyme immobilized trypsin beads than that of dND-trypsin particles. Meanwhile, the surface of poroszyme may be lead to the adsorption of peptides, which was avoided by washing the beads before MS analysis in the manufacturers' instruction. However, the high binding rate of enzyme immobilized onto dNDs reduced the adsorption of peptides on particles. Table 1 compares the MALDI-TOF MS results obtained from 5 min digestion using dND-trypsin, 12 h in-solution digestion and 5 min digestion using poroszyme immobilized trypsin beads (Applied Biosystems). These results show dND-trypsin particles offers more efficient proteolysis than others digestion approach, which attributed to the reasons as following: (1) the use of high enzyme concentration yielding shorter digestion times and reducing the interference of enzyme fragments; (2) the high dispersibility of dND-trypsin in solution increases its affinity to substrates; (3) the small particle size and the surface functional groups of dNDs provide higher binding rate and much more enzyme than poroszyme beads. Therefore, dND-enzyme has a potential application for proteome analysis.

3.4. Application of dND-PNGase F for digestion

PNGase F is widely used to remove *N*-glycans from glycoproteins or glycopeptides for the identification of glycosylation sites and oligosaccharide heterogeneity in glycoproteins. To evaluate the feasibility of immobilized method, PNGase F was also covalently immobilized onto dNDs. The tryptic digestions of fetuin were used to test the performance of dND-PNGase F particles. Fig. 5 shows the mass spectra of tryptic fetuin peptides before and after incubation with PNGase F. The tryptic glycopeptides of fetuin at m/z 5004.6 (the peptide Val_{160}–Arg_{187} containing $Hex_6HexNAc_5$ at N_{176}) and its deglyco-peptide at m/z 3017.2 (^{160}VVHAVEVALATFNAES***N***GSYLQLVEISR^{187}) were all observed in mass spectra of tryptic fetuin peptides (Fig. 5(a)). The MS/MS fragmentation of isolated glycopeptides ions at *m*/*z* 5004.6 was displayed in Figure S2 (Supporting Information). After incubation for 6 h with free PNGase F in-solution, the glycopeptides (at

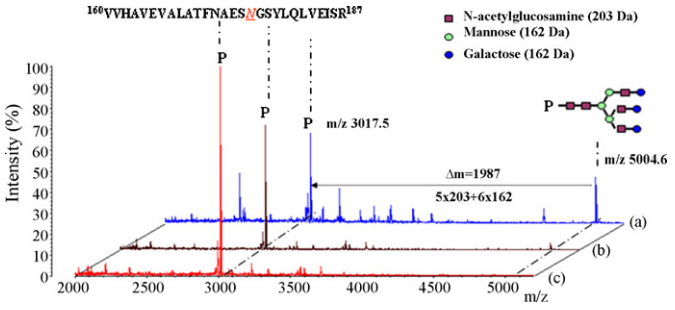


Fig. 5. MALDI-QIT-TOF mass spectra of tryptic fetuin peptides (a) before incubation with PNGase F enzyme, (b) after incubation with the free PNGase F in-solution for 6 h and (c) after incubation with dND-PNGase F particles for 10 min.

m/*z* 5004.6) was partly deglycosylated, so the signal intensity of glycopeptide (at *m*/*z* 5004.6) was decreased but still alive, and that of deglyco-peptide (at *m*/*z* 3017.2) was increased (Fig. 5(b)). However, after the tryptic fetuin peptides was treated by dND-PNGase F particles for 10 min, the peak of glycopeptides (at *m*/*z* 5004.6) was almost disappeared and the signal intensity of deglycopeptide (at *m*/*z* 3017.2) was obviously increased (Fig. 5 (c)). Therefore, the PNGase F immobilized onto dNDs can also successfully applied in the deglycan proteolysis of glycopeptides within a short time.

4. Conclusion

In summary, enzyme immobilized on dNDs (3–10 nm) has been prepared by a simple and one step reaction. The binding rate and amount of enzyme immobilized on dNDs with high surface/mass ratio and large amount of stabilizer (i.e., carboxylic acid groups) was higher than those of micro- and macroscale supports. Compared with free enzyme, the immobilized enzyme showed higher stability to temperature, acid, alkali and ethanol, and exhibited good operational stability. Meanwhile, the dND-trypsin coupled with MALDI-TOF MS demonstrates a promising strategy for the efficient proteolysis of protein. In this modified manner, very short digestion time with the high sequence coverage was achieved. Furthermore, using dND-PNGase F, *N*-glycans were effectively removed from glycopeptides in a short time. These results are expected to open up a new application of dNDs in proteomics. And, it is worth noting that, since the surface of dNDs provides a unique platform for conjugation of biological molecules, the application approach of dNDs may find much potential in proteomic study.

Acknowledgments

This study was supported by National Science and Technology Key Project of China (2007CB914100, 2009CB825607 and 2008ZX10207), National Natural Science Foundation of China (20875016, 30672394 and 30530040), Ministry of Education of China (20080246011 and NCET), Shanghai Leading Academic Discipline (B109) and Shanghai Projects (08DZ2293601).

Appendix A. Supplementary data

Supplementary data associated with this article can be found, in the online version, at doi:10.1016/j.talanta.2009.09.029.

References

[1] M. Tyers, M. Mann, Nature 422 (2003) 193.
[2] H. Schaefer, D.C. Chamrad, K. Marcus, K.A. Reidegeld, M. Blu¨ggel, H.E. Meyer, Proteomics 5 (2005) 846.
[3] N. Lundell, T. Schreitmüller, Anal. Biochem. 266 (1999) 31.
[4] C. Wang, R. Oleschuk, F. Ouchen, J. Li, P. Thibault, D.J. Harrison, Rapid Commun. Mass Sepctrom. 14 (2000) 1377.
[5] R.K. Blackburn, R.J. Anderegg, J. Am. Soc. Mass Spectrom. 8 (1997) 483.
[6] E. ŁHostis, P.E. Michel, G.C. Fiaccabrino, D.J. Strike, N.F. De Rooij, M. Koudelka-Hep, Sens. Actuators B 64 (2000) 156.
[7] L. Qiao, Y. Liu, S.P. Hudson, P. Yang, E. Magner, B. Liu, Chem. Eur. J. 14 (2008) 151.
[8] Y.H. Zhang, Y. Liu, J.L. Kong, P.Y. Yang, Y. Tang, B.H. Liu, Small 2 (2006) 1170.
[9] H.L. Wu, Y.P. Tian, B.H. Liu, H.J. Lu, X.Y. Wang, J.J. Zhai, H. Jin, P.Y. Yang, X.J. Xu, H.H. Wang, J. Proteome Res. 3 (2004) 1201.
[10] Y. Jiang, C.S. Lee, J. Chromatogr. A 924 (2001) 315.
[11] Y. Li, X.Q. Xu, C.H. Deng, P.Y. Yang, X.M. Zhang, J. Proteome Res. 6 (2007) 2367.
[12] S. Xie, F. Svec, J.M. Fréchet, Biotechnol. Bioeng. 62 (1999) 30.
[13] A. Palm, M.V. Novotny, Rapid Commun. Mass Sepctrom. 18 (2004) 1374.
[14] J.M. Palomo, C. Ortiz, M. Fuentes, G. Fernández-Lorente, J.M. Guisán, R. Fernández-Lafuente, J. Chromatogr. A 1038 (2004) 267.
[15] L.L. Manza, S.L. Stamer, A.J.L. Ham, S.G. Codreanu, Proteomics 5 (2005) 1742.
[16] H.M. Ding, L. Shao, R.J. Liu, Q.G. Xiao, J.F. Chen, J. Colloid Interface Sci. 290 (2005) 102.
[17] M. Kato, K. Inuzuka, K. Sakai-Kato, T. Toyo'oka, Anal. Chem. 77 (2005) 1813.
[18] J.J. Li, Q. Wang, V.G. Gavalas, D.A. Atwood, L.G. Bachas, Nano Lett. 3 (2003) 55.
[19] S. Yu, M.W. Kang, H.C. Chang, K.M. Chen, Y.C. Yu, J. Am. Chem. Soc. 127 (2005) 17604.
[20] K.K. Liu, C.L. Cheng, C.C. Chang, J.I. Chao, Nanotechnology 18 (2007) 325102.
[21] K.K. Liu, M.F. Chen, P.Y. Chen, T.J.F. Lee, C.C. Cheng, C.C. Chang, Y.P. Ho, J.I. Chao, Nanotechnology 19 (2008) 205102.
[22] K. Ushizawa, Y. Sato, T. Mitsumori, T. Machinami, T. Ueda, T. Ando, Chem. Phys. Lett. 351 (2002) 105.
[23] N. Kossovsky, A. Gelman, H.J. Hnatyszyn, S. Rajguru, R.L. Garrell, S. Torbati, S.S.F. Freitas, G.M. Chow, Bioconjugate Chem. 6 (1995) 507.
[24] L.C. Huang, H.C. Chang, Langmuir 20 (2004) 5879.
[25] C.Y. Cheng, E. Perevedentseva, J.S. Tu, P.H. Chung, C.L. Cheng, K.K. Liu, J.I. Chao, P.H. Chen, C.C. Chang, Appl. Phys. Lett. 90 (2007) 163903.
[26] A. Krueger, J. Stegk, Y. Liang, L. Lu, G. Jarre, Langmuir 24 (2008) 4200.
[27] W.S. Yeap, Y.Y. Tan, K.P. Loh, Anal. Chem. 80 (2008) 4659.
[28] W.J. Huang, S. Taylor, K.F. Fu, D.H. Zhang, T.W. Hanks, A.M. Rao, Y.P. Sun, Nano Lett. 2 (2002) 311.
[29] S.S. Wong, A.T. Woolley, E. Joselevich, C.L. Cheung, C.M. Lieber, J. Am. Chem. Soc. 120 (1998) 8557.
[30] M.M. Bradford, Anal. Biochem. 72 (1976) 248.
[31] L. Keay, B.S. Wildi, Biotechnol. Bioeng. 12 (1970) 179.
[32] S. Lin, G. Yao, D. Qi, C. Deng, P. Yang, X. Zhang, Anal. Chem. 80 (2008) 3655.
[33] R. Kleine, P. Spangenberg, C. Flemming, Physiol. Chem. 357 (1976) 629.
[34] H.A. Chase, Y. Yang, Biotechnol. Appl. Biochem. 27 (1998) 205.
[35] S.J. Ge, L.X. Zhang, Acta Biotechnol. 13 (1993) 151.
[36] D.H. Chen, M.H. Liao, J. Mol. Catal., B: Enzyme 16 (2002) 283.
[37] Y. Li, X.Q. Xu, C.H. Deng, P.Y. Yang, X.M. Zhang, J. Proteome Res. 6 (2007) 3849.

Talanta 80 (2010) 1305–1310

Contents lists available at ScienceDirect

Talanta

journal homepage: www.elsevier.com/locate/talanta

Preparation of a new Cd(II)-imprinted polymer and its application to determination of cadmium(II) via flow-injection-flame atomic absorption spectrometry

Marta Gawin, Jadwiga Konefał, Bartosz Trzewik, Stanisław Walas*, Anna Tobiasz, Halina Mrowiec, Ewa Witek

Jagiellonian University, Faculty of Chemistry, Ingardena 3, 30-060 Krakow, Poland

ARTICLE INFO

Article history:
Received 10 June 2009
Received in revised form 2 September 2009
Accepted 14 September 2009
Available online 19 September 2009

Keywords:
Cadmium(II)
Imprinted polymer
Preconcentration
Flow-injection-flame atomic absorption spectrometry (FI-FAAS)

ABSTRACT

A new cadmium(II)-imprinted polymer based on cadmium(II) 2,2′-{ethane-1,2-diylbis[nitrilo(*E*)methylylidene]} diphenolate-4-vinylpyridine complex was obtained via suspension polymerization. The beads were used as a minicolumn packing for flow-injection-flame atomic absorption spectrometry (FI-FAAS) determination of cadmium(II) in water samples. Sorption effectiveness was optimal within pH range of 6.6–7.7. Nitric acid, 0.5% (v/v) was used as eluent. Fast cadmium(II) sorption by the proposed material enabled to apply sample flow rates up to 10 mL min^{-1} without loss in sorption effectiveness. Enrichment factor (EF), concentration efficiency (CE) and limit of detection (LOD, 3σ) found for 120-s sorption time were 117, 39.1 min^{-1} and 0.11 μg L^{-1}, respectively. Sorbent stability was proved for at least 100 preconcentration cycles (RSD = 2.9%). When compared to non-imprinted polymer the new Cd(II)-imprinted polymer exhibited improved selectivity towards cadmium(II) against other heavy metal ions, especially Cu(II) and Pb(II), as well as light metal ions. Accuracy of the method was tested for ground water and waste water certified reference materials and fortified water. The method was applied to Cd(II) determination in natural water samples.

© 2009 Elsevier B.V. All rights reserved.

1. Introduction

Cadmium presence in biosphere is related to both natural (mainly volcanic activity and rock weathering) and anthropogenic emission sources. Elevated cadmium concentration in waters, soil and as a consequence in food is caused by its various applications in many branches of industry. The metal is used in electroplating, in nickel–cadmium batteries, alloys and as a coating for other metals. Cadmium compounds have been mainly applied as pigments, they are also used as semiconductors [1].

Exposure to cadmium has been proved to have adverse effect on heart, lungs, bones and especially kidneys. Having been accumulated in liver and kidneys it is excreted very slowly and the process may last even for 20–30 years [2,3]. Moreover, cadmium has been classified as a carcinogen (Group IA) by International Agency for Research on Cancer [4]. Due to its toxicity both to humans and animals cadmium concentration in the environment should be monitored, hence appropriate guideline values for cadmium content have been introduced; for drinking water they are as follow: WHO 3 μg L^{-1} [5], EU 5 μg L^{-1} [6], US EPA 5 μg L^{-1} [7].

For many years flame atomic absorption spectrometry (FAAS) has been a standard analytical tool for determination of metals in various matrices owing to its wide application range, simplicity in operation and low cost of analysis [8]. However, cadmium content in many natural water samples is frequently below the quantification limit achieved with this technique, therefore introducing a preconcentration step prior to FAAS determination is required. Coupling flame atomic absorption spectrometer with flow-injection system (FI-FAAS) for on-line column preconcentration of metal ions is an interesting alternative to classic off-line solid-phase extraction (SPE) technique [9]. The system is generally a cheaper alternative to graphite-furnace atomic absorption spectrometry (GFAAS)—it enables to achieve comparable parameters and allows to eliminate some interference effects. FI separation and preconcentration methods offer several favorable features, among them: high sample throughput and enrichment efficiencies, low sample and reagent consumption, high reproducibility, low risk of contamination and simple automated operation [10].

The search of selective sorbents and their application to cadmium ions separation and preconcentration still attracts much attention [11]. One of the most promising groups of new sorbents are ion-imprinted polymers (IIPs). Ion-imprinting idea is based on formation of a complex of given metal ion (serving as a template) with an appropriate ligand and its subsequent immobilization in

* Corresponding author. Tel.: +48 12 663 22 33; fax: +48 12 663 22 32.
E-mail address: walas@chemia.uj.edu.pl (S. Walas).

0039-9140/$ – see front matter © 2009 Elsevier B.V. All rights reserved.
doi:10.1016/j.talanta.2009.09.021

a cross-linked polymeric matrix. Upon metal ion extraction from the polymeric body spatially prearranged binding sites are left in the sorbent structure. Therefore, due to their predetermined selectivity thus obtained synthetic materials are able to recognize and preferentially bind the metal ion which was used as a template in the polymerization process which offers new possibilities in separation science. Analytical applications of IIPs have been reviewed by Rao et al. [12,13].

A number of ion-imprinted polymers have already been proposed for separation and preconcentration of various metal ions; however, the highest interests have been shown to transition elements and actinides and lanthanides. Recently, Saraji and Yousefi reported synthesis of a new Ni(II)-imprinted polymer dedicated to selective solid-phase extraction of nickel(II) from water samples [14]. The polymer was based on Ni(II)-dithizone complex trapped in copolymer of 4-vinylpyridine and ethyleneglycol dimethacrylate. Dakova et al. presented a new sorbent for preconcentration and speciation of mercury obtained via copolymerization of methacrylic acid and trimetylolpropane trimethacrylate in the presence of Hg(II)-1-(2-thiazoylazo)-2-naphtol complex [15]. The polymer was used for Hg(II) and total Hg preconcentration and determination in water samples with the use of CV-AAS. A new cadmium(II)-imprinted polymer was recently obtained by Singh and Mishra who immobilized Cd(II)-(*p*-sulphophenylazo)-1,8-dihydroxynaphtalene-3,6-disulphonate (Cd(II)-SPANDS) in phenyl-formaldehyde resin [16]. Zhai et al. presented a Cu(II)-imprinted polymer for selective enrichment of trace copper(II) from biological and natural water samples by solid-phase extraction: (2*Z*)-*N*,*N*′-bis-(2-aminoethylic)-but-2-enediamine was used as a chelating ligand and pentaerythritol triacrylate was chosen for a crosslinker [17]. Shirvani-Arani et al. described synthesis of a nanopore samarium(III) imprinted polymer along with its application to Sm(III) separation from other lanthanide ions and preconcentration via solid-phase extraction [18]. The sorbent is based on a ternary complex of samarium(III) with 5,7-dichloroquinoline-8-ol and 4-vinylpyridine embedded in styrene-divinylbenzene matrix.

Herein, synthesis of a new Cd(II)-imprinted polymer has been presented along with its analytical characteristics and applicability to determination of trace cadmium in water samples with the use of flow-injection-flame atomic absorption spectrometry technique.

2. Experimental

2.1. Reagents and solutions

For synthesis of the complex cadmium oxide extra pure was obtained from Merck (Darmstadt, Germany), salicyl aldehyde pure, etylenediamine pure for analysis and pyridine pure for analysis were purchased from Aldrich (Milwaukee, WI, USA). Sodium chloride pure for analysis, dimethylsulfoxide min. 99.5% (DMSO), benzoylperoxide (BPO) 75% and 4-vinylpyridine 95% for the sorbent synthesis were obtained from POCh (Gliwice, Poland), Riedel-de Haën (Seelze, Germany), Merck and Aldrich, respectively. Styrene and divinylbenzene 55% were purchased from Fluka (Buchs, Switzerland). Gelatin was used as protecting colloid.

Cadmium(II), copper(II), zinc(II), iron(III), lead(II), nickel(II), manganese(II), calcium(II), magnesium(II) and potassium(I) standards were prepared from Titrisol® solutions (Merck). Britton-Robinson buffers (a mixture of 0.04 mol L^{-1} acetic acid, 0.04 mol L^{-1} phosphoric acid, 0.04 mol L^{-1} boric acid and 0.2 mol L^{-1} sodium hydroxide in appropriate ratios) were used for buffering purposes. Sodium hydroxide, acetic acid and boric acid were obtained from POCh. Nitric acid and hydrochloric acid, both of analytical grade, were obtained from Merck. Deionized water after reversed osmosis was used throughout the work. Composition of the fortified water used in applicability studies corresponded to SPS-SW2 Batch 105 (Reference Material for Measurement of Elements in Surface Water), Spectrapure Standards AS (Oslo, Norway). Two certified reference materials (CRMs), namely EnviroMAT Ground Water, High (ES-H-2 CRM) and EnviroMAT Waste Water, High (EU-H-3 CRM), SCP Science, Canada were applied to evaluate the method accuracy.

2.2. Instrumentation

FIAS 400 (PerkinElmer) coupled with PE 3100 flame atomic absorption spectrometer (PerkinElmer) was used for metal ions preconcentration and determination. Cadmium was determined at 228.8 nm and air-acetylene flame was used with the gases flow rates as recommended by the manufacturer. Deuterium background correction was used for all measurements. Inductively Coupled Plasma Mass Spectrometer (ICP-MS), ELAN DRC-e (PerkinElmer) was applied to additional cadmium determinations at ultra-trace concentrations. A home-made microcolumn (5 mm × 3 mm i.d.) and Tygon (Saint-Gobain Performance Plastics, Charny, France) red–red tubings (1.14 mm i.d.) were used in the study. Elmetron CPI-551 pH-meter (Zabrze, Poland) was used for pH measurements. IR spectra and elemental analyses were obtained with IFS 48 spectrometer (Bruker) and EuroEA 3000 Elemental Analyzer, respectively.

2.3. Preparation of salen/Cd(II) complex

Salen/Cd(II) complex (cadmium(II) 2,2′-{ethane-1,2-diylbis[nitrilo(*E*)methylylidene]} diphenolate) was obtained in a four-step procedure as follows. A suspension of CdO powder (0.05 mol; 6.42 g) in salicylic aldehyde (0.10 mol; 12.21 g; 10.6 mL) and a small amount of water (2 mL) was heated at 110 °C for 6 h. The crude cadmium(II) bis(2-formylphenolate) was collected under reduced pressure and recrystallized from pyridine to give cadmium(II) bis(2-formylphenolate)–pyridine (1:1) complex [19]. The complex was then heated in an open flask in an oil-bath at 180 °C for 2 h to remove pyridine completely. The pure cadmium(II) bis(2-formylphenolate) (0.01 mol; 3.55 g) was refluxed (6 h) with 1.2-fold molar excess of ethylenediamine (0.36 g; 0.40 mL; 0.006 mol) in EtOH (30 mL). The resulting complex was collected under reduced pressure. Elemental analysis indicated 90% conversion of cadmium(II) bis(2-formylphenolate) into the complex. Yield 3.01 g (80%): yellow powder. IR (KBr): 3055, 3014, 2894, 2855, 1631, 1596, 1542, 1471, 1443 cm^{-1}. Calculated for $0.9\,C_{16}H_{14}N_2O_2Cd{\cdot}0.1\,C_{14}H_{10}O_4Cd$ (%): C, 50.41; H, 3.64; N, 6.66. Found: C, 50.14; H, 3.58; N, 6.69.

2.4. Preparation of sal/Cd-4VP-S/DVB beads

Sorbent beads were prepared via suspension polymerization. Dispersion medium consisting of 0.34 g of NaCl, 2.6 g of gelatine and 125 mL of distilled water was placed in a thermostatted reactor and heated up to 90 °C upon stirring (600 rpm). Salen/Cd(II) complex (0.151 g, 0.398 mmol) was dissolved in 7.5 mL of DMSO, then 0.09 mL (0.776 mmol) of 4-VP was added and the whole was thoroughly mixed. Organic phase comprised 3 mL of styrene (25.8 mmol), 7 mL of divinylbenzene (25.8 mmol), 0.38 g of BPO and solution of the complex. The organic phase was purged with argon for 5 min and subsequently added dropwise to the aqueous medium. Polymerization mixture was heated over 5 h upon mechanical stirring. Thus obtained spherical beads were filtered, thoroughly washed with hot water and dried in a vacuum dryer. Prior to analytical application the polymer was sieved and the

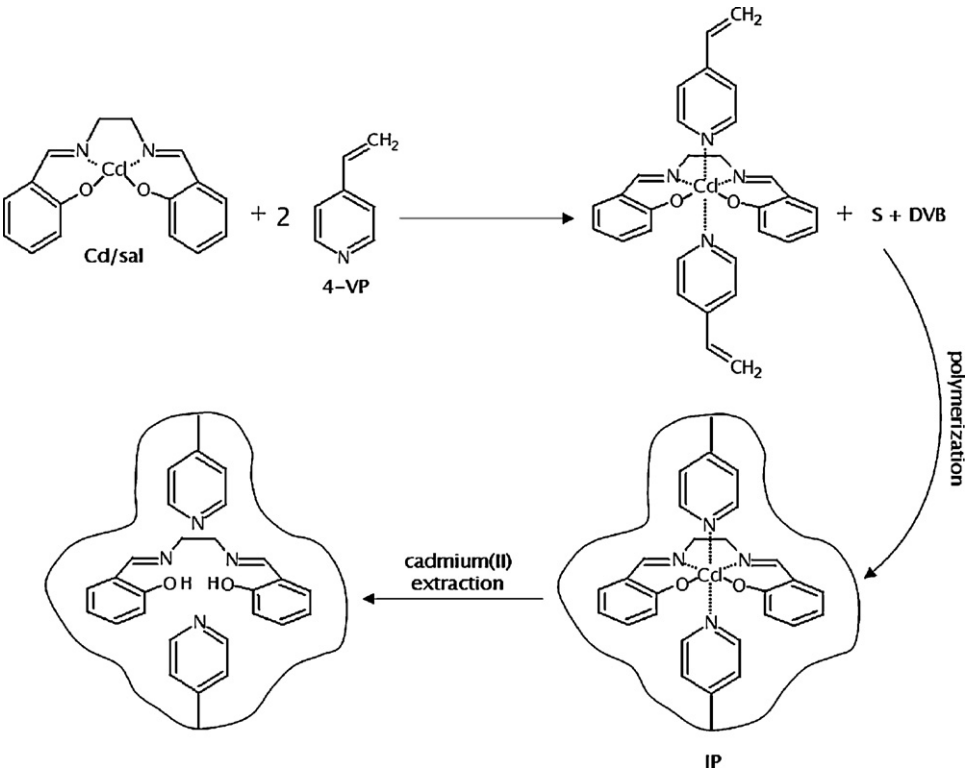


Fig. 1. Schematic representation of ion-imprinting process for the new cadmium(II)-imprinted polymer.

following fractions were collected: >80 μm: 49.2%, 63–80 μm: 30.1%, <63 μm: 20.7%. To avoid column backpressure the fraction 63–80 μm was used as a packing material. Cadmium ions built into the polymeric matrix in the imprinting process were extracted with 1 M HCl. Non-imprinted polymer was prepared in a similar way, however salen (0.102 g, 0.382 mmol) was added instead of salen/Cd complex. The proposed structure of the obtained cadmium(II)-imprinted polymer was presented in Fig. 1.

2.5. Sample preparation

All solutions for preliminary studies (including optimalization process and analytical characteristics of the sorbent) were prepared via dilution of cadmium(II) stock solution with deionized water and were buffered to appropriate pH.

Tap water was collected from laboratory installation and used without any additional preparation. Vistula River water was filtered through 0.45 μm cellulose acetate membrane filters (Sartorius, Goettingen, Germany) and refrigerated until used. All samples were adjusted to appropriate pH with Britton-Robinson buffer.

2.6. Preconcentration procedure

The measuring set-up consisted of two peristaltic pumps, a cylindrical minicolumn filled with the polymer, a two-positional valve and a flame atomic absorption spectrometer. Each preconcentration cycle comprised three steps: preconditioning, sorption and elution. In the preconditioning step pump 1 was activated for the time needed for a sample to fill the tubes before the minicolumn, then the valve position was changed (pump 1 stopped, pump 2 activated) and acid solution was passed through the sorbent for conditioning purposes. In the second step pump 1 was activated for the required sorption time and the sample was loaded onto the polymeric bed. Ten seconds before changing the valve position pump 2 was activated and acid was transferred via a capillary to the nebuliser and the signal was set zero. In the last step pump 1 was stopped, the valve position changed to *inject*, the eluate was directed to the nebulizer and analytical signal was recorded. Schematic representation of the set-up and the detailed program were described elsewhere [20]. If not otherwise stated all results refer to 35 mg of the sorbent. In preliminary studies 15 s loading time was applied to increase sample throughput. For evaluation of the figures of merit and for CRMs and real water analysis (Sections 3.7 and 3.8) loading time was elongated to 120 s.

3. Results and discussion

3.1. Elution conditions

Nitric and hydrochloric acid solutions within concentration range of 0.1–2% (v/v) were tested as eluent. Cadmium(II) standard (50 μg L^{-1}, pH 6.8) was loaded onto the sorbent, then eluted with a given acid solution (elution time: 30 s) and analytical signal was measured. It was proved that starting from eluent concentration of 0.5% (v/v) the kind and concentration of acid did not improve Cd(II) elution effectiveness which was equal for both acids. Nitric acid 1% (v/v) was chosen as eluent for further studies.

3.2. Optimal pH

As sorption effectiveness of an analyte on a given sorbent may vary depending on the loading solution pH, finding the proper pH is one of the most crucial issues in working conditions optimization. For this reason a set of Cd(II) solutions (50 μg L^{-1}) was prepared within pH range of 4–9 and subjected to the preconcentration procedure. The influence of the solution pH on analytical signal presented in Fig. 2 indicates that sorption was the most effective within the pH range of 6.6–7.7, therefore for further studies all samples were buffered to pH 6.8.

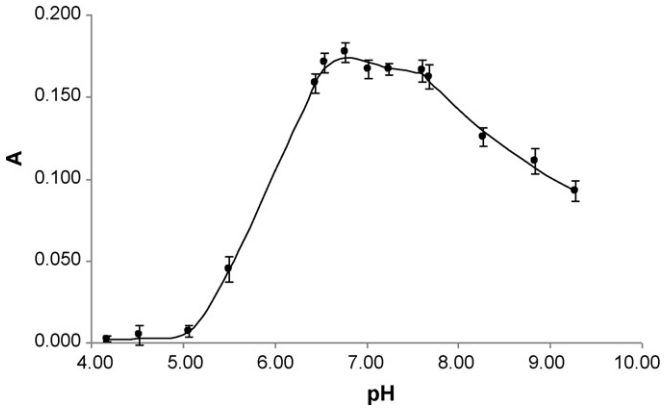


Fig. 2. Dependence of analytical signal on the loading solution pH; loading time: 15 s, eluent: 0.5% HNO_3.

3.3. Sorbent stability test

For sorbent stability evaluation Cd(II) solution (50 μg L^{-1}, pH 6.8) was loaded onto the sorbent and 0.5% HNO_3 was applied as an eluent. Analytical signal (absorbance) was recorded for each preconcentration cycle. No descending trend was observed for at least 100 consecutive preconcentration cycles (RSD 2.9%) which proves good stability of the sorbent in the working conditions.

3.4. Sample flow rate and sorption efficiency

On-line preconcentration as a non-equilibrium process requires special attention to be paid to sample flow rate. In set sorption time applying high sample flow rate may seem favorable in terms of obtaining high enrichment factor due to higher sample volume loaded onto the column. However, sorption effectiveness, being limited by the sorption kinetics, may be deteriorated. For the presented sorbent the dependence of sorption effectiveness on sample flow rate was evaluated for constant sample volume passing through the column bed (i.e. 4 mL) and variable sorption time. No signal decrease was observed upon raising the sample flow rate in the whole tested range, i.e. 4–10 mL min^{-1}. Sample flow rate of 8.0 mL min^{-1} was applied in further studies.

Table 2
Analytical figures of merit of the proposed method.

Parameter	
Preconcentration time (s)	120
Elution time (s)	30
Enrichment factor, EF	117
Consumptive index, CI (mL)	0.14
Sampling frequency, f (h^{-1})	20
Concentration efficiency, CE (min^{-1})	39.1
Calibration range (μg L^{-1})	1–10
Correlation coefficient, R^2	0.9979
Precision (RSD, n = 5) (%)	6.3 (1 μg L^{-1})
Limit of detection (LOD, 3σ) (μg L^{-1})	0.11
Limit of quantification (LOQ, 10σ) (μg L^{-1})	0.36

CI = V_s/EF. V_s = the volume of a sample consumed to achieve the EF value. CE = EF × (f/60).

Table 3
Application of the proposed method to cadmium(II) analysis in water samples.

Sample	FI-FAAS (μg L^{-1})	ICP-MS (μg L^{-1})	RE (%)
Tap water	2.08 ± 0.12	1.94 ± 0.03	6.7
Spring water	2.30 ± 0.07	2.15 ± 0.05	6.8
River water	2.21 ± 0.19	2.26 ± 0.05	−2.3
Fortified water	2.34 ± 0.07	2.54 ± 0.04	−7.8

CRM	FI-FAAS (mg L^{-1})	CRM certified value (mg L^{-1})	CRM confidence interval
ES-H-2	0.205 ± 0.022	0.200	0.194–0.205
EU-H-3	0.245 ± 0.009	0.228	0.207–0.249[a]

[a] Tolerance interval.

Table 1
Sorbent selectivity test: Cd(II)-imprinted polymer (IP), non-imprinted polymer (NIP); pH 6.8, loading time: 15 s, Cd(II) 50 μg L^{-1}. Recovery values exceeding 90% were considered as acceptable and bolded.

Cu(II) added (mg L^{-1})	Cd(II) recovered (%)		Zn(II) added (mg L^{-1})	Cd(II) recovered (%)		Ni(II) added (mg L^{-1})	Cd(II) recovered (%)	
	IP	NIP		IP	NIP		IP	NIP
0.1	**105.0**	79.7	0.1	**108.2**	**96.7**	0.1	**98.4**	76.9
0.2	**111.6**	71.7	0.2	**102.1**	83.3	0.2	**98.7**	63.2
0.5	**108.0**	49.3	0.5	**107.8**	68.1	0.5	**91.3**	52.6
1.0	**93.7**	36.4	1.0	83.6	49.1	1.0	80.8	40.5
2.0	**96.4**	25.2	2.0	57.7	35.2	2.0	60.7	27.2
5.0	**99.2**	42.6	5.0	35.5	21.4	5.0	34.6	20.4
Fe(III) added (mg L^{-1})	**Cd(II) recovered (%)**		**Mn(II) added (mg L^{-1})**	**Cd(II) recovered (%)**		**Pb(II) added (mg L^{-1})**	**Cd(II) recovered (%)**	
	IP	NIP		IP	NIP		IP	NIP
0.1	**102.5**	**100.3**	0.1	**102.8**	**103.3**	0.1	**98.5**	**96.6**
0.2	**99.7**	**93.4**	0.2	**96.5**	**103.6**	0.2	**97.5**	78.2
0.5	81.3	64.7	0.5	**101.9**	**106.8**	0.5	**97.5**	72.2
1.0	64.2	52.5	1.0	**100.5**	**100.8**	1.0	**95.9**	62.2
2.0	63.2	43.1	2.0	**99.8**	82.6	2.0	**92.4**	77.8
5.0	52.0	35.7	5.0	**96.6**	89.3			
Ca(II) added (mg L^{-1})	**Cd(II) recovered (%)**		**Mg(II) added (mg L^{-1})**	**Cd(II) recovered (%)**		**K(I) added (mg L^{-1})**	**Cd(II) recovered (%)**	
	IP	NIP		IP	NIP		IP	NIP
10.0	**98.5**	**100.8**	1.0	**102.5**	**97.9**	1.0	**103.6**	**97.8**
20.0	**99.7**	75.4	2.0	**103.3**	**91.6**	2.0	**97.8**	**91.1**
40.0	**105.9**	67.9	5.0	**98.6**	85.1	5.0	**102.9**	**96.3**
60.0	**105.5**	66.3	10.0	**103.3**	73.7	10.0	**98.0**	**100.2**
			20.0	**107.6**	77.4	20.0	**97.4**	**94.2**
			30.0	**99.8**	61.7	30.0	**95.2**	**95.8**

Table 4
Comparison of analytical performance of the presented sorbent with other reported cadmium(II)-imprinted polymers.

Cadmium(II)-imprinted polymer	Optimal sorption pH	Equilibrium sorption time (min)	LOQ (10σ) ($\mu g\,L^{-1}$)	RSD (%)	EF; sample volume (mL)	Stability (no. cycles)	Ref.
PF-Cd(II)-SPANDS	6.0	50	–	–	–	5 (recovery ca. 95%)	[16]
Poly-Cd(II)-DAAB-VP	6.0	60 (recovery ≥ 95%)	0.21	3.7 (100 $\mu g\,L^{-1}$)	200; 2000	20 (2–5% error)	[21]
Cd(II)-IP based on a dual-ligand monomer	6.0	20 (recovery 95%)	0.47	2.4 (10 $\mu g\,L^{-1}$)	200; 1000	15	[22]
sal/Cd-4VP-S/DVB	6.6–7.7	20	0.36	2.9 (50 $\mu g\,L^{-1}$)	117; 16	100	This work

Sorption efficiency was evaluated for sample flow rate of 8.0 mL min^{-1}, Cd(II) 50 $\mu g\,L^{-1}$, pH 6.8 and sorption time 15 s. Cadmium(II) standard was loaded onto the sorbent, the filtrate was collected and Cd(II) content was determined by ICP-MS. The procedure was repeated four times. Sorption efficiency was found at 95.3%.

3.5. Sorption capacity

To assess the equilibrium sorption time for the Cd(II)-imprinted polymer, 35 mg of the sorbent was packed in a minicolumn, then a portion of Cd(II) standard solution (1 mg L^{-1}, pH 6.8, 5 mL) was loaded onto the bed (flow rate 8.0 mL min^{-1}) in a closed circuit for loading time from 1 to 60 min. Afterwards cadmium(II) content was determined in each standard portion with the use of FAAS. It was found that the amount of cadmium(II) ions sorbed onto the polymer was constant starting from 20-min loading time.

For sorption capacity evaluation cadmium(II) standard solutions at concentration up to 130 mg L^{-1} (pH 6.8, portion volume 5 mL) were loaded onto the bed in a closed circuit for 30 min. The initial and equilibrium cadmium(II) concentration in a portion of a given standard solution were determined via FAAS. The maximum sorption capacity of the sorbent was found from Langmuir isotherm according to Eq. (1):

$$\frac{C_e}{Q} = \frac{C_e}{Q_{max}} + \left(\frac{1}{Q_{max}}\right) \times b \quad (1)$$

where C_e stands for equilibrium concentration (mg L^{-1}), Q is the amount of Cd(II) ions sorbed per 1 g of the sorbent (mg g^{-1}), Q_{max} denotes the maximum sorption capacity (mg g^{-1}) and b is Langmuir sorption equilibrium constant.

The maximum sorption capacity found for the presented Cd(II)-imprinted polymer was 0.48 mg g^{-1} (4.27 μmol g^{-1}).

3.6. Sorbent selectivity study

Selectivity study was performed for nine potential interfering ions including heavy metal ions (Cu(II), Zn(II), Ni(II), Fe(III), Mn(II), Pb(II)), alkaline and alkaline earth ions (K(I), Mg(II), Ca(II)). The results obtained both for the imprinted (IP) and the non-imprinted polymer (NIP) have been collected in Table 1.

When compared to the non-imprinted polymer the new cadmium(II)-imprinted polymer was found to be considerably less prone to interferences from other heavy metal ions as well as from light metal ions. The strongest effect was observed for Cu(II) and Pb(II) ions.

3.7. Analytical figures of merit

Analytical characteristics of the method obtained for 120-s sorption time has been presented in Table 2. Enrichment factor (EF) was calculated as a ratio of the calibration line slope found when applying preconcentration step ($S_{FI\text{-}FAAS}$) to the one obtained without it (S_{FAAS}) (2). Consumptive index (CI) was characterized as the volume of a sample (V_s) consumed to achieve a unit EF (3). Concentration efficiency (CE) was calculated as the product of EF and the sampling frequency f expressed in samples analyzed per minute (4):

$$EF = \frac{S_{FI\text{-}FAAS}}{S_{FAAS}} \quad (2)$$

$$CI = \frac{V_s}{EF} \quad (3)$$

$$CE = EF \times \left(\frac{f}{60}\right) \quad (4)$$

Limit of detection and limit of quantification were found for 3σ (LOD) and 10σ (LOQ) divided by the calibration line slope ($S_{FI\text{-}FAAS}$), where σ stands for standard deviation of signal for the blank.

3.8. Application to cadmium(II) determination in water samples

The method accuracy was examined with the use of fortified water and two certified reference materials: ground water (ES-H-2) and waste water (EU-H-3). Cadmium(II) content found in CRMs was in good agreement with the certified values which proves the method accuracy. The presented method was applied to cadmium(II) determination in several water samples: tap water, river water and spring water. As cadmium content in the real samples used in the study was below the quantification limit of the method the samples were beforehand spiked with cadmium. The FI-FAAS results were compared with those obtained by ICP-MS (reference technique) and relative error was calculated. The standard addition method (SAM) was employed for calibration purposes. The obtained results (Table 3) indicate that the presented method may be successfully applied to trace cadmium(II) determination in water samples.

4. Conclusions

The paper reports synthesis and analytical application of a new sorbent dedicated to on-line flow-injection preconcentration and flame atomic absorption spectrometry determination of cadmium(II). The new Cd(II)-imprinted polymer exhibits good sorption properties which combined with its high working stability makes it a suitable packing material for minicolumn preconcentration of cadmium(II). The presented method enables to achieve high enrichment factor and limit of quantification sufficient for trace cadmium analysis. Employing the ion-imprinting technique resulted in achieving a polymer of enhanced selectivity towards cadmium(II) over all investigated metal ions, especially lead(II) and copper(II). Application of sal/Cd-4VP-S/DVB beads as a new sorbent in flow-injection system enabled FAAS cadmium(II) determination at levels found in natural water samples.

When compared to other reported cadmium(II)-imprinted polymers, sal/Cd-4VP-S/DVB beads offer comparable LOQ and RSD along with superior sorption kinetics and the sorbent stability (Table 4). Employing flow-injection system, apart from the obvious benefit of the process automation, enabled cadmium(II) preconcentration with high enrichment factor obtained with low sample consumption and satisfactory sample throughput.

References

[1] R. Bruce King (Editor-in-Chief), Encyclopedia of Inorganic Chemistry, vol. 1, John Wiley & Sons, Chichester, 1994, p. 455.
[2] Philip Wexler (Editor-in-Chief), Encyclopedia of Toxicology, 2nd ed., Elsevier Ltd., Oxford, 2005, p. 375.
[3] P. Patnaik, A Comprehensive Guide to the Hazardous Properties of Chemical substances, 3rd ed., John Wiley & Sons, Inc., 2007, pp. 652–653.
[4] World Health Organization, IARC Monographs on the Evaluation of Carcinogenic Risks to Humans, vol. 58, Geneva, 1993.
[5] World Health Organization, Guidelines for Drinking-Water Quality, 3rd ed., vol. 1, Recommendations, Geneva, 2006.
[6] Official Journal of the European Communities, Council Directive 98/83/EC of 3 November 1998 on the Quality of Water Intended for Human Consumption.
[7] Unites States Environmental Protection Agency, National Primary Drinking Water Standards, June 2003.
[8] B. Welz, M. Sperling, Atomic Absorption Spectrometry, 3rd compl. rev. ed., Wiley-VCH, Weinheim, 1999.
[9] Z. Fang, Flow Injection Atomic Absorption Spectrometry, John Wiley & Sons, Chichester, 1995.
[10] Z. Fang, Flow Injection Separation and Preconcentration, VCH, Weinheim, 1993.
[11] K. Pyrzyńska, K. Kilian, Water Res. 41 (2007) 2839.
[12] T.P. Rao, S. Daniel, J.M. Gladis, Trends Anal. Chem. 23 (2004) 28.
[13] T.P. Rao, R. Kala, S. Daniel, Anal. Chim. Acta 578 (2006) 105.
[14] M. Saraji, H. Yousefi, J. Hazard. Mater. 167 (2009) 1152.
[15] I. Dakova, I. Karadjova, V. Georgieva, G. Georgiev, Talanta 78 (2009) 523.
[16] D.K. Singh, S. Mishra, J. Hazard. Mater. 164 (2009) 1547.
[17] Y. Zhai, D. Yang, X. Chang, Y. Liu, Q. He, J. Sep. Sci. 31 (2008) 1195.
[18] S. Shirvani-Arani, S.J. Ahmadi, A. Bahrami-Samani, M. Ghannadi-Maragheh, Anal. Chim. Acta 623 (2008) 82.
[19] P. Pfeiffer, E. Breith, E. Lübbe, T. Tsumaki, Justus Liebigs Ann. Chem. 503 (1933) 84–121.
[20] S. Walas, A. Tobiasz, M. Gawin, B. Trzewik, M. Strojny, H. Mrowiec, Talanta 76 (2008) 96.
[21] Y. Liu, X. Chang, S. Wang, Y. Guo, B. Din, S. Meng, Anal. Chim. Acta 519 (2004) 173–179.
[22] Y. Zhai, Y. Liu, X. Chang, S. Chen, X. Huang, Anal. Chim. Acta 593 (2007) 123–128.

Talanta 80 (2010) 1311–1317

Contents lists available at ScienceDirect

Talanta

journal homepage: www.elsevier.com/locate/talanta

Comparison of tetraethylborate and tetraphenylborate for selenite determination in human urine by gas chromatography mass spectrometry, after headspace solid phase microextraction

D.C. Kapsimali, G.A. Zachariadis*

Laboratory of Analytical Chemistry, Aristotle University, Thessaloniki GR-54124, Greece

ARTICLE INFO

Article history:
Received 27 May 2009
Received in revised form 1 September 2009
Accepted 14 September 2009
Available online 19 September 2009

Keywords:
Headspace solid phase microextraction
Gas chromatography mass spectrometry
Selenite
Ethylation
Phenylation
Urine

ABSTRACT

Two different derivatizing reagents were tested for the development of a fast and sensitive method for the determination of selenites (Se^{IV}) in human urine. The reagents were sodium tetraethylborate ($NaBEt_4$) and tetraphenylborate ($NaBPh_4$), respectively, and the procedure is based on in situ derivatization of selenites in aqueous medium. Selenite ions are converted to diethylselenide (DESe) or diphenylselenide (DPhSe) and subsequently collected from the headspace by solid phase microextraction using a silica fiber coated with polydimethylsiloxane (HS-SPME). Finally, they are quantitated by GC/MS in SIM mode. Ethylation over phenylation was proved preferable for the headspace extraction because of the higher volatility of the diethyl-derivative of selenites. The optimization of the HS-SPME conditions was performed both in aqueous and urinary solutions. Under the optimum conditions for HS-SPME, the gas chromatographic conditions were also optimized. Between the two alkylation reagents tetraethylborate was proved more efficient and the quantitation was satisfactory. Aqueous certified reference materials were analyzed to evaluate the accuracy of the method. The precision of the method was 4.2% and the calculated detection limit was 0.05 $\mu g\,L^{-1}$ for human urine.

© 2009 Elsevier B.V. All rights reserved.

1. Introduction

Selenium is a challenging element, because it is essential at low levels and toxic at higher levels. This range is very narrow depending on its various chemical forms like species or oxidation state [1–3]. Selenites are found in water, environmental and biological matrices and are the most important form either as nutrient or as a possibly toxic species [4]. Consequently, the quantification of selenium species is of increasing importance and accurate analytical methods are necessary for its monitoring [1,3,5].

The determination of selenites is usually based on sensitive analytical techniques like hydride generation atomic absorption spectrometry [6–9] or hyphenated techniques, including capillary electrophoresis [10,11] and gas or liquid chromatography [4,12,13]. The gas chromatographic determination of selenium is based on coupling GC by one or more of several commercially available detectors. Gas chromatography is very promising because it eliminates potential interferences and can serve also as a powerful separation technique for speciation studies. In several reports the GC has been directly coupled to various detectors like AED [12], MIP/AED [2,13], AAS [14], ICP/MS [15,16], MS [4,17] or FID [17]. Liquid chromatography is preferred for the separation of selenoaminoacids, which are coupled to different detectors such as ICP/MS [18,19], MS/MS [7], UV or AFS [20] and amperometric detection [21]. In addition, other techniques were used for organoselenium speciation like IC-ICP-MS [22], ID-ICP-MS [23], ETV-ICP-MS [24], ETAAS [25], CE-ICP-MS [10], HG-ICP-MS [26] and HG-AFS [27].

Also, preconcentration techniques are used for the determination of inorganic and organic selenium. Conventional preconcetration techniques are liquid–liquid extraction and solid phase extraction. Modern preconcentration methods of selenium determination such as solid phase extraction, solid phase microextraction, isotachophoresis and cryogenic trapping were reviewed by Wake et al. [28]. Also, dispersive liquid–liquid microextraction was able to use for the extraction of selenium derivative [29].

SPME is a very helpful tool for chromatographic separations. Solid phase microextraction (SPME) appears as an interesting separation and preconcentration technique for both inorganic and organoselenium compounds. It can be regarded as an environmental friendly technique, due to elimination of use of liquid solvents. Nevertheless, its precision is poor as compared to liquid–liquid extraction. SPME with a derivatization procedure has been used for the speciation of organoselenium and various other organometallic compounds [30–34]. The derivatives are collected directly or from the headspace on a silica fiber coated with polydimethylsiloxane

* Corresponding author.
E-mail address: zacharia@chem.auth.gr (G.A. Zachariadis).

0039-9140/$ – see front matter © 2009 Elsevier B.V. All rights reserved.
doi:10.1016/j.talanta.2009.09.022

Table 1
Optimum operating conditions for GC-MS with HS-SPME.

Operating conditions	Ethylation	Phenylation
Column DB-5MS	30 m × 0.25 mm i.d. × 0.10 μm	30 m × 0.25 mm i.d. × 0.10 μm
Injection mode	Splitless	Splitless
Injector port temperature	230 °C	250 °C
Oven temperature	40 °C (1 min) to 250 °C (0 min)	40 °C (1 min) to 250 °C (1 min)
Ramp	45 °C min^{-1} ramp	30 °C min^{-1} ramp
Carrier gas	Helium; 4.2 mL min^{-1}	Helium; 4.2 mL min^{-1}
Pressure conditions	Constant pressure at 39.8 psi	Constant pressure at 39.8 psi
Transfer line temperature	250 °C	250 °C
MS model	5973 MSD	5973 MSD
SIM ions (m/z)	78, 80, 82 (selenium) 107, 110, 111 (ethylselenide) 136, 138, 139, 140 (diethylselenide)	78, 80, 82 (selenium) 152, 153, 154, 155, 157 (phenylselenide) 232, 233, 234 (diphenylselenide)
Electron ionization	70 keV	70 keV
SIM dwell time	50 ms	50 ms
MS quad/source temperature	150 °C/230 °C	150 °C/230 °C

(PDMS). In this way, SPME can be successfully applied for one-step preconcentration and extraction of analytes.

Selenite ions (Se^{IV}) can be measured by GC if a derivatization reagent is employed. They can be transformed by ethylation reagents to diethylselenide (DESe), a more volatile and less polar compound, which is amenable for gas chromatography to be carried out. Suitable and useful reagents for alkylation purpose are sodium tetraethylborate ($NaBEt_4$) and sodium tetrapropylborate ($NaBPr_4$) [3,4,14]. Another group of reagents which was reported for increased sensitivity is 4-chloro-o-phenylenediamine or 4,5-dichloro-1,2-phenylenediamine compounds, however, sodium tetraethylborate ($NaBEt_4$) can be generally recommended [12]. Practically selenates (Se^{VI}) could not be derivatized with the developed method, and a small peak, not always measurable, was observed in the chromatogram just after that of selenite. This observation is in agreement with the remarks of Guidotti [4] according to which selenates are not derivatized as selenites in SPME and GC separations.

The aim of this work is to investigate and compare the performance of two different derivatization reagents, i.e. sodium tetraethylborate ($NaBEt_4$) and sodium tetraphenylborate ($NaBPh_4$), respectively, for the development of a fast and sensitive method for selenium determination in human urine by HS-SPME coupled to GC/MS.

2. Experimental

2.1. Instrumentation

An Agilent quadrupole mass spectrometer MSD 5973 (Hewlett Packard, Waldbronn, Germany) was used as detector for selenium determination. An Agilent 6873 K gas chromatograph equipped with a DB-5MS (30 m length, 0.25 mm i.d., 0.1 μm film, Supelco) capillary column was employed. Helium was the carrier gas. The GC/MS optimum operating conditions are listed briefly in Table 1. The manual SPME fiber holder (57330-U) and polymer-coated fibers (Supelco 57342-U) were purchased from Supelco (Deisenhofen, Germany). The fibers were coated with a 100 μm film of polydimethylsiloxane (PDMS). 15-mL glass vials closed with PTFE-coated silicone rubber septa were employed for the solid phase extraction procedure.

2.2. Reagents and materials

A stock solution of selenite (Na_2SeO_3) containing 1000 mg L^{-1} Se in 0.5 mol L^{-1} HNO_3 (Merck, Darmstadt, Germany) was used. Lowercase selenite standards with concentrations ranging from 1 mg L^{-1} down to 0.1 μg L^{-1} (as Se) were prepared by diluting with Milli-Q ultrapure water (18.2 MΩ cm, 25 °C, Millipore, USA). The solutions were stored at 4 °C.

Sodium tetraethylborate ($NaBEt_4$) and sodium tetraphenylborate ($NaBPh_4$) both were purchased from (99.5%) Sigma–Aldrich Newburgport, MA, USA. A 20% (m/v) solution was freshly prepared by dissolving 0.40 g $NaBEt_4$ in 2 mL Milli-Q water, and was always kept at 4 °C. Similar solution of $NaBPh_4$ was also freshly prepared. Acetate buffer solution with pH values of 5.2 ± 0.1 was prepared by mixing appropriate amounts of sodium acetate (CH_3COONa) (2 mol L^{-1}) and acetic acid (CH_3COOH) (2 mol L^{-1}) in a final volume of 1 L. For optimization of pH in the range 3.0 to 8.4, addition of acetic acid and sodium hydroxide was required.

The accuracy of the method was validated using aqueous certified reference materials NIST 1643e Trace elements in water and standard reference material 2670 Freeze-Dried Urine.

2.3. Ethylation/phenylation and SPME

Variable volumes of the acetate buffer and equal volumes of Milli-Q water or standard solution or urine were transferred into glass vials. Suitable quantity of $NaBEt_4$ or $NaBPr_4$ solution was added and the vials were closed with PTFE-coated septum. The contents of the vial were stirred at 900 rpm with a 6-mm magnetic bar.

The PDMS fiber was exposed to the headspace at 25 °C (for $NaBEt_4$) or 65 °C (for $NaBPr_4$) for 20 min. The fiber was removed from the vial and immediately transferred into the GC injection port at 230 °C (for $NaBEt_4$) or 250 °C (for $NaBPr_4$) and left there for complete desorption of the analytes (4 min).

Three different total mixture volumes were examined: 6 or 10 mL in 15-mL glass vials and 25 mL in 40-mL glass vial, respectively. 15-mL glass vial was finally chosen because of better reproducibility observed in comparison to 40-mL vial either using $NaBEt_4$ or $NaBPr_4$ for alkylation. In addition, 10 mL total mixture volume (headspace/liquid ratio, 1:2) was proved preferable over 6 mL (headspace/liquid ratio, 3:2) because of better sensitivity and repeatability.

3. Results and discussion

Gas chromatographic parameters were optimized by varying one parameter while holding the others constant. The transfer line from column to MS was also heated at 250 °C. Under the optimum conditions the peak of selenite as diethylselenide appears after 1.82 min while that of diphenylselenide appears after 6.61 min (Fig. 1). The optimization of GC and HS-SPME parameters was per-

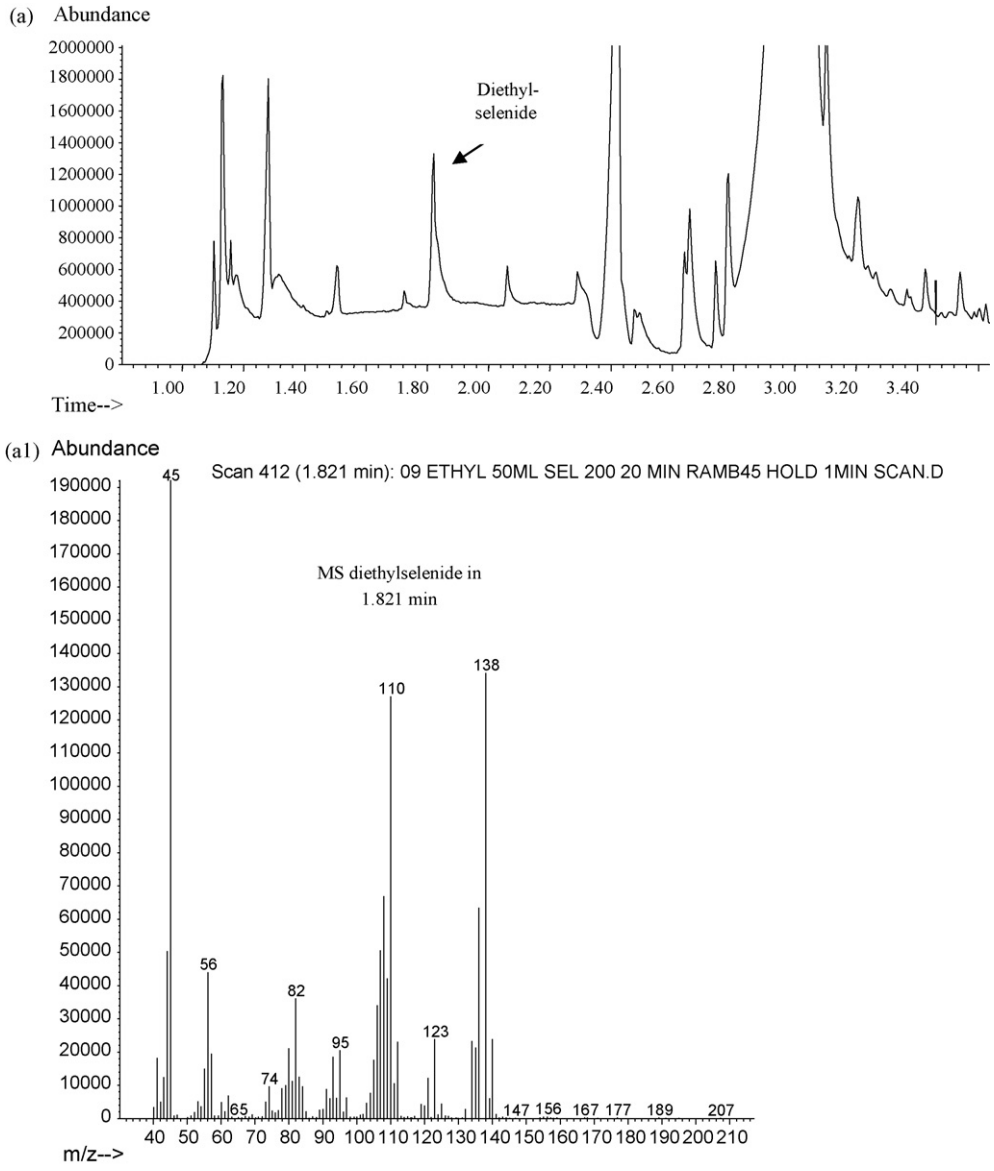


Fig. 1. Typical chromatograms obtained from the determination of selenite by HS-SPME and GC/MS. (a) Chromatogram with the peak of diethylselenide, (a1) MS diethylselenide in 1.821 min, (a2) MS boroxine, triethyl in 3.041 min. (b) Chromatogram with the peak of diphenylselenide.

formed in the scan mode while for quantification the selected ion monitoring (SIM) mode was applied using ions with m/z values listed in Table 1. The two alkylation processes were optimized as it is described below.

3.1. Optimization of GC/MS and HS-SPME with $NaBEt_4$

3.1.1. Optimization of GC parameters

The helium flow conditions were selected under constant pressure and variable flow rate. Helium flow rate was studied at three levels, i.e. 2.2 mL min^{-1} (17.4 psi), 4.2 mL min^{-1} (29.73 psi) and 6.2 mL min^{-1} (39.3 psi), respectively. The results are illustrated in Fig. 2a. It is shown that at higher flow rate of helium (6.2 mL min^{-1}) smaller peak area is obtained. On the one hand with higher carrier gas flow rate, selenite as diethylselenide is coming faster and on the other hand at 2.2 mL min^{-1} no well-resolved peak was obtained. Thus, the flow rate was adjusted to 4.2 mL min^{-1} for subsequent work.

The temperature program of the GC capillary column was subsequently investigated. Initial temperature was selected to be at 40 °C because selenite as diethylselenide is a volatile compound. Hold times at 40 °C were studied in the range of 1–4 min and the results are shown in Fig. 2b. The sensitivity was better at 1 min hold time for diethylselenide and sharper peaks are obtained.

The temperature ramp from 40 to 250 °C was then optimized keeping the above two conditions constant. The fast ramp (i.e. 45 °C min^{-1}) was preferred than the slower one (e.g. 15 °C min^{-1}) (Fig. 2c). Use of 45 °C min^{-1} resulted in narrow peaks without tailing. In addition, the peak of diethylselenide was not overlapped with other compounds. The total chromatographic time with hold time 1 min at 40 °C and ramp 45 °C min^{-1} up to 250 °C was 5.87 min. Selenite as diethylselenide is coming at 1.821 min. All the above optimum parameters were maintained constant during the following HS-SPME optimization.

3.1.2. Optimization of HS-SPME parameters

All the experiments for optimization of HS-SPME parameters were done using 100 μm PDMS fiber, based on the results of Dimitrakakis et al. [3] according to which among four different types of

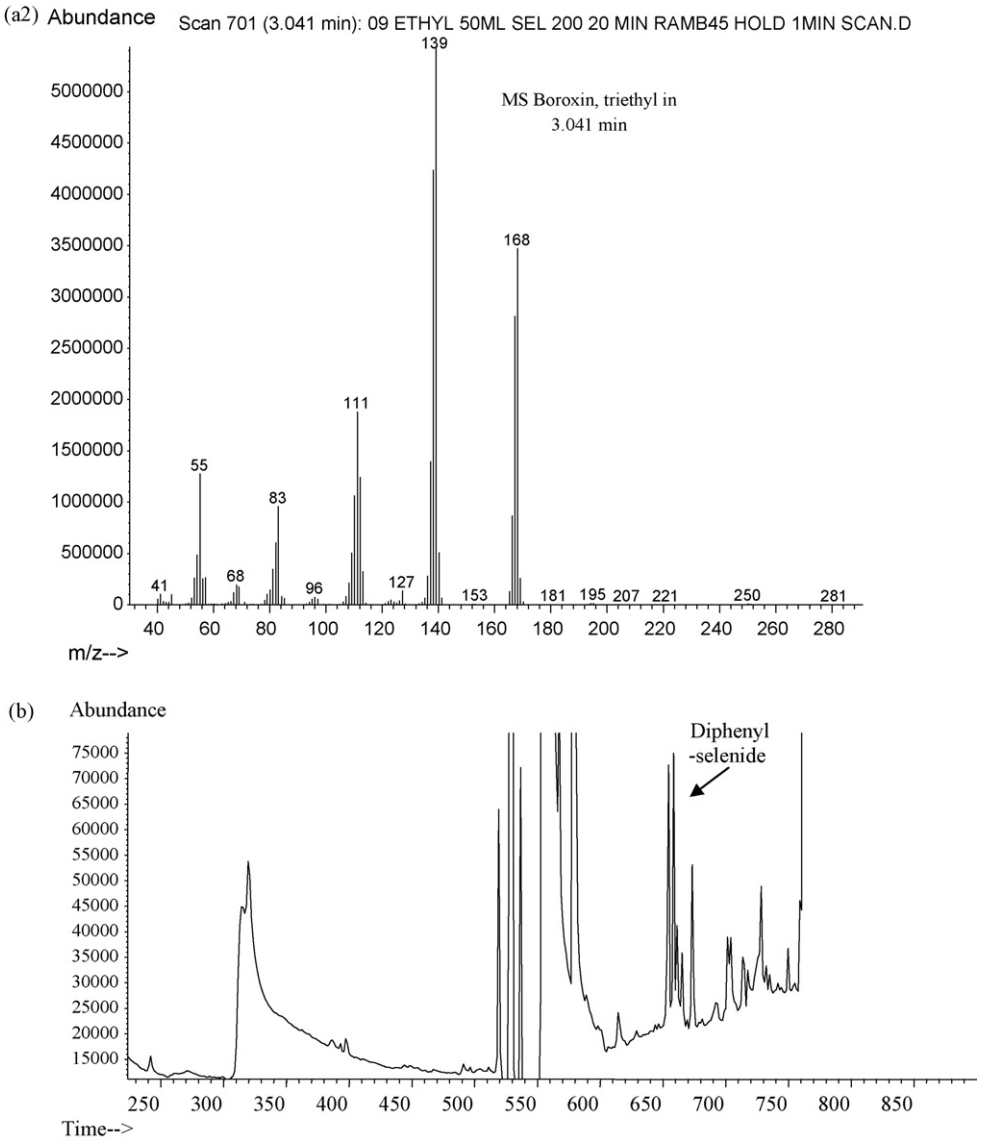


Fig. 1. (*Continued*).

SPME fibers the 100 μm PDMS was proved more efficient because of its constant response and best repeatability.

The pH of the acetate buffer solution was studied in the range of pH 3.0–8.4. This is a very important parameter which defines the efficiency of the derivatization reaction. The optimum value was found to be 5.2 ± 0.1. This finding is in accordance with previously reported values for ethylation by tetraethylborate [3,12].

The effect of temperature was studied for ethylation of selenite and HS-SPME sampling at 25, 45 and 65 °C respectively (Fig. 3a). Eventually, 25 °C was found to be preferable in terms of higher sensitivity obtained. At this temperature, selenite was extracted efficiently without peak overlapping with other compounds, for example, boroxine, which is formed during the ethylation reaction. Ethylated selenite and boroxine (B_3O_3 M.W. = 81) give ions with similar *m*/*z* in MS spectrum. A useful difference to distinguish is ion *m*/*z* 168 (triethylboroxine) which appears only in boroxine in contrast to selenite.

The effect of increasing the extraction time (10, 20 and 30 min) was studied at 25 °C and the results are presented in Fig. 3b. The duration of HS-SPME defines the efficiency to collect selenite from the solution. The signal obtained at ten minutes extraction is only 50–60% of the one obtained at thirty minutes sampling. At 20 min most selenite was extracted as diethylselenide, thus all further analyses were conducted with this extraction time as a compromise to avoid time consumption.

The amount of $NaBEt_4$ was studied using 25, 50, 75, 100 μL of a 20% (m/v) solution. 50 μL was eventually chosen in order also to limit high production of boroxine product when the derivatization reagent is used in excess (Fig. 3c).

The inlet port temperature was examined in order to achieve quantitative desorption of the analyte from PDMS fiber. Variable desorption temperatures in the range 210–250 °C were studied and 230 °C was found as optimum.

3.2. Optimization of the GC/MS and HS-SPME with $NaBPh_4$

Following the same procedure as described above, the use of $NaBPh_4$ was optimized as alkylation reagent. Several of the above-described optimum parameters (volume of solution 10 mL, 15-mL vials) were maintained the same throughout this optimization. Tetraphenylborate ($NaBPh_4$) is capable of converting selenite to diphenylselenide (DPhSe). Diphenylselenide has higher molecular weight and certainly is less volatile as compared to diethylselenide. After preliminary experimentation in the range 190–250 °C,

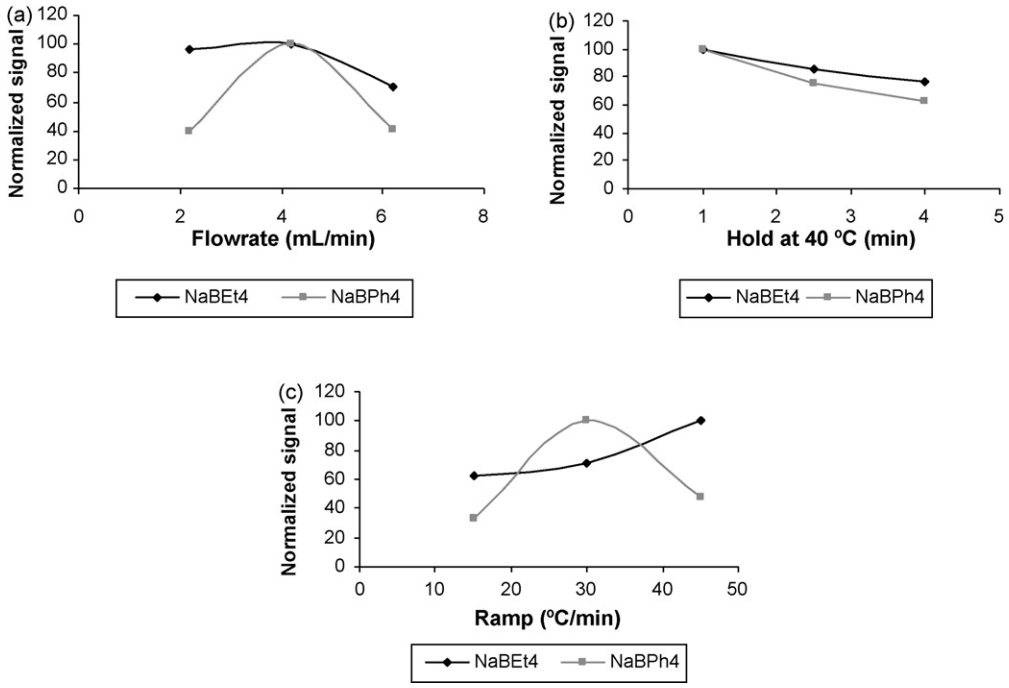


Fig. 2. Optimization of GC/MS with $NaBEt_4$ or $NaBPh_4$ of (a) helium flow rate under constant pressure for selenite determination, (b) hold time at initial temperature 40 °C, (c) ramp from 40 to 250 °C.

the inlet port temperature was set at 250 °C, in order to ensure complete desorption of the less volatile diphenylselenide from the PDMS fiber.

3.2.1. Optimization of GC parameters

As regards to the GC oven program, the same parameters were examined as from $NaBEt_4$. The helium flow conditions were examined under constant pressure and variable flow rate of helium. The effect on the signal is the same as in the ethylation process (Fig. 2a) thus 4.2 mL min^{-1} was selected for further investigation. Hold times at 40 °C were studied in the range of 1–4 and 1 min was selected (Fig. 2b). The temperature ramp from was also optimized among 15, 30, 45 and 30 °C min^{-1} was eventually selected (Fig. 2c).

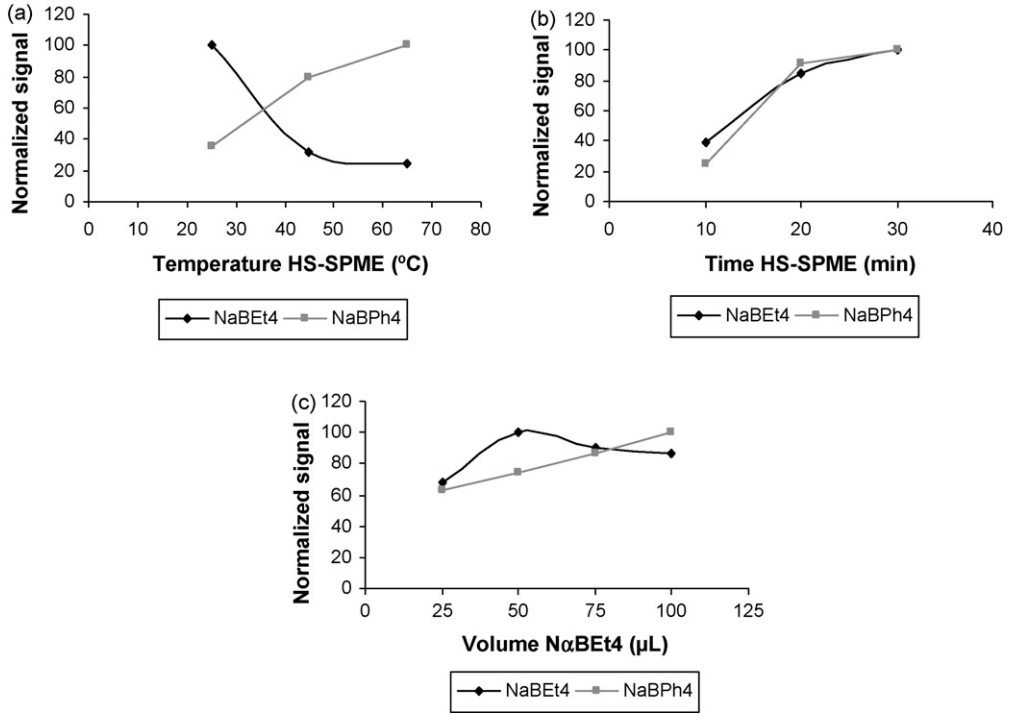


Fig. 3. Comparative curves for the optimization of HS-SPME with $NaBEt_4$ or $NaBPh_4$. Effect of (a) extraction temperature, (b) the extraction time during HS-SPME on selenite normalized signal and (c) 20% (m/v) $NaBEt_4$ volume used in HS-SPME on selenite normalized signal.

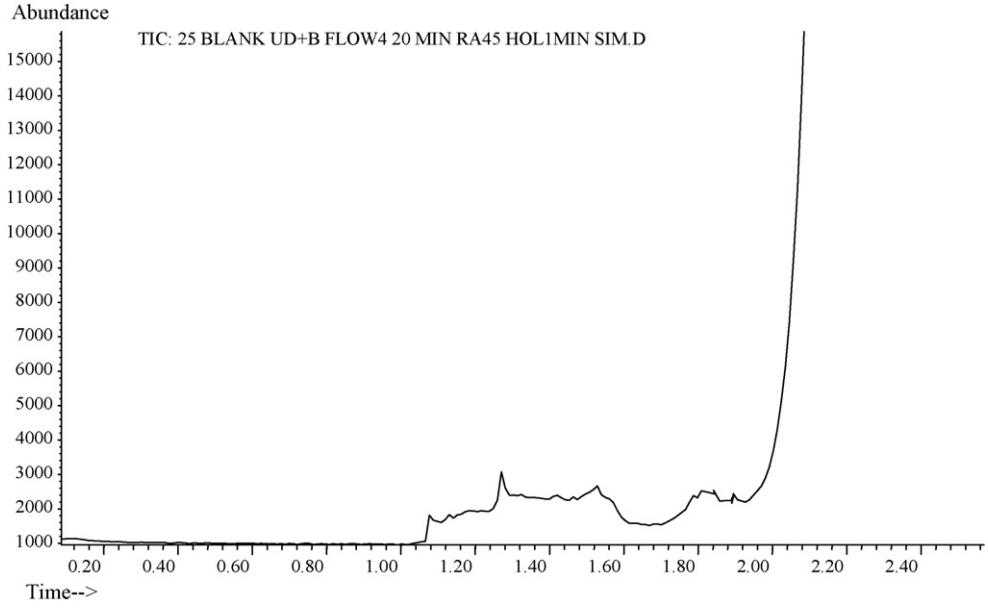


Fig. 4. Chromatogram of blank urine matrix from which selenium was removed by preliminary ethylation and one-hour degassing.

3.2.2. Optimization of HS-SPME parameters

The effect of temperature of the HS-SPME was investigated and the higher signal in the examined range was obtained at 65 °C (Fig. 3a), which are in accordance with previously reported observations about the use of tetraphenylborate for other analytes [20–22]. After experimentation in the range 10–30 min, 20 min was chosen as compromised extraction time (Fig. 3b). The volume of derivatization reagent was also investigated and the higher signal was obtained using 100 μL volume of the phenylation reagent (Fig. 3c).

3.3. Comparative calibration studies for ethylation and phenylation

Calibration curves for the determination of selenite after ethylation or phenylation and HS-SPME were done under optimum conditions for aqueous solutions. The regression equation was $[y = (444 \pm 6.6) \times 10^2\ c_{Se} + 20.3 \times 10^2]$ and the correlation coefficient $r = 0.9997$. Phenylation procedure can be useful in case of selenium speciation in samples where diethylselenide is to be determined. The regression equation for the phenylation was $[y = (69 \pm 4.3) \times 10^2\ c_{Se} + 12 \times 10^2]$ and the correlation coefficient $r = 0.9943$. It is evident that in terms of sensitivity, the ethylation procedure was preferable over the phenylation one by an order of magnitude and consequently it was applied for the determination of selenite in urine.

Next, the standard addition procedure was applied to blank urine matrix from which selenium was completely removed by preliminary ethylation and one-hour degassing (Fig. 4). It is worth mentioning that at 1.821 min no measurable peak was obtained. The regression equation was in this case $[y = (414 \pm 9.5) \times 10^2\ c_{Se} + 59 \times 10^2]$ and the correlation coefficient $r = 0.9995$. As there is no remarkable difference in sensitivity obtained in urine matrix as compared to that in aqueous matrix, it is reasonable to conclude that the compounds which are normally present in human urine do not interfere significantly with the determination of selenite. The detection limits were calculated by the 3 s criterion (i.e. three times the standard deviation of a series of blank measurements) for both procedures and are given in Table 2.

Table 2
The analytical performance characteristics of the proposed method.

Parameter	Water	Urine
Range ($\mu g\,L^{-1}$)	0.08–10	0.10–20
Regression coefficient (r)	0.9996	0.9995
Sensitivity	$(444 \pm 6.5) \times 10^2$	$(414 \pm 9.4) \times 10^2$
Recovery (%) [$n = 5$, $\gamma = 2.5\ \mu g\,L^{-1}$]	101 ± 5.0	95.0 ± 5.7
LOD (c_L, $\mu g\,L^{-1}$)	0.03	0.05
RSD (s_r, %, $n = 5$)	5.5	4.2

The accuracy of the method was studied by analyzing two certified referents materials. In standard reference material Trace elements in Water NIST-1643e the certified concentration was $11.97 \pm 0.14\ \mu g\,L^{-1}$ and the calculated recovery was 97.0 ± 3.7 and $87.8 \pm 3.0\%$ using $NaBEt_4$ and $NaBPh_4$, respectively. The standard reference material 2670 Freeze-Dried Urine had a certified value of $0.030 \pm 0.008\ \mu g\,mL^{-1}$ and the found value using $NaBEt_4$ was $0.029\ \mu g\,mL^{-1}$, i.e. $96.7 \pm 7.7\%$ recovery. The performance characteristics of the developed method were compared to those reported in literature and listed in Table 3. Concerning urine matrix, the limit of detection for Se was calculated as $0.05\ \mu g\,L^{-1}$, the precision (RSD) was 4.2% and the mean recovery after 5 replicates was $95.0 \pm 5.7\%$.

Table 3
Comparison of the performance of several SPME-GC methods for selenites.

Ref.	Technique	Matrix	RSD (%)	c_L of selenite ($\mu g\,L^{-1}$)
This work	HS-SPME-GC-MS	Water	5.5	0.03 (ethylation)
This work	HS-SPME-GC-MS	Urine	4.2	0.05 (ethylation)
[3]	HS-SPME-GC-MIP-AED	Water	6.9	2.7 (ethylation)
[3]	HS-SPME-GC-MIP-AED	Water	4.4	1.8 (propylation)
[5]	HS-SPME-GC-MS	Water	10.1	0.08
[10]	HS-SPME-GC-AED	Water		0.0073 (ethylation)
[10]	HS-SPME-GC-AED	Water		0.055 (4,5-dichloro-1,2-phenylenediamine)

4. Conclusions

Determination of selenites in human urine samples can be performed directly in the urine matrix after alkylation using tetralkylate reagents. Both tetraethylborate and tetraphenylborate reagents were capable to alkylate selenites in moderate acidic solutions in reasonable extraction time. Under optimized conditions of HS-SPME, the performance of sodium tetraethylborate was proved better than that of tetraphenylborate in all terms. The use of phenylation could be recommended as an alternative procedure only in case of presence of diethylselenide in the sample matrix. The analytical performance characteristics of the proposed method make the method useful as a screening and monitoring method for the determination of selenite in urine samples.

References

[1] E. Dumont, F. Vanhaecke, R. Cornelis, Anal. Bioanal. Chem. 385 (2006) 1304.
[2] C. Dietz, J. Sanz Landaluze, P. Ximenez-Embun, Y. Madrid-Albarran, C. Camara, J. Anal. At. Spectrom. 19 (2004) 260.
[3] E. Dimitrakakis, C. Haberhauer-Troyer, Yo Abe, M. Ochsenkuhn-Petropoulou, E. Rosenberg, Anal. Bioanal. Chem. 379 (2004) 842.
[4] M. Guidotti, J. AOAC 83 (2000) 1082.
[5] P. Jitaru, G. Cozzi, A. Gambaro, P. Cescon, C. Barbante, Anal. Bioanal. Chem. 391 (2008) 661.
[6] T. Lindemann, A. Prange, W. Dannecker, B. Neidhart, Fresenius J. Anal. Chem. 364 (1999) 462.
[7] T. Lindemann, H. Hintelmann, Anal. Bioanal. Chem. 372 (2002) 486.
[8] I. Ipolyi, Z. Stefanka, P. Fodor, Anal. Chim. Acta 435 (2001) 367.
[9] I. Ipolyi, P. Fodor, Anal. Chim. Acta 413 (2000) 13.
[10] K. Pyrzynska, Talanta 55 (2001) 657.
[11] O. Schramel, B. Michalke, A. Kettrup, Fresenius J. Anal. Chem. 363 (1999) 452.
[12] N. Campillo, R. Penalver, M. Hernandez-Cordoba, B. Perez-Sirvent, M. Martınez-Sanchez, J. Chromatogr. A 1165 (2007) 191.
[13] C. Dietz, J. Landaluze, P. Ximenez-Embun, Y. Madrid-Albarran, C. Camara, Anal. Chim. Acta 501 (2004) 157.
[14] S. Clark, P. Craig, J. Microchim. Acta 109 (1992) 141.
[15] C. Dietz, T. Perez-Corona, Y. Madrid-Albarran, C. Camara, J. Anal. At. Spectrom. 18 (2003) 467.
[16] A. Vonderheide, M. Montes-Bayon, J. Caruso, Analyst 127 (2002) 49.
[17] L. Jungin, J. Finley, J. Harnly, J. Agric. Food Chem. 53 (2005) 9105.
[18] S. Bird, G. Honghong, P. Uden, J. Tyson, E. Block, E. Denoyer, J. Chromatogr. A 789 (1997) 349.
[19] T. Grant, M. Montes-Bayon, D. LeDuc, M. Fricke, N. Terry, J. Caruso, J. Chromatogr. A 1026 (2004) 159.
[20] M. Czauderna, J. Kowalczyk, M. Niedzwiedzn, I. Wasowska, J. Anim. Feed Sci. 12 (2003) 199.
[21] L. Liang, S. Mo, Y. Cai, S. Mou, G. Jiang, M. Wen, J. Chromatogr. A 1118 (2006) 134.
[22] R.Y. Wang, Y.L. Hsu, L.F. Chang, S.J. Jiang, Anal. Chim. Acta 590 (2007) 239.
[23] L. Hinojosa Reyes, J.M. Marchante Gayon, J.I. Garcia Alonso, A. Sanz-Medel, J. Anal. At. Spectrom. 18 (2003) 11.
[24] J. Turner, S.J. Hill, E. Hywei Evans, B. Fairman, J. Anal. At. Spectrom. 14 (1999) 121.
[25] J. Mierzwa, S.B. Adeloju, H.S. Dhindsa, Anal. Sci. 13 (1997) 189.
[26] C. Moor, J.M.H. Lam, R.E. Sturgeon, J. Anal. At. Spectrom. 15 (2000) 143.
[27] Y. Chen, L. Li, A. D'Ulivo, N. Belzile, Acta Anal.Chim. 577 (2006) 126.
[28] B. Wake, A. Bowie, E. Butler, P. Haddad, Trends Anal. Chem. 23 (2004) 491.
[29] A. Bidari, P. Hemmatkhah, S. Jafarvand, M.R.M. Hosseini, Y. Assadi, Microchim. Acta 163 (2008) 243.
[30] S. Nazari, Microchem. J. 90 (2008) 107.
[31] A. Carro, I. Neira, R. Rodil, R. Lorenzo, Chromatographia 56 (2002) 733.
[32] R. Rodil, A.M. Carro, R.A. Lorenzo, M. Abuın, R. Cela, J. Chromatogr. A 963 (2002) 313.
[33] P. Hutchinson, L. Setkova, J. Pawliszyn, J. Chromatogr. A 1149 (2007) 127.
[34] D. Vuckovic, E. Cudjoe, D. Hein, J. Pawliszyn, Anal. Chem. 80 (2008) 6870.

Talanta 80 (2010) 1318–1325

Contents lists available at ScienceDirect

Talanta

journal homepage: www.elsevier.com/locate/talanta

Design of a new electrogenerated polyquinone film substituted with glutathione. Towards direct electrochemical biosensors

S. Reisberg[a], D.F. Acevedo[b], A. Korovitch[a], B. Piro[a], V. Noel[a], I. Buchet[a], L.D. Tran[c], C.A. Barbero[b], M.C. Pham[a,*]

[a] Laboratoire Interfaces-Traitements-Organisation et Dynamique des Systèmes (ITODYS), Université Paris-Diderot, associé au CNRS, UMR 7086, 15 rue Jean-Antoine de Baïf, 75205 Paris, France
[b] Departamento de Quimica, Universidad Nacional de Rio Cuarto-Ruta 8, km601, 5800 Rio Cuarto, Argentina
[c] Faculté de Technologie Chimique, Institut Polytechnique de Hanoi, 1 rue Dai Co Viet, C1-408, DHBK, Vienam

ARTICLE INFO

Article history:
Received 28 May 2009
Received in revised form 3 September 2009
Accepted 14 September 2009
Available online 2 October 2009

Keywords:
Glutathione
Conducting polymer
Electrochemical DNA sensor
Direct detection
Oligopeptide grafting

ABSTRACT

We developed a method to graft a tripeptide (glutathione) onto 5-hydroxy-1,4-naphthoquinone, an electropolymerizable molecule. The resulting thin conducting polymer presents a well-defined and stable electroactivity in neutral buffered solution, due to the embedded quinone group, and is able to covalently graft amino-modified DNA probe strands. It is shown that the bioelectrode presents positive current change following DNA hybridization. This makes a "signal-on" direct electrochemical DNA sensor. The results were obtained with low target concentration (50 nM) and the selectivity is excellent as a single-mismatch sequence can be discriminated from the full-complementary target.

© 2009 Elsevier B.V. All rights reserved.

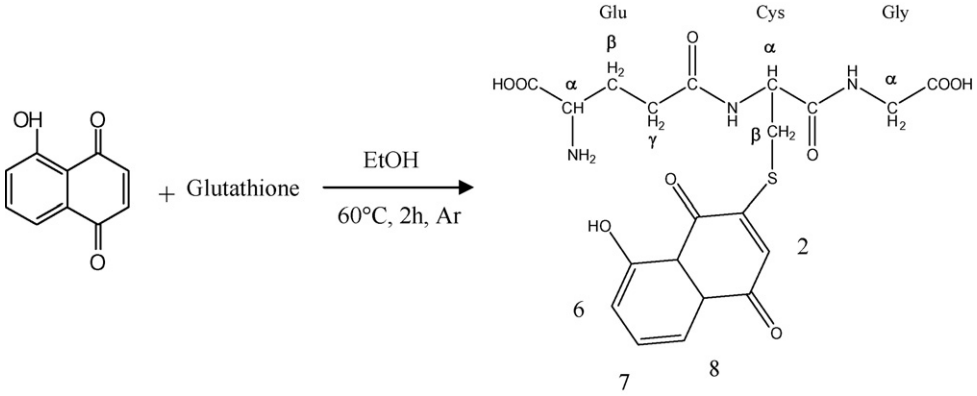
1. Introduction

Biosensors are of great interest nowadays. These devices need immobilization of biomolecules (bioprobes) on the sensor surface. To achieve this, several procedures are currently described [1]. One can use adsorption on the surface [2], inclusion into an organic [3] or an inorganic [4] matrix, covalent binding [3,5], complexation (using biotin–avidin association for example) [6]. Adsorption is simple to achieve, but generally poorly reproducible, and unstable. Inclusion into polymer or inorganic matrixes usually makes bioprobes, in particular DNA, inaccessible for subsequent reactions. Complexation using antibody–antigen association is efficient and widely used, as this avoids any risk of bioprobe denaturation due to immobilization. However, in this configuration, the antibody–antigen system (which is heavy) is inserted between the biosensor surface and the bioprobe, then hinders some interactions between the surface and the probe. Therefore, the direct covalent binding of the biomolecule onto the biosensor surface seems more pertinent and presents the advantage to be irreversible, i.e. more stable during the biosensor lifetime, and 'keeps in contact' the biomolecule and the surface. Its eventual drawback is that it may denaturate the immobilized bioprobe due to a lack of control of the linking regions and the linker reactivity. That is why the choice of the linker (the molecule or the reactive group which belongs to the sensor surface and binds the bioprobe) is of great importance.

Glutathione (γ-L-glutamyl-L-cysteinyl-glycine) is a tripeptide, bearing one primary amine, two amide groups, two carboxylic groups and one thiol group (see Scheme 1). It contains an unusual peptide link between the amine group of cysteine and the carboxyl group of the glutamyl side chain. The thiol group carried by this molecule is one of the most stable thiol group in a biomolecule. For this reason, glutathione is well-known to have antioxidant properties. Glutathione is then currently associated with drugs, in order to protect them from oxidizing species (free radicals for example), and, in addition, make them more soluble in water. The p*K*a associated to the carboxylic acid, the thiol and the primary amine groups are, respectively, 2.1 (COOH on glutamyl), 3.5 (COOH on glycine), 9.6 (SH) and 8.7 (NH_2) [7]. Therefore, at neutral pH, the molecule carries the equivalent of one negative charge. As glutathione is an oligopeptide bearing reactive amine, carboxylic groups and considering properties described above, this molecule of interest has been described in the literature as a linker for biomolecules immobilization on surfaces [8–10]. However, very few works reported electrochemical biosensor using glutathione as the binding element [9].

* Corresponding author. Tel.: +33 1 44276961; fax: +33 1 44276814.
E-mail address: mcpham@univ-paris-diderot.fr (M.C. Pham).

0039-9140/$ – see front matter © 2009 Elsevier B.V. All rights reserved.
doi:10.1016/j.talanta.2009.09.025



Scheme 1. Synthesis of 5-hydroxy-3-γ-L-glutamyl-L-cysteinyl-glycine-1,4-naphtoquinone (HNQ–Glu) from HNQ and glutathione, in one step. Proton's numbering corresponding to NMR attribution.

In this work, we developed a new electrogenerated polyquinone film substituted by glutathione. An original and direct procedure was used to chemically graft glutathione on 5-hydroxy-1,4-naphthoquinone. The resulting 3-(γ-L-glutamyl-L-cysteinyl-glycine)-5-hydroxy-1,4-naphthoquinone (HNQ–Glu) presents 3 functional groups: the hydroxyl group for electropolymerization (molecules of the hydroxynaphthoquinone family present the property to electropolymerize into a conducting polymer, via the hydroxyl group [11,12]), the quinone group for its redox and sensing properties, and the glutathione oligopeptide as a precursor for subsequent biomolecule linkage, via amine or carboxylic groups.

The synthesis and characterizations of the HNQ–Glu monomer are first described. After that, electrosynthesis of a conducting polymer is performed, by co-electropolymerization of a mixture of HNQ–Glu and unmodified HNQ, leading to poly[5-hydroxy-1,4-naphthoquinone-*co*-3-(γ-L-glutamyl-L-cysteinyl-glycine)-5-hydroxy-1,4-naphthoquinone], so-called poly(HNQ-*co*-HNQ–Glu) in the following. By this method, the quinone, carboxylic and amine functions are preserved in the polymer. The electroactivity of poly(HNQ-*co*-HNQ–Glu) film is investigated in neutral aqueous phosphate buffer (PBS), the modified electrode presents a well-defined, stable and reversible redox couple.

The quinone is well-known to be particularly sensitive to its chemical environment, in terms of pH or redox state. Therefore, the quinone group of poly(HNQ-*co*-HNQ–Glu) can be used as a redox reporter for chemical or electrochemical modifications of its vicinity. These modifications can be generated by change in ion concentration, for example. It has been shown in a previous work that in PBS the quinone groups of a poly(quinone) film exchange mainly sodium cations [13]. Therefore, the cyclic voltammograms of a poly(HNQ-*co*-HNQ–Glu) film, in the quinone redox domain, must change if sodium cation diffusion is modified. This can be generated by heavy molecules or charged molecules immobilized at the vicinity of the film surface, influencing the diffusion layer by steric hindrance or electrostatic effect. The transduction mechanism has been thoroughly investigated in some of our previous papers [14,15].

In this work, DNA probe strands (modified by an amine group at their 3′-end) are linked to the poly(HNQ-*co*-HNQ–Glu) copolymer via a free carboxylic group of the Glu moiety. After hybridization, the biosensor presents an increase in the redox current of the quinone group. As these current changes are mainly due to the faradic component instead of the capacitive one, Square Wave Voltammetry (SWV) is employed instead of classical voltammetry to characterize and emphasize the current variations. Addition of a probe strand which is perfectly complementary to the immobilized probe strand leads to a clear signal increase, whereas addition of a non-complementary sequence (random) or even a single-mismatch one does not generate significant change in current.

2. Materials and methods

2.1. Chemicals

N′-(3-Dimethylaminopropyl)-N-ethylcarbodiimide hydrochloride (EDC), N-hydroxysuccinimide (NHS) and phosphate buffer saline (PBS, 0.137 M NaCl; 0.0027 M KCl; 0.0081 M Na_2HPO_4; 0.00147 M KH_2PO_4, pH 7.4) were provided by Sigma. Aqueous solutions were made with ultrapure (18 MΩ) water. 5-Hydroxy-1,4-naphthoquinone (HNQ) 1-naphthol (1-NAP) and L-glutathione were purchased from Fluka. Acetonitrile (ACN, HPLC grade) was supplied by Aldrich. All other reagents used were of analytical grade. Oligonucleotides were provided by Eurogentec. The probe strand (PROBE) is a 37-mer sequence bearing an amino group on its 3′-end (5′-TC-CCT CAT AGT CGC ACC CAT CTC TCT CCT TCT-AGCCT-3′C_7NH_2). Targets are 30-mer sequences: COMP (3′-GGA GTA TCA GCG TGG GTA GAG AGA GGA AGA-5′) is the complementary one. MISMATCH (3′-GGA GTA TCA GCG TGG GTA AAG AGA GGA AGA-3′) presents one mismatch base, and the random sequence RANDOM (3′-TTG AAC CAG TAT CCA TGC ATT CCG CCT AAG-5′) is non-complementary. As explained above, the transduction mechanism of this biosensor is closely related to the conformational changes of the ODN strands upon hybridization. For this reason, in this work, we preferred to have a total control of the spatial conformation of the probe-target hybrid (double strand). For this, we needed to use probe and targets of ca. the same length. However, our probe was chosen slightly longer (37b) than the target sequences (30b) to let some bases as spacers at both ends of the probe.

2.2. Electrochemical methods

For electrochemical experiments, a conventional one-compartment, three-electrode cell was employed. An *EG&G 263A* potentiostat was used with the *Echem* software (Ecochemie). The working electrodes were glassy carbon (GC) disks (Aldrich) of 0,07 cm^2 area or gold plates (2 cm^2 area) for FTIR and XPS characterizations. The auxiliary electrode was a platinum grid and the reference electrode a commercial Saturated Calomel Electrode (SCE, MetrOhm, France). Electrodes were polished prior to each use with alumina slurry (1 then 0.3 μm).

The electrochemical synthesis of this copolymer poly(HNQ-*co*-HNQ–Glu) was carried out by electrooxidation of 5×10^{-2} M HNQ + 5×10^{-2} M HNQ–Glu + 10^{-3} M 1-naphthol (1-NAP) + 0.1 M $LiClO_4$ in acetonitrile, on gold or GC electrodes, under a dried argon atmosphere, by potential scans at 50 mV s^{-1} from 0.4 to 1.05 V

versus SCE. Without 1-NAP, no polymerization occurs, while electrooxidation of a solution containing only 10^{-3} M 1-NAP does not lead to any film. This indicates that 1-NAP acts as an electropolymerization initiator.

Hybridization was detected by recording the modification of the redox process of the quinone group, using Square Wave Voltammetry (SWV). The following parameters were used: pulse height 50 mV, pulse width 50 ms, scan increment 2 mV, frequency 12.5 Hz. The medium was PBS, bubbled with argon for 20 min before and during SWV measurements. The SWV scans were repeated (usually two or three times) until complete stabilization of the signal (i.e. no difference observed between two successive responses). Differential currents (Δi) were calculated by subtracting the current obtained after probe grafting from the current obtained after the considered experiment.

All electrochemical experiments were conducted at room temperature (22 °C). After modifications, electrodes were kept in the dark, away from oxygen and humidity in a dry argon atmosphere. In these conditions, the electrodes are stable (no significant decrease of its electroactivity) for ca. 2 weeks. The modified electrodes were used only for one cycle of electropolymerization-probe grafting-hybridization, then polished prior to re-use.

2.3. X-ray photoelectron spectroscopy (XPS)

X-ray Photoelectron Spectroscopy (XPS) data were recorded on a Thermo VG Escalab 250 (Al anode). XPS signals were fitted with a sum of Gaussian (70%)/Lorenzian (30%) functions, and calibrated by assuming a 285 eV binding energy for aromatic and aliphatic carbons.

2.4. NMR

All NMR spectra were recorded on a Bruker Avance III 300 MHz spectrometer. D_2O was used as solvent for all NMR measurements. The temperature was set at 298 K. Water resonance was suppressed with a low-power presaturation [16]. Data were processed using TOPSPIN 2.1 software (Bruker). Proton chemical shifts are referenced using residual HDO as an internal standard (4.70 ppm).

2.5. Grafting and hybridization conditions

As described before, poly(HNQ-*co*-HNQ–Glu) films present two carboxylic functions which are free to react with a coupling agent. As γ-L-glutamyl-L-cysteinyl-glycine is a peptide, it was natural to use a binding reaction currently used in peptide chemistry, i.e. formation of an amide bond from a carboxylic group and a primary amine (amidation). Under normal conditions, amidation is slow. To increase reactivity, the carboxyl group can be transformed into an ester group with the coupling agent N′-(3-dimethylaminopropyl)-N-ethylcarbodiimide hydrochloride (EDC). In aqueous solution, to obtain a better reactivity of the intermediate ester towards the primary amine carried on the DNA probe, another molecule must be used: N-hydroxysuccinimide (NHS). Indeed, water molecules act as nucleophilic molecules and induce hydrolysis of the intermediate ester. NHS competes with water and therefore increases the coupling yield.

Practically, poly(HNQ-*co*-HNQ–Glu) films were dipped into 1 mL of distilled water containing 0.1 μM probe (PROBE), 1.5×10^{-2} M EDC and 3×10^{-2} M NHS at 37 °C. After 20 h, the ODN immobilization reaction was stopped: the electrode was washed with distilled water (5 min) then with PBS (2 h at 37 °C) in order to remove non-covalently bound ODN.

At this stage, the electrodes were characterized by SWV, as explained in Section 2.2. Only those which present peak currents of 3 ± 0.5 μA were selected for the following steps.

For hybridization experiments, 1 mL of PBS solutions containing 50 nM of target (COMP, MISMATCH or RANDOM) were used. The electrode bearing the probe strand was dipped in the target solution then heated at a temperature above the melting temperature of the corresponding duplex (e.g. 72 °C for the PROBE/COMP duplex) during 2 h, and slowly cooled down to room temperature. After that, the electrode was washed in PBS for 1 h at 25 °C in order to remove the non-hybridized strands.

2.6. Fluorescence experiments

The apparatus used is an *Aminco-Bowman* Series 2 spectrofluorometer. Fluorescent targets (COMP*, MISMATCH* and RANDOM*) are modified with fluorescein (*Eurogentec*) on their 5′-end. These labeled targets were used following the same hybridization protocol than for the unlabelled targets, using 2 cm^2 GC plates as electrodes instead of 0.07 cm^2 GC disks. For quantification, dehybridization was performed in order to make spectrofluorometric analysis in solution and not directly onto the polymer surface.

The dehybridization protocol consists in a washing procedure made of 4 steps. To remove unspecific association, the three first steps consist in soaking the film in 2 mL of PBS, at 25 °C, under magnetic stirring, during 5 min (step 1), 10 more min (step 2), and 30 more min (step 3). After each step, the 2-mL solution is removed, stored for subsequent fluorescence experiments, and replaced by a fresh one. After these extensive washing steps, the fourth step consists in soaking the film in 2 mL of pure water at 80 °C during 10 min. Under these very stringent conditions, the hybrids which are present on the film are denatured and the target strands withdrawn towards the solution, which is stored for subsequent fluorescence experiments.

To determine the ODN concentration in these solutions, calibration curves were first obtained, for each fluorescent strand (in the range 0.25–10 nM). ODN concentrations were then converted into surface concentrations, which were found in the 0–15 pmol cm^{-2} range.

3. Results and discussion

3.1. Synthesis of HNQ–glutathione (HNQ–Glu)

3.1.1. Synthesis of 5-hydroxy-3-γ-L-glutamyl-L-cysteinyl-glycine-1,4-naphthoquinone (HNQ–Glu)

The reaction of thiols on various hydroxynaphthoquinone derivatives led, in one step, to substituted quinone rings, under mild conditions [17]. It is one of the most elegant substitution reactions on quinone rings, which are known to be quite unreactive in usual conditions. Therefore, the grafting reaction of glutathione onto hydroxynaphthoquinone derivatives appears highly interesting and original (to our knowledge, this reaction has not been described elsewhere).

5-Hydroxy-3-γ-L-glutamyl-L-cysteinyl-glycine-1,4-naphthoquinone (HNQ–Glu) was synthesized in one step from 1 equiv. of 5-hydroxy-1,4-naphthoquinone (HNQ) and 2 equiv. of γ-L-glutamyl-L-cysteinyl-glycine in 25 mL ethanol at 60 °C (Scheme 1). The solution was stirred for 15 min at this temperature and cooled at room temperature. The mixture was then allowed to stand for 2–3 days at 5 °C in the dark. The precipitate obtained was filtered and washed with ethanol. Evaporation of the solvent led to a brown/orange powder. Finally, a recrystallization step was made. The powder was dissolved in hot ethanol, filtered, then activated charcoal was added, and the mixture was filtered again. After one or 2 days at 4 °C, needles appeared at the bottom of the flask, which were separated by filtration, washed with cold ethanol (−18 °C) and kept for further analysis.

Table 1
NMR chemical shifts and multiplicity in D_2O at 298 K.

Proton	δ (ppm)	Multiplicity
Glu-H_α	3.76	t
Glu-$H_{\beta1}/H_{\beta2}$	2.13	m
Glu-$H_{\gamma1}/H_{\gamma2}$	2.52–2.51	m
Cys-H_α	4.53	d
Cys-$H_{\beta1}/H_{\beta2}$	2.92–2.90	m
Gly-H_α	3.92	s
H_2	–	–
H_8	7.72	d.d
H_7	7.78	t
H_6	7.40	d.d

The yield is ca. 40%. The purity of HNQ–Glu was verified by TLC and its structure was confirmed by FTIR (in KBr pellets, ν/cm^{-1}): 3028 [ν(N—H), weak]; 2975,2932 [asym. and sym. ν(C—H) of –CH_2–, strong], 1713 [ν(C—O), acid, strong]; 1661, 1559 [ν(C—C_{ar}), strong], 1630 [ν(C—O) of quinone, strong], 930 (δC—H_{ar}, 1H, weak), 759 (δC—H_{ar}, 3 adj. H, weak). A typical band of the ν(C—S) bond was found at 550 cm^{-1} (weak). The HNQ–Glu melting point is 250 °C versus 164 °C for HNQ.

NMR was performed in several deutered solvents, as MeOD, CD_2Cl_2 or D_2O. It was found that the whole HNQ–Glu molecule is only partially soluble in organic MeOD or CD_2Cl_2, whereas its solubility is acceptable in D_2O. This is due to the opposed behaviour between the glutathione part and the juglone part. If the second one is easily soluble in organic solvents, that is not the case for the glutathione moiety. The NMR identification was therefore performed in D_2O. L-Glutathione (Glu) and 5-hydroxy-1,4-naphthoquinone (Jug) were analyzed in D_2O and used as references. Their NMR spectra were compared to that of HNQ–Glu. Their profiles are identical. Proton's chemical shifts and attributions of HNQ–Glu are reported in Table 1 (see Scheme 1 for numbering). It can be noted that β protons of the glutamic acid present the same chemical shift (2.13 ppm) whereas the γ ones are slightly different (2.52–5.51 ppm), as well as the β protons of the cysteine moiety (2.92–2.90 ppm). The H_2 proton was expected but cannot be seen. This can be explained by interactions with the Glu moiety at close vicinity.

3.1.2. Electrosynthesis of poly(HNQ-co-HNQ–Glu)

Due to its relatively high molecular weight, the glutathione moiety induces a strong steric hindrance on the HNQ moiety. Moreover, the carboxylic acids (negatively charged) may change the ion-exchange properties of the polymer. This is why we chose to make a copolymer with an equivalent proportion (1:1) of HNQ and HNQ–Glu instead of poly(HNQ–Glu). Conditions are described in Section 2.2.

The voltammograms obtained during electrosynthesis of poly(HNQ-*co*-HNQ–Glu) films present during the first cycles an oxidation wave situated above 1 V. After a few cycles, a redox couple appears around 0.85/0.90 V. Currents increase gradually with potential scans (Fig. 1).

The FTIR spectrum of the resulting film (synthesized on a gold plate) is presented on Fig. 2. A peak at 3059 cm^{-1} of medium intensity can be attributed to free N—H stretch (asymmetric vib.). Bands situated between 3000 cm^{-1} and 2800 cm^{-1} concern CH_2 stretching vibrations. The presence of several peaks (asym. νCH_2, 2954 cm^{-1} and 2924 cm^{-1}; sym. νCH_2, 2860 cm^{-1} and 2870 cm^{-1}) shows that two different –CH_2– groups are present in the glutathione moiety: –CH_2– close to carboxyl groups and –CH_2– close to amine groups. The bands present in the 2000–700 cm^{-1} range are typical for the HNQ moiety, with a shoulder at 1737 cm^{-1} due to ν(C=0) of the carboxylic acid group, two strong bands at 1670

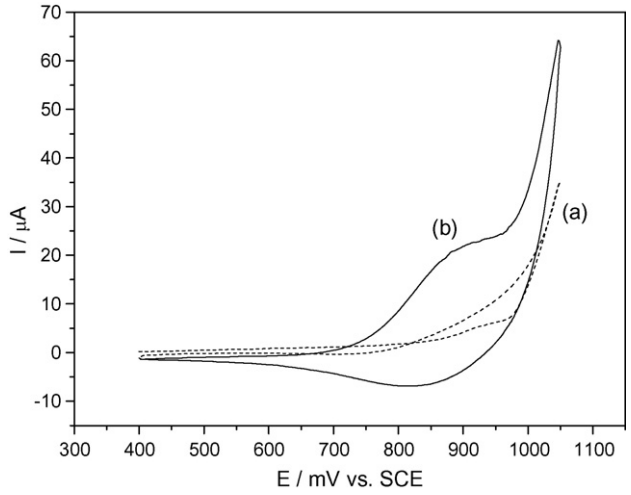


Fig. 1. Cyclic voltammograms recorded during electrosynthesis of a poly(HNQ-*co*-HNQ–Glu) film in ACN + 0.1 M $LiClO_4$ + 5×10^{-2} M HNQ + 5×10^{-2} M HNQ–Glu + 2×10^{-3} M 1-naphthol on a GC electrode under argon atmosphere. Scan rate: 50 mV s^{-1}. Electrode surface: 0.07 cm^2. (a, dashed line), fist cycle; (b, plain line) 50th cycle. Film thickness after 50 scans: ca. 100 nm (measured by SEM).

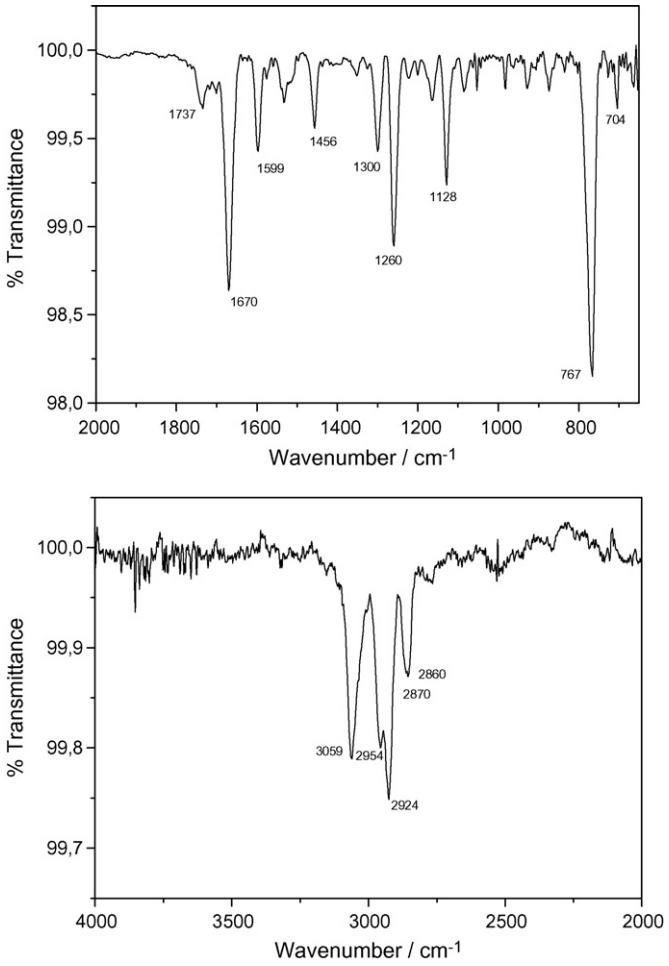


Fig. 2. FTIR spectra of the poly(HNQ-*co*-HNQ–Glu) film electrodeposited on a gold substrate, in the 650–2000 cm^{-1} and 2000–4000 cm^{-1}.

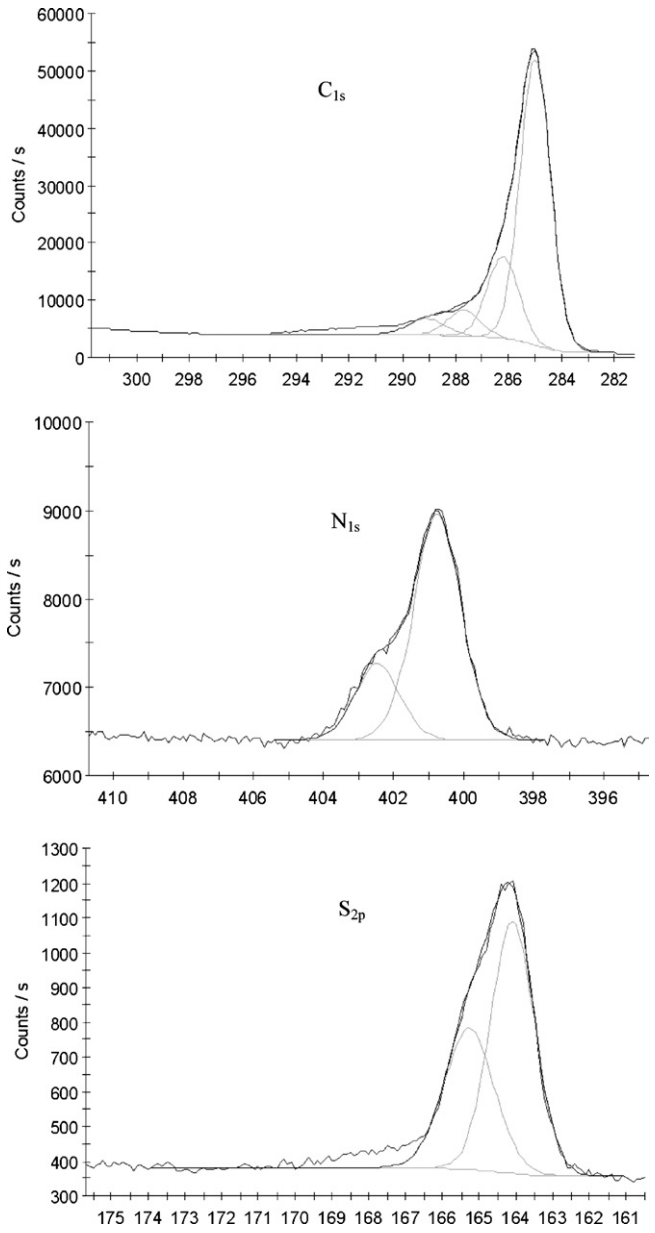


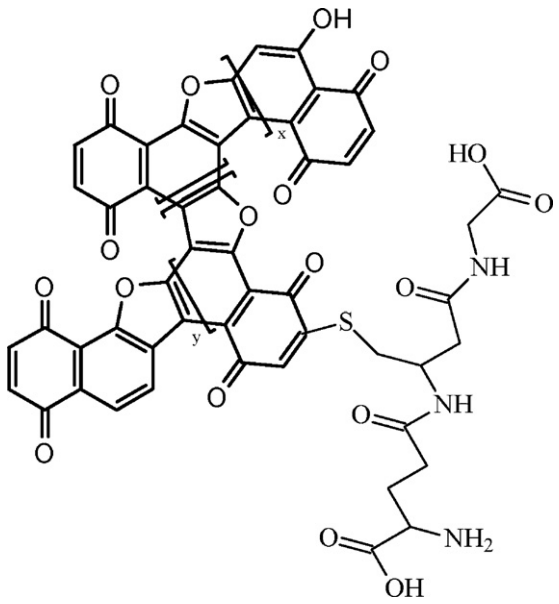
Fig. 3. XPS spectra of the poly(HNQ-*co*-HNQ–Glu) film for C, N and S elements.

and 1599 cm^{-1} are due to $\nu(C{=}C)_{ar}$ of the aromatic structure and of the quinone group, bands at 1260 and 1300 cm^{-1} are attributed to $\nu(C{-}O{-}C)_{as}$ of the furan cycle and a strong band at 767 cm^{-1} is typical for naphthalene structure.

3.2. XPS characterization of poly(HNQ-co-HNQ–Glu) films

The poly(HNQ-*co*-HNQ–Glu) films were analyzed by X-Ray Photoelectron Spectroscopy (XPS). Fig. 3 presents spectra of C, N and S. Carbon atoms are present in the polymer structure as well as in the Glu moiety whereas nitrogen and sulfur belong only to Glu.

The C1s spectrum displays four peaks, at 285 eV, 286.2 eV, 287.7 eV and 289.1 eV. They can be respectively attributed to C—C and C=C (present into the polymer backbone and the Glu moiety), C—O, C—S and C—N (polymer backbone and Glu), C=C (of the quinone group), and O—C=C or O=C—N (of the carboxylic and amide groups belonging to the Glu moiety).



Scheme 2. The proposed structure for poly(HNQ-*co*-HNQ–Glu).

The N1s spectrum displays 2 peaks, at 400.7 eV and 402.5 eV. These peaks can be attributed to the amide (–NH—C=C) and amine groups ($-NH_2$) respectively.

The S2p spectrum displays two peaks (as it is a 2p level) at 164.1 eV and 165.3 eV. It corresponds to the only sulfur present in the Glu moiety, which binds Glu and HNQ via a C—S bond.

The calculations from the peak surfaces, using the sensitivities for C, N and S which are respectively 1, 1.80 and 1.67, give an experimental atomic ratio N/S of 2.95. This ratio corroborates very well with the theoretical ratio (3:1) of the Glu structure. The experimental C/S ratio equals to 99. The theoretical one equals to 20:1 for the HNQ–Glu moiety, whereas no sulfur belongs to the HNQ molecule. This indicates that the ratio between the HNQ moieties and the HNQ–Glu moieties in the copolymer is around 4, that means 1 HNQ–Glu for 4 HNQ. Scheme 2 presents a proposed structure for poly(HNQ-*co*-HNQ–Glu) film, deduced from XPS and FTIR results.

3.3. Electroactivity of poly(HNQ-co-HNQ–Glu) films

The electroactivity of the copolymer film was investigated in phosphate buffer saline (PBS). In the cathodic potential domain of potential (between −0.9 V and 0.25 V), a redox couple develops at −0.51/−0.63 V (Fig. 4a).

The observed peaks are due to quinone electroactivity. By charge integration, 5×10^{-10} mol cm^{-2} of quinone are estimated to be electroactive for a 100-nm thick film (thickness determined by SEM at grazing angle). The redox systems present excellent stability upon cycling (several hundreds of cycles without significant current decrease, as shown in Fig. 4a). Of interest is the fact that the potential range is low enough to avoid interference with many electroactive species that can be present in biological media. Moreover, in applications for DNA grafting and hybridization detection, this behaviour avoids any risk of nucleobases oxidation, as they are oxidized at much higher potentials. At last, it is known that the redox system of the quinone group exchanges cation and not anion. More precisely, it has been shown by electrogravimetric experiments [13] that quinone exchanges mainly sodium cations in neutral PBS medium. This behaviour is a strong advantage of poly(HNQ-*co*-HNQ–Glu) film over other more classical polymer films. Indeed, DNA strands (which are negatively charged) are not able to play the role of counterions for this polymer which

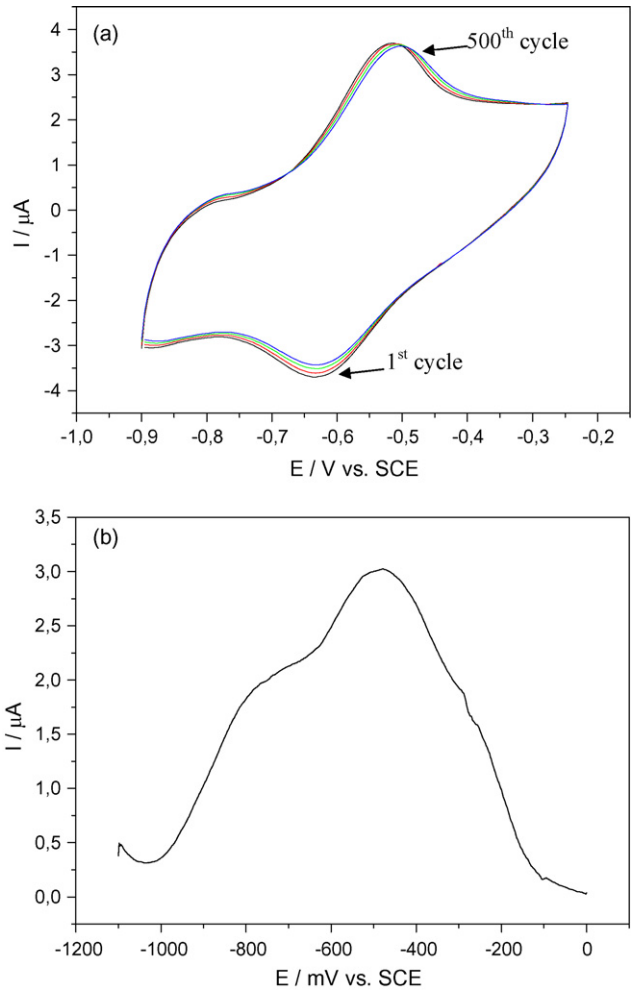


Fig. 4. (a) Cyclic voltammograms of a poly(HNQ-*co*-HNQ–Glu)-modified electrode recorded in PBS under argon atmosphere. Scan rate: 50 mV s^{-1}. Electrode surface: 0.07 cm^2. Film thickness: 100 nm. Several voltammograms were recorded between the first and the 500th without significant current decrease. (b) Square wave voltammogram (SWV) of a poly(HNQ-*co*-HNQ–Glu)-modified electrode recorded in PBS under argon atmosphere. Parameters: pulse height 50 mV, pulse width 50 ms, scan increment 2 mV, frequency 12.5 Hz, potential domain (−1.1 V; 0 V vs. SCE).

exchanges cations. As poly(HNQ-*co*-HNQ–Glu) polymer is neutral or negatively charged, it repels probe DNA strands (which still remain available for hybridization), and prevents non-specific adsorption of target strands. This property is interesting for the film to be used in biosensor matrix.

3.4. SWV of poly(HNQ-co-HNQ–Glu) films

As shown on Fig. 4a, the voltammograms present a strong capacitive component. We have shown in a previous work that DNA hybridization induces more change on the faradic current than on the capacitive current [13]. Therefore, square wave voltammetry (SWV), which is able to suppress much of the capacitive component, was chosen as the best analytical tool to study the influence of DNA grafting or hybridization on the film electroactivity. SWV was performed on the poly(HNQ-*co*-HNQ–Glu)-modified electrode before treatment with the ODN probe (Fig. 4b). The potential was swept from −1100 mV versus SCE to 0 V versus SCE (oxidation scan). Two oxidation peaks appear in this range. The main peak presents a maximum at around −500 mV/SCE, and the second one appears as a shoulder at around −800 mV/SCE. These peaks correspond to the redox process of the quinone group.

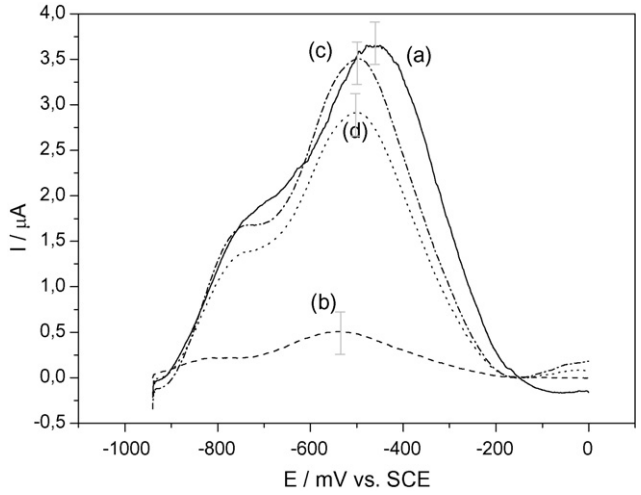


Fig. 5. SWV of a poly(HNQ-*co*-HNQ–Glu)-modified electrode. (a) Before PROBE grafting; (b) after PROBE grafting; (c) after incubation with PROBE without EDC nor NHS; (d) after incubation with EDC and NHS, without PROBE. Medium: PBS, under argon atmosphere. Parameters: pulse height 50 mV, pulse width 50 ms, scan increment 2 mV, frequency 12.5 Hz, potential domain −0.95/0 V versus SCE. Results obtained from 3 sets of independent experiments. Reproducibility is materialized by error bars.

This electroactivity involves ion exchange at the polymer/solution interface. Therefore, changes made on this interface will affect electroactivity. The presence of DNA at the interface strongly influences the ionic flux, therefore the switching rate of the polymer, and as a consequence the recorded current.

Two main explanations for the current change could be envisaged: electrostatic effect (due to the polyelectrolyte character of ODN strands) and/or steric effect (due to the fact that ODN are relatively large molecules). Due to the strong ionic force used in our experiments, the charges localized on the double-stranded ODN (dsODN) backbone are totally screened. The electrostatic effect can be neglected. The steric effect is therefore predominant.

An interesting particularity of ODN is that the double-stranded state (after hybridization) presents a conformation which is very different from the single-stranded state (before hybridization). One can assume that the single-stranded ODN (ssODN) behaves as a classical polymer chain. This means that it is folded as a statistical coil. On the contrary, the double-stranded ODN can be modeled as a rigid cylinder [18–20]. Therefore, steric hindrances generated by ssODN or dsODN are very different. This influences the ionic transport dynamics.

This model has been thoroughly developed in previous papers [14,15] and is the basic principle of the transduction mechanism which is concerned in this work. We have shown that, under certain conditions, dsODN generate a lower steric hindrance than ssODN. Considering that the peak current is controlled by ions transport through the polymer/solution interface, this allows to conclude that ssODN grafting onto the surface generates a current drop; Conversely, the hybridization event (i.e. formation of dsODN) will lead to a current increase.

3.5. Electrochemical detection

3.5.1. Probe grafting

The probe ODN (PROBE) was grafted as described in Section 2. SWV was used to characterize grafting. A SWV curve was recorded before PROBE grafting, and another one was recorded, in the same conditions, after PROBE grafting. As shown on Fig. 5, the current intensity is high for the unmodified film (before grafting, curve a, plain line), and strongly diminishes after grafting (curve b, dashed

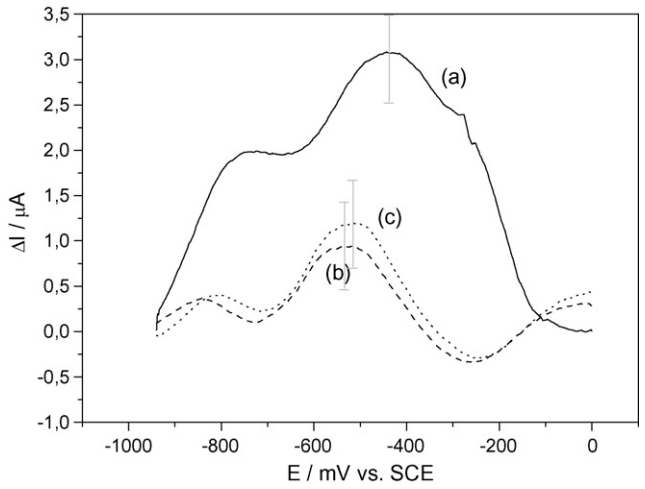


Fig. 6. Differential SWV (Δi) obtained after incubation of the probe-grafted poly(HNQ-*co*-HNQ–Glu) with complementary TARGET (curve a); incubation with RANDOM (curve b); incubation with MISMATCH (curve c). Medium: PBS, under argon atmosphere. Parameters: pulse height 50 mV, pulse width 50 ms, scan increment 2 mV, frequency 12.5 Hz, potential domain −0.95/0 V versus SCE. Differential currents (Δi) were obtained by subtraction of the current obtained after probe grafting. Results were obtained from 3 sets of independent experiments. Reproducibility is materialized by error bars.

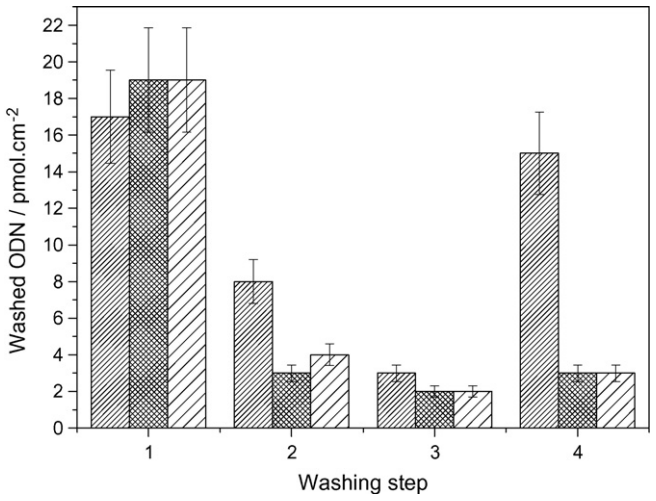


Fig. 7. ODN surface concentration deduced from fluorescence analysis. The fluorescence measurements were made as explained in Section 2, by 3 steps: (1) washing in PBS at 37 °C during 5 min; (2) washing in PBS at 37 °C during 10 additional min; (3) washing in PBS at 37 °C during 30 additional min; (4) washing in pure water at 80 °C during 15 min. The left-handed bars correspond to the COMP target; The central bars correspond to the RANDOM target; The right-handed bars correspond to the MISMATCH target. Results obtained from 3 sets of independent experiments. Reproducibility is materialized by error bars.

line). This can be attributed to the steric hindrance generated by the PROBE strands immobilized on the film surface. As shown, only 10% of the initial electroactivity remains after grafting.

During probe grafting, the electrodes were dipped into three different media: water containing reactants, pure water, and then PBS. To be sure that the current change is only due to probe grafting, blank experiments were performed. The first consisted of the same experiment as above, without NHS nor EDC. The second consisted of the same experiment as above, without ODN probe. The only case for which a significant current change occurs is for probe grafting. Probe alone in solution (curve c) does not lead to any change (this could indicate that there is no probe adsorption), whereas esterification with NHS and EDC (without ODN probe) leads only to a slight (20%) current drop (curve d).

We do no discuss the potential shift which appears between SWV (Figs. 5 and 6), because it cannot be interpreted as it would be for classical voltammetry. Indeed, SWV is a complex technique which subtracts what is called a reverse current (Ir, negative) from a forward current (If, positive).

3.5.2. Hybridization and selectivity

A similar experiment was performed to characterize target hybridization onto the grafted film. A SWV was recorded after PROBE grafting, before addition of the COMP target; another SWV experiment was recorded, in the same conditions, after COMP hybridization (target concentration: 50 nM). To make changes more visible, differential currents (Δi) were plotted. Δi corresponds to the current difference between two SWV recorded for two different electrode states. For example, the Δi which characterizes COMP hybridization corresponds to the difference between the SWV recorded after COMP hybridization and the one recorded before COMP addition.

As shown on Fig. 6 (curve a), a positive response ($\Delta i > 0$, meaning that the current increases upon hybridization) is obtained consecutively to addition of the full-complementary strand.

To be sure that the positive response is truly due to hybridization and not an artefact, a similar experiment was performed under the same conditions, with a non-complementary (RANDOM) strand. As previously, SWV was recorded before and after RANDOM addition. The resulting differential current is plotted on Fig. 6, curve b. As shown, current variations are weak. This result indicates that the current change observed after addition of the COMP sequence is truly due to hybridization.

In a last experiment, the selectivity was checked. A similar experiment than above was performed and a MISMATCH sequence was added (i.e. a sequence which differs from the COMP sequence by only one base, a G being replaced by a A). As shown on Fig. 6, curve c, the current change is weak. This means that the biosensor is selective and discriminates one mismatching base in a 30-bases sequence.

3.5.3. Sensitivity

The results concerning hybridization with a full-complementary target were obtained with a target concentration of 50 nM, in 1 mL PBS solution, at 72 °C for 2 h. As shown in Fig. 6, the current change upon hybridization is ca. 3 μA in these conditions, with a S/N ratio of around 3. This sensitivity is comparable to that obtained on another system developed by our group [15]. We have tested with various target concentrations, with 10 nM, the S/N ration is around 2 while with 1000 nM target concentration, the current change recorded is not more than 3 μA, but is reached faster, after 30 min instead of 2 h. These results illustrate the fact that the current change is limited by the surface concentration of hybrids, i.e. the probe surface concentration and not by the target concentration, as soon as the quantity of target is sufficient. For example, 1 mL at 1 nM contains 1 pmol of target, which corresponds approximately to the probe quantity on our electrodes.

3.5.4. Fluorescence experiments

Besides the electrochemical experiments, we have performed fluorescence experiments in order to demonstrate the stability of the probe grafting as well as the selectivity of the target hybridization.

A systematic procedure was followed, in four steps, as described in Section 2. Three different targets were studied: COMP*, MISMATCH* and RANDOM*. As shown in Fig. 7, the first wash removes quite high quantities (around 18 pmol cm^{-2}) for the three targets. This corresponds to elimination of unspecifically adsorbed ODN. Since the second wash (still under mild conditions, 37 °C), the

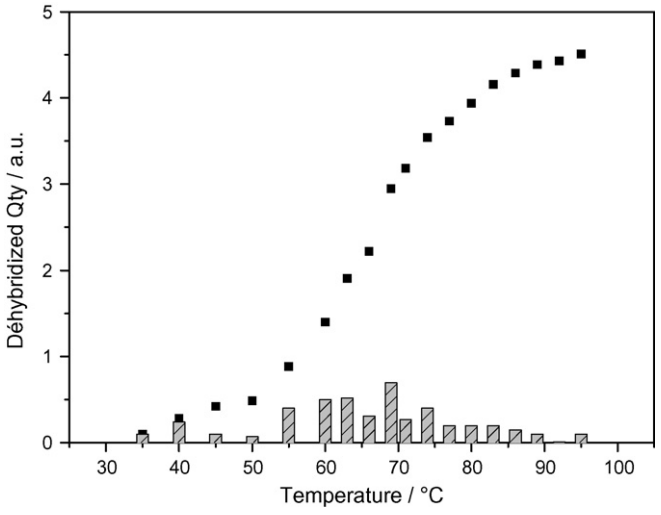


Fig. 8. Dehybridized COMP sequence as a function of the temperature. Nineteen washes were performed, from 35 °C up to 95 °C, in PBS. Bars indicate the dehybridized quantity (fluorescence intensity) corresponding to each wash at a given temperature. The curve (in black squares) is obtained by successive integration of dehybridized quantities.

results begin to be sequence-specific. Indeed, there are at least two times more desorbed COMP* sequences (equivalent to around 8 pmol cm^{-2}) than MISMATCH* or RANDOM* ones (equivalent to around 4 pmol cm^{-2}). We suppose that a part of hybridized COMP* targets may dehybridize even under these mild conditions. At the third wash, desorption is low for all (around 2 pmol cm^{-2}).

The results are different for the 4th step (dehybridization under stringent conditions, 80 °C in pure water. At this temperature, one can assume that all previously hybridized COMP* are denatured). Fluorescence remains low for MISMATCH* and RANDOM* targets (equivalent to around 3 pmol cm^{-2}), whereas it reaches five times more, i.e. 15 pmol cm^{-2} for COMP*. These data show that hybridization occurs efficiently on the modified electrode, and is highly sequence-specific.

In addition to these results, we performed an original and complementary experiment. This time, dehybridization was performed in PBS instead of pure H_2O, not only at 80 °C but at increasing temperatures from 35 °C up to 95 °C and fluorescence was followed stepwise, as a function if temperature. As shown (Fig. 8), fluorescence increases significantly for temperatures above 55 °C. The shape of the curve corresponds to the melting temperature of the PROBE-COMP* duplex (given at 72 °C in homogenous conditions). This result demonstrates without any doubt that dehybridization is responsible for this behaviour.

4. Conclusion

The modification of 5-hydroxy-1,4-naphthoquinone by γ-L-glutamyl-L-cysteinyl-glycine (glutathione) has been obtained by a direct and elegant method. The resulting 2-(γ-L-glutamyl-L-cysteinyl-glycine)-5-hydroxy-1,4-naphthoquinone (HNQ–Glu) presents 3 functional groups: the hydroxyl group for electropolymerization, the quinone group as the redox reporter, and the glutathione oligopeptide as a precursor for subsequent biomolecule linkage, via amine or carboxylic groups.

It is shown that the co-electrooxidation of HNQ–Glu and unmodified HNQ leads to poly(HNQ-*co*-HNQ–Glu), into which the quinone group remains electroactive, even in neutral buffered solution.

The poly(HNQ-*co*-HNQ–Glu)-modified electrode allows to detect directly DNA hybridization with a "signal-on" current (i.e. a current increase in Square Wave Voltammetry curve).

This DNA sensor is selective as a positive response is detected when a complementary DNA strand is added, while no significant signal change is observed consecutively to addition of a non-complementary or a mismatch sequence.

The molecular recognition is detected by changes in the electroactivity of the quinone group. This is due to the fact that DNA strands generate both steric hindrance and electrostatic effect on the electrode surface, which influences the quinone electroactivity.

The high selectivity could be explained by the fact that as the Glu moiety is negatively charged and poly(HNQ-*co*-HNQ–Glu) film is a cation (sodium) exchanger, non-specific adsorption of DNA strands are prevented.

The high selectivity as well as the "signal-on" response make this film original and efficient to be used in a direct DNA biosensor. This is, to our knowledge, the only work reported in the literature concerning an electrochemical DNA sensor using glutathione as the binding element. This approach can be generalized with other polypeptides, providing that a thiol group is available.

Acknowledgments

The authors thank ECOS Sud (France) and SECYT (Argentina) for the support of the collaboration between ITODYS (Paris) and the Department of Chemistry-Universidad Nacional de Rio Cuarto (Argentina). S. Reisberg thanks University Paris – Diderot for a post-doctoral position.

References

[1] W.M. Albers, I. Vikholm, T. Viitala, J. Peltonen, Handbook Surface Interf. Mater. 5 (2001) 1–31.
[2] I. Palchetti, M. Mascini, Topics Curr. Chem. 261 (2005) 27–43.
[3] S. Cosnier, Anal. Lett. 40 (2007) 1260–1279.
[4] V.B. Kandimalla, V.S. Tripathi, H. Ju, Crit. Rev. Anal. Chem. 36 (2006) 73–106.
[5] S. Griveau, D. Mercier, C. Vautrin-Ul, A. Chausse, Electrochem. Commun. 9 (2007) 2768–2773.
[6] M.I. Pividori, A. Lermo, E. Zacco, S. Hernandez, S. Fabiano, S. Alegret, Thin Solid Films 516 (2007) 284–292.
[7] N.W. Pirie, K.G. Pinhey, J. Biol. Chem. 84 (1929) 321–333.
[8] H.H. Tai, S.O. Jung, J.M. Lee, K.Y. Lee, Y. Lee, J.S. Park, B.H. Chung, Anal. Chem. 79 (2007) 546–556.
[9] S. Akella, C.K. Mitra, Indian J. Biochem. Biophys. 44 (2007) 82–87.
[10] M. Musameh, N. Moezzi, L.M. Schauman, M.E. Meyerhoff, Electroanalysis 18 (2006) 2043–2048.
[11] M.C. Pham, J. Moslih, P.C. Lacaze, J. Electrochem. Soc. 138 (1991) 449–454.
[12] B. Piro, J. Haccoun, M.C. Pham, L.D. Tran, A. Rubin, H. Perrot, C. Gabrielli, J. Electronal. Chem. 577 (2005) 155–165.
[13] A. Rubin, H. Perrot, C. Gabrielli, M.C. Pham, B. Piro, Electrochimica Acta, submitted.
[14] B. Piro, S. Reisberg, V. Noel, M.C. Pham, Biosens. Bioelectron. 22 (2007) 3126–3131.
[15] S. Reisberg, B. Piro, V. Noel, M.C. Pham, Bioelectrochemistry 69 (2006) 172–179.
[16] M. Gueron, P. Plateau, M. Decorps, Prog. NMR Spectrosc. 23 (1991) 135–209.
[17] F.G. Rothman, Chem. Mater. 23 (1958) 1049–1051.
[18] S.B. Smith, Y. Cui, C. Bustamante, Science 271 (1996) 795–799.
[19] B. Tinland, A. Pluen, J. Sturm, G. Weill, Macromolecules 30 (1997) 5763–5765.
[20] M.D. Frank-Kamenetskii, Phys. Rep. 288 (1997) 13–60.

Talanta 80 (2010) 1326–1332

Contents lists available at ScienceDirect

Talanta

journal homepage: www.elsevier.com/locate/talanta

Single interface flow system with potentiometric detection for the determination of nitrate in water and vegetables

João Rodrigo Santos, João L.M. Santos*, José L.F.C. Lima

REQUIMTE, Serviço de Química-Física, Faculdade de Farmácia, Universidade do Porto, R. Aníbal Cunha, 164, 4099-030 Porto, Portugal

ARTICLE INFO

Article history:
Received 12 May 2009
Received in revised form
10 September 2009
Accepted 18 September 2009
Available online 24 September 2009

Keywords:
Single interface flow analysis (SIFA)
Potentiometry
Nitrate ion
Tubular electrodes

ABSTRACT

In this work a single interface flow system (SIFA) with potentiometric detection was for the first time implemented and applied to the determination of nitrate in waters and plant extracts. The analytical potential of the SIFA system was exploited not only to transport the sample towards detection but also to carry out, in a reproducible and automated way, the tasks associated with sample pre-treatment, namely ionic strength, pH adjustment and interfering species suppression. The advantageous aspects of combining a SIFA system with potentiometry with enhanced simplicity, ease of implementation and automation were further discussed and emphasised.

The obtained results showed relative deviations lower than 5%, for both types of samples, with sampling rates of about 40 h^{-1}.

In addition, an innovative and straightforward process for constructing plastic membrane ion selective electrodes with a tubular configuration able to be coupled to flow-based analytical systems is also proposed. The developed approach, consisting of assembling the electrode inside a flow tubing connector is very simple to implement, robust, particularly adequate to be combined with flow methodologies and maintains all dynamic and analytical characteristics exhibited by previous assembling processes.

© 2009 Elsevier B.V. All rights reserved.

1. Introduction

Single interface flow analysis (SIFA) was recently proposed by Ribeiro et al. [1] as a new flow strategy for the automated handling of solutions and implementation of reaction schemes. This flow approach relies on the establishment of two dynamic concentration gradients between two adjoining solutions (sample and reagent) at the single interface where these are put in contact for reaction development prior to transport towards detection.

The formed concentration gradients are a consequence of the mutual penetration/interdispersion of the neighbouring zones due to the higher velocity of the flowing stream at its central zone, when compared to more peripheral ones, characteristic of a laminar flow. In opposition to more conventional flow techniques, in SIFA systems, whatever might be the residence time, a physical or a chemical equilibrium is never attained. In fact, the interface or reaction zone progresses continuously in opposite directions with time, as more and more solutions zones are involved in the mutual penetration process. This way, the width of the reaction zone increases and since there is a continuous supply of fresh sample and reagent solutions the analytical signal becomes broader although its magnitude is almost unaffected by dilution phenomena. Parameters such as flow rate and reactor length that affect zone penetration also influence analytical peak broadness. With respect to the profile of the analytical signal obtained, it could vary from an almost Gaussian peak, if a spectrophotometer is used and a coloured product reaction is formed at the single interface, to a typical sigmoid curve, in the case of for instance a potentiometric detector, the sigmoidal shape (Fig. 1) portraying the intermixing process between the adjoining solutions [2]. Nevertheless, the profile of the analytical signal is representative of the continuous point-to-point molar ratio variation that results from the mixing of the individual solutions at the interface. This feature provides a high analytical versatility since it makes possible to select any point of the analytical profile, referenced in terms of a detection time (t_D), which may be regarded as combining the most favourable reaction conditions concerning sample and reagent concentrations. Another important advantage of SIFA systems is their operational simplicity. This arises from the fact that no compelling sample or reagent volumes have to be used, in opposition to other flow techniques, which simplifies analytical system implementation and optimisation. Moreover, since no specific sample and reagent insertion devices are required, the number of flow manifold components is reduced with a concomitant restraint in the potential sources of errors or malfunctions.

* Corresponding author. Tel.: +351 22 2087132; fax: +351 222078961.
E-mail address: joaolms@ff.up.pt (J.L.M. Santos).

0039-9140/$ – see front matter © 2009 Elsevier B.V. All rights reserved.
doi:10.1016/j.talanta.2009.09.031

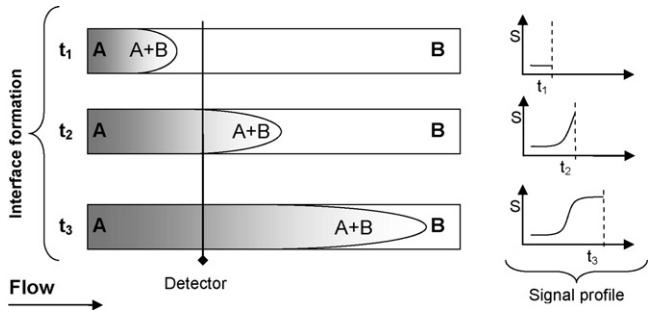


Fig. 1. Scheme of the single interface formation between two adjoining solutions (A and B) and analytical signal profile obtained for increasing detection time (t_1 to t_3).

These characteristics make SIFA systems very attractive for coupling with potentiometric detectors where the single interface could be exploited for sample pre-treatment, such as pH and ionic strength adjustment or interferences suppression, for the formation of electroactive species, for carrying out standard addition methods, to increase detector selectivity or to implement titrimetric methodologies.

Potentiometric techniques have a widespread use in routine analysis although most of the times they rely on direct potentiometric measurements carried out in batch procedures by using well defined volumes of sample that frequently require a previous conditioning. These aspects could constitute an important shortcoming in terms of analytical efficiency that could be overcome by resorting to a flow-based technique. The simplicity and efficiency of coupling flow-based techniques with potentiometric detection has been demonstrated with distinct analytical purposes [3]. The enhanced detector selectivity prevents the need for extensive sample pre-treatments and greatly simplifies flow manifold configuration. At the same time, the expeditious sample handling provided by flow analysis capitalises the fast potentiometric detector response enabling a high sampling rate, while repeatability is favoured by the continuous detector conditioning that the flowing stream is able to assure.

In this work, a SIFA system was for the first time coupled to a potentiometric detector, more specifically a tubular ion selective electrode with plastic membrane, and the analytical capability of this association was assessed in the determination of nitrate ion in waters and plant extracts. Moreover, a new strategy for constructing plastic membrane electrodes with a tubular configuration and without internal reference solution is proposed.

2. Experimental

2.1. Reagents and solutions

All reagents were of analytical quality grade or equivalent. Solutions were prepared with water (specific conductivity <0.1 μS cm^{-1}) obtained from a Milli-Q (Millipore) equipment. Ions stock solutions were prepared by rigorous weighing and dissolution of appropriate salts amounts. Working solutions were subsequently obtained by accurate dilution.

Nitrate ion sensor was prepared by mixing 0.2 g of a mixture of 4,7-diphenyl-1,10-phenantroline/nickel complex in 2-nitrophenyl octyl ether [4] (Fluka) with 0.08 g of vinyl polychloride (Fluka) previously dissolved in tetrahydrofuran (Fluka).

For obtaining the non-conductive epoxy resin, Araldit M (Fluka) and Ren HY5162 (Huntsman Advanced Materials) hardener were mixed in a 100:40 mass ratio. The graphite based conductive resin was prepared by adding graphite (Merck) to the non-conductive epoxy resin in a 1.4:1 mass ratio.

2.2. Equipment

The plastic membrane tubular detectors were constructed by using Gilson connectors (ref. F1410153) as the physical supports that accommodate the graphite based conductive resin. The detector was coupled to the flow system by means of Gilson end-fittings (ref. 4911031) and rubber rings of 1.6 and 2.0 mm of internal and external diameter, respectively.

The flow system comprised a B-2031 automatic burette (Crison Instruments) equipped with a 5 mL syringe (Hamilton), a 3-way solenoid valve (ref. 161T031, NResearch) and a detection system combining a tubular electrode selective to nitrate, a double junction reference electrode AgCl/Ag (ref. 90-02, ThermoOrion) filled with a ref 90-00-02 internal solution (ThermoOrion) and a ref. 90-00-03 external solution (ThermoOrion) and a potentiometer (ref. 2002, Crison Instruments). The reference electrode was coupled to the flow system by employing a homemade [5] acrylic support. All tubing, including the reaction coil, was made of PTFE with 0.8 mm i.d. (Omnifit). A Kipp & Zonnen BD 111 recorder was used to trace the analytical signals, when required.

Control of the analytical system and data acquisition and processing was achieved by means of a microcomputer equipped with a PCL711B interface card (Advantech). The control software was developed in QuickBasic 4.5 and permitted to operate the automatic burette (by RS232C protocol) as well as the solenoid valve. The latter was actuated by TTL signals by resorting to a CoolDrive (NResearch) power drive.

The determination of nitrate in water samples by the reference method was carried out by resorting to a PerkinElmer 50 spectrophotometer and the determination of the same ion in plant extracts was accomplished by using a model 761 Compact IC ion chromatographer (Metrohm) equipped with a Metrosep Anion Dual ref. 6.1006.020 column (Metrohm) and a conductimetric detector.

2.3. Construction of the tubular electrode

The utilisation of a common tubing connector as the assembling support piece for the plastic membrane nitrate ion selective electrode has main advantages, namely low cost, commercial availability and ease of inclusion in a flow manifold. The tubular electrode was constructed in a sequence of steps that included (Fig. 2): (i) transversal perforation of the connector for insertion of a coaxial cable; (ii) filling of the central interior zone of the connector with graphite based conductive epoxy resin; (iii) connection of the coaxial cable to the resin through the transversal hole; (iv) hardening of the epoxy resin; (v) electric insulating of both exposed

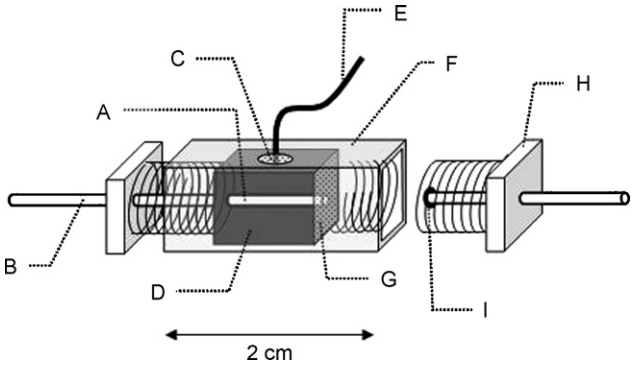


Fig. 2. Scheme of the tubular electrode selective to nitrate ion. A—nitrate ion sensor deposited inside a 1.0 mm internal diameter channel; B—flanged PTFE tubing; C and D—graphite based conductive resin; E—coaxial electric cable; F—connector; G—non-conductive epoxy resin; H—end-fitting; I—rubber o-ring.

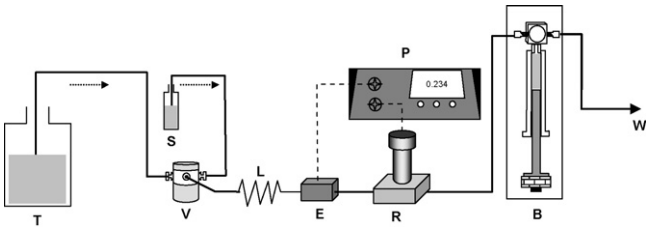


Fig. 3. Scheme of the SIFA flow manifold developed for nitrate ion determination. T—TISAB; S—sample; V—solenoid valve; L—reactor; E—nitrate ion selective electrode; R—reference electrode; P—potentiometer; B—automatic burette; W—waste.

surfaces of the conductive epoxy resin as well as the transversal hole by covering them with non-conductive resin; (vi) hardening of the non-conductive resin; (vii) perforation of a 1.0 mm-diameter longitudinal hole through the resin layers at the centre of the connector; (viii) deposition of a few drops of nitrate sensor solution on both extremities of the hole; (ix) dry out of the electrode overnight.

The sensor was coupled to the flow system by means of two end-fittings and rubber o-rings.

2.4. Sample preparation

Water samples were analysed by both the reference method and the developed procedure without any additional treatment.

Plant extracts were prepared by using the following procedure: to 0.1 g of plant leaves, previously dried and powdered, 150 mL of water were added and the suspension stirred for 30 min at room temperature. After being diluted to 200 mL in a volumetric flask the suspension was passed through a 0.45 μm filter.

2.5. Flow system

The analytical flow system, pictured in Fig. 3, was kept as simple as possible in order to emphasise the analytical potential of the single interface flow approach. With this purpose the solutions were propelled by aspiration instead of propulsion, which would require further manifold components and a more complex configuration. Indeed, the utilisation of an additional burette for sample insertion and propulsion would increase significantly the time required for the analysis, considering that each sample replacement would be a time-consuming step, and it would result as well in the consumption of larger sample volumes.

In order to guarantee a reproducible steady stream assuring a well definition of the interface contour without irregularities or fluctuations, an automatic burette equipped with a 5 mL syringe was selected as solutions propelling unit (by aspiration).

The interface was established between the sample and a total ionic strength adjustment buffer (TISAB). This way, pH buffering, ionic strength adjustment and interferences suppression can be performed on-line (along with the interface generation) carrying out the necessary sample conditioning before potentiometric detection.

In terms of operation of the developed flow system, the establishment of the interface between the sample and the total ionic strength adjustment buffer (TISAB) could have been achieved in two distinct arrangements: either by aspirating first the sample (leading solution) and then the TISAB solution (tailing solution) or by inverting the sequence of insertion, being the TISAB solution the leading one. The solution that was inserted in the reaction coil was determined by the solenoid valve position. Since the first option determined lower sample consumption and reduced the electrode exposure to sample matrix constituents it was the one selected for the assays.

The analytical cycle (Table 1) started by switching off the solenoid valve and insertion of the sample solution for cleaning the sample channel. Subsequently, the solenoid valve was switched on and the TISAB solution was aspirated into the analytical system for cleaning, electrode conditioning and baseline establishment. In a third step, the solenoid valve was again switched off and the sample solution was inserted in the analytical path, establishing a single reaction interface that produced an analytical signal when passed through the tubular electrode.

2.6. Reference procedure

For the determination of nitrate in waters the reference methodology described in "Standards Methods for the Examination of Waters and Wastewaters", 20th Ed. (1998), was followed. This is based on direct spectrophotometric measurement of sample absorption at 220 nm.

The determination of nitrate in plant extracts was carried out by ion chromatography with conductimetric detection similar to [6], by using a solution of Na_2CO_3 2.0×10^{-3} mol L^{-1} and $NaHCO_3$ 2.4×10^{-3} mol L^{-1} as mobile phase, at a flow rate of 0.5 mL min^{-1}. Sample volume was 20 μL.

3. Results and discussion

3.1. Evaluation of the nitrate ion selective electrode intrinsic characteristics

The developed tubular electrodes selective to nitrate ion were evaluated concerning their dynamic and analytical characteristics in a single-channel low dispersion flow injection system by using nitrate standard solutions prepared in Na_2SO_4 0.033 mol L^{-1} as

Table 1
Experimental conditions used for the potentiometric determination of nitrate ion by using a SIFA based analytical flow system and the corresponding analytical figures of merit.

Reactor length: 10 cm
TISAB solution composition: PbO, 0.01 mol L^{-1}; $Pb(CH_3COO)_2$, 0.02 mol L^{-1}; NH_4SO_3, 0.015 mol L^{-1}; $NaNO_3$, 1×10^{-5} mol L^{-1}

Step	Solenoid valve	Flow rate (mL min^{-1})	Inserted volume (μL)	Description
Experimental protocol				
1	Off	1.70	160	Sample replacement
2	On	1.70	1000	Reactor cleaning and electrode conditioning
3	Off	0.800	140	Sample analysis

Analytical figures of merit
Sampling rate: 40 h^{-1}
Sample volume used in the analysis: 300 μL
Detection limit: 1.6×10^{-4} mol L^{-1} (6 s); 4×10^{-5} mol L^{-1} (8 s); 2×10^{-5} mol L^{-1} (10 s)
Lower limit of linear regression: 3×10^{-4} mol L^{-1} (6 s); 7×10^{-5} mol L^{-1} (8 s); 3×10^{-5} mol L^{-1} (10 s)

ionic strength adjuster, as described in a previous work [7]. Suitable and efficient coupling was attained as no leaking was observed. Additionally, baseline potential value variation was not higher than 0.2 mV, highlighting the construction procedure adopted. The obtained results were similar, both in terms of dynamic and analytical characteristics, to those presented in the referred work for tubular electrodes operated under similar experimental conditions. Therefore, this aspect will not be further discussed.

During the flow methodology development the constructed detector was periodically tested in order to assess its intrinsic response characteristics. The detectors constructed were substituted, or the plastic membrane replaced, whenever the slope observed was inferior to 45 mV dec^{-1} or when the response time became significantly higher than the original values.

3.2. System performance

System performance assays were carried out with aqueous solutions solely, assuring that no significant differences of density between the different standards were verified. This aspect is of utmost importance considering the flow strategy here explored, since the profile generated by two adjoining solutions moving along the flow system is different for solutions with distinct density.

With the purpose of evaluating the influence of the reactor length and flow rate on the single interface profile, studies were carried out involving the utilisation of solutions with different nitrate ion concentrations. The selected concentration values, between 3.00×10^{-5} and 1.00×10^{-2} mol L^{-1}, corresponded to nitrate values usually found in water samples and plant extracts and lay within the nitrate electrode linear working range. Reactors with 10, 20 and 30 cm length and flow rates of 800, 320 and 160 μL min^{-1} were assessed in this study.

The obtained results showed that, as expected, the broadness of the interface increased for longer reaction coils and for lower flow rates. This behaviour is a direct consequence of the greater residence time of the interface within the flow system and the subsequent increase in the mutual interpenetration of the neighbouring conditioning and nitrate standard solutions.

From the results obtained in these studies it was evident that the proposed flow system enabled a simple, fast and reproducible (analytical signal variation was lower than 0.3 mV) single interface implementation. Moreover, it was also realised that the electrode showed a Nernstian behaviour, which made possible to calibrate the flow system by correlating, for a given detection time (t_D, time interval between sample insertion and measurement), analytical signal height and nitrate concentration, being clear that the found slope increased with t_D until a value equivalent to the one obtained under stationary conditions. This performance was observed for all assayed experimental conditions. As an example, Fig. 4 exhibits the calibration curves obtained for 4 distinct t_D (6, 8, 10 and 12 s) when using a 10 cm reactor and a 800 μL min^{-1} flow rate. This feature could represent a valuable asset in terms of analytical capability since it enables the gathering of multiple calibration curves at variable t_D for the same set of standard solutions, which could be used for accuracy assessment purposes.

The obtained results have also demonstrated that a wide range of t_D, covering almost the entire interface span, could be used for calibrating the single interface flow system. Effectively, this time interval is limited by both a minimum value below which the sensitivity of the detector is gradually lower and a maximum value above which the ionic strength adjustment is inappropriate or, considering a more global perspective, sample pre-treatment is insufficient. Nevertheless, the possibility of utilisation of a variety of t_D, with similar system performance, could be considered interesting in a sense that, depending on the purpose of the analysis or, for instance, the number of samples to be analysed a shorter or a longer t_D could be used, which would yield different sampling rates or sensitivity. On the other hand, the selection of a given t_D to calibrate the analytical system should also take into account the characteristics of the sample matrix. Anticipating a high analyte concentration along with a high interferences level, a short t_D close to the lower boundary of the interface zone should be selected. This way, the higher dispersion endured by the sample in the TISAB solution (present in a higher concentration ratio) allowed a more efficient sample conditioning. On the contrary, if the sample presents both low analyte and low interferences concentration levels, then a higher t_D within the upper interface zone should be used. In these conditions, despite the lower TISAB/sample concentration ratio, TISAB levels are high enough to assure a proper sample conditioning. Moreover, since in this zone of the interface sample dispersion is minimal it assures an increment in the sensitivity thus a lower detection limit.

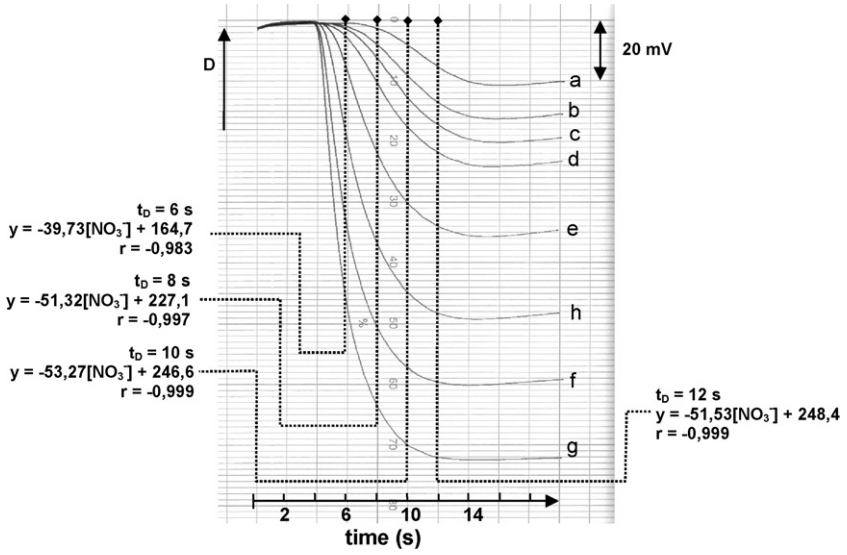


Fig. 4. Analytical signal profiles obtained at increasing detection times for nitrate ion standard solutions with distinct concentrations (mol L^{-1}): a—3.00×10^{-5}; b—5.00×10^{-5}; c—7.00×10^{-5}; d—1.00×10^{-4}; e—3.00×10^{-4}; f—1.00×10^{-3}; g—3.00×10^{-3}; h—1.00×10^{-2}. Experimental conditions: reactor length = 10 cm; flow rate = 800 μL min^{-1}. Calibration curves, representing $E = m \times \log[NO_3^-] + b$, correspond to each of the detection times assayed. D—dispersion coefficient.

Table 2
Concentration of interferences in the solutions assayed (mol L^{-1}).

Interferences	Solution I	Solution II	Solution III
Cl^-	1.00×10^{-4}	1.00×10^{-3}	1.00×10^{-2}
HCO_3^-	5.00×10^{-4}	1.00×10^{-3}	5.00×10^{-3}
NO_2^-	1.00×10^{-5}	5.00×10^{-5}	1.00×10^{-4}

Furthermore, the flow system configuration and the selected experimental procedure guaranteed no carry over effects during the analysis of samples or standards. The volumes aspirated provided an efficient cleaning of sample tubing, reactor as well as good electrode conditioning.

3.3. Interferences suppression

Despite the intrinsic selectivity, the nitrate ion selective electrode with the sensor based in the 4,7-diphenyl-1,10-phenanthroline/nickel complex exhibit a lack of selectivity mainly in the presence of chloride, nitrite and hydrogencarbonate [4,8,9]. Aiming at minimising the interfering effect of these species, Mitrakas and Alexiades [10] proposed the TISAB solution composed of PbO, 0.01 mol L^{-1}, $Pb(CH_3COO)_2$, 0.02 mol L^{-1}, KCH_3COO, 0.01 mol L^{-1} and NH_2SO_3H, 0.01 mol L^{-1} (pH 6.8). Lead(II) oxide and lead(II) acetate enabled the flocculation of organic compounds as well as the precipitation and/or complexation of chloride and the removal of hydrogencarbonate. Sulfamic acid is used to eliminate nitrite while potassium acetate facilitates pH buffering and ionic strength adjustment. When using a direct potentiometric batch procedure, well defined volumes of TISAB of known concentration are used. Moreover, the final solution is homogeneous. On the contrary, in a SIFA system no definite solutions volumes are used and no physical equilibrium is ever reached. Therefore, a study of TISAB solution efficiency in removing interferences in the developed flow approach was carried out by preparing various nitrate solutions with concentrations of 1.00×10^{-4}, 1.00×10^{-3} and 1.00×10^{-2} mol L^{-1}, respectively, with the referred interfering species present at different concentrations, as presented in Table 2. It should be noted that the highest concentration values tested for hydrogencarbonate concentration exceeded the values found in Portuguese potable waters, while for chloride (7.0×10^{-3} mol L^{-1}) and nitrite (1.1×10^{-5} mol L^{-1}) exceeded the allowed maxima defined by the European Union legislation [11].

The results obtained in the analysis of the prepared solutions by using the developed procedure (with a 10-cm reactor and at a flow rate of 800 μL min^{-1}, in order to maximize sampling rate) showed that at high hydrogencarbonate concentrations a $Pb(HCO_3)_2$ precipitate was formed, which affected repeatability due mainly to accumulation of the solid all over the flow system. To overcome this situation the TISAB solution was tested for pH values of 4.5, 4.0 and 3.5 obtained upon addition of further sulfamic acid. It was verified that the formation of precipitate actually diminished although for pH 4.0 and 3.5 an unwanted pronounced reduction of the analytical signal was also observed.

Table 3
Nitrate ion concentration values found in water samples by using the reference methodology and the developed flow approach (t_D = 10 s).

Water sample	$[NO_3^-]_{ref.\ meth.}$[a] (±SD) (mol L^{-1})	$[NO_3^-]_{flow}$[a] (±SD) (mol L^{-1})	RD (%)
1	$2.8\ (\pm0.1) \times 10^{-5}$	$2.9\ (\pm0.1) \times 10^{-5}$	3.4
2	$3.7\ (\pm0.1) \times 10^{-5}$	$3.5\ (\pm0.2) \times 10^{-5}$	−5.4
3	$3.8\ (\pm0.1) \times 10^{-5}$	$3.7\ (\pm0.1) \times 10^{-5}$	−2.6
4	$8.3\ (\pm0.1) \times 10^{-5}$	$7.8\ (\pm0.1) \times 10^{-5}$	−6.0
5	$1.1\ (\pm0.1) \times 10^{-5}$	<d.l.[b]	–

[a] Triplicate average values.
[b] Lower than the detection limit.

Since the residence time determines the sample/TISAB mutual interdispersion the influence of flow rate on TISAB solution ability to suppress the interfering effects, was also object of study. Flow rates of 800, 320 and 160 μL min^{-1} were evaluated. It was anticipated that a lower flow rate would provide an improved mutual dispersion along with an enhanced reaction development that would contribute to a more efficient suppression of interferences. For the distinct levels of interferences assayed it was confirmed that the interfering effect increased as the interference/nitrate molar ratio increased. In fact, for nitrate concentrations of 1.00×10^{-3} mol L^{-1} and 1.00×10^{-2} mol L^{-1}, the profile of the potentiometric signals obtained in the presence or absence of interference was identical up to a dispersion coefficient of about 2.2. For these concentration levels this behaviour was similar for the three assayed flow rates. In opposition, for nitrate 1.00×10^{-4} mol L^{-1}, the interferences produced a more pronounced deviation than the one observed for higher nitrate concentrations. Moreover, the deviation was more prominent for the lower flow rate. Fig. 5 shows that the solutions prepared with interferences concentrations signalled as I and II in Table 1 exhibit signal profiles that were identical to the signal profile obtained in the absence of interferences, up to a dispersion coefficient of about 2. For the lower assessed flow rate that was not verified. These results demonstrated the faster response of the electrode for the primary ion with respect to the interfering species, which enabled the attenuation of the potentiometric signal deviation induced by the latter and are in agreement with the results described by Trojanowickz and co-workers [12] that applied the same strategy to improve the selectivity of electrodes sensitive to chloride ion.

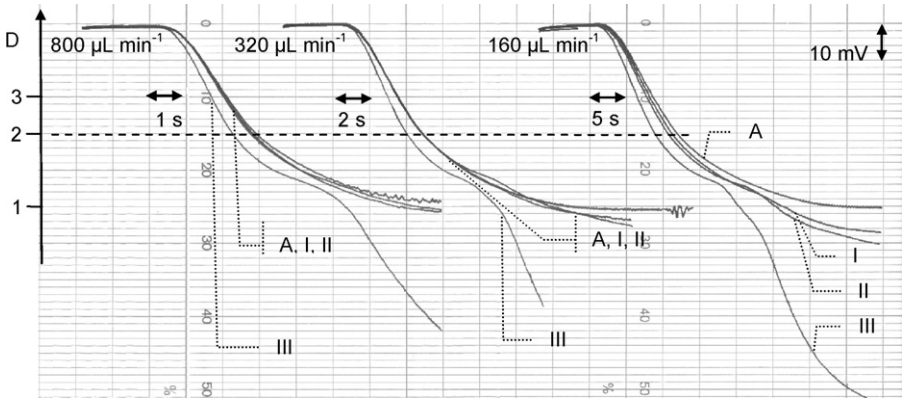


Fig. 5. Study of the influence of flow rate in the interface signal profile carried out by using a nitrate ion solution 1.00×10^{-4} mol L^{-1} in the absence (A) and in the presence of distinct interfering species concentrations referred as I, II and III (see Table 1 for composition). D—dispersion coefficient.

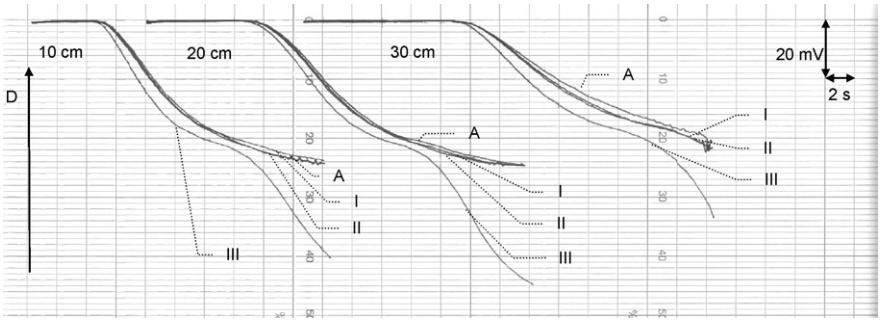


Fig. 6. Study of the influence of reactor length (10, 20 and 30 cm) in the interface signal profile carried out by using a nitrate ion solution 1.00×10^{-4} mol L^{-1} in the absence (A) and in the presence of distinct interfering species concentrations referred as I, II and III (see Table 1 for composition). D—dispersion coefficient.

It was also assessed the possibility of reduction of the analytical signal deviation by increasing reactor length, which would increase the reaction time between the sample and TISAB solution and therefore reduce the interfering effect. By using 20 and 30 cm reaction coils it was observed that for the same dispersion coefficient the deviation in the signal profile was more pronounced for longer reactors (Fig. 6). This behaviour can be justified by the fact that long coils originated broader interfaces and thus the residence time required to reach a given dispersion coefficient was raised, which concomitantly increases electrode exposure to interferences. Accordingly, a 10 cm reactor was selected for the analysis, which also assured higher sampling rates.

The results obtained in the interferences suppression study put in evidence the importance of the flow system operational interval calibration, previously discussed. The selection of a given t_D should take into account the interferences level usually found in the samples in order to enhance accuracy. Table 1 presents the experimental conditions selected for the determination of nitrate in water samples as well as the respective analytical figures of merit considering distinct sampling times.

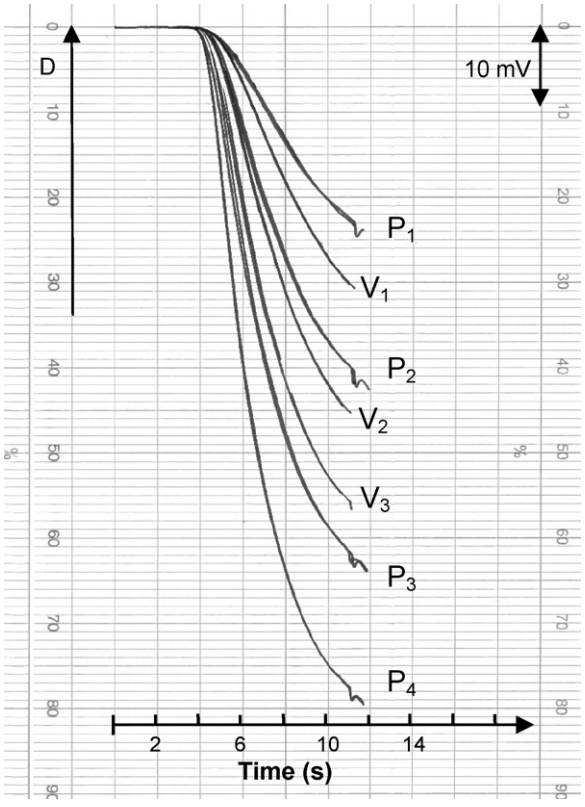


Fig. 7. Analytical signal profiles obtained in the determination of nitrate ion concentration in vegetable extracts. P_1, P_2, P_3 and P_4—nitrate standard solutions of 1.00×10^{-4}, 2.00×10^{-4}, 5.00×10^{-4} and 1.00×10^{-3} mol L^{-1}, respectively; V_1—sprout extract; V_2—parsley extract; V_3—lettuce extract. Experimental conditions as described in Table 1 and Fig. 3.

3.4. Sample analysis

Bearing in mind the low concentration of ions usually found in water samples the analyses were carried out by using a t_D of 10 s, which permitted to measure low nitrate levels, required by the regulations for water quality, without impairing sample conditioning. The obtained results are displayed in Table 3. No significant statistical differences were found for the results obtained by both the developed and the reference methodologies as confirmed by a paired Student's t-test ($t_{found} = 1.21 < t_{tabulated} = 3.18$; $n = 4$; 95% confidence level). These results demonstrate the efficient sample on-line treatment regarding ionic strength adjustment, pH buffering and interferences suppression. Precision of the SIFA system was also adequate as corroborated by r.s.d. < 3%.

Sampling rate was about 40 h^{-1}, appreciably higher than the one afforded by the reference methodology (20 h^{-1}).

Due to the greater matrix complexity, for the determination of nitrate in plant extracts t_D values of 7, 8 and 10 s were assayed, in order to find out the most appropriate (Fig. 7). The obtained results showed deviations that were more pronounced for higher t_D. These results demonstrated that for a convenient sample pretreatment a higher dispersion of the sample in the TISAB solution would have to be accomplished. Thus, a 7 s t_D was selected for the analysis. Under these circumstances relative deviations lower than 6% were obtained for all samples analysed (Table 4) revealing that an effective sample on-line treatment occurs within the time period selected. The accuracy of the developed procedure was confirmed by a paired Student's t-test ($t_{found} = 2.15 < t_{tabulated} = 2.57$; $n = 6$; 95% confidence level). r.s.d. was lower than 5%.

The nitrate levels found in this type of samples were comparable to those previously published [10,13,14]. The developed flow methodology revealed noteworthy advantages regarding the chromatographic method supported on higher sampling rate (40 h^{-1}

Table 4
Concentration values (g kg^{-1} of dry matter) obtained in the determination of nitrate ion in plant extracts by both ionic chromatography (I.C.) and the developed flow approach, at a detection time of 7 s.

Sample	I.C.[a] (g kg^{-1}) (±SD)	Flow approach[a] (g kg^{-1}) (±SD)	RD (%)
Lettuce	49.1 (±0.1)	48.2 (±1.9)	−1.8
Parsley	32.1 (±0.1)	30.5 (±0.2)	−5.0
Turnip	19.8 (±0.1)	20.7 (±0.3)	4.5
Sprout	15.5 (±0.2)	15.9 (±0.1)	2.6
Cabbage	32.6 (±0.2)	31.4 (±1.0)	−3.7
Spinach	16.2 (±0.2)	17.0 (±0.1)	4.9

[a] Triplicate average values.

versus 4 h^{-1}) and lower cost of implementation, maintenance and analysis.

4. Conclusions

SIFA approach enables the implementation of analytical flow systems with simplified optimisation and operation. These advantageous features arise from the fact that neither a specific sample insertion device nor a compelling sample volume are required for a reliable system performance. In the developed procedure solutions management was achieved by means of just a single propelling unit and a single solenoid valve. This characteristic is advantageous both in terms of cost-effectiveness, ease of miniaturisation and operational errors minimisation since the number of manifold components is reduced and no rigorous reproducible volumes have to be measured. SIFA techniques are easily coupled to potentiometric detectors with an additional advantage that is the possibility of selection of any point of the analytical signal profile, corresponding to a given residence time or to particular dispersion conditions, to carry out the measurements or to assure an adequate sample pre-conditioning.

The developed procedure was applied to the determination of nitrate in waters and plant extracts guaranteeing that all steps of sample pre-treatment, namely pH and ionic strength adjustment and interferences suppression, were adequately achieved at the single interface.

The proposed process for the construction of tubular electrodes selective to nitrate is simple, cost-effective, does not require expensive equipment and enabled the easy coupling of the electrodes to flow-based analytical systems. Despite this simplicity, the developed electrodes exhibit an analytical performance similar to those obtained by more intricate or expensive processes. Moreover, being a generic construction method it can be easily applied to the preparation of plastic membrane electrodes selective to other species simply by selecting the appropriate sensor.

In the developed application, the constructed electrode could be used for more than 2 months without loosing its response characteristics.

Acknowledgement

The authors are grateful to Fundação para a Ciência e Tecnologia (FCT) for the financial support under the project PTDC/QUI-QUI/105514/2008.

References

[1] M.F.T. Ribeiro, J.L.M. Santos, J.L.F.C. Lima, A.C.B. Dias, E.A.G. Zagatto, Talanta 68 (2005) 351.
[2] J. Ruzicka, E.H. Hansen, Flow Injection Analysis, 2nd ed., John Wiley & Sons, New York, 1988.
[3] I.M.P.L.V.O. Ferreira, J.L.F.C. Lima, J. Flow Inject. Anal. 10 (1993) 17.
[4] J. Alonso-Chamarro, J. Bartroli, S. Jun, J.L.F.C. Lima, M.C.B.S.M. Montenegro, Analyst 118 (1993) 1527.
[5] S. Alegret, J. Alonso, J. Bartroli, J.L.F.C. Lima, A.A.S.C. Machado, J.M. Paulis, Quim. Anal. 6 (1987) 278.
[6] E.G. Bradfield, D.T. Cooke, Analyst 110 (1985) 1409.
[7] I.M.P.L.V.O. Ferreira, J.L.F.C. Lima, L.S.M. Rocha, Fresenius J. Anal. Chem. 347 (1993) 314.
[8] S. Alegret, J. Alonso, J. Bartroli, J.L.F.C. Lima, A.A.S.C. Machado, J.M. Paulis, Anal. Lett. 18 (1985) 2291.
[9] J.L. Paul, R.M. Carlson, J. Agric. Food Chem. 16 (1968) 766.
[10] M.G. Mitrakas, C.A. Alexiades, Mikrochim. Acta 19 (1990) 7.
[11] Council of European Union, Council Directive 98/83/EC, Quality of water intended for human consumption, Off. J. Eur. Commun. L330 (1998) 32.
[12] T.K. Krawczyk, M. Trojanowickz, N. El-Murr, Lab. Rob. Autom. 12 (2000) 205.
[13] P.K.T. Lin, A.N. Araujo, M.C.B.S.M. Montenegro, R. Pérez-Olmos, J. Agric. Food Chem. 53 (2005) 211.
[14] J.L.F.C. Lima, A.O.S.S. Rangel, M.R.S. Souto, J. Agric. Food Chem. 43 (1995) 704.

Talanta 80 (2010) 1333–1340

Contents lists available at ScienceDirect

Talanta

journal homepage: www.elsevier.com/locate/talanta

Interfacing on-line solid phase extraction with monolithic column multisyringe chromatography and chemiluminescence detection: An effective tool for fast, sensitive and selective determination of thiazide diuretics

Fernando Maya, José Manuel Estela, Víctor Cerdà*

Department of Chemistry, Faculty of Sciences, University of the Balearic Islands, Carretera de Valldemossa km 7.5, E-07122 Palma de Mallorca, Illes Balears, Spain

ARTICLE INFO

Article history:
Received 3 June 2009
Received in revised form 7 September 2009
Accepted 18 September 2009
Available online 24 September 2009

Keywords:
Solid phase extraction
Monolithic column
Multisyringe chromatography
Chemiluminescence
Thiazide diuretics

ABSTRACT

A new, multisyringe flow injection set-up has been developed for the completely automated determination of trace thiazide compounds with diuretic action in different types of samples. The proposed instrumental set-up exploits for the first time, a low pressure on-line solid phase extraction–liquid chromatography–chemiluminescence detection method. This novel combination of sample treatments in flow systems expands the current applicability of low pressure liquid chromatography due to the isolation/preconcentration of the target compounds, besides high selectivity and sensitivity.

For the determination of three thiazide compounds named hydroflumethiazide, furosemide and bendroflumethiazide, the proposed set-up provided with the preconcentration of only 1 mL of sample, limits of detection of 3, 60 and 40 $\mu g\,L^{-1}$, respectively. Furthermore wide linear dynamic ranges of 6–4000, 140–20,000 and 90–40,000 $\mu g\,L^{-1}$, respectively, were obtained. Besides of this, a high injection throughput of $12\,h^{-1}$ was also achieved. As in sports, thiazide diuretics are prohibited substances, the proposed method has been applied to their determination in urine samples. Furthermore the potential of the proposed method as a fast-screening approach for emerging contaminants in waters has been also tested by applying it to well water and leachates from a solid waste landfill.

© 2009 Elsevier B.V. All rights reserved.

1. Introduction

Flow injection/sequential injection techniques (FI/SI) [1] are well established tools for the automation of analytical methodologies, but their initial capability for multi-analyte determinations, is basically limited to (i) simple two analyte determinations based on speciation [2], (ii) the chemometric deconvolution of overlapped spectras [3] and (iii) determinations based on the sum parameters or total indices [4,5].

Initially, the separation and quantification of several organic compounds with similar molecular structures in a FI/SI manifold was not a feasible task. Nonetheless, the development of hybrid porous silica monolithic columns (MC) [6] for liquid chromatography (LC), provided high performance LC separations at relatively lower back-pressures, making feasible its accomplishment in Sequential Injection Analysis (SIA) systems [7,8]. This technique was defined as Sequential Injection Chromatography (SIC) [9,10], allowing faster, cheaper and environmentally friendlier [11] LC separations.

Among the different FI techniques, Multisyringe Flow Injection Analysis (MSFIA) [12–15] also revealed its potential for the accomplishment of LC schemes [16], this variant was named Multisyringe Chromatography technique (MSC) [17]. Due to its inherent characteristics the MSC technique owns high capabilities in terms of versatility, simplifying the implementation of in-line pre- and post-column sample treatments commonly used in LC separations. But at the moment the major part of the current applications of this technique have been focused to the direct analysis with UV spectrophotometric detection of pharmaceuticals (in pharmaceutical formulations) [18–20]. So the high versatility of SIC and overcoat MSC techniques for the implementation of automated sample treatments has been scarcely exploited.

On the one hand, the few studies accomplished by the moment about this topic, are based on: (i) the determination of amino acids after automated derivatization with o-phthalaldehyde by using SIC technique [21], (ii) the automated sample filtration and dilution for the accomplishment of pharmacological studies about acyclovir also exploiting SIC [22], (iii) the development of an hybrid FIA-HPLC system with chemiluminescence (CL) detection for the generation of solvent gradients [23], or the (iv) implementation of in-line solid phase extraction (SPE) on the MSC technique for the determination of hydrochlorothiazide and losartan potassium in different types of water samples containing high loads of them [24].

* Corresponding author. Tel.: +34 971173261; fax: +34 971173426.
E-mail address: victor.cerda@uib.es (V. Cerdà).

0039-9140/$ – see front matter © 2009 Elsevier B.V. All rights reserved.
doi:10.1016/j.talanta.2009.09.033

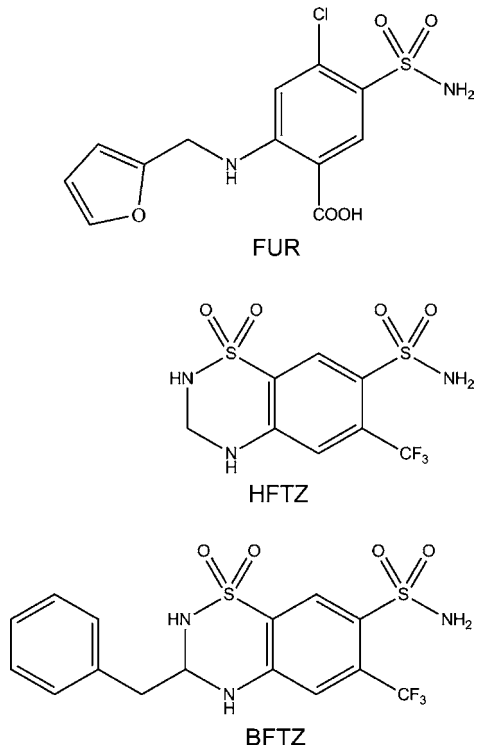


Fig. 1. Molecular structures of: furosemide (FUR, $pK_{a_1} = 3.9$), hydroflumethiazide (HFTZ, $pK_{a_1} = 8.9$), and bendroflumethiazide (BFTZ, $pK_{a_1} = 8.5$).

On the other hand, the relatively low selectivity and sensitivity achieved by this type of techniques remains a drawback. It is widely known that some very advantageous sample treatments for improved selectivity and sensitivity are SPE and CL detection. The development of a SPE–LC–CL system would be a complicated task, but this could be simplified, exploiting the high versatility of the MSC technique.

The development of a fast SPE–LC–CL system could be a powerful tool for the determination, as for example, of thiazide compounds such as hydroflumethiazide (HFTZ), furosemide (FUR) and bendroflumethiazide (BFTZ) (Fig. 1), which present a diuretic action in humans. These compounds present CL emission by reaction with Tris(2,2′-bipyridylruthenium(III)) ($[Ru(bipy)_3]^{3+}$) [25,26]. Diuretics are a group of substances with pharmacological action over hypertension and heart or renal failure [27], but also are misused by athletes for fast weight loss (before competition in sports divided by weight categories) and also for dilution of other doping agents in the urine (prior to anti-doping controls). Diuretics are on the list of forbidden substances by the World Anti-Doping Agency (WADA) [28]. By this reason, fast and quick methods for the determination of diuretics in human urine samples are essential. The most recently developed analytical methodologies for the determination of diuretics in urine are based on complex methodologies and instrumentation, such as: (i) capillary electrophoresis–electrospray ionization–mass spectrometry [29], (ii) gas chromatography–mass spectrometry (after derivatization) [30], (iii) capillary electrophoresis–amperometric detection [31] or (iv) hollow fiber-based liquid–liquid–liquid microextraction coupled to high performance liquid chromatography with UV detection [32]. Beside this, several pharmaceuticals used commonly as diuretics are recognized as emerging contaminants in waste wasters [33]. In fact, in several cities from Italy, some diuretics have been detected in wastewaters by means of SPE combined with HPLC–MS/MS [34]. They have been found even at low $\mu g\ L^{-1}$ concentrations.

This work is aimed to solve an important drawback of low pressure chromatographic techniques, this is their limited selectivity and sensitivity. By this reason, the first on-line SPE–MSC–CL system has been developed and characterized for the determination of diuretics in potentially polluted well water, wastewater and human urine samples.

2. Experimental

2.1. Reagents and sorbents

Hydroflumethiazide (HFTZ), furosemide (FUR) and bendroflumethiazide (BFTZ) were purchased from Sigma–Aldrich (Germany). Stock solutions of 1000 mg L^{-1} HFTZ, BFTZ and FUR were prepared in methanol (Scharlau, Spain) and were stored at 4 °C in dark glass flasks. Standards were obtained from proper dilution of stock solutions and acidified to pH = 3 with H_2SO_4.

Other chemicals were of analytical-grade quality and they were used without purification. Millipore-quality water was used to prepare solutions. Acidified water to pH = 3 by using H_2SO_4 (Scharlau) was used as carrier for SPE. The $[Ru(bipy)_3]^{2+}$ reagent 10 mmol L^{-1} stock solution was prepared by dissolving 0.374 g Tris(2,2′-bipyridyl)dichlororuthenium(II) hexahydrate 99.95% metals basis (Sigma–Aldrich) in 0.05 L water. The oxidant 20 mmol L^{-1} stock solution was prepared by dissolving 0.664 g of ammonium cerium(IV) sulfate dihydrate 95% (Sigma–Aldrich) in 0.05 L of diluted H_2SO_4.

Acetonitrile (Scharlau) was used as mobile phase organic modifier. Potassium dihydrogen phosphate (Scharlau) 10 mmol L^{-1} is used as mobile phase buffer. Mobile phase was degassed for 15 min in an ultrasonic bath and filtered through a 0.45-μm Nylon membrane.

The solid reversed-phase materials tested for SPE were C18 (octadecyl), SDB-XC (poly(styrenedivinylbenzene)) and SDB-RPS (poly(styrenedivinylbenzene) modified with sulphonic groups) sorbent disks (Empore 3M, St. Paul, MN).

2.2. Instrumentation and software

Fig. 2 depicts the proposed flow system. A multisyringe automatic burette (MS) from Crison (Alella, Barcelona, Spain) was used to drive the liquids to the flow network. The burette was equipped with four syringes (S1–S4), which were all mounted on a common metallic bar and every one of them were provided with a solenoid valve (V1–V4); as a result, the four syringes were operated simultaneously. Depending on the position of the solenoid valves, the fluids contained in syringes were loaded (PK, pickup) or dispensed (DP, dispense) to the flow network (on) or the reservoirs (off). Syringe S1 (5 mL) acted as a flow carrier and was connected to an additional three-way solenoid valve (V5, MTV-3-N1/4UKG, 2 bar maximum pressure, Takasago, Japan) allowing the sample introduction into the flow network. A second syringe of 5 mL (S2) is used for the handling of the mobile phase for the elution, separation and detection of the previously isolated target compounds. S3 and S4 are both of 1 mL, and are used for the post-column injection of the two reagents required for the CL emission. V1, V3 and V4 do not suffer any significantly high pressure, so N-Research (West Caldwell, NJ) solenoid valves (maximum pressure 2 bar) were used. V2 suffers higher pressures than 2 bar, by this reason a two way connector made of polyoxymethylene was used to connect S2 with V2, which is situated outside the MS module. V2 is a Takasago MTV-3-1/4UKGH (Takasago), which allows a maximum pressure of 6 bar.

All the tubing of the system was made of polytetrafluoroethylene (PTFE) 0.8 mm i.d. except the holding coil (HC), which is a

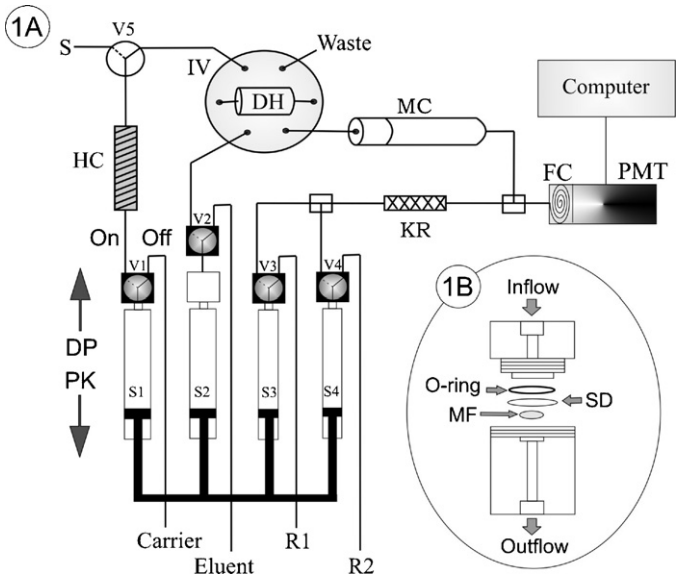


Fig. 2. Schematic depiction of the proposed multisyringe flow set-up for the determination of thiazide compounds. (A) General set-up: S, sample; HC, holding coil; V1–V5, three-way solenoid valves; DP, dispense; PK, pickup; off, normally open position of the solenoid valves (syringes connected with the reservoirs); On, normally closed position of the solenoid valves (syringes connected to the flow network); S1–S4, syringes; R1, Tris(2,2′-bipyridyl)dichlororuthenium(II) solution; R2, cerium(IV) solution; IV, injection valve; DH, disk holder for SPE; MC, monolithic column; KR, knotted reactor; FC, spiral-shaped flow cell; PMT, photomultiplier. (B) Amplified view of the DH: SD, sorbent disk; MF; microporous silica frit.

4 m long × 1.5 mm i.d. PTFE tube (7 mL volume). The two three-way confluence points were made also from PTFE.

A six-port injection valve (IV) (Crison) is used as interface between the sample loading – SPE – waste and the elution–LC–CL flow networks. In the injection loop of the IV is placed a miniaturized SPE device (Sciware, Palma de Mallorca, Spain) (Fig. 2), which is named disk holder (DH). The DH was a polyoxymethylene cylindrical block (2 cm long × 0.8 mm i.d.) with a central cavity of 1 cm diameter, in which an extraction disk of 0.9 cm diameter was accommodated in order to pass through it the different fluids involved in the SPE.

Extracted compounds are separated at room temperature by means of LC on a reversed-phase monolithic porous silica MC functionalized with octadecyl (C18) groups (25 mm length × 4.6 mm i.d.; Phenomenex) coupled with a guard column of the same material (5 mm length × 4.6 mm i.d.). The column was conditioned and cleaned according to the specifications of the manufacturer. A knotted reactor (KR; 60 cm length × 0.8 mm i.d.) is used for the generation of the $[Ru(bipy)_3]^{3+}$ from $[Ru(bipy)_3]^{2+}$ and Ce^{4+}.

The flow cell (FC; Sciware) was made from a PEEK plate to keep a PTFE body airtight. To this end, a spiral-shaped channel (4 cm long, 0.14 cm wide, 0.09 cm deep, 50 μl inner volume, 0.8 cm^2 effective light emission surface area) was carved into it; the spiral diameter was 0.9 cm. The FC was placed in front of a model H5784 photomultiplier tube (PMT, Hamamatsu, Japan) with a photosensitive wavelength range 04 (195–850 nm) and a photosensitive area of 0.5 cm^2. No wavelength discrimination was done in the detector. The FC and the PMT were both accommodated in a black plastic box protecting the detection system from external light.

A signal amplifier module [35] (Sciware) was used to supply the PMT with a feedback voltage of 0.3–0.8 V and obtain a signal gain (G) linear over the range 1–1000. The best results were obtained using a voltage of 0.80 V (G = 1000). The resultant scale for CL measurements is from 0 to 10000 counts. Instrumental control and data acquisition were accomplished by using the AutoAnalysis 5.0 (Sciware), which is based on dynamic link libraries (DLLs) [36] appropriate DLLs were used to operate the MS, the IV and the CL detector. MS DLL contemplates the use of the additional V5.

2.3. Analytical procedure

Table 1 summarizes the analytical procedure developed for the determination of HFTZ, FUR and BFTZ with the proposed SPE–MSC–CL system. The entire procedure complains 12 steps. On the steps 1–5 the SPE procedure is carried out, adjusting the volumes or repeating the steps, the volume of preconcentration can be easily modified. Once the sample matrix is isolated from the flow network, the elution of the previously retained species in the DH is accomplished, followed by LC with CL detection (steps 6–12).

3. Results and discussion

3.1. Chemiluminescence detection of diuretics

For the sensitive detection of the target compounds, chemiluminescence detection was chosen. The MSFIA technique is a useful tool for the micro-fluidic handling of complex matrix samples prior to CL detection [37].

The on-line chemical generation of $[Ru(bipy)_3]^{3+}$ from $[Ru(bipy)_3]^{2+}$ and Ce^{4+} was selected as a potentially appropriate detection system for the target compounds and preliminary studies were carried out by direct CL measurements (100 μL of sample were loaded into the HC and subsequently injected to the detector). The initial conditions were: 10 mmol L^{-1} $[Ru(bipy)_3]^{2+}$; 20 mmol L^{-1} Ce^{4+} in 0.25 mol L^{-1} H_2SO_4; 1 mg L^{-1} HFTZ, 10 mg L^{-1} FUR and 10 mg L^{-1} BFTZ, injection flow rate = 7 mL min^{-1}. With these experimental conditions the three target compounds exhibited repeatable CL signal (RSD's: HFTZ = 2.3%, FUR = 3.7%, BFTZ = 2.1%).

The concentration of $[Ru(bipy)_3]^{2+}$ was studied between 1 and 10 mmol L^{-1} (Fig. 3A) and a concentration of 7.5 mmol L^{-1} was selected. Once the previous concentration was adopted, the con-

Table 1
Main steps of the Autoanalysis 5.0 standard analytical SPE–MSC–CL procedure for the determination of HFTZ, FUR and BFTZ (for a sample volume of 1 mL).

Step	Inst	System protocol	Analytical description
1	MS	DP 1 mL at 15 mL min^{-1} (off/off/off/off/off)	Adjustment of syringe volumes
2	MS	PK 1 mL at 5 mL min^{-1} (on/off/off/off/on)	Sample loading
3	IV	Move to "Load" position	Connecting S1 with SPE unit and waste
4	MS	DP 1.5 mL at 2.5 mL min^{-1} (on/off/off/off/off)	SPE of the target compounds
5	MS	PK 1.5 mL at 15 mL min^{-1} (off/off/off/off/off)	Adjustment of syringe volumes
6	IV	Move to "Inject" position	Connecting S2 with SPE unit and LC–CL system
7	CL	Starts data acquisition every 0.1 s	
8	MS	DP 1.0 mL at 1.30 mL min^{-1} (off/on/off/off/off)	Elution from disk and LC separation
9	MS	DP 3.0 mL at 1.30 mL min^{-1} (off/on/on/on/off)	Continue the LC separation, and start the injection of reagents
10	MS	DP 0.7 mL at 1.30 mL min^{-1} (off/on/off/off/off)	System cleaning
11	CL	Stop data acquisition	
12	MS	PK 4.7 mL at 15 mL min^{-1} (off/off/off/off/off)	Adjustment of syringe volumes

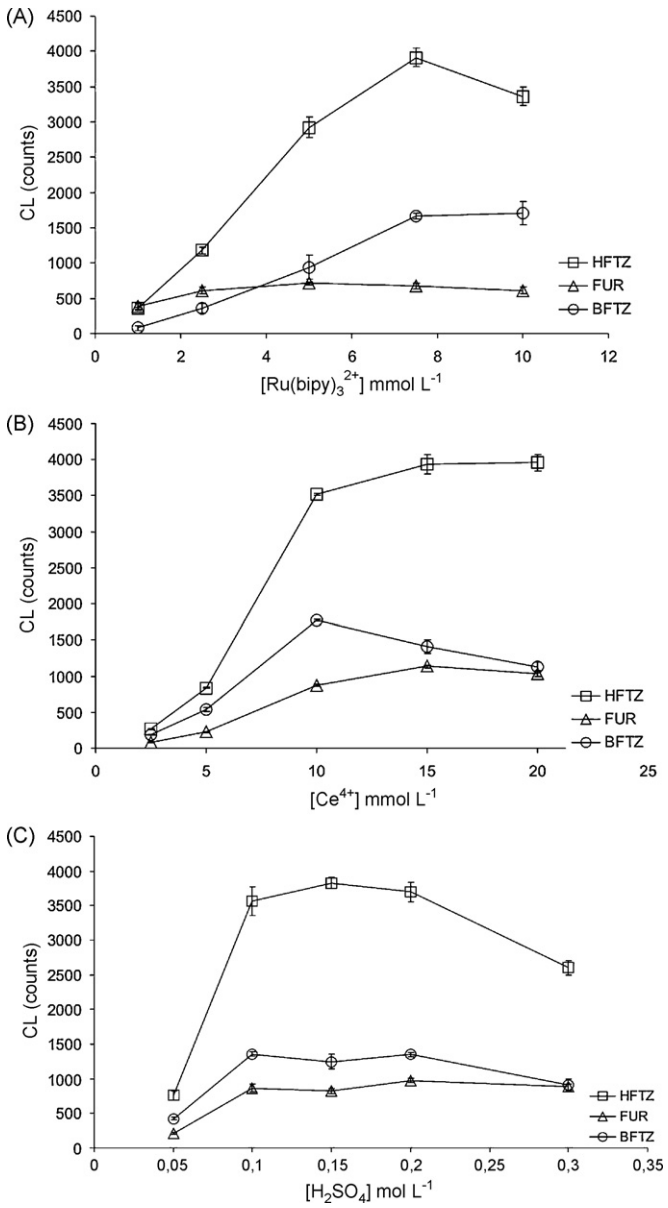


Fig. 3. Influence on the emitted CL (peak height) of (A) the concentration of Tris(2,2′-bipyridyl)dichlororuthenium(II) in S3, (B) the concentration of Ce^{4+} in S4 and (C) the concentration of H_2SO_4 in S4.

centration of Ce^{4+} was studied in the range of 2.5–20 mmol L^{-1}, as is shown in Fig. 3B a concentration of 10 mmol L^{-1} Ce^{4+} was selected for further experiments. The next experiment consists in the adjustment of the H_2SO_4 concentration of the Ce^{4+} solution, this was studied between 0.05 and 0.3 mol L^{-1} (Fig. 3C), lower H_2SO_4 concentrations induced short-term stability of Ce^{4+} solution, in a compromise between signal peak height and solution stability, a concentration of 0.2 mol L^{-1} H_2SO_4 was adopted for further experiments.

3.2. Solid phase extraction

In order to achieve the SPE of the target compounds for sample matrix clean-up and/or preconcentration, thus accomplishing it without increase significantly the back-pressure, sorbent disks were chosen instead of particulate resins. By this way, from the 6 bar maximum pressure allowed by V2, only 0.25 bar are employed for SPE procedure. Remaining a total of 5.75 free bars, that could be employed for the post-SPE liquid chromatographic separation. The three target compounds are highly polar by this reason an appropriate sorbent material could be SDB-RPS disks, but also were tested SDB-XC and C18 disks. The three types of disks were of an initial diameter of 47 mm, of which a smaller portion of 0.9 mm diameter is placed on the miniaturized SPE device, being the final effective surface extraction area of 0.6 mm diameter.

Changing the initial carrier composition by a mixture of 0.01 mol L^{-1} H_3PO_4–$H_2PO_4^-$/ACN (60:40) adjusted to pH = 3, no significant differences are observed in the obtained CL signals. So this was selected as the initial composition of eluent, and also 2 mL min^{-1} flow rates for preconcentration and elution were initially adopted. ACN was selected as organic modifier according to the specifications of the MC manufacturer. A preconcentration volume of 1 mL of sample was adopted.

The instrumental set-up for these experiments is the same as in Fig. 2, but without the MC. So, with this SPE–CL instrumental set-up, the three types of disks were tested. As can be seen in Table 2, SDB-RPS disks showed the best performance in terms of repeatability, obtaining adequate standard deviation values for the three target diuretics (RSD ≤ 3%). RSD's higher than a 5% were obtained for BFTZ using SDB-XC and for BFTZ and HFTZ using C18. In terms of sensitivity, higher signals were obtained for HFTZ and BFTZ by using SDB-RPS, but for FUR higher signals were obtained by using C18. Finally, SDB-RPS disks (90% adsorbent particles linked by 10% PTFE, 0.5 ± 0.05 mm in width, 60 Å pore diameter, 450 m^2 g^{-1} surface area and 12 μm average particle size) were chosen for further experiments.

The flow rate for the preconcentration of the target compounds was studied (Fig. 4A) in the range of 1–3 mL min^{-1}. Higher flow rates caused higher RSD's and a decrease of the life time of the sorbent disk. A flow rate of 2.5 mL min^{-1} was selected for further experiments. The percentage of organic modifier for the elution of the target compounds from the sorbent disk was studied between 20 and 50% ACN, as is seen in Fig. 4B, at least a 30% ACN is required in the mobile phase for the satisfactory elution of the three compounds.

In order to study the durability of the sorbent disk, a standard solution (mixture of 1 mg L^{-1} HFTZ, 10 mg L^{-1} FUR, 10 mg L^{-1} BFTZ) was analyzed 40 times with the same disk portion. For the first ten injections, the RSD was a 3%. For the next ten injection series, the RSD's were of 3.5% (11–20 injections), 4.5% (21–30 injections) and slightly higher than a 5% (31–40 injections). In conclusion, the same disk portion could be used satisfactorily for at least 30 injections.

3.3. Chromatographic separation

By using the complete SPE–MSC–CL set-up, the separation of the target compounds in the short 25 × 4.6 mm MC was studied follow-

Table 2
Results obtained in the selection of an appropriate sorbent material for SPE of HFTZ, FUR and BFTZ (n = 3). CL emission is expressed in hundreds of counts.

Sorbent material	HFTZ (1 mg L^{-1})		FUR (10 mg L^{-1})		BFTZ (10 mg L^{-1})	
	RSD (%)	CL emission	RSD (%)	CL emission	RSD (%)	CL emission
SDB-RPS	1.6	17	3.0	6	1.4	15
SDB-XC	0.6	10	2.6	6	8.2	5
C18	9.2	3	1.5	12	7.0	10

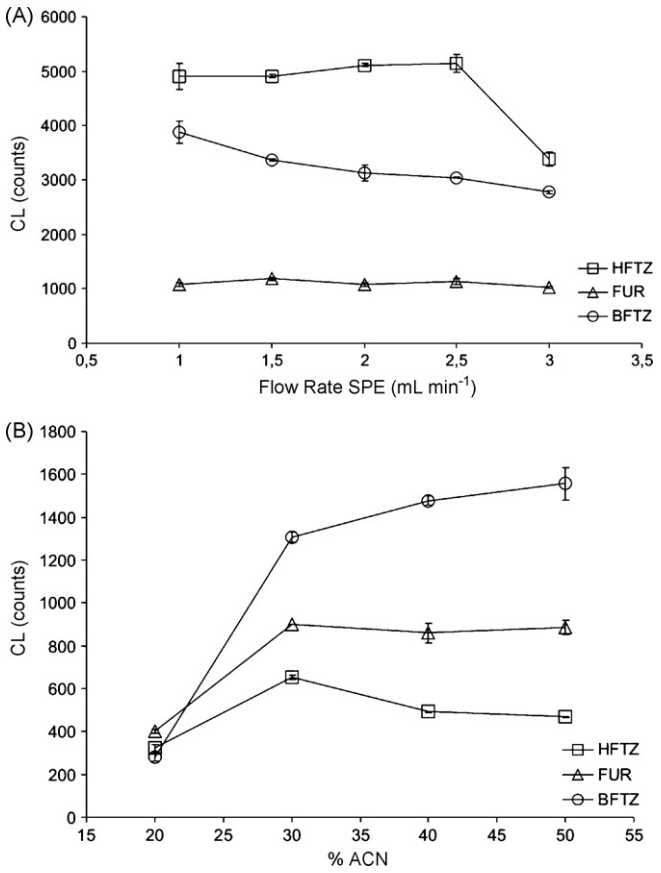


Fig. 4. Influence on the emitted CL (peak height) of (A) the flow rate for the SPE of the target compounds and (B) the percentage of organic modifier.

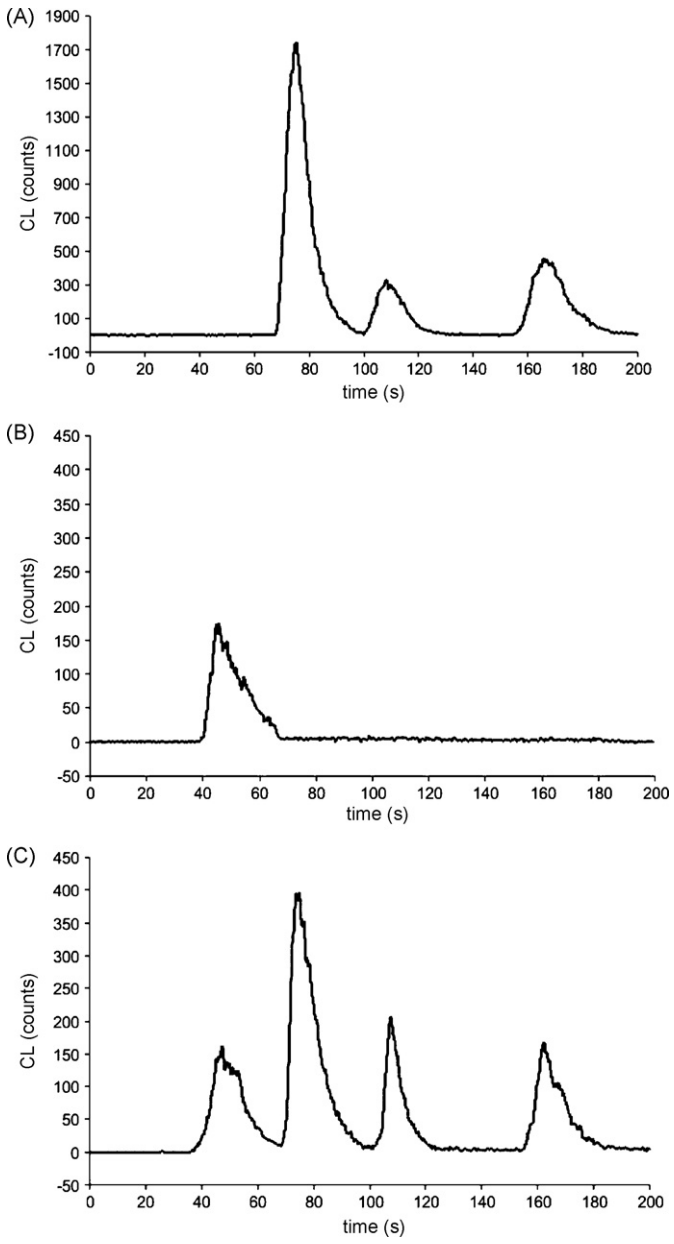


Fig. 5. Some examples of the obtained chromatograms working with the proposed SPE–MSC–CL system under the final experimental conditions. (A) Standard solution (HFTZ = 1.5 mg L^{-1}, FUR = 5 mg L^{-1}, BFTZ = 5 mg L^{-1}), (B) blank of an urine sample, (C) spiked urine sample (HFTZ = 1 mg L^{-1}, FUR = 10 mg L^{-1}, BFTZ = 5 mg L^{-1}). Standard/sample volume in (A) is 1 mL, in (B) and (C) is 3 mL. (B) and (C) have been diluted 10-fold.

ing the procedure detailed in Table 1. The maximum mobile phase flow rate allowed by V2 (maximum pressure 6 bar) was estimated measuring the column back-pressure and increasing the flow rate. The maximum allowable flow rate (for mobile phases containing between 20 and 50% ACN) was 1.5 mL min^{-1} (pressure = 5.75 bar). Finally, in order to avoid short-term damage of V2, a final flow rate for the LC separation of 1.3 mL min^{-1} was selected for further experiments.

The percentage of organic modifier (ACN) was studied in the range of 20–50% ACN. By using a 20% ACN the three peaks were separated. Increasing the content of ACN to a 30%, no peak overlapping was observed, thus improved separation conditions were achieved. With a 40% ACN, HFTZ and FUR peaks partially co-eluted obtaining these two signals overlapped, and with a 50% ACN, the three compounds co-eluted in a single peak. Finally a 35% ACN was tested, achieving a good peak separation and a reduced mobile phase and reagents consumption.

In order to improve the LC procedure, the addition of methanol to the mobile phase was studied between 1 and 10% methanol. Best results were obtained with a 10% methanol, but this induced a severe precipitation of Ce^{4+} inside the flow cell, causing overpressure problems and decreasing signal repeatability. Finally, a 3% methanol was selected. The final eluent composition is H_3PO_4–$H_2PO_4^-$/ACN/CH_3OH (62:35:3) adjusted to pH = 3. By the addition of methanol peak tailing was reduced, thus signal peak height and elution of BFTZ were slightly improved. The selected composition of the mobile phase showed good compatibility with the CL reagents, a factor to have in consideration as one of the main sources of problems in LC–CL systems. Fig. 5A shows a typical chromatogram obtained by working under the selected conditions.

Mass calibration was done injecting sample volumes between 1 – 20 mL containing an identical amount of total mass (2 μg HFTZ, 2 μg FUR, 2 μg BFTZ). No significant analyte loss (<5%) was observed when the preconcentration volume was increased from 1 to 7.5 mL. If the volume is increased up to 10 mL, a 10% analyte loss for HFTZ is observed, and FUR and BFTZ are still completely retained. Finally for a 20 mL sample volume, a 50% and a 60% of analyte breakthrough are observed for HFTZ and FUR, respectively, while no significant breakthrough is observed for BFTZ.

3.4. Analytical performance

Once the final instrumental set-up was established and the influence of the main variables examined, the performance of the

Table 3
Figures of merit of the proposed SPE–MSC–CL system. Parameters were calculated by using 1 mL of sample volume.

Analytical parameter	HFTZ	FUR	BFTZ
Linear dynamic range ($\mu g\,L^{-1}$)	6–4000	140–20,000	90–40,000
Limit of detection ($\mu g\,L^{-1}$)	3	60	40
Limit of quantification ($\mu g\,L^{-1}$)	6	140	90
Repeatability (%) ($n = 10$)	4.6	4.9	3.5
Sensitivity ($L\,\mu g^{-1}$) ($n = 6$)	1.244 ± 0.059	0.066 ± 0.002	0.093 ± 0.001
Regression coefficient ($n = 6$)	0.997 ± 0.002	0.994 ± 0.002	0.996 ± 0.003
Retention time (s)	75	108	165

proposed methodology was assessed. The analytical figures of merit of the proposed set-up are summarized in Table 3. Wide linear working ranges were achieved for the three analytes, which is typical in methods based on CL detection. The limits of detection (LOD) and quantification (LOQ) were estimated as 3 and 10 times the standard deviation of the absorbance for 10 injections of the blank. LOD and LOQ were calculated by using a sample volume of 1 mL, and they could be improved by increasing sample volume, in accordance with the mass calibration done. The repeatability of the proposed method was estimated as the relative standard deviation (RSD) for 10 consecutive injections of a standard containing 1 mg L^{-1} HFTZ, 10 mg L^{-1} FUR and 10 mg L^{-1} BFTZ. The sensitivity (slope) and regression coefficient were calculated from six day-to-day regression curves. The injection throughput (IT) obtained by using the entire SPE–MSC–CL method was 12 h^{-1}, if a sample volume of 1 mL is used (it is decreased to 7 and 5 h^{-1} for sample volumes of 5 and 10 mL, respectively). Another highlight of the proposed system is the low mobile phase consumption, with the concomitant saving of organic solvents. Only are required 1.65 mL ACN and 0.14 mL MeOH per determination. Furthermore is also presented a low consumption of CL reagents being achieved 400 determinations with only 1 g of $[Ru(bipy)_3]^{2+}$.

3.5. Interference tests

The CL evoked by $[Ru(bipy)_3]^{2+}$ can be used to determine a wide variety of organic compounds, but also, this CL reaction system cannot be applied directly to samples with a matrix of high complexity. In this work, we attempt to remove the potential interferences by means of on-line SPE–MSC prior CL detection, expanding by this way the analytical applicability of this CL reaction system. By this reason, in order to ensure this selectivity, a group of chemical compounds were tested as potential interfering compounds.

In order to do this, 100 mg L^{-1} standards of each one of the selected compounds were prepared and analyzed with the proposed configuration of the SPE–MSC–CL set-up. Different types of responses were obtained:

(1) Compounds which are removed by SPE and/or LC, or that are no CL emitters in the proposed experimental conditions. This was observed when ibuprofen, ketoprofen, trimethylamine, uric acid, glycine, phenol, ethylenediaminetetraacetic acid and p-aminocinnamic acid standards were analyzed.
(2) Compounds that exhibited CL emission with the proposed experimental conditions, but does not interfere due to their different retention times in the MC. This was observed analyzing a standard of Naproxen, this compound was extracted by SPE and quantified with good sensitivity by MSC–CL, obtaining similar results in sensitivity than for BFTZ, but with a retention time (tret = 192 s) higher than those of BFTZ.
(3) Compounds as oxalic acid, ascorbic acid or hydrazine that evoke intense CL emission with $[Ru(bipy)_3]^{2+}$ but are poorly retained by SPE and MC (approximately tret = 50 s). Experimental results confirmed that oxalic and ascorbic acids are almost totally removed by SPE, and due to the high concentration of the tested standard, only a small residual part of them arrives to the detector. Anyway, the retention times of these compounds are lower than those of HFTZ, not being interferences. Considerably higher concentration than 100 mg L^{-1} of these compounds could be a real interference. Nonetheless, hydrazine seems that is slightly more retained by SPE than oxalic and ascorbic acids. A concentration of hydrazine 20-fold higher than HFTZ causes a positive interference of a 5%, if the concentration of hydrazine is higher than 1 mg L^{-1}.
(4) Compounds which were CL emitters in the proposed experimental conditions, and have similar retention times than some of the analytes. This is the case of the thiazide diuretic hydrochlorothiazide (HCTZ), which has a retention time similar than HFTZ. The interference of 1-fold HCTZ over HFTZ is a 8%, if HCTZ concentration is at least 0.1 mg L^{-1}.

3.6. Application of the proposed SPE–MSC–CL system

The proposed methodology was assessed by analyzing HFTZ, FUR and BFTZ in spiked environmental and biological samples. The two environmental samples were a water sample from a well located in the vicinity of an urban solid waste landfill and a leachate from a solid urban waste landfill. The two biological samples were two human urine samples collected from healthy volunteers.

All samples were filtered through a 0.45 μm pore filter, spiked with a concrete amount of target compounds and adjusted to pH = 3. Furthermore, non-spiked samples were analyzed in order to test the baseline behavior and if they contain significant interferences. None of the two environmental samples exhibited significantly higher CL emission than the blank, nonetheless the two urine samples exhibited CL emission at low retention times, this drawback was avoided by means of diluting 10-fold the urine samples, avoiding possible interferences with the HFTZ signal peak. An example of a blank and a spiked urine samples are shown in Fig. 5B and C, respectively.

Table 4 shows the results obtained from the analysis of the detailed spiked samples with the proposed system. Environmental samples were spiked at the $\mu g\,L^{-1}$ level and a volume of 5 mL of sample was used. Urine samples were spiked at the mg L^{-1} level, and after dilution, a volume of 2.5 mL of urine 1 and 1 mL of urine 2 were used. In all instances, relative standard deviations between 1.8 and 4.4% for environmental and 2.7–5.5% for urine samples, were obtained. Furthermore, the absolute recoveries were between 94 and 108% in all instances.

The proposed method due to its wide linear dynamic range, can be applied satisfactorily to samples containing $\mu g\,L^{-1}$ levels of the target compounds, and also at mg L^{-1} level in high concentrated matrices, allowing sample dilution.

3.7. Comparison with other current analytical methodologies for the determination of diuretics

Due to the current relevance about the determination of diuretics in urine samples for anti-doping controls, several improved methodologies have been developed recently [29–32]. They are

Table 4
Results obtained in the determination of HFTZ, FUR and BFTZ in spiked environmental and biological samples by means of the proposed SPE–MSC–CL system. For all samples $n = 3$.

	Samples			
	Added ($\mu g\,L^{-1}$)	Found ($\mu g\,L^{-1}$)	RSD (%)	Absolute recovery (%)
Environmental				
HFTZ				
Well	2	2.13	4.3	107
Leach	5	5.06	3.4	101
FUR				
Well	20	20.6	4.4	103
Leach	50	53.4	2.9	107
BFTZ				
Well	20	21.4	3.1	107
Leach	50	49.6	1.8	99
	Samples			
	Added ($mg\,L^{-1}$)	Found ($mg\,L^{-1}$)	RSD (%)	Absolute recovery (%)
Human urine				
HFTZ				
Urine 1	1	1.03	5.5	103
Urine 2	10	10.8	4.5	108
FUR				
Urine 1	1	0.94	4.1	94
Urine 2	10	10.2	2.7	102
BFTZ				
Urine 1	1	1.06	3.9	106
Urine 2	10	9.57	4.1	96

based on highly expensive and time-consuming instrumentation, thus lower levels in terms of automation, being required in some cases time-consuming manual sample derivatization (at least 2 h) [30] or extraction (50 min) [32] treatments prior to GC–MS and HPLC-UV, respectively.

As an alternative to chromatography, recently developed capillary electrophoresis (CE) methods for diuretics have provided improved injection throughputs, as for example a highly selective and sensitive CE-ESI-MS method for the determination of 12 diuretics [29], providing almost no sample pretreatment and an IT = 3 h^{-1}. Another alternative is based on CE with amperometric detection [31], which provides an improved IT = 6 h^{-1} and a wider linear dynamic range of three order of magnitude, but with a concomitant lower selectivity than CE-ESI-MS.

On the one hand, the proposed SPE–MSC–CL system provides a higher automation degree in front of the previously commented systems, is a low cost system, both referring to the low cost of the used instrumentation and furthermore the low cost per analysis. It provides a wide linear range as with CE-amperometry, and similar sensitivity than the previous systems with only 1 mL of sample. The proposed method provides higher injection throughputs (IT = 12 h^{-1}), and is highly versatile being easily adapted to different preconcentration volumes or types of samples.

On the other hand, the multi-analyte determination by the proposed system becomes limited in comparison with high performance chromatographic or electrophoretic techniques coupled with mass spectrometric detectors. But having in account the necessity to have fast-screening systems for organic compounds (pharmaceuticals, pesticides, personal care products, etc.), the proposed system provides an standard analytical tool – which is applied in this work to the determination of some thiazide diuretics – that meets the main corollaries for fast-screening, such as: rapid and reliable response, simplification of operations, thus avoiding the extensive use of high cost and maintenance instrumentation.

If we are talking about the development of simplified methodologies for the determination of emerging organic pollutants in environmental samples, the proposed SPE–MSC–CL provides an smart, versatile and downsized efficient instrument to carry out analytical tasks in this field, but it is still work to be done in this field, in terms of selectivity, and overcoat in the obtention of improved sensitivity to the low ng L^{-1} range.

4. Conclusions

For the first time, the potential of the versatility of monolithic column-based chromatographic separations in low/medium-pressure flow systems have been fully exploited, allowing the implementation of on-line pre- and post-column sample treatments in a smart, miniaturized and expeditious fashion, being this achieved through the versatile fluidic handling allowed by the MSFIA technique. To prove this, a novel methodology for the determination of three known diuretics (HFTZ, FUR and BFTZ) has been developed. The proposed method is the first on-line completely automated method which combines SPE with low pressure LC and CL detection. This allowed the fast, selective and sensitive determination of the target compounds, thus a concomitant saving of reagents/solvents. This improved performance, allowed for the first time the application of syringe-based (SIC and MSC techniques) multicommuted LC separations to the determination of target compounds in complex samples (environmental and human urine samples) at the $\mu g\,L^{-1}$ level, instead their usual applications in simple commercial formulations of pharmaceuticals, herbicides and other types of products at the $mg\,L^{-1}$ level. This is transduced in an improved applicability of this type of techniques, being fast and low cost screening valuable tools, for vanguard strategies to carry out difficult tasks as the anti-doping controls, or the detection of emerging contaminants in waters.

Acknowledgements

This work was supported from the “Ministerio de Educación y Ciencia, Gobierno de España” through the project CTQ2007-64331. F. Maya is very grateful to the “Conselleria d’Economia, Hisenda i

Innovació, Govern de les Illes Balears", for its support through a PhD grant.

References

[1] M. Trojanowicz, Advances in Flow Analysis, Wiley–VCH, Weinheim, 2008.
[2] D.G. Themelis, F.S. Kika, A. Economou, Talanta 69 (2006) 615–620.
[3] M. Manera, M. Miró, J.M. Estela, V. Cerdà, M.A. Segundo, J.L.F.C. Lima, Anal. Chim. Acta 600 (2007) 155–163.
[4] F. Maya, J.M. Estela, V. Cerdà, Anal. Chem. 80 (2008) 5799–5805.
[5] H.M. Oliveira, M.A. Segundo, S. Reis, J.L.F.C. Lima, Microchim. Acta 150 (2005) 187–196.
[6] N. Tanaka, H. Kobayashi, N. Ishizuka, H. Minakuchi, K. Nakanishi, K. Hosoya, T. Ikegami, J. Chromatogr. A 965 (2002) 35–49.
[7] J. Ruzicka, G.D. Marshall, Anal. Chim. Acta 237 (1990) 329–343.
[8] C.E. Lenehan, N.W. Barnett, S.W. Lewis, Analyst 127 (2002) 997–1020.
[9] D. Satinsky, P. Solich, P. Chocholous, R. Karlicek, Anal. Chim. Acta 499 (2003) 205–214.
[10] D. Satinsky, J. Huclova, P. Solich, R. Karlicek, J. Chromatogr. A 1015 (2003) 239–244.
[11] S. Armenta, S. Garrigues, M. de la Guardia, Trends Anal. Chem. 27 (2008) 497–511.
[12] V. Cerdà, J.M. Estela, R. Forteza, A. Cladera, E. Becerra, P. Altamira, P. Sitjar, Talanta 50 (1999) 695–705.
[13] M. Miró, V. Cerdà, J.M. Estela, Trends Anal. Chem. 21 (2002) 199–210.
[14] B. Horstkotte, O. Elsholz, V. Cerdà, J. Flow Injection Anal. 22 (2005) 99–109.
[15] M.A. Segundo, L.M. Magalhaes, Anal. Sci. 22 (2006) 3–8.
[16] H.M. González-San Miguel, M. Fernández, J.M. Estela, V. Cerdà, Trends Anal. Chem. 28 (2009) 336–346.
[17] H.M. González-San Miguel, J.M. Alpízar-Lorenzo, V. Cerdà-Martín, Talanta 72 (2007) 296–300.
[18] H.M.G.S. Miguel, J.M. Alpízar-Lorenzo, V. Cerdà, Anal. Bioanal. Chem. 387 (2007) 663–671.
[19] M. Fernández, M. Miro, H.M. González, V. Cerdà, Anal. Bioanal. Chem. 391 (2008) 817–825.
[20] M.A. Obando, J.M. Estela, V. Cerdà, Anal. Bioanal. Chem. 391 (2008) 2349–2356.
[21] M. Rigobello-Masini, J.C.P. Penteado, C.W. Liria, M.T.M. Miranda, J.C. Masini, Anal. Chim. Acta 628 (2008) 123–132.
[22] C.K. Zacharis, A. Verdoukas, P.D. Tzanavaras, D.G. Themelis, J. Pharm. Biomed. Anal. 49 (2009) 726–732.
[23] J.L. Adcock, P.S. Francis, K.M. Agg, G.D. Marshall, N.W. Barnett, Anal. Chim. Acta 600 (2007) 136–141.
[24] M.A. Obando, J.M. Estela, V. Cerdà, J. Pharm. Biomed. Anal. 48 (2008) 212–217.
[25] R.D. Gerardi, N.W. Barnett, S.W. Lewis, Anal. Chim. Acta 378 (1999) 1–41.
[26] B.A. Gorman, P.S. Francis, N.W. Barnett, Analyst 131 (2006) 616–639.
[27] J.G. Hardman, L.E. Limbird, Goodman and Gilman's Pharmacological Basis of Therapeutics, 9th ed., McGraw-Hill, New York, 1996.
[28] The World Anti-Doping Code. The 2004 Prohibited List, International Standard, WADA, Canada, 2004.
[29] M.H. Lu, P. Tong, H. Xiao, S.F. Xia, X.Y. Zheng, W. Liu, L. Zhang, G.N. Chen, Electrophoresis 28 (2007) 1461–1471.
[30] V. Morra, P. David, R. Capra, M. Vincenti, A. Di Stilo, F. Botre, J. Chromatogr. A 1135 (2006) 219–229.
[31] X.Y. Zheng, M.H. Lu, L. Zhang, Y.W. Chi, L.H. Zheng, G.N. Chen, Talanta 76 (2008) 15–20.
[32] Z.M. Zhang, D.P. Wang, L. Zhang, M. Du, G.N. Chen, Analyst 133 (2008) 1187–1194.
[33] S. Castiglioni, R. Bagnati, R. Fanelli, F. Pomati, D. Calamari, E. Zuccato, Environ. Sci. Technol. 40 (2006) 357–363.
[34] S. Castiglioni, R. Bagnati, D. Calamari, R. Fanelli, E. Zuccato, J. Chromatogr. A 1092 (2005) 206–215.
[35] M. Miró, J.M. Estela, V. Cerdà, Anal. Chim. Acta 541 (2005) 55–66.
[36] E. Becerra, A. Cladera, V. Cerdà, Lab. Rob. Autom. 11 (1999) 131–140.
[37] F. Maya, J.M. Estela, V. Cerdà, Anal. Chim. Acta 601 (2007) 87–94.

Talanta 80 (2010) 1341–1346

Contents lists available at ScienceDirect

Talanta

journal homepage: www.elsevier.com/locate/talanta

A multisyringe flow injection Winkler-based spectrophotometric analyzer for in-line monitoring of dissolved oxygen in seawater

Burkhard Horstkotte[a], Juan Carlos Alonso[b], Manuel Miró[a], Víctor Cerdà[a,*]

[a] University of the Balearic Islands, Department of Chemistry, Carreterra de Valldemossa km 7,5, E-07122 Palma de Mallorca, Spain
[b] Institut Mediterrani d'Estudis Avançats IMEDEA, Calle Miquel Marques 21, E-07190 Esporles, Spain

ARTICLE INFO

Article history:
Received 16 June 2009
Received in revised form 9 September 2009
Accepted 18 September 2009
Available online 24 September 2009

Keywords:
Multisyringe flow injection analysis
Dissolved oxygen
Winkler method
On-line monitoring
Seawater

ABSTRACT

An integrated analyzer based on the multisyringe flow injection analysis approach is proposed for the automated determination of dissolved oxygen in seawater. The entire Winkler method including precipitation of manganese(II) hydroxide, fixation of dissolved oxygen, dissolution of the oxidized manganese hydroxide precipitate, and generation of iodine and tri-iodide ion are in-line effected within the flow network. Spectrophotometric quantification of iodine and tri-iodide at the isosbestic wavelength of 466 nm renders enhanced method reliability. The calibration function is linear up to 19 mg L^{-1} dissolved oxygen and an injection frequency of 17 per hour is achieved. The multisyringe system features a highly satisfying signal stability with repeatabilities of 2.2% RSD that make it suitable for continuous determination of dissolved oxygen in seawater. Compared to the manual starch-end-point titrimetric Winkler method and early reported automated systems, concentrations and consumption of reagents and sample are reduced up to hundredfold. The versatility of the multisyringe assembly was exploited in the implementation of an ancillary automatic batch-wise Winkler titrator using a single syringe of the module for accurate titration of the released iodine/tri-iodide with thiosulfate.

© 2009 Elsevier B.V. All rights reserved.

1. Introduction

Determination of dissolved oxygen (DO) in natural waters is of high importance in the evaluation of water quality and in getting knowledge on the atmospheric gas diffusion processes, the circulation of water masses, and the occurrence of biological and chemical reactions. It is thereby an important indicator of the metabolism activity [1]. DO is consumed in the metabolic degradation of biomass and in the respiratory activity of specimens. On the contrary, DO concentration increases by the photosynthetic activity of phytoplankton, which can in superficial layers even lead to an over-saturation of oxygen with respect to steady-state conditions at a given temperature and salt content [1,2]

In the classical end-point Winkler titration method [3], dissolved oxygen is chemically bound to manganese(II) hydroxide precipitate (1) in a strongly alkaline milieu, which results in a brownish oxidized manganese oxyhydroxide precipitate (2). Following the fixation of DO, the acidification of the reactant mixture leads to the oxidation of previously added iodide in the liquid phase to molecular iodine (3). Iodine forms the tri-iodide complex with surplus of iodide ions (4). The liberated tri-iodide is then titrated with standardized thiosulfate using either potentiometric-assisted or starch-based end-point detection (5) [3–6].

$$Mn^{2+} + 2OH^- \rightarrow Mn(OH)_2\downarrow \quad (1)$$

$$Mn(OH)_2\downarrow + (1/2)O_2 \rightarrow MnO(OH)_2\downarrow \quad (2)$$

$$MnO(OH)_2\downarrow + 4H^+ + 2I^- \rightarrow Mn^{2+} + 3H_2O + I_2 \quad (3)$$

$$I^- + I_2 \leftrightarrow I_3^- \quad (4)$$

$$I_3^- + 2S_2O_3^{2-} \rightarrow 3I^- + S_4O_6^{2-} \quad (5)$$

The Winkler titration method has proven precise and robust for determination of DO regardless of the actual matrix components of the sample, e.g., the contents of dissolved salts or organic matter, which in contrast can severely influence the diffusive membrane passage of oxygen when resorting to amperometric detection by the Clark electrode. The electrode further requires a constant approach flow of the sample to the membrane. Due to a considerable delay time and the consumption of DO by the sensor itself, its application to small changes in the concentration or low contents of DO is troublesome [1,4]. The Winkler method is however not free from drawbacks. It is a lengthy steady-state procedure involving a large number of manual operations and the consumption of considerable amounts of reagents along with the requirement of a precisely metered sample volume for accurate results. As a result, the classical method lacks suitability for expeditious on-board measurements in monitoring campaigns.

* Corresponding author. Tel.: +34 971 173 260; fax: +34 971 173 426.
E-mail address: Victor.cerda@uib.es (V. Cerdà).

0039-9140/$ – see front matter © 2009 Elsevier B.V. All rights reserved.
doi:10.1016/j.talanta.2009.09.034

Several researchers selected spectrophotometric detection as an improvement of the end-point detection compared with the use of visual starch indicator or potentiometric assistance in terms of reduction of sample handling, accuracy, sample throughput, easiness of the assays, and avoidance of the human factor on reliability [7,8].

However, the choice of the appropriate detection wavelength has been a matter of controversy. Labasque et al. [9] have recently confirmed that detection at 466 nm, that is, the isosbestic point of molecular iodine and tri-iodide, provides sufficient sensitivity for the determination of DO at the expected concentration range in fresh and marine waters (5–15 mg L^{-1} DO). Further, measurement at the isosbestic point renders enhanced method ruggedness with no need to cope with the usage of surplus of iodide.

To expedite the Winkler method while assuring decreased consumption of chemicals and minimum risks of sample contamination, flow-based kinetic methods should be regarded as appealing alternatives to the batch-wise classical titration. Flow approaches have been proven suitable in the mechanization of sample preparation methods as well as wet-chemical based analytical procedures. Analytical flow-based procedures are of widespread use whenever fast, economic, reliable and automated analyses of a large number of samples of similar origin are called for. Distinct flow techniques have been proposed over the last three decades differing in the way of liquid propulsion, sample introduction, operation schemes, flow pattern, and manifold configurations, as extensively described in recent monographs [10–13].

A survey in the literature revealed the lack of robust, fully automatic flow-based setups capitalized on the Winkler method for determination of DO. In fact, there are only two reports on the implementation of the Winkler chemistry in flow injection setups [14,15]. Yet, several semi-automated methods comprising a manual step for fixation of molecular oxygen with further in-line optical or electrochemical detection of the evolved iodine/tri-iodide have been reported and characterized [16–18]. This is most likely due to the formation of water insoluble manganese hydroxides within the flow network and the eventual accumulation of the precipitates in the reaction coils that demands for a thorough rinsing of the manifold to prevent clogging of the flow conduits [14].

In this work, multisyringe flow injection analysis (MSFIA) launched in 1999 [19,20] and reviewed lately [21,22] is exploited as an analytical tool for construction of a compact, portable, and multipurpose Winkler-based spectrophotometric flow-through analyzer with the capability of operating as an automatic batch titrator as well. The overall Winkler method encompassing in-line precipitation of manganese(II) hydroxide, reaction with dissolved oxygen in the sample, in-line dissolution of the evolved oxidized manganese oxyhydroxide, generation of molecular iodine and tri-iodide and downstream spectrophotometric detection of the colored iodine species is fully integrated in a single MSFIA assembly. The advantages of MSFIA with respect to former flow injection systems for DO determination [14,23] include the instrumental robustness and versatility in fluid handling as a result of the use of a syringe pump rather than a peristaltic pump as liquid driver, software-assisted system configuration with no need for manifold re-design, integration of multicommutation valves, and – as a multichannel flow technique – the possibility of usage of merging flows at will.

2. Materials and methods

2.1. Reagents

Distilled water was used throughout for the preparation of the overall solutions. All chemicals were of analytical-reagent grade (Scharlab, Barcelona, Spain) and used as received. A solution of 0.25 mol L^{-1} manganese chloride was used as a reagent 1 (R1) in syringe 2. A solution composed of 1.0 mol L^{-1} sodium iodide and 0.8 mol L^{-1} sodium hydroxide solution was used as reagent 2 (R2) in syringe 3. Reagent 3 (R3) being 2.0 mol L^{-1} sulfuric acid was pumped by syringe 4. A 0.1 mol L^{-1} sulfuric acid used as a carrier solution was propelled by syringe 1. The reagents were not sparged with nitrogen prior to use as this would be impracticable in shipboard assays.

Chemicals for the classical Winkler titrimetric procedure are detailed as follows: 3.0 mol L^{-1} manganese chloride (R1c), 4.0 mol L^{-1} sodium iodide and 8.0 mol L^{-1} sodium hydroxide (R2c), and 5.0 mol L^{-1} sulfuric acid (R3c). Potassium iodate was dried at 105 °C overnight and used to prepare a 0.0023 mol L^{-1} KIO_3 solution. A 0.2 mol L^{-1} sodium thiosulfate solution was used as a titrant of iodine/tri-iodide and standardized against 10 mL of 0.0023 mol L^{-1} potassium iodate, which was previously mixed with 1 mL of R3c and 1 mL of R2c according to the standard protocol [5]. A 30% (w/v) starch solution in glycerol was used as iodine end-point indicator.

Surrogate seawater (SSW) was prepared as detailed elsewhere [1] by dissolving the following components in distilled water: 3.0 mg L^{-1} NaF, 20 mg L^{-1} $SrCl_2{\cdot}6H_2O$, 30 mg L^{-1} H_3BO_3, 100 mg L^{-1} KBr, 700 mg L^{-1} KCl, 1470 mg L^{-1} $CaCL_2{\cdot}2H_2O$, 4000 mg L^{-1} Na_2SO_4, 10,780 mg L^{-1} $MgCl_2{\cdot}6H_2O$, 23,500 mg L^{-1} NaCl, 20 mg L^{-1} $Na_2SiO_3{\cdot}9H_2O$, and 200 mg L^{-1} $NaHCO_3$.

For calibration purposes, standards were prepared by sparging SSW with nitrogen, air, or oxygen for at least 15 min. Oxygen was generated in the laboratory by the catalytic decomposition of hydrogen peroxide (about 10% (v/v)) continuously added to an initial small volume of potassium permanganate solution. A solution of 0.1 g L^{-1} methylene blue was used for visual inspection of displaced volumes in the flow network.

2.2. Flow analyzer

The implemented MSFIA system for in-line determination of DO is depicted in Fig. 1 wherein the tubing dimensions are indicated. A multisyringe piston pump module (model Bu4S) [19,21] was purchased from Crison Instruments S.A. (Allela, Barcelona, Spain). The module was equipped with three glass syringes of 1 mL each (S2, S3, S4) from Hamilton Bonaduz AG (Bonaduz, Switzerland) and one polypropylene syringe of 10 mL (S1) from Sciware SL (Palma de Mallorca, Spain). Solenoid head valves allowed the connection of each syringe either with the manifold (ON) or with the respective solution reservoir (OFF) for refilling. Two additional 3-way solenoid valves (V5 and V6) were powered by 12 V supply ports of the syringe module. The module was connected in series via a RS232C serial interface to a PC for remote software control.

All liquid contacted parts such as confluences and valve components were of chemical resistant polymers, namely, ETFE, PMMA, PEEK, and PTFE. PTFE tubing was used for the flow lines of the manifold.

An USB-2000 miniature spectrophotometer from Ocean Optics Inc. (Dunedin, FL, USA) had been integrated into the multisyringe module and was directly attached to a cuvette support (Sciware SL) holding a 1.0-cm pathlength flow cuvette from Starna (type 75.15 SOG, Essex, UK). A white LED was used as light source and powered by a stabilized constant current source (Sciware SL). Dual-wavelength detection was done for compensation of the schlieren effect using a reference wavelength of 620 nm. The analytical wavelength was affixed at 466 nm, that is, the isosbestic point wavelength of tri-iodide and iodine. So, the difference of the absorbance at 466 nm and absorbance at 620 nm was applied as analytical signal throughout.

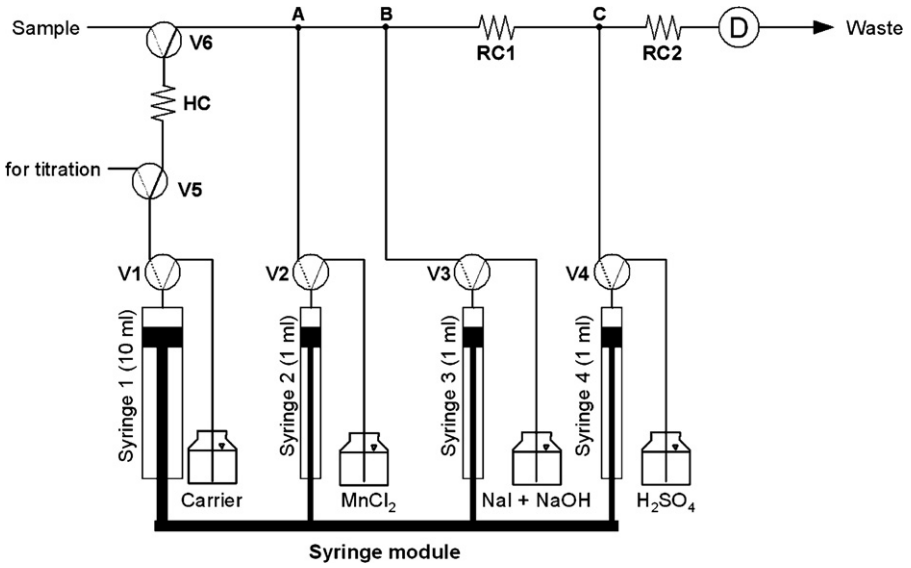


Fig. 1. Schematic illustration of the MSFIA system and batch-wise titrator for automatic Winkler determination of dissolved oxygen. HC: holding coil (280 cm, 1.5 mm i.d.) RC1: reaction coil 1 (120 cm, 1.5 mm i.d.), RC2: reaction coil 2 (75 cm, 0.8 mm i.d.), D: detector: integrated flow-through spectrophotometer (λ_{Det}: 466 nm, λ_{Ref}: 620 nm) with white LED. V1–V6: 3-way multicommutation solenoid valves with normally closed position (ON, activated) dotted and normally open (OFF, deactivated) straight. A, B, C: confluences for reagents, the distance between A and B was about 4 cm.

2.3. Software

The software package AutoAnalysis 5.0 (Sciware SL) was used for instrumental control, data acquisition, and integration of the analytical readouts [24]. The basic protocol can be adapted to the individual instrumental assembly by additional dynamic link libraries, which are amenable to communicate with the assembled instruments and detector devices. User-friendly software tools for method development such as loops, procedures, variables, user inquiries, waiting steps, and conditional definitions are available for method creation.

2.4. Analytical protocol

The main steps of the analytical protocol are given and commented in Table 1. In brief, after cleaning of the sample channel, if required, a large sample volume (4 mL) was aspirated into the holding coil. Afterwards, a 600 μL of the sample volume were propelled forward towards the confluences A and B (see Fig. 1). Volumes of 35 μL of R1 (manganese chloride) and R2 (sodium hydroxide and sodium iodide), respectively, were then injected simultaneously into a continuous flow of 350 μL sample. The composite plug (350 μL sample merged with 35 μL of each R1 and R2) was dispensed further in RC1 in order to promote the mixing between the DO and in situ generated manganese(II) hydroxide precipitate and increase the dispersion of injected solutions. After refilling of the syringes and halting the flow for 80 s in order to promote the reaction, the manganese oxyhydroxide precipitate was pushed downstream to merge with sulfuric acid at the confluence C. This led to the dissolution of the precipitate whereupon the iodide in the composite segment was in-line oxidized to iodine/tri-iodide prior to reaching the spectrophotometric detector. After each aspiration step, a waiting time of 1 s was implemented to release negative pressure in the manifold and to improve the repeatability of the procedure.

By the integration of the solenoid valve 5 (generally not used), S1 (10 mL) could be alternatively used as a high-precision burette for automatic batch titration of released iodine/tri-iodide in the classical Winkler procedure exploiting sodium thiosulfate as titrant. A software protocol was programmed for repeated user-defined dispensing of titrant volumes as low as 5 μL along with the automated refilling of the syringe and summation of the total volume of titrant consumed for end-point detection. The titration of 2 mL of 0.023 mol L^{-1} potassium iodate in surplus of iodide gave a relative standard deviation better than 0.3%.

2.5. Calibration method

External calibration was effected with about 300 mL SSW solutions purged with nitrogen, air, and oxygen and mixtures thereof. A sparging time of 15 min was proven sufficient for steady-state gas saturation. After in-line analysis of the standards, the unknown content of oxygen was determined by the application of the classical Winkler titration protocol. Hence, Winkler bottles of approximately 100 mL were filled carefully with the calibration standards, to which 0.5 mL of R1c and 0.5 mL of R2c were added. The bottles were sealed and incubated for at least 1 h at room temperature in the darkness. Thereafter, 0.5 mL of R3 was added and the formed iodine/tri-iodide was quantified by titration with thiosulfate using starch as indicator.

3. Results and discussion

3.1. System configuration and preliminary considerations

Of particular challenge in this work was the injection of minute, well-defined volumes of both R1 and R2 into the sample to create a single composite mixing zone. Therefore, syringes of 1 mL were used for injection of both R1 and R2 in adjacent confluences and a 10 mL syringe for the sample whereby the maximal achievable reagent to sample volume ratio in the assembled multisyringe set-up was 1:10. To avoid a severe dilution of the composite reaction zone by the downstream addition of acid in order to dissolve the manganese precipitates a small syringe (1 mL capacity) was utilized for reagent addition.

The analytical procedure was set to utilize a large sample volume, into which small volumes of R1 and R2 were injected. This was done in order to prevent the reactant zone to be affected by the oxygen content in the carrier solution during sample aspiration and propelling into the reaction coil. As the maximal usable volume of sample was limited by the volume of RC1 but former

Table 1
Automated procedure for in-line dissolved oxygen quantification exploiting multisyringe flow injection analysis.

Instrument	Instruction[a]	Description
MS[b]	Pickup 10 μL at 1.5 mL min^{-1} [1-Off 2-Off 3-Off 4-Off 6-Off]	Overcome of syringe backlash
MS	Pickup 400 μL at 0.4 mL min^{-1} [1-On 2-Off 3-Off 4-Off 6-On]	Aspiration of 4 mL sample
MS	Dispense 60 μL at 1.0 mL min^{-1} [1-On 2-Off 3-Off 4-Off 6-Off]	Dispense of 600 μL sample to the reagents' confluence
MS	Dispense 35 μL at 1.0 mL min^{-1} [1-On 2-On 3-On 4-On 6-Off]	Confluent injection of R1 and R2 into sample flow
MS	Dispense 65 μL at 1.0 mL min^{-1} [1-On 2-Off 3-Off 4-On 6-Off]	Dispersion of precipitate and mixing with dissolved oxygen by further dispensing of 650 μL sample
MS	Full aspiration at 1.5 mL min^{-1} [1-Off 2-Off 3-Off 4-Off 6-Off]	Syringe refilling
Wait	Wait 80 s	Reaction time for oxygen fixation
Spectrophotometer	λ_{Det}: 466 nm/λ_{Ref}: 620 nm at 3.3 Hz	Measurement start
MS	Dispense 350 μL at 0.4 mL min^{-1} [1-On 2-Off 3-Off 4-On 6-Off]	Dissolution of $MnO(OH)_2$ by acid merging flow and in-line detection of formed iodine/tri-iodide
Spectrophotometer	Stop measure	Measurement stop

[a] All volumes and flow rates refer to a syringe size of 1 mL. For syringe 1, a factor of 10 has to be taken into account. The solenoid valve V5 was set to position "Off" throughout this procedure.
[b] MS: multisyringe module.

dispersion in the HC had to be considered, a 4-fold larger volume of sample than RC1 of sample was applied.

The handling of the manganese precipitates in the flow-through manifold might be cumbersome as well. Thus, the reaction coil was made of PTFE tubing with an inner diameter of 1.5 mm in order to minimize the risk of tubing blockage by the in-line generated precipitates.

Analytical detection was effected at the isosbestic wavelength of iodine and tri-iodide, that is, 466 nm, aimed at operating at a dynamic working range of 0–15 mg L^{-1} DO while keeping the blank value as low as possible, and at preventing eventual errors as a result of the different molecular absorptivity of iodine and tri-iodide. In addition, a reference wavelength at 620 nm was selected to overcome potential interferences from schlieren effects.

3.2. Selection of chemical variables

Exploration of the effect of the reagent concentrations on the analytical response in the multisyringe-flow procedure was done in a univariate mode in the order of reagent addition of the classical Winkler method. The overall reagents were used in excess to the actual concentrations of the parameter investigated for a stoichiometric ratio of Mn^{2+}:OH^-:I^-:H^+ of 1:2:3:4 (see reactions under Section 1). The idea behind this investigation was to keep the blank readouts at the lowest possible level, yet with sufficient analytical sensitivity to analyze hypoxic seawater samples. To this end, surrogate seawaters sparged with nitrogen, air, and oxygen were analyzed for each combination of experimental factors. Analytical results are compiled in Table 2.

Diluted sulfuric acid fixed to a concentration of 0.1 mol L^{-1} was selected as a carrier to serve concomitantly as a washing solution for precluding the accumulation of precipitate onto the inner walls of the manifold tubing. As a result, an additional step for manifold cleaning as elsewhere reported [14] was not required. Adverse effects of the chemical composition of the carrier on the chemical yield of formation of manganese oxyhydroxide were avoided by isolation of the reactant zone from the carrier by the sample segment itself.

To mimic the addition of 1.0 mL of 3.0 mol L^{-1} Mn(II) to 125 mL Winkler bottles in the standard protocol [6], the concentration of R1 was originally affixed to 0.25 mol L^{-1} Mn(II) to cope with the 10-fold dilution of the reagent in the multisyringe flow setup. The influence of the Mn(II) concentration in R1 on the analytical response was studied over the range of 0.06–0.48 mol L^{-1}. Increased concentrations were not assayed to prevent the undue formation of the manganese(II) hydroxide precipitate. Experimental results are given in Table 2. While the blank value was not affected significantly, peak height of oxygen saturated SSW increased about 80% and reached a plateau level at a concentration of 0.24 mol L^{-1} and onwards. Therefore, the original concentration of 0.25 mol L^{-1} was selected for further experiments.

The effect of increasing concentrations of sodium hydroxide in the range of 0.3–1 mol L^{-1} on the peak signals of nitrogen and air saturated SSW was not significant, yet, the analytical readouts for oxygen saturated SSW increased linearly up to 0.8 mol L^{-1} (see Table 2), which was therefore chosen for the remainder of the work.

As to the concentration of iodide studied over the range of 0.5–2 mol L^{-1}, the peak height of oxygen saturated SSW increased up to 1.25 mol L^{-1} and decreased slightly for higher concentrations. The peak height of nitrogen saturated SSW decreased to a stable level from 0.5 to 1.0 mol L^{-1} NaI, the latter being selected to attain a robust blank signal.

Table 2
Effect of the reagent concentrations on the analytical readouts in the multisyringe flow-based determination of dissolved oxygen.

	N_2 sat. SSW [AU]	Air sat. SSW [AU]	O_2 sat. SSW [AU]
Concentration $MnCl_2$ (mol L^{-1})[a]			
0.06	0.61 ± 0.03	0.75 ± 0.04	1.13 ± 0.06
0.12	0.62 ± 0.04	0.75 ± 0.02	1.59 ± 0.11
0.18	0.61 ± 0.04	0.84 ± 0.02	1.74 ± 0.02
0.24	0.60 ± 0.04	0.87 ± 0.08	1.86 ± 0.04
0.36	0.61 ± 0.03	0.87 ± 0.02	1.79 ± 0.03
0.48	0.63 ± 0.03	0.86 ± 0.02	1.77 ± 0.04
Concentration NaOH (mol L^{-1})[b]			
0.30	0.58 ± 0.02	0.77 ± 0.01	1.34 ± 0.04
0.50	0.56 ± 0.03	0.77 ± 0.02	1.45 ± 0.05
0.60	0.56 ± 0.03	0.78 ± 0.02	1.49 ± 0.02
0.70	0.55 ± 0.03	0.77 ± 0.01	1.57 ± 0.02
0.80	0.57 ± 0.04	0.79 ± 0.01	1.60 ± 0.01
1.00	0.57 ± 0.03	0.78 ± 0.02	1.61 ± 0.02
Concentration NaI (mol L^{-1})[c]			
0.50	0.56 ± 0.02	0.73 ± 0.01	1.38 ± 0.10
0.75	0.47 ± 0.01	0.71 ± 0.02	1.66 ± 0.14
1.00	0.45 ± 0.01	0.75 ± 0.01	1.75 ± 0.03
1.25	0.43 ± 0.02	0.73 ± 0.00	1.80 ± 0.03
1.50	0.44 ± 0.00	0.76 ± 0.04	1.77 ± 0.01
2.00	0.44 ± 0.01	0.74 ± 0.03	1.70 ± 0.08
Concentration H_2SO_4 (mol L^{-1})[d]			
1.00	0.58 ± 0.03	0.87 ± 0.02	
1.50	0.54 ± 0.05	0.90 ± 0.02	
2.00	0.51 ± 0.04	0.84 ± 0.02	
2.50	0.51 ± 0.06	0.84 ± 0.02	
3.00	0.56 ± 0.09	0.85 ± 0.01	

Results are given as mean peak height of five replicates ± standard deviation.
[a] [NaOH]: 1.2 mol L^{-1}; [NaI]: 2.0 mol L^{-1}; [H_2SO_4]: 5.0 mol L^{-1}.
[b] [Mn(II)]: 0.25 mol L^{-1}; [NaI]: 2.0 mol L^{-1}; [H_2SO_4]: 5.0 mol L^{-1}.
[c] [Mn(II)]: 0.25 mol L^{-1}; [NaOH]: 0.8 mol L^{-1}; [H_2SO_4]: 5.0 mol L^{-1}.
[d] [Mn(II)]: 0.25 mol L^{-1}; [NaOH]: 0.8 mol L^{-1}; [NaI]: 1.0 mol L^{-1}.

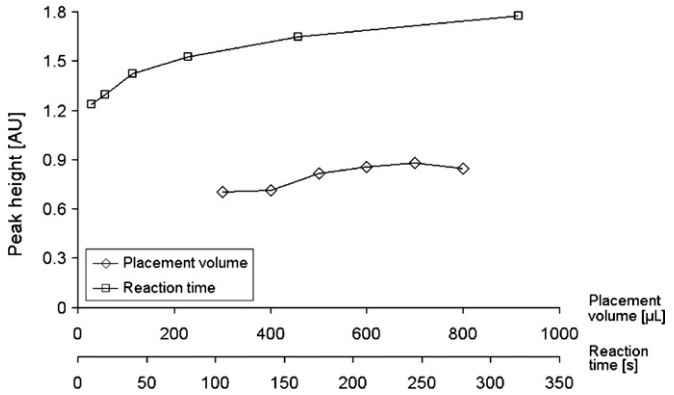


Fig. 2. Evaluation of the effect of placement volume and reaction time on the analytical readouts for air and oxygen saturated SSW, respectively, applying injection volumes for both R1 and R2 of 65 µL.

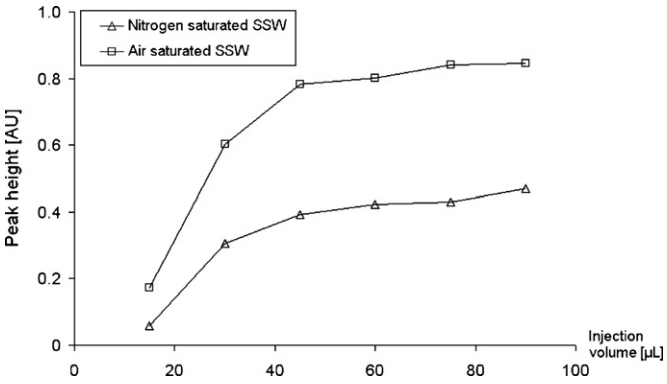


Fig. 3. Evaluation of the influence of the injection volumes of R1 (0.25 mol L^{-1} $MnCl_2$) and R2 (0.8 mol L^{-1} NaOH and 1 mol L^{-1} NaI) for a reaction time of 80 s on the analytical readouts.

The influence of the sulfuric acid concentration in R3 was studied over the range of 1–3 mol L^{-1}. In order to warrant a fast and quantitative in-line dissolution of the generated manganese oxyhydroxide precipitate along with the minimization in the consumption of acid, a concentration of 2.0 mol L^{-1} sulfuric acid was selected as R3.

3.3. Selection of physical variables

The dependences of the reagent volumes, injection mode and flow rates upon the method's sensitivity were investigated. For the final dispense step including in-line acid merging, dissolution of the manganese hydroxides, and formation of iodine/tri-iodide, the peak heights of air saturated SSW decreased linear with increasing flow rates (for S1) in the range of 3–8 mL min^{-1} by about 10%. Therefore, a flow rate of 4 mL min^{-1} was applied as a compromise between time of analysis and signal height.

For sample aspiration, likewise a flow rate of 4 mL min^{-1} was applied as a compromise between time of analysis and bubble evolving. For further flow operations, flow rates of 10 mL min^{-1} were utilized as a compromise between flow in the system backpressure and sample throughput.

After aspiration a total sample volume of 4 mL, a first sample fraction was dispensed to confluences A and B before the injection of R1 and R2, whose effect on the analytical response was studied over the range of 300–800 µL. Experimental results are shown in Fig. 2. The sensitivity was maximal for a displacement volume of 600 µL and onwards due to the decreased contact of the leading edge of the composite reaction zone with the acidic carrier in the manifold tubing.

The influence of halting the flow in RC1 for development of the reaction between dissolved oxygen and the in-line formed manganese(II) hydroxide was evaluated over the range of 10–320 s. The longer the reaction time the better were the yields of formation of manganese oxyhydroxide, whereas the blank value did not increase significantly. Experimental data are given in Fig. 2. As a compromise between time of analysis and sensitivity, a fixation time for dissolved oxygen of 80 s was chosen for further experiments.

The simultaneous injection of equal volumes of R1 and R2 into the sample flow was studied over the range of 15–90 µL each. The injection of reagents was followed by a forward flow of further sample in RC1 in order to increase the dispersion and thus promoting the reactions. This ancillary sample volume had to be limited to 1080 µL minus the volume of the injection step to prevent the flowing of the manganese precipitates ahead of the confluence C. The evaluation of the dependence of reagent volumes upon the blank and the analytical signal is shown in Fig. 3. The increase in reagent volumes lead to enhanced signals for both nitrogen and air saturated SSW up to ca. 50 µL. Aiming at affixing the blank value down to 0.4 AU, that is, one fourth of the response working range, a confluent injection of 35 µL for both R1 and R2 into 350 µL sample followed by a sample forward flow of 650 µL was selected for the remainder of the work. It should be noted that integrated absorbance peaks were in all instances $\leq$1.5 AU to prevent operating in the range of maximum photometric uncertainty.

3.4. Analytical performance and real sample analysis

The analytical curve was constructed by using six standard solutions prepared in sparged SSW as described in Section 2.5. A linear response was encountered up to 19 mg L^{-1} with a mean sensitivity of $0.029 \pm 0.002 \cdot AU \cdot [O_2]^{-1}$ and a mean blank value of 0.33 AU. If needed, ca. 2.2-fold improved sensitivity can be obtained by selection of a wavelength down to 440 nm as reported by Muangkaew et al. [15]. Compared with this later work, blank and sensitivity values were about 33% lower in this work yet significant improvements were achieved with respect to reproducibility and reagents' consumption, thus demonstrating the green chemical credentials of the devised multisyringe-based assembly.

The relative standard deviations of ten consecutively performed measurements of air saturated and nitrogen saturated SSW were 2.1% and 2.3%, respectively. A detection limit of 0.8 mg L^{-1} was calculated as the concentration of dissolved oxygen yielding a signal equal to the blank plus three times the standard deviation of the blank.

The multisyringe flow analyzer features an injection throughput of 17 h^{-1} where the sample aspiration and fixation time of dissolved oxygen were the limiting steps. It has to be noted that the sample had to aspirated at a reduced flow rate in order to avoid the evolvement of gas bubbles as a consequence of the negative pressure in the holding coil.

It has been proven that the blank signals did not depend upon the oxygen content of the reagents as sparging with nitrogen did not alter the signals significantly. Sparging of the sample carrier with nitrogen led to a signal decrease of 5%. The acid catalyzed oxidation of iodide to iodine was also negligible as demonstrated by replacing the manganese reagent R1 by water. The blank signal was likely attributed to the permeability to atmospheric oxygen of the 350 µm-thick PTFE connecting tubes (dead volume ca. 60 µL) from S2 and S3 to the confluences A and B, respectively, where the reagents remain for >6 min reaching oxygen saturation before being injected. This would further explain the decrease of the blank signal at high concentrations of iodide because the higher is the ionic strength the lower is the dissolved concentration of oxygen in aqueous solutions.

Table 3
Comparison of results obtained by the multisyringe flow-based determination of dissolved oxygen with those obtained with the classical Winkler titration method.

Sample	Classical Winkler [mg L^{-1}][a]	MSFIA-analyzer [mg L^{-1}]	Difference [%]	Salinity [%][b]
Seawater 1	6.60	6.96 ± 0.04	+5.6%	3.7
Seawater 2	6.39	6.54 ± 0.08	+2.4%	3.8
Seawater 3	6.48	6.24 ± 0.07	−3.7%	3.8
Seawater 4	6.53	6.67 ± 0.15	+2.1%	3.7
Seawater 5	4.63	4.69 ± 0.12	+1.3%	3.1
Seawater 6	5.94	6.41 ± 0.11	+8.0%	3.9
Seawater 7	4.90	5.34 ± 0.06	+8.9%	3.7
Seawater 8	6.28	6.08 ± 0.07	−3.2%	4.0
Seawater 9	3.80	3.58 ± 0.05	−5.8%	3.7
Seawater 10	1.21	1.30 ± 0.02	+7.3%	3.7
Seawater 11	1.76	1.89 ± 0.04	+7.1%	3.9

From seawater samples 10, 11, and 12 oxygen was partly stripped out by gasification with nitrogen.
[a] The titrant volume error was ±5 μL, representing in the present case an SD of 0.02 mg L^{-1}.
[b] Determined as the dry substance of 0.45 μm pore-filtered seawater after 24 h at 150 °C.

A slight memory effect has been observed after analyzing samples with high oxygen content, which mostly affected the first peak of repeated measurements. This effect was likely due to the permeation of oxygen into the pores of the PTFE tubing. Remains of oxidized manganese precipitate onto the tubing walls of the flow system as reported elsewhere [15] were not observed in our flow setup as a consequence of the usage of an acidic carrier.

For ascertainment of the accuracy of the proposed flow system and evaluation of matrix effects on the content of dissolved oxygen, 11 coastal Mediterranean surface seawater sample (air saturated) were analyzed and the results compared with the classical Winkler method. The samples were analyzed without any prior treatment as recommended by Grasshoff et al. (1999) [6]. To cover the concentration working range, three seawater samples were sparged with nitrogen for 1–2 min, decreasing by this the original oxygen content. A good agreement was found as shown in Table 3 between both methods with relative deviations between −5.8% and +8.9% (average 5%). It should be pointed out that an important error source was surely the transfer of the in-line evaluated samples to smaller Winkler bottles for verification by the classical Winkler method. The averaged RSD for sample measurements ($n = 5$) by resorting to the proposed analyzer was generally <2%. The *t*-test of comparison of means revealed the inexistence of significant differences at a 95% confidence level, thus, demonstrating the accuracy of the in-line Winkler procedure.

4. Conclusion

A versatile flow-through analyzer based on multisyringe flow injection analysis has been proposed for the determination of dissolved oxygen in seawater. It features the implementation of the entire Winkler methodology in a completely enclosed, automated tubing set-up. Physical and chemical parameters were studied thoroughly; the optimized system featured high sample frequency and satisfying sensitivity and repeatability with a remarkable decrease in the consumption of reagents and sample compared to the classical Winkler method. The analyzer can further be tuned to operate as a high-precision, automatic batch titrator of the iodine/tri-iodide with sodium thiosulfate generated in the classical Winkler procedure. The multisyringe flow system was successfully applied to the analysis of seawater samples with results in good agreement with the classical Winkler method. Due to its intrinsic characteristics and low frequency of maintenance, this analyzer is particularly suited to semi-continuous monitoring of dissolved oxygen in shipboard analysis. However, as common in all flow techniques, variation of the ambient temperature have to be named as a possible error source, altering both the reaction rate and the viscosity of the solutions with consequent changes in dispersion and mixing as well as in the solubility of oxygen. Temperature control bears the potential to increase the reproducibility required for shipboard monitoring purposes.

Acknowledgements

This work contributed to the project “Design and application of analytical systems for the quantification of trace elements in the ocean” supported by the Government of the Balearic Islands (CAIB Progecib-5C).

References

[1] R.G. Weztel, G. Likens, Limnological Analysis, 2nd edition, Springer, New York, 1991.
[2] APHA, AWWA, WPCF, in: L.S. Clesceri, A.E. Greenberg, R. Rhodes Trussell (Eds.), Standard Methods for the Examination of Water and Wastewater, 20th edition, Washington, DC, 1998.
[3] L.W. Winkler, Chem. Ber. 27 (1888) 2843.
[4] W. Granéli, E. Granéli, Mar. Biol. 108 (1991) 341.
[5] A.G. Dickson, Determination of dissolved oxygen in sea water by Winkler titration. WOCE Operations Manual. Part 3.1.3 Operations & Methods, WHP Office Report WHPO 91-1, 1995.
[6] K. Grasshoff, K. Kremling, M. Ehrhardt, Methods of Seawater Analysis, 3rd edition, Wiley–VCH, Weinheim, 1976.
[7] F. Roland, N.F. Caraco, J.J. Cole, Limnol. Oceanogr. 44 (1999) 1148.
[8] S.-C. Pai, G.-C. Gong, K.-K. Liu, Mar. Chem. 41 (1993) 343.
[9] T. Labasque, C. Chaumery, A. Aminot, G. Kergoat, Mar. Chem. 88 (2004) 53.
[10] S.D. Kolev, I.D. McKelvie (Eds.), Advances in Flow Injection Analysis and Related Techniques. Comprehensive Analytical Chemistry, Elsevier, The Netherlands, 2008, p. 54.
[11] A. Cerdà, V. Cerdà, An Introduction to Flow Analysis, Sciware, Palma de Mallorca, 2009.
[12] M. Trojanowicz (Ed.), Flow Injection Analysis. Instrumentation and Applications, World Scientific Publishing, Singapore, 2000.
[13] M. Trojanowicz (Ed.), Advances in Flow Methods of Analysis, Wiley–VCH, Weinheim, 2008.
[14] T. Reinthaler, K. Bakker, R. Manuels, J. van Ooijen, G.J. Herndl, Limn. Oceanogr. Meth. 4 (2006) 358.
[15] S. Muangkaew, I.D. McKelvie, M.R. Grace, M. Rayanakorn, K. Grudpan, J. Jakmunee, D. Nacapricha, Talanta 58 (2002) 1285.
[16] T. Sakai, S. Piao, N. Teshima, T. Kuroishi, K. Grudpan, Talanta 63 (2004) 893.
[17] T. Sakai, H. Takio, N. Teshima, N. Nishikawa, Anal. Chim. Acta 438 (2001) 117.
[18] M. Novic, B. Pihlar, M. Dular, Fresenius J. Anal. Chem. 332 (1988) 750.
[19] V. Cerdà, J.M. Estela, R. Forteza, A. Cladera, E. Becerra, P. Altimira, P. Sitjar, Talanta 50 (1999) 695.
[20] F. Albertús, B. Horstkotte, A. Cladera, V. Cerdà, Analyst 15 (1999) 1373.
[21] B. Horstkotte, O. Elsholz, V. Cerdà, J. Flow Injection Anal. 22 (2005) 99.
[22] M. Miró, V. Cerdà, J.M. Estela, Trends 21 (2002) 199.
[23] A. Sanz-Martinez, A. Rios, M. Valcarcel, Anal. Chim. Acta 284 (1993) 189.
[24] E. Becerra, A. Cladera, V. Cerda, Lab. Robotics Automat. 58 (1999) 131.

Talanta 80 (2010) 1347–1355

Contents lists available at ScienceDirect

Talanta

journal homepage: www.elsevier.com/locate/talanta

Voltammetric studies on the potent carcinogen, 7,12-dimethylbenz[*a*]anthracene: Adsorptive stripping voltammetric determination in bulk aqueous forms and human urine samples and detection of DNA interaction on pencil graphite electrode

Y. Yardım[a], E. Keskin[a], A. Levent[a], M. Özsöz[b], Z. Şentürk[a,*]

[a] *Yüzüncü Yıl University, Faculty of Science and Letter, Department of Analytical Chemistry, Campus Zeve, 65080 Van, Turkey*
[b] *Ege University, Faculty of Pharmacy, Department of Analytical Chemistry, 35100 Izmir, Turkey*

ARTICLE INFO

Article history:
Received 18 July 2009
Received in revised form 7 September 2009
Accepted 18 September 2009
Available online 24 September 2009

Keywords:
7,12-Dimethylbenz[*a*]anthracene (DMBA)
Cyclic voltammetry
Adsorptive stripping square-wave voltammetry
Non-aqueous and aqueous media
Urine
DNA interaction
Glassy carbon and pencil graphite electrodes

ABSTRACT

7,12-Dimethylbenz[*a*]anthracene (DMBA), is a widely studied polycyclic aromatic hydrocarbon that has long been recognized as a very potent carcinogen. Initially, the electrochemical oxidation of DMBA at the glassy carbon and pencil graphite electrodes in non-aqueous media (dimethylsulphoxide with lithium perchlorate) was studied by cyclic voltammetry. DMBA was irreversibly oxidized in two steps at high positive potentials, resulting in the ill-resolved formation of a couple with a reduction and re-oxidation wave at much lower potentials. Special attention was given to the use of adsorptive stripping voltammetry together with a medium exchange procedure on disposable pencil graphite electrode in aqueous solutions over the pH range of 3.0–9.0. The response was characterized with respect to pH of the supporting electrolyte, pre-concentration time and accumulation potential. Using square-wave stripping mode, the compound yielded a well-defined voltammetric response in acetate buffer, pH 4.8 at +1.15 V (vs. Ag/AgCl) (a pre-concentration step being carried out at a fixed potential of +0.60 V for 360 s). The process could be used to determine DMBA concentrations in the range 2–10 nM, with an extremely low detection limit of 0.194 nM (49.7 ng L^{-1}). The applicability to assay of spiked human urine samples was also illustrated. Finally, the interaction of DMBA with fish sperm double-stranded DNA based on decreasing of the oxidation signal of adenine base was studied electrochemically by using differential pulse voltammetry with a pencil graphite electrode at the surface and also in solution. The favorable signal-to-noise characteristics of biosensor resulted in low detection limit (*ca.* 46 nM) following a 300-s interaction. These results displayed that the electrochemical DNA-based biosensor could be used for the sensitive, rapid, simple and cost effective detection of DMBA–DNA interaction.

© 2009 Elsevier B.V. All rights reserved.

1. Introduction

Polycyclic aromatic hydrocarbons (PAHs) are a large group of organic compounds with two or more fused aromatic rings. They are widespread environmental contaminants resulting from incomplete combustion of organic materials during both natural events and human activities, such as forest fires and volcanic eruptions, and burning of fossil fuels and petroleum products during industrial production, food processing, of machinery operation, including automobiles, airplanes and ships [1]. In view of the large amount of environment pollution studies being carried out on PAHs because some of these compounds are highly carcinogenic and mutagenic, the need has arisen for developing suitable quantitative methods for their determination and monitoring in various types of matrices. PAHs themselves are relatively non-reactive chemicals toward biological macromolecules under physiological conditions. In mammalian system they are metabolized principally in the liver to yield both detoxification products, which are more polar and excretal, and bioactivation products, which are more reactive and genotoxic. Their biological effects are actually attributed to the oxidation process that occurs during biotransformation of the mother compounds. PAH metabolites, including bay-region diol epoxides and free radical cation intermediates formed by monooxygenation and one-electron oxidation, respectively, are molecules that may bind to cellular DNA forming covalent DNA adducts responsible for carcinogenic process [2–5]. Some PAHs are activated exclusively by one of these mechanisms, and others are activated by a combination of both. Recent studies have demonstrated that activation of PAHs can also be achieved by light irradiation [2]. When the skin concomitantly exposed to environmental contaminants and

* Corresponding author. Tel.: +90 432 2251661; fax: +90 432 2251663.
E-mail address: zuhresenturk@hotmail.com (Z. Şentürk).

0039-9140/$ – see front matter © 2009 Elsevier B.V. All rights reserved.
doi:10.1016/j.talanta.2009.09.035

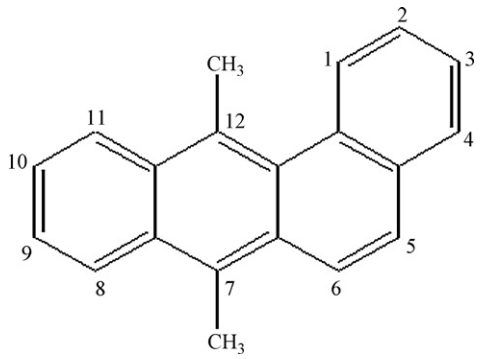


Fig. 1. Chemical structure of DMBA.

sunlight, these chemicals may be activated by photo-irradiation to cause cellular damages and exert toxicity including carcinogenicity.

DNA adducts generated by carcinogenic chemicals or their metabolites are directly related to tumor formation. Therefore, the investigation of DNA interactions is of great importance in order to understand the action mechanisms of some DNA-damaging agents and the design of preventive strategies [3,6–8]. Furthermore, this interaction could be used for rapid detection and quantitative determination of compounds hazardous for all living organisms in the environment, food and clinical samples [9–13].

7,12-Dimethylbenz[*a*] anthracene (DMBA) (its structure is shown in Fig. 1) is one of the PAHs used extensively in experimental studies as a presumptive prototype mutagen, a signal transduction modulator and a known breast and skin carcinogen [14]. The CH_3 groups at C-7 and-12 play an important role in the carcinogenic activation of DMBA [15]. The relationship between the interaction of DMBA with DNA and its carcinogenic potency has been recognized for over 40 years [16]. This compound has been investigated more intensively than any other PAH in terms of its biological activities and biotransformation.

For the above reasons, mostly analytical methods have been employed to characterize and determine DMBA–DNA adducts, and to understand the mechanism of metabolic activation of PAHs in living organisms. So far, chromatographic methods such as GC and HPLC [4,17–24], fluorescence, NMR and mass spectroscopic studies [4,18,25–28], ^{32}P-postlabeling methods [29–32], immunoassay and immunohistochemistry [33–35] are used for these purposes. However, since experimental complications and tediousness or high-cost, most of these methods are not affordable for most laboratories. Although electrochemical techniques were introduced in DNA biosensor technology with a certain delay, as compared to other sophisticated methods, there is a growing interest for design of electrochemical genosensors for biomedical, environmental and forensic applications during the last years. In addition to their useful role in environmental applications, it seems straightforward to employ such electrodes in cancer chemotherapy where DNA is main target. This is mainly due to the capability of fast and sensitive detection by using a relatively low-cost, low-power and pocket-size portable instrumentation. Nonetheless, electrochemical biosensors that detect toxins, pollutants and carcinogenic or mutagenic agents, in particular PAHs [36–41], based on the changes in the oxidation peak of the bases caused by the interaction DNA-analyte, have been scarce so far.

A survey of the literature indicates that very little attention has been paid to the redox behavior of DMBA. In those early reports, electrochemical properties of DMBA was not well documented, only the oxidation potentials of DMBA and related polycyclic carcinogenic hydrocarbons have been studied in non-aqueous medium by cyclic voltammetry using platinum or glassy carbon electrodes [42,43]. Furthermore, there have not yet been any literature reports about the electrochemical detection of the interaction between DMBA and DNA. Therefore, this study is the first attempt describing the detailed voltammetric assay of DMBA and electrochemical investigation of its interaction with DNA.

The current paper is broadly divided into three sections. The first part involves cyclic voltammetric studies of DMBA in non-aqueous solvent at surface of glassy carbon and pencil graphite electrodes. Secondly, special attention will be given to the use of adsorptive stripping voltammetry on disposable pencil graphite electrode in aqueous solutions for the quantification of DMBA in bulk forms and spiked human urine samples. Finally the detection of DMBA–DNA interaction based on the changes of adenine signal using differential pulse voltammetry on pencil graphite electrode will be discussed.

2. Experimental

2.1. Caution

DMBA is a hazardous chemical and should be handled with extreme caution using the guidelines for carcinogenic materials developed by National Cancer Institute [44].

2.2. Apparatus

Cyclic voltammetry (CV) on the glassy carbon electrode (GCE, φ: 3 mm) was performed with BAS 100B/W electrochemical analyzer (Bioanalytical System, USA). Voltammetric measurements with the pencil graphite electrode (PGE) were carried out using electrochemical system μAutolab type III (EcoChemie, The Netherlands) driven by a GPES software version 4.9 (EcoChemie) in connection with a personal computer. The raw voltammograms of differential pulse (DPV) and square-wave (SWV) voltammetry were treated by using Savitzky and Golay filter (level 2) of the GPES software, followed by the moving average baseline correction with a peak width of 0.01 V.

In all measurements, the reference electrode was an Ag/AgCl (3 M NaCl) (Model RE-1, BAS, USA) and the auxiliary electrode was a platinum wire. The measurements with the GCE and PGE were carried out in a standard 10 mL and homemade 5 mL glass one-compartment voltammetric cell, respectively, at a laboratory temperature (20 °C). For stripping analysis, two cells were used, a pre-concentration cell containing the analyte solution and measurement cells containing a blank background electrolyte. Before use, glass cells were soaked into 3 M HNO_3, and rinsed several times with water and working buffer. If no stated otherwise, the convective transport was provided with a magnetic stirring of 400 rpm.

2.3. Chemicals

DMBA standard and native double-stranded fish sperm DNA (ds-DNA) were kindly provided by Merck and Sigma, respectively. All other reagents were of analytical grade quality. Stock solutions of 4×10^{-3} M (corresponding to *ca.* 1 mg mL^{-1}) DMBA were prepared daily by dissolving appropriate amounts of the compound in dimethylsulphoxide (DMSO). When it was necessary, more dilution of working solutions was prepared with the use of same solvent. CV experiments were recorded in DMSO and ionic strength was maintained at 0.1 M with lithium perchlorate ($LiClO_4$) as the supporting electrolyte. In case of stripping analysis in aqueous solutions, three different supporting electrolytes, namely acetate (0.1 M, pH 4.8), phosphate (0.1 M, pH 3, 7.4 and 9) and Britton–Robinson (0.1 M, pH 6) buffer solutions containing 0.02 M NaCl were used. The supporting electrolyte under voltammetric investigation of the DMBA–DNA interaction was a phosphate buffer solution (0.05 M, pH 7.4) containing 0.02 M NaCl, which served as physiological

medium. The stock solution of the ds-DNA (1 mg mL^{-1}) was prepared in TE solution (10 mM Tris–HCl, 1 mM EDTA, pH 8.00).

Solutions at all stages of the study were made with deionized water (Milli-Q quality), and were kept in the dark and in refrigerator.

2.4. Procedures

2.4.1. Pretreatment of glassy carbon electrode

Before each measurement, GCE was thoroughly polished with aqueous slurry of alumina powder (φ: 0.01 μm) on a damp smooth polishing cloth (BAS velvet polishing pad), and then was subjected to an electrochemical treatment by keeping it for 60 s at +1.6 V in DMSO/0.1 M $LiClO_4$ mixture.

2.4.2. Fabrication and pretreatment of pencil graphite electrode

The preparation of PGE was carried out as described earlier [45]. In brief, a mechanical pencil Model T 0.5 (Rotring, Germany), was used as a holder for pencil lead (Tombo, Japan), which were purchased from a local bookstore. All leads had a total length of 60 mm and a diameter of 0.5 mm. Electrical contact to the lead was achieved by wrapping a metallic wire around the metallic part of the pencil. A total of 10 mm of lead was immersed in solution per measurement. Such length corresponds to an active electrode area of 15.9 mm^2. Each measurement was performed using a new pencil surface.

To obtain a more sensitive and stable analytical signal, PGE surface was pretreated by applying a potential of +1.4 V for 60 s (in case of cyclic voltammetric studies, +1.6 V for 90 s) in the selected supporting electrolyte without stirring.

2.4.3. Adsorptive stripping voltammetric procedure

For stripping studies, the pre-concentration/medium exchange/voltammetry scheme was adopted. Required aliquot of the DMBA working solutions were placed in a pre-concentration cell containing a buffer solution. The pretreated bare PGE (unless otherwise indicated) was kept in the cell, and the solution was stirred at a chosen accumulation potential throughout the selected the accumulation period. The electrode was then placed in the measurement cell containing the same buffer solution, previously washed with water and with the blank background electrolyte. Subsequently, an anodic sweep was carried out towards more positive potentials using the selected voltammetric technique. The measurements were made at room temperature. The common instrumental parameters for SWV (unless otherwise indicated) were as follows: pulse amplitude, 25 mV; frequency, 50 Hz; step potential, 16 mV; rest period, 10 s; stirring rate, 400 rpm.

2.4.4. Determination in spiked urine samples

Blank urine samples were obtained from a healthy and non-smoking donor (male, age 30 years). An aliquot volume of sample was fortified with DMBA dissolved in DMSO to achieve final concentration of 4×10^{-5} M, and treated with 4.95 mL acetonitrile then the volume was completed to 10 mL with the same urine sample. The samples tubes were vortexed for 1 min and then centrifuged for 10 min at 5000 rpm for removing of unknown endogenous chemicals (an unspiked sample of the same urine was kept as a blank). Appropriate volumes of the supernatant were mixed with the acetate buffer (0.1 M, pH 4.8)/0.02 M NaCl in the voltammetric cell. The pretreated bare PGE was immersed in the solution for 360 s at a fixed potential of +0.60 V using 400 rpm stirring rate (pre-concentration step). The electrode was then washed with water and with the blank acetate buffer (pH 4.8), and transferred into the measurement cell containing the acetate buffer at pH 4.8 (with 0.02 M NaCl). Subsequently, the square-wave voltammogram was recorded from +0.40 to +1.40 V in steps of 16 mV at 50 Hz with a pulse amplitude of 25 mV. Successive measurements were carried out by repeating the above assay protocol on a new PGE surface using a new pre-concentration solution.

2.4.5. Electrode preparation for DMBA-DNA interaction studies

DNA immobilization: The ds-DNA was immobilized onto the pretreated PGE surface by adsorptive accumulation for 300 s at +0.5 V in supporting electrolyte containing 10 μg mL^{-1} of DNA under stirred conditions. The electrode was then gently rinsed with a clean supporting electrolyte for 5 s for removal of the unbound ds-DNA at the electrode surface.

Interaction of surface-confined DNA with DMBA: After the DNA immobilization step described above, the ds-DNA-coated PGE was transferred to the stirred supporting electrolyte containing DMBA concentration of 1 μg mL^{-1} (unless otherwise indicated). The adsorption, at open circuit conditions, was allowed to proceed for 300 s (unless otherwise indicated). The biosensor was then rinsed for 5 s in a clean supporting electrolyte.

Interaction of solution-phase DNA with DMBA: DMBA in the concentration level of 1 μg mL^{-1} was added to supporting electrolyte containing DNA at a concentration of 10 μg mL^{-1}. A PGE was first pretreated as described above and subsequently immersed into the mixture solution. The accumulation of the mixture was performed for 300 s while holding the potential at +0.5 V under stirred conditions. The electrode was then washed with a clean supporting electrolyte for 5 s.

Signal transduction: The oxidation signals of DMBA and adenine were measured by using DPV (amplitude: 50 mV; step potential: 8 mV; scan rate: 16 mV s^{-1}) between +0.45 and +1.40 V in a fresh supporting electrolyte.

Successive measurements were carried out by repeating the above assay protocol on a new PGE surface using a new pre-concentration solution.

3. Results and discussion

3.1. Cyclic voltammetry on the glassy carbon and pencil graphite electrodes in non-aqueous solution

The voltammetric oxidation of 8×10^{-4} M DMBA solution on the GCE and PGE was investigated in DMSO without prior accumulation time. DMBA exhibited one distinct and well-defined oxidation peak (peak I) with a maximum at about +1.15 V and one broad peak (peak II) at more positive potential (*ca.* +1.33 V) at scan rate of 100 mV s^{-1} for both electrodes as depicted by cyclic voltammograms given in Fig. 2A and B. It seems to be relatively high background current of PGE arising from clays and polymers present in pencil graphite. However, its usage was proved to be much more sensitive, yielding current densities (obtained by subtracting the background currents from the recorded currents) *ca.* two times higher than those obtained by using GCE.

The initial oxidation step (peak I) could be due to the one-electron transfer which corresponds to the formation of DMBA radical cation intermediate, benzylic radical. As reported on the literature data [15], the CV of DMBA in dimethylformamide under reversible conditions revealed that the oxidation of this compound involves only one electron. The point concerning the broad peak (peak II), which follows the initial oxidation of DMBA, remained obscure. Bearing in mind the anodic voltammetric behavior of benzo[*a*]pyrene, unsubstituted PAH compound, in non-aqueous solvents which has been previously discussed [46], we suggest that peak II could be attributed to either the oxidation of the product from solvent interaction with the DMBA cation radical or the formation of DMBA dication. No corresponding reduction peaks were observed on scan reversal, indicating irreversibility of

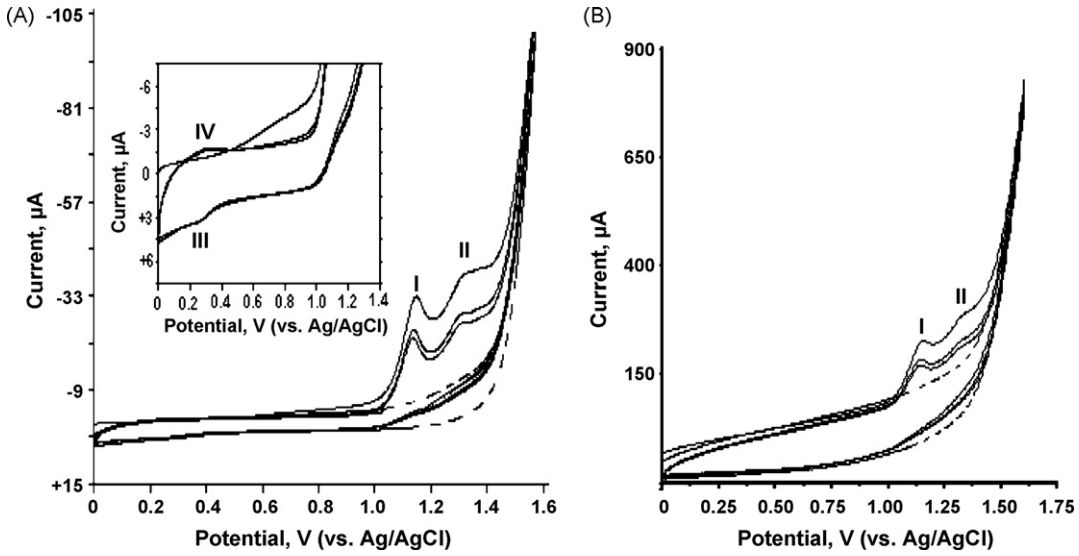


Fig. 2. Repetitive cyclic voltammograms of 8×10^{-4} M DMBA solutions in DMSO for GCE (A) and for PGE (B). Scan rate, 100 mV s^{-1}. Inset: enlargement of reversible redox couple for A. Dashed lines represent background current.

the processes. At lower concentrations of DMBA, these two processes became ill-defined waves, their shape changing from peak to sigmoidal. For the reverse scan and in subsequent scans, a new reversible redox couple producing a reduction (wave III) and re-oxidation (wave IV) wave, appeared in considerably lower positive potential region (Fig. 2A, see inset: enlargement of reversible redox couple). However, this couple was poorly defined in DMSO, where the product solubility may be low. The appearance of these closely spaced waves supported that a chemical reaction subsequent to the electron step occurs, giving rise to species more readily oxidized than DMBA. If successive scans are made, it can be observed that the oxidation process at more positive potentials decreases as the number of scans increase, while the intensity of this couple increases slightly, which confirms this couple arises from the product of follow-up chemical reaction of the DMBA oxidation. Such behavior was also observed and became more pronounced for the oxidation of benzo[*a*]pyrene in the same solvent (our unpublished results will be reported elsewhere soon).

Since the initial oxidation step was more intense, it was selected for analysis purposes. When the scan rate was varied from 5 to 1000 mV s^{-1} at GCE, a 160-mV positive shift in the peak potential was observed as expected for an irreversible oxidation with the simultaneous increase in the peak current. Plotting the logarithm of peak current versus logarithm of scan rate gave up a straight line (correlation coefficient 0.997) with a slope of 0.51. The slope means that process is predominantly controlled by diffusion, although partially coupled to weak adsorption in the whole scan rate range studied. Furthermore, a linear dependence of the peak current upon the square root of the scan rate (correlation coefficient 0.994) was found, demonstrating a diffusional behavior.

3.2. Stripping analysis on the pencil graphite electrode in aqueous solution

Under the voltammetric investigation leading to analytical methodologies, we planned to study in aqueous samples, not only to alleviate the need for a high volume of organic solvents but in order to make possible the application of proposed method in PAHs-contaminated aquatic environments. For this reason the diluted aqueous solutions of DMBA ($\leq 4 \times 10^{-5}$ M) were used due to its low solubility in water. In order to confirm the adsorption of DMBA on working electrodes, preliminary medium exchange experiences were then performed. The PGE electrode was kept in contact with a quiescent solution of assayed concentration of DMBA in background electrolyte for a fixed accumulation time under open circuit. Then it was transferred to another cell containing only the clean electrolyte and the voltammogram was recorded. On the contrary, when the experiment was repeated maintaining the electrode in a stirred solution of DMBA, the voltammogram recorded presented higher peak current. These facts indicate that DMBA undergoes an adsorptive pre-concentration on the electrode surface. Adsorptive stripping voltammetric (AdSV) behavior of DMBA was studied by CV, DPV and SWV techniques after medium exchange.

At first, basic voltammetric behavior of DMBA in aqueous solutions was investigated using CV measurements. Before the measurements, 4×10^{-5} M DMBA in stirred various types of electrolyte solutions (all in 0.1 M containing 0.02 M NaCl), including acetate, phosphate and Britton–Robinson buffers over the pH range of 3–9 was accumulated on the working electrodes (PGE or GCE) using a 300-s open circuit accumulation. Cyclic voltammograms were recorded in the potential range of 0 V to +1.6 V at scan rate of 100 mV s^{-1}. In all of the investigated pH values, two anodic peaks observed in concentrated non-aqueous solutions merged into a single one (Fig. 3A). No peaks were observed in the cathodic scan which indicated that the process was irreversible. Since the DMBA concentration was lower, redox couple could not also be detected. Cyclic voltammogram obtained using the GCE exhibited a similar behavior at comparable potentials; however the peak separation from the background was not better, giving rise to inaccurate measurements of the currents. Furthermore, the GCE severed surface contamination, and the single-use PGE was much superior. For this reason, further electroanalytical experiments were realized using PGE.

The attention was then turned to the effect of solution condition such as pH, which is a critical factor affecting both the rate and equilibrium state of the accumulation process and the rate of the electrode reaction. Due to the poorly resolved stripping signals obtained by CV, the effect of solution acidity on oxidation process was studied using DPV and SWV. Voltammograms were carried out in stirred 4×10^{-5} M DMBA solution with an open circuit mode at 300 s. In application of both DPV and SWV, the appearance of two distinct anodic peaks, together with the improvement of their shapes could be seen between pH 3–7.4. Fig. 3B obtained by applying square-wave scan is representative. At pH 9.0, the second peak

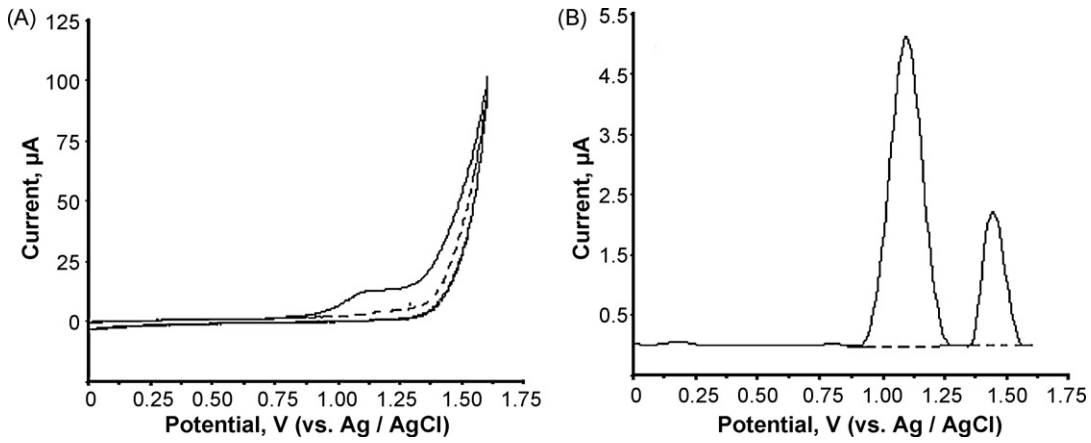


Fig. 3. Cyclic (A) and square-wave (B) voltammograms of 4×10^{-5} M DMBA solution in acetate buffer pH 4.80. CV conditions: scan rate, 100 mV s^{-1}; SWV conditions: pulse amplitude, 20 mV, frequency, 25 Hz, step potential, 8 mV. Dashed lines represent background current.

was not extracted from the background discharge that occurred at less positive potential. The pH did not indicate a significant change in the peak potential over the range studied. For the first peak, a 55- and 70-mV negative shift was only observed upon increasing the pH from 3 to 9 using DPV and SWV, respectively. For the first oxidation step, the peak intensities reached a maximum in acetate buffer pH 4.8. Moreover, the application of square-wave mode for the stripping of adsorbed DMBA was proved to be much more sensitive, yielding signals *ca.* 2.5 times higher than those obtained by applying differential pulse scan. The second oxidation step exhibited a similar behavior however the peak currents were smaller than those of the first one. For remainder of the work, SWV technique was applied in acetate buffer at pH 4.8 by considering the primary oxidation peak.

Further optimization of the analytical signal focused on studying the effect of pre-concentration/stripping conditions, such as accumulation potential and time. The influence of the accumulation potential either at open circuit potential or at a potential range from +0.1 V to +0.8 V was studied with accumulation time of 300 s in stirred 4×10^{-5} M DMBA solution. The value for the stripping current obtained at +0.1 V was nearly equal to the value obtained at open circuit voltage. The maximum peak current was obtained at an accumulation potential of +0.6 V because of an increased accumulation rate, due to more favorable alignment of the molecule by the electric field at the electrode–solution interface. After fixing the accumulation potential at this value, the deposition time was varied between 30 and 480 s. The increasing the peak currents were obtained at a fast rate up to about 360 s and starting to level off for longer times above this value. The peak potentials undergo a small displacement towards more negative potentials; this indicates the need of a larger energy to attain the stripping of the adsorbate from the electrode. For further analytical studies, the deposition stage was carried out at +0.6 V for a pre-concentration time of 360 s.

Square-wave stripping voltammograms at different concentrations of DMBA were recorded under the maximum current experimental conditions. The use of DMBA oxidation at about +1.15 V as the first analytical peak allowed quantification in the range of 2 nM to 10 nM with a regression equation of i_p (μA) = 0.217 C (nM) − 0.134 (correlation coefficient, 0.992). A detection limit of 0.194 nM was estimated based on signal-to-noise characteristics of the data for S/N = 3. The repeatability of the stripping signal was realized in terms of relative standard deviation for ten identical measurements carried out at a concentration level of 6 nM DMBA of a new PGE surface using a new solution in the cell and found to be 5.1%. A variation of the DMBA concentration was found to have a slight influence on the peak potential. The peak potential shifted towards more negative values when the concentration was increased.

The selectivity of such determination could be limited by interactions of structurally similar compounds with DMBA. However, this is not a case of samples with one class of compounds or one analyte present.

Since DMBA solutions undergo photooxidation in air and light, they were freshly prepared and kept in dark-colored, tightly closed containers. However, to check its stability, the voltammograms of stock solutions in DMSO stored in the dark and in refrigerator were recorded after two-week periods. When the voltammograms were compared with those of samples freshly prepared they did not show any appreciable change, demonstrating that DMBA solutions were stable for this period. Taking into account that the stability of aqueous solutions containing PAHs is a major problem due to their tendency to be absorbed on surfaces of polyethylene containers [47], all solutions were stored in glass vials. In daily laboratory practice, no significant decrease was evident among the calibration samples throughout the study period.

In view of the sensitivity (extremely low detection limit) of the proposed method, PGE electrode was applied to the determination of DMBA in simulated human urine.

The presence of proteins, major components of the sample matrix which could be adsorbed on the electrode surface together with analyte is an important drawback of adsorptive voltammetric techniques. In case of our study, when the voltammograms were recorded in 1:100 blank urine dilutions smooth curves were not obtained in the potential range from +0.4 to +1.4 V comparing to those of the background electrolyte. To obviate this problem, the extraction with acetonitrile followed by centrifugation protocol, that was quick and easy, was applied together with a medium exchange procedure. After medium exchange technique (analogous to solid phase extraction methods), none of the potentially interfering electroactive urine components contributed to the response and DMBA could easily be measured as shown in Fig. 4.

In order to check if the linearity persists, a new calibration plot was carried out in urine samples. In this case, the voltammetric response measured in urine was linearly related to the concentration of DMBA within the range of 0.2–0.8 μM according to the equation: i_p (μA) = 2.39 C (μM) + 0.025 (correlation coefficient, 0.999) with a detection limit of 0.04 μM. Under these conditions a decrease in the signal was observed comparing to that obtained in aqueous solution without urine. The matrix of the sample did not reduced the reproducibility of the signal as demonstrated by recording three voltammograms for each of the urine samples containing DMBA in the concentration range mentioned above. In

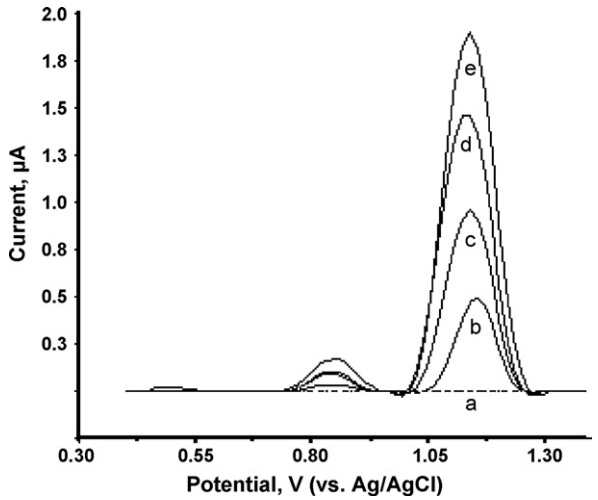


Fig. 4. Square-wave voltammograms obtained for the determination of DMBA in spiked urine. Blank urine (a), urine spiked at a DMBA level of 0.2 μM (b), 0.4 μM (c), 0.6 μM (d), 0.8 μM (e). For operating conditions, see Section 2.4.4.

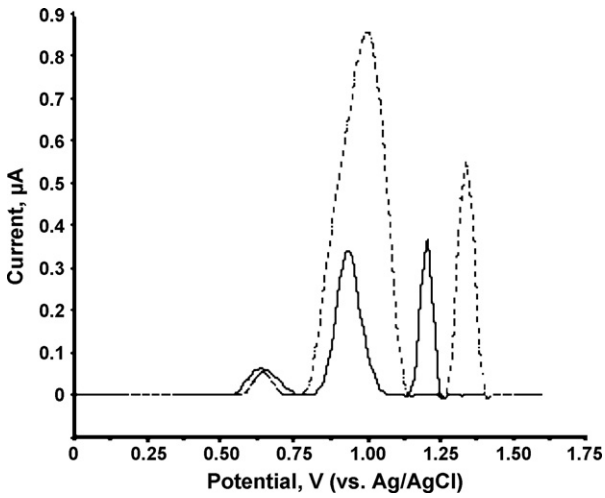


Fig. 5. Differential pulse voltammograms for 4×10^{-5} M (10.3 μg mL^{-1}) DMBA (dashed line) and 10 μg mL^{-1} DNA (solid line). Supporting electrolyte, phosphate buffer pH 7.40.

urine, results were characterized by higher precision comparing to those obtained in aqueous solutions, probably due to the fact that concentration in urine samples was relatively higher. An average relative standard deviation was found to be 2.9%. There was no degradation of the DMBA in solution during the experiments.

3.3. Interaction with DNA on the pencil graphite electrode

Before interaction differential pulse voltammograms for DNA and DMBA in phosphate buffer (pH 7.40) are shown in Fig. 5. Under the conditions of the experiment, the redox behavior of original ds-DNA immobilized PGE exhibited two oxidation processes of guanine (G, *ca.* +0.93 V) and adenine (A, *ca.* +1.20 V) residues. DMBA produced two oxidation peaks at around +1.05 and +1.40 V with a pre-concentration step on PGE at open circuit condition for 300 s in a stirred supporting electrolyte (explained above). Guanine and DMBA (first peak) oxidation peaks coincided with each other, whereas separation of adenine and DMBA (first and second peaks) oxidation peaks was possible even if at high concentration of DMBA. That is why we could compare only adenine oxidation peak changes.

Fig. 6 displays the DPV signals, which were monitored in blank supporting electrolyte, obtained before/after interaction of 1 μg mL^{-1} DMBA with 10 μg mL^{-1} ds-DNA both at the electrode surface and in solution. In the case of both interaction protocols (following the association with DMBA), a considerable diminution in peak current was observed.

It is known that planar condensed aromatic ring systems play a major role in their intercalative DNA binding, primarily involving stacking interactions. Binding of the intercalators to DNA results in a significant change in DNA conformation, and can be followed by electrochemical methods [48,49]. On the other hand, it is reported the synthesis of two detectable DNA adducts by the electrochemical oxidation of DMBA in the presence of dA. A covalent bond is formed specifically at the 12-CH_3 and 7-CH_3 group of DMBA for the N-7 and N-3 position of adenine, respectively [15]. Taking into account these findings, the decrease in the adenine signal could be attributed to either the penetration into the DNA double-helix between adjacent base pairs (non-covalent interaction) or forming adducts through covalently binding to sites in DNA.

The reproducibility of DNA biosensor protocol was also evaluated from three repetitive measurements for the concentration 10 μg mL^{-1} DNA and 1 μg mL^{-1} DMBA. In the absence of DMBA, measurements yielded a reproducible result with a mean peak height of 374 nA and a relative standard deviation of 3.74%, indicating that the preparation of working electrode was satisfactory. After interaction of DMBA at electrode surface or in solution, the series resulted in mean peak heights of 166 and 159 nA and relative standard deviations of 4.86 and 13.46%, respectively. Following a 5 min accumulation, the detection limits of DMBA, which were esti-

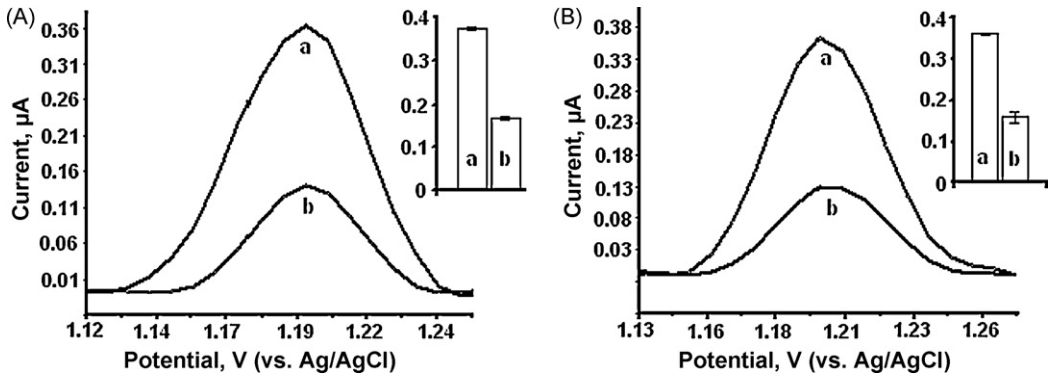


Fig. 6. Differential pulse voltammograms for 0 (a) and 1 μg mL^{-1} (b) DMBA after the interaction of surface-confined DNA (A) and solution-phase DNA (B) at a 5-min accumulation. Inset: the results were also demonstrated with bar charts. For operating conditions, see Section 2.4.5.

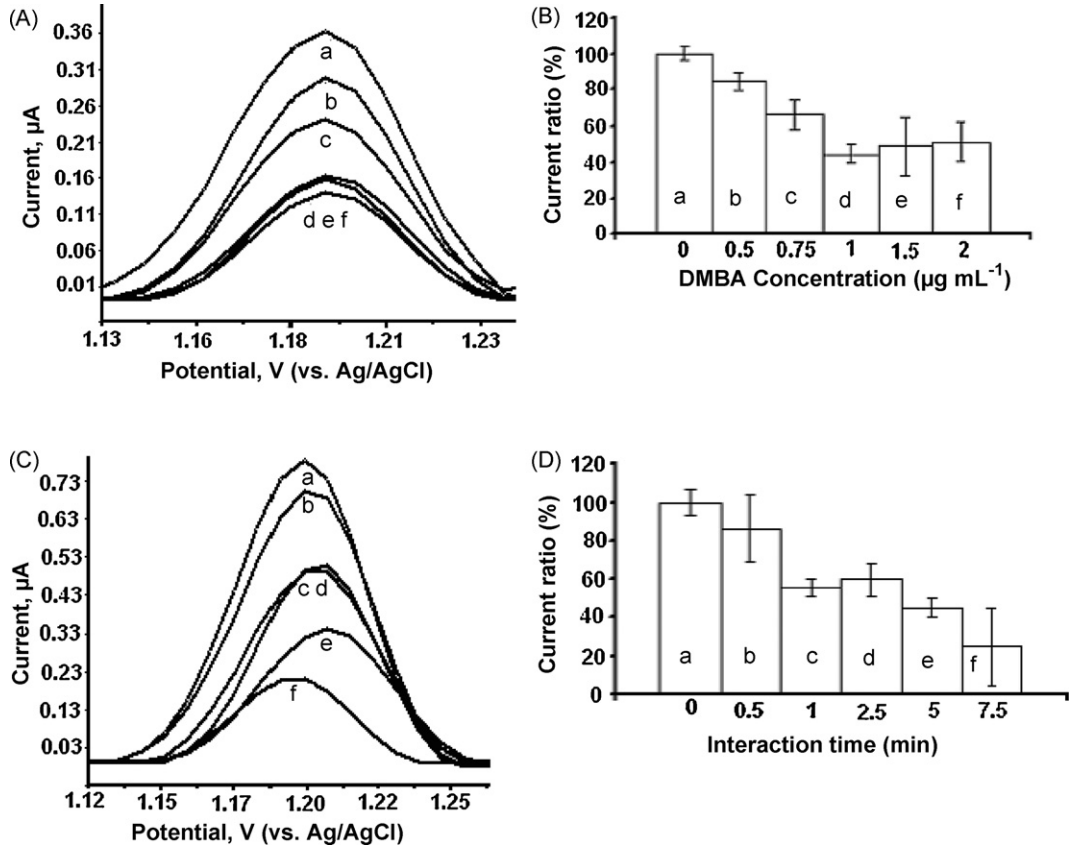


Fig. 7. The effect of DMBA concentration (A) and accumulation time (C) upon the DPV response of adenine after interaction of surface-confined DNA for 5 min (A) and with 1 μg mL^{-1} DMBA (C). The results were also shown as the peak current ratio (B and D). For operating conditions, see Section 2.4.5.

mated from the signal-to-noise characteristics of the data (S/N = 3), were found as 11.8 and 11.9 ng mL^{-1} (corresponding to *ca.* 46 nM) for interaction of surface-confined and solution-phase ds-DNA, respectively. Bearing in mind that the size (ring number), and conformation of the molecule play a major role in its DNA binding [40,50], four-ring structure of DMBA may account for its higher sensitivity. Such detection limits are low enough for assays of polluted environmental samples. The results obtained by the interaction in solution phase were found to be less suitable for this study because of the relatively poor reproducibility. Thus, the assay protocol at the electrode surface was chosen for remaining parts.

The dependence of DMBA concentration (in the range 0–2 μg mL^{-1}) on the adenine signal was shown in Fig. 7A and B. In the presence of DMBA, adenine oxidation peaks decreased linearly with concentration up to 1 μg mL^{-1} according to the equation: i_p (μA) = −0.294 C (μg mL^{-1}) + 0.465 (correlation coefficient, 0.999), and almost leveled off for more concentrated solutions. In repetitive measurements, the relative standard deviation values of DMBA measurements did not exceed 8% in the range 0.5–1 μg mL^{-1}, whereas the higher values (above 10%) occurred at the concentration above the linearity of calibration curve. Since the linear range looks shorter, the improvement in application of assay protocol would be resulting in relatively wide range of DMBA concentration.

Fig. 7C and D displays the influence of DMBA interaction time (in the range 0–7.5 min) at ds-DNA immobilized PGE surface upon the changes in the adenine signal. There was a decrease on adenine signal till 1 min. The response remained nearly constant from 1 min to 2.5 min then decreased again. The time-dependent profile which differs from compound to compound is due to the binding kinetics of the analyte-DNA interaction [49]. The optimum time for interaction of DMBA with ds-DNA was found as 5 min, since the changes at the adenine peak before/after the interaction with DMBA could clearly be observed following this accumulation time.

4. Conclusion

In the present study, the DMBA molecule was chosen for two specific reasons. First, it is a highly interesting and valuable tool in investigations of bioactivation processes as they relate to the etiology of several important pathological conditions. Second, it is a synthetic model PAH compound of controlled laboratory environment. Thus, the present observations dealing with voltammetric studies on DMBA may be similar to the finding of other large hydrocarbon systems.

We note that elucidating the mechanism of DMBA electrochemical oxidation is not an easy task and is beyond the scope of the present work. It only shows how the compound is oxidized in aqueous and non-aqueous media at carbon-based electrodes. Although the sufficient data are not available to determine the exact oxidation mechanism, it is hoped that knowledge of the voltammetric oxidation behavior of DMBA would help with a better understanding of the carcinogenic and oxidative pathways of PAHs in their metabolism and provide a more comprehensive picture.

The anodic voltammetry of aromatic hydrocarbons has been studied in great detail in acetonitrile, dimethylformamide, methylene chloride, propylene carbonate and nitrobenzene. The stability of the intermediates formed is affected markedly by the solvent, undergoing a series of chemical and additional electrochemical steps. In case of our study, DMSO was selected as the solvent. For medicine purposes, DMSO has proved a popular choice due to its suitability as fatty emulsions for the intravenous administration of

DMBA, maintaining the stability [51]. This encouraged its use in a clinical measurement sensor for the animal assays in future.

GCE is the most common carbon-based electrode in current use. However, anodic voltammetry at GCE is more frequently used for research purposes than for routine analytical determinations because of its passivation which can decrease of the sensitivity. Although disposable PGE is relatively new type of carbon electrode, it has become of interest in the field of sensitive and simple monitoring of toxic compounds including carcinogenic compounds by virtue of its high electrochemical reactivity, good mechanical rigidity, low-cost, low technology and ease of modification. In the environmental sense, disposable PGE in combination with field-based experiments can be much more attractive than the electrodes commonly used in the laboratory, i.e. GCE, because of the avoiding the need for extensive time delays, and considerable risk of contamination or loss of analyte of interest [52]. In this study, the PGE combined with more highly sensitive and accurate AdSV could allowed to an attractive trace analysis of DMBA from the aqueous solutions with the detection limit that reached the level as low as 0.194 nM (49.7 ng L^{-1}). This value is comparable to those obtained by commonly used chromatographic techniques for environmental carcinogens [53]. Therefore this technique could not only be used for monitoring the efficiency of destruction of DMBA in laboratory wastes, but serve as a model for the determination of trace risk chemicals in contaminated aquatic environments [54].

Following PAHs exposure, most of the absorbed compounds via different exposure pathways, i.e. inhalation, dermal contact, and ingestion of contaminated food are metabolized and eliminated in urine as phenols [55] while only a smaller amount is excreted unchanged in urine [56]. However, measurement of unmetabolized PAHs, instead of metabolites, in urine can be very useful for several reasons: their elimination is directly associated to previous exposure; they are less susceptible to intra-individual variability; they are characterized by a high degree of specificity [57]. With this aim, the possibility of measuring the DMBA in simulated human urine was also demonstrated. Owing to the complexity of the biological samples in which chemical carcinogens are sought, conventional biomonitoring methods are often time-consuming, labor intensive and expensive. They often incorporate a preliminary separation, involving extraction, filtration, fractionation, drying of extracts, redissolution and other steps. Using proposed technique, no sample pretreatment was required, other than precipitation in the presence of *ca.* 50% acetonitrile and dilution steps. Solvent addition is expected to increase DMBA solubility and reduce its absorption on container walls as well as to eliminate the influence of proteins. The performance of the stripping step in clean electrolyte was very convenient from the point of eliminating possible interferences with similar redox potential (not or slightly adsorbed) in urine. However, its detection limit found urine samples (0.04 μM corresponding to 10.3 μg L^{-1}) was not low enough to reach the levels expected in urine after the exposure to PAHs through especially multiple media [55]. We plan to undertake the investigations to improve the sensitivity together with the selectivity by combining HPLC with proposed adsorptive stripping technique at PGE.

In this study it was also presented for the first time a new screening tool for DMBA. Such use of DNA interaction as a basis for electrochemical biosensor results in a simple, cost effective, rapid, reliable and sensitive detection of DMBA. This promising approach might be a key step not only to detect very low concentrations of DMBA, but also to clarify its reaction mechanism concerning its role in the tumor formation.

Due to the fact that PAHs are very hydrophobic, they tend to be stored in fat tissue, liver and kidney (common target organs) [51]. Considering this knowledge, the preliminary investigation (experiments in vitro) was performed in these tissues of the rats which were first treated with DMBA dissolved in olive oil as orally, and then followed for tumor production. The use of proposed method represented satisfactory results giving well-defined voltammetric responses in the tissue extracts. Studies on laboratory animals are continuing in the development of these measurements.

Acknowledgements

This work was supported by the Yüzüncü Yıl University Scientific Research Foundation (Project no. 2007-FED-B44). It is produced from PhD thesis of Yavuz Yardım and Ertuğrul Keskin (Yüzüncü Yıl University, Institute of Natural and Applied Sciences). The authors thank to Gökhan Oto, PhD (Yüzüncü Yıl University Faculty of Medicine) for his kind help on partially supplying DMBA standard sample.

References

[1] R.G. Harvey, Polycyclic Aromatic Hydrocarbons, Wiley-VCH, New York, 1991.
[2] H. Yu, J. Environ. Sci. Health C20 (2002) 149–183.
[3] W.M. Baird, L.A. Hooven, B. Mahadevan, Environ. Mol. Mutagen 45 (2005) 106–114.
[4] R. Todorovic, F. Ariese, P. Devanesan, R. Jankowiak, G.J. Small, E. Rogan, E. Cavalieri, Chem. Res. Toxicol. 10 (1997) 941–947.
[5] N. Yusuf, L. Timares, M.D. Seibert, H. Xu, C.A. Elmets, Toxicol. Appl. Pharmacol. 224 (2007) 308–312.
[6] M.C. Poirier, R.M. Santella, A. Weston, Carcinogenesis 21 (2000) 353–359.
[7] E.F. Madden, Rev. Environ. Health 18 (2003) 91–109.
[8] G.N. Wogan, S.S. Hecht, J.S. Felton, A.H. Conney, L.A. Loeb, Sem. Cancer Biol. 14 (2004) 473–486.
[9] M. Mascini, Pure Appl. Chem. 73 (2001) 23–30.
[10] T. Ohe, T. Watanabe, K. Wakabayashi, Mutat. Res. 567 (2004) 109–149.
[11] M. Jakubowski, M. Trzcinka-Ochocka, J. Occup. Health 47 (2005) 22–48.
[12] S.K. Hyung, H.B. Soo, M.L. Byung, J. Toxicol. Environ. Health Part A 68 (23) (2005) 2081–2095.
[13] S. Zhang, P.W. Villalta, M. Wang, S.S. Hecht, Chem. Res. Toxicol. 20 (2007) 565–571.
[14] S. De Flora, S. Scarfi, A. Izzotti, F. D'agostini, C.-C. Chang, M. Bagnasco, A. De Flora, J.E. Trosko, Int. J. Oncol. 29 (2006) 521–529.
[15] N.V.S. RamaKrishna, E.L. Cavalieri, E.G. Rogan, G. Dolnikowski, R.L. Cerny, M.L. Gross, H. Jeong, R. Jankowiak, G.J. Small, J. Am. Chem. Soc. 114 (1992) 1863–1874.
[16] P. Brookes, P.D. Lawley, Nature 202 (1964) 781–784.
[17] Y.L. Ha, N.K. Grimm, M.W. Pariza, Carcinogenesis 8 (1987) 1881–1887.
[18] N.V.S. RamaKrishna, P.D. Devanesan, E.G. Rogan, E.L. Cavalieri, H. Jeong, R. Jankowiak, G.J. Small, Chem. Res. Toxicol. 5 (1992) 220–226.
[19] M. Miyata, M. Furukawa, K. Takahashi, F.J. Gonzalez, Y. Yamazoe, Jpn. J. Pharmacol. 86 (2001) 302–309.
[20] H.E. Kleiner, S.V. Vulimiri, M.J. Reed, A. Uberecken, J. DiGiovanni, Chem. Res. Toxicol. 15 (2002) 226–235.
[21] J.D. Moody, P.P. Fu, J.P. Freeman, C.E. Cerniglia, Appl. Environ. Microbiol. 69 (2003) 3924–3931.
[22] J. Gao, F.T. Lauer, L.A. Mitcell, S.W. Burchiel, Toxicol. Sci. 98 (2007) 137–144.
[23] Y.S. Kim, K.N. Bahn, C.K. Hah, H.I. Gang, Y.L. Ha, J. Food Sci. 73 (2008) T16–T20.
[24] Y. Cai, H. Kleiner, D. Johnston, A. Dubowski, S. Bostic, W. Ivie, J. DiGiovanni, Carcinogenesis 18 (1997) 1521–1527.
[25] R.C. Moschel, M.A. Piggot, N. Constantino, A. Dipple, Carcinogenesis 4 (1983) 1201–1204.
[26] P. Vigny, A. Brunissen, D.H. Phillips, C.S. Cooper, A. Hewer, P.L. Grover, P. Sims, Cancer Lett. 26 (1985) 51–59.
[27] P.P.J. Mulder, L. Chen, B.C. Sekhar, M. George, M.L. Gross, E.G. Rogan, E.L. Cavalieri, Chem. Res. Toxicol. 9 (1996) 1264–1277.
[28] J.J. Li, D. Papa, M.F. Davis, S.J. Weroha, C.M. Aldaz, K. El-Bayoumy, J. Ballenger, O. Tawfik, S.A. Li, Mol. Carcinog. 33 (2002) 56–65.
[29] K. Randerath, P. Sriram, B. Moorthy, J.P. Aston, R.A. Baan, P.T.M. Van Den Berg, E.D. Booth, W.P. Watson, Chem. Biol. Interact. 110 (1998) 85–102.
[30] M.V. Vadhanam, J.W. HornFlesher, R.C. Gupta, Chem. Biol. Interact. 146 (2003) 81–87.
[31] D. Malejka-Giganti, K.K. Bennett, S.J. Culp, F.A. Beland, H. Shinozuka, R.L. Bliss, Cancer Detect. Prev. 29 (2005) 338–347.
[32] H. Yu, J. Yan, Y. Jiao, P.P. Fu, Int. J. Environ. Res. Public Health 2 (2005) 114–122.
[33] L. Teodori, F. Tagliaferri, F. Stipa, M.G. Valente, D. Coletti, A. Manganelli, M. Guglielmi, L.S. D'Angelo, H. Schafer, W. Göhde, In Vitro Cell Dev. Biol. Anim. 36 (2000) 153–162.
[34] L. Sivaraman, J. Gay, S.G. Hilsenbeck, H.D. Shine, O.M. Conneely, D. Medina, B.W. O'Malley, Breast Cancer Res. Treat. 73 (2002) 75–83.
[35] Y.K. Chen, S.S. Hsue, L.M. Lin, Arch. Oral Biol. 47 (2002) 695–699.
[36] S. Bagni, M. Hernandez, E. Mascini, P. Sturchio, S. Boccia, Marconi, Sensors 5 (2005) 394–410.
[37] K. Kerman, B. Meric, D. Ozkan, P. Kara, A. Erdem, M. Ozsoz, Anal. Chim. Acta 450 (2001) 45–52.

[38] F. Lucarelli, A. Kicela, I. Palchetti, G. Marrazza, M. Mascini, Bioelectrochem 58 (2002) 113–118.
[39] F. Lucarelli, L. Authier, G. Bagni, G. Marrazza, T. Baussant, E. Aas, M. Mascini, Anal. Lett. 36 (2003) 1887–1901.
[40] G. Bagni, T. Baussant, G. Jonsson, J. Barsiene, M. Mascini, Anal. Lett. 38 (2005) 2639–2652.
[41] M. Del Carlo, M. Di Marcello, M. Perugini, V. Ponzielli, M. Sergi, M. Mascini, D. Compagnone, Microchim. Acta 163 (2008) 163–169.
[42] V. Podany, E. Rezabkova, L. Bahna, Neoplasma 25 (1978) 57–65.
[43] P. Cremonesi, E. Rogan, E. Cavalieri, Chem. Res. Toxicol. 5 (1992) 346–355.
[44] NIH Guidelines for the Laboratory Use of Chemical Carcinogens, NIH Publication No. 81-2385. U. S. Government Printing Office, Washington, D.C. 1981.
[45] J. Wang, A.N. Kawde, E. Sahlin, Analyst 125 (2000) 5–7.
[46] L. Jeftic, R.N. Adams, J. Am. Chem. Soc. 92 (1970) 1332–1337.
[47] L. Campo, R. Mercadante, F. Rossella, S. Fustinoni, Anal. Chim. Acta 631 (2009) 196–205.
[48] M. Fojta, L. Havran, J. Fulneckova, T. Kubicarova, Electroanalysis 12 (2000) 926–934.
[49] M. Fojta, Electroanalysis 14 (2002) 1449–1463.
[50] J. Wang, G. Rivas, D. Luo, X. Chai, F.S. Valera, N. Dontha, Anal. Chem. 68 (1996) 4365–4369.
[51] J. Digiovanni, M.R. Juchau, Drug. Metab. Rev. 11 (1980) 61–101.
[52] A.M. Bond, P.J. Mahon, J. Schiewe, V. Vincente-Beckett, Anal. Chim. Acta 345 (1997) 67–74.
[53] J. Barek, J. Cvacka, A. Muck, V. Quaiserova, J. Zima, Fresenius J. Anal. Chem. 369 (2001) 556–562.
[54] K. Srogi, Environ. Chem. Lett. 5 (2007) 169–195.
[55] J. Angerer, C. Mannschreck, J. Gündel, Int. Arch. Occup. Environ. Health 70 (1997) 365–377.
[56] G. Becher, A. Bjørseth, Cancer Lett. 17 (1983) 301–311.
[57] L. Campo, L. Addario, M. Buratti, L. Scibetta, O. Longhi, C. Valla, P.E. Cirla, I. Martinotti, V. Foa, S. Fustinoni, Toxicol. Lett. 162 (2006) 132–138.

Talanta 80 (2010) 1356–1363

Contents lists available at ScienceDirect

Talanta

journal homepage: www.elsevier.com/locate/talanta

Batch and hydrodynamic monitoring of vitamin C using novel periodate selective sensors based on a newly synthesized Ni(II)-Schiff bases complexes as a neutral receptors

Ayman A. Abdel Aziz, Ayman H. Kamel *

Chemistry Department, Faculty of Science, Ain Shams University, Cairo, Egypt

ARTICLE INFO

Article history:
Received 25 July 2009
Received in revised form
16 September 2009
Accepted 18 September 2009
Available online 24 September 2009

Keywords:
Schiff bases
Potentiometric sensors
Periodate
Ascorbic acid
Flow injection analysis (FIA)
Flavored water

ABSTRACT

A highly selective membrane electrodes based on a two newly synthesized nickel (II) Schiff bases, [NiL^1] and [NiL^2] where L^1 and L^2 are N,N/bis(salicylaldehyde)4,5-dimethyl-1,2-phenylenediamine (H_2L^1) and N,N/bis(salicylaldehyde)4,5-dichloro-1,2-phenylenediamine (H_2L^2) were used as a neutral carrier ionophores for static and hydrodynamic potentiometric mode of operations for the determination of periodate. Under static mode of operation, the sensors displayed a near-Nernstian slope of -66.1 ± 0.8 and -59.9 ± 1.1 mV decade^{-1} of activity and detection limits to 5.2×10^{-6} and 7.3×10^{-6} mol L^{-1} for the sensors based on [NiL^1] and [NiL^2], respectively. Under hydrodynamic mode of operation (FIA), the slope of the calibration plot, limit of detection, and working linear range were -71.1 mVdecade^{-1} of activity, 7.3×10^{-6} and 1.0×10^{-5} to 1.0×10^{-3} mol L^{-1}, respectively. The response time of the sensors in whole concentration ranges was very short (<10 s). The response of the sensors was independent on the pH range of 3–8. A tubular version was further developed and coupled to a flow injection system for ascorbic acid (AA) determination in beverages and pharmaceutical preparations. This approach was achieved by selecting a 50-cm reactor and an overall flow of 3 mL min^{-1}, and injecting volume 100 μL of AA standards in a 1.0×10^{-4} mol L^{-1} IO_4^- solution. Under these conditions, a linearity range of 2–13 μg mL^{-1}, with a slope of 4.97 mV (mg/L)$^{-1}$ ($r^2 = 0.9995$), detection limit 0.9 mg L^{-1} and a reproducibility of ±1.1 mV ($n = 5$) was recorded. This simple and inexpensive flow injection analysis manifold, with a good potentiometric detector, enabled the analysis of ~50 samples h^{-1} without requiring pretreatment procedures. An average recovery of 98.8% and a mean standard deviation of 1.3% were obtained.

© 2009 Elsevier B.V. All rights reserved.

1. Introduction

L-Ascorbic acid (Vitamin C) is a γ-lactone synthesized by plants and many animals (except primates). It is a water-soluble vitamin usually used as a dietary supplement in pharmaceutical preparations and in manufactured food and beverages as an antioxidant, preventing color changes and alterations of aroma and flavor as well as extending the storage time of the products [1]. This vitamin is among the compound of major biological importance, it plays a key role in the protection against biological oxidation processes participating in many metabolic reactions. It has also been used in the treatment and prevention of common cold, mental illness and infertility. Traditionally, ascorbic acid has been used clinically in the treatment and prevention of scurvy, but it is also important in the regulation of the immunological system and in the tissue reconstruction, which assist the formation of collagen. However, an excess of ascorbic acid can cause gastric irritation and diarrhea and it is metabolized to oxalic acid, which can cause renal problems [2]. On the other hand, the ascorbic acid ingestion is associated to increase absorption of metal transition (as inorganic iron and copper), metabolism of folic acid, amino acid and in biosynthesis of suprarenal hormone, minimizing the stress effect [1].

There is a frequent citation about ascorbic acid as an important exogenous antioxidant. Its chemoprotective action is attributed to two mechanisms of action. It is indeed a good scavenger of free radicals and several reactive oxygen species produced during the metabolic pathways of detoxification [3]. It justifies its association to protection against cancer agents by the prevention of formation of carcinogens precursors' compound [4]. In addition, AA has a reducing property by donation of one electron giving the semi-dehydroascorbate radical (DHA). It also regenerates tocopherol from tocopheroxyl radical providing membrane protection [5,6]. Thus, vitamin C determination is very important for biological and food industry.

Ascorbic acid has been monitored by different analytical methods in pharmaceutical formulations, foods and biological fluids.

* Corresponding author. Tel.: +20100743328.
E-mail address: ahkamel76@yahoo.com (A.H. Kamel).

0039-9140/$ – see front matter © 2009 Elsevier B.V. All rights reserved.
doi:10.1016/j.talanta.2009.09.036

Some of these methods are based on spectrophotometry [7,8], chromatography [9–11], electrophoresis [12,13] and electrochemistry [14–17]. Most of these methods, however, utilize expensive instrumentation, suffer from lack of selectivity, involve careful control of the reaction conditions or derivatization reactions, and require time-consuming pretreatment steps which are not easily applied to colored or turbid samples and affect their usefulness for routine analysis.

Therefore, a more rapid, accurate and simple method is always a target of research. This justifies the attention attracted by electrochemical methods; they possess quick response, low cost, simplicity of instrumentation, high sensitivity and possibility of miniaturization.

Periodate is a good oxidizing agent for α-diols, α-aminoalcohols, and similar compounds. The reaction proceeds at room temperature and usually takes place under mild conditions. Periodate potentiometric sensors have been reported for determination of different compounds, namely dopamine [18], glycerol [19,20], 2,3-butanediol [21], carbohydrates [22], and metal ions [23]. The same principal could be applied to ascorbic acid determination, avoiding tedious sampling pre-treating procedures and enhancing the selectivity and quickness of the procedure. In addition, for an industrial routine control of the analyte the continuous mode of operation is of regular selection. This may be achieved by means of flow injection systems that are particularly attractive in view of their versatility, simplicity and suitability for large-scale analyses.

The goal of the present work is to devise a highly selective periodate membrane electrode with good response properties, such as slope and response time, using the selective coordination chemistry between Schiff bases and Ni(II). Salophens have been found to be potentially useful for this purpose, due to the relative simplicity for their synthesis and the promising results already obtained for periodate based on Ni(II)-salophens. Accordingly in this work, two Ni(II)-salophen structures have been synthesized, well characterized and examined for preparation of periodate selective membrane electrodes.

2. Experimental

2.1. Reagents

$Ni(CH_3COO)_2.4H_2O$, salicylaldehyde, 4,5-dimethyl-*o*-phenylenediamine and 4,5-dichloro-*o*-phenylenediamine were supplied by Aldrich (St. Louis, MO). Tridodecylmethylammonium chloride (TDMAC), *o*-nitrophenyloctyl ether (*o*-NPOE), poly(vinyl chloride) (PVC) were used as received from Fluka (Ronkonkoma, NY). All anions used in selectivity measurements were in the form of sodium or potasium salt and used as received from Aldrich (St. Louis, MO). Tetrahydrofuran (THF) employed to cast membranes was from Sigma-Aldrich. L(+) Ascorbic acid was purchased from Riedel-de Haën. All potentiometric measurements were carried out in 1.0×10^{-2} mol L^{-1} acetate buffer solution adjusted to pH 4.7.

2.2. Equipment

All potentiometric measurements were made at 25 °C with an Orion pH/mV meter (model SA 720) and periodate PVC membrane sensors in conjunction with an Orion Ag/AgCl double junction reference electrode (model 90-02) with 10% (w/v) KNO_3 in the outer compartment. A combination Ross glass pH electrode (Orion 81-02) was used for all pH measurements. The analytical output signal was transferred to a commutation point that enabled the reconnection of the signal to one of six ways out. Each way presented an electrical antenna connector that provided suitable adaptation to one selective electrode. The selective electrodes had no internal reference solution and an epoxy-graphite matrix as conductive solid contact [24]. Batch trials were carried out with electrodes of conventional configuration, and flow ones with electrodes of tubular shape.

The flow injection analysis (FIA) system manifold consisted of a two-channel Ismatech MSREGLO model peristaltic pump. The manifold was connected with polyethylene tubing (Tygon, 0.7 mm i.d.) and an Omnifit injection valve (Rheodyne, Model 7125) with sample loop of 100 μL volume. The potential signals were recorded using an Orion pH/mV meter (model SA 720) connected to a PC through the interface ADC 16 (Pico Technology, UK) and PicoLog for windows (version 5.07) software.

IR measurements (KBr Pellets) were carried out on a Unicam-Mattson 1000 FT-IR. Elemental analyses were carried out on Elementar Vario EL. Ni-content was determined by Perkin Elmer Atomic Absorption Spectrometer. ^1H NMR measurements were performed on JEOL-270 MHz NMR DMSO-d_6 as a solvent and TMS as an internal reference. Molar conductivities of complexes were measured by using Jenway 4010 conductivity meter. Magnetic moments were determined on a Sherwood Scientific magnetic moment balance (Model ML1) at room temperature using Hg $[Co(SCN)_4]$ as a calibrant.

2.3. Syntheses of the ligands

The ligands H_2L^1 as described as in literature [25] and H_2L^2 were synthesized by a similar way according to the synthetic route shown in Scheme 1.

To a hot methanolic solution containing 10 mmol of the amine, 2.11 mL (20 mmol) of salicylaldehyde was added dropwise. The yellow solution obtained was refluxed for 2 h. After cooling, the precipitate Schiff base was collected by filtration and recrystallized from methanol. The ligands were dried in a desiccator over anhydrous $CaCl_2$ under vacuum.

Characteristics of the ligands are as follows:

H_2L^1 ($C_{22}H_{20}N_2O_2$): Yield 63%. Color Yellow. M.P. 148–150 °C. Elemental analysis Calc.(%): C, 76.72; H 5.85; N 8.13. Found: C 76.21; H 5.72; N 7.98. IR (KBr pellet. cm^{-1}): 3428 (ν_{OH}); 1617 ($\nu_{HC=N}$); 1278 ($\nu_{C\text{-}O}$). ^1H NMR (DMSO-d_6, 270 MHz): δ 11.80 (s, 2H; OH); 8.88 (s, 2H; HC=N); 7.50–7.80 (m, 8H; aromatic); 7.30 (s, 2H, aromatic); 2.46 (s 6H; CH_3 attached to diamine benzene ring).

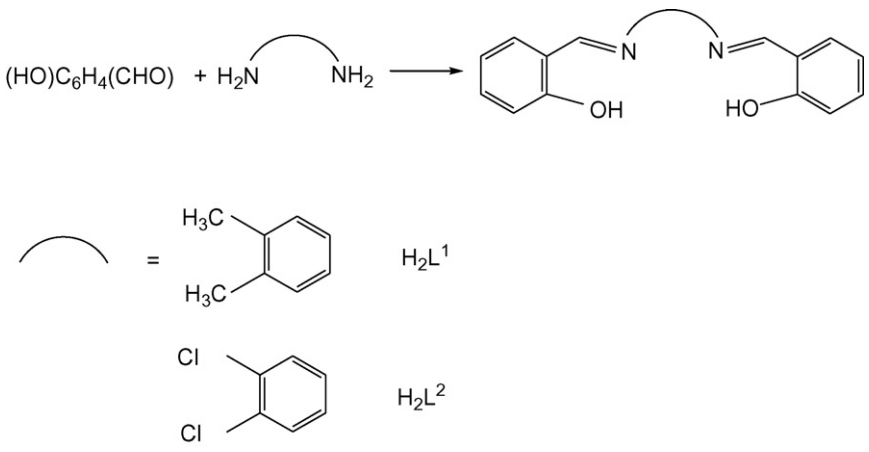
H_2L^2 ($C_{20}H_{14}N_2O_2Cl_2$): Yield 70%. Color Yellow. M.P. 142–144 °C. Elemental analysis Calc.(%): C, 62.35; H 3.66; N 7.27; Cl 18.40. Found: C 62.19; H 3.60; N 7.25; Cl 18.38. IR (KBr pellet. cm^{-1}): 3444 (ν_{OH}); 1616 ($\nu_{HC=N}$); 1279 (ν_{C-O}). ^1H NMR (DMSO-d_6, 270 MHz): δ 10.90 (s, 2H; OH); 8.92 (s, 2H; HC=N); 7.65–7.80 (m, 8H; aromatic); 7.35 (s, 2H, aromatic).

2.4. Syntheses of the complexes

To a hot 20 mL methanolic solution containing 10 mmol of the ligand, 20 mL of a methanolic solution containing 2.48 g (10 mmol) of $Ni(CH_3COO)_2.4H_2O$ was added. A red precipitate appears immediately. After stirring for 1 h the formed red complexes were filtered, collected and then washed for several times with hot methanol until the filterate became colorless. The complexes were dried in a desiccator over anhydrous $CaCl_2$ under vacuum.

The dried ligands and complexes were subjected to elemental and spectroscopic analyses. The complexes are air-stable, non-hygroscopic, insoluble in H_2O, partly soluble in ethanol, methanol and completely soluble in DMSO, DMF and CH_2CL_2. Decomposition occurs with concentrated nitric acid, and the resultant solution was used after suitable dilution for metal analysis. Characteristics of the complexes are as follows:

NiL^1 ($C_{22}H_{18}N_2O_2Ni$): Yield 80%. Color Red. M.P. >300 °C. Λ_m (Ω^{-1} cm^{-1} mol^{-1}) 4.2. Elemental analysis Calc.(%): C, 65.87; H 4.52; N 6.98; Ni 14.63. Found: C 65.73; H 4.52; N 6.77; Ni 14.58. IR (KBr pellet. cm^{-1}): 1613 ($\nu_{HC=N}$); 1288 (ν_{C-O}); 542 (ν_{Ni-N}); 412 (ν_{Ni-O}).



Scheme 1.

^{1}H NMR (DMSO-d_6, 270 MHz): δ 8.79 (s, 2H; HC=N); 7.60–7.85 (m, 8H; aromatic); 7.40 (s, 2H, aromatic); 2.46 (s 6H; CH_3 attached to diamine benzene ring).

NiL^2 ($C_{20}H_{12}N_2O_2Cl_2Ni$): Yield 76%. Color Red. M.P. >300 °C. Λ_m (Ω^{-1} cm^{-1} mol^{-1}) 6.7. Elemental analysis Calc.(%): C, 54.35; H 2.73; N 6.33; Cl 16.04; Ni 13.28. Found: C 54.05; H 2.67; N 6.30; Cl 15.95; Ni 13.10. IR (KBr pellet. cm^{-1}): 1615 ($\nu_{HC=N}$); 1290 (ν_{C-O}); 536 (ν_{Ni-N}); 419 (ν_{Ni-O}). H NMR (DMSO-d_6, 270 MHz): δ 8.89 (s, 2H; HC=N); 7.70–7.85 (m, 8H; aromatic); 7.4 (s, 2H, aromatic).

2.5. Membrane sensors formation and EMF measurements

A 10 mg portion of either [NiL^1] or [NiL^2] complex was mixed with 5 mg TDMAC, 350 mg of the plasticizer and 190 mg of PVC. The mixture was dissolved in ~5 mL THF. The membrane solutions were cast into conductive supports of conventional or tubular shapes and left drying overnight. The sensors were conditioned before use by soaking in 10^{-2} mol L^{-1} IO_4^- solution (for at least 12 h) and stored in the same solution when not in use. Calibration was made by immersing the periodate membrane sensor in conjunction with a double junction Ag/AgCl reference electrode in 50 mL beakers containing 10 mL aliquots of standard 1.0×10^{-6}–1.0×10^{-2} mol L^{-1} IO_4^- solution. The pH of the solutions was adjusted to 4.7 using 0.01 mol L^{-1} acetate buffer. Potential readings were carried out for periodate starting from low to high concentrations until stabilization occurred. The potential response was plotted as a function of the logarithm of IO_4^- concentrations. The calibration plot was used for subsequent measurements of unknown IO_4^- concentrations.

For FIA measurements, a series of portions (100 μL) of IO_4^- test solutions covering the range 1.0×10^{-2}–1.0×10^{-6} mol L^{-1} was injected into a flow stream of 10^{-2} mol L^{-1} acetate buffer of pH 4.7, flowing at 3 mL min^{-1}. The periodate sensor was used as a working sensor against Ag/AgCl double junction reference electrode. Each solution was measured in triplicate. The average potentials at maximum heights were plotted against log [IO_4^-].

2.6. Ascorbic acid determination

A 10 mL portion of a standard 5.0×10^{-4} mol L^{-1} $NaIO_4$ solution was transferred into a 50-mL beaker and the periodate sensor in conjunction with the reference electrode was immersed in the solution. After stabilization of the potential within ± 2 mV, a 1.0 mL aliquot containing 0.5–50 mg mL^{-1} of ascorbic acid (pH 3–6) was added, the solution stirred and the potential reading recorded after 60 s. A blank experiment was conducted under the same conditions using a 1.0 mL aliquot of water instead of the sample test solution. The potential reading was recorded after the same reaction time. The concentrations of IO_4^- in the presence and absence of ascorbic acid were calculated from the calibration graph. The concentration of the reducing compounds was calculated from the concentration of periodate consumed: 1 mol of IO_4^- = 1.0 mol of ascorbic acid.

For continuous measurements (FIA), a flow stream of 0.01 mol L^{-1} acetate buffer of pH 4.7 carrier solution and 1.0×10^{-4} mol L^{-1} periodate solution were allowed to pass through the flow-cell at a flow rate 3 mL min^{-1}. Successive 100 μL aliquots of the standard ascorbic acid and unknown test sample solutions were injected into the flowing stream. The corresponding potential change was measured and recorded versus time. A typical calibration plot was made and used to determine the concentration of ascorbic acid in the unknown samples.

3. Results and discussions

3.1. Elucidation structure of the complexes

Physical characteristics, elemental analysis and magnetic susceptibility data of the ligands and complexes show the formation of 1:1 [Ni:L]. Magnetic susceptibility values of the complexes at room temperature are consistent with square planar geometry around Ni(II) ion. The molar conductance values of the synthesized complexes were determined using 1×10^{-3} mol L^{-1} DMF solution are in the range 4.2–6.7 Ω^{-1}cm^2 mol^{-1}. These results suggest the presence of a non-electrolytic nature in the same solvent [26]. Also these values indicate that there are no anions existing in the outer sphere coordination.

The IR spectra of the complexes, in comparison with those of the free ligands, display certain changes, which give an idea about the type of coordination and their structure. Free Schiff bases show a very strong absorption at 1616 and 1617 cm^{-1} characteristic of azomethine ($\nu_{C=N}$) group [27]. Coordination of the Schiff bases to the nickel ion through the azomethine nitrogen atom is expected to reduce the electron density in the azomethine link and thus, lower the $\nu_{C=N}$ absorption frequency. Hence this band undergoes a shift to lower frequency to 1608–1615 cm^{-1} after complexation, indicating coordination of the azomethine nitrogen to nickel [28,29]. The free ligands exhibit a broad band at 3418–3444 cm^{-1}, which may be assigned to the ν(OH) and this band is absent in the spectra of all the complexes, conferring the deprotonation of the Schiff bases prior to coordination. The hydroxy protons are displaced by the metal leading to higher ν(C—O) (1288–1290 cm^{-1}) compared to the IR of the free ligands, suggesting that the other coordinating atom is phenolic

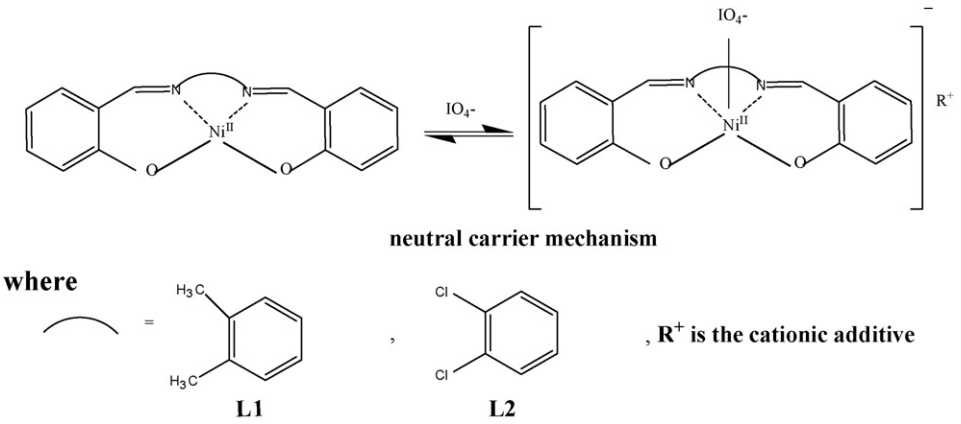


Fig. 1. Proposed mechanism for the potentiometric response of either NiL^1 or NiL^2-based PVC membrane sensors towards periodate.

oxygen [30]. The binding of the metal to the ligand through nitrogen and oxygen atom is further supported by the appearance of new band in 534–542 cm^{-1} and 412–419 cm^{-1} ranges due to ν(M-N) and ν(M-O) [31], respectively, in the spectra of all the complexes.

The IR spectral evidences were further substantiated by ^1H NMR of the free ligands and their Ni(II) complexes. The Chemical shift observed for the OH protons in the free ligands was not observed in any of the complexes. This confirms the bonding of oxygen to the metal ion (C—O—Ni).

The presence of a sharp singlet for the —C(H)═N proton in both the free ligands and their Ni(II) complexes clearly indicates that the magnetic environment is equivalent for all such protons, suggesting that the presence of a planar ligand in these complexes[32]. The multiplets of aromatic protons appearing within the range are less affected by chelation. In the ligand H_2L^1 the signal of —CH_3 is unaffected by chelation.

On The basis of the physical and spectral data of the Schiff bases and The complexes discussed above, one can assume that Ni(II) ions are bonded to the Schiff bases via the phenolic oxygen and the imino nitrogen as illustrated in Fig. 1.

3.2. Response characteristics of periodate sensors

The potentiometric response characteristics of the electrodes assembled with the different membranes are shown in Fig. 2. The sensor based on [NiL^1] shows a linear response towards periodate over the concentration range of 9.0×10^{-6}–1.0×10^{-3} mol L^{-1} in a 0.01 mol L^{-1} acetate buffer solution of pH 4.7 with a slope of -48.7 ± 1.2 mV decade^{-1} of activity and detection limit 7.2×10^{-6} mol L^{-1}. The sensor assembled with [NiL^2] displays a linear response towards periodate ranging from 3.2×10^{-5}–1.0×10^{-3} mol L^{-1} with a slope of -49.2 ± 0.7 mV decade^{-1} of activity and detection limit 1.78×10^{-5} mol L^{-1}.

On the other hand, the addition of ionic additive (e.g. TDMAC) improves the potentiometric properties of anion-selective sensors. This is in accordance with the results reported previously that the cationic sites in neutral carrier-based electrodes can stabilize the formation of the negatively charged product (NiL^1-IO_4^-) in the membrane phase as well as lower the electrical membrane resistance and improve the potentiometric response characteristics of the membrane electrodes [33–35]. Addition of 10 mol% of TDMAC relative to the ionophore to the membranes showed an enhancement of the potentiometric response characteristics. These membrane electrodes exhibited a slope of -66.1 ± 0.8 and -59.9 ± 1.1 mV decade^{-1} of activity, and decreased the detection limits to 5.2×10^{-6} and 7.3×10^{-6} mol L^{-1} for the sensors based on [NiL^1] and [NiL^2], respectively.

The influence of the pH on the potentiometric response of periodate-based membrane sensors was tested using 10^{-4} and 10^{-3} mol L^{-1} IO_4^- solutions over the pH range 2–10. Adjustment of pH was carried out using NaOH and/or HCl. From pH-potential profiles, it is apparent that there is no change in potential response within the pH range 3–8 for both [NiL^1] and [NiL^2] membrane-based sensors. The sensor significant response at high pH values (>8.5), which outcomes probably from the ability of hydroxide ions to compete favorably for the axial coordination site of the central metal. At pH <3, there was also interference due to the increase of hydrogen ion concentration.

Dynamic response time is an important factor for any ion selective electrode. In this study, the practical response time was recorded by immediate changing of IO_4^- concentration from 1.0×10^{-6} to 1.0×10^{-3} mol L^{-1}. The actual potential versus time trace showed in whole concentrations range that the sensors reach the equilibrium response in a very short time (<10 s). These results

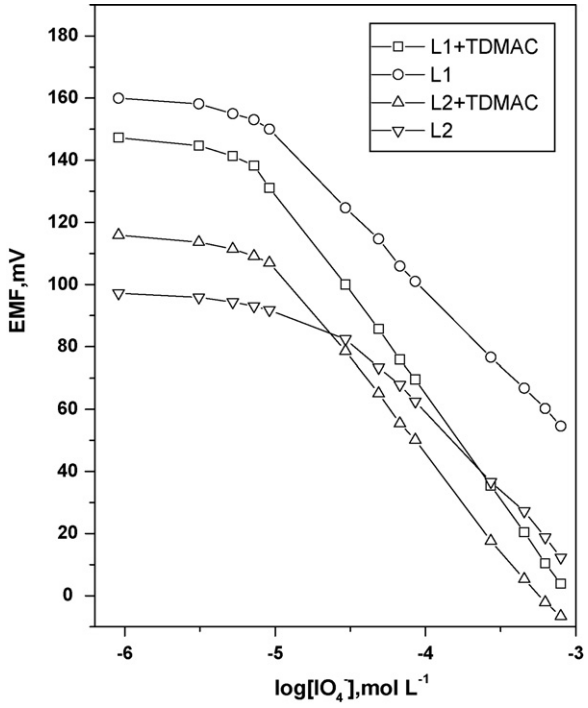


Fig. 2. Potentiometric response of periodate based membrane sensors in 0.01 mol L^{-1} acetate buffer, pH 4.7.

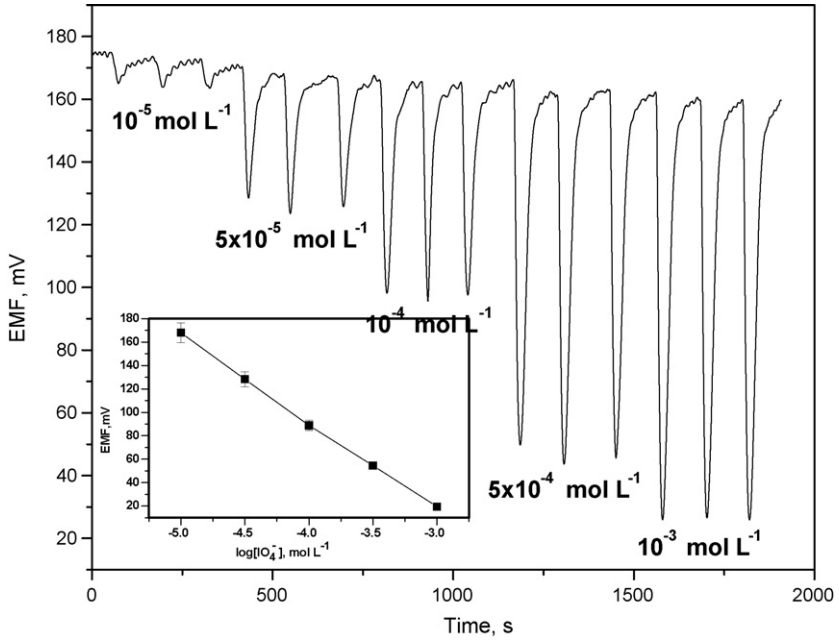


Fig. 3. Transient potentiometric signals obtained in triplicate for periodate membrane based sensor. Conditions: carrier solution, 0.0.1 mol L^{-1} acetate buffer pH 4.7 flow rate, 3.0 mL min^{-1}; injection valve, 100 μL.

indicate that both sensors are amenable for use with automated systems.

For continuous periodate measurements, a tubular-type detector incorporating a [NiL^1] + TDMAC based membrane sensor was prepared and used under hydrodynamic mode of operation for continuous IO_4^- quantification. The general intrinsic response features of the detector revealed that the dependency of the peak height, peak width, and time to recover the base line depend on the flow rate of the carrier buffer solution and the sampling volume. The linear response range of the detector was evaluated by using a set of sodium periodate solutions (1.0×10^{-6}–1.0×10^{-3} mol L^{-1}), with 0.01 mol L^{-1} acetate buffer of pH 4.7, sample loop volume 100 μL and flow rate 3 mL min^{-1}. It was found that the detection unit presented a Nernstian response with concentrations ranging from 1.0×10^{-5} to 10^{-3} mol L^{-1} with a detection limit 7.3×10^{-6} mol L^{-1}, slope of -71.9 ± 0.8 mV $decade^{-1}$ of activity and a reproducibility of ±0.9 mV ($n = 6$). A typical FI-diagram is shown in Fig. 3. These good analytical features of the detector opened the possibility of its application to the indirect determination of ascorbic acid by monitoring the periodate concentration changes caused by the oxidation reaction of the analytes.

3.3. Sensor selectivity

The selectivity of potentiometric anion sensors is introduced via an ion-selective membrane deposited on top of the transducer element. Because sensors are often designed for certain applications and well-defined conditions, this membrane does not necessarily have to be specific for the analyte as long as strong interferents are absent or present only in low concentrations. Receptors with Lewis acidic metal centers as anion binding sites are often applied for anion sensors with selectivities deviating from the Hofmeister series. The metal center can be either ionic (complexed in an organic ligand), or can be covalently bound as part of an organometallic structure. Depending on the organic ligand and the metal center this class of receptors applied in ISEs contains both charged and neutral receptors.

In the present work the selectivity of the sensors has been determined by the matched potential method (MPM) [36]. By this method, the selectivity coefficient is defined as the activity ratio of the primary ion ($A = 1.0 \times 10^{-5}$ mol L^{-1} IO_4^- ions) and the interfering ion ($B = 10^{-2}$ mol L^{-1}) that gives the same potential change in a reference solution (1.0×10^{-6} mol L^{-1} IO_4^- ions). All potentiometric measurements are carried out in 10^{-2} mol L^{-1} acetate buffer pH 4.5. First, the change in potential upon changing the primary ion activity is measured. Then, the interfering ion would be added to an identical reference solution until the same potential change is obtained. The selectivity coefficient K is determined as:

$$K^{pot} = \frac{\Delta A}{aB} \quad (1)$$

where $\Delta A = \acute{a}A - aA$, aA is the initial primary ion activity and $\acute{a}A$ is the activity of A, in the presence of the interfering ion, aB. The selectivity coefficient values determined were compiled in Table 1. The selectivity coefficients of [NiL^1] and [NiL^2] membrane sensor without membrane additives were in the order: $IO_4^- > SCN^- > I^- > ClO_4^- > NO_3^- > NO_2^- > Br^- > IO_3^- > F^- = Cl^-$ > Ascorbate > SO_4^{2-} and $IO_4^- > SCN^- > I^- > ClO_4^- > Cl^- > Br^- > NO_3^- > IO_3^- > NO_2^-$ > Ascorbate > $F^- > SO_4^{2-}$, respectively. Membrane electrodes doped with cationic sites (e.g. TDMAC 10 mol%) exhibited almost the same selectivity order of membranes containing no additives with an improvement in the potentiometric selectivity

Table 1
Selectivity coefficients (K^{pot}, j) of periodate PVC membrane sensors.

Ion	[NiL^1]	[NiL^1]+TDMAC	[NiL^2]	[NiL^2]+TDMAC
IO_4^-	0	0	0	0
IO_3^-	−3.12	−3.21	−2.78	−2.85
Ascorbate	−3.49	−3.27	−3.14	−3.21
ClO_4^-	−2.08	−2.15	−2.12	−2.21
I^-	−1.66	−1.77	−1.48	−1.49
NO_3^-	−2.81	−2.41	−2.76	−2.40
NO_2^-	−2.76	−2.66	−2.88	−2.68
Cl^-	−3.34	−2.90	−2.36	−2.12
Br^-	−2.87	−2.86	−2.64	−2.61
F^-	−3.33	−3.45	−3.53	−3.5
SCN^-	−0.95	−1.02	−0.74	−0.88
SO_4^{2-}	−3.64	−3.42	−3.77	−3.31

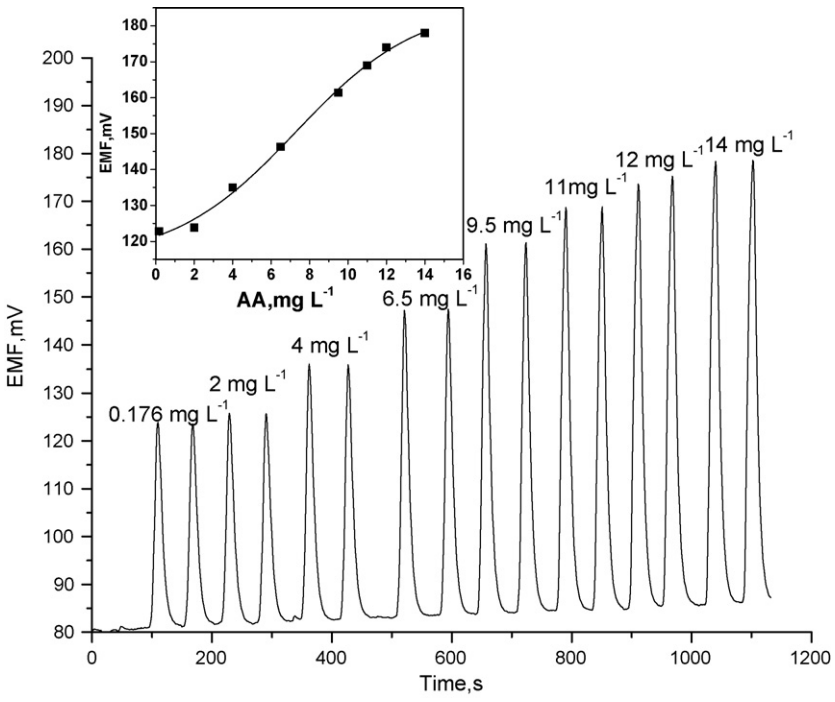


Fig. 4. Transient potentiometric signals obtained in triplicate for periodate membrane based sensor. Conditions: carrier solutions, 0.01 mol L^{-1} acetate buffer pH 4.7 and 1.0×10^{-4} mol L^{-1} IO_4^- solution; flow rate, 3.0 mL min^{-1}; injection valve, 100 μL.

towards periodate anion, in comparison with membrane sensors prepared without cationic additive site. The improvement was obtained over perchlorate, iodide, iodate, and thiocyanate (i.e., the lipophilic anions), whereas no improvement was obtained over the other anions. This selectivity order clearly showed that the response mechanism is neutral carrier mechanism and due to strong coordination affinity between the metal center in the ionophore and the anion leading to a non-Hofmeister selectivity sequence.

3.4. Hydrodynamic monitoring of ascorbic acid

The injection of ascorbic acid in a periodate carrier solution provides the oxidation of periodate within the carrier. The subsequent increase in periodate concentration is detected by a positive potential change at the potentiometric sensor. The relative consumption of periodate may therefore be used to the indirect monitoring of ascorbic acid. The overall reaction expressed in Eq. (2), where k is the overall reaction rate constant and AA ascorbic acid.

$$IO_4^- + AA \xrightarrow{k} IO_3^- + \text{Product} \quad (2)$$

Under specific pH conditions, the reaction kinetics follows a second order behavior expressed as follows:

$$\frac{d[IO_4^-]}{dt} = -k\,[IO_4^-][AA] \quad (3)$$

The potential E of periodate sensor used for monitoring the reaction is given by Nernest equation:

$$E = K' - \text{Slope}\,\ln[IO_4^-] \quad (4)$$

Differentiating Eq. (4) with time gives:

$$\frac{dE}{dt} = -\text{Slope} \times \frac{1}{[IO_4^-] \times d[IO_4^-]/dt} \quad (5)$$

Combination of Eqs. (5) and (3) shows that the change in potential with time depends on AA concentration.

Periodate concentration was an important parameter in the procedure for AA determination. With a concentration lower than 10^{-5} mol L^{-1} in the flow system, the baseline was noisy and recorded peak heights were not measurable because the remaining periodate concentration approached the practical limit of detection. For periodate concentrations within the 10^{-4}–10^{-2} mol L^{-1} range, baseline noise was about ±1.8 mV, washing time reached

Table 2
Ascorbic acid content in some commercially flavored water and juice samples.

Product	Flavor	AA content (μg mL^{-1})[a]		
		Static	Hydrodynamic	Standard method [37]
SAN BENDETTO (Italy)	Orange and mandarin	535.0 ± 0.8	532.0 ± 0.4	538.0 ± 0.4
	Lemon	352.0 ± 0.7	350.0 ± 0.9	347.0 ± 0.9
	Green tea	363.0 ± 0.5	360.0 ± 0.4	366.0 ± 0.8
	Grape	273.0 ± 0.6	277.0 ± 0.2	279.0 ± 0.9
G2 (Gatotrade, USA)	Apple	262.0 ± 0.4	266.0 ± 0.3	265.0 ± 0.9
TOP (United Food Ind., Egypt)	Orange	265.0 ± 0.6	260.0 ± 0.9	267.0 ± 0.3
	Mango	261.7 ± 0.9	260.1 ± 0.3	257.9 ± 0.3
	Cocktail	260.3 ± 0.3	263.8 ± 0.6	267.1 ± 0.1
	Guava	263.2 ± 0.6	264.7 ± 0.9	269.1 ± 0.5

[a] Average of five measurements.

Table 3
Potentiometric determination of ascorbic acid using periodate sensor.

Commercial products	Label (mg tablet^{-1})	Found (mg tablet^{-1})[a]		
		Static	Hydrodynamic	Standard method [37]
Vitacid (Chemical Industrial Development, Egypt) C-Retard (Alkan Pharma S.A.E., Egypt)	100	97.1 ± 0.5	98.4 ± 0.6	98.8 ± 0.9
Vitamin C 500 CR (EPCI, Egypt)	200	198.4 ± 0.8	195.8±0.7	197.8 ± 0.3
Cevarol (Memphis, Egypt)	500	495.1 ± 0.7	501.6 ± 0.9	498.6 ± 0.5
Ascorbovit (Pharco, Alex, Egypt)	500	497.2 ± 0.9	493.1 ± 0.4	498.3 ± 0.2
	1000	993.1 ± 0.6	991.5 ± 0.3	995.3 ± 0.4

[a] Mean of five determinations.

a constant value of 11 sets, and the tendency for linearization of the relation between AA concentration and recorded peak height was observed. This was due to the combination of Nernstian response of the electrode and kinetics of AA oxidation which, in the initial development steps, tends to be of first order relatively to periodate. Better linearity ($r^2 > 0.995$) was observed for $IO_4^- = 1.0 \times 10^{-4}$ mol L^{-1}. For periodate concentrations higher than 10^{-3} mol L^{-1}, linearity decreased and lower peaks were recorded. In this situation, AA concentrations were very low relative to periodate, so that the relative oxidant consumption underwent a pronounced reduction. Also, an oscillating baseline was observed, probably due to inefficient mixing conditions associated with the fast electrode response.

As can be seen in Fig. 4 with an injected volume 100 μL, it gives a linearity range from 2.0 to 13 mg mL^{-1} with a slope = 4.97 mV (mg/L)$^{-1}$ ($r^2 = 0.9995$) and detection limit 0.9 mg L^{-1}.

The influence of some excipients commonly present in injection forms of pharmaceutical preparations was evaluated. Glucose, saccharose, fructose, sodium chloride, and poly(ethylene glycol) were selected for this evaluation. This study was based on performing recovery trials of AA solutions with the excipients just mentioned. The influence of the interfering substances was evaluated at interferent/AA concentration ratios of 1:1, 1:10, and 1:100 (w/w) for AA concentrations of 5.0×10^{-4} and 1.50×10^{-2} mol L^{-1}. The recorded values showed that the interference of these excipients was generally not perceptible. However, the interference of this preservative was not recorded on the analyzed injection forms because a −0.3% relative error was obtained by an independent method and its concentration was not specified in these preparations.

3.5. Ascorbic acid determination in pharmaceuticals and beverages

In order to check the usefulness of the proposed sensors for resolving real samples, we addressed the determination of AA in real food samples as soft drinks as well as pharmaceuticals under static and hydrodynamic mode of operations. Many marketed beverages have the intentional addition of ascorbic acid, either by its antioxidant properties or by a supplementary vitamin addition. The samples analyzed by the proposed method were obtained from the local market and their content in ascorbic acid estimated by the proposed potentiometric method is presented in Table 2. A blank sample was used to control and ascertain the accuracy of the analytical results. Analytical data support the application of the proposed potentiometric method for the routine control ascorbic acid.

To widen the range of application of the proposed method, the analysis of pharmaceuticals was also established. Generally, these samples have high vitamin C contents. A different marketed formulation was used as a case study to prove this possible application. Table 3 gives the mean results obtained by either static or hydrodynamic modes of operations. Average values obtained varied between 98.5 and 99.1% of labeled amounts. The potentiometric method is well compared with the standard method [37]. Considering as null hypothesis that the two methods agree, a paired two-tail test for 5% level of significance gave a calculated $t_{(0.662)}$ below the tabulated one ($t_{0.025,11} = 2.20$), therefore accepting the null hypothesis. Comparison of variances attained for each sample was made by the *F*-test using the same assumptions as for the Student's *t*-test.

Table 4
Comparison of the proposed sensor with some other reported methods.

Technique	Linear range, μg mL^{-1}	LOD, μg mL^{-1}	Ref.
Spectrophotometry (FIA)	5.7–600	1.7	[7]
Spectrophotometry (Paptode)	20–220	1	[8]
HPLC (UV-detector)	0.2–20	0.01	[10]
HPLC (UV-detector)	–	2–6	[11]
Electrophoresis	1–1000	0.2	[12]
Electrophoresis	–	1	[13]
Cyclic voltammetry	1–176	0.38	[15]
Potentiometry (FIA)	2–13	0.9	This work

4. Conclusions

Potentiometric membrane sensors for periodate based on a newly synthesized and well characterized Ni(II)-Schiff bases with high sensitivity and good selectivity were developed and utilized in batch and hydrodynamic modes of operation. The sensors offer the advantages of fast response, reasonable selectivity, low cost and possible interfacings with computerized and automated systems. Interfacing the sensor in a flow injection analysis system offers adequate analysis speed, good reproducibility, high sample throughputs and excellent response characteristics. Direct analysis of ascorbic acid was possible under static and hydrodynamic mode of operations with a linear range 2.0–13 μg mL^{-1} with a sample rate ~50–55 sample h^{-1}. Some of the analytical features of developed method were compared with other methods based on different techniques (Table 4). As this table shows, our simple and inexpensive method is comparable with other complicated and expensive methods. Most of these methods, however, utilize expensive instrumentation [10–13,15], suffer from lack of selectivity [7,8,15], involve careful control of the reaction conditions or derivatization reactions [7,8,12,13], and require time-consuming pretreatment steps which are not easily applied to colored or turbid samples and affect their usefulness for routine analysis [7,8].

References

[1] M.W. Davey, M. Van Montagu, D. Inze, M. Sanmartin, A. Kanellis, N. Smirnoff, I.J.J. Benzie, J.J. Strain, D. Favell, J. Fletcher, J. Sci. Food Agric. 80 (2000) 825.
[2] N. Smirnoff, Curr. Opin. Plant Biol. 3 (2000) 229.
[3] A.H. Kamel, F.T.C. Moreira, C. Delerue-Matos, M.G.F. Sales, Biosens. Bioelectron. 24 (2008) 591.
[4] W. Lee, K.A. Davis, R.L. Rettmer, R.F. Lable, Am. J. Clin. Nutr. 48 (1988) 289.
[5] G.R. Buettner, Arch. Biochem. Biophys. 300 (1993) 535.
[6] N. Smirnoff, J.E. Pallanca, Biochem. Soc. Trans. 24 (1996) 472.
[7] D.G. Themelis, P.D. Tzanavaras, F.S. Kika, Talanta 55 (2001) 127.
[8] A. Abbaspour, A. Khajehzadeh, A. Noori, Anal. Sci. 24 (2008) 721.
[9] E.J. Oliveira, D.G. Watson, J. Chromatogr. B: Biomed. Appl. 764 (2001) 3.

[10] A. Rodríguez-Bernaldo de Quirós, M. Fernández-Arias, J. López-Hernández, Food Chem. 116 (2009) 509.
[11] A. Balaguer, A. Chisvert, A. Salvador, J. Sep. Sci. 31 (2008) 229.
[12] Y. Peng, Y. Zhang, J. Ye, J. Agric. Food Chem. 56 (2008) 1838.
[13] T. Wu, Y. Guan, J. Ye, Food Chem. 100 (2007) 1573.
[14] H. Guo, T. Yin, Q. Su, W. Qin, Talanta 75 (2008) 851.
[15] T.R.L.C. Paixao, M. Bertotti, J. Pharm. Biomed. Anal. 46 (2008) 528.
[16] N. Pejic, S. Blagojevic, S. Anic, L. Kolar-Anic, Anal. Bioanal. Chem. 389 (2007) 2009.
[17] G. Wang, J. Meng, H. Liu, S. Jiao, W. Zhang, D. Chen, B. Fang, Electrochim. Acta 53 (2008) 2837.
[18] M.C.B.S.M. Montenegro, M.G.F. Sales, J. Pharm. Sci. 89 (2000) 876.
[19] M.C.B.S.M. Montenegro, J.L.F.C. Lima, Talanta 40 (1993) 1563.
[20] V.H. Hartofylax, C.E. Efstathiou, Anal. Chim. Acta 167 (1985) 375.
[21] G.C. Luca, B.F. Reis, E.A.G. Zagatto, M.C.B.S.M. Montenegro, Anal. Chim. Acta 336 (1998) 193.
[22] C.E. Efstathiou, T.P. Hadjiioannou, Ana. Chim. Acta 89 (1977) 55.
[23] C.E. Efstathiou, T.P. Hadjiioannou, Talanta 24 (1977) 270.
[24] A.H. Kamel, M.G.F. Sales, S.A.A. Almeida, F. Teixeira, Anal. Sci. 25 (2009) 365.
[25] A.A.H. Saeed, E.K. Ebraheem, A.A. Tossonian, Thermochim. Acta 97 (1986) 337.
[26] N. Raman, Y.P. Raja, A. Kulandaisory, Indian Acad. Sci. 113 (2001) 1873.
[27] K.N. Kumar, R. Ramesh, Spectrochim. Acta A 60 (2004) 2913.
[28] R. Ramesh, M. Sivagamasundari, Synth. React. Inorg. Met. -Org. Chem. 33 (2003) 899.
[29] S.N. Pal, S. Pal, J. Chem. Soc. Dalton Trans. (2002) 2102.
[30] R.C. Maurya, P. Patel, S. Rajput, Synth. React. Inorg. Met. -Org. Chem. 23 (2003) 817.
[31] K. Nakamoto, Infrared and Raman Spectra of Inorganic and Coordination Compounds, Wiley-Interscience, New York, 1971.
[32] R.A. Siddiqui, P. Raj, A.K. Saxena, Synth. React. Inorg. Met. -Org. Chem. 26 (1996) 1189.
[33] E. Bakker, E. Malinowska, R.D. Schiller, M.E. Meyerhoff, Talanta 41 (1994) 881.
[34] R. Eugster, P.M. Gehrig, W.E. Morf, U.E. Spichiger, W. Simon, Anal. Chem. 63 (1991) 2285.
[35] U. Schaller, E. Bakker, U.E. Spichiger, E. Pretsch, Anal. Chem. 66 (1994) 391.
[36] S. Amemiya, P. Buhlmann, E. Pretsch, B. Rusterholz, Y. Umezawa, Anal. Chem. 72 (2000) 1618.
[37] T. Kleszczewski, E. Kleszczewska, J. Pharm. Biomed. Anal. 29 (2002) 755.

Talanta 80 (2010) 1364–1370

Contents lists available at ScienceDirect

Talanta

journal homepage: www.elsevier.com/locate/talanta

A sensitive and selective method for determination of gold(III) based on electrothermal atomic absorption spectrometry in combination with dispersive liquid–liquid microextraction using dicyclohexylamine

Shigehiro Kagaya[a,*], Daisuke Takata[a], Torajiro Yoshimori[a], Takaki Kanbara[b], Koji Tohda[a]

[a] Graduate School of Science and Engineering for Research, University of Toyama, Gofuku 3190, Toyama 930-8555, Japan
[b] Tsukuba Research Center for Interdisciplinary Materials Science (TIMS), University of Tsukuba, Tennoudai 1-1-1, Tsukuba 305-8573, Japan

ARTICLE INFO

Article history:
Received 8 August 2009
Received in revised form
15 September 2009
Accepted 18 September 2009
Available online 24 September 2009

Keywords:
Gold(III)
Homogeneous liquid–liquid extraction
Dispersive liquid–liquid microextraction
Dicyclohexylamine
Electrothermal atomic absorption spectrometry

ABSTRACT

A combined method with dispersive liquid–liquid microextraction (DLLME) and electrothermal atomic absorption spectrometry (ETAAS) has been developed for determining gold(III). Dicyclohexylamine, a new extractant for gold(III), showed excellent performance in DLLME. Acetone was indispensable to the quantitative extraction of gold(III), contributing to decrease in hydration, decrease in the difference in the dielectric constants between the supernatant phase and the sedimented phase, and dissolution of a part of chloroform as an extraction solvent to the supernatant phase as well as improvement of dipersibility. In DLLME using a mixture of 1.0 mL of acetone and 100 μL of chloroform containing 50 mmol L^{-1} of dicyclohexylamine, gold(III) could be extracted selectively and effectively from 8 mL of a sample solution in the presence of iron(III), cobalt(II), nickel(II), copper(II), palladium(II), and platinum(IV) at pH 1. The extracted gold(III) was determinable by ETAAS; the detection limit was 0.002 μg L^{-1} (three times the standard deviation of the blank values, $n = 8$) as a gold(III) concentration in 8 mL of sample solution. The proposed method was applicable to the determination of gold in platinum metal and its alloy as well as effluent without any interference by the matrices.

© 2009 Elsevier B.V. All rights reserved.

1. Introduction

Gold, which has important characteristics such as high ductility, corrosion resistance, low impedance, and catalytic properties, is widely utilized in the electronic, electroplating, fine-chemical, and jewelry industries [1]. Because it is precious, gold is carefully recovered after use through various techniques such as electrolysis and ion exchange [2,3]; however, complete recovery cannot be achieved, and a small amount of gold is lost through routes such as effluents. To estimate the amount of gold lost through an effluent, a method in which gold can be sensitively determined without any interference by the major ions generally contained in the effluent is necessary.

Other precious metals, including platinum, are also key materials for various industries [1]. With the expansion of its applications, such as in fuel cells, a growing demand for high-purity platinum is expected [4,5]. Because platinum metal contains significant impurities, including gold, an accurate and precise method of analysis is required.

For the determination of gold, electrothermal atomic absorption spectrometry (ETAAS) is a powerful tool [6]; however, the sensitivity is sometimes insufficient and the presence of matrices seriously interferes with the analyses of effluents, metals, and alloys. Therefore, a separation and preconcentration technique is extensively applied to the ETAAS determination of gold [6].

Liquid–liquid extraction (LLE) is an effective method for the separation and preconcentration of gold(III) [7–12]. Amine compounds, including *n*-trioctylamine [9], *n*-octylaniline [10], *N*-phenylbenzylamine [11], and *N*-*n*-octylaniline [12], are conveniently utilized for the extraction of gold(III) and other elements. However, there are some problems with the use of LLE, including the large amounts of harmful organic solvents needed, the long extraction time required for quantitative extraction, and difficulty in the treatment of wastewater generated after extraction.

To overcome these problems, various types of LLE techniques have been proposed. Among them, microextraction techniques have been investigated intensely. Homogeneous liquid–liquid extraction (HoLLE) based on a ternary solvent system [13–17] is one of the most useful microextraction techniques. HoLLE utilizes the phase separation phenomenon from a homogeneous solution, and the analytes are rapidly and efficiently extracted into a separated phase. HoLLE is available for the separation and

* Corresponding author. Tel.: +81 76 445 6865; fax: +81 76 445 6703.
E-mail address: kagaya@eng.u-toyama.ac.jp (S. Kagaya).

0039-9140/$ – see front matter © 2009 Elsevier B.V. All rights reserved.
doi:10.1016/j.talanta.2009.09.037

preconcentration of some elements [14–17], but there has been no report on the separation and preconcentration of gold(III). Dispersive liquid–liquid microextraction (DLLME) [18] has also attracted attention recently [19–27]. In DLLME, as in HoLLE, an aqueous sample solution, a water-miscible organic solvent as the disperser solvent, and a water-immiscible organic solvent as the extraction solvent are used; however, the extraction solvent has only to disperse finely into solution. In general, a mixture of disperser solvent and extraction solvent is swiftly injected using a microsyringe, and a gentle shaking is applied to extract the analyte quantitatively into the dispersed extraction solvent. The selection of a dispersive solvent which gives favorable dispersibility of the extraction solvent is important to achieve effective extraction of analyte [18–27]. DLLME is conveniently applicable to the separation and preconcentration of various elements prior to their ETAAS determination [19–27]; for gold(III), however, only DLLME using victoria blue R has been reported [25].

In this work, we investigated a combined method with DLLME and ETAAS for determining gold(III). For DLLME using acetone as a water-miscible organic solvent and chloroform as a water-immiscible organic solvent, we tested 11 kinds of amine compounds as extractants and found that dicyclohexylamine, which has not been used for the extraction of gold(III), was excellent. It is noteworthy that DLLME using dicyclohexylamine has rather high selectivity; gold(III) could be determined by ETAAS without any interference even in the presence of large amounts of other elements. In this paper, we report the results of investigations of the DLLME of gold(III) with amine compounds and discuss the role of acetone as a water-miscible organic solvent in the extraction of gold(III) with dicyclohexylamine. The potential of ETAAS combined with DLLME using dicyclohexylamine is also demonstrated through the determination of gold in effluent, platinum metal, and platinum alloy.

2. Experimental

2.1. Apparatus

A Hitachi 180-80 polarized Zeeman atomic absorption spectrometer (flame- and electrothermal-type) was used to measure gold and other elements. The pH measurement and ultrasonic irradiation were carried out using a Horiba F-22 pH meter and an AS ONE US-2 ultrasonic cleaner (120 W, 38 kHz), respectively. A Kubota Model 5400 centrifuge was used to form the sedimented phase.

2.2. Reagents

Purified water obtained by a Simplicity UV (Millipore) was used for all experiments. Standard solutions of gold(III) and the other elements (1000 mg L^{-1}) were purchased from Kanto Chemical. Eleven kinds of amine compounds, ethylenediamine (guaranteed reagent grade, GR, Wako Pure Chemical Industries), diethylenetriamine (GR, Wako Pure Chemical Industries), *N*-butyldimethylamine (>98%, Tokyo Chemical Industry), triphenylamine (GR, Kanto Chemical), *N*-methyldiphenylamine (97%, Acros Organics), *N*-methylaniline (GR, Kanto Chemical), *N*-phenylbenzylamine (99%, Acros Organics), benzylamine (GR, Kanto Chemical), dibenzylamine (>97%, Tokyo Chemical Industry), cyclohexylamine (>99%, Tokyo Chemical Industry), and dicyclohexylamine (>99%, Tokyo Chemical Industry), were used as extractants without any further purification (the structures are summarized in Fig. 1S in the Supplementary Material). The other reagents, including chloroform, acetone, hydrochloric acid, and sodium hydroxide, were of GR or analytical reagent grade.

Table 1
Operating conditions for FAAS and ETAAS.

Analytical wavelength (nm)	242.8
Lamp current (mA)	10
Slit width (nm)	1.3
<FAAS>	
Flame conditions	
Air pressure (kPa)	160
Acetylene pressure (kPa)	20
<ETAAS>	
Cuvette	Pyro-coated graphite tube
Carrier gas (Ar) flow rate (mL min^{-1})	200
Injection volume (μL)	10
Atomizer program	
Dry (°C, s)	80–120, 30
Ash (°C, s)	400, 30
Atomize (°C, s)	2700, 7
Clean (°C, s)	2800, 3

2.3. Procedures

2.3.1. Extraction behavior of gold(III) with some amine compounds

As a test solution, 0.1 mol L^{-1} hydrochloric acid spiked with gold(III) (4 mg L^{-1} or 10 μg L^{-1}) was used.

For DLLME, the test solution (5 mL) was taken into a 10 mL glass centrifuge tube. To the solution, a mixture of 0.90 mL of acetone and 90 μL of chloroform containing 50 or 200 mmol L^{-1} of amine compound was swiftly injected using a glass syringe equipped with a stainless needle. After the cloudy solution was gently shaken by hand for approximately 10 s, the solution was centrifuged at 3000 rpm for 8 min. Gold in the supernatant phase was determined using flame atomic absorption spectrometry (FAAS) under the operating conditions shown in Table 1. The extraction percentage was calculated based on the initial amount of gold in the test solution and the amount in the supernatant phase, which was calibrated using the supernatant phase spiked with an appropriate amount of gold(III) after the blank test.

For LLE, 1 mL of chloroform containing 1–200 mmol L^{-1} of amine compounds and 0–10 mL of acetone was added to 50 mL of the test solution containing 4 mg L^{-1} of gold(III). The solution was then stirred vigorously. The concentration of gold(III) in the supernatant solution was measured using FAAS after centrifugation. The extraction percentage was calculated in the same manner for DLLME.

2.3.2. Determination of gold by ETAAS after DLLME using dicyclohexylamine

For the optimization of the extraction conditions, a purified water-based solution containing 10 μg L^{-1} or 0.2 μg L^{-1} of gold(III), in which the pH was adjusted using hydrochloric acid and/or sodium hydroxide solution, was used as a test solution. Effluent samples, which were obtained from a jewelry factory, were digested with hydrochloric acid on heating [28] after filtration using a membrane filter (Nihon Millipore, Omnipore membrane, pore size of 0.45 μm). The pH of the sample solutions was approximately 1. For analyses of platinum metal and its alloy, approximately 0.1 g of a platinum metal (Pt, 99.95%) or platinum alloy (Pt, 94.82%; Cu, 5.16%) was dissolved in 20 mL of aqua regia on heating. The solution was then diluted with 0.1 mol L^{-1} hydrochloric acid.

To 8 mL of the test solution or the sample solution, a mixture of 1.0 mL of acetone and 100 μL of chloroform containing 50 mmol L^{-1} of dicyclohexylamine was swiftly injected. The cloudy solution was gently shaken, and ultrasonic irradiation was carried out for 5 min. The solution was then centrifuged.

Gold in the sedimented phase was determined using ETAAS under the operating conditions summarized in Table 1. Solutions

for the calibration curve were prepared using 8 mL of 0.1 mol L^{-1} hydrochloric acid spiked with appropriate amounts of gold(III). A blank test was also carried out using 0.1 mol L^{-1} hydrochloric acid or the purified water-based solution after the treatment with hydrochloric acid or aqua regia. To optimize the extraction conditions, gold in the supernatant phase was determined using ETAAS. The extraction percentage was evaluated in a manner similar to that used for the extraction behavior of gold(III), as mentioned above.

3. Results and discussion

3.1. Extraction of gold(III) with some amine compounds

The extraction of gold(III) using 11 kinds of amine compounds was investigated using DLLME as well as LLE in order to select the appropriate amine compound for the extraction. Since the extraction of gold(III) with amine compounds has been carried out in the acidic region [9–12], 0.1 mol L^{-1} hydrochloric acid was used for the experiments. As a water-miscible organic solvent, acetone was chosen because it has been widely utilized as a disperser solvent for DLLME [18,19,24,25].

3.1.1. Comparison of extraction behavior of gold(III) by LLE and DLLME

The results of the extraction of gold(III) using a series of amine compounds by LLE, in which 50 mL of the test solution containing 4 mg L^{-1} of gold(III) and 1 mL of chloroform containing an amine compound were used without acetone, are shown in Fig. 1. For *N*-methylaniline and *N*-phenylbenzylamine [11], gold(III) was quantitatively extracted. *N*-Methyldiphenylamine gave 57% of the extraction. For the other amine compounds, however, less than 30% of gold(III) was extracted, and no extraction of gold (III) was observed for dicyclohexylamine.

The results for DLLME of gold(III) using the amine compounds are summarized in Fig. 1. For aromatic amines, including *N*-methylaniline and *N*-phenylbenzylamine [11], the extraction percentages decreased compared to those for LLE when a mixture of 0.9 mL of acetone and 90 μL of chloroform containing 200 mmol L^{-1} of the corresponding amine compound was added to 5 mL of the test solution. In contrast, the extraction percentages were considerably improved with the use of *N*-butyldimethylamine, benzylamine, dibenzylamine, cyclohexylamine, and dicyclohexylamine. From the results of DLLME, the extraction of gold(III) with dibenzylamine and dicyclohexylamine, which gave more than 80% of the extraction, was further investigated using 5 mL of the test solution containing a much lower concentration of gold(III) (10 μg L^{-1}). The extraction of gold(III) was almost 100% with the use of both 50 and 200 mmol L^{-1} of dicyclohexylamine in chloroform, whereas 50 and 200 mmol L^{-1} of dibenzylamine extracted 67% and 88% of gold(III), respectively. These results indicate that dicyclohexylamine is an excellent extractant for DLLME of gold(III). The molecular-structural characteristics, including bulkiness, the strong basicity (pK_a = 10.4 [29]), and the high lipophilicity of dicyclohexylamine may contribute to the effective extraction of gold(III).

3.1.2. Role of acetone on extraction of gold(III) with dicyclohexylamine

In DLLME, a water-miscible organic solvent is used to disperse the water-immiscible organic solvent as an extraction solvent [18–27]. The efficient dispersion of the extraction solvent accelerates the extraction of analytes. In our experiments using acetone as a disperser solvent, however, the extraction efficiency in DLLME using amine compounds was not necessarily improved compared with that in LLE as shown in Fig. 1, which suggests that acetone may also have other functions in the extraction. The role of acetone in the extraction of gold(III) with dicyclohexylamine was therefore examined using the LLE technique.

The effect of the stirring time on the extraction of gold(III) with dicyclohexylamine using 0–10 mL of acetone is shown in Fig. 2. In the absence of acetone, gold(III) was not extracted after stirring for 2 h; the extraction percentages retained almost 0% for at least 24 h. In contrast, the extractability was dramatically improved in the presence of acetone (Fig. 2). When 1–10 mL of acetone was used, the solution became cloudy just after the stirring was started. The extraction percentages increased as the amount of acetone added was increased. In these cases, gold(III) was extracted after 1 min, and the extraction percentages were almost constant when further stirring was carried out (Fig. 2). The extraction of gold(III) was also observed without dicyclohexylamine; the extraction percentages after stirring for 1 h were 0.4% for 4 mL of acetone, 3.1% for 8 mL, and 11% for 10 mL. On the other hand, 68% of gold(III) was extracted even when 1 mL of chloroform containing 200 mmol L^{-1} of dicyclohexylamine was slowly added to a mixture of 50 mL of 0.1 mol L^{-1} hydrochloric acid containing 4 mg L^{-1} of gold(III) and 10 mL of acetone and the mixture was allowed to stand statically

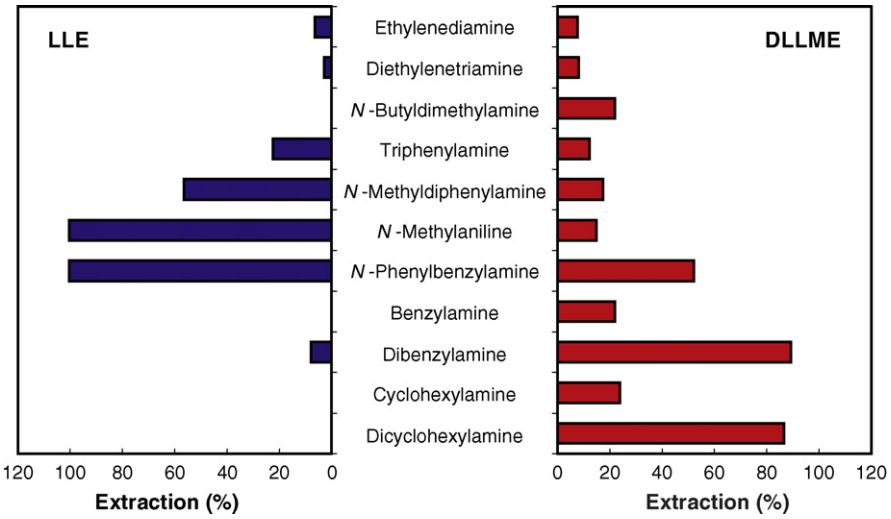


Fig. 1. Extraction of gold(III) with 11 kinds of amine compounds using normal LLE and DLLME techniques. Aqueous phase, 0.1 mol L^{-1} HCl containing 4 mg L^{-1} of Au(III); organic phase, chloroform containing 200 mmol L^{-1} of amine compound. LLE: 50 mL of aqueous phase and 1 mL of organic phase was stirred for 1 h. DLLME: 1 mL of the mixture of 0.90 mL of acetone and 90 μL of organic phase was injected swiftly to 5 mL of aqueous phase, and the cloudy solution was gently shaking for 10 s.

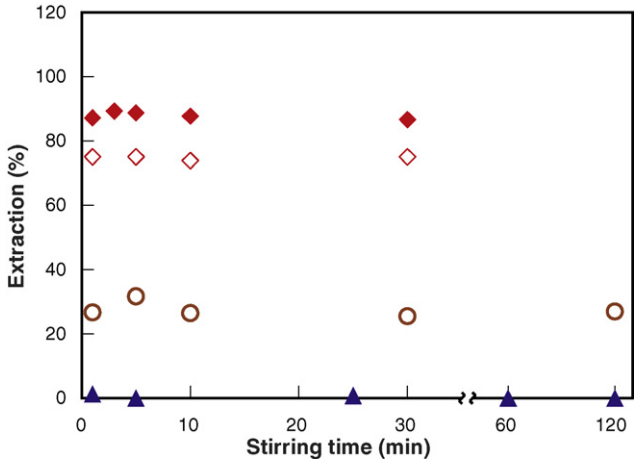


Fig. 2. Extraction percentage of gold(III) as a function of stirring time on LLE. Aqueous phase, 50 mL of 0.1 mol L^{-1} HCl containing 4 mg L^{-1} of Au(III); organic phase, 1 mL of chloroform containing 200 mmol L^{-1} of amine compound. Acetone, 10 mL (♦), 8 mL (◊), 1 mL (○), or not added (▲).

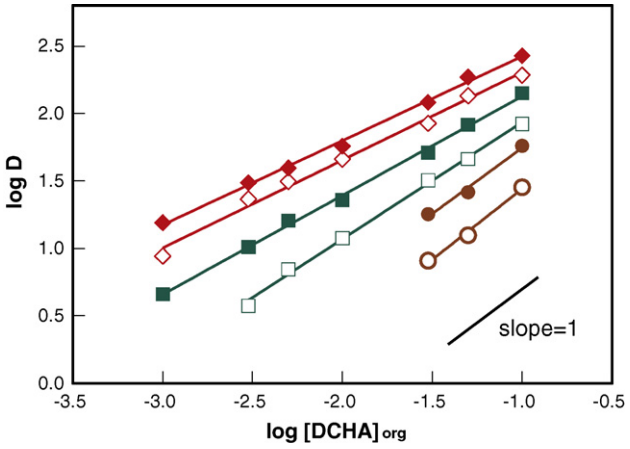


Fig. 3. Relationship between the distribution ratio of gold(III) (D) and the initial concentration of dicyclohexylamine in chloroform ($[DCHA]_{org}$) on LLE using various amounts of acetone. Aqueous phase, 50 mL of 0.1 mol L^{-1} HCl containing 4 mg L^{-1} of Au(III); organic phase, 1 mL of chloroform containing 200 mmol L^{-1} of amine compound. Acetone, 10 mL (♦), 8 mL (◊), 4 mL (■), 3 mL (□), 2 mL (●), 1 mL (○).

for 260 h, whereas the extraction of gold(III) was not observed in the absence of acetone. These results suggest that acetone is not merely the disperser.

It has been reported that in the extraction of some elements with aliphatic tertiary amines [30–32], the extraction percentages were considerably improved by the addition of water-miscible organic solvents, including methanol, ethanol, and acetone, which are generally utilized as disperser solvents in DLLME [18–27]. Such phenomena have been attributed to the decrease in hydration as the mole fraction of water decreased [30–32], resulting in the increased stability of negatively charged chloro-complexes in solution [31]. The enhancement of the extraction percentage is also discussed from the standpoint of the differences in the dielectric constants between the aqueous phase and the organic phase [32]. The contents of water and the water-miscible organic solvent in the organic phase as well as that of the water-miscible organic solvent in the aqueous phase increased as the added amount of water-miscible organic solvent was increased. The difference in the dielectric constants between the aqueous phase and the organic phase was therefore decreased. The decreases in hydration and in the differences in the dielectric constants resulted in the effective extraction of some elements [32]. In the case of the gold(III) extraction with dicyclohexylamine, acetone would play similar roles in addition to acting as a disperser solvent.

When the added amount of acetone increased, the volume of the sedimented phase increased due to the increase in the distribution of acetone and water to chloroform [32]. In our experiment, a similar tendency was observed, but all the volumes of the sedimented phases with various amounts of acetone were less than those of chloroform added. These results indicate that the supernatant phase is a homogeneous ternary solvent mixture containing water, acetone, and chloroform; that is, acetone promotes the dissolution of chloroform into the supernatant phase. The dissolution of chloroform to the supernatant solution and the phase separation arise reversibly, and the separated chloroform is expected to extract gold(III) effectively. Such an extraction, which is inherently similar to HoLLE [13–16], would also take place in DLLME of gold(III) with dicyclohexylamine.

The relationship between the distribution ratio of gold(III) (D) and the initial concentration of dicyclohexylamine in chloroform ($[DCHA]_{org}$) was examined in the presence of 1–10 mL of acetone. The D value was corrected based on the volume of the sedimented phase. As shown in Fig. 3, linear relationships between log D and log $[DCHA]_{org}$ were obtained under all amounts of acetone. The slopes for 1 mL and 2 mL of acetone were 1.05 and 0.98, respectively. These results indicate that the dominant extracted species of gold(III) should be 1:1 for tetrachloroaurate(III) ion:protonated dicyclohexylamine under these conditions. The extraction of gold(III) with dicyclohexylamine may obey the ion-pair mechanism, as it does with the other amine compounds [9–12]. However, the slope gradually decreased with an increase in the amount of acetone, which may have been caused, in part, by a dissociation of the extracted species occurring in the sedimented phase. The variation of the dicyclohexylamine concentration in the sedimented phase and the extraction of gold(III) without dicyclohexylamine would also be possible reasons.

3.2. Optimum conditions for DLLME of gold(III) with dicyclohexylamine

As mentioned above, dicyclohexylamine was useful as an extractant for the DLLME of gold(III). We optimized the conditions for DLLME of gold(III) with dicyclohexylamine using 8 mL of the test solution.

3.2.1. Water-miscible organic solvent

The influence of some water-miscible organic solvents, including acetone, acetonitrile, methanol, and acetic acid, was investigated. As shown in Fig. 4, acetone was the most suitable of the investigated solvents in terms of effective extraction and ease of handling. The extraction percentage of gold(III) increased with an increase in the amount of acetone used, whereas gold(III) was not extracted in the absence of acetone. The quantitative extraction of gold(III) was achieved using 1.0–1.5 mL of acetone. Therefore, 1.0 mL of acetone was used in this method.

3.2.2. Water-immiscible organic solvent as extraction solvent

Chloroform was a convenient extraction solvent in gold(III) extraction using dicyclohexylamine because of the easy dissolution of dicyclohexylamine and the efficient extraction of gold(III). Fig. 5 shows the effect of the volume of chloroform, which contained 50 mmol L^{-1} of dicyclohexylamine, on both the extraction of gold(III) and the volume of the sedimented phase. The extraction percentage of gold(III) increased with an increase in the volume of chloroform and reached approximately 100% when more than 100 μL of chloroform was used. Additionally, the volume of the sedimented phase increased with an increase in the volume of chloroform used, whereas each volume of the sedimented phase after

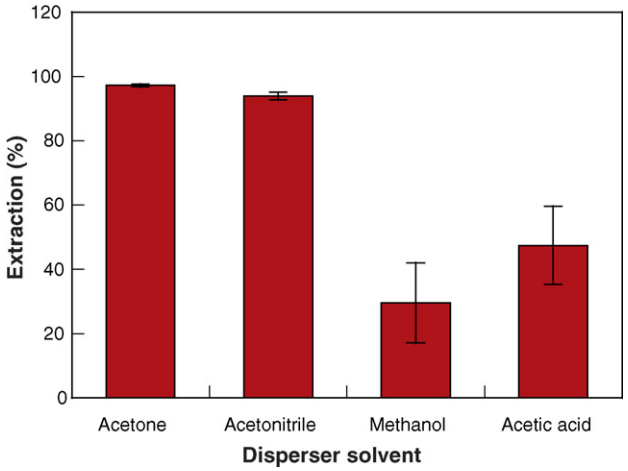


Fig. 4. Effect of some disperser solvents on DLLME of gold(III) with dicyclohexylamine. Aqueous phase, 8 mL of 0.1 mol L^{-1} HCl containing 10 μg L^{-1} of Au(III); mixture solution, 1.0 mL of disperser solvent and 100 μL of chloroform containing 50 mmol L^{-1} of dicyclohexylamine; shaking, 10 s; ultrasonic irradiation, 5 min. The results were shown at mean ± standard deviation (n = 3).

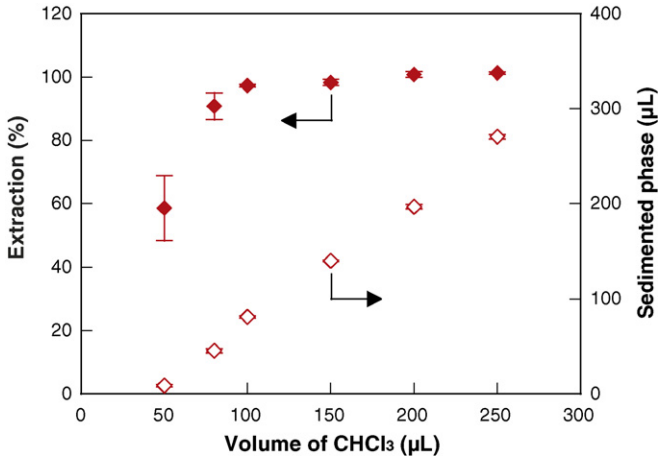


Fig. 5. Effect of volume of chloroform on DLLME of gold(III) with dicyclohexylamine. Aqueous phase, 8 mL of 0.1 mol L^{-1} HCl containing 10 μg L^{-1} of Au(III); mixture solution, 1.0 mL of acetone and 50–250 μL of chloroform containing 50 mmol L^{-1} of dicyclohexylamine; shaking, 10 s; ultrasonic irradiation, 5 min. The results were shown at mean ± standard deviation (n = 3).

the extraction scarcely varied. Due to the quantitative extraction of gold(III) and the high enrichment factor, 100 μL of chloroform was used in this method.

3.2.3. Dicyclohexylamine

When the extraction was carried out using a mixture of acetone and chloroform not containing dicyclohexylamine, 26 ± 2.8% (mean ± standard deviation, n = 3) of gold(III) was extracted. The extraction percentage increased with an increase in the concentration of dicyclohexylamine; more than 90% of gold(III) was extracted with the use of more than 30 mmol L^{-1} of dicyclohexylamine in chloroform. In this method, 50 mmol L^{-1} of dicyclohexylamine was used.

3.2.4. Extraction time

When a mixture of 1.0 mL of acetone and 100 μL of chloroform containing 50 mmol L^{-1} dicyclohexylamine was injected, the extraction percentage of gold(III) was 66 ± 7.1% (n = 3) without shaking due to the insufficient dispersibility of chloroform [19]. However, the extraction percentage of gold(III) was significantly improved to 95 ± 1.6% (n = 3) when the mixture was gently shaken by hand for a few seconds. In this method, ultrasonic irradiation was applied after the gentle shaking for just in case. Since the irradiation time, ranging from 1 to 30 min, did not affect the extraction percentages, ultrasonic irradiation for 5 min was employed. It may be possible to omit the ultrasonic irradiation, depending on the sample.

3.2.5. Extraction pH

The relationship between the extraction percentage of gold(III) and the pH or acidity of the test solution is shown in Fig. 6. In the initial pH range of 1–3, gold(III) was quantitatively extracted. The extraction percentage of gold(III) decreased with an increase in the concentration of hydrochloric acid in the range of 1–3 mol L^{-1}, which might be due to the formation of tetrachloroauric acid ($HAuCl_4$) and/or interference by chloride ions. On the other hand, the extraction percentage also decreased with an increase in the initial pH in the range of 3–7. In this range, the pH in the supernatant phase was significantly shifted to the basic region after the extraction, whereas the pH shift was slight or negligible at an initial pH below 3. The insufficient extraction at an initial pH above 3 would be due to a lack of the protonated form of dicyclohexylamine as well as the ligand displacement of tetrachloroaurate(III) ion in the test solution. In this method, the extraction was carried out using a sample solution adjusted to pH 1.

3.2.6. Selectivity

The extraction of other elements, including iron(III), cobalt(II), nickel(II), copper(II), palladium(II), and platinum(IV), was also investigated at an initial pH range of 1–3 and an acid concentration range of 1–3 mol L^{-1}. Iron(III), cobalt(II), nickel(II), and

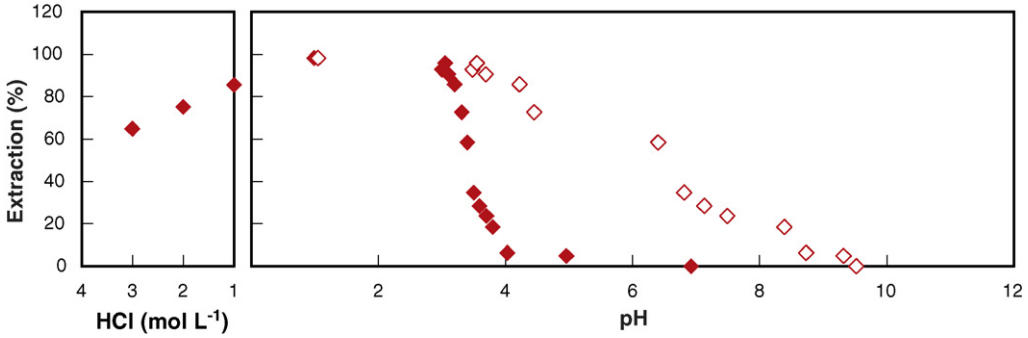


Fig. 6. Effect of HCl concentration and pH on DLLME of gold(III) with dicyclohexylamine. Aqueous phase, 8 mL of 0.1 mol L^{-1} HCl containing 10 μg L^{-1} of Au(III); mixture solution, 1.0 mL of disperser solvent and 100 μL of chloroform containing 50 mmol L^{-1} of dicyclohexylamine; shaking, 10 s; ultrasonic irradiation, 5 min. The extraction percentage was plotted as a function of the initial (♦) or final (◊) pH.

Table 2
Results for determination of gold(III) in effluent.

Sample[a]	Au added (ng in 8 mL)	Au found[b] (ng in 8 mL)	Au concentration ($\mu g\,L^{-1}$)	Au recovery (%)
Effluent 1[c]	–	2.3 ± 0.14	5.7	
	0.8	3.0 ± 0.06		98
Effluent 2[c]	–	1.4 ± 0.07	3.4	
	0.8	2.1 ± 0.07		96
Effluent 3	–	2.9 ± 0.12	0.36	
	0.8	3.7 ± 0.08		103

[a] Effluents were sampled at different time in the same day.
[b] Mean ± standard deviation ($n = 3$).
[c] Effluent was diluted to 20 times with 0.1 mol L^{-1} hydrochloric acid after the digestion.

Table 3
Results for determination of gold in platinum metal and platinum alloy.

Sample	Au added (ng in 8 mL)	Au found[a] (ng in 8 mL)	Au content ($\mu g\,g^{-1}$)	Au recovery (%)
Pt metal	–	0.76 ± 0.03	39.9	
	0.8	1.58 ± 0.03		104
Pt alloy	–	0.57 ± 0.02	28.1	
	0.8	1.36 ± 0.02		99

[a] Mean ± standard deviation ($n = 3$).

copper(II) were scarcely extracted under the conditions used for the investigation (the obtained results are shown in Fig. 2S in the Supplementary Material). For palladium(II), the extraction was negligible at an initial pH below 1, whereas the formation of the precipitate was observed at an initial pH above 3 (Fig. 2S). Although the extraction percentage of platinum(IV) slightly increased with an increase in acidity in the test solution, platinum(IV) was not extracted at an initial pH of 1–3 (Fig. 2S). These results indicate that DLLME using dicyclohexylamine is quite selective for gold(III). It is known that the extractability of gold(III) is higher than those of palladium(II) and platinum(IV) in the ion-pair extraction of their chloro-complexes [33]. In our experiments, the selectivity might have been emphasized by the use of small amounts of dicyclohexylamine.

3.3. Calibration curve and detection limit

The relationship between the absorbance of gold in the ETAAS measurement and the concentration of gold(III) was investigated. A straight line ($R^2 = 0.996$) was obtained with the use of 8 mL of the test solution containing 0.02–1.0 $\mu g\,L^{-1}$ of gold(III). The enrichment factor, which was calculated based on the slopes for the calibration curves with or without the extraction [25], was 60. The detection limit, defined as three times the standard deviation for the procedural blank ($n = 8$), was 0.002 $\mu g\,L^{-1}$ of gold(III) in 8 mL of sample solution; this value was slightly lower than the detection limit in the combined method with DLLME and ETAAS reported previously [25].

3.4. Interference

The effect of ions generally contained in various water samples on the extraction of gold(III) was investigated. The concentration of the ions (1.1×10^7 $\mu g\,L^{-1}$ of sodium, 4.1×10^5 $\mu g\,L^{-1}$ of potassium, 1.3×10^6 $\mu g\,L^{-1}$ of magnesium, 4.2×10^5 $\mu g\,L^{-1}$ of calcium, 1.6×10^6 $\mu g\,L^{-1}$ of phosphate, and 2.8×10^6 $\mu g\,L^{-1}$ of sulfate) in the test solution used for the investigation was nearly equal to that in seawater [1]. More than 87% of gold(III) was extracted in the presence of large amounts of these ions (Table 1S in the Supplementary Material). The obtained results indicate that the method proposed here is useful for determining gold(III) in various water samples, including effluents.

The effect of excessive amounts of platinum(IV) and copper(II), which were scarcely extracted at an initial pH of 1 (Fig. 2S), was also investigated. Gold(III) was extracted at more than 92% in the presence of 2000 $\mu g\,L^{-1}$ of platinum(IV) and copper(II) (Table 2S in the Supplementary Material). These results indicate that the proposed method is also applicable to the determination of gold as an impurity in platinum metal and alloys containing platinum and copper.

3.5. Application

The method proposed here was applied to the determination of gold(III) in effluents. The obtained results are shown in Table 2. In all of the effluent samples, gold(III) was precisely determined. The gold(III) spiked to the effluent samples was quantitatively recovered, and no significant interference was observed.

The determination of gold in platinum metal and its alloy was also attempted. As shown in Table 3, gold was determined in both samples, and satisfactory results were obtained in the recovery tests.

4. Conclusion

Dicyclohexylamine as an extractant for gold(III) showed excellent performance in DLLME using acetone as a disperser solvent and chloroform as an extraction solvent. The results of the investigation using the LLE technique suggest that acetone used as a disperser solvent in DLLME also contributes to decrease in hydration, decrease in the difference in the dielectric constants between the supernatant phase and the sedimented phase, and dissolution of a part of chloroform as an extraction solvent to the supernatant phase. The extraction of gold(III) in DLLME using dicyclohexylamine is, therefore, quite efficient. Gold(III) can be selectively extracted from a sample solution at pH 1 even in the presence of other elements, such as iron(III), cobalt(II), nickel(II), copper(II), palladium(II), and platinum(IV). The combined method with DLLME and ETAAS can readily determine gold(III) at a sub-$\mu g\,L^{-1}$ level using only 8 mL of the sample solution without interference by the matrices and can be applied to the determination of gold in platinum metal and its alloy as well as effluent. The proposed method should be useful for the analyses of other water samples and the determination of gold in various materials, including metals, alloys, and salts.

Acknowledgements

The authors are grateful to Prof. Shukuro Igarashi of Ibaraki University for his valuable suggestion and helpful discussion about homogeneous liquid–liquid extraction.

Appendix A. Supplementary data

Supplementary data associated with this article can be found, in the online version, at doi:10.1016/j.talanta.2009.09.037.

References

[1] C. Reimann, P. de Caritat, Chemical Elements in the Environment, Springer, Berlin, 1998.
[2] I. Dobrevski, M. Dimova-Todorova, T. Panayotova, Environ. Protect. Eng. 18 (1994) 81.
[3] M. Spitzer, R. Bertazzoli, Hydrometallurgy 74 (2004) 233.
[4] S.J. Paddison, K.S. Promislow, Topics in Applied Physics, Device and Materials Modeling in PEM Fuel Cells, vol. 113, Springer, Berlin, 2009.
[5] T. Okada, M. Kaneko, Springer Series in Material Science, Molecular Catalysts for Energy Conversion, vol. 111, Springer, Berlin, 2009.
[6] K. Pyrzynska, Spectrochim. Acta Part B 60 (2005) 1316.
[7] N.R. Das, S.N. Bhattacharyya, Talanta 23 (1976) 535.
[8] J.D. Miller, M.B. Mooiman, Sep. Sci. Technol. 19 (1984) 895.
[9] J. Adam, R. Pribil, Talanta 18 (1971) 405.
[10] A.A. Vasilyeva, I.G. Yudelevich, L.M. Gindin, T.V. Lanbina, R.S. Shulaman, I.L. Kotlarevsky, V.N. Andrievsky, Talanta 22 (1975) 745.
[11] T. Ohara, S. Matsumoto, H. Yamamoto, J. Shibata, Y. Baba, Solv. Extr. Res. Dev., Jpn. 3 (1996) 213.
[12] S.S. Kolekar, M.A. Anuse, Gold Bull. 34 (2001) 50.
[13] S. Igarashi, S. Oshite, Bunseki (1997) 702.
[14] S. Igarashi, T. Arai, T. Kawakami, Bunseki Kagaku 43 (1994) 1183.
[15] S. Igarashi, N. Ide, Y. Takagai, Anal. Chim. Acta 424 (2000) 263.
[16] S. Igarashi, N. Ide, K. Takahata, Y. Takagai, Bunseki Kagaku 48 (1999) 1115.
[17] M.A. Farajzadeh, M. Bahram, S. Zorita, B.G. Mehr, J. Hazard. Mater. 161 (2009) 1535.
[18] M. Rezaee, Y. Assadi, M.-R.M. Hosseini, E. Aghaee, F. Ahmadi, S. Berijani, J. Chromatogr. A 1116 (2006) 1.
[19] F. Pena-Pereira, I. Lavilla, C. Bendicho, Spectrochim. Acta Part B 64 (2009) 1.
[20] E.Z. Jahromi, A. Bidari, Y. Assadi, M.R.M. Hosseini, M.R. Jamali, Anal. Chim. Acta 585 (2007) 305.
[21] A. Bidari, E.Z. Jahromi, Y. Assadi, M.R.M. Hosseini, Microchem. J. 87 (2007) 6.
[22] H. Jiang, Y. Qin, B. Hu, Talanta 74 (2008) 1160.
[23] A. Moghimi, J. Chin. Chem. Soc. 55 (2008) 369.
[24] M.T. Naseri, M.R. Milani Hosseini, Y. Assadi, A. Kiani, Talanta 75 (2008) 56.
[25] M. Shamsipur, M. Ramezani, Talanta 75 (2008) 294.
[26] P. Liang, E. Zhao, F. Li, Talanta 77 (2009) 1854.
[27] R.E. Rivas, I. Lopez-Garcia, M. Hernandez-Cordoba, Spectrochim. Acta Part B 64 (2009) 329.
[28] Japan Industrial Standards, Testing Methods for Industrial Wastewater, K0102, Japan Industrial Standards, 1998.
[29] B.G. Tehan, E.J. Lloyd, M.G. Wong, W.R. Pitt, E. Gancia, D.T. Manallack, Quant. Struct.—Act. Relat. 21 (2002) 473.
[30] A. Alian, W. Sanad, Talanta 14 (1967) 659.
[31] A. Alian, W. Sanad, R. Shabana, Talanta 15 (1968) 639.
[32] R. Azzam, R. Shabana, A. Alian, Microchem. J. 16 (1971) 376.
[33] J. Chen, Y. Zhang, Precious Met. 19 (1995) 29.

Talanta 80 (2010) 1371–1377

Contents lists available at ScienceDirect

Talanta

journal homepage: www.elsevier.com/locate/talanta

The porous CuO electrode fabricated by hydrogen bubble evolution and its application to highly sensitive non-enzymatic glucose detection

Serhiy Cherevko, Chan-Hwa Chung*

Advanced Materials and Process Research Center for IT, School of Chemical Engineering, Sungkyunkwan University, Suwon, 440-746, Republic of Korea

ARTICLE INFO

Article history:
Received 22 June 2009
Received in revised form
15 September 2009
Accepted 18 September 2009
Available online 24 September 2009

Keywords:
Copper oxide
Porous film
Non-enzymatic sensor
Glucose
Amperometry

ABSTRACT

The porous Cu film was deposited on a Pt/Ti/Si substrate by electrochemical deposition accompanied by hydrogen evolution at very high current densities. CuO films with similar morphologies were obtained by subsequent annealing of the porous copper films. The morphology, composition and structure of the porous Cu and porous CuO were investigated by FE-SEM, EDS and XRD methods. The complete transformation of Cu to CuO after annealing was indicated. The sensing performances of the porous CuO film were evaluated in alkaline solution with the porous CuO film showing a wide linearity range from 1 μM to 2.5 mM with sensitivity of 2.9 mA cm^{-2} mM^{-1}, and detection limit of 0.14 μM. The sensor showed good selectivity to conventional intermediates such as AA and UA and long term stability.

© 2009 Elsevier B.V. All rights reserved.

1. Introduction

Research on the development and improvement of existing amperometric glucose sensors has been performed over at least the past 45 years since Clark and Lyons reported on the first enzyme electrode [1]. The majority of known amperometric glucose sensors is based on the immobilization of enzymes, such as glucose oxidase (GO_x), and electrochemical detection of hydrogen peroxide or they are based on the use of redox mediators [2–4]. Even though enzymatic sensors show good sensitivity and excellent selectivity, such sensors suffer from the intrinsic nature of enzymes which results in bad long term stability [2]. To overcome this limitation numerous non-enzymatic sensors were proposed recently. Most of these sensors are based on the utilization of precious metals like bare platinum or gold electrodes [3–6]. However, these electrodes were also not optimal as they showed low sensitivity, poor selectivity and were poisoned by intermediates and chloride [7]. More recently, some of these drawbacks were overcome by taking advantages of special physical and chemical properties of different nanomaterials, such as nanoparticles [8–11], nanowires [12], and nanoporous films [13,14]. When utilizing nanomaterials, it becomes possible to minimize the influence of interferences such as ascorbic acid and uric acid [15]. Nonetheless, low sensitivity and costliness still limits the practical application of many nanomaterials based sensors.

Recently, nanostructured cupric oxide (CuO) was investigated for glucose sensing. Zhuang et al. reported CuO nanowires grown on a copper electrode for glucose detection [16]. The obtained sensor showed very high sensitivity and good stability. However, the synthesis of CuO nanowires was still tedious and involved multiple steps. The instability of copper in air and in the electrolyte may also affect sensing properties of such a sensor. The use of copper (II) oxide nanorod bundles modified basal plane pyrolytic graphite electrode (bppg) toward carbohydrates sensing was also reported [17]. A more robust sensor was prepared by modification of glassy carbon (GC) electrode with Nafion by CuO nanospheres [18]. The analytical performance, mainly sensitivity and response time, is still significantly lower than that of CuO nanowire electrode.

In this paper, we report on a highly sensitive and robust porous CuO glucose sensor fabricated by utilization of porous CuO electrode. Porous CuO electrode was prepared by deposition of porous Cu and subsequent annealing. The analytical performance was investigated by characterizing the sensitivity, detection limit, linearity range, selectivity, and stability of the sensor.

2. Experimental details

2.1. Reagents

Sulfuric acid, hydrochloric acid, copper (II) sulfate pentahydrate, and sodium hydroxide were obtained from Duksan Pure Chemicals (Korea). L-Ascorbic acid (AA), uric acid (UA), and D-(+)-glucose were

* Corresponding author. Tel.: +82 31 290 7260; fax: +82 31 290 7272.
E-mail address: chchung@skku.edu (C.-H. Chung).

0039-9140/$ – see front matter © 2009 Elsevier B.V. All rights reserved.
doi:10.1016/j.talanta.2009.09.038

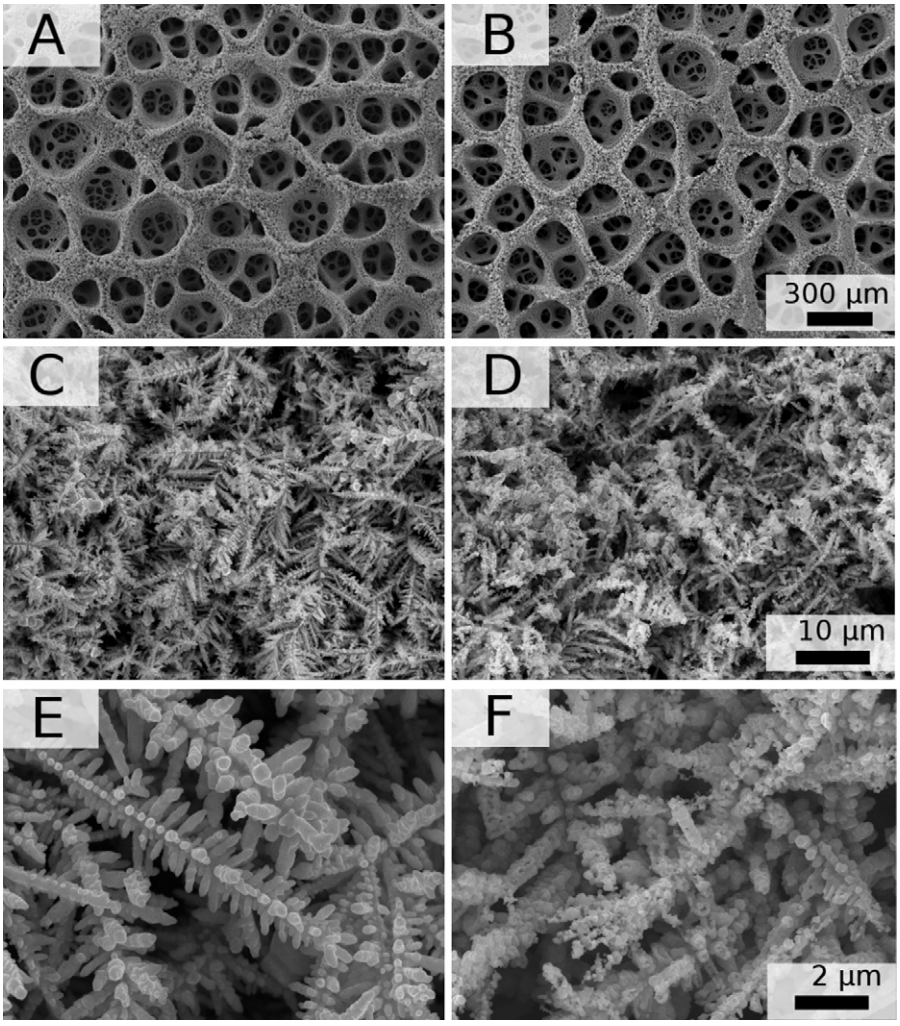


Fig. 1. FE-SEM images of as-deposited porous copper film (A, C, and E) and cupric oxide structures obtained after heating porous copper (B, D, and F) taken with magnifications 60 (A, B), 2000 (C, D), and 15,000 (E, F).

purchased from Sigma–Aldrich. All of the solutions were prepared in deionized (DI) water. All chemicals were used as received.

2.2. Instruments

The electrochemical experiments were performed using an electrochemical workstation (Zahner® Elektrik IM6ex, Germany). Hg/HgO (0.098 V *vs*. NHE) and Pt plate were used as the reference and counter electrodes, respectively. The chemical composition was measured by energy dispersive X-ray analysis (EDS) performed in a field emission scanning electron microscope (FE-SEM) (JEOL JSM-7000F) with which the morphology of the deposited films was also examined. The structural properties were examined by X-ray diffractometry (XRD) (Bruker AXS with Cu Kα radiation at 40 kV and 40 mA).

2.3. Electrode preparation

With a thin 10 nm thick Ti layer used for adhesion, a 200 nm thick Pt thin film was deposited onto a Si (1 0 0) oriented wafer by using electron beam evaporation after which the wafer was diced into 5 mm × 25 mm pieces. To prepare the working electrode, a strip of sticky tape with a hole of 2 mm diameter was put on the surface of Pt/Ti/Si slide, and then the edges and the back side of the slide were covered by insulating varnish. Prior to copper deposition, the slides were electrochemically cleaned in 1 M H_2SO_4 solution by cycling potential in the potential window 0.4–1.6 V *vs*. Hg/HgO. The porous copper films were galvanostatically (current density was controlled as 3 A cm^{-2}) electrodeposited on the tape covered Pt/Ti/Si structure from a solution containing 0.4 M $CuSO_4 \times 5H_2SO_4$, 1.5 M H_2SO_4 and 50 mM HCl [19]. The deposition was performed at room temperature from an unstirred solution for 20 s. After deposition the porous Cu/Pt/Ti/Si substrate (porous Cu electrode) was washed with DI water and dried in nitrogen. Before annealing, the tape and varnish were removed from the slide. Porous CuO was obtained by heating the porous copper at $T = 500\,^{\circ}C$ for 5 h in ambient environment. To eliminate any possible influence of the Pt substrate on the electrochemical experiments, Pt was covered by varnish again

2.4. Electrochemical experiments

All of the electrochemical experiments were carried out at room temperature in a standard three-electrode system. The porous CuO/Pt/Ti/Si electrode (porous CuO electrode) was evaluated as a glucose sensor in 0.1 M NaOH solution. Cyclic voltammetry (CV) measurements were carried out in the potential range of 0–0.8 V *vs*. Hg/HgO. The amperometric curves were obtained after adding the desired amount of glucose with the solution being stirred constantly. The current density in this paper was reported as the ratio

of the recorded current to the geometrical area of the electrode. All potentials are quoted against Hg/HgO reference electrode.

3. Results and discussion

3.1. Preparation and characterization of the porous CuO electrode

The porous Cu films were deposited by hydrogen bubble dynamic synthesis [20]. This technique involves extremely fast electrochemical deposition of metal along with hydrogen evolution at very high cathodic current densities. Previously it was reported that Au substrate which has much lower overpotential for the hydrogen evolution than Cu, should be used to obtain porous structure, where pore sizes of the copper increase with the distance away from the substrate [19]. This type of structure, where big pores are located near the top of an electrode and sub-layers with smaller pores located near the substrate is ideal for sensing of highly active electrochemical species. The main advantage of highly porous film is high surface area. Whereas in most porous films the distribution of pores is uniform resulting in difficulties of the transport of electroactive species to the inner space of the porous film because of the small pores on the top, here that problem is overcome since wide pores at the top allow the species to enter the porous film more efficiently. Recently, Zhuang et al. showed that the oxidation of glucose on CuO nanowires is diffusion controlled [16]. We have come to the same conclusion for the CuO porous film in our experiments (the linear dependence of glucose oxidation peak current on the square root of sweep rate was obtained) (not shown). It means that using porous films with non-uniform pores would result in better efficiency compared to traditional porous films. Following [19] we performed electrodeposition of porous Cu on gold (Au/Si/Ti) substrate. However, after heating at $T = 500\,^{\circ}C$ the thin layer of gold becomes non-conductive, which makes it unsuitable for use as a working electrode in electrochemical experiments. As platinum also has a much lower overpotential for the hydrogen evolution compare to Cu, the Au thin film was replaced by a thin layer of Pt.

Fig. 1(A, C, and E) shows the FE-SEM images of porous Cu film electrodeposited on the Pt/Ti/Si structure taken at different magnifications. It can be seen that the top layer of the porous film consists of pores of about 200–300 μm in diameter and smaller holes could be seen in the inner sub-layers. The walls of the structure are composed of dense ramified deposits (see Fig. 1C and D). The branch size is smaller than 100 nm, which is similar to the porous copper deposited on Au substrate [19]. The porous CuO structures obtained after heating of porous Cu is shown in Fig. 1(B, D, and F). As can be seen by comparing images of porous Cu (Fig. 1A and B) the obtained CuO film retained the structure of the porous Cu template. The entire dense structure was also retained. At high magnification one can see that the nanoscale morphology was slightly different (Fig. 1E and F). The as-deposited films have dendrite structure and consist of branches about 10 μm long with smaller branches of about 1 μm long and 70–100 nm in diameter. Porous branches were formed after the heat treatment. It is believed that the formation of such voids in the branches is due to the Kirkendall effect [21,22].

The X-ray diffraction peaks of as-deposited porous copper and porous CuO are shown in Fig. 2(A). For comparison the standard diffraction patterns for Cu and CuO (JCPDS 004-0836 and 045-0937) are also presented. The as-deposited copper film is indexed as (fcc) phase. It is believed that since copper easily oxidizes in air and more so in this cause due to the very high surface area, the small peak at *ca.* 36° for as-deposited film is from copper oxide. It can be seen that after heating at 500 °C copper is completely converted to pure monoclinic CuO with the lattice constants $a = 4.686$, $b = 3.427$, $c = 5.129$ Å, and $\beta = 99.53°$, which match well the standard XRD

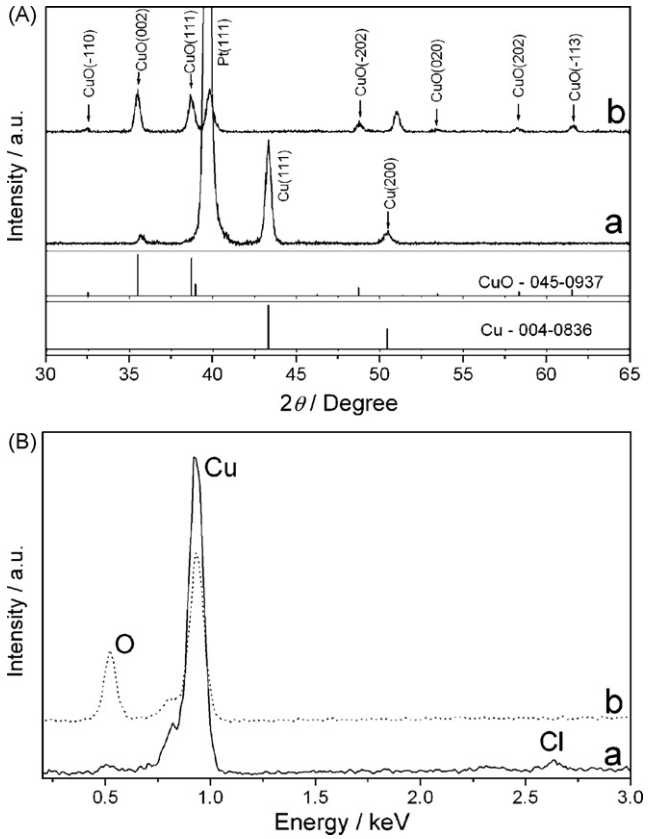


Fig. 2. (A) XRD patterns and (B) EDS spectra of (a) as-deposited porous copper and (b) porous CuO film formed after heat treatment.

data (JCPDS 045-0937). The peak around 51.3° could be indexed as (1 1 2), though the intensity of this peak from the standard polycrystalline sample should be very low. To examine chemical purity and composition of as-deposited and annealed samples, EDS was also performed. Fig. 2(B) shows the EDS spectra of porous films (a) before and (b) after heat treatment.

The as-deposited copper film consists of copper with some traces of oxygen and chlorine and no chlorine was observed after heat treatment. The observed oxygen is likely due to the presence of surface oxides and chlorine is from HCl. The composition of CuO samples was found to be Cu:O = 56.6 ± 0.4:43.4 ± 0.4 (for four samples). The XRD and EDS results confirm that porous Cu was completely transformed to CuO.

3.2. Electrocatalytic oxidation of glucose

Voltammetry in the potential window from 0 V to 0.8 V was used to investigate and compare the catalytic activities of bare platinum film, copper film, and porous CuO electrodes. Fig. 3(A) shows CVs for (a) bare platinum film, (b) copper film, and (c) porous CuO electrodes in a 0.1 M NaOH solution with presence of 2.5 mM of glucose.

It is clear (Fig. 3(A) (a)) that the bare platinum film electrode is not active for glucose oxidation in applied potential window, as only small background current was observed. The typical voltammogram of glucose oxidation on copper was observed when the copper film was used. It should be noted that in alkaline solution the potential of copper oxidation is lower than the onset of glucose oxidation, which means that a thin film of copper oxide was formed and copper oxide instead of copper should be considered. The oxidation of glucose on the copper film electrode starts at approximately 0.35 V with broad peak at around 0.69 V. On the

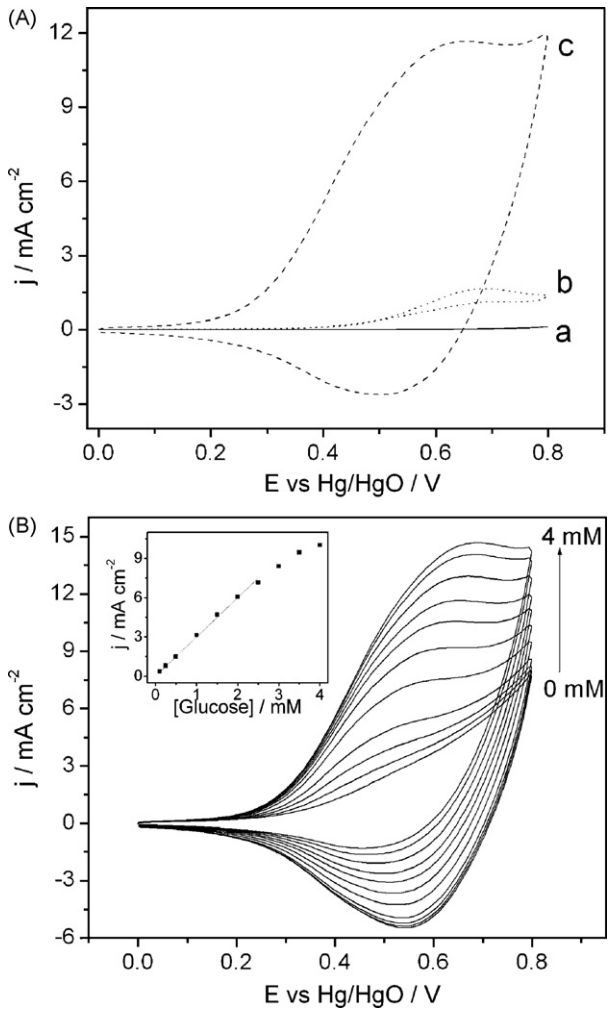


Fig. 3. (A) CVs of (a) bare platinum electrode, (b) bare copper electrode, and (c) porous CuO electrode in the 0.1 M NaOH + 2.5 mM glucose solution. (B) Shows the voltammetric response of a porous CuO electrode to the addition of 0.1 mM, 0.15 mM, 0. 25 mM, and subsequent addition of 0.5 mM of glucose until total concentration of 4 mM was obtained. Inset shows the dependence of the current at $E = 0.65$ V on the concentration of glucose. The scan rate was 50 mV/s.

other hand, the oxidation of glucose on a porous CuO electrode commences at more negative potential *ca.* 0.2 V with peak at around 0.64 V, indicating the enhanced catalytic properties of porous CuO electrode toward oxidation of glucose.

The concentration dependence of electrochemical activity of porous CuO electrode toward oxidation of glucose was also studied. Fig. 3(B) presents the CVs of the porous CuO electrode recorded in 0.1 M NaOH electrolyte in the absence of glucose and in presence of 0.1 mM, 0.25 mM, 0.5 mM and so on until 4 mM with successive addition of 0.5 mM. The increase of glucose concentration produces the gradual increase of current around 0.65 V. The current at chosen voltage of 0.65 V was found to be linear in the range of 0.1–2.5 mM with the correlation coefficient of 0.998 (Fig. 3(B) inset). This linear dependence can be used for calibration in analytical application of porous cupric oxide electrode.

3.3. Amperometric sensing of glucose

To find the optimal conditions for the amperometric sensing of glucose, the effect of applied potential on the response current of the sensor was investigated. Fig. 4 shows the amperometric curves of cupric oxide electrode in 0.1 M NaOH solution with successive addition of 0.5 mM glucose at applied potentials of 0.55–0.7 V. In the range of 0.55–0.65 V the oxidation current of glucose increased with increasing potential. With increasing potential further the side reaction takes place on the electrode, which results in the increase of the background current and leads to the inhibition of glucose oxidation. Thus a constant potential of 0.65 V was chosen for further amperometric investigations.

Fig. 5(A) illustrates typical amperometric responses to successive addition of glucose concentration indicated. The lower right inset shows the increased section of amperometric curve after addition of low concentration of glucose. The upper left inset presents a typical current–time curve of cupric oxide electrode under successive injections of 10 μM of glucose. The corresponding dependence of oxidation current on the concentration of glucose is shown in Fig. 5(B). The oxidation current increased with each addition of glucose until saturation at concentrations higher than 20 mM was observed. For comparison the dependence of oxidation current on the concentration of glucose for platinum film electrode is also presented. It can be seen that platinum is not active for glucose oxidation. The inset shows the calibration curve of glucose oxidation on the porous cupric oxide electrode in the concentration range of 1 μM to 2.5 mM. One can see that oxidation current linearly increases in this range of concentrations

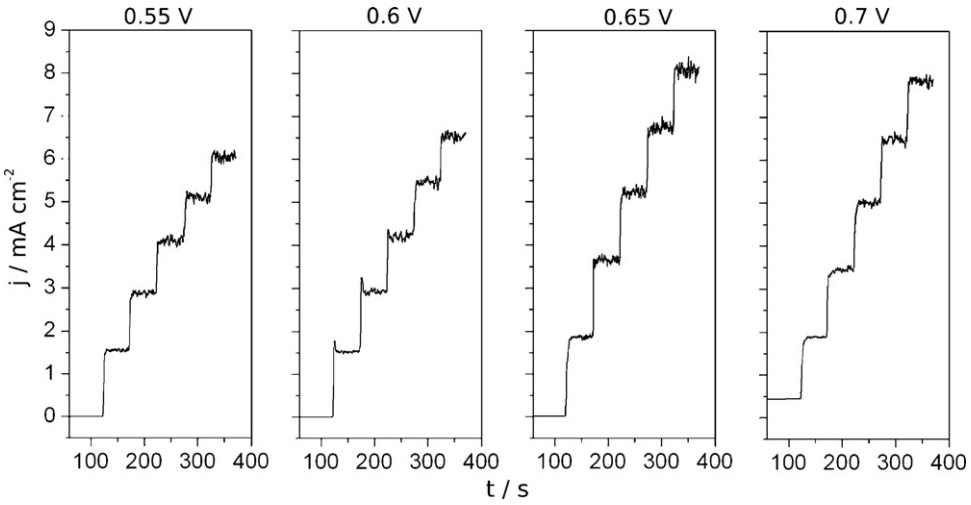


Fig. 4. Amperometric response of a porous CuO electrode with successive addition of 0.5 mM glucose to 0.1 M NaOH at different applied potentials.

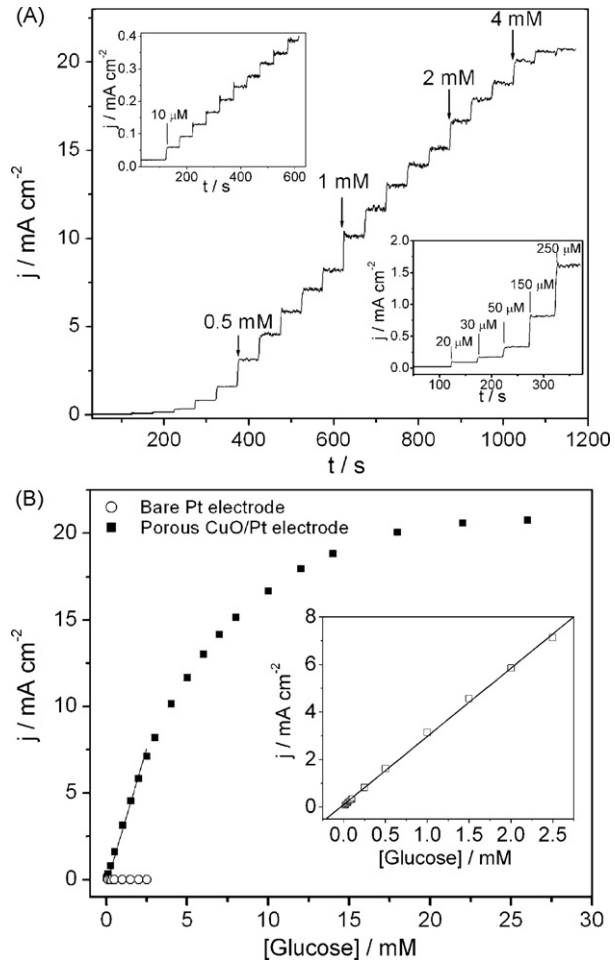


Fig. 5. (A) Amperometric response of a porous CuO electrode at 0.65 V on the addition of glucose indicated. The lower right inset shows the magnified view of the amperometric response at low concentrations of glucose. The upper left inset shows the response of a porous CuO electrode to successive addition of 10 μM glucose. (B) The calibration curve of the porous CuO electrode toward glucose. Inset—the linear range of the calibration curve.

with correlation coefficient 0.999. The sensitivity of porous CuO electrode is 2.9 mA cm^{-2} mM^{-1}, which is higher than 0.4 and similar to 2.45 mA cm^{-2} mM^{-1} for CuO nanospheres [18] and CuO nanowires [16] electrodes, respectively. Also the sensitivity of porous CuO electrode is significantly higher than that of other glucose sensors based on the use of precious metal nanomaterials [8,12,13,15,23–26] and enzymes [27–32]. The important analytical performances of our porous CuO electrode were compared with other Cu or Cu oxide based sensors as summarized in Table 1. As one can see the porous CuO electrode shows the highest sensitivity. The high sensitivity for this CuO electrode can be attributed to the high surface area of the electrode and high efficiency of the electrode morphology. A detection limit of 1.4×10^{-7} M was obtained

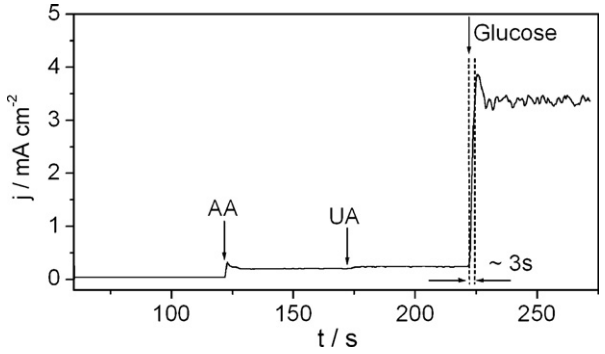


Fig. 6. Current–time profile of a porous CuO electrode with addition of 0.05 mM AA, 0.1 mM UA, and 1 mM glucose.

(detection limit (*dl*) was calculated as $dl = 3\sigma_b/m$, where σ_b is the standard deviation of the background current, and m the slope of the linear part of the calibration curve [30]).

3.4. Selectivity and response time

It was reported that the presence of chloride ions in the solution can significantly affect the glucose oxidation [18]. To investigate this, voltammetric and amperometric response to 0.5 mM of glucose in 0.1 M NaOH with presence and absence of 0.15 M NaCl was also investigated (data not shown). The change of both voltammetric and amperometric responses was found to be negligible in the presence of chloride, indicating the tolerance of CuO electrode to the presence of chloride ions in the solution.

It is also well known that the non-enzymatic sensor usually suffers from the interfering species, such as AA and UA. The normal physiological level of glucose is 3–8 mM and that of AA and UA is about 0.1 mM [16]. However, usually due to the high electron transfer rate, the interference oxidation current can be comparable with the one of glucose oxidation. Therefore, the selectivity of the porous CuO electrode was investigated against AA and UA. Fig. 6 presents amperometric curve for the porous CuO electrode in 0.1 M NaOH with successive additions of 0.05 mM AA, 0.1 mM UA, and 1 mM glucose. The defined concentrations were chosen to compare obtained data with results obtained on the CuO nanowrires and CuO nanospheres electrodes [16,18]. By setting the current density of the porous CuO electrode to 1 mM glucose at 100%, the response to the addition of 0.05 mM AA, and 0.1 mM UA was 5.1% and 1.1%, respectively. The obtained selectivity is even better than that found for the CuO nanospheres electrode, where Nafion, which sometimes is utilized for improvements of selectivity, was used. A similar result was observed when the opposite sequence (glucose, UA, and AA) was used (not shown). This result demonstrates that amperometric detection of glucose on the porous CuO electrode can be performed with negligible interference from AA, and UA.

Also, the ability of the glucose sensing in real blood serum samples was evaluated. Here 0.4 mL of serum samples were added

Table 1
Comparison of the performance of the porous CuO glucose sensor with that of reported glucose sensors base on utilization of Cu or Cu oxide in NaOH solution.

Electrode materials	Reference electrode	Potential (V)	Sensitivity (mA cm^{-2} mM^{-1})	Dynamic range (M)	Detection limit (M)	References
DMG-CuNPs	SCE	0.65	0.7	1.0×10^{-6} to 5.0×10^{-3}	5.0×10^{-7}	[35]
CuO NWs	Ag/AgCl	0.33	2.45	4.0×10^{-7} to 2.0×10^{-3}	4.9×10^{-8}	[16]
PVP-CuNPs	Ag/AgCl	0.45	–	1.0×10^{-6} to 2.5×10^{-3}	–	[36]
Cu-CNTs	Ag/AgCl	0.65	0.25	7.0×10^{-7} to 3.5×10^{-3}	2.1×10^{-7}	[33]
CuO nanospheres	Ag/AgCl	0.6	0.4	Up to 2.55×10^{-3}	1.0×10^{-6}	[18]
CuO nanorods	SCE	0.6	2.3 in the range 0–100 μM	Up to 1×10^{-3}	1.2×10^{-6}	[17]
Porous CuO	Hg/HgO	0.65	2.9	1.0×10^{-6} to 2.5×10^{-3}	1.4×10^{-7}	This work

DMG: dimethylglycoxime; NP: nanoparticles; PVP: polyvinylpyrrolidone; CNT: carbon nanotubes.

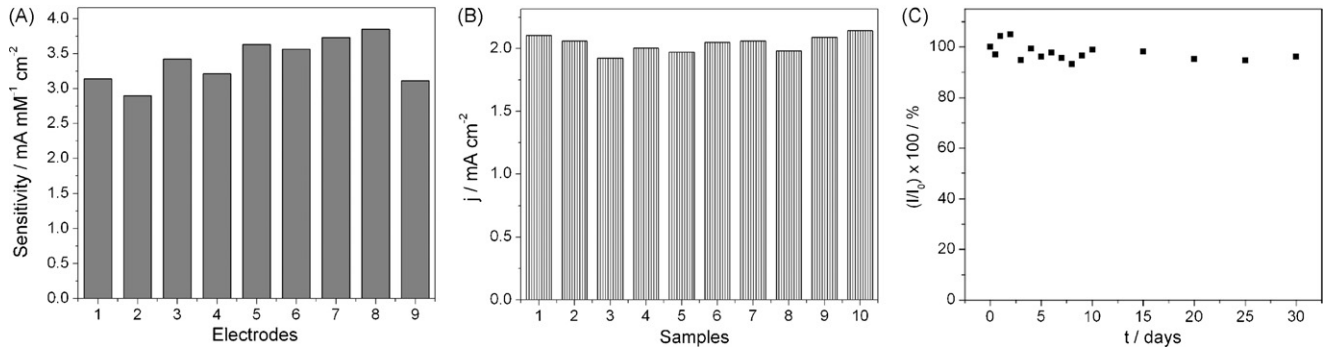


Fig. 7. (A) Sensitivity values measured on nine different porous CuO electrodes in glucose concentration range 0.5–2.5 mM. (B) The amperometric response of one porous CuO electrodes to ten 0.5 mM glucose samples. (C) The variation of amperometric response taken over 1 month of a CuO electrode to addition of 0.5 mM glucose.

to 10 mL of 0.1 M NaOH solution and the amperometric response was recorded at 0.65 V. According to the calibration curve the current response corresponded to the glucose concentration around 6.5 mM. The hospital analysis, however, showed that the glucose level in the blood sample was 4.6 mM. This result demonstrates that beside the interference from the AA and UA there are, probably, other compounds that have to be taken into account. It is of interest that when CuO nanowires [16] or copper nanocluster/multiwall carbon nanotube [33] modified electrodes were used for the detection of glucose the deviation between experimentally and clinically obtained data was small. So far the exact reason of the unexpected high oxidation currents obtained on the CuO porous electrode when blood serum was added is not clear, however, we believe that it is related to the high surface area of the CuO porous electrode. Thus, the kinetics of glucose oxidation on CuO was estimated as described below.

Even though the exact mechanism of glucose oxidation on the CuO is not clearly known [16,33] it can be proposed that the kinetics of this process is faster than the oxidation of glucose on precious metals, as it was found that this process is diffusion controlled (described above). In the case of precious metals high roughness electrodes were proposed which resulted in an increase of the response of sluggish oxidation of glucose [12,15]. This reaction is proportional to the real surface area of the electrode. On the other hand, fast oxidation of intermediates such as AA takes place on the outer surface of electrode and is thus proportional to the geometrical area of the electrode. In the case of CuO electrode, however, the kinetics of glucose and AA oxidation are probably different. To study this, the kinetics for glucose, AA, and UA oxidation on a porous CuO electrode were determined by the Tafel plots. The Tafel slopes were obtained as about 120 mV dec^{-1}, 190 mV dec^{-1}, and 260 mV dec^{-1} for glucose, AA, and UA, respectively. The results show that the reaction activity of glucose oxidation on a porous CuO electrode is higher than that for AA and UA. Also, from the kinetic theory of electrode reaction, the value of Tafel slope about 118 mV dec^{-1} for glucose oxidation on porous CuO electrodes indicates that a single electron exchange is involved in the rate-determining step (assuming a transfer coefficient of $\alpha = 0.5$). Assuming that the glucose oxidation mechanism is similar with the one described by Fleischmann et al. [34], the abstraction of hydrogen atom from the α-carbon with electron transfer to the electrode is most likely to be the rate-determining step of glucose oxidation.

We can conclude that due to the high activity of glucose oxidation on CuO the area of porous electrode could be involved in this reaction only partially. On the other hand for the oxidation of intermediate compounds with sluggish reaction activity the efficiency of utilization of whole surface area is higher. This is probably the reason of higher responses obtained for real blood samples. Additional experiments are needed to find the role of blood components in the CuO sensor response.

The response time defined as 95% of the response current density was within 3 s (see Fig. 6), which is smaller than the response time for most glucose sensors.

3.5. Reproducibility and stability

The reproducibility and stability of the amperometric glucose sensor were also evaluated. The sensitivity for nine porous CuO electrodes in the glucose concentration range of 0.5–2.5 mM was measured (Fig. 7(A)). The relative standard deviation (RSD) was 15.45%, which is relatively high. The mean value of sensitivity was 3.43 ± 0.53 mA cm^{-2} mM^{-1}. The high value of RSD can be related to the dendrite nature of the growth. It is believed that sensitivity is strongly dependent on the morphology of porous electrode at the nanoscale. By analyzing porous Cu and porous CuO films by FE-SEM we found that the sizes of smallest branches vary in size at different electrodes. Probably this is why we obtained slight deviation between different electrodes. Further investigations on the optimization of deposition conditions are needed to improve the reproducibility.

Ten successive measurements of current density response to the addition of 0.5 mM of glucose at one chosen porous CuO electrode yielded an RSD of 3.35%, demonstrating that the porous CuO sensor is stable and suitable for repeated detection of glucose (Fig. 7(B)). The long term stability was investigated by measuring the response to 0.5 mM glucose over 1 month. The sensor was stored in air and was tested each day for 10 days and every fifth day over the next 20 days. Fig. 7(C) shows the variation of current during the investigation. For convenience the response on the first day was set to 100%. The results demonstrate that the response was almost the same over the entire investigation period, implying that the electrode can be used in long term routine applications. It is worthy to mention that even after 6 months of storage in air the response of the sensors did not change. The good reproducibility and long term stability of porous CuO electrode can be attributed to both the good stability of CuO in the alkaline solution [18] and good stability of the porous structure itself.

4. Conclusions

In this paper the porous CuO film was prepared by a simple method, comprised electrochemical deposition of Cu on Pt/Ti/Si substrate and subsequent annealing in air. The porous CuO film was evaluated as a glucose sensor. The prepared sensor shows excellent analytical performances including robustness, high sensitivity, wide range of linearity, low detection limit, good selectivity and stability and can be reliably used for the detection of glucose in analytical purposes. Due to the high efficiency of the electrode morphology the highest sensitivity among non-enzymatic sensors based on Cu or CuO was achieved. Moreover, the sensor preparation

technique is very simple and can be easily arranged for the mass production. We believe that the proposed technique can be used for the preparation of other metal oxide based electrochemical sensors

Acknowledgement

This work was supported by a Korea Science and Engineering Foundation (KOSEF) grant funded by the Korea government (MOST) (No. R01-2007-000-10322-0). S.C. thanks Soyoung Kim for the help in real blood serum analysis.

References

[1] L.C. Clark Jr., C. Lyons, Ann. N.Y. Acad. Sci. 102 (1962) 29.
[2] Y.B. Vassilyev, O.A. Khazova, N.N. Nikolaeva, J. Electroanal. Chem. 196 (1985) 105.
[3] I.T. Bae, E. Yeager, X. Xing, C.C. Liu, J. Electroanal. Chem. 309 (1991) 131.
[4] R.R. Adzic, M.W. Hsiao, E.B. Yeager, J. Electroanal. Chem. 260 (1989) 475.
[5] M.W. Hsiao, R.R. Adzic, E.B. Yeager, Electrochim. Acta 37 (1992) 357.
[6] M.W. Hsiao, R.R. Adzic, E.B. Yeager, J. Electrochem. Soc. 143 (1996) 759.
[7] S. Park, H. Boo, T.D. Chung, Anal. Chim. Acta 556 (2006) 46.
[8] C.R.R. Bikash Kumar Jena, Chem. Eur. J. 12 (2006) 2702.
[9] H.-F. Cui, J.-S. Ye, W.-D. Zhang, C.-M. Li, J.H.T. Luong, F.-S. Sheu, Anal. Chim. Acta 594 (2007) 175.
[10] B.K. Jena, C.R. Raj, Chem. Eur. J. 12 (2006) 2702.
[11] X. Kang, Z. Mai, X. Zou, P. Cai, J. Mo, Talanta 74 (2008) 879.
[12] Y. Bai, Y. Sun, C. Sun, Biosens. Bioelectron. 24 (2008) 579.
[13] Y. Bai, W. Yang, Y. Sun, C. Sun, Sens. Actuators B: Chem. 134 (2008) 471.
[14] Y. Deng, W. Huang, X. Chen, Z. Li, Electrochem. Commun. 10 (2008) 810.
[15] S. Park, T.D. Chung, H.C. Kim, Anal. Chem. 75 (2003) 3046.
[16] Z. Zhuang, X. Su, H. Yuan, Q. Sun, D. Xiao, M.M.F. Choi, Analyst 133 (2008) 126.
[17] C. Batchelor-McAuley, Y. Du, G.G. Wildgoose, R.G. Compton, Sens. Actuators B: Chem. 135 (2008) 230.
[18] E. Reitz, W. Jia, M. Gentile, Y. Wang, Y. Lei, Electroanalysis 20 (2008) 2482.
[19] H.-C. Shin, M. Liu, Chem. Mater. 16 (2004) 5460.
[20] H.-C. Shin, J. Dong, M. Liu, Adv. Mater. 15 (2003) 1610.
[21] H.J. Fan, U. Gösele, M. Zacharias, Small 3 (2007) 1660.
[22] Y. Yin, R.M. Rioux, C.K. Erdonmez, S. Hughes, G.A. Somorjai, A.P. Alivisatos, Science 304 (2004) 711.
[23] Y.-G. Zhou, S. Yang, Q.-Y. Qian, X.-H. Xia, Electrochem. Commun. 11 (2009) 216.
[24] J. Wang, P. Holt-Hindle, D. MacDonald, D.F. Thomas, A. Chen, Electrochim. Acta 53 (2008) 6944.
[25] Y.-Y. Song, D. Zhang, W. Gao, X.-H. Xia, Chem. Eur. J. 11 (2005) 2177.
[26] Y. Li, Y.-Y. Song, C. Yang, X.-H. Xia, Electrochem. Commun. 9 (2007) 981.
[27] S.A. Miscoria, G.D. Barrera, G.A. Rivas, Sens. Actuators B: Chem. 115 (2006) 205.
[28] P. Benvenuto, A.K.M. Kafi, A. Chen, J. Electroanal. Chem. 627 (2009) 76.
[29] G.L. Luque, M.C. Rodríguez, G.A. Rivas, Talanta 66 (2005) 467.
[30] D. Xinyi Zhang, L. Li, H. Bourgeois, P.A. Wang, Webley, ChemPhysChem 10 (2009) 436.
[31] Y. Sun, F. Yan, W. Yang, C. Sun, Biomaterials 27 (2006) 4042.
[32] S. Zhang, W. Yang, Y. Niu, C. Sun, Anal. Chim. Acta 523 (2004) 209.
[33] X. Kang, Z. Mai, X. Zou, P. Cai, J. Mo, Anal. Biochem. 363 (2007) 143.
[34] M. Fleischmann, K. Korinek, D. Pletcher, J. Chem. Soc., Perkin Trans. 2 (1972) 1396.
[35] Q. Xu, Y. Zhao, J.Z. Xu, J.-J. Zhu, Sens. Actuators B: Chem. 114 (2006) 379.
[36] H. Liu, X. Su, X. Tian, Z. Huang, W. Song, J. Zhao, Electroanalysis 18 (2006) 2055.

Talanta 80 (2010) 1378–1384

Contents lists available at ScienceDirect

Talanta

journal homepage: www.elsevier.com/locate/talanta

Fabrication and evaluation of chiral monolithic column modified by β-cyclodextrin derivatives

Yingjie Li[a,b], Chunhui Song[b], Lingyi Zhang[c], Weibing Zhang[c], Honggang Fu[a,*]

[a] Key Laboratory of Functional Inorganic Material Chemistry, Ministry of Education of the People's Republic of China, Heilongjiang University, Xuefu Road 74, Harbin 150080, Nangang District, Heilongjiang, PR China
[b] College of Chemistry and Chemical Engineering, Qiqihar University, Qiqihar 161006, PR China
[c] School of Chemistry and Molecular Engineering, East China University of Science and Technology, Shanghai 200237, PR China

ARTICLE INFO

Article history:
Received 18 May 2009
Received in revised form
18 September 2009
Accepted 24 September 2009
Available online 30 September 2009

Keywords:
Capillary electrochromatography
Chiral separation
β-Cyclodextrin
Derivative
Monolith

ABSTRACT

Based on combination of chiral recognition ability of β-cyclodextrin (β-CD) derivatives and flexibility of monolithic material, a series of chiral stationary phases (CSPs) were prepared by the immobilization of β-CD and three of its derivatives to the epoxy-activated poly(glycidyl methacrylate-co-ethylene dimethacrylate) monolith under mild condition. Immobilization condition for the connection reaction by different functional groups and bonding ways was studied to obtain good enantiomer selectivity. Prepared CSPs were evaluated by separating racemic mixtures of eight amino acids and two chiral drugs with capillary electrochromatography (CEC).

© 2009 Elsevier B.V. All rights reserved.

1. Introduction

Chiral separation comprises one of the most attractive tasks of modern day chemistry because of the quintessential nature of life [1]. The development of life science, modern pharmaceutical industry, and asymmetric synthesis raises more requests for chiral recognition and separation.

Chromatographic technique has proven to be one of the best methods for the direct separation and analysis of enantiomers. Chiral stationary phases based on proteins, cyclodextrins, cellulose derivatives and macrocyclic antibiotics are widely used in the separation of chiral compounds [2,3]. Native cyclodextrins (α, β, and γ-CD) and modified cyclodextrins (CDs) are classical chiral selectors which were first employed in 1982 [4] as mobile phase additives in high performance liquid chromatography (HPLC). The hydroxyl groups of CDs can be functionalized with hydrophobic or hydrophilic groups to further enhance complex forming ability and selectivity towards certain analytes. Shortly after, the versatility of CDs as chiral selectors in chromatography was exploited in different electromigration methods. CDs and their derivatives have already been used in many electroseparation modes [5–25] such as capillary zone electrophoresis (CZE) [5,6], capillary gel electrophoresis (CGE) [7], isotachophoresis (ITP) [8], micellar electrokinetic chromatography (MEKC) [9] and capillary electrochromatography (CEC) [10].

CEC, a hybrid method of capillary electrophoresis (CE) and HPLC, has received considerable attention in recent years and has evolved as a powerful technique in the analysis of enantiomers. For the first time, Mayer and Schurig [10] separated enantiomers by opentube-capillary electrochromatography (o-CEC) using capillaries coated with a polydimethylsiloxane (PDMS) bound permethylated CD (Chirasil-Dex). In particle packed CEC, CDs are employed either as a mobile phase additive or are directly bonded to the packing material. Immobilized CDs and their various neutral, positively or negatively charged derivatives become suitable chiral selectors in CEC.

The monolithic stationary phase [11,12], has attracted increasing attention because of its easy preparation, excellent properties and high performance for chiral separation. The monolithic stationary phase is directly bonded to the inner wall of the capillary, and no supporting frits are necessary. In addition, the pore structure of the monolith could be easily controlled through adjusting the composition of reaction mixture to ensure good permeability. A further improvement was achieved by utilizing CDs as chiral selectors in monolithic stationary phases [13] as it was described earlier for HPLC [14].

* Corresponding author. Tel.: +86 451 86608616; fax: +86 451 86608616.
E-mail address: fuhg@vip.sina.com (H. Fu).

0039-9140/$ – see front matter © 2009 Elsevier B.V. All rights reserved.
doi:10.1016/j.talanta.2009.09.039

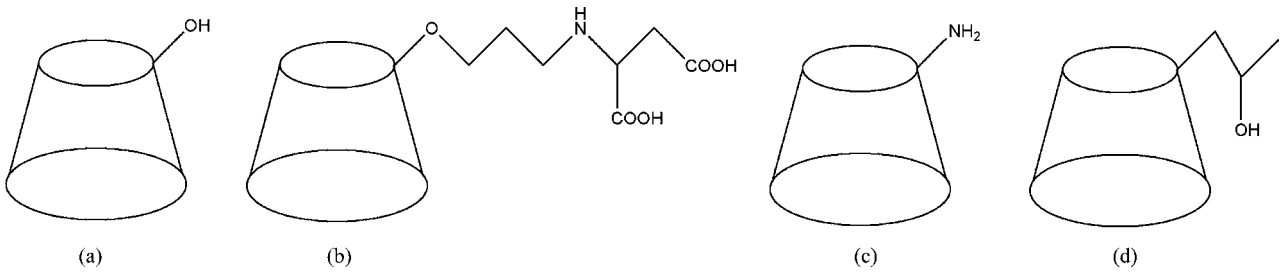


Fig. 1. Structure of derivatives of β-CD. (a) β-CD; (b) Asp-β-CD; (c) NH_2-β-CD; (d) HP-β-CD.

Organic polymeric monolithic material [15–24] possessing a bimodal structure, large through pores, and small diffusion pores has benefits of good permeability, a fast mass transfer property, a strong enrichment capability, high stability and ease of modification, which can be widely used as the stationary phase for CEC and microcolumn HPLC (m-HPLC). The chiral selectors can be immobilized by grafting through polymerization [15–21] or copolymerized [22–24]. Polyrotaxane [15], polyacrylic [19], poly(cyclopentadiylvinylene) [20], polymethacrylate [15,18,21–23] and polyacrylamides [16,17,24] polymer monolith were employed to immobilize CD for chiral recognition. In previous researches of monolithic column with CDs as chiral selectors, only few of modified β-CDs were coated onto the monolith matrix by reaction of hydroxy group. The advantages of β-CD derivatives, such as multi-functional group, diversified chiral selectivity, have not been fully utilized to extend application range.

Based on combination of chiral recognition ability of β-CD derivatives and flexibility of monolithic material, organic polymer chiral monolith poly(glycidyl methacrylate-co-ethylene dimethacrylate) was prepared by chemical grafting of the β-CD and series of its derivatives to surface of monoliths by different functional groups through direct or indirect bonding ways. Aspartate-β-CD, a new β-CD derivative, was immobilized to stationary phase as chiral selector. The synthesis conditions were investigated carefully. The novel monolithic CSP was evaluated by the separation of several racemic drugs and amino acids in CEC modes.

2. Materials and methods

2.1. Chemicals and materials

Glycidyl methacrylate (GMA), ethylene dimethacrylate (EDMA), γ-methacryloxypropyltrimethoxysilane (γ-MAPS), and cyclohexanol, 1-dodeanol and azobisisobutyronitrile (AIBN) were ordered from Acros Chemical Co. (NJ, USA). Deionised water (18 MΩ) was prepared using a CLEAR SG system (Barsbüttel, Germany). β-CD was ordered from Tianjin Kermel chemical reagents development centre (Tianjin, China). NH_2-β-CD and hydroxypropyl-β-CD (HP-β-CD) were synthesized according to the procedures described in Refs. [25,26]. Aspartate-β-CD (Asp-β-CD) was designed and synthesized firstly in our previous research [27]. Fig. 1 shows the structure of β-CD and its derivatives. All the other reagents used in experiments were of chromatographic grade.

Fused silica capillaries with 75 μm I.D. and 375 μm O.D. were purchased from Yongnian Optical Fiber Factory (Hebei, China).

The C_{18} solid-phase extraction column was conditioned with 3 ml methanol followed by 3 ml distilled water. 0.1 M NaOH solution (0.1 ml) was added to 1.0 ml human plasma sample including mexiletine, then vortex-mixed. The treated sample, after centrifugation (10 min, 4000 r/min), was applied to the column and adjusted the flow rate about 1 ml/min. The column was then washed with 2 ml hexane and 2 ml ether, respectively. The ether-eluent was collected in test-tube, then was blow-dried by nitrogen gas in 60 °C water bath. The residue was resolved in pH 4.5 buffer (0.5 ml, 5 mM), then filtered by 0.45 μm millipore filter after 10 min ultrasonic extraction for injected.

2.2. Instrumentation

Electrophoresis experiments were performed on Agilent CE instrument equipped with ultraviolet detector set at 200 nm (CA, USA). An HPLC pump, Elite P200 (Dalian, China) was used to flush the columns during the preparation. Scanning electron microscope, S-4300 (Hitachi, Japan), was adopted to observe the structure of the monolithic stationary phase. IR spectrometer (SpectrumOne, PE Co., USA) was used to verify the connections of chiral selectors.

2.3. Preparation of monolithic columns

The capillary was washed in turn by 0.1 M HCl and 0.1 M NaOH for 30 min, respectively. After the subsequent flushing by H_2O for 10 min, it was dried by nitrogen gas. A solution of 50% (v/v) γ-MAPS dissolved in acetone was prepared and purged with nitrogen for 10 min. The capillary was then washed with 10-column-volume of the solution. Thereafter, the capillary was placed at room temperature for 24 h with both ends sealed. Finally, the capillary was washed with acetone to remove the residual reagents and dried by a nitrogen stream. Thus, the inner wall of the capillary was modified by a layer of γ-MAPS.

The mixture of EDMA (0.12 g), GMA (0.18 g), cyclohexanol (0.405 g) and 1-dodeanol (0.045 g) were prepared with AIBN (1 wt% with respect to the monomers) in it. The homogeneous mixtures were purged with nitrogen for 10 min. After that, the mixture was introduced into a modified capillary to a length of 25 cm with another 8.5 cm empty. Then with both ends sealed, the capillary was heated at 40 °C by water bath for 12 h. After the polymerization, the column was washed by ethanol and water in turn.

2.4. Immobilization of derivatives of β-CD having amino group

2.4.1. Direct chemical bonding

The monolithic column was filled with solution of NH_2-β-CD (0.1 g/ml) or Asp-β-CD (0.03 g/ml) containing 0.1 M Na_2CO_3 (pH 10.5). With both ends of the capillary sealed, the capillary was heated at 60 °C by water bath for 16 h to bond derivatives of β-CD to epoxy group. Scheme of chemical bonding procedure was shown in Fig. 2(a).

2.4.2. Indirect chemical bonding by glutaraldehyde spacer

The bare monolithic column was filled with 1 M $NH_3{\cdot}H_2O$ for 6 h at 60 °C to open the epoxy group. After that, the column was washed by water to remove excessive $NH_3{\cdot}H_2O$. Then the column was filled with 10% glutaraldehyde solution for 12 h at room temperature to bond aldehyde group with amino group. After washing

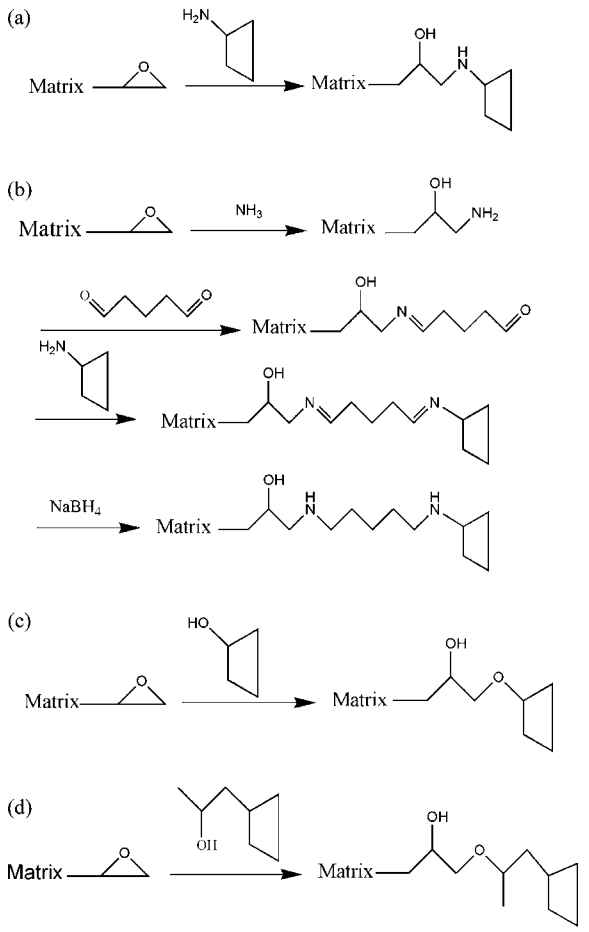


Fig. 2. Scheme of chemical bonding procedure. (a) Direct bonding by amino group, (b) indirect bonding by amino group, (c) bonding with β-CD, and (d) bonding with HP-β-CD.

with water to remove glutaraldehyde residual, the capillary was eluted by solution of derived β-CD (NH_2-β-CD 0.1 g/ml or Asp-β-CD 0.03 g/ml) at least 12 h to bond derivatives of β-CD to glutaraldehyde. Afterwards, the column was washed by water to remove residual of reactants. 2% $NaBH_4$ phosphate solution (pH 8.2) was used to reduce double bond C=N to single bond C–N. Scheme of chemical bonding procedure was shown in Fig. 2(b).

2.5. Immobilization of β-CD and its derivatives by hydroxyl

The monolith was flushed by solution of β-CD or HP-β-CD (both 60 mg/ml) containing 3.5% M NaOH slowly for 16 h to bond β-CD to epoxy group. Afterwards, the column was washed by water to remove residual of reactants. Scheme of chemical bonding procedure was shown in Fig. 2(c and d).

2.6. CEC procedure

After reaction, the column was washed by water to remove the residual of reactants. A detection window was later made by removing the outer coat of capillary with a razor. The monolithic chiral column was equilibrated by buffer for 30 min. The capillary column was installed on the CE instrument and equilibrated by applying a potential difference of 10 kV until the current was stable (about 7 mA). UV absorption wavelength was set at 200 nm. The mobile phase was 5 mM phosphate buffer or acetate buffer (pH 3.5–8.5). Voltage −10 kV was applied to the columns fabricated with NH_2-β-CD and Asp-β-CD. +10 kV was applied to the columns fabricated with β-CD and HP-β-CD. Electrokinetic injections were made at ±2 kV for 2 s.

Table 1
Immobilization conditions.

	Bonding way	Temperature (°C)	Reaction time (h)	Concentration (mg/ml)
NH_2-β-CD	Direct	60	16	30
	Indirect	Room temperature	12	30
Asp-β-CD	Direct	60	16	100
	Indirect	Room temperature	12	100
β-CD	Direct	Room temperature	16	60
HP-β-CD	Direct	Room temperature	16	60

3. Results and discussion

3.1. Preparation and optimization of chiral monolithic column with β-CD and its derivatives

A number of factors could control the immobilization rate and efficiency including the temperature of reaction and concentration of reactants, pH, solvent nature and reaction time. The concentrations of reactants, reaction time and temperature were found to be the determining factors in the preparation of chiral stationary phase. The optimized reaction conditions are listed in Table 1.

3.1.1. Direct and indirect immobilization

The immobilization could be carried out either by direct or indirect ways. The spacer glutaraldehyde could help to overcome the steric hindrance effect and provide other possibility to chemical bond functionalized chiral selectors. According to our experiments, there were no significant differences between the CSPs prepared by glutaraldehyde spacer and direct grafting. Both of the chiral columns could accomplish separation of enantiomers. In addition, indirect immobilization procedure was performed at room temperature, which is beneficial to stability of monolithic matrix.

3.1.2. Influence of reaction temperature

The temperature is important for the direct immobilization of derivatives of β-CD by amino group because that high temperature can improve the reaction of amino group and epoxy group. We grafted the NH_2-β-CD and Asp-β-CD to bare monolith at four different temperatures, room temperature, 50 °C, 60 °C and 70 °C. The CSP prepared at room temperature showed no chiral separation ability at all. At the other three conditions, all the stationary phases can easily accomplish separation of D,L-phenylalanine. But, better symmetry of peaks and separation efficiency was achieved by the monolithic column prepared at 60 °C. Higher temperature may cause the deconstruction of polymer matrix. Mild reaction condition is preferred to acquire better long-term stability.

Although hydroxy is weaker nucleophilic reagent than amino group, the immobilization by hydroxy was performed well at room temperature in our experiments. When indirect chemical bonding by amino group was employed, the grafting was implemented by reaction of aldehyde group with amino group which could be performed well enough at room temperature.

3.1.3. Optimization of reaction time

Reaction time can also affect the immobilization. When the reaction time is not long enough, the immobilization quantities of β-CD and its derivatives were not sufficient for the chiral separation. Meanwhile, longer reaction time might cause the converse disconnection of functional groups at high temperatures. In case of the immobilization of derivatives of β-CD by amino group, 16 h is the optimized reaction condition compared to 14 h and 18 h. For

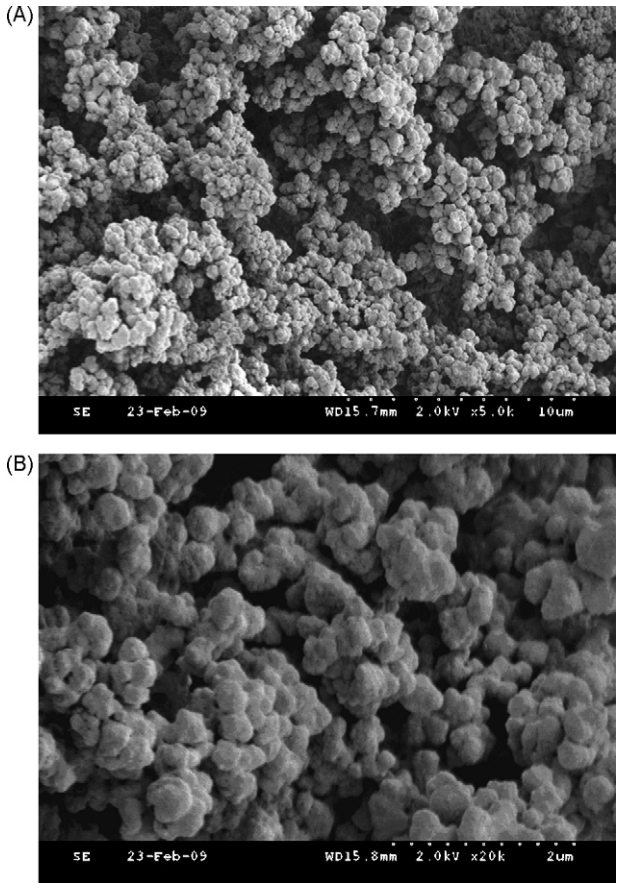


Fig. 3. Electron micrograph scanning of the monolith. (a) 5000× and (b) 20,000×.

indirectly chemical bonding, 12 h were found sufficient for reaction of aldehyde group and amino group.

Considering immobilization quantity of β-CD by hydroxy and time consume, 16 h showed the best immobilization effect. Both β-CD and HP-β-CD can be grafted to monolith matrix successfully to achieve chiral separation ability with 16 h reactions at room temperature.

3.1.4. Effect of concentration of reactant solution

The concentration of reactants solution can affect the immobilization significantly. Higher concentrations of β-CD amino derivatives will improve their nucleophilic attack ability by increasing the density of reactants. When the concentration reaches close to saturation, the derivatives incline to separate out from the solution and block the pore of monolithic column. Three concentrations were investigated to select optimized concentration of reactants. The highest concentrations in both the derivatives (Asp-β-CD, 0.03 g/ml; NH_2-β-CD, 0.10 g/ml) are close to the saturation concentration. In following experiments, they were chosen as the optimized conditions for Asp-β-CD and NH_2-β-CD for both direct and indirect bonding, respectively.

The separation results of columns immobilized β-CD and HP-β-CD showed that concentrations higher than 60 mg/ml could get maximum immobilization quantity. Further increase in concentration of β-CD and HP-β-CD would cause higher solution viscosity which leads to the poor permeability during the grafting.

3.2. Characterization of chiral monolith

3.2.1. Structure of monolithic stationary phase

SEM was used to study the morphology of the monolithic stationary phases. Short lengths of the capillary columns were sectioned and sputtered with gold for observing the cross-section of the monolithic columns. The scanning electron micrograph shown in Fig. 3 reveals the structure of chiral monolithic stationary phase, which forms a dense network of polymer bundles that are highly convoluted. The pore size distribution of the monolith is characterized by mercury intrusion porosimeter. It could be seen that rather large pores are formed (Fig. 4). By measurement, the total pore volume of the porous polymer is 1.65 cm^3/g, and the specific surface area is 64 m^2/g. According to the pore size distribution curve, the pores radius smaller than 150 nm represent 8.6%, and the diameters of more than 88% pores are through the range of 100–2400 nm. Such a large pore structure could enable the fast transfer of molecules in it.

3.2.2. Infrared spectroscopy

Fig. 5 shows the infrared spectroscopy of bare monolithic material and chiral stationary phases immobilized chiral selec-

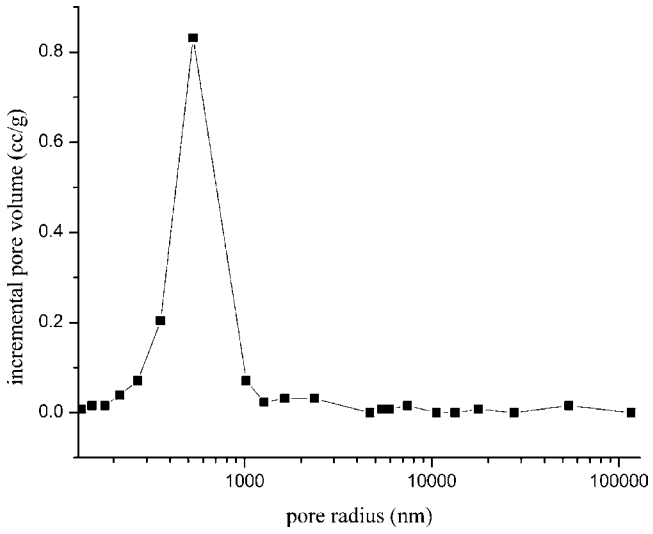


Fig. 4. Pore size distribution curve of the monolith measured by mercury intrusion porosimeter.

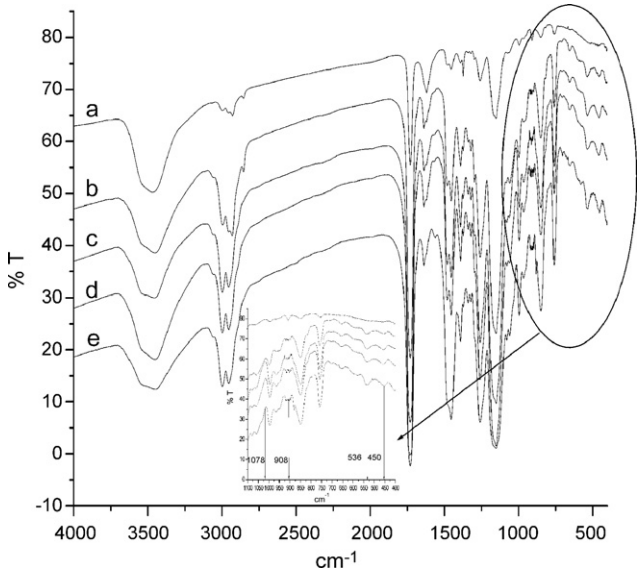


Fig. 5. Infrared spectroscopy of bare monolith and chiral stationary phases. (a) Bare column; (b) with Asp-β-CD; (c) with NH_2-β-CD; (d) with HP-β-CD; (e) with β-CD.

Table 2
Effect of pH on the separation with Asp-β-CD fabricated column.

Sample	pH	t_D (min)	t_L (min)	α
Phenylalanine	3.5	4.770	9.545	2.001
	4.5	2.587	4.038	1.561
	5.5	2.445	2.575	1.053
	6.5	2.125	3.912	1.841
	7.5	2.007	4.360	2.172
	8.5	1.470	2.217	1.508
Sample	pH	t_1 (min)	t_2 (min)	α
Mexiletine hydrochloride	3.5	No separation		
	4.5	4.800	9.184	1.913
	5.5	1.949	2.427	1.245
	6.5	2.447	4.881	1.995
	7.5	8.232	8.667	1.053
	8.5	No separation		

t: retention time. α: separation factor.

tors. The characteristic absorptions of bare GMA/EDMA matrix were 2928 cm^{-1}, 1729 cm^{-1}, 1258 cm^{-1}, 1151 cm^{-1}, and 908 cm^{-1}. According to the structure of material, 2928 cm^{-1} is assigned to stretching vibration of $-CH_2-$, 1729 cm^{-1} and 1151 cm^{-1} are the stretching vibration adsorption peak of carbonyl group and asymmetric stretching vibration absorption peak of –C–O–C–, respectively, 908 cm^{-1} confirms the existence of epoxy group. After immobilizing β-CD and its derivatives, disappearance of characteristic absorption 908 cm^{-1} proves that chiral selector is connected to epoxy group. Meanwhile, 1078 cm^{-1}, 536 cm^{-1} and 450 cm^{-1} showed in chiral stationary phase according to the characteristic absorption of β-CD which confirms successful immobilization of chiral selector.

3.3. Evaluation of chiral monolith

3.3.1. Investigation of separation condition

Since various parameters might affect the elution and separation of analytes, optimization of the operation conditions should be carried out to achieve better separation.

3.3.1.1. Effect of pH. The pH of mobile phase showed obvious effect on separation of charged analytes. Samples with different p*I* or pKa will have different electrophoresis behaviors under different pH environments. Amine and aspartate moieties of NH_2-β-CD and Asp-β-CD provide not only immobilization sites but also electric interactions. To obtain the optimum separation result, the effects of pH value of the mobile phase were studied in the range from 3.5 to 8.5 when amino acid and chiral drug were selected as sample. From Table 2, we could see that the variation of pH influenced the separation significantly. With the consideration of both analysis time and the detection sensitivity, pH 5.5–8.5 was chosen as the optimum condition.

3.3.1.2. Selection of the separation buffer. In our work, we also found that there were no obvious differences on the peak shape and the resolution of with either acetate or phosphate as the buffer. However, as far as the detection of the chiral compounds, Joule heat effect and the pH range of buffer were concerned, the phosphate was chosen as the running buffer in the following separation.

3.3.1.3. Effect of separation temperature. Temperature of column during separation procedure will also affect the migration time and resolution. Fig. 6 shows the heating effect on separation of phenylalanine on the Asp-β-CD fabricated column. Appropriate

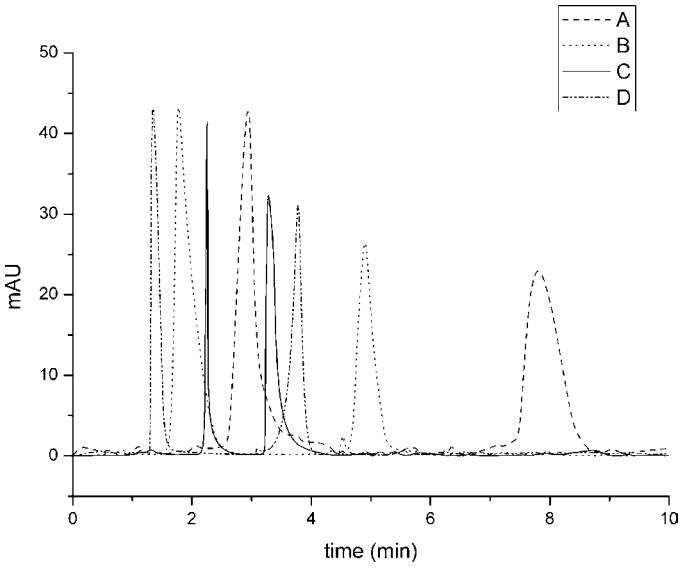


Fig. 6. Effect of separation temperature. (A) 10 °C; (B) 15 °C; (C) 20 °C; (D) 25 °C. *Column*: fabricated with Asp-β-CD; *sample*: phenylalanine; *voltage*: −10 kV; *injection*: −2 kV, 2 s; *mobile phase*: phosphate, 5 mM, pH = 6.5.

heating improved the chiral separation by decreasing the viscosity of mobile phase to short the migration time. But at the same time, over heating would lead to deterioration of the separation by Joule heat effect. When temperature increased from 10 °C to 20 °C, the migration time shortened significantly. But, when the temperature was raised to 25 °C, the symmetry and column efficiency was deteriorated compared to 20 °C.

3.3.2. Evaluation of chiral monolithic stationary phase by separating amino acids and racemic drugs

Racemic mixtures of eight amino acids and two drugs were separated by prepared chiral capillary monolithic columns. The p*I* of amino acids is varying from 5.5 to 10.76. All the samples could be baseline separated under selected condition, demonstrating the prospect of monolithic chiral stationary phase in the separation of enantiomers. Separation time, separation factors and resolution are shown in Table 3. Based on Table 3, monolithic columns fabricated with Asp-β-CD and HP-β-CD showed stronger separation abilities compared to other two types of columns.

All the derivatives have the same hydrophobic cavity as β-CD, but functional groups can also provide other interaction to

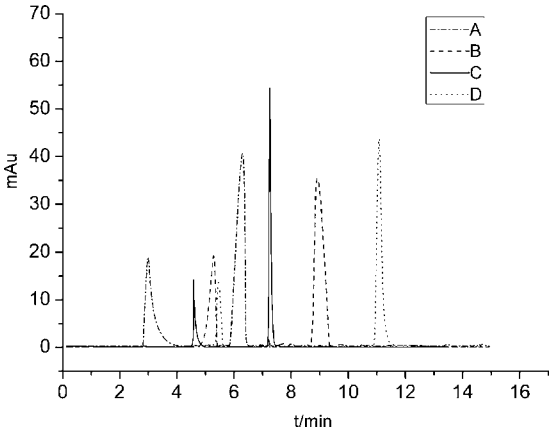


Fig. 7. Separation of D,L-phenylalanine by four CSPs. (A) Fabricated with NH_2-β-CD; (B) fabricated with β-CD; (C) fabricated with Asp-β-CD; (D) fabricated with HP-β-CD. *Temperature*: 20 °C; other conditions see Fig. 6.

Table 3
Results of the chromatographic separation of racemates using four monolithic chiral stationary phases.

Column types	Racemates	t_D (min)	t_L (min)	α	R_S
HP-β-CD	Phenylalanine	2.240	4.872	2.174	5.285
	Tyrosine	2.078	7.727	3.718	4.112
	Tryptophan	1.390	4.362	1.333	4.235
	Alanine	12.170	8.512	1.429	2.145
	Lysine	11.444	8.675	1.319	1.958
	Histidine	4.723	8.159	1.727	5.826
	Arginine	7.401	9.784	1.322	2.177
Asp-β-CD	Phenylalanine	2.102	3.922	1.866	2.672
	Tyrosine	1.389	4.071	2.930	2.457
	Tryptophan	1.395	4.079	2.924	3.134
	Serine	3.600	1.022	3.522	4.151
NH_2-β-CD	Phenylalanine	2.731	4.961	1.816	1.367
	Tyrosine	7.003	8.648	1.235	2.378
	Tryptophan	1.574	6.151	3.907	0.852
β-CD	Phenylalanine	10.375	14.948	1.441	3.481
	Tyrosine	2.427	3.610	1.487	1.534
	Tryptophan	1.470	2.212	1.505	3.27

Column types	Chiral drugs	t_1	t_2	α	R_S
Asp-β-CD	Mexiletine hydrochloride	1.040	2.429	2.335	2.672
	Oxybutynin chloride	1.919	3.023	1.575	6.240
NH_2-β-CD	Mexiletine hydrochloride	8.230	8.663	1.053	0.674
	Oxybutynin chloride	0.542	4.781	8.821	3.157
β-CD	Mexiletine hydrochloride	1.934	2.355	1.212	1.324

R_S: resolution factor.

improve the chiral separation. For Asp-β-CD, aspartic acid itself has strong stereoselectivity which also contributes to the chiral selection. The hydroxyl of introduced hydroxypropyl group in HP-β-CD could improve the combination of β-CD and guest molecule, increase the solubility of β-CD, form intermolecular hydrogen bond to increase the interaction between chiral selector and enantiomers.

Separation results demonstrate that functional groups of β-CD derivatives promote the chiral recognition significantly. As an example, the electropherograms of D,L-phenylalanine by four different monolith columns are shown in Fig. 7.

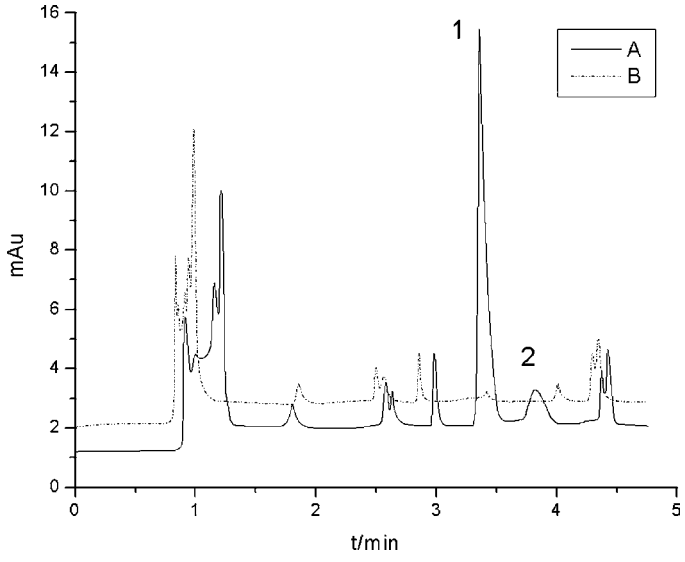


Fig. 8. Separation of mexiletine hydrochloride in human plasma sample by Asp-β-CD fabricated monolithic column. (A) Plasma sample; (B) free plasma. 1 and 2, the enantiomers' peaks of mexiletine hydrochloride. Mobile phase: phosphate/trolamine buffer, 5 mM, pH = 4.5; *temperature*: 20 °C; *voltage*: −10 kV; *injection*: −2 kV, 2 s.

3.3.3. Application

Monolithic column fabricated with Asp-β-CD was applied to the separation of mexiletine hydrochloride enantiomers in human plasma sample. Because of complex matrixes, as little as possible trolamine was added to phosphate buffer to decrease absorption between the sample and the solid phase. Fig. 8 shows the electropherogram of mexiletine hydrochloride extracted from the plasma sample. From Fig. 8, two enantiomers were separated by baseline, the migrate times were 3.46 and 3.84 min, respectively. Some components in plasma were determined, too. But they did not interfere the determination of the enantiomers. Thus, the method was applied to the complex matrix sample, and the column had good selectivity.

4. Conclusion

Based on combination of chiral recognition ability of β-CD derivatives and flexibility of monolithic material, a novel type of monolithic chiral column modified with β-CD and its derivatives has been developed and evaluated by separations of chiral compounds. Prepared chiral monolithic stationary phases showed promising potential in HPLC, preparative chromatography and industry production.

Acknowledgement

We gratefully acknowledge the support of this research by the Key Program Projects of the National Natural Science Foundation of China (No. 20431030), the National Natural Science Foundation of China (No. 20671032), The Cultivation Fund of the Key Scientific and Technical Innovation Project, Ministry of Education of China (No. 708029), the Key Program Projects of the Province Natural Science Foundation of Heilongjiang Province (No. ZJG0602-01).

References

[1] R. Vespalec, P. Bocek, Chem. Rev. 100 (2000) 3715.

[2] Chirobiotic Handbook, A Guide to Using Macrocyclic Glycopeptide Bonded Phases for Chiral LC Separations, fifth ed., Advanced Separation Technologies Inc., Whippany, USA, 2004.
[3] Y. Zhao, Z. Guo, Y. Zhang, X. Xue, Q. Xu, X. Li, X. Liang, Y. Zhang, Talanta 78 (2009) 916.
[4] W. Dorothee, S. Volker, J. Sep. Sci. 29 (2006) 1344.
[5] J. Marak, P. Mikus, K. Marakova, D. Kaniansky, I. Valaskova, E. Havranek, Electrophoresis 28 (2007) 2738.
[6] N. Mofaddel, H. Krajian, D. Villemin, P.L. Desbène, Talanta 78 (2009) 631.
[7] J.M. Lin, N. Tatsuro, O. Hitoshi, X.Z. Wu, H. Toshiyuki, Fresenius' J. Anal. Chem. 354 (1996) 451.
[8] M. Urbanek, A. Varenne, P. Gebauer, L. Krivankova, P. Gareil, Electrophoresis 27 (2006) 4859.
[9] W.A.W. Ibrahim, D. Hermawan, M.M. Sanagi, J. Chromatogr. A 1170 (2007) 107.
[10] S. Mayer, V. Schurig, J. High Resolut. Chromatogr. 15 (1992) 129.
[11] F. Svec, J. Sep. Sci 28 (2005) 729.
[12] M.L. Hsieh, G.Y. Li, L.K. Chau, Y.S. Hon, J. Sep. Sci. 31 (2008) 1819.
[13] C.V. Fujimoto, Anal. Sci. 18 (2002) 19.
[14] D. Lubda, K. Cabrera, K. Nakanishi, W. Lindner, Anal. Bioanal. Chem. 377 (2003) 892.
[15] A. Wahl, F. Al-Rimawi, I. Schnell, O. Kornysova, A. Maruska, U. Pyell, J. Sep. Sci. 31 (2008) 1519.
[16] H.L. Zeng, H.F. Li, J.M. Lin, Anal. Chim. Acta 551 (2005) 1.
[17] H.L. Zeng, H.F. Li, W. Xu, J.M. Lin, Talanta 69 (2006) 226.
[18] E.C. Peters, K. Lewandowski, M. Petro, F. Svec, J.M.J. Fréchet, Anal. Commun. 35 (1998) 83.
[19] M. Pumera, I. Jelinek, J. Jindrich, O. Benada, J. Liq. Chromatogr. Rel. Tech. 25 (2002) 2473.
[20] F.M. Sinner, M.R. Buchmeiser, Angew. Chem. Int. Ed. 39 (2000) 1433.
[21] R. Zhu, W. Xu, The Analyst 133 (2008) 1722.
[22] M. Lämmerhofer, E.C. Peters, C. Yu, F. Svec, J.M.J. Fre'chet, Anal. Chem. 72 (2000) 4614.
[23] M. Lämmerhofer, E. Tobler, E. Zarbl, W. Lindner, W. Lindner, F. Svec, M.J.J. Frechet, Electrophoresis 24 (2003) 2986.
[24] Á. Végvári, A. Földesi, C. Hetényi, O. Kocnegarova, M.G. Schmid, V. Kudirkaite, S. Hjertén, Electrophoresis 21 (2000) 3116.
[25] C.P. Ramos, E. Alvarez-Parrilla, F.L. Meijide, Langmuir 15 (1999) 5489.
[26] J. Pitha, J. Milecki, H. Fales, L. Pannell, K. Uekama, Int. J. Pharm. 29 (1986) 73.
[27] Z. Chen, Y. Li, Chem. Eng. 10 (2007) 55 (Chinese).

Talanta 80 (2010) 1385–1391

Contents lists available at ScienceDirect

Talanta

journal homepage: www.elsevier.com/locate/talanta

Electrochemical immunoassay of hepatitis B surface antigen by the amplification of gold nanoparticles based on the nanoporous gold electrode

Caifeng Ding[a,b], Hui Li[b], Kongcheng Hu[c], Jin-Ming Lin[a,*]

[a] The Key Laboratory of Bioorganic Phosphorus Chemistry & Chemical Biology, Department of Chemistry, Tsinghua University, Beijing 100084, PR China
[b] Key Laboratory of Eco-chemical Engineering, Ministry of Education, College of Chemistry and Molecular Engineering, Qingdao University of Science and Technology, Qingdao 266042, PR China
[c] College of Life Science and Pharmaceutical Engineering, Nanjing University of Technology, Nanjing 210009, PR China

ARTICLE INFO

Article history:
Received 25 May 2009
Received in revised form
19 September 2009
Accepted 24 September 2009
Available online 13 October 2009

Keywords:
Electrochemical immunoassay
Hepatitis B surface antigen (HBsAg)
Nanoporous gold (NPG) electrode
Gold nanoparticle
o-Phenylenediamine (OPD)

ABSTRACT

We describe herein the combination of electrochemical immunoassay using nanoporous gold (NPG) electrode with horseradish peroxidase (HRP) labeled secondary antibody–gold nanoparticles (AuNPs) bioconjugates for highly sensitive detection of protein in serum. The electroactive product of *o*-phenylenediamine (OPD) oxidized with H_2O_2 catalyzed by HRP was reduced in the Britton–Robinson (BR) buffer and the peak current of which was used to determine the concentration of antigen (Ag) in the analyte. The active surface area of NPG electrode was larger than that of a bare flat one. The presence of AuNPs enhanced the immobilized amount of HRP labeled antibody (Ab), which improved the sensitivity of the immunoassay when used as the secondary antibodies. As a result of these two combined effects, the sensitivity of the immunoassay for the determination of target protein was increased significantly. Using hepatitis B surface antigen (HBsAg) as a model, we demonstrate a dose response in the range of 0.01–1.0 ng/mL with a detection limit of 2.3 pg/mL. Analytical results of several human serum samples obtained using the developing technique are in satisfactory agreement with those given by enzyme-linked immune-absorbent assays (ELISA). In addition, the technique was about 100 times more sensitive in the detection of HBsAg than ELISA. All these demonstrated the feasibility of the present immunoassay method for clinical diagnosis.

© 2009 Elsevier B.V. All rights reserved.

1. Introduction

Sensitive measurement of proteins is a critical need in many aspects of modern biochemical and biomedical research, especially in early cancer detection, while maintaining minimum sample amount and operational simplicity [1–5]. Due to the highly sensitive and selective nature of the recognition between antigen (Ag) and antibody (Ab), immunoassay has been considered as a major analytical method for the determination of proteins [6–9]. Signal amplification and noise reduction are crucial for obtaining low detection limits and high sensitivity in clinical immunoassays [10]. Much attention has been focused on signal amplification by using an enzyme such as horseradish peroxidase (HRP) and alkaline phosphatase [11–14]. The detection methods commonly used in enzyme amplification immunoassay are amperometry [15,16], spectrophotometry [17], fluorometry [18], and chemiluminometry [19]. Electrochemical method has attracted increasing interest for the high sensitivity, low cost, and reliable results.

In the past decade, the applications based on nanoparticles (NPs) in immunoassay have attracted wide interest due to their unique optical, electronic, and mechanic properties. Various NPs such as gold, silver, silica, and quantum dots have been extensively used for ultrasensitive optical and electrochemical bioassays. Among them, gold nanoparticles (AuNPs) have been used for analytical and biomedical purposes for many years due to the advantage of rapid and simple chemical synthesis, a narrow size distribution, and efficient coating by thiols or other biomolecules. Recently, AuNPs have been widely used for signal amplification in DNA biosensors and clinical immunoassays [20–26].

Hepatitis B virus (HBV) is one of the most important causes of liver disease, and it can induce chronic or acute hepatitis. A total of nine HBV serotypes have been described [27]. The first virological marker to appear in the circulation, hepatitis B surface antigen (HBsAg), can be found in filamentous or spherical surface antigen particles in addition to virions. It is generally accepted that the diagnosis of infection by hepatitis B virus (HBV) is based on the presence of the HBsAg in the blood, since that it can generally be detected while still in the incubation period [28]. On the fast development of the clinical diagnostic technologies, there were some case reports on detection of HBsAg in human serum using capillary

* Corresponding author. Tel.: +86 010 62792343; fax: +86 010 62792343.
E-mail address: jmlin@mail.tsinghua.edu.cn (J.-M. Lin).

0039-9140/$ – see front matter © 2009 Elsevier B.V. All rights reserved.
doi:10.1016/j.talanta.2009.09.040

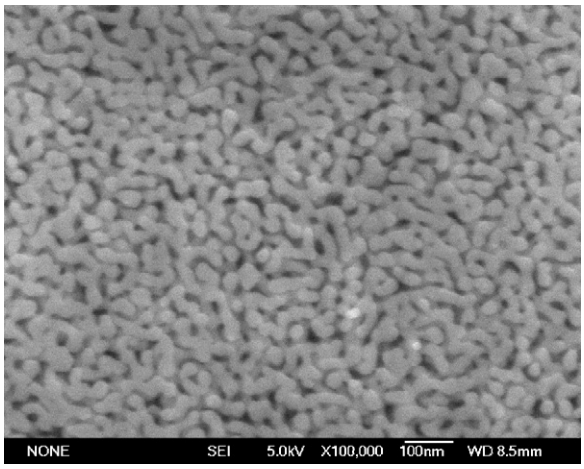
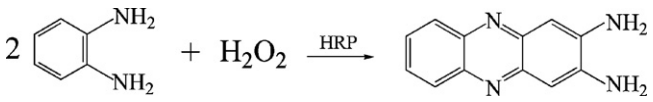


Fig. 1. SEM image of the NPG structures.

electrophoresis with chemiluminescence detection [29], as well as the nanoparticle-based time-resolved detection method [30,31]. Currently, electrochemical immunosensor based on gold nanoparticle or chitosan membranes [32–36], cross-flow chromatography [37] and photolithography [38] technologies were reported, while enzyme-linked immunosorbent assay (ELISA) was still the main means to clinically diagnose HBV [39,40]. However, ELISA method has the shortcoming of low sensitivity. Therefore, it is necessary to develop more sensitive assays to detect the low concentration of HBsAg in clinical serum samples.

Our group had constructed a sensitive electrochemical DNA sensor based on nanoporous gold (NPG) electrode and multifunctional encoded AuNPs [41]. The active surface area of NPG electrode was ~9 times higher than that of a bare flat one. In present work, an electrochemical immunosensor using NPG electrode with HRP label secondary antibody–AuNPs bioconjugates for highly sensitive detection of protein was established. As a platform model, measurements of HBsAg were performed in the range of 0.01–1.0 ng mL^{-1} with a detection limit of 2.3 pg/mL. The immunosensors were used to analyze HBsAg in human serum samples. Analytical results of clinical samples show that the developed



Scheme 2. The reaction equation of OPD and H_2O_2 catalyzed by HRP.

immunoassay is comparable with the ELISA method, implying a promising alternative approach for detecting HBsAg in the clinical diagnosis.

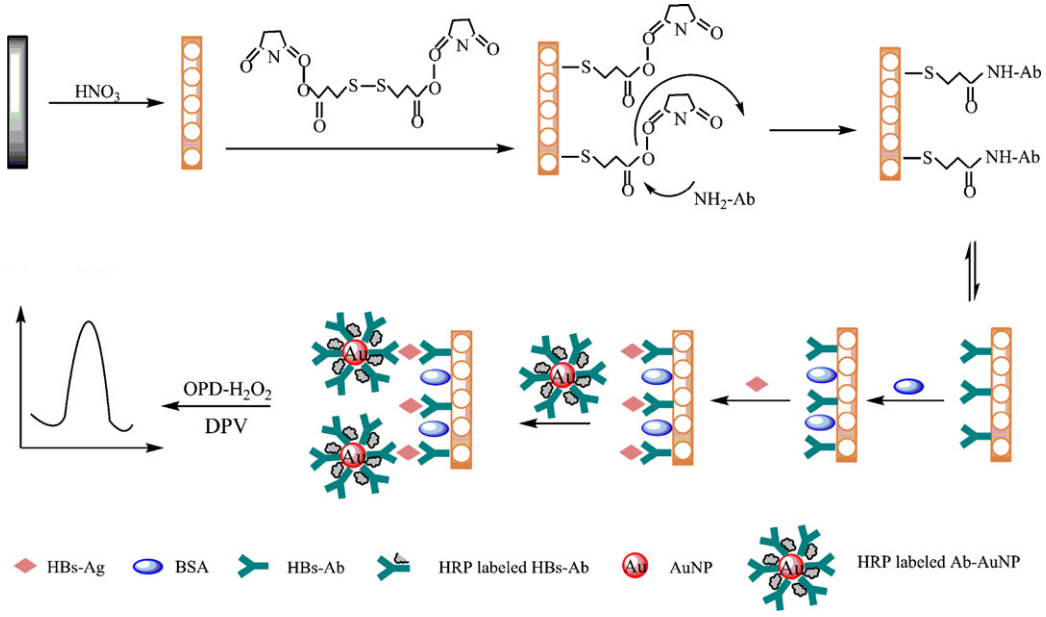
2. Experimental

2.1. Materials

HBs Ag, HBs Ab, and HRP labeled HBs secondary Ab were purchased from Maybio Co. Ltd. (China). 3,3′-Dithiodipropionic acid di (*N*-succinimidyl ester) (DTSP) was purchased from Tokyo Chemical Industry Co. Ltd. (Japan). DTSP solution (4 mM) was prepared in dimethylsulfoxide (DMSO). PBS buffer (10 mM, pH 7.4) was employed for preparing HBsAg and HBsAb solution. Hydrogen tetrachloroaurate (III) trihydrate ($HAuCl_4{\cdot}3H_2O$, 99.9%) and trisodium citrate were used for preparing AuNPs. Other solutions such as 3% bovine serum albumin (BSA), H_2O_2 (4.0×10^{-3} M), *o*-pheneylenediamine (OPD) (5.0×10^{-2} M, prepared in methanol), HAc–NaAc buffer (pH 4.8) and Britton–Robinson (BR) buffer (pH 7.8) were also used. All the reagents were analytical grade and used without further purification. Deionized and doubly distilled water was used throughout.

2.2. Apparatus

Cyclic voltammetry (CV) and electrochemical impedance spectroscopy (EIS) measurement were performed on a CHI 660C electrochemical working station (CH Instrument Company, USA) with a conventional three-electrode system comprised of platinum wire as auxiliary electrode, Ag/AgCl electrode as reference electrode, and different modified NPG electrode as working electrode. Differential pulse voltammetry (DPV) measurement was carried out by CHI 832B electrochemical analyzer (CH Instrument Company, USA) with a three-electrode system consisted of a glassy carbon electrode (GCE) as working electrode, an Ag/AgCl



Scheme 1. Schematic illustration of the stepwise process of modified electrode.

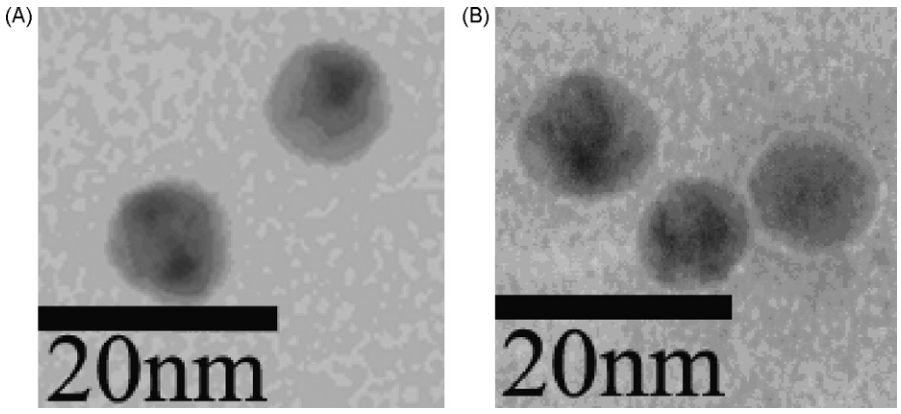


Fig. 2. TEM images of AuNPs (A), HRP labeled Ab–AuNPs (B).

electrode as reference electrode, and a platinum wire as an auxiliary electrode. UV–vis spectra were carried out on a Cary 50 UV–vis–NIR spectrophotometer (Varian). Transmission electron microscopy (TEM) image was taken with a JEOL JEM-1200EX instrument (HITACHI).

2.3. Procedure

2.3.1. Preparation of NPG electrode

NPG was prepared according to the previous work of our group by selective dissolution of silver from silver/gold alloy [41]. Briefly, a piece of commercially available 9-carat white gold leaf (Au/Ag alloy, 50:50 wt%, 100 nm thick) was floated onto 1:1 concentrated nitric acid for 1 h. Then the NPG foil was carefully coated onto pretreated GCE using a variation of electroless deposition in which the leaf adhered on the GCE surface via physical adsorption after being washed repeatedly with triply distilled water to remove the NO_3^- and Ag^+ which would interfere signal detection during electrochemical analysis. The electrode was then intentionally parched in infrared light for 1 h. Thus, NPG was modified onto the GCE to get the NPG electrode.

2.3.2. Synthesis of AuNPs

AuNPs were synthesized by reducing tetracholoroauric acid with trisodium citrate referred to literature [42]. Briefly, 100 mL of 0.01% $HAuCl_4$ solution was boiled with stirring and 2.5 mL 1% trisodium citrate solution was added quickly to the boiling solution. After reaction for 10 min, the solution was left for stirring and cooling down. The AuNPs solution was stored at 4 °C when not in use.

2.3.3. Preparation of HRP labeled HBs secondary Ab modified Au nanoparticles (HRP labeled Ab–AuNPs)

HRP labeled Ab–AuNPs bioconjugate was prepared according to the published procedure [43]. First, the pH of AuNPs solution was adjusted to 9 with 0.1 M NaOH, and then 30 μL HRP labeled HBsAb solution was added into 500 μL AuNPs solution without dilution. After stirring for 15 min, the AuNPs were tagged with HRP labeled Ab on the surface. The excess of Ab was removed by centrifugating the mixture at 10,000 rpm for 20 min. After being washed one more time in PBS (pH 7.4), HRP labeled Ab–AuNPs was dispersed to 100 μL PBS (pH 7.4) and was stored at 4 °C for further use.

2.3.4. Sandwich immunoassay procedures

After careful cleaning by deionized and doubly distilled water and PBS, respectively, the NPG electrode was dipped into a 4 mM DTSP solution to create Au–S bond between the NPG electrode and DTSP for 2 h [44]. After thorough rinsing with acetone to remove physically adsorbed DTSP, a drop of 250 μg/mL HBsAb solution was dripped onto the surface of the DTSP/NPG electrode and the modified electrode was stored at room temperature overnight. The unbound HBsAb was washed away by PBS and then BSA was employed to block the unreacted succinimidyl groups by soaking the Ab/DTSP/NPG electrode into 500 μL 3% BSA solution for 3 h. After the electrode was rinsed once again, the reaction between HBsAb and HBsAg was performed by immersing the modified electrode into 500 μL different concentrations of HBsAg solution and incubated for 60 min at 37 °C. Finally a drop of HRP labeled Ab–AuNPs solution was dripped onto the Ag/Ab/DTSP/NPG electrode to perform the sandwich immunocomplex for 90 min.

2.3.5. Electrochemical analysis

1 mL 5.0×10^{-2} M OPD solution, 2 mL 4.0×10^{-3} M H_2O_2 solution, 2 mL HAc–NaAc buffer (pH 4.8), and double distilled water were added to the 10 mL colorimetric tube in turn and the mixture was vibrated to get a uniform solution. The modified electrode was dipped into 300 μL of above substrate solution at 37 °C to catalyze the reaction between OPD and H_2O_2.

After the redox reaction between OPD and H_2O_2 catalyzed by HRP labeled on the modified electrode was finished 1 h later, 1 mL 0.2 M BR buffer (pH 7.8) was added into reaction cell for DPV measurement of the reduction signal of the product of OPD. DPV was performed in the degassed solution by scanning the potential from

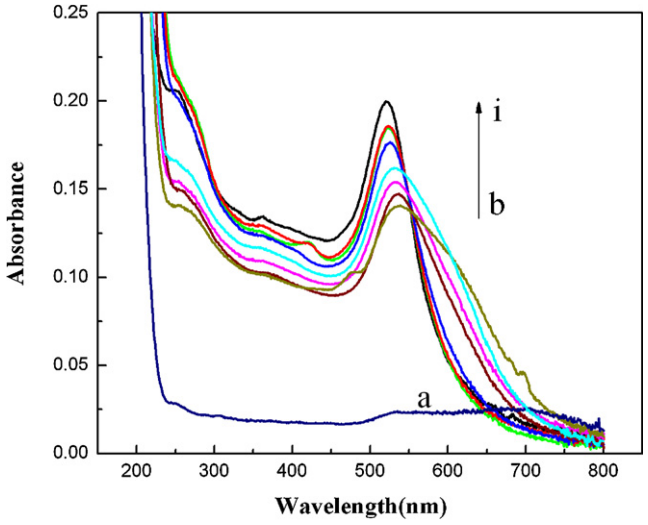


Fig. 3. Ultraviolet spectroscopy of (a) AuNPs, (b–h) HRP labeled Ab–AuNPs (1, 2.5, 5, 10, 20, 30 L, and 40 μL HRP labeled Ab were added to AuNPs solution).

−0.3 to −0.8 V with amplitude of 25 mV and a step potential of 12 mV at 5 Hz. All experiments were conducted at room temperature.

3. Results and discussion

In the current study, NPG electrode and AuNPs modified with the HRP labeled secondary Ab were used to perform an immunoassay for the determination of HBsAg. The characteristics of the NPG electrode surface are shown in Fig. 1. The new electrochemical immunoassay involves a binding event between DTSP-coated NPG electrode and HBsAb, and the formation of sandwich immunocomplex between the HBsAb labeled on the NPG electrode and the HRP labeled HBsAb–AuNPs is shown in Scheme 1. The electroactive product of OPD oxidized with H_2O_2 catalyzed by HRP tagged on the immunocomplex was reduced in the BR buffer and its peak current was used to determine the concentration of antigen (Ag) in the analyte. The product of H_2O_2–OPD redox system catalyzed by HRP is 2,3-diaminophenazine (DAP) and the equation is shown in Scheme 2.

3.1. The characterization of the HRP labeled Ab–AuNPs conjugate

TEM were recorded to prove the formation of HRP labeled Ab–AuNPs conjugate as shown in Fig. 2A and B. There were distinct differences between the TEM images of AuNPs and HRP labeled Ab–AuNPs because the electron beam could permeate HRP labeled Ab but could not permeate AuNPs after dyed with acetate uranium. Obviously, HRP labeled Ab–AuNPs were surrounded by a transparent ring indicating that HRP labeled HBs Ab had tagged onto the surface of AuNPs.

UV–vis spectrum was also performed to characterize the formation of the HRP labeled Ab–AuNPs conjugate as shown in Fig. 3. The presence of NaCl could cause the aggregation of AuNPs, and the aggregation could be prevented when the AuNPs were functionalized with HRP labeled Ab [43]. The increase in HRP labeled Ab stabilizes the AuNPs by preventing their aggregation that is visible from the shift of the maximum absorbance peak from curve a (AuNPs aggregated with NaCl) to curve i (pure AuNPs). It can be seen that the spectrum of HRP labeled Ab–AuNPs conjugate solutions (curves b–h) became more and more similar to that of pure AuNPs when the volume of HRP labeled HBs Ab added to AuNPs solution was ranged from 1 to 40 μL. Furthermore, the absorbance of curves g and h became almost the same. The results showed that the Ab–AuNPs conjugate was formed and 30 μL HRP labeled Ab was selected as the optimal volume.

3.2. Electrochemical characterization of the fabrication process of the immnuocomplex

CV and EIS measurements were performed in PBS (10 mM, pH 7.4) solution containing 0.1 M KCl and 5 mM $Fe(CN)_6^{3-}/Fe(CN)_6^{4-}$. The CV of ferricyanide was chosen as a marker to investigate the changes of the electrode behavior after each assembly step. The CV curves showed the changes of the electrode behavior after each assembly step. As shown in Fig. 4A, stepwise modification on the NPG electrode was accompanied by a decrease in the amperometric response and an increase in the peak-to-peak separation between the cathodic and anodic waves, showing the electron-transfer kinetics of $Fe(CN)_6^{3-}/Fe(CN)_6^{4-}$ is obstructed. After the NPG electrode was functionalized with DTSP, the electron transfer between the electrochemical probe and electrode surface was inhibited, owing to the electrostatic repulsion of DTSP and the negatively charged electrochemical probe. When HBsAb and BSA were immobilized on the electrode surface, the peak currents of the

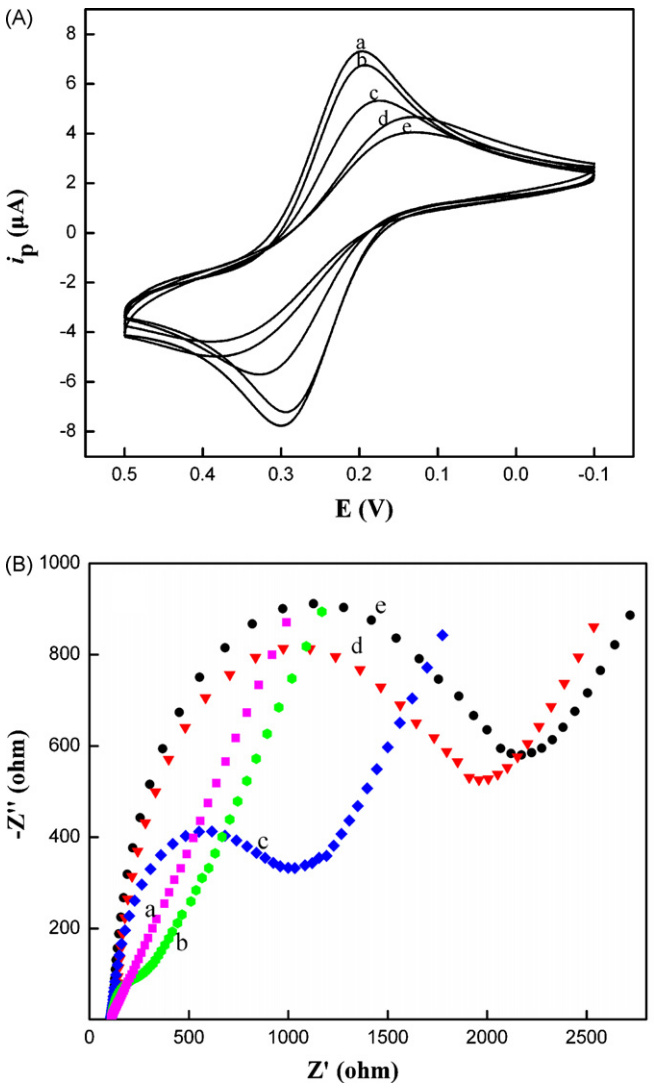


Fig. 4. Cyclic voltammograms (A) and electrochemical impedance spectroscopy (B) of the modified NPG electrode recorded in PBS (10 mM, pH 7.4) containing 0.1 M KCl and 5 mM $Fe(CN)_6^{3-}/Fe(CN)_6^{4-}$. (a) NPG electrode, (b) DTSP/NPG electrode, (c) Ab/DTSP/NPG electrode, (d) Ag/Ab/DTSP/NPG electrode, and (e) HRP labeled Ab–AuNPs/Ag/Ab/DTSP/NPG electrode. The scan rate was 100 mV s^{-1}; the frequency range was from 0.1 Hz to 10 kHz with a signal amplitude of 5 mV and the scan rate was 100 mV s^{-1}.

redox couple of $Fe(CN)_6^{3-}/Fe(CN)_6^{4-}$ decreased again. In particular, after HBs antigen molecules were combined with the antibody molecules, and the HRP labeled Ab–AuNPs were combined with the HBsAg, an obvious disappearance of the anodic peak and cathodic peak was observed.

EIS can also give detailed information on the impedance changes in the modification process. The semicircle portion of the impedance spectra, corresponding to the electron-transfer-limited process, became larger and larger after each modification step, as shown in Fig. 4B. Both CV and EIS showed the successful conjugation on the electrode surface.

3.3. Optimization of experimental conditions

In order to achieve maximum electrochemical response, several factors such as Ab concentration, incubation time, and pH of DPV measurement were investigated.

The effect of Ab concentration was studied in the range of 10–250 μg/mL. The Ab/DTSP/NPG electrodes with different Ab

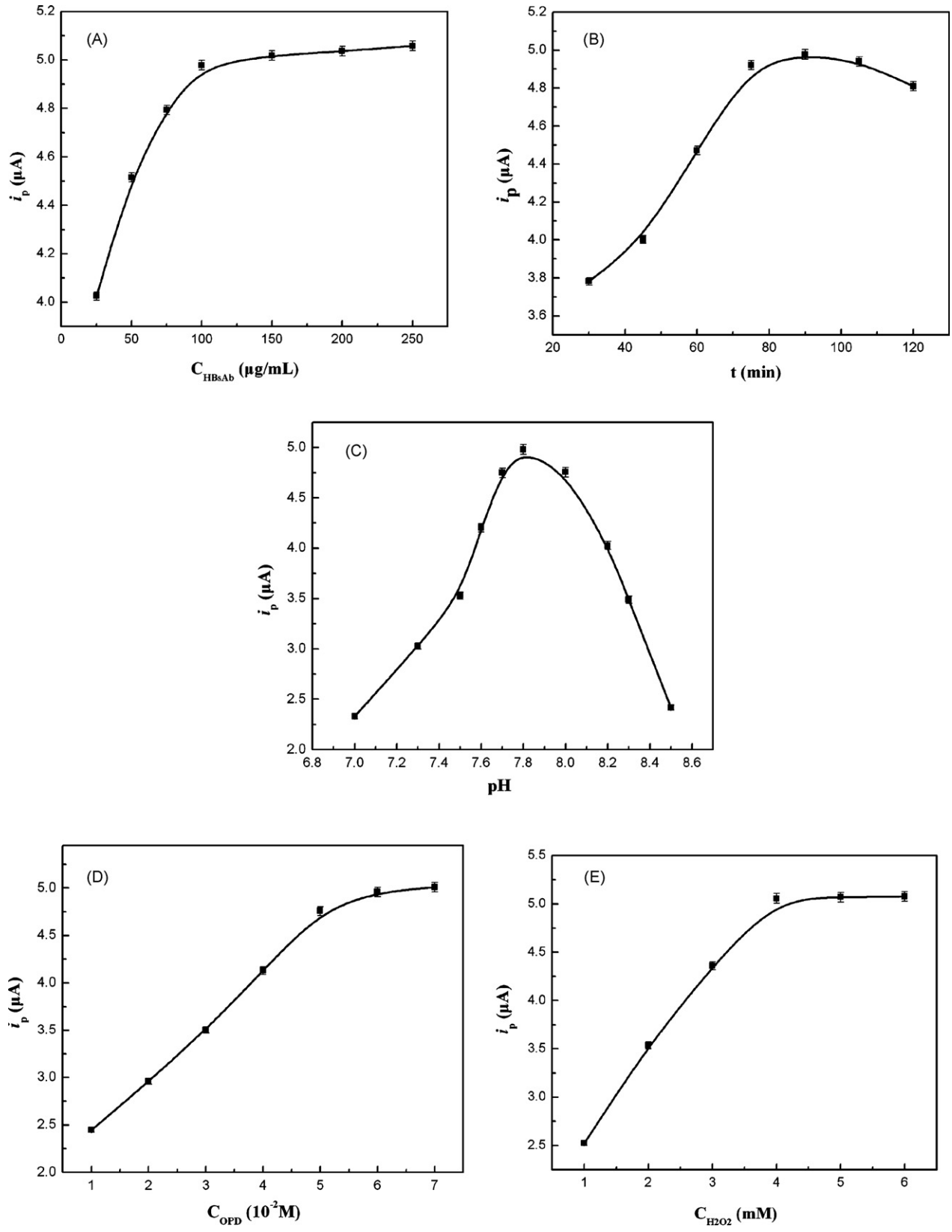


Fig. 5. Dependence of DPV peak currents of the enzyme-catalyzed analysis on Ab concentration (A), incubation time of Ag/Ab/DTSP/NPG electrode and HRP labeled Ab–AuNPs (B), pH value of BR buffer (C), OPD concentration (D), and H_2O_2 concentration (E), when one parameter changes while the others were under their optimal conditions.

concentration were immersed in 0.5 ng/mL HBs Ag solution respectively and then reaction to HRP labeled Ab–AuNPs. As shown in Fig. 5A, DPV response increased with the increase in concentration of Ab and then reached a plateau at 250 μg/mL. So 250 μg/mL of Ab solution were chosen as the optimal concentration.

The incubation time between HRP labeled Ab–AuNPs and Ag/Ab/DTSP/NPG electrode was another important parameter for the immunoassay. The influence of the incubation time was investigated as shown in Fig. 5B, when the concentrations of the HBsAg and HBsAb were 0.5 ng/mL and 250 μg/mL, respectively. The DPV response increased rapidly at first and reached on an equilibration step after 90 min, and then decreased slowly. Thus, the incubation time of 90 min was selected for the subsequent assays.

The pH value for DPV measurement was an important factor to the current response which was studied as shown in Fig. 5C. The immunoassay demonstrated the maximum response was obtained when the pH of the substrate solution was coordinated by adding 1 mL pH 7.8 BR buffer.

The effect of the concentrations of H_2O_2 and OPD were also studied as shown in Fig. 5D and E. 8×10^{-4} M H_2O_2 and 5 mM OPD was used as an optimal condition.

3.4. Detection of HBsAg

The product of OPD oxidized with H_2O_2 catalyzed by HRP was easily undergone the reductive reaction at −0.56 V at the experiment condition and the DPV response was in proportion to the concentration of the product as shown in Fig. 6.

The DPV response was enhanced by employing the AuNPs as the supporting material for the secondary HBsAb because one AuNP could be labeled by several HRP labeled Ab molecules. The results showed that the DPV response increased with the increase in the concentration of the target Ag ranging from 0.01 to 1.0 ng/mL based on the amplification of AuNPs (Fig. 6A). The linear range for target Ag was 0.01–0.1 ng/mL with the equation of $\Delta i_p = 1.3555 + 25.5077 C_{Ag}$ (ng/mL) ($R = 0.9976$; Fig. 6B). The relative standard deviation (RSD) was obtained to be 7.6% at a target Ag concentration of 0.01 ng/mL with 11 independent experiments. A detection limit of 2.3 pg/mL of target Ag could be further estimated using 3σ.

3.5. Reproducibility of the immunoassay

The reproducibility of current method was investigated with intraassay and interassay precision. The intraassay precision was evaluated by assaying one HBs level for three reduplicate measurements, whereas the interassay precision was estimated by measuring one HBs level with three different electrode prepared independently at the same experimental conditions. The intraassay and interassay variation coefficient obtained from 0.5 ng/ml HBsAg were 2.5% and 4.7%, respectively. These results showed the good reproducibility of the immunoassay.

3.6. The selectivity of the immunoassay

The selectivity of the immunoassay was also studied in the incubation solution with 0.05 ng/mL HBsAg and with some possible interfering substances, i.e., L-glutamic acid, D-glucose, hemoglobin, C-reactive protein, AFP, and BSA as shown in Table 1. When the concentrations of the interferences were much higher than the concentration of HBsAg, the relative deviation of the HBsAg solution was less than 3.0% compared with the concentration of HBsAg without the interference. From the results, we could demonstrate that the current immunoassay could response to HBsAg specifically.

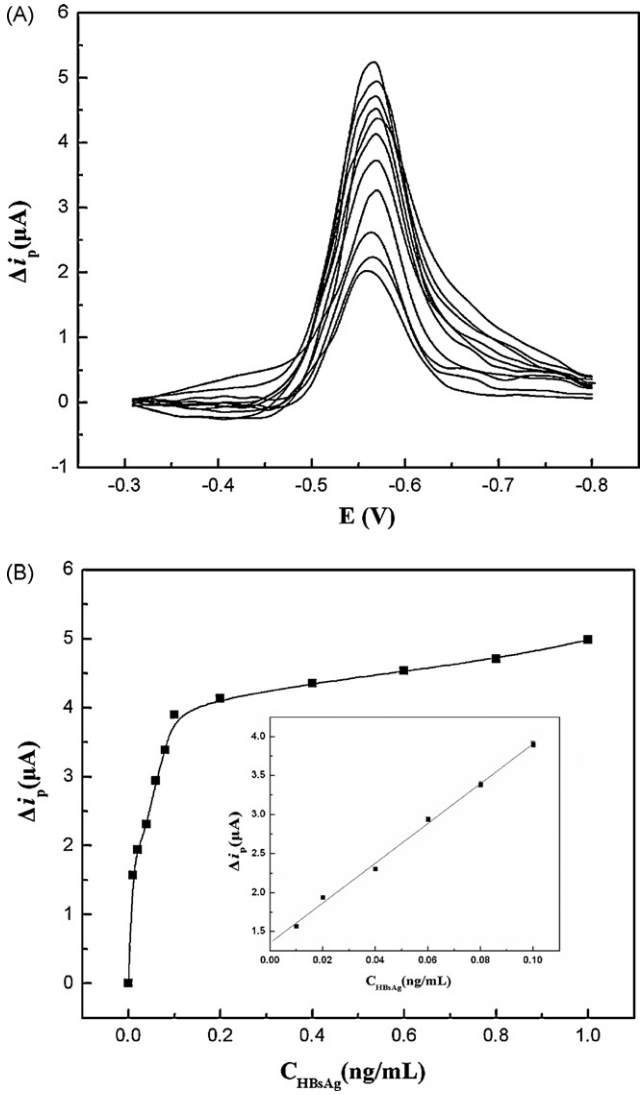


Fig. 6. DPV curves of HRP labeled Ab–AuNPs/Ag/Ab/DTSP/NPG electrode obtained with HBsAg concentrations of 0.01, 0.02, 0.04, 0.06, 0.08, 0.1, 0.2, 0.4, 0.6, 0.8, and 1.0 ng/mL (A), and calibration curves for sandwich immunoassay of HBs Ag (B). (Inset) Plot of DPV peak current vs HBsAg concentration from 0 to 0.1 ng/mL.

3.7. Detection of HBs Ag in clinical serum samples

In order to investigate the possibility of the newly developed technique to be applied for clinical analysis, several serum specimens, which were obtained from our college hospital, were examined by the developed immunoassay and the ELISA method. The HBs Ag level in some samples was beyond the kinetic range of the proposed method, thus appropriate dilution before assay

Table 1
Comparison of serum HBsAg levels determined using two different methods.[a]

Sample	Proposed method (ng/mL)	ELISA (ng/mL)	Relative deviation (%)
1	162	174	−6.8
2	233	214	8.8
3	541	515	5.0
4	0.056	–[b]	–
5	0.09	–	–
6	0.958	1	−4.4

[a] Each value is the average of three measurements.
[b] The concentraton of HBsAg was too low to be detected by ELISA. When the HBsAg concentration was more than 1 ng/mL, an appropriate dilution of sample was needed in the pre-incubation step in the proposed method.

Table 2
The relative responses of 0.05 ng/mL HBsAg in the presence of interference on the established bioassay (compared to the response mere 0.05 ng/mL HBsAg).[a].

Possible interference	Interfering concentration (μg/mL)	Current ratio
L-Glutamic acid	1	1.0125
D-Glucose	1	0.9924
Hemoglobin	140	1.0200
C-reactive protein	1	0.9789
AFP	1	1.0153
BSA	10	0.9867

[a] Each value is the average of three measurements.

was necessary. As shown in Table 2, there is no significant difference between the results given by two methods which are in concordance with the results obtained using the standard methods proposed by ELISA, that is, the developed immunoassays may provide a feasible alternative tool for determining HBs Ag in human serum in clinical laboratory.

Safety precaution: Patients with a high serum HBs Ag concentration often suffer from infectious blood liver disease. Thus, all tools in contact with clinical sera were disinfected after use.

4. Conclusion

In the present work, a novel ultrasensitive method based on NPG electrode and AuNPs was used for electrochemical determination of HBs Ag. The combination of the big active surface area of NPG electrode and the advantages of the AuNPs, including biocompatibility and amplification, enhanced the sensitivity of the method significantly. The results showed that the method was sensitive enough for determination of HBsAg in human serum samples with good precision and accuracy. The samples could be diluted to minimum even eliminate the disturbance of other proteins in serum to meet the low detection limit of this method. It can be expected that the new method would be widely used for highly sensitive clinical analysis and other biotechnology applications.

Acknowledgments

This work was supported by the Excellent Young Scientists Encouragement Foundation of Shandong Province (no. 2008BS05004), the Educational Administration of Shandong Province (no. J07YC09), and the National Natural Science Foundation of China (no. 20775038).

References

[1] E.V. Stevens, L.A. Liotta, E.C. Kohn, Int. J. Gynecol. Cancer 13 (2003) 133.
[2] D.S. Wilson, S. Nock, Angew. Chem. Int. Ed. 42 (2003) 494.
[3] Z. Xiao, D. Prieto, T.P. Conrads, T.D. Veenstra, H.J. Issaq, Mol. Cell. Endocrinol. 230 (2005) 95.
[4] A.D. Weston, L.J. Hood, Proteome Res. 3 (2004) 179.
[5] P.D. Wagner, M. Verma, S. Srivastava, Ann. N. Y. Acad. Sci. 1022 (2004) 9.
[6] S.F. Wang, D. Du, Sensors 2 (2002) 41.
[7] C. Valat, B. Limoges, D. Huet, J.L. Romette, Anal. Chim. Acta 404 (2000) 187.
[8] A. Roda, A.C. Manetta, F. Piazza, P. Simoni, R. Lelli, Talanta 52 (2000) 311.
[9] T.C. Tang, A. Deng, H.J. Huang, Anal. Chem. 74 (2002) 2617.
[10] H. Tang, H. Haisall, W. Heineman, Clin. Chem. 37 (1991) 24524.
[11] X. Yu, B. Munge, V. Patel, G. Jensen, A. Bhirde, J. Gong, S.N. Kim, J. Gillespie, J.S. Gutkind, F. Papadimitrakopoulos, J.F. Rusling, J. Am. Chem. Soc. 128 (2006) 11199.
[12] M. Wilson, W. Nie, Anal. Chem. 78 (2006) 6476.
[13] M.S. Wilson, W.Y. Nie, Anal. Chem. 78 (2006) 2507.
[14] J. Wu, F. Yan, J. Tang, C. Zhai, H. Ju, Clin. Chem. 53 (2007) 1495.
[15] W. Sun, K. Jiao, S.S. Zhang, C.L. Zhang, Z.F. Zhang, Anal. Chim. Acta 434 (2001) 43.
[16] S. Korkut, B. Keskinler, E. Erhan, Talanta 76 (2008) 1147.
[17] E.H.J.M. Jansen, J.J. Bergman, R.H.V.D. Berg, G. Zomer, Anal. Chim. Acta 227 (1989) 109.
[18] X.Q. Guo, F.N. Castellano, L. Li, J.R. Lakowicz, Anal. Chem. 70 (1998) 632.
[19] F.G. Sánchez, A.N. Díaz, C.D. Téllez, M. Algarra, Talanta 77 (2008) 294.
[20] H. Tang, J. Chen, L. Nie, Y. Kuang, S. Yao, Biosens. Bioelectron. 22 (2007) 1061.
[21] J. Das, M. Aziz, H.J. Yang, Am. Chem. Soc. 128 (2006) 16022.
[22] Z. Wang, J. Hu, Y. Jin, X. Yao, J. Li, Clin. Chem. 52 (2006) 1958.
[23] C.F. Ding, F. Zhao, R. Ren, J.M. Lin, Talanta 78 (2009) 1148.
[24] D.Y. Tian, C.F. Duan, W. Wang, N. Li, H. Zhang, H. Cui, Y.Y. Lu, Talanta 78 (2009) 399.
[25] F. He, Q. Shen, H. Jiang, J. Zhou, J. Cheng, D.D. Guo, Q.N. Li, X.M. Wang, D.G. Fu, B.A. Chen, Talanta 77 (2009) 1009.
[26] S.S. Zhang, H. Zhong, C.F. Ding, Anal. Chem. 80 (2008) 7206.
[27] A.M. Courouce-Pauty, A. Plancon, J.P. Soulier, Vox Sang. 35 (1983) 197.
[28] S. Badur, A. Akgun, J. Clin. Virol. 21 (2001) 229.
[29] Y.X. Zhang, Z.J. Zhang, F.J. Yang, Chromatogr. B 857 (2007) 100.
[30] A. Valanne, S. Huopalahti, R. Vainionpää, T. Lövgren, H.J. Härmä, Virol. Methods 129 (2005) 83.
[31] H. Zhang, Y. Xu, W. Yang, Q.G. Li, Chem. Mater. 19 (2007) 5875.
[32] D.P. Tang, R. Yuan, Y.Q. Chai, Y.Z. Fu, J.Y. Dai, Y. Liu, X. Zhong, Biosens. Bioelectron. 21 (2005) 539.
[33] M.J. Wang, L.Y. Wang, G. Wang, X.H. Ji, Y.B. Bai, T.J. Li, S.Y. Gong, J.H. Li, Biosens. Bioelectron. 19 (2004) 575.
[34] D.P. Tang, R. Yuan, Y.Q. Chai, X. Zhong, Y. Liu, J.Y. Dai, L.Y. Zhang, Anal. Biochem. 333 (2004) 345.
[35] R.P. Liang, H.Z. Peng, J.D. Qiu, J. Colloid Interface Sci. 320 (2008) 125.
[36] D.P. Tang, R. Yuan, Y.Q. Chai, X. Zhong, Y. Liu, J.Y. Dai, Clin. Biochem. 39 (2006) 309.
[37] J.H. Cho, E.H. Paek, I.H. Cho, S.H. Paek, Anal. Chem. 77 (2005) 4091.
[38] T. Konry, B. Hadad, Y. Shemer-Avni, S. Cosnier, R.S. Marks, Talanta 75 (2008) 564.
[39] T. Moriya, I.K. Kuramoto, H. Yoshizawa, P.V. Holland, J. Clin. Microbiol. 40 (2002) 877.
[40] J. Pal, L. Palinkas, Z. Nyarady, T. Czömpöly, L. Marczinovits, G. Lustyik, Y.S. Ali, G. Berencsi, R. Chen, R. Varro, A. Par, P. Nemeth, J. Immunol. Methods 306 (2005) 183.
[41] K.C. Hu, D.X. Lan, X.M. Li, S.S. Zhang, Anal. Chem. 80 (2008) 9124.
[42] J. Turkevich, P. Stevenson, J. Hillier, J. Discuss. Faraday Soc. 11 (1951) 55.
[43] A. Ambrosi, M.T. Castañeda, A.J. Killard, M.R. Smyth, S. Alegret, A. Merkoci, Anal. Chem. 79 (2007) 5232.
[44] O.A. Loaiza, S. Campuzano, M. Pedrero, J.M. Pingarroïn, Talanta 73 (2007) 838.

Talanta 80 (2010) 1392–1399

Contents lists available at ScienceDirect

Talanta

journal homepage: www.elsevier.com/locate/talanta

Dual-sensitive probe 1-imidazole-2-(5-benzoacridine)-ethanone for the determination of amines in environmental water using HPLC with fluorescence detection and online atmospheric chemical ionization-mass spectrometry identification

Jinmao You[a,b,*], Cuihua Song[b], Yanyan Fu[b], Zhiwei Sun[a,c], Lian Xia[a], Yulin Li[a], Yourui Suo[a]

[a] Northwest Plateau Institute of Biology, Chinese Academy of Sciences, Xining 810001, PR China
[b] The Key Laboratory of Life-Organic Analysis, Qufu Normal University, Qufu, Shandong 273165, PR China
[c] Graduate University of the Chinese Academy of science, Beijing 100049, PR China

ARTICLE INFO

Article history:
Received 4 June 2009
Received in revised form
20 September 2009
Accepted 24 September 2009
Available online 30 September 2009

Keywords:
HPLC
Amines
Fluorescence
Mass spectrometry
2-(Benzoacridine)-5-acetic acid (BAAA)
1-Imidazole-2-(5-benzoacridine)-ethanone (IBAE)

ABSTRACT

Dual-sensitive probe of 1-imidazole-2-(5-benzoacridine)-ethanone (IBAE) for the determination of free amines with fluorescence detection and online highly sensitive atmospheric chemical ionization-mass spectrometry identification (APCI-MS) has been developed. 2-(Benzoacridine)-5-acetic acid (BAAA) reacts with coupling agent *N,N′*-carbonyldiimidazole (CDI) to form a highly activated amide intermediate 1-imidazole-2-(5-benzoacridine)-ethanone (IBAE), which is dual-sensitive probe. The amide intermediate (IBAE) reacts preferably with amines in dimethylformamide (DMF) solvent to give the high yields of derivatives. IBAE-amine derivatives are not only sensitive to fluorescence but also to MS ionizable efficiency. The percent ionization δ values change from 0 to 57.32% in aqueous acetonitrile and from 0 to 62.14% in aqueous methanol. The relative standard deviations of the peak areas with fluorescence detection for each amine are <1.24% (40 ng/ml, $n=6$). The fluorescence detection limits (at a signal-to-noise ratio of 3) are in the range of 0.15–0.50 ng/ml. The online APCI-MS detection limits are in the range of 2.07–8.51 ng/ml (at a signal-to-noise ratio of 3). Therefore, the facile IBAE intermediate derivatization allowed the development of a highly sensitive and specific method for the quantitative analysis of trace levels of amines in environmental water.

© 2009 Elsevier B.V. All rights reserved.

1. Introduction

Most aliphatic and aromatic amines may occur as biodegradation products of organic matter such as proteins, amino acids, and other nitrogen containing organic compounds. Volatile amines not only have an unpleasant smell but also possess hazards. Moreover, they may react with nitrosating agents, leading to the formation of potentially carcinogenic *N*-nitrosamine compounds [1–5]. Therefore, it is important to determine certain amino compounds in real environmental samples. Gas chromatography is frequently used to determine amines using various derivatization reagents [6]. Other methods including enzymatic [7,8] and ion-exchange chromatographic detection [9] have been described for the determination of amines in various matrixes. These methods usually have limitations because of low sensitivity. Therefore, chemical derivatization is necessary in order to increase detection sensitivity and improve selectivity by pre-column or post-column HPLC derivatization methods [10,11]. Other techniques used to improve detection limits are microcolumn LC [12] and capillary electrophoresis [13]. Several common fluorescent derivatizing reagents [14–20] have also been developed fully. However, there have also been many reports describing various shortcomings in application, and to date no method has been shown to overcome all these problems. For example, the (2-phthalimidyl)benzoyl chloride (PIB-Cl) method offers high sensitivity, but it is not suitable for aromatic amines [21,22]. Although 7-fluoro-4-nitrobenzo-2-oxa-1,3-diazole (NBDF) is more reactive than 7-chloro-4-nitrobenzo-2-oxa-1,3-diazole (NBD-Cl) for amino compounds, data reported previously indicate that the two reagents themselves show ~30–50% decomposition in methanol–water solution within 25 min when exposed to daylight [23]. Recently 9-fluorenylmethyl chloroformate (FMOC) [24], 1-(9-fluorenyl)ethyl chloroformate (FLEC) [25], and 2-(9-anthryl)ethyl chloroformate (AEOC) [26] reagents have been used for the derivatization of amines, amino acids, and peptides for chiral or nonchiral separation in LC or CE. These reagents result in good UV absorption and very high sensitivity with laser-induced fluorescence detection. However, for effective derivatization, an

* Corresponding author at: Northwest Plateau Institute of Biology, Chinese Academy of Sciences, Xining 810001, PR China.
E-mail address: Jmyou6304@163.com (J. You).

0039-9140/$ – see front matter © 2009 Elsevier B.V. All rights reserved.
doi:10.1016/j.talanta.2009.09.041

excess of reagent must be used, and the derivatized solution must be extracted with pentane to remove an excess of reagent [27,28], because it interferes with the separation of derivatives and is detrimental to column performance. The 6-aminoquinolyl-*N*-hydroxysuccinimidyl carbamate (AQC) method is rapid and convenient and gives stable derivatives. However, only 10% of the fluorescent intensity in aqueous solution relative to that in pure acetonitrile solution is observed for its derivatives. Thus, the detection limits for the early eluted amine derivatives are usually higher than those for later ones [29].

In our previous studies [1,30–33], we described the synthesis of several fluorescent labeling reagents and their applications for common amino compound analysis. These probes exhibited very high fluorescence sensitivities; however, they gave relatively low MS ionization potential and were great disadvantage to online highly sensitive MS identification. The principal purpose of this study is to develop a new dual-sensitive probe for the rapid determination of amino compounds with fluorescence detection and online highly sensitive MS identification. The results indicate that the prepared 1-imidazole-2-(5-benzoacridine)-ethanone (IBAE) intermediate is a dual-sensitive probe, and reacts rapidly with amino compounds to give the high yields of derivatives without the need of catalysts. Derivatives are not only sensitive to fluorescence but also to MS ionizable potential with little matrix interference. To the best of our knowledge, this is the first time that IBAE probe and its further applications for the determination of amino compounds have been reported.

2. Experimental

2.1. Instrumentation

Experiments were performed using a 1100 Series LC/MSD-Trap-SL electrospray ion trap liquid chromatography/mass spectrometry consisted of a vacuum degasser (model G1322A), a quaternary pump (model G1311A), an autosampler (model G1329A), a fluorescence detector (FLD) (model G1321A), and a diode array detector (DAD) (model G1315A). The mass spectrometer from Bruker Daltonik (Bremen, Germany) was equipped with an atmospheric pressure chemical ionization (APCI). Fluorescence excitation and emission spectra were obtained at an F-7000 fluorescence spectrophotometer (Hitachi, Japan). The semi-preparative HPLC system, which used to obtain the single IBAE-butylamine derivative, was Waters Delta 600 (Waters, USA).

2.2. Materials and reagents

Acetonitrile and methanol were of chromatographic grade from Jining Chemical Reagent Co. (Shandong, China). All reagents used in this study were of analytical grade unless otherwise stated. Catalysts including triethylamine, pyridine, 4-dimethylaminopyridine (DMAP) were purchased from Shanghai Chemical Reagent Co. (Shanghai, China). *N*,*N*′-Carbonyldiimidazole (CDI) was purchased from Sigma Chemical Co. (St. Louis, MO). Dichloromethane, chloroform, DMF and other reagents were of analytical reagent grade. All amines used in experiments were of chromatographic grade and purchased from Jining Chemical Reagent Co.

2.3. Synthesis of 1-imidazole-2-(5-benzoacridine)-ethanone (IBAE)

2.3.1. Synthesis of 2-(benzoacridine)-5-acetic acid (BAAA)

Benzoacridine was conveniently prepared according to the method as previously described [34]. 2-(Benzoacridine)-5-acetic acid (BAAA) was synthesized as follows: benzoacridine (10 g), KOH (13 g) and dimethylsulfoxide (80 ml) were mixed in a 250-ml round-bottom flask and rapidly heated to 100–110 °C for 60 min with vigorous stirring. A solution of 13 ml ethyl bromoacetate in 30 ml dimethylsulfoxide was added dropwise within 1 h with stirring. The contents of the flask were continuously heated at 100–110 °C for 30 min. After cooling, the mixture was transferred into a solution containing 300 ml water and 20 g KOH, and continuously heated at 100 °C for 30 min. After the solution was cooled to ambient temperature, the mixture was filtrated; the result solution was adjusted to pH 3.0 with 4 mol/l HCL solution. The precipitated solid was recovered by filtration, washed with water. The crude product was dried at room temperature for 48 h and recrystallized twice from acetic acid to afford a yellow crystal 6.7 g, yield 56.8%. m.p. 289.1–289.4 °C. Found: C: 78.89%, H: 5.22%, N: 4.85%. Calculated: C: 78.87%, H: 5.23%, N: 4.84%. IR (KBr): 3320.98 (ν_{O-H}), 3023.15 (ν_{Ar-H}), 1605.94 (Ph–C=O), 1571.62, 1488.63, 1449.10, 1383.14, 1293.15, 757.07, 658.65. LC–APCI-MS: *m*/*z* 304.2 $[M+H]^+$ in positive-ion mode; MS/MS: *m*/*z* 246.0 (molecular core moiety).

2.3.2. Synthesis of intermediate of 1-imidazole-2-(5-benzoacridine)-ethanone (IBAE)

IBAE was prepared by the reaction of BAAA with CDI as follows: To a solution of BAAA (2.0 g) in 50 ml acetonitrile in a 100 ml round-bottom flask, CDI (3.0 g) was added. The contents of the flask were rapidly heated to reflux. After a 60 min period, the mixture was transferred into 300 ml of ice-water with stirring for 10 min; the precipitated solid was recovered by filtration, washed with water, and dried at room temperature for 48 h. The crude product was recrystallized 3 times from acetonitrile (3 × 30 ml) to afford a yellow crystal 1.9 g, yield (81.54%). m.p. >239 °C (decomposition). Found: C: 74.52%, H: 4.20%, N: 11.94%. Calculated: C: 74.78%, H: 4.25%, N: 11.89%. IR (KBr): 3040.5, 3022.36 (Ar), 1747.82 (–C=O in carboxylic group), 1643.00 (–C=O in acridine ring), 1485.83, 1398.86, 1292.55, 1226.79, 750.64. LC–APCI-MS: *m*/*z* 354.0 $[M+H]^+$ in positive-ion mode; MS/MS: *m*/*z* 246.0 (molecular core moiety).

2.4. Preparation of standard solutions

The standard solutions of BAAA and IBAE (approximate 4.0×10^{-3} mol/l) were prepared by dissolving appropriate amounts of BAAA and IBAE in 10 ml of acetonitrile or DMF solvents, respectively. Standard solutions (50 ng/ml) of amines from methylamine to dodecylamine were prepared by the dilution of the stock acetonitrile solutions of each amine (1 mg/ml) with acetonitrile. A standard solution of the coupling agent CDI (10 mg/ml) was prepared by dissolving 0.1 g CDI in 10 ml of acetonitrile.

2.5. Chromatographic method and MS condition

HPLC separation of amine derivatives was carried out on an Hypersil BDS C_{18} column (200 mm × 4.6 mm i.d, 5 μm) by a gradient elution. Eluent A was 30% of acetonitrile consisting of 10 mM ammonium/formic acid buffer (pH 3.75); B was 95% acetonitrile. Gradient conditions: initial = 90% A + 10% B; 0–30 min = from 90% A + 10% B to 100% B (kept for 10 min, injection 10 μl). The flow rate was constant at 1.0 ml min^{-1}. The fluorescence excitation and emission wavelengths were set at λ_{ex} = 272 and λ_{em} = 505 nm, respectively. Online MS ion source: dry gas temperature, 350 °C; nebulizer pressure, 60.0 psi; dry gas flow, 5.0 l/min; APCI Vap Temp 450 °C; corona current (nA) 4000 (pos); capillary voltage, 3500 V.

2.6. Derivatization procedure

Method A: To 100 μl of a standard mixture of amines was successively added 100 μl each of derivatizing reagent (BAAA, 4.0×10^{-3} mol/l), and CDI solution into a screw-capped tube. The mixture was allowed to react in a water-bath at 80 °C for 5 min.

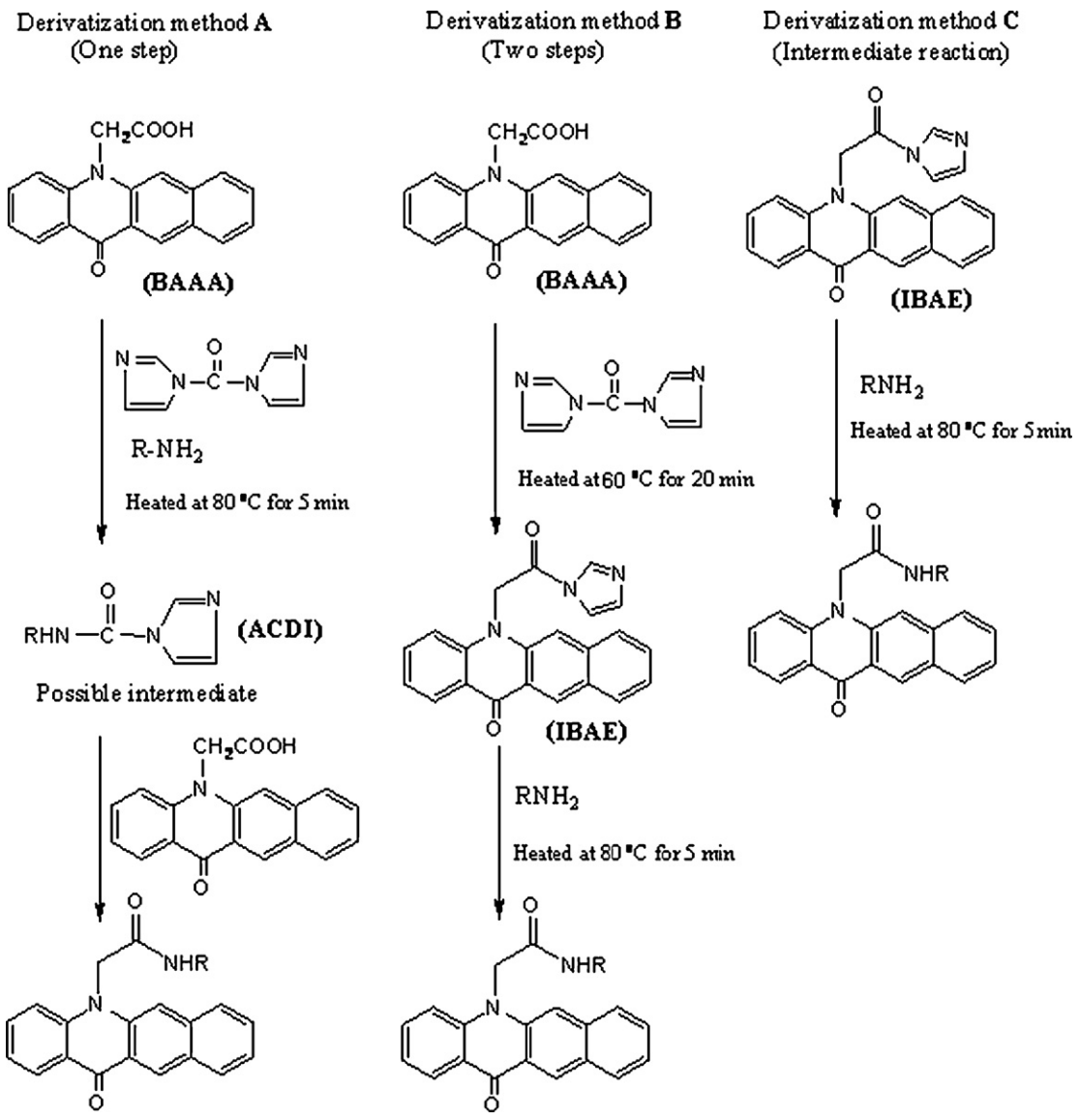


Fig. 1. The scheme of derivatization procedure using three kinds of different methods.

After the reaction was completed, the mixture was cooled to room temperature in a water-bath. A 10-μl volume of the crude reaction mixture was diluted to 100 μl with acetonitrile. The diluted solution (10 μl) was injected directly onto the chromatograph (Fig. 1, Method A).

Method B: To 100 μl of BAAA acetonitrile solution (BAAA, 4.0×10^{-3} mol/l), 100 μl CDI was added. This mixture was allowed to react at 60 °C for 20 min to form an activated amide intermediate without further purification. After activation of BAAA, 100 μl of standard mixture of amines was added, and the tube was sealed again and heated at 80 °C for 5 min. After the reaction was completed, the mixture was cooled to room temperature in a water-bath, and diluted with acetonitrile and injected directly onto the chromatograph (Fig. 1, Method B).

Method C: To 100 μl of a standard intermediate solution (IBAE: 4.0×10^{-3} mol/l), 100 μl amine solution was added. The mixture was allowed to react in a water-bath at 80 °C for 5 min. After the reaction was completed, the mixture was cooled to room temperature in a water-bath, and diluted with acetonitrile. A 10 μl volume of solution was injected directly onto the chromatograph (Fig. 1, Method C).

2.7. Samples preparation

Water samples collected from different sampling sites were analyzed using the developed method. Once water samples (50 ml) had been collected, they were immediately neutralize to pH 3.0 with 0.2 mol/l HCl and filtered through a 0.45-μm membrane filter. The neutralized solution was concentrated to dryness by a rotary evaporator. The residue was re-dissolved with 80% aqueous acetonitrile (ACN/H_2O, v/v). The resulting solution was then immediately cooled to 0–5 °C to avoid volatilization of amines, and stored in brown glass bottles in a refrigerator. All analyses were immediately subjected to derivatization and analysis by HPLC within one day after sampling.

2.8. Theoretical parts: estimation of the percent ionization fraction (δ)

The intramolecular isomerization of probe molecule **A** is shown in Fig. 2. The formation of quaternary ammonium ion **AB** results in the corresponding fluorescence quenching. The ionization δ values of the quaternary ammonium ion **AB** can be easily obtained by the

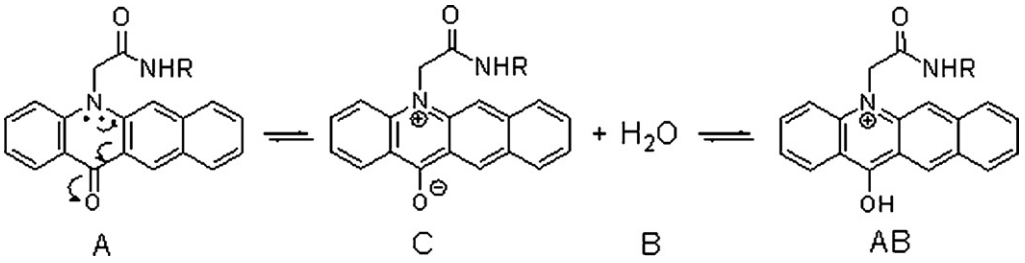


Fig. 2. The scheme of intramolecular keto–enol isomerization.

determination of the differences in fluorescence intensity in the presence of various amount of water in acetonitrile or methanol. When probe **A** is dissolved in aqueous acetonitrile or methanol, the forward and reverse reactions occur at equal rates, so the chemical equilibrium can be expressed as:

$$\mathbf{A} + \mathbf{B} \Leftrightarrow \mathbf{AB} \tag{1}$$

where **A** and **B** are the reactants, **A** is the fluorescence probe, **B** is the proton-solvent (proton donor, H_2O) and **AB** is the product (proton acceptor). When equilibrium is achieved, the quenching constant K in aqueous acetonitrile is given by

$$K = \frac{[\mathrm{AB}]}{[\mathrm{A}][\mathrm{B}]} \tag{2}$$

where [A], [B] and [AB] are the corresponding equilibrium concentrations in the aqueous acetonitrile, respectively. According to the law of conservation of mass, the percentage of ionization fraction δ can be defined as:

$$\delta = \frac{[\mathrm{AB}]}{[\mathrm{A}]_0} = \frac{[\mathrm{AB}]}{[\mathrm{A}] + [\mathrm{AB}]} \tag{3}$$

We also suppose that initial concentration of **A** in pure acetonitrile is $[A]_0$, corresponding fluorescence intensity is F_0, the relationship between fluorescence intensity and the concentration of probe **A** can be expressed:

$$F_0 = K'\phi_f[\mathrm{A}]_0 \tag{4}$$

where K' is the constant depended on the relative parameters of instruments, ϕ_f is the quantum yield of **A.** When **A** is partially ionized by **B** to form corresponding quaternary ammonium ion **AB**, the fluorescence intensity of unionized probe **A** is F, in this case, the fluorescence intensity F can be expressed quantitatively as:

$$F = K'\phi_f(1-\delta)[\mathrm{A}_0] \tag{5}$$

where $\delta = [\mathrm{AB}]/[\mathrm{A}]_0$.

By combination of Eqs. (4) and (5) we obtained:

$$\frac{F_0 - F}{F} = \frac{K'\delta[\mathrm{A}]_0}{K'(1-\delta)[\mathrm{A}]_0} \tag{6}$$

This Eq. (6) can be reorganized into:

$$\frac{F_0 - F}{F} = \frac{\delta}{1-\delta} \tag{7}$$

This Eq. (7) can be reorganized into:

$$\delta = \frac{F_0/F - 1}{F_0/F} \tag{8}$$

Thus, the percent ionization fraction δ value can be calculated by Eq. (8) by the combination of each F value obtained in the presence of various volume percentage of water (here, assumption that the percent ionization fraction $\delta = 0$ in pure acetonitrile and pure methanol).

3. Results and discussion

3.1. Fluorescence for representative IBAE-butylamine derivative

The recorded spectra of IBAE-butylamine derivative in aqueous acetonitrile (50%, ACN/H_2O, v/v) showed an excitation maximum at λ_{ex} 272 nm and an emission maximum at λ_{em} 505 nm. An increase in solvent polarity resulted in obvious red-shift in fluorescent emission spectra. The emission intensities in pure methanol and acetonitrile exhibited 2.64–2.34 times stronger than that in pure water with peak red-shift about 12 and 47 nm, respectively. The quenching in aqueous acetonitrile and methanol for IBAE-amine derivative should be attributed to the formation of quaternary ammonium ion AB by the protonation reaction with H_2O as described in Fig. 2.

3.2. Effect of temperature on fluorescence intensity in various solvents

The effects of temperature on the fluorescence spectra of IBAE-butylamine in solvents from group 1 to group 5 were investigated over the temperature range from 10 to 70 °C in 10 °C increments. The analysis of fluorescence intensity (I_{em}) of IBAE-butylamine derivative at different temperature in various solvents led to a linear correlation between I_{em} and T (see Table 1). With solvents from group 1 to group 5, IBAE-butylamine fluorescence intensity remarkably decreased with increasing temperature from 10 to 70 °C. There was an exception of methanol, the fluorescent intensities of IBAE-butylamine in methanol solvent increased with increasing temperature. In addition, the formic acid from group 3 was irreversible to fluorescence; this was probably due to the fact that the derivative was mostly protonated by its nitrogen atoms in molecular core structure in relatively strong formic acid solvent, resulting in the irreversible fluorescence emission. When aqueous organic solvents were used, such as aqueous acetonitrile or aqueous methanol, fluorescence intensities constantly increased with increasing solvent temperature. It was probably due to the fact that the IBAE-butylamine molecules were first solvated by several H_2O molecules by hydrogen bond acting force and resulted in the decrease of direct collision frequency between IBAE-butylamine and solvent molecules. Methanol was a kind of protic solvent and similar to water (HOH), where one of the hydrogens was replaced with the methyl group. Therefore IBAE-butylamine molecules could also be solvated by methanol molecules as did of water molecules resulting in an increase of fluorescence with the increase of solvent temperature. It was similar to the case of aqueous acetonitrile and aqueous methanol. In addition, the tested solvent volume in cell (4-mL) increased with increasing temperature from 10 to 40 °C or 10 to 70 °C; however, the tested temperatures for these solvents were below their boiling points and resulted in a very small change to IBAE-butylamine concentration. Therefore, the influence of the volume change of solvent on the fluorescence intensity could be ignored.

Table 1
Effects of temperature on fluorescence intensity of IBAE-butylamine derivative in various solvents[a].

Solvent	Fluorescence intensity							$I_{em} = A + B \times T$		
	10 °C	20 °C	30 °C	40 °C	50 °C	60 °C	70 °C	A	B	Coefficient (r^2)
Group 1										
Methanol	566	602	629	653	675	707	[b]	−195.57	2.708	0.9928
Ethanol	627	613	601	593	584	575	[b]	911.23	−1.014	0.9859
1-Propanol	656	641	628	614	606	596	590	965.25	−1.107	0.9776
1-Butanol	761	745	733	723	713	703	695	10,162.37	−1.078	0.9875
1-Pentanol	559	546	535	523	513	503	493	866.64	−1.093	0.9973
1-Hexanol	710	694	680	665	654	643	631	1076.16	−1.303	0.9938
1-Heptanol	515	506	500	494	489	484	480	674.28	−0.571	0.9826
Group 2										
Methylamine	50	48	46	44	42	40	38	106.60	−0.200	1.00
Ethylamine	403	380	356	336	319	300	286	952.58	−1.957	0.9919
1-Propylamine	348	330	315	302	[b]	[b]	[b]	779.69	−1.537	0.9919
1-Butylamine	95	88	82	78	73	68	64	237.02	−0.507	0.9913
Group 3										
Formic acid[c]	16	15	14	13	13	13	13	40.06	−0.086	0.9554
Glacial acid	[d]	622	601	580	557	533	513	1269.08	−2.206	0.9992
Propionic acid	156	150	145	140	137	133	130	275.71	−0.428	0.9829
Butyric acid	166	161	157	153	148	145	141	282.67	−0.414	0.9964
Pentoic acid	60	59	58	57	56	55	54	88.30	−0.170	1.00
Group 4										
Dichloromethane	446	427	412	[b]	[b]	[b]	[b]	926.43	−1.770	0.9908
Chloroform	538	512	483	456	436	[b]	[b]	1272.08	−2.600	0.9953
Tetrachloromethane	109	84	65	48	35	26	[b]	570.68	−1.654	0.9671
Group 5										
Methyl sulfoxide	[d]	586	563	537	512	481	457	1354.92	−2.617	0.9980
Tetrahydrofuran	28	26	24	22	20	19	[b]	80.36	−0.186	0.9902
DMF	614	581	549	524	496	466	440	1424.16	−2.875	0.9983
Acetonitrile	458	433	409	388	370	354	340	1009.08	−1.967	0.9866

[a] Concentration of IBAE-butylamine in each solvent is kept at 5.0×10^{-7} mol/l.
[b] The test is not carried out as the temperature is close to or beyond the boiling point.
[c] Linear regression was carried out at the temperature range of 10–40 °C.
[d] The test is not carried out because the temperature is below the freezing point.

3.3. Effects of solvent and basic catalyst on derivatization

Several types of solvents were tested in this study for derivatization, including acetonitrile, ethyl acetate, acetone, chloroform, dichloromethane, DMF and methyl sulfoxide (DMSO). Derivatization was carried out at 80 °C for 5 min using DMAP as basic catalyst. Each value was an average of six runs with DMF solvent taken as 100%. The results indicated that DMF gave the highest detector responses. All derivatization was, therefore, performed by the use of DMF as reaction co-solvent. In addition, DMF was used as the derivatization co-solvent in preference to other solvents as it easily avoided the problem of precipitation of hydrophobic long chain amine derivatives. Several base catalysts, including triethylamine, pyridine and DMAP were evaluated as reaction catalysts. The results indicated that the derivatization yields in the absence of the basic catalysts were in good agreement with the cases of using triethylamine, pyridine and DMAP. Therefore, catalysts were not used for all subsequent derivatization experiments.

3.4. Temperature conditions, time effects and reagent concentration for derivatization

The peak heights for all amines became constant at 80 °C for 5 min. When below 80 °C the reaction rate was decreased and led to a long derivatization time. Therefore, derivatization temperature selected was set at 80 °C for all experiments. Constant fluorescence intensity could be obtained with the addition of 3–4-fold molar reagent excess to total molar amines; further increasing the excess of reagent did not significantly alter the reaction time and temperature needed for the derivatization reaction to be completed.

3.5. Percent ionization and MS cleavage mode of IBAE-amine derivatives

IBAE-amine derivatives actually exhibited excellent ionization efficiency under LC–MS conditions. This should be attributed to the intramolecular keto–enol isomerization as described in Fig. 2. This property was of great importance to perform a sensitive MS detection as the main characteristic of APCI derived from the fact that the molecule in MS ion chamber was first solvated by water molecules [35]. The fluorescence intensity of probe **A** molecule in the presence of varying amount of water is shown in Table 2. On the basis of the obtained data, the percentage of ionization (δ) values for representative IBAE-C4 was evaluated according to the Eq. (8), which indicated that the estimated δ values in aqueous acetonitrile were in the range of 0–57.32% with increasing amount of water from 0 to 100% (v/v). The δ values in aqueous methanol were in the range of 0–62.14% with increasing amount of water from 0 to 100% (v/v).

With aqueous acetonitrile as solvent, the percent ionization δ values versus the added volume percent of water showed a good linear relationship in the range 0–60% of water ($\delta = 0.763 + 0.256v$, $r = 0.9927$, v : the added volume percent of water). Although a good linear relationship in the range 60–100% of water was also observed ($\delta = -47.35 + 1.018v$, $r = 0.9893$), the linear relationship had been deviated from the original curve. It could not express the linear relationship of actual concentration of initial form **A** versus fluorescence. This should be attributed to the fact that the molecules of IBAE-amine derivatives in the presence of water (<60%) existed mainly as form **A** as described in Fig. 2. When the percentage of water is >60%, molecular structure of form **A** had been partially converted to no-fluorescent quaternary ammonium ion **AB** (see Fig. 2). In other words, the actual concentration of form **A** in the

Table 2
The fluorescence intensity of IBAE-butylamine in the presence of varying amount of water and corresponding calculated ionization fraction δ values (IBAE-butylamine concentrations were kept constant at 5.0×10^{-7} mol/l for each tested solution).

H_2O% (v/v)	Solvent					
	Acetonitrile			Methanol		
	Emission wavelength (nm)	Relative intensity	Ionization fraction, δ (%)	Emission wavelength (nm)	Relative intensity	Ionization potential, δ (%)
100	520	309	57.32	518	265	62.14
90	515	419	42.13	517	318	54.57
80	511	496	31.49	516	388	44.57
70	507	550	24.03	515	481	31.29
60	506	612	15.47	514	556	20.57
50	505	629	13.12	511	586	16.29
40	503	639	11.74	509	602	14.00
30	501	656	9.39	508	626	10.57
20	499	680	6.08	506	647	7.57
10	495	700	3.31	506	662	5.43
0	473	724	0	506	700	0

presence of water (>60%) is lower than the initial concentration of the probe molecule **A**. This result was also similar to the case of using aqueous methanol (<50%, MeOH/H_2O, v/v). In aqueous methanol, $\delta = 1.108 + 0.315\nu$ ($r = 0.9914$, ν : the added volume percent of water in methanol in the range of 0–50%). The estimation of percent ionization δ values revealed that the probe molecule **A** provided the desired ionization efficiency in commonly used aqueous acetonitrile or methanol, which was usually used in LC–MS separation as mobile phase composition. To evaluate the effects of pH on fluorescence and ionization efficiency in APCI-MS ion source, two mobile phase compositions containing 10 mM of aqueous ammonium/formic acid buffer–acetonitrile in 70:30 volume ratios were used and their pH values were, respectively, adjusted to pH 3.75 and 8.65 by adding an appropriate amount of ammonium and formic acid. The results indicated that fluorescence intensities for all 12 amine derivatives with pH 3.75 mobile phase were 1.42 times less than those obtained with pH 8.65 mobile phase (chromatogram was not shown). MS ion current responses at pH 3.75 and 8.65 were also compared under the same APCI-MS conditions proposed. With pH 3.75 mobile phase, the strong MS ion current responses for amine-derivatives were observed (Fig. 3a). However, no ion current responses for amine-derivatives were observed when mobile phase pH was adjusted to pH 8.65 (Fig. 3b). The main merits of the prepared probe molecule compared with our previously reported [30–33] indicated that IBAE-amines could be easily obtained a sensitive fluorescent detection using relatively high pH buffers (pH > 4.0), at the same time, it could also be achieved highly sensitive APCI-MS identification using relatively low pH buffers (pH < 8.65). Our experiments also indicated that the mobile phases with a pH range of 4.0–6.0 did not cause significant changes in retention values for all IBAE-amine derivatives tested in LC separation (data are not shown).

As expected, the IBAE-amine derivative produced an intense molecular ion peak at m/z $[M+H]^+$ under APCI-MS in positive-ion mode. The collision-induced dissociation spectra of m/z $[M+H]^+$ produced the fragment ions at m/z 258.6, m/z 245.5 and m/z 230.6, respectively. MS ion current chromatogram and corresponding cleavage mode for the representative IBAE-C_8 derivative are shown in Fig. 4(a: MS/MS, b: MS). The fragment ion at m/z 258.6 derived from the cleavage of C–CO bond of the N-linked side chain. A modified McLafferty rearrangement mechanism gave the specific fragment ion at m/z 245.5, the characteristic fragment ion derived from the cleavage of N–C bond of the N-linked side chain, followed by the rearrangement of one hydrogen atom toward the benzoacridine core structure. The selected reaction monitoring, based on the m/z $[M+H]^+ \rightarrow m/z$ 258.6 and m/z 245.5 transitions, was specific for IBAE-amine derivatives.

3.6. Analytical performance

A standard consisting of 40 ng/ml amine derivatives (C_1–C_{12} amines) was prepared to examine the method repeatability. The relative standard deviations (R.S.D.s; $n = 6$) of the peak areas and retention times were <1.24% and <0.086%, respectively.

Precision and accuracy: The precision and accuracy values for all 3-day validated quality control for the 12 amines were examined by using triplicate set of spiked blank water samples at the concentration of 15, 25, and 40 ng/ml (low, medium, and high),

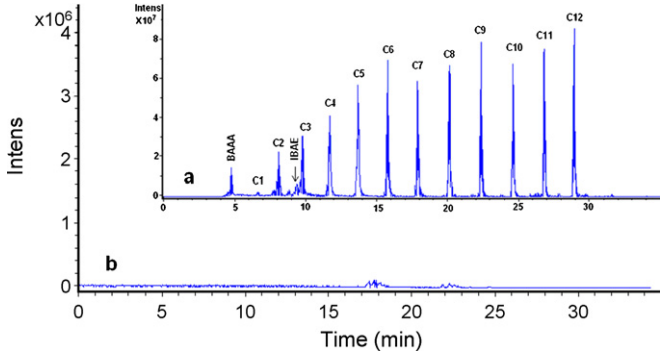


Fig. 3. (a and b) Ion current chromatogram for standard amine derivatives (20 pmol, 10 μl injection and followed into post-column mass spectrometer, **a** at pH 3.75; **b** at pH 8.65). Ion peaks: C1, methylamine; C2, ethylamine; C3, propylamine; C4, butylamine; C5, pentylamine; C6, hexylamine; C7, heptylamine; C8, octylamine; C9, nonylamine; C10, decylamine; C11, undecylamine; C12, dodecylamine; BAAA: 2-(benzoacridine)-5-acetic acid; IBAE: 1-imidazole-2-(5-benzoacridine)-ethanone.

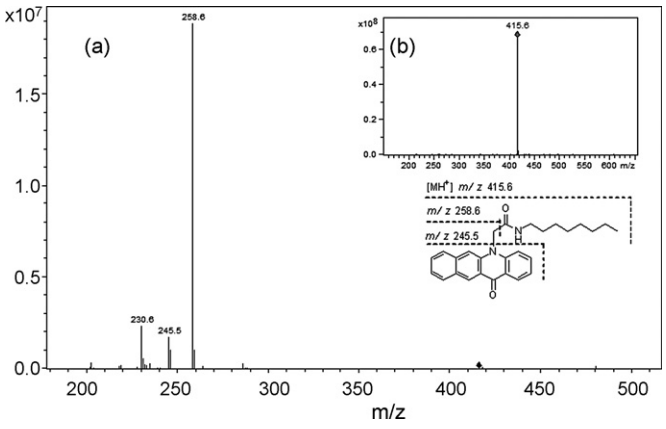


Fig. 4. MS spectra of representative C8-amine derivative (MS/MS: **a**; MS: **b**).

Table 3
Linear dynamic ranges and procedural LODs of amines determined using derivatization C.

Compound	Linear range (ng/ml)	R.S.D.[a] (%) peak area (n = 6)	(r)	LODs (ng/ml)[b] fluorescence	LODs (ng/ml)[b] APCI-MS
Methylamine	0.240–35.65	1.24	0.9995	0.16	2.43
Ethylamine	0.203–51.75	0.96	0.9999	0.15	2.07
Propylamine	0.267–271.4	1.14	0.9999	0.20	2.71
Butylamine	0.328–335.8	0.80	0.9999	0.26	3.36
Pentylamine	0.392–100.05	0.86	0.9998	0.33	4.00
Hexylamine	0.454–29.04	1.07	0.9996	0.28	4.65
Heptylamine	0.517–132.29	0.95	0.9999	0.45	5.29
Octylamine	0.581–148.35	0.96	0.9998	0.37	5.93
Nonylamine	0.644–657.8	1.08	0.9998	0.47	6.58
Decylamine	0.707–180.55	0.94	0.9997	0.49	7.22
Undecylamine	0.770–196.65	0.96	0.9999	0.50	7.87
Dodecylamine	0.833–212.75	1.16	0.9999	0.50	8.51

[a] Relative standard deviation was determined at 40 ng/ml of each IBAE-derivatives (n = 6).
[b] Signal-to-noise ratio of 3.

respectively. The intra- and inter-assay accuracy, determined at each quality control level throughout the validated runs (each batch, n = 6), remained below 103.6% and 104.91%. The mean intra- and inter-assay precision for all amines levels were <4.32% and 4.84%, respectively.

The linearity was established over a 1000-fold concentration range for amines with analysis of serial standards in the concentration range of 0.1–200 ng/ml (corresponding injected amounts of amines from 1.0 to 2000 pg). Linear ranges and detection limits using fluorescence detection for amines by methods C are listed in Table 3. All of the amines were found to give linear responses over this range, with correlation coefficients of >0.9995. The linear regression analysis for higher concentrations of amines was not tested as the responses were over the range of linearity. As expected, amines exhibited a wide linear range. The fluorescence detection limits were in the range of 0.15–0.50 ng/ml. The online APCI-MS detection limits were in the range of 2.07–8.51 ng/ml.

Discrimination using derivatization methods A, B and C for labeling amines based on the fluorescence responses is significantly observed. The chromatograms are shown in Fig. 5a–c. A significant decrease in detector response in method A for the labeled IBAE-amine derivatives is observed. It is possible that amino functional groups of alkylamines are superior to a carboxylic group from BAAA molecules when reacting with CDI. This procedure probably forms another intermediate *N*-alkylcarbonylimidazole ACDI (see Fig. 1). Subsequently, the condensation reaction of ACDI with BAAA molecules is a slow reaction because the carboxylic ions from BAAA molecules are weak basicity, which results in remarkably

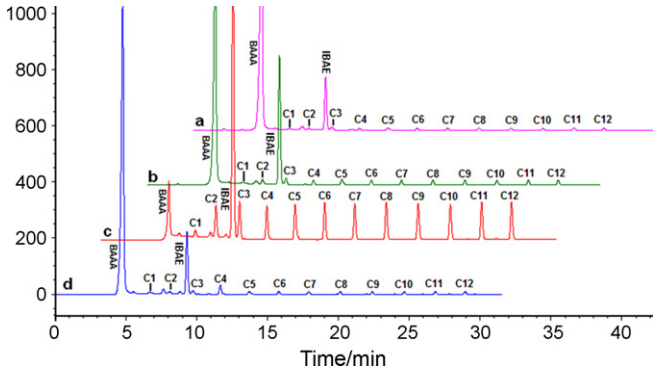


Fig. 5. (a–d) Chromatograms for amine standard solutions derivatized by applying: (a) method A; (b) method B; (c) method C; (d) method C in the presence of small quantity of water (>10%, w/w) in derivatization solution. C1, methylamine; C2, ethylamine; C3, propylamine; C4, butylamine; C5, pentylamine; C6, hexylamine; C7, heptylamine; C8, octylamine; C9, nonylamine; C10, decylamine; C11, undecylamine; C12, dodecylamine; DMA, dimethylamine; BAAA, benzoacridine-5-acetic acid; IBAE, 1-imidazole-2-(5-benzoacridine)-ethanone.

low detection responses for amine derivatives (Fig. 5a). Method C gives the highest fluorescence responses; it is probably because the derivatization in method C (direct intermediate reaction) is a rapid nucleophilic substitution reaction (Fig. 5c). In method B (two steps method), an obvious decreases in detector responses for the labeled IBAE-amine derivatives are observed (Fig. 5b). This result derives from the reason that the intermediate solution contains an excess amount of CDI coupling agent. When amines are subsequently added into the intermediate solution, amines, at least in part, firstly react with the excess amount of CDI to give, in part, the intermediate ACDI as described in method A. It is obvious that method C is superior to methods A and B, and therefore, the derivatization method C is selected in all cases in this study. In addition, derivatization in the presence of a small quantity of water in derivatization solution has been tested and compared with method C. When the amount of water in derivatization solution is >10% (w/w), a significant degradation in detector responses is observed (see Fig. 5d). The peak of intermediate IBAE is significantly reduced, the corresponding peak height of by-product BAAA is simultaneously intensified. It should be attributed to the reagent hydrolysis to form corresponding BAAA (m/z 289.8 $[M+H]^+$; MS/MS: m/z 246.0, molecular core moiety). If the amount of water in derivatization solution in method C is less than 5% (w/w), the derivatization yields for amine-derivatives are similar to the case of without water. As observed, the presence of BAAA (major by-product) does not interfere with the separation of amine derivatives. The similar results for the MS ion current chromatogram are also observed (ion current chromatogram is not shown). Comparing of derivatization of primary with secondary amine such as ethylamine/dimethylamine and butylamine/diethylamine, a greater degree of deviation for the detection response is observed, where the latter is 10–12 times less reactive than the former. The common trait of this type of nucleophilic substitution reaction is steric requirements for solute molecules. Secondary amines possess two alkyl groups around the nitrogen atom, which can assume much more spatially demanding configurations than those of primary amines for a nucleophilic substitution reaction. Aniline and benzenic ethylamine as representative aromatic amines are also evaluated, where the latter is similar to the case of alkylamines such as methylamine or ethylamine. But, aniline hardly reacts with the intermediate. There is no denying the fact that the basicities of amino functional groups of aromatic amines are weaker than those of alkylamines [35], which result in low detection responses.

3.7. The application of the method C

Fig. 6 shows the application of this method for the determination of amines present in an environmental wastewater. The contents of amines from two different sampling sites are listed in Table 4. The

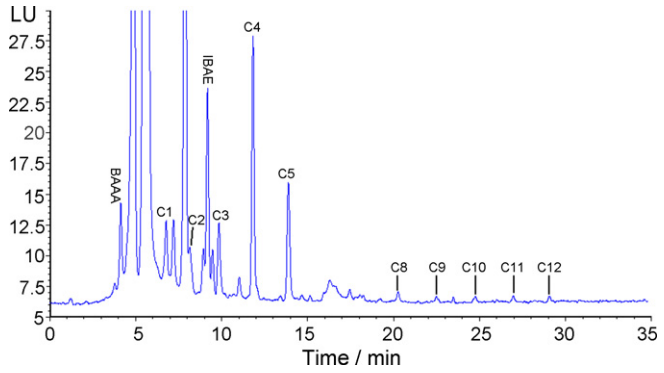


Fig. 6. Chromatogram of environmental wastewater (peaks were the same as Fig. 5c).

Table 4
Analysis of amines from water examples.

Amine	ng/ml[a]	R.S.D.s (%) (n = 6)	ID[b]	ng/ml[c]	R.S.D.s (%) (n = 6)	ID[b]
Methylamine	78.90	1.84	Yes	2.26	2.34	Yes
Ethylamine	13.45	2.23	Yes	0.14[d]	4.20	
Propylamine	32.69	2.04	Yes	0.085[d]	4.82	
Butylamine	164.21	1.21	Yes	84.6	2.08	Yes
Pentylamine	84.52	1.63	Yes	63.5	2.12	Yes
Hexylamine	[e]			[e]		
Heptylamine	[e]			[e]		
Octylamine	7.16	2.34	Yes	6.54	2.37	Yes
Nonylamine	2.08	2.64	Yes	1.42	2.68	Yes
Decylamine	4.91	2.55	Yes	3.94	2.57	Yes
Undecylamine	5.03	2.67	Yes	4.62	2.84	Yes
Dodecylamine	2.41	2.96	Yes	2.64	2.98	Yes

[a] Wastewater from pharmaceutical factory of Qufu City (Qufu Shandong, China).
[b] 'Yes": corresponding components were simultaneously identified by online APCI-MS in positive-ion mode using specific fragment ion transitions as observed in text.
[c] Wastewater from pharmaceutical factory Jining City (Jining Shandong, China).
[d] To measure ethylamine and propylamine, the injection amounts were 3 times relative to that of other amines.
[e] Not detectable or below detection limits (LOQ).

quantitative analysis is carried out by fluorescence, corresponding components are simultaneously identified by online APCI-MS. Generally, the amine compositions depend on the type of wastewater samples. While C1–C5 amines in wastewater samples remain the high levels. The contents of >C5 amines in wastewater are also detected with the exception of being C6 and C7 amines are not determined in wastewater. As can be seen from Fig. 6, ethylamine (C2) is, in part, co-eluted with an impurity, and thus the quantitative analysis of ethylamine is performed by the corresponding peak height. Because the certified reference material was not available, therefore, the established IBAE method was compared with our previously reported method using BCEOC-Cl as labeling reagent for the determination of amines in the same sample (No. 2). The results with IBAE derivatization were in good agreement with those obtained using BCEOC-Cl as labeling reagent (data were not shown).

4. Conclusions

Although amine compound analysis is a relatively mature technique, current liquid chromatographic technology still needs improvement in the speed, accuracy and sensitivity of the analysis. The proposed method offers a number of advantages: (1) derivatization of amines used intermediate IBAE is relatively simple with little matrix interference; (2) derivatives are not only sensitive to fluorescence but also to MS ionizable efficiency with only changing mobile phase pH values; (3) maximal yields close to 100% are observed with a 4–6-fold molar reagent excess; (4) catalysts are not required for the derivatization. A possible disadvantage of this method is that the reaction of IBAE with amines in derivatization solution must be kept as small quantity of water as possible. Complete derivatization for further higher chain amines (>C12), in fact, can easily be achieved under the HPLC derivatization conditions proposed. The proposed method has been successfully applied to the determination of free amines in environmental wastewater with satisfactory results. In this study, the developed LC–MS technology was only used for the sensitive identification of amine derivatives. In addition, a possible advantage of this method is that the reagent IBAE may be used by on-line and on-column derivatization; corresponding work is in progress in our laboratory.

Acknowledgments

This work was supported by the National Science Foundation of China (No. 20075016) and supported by 100 Talents Programme of The Chinese Academy of Sciences (No. 328).

References

[1] J. You, X. Fan, W. Lao, Q. Ou, Q. Zhu, Talanta 48 (1999) 437–449.
[2] F. Sacher, S. Lenz, H. Brauch, J. Chromatogr. A 764 (1997) 85–93.
[3] G.W. Schade, P.J. Crutzen, J. Atmos. Chem. 22 (1995) 319–346.
[4] A. Terashi, Y. Hanada, A. Kido, R. Shinohara, J. Chromatogr. 503 (1990) 369–375.
[5] M. Abalos, J.N. Bayona, F. Ventura, Anal. Chem. 71 (1999) 3531–3537.
[6] D.R. Knapp, Handbook of Analytical Derivatization Reactions, Wiley-Interscience, New York, USA, 1979.
[7] B. Vinet, Clin. Chem. 33 (1987) 2204–2208.
[8] Y. Sekine, M. Suzuki, T. Takeuchi, E. Tamiya, I. Karube, Anal. Chim. Acta 280 (1993) 179–184.
[9] M.C. Gennaro, E. Mentasti, C. Sarzanini, V. Porta, Chromatographia 25 (1988) 117–124.
[10] B. Valeur, in: S.G. Schulman (Ed.), Molecular Luminescence Spectroscopy, Wiley, USA, 1993, pp. 25–84 (Part 3).
[11] Q.-Z. Zhu, F. Li, X.-Q. Guo, J.-G. Xu, W.-Y. Li, Analyst 122 (1997) 937–940.
[12] M.D. Oates, J.W. Jorgenson, Anal. Chem. 61 (1989) 432–435.
[13] Y.-F. Cheng, N.J. Docichi, Science 242 (1988) 562–564.
[14] Y. Yamada, Y. Aizawa, J. Pharmacol. Methods 9 (1983) 1–6.
[15] Y. Moliner Martinez, C. Molins Legua, P. Campíns Falcó, Talanta 62 (2004) 373–382.
[16] T. Ishida, M. Yamaguchi, T. Iwata, M. Nakamura, Anal. Chim. Acta 223 (1989) 319–326.
[17] Y. Tsuruta, K. Kohashi, Anal. Chim. Acta 192 (1987) 309–313.
[18] P. Lindroth, K. Mopper, Anal. Chem. 51 (1979) 1667–1674.
[19] D.W. Hill, F.H. Walters, T.D. Wilson, J.D. Stuart, Anal. Chem. 51 (1979) 1338–1341.
[20] H.G. Barth, W.E. Barber, C.H. Lochmuller, R.E. Majors, F.E. Regnier, Anal. Chem. 60 (1988) 387–435.
[21] M.H. Zheng, H.D. Xu, C.G. Fu, Chin. J. Chromatogr. 12 (1994) 186–187.
[22] M. Zheng, C. Fu, H. Xu, Analyst 118 (1993) 269–271.
[23] M. Ahnoff, I. Grundevik, A. Arfwidsson, J. Fonselius, B.-A. Persson, Anal. Chem. 53 (1981) 485–489.
[24] A. Engstrom, P.E. Anderson, B. Jossfsson, W.D. Pfeffer, Anal. Chem. 67 (1995) 3018–3022.
[25] S. Einarsson, B. Josefsson, P. Moller, D. Sanchez, Anal. Chem. 59 (1987) 1191–1195.
[26] A.J. Faulkner, H. Veening, H.D. Becker, Anal. Chem. 63 (1991) 292–296.
[27] D.S. Burgi, R.L. Chien, Anal. Biochem. 202 (1992) 306–309.
[28] C. Schwer, B. Gas, F. Lottspeich, E. Kenndler, Anal. Chem. 65 (1993) 2108–2115.
[29] S.A. Cohen, D.P. Michaud, Anal. Biochem. 211 (1993) 279–287.
[30] J. You, X.-E. Zhao, Y. Suo, H. Wang, Y. Li, J. Sun, Anal. Chim. Acta 565 (2006) 168–177.
[31] J.M. You, W. Zhao, L. Liu, X. Zhao, Y. Suo, H. Wang, Y. Li, C. Ding, Talanta 72 (2007) 914–925.
[32] J. You, X. Chen, W. Zhao, L. Liu, X. Zhao, Y. Suo, H. Wang, Y. Li, J. Sun, Chromatographia 63 (2006) 337–343.
[33] J. You, H. Zhao, Z. Sun, L. Xia, T. Yan, Y. Suo, Y. Li, J. Sep. Sci. 32 (2009) 1351–1362.
[34] D.A. Shirley, W.E. Tatum, J. Org. Chem. 25 (1960) 2238–2240.
[35] J. Sunner, G. Nicol, P. Kebarle, Anal. Chem. 60 (1988) 1300–1307.

Talanta 80 (2010) 1400–1405

Contents lists available at ScienceDirect

Talanta

journal homepage: www.elsevier.com/locate/talanta

Cuprous oxide nanospheres as probes for light scattering imaging analysis of live cells and for conformation identification of proteins

Wen Jing Qi [a], Cheng Zhi Huang [a,b,*], Li Qiang Chen [c]

[a] Education Ministry Key Laboratory on Luminescence and Real-Time Analysis, College of Chemistry and Chemical Engineering, Southwest University, Chongqing 400715, PR China
[b] College of Pharmaceutical Sciences, Southwest University, Chongqing 400715, PR China
[c] College of Life Science, Southwest University, Chongqing 400715, PR China

ARTICLE INFO

Article history:
Received 30 May 2009
Received in revised form
22 September 2009
Accepted 24 September 2009
Available online 30 September 2009

Keywords:
Cu_2O nanospheres (Cu_2O NPs)
Morphology
Scanning electron microscopy (SEM)
Light scattering (LS)
Dark-field light scattering images

ABSTRACT

A facile solution-phase synthesis route of highly uniform Cu_2O nanospheres (Cu_2O NPs) with the size of 57.7 ± 4.7 nm was developed, and then the nanoparticles were applied to live cell imaging under a common dark-field microscope. Starting from copper(II) salts, the synthesis of Cu_2O NPs was made in the presence of cetyltrimethylammonium bromide (CTAB) by reducing the copper(II) with sodium borohydride ($NaBH_4$) in aqueous medium and by aging process in the air. Monitoring of morphology evolution process of Cu_2O NPs with scanning electron microscopy (SEM) and measuring of the UV–visible spectra showed that the synthesis of Cu_2O NPs follows the reduction–oxidation coupled process of Cu^{2+} into Cu^0 species at first and then the resulted Cu^0 species into Cu_2O NPs in the air. Light scattering (LS) features have been measured with a common spectrofluorometer and a common dark-field microscope, and it was found that the as-prepared Cu_2O NPs display strong blue scattering light and can be applied for cell imaging. If incubated with human bone marrow neuroblastoma, transferrin-conjugated Cu_2O NPs can get into the cells and show strong pure blue light in cytoplasm. Further investigations showed that the Cu_2O NPs could be applied for probes for conformation of proteins.

© 2009 Elsevier B.V. All rights reserved.

1. Introduction

Copper oxide, a p-type metal oxide semiconductor with a direct band gap about 2.2 eV, has attracted interest of researchers due to its unique optical properties [1] and applications in photodegradation [2], gas sensing [3], catalysis such as a catalyst of a carbon nanofibers [4]. Therefore, efforts on the syntheses and applications of nanoparticles related to copper element have been made recently. Methods such as γ-ray irradiation reduction [5], electrochemical deposition [6], solid-state [7] or liquid-phase [8,9] have been reported for the synthesis of cuprous oxide nanoparticles (Cu_2O NPs). Of these methods, a variety of capping agents such as sodium dodecyl sulfate [10] and reducing agents such as ascorbic acid [11–13] have been employed [1,3,5,8,9,13–17], and the following synthesis generally involves in the step that directly reduces the copper(II) salt into Cu_2O NPs, which, however, needs complicated multiple procedures [4,18] or to be in a medium of organic solvents participating in [1,3]. However, we recently noticed an indirect method, that is at first reducing copper(II) into Cu^0 species and then oxidizing the Cu^0 species into Cu_2O NPs [8], which, although indirect, is interesting since it is based on the slow oxidation of Cu^0 state into Cu^+ state in the air and only once addition of all reactants needed without annealing step involved, making operation so easy to handle that different morphology of Cu_2O NPs could be available [8].

Light scattering (LS) features of metallic nanoparticles (NPs) are unique and it has increasingly reported that metallic nanoparticles have become promising optical probes due to their photostability and colorful features. Recent efforts on light scattering optical properties of metallic nanoparticles with dark-field microscopy have prompted our interest since that could supply good imaging ways [19–21]. Up to now, the light scattering imaging of metallic nanoparticles is mainly concentrated on gold and silver nanoparticles [22–25]. It is regretted that gold NPs have relatively low light scattering power [26], and silver nanoparticles, although having strong light scattering ability, cannot supply stable light scattering features because general synthesis protocols of silver nanoparticles are apt to produce somewhat faceted particles with slightly different shapes [27]. Therefore, finding a substitute with high scattering power through simple process is meaningful and compulsory.

Herein, we report a facile low-cost solution-phase synthesis method of Cu_2O NPs in ambient conditions by reducing copper(II) salts in water in the presence of CTAB with $NaBH_4$ and then by

* Corresponding author at: Education Ministry Key Laboratory on Luminescence and Real-Time Analysis, College of Chemistry and Chemical Engineering and College of Pharmaceutical Science, Southwest University, Chongqing 400715, PR China. Tel.: +86 23 68254659; fax: +86 23 688866796.
E-mail address: chengzhi@swu.edu.cn (C.Z. Huang).

0039-9140/$ – see front matter © 2009 Elsevier B.V. All rights reserved.
doi:10.1016/j.talanta.2009.09.042

aging the produced Cu^0 species in the air. The available Cu_2O NPs are highly uniform with the size of 57.7 ± 4.7 nm, and can scatter strong blue color light. Due to the high scattering power, we apply the as-prepared Cu_2O NPs for scattering imaging of live cell by using the human bone marrow neuroblastoma as model cells.

2. Experimental

2.1. Materials

All regents were prepared by dissolving their commercial products in doubly distilled water (18.2 MΩ). Sodium borohydride ($NaBH_4$) and copper sulfate ($CuSO_4{\cdot}5H_2O$) were commercially obtained from Huanwei Fine Chemical Co., Ltd. (Tianjin, China) and Chujiang Chemical Co., Ltd. (Wuhan, China), respectively. Cetyltrimethylammonium bromide (CTAB) was purchased from Sinopharm Group Chemical Regent Co., Ltd. (Shanghai, China). Polystyrene sulfonate (PSS, MW 20 kD) and Transferrin was purchased from Sigma–Aldrich Co., Ltd. (Shanghai, China). Proteins BSA, lysozyme and trypsin were commercially obtained from Sigma (Steinheim, Germany). Prion protein (PrP^C) was prepared in our laboratory. HEPES buffer (1.0 mM, pH 7.4) was used to control the acidity. Glass slides (12.7 mm × 76.2 mm × 1 mm) for the light scattering imaging were commercially obtained from Shitai Experimental Instrument Co. Ltd., Haimen (Jiangsu, China).

2.2. Apparatus

The absorption and light scattering spectra were measured with a Hitachi U-3010 spectrophotometer and a Hitachi F-4500 fluorescence spectrophotometer (Hitachi Ltd., Tokyo, Japan), respectively. For the measurements of light scattering spectra, the excitation and emission monochromators of the spectrofluorometer should be coupled and simultaneously scanned by keeping $\lambda_{em} = \lambda_{ex}$. An S-4800 scanning electron microscope (SEM, Hitachi Ltd., Tokyo, Japan) was employed for monitoring the morphology change of Cu_2O NPs during the whole synthesis process. The optical light scattering imaging of Cu_2O NPs was made with an Olympus BX51 inverted microscope coupled with a tungsten lamp and a highly numerical dark-field condenser (U-DCW, 1.2-1.4, Tokyo, Japan) and the images were captured with a Nikon Coolpix-4500 digital camera. In order to get the dark-field light scattering spectra of single nanoparticle, an imaging spectrograph (Micro Spec TM 2300i, Acton Research Corporation) coupled with a CCD detector (Roper Scientific, Inc.) were employed. A 100 × /1.3 oil Iris objective (UPLANFLN) was used for subsequent collection of dark-field light scattering signals of the single nanoparticle. All circular dichroism (CD) measurements are obtained on a J-810 CD spectrometer. The phase structures of the Cu_2O NPs were analyzed by X-ray powder diffraction (XD-3 system, Purkinje General Instrument Co. Ltd., Beijing, China) with Cu Kα (1.5405 Å) radiation source. An MVS-1 vortex mixer (Beide Scientific Instrumental Ltd., Beijing, China) was employed to mix the solutions.

2.3. Synthesis of Cu_2O NPs

Cu_2O NPs were prepared as the method of preparing positively charged Au nanospheres [28] following a solution-phase process [1,9]. Firstly, 0.16 mL of 0.1 M copper sulfate, 1.6 mL of 0.1 M CTAB and 1.24 mL of doubly distilled water were added into a 10-mL clean test tube. After shaking vigorously for several seconds by vortex mixer, 7 mL of 0.04 M freshly prepared ice-cold $NaBH_4$ was added. By keeping the vigorous shaking, the mixture initially displays light brown and then deep red after 15 min. The mixture solution was then left undisturbed allowing slow oxidation of air by keeping in a 27 °C water bath throughout the procedure under which temperature the crystallization of CTAB could be prevented. About 9 h after the reaction started, some yellow flocculent precipitates get produced, and about 16 h, a bright yellow transparent solution of Cu_2O NPs could be obtained. The yielding products are stable at least 1 month if stored in a 4 °C refrigerator. Samples prepared for SEM and dark-field imaging were made by separating Cu_2O NPs from excessive CTAB by centrifuging at 27 °C for 15 min at 12,000 rpm. After repeating the centrifugation twice, the precipitate was collected and redispersed in about 200 μL of deionized water for characterization.

Drops of 5 μL of redispersed solution were pipetted onto the aluminum foils and the glass slides respectively for the measurements of SEM and dark-field scattering light imaging after they dried in the air. SEM measurements were performed with a voltage of 20 kV and a working current of 10.0 μA. Dark-field light scattering image was performed on the Olympus BX51 inverted microscope fitted with a transmitted dark-field condenser and a 100× objective.

2.4. Preparation of transferrin-conjugated Cu_2O NPs

Cu_2O NPs were functionalized with transferrin following the report previously with minor modifications [24]. Briefly, 10 mg/mL polystyrene sulfonate solution containing 1.0 mM NaCl was added to the Cu_2O NPs suspension with a 1:10 volume ratio and allowed to react for 30 min. The particles were then collected *via* centrifugation at 9000 rpm for 10 min, resuspended in HEPS buffer. Transferrin solution, which had been previously diluted in the same HEPES buffer, was then mixed with PSS-capped nanoparticles and allowed to react for 45 min. The nanoparticles were then centrifuged and redispersed into PBS buffer (pH 7.4) to form a stock solution.

2.5. Cell culture for imaging analysis

Human bone marrow neuroblastoma (SK-N-SH cells) was cultured in DMEM medium plus 5% fetal bovine serum at 37 °C under 5% CO_2. Typically, a 1-mL suspension of SK-N-SH cells (about 10^5 cells/mL) was plated onto a cover slip, grown for 2–3 days, then treated with 0.1 mM transferrin-conjugated Cu_2O NPs for 3 h, rinsed with PBS buffer, fixed with paraformaldehyde and sealed with a small amount of glycerol.

2.6. Cu_2O NPs as probes for configuration of proteins

Into a 1.5-mL plastic vial, 40 μL of HEPES buffer (pH 7.4), 80 μL of the prepared Cu_2O NPs, which was centrifuged for 10 min at a speed of 8000 rpm in order to remove CTAB and redispersed with the same amount of ultra pure water (18.2 MΩ), and an appropriate volume of proteins including bovine serum albumin (BSA), lysozyme, trypsin and prion (PrP^C) were added. The above mixture was finally diluted with ultra pure water to the total volume of 400 μL. After vortex-mixed and placed for 30 min at room temperature, the mixture was transferred to CD measurements.

3. Results and discussion

3.1. Synthesis of Cu_2O NPs

Our preparation of Cu_2O NPs starts by using copper(II) salts in water in the presence of CTAB with $NaBH_4$. 15 min later after the start of the redox reaction, we found that the mixture gets deep red, and following undisturbed placement in the air makes the color of mixture get changes gradually. By monitoring the UV–visible absorption changes in the following processes, we found that an absorption band at 568 nm (Fig. 1), which is the characteristics of

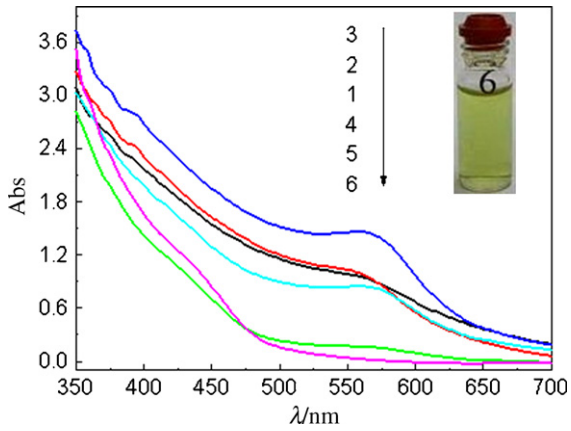


Fig. 1. UV–visible absorption spectra of the reaction mixture when exposing to air. Blue curve, 15 min; red curve, 2 h; black curve, 9 h; cyan curve, 11 h; green curve, 12 h; magenta curve, 16 h. All the molar ratio of CTAB/$NaBH_4$ is 0.57. (For interpretation of the references to color in this figure legend, the reader is referred to the web version of the article.)

the plasmon resonance absorption (PRA) band of copper nanoparticles (Cu^0 NPs) [8,29,30], gradually appears. After 12 h, however, the PRA band gradually decreases, indicating that depletion of Cu^0 NPs occurs. At 16 h, a broad absorption from 370 nm to 450 nm increases, indicating that Cu_2O NPs have formed (see following further identification with XRD analysis). During the slow oxidation process in the air, the appearance and disappearance of the 568 nm PRA band indicate our preparation of Cu_2O NPs proceeds by the way of the formation of Cu^0 [8].

The synthesis of Cu_2O NPs by the way of the formation of Cu^0 starting from the reduction of Cu^{2+} species into Cu^0 species and then completion after the oxidation of the Cu^0 species into Cu^+ species could be further monitored in terms of the state of the formed species at various stages by SEM. Fig. 2A–C shows images of the reaction mixture after the reaction occurred at 2 h, 8 h and 16 h. It was found that particles were so small that it was difficult to be precipitated by centrifuging at the initial time. At 2 h, it was observed that the particles are irregularly spherical with the size about 15 nm (Fig. 2A). In the following period, these spheres gradually grew up to the size of about 50 nm (Fig. 2B), and there are some cubic particles having rough surfaces with the size of about 100 nm (which are marked in red circles in Fig. 2B). Fig. 2C shows that cubic particles are dissolved and highly uniform spheres with smooth surface if the aging is made further are available. These nanospheres are 57.7 ± 4.7 nm in size by averaging 20 particles at random.

From SEM images above, we could confirm that morphology evolution of the Cu_2O NPs was time-dependent and involves in a dynamic mutative process. After the initial formation of the red solutions immediately, the reaction mixture kept red up to 8 h. During this period, Cu^0 species are in the solutions owing to the excessive reducing agent of $NaBH_4$. After the reaction occurred at 8 h, however, the deep red color diminished gradually and yellow flocculent precipitates appear, indicating the beginning of oxidation process. It could be visually observed that the oxidation process occurred preferentially in the upper solution and then continuously extended to the whole solution because Cu^0 species in the upper solution can react relatively sufficiently with oxygen in the air. The process undergoes such transition state and these yellow flocculent precipitates are corresponding to cubic particles even if larger

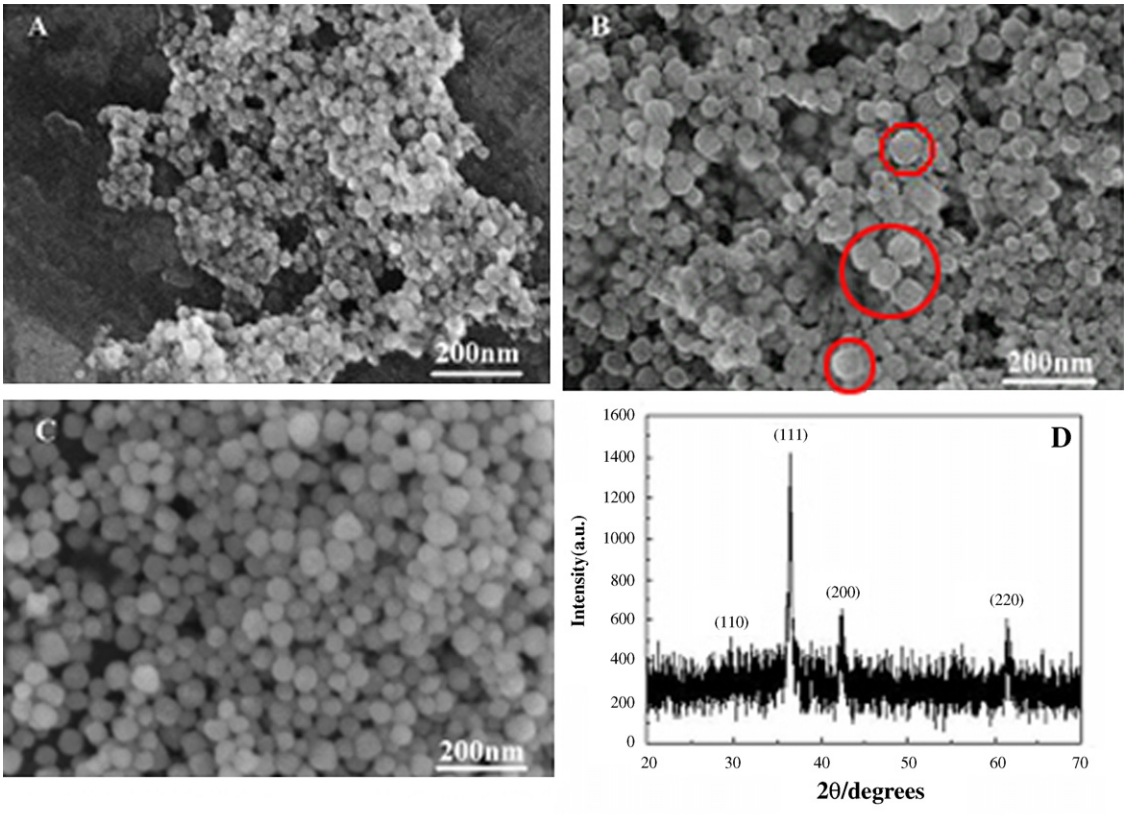


Fig. 2. Time-course of the oxidation process of Cu^0 NPs into Cu_2O NPs as monitored by SEM imaging. 2 h for (A), 8 h for (B) and 16 h for (C). (A) Cu^0 NPs, deep red; (B) the transition state with yellow flocculent precipitates, and the red circles indicate some large particles formed; (C) Cu_2O NPs, which is bright yellow transparent solution and it is obviously that the large particles in (B) are obviously dissolved. All the molar ratio of CTAB/$NaBH_4$ in (A), (B) and (C) is 0.57. (D) XRD pattern of the as-prepared Cu_2O NPs. (For interpretation of the references to color in this figure legend, the reader is referred to the web version of the article.)

than 100 nm in SEM images (Fig. 2B marked in red circles). After the reaction occurred at 16 h, yellow flocculent precipitates dissolved gradually and regular spherical products could be gained.

Fig. 2D displays the XRD pattern of the as-prepared Cu_2O NPs when the molar ratio of CTAB/$NaBH_4$ is 0.57. All the three diffraction peaks are indexed according to pure cubic phase of Cu_2O, which is consistent with the values in the standard card (JCPDF 05-0667). No other diffraction peaks arising from possible impurities such as Cu^0 and CuO species are detected, indicating that only Cu_2O NPs were obtained. The relative intensity of planes {1 1 1}, {2 0 0}, {2 2 0} is 1:0.44:0.43, being identical to the typical relative intensity of 1:0.40:0.43, indicating the equal growth rate for various faces.

By optimizing the experimental conditions, we got a conclusion that Cu_2O NPs are highly uniform and have smooth surfaces when the molar ratio of CTAB/$NaBH_4$ is 0.57, and else we could get irregular aggregations and the products are even inhomogeneous. It has been well known that CTAB can effectively prevent nanoparticles from aggregation. So we can control oxidation growth speed and aggregation by adjusting the molar ratios of CTAB/$NaBH_4$. This is one important factor influencing the morphology of Cu_2O NPs.

It has been known that the preparation of gold seeds at the initial time is very important in the synthesis of gold nanoparticles [11]. Similarly, Cu^0 nanoparticles at the initial time should be small and homogeneous. Under the conditions of high reaction temperature or slow addition of $NaBH_4$, the nucleation is so rapid that morphology of initial seed nanoparticles would be inhomogeneous, influencing the oxidation process of Cu_2O NPs. In addition, the temperature during the preparation should be controlled since crystallization of CTAB should occur if the temperature is too low. So we should control the reaction at 27 °C, which could not only prevent CTAB from crystallization but also can slow down the formation speed of nuclei.

3.2. *Plasmon resonance light scattering features of Cu_2O nanoparticles*

Fig. 3 displays the characteristics of the light scattering spectra during the oxidation process. From the results in Fig. 3, we can find LS intensity of Cu_2O NPs in solution is strong compared with the initial solution. It has reported that silver and gold are efficient plasmon scatterers following the order of Ag > Au > Cu > Al [26]. In other words, Cu NPs have weak plasmon scattering power. Before the reaction occurred at 9 h, Cu^0 species are dominant in the mixture, so the solution LS intensity is weak. At 11 h, a weak LS peak

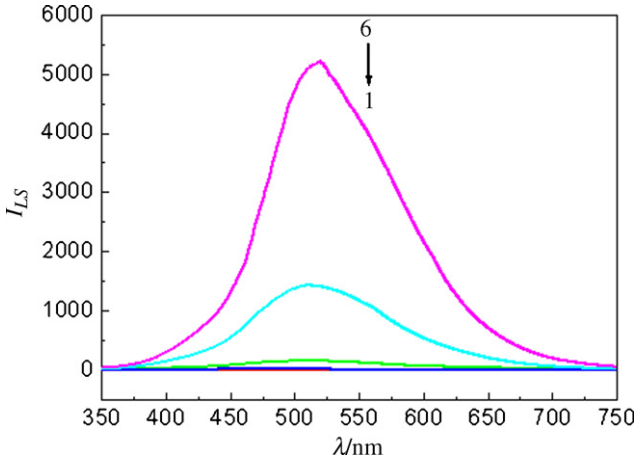


Fig. 3. The corresponding light scattering spectra of reaction mixture at different time: curve 1, 15 min; curve 2, 2 h; curve 3, 9 h; curve 4, 11 h; curve 5, 12 h and curve 6, 16 h. Curves 1–3 overlapped throughout. All the molar ratio of CTAB/$NaBH_4$ is 0.57.

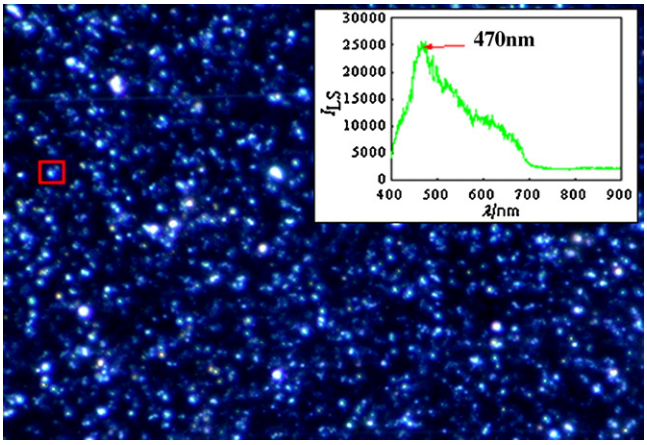


Fig. 4. Dark-field light scattering images of the as-prepared Cu_2O NPs. The molar ratio of CTAB/$NaBH_4$ is 0.57. The inserted picture is the dark-field light scattering spectrum of single Cu_2O in the square.

at 520 nm emerges, indicating the formation of Cu^+ species. At last, a very strong LS peak located at 520 nm is observed, indicating the formation of Cu_2O NPs. From the investigations on the LS spectra during the oxidation process, we can conclude that the LS intensity of the solution gets increased after the oxidation process and we can get promising Cu_2O NPs with special scattering properties.

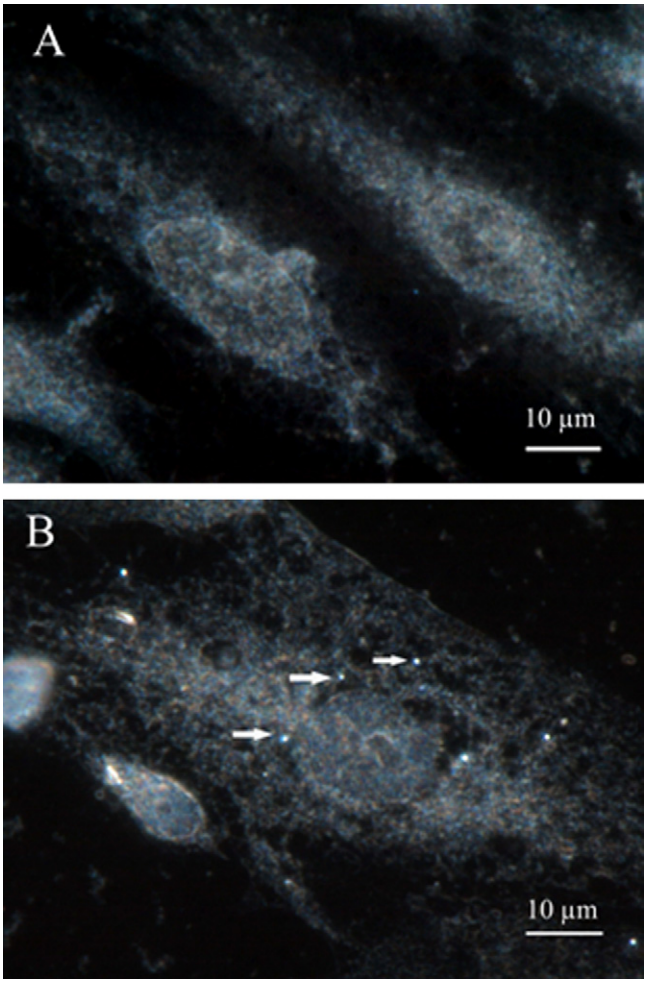


Fig. 5. Dark-field light scattering images of SK-N-SH cells after incubation with CTAB-capped Cu_2O NPs (A) and transferrin-conjugated Cu_2O NPs (B) for 3 h, respectively. Arrows indicate the Cu_2O NPs entered into cytoplasm in image (B).

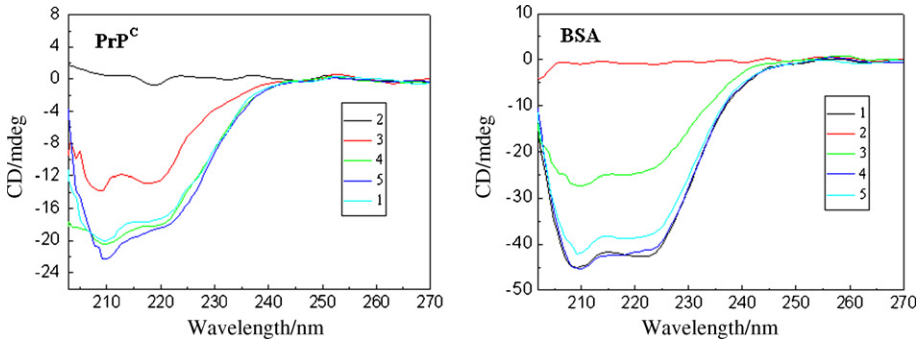


Fig. 6. CD properties of PrP^C and BSA after their interaction with Cu_2O NPs, CTAB and Cu^{2+} ion. Curves 1–5 are respectively protein, Cu_2O NPs, Cu_2O NPs and protein, Cu_2O NPs and Cu^{2+} ion, Cu_2O NPs and CTAB. Concentration of PrP^C, and BSA is 0.07 mg/mL and 0.05 mg/mL. The amount of copper element and CTAB is in accordance with those contained in the corresponding Cu_2O NPs solution. All the acid condition is HEPES buffer pH 7.4.

3.3. Dark-field light scattering imaging of cells

Resonance light scattering features from metallic nanoparticles are specific and it has increasing number of reports showing that elastic light scattering features from metallic nanoparticles can be measured so as to infer the position and local environments of nanoparticle, or relative orientation (in the case of nanorods) [31]. Considering the special applications of light scattering in those fields, we made efforts to investigate the light scattering optical properties of Cu_2O NPs.

From dark-field light scattering images in Fig. 4, we can see that Cu_2O NPs scatter pure blue light without any other interference color. The light scattering color of Cu_2O NPs is monochromic, which is different from silver colloids whose scattering colors are various. The inserted picture in Fig. 4 displays the light scattering spectrum of single Cu_2O nanoparticle deposited on the surface of a glass slide. It has a light scattering peak located at 470.0 nm in the blue region. Comparison with the light scattering features of Cu_2O NPs in solution, the light scattering spectrum of single nanoparticle on the glass substrate has 50 nm blue-shifted. One possible reason for the blue shift concerns the dielectric function at the metal/surface or metal/solvent interface [19,32]. It is probably associated with strong fields away from the substrate [23]. In addition, this measured shift is physically possible to the different response of the detectors of spectrofluorometer and CCD. Even though, the strong light scattering light emission of Cu_2O NPs could be identified and could be further applied. In such case, we consider applying Cu_2O NPs as an optical probe for live cell imaging with the light scattering properties by dark-field microscopy.

Fig. 5 shows the light scattering images of the human bone marrow neuroblastoma after incubation with CTAB-capped Cu_2O NPs (A) and transferrin-conjugated Cu_2O NPs (B) for 3 h, respectively. As indicated by the arrows in Fig. 5B, the transferrin-conjugated Cu_2O NPs can get into the cells and show strong pure blue light in cytoplasm since the uptake of transferrin-conjugated Cu_2O NPs may be due to the receptor-mediated endocytosis, while the CTAB-capped Cu_2O NPs cannot get into the cells (Fig. 5A). It is obviously that our present work identifies the possibility of Cu_2O NPs as a novel optical probe to image the proteins in living cells due to its special light scattering optical properties.

3.4. Cu_2O NPs as probes for configuration of proteins

In the experiment, we unexpectedly found that the prepared Cu_2O NPs can not only show their application in imaging protein in living cells but also can lead to CD property changes of proteins. In the control experiment we investigate the effect of CTAB and Cu^{2+} ion on the CD characteristics of proteins. After the individual interaction of PrP^C, BSA, lysozyme and trypsin with CTAB and Cu^{2+} ion under the experimental condition, four kinds of proteins show no obvious CD changes. However, to some extent, Cu_2O NPs can selectively lead to obvious CD changes with proteins such as PrP^C and BSA (Fig. 6) but lysozyme and trypsin cannot. Decreasing of CD indicates that the tertiary structure of proteins does not show obvious changes while a local structural alteration of proteins occurs [33,34]. This local alteration is maybe due to the hydrolytic ability of proteins on the substrate.

4. Conclusion

In this contribution, we obtained highly uniform Cu_2O NPs upon slow oxidation of Cu nanostructures *via* a facile low-cost solution-phase method at 27 °C. To our knowledge, this is the first report about the investigations on the light scattering properties of Cu_2O NPs *via* dark-field light scattering images and light scattering spectrum of a single particle. The results showed that Cu_2O NPs have relatively strong pure blue light scattering emission after undergoing the oxidation process. Furthermore, the present application of Cu_2O NPs shows high promise for Cu_2O NPs which possibly not only lead to the local structural alteration of proteins but also act as a novel optical probe applied in cell or molecular biology imaging due to their special scattering optical properties.

Acknowledgements

The authors herein express their deep thanks for the financial supports from the Ministry of Science and Technology of the People's Republic of China (2006CB 933100), the National Natural Science Foundation of China (NSFC, 20675065), and Chongqing Science and Commission for the Municipal Key Laboratory on Luminescence and Real-Time Analysis ([2006]-13-44).

References

[1] M. Yin, C.-K. Wu, Y. Lou, C. Burda, J.T. Koberstein, Y. Zhu, S. O'Brien, J. Am. Chem. Soc. 127 (2005) 9506.
[2] Y.G. Zhang, L.L. Ma, J.L. Li, Y. Yu, Environ. Sci. Technol. 41 (2007) 6264.
[3] J. Zhang, J. Liu, Q. Peng, X. Wang, Y. Li, Chem. Mater. 18 (2006) 867.
[4] H. Zhang, X. Ren, Z. Cui, J. Crystal. Growth 304 (2007) 206.
[5] W.T. Wu, Y.S. Wang, L. Shi, W.M. Pang, Q.R. Zhu, G.Y. Xu, F. Lu, J. Phys. Chem. B 110 (2006) 14702.
[6] P.E.d. Jongh, D. Vanmaekelbergh, J.J. Kelly, Chem. Mater. 11 (1999) 3512.
[7] W. Yao, S.H. Yu, Y. Zhou, J. Jiang, Q.S. Wu, L. Zhang, J. Jiang, J. Phys. Chem. B 109 (2005) 14011.
[8] C.H. Bernard Ng, W.Y. Fan, J. Phys. Chem. B 110 (2006) 20801.
[9] L. Gou, C.J. Murphy, Nano Lett. 3 (2003) 231.
[10] Y. Xiong, Z. Li, R. Zhang, Y. Xie, J. Yang, C. Wu, J. Phys. Chem. B 107 (2003) 3697.
[11] J.H. Lee, K. Kamada, N. Enomoto, J. Hojo, J. Colloid. Interf. Sci. 316 (2007) 887.
[12] F. Luo, D. Wu, L. Gao, S. Lian, E. Wang, Z. Kang, Y. Lan, L. Xu, J. Cryst. Growth. 285 (2005) 534.
[13] L. Gou, C.J. Murphy, J. Mater. Chem. 14 (2004) 735.

[14] I. Prakash, P. Muralidharan, N. Nallamuthu, M. Venkateswarlu, N. Satyanarayana, Mater. Res. Bull. 42 (2007) 1619.
[15] W. Wang, G. Wang, X. Wang, Y. Zhan, Y. Liu, C. Zheng, Adv. Mater. 14 (2002) 67.
[16] H. Xu, W. Wang, W. Zhu, J. Phys. Chem. B 110 (2006) 13829.
[17] J.J. Teo, Y. Chang, H.C. Zeng, Langmuir 22 (2006) 7369.
[18] J. Pike, S.W. Chan, F. Zhang, X.Q. Wang, J. Hanson, Appl. Catal. A 303 (2006) 273.
[19] L.J. Sherry, S.-H. Chang, G.C. Schatz, R.P.V. Duyne, Nano Lett. 5 (2005) 2034.
[20] A.D. McFarland, R.P.V. Duyne, Nano Lett. 3 (2003) 1057.
[21] J.J. Mock, D.R. Smith, S. Schultz, Nano Lett. 3 (2003) 485.
[22] A.K. Oyelere, P.C. Chen, X. Huang, I.H. El-Sayed, M.A. El-Sayed, Bioconjugate. Chem. 18 (2007) 1490.
[23] B.J. Wiley, Y. Chen, J. McLellan, Y.J. Xiong, Z.Y. Li, D. Ginger, Y.N. Xia, Nano Lett. 7 (2007) 1032.
[24] X. Huang, I.H. El-Sayed, W. Qian, M.A. El-Sayed, J. Am. Chem. Soc. 128 (2006) 2115.
[25] J.W. Stone, P.N. Sisco, E.C. Goldsmith, S.C. Baxter, C.J. Murphy, Nano Lett. 7 (2007) 116.
[26] K. Aslan, J.R. Lakowicz, C.D. Geddes, Curr. Opin. Chem. Biol. 9 (2005) 538.
[27] K. Munechika, J.M. Smith, Y. Chen, D.S. Ginger, J. Phys. Chem. C 111 (2007) 18906.
[28] T.K. Sau, C.J. Murphy, J. Am. Chem. Soc. 126 (2004) 8648.
[29] S. Kapoor, R. Joshi, T. Mukherjee, Chem. Phys. Lett. 354 (2002) 443.
[30] C. Salzemann, I. Lisiecki, A. Brioude, J. Urban, M.-P. Pileni, J. Phys. Chem. B 108 (2004) 13242.
[31] C.J. Murphy, T.K. Sau, A.M. Gole, C.J. Orendorff, J. Gao, L. Gou, S.E. Hunyadi, T. Li, J. Phys. Chem. B 109 (2005) 13857.
[32] M.D. Malinsky, K.L. Kelly, G.C. Schatz, R.P.V. Duyne, J. Phys. Chem. B 105 (2001) 2343.
[33] S.W. Provencher, J. Glöckner, Biochemistry 20 (1981) 33.
[34] P.C. Kahn, Method Enzymol. 61 (1979) 339.

Talanta 80 (2010) 1406–1412

Contents lists available at ScienceDirect

Talanta

journal homepage: www.elsevier.com/locate/talanta

Investigation of the effects of 24 bio-matrices on the LC–MS/MS analysis of morinidazole

Wenxu Lv*

Shanghai Institute of Materia Medica, Chinese Academy of Sciences, 646 SongTao Road, Shanghai 201203, PR China

ARTICLE INFO

Article history:
Received 29 July 2009
Received in revised form
17 September 2009
Accepted 24 September 2009
Available online 30 September 2009

Keywords:
Matrix effects
Bio-matrices
Pulse gradient with ammonium formate effects
Pharmacokinetic study
LC–ESI-MS/MS
Protein precipitation

ABSTRACT

This study compares and evaluates the effect of various matrices on liquid chromatography (LC) coupled with tandem mass spectrometry (MS/MS) analysis. Permanent post-column infusion (PCI) was used to quantify matrix effects. In this way, the suppressed or enhanced signal of the target material resulting from different co-eluting matrix components could be assessed. Twenty-four biological samples from *in vivo* and *in vitro* experiments were selected for this study. In addition, 7 sample components were further analyzed after sample preparation by protein precipitation. Multiple regression analysis was used to investigate the collinear relationship between matrix effects and co-eluted components at different time intervals. We found that salt was the dominant factor which impacted changes in signal detection. In order to eliminate it, we used ammonium formate as a modifier of the mobile phase which resulted in charge-state redistribution profiles so that a homogeneous matrix formed. By employing pulse gradient chromatography in the presence of 5 mM ammonium formate, favorable improvements of enhanced signal intensity and reduced matrix effects were obtained. These experiments also indicated the feasibility of using analogue IS during bio-analysis which contributed to an overall faster assay that would be suitable for drug discovery and development purposes.

© 2009 Elsevier B.V. All rights reserved.

1. Introduction

Evaluating matrix effects is of the utmost importance when developing a quantitative liquid chromatography/tandem mass spectrometry (LC–MS/MS) method. Co-eluting compounds originating from the matrix can cause signal enhancement or suppression. When the compounds and target material enter the ion source at the same time, the ionization efficiency of the target material might be influenced [1]. In this way, the matrix can affect the reproducibility and accuracy of the method. With an increase in the number and types of biological samples required for pharmacokinetic studies, an understanding of the matrix effects becomes increasingly important in order to obtain timely and accurate bio-analysis [2–7].

Several solutions can be employed to minimize the interference caused by matrix components. Extensive cleanup procedures prior to LC–MS/MS analysis can help to reduce the introduction of matrix components [8,9]. Improved chromatographic separation can often reduce the interference of the matrix components with the target materials [10]. Another approach is to dilute the final sample extract as much as possible in order to simultaneously dilute the matrix components [11,12]. Standard additions of each material of interest into the sample may also be used to compensate for matrix effects [13]. In some cases, researchers opt to use an ionization source, such as APCI, which is less sensitive, thus minimizing the matrix effects [14]. One of the most effective options to compensate for signal changes is the use of isotope-labeled analogues [15]. However, in most cases, the matrix effects cannot be completely eliminated, despite the use of the aforementioned operational strategies. In addition, most of the approaches are time-consuming, laborious and do not contribute to efficient analytical performance. Moreover, isotope-labeled internal standard (IS) may not be available for some materials because of difficulties in synthesis and/or cost, especially for pharmacokinetic screening study experiments.

There is a need for more simple solutions to the problem of matrix effects. Dilute and shoot and protein precipitation (PPT) are popular techniques because of their simplicity. Sample preparation with PPT is widely used in bio-analysis of plasma samples. Overall, PPT offers a generic and fast sample preparation technique that can be easily automated to deal with biological samples. Fast gradients and short columns can be utilized during high-throughput LC–MS/MS assays to reduce run time. Electro-spray ionization (ESI) techniques have achieved great popularity because of their high selectivity and sensitivity for the determination of trace substances.

* Tel.: +86 21 54668788; fax: +86 21 54668700.
E-mail addresses: lvwenxu@hotmail.com, lvwenxu@126.com.

0039-9140/$ – see front matter © 2009 Elsevier B.V. All rights reserved.
doi:10.1016/j.talanta.2009.09.043

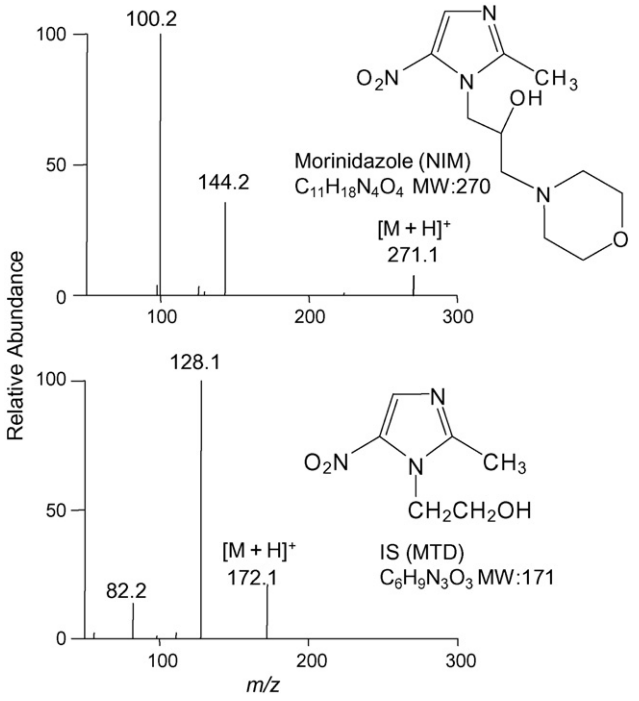


Fig. 1. MS/MS product ion spectra of the protonated molecules ([M+H]$^+$) of morinidazole (NIM) and IS (metronidazole: MTD), as well as their chemical structures.

In this study, we first investigated matrix effects stemming from 24 biological matrices from both *in vivo* and *in vitro* studies of morinidazole (NIM, Fig. 1), a National Class I Antimicrobial Drug. It belongs to the nitroimidazole group of antibiotics, and is mainly used in amoebas, trichomoniasis and anaerobic bacterial infections. First the percentage of morinidazole in each matrix was analyzed. Then multiple regression analyses were used to identify the collinear relationship between matrix effects and co-eluted matrices components during different time points of special pulse gradient chromatography. A pulse gradient with ammonium formate was utilized and was found to eliminate matrix effects. The feasibility of using an analogue IS metronidazole (MTD, Fig. 1) for the rapid bio-analysis of morinidazole was also evaluated. It is hoped that the work presented here will help to establish methods for efficient LC–ESI-MS/MS bio-analytical assays.

2. Experimental

2.1. Chemicals

Analytical reference standards of morinidazole and metronidazole were supplied by Jiangsu HengRui Medicine Co., Ltd. (Lianyungang, China). HPLC-grade methanol was purchased from Merck (Darmstadt, Germany). Ammonium formate was obtained from Aldrich (Milwaukee, WI, USA). Other organic solvents and chemicals used were of analytical grade and were obtained from Shanghai Chemical Reagent Co. (Shanghai, China). Deionized water was generated from a Millipore Direct-Q® 3 UV water purifying system (Bedford, USA). Hank's balanced salt solution (HBSS) was purchased from Sigma–Aldrich. Human liver microsomes were obtained from DB Gentest (USA), the other microsomes were prepared in our laboratory according to the method of differential centrifugation. Animal samples obtained by experiments which were conducted according to protocols approved by the Review Committee of Animal Care and Use at the Shanghai Institute of Materia Medica (Shanghai, China). Human plasma samples were provided by Renji Hospital (Shanghai, China) and approved by ethical committee. Healthy volunteers were enrolled in this study after providing written informed consent.

All biological material was stored at −80 °C until use.

2.2. Instrumentation

A TSQ Quantum triple stage quadrupole mass spectrometer (Thermo Finnigan, San Jose, CA, USA) was interfaced via an ESI probe with an Agilent 1100 series liquid chromatograph that included a vacuum degasser, a binary pump, an autosampler, and a thermostatted column compartment (Waldbronn, German). The Agilent Chemstation and Finnigan Xcalibur software packages were used for controlling the LC–MS/MS system, data acquisition and processing. Protein concentration was determined using the Bradford method by measuring the absorbance at 595 nm with a Bio-Rad 550 Microplate Spectrophotometer (BIO-TEK Instruments, Inc., USA). An automated biochemical analyzer (Hitachi-7080) was used for the component analyses of the matrices.

2.3. LC–MS/MS conditions

An Agilent Zobax SB C18 LC column (50 mm × 2.1 mm, 5 μm) with a solvent flow rate of 0.35 mL/min was used. The sample injection volume was 10 μL. Approximately 63 mg of ammonium formate was dissolved in 10 mL of water to prepare the stock solution at a concentration of 100 mM. Mobile phase A (ACN/H_2O, 2:98, v/v, 5 mM $HCOONH_4$) and mobile phase B (ACN/H_2O, 90:10, v/v, 5 mM $HCOONH_4$) were prepared by the addition of ammonium formate stock solution and the required volume of water or ACN. The solvent gradient adopted was as follows: 0–0.1 min, linear from 0 to 100% B; 0.1–0.4 min, isocratic 100% B; 0.4–0.41 min, linear from 100 to 0% B; and 0.41–4 min, isocratic 0% B. All MS/MS data for morinidazole were collected in positive ion mode by selected reaction monitoring (SRM) of the transition m/z 271 → 100; for metronidazole the transition m/z 172 → 128 was monitored. The ESI-MS was operated in positive ion mode with the following instrument settings: spray voltage, 4700 eV; sheath gas pressure, 35(a.u.); aux gas pressure, 10(a.u.); capillary temperature, 300 °C.

2.4. Sample preparation

Protein precipitation extraction was performed using a 4:1 ratio of methanol to sample. In brief, a 20 μL aliquot of each sample was mixed with 80 μL of MeOH, vortexed for 5 min, and then centrifuged at 21 885 × g for 10 min. The resulting supernatant (10 μL) was used directly for LC–MS/MS analysis.

Selected tissues including the abdominal fat, testicle, bladder, spleen, stomach, ileum, colon, kidney, liver, lung, heart, and brain were excised from SD rats, rinsed in ice-cold saline before gentle blotting on absorbent paper and weighing. The tissues were homogenized in 4 volumes of ice-cold saline. The tissue homogenate samples were stored at −80 °C until analysis. The plasma samples were derived from mouse, rat, rabbit, dog, monkey, and human, respectively.

2.5. Post-column infusion experiments

A blank pretreated biological sample was injected during continuous post-column infusion of a 100 ng/mL solution of morinidazole and metronidazole at a flow rate of 5 μL/min. The chromatographic area of interest was determined by comparing the SRM chromatographic profiles for morinidazole or metronidazole obtained with an injection of the blank pretreated biological sample and an equivalent injection of mobile phase. Each experiment was performed in duplicate. The instrumental setup for permanent

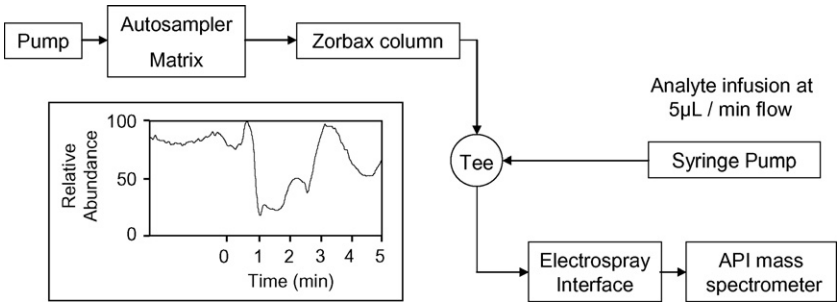


Fig. 2. The instrumental setup for permanent post-column infusion and the chromatographic run map for infusion profiles of analyte standards after injection of bio-matrices.

post-column infusion and the chromatographic run map is shown in Fig. 2.

2.6. Matrices component determination

The concentration of albumin (ALB) in the sample prepared by protein precipitation was determined by Bradford quantification at 595 nm. The linear range of protein assayed by the Bradford method was 25–400 ng/mL (R^2 = 0.996). The content of triglyceride (TG), total cholesterol (TC), Na, K, P, and Cl was determined using an auto biochemical analyzer.

2.7. Multiple regression analysis

SPSS Statistics 14.0 software was employed for multiple regression analysis to identify collinear relationships between the variables measured. The percentage of enhancement or suppression of the signal at different times in the chromatogram is related to the different matrices components co-eluted at the different time intervals.

3. Results and discussion

3.1. Analysis of pharmacokinetic samples by a post-column infusion method using pulse gradient chromatography in the presence of 24 different bio-matrices

The matrix effects were evaluated during method development of the simultaneous analysis of morinidazole and metronidazole in 24 biological samples. The differences in the RICs illustrate signal suppression of −52 to 100% from 1 to 2 min, −90 to 300% from 2 to 3 min, and −40 to 300% from 3 to 5 min.

Table 1 provides an overview of the results obtained with the continuous post-column infusion experiments. The different time intervals where the matrix impacted the chromatographic analysis are documented for each combination of bio-fluid, sample preparation technique, and ionization type. For reporting purposes, the matrix effect was expressed as the percentage of suppression or enhancement of the signal. Because of the variable nature of the matrix effect, the percent matrix effect is a relative indicator of the degree of suppression or enhancement.

The data indicates that the representation of matrix effects is variable in different biological samples and both signal suppression and enhancement occurred. Signal suppression was more common than signal enhancement in our study. The variety of matrix effects was unpredictable and unsystematic across the time span of chromatographic analysis. For example, within 2–3 min of retention time, the signal changed from 90% suppression to 300% enhancement. These types of results can lead to large variances in exposure assays and thus influence the estimate of drug concentrations during preclinical development experiments.

In our study, a special pulse gradient was used for quick and reliable quantification of morinidazole and metronidazole in biomatrices. The start proportion and the elution proportion were set at 0% B and 100% B, the start proportion segment (SPS) was very short (0.1 min) and the elution proportion segment was only 0.3 min. The column equilibrium segment lasted from 0.4 to 4 min (Fig. 3, top). The retention time of NIM and IS was almost the same (Fig. 3, bottom). The pulse gradient method was extremely simple to optimize. Separation of the analytes from the sample matrix components and organic solvent was optimized by simply tuning the SPS, rather than tuning the mobile phase composition (for isocratic elution) or gradient steepness (for conventional gradient elution). In addition, the pulse gradient method overcomes eluotropic effects more effectively than isocratic and conventional gradient methods.

3.2. Matrices component analysis results

The mechanism and the origin of the matrix effect are not fully understood, but it may originate from the competition between an analyte and the co-eluting, undetected matrix components reacting with primary ions formed in the HPLC–MS/MS interface. Matrix ion-suppression or enhancement is considered to more likely be a problem when using protein precipitation, which is often used as a routine sample preparation procedure for LC–MS/MS assays in drug discovery because of its simplicity [16]. The use of protein precipitation may cause ion-suppression or enhancement in ESI due to a lack of selectivity (co-elution of endogenous compounds such as lipids, phospholipids, fatty acids, and inorganic salts) that affect the ESI droplet de-solvation process [17,18]. Thus, we investigated the concentration of TG, TC, ALB, P, Na, K, and Cl in different blank matrices prepared by protein precipitation. The result is shown in Table 2. The data indicated that different matrices samples had different concentration of components.

3.3. Correlations of matrix effects and matrices components under a special pulse gradient chromatography by multiple regression analysis

The results of matrix effects and the determination of matrices components had several general trends. First, the variability in matrix effects observed in plasma from different species was caused by different concentrations of ALB. In addition, the variability in matrix effects observed in different lots of plasma was also believed to be from variations in protein content. Protein and TG in the tissue homogenate samples likely accounted for differences in the signal at the MS interface. Similar components resulted in similar matrix effects in post-column chromatography. For example, high concentrations of salts restrained the intensity of the signal of NIM and IS. Lipids, phospholipids, fatty acids, amino acids, and proteins caused both an enhancement and suppression of signals in the mass spectra. We then introduced multiple regression anal-

Table 1
Results of post-column infusion experiments, showing time (min) and extent (−%: suppression; +%: enhancement) of the observed matrix effects.

Preclinical samples	0–1 min		1–2 min		2–3 min		3–5 min	
	NIM	MTD	NIM	MTD	NIM	MTD	NIM	MTD
Plasma								
Mouse	230	0	0	−63	0	−27	111	−56
Rat	235	−72	0	−50	87	−58	0	−65
Rabbit	200	−71	0	−14	75	−50	0	−50
Dog	280	−80	0	−50	35	−49	0	−64
Monkey	280	−82	0	−55	100	−58	0	−64
Human	350	−70	0	−45	150	−9	−22	−68
Bladder	−50	−70	0	0	−50	−70	−23	−60
Brain	−33	−63	0	−25	−40	−67	0	−30
Testicle	14	−70	−20	−50	−52	−70	−26	−63
Fat	−51	−70	0	0	−40	−62	−13	−56
Small intestine	90	−50	0	−60	78	−70	122	−33
Liver	−28	−60	−30	−33	−70	−73	−40	−53
Uterus	22	−70	22	−50	−50	−70	−20	−65
Heart	0	−66	−20	−33	−67	−80	25	−44
Large intestine	0	−64	0	−52	100	−70	185	−50
Stomach	0	−60	−23	−55	−54	−74	92	−42
Skeletal muscle	20	−70	−28	−40	185	100	185	−40
Spleen	0	−76	−14	−35	90	−70	138	−55
Ovary	36	−72	0	−20	−36	−72	30	−75
Lung	86	−50	0	−47	90	−67	138	−40
Kidney	43	−63	−23	−54	126	−60	138	−50
Urine	40	−64	−23	−60	−30	−64	−27	−64
Feces	82	30	0	33	−54	−76	0	−60
Bile	100	−82	100	−60	84	−88	−20	−76
Microsome-system	25	−80	−30	−30	150	85	165	−52
Caco-2 cell system	150	−40	0	−50	0	−76	−25	−70
Cerebral MDS	220	0	0	−75	90	−30	10	−82
Plasma filtrate	0	−80	−52	−80	300	−55	300	−38
Serum	133	−75	0	−50	200	−52	233	−40

NIM: morinidazole; MTD: metronidazole(IS); microsome-system: liver microsome; Caco-2 cell system: Hank's balanced salt solution (HBSS); cerebral MDS: cerebral microdialysate.

ysis in order to investigate possible correlations between the many simultaneous variables which were measured.

Multiple regression procedures estimated a linear equation of the form:

$$Y = a + b1 \times X1 + b2 \times X2 + \ldots + bp \times Xp$$

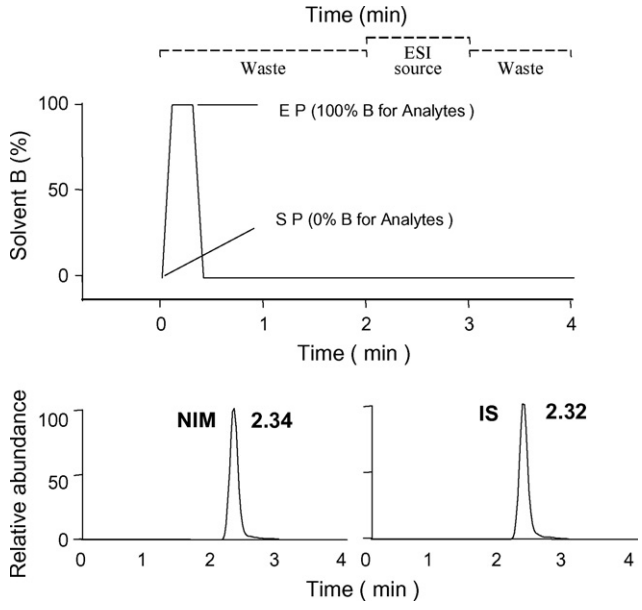


Fig. 3. Pulse gradient program (top) and LC–ESI-MS/MS chromatograms for NIM and IS (bottom).

where *Y*, extent of matrix effects (−%: suppression; +%: enhancement); *X*1, *X*2, . . ., *Xp*, the different matrices components; *a* is a constant; *b* is the regression coefficient (or *B* coefficient(s)). If the *B* coefficient is positive, then the relationship of this variable with the dependent variable is positive; if the *B* coefficient is negative then the relationship is negative; if the *B* coefficient is equal to 0 then there is no relationship between the variables.

We investigated the relationship of matrix effects and matrices components at different time intervals under a special gradient system using SPSS. In the time interval of 0–1, 1–2 and 3–5 min, the tolerance of variables was all greater than 0.1, which means there was an absence of a linear relationship among the matrix effects, matrices components and different times of the chromatogram map. For the region of 2–3 min (the retention time), regarding TG, TC and ALB, the tolerance was also greater than 0.1; regarding P, Na, K, and Cl, the tolerance was smaller than 0.1. The data showed that collinearity was present among P, Na, K, Cl and matrix effects at the specified retention time. The linear equation was as follows:

$$E\ (\mathrm{NIM}) = 53.887\,\mathrm{P} + 10.336\,\mathrm{Na} - 23.284\,\mathrm{K} - 8.997\mathrm{Cl}$$

$$E\ (\mathrm{TMD}) = 25.657\,\mathrm{P} + 1.613\,\mathrm{Na} - 9.217\,\mathrm{K} - 2.004\,\mathrm{Cl}$$

This indicated that salt was the major agent responsible for matrix effects and different inorganic salts contributed differently within various retention time intervals. P and Na enhanced the signal intensity in the mass spectra while K and Cl suppressed it. Thus the neutral salt ammonium formate was used a mobile phase modifier to alter the signal intensity of the target material in the mass spectra.

Table 2
The concentration of triglyceride (TG), total cholesterol (TC), albumin (ALB), P, Na, K, and Cl in different matrices.

Matrices	TG (mM)	TC (mM)	ALB (μg/mL)	P (mM)	Na (mM)	K (mM)	Cl (Ku/L)
Mouse plasma	0.02	0.21	142	0.09	37	1.6	24
Rat plasma	0.03	0.1	74	0.1	36	1	22
Rabbit plasma	0.01	0.09	32	0.07	37	1	23
Dog plasma	0.01	0.22	68	0.07	36	1	25
Monkey plasma	0.01	0.17	110	0.07	35	0.8	24
Human plasma	0.01	0.11	101	0.28	40	0.9	16
Bladder	0.03	0.03	26	0.23	2	0.5	2
Brain	0.03	0.43	108	1.26	5	3.7	3
Testicle	0.03	0.21	64	1.34	5	4	4
Fat	0.08	0	0	0.11	2	0.2	2
Small intestine	0.21	0.19	191	1.86	6	2.5	4
Liver	0.02	0.22	114	1.69	4	4.3	3
Womb	0.04	0.17	0	0.85	5	2.8	4
Heart	0.02	0.06	55	1.22	5	2.9	3
Large intestine	0.17	0.24	131	1.15	6	2.9	5
Stomach	0.14	0.25	99	1.58	5	3.7	4
Skeletal muscle	0.02	0	0	2.34	4	5.1	3
Spleen	0.03	0.35	69	1.8	4	4.5	3
Ovary	0.04	0.07	0	0.37	2	0.8	2
Lung	0.08	0.4	37	1.5	5	3.3	4
Kidney	0.02	0.37	43	1.95	6	3.2	4
Urine	0.01	0	0	4.2	5	11.6	7
Feces	0.02	0.06	42	0.08	2	0.7	2
Bile	0.01	0.15	111	0.06	41	1.4	21
Microsome-system	0.02	0.04	0	17.72	5	33.9	3
Caco-2 cell system	0	0	0	0.08	40	1.6	33
Cerebral MDS	0.01	0.05	0	0.46	34	0.8	27
Plasma filtrate	0	0	0	0.24	39	1.1	25
Serum	0.02	0.17	36	0.11	35	1.2	22

3.4. Ammonium formate enhances signal intensity

To enhance analytical performance, the LC-electrolyte effects [19–21] were studied by modifying the acetonitrile/H_2O-based mobile phases with various concentrations of electrolytes (e.g. $HCOONH_4$), and testing the analyte response and matrix effect levels. The data showed that the positive ion ESI response for morinidazole and metronidazole varied as the concentrations of the tested electrolytes changed providing different spectra for the analyte response. These results indicate that the magnitude of the LC-electrolyte effect on the analyte response depends on the concentration of the electrolyte modifier in the mobile phase. For $HCOONH_4$, the maximum positive ion ESI response of the analyte was observed when the electrolyte concentration in the mobile phase was 0.2 mM and the response increased by 7.4-fold. Further decreasing the $HCOONH_4$ concentration to 0.04 mM did not improve the ESI response compared with that obtained at 0.2 mM. A significant increase in the analyte response was observed when the $HCOONH_4$ concentration in the mobile phase was between 0 and 25 mM, ranging from 3.7 to 5.7 times higher than the results obtained in an experimental run containing no electrolyte.

3.5. Use of a special pulse gradient in the presence of ammonium formate to minimize matrix effects

The favorable effect of the special pulse gradient in the presence of ammonium formate effects in reducing matrix effects was found to depend on the concentration of the utilized electrolyte modifier. Fig. 4 shows that the matrix effects which resulted from rat plasma were minimized more when the concentration of ammonium formate was increased. The use of a lower concentration of $HCOONH_4$ (0.04 mM) failed to significantly reduce the duration of ionization suppression. The best result was achieved with a 5 mM $HCOONH_4$-modified mobile phase and showed that suppression was maintained for less than 1 min, making fast LC analysis possible. $HCOONH_4$ acts to redistributes the charges in the mobile phase to a homogeneous state.

By weighting these two factors, we utilized 5 mM $HCOONH_4$ (rather than 0.2 mM) in the mobile phase because it provided both reproducible chromatographic retention times and a favorable high detection response for morinidazole and IS. Fig. 5 shows the extent of enhancement and suppression contributed by 24 blank biological samples prepared using protein precipitation at different chromatographic time intervals obtained with the continuous post-column infusion of NIM and IS (MTD). To NIM, there was about 60% suppression in most biological samples from 0 to 1 min; there were 47% enhancement or 17% suppression during the retention time interval of 2–3 min. To IS, there were 80% suppression from 0 to 1 min and 43% suppression from 2 to 3 min. A 5 mM $HCOONH_4$-modified mobile phase minimized the matrix effects contributed by most biological samples obtained from preclinical pharmacokinetic experiments.

Multiple regression analysis was also used to examine the collinear relationship among the experimental variables for pulse

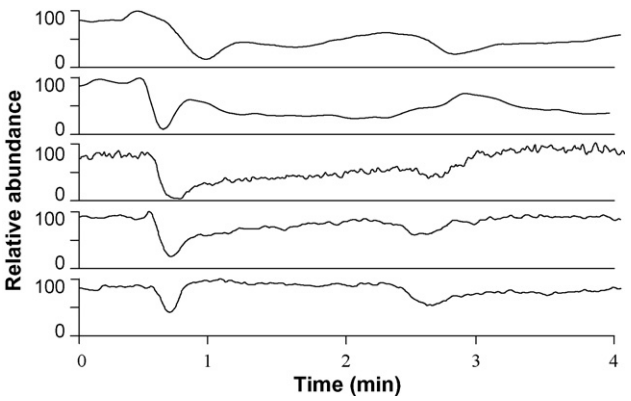


Fig. 4. Infusion chromatograms exhibiting the effect of rat plasma on the response to post-column infusion of NIM (100 ng/mL) in the positive ion ESI mode. The concentration of $HCOOCH_4$ in the mobile phase from top to bottom is: 0, 0.04, 0.2, 1, and 5 mM.

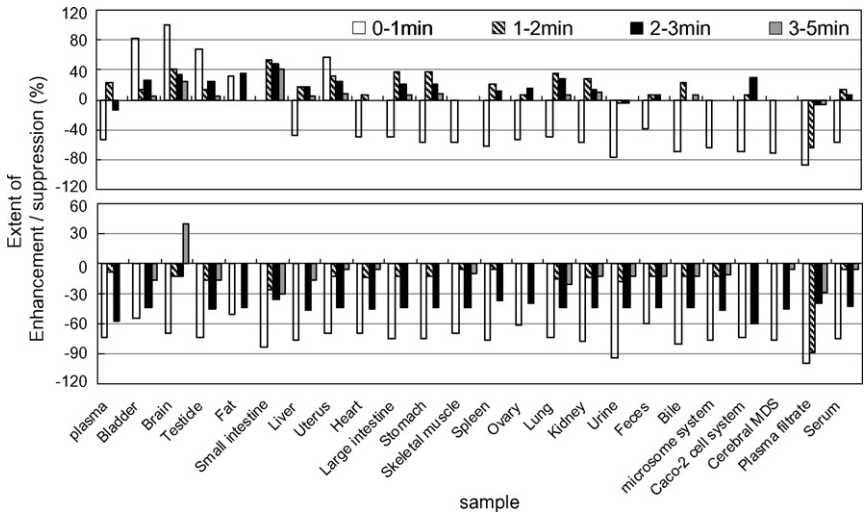


Fig. 5. Extent of enhancement/suppression contributed by 24 blank biological samples at different times of the chromatogram map obtained with the continuous post-column infusion of NIM (top) and IS (bottom) under the special pulse gradient with 5 mM $HCOONH_4$ in the mobile phase.

gradient chromatography in the presence of 5 mM $HCOONH_4$. During the interval of 2–3 min (the retention time), for TG, TC and ALB, the tolerance was also greater than 0.1; for P, Na, K, and Cl, the tolerance was smaller than 0.1. The data showed that collinearity was present among P, Na, K, Cl and the matrix effects at the retention time of interest. The linear equation was the following:

$$E(NIM)_{add} = 3.955\,P - 0.42\,Na - 2.586\,K - 0.087\,Cl$$

$$E(TMD)_{add} = -1.025\,P + 0.008\,Na + 0.451\,K - 0.432\,Cl$$

This indicated that salt was still the major agent to cause matrix effects but the influence on signal intensity was much smaller than without $HCOONH_4$ in the mobile phase. We concluded that ammonium formate was a suitable mobile phase modifier resulting in charge-state redistribution profiles and a homogeneous matrix.

3.6. Ammonium formate contributes to the feasibility of using structural analogue IS

Differences in ion-suppression between analytes and structurally different IS may also be problematic. The presence of a matrix effect can dramatically shift the response of the target analyte, thus affecting sensitivity, or it can adversely affect the accuracy/precision of a bio-analytical method by impacting the analyte/IS response ratio. Normally, the use of a co-eluting stable isotope analog as an IS is considered to solve the accuracy/precision problem since the analyte/IS response ratio is expected to remain unaffected even when the absolute responses of the analyte and IS are affected significantly. Wang et al. demonstrated that a slight difference in retention times between the analyte and the SIL IS was significant enough to change the analyte to IS peak area ratio and affect the accuracy of the method [22]. However, isotopically labeled IS may not be available for some analytes due to difficulties associated with synthesis and/or cost. Alternatively, a structural analogue can be used, but the IS has to elute close to the compound of interest and preferably show similar behavior in the source to compensate for any matrix effects.

We selected the structural analogue metronidazole as an IS for the correction of ion-suppression or enhancement effect. The data indicates that they have similar physical characteristics; moreover, their chromatographic retention time is very close: the analyte is 2.32 min, IS is 2.34 min. However, as shown in Table 1, the matrix effects between NIM and MTD were distinctively different. The variability of the analyte/IS response ratio is severe: it varied from 0.25 to 9.2 in different biological samples. The results are shown in Fig. 6.

In our study, the presence of ammonium formate impacted the use of a structural analogue as the IS. The RSD was calculated to show the variability of the target material/IS response ratio in different biological samples. As a result, because of ammonium formate, the variance of the ratio changed. The RSD in plasma from different species changed from 6.7 to 37.1 and the RSD in 24 different matrices samples varied from 7.3 to 77.8. Therefore, it was concluded that a structural analogue can serve as an IS to compensate and correct for the response of the target material in the ion source.

3.7. Analytical method validation and application for analysis of NIM in 24 bio-matrices

Method validation was performed, including sensitivity, linearity, and precision. The experiments on plasma standard solutions were carried out using the conditions reported in Section 2. Sensitivity was expressed by the instrumental limit of detection (LOD) and limit of quantitation (LOQ) for the target compound. LOD and LOQ were defined as the lowest analyte amount with a signal-to-noise ratio (S/N) of 3 and 10, respectively. LOD was found to be 80 pg/mL and the LOQ was 250 pg/mL. To assess the linearity, five point calibration curves were calculated over the linear range of the instrument response. Linear regression plots were calculated using peak area versus absolute injected amount; five replicates were analyzed for each concentration. The linear regression equa-

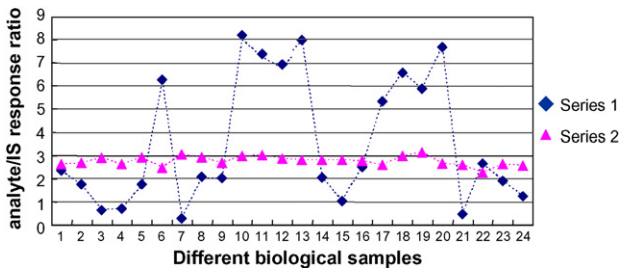


Fig. 6. The analyte/IS response ratio in 24 different animal tissues. Series 1: no electrolyte in the mobile phase. Series 2: 5 mM $HCOONH_4$ in the mobile phase. Samples 1–24: plasma, bladder, brain, testicle, fat, small intestine, liver, liver, large intestine, stomach, muscle, spleen, ovary, plasma filtrate, cerebral MDS, Caco-2 cell system, kidney, lung, serum, feces, urine, bile, and microsome.

tion was $Y = 0.0714626 + 0.109117X$. Linearity was expressed as the squared correlation coefficient (R^2) where values higher than 0.9953 were obtained. In this study, NIM was spiked in 24 biological matrices at 3 concentrations (1, 10, 100 ng) and its concentration was redetermined. Using the above linear regression equation, precision was calculated as the intraday and inter-day repeatability of the method provided the % RSD values less than or equal to 10% for the plasma samples from six different species (mouse, rat, rabbit, dog, monkey, and human). The % RSD values were less than 15% for all the 24 biological samples, indicating a satisfactory level of precision at the selected concentration levels.

4. Conclusions

Matrix effects during HPLC–MS/MS analysis of large numbers of biological samples from preclinical pharmacokinetic drug studies were investigated. It was determined that the shift in the MS signal for co-eluted compounds follow a co-linear relationship with regards to retention time. Using pulse gradient chromatography with 5 mM $HCOONH_4$ as the mobile phase modifier resulted in a charge-state redistribution profile and a homogeneous matrix. The combination of a special pulse gradient with ammonium formate was favorable towards reducing matrix effects and contributed to the use of a structural analogue IS. These results suggest that an ideal ESI modifier and an appropriate pulse gradient would be valuable towards developing a simple and rapid bioanalysis method for the analysis of preclinical pharmacokinetics samples.

Acknowledgments

This work was supported by the Chinese Ministry of Science and Technology (2004CB518902 and 2005CB523403) and the Science & Technology Commission of Shanghai Municipality (04DZ19215). We also acknowledge Professor Chuan Li (Shanghai Institute of Materia Medica, Chinese Academy of Sciences) for providing some apparatus and his advice on pulse gradient chromatography.

References

[1] P.J. Taylor, Clin. Biochem. 38 (2005) 328–334.
[2] B.K. Matuszewski, M.L. Constanzer, C.M. Chavez-Eng, Anal. Chem. 70 (1998) 882–889.
[3] S. Briem, S. Martinsson, T. Bueters, E. Skoglund, Rapid Commun. Mass Spectrom. 21 (2007) 1965–1972.
[4] S.S. Singh, Curr. Drug Metab. 7 (2006) 165–182.
[5] R.N. Xu, L.M. Fan, M.J. Rieser, T.A. El-Shourbagy, J. Pharm. Biomed. Anal. 44 (2007) 342–355.
[6] G. Hopfgartner, E. Bourgogne, Mass Spectrom. Rev. 22 (2003) 95–214.
[7] D.B. Kassel, Curr. Opin. Chem. Biol. 8 (2004) 339–345.
[8] M. Urpí-Sardà, O. Jáuregui, R.M. Lamuela-Raventós, W. Jaeger, M. Miksits, M.I. Covas, C. Andres-Lacueva, Anal. Chem. 77 (2005) 3149–3155.
[9] B. Guo, C. Li, Z. Deng, S. Chen, Z. Ji, J. Zhang, M. Chen, Rapid Commun. Mass Spectrom. 19 (2005) 2840–2848.
[10] A. Kloepfer, J.B. Quintana, T. Reemtsma, J. Chromatogr. A 1067 (2005) 153–160.
[11] N. Lindegardh, W. Hanpithakpong, Y. Wattanagoon, P. Singhasivanon, N.J. White, N.P. Day, J. Chromatogr. B 859 (2007) 74–83.
[12] N. Lindegardh, A. Annerberg, N.J. White, N.P. Day, J. Chromatogr. B 862 (2008) 227–236.
[13] M. Antler, E.J. Maxwell, D.A. Duford, E.D. Salin, Anal. Chem. 79 (2007) 688–694.
[14] H.R. Liang, T. Takagaki, R.L. Foltz, P. Bennett, Rapid Commun. Mass Spectrom. 19 (2005) 2284–2294.
[15] E. Stokvis, H. Rosing, J.H. Beijnen, Rapid Commun. Mass Spectrom. 19 (2005) 401–407.
[16] E. Chambers, D.M. Wagrowski-Diehl, Z. Lu, J.R. Mazzeo, J. Chromatogr. B 852 (2007) 22–34.
[17] O.A. Ismaiel, M.S. Halquist, M.Y. Elmamlyb, A. Shalaby, H.T. Karnes, J. Chromatogr. B 859 (2007) 84–93.
[18] R. King, R. Bonfiglio, F.M. Carmen, M.S. Cynthia, O. Timothy, J. Am. Soc. Mass Spectrom. 11 (2000) 942–950.
[19] L. Wang, Y. Sun, F. Du, W. Niu, T. Lu, J. Kan, F. Xu, K. Yuan, T. Qin, C. Liu, C. Li, Rapid Commun. Mass Spectrom. 21 (2007) 2573–2584.
[20] Y. Li, Y. Sun, F. Du, K. Yuan, C. Li, J. Chromatogr. A 1193 (2008) 109–116.
[21] Y. Zhao, L. Wang, Y. Bao, C. Li, Rapid Commun. Mass Spectrom. 21 (2007) 971–981.
[22] S. Wang, M. Cyronak, E. Yang, J. Pharm. Biomed. Anal. 43 (2007) 701–707.

Talanta 80 (2010) 1413–1420

Contents lists available at ScienceDirect

Talanta

journal homepage: www.elsevier.com/locate/talanta

Development and validation of a quantitative method for the selective determination of tin species in tin octoate by differential pulse polarography

C. Hubert*,[1], E. Ziémons[1], E. Rozet, A. Breuer, A. Lambert, C. Jasselette, C. De Bleye, R. Lejeune, Ph. Hubert

Laboratory of Analytical Chemistry, CIRM, Department of Pharmacy, University of Liège, Avenue de l'Hôpital 1, B36, 4000 Liège, Belgium

ARTICLE INFO

Article history:
Received 3 July 2009
Received in revised form
15 September 2009
Accepted 25 September 2009
Available online 3 October 2009

Keywords:
Speciation
Stannous
Stannic
Tin octoate
Differential pulse polarography
DPP

ABSTRACT

Tin octoate is used as a catalyst in the synthesis of polydimethylsiloxane (PDMS), a room temperature vulcanizing (RTV) silicone rubber. This rubber is largely used in the medical field due to its great biocompatibility. In this framework, a high-speed and costless analytical method for the determination of stannic ions, Sn(IV), in the presence of stannous ions, Sn(II), has been developed.

The separation of these two ions was carried out using differential pulse polarography (DPP). For this purpose, the tin species contents in the catalyst is quantitatively extracted under inert condition to avoid any changes in the ratio Sn(IV)/Sn(II). Polarography showed well-shaped oxidation and reduction peaks respectively at −650 and −860 mV for stannous ions. The peak of the stannic ion was well separated and appeared at −1210 mV. Many parameters such as extraction process, extraction time, pH, chelating agents and polarographic conditions were optimized. We have also demonstrated that no oxidation of the stannous ions occurred during the sample preparation.

The dosing range considered in this study extends between 10 and 40 μg/mL, corresponding to 6.8% and 27.2% of the degradation product (Sn(IV)) in the catalyst, regarding to the sampling. Finally this method was successfully validated using the total error concept.

© 2009 Elsevier B.V. All rights reserved.

1. Introduction

Silicone polymers are used in medical and pharmaceutical applications since the 1960s. Common silicon medical components and assemblies includes airways, balloon catheter, tubing for feeding, drainage,. . .. Silicone elastomers are one of the mostly used synthetic and nondegradable polymers. Reasons for their widespread use in medical and pharmaceutical applications are biocompatibility, minimal tissue reaction, biological inertness, chemical and thermal stability, good mechanical properties, easy processability and sterilizability. Due to the excellent diffusional properties, they allow drugs to be delivered in a therapeutic amount that might have not been possible with other polymer systems. For all these reasons, they have been used in many implants and in particularly in silicone-enzyme elastomers such as lipase silicone elastomers. In such delivery system, the enzyme was added as a powder and mixed with the resin before curing in the presence of stannous octoate (catalyst) [1].

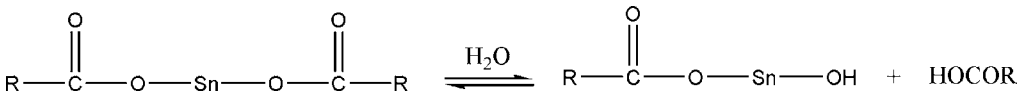
Tin-2-ethylhexanoate or tin octoate ($Sn(Oct)_2$) is commonly used as catalyst for long-term implant products made of a 50/50 (w/w) mixture of poly(dimethylsiloxane) (PDMS) and an active substance. This kind of elastomer is generally prepared by mixing 3 components: the silicone base (hydroxyterminated PDMS), a crosslinker and a catalyst (Fig. 1).

In our awaited use of the elastomer, this one plays the role of reservoir for the substance as well as the matrix for the controlled drug release. In this way the mechanical properties of these room temperature vulcanisation (RTV) silicone rubbers are extremely important and a particular attention must be done on its synthesis. As it is well known, the catalyst takes an important place in the polymerisation process and it may lead to poor quality of the product if no attention is paid to its purity and its storage. So, several parameters such as moisture, oxidation conditions and age of the catalyst are very important to control. The studies of Labouriau et al. [2], and related papers [3,4], suggest that degradation by oxidation and/or by hydrolysis might be important points. Indeed, as shown below, tin octoate in the presence of moisture produces hydroxyl derivative (1) or tin hydroxyoctoate, and also 2-ethylhexanoic acid

* Corresponding author. Fax: +32 4 3664317.
E-mail address: chubert@ulg.ac.be (C. Hubert).
[1] These authors contributed equally to this work.

0039-9140/$ – see front matter © 2009 Elsevier B.V. All rights reserved.
doi:10.1016/j.talanta.2009.09.045

or octanoic acid



(1)

Moreover, octanoic acid is always formed when tin octoate is allowed to age in an open flask. The presence of this carboxylic acid in RTV silicones can lead to degradation by protonating the siloxane chain and then reducing the barrier for hydrolysis of the polymer. Furthermore, these authors have clearly demonstrated that for an aging or a degraded catalyst, the amount of stannic ions (Sn(IV)) is directly linked to the importance of these phenomena.

For all these reasons, and considering their economic impact on a silicone-enzyme elastomers manufacture, it seems very important to develop a method for the determination of stannic ions in the catalyst before its use in such polymerisation process. This method will have to allow the selective determination of stannic ions in presence of stannous ions. Already in the sixties, Fritz and Latwesen [5] have proposed a separation of tin ions from other metallic elements by partition chromatography but only in its more oxidative state. In such a way, no selective determination of a specific oxidation state of tin could be achieved.

In order to avoid the formation of Sn(IV) due to the oxidation of Sn(II) and also to ensure accurate measurements, the determination of stannic ions should be as direct as possible without preliminary separation of Sn(IV) and Sn(II) and/or preconcentration of stannic ions. In the scope of this study, a simple mathematical approach (univariate treatment) is more appropriate than a partial least square multivariate calibration as proposed in the work of González et al. [6] and was thus selected.

Considering a direct and selective determination of stannic ions in the presence of stannous ions, only two methods seem to be suitable: redox titration and polarography. Several polarographic methods [7–14] were published before the years 2000, but they are generally complex, time-consuming or not adapted to the simultaneous determination of tin species.

On the other hand, inductive coupled plasma–mass spectroscopy (ICP–MS) methods can only determine the total tin concentration, and are not suitable. This technique seems to be more relevant for the selective determination of different organotin rather than inorganic tin species [15,16]. Gas chromatography coupled with mass spectrometry (GC/MS) for the determination of mercury and tin compounds (especially organometalics) are published [17,18]. However, these methods are expensive and are not able to selectively determine stannous and stannic ions. Furthermore, several methods have been reported for the determination of tin by ion chromatography but they do not seem promising for the simultaneous determination of tin species [19,20].

More recently, Gholivand et al. showed that atomic absorption spectroscopy (AAS) can be applied for the determination of stannous ions in the presence of stannic ions or for a total tin determination [21]. This assay requires extraction (mixed micelle-mediated cloud point extraction) of Sn(II) or total tin species using a complexing agent. Although this method allows the determination of Sn(II) in samples containing Sn(IV), the determination of stannic ions has to be calculated using total tin determination. Thus, tin species are not really selectively determined.

Consequently, a new method allowing the separation of stannic ions from stannous ions in order to monitor the degradation product, i.e. the stannic ions, has been developed and fully validated [22–24]. The selected method is based on differential

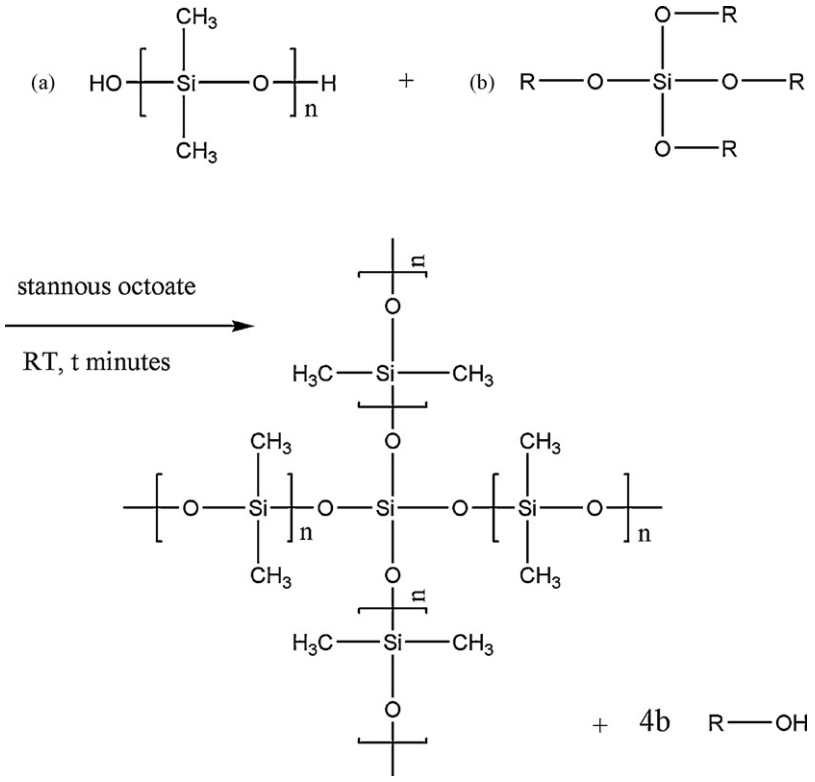


Fig. 1. Representation of a silicone condensation cure mechanism. Coefficients (a and b) related to the polymerisation process, RT: room temperature, *t*: reaction time.

pulse polarography (DPP) that enables the selective separation of tin species, and allowed the accurate determination of stannic ions.

2. Experimental

2.1. Reagents and apparatus

2.1.1. Reagents

Water used for the preparation and dilution of all aqueous solutions was of Milli-Q grade (Millipore, Bedford, MA, USA). Nitrogen (alphagaz 1, 99.999%) purchased from Air Liquide (Milmort, Belgium) was used to remove the dissolved oxygen.

Solution of hydrochloric acid 2 M and sodium hydroxide 2 M were prepared for adjusting the pH of analysed solutions. Analytical grade of these acid and base were obtained from Merck (Darmstadt, Germany). Sodium malonate (99.0%) was acquired from Fluka (Buchs, Switzerland). Sodium carbonate and sodium hydrogencarbonate (99.8% and 99.7% respectively), constituting the buffer solution, were both purchased from Riedel-de Haën (Seelze, Germany). Appropriate amounts of sodium malonate, sodium carbonate and sodium hydrogencarbonate were dissolved to reach final concentrations of 0.5, 0.2 and 0.2 M, respectively.

Liquid/liquid extractions were performed using heptane (for spectroscopy, 99.3%, Merck) as the organic phase.

During the development phase, Oxygen (alphagaz 1, 99.995%) supplied by Air Liquide was used to modify the tin species ratio in aqueous solutions. Standard stock solutions of Sn(II) were prepared by dissolving appropriate amounts of chloride stannous (99%, Sigma–Aldrich, Saint Louis, MO, USA) in hydrochloric acid 0.2 M.

Standard reference of stannic ions at 1000 μg/mL was obtained from Merck. Tin octoate was purchased from NuSil Technology (Carpinteria, CA, USA).

2.1.2. Apparatus

The polarograms were obtained with a Metrohm Model 746 VA processor (Metrohm AG, Herisau, Switzerland) and a Metrohm 694 VA stand with a multimode electrode (MME) operating in Static Mercury Drop Electrode (SMDE) mode. The three electrodes system was completed by means of a Ag/AgCl (3 M KCl) reference electrode and a Pt auxiliary electrode.

The pH of the analysed solutions was measured with a Radiometer analytical IONcheck 10 (Villeurbanne, France) pH meter. The apparatus was daily calibrated using 3 buffers solutions at pH 4.01, 7.00 and 9.21 (Mettler-Toledo, Urdorf, Switzerland).

2.2. Procedure

2.2.1. Extraction step from tin octoate

Liquid/liquid extractions were achieved with a homemade extraction cell (Fig. 2) allowing transfer of tin species in aqueous medium, from the organic matrix, under inert conditions. An aliquot of tin octoate (250 mg) was introduced in the extraction cell and dissolved in 50 mL of deoxygenated heptane. The extraction process was performed under nitrogen, to avoid oxidation of stannous ions, with 50.0 mL of 2 M aqueous hydrochloric acid. The stirring is carried out by bubbling of nitrogen with a flow rate of 20 L/h. The extraction step is performed during 5 min.

2.2.2. Electrochemical determination conditions

Polarographic measurements were carried out using the following procedure: 5.0 mL of aqueous phase resulting from the extraction step was transferred into a 50.0 mL volumetric flask containing 35 mL of degassed sodium malonate (0.5 M) in buffer solution ($NaHCO_3/Na_2CO_3$, 0.2 M both). 5 mL of sodium hydroxide solution (2 M) was previously introduced into the volumetric flask in order to ensure a pH near 9.8 after the addition of the sample. A pH adjustment at 9.8 was made in the volumetric flask by addition of 2 M sodium hydroxide solution. The polarographic measurement is performed on an aliquot of 10 mL. The values of the instrumental parameters are described in Table 1.

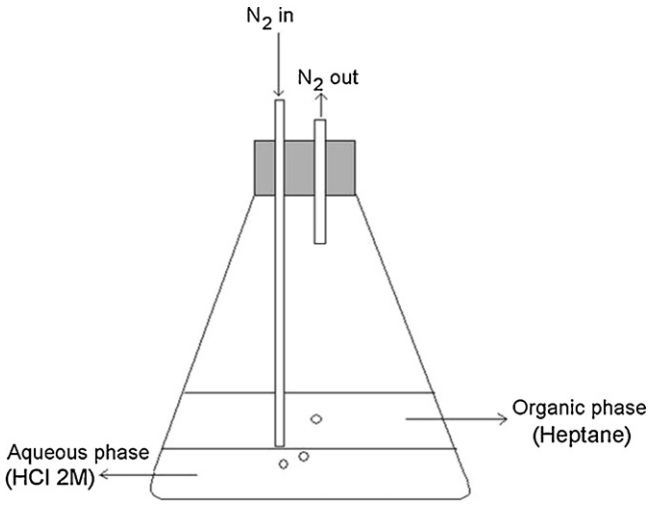


Fig. 2. Tailor-made extraction cell for the liquid/liquid extraction of tin species.

2.2.3. Standard solutions

Standards references of stannic ions at 996 and 999 μg/mL were employed as independent stock solutions for the preparation of the calibration and the validation standards, respectively. Dilutions of the first one were performed in volumetric flasks containing the complexing agent in the pH 9.8 buffer to reach final concentrations of 9.96, 14.94, 19.92 and 39.84 μg/mL. These solutions are used as calibration standards (CSs).

The second stock solution was diluted in 2 M aqueous hydrochloric acid to reach final concentrations of 99.9, 149.5, 199.8 and 399.6 μg/mL. These solutions are used as the aqueous phase in the liquid/liquid extraction of different portions of 250 mg of stannous octoate. After an extraction of 5 min, 5.0 mL of the aqueous phase are diluted in a 50.0 mL volumetric flask containing the complexing agent in the pH 9.8 buffer. These solutions are used as validation standards (VSs) and prepared in duplicates ($n = 2$) from two stock solutions available.

Two independent extractions of 250 mg of stannous octoate in presence of 2 M aqueous hydrochloric acid as the aqueous phase are also performed. These solutions are used as the initial point of the standard addition method (see Section 3.2.1). The resulting mean response was subtracted from all the responses obtained for the analyses of the VSs.

All CSs and VSs were extemporaneously prepared under nitrogen. The concentration levels targeted for the VSs were of 10, 15, 20 and 40 μg/mL representing a degradation of the catalyst of 6.8%, 10.2%, 13.6% and 27.2% for tin octoate sample of 250 mg.

Table 1
Setting of the instrumental parameters for the determination of stannic ions by differential pulse polarography.

Polarographic mode	SMDE	Potential step	6 mV
T step	0.6 s	Sweep rate	10 mV s^{-1}
Pulse amplitude	−50 mV	Sweep start potential	−1000 mV
Pulse time	10 ms	Sweep end potential	−1450 mV
Measure time	5 ms	*E* peak	−1250 mV

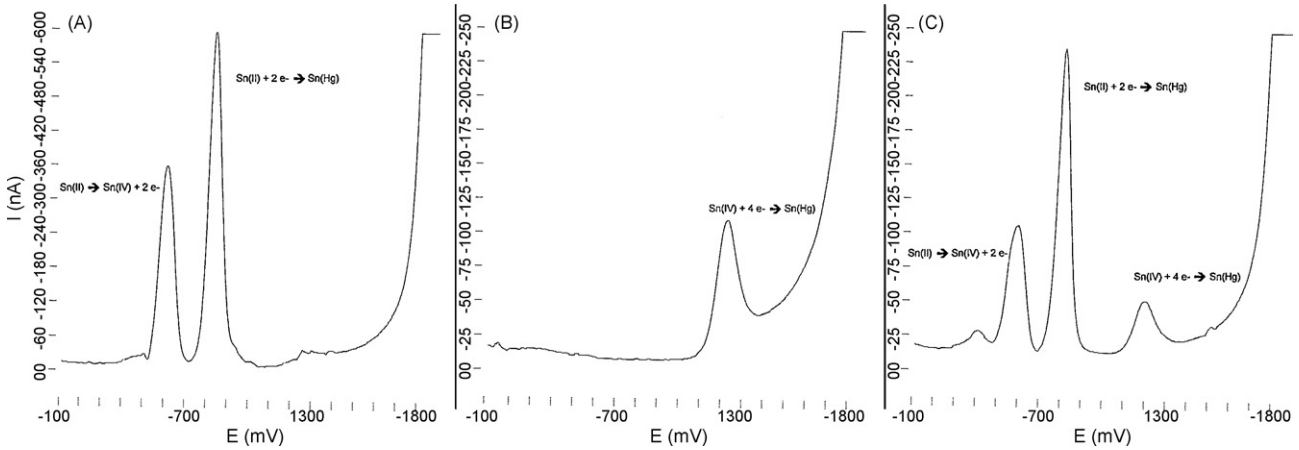


Fig. 3. Polarograms of tin species solutions in carbonate/bicarbonate solution (0.2 M) and malonate ions (0.5 M). (A) Stannous ions at 30 μg/mL, (B) stannic ions at 30 μg/mL and (C) stannous and stannic ions both at 10 μg/mL.

2.2.4. Computations

The e.noval software v2.0 (Arlenda, Liège, Belgium) was used to compute the validation results of the analytical method as well as to get the accuracy profiles.

3. Result and discussion

3.1. Method development

The separation of tin species by differential pulse polarography is only achievable if a chelating agent is used. Previously, Lejeune et al. [25] have reported the use of sodium fluoride for the analysis of stannous ions in the presence of stannic ions. However, fluoride forms a strong complex with tin species resulting on a rejection of polarographics waves to very low negatives potentials, particularly for stannic ions. Indeed, only the stannous ions are detected at −790 and −654 mV for the oxidation wave ($Sn^{2+} \rightarrow Sn^{4+}$) and the reduction wave ($Sn^{2+} \rightarrow Sn^{0}$), respectively [25]. In our case, stannic ions are the degradation product of tin octoate. It thus seems more suitable to follow the abundance of these ions rather than the decrease of stannous ions. So, in order to achieve the direct and specific determination of stannic ions in presence of stannous ions, other chelating agent must be chosen. Moreover, the tin species of the catalyst must be extracted to ensure their polarographic analysis in an aqueous medium. Thus, to find the optimum extraction and analysis conditions, the influence of various parameters was investigated.

3.1.1. Malonate ions, the chelating agent allowing the separation of tin species

In order to reduce the rejection of the Sn(IV) wave when using fluorides, another chelating agent that forms weaker complex had to be selected. According to Handbook Series in Inorganic Electrochemistry [26], the malonate ions (mal) seem to be adequate. Sn(II) and Sn(IV) reacts with sodium malonate, in presence of carbonate ions, to form stable complex with a different complex constant in basic medium. However, in high pH conditions, malonate form with Sn(II) and Sn(IV) complexes of relatively low stability ($\log K_{ML} < 6$) while carbonate allows the formation of very stable complexes ($\log K_{ML} > 15$). Moreover, carbonate forms stable hydroxo-complexes that allow the metal to remain in aqueous solution. On the other hand, the use of carbonate as chelating agent without malonate ions leads to drastically different results and avoid a selective determination of stannic ions in presence of stannous ions. So, it seems that in basic medium, both ions (malonate and carbonate) are involved in the chelating process allowing the separation of tin species. As can be seen from Fig. 3, in a supporting electrolyte composed by malonate, carbonate and hydrogencarbonate at pH 9.8, two waves for stannous ions are detected at −610 and −840 mV (Fig. 3A), due to the oxidation and the reduction waves respectively.

Oxidation wave : $Sn^{2+} \rightarrow Sn^{4+} + 2e^{-}$

Reduction wave : $Sn^{2+} + 2e^{-} \rightarrow Sn(Hg)$

Moreover, stannic ions wave (at −1210 mV) is well separated from two others (at −610 and −840 mV (Fig. 3B)), proving in this way that the separation of both ions is achievable by polarographic method (Fig. 3C).

Reduction wave : $Sn^{4+} + 4e^{-} \rightarrow Sn(Hg)$

3.1.2. Influence of extraction step on stannous and stannic ions

As the selective determination of the tin species is possible in an aqueous medium by polarographic method, an adequate extraction step must be selected and developed [27]. However, extraction procedure of the tin species is the main restricting step in this analytical process. Indeed, a controlled inert atmosphere is necessary to prevent a modification of the Sn(II)/Sn(IV) ratio. Oxygen, in solvents part as well as in the extraction cell, quickly reacts with stannous ions leading to the increase of stannic species and thus impairing a reliable quantitative analysis of the Sn(II)/Sn(IV) ratio in the raw catalyst.

To avoid this, a tailor-made extraction cell has been used (Fig. 2). Two glass tubes (the nitrogen inlet and outlet) create and maintain inert condition into the extraction cell. Moreover, the nitrogen inlet tube is placed at the border of the two phases in order to mix them together and thus to allow the extraction of tin species from organic to aqueous medium.

This original device avoids the modification of the tin ratio as demonstrated by the following results. Indeed, portions of several aqueous stannous solutions containing 500 μg/mL, were either submitted to the extraction process or not and then analysed as previously described. The ratio of stannic ions detected for the same stannous solution was computed and showed a mean percentage of degradation caused by the extraction process of $5.1 \pm 0.7\%$ ($n = 11$). This result is acceptable regarding to the final objective of the method. In a second time the same experiments were performed on aqueous stannic solutions in order to demonstrate that stannic ions were not affected by the extraction procedure. These experiments were performed on stannous solution at 10, 20 and 40 μg/mL. For

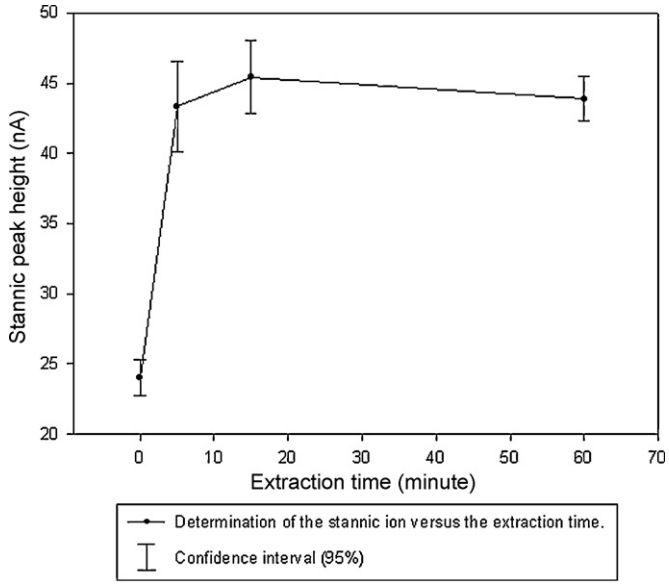


Fig. 4. Determination of the optimal extraction time of stannic ions ($n = 3$).

these concentration levels the mean percentage of degradation was $0.5 \pm 3.0\%$ ($n = 28$). These experiments clearly demonstrate that stannic ions are not affected by the extraction procedure.

3.1.3. Determination of the optimal extraction time

Regarding the rapid oxidation problem of the stannous catalyst part, the extraction time must be as short as possible while being quantitative.

Four extraction times have been tested: 0, 5, 15 and 60 min. A very light hand agitation of the extraction cell without bubbling was carried out to represent the 0 min extraction time point. This experiment is realised as previously described on several portions (250 mg) of the same catalyst to monitor the stannic ions recovered after the extraction step.

The transfer of the mineral compounds (like tin) is quickly achieved. As it can be seen from Fig. 4, a plate of maximum extraction is reached after only 5 min. This is demonstrated by the confidence interval (95%) analysis from each extraction time (0, 5, 15 and 60 min). By this analysis, only the 0 min extraction time point can be differentiated from the others, showing that within only 5 min, stannic ions extraction is completed.

Regarding the results, an extraction time of 5 min was selected to achieve a quantitative and rapid extraction while always keeping in mind that a short time of treatment decreases the risk of a change in the tin species ratio.

3.1.4. Influence of pH on stannic polarographic response

The supporting electrolyte is an important part of the analytical system. Indeed, an ionic medium is necessary to obtain an analytical response. However the supporting electrolyte takes often place in the electrochemical reaction itself. As previously mentioned, malonate and carbonate allow the separation of the stannous and the stannic compounds in the basic medium envisaged. Moreover, it seems obvious that in such ionic solution, pH is a critical parameter to study.

So, three independent solutions of stannic ion standard at a concentration of 30 μg/mL were analysed at pH: 9.0, 9.2, 9.4, 9.6, 9.8 and 10.0 (number of replicate in each series = 3) in the presence of bicarbonate/carbonate solutions at 0.2 M and malonate at 0.5 M.

These experiments highlight that the intensity of the response depends on the pH at which complex formation occurs. As illustrated in Fig. 5, the analytical response for the stannic peak is dramatically influenced by the increase of the pH of the buffered supporting electrolyte. However, a too high pH involves a decrease in the analytical response due to a competition between the complex stability at this pH and the hydroxide precipitation of tin.

In conclusion, the optimal pH for the analysis of the stannic ions is equal to 9.8.

3.2. Analytical method validation

3.2.1. Standards preparation

Analytical method validation is an essential step in the life cycle of any analytical method. The experimental conditions used to assess the validity of a method should be as representative as possible of its future routine application. One condition is to prepare the validation standards in the matrix in which the analyte of interest will be present in the forthcoming daily application of

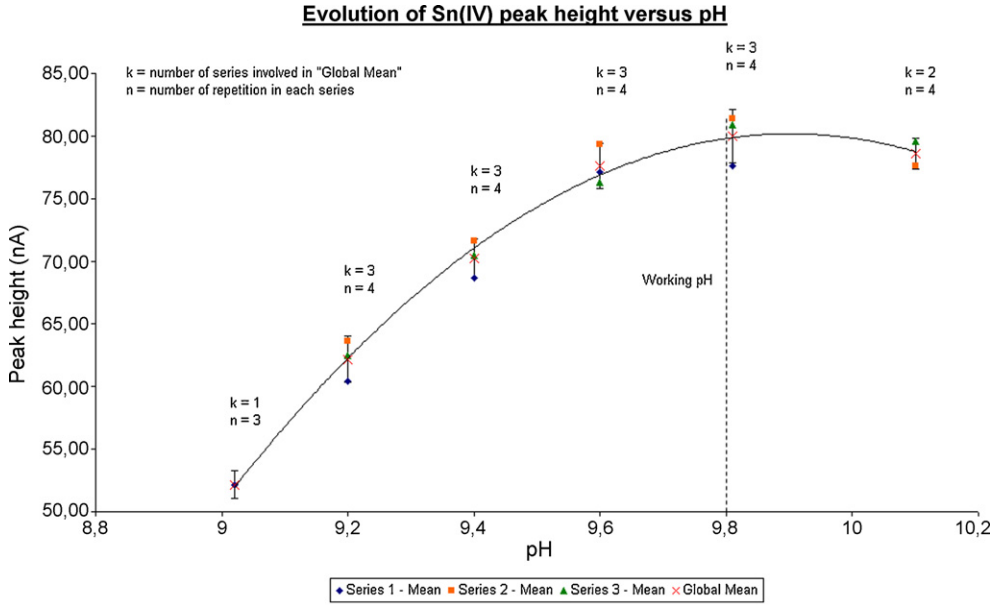


Fig. 5. Influence of the working pH on the intensity of the stannic peak response.

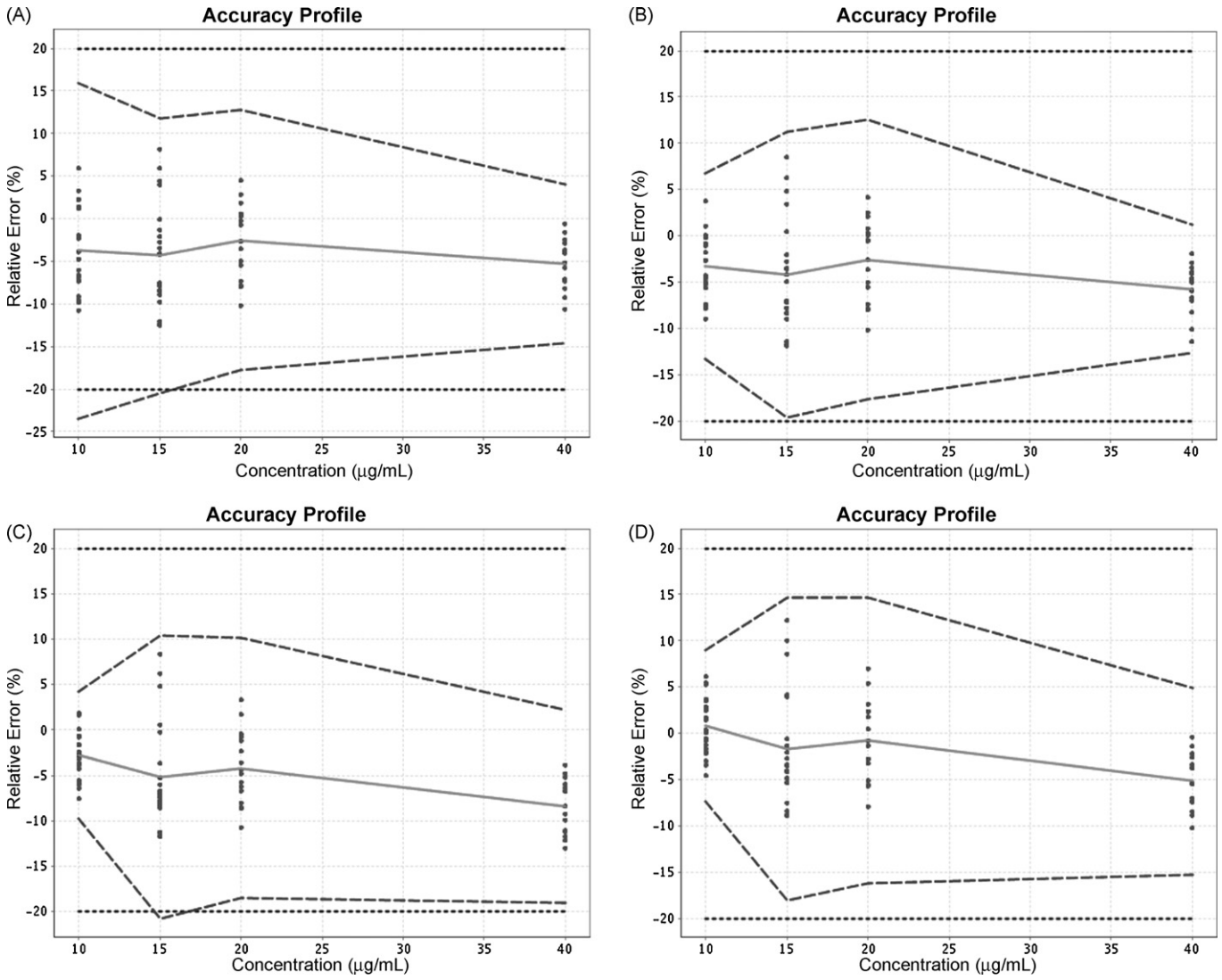


Fig. 6. Accuracy profile obtained for the validation study of the method considering (A) linear regression, (B) weighted $1/x^2$ linear regression, (C) linear regression through 0 fitted using only the smallest concentration level, (D) linear regression through 0 fitted using only the highest concentration level; plain line: relative bias, dashed lines: 95% β-expectation tolerance limits, dotted curves: ±20% acceptance limit and dots: relative back-calculated concentrations of the validation standards.

the method. Nonetheless, the reconstitution of the matrix without the tin parts is difficult and irrelevant. Thus the use of the stannous octoate as matrix was selected. However, a natural degradation of the product is always present leading to the presence of a natural amount of stannic ions from the matrix itself that would interfere with the preparation of the VSs. To circumvent this, the standard addition method was used on the validation standards in order to adequately estimate the analytical signal due to the endogenous stannic ions of the matrix. Once estimated, this signal was substracted to the response of each validation standard analysed. In a preliminary study no matrix effect on the CSs was highlighted. The CSs were therefore prepared directly in the supporting electrolyte.

3.2.2. Method performance

The method validation was carried out using the accuracy profile approach based on tolerance intervals for the total measurement error [24,28,29]. This approach reflects more directly the performance of individual assays and will result in fewer rejected in-study runs than the current procedure that compares point estimates of observed bias and precision. The concept of accuracy profile was also used to select the most appropriate regression model for calibration, to evaluate matrix effect, to determine the lower limit of quantitation (LLOQ) and the range over which the method can be considered as valid. For this approach two parameters must be set by the analyst, the acceptance limits on one hand and the risk of having future measurements falling outside those acceptance limits on the other hand $(1-\beta)$.

Due to the objective of this method (determination of the degradation product of a catalyst), the present acceptance limits were set at ± 20% and the risk (=$1-\beta$%) of having future results outside the acceptance limits was set at 5% maximum. The calibration curve was prepared in the supporting electrolyte in order to reach four concentration levels of stannic ion ranging from 10 to 40 µg/mL. Triplicate calibration standards were analysed at each concentration level for 3 runs.

Several regression models were tested in order to select for the most appropriate response function. This was achieved by preparing validation standard, in presence of stannous octoate during the extraction step, at the same four concentration levels and analysing them in four replicates during 3 runs. The concentrations of the validation standards were back-calculated using the various response

Table 2
Validation results of the polarographic method with the linear regression through 0 fitted using only the highest concentration level as standard curve.

Response function ($p=3$; $n=3$)	Linear regression through 0 fitted using only the highest concentration level model; calibration range ($m=4$): 10–40 μg/mL		
	Run 1	Run 2	Run 3
Slope	2.841	2.917	3.218
Trueness ($p=3$; $n=8$) (μg/mL)		Relative bias (%)	
10		0.8	
15		−1.8	
20		−0.8	
40		−5.2	
Precision ($p=3$; $n=8$) (μg/mL)	Repeatability (RSD%)	Intermediate precision (RSD%)	
10	2.4	3.2	
15	5.0	6.5	
20	2.7	4.8	
40	2.3	3.5	
Accuracy ($p=3$; $n=8$) (μg/mL)		β-Expectation tolerance limits (%)	
10		[−7.4, 9.1]	
15		[−18.0, 14.7]	
20		[−16.2, 14.7]	
40		[−15.3,5.0]	
Linearity ($p=3$; $n=8$)			
Range (μg/mL)		[10; 40]	
Slope		0.928	
Intercept		0.904	
r^2		0.9932	
LOD (μg/mL)		1.51	
LOQ (μg/mL)		10.00	

p: number of series of experiments, m: number of concentration levels, n: number of replicates per concentration levels and per series.

functions tested in order to determine, by concentration level, the mean relative bias, the standard deviation intermediate precision as well as the upper and the lower β-expectation tolerance limits at 95% level and finally draw their corresponding accuracy profiles [24,28,29] (cf. Fig. 6).

As shown in Fig. 6, the linear regression (Fig. 6A) and the linear regression through 0 fitted using only the smallest concentration level (Fig. 6C) response functions were not acceptable at the lower concentration. Two other models were evaluated and presented an acceptable accuracy profile: the weighted ($1/x^2$) linear regression (Fig. 6B) and the linear regression through 0 fitted using only the highest concentration level (Fig. 6D) model. Nevertheless, only the last one lead to the lowest bias over the whole dosing range while keeping an acceptable variability. Furthermore, this regression model is the simplest one and will allow a calibration with only the highest level concentration in routine use. The response function obtained by applying this regression model is presented in Table 2.

Trueness [23,28–30] expressed in terms of relative bias (%) was then assessed from the validation standards at the four concentration levels. As can be seen in Table 2, the bias did not exceed the value of 2.0% for the concentrations between 10 and 20 μg/mL and was near 5.0% for the highest concentration level.

The precision of the analytical method was determined by computing the relative standard deviations (RSD) for repeatability and time-different intermediate precision at each concentration level of the validation standards [22–24,28,30–32]. The RSD values presented in Table 2 did not exceed 6.5%.

Accuracy takes into account the total error, i.e. the sum of systematic and random errors, related to the test result [22–24,28,30].

Table 3
Determination of Sn(IV) in independent sample of stannous octoate.

Sample	Concentration of stannic ions (μg/mL)	Mean concentration per Batches ± SD (μg/mL)	Percentage of degradation (%)
Batch-A 1 (T0)[a]	10.04	10.09 ± 0.05 ($n=3$)	6.9
Batch-A 2 (T0)	10.08		
Batch-A 3 (T0)	10.14		
Batch-B 1 (T0)	11.75	11.90 ± 0.13 ($n=3$)	8.1
Batch-B 2 (T0)	11.93		
Batch-B 3 (T0)	12.01		
Batch-A 4 (T3)	13.19	13.54 ± 0.22 ($n=6$)	9.2
Batch-A 5 (T3)	13.79		
Batch-A 6 (T3)	13.37		
Batch-A 7 (T3)	13.54		
Batch-A 8 (T3)	13.65		
Batch-A 9 (T3)	13.67		

[a] Time after first use of the catalyst flask; T0: first use; T3: use after 3 months.

As shown in Table 2, the relative upper and lower β-expectation tolerance limits (%) did not exceed the acceptance limits settled at ±20% for each concentration level.

The analytical method can be considered as valid over the concentration range investigated [22–24,28,30]. Therefore, the lowest amount of stannic ions that can be quantitatively determined under the experimental conditions with a well-defined accuracy, i.e. the lower limit of quantification, is equal to 10 μg/mL [23,24,28,29].

The most important conclusion that can be made at the end of this validation phase is that, thanks to the predictive attribute of the β-expectation tolerance interval, it is expected that during the routine use of the validated analytical method less than 5% of future results will fall outside the tolerance limits and thus outside the acceptance limits of ±20%.

3.3. Results obtained during routine use

This method was then used in routine. As stated in the validation section, the linear regression through 0 fitted using only the highest concentration was selected as response function. The calibration standard at 40 μg/mL was prepared in the supporting electrolyte as previously described.

Two batches (named Batch-A and Batch-B, respectively) of stannous octoate (29.30% of Sn) were analysed. The Batch-A was used during 3 months for multiple polymerisations before being re-analysed. After each use of the catalyst, it was stored under inert atmosphere by bubbling of nitrogen during 15 min.

As can be seen in Table 3, the concentration of stannic ions in the catalyst in Batch-A and Batch-B was equal to 10.09 ± 0.05 μg/mL ($n = 3$) and 11.90 ± 0.13 μg/mL ($n = 3$) respectively. Considering the sampling, the degradation of the stannous octoate was 6.9% and 8.1% respectively. After a 3 months use of the first catalyst (i.e. Batch-A), the concentration of stannic ions reached 13.54 ± 0.22 μg/mL, corresponding to a degradation of the catalyst of 9.2%.

4. Conclusions

Our study has showed that a separation of stannous and stannic ions can be achieved from stannous octoate (catalyst) with simplicity, rapidity and accuracy.

Indeed, after a liquid/liquid extraction procedure of 5 min in inert atmosphere, a simple differential pulse polarography analysis in aqueous medium is performed. The electrolyte support used for this analysis contains malonate and carbonate ions both contributing to the chelating process. Two well-defined oxidation and reduction peak of stannous ions (−610 and −840 mV) and a well separate reduction peak of stannic ions (−1210 mV) were observed.

Finally, the developed method was successfully validated according to regulatory authorities' requirements and shows acceptable trueness and precision regarding to the final objective of the method.

Moreover, this method could allow to investigate the link between the Sn(IV)/Sn(II) ratio and the polymerisation performance of the catalyst.

Acknowledgments

The authors acknowledge Mithra Pharmaceuticals S.A. for financial support as well as Dr. F. Wijzen and Dr. A. Ceccato for valuable scientific discussions. The authors are very grateful to the anonymous reviewers for providing important comments that led to significant improvements of this article. A research grant from the Belgium National Fund for Scientific Research (FRS-FNRS) to E. Rozet is gratefully acknowledged.

References

[1] A.M. Ragheb, M.A. Brook, M. Hrynyk, Biomaterials 26 (2005) 1653.
[2] A. Labouriau, D. Taylor, T.S. Stephens, M. Pasternak, Polym. Degrad. Stab. 91 (2006) 1896.
[3] F.W. Van der Weij, Makromol. Chem. 12 (1980) 2541.
[4] M. Cypryk, Y. Apeloig, Organometallics 21 (2002) 2165.
[5] J.S. Fritz, G.L. Latwesen, Talanta 14 (1967) 529.
[6] M.J.G. González, O.D. Renedo, M.J.A. Martínez, Talanta 71 (2007) 691.
[7] S.B.O. Adeloju, F. Pablo, Anal. Chim. Acta 270 (1992) 143.
[8] A.M. Bond, Anal. Chem. 42 (1970) 1165.
[9] K. Boutakrit, Z.P. Yang, J.M. Kauffmann, Talanta 42 (1995) 1883.
[10] E. Desimoni, F. Palmisano, L. Sabbatini, Anal. Chem. 52 (1980) 1889.
[11] J.H. Mendez, R.C. Martinez, M.E.G. Lopez, Anal. Chim. Acta 138 (1982) 47.
[12] S.L. Phillips, I. Shain, Anal. Chem. 34 (1962) 262.
[13] G. Somer, A. Arslantas, Analyst 119 (1994) 1257.
[14] C.M.G. Van den Berg, S.H. Khan, J.P. Riley, Anal. Chim. Acta 222 (1989) 43.
[15] M. Üveges, L. Abrankó, P. Fodor, Talanta 73 (2007) 490.
[16] N.P. Vela, J.A. Caruso, J. Biochem. Biophys. Methods 43 (2000) 45.
[17] J. Muñoz, M. Gallego, M. Valcárcel, Anal. Chim. Acta 548 (2005) 66.
[18] J. Muñoz, J.R. Baena, M. Gallego, M. Valcárcel, J. Chromatogr. A 1023 (2004) 175.
[19] J.S. Fritz, R.C. Freeze, M.J. Thornton, D.T. Gjerde, J. Chromatogr. A 739 (1996) 57.
[20] Q. Sun, H. Wang, S. Mou, J. Chromatogr. A 708 (1995) 99.
[21] M.B. Gholivand, A. Babakhanian, E. Rafiee, Talanta 76 (2008) 503.
[22] International Conference on Harmonization (ICH) of Technical Requirements for registration of Pharmaceuticals for Human Use, Topic Q2 (R1): Validation of Analytical Procedures: Text and Methodology, Geneva, November 2005.
[23] E. Rozet, A. Ceccato, C. Hubert, E. Ziemons, R. Oprean, S. Rudaz, B. Boulanger, Ph. Hubert, J. Chromatogr. A 1158 (2007) 111.
[24] Ph. Hubert, J.-J. Nguyen-Huu, B. Boulanger, E. Chapuzet, P. Chiap, N. Cohen, P.-A. Compagnon, W. Dewe, M. Feinberg, M. Lallier, M. Laurentie, N. Mercier, G. Muzard, C. Nivet, L. Valat, J. Pharm. Biomed. Anal. 36 (2004) 579.
[25] R. Lejeune, J. Thunus, L. Thunus, Anal. Chim. Acta 332 (1996) 67.
[26] L. Meites, P. Zuman, E.B. Rupp, T.L. Fenner, A. Narayanan, Handbook Series in Inorganic Electrochemistry, vol. VII, Se-Tm, CRC Press, Inc., Florida, 1986.
[27] C. Dietz, J. Sanz, E. Sanz, R. Muñoz-Olivas, C. Cámara, J. Chromatogr. A 1153 (2007) 114.
[28] Ph. Hubert, J.-J. Nguyen-Huu, B. Boulanger, E. Chapuzet, P. Chiap, N. Cohen, P.-A. Compagnon, W. Dewe, M. Feinberg, M. Lallier, M. Laurentie, N. Mercier, G. Muzard, C. Nivet, L. Valat, STP Pharma Pratiques 13 (2003) 101.
[29] Ph. Hubert, J.-J. Nguyen-Huu, B. Boulanger, E. Chapuzet, P. Chiap, N. Cohen, P.-A. Compagnon, W. Dewe, M. Feinberg, M. Lallier, M. Laurentie, N. Mercier, G. Muzard, C. Nivet, L. Valat, STP Pharma Pratiques 16 (2006) 28.
[30] ISO 5725-1, Application of the Statistics-Accuracy (Trueness and Precision) of the Results and Methods of Measurement—Part 1: General Principles and Definitions, International Organization for Standardization (ISO), Geneva, 1994.
[31] Ph. Hubert, P. Chiap, J. Crommen, B. Boulanger, E. Chapuzet, N. Mercier, S. Bervoas-Martin, P. Chevalier, D. Grandjean, P. Lagorce, M. Lallier, M.C. Lapara, M. Laurentie, J.C. Nivet, Anal. Chim. Acta 391 (1999) 135.
[32] Guidance for Industry: Bioanalytical Method Validation, US Department of Health and Human Services, Food and Drug Administration, Center for Drug Evaluation and Research (CDER), Center for Biologics Evaluation and Research (CBER), Rockville, MD, May 2001.

Talanta 80 (2010) 1421–1427

Contents lists available at ScienceDirect

Talanta

journal homepage: www.elsevier.com/locate/talanta

Retention of arsenate using genetically modified coryneform bacteria and determination of arsenic in solid samples by ICP-MS

A.F. Villadangos[a], E. Ordóñez[a], M.I. Muñoz[b], I.M. Pastrana[b], M. Fiuza[a], J.A. Gil[a], L.M. Mateos[a], A.J. Aller[b,*]

[a] Department of Molecular Biology, Area of Microbiology, University of León, E-24071 León, Spain
[b] Department of Applied Chemistry and Physics, Area of Analytical Chemistry, University of León, E-24071 León, Spain

ARTICLE INFO

Article history:
Received 11 May 2009
Received in revised form
19 September 2009
Accepted 25 September 2009
Available online 1 October 2009

Keywords:
Arsenate
Corynebacterium glutamicum
Genetically modified bacteria
Mathematical modeling
ICP-MS

ABSTRACT

A novel method for the retention of arsenate [As(V)] combining time-controlled solid-phase extraction with living bacterial biomass is presented. As(V) retention was carried out by exposing the extractant, consisting of a living double-mutant of *Corynebacterium glutamicum* strain ArsC1-C2, to the sample for a retention time of 1–7 min, before the arsenic distribution equilibrium between the sample solution and the extractant was established. The amount of As(V) retained in the biomass was measured by inductively coupled plasma-mass spectrometry (ICP-MS) after the sample had been treated with nitric acid. A theoretical model of the retention process was developed to describe the experimental retention-time profiles obtained with the bacterial cells. This relationship provided a feasible quantification of the retention process before steady-state was reached, providing that the agitation conditions and the retention time had been controlled. An analytical procedure for the retention/quantification of As(V) was then developed; the detection limit was 0.1 ng As(V) mL^{-1} and the relative standard deviation 2.4–3.0%. The maximum effective retention capacity for As(V) was about 12.5 mg As (g biomass)$^{-1}$. The developed procedure was applied to the determination of total arsenic in coal fly ash, using a sample that had undergone oxidative pre-treatment.

© 2009 Elsevier B.V. All rights reserved.

1. Introduction

Arsenic is a ubiquitous and extremely toxic metalloid that enters the environment from natural and anthropogenic sources [1]. The adverse health effects that arsenic can produce in living creatures are well known [2], as its concentration-dependent beneficial effects in treating infections in humans [3]. However, the biological implications of arsenic differ with the chemical form involved [4], and the many species of arsenic have posed a great challenge in the development of analytical tools for their isolation. Interest in measuring the chemical species of arsenic in environmental samples has recently grown, as speciation plays an important role in the toxicity and mobility of arsenic. Therefore, effective methodologies to monitor total As content and/or particular As species leaching from environmental solid samples, such as coal fly ash, are crucial, especially in evaluating the potential impact of As on groundwater quality.

Many techniques have been tested for their ability to fractionate arsenic species, including the most common instrumental techniques of voltammetry [5], spectrophotometry [6], inductively coupled plasma-mass spectrometry (ICP-MS) [7–9], and atomic absorption spectrometry (AAS) [10–12]. These techniques are frequently used in combination with a previous separation technique, mainly electrophoresis and chromatography [8–14]; the use of solid phases in arsenic preconcentration/separation procedures prior to its determination with ICP-MS has also been exploited [15,16]. Other analytical developments have been based on advances in the use of microorganisms, such as yeast, algae, fungi, and bacteria, as specific sorbents [17–19]. In these applications, bacteria have proven to be advantageous because they are relatively small, simple, with fast rates of division and tremendous metabolic/catalytic diversity especially in extreme environments. In addition, many bacterial species are environmentally benign and able to use nutrients unavailable to other organisms.

Bacteria can be used for analytical purposes either as dead (suspension and immobilized) [20,21] or living [22] preparations. However, with living bacteria, genetic manipulation of bacterial metabolic processes allows for improvements in both the specificity of the retention process and the accumulation of analyte. The ability of bacteria to retain arsenic involves genetic determinants typically organized in an *ars* operon [23]. The arsenic operon generally comprises either three (*arsRBC*) or five (*arsRDABC*) genes organized into a single transcriptional unit. The three-gene system (the most common) encodes the arsenic transcriptional

* Corresponding author. Tel.: +0034 987 291536; fax: +0034 987 291883.
E-mail address: aj.aller@unileon.es (A.J. Aller).

0039-9140/$ – see front matter © 2009 Elsevier B.V. All rights reserved.
doi:10.1016/j.talanta.2009.09.046

repressor (*arsR*), a membrane-located arsenite permease (*arsB/acr3*) that functions as an arsenite efflux pump, and an arsenate reductase (*arsC*) that converts arsenate [As(V)] to arsenite [As(III)] before it is pumped out of the cell. The genes of the five-gene *ars* operon and those of numerous *ars*-type operons are configured according to many variations [23,24]. Genetically modified bacteria have been shown to improve the retention of As in studies in which phosphate uptake [25] and the arsenic detoxification pathway [26] have been exploited. The high affinity and specificity of the arsenic regulatory protein ArsR and of other *ars*-encoded proteins, such as ArsB, have been exploited in the development of whole-cell bacterial biosensors for arsenic by their incorporation into fusion constructs containing the bacterial luciferase genes (*lux* and *luc* operons) [27,28].

The Gram-positive saprophytic soil bacterium *Corynebacterium glutamicum* is a member of the Actinobacteria and highly As-resistant. The As(III) resistance of *C. glutamicum* is due to the lack of the aquaglyceroporin system (*glpF*) [23] involved in the uptake of As(III) [29]; the As(V) resistance is accomplished by the presence of two arsenate reductases (ArsC1 and ArsC2) responsible of the intracellular chemical reduction of As(V) to As(III) [23,29,30] with a further efficiently release of As(III) due to the presence of the arsenite permease pumps (Acr3-1 and Acr3-2) [31]. A *C. glutamicum* double-mutant strain was recently obtained by disruption of the *arsC1-arsC2* genes [32]. This mutant strain might be able to selectively retain large amount of As(V), as the intracellular reduction of As(V) and the uptake of As(III) would be now inactive processes. The aim of this work was to use this novel coryneform double-mutant strain, lacking in the ArsC1 and ArsC2 arsenate reductases, as an efficient extractant for As(V) for very short retention times, before partitioning equilibrium is reached. The As(V)-retention process before the steady-state situation was adopted to develop an analytical procedure based on the selective retention of As(V) on complex matrices, prior to the determination of arsenic in the bacterial biomass by ICP-MS.

2. Theoretical considerations

Mathematical modeling of analyte–cell interactions helps in understanding and predicting their behavior, and thus in meaningfully guiding experimental work. For very long sampling times, a steady-state situation is usually reached for any retention process, which is characterized by the partitioning equilibrium constant. However, for short sampling times, net retention by the cells of the analyte species formerly present in the solution can, under controlled conditions at a diffusion-limited rate, be described by the following exponential equation [22]:

$$q = [1 - e^{-Abt}] \left[\frac{C_0}{b}\right] \quad (1)$$

where q is the amount of the analyte retained at any time by the bacterial cells, and the parameters A and b are related to the area of the retention surface, the diffusion-layer thicknesses, the diffusion coefficients of the analyte, the volumes of the liquid and solid phases, and the partition constant. However, for the initial phases of the retention process, Taylor's approximation, $e^{-E} \approx 1 - E$, can be applied such that Eq. (1) can be simplified as:

$$q = AtC_0 \quad (2)$$

that is, for a t constant value, proportionality between q and C_0 allows a quantitative analysis to be carried out until retention equilibrium is reached.

In contrast to the above-described scenario, for active-transport systems, many of the cellular homeostatic mechanisms are directly linked to solute transport, since the retention of chemical species usually requires metabolic energy, and transport processes are regulated by the energy states of cells. In these cases, retention is a non-diffusion-limited process with a metabolic-energy-limited rate. This process is typically modeled by a hyperbolic function similar to that describing the autocatalytic biomass growth rate, which follows Monod-type kinetics:

$$q = \frac{q_m C}{q_{1/2} + C} \quad (3)$$

where q is the amount of the analyte retained during uptake, q_m the maximum retention amount, $q_{1/2}$ the analyte concentration in the sample solution corresponding to the half-retention value, and C is the analyte concentration in the sample solution at any time. However, for values of $C < q_{1/2}$, the hyperbolic rate model can be reduced to a first-order rate equation:

$$-\frac{dC}{dt} = q_m C \quad (4)$$

Reordering and carrying out integrations with the following initial ($C = C_0$, $t = 0$) and boundary ($C = C$, $t = t$) conditions, one obtains:

$$C = C_0 e^{-q_m t} \quad (5)$$

After the following transformation

$$C_0 - C = C_0(1 - e^{-q_m t}) \quad (6)$$

has been made and considering that $q = ((C_0 - C)/m)V$ is the amount of analyte retained by mass, m, units (dry weight) of bacteria and, V, the sample volume, then

$$q = \frac{V}{m} C_0 (1 - e^{-q_m t}) \quad (7)$$

After Taylor's transformation, which is possible for the first moments of the retention process, an equation similar to Eq. (2) is derived:

$$q = \frac{V}{m} q_m t C_0 \quad (2')$$

This clearly shows that the amount of retained analyte at non-steady-state conditions for a t constant value is linearly proportional to the initial concentration, C_0, in the liquid solution. This result indicates that a quantitative analysis can be carried out before the retention equilibrium is reached.

3. Experimental

3.1. Instruments and operating conditions

Retained As was measured by ICP-MS using a Varian spectrophotometer (Varian Inc., Palo Alto, CA). The sample solutions were pumped by a peristaltic pump from tubes arranged on an ASX 500 model 510 autosampler (CETAC, Omaha, NE) and aspirated into the argon plasma. Further details of the instrumental settings are given in Table 1. The torch position and ion lenses were optimized and tested daily by short-term stability testing in the standard mode to maximize ion signals and stability. The mass-scanning data acquisition mode was used for optimization and a mixed internal-standard solution (5 μg L^{-1}) of ^{89}Y and ^{115}In was used to correct short-term drift.

The optical density ($OD_{600\,nm}$) of the growing cell culture was measured on a UV–vis spectrophotometer (Hitachi V-200). Temperature was controlled by a "digital dry bath" (Labnet International D1100). The acidity of the aqueous phase was measured, when necessary, with a pH-meter (Crison model Digit 505). Chemicals and bacterial biomass (dry weight) were weighed on a Mettler AE 240 semi-microanalytical balance (sensitivity ±0.01 mg).

Table 1
Instrument conditions for ICP-MS.

Plasma	ICP-MS
Rf power (kW)	1.40
Plasma flow rate (L min^{-1})	Ar 18
Auxiliary flow rate (L min^{-1})	Ar 1.8
Nebulizer flow rate (L min^{-1})	Ar 1.05
Sheath flow (L min^{-1})	Ar 0.15
Measured (m/z)	^{75}As
Sampling conditions	
Spray-chamber temperature (°C)	5
Sampling depth (mm)	5
Pump rate (rpm)	15
Stabilization time (s)	0
Sample injection	Peristaltic pumping, natural aspirate

3.2. Chemicals

Arsenite and arsenate stock solutions (1000 mg L^{-1}) were prepared by dissolving, respectively, suitable amounts of sodium arsenite and *di*-sodium hydrogen arsenate in appropriate volumes of de-mineralized water. Standard stock solutions (1000 mg L^{-1}) of other elements were prepared from their salts by a conventional method. Working solutions were prepared immediately prior to their use by appropriately diluting the stock solutions.

Tryptone soy agar (TSA; Oxoid) medium (40 g L^{-1}) was composed of tryptone (1.5%, w/w), soy peptone (0.5%, w/w), sodium chloride (0.5%, w/w), and agar (1.5%, w/w) and adjusted to pH 7.3 ± 0.2; TSB medium (tryptone soy broth) was the same as TSA but without agar. Minimal medium for corynebacteria low in phosphate (MMCLP) consisted of the following: glucose (20 g L^{-1}), ammonium sulfate (10 g L^{-1}), urea (3 g L^{-1}), monopotassium phosphate (0.1 g L^{-1}), magnesium sulfate heptahydrate (0.41 g L^{-1}), sodium chloride (50 mg L^{-1}), iron(II) sulfate monohydrate (2 mg L^{-1}), manganese sulfate monohydrate (2 mg L^{-1}), biotin (50 μg L^{-1}), and thiamine (200 μg L^{-1}) for liquid MMCLP, with the addition of 1.5% of agar for solid MMCLP. This medium contained ten times less phosphate than conventional minimal medium for corynebacteria (MMC) [33].

All media were sterilized by autoclaving for 20 min at 120 °C. Chemicals used in this study were of analytical reagent grade and were obtained from Merck. Distilled, deionized water (resistance 18 MΩ cm) was used to prepare the samples and standards. The pH of the sample was adjusted as necessary with HCl and NaOH and buffered using TAB solution. TAB solution consisted of *N*-(2-hydroxyethyl)-piperazine-*N*′-2-ethanesulfonic acid (HEPES) (75 mM), potassium chloride (150 mM), and magnesium chloride (1 mM) at pH 7.3 ± 0.2 [25].

3.3. Bacterial strains and mutants

C. glutamicum RES167 (a restriction-deficient strain derived from *C. glutamicum* ATCC 13032) was used as the type strain for the arsenic studies. *E. coli* DH5α and S17-1 strains were used, respectively, for subcloning and as the donor strain in conjugation experiments [34]. Bacterial cultures were grown in complex (TSA/TSB) or defined (MMCLP) medium for 24–48 h at 37 °C (*E. coli*) or 30 °C (corynebacteria). When necessary, antibiotics kanamycin (Kan) and apramycin (Apr) were added to the cultures at final concentrations of 12.5 mg L^{-1} for corynebacteria and 50 mg L^{-1} for *E. coli*. Construction of the double-mutant strain *C. glutamicum* ArsC1-C2 was recently reported [32]. Briefly, small internal fragments from the *C. glutamicum* arsenate reductase genes *arsC1* and *arsC2* (both involved in the conversion of arsenate to arsenite) were PCR-amplified and subcloned into the *E. coli* mobilizable vectors pK18mob and pOJ260 [35], yielding plasmids pKC1int and pOJC2int, respectively. Both plasmids were transferred from the donor strain *E. coli* S17-1 to the recipient strain *C. glutamicum* RES167, and the transconjugant *C. glutamicum* ArsC1-C2 was selected under antibiotic pressure. Since pKC1int and pOJC2int are suicide plasmids for *C. glutamicum*, the transconjugant *C. glutamicum* ArsC1-C2 was obtained only after integration of the vectors into the chromosomal *arsC* genes (see Fig. 1 for details). The resulting mutant, ArsC1-C2, is unable to transform As(V) to As(III) such that the former As species accumulates intracellularly.

3.4. Procedures

3.4.1. Bacterial cultivation

C. glutamicum strains (wild-type and mutant strain ArsC1-C2) were precultured overnight in TSB medium, and the precultures (0.6 mL) used to inoculate 60 mL of MMCLP medium in 250-mL Erlenmeyer flasks. These cultures were incubated with continuous stirring (200 rev min^{-1}) until they reached an OD_{600} = 2. Cells were harvested, washed twice in 30 mL of TAB solution, and resuspended in 2 mL of TAB solution, which allowed storage of the cells in a non-growing state ("resting cells") until needed for further analyses.

3.4.2. As retention

A volume of 100 μL of "resting cells" was added to 900 μL of sample solution at pH 7.3 ± 0.2 for retention times of 1–7 min (or as indicated) at a temperature of 37 °C. The slurry was filtered through nitrocellulose filters (0.45-μm pore diameter; Whatman) and the cells retained on the filters were washed twice with 5 mL of TAB solution. Filtering and washing were carried out using a "ten place filter manifold" (Hoefer FH 225V) connected to a vacuum pump (ILMVAC GmbH, diaphragm pump MP104E). The filters, which contained the retained cells, were treated with 0.2 mLof 70% nitric acid at 70 °C for 120 min. The digested material (filter and cells) was diluted with water of high-pressure liquid chromatography quality (HPLC-quality water) to bring each sample to a final volume of 10 mL with 1% of HNO_3. The amount of arsenic retained by the "resting cells" biomass was directly determined by ICP-MS. The amount of As present in the supernatant fraction was measured (when necessary) by treating an aliquot of the liquid obtained from the filtered sample (including the washing steps) with 70% nitric acid at 70 °C for 120 min and then subjecting the sample to ICP-MS. The digestion procedure with 70% nitric acid at 70 °C, prior to the analysis stage, ensures the volatilization of chloride ions [36,37] and allowed an accurate determination of As by ICP-MS without any noticeable effect from ^{75}Ar–Cl species. The included experimental data represent the mean of three independent assays.

3.4.3. Coal fly ash preparation

The coal fly ash reference material was prepared as follows. Air-dried coal fly ash samples were ground fine enough to pass through a 200-mesh (74-μm) sieve and then ashed at 750 °C for 1 h to remove carbonaceous material. A sample containing 0.1 g of fly ash was placed in an open Teflon capsule together with 10 mL of hydrofluoric acid (d = 1.13, 40% (w/w)) and the mixture heated until near dryness. To ensure complete oxidation of the organic matter, 20 mL of sulfuric acid (d = 1.84, 96% (w/w)) and 20 mL of nitric acid (d = 1.42, 69.8% (w/w)) were added to the capsule and the sample was allowed to evaporate to dryness. Next, 25 mL of hydrochloric acid (d = 1.19, 37.9% (w/w)) and 10 mL of hydrogen peroxide (33%) were added and the sample was heated until complete dissolution of the residue. The pH was adjusted to 7.3 ± 0.2 using NaOH, with sufficient sodium tartrate added so as to avoid precipitation. Spiking studies with NIST material were carried out by treating solid samples with different amounts of As(V) standard solutions prior to the dissolution procedure. Measurements were calibrated either

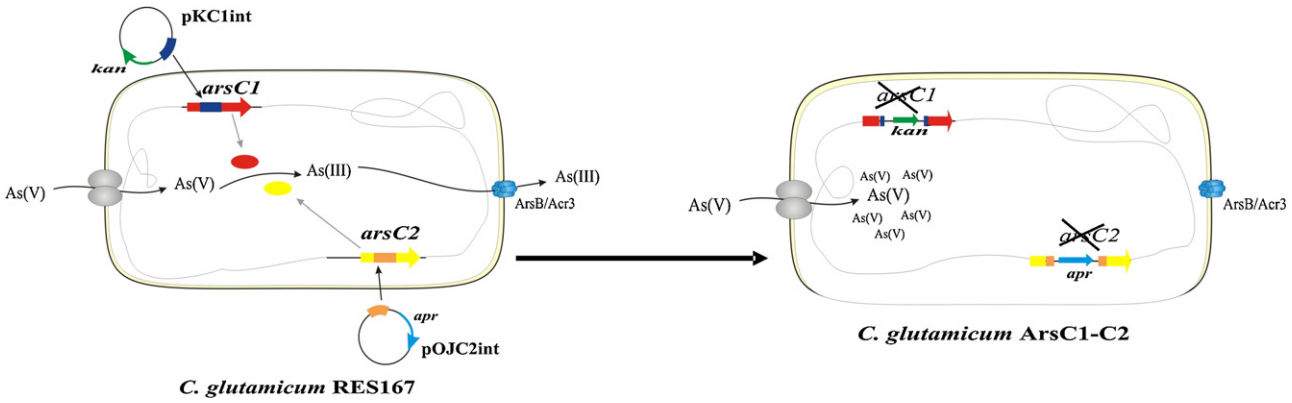


Fig. 1. Construction of the double-mutant *C. glutamicum* ArsC1-C2. Suicide plasmids pKC1int and pOJC2int contain internal fragments of the *arsC1* and *arsC2* genes. Disruption of the *arsC* genes in strain ArsC1-C2 allows the selective retention/accumulation of As(V) by the mutant.

by treating the As(V) standards in the same way as the samples via bacterial preconcentration, or by directly using As(V) standard aqueous solutions.

4. Results and discussion

4.1. Optimization of the retention system

The effect of phosphate present in the sample solution on As(V) retention by the mutant *C. glutamicum* ArsC1-C2 at pH 7.3 and temperature of 37 °C is shown in Fig. 2 for several retention times. An inverse relationship between phosphate concentration and retained As(V) was noted even for retention times as long as 3 h (data not shown), in agreement with the fact that cellular incorporation of As(V) proceeds by the same pathway as phosphate uptake [25]. However, in repeat experiments with As(III) alone and mixtures of As(V) and As(III), only minor amounts of As(III) were retained (Fig. 3) independent of the phosphate concentration present in the sample solution. Strain ArsC1-C2 is unable to accumulate As(III) due to the presence of arsenite permease pumps (Acr3/ArsB) involved in the removal of As(III) from the cell (see Fig. 1) [23,31]. Therefore, the mutant *C. glutamicum* ArsC1-C2 accumulates As(V) rather than As(III) under phosphate-free conditions even at As(III) concentrations 75 times higher than those of As(V). The effect of Sb(III) and Sb(V) on As(V) retention was similar to that of As(III) (Fig. 3).

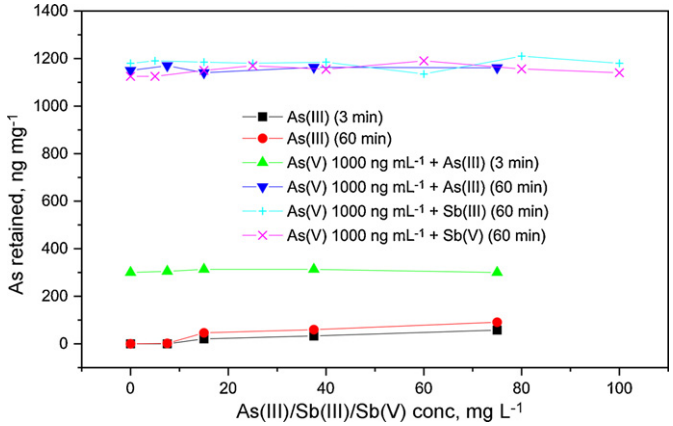


Fig. 3. Effect of As(III), Sb(III) and Sb(V) concentrations on As(V) retention (in the absence of phosphate) by the mutant strain ArsC1-C2 at the selected conditions (pH 7.3 and 37 °C) as measured during two retention times.

The effect of temperature on As(V) retention was also studied in the range of 4–38 °C. As(V) retention initially increased with increasing temperature, but became nearly constant between 20 and 38 °C (data not shown). For this reason, all subsequent As-retention experiments were carried out at 37 °C. Another important factor with respect to the cellular environment was the pH of the sample solution, since As(V) retention was greatly improved at neutral pH (Fig. 4), with pH 7.3 optimal for the experimental conditions

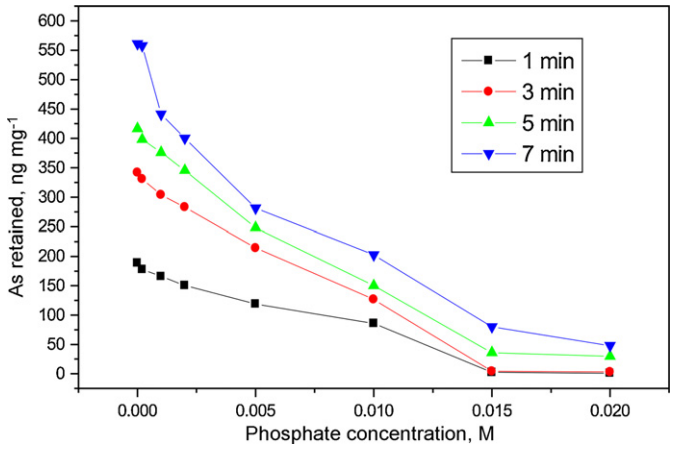


Fig. 2. Effect of phosphate concentration on the retention of As(V) (1000 ng mL^{-1}) by the mutant strain ArsC1-C2, at the selected conditions (pH 7.3 and 37 °C) as measured during four retention times.

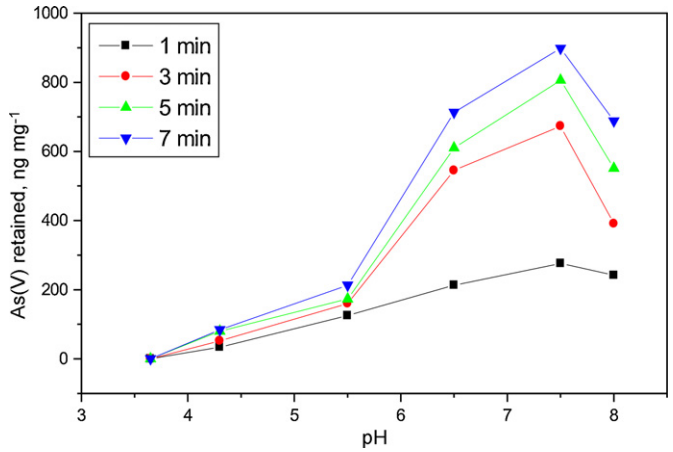


Fig. 4. Effect of pH on the retention of As(V) (1000 ng mL^{-1}) in the absence of phosphate at 37 °C by the mutant strain ArsC1-C2, as measured during four retention times.

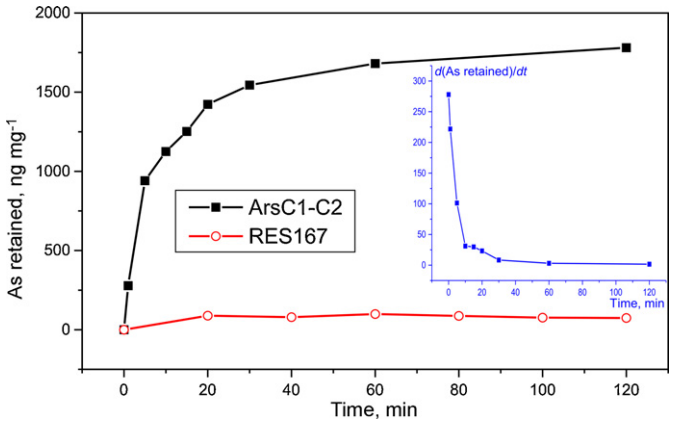


Fig. 5. Effect of time on the retention of As(V) (1000 ng mL^{-1}) by the ArsC1-C2 mutant strain and by the parent strain *C. glutamicum* RES167 at the selected conditions (pH 7.3 and 37 °C). The inset shows the corresponding derivative plot for the ArsC1-C2 mutant.

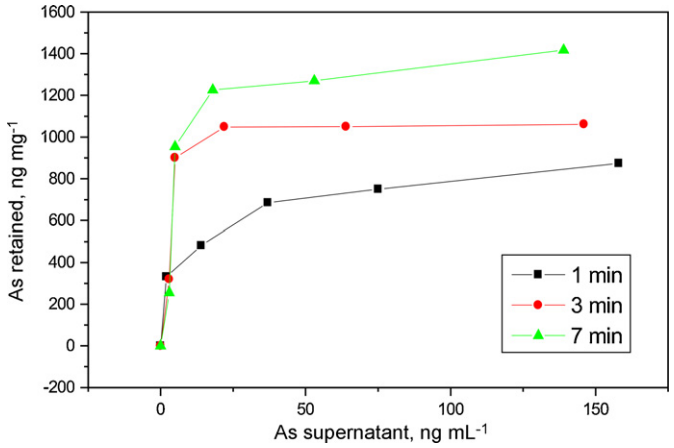


Fig. 6. Plot of the amount of As(V) retained by the mutant strain ArsC1-C2 *vs.* the concentration of nonretained As(V) present in the supernatant, at the selected conditions (pH 7.3 and 37 °C) and for three retention times.

used in this study. Working at this pH, the retention process occurs with no pH variation. Nonetheless, the retention procedure was always carried out using TAB-buffered samples.

The effect of time on As(V) retention is shown in Fig. 5. The arsenic retention profile showed two well-differentiated stages. The first stage covered the initial 20 min, when the amount of arsenic retained increased rapidly, while during the second stage, from 20 to 120 min (Fig. 5), arsenic retention increased more slowly. The inserted derivative plot in Fig. 5 confirms this conclusion, showing that the retention rate was highest during the early stage of the retention process. Fig. 5 also shows that the mutant strain ArsC1-C2 accumulated up to 25-fold more As(V) that the parent strain *C. glutamicum* RES167.

4.2. Retention equilibrium

The retention percentage was derived by comparing the amount of As(V) retained by the biomass with the total arsenic content in the original sample solution. As expected, the retention percentage decreased with increasing amounts of As(V) present in the sample solution. Consequently, a more useful parameter, q_m, the maximum amount of As(V) retained per mass unit (dry weight) of bacterial cells, was determined for several As(V) concentrations and retention times. Thus, the amount of As(V) retained by the bacterial biomass was mathematically modeled, fitting the equations according to Marquardt nonlinear regression techniques (MicroCal Origin). The χ^2 value and the smallest relative error, as indicated by the values of the derived variables, were used to ascertain the suitability of the models' fit with the experimental data. The results showed that hyperbolic equations were the best theoretical model to describe the retention of As(V) by the corynebacterial "resting cells" (Table 2). This, in turn, allowed determination of the parameter q_m. However, for As(V) concentrations below $q_{1/2}$, it was theoretically derived that a first-order rate equation could also be used to describe the retention process. Accordingly, the amount [q, in mg As (g bacteria)$^{-1}$] of arsenic retained per mass unit (dry weight) of bacterial cells increased linearly, $q = (0.52 \pm 0.08) \times 10^{-3}\ C_0$, at As(V) concentrations (C_0, ng mL^{-1}) in the original sample solution in the range of 0–1500 ng mL^{-1} ($r = 0.98909$). This relationship shows that, at least for analytical purposes, "resting cells" can be successfully used as the extractant for As(V) and that the amount of the analyte retained at saturation will not be fully reached within the concentration range established in this study.

Fig. 6 shows the retention isotherms of As(V) for the "resting cells". The Langmuirian shape indicates that the data fit reasonably well with a two-site Langmuir model, implying that the tendency of As(V) to be retained decreased with increased As(V) loading of the bacterial mass. However, assuming a one-site Langmuirian sorption and solutions in which the As(V) concentration is low, the results explain the retention of As(V) with good precision (Table 3). The equilibrium constant, b, determined from low concentrations of As(V), is of greater general interest for analytical applications and was obtained from the experimental data (slope of the plot $1/q$ versus $1/C$ in the Langmuir isotherms). The theoretical maximum monolayer retention capacity, q_m (mg g^{-1}), was also derived, while the essential characteristics of the Langmuir isotherm could be expressed in terms of the dimensionless constant separation factor, $R_L = 1/(1 + bC_0)$. The value of R_L in the range of 0–1 at all initial analyte concentrations confirms the favorable retention of arsenic process. The Gibbs free energy of the retention process was $\Delta G = -RT\,Lnb$, where b (in L mol^{-1}) is the equilibrium constant for the Langmuir isotherm. The parameters for the As(V)-bacterium system are given in Table 3, which shows the favorable, very-high-affinity retention of the bacterial cells for As(V). The negative value of the Gibbs free energy indicates the spontaneity of the retention process, in agreement with the values obtained from the hyperbolic model (Table 2), showing that "resting cells" exhibit large preconcentration abilities for short retention times.

Table 2
Values obtained for each parameter after fitting the experimental retention and kinetics data to hyperbolic functions.

Parameter	Value	
q_m or q'_m (mg g^{-1})	3.54 ± 0.5	2.2 ± 0.4
$q_{1/2}$ (mg L^{-1}) or $q'_{1/2}$(min)	1.8 ± 0.3	4.2 ± 0.3
χ^2	0.37812	0.18432
Equations used	Retention, $q = \frac{q_m C}{q_{1/2}+C}$	Kinetics, $q = \frac{q'_m t}{q'_{1/2}+t}$

Table 3
Parameters obtained for the Langmuir isotherm used to model the retention process.

Langmuir isotherm, $\frac{1}{q} = \frac{1}{q_m bC} + \frac{1}{q_m}$	
Parameter	Value
b (L mg^{-1})	0.81
q_m (mg g^{-1})	3.9
R_L	0.08–0.62
r	0.9899
ΔG (kJ mol^{-1})	−0.3

Table 4
Spiking studies ($n = 3$).

Sample	Content ($ng\,mL^{-1}$)	Added ($ng\,mL^{-1}$)	Found ($ng\,mL^{-1}$)	Recovery (%)
Deionized water	–	10	10.2 ± 0.4	102.0
		20	19.5 ± 0.7	97.5
		30	30.6 ± 0.8	102.0
		40	40.2 ± 0.8	100.5
	Content ($ng\,mg^{-1}$)	Added ($ng\,mg^{-1}$)	Found ($ng\,mg^{-1}$)	Recovery (%)
NIST SRM 1633a	145 ± 15	0	144.8 ± 4.4	99.86
		100	247.3 ± 5.6	100.94
		200	347.6 ± 4.3	100.75
		400	547.9 ± 4.9	100.53

Alternatively, the amount of As(V) retained at equilibrium can be evaluated using the distribution coefficient (K_D) of As(V) between the bacterial cells and the aqueous phase. The K_D ($= 25.4\,L\,g^{-1}$) value obtained ($r = 0.9907$) was affected by the concentration of As(V) [C_0 ($ng\,mL^{-1}$)] in the original sample solution and decreased with the initial As(V) concentration ($ng\,mL^{-1}$). The best-fitting equation obtained was: $\log K_D = (-1.5 \pm 0.1)\ \log C + (5.6 \pm 0.5)$ ($r = 0.9909$), from which it is possible to derive a very high theoretical value for K_D, as in the case of strongly diluted solutions. The K_D values determined at low concentrations of As(V) were higher than those previously reported for other inorganic species and bacteria [22,38,39]. This result indicated that, under the established conditions, bacterial cells were far from having reached As(V) saturation. A maximum value for the amount of As(V) retained per mass unit of bacterial cells was experimentally established as $12.5\,mg\,As\,(g\,cells)^{-1}$, in accordance with the above comments.

4.3. Kinetic modeling

The As(V) retained by "resting cells" with time was theoretically better modeled according to a hyperbolic function (Table 2). The half-retention time was very short, indicating that the retention kinetics is very rapid. The same conclusion was derived from the data in Fig. 5 (inserted graph), which shows that the specific retention rate reaches a maximum value at early phases of the retention process but then sharply decreases after 15 min. Fig. 5 also shows that, as a whole, As(V) retention follows a two-step process, in which the surface binding of As(V) is initially very rapid and can be described by an external diffusion-controlled model. The experimental data obtained from this early stage of the retention process fit well along a straight line, $q = (0.27 \pm 0.02)t$ ($r = 0.99812$), where q is the amount of As(V) retained ($mg\,g^{-1}$) and t is the retention time (min) in the range 0–10. Afterwards, in the second step, retention increased slowly, eventually reaching with the bacterial surface pseudo-equilibrium that was controlled by an intracellular diffusion process.

4.4. Analytical applications

As theoretically stated in Eq. (2) and experimentally demonstrated above, the amount of As(V) retained by corynebacterial mutant "resting cells" is simultaneously dependent upon the initial As(V) concentration and the retention time. This means that it would be possible to retain the same amount of As(V) under a variety of external conditions. It is clear that the amount of As(V) retained is improved with longer retention times. However, in most analytical applications, short analysis times are preferable. Consequently, in the following, all data characterizing the performance of the analytical procedure for As(V), carried out under optimal conditions, were based on a 3-min retention time. The precision for 10 replicate determinations of 50 ng As(V) mL^{-1} was 2.4% relative standard deviation (R.S.D.). The lower limit of detection under the selected optimal conditions was 0.1 $ng\,mL^{-1}$ (3σ). The enhancement factor, which is based on the ratio of the slope of the calibration line derived from the preconcentration procedure using the "resting cells" to the slope obtained from direct measurements of aqueous standards solutions, was found to be about 25. The between-batch precision ($n = 7$) was better than 3.0% for As(V) concentrations of 50 $ng\,mL^{-1}$. These results show that the procedure described herein can be used routinely and that it does not require the use of time-consuming methods.

The effect of several ions, Na(I), K(I), Ca(II), Mg(II), Hg(II), Cd(II), Ni(II), Fe(III), Cu(II), Mn(II), Zn(II), V(V), Cr(VI), Al(III), Si(IV), and Pb(II), as well as tartrate and chloride anions, on the retention of As(V) was evaluated individually and in combination. When added in concentrations of up to 100 $mg\,L^{-1}$, none of these ions interfered (<5%) in the retention/determination of As(V). The effect of the presence of different concentrations of As(III), Sb(III), and Sb(V) on the retention of As(V) was also studied, but again no interference was observed.

For practical applications of the developed procedure, phosphate-free samples are the most appropriate for As(V) fractionation. However, samples containing known amounts of phosphate can also be studied, as long as phosphate-matched standards are used. Nonetheless, the retention capacity of the bacterial cells is decreased in the presence of phosphate. In this study, the reliability of the procedure was tested using a phosphate-free reference coal fly ash sample (NIST SRM 1633a coal fly ash), which served as a suitable complex matrix for a preliminary application. The coal fly ash reference material was certified for total As, but the sample treatment described in Section 3.4.3 assured full transformation of total arsenic into As(V). The assayed value ($144.8 \pm 4.4\,ng\,mg^{-1}$) of the arsenic in the NIST standard reference material was in close agreement with the certified value ($145 \pm 15\,ng\,mg^{-1}$). The recovery of arsenic from artificial samples (Table 4) and from the reference coal fly ash was between 97.5% and 102.0%. These results demonstrate the utility of the mutant strain for the retention of As(V), and its accurate determination with no matrix effect.

5. Conclusion

A novel methodology for the selective retention of arsenate at non-steady-state conditions using a double-mutant strain of corynebacteria was optimized. Moreover, our study demonstrated not only that the double-mutant strain *C. glutamicum* ArsC1-C2 is a good biomaterial for the efficient extraction of As(V), particularly from phosphate-free matrices, but also that the method can be used for screening purposes in aqueous samples. The results showed that the developed analytical procedure based on the selective retention of As(V) on complex matrices, such as coal fly ashes, allowed the accurate determination of total arsenic by ICP-MS, when a previous oxidation to As(V) is ensured. The method is generally applicable to specialised facilities for the use of the bacterial cells, which

represents an important drawback for general analytical laboratories set-ups. The good analytical characteristics, obtained with these engineered bacterial cells when used as extractants, provide the basis for new, improved analytical applications using this and similar kinds of materials.

Acknowledgements

This work was supported by funding provided by grants from the Junta de Castilla y León, Consejería de Educación, Ref.: LE050A06, and the Spanish Ministerio de Educación y Ciencia, Ref.: BIO2005-02723. The authors are grateful to the Spanish Ministerio de Educación y Ciencia (MIM, MF) and the Junta de Castilla y León (AFV, EO) for fellowships supporting this research.

References

[1] C.J. Langdon, T.G. Piearce, A.A. Meharg, K.T. Semple, Environ. Pollut. 124 (2003) 361.
[2] A.A. Duker, E.J.M. Carranza, M. Hale, Environ. Int. 31 (2005) 631.
[3] G. Przygoda, J. Feldmann, W.R. Cullen, Appl.Organometall. Chem. 15 (2001) 457.
[4] K.S. Squibb, B.A. Fowler, in: B.A. Fowler (Ed.), Biological and Environmental Effects of Arsenic, Elsevier, Amsterdam, 1983, p. 233.
[5] G. Henze, W. Wagner, S. Sander, Fresenius J. Anal. Chem. 358 (1997) 741.
[6] K. Palanivelu, N. Balasubramanian, T.V. Ramakrishnan, Talanta 39 (1992) 555.
[7] J.R. Pretty, E.A. Blubaugh, J.A. Caruso, Anal. Chem. 65 (1993) 3396.
[8] Y. Lin, U. López-Avila, J.J. Zhu, D. Wiederin, W.F. Bechert, Anal. Chem. 67 (1995) 2020.
[9] M.L. Magnuson, J.T. Creed, C.A. Brockhoff, Analyst 122 (1997) 1057.
[10] S.H. Hansen, E.H. Larsen, G. Pritzl, C. Cornett, J. Anal. Atom. Spectrom. 7 (1992) 629.
[11] E. Hakala, L. Pyy, J. Anal. Atom. Spectrom. 7 (1992) 191.
[12] M.A. López, M.M. Gómez, M.A. Palacios, C. Cámara, Fresenius J. Anal. Chem. 346 (1993) 643.
[13] G. Koellensperger, J. Nurmi, S. Hann, G. Stingeder, W.J. Fitz, W.W. Wenzel, J. Anal. At. Spectrom. 17 (2002) 1042.
[14] Y. Morita, T. Kobayashi, T. Kuroiwa, T. Narukawa, Talanta 73 (2007) 81.
[15] C. Yu, Q. Cai, Z.-X. Guo, Z. Yang, S.B. Khoo, Spectrochim. Acta Part B 58 (2003) 1335.
[16] S. Chen, X. Zhan, D. Lu, C. Liu, L. Zhu, Anal. Chim. Acta 634 (2009) 192.
[17] A. Martín-Esteban, P. Fernández, C. Cámara, Anal. Chem. 69 (1997) 3267.
[18] H.A.M. Elmahadi, G.M. Greenway, J. Anal. Atom. Spectrom. 9 (1994) 547.
[19] A.J. Aller, M.A. Castro, Trends Anal. Chem. 25 (2006) 887.
[20] L.C. Robles, A.J. Aller, J. Anal. At. Spectrom. 9 (1994) 871.
[21] L.C. Robles, A.J. Aller, Quim. Anal. 15 (1996) 21.
[22] A.J. Aller, L.C. Robles, Analyst 123 (1998) 919.
[23] L.M. Mateos, E. Ordóñez, M. Letek, J.A. Gil, Int. Microbiol. 9 (2006) 207.
[24] D. Páez-Espino, J. Tamames, V. de Lorenzo, D. Cánovas, Biometals 22 (2009) 117.
[25] J.C. Feo, E. Ordoñez, M. Letek, M.A. Castro, M.I. Muñoz, J.A. Gil, L.M. Mateos, A.J. Aller, Water Res. 41 (2007) 531.
[26] J. Kostal, R. Yang, C.H. Wu, A. Mulchandani, W. Chen, Appl. Environ. Microbiol. 70 (2004) 4582.
[27] F.F. Roberto, J.M. Barnes, D.F. Bruhn, Talanta 58 (2002) 181.
[28] A. Tauriainen, M. Virta, W. Chang, M. Karp, Anal. Biochem. 272 (1999) 191.
[29] Y.L. Meng, Z. Liu, B.P. Rosen, J. Biol. Chem. 279 (2004) 18334.
[30] E. Ordóñez, M. Letek, N. Valbuena, J.A. Gil, L.M. Mateos, Appl. Environ. Microbiol. 71 (2005) 6206.
[31] H.L. Fu, Y. Meng, E. Ordóñez, A.F. Villadangos, H. Bhattacharjee, J.A. Gil, L.M. Mateos, B.P. Rosen, J. Biol. Chem. 284 (2009) 19887.
[32] E. Ordóñez, K. Van Belle, G. Roos, S. De Galan, M. Letek, J.A. Gil, L. Wyns, L.M. Mateos, J. Messens, J. Biol. Chem. 284 (2009) 15107.
[33] H. Kaneko, K. Sakaguchi, Agric. Biol. Chem. 43 (1979) 1007.
[34] C. Fernández-González, J.A. Gil, L.M. Mateos, A. Schwarzer, A. Schäfer, J. Kalinowski, A. Pühler, J.F. Martín, Appl. Microbiol. Biotechnol. 46 (1996) 554.
[35] M. Letek, N. Valbuena, A. Ramos, E. Ordóñez, J.A. Gil, L.M. Mateos, J. Bacteriol. 188 (2006) 409.
[36] M. Bettinelli, C. Baffi, G.M. Beone, S. Spezia, At. Spectrosc. 21 (2000) 60.
[37] M. Hoenig, Talanta 54 (2001) 1021.
[38] A.J. Aller, J.M. Lumbreras, L.C. Robles, G.M. Fernández, Anal. Chim. Acta 330 (1996) 89.
[39] A.J. Aller, L.C. Robles, J. Anal. At. Spectrom. 13 (1998) 469.

Talanta 80 (2010) 1428–1435

Contents lists available at ScienceDirect

Talanta

journal homepage: www.elsevier.com/locate/talanta

Two analyte calibrations from the transient response of a single potentiometric sensor employed with the SIA technique

Raul Cartas [a], Aitor Mimendia [a], Andrey Legin [b], Manel del Valle [a,*]

[a] Sensors and Biosensors Group, Chemistry Department, Universitat Autònoma de Barcelona, Edifici Cn, 08193 Bellaterra, Barcelona, Spain
[b] Chemistry Dept, St. Petersburg University, Universitetskaya nab. 7/9, 199034 St. Petersburg, Russia

ARTICLE INFO

Article history:
Received 29 May 2009
Received in revised form
21 September 2009
Accepted 25 September 2009
Available online 3 October 2009

Keywords:
Wavelet transform
Artificial neural networks
Multi-analyte calibration
SIA
Potentiometry

ABSTRACT

Simultaneous quantification of Cd^{2+} and Pb^{2+} in solution has been correctly targeted using the kinetic information from a single non-specific potentiometric sensor. Dual quantification was accomplished from the complex information in the transient response of an electrode used in a Sequential Injection Analysis (SIA) system and recorded after step injection of sample. Data was firstly preprocessed with the Discrete Wavelet Transform (DWT) to extract significant features and then fed into an Artificial Neural Network (ANN) for building the calibration model. DWT stage was optimized regarding the wavelet function and decomposition level, while the ANN stage was optimized on its structure. To simultaneously corroborate the effectiveness of the approach, two different potentiometric sensors were used as study case, one using a glass selective to Cd^{2+} and another a PVC membrane selective to Pb^{2+}.

© 2009 Elsevier B.V. All rights reserved.

1. Introduction

Automated systems based on flow-injection techniques, namely Flow-Injection Analysis (FIA) and Sequential Injection Analysis (SIA), have been used in analytical chemistry during the last three decades [1,2]. With these, species detection for either qualitative or quantitative purposes can be accomplished by using different detection principles; when the systems employ sensors at the detection stage, specially simple and efficient analytical systems can be devised. Selectivity of used sensors plays an important role given it determines discrimination capability [3]. Early applications based on flow-injection techniques were developed using highly selective sensors, but the lack of availability of specific sensors for all needs fostered the proposal of a new approach. This alternate solution to the lack of sensor variety is the use of sensors with less restrictive response characteristics and the attempt to take advantage of multidimensional information that they can provide [4].

Detection of a single analyte in the simpler cases does not represent a challenge for low-selective sensors; but for multi-species detection in complex matrices, these sensors provide signals with multiple analyte dependence that makes mandatory the use of chemometric tools for deconvolution. This multicomponent aspect can be derived either from a high dimensional signal [5,6] or from the use of sensor arrays [7].

Calibration models for multiple component determinations have been built with different multivariate tools such as Multiple Linear Regression [8–10], Multivariate Curve Resolution [11,12], Principal Component Regression [13–15], Partial Least Squares [13,16–18], Non-linear Iteratively Partial Least Squares [10], Non-linear Least Squares [9], Support Vector Machines [19] and Artificial Neural Networks (ANNs) [20–23]. From this set of tools, ANNs have outstood due to its ability to model both linear and non-linear responses (with respect to the analytes). Models based on ANNs are sometimes created from high-dimensionality information, for example a mass spectra or a voltammogram. In such cases, preprocessing must be done to compress the signals while preserving enough amount of relevant information. Usual approaches for data preprocessing are Principal Component Analysis (PCA) [2,13,15,18,24], Fourier Transform [20] and Discrete Wavelet Transform (DWT) [25]. Among these tools, DWT has certain interesting advantages because, besides to compression, the technique also filters and smoothes signals.

Analytical use of sensors is carried out normally in steady state conditions, but recent applications have explored the advantages of using their dynamic signals. These can be derived from chemical kinetics or from their use immersed in flowing solutions. This additional characteristic represents an advantage, since the richer content of information supplied by the dynamic response of a sensor after, e.g. a step profile insertion of the sample improves the discrimination ability between primary and interfering species [13,26].

* Corresponding author. Tel.: +34 93 5811017; fax: +34 93 5812379.
E-mail address: manel.delvalle@uab.es (M. del Valle).

0039-9140/$ – see front matter © 2009 Elsevier B.V. All rights reserved.
doi:10.1016/j.talanta.2009.09.048

From this departure point, FIA systems combined with spectrophotometric detection were applied to resolve ternary mixtures of metallic cations [14] or binary mixtures of antibiotics [16]. Dynamic signals recorded from an array of potentiometric sensors coupled to an SIA system were reported for the resolution of ternary and quaternary mixtures of cations in water samples [20]. Heavy metals have also been the goal of multi-species determination based on transient signals. Relevant to this communication is the work reported in [26], where a flow-injection system coupled to a sensor array was used for the simultaneous quantification of two metallic ions in solution from the dynamic sensor recordings. Similarly, dynamic signals obtained with two different biosensor-based FIA systems have been used for the binary determinations of glucose/pH or urea/pH pairs [21]. The same methodology was successfully applied later for the quantification of several concentrations of penicillin [22]. In all the described cases, transient signal is directly processed, without any data pre-treatment.

This work describes the use of a potentiometric sensor in a SIA system, which after a chemometric treatment of its transient signal, permits to simultaneously quantify two analytes. The advanced approach suggested takes advantage of the dynamic response and cross-sensitivity contained in a single non-specific sensor to resolve a binary mixture. As case study, quantification of cadmium and lead is performed departing from the signal recorded from one sensor only, after the high reproducible step injection of a sample employing the SIA system.

In the data treatment aspect, it is difficult to build calibration models from dynamic responses, given the increased complexity of the signals after addition of the kinetic dimension. In this work, the difficulty was surpassed by first preprocessing the recordings using DWT to reduce their size and extract significant features [25]. Compressed information was later fed to an Artificial Neural Network (ANN) to finally build the calibration model. The utility of the approach is shown by modelling both analytes in two different study cases: two potentiometric sensors from different nature, PVC or glass membrane, were used to illustrate the concept. The final aim of the work is to enrich the type of information to be used by electronic tongues with multiple sensors, to better resolve the most complex cases.

2. Experimental

2.1. Equipment

Quantification of two heavy metals in solution was the goal of this application. A total of 45 different combinations for cadmium and lead were randomly generated using Excel and then programmed for being automatically prepared (by dilution from stocks) and injected into a cell by a SIA system available at our laboratory [20]. Composition of mixed solutions is available for downloading as Supplementary information. The SIA system shown in Fig. 1 is formed by a fluidic stage and a measurement stage. The former consists of an automatic microburette (Crison 2030 microburette, Crison, Spain) equipped with a 5 ml syringe (Hamilton, Switzerland), a holding coil (5 ml volume, 1 mm Ø PTFE tube, Bioblock, France), an 8 way Hamilton MVP valve (Hamilton, Switzerland) and a 7 ml home-made Perspex mixing cell with a magnetic stirrer. The measurement stage comprises the sensors, a reference electrode (Thermoelectron 900200, MA, USA) and an 8-channel signal conditioning circuit connected to a Data Acquisition System (National Instruments NI 6221 Multifunction DAQ, TX, USA). All active elements involved in the SIA system are controlled using a virtual instrument developed in LabView [20] through the RS-232 port of a PC Pentium III at 600 MHz.

2.2. Reagents and solutions

Standards were prepared by the SIA system using a 0.05 M acetic/acetate buffer at pH 4.5 as carrier and diluting solution. Analytes were in ranges 0–2.44×10^{-4} M for Cd^{2+} and 0–4.97×10^{-5} M for Pb^{2+}. These ranges were determined by the optimal working range of the sensors used. Studied concentrations, although low for conventional potentiometric sensors, are higher than those permitted by the Environmental Protection Agency. It is also worth noticing that for heavy metals these permitted levels are extremely low (75 nM for lead and 45 nM for cadmium). All solutions carrier were prepared using doubly distilled water and analytical grade (or similar) reagents.

2.3. Sensors and procedure

The measuring cell incorporated two ion selective electrodes (ISEs) with cross response to the tested heavy metals, and a Ag–AgCl reference electrode. One ISE was based on a potentiometric Pb^{2+} PVC membrane with trioctylphosphine oxide as ionophore, and the other was based on a chalcogenide glass selective to Cd^{2+}. ISEs were fabricated at the Chemistry Department of St. Petersburg University.

Each ISE was characterized in static and flow conditions. Batch analysis measurements were firstly done in distilled water and later in single ion solutions at different concentrations. Linear working

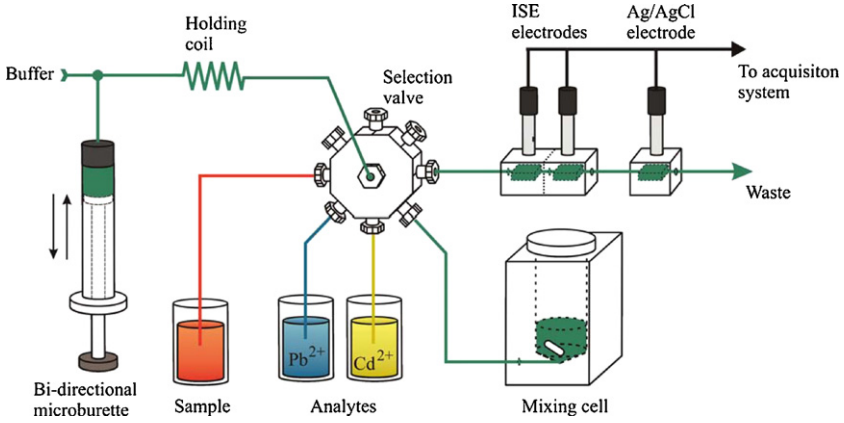


Fig. 1. Scheme of the SIA system employed. The measurement part comprises the ISEs, the reference electrode and the acquisition system (not shown in the figure). The fluidic part is formed by the microburette, the holding coil, the selection valve and the mixing cell with magnetic stirrer.

Table 1
Summary of data calibration results for the Cd-ISE and Pb-ISE in static conditions according to Nernstian model. Slope and intercept values obtained from the linear fit of the linear response zone.

Sensor	Response to distilled water (mV)	Linear fit data	
		Intercept (mV)	Slope (mV/dec)
Cd^{2+}	−365.9	−272.19	16.55
Pb^{2+}	138.7	321.29	26.45

zone was determined from the calibration curves for each sensor. Slope and intercept describing the linear response for each sensor are contained in Table 1. Characterization in flow condition was done by firstly examining the sensors in distilled water, then in acetate buffer and lastly integrating them in the flow cells to determine the responses to single metal solutions automatically prepared by the SIA system. Detection limit was taken at the point of intersection of the two asymptotic behaviours of calibration curves, as recommended by IUPAC. Calibration results are summarized in Table 2. Characterization shows that cadmium electrode response to Cd^{2+} ion presents poor response, having a sensitivity value lower than the theoretical one for double charged ions (29 mV/dec). Despite this bad response, the electrode was not replaced given that was the only one available.

After characterization, the cell containing the set of electrodes was subject to injections of binary mixtures of heavy metals. Samples were injected into the cell with a step profile and the transient response for each ISE was simultaneously recorded during 60 s per sample in time steps of 0.1 s, obtaining two data sets of potentials, one per ISE.

2.4. Information processing and modelling

Both matrices of potentials were preprocessed by DWT to reduce the number of variables before entering the ANN. Preprocessing and modelling were done using MATLAB. DWT was carried out with the Wavelet Toolbox. DWT is implemented in MATLAB using Mallat's pyramidal algorithm (Fig. 2). This signal processing technique operates over a single discrete signal by applying two digital complementary filters performing low-pass and high-pass filtering followed by downsampling. The result of the decomposition is two sets of coefficients named approximation and detail coefficients, each one correlated with the low- and high-frequency content of the signal, respectively. The size of each set after transforming the signal is approximately half the original size. The process can be repeatedly applied on either set of coefficients, taking the decomposition procedure one level down and obtaining two more sets of coefficients (approximation and detail) each time the transformation is carried out. In this work, compression was accomplished by retaining the approximation coefficients resulting from this transformation and discarding the detail coefficients.

The full set of discrete wavelets available in MATLAB's toolbox (the four families Daubechies, Coiflets, Symlets and Biorthogonal Spline) was evaluated with decomposition levels ranging from 1 up to 9. The goal was to find the combination that performed the best in terms of retaining most of the original information with the fewer number of components for correctly modelling the next step. The number of combinations evaluated was 324, considering each Wavelet family was also assayed at different orders.

Calibration model was based on an ANN built with the Neural Network Toolbox. Several ANNs were also attempted in order to find the optimum structure. In all cases, ANNs were feedforward

Table 2
Summary of data calibration results for the Cd^{2+} and Pb^{2+} ISEs in flowing conditions. Sensitivities expressed as slopes obtained from linear fit of the linear working zone.

Sensor	Sensitivity to Cd^{2+} ion (mV/dec)	Sensitivity to Pb^{2+} ion (mV/dec)	Potentiometric selectivity coefficient log $\left(K_{x,y}^{pot}\right)$ [a]	Detection limit (M)[b]
Cd^{2+}	8.51	6.05	1.2 ± 0.1	2.00×10^{-6}
Pb^{2+}	8.97	20.58	-3.2 ± 0.2	4.48×10^{-5}

[a] Uncertainty intervals calculated at 95% of confidence level.
[b] Determined as the intercept between the linear Nernstian behaviour and the horizontal line in absence of response.

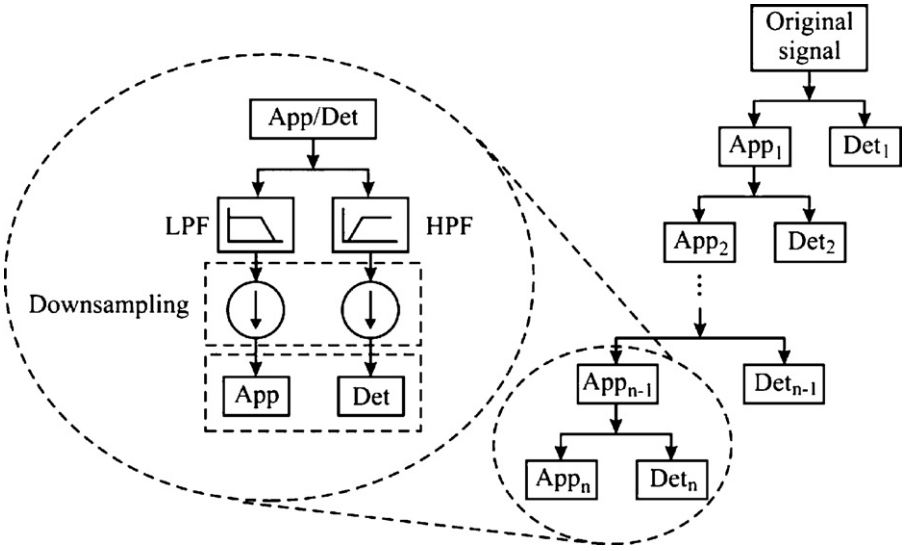


Fig. 2. Mallat's pyramidal algorithm implemented in MATLAB's Wavelet Toolbox. Approximation and detail coefficients are indicated by App and Det, respectively. Subindexes denote decomposition level up to an *n*-th level. LPF and HPF stand for low-pass and high-pass filters, respectively. Downsampling is represented by a circle with a centred arrow pointing downwards.

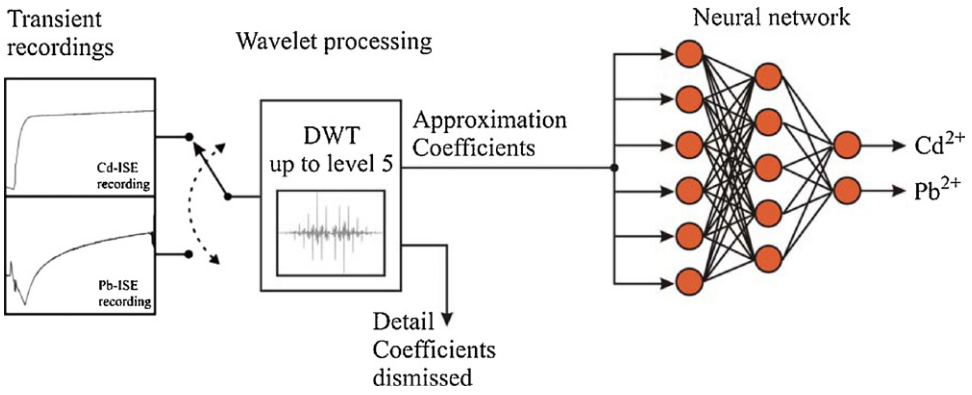


Fig. 3. Scheme depicting both the information processing and modelling stages. Recordings are processed by the DWT and the approximation coefficients obtained from the decomposition are used to feed the ANN for building the calibration model.

type trained with the Bayesian regularization algorithm for better fitting the test set. Approximation coefficients were taken as inputs, and concentrations of cadmium and lead as targets. Sets of inputs and targets were split into two subsets for training and testing purposes. Structures with one and two hidden layers, different number of neurons (from 6 up to 30) and different non-linear transfer functions in their hidden layers were tested. A scheme showing the coupling of preprocessing and modelling stages is depicted in Fig. 3.

3. Results

The departure universe of data consisted of two input matrices (one per ISE) formed by the transient recordings (600 data values) obtained with the 45 samples, plus a target matrix formed by the corresponding concentrations of each binary mixture of heavy metals. The size of each recording made mandatory the compression before building the calibration model with the ANN. As reference, two recordings are shown in Fig. 4, one per each ISE, where one can visualize that the glass membrane ISE (the Cd^{2+} electrode) displays a faster response than the polymeric membrane type (the Pb-ISE).

The combination of wavelet and decomposition level used in our application was chosen based on the compression ratio, percentage of total energy retained by approximation coefficients after each decomposition and degree of similarity between the original recording and the one reconstructed using only the coefficients retained. Compression ratio is the relationship between the original data size to the number of approximation coefficients

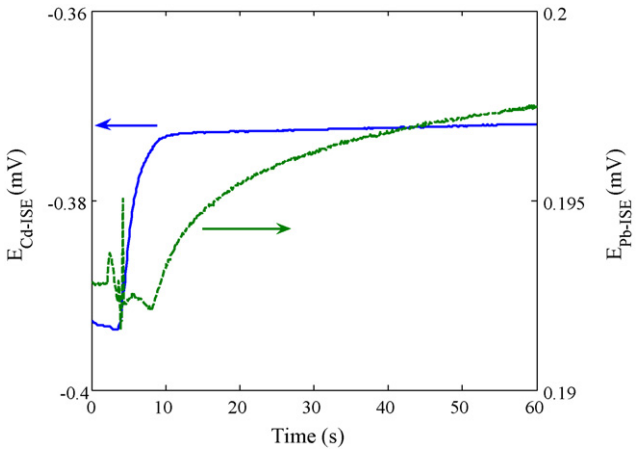


Fig. 4. Example of two transient signals recorded with the ISEs after step insertion of a sample into the cell. Analyte mixture corresponds to concentrations (lead and cadmium) 85.7 and 49.4 μM, respectively.

obtained after decomposition. Total energy is defined as the sum of all squared detail coefficients over all scales plus the square of the remaining approximation coefficients. Finally, comparisons between the original and reconstructed recordings were carried out at all levels of decomposition. This evaluation is proposed since we have loss of information after dismissing the detail coefficients.

Compression ratios reported values as low as 1.9 for Coiflets Wavelet of fifth order and decomposition level 1, to as high as 300 for Daubechies Wavelet of first order and decomposition level 9. Bar graphs in Fig. 5 show the number of approximation coefficients obtained by DWT for the 326 combinations detailed above. Energy retained by approximation coefficients was over 99% of total energy contained in the complete set of coefficients for all decomposition levels, meaning that almost no high-frequency components are contained in raw recordings (most of the high-frequency components are noise).

Degree of similarity between original and reconstructed signals was evaluated by running a test described in [25]. The test compares two discrete signals of the same size and yields a result between 0 and 1 depending on how they match. The result is 0 when the two signals have nothing in common and increases with its matching. Results along the different tests done ranged from 0.746 for signals processed with the Coiflets Wavelet of first order, up to 0.999 for signals processed with the set of second order filters (for decomposition and reconstruction) contained in the Biorthogonal Spline Wavelet, being the latter the family showing best performance.

Approximation coefficients from decomposition levels 1 to 4 and 6 to 9 for all wavelets were not considered for ANN modelling given that (i) the large amount of coefficients from levels 1 to 4 made the network training last too long, (ii) the coefficients from level 6 did not helped the network to converge to the desired error during training and (iii) signals reconstructed with coefficients from levels 6 to 9 yielded similarity values below 0.95. This threshold, imposed to assure a faithful representation in the compression stage, was the reason that only approximation coefficients obtained at decomposition level 5 were used for building the calibration model.

Among the tests, the wavelet function that best performed was the Biorthogonal Spline Wavelet of order 3 for decomposition and order 1 for reconstruction ('bior3.1', according to MATLAB's nomenclature). The number of approximation coefficients retained after decomposition was 23, yielding a final data matrix of size 23×45 for each set of transient signals. Mean degree of similarity was 0.985 for Cd^{2+} ISE and 0.991 for Pb^{2+} ISE. For comparison purposes, Fig. 6 shows two plots for the degree of similarity obtained when original signals from Cd-ISE and Pb-ISE were compared against their corresponding signals reconstructed using the approximation coefficients after wavelet decomposition. Only wavelets of order 3 are

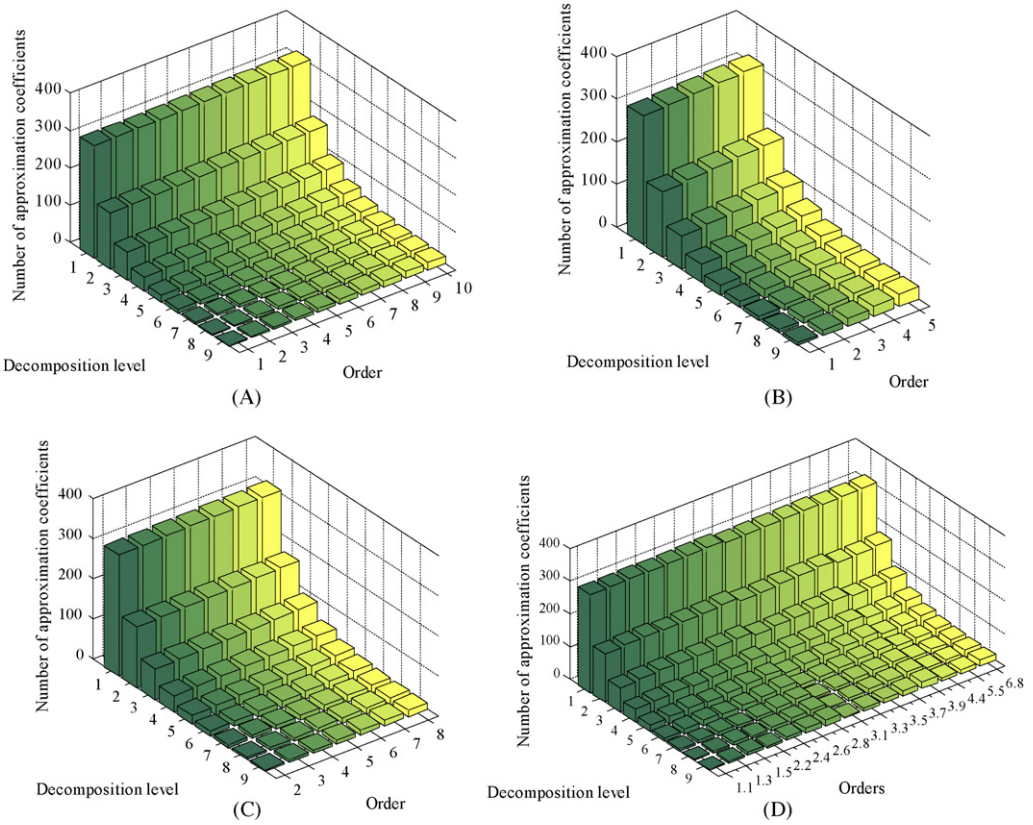


Fig. 5. Bar graphs showing the number of approximation coefficients obtained with nine decomposition levels using discrete wavelet families (A) Daubechies, (B) Coiflets, (C) Symlets and (D) Biorthogonal Spline. All wavelets were tested at all orders available. For the case of the Biorthogonal Spline family, the format used to indicate the orders is as follows, the first number corresponds to the order for decomposition and the second number to the order of reconstruction.

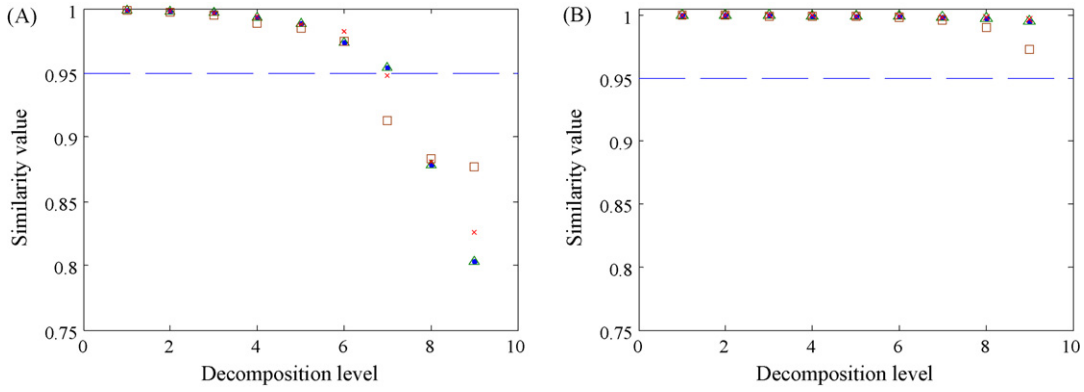


Fig. 6. Plots for similarity values from reconstructed and original recordings obtained with (A) Cd-ISE and (B) Pb-ISE. The dashed line marks the 0.95 value imposed as limit. The markers identify the wavelet family: (●) Daubechies, (△) Symlets, (+) Coiflets, (□) Biorthogonal Spline. Plots were obtained with wavelets of third order for comparison purposes.

indicated since the chosen wavelet is of order 3 for decomposition.

Regarding the calibration model, all trained networks had structures with one or two hidden layers and one output layer. Non-linear activation functions of sigmoidal type were used in hidden layers while linear activation function was used in the output layer. Neurons for the one hidden layer case varied from 6 up to 30. Neurons for the two hidden layers case varied from 6–24 up to 24–6. These combinations were obtained by increasing in one the neurons in the first hidden layer while decreasing in one the neurons in the second hidden layer. Structures with one output for independently modelling each metal ion were proposed, as well as structures with two outputs for simultaneous quantification of cadmium and lead.

Wavelet coefficients and concentrations were randomly split into two subsets for training and testing purposes, 75% of total information was used to determine the parameters of the model while the remaining was used for testing its generalization capability. No third subset was used for internal validation, given the training algorithm used (Bayesian regularization) prevents overfitting by other means. In order to facilitate convergence, input and output data in training subset were firstly normalized in the interval [−1,1]. Data normalization of testing subset was done according to maximum and minimum values obtained from training subset. The sum of squared errors (SSE), from the differences between the expected and calculated values, was used for tracking convergence during training. Error goal was set to 0.09 since this value had proven to avoid overfitting in our work and yielded low dispersion

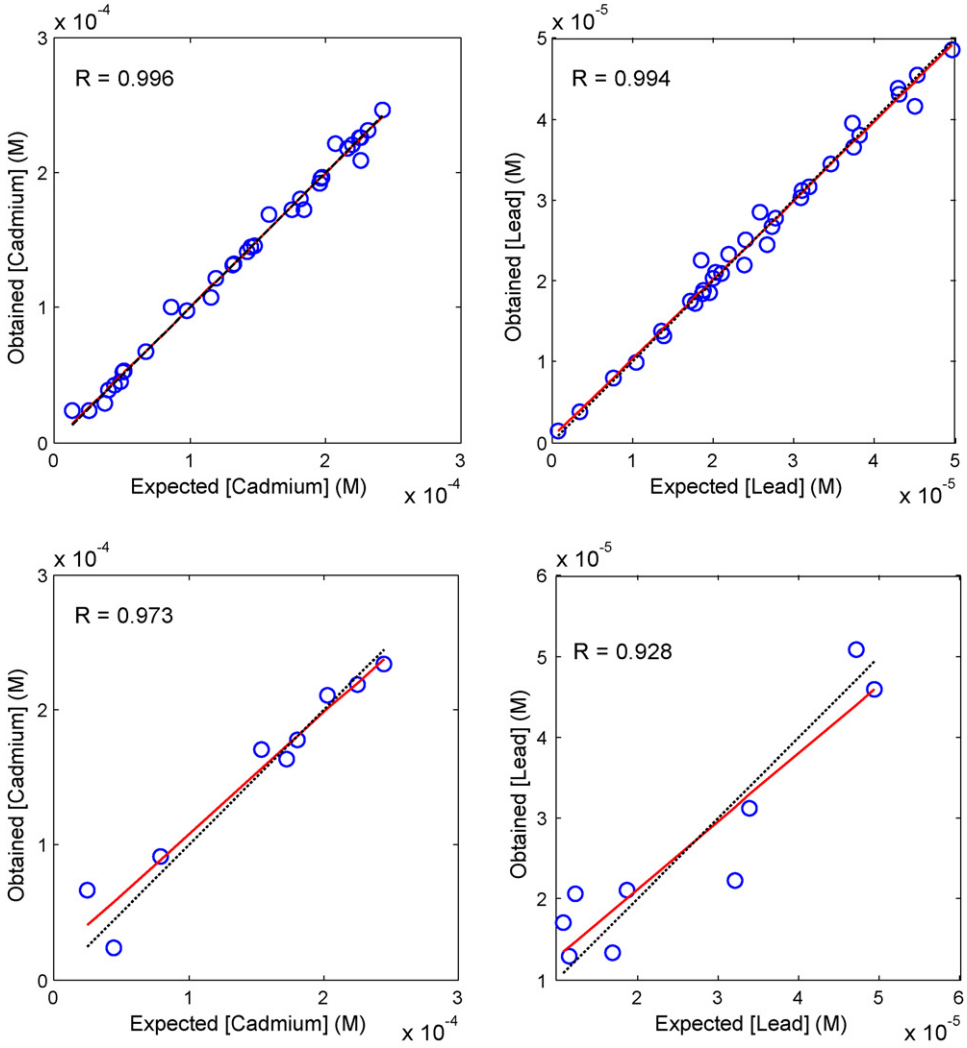


Fig. 7. Comparison of obtained vs. expected concentration for cadmium (left) and lead (right) using the recordings from the Cd-ISE. Dashed line corresponds to ideality and solid line corresponds to the obtained fit. Plots in the upper row are the results for training, plots in the lower row are the results for testing.

when linear regression analysis is performed between the obtained and expected values. SSE and correlation coefficients of the previous comparison were also used as figures of merit when the trained networks were tested.

None of the network structures with two outputs, as well as structures with one hidden layer and two outputs performed well in testing although training was fulfilled. For these cases, error goal was met in almost 50% of training runs but correlation coefficients obtained in testing were below 0.6 and even negative.

Networks with one output for single analyte quantification were those showing better performance. The structure that worked the best had 10 neurons in the first hidden layer, 4 neurons in the second hidden layer, and one neuron in its output layer, both for Cd and for Pb sensor signals. Hyperbolic tangent sigmoid function was used as transfer function in both hidden layers, and linear transfer function in the output layer. Simultaneous analyte determination was accomplished using two parallel networks with the aforementioned structure, one per metal ion and fed with the same DWT reduced transient. Fig. 7 shows the regression plots between the expected and predicted concentration for cadmium and lead obtained with the Cd^{2+} electrode, Fig. 8 are the equivalent plots for the Pb^{2+} electrode, an ISE with a completely different membrane type, and very different intrinsic response rate. Cd^{2+} sensor employed a chalcogenide glass and was fast responding, while Pb^{2+} sensor used a potentiometric PVC membrane and was much slower.

Effectiveness of the data processing methodology was corroborated by doing 25 additional trainings with a 9-fold cross validation over each electrode's recordings. Input and output data were randomly split into five parts, four fifths were taken for training and one fifth for testing. As previously, training data was firstly normalized and then testing data. Error goal was met in all cases. Results obtained yielded mean SSE in testing as low as $0.259 \pm 0.029\,mol^2\,l^2$ for lead prediction using the Pb-ISE, to as high as $0.725 \pm 0.049\,mol^2\,l^2$ for cadmium prediction with the same electrode. Average values for SSEs and correlation coefficients obtained with Cd-ISE are shown in Table 3; Table 4 presents the results obtained with Pb-ISE. Indicated uncertainties correspond to the 95% confidence interval for the 25 replicate training cases.

The proposed methodology was compared against the approach based on PCA preprocessing followed by ANN modelling to provide some reference. PCA was performed on both sets of recordings using the MATLAB's Statistics Toolbox. The analysis of the decomposition showed that for any of the two data sets more than 98% of variance was accounted for by the first two principal components. Two matrices were built with the two principal components from each data set and independently used for modelling. When neural networks with equivalent structures to those above were trained with this PCA preprocessed matrix, none of the networks converged to the desired error goal during training. These results, we believe, highlight the difficulties of the chemometric treatment.

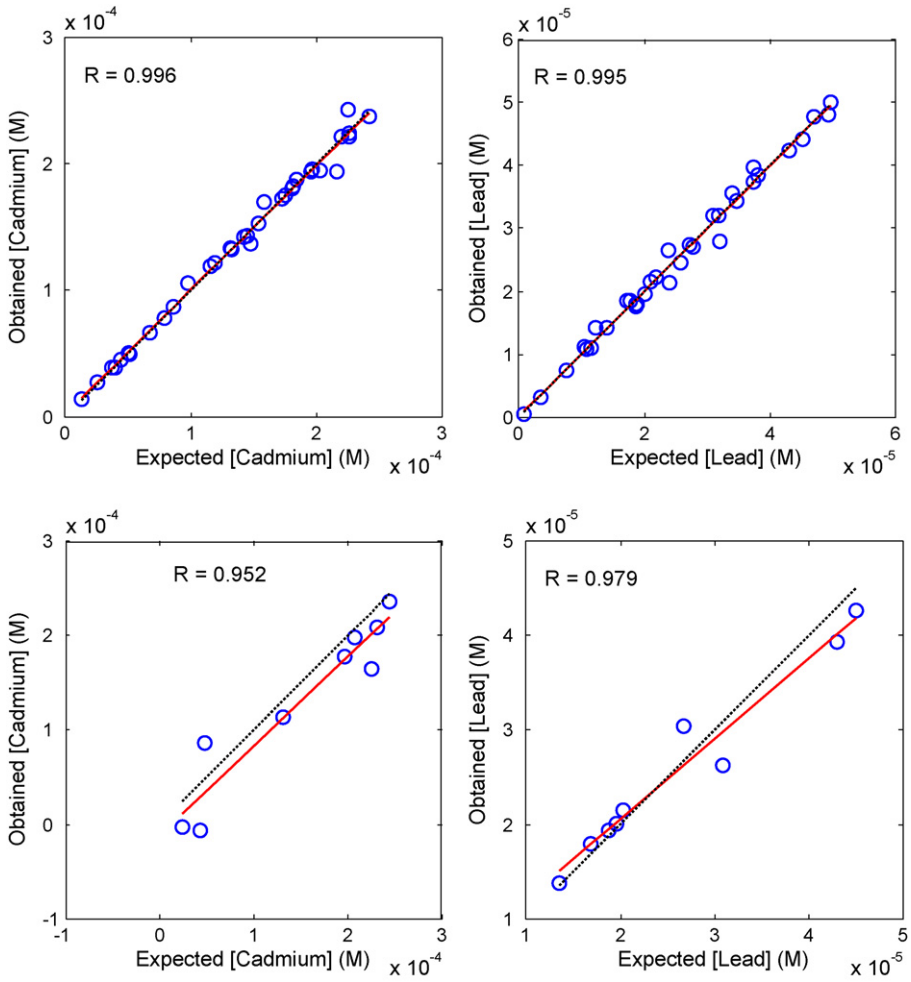


Fig. 8. Comparison of obtained vs. expected concentration for cadmium (left) and lead (right) using the recordings from the Pb-ISE. Dashed line corresponds to ideality and solid line corresponds to the obtained fit. Plots in the upper row are the results for training, plots in the lower row are the results for testing.

Table 3
Mean values for the SSE and correlation coefficient (R) obtained with the cross validation process using the Cd-ISE. Uncertainty intervals calculated at 95% confidence level.

Analyte	Training		Testing	
	SSE ($mol^2\ l^{-2}$)	R	SSE ($mol^2\ l^{-2}$)	R
Cd^{2+}	$0.0980 \pm 3 \times 10^{-4}$	$0.996 \pm 9.9 \times 10^{-4}$	0.544 ± 0.062	0.917 ± 0.019
Pb^{2+}	$0.0977 \pm 5 \times 10^{-4}$	$0.995 \pm 1 \times 10^{-4}$	0.715 ± 0.044	0.844 ± 0.029

Table 4
Mean values for the SSE and correlation coefficient (R) obtained with the cross validation process using the Pb-ISE. Uncertainty intervals calculated at 95% of confidence interval.

Analyte	Training		Testing	
	SSE ($mol^2\ l^{-2}$)	R	SSE ($mol^2\ l^{-2}$)	R
Cd^{2+}	$0.0978 \pm 5 \times 10^{-4}$	$0.996 \pm 3 \times 10^{-4}$	0.725 ± 0.049	0.926 ± 0.004
Pb^{2+}	$0.0976 \pm 4 \times 10^{-4}$	$0.995 \pm 1 \times 10^{-4}$	0.259 ± 0.029	0.934 ± 0.031

4. Conclusions

The present work shows a procedure for simultaneous quantitative determination of a binary mixture using the transient recording from a single electrode. The procedure was carried out twice with sensors of different nature to demonstrate its applicability. Our approach takes advantage of the kinetic information of the interference produced on a sensor to develop the calibration models; in the study, any of the Cd^{2+} or Pb^{2+} electrode could be used to resolve a binary mixture of the two heavy metals.

The calibration model is built by first extracting significant features employing the DWT, then evaluating the information obtained after wavelet transformation for getting a good compression/reconstruction relationship, and finally building the calibration model with an ANN. The DWT processing of the recordings has permitted the reduction of the acquired data from each electrode in a factor ca. 26. The aim of the developed application is to improve performance of existing electronic tongue systems, which may be employing signals from fewer sensors but exploiting their dynamic resolution.

Acknowledgements

This work was supported by Spanish Ministry of Science and Innovation, through project TEC2007-68012-c03-02/MIC and by CONACyT (México) through PhD scholarship 144044 for R. Cartas.

Appendix A. Supplementary data

Supplementary data associated with this article can be found, in the online version, at doi:10.1016/j.talanta.2009.09.048.

References

[1] A. Gutés, F. Céspedes, M. del Valle, Anal. Chim. Acta 600 (2007) 90–96.
[2] J. Ruzicka, E.H. Hansen, Anal. Chem. 72 (2000) 212A–217A.
[3] Yu. Vlasov, A. Legin, A. Rudniskaya, C. Di Natale, A. D'amico, Pure Appl. Chem. 77 (2005) 1965–1983.
[4] J. Gallardo, S. Alegret, M. del Valle, Talanta 66 (2005) 1303–1309.
[5] J. Saurina, S. Hernández-Cassou, Anal. Chim. Acta 438 (2001) 335.
[6] A. Ruiz-Medina, M.L. Fernández-de Córdoba, M.J. Ayora-Cañada, M.I. Pascual-Reguera, A. Molina-Díaz, Anal. Chim. Acta 404 (2000) 131–139.
[7] P. Ciosek, Z. Brzózka, W. Wróblewski, Sens. Actuators B 118 (2006) 454–460.
[8] R. Schindler, M. Watkins, R. Vonach, B. Lendl, R. Kellner, Anal. Chem. 70 (1998) 226–231.
[9] C. Di Natale, A. Macagnano, F. Davide, A. D'Amico, A. Legin, Y. Vlasov, A. Rudnitskaya, B. Selezenev, Sens. Actuators B 44 (1997) 423–428.
[10] E. Richards, C. Bessant, S. Saini, Electroanalysis 14 (2002) 1533–1542.
[11] P. Ciosek, W. Wróblewski, Talanta 71 (2007) 738–746.
[12] A. Pasamontes, M.P. Callao, Anal. Sci. 22 (2006) 131–135.
[13] V. Pravdová, M. Pravda, G.G. Guilbault, Anal. Lett. 35 (2002) 2389–2419.
[14] M. Blanco, J. Coello, H. Iturriaga, S. Maspoch, M. Redón, Anal. Chem. 67 (1995) 4477–4483.
[15] L. Lvova, S.S. Kim, A. Legin, Y. Vlasov, J.S. Yang, G.S. Cha, H. Nam, Anal. Chim. Acta 468 (2002) 303–314.
[16] J. Polster, G. Prestel, M. Wollenweber, G. Kraus, G. Gauglitz, Talanta 42 (1995) 2065–2072.
[17] J. Mortensen, A. Legin, A. Ipatov, A. Rudnitskaya, Y. Vlasov, K. Hjuler, Anal. Chim. Acta 403 (2000) 273–277.
[18] M.J. Culzoni, H.C. Goicoechea, Anal. Bioanal. Chem. 389 (2007) 2217–2225.
[19] P. Ciosek, K. Brudzewski, W. Wróblewski, Meas. Sci. Technol. 17 (2006) 1379–1384.
[20] D. Calvo, A. Durán, M. del Valle, Sens. Actuators B 131 (2008) 77–84.
[21] B. Hitzmann, A. Ritzka, R. Ulber, T. Scheper, K. Schügerl, Anal. Chim. Acta 348 (1997) 135–141.
[22] B. Hitzmann, A. Ritzka, R. Ulber, K. Schöngarth, O. Broxtermann, J. Biotechnol. 65 (1998) 15–22.
[23] L.S. Ferreira, M.B. De Souza Jr., J.O. Trierweiler, O. Broxtermann, R.O.M. Folly, B. Hitzmann, Comput. Chem. Eng. 27 (2003) 1165–1173.
[24] R.M. de Carvalho, C. Mello, L.T. Kubota, Anal. Chim. Acta 420 (2000) 109–212.
[25] L. Moreno-Barón, R. Cartas, A. Merkoçi, S. Alegret, M. del Valle, L. Leija, P.R. Hernández, R. Muñoz, Sens. Actuators B 113 (2006) 487–499.
[26] A.V. Legin, A.M. Rudnitskaya, K.A. Legin, A.V. Ipatov, Yu.G. Vlasov, Russ. J. Appl. Chem. 78 (2005) 89–95.

Talanta 80 (2010) 1436–1440

Contents lists available at ScienceDirect

Talanta

journal homepage: www.elsevier.com/locate/talanta

Simultaneous kinetic determination of 3-hydroxybutyrate and 3-hydroxyvalerate in biopolymer degradation processes

C. García de María*, K.B. Hueso Domínguez

Dpto. de Química Analítica, Nutrición y Bromatología, University of Salamanca, Plaza de la Merced s/n, E-37008 Salamanca, Spain

ARTICLE INFO

Article history:
Received 11 June 2009
Received in revised form
21 September 2009
Accepted 25 September 2009
Available online 3 October 2009

Keywords:
Biopolymer
3-Hydroxybutyrate
3-Hydroxyvalerate
Flow injection
Immobilised enzyme
3-Hydroxybutyrate dehydrogenase

ABSTRACT

A new kinetic method is proposed for the simultaneous determination of 3-hydroxybutyrate (3HB) and 3-hydroxyvalerate (3HV) based on the different rate of the 3-hydroxybutyrate dehydrogenase-catalysed reactions of these compounds with coenzyme NAD^+. A flow injection system with two reactors of immobilised 3-hydroxybutyrate dehydrogenase and dual detection is used. The concentrations of NADH produced after two different reaction times are measured by fluorometry or spectrophotometry and multivariate linear calibration is applied for quantification. Concentrations of 3HB and 3HV between 1×10^{-6} and 1×10^{-4} M can be determined at an average sampling frequency of 20 h^{-1}. In contrast to usual methods, the proposed here makes possible the discrimination of 3HB and 3HV without previous separation so that usual extraction with chlorinated solvents and/or chromatographic separation is not required. The method is of interest in a wide variety of fields concerning PHAs, as it can provide information on the degradation rate and mechanism, composition and structure of these polymers. Its applicability has been proved through the determination of 3HB and 3HV in the digests of some chemically degraded commercial PHAs.

© 2009 Elsevier B.V. All rights reserved.

1. Introduction

Polyhydroxyalkanoates (PHAs) [1,2] are a large group of natural polymers that are synthesized by numerous bacteria under unfavourable growth conditions. Tailor-made PHAs, with controlled composition, structure and properties, are industrially produced with genetically modified bacteria. PHAs have thermoplastics properties but unlike synthetic plastics, they are biodegradable and biocompatible. Most current applications of PHAs are based on these features and are effected in the environmental and medical fields [3,4]. PHAs are ecological plastics that are used in packaging and coating as substitutes for non-biodegradable petrochemical polymers. Their main medical applications are the fabrication of biodegradable body implants and the control of drug delivery, this being used also in pharmacy, agriculture and veterinary. Moreover, the degradation of PHAs is a source of optically active monomers of hydroxyalkanoic acids [5] that can be used to synthesize chiral compounds such as aminoacids, vitamins, antibiotics, pheromones, perfumes or biodegradable solvents. PHAs can be degraded by enzymes (biodegradation) but also by chemical or thermal processes. From an applicative point of view, the degradation kinetics is essential since the degradation rate or the resultant products can determine the potential applications. Chemical hydrolysis is also a crucial stage of methods for indirect analysis of PHAs.

Although more than 150 different monomers of hydroxyalkanoic acids can be combined to give PHAs, only very few of them are actually used. The commonest PHA is poly(3-hydroxybutyrate) (PHB), a homopolymer of (R)-3-hydroxybutyric acid (3HB). The high cost and some disadvantages of PHB have lead to the production of copolymers of 3HB and other hydroxyalkanoic acids. The most widespread commercial products are the copolymers of 3HB and (R)-3-hydroxyvaleric acid (3HV) with variable properties depending on the percentage of poly(3-hydroxyvalerate) (PHV). Experimental products include also blends of PHAs (homopolymers, copolymers or both) and blends of PHAs with other biodegradable polymers. As PHB and PHV are by far the commonest components of PHAs, 3HB and/or 3HV are generally among the ultimate degradation products. The quantification of these monomers can provide information not only on the degradation rate and mechanism but also on the composition and structure of PHAs. Indirect quantification of PHB, PHV and their copolymers is commonly performed after alcoholysis with methanol, ethanol or propanol in sulphuric or hydrochloric acids. The polymers are quantitatively transformed into the esters of 3HB and/or 3HV which can be extracted with chloroform or other solvents and determined by gas chromatography with flame ionization (GC–FID) or mass spectrometry (GC–MS) detection [6,7]. In these methods, the recoveries of PHB and PHV are not complete, due to the partition of the esters between the aqueous and organic phases. Alternatively, the

* Corresponding author. Tel.: +34 923294483.

0039-9140/$ – see front matter © 2009 Elsevier B.V. All rights reserved.
doi:10.1016/j.talanta.2009.09.049

esters can be hydrolysed to their respective hydroxyacids which are then determined directly in aqueous solution by ion-exchange chromatography with conductivity detection [8]. In concentrated sulphuric acid, PHB is quantitatively converted into crotonic acid that can be analysed by HPLC with ultraviolet detection [9]; this is not applicable to PHV [10]. Alkaline hydrolysis of PHB gives a mixture of crotonic acid and 3HB while PHV is converted into 3HV; these products are then usually determined also by chromatographic methods [9,11]. Whatever the degradation process, the 3HB formed can be determined directly in aqueous solution by enzymatic analysis, this being a rapid alternative to chromatographic methods. Enzymatic determinations are based on the selective action of the enzyme (R)-3-hydroxybutyrate dehydrogenase (3-HBDH) which catalyses the oxidation of 3HB with NAD^+ to give acetoacetic acid and NADH. First described by Williamson et al. [12], this reaction is also the basis of a wide variety of methods for the determination of 3HB in biological samples such as blood, serum, urine or milk for clinical or veterinary purposes [12–16]. In its biopolymer applications, the NADH produced is measured directly by photometry at 340 nm [17] or after coupling with other enzymatic reactions using photometric [8] or amperometric detection [18]. The catalytic action of 3-HBDH is highly selective, but not specific for the R-isomer of 3HB. Although the S-isomer does not react, other (R)-3-hydroxyacids, such as (R)-3-hydroxyvaleric or (R)-3-hydroxyhexanoic acids, can also be transformed at slower rates [19]. The existing enzymatic methods are based on measurements under equilibrium conditions (i.e., when the enzymatic reaction is complete) and the quantification of 3HB is only possible if other interfering hydroxyacids are not present. An enzymatic method has been proposed [8] for the determination of the total sum of 3HB and 3HV although these compounds cannot be individually quantified.

In this article, an enzymatic method is described which makes possible the individual determination of 3HB and 3HV in mixtures of these compounds. It is based on the different rate of the about mentioned 3-HBDH-catalysed reactions:

$$3HB + NAD^+ \overset{3\text{-HBDH}}{\longleftrightarrow} \text{acetoacetate} + NADH^+ + H^+ \quad (1)$$

$$3HV + NAD^+ \overset{3\text{-HBDH}}{\longleftrightarrow} \text{3-ketovalerate} + NADH + H^+ \quad (2)$$

The total NADH produced is measured under two different kinetic conditions and the concentrations of 3HB and 3HV are calculated by mathematical computation using multivariate linear calibration. Highly reproducible measurements are achieved using flow injection analysis with immobilised 3-HBDH. The proposed procedure is applied to the determination of 3HB and 3HV in chemically degraded commercial PHAs.

2. Experimental

2.1. Apparatus and materials

A RF-10AXL fluorescence detector and a SPD 6AV UV–vis spectrophotometric detector were used. Both detectors were simultaneously connected to a SCL-10AVP System Controller and a computer with LC Solution software (all from Shimadzu, Madrid) for data acquisition. Reagents were propelled with a Minipuls 2-HP4 peristaltic pump (Gilson, Madrid) with calibrated vinyl pump tubes (0.60 $cm^3\ m^{-1}$). Samples and standards were injected with a V-1451 injection valve (Upchurch Scientific, Barcelona, Spain) electronically actuated and provided with loops of different volume; the sample loop was fed with another peristaltic pump. Flangeless fittings, unions and tees (Upchurch Scientific) and 0.5 mm i.d. PTFE tubing were used in the flow system. The working temperature was controlled with a Lauda E-103 circulation thermostat (Hucoa-Erlöss, Madrid). Statistica 6 software (StatSoft, Tulsa, USA) was used for statistical computation.

2.2. Reagents

The following chemicals were supplied by Sigma–Aldrich (Madrid): controlled-pore glass PG 240-120, pore size 240, mesh size 80–120; 3-aminopropyltriethoxysilane; glutaraldehyde, 50% (w/v), aqueous solution; (R)-(−)-3-hydroxybutyric acid, sodium salt; (R)-3-hydroxybutyrate dehydrogenase (E.C. 1.1.1.30); (−)-methyl (R)-3-hydroxyvalerate, >98%; crotonic acid (trans-2-butenoic acid), 98%; Trizma® hydrochloride (Tris(hydroxymethyl)aminomethane hydrochloride), reagent grade, >99%. Oxidized β-nicotinamide-adenine dinucleotide, NAD^+, free acid, grade I, 100%, was from Roche Diagnostics (Barcelona). All other chemicals were of analytical-reagent grade. Working solutions of 3-hydroxybutyrate were prepared from a stock solution (5.0×10^{-3} M) that was renewed daily. Stock solutions of 3-hydroxyvalerate (1.8×10^{-3} M) were freshly prepared by the hydrolysis of the methyl-ester in 0.05 M sodium hydroxide (30 min at room temperature).

2.3. Enzyme reactors

The enzyme 3-HBDH (100 U) was immobilised on controlled-pore glass (CPG, 0.1 g) by indirect covalent binding, as described earlier [20]. The immobilised enzyme was stored wet (in deoxygenated 0.1 M phosphate buffer, pH 6.0) and refrigerated (4 °C) in sealed bottles. Under such conditions, 3-HBDH was very stable: after more than 2 years, the stored immobilised enzyme showed about 55% of its initial activity (activities were compared under the proposed working conditions with newly made enzyme reactors). Enzyme reactors were made by packing the CPG-immobilised enzyme into PTFE tubes (1 mm i.d., 5–6 cm long) with 10 μm frits (Upchurch Scientific) at the ends. The reactors showed no measurable loss of activity after at least 150 injections under the proposed working conditions.

2.4. Samples and sample preparation

Three commercial PHAs were used (Goodfellow, Huntingdon, England). One of them (sample BP-1) was described as polyhydroxybutyrate/polyhydroxyvalerate 12%-biopolymer (PHB88/PHV12), granule, 10% plasticised pellets (citric ester). The second product (sample BP-2) was described as polyhydroxybutyrate-biopolymer (PHB) sheet, technical grade. The label of the third product (sample BP-3) described a polyhydroxybutyrate-biopolymer (PHB), non-woven fabric, research grade. Since the information given was ambiguous or incomplete, the samples were analysed by NMR to estimate their composition. The commercial products were dissolved in deuterated chloroform and their ^1H NMR spectra were registered in a Varian 200 VX spectrometer at 200 MHz. In sample BP-1, the molar ratio PHB:PHV was found to be 7.6:1 and the plasticiser was identified as tributyl O-acetylcitrate. The NMR analysis indicated that both BP-2 and BP-3 were in fact copolymers of 3HB and 3HV with an approximate molar ratio PHB:PHV of 4.2:1 and 4.1:1, respectively.

An adequate amount (20–40 mg) of commercial product was dissolved in 1 mL of chloroform in the 100 mL round bottom flask of a reflux setup. After chloroform was evaporated by heating at 40 °C, 4 mL of propanol and 1 mL of concentrated hydrochloric acid were added and reflux was applied for 3 h at 90 °C to perform propanolysis. After diluting and cooling with 80 mL of water, 4 mL of 5 M sodium hydroxide was added to hydrolyse the propyl esters. The mixture was left for 30 min at room temperature and then it was neutralized (pH 7) with hydrochloric acid and made up to 100 mL with water. The resultant sample solutions were analysed for 3HB and 3HV according to the proposed flow injection procedure.

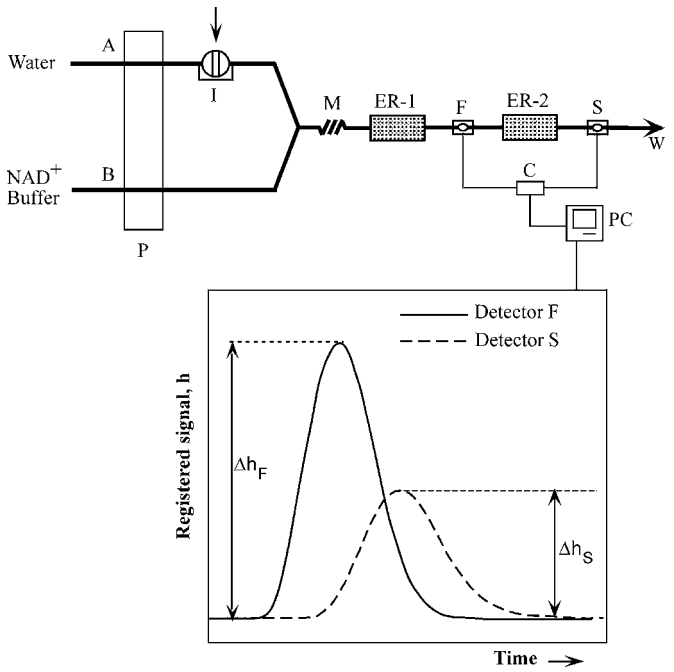


Fig. 1. Diagram of the flow injection system and registered signals. A and B = channels; P = peristaltic pump; I = injection valve; M = mixing coil; ER = enzyme reactors; F = fluorometer; S = spectrophotometer; W = waste; C = control module; PC = computer; Δh_F = fluorescence peak height; Δh_S = absorbance peak height.

2.5. Flow system

The working system is depicted in Fig. 1. It consisted of a flow injection manifold with two enzyme reactors (ER-1, ER-2) containing immobilised 3-HBDH, and two detectors, a fluorometer (F) and a spectrophotometer (S). Both detectors were set for the determination of NADH and were simultaneously connected to a multi-channel data acquisition system where a double real-time signal was registered. Solutions containing 3HB, 3HV or both were injected into a carrier stream (A), merged with the reagent (B, NAD^+ buffered solution) and reacted for two sequential periods as they passed through the enzyme reactors. Every injected solution gave a peak at each detector. The fluorescence peak height (Δh_F) was proportional to the concentration of NADH produced in the first enzyme reactor according to reactions (1) and/or (2). The absorbance peak height (Δh_S) was proportional to the total NADH accumulated after the second enzyme reactor (i.e., after the two reaction periods). With the proposed configuration, the lower sensitivity of the spectrophotometer in comparison with that of the fluorometer was partly compensated by the higher concentrations of NADH to be measured after the second enzyme reactor. The working temperature was controlled by keeping all the solutions (carrier, reagent and injected samples), the mixing coil (M), and the enzyme reactors at constant temperature by means of a circulation thermostat.

2.6. Experimental procedure

The working conditions for the flow system were first established. Some of them (flow rates, sample volume, size of the enzyme reactors and temperature) were fixed after preliminary experiments. The variables of the reagent solution (pH and concentration of NAD^+) were studied and set to get maximum signals. Under the proposed conditions, standard samples containing 3HB, 3HV or both were used to establish the calibration equations for the independent or simultaneous determination of these compounds. Quantifications were based on Δh_F, on Δh_S or on both. The proposed procedure was applied to the determination of 3HB and 3HV in the digests of chemically degraded commercial PHAs.

3. Results and discussion

3.1. Effect of variables

The variables studied and their experimental ranges are summarized in Table 1. The size of the enzyme reactors, the flow rates and the injected sample volume were fixed after preliminary experiments. In the proposed flow system, the registered signals increased on increasing the reaction periods, these being determined by the size of the enzyme reactors and the flow rate through them. Short enzyme reactors were observed to give poor signals unless slow flow rates were used, this giving low sampling frequencies. On the other side, long reactors gave better sensitivity and sampling frequency at moderate flow rates but they produced leaks and became finally obstructed. Predictably, for fixed flow rate and reactors, higher signals but lower sampling frequencies were obtained on increasing the sample volume. The proposed reactors, flow rate and sample volume provided acceptable signals and sampling frequency without flow drawbacks. These conditions can obviously be modified depending on the analytical requirements.

Also predictably, higher fluorescence and absorbance signals were obtained on increasing the working temperature as a result of the increased enzyme activity. However, the rising of temperature produced also less and less reproducible fluorescence peaks. This effect, that was not significant for the absorbance signals, was probably due to the temperature-dependence of the fluorescence of NADH [21] since the flow cell at the fluorometer was not thermostatable. To minimize this effect, a working temperature close to that of the laboratory was proposed.

Once the above mentioned variables were fixed, the influence of pH on the catalytic activity of 3-HBDH for reactions (1) and (2) was first considered. The pH of the reagent solution (1.5×10^{-3} M NAD^+, 0.10 M Trizma®) was varied in the 7.0–9.0 range and 5.0×10^{-5} M solutions of 3HB or 3HV were injected for each pH value. The peak heights obtained at the fluorescence detector are compared in Fig. 2 (a similar graph was obtained from the spectrophotometric detector). The pH profiles indicate that the maximum catalytic activity of 3-HBDH took place at pH close to 8.3 for both 3HB and 3HV. The profiles also indicate that, as expected, 3HV was transformed at lower rate than 3HB.

Table 1
Experimental variables fixed or investigated.

Variable	Experimental range	Fixed/proposed value
Fluorometric detection		
Excitation wavelength		340 nm
Emission wavelength		460 nm
Spectrophotometric detection		340 nm
Flow rates (mL min^{-1})		
A and B	0.10–0.75	0.20
Reactor size (cm)		
M		125
ER-1	1–10	5
ER-2	1–10	6
Sample volume (μL)	35–250	115
Temperature (°C)	20–40	25
pH	7.0–9.0	8.3
NAD^+ (M)	1.5×10^{-4} to 5.0×10^{-3}	1.5×10^{-3}

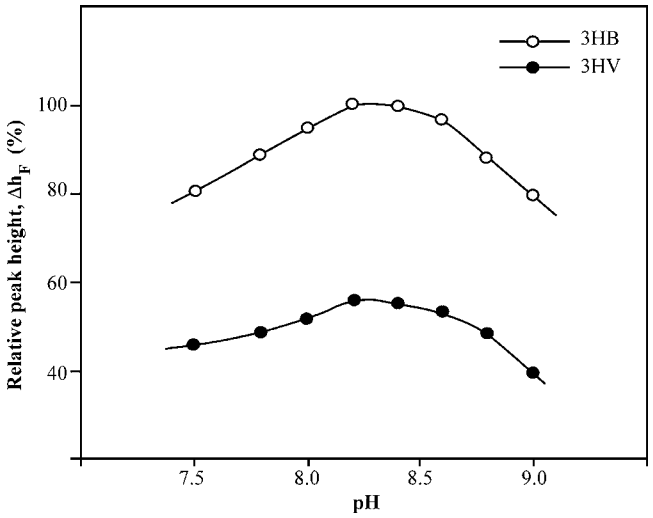


Fig. 2. Effect of pH on the catalytic activity of 3-HBDH. Fluorescence signals for 5.0×10^{-5} M 3HB and 3HV at different pHs.

The concentration of NAD^+ in the reagent solution (0.10 M Trizma®, pH 8.3) varied between 1.5×10^{-4} and 5.0×10^{-3} M. The heights of the peaks registered for both 3HB and 3HV were observed to increase gradually with increasing the concentration of NAD^+, this effect being less pronounced for concentrations higher than 1.5×10^{-3} M. This value was chosen for all subsequent experiments as it provided reduced NAD^+ consumption without a significant loss of sensitivity.

3.2. Quantification of 3HB and 3HV

The calibration equations for these compounds in aqueous solution are summarized in Table 2. For samples containing only 3HB or 3HV, both Δh_F and Δh_S were linearly related with the concentrations of 3HB or 3HV injected. The slope values of equations in Table 2 indicate that the detection of 3HV was less sensitive than that of 3HB, this being an expected result because of the lower reaction rate of 3HV. The calculated limits of detection were in the range from 2×10^{-8} to 5×10^{-8} M (the limits of detection were calculated from the expression LOD = $3\sigma_B/b$, where σ_B was the standard deviation ($n = 10$) of the blank peak height that was obtained when water was injected, and b was the slope of the proposed equation). Relative standard deviations ($n = 10$) between 0.8% and 1.5% were found for the peak heights of samples 1.0×10^{-5} M. The average sampling frequency was 20 h^{-1}.

For samples containing both 3HB and 3HV, the peak heights Δh_F and Δh_S were predicted by multiple linear regression, this being only valid when the total concentration of 3HB + 3HV was below 1×10^{-4} M, approximately. The partial regression coefficients of the multilinear equations (Table 2) were coincident with the individual coefficients found for samples of only 3HB or 3HV. This indicated that the signals of 3HB and 3HV were additive so that the fluorometric or spectrophotometric signals of any mixture of 3HB and 3HV could be calculated by the addition of the signals given by the equivalent individual samples containing only 3HB or 3HV. Apart from not being predictable by multiple linear regression, negative deviations from the additivity were observed for the signals of mixtures with concentrations of 3HB + 3HV higher than 1×10^{-4} M, particularly when the 3HB:3HV molar ratio was close to unity. This suggested some kind of interaction between 3HB and 3HV, probably due to the competition of both substrates for the catalytic site on the immobilised enzyme.

4. Application to PHAs

The above proposed procedure was applied to the determination of 3HB and 3HV in solutions produced by propanolic digestion of commercial PHAs. Propanolysis can convert PHB/PHV stoichiometrically into the propyl esters of 3HB/3HV [6,7] although the degradation kinetics and products may depend on the composition and crystallinity of the polymer or just on the applied degradation conditions (digestion time, temperature, etc.) [8,9].

The possible interferences of citrate and crotonic acid were considered. Citrate was a component of sample BP-1 while crotonic acid is usually produced in chemical degradations of PHB. The injection of solutions up to 1.5×10^{-4} M citrate or crotonic acid gave no measurable peaks, so the interference of these compounds by their contribution to the measured signals was discarded. Their possible interference by reaction with 3HB or 3HV was also investigated. To this end, freshly prepared 2.0×10^{-5} M solutions of 3HB or 3HV with or without 1.5×10^{-4} M citrate or crotonic acid at pH 8.3 were left for 1 h at room temperature and then analysed according to the proposed procedure. As no significant

Table 2
Calibration equations for the determination of 3HB and/or 3HV.

Analyte	Detection	Application range (M)/equation[a]
3HB	F	8×10^{-7} to 1×10^{-4} $\Delta h_F = (2.1 \pm 5.7) \times 10^2 + (1.42 \pm 0.02) \times 10^9$ [3HB] $R^2 = 0.9999$; $n = 10$
	S	8×10^{-7} to 1×10^{-4} $\Delta h_S = (-1.6 \pm 1.8) \times 10^2 + (6.52 \pm 0.04) \times 10^8$ [3HB] $R^2 = 0.9999$; $n = 10$
3HV	F	1×10^{-6} to 1×10^{-4} $\Delta h_F = (2.1 \pm 4.6) \times 10^2 + (9.36 \pm 0.10) \times 10^8$ [3HV] $R^2 = 0.9999$; $n = 9$
	S	1×10^{-6} to 1×10^{-4} $\Delta h_S = (0.8 \pm 3.3) \times 10^2 + (4.93 \pm 0.07) \times 10^8$ [3HV] $R^2 = 0.9998$; $n = 9$
3HB and 3HV	F	$1 \times 10^{-6} < [3HB] + [3HV] < 1 \times 10^{-4}$ $\Delta h_F = (3.1 \pm 3.2) \times 10^2 + (1.41 \pm 0.01) \times 10^9$ [3HB] + $(9.30 \pm 0.09) \times 10^8$ [3HV] $R^2 = 0.9998$; $n = 28$
	S	$1 \times 10^{-6} < [3HB] + [3HV] < 1 \times 10^{-4}$ $\Delta h_S = (-0.1 \pm 1.3) \times 10^2 + (6.51 \pm 0.04) \times 10^8$ [3HB] + $(4.94 \pm 0.04) \times 10^8$ [3HV] $R^2 = 0.9999$; $n = 28$

[a] Δh_F and Δh_S in μV; 1×10^3 μV = 1 fluorescence unit; 4×10^5 μV = 1 absorbance unit; n = number of standards; regression coefficients are expressed with 95% confidence limits.

Table 3
Analysis of chemically degraded commercial PHAs. Concentrations estimated, added and found in the analysed samples.

Sample	Concentration[a], M × 10^5					
	Estimated		Added		Found[b]	
	HB	HV	HB	HV	HB	HV
BP-1	5.23	0.69	–	–	5.2 ± 0.2	0.8 ± 0.2
BP-1			1.00	–	6.2 ± 0.2	0.7 ± 0.2
BP-1			–	1.47	5.3 ± 0.2	2.1 ± 0.2
BP-2	3.23	0.77	–	–	2.9 ± 0.1	0.7 ± 0.2
BP-2			1.00	–	3.9 ± 0.1	0.6 ± 0.2
BP-2			–	1.47	3.0 ± 0.1	2.0 ± 0.2
BP-2			1.00	1.47	3.9 ± 0.1	2.2 ± 0.2
BP-3	2.56	0.62	–	–	2.1 ± 0.1	0.7 ± 0.2
BP-3			1.00	–	3.0 ± 0.1	0.9 ± 0.2
BP-3			–	1.47	2.3 ± 0.1	2.1 ± 0.2
BP-3			1.00	1.47	3.2 ± 0.1	2.3 ± 0.2

[a] Values refer to the injected solutions.
[b] Mean values of three determinations with 95% confidence limits.

differences were observed between the signals of samples with and without citrate or crotonic acid, the possible interference of these compounds by interaction with 3HB or 3HV was also discarded.

Since the degradation was not certain to yield stoichiometric amounts of 3HB and 3HV, standard addition experiments were performed to validate the procedure. To this end, adequate volumes of sample and standard solutions were mixed, properly diluted with water and finally injected into the flow system. Results are summarized in Table 3. All the concentration values in this table refer to the injected solutions. The estimated concentrations were calculated from the initial NMR analysis supposing full conversion of PHB/PHV into 3HB/3HV. The comparison of the concentrations found with the estimated values indicates that the conversion of PHV into 3HV was seemingly complete in all the samples while that of PHB into 3HB was quantitative only in sample BP-1. The different degradation of samples was undoubtedly due to their different composition and structure; in comparison with BP-1, for example, BP-2 and BP-3 were not-plasticised polymers with higher proportion of PHV.

Whatever the conversion degree or the degradation kinetics, the concentrations of 3HB and 3HV found in all the experiments were in agreement with the effected standard additions. Results therefore indicate that the proposed procedure was adequate to discriminate the concentrations of 3HB and 3HV produced in the degradation of the commercial PHAs.

5. Conclusions

The described enzymatic method makes possible the direct determination and discrimination of 3HB and 3HV. In contrast to the methods commonly used for these compounds, previous separation by extraction with chlorinated solvents and/or chromatography is not required. The method is of interest in a wide variety of fields concerning PHAs, as it can provide information on the degradation rate and mechanism, composition and structure of these polymers. Its applicability has been proved through the determination of 3HB and 3HV in the digests of some chemically degraded commercial PHAs.

Acknowledgments

This work was supported by the Spanish Ministerio de Ciencia e Innovación (Ref.: BQU2002-02332). Karina B. Hueso Domínguez thanks the Spanish Ministerio de Ciencia e Innovación for the grant BES-2003-1012.

References

[1] T. Volova, Polyhydroxyalkanoates—Plastic Materials of the 21st Century: Production, Properties and Application, 1st edition, Nova Science Publishers, Hauppauge, New York, 2004.
[2] I. Vroman, L. Tighzert, Biodegradable Polymers, Materials, vol. 2, 2009, doi:10.3390/ma2020307, p. 307.
[3] B. Hazer, A. Steinbüchel, Appl. Microbiol. Biotechnol. 74 (2007) 1.
[4] H. Ueda, Y. Tabata, Adv. Drug Deliv. Rev. 55 (2003) 501.
[5] G.-Q. Chen, Q. Wu, Appl. Microbiol. Biotechnol. 67 (2005) 592.
[6] A. Oehmen, B. Keller-Lehmann, R.J. Zeng, Z. Yuan, J. Keller, J. Chromatogr. A 1070 (2005) 131.
[7] P. Furrer, R. Hany, D. Rentsch, A. Grubelnik, K. Ruth, S. Panke, M. Zinn, J. Chromatogr. A 1143 (2007) 199.
[8] R.P.X. Hesselmann, T. Fleischmann, R. Hany, A.J.B. Zehnder, J. Microbiol. Methods 35 (1999) 111.
[9] J. Yu, D. Plackett, L.X.L. Chen, Polym. Degrad. Stabil. 89 (2005) 289.
[10] D. Seebach, M.G. Fritz, Int. J. Biol. Macromol. 25 (1999) 217.
[11] S. Karlsson, C. Sares, R. Renstad, A.-C. Albertsson, J. Chromatogr. A 669 (1994) 97.
[12] D.H. Williamson, J. Mellanby, H.A. Krebs, Biochem. J. 82 (1962) 90.
[13] N. Kiba, H. Koemado, M. Furusawa, Talanta 41 (1994) 1583.
[14] N. Kiba, Y. Inoue, M. Tachibana, K. Tani, H. Koizumi, Anal. Sci. 19 (2003) 1203.
[15] C.K. Pires, P.B. Martelli, B.F. Reis, J.L. Lima, M.L. Saraiva, J. Agric. Food Chem. 51 (2003) 2457.
[16] R.C.H. Kwan, P.Y.T. Hon, W.C. Mak, L.Y. Law, J. Hu, R. Renneberg, Biosens. Bioelectron. 21 (2006) 1101.
[17] Y. Cui, J.P. Barford, R. Renneberg, Anal. Lett. 39 (2006) 2429.
[18] Y. Cui, J.P. Barford, R. Renneberg, Anal. Sci. 22 (2006) 1323.
[19] H.A. Krebs, K. Gawehn, D.H. Williamson, H.U. Bergmeyer, Methods Enzymol. 14 (1969) 222.
[20] M. Masoom, A. Townshend, Anal. Chim. Acta 171 (1985) 185.
[21] R.V. Hull, P.S. Conger III, R.J. Hoobler, Biophys. Chem. 90 (2001) 9.

Talanta 80 (2010) 1441–1444

Contents lists available at ScienceDirect

Talanta

journal homepage: www.elsevier.com/locate/talanta

Arsenic species in certified reference material MURST-ISS-A2 (Antarctic krill)

Marco Grotti[a,*], Francesco Soggia[a], Walter Goessler[b], Silvia Findenig[b], Kevin A. Francesconi[b]

[a] Department of Chemistry and Industrial Chemistry, University of Genoa, Via Dodecaneso 31, 16146 Genova, Italy
[b] Karl-Franzens-University Graz, Institute of Chemistry-Analytical Chemistry, Universitaetsplatz 1, 8010 Graz, Austria

ARTICLE INFO

Article history:
Received 29 June 2009
Received in revised form
15 September 2009
Accepted 25 September 2009
Available online 3 October 2009

Keywords:
Arsenic
Speciation
Reference materials
Inductively coupled plasma mass spectrometry
Antarctica

ABSTRACT

Arsenic compounds were quantified in the certified reference material MURST-ISS-A2 (Antarctic krill) using HPLC/ICPMS. The data should prove useful for assessing the accuracy of arsenic speciation procedures.

© 2009 Elsevier B.V. All rights reserved.

1. Introduction

With an estimated biomass of 120–700 million tons, the planktonic crustacean *Euphausia superba* (Antarctic krill) is probably the most abundant animal species on the planet and the keystone organism in the Antarctic marine ecosystem [1]. Swimming in large groups over long distances, the Antarctic krill feeds on phytoplankton floating in the Southern Ocean and represents the primary food source for whales, seals, cephalopods, penguins and seabirds. Antarctic krill also has economic importance through its use as a human and animal food. In addition, it has been used in ecological studies as a biomonitor of Antarctic ecosystems [2]. For these reasons, a certified reference material (MURST-ISS-A2) based on this matrix was produced [3] and it is currently available on request from the Antarctic Environmental Specimen Bank (www.bcaa.unige.it).

Our ongoing investigation on the occurrence of arsenic compounds in Antarctic marine biota has produced a need for a relevant certified reference material. As a first step to achieving this goal, we present arsenic speciation data for the reference material MURST-ISS-A2 (Antarctic krill).

2. Experimental

2.1. Samples

The certified reference material MURST-ISS-A2 [3] was produced in the frame of the Italian National Programme for Research in Antarctica, under the coordination of the Istituto Superiore di Sanità (ISS), Rome, Italy, and of the Institute for Reference Materials and Measurements of the Joint Research Centre, European Commission (EC-JRCIRMM), Geel, Belgium. This material is certified for a number of trace elements (total concentration only) including arsenic. In this study, three 500-mg batches were considered, each of which was split into four parts (*ca* 100 mg weighed with a precision of ±0.1 mg).

2.2. Reagents and standards

Standard solutions containing 1000 mg As l^{-1} of each of the following compounds were prepared in Milli-Q water (Millipore, El Paso, TX, USA): arsenate as $Na_2HAsO_4{\cdot}7H_2O$ (Merck, Darmstadt, Germany); arsenite as $NaAsO_2$ (Merck), dimethylarsinate as $C_2H_6AsNaO_2{\cdot}3H_2O$ (Sigma–Aldrich, St. Louis, MO, USA) and methylarsonate as $Na_2CH_3AsO_3{\cdot}6H_2O$ (Chem Service, West Chester, PA, USA). Arsenobetaine standard solution (BCR626 certified reference material) was purchased from Sigma–Aldrich. Arsenocholine [4] trimethylarsoniopropionate [5], trimethylarsine oxide [6], oxo-arsenosugar-glycerol [7], oxo-arsenosugar-sulfate

* Corresponding author.
E-mail address: grotti@chimica.unige.it (M. Grotti).

0039-9140/$ – see front matter © 2009 Elsevier B.V. All rights reserved.
doi:10.1016/j.talanta.2009.09.050

[8] and oxo-arsenosugar-sulfonate [8] were synthesised as previously reported. Oxo-arsenosugar-phosphate was isolated from natural sources [9]. Thio-arsenosugar-glycerol was prepared in house in Graz by blowing H_2S over the surface of a solution of oxo-arsenosugar-glycerol for a few seconds. The vial was closed and shaken, and the surplus H_2S was removed by purging with argon. Formic acid (p.a.) was obtained from Sigma–Aldrich. Methanol (p.a.), ammonium dihydrogen phosphate (p.a.), pyridine (p.a.), aqueous ammonia solution (25%, Suprapur), hydrogen peroxide (30%, Suprapur), hydrochloric acid (37%, Suprapur), and nitric acid (60%, Suprapur) were purchased from Merck. Ammonium formate (p.a.) was purchased from Fluka (Buchs, Switzerland).

The certified reference material DORM-2 was purchased from the National Research Council Canada (Ontario, Canada), and the reference algal sample was from a batch of *Fucus serratus* (brown alga) extracts as described by Madsen et al. [10].

2.3. Determination of total arsenic

The total arsenic concentration in the reference material was determined by microwave-assisted acid dissolution and ICP-AES analysis, according to a procedure previously reported [11]. The found concentration was $5.29 \pm 0.44\ \mu g\ g^{-1}$ (mean ± SD, $n = 3$), in agreement with the certified value $5.02 \pm 0.44\ \mu g\ g^{-1}$ (mean ± SD). The total arsenic concentration in each extract was determined by ICPMS after microwave-assisted acid dissolution with nitric acid.

2.4. Determination of arsenic species

Each sub-sample (*ca* 100 mg weighed with a precision of ±0.1 mg) was weighed directly into a 15-ml polypropylene tube and methanol/water (4.90 g, 1 + 4, w/w) was added. The mixture was shaken top over bottom at ambient temperature overnight, then centrifuged (4500 rpm × 15 min) and filtered through a 0.45 μm hydrophilic PVDF filter (Millipore, El Paso, TX, USA). Arsenic speciation analyses were performed by HPLC/ICPMS on the extracts. Chromatographic conditions are summarized in Table 1. Two instrumental systems were employed: (a) Perkin Elmer-Sciex (Concord, Ontario, Canada) Series 200 HPLC coupled to a Perkin Elmer-Sciex Elan DRC II ICPMS, via a pneumatic nebulizer/cyclonic spray chamber; (b) Agilent (Waldbronn, Germany) 1100 Series HPLC system coupled to an Agilent 7500ce ICPMS via an Ari Mist HP nebulizer (Burgener Research International, Berkshire, England)/Scott double pass spray chamber. The ion intensities at m/z 75 (^{75}As) and m/z 77 ($^{40}Ar^{37}Cl$) were monitored with the time resolved analysis software.

Structures of the investigated arsenic compounds are shown in Fig. 1. Arsenic species in sample solutions were identified by retention time matching and, on occasions, by co-chromatography; they were quantified by external calibration against the standard arsenical prepared in methanol/water (1 + 4, w/w). The anionic arsenic species were quantified by calibration against arsenate, arsenite, methylarsonate and dimethylarsinate standards chromatographed under identical conditions. The responses for the four arsenic species were the same (within 5%) and the mean of the slopes was hence used. The accuracy of HPLC/ICPMS quantification was checked by the analysis of arsenic species in DORM-2 and in the reference algal extract reported by Madsen et al. [10]. For DORM-2 ($n = 3$) we obtained $16.0 \pm 0.5\ \mu g\ As\ g^{-1}$ for arsenobetaine and $0.260 \pm 0.005\ \mu g\ As\ g^{-1}$ for tetramethylarsonium ion (certified values are $16.4 \pm 1.1\ \mu g\ As\ g^{-1}$ and $0.248 \pm 0.054\ \mu g\ As\ g^{-1}$, respectively). Because DORM-2 is certified only for arsenobetaine and tetramethylarsonium ion, we also checked our method for arsenosugars and DMA using the *Fucus* extract that has been fully characterized by HPLC/ICPMS and HPLC/electrospray MS [10]. Measured oxo-arsenosugar-phosphate, oxo-arsenosugar-glycerol and dimethylarsinate amounts were 0.090, 0.095 and 0.004 μg As, respectively, in good agreement with the reported values (0.086 μg As ±2.9%, 0.10 μg As ±3.6% and 0.005 μg As ±20%, respectively).

3. Results and discussion

The total extracted arsenic was $3.6 \pm 0.1\ \mu g\ g^{-1}$ ($n = 4$) corresponding to an extraction efficiency of 71%. Anion-exchange HPLC/ICPMS showed the presence of dimethylarsinate, oxo-arsenosugar-phosphate, arsenate, and oxo-arsenosugar-sulfate; a large quantity of arsenic, presumably present as cationic species, eluted at the void volume (Fig. 2). Cation-exchange chromatography (Fig. 3) demonstrated the presence of significant cationic arsenicals, namely arsenobetaine, oxo-arsenosugar-glycerol and trimethylarsoniopropionate (dimethylarsinate also runs as a cation under these conditions since the arsinoyl group protonates at the low pH employed).

The concentrations of the quantified arsenic species are reported in Table 2. In order to improve the confidence in the analytical results, the samples were analysed in two laboratories using different instrumental systems (see Section 2 for details). An excellent agreement between the results may be observed. The sum of the quantified species corresponded to about 95% of the total extracted arsenic. The variability of the main arsenic species within each batch was also considered. RSD% values ranged from 1–5% for arsenobetaine, trimethylarsoniopropionate and oxo-arsenosugar-phosphate to 10–15% for dimethylarsinate and oxo-arsenosugar-glycerol.

From Table 2, it can be seen that arsenobetaine was the major arsenical in the Antarctic krill sample, with a concentration of $1.9\ \mu g\ g^{-1}$, corresponding to about 45% of the extracted arsenic. Dimethylarsinate and trimethylarsoniopropionate were present as minor but significant constituents (about 5% and 10% of the total extractable arsenic, respectively), as well as oxo-arsenosugars (about 20%). The other investigated species were either below the limit of detection (about $0.02\ \mu g\ As\ g^{-1}$ dry mass) or, when detectable, they contributed less than 1% of the total extracted arsenic.

The presence of arsenobetaine as the dominant species in crustacean is well documented [12–16] as well as the occurrence of

Table 1
Chromatographic conditions used for arsenic speciation analysis.

	Anion-exchange HPLC Hamilton PRP-X100	Cation-exchange HPLC Zorbax 300-SCX	Reversed phase HPLC Atlantis® dC18
	4.1 mm × 250 mm	4.6 mm × 250 mm	4.6 mm × 150 mm
Mobile phase	20 mM $NH_4H_2PO_4$	10 mM pyridine	20 mM NH_4COOH
pH	6.0	2.3	3.0
Temperature	40 °C	30 °C	30 °C
Injection volume	20 μl	20 μl	20 μl
Flow rate	1 ml min^{-1}	1.5 ml min^{-1}	1 ml min^{-1}

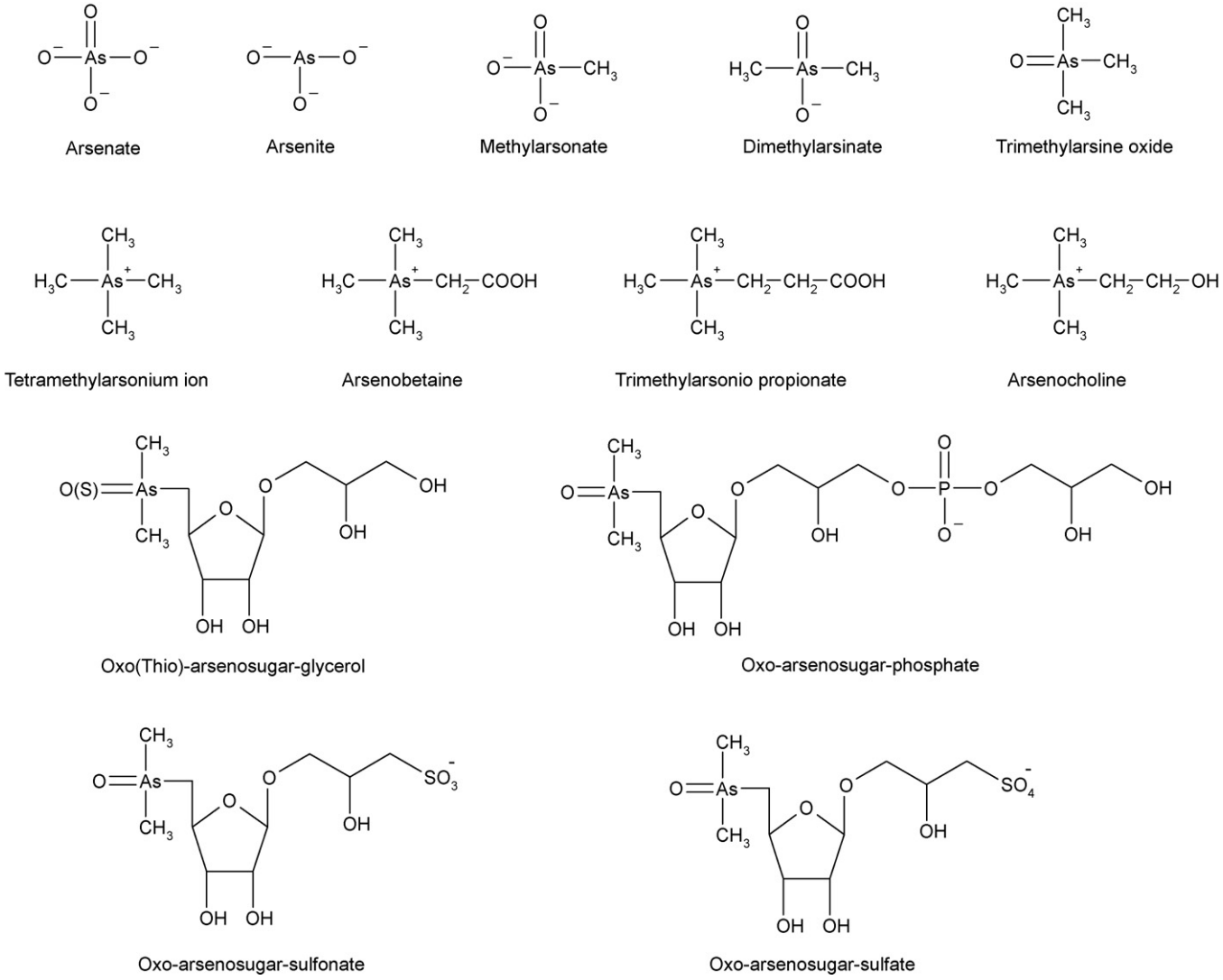


Fig. 1. Structures of arsenic species referred in text.

dimethylarsinate [15] and arsenosugars [13,14]. It has been suggested [13] that the arsenic speciation in marine zooplankton could depend on their feeding habits. Higher arsenobetaine concentrations have been reported for carnivorous species compared with herbivorous ones, and the opposite trend has been observed for the arsenosugars [13]. The Antarctic krill is predominantly herbivorous, feeding directly on phytoplankton and ice-algae, although filtering of other particles, such as eggs, larvae, fecal pellets and small zooplankton cannot be excluded. Hence, it is not surprising that this organism contained significant amounts of both arsenobetaine and arsenosugars. The occurrence of trimethylarsoniopropionate as a minor constituent could be linked to the biosynthesis of arsenobetaine, as proposed for aliphatic dimethylarsinoyl compounds [17].

In conclusion, the arsenic speciation data obtained for the certified reference material MURST-ISS-A2 (Antarctic krill) appear to be

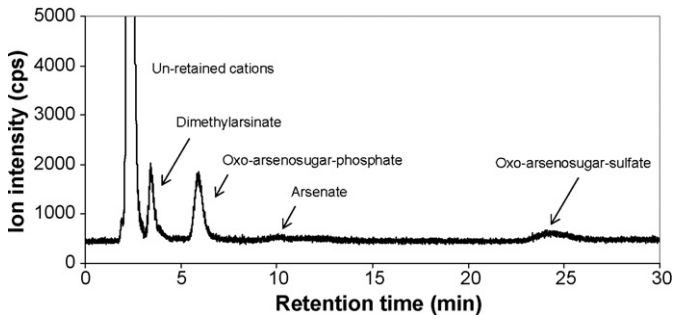


Fig. 2. Anion-exchange HPLC/ICPMS chromatogram of extract from MURST-ISS-A2 (Antarctic krill). Column: Hamilton PRP-X100; column temperature: 40 °C; mobile phase: 20 mM $NH_4H_2PO_4$ at pH 6.0; injection volume: 20 μl; flow rate: 1 ml min^{-1}.

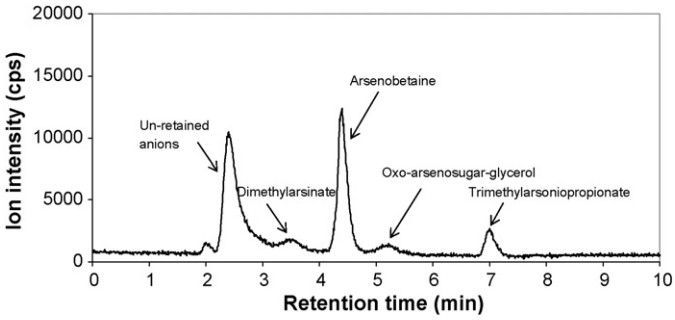


Fig. 3. Cation-exchange HPLC/ICPMS chromatogram of extract from MURST-ISS-A2 (Antarctic krill). Column: Zorbax 300-SCX; column temperature: 30 °C; mobile phase: 10 mM pyridine at pH 2.3; injection volume: 20 μl; flow rate: 1.5 ml min^{-1}.

Table 2
Arsenic compounds (μg As g^{-1} dry mass) in the certified reference material MURST-ISS-A2 (Antarctic krill).

Arsenic species	As concentrations (μg g^{-1} dry mass)	
	Analysis 1[a] ($n = 12$)	Analysis 2[b] ($n = 4$)
Dimethylarsinate	0.22 ± 0.04	0.22 ± 0.07
Oxo-arsenosugar-phosphate	0.31 ± 0.08	0.28 ± 0.05
Oxo-arsenosugar-glycerol	0.24 ± 0.03	0.29 ± 0.01
Arsenobetaine	1.91 ± 0.03	1.92 ± 0.02
Trimethylarsoniopropionate	0.41 ± 0.02	0.40 ± 0.01
Arsenite	<0.02[c]	<0.02
Arsenate	<0.02	0.03 ± 0.01
Methylarsonate	<0.02	<0.02
Arsenocholine	<0.02	0.03 ± 0.01
Trimethylarsine oxide	<0.02	<0.02
Tetramethylarsonium ion	<0.02	<0.02
Oxo-arsenosugar-sulfate	–	0.13 ± 0.02
Oxo-arsenosugar-sulfonate	–	0.03 ± 0.01
Thio-arsenosugar-glycerol	–	∼0.04

[a] HPLC/ICPMS analyses carried out at the Genoa laboratory using a Series 200 HPLC coupled to an ICPMS Elan DRC II, both from Perkin Elmer-Sciex.
[b] HPLC/ICPMS analyses carried out at the Graz laboratory using a Series 1100 HPLC coupled to an ICPMS 7500ce, both from Agilent Technologies.
[c] Quantification limit.

consistent with previous data for crustaceans in general. The quantitative data for a number of arsenicals provided for this reference material should prove useful for checking analytical procedures employed in arsenic speciation studies.

References

[1] D.G.M. Miller, I. Hampton, Biology and ecology of the Antarctic krill (*Euphausia superba*): a review. BIOMASS Scientific Series, vol. 9, Scientific Committee on Antarctic Research, Cambridge, England, 1989, 168 pp.
[2] K. Reid, J.P. Croxall, D.R. Briggs, E.J. Murphy, ICES J. Mar. Sci. 62 (2005) 366–373.
[3] S. Caroli, O. Senofonte, S. Caimi, J. Pauwels, G.N. Kramer, P. Robouch, J. Anal. Atom Spectrom. 10 (2001) 1142–1146.
[4] W.J. McShane, Ph.D. Thesis, Department of Chemistry, Texas, A&M University, College Station, Texas, USA, 1982.
[5] K.A. Francesconi, J. Gailer, J.S. Edmonds, W. Goessler, K.J. Irgolic, Comp. Biochem. Phys. C 122 (1999) 131–137.
[6] R.A. Zingaro, in: W.A. Herman, G. Brauer (Eds.), Phosphorus, Arsenic, Antimony, and Bismuth, vol. 3, Thieme Verlag, Stuttgard, 1996.
[7] P. Traar, K.A. Francesconi, Tetrahedron Lett. 47 (2006) 5293–5296.
[8] P. Traar, A. Rumpler, T. Madl, G. Saischek, K.A. Francesconi, K.A. Aust, J. Chem. 62 (2009) 538–545.
[9] K.A. Francesconi, J.S. Edmonds, R.V. Stick, B.W. Skelton, A.H. White, J. Chem. Soc., Perkin Trans. 1 (1991) 2707–2716.
[10] A.D. Madsen, W. Goessler, S.N. Pedersen, K.A. Francesconi, J. Anal. Atom Spectrom. 15 (2000) 657–662.
[11] M. Grotti, F. Soggia, C. Lagomarsino, S. Dalla Riva, W. Goessler, K. Francesconi, Antarctic Sci. 20 (2008) 39–51.
[12] K.A. Francesconi, J.S. Edmonds, Adv. Inorg. Chem. 44 (1997) 147–189.
[13] Y. Shibata, M. Sekiguchi, A. Otsuki, M. Morita, Appl. Organomet. Chem. 10 (1996) 713–719.
[14] S. Foster, W. Maher, A. Taylor, F. Krikowa, K. Telford, Environ. Chem. 2 (2005) 177–189.
[15] S. Rattanachongkiat, G.E. Millward, M.E. Foulkes, J. Environ. Monit. 6 (2004) 254–261.
[16] S.X.C. Le, W.R. Cullen, K.J. Reimer, Environ. Sci. Technol. 28 (1994) 1598–1604.
[17] J.J. Sloth, E.H. Larsen, K. Julshamn, Rapid Commun. Mass Spectrom. 19 (2005) 227–235.

Talanta 80 (2010) 1445–1451

Contents lists available at ScienceDirect

Talanta

journal homepage: www.elsevier.com/locate/talanta

Analysis of commercial beverage products by size exclusion chromatography coupled with UV–vis absorbance detection and dynamic surface tension detection

Karisa M. Pierce[a,*], Emilia Bramanti[b], Massimo Onor[b], Roberto Spiniello[b], Alexandra Kangas[a], Kristen J. Skogerboe[c], Robert E. Synovec[d]

[a] Department of Chemistry and Biochemistry, 3307 Third Avenue West, Suite 205, Seattle Pacific University, Seattle, WA 98119, USA
[b] National Research Council of Italy (CNR), Istituto per i Processi Chimico-Fisici, Laboratory of Instrumental Analytical Chemistry, Via G. Moruzzi 1, 56124 Pisa, Italy
[c] Department of Chemistry, Seattle University, Seattle, WA 98122, USA
[d] Department of Chemistry, Box 351700, Center for Process Analytical Chemistry, University of Washington, Seattle, WA 98195, USA

ARTICLE INFO

Article history:
Received 16 June 2009
Received in revised form
24 September 2009
Accepted 25 September 2009
Available online 3 October 2009

Keywords:
Instant coffee
Surface tension
Tetrabutylammonium (TBA)
Liquid chromatography
Proteins

ABSTRACT

Multidimensional analysis of instant coffee and barley beverage samples using size exclusion chromatography (SEC) combined with a dynamic surface tension detector (DSTD) and a UV–vis absorbance detector (UV) is reported. A unique finding of this study was the action of the tetrabutylammonium (TBA) cation as a modifying agent (with bromide as the counter anion) that substantially increased the surface pressure signal and sensitivity of many of the proteins in the chromatographically separated samples. The tetrabutylammonium bromide (TBAB) enhancement of the surface pressure signal was further investigated by studying the response of 12 commercial standard proteins (α-lactalbumin, β-lactoglobulin, human serum albumin (HSA), albumin from chicken egg white (OVA), bovine serum albumin (BSA), hemoglobin, α-chymotrypsinogen A, cytochrome *C*, myoglobin, RNase A, carbonic anhydrase, and lysozyme) in buffer performed using flow injection analysis (FIA) coupled with the DSTD with and without various concentrations of TBAB. The FIA-DSTD data show that 1 mM TBAB enhances sensitivity of HSA detection, by lowering the limit of detection (LOD) from 2 mg/mL to 0.1 mg/mL. Similarly, the LOD for BSA was reduced from 1 mg/mL to 0.2 mg/mL. These FIA-DSTD experiments allowed the detection conditions to be optimized for further SEC-UV/DSTD experiments. Thus, the SEC-UV/DSTD system has been optimized and successfully applied to the selective analysis of surface-active protein fractions in a commercial instant coffee sample and in a soluble barley sample. The complementary selectivity of using the DSTD relative to an absorbance detector is also demonstrated.

© 2009 Elsevier B.V. All rights reserved.

1. Introduction

The direct measurement of surface tension is of interest in the investigation of molecular interactions at the air–liquid interface, the study of thermodynamic kinetics of protein denaturation at the air–liquid interface, and in determining foaming capabilities of foods and beverages. Proteins play a key role in the stabilization of foams, emulsions, and composite systems in food products and in cosmetics [1–7]. The creation of emulsions and foams in food products represent dynamic processes and the dynamic surface-active properties of protein solutions are considered to play an important role in the formation and stabilization of these systems [6,8,9].

Traditional methods of quantifying surface tension are based on optical observations of drop growth, optical imaging, tensiometry, and manual observations of foam performance [10–12]. Most of these techniques are restricted to static measurements and cannot assess the dynamic nature of foams and emulsions. Additionally there may be other limitations of these methods such as protein adsorption [13] or lack of compatibility with flow injection analysis (FIA) or liquid chromatographic systems [14].

The limitations of previous methods have led to the development of a versatile technique to assess the dynamic surface pressure of flowing liquids. The dynamic surface tension detector (DSTD) is a high-throughput automated chemical analyzer capable of quantifying the surface tension of a complex sample [13–17]. The surface-tension-lowering response observed by the DSTD is converted to a quantity known as the surface pressure. The DSTD provides real-time surface pressure data for surface-active sample

* Corresponding author. Tel.: +1 206 281 2102.
E-mail address: pierck1@spu.edu (K.M. Pierce).

0039-9140/$ – see front matter © 2009 Elsevier B.V. All rights reserved.
doi:10.1016/j.talanta.2009.09.051

compounds as they migrate to the surface of the drop or as macromolecules such as proteins denature and interact at the air–liquid interface of every drop of sample as it elutes, forms, and is detached. The DSTD is described in more detail and the procedure for calibrating the DSTD with aqueous standard when the sample mobile phase is different is described in Refs. [17–19].

Coffee is a popular beverage worldwide and the surface properties of coffee beverages are of interest to food chemists. The foam present on the top of a cup of coffee (crema) is important for trapping volatilized aromas and improving coffee quality. Researchers have studied the influence of polysaccharide composition on foam stability of espresso coffees by timing how long it takes for the foam layer to disappear during cooling [20]. Another report indicates that this "crema" is important because it is quantitatively related to surface tension phenomena [21]. Instrumental methods have also been used to study how coffee brewing affects foam formation and stabilization [12,21]. Polysaccharides, proteins and melanoidins have been shown to influence foaming capability and foam stability of the beverages [20,21]. Coffee quality and aroma have been shown to be related to foam and viscosity levels, and associated with the presence of oligosaccharides and polysaccharides [21]. In addition to affecting coffee beverage quality, the carbohydrates have also been shown to possess various biological and antibacterial activities [22].

In this report, FIA is coupled to DSTD to provide a means of quickly and accurately investigating the total real-time surface activity of water soluble coffee samples. Additionally, liquid chromatography (LC) is coupled to a UV/Vis absorbance detector and a DSTD to evaluate the surface activity associated with compounds in soluble coffee samples. Since polysaccharides and proteins are important compounds involved in the foaming capability and foam stability of the beverages [20], size exclusion chromatography (SEC) is used to separate these two classes of compounds.

In previous work, we employed denaturing agents in a post-column derivatization SEC-DSTD system in order to increase surface activity of proteins and enhance their DSTD signal [14]. The use of denaturants as post-column modifiers was preferred to the addition of denaturing agents in the mobile phase of SEC because denatured proteins may have a different elution pattern in SEC than the native proteins.

The report herein describes the first use of tetrabutylammonium bromide (TBAB) to increase surface activity of proteins from coffee beverages analyzed by FIA-DSTD and SEC-UV/DSTD. Previous literature reports related to the effect of tetrabutylammonium (TBA) salts on protein conformation [23–25] do not address its effect on protein surface activity. Jain and Ahluwalia reported that tetrabutylammonium (TBA) at a concentration less than or equal to 0.25 M destabilize lysozyme to a greater degree than urea and that polyols are not sufficient to counteract the destabilization effect of TBA [25]. They also found that the destabilization effect increases with increasing concentration and increasing alkyl chain length. This effect was attributed to the hydrophobic interactions between the tail of TBA and the hydrophobic regions of the protein. We also observed that TBA is an enhancer of the surface activity of surfactants like sodium dodecyl sulfate, and of ions like Cr(III), presumably because the tetrabutylammonium cation acts as a counter ion in the formation of ion pairs [26]. In this report, TBAB at concentrations less than or equal to 5 mM were employed both for the solubilization of standard proteins and raw soluble coffee samples and in the mobile phase buffers of SEC separations. The SEC-UV/DSTD configuration provides additional analyte selectivity over traditional detection methods such as absorbance detection, and enables the analyst to obtain analyte-specific information, with potential use in formulation science and quality control applications.

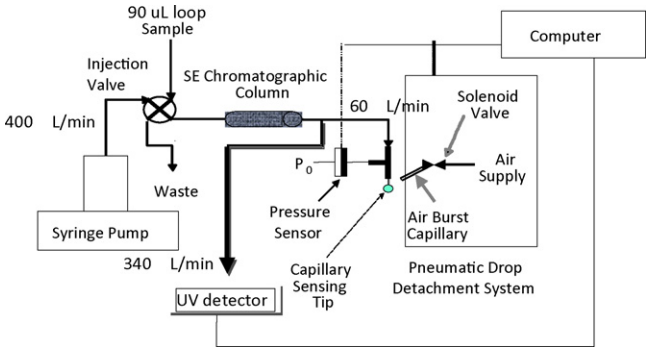


Fig. 1. SEC-DSTD instrument configuration. The flow splitter delivers 60 μL/min to the DSTD and 340 μL/min to the diode array UV–vis absorbance detector (abbreviated as UV in text). The differential pressure, $P(t)$, across the liquid–air interface of each eluting drop, is measured with respect to the atmospheric pressure, P_0 by a pressure transducer on a side arm of the DSTD capillary sensor tip. A small capillary directs a short burst of air regulated to 25 psi at a 45° angle via a computer-controlled solenoid valve and pneumatically detaches the eluent from the sensor tip.

2. Materials and methods

Carbonic anhydrase from bovine erythrocytes (CA, 21803) was purchased from Fluka (Buchs, Switzerland); bovine serum albumin (BSA, A-0281), albumin from chicken egg white (OVA, A-5503), human serum albumin (HSA, A-1887), β-lactoglobulin (β-LG, L-3908) and α-lactalbumin from bovine milk (α-Lac, L-6010), myoglobin from equine skeletal muscle (Myo, M-0630), α-chymotrypsinogen A from bovine pancreas (α-Chy, C-4879), lysozyme from chicken egg white (Lys, L-6876), human hemoglobin (Hb, H-7379), cytochrome *C* from equine heart (CytC, C-7752) and ribonuclease A from bovine pancreas (RNase A, R5125) were purchased from Sigma, Chemical Co. (St. Louis, MO, USA). The buffer solutions were prepared from monobasic monohydrate sodium phosphate, dibasic anhydrous potassium phosphate (BDH Laboratory Supplies, Poole, England), and TBAB (Sigma Chemical Co., P.O. 14508, St. Louis, MO 63178, USA). The phosphate buffer solution (PBS) contained 0.1 M phosphate at a pH of 6.8 or 7.8 as specified. Water deionized with a Milli-Q system (Millipore, 80 Ashby Road, Bedford, MA 01730-2271, USA) was used throughout and degassed prior to use. A Biosep SEC S2000 HPLC column (Phenomenex, Chemtek, Bologna, Italy), with dimensions of 300 mm long by 7.8 mm inside diameter was used for all the SEC experiments with calculated ~5 mL void volume.

Protein solutions were prepared by dissolving lyophilized powder in PBS at the concentration indicated. TBAB-modified protein working solutions were prepared freshly by dissolving protein lyophilized powder in PBS, containing TBAB at the indicated concentration. Samples were injected less than 10 min after preparation, in order to not show significant variation at the DSTD and UV absorbance detector during the working day. The proteins were α-lactalbumin, β-lactoglobulin, HSA, OVA, BSA, hemoglobin, α-chymotrypsinogen A, cytochrome *C*, myoglobin, RNase A, carbonic anhydrase, and lysozyme. Commercial samples of instant coffees (Nescafe and Nescafe Classic from Nestle), soluble barley beverage (Crastan), and milk powder (Kroger) were purchased at the grocery store and were prepared for analysis by dissolving a weighed portion in PBS or PBS/TBAB, and filtering using 0.22 μm Millipore syringe filters, followed by SEC-UV/DSTD analysis.

A detailed schematic of the DSTD configuration with pneumatic detachment is shown in Fig. 1. A narrow bore HPLC gradient pump (P2000, ThermoQuest) equipped with a mechanical degassing system (SC1000, ThermoQuest) was connected to a diode array UV–vis absorbance detector (UV6000, ThermoQuest). A total flow of 0.4 mL/min was split in order to provide 340 μL/min to the UV

detector and 60 μL/min to the DSTD. Samples were introduced via a ten-port injection valve (Rheodyne PR700-102-1, Cotati, CA). A poly(etheretherketone) (PEEK) injection loop of 100 μL of tubing (Upchurch, Oak Harbor, WA) was used for all experiments. The pneumatic detachment apparatus for the DSTD, shown in Fig. 1, consists of a small capillary directing a repeated short burst of in-house air at 45° angle to the capillary sensing tip via a computer-controlled solenoid valve to detach drops from the sensor tip capillary at controlled time intervals. Pneumatic detachment was performed every 2 s, corresponding to 2 μL drops at 60 μL/min, using a solenoid valve (MBD002, Skinner Valve, New Britain, CT, USA). The pressure sensor (Validyne P305D-20-2369, Northridge, CA) was configured with a sensing membrane (Validyne diaphragm 3-36, Northridge, CA) that was optimized for the response time of the DSTD measurements of interfacial kinetics. The sensor capillary tip was made from a short piece of PEEK tubing, 457 μm ID and 635 μm OD. All data were collected at 20 kHz with a personal computer (Intel Centrino® Duo, Intel Corporation, Santa Clara, CA) equipped with a data acquisition card (AT-MIO-16XE-50, National Instruments, Austin, TX). The data were averaged to 50 points/s and collected using LABVIEW (Version 6, National Instruments, Austin, TX) with programs written in-house. Subsequent data analysis was performed using MATLAB 7.0 (MathWorks, Natick, MA). UV–vis absorbance measurements were performed using a Beckman DU-600 spectrophotometer.

Typical raw pressure data from the DSTD have been reported in detail previously [13–15,17]. Four drop profiles are necessary in the dual-mobile phase calibration to obtain the dynamic surface pressure of a protein sample in TBAB: the drop profile of TBAB in 0.1 M phosphate buffer; the drop profile of sample in TBAB with phosphate buffer; the drop profiles of water; the drop profile of the standard 5% acetic acid in water. The four drop profiles and the surface pressure of the 5% acetic acid standard in water (10.3 dyn/cm) were applied yielding the Π value. Additionally, the Π_{mean} value is defined as the surface pressure signal averaged over the last 0.2 s at the end of the 2 s drop.

In all SEC-UV/DSTD experiments, 1 mM TBAB was kept constant in the mobile phase in order to increase the surface pressure signal of protein samples. The elution conditions were the following: 30 min isocratic elution in PBS, 1 mM TBAB at 20 ± 1 °C with a flow rate of 0.4 mL/min in the column. The mobile phase was filtered by a 0.45 μm cellulose acetate filter (Millipore) and degassed (for 10 min) before using.

3. Results and discussion

3.1. FIA-DSTD analysis of standard protein solutions and instant coffee samples: effect of TBAB

It is well known that proteins differ significantly in their surface activity due to differences in structural properties (size, shape, and charge distribution), stability and flexibility [4,27]. It has also been shown that the surface activity of proteins varies with changes in these properties [27–29]. Typically, surface activity increases as the hydrophobic character of the protein is exposed upon denaturation [14,15]. On this basis, we investigated the effect of sub-denaturant concentrations of TBAB on protein surface tension with the aim of employing TBAB as an additive in the mobile phase of SEC to increase DSTD signal of proteins, without inducing protein denaturation. Experiments were initially performed using the FIA-DSTD system to investigate the surface activity of 12 commercial standard proteins at various concentrations of TBAB.

Fig. 2A shows the surface pressure data (Π_{mean}) of a representative protein, β-lactoglobulin (500 mg/L) as a function of the TBAB concentration in 0.1 M PBS (panel A). Concentrations of

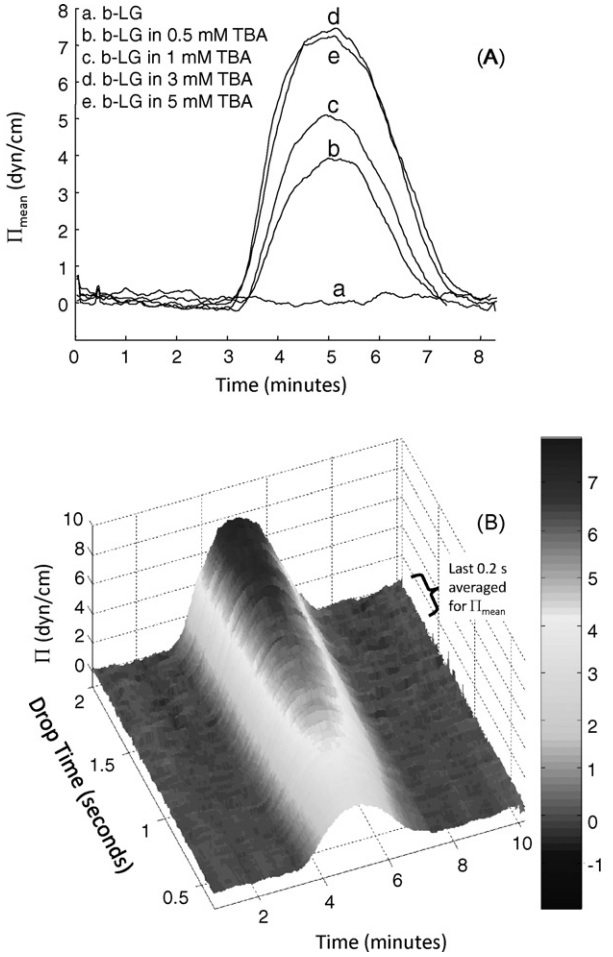


Fig. 2. FIA-DSTD experiments on β-LG (all in pH 6.8 buffer). (A) Dynamic surface pressure plots of β-LG (500 mg/L) in (a) 0.1 M PBS, (b) 0.1 M PBS with 0.5 mM TBAB, (c) 0.1 M PBS with 1 mM TBAB, (d) 0.1 M PBS with 3 mM TBAB, (e) 0.1 M PBS with 5 mM TBAB. Π_{mean} represents the surface pressure signal averaged over the last 10 points at the end of the 2 s drop (i.e., average values from 1.8 to 2.0 s). (B) Surface pressure plot of 500 mg/L β-LG in 0.1 M PBS with 3 mM TBAB; surface pressure values are reported as a function of drop time and elution time, Π_{mean} = 7.4 dyn/cm.

TBAB ≤ 3 mM did not yield a signal, while 5 mM TBAB produced a peak height of ~1.5 dyn/cm, and this background signal contribution was subtracted from the observed sample signal for other samples, as appropriate. As the TBAB concentration was increased, the surface activity of β-LG increased. In Fig. 2B the data show the relatively slow adsorption and diffusion kinetics at the air–liquid interface of TBAB-modified β-LG during the 2 s drop time. The change in the surface pressure signal over the growth of a single drop is attributed to the finite time required for diffusion, adsorption and molecular arrangement of the protein at the air–liquid interface, as has been discussed in another study [29].

Fig. 3A shows the trend of Π_{mean} as a function of TBAB concentration for α-lactalbumin, β-lactoglobulin, HSA, OVA and BSA. At a concentration of 500 mg/L, these proteins showed an increase in surface pressure until a *plateau* value was reached, which was reached between 1 and 3 mM TBA. Hemoglobin (not shown) showed a small increase in its surface activity in this concentration range. The other proteins (α-chymotrypsinogen A, cytochrome *C*, myoglobin, RNase A, carbonic anhydrase, and lysozyme) did not show any increase in surface activity up to 5 mM TBA. The plateau result was pH dependent. By increasing the pH from 6.8 to 7.8 carbonic anhydrase increased its surface activity reaching a plateau value of 2.7 dyn/cm. Hemoglobin and ribonuclease A reached a maximum signal of 8.8 dyn/cm and 4.5 dyn/cm, respectively, for

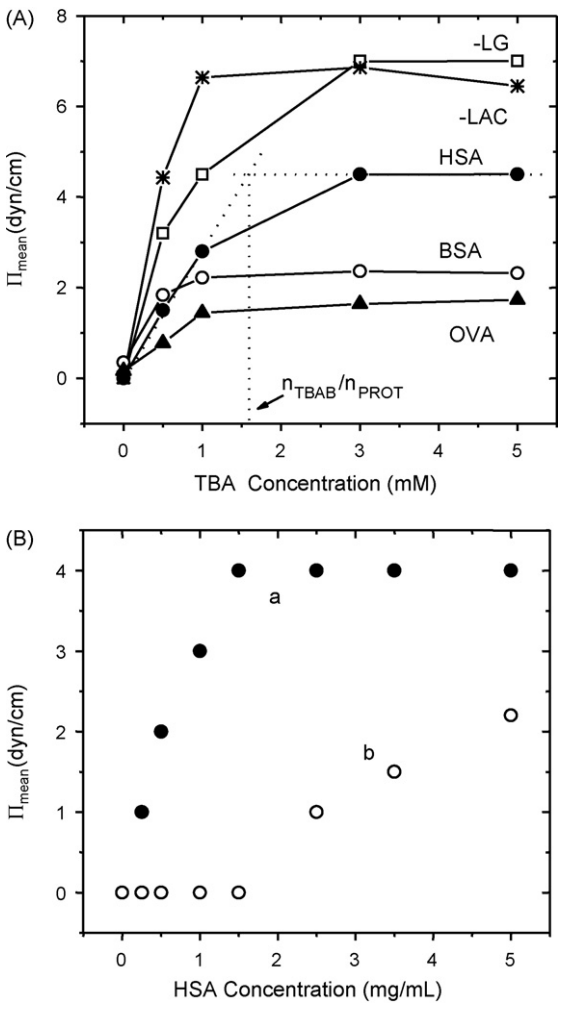


Fig. 3. FIA-DSTD experiments of standard proteins. (A) Surface pressure of 500 mg/L OVA, 500 mg/L BSA, 500 mg/L HSA, 500 mg/L α-Lac and 500 mg/L β-LG as a function of increasing concentration of TBAB. (B) Calibration plot for surface pressure of HSA in 0.1 M PBS, pH 6.8 with (a) or without (b) 1 mM TBAB. A significant enhancement of the surface pressure of these proteins due to TBAB is observed.

3 mM TBA. Table 1 summarizes the maximum value of Π_{mean} for all proteins studied at pH 6.8 and 7.8.

No comparative data are reported in the literature regarding surface activity of TBA-modified proteins. Tetra alkylammonium salts at concentrations ≥0.25 M were found to influence surface activity. This effect was attributed to the hydrophobic interaction between the buffer and the hydrophobic regions of the protein [26], although additional study is warranted. We were using much lower concentrations of TBAB (1–5 mM). It is possible that the increase of protein surface activity is due to ion pair formation with anionic charges located on the protein surface rather than to the interaction of aliphatic chains of TBA with hydrophobic portions of the protein [30], however, additional study is warranted to draw conclusions. Indeed, the five proteins that qualitatively increase surface activity in the presence of 1 mM TBAB in the mobile phase are all characterized by an isoelectric point lower than the pH 6.8 of the mobile phase (Table 1) [31–35]. At pH 6.8, these proteins are all negatively charged. With the exception of myoglobin, all proteins with an isoelectric point greater than pH 6.8 were presumably positively charged, and unlikely to interact as strongly with the tetrabutylammonium cations. Indeed, by increasing the mobile phase to pH 7.8, carbonic anhydrase, hemoglobin and RNase A did yield increased surface tension signals in the presence of TBAB as shown in Table 1.

Referring back to Fig. 3A and an observed trend of Π_{mean} as a function of TBAB concentration for various proteins, correspondingly, Table 1 indicates the molar ratio of TBAB and protein (n_{TBAB}/n_{PROT}) calculated from the intersection of the lines fit to the curves in Fig. 3A. The values of n_{TBAB}/n_{PROT} likely indicate the approximate number of TBA ions associated with each molecule of protein. If so, it may correlate with the number of negative surface charges at the particular pH [30].

Although the effect of TBAB on protein surface activity is not universal, the increase in detection sensitivity for several proteins provided by the TBAB is a very important finding for applying the DSTD as an HPLC detector. Fig. 3B shows the results of calibration experiments performed by the FIA-DSTD system on standard solutions of native HSA in 0.1 M PBS, pH 6.8 (curve b) and TBAB-modified HSA (0.1 M PBS, pH 6.8, 1 mM TBA, curve a). Calibration curves have been obtained by plotting the surface pressure data at the end of the 2 μL drop (Π_{mean}) as a function of the concentration of untreated (native) and TBAB-modified protein. Data show that 1 mM TBAB enhances sensitivity of HSA detection, by lowering the limit of detection (LOD) from 2 mg/mL to 0.1 mg/mL. Taking into account the flow splitting in the apparatus of Fig. 1, with only 15% of the effluent delivered to the detector, the mass LOD for HSA is 3 μg of injected protein and 450 ng of the protein at the DSTD. Likewise, the LOD for BSA was reduced from 1 mg/mL to 0.2 mg/mL. Furthermore, the LOD for RNase A was reduced from 0.3 mg/mL to 0.1 mg/mL, and the LOD for carbonic anhydrase was reduced from 0.4 mg/mL to 0.2 mg/mL. Standard protein solutions were prepared with and without 1 mM TBA in phosphate buffer at various protein concentrations of 5 mg/mL, 2.5 mg/mL, 1.25 mg/mL, 0.625 mg/mL, 0.313 mg/mL, and 0.156 mg/mL. The slope of the linear fit for the HSA calibration with TBA was 0.844 (R^2 = 0.944), while the slope for HSA without TBA was 0.697 (R^2 = 0.931). The HSA signals with TBA were greater than the HSA signals without TBA, and the DSTD

Table 1
Maximum value of Π_{mean} vs. TBAB concentration plots for 12 standard proteins (500 mg/L) investigated by FIA-DSTD at pH 6.8 and 7.8. The molecular weight (MW) of the protein and the molar ratio n_{TBAB}/n_{PROT}, calculated as described in the text, is also reported.

Protein	MW (kDa)	Isoelectric point [reference]	Maximum Π_{mean} in TBAB, PBS, pH 6.8	Maximum Π_{mean} in TBAB, PBS, pH 7.8	n_{TBAB}/n_{PROT}, pH 6.8	n_{TBAB}/n_{PROT}, pH 7.8
α-Lactalbumin	14.0	4.2	6.9		56	
OVA	42.7	4.7 [31]	1.6		78	
BSA	77.5	4.7	2.4		155	
β-Lactoglobulin	18.4	5.1–5.34 [32]	7.4		55	
HSA	69.0	5.3–5.85 [32]	4.5		208	
Myoglobin	16.9	6.88–7.45 [33,34]	0	1.7		34
Carbonic anhydrase	29.0	5.4–7.4	0	2.7	–	58
Hemoglobin	64.5	6.8–7.05 [35]	0.5	8.8	–	385
RNase A	13.5	8.9 [32]	0	4.5	–	76
α-Chymotrypsinogen A	25.7	8.8–9.6 [32]	0	0	–	
Cytochrome *C*	12.4	9–9.4 [32]	0		–	
Lysozyme	14.3	10–11 [32]	0		–	

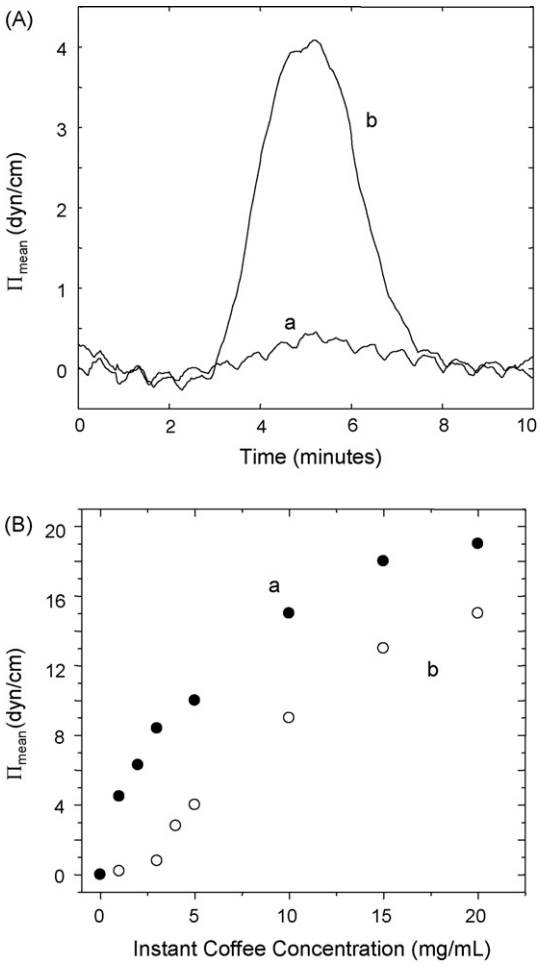


Fig. 4. (A) FIA-DSTD experiments of an instant coffee sample (1 mg/mL) solubilized in 0.1 M PBS, pH 6.8 (curve a) and 1 mM TBAB in 0.1 M PBS, pH 6.8 (curve b). (B) Calibration plot for surface pressure of the coffee sample in 0.1 M PBS, pH 6.8 (curve b) and 1 mM TBAB in 0.1 M PBS, pH 6.8 (curve a).

sensitivity with TBA was greater than the sensitivity without TBA, as shown by the relative slopes. Linear fitting for DSTD calibration is justified in Ref. [17]. The same calibration was performed with other proteins to show that TBA increases the DSTD sensitivity. The slope of the linear fit for BSA calibration with TBA was 1.352 (R^2 = 0.953), while the slope of the linear fit for BSA without TBA was 0.885 (R^2 = 0.914). The slope of the linear fit for OVA calibration with TBA was 1.132 (R^2 = 0.974), while the slope for OVA without TBA was 0.517 (R^2 = 0.959). The slope of the linear fit for α-lactalbumin with TBA was 1.486 (R^2 = 0.982), while the slope for α-lactalbumin without TBA was 1.287 (R^2 = 0.986).

3.2. FIA-DSTD and SEC-UV/DSTD of standard proteins and instant coffee samples

In Fig. 4, FIA-DSTD of an instant coffee sample (1 mg/mL) solubilized in 0.1 M PBS, pH 6.8 (curve a) and 1 mM TBAB in 0.1 M PBS, pH 6.8 (curve b) demonstrates the significant benefit of using the TBAB as a mobile phase additive to enhance sensitivity, ultimately useful for SEC-UV/DSTD. The FIA results indicate that without the TBAB present in the mobile phase, there is likely to be insufficient sensitivity to observe the surface-active compounds in the instant coffee and barley samples while doing SEC. Based on these results, the DSTD was optimized and successfully coupled to SEC for the analysis of protein standards, and several commercially available instant beverage samples. SEC separations of standard

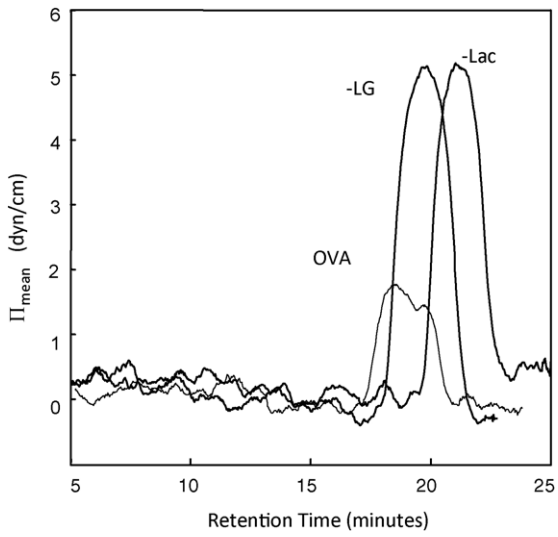


Fig. 5. SEC-DSTD chromatograms of OVA (4 mg/mL and MW = 42.7 kDa), β-LG (2.5 mg/mL and MW = 18.4 kDa), and α-Lac (2.8 mg/mL and MW = 14.2 kDa) in 0.1 M PBS, pH 6.8 with 1 mM TBAB.

proteins in 1.0 mM TBAB were obtained in order to estimate molecular weights for compounds of the beverage samples based on retention times. Three of the standard protein chromatographic responses are shown in Fig. 5, in terms of Π_{mean} as a function of the elution time. OVA (42.7 kDa) eluted at approximately 18 min, β-LG (18.4 kDa) eluted at approximately 20 min, and α-Lac (14.2 kDa) eluted at approximately 21.5 min.

Figs. 6 and 7 show SEC-UV/DSTD chromatograms of a commercial instant coffee sample and a soluble barley beverage, respectively. In these figures, the typical UV absorbance chromatograms at 280 nm are compared with the simultaneously acquired SEC-DSTD chromatograms plotted as Π_{mean} as a function of the elution time. For the Nescafe instant coffee beverage shown in Fig. 6, the UV chromatogram shows one complex band (eluting between 17 min and 24 min) and four peaks (eluting at approximately 25 min, 29 min, 32 min, and 37 min). However, the

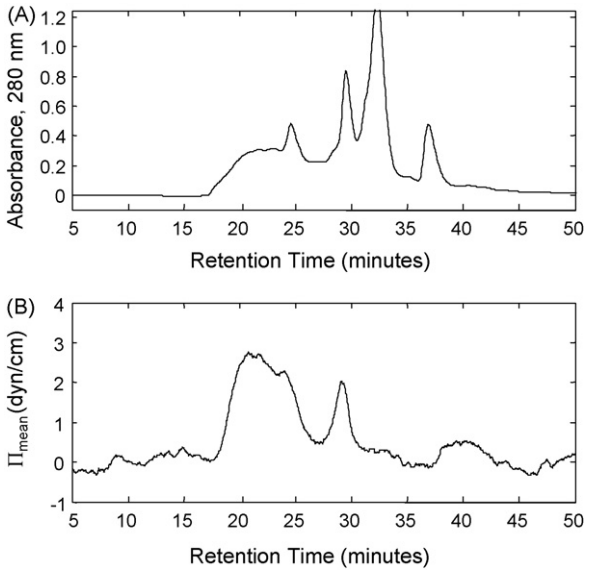


Fig. 6. SEC-UV/DSTD chromatograms of beverage samples. (A) UV absorbance chromatogram at 280 nm for Nescafe instant coffee sample (20 mg/mL in 0.1 M PBS, pH 6.8 with 1 mM TBAB). (B) Simultaneously acquired SEC-DSTD chromatogram with π mean as a function of elution time for the commercial instant coffee sample.

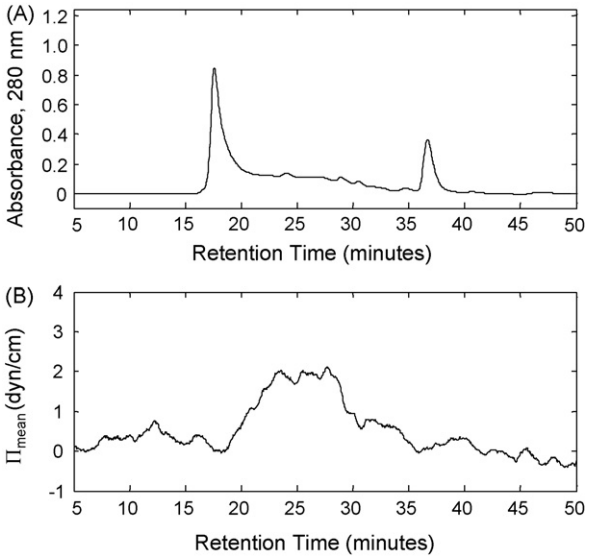


Fig. 7. (A) UV absorbance chromatogram at 280 nm for soluble barley beverage (20 mg/mL in 0.1 M PBS, pH 6.8 with 1 mM TBAB). (B) Simultaneously acquired SEC-DSTD chromatogram with π mean as a function of elution time for the soluble barley beverage.

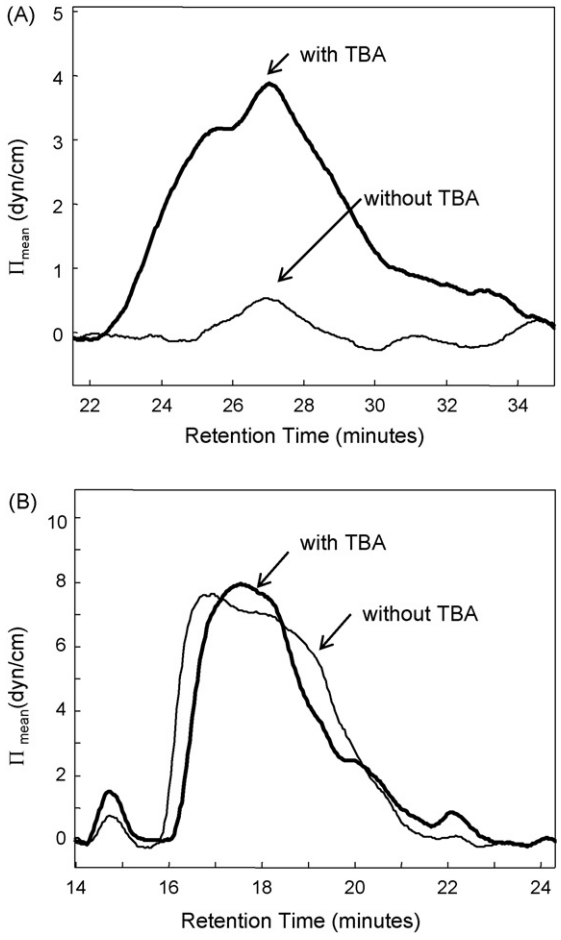


Fig. 8. (A) SEC-DSTD chromatogram for 10 mg/mL Nescafe Classic instant coffee sample with and without 1 mM TBAB. (B) SEC-DSTD chromatogram for 10 mg/mL powdered milk sample with and without 1 mM TBAB.

DSTD chromatogram of the instant coffee indicates that only compounds eluting between 17 min and 29 min were surface active. According to the retention time calibration of the SEC column, the molecular weight of the surface-active compounds in the instant coffee beverage sample corresponded to a range of approximately 1–45 kDa. For the barley beverage sample in Fig. 7, the UV chromatogram shows peaks at 18 min and 37 min with a complex band between these peaks. However, the DSTD chromatogram of this barley sample indicates that only the compounds eluting between 20 min and 30 min were surface active. Thus, the selectivity of the DSTD with respect to UV absorbance detection provided unique surface activity information for these mixtures. SEC-UV/DSTD analyses of these samples eluted in the absence of TBAB yielded the same UV absorbance chromatogram and close to zero signal at the DSTD detector. These results demonstrate that 1 mM TBAB in the mobile phase increased the surface activity of the coffee and barley samples at the DSTD without affecting the SEC separation.

TBAB can increase the signal of sample components to varying degrees, as shown in Fig. 8 where the SEC separations of 10 mg/mL Nescafe Classic instant coffee or powdered milk are shown with and without 1 mM TBAB. In Fig. 8A the DSTD signal for the coffee component was increased from 0.5 dyn/cm without TBAB to 3.8 dyn/cm with TBAB. In Fig. 8B the DSTD signal for the powdered milk component at 14.8 min increased from 0.7 dyn/cm to 1.5 dyn/cm when TBAB was present. The DSTD signal for the powdered milk component at 22 min increased from 0.1 dyn/cm to 0.8 dyn/cm when TBAB was present.

The application of the SEC-DSTD method to commercial food products like instant beverage samples provides a selective view of the surface-active compounds that may differ significantly among the examined samples. For example, it is worth noting that the number and the concentration of surface-active proteins in barley and coffee samples are substantially different. In summary, the DSTD coupled with TBAB as a protein modifier offers a novel tool for improving the sensitive detection of the surface activity of food products such as instant coffee.

4. Conclusions

The SEC-DSTD/UV instrument is chemically selective and provides surface activity information complementary to absorbance data for constituent analysis of commercial coffee and commercial soluble barley samples. Furthermore, the LOD was selectively enhanced (reduced to parts-per-thousand protein concentration) when proteins were combined with mM concentrations of TBAB. This instrument has the potential to be a fundamental tool for quality control during all the steps of food processing (from the raw materials to the processed foodstuff), as well as in the pharmaceutical industry and in environmental chemistry where surface property phenomena of individual compounds in a complex mixture are of interest.

Acknowledgments

We thank the Center for Process Analytical Chemistry (CPAC) at the University of Washington for financial support. We also thank the Montana Family Endowment and the M.J. Murdock Charitable Trust for financial support.

References

[1] M.E. Mangino, in: N.S. Hettiarachchy, G.R. Ziegler (Eds.), Protein Functionality in Food Systems, Marcel Dekker, New York, 1994, pp. 147–179.
[2] J.B. German, L. Phillips, in: N.S. Hettiarachchy, G.R. Ziegler (Eds.), Protein Functionality in Food Systems, Marcel Dekker, New York, 1994, pp. 181–208.
[3] L.G. Phillips, D.M. Whitehead, J. Kinsella, Structure–Function Properties of Food Proteins, Academic Press, London, 1994, p. 271.

[4] S. Damodaran, in: S. Damodaran, A. Paraf (Eds.), Food Proteins and their Applications, Marcel Dekker, New York, 1997, p. 57.
[5] N. Garti, Colloids Surf. A: Physicochem. Eng. Asp. 152 (1999) 125–146.
[6] E. Dickinson, An Introduction to Food Colloids, Oxford University Press, Oxford, UK, 1992.
[7] P.J. Halling, Crit. Rev. Food Sci. Nutr. 13 (1981) 155–203.
[8] B.S. Murray, E. Dickinson, Food Sci. Technol. Inst. 2 (1996) 131.
[9] S. Damodaran, Adv. Food Nutr. Res. 1 (1990) 34.
[10] M.J. Rosen, Surfactants and Interfacial Phenomena, second ed., Wiley, New York, 1989.
[11] A.W. Adamson, Physical Chemistry of Surfaces, fifth ed., Wiley, New York, 1990.
[12] M. Ferrari, L. Navarini, L. Liggieri, F. Ravera, F.S. Liverani, Food Hydrocoll. 21 (2007) 1374–1378.
[13] B.A. Staggemeier, E. Bramanti, C. Allegrini, K.J. Skogerboe, R.E. Synovec, Anal. Chem. 77 (2005) 250–258.
[14] E. Bramanti, C. Allegrini, M. Onor, G. Raspi, K.J. Skogerboe, R.E. Synovec, Anal. Biochem. 351 (2006) 100–113.
[15] W.W.C. Quigley, E. Bramanti, B.A. Staggemeier, K.E. Miller, A. Nabi, K.J. Skogerboe, R.E. Synovec, Anal. Bioanal. Chem. 378 (2004) 134–143.
[16] K.E. Miller, E. Bramanti, B.J. Prazen, M. Prezhdo, K.J. Skogerboe, R.E. Synovec, Anal. Chem. 72 (2000) 4372–4380.
[17] E. Bramanti, W.W.C. Quigley, C. Sortino, F. Beni, M. Onor, G. Raspi, R.E. Synovec, J. Chromatogr. A 1023 (2004) 79–91.
[18] W.W.C. Quigley, A.J. Nabi, N. Lenghor, K. Grudpan, R.E. Synovec, Talanta 55 (2001) 551–560.
[19] K.E. Miller, K.J. Skogerboe, R.E. Synovec, Talanta 50 (1999) 1045–1056.
[20] A. D'Agostina, G. Boschin, F. Bacchini, A. Arnoldi, J. Agric. Food Chem. 52 (2004) 7118–7125.
[21] M. Arya, L.J.M. Rao, Crit. Rev. Food Sci. Nutr. 47 (2007) 51–67.
[22] M. Daglia, A. Papetti, C. Dacarro, G. Gazzani, J. Pharm. Biomed. Anal. 18 (1998) 219–225.
[23] P.H. von Hippel, K.-Y. Wong, J. Biol. Chem. 240 (1965) 3909–3923.
[24] S. Jain, J.C. Ahluwalia, Thermochim. Acta 302 (1997) 17–24.
[25] S. Jain, J.C. Ahluwalia, Biophys. Chem. 59 (1996) 171–177.
[26] R.E. Synovec, B.A. Staggemeier, E. Bramanti, W.W.C. Quigley, B.J. Prazen, in: A.M. Striegel (Ed.), ACS Symposium Series 893, N. 16, American Chemical Society, Washington, DC, 2004, ISBN 0-8412-3878-2, pp. 266–280.
[27] K.D. Schwenke, in: S. Magdassi (Ed.), Surface Activity of Proteins: Chemical and Physiochemical Modifications, Marcel Dekker, New York, 1996, p. 61.
[28] V.N. Izmailova, G.P. Yampolskaya, in: D. Mobius, R. Miller (Eds.), Protein at Liquid Interfaces, Elsevier, Amsterdam, 1998, p. 103.
[29] P.A. Wierenga, M.B.J. Meinders, M.R. Egmond, A.G.J. Voragen, H.H.J. de Jongh, J. Phys. Chem. B 109 (2005) 16946–16952.
[30] D. Horn, C.-C. Heuck, J. Biol. Chem. 254 (1983) 1665–1670.
[31] A. Conway-Jacobs, L.M. Lewin, Anal. Biochem. 43 (1971) 394–400.
[32] P.G. Righetti, T. Caravaggio, J. Chromatogr. 127 (1976) 1–28.
[33] B.J. Radola, Biochim. Biophys. Acta 295 (1973) 412–428.
[34] E.T. Nakhleh, S.A. Samra, Z.L. Awdeh, Anal. Biochem. 49 (1972) 218–224.
[35] P.G. Righetti, G. Tudor, K. Ek, J. Chromatogr. 220 (1981) 115–194.

Talanta 80 (2010) 1452–1460

Contents lists available at ScienceDirect

Talanta

journal homepage: www.elsevier.com/locate/talanta

Sorption of As(V) from waters using chitosan and chitosan-immobilized sodium silicate prior to atomic spectrometric determination

Ezel Boyacı[a], Ahmet E. Eroğlu[a,*], Talal Shahwan[a,b]

[a] Department of Chemistry, İzmir Institute of Technology, Gulbahce, Urla 35430, İzmir, Turkey
[b] Department of Chemistry, Birzeit University, Ramallah, West Bank, Palestine

ARTICLE INFO

Article history:
Received 30 April 2009
Received in revised form
14 September 2009
Accepted 25 September 2009
Available online 3 October 2009

Keywords:
As(V)
As(III)
Sorption
Chitosan
Chitosan-immobilized sodium silicate

ABSTRACT

A natural biosorbent containing amine functional groups, chitosan, and a novel sorbent, chitosan-immobilized sodium silicate, were prepared and utilized for the selective sorption of As(V) from waters prior to its determination by atomic spectrometric techniques, namely, hydride generation atomic absorption spectrometry (HGAAS) and inductively coupled plasma mass spectrometry (ICP-MS). Chitosan was synthesized from chitin and sodium silicate was used as the immobilization matrix due to its straightforward synthesis. Through sequential sorption studies, it was shown that chitosan-immobilized sodium silicate has exhibited a better chemical stability than the chitosan itself which demonstrates the advantage of immobilization method. Both chitosan and chitosan-immobilized sodium silicate were shown to selectively adsorb As(V), arsenate, from waters at pH 3.0 at which neither chitin nor sodium silicate displayed any sorption towards As(V). The sorption of arsenate by chitosan is supposed to have electrostatic nature since pH of 3.0 is both the point at which the amino groups in chitosan are protonated and also the predominant form of As(V) is $H_2AsO_4^-$. A pre-oxidation step is required if both As(III) and As(V) are to be determined. Desorption from the sorbents was realized with 1.0% (w/v) L-cysteine prepared in a pH 3.0 solution adjusted with HCl. Among the possible interfering species tested, only Te(IV) and Sb(III) were shown to cause a decrease in the sorption capacity especially at high interferant concentrations. High concentrations of Sb(III) also resulted in gas phase interference during hydride generation.

The validity of the method was checked both via spike recovery experiments and also through the analysis of a standard reference material. Spike recovery tests were carried out with four different types of water; namely, ultra-pure, bottled drinking, tap, and sea water; and percent recovery values were found to be 114 (±4), 112 (±2), 43 (±4), and 0 (±1), respectively. It was concluded that the proposed methodology can be applied efficiently to low-to-medium ionic strength solutions, such as most drinking waters. The accuracy of the method was additionally investigated through the analysis of a standard reference material and a good correlation was found between the determined ($26.6 \pm 2.4\ \mu g\ L^{-1}$) and the certified ($26.67\ \mu g\ L^{-1}$) value.

© 2009 Elsevier B.V. All rights reserved.

1. Introduction

In nature, arsenic can be found in food, water and air in organic and inorganic forms [1] and exists in the −3, 0, +3 and +5 oxidation states [2–4]. Inorganic arsenic species occur as arsenite, As(III), with primary form of H_3AsO_3 and arsenate, As(V), with primary forms of $H_2AsO_4^-$ and $HAsO_4^{2-}$ in natural waters [1]. Arsenates are stable under aerobic (oxidizing) conditions whereas arsenites are predominant under anaerobic (reducing) conditions [3,5].

Both natural and anthropogenic sources contribute to the arsenic levels in the environment, which is distributed throughout earth crust, soil, water, air and living organisms [5]. The presence of arsenic in drinking water is related to the dissolution of minerals and ores [6]. Waste discharges from industrial and mining activities, agricultural use of arsenical pesticides and use of chromated copper arsenate (CCA) wood preservative may enhance the anthropogenic arsenic contamination in air, water and soil [5]. Long term consumption of drinking water contaminated with arsenic is reported to cause cancers of the skin, lungs, kidney and liver. Short term exposure to arsenic may result in vomiting, oesophageal, and abdominal pain, and "rice water" diarrhea [2,6]. Hence, drinking water containing arsenic is a potential threat to the health of humans. The World Health Organization (WHO) revised the guide-

* Corresponding author. Tel.: +90 232 7507533; fax: +90 232 7507509.
E-mail address: ahmeteroglu@iyte.edu.tr (A.E. Eroğlu).

0039-9140/$ – see front matter © 2009 Elsevier B.V. All rights reserved.
doi:10.1016/j.talanta.2009.09.053

line for arsenic in drinking water from 0.05 to 0.01 mg L^{-1} and has classified arsenic as the most toxic chemical with carcinogenic effects [6].

Because of the undesired health effects mentioned above, finding/devicing economic, easily operable and nontoxic technologies for removal of arsenic are a major goal especially when clean water sources are scarce. Arsenic removal methods from drinking water including precipitation, adsorption, ion exchange, membrane filtration and some other alternative processes have been reviewed [1,2,7]. All processes are limited with lower efficiency for arsenite removal because of the uncharged state of the species under pH 8 which necessitates the oxidation of As(III) before the removal step. In last years, nanozero valent iron has become one of the most attractive materials for arsenic removal which effectively removes both inorganic forms [8,9]. Application of various biomasses in arsenic removal has been reviewed by Mohan and Pittman [2]. Among numerous polysaccarides, cellulose and chitin are the most abundant organic compounds on the earth, with the largest amounts of production per year [10]. The shells of marine crustaceans such as crabs and shrimps are available as waste from the seafood processing industry and are used for commercial production of chitin. Chitosan, the N-deacetylated form of chitin, is an attractive material with unique properties of non-toxicity, film and fiber forming properties, adsorption of metal ions, coagulation of suspensions or solutes, and distinctive biological activities [10,11] and is produced by thermochemical alkaline treatment of chitin. Chitosan has been used as a sorbent for arsenic removal. For example, Kartal and Imamura studied arsenic removal from chromated copper arsenate (CCA)-treated wood via biosorption by chitin and chitosan in 1, 5 and 10 days periods; however, a quantitative removal was not obtained [12]. Chitosan was modified with molybdate and it was shown that the modification increased the sorption capacity by the ability of molybdate ion to complex As(V) [13–16]. Chitosan was also used as a resin for arsenic sorption in column studies with improved resistance to shrinkage which was obtained by cross-linked chitosan functionalized with 3,4-diamino benzoic acid [17]. Boddu et al. used ceramic alumina dip-coated with chitosan for As(III) and As(V) removal in column and an improved sorption capacity was reported for As(III) [18].

As revealed in the literature, effective use of chitosan as a sorbent can be based on the enhancement of its capacity through particular modifications. In the meantime, the resistance of the biomaterial to shrinkage may be improved. Immobilization of chitosan onto a supporting surface increases the surface area of sorbent (compared to chitosan itself) with a corresponding increase in the number of functional groups available for sorption. Using sodium silicate as an immobilization matrix has the advantage of tuning the immobilized amount of functional groups in a narrow synthesis time. Ease of the application and availability of low-cost chemicals are among the other advantages of the silicate-immobilization method. In this study, both chitosan as synthesized and chitosan-immobilized sodium silicate were used in the sorption of As(V) from waters prior to determination by hydride generation atomic absorption spectrometry (HGAAS) and inductively coupled plasma mass spectrometry (ICP-MS).

2. Experimental

2.1. Instrumentation and apparatus

A Thermo Elemental Solaar M6 Series atomic absorption spectrometer (Cambridge, UK) with an air-acetylene burner was used in arsenic determination utilizing the Segmented Flow Injection Hydride Generation (SFI-HGAAS) unit. An arsenic hollow cathode lamp at the wavelength of 193.7 nm and a deuterium lamp were employed as the source line and for background correction, respectively. In HGAAS, the quartz tube atomizer was 10 cm long, 8 mm in internal diameter and 10 mm in external diameter with a 4 mm bore inlet tube fused at the middle for sample introduction. Air-acetylene flame was used for heating the quartz tube externally and nitrogen was used as the carrier gas. Operating parameters for the HGAAS system were as follows: 200 mL min^{-1} carrier gas (N_2) flow rate, 6.1 mL min^{-1} HCl flow rate, 2.0% (v/v) HCl concentration, 3.0 mL min^{-1} $NaBH_4$ flow rate, 1.0% (w/v) $NaBH_4$ concentration (stabilized with 0.1%, w/v, NaOH), 7–8 mL min^{-1} sample flow rate. In addition to HGAAS, ICP-MS (Agilent 7500ce Series, Tokyo, Japan) was also employed in validation and interference studies.

In batch sorption studies, GFL 1083 water bath shaker (Burgwedel, Germany) equipped with a microprocessor thermostat was used for mixing. The elemental composition of chitosan was determined by a LECO-CHNS-932 elemental analyzer (Mönchengladbach, Germany). Determination of the molecular weight was realized using a Petrotest capillary viscosimeter (Dahlewitz, Germany). The crystallographic structure of the sorbent was elucidated by a Philips X'Pert Pro X-Ray Diffractometer (Eindhoven, The Netherlands). The pH adjustments were performed with Ino Lab Level 1 pH meter (Weilheim, Germany). Microimages of sorbents were taken utilizing a Philips XL-30S FEG scanning electron microscope (Eindhoven, The Netherlands). The thermal properties of sorbents were analyzed using a Perkin Elmer Pyris Diamond TG/DTA (Boston, MA, USA). The point of zero charge of chitosan flakes was determined with a Zeta-Meter 3.0+ equipment (Staunton, USA).

2.2. Reagents and solutions

All the chemicals were of analytical reagent grade. Ultra-pure water (18.2 MΩ) was used throughout the study. Glassware and plastic containers were cleaned by soaking in 10% (v/v) nitric acid for 24 h and rinsed with deionized water prior to use.

Stock standard solutions of As(V) and As(III), 2000.0 mg L^{-1}, were prepared by dissolving As_2O_5 (Merck, product code: 1.09939, CAS no.: [1303-28-2]) and As_2O_3 (Fischer, CAS no.: [1327-53-3]), respectively, in ultra-pure water. Stock standard solution of Te(IV), 500.0 mg L^{-1} was prepared by pre-reduction of Te(VI) (Aldrich, product code: 41058-6, CAS no.: [26006-71-3]) by boiling with 6.0 M HCl. Stock solutions of Se(VI), Se(IV), Sb(III) and Sb(V), 1000.0 mg L^{-1}, were prepared by dissolving Na_2SeO_4 (Fluka, product code: 71948, CAS no.: [13410-01-0]), $Na_2SeO_3 \cdot 5H_2O$ (Merck, product code: 1.06607, CAS no.: [26970-82-1]), $C_8H_4K_2O_{12}Sb_2 \cdot 3H_2O$ (Sigma–Aldrich, product code: P-6949, CAS no.: [28300-74-5]) and $KSb(OH)_6$ (Riedel-de Haen, product code: 31149, CAS no.: [12208-13-8]), respectively, in ultra-pure water. Mo(VI) and V(V), 1000.0 mg L^{-1} standard stock solutions were supplied from High-Purity Standards (product code: 100065-1) and Merck (product code: 1.70227), respectively. Lower concentration standard solutions were prepared daily by appropriate dilution from their stock standards before use.

Chitosan flakes were synthesized from practical grade chitin (Sigma, product code: C923, CAS no.: [1398-61-4]).

Sodium borohydride solution was prepared for a daily use from fine granular product (Merck, product code: 8.06373, CAS no.: [16940-66-2]) and stabilized by NaOH (Merck, product code: 1.06498, CAS no.: [1310-73-2]) in water. L-cysteine (Merck, product code: 1.02838, CAS no.: [52-90-4]) was added to all standards and samples to reduce As(V) to As(III) before HGAAS determination.

N,N-Dimethylacetamide (Sigma, product code: D 5511, CAS no.: [127-19-5]) containing 5.0% (w/v) LiCl (Aldrich, product code: 310468, CAS no.: [7447-41-8]) and 0.200 M NaCl (Riedel-de Haen, product code: 13423, CAS no.: [7647-14-5]) containing 0.100 M acetic acid (Riedel-de Haen, product code: 27225, CAS no.: [64-

19-7]) were used in molecular weight determination of chitin and chitosan, respectively.

$BaCl_2 \cdot 2H_2O$ (Riedel-de Haen, product code:11411, CAS no.: [10326-27-9]) was used to prepare 0.1 M solution by dissolving appropriate amount in distilled water. Silicate-immobilization matrix was prepared from sodium silicate solution (Sigma–Aldrich, product code: 338443, CAS no.: [1344-09-8]).

2.3. Synthesis and characterization of chitosan

2.3.1. Synthesis of chitosan

Chitosan flakes were synthesized from chitin under inert atmosphere by the method of Rigby and Wolfrom given in the monograph by Muzzarelli [19]. Briefly, 15.0 g of chitin was treated with 720 mL of 40.0% (w/w) aqueous NaOH solution in a 1-L three-necked round bottomed flask with reflux condenser connected to its middle neck. A thermometer was connected to control the temperature during the reaction and N_2 gas was bubbled through the solution from the side arm to provide inert atmosphere in the reaction medium. Constant reflux was obtained at 115 °C and continued for 6 h. After cooling the alkaline mixture to room temperature, chitosan flakes were washed with distilled water until a neutral filtrate was obtained. The resulting chitosan flakes were dried at 60 °C for 2 h before use.

2.3.2. Characterization of chitosan

A variety of methods were applied for the characterization of synthesized chitosan flakes. Elemental analysis and potentiometric titrimetry were used for the determination of the degree of deacetylation as reported in the literature [20,21]. The molecular weights of chitin and chitosan were determined by viscosimetric method which relates intrinsic viscosity of polymer to its molecular weight according to Mark–Houwink–Sakurada relation as described in the literature [21–26]. Images of chitosan, sodium silicate, and chitosan-immobilized sodium silicate were taken with scanning electron microscopy (SEM). XRD crystallographic properties and thermal gravimetric degradation were also investigated.

2.4. Immobilization of chitosan on sodium silicate

Chitosan was immobilized on polysilicate matrix after slight modification in the method described by Karunasagar et al. [27] in which sodium silicate was used as the immobilization matrix for the plant *Coriandrum sativum*. In the present study, the immobilization procedure was as follows: 6.0% (w/w) sodium silicate was added dropwise into 15.0 mL of 5.0% (v/v) H_2SO_4 until pH rose to 2. The solution pH was checked with pH paper instead of pH meter in order not to cause any damage to the electrode system due to use of silicate solution. Then, 50.0 mL of 2.0% (w/v) chitosan dissolved in 2.0% (v/v) acetic acid was added dropwise to the silicate solution and the mixture was stirred for 15 min. The polymer gel was formed by increasing the pH to 7 by dropwise addition of sodium silicate solution. Formed gel was washed with ultra-pure water until the solution is free of sulphate ion. This was checked by the addition of 0.200 M $BaCl_2$ solution to the filtrate. Usually cloudiness is observed as a result of precipitation reaction between barium and sulphate ions when sulphate is at an appreciable concentration. After the immobilization procedure had been completed, the chitosan-immobilized sodium silicate was dried at 50 °C overnight and ground by mortar and pestle prior to use.

2.5. Sorption studies

Sorption studies were performed for all the sorbents prepared; namely, chitin, chitosan, sodium silicate and chitosan-immobilized sodium silicate through batch process. Effect of the sorbent amount, shaking time, solution pH, reaction temperature and successive loadings was investigated. In all these experiments, batch sorption was followed by the filtration of the mixture through blue-band filter paper and analysis of the filtrate for its arsenic content using HGAAS. Before HGAAS measurements all samples and standard solutions were acidified with the addition of appropriate amount of concentrated HCl to produce 1.0% (v/v) HCl in the final solution. For As(V) determination, L-cysteine was also added to all solutions so as to have 0.5% (w/v) concentration in the final solution which guaranteed the pre-reduction of As(V) to As(III).

2.6. Sorption isotherm models

Sorption isotherm is a constant-temperature curve that describes the retention of a substance on a solid at various concentrations and is used to predict the mobility of the substance in the environment [28]. Sorption isotherm defined by Langmuir assumes that the energy of sorption is constant and sorption occurs at a fixed number of definite localized homogeneous sites with monolayer coverage [28–30]. The nonlinear form of Langmuir isotherm is given in Eq. (1):

$$Q_e = Q_{max} \frac{bC_e}{1 + bC_e} \quad (1)$$

Here, Q_{max} (mmol/g) and b (L/mmol) are Langmuir constants; Q_{max} is the amount of arsenate ion sorption corresponding to monolayer coverage, b is the affinity of arsenate for the sorbent, C_e (mmol/L) is the amount of arsenate in liquid phase at equilibrium and Q_e is the amount of arsenate adsorbed on the surface of sorbent (mmol/g) at equilibrium. The values of constants were evaluated from the linearized form of the equation which is given in Eq. (2):

$$\frac{1}{Q_e} = \frac{1}{Q_{max}} + \frac{1}{Q_{max} bC_e} \quad (2)$$

The intercept and slope of the plot of $1/Q_e$ versus $1/C_e$ were used for determination of Q_{max} and b.

Freundlich isotherm is among the most widely applied isotherms. This isotherm can be applied for heterogeneous surfaces over a wide range of concentrations. The nonlinear form of this isotherm is described by Eq. (3) [31]:

$$Q_e = K_F C_e^{1/n} \quad (3)$$

where K_F and n are constants for a given sorbent–sorbate system. These constants can be evaluated from the linearized form of Eq. (3) given as follows:

$$\log Q_e = \log K_F + \frac{1}{n} \log C_e \quad (4)$$

The intercept and slope of the plot of $\log Q_e$ versus $\log C_e$ in Eq. (4), give K_F and $1/n$, respectively.

Dubinin–Radushkevich (D–R) isotherm model assumes that the ionic species bind preferentially to most energetically favorable sites of sorbent material and allows for multilayer sorption of ions [13]. D–R isotherm is generally described by Eq. (5) [32]:

$$Q_e = q_s \exp(-B\varepsilon^2) \quad (5)$$

where

$$\varepsilon = RT \ln\left(1 + \frac{1}{C_e}\right) \quad (6)$$

The D–R parameter, B, provides information about the mean free energy of sorption defined as the energy required to transfer one mole of ions to the surface of the solid from infinity in the solution. The constant, q_s corresponds to the sorption monolayer capacity

[33]. The mean free energy of sorption can be calculated from D–R parameter B using Eq. (7):

$$E = (2B)^{-1/2} \quad (7)$$

The q_s and B constants are, respectively, obtainable from the intercept and the slope of the experimental plot of $\ln Q_e$ versus ε^2.

2.7. Desorption/dissolution studies

Two different strategies were followed to take the adsorbed arsenate ion back into solution from chitosan or chitosan-immobilized sodium silicate. Firstly, 2% (v/v) acetic acid in which chitosan was completely soluble was used. Secondly, desorption was carried out in L-cysteine which reduces the adsorbed form of arsenic (As(V), arsenate) to the non-adsorbed form (As(III), arsenite). In both strategies, calibration standards were also prepared in the same matrixes using the same method of preparation (matrix-matched standards). Before HGAAS measurements both samples and standards were acidified with concentrated HCl to produce 1.0% (v/v) of HCl in the final solution. For reduction of As(V) to As(III) L-cysteine was added to produce 0.5% (w/v) in the solution (This step was skipped if desorption matrix had already contained L-cysteine.).

2.8. Interference studies

Interference effects of two groups of compounds on arsenic determination were investigated. The first group contained hydride forming ions possessing different oxidation states of several elements; namely, Sb(III), Sb(V), Te(IV), Te(VI), Se(IV), and Se(VI) ions. The second group included Mo(VI) and V(V) for which chitosan is presumed to show sorption affinity [17,34]. Two types of interferences were expected: firstly, during the sorption of arsenate, and secondly, during hydride generation [35].

Initially, the sorption characteristics of chitosan towards each of the possible interfering ions were investigated in the absence of arsenate. For this purpose, 100.0 and 1000.0 $\mu g\,L^{-1}$ concentrations of the ions were mixed with chitosan and shaken under the conditions optimized for arsenate sorption. The percent sorption of each ion was determined by ICP-MS after acidification with concentrated HNO_3 so as to have 1.0% (w/v) acid concentration in the final solution.

In addition, 10.0, 100.0, 1000.0 $\mu g\,L^{-1}$ of each of the interfering species were added in separate experiments into both 10.0 and 100.0 $\mu g\,L^{-1}$ As(V) solutions in order to see the interference effect in presence of arsenate. The sorption experiments were performed under optimized conditions for arsenate described in the previous paragraph. After proper acidification and pre-reduction (L-cysteine) steps, ICP-MS and HGAAS were used for the analyses.

2.9. Method validation

The proposed methodology was validated both through the analysis of a standard reference material (SRM from NIST, Natural Water – Trace Elements, Cat. No. 1640) and via spike recovery experiments. Due to the absence of any information about the oxidation state of arsenic in the SRM, initial experiments were carried out in two ways: shaking with chitosan first directly, and second, after a pre-oxidation step with concentrated HNO_3. The oxidation was carried out by diluting 5.0 mL of SRM with 10.0 mL of ultra-pure water in a teflon beaker. After addition of 3.0 mL concentrated HNO_3, heating was applied on hot plate until evaporation of solution was completed. The remaining residue was dissolved in about 10 mL of ultra-pure water and after pH was adjusted to 3.0, the solution was diluted to exactly 15.0 mL to provide an As(V) concentration of 9.0 $\mu g\,L^{-1}$ in the final solution. The same procedure was also applied to the SRM directly without pre-oxidation step. In line with these experiments, both As(III) and As(V) standard solutions were also subjected to the same procedure; namely, with or without pre-oxidation with HNO_3.

Spike recovery tests were performed with four different types of water; namely, tap, distilled, sea and bottled drinking water. Spiked samples were subjected to the same sorption/elution cycles as previously and recoveries were calculated.

In addition to the validation tests described above, solutions containing both As(III) and As(V) were analyzed with the proposed method to see if there is a mutual interference. In these experiments, both chitosan and chitosan-immobilized sodium silicate were used in a two-stage batch type process. Three different solutions, namely, As(III) only, As(V) only and the mixture of As(III) and As(V) were prepared in a way that the concentrations of the species were 100.0 $\mu g\,L^{-1}$ in each case. After the addition of 50.0 mg of chitosan or chitosan-immobilized sodium silicate, the mixture was shaken for 30 min and then was filtered through blue-band filter paper. The solid and the liquid parts were separated and the filtrate was kept for determination of its arsenic concentration. Solid chitosan (or chitosan-immobilized sodium silicate) remained on the filter paper was taken into 30.0 mL of 1.0% (w/v) L-cysteine solution of which pH was adjusted to 3.0 and shaking was continued for a further 30 min for desorption. This eluate was analyzed by ICP-MS for its arsenic concentration by using matrix-matched standards which were prepared under the same sorption/desorption conditions described above.

3. Results and discussion

3.1. Characterization of chitosan

Surface morphology of chitosan flakes, sodium silicate and chitosan-immobilized sodium silicate was examined from different locations on their surfaces using SEM. The images (not shown) reveal the increasing surface porosity of chitosan-immobilized sodium silicate in comparison to chitosan.

The thermal gravimetric analysis of chitosan shows two notable weight loss stages (Fig. 1). The first stage results in about 9% loss in weight and corresponds to the weight loss of water molecules adsorbed onto surface (25–98 °C) and weight loss of bonded water (98–266 °C). The second stage weight loss occurred between 266 and 328 °C due to rapid thermal degradation of chitosan and resulted in 33% weight loss. The results are in agreement with thermal gravimetric analysis reported for chitosan by different studies in the literature [36,37]. As in the case of chitosan, sodium silicate matrix shows a weight loss of about 9% in the same temperature range due to release of water molecules from the structure. The chitosan-immobilized sodium silicate demonstrates intermediate thermal characteristics between chitosan and immobilization

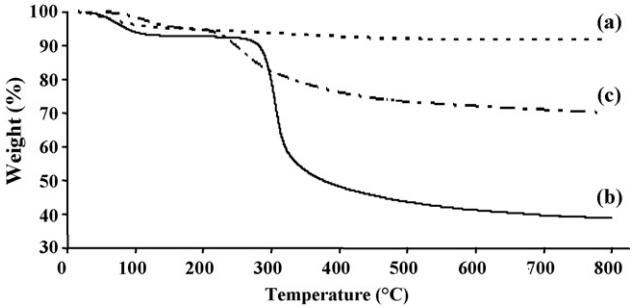


Fig. 1. TGA curves of (a) sodium silicate, (b) chitosan and (c) chitosan-immobilized sodium silicate.

matrix. Careful investigation of the weight loss percentages in thermograms is also indicative of around 30% (w/w) of chitosan in the immobilization matrix of silicate.

The degree of deacetylation of chitosan was determined by two methods: elemental analysis and titrimetry, and the results obtained were in good agreement (84.7% versus 85.4%, respectively). In addition, the percentage of chitosan-immobilized onto sodium silicate was calculated from the carbon ratios of chitosan-immobilized sodium silicate to pure chitosan sample. The amount of chitosan in sodium silicate matrix was calculated as 33.3% in the total mass which is also in accordance with TGA results.

Molecular weights of chitin and chitosan were determined using the Mark–Houwink–Sakurada equation [21–26] and found to be 1215 and 910 kDa, respectively. These results are in accordance with the results in the literature where very scattered molecular weights are reported. The wide range of the reported molecular weight values, especially for chitin, is thought to be arising from the limited solubility of chitin in the given solvent system which prevents accurate determination of the molecular weight. As reported in [26 and the references therein], two factors are effective on incomplete dissolution. Firstly, high molecular weight chitin chains are not soluble, and secondly, the presence of proteins in the unpurified chitin may associate with the N-acetyl groups in the structure and make the product insoluble. To eliminate the possible error in the determination of the molecular weight of the chitin, the insoluble part was filtered, dried, and weighed as suggested in [26]; and the true molecular weight of the chitin was calculated after subtracting the weight of the insoluble part from the total weight taken at the beginning. The calculated molecular weights indicate that the chitin used in this study is of high molecular weight and the deacetylation process not only removes the acetyl groups but also decreases the molecular weight of chitosan by cleavage of glycosidic bonds.

The X-ray diffraction patterns for chitin and chitosan are given in Fig. 2. The most significant difference observed between the two XRD patterns is the decreasing crystallinity of the compound after deacetylation process. Deacetylation procedure involves the disappearance of small peaks; only the peaks at $2\theta = 9–10^\circ$ and $2\theta = 19–20^\circ$ remain. The decrease in the crystallinity when going from chitin to chitosan was also observed by different research groups in the literature who reported that the retained peaks corresponded to hydrated crystals of chitosan [38,39].

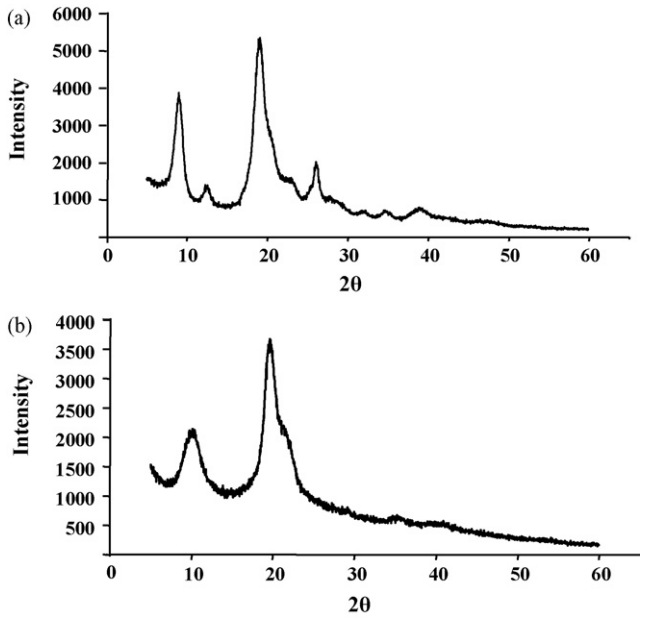


Fig. 2. X-ray diffraction patterns for (a) chitin and (b) chitosan.

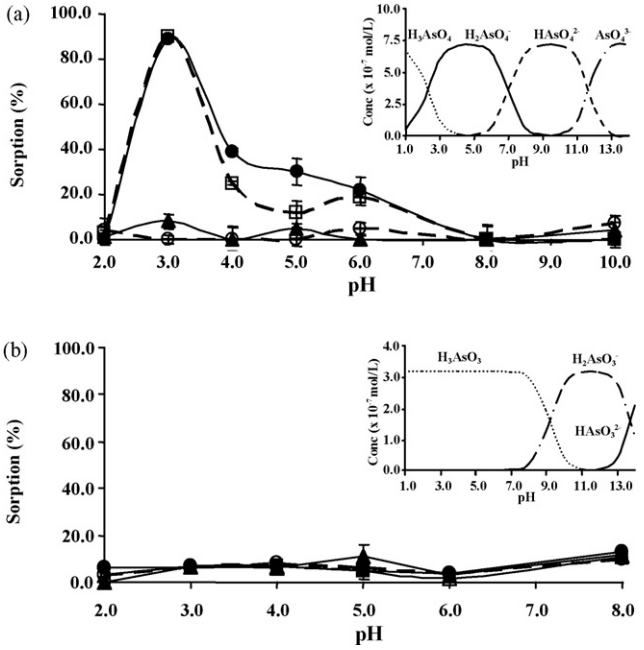


Fig. 3. Effect of pH on the sorption of (a) 100.0 μg L^{-1} As(V) and (b) 40.0 μg L^{-1} As(III) solutions. (●) chitosan, (○) sodium silicate, (▲) chitin, (□) chitosan-immobilized sodium silicate, $n = 3$. Reaction conditions: 30.0 mL sample volume, 30 min shaking time, 50.0 mg sorbent, 25 °C sorption temperature. The insets obtained with VISUAL MINTEQ software show speciation diagrams of As(V) and As(III).

3.2. Sorption studies

3.2.1. Effect of pH on sorption of As(V) and As(III)

The sorption characteristics of chitin, chitosan, sodium silicate and chitosan-immobilized sodium silicate towards As(V) and As(III) are given in Fig. 3. Chitosan and chitosan-immobilized sodium silicate have maximum sorption at pH 3.0 while sodium silicate and chitin do not show any affinity for As(V) as indicated in the figure. In case of As(III), all sorbents showed the same trend; arsenite ions were not adsorbed significantly (<15% sorption) by any of the sorbents under the working conditions applied. The nature of sorption behavior of chitosan at pH 3.0 can be explained by the electrostatic attraction between the protonated amine groups of chitosan and $H_2AsO_4^-$ ion, which is the main (approximately 85% of the As(V)) species at pH 3.0 (Fig. 3a inset). Chitosan flakes start to dissolve below pH 3 and this property precludes the possibility of them to be used as a biosorption material below this pH. Through zeta potential measurements, the isoelectric point of chitosan was determined to be 4.8–4.9. As the pH of the solution was lowered, positive charge on chitosan flakes increased. This also supported the electrostatic nature of the sorption. As can be seen from the speciation graphs of As(V) and As(III) (Fig. 3 insets), there is no any other pH with the same electrostatic behavior that biosorbent and arsenic species have opposite charges.

3.2.2. Effect of sorbent amount and shaking time on the sorption of As(V)

The percentage sorption of As(V) as a function of different amounts of chitosan and chitosan-immobilized sodium silicate is given in Fig. 4. As seen from the figure, similar sorption percentages were obtained with both sorbents at each amount tested; and 50.0 mg appeared to be the optimum amount for both sorbents under the conditions applied (the concentrations employed were

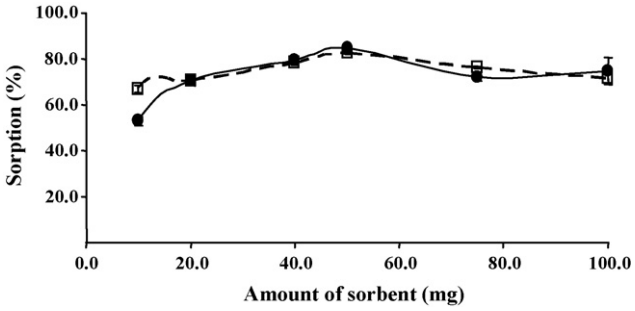


Fig. 4. Effect of sorbent amount on the sorption of 30.0 mL 100.0 μg L^{-1} As(V) solution at pH 3.0, 25 °C sorption temperature. (●) chitosan, (□) chitosan-immobilized sodium silicate, $n = 3$.

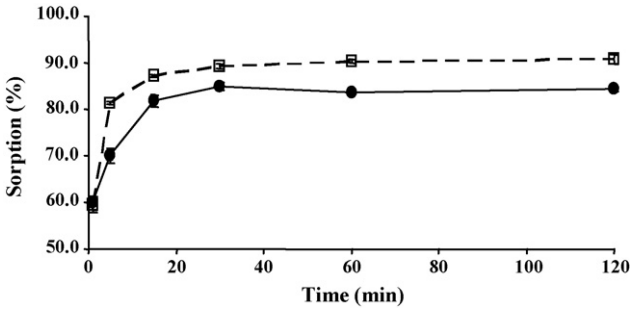


Fig. 5. Effect of shaking time for 50.0 mg sorbent at pH 3.0 in 30.0 mL 100.0 μg L^{-1} As(V) solution at 25 °C sorption temperature. (●) chitosan, (□) chitosan-immobilized sodium silicate, $n = 3$.

lower than the sorption capacity of the sorbents). Otherwise, the amount of chitosan-immobilized sodium silicate would be about three times that of the chitosan itself since the immobilized sorbent contains about 33% chitosan. This behavior can also be explained by the increased surface area of the immobilized sorbent (32.6 m^2/g) compared to that of chitosan (9.1 m^2/g).

Effect of shaking time on the percentage sorption was investigated for 1, 5, 15, 30, 60 and 120 min; the results are given in Fig. 5. As seen in the figure, the results are very similar for both sorbents especially after 15 min which can be taken as the equilibration time. However, the sorption rate before 15 min for the immobilized sorbent was sharper than that of chitosan which can be the indication of less diffusion restricted sorption in chitosan-immobilized sodium silicate.

3.2.3. Effect of solution temperature on the sorption of As(V)

The extent of sorption of As(V) by chitosan and chitosan-immobilized sodium silicate decreases as temperature increases. This behavior is reflected into the negative values of ΔH^o, given in Table 1, which designate the exothermic nature of sorption. The negative ΔS^o values suggest that sorption is associated with a decrease in system entropy probably due to the restriction on the mobility of the sorbate ions that results from binding to the sorbent surface. The process thus appears to be enthalpy-driven. Both parameters contribute to negative ΔG^o values which in turn results when the equilibrium position of a reaction occurs closer to the products.

Table 1
Thermodynamic parameters of chitosan and chitosan-immobilized sodium silicate (50.0 mg sorbent, 30.0 mL of 100.0 μg L^{-1} As(V) at pH 3.0, $n = 3$).

	ΔG^o (kJ/mol)		ΔH^o (kJ/mol)	ΔS^o (J/mol K)	
	298 K	323 K		298 K	323 K
Chitosan	−20.2	−19.8	−24.7	−15.1	−15.1
Chitosan-immobilized sodium silicate	−21.1	−20.9	−23.8	−9.1	−9.1

3.2.4. Successive loading

Sequential sorption of arsenate by chitosan and chitosan-immobilized sodium silicate for two different concentrations was investigated. It can be seen from Fig. 6a that the sorption percentage starts to decrease with the third loading and previously sorbed arsenate even starts to be released from chitosan surface after the sixth loading. This observation cannot be related to the sorption capacity of chitosan since a similar trend was observed for both 100.0 and 1000.0 μg L^{-1} concentrations. In order to clarify this further, the cumulative amount of arsenate on the sorbent was also determined which was approximately 0.015 mmol/g at the sixth load. This amount is still lower than the maximum sorption capacity of chitosan. Several reasons can be suggested to explain the decrease in sorption capacity. Firstly, a gradual dissolution of flakes was observed after each loading which might have caused a decrease in the sorption capacity. More importantly, the dissolution of chitosan flakes must have been associated with the release of previously adsorbed species from the surface which eventually increased the arsenate concentration in the solution. Secondly, although it needs further consideration, it can be speculated that the surface positive charge of chitosan after each loading could have been reduced which might also have resulted in a decrease in the sorption percentage after each step.

In contrast to chitosan, chitosan-immobilized sodium silicate has shown a better chemical stability in a way that no negative sorption (no release from chitosan surface) was observed although the sorption percentage started to decrease after the second load for both concentrations (Fig. 6b). As in the case of chitosan, the decrease in the sorption percentage of chitosan-immobilized sodium silicate cannot be explained by the reduction in the sorption capacity of the immobilized sorbent. Similarly, from the cumulative amount of arsenate on the immobilized sorbent, the amount of arsenate even at the tenth load is approximately 0.016 mmol/g which is about half of the maximum sorption capacity of chitosan-immobilized sodium silicate.

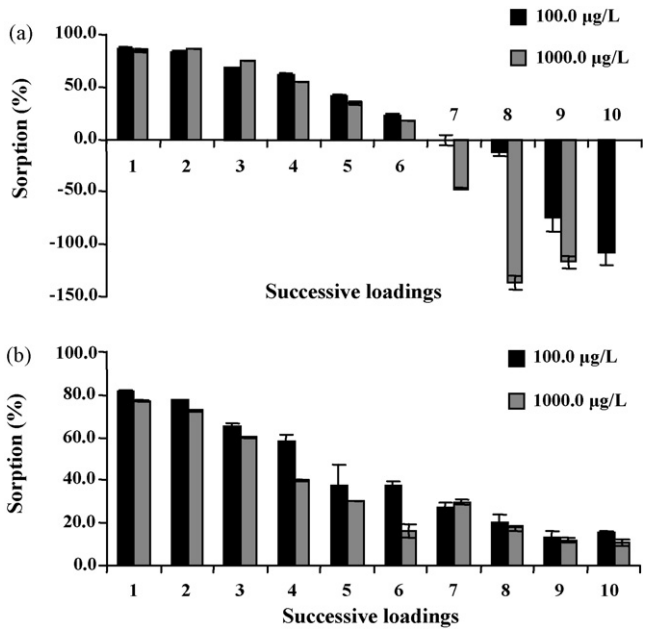


Fig. 6. Percent sorption of (a) chitosan and (b) chitosan-immobilized sodium silicate for 10 successive loadings in pH 3.0, 30.0 mL of 100.0 and 1000.0 μg L^{-1} As(V) concentrations, 50.0 mg sorbent, 30 min at 25 °C batch sorption, $n = 3$.

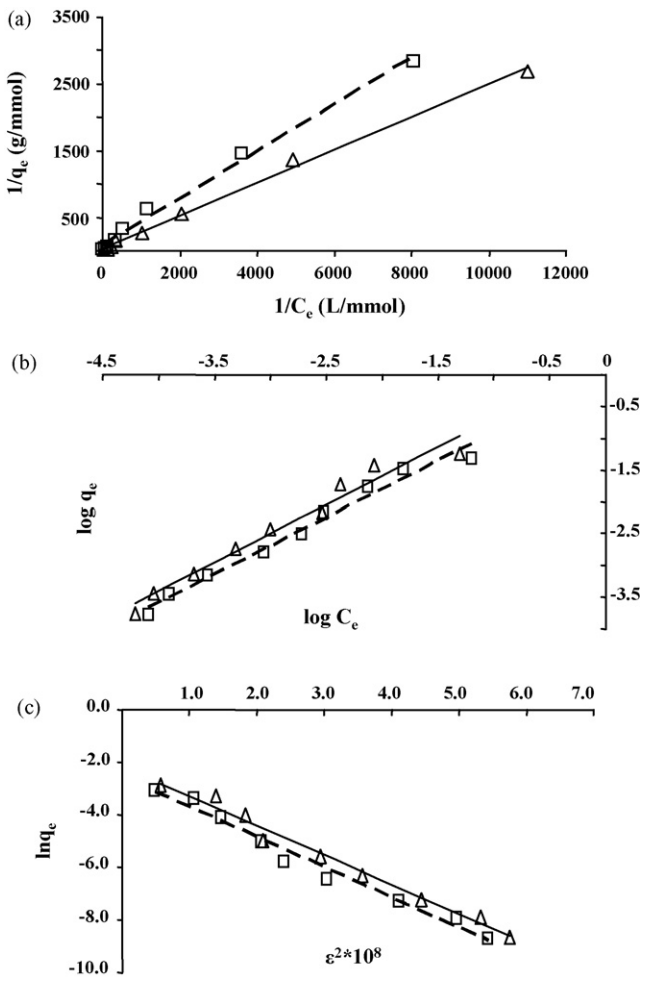


Fig. 7. Linear fits of (a) Langmuir, (b) Freundlich, (c) Dubinin–Radushkevich models for arsenate sorption by (△) chitosan and (□) chitosan-immobilized sodium silicate.

3.3. Sorption isotherm models

Freundlich, Dubinin–Radushkevich and Langmuir isotherm models were tested for sorption of arsenate by chitosan and chitosan-immobilized sodium silicate. The linearized forms of models (Fig. 7) were used for the calculation of coefficients and the results are summarized in Table 2. According to the linear correlation coefficients (R^2), Langmuir model, with R^2 close to unity, appears as the most suitable isotherm for describing the sorption of arsenate on chitosan and chitosan-immobilized sodium silicate. However, D–R isotherm can be considered also to provide adequate description of the sorption data.

3.4. Desorption studies

As described in Section 2.7, two different elution strategies were followed to take the sorbed arsenate ion back into solution from chitosan or chitosan-immobilized sodium silicate. In the first method, 2% (v/v) acetic acid was used and chitosan was completely dissolved together with the previously sorbed arsenate. On the other hand, in the case of chitosan-immobilized sodium silicate, acetic acid was not effective even though acid concentration and volume, and desorption time were doubled. Therefore, as a second method, 1.0% (w/v) L-cysteine prepared in a pH 3.0 solution adjusted with HCl was used as the eluent which was expected to reduce the adsorbed arsenate (As(V)) to arsenite (As(III), non-adsorbed form) through the thiol groups [35 and the references therein]. In the meantime, arsenic in the solution was converted to the hydride forming form. This eluent worked with 100% efficiency and was used in all desorption studies.

3.5. Interference studies

As explained in Section 2.8, two groups of possible interferants were prepared; the first group contained the hydride forming elements; namely, Sb(III), Sb(V), Te(IV), Te(VI), Se(IV), and Se(VI) ions, and the second group included the oxyions of Mo(VI) and V(V) which are expected to be adsorbed by chitosan. It should also be mentioned that the interference effect was classified into two: firstly, whether the ion caused the sorption to increase-or-decrease at least 30% of the original signal obtained with As(V) only, and secondly, the adsorbed ion caused at least 30% increase-or-decrease in the hydride signal of As. For this purpose, all the solutions were analyzed with both HGAAS and ICP-MS.

As a starting point, the sorption of chitosan towards each of the ions mentioned above was investigated under the conditions optimized for arsenate sorption but in the absence of arsenate; and it was found that chitosan shows affinity to all species except Te. The sorption percentage was almost 100% for Mo(VI), V(V) and Se(VI) in both concentrations; namely, 100.0 and 1000.0 $\mu g\,L^{-1}$. These results were in agreement with several studies of Guibal et al. in which they report that the sorption of Mo(VI) by cross-linked chitosan beads was maximum at pH 3 [13]. Similarly Qian et al. found that optimum pH value for maximum sorption of V(V) ions was 3 [40].

No interference was observed from neither Se(IV) nor Se(VI) for an As(V) concentration of 10.0 $\mu g\,L^{-1}$ although chitosan shows high affinity for Se(VI). On the other hand, when As(V) concentration was 100.0 $\mu g\,L^{-1}$, a decrease in sorption percentage was observed in the presence of 1000.0 $\mu g\,L^{-1}$ Se(IV). Sb(V) and Sb(III)

Table 2
Summary of models coefficients (Solution volume, shaking time, solution pH, sorbent amount and reaction temperature were 30.0 mL, 30 min, pH 3.0, 50.0 mg, and 25 °C, respectively, $n = 3$.).

Adsorption model	Parameter	Chitosan	Chitosan-immobilized sodium silicate
Langmuir	R^2	0.9963	0.9918
	Q_{max} (mmol/g)	0.03038	0.01276
	B (L/mmol)	133.43	222.25
Freundlich	R^2	0.9649	0.9781
	K_F	1.655	0.9309
	$1/n$	0.9054	0.8883
Dubinin–Radushkevich	R^2	0.9822	0.9804
	B (mol/kJ)^2	1×10^{-8}	1×10^{-8}
	q_s	0.1166	0.0781
	E (kJ/mol)	7.07	7.07

Table 3
The comparative spike recovery of As(V) and As(III) ions from chitosan and chitosan-immobilized sodium silicate (Sorption conditions: solution volume, shaking time, solution pH, sorbent amount and reaction temperature were 30.0 mL, 30 min, pH 3.0, 50.0 mg, and 25 °C, respectively, $n = 3$; elution conditions: eluent volume, shaking time, solution pH and reaction temperature were 30.0 mL of 1.0% (w/v) L-cysteine solution, 30 min, pH 3.0 and 25 °C, respectively, $n = 3$.).

Solution	Spike recovery (%)			
	Chitosan		Chitosan-immobilized sodium silicate	
	ICP-MS	HGAAS	ICP-MS	HGAAS
100.0 μg L^{-1} As(V)	110.0 (±3.7)	96.3 (±2.5)	104.6 (±3.5)	102.2 (±5.8)
100.0 μg L^{-1} As(III)	10.6 (±0.4)	10.0 (±0.7)	13.1 (±0.2)	13.6 (±2.3)
100.0 μg L^{-1} As(V) + 100.0 μg L^{-1} As(III)	111.2 (±2.4)	95.9 (±3.3)	104.1 (±1.0)	102.4 (±2.7)

behaved differently from the other hydride forming elements in a way that they caused a decrease in hydride signal of arsenic when their concentrations were 1000.0 μg L^{-1}. This finding is in accordance with the results obtained in one of our earlier studies which was about the gas phase interference of Sb(III) during hydride formation in HGAAS system [41]. The interference caused only during hydride formation can be eliminated with the use of ICP-MS if it is available in the laboratory. An unexpected interference (decrease in the arsenate sorption percentage by chitosan) was observed for both As(V) concentrations in the presence of 1000.0 μg L^{-1} Te(IV). As mentioned in the previous paragraph, chitosan demonstrates a very low affinity to Te(IV) (<1%) under the optimized sorption conditions for As(V). It should not be speculated much on this observation; but it can be stated that the presence of Te(IV) may change the reaction conditions during the sorption of As(V) by chitosan which needs further investigation. Although chitosan showed high affinity for V(V), this property did not cause any reduction in the signal due to the high capacity of chitosan. Instead, V(V) caused a small increase in As(V) sorption which necessitates the close control of this oxyion in the sample matrixes. Totally different behavior was obtained in the case of Mo(VI) for two different As(V) concentrations; when As(V) was only 10.0 μg L^{-1}, none of the Mo(VI) concentrations caused interference. However, when As(V) and Mo(VI) concentrations were both 100.0 μg L^{-1}, a decrease in the sorption capacity of chitosan towards As(V) was observed.

3.6. Method validation

The proposed methodology was validated, as explained in Section 2.9, both via spike recovery experiments and also through the analysis of a standard reference material. Initially, arsenate/arsenite speciation was performed using chitosan and chitosan-immobilized sodium silicate. As seen in Table 3, both chitosan and chitosan-immobilized sodium silicate have been found effective in arsenate recovery from spiked solutions whereas they have demonstrated a very low sorption (about 10%) towards arsenite. In addition to the above solutions containing only one arsenic species, either As(V) or As(III), solutions containing both As(III) and As(V) were analyzed with the proposed method to see if the presence of As(III) affected the sorption of As(V). The results indicate that sorption of As(V) is not affected from the presence of As(III) under the conditions employed as expected and this demonstrates the arsenic speciation capability of the chitosan and the chitosan-immobilized sodium silicate.

Subsequently, spike recovery tests were also carried out with four different types of water; namely, ultra-pure, bottled drinking, tap, and sea water. Spiked samples were subjected to the same sorption/elution cycles as previously. The results given in Table 4 show that the proposed methodology works efficiently for ultra-pure and bottled drinking water samples where the recovery values were very close to 100%. The municipality tap water of Urla where the IYTE campus is situated is very hard with high carbonate content. The hard matrix of this tap water had caused a change in Sb(III)/Sb(V) equilibrium in a previous study in which the use of L-cysteine was required to reduce Sb(V) to Sb(III) before the sorption of Sb(III) by Duolite GT-73 chelating resin [42]. Here, the low recovery value given in Table 4 (43.2%) is thought to be due to the high ionic strength of the tap water rather than its effect on the As(III)/As(V) equilibrium. The situation was even worst in the case of spiked sea water in which arsenate could not be recovered because of the very high ionic strength of the solution.

Finally, the accuracy of the proposed methodology was investigated through the analysis of a standard reference material, SRM from NIST (Natural Water – Trace Elements, Cat. No. 1640). Since the oxidation state of arsenic was not stated in the certificate, the SRM was analyzed both with and without a pre-oxidation step and the results compared. The same strategy was also followed with both As(III) and As(V) standard solutions to see the effect of the pre-oxidation step. As expected, SRM and As(III) solutions gave almost the same recovery value of 0% which also showed the importance of pre-oxidation step for unknown samples. When HNO_3 pre-oxidation step was applied, As(V) signal was assumed to be the reference (matrix-matched standard) and As(III) signal was compared to this signal after being oxidized to As(V). A conversion of 95% indicated the success of the oxidation process which also guaranteed the As(III) → As(V) conversion in the SRM. The results demonstrate the good agreement between the result of the proposed method (26.6 ± 2.4 μg L^{-1}) and the certified value (26.67 μg L^{-1}). This strong agreement may also indicate the validity of the method to the natural water samples of low and intermediate ionic strength.

Table 4
Percent recovery for spiked arsenate ion with ultra-pure, bottled, tap and sea water samples after desorption from chitosan (Sorption parameters: solution volume, shaking time, solution pH, sorbent amount and reaction temperature were 15.0 mL, 30 min, pH 3.0, 50.0 mg, and 25 °C, respectively, $n = 3$.).

Water type	Spiked As(V) concentration (μg L^{-1})		
	Initial	Final	Recovery %
Ultra-pure	10.0	11.4 (±0.5)	114.2 (±4.5)
Bottled drinking	10.0	11.2 (±0.2)	112.3 (±1.6)
Tap	10.0	4.3 (±0.4)	43.2 (±4.2)
Sea	10.0	0.0 (±0.1)	0.0 (±0.8)

4. Conclusions

It has been shown that chitosan and chitosan-immobilized sodium silicate can be applied in the sorption of As(V) from several water types. Sodium silicate as an immobilization matrix has the advantage of tuning the immobilized amount of biomass, in this case chitosan, in a narrow synthesis time. The optimum pH for As(V) sorption for both the chitosan and chitosan-immobilized sodium silicate was shown to be 3.0 at which amino groups of chitosan are protonated and the predominant form of As(V) is $H_2AsO_4^-$. Therefore, sorption was assumed to be electrostatic in nature. Speciation of As species was shown to be feasible since no sorption was obtained for As(III) at any pH investigated. If both As(III) and As(V) are to be determined, a pre-oxidation step is necessary. Desorption from the sorbents was realized with 1.0% (w/v) L-cysteine prepared in a pH 3.0 solution adjusted with HCl.

Among the isotherm models tested, Langmuir model appeared to be the most appropriate. Sorption of As(V) by the two sorbents decreased with increase in solution temperature. This exothermic behavior is associated with a decrease in system entropy. Through sequential sorption studies, it was shown that chitosan-immobilized sodium silicate has exhibited a better chemical stability than the chitosan itself which demonstrates the advantage of immobilization strategy.

The results of the interference study have shown that As(V) sorption by chitosan can be decreased especially at high interferant concentration. An exception to this observation was obtained with Sb species which caused gas phase interference during hydride generation rather than decreasing the sorption percentage. In addition, when the concentration of As(V) is 100.0 $\mu g\,L^{-1}$, the presence of V(V) in the samples causes an increase in As(V) sorption.

It can be concluded that the chitosan and chitosan-immobilized sodium silicate sorbents can be used in the sorption/speciation of As(V) from medium-to-low ionic strength solutions prior to its determination with atomic spectrometric techniques like AAS, ICP-AES, or ICP-MS. In addition, the sorbents can be used in the removal of As(V) (or As(III) after a proper oxidation step) from drinking water.

Acknowledgements

The authors would like to thank the Center of Material Research and the Environmental Research Center at İzmir Institute of Technology for the facilities SEM, TGA, XRD, and ICP-MS measurements, respectively.

References

[1] United States Environmental Protection Agency, UESPA, 1999. Doc. EPA 815-P-01-001.
[2] D. Mohan, C.U. Pittmant, J. Hazard. Mater. 142 (2007) 1.
[3] P.L. Smedley, D.G. Kinniburgh, Appl. Geochem. 17 (2001) 517.
[4] L. Ebdon, L. Pitts, R. Cornelis, H. Crews, O.F.X. Donard, P. Quevauviller, Trace Element Speciation for Environment, Food and Health, The Royal Society of Chemistry, Cambridge, 2001.
[5] B.K. Mandaland, K.T. Suzuki, Talanta 58 (2002) 201.
[6] World Health Organization, Guidelines for Drinking-water Quality [electronic resource]: Incorporating First Addendum, vol.1, Recommendations, 3rd ed., 2006.
[7] T.S.Y. Choong, T.G. Chuah, Y. Robiah, F.L.G. Koay, I. Azni, Desalination 217 (2007) 139.
[8] V.T. Nguyen, S. Vigneswaran, H.H. Ngo, H.K. Shon, J. Kandasamy, Desalination 236 (2009) 363.
[9] M.E. Morgada, I.K. Levy, V. Salomone, S.S. Farıas, G. Lopez, M.I. Litter, Catal. Today (2008), doi:10.1016/j.cattod.2008.09.038.
[10] K. Kurita, Mar. Biotechnol. 8 (2006) 203.
[11] M.N.V. Kumar, React. Funct. Polym. 46 (2000) 1.
[12] S.N. Kartal, Y. Imamura, Bioresour. Technol. 96 (2005) 389.
[13] E. Guibal, S. Milot, J.M. Tobin, Ind. Eng. Chem. Res. 37 (1998) 1453.
[14] L. Dambies, T. Vincent, A. Domard, E. Guibal, Biomacromolecules 2 (2001) 1198.
[15] L. Dambies, T. Vincent, E. Guibal, Water Res. 36 (2002) 3699.
[16] P. Chassary, T. Vincent, E. Guibal, React. Funct. Polym. 60 (2004) 137.
[17] A. Sabarudin, K. Oshita, M. Oshima, S. Motomizu, Anal. Chim. Acta 542 (2005) 207.
[18] V.M. Boddu, K. Abburi, J.L. Talbott, E.D. Smith, R. Haasch, Water Res. 42 (3) (2007) 633.
[19] R.A.A. Muzzarelli, Natural Chelating Polymers, Pergamon Press, Hungary, 1973.
[20] A. Tolaimate, J. Desbrieres, M. Rhazi, A. Alagui, M. Vincendon, P. Vottero, Polymer 41 (2000) 2463.
[21] M.R. Kasaai, J. Arul, G. Charlet, J. Polym. Sci. Polym. Phys. 38 (2000) 2591.
[22] M.R. Kasaai, Carbohydr. Polym. 68 (2007) 477.
[23] M.L. Tsaih, R.H. Chen, J. Appl. Polym. Sci. 71 (1999) 1905.
[24] S.M. Taghizadeh, G. Davari, Carbohydr. Polym. 64 (2006) 9.
[25] R.F. Weska, J.M. Moura, L.M. Batista, J. Rizzi, L.A.A. Pinto, J. Food Eng. 80 (2007) 749.
[26] M. Poirier, G. Charlet, Carbohydr. Polym. 50 (2002) 363.
[27] D. Karunasagar, M.V.B. Krishna, S.V. Rao, J. Arunachalam, J. Hazard. Mater. 18 (2005) 133.
[28] G. Limousin, J.P. Gaudet, L. Charlet, S. Szenknect, V. Barthes, M. Krimissa, Appl. Geochem. 22 (2007) 249.
[29] L. Qi, Z. Xu, Colloid Surf. A 251 (2004) 183.
[30] S. Gueu, B. Yao, K. Adouby, G. Ado, Int. J. Environ. Sci. Technol. 4 (2007) 11.
[31] R.J. Umplebay II, S.C. Baxter, M. Bode, J.K. Berch Jr., R.N. Shaha, K.D. Shimizu, Anal. Chim. Acta 435 (2001) 35.
[32] D. Kavitha, C. Namasivayam, Dyes Pigments 74 (2007) 237.
[33] A. Şeker, T. Shahwan, A.E. Eroğlu, S. Yılmaz, Z. Demirel, M.C. Dalay, J. Hazard. Mater. 154 (2008) 973.
[34] E. Guibal, Sep. Purif. Technol. 38 (2004) 43.
[35] J. Dedina, D.L. Tsalev, Hydride Generation Atomic Absorption Spectrometry, Willey, Chichester, 1995.
[36] G. Huacai, P. Wan, L. Dengke, Carbohydr. Polym. 66 (2006) 372.
[37] F.A.A. Tirkistani, Polym. Degrad. Stabil. 60 (1998) 67.
[38] M. Jaworska, K. Sakurai, P. Gaudon, E. Guibal, Polym. Int. 52 (2003) 198.
[39] K. Ogawa, Agric. Biol. Chem. 55 (1991) 2375.
[40] S. Qian, H. Wang, G. Huang, S. Mo, W. Wei, J. Appl. Polym. Sci. 92 (2004) 1584.
[41] M. Yersel, A. Erdem, A.E. Eroğlu, T. Shahwan, Anal. Chim. Acta 534 (2005) 293.
[42] A. Erdem, A.E. Eroğlu, Talanta 68 (2005) 86.

Talanta 80 (2010) 1461–1466

Contents lists available at ScienceDirect

Talanta

journal homepage: www.elsevier.com/locate/talanta

Cu nanoparticles incorporated polypyrrole modified GCE for sensitive simultaneous determination of dopamine and uric acid

Şükriye Ulubay, Zekerya Dursun*

Ege University, Science Faculty, Department of Chemistry, 35100 Bornova, İzmir, Turkey

ARTICLE INFO

Article history:
Received 13 May 2009
Received in revised form
14 September 2009
Accepted 25 September 2009
Available online 3 October 2009

Keywords:
Metal nanoparticles
Nano-copper
Polypyrrole
Modified electrode
Dopamine
Uric acid

ABSTRACT

Cu nanoparticles have been electrochemically incorporated polypyrrole film that was used for modification of the glassy carbon electrode surface. The performance of the electrode has been characterized by cyclic voltammetry and atomic force microscopy. The electrode has shown high electrocatalytic activity towards the oxidation of dopamine (DA) and uric acid (UA) simultaneously in a phosphate buffer solution (pH 7.00). The electrocatalytic oxidation currents of UA and DA were found linearly related to concentration over the range 1×10^{-9} to 1×10^{-5} M for UA and 1×10^{-9} to 1×10^{-7} M for DA using DPVs method. The detection limits were determined as 8×10^{-10} M (s/n = 3) for UA and 8.5×10^{-10} M (s/n = 3) for DA at a signal-to-noise ratio of 3.

© 2009 Elsevier B.V. All rights reserved.

1. Introduction

Dopamine (DA), one of the naturally occurring catecholamines, plays an important role as a neurotransmitter in the renal, hormonal, cardiovascular and central nervous systems. Low levels of DA can lead to brain disorders such as schizophrenia and Parkinson's disease [1–3]. Uric acid (2,6,8-trihydroxypurine) on the other hand, is the main final product of purine metabolism in the human body. Extreme abnormalities of UA levels cause many diseases, such as gout, hyperuricaemia and Lesch–Nyan disease [4–6]. Therefore a simple, sensitive and accurate analytical method for the quantization of DA and UA would be useful for physiological investigations as well as early diagnosis of diseases [7]. Voltammetric techniques offer a powerful tool for the simultaneous determinations of DA and UA in buffered solutions [8–10]. However, the presence of ascorbic acid (AA) in such samples including both DA and UA, the electrochemical oxidation peak of AA takes place at very close potentials and then, homogeneous electron transfer reaction have been observed at bare electrodes [2,11–13]. As well known, modified electrodes may offer higher selectivity, sensitivity, greater time efficiency and higher stability than the bare electrodes. Therefore, several modifier materials such as polymers [14–17], DNA doped polymers [18], dye doped sol–gels [19], metal oxides [20], carbon nanotubes [21–23] and metal nanoparticles (MNPs) [24–26] have been used to overcome this problem.

Among them, MNPs modified electrodes have drawn particular attention due to their high surface area, effective mass transport, catalysis and control over local microenvironment compared to macro-electrodes [27,28]. However, the MNPs at the electrode surface can be fragile in the absence of stabilizing conductive material. To solve this problem, in the first step, the electrode surface can be modified with some conductive stabilizing materials such as ligands, carbon nanotubes and polymers [29,30]. Then, the MNPs are attached to the modified electrode surface. Moreover, the porous structure of conducting polymer allows dispersing of the metal nanoparticles into the polymer matrix and generates additional electrocatalytic sites [31–33]. Polypyrrole (PPy) is one of the most important conducting polymers to support the metal nanoparticles. Some metal nanoparticles–polypyrrole composites have already been reported at PPy/Pt [34,35], PPy/Ag [36], PPy/Ti [37] and PPy/Au [38,39] conducting composites. According to our knowledge, there is no any reported data for the simultaneous determination of DA and UA at nano-Cu/PPy/GCE.

In the present study, a modified electrode was prepared by electrochemical deposition of Cu-metal nanoparticles in over-oxidized polypyrrole film modified GCE and the performance of the electrode developed was characterized by cyclic voltammetry and close surface examination was made by atomic force microscopy (AFM). The Cu nanoparticles incorporated polypyrrole modified GCE was

* Corresponding author. Tel.: +90 2323884000/2365.
E-mail addresses: zekerya.dursun@ege.edu.tr, dursunz@hotmail.com (Z. Dursun).

0039-9140/$ – see front matter © 2009 Elsevier B.V. All rights reserved.
doi:10.1016/j.talanta.2009.09.054

utilized as the sensing matrix for the simultaneous determination of DA and UA at nanomolar levels.

2. Experimental

2.1. Reagents

Pyrrole, dopamine and uric acid were purchased from Sigma and used without further purification. Pyrrole (Py) was triply distilled until a colorless liquid was obtained and it was then stored under nitrogen before use. Sodium dodecylsulfate (SDS), $CuSO_4$, H_2SO_4, NaOH, ethanol were of analytical-reagent grade and supplied from Sigma. All of the solutions were prepared using ultrapure water provided from an 18 MΩ cm Milli-Q system. All experiments were carried out at ambient temperature and highly pure nitrogen was kept flowing over the solution during electrochemical experiments.

2.2. Apparatus

Voltammetric measurements were carried out using a Bass 100B Electrochemical Analyser and Ivium Stat Electrochemical Interface equipped with a three electrode system consisting of a working electrode (GCE, PPy/GCE and nano-Cu/PPy/GCE), an auxiliary platinum electrode and an Ag/AgCl (sat. KCl) were used as reference electrode. Cyclic, differential pulse (dp) and time base modes were utilized throughout the studies. The pH measurements were made with WTW handheld meter pH 330i ion analyser. Ambios Q-Scope Atomic Force Microscopy was used for the characterization of metal nanoparticles on the electrode surfaces. Bandelin Sonorex model ultrasonic bath was used for cleaning the electrodes.

2.3. Preparation of polypyrrole film modified GCE

A bare GCE was polished successively with different grades of Al_2O_3 slurry (0.05–3 μm) on a synthetic cloth, rinsed with pure water, and sonicated subsequently in a 1:1 ultrapure water and ethanol for 5 min. Electrochemical deposition of polypyrrole (PPy) on GCE was performed using cyclic voltammetry in a solution of 0.1 M Py + 0.01 M SDS in a potential range of −0.35 to 0.85 V versus Ag/AgCl (sat. KCl) at a scan rate of 20 mV s^{-1} in a period of three cycles [40]. Then, the modified electrode was rinsed thoroughly with ultrapure water and transferred into a voltammetric cell containing 0.1 M NaOH solution for electrochemical over-oxidation of the conductive PPy film at +1.0 V for 300 s. The obtained electrode was ready for use after a final wash with ultrapure water and denoted as PPy/GCE.

2.4. Preparation of metal nano-clusters modified polypyrrole film GCE

The Cu-metal nanoparticles (Cu-MNPs) were electrochemically deposited on the PPy/GCE surface by cycling the potential from 0.00 to 1.10 V in 1 mM $CuSO_4 + H_2SO_4$ solution at a scan rate of 50 mV s^{-1} for 10 times. The obtained Cu nanoparticles modified polypyrrole film electrode was washed with ultrapure water and indicated as nano-Cu/PPy/GCE.

3. Results and discussion

3.1. Characterization of surface morphology modified GCE with PPy and nano-Cu/PPy

As well known, the thickness of polymeric film on the electrode surface can be changed by controlling the amount of charge passed [41–43]. Here, 24 mC cm^{-2} integrated charge was used to generate 0.10 μm film thickness in the polymerization procedure. The bare GCE, PPy/GCE and nano-Cu/PPy/GCE surfaces were characterized using AFM measurements. Large pores on the PPy film were obtained by using dodecylsulfate as doping ions as indicated in the literature [40].

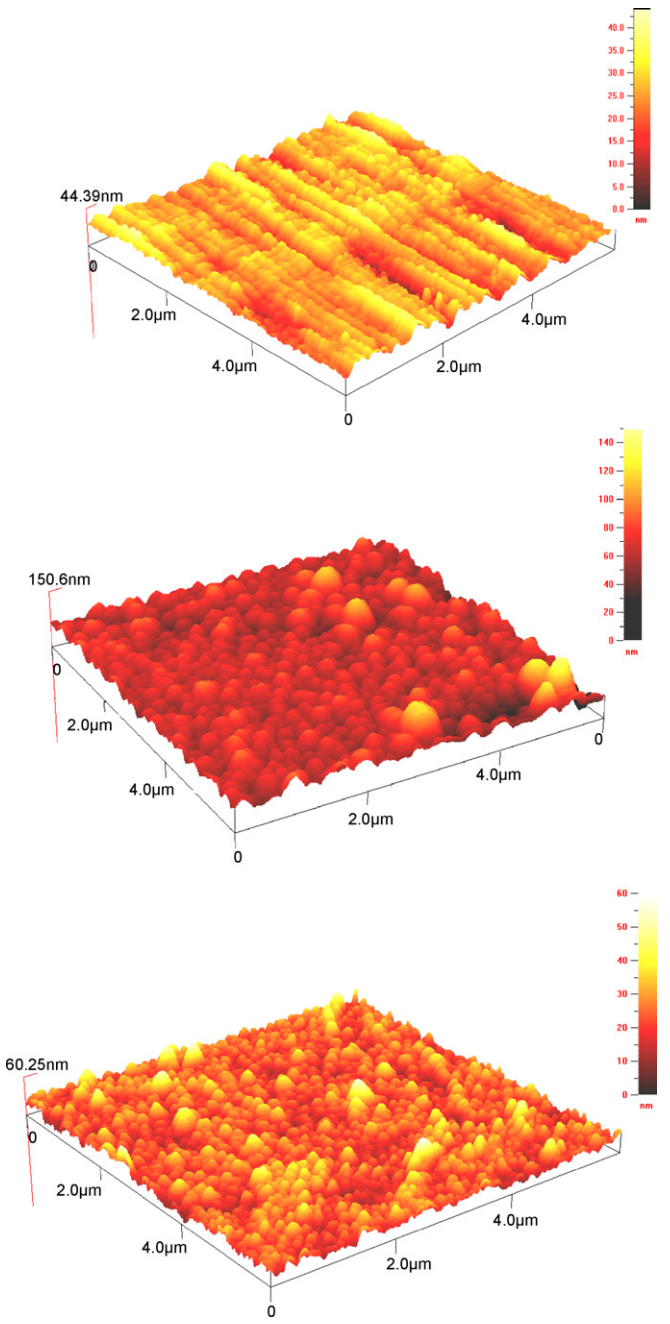


Fig. 1. AFM images of the (A) bare GCE, (B) PPy/GCE, and (C) nano-Cu/PPy/GCE surfaces as three-dimensional views.

The atomic force microscopy (AFM) images have shown the surface morphology and film thickness of the bare and modified electrodes (Fig. 1). Three-dimensional images clearly displayed partially rough surface of the bare GCE (Fig. 1A) and after the modification of the surface with PPy film, even rougher surface image was obtained with irregular islands (Fig. 1B). The average film thickness was measured as ~100 nm with three-dimensional AFM analyses. From Fig. 1C it was evident that the Cu nanoparticles with a 60 nm average diameter were homogeneously distributed throughout the film.

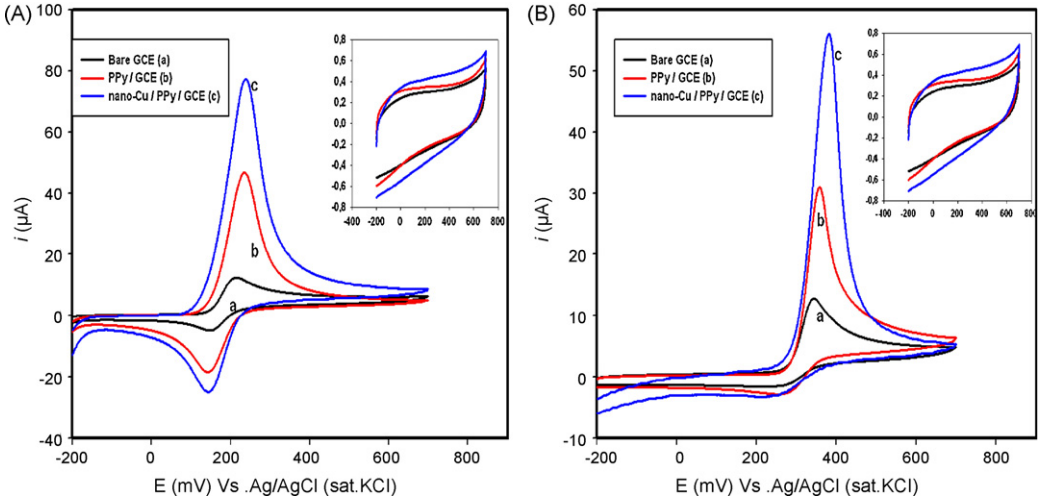


Fig. 2. Cyclic voltammograms obtained at bare GCE (a), PPy/GCE (b), and nano-Cu/PPy/GCE (c) in the absence (inset) and in the presence of (A) 5×10^{-4} M DA and (B) 5×10^{-4} M UA with a scan rate of 50 mV s^{-1} in 0.1 M pH 7.00 PBS.

3.2. Electrocatalytic oxidation of DA and UA on nano-Cu/PPy/GCE

In order to achieve optimal conditions for voltammetric determination of DA and UA, main parameters related to the film formation and solution characteristics were evaluated. These parameters were selected as the pyrrole concentration, electrochemical over-oxidation time of polypyrrole, NaOH concentration, cycle number that effect on electrodeposition of Cu nano-clusters and the pH of supporting electrolyte solution. Optimal conditions were elucidated by means of measuring the peak currents of both compounds with one variable at time method and determined as follows: 0.1 M pyrrole, 300 s, 0.1 M NaOH, 10 cycles for electrodeposition of Cu nanoparticles and pH 7.0 for electrolyte medium, respectively.

Fig. 2 shows the cyclic voltammograms recorded at PPy/GCE and nano-Cu/PPy/GCE in comparison to the bare GCE. Clear background signal was obtained in the absence of DA (Fig. 2A-inset) for the bare and modified electrodes. Upon addition of DA to be 5×10^{-4} M in the cell, oxidation and subsequent reduction peaks have appeared at 0.24 and 0.16 V, respectively indicating a quasireversible electrode process probably due to the diffusion barrier of the polymeric film. Similar peak potentials have been obtained with bare electrode with much smaller peak currents. Electrochemical reaction kinetics were improved as the copper nanoparticles were inserted to the polymeric film matrix by subsequent cycling of the potential in a range of 0–1.1 V. Therefore, nano-Cu/PPy/GCE has exhibited a large peak to peak separation with almost reversible electrochemical behavior ($\Delta E_p = 0.08$ V). The peak currents have also increased 7 times compared with bare GCE and twice as the PPy/GCE. So far the peak characteristics have clearly indicated an electrocatalytic oxidation of DA at PPy modified electrodes by the gain of a more active surface compared to the bare GCE. The increase in the analytical determination sensitivity of DA is a clear indication of the enlargement of active surface area of the electrode modified by PPy and nano-Cu clusters.

The influence of pH solution on the electrochemistry of DA oxidation was studied. The anodic peak potential was shifted linearly with the increase of solution pH with a slope of 0.053 V/pH. The magnitude of the slope for DA oxidation most probably points out that two protons could be involved in the electrode reaction.

Cyclic voltammograms of UA in pH 7.0 phosphate buffer solution at bare GCE, PPy and nano-Cu/PPy/GCE are given in Fig. 2B. UA has shown a quasireversible electrochemical behavior with an anodic peak potential of about 0.35, 0.36 and 0.38 V, respectively. All three voltammograms have displayed a small cathodic peak at 0.28 V indicating a sluggish cathodic electron transfer. Under identical conditions, both PPy/GCE and nano-Cu/PPy/GCE offer significantly increased peak current to UA oxidation. The results suggest a more efficient oxidation reaction of UA at nano-Cu/PPy/GCE probably due to the effective surface area supplied by both polymeric film and Cu nanoparticles on the GCE.

The effect of pH of electrolyte solutions might have a pronounced effect on the response and therefore, oxidation process of 5×10^{-4} M UA was studied in different electrolyte media by cyclic voltammetry. The pH dependencies of E_a clearly illustrate that the electrocatalytic oxidation peak shifts to more negative potentials with increasing the pH. The slope of 0.054 V per pH unit for UA oxidation showed that two protons were involved in the electrode reaction at nano-Cu/PPy/GCE. The highest oxidation current was obtained in neutral pH. The oxidation current was decreased at both lower pH and higher pH than 8 due to the instability of UA under both acidic and alkaline solutions.

3.3. Separation of electrochemical response of DA and UA at modified electrodes

Curves in Fig. 3a–c the cyclic voltammograms of a 5×10^{-4} M DA and UA mixture at bare GCE, PPy/GCE and nano-Cu/PPy/GCE, respectively. Two broad peaks were obtained in ongoing scan and convolution of the oxidation peaks has limited the selectivity and sensitivity of simultaneous determination of DA and UA at a bare GCE. Fig. 3b and c shows that modification of GCE surface with PPy film and incorporation of Cu nanoparticles have resolved the merged voltammetric peaks into two well-defined oxidation peaks at 0.20 and 0.35 V for DA and UA, respectively. The separation of the two oxidation peaks offers the simultaneous determination of DA and UA in a homogeneous solution. Cu nanoparticles deposition also enhanced the catalytic activity of PPy/GCE for oxidation of a DA and UA mixture in both way of oxidation potentials and peak currents. This increase in the catalytic current can be explained by a higher density of carbonyl groups generated on the PPy film after the electrochemical over-oxidation process. The existence of dense carbonyl groups on the PPy film could provide a selective interface for the molecular interaction of DA and UA via hydrogen bonds with the proton donating group of –NH [16].

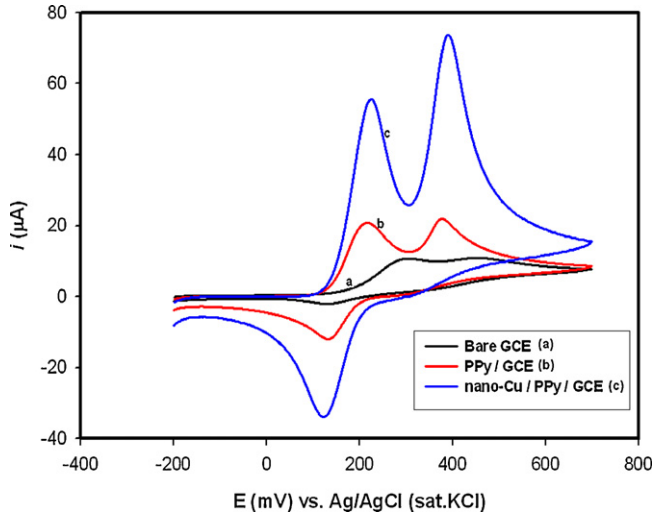


Fig. 3. Cyclic voltammograms of 5×10^{-4} M UA + 5×10^{-4} M DA at bare GCE (a), PPy/GCE (b), and nano-Cu/PPy/GCE (c) with a scan rate of 50 mV s^{-1}.

3.4. Differential pulse voltammetric determination of uric acid and dopamine

Differential pulse voltammetry (DPV) has a discrimination against background noise and offers much higher current sensitivity and better peak separation than cyclic voltammetry. Therefore, DPV was used for the sensitive determination of UA and DA at nano-Cu/PPy/GCE and compared with both PPy/GCE and bare GCE. Under the optimal conditions, the electrocatalytic oxidation currents of UA and DA were linearly related to concentration over the range 1×10^{-9} to 1×10^{-5} M with a coefficient of determination of 0.9973 for UA (figure not shown), and 1×10^{-9} to 1×10^{-7} M with a coefficient of determination of 0.9973 for DA (figure not shown). The regression equations were $i_{pa} = 0.026 + 2.22C$ (i_{pa}: μA, C: μmol/L) and the detection limit 8×10^{-10} M (s/n = 3) for UA and $i_{pa} = 13.761C - 0.024$ and the detection limit was found to be 8.5×10^{-10} M for DA (s/n = 3).

3.5. Selective determination of DA in the presence of a fixed concentration of UA

Fig. 4 displays the DPV obtained for the different concentrations of DA in the presence of 5.0×10^{-6} M concentration of UA at nano-Cu/PPy/GCE. The oxidation peaks with adequate resolution for both compounds were obtained at 0.17 V for DA and 0.36 V for UA using nano-Cu/PPy/GCE. The oxidation peak current of DA has built up linearly ($R^2 = 0.9945$) with increasing concentration in the range of 8.0×10^{-8} to 1.0×10^{-5} M, whereas the voltammetric peak current of UA remained the same.

Similarly, voltammetric determination of UA was carried out in the presence of DA at fixed concentration being 5.0×10^{-6} M. As shown in Fig. 5, no obvious change in the oxidation current of DA was observed while varying concentration of UA and the peak current of UA increased linearly with increasing of UA concentration (8.0×10^{-8} to 1.0×10^{-5} M) with a coefficient of determination of 0.9941.

Detection limits were estimated to be 3.0×10^{-9} mol/L for DA and 4.0×10^{-9} mol/L for UA using 3σ/slope ratio, where σ is the standard deviation of the mean value for 5 independent voltammograms of the blank solution. Stable peak observations at fixed concentration while increasing the other analyte concentration indicated that the oxidation of DA and UA at nano-Cu/PPy/GCE is relatively concentration independent.

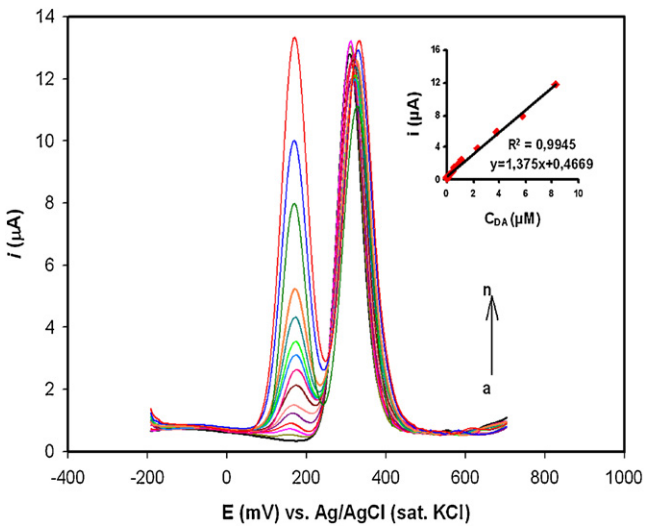


Fig. 4. Differential pulse voltammograms of DA in the presence of UA (5×10^{-6} M) at nano-Cu/PPy/GCE in 0.1 M pH 7.00 PBS with scan rate 20 mV s^{-1} and pulse amplitude 50 mV. DA (a–n): 0.00, 1.0×10^{-8}, 3.0×10^{-8}, 5.0×10^{-8}, 7.0×10^{-8}, 1.0×10^{-7}, 2.0×10^{-7}, 4.0×10^{-7}, 6.0×10^{-7}, 8.0×10^{-7}, 1.0×10^{-6}, 2.0×10^{-6}, 4.0×10^{-6}, 6.0×10^{-6}, and 8.0×10^{-6} M. The inset shows the plot of current versus concentration of DA.

3.6. DPV of DA and UA in the presence of AA

Electrochemical behavior of DA and UA was examined in the presence of AA at PPy/GCE and nano-Cu/PPy/GCE in comparison to the bare glassy carbon electrode. As can be seen from Fig. 6, two peaks at 0.19 V for AA and DA and at 0.38 V for UA (curves a and b) can be detected. Most sensitive results were obtained with nano-Cu/PPy/GCE modified electrode however, these electrodes cannot separate AA and DA oxidation peaks. To avoid the interference of AA on the DA determination at nano-Cu/PPy/GCE, the Cu nanoparticles deposited to the electrode surface was performed in the presence of methionine compound. Therefore, the Cu nanoparticles modified PPy/GCE electrode has accomplished to separate the AA, DA and UA responses into three well-defined peaks with an additional peak at

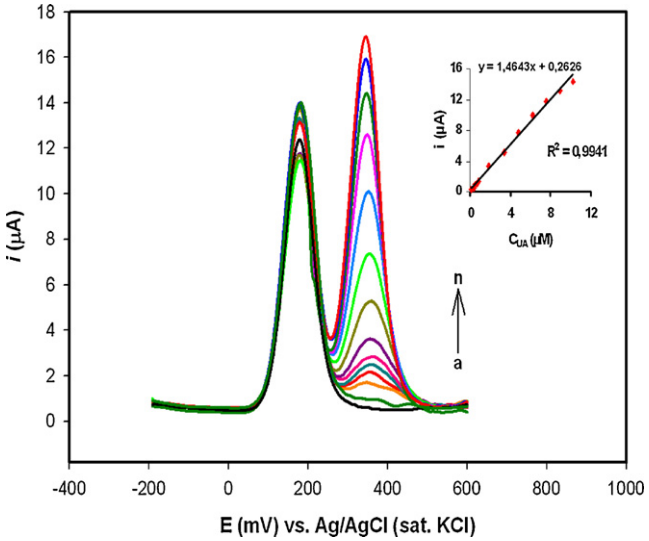


Fig. 5. Differential pulse voltammograms of UA in the presence of DA (5×10^{-6} M) at nano-Cu/PPy/GCE in 0.1 M pH 7.00 PBS with scan rate 20 mV s^{-1} and pulse amplitude 50 mV. UA (a–n): 0.00, 8.0×10^{-8}, 1.0×10^{-7}, 3.0×10^{-7}, 5.0×10^{-7}, 6.0×10^{-7}, 8.0×10^{-7}, 9.6×10^{-7}, 1×10^{-6}, 2×10^{-6}, 4×10^{-6}, 6.0×10^{-6}, 8.0×10^{-6}, and 1.0×10^{-5} M. The inset shows the plot of current versus concentration of UA.

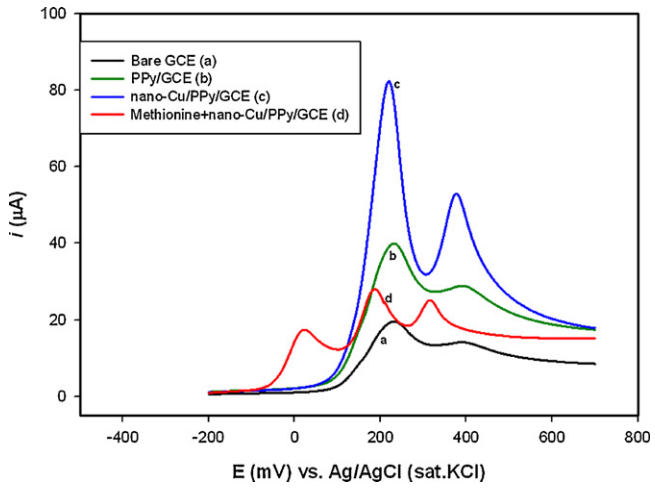


Fig. 6. Differential pulse voltammograms obtained at bare GCE (a), PPy/GCE (b), nano-Cu/PPy/GCE (c) and methionine + nano-Cu/PPy/GCE (d) in the presence of 5×10^{-5} M UA + 5×10^{-5} M DA, 5×10^{-5} M AA with a scan rate of 20 mV s^{-1} in 0.1 M pH 7.00 PBS.

0.0 V for AA with rather less sensitive results. As the main goal was to determine DA and UA, the performance of the method developed was found most satisfactory. In case of any interference of AA, the use of methionine would be the proper answer to the problem.

3.7. Stability of nano-Cu/PPy/GCE

A long-term storage stability of the nano-Cu/PPy/GCE was studied by keeping the electrode in phosphate buffer solution (pH 7.0) at room temperature. The performance of Cu nanoparticles/PPy/GCE for the detection of 5×10^{-7} M UA was tested in PBS of pH 7 for a week. Over the first 2 days, the oxidation of UA signal decreased by 1.3% and the oxidation current response maintained 90.2% of the original peak current value after 1 week. The experiments were repeated for DA and UA mixture and similar stable signals were obtained. These results prove that nano-Cu/PPy/GCE is stable and the voltammetric studies could be replicated for the selective and sensitive determination of DA and UA.

3.8. Real sample analysis

The nano-Cu/PPy/GCE for the determination of DA and UA in practical samples such as DA injection solution and human urine samples was tested. The dopamine hydrochloride injection (DHI) solution (specified content of DA is 40 mg mL^{-1}) was diluted to 10 mL with ultrapure water and 100 μL diluted DHI or some amount of standard DA solutions were injected into each of a series of was piped into each of series of 10 mL measuring flasks and made up to volume phosphate buffer (pH 7.00). An aliquot of 50 μL of those solutions was placed in an electrochemical cell for the determination of DA using differential pulse voltammetry. The results are listed in Table 1. Uric acid analysis was performed as follows: 1.0 mL urine sample was diluted to 10 mL with 0.1 M NaOH solution. An aliquot mL of the diluted solution was injected to electrochemical cell and made up 10 mL with phosphate buffer solution (pH 7.00)

Table 1
Determination of DA in dopamine hydrochloride injection ($n = 3$).

Samples	Added (μM)	Found (μM)	RSD (%)
1	10.50	10.37	1.92
2	15.70	16.00	1.99
3	21.00	21.32	1.97

Table 2
UA analysis in human urine sample ($n = 3$).

	Proposed method (10^{-4} M)	% RSD	Standard method (10^{-4} M)	% RSD
Sample 1	3.10	1.98	3.09	2.01
Sample 2	3.30	1.95	3.40	1.98

for the determination of uric acid in urine sample. The results were compared with standard spectrophotometric method as shown in Table 2. Uric acid in human urine samples was compared. Here the DPV technique was used in the experiments. The real sample analysis data for dopamine injection solution (DOPAMIN, 40 mg/mL) and human urine sample results are listed in Tables 1 and 2. From these results, it shows that the nano-Cu/PPy/GCE shows good catalytic activity for real sample analysis.

4. Conclusion

In the present study reported, a new composite electrode nano Cu/PPy/GCE was prepared by electropolymerization and electrodeposition methods. It was shown that this composite electrode improved the electrocatalytic activities towards the oxidation of DA and UA. The catalytic activity of bare GCE towards DA and UA oxidation was improved by the formation of a uniform PPy film which was incorporated with Cu nanoparticles on the electrode surface due to the increasing electronic conductivity and effective surface area. In the differential pulse voltammetric determination, the detection limits of DA and UA were estimated as 3.0×10^{-9} and 4.0×10^{-9} mol/L, respectively. Thus, Cu nanoparticles modified polypyrrole film electrode showed excellent sensitivity, selectivity and anti-fouling properties for the voltammetric determination of DA and UA individually and simultaneously. The proposed method was demonstrated for DA and UA determination in real samples with satisfactory results.

Acknowledgements

The authors are grateful for the careful review of the manuscript by Associate Prof. Dr. Stephan Astley, Prof. Dr. F. Nil Ertaş and Dr. Armağan Kınal.

References

[1] T.E. Smith, in: T.M. Devlin (Ed.), Textbook of Biochemistry with Clinical Correlations, Wiley/Liss, New York, 1992, p. 929.
[2] R.D. O'Neill, Analyst 119 (1994) 767.
[3] A.J. Downard, A.D. Roddick, A.M. Bond, Anal. Chim. Acta 317 (1995) 303.
[4] E. Miland, A.J.M. Ordieres, P.T. Blanco, M.R. Smyth, C.O. Fagain, Talanta 43 (1996) 785.
[5] K. Shi, K.-K. Shiu, Electroanalysis 13 (2001) 1319.
[6] L. Zheng, S. Wu, X. Lin, L. Nie, L. Rui, Electroanalysis 13 (2001) 1351.
[7] L.A. Paschla, L.D. Reynolds, S. Wright, P.T. Kissinger, J. Assoc. Off. Anal. Chem. 70 (1987) 1.
[8] J.S.N. Dutt, M.F. Cardosi, C. Livingstone, J. Davis, Electroanalysis 17 (2005) 1233.
[9] G.A. Rivas, M.D. Rubianes, M.C. Rodrigues, N.F. Ferreyra, G.L. Lugue, M.L. Pedano, S.A. Miscoria, C. Parrado, Talanta 74 (2007) 291.
[10] R. Bravo, Ch.Ch. Hsueh, A. Jaramillo, A. Brajter-Toth, Analyst 123 (1998) 1625.
[11] R.N. Adams, Anal. Chem. 48 (1976) 1126A.
[12] J.A. Stamford, J.B. Justice Jr., Anal. Chem. 68 (1996) 359A.
[13] F. Gonon, M. Buda, R. Cespuglio, M. Jouvert, J. Pajol, Nature 286 (1980) 902.
[14] G. Jin, Y. Zhang, W. Cheng, Sens. Actuator B: Chem. 107 (2005) 528.
[15] H. Zhao, Y. Zhang, Z. Yuan, Anal. Chim. Acta 441 (2001) 117.
[16] J. Li, X. Lin, Sens. Actuator B: Chem. 124 (2007) 486.
[17] J. Mathiyarasu, S. Senthilkumar, K.L.N. Phani, V. Yegnaraman, Mater. Lett. 62 (2008) 571.
[18] L. Lu, X. Lin, Electrochem. Commun. 10 (2008) 704.
[19] S.B. Khoo, F. Chen, Anal. Chem. 74 (2002) 5734.
[20] P. Shakkthivel, S.M. Chen, Biosens. Bioelectron. 22 (2007) 1680.
[21] S. Jo, H. Jeong, S.R. Bae, S. Jeon, Microchem. J. 88 (2008) 1.
[22] A. Liu, I. Honma, H. Zhou, Biosens. Bioelectron. 23 (2007) 74.
[23] S. Jiao, M. Li, C. Wang, D. Chen, B. Fang, Electrochim. Acta 52 (2007) 5939.

[24] A. Sivanesan, P. Kannan, S. Abraham John, Electrochim. Acta 52 (2007) 8118.
[25] C.R. Raj, T. Okajima, T. Ohsaka, J. Electroanal. Chem. 543 (2003) 127.
[26] L. Zhang, R. Yuan, Y. Chai, X. Li, Anal. Chim. Acta 596 (2007) 99.
[27] A. Safavi, N. Maleki, F. Tajabadi, E. Farjami, Electrochem. Commun. 9 (2007) 1963.
[28] A.N. Shipway, M. Lahav, I. Willner, Adv. Mater. 12 (2000) 993.
[29] D.N. Muraviev, Contrib. Sci. 3 (2005) 19.
[30] Y. Ohnuki, T. Ohsaka, H. Matsuda, N. Oyama, J. Electroanal. Chem. 158 (1983) 55.
[31] S. Tian, J. Liu, T. Zhu, W. Knoll, Chem. Mater. 16 (2004) 4103.
[32] L. Zhang, M. Wan, J. Phys. Chem. B 107 (2003) 6748.
[33] R. Davies, G.A. Schurr, P. Meenan, R.D. Nelson, H.E. Bergna, C.A.S. Brevett, R.H. Goldbaum, Adv. Mater. 10 (1998) 1264.
[34] C.S.C. Bose, K. Rajeshwar, J. Electroanal. Chem. 333 (1992) 235.
[35] J. Li, X. Lin, Microchem. J. 87 (2007) 41.
[36] Y.C. Liu, H.T. Lee, S.J. Yang, Electrochim. Acta 51 (2006) 3441.
[37] S. Roux, G.J. de, A.A. Soler-Illia, S. Demoustier-Champagne, P. Audebert, C. Sanchez, Adv. Mater. 15 (2003) 217.
[38] W. Chen, C.M. Li, P. Chena, C.Q. Sun, Electrochim. Acta 52 (2007) 2845.
[39] J. Njagi, S. Andreescu, Biosens. Bioelectron. 23 (2007) 168.
[40] J. Li, X.O. Lin, Anal. Chim. Acta 596 (2007) 222.
[41] A.F. Diaz, J.I. Castillo, J.C.S. Chem. Commun. (1980) 397;
Ai-L. Lui, S.B. Zhang, W. Chen, X.-H. Lin, X.-H. Xia, Biosens. Bioelectron. 23 (2008) 1495.
[42] R.A. Bull, F.R. Fan, A.J. Bard, J. Electrochem. Soc. 129 (1982) 1009.
[43] R.N. Singh, B. Lal, M. Malviya, Electrochim. Acta 49 (2004) 4605.

Talanta 80 (2010) 1467–1469

Contents lists available at ScienceDirect

Talanta

journal homepage: www.elsevier.com/locate/talanta

Short communication

The reference materials syndrome

Michael S. Epstein*

Department of Science, Mount Saint Mary's University, Emmitsburg, MD 21727, United States

ARTICLE INFO

Article history:
Received 19 August 2009
Received in revised form
13 September 2009
Accepted 14 September 2009
Available online 19 September 2009

Keywords:
Reference materials
Spectroscopy
Certified values
SRM 1648
SRM 1645

ABSTRACT

This paper examines specific cases in the literature where analysts using spectroscopic instrumentation report elemental concentrations that agree with information values reported in reference material certificates that are subsequently found to be incorrect.

© 2009 Elsevier B.V. All rights reserved.

1. Introduction

The term "Standard Reference Materials (SRM) Syndrome" was coined by F.P. Byrne [1] in 1974 to characterize the incidents where analysts succeed in accurately measuring the concentration of certified constituents in reference materials for which they know the true constituent concentrations, but fail when such samples are presented as blind unknowns. It is common knowledge that inter-laboratory round-robin analysis results for samples of known concentration are more often in agreement than for samples of unknown concentration. Of course the most logical explanation is that an analyst who obtains an incorrect concentration for a reference material investigates the cause of the error and corrects it. But is there also an element of self-deception or dishonesty involved in this phenomenon?

In order to study this syndrome, two instances were evaluated where information or matrix concentrations for elements listed in SRM certificates were later found to be incorrect and changed in later editions of the certificates. The two elements studied, manganese and magnesium, were chosen for their known certificate discrepancies as well as because the determination of these elements should be simple using most analytical techniques.

While the analytical community accepts certified element concentrations as inherently correct, within the stated uncertainty limits, this aura of validity was often incorrectly carried over to information values because of the status of the certifying body. At the National Institute of Standards and Technology (NIST, formerly the National Bureau of Standards), information values were not certified because they were not determined by a definitive method [2] or by at least two agreeing independent methods [3]. In many cases, the information values were based on either one analytical method or a significant difference existed between two independent analytical method results that implied a systematic bias in one or both of the methods. Since information values were sometimes misinterpreted by the end users as certified values in the validation of new analytical techniques or methodologies in the scientific literature, a unique opportunity is provided to validate the reference material syndrome. This study is based on a compilation of elemental concentration values in the literature [4] as well as the author's extensive involvement in the certification of reference materials.

2. Results

One of the best examples of a change in the information value occurred in the case of SRM 1648, Urban Particulate Matter. The original certificate from 1978 [5] as well as the revised certificate from 1991 [6] reported an information value for manganese of 860 μg/g. This value was based on disagreement between three analytical methods: atomic absorption spectroscopy, neutron activation analysis, and direct current plasma emission spectrometry. (The 1991 certificate incorrectly listed flame emission spectrometry as the certifying method instead of direct current plasma emission spectrometry.) The discrepancy was eventually resolved as reported in the 1998 certificate [7] in which the concentration of manganese was reported as 786 ± 17 mg/kg (μg/g). The

* Tel.: +1 301 447 5376x4568; fax: +1 301 447 5021.
E-mail address: epstein@msmary.edu.

0039-9140/$ – see front matter © 2009 Elsevier B.V. All rights reserved.
doi:10.1016/j.talanta.2009.09.028

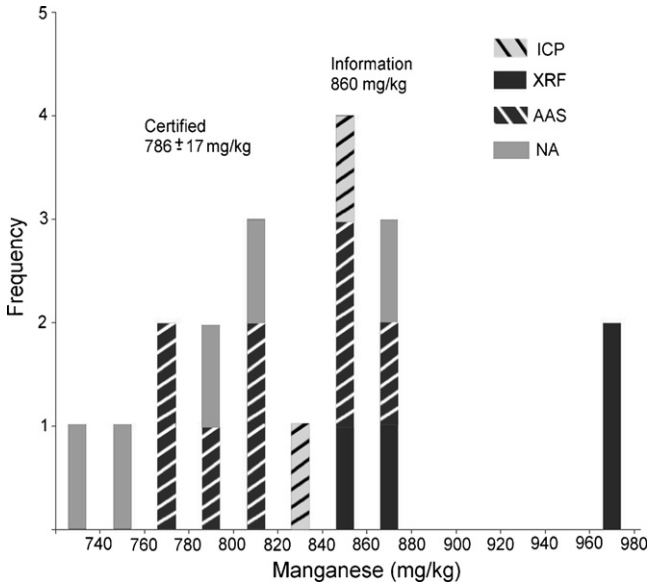


Fig. 1. Histogram of the distribution of literature values for the determination of manganese in SRM 1648 (urban particulates), including analysis techniques (XRF, X-ray fluorescence methods; ICP, inductively-coupled plasma emission spectrometry; AAS, atomic absorption spectrometry; NA, neutron activation methods).

discrepancy was traced to an impure manganese standard used by one of the analytical methods.

Shown in Fig. 1 is a histogram of literature values reported for manganese in SRM 1648 from 1977 to 1984, segmented by analytical technique. The distribution is skewed towards the correct concentration with the maximum at the incorrect information value. There is no question that the reference materials syndrome is a real phenomena. The more important question to ask is why it occurred. Based on the distribution of analytical techniques, there is no obvious technique-based bias. While it is possible that some data may have been fraudulent, it is likely that many errors were made for the same reason that the NIST information value was in error, because of an impure manganese standard. Furthermore, since this time period corresponded to the development of new analytical techniques, such as inductively-coupled plasma emission spectrometry (ICPES), it is also feasible that spectral interferences might have been ignored because the presumably correct answer was obtained. Such interferences would have resulted in concentrations higher than the certified value.

Fig. 2 is a histogram of literature values for magnesium, one of 4 components of SRM 1645, River Sediment, again segmented by analytical techniques. The matrix composition for this SRM was described in the 1978 certificate of analysis [8] as 4% MgO, 4% Al_2O_3, and 4% CaO. These numbers correspond to elemental concentrations of 2.4% Mg, 2.1% Al, and 2.9% Ca and were specifically listed only to "describe the matrix of the material" and not intended as certified or information numbers. A later certificate in 1982 [9] reported a certified value of 2.26 ± 0.04 wt. percent aluminum, 0.74 ± 0.02 wt. percent magnesium, and an information value of 2.9 wt. percent calcium. Thus the initially reported matrix concentration of MgO of 4% was incorrect, and should have been 1.2%. The histogram shows several interesting components. First, there is no specific analytical technique bias. Second, several reported values corresponded to an incorrectly calculated concentration of magnesium (2.4%) based on the matrix composition of 4% MgO. Finally, one analytical method reported a concentration of 4.1% magnesium, corresponding to the incorrect matrix composition of MgO. That same analytical method reported concentrations of 4.2% calcium and 3.9% aluminum. Furthermore, their analysis of SRM 1648 reported a concentration of manganese of 851 μg/g.

3. Conclusion

It is impossible to assign causes to specific cases of the reference materials syndrome, of which there are undoubtedly many. Certainly the primary cause is the tendency of the analyst to implicitly trust the source of the reference material certificate and a misunderstanding of the validity of the numbers reported therein. The period examined corresponded to the development of new analytical techniques, such as ICPES, as well as more mature techniques such as X-ray fluorescence, where the inexperienced analyst could easily be in error. The primary lesson is one that Byrne delineated in

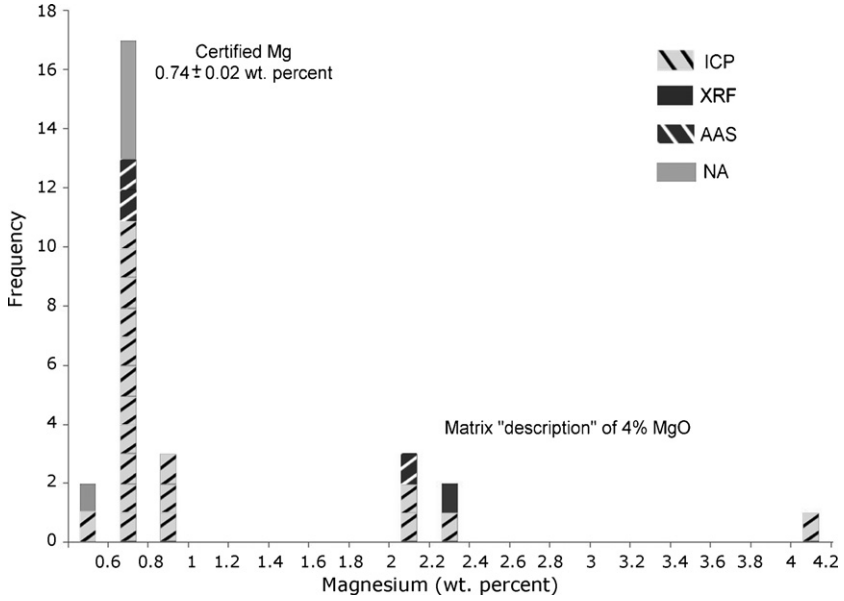


Fig. 2. Histogram of the distribution of literature values for the determination of magnesium in SRM 1645 (River Sediment), including analysis techniques (XRF, X-ray fluorescence methods; ICP, inductively-coupled plasma emission spectrometry; AAS, atomic absorption spectrometry; NA, neutron activation methods including photon activation).

that "the analyst must always be conscious of the human element" and "that he must design his methods testing in such a way that his subconscious will not know the expected result."

References

[1] F.P. Byrne, Introductory Statement: Some Fundamentals of Analytical Chemistry, ASTM STP 564, American Society for Testing and Materials, Philadelphia, 1974, pp. 1-5.
[2] J.R. Moody, M.S. Epstein, Spectrochim. Acta 46B (1991) 1571–1575.
[3] M.S. Epstein, Spectrochim. Acta 46B (1991) 1583–1591.
[4] E.S. Gladney, B.T. O'Malley, I. Roelandts, T.E. Gills, Standard Reference Materials: Compilation of Elemental Concentration Data for NBS Clinical, Biological, Geological, and Environmental Standard Reference Materials, NBS Special Publication 260-11, Washington DC, 1987.
[5] Standard Reference Material 1648, Urban Particulate Matter, Certificate of Analysis, National Bureau of Standards, Washington D.C., November 16, 1978.
[6] Standard Reference Material 1648, Urban Particulate Matter, Certificate of Analysis, National Institute of Standards and Technology, Gaithersburg, MD, August 30, 1991.
[7] Standard Reference Material 1648, Urban Particulate Matter, Certificate of Analysis, National Institute of Standards and Technology, Gaithersburg, MD, April 28, 1998.
[8] Standard Reference Material 1645, River Sediment, Certificate of Analysis, National Bureau of Standards, Washington D.C., November 16, 1978.
[9] Standard Reference Material 1645, River Sediment, Certificate of Analysis, National Bureau of Standards, Washington D.C., May 5, 1982.

Talanta 80 (2010) 1470–1474

Contents lists available at ScienceDirect

Talanta

journal homepage: www.elsevier.com/locate/talanta

Short communication

Enantiomer analysis of chiral carboxylic acids by AIE molecules bearing optically pure aminol groups

Yan-Song Zheng*, Yu-Jian Hu, Dong-Mi Li, Yi-Chang Chen

Department of Chemistry, Huazhong University of Science and Technology, Wuhan 430074, PR China

ARTICLE INFO

Article history:
Received 15 July 2009
Received in revised form
11 September 2009
Accepted 16 September 2009
Available online 24 September 2009

Keywords:
Aggregation-induced emission
Chiral recognition
Quantitative analysis of enantiomer
Fluorescence
Carboxylic acids

ABSTRACT

Pure enantiomers of carboxylic acids are a class of important biomolecules, chiral drugs, chiral reagents, etc. Analysis of the enantiomers usually needs expensive instrument or complex chiral receptors. However, to develop simple and reliable methods for the enantiomer analysis of acids is difficult. In this paper, chiral recognition of 2,3-dibenzoyltartaric acid and mandelic acid was first carried out by aggregation-induced emission molecules bearing optically pure aminol group, which was easily synthesized. The chiral recognition is not only seen by naked eyes but also measured by fluorophotometer. The difference of fluorescence intensity between the two enantiomers of the acids aroused by the aggregation-induced emission molecules was up to 598. The chiral recognition could be applied to quantitative analysis of enantiomer content of chiral acids. More chiral AIE amines need to be developed for enantiomer analysis of more carboxylic acids.

© 2009 Elsevier B.V. All rights reserved.

1. Introduction

Pure enantiomers of carboxylic acids are a class of important biomolecules, chiral drugs, catalysts, chiral building blocks, etc. Conventional enantiomer analyses usually need expensive instrument or complex chiral reagents, and are also time-consuming in practice. However, to develop simple and reliable methods for the enantiomer analysis of acids is difficult. Chiral recognition of carboxylic acids in fluorescence can provide time-efficient, accurate, and sensitive enantiomer determination [1]. Especially, fluorescent receptors that are capable of differentiating the two enantiomers of a chiral acid would provide a real time technique in the rapid chiral assays of high throughput drug discovery and catalyst screening. However, to design and synthesize excellent chiral fluorescent receptors for enantiomers of carboxylic acids are still a challenge [1,2].

Recently, a new class of organic compounds with an amazing property of aggregation-induced emission (AIE) or aggregation-induced emission enhancement (AIEE) have been found [3–19]. These compounds have not the quenching problem in the solid state, therefore they not only show a great potential in optoelectronic materials [4,5], but also will act as highly selective and stable fluorescence sensors for protein [6,7], DNA [8,9], organic vapor [10–12], heparin [13], metal ions [14], chlorine [15], immunoassay [16] and even layer-by-layer self-assembling process [17], and so on. Although chiral AIE compounds bearing cholesteryl groups [18,19] were reported as crystal light-emitting materials, research work related to chiral recognition based on AIE or AIEE characters is not reported. During studying chiral recognition [20–22], it occurred to us that novel chiral fluorescent receptors would be obtained if one molecule having AIE character and another molecule having chiral recognition ability were connected. Here we first report that the AIE compound bearing optically pure aminol group can enantioselectively aggregate with one enantiomer of chiral carboxylic acid and results in big fluorescence intensity difference up to more than 200-fold which can be used in quantitative analysis of enantiomer composition.

2. Experimental

2.1. Materials and measurements

All reagents and solvents were chemical pure (CP) grade or analytical reagent (AR) grade and were used as received. ^{1}H NMR and ^{13}C NMR spectra were measured on a 400 MHz spectrometer at 298 K in $CDCl_3$. Absorption spectra were recorded on a UV–vis spectrophotometer. Mass spectrum was measured on a FTMS instrument. Field emission scanning electron microscopy (FE-SEM) images were taken on an electron microscope operating at 10 kV. The suspension or solution of sample was dropped onto a slide and air-dried. Fluorescent emission spectra were collected on a fluorophotometer at 298 K. The fluorescence spec-

* Corresponding author. Fax: +86 27 87543632.
E-mail address: zyansong@hotmail.com (Y.-S. Zheng).

0039-9140/$ – see front matter © 2009 Elsevier B.V. All rights reserved.
doi:10.1016/j.talanta.2009.09.030

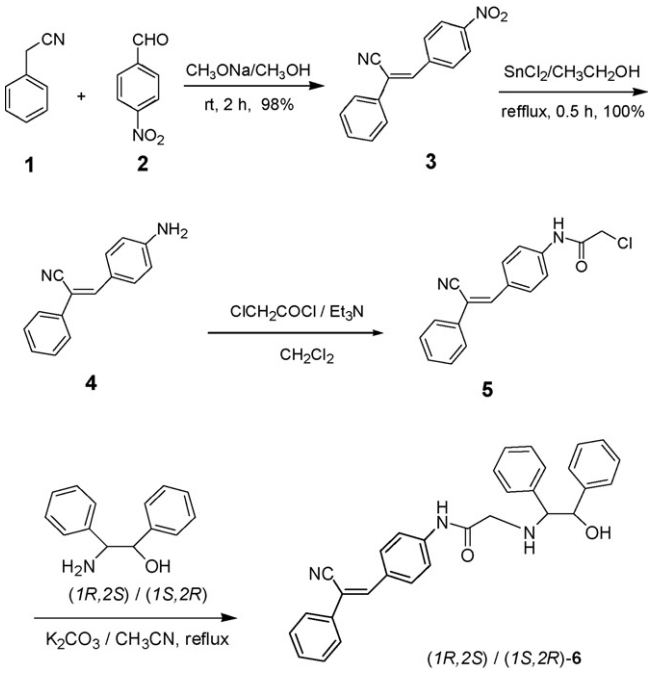
trum was measured after the aggregation appeared and stood for 1 h.

2.2. Synthesis of chiral AIE amines

The synthetic route is as Scheme 1.

Synthesis of compound **5**: a solution of **4** (2.2 g, 0.01 mol) and triethylamine (1.5 g, 0.015 mol) in dichloromethane (40 mL) was cooled with iced bath. To the solution chloroacetyl chloride (1.7 g, 0.015 mol) was added during 0.5 h under stirring. The mixture was continued to stir at the iced temperature for about 3 h until **4** disappeared (monitored by silica gel thin layer chromatography; eluent:chloroform). Then the pH of the reaction mixture was adjusted to neutral with 1 M HCl. After organic phase was separated the aqueous phase was extracted with chloroform. The combined organic phase was dried over anhydrous Na_2SO_4, filtered and evaporated to dryness. The residue was recrystallized with THF and methanol to give yellow powder (2.0 g, yield 70%). Mp: 182–184 °C; IR (KBr) ν 3305, 3279, 3184, 3106, 3050, 2954, 2223, 1690, 1601, 1536 cm^{-1}; ^1H NMR (400 MHz, $CDCl_3$): δ 8.37 (s, 1H), 7.93 (d, J = 8.4 Hz, 2H), 7.69 (t, J = 7.6 Hz, 4H), 7.50–7.40 (m, 4H), 4.23 (s, 2H).

Synthesis of compound (*1S,2R*)-**6**: to the flask was added **5** (1.19 g, 0.004 mol), (*1S,2R*)-2-amino-1,2-diphenylethanol (0.852 g, 0.004 mol), triethylamine (1.22 g, 0.012 mol) and dried THF (15 mL). The mixture was refluxed for about 48 h until **5** disappeared (monitored by silica gel TLC, chloroform:ethyl acetate 3:1). After concentrated, the residue was subjected to flash column chromatography (silica gel thin layer chromatography; eluent:chloroform:ethyl acetate 5:1) to give light yellow powder (1.23 g, yield 65%). Mp: 195–197 °C; $[\alpha]_D^{20}$ = −29.9 (*c* 1.0, THF); IR (KBr) ν 3447, 3355, 3271, 3055, 3029, 2903, 2216, 1678, 1604, 1571, 1525, 1049; ^1H NMR (400 MHz, $CDCl_3$) δ 9.37 (s, 1H), 7.85 (d, J = 8.8 Hz, 2H), 7.66 (d, J = 8.8 Hz, 2H), 7.52 (d, J = 8.4 Hz, 2H), 7.5–7.17 (m, 14 H), 4.93 (d, J = 6 Hz, 1H), 3.94 (d, J = 6 Hz, 1H), 3.34, 3.22 (2d, J = 17.6 Hz, 2H), 2.20 (br, 2H); ^{13}C NMR (100 MHz, $CDCl_3$) δ 169.6, 141.6, 140.4, 139.6, 134.7, 130.3, 129.4, 129.0, 128.8, 128.5, 128.5, 128.4, 128.1, 127.1, 126.0, 119.4, 118.3, 110.0, 77.2, 69.0, 50.4; ESI^+ MS m/z calcd for $C_{31}H_{27}N_3O_2$ 473 [M], found 474 $[(M+1)]^+$. Anal. Calcd for $C_{31}H_{27}N_3O_2$: C, 78.62; H, 5.75; N, 8.87. Found: C, 78.27; H, 5.30; N, 8.25.



Scheme 1. Synthesis of chiral AIE compounds (*1R,2S*)-**6** and (*1S,2R*)-**6**.

Synthesis of compound (*1R,2S*)-**6**: the method was the same as (*1S,2R*)-6, yellow powder, yield 67%; Mp: 194–196 °C; $[\alpha]_D^{20}$ = +29.3 (*c* 1.0, THF); IR (KBr) ν 3447, 3357, 3271, 3054, 3030, 2903, 2217, 1678, 1606, 1570, 1526, 1050 cm^{-1}; ^1H NMR (400 MHz, $CDCl_3$) δ 9.34 (s, 1H), 7.88 (d, J = 8.4 Hz, 2H), 7.68 (d, J = 7.6 Hz, 2H), 7.53 (d, J = 6.4 Hz, 2H), 7.6–7.29 (m, 12H), 7.23 (d, J = 6.4 Hz, 2H), 4.91 (d, J = 6.4 Hz, 1H), 3.94 (d, J = 6.4 Hz, 1H), 3.35, 3.19 (2d, J = 17 Hz, 2H), 2.21 (br, 2H); ^{13}C NMR (100 MHz, $CDCl_3$) δ 169.8, 141.6, 140.4, 139.6, 138.4, 134.7, 130.3, 129.4, 129.1, 129.0, 128.8, 128.5, 128.5, 128.4, 128.0, 127.1, 125.9, 119.4, 118.3, 109.9, 77.2, 68.9, 50.4; ESI^+ MS m/z calcd for $C_{31}H_{27}N_3O_2$ 473 [M], found 474 $[(M+1)]^+$. Anal. Calcd for $C_{31}H_{27}N_3O_2$: C, 78.62; H, 5.75; N, 8.87. Found: C, 78.22; H, 5.27; N, 8.22.

3. Results and discussion

3.1. AIE character of chiral amines **6**

2-Phenyl-3-(*p*-aminophenyl)acrylonitrile **4** is one of cyano-containing AIE molecules, which does not emit fluorescence in solution but emits strong one in solid state [10,23]. It reacted with chloroacetylchloride to give **5** which was easily attached by an optically pure amine to get chiral AIE compound **6** (Scheme 1). The structure of both (*1S,2R*)-**6** and (*1R,2S*)-**6** were fully characterized by ^1H and ^{13}C NMR, MS, elemental analysis and polarimetry.

(*1S,2R*)-**6** and (*1R,2S*)-**6** are soluble in common organic solvents such as ethanol, THF, chloroform and 1,2-dichloroethane, but insoluble in water and in nonpolar solvent such as petroleum ether, *n*-hexane. As expected, just like AIE compound **4**, while dilute solution of (*1S,2R*)-**6** or (*1R,2S*)-**6** in ethanol or 1,2-dichloroethane was almost no fluorescent, the resultant solid after solvents were evaporated exhibited strong blue emission under a UV lamp. When water was added into the solution of (*1S,2R*)-**6** or (*1R,2S*)-**6** in ethanol, or petroleum ether was added into the solution in 1,2-dichloroethane, the resultant suspension also emitted strong fluorescence. As shown in Fig. 1A, the fluorescence intensity of (*1S,2R*)-**6** increased little with increasing the volume ratio of petroleum ether vs 1,2-dichloroethane in the range of less than 80:20. But when the ratio was more than 80:20 the fluorescence intensity increased swiftly. At the ratio of 95:5, the fluorescence intensity of the resultant suspension got up to 536 at λ_{max} = 460 nm which was 2680 times as large as the solution in 1,2-dichloroethane without petroleum ether (intensity 0.2). From macroscopic observation, the solution at the ratio less than 80:20 was homogeneous, but it became suspension at volume ratio larger than 80:20. Therefore, (*1S,2R*)-**6** and (*1R,2S*)-**6** display an AIE character. The absorbance of (*1S,2R*)-**6** almost had not change with increasing content of petroleum ether in 1,2-dichloroethane when the volume ratio of petroleum ether vs 1,2-dichloroethane was less than 70:30 (Fig. 1B). But after the ratio was lager than 80:20, the absorbance of (*1S,2R*)-**6** rapidly decreased. Although the absorbance decreased with increasing petroleum ether the fluorescence intensity greatly increased. This result confirmed that (*1S,2R*)-**6** was truly a AIE compound.

In addition, although the absorption band of the suspension at λ_{max} = 327 nm exhibited a little blue-shift of 3 nm compared with the solution at λ_{max} = 330 nm which probably was ascribed to the solvent effect, the emission band of the suspension at λ_{max} = 460 nm in mixed solvent of petroleum ether and 1,2-dichloroethane (95:5) showed a large red-shift of 18 nm compared with the solution in 1,2-dichloroethane at λ_{max} = 442 nm. Moreover, in a mixed solvent of water and ethanol the maximum emission peak had a red-shift of 35 nm and the maximum absorption peak also displayed a red-shift of 8 nm from solution to suspension (Figs. S9 and S10 in Support Information). This result is in accordance with literature

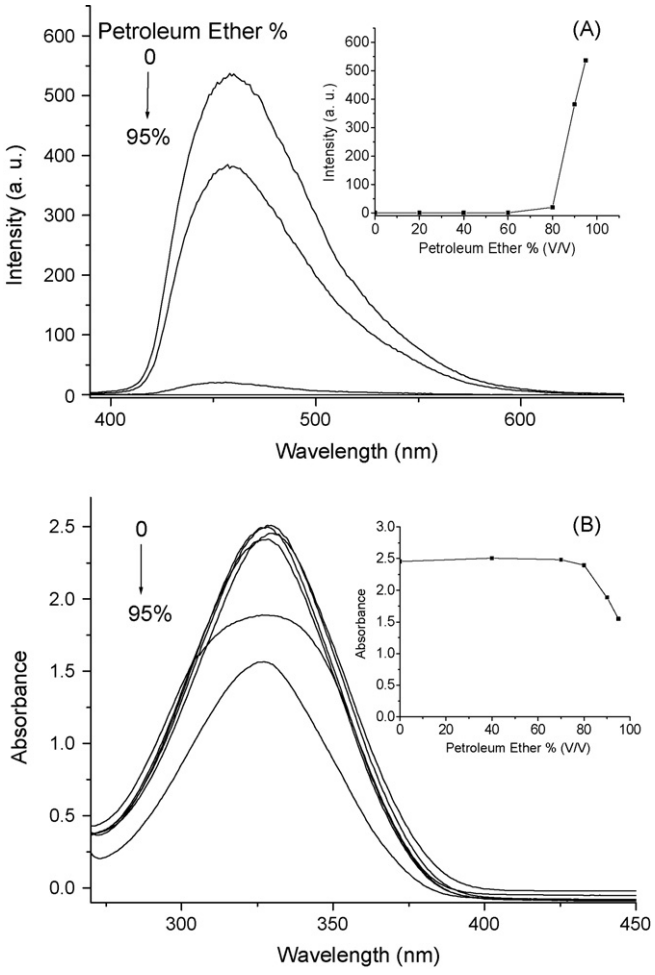
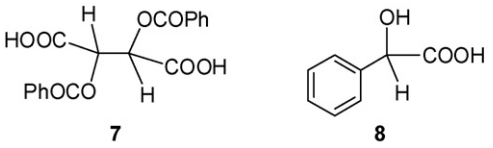


Fig. 1. Change of fluorescence and absorption spectra of (*1S,2R*)-**6** (1.0×10^{-4} M) with increasing content of petroleum ether in 1,2-dichloroethane. (A) Fluorescence spectra. λ_{ex} = 345 nm, ex/em slits = 3/3 nm. Inset, curve of intensity changed with petroleum ether percentage. (B) Absorption spectra. Inset, curve of absorbance changed with petroleum ether percent.

reports, in which addition of water into organic solvent ethanol or THF would arise a red-shift of maximum emission and absorption peak [10,18,24,25]. Therefore, the aggregation in solution by addition of nonsolvent should be one through head to tail stack (J-aggregation) of compound **6** [24,25]. Due to the J-aggregation, the intramolecular vibrational and rotational motions, which behave strongly in a twisted conjugation molecule and will lead to the fast nonradiative relaxation and reduce fluorescence intensity in a solution, are restricted. Meanwhile, the bulky substituents, especially the cyano group[2c,4g], at the carbon-carbon double bond of **6** prevent the molecule from forming excimer which usually results in quenching in solid state, so that the fluorescence increases when this sort of molecule aggregates.

3.2. Chiral recognition

The chiral recognition property of **6** was initially studied with interaction of (*1S,2R*)-**6** and the two enantiomers of a chiral carboxylic acid. As expected, enantioselective aggregates formed when (*1S,2R*)-**6** and chiral carboxylic acid were mixed in 1,2-dichloroethane. When equal volumes of (*1S,2R*)-**6** (0.02 M in 1,2-dichloroethane) and *D*-**7** (Scheme 2, 0.02 M in 1,2-dichloroethane) were mixed and let the solution stand for 0.5 h at room temperature, a suspension appeared. But the mixture of (*1S,2R*)-**6** and *L*-**7** in 1,2-dichloroethane was a clear solution even



Scheme 2. Structure of carboxylic acids used in chiral recognition.

after standing for more than 1 day. Under the same conditions, interaction of (*1S,2R*)-**6** and (*S*)-**8** (Scheme 2) led to a suspension, but the mixture of (*1S,2R*)-**6** and (*R*)-**8** remained a clear solution. Very importantly, the enantioselective aggregation in 1,2-dichloroethane could not only be visualized by naked eyes but also be quantitatively observed by fluorophotometer due to AIE effect of **6** as shown in Fig. 2A and B. The suspension of (*1S,2R*)-**6** and *D*-**7** had a fluorescence intensity of 515, but the solution of (*1S,2R*)-**6** and *L*-**7** showed only 2.6 at λ_{max} = 421 nm, providing this system with a very high enantiomer fluorescence intensity ratio 196 ($I_{D\text{-}7}/I_{L\text{-}7}$). For mandelic acid **8**, the fluorescence intensity ratio of their two enantiomers was as high as $I_{(S)\text{-}8}/I_{(R)\text{-}8}$ = 598.

To confirm that the enantioselective aggregation was the result of chiral recognition by the chiral receptor, the interaction of chiral carboxylic acids with (*1R,2S*)-**6** was also studied. Under the same conditions as that with (*1S,2R*)-**6**, interaction of (*1R,2S*)-**6** with **7** and **8** just led to opposite results, that is, mixture of (*1R,2S*)-**6** with *L*-**7** or (*R*)-**8** gave a suspension but the diastereomeric mixing of (*1R,2S*)-**6** with *D*-**7** or (*S*)-**8** led to a clear solution. And similarly, the suspensions had stronger fluorescence than the solutions (Fig 2C and D). Similarly, the fluorescence intensity ratio for the mixture of (*1R,2S*)-**6** with enantiomers of **7** ($I_{L\text{-}7}/I_{D\text{-}7}$) was as high as 506, and the ratio of $I_{(R)\text{-}8}/I_{(S)\text{-}8}$ got up to160. In addition, FE-SEM revealed that the aggregates in suspension of (*1S,2R*)-**6** and *D*-**7** were composed of nanofibers with a length of 5–20 μm and a width of 50–150 nm, but the solid resulted from evaporation of the solution of (*1S,2R*)-**6** and *L*-**7** was amorphous (Figs. S11 and S12 in Support Information). Therefore the above results demonstrate that the interaction of chiral receptor **6** with chiral acids is indeed highly enantioselective and can lead to strong enantioselectively aggregation-induced emission.

3.3. Quantitative analysis of enantiomer content

In order to ascertain if the fluorescence difference resulted from the enantioselective aggregation could be applied to determination of enantiomer composition, fluorescence intensity of the suspension of (*1S,2R*)-**6** and *D*-**7** in different concentration was measured. As shown in Fig. 3, the fluorescence intensity of suspension increased with increasing the concentration of mixture of (*1S,2R*)-**6** and *D*-**7**. Notably, in the range of concentration less than 2.0×10^{-3} M, the fluorescence intensity linearly increased with the concentration of mixture of (*1S,2R*)-**6** and *D*-**7** as shown in inset of Fig. 3. This is valuable because the concentration of complex of (*1S,2R*)-**6** with *D*-**7** could be conveniently measured by its fluorescence intensity.

Due to direct proportion of fluorescence intensity and concentration in less than 2.0×10^{-3} M, therefore, kept total concentration of both (*1S,2R*)-**6** with *D*-**7** at 2.0×10^{-4} M, the change of fluorescence intensity with content of *D*-**7** in the two enantiomers of **7** was studied. As displayed in Fig. 4, the mixture of (*1S,2R*)-**6** and **7** almost emitted no fluorescence with increasing the molar percentage of *D*-**7** in enantiomer composition of **7** when the percentage of *D*-**7** was less than 50%, but when it was more than 50%, the fluorescence intensity increased with the molar percentage of *D*-**7**. Similarly, when the molar percentage of *L*-**7** was more than 50% the fluorescence intensity of mixture of (*1R,2S*)-**6** and **7** increased with

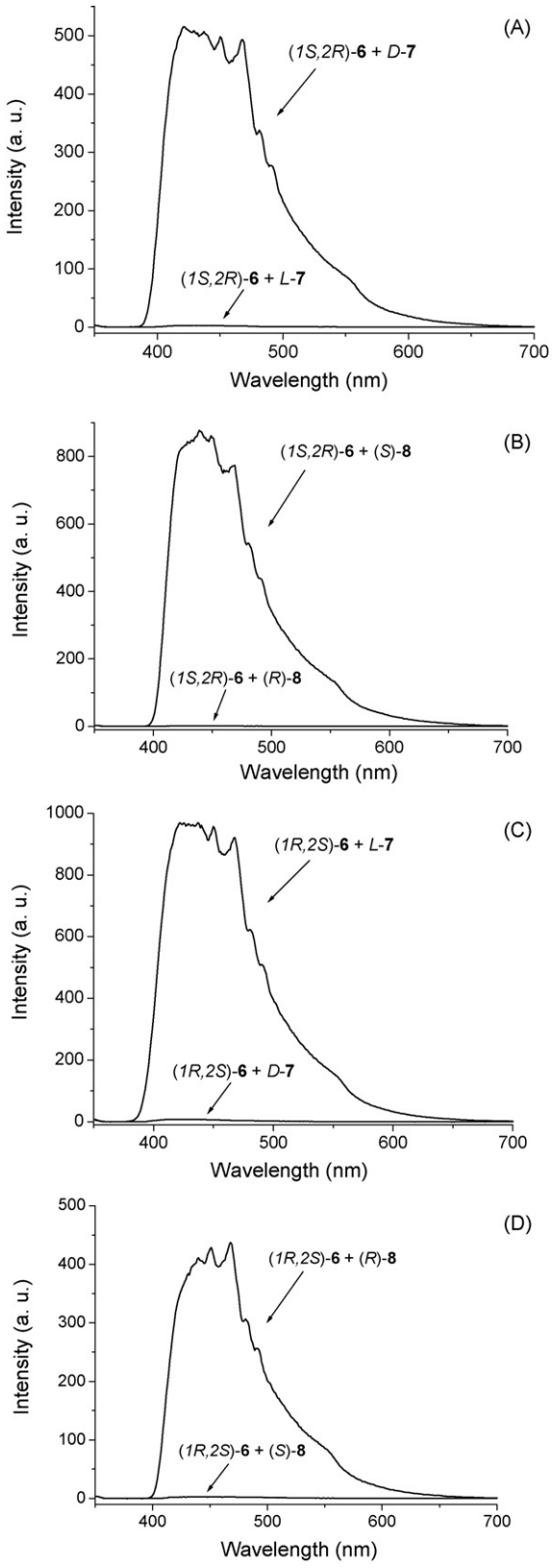


Fig. 2. Fluorescence spectra of mixture of **6** and enantiomers of chiral acids in 1,2-dichloroethane ([**6**] = [**7**] = [**8**] = 0.01 M, λ_{ex} = 345 nm, ex/em slits = 10/5 nm). (A) of (*1S,2R*)-**6** with **7**; (B) of (*1S,2R*)-**6** with **8**; (C) of (*1R,2S*)-**6** with **7**; (D) of (*1R,2S*)-**6** with **8**.

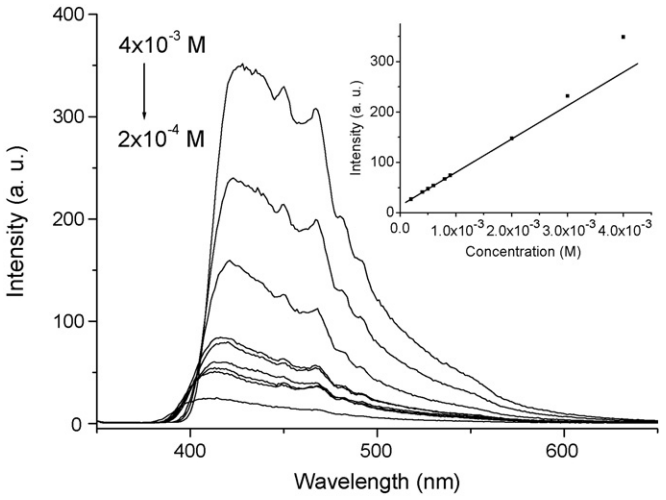


Fig. 3. Change of fluorescence spectra of mixture of (*1S,2R*)-**6** and *D*-**7** with concentration from 2.0×10^{-4} to 4.0×10^{-3} M in 1,2-dichloroethane([(*1S,2R*)-**6**] = [*D*-**7**], λ_{ex} = 345 nm, ex/em slits = 10/5 nm). Inset, curve of intensity changed with concentration.

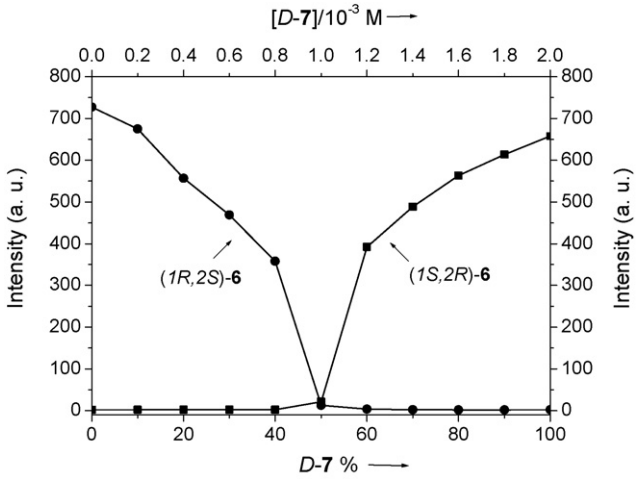


Fig. 4. Change of fluorescence intensity of mixture of amine **6** and acid **7** with enantiomer content of acid **7**. [**6**] = total concentration of two enantiomers of **7** = 2.0×10^{-3} M in 1,2-dichloroethane; λ_{ex} = 345 nm, ex/em slits = 10/5 nm.

the molar percentage of *L*-**7**. As a result, two standard curves were drawn and any enantiomeric composition of **7** could be obtained. This is very important for high throughput analysis of chiral drugs and reagents. By the same method, the enantiomer composition of other chiral acids such as **8** could be also analyzed.

4. Conclusions

In conclusion, combination of AIE component and optically pure amine group could result in excellent chiral receptors for fluorescent chiral recognition of carboxylic acids. This finding provides a totally new and simple methodology for design of fluorescent chiral receptor which can be applied to quantitative determination of enantiomer content, although only two chiral carboxylic acids were tested. Other chiral AIE amines that can analyze enantiomers of more carboxylic acids need to be developed.

Acknowledgements

The authors thank National Natural Science Foundation of China (No. 20872040) for financial support, and thank the Analytical and

Testing Centre at Huazhong University of Science and Technology for measurement.

Appendix A. Supplementary data

Supplementary data associated with this article can be found, in the online version, at doi:10.1016/j.talanta.2009.09.030.

References

[1] L. Pu, Chem. Rev. 104 (2004) 1687–1716.
[2] H.-L. Liu, X.-L. Hou, L. Pu, Angew. Chem. Int. Ed. 47 (2008) 1–5.
[3] J. Luo, Z. Xie, J.W.Y. Lam, L. Cheng, H. Chen, C. Qiu, H.S. Kwok, X. Zhan, Y. Liu, D. Zhu, B.Z. Tang, Chem. Commun. (2001) 1740–1741.
[4] H. Chen, J.W.Y. Lam, J. Luo, Y.L. Ho, B.Z. Tang, D. Zhu, M. Wong, H.S. Kwok, Appl. Phys. Lett. 81 (2002) 774–776.
[5] G. Qian, B. Dai, M. Luo, D. Yu, J. Zhan, Z. Zhang, D. Ma, Z.Y. Wang, Chem. Mater. 20 (2008) 6208–6216.
[6] H. Tong, Y. Hong, Y. Dong, M. Haussler, Z. Li, J.W.Y. Lam, Y. Dong, H.H.-Y. Sung, I.D. Williams, B.Z. Tang, J. Phys. Chem. B 111 (2007) 11817–11823.
[7] H. Tong, Y. Hong, Y. Dong, M. Haussler, J.W.Y. Lam, Z. Li, Z. Guo, Z. Guo, B.Z. Tang, Chem. Commun. (2006) 3701–3705.
[8] Y. Hong, M. Häußbler, J.W.Y. Lam, Z. Li, K.K. Sin, Y. Dong, H. Tong, J. Liu, A. Qin, R. Renneberg, B.Z. Tang, Chem. Eur. J. 14 (2008) 6428–6437.
[9] M. Wang, D. Zhang, G. Zhang, Y. Tang, S. Wang, D. Zhu, Anal. Chem. 80 (2008) 6443–6448.
[10] B.-K. An, S.-K. Kwon, S.-D. Jung, S.Y. Park, J. Am. Chem. Soc. 124 (2002) 14410–14415.
[11] K. Itami, J. Yoshida, Chem. Eur. J. 12 (2006) 3966–3974.
[12] H. Tong, Y. Dong, M. Haussler, J.W.Y. Lam, B.Z. Tang, Nonlinear Opt., Quantum Opt. 35 (2006) 147–154.
[13] M. Wang, D. Zhang, G. Zhang, D. Zhu, Chem. Commun. (2008) 4469–4471.
[14] L. Liu, G. Zhang, J. Xiang, D. Zhang, D. Zhu, Org. Lett. 10 (2008) 4581–4584.
[15] Z. Ning, Z. Chen, Q. Zhang, Y. Yan, S. Qian, Y. Cao, H. Tian, Adv. Funct. Mater. 17 (2007) 3799–3807.
[16] C.P. Chan, M. Haeussler, B.Z. Tang, Y. Dong, K.K. Sin, W.C. Mak, D. Trau, M. Seydack, R. Renneberg, J. Immunol. Methods 295 (2004) 111–118.
[17] J.-K. Jin, J.-Z. Sun, Y.-Q. Dong, H.-P. Xu, W.-Z. Yuan, B.Z. Tang, J. Lumin. 129 (2008) 19–23.
[18] P. Xue, R. Lu, G. Chen, Y. Zhang, H. Nomoto, M. Takafuji, H. Ihara, Chem. Eur. J. 13 (2007) 8231–8239.
[19] H. Tong, Y. Hong, Y. Dong, Y. Ren, M. Haussler, J.W.Y. Lam, K.S. Wong, B.Z. Tang, J. Phys. Chem. B 111 (2007) 2000–2007.
[20] Y.-S. Zheng, A. Ji, X.-J. Chen, J.-L. Zhou, Chem. Commun. (2007) 3398–3400.
[21] X.-X. Liu, Y.-S. Zheng, Tetrahedron Lett. 47 (2006) 6357–6360.
[22] Y.-S. Zheng, C. Zhang, Org. Lett. 6 (2004) 1189–1192.
[23] Y. Li, F. Li, H. Zhang, Z. Xie, W. Xie, H. Xu, B. Li, F. Shen, L. Ye, M. Hanif, D. Ma, Y. Ma, Chem. Commun. (2007) 231–233.
[24] W.I. Gruszecki, J. Biol. Phys. 18 (1991) 99–109.
[25] A. Chowdhury, S. Wachsmann-Hogiu, P.R. Bangal, I. Raheem, L.A. Peteanu, J. Phys. Chem. B 105 (2001) 12196–12201.

Talanta 80 (2010) 1475

Contents lists available at ScienceDirect

Talanta

journal homepage: www.elsevier.com/locate/talanta

Foreword

The role of analytical chemists in the XXI century is becoming critical to help colleagues from other areas of research, such as in medicine, biology, genetics or toxicology, to understand the performances of modern analytical techniques and to outline how to properly apply these methods in their own workflows.

The field of Analytical Proteomics is growing constantly and is becoming a major instrument of support for progress in System Biology or Medical Chemistry. The improvements driven by Analytical Chemistry, through techniques such as mass spectrometry or near magnetic resonance, are quickly implemented in Proteomics. The advances in sample treatment for proteomics allow the handling of more samples in less time and in a non-intensive labour fashion.

It is said in the legend that Atalanta refused to compete with Hippomenes, who finally, helped by the goddess of love, Aphrodite, wins her hand in marriage.

Nowadays Atalanta's role is played by Analytical Chemistry whilst Hippomenes' role is played by the modern Society, which is asking for a skilled use of the tools that are provided to the researchers. Modern methods of analysis can be applied to solve many present problems encountered by our Society, but only if they are married with analytical chemists.

I am grateful to the editors of Talanta who have agreed to publish this special issue on Analytical Proteomics and for allowing Carlos Lodeiro, Hugo Santos and myself to act as Guest Editors.

J.L. Capelo [a,b,*]
C. Lodeiro [c]
H.M. Santos [b]

[a] *Nutrition and Bromatology Group, Department of Analytical and Food Chemistry, Faculty of Science, University of Vigo at Ourense Campus, 32004, Ourense, Spain*

[b] *REQUIMTE, Departamento de Química, Faculdade de Ciências e Tecnologia, Universidade Nova de Lisboa, 2829-516, Monte de Caparica, Portugal*

[c] *Physical Chemistry Department, Faculty of Science, University of Vigo at Ourense Campus, E-32004, Ourense, Spain*

* Corresponding author. Tel.: +351 212 949649; fax: +351 212948550.
E-mail address: jlcapelom@dq.fct.unl.pt (J.L. Capelo)

Available online 20 August 2009

0039-9140/$ – see front matter © 2009 Elsevier B.V. All rights reserved.
doi:10.1016/j.talanta.2009.08.013

Talanta 80 (2010) 1476–1486

Contents lists available at ScienceDirect

Talanta

journal homepage: www.elsevier.com/locate/talanta

Review

Latest developments in sample treatment for ^{18}O-isotopic labeling for proteomics mass spectrometry-based approaches: A critical review

J.L. Capelo[a,b,*,1], R.J. Carreira[a,1], L. Fernandes[a,1], C. Lodeiro[a,c,1], H.M. Santos[a,1], J. Simal-Gandara[b,1]

[a] REQUIMTE, Departamento de Química, Faculdade de Ciências e Tecnologia, Universidade Nova de Lisboa, 2829-516, Monte de Caparica, Portugal
[b] Nutrition and Bromatology Group, Analytical and Food Chemistry Department, Faculty of Food Science and Technology, University of Vigo, Ourense Campus, 32004, Ourense, Spain
[c] Physical Chemistry Department, Science Faculty, University of Vigo, E-32004, Ourense, Spain

ARTICLE INFO

Article history:
Available online 3 May 2009

Keywords:
Proteomics
Review
^{18}O
Isotopic labeling
Protein quantification

ABSTRACT

Nowadays isotopic ^{18}O-labeling of peptides has recalled the attention of researchers due to its simplicity of application and high versatility for proteomics studies. Protein quantification, differential peptide mass mapping, studies regarding proteins overexpressed or underexpressed, or the searching of biomarkers can be accomplished by using ^{18}O-labeling. In this critical review we comment on the different ways in which ^{18}O-labeling can be done, highlighting the key parameters of the different sample treatments to obtain a reliable and reproducible labeling. In addition we describe and compare the latest improvement in terms of sample treatment that allows to reduce the handling and to increase the throughput for this sample treatment. Finally, we hypothesize on the future trends of these methods under the light of the new technological advances to speed protein cleavage.

© 2009 Elsevier B.V. All rights reserved.

Contents

1. Introduction 1477
2. The ^{18}O-isotopic labeling 1477
3. The different ways of labeling 1478
   3.1. The direct labeling 1478
   3.2. The decoupling procedure 1478
   3.3. The use of immobilized enzymes 1479
4. The problem of the ^{18}O-labeling efficiency 1479
5. Algorithms for calculating isotopic labeling correction 1479
6. The enzymes used for ^{18}O-labeling 1481
7. The influence of the pH 1481
8. Accelerating and simplifying the sample treatment 1481
   8.1. Heating 1482
   8.2. Micro-spin columns 1482
   8.3. Ultrasonic energy 1482
   8.4. High pressure 1482
9. Applications of the ^{18}O-labeling 1482
   9.1. Inverse labeling 1482
   9.2. Applications to gel-separated proteins 1483
   9.3. Applications to proteins in solution 1484
10. Future trends 1484
   10.1. Micro-scaling the labeling 1484
   10.2. The use of infrared radiation and microwave energy 1485

* Corresponding author at: Nutrition and Bromatology Group, Analytical and Food Chemistry Department, Faculty of Food Science and Technology, University of Vigo, Ourense Campus, 32004, Ourense, Spain. Tel.: +34 610 835 903; fax: +34 610 835.
E-mail address: jlcapelom@uvigo.es (J.L. Capelo).
[1] All authors have contributed equally to this work.

0039-9140/$ – see front matter © 2009 Elsevier B.V. All rights reserved.
doi:10.1016/j.talanta.2009.04.053

11. Conclusions 1485
Acknowledgements 1485
References 1485

1. Introduction

Mass spectrometry is nowadays a powerful tool for protein quantification, both in a relative or absolute manner, with a continuously growing interest among the research community, as it is showed by the large amount of reviews published regarding this item in the last years, 124 since 2005 (key searching words: protein quantification and mass spectrometry; searching engine: scopus). Those reviews cover a broad area of research activities, including proteomics, genomics and medical care or food chemistry [1–6].

The different strategies that can nowadays be followed for protein quantification are briefly addressed in Table 1, along with their main advantages and drawbacks.

Protein quantification using isotopic labeling of peptides with ^{18}O has recently recalled the attention in research due to its almost perfect characteristics to be used for protein differential expression and for relative protein quantification. Enzymatic labeling with ^{18}O-water is easy to do, all peptides formed during the protein cleavage are labeled, and all that is required is the presence of ^{18}O-water, avoiding extra-reagents or synthetic steps. Indeed some authors, as we will see in the next sections, have claimed absolute protein quantification using this labeling tool for non-gel-based approaches.

Time-consuming and labor-intensive are drawbacks of the ^{18}O-labeling. Therefore, during the last years researchers have focused on how to perform ^{18}O-labeling in a fast and reproducible fashion, using different tools to speed and to simplify the sample handling, such as heating, ultrasonic energy, or centrifugation.

Since most approaches currently used fast ^{18}O-labeling have been developed during the last 5 years, reported conclusions are sometimes inconclusive or even contradictory. Therefore, in this work, we present a critical overview of the last trends in ^{18}O-labeling, focusing on the main drawbacks of the sample treatments and giving advises about how to overcome them. In addition the latest developments to speed the labeling procedure are presented and are critically commented. Finally, future trends based on recent findings for the simplification of protein digestions are addressed for their application in ^{18}O-labeling.

2. The ^{18}O-isotopic labeling

It is generally agreed that the ^{18}O-isotopic labeling of peptides can be considered as consisting in two different chemical reactions. The first one is an amide bond cleavage whilst the second reaction is a carboxyl oxygen exchange. Both chemical reactions can be written as follows:

(i) First reaction: amide bond cleavage

$$RC^{16}ONHR' + H_2{}^{18}O \rightarrow [RC^{16}O^{18}O]^- + [H_3NR']$$

(ii) second reaction: carboxyl oxygen exchange

$$[RC^{16}O^{18}O]^- + H_2{}^{18}O \rightarrow [RC^{18}O^{18}O]^- + H_2{}^{16}O$$

As may be seen peptides incorporate one ^{18}O in the first reaction, during the enzymatic cleavage. If this reaction is done in pure ^{18}O-water (normally 95% reach in $H_2{}^{18}O$) then it can be considered that almost 100% of the peptides will be labeled with one ^{18}O. If the reaction is done in mixed $^{16}O/^{18}O$-water, then the labeling ratio will be proportional to the percentage of $H_2{}^{18}O$ in solution: the higher the amount of $H_2{}^{18}O$ the higher the percentage of peptides labeled. This is the reason why accuracy is solely guaranteed when the labeling is done in pure $H_2{}^{18}O$ (generally 95%). In any case, the labeling cannot be studied without taking into consideration the second reaction, the carboxyl oxygen exchange. This reaction is an equilibrium, that ideally should be displaced towards the double oxygen incorporation, since the introduction of two oxygen in a peptide shifts its mass 4 Da, facilitating the identification of the labeled peptide and its quantification by mass spectrometry-based techniques. Both, the amide bond cleavage and the carboxyl oxygen exchange reactions, can take place at the same time, which is the principle of the direct ^{18}O-labeling procedure; or separately, in two steps, which is the basis for the decoupling method. In the next sections we are going to comment the differences of both procedures along with the variables affecting the performance of each one.

Table 1
Main modern strategies for protein quantification in absolute or relative manner: basics, advantages and pitfalls.

SILAC™	ICAT™	ITRAQ™	^{18}O-labeling
Basic concepts			
Metabolic labeling	Chemical labeling	Chemical labeling	Enzymatic labeling
Labeling at selected amino acids (normally arginine, leucine and lysine)	Labeling at cysteines	Labeling at peptide N-terminus and lysine side chain	Labeling at peptide C-terminus
Labeling occurs during cell growth	Labeling occurs before protein digestion	Labeling occurs after protein digestion	Labeling occurs during protein digestion
Labeling at protein level	Labeling at protein level	Labeling at peptide level	Labeling at peptide level
Advantages and disadvantages			
Uniform labeling of every protein	Only peptides with cysteines are labeled	All peptides are labeled	All peptides are labeled
No reduction of sample complexity	Reduction of sample complexity	No reduction of sample complexity	No reduction of sample complexity
Not applicable to human samples	No sample restriction	No sample restriction	No sample restriction
Mixing of differentially treated samples at intact cell level	Mixing of differentially treated samples at protein level	Mixing of differentially treated samples at peptide level	Mixing of differentially treated samples at peptide level
Interconversion of arginine to proline	Side reactions with methionines	Side reactions with thiols and primary amines	No side reactions
MS quantification	MS quantification	MS/MS quantification	MS quantification

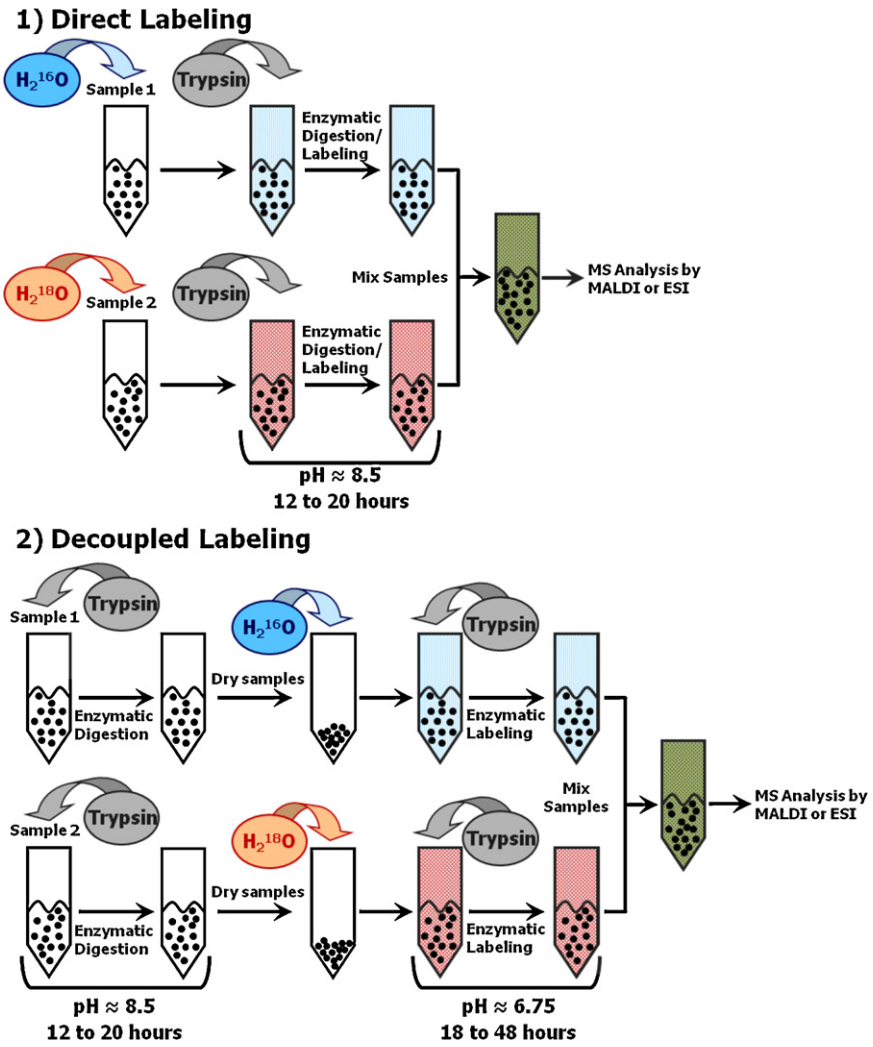


Fig. 1. Comprehensive scheme for the isotopic labeling sample treatment. (1) The direct labeling: samples are dissolved/recomposed in NH_4HCO_3 buffer (25 mM). Then samples are (i) denaturated with acetonitrile, (ii) reduced with DTT, and (iii) alkylated with IAA. Each step is done under the effects of an ultrasonic field provided by a sonoreactor. Then the enzyme is added and the peptides are labeled as the protein is digested. This step is done overnight or with the aid of an ultrasonic bath during 30 min (130 kHz of sonication frequency; 70% sonication amplitude; 60 °C temperature). Finally samples are pooled and are ready to be measured by MS. For more details refer Ref. [7]. (2) The decoupling procedure: the first part of the decoupling procedure is done as in the direct procedure, but samples are digested in ^{16}O-water. Then samples are evaporated to dryness and then they are recomposed in a new solution with a lower pH to speed and facilitate the labeling through oxygen interchange. Samples are evaporated to dryness again and then are recomposed in ^{16}O-water or in ^{18}O-water for the peptide labeling.

3. The different ways of labeling

3.1. The direct labeling

The direct labeling typically done in our laboratory is depicted in Fig. 1. The whole sample treatment entails four main steps [7]: (i) protein dissolution/denaturation; (ii) protein reduction; (iii) protein alkylation and (iv) protein digestion/peptide labeling. The direct labeling can be done accelerating each step with the aid of ultrasonic energy or not [7,8]. As may be seen in Fig. 1, the protein cleavage is done in ^{18}O-water, thus during the protein digestion process, when the peptide bond is broken, one heavy oxygen is incorporated. Further incorporation is done trough the carboxyl oxygen exchange at the same time. The main advantage of this procedure is simplicity and speed. In addition, it can be used in on-line approaches. The main drawback is the lack in labeling efficiency, which makes direct labeling suitable only for relative quantification and for studies regarding proteins overexpressed or underexpressed.

3.2. The decoupling procedure

The decoupling procedure was first proposed by Yao et al. who have demonstrated that the cleavage of the protein can be done separately from the labeling in such a way that almost total double oxygen incorporation can be achieved using the carboxyl oxygen exchange process only [9]. The variant of this procedure usually done in our laboratory is shown in Fig. 1 (manuscript in progress). As may be seen, the decoupling procedure consists in a more elaborated, labor-intensive and time-consuming protocol. In addition to the four main steps of the direct procedure, as described above, it is necessary to dry the sample, once the protein has been digested. Then the sample is recomposed in a solution of acetonitrile/ambic, that facilitates peptide solubilization and that lowered the pH of the solution to speed the subsequent carboxyl oxygen exchange process. Then the sample is dried again and finally recomposed in ^{18}O-water. Finally, the labeling takes place. The advantage of this procedure is that a higher degree of peptides are double labeled in an efficient fashion, which is extremely important for the accuracy

of the quantification, as it will be shown in the next sections. Nevertheless this procedure takes longer than the direct method, usually 12 h, if ultrasonication is used to speed the protein digestion step, otherwise it takes 24–48 h. In addition, it cannot be done on-line, and consequently it is of hard automation.

3.3. The use of immobilized enzymes

Enzymes, such as trypsin, can be immobilized in solid supports that can be used either for protein digestion/labeling in a single step (direct labeling) or in different ones (decoupling procedure). The main advantage of using immobilized enzymes is that once the solution is separated from the solid support, then the protein digestion is stopped and the carboxyl oxygen exchanges is slowed down to almost a negligible effect. This is very important for on-line approaches, where the sample will be mixed with solvents containing ^{16}O-water. This means that some ^{16}O/^{18}O interchange will happen, thus interfering with the quantification process. If the enzyme is not present in the solution the interchange can be consider small to have a significant effect on the quantification process. In addition, the presence of peptides coming from the autolysis of the enzyme is negligible and thus the interferences that they may cause in the subsequent measurements by mass spectrometry are avoided [10].

4. The problem of the ^{18}O-labeling efficiency

The ^{18}O-labeling of peptides following any of the approaches described in Section 3 results in a mixture of non-labeled, single labeled or double labeled peptides. The efficiency in the labeling depends not only on the protocol followed, but also in different variables affecting each protocol, such as pH, type of enzyme used, peptide characteristics, labeling time and conditions of labeling. In addition, the contribution to the peak intensities from the naturally occurring isotopes, others than ^{18}O, such as ^{13}C and ^{15}N, needs also to be considered. The aforementioned variables make ^{18}O-spectra difficult to be interpreted. The influence of sample treatment, as depicted in Fig. 1, on ^{18}O-labeling efficiency of proteins is shown in Fig. 2 through the direct procedure and peptide YLYEIAR ([M+H]$^+$ 927 m/z) from BSA, and Fig. 3, through the decoupling procedure and spectra of peptides LGEYGFQNALIVR ([M+H]$^+$ 1479 m/z) and CEVFR ([M+H]$^+$ 710 m/z) from BSA and α-lactalbumin respectively. As may be seen from Figs. 2 and 3, the decoupling procedure is a robust method that performs the labeling with a better efficiency than the direct procedure. The different conditions used in the labeling step do not affect the double labeling efficiency that was always higher than 90%. On the other hand, the efficiency for protein α-lactalbumin is severely affected when not enough time is given to the labeling reaction, as may be seen in Fig. 3h. This variability in the labeling efficiency makes extremely difficult the interpretation of data from complex protein mixtures, such as proteomes, making hard to distinguish highly up-regulated from highly down-regulated or C-terminal peptides, in studies regarding differential proteomics. This problem is even worst when the direct method is the choice to perform the labeling. As may be seen in Fig. 2, the efficiency in the double labeling is, c.a. 70%. To overcome the labeling efficiency problem, different algorithms have been proposed, as we will see in Section 5 [11]. Other approaches to solve this problem focus on the sample treatment itself, trying to make the labeling as complete as possible, thus minimizing the effects on the efficiency to a residual level.

5. Algorithms for calculating isotopic labeling correction

The basic formula used for ^{18}O-isotopic labeling peak deconvolution is as follows:

$$^{16}\mathrm{O}/^{18}\mathrm{Oratio} = I_0/[I_4 - (M_4 I_0/M_0) - (M_2/M_0(I_2 - (M_2 I_0/M_0))) + (I_2 - (M_2 I_0/M_0))]$$

This formula is explained by looking at Fig. 2 where I_0, I_2 and I_4 represent the experimental (observed) intensities of the monoisotopic peak, named as I_0, and the peaks at 2 and 4 Da, I_2 and I_4, respectively. The theoretical intensities of these peaks corresponding to M_0, M_2 and M_4 are calculated from dedicated software following

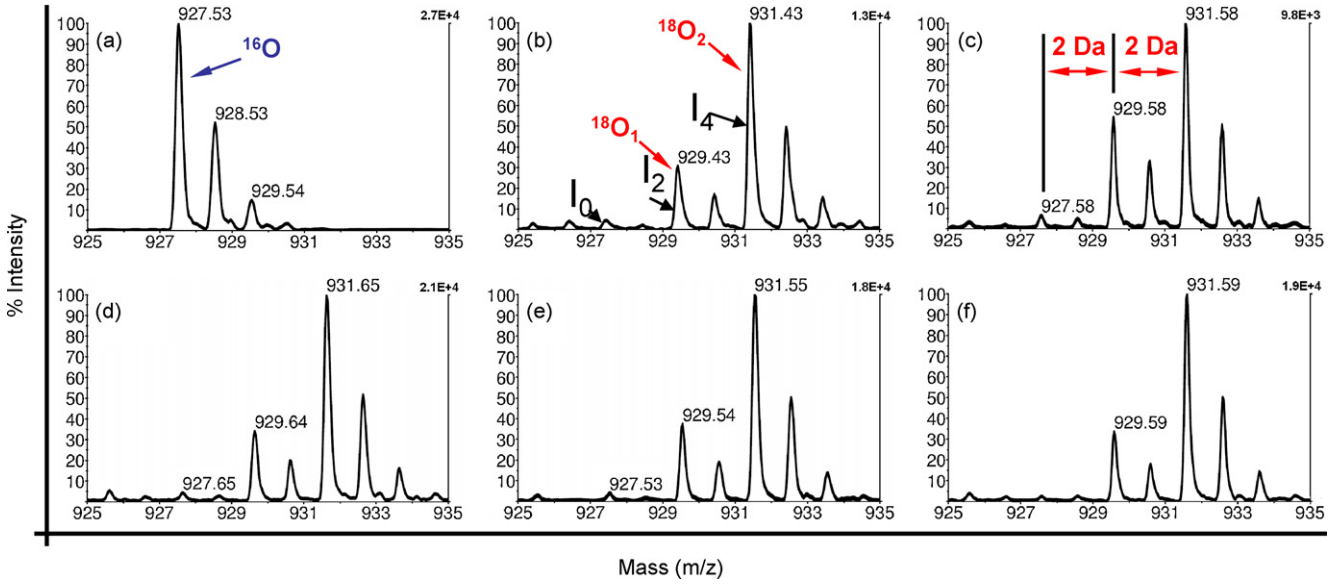


Fig. 2. Reflector positive ion mode MALDI-TOF mass spectra of the peptide fragment (YLYEIAR)H$^+$ obtained in the tryptic digest of BSA. (a) Overnight digestion in 100% $H_2{}^{16}O$ buffer solution at 37 °C (c.a. 12 h); (b) overnight digestion in 95% $H_2{}^{18}O$ buffer solution at 37 °C (c.a. 12 h); (c) ultrasonic bath digestion in 95% $H_2{}^{18}O$ buffer solution at 60 °C (35 kHz frequency; 70% amplitude; 30 min); (d) ultrasonic bath digestion in 95% $H_2{}^{18}O$ buffer solution at 60 °C (130 kHz frequency; 70% amplitude; 15 min); (e) ultrasonic bath digestion in 95% $H_2{}^{18}O$ buffer solution at 60 °C (130 kHz frequency; 70% amplitude; 30 min); (f) water bath digestion in 95% $H_2{}^{18}O$ buffer solution at 60 °C (30 min). Reproduced from Ref. [7].

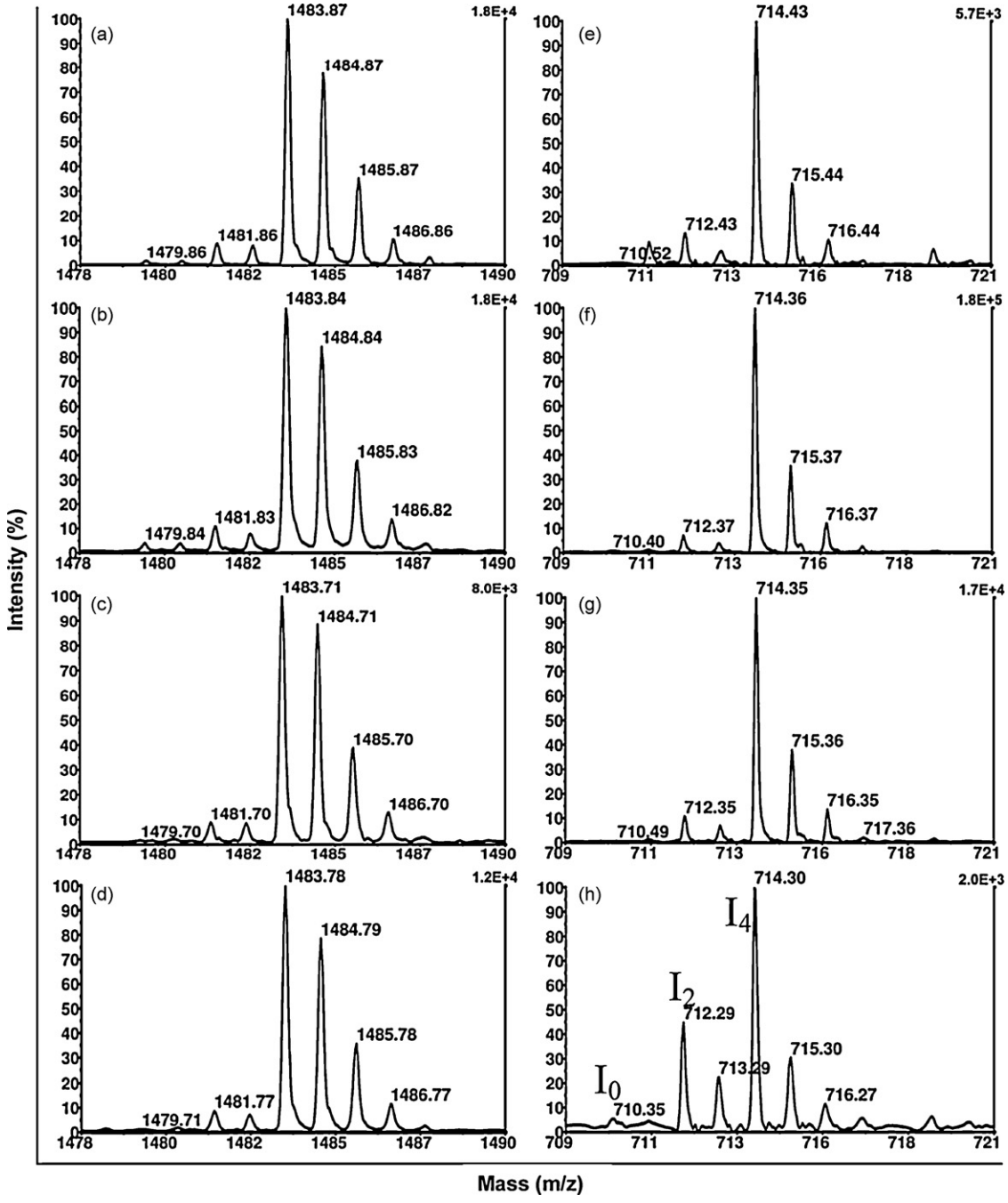


Fig. 3. MALDI-TOF spectra of the peptides LGEYGFQNALIVR ([M+H]$^+$ 1479.80 m/z) and CEVFR ([M+H]$^+$ 710.33 m/z) from BSA and α-lactalbumin, respectively, obtained after ^{18}O-labeling by the decoupling procedure. (a) BSA overnight labeling (6 + 6 h) at 37 °C; (b) sonoreactor labeling of BSA for 15 + 15 min (50% amplitude); (c) sonoreactor labeling of BSA for 5 + 5 min (50% amplitude); (d) sonoreactor labeling of BSA for 2.5 + 2.5 min (50% amplitude); (e) α-lactalbumin overnight labeling (6 + 6 h) at 37 °C; (f) sonoreactor labeling of α-lactalbumin for 15 + 15 min (50% amplitude); (g) sonoreactor labeling of α-lactalbumin for 5 + 5 min (50% amplitude); (h) sonoreactor labeling of α-lactalbumin for 2.5 + 2.5 min (50% amplitude).

peptide identification [12,13]. The isotopic peaks annotated as I_0, I_2, and I_4 are the peaks used for quantification. The non-annotated peaks are primarily composed of $^{13}C_1$ contributions related to the annotated peaks [14].

As may be understood, in most of the modern proteomics approaches the number of peptides to be treated is enormous. Consequently, algorithms have been proposed by different authors, based on the formula described above, accounting for skewed isotopic distributions due to partial single labeling and double labeling, thus variants of the above-mentioned formula are reported from time to time [9,14–16].

QUIL software has been proposed by Wang et al. as an automated quantification tool for high-throughput proteomics using stable isotope labeling and LC–MS^n [17]. QUIL accounts for the dynamic nature of spectral background and subtracts this background accordingly during ion chromatogram reconstruction. For elution profile identification, QUIL minimizes the inclusion of coeluted neighbor peaks, yet tolerated imperfect peak shapes.

Wan et al. have proposed a method for the quantification of proteins with a correction being made for incomplete isotope incorporation due to either ^{16}O-to-$^{18}O_1$ or $^{18}O_1$-to-$^{18}O_2$ exchange effects [18].

As a final example, Eckel-Passow et al. described two multivariate linear regression models for $^{16}O/^{18}O$ stable-isotope labeled data that joint model pairs of resolved isotopic clusters from the same peptide and quantify the abundance present in each of the two biological samples whilst concurrently accounting for peptide–specific incorporation rates of the heavy isotope [19].

6. The enzymes used for ^{18}O-labeling

The enzyme trypsin, a serine protease that predominantly cleaves peptide chains at the carboxyl side of amino acids lysine and arginine, is the enzyme most commonly used for ^{18}O-isotopic labeling. Other two enzymes, the endoproteinase Lys-C that specifically cleaves peptide bonds C-terminally at lysine; and the endoproteinase Glu-C, that cleaves peptide bonds C-terminally at glutamic and aspartic acids are also frequently used.

Trypsin, Lys-C and Glu-C have been reported to incorporate two ^{18}O atoms into the carboxyl termini of all peptides, except the original carboxyl termini [20–24]. However, lysine terminated peptides do not incorporate two oxygen efficiently [25,26]. Chemotrypsin has been claimed as being only capable of label peptides with one oxygen, however, it seems that this process is dependant of the experimental conditions. Thus, it has been demonstrated by Yao et al. that chemotrypsin can double label peptides in a decoupling procedure [9].

Asp-N was used to perform the in-gel digestion of proteins, in 50% of $H_2{}^{18}O$ buffer solution, to characterize and identify five C-terminal peptides out of seven C-terminally processed enolase 2 forms [44].

7. The influence of the pH

The influence of the pH on the labeling process depends on the way in which this is done. In the direct process, the protein is labeled at the same time that is cleaved. To guarantee the efficiency of the process, the pH must be the optimum at which the enzyme cleaves the protein, for instance the optimum pH for the enzyme trypsin is about 8. If the cleavage is done in pure ^{18}O-water, then all peptides will have one ^{18}O at the C-termini at least. Interestingly, the double ^{18}O incorporation will depend on various factors, such as the type of peptide and the pH of the solution. For instance, lysine terminated peptides do not incorporate two oxygen efficiently. In addition, Yao et al. have demonstrated that by lowering the pH of the solution, the double incorporation can be done faster and with higher efficiency [9]. Precisely, the possibility to separate the protein cleavage from the isotopic incorporation doing both separately at different pH is the basis of the decoupling procedure, as proposed by the former mentioned authors. Thus, the first step is the protein cleavage, which is done at the optimum pH of the enzyme used. In addition, this step is generally done in ^{16}O-water, lowering costs, since ^{18}O-water is an expensive reagent. In the second step, after drying, the sample is recomposed in ^{18}O-water at an acidic pH and further enzyme is used to speed the double ^{18}O incorporation. The recommended pH for this step is in between 4.5 and 5.5. In this approach some peptides will be hardly recomposed due to their hydrophobic characteristics, and therefore some peptides will remain unlabeled or will be labeled inefficiently. For this reason, before reconstitution of peptide mixtures in $H_2{}^{18}O$ buffers for the exchange reaction, dissolution of the entire mixture with a strong solvent such as DMSO is critical to get successful homogeneous labeling [9]. Once the labeling protocol has been done using any of the procedures already described, it is mandatory to stop the enzymatic activity. It must be considered that the labeled samples (in ^{18}O) are mixed with their unlabeled counterparts (in ^{16}O) prior to analysis by mass spectrometry to measure their relative ratios. This means that $^{16}O/^{18}O$ chemical back exchange will occur in some degree during the mixing process. The presence of any remaining trypsin at this stage will accelerate the $^{16}O/^{18}O$ carboxyl oxygen exchange. To avoid this problem some authors have suggested lowering the pH of the solutions below 2, since the activity of trypsin and other proteases at that pH is negligible [27]. By this way the problem of oxygen interchange is reduced to a minimum. However, other authors have claimed indeed that lowering pH, even below 2, is not enough to overcome this problem. Thus, Staes et al. [28] have found necessary to destroy the trypsin structure by covalent modification of its thiol group using trypsin inhibitors, to avoid any re-naturation at every step of the subsequent peptide isolation procedure. To complicate things more, Sevinsky et al. reported the failure of covalent trypsin inhibitors in their approach to quantitative proteomics making use of ^{18}O-labeling [29]. In fact the aforementioned authors have proposed the use of immobilized trypsin in the digestion step as the best method to avoid the subsequent chemical exchange, due to residual trypsin.

The carboxyl oxygen exchange is a problem to deal with when a complex mixture of peptides is separated through chromatography. In this case the contact of the labeled peptides with reagents prepared in ^{16}O-water last for long time, as long as the chromatographic separation needs to efficiently separate the mixture of peptides. This contact hinders the double labeling ratios and thus makes the application of this protocol to investigations related to protein expression levels useless. An additional problem is addressed by the method by which the chromatographic separation is done. Some authors have proposed the use of multidimensional chromatography using strong cation exchange (SCX) either as an on-line technology, called MudPIT [30], or as an off-line technique, named 2D-LC [31]. Regarding the aforementioned approaches it has been suggested that the off-line approach is preferable, since the linear gradient that can be used in off-line approaches has higher resolution than the regular step-gradient commonly used in on-line procedures. In addition, off-line methods allow using higher ACN concentrations, and so more fractions can be collected from a single experiment using off-line strategies. Researchers are aware that off-line 2 dimensional chromatographic approaches imply that the samples are dried after the first dimension or that hydrophilic peptides may be lost in the second dimension. Lassman et al. have studied the possibility of ^{18}O-exchange during the course of typical reversed phase chromatography experiments, as well as strong cation exchange separations, and they have found that with appropriate sample handling, the use of ^{18}O-labeling for differential expression analysis can be extended to multi-dimensional chromatography experiments [32]. Thus, they suggest that peptide separation with minimum back exchange is obtained if SCX buffer (5 mM phosphate/25% ACN pH 2.8, column 1.0 mm × 100 mm of polysulfoethyl aspartamide, poly LC) acidified with 5% formic acid pH < 2 is used.

From a critical point of view, the most useful way to perform the labeling is using immobilized trypsin, since once the solution has been separated from the trypsin there is no risk of back exchange or the risk is reduced to a negligible effect.

8. Accelerating and simplifying the sample treatment

As may be seen in Fig. 1, the ^{18}O-labeling handling presents two main drawbacks. On the one hand is labor-intensive and on the other one is time consuming. For those reasons, in the last years, many researchers have focused on how to simplify and to speed the different steps of the ^{18}O-labeling protocols. In the next sections we are going to discuss the advantages and drawbacks of the modern approaches to accelerate and to simplify the isotopic labeling.

8.1. Heating

It is well known that enzymes can perform better at an optimum temperature. Overnight at 37 °C is the handling protocol commonly used to perform protein cleavage. However, Havlis et al. proposed a methodology that enables the digestion of proteins in 30–60 min by warming the sample at 58 °C without compromising the peptide yield and the sensitivity when compared to conventional protocols relying upon overnight enzymatic cleavage [10,33]. The warming was done in a water bath. Variants of this protocol have been proposed from time to time by just changing the heating systems. Thus, Turapov et al. [34] have proposed the use of a PCR thermocycler and a temperature gradient to digest native proteins in less that 5 min. They claimed to be able to perform protein identification using micro-scale amounts of sample (3 μL) without the need of denaturating agents. After treatment, samples were directly spotted on the MALDI target plate, without additional purification. Although these could be a promising approach, the authors did not test the system with a complex sample neither used the method for the digestion of proteins separated through gel electrophoresis.

The above-described methods to speed the protein digestion through warming the solutions are a way to speed the first part of the decoupling procedure as depicted in Fig. 1. However there is a lack on works dealing with the specific purpose of ^{18}O-labeling and warming. Finally, Carreira et al. have stressed the inefficiency to speed the labeling through warming at 60 °C during 30 min in the direct approach [7].

8.2. Micro-spin columns

Mirza et al. [35] have showed the possibility to accelerate the isotopic labeling using immobilized trypsin on micro-spin columns to speed up the enzyme-mediated oxygen substitution. They claimed to be able to complete the labeling for a four protein mixture and whole cell lysate from rat vascular endothelial cells in 15 min. The Sigma company also offers a similar method through its ^{18}O proteome profiler kit® including micro-spin columns (sigma product code P3623. Disclaimer: specific company, product and equipment names are given to provide useful information; their mention does not imply recommendation or endorsement by the authors). However, the procedure described by sigma lasts for 24–48 h.

8.3. Ultrasonic energy

The utilization of ultrasonic energy provided by an ultrasonic probe was first described in 2005 as a method to accelerate the enzymatic cleavage of proteins from overnight to a few minutes [36]. The methodology has been named ultrasonic assisted enzymatic digestion (USAED). The acceleration method using ultrasound can be applied either to proteins dissolved in liquids, to proteins separated by gel electrophoresis [37] and whole proteomes [38]. The physical and chemical properties of enzymatic and chemical reactions are greatly modified with the presence of an ultrasonic field. The mechanisms by which the enzymatic reactions are accelerated by means of ultrasonication are due to the acceleration of the diffusion coefficients because ultrasound (1) increases the temperature of the medium in which it is applied, which increases the velocities of reaction and (2) mix the material present in the solution, making the enzymes becoming in deep contact with the present substances, causing a large increase in the total contact area. It must be remarked that ultrasounds reduce the size of the solids present in solution, incrementing the available contact surface [39,40].

The USAED method can be done using direct in-solution sonication, with an ultrasonic probe, meaning the probe is in contact with the solution, or by using the sonoreactor technology, which allows indirect ultrasonic irradiation of the sample, meaning the solution is treated in sealed cups. Recently, the method has also been applied to accelerate the isotopic labeling with ^{18}O-water in standards of proteins and purified proteins from complex samples using the direct labeling [7] or in standards of proteins and whole proteomes using the decoupling procedure [41]. Regarding the decoupling procedure, it must be stressed, in contrast with the work done by López-Ferrer et al. [41], that on-going work developed in our laboratory suggests that there is no improvement in using ultrasonication to enhance the performance of the labeling step, and that the labeling efficiency obtained is the same with or without sonication as shown in Table 2.

8.4. High pressure

An efficient on-line digestion system that reduces the number of sample manipulation steps for high-throughput proteomics based on high pressure has been reported. By incorporating a pressurized sample loop into a liquid chromatography separation system, both sample and enzyme (e.g. trypsin) can be simultaneously introduced to produce a complete, yet rapid digestion. Both standard proteins and a complex *Shewanella oneidensis* global protein extract were digested and analyzed using the automated on-line pressurized digestion system coupled to an ion mobility time-of-flight mass spectrometer, to an ion trap mass spectrometer, or both. The system denatures, digests, and separates product peptides in a manner of minutes, making it amenable to on-line high-throughput applications. The system was easy to implement and no cross-contamination was observed among samples [42].

9. Applications of the ^{18}O-labeling

9.1. Inverse labeling

The ^{18}O-labeling method has many problems, i.e., tedious data analysis, ambiguity in detection of extreme changes in expression,

Table 2
Comparison between the different methods tested for the ^{18}O-labeling of BSA and α-lactalbumin with the decoupling procedure. The results refer to the average percentage of the double ^{18}O incorporation from the total of peptides labeled in the C-terminal group of selected peptides from BSA and α-lactalbumin (n = 3).

Ultrasound (sonoreactor 50% amplitude)					No ultrasound			Peptides
2.5 + 2.5 min	5 min	5 + 5 min	15 + 15 min	30 min	6 + 6 h (37 °C)	2.5 + 2.5 min (RT)	5 + 5 min (RT)	
BSA								
89.85 ± 3.92	96.13 ± 3,03	95.03 ± 3.48	95.45 ± 2.80	94.10 ± 3.94	94.72 ± 2.44	90.86 ± 1.43	93.83 ± 1.58	YLYEIAR
88.17 ± 5.40	94.05 ± 1.74	93.20 ± 3.92	92.22 ± 0.76	93.03 ± 0,61	88.62 ± 11.67	88.95 ± 4.86	92.23 ± 0.32	RHPEYAVSVLLR
91.26 ± 0.83	91.87 ± 0.06	92.96 ± 0.60	91.61 ± 0.91	92.35 ± 0.34	90.76 ± 0.11	93.81 ± 1.80	92.43 ± 1.90	LGEYGFQNALIVR
92.72 ± 1.89	79.16 ± 22.52	89.49 ± 1.82	94.25 ± 8.13	79.26 ± 15.99	88.65 ± 16.05	90.29 ± 1.40	91.30 ± 1.45	KVPQVSTPTLVEVSR
α-Lactalbumin								
69.89 ± 0.45	83.15 ± 1.60	90.50 ± 2.96	91.51 ± 0.42	93.27 ± 3.47	91.98 ± 1.78	71.92 ± 2.26	88.26 ± 0.10	CEVFR
22.11 ± 1.26	43.25 ± 0.19	61.57 ± 0.94	86.73 ± 0.64	70.44 ± 0.27	90.37 ± 0.54	22.57 ± 1.90	61.29 ± 1.58	VGINYWLAHK
9.48 ± 0.29	20.56 ± 3.34	41.80 ± 1.52	76.03 ± .167	50.08 ± 1.24	58.19 ± 6.37	9.57 ± 4.18	40.58 ± 0.68	ILDKVGINYWLAHK

and inability to detect protein modifications due to perturbation. In addition, the method has additional complexities due to ^{13}C effect and its interference on the ^{18}O signals. The ^{13}C effect can make interpretation of a down-regulation very difficult since weak ^{18}O signals can be buried under the normal ^{13}C pattern, and the signals can be easily misinterpreted as non-labeled C-terminal peptides. Since the goal of a protein differential analysis is to extract and to identify the small number of proteins that deviate in expression level upon a perturbation, any method that enables subtractive analysis of protein signals with unaltered levels would be of great value. This is the base of the method called ⟨⟨Inverse ^{18}O-labeling⟩⟩ as first reported by Wang et al. [22]. Inverse ^{18}O-labeling offers a number of merits when applied to a labeling-based proteomic strategy. It offers the rapid identification of the signals from the differentially expressed proteins through quick pattern recognition. It eliminates the ambiguity in detection of proteins with extreme changes in expression caused by the limitation of dynamic range of detection. It also resolves the detection problems associated with protein modifications due to perturbation, where unpaired peaks are detected. Fig. 4 gives a detailed explanation of this approach. Since it was first reported, the inverse ^{18}O-labeling has been applied from time to time in studies regarding proteins overexpressed or underexpressed. Thus, Wang et al. [43] used the direct and inverse labeling in an integrated fashion with solution isoelectric focusing and capillary LC–tandem mass spectrometry to study abundance changes in mitochondrial proteins associated with drug resistance in MCF-7 human cancer cells whilst Ang et al., have used the reverse approach to determine the effect of biofilm culture on the cell envelope proteome of *Porphyromonas gingibalis* W50 [44].

9.2. Applications to gel-separated proteins

The absolute quantification of proteins separated in polyacrylamide gels lacks in efficiency and accuracy, as it was demonstrated by Havlis and Shevchenko [45]. However this method is a powerful tool when applied for relative quantification. The best sample treatment for relative quantification of proteins separated in polyacrylamide gels consists firstly in digest the gel spots containing the control sample, a certain amount of a known protein, and the target sample in ^{16}O-water, afterward the extracted pool of peptides is dried in a speed vacuum. Finally, the control sample is recomposed in ^{18}O-water whilst the target sample is recomposed in ^{16}O-water. The same amount of both samples is then mixed and submitted to mass spectrometry-based techniques. The signal intensities of the same peptides are then compared and the relative $^{16}O/^{18}O$ ratios are used to calculate the concentration of the unknown protein. By carrying out ^{18}O-labeling post proteolysis, the amount of ^{18}O-water required is substantially reduced, since the labeling is performed on the extracted and dried peptides not on the excised gel pieces [22]. The ^{18}O-labeling of N-glycosylation sites during in-gel deglucosylation has been claimed as a way to extend the capabilities of MALDI peptide mass mapping and database searching for the identification of gel-separated proteins [46]. There are also some studies that report in-gel ^{18}O-labeling as a tool for protein quantification and characterization. For instance, Kosaka et al. [47] reported a method for the C-terminal characterization and identification of proteins separated by two-dimensional polyacrylamide gel electrophoresis (2D-PAGE), based on in-gel digestion/labeling of proteins. After 2D-PAGE of a cell lysate of rat liver, 10 different protein spots were

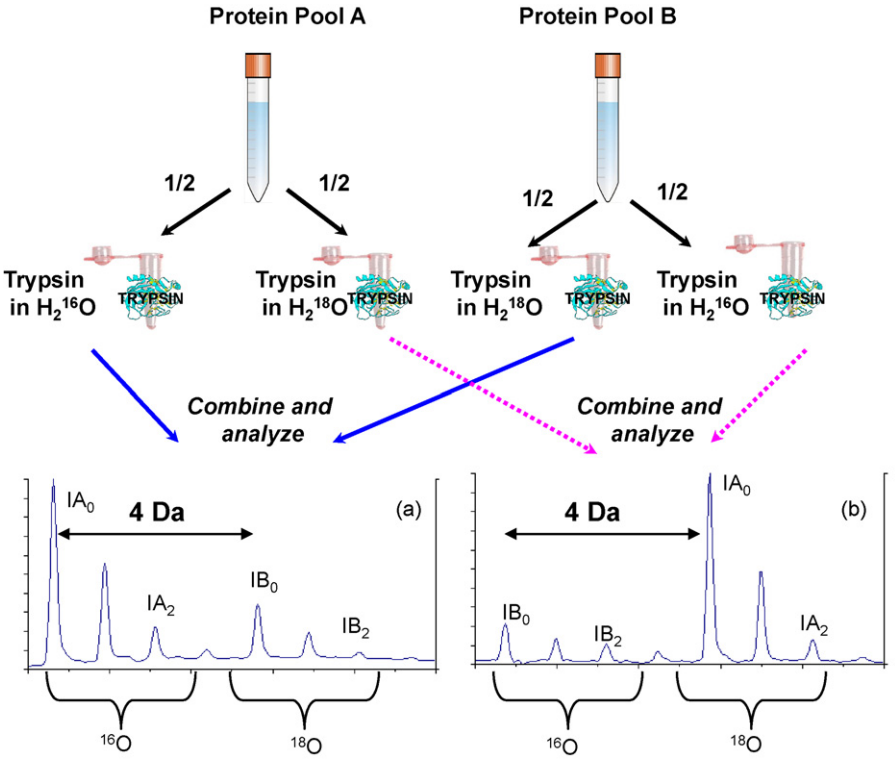


Fig. 4. Inverse labeling. The labeling is swapped between two samples, for instance a target sample (sample A) and a control sample (sample B). In the example provided, sample A correspond to crucian carp (*Ciprinus carpio*) exposed to endocrine disruptors whilst sample B corresponds to non-exposed fish. The example is given through one peptide from the protein vitalogenin, which is overexpressed by crucian carps when they are exposed to endocrine disruptors. As may be seen the overexpression of vitalogenin in the exposed fish is unambiguously verified. Thus in spectrum a the peptide coming from the exposed fish present a intensity (IA_0) three times higher that its counterpart from the non-exposed fish (IB_0), shifted 4 Da thanks to the ^{18}O-labeling. This up-regulation of the protein is verified in the second experiment, spectrum b, where now the vitalogenin's peptide from the exposed fish is shifted 4 Da as now this is the sample isotopically labeled. This time the intensity was also clearly higher in agreement with the information given the inverse experiment. Thus, by comparing the results of the two experiments it is possible quickly to identify those differentially express proteins present in complex mixtures.

in-gel digested during overnight with trypsin in a buffer solution of 50% ^{18}O enriched water, and analyzed by nano-electrospary Fourier transform ion cyclotron resonance mass spectroscopy (nano-ES FT-ICR MS). Due to the high resolution of FT-ICR MS and since the C-terminal peptides were the only unlabeled peptides in the protein digests, the authors were able to identify and characterize the C-termini of 8 proteins, from the initial 10 chosen, with a high level of confidence. On the other side, and following the same strategy, Larsen et al. [48] were unable to characterize and identify by MALDI the C-terminal peptides of different enolase-2-forms form stressed cells of *Saccharomyces cerevisiae*, when using trypsin to digest the separated proteins from 2D-PAGE. However, when the endoproteinase Asp-N was used to perform the in-gel digestion of proteins, in 50% of $H_2{}^{18}O$ buffer solution, they were able to fully characterize and identify five C-terminal peptides out of seven C-terminally processed enolase 2 forms. These results show how important it is the choice of the correct enzyme to perform protein digestion and labeling. In this case the authors were only concerned in distinguishing the unlabeled C-terminal peptide from the labeled internal peptides, so they use an enzyme, endoproteinase Asp-N that only incorporates one ^{18}O atom in the carboxylic group of the peptide whilst trypsin incorporates one or two ^{18}O. This way, they were able to control the oxygen incorporation in the peptides, avoiding the presence of a mixture of single and double labeled peptides which would be responsible for the spreading of the peptide signal over more peaks, thus reducing the intensity in the mass spectra and compromising a correct identification.

The previous examples demonstrate the potential of ^{18}O-isotopic labeling in the detection of modified peptides by mass spectrometry thus enhancing the characterization of protein modifications, many of them implicated in a large number of disease states. On the other hand, there are also a few examples where in-gel ^{18}O-labeling was successfully used for protein quantification and to identify potential biomarkers of disease states. Using a combination between in-gel ^{18}O-labeling and nano-LC/MS/MS, Körbel et al. [49] were able to identify and quantify approximately 180 low-expressed erythropoietin (EPO) receptor-dependent proteins, which are related with signaling pathways and EPO-dependent cellular responses like cell differentiation and proliferation. The developed method relies on immunoaffinity and 1D-PAGE for protein separation; in-gel protein digestion in the presence of in $H_2{}^{16}O$ or $H_2{}^{18}O$ (95% ^{18}O abundance) with non-methylated (non-stabilized) trypsin to avoid post-digestion $^{18}O/^{16}O$ back-exchange; and nano-LC–MS/MS techniques for the detection of low-fentomole proteins. More recently, Chaerkady et al. [50] used lectin affinity enrichment and 1D-PAGE to purify and separate glycosylated proteins from liver tissues of healthy patients and patients with hepatocellular carcinoma. After in-gel digestion with trypsin in the presence of $H_2{}^{16}O$ or $H_2{}^{18}O$ and LC–MS/MS analysis they were able to perform relative quantification and find differential expressed proteins from non-tumor/tumor samples. Finally, the application of in-gel ^{18}O-labeling has been used by Ang et al. [44] in the study of the *Porphyromonas gingivalis* proteome, an oral pathogen related with chronic periodontitis. Based on an inverse labeling strategy, where the control sample was first digested in $H_2{}^{16}O$ and the experimental sample digested in $H_2{}^{18}O$, whilst in the inverse experiment the control sample was digested in $H_2{}^{18}O$ and the experimental in $H_2{}^{16}O$, they found 24 proteins up-regulated and 18 proteins down-regulated in experimental sample. Once more, these examples show the reliability and applicability of the in-gel ^{18}O-labeling technique when applied to comparative proteomic studies.

9.3. Applications to proteins in solution

This is by far the most reported use given to ^{18}O-labeling. A combination of tandem mass spectrometry and ^{18}O-labeled internal standards provide absolute or relative quantification of simple or complex mixtures of proteins in solution. Internal standards could be directly obtained by digesting in ^{18}O-water a stock solution of known concentration of the protein of interest. Since many peptides are quantified in parallel, the resulting estimate of the protein concentration is robust and would also be applicable to complex protein mixtures, when combined with MS/MS spectrometry, if powered by appropriate software [45].

The application of ^{18}O-labeling in assisting sequencing of peptides by helping to distinguish a-type ions from b-type ions in tandem mass spectrometry has been reported by different authors [51,52]. The isomerization of aspartic acid (Asp) to isoaspartic acid (IsoAsp) is a spontaneous reaction that can alter protein structure and function, and for this reason the identification of this phenomenon in proteins is a biochemical challenge. Xiao et al. [53] have proposed a method for the identification and quantification of the above-mentioned reaction based on the utilization of ^{18}O-labeling and tandem mass spectrometry. Wa et al. have proposed a method for the study of the binding sites of proteins when they are immobilized in solid supports. The method is simple: the free protein is cleaved in ^{18}O-water whilst, after its immobilization, the protein is digested in ^{16}O-water. The two digests are mixed and then analyzed by mass spectrometry. Peptides having significantly higher $^{18}O/^{16}O$ ratios than other peptides in the same digest are involved in the immobilization [54]. Another interesting application consists in using the ^{18}O-labeling for the quantification of ribonucleic acids using ^{18}O. RNA labeled and non-labeled samples are mixed and then the intensities of the ^{16}O and $^{18}O_1$ monoisotopic peaks are then correlated through a proposed formula. It must be taken into account that for this biomolecules, the labeling is only single [55]. Havlis et al. have systematically demonstrated that absolute quantification of proteins can be done using ^{18}O-labeling in non-gel-based approaches [45]. In the same work they also compared the performance of the labeling using MALDI or nano-LC-ESI, concluding that both methods produced consistent results; however, the nano-ESI method was more accurate and allowed relatively straightforward quantification in simple protein mixtures. Finally they stressed that for quantifying protein mixtures of higher complexity, LC–MS/MS capabilities are indispensable.

10. Future trends

10.1. Micro-scaling the labeling

One of the main drawbacks related to proteomic approaches deals with the low amount of sample available for handling. In addition ^{18}O-water is an expensive reagent. For this reasons micro-scaling the labeling is an alternative to conventional sample treatments that has the advantages of automation and low sample/reagent consumptions.

Lee et al. have recently described an automated digestion system based on a microfluidic chip for MALDI-TOF-MS [56]. The chip has a bioreactor, 100 μm wide, 100 μm deep and 4 cm effective channel, containing immobilized trypsin. The chip was operated by pressure-driven flow and mounted on a robotic fraction collector system. Advantages of the system are sample consumption at the micro-scale level (flow rate 1 μL/min) and a reaction time of 24 s. The system entails automation for digestion and accomplishment to MALDI droplet deposition system. This approach could also be used for labeling the peptides by just adding some more channels for the introduction of the ^{18}O-water, thus reducing the consumption or reagents and facilitating automation.

10.2. The use of infrared radiation and microwave energy

Bao et al. and Wang et al. have proposed the use of infrared radiation for the digestion of proteins in solution or proteins separated by gel electrophoresis [57,58] respectively. The authors claimed a total time for the digestion of 5 min. The maximum temperature allowed to reach using the infrared radiation was 37 °C. The authors explained that the enhanced activity of the enzyme could be explained considering that vibrations of N–H, C=O and C–N bonds in proteins would led to the vibrations of peptide bonds. These vibrations could increase the frequency of the interaction between the enzyme and the peptide bonds in proteins molecules, resulting in highly efficient proteolysis. In addition, the vibrations could also expose more cleavage sites to the enzyme. Although the aforementioned explanation can be applied to proteins in solution, the sample treatment proposed for proteins separated by gel electrophoresis, as described by Bao et al., included also a step with ultrasonication [58]. Therefore, in the last case it remains unclear if the enhancement in the enzymatic activity was due to the infrared radiation, to the ultrasonication or to the combination of both. Finally, the most recent contribution reported regarding IR deals with its application to on-plate proteolysis for MALDI-TOF-MS peptide mapping. Protein solutions containing trypsin were allowed to digest directly on the spots of matrix-assisted laser desorption/ionization (MALDI) plates under IR radiation. The suitability of IR-assisted on-plate proteolysis to complex proteins was demonstrated by digesting human serum and casein extracted from commercially available milk sample [59]. As it can be seen, the application of IR to speed the direct labeling or to speed the digestion step in a decoupling procedure is a promising methodology that deserves to be investigated.

In the same way as IR, microwave has been used to speed protein digestion of proteins. Fenselau et al. [60,61] pioneered the utilization of microwave energy in proteomics sample treatments and the works of this author dealing with this subject are strongly recommended. It is expected in the near future the linkage between microwave energy and ^{18}O-labeling due to the potential of simplicity, speed and throughput that jointing both it will be obtained.

11. Conclusions

^{18}O-labeling of peptides is an approach that nowadays offers a simply way to perform many different proteomic tasks, including protein quantification in a relative or absolute manner, differential peptide mass mapping or the searching for biomarkers.

The modern technological advances available currently, such as ultrasonic energy, microwave energy, ultracentrifugation, and infrared energy offer many real or potential methods, to speed the labeling, to increase the throughput and to simplify the handling, for this methodology.

From data reported to date and from our own experience the most robust way to perform ^{18}O-labeling seems to be the decoupling procedure jointed to ultrasonication. With this accomplishment peptides are double labeled in more than a 90%.

Finally, the application of the inverse labeling in conjunction with immobilized trypsin to digest the proteins and to label the ones seems to be the most promising approach for unambiguous studies regarding proteins overexpressed or underexpressed,, biomarker discovery and protein quantification.

Acknowledgements

H.M. Santos and R. Carreira acknowledge the doctoral grants SRFH/BD/38509/2007 and SFRH/BD/28563/2006, respectively, from FCT (Science and Technological Foundation) from Portugal. The research findings here reported regarding ultrasonication and enzymes are protected under patent pendings PCT/IB2006/052314 and PT 103 303. FCT is acknowledged for financial support under the project POCI/QUI/55519/2004 FCT-FEDER and PTDC/QUI-QUI/099907/2008. J.L. Capelo and C. Lodeiro acknowledge the Isidro Parga Pondal Program from Xunta de Galicia, Spain.

References

[1] S.E. Ong, M. Mann, Nat. Chem. Biol. 1 (2005) 252.
[2] E. Langenfeld, H.E. Meyer, K. Marcus, Anal. Bioanal. Chem. 392 (2008) 1123.
[3] A. Nita-Lazar, H. Saito-Benz, F.M. White, Proteomics 8 (2008) 4433.
[4] A. Doucet, G.S. Butler, D. Rodriguez, A. Prudova, C.M. Overall, Curr. Proteomics 5 (2008) 146.
[5] I. van den Broek, R.W. Sparidans, J.H.M. Schellens, J.H. Beijnen, J. Chromatogr. B 872 (2008) 1.
[6] M. Del Mar Contreras, I. Lopez-Exposito, B. Hernandez-Ledesma, M. Ramos, I. Recio, J. AOAC Int. 91 (2008) 981.
[7] R.J. Carreira, R. Rial-Otero I, D. Lopez-Ferrer, C. Lodeiro, J.L. Capelo, Talanta 76 (2008) 400.
[8] F.M. Cordeiro, R.J. Carreira, R. Rial-Otero, M.G. Rivas, I. Moura, J.L. Capelo, Rapid Commun. Mass Spectrom. 21 (2007) 3269.
[9] X. Yao, C. Afonso, C. Fenselau, J. Proteome Res. 2 (2003) 147.
[10] J.R. Sevinsky, K.J. Brown, B.J. Cargile, J.L. Bundy, J.L. Stephenson, Anal. Chem. 79 (2007) 2158.
[11] C.J. Mason, T.M. Therneau, J.E. Eckel-Passow, K.L. Johnson, A.L. Oberg, J.E. Olson, K.S. Nair, D.C. Muddiman, H.R. Bergen, Mol. Cell. Proteomics 6 (2007) 305.
[12] Applied Biosystems Data Explorer Software User's Guide, section 3, pp. 45–47.
[13] GPMAW Version 6.0, General protein/mass analysis for windows. Lighthouse Data 2003, Odense, Denmark.
[14] K.L. Johnson, D.C. Muddiman, J. Am. Soc. Mass Spectrom. 15 (2004) 437.
[15] A. Ramos-Fernandez, D. Lopez-Ferrer, J. Vazquez, Mol. Cell. Proteomics 6 (2007) 1274.
[16] I. Jorge, P. Navarro, P. Martínez-Acedo, E. Núñez, H. Serrano, A. Alfranca, J.M. Redondo, J. Vazquez, Mol. Cell. Proteomics (2009), doi:10.1074/mcp.M800260-MCP200.
[17] G. Wang, W.W. Wu, T. Pisitkun, J.D. Hoffert, M.A. Knepper, R.F. Shen, Anal. Chem. 78 (2006) 5752.
[18] C. Wan, R.L. Cerny, D.S. Hage, Anal. Chem. 78 (2006) 7967.
[19] J.E. Ekel.Passow, A.L. Oberg, T.M. Therneau, C.J. Mason, D.W. Mahoney, K.L. Johnson, J.E. Olson, H.R. Bergen, Bioinformatics 22 (2006) 2739–2745.
[20] X. Yao, A. Freas, J. Ramirez, P.A. Demirev, C. Fenselau, Anal. Chem. 73 (2001) 2836.
[21] K. Reynolds, X. Yao, C. Fenselau, J. Proteome Res. 1 (2002) 27.
[22] Y.K. Wang, Z. Ma, D.F. Quinn, E.W. Fu, Anal. Chem. 73 (2001) 3742.
[23] K. Rose, L.A. Savoy, M.G. Simona, R.E. Offord, P. Wingfield, Biochem. J. 250 (1988) 253.
[24] M. Schnolzer, P. Jedrzejewski, W.D. Lehmann, Electrophoresis 17 (1996) 945.
[25] A. Shevchenko, A. Shevchenko, Anal. Biochem. 296 (2001) 279.
[26] F.E. Regnier, L. Riggs, R. Zhang, L. Xiong, P. Liu, A. Chakraborty, E. Seeley, C. Sioma, R.A. Thompson, J. Mass Spectrom. 37 (2002) 133.
[27] I.I. Stewart, T. Thomson, D. Figeys, Rapid Commun. Mass Spectrom. 15 (2001) 2456.
[28] A. Staes, H. Demol, J. Van Damme, L. Martens, J. Vandekerckhove, K. Gevaert, J. Proteome Res. 3 (2004) 786.
[29] J.R. Sevinsky, K.J. Brown, B.J. Cargile, J.L. Bundy, J.L. Stephenson, Anal. Chem. 79 (2007) 2158–2162.
[30] M.P. Washburn, D. Wolters, J.R. Yates, Nat. Biotechnol. 19 (2001) 242.
[31] J. Blonder, M.L. Hale, K.C. Chan, L.R. Yu, D.A. Lucas, T.P. Conrads, M. Zhou, M.R. Popoff, H.J. Issaq, B.G. Stiles, T.D. Veenstra, J. Proteome Res. 4 (2005) 523.
[32] M.E. Lassman, A. Rahbar, I.L. Medintz, F.S. Ligler, Anal. Lett. 40 (2007) 1864.
[33] J. Havlis, H. Thomas, M. Sebela, A. Shevchenko, Anal. Chem. 75 (2003) 1300.
[34] O.A. Turapov, G.V. Mukamolova, A.R. Bottrill, M.K. Pangburn, Anal. Chem. 80 (2008) 6093.
[35] S.P. Mirza, A.S. Greene, M. Olivier, J. Proteome Res. 7 (2008) 3042.
[36] D. Lopez-Ferrer, J.L. Capelo, J. Vazquez, J. Proteome Res. 4 (2005) 1569.
[37] M. Galesio, D.V. Vieira, R. Rial-Otero, C. Lodeiro, I. Moura, J.L. Capelo, J. Proteome Res. 7 (2008) 987.
[38] R. Rial-Otero, R.J. Carreira, F.M. Cordeiro, A.J. Moro, M.G. Rivas, L. Fernandez, I. Moura, J.L. Capelo, J. Proteome Res. 6 (2007) 909.
[39] J.L. Capelo (Ed.), Ultrasound in Chemistry. Analytical Applications, Wiley, Germany, 2009.
[40] H.M. Santos, J.L. Capelo, Talanta 73 (2007) 795.
[41] D. López-Ferrer, T.H. Heibeck, K. Petritis, K.K. Hixson, W. Qian, M.E. Monroe, A. Mayampurath, R.J. Moore, M.E. Belov, D.G. Camp II, R.D. Smith, J. Proteome Res. 7 (2008) 3860.
[42] D. Lopez-Ferrer, K. Petritis, N.M. Lourette, B. Clowers, K.K. Hixson, T. Heibeck, D.C. Prior, L. Pasa-Tolic, D.G. Camp, M.E. Belov, R.D. Smith, Anal. Chem. 80 (2008) 8930.
[43] J. Wang, P. Gutierrez, N. Edwards, C. Fenselau, J. Proteome Res. 6 (2007) 4601.
[44] C.S. Ang, P.D. Veith, S.G. Dashper, E.C. Reynolds, Proteomics 8 (2008) 1645.
[45] J. Havlis, A. Shevchenko, Anal. Chem. 76 (2004) 3029.

[46] B. Kuster, M. Mann, Anal. Chem. 71 (1999) 1431.
[47] T. Kosaka, T. Takazawa, T. Nakamura, Anal. Chem. 72 (2000) 1179.
[48] R.M. Larsen, P.M. Larsen, S.J. Fey, P. Roepstorff, Electrophoresis 22 (2001) 566.
[49] S. Körbel, M. Schümann, T. Bittorf, E. Krause, Rapid Commun. Mass Spectrom. 19 (2005) 2259.
[50] R. Chaerkady, P.J. Thuluvath, M.S. Kim, A. Nalli, P. Vivekanandan, J. Simmers, M. Torbenson, A. Pandey, Clin. Proteomics 4 (2008) 137.
[51] S. Uttenweiler-Joseph, G. Neubauer, S. Christoforidis, M. Zerial, M. Wilm, Proteomics 1 (2001) 668.
[52] A. Shevchenko, I. Chernushevich, K.G. Standing, B. Thomson, M. Wilm, M. Mann, Rapid Commun. Mass Spectrom. 11 (1997) 1015.
[53] G. Xiao, P.V. Bondarenko, J. Jacob, G.C. Chu, D. Chelius, Anal. Chem. 79 (2007) 2714.
[54] C. Wa, R.L. Cerny, D.S. Hage, Anal. Chem. 78 (2006) 7967.
[55] Z. Meng, P.A. Limbach, Anal. Chem. 77 (2005) 1981.
[56] J. Lee, H.K. Musyimi, S.A. Soper, K.K. Murray, J. Am. Soc. Mass. Spectrom. 19 (2008) 964.
[57] H. Bao, T. Liu, X. Chen, G. Chen, J. Proteome Res. 7 (2008) 5339.
[58] S. Wang, T. Liu, L. Zhang, G. Chen, J. Proteome Res. (2008), doi:10.1021/pr800476s.
[59] S. Wang, H. Bao, L. Zhang, P. Yang, G. Chen, Anal. Chem. 80 (2008) 5640.
[60] S. Swatkoski, P. Gutierrez, J. Ginter, A. Petrov, J.D. Dinman, N. Edwards, C. Fenselau, J. Protoeme Res. 6 (2007) 4525.
[61] S. Swatkoski, P. Gutierrez, C. Wynne, A. Petrov, J.D. Dinman, N. Edwards, C. Fenselau, J. Protoeme Res. 7 (2008) 579.

Talanta 80 (2010) 1487–1495

Contents lists available at ScienceDirect

Talanta

journal homepage: www.elsevier.com/locate/talanta

Isotope coded protein label quantification of serum proteins—Comparison with the label-free LC–MS and validation using the MRM approach

A. Turtoi[*,1], G.D. Mazzucchelli[1], E. De Pauw

University of Liege, Mass Spectrometry Laboratory, Dept. of Chemistry, Bat. B6c, B-4000 Liege, Belgium

ARTICLE INFO

Article history:
Available online 25 July 2009

Keywords:
Protein quantification
ICPL
Label-free quantification
Serum

ABSTRACT

Protein quantification based upon mass spectrometry is gaining ground in diverse applications of biological and clinical relevance. The present article focuses on one of the most complex biological fluids – serum – and provides a novel ICPL based quantification protocol. The results are compared to a label-free (data independent alternate scanning) absolute quantification method. The validation is performed using MRM based protein quantification technique. Regarding the ICPL approach, serum samples used in this study were depleted of high abundant proteins, labeled with ICPL and fractionated according to their respective pI (3–5, 5–7 and 7–12). The samples were further subjected to tryptic digestion followed by treatment with the Glu-C enzyme. The peptides were analyzed on a 2D-nano-LC system using four different concentrations of salt injections (45, 75, 150 and 500 mM ammonium acetate). The LC system was connected *on-line* with the electrospray ion-trap mass spectrometer. For the label-free quantification the serum samples were depleted and digested with trypsin. A proteome-wide comparison was performed using highly reproducible LC and data independent alternate scanning in conjunction with a high mass accuracy orthogonal time-of-flight mass spectrometer. Selected proteins, found by both methods, were validated using the MRM approach. For this purpose non-depleted tryptically digested serum samples were analyzed by LC coupled with a triple-quadrupole MS. The relative protein quantification using ICPL and mass spectrometry allowed for the detection of approximately 200 proteins, whereas about 2/3 of those contained the ICPL label and could therefore be quantified. Label-free approach used no fractionation, less sample and was able to identify and quantify over 110 proteins. The identified proteins covered generally 3–4 orders of magnitude of protein concentration in human serum. Changes in relative abundance of eight proteins were validated using MRM. This study, for the first time, shows the ability of the relative protein quantification based upon ICPL and 2D-LC–MS/MS to quantify serum biomarkers. It provides two additional label-free approaches that could validate and bring additional value to the label-based results, offering a starting point for comprehensive proteomics studies aiming at revealing biomarkers of clinical relevance.

© 2009 Elsevier B.V. All rights reserved.

1. Introduction

Serum samples are complex protein mixtures with concentrations spanning up to 10 orders of magnitude leading to difficulties in reliable protein identification and quantification [1–3]. Up until now, several quantification strategies have been described for serum samples. As far as the quantification of specific individual proteins is concerned, methods for spiking isotope-labeled or cloning of concatenated peptides have been developed. After sample digestion, a comparison of the MS signal of the endogenous peptide to the synthetic standard delivers the desired quantification result. Triple-quadrupole instruments and MRM methodologies are particularly suitable tools. For unselective, proteome-wide comparisons, primarily chemical labeling approaches are employed. For example, methanol (substituted with hydrogen or deuterium) esterification reactions [4], tryptic digestion in the presence of $H_2{}^{(16/18)}O$ [5], $^{12/13}$C-acrylamide–cysteine labeling [6], ICAT (isotope coded affinity tags) [7], iTRAQ (isobaric tag for relative and absolute quantitation) [8] and ICPL [9] have been applied. In spite of promising results, several difficulties are associated with some of these quantification methods. It is recognized that chemical labeling bares the drawback of unexpected side reactions and chemical products which complicate the quantification results [10]. Specifically ICAT and other chemical moieties that selectively label cysteine residues cannot be used to quantify proteins that contain none or few cysteines. Isotope coded tags based on N-hydroxysuccinimide (NHS) chemistry like iTRAQ and ICPL have the

* Corresponding author. Fax: +32 4 3663413.
E-mail address: a.turtoi@ulg.ac.be (A. Turtoi).
[1] oth authors contributed equally to the work.

0039-9140/$ – see front matter © 2009 Elsevier B.V. All rights reserved.
doi:10.1016/j.talanta.2009.07.035

potential to bridge these difficulties. These reagents target primary amino groups (e.g. lysine residues that are more abundant that cysteines) enabling the quantification of larger number of proteins. Hergenroeder et al. [11] have shown the application of iTRAQ to identify novel brain injury biomarkers in serum samples. One limitation associated with iTRAQ is the restricted ability to be used in conventional ion-trap instruments because of the reporter masses that are usually in the region of the 1/3 m/z precursor to product ion cut off. The novel stable isotope labeling method, termed ICPL, has emerged as a promising technique to relatively quantify proteins within complex protein mixtures [9,12]. The ICPL reagent is non-cleavable resulting in the permanent mass shift of the labeled peptide. This technique has provided the means to improve the accuracy, sensitivity and dynamic range of existing methods [13]. Up to date there has been no study related to the application of ICPL to quantify serum proteins. To this end, the primary goal of this work is to show the ability of the ICPL and 2D-LC–MS/MS method to relatively quantify serum proteins.

Because of the mentioned drawbacks concerning the label-based methods there is an increasing trend towards label-free quantification techniques. These are predominantly based either on the (i) measurement of MS signal ion intensity of peptide precursors or on the (ii) counting of the fragment ion spectra corresponding to a given protein. The first method consists of the peak area integration of the extracted ion chromatogram for a particular peptide. This value is then compared with the corresponding one in other experiments, in order perform a relative quantification. Although different algorithms and strategies have been employed to analyze the data, a series of inherent sources of error have been identified. The uncertainty arises primarily from the fact that only a limited number of data points across a peak can be acquired per unit of time. This can be associated to limitation of the duty cycle in the MS/MS acquisition mode. Problems resulting from the mass accuracy and resolution of the instrument employed as well as the reproducibility of the chromatographic separation further complicate reliable quantification. The second label-free quantification approach of spectral counting is based on the assumption that the more one protein is present in the mixture the greater is the chance that its peptide would be picked for an MS/MS fragmentation. Here one of the most obvious problems is that this method does not consider any physical properties of the peptide in question. Therefore ionisation differences, changes in the chromatographic peak width are some of the conundrums encountered. Taken together both techniques mentioned have their strengths but offer also significant pitfalls that could cumulate in misleading quantification results. In order to bridge these difficulties novel instrumentation is needed along with a significant improvement in the statistical data evaluation. Recently a novel MS and LC instrument, as well as special software algorithm, was developed with a potential to overcome the problems mentioned [14–16]. The accomplishment is based on highly reproducible LC and data independent, alternate scanning in conjunction with high mass accuracy measurements provided by an orthogonal time-of-flight mass spectrometer. The technique is based on the detection and correlation of all detectable precursor and fragment ions that share the same chromatographic profile. This is achieved by a rapid alteration between low- and elevated-energy states applied to the collision cell [15], which subsequently allows for the simultaneous quantification and identification of proteins in a single experiment. This method has already been applied to complex protein mixtures like the plant secretome [17], exosomes research [18], human serum [19] and the identification of novel MMP-9 substrates in cancer cells [20]. In the present study a functional protocol has been presented for rapid label-free serum proteins quantification, with the goal to compare this novel method with the label-based ICPL protocol. Selected ICPL and label-free data were validated regarding the accuracy of the relative quantification using the MRM as an established targeted quantification technique. For this purpose no synthetic peptides were employed as internal standards but a set of two proteins which served as a pseudo internal standard was used. The technique was put forward by Tabata et al. [21] which demonstrated that the usage of "housekeeping proteins" as normalization standards is a valid quantitative approach. The experimental design is detailed in Fig. 1. The current work offers scientists two independent ways to proceed from the biomarker discovery to their validation in a fast and accurate manner.

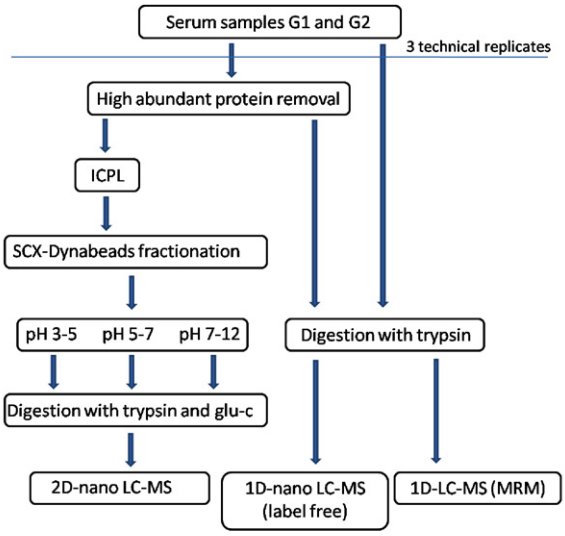


Fig. 1. Schematic representation of the experimental setup. The MRM experiments were conducted without prior removal of the most abundant proteins. In contrast to the label-free method, the label-based ICPL approach involved a pre-fractionation according to different pI of the proteins and subsequent digestion using two different proteolytic enzymes (trypsin and Glu-c).

2. Materials and methods

Unless otherwise indicated all the chemicals were purchased from Sigma–Aldrich (St. Louis, MO, USA) and had at least p.a. and higher quality. Human serum samples used here consisted of two groups of patients (G1 and G2) involving 10 patients each within a clinical trial for analysis of frailty markers (SENEGENE project, Walloon Region, Belgium) at the Catholic University of Louvain, Mont-Godinne University Hospital. The project was approved by the ethics committee and written consent was obtained from all the human individuals involved in the study. Per quantification method at least three technical replicates were performed (see Fig. 1).

2.1. Depletion of the most abundant proteins from the serum samples

A volume of 20 μL of the serum sample was depleted of high abundant proteins using the IgY-12 kit (Beckman Coulter, Fullerton, CA, USA). Unless otherwise indicated all components originate from the above mentioned IgY-12 kit. For long-term storage, the serum samples were kept frozen at −20 °C. Prior to depletion they were thawed at +4 °C for 1–2 h, vortexed briefly and centrifuged for 5 min at 13,000 × *g* (Eppendorf, Hamburg, Germany). Subsequently, 20 μL of each serum sample was mixed with 480 μL of dilution buffer and was added to the freshly reconditioned IgY-12 column. Following this, the samples were incubated for 15 min at RT under constant shaking and subsequently the column was centrifuged for 30 s at 400 × *g*. The filtrate contained the depleted serum proteins (V = 400 μL). The highly abundant proteins bound to the column

were stripped off with 2× 500 μL of stripping buffer and discarded. Subsequently, the column was neutralized with 600 μL of 1:10 diluted neutralization buffer and reconditioned in 500 μL of dilution buffer. After the depletion of 20 μL of serum sample, 96 ± 1% of the initial total protein content was removed. The depleted proteins were precipitated using the 2D Clean-Up kit (GE Healthcare, Piscataway, NJ, USA) and dissolved in 20 μL of sample buffer (Serva, Heidelberg, Germany). The concentration of the samples was set to 5 mg/mL and the pH to 8.5 ± 0.1.

2.2. ICPL labeling, fractionation and digestion of the serum samples

Unless otherwise indicated, all the components used were part of the ICPL kit. An amount of 0.5 μL of the ICPL-reduction solution was added to each of the depleted serum samples followed by 30 min incubation under mild shaking (600 rpm, Thermomixer [Eppendorf]) at 60 °C. Subsequently, 0.5 μL of ICPL-alkylation reagent was added and the samples were incubated for further 30 min at 25 °C protected from the light. After 30 min the reaction was stopped following the addition of 1 μL of ICPL-stop solution and 15 min incubation at 25 °C. The reduced and alkylated protein samples were labeled using 3 μL of ^{12}C-Nic- or ^{13}C-nic-reagent solution for the respective sample. Subsequently, both samples were overlaid with nitrogen gas, vortexed for 10 s and sonicated for 1 min in the ultrasonic bath (Branson, Danbury, CT, USA). The samples were incubated for 2 h at 25 °C. The reaction was stopped by addition of 2 μL of ICPL-stop solution. The samples were incubated for further 20 min at 25 °C and combined together by vortexing. The pH of the mixture was adjusted to 11.9 by adding approximately 1 μL of 2 M NaOH. After 20 min the same amount of 2 M HCl was added to neutralize the samples. This was necessary in order to destroy the surplus label in the sample and prevent any subsequent unspecific reaction. An amount of 100 μg of total protein (considering both samples) was taken for subsequent analysis.

After the ICPL, serum proteins were fractionated according to their respective pI. For this purpose, SCX material immobilized on magnetic beads (Dynabeads [Invitrogen, Carlsbad, CA, USA]) was employed; the beads were separated from the liquid phase by a strong magnet (part no. 105.13D, Invitrogen). Approximately 1 mg of Dynabeads (corresponding to 80 μL beads suspension) was transferred in a reaction tube. The beads were reconditioned twice with 100 μL of pre-loading solution (50 mM HEPES buffer [pH 8.0] and 1 M NaCl). After this step the beads were suspended for 2 times in 100 μL of adsorption solution (20 mM citric acid [pH 3] and 10 mM NaCl). The labeled sample was added to the reconditioned beads and the volume was adjusted with ads. sol. to 200 μL (pH 3). The samples were incubated for 2 min at RT and subsequently the supernatant was removed and saved as fraction 1; the beads were suspended for one more time in 100 μL of ads. sol. and the supernatant was joined with the fraction 1. Following this step further fractions were eluted by mixing 50 μL of corresponding desorption solution (1. 50 mM PBS, pH 7 and 2. 20 mM ammonium acetate, pH 9.5) followed by 2 min incubation at RT. This step yielded fractions no. 2 and 3. Finally the beads were suspended in 50 μL of 100 mM NaOH in order to detach the remaining proteins bound to the Dynabeads. This last fraction was joined with the previous one (no. 3, pH 9.5). As the elution buffers were not compatible with the subsequent enzymatic digestion (outlined below) the proteins found in each fraction were subjected to precipitation using the 2D Clean-Up kit.

The samples were first subjected to tryptic digestion followed by digestion with Glu-C (both recombinant enzymes were supplied by Roche, Basel, Switzerland). To the protein pellets, a volume of 20 μL of 1 M urea and 25 mM NH_4HCO_3 buffer (pH 8) was added. The samples were suspended and sonicated for 1 min in the ultrasonic bath (Branson, Danbury, CT, USA). After sonication 1 μg of trypsin was added and the samples were incubated at 37 °C overnight. Following the 16 h period, 0.5 μg of fresh trypsin was added and the incubation was extended for additional 4 h at 37 °C. Subsequently, 2 μg of Glu-C enzyme was added to each sample. The samples were digested for additional 6 h at 25 °C. To stop the digestion, 20 μL of water containing 0.5% formic acid (pH 2) was added. The samples were desalted using the C18 ZipTips (Millipore, Billerica, MA, USA) and analyzed with the 2D-LC–MS system.

2.2.1. MS analysis and relative quantification of the ICPL labeled peptides

The peptide samples were analyzed on the 2D-nano-LC system Ulimate 3000 (Dionex, Sunnyvale, CA, USA). The LC system was connected *on-line* with the electrospray ion-trap mass spectrometer Esquire HCT ultra (Bruker Daltonics, Bremen, Germany). For the MS analysis, approximately 5 μg of digested protein sample was loaded on the Bio-X-SCX column (500 μm i.d. × 15 mm; Dionex). Subsequently, four different concentrations of salt injections were performed (45, 75, 150 and 500 mM ammonium acetate, 0.1% formic acid). After each salt injection, the eluted peptides from the SCX column were trapped on a C18 pre-column (Acclaim PepMap, 300 μm i.d. × 5 mm; Dionex) and desalted for 5 min at the flow rate of 30 μL/min using solvent A (97.9% water, 2% acetonitrile and 0.1% formic acid). Following this, the separation of the peptides was conducted on the C18 analytical column (Acclaim 75 μm × 150 mm; Dionex) using a 120 min solvent gradient (t = 0 min, 0% B [B: 80% acetonitrile, 19.9% water and 0.1% formic acid]; t = 120 min, 40% B) at the flow rate of 0.3 μL/min. The MS scanned the mass range from 200 to 1600 m/z. The four most intense peptides found in this mass range (bearing +2 and +3 charges) were selected automatically and fragmented in MS/MS mode (m/z range 100–2500). The acquired spectra from all the samples were combined in one raw data file using Analysis Combiner (Bruker) software tool and were deconvoluted with the Data Analysis software (Bruker). The processed data were loaded in the WarpLC software (Bruker) and protein identification and quantitation was conducted with the help of the Mascot search engine (Matrix Sciences, Boston, MA, USA) and the human non-redundant and non-identical protein database Swiss-Prot (Swiss Institute for Bioinformatics, Basel, Switzerland, release 57.0; 20,334 entries). The following parameters were used: MS and MS/MS tolerance 0.6 and 0.3 Da respectively, 1 missed cleavage was allowed and a novel enzyme entry (trypsin + Glu-C) was made in the Mascot engine allowing for lysine, arginine and glutamic acid cleavage sites. The ratios of heavy and light ICPL labeled peptides allowed for the relative quantitation (Table 1).

2.3. Serum sample preparation for label-free quantification

The samples were depleted as described in Section 2.1. A total of 50 μg of proteins per sample were reduced with 25 mM DTT for 30 min at 60 °C and alkylated with 50 mM iodoacetamide for 30 min at RT. After precipitation (as described in Section 2.1), the protein pellet was dissolved in 20 μL of 1 M urea and 25 mM ammonium bicarbonate (pH 8) and sonicated for 1 min in the ultrasonic water bath. To the dissolved proteins, 1 μg of trypsin was added and the samples were incubated overnight at 37 °C. Following the initial period of incubation, 0.5 μg of fresh trypsin was added and the incubation was extended for additional 4 h. The samples were then diluted with 30 μL water containing 0.5% formic acid (pH 2), desalted using C18 ZipTips and analyzed with the 1D-LC–MS system.

Table 1
ICPL based relative protein quantification of serum samples G1 and G2. The value of the ratio displayed refers to G2/G1 comparison. The number of the labeled peptides (H/L) is the mean value of three independent replicates. The standard deviation (SD) of means is based on the respective ratios of the labeled peptides. Score, sequence coverage (SC, %) and the number of peptides are average values ($n = 3$) obtained through Mascot/Swiss-Prot database search.

No.	Protein	MW (kDa)	pI	Score	SC (%)	No. pept.	No. H/L	Ratio	SD
1	6PGD	53.1	7.0	55.2	9.9	4	1	1.41	n.a.
2	A1AG2	23.6	4.9	365.1	21.4	10	5	0.40	0.03
3	A1AT	46.7	5.3	146.9	24.4	11	5	1.15	0.03
4	A1BG	54.2	5.5	663.6	34.3	31	4	1.25	0.04
5	A26CA	121.3	5.8	93.6	14.5	15	1	0.04	n.a.
6	A26CB	121.3	5.8	93.6	14.5	15	2	0.57	0.10
7	A2AP	54.5	5.9	208.3	27.1	12	2	0.91	0.15
8	A2GL	38.2	6.5	287.4	28.5	12	2	0.97	0.05
9	A2MG	163.2	6.0	1849.3	34.8	112	34	0.78	0.03
10	AACT	47.6	5.2	1525.3	31.9	71	31	0.78	0.04
11	ACTG	41.8	5.2	166.9	40.8	14	1	0.04	n.a.
12	AFAM	69.0	5.6	116.6	21.7	20	2	4.93	2.80
13	ALBU	69.3	5.9	1064.1	43.0	72	4	1.34	0.11
14	ANGT	53.1	5.9	208.8	42.9	16	4	1.03	0.04
15	ANT3	52.6	6.3	769.9	42.0	49	8	1.55	0.12
16	ANXA2	38.6	8.5	90.2	13.3	9	2	0.14	0.06
17	APOA1	30.8	5.5	124.0	13.1	6	1	1.53	n.a.
18	APOA2	11.2	7.1	152.5	19.0	4	2	1.43	0.21
19	APOA4	45.4	5.2	298.0	25.3	19	4	0.87	0.20
20	APOB	515.2	6.6	193.6	10.3	53	2	69.31	5.10
21	APOH	38.3	9.5	214.9	35.1	23	6	1.31	0.16
22	C1R	80.1	5.9	262.2	13.0	10	2	1.30	0.07
23	C1S	76.6	4.7	365.7	33.9	22	3	1.07	0.13
24	C4BP	67.0	7.9	438.0	35.8	39	11	0.98	0.04
25	C4BPA	67.0	7.9	525.8	33.5	32	7	1.09	0.05
26	CERU	122.1	5.4	1410.9	42.1	93	20	0.93	0.05
27	CFAB	85.5	6.7	1313.8	47.8	94	21	0.95	0.04
28	CFAH	139.0	6.2	791.3	32.0	59	19	1.05	0.04
29	CFAI	65.7	9.0	112.9	16.1	13	2	0.99	0.06
30	CLUS	52.5	5.9	105.8	16.5	10	2	0.85	0.06
31	CO2	83.2	7.9	248.3	9.2	7	2	0.88	0.05
32	CO3	187.0	6.0	4924.4	47.8	224	61	1.15	0.12
33	CO4A	192.7	6.7	3148.2	36.8	123	24	0.98	0.05
34	CO4B	192.7	6.8	2954.3	41.1	122	20	1.02	0.03
35	CO5	188.2	6.1	348.2	12.2	23	8	1.04	0.08
36	CO6	104.7	6.4	149.9	14.9	22	4	1.20	0.13
37	CO7	93.5	6.1	425.2	31.4	26	5	0.85	0.06
38	CO8A	65.1	6.1	83.4	12.2	8	2	1.03	0.03
39	CO8G	22.3	9.4	412.0	41.1	12	2	1.94	0.37
40	CO9	63.1	5.3	392.6	32.4	32	6	1.05	0.08
41	CPN2	60.6	5.6	222.2	17.4	11	2	0.71	0.03
42	CRP	25.0	5.3	626.6	45.5	26	5	0.84	0.03
43	DCD	11.3	6.1	75.5	54.5	7	1	0.87	n.a.
44	DESP	331.6	6.4	384.7	15.7	41	2	0.35	0.12
45	DOP2	258.0	5.9	54.6	9.8	28	2	13.16	2.34
46	DSC1	100.0	5.1	288.1	14.2	15	2	0.57	0.04
47	DSG1	113.6	4.8	272.6	15.6	19	2	14.08	1.84
48	ECM29	204.2	6.8	55.9	19.0	22	1	0.06	n.a.
49	ENO1B	49.4	5.7	58.4	19.9	7	1	27.19	n.a.
50	ENOA	47.1	7.7	58.4	11.5	6	2	0.37	0.10
51	FA12	67.8	9.4	193.9	20.8	10	2	0.84	0.04
52	FA9	51.7	5.2	52.9	19.7	9	3	0.50	0.06
53	FABP4	14.7	7.5	153.5	43.2	6	1	63.09	n.a.
54	FCGBP	571.7	5.0	57.3	7.4	26	2	0.34	0.03
55	FETUA	39.3	5.4	241.0	22.3	16	3	1.16	0.07
56	FHR1	37.6	9.0	111.6	29.4	13	2	1.17	0.02
57	FHR3	37.3	8.9	70.6	31.5	9	2	1.20	0.07
58	FHR5	64.4	7.0	56.1	12.5	5	2	0.95	0.01
59	FIBA	94.9	5.6	2259.3	39.1	108	32	1.06	0.04
60	FIBB	55.9	9.3	1758.5	42.4	98	26	1.12	0.05
61	FIBG	51.5	5.3	424.4	32.7	56	12	1.11	0.05
62	FILA2	247.9	9.2	102.9	7.1	23	1	0.06	n.a.
63	FINC	262.4	5.4	1297.2	31.3	65	3	2.15	0.18
64	FPGT	66.6	6.1	45.7	24.7	18	2	5.29	1.11
65	GELS	85.6	5.9	144.8	18.0	14	2	1.51	0.03
66	GRP78	72.3	4.9	50.7	11.6	8	2	5.62	1.64
67	H2B3B	13.9	10.8	123.8	36.5	6	1	0.10	n.a.
68	HBB	16.0	6.9	60.6	50.3	6	2	0.44	0.05
69	HEMO	51.6	6.6	1168.2	23.8	71	13	0.87	0.05
70	HPT	45.2	6.1	815.9	37.7	42	13	0.47	0.03
71	HRG	59.5	7.2	46.6	2.9	1	1	1.82	n.a.
72	HS71L	70.3	5.7	50.7	11.4	6	1	21.53	n.a.
73	HSP72	70.0	5.4	50.7	14.1	8	2	1.12	0.07
74	HV315	0.0	9.2	108.6	36.8	7	2	1.30	0.20

Table 1 (*Continued*)

No.	Protein	MW (kDa)	pI	Score	SC (%)	No. pept.	No. H/L	Ratio	SD
75	HV319	12.6	10.2	66.6	33.9	5	2	0.99	0.14
76	IC1	55.1	6.1	505.3	21.6	26	8	1.01	0.05
77	IGHA1	37.6	6.1	600.2	37.7	22	9	0.90	0.03
78	IGHA2	36.5	5.7	548.7	39.1	21	9	0.86	0.02
79	IGHG1	36.1	9.4	237.5	28.5	25	6	1.04	0.06
80	IGHG2	35.9	8.8	195.7	23.3	15	2	0.92	0.03
81	IGHG4	35.9	7.8	71.0	13.8	9	2	0.77	0.10
82	IQEC3	0.0	6.1	44.3	10.3	13	4	0.04	0.01
83	ITIH1	101.3	6.3	473.7	21.8	29	4	1.21	0.14
84	ITIH2	106.4	6.4	730.0	28.1	48	15	1.58	0.10
85	ITIH3	99.1	5.5	505.0	16.7	20	5	0.92	0.05
86	ITIH4	103.3	6.5	1112.5	42.8	66	12	0.92	0.04
87	K1C14	51.6	4.9	1069.8	40.9	40	2	2.46	0.01
88	K1C25	49.3	4.9	66.6	6.9	5	1	12.20	n.a.
89	K1C28	50.6	5.2	66.6	14.0	10	2	0.04	0.00
90	K22E	65.8	8.9	2211.4	39.8	82	1	2.26	n.a.
91	K2C1	66.0	8.8	5750.7	50.5	193	1	8.69	n.a.
92	K2C74	57.8	8.6	81.2	12.5	10	1	0.49	n.a.
93	K2C80	50.5	5.4	65.8	18.4	14	1	0.12	n.a.
94	KAC	11.6	5.5	193.4	54.7	16	6	0.99	0.06
95	KLKB1	71.3	9.7	85.0	17.7	13	2	1.32	0.06
96	KNG1	71.9	6.4	232.9	23.4	32	10	1.20	0.08
97	KRT34	44.7	4.6	123.2	22.1	9	1	0.04	n.a.
98	KT33B	46.2	4.7	136.8	20.5	8	1	1.41	n.a.
99	LAC	11.2	7.6	63.9	30.5	10	2	0.91	0.04
100	LBP	53.3	6.2	57.8	19.5	10	1	0.18	n.a.
101	LG3BP	65.3	5.0	153.6	8.0	5	1	0.99	n.a.
102	LUM	38.4	6.2	119.6	25.7	20	2	1.05	0.26
103	MACF4	669.7	5.1	45.3	10.3	70	2	0.19	0.01
104	MUC	49.5	6.4	251.8	36.3	22	3	0.94	0.09
105	MUCB	43.0	5.0	91.2	15.6	4	1	5.79	n.a.
106	NSD2	152.2	10.1	50.6	18.1	33	3	0.04	0.01
107	PEDF	46.3	6.0	83.6	12.2	4	2	0.43	0.16
108	PIWL2	109.8	10.0	46.3	3.4	6	3	4.51	1.14
109	PK3CA	124.2	7.0	52.0	12.3	17	2	0.79	0.11
110	PKP1	82.8	10.1	122.4	22.1	13	1	36.13	n.a.
111	PLMN	90.5	7.3	393.0	28.4	28	3	1.08	0.13
112	PRDX1	22.1	9.2	52.4	20.1	13	2	0.60	0.14
113	PRG4	151.0	10.2	85.1	29.8	35	2	0.96	0.07
114	PROS	75.1	5.4	65.9	27.2	11	2	1.45	0.17
115	PRP31	55.4	5.5	46.2	13.4	10	1	10.07	n.a.
116	PZP	163.7	5.9	217.6	21.4	31	5	0.88	0.13
117	SAA	13.5	6.4	76.0	53.3	8	1	0.29	n.a.
118	SAMP	25.4	6.1	126.1	22.0	14	6	0.93	0.05
119	SCUB2	109.9	6.2	43.8	15.2	14	3	0.18	0.01
120	SLK	142.6	4.9	51.3	8.7	14	4	0.17	0.05
121	THBG	46.3	5.9	91.7	14.2	8	2	3.72	0.29
122	THEM2	15.0	10.0	44.4	27.1	5	2	0.94	0.01
123	THRB	70.0	5.6	1601.3	38.6	50	9	1.22	0.05
124	TITIN	3813.8	6.0	51.3	12.4	430	3	13.29	1.25
125	TTHY	15.9	5.4	89.2	41.5	5	1	7.90	n.a.
126	VTDB	52.9	5.3	496.5	43.0	45	6	1.04	0.06
127	VTNC	54.3	5.5	561.9	32.6	34	7	1.16	0.04
128	VWF	309.1	5.2	94.1	15.1	37	2	5.18	1.21

2.3.1. MS analysis and absolute quantification of label-free peptides

The samples were analyzed using a nanoAcquity system (Waters Corporation, Milford, MA, USA) coupled with the SYNAPT mass spectrometer (Waters Corporation, Manchester, UK). An amount of 10 μg of each of the digested serum samples was diluted in 40 μL of 0.1% formic acid in water to a concentration of 0.25 μg/μL. Samples were spiked with yeast alcohol dehydrogenase tryptic digest (final concentration 77 fmol/μL). Finally, 1 μL of the sample was injected, corresponding to an estimated sample load of 250 ng. The LC system configuration was as follows: trap column Symmetry C18 5 μm, 180 μm × 20 mm (Waters Corporation), analytical column BEH C18 1.7 μm, 75 μm × 250 mm (Waters Corporation), solvent A (0.1% formic acid in water), solvent B (0.1% formic acid in acetonitrile) and flow rate 300 nL/min (gradient: 0 min, 97% A; 90 min, 60% A). The following acquisition parameters were set for the SYNAPT mass spectrometer: data independent, alternate scanning (MS^E) mode, 50–1990 *m/z* range, ESI+, V optics, scan time 1 s, cone 24 V and lock mass [Glu1]-Fibrinopeptide B $[M+2H]^{2+}$ 785.8426 *m/z*.

ProteinLynx GlobalSERVER v2.3 was used to process raw data for subsequent protein identification and quantitation. The processing parameters were as follows: MS TOF resolution and the chromatographic peak width were set to automatic, low-/elevated-energy detection threshold to 150/50 counts, identification intensity threshold to 1000 counts and lock mass window to 785.8426/0.25 Da. The Swiss-Prot human database (release 57.0; 20,334 entries) served as the reference. The search tolerances were automatically read from the data and were approximately 9 and 23 ppm for the precursor and product ions, respectively. Peptide modifications carbamidomethylation, deamidation (N/Q) and oxidation (M) were set as variable. One missed cleavage for trypsin digestion was allowed (Table 2).

Table 2
Label-free relative protein quantification of depleted serum samples G1 and G2 (ratio G2/G1). The SD represents the standard deviation of means ($n = 3$). The score was calculated for each individual protein using the identification and quantification software embedded in ProteinLynx GlobalSERVER v2.3.

No.	Protein	MW (kDa)	pI	Score	Ratio	SD
1	A1AG1	23.5	4.9	518.0	0.06	0.10
2	A1AG2	23.6	4.9	317.9	0.41	0.09
3	A1AT	46.7	5.3	179.9	1.03	0.16
4	A1BG	54.2	5.5	1131.1	1.25	0.03
5	A2AP	54.5	5.9	234.0	1.54	0.11
6	A2GL	38.2	6.5	411.5	1.02	0.07
7	A2MG	163.2	6.0	5186.9	0.88	0.02
8	AACT	47.6	5.2	1836.6	0.73	0.01
9	AFAM	69.0	5.6	111.0	1.77	0.10
10	ALBU	69.3	5.9	438.1	1.65	0.06
11	AMBP	40.0	6.0	508.9	1.39	0.05
12	ANGT	53.1	5.9	906.4	1.21	0.04
13	ANT3	52.6	6.3	992.7	1.45	0.06
14	APOA4	45.4	5.2	484.1	0.99	0.07
15	APOC3	10.9	5.2	105.5	1.38	0.41
16	APOH	38.3	9.5	290.3	1.34	0.05
17	C1QB	26.5	8.8	168.1	1.07	0.11
18	C1QC	25.8	8.6	167.9	1.08	0.13
19	C1R	80.1	5.9	172.6	1.80	0.09
20	C1S	76.6	4.7	168.6	1.31	0.09
21	C4BP	67.0	7.9	624.7	1.06	0.04
22	CERU	122.1	5.4	3135.0	1.09	0.02
23	CFAB	85.5	6.7	1437.8	0.97	0.03
24	CFAH	139.0	6.2	1638.8	0.94	0.03
25	CFAT	65.7	9.0	221.7	1.04	0.11
26	CLUS	52.5	5.9	289.8	0.95	0.10
27	CO2	83.2	7.9	161.1	1.09	0.16
28	CO3	187.0	6.0	6463.5	1.01	0.02
29	CO4A	192.7	6.7	2718.2	1.15	0.03
30	CO4B	192.7	6.8	2802.1	1.14	0.03
31	CO5	188.2	6.1	991.4	1.11	0.05
32	CO6	104.7	6.4	248.6	1.38	0.08
33	CO7	93.5	6.1	450.9	0.88	0.07
34	CO8A	65.1	6.1	199.8	1.34	0.10
35	CO8B	67.0	8.5	185.5	1.55	0.14
36	CO8G	22.3	9.4	184.5	1.32	0.12
37	CO9	63.1	5.3	471.5	0.92	0.06
38	CPN2	60.6	5.6	190.7	1.22	0.17
39	CRP	25.0	5.3	389.0	0.84	0.04
40	FA12	67.8	9.4	120.0	1.40	0.16
41	FETUA	39.3	5.4	181.1	1.73	0.10
42	FHR1	37.6	9.0	139.1	0.98	0.10
43	FIBA	94.9	5.6	1835.4	1.09	0.02
44	FIBB	55.9	9.3	2512.6	1.17	0.02
45	FIBG	51.5	5.3	2263.5	1.23	0.02
46	GELS	85.6	5.9	220.9	1.39	0.08
47	HBA	15.3	8.7	63.4	1.92	0.12
48	HBB	16.0	6.9	213.1	1.67	0.09
49	HBD	16.0	7.8	84.7	1.36	0.18
50	HEMO	51.6	6.6	1690.6	0.89	0.01
51	HEP2	57.1	6.4	82.3	0.99	0.08
52	HPT	45.2	6.1	1683.7	0.43	0.02
53	HPTR	39.0	6.4	617.0	0.43	0.04
54	HRG	59.5	7.2	129.0	2.53	0.13
55	IC1	55.1	6.1	828.6	0.96	0.04
56	IGHA1	37.6	6.1	235.7	0.89	0.05
57	IGHA2	36.5	5.7	179.6	0.98	0.12
58	IGHG1	36.1	9.4	205.9	1.40	0.09
59	IGHG4	35.9	7.8	76.9	1.54	0.30
60	ITIH1	101.3	6.3	939.1	1.49	0.04
61	ITIH2	106.4	6.4	611.9	1.95	0.04
62	ITIH3	99.1	5.5	409.9	0.96	0.07
63	ITIH4	103.3	6.5	1754.1	0.92	0.03
64	KAC	11.6	5.5	245.4	0.70	0.10
65	KNG1	71.9	6.4	699.3	1.09	0.04
66	LAC	11.2	7.6	182.3	0.94	0.13
67	LUM	38.4	6.2	113.5	1.52	0.14
68	MUG	49.5	6.4	467.3	1.07	0.05
69	MUCB	43.0	5.0	231.3	1.07	0.06
70	PEDF	46.3	6.0	130.5	1.17	0.09
71	PLMN	90.5	7.3	462.2	1.17	0.08
72	PZP	163.7	5.9	219.4	0.90	0.06
73	RETBP	23.0	5.8	163.6	1.22	0.09
74	THBG	46.3	5.9	201.6	1.32	0.13
75	THRB	70.0	5.6	1310.1	1.08	0.03
76	VTDB	52.9	5.3	1978.8	1.12	0.02
77	VTNC	54.3	5.5	217.3	1.42	0.05

Table 3
Proteins and their respective peptides quantified with the MRM method. The A2GL and IC1 proteins served as pseudo internal standards. Observed retention times (t) are indicated for each of the peptides.

Protein	Precursor (m/z)		Product (m/z)		Peptide sequence	t (min)
	$[M+H]^+$	$[M+2H]^{2+}$	$[M+H]^+$	$[M+H]^+$		
A2GL	989.55	495.28	819.45 (y8)	748.41 (y7)	VAAGAFQGLR	5.5
IC1	1116.59	558.80	890.42 (y8)	575.28 (y5)	LLDSLPSDTR	6.1
A1AG2	1160.59	580.80	827.44 (y7)	551.30 (y5)	WFYIASAFR	8.4
A1BG	1088.58	544.79	916.50 (y9)	730.42 (y8)	ATWSGAVIAGR	6.2
A2AP	1176.58	588.79	960.49 (y9)	832.43 (y8)	LCQDLGPGAFR	6.3
CO8G	1620.82	810.91	836.43 (y7)	723.34 (y6)	SLPVSDSVLSGFEQR	7.8
FIBB	1275.56	638.28	688.36 (y6)	575.28 (y5)	DNDGWLTSDPR	6.4
PEDF	1055.65	528.33	855.53 (y8)	727.47 (y7)	TVQAVLTVPK	4.2
THBG	1121.64	561.32	887.53 (y7)	756.49 (y6)	SFMLLILER	9.3
VTNC	1422.65	711.83	875.43 (y7)	647.32 (y5)	FEDGVLDPDYPR	6.9

2.4. Serum sample preparation for quantification based upon MRM

A volume of 100 μL of serum diluted with 100 μL of water was subjected to reduction and alkylation (25 mM DTT for 30 min at 60 °C and 50 mM iodoacetamide for 30 min at RT) followed by addition of 3 μg of trypsin. The samples were incubated at 37 °C overnight. After the initial incubation period, 1.5 μL of trypsin was freshly added and the samples were incubated at 37 °C for additional 4 h. Subsequently, the samples were diluted with 3 volumes of water containing 0.2% formic acid and the MS analysis was conducted as described in Section 2.4.1.

2.4.1. MRM assisted quantification using the triple-quadrupole MS

Waters Alliance 2690 liquid chromatography system coupled with a Quattro Ultima Platinum triple-quadrupole MS instrument (Waters Corporation) was employed for the MRM analysis. Approximately 50 μg of the digested sample was injected on C18 column, Polaris C18, 3 μm beads, 200 Å pore size, 2.1 mm × 150 mm (Varian Inc., Palo Alto, CA, USA). The flow rate was 400 μL/min. Linear separation gradient was used: t = 0 min, 100% water (0.1%, v/v acetic acid) and t = 20 min, 60% water and 40% acetonitrile (0.1%, v/v acetic acid). The eluent flow rate was split to 50% prior to the ESI ionisation. The triple-quadrupole MS instrument was set in the MRM mode, capillary voltage was 2.6 kV, desolvation temperature 250 °C, cone desolvation gas 630 L/h, collision cell pressure 2 μbar, collision energy 15 (for all the peptides selected) and resolution at quadrupole 1 was ±1 Da. The data were accrued and evaluated using the MassLynx (v 4.0) software. Two proteins whose quantities proved to be unchanged between the two groups (both with the label-free and ICPL quantification), namely A2GL and IC1, were used as internal standards to normalize ion intensities between both samples. Proteins selected for quantification as well as their respective peptides and fragments used for MRM are outlined in Table 3.

3. Results and discussion

The application of ICPL combined with the 2D-LC–MS method, including in addition the fractionation of the labeled proteins according to their pI value, enabled the identification of 211 proteins, with a false positive rate (FPR) of 5.3%, in human serum samples. This represents a group of non-redundant proteins in two out of three independent replicates. Of these, 128 (61%) proteins were quantified as they had one or more labeled peptides. The remaining proteins were identified with one or more peptides that did not contain any lysines. Hence, this information was lost and could not contribute to the quantification. Therefore the limiting factor of the ICPL technique is the number of the labeled peptides per protein of interest. Moreover, as ICPL specifically labels all the lysine residues and the positive charge is lost the pI of the respective proteins is shifted towards the acidic end. This results in the fact that the greatest part of the proteome is found in the relatively narrow pH range starting from very acidic to a pH of approximately 6. Nevertheless, very basic proteins (with pI above 10) shifted to lower pI values and were generally found in the fractions between pH 6 and 10. In the acidic environment during the LC–MS analysis, effective fractionation of the labeled proteins on the SCX column proved to be difficult. This was most probably due to the loss of charged lysines and hence the peptides were predominantly eluting in a narrow window of low ionic strength. In order to counteract this, an additional fractionation step was employed at the protein level, according to the respective pI value, which simplified the protein mixture but increased the analysis time. An additional conundrum inherent to the ICPL method was the sequestration of the lysine cleaving sites for the endo-protease trypsin. Hence trypsin cleaves only at arginine sites which results in fragments with large molecular weights. The MS analysis of such large fragments using conventional ion-trap MS is difficult for several reasons. Firstly, the scanning m/z window must be increased which will lead to longer cycle times. Secondly, these large peptides are probably carrying more than 3 charges which cause difficulties related to the resolution power of the mass spectrometer used. In order to try to avoid these problems and to reduce the size of such large fragments an additional enzyme has been employed, namely Glu-C protease, which cleaved the proteins at glutamic acid sites when used in bicarbonate buffer.

In comparison to ICPL, the label-free method did not employ any pre-fractionation and could identify 114 proteins. Considering two out of three independent replicates, 77 (68%) commonly identified proteins (present both in G1 and G2) were quantified. In contrast to the ICPL method, where no quantitative data were available on approximately 1/3 of all proteins identified, label-free approach could provide the quantitative data even for the remaining proteins that were identified in only one out of three replicates. These were of limited significance but could still offer valuable information that can be subject to future validation. One of the possible methods is the MRM approach which was used for selected number of proteins in the present work. Along these lines, the label-free approach offered insights into the actual reproducibility of the technique, due to the absolute quantification of individual samples and replicates. Regarding sample G1, 81 proteins were confidently identified in at least 2 out of 3 replicates. The calculated protein identification false positive rate of the experiment was 1.23% and the peptide FPR of identification 0.34%, including replicating as filter for both the protein and peptide FPR calculations and in addition the number of identified peptides, which had to be at least 2, for the protein FPR calculation. The average column sample loading was calculated to be 116.8 ng using the absolute quantification function afforded

by the search algorithm [22]. The absolute quantity of the individual proteins ranged from 0.007 to 13.7 ng. In the sample G2, 83 proteins were identified. The protein and peptide FPR were both 0%, and the average sample loading 143.1 ng. In this instance, the quantity of the individual proteins ranged from 0.01 to 16.2 ng. It is important to note that these identifications mount from relatively low column loadings and it should therefore be expected that a greater number of proteins can be identified and quantified with either more optimized loadings or a 2D-HPLC approache (the latter was not available at the time of the manuscript preparation). Taken together, for both samples, the mean mass precision of the peptides of the technical replicates was approximately 2.13 ppm and the mean retention time reproducibility approximately 0.1% CV. Injection comparisons between the G2 vs. G1 triplicate analyses using log/log normal intensity plots showed a high inter-injection reproducibility (all results not shown here).

One further important difference between the two quantification approaches was found in the normalization techniques employed. In the case of the ICPL data, there was no need to normalize the signal intensity difference between each of the replicate analysis, since both conditions were introduced at the same time in the MS. The data were solely normalized according to the Gaussian distribution under the assumption that most of the proteins quantified will not change between the two conditions. Regarding the label-free data, an alternative approach was necessary as each of the samples and the replicates was analyzed separately. The observed peptide intensity measurements are normalized to the intensity measurement of the identified peptides of the digested internal standard. Next, the redundant, proteotypic quantitative measurements provided by the multiple tryptic peptide identifications from each protein were used to determine an average, relative protein fold-change. The algorithm performs binary comparisons for each of the conditions to generate an average normalized intensity ratio for all matched proteins. Proteins with a likelihood of quantification smaller than 0.05 were considered to be significantly regulated [14]. The normalization method for the label-free experiment is similar to the one conducted for the ICPL data and is also based on the assumption of a normal distribution.

It is not unreasonable to assume that the standard protocol used for the label-free application, where the tryptic digest is spiked in the peptide mixture of the previously digested sample, may fail to account for differences in the degree of the tryptic digestion as well as for a possible bias introduced in the subsequent fractionation steps. In the attempt to balance these effects out, the method described here does not use any fractionation steps prior or after the digestion. Nevertheless, for future applications we suggest to consider spiking the internal standard prior to sample digestion as this would lead to more robustness in the method workflow and allow for new possibilities in the sample preparation. A combination of several standards as well the consideration of some possible endogenous standard proteins (those that would most probably stay unchanged due to their biology) may further improve the accuracy of the method.

Eight regulated proteins comprising those displaying significant differences or similarities with regard to the relative quantification ratios calculated with ICPL and label-free techniques were selected to be validated employing the MRM approach. The initial ICPL analysis delivered protein identifications along with masses of peptides (MS) and their fragments (MS/MS) that were used in the MRM experiment (see Table 3). These so-called transitions (fragmentation of precursor to product ions) were employed to selectively isolate and quantify proteins using the tandem MS. The choice of the MRM suitable peptides was guided primarily by four important criteria: the peptides should (i) be tryptic and contain no missed cleavage sites, (ii) have a high score (Mascot), (iii) contain no cysteine residues (avoid carbamidomethylation) and (iv) have the sequence specific for the selected protein (all the sequences were checked using the BLAST program (NCBI) and compared with the Swiss-Prot human database). Peptides which fulfilled these requirements were further sorted according to their respective product ion spectra and the ones that contained the most intense "y" series fragments were selected. The respective peptides of two proteins that appeared to have the same concentration in both samples (considering the label-free and ICPL data, Fig. 1) were assigned to serve as a pseudo internal control (A2GL and IC1). Inherent to this approach these pseudo internal standards were used to also account for differences that might result during the tryptic digestion. Peptide ionisation differences were normalized by calculating the average peak area ratio of the internal control peptides between individual injections. This value was employed as the correction factor for the ratio calculations of the remaining eight proteins (A1AG2, A1BG, A2AP, CO8G, FIBB, PEDF, THBG and VTNC). Generally the MRM based quantification correlated well with both methods. In particular for the proteins that have shown opposing quantification results (A2AP, PEDF and THBG) the MRM data were more supportive of the label-free quantification results. One exception was CO8G protein where the MRM quantification was closer to the result obtained by the ICPL method (Table 4). Taken together 66 proteins that were found in common to the two quantification strategies (ICPL and label-free). Of these 7 proteins showed discrepant results. Considering the ICPL data these proteins have been quantified mainly by 2 or more labeled peptides, which shows that successful ICPL quantification is not dependent only on the number of labeled peptides. Apparently other factors like signal to noise ratio (S/N) of the MS spectra appeared to be decisive. Indeed the proteins in question were quantified using predominantly peptides that had an average S/N of 15. Good quantification results were achieved with peptides that had an S/N above 30. The trend was observed throughout the ICPL experiments (data not shown here) and points at the need to assess each of the peptides on individual basis.

In contrast to the sample preparation for the ICPL and the label-free method, the MRM quantification was performed without prior depletion of the major serum proteins. This offered a good basis for an overall evaluation of the sample preparation. The IgY-12 kit was used to selectively remove 12 highly abundant proteins from the serum samples. These proteins are: ALBU, IGHG, IGHM, IGHA, TRFE, HPT, A1AT, FIB(A/B), A1AG(1/2) and A2MG. Of these FIBB and A1AG2 were evaluated in all three quantification methods and yielded similar results. Others (except IGHG1 and IGHG4) have also shown consistent results using the ICPL and the label-free technique. This may indicate that the depletion of the abundant proteins using the IgY-12 kit did not alter the original relationship of these proteins in the serum sample. Moreover the technique proved to be reproducible results are obtained within technical replicates. Along these lines, the MRM together with the label-free results have shown that the additional fractionation with SCX Dynabeads and subsequent double enzymatic digestion (trypsin and Glu-c) employed in the ICPL method did not alter the quantification results.

Table 4
MRM quantification of the eight selected proteins. The SD indicates the standard deviation of means ($n = 3$).

Protein	MRM quantification	
	Ratio	SD
A1AG2	0.54	0.09
A1BG	1.24	0.01
A2AP	1.63	0.29
CO8G	2.77	0.07
FIBB	1.24	0.25
PEDF	1.40	0.38
THBG	0.95	0.13
VTNC	2.37	0.35

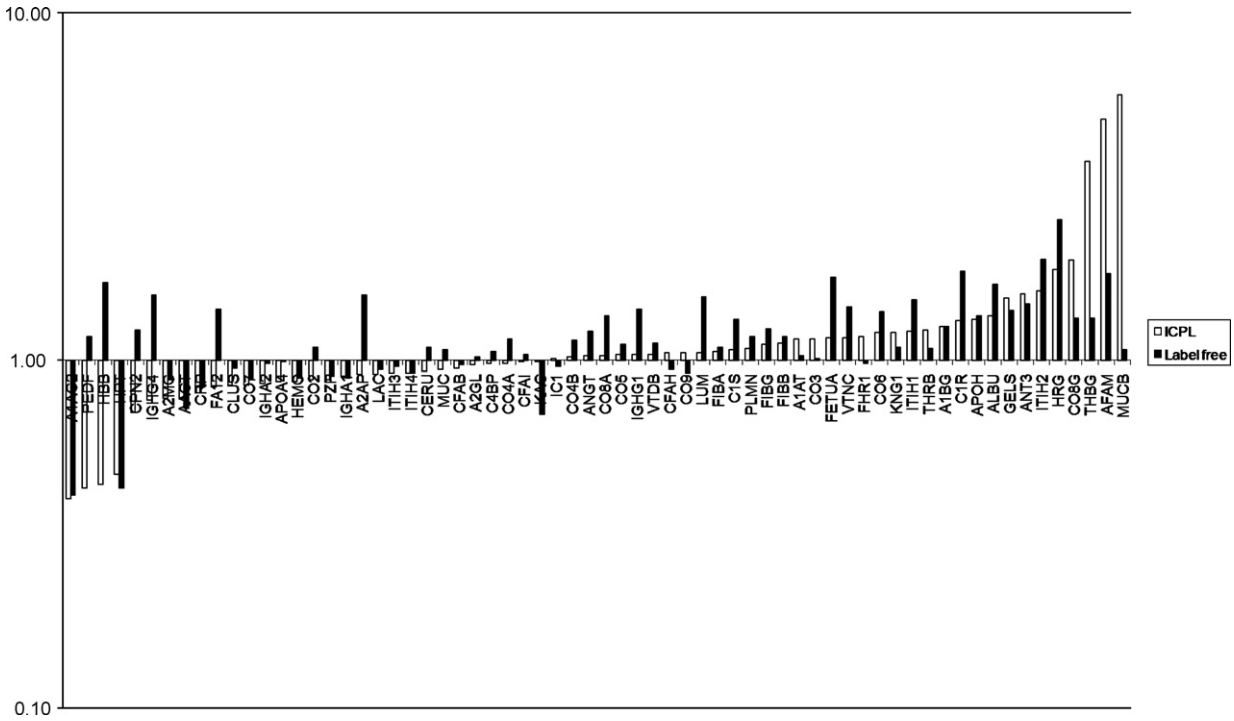


Fig. 2. The comparison of the relative quantification of the G2 vs. G1 sample using the ICPL and the label-free method. In total 66 commonly identified and quantified proteins have been displayed.

4. Summary and perspectives

Considering all the results presented here both ICPL and label-free approach are promising techniques for protein quantification in complex mixtures. In direct comparison label-free approach does seem to a certain extent more advantageous since:

(i) the sample preparation method was simpler (see Fig. 1), the instrumentation required less amount of sample (column load of approximately 0.2 ng was sufficient compared with ICPL where 5 μg were used),
(ii) the quantification appeared to be more accurate (7/8 proteins were validated compared to ICPL where 5/8 proteins showed the similar ratio as the MRM technique; see Fig. 2) and
(iii) quantitative information was provided for all identified proteins in at least one out of three replicates (ICPL could provide the quantification only if the peptides contained the label).

Regarding the serum sample, being characterized with the large dynamic range of protein concentrations, extensive fractionation has clearly shown to improve the number of proteins identified. The MRM strategy, well known as a method of choice for the quantification of small molecules, has proved to be of great value for relative label-free quantification of specific proteins. Future studies should consider the development of suitable pre-fractionation techniques that could be used with the label-free quantification methods. The emphasis in further development of both quantification methods should ideally be laid on functional protein separation (phospho-, glycoproteins, etc.) as this is of significant biological relevance.

Acknowledgments

The authors are grateful to the Walloon Region for the funding of the SENEGENE project, to Dr. Marie de Saint-Hubert and Prof. Christian Swine from the Catholic University of Louvain, Mont-Godinne University Hospital, for providing the serum samples. The authors acknowledge GIGA consortium and the proteomics platform of the University of Liege for providing material help.

References

[1] M.V. Faca, S.J. Pitteri, L. Newcomb, V. Glukhova, D. Phanstiel, A. Krasnoselsky, Q. Zhang, J. Struthers, H. Wang, J. Eng, M. Fitzgibbon, M. McIntosh, S. Hanash, J. Proteome Res. 6 (9) (2007) 3558–3565.
[2] S.J. Pitteri, V.M. Faca, K.S. Kelly-Spratt, A.E. Kasarda, H. Wang, Q. Zhang, L. Newcomb, A. Krasnoselsky, S. Paczesny, G. Choi, M. Fitzgibbon, M.W. McIntosh, C.J. Kemp, S.M. Hanash, J. Proteome Res. 7 (4) (2007) 1481–1489.
[3] S.M. Hanash, S.J. Pitteri, M.V. Faca, Nature 452 (2008) 571–579.
[4] D.R. Goodlett, A. Keller, J.D. Watts, R. Newitt, E.C. Yi, S. Purvine, J.K. Eng, P. von Haller, R. Aebersold, E. Kolker, Rapid Commun. Mass Spectrom. 15 (14) (2001) 1214–1221.
[5] M. Heller, H. Mattou, C. Menzel, X. Yao, J. Am. Soc. Mass Spectrom. 14 (7) (2003) 704–718.
[6] S. Sechi, Rapid Commun. Mass Spectrom. 16 (15) (2002) 1416–1424.
[7] S.P. Gygi, B. Rist, S.A. Gerber, F. Turecek, M.H. Gelb, R. Aebersold, Nat. Biotechnol. 17 (10) (1999) 994–999.
[8] P.L. Ross, Y.N. Huang, J.N. Marchese, B. Williamson, K. Parker, S. Hattan, N. Khainovski, S. Pillai, S. Dey, S. Daniels, S. Purkayastha, P. Juhasz, S. Martin, M. Bartlet-Jones, F. He, A. Jacobson, D.J. Pappin, Mol. Cell. Proteomics 3 (12) (2004) 1154–1169.
[9] A. Schmidt, J. Kellermann, F. Lottspeich, Proteomics 5 (1) (2005) 4–15, Erratum in: Proteomics 5 (3) 826.
[10] M. Bantscheff, M. Schirle, G. Sweetman, J. Rick, B. Kuster, Anal. Bioanal. Chem. 389 (4) (2007) 1017–1031.
[11] G. Hergenroeder, J.B. Redell, A.N. Moore, W.P. Dubinsky, R.T. Funk, J. Crommett, G.L. Clifton, R. Levine, A. Valadka, P.K. Dash, J. Neurotrauma 25 (2) (2008) 79–93.
[12] A. Schmidt, B. Bisle, T. Kislinger, Methods Mol. Biol. 492 (2009) 21–38.
[13] J. Kellermann, Methods Mol. Biol. 424 (2008) 113–123.
[14] J. Silva, R. Denny, C. Dorschel, M. Gorenstein, I. Kass, G.Z. Li, T. McKenna, M. Nold, K. Richardson, P. Young, S.J. Geromanos, Anal. Chem. 77 (2005) 2187–2200.
[15] S.J. Geromanos, J.P. Vissers, J.C. Silva, C.A. Dorschel, G.-Z. Li, M.V. Gorenstein, R.H. Bateman, J.I. Langridge, Proteomics 9 (6) (2009) 1683–1695.
[16] G.-Z. Li, J.P. Vissers, J.C. Silva, D. Golick, M.V. Gorenstein, S.J. Geromanos, Proteomics 9 (6) (2009) 1696–1719.
[17] F.Y. Cheng, K. Blackburn, Y.M. Lin, M.B. Goshe, J.D. Williamson, J. Proteome Res. 8 (1) (2009) 82–93.
[18] E.-M. Krämer-Albers, N. Bretz, S. Tenzer, C. Winterstein, W. Möbius, H. Berger, K.-A. Nave, H. Schild, J. Trotter, Proteomics 1 (11) (2007) 1446–1461.
[19] J.P. Vissers, J.I. Langridge, J.M. Aerts, Mol. Cell. Proteomics 6 (5) (2007) 755–766.
[20] D. Xu, N. Suenaga, M.J. Edelmann, R. Fridman, R.J. Muschel, B.M. Kessler, Mol. Cell. Proteomics 7 (2008) 2215–2228.
[21] T. Tabata, T. Sato, J. Kuromitsu, Y. Oda, Anal. Chem. 79 (22) (2007) 8440–8445.
[22] J.C. Silva, M.V. Gorenstein, G.-Z. Li, J.P. Vissers, S.J. Geromanos, Mol. Cell. Proteomics 5 (2006) 144–156.

Talanta 80 (2010) 1496–1502

Contents lists available at ScienceDirect

Talanta

journal homepage: www.elsevier.com/locate/talanta

Evaluation of isotope-coded protein labeling (ICPL) in the quantitative analysis of complex proteomes

Alberto Paradela[a,*], Miguel Marcilla[a], Rosana Navajas[a], Laura Ferreira[c], Antonio Ramos-Fernandez[a], Marisol Fernández[a], Javier Fernando Mariscotti[b], Francisco García-del Portillo[b], Juan Pablo Albar[a]

[a] Laboratorio de Proteómica, Centro Nacional de Biotecnología, Consejo Superior de Investigaciones Científicas (CSIC), Madrid, Spain
[b] Departamento de Biotecnología Microbiana, Centro Nacional de Biotecnología, Consejo Superior de Investigaciones Científicas (CSIC), Madrid, Spain
[c] Unidad de Investigación, Hospital Universitario, Salamanca, Spain

ARTICLE INFO

Article history:
Available online 9 July 2009

Keywords:
Stable isotopic labeling
Mass spectrometry
Quantitative proteomics
ICPL

ABSTRACT

An evaluation of the ICPL (isotope-coded protein labeling) non-isobaric labeling technique was performed using two different biological models. Two samples containing phage T4 capsids were mixed in a 1:1 ratio after being labeled with the light or heavy versions of the ICPL reagent. The analysis of this proteome demonstrated the feasibility of this approach for differential quantitative proteomics and was employed to optimize the experimental parameters of the ICPL workflow. ICPL-mediated analysis of two more complex proteomes, those of a *Salmonella enterica* serovar Typhimurium virulent strain and an isogenic attenuated mutant, and its comparison with the results obtained in a 2D-PAGE "classical" approach confirmed that ICPL is a valuable alternative to other labeling techniques currently in use. In addition, our results suggest that labeling at the peptide level instead of following the standard ICPL workflow should increase both the number of proteins quantified and the reliability of the quantification.

© 2009 Elsevier B.V. All rights reserved.

1. Introduction

The development of new quantitative tools for the analysis and comparison of whole proteomes (differential proteomics) has been continuous during the past years. Traditional approaches, based on previous fractionation of complex proteomes by 2D-gel electrophoresis and comparison of the gel images generated thereby, are being complemented by new techniques that commonly make use of isotopic labeling of the samples to be compared, followed by liquid chromatography coupled to electrospray tandem mass spectrometry [1,2]. Isotopic labeling can be performed *in vivo* (e.g., SILAC [3]), chemically (e.g., ICAT [4], cICAT [5], iTRAQ [6], Lys-tag [7], ICPL [8], TMT [9]) or enzymatically (e.g., $^{16}O/^{18}O$ [10,11]). In addition, label-free techniques show increasing acceptance as ultra-high performance liquid chromatography systems are becoming available and software developments required to compare multiple LC–MS runs are gaining efficiency and reliability [12].

Among differential proteomics methods based on stable isotopic labeling, ICPL is a non-isobaric technique devised to efficiently label primary amines profusely found in proteins. Relative quantification is achieved by comparison of the relative abundance (regarded as either peak intensity or area) of the differentially labeled peptides. The latest version of this reagent allows the comparison of up to four samples at the same time. Theoretically, ICPL overcomes some of the disadvantages found in other chemical labeling techniques, such as iTRAQ (poor detectability of the reporter ions in several types of mass spectrometers) or ICAT (low number of potentially labelable residues). However, the number of articles published to date using ICPL is noticeably low [13–15] when compared with other methods and no clear consensus exists on its feasibility as a quantitative tool. Here we describe a comprehensive evaluation of this technique using two different biological models. First, the proteome of the bacteriophage T4 capsid was labeled with the light or heavy version of ICPL and mixed in a 1:1 ratio. This sample was then used to evaluate the viability and robustness of the ICPL approach as well as to determine the optimal experimental parameters. In the second case, we compared a more complex sample composed of whole proteomes from a *Salmonella enterica* serovar Typhimurium virulent strain and an isogenic strain harboring a mutation in the Intracellular-growth-attenuator-A (*IgaA1*). The Intracellular-growth-attenuator-A (*IgaA*) is a *S. enterica* membrane protein that inhibits the RcsC-YojN-RcsB regulatory system preventing its over activation. Mutations in *IgaA* have been shown to drastically alter the bacterial transcriptome

Abbreviations: CID, collision-induced dissociation; 2D-PAGE, bidimensional polyacrilamide gel electrophoresis; ICAT, isotope-coded affinity tag; ICPL, isotope-coded protein labeling; iTRAQ, isotope tagging for relative and absolute quantification; LC ESI-MS/MS, liquid chromatography coupled to electrospray tandem mass spectrometry; MALDI-TOF, matrix-assisted laser desorption-ionization time-of-flight; ORF, open-reading frame; SILAC, stable isotope labeling with amino acids in cell culture.

* Corresponding author.
E-mail address: alberto.paradela@cnb.csic.es (A. Paradela).

0039-9140/$ – see front matter © 2009 Elsevier B.V. All rights reserved.
doi:10.1016/j.talanta.2009.06.083

[16]. Using this approach, more than 500 different proteins were identified and about 150 could be quantified as well. Our results demonstrate that ICPL may be a very valuable alternative to iTRAQ when the analysis of iTRAQ specific reporter ions is not possible and clearly overcomes the limitations imposed by other non-isobaric labeling approaches, such as ICAT. However, our data also point out that the number of proteins quantified and the reliability of the quantification results would benefit from modifications in the standard experimental workflow.

2. Experimental

2.1. Chemicals and reagents

ICPL-labeling kit including all the reagents needed to differentially label two samples was purchased from Serva Electrophoresis (Heidelberg, Germany). Labeling was performed according to manufacturer's instructions. A more detailed description of the protocol can be found elsewhere [8,14,17]. Recombinant trypsin (proteomics grade) was purchased from Roche Diagnostics GmbH (Mannheim, Germany). Mass spectrometry-grade water, acetonitrile and formic acid used in LC ESI-MS/MS analysis were supplied by Fluka Analytical (Buchs, Switzerland). Except when indicated, all the reagents used in 2D-PAGE analysis were obtained from Amersham Biosciences (Uppsala, Sweden).

2.2. Samples

The T4 bacteriphage capsid proteome was a generous gift of Dr. Peter James (Lund University, Sweden). This sample comprises 37 different proteins with copy numbers ranging between 3 and 960 and molecular weight ranging between 2.5 and 140 kDa. The two different *S. enterica* serovar Typhimurium strains (wild-type and *IgaA1* mutant [16]) were grown in LB medium until stationary phase was reached.

2.3. 2D-PAGE analysis

Sample aliquots (100 μg) were mixed with Rehydration buffer (7 M urea, 2 M thiourea, 4% CHAPS, 0.5% carrier ampholites pH 4–7, 50 mM DTT) in a final volume of 350 μl and applied to a dry IPG strip (18 cm, 4–7 L, General Electric Healthcare, Uppsala, Sweden) for reswelling. Focusing was carried out on an Ettan IPGphor system (General Electric Healthcare) by increasing voltage as follows: 30 V/h for 7 h, 60 V/h for 7 h, 120 V/h for 1 h, 250 V/h for 1 h, 500 V/h for 1 h, 1000 V/h for 1 h, then voltage was increased from 1000 to 8000 V in 0.5 h, and kept constant at 8000 V until a total of 35,000 V was reached. After IEF separation, the strips were equilibrated twice for 10 min in 50 mM Tris–HCl (pH 8.8), 6 M urea, 30% glycerol, 2% SDS, and trace amounts of bromophenol blue. The first equilibration solution contained 1% DTT while the second contained 4% iodoacetamide (IAA). The second dimension (SDS-PAGE) was performed on 12.5% polyacrylamide gels (1 mm, 16 cm × 15 cm). Gels were run at 7 mA per gel overnight maintaining buffer temperature at 4 °C. Staining was carried out with SYPRO Ruby Protein Gel Stain (Sigma–Aldrich, St Louis, MO) as follows: gel was fixed in 10% methanol, 7% acetic acid for 30 min, incubated overnight in SYPRO Ruby staining solution, washed twice with 10% methanol, 7% acetic acid for 30 min, and finally, washed twice with water for 10 min.

Gels were then scanned in a Typhoon™ 9400 Variable Mode Imager (General Electric Healthcare) equipped with a 532 nm excitation laser with the emission filter adjusted to 610 nm and 100 μm resolution. The photomultiplier tube settings were modified to optimize sensitivity to background ratios (600 V for SYPRO-R). 2D-PAGE images were analyzed with Image Master 2D-Platinum 5.0 (General Electric, Healthcare).

2.4. Digestion

ICPL-labeled bacteriophage T4 proteome was dissolved in 2 M Urea, 25 mM ammonium bicarbonate and 10 μg were digested with trypsin (ratio 20:1) for 6 h at 37 °C.

ICPL-labeled *S. enterica* proteome was fractionated in a 12% SDS-PAGE gel. About 25–30 slices were excised manually, deposited in 96-well plates and processed automatically in a Proteineer DP (Bruker Daltonics, Bremen, Germany). The digestion protocol used was described by Shevchenko et al. [18] but the following minor variations were introduced: gel plugs were washed first with 50 mM ammonium bicarbonate and then with acetonitrile prior to reduction with 10 mM DTT in 25 mM ammonium bicarbonate; alkylation was carried out with 55 mM IAA in 50 mM ammonium bicarbonate. Gel pieces were then rinsed with 50 mM ammonium bicarbonate and with 100% acetonitrile, and then dried under a stream of nitrogen. Modified porcine trypsin (sequencing grade; Promega, Madison WI) or endoGluC (Roche, Mannheim, Germany) was added at a final concentration of 16 or 25 ng/μl, respectively, in 25% acetonitrile, 50 mM ammonium bicarbonate and digestion proceeded for 6 h at 37 °C. The reaction was stopped by adding 0.5% TFA for peptide extraction. Tryptic peptides were dried by speed-vacuum centrifugation and resuspended in mobile phase A (0.1% formic acid in water) for LC ESI-MS/MS. In the case of the 2D-PAGE analysis, spots of interest were excised automatically using an Ettan Spot Picker Workstation (GE), deposited into 96-well plates and processed automatically as previously described.

2.5. Peptide mass fingerprint

For the identification of 2D-PAGE spots, MALDI-TOF mass spectra were acquired automatically on a Bruker Reflex IV MALDI-TOF mass spectrometer (Bruker Daltonics, Bremen, Germany) using FlexControl 1.1 and then processed with Xtof 5.1.1. Each spectrum was calibrated internally with two trypsin autolysis reference ions at m/z 842.510 and 2211.105 reaching typically an accuracy of ±30 ppm in the 800–3000 m/z range. All signals corresponding to known contaminants were excluded during the process and signal-to-noise threshold was limited to 20. Tryptic peptide masses were transferred to BioTools 2.0 (Bruker Daltonics) for searching against the Salmonella database using a licensed version of Mascot v.2.2.04 (www.matrixscience.com; Matrix Science, London, UK) as search engine. Search parameters were set as follows: carbamidomethylated cysteins as fixed modification and oxidized methionines as variable one, peptide mass tolerance was set to 80 ppm and one missed cleavage was allowed. In all protein identifications, the probability mowse scores were greater than the minimum score fixed as significant with a p-value below 0.05.

2.6. LC ESI-MS/MS analysis

LC ESI-MS/MS analysis was performed on an Ultimate 3000 nanoHPLC (Dionex, Sunnyvale, California) coupled to an HCT Ultra ion-trap mass spectrometer (Bruker Daltonics, Bremen, Germany). The analytical column used was a silica-based reversed phase column C18 PepMap 75 μm × 15 cm, 3 μm particle size and 100 Å pore size (Dionex, Sunnyvale, California). The trap column was a C18 PepMap (Dionex, Sunnyvale, California), 5 μm particle diameter, 100 Å pore size, switched on-line with the analytical column after a 5 min loading time. The loading pump delivered a solution of 0.1% trifluoroacetic acid in 98% water/2% acetonitrile at 30 μl/min. The nanopump provided a flow-rate of 300 nl/min and was operated under gradient elution conditions, using 0.1% formic acid as mobile phase A, and 0.1% formic acid in 80% acetonitrile, 20% water

as mobile phase B. Gradient elution was performed according the following scheme: isocratic conditions of 4% B for 5 min, a linear increase to 40% B in 60 min, a linear increase to 95% B in 1 min and isocratic conditions of 95% B for 7 min. Injection volume was 5 μl and absorbance was monitored at 214 and 280 nm.

The LC system was coupled via a nanospray source to the ion trap mass spectrometer operating in positive ion mode with the capillary voltage set at 1400 V. Two different automatic data-dependent acquisition methods were used for the T4 bacteriophage sample. In both a full scan (m/z 350–1500) MS analysis was performed and then, either the four most abundant ions were isolated for CID fragmentation (non-SILE method), or the two most abundant ions and their putative ICPL-labeled counterparts according to their measured masses were fragmented (SILE method). In both cases, a dynamic exclusion was applied which prevented the same m/z from being isolated for 1 min after its fragmentation. For the *S. enterica* serovar Typhimurium samples, only the SILE method was used. Raw LC–MS data were processed using DataAnalysis 3.4 (Bruker Daltonics, Bremen, Germany). When samples were first fractionated by monodimensional SDS-PAGE, the data obtained from the LC runs corresponding to different gel slices were merged using the Analysis Combiner tool before processing them as a single experiment. Processed files were analyzed using WARP-LC 1.1 (Bruker Daltonics) for their qualitative and quantitative analysis. For protein identification, LC ESI-MS/MS spectra were searched against the SwissProt database or against a homemade Salmonella SL1344 database containing 5065 ORFs using Mascot. Search parameters were set as follows: carbamidomethylated cysteines as fixed modification, oxidized methionines and ICPL-light (+105.02 Da) and -heavy (+111.04 Da) labeled lysine residues or protein amino termini as variable ones. Peptide mass tolerance was set to 0.5 Da both in MS and MS/MS mode, and one missed cleavage was allowed. Typically, an accuracy of ±0.1–0.2 Da was found both for MS and MS/MS spectra. For quantitative analysis, extracted ion chromatograms of those peptides identified with Mascot scores ≥25 were considered. When only one ICPL-labeled peptide was identified, the extracted ion chromatogram of its putative partner was used for quantification. Putative ICPL pairs were determined allowing a mass tolerance of 0.5 Da and a retention time tolerance of 40 s. Relative ratios between the heavy and light counterparts of ICPL-labeled peptides were calculated using the intensity of their respective monoisotopic peaks.

3. Results and discussion

3.1. Differential proteomics analysis of the T4 bacteriophage capsid proteome

To evaluate the feasibility of the ICPL approach in quantitative proteomics, we first analyzed the T4 bacteriophage capsid proteome. 100 μg of purified T4 bacteriophage capsid were labeled either with the light or the heavy version of the ICPL reagent, mixed in a 1:1 ratio and digested in solution with trypsin (Fig. 1). 2 μg of the mixture were analyzed in each LC ESI-MS/MS run and two different LC ESI-MS/MS acquisition methods were employed (see Section 2): (1) the two most prominent signals in each survey scan as well as their putative ICPL-labeled partners were isolated and fragmented (SILE method) and (2) the four most abundant ions of each MS spectrum were isolated and fragmented (non-SILE method). Two independent LC ESI-MS/MS analysis were performed in each case and raw data were combined using the Analysis Combiner tool included in WARP-LC before their processing for protein identification and quantification. Results obtained in both experiments are summarized in Table 1. A total number of 20 and 23 different proteins, respectively, were identified with Mascot scores ranging from 32 to 1146. In each case, the number of identified

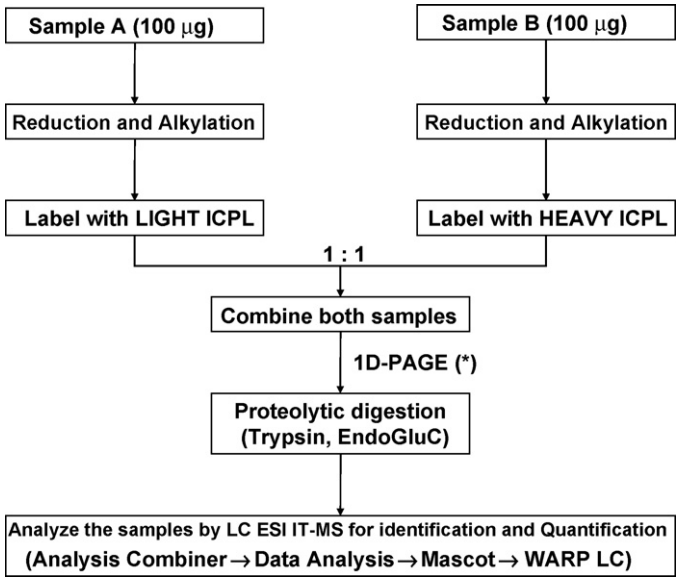


Fig. 1. Diagram of the standard experimental workflow used in the analysis of ICPL-labeled samples. An additional fractionation step (e.g., by 1D-PAGE) is mandatory for the analysis of complex samples.

peptides, either labeled or unlabeled, was very similar as it was the fraction of ICPL-labeled peptides, 37% and 34% for the SILE and non-SILE approach, respectively. This result indicates that none of the approaches offers a truly significant improvement. In terms of protein identification, three additional proteins were identified when the non-SILE method was used. Other minor differences were found: sequence coverage values were higher for 15 out of 23 proteins in the non-SILE dataset while these values were higher for six proteins in the SILE one. ICPL-labeling did not affect significantly the identity score of the peptides, as it was demonstrated by comparing the averaged scores of ICPL-labeled and non-labeled peptides (data not shown). Similarly, the chromatographic behavior of the peptides labeled with the light or heavy versions of the ICPL reagent were near identical, and no differences regarding the retention times of light and heavy ICPL pairs could be detected (data not shown). This feature contrasts with the lack of chromatographic reproducibility introduced by other non-isobaric reagents such as deuterated ICAT [19,20] and increases the reliability of ICPL as a differential proteomics tool.

Regarding protein quantification, no significant differences were found between both datasets. About 2/3 of the identified peptides were not labeled and, thus, did not contribute to the quantification of the protein mixture irrespectively of the acquisition method used (Table 1). When using the SILE acquisition method 19 out of 20 proteins were quantified with ICPL-heavy/ICPL-light (H/L) ratios ranging between 0.73 and 1.24, very close to the expected 1:1 ratio. Similarly, in the non-SILE dataset, 16 out of 20 quantified proteins showed H/L ratios ranging between 0.79 and 1.39. Nonetheless, some significant deviations from the expected values were found. These were caused by different factors, being the most common the coelution of the ICPL-labeled peptides and another molecular species with almost identical m/z value and to the inability of the mass spectrometer and the data processing software to discriminate them. For example, P12726 expression rate is drastically increased by the contribution of a single ICPL-labeled peptide pair, QYKIDACMLR (Table 2). Consistently, the H/L ratio of this protein in the non-SILE analysis (0.98), where the peptide QYKIDACMLR could not be identified, is extremely close to the expected one (Table 2). Fig. 2A shows that this peptide pair elutes very close (elution time 126.9–127.2) to an unidentified charge 3+

Table 1
Differential proteomics analysis of the T4 bacteriophage sample. The protein name, accession number, number of peptides identified (# Pept), number of peptides labeled with ICPL (# Pept (ICPL)), heavy/light ratio (H/L), sequence coverage (Cov (%)) and Mascot score (Score) is given for each protein identified using the SILE and the non-SILE approaches.

Protein name	Accession number	SILE method					Non-SILE method				
		# Pept	# Pept (ICPL)	H/L	Cov (%)	Score	# Pept	# Pept (ICPL)	H/L	Cov (%)	Score
17 kDa prohead core protein	P04538	12	3	1.10	24.8	191.5	12	6	1.03	24.1	206.6
Baseplate structural protein Gp11	P10929						2	2	1.37	5.5	79.4
Baseplate structural protein Gp6	P19060	6	3	1.24	6.8	181.6	2	1	0.95	3.8	111.1
Baseplate structural protein Gp7	P19061	9	2	0.91	2.8	162.0	8	3	0.84	4.0	179.5
Baseplate structural protein Gp8	P19062	6	2	0.95	4.8	87.5	4	3	1.35	12.3	90.2
Fibritin	P10104	5	2	0.73	17.5	261.8	5	2	0.58	10.9	234.7
Gene 57B protein	P04533						2	1	44.71	13.8	80.1
Head vertex protein Gp24	P19896	19	8	0.99	13.8	386.0	8	6	1.31	14.8	362.5
Highly immunogenic outer capsid protein	P18056	3	2	0.82	5.1	83.9	1			3.7	32.3
Internal protein III	P13302	2	2	0.78	7.3	87.7	3	3	0.79	16.6	165.0
Large tail fiber protein p34	P18771	17	6	1.01	11.6	519.5	19	8	0.89	15.4	816.4
Long tail fiber protein p37	P03744	22	7	0.88	9.7	536.0	16	4	0.98	9.5	587.2
Major capsid protein	P04535	49	19	1.02	34.9	707.2	39	13	1.52	31.3	788.0
NAD-protein ADP-ribosyltransferase	P12726	11	6	2.31	6.7	310.0	12	4	0.98	13.5	475.5
Neck protein Gp13	P11110	4	1	1.09	7.1	89.9	4	1	2.51	12.0	169.0
Short tail fiber protein	P10930	14	4	1.13	16.1	478.5	19	3	1.05	22.2	629.9
Small outer capsid protein	P03715	4	2	0.74	18.8	60.0	3	1	0.93	18.8	42.2
Structural protein of head	P13334	1	1	1.04	3.6	62.2	6	1	1.13	7.1	211.6
Tail connector protein Gp15	P11112						1			4.0	74.3
Tail fiber protein p36	P03743	3	3	0.93	15.8	71.2	10	4	1.1	25.3	373.8
Tail sheath protein Gp18	P13332	23	8	1.21	16.5	711.1	36	9	1.39	28.4	1146.6
Tail tube protein Gp19	P13333	18	5	0.82	20.9	228.5	16	4	0.89	20.9	220.2
Tail-tube assembly protein Gp48	P13339	5	1	0.85	6.0	155.6	2			6.3	146.9
		233	87				230	79			

peptide pair (Fig. 2B, elution time minute 127.3–127.6). Although elution times do not overlap precisely they are close enough to get mixed up when quantifying with the WARP-LC standard parameters (Fig. 2C). These were set to consider peptide signals with similar m/z value (± 0.5) and retention time ($\pm$ 20 s) as corresponding to the same molecular species. It should be noted that these parameters were not set arbitrarily but according to the technical specifications of the LC ESI-MS/MS equipment employed. An even more drastic situation was found in other cases (e.g., P04533, data not shown).

3.2. Differential proteomics analysis of the S. enterica serovar Typhimurium proteome

To evaluate the performance of ICPL in the relative quantitation of complex proteomes, we compared two different *S. enterica* serovar Typhimurium proteomes (wild-type and *IgaA1* mutant). Protein extracts prepared from wild-type and mutant *IgaA1* strains were labeled with the light and heavy versions of the ICPL reagent, respectively. The experimental workflow used was similar to that described for the analysis of the bacteriophage T4. As the complex-

Table 2
Summary of the results obtained for the T4 bacteriophage protein P12726. The peptide sequence, ICPL labeling (ICPL), calculated m/z value (m/z (calc)), delta mass (Δm (Da)), charge (z), Mascot score (score), signal to noise ratio (S/N), and heavy/light ratio (H/L) is given for each peptide identified using the SILE and non-SILE approaches. ICPL-labeled lysine residues are shown in bold.

Sequence	ICPL	m/z (calc)	Δm (Da)	z	Score	S/N	H/L
SILE							
AIAQSQSLESSR	–	638.83	0.10	2	98.93	150.6	–
AIAQSQSLESSR	–	638.83	0.21	2	88.33	110.0	–
IL**K**S**K**TAGQAR	Light	691.88	−0.10	2	69.64	42.9	1.10
	Heavy	697.90	−0.13	2	72.97	55.0	
IL**K**S**K**TAGQAR	Light	691.88	0.26	2	76.35	70.1	1.13
	Heavy	697.90	0.26	2	80.51	79.3	
QY**K**IDACMLR	Light	701.83	0.02	2	29.80	25.1	5.49
	Light	701.83	0.22	2	46.90	17.7	4.27
MLPSIYEAMV**K**NR	Light	552.95	0.10	3	46.85	3.6	1.21
MLP-SIYEAMV**K**NR	Light	828.92	0.30	2	88.73	15.2	1.00
	Light	552.95	0.46	3	38.77	24.5	1.00
Non-SILE							
QIQVIADR	–	471.77	0.15	2	49.01	33.3	–
QIQVIADR	–	471.77	0.17	2	46.97	42.1	–
AIAQSQSLESSR	–	638.83	0.39	2	96.18	34.2	–
RAIAQSQSLESSR	–	716.88	0.27	2	78.29	61.1	–
RAIAQSQSLESSR	–	716.88	0.34	2	72.2	28.1	–
EYVGSGYVDINNALLGLYNPDER	–	857.75	0.43	3	53.48	24.7	–
EASI-IPED**K**ESIINAEI**K**N**K**ALER	Light	1009.18	0.20	3	28.38	20.3	0.91
	Heavy	1015.20	0.14	3	43.02	12.3	
ILKS**K**TAGQAR	Light	691.88	0.22	2	69.42	28.3	0.92
	Heavy	697.90	0.31	2	80.28	27.9	
ILKS**K**TAGQAR	Heavy	697.90	0.32	2	80.46	24	1.04
MLPSIYEAMV**K**NR	Light	828.92	0.29	2	82.67	39.4	1.06

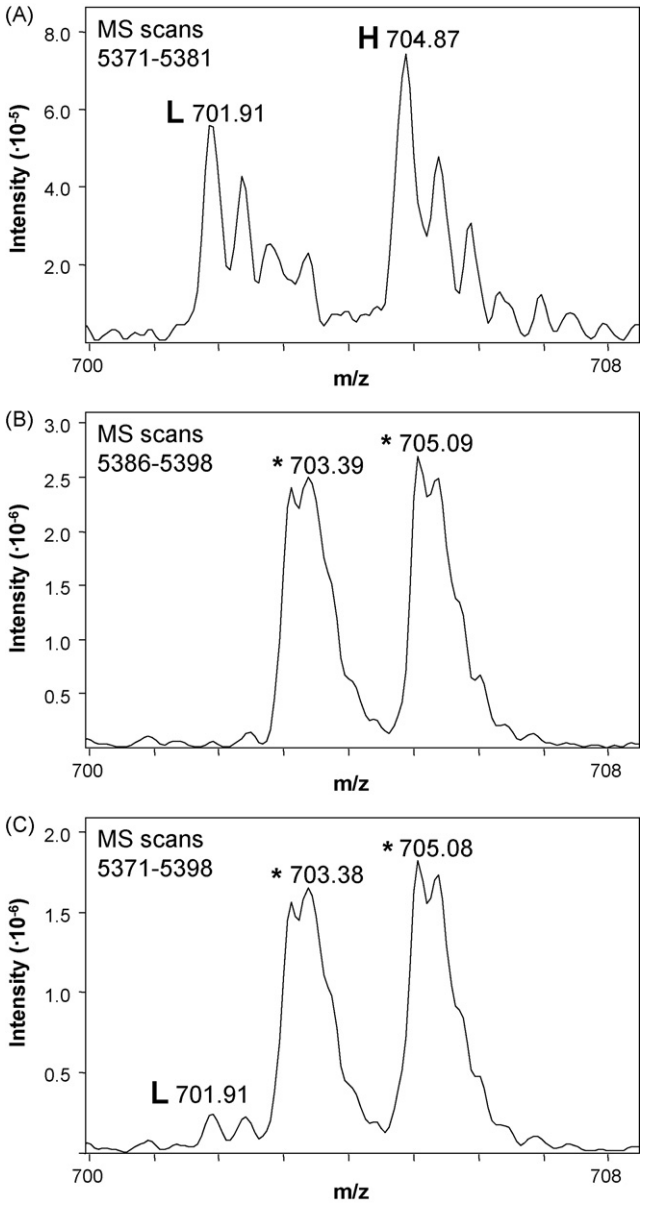


Fig. 2. Averaged survey scans of (A) MS scans 5371–5381 corresponding to the doubly charged peptide QYKIDACMLR labeled with light ICPL (m/z = 701.91) and heavy ICPL (m/z = 704.87); (B) MS scans 5386–5398 corresponding to an unidentified charge 3+ MS signal (m/z = 703.39 and m/z = 705.08) and (C) MS scans 5371–5398. Note that the coelution of m/z signals 703.39 and 705.08 interferes with the calculation of the H/L ratio corresponding to QYKIDACMLR.

ity of the bacterial proteome was much higher, an additional 1D SDS-PAGE fractionation step was carried out after mixing the ICPL-labeled samples (Fig. 1) and, since no significant differences were detected, only the SILE acquisition method was used. In the first experiment, 26 gel-slices were excised and 50% of each slice was digested using trypsin or endoGluC. The resulting peptide mixture was independently analyzed by LC ESI-MS/MS. In a second labeling experiment, 29 slices obtained after 1D SDS-PAGE fractionation of ICPL-labeled samples were digested with trypsin and analyzed by LC ESI-MS/MS. In all cases, the individual MS and MS/MS data obtained from each gel slice were combined using the Analysis Combiner tool available in WARP LC 1.1 and processed as a single file. As shown in Table 3, a total number of 376, 363 and 439 different proteins were identified in each experiment, respectively. However, only between 54% and 64% of the identified proteins were

Table 3
Summary of the results obtained in the *Salmonella enterica* serovar Typhimurium differential proteomics analysis. .

	Experiment #1		Experiment #2
	Trypsin	endoGluC	Trypsin
Proteins identified	376	363	439
Proteins quantified (# pept ≥ 1)	205 (54%)	178 (49%)	281 (64%)
Proteins quantified (# pept ≥ 2)	94 (25%)	79 (22%)	167 (38%)

amenable to quantification, namely those that included at least one ICPL-labeled peptide. Furthermore, the percentage of proteins that could be quantified dropped to values between 22% and 38% when more restrictive criteria were established, such as the use of at least two ICPL-labeled peptides. These results underline the fact that modifying the standard ICPL workflow may be necessary when analyzing complex proteomes (i.e., labeling at the peptide level in order to increase the fraction of labeled peptides and, thus, the number of proteins amenable to quantification). It is also noticeable that the relative number of identified and quantified proteins was very similar for both trypsin and endoGluC digested samples (54% and 49%, respectively). Interestingly, there is a significant set of proteins that were only identified and quantified when a particular protease, endoGluC or trypsin was used, pointing out that the use of several proteases increases the total number of proteins identified. However, this is at expense of a notorious increase in the time and complexity of the analysis.

Table 4 summarizes the results obtained in the three experiments. Only those proteins identified and quantified using at least three peptides in at least two individual experiments are shown (see Supplementary data for additional information). According to their quantitative ratios, proteins were arbitrarily divided in four groups: unaltered (0.5 < ratio < 2); up regulated (ratio >2); down regulated (ratio < 0.5) and a fourth set that includes all those proteins that did not fit any of the previous groups (i.e., quantification values from different experiments were not consistent). Although the specific causes of the inconsistent results in the later group have not been investigated in detail we speculate that, as described for the T4 bacteriophage model, the coelution of ICPL-labeled peptides and other molecular species with almost identical m/z value could explain most of the variability described. In fact, the percentage of proteins showing inconsistent results is very similar in both cases (3 out of 22 (14%) for the T4 model and 12 out of 79 (15%) for the analysis of *Salmonella)*. For each labeling experiment, the number of ICPL-labeled peptide pairs used for quantification and the averaged H/L ratio (*IgaA1*/wild-type) are shown. The results obtained in a 2D-PAGE experiment are also included to compare both strategies and to validate the results obtained in the ICPL approach. In general, both approaches yielded similar results, demonstrating that ICPL quantification values obtained were reproducible and equivalent to that obtained with the "classical" 2D-PAGE workflow. This fact is particularly evident when up regulated or down regulated proteins are considered. Nevertheless, some differences in the absolute values were observed that could be caused by a multiplicity of factors. For example, digestion with endoGluC or trypsin may produce different peptide sets, modulating the effect that outliers may exert in the final averaged value. Additionally, signal to noise ratios may differ among individual experiments, altering the final H/L values. Finally, it should be considered that the ratios calculated for specific proteins in the ICPL experimental approach may correspond actually to the averaged expression ratios of different protein isoforms. These isoforms, that are hardly distinguishable for shotgun proteomics techniques, can be separated and changes in their expression can be individually measured by means of the 2D-PAGE. However, since the presence of protein isoforms is much less frequent in prokaryotes than in higher organisms the multi-

Table 4
Comparison of ICPL and 2D-PAGE quantitative approaches in the *Salmonella enterica serovar typhimurium* analysis.

Systematic gene name	Gene	ICPL analysis						2D-PAGE analysis			
		Experiment 1				Experiment 2		Spot 1	Spot 2	Spot 3	Spot 4
		endoGluC		Trypsin		Trypsin					
		Average	# Pept. (ICPL)	Average	# Pept. (ICPL)	Average	# Pept. (ICPL)				
Unmodified (0.5 < average < 2)											
STM1780	prsA			1.66	4	1.81	3	N.Q.			STM1780
STM1238	icdA	1.08	9			1.02	5	1.11	0.79	1.31	
STM0959	lrp			1.29	3	1.57	3	N.F.			
STM1070	ompA	1.66	11	1.2	18	1.69	23	1.22	1.13	1.09	1.16
STM0739	sucD	1.49	7	1.1	7			1.17			
STM0737	sucB	0.98	2			0.69	10	N.F.			
STM0736	sucA			1.31	5	1.35	13	N.F.			
STM0730	gltA	1.91	6			1.63	5	N.F.			
STM0981	rpsA	1.12	12	1.1	8	1.06	15	1.65	0.96	0.89	
STM2952	eno	1.47	14			0.95	6	0.99			
STM2090	rfbH	1.83	7			1.32	2	1.15			
STM2660	clpB	1.22	3	1.08	4	1.13	6	2.22			
STM4364	hflC			1.93	7	0.71	7	N.F.			
STM0487.S	htpG	0.77	8	0.5	5	0.58	8	0.91	0.96		
STM0447	tig	0.73	15	0.72	14	0.74	14	0.79	0.73	0.73	
STM0232	accA	0.99	2	0.82	2	0.53	2	0.62			
STM0224	yaeT	0.88	2	1.48	3	1.17	2	0.71	0.97		
STM0217	tsf	1.29	21	0.78	5	1.26	2	0.87			
STM0216	rpsB	0.95	5	0.89	6	0.93	7	N.F.			
STM0158	acnB	1.01	7			1.11	6	1.62	1.55	1.37	
STM0153	aceF	1.71	19	1.58	4	1.08	13	N.F.			
STM4394	rplI	0.64	3	0.94	2	0.83	3	N.F.			
STM4343	frdA			1.47	4	1.61	9	1.47			
STM0012	dnaK	0.73	17	0.6	21	0.66	28	0.75	0.74	0.64	
STM0007	talB			1.66	8	1.37	6	N.F.			
STM4581	yjjK			1.91	4	1.41	5	N.F.			
STM4151	rplJ	1.85	6	1.47	3			N.F.			
STM4146	tuf	1.75	13	1.33	14	1.57	49	1.14	1.37	1.54	0.83
STM4086	glpK	1.44	5	1.48	4	1.23	20	1.11	1.25	1.09	1.07
STM4150	rplA	0.81	6	0.64	2			N.F.			
STM3869	atpF	1.47	2			1.18	8	N.F.			
STM3287	nusA			1.95	3	1.56	3	1.15			
STM4330	groEL	1.31	47	1.03	41	1.39	35	1.07	1.37	1.15	
STM3865	atpD	1.27	2			1.08	5	1.12	0.68		
STM3655	glyS			1.06	3	1.43	5	N.F.			
STM3500	pckA	1.1	6	1.27	5	1.08	9	0.9	0.95	0.92	
STM3416	rpsD	1.81	2	1.93	12	1.7	6	N.F.			
STM3428	rplE			0.69	5	1.05	4	N.F.			
STM3423	rpsE			1.66	6	1.07	7	N.F.			
STM3439	rplD			1.31	12	0.87	5	N.F.			
Down regulated (0.5 > average)											
STM3359	mdh	0.63	4	0.4	8			0	0.57	0.55	
STM1572	nmpC	0.33	4			0.21	10	0.47			
STM1959	fliC	0.08	7	0.17	7	0.14	6	0	0	0	0
STM2190	mglB	0.38	7	0.3	8			0.62	0.39		
STM2771	fljB			0.24	8	0.14	6	N.F.			
Up regulated (average > 2)											
STM3526	glpD			3.4	9	2.7	33	N.F.			
STM3437	rplB			2.52	5	2.12	18	N.F.			
STM3157	yghA	3.17	2	10.27	16	8.15	12	N.F.			
STM3434	rpsC			2.42	10	2.46	13	N.F.			
STM3040	lysS	2.18	2	2.47	5	2.27	4	N.F.			
STM3422	rpmD			2.3	2	2.02	14	N.F.			
STM1730	yciE	24.13	3			14.49	3	N.F.			
STM1378	pykF			2.4	2	2.24	5	2.59			
STM1349	pps	5.24	2	3.77	11	2.88	10	N.F.			
STM1311	osmE	5.75	5	2.91	2			N.F.			
CNB1344-0716	CNB1344-0716			2.33	7	1.8	35	N.F.			
STM0973	pflB	2.57	3	3.56	3	2.21	8	1.8			
STM2827	alaS	3.24	2	1.75	2	2.16	6	N.F.			
STM2430	cysK	1.99	3	3.7	4	2.42	3	N.F.			
STM2432	ptsI	2.09	4			2.08	4	1.68			
STM0152	aceE	2.02	6	2.26	2	1.94	5	N.F.			
STM0067	carB			3.45	5	2.27	9	N.F.			
STM4561	osmY	7.3	13	3.26	3			N.F.			
STM4519	STM4519	4.31	3			3.29	6	N.F.			
STM4154	rpoC	2.47	3	3.13	19	2.5	35	N.F.			
STM4153	rpoB	2.61	9	2.28	15	1.75	28	N.F.			
STM2474	tktB			2.47	2	9.31	3	3.11			

Table 4 (*Continued*)

Systematic gene name	Gene	ICPL analysis						2D-PAGE analysis			
		Experiment 1				Experiment 2		Spot 1	Spot 2	Spot 3	Spot 4
		endoGluC		Trypsin		Trypsin					
		Average	# Pept. (ICPL)	Average	# Pept. (ICPL)	Average	# Pept. (ICPL)				
Unconsistent											
STM4326	aspA	1.27	3	2.28	6	1.12	5	0.97	0.95		
STM3867	atpA	2.57	8	2.46	5	1.62	13	1.82	1.09	1.31	1.37
STM3415	rpoA	2.54	4			1.32	3	1.35	1.01	1.31	
STM3286	infB	2.83	7	2.7	6	1.54	19	N.F.			
STM3283	rpsO	2.15	5			1.01	8	1.95	1.01	1.88	
STM3440	rplC			2.63	4	1.68	3	N.F.			
STM3053	gcvP			2.99	4	1.86	9	N.F.			
STM0772	gpmA	2.27	6	1.28	2			1.06			
STM2272	gyrA			1.28	2	2.15	7	N.F.			
STM4366	purA	2.1	2			1.03	4	N.F.			
STM0154	lpdA	2.48	4			1.38	5	1.47	4.15		
STM0831	dps			2.17	5	1.65	2	1.14			

Average H/L ratios (Average) and number of peptides labeled with ICPL (# Pept (ICPL)) are shown for the three independent experiments performed using ICPL. Mutant/wild-type ratios for proteins detected in the 2D-PAGE analysis are also included. Note that several proteins were detected in more than one individual spot in the 2D gel.

plicity of spots found for the same protein may also correspond to artefactual modifications, (e.g., deamidation). Nevertheless, similar differences between approaches based on stable isotopic labeling and 2D-PAGE strategies are not unusual and have been described before [21–23].

4. Conclusions

In summary, our results demonstrate that ICPL is a useful and reliable alternative for the isotopic labeling of complex proteomes and the subsequent estimation of protein expression levels. ICPL overcomes some limitations found in other labeling strategies, such as the low number of peptides amenable for labeling with ICAT or the difficulty to analyze iTRAQ specific reporter ions in many mass spectrometers currently in use. ICPL reaction labeling was found to be very specific and efficient, with no apparent byproducts or undesired side reactions. The chromatographic properties of light and heavy labeled peptides were almost indistinguishable. Similarly, comparable identification scores were determined for both labeled and unlabeled peptides, demonstrating that ICPL labeling does not alter the quality of MS/MS spectra. Nevertheless, our data make evident that further improvements are required to increase the usefulness of ICPL in differential proteomics. Among them, the fraction of labeled peptides should be notably higher (ideally close to 100%) in order to increase the number of quantified proteins and, in parallel, the average number of labeled peptides per protein, since this would result in much more reliable differential expression rates. This may be achieved by labeling at the peptide level, right after protein digestion, instead of employing the standard workflow, in which labeling occurs at the protein level.

Acknowledgements

We wish to thank our colleague Dr. Peter James (Lund University, Sweden) for providing purified T4 bacteriophage capsid used in this study. This works was supported by grants S-GEN-0166-2006 from the Comunidad Autónoma de Madrid (to J.P.A.) and BIO2007-67457-C02-01 from the Spanish Ministry for Science and Innovation (to F.G.-P.). The Proteomics Facility of CNB is a member of ProteoRed-Spanish National Institute for Proteomics and follows the quality criteria set up by ProteoRed standards

Appendix A. Supplementary data

Supplementary data associated with this article can be found, in the online version, at doi:10.1016/j.talanta.2009.06.083.

References

[1] K. Gevaert, F. Impens, B. Ghesquiere, P. Van Damme, A. Lambrechts, J. Vandekerckhove, Proteomics 8 (2008) 4873.
[2] S.E. Ong, M. Mann, Nat. Chem. Biol. 1 (2005) 252.
[3] S.E. Ong, B. Blagoev, I. Kratchmarova, D.B. Kristensen, H. Steen, A. Pandey, M. Mann, Mol. Cell. Proteomics 1 (2002) 376.
[4] S.P. Gygi, B. Rist, S.A. Gerber, F. Turecek, M.H. Gelb, R. Aebersold, Nat. Biotechnol. 17 (1999) 994.
[5] N. Gupta, B. Wollscheid, J.D. Watts, B. Scheer, R. Aebersold, A.L. DeFranco, Nat. Immunol. 7 (2006) 625.
[6] P.L. Ross, Y.N. Huang, J.N. Marchese, B. Williamson, K. Parker, S. Hattan, N. Khainovski, S. Pillai, S. Dey, S. Daniels, S. Purkayastha, P. Juhasz, S. Martin, M. Bartlet-Jones, F. He, A. Jacobson, D.J. Pappin, Mol. Cell. Proteomics 3 (2004) 1154.
[7] P. Conrotto, U. Hellman, Rapid Commun. Mass Spectrom. 22 (2008) 1823.
[8] A. Schmidt, J. Kellermann, F. Lottspeich, Proteomics 5 (2005) 4.
[9] L. Dayon, A. Hainard, V. Licker, N. Turck, K. Kuhn, D.F. Hochstrasser, P.R. Burkhard, J.C. Sanchez, Anal. Chem. 80 (2008) 2921.
[10] D. Lopez-Ferrer, A. Ramos-Fernandez, S. Martinez-Bartolome, P. Garcia-Ruiz, J. Vazquez, Proteomics 6 (Suppl. 1) (2006) S4.
[11] A. Ramos-Fernandez, D. Lopez-Ferrer, J. Vazquez, Mol. Cell. Proteomics 6 (2007) 1274.
[12] Y.J. Kim, P. Zhan, B. Feild, S.M. Ruben, T. He, Anal. Chem. 79 (2007) 5651.
[13] T. Nakatsuji, Y. Shi, W. Zhu, C.P. Huang, Y.R. Chen, D.Y. Lee, J.W. Smith, C.C. Zouboulis, R.L. Gallo, C.M. Huang, Proteomics 8 (2008) 3406.
[14] H. Sarioglu, S. Brandner, C. Jacobsen, T. Meindl, A. Schmidt, J. Kellermann, F. Lottspeich, U. Andrae, Proteomics 6 (2006) 2407.
[15] Y. Shi, C.A. Elmets, J.W. Smith, Y.T. Liu, Y.R. Chen, C.P. Huang, W. Zhu, H.N. Ananthaswamy, R.L. Gallo, C.M. Huang, Proteomics 7 (2007) 4589.
[16] J.F. Mariscotti, F. García-del Portillo, J. Bacteriol. 191 (2009) 1855.
[17] J. Kellermann, Methods Mol. Biol. 424 (2008) 113.
[18] A. Shevchenko, M. Wilm, O. Vorm, M. Mann, Anal. Chem. 68 (1996) 850.
[19] R. Zhang, C.S. Sioma, R.A. Thompson, L. Xiong, F.E. Regnier, Anal. Chem. 74 (2002) 3662.
[20] R. Zhang, C.S. Sioma, S. Wang, F.E. Regnier, Anal. Chem. 73 (2001) 5142.
[21] A.S. Haqqani, J. Kelly, E. Baumann, R.F. Haseloff, I.E. Blasig, D.B. Stanimirovic, J. Proteome Res. 6 (2007) 226.
[22] P.M. Uitto, B.K. Lance, G.R. Wood, J. Sherman, M.S. Baker, M.P. Molloy, J. Proteome Res. 6 (2007) 2105.
[23] W.W. Wu, G. Wang, S.J. Baek, R.F. Shen, J. Proteome Res. 5 (2006) 651.

Talanta 80 (2010) 1503–1512

Contents lists available at ScienceDirect

Talanta

journal homepage: www.elsevier.com/locate/talanta

Chemical labeling and enrichment of nitrotyrosine-containing peptides

Nicolas Abello[a], Begona Barroso[a,1], Huib A.M. Kerstjens[b], Dirkje S. Postma[b], Rainer Bischoff[a,*]

[a] Department of Pharmacy, Analytical Biochemistry, University of Groningen, A. Deusinglaan 1, 9713 AV Groningen, The Netherlands
[b] Department of Pulmonary Diseases, University Medical Center Groningen, University of Groningen, Hanzeplein 1, 9700 RB Groningen, The Netherlands

ARTICLE INFO

Article history:
Available online 10 February 2009

Keywords:
Nitrotyrosine
Tyrosine nitration
NHS-acetate
NHS-biotin
Mass spectrometry
Peroxynitrite

ABSTRACT

Protein tyrosine nitration (PTN) is a post-translational modification of proteins associated with a number of inflammatory diseases. While PTN is rather selective (not all proteins are modified and within a protein, only certain tyrosines are subject to nitration), no consensus sequence has been identified. Since PTN is a low-abundance post-translational modification, it is necessary to enrich modified proteins and/or to detect them with high selectivity and sensitivity. Until now this has been mostly accomplished with anti-nitrotyrosine antibodies in combination with two-dimensional gel electrophoresis and mass spectrometry. We propose a chemical labeling approach designed to allow enrichment of tyrosine-nitrated peptides independent of the sequence context, which is a potential shortcoming of antibody-based approaches. In this procedure, all amines are blocked by acetylation followed by conversion of nitrotyrosine to aminotyrosine and biotinylation of aminotyrosine. The entire reaction sequence is performed in a single buffer with no need for sample cleanup or pH changes thereby reducing sample loss. Free biotin is subsequently removed with a strong cation exchanger, the labeled peptides are enriched on an immobilized avidin column and the enriched peptides analyzed by LC–MS/MS. As a proof of concept, this method was successfully applied to the enrichment of tyrosine-nitrated angiotensin II in a tryptic digest of bovine serum albumin (BSA). The approach presented here is well adapted to peptide analysis, for instance in shotgun proteomics.

© 2009 Elsevier B.V. All rights reserved.

1. Introduction

Nitrotyrosine is formed by the reaction of tyrosine with nitrating species, particularly peroxynitrite ($ONOO^-$), which is mostly formed by the combination of a superoxide radical anion ($^{\bullet}O_2^-$) with nitric oxide ($^{\bullet}NO$). Protein tyrosine nitration (PTN) is therefore a post-translational modification of proteins associated with $^{\bullet}NO$-dependent oxidative stress [1]. PTN occurs under physiological conditions and its level (both as protein-bound residue and in its free amino acid form) is increased in at least 50 human diseases [2]. It has been associated with a change in function of several proteins (generally a loss of function), enhanced immunogenicity or an increased protein turn-over [3–5]. PTN is a rather selective process, despite of the reactivity of nitrating agents such as peroxynitrite. Some proteins are preferentially nitrated but the abundance of a given protein or the number of tyrosine residues does not determine susceptibility for nitration [5,6].

Many of the methods developed so far to investigate PTN have focused on the detection and quantification of 3-nitrotyrosine in its circulating free form or after its release by protein hydrolysis (see reviews by Herce-Pagliai et al. [7], Greenacre and Ischiropoulos [2], Duncan [8], Tsikas and Caidahl [9] and Ryberg and Caidahl [10]). While such analyses give an assessment of the overall nitration of tyrosine in proteins, they do not allow to discriminate between individual nitrated proteins nor do they allow determination of their respective levels in a biological sample [11]. The identification of *in vivo* targets for PTN would provide insight into structure–function relationships and advance our understanding how the addition of a nitro group may alter the function or immunogenicity of a given protein. It would also open the possibility to study the association between specific nitrated proteins and a pathological phenotype [5]. Most methods developed to address PTN in individual proteins are based on immunochemical approaches (Western blotting, immunoprecipitation) in combination with gel electrophoresis (in-solution isoelectrofocusing followed by SDS-PAGE [12–14], immunoprecipitation followed by SDS-PAGE [12,15], or 2D-gel electrophoresis [12,15–32]) followed by mass spectrometric (MS) analysis. Despite their relevance, these methods have limitations commonly associated with gel electrophoresis and immunochemistry such as gel-to-gel reproducibility, the detection of low-abundance proteins and the fact that one protein spot may contain several proteins, which complicates interpretation of the MS data [33,34]. The unambiguous immunochemical recognition of nitrotyrosine in proteins generally requires a step of nitrotyro-

* Corresponding author. Tel.: +31 503 633 338; fax: +31 503 637 582.
E-mail address: r.p.h.bischoff@rug.nl (R. Bischoff).
[1] Present address: Astellas B.V., Exploratory Development Department, Elisabethhof 1, 2353 EW Leiderdorp, The Netherlands.

0039-9140/$ – see front matter © 2009 Elsevier B.V. All rights reserved.
doi:10.1016/j.talanta.2009.02.002

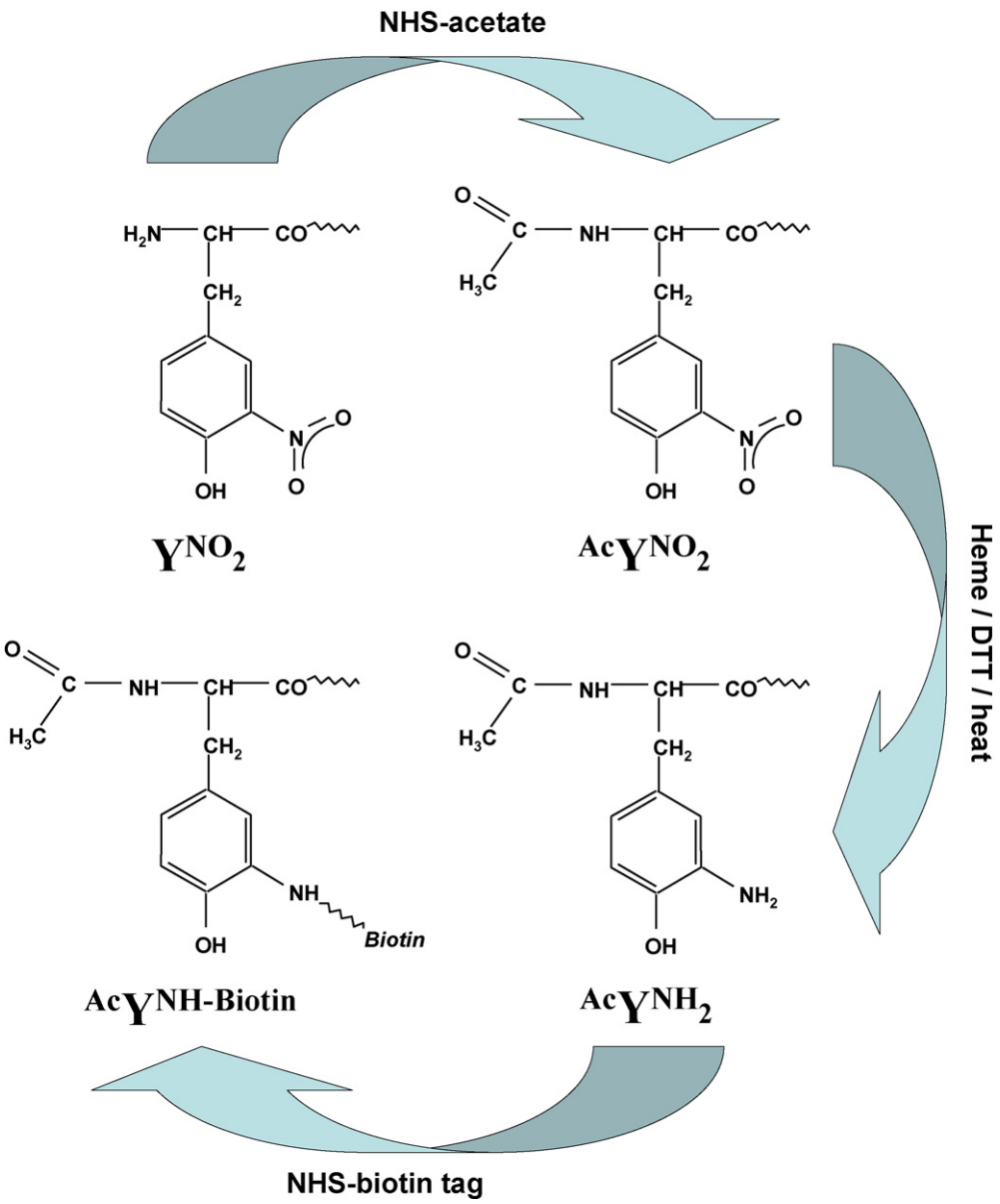


Fig. 1. Reaction scheme of the chemical labeling method as exemplified with an N-terminal nitrotyrosine residue. Blocking all amines by acetylation with NHS-acetate is followed by the reduction of nitrotyrosine to aminotyrosine with heme and DTT in a boiling water bath. The reaction sequence is completed by biotinylation of aminotyrosine with NHS-biotin.

sine reduction in order to ascertain the specificity of the antibody further complicating this approach [16].

In a recent report, Nikov et al. proposed a new approach to enrich nitrotyrosine-containing proteins from a complex mixture [35]. This gel-free, antibody-free method is based on the reduction of nitrotyrosine to aminotyrosine followed by the exploitation of the pK_a difference between the aromatic amine (pK_a = 4.75) [36] and other aliphatic amines that are present in proteins and peptides (pK_a of 8.0 for α-amines and 10.5 for ε-amine) [37] to label aminotyrosine at pH 5.0 with a biotin-containing tag. While an intriguing approach, that may allow enrichment and identification of nitrotyrosine-containing proteins independent of antibodies, it did not prove selective enough, since α- and ε-amines were partially modified by the recommended N-hydroxysuccinimide esters at pH 5.0 (our own results and Refs. [38,39]). Since selectivity of a labeling method is of primary importance when it comes to studying low-abundance post-translational modifications, we designed a multi-step, one-pot chemical labeling approach with the goal of reaching close to 100% conversion at each step (see Fig. 1). The reaction sequence is as follows: (1) blocking of all amines by acetylation, (2) conversion of nitrotyrosine to aminotyrosine, and (3) biotinylation of the amine group of aminotyrosine. Subsequent enrichment of biotinylated peptides using avidin-based affinity chromatography and analysis by LC–MS/MS completes the procedure. This methodology was evaluated in a proof-of-concept study, where nitrated angiotensin II was selectively labeled and enriched from a matrix of trypsin-digested bovine serum albumin (BSA).

2. Materials and methods

2.1. Materials and reagents

Acetic acid N-hydroxysuccinimide ester (NHS-acetate) was from MP Biomedicals (Illkirch, France). Monomeric avidin immobilized on agarose beads was from Pierce (Perbio Science, Etten-Leur, The Netherlands) and dimethyl sulfoxide (DMSO), sodium dihydrogen

phosphate monohydrate, di-sodium hydrogen phosphate dihydrate and formic acid (FA) were from Merck KGaA (Darmstadt, Germany). HPLC-S gradient grade acetonitrile and methanol were from Biosolve (Valkenswaard, The Netherlands). Angiotensin II (human) acetate, bovine serum albumin, dithiothreitol (DTT), biotinyl N-hydroxysuccinimide ester (NHS-biotin) were from Sigma (Zwijndrecht, The Netherlands). Hemin was purchased from Sigma–Fluka (Zwijndrecht, The Netherlands) and peroxynitrite from Calbiochem (Merck Chemicals Ltd., Nottingham, UK). Ultra-pure water (conductivity: 18.2 MΩ) was obtained from a Maxima System (Elga Labwater, Ede, The Netherlands). All incubations at 25 and 37 °C were performed in a Thermomixer (Eppendorf, Hamburg, Germany) at 450 rpm.

2.2. Sample preparation

2.2.1. Nitration of angiotensin II

20 μL of angiotensin II (DRVYIHPF; 500 μM in water) was diluted with 940 μL 500 mM sodium phosphate buffer, pH 7.5. 40 μL of peroxynitrite solution (160–200 mM in 4.7% NaOH) were added and the solution was immediately vortexed for 1 min. The sample was subjected to solid-phase extraction on an Oasis HLB column (Waters, Etten-Leur, The Netherlands) previously conditioned with 1 mL methanol and 1 mL water. After washing the column with 1 mL 5% methanol, the peptides were eluted with 80% methanol in water and dried under nitrogen.

2.2.2. Preparation of trypsin-digested BSA

BSA (1 mg/mL in 100 mM sodium phosphate, pH 8) was digested at 37 °C for 4 h with trypsin at a ratio of 1/20 (trypsin/BSA) by weight. A 1 mL sample was subjected to solid-phase extraction on an Oasis HLB column as described above for angiotensin II.

2.2.3. Addition of nitrated angiotensin II to the digested BSA matrix

The content of a tube of dried nitrated peptide was resuspended in 1 mL 250 mM sodium phosphate, pH 8 (final peptide concentration: 10 μM). After completion, the liquid was transferred to another tube containing the dried BSA digest (final concentration: 1 mg/mL, i.e. 15 μM).

2.3. Chemical labeling

2.3.1. Acetylation of primary amines

10 μL of 500 mM NHS-acetate in DMSO (final concentration: 25 mM) was added to 190 μL of nitrated angiotensin II. The sample was incubated for 2 h at 25 °C and subsequently treated for 15 min in a boiling water bath to hydrolyze remaining reagent and to reverse O-acylations, as previously described [40].

2.3.2. Reduction of nitrotyrosine to aminotyrosine

10 μL of 440 mM DTT (final concentration: 20 mM) and 10 μL of 550 μM hemin (final concentration: 25 μM) were added to the sample prior to incubation for 15 min in a boiling water bath.

2.3.3. Biotinylation of aminotyrosine

10 μL of 115 mM NHS-biotin in DMSO (final concentration: 5 mM) was added to the sample. After 2 h at 25 °C, the sample was incubated for another 15 min in a boiling water bath and supplemented with 170 μL 1% (v/v) FA.

2.4. Removal of excess biotin

The sample was diluted to 1 mL with 11 mM (0.425‰, v/v) FA and applied to a strong cation exchange (SCX) cartridge (3-mL LiChrolut SCX; Merck, Germany), previously conditioned with 3 mL methanol and 3 mL 11 mM FA, to remove the excess of free biotin. After washing the column with 7 mL 11 mM FA, the peptides were eluted in 1.4 mL of 300 mM sodium phosphate, pH 8.0, 150 mM NaCl:methanol (7:3) and collected in a tube of known weight. The samples were concentrated in a vacuum centrifuge (Concentrator 5301; Eppendorf, Hamburg, Germany) at 40 °C until their residual volume was ~600 μL (based on their weight, considering a density of 1 g/mL). Water was subsequently added to 1 mL.

2.5. Enrichment of biotinylated peptides

100 μL of a 50% slurry of monomeric avidin immobilized on agarose beads were washed with 2× 1 mL phosphate buffer saline (PBS) prior to being added to the sample. After 1 h on a rotary shaker at room temperature, an aliquot (40 μL) of the supernatant was removed, diluted with an equal volume of 1% FA, and stored on ice for further analysis ("flow-through fraction"). The beads were packed into a gel loader tip without letting them dry, washed with 5 mL PBS and the retained peptides eluted with 100 μL 8 M guanidinium–HCl, pH 1.4. The eluate was diluted with an equal volume of 1% FA prior to LC–MS/MS analysis ("bound fraction").

2.6. LC–MS/MS

The HPLC part of the LC–MS/MS system consisted of an Agilent series 1100 capillary LC (Waldbronn, Germany) comprising a degasser, a binary pump with stream splitter and flow controller, a temperature-controlled autosampler (4 °C) and a temperature-controlled column compartment (40 °C). A diode array detector set at 214, 280 and 365 nm was used to ascertain nitration of angiotensin II after treatment with peroxynitrite. Chromatographic separation took place in an Atlantis dC18 column (Waters, Etten-Leur, The Netherlands; 1.0 mm i.d. × 150 mm length, particle size 3 μm) operated at 20 μL/min flow rate. Mobile phase A consisted of 0.1% (v/v) FA in ultra-pure water and mobile phase B of 0.1% (v/v) FA in acetonitrile.

All samples obtained after chemical labeling (including the biotinylation step) were diluted to 400 μL with 1% (v/v) FA prior to LC–MS/MS analysis. All other samples were diluted with an equal volume of 1% (v/v) FA. Unless stated otherwise, an injection volume of 4 μL was used, and the separation was performed with an increasing gradient of B (2–47% at 0.5%/min). The analytes were detected by an Agilent SL ion-trap mass spectrometer equipped with an electrospray ionization source operated in positive mode. MS data were acquired over a scan range of 200–1200 m/z. Molecules of interest were selected as precursor ions (preferentially doubly charged states were used, when applicable; isolation width of 2 amu) and analyzed by MS/MS at a fragmentation amplitude of 1 V. Daughter ions were acquired over a scan range of 50–1200 m/z.

All displayed chromatograms underwent one cycle of three-point smoothing based on a Gaussian algorithm and all extracted ion chromatograms (EICs) were retrieved with a tolerance of ±0.2 m/z.

3. Results

3.1. Nitration of angiotensin II

In order to assess the efficiency and selectivity of the labeling method, we applied it to chemically nitrated angiotensin II in a matrix of trypsin-digested BSA. After exposure to peroxynitrite, angiotensin II (native form: "Y"; Fig. 2B, first and second panels) was found to be partially (about 50%) nitrated ("Y^{NO_2}"; Fig. 2B, third and fourth panels). Nitration was accompanied by a shift to a higher retention time upon reversed-phase HPLC and a 45-Da increase

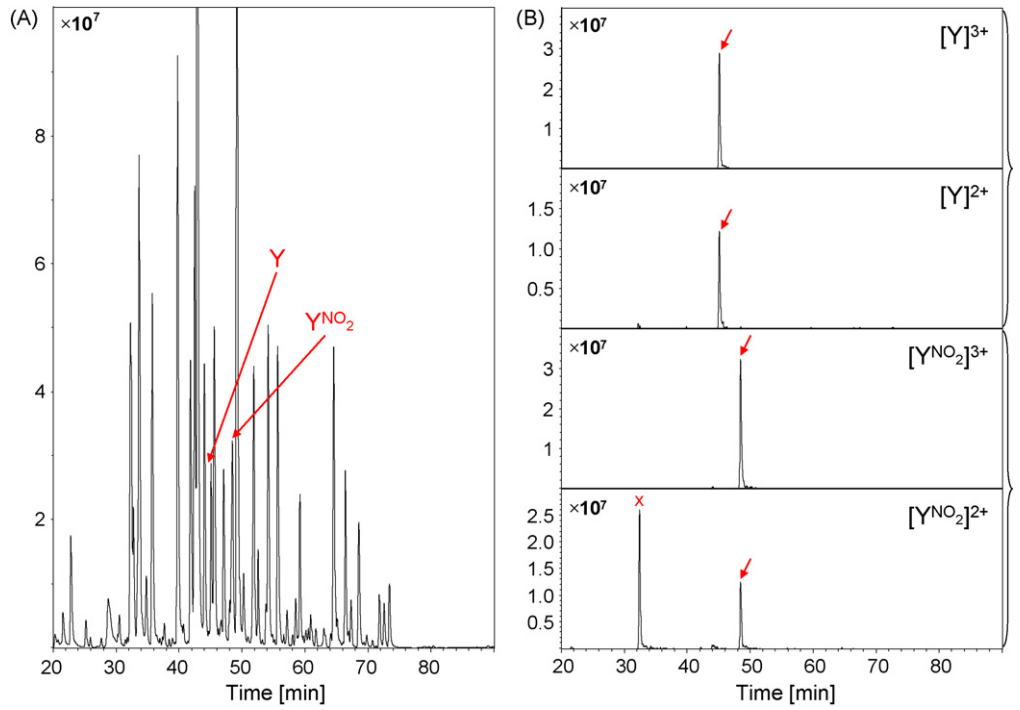


Fig. 2. LC–MS analysis of nitrated angiotensin II in a tryptic digest of BSA: A (left)—base peak chromatogram; B (right)—extracted ion chromatograms (±0.2 amu) of non-modified [Y] and tyrosine-nitrated [Y^{NO_2}] angiotensin II. First and second panels: triply (*m*/*z* 349.8) and doubly (*m*/*z* 523.9) charged molecular ions of [Y] (45.1 min); third and fourth panels: triply (*m*/*z* 364.7) and doubly (*m*/*z* 546.4) charged molecular ions of [Y^{NO_2}] (48.5 min). The peak marked "X" has an *m*/*z* of 546.3. Its isotopic distribution indicates a higher charge state, although resolution of the ion-trap mass analyzer was insufficient to assign the charge state.

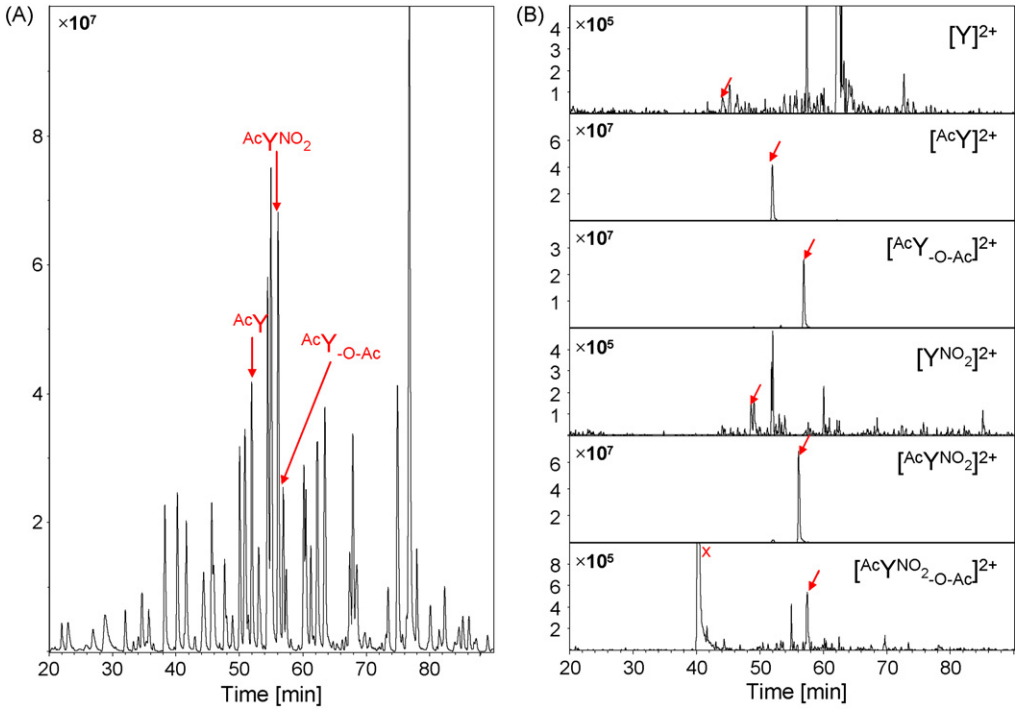


Fig. 3. LC–MS analysis after acetylation of primary amines: A (left)—base peak chromatogram; B (right)—extracted ion chromatograms (±0.2 amu); first panel: doubly charged molecular ion of remaining, non-nitrated angiotensin II ("Y", *m*/*z* 523.9, 45.1 min); second panel: doubly charged molecular ion of non-nitrated, N-acetylated angiotensin II ("^{Ac}Y", *m*/*z* 545.1, 51.9 min); third panel: doubly charged molecular ion of non-nitrated, N-,O-diacetylated angiotensin II ("$^{Ac}Y_{-O-Ac}$", *m*/*z* 566.1, 56.9 min); fourth panel: doubly charged molecular ion of tyrosine-nitrated angiotensin II ("Y^{NO_2}", *m*/*z* 546.4, 45.5 min); fifth panel: doubly charged molecular ion of tyrosine-nitrated, N-acetylated angiotensin II ("$^{Ac}Y^{NO_2}$", *m*/*z* 567.6, 56.1 min); sixth panel: doubly charged molecular ion of tyrosine-nitrated, N-,O-diacetylated angiotensin II ("$^{Ac}Y^{NO_2}$", *m*/*z* 588.4, 57.4 min). The peak marked "X" has an *m*/*z* of 588.5. It is an isotopic peak of a compound of which the molecular ion is of 587.5 *m*/*z*, and which is singly charged, according to its isotopic distribution.

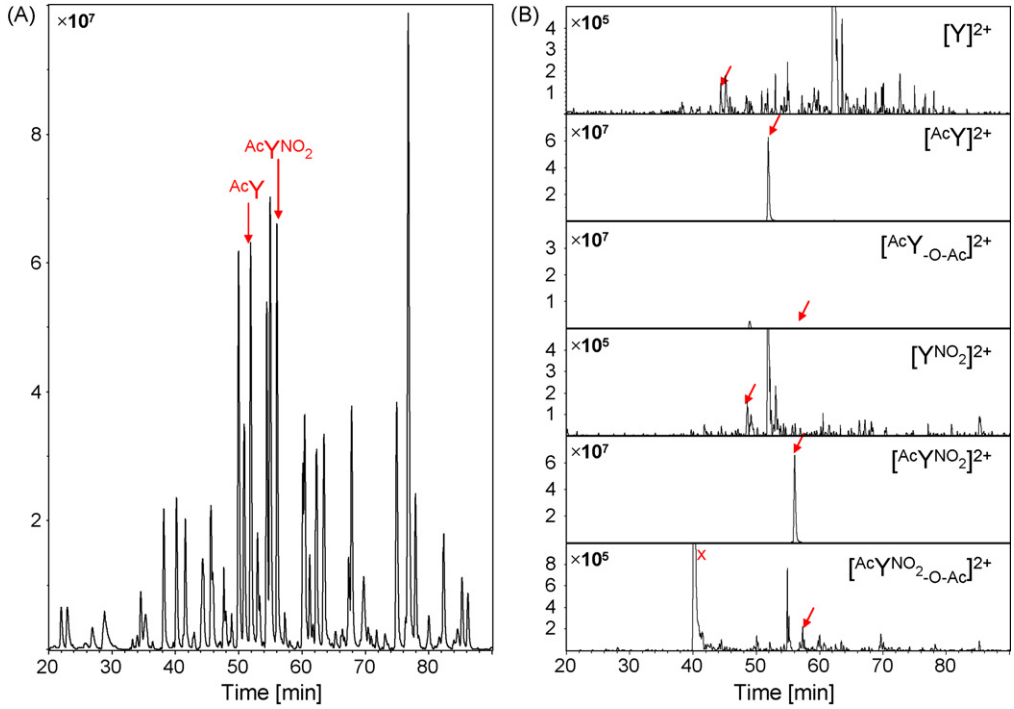


Fig. 4. LC–MS analysis after removal of O-acyl groups: A (left)—base peak chromatogram; B (right)—extracted ion chromatograms (±0.2 amu); first panel: doubly charged molecular ion of non-nitrated angiotensin II ("Y", *m*/*z* 523.9, 45.1 min); second panel: doubly charged molecular ion of non-nitrated, N-acetylated angiotensin II ("^{Ac}Y", *m*/*z* 545.1, 51.9 min); third panel: doubly charged molecular ion of remaining non-nitrated, N-,O-diacetylated angiotensin II ("$^{Ac}Y_{-O-Ac}$", *m*/*z* 566.1, 56.9 min); fourth panel: doubly charged molecular ion of tyrosine-nitrated angiotensin II ("Y^{NO_2}", *m*/*z* 546.4, 45.5 min); fifth panel: doubly charged molecular ion of tyrosine-nitrated, N-acetylated angiotensin II ("$^{Ac}Y^{NO_2}$", *m*/*z* 567.6, 56.1 min); sixth panel: doubly charged molecular ion of remaining tyrosine-nitrated, N-,O-diacetylated angiotensin II ("$^{Ac}Y^{NO_2}$", *m*/*z* 588.4). The peak marked "X" has an *m*/*z* of 588.5 and is singly charged according to its isotopic distribution.

in molecular weight. Using a DAD detector, we also observed an absorbance peak at 365 nm, which is the maximum of absorbance of nitrotyrosine in acidic media (data not shown) [41,42].

3.2. Acetylation of primary amines

The mixture of nitrated and non-nitrated angiotensin II was added to a tryptic digest of BSA to evaluate the selectivity of our labeling and enrichment methodology. In order to avoid side reactions with NHS-biotin, we blocked all primary amines with an excess of NHS-acetate. LC–MS analysis showed that acetylation was complete when investigating the angiotensin II-related peaks (see Fig. 3). Based on previous reports [40,43], angiotensin II (DRVYIHPF) was expected to be mostly doubly acetylated on its N-terminus and the tyrosine hydroxyl group. The non-nitrated peptide was indeed found to be both singly acetylated ("^{Ac}Y"; Fig. 3B, second panel) and doubly acetylated at both the N-terminus and the phenolic hydroxyl group of tyrosine ("$^{Ac}Y_{-O-Ac}$"; Fig. 3B, third panel). In contrast, the nitrated version of the peptide was principally found as singly acetylated derivative ("$^{Ac}Y^{NO_2}$"; Fig. 3B). This difference in reactivity may be explained by a shift of the pK_a of the phenolic hydroxyl group from 10.1 to 7.2 upon nitration [36]. It is thus mostly found in its phenolate form at pH 8, which appears to be less reactive towards NHS-acetate. An alternative explanation for the reduced reactivity might be that steric hindrance of the adjacent nitro group interferes with acetylation.

As shown previously [40], all O-acetyl groups were hydrolyzed after 15 min of incubation in a boiling water bath resulting in singly acetylated angiotensin II ("^{Ac}Y" and "$^{Ac}Y^{NO_2}$"; Fig. 4B, respectively second and fifth panels). The N-acetyl blocking groups withstood this treatment, as shown by the very low-intensity signals (calculated by peak integration to equal respectively 0.7% and 1.1% with respect to the starting material) for non-modified angiotensin II (nitrated "Y^{NO_2}" and non-nitrated "Y", respectively; Fig. 4B, first and fourth panel). By comparing the base peak chromatograms (BPCs) before and after acetylation as well as after the removal of O-acetyl groups (Figs. 2A and 4A) it appears that peak intensities for both native and nitrated angiotensin II doubled upon N-terminal acetylation indicating an increased ionization efficiency.

3.3. Reduction of nitrotyrosine to aminotyrosine

Although the conversion of nitrotyrosine to aminotyrosine is generally performed with sodium dithionite as proposed by Sokolovsky et al. [36], we decided to exploit an alternative reduction reaction previously described by Balabanli et al., due to its better controllability and the lower risk of side-reactions (see Section 4) [44]. Balabanli et al. showed that nitrotyrosine is readily converted into aminotyrosine at physiological pH and high temperature in presence of heme (or hemoproteins) and DTT. This reaction proved to be very efficient, since singly acetylated, aminotyrosine-containing angiotensin II ("$^{Ac}Y^{NH_2}$"; Fig. 5B, second and third panels) was readily detected whereas $^{Ac}Y^{NO_2}$ was barely detectable after reduction (Fig. 5B, first panel). By comparing the BPCs before and after nitrotyrosine reduction (Figs. 4A and 5A) we estimate that the reduction of nitrated angiotensin II decreases peak intensity by roughly a factor three indicating a reduction in ionization efficiency.

3.4. Biotinylation of aminotyrosine

Biotinylation of the aromatic amine in aminotyrosine with an excess of NHS-biotin followed by 15 min incubation in a boiling water bath appeared to be complete as judged by the disap-

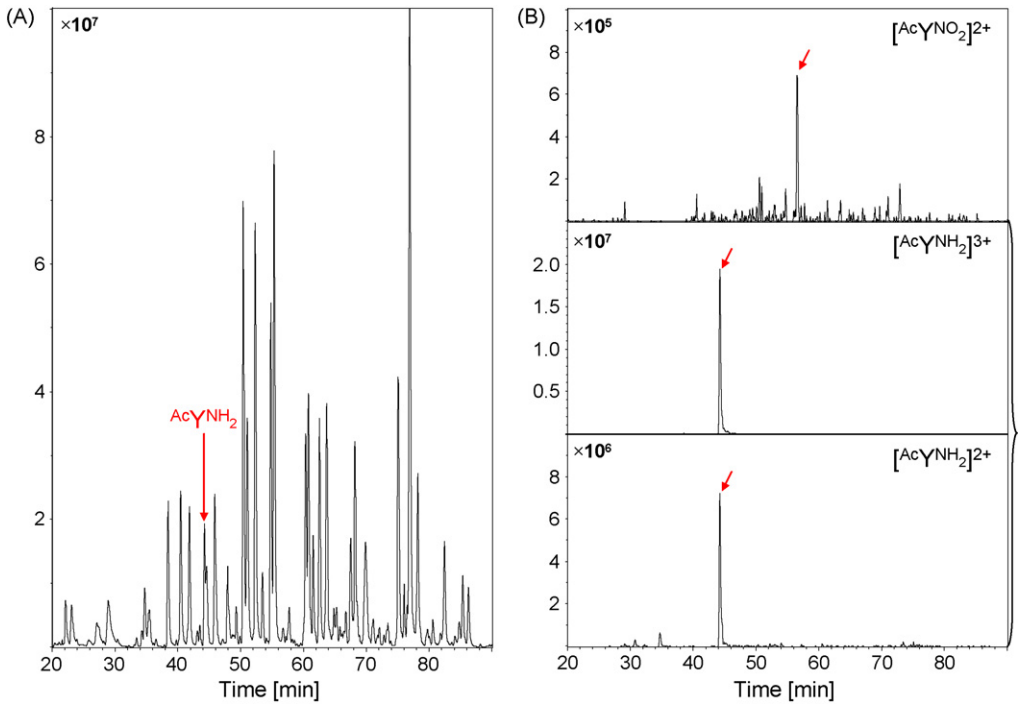


Fig. 5. LC–MS analysis after reduction of nitrotyrosine to aminotyrosine in angiotensin II: A (left)—base peak chromatogram; B (right)—extracted ion chromatograms (±0.2 amu); first panel: doubly charged molecular ion of tyrosine-nitrated, N-acetylated angiotensin II ("$^{Ac}Y^{NO_2}$", *m/z* 567.4, 56.5 min); second and third panels: triply (*m/z* 368.8) and doubly (*m/z* 552.4) charged molecular ions of N-acetylated, aminotyrosine-containing angiotensin II ("$^{Ac}Y^{NH_2}$", 44.2 min).

pearance of the peak corresponding to aminotyrosine-containing angiotensin II ("$^{Ac}Y^{NH_2}$"; Fig. 6B, third and fourth panels). The expected final product of the overall reaction ("$^{Ac}Y^{NH\text{-biotin}}$"; Fig. 6B, fifth and sixth panels) was primarily detected as doubly charged molecular ion. Some O-biotinylated, N-acetylated peptide was still observed ("$^{Ac}Y_{\text{-O-biotin}}$"; Fig. 6B, second panel) indicating that hydrolysis of the O-biotin ester is somewhat slower than for O-acetate. The O-biotin ester was, however, completely removed after

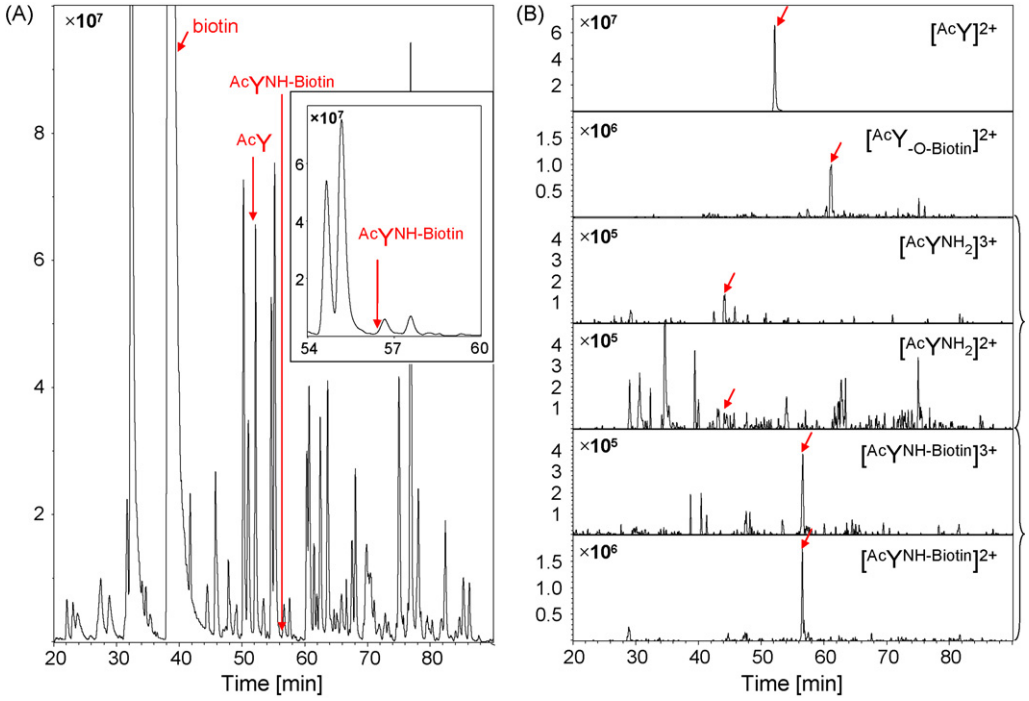


Fig. 6. LC–MS analysis after biotinylation of aminotyrosine-containing angiotensin II: A (left)—base peak chromatogram; B (right)—extracted ion chromatograms (±0.2 amu); first panel: doubly charged molecular ion of N-acetylated angiotensin II ("^{Ac}Y", *m/z* 545.1, 52.1 min); second panel: doubly charged molecular ion of N-acetylated and tyrosine O-biotinylated angiotensin II ("$^{Ac}Y_{\text{-O-biotin}}$", *m/z* 658.3, 61.2 min); third and fourth panels: triply (*m/z* 368.8) and doubly (*m/z* 552.4) charged molecular ions of N-acetylated, aminotyrosine-containing angiotensin II ("$^{Ac}Y^{NH_2}$", 44.2 min); fifth and sixth panels: triply (*m/z* 444.1) and doubly (*m/z* 665.6) charged molecular ions of N-acetylated and aminotyrosine N-biotinylated angiotensin II ("$^{Ac}Y^{NH\text{-biotin}}$", 56.5 min). The peak of free biotin (*m/z* 245.2 $[M+H^+]^{1+}$ and *m/z* 489.2 $[2M+H^+]^{1+}$, 38.3 min) has been truncated in Fig. 6A (actual intensity value: 7.75×10^8).

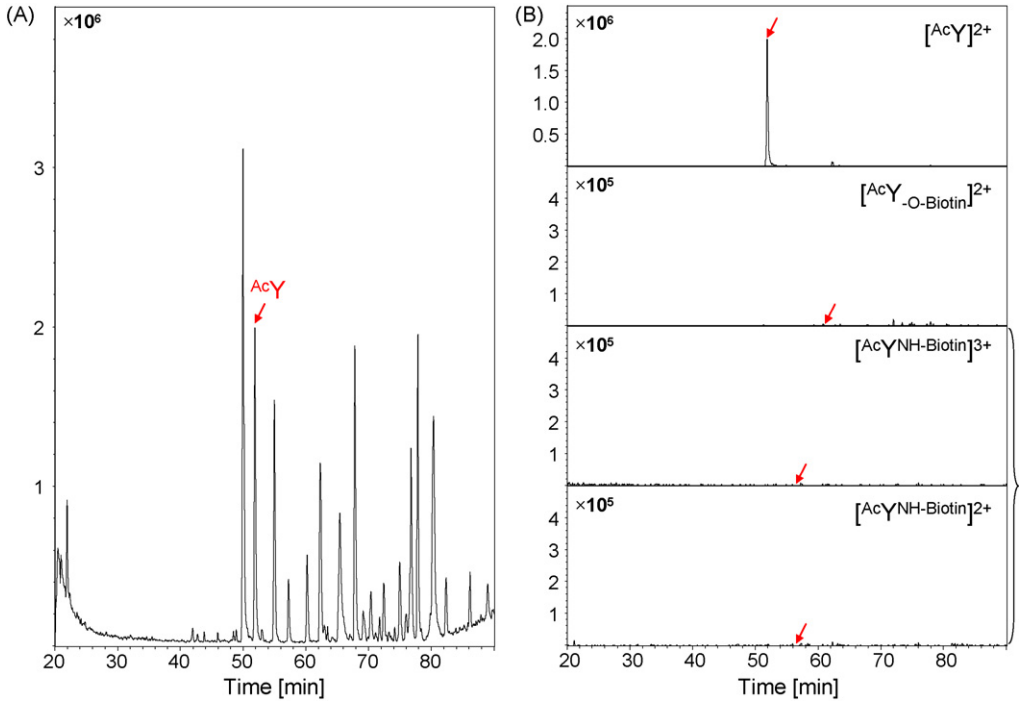


Fig. 7. LC–MS analysis of the flow-through fraction after avidin-based enrichment of biotinylated peptides: A (left)—base peak chromatogram; B (right)—extracted ion chromatograms (±0.2 amu); first panel: doubly charged molecular ion of N-acetylated angiotensin II ("^{Ac}Y", *m*/*z* 545.1, 51.9 min); second panel: doubly charged molecular ion of N-acetylated and tyrosine O-biotinylated angiotensin II ("^{Ac}Y$_{\text{-O-biotin}}$", *m*/*z* 658.3, 61.2 min); third and fourth panels: triply (*m*/*z* 444.1) and doubly (*m*/*z* 665.6) charged molecular ions of N-acetylated and aminotyrosine N-biotinylated angiotensin II ("^{Ac}Y$^{\text{NH-biotin}}$", 56.5 min).

incubation in a boiling water bath for 60 min (Fig. S-1 in Supplementary Material). The excess of free biotin (released after hydrolysis of NHS-biotin) is also retained on the C_{18} reversed-phase column and elutes slightly before the acetylated peptides (Fig. 6A).

3.5. Removal of excess biotin and enrichment of biotinylated, aminotyrosine-containing peptides

Since the large excess of biotin interferes with the subsequent enrichment step on a monomeric avidin column, it was removed

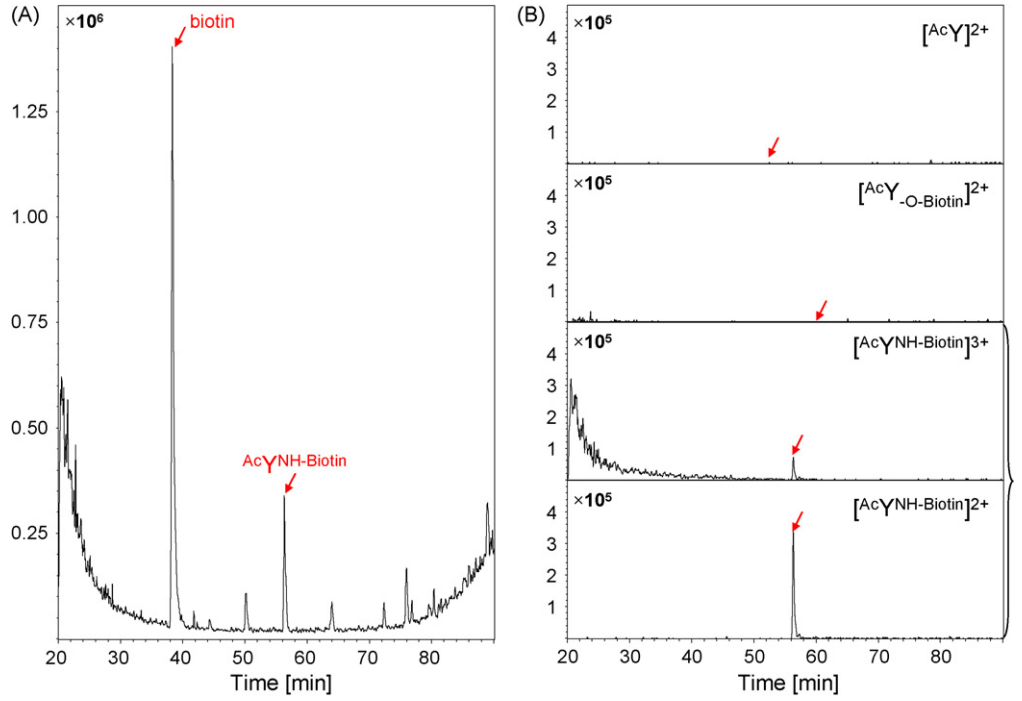


Fig. 8. LC–MS analysis of biotinylated peptides after enrichment on a monomeric avidin column (bound fraction): A (left)—base peak chromatogram; B (right)—extracted ion chromatograms; first panel: doubly charged molecular ion of N-acetylated angiotensin II ("^{Ac}Y", *m*/*z* 545.1, 51.9 min); second panel: doubly charged molecular ion of N-acetylated and tyrosine O-biotinylated angiotensin II ("^{Ac}Y$_{\text{-O-biotin}}$", *m*/*z* 658.3, 61.2 min); third and fourth panels: triply (*m*/*z* 444.1) and doubly (*m*/*z* 665.6) charged molecular ions of N-acetylated and aminotyrosine N-biotinylated angiotensin II ("^{Ac}Y$^{\text{NH-biotin}}$", 56.2 min).

by solid-phase extraction over a strong cation exchange cartridge at acidic pH based on the fact that biotin is expected to be neutral under these conditions while most peptides are positively charged and thus retained. After extensive washing of the SPE cartridge, peptides were eluted with an increased salt concentration at pH 8 in the presence of an organic modifier. The eluate was applied to a monomeric avidin column. Analysis of the flow-through of the avidin column showed that the biotinylated, aminotyrosine-containing angiotensin II was retained while the non-biotinylated, non-nitrated angiotensin II as well as most of the BSA-derived peptides were retrieved in this fraction as expected (Fig. 7). It is noteworthy that the early-eluting BSA-derived peptides were no longer visible in the flow-through fraction indicating that they were lost during the biotin-removal step. This step requires therefore further optimization prior to application of the procedure to endogenously tyrosine-nitrated proteins and peptides.

The relatively small amount of remaining biotin and the biotinylated, aminotyrosine-containing angiotensin II were eluted from the avidin affinity column with 8 M guanidinium hydrochloride at pH 1.4 (Fig. 8). It is noteworthy that none of the "background" peptides derived from trypsin-digested BSA were detected in the eluate indicating strongly that the initial acetylation reaction proceeded to completion. Detection of some biotin showed, however, that biotin removal by SCX was not complete albeit quite efficient when comparing the remaining amount to the large initial excess (Fig. 8A). The identity of $^{Ac}Y^{NH\text{-}biotin}$ was confirmed by MS/MS (Fig. S-2 in Supplementary Material). A few additional small peaks were observed in the base peak chromatogram of the eluate (Fig. 8A). MS/MS analysis revealed that these were mostly low molecular weight contaminants possibly originating from the guanidine solution or the avidin beads. This result shows that nitrated angiotensin II was selectively labeled and enriched from an excess of BSA-derived tryptic peptides.

4. Discussion

Nikov et al. [35] investigated the possibility of selective labeling of nitrotyrosine after reducing it to aminotyrosine followed by reaction with NHS-SS-biotin at pH 5. Selectivity was entirely based on the pK_a difference between the aromatic amine (pK_a = 4.75) [36] and other aliphatic amines present in proteins and peptides (pK_a of 8.0 for α-amines and 10.5 for ε-amines) [37]. The selectivity of a labeling method is of prime importance when it comes to the study of low-abundance post-translational modifications. In agreement with reports by other investigators [38,39], we observed that aliphatic amines reacted with NHS esters to a certain extent at pH 5 (data not shown) indicating that the method of Nikov et al. is not selective enough in the case of a low-abundance post-translational modification such as nitrotyrosine. Amoresano et al. [45] recently described a method for the labeling of *in vitro* nitrated milk proteins and endogenously nitrated *E. coli* proteins with dansyl chloride at pH 5 after reduction of nitrotyrosine to aminotyrosine. Non-selective labeling of primary amines was avoided at the expense of a reduced labeling yield (60%). Although the combination of precursor ion and MS^3 scan modes to detect dansyl-specific fragment ions proved to be a powerful and selective detection technique, this method does not allow enrichment of nitrated peptides. Since tyrosine nitration is a low-abundance protein post-translational modification, similar to protein phosphorylation, it is critical that proteins be enriched prior to LC–MS/MS analysis to overcome limitations in terms of loading capacity of the chromatographic column.

Here we report the further development of a chemical approach for the biotinylation of nitrotyrosine residues in peptides with each step reaching a yield close to 100% as determined by LC–MS. Having a quantitative and selective method is critical to avoid labeling of other functional groups, such as primary amines, thiols or hydroxyl groups, which are much more abundant than nitrotyrosine and would thus lead to the enrichment of many non-nitrotyrosine-containing peptides. All reactions were performed sequentially in the same buffer (250 mM sodium phosphate, pH 8). This amine-free buffer (i) does not interfere with NHS ester-based acylations, (ii) is concentrated enough to prevent pH variation due to the release of acetic acid after hydrolysis of the excess of NHS-acetate and (iii) its pH is compatible with NHS ester-based amine acylations, with the hydrolysis of O-acyl groups upon incubation in a boiling water bath as well as with the non-enzymatic heme-based reduction of nitrotyrosine to aminotyrosine.

Recently Zhang et al. [39] published an approach for the chemical labeling and enrichment of nitrotyrosine-containing peptides independently of our work, based on acetylation of primary amines with acetic acid anhydride followed by reduction of nitrotyrosine with sodium dithionite and the acylation of aminotyrosine with NHS S-acetylthioacetate (SATA). In the following we discuss our results and methodology and compare it to the methodology described by Zhang et al., where appropriate.

4.1. Acetylation of primary amines

The first step of our methodology consists of the quantitative acetylation of all primary amines to avoid subsequent biotinylation of these residues. Using a high molar excess of NHS-acetate allowed to reach a yield of more than 99% (Fig. 3), while Zhang et al. estimated their yield at 91% after reaction with acetic anhydride, which leaves approximately 9% of all reactive amines unprotected [39]. Due to the large excess of primary amines over nitrotyrosine residues in peptides, it is critical to block all sides that will give rise to side reactions (non-selective labeling). Since only one tyrosine (natural occurrence in proteins: 3.2%) [46] in 10,000 is nitrated under inflammatory conditions [1], but 6.0% of amino acids in proteins are lysine [46], there is an 18,750-fold molar excess of ε-amines with respect to aminotyrosines (considering 100% conversion of nitrotyrosine to aminotyrosine). Moreover, if labeling is performed on a trypsin digest, every peptide will bear an additional reactive α-amine (a further 9.1% of all amino acid residues considering an average length of 11 amino acids for a tryptic peptide) [47], resulting in an approximate 28,450-fold molar excess of primary amines over aminotyrosines. Even a moderate percentage of non-acetylated or otherwise reactive aliphatic amines would therefore result in a majority of labeled peptides being devoid of nitrotyrosine. As a result, acetylation of all primary amines must be as close as possible to 100%.

4.2. Reduction of nitrotyrosine to aminotyrosine

The second step of our approach consists of the reduction of nitrotyrosine to aminotyrosine. Although this reaction is generally performed with sodium dithionite [36], we used hemin (i.e. chloroprotoporphyrin IX iron(III)) and DTT as previously described by Balabanli et al. [44]. The advantage of this reaction is that it proceeds to completion within a couple of minutes in a boiling water bath at the same pH as the acetylation reaction. Incidentally, Ghesquière et al. [38] used Fe^{2+}-charged cytochrome *C* as the reducing agent and showed it to be preferable to sodium dithionite, since the latter leads to partial sulfation of tyrosine, as suggested by an 80-Da increase in mass, hence complicating chromatograms and mass spectra.

4.3. Biotinylation of aminotyrosine

NHS-biotin was used to biotinylate aminotyrosine. Due to the blocking of primary amines in step 1 aminotyrosine should be, at this stage, the only amine available for biotinylation. While the

expected biotinylated peptide was observed (Fig. 6B, fifth and sixth panels), signal intensity was rather low, notwithstanding the fact that no starting material was left. We did not observe any side reactions that might explain a major loss of aminotyrosine-containing peptide and assume that the introduction of the biotin moiety at the aminotyrosine residue dramatically decreased ionization efficiency.

The phenolic hydroxyl group of tyrosine reacts as well with NHS-activated esters under the described conditions. By incubating for 60 min in a boiling water bath we assured that all O-biotinylated peptide was removed (Fig. S-1 in Supplementary Material). Although the phenolic hydroxyl group of aminotyrosine has an almost identical pK_a as in tyrosine (10.0 and 10.1, respectively [36]), we did not observe the O-biotinylated side product in this case (Fig. 6B, fifth and sixth panels). This is likely due to the fact that the aromatic amine is more reactive than the hydroxyl group making subsequent biotinylation of the adjacent OH-group sterically unfavorable.

4.4. Removal of excess biotin prior to enrichment on a monomeric avidin column

The binding capacity of the monomeric avidin resin is relatively low (1.2 mg BSA, i.e. 18 nmol/mL of settled resin corresponding to 0.9 nmol for the 100 μL of a 50% slurry of resin that we used). Thus, the resin would be very easily saturated by the 5 mM (1.15 μmol) of NHS-biotin (hydrolyzed to biotin during the boiling step) used during the last step of chemical labeling. We therefore wished to remove the excess of biotin prior to the final enrichment step. Several methods were not deemed optimal. Size-based separation methods (dialysis, gel filtration, ultrafiltration) were not possible because of the small size difference between free biotin (244 Da) and the target peptide (1329 Da). Solid-phase extraction with reverse-phase materials was no option since both molecules have similar retention characteristics (see retention on the C_{18} reversed-phase column; Fig. 6). Anion exchange was also not optimal, since both peptides and biotin contain at least one carboxylic acid moiety. Consequently we exploited SPE on a strong cation exchange resin based on the fact that biotin cannot acquire a positive charge at acidic pH, whereas most peptides can be protonated at histidine or arginine residues, despite the fact that all primary amines have been acetylated. This separation step proved to be efficient, although biotin still resulted in the highest peak upon LC–MS after the SCX step (Fig. 8A), considering that the remaining biotin is only a very small fraction of the initial amount that was present after biotinylation (Fig. 6A). Unfortunately, this cleanup step is also the cause for some peptide loss and requires further study. Comparison of the BPCs before (Fig. 6) and after SCX (flow-through of the avidin-based extraction, Fig. 7) reveals that the peak intensity for $[^{Ac}Y]^{2+}$ is reduced by a factor 30 although the peptide solution was only diluted by about a factor of 2.5. This signal reduction after the SCX column is consistent with the observation that the signal for the labeled peptide decreased by about a factor 5 although it is recovered in a volume that is only two times smaller than that of the biotinylation step (Figs. 6 and 8). Moreover, it appears that certain BSA-derived peptides are no longer observed after SCX, neither in the flow-through nor in the eluate of the avidin-based enrichment.

To circumvent this problem we are presently evaluating ways to perform the chemical labeling at the protein level and to use molecular size-based methods for biotin removal. Initial experiments show that it is possible to perform our sequence of reactions, including the boiling steps, with proteins in a solution containing 6 M guanidinium hydrochloride, so further investigations are warranted.

It is noteworthy that the labeled peptide of interest was recovered as the major peptide in the eluate of the avidin-based resin. No BSA-derived peptides were observed, reflecting the high selectivity of the chemical labeling and enrichment procedure.

5. Conclusion

We describe a methodology for the selective labeling and enrichment of tyrosine-nitrated angiotensin II in a matrix of BSA tryptic peptides. This method constitutes an improvement over previous reports by Nikov et al. [35] and Zhang et al. [39]. First, all chemical reactions proceeded with yields approximating 100%. This reduces the chance of enriching peptides that do not contain nitrotyrosine, which is of prime importance when targeting a low-abundance protein post-translational modification. Second, neither sample cleanup nor change of pH are required until the biotin-removal step. Considering that proteomic samples are often small in volume and contain low amounts of peptides, this is a major advantage.

Our chemical labeling approach is well adapted to the analysis of tyrosine nitration at the peptide level, for instance in shotgun proteomics. We are presently pursuing experiments to perform the labeling reactions at the protein level prior to digestion, notably to facilitate biotin removal.

Acknowledgments

The authors thank Dr. L. Rieux (University of Groningen, Department of Pharmacy, Pharmaceutical Analysis) for his expert technical help and useful discussions. N. Abello is the recipient of an Ubbo Emmius fellowship (University of Groningen). The Netherlands Proteomics Center (NPC) is gratefully acknowledged for financial support.

Appendix A. Supplementary data

Supplementary data associated with this article can be found, in the online version, at doi:10.1016/j.talanta.2009.02.002.

References

[1] R. Radi, Proc. Natl. Acad. Sci. U.S.A. 101 (2004) 4003.
[2] S.A. Greenacre, H. Ischiropoulos, Free Radic. Res. 34 (2001) 541.
[3] J.S. Beckman, Chem. Res. Toxicol. 9 (1996) 836.
[4] H. Ischiropoulos, Arch. Biochem. Biophys. 356 (1998) 1.
[5] H. Ischiropoulos, Biochem. Biophys. Res. Commun. 305 (2003) 776.
[6] J.M. Souza, E. Daikhin, M. Yudkoff, C.S. Raman, H. Ischiropoulos, Arch. Biochem. Biophys. 371 (1999) 169.
[7] C. Herce-Pagliai, S. Kotecha, D.E. Shuker, Nitric Oxide 2 (1998) 324.
[8] M.W. Duncan, Amino Acids 25 (2003) 351.
[9] D. Tsikas, K. Caidahl, J. Chromatogr. B: Anal. Technol. Biomed. Life Sci. 814 (2005) 1.
[10] H. Ryberg, K. Caidahl, J. Chromatogr. B 851 (2007) 160.
[11] D. Tsikas, J. Biochem. Biophys. Methods 49 (2001) 705.
[12] G. Gokulrangan, A. Zaidi, M.L. Michaelis, C. Schoneich, J. Neurochem. 100 (2007) 1494.
[13] J. Kanski, S.J. Hong, C. Schoneich, J. Biol. Chem. 280 (2005) 24261.
[14] S.J. Hong, G. Gokulrangan, C. Schoneich, Exp. Gerontol. 42 (2007) 639.
[15] J. Kanski, A. Behring, J. Pelling, C. Schoneich, Am. J. Physiol. Heart Circ. Physiol. 288 (2005) H371.
[16] K.S. Aulak, M. Miyagi, L. Yan, K.A. West, D. Massillon, J.W. Crabb, D.J. Stuehr, Proc. Natl. Acad. Sci. U.S.A. 98 (2001) 12056.
[17] A. Castegna, V. Thongboonkerd, J.B. Klein, B. Lynn, W.R. Markesbery, D.A. Butterfield, J. Neurochem. 85 (2003) 1394.
[18] J. Kanski, M.A. Alterman, C. Schoneich, Free Radic. Biol. Med. 35 (2003) 1229.
[19] J. Murray, S.W. Taylor, B. Zhang, S.S. Ghosh, R.A. Capaldi, J. Biol. Chem. 278 (2003) 37223.
[20] I.V. Turko, L. Li, K.S. Aulak, D.J. Stuehr, J.Y. Chang, F. Murad, J. Biol. Chem. 278 (2003) 33972.
[21] K.S. Aulak, T. Koeck, J.W. Crabb, D.J. Stuehr, Am. J. Physiol. Heart Circ. Physiol. 286 (2004) H30.
[22] S.L. Elfering, V.L. Haynes, N.J. Traaseth, A. Ettl, C. Giulivi, Am. J. Physiol. Heart Circ. Physiol. 286 (2004) H22.
[23] T. Koeck, X. Fu, S.L. Hazen, J.W. Crabb, D.J. Stuehr, K.S. Aulak, J. Biol. Chem. 279 (2004) 27257.
[24] T. Koeck, B. Levison, S.L. Hazen, J.W. Crabb, D.J. Stuehr, K.S. Aulak, Mol. Cell. Proteomics 3 (2004) 548.

[25] X. Zhan, D.M. Desiderio, Biochem. Biophys. Res. Commun. 325 (2004) 1180.
[26] Y. Suzuki, M. Tanaka, M. Sohmiya, S. Ichinose, A. Omori, K. Okamoto, Neurol. Res. 27 (2005) 630.
[27] S. Ghosh, A.J. Janocha, M.A. Aronica, S. Swaidani, S.A.A. Comhair, W. Xu, L. Zheng, S. Kaveti, M. Kinter, S.L. Hazen, S.C. Erzurum, J. Immunol. 176 (2006) 5587.
[28] R. Sultana, H.F. Poon, J. Cai, W.M. Pierce, M. Merchant, J.B. Klein, W.R. Markesbery, D.A. Butterfield, Neurobiol. Dis. 22 (2006) 76.
[29] G. Tedeschi, G. Cappelletti, S. Nonnis, F. Taverna, A. Negri, C. Ronchi, S. Ronchi, Neurochem. Res. 32 (2007) 433.
[30] X. Zhan, D.M. Desiderio, Int. J. Mass Spectrom. 259 (2007) 96.
[31] T.T. Reed, J. Owen, W.M. Pierce, A. Sebastian, P.G. Sullivan, D.A. Butterfield, J. Neurosci. Res., in press, doi:10.1002/jnr.21872.
[32] T.T. Reed, W.M.J. Pierce, D.M. Turner, W.R. Markesbery, D.A. Butterfield, J. Cell. Mol. Med., in press doi:10.1111/j.1582-4934.2008.00478.x.
[33] S. Garbis, G. Lubec, M. Fountoulakis, J. Chromatogr. A 1077 (2005) 1.
[34] S.P. Gygi, G.L. Corthals, Y. Zhang, Y. Rochon, R. Aebersold, Proc. Natl. Acad. Sci. U.S.A. 97 (2000) 9390.
[35] G. Nikov, V. Bhat, J.S. Wishnok, S.R. Tannenbaum, Anal. Biochem. 320 (2003) 214.
[36] M. Sokolovsky, J.F. Riordan, B.L. Vallee, Biochem. Biophys. Res. Commun. 27 (1967) 20.
[37] R. Wetzel, R. Halualani, J.T. Stults, C. Quan, Bioconjug. Chem. 1 (1990) 114.
[38] B. Ghesquière, M. Goethals, J. Van Damme, A. Staes, E. Timmerman, J. Vandekerckhove, K. Gevaert, Rapid Commun. Mass Spectrom. 20 (2006) 2885.
[39] Q. Zhang, W.J. Qian, T.V. Knyushko, T.R.W. Clauss, S.O. Purvine, R.J. Moore, C.A. Sacksteder, M.H. Chin, D.J. Smith, D.G. Camp, D.J. Bigelow, R.D. Smith, J. Proteome Res. 6 (2007) 2257.
[40] N. Abello, H.A. Kerstjens, D.S. Postma, R. Bischoff, J. Proteome Res. 6 (2007) 4770.
[41] A. van der Vliet, J.P. Eiserich, H. Kaur, C.E. Cross, B. Halliwell, Methods Enzymol. 269 (1996) 175.
[42] J.P. Crow, H. Ischiropoulos, Methods Enzymol. 269 (1996) 185.
[43] B.T. Miller, Biochem. Biophys. Res. Commun. 218 (1996) 377.
[44] B. Balabanli, Y. Kamisaki, E. Martin, F. Murad, Proc. Natl. Acad. Sci. U.S.A. 96 (1999) 13136.
[45] A. Amoresano, G. Chiappetta, P. Pucci, M. D'Ischia, G. Marino, Anal. Chem. 79 (2007) 2109.
[46] C. Clementi, P. Carloni, A. Maritan, Proc. Natl. Acad. Sci. U.S.A. 96 (1999) 9616.
[47] A. Shevchenko, S. Sunyaev, A. Loboda, P. Bork, W. Ens, K.G. Standing, Anal. Chem. 73 (2001) 1917.

Talanta 80 (2010) 1513–1525

Contents lists available at ScienceDirect

Talanta

journal homepage: www.elsevier.com/locate/talanta

Protein phosphorylation stoichiometry by simultaneous ICP-QMS determination of phosphorus and sulfur oxide ions: A multivariate optimization of plasma operating conditions

Domenico Ciavardelli[a,b], Paolo Sacchetta[b], Giorgio Federici[c,d], Carmine Di Ilio[a,b], Andrea Urbani[c,d,*]

[a] Centro Studi sull'Invecchiamento (Ce.S.I.), Chieti, Italy
[b] Dipartimento di Scienze Biomediche, Università "G. D'Annunzio" di Chieti-Pescara, Italy
[c] IRCCS-Fondazione Santa Lucia Centro di Ricerca sul Cervello, Rome, Italy
[d] Dipartimento di Medicina Interna, Università di Roma "Tor Vergata", Rome, Italy

ARTICLE INFO

Article history:
Received 31 October 2008
Received in revised form 11 June 2009
Accepted 29 June 2009
Available online 10 July 2009

Keywords:
Phosphorylation
Proteomics
ICP-MS
Mass spectrometry
MALDI-TOF-MS

ABSTRACT

Molecular mass spectrometry (MS) analysis of protein phosphorylation is partially limited by the molecular specie specificity of the analytical responses that might impair both qualitative and quantitative performances. Elemental MS, such as inductively coupled plasma mass spectrometry (ICP-MS) can overcome these drawbacks; in fact, analytical performance is theoretically independent of the molecular structure of a target analyte naturally containing the elements of interest. Nevertheless, isobaric interferences derived from sample matrix and laboratory environment can hinder the quantitative determination of both phosphorus (P) and sulfur (S) as $^{31}P^+$ and $^{32}S^+$ by inductively coupled plasma quadrupole mass spectrometry (ICP-QMS) under standard plasma conditions. These interferences may be overcome by quantifying P and S as oxide ions $^{31}P^{16}O^+$ and $^{32}S^{16}O^+$, respectively.

In this study, we present a systematic investigation on the effect of plasma instrumental conditions on the oxide ion responses by a design of experiment approach for the simultaneous ICP-QMS determination of P and S ($^{31}P^{16}O^+$ and $^{32}S^{16}O^+$, respectively) in protein samples without the use of dynamic reaction, collision reaction cells or pre-addition of oxygen as reactant gas in the torch. The proposed method was evaluated in terms of limit of detection, limit of quantification, linearity, repeatability, and trueness. Moreover, detection and quantification capabilities of the optimized method were compared to the standard plasma mode for determination of $^{31}P^+$ and $^{34}S^+$. Spectral and non-spectral interferences affecting the quantification of $^{31}P^+$, $^{31}P^{16}O^+$ and $^{32}S^{16}O^+$ were also studied. The suitability of inorganic elemental standards for P and S quantification in proteins was assessed. The method was applied to quantify the phosphorylation stoichiometry of commercially available caseins (bovine β-casein, native and dephosphorylated α-casein) and results were confirmed by Matrix Assisted Laser Desorption Ionization Time of Flight MS analysis.

We demonstrate that ICP-QMS, by quantifying P and S as oxide ions, was able to accurately calculate the degree of phosphorylation of β-casein and α-casein and to detect specific partial enzymatic dephosphorylation. The collected results might lead to further development of ICP-QMS interfaces optimized for protein phosphorylation studies and for proteomics investigations.

© 2009 Elsevier B.V. All rights reserved.

1. Introduction

Reversible protein phosphorylation is one of the most important post-translational modifications that plays a key role in many cellular metabolic pathways and strictly regulates protein functions [1,2]. The extent of phosphorylation for a specific protein depends on the cell status and can dynamically change over time. A protein can be phosphorylated and dephosphorylated by kinases and phosphatases, respectively, on different sites at different times. It is estimated that about 25–30% of the proteins present in eukaryotic cells are phosphorylated at some point in their life cycle [3]. Such a scenario makes quantitative determination of protein phosphorylation degree of great interest in proteomics investigations. Nevertheless currently this is a challenging task and is far to be routinely surveyed in mass spectrometry (MS) based proteomics. Molecular MS, such as Electrospray Ionization MS (ESI-MS) and Matrix Assisted Laser Desorption Ionization MS (MALDI-MS), are

* Corresponding author at: Department of Internal Medicine, University of Rome "Tor Vergata", Via del Fosso di Fiorano 65, 00149 Roma, Italy. Fax: +39 06 501703332.
E-mail address: andrea.urbani@uniroma2.it (A. Urbani).

0039-9140/$ – see front matter © 2009 Elsevier B.V. All rights reserved.
doi:10.1016/j.talanta.2009.06.082

the most useful tools for protein identification, sequencing, and site specific modification studies. However, some applications in the field of post-translational modification study are difficult. In the case of protein phosphorylation, the main problem affecting molecular MS in phosphoproteomics studies is the species specificity of the analytical responses that limits both qualitative and quantitative performance [4]. This is a general limitation of molecular MS because the signal obtained by MALDI or ESI ion source strongly depends on the molecular features of the ionized species and on the sample matrix. In particular phosphoproteins and phosphopeptides exhibit a lower MALDI-MS and ESI-MS sensitivity with respect to the unmodified peptides and are often not detectable in complex mixtures under standard operating conditions. In addition, the lack of suitable external standards limits quantitative applications and usually only relative quantification is possible. A great effort has been made to overcome these problems and enrichment procedures or selective tagging in the case of phosphorylated proteins and peptides have been proposed [5].

Theoretically, elemental MS, such as inductively coupled plasma MS (ICP-MS) can overcome these drawbacks. In fact, in this case the analytical sensitivity is theoretically independent from the molecular structure of a target analyte containing a natural elemental tag and quantification can be performed by using species-unspecific standards, i.e. inorganics [6–8]. Recently, Pereira-Navaza et al. described the accurate quantification of phosphorylated peptides in complex peptide mixtures by using elemental phosphorus (P) standard [9,10]. Furthermore, ICP-MS was proposed for detection not only of phosphorylation that occurs at the hydroxyl groups of serine (Ser), threonine (Thr), and tyrosine (Tyr) residues but also of acid labile phosphorylation of the side chains of arginine (Arg), aspartic acid (Asp), lysine (Lys), and histidine (Hys) residues often not detectable by MALDI or ESI-MS [11].

Another potential advantage of ICP-MS is the possibility of protein quantification by determination of sulfur (S) [12]. Absolute protein quantification is a challenging task in analytical chemistry and is pivotal for the understanding of proteome variations in living systems [13]. S naturally occurs in cysteine (Cys) and methionine (Met) side chains and constitutes a natural tag that did not require any reaction to be detected in contrast to other quantitative techniques as isotope-coded affinity tagging (ICAT) [14] and metal-coded affinity tagging (MECAT) [15]. Recently, the potentials of this approach were assessed by Schaumlöffel et al. [16] and Wang et al. [17]. They proposed isotope dilution analysis of S as a method for absolute quantification of peptides and proteins, respectively. Furthermore, S was used as an internal standard for quantitative determination of heteroatom/protein stoichiometric ratios. However, quantitative determination of P as $^{31}P^+$ and S as $^{32}S^+$ and/or $^{34}S^+$ by inductively coupled plasma quadrupole mass spectrometry (ICP-QMS) is hindered by severe nitrogen ($^{15}N^{16}O^+$, $^{14}N^{17}O^+$, $^{14}N^{16}O^1H^+$, $^{14}N^{18}O^+$, $^{15}N^{16}O^1H^+$) and oxygen ($^{16}O_2{}^+$) based isobaric interferences derived from sample matrix and laboratory environment. The problem of spectral interferences is less relevant in the case of P. ICP-QMS without collision/reaction cell technology was applied to quantify P as $^{31}P^+$ at trace level in different matrices or tagged molecules under standard plasma conditions [18–20]. This is not the case for S for which interferences hinder accurate quantification as $^{32}S^+$ and $^{34}S^+$ by ICP-QMS, discouraging potential applications for quantification. Spectral interferences of the major isotope ^{32}S can be efficiently resolved by using different instruments. Sector field mass spectrometer was successfully applied to quantify S and other elements in peptides and proteins [21,22]. Since the advent of dynamic reaction and collision reaction cells (DRC/CRC), ICP-QMS instruments can be used to quantitate P and S as oxide ions. In particular, the pioneering work of Bandura et al. [23] describes the quantification of protein phosphorylation by simultaneous ICP-QMS determination of P and S as oxide ions with excellent detection capability. However, only few papers report the quantification of S by ICP-QMS without collision/reaction cell. Menegario et al. [24] used ICP-QMS to determine $^{34}S/^{32}S$ isotope ratio from oxide ions $^{34}S^{16}O^+$ and $^{32}S^{16}O^+$ at m/z 50 and 48, respectively to resolve spectral interferences affecting the corresponding $^{32}S^+$ and $^{34}S^+$ singly charged ions. This approach was proposed by Menegario and Giné for quantification of S in plant digest [25], by Dviak and Goessler [26] for the quantitative determination of inorganic S species by ion chromatography coupled with ICP-QMS, and by Koplík et al. [27] for simultaneous P and S quantification in different matrices. In these works, plasma-operating conditions were optimized to give the maximum oxide ion formation ratio by using one factor at a time (OFAT) approach. Recently, design of experiment (DOE) has been proposed for the multivariate optimization of plasma conditions [28,29]. This approach has several advantages with respect to OFAT optimization process: the evaluation of effects of several factors is less time consuming and significant interactions between factors can be assessed with a lower risk of misinterpreting the results [30,31].

Here we present an optimization of oxide ion detection method that results in a significant improvement of simultaneous quantification of P and S in protein samples allowing to quantification of protein phosphorylation. The factors considered in the optimization procedure (i.e., sample depth, sample uptake flow, extraction lens 1 voltage, and plasma power) were optimized to maximize $^{31}P^{16}O^+$ and $^{32}S^{16}O^+$ yields without using oxygen as reactant gas.

Several assays were performed to compare our optimized conditions with standard plasma conditions. For both analytes the effective advantages of quantification as oxide ion under our conditions were verified by comparing background equivalent concentration (BEC), limit of detection (LOD), and limit of quantification (LOQ) with P and S determined as $^{31}P^+$ and $^{34}S^+$ under standard plasma conditions. In fact, this method has been widely reported for ICP-MS quantification of P [18–20]. While $^{34}S^+$, which is less interfered than $^{32}S^+$, could be potentially used as the analyte ion for S quantification by ICP-QMS under standard experimental conditions. Moreover, spectral and non-spectral interferences affecting the determination of P as $^{31}P^{16}O^+$ and S as $^{32}S^{16}O^+$ under our optimized conditions were studied. In fact, carbon (C), nitrogen (N), silicon (Si), magnesium (Mg), calcium (Ca), and titanium (Ti) are potential sources of spectral interferences at m/z 47 and 48 (Table 1) [32,33]. In particular, C and N polyatomic species were reported as interfering ions at m/z 47 and 48 affecting the analytical

Table 1
Isobaric interferences at m/z 47 and 48.

m/z	Interference
47	$^{12}C^{35}Cl^+$ [a]
	$^{13}C^{16}O^{18}O^+$ [b]
	$^{12}C^{16}O^{18}OH^+$ [b]
	$^{14}N^{16}O^{16}OH^+$ [a,b]
	$^{14}N^{16}O^{17}O^+$ [b]
	$^{15}N^{16}O_2{}^+$ [a,b]
	$^{30}Si^{16}OH^+$ [a]
	$^{47}Ti^+$
48	$^{12}C_4{}^+$ [a]
	$^{13}C^{35}Cl^+$ [a]
	$^{36}Ar^{12}C^+$ [a]
	$^{14}N^{16}O^{18}O^+$ [a]
	$^{14}N^{17}O_2{}^+$ [a]
	$^{24}Mg^{24}Mg^+$
	$^{48}Ca^+$
	$^{48}Ti^+$

[a] Ref. [32].
[b] Ref. [33].

performance in terms of sensitivity and trueness in carbon and nitrogen rich matrices [33]. Furthermore, C can also affect the analyte ionization in a species-specific fashion, usually enhancing non metal sensitivity and suppressing metal ionization [9,16,21,34,35]. For P the potential interference sources were also studied when analyzed as $^{31}P^+$ under standard plasma conditions. Performance evaluations for both ionization modes were performed in the same analysis by switching between oxide ion mode and normal plasma conditions, instead of performing the two analyses independently.

Finally, the method was applied to quantify the phosphorylation degree of commercially available caseins (bovine β-casein, native and dephosphorylated α-casein) and results were confirmed by MALDI-MS analysis demonstrating that this method can yield results thus far obtained on more complex instrumental set-up including DRC/CRC system.

2. Experimental

2.1. Chemicals and reagents

Deionized water with a specific resistance of 18.2 MΩ cm (Milli-Q system, Millipore, Watford, Hertfordshire, UK) was used for preparing all solutions and diluting the samples. P (H_3PO_4, 1000 mg L^{-1}, H_2O) and S (Na_2SO_4, 1000 mg L^{-1}, H_2O) stock solutions were purchased by Merck (Darmstadt, Germany) and Romil (Cambridge, UK), respectively. Standard solutions were prepared daily from the stock. Internal standard stock solution (Sc, Ge, Y, In, Tb, Bi, 10 mg L^{-1}, 1% HNO_3) and tuning solution (Li, Y, Ce, Tl, 10 μg L^{-1}, 2% HNO_3) were acquired from Agilent Technology (Palo Alto, California, USA). Tris(hydroxymethyl)-aminomethane (Tris) was obtained from Bio Rad Laboratories (Hercules, CA, USA). Barium hydroxide, acetonitrile, trifluoroacetic acid (TFA), acetic acid, Triton X100, bovine serum albumin (BSA, purity 99%), bovine β-casein (total protein 92%, purity 94%), bovine α-casein (total protein 98.8%, purity 96.9%), enzymatically dephosphorylated α-casein (total protein 87%, purity 87%), and sequence grade modified trypsin were purchased from Sigma–Aldrich (Shnelldorf, Germany). Rhodium stock solution (Rh, 10 mg L^{-1}), sinapinic acid, α-cyano-4-hydroxycinnamic acid (CHCA), L-cysteine (Cys, purity ≥99.5%) and O-phospho-DL-serine (P-Ser, purity ≥99%) were purchased from Fluka BioChemika (Shnelldorf, Germany).

2.2. Sample preparation

Proteins and amino acids were accurately weighed using a Mettler Toledo AX26 DeltaRange™ balance with the readability of 1 μg and then dissolved in 18 MΩ water to give a concentration of at least 1 mg mL^{-1}. Class A volumetric flasks (Assistent, Sondheim, Germany) previously soaked with 10% HNO_3, were used to prepare stock solutions. Stocks were stored at −80 °C until use. Stock solutions were suitably diluted and analyzed by ICP-MS without any further purification. Enzymatic hydrolysis for peptide mass fingerprint (PMF) analysis of caseins was performed by using trypsin. Bovine β-casein, bovine α-casein, and enzymatically dephosphorylated bovine α-casein, 1 μmol L^{-1} in 50 mM ammonium carbonate/2 M urea at pH 8.3, were incubated overnight at 37 °C with trypsin at an enzyme/substrate ratio of 1:100 to produce tryptic digest for MALDI-TOF-MS analysis. Reaction was stopped by addition of 0.1% TFA and 10 μL of solution, corresponding to 10 pmol of peptides, were desalted on Zip-Tip™ C18 micro-columns (Millipore, Watford, Hertfordshire, UK) and eluted with 2 μL saturated CHCA matrix solution (50% CH_3CN, 0.1% TFA) onto the MALDI target. β-Elimination of intact proteins was performed on 50 μmol L^{-1} casein solutions (30 μL) in 2 M urea by adding 15 μL of saturated $Ba(OH)_2$. After 15 min at 37 °C, 5 μL of 10% (v/v) acetic acid was added. Sample desalting was performed by ZipTip™ C4 micro-columns (Millipore, Watford, Hertfordshire, UK). Protein elution with 2 μL of saturated sinapinic acid matrix solution (50% CH_3CN) was performed directly onto the MALDI target.

Table 2
ICP-MS operating conditions.

	Standard plasma mode	Oxide ion mode
Plasma power (W)	1200	960[a]
Carrier gas flow rate (L/min)	1.15	1.15
Sample depth	7.5	4.5[a]
Sample flow rate (mL/min)	0.40	0.88[a]
Spray chamber temperature (°C)	2	2
Extraction lens 1 (V)	−150	−135.2[a]
Extraction lens 2 (V)	−70	−70
Element (ion, *m*/*z*)	P ($^{31}P^+$, 31), S ($^{34}S^+$, 34)	P ($^{31}P^{16}O^+$, 47), S ($^{32}S^{16}O^+$, 48)
Integration time per point (s)	0.1	0.3
Point per mass	3	3

[a] Optimized by DOE.

2.3. ICP-MS analysis

The analysis equipment employed was an inductively coupled plasma mass spectrometer, model 7500A (Agilent Technologies, Tokyo, Japan) fitted with an ASX-510 autosampler (CETAC, Omaha, NE, USA) and a peristaltic pump. A Babington nebulizer with a Scott spray chamber (Agilent Technologies) was used for sample introduction. A multi-tune method based on the automatic switching between the two operating conditions in the same analysis was used for the simultaneous determination of P and S as $^{31}P^+$, $^{34}S^+$ and $^{31}P^{16}O^+$, $^{32}S^{16}O^+$ under normal and optimized conditions, respectively. The stabilization time after switching was 25 s. Operating conditions are described in Table 2. Normal plasma conditions were optimized for the best sensitivity of 10 μg L^{-1} of ^7Li, ^{89}Y and ^{205}Tl and for the reduction of $^{140}CeO^+/^{140}Ce^+$ and $^{140}Ce^{2+}/^{140}Ce^+$ ratios below 1% and 3%, respectively. While the DOE was used to optimize sample depth, sample uptake flow, extraction lens 1 voltage, and plasma power for $^{31}P^{16}O^+$ and $^{32}S^{16}O^+$ formation. An internal standard solution (Sc, Ge, Y, Rh, In, Tb, Bi, 50 μg L^{-1}) was added on line in a T-piece. Washing of sample introduction system was performed with 18 MΩ cm water. Data analysis was performed using ChemStation software (Agilent Technologies).

2.4. MALDI-TOF-MS analysis

All MALDI-Time of Flight-MS (MALDI-TOF-MS) analyses were performed on a MALDI-TOF-MS Reflex IV (Bruker Daltonics, Bremen, Germany) spectrometer equipped with an MTP multiprobe and a nitrogen laser pulsing operating at 337 nm. Positive ion mass spectra (*m*/*z* range = 700–4000) for PMF analysis were acquired operating in reflectron mode by summing at least 200 single laser shots with a repetition rate of 6 Hz. Source voltages were 20.00, 16.80 and 8.9 kV and reflectron voltage was 23 kV. Angiotensin I (1296.68 Da), ACTH 8–39 (2465.19 Da), Bradichinin (fragments 1–9, 1060.57 Da), and Renin substrate (1758.93 Da) were used as external standard for mass calibration. Acquired spectra were processed with FlexAnalysis 2.3 and BioTools 3.0 software (Bruker Daltonics). Database searches were performed against the nonredundant protein sequence database NCBInr using the peptide search algorithm MASCOT (Matrix Science, http://www.matrixscience.com). A mass tolerance of 100 ppm was allowed during processing of MS data for PMF. Oxidation of Met and phosphorylation of Ser were chosen as optional modifications. One enzyme missed cleavage was chosen for all searches performed without taxonomic restriction.

Table 3
Design matrix and responses from central composite design. Real values for the selected factors are reported in parentheses. Responses were blank subtracted and are mean value from triplicate measurements (standard deviation in parentheses). Six analyses were performed at centre of experimental domain.

X_1 (sample depth, mm)	X_2 (sample uptake flow, mL min^{-1})	X_3 (extraction lens 1, V)	X_4 (plasma power, W)	$^{31}P^{16}O^+$ (counts s^{-1})	$^{32}S^{16}O^+$ (counts s^{-1})
−1 (5.00)	−1 (0.4)	−1 (−160)	−1 (1000)	4648 (58)	22,174 (394)
−1 (5.00)	−1 (0.4)	−1 (−160)	1 (1300)	2029 (20)	8,098 (84)
−1 (5.00)	−1 (0.4)	1 (−140)	−1 (1000)	5360 (28)	23,435 (284)
−1 (5.00)	−1 (0.4)	1 (−140)	1 (1300)	2532 (10)	10,368 (312)
−1 (5.00)	1 (0.8)	−1 (−160)	−1 (1000)	6185 (9)	29,545 (320)
−1 (5.00)	1 (0.8)	−1 (−160)	1 (1300)	3324 (18)	13,542 (238)
−1 (5.00)	1 (0.8)	1 (−140)	−1 (1000)	6683 (6)	32,945 (73)
−1 (5.00)	1 (0.8)	1 (−140)	1 (1300)	3903 (10)	16,391 (288)
1 (7.00)	−1 (0.4)	−1 (−160)	−1 (1000)	4145 (73)	17,584 (230)
1 (7.00)	−1 (0.4)	−1 (−160)	1 (1300)	572 (6)	1,400 (29)
1 (7.00)	−1 (0.4)	1 (−140)	−1 (1000)	5141 (49)	22,070 (141)
1 (7.00)	−1 (0.4)	1 (−140)	1 (1300)	691 (8)	1,706 (28)
1 (7.00)	1 (0.8)	−1 (−160)	−1 (1000)	4823 (2)	20,611 (6)
1 (7.00)	1 (0.8)	−1 (−160)	1 (1300)	1153 (6)	3,019 (62)
1 (7.00)	1 (0.8)	1 (−140)	−1 (1000)	4635 (31)	20,336 (25)
1 (7.00)	1 (0.8)	1 (−140)	1 (1300)	1391 (13)	3,573 (10)
−1.48 (4.50)	0 (0.6)	0 (−150)	0 (1150)	4644 (4)	21,535 (50)
1.48 (7.50)	0 (0.6)	0 (−150)	0 (1150)	2574 (5)	7,785 (53)
0 (6.00)	−1.48 (0.32)	0 (−150)	0 (1150)	2751 (19)	10,785 (141)
0 (6.00)	1.48 (0.88)	0 (−150)	0 (1150)	5375 (60)	23,444 (281)
0 (6.00)	0 (0.6)	−1.48 (−164.8)	0 (1150)	3486 (338)	15,111 (30)
0 (6.00)	0 (0.6)	1.48 (135.2)	0 (1150)	4889 (50)	20,514 (555)
0 (6.00)	0 (0.6)	0 (−150)	−1.48 (930)	4322 (30)	20,788 (187)
0 (6.00)	0 (0.6)	0 (−150)	1.48 (1370)	1656 (117)	5,419 (53)
0 (6.00)	0 (0.6)	0 (−150)	0 (1150)	4019 (109)	16,313 (770)

Intact mass determination of native caseins and dephosphorylated β-elimination products were performed operating in linear mode with detection of positive ions (m/z range = 7000–35,000). Source voltages were 20.00, 18.00, and 9.4 kV. External mass calibration was performed using molecular and doubly charged ions of human hemoglobin α (m/z 15,127 and 7564, respectively) and β-chains (m/z 15,868 and 7934, respectively). At least 200 single pulse spectra were summed with a repetition rate of 9 Hz.

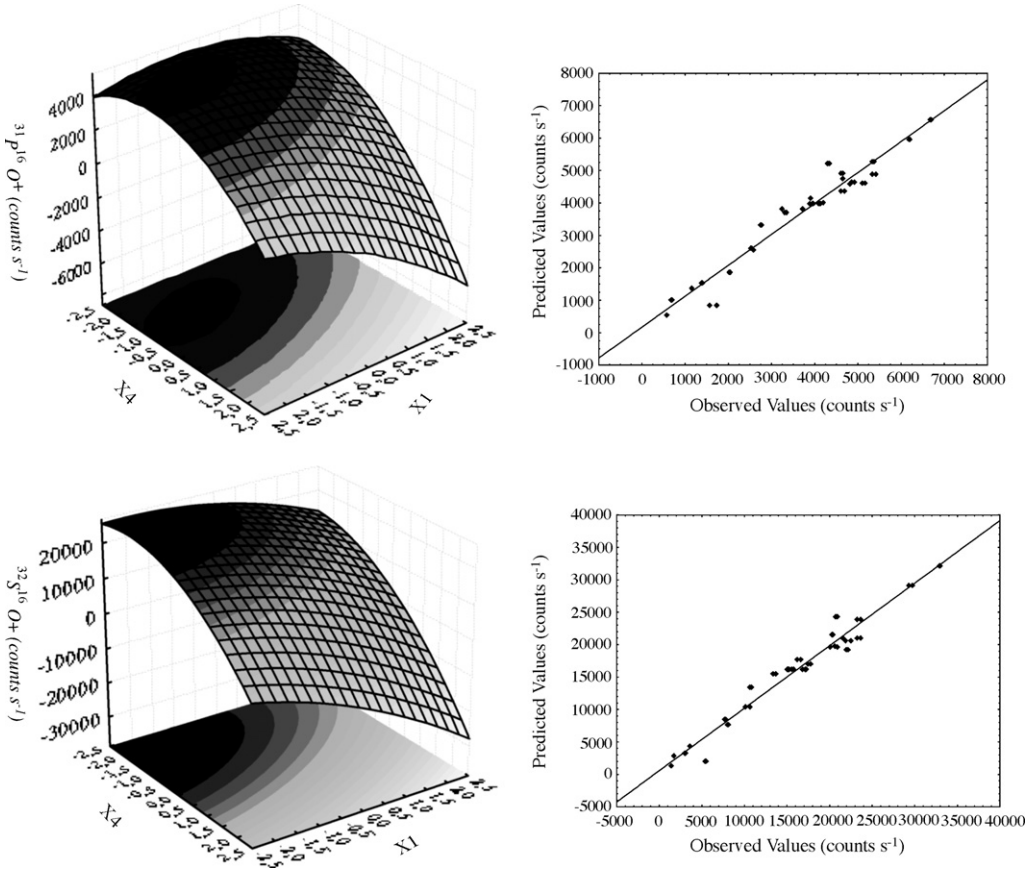


Fig. 1. Response surfaces of $^{31}P^{16}O^+$ and $^{32}S^{16}O^+$ signals as function of plasma power (X_4) and sample depth (X_1) and observed versus predicted values from central composite design.

Table 4
Polynomial functions and correlation coefficients calculated using the standard least squares regression method. Standard errors are in parentheses (X_1 = sample depth, X_2 = sample uptake flow, X_3 = lens 1 voltage, X_4 = plasma power).

$^{31}P^{16}O^+$
$Y = 3,992(\pm83) - 744X_1(\pm63) + 533X_2(\pm63) + 271X_3(\pm63) - 1,470X_4(\pm63) - 254X_1X_2(\pm71) - 241X1X4(\pm71) - 432X_4^2(\pm86)$
$R^2 = 0.945$

$^{32}S^{16}O^+$
$Y = 16,097(\pm442) - 4,245X_1(\pm277) + 2,544X_2(\pm277) + 1,121X_3(\pm277) - 7,521X_4(\pm277) - 1,473X_1X_2(\pm314) - 700X_1X_4(\pm314) + 746X_3^2(\pm384) - 1,396X_4^2(\pm384)$
$R^2 = 0.959$

2.5. Experimental design

A 2^4 two-level full factorial design (FFD) was used to investigate the main and interaction effects of sample depth (X_1, mm), sample uptake flow (X_2, mL min^{-1}), extraction lens 1 voltage (X_3, V) and plasma power (X_4, W) on the $^{31}P^{16}O^+$ and $^{32}S^{16}O^+$ signals (counts s^{-1}) at m/z 47 and 48, respectively. Aqueous standards containing 30 and 300 μg L^{-1} of P and S, respectively, were analysed. Instrumental blank (18 MΩ cm water) signal was measured under each experimental condition and subtracted from the corresponding standard signal. Low (−1) and high (+1) levels were: X_1 = [5–7] mm, X_2 = [0.4–0.8] mL min^{-1}, X_3 = [(−170)–(−140)] V, X_4 = [1000–1300] W. Torch position was automatically adjusted at each sample depth to maximize intensities at m/z 47 and 48. Experimental domains were defined for all the investigated factors on the basis of technical limitation of the system and acceptable signal stability below 5%. Experiments were performed in random order to avoid trends and three replicate measurements were done for all the experimental conditions to check the repeatability. Significant main and interaction effects were evaluated by single factor analysis of variance (ANOVA) of responses and standard least squares regression was used to calculate the best first order fit. Six measurements were also performed at the centre of experimental domain to check the relevant quadratic effect by a lack of fit test. A 95% confidence level was chosen in every case. Star points were added to the full factorial plan when a significant quadratic effect was detected. The axial distance (α) between star points and centre of experimental domain was calculated to obtain an orthogonal central composite design (CCD). The best regression model and coefficients of determination R^2 were then calculated by using all the experiments performed in both phases of experimental design. The desirability function approach was used for multiple response optimization [36]. The overall desirability, D, was calculated as the geometric mean of individual desirabilities:

$$D = [d_1(\hat{Y}_1) \times d_2(\hat{Y}_2) \times \cdots \times d_i(\hat{Y}_i)]^{1/i} \quad (1)$$

where d_i is the desirability associated to the ith fitted response value, $\hat{Y}_i$. Individual desirabilities were defined as follow:

$$d_i(\hat{Y}_i) = 0 \quad \text{if } \hat{Y}_i \le 0 \quad (2)$$

$$d_i(\hat{Y}_i) = \frac{\hat{Y}_i}{1.2 \times \hat{Y}_{i,\max}} \quad \text{if } 0 < \hat{Y}_i < 1.2 \times \hat{Y}_{i,\max} \quad (3)$$

$$d_i(\hat{Y}_i) = 1 \quad \text{if } \hat{Y}_i = 1.2 \times \hat{Y}_{i,\max} \quad (4)$$

The overall desirability D was then maximized by grid search algorithm. All statistical analyses were performed with STATISTICA 6.0 software (StatSoft Inc., Tulsa, OK)

2.6. Method development

Detection limit (LOD) and quantification limit (LOQ) were expressed as signals (y_D and y_Q) on the basis of the mean value ($\bar{y}_b$) and standard deviation (s_b) of the blank responses (n = 20):

$$y_D = \bar{y}_b + 2ts_b \qquad y_Q = \bar{y}_b + 10s_b \quad (5)$$

where t is the constant from the one sided Student's t-test at 95% confidence level for $n-1$ degrees of freedom. The corresponding concentration values were obtained by using an appropriate calibration curve satisfying the relationship: $0.5x_1 < \text{LOD} < x_1$, where x_1 is the concentration of the first calibration level [37]. Linearity was studied according to IUPAC guidelines [38]. Homoscedasticity was verified by applying Bartlett's test. Linearity of calibration functions was verified by the calculation of coefficient of determination (R^2) and Mandel's fitting test. Two-sided t-test was used to confirm the significance of the intercept. Precision was calculated in term of repeatability as relative standard deviation (RSD%) [37]. Trueness was evaluated by recovery tests [37]. A standard of BSA and P-Ser corresponding to the theoretical concentrations of 200 and 50 μg L^{-1} for S and P, respectively, was spiked with known amounts of the same organic standards. Quantification was performed by means of the calculated inorganic standard calibrations. Three spike levels were analysed (n = 3).

Statistical analysis was performed with XLStat and Microsoft Excel.

3. Results and discussion

3.1. Optimization of plasma-operating conditions by design of experiment

Oxide ions are one of the main spectral interferences limiting the multi-element capability of ICP-QMS. Their origin in the argon plasma has been well investigated [39,40]. Usually instrumental parameters were adjusted to minimize their formation maximizing singly charged ion M^+ intensities. However, oxide ions have been proposed as analyte ions to chemically resolve spectral interferences of the corresponding elemental ion [41,42]. In particular, the use of oxygen as reactant gas in DRC systems was successfully proposed for quantification of P and S in native protein sample by low resolution ICP-MS with excellent detection capability [23]. Plasma conditions could also be optimized to enhance oxide ion formation without any DRC system or pre-addition of oxygen as reactant gas

Table 5
Background equivalent concentration (BEC), instrumental limit of detection (LOD) and quantification (LOQ) calculated for P and S under the standard plasma and optimized conditions.

Element (ion, m/z)	BEC (μg L^{-1})[a]	LOD (μg L^{-1})[b]	LOQ (μg L^{-1})[c]
P ($^{31}P^+$, 31)[d]	6.3 (0.2)	1	5
S ($^{34}S^+$, 34)[d]	464 (56)	114	402
P ($^{31}P^{16}O^+$, 47)[e]	4.6 (0.2)	0.4	1.1
S ($^{32}S^{16}O^+$, 48)[e]	84 (5)	13	47

[a] Calculated as $[y_B/(y_{ex} - y_B)] \times x_{ex}$(μg L^{-1}), y_B = blank signal (n = 20), y_{ex} = external standard signal (n = 5), x_{ex} = concentration level (30 and 300 μg L^{-1} for P and S, respectively).
[b] Calculated as concentration corresponding to the signal $y = y_B + 2ts_B$, y_B = average blank signal (n = 20), s_B = standard deviation, t = critical value of t distribution (one tailed, 95% confidence level, 19) = 1.729.
[c] Calculated as concentration corresponding to the signal $y = y_B + 10s_B$, y_B = average blank signal (n = 20), s_B = standard deviation.
[d] Measured under standard plasma conditions.
[e] Measured using the optimized oxide ion mode.

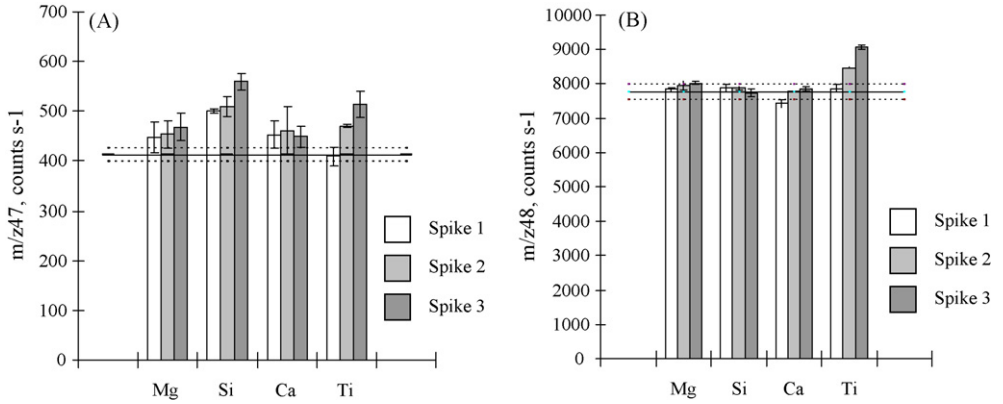


Fig. 2. Evaluation of Mg, Si, Ca, and Ti based spectral interferences at m/z 47 and 48. Data are the mean signal corresponding to increasing concentrations (nmol L^{-1}) of the potential interfering species. Bars are standard deviations ($n = 3$). Solid and dotted lines represent the mean signals and the confidence intervals at 95% confidence level, respectively, of 18 MΩ cm water.

in the torch. This approach has been applied for P and S quantification but optimization has been made by an OFAT approach without taking into account a possible interaction between the studied factors. In this work experimental design was applied to investigate main and interaction effects of sample depth, sample uptake flow, extraction lens 1 voltage and plasma power on $^{31}P^{16}O^+$ and $^{32}S^{16}O^+$ ions formation. It is known that factors affecting residence time of ion in the plasma e.g. carrier gas flow, sample depth, sample uptake flow and the plasma power can have a significant effect on the oxide ion formation. Reducing the residence time and plasma power gives usually increased MO^+/M^+ intensity ratios. In accordance with previous reports, preliminary experiments showed that carrier gas flow was the most important factor affecting oxide ion formation with a high significant positive effect. Small increases of carrier gas flow give significant increase of oxide ion yield and the corresponding experimental domain would be too narrow. Therefore, all measurements were performed by setting carrier gas flow at 1.35 L min^{-1} achieving acceptable short time signal repeatability. The experimental plan and the analytical responses are showed in Table 3. The analytical responses were the net signals for $^{31}P^{16}O^+$ and $^{32}S^{16}O^+$ calculated from the standard signals by subtracting the corresponding blank at each experimental condition. In this way, signals depend only on the analyte ions without any contribution of background that also changes at different experimental conditions. A significant curvature effect was detected by a Lack of Fit test ($p < 0.05$) for analyte ions. Star points were then added to the full factorial experimental design to estimate square terms. Fig. 1 shows the response surface and the corresponding residual plots while the calculated polynomial functions and the correlation coefficients were reported in Table 4. Residual plots (Fig. 1) and the calculated R^2 (Table 4) attest an acceptable descriptive and predictive ability of the calculated model for both analytes. The calculated models were used for the multiple response optimizations by means of the desirability function and the optimal experimental conditions were $X_1 = 4.5$ mm, $X_2 = 0.88$ mL min^{-1}, $X_3 = 135.2$ V and $X_4 = 959$ W corresponding to an overall desirability $D = 0.97$. The excellent global desirability (D) demonstrated that these experimental conditions were optimal for the simultaneous $^{31}P^{16}O^+$ and $^{32}S^{16}O^+$ formation. As expected, a low plasma power and the lowest sample depth within the experimental domain increase oxide ion level. In fact, reducing the distance between the torch and the sample cone the permanence time of ions in cooler plasma is also reduced and the probability of polyatomic ion detection increased. A significant effect of the sample loading flow was also observed. Increasing the sample uptake flow at the highest value within the experimental domain, increased oxide ion intensities were observed. By increasing sample loading flow rate, more aerosol was introduced in the plasma and the mass transport rate simultaneously increased for analyte and solvent [43]. Higher water vapours generate higher oxygen level in plasma enhancing oxide ion formation. Furthermore, water reduced plasma temperature, and ionization efficiency with the same effect [44]. Surprisingly, no significant interaction effect between extraction lens 1 voltage and the other factors was observed. The optimal extraction lens voltage, i.e. the higher value in the investigated experimental domain could be probably explained on the basis of the best compromise between analyte and blank signals. The reliability of the predictive model was evaluated by comparing the predicted responses (7552 ± 904 and $39{,}626 \pm 4006$ counts s^{-1} for $^{31}P^{16}O^+$ and $^{32}S^{16}O^+$, respectively; mean ± CI, 95% confidence level) with the experimental signals at m/z 47 and 48 measured under the optimized operating conditions. The measured signal blank subtracted was 7048 ± 54 and $40{,}533 \pm 372$ counts s^{-1} (mean ± CI, $n = 5$, 95% confidence level) at m/z 47 and 48, respectively. These results agreed with the predicted responses.

Background equivalent concentrations (BEC, μg L^{-1}), instrumental limits of detection (LOD, μg L^{-1}) and quantification (LOQ, μg L^{-1}) were calculated under the optimized conditions and compared with values calculated at mass m/z 31 and 34 corresponding to isotopes ^{31}P and ^{34}S analyzed under standard plasma conditions (Table 5). Analysis of 20 instrumental blanks (18 MΩ cm water) was carried out in multi-tune mode with two sequential steps for every acquisition: first standard operating conditions and then plasma conditions optimized for detection of oxide ions. A significant improvement of BEC, LOD, and LOQ was observed for S by measuring the oxide ion $^{32}S^{16}O^+$ under the optimized conditions with respect to normal plasma conditions even if BEC and LOD were higher than previously published data obtained measuring S as $^{32}S^{16}O^+$ with DRC–ICP-QMS [23]. However, the calculated LOD is of the same order of magnitude obtained measuring $^{32}S^+$ and $^{34}S^+$ with CRC–ICP-QMS with H_2 or Xe as reactant gas and He as collision gas [45]. On the other hand, the calculated LOD for P measured as $^{31}P^{16}O^+$ was of the same order of magnitude of that previously reported [23]. However, higher BEC was calculated in the present case. The effect of higher BEC on LOD was negligible. This is probably related to the higher acquisition time (Table 2) that improved precision of background measurement for oxide ions.

In contrast with S measured as $^{34}S^+$, acceptable LOD and LOQ were calculated for P measured as $^{31}P^+$ under normal plasma conditions. Therefore, both the operating conditions were suitable for quantitative determination of P at trace (μg L^{-1}) levels and could be alternatively used depending on specific sample matrix and related interferences.

Table 6
Calibration functions calculated for P measured as $^{31}P^+$ and $^{31}P^{16}O^+$ and for S measured as $^{32}S^{16}O^+$ using inorganic elemental standards, amino acids P-Ser and Cys (P-Ser/Cys), and BSA spiked with P-Ser (P-Ser/BSA). Blank matrix and five concentration levels ($n = 3$) between 50–300 and 200–1200 ng mL^{-1} for P and S, respectively, were analysed. R^2 values were better than 0.99 for all curves. Significant p values are bold. ND: not determined. CI: 95% confidence interval.

Element (ion, m/z), matrix	Inorganic standards		P-Ser/Cys		P-Ser/BSA	
	b_1(CI)	Mandel's fitting test, p[a]	b_1(CI)	Mandel's fitting test, p[a]	b_1(CI)	Mandel's fitting test, p[a]
P ($^{31}P^+$, 31), 18 MΩ cm water[b]	1222(39)	0.303	1205(17)	0.927	1223(39)	0.217
P ($^{31}P^{16}O^+$, 47), 18 MΩ cm water[c]	403(8)	0.096	402(4)	0.101	437(8)	0.052
P ($^{31}P^{16}O^+$, 47), 50 mmol L^{-1} Tris/HNO_3[c]	352(6)	0.082	ND	ND	355(6)	0.098
S ($^{32}S^{16}O^+$, 48), 18 MΩ cm water[c]	179(4)	0.391	184(2)	0.183	183(9)	**0.007**
S ($^{32}S^{16}O^+$, 48), 50 mmol L^{-1} Tris/HNO_3[c]	140(2)	0.461	ND	ND	141(5)	**0.001**
S ($^{32}S^{16}O^+$48), 40 mmol L^{-1} Tris/HNO_3–0.1% Triton X100[c]	129(4)	0.062	ND	ND	127(2)	0.106

[a] 95% confidence level.
[b] Measured under standard plasma conditions.
[c] Measured using the optimized oxide ion mode.

3.2. Study of spectral interferences

Mg, Ca, Si, and Ti based spectral interferences might affect background at m/z 47 and 48 (Table 1). Ca and Ti based interferences can be chemically resolved using DRC–ICP-MS instruments via thermodynamically allowed reactions with oxygen resulting in the corresponding oxide ions. In our experimental conditions we simultaneously maximize the yield of both $^{31}P^{16}O^+$ and $^{32}S^{16}O^+$. However, we cannot exclude that this also resulted in the formation of potential interfering species. Furthermore, Si and Mg can give the corresponding $SiOH^+$ hydroxide ions and $^{24}Mg^{24}Mg^+$ dimers that can interfere at m/z 47 and 48, respectively. Therefore, the potential contribution of these elements on the background has been investigated. Equimolar solutions of Mg, Ca, Ti (5, 10 and 20 nmol L^{-1}, respectively), and Si solutions (200, 400 and 800 nmol L^{-1}) were analyzed. The concentrations of these elements used in our experiments were at least ten fold higher than the typical concentration found in the 18 MΩ cm water [46]. As can be seen in Fig. 2, Mg and Ca do not significantly affect the signal at m/z 48 at these concentration levels. However, the effect of these potential interferences should be checked if analyses have to be performed in buffers containing higher concentration of Mg and Ca instead water. An increase of signal at m/z 47 was observed for Si and Ti spikes. Ti also increases signal at m/z 48. This is probably due to the incomplete oxidation of Ti^+ under these experimental conditions. While Ti was probably not a major problem, since Ti concentration in protein samples can be expected to be low if care is taken to avoid Ti contamination in chemicals used for sample preparation. On the contrary Si might represent an important potential interference. Indeed it is not surprising that Si increased background signal at m/z 47; in fact, the isobaric hydroxide ion $SiOH^+$ is known to be generated in plasma to a level suitable for Si ICP-QMS quantification [47]. Furthermore, Si is very common in nature and constitutes one of the main inorganic components of ultrapure water. For this, Si contribution to the background at m/z 47 could be relevant.

3.3. Study of non-spectral interferences

Organic compounds as proteins are potential sources of non-spectral interferences affecting analyte signals because C naturally occurring in biomolecules might affect the ionization of the heteroatoms bound to proteins. On the other hand, proteins can change physical properties (density, viscosity, and surface tension) of aqueous solutions with respect to aqueous inorganic standard used for quantification, affecting the aerosol transport rate, the vapour mass load, and/or the nebulization processes.

To check possible non-spectral C based interferences and assess the suitability of inorganic element standards for P and S quantification in proteins, we calculated calibration curves for P as $^{31}P^+$ and $^{31}P^{16}O^+$ and S as $^{32}S^{16}O^+$ by analyzing aqueous inorganic standards, amino acids P-Ser/Cys and P-Ser/BSA standards. BSA spiked with known amount of P-Ser was used as a surrogate of phosphoprotein because of high purity of the standards available. This approach was successfully proposed to verify the feasibility of protein quantification via inductively coupled plasma-atomic emission spectroscopy (ICP-AES) analysis of S by using inorganic elemental standard [48]. Table 6 shows the slopes of calculated calibration curves, showing that inorganic phosphate was a suitable external standard for quantification of P as $^{31}P^+$ under normal plasma conditions in aqueous solutions of biomolecules. On the other hand, the slopes of inorganic and P-Ser/Cys calibrations differ at 95% confidence level with slope of P-Ser/BSA calibration when P was determined as $^{31}P^{16}O^+$. This is probably due to the contribution of C based interferences to the signal at m/z 47 that proportionally increases with protein concentration. Therefore, protein levels affect P sensitivity and inorganic standards cannot be used for accurate quantification of P as $^{31}P^{16}O^+$ in aqueous samples of phosphoproteins. In addition data shown in Table 6 demonstrate that a first order calibration function, verified by Mandel's fitting test, correctly describes the relationship between signal and element concentration for P measured under both the ionization modes. In contrast for S a significant curvature was observed when BSA was used as organic standard. The plot of residuals for the BSA calibration (Fig. 3A) in water showed systematic deviations from the linear model indicating that a first order function was inadequate in this case. However, the sensitivities did not significantly differ because the slope of BSA calibration curve overlaps at 95% confidence level with the slope of calibration obtained from inorganic standards (Table 6). Interestingly, deviation from linearity was not observed when using Cys as organic standard (Table 6). This finding suggested that the chemical properties of the protein polymer may clearly affect plasma response of the covalently bound S. Such an effect cannot be corrected by internal standardization or by standard addition method using inorganic or amino acid spikes (data not shown). Possible size-dependent effects on the nebulization, changes of solution properties or unspecific protein losses should be taken into account. Furthermore, we observed an ionic suppression below 4% for inorganic S spikes in BSA (data not shown). This could be an effect of increased C concentrations. In addition plot of residuals showed a significant underestimation of S concentrations at lower BSA levels. If this signal suppression is mainly due to C naturally occurring in proteins, we can expect that this effect will be lower at lower BSA concentrations. However, signal enhancement or suppression also depended on the analyte concentration. Therefore, the effect of the same amount of C might be more important at lower S concentrations. We therefore evaluated the effect of increasing C levels on different concentrations of inorganic P and S. Experiments were performed using Tris as a

carbon source because in contrast with organic solvents it should not increase sample loading resulting in an erroneous evaluation of carbon effects. Tris concentrations were chosen to give C concentrations identical to the analyzed BSA samples, i.e. 0.7–7 mmol L^{-1}. As can be seen in Fig. 4, the effect of increasing C concentrations strictly depended on the analyte levels; indeed lower analyte concentrations showed a more pronounced signal enhancement. However, at 50 mmol L^{-1} or higher Tris comparable signal intensities were measured regardless of the analyte concentrations. Moreover, the slopes of inorganic standards and P-Ser/BSA calibrations for P measured as oxide ion did not significantly differ when 50 mmol L^{-1} of Tris was used (Table 6). Therefore, this concentration of organic modifier can be used to buffer carbon concentration changes in protein samples resolving the observed interferences for P measured as $^{31}P^{16}O^+$. A decrease of sensitivity was observed for P measured as $^{31}P^+$ but the slopes of inorganic standards and P-Ser/BSA calibrations did not significantly differ showing that inorganic standards

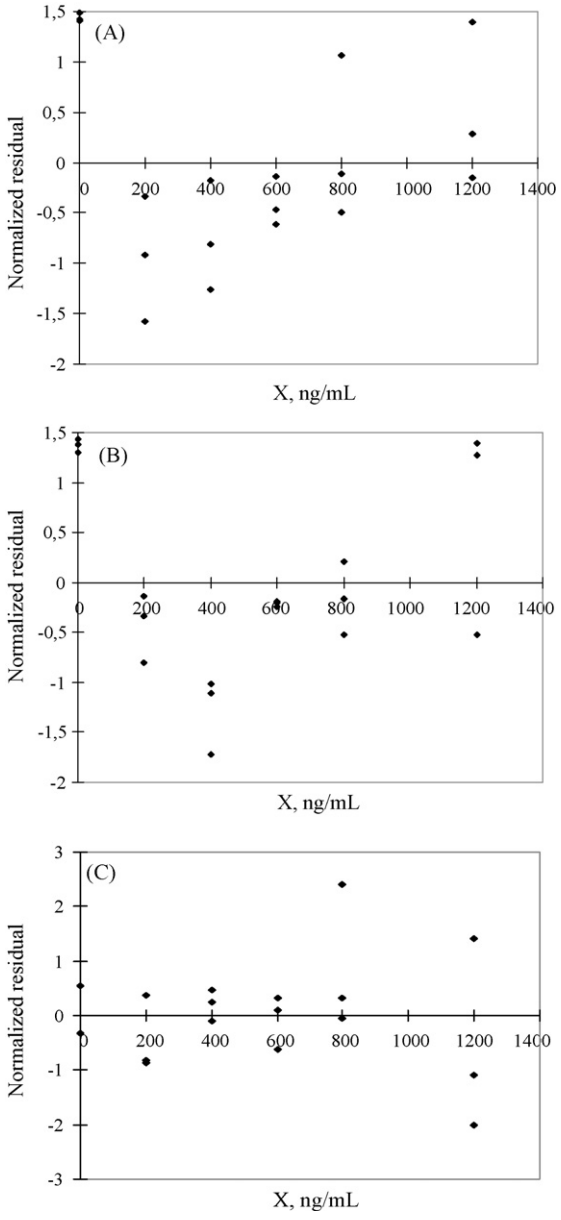


Fig. 3. Plots of normalized residuals (mean zero, standard deviation unity) for S measured as $^{32}S^{16}O^+$ using the optimized ion mode and BSA as organic standard in (A) 18 MΩ cm water, (B) Tris–HNO_3 50 mmol L^{-1}, and (C) 40 mmol L^{-1} Tris–HNO_3–0.1% Triton X100.

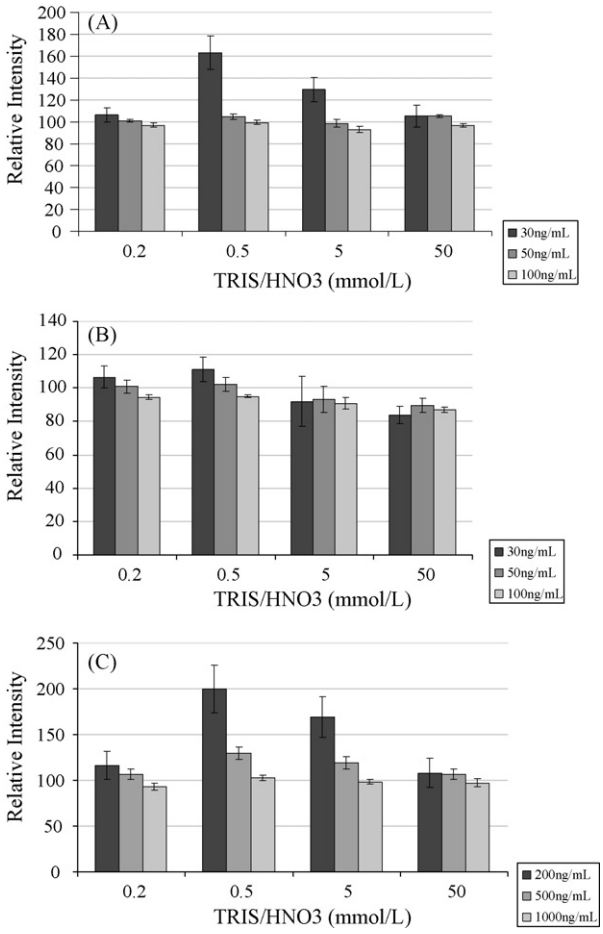


Fig. 4. Effect of increasing C concentration on the analyte signals at different analyte concentration levels. (A) P measured as $^{31}P^+$ under standard plasma conditions. (B) P measured as $^{31}P^{16}O^+$ using the optimized oxide ion mode. (C) S measured as $^{32}S^{16}O^+$ using the optimized oxide ion mode. Data are relative intensity calculated as $[y_{iMj}\ (\text{counts s}^{-1})/y_{iW}\ (\text{counts s}^{-1})] \times 100$, where y_{iMj} and y_{iW} are the net signals for the ith analyte concentration in the jth carbon matrix and 18 MΩ cm water, respectively. Net signals are calculated by subtracting the corresponding blank signal. Data are mean values from triplicate measurement. Bars correspond to standard deviations.

were suitable for P as $^{31}P^+$ quantification under standard plasma conditions (data not shown). In addition, the use of Tris theoretically increases potential applications of this method since normally protein samples are rarely obtainable in water. Furthermore, Tris is widely used as mobile phase for hyphenated chromatography with ICP-MS, thus does not require changes of the sample introduction system and consequent additional optimization works. However, Tris was not able to completely resolve the interference observed for S measured as $^{32}S^{16}O^+$. In fact, residual plot for BSA calibration in 50 mM TRIS (Fig. 3B) revealed systematic deviation from linearity. However, since negative residuals were calculated at low BSA concentrations this cannot be due to a simple C effect on ionization. Therefore, deviations from linearity could be due to changes in solution properties such as viscosity and superficial tension affecting aerosol formation and ion transmission or to unspecific protein loss in the sample introduction phase. We therefore reasoned that detergents, surfactants or organic solvents could be used to reduce these effects, and used a mixture of 40 mmol L^{-1} Tris–0.1% (v/v) Triton X100 in our experiment. Triton X100 was chosen because it has been successfully and extensively used in ICP-MS determination of non-metals in different protein rich matrix [49]. The relative amount of the two organic modifiers was chosen to give a C concentration equivalent to 50 mmol L^{-1} Tris to prevent the effects of carbon on the analyte ionization and at the same time limit Triton

Table 7
LOD, LOQ and external calibration curves calculated using inorganic elemental standards for P measured as $^{31}P^+$ and $^{31}P^{16}O^+$ and for S measured as $^{32}S^{16}O^+$ using the optimized oxide ion mode in 40 mmol L^{-1} Tris–0.1% Triton X100.[a].

Element (ion, m/z)	LOD[b] ($\mu g\,L^{-1}$)	LOQ[c] ($\mu g\,L^{-1}$)	Concentration range ($\mu g\,L^{-1}$)	Homoscedasticity, p[d]	Mandel's fitting test, p[d]	b_0 ($\pm s_{b0}$)[e]	b_1 ($\pm s_{b1}$)[e]	R^2 ($n=40$)
P ($^{31}P^+$, 31)[f]	3	9	20–1000	0.061	0.217	12,031 (1195)	845 (6)	0.999
P ($^{31}P^{16}O^+$, 47)[g]	6	16	20–1000	0.809	0.079	21,140 (465)	342 (2)	0.999
S ($^{32}S^{16}O^+$, 48)[g]	25	95	100–2000	0.076	0.124	21,067 (1015)	128 (1)	0.999

[a] Calibration fit: $y = b_0 + b_1 x$, no internal standard correction.
[b] Calculated as concentration corresponding to the signal $y = y_B + 2ts_B$, y_B = average blank signal ($n = 10$), s_B = standard deviation, t = critical value of t distribution (one tailed, 95% confidence level, 9) = 1833.
[c] Calculated as concentration corresponding to the signal $y = y_B + 10s_B$, y_B = average blank signal ($n = 10$), s_B = standard deviation.
[d] 95% confidence level.
[e] Average ± standard deviation.
[f] Measured under standard plasma conditions.
[g] Measured using the optimized oxide ion mode.

Table 8
Precision and trueness: relative standard deviation ($n = 3$) from analysis and recovery ($n = 3$) obtained under repeatability conditions. Spike-recovery calculations were performed on a standard of P-Ser/BSA corresponding to 50 ng mL^{-1} and 200 ng mL^{-1} of P and S (spike level = 0 ng mL^{-1}). Spiking was made with same organic P and S standards.

Element (ion, m/z)	Spike (ng mL^{-1})	Experimental (ng mL^{-1})[a]	RSD%	R%[a]
P ($^{31}P^+$, 31)[b]	0	36(1)	4	
	50	85(2)	3	97(5)
	150	186(6)	3	100(4)
	250	272(4)	2	94(2)
P ($^{31}P^{16}O^+$, 47)[c]	0	46(3)	6	
	50	96(1)	1	99(4)
	150	193(4)	2	98(2)
	250	284(2)	1	95(1)
S ($^{32}S^{16}O^+$, 48)[c]	0	194(7)	4	
	200	401(3)	1	103(4)
	600	816(13)	2	104(2)
	1000	1190(19)	2	100(1)

[a] Mean (SD) ($n = 3$).
[b] Measured under standard plasma conditions.
[c] Measured using the optimized oxide ion mode.

X100 concentration reducing the risk of possible soot deposition. The plot of residuals of BSA calibration in this buffer (Fig. 3C) did not show systematic deviations and a first order calibration function can be used to fit the model (Table 6). This effect of Triton X100 may be, at least partially, explained by a reduction of unspecific protein loss. However, additional effects on density or viscosity of protein solutions and protein transport in the plasma cannot be excluded.

3.4. Analytical figures of merit and determination of casein phosphorylation degree

Table 7 shows LOD and LOQ calculated in 40 mmol L^{-1} Tris/HNO_3–0.1% Triton X100. As expected, higher values with respect to water were calculated. This is particularly evident in the case of P measured as $^{31}P^{16}O^+$. This buffer yields better LOD and LOQ compared to 50 mM Tris (data not shown), probably due to the lower content of N, a more important source of interferences at m/z 47 with respect to C. In all conditions used, an increase of LOD and LOQ was paralleled by a proportional increase of BEC (data not shown). This did not represent a problem for P quantification but it did for S determination thus remaining the limiting factor of ICP-QMS quantification of protein phosphorylation.

For the calculation of a reliable calibration model matrix blanks and seven concentration levels within the specified concentration range (Table 7) were analyzed. Linearity of the calculated calibration functions was demonstrated by assessing homoscedasticity throughout the range tested and by applying the Mandel's fitting test. The homogeneities of variance were verified by Bartlett's test at 95% confidence level ($p > 0.05$) for each analyte ion. The calculated R^2 were higher than 0.99 in all cases. Furthermore, Mandel's fitting test at 95% confidence level provided p values greater than 0.05 confirming the linearity of the calibration curves. As shown, the slopes of established calibration curves were lower than the slopes calculated in 18 MΩ cm water and 50 mM Tris (Table 6). The addition of Triton X100 suppresses sensitivity with respect to 50 mM Tris under both the operating conditions. This effect could not have

Table 9
Determination of casein phosphorylation degree by ICP-QMS measurement of P and S as $^{31}P^{16}O^+$ and $^{32}S^{16}O^+$, respectively, using the optimized plasma conditions.

Protein	$\mu g\,mL^{-1}$	pmol mL^{-1}[a]	Theoretical S (ng mL^{-1})[b]	Experimental S (ng mL^{-1})[c]	RSD%[d]	Experimental P (ng mL^{-1})[c]	RSD%[d]	$mol_P/mol_{protein}$	RSD%[d]
Bovine β-casein	15	636	122	121(8)	7	86 (5)	6	4.6 (0.4)	8.6
	30	1,272	245	254 (12)	5	209 (10)	4	5.12 (0.03)	0.56
	60	2,544	489	529(3)	1	428 (3)	1	5.03 (0.02)	0.34
Bovine α-casein	15	653	105	94 (5)	5	143 (4)	3	7.9 (0.1)	1.1
	30	1,305	209	172(7)	4	268 (11)	4	8.09 (0.04)	0.48
	60	2,611	419	365(4)	1	570(6)	1	8.09 (0.01)	0.17
Enzymatically dephosphorylated bovine α-casein	15	653	100	ND[e]		ND[e]			
	30	1,305	201	148 (1)	1	19 (1)	7	0.66 (0.05)	7.88
	60	2,611	401	320 (1)	1	42.7 (0.3)	0.6	0.691 (0.003)	0.49

[a] Calculated on the basis of the theoretical molecular weight of unmodified proteins, i.e. 23,583 and 22,975 Da for bovine β-casein and bovine α-casein S1 variant, respectively.
[b] Calculated on the basis of the number of sulfhydryl residues, i.e. 6 and 5 for bovine β-casein and bovine α-casein S1 variant, respectively.
[c] Mean (SD) ($n = 5$).
[d] Relative standard deviation ($n = 5$).
[e] Not detected.

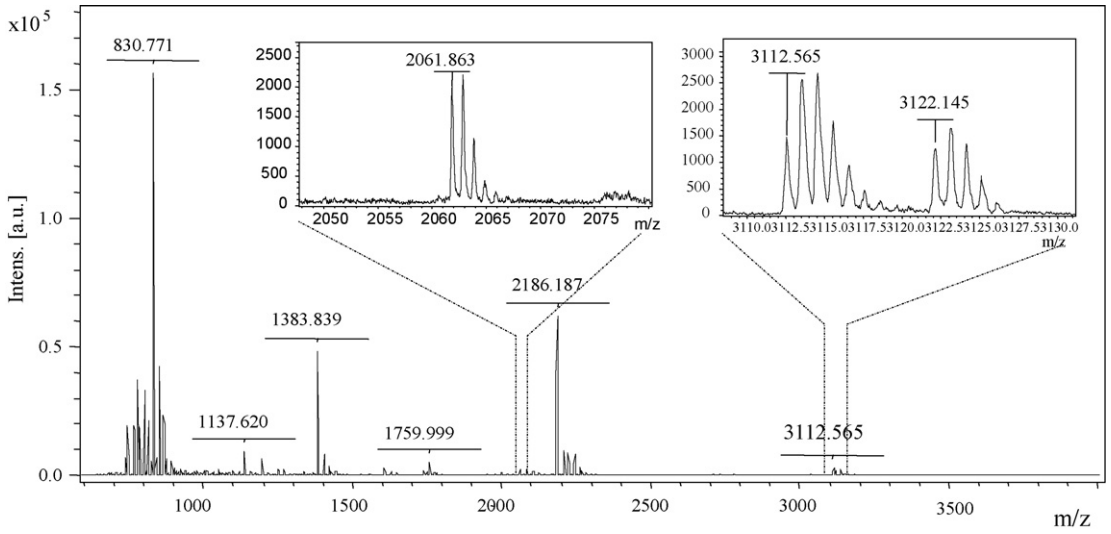


Fig. 5. Positive MALDI-TOF-MS spectrum of tryptic peptides (10 pmol) from bovine β-casein. The insets show phosphopeptides signals at *m*/*z* 2061.863 and 3122.145, respectively.

been due to changes of C content that was maintained constant and was probably related to the molecular size of the organic modifier that contained an aromatic ring which is more difficult to break [50].

Repeatability and trueness were calculated by analyzing P-Ser/BSA standards (Table 8) quantifying P as $^{31}P^{+}$ and $^{31}P^{16}O^{+}$ under standard plasma and oxide ion conditions, respectively and S as $^{32}S^{16}O^{+}$ using the oxide ion mode by means of the calculated

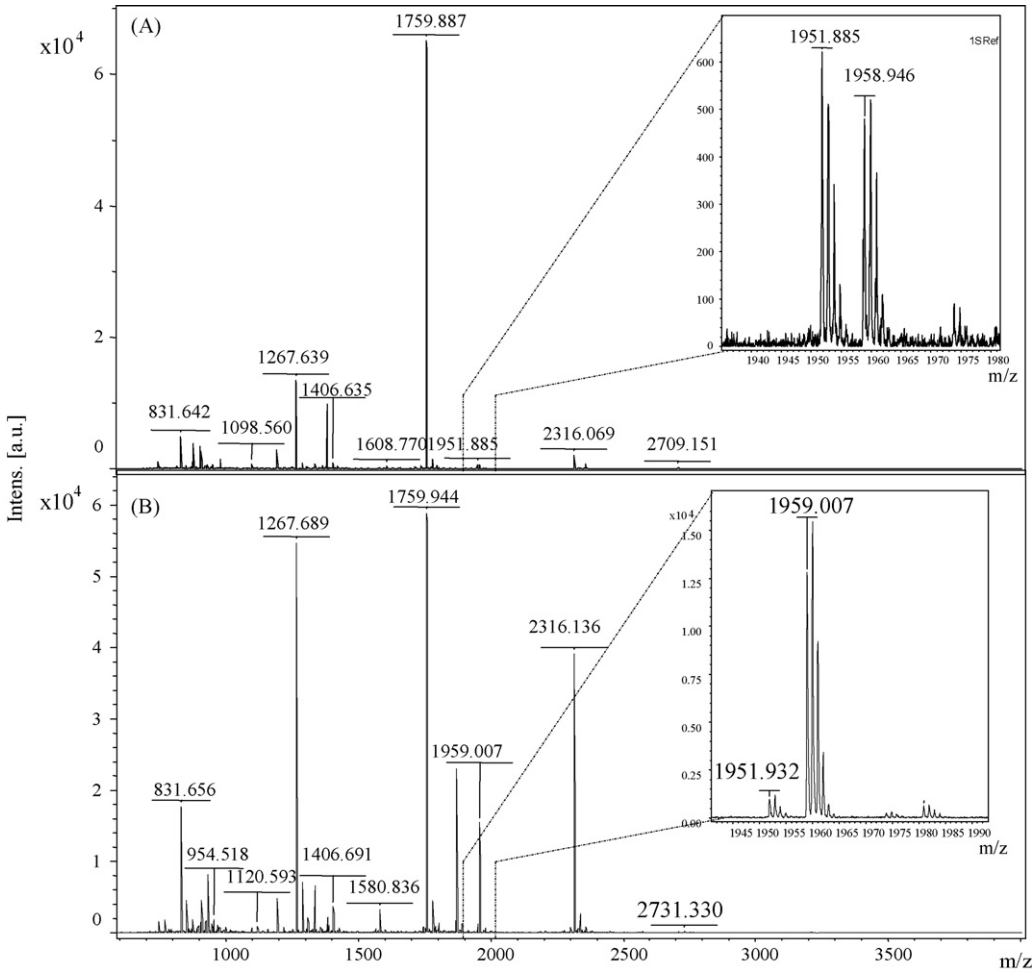


Fig. 6. Positive MALDI-TOF-MS spectra of tryptic peptides (10 pmol) from native bovine α-casein (A) and enzymatically dephosphorylated bovine α-casein (B). The insets show signal of the only phosphopeptide detected in both proteins at *m*/*z* 1951.

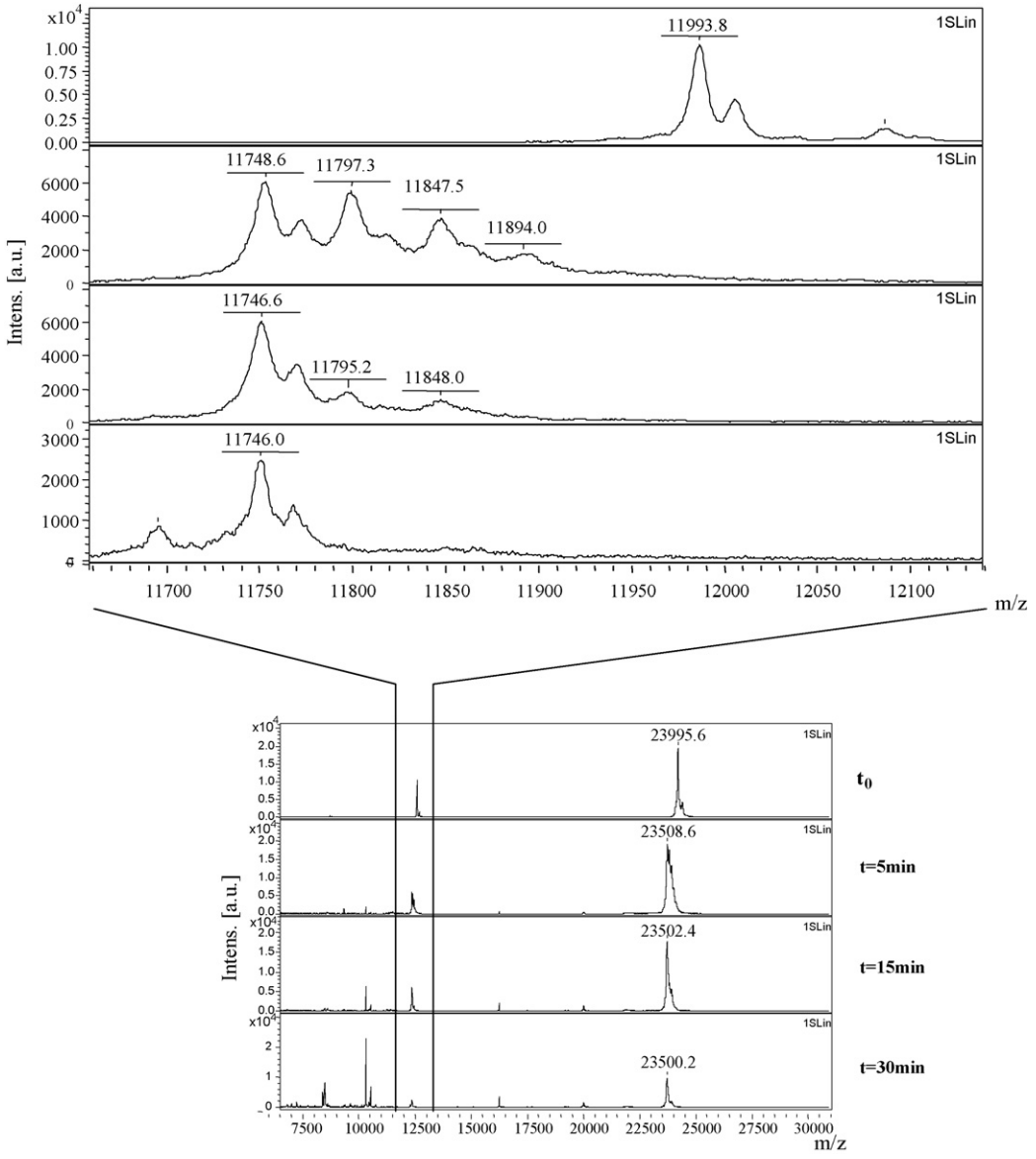


Fig. 7. Study of Ba^{2+} catalysed β-elimination of bovine β-casein by linear positive MALDI-TOF-MS. The portions of spectra containing the doubly charged ions are enlarged.

calibration function based on inorganic P and S standards. Excellent repeatability was observed for each analyte at the analyzed concentration levels. As expected on the basis of similarity between the slopes of inorganic standard and P-Ser/BSA calibrations, satisfactory recoveries were calculated for S. Better recoveries were calculated for P measured as oxide ion. In this case, the calculated concentrations for the reference standard corresponding to an actual concentration of 50 ng mL^{-1} were in accordance with the theoretical concentrations. Actual carbon concentration did not affect trueness.

For this reason, casein samples were analyzed under the optimized conditions measuring P and S as oxide ions. Increasing protein amounts were analyzed to assess the effect of protein concentrations on the measurement of phosphorylation degree. As can be seen in Table 9, calculated protein concentrations were in good agreement with the predicted concentration especially in the case of bovine β-casein that was available at higher purity. Moreover, results for native and enzymatically dephosphorylated α-caseins were consistent with the specifications provided by the suppliers. Phosphorylation degrees were calculated with an excellent precision for β and α-casein and did not significantly differ from the predicted stoichiometric P/protein ratio of 5 and 8, respectively. Unexpectedly, P was quantified also in enzymatically dephosphorylated α-casein. This could have been due either to partial dephosphorylation or to non-covalent phosphate adducts [51,52]. However, as demonstrated in the following paragraphs, in this case this was due to partial enzymatic dephosphorylation.

3.5. Determination of casein phosphorylation degree by MALDI-TOF-MS

On the basis of the calculated phosphorylation degree, increase of 399.8 and 639.7 Da of the molecular weights (MW) of bovine β-casein and intact α-casein, respectively, can be predicted and can be assessed by molecular MS. Bovine β-casein has been proposed as a model in several studies and was used to check the feasibility of standard PMF procedure. β-Casein gives two phosphopeptides after treatment with trypsin (a tetra-phosphorylated peptide 2-ELEELNVPGEIVE[P-Ser]L[P-Ser][P-Ser][P-Ser]EESITR-25 (2965.2 Da) and a mono-phosphorylated peptide 48-FQ[P-Ser]EEQQQTEDELQDK-63 (2060.8 Da)) that can be detected with different MALDI sensitivities. In particular, the

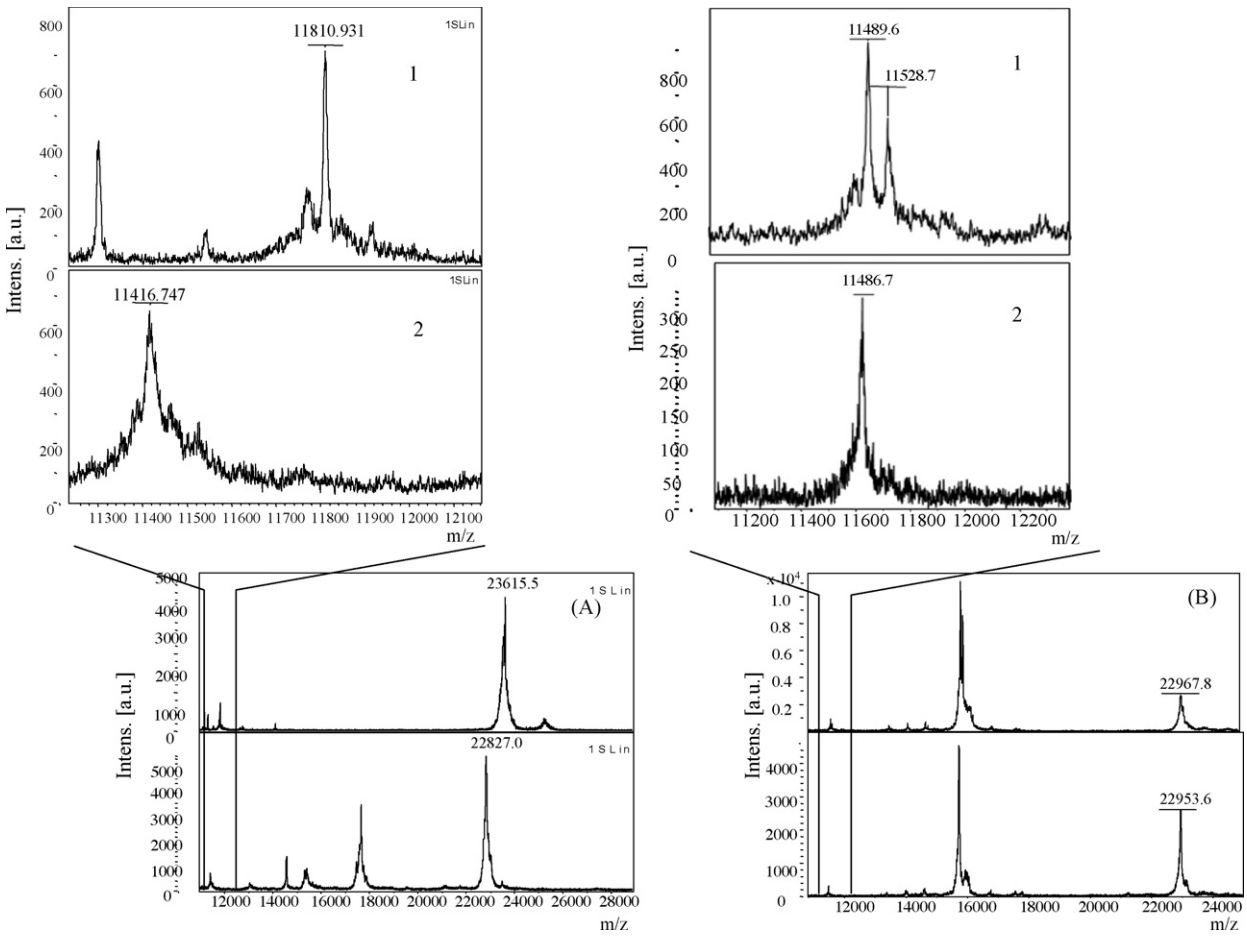


Fig. 8. Linear positive MALDI-TOF-MS spectra of intact (A) and enzymatically dephosphorylated (B) bovine α-casein before (1) and after β-elimination reaction (2). The insets show signals corresponding to the doubly charged ions.

reported MALDI-MS detection limits for the tetra-phosphorylated peptide range between five orders of magnitude depending on the acquisition mode and sample preparation procedure [53–55]. On the basis of these published results, a PMF experiment was performed using 10 pmol tryptic β-casein digest. Fig. 5 shows the mass spectra of tryptic digest of bovine β-casein. Signals at *m*/*z* 2061.83 and 3122.14 correspond to the mono-phosphorylated 48–63 peptide and to the tetraphosphorylated 1-RELEELNVPGEIVE[P-Ser]L[P-Ser][P-Ser][P-Ser]EESITR-25 peptide containing a missed cleavage site. This data confirm the ICP-QMS results. The same amounts of peptides from native and dephosphorylated α-caseins were then analyzed. Digestion of bovine α-casein using trypsin theoretically provides four phosphopeptides: 35-EKVNEL[P-Ser]K-42 (1025.47 Da), 43-DIG[P-Ser]E[P-Ser]TEDQAMEDIK-58 (1926.68 Da), 59-QMEAE[P-Ser]I[P-Ser][P-Ser][P-Ser]EEIVPN[P-Ser]VEQK-79 (2719.90 Da), and 106-VPQLEIVPN[P-Ser]AEER-119 (1659.78 Da). Only the phosphopeptide 104-YKVPQLEIVPN[P-Ser]AEER-119 containing a missed cleavage site was detected (Fig. 6A). Again, the same signal appeared in the mass spectrum of dephosphorylated α-casein (Fig. 6B). Therefore, detection of the mono-phosphorylated peptide was consistent with P measurement by ICP-QMS in this case. It is important to emphasize that in both cases proteins were successfully identified as bovine α-S1-casein isoform by database search (data not shown) but assessment of phosphorylation degree was not directly possible for native α-casein. This was not surprising because all phosphopeptides of native α-casein were often detected by applying different experimental procedures [56,57].

An alternative strategy based on chemical dephosporylation and MALDI-TOF-MS operating in linear mode was proposed. This approach relies on the well-established β-elimination of phosphoserine residues to give dehydroalanine with a loss of 97 Da under basic conditions [58]. The optimum reaction time was estimated by monitoring the reaction products of β-casein. MALDI-TOF-MS was preferred to ESI-MS because of a simpler sample preparation and lower analysis time.

Fig. 7 shows the mass spectra obtained at different reaction times. In the case of caseins, molecular weights were sufficiently low to detect the doubly charged ions with a sufficient resolution (i.e. $m/\Delta m \sim 10{,}000$) and estimate with acceptable accuracy the molecular masses of native proteins and β-elimination products. As can be seen, complete dephosphorylation was obtained after 15 min. This reaction time was chosen to reduce protein degradation due to base hydrolysis of peptide backbone. It is important to note that the experimental MW (23,983 Da) of native β-casein (theoretical MW = 23,583.2 Da), calculated from the doubly charged ion mass, was consistent with the molecular weight calculated on the basis of the phosphorylation degree by ICP-QMS. Fig. 8 shows linear MALDI-TOF-MS mass spectra of β-elimination products of native and dephosphorylated α-caseins. As observed for β-casein, the experimental MW (23,612 Da) of intact α-casein S1 isoform (theoretical MW = 22,974.8 Da) before β-elimination completely agrees with the molecular weights predicted on the basis of ICP-QMS analysis. Molecular weight of α-casein decreased of 788 Da corresponding to the β-elimination of height P-Ser residues, as predicted from ICP-QMS data.

Two signals at m/z 11,489.6 and 11,528.7 were detected in the spectrum of enzymatically dephosphorylated α-casein (Fig. 8B). The signal at m/z 11,528.7 corresponded to the doubly charged ions of mono-phosporylated α-S1-casein isoform. In fact, this signal disappeared under base catalyzed β-elimination demonstrating that this sample contains both dephosphorylated and mono-phosphorylated isoforms of α-casein. Interestingly, the relative intensity of the mono-phosphorylated isoform (∼0.70) in the MALDI-TOF spectrum was consistent with the degree of phosphorylation obtained by ICP-QMS. Moreover, it is important to emphasize that ICP-QMS was able to quantify the degree of phosphorylation of intact caseins and detect partial enzymatic dephosphorylation at protein concentrations significantly lower than those used in MALDI-TOF-MS experiments.

4. Conclusions

In this paper, we showed that without using reaction or collision gas low resolution ICP-QMS was a suitable technology to investigate protein phosphorylation stoichiometries with high confidence and sensitivity and yields better results than standard PMF analysis. Nevertheless, the subtle interferences which might affect the plasma performances must be taken into account in order to actually push forward the analytical capacities in quantifying P and S. We acknowledge that the main limiting factors preventing wider applications in proteomics were the high calculated LOQ for S and the total protein amounts required with the sample introduction device used. However, the results presented in our manuscript demonstrate that quantitative analysis of protein phosphorylation is feasible with the proposed instrumental set-up and data obtained are in accordance with data obtained with molecular MS. While we are aware that better results can be obtained using ICP-HRMS or ICP-DRC/CRC-MS systems, we propose that the presented optimization procedure might be employed to evaluate the performance of highly efficient ICP interfaces in order to further improve protein elemental investigations by less expensive and quadrupole based ICP-MS systems which are more widely available to the scientific community.

Acknowledgements

We would like to thank Prof. Vincenzo De Laurenzi for his insightful discussions and Dr. Peter A. Mattei for his help in preparing the final version of the manuscript.

References

[1] T. Hunter, Cell 100 (2000) 113.
[2] P. Cohen, TIBS 25 (2000) 596.
[3] S. Zolnierowicz, M. Bollen, EMBO J. 19 (2000) 483.
[4] M.J. MacCross, D.L. Matthews, Anal. Chem. 77 (2005) 295A.
[5] A. Paradela, J.P. Albar, J. Proteome Res. 7 (2007) 1809.
[6] B.O. Axelsson, M. Jörnten-Karlsson, P. Michelsen, F. Abou-Shakra, Rapid. Commun. Mass Spectrom. 15 (2001) 375.
[7] J. Bettmer, N. Jakubowski, A. Prange, Anal. Bioanal. Chem. 386 (2006) 7.
[8] A. Sanz-Medel, Anal. Bioanal. Chem 391 (2008) 885.
[9] A. Pereira-Navaza, J. Ruiz Encinar, A. Sanz-Medel, Angew. Chem. Int. Ed. 45 (2006) 1.
[10] A. Pereira-Navaza, J. Ruiz Encinar, M. Carrascal, J. Abián, A. Sanz-Medel, Anal. Chem. 80 (2008) 1777.
[11] M. Wind, A. Wegener, R. Kellner, W.D. Lehmann, Anal. Chem. 77 (2005) 1957.
[12] M. Wind, A. Wegener, A. Eisenmenger, R. Kellner, W.D. Lehmann, Angew. Chem. Int. Ed. 42 (2003) 3425.
[13] E. Kolker, R. Higdon, J.M. Hogan, Trends Microbiol. 14 (2006) 229.
[14] S.P. Gygi, B. Rist, S.A. Gerber, F. Turecek, M.H. Gelb, R. Aebersold, Nat. Biotechnol. 17 (1999) 994.
[15] R. Ahrends, S. Pieper, A. Kühn, H. Weisshoff, M. Hamester, T. Lindemann, C. Scheler, K. Lehmann, K. Taubner, M.W. Linscheid, Mol. Cell. Proteomics 6 (2007) 1907.
[16] D. Schaumlöffel, P. Giusti, H. Preud'Homme, J. Szpunar, R. Lobiński, Anal. Chem. 79 (2008) 2859.
[17] M. Wang, W. Feng, W. Lu, B. Li, B. Wang, M. Zhu, Y. Wang, H. Yuan, Y. Zhao, Z. Chai, Anal. Chem. 79 (2008) 2859.
[18] J.S. Becker, S.F. Boulyga, C. Pickhardt, J. Becker, S. Buddrus, M. Przybylski, Anal. Bioanal. Chem. 375 (2003) 561.
[19] M. Kovačevič, A. Gartner, M. Novič, J. Chromatogr. A 1039 (2004) 77.
[20] R.G. Wuilloud, M. Shah, S.S. Kannamkumarath, J.C. Altamirano, Electrophoresis 26 (2005) 1598.
[21] M. Wind, H. Wesch, W.D. Lehmann, Anal. Chem. 73 (2001) 3006.
[22] S. Hann, G. Koellensperger, C. Obinger, P.G. Furtmüller, G. Stingeder, J. Anal. At. Spectrom. 19 (2004) 74.
[23] D.R. Bandura, V.I. Baranov, S.D. Tanner, Anal. Chem. 74 (2002) 1497.
[24] A.A. Menegario, M.F. Giné, J.A. Bendassolli, A.C.S. Bellato, P.C.O. Trivelin, J. Anal. At. Spectrom. 13 (1998) 1065.
[25] A.A. Menegario, M.F. Giné, J. Anal. At. Spectrom. 12 (1997) 671.
[26] B. Divjak, W. Goessler, J. Chromatogr. A 844 (1999) 161.
[27] R. Koplíc, H. Pavelková, J. Cicinbuchová, O. Mestek, F. Kvasnička, M. Suchánek, J. Chromatogr. B 770 (2002) 261.
[28] F. Bianchi, M. Careri, M. Maffini, A. Mangia, C. Mucchino, Rapid Commun. Mass Spectrom. 17 (2003) 251.
[29] R. Brennetot, A. Becquet, H. Isnard, C. Caussignac, D. Vailhen, F. Chartier, J. Anal. At. Spectrom. 20 (2005) 500.
[30] V. Czitrom, Am. Statistician 53 (1999) 126.
[31] P.W. Araujo, R.G. Brereton, Trend Anal. Chem. 15 (1996) 63.
[32] N.M. Reed, R.O. Cairns, R.C. Hutton, J. Anal. At. Spectrom. 9 (1994) 881.
[33] M. Kovačevič, W. Goessler, N. Mikac, Anal. Bioanal. Chem. 383 (2005) 145.
[34] J.E. Carr, K. Kwok, G.K. Webster, J.W. Carnahan, J. Pharm. Biomed. 40 (2006) 42.
[35] M. Wind, A. Eisenmenger, W.D. Lehmann, J. Anal. At. Spectrom. 17 (2002) 21.
[36] G. Derringer, R. Suich, J. Qual. Technol. 12 (1980) 214.
[37] The Fitness for Purpose of Analytical Methods: A Laboratory Guide to Method Validation and Related Topics, Eurachem Guide, 1st English edition, LGC: Teddington Ltd., 1998.
[38] K. Danzer, L.A. Currie, Pure Appl. Chem. 70 (1998) 993.
[39] S.D. Tanner, J. Anal. At. Spectrom. 8 (1993) 891.
[40] E. Poussel, J. Mermet, J. Anal. At. Spectrom. 9 (1994) 61.
[41] D.R. Bandura, V.I. Baranov, S.D. Tanner, Fresenius J. Anal. Chem. 370 (2001) 454.
[42] J.S. Becker, H. Dietze, Int. J. Mass Spectrom. 202 (2000) 69.
[43] R.F. Browner, A.W. Boorn, Anal. Chem. 86 (1984) 786A.
[44] R.C. Hutton, A.N. Eaton, J. Anal. At. Spectrom. 2 (1987) 595.
[45] P.R.D. Mason, K. Kaspers, M.J. van Bergen, J. Anal. At. Spectrom. 14 (1999) 1067.
[46] I. Kano, D. Darbouret, R&D Notebook, Millipore RD003, 2000.
[47] C.H. Yang, S.H. Jiang, Spectrochim. Acta Part B 59 (2004) 1389.
[48] E. Swantesson, J. Pettersson, K.E. Markides, J. Anal. At. Spectrom. 17 (2002) 491.
[49] J.P. Goullé, L. Mathieu, J. Costermant, N. Neveu, L. Bonneau, G. Lainé, D. Bouige, C. Lacroix, Forensic Sci. Int. 153 (2005) 39.
[50] S. Liu, D. Beauchemin, Spectrochim. Acta Part B 61 (2006) 319.
[51] M. Wind, I. Feldmann, N. Jakubowski, W.D. Lehmann, Electrophoresis 24 (2003) 1276.
[52] S.K. Chowdhury, V. Katta, R.C. Beavis, B. Chait, J. Am. Soc. Mass Spectrom. 1 (1990) 382.
[53] K. Janek, H. Wenschuh, M. Bienert, E. Krause, Rapid Commun. Mass Spectrom. 15 (2001) 1593.
[54] C.H. Lee, M.E. McComb, M. Bromirski, A. Jilkine, W. Ens, K.G. Standig, H. Perreault, Rapid Commun. Mass Spectrom. 15 (2001) 191.
[55] Y. Ma, Y. Lu, H. Zeng, D. Ron, W. Mo, T.A. Neubert, Rapid Commun. Mass Spectrom. 15 (2001) 1693.
[56] S.S. Jensen, M.R. Larsen, Rapid Commun. Mass Spectrom. 21 (2007) 3635.
[57] S.Y. Imanishi, V. Kochin, J.E. Eriksson, Proteomics 7 (2007) 174.
[58] M.F. Byford, Biochem. J. 280 (1991) 261.

Talanta 80 (2010) 1526–1531

Contents lists available at ScienceDirect

Talanta

journal homepage: www.elsevier.com/locate/talanta

Analysis of low-abundance proteins using the proteomic reactor with pH fractionation

Hu Zhou[a,b], Weimin Hou[a,c], Jean-Philippe Lambert[a,b], Ruijun Tian[a,b], Daniel Figeys[a,b,c,*]

[a] Ottawa Institute of Systems Biology, Faculty of Medicine, University of Ottawa, 451 Smyth Road, Ottawa, Ontario, Canada K1H 8M5
[b] Department of Biochemistry, Microbiology and Immunology, Faculty of Medicine, University of Ottawa, 451 Smyth Road, Ottawa, Ontario, Canada K1H 8M5
[c] Department of Chemistry, Faculty of Science, University of Ottawa, 10 Marie Curie, D'Iorio Hall, Ottawa, ON, Canada K1N 6N5

ARTICLE INFO

Article history:
Available online 14 July 2009

Keywords:
Proteomic reactor
pH fractionation
Low-abundance protein
Liquid chromatography
Mass spectrometry

ABSTRACT

We developed a new method consisting of the proteomic reactor coupled with step pH fractionation for the analysis of low-abundance proteins from minute amount of sample. These new reactors were implemented using both SAX and SCX materials. The pH fractions from the SAX reactor provided higher peptide and protein identification than SCX reactor and conventional solution digestion. Interestingly, the physical characteristics (pI, molecular weight, missed cleavage site and grand average hydrophobicity (GRAVY) index, and number of acid and basic amino acid) of the peptides obtained from the SAX and SCX proteomic reactors are drastically different. Furthermore, nearly half of the peptides observed from the pH fractionations from the SAX reactor are of low abundance while only 22% low-abundance proteins are observed with conventional in-solution digestion following 2D LC–MS/MS analysis.

© 2009 Elsevier B.V. All rights reserved.

1. Introduction

One major challenge in proteomics is the identification of low-abundance proteins in complex mixtures. Currently, up to 50% of the proteins in any tissues or cells proteome have concentration below the detection limits of proteomic methodologies [1–3]. However, low-abundance proteins are often the key molecules in signal transduction pathway. As well, many clinical biomarkers of disease stages or disease progression are of low abundance [4–6]. Fractionation techniques have been used to reduce the sample complexity and dynamic range with the hope of then observing an increase number of low-abundance proteins. Approaches have been developed to fractionate protein and peptides. At the protein level, affinity-depletion [7–10], narrow-range isoelectric focusing (IEF) [11,12], free flow electrophoresis (FFE) [9,13,14], and multiple dimensional liquid chromatography [4,6,15] have been employed to enrich low-abundance proteins. These techniques are also employed for peptide fractionation, for example, the Agilent OFFGEL system, using immobilized pI strips for peptide separation, which is an attractive alternative to in-gel protein digestion in proteome analysis [16]. However, at the peptide level, multidimensional protein identification technology (MudPIT) [17,18] is the most popular method in mass spectrometry-based proteomics. This approach uses strong cation exchange as first dimension and reversed phase as second dimension. SCX chromatography has been routinely employed for peptide fractionation based on salt gradient [19–21]. Furthermore, pH gradients are also suitable for SCX fractionation [22–24]. SAX is another promising type of ion exchange chromatography for peptide fractionation, particularly for phosphopeptide analysis [25–29].

In many applications the amount of proteins available is not a limiting factor with micrograms to milligrams of material readily available. In these instances, the protein fractionation methods can be used to identify low-abundance proteins. Although these preparative methods can cause sample losses, it only becomes a significant issue for minute sample amount. In many instances, such as rare cells and specific regions of tissue slides, only minute amount of samples are available. A pressing issue is the analysis of low-abundance proteins from samples in the low to sub-microgram level.

We have recently introduced a novel proteomic sample processing device for minute protein sample termed the proteomic reactor [30]. The proteomic reactor allows the enrichment, clean-up, and chemical and enzymatic processing of proteomic samples in as little as 50-nL volume. In our recent implementation of the proteomic reactor, we have successfully employed step pH gradient in SCX proteomic reactor for glycopeptides fraction [31]. We also demonstrated that proteomic reactor using polymer-based strong anion exchange (SAX) was a powerful tool for protein identification [in

Abbreviations: SAX, strong anion exchange; SCX, strong cation exchange; GRAVY, grand average hydrophobicity; IEF, isoelectric focusing; FFE, free flow electrophoresis; MudPIT, multidimensional protein identification technology; DTT, dithiothreitol; IAA, iodoacetamide; CAI, codon adaptation index; LC–MS/MS, liquid chromatography–tandem mass spectrometry.

* Corresponding author at: Ottawa Institute of Systems Biology, Faculty of Medicine, University of Ottawa, 451 Smyth Road, Ottawa, Ontario, Canada K1H 8M5.
E-mail address: dfigeys@uottawa.ca (D. Figeys).

0039-9140/$ – see front matter © 2009 Elsevier B.V. All rights reserved.
doi:10.1016/j.talanta.2009.07.018

preparation]. In this study, we will employ pH fractionation on both SAX and SCX proteomic reactors to identify low-abundance proteins contained in minute amount of sample.

2. Materials and methods

2.1. Materials

Water used in the study was prepared from a Milli-Q system. Ammonium bicarbonate and dithiothreitol (DTT) were purchased from EMD Chemicals, Inc. (Darmstadt, Germany). Iodoacetamide (IAA), HEPES, magnesium acetate, EGTA, EDTA and NP-40 were obtained from Sigma–Aldrich (Saint Louis, MO). Glycerol was purchased from MP Biomedicals. YPD medium was home made following common practices [32]. Trypsin was purchased from Promega (Madison, WI). Strong cation exchange and strong anion exchange beads were obtained from Polymer Laboratories, Varian, Inc. The pH buffer kits were obtained from Column Technology, Inc. (Fremont, CA). Acetonitrile with 0.1% formic acid and water with 0.1% formic acid were purchased from J.T. Baker (Phillipsburg, NJ).

2.2. Yeast sample preparation

The yeast extracts were prepared as previously described [32] with minor modifications. Briefly, a 200 mL culture of yeast was grown to an OD_{600} of 0.8 at which point they were harvest by centrifugation and the cells pellet washed with water. Cell pellets were frozen at −80 °C until ready to be used. The cell pellets were resuspended in 1 volume of lysis buffer (100 mM HEPES pH 8.0, 20 mM magnesium acetate, 10% glycerol (V/V), 10 mM EGTA, 0.1 mM EDTA + fresh yeast protease inhibitors cocktail (Sigma–Aldrich, USA) and frozen in liquid nitrogen in small droplets and lysed using a coffee grinder half-filled with dry ice for 1 min. The dry ice was allowed to evaporate and the resulting whole cell extract was sonicated three times for 30 s with at least 1 min on ice between each pulse. Nonidet P-40 (NP-40) was added to a final concentration of 0.4% and the sample was manually mixed for 30 s. The extract was clarified by centrifugation at 14,000 rpm for 15 min (4 °C) and the supernatant transferred to a fresh tube. The final protein concentration was determined using a Bradford protein assay kit (Bio-Rad).

2.3. pH fractionated proteomic reactor

A capillary tubing (200-μm i.d. and 700-μm i.d) was used to create the proteomic reactor. Briefly, a frit was formed at one end of a fused silica tubing using a mixture of potassium silicate (KASIL 1, PQ Corporation, Valley Forge, PA) and formamide (11/2 volume ratio) as previous report protocol [33]. Then, a 5 cm long reactor was constructed in the capillary by pressure packing (400 psi) a slurry of SAX or SCX beads (10 μm, Polymer Laboratories, Varian, Inc.) from the open end of the capillary tubing. As shown in Fig. 1, the SAX and SCX reactor was washed with alkaline buffer (3N ammonium hydroxide, pH 12) and acid buffer (0.5% formic acid, pH 2.5) prior to their utilities, respectively. The reactor digestion was performed according to the published protocol [30] with some modifications. Fifty micrograms of yeast protein sample and 10 μg trypsin were mixed, alkalified (pH 12) or acidified (pH 2.5), and loaded on the 700-μm i.d. SAX or SCX reactor using a pressurized vessel with 150 psi N_2. The SAX and SCX reactors were then washed with alkaline buffer (3N ammonium hydroxide, pH 12, 20 μL) and acid buffer (0.5% formic acid, pH 2.5), respectively. The proteins present on the reactor were subjected to disulfide bond reduction by introducing the reduction buffer (50 mM dithiothreitol, 20 mM ammonium bicarbonate, pH 8.0) in the reactor for 30 min at room temperature. The reactors were again washed with 10 μL of 20 mM ammonium bicarbonate buffer (pH 8.0) to quench the reaction and dried. Proteins were subjected to simultaneous alkylation and trypsin digestions by introducing the digestion buffer (10 mM iodoacetamide, 20 mM ammonium bicarbonate, pH 8.0) in the reactor for 2 h at 37 °C. The resulting peptides were eluted with 35 μL of step pH buffers (pH 2.5, 3.0, 3.5, 4.0, 4.5, 5.0, 5.5, 6.0, 8.0, 12; For SAX reactor: pH from 12 to 2.5; For SCX reactor: pH from 2.5 to 12).

2.4. In-solution digestion

A total of 50 μg yeast protein sample was dissolved in 100 μL reducing buffer containing 8 M urea, 1% Triton X-100, 40 mM Tris–HCl, and 10 mM dithiothreitol (pH 8.3). After incubation at 37 °C for 2 h, 2.5 μL of 1 M iodoacetamide was added to the protein solution and incubated in the dark for additional 30 min at room temperature. The sample was then diluted four times using 40 mM Tris–HCl (pH 8.3), reducing the urea concentration to 2 M and digested with trypsin (1/5 amount of the protein) at 37 °C overnight. The tryptic digestion was quenched by adding formic acid to final concentration of 2%. The resulting peptides were desalted using Sep-Pak C18 column (WAT023590, Waters, Milford, MA), then dried by speed vac, redisolved in 40 μL of 5% formic acid solution, and used for 2D-LC–MS/MS analysis.

2.5. LC–MS/MS

The LC–MS/MS was performed as previous described [33]. Each peptide fraction from the SAX or SCX reactor was acidified with formic acid to a final concentration of 5% (v/v) and loaded on a 200 μm × 50 mm fused silica precolumn packed in-house with 5 cm of 5-μm YMC ODS-A C18 beads (Waters Co., Milford, MA) using an 1100 micro-HPLC system (Agilent Technologies, Santa Clara, CA). Following a desalting step, the flow was split, and peptides were eluted through a second 75 μm × 50 mm column packed with the same beads at approximately 200 nL/min. The peptides were eluted using a 2-h gradient (5-80% acetonitrile with 0.1% formic acid) into an ESI LTQ linear ion trap mass spectrometer (Thermo Electron, Waltham, MA). MS/MS spectra were acquired in a data-dependent acquisition mode that automatically selected and fragmented the 10 most intense peaks from each MS spectrum generated.

2.6. 2D LC–MS/MS

All the setting is the same as mentioned above, except for the precolumn. The precolumn was packed in-house first with 5 cm of 5-μm YMC ODS-A C18 beads (Waters Co., Milford, MA) in the front and the n with 8 cm of 10-μm SCX beads (Polymer Laboratories, Varian, Inc.) in the back. The flow-through of the first sample loading was labelled 0 mM salt elution. Then, nine-step salt elutions were performed using 50, 100, 150, 200, 300, 400, 600, 800 and 1000 mM of ammonium acetate solution (pH 2.7), respectively.

2.7. Data analysis

The acquired MS/MS spectra were searched against the decoyed Saccharomyces Genome Database (http://www.yeastgenome.org/, 6716 protein entries, released December 2, 2008) augmented with the reversed sequence of each entry in the forward database. Mascot Distiller was used to generate peak list from raw file, and Mascot 2.2.02 (Matrix Science) was used to search the protein sequence database using the following parameters: carbamidomethyl (C) was set as a fixed modification, while oxidation (M, +15.99492 Da) was set as a variable modification. The precursor and fragment mass tolerances for the LTQ data were set at 2.0 and 0.8 Da, respectively. Trypsin was selected as the enzyme with two potential missed cleavages. Only fully tryptic peptides were accepted in our database

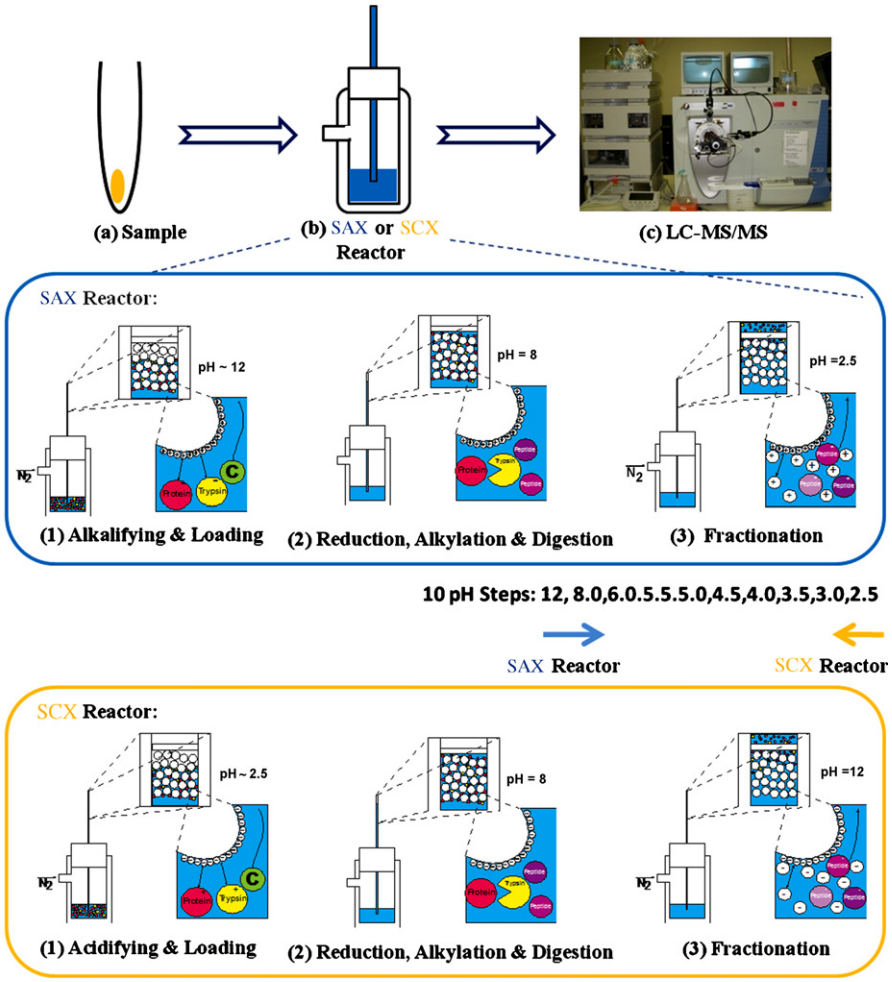


Fig. 1. Flowchart of proteomic reactor based on step pH gradient elution. (A) Yeast protein sample preparation. (B) SAX or SCX reactor: (1) yeast protein sample was mixed with trypsin (5/1, w/w), alkalified or acidified by adding ammonium hydroxide or formic acid, and loaded onto the SAX or SCX reactor; (2) after washing and drying, the reduction buffer (50 mM dithiothreitol, 20 mM ammonium bicarbonate, pH 8.0) was introduced onto the reactor, and the proteins present on the reactor were subjected to disulfide bond reduction; after another washing (10 μL of 20 mM ammonium bicarbonate, pH 8.0) and drying, the digestion buffer (10 mM iodoacetamide, 20 mM ammonium bicarbonate, pH 8.0) was introduced onto the reactor to perform alkylation and tryptic digestion; (3) the resulting peptides were then eluted with 10-step pH gradient buffers (pH 2.5, 3.0, 3.5, 4.0, 4.5, 5.0, 5.5, 6.0, 8.0, 12; SAX reactor from pH 12 to 2.5; SCX reactor from pH 2.5 to 12). (C) The resulting peptides from the SAX or SCX reactor were analyzed by LC–MS/MS.

searching results. Mascot cutoff scores were set to 30. Furthermore, only the peptides ranked first with a probability-based Mowse (expect) *P*-value smaller than 0.05 were accepted. The false positive rate was controlled to be less than 0.5%.

3. Results and discussion

We have combined two versions of the proteomics reactor (SCX and SAX) coupled with pH elution followed by LC–MS analysis for proteomic studies (Fig. 1). The expectation was that this would increase the number of proteins identified due to the reducing of the complexity of peptides in each individual fraction. The initial protocol for the proteomic reactor was not compatible with pH fractionation [30,34,35]. In these earlier versions, 100 mM Tris–HCl (pH 8.0) was used as digestion buffer and 200 mM ammonium bicarbonate was used as elution buffer, which are obviously incompatible with step salt or pH gradient elution. We also previously reported that the ammonium bicarbonate buffer is expected to be incompatible for direct and effective separation by SCX chromatography because the cationic ammonium ion and the elevated pH of the buffer (pH 8) will hinder peptide interactions with the SCX matrix [36]. The concentration of ammonium bicarbonate is the key issue for sample loss and band broadening in SCX chromatography. Therefore, we developed a revised protocol for the proteomic reactor that is compatible with pH fractionation. In this study, 20 mM ammonium bicarbonate was selected as digestion buffer in both SCX and SAX reactors, which are suitable for step pH gradient elution. Furthermore, the elution buffers for the SCX and SAX proteomic reactors were modified to provide 10 fractions ranging from pH 2.5 to 12. Here we demonstrate that the proteomic reactors combined with pH fractionation increases the number of protein identified and the likelihood to identify low-abundance proteins in comparison with conventional proteomic approaches.

3.1. Peptide and protein identifications by pH fractionated SAX and SCX reactors

We initially compared the performance of the modified reactors with conventional sample processing approaches. Briefly, identical amount of 50-μg yeast lysate were processed on the proteomic reactors (SAX and SCX) followed by 10 pH elution steps. As well, the same amount of 50-μg yeast lysate was processed by solution digestion followed by 10 step of salt elution in 2D LC–MS/MS analysis. Table 1 compares the peptides, unique peptides and proteins identified in each fraction from the modified proteomic reactors, and the results obtained from the 10 conventional analysis of yeast

Table 1
Identification summary of SAX and SCX reactors using pH fractionation and 2D LC–MS/MS of in-solution digested yeast proteins.

	pH fractions										
	pH 2.5	pH 3.0	pH 3.5	pH 4.0	pH 4.5	pH 5.0	pH 5.5	pH 6.0	pH 8.0	pH 12	Combined
SAX reactor (FPR: 0.27%)											
Peptides	668	698	725	791	981	1152	1259	1001	692	965	8,932
Unique peptides	410	388	434	439	511	569	520	514	367	505	2,919
Proteins	302	268	290	313	360	355	341	287	193	220	1,106
SCX reactor (FPR: 0.49%)											
Peptides	640	443	616	829	993	1153	945	1004	583	558	7,764
Unique peptides	350	347	474	574	594	469	435	445	356	289	2,265
Proteins	215	229	302	332	288	234	186	176	152	108	685
	Salt fractions (mM)										
	0	50	100	150	200	300	400	600	800	1000	Combined
MudPIT (FPR: 0.32%)											
Peptides	1123	1366	1628	1340	1300	1316	1270	1270	1313	1047	12,973
Unique peptides	558	579	519	414	380	392	334	344	344	344	2,146
Proteins	261	270	267	213	211	227	186	189	189	198	613

sample. A total of 2919 unique peptides were identified by SAX reactor, resulting in 1106 proteins. As well, 2265 unique peptides were identified by SCX reactor, resulting in 684 proteins. There were three fractions (pH 5.0, 5.5 and 6.0) with more than 1000 peptides identified by SAX reactor, and only two fractions (pH 5.0 and 6.0) by SCX reactor. Theoretically, all peptides should be bound to the SAX reactor at pH 12 and to the SCX reactor at pH 2.5. However, 965 peptide were identified in the fraction of pH 12 in SAX reactor and 640 peptide were identified in the fraction of pH 2.5 in SCX reactor. One possible reason for explaining this phenomenon might be that the trypsin digestion was performed in the buffer of 20 mM ammonium bicarbonate at pH 8.0. As a result, even though the pH of elution buffer for the first fraction is at 2.5 and 12 for SCX and SAX, respectively, the actual pH probably is affected by the residual buffer retained on the SCX and SAX reactors. In contrast, 2146 unique peptides were identified by conventional in-solution digestion and 2D LC–MS/MS analysis, resulting in 613 proteins. The striking feature from this analysis is the improvement that the SAX and SCX proteomic reactors provide over the conventional solution-based approach. First, 30% of the MS/MS generated by the SAX and SCX reactor led to unique peptide identification while only 15% of the MS/MS generated by the conventional approach led to the identification of unique peptides. More importantly, the number of unique protein identified is respectively 80% and 12% higher using the SAX and SCX proteomic reactor over the conventional solution-based approach. This clearly illustrates the improved performance of the proteomic reactor with pH fractionation.

3.2. Efficiency of pH fractionation in SAX and SCX reactors

Proteomic analysis by LC–MS does not identify all the proteins present in the samples in one experiment because of limitation due to dynamic range and duty cycle of the mass spectrometer. However, it has been reported that repetitive analysis of the same sample can increase the number of identified unique peptides and proteins. As reported by Liu et al. [37], 95% saturation in protein identifications can be achieved from 10 replicate runs of yeast soluble cell lysate. We evaluated the saturation effect on unique peptide identification across different pH fractions. To evaluate the efficiency of pH fractionation, overlapping unique peptides across different pH steps was displayed in Fig. 2. The number of unique peptides varied between different pH steps, so the overlapping unique peptides were normalized using the following formula:

$$\text{Overlapping rate} = \frac{\text{overlapping unique peptides between fractions A and B}}{\text{unique peptides of fraction A} + \text{unique peptide of fraction B} - \text{overlapping unique peptides between fractions A and B}}$$

Heatmaps were generated to compare the unique peptide overlaps between the different pH elution. Fig. 2A and B illustrates the heatmaps for the unique peptides from the SAX and SCX proteomic reactor. While there are some overlaps in neighbouring pH fractionation the overlaps between distal fractions is nearly zero. The comparison of the overlap between the 10 salt steps used in conventional analysis is very informative (Fig. 2C). In this case not only are the overlaps between some neighbouring salt steps high (about 45%) but also the overlaps between many distal fractions (for example, 50 and 150, 100 and 800 mM) still remain over 40%. This clearly illustrate that the pH fractionation approach on the proteomic reactor provides a tremendous improvement in peptide separation and hence in dynamic range coverage over conventional solution-based processing of samples.

3.3. Comparison of characteristics of peptides in each fraction obtained through pH fractionated SAX, SCX reactors and conventional 2D LC–MS/MS

We were also interested in the characteristic of the peptides in the pH fractions and if there were any notable differences between the peptides observed from the SAX, SCX proteomic reactors and conventional 2D LC–MS/MS. For every peptide in the pH fractionations we calculated the pI, molecular weight, missed cleavage site GRAVY index, as well as the average number of acid amino acids and basic amino acids. Our analysis of these physical characteristics of the unique peptides surprisingly reveal that the properties of the eluting peptides in the different pH fractions are different between the SAX and SCX proteomic reactors (Fig. 3A–F). Furthermore, the key physical characteristics are different. For example, the unique peptides eluting from pH fractionation of the SAX proteomic reactor shows strong correlation between their pI (correlation coefficient of 0.95), GRAVY index (inverse correlation coefficient of 0.97), number of acidic amino acid (inverse correlation coefficient of 0.95), and molecular weight (inverse correlation coefficient of 0.92) with the pH of the fraction. Interestingly, the unique peptides eluting from pH fractionation of the SCX proteomic reactor show no similar correlation with the pI, the GRAVY index, nor the number of acidic amino acid. Furthermore in contrast to the SAX proteomic reactor, the peptides molecular weight (correlation coefficient of 0.85), the number of basic amino acids (correlation coefficient of 0.77), and the number of miss-cleavage sites (correlation coefficient of

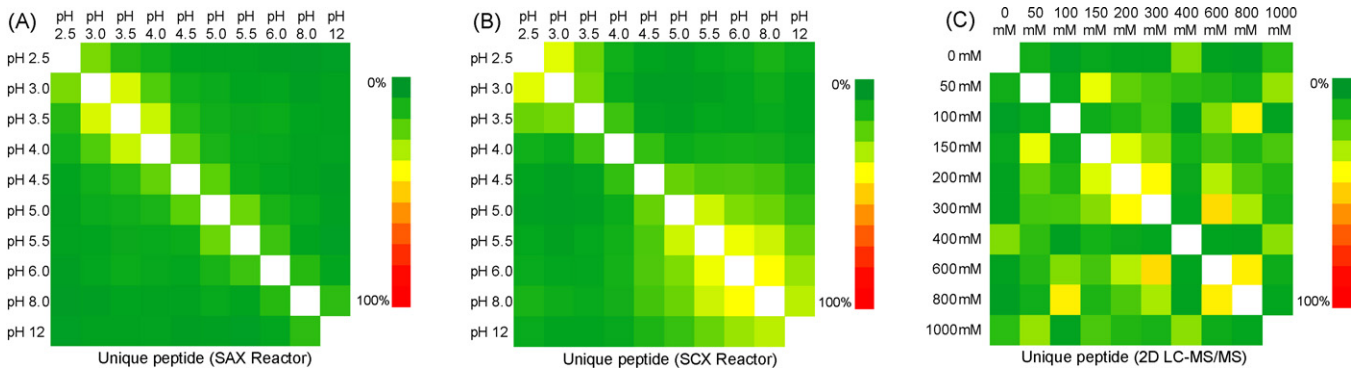


Fig. 2. Heatmap of unique peptide overlap between two fractions in SAX reactor (A), SCX reactor (B) and 2D LC–MS/MS (C).

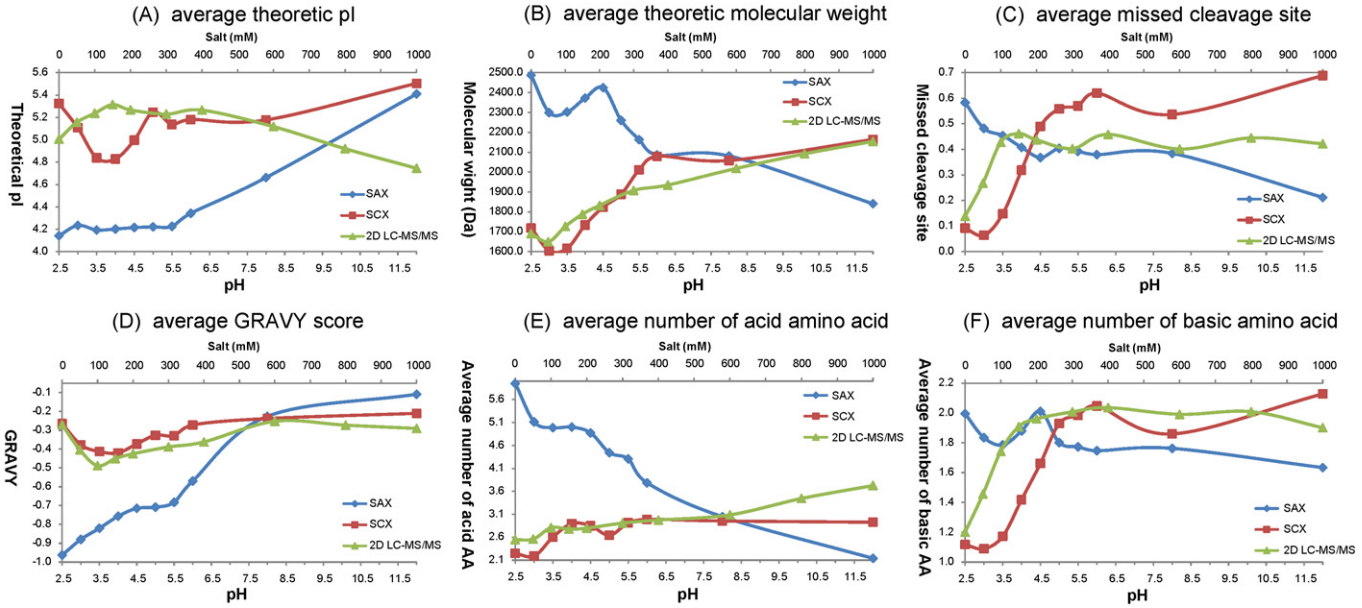


Fig. 3. Distributions of average pI (A), molecular weight (B), missed cleavage site (C), GRAVY (D) and average number of acid (E) and basic (F) amino acid of unique peptides from each fraction in SAX reactor, SCX reactor and 2D LC–MS/MS. F1–F10: pH 2.5, 3.0, 3.5, 4.0, 4.5, 5.0, 5.5, 6.0, 8.0 and 12 for SAX and SCX reactors; 0, 50, 100, 150, 200, 300, 400, 600, 800 and 1000 mM ammonium acetate for 2D LC–MS/MS.

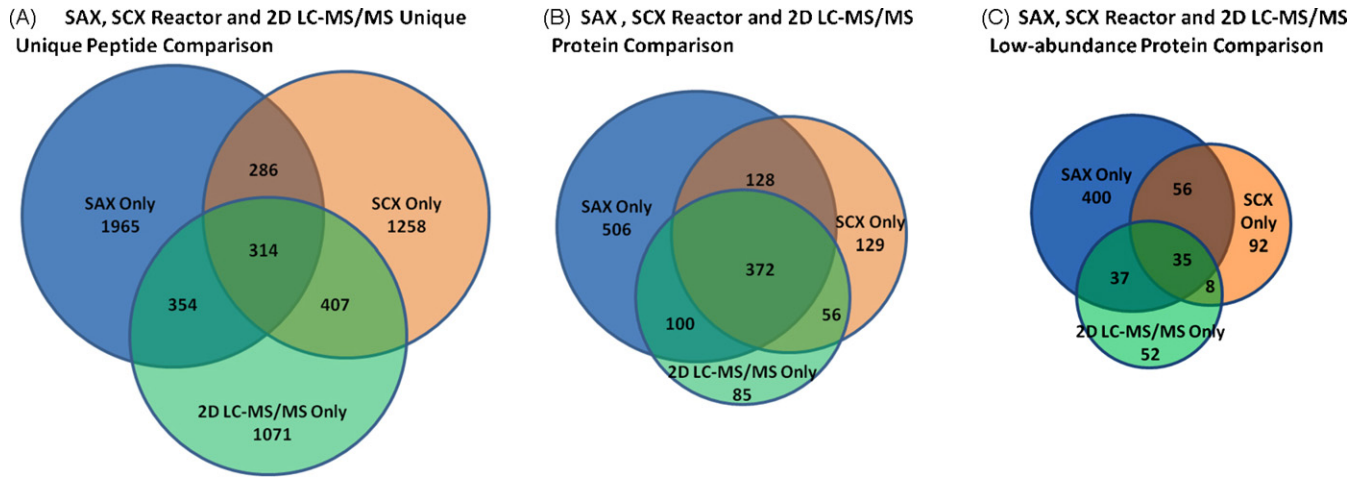


Fig. 4. Overlap between SAX reactor, SCX reactor and 2D LC–MS/MS at the levels of identified unique peptides (A) proteins (B) and low-abundance proteins (C).

0.77) increases with the pH of the fraction. As a control, the unique peptides eluting from step salt gradient elution of the SCX column show no similar correlation with the pI, the GRAVY index, the number of basic amino acid, nor the number of miss-cleavage sites. The peptides molecular weight (correlation coefficient of 0.97) and the number of acidic amino acid (correlation coefficient of 0.98) increases with the salt concentration of the elution. Although, as the name implies, the major separation mechanism of SAX or SCX is electrostatic in nature, ion-exchange packing material is polymer-based, i.e., poly(styrene–divinylbenzene) (PS-DVB), and also exhibit significant hydrophobic characteristics, giving rise to mixed-mode contribution to peptide separation [38,39]. The SCX beads might display stronger hydrophobic interaction than the SAX beads, which could be the reason for the lack of a correlation between the theoretical peptide pIs and the pH of the fractions in the SCX reactor. Clearly, there are cross-correlations between Fig. 3B, C and F. The protein samples were digested by trypsin, i.e., at the residues of K and R. As shown in Fig. 3C, when the missed cleavage sites increase in the fractions of SCX column either by raising the salt concentration or by increasing the pH, the molecular weight and the average number of basic amino acid also increase; and vice versa for the SAX column (Fig. 3B and F). The correlation of pI and the average number of acid amino acid in the fractions of SAX reactor is very strong (inverse correlation coefficient of 0.88, Fig. 3A and E), which indicates that the acid amino acid number of a peptide might be the key issue in pH gradient-based fractionation of SAX column. Clearly the peptides eluted by pH fractionations off the SAX and SCX proteomic reactors have distinct physical properties. This is further illustrated by the limited overlap between the unique peptides (13%) and proteins (39%) observed by the SAX and SCX proteomic reactors (Fig. 4A and B).

4. Identification of low-abundance protein by pH fractionation coupled with the SAX and SCX reactors

The codon adaptation index (CAI), a measurement of codon usage, can be used to predict the expression of a gene, which is positively correlated to protein abundance [40–43]. Usually, yeast proteins with CAI of less than 0.2 are defined as low-abundance protein [13,16,41,44]. Among the 6716 proteins reported in the Saccharomyces Genome Database (http://www.yeastgenome.org/), 6624 proteins (98.6% of the total) are annotated with codon adaptation index (CAI) value. We compared the CAI for protein identified by the modified proteomic reactors and the conventional solution-based proteomics. Interestingly, 48% and 28% of the proteins identified in the pH fractions from the SAX and SCX proteomic reactor have CAI lower than 0.2 (Supplementary Table). In contrast, only 22% of the proteins identified from the conventional solution method (2D LC–MS/MS runs using 10 salt steps) have a CAI lower than 0.2 (Supplementary Table). As shown in Fig. 4C, there are 680 low-abundance proteins (CAI <0.2) identified by the three techniques. Of these, only 5% are common to the three techniques, while 59% of the low-abundance proteins are only identified by the SAX proteomic reactor, 14% by the SCX proteomic reactor and 8% by the conventional approach. These results indicated that the proteomic reactor based on pH elution, particularly the SAX reactor, facilitated the identifications of low-abundance proteins.

5. Conclusion

In this study, we demonstrate for the first time that step pH gradient elution is an efficient fractionation method for routine proteomic reactor. In addition, we have shown that the characteristics of the unique peptides from the pH gradient elution of SAX and SCX reactor are very different which leads to limited overlaps in identified peptides. Finally, our results demonstrate that the proteomic reactor with pH fractionation is a powerful and promising tool for the identification of low-abundance proteins from minute amount of sample.

Acknowledgements

This project was funded by Genome Canada through the Ontario Genomics Institute (2008-OGI-TD-01), NSERC, The Province of Ontario, and the University of Ottawa. Daniel Figeys is a Canada Research Chair in Proteomics and Systems Biology, a Professor in the Department of Biochemistry, Microbiology, and Immunology, and Director of the Ottawa Institute of Systems Biology at the University of Ottawa.

Appendix A. Supplementary data

Supplementary data associated with this article can be found, in the online version, at doi:10.1016/j.talanta.2009.07.018.

References

[1] E. Boschetti, P. Giorgio Righetti, Biotechniques 44 (5) (2008) 663–665.
[2] E. Boschetti, P.G. Righetti, J. Proteomics 71 (3) (2008) 255–264.
[3] E. Boschetti, P.G. Righetti, Proteomics 9 (6) (2009) 1492–1510.
[4] H.J. Lee, et al., Curr. Opin. Chem. Biol. 10 (1) (2006) 42–49.
[5] J.R. Wisniewski, Arch. Pathol. Lab. Med. 132 (10) (2008) 1566–1569.
[6] S.A. Hoffman, et al., J. Chromatogr. B Anal. Technol. Biomed. Life Sci. 849 (1–2) (2007) 43–52.
[7] S.W. Tam, J. Pirro, D. Hinerfeld, Exp. Rev. Proteomics 1 (4) (2004) 411–420.
[8] N. Ahmed, et al., Proteomics 3 (10) (2003) 1980–1987.
[9] S.Y. Cho, et al., Proteomics 5 (13) (2005) 3386–3396.
[10] L.A. Echan, et al., Proteomics 5 (13) (2005) 3292–3303.
[11] S. Hoving, H. Voshol, J. van Oostrum, Electrophoresis 21 (13) (2000) 2617–2621.
[12] J.A. Westbrook, et al., Electrophoresis 22 (14) (2001) 2865–2871.
[13] R.X. Li, et al., J. Proteome Res. 4 (4) (2005) 1256–1264.
[14] P. Hoffmann, et al., Proteomics 1 (7) (2001) 807–818.
[15] Z.B. Ning, et al., J. Proteome Res. 7 (10) (2008) 4525–4537.
[16] N.C. Hubner, S. Ren, M. Mann, Proteomics 8 (23–24) (2008) 4862–4872.
[17] M.P. Washburn, D. Wolters, J.R. Yates III, Nat. Biotechnol. 19 (3) (2001) 242–247.
[18] A.J. Link, et al., Nat. Biotechnol. 17 (7) (1999) 676–682.
[19] R.J. Slebos, et al., J. Proteome Res. (2008).
[20] J. Tang, et al., J. Chromatogr. B Anal. Technol. Biomed. Life Sci. 866 (1–2) (2008) 123–132.
[21] D. Winter, et al., J. Proteome Res. (2008).
[22] J. Dai, et al., J. Proteome Res. 6 (1) (2007) 250–262.
[23] M. Pepaj, et al., J. Chromatogr. A 1120 (1–2) (2006) 132–141.
[24] H. Zhou, et al., Electrophoresis 28 (23) (2007) 4311–4319.
[25] J. Dai, et al., J. Proteome Res. (2008).
[26] G. Han, et al., Proteomics 8 (7) (2008) 1346–1361.
[27] X. Li, et al., Proteomics 5 (13) (2005) 3423–3441.
[28] A. Mange, et al., J. Chromatogr. B Anal. Technol. Biomed. Life Sci. 876 (2) (2008) 252–256.
[29] C. Oh, et al., Bioinformatics 23 (1) (2007) 114–118.
[30] M. Ethier, et al., J. Proteome Res. 5 (10) (2006) 2754–2759.
[31] H. Zhou, et al., J. Proteome Res. 8 (2) (2009) 556–566.
[32] J.P. Lambert, et al., Mol. Cell Proteomics (2008).
[33] H. Zhou, et al., J. Proteome Res. (2008).
[34] W. Hou, et al., Anal. Chem. 79 (1) (2007) 39–44.
[35] J. Vasilescu, et al., J. Proteome Res. 6 (1) (2007) 298–305.
[36] T. Le Bihan, H.S. Duewel, D. Figeys, J. Am. Soc. Mass Spectrom. 14 (7) (2003) 719–727.
[37] H. Liu, R.G. Sadygov, J.R. Yates III, Anal. Chem. 76 (14) (2004) 4193–4201.
[38] T.W. Burke, et al., J. Chromatogr. 476 (1989) 377–389.
[39] L.A. Kennedy, W. Kopaciewicz, F.E. Regnier, J. Chromatogr. 359 (1986) 73–84.
[40] A. Coghlan, K.H. Wolfe, Yeast 16 (12) (2000) 1131–1145.
[41] S. Ghaemmaghami, et al., Nature 425 (6959) (2003) 737–741.
[42] R. Jansen, H.J. Bussemaker, M. Gerstein, Nucleic Acids Res. 31 (8) (2003) 2242–2251.
[43] P.M. Sharp, W.H. Li, Nucleic Acids Res. 15 (3) (1987) 1281–1295.
[44] L.M. de Godoy, et al., Nature 455 (7217) (2008) 1251–1254.

Talanta 80 (2010) 1532–1538

Contents lists available at ScienceDirect

Talanta

journal homepage: www.elsevier.com/locate/talanta

Enhancing plasma peptide MALDI-TOF-MS profiling by mesoporous silica assisted crystallization

Rosa Terracciano[a,*], Francesca Casadonte[a], Luigi Pasqua[b], Patrizio Candeloro[a], Enzo Di Fabrizio[a], Andrea Urbani[c], Rocco Savino[a]

[a] Department of Experimental and Clinical Medicine, "Magna Graecia" University of Catanzaro, 88100 Catanzaro, Italy
[b] Department of Chemical Engineering and Materials, University of Calabria, 87036 Cosenza, Italy
[c] University of Rome "Tor Vergata", Department of Internal Medicine and S. Lucia Foundation - IRCCS, Rome, Italy

ARTICLE INFO

Article history:
Available online 5 April 2009

Keywords:
Clinical proteomics
Biomarkers discovery
MALDI-TOF-MS
Mesoporous materials
Human plasma

ABSTRACT

Promising profiling techniques based on new material/solid phase extraction for capturing "molecular signatures" from body fluids are being coupled to MALDI-TOF-MS. Sample preparation significantly influences spectrum quality in this ionization method. Mesoporous silica beads (MSB), by the means of nano-sized porous channels with high surface area, enable harvesting of peptides from plasma and serum excluding large size proteins. We have investigated the morphology of a sample slurry, developed as a new tool for plasma peptides enrichment based on mesoporous materials. Our study highlights a correlation between crystals morphology and enhanced performances in MALDI-TOF-MS analysis. This is the first report which correlates the increase in signal intensity with crystal formation in samples preparations which make use of various kinds of slurries for the analysis of samples clinically relevant like human plasma.

© 2009 Elsevier B.V. All rights reserved.

1. Introduction

Discovery of biomarkers for disease diagnosis is the major task for modern predictive medicine. Besides traditional and well-established immunoassays (ELISA, RIA) and other technologies used for the detection of a single over-expressed molecule, proteome profiling of human body fluids based on mass spectrometry (MS) is now becoming an important method for investigating and detecting novel disease-associated markers [1–4]. The ability to screen and discover multiple biomarkers simultaneously has been advanced by the recent success of MS, especially surface-enhanced laser desorption/ionization time-of-flight (SELDI-TOF) MS and matrix-assisted laser desorption/ionization time-of-flight (MALDI-TOF) MS [5]. The demand for reducing sample complexity in order to increase the detection of low-abundance proteins has generated the development and implementation of proteomic technologies in the field of protein biomarker discovery. Most of these proteomic technology platforms are centered on the implementation of MS in conjunction with several other analytical techniques, such as solid phase extraction, chromatography and electrophoresis [6]. A new emerging field of study is addressed to development, improvement and standardization of pre-MS separations approaches. Among well-established methods for sample preparation such as magnetic beads (MB) [7], or surface-derivatized chips (SELDI) [8], new separation/fractionation platforms are based on innovative application of both traditional and novel materials for selective capture of low molecular weight peptides and polypeptides from biofluid samples [9–12]. Material science is a mine of richness not yet exploited by proteomic community which could contain premises and promises for future generations of "biomarker discovery" pioneers. That is why the design and generation of material-based platforms for capturing "molecular signatures" from body fluids has gained increasing interest in recent years. Sample preparation is crucial step to generate reproducible and good quality mass spectra which are essential prerequisites for successful proteomic pattern analysis. Therefore optimization and more comprehensive investigations of sample preparation methods could be of high impact for MALDI-TOF-MS analysis of biofluids proteome.

We report herein further investigations and optimization of our recently developed procedure based on mesoporous silica particles for selective binding and enrichment of low molecular weight plasma/serum proteins by MALDI-TOF-MS analysis [11]. Mesoporous silica beads (MSB) are incubated with the sample, washed, then suspension in α-cyano-4-hydroxycinnamic acid (CHCA) is loaded on the MALDI target plate. In comparison to the previous standard protocol [11], the results emphasize a significant increase in signal intensity and decrease in background by new modified

* Corresponding author at: Department of Experimental and Clinical Medicine, "Magna Graecia", Laboratory of Mass Spectrometry and Proteomics, University of Catanzaro, University Campus, Europa Avenue, 88100, Germaneto, Catanzaro, Italy. Tel.: +39 09613694080; fax: +39 09613694090.
E-mail address: terracciano@unicz.it (R. Terracciano).

0039-9140/$ – see front matter © 2009 Elsevier B.V. All rights reserved.
doi:10.1016/j.talanta.2009.03.060

procedure. We have additionally investigated by scanning electron microscopy (SEM) on MALDI samples spots obtained from two different preparation procedures based on MSB. A different behavior in matrix crystallization is observed when sample is spotted on MALDI target plate as matrix-particles suspension, which changes dramatically plasma analysis performances.

2. Experimental

2.1. Material preparation and characterization

The synthesis of MSB was performed under hydrothermal condition in presence of cationic surfactant dodecyltrimethylammonium bromide [$C_{12}H_{25}N(CH_3)_3Br$] (CTABr). The molar composition of the starting mixture was: SiO_2:0.2 CTABr, 0.2 NaOH, 0.04 $Al(OH)_3$, 40 H_2O. 10 g of fumed silica were added to a solution of 0.52 g of $Al(OH)_3$, 12.1 g of CTABr, and 1.35 g of NaOH in 120 g of H_2O. The gel was aged for 2 h at room temperature and then heated in oven for 24 h at 140 °C. The product obtained was filtered, washed with deionized water, and dried at 80 °C for 12 h. The activated sample was obtained by solvent extraction in a Soxhlet apparatus. The nitrogen adsorption–desorption volumetric isotherms at 77 K were measured on a Micrometritics Asap 2010 apparatus. Surface area of the samples was obtained by Brunauer–Emmet and Teller (BET) linearization.

2.2. Plasma collection

Blood intended for plasma preparation was collected into the following tubes: BD Plus Plastic K2EDTA, 10 mL, # 367525. The samples were centrifuged at 1300 × *g* for 10 min under refrigerated conditions (2–6 °C), within 15 min of the draw. The resultant plasma was pooled into one secondary conical bottom BD (TM) Falcon tube. The secondary tube was centrifuged at 2400 × *g* for 15 min to remove potentially remaining cellular material and to prepare platelet poor plasma. Samples were then aliquoted and immediately frozen at −80 °C. All experiments were performed on aliquots of first-thawed poor platelet plasma.

2.3. Experimental procedures

Substance P was spiked in human plasma at a concentration of 12.5 ng/ml. Plasma-Substance P was diluted 1:5 (40 μL of plasma in 160 μL of deionized water), MSB (2 mg) were mixed with diluted human plasma-Substance P sample and shaken at room temperature for 1 h. The suspension was centrifuged at 2000 × *g* for 2 min, and then MSB were separated from the supernatant and washed with deionized water (4× 30 μL). After the last wash, bound species were directly extracted in CHCA (30 μL of a 4 mg/mL solution prepared dissolving the matrix in a 1:1 mixture of acetonitrile and 0.1% trifluoroacetic acid). A volume of the above slurry (1 μL) was loaded on MALDI target plate in the "suspension" procedure, otherwise, after centrifugation at 2000 × *g* for 2 min, 1 μL of supernatant solution (30 μL) with extracted peptides, was deposited on MALDI probe ("elution" procedure). Both in suspension and in elution procedure, equal volume of matrix solution (30 μL) was used for extracting bound species from beads, and in both cases 1 μL was deposited on MALDI probe.

Protein concentrations were determined using the Bio-Rad Laboratories (Hercules, CA, USA) protein assay kit (Bradford method) and bovine gamma-globulin as standard following the instructions furnished by the manufacturer.

Standard solution was prepared by mixing 100 μL of a 1 mg/mL stock solution of Substance P, with 100 μL of a 1 mg/mL stock solution of Dynorfine and with 100 μL of a 1 mg/mL stock solution of Insuline (bovine). Stock solutions of standard peptides were all prepared in 0.1% of TFA. 1 μL of standard solution was directly spotted onto a well of MALDI plate and air-dried. Then 1 μL of CHCA matrix solution (prepared as described above) was overlaid on the sample and air-dried. In parallel, 1 mg of MSB was added to100 μL of standard solution, then 1 μL of this suspension was spotted onto a well of MALDI plate and air-dried. Then 1 μL of CHCA matrix solution was overlaid on the sample and air-dried.

2.4. MALDI-TOF-MS analysis

MALDI-TOF-MS analysis was performed on a mass spectrometer (Voyager-DE STR, Applied Biosystems, Foster City, CA, USA) equipped with a 337 nm nitrogen laser. Analyses were performed in linear positive-ion mode, using delayed extraction. The acceleration voltage was 20 kV, guide wire was 0.05% of the accelerating voltage, grid voltage was 91.5%, and the delay time was 220 ns. Same TOF-MS settings and laser shot acquisition of the sample spots were applied to carefully compare spectral read-outs from different MALDI preparations. In particular five 100-laser shots were averaged for each mass spectrum to obtain a good statistical analysis. All spectra were normalized to the base peak and a baseline correction was performed using Data Explorer 4.0 (Applied Biosystems, Framingham, MA, USA). All experiments were carried out at least in triplicate to ensure the reproducibility of the spectra. Same instrument settings were used for both elution and suspension procedures.

2.5. Scanning electron microscopy

The samples were first prepared on MALDI stainless steel target plate following the same procedures of the samples for MALDI-TOF-MS analysis. The samples topography was characterized by scanning electron microscopy, using the electron column of a dual beam system (FEI Nova 600 Nanolab) equipped with a thermal field emitter as electron source. Low beam currents in combination with

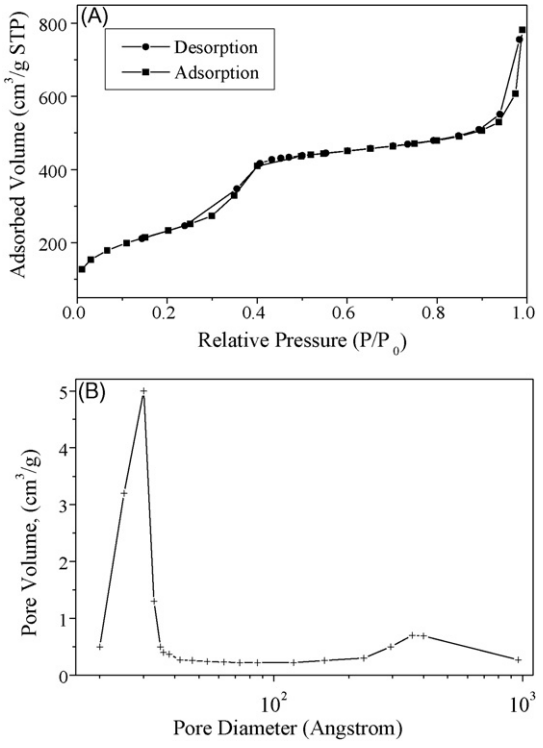


Fig. 1. (A) Nitrogen adsorption–desorption isotherms and (B) Barret–Joyner–Halenda (BJH) pore size distribution of mesoporous silica beads used in proteomic experiments.

a small accelerating voltage of 5 kV were employed in order to prevent the sample from any possible damage. Furthermore, the low beam currents limited the charging effects and consequently no previous metal coating of the sample was required for the analysis.

3. Results and discussion

Mesoporous materials constitute a new generation of materials that show ordered arrangements of channels and cavities of different geometry built up from SiO_2 unities [13]. The pore size is variable ($2\,nm < \Phi_p < 50\,nm$) and can be controlled and modified, in a reasonable range, using in situ [14] and ex situ [15] synthetic strategies. These materials find many uses in catalysis, metal ion extraction, optical applications. Moreover silica particles with highly ordered mesostructures, for example, M41s [16] and SBA-15 [17], have been widely applied in the fields of separation and adsorption [18–20].

MSB used in the experiments hereby described belong to highly ordered mesoporous silica particles synthesized according to reported procedure [21]. Representative nitrogen adsorption–desorption isotherms (Fig. 1, panel A) and the pore size distribution diagram for MSB (Fig. 1, panel B) demonstrate the existence of highly ordered mesopores running along the same direction. In particular nitrogen adsorption–desorption isotherms of sample ($S_{BET} = 848\,m^2/g$, pore volume = $1.21\,cm^3/g$, show two mesopore filling steps at P/P_0 range 0.2–0.4 and 0.9–1.0, indicating a bimodal pore system. The Barret–Joyner–Halenda (BJH) pore size distribution is centered at 25 and 390 Å. The first peak is associated with primary mesopores generated by surfactant micelles, the second one is associated with secondary mesopores resulting from secondary silica condensation.

Here we extended our previous studies in which we developed a strategy based on MSB for plasma peptides profiling [11]. Given the high surface area mesoporous silicates offer the desired adsorptive capacity for binding and enrichment of low molecular weight peptides present in body fluids. Tuning the pore size distribution and surface adsorptive properties, MSB selectively capture peptides and small size molecules excluding large size proteins such as Human Serum Albumin. Plasma samples are exposed to mesopores, then captured molecular species are extracted and profiled by MALDI-TOF-MS. In order to make the analysis more rapid and to circumvents the risk of sample loss, we refined the previous protocol by direct spotting of MSB-loaded suspension on the MALDI target plate. As illustrated in Fig. 2 we called "elution" procedure the previous protocol in order to distinguish from the new modified procedure called "suspension" procedure. A detailed description of procedure is summarized in experimental section. We prepared our samples with CHCA given its optimal chemical–physical properties as a matrix for the MALDI mass spectrometric analysis of peptides.

A comparison of the performance in MALDI-TOF-MS analysis of human plasma, between the "suspension" procedure and the "elution" procedure is shown in Fig. 3 where the MALDI-TOF-MS spectra are evaluated in absolute ion counts units for the same m/z range. A significant enhancement in signal intensity as well as the

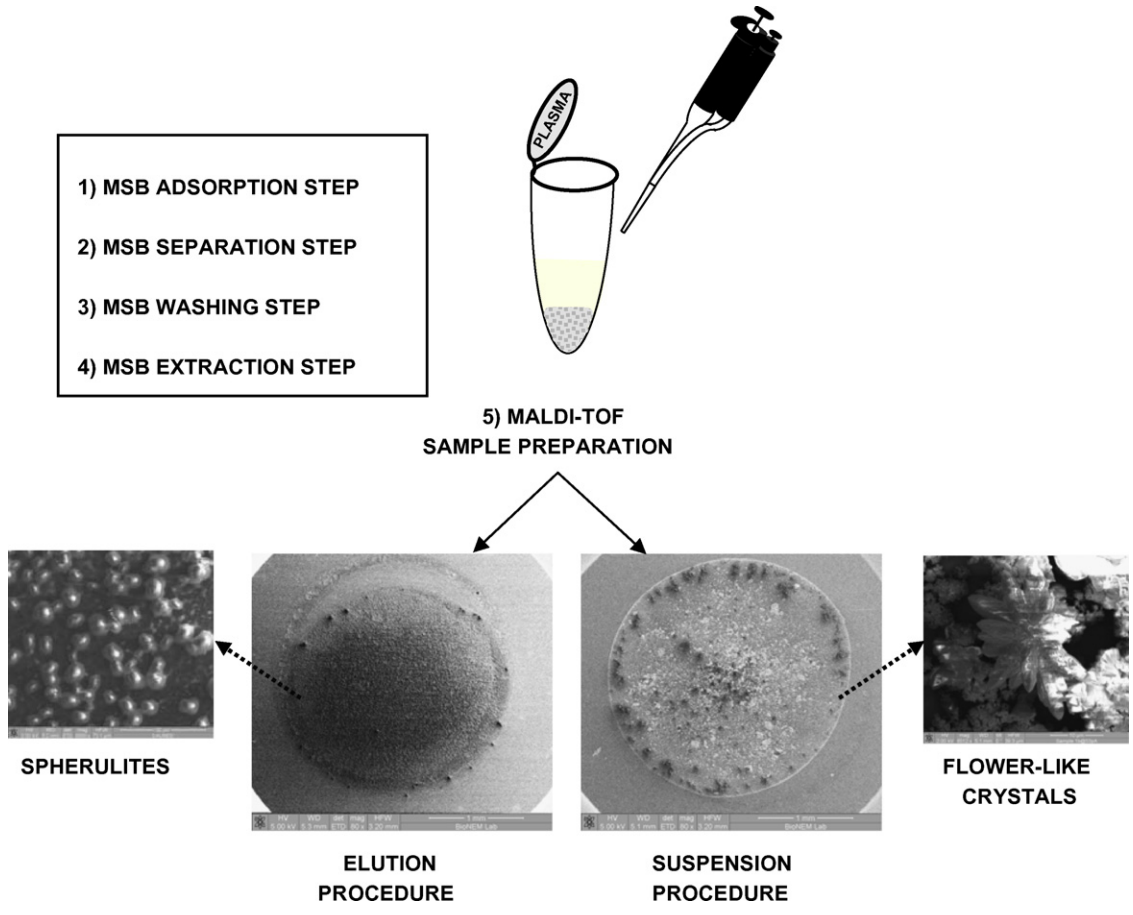


Fig. 2. Extraction of plasma peptides by MSB and MALDI sample preparation on-target plate by "elution" and "suspension" procedure. MSB were mixed with diluted human plasma and shaken at room temperature for 1 h (adsorption step). The suspension was centrifuged, the MSB were separated from the supernatant (separation step) and washed with deionized water (washing step). After the last wash, bound species were directly extracted in CHCA (extraction step). 1 μL of the above slurry was loaded on MALDI target plate in the "suspension" procedure, otherwise, after centrifugation 1 μL of supernatant solution, was deposited on MALDI probe ("elution" procedure). SEM images of two different preparations with magnification inserts are provided.

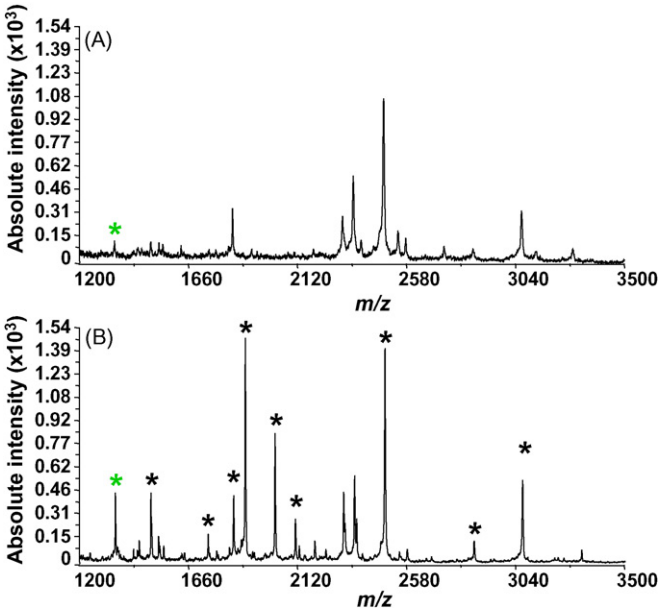


Fig. 3. Performance of the "elution" and "suspension" procedures in MALDI-TOF-MS analysis. (A) MSB were incubated with the sample, washed, captured peptides were eluted and analyzed ("elution" procedure). (B) MSB were incubated with the sample, washed, matrix solution was added and finally 1 μL of slurry was loaded on MALDI target plate. In both cases Substance P was spiked at 12.5 ng/ml (green asterisk). High, medium, and low intensity peaks within the mass range of *m*/*z* 1200–3500 were randomly selected (asterisks) for the variability assessment. Signal intensity is plotted in the same absolute units for both procedures.

number of peaks detected is clearly visible in the new "suspension procedure" (Fig. 3, panel B). A typical effect observed in the MALDI technique is that the spectra do not show good stability of the ion current intensity, therefore to obtain a good statistical analysis we used five hundreds laser pulses to average the mass spectra. Moreover, to carefully compare spectral read-outs from different MALDI preparations, same TOF-MS conditions and laser shot acquisition of the sample spots were applied both in "suspension" and "'elution" procedure.

In order to evaluate the increased detection sensitivity achieved by suspension procedure, Substance P was added to human plasma sample at the concentration of 12.5 ng/ml in both elution and suspension procedures. Substance P was detected with a signal over 10-fold higher when the sample was deposited on MALDI probe as slurry instead of as simple solution (Table 1 and Fig. 3).

In order to better discriminate whether the enhancement in signal intensity we observed was due to different analyte concentration, total protein concentration of the samples spotted on MALDI plate was measured by Bradford assay in three different experiments. Interestingly we found that the supernatant solution by the "elution procedure" contained a total protein concentration of 3.9 ± 0.1 μg/μL, while, in the case of the slurry, the measured protein concentration was 3.68 ± 0.03 μg/μL. Therefore, we consider highly unlikely that the poorer mass spectrum observed in the "elution" procedure may be due to lower analyte concentration.

To better analyze the gain in ion yield, we randomly selected a list of ten peaks (indicated with asterisk in Fig. 3, panel B) of low, medium and high intensity in a set of three replicate experiments. The results are illustrated in Table 1, which shows average absolute areas and area ratios of peaks obtained with suspension and elution procedure. We observed a substantial enhancement in peak areas which for some peaks resulted more than hundred fold, whereas a minority of peaks were detected with roughly the same intensity (Table 1). Although mass accuracy was slightly lower in "suspension procedure", we found a higher reproducibility in peaks area in "suspension procedure" (see percentage coefficient of variance in Table 1).

In the higher *m*/*z* range between 3500 and 7500, the MALDI mass spectrum from suspension procedure (Fig. 4, panel B) shows more spectral features with higher S/N when compared to the MALDI-TOF-MS spectrum from elution preparation (Fig. 4, panel A), even though we notice the presence of some isolated little peaks, more evident in elution preparation, marked with red arrows in Fig. 4, panel A. The superior performance of suspension preparation is evident as the highest signal intensities were gained with almost no background noise (Fig. 4, panel B). Signal-to-noise ratio was increased ninefold for the *m*/*z* 3519 peak (from 4.7 to 43.4), and 16-fold for the *m*/*z* 3830 peak (from 5 to 83) when slurry was used

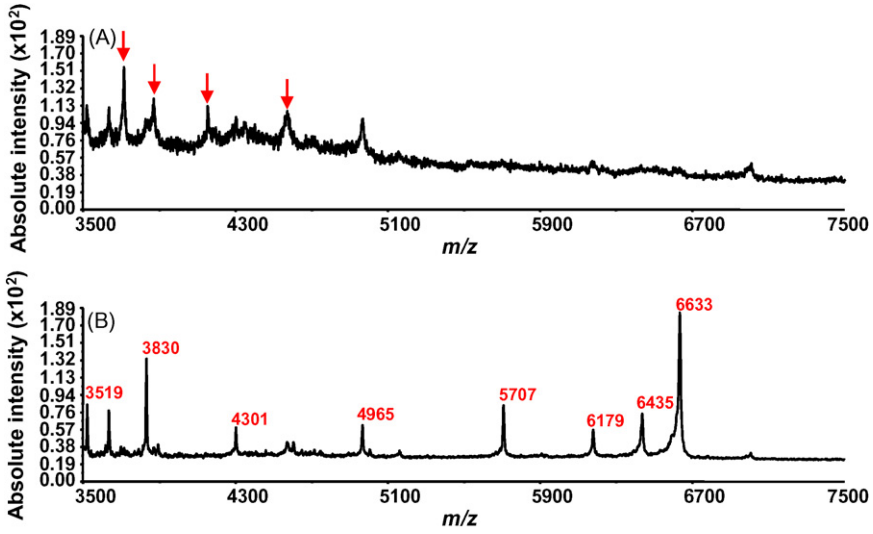


Fig. 4. MALDI-TOF mass spectra of human plasma treated with MSB and spotted on MALDI probe with "elution" (A) and "suspension" (B) procedures in the mass range of *m*/*z* 3500-7500. Same amount of plasma and MSB were used in both procedures as well as the volume of matrix solution used for extraction and for MALDI sample preparation on the probe. Instrument settings were the same in both experiments. Red arrows in panel A show little isolated peaks more evident in "elution" vs. "suspension" procedure. Signal intensity is plotted in the same absolute units for both spectra.

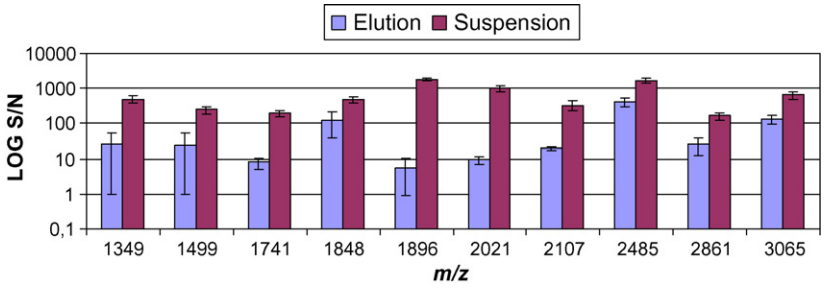


Fig. 5. Comparison of S/N ratio for "elution" (cyan) and "suspension" (magenta) procedures. The values were averaged on three independent experiments and reported, with error bars, on logarithmic scale.

in sample preparation. Enhancement of S/N was also estimated for peaks 4301 (from 8 to 22) and 4965 (from 6 to 25) in suspension preparation as well as the peaks 5707, 6179, 6435 and 6633 were lost in elution preparation (Fig. 4, panel A and B).

To complete MS spectra analysis we also evaluated signal to noise ratios for the same set of peaks of Table 1. Fig. 5 illustrates the stringent increase of performance in suspension procedure with respect to elution procedure with S/N values which increases several fold (over 100-fold for peaks 1896 and 2021).

To gain deeper insight in the mechanisms determining the increased performance of the "suspension procedure", inspection of sample morphology of the two different preparations on MALDI plate was investigated by SEM. This study revealed a higher density of CHCA crystals over the entire well area of sample in the new

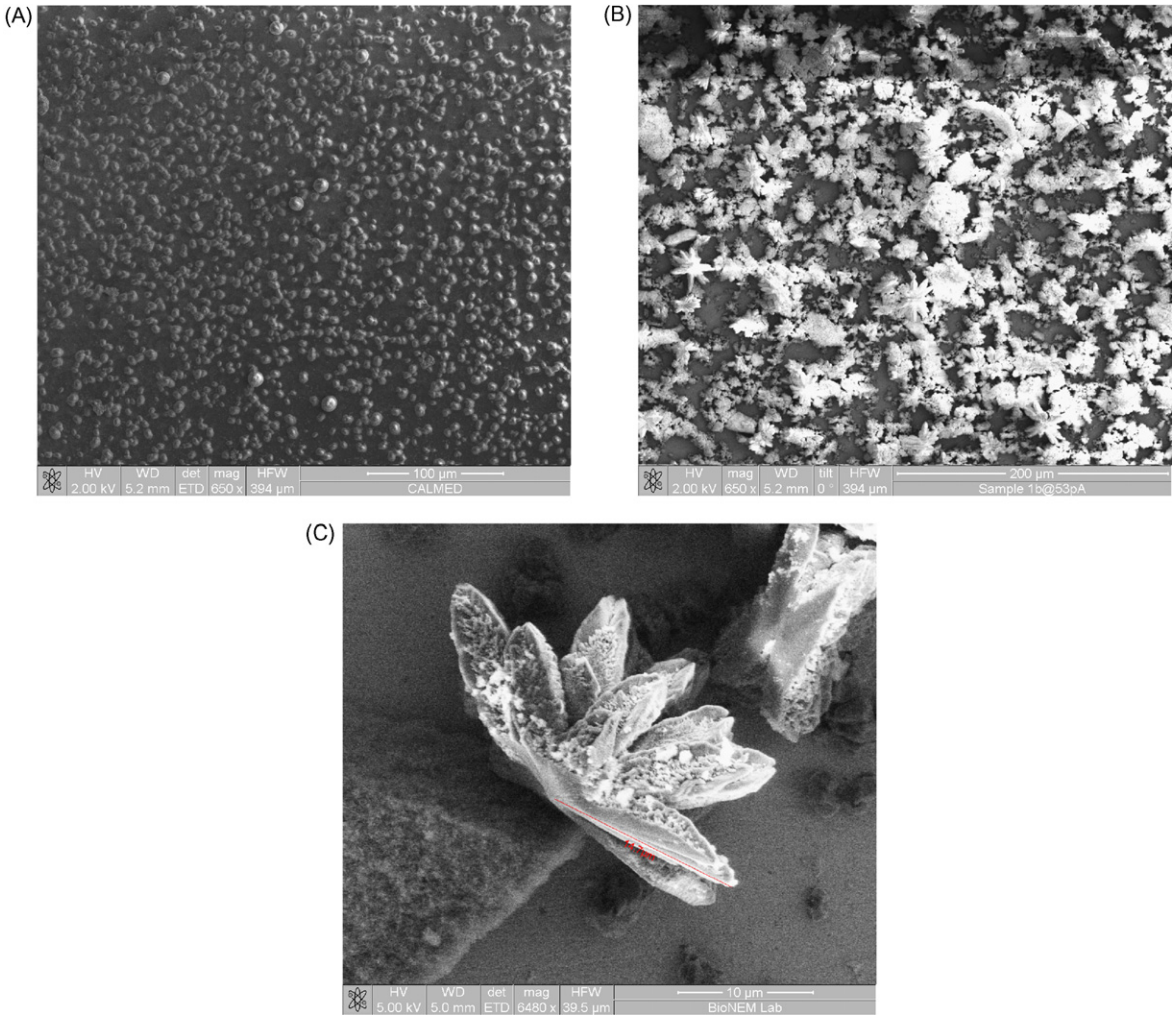


Fig. 6. SEM analysis. (A) SEM image of on-target sample preparation by "elution" procedure; (B) SEM image of on-target sample preparation by "suspension" procedure; (C) A superb flower-shaped crystal obtained from analytes in α-cyano-4-hydroxycinnamic acid matrix, grown among mesoporous silica beads on a typical stainless steel MALDI probe. The crystals radially grow around a bud and a flower-shaped crystal consists of approximately 20 crystalline parts looking like "petals" of the flowers. Promotion of these micron-sized crystals significantly improves MALDI mass spectral read-outs of human plasma peptides extracted by mesoporous silica beads and deposited as slurry on MALDI probe.

Table 1
Comparison of mass accuracy and absolute peak areas in suspension and elution procedure.

m/z[a]	%CV on mass accuracy[b]	%CV on mass accuracy[c]	Average peak area[b] (%CV)	Average peak area[c] (%CV)	Peak area ratio[d]
1349	0.00 (i.s.)[e]	0.00 (i.s.)[e]	10347 (12.39)	718 (19.77)	14.40
1499	0.033	0.041	16859 (24.55)	688 (36.30)	24.51
1741	0.0094	0.016	6462 (3.17)	609 (1.65)	10.61
1848	0.043	0.030	18667 (5.21)	14853 (6.88)	1.26
1896	0.044	0.029	84094 (15.45)	364 (15.33)	231.09
2021	0.048	0.027	44434 (11.45)	432 (20.50)	102.87
2107	0.052	0.043	19874 (23.39)	915 (25.72)	21.71
2485	0.025	0.029	78137 (7.82)	68071 (23.86)	1.15
2861	0.060	0.012	8140(9.17)	3658 (36.85)	2.22
3065	0.047	0.016	32487 (3.65)	19099 (29.92)	1.70
Mean	0.036	0.024	%CV = 11.62	%CV = 21.68	41.15

[a] Analysis and variability assessment for peak areas are performed on MALDI-TOF spectra acquired from replicate analyses ($n = 3$).
[b] Suspension procedure.
[c] Elution procedure. %Coefficient of variance is in parentheses.
[d] Suspension vs. elution peak area ratios.
[e] Internal standard.

"suspension procedure", whereas typically "sweet spots" are observed at the edge of the spot in the standard procedure (see Supplementary material Fig. 1). We speculate that when silica particles are present in sample preparation they represent centers of nucleation for crystals growth after the deposition on MALDI probe. When the particles are absent, as it happens in elution procedure, the crystallization takes place on the smooth surface of the stainless-steel probe thus determining a lower density of crystals per unit area. We observed with SEM that matrix-analytes solution (elution procedure) and matrix-analytes-particles suspension (suspension procedure) crystallize in different shapes and dimensions (Fig. 6). In the case of elution procedure crystallites with roughly spherical shapes are predominant with an average diameter of 7 μm (Supplementary material Fig. 2), whereas larger flower-like crystals are predominant in the suspension procedure (Fig. 6, panel B and C). Careful inspection by SEM revealed that these flowers have different sizes and shapes with petals from 10 to 20 μm (Fig. 6, panel C and Supplementary material Fig. 3).

To further support the hypothesis that the increased performance observed in the case of the "suspension procedure" is due mainly to the crystal shape and not to other reasons (for instance, different analyte concentration) we performed an additional experiment in which MSB were exclusively used for assisting crystallization and not for peptide harvesting. A standard solution containing Substance P, Dynorfine and Insuline was deposited on MALDI probe with and without mesoporous silica, air-dried and then covered with a CHCA solution. As shown in Fig. 7, MALDI and SEM data confirmed the results obtained with human plasma peptides. An enhancement in signal intensity (Fig. 7, panels A and C) was observed in the presence of MSB, which correlated with the appearance of flower-like crystals (Fig. 7, panel B); considering that in this case the peptide concentration is identical in the two samples, the most likely explanation for the observed difference is the different crystal shapes obtained from two sample preparations (Fig. 7, panels B and D and supplementary material Fig. 4). It is important to underline that the crystals obtained in this

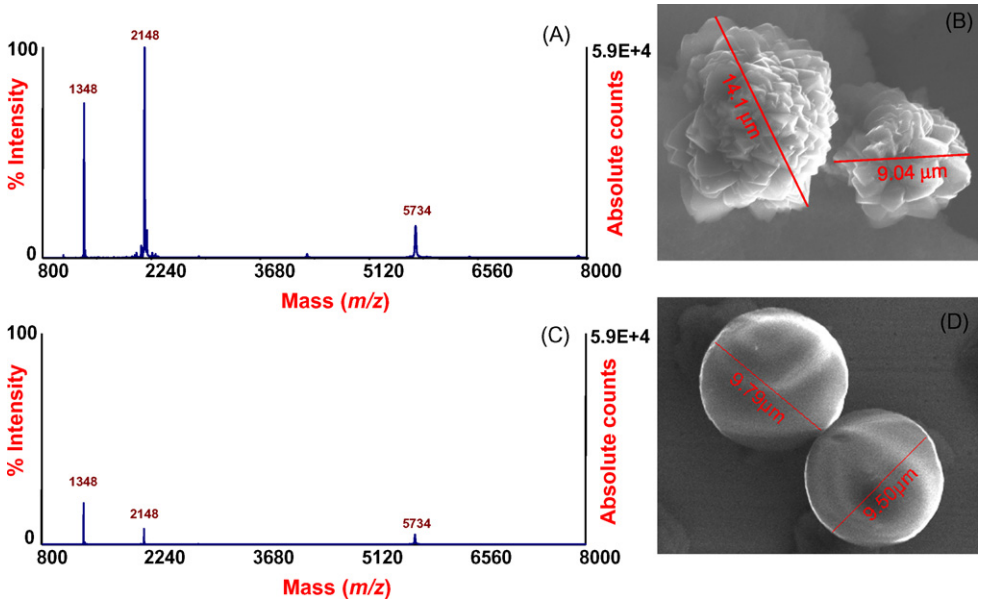


Fig. 7. MALDI-TOF MS spectra and SEM images of a standard solution from two different preparations on MALDI probe. The standard solution was prepared with Substance P (m/z 1348), Dynorfine (m/z 2148) and Insuline (m/z 5734); each peptide at a concentration of 0.33 μg/μL. Panel A illustrates the mass spectrum obtained when 1 μL of standard solution containing mesoporous silica particles was deposited on MALDI plate, air-dried and then the solution of CHCA was added. Panel B shows a high magnification SEM image of floral-shaped crystals obtained from above described preparation. Panel C illustrates the mass spectrum obtained when 1 μL of standard solution without mesoporous silica particles was deposited on MALDI plate, air-dried and then the solution of CHCA was added. MALDI spectra are compared at the same absolute counts. Panel D shows a high magnification SEM image of spherulitic crystals obtained from preparation without silica particles.

experiment, with the standard solution in absence of MSB, retain the spherical shape already observed in the "elution" procedure. Flower-like shapes are still observed when MSB are used, but in comparison to previously described suspension procedure, these flowers are obviously slightly different, due to the different crystallization conditions.

Sample morphology is considered critical in determining the ion yield in MALDI-MS of proteins [22]. It is tempting to speculate that the shape of the crystals obtained with the "suspension procedure", with a more favorable surface to volume ratio, offers a larger surface to the laser beam, allowing a more efficient desorption/ionization process compared to the crystals obtained with the "elution procedure".

Although MALDI is a very popular mass analysis technique, it is still a poorly understood process and one has to be cautious in extrapolating the results. Our experimental observations regarding the possible correlation between the crystals/analyte distribution and resultant MALDI signals have been reported in other systems [23]. Even if other studies investigated on the dependence of matrix crystal morphology on analyte ion yield [24], this is the first report which correlates the increase in signal intensity with crystal formation in samples preparations which make use of various kinds of slurries for the analysis of samples clinically relevant like human plasma.

Materials with micrometer-scale regularity are of great technological applications in microelectronics, information storage, optics, biomedical implants, catalysis and separation technologies [25]. It is hoped that this study would ultimately lead to rational design of improved methods for sample preparation by controlling crystallization conditions in the wide range of biofluid proteomics applications. Detailed studies on influence of particles suspension on matrix-analytes crystallization as well as inspection of the crystallites morphology might help elucidating the mechanisms and facilitating MS-based proteomics research.

Acknowledgment

This work was supported by an AIRC 2005 grant and a Ministero della Salute, Dipartimento dell'Innovazione (Direzione Generale della Ricerca Scientifica e Tecnologica) 2006 grant.

Appendix A. Supplementary data

Supplementary data associated with this article can be found, in the online version, at doi:10.1016/j.talanta.2009.03.060.

References

[1] J. Villanueva, J. Philip, D. Entenberg, C.A. Chaparro, M.K. Tanwar, E.C. Holland, P. Tempst, Anal. Chem. 76 (2004) 1560–1570.
[2] X. Zhang, S.M. Leung, C.R. Morris, M.K. Shigenaga, J. Biomol. Technol. 15 (2004) 167–175.
[3] G.L. Hortin, Clin. Chem. 52 (2006) 1223–1237.
[4] G.L. Hortin, S.A. Jortani, J.C. Ritchie, R. Valdes, D.W. Chan, Clin. Chem. 52 (2006) 1218–1222.
[5] R.E. Banks, M.J. Dunn, D.F. Horchstrasser, J.C. Sanchez, W. Blackstock, D.J. Pappin, P.J. Selby, Lancet 356 (2000) 1749–1756.
[6] J.L. Luque-Garcia, T.A. Neubert, J. Chromatogr. A 1153 (2007) 259–276.
[7] J. Villanueva, J. Philip, C.A. Chaparro, Y. Li, R. Toledo-Crow, L. De Noyer, M. Fleisher, R.J. Robbins, P. Tempst, J. Proteome Res. 4 (2005) 1060–1072.
[8] T.W. Hutchens, T.T. Yip, Rapid Commun. Mass. Spectrom. 7 (1993) 576–580.
[9] I. Feuerstein, M. Rainer, K. Bernardo, G. Stecher, C.W. Huck, K. Kofler, A. Pelzer, W. Horninger, H. Klocker, G. Bartsch, G.K. Bonn, J. Proteome Res. 4 (2005) 2320–2326.
[10] X.L. Kong, L.C.L. Huang, C.M. Hsu, W.H. Chen, C.C. Han, H.C. Chang, Anal. Chem. 77 (2005) 259–265.
[11] R. Terracciano, M. Gaspari, F. Testa, L. Pasqua, G. Cuda, P. Tagliaferri, M.C. Cheng, A.J. Nijdam, E.F. Petricoin, L.A. Liotta, M. Ferrari, S. Venuta, Proteomics 6 (2006) 3243–3250.
[12] H. Chen, X. Xu, N. Yao, C. Deng, P. Yang, X. Zhang, Proteomics 8 (2008) 2778–2784.
[13] J.S. Beck, J.C. Vartuli, W.J. Roth, M.E. Leonowicz, C.T. Kresge, K.D. Schmitt, C.T.W. Chu, D.H. Olson, E.W. Sheppard, S.B. Higgins, J.L. Schlenker, J. Am. Chem. Soc. 114 (1992) 10834–10843.
[14] X.S. Zhao, G.Q. Lu, X. Hu, Chem. Commun. (1999) 1391–1392.
[15] A. Firouzi, F. Atef, A.G. Oertly, G.D. Stucky, B. Chmelka, J. Am. Chem. Soc. 119 (1997) 3596–3610.
[16] C.T. Kresge, M.E. Leonowicz, W.J. Roth, J.C. Vartuli, J.S. Beck, Nature 359 (1992) 710–712.
[17] D.Y. Zhao, J.L. Feng, Q.S. Huo, N. Melosh, G.H. Fredrickson, B.F. Chmelka, G.D. Stucky, Science 279 (1998) 548–552.
[18] M. Hartmann, Chem. Mater. 17 (2005) 4577–4593.
[19] G. Buchel, M. Grun, K.K. Unger, A. Matsumoto, K. Tsutsumi, Supramol. Sci. 5 (1998) 253–259.
[20] M. Grun, C. Buchel, D. Kumar, K. Schumacher, B. Bidlingmaier, K.K. Unger, Stud. Surf. Sci. Catal. 128 (2000) 155.
[21] L. Pasqua, F. Testa, R. Aiello, Stud. Surf. Sci. Catal. 146 (2003) 497–500.
[22] M. Sadeghi, A. Vertes, Appl. Surf. Sci. 127–129 (1998) 226–234.
[23] Y. Day, R.M. Whittal, L. Li, Anal. Chem. 68 (1996) 2494–2500.
[24] I.D. Figueroa, O. Torres, D.H. Russell, Anal. Chem. 70 (1998) 4527–4533.
[25] V. Gupta, P. Scharff, N. Miura, Mater. Lett. 60 (2006) 2278–2281.

Talanta 80 (2010) 1539–1544

Contents lists available at ScienceDirect

Talanta

journal homepage: www.elsevier.com/locate/talanta

Combined RNA-expression and 2D-PAGE-screening identifies comprehensive interaction networks affected after bortezomib or enzastaurin exposure of mantle cell lymphoma

Marc Weinkauf[a], Grit Hutter[a], Yvonne Zimmermann[a], Elena Hartmann[b], Andreas Rosenwald[b], Martin Dreyling[a,*]

[a] Clinical Cooperative Group Leukemia, Campus Großhadern Medical Clinic III and Helmholtz Center Munich, Marchioninistr. 25, 81377 Munich, Germany
[b] Institute of Pathology, University of Wuerzburg, Josef-Schneider-Str. 2, 97080 Wuerzburg, Germany

ARTICLE INFO

Article history:
Available online 17 June 2009

Keywords:
Network anaylsis
Proteomics
RNA-expression array
Mantle cell lymphoma
Bortezomib
Enzastaurin

ABSTRACT

Despite recent advances in treatment, mantle cell lymphoma (MCL) still represents a disease with dismal prognosis due to its progressive clinical course, high rate of therapy refractory cases and frequent relapses. During recent years, the proteasome inhibitor bortezomib and enzastaurin, an inhibitor of protein kinase c have been explored in MCL. In relapsed disease enzastaurin achieved disease stabilization in a subset of patients. Bortezomib in relapsed and refractory MCL achieves response rates of 30–40%. To identify signal pathways and manifold interactions regulating cellular response to molecular targeted approaches several high throughput screening methods were applied. A combined network analysis of the identified target molecules based on both RNA array expression data and a survey of cellular protein levels resulted in a unified interaction network more comprehensive (bortezomib: 394 and enzastaurin: 174 molecules) than the networks of the individual screening techniques (329/44 and 117/36 molecules respectively). Interestingly, although none of the target molecules were matched in both RNA-expression and protein level analysis they were mapped nonetheless to common pathways. Additionally, the ranking of identified pathways allowed an improved characterization of the observed induction of cell apoptosis.
© 2009 Elsevier B.V. All rights reserved.

1. Introduction/background

Mantle cell lymphoma (MCL) is an aggressive lymphoma characterized by a high incidence of refractory cases and constant relapses after initial treatment. Prognosis for MCL patients remains poor [1]. To address the need for new treatment options, several molecularly targeted approaches have reached the clinical testing phase. Among the more promising biologicals rank the proteasome inhibitor bortezomib [2] and the protein kinase c beta inhibitor enzastaurin [3]. Both substances achieve significant treatment responses in subsets of MCL patients and, while their primary targets are well known, comprehensive understanding of their effects are still to be elucidated [4,5].

To characterize the interaction of signalling and physiological function various screening approaches have been developed. In most cases, these screening approaches focus either on RNA-expression analysis (e.g. expression arrays) or directly detect cellular protein levels (e.g. 2D-PAGE or protein arrays). However, each individual screening method lacks important information. Focussing exclusively on RNA-expression analysis misses all post-translational events that directly influence protein expression. Likewise, analysis of the protein level only neglects transcriptional regulation. Thus the optimal approach is a unified interaction network analysis of both, the pooled protein level and RNA-expression data.

2. Material/methods

The well characterized mantle cell lymphoma cell lines Granta 519, HBL-2, Jeko-1 and Rec-1 were treated at a previously defined concentration either with the proteasome inhibitor bortezomib (25 nM) [6] or the protein kinase c beta inhibitor enzastaurin (10 nM). Target molecule identifications by 2D-PAGE and subsequent MALDI-TOF mass spectrometry (4700 Proteomics Discovery System with Mascot™, Applied Biosystems, Foster City, USA) were performed as described previously [7,8]. Briefly, whole cell lysates consisting of 5×10^6 treated or control cells were harvested after 2, 4 and 8 h for 2D-PAGE analysis. The resulting triplicate protein maps were compared for altered protein spot patterns and indicated protein spots selected for mass spectrometry. In parallel, RNA-expression analysis was performed as described previously

* Corresponding author at: Medizinische Klinik III der Universität München - Grosshadern, Marchioninistrasse 15, D-81377 München, Germany.
Tel.: +49 89 7095 2202; fax: +49 89 7095 2201.
E-mail address: martin.dreyling@med.uni-muenchen.de (M. Dreyling).

0039-9140/$ – see front matter © 2009 Elsevier B.V. All rights reserved.
doi:10.1016/j.talanta.2009.06.023

[9]. Again, of each individual treated cell line 5×10^6 cells were harvested after 4 and 8 h and processed. The resulting lists of affected gene expression and protein levels were pooled and submitted for network analysis (IPA, Ingenuity Systems; GenomatixSuite, Genomatix).

3. Results

As previously reported, our group analyzed the effect of the proteasome inhibitor bortezomib [8] on a panel of mantle cell lymphoma cell lines, screening for both alterations of the cel-

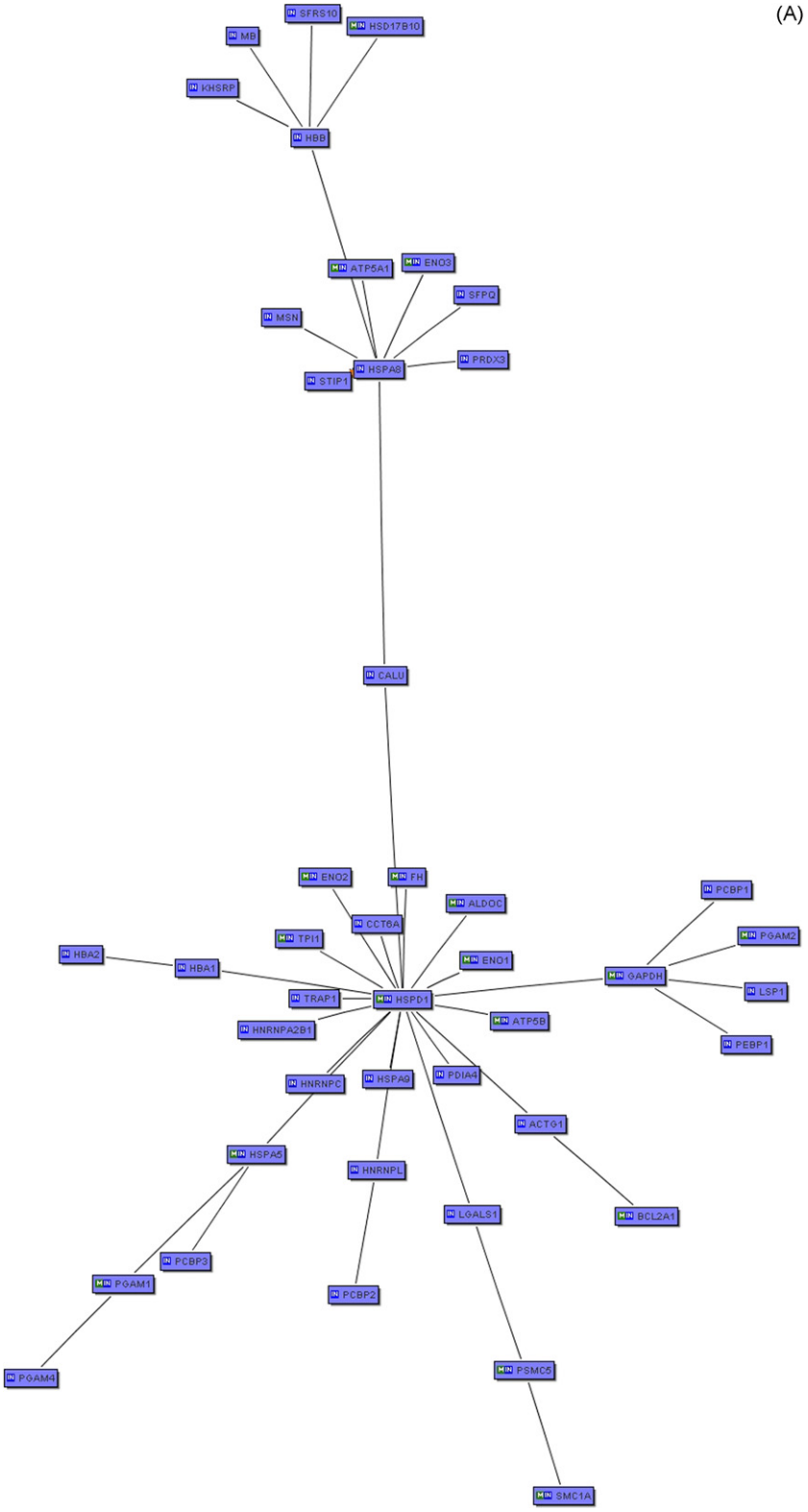


Fig. 1. Example of a network representation of bortezomib treated mantle cell lymphoma cell lines analyzed by BiblioSphere Pathway Analysis (Genomatix, Munich). (A) Interaction network of proteins identified by 2D-PAGE and MALDI-TOF-TOF mass spectrometry. (B) Interaction network of gene expression identified by Affymetrix RNA-expression array. (C) Interaction network of combined lists of RNA-expression and proteomics analysis.

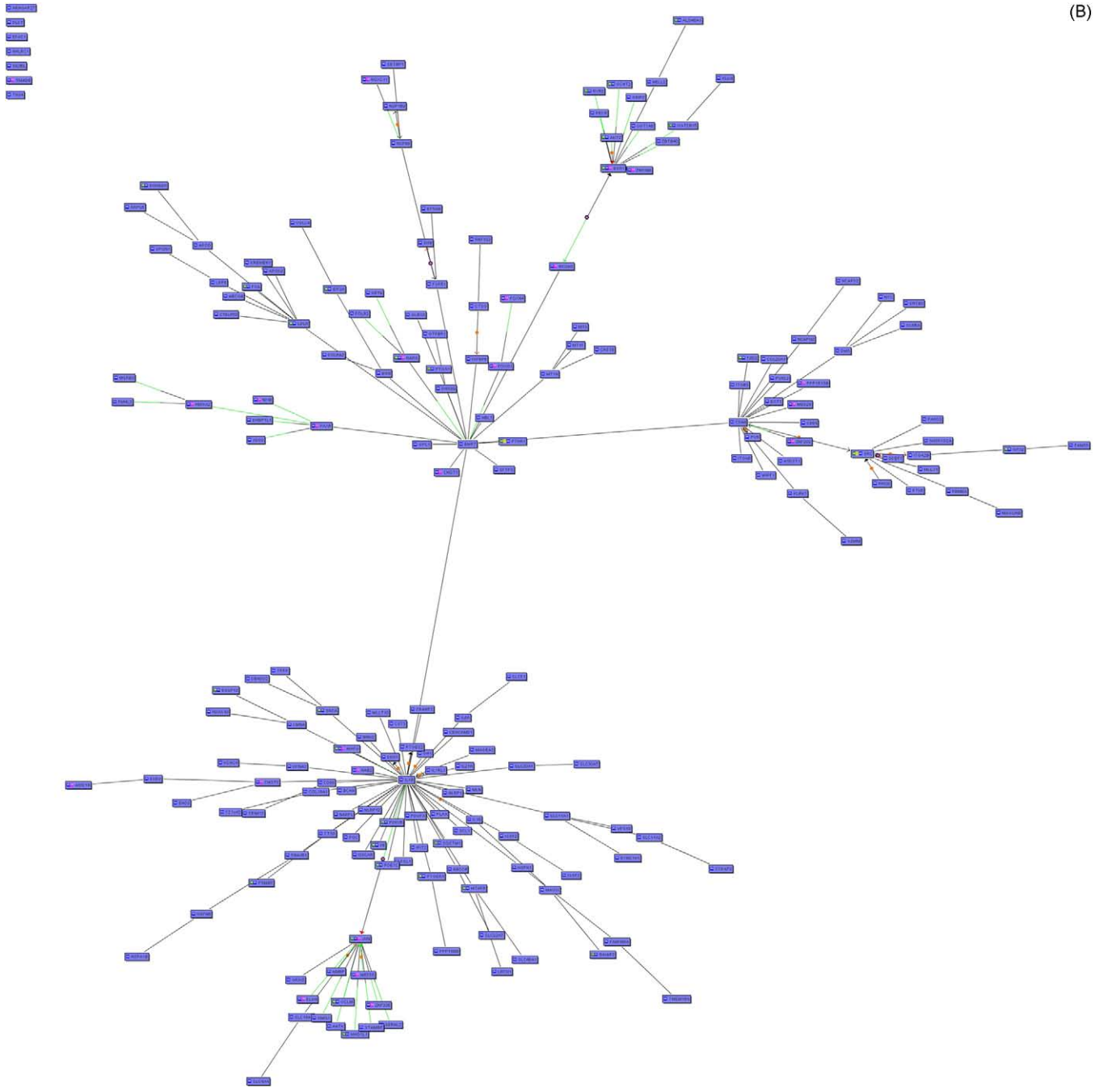


Fig. 1. (*Continued*)

lular protein levels by 2D-PAGE and RNA-expression changes by Affymetrix array 2–8 h after treatment. In addition, we screened for the impact of the protein kinase c beta inhibitor enzastaurin in the same panel of cell lines. Interestingly, the resulting lists of target molecules of each study exhibited no matches between RNA-expression and protein levels but identified a similar set of affected pathways. To elucidate the comprehensive interaction of RNA-expression and cellular protein levels, we created combined lists of gene expression array data and 2D-PAGE-based analysis of cellular protein levels and applied subsequent interaction network analysis in the resulting master list of regulated molecules. In line with our hypothesis, most molecules identified either on the protein level or by RNA array analysis mapped into a combined functional interaction network.

While combining the lists of 75 identified candidate proteins for bortezomib treated MCL with the corresponding gene lists of the RNA-expression array analysis (393 genes) did not identify additional pathways, it highlighted certain cellular regulations (e.g. apoptosis, DNA repair, gene expression) as the impact ranking of certain pathways shifted due to involvement of additional candidate proteins in the network. Using Genomatix BiblioSphere (Genomatix, Munich) for the literature-based network analysis, the individual analysis of the bortezomib proteomics data resulted in a network containing 44 connected proteins of 59 analyzed (Fig. 1A). Additional 15 proteins (25%) remained unrelated to this network. Analysis of the accompanying RNA-microarray analysis resulted in a network of 329 functionally interacting genes (Fig. 1B) with additional 54 independent genes (16%). Combining both sets of genes,

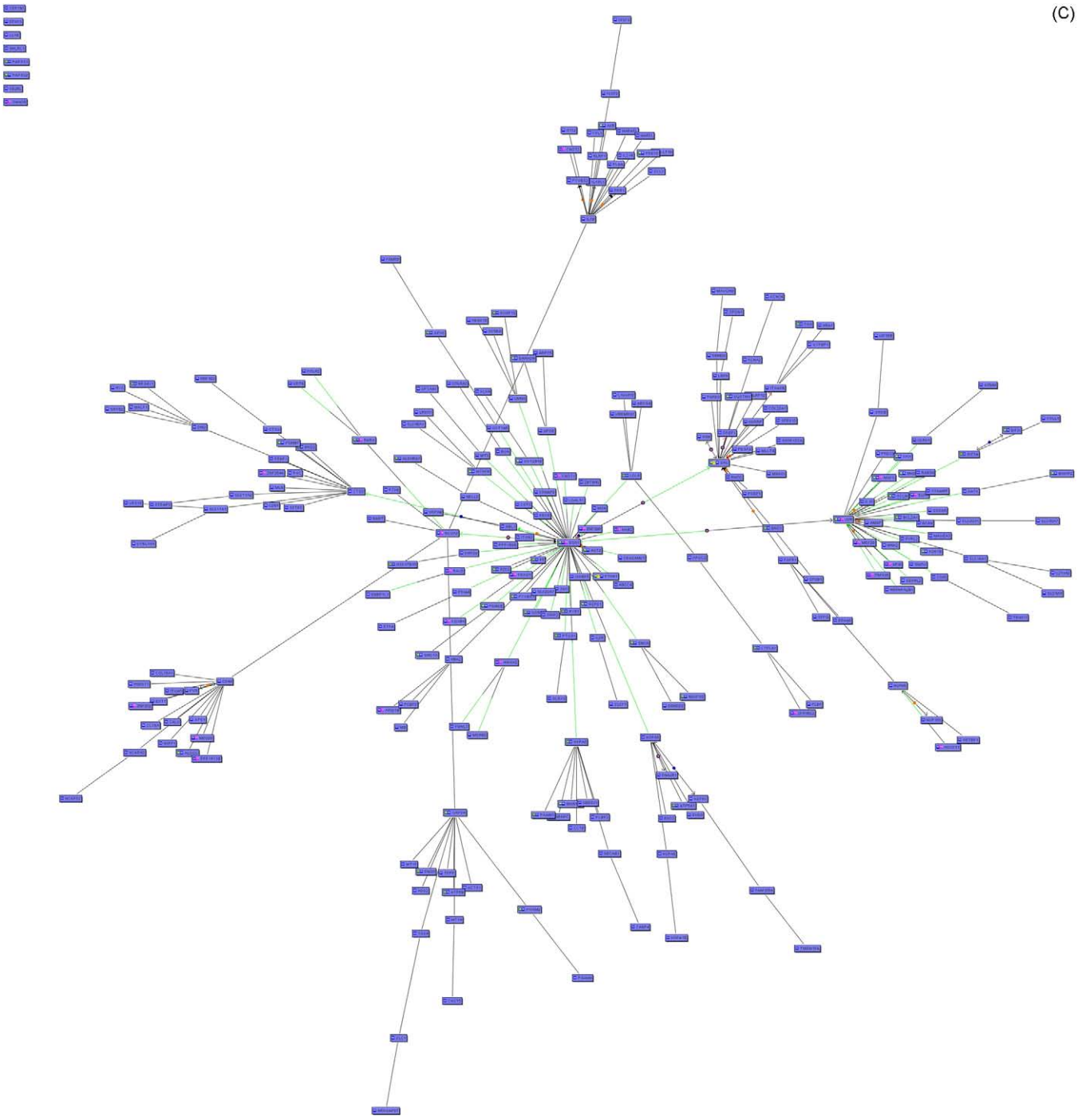


Fig. 1. (*Continued*).

the resulting network encompassed 394 functionally interacting molecules (Fig. 1C), with an additional 51 analyzed genes (13%). Thus, even though the total number of identified molecules did not increase, the number of functionally connected molecules of the interaction network rose to 394. Interestingly, the ranking of involved pathways (based on the number of molecules mapped to a pathway) shifted in the combined analysis to correspond better with the known mode of action of the investigated therapeutics (Fig. 2).

Similar results were also found for enzastaurin treated MCL cells (data not shown).

Combining the lists of 71 candidate proteins for enzastaurin treated MCL identified by 2D-PAGE and mass spectrometry with the corresponding gene lists of the RNA-expression array analysis (180 genes) also highlighted certain cellular regulations (e.g. apoptosis, DNA repair, gene expression) as the impact ranking of certain pathways shifted due to involvement of additional candidate proteins in the network.

In individual analysis, 36 of 56 analyzed proteins identified by 2D-PAGE and mass spectrometry mapped to an interaction network, leaving 20 unrelated proteins. In parallel, RNA-microarray analysis mapped 71 genes to an interaction network with additional 46 independent genes. Combined analysis of proteomics and RNA-expression data again resulted in 14 additional molecules mapped to the interaction network, creating a network of 121 interacting genes. The rate of unrelated molecules in this analysis was also

Proteomics (P) - Score	RNA-Array (R) - Score	Combined Analysis - Score	Pathway
4	10	**14**	**Huntington's Disease Signaling**
0	13	**13**	Axonal Guidance Signaling
3	8	**11**	**Glucocorticoid Receptor Signaling**
9	2	**11**	**Glycolysis/Gluconeogenesis**
1	10	**11**	Integrin Signaling
2	8	**10**	**Actin Cytoskeleton Signaling**
0	9	**9**	Aryl Hydrocarbon Receptor Signaling
0	9	**9**	LPS/IL-1 Mediated Inhibition of RXR Function
2	7	**9**	**NRF2-mediated Oxidative Stress Response**
1	8	**9**	RAR Activation
0	8	**8**	Acute Phase Response Signaling
1	7	**8**	Clatrin-mediated Endocytosis
0	8	**8**	Ephrin Receptor Signaling
2	6	**8**	**Leukocyte Extravasation Signaling**
5	3	**8**	**Purine Metabolism**
1	6	**7**	TR/RXR Activation
0	7	**7**	Xenobiotic Metabolism Signaling
0	6	**6**	14-3-3-mediated Signaling
1	5	**6**	Macropinocytosis
5	1	**6**	Mitochondrial Dysfunction
2	4	**6**	**Tight Junction Signaling**
1	5	**6**	VDR/RXR Activation
0	6	**6**	Wnt/β-catenin Signaling
1	4	**5**	Caveolar-mediated Endocytosis
1	4	**5**	Fcγ Receptor-mediated Phagocytosis in Macrophages and Monocytes
0	5	**5**	FXR/RXR Activation
0	5	**5**	G-Protein Coupled Receptor Signaling
0	5	**5**	Hepatic Fibrosis / Hepatic Stellate Cell Activation
0	5	**5**	IGF-1 Signaling
0	5	**5**	IL-8 Signaling
3	2	**5**	**Protein Ubiquitination Pathway**

Fig. 2. Detail on the functional pathway ranking lists (bortezomib treated MCL cell lines) for proteomics data (P), RNA-microarray data (R) and combined network analysis of both. Pathway rankings reflect the number of genes mapped to this pathway. Pathways indicated exclusively by one analysis method are marked dark grey and white lettering, lighter shades (black lettering) indicate increasingly more additional genes mapped to the pathway due to combined analysis of RNA- and protein level alterations.

reduced (53 molecules; 31% for combined versus 20 (36%) and 46 (39%) for individual analysis runs). Again, the shifted ranking of involved pathways corresponds well with the known mode of action of the investigated therapeutics (data not shown).

4. Discussion

MCL is characterized by a rapid clinical progression and incidence of treatment refractory cases. Although the addition of the anti-CD20 antibody Rituximab to standard chemotherapy regimens has been shown to increase initial response rates, therapy options remain limited [1].

The proteasome inhibitor bortezomib is the first biological compound to gain approval of the FDA for treatment of relapsed and refractory MCL [2]. In addition it has been reported to act synergistically with several other biological compounds [10,11] as well as standard therapy regimens [6,12]. Enzastaurin, another promising new compound achieved disease stabilization in relapsed and refractory MCL [3].

Characterization of the drug effect, including primary target molecules as well as the affected signalling pathways will finally allow prediction of susceptibility as well as development of optimal combinations of biologicals targeting interacting pathways thereby acting synergistic. One example may be the combination of cell cycle inhibitors and proapoptotic compounds [13]. Especially in MCL, with the variable degree of cell cycle alteration in different tumours and accordingly varying susceptibility to treatment, another layer of complexity is added. Thus it is essential to concisely elucidate the affected signalling pathways and molecular functions.

Existing screening methods achieve this goal to a certain degree, but represent a view biased by the analyzed molecule. Proteomics commonly suffers from experimental bias as certain proteins possess limited solubility or might remain attached to plasma membranes and are thus not resolved by 2D-PAGE. On the other hand, RNA-expression arrays miss post-transcriptional processes, such as the regulation of cellular damage pathways. Such cellular damage signalling can be divided in two distinct but inter-connected stages: a fast emergency shutdown of cellular progression mediated by a disruption of normal protein homeostasis to prevent further damage and a slightly slower induction of physiological cellular repair mechanisms by activation of damage-signalling dependent gene expression [14]. In these two cell programmes altered protein levels act as inducers of gene expression and vice versa. Especially in most cases of therapeutic cancer treatment normal cellular function is massively disrupted by induction of DNA-damage (alkylating agents), inactivation of essential cellular enzymes (inhibition of the proteasome or cellular phosphatases) or direct activation of external death signals (therapeutic antibodies), resulting in cell death or growth inhibition.

We combined the involved candidate molecules of simultaneous RNA-expression-array- and protein-expression analysis in a comprehensive interaction network analysis. Especially for the proteasome inhibitor bortezomib most expression alterations are

represented on the protein level. Therefore, we selected an early time-point (4 h) to minimize the secondary influence of altered RNA-expression on the protein level, while still detecting early RNA-expression alterations in the microarray analysis. The absence of genes indicated simultaneously by protein and RNA screening confirms that the secondary impact of gene expression on the cellular protein levels is still limited at this early time-point. Thus our study represents two distinct regulation pathways of cellular response targeting either gene transcription identified by RNA array analysis or direct protein interaction as detected by 2D-PAGE analysis. However, the identified candidate molecules map to common interaction pathway networks.

Especially in the case of unspecific therapeutic agents, alternate unrelated triggering events might also converge to signal in a common response pathway and passing parallel checkpoints [4,5,15]. The combined analysis of these two mechanisms of cellular response resulted in a more comprehensive interaction network than the analysis on RNA or protein level. This is reflected by the involvement of additional molecules in the identified interaction network. In our study such a combined approach resulted in 21 additional molecules included into the identified interaction networks in bortezomib treated MCL cell lines. Accordingly, the number of unmapped genes was significantly diminished (25% and 16% respectively to 13%). Whether these observations may be also transferred to DNA-damaging agents or gene therapy approaches (including therapeutic anti-sense oligonucleotides) remains to be confirmed, as those treatment strategies directly interfere with gene expression, thereby avoiding direct protein-mediated regulation.

Role of the funding source

This work was supported by the European Union: 6.FP, Translational research on promising predictive and prognostic markers: “European MCL Network” (contract no. 503351).

E.H. and A.R. are supported by the Interdisciplinary Center for Clinical Research (IZKF) of the University of Wuerzburg, Germany.

The authors have declared no conflict of interest due to the funding sources.

Disclosure

There is no conflict of interest concerning this publication (all authors).

References

[1] M. Dreyling, O. Weigert, W. Hiddemann, Ann. Oncol. 19 (Suppl. 4) (2008) iv41–iv44.
[2] A. Goy, S.H. Bernstein, B.S. Kahl, B. Djulbegovic, M.J. Robertson, S. de Vos, E. Epner, A. Krishnan, J.P. Leonard, S. Lonial, S. Nasta, O.A. O'Connor, H. Shi, A.L. Boral, R.I. Fisher, Ann. Oncol. 20 (2009) 520–525.
[3] F. Morschhauser, J.F. Seymour, H.C. Kluin-Nelemans, A. Grigg, M. Wolf, M. Pfreundschuh, H. Tilly, J. Raemaekers, M.B. van't Veer, N. Milpied, G. Cartron, A. Pezzutto, A. Spencer, F. Reyes, M. Dreyling, Ann. Oncol. 19 (2008) 247–253.
[4] P. Perez-Galan, G. Roue, N. Villamor, E. Campo, D. Colomer, Blood 109 (2007) 4441–4449.
[5] K.W. Lee, S.G. Kim, H.P. Kim, E. Kwon, J. You, H.J. Choi, J.H. Park, B.C. Kang, S.A. Im, T.Y. Kim, W.H. Kim, Y.J. Bang, Cancer Res. 68 (2008) 1916–1926.
[6] O. Weigert, A. Pastore, M. Rieken, N. Lang, W. Hiddemann, M. Dreyling, Leukemia 21 (2007) 524–528.
[7] M. Weinkauf, M. Christopeit, W. Hiddemann, M. Dreyling, Electrophoresis 28 (2007) 4416–4426.
[8] M. Weinkauf, Y. Zimmermann, E. Hartmann, A. Rosenwald, M. Rieken, A. Pastore, G. Hutter, W. Hiddemann, M. Dreyling, Electrophoresis 30 (2009) 974–986.
[9] A. Rosenwald, L.M. Staudt, Leuk. Lymphoma 44 (Suppl. 3) (2003) S41–S47.
[10] L. Paoluzzi, M. Gonen, G. Bhagat, R.R. Furman, J.R. Gardner, L. Scotto, V.D. Gueorguiev, M.L. Heaney, K. Manova, O.A. O'Connor, Blood 112 (2008) 2906–2916.
[11] U. Heider, I. von Metzler, M. Kaiser, M. Rosche, J. Sterz, S. Rotzer, J. Rademacher, C. Jakob, C. Fleissner, U. Kuckelkorn, P.M. Kloetzel, O. Sezer, Eur. J. Haematol. 80 (2008) 133–142.
[12] M. Wang, X.H. Han, L. Zhang, J. Yang, J.F. Qian, Y.K. Shi, L.W. Kwak, J. Romaguera, Q. Yi, Leukemia 22 (2008) 179–185.
[13] V. Fernandez, E. Hartmann, G. Ott, E. Campo, A. Rosenwald, J. Clin. Oncol. 23 (2005) 6364–6369.
[14] M. Blank, Y. Shiloh, Cell Cycle 6 (2007) 686–695.
[15] D.J. McConkey, K. Zhu, Drug Resist. Updat. 11 (2008) 164–179.

Talanta 80 (2010) 1545–1551

Contents lists available at ScienceDirect

Talanta

journal homepage: www.elsevier.com/locate/talanta

Evaluation of sample preparation protocols for proteomic analysis of sunflower leaves

Marcelo Anselmo Oseas da Silva[a,b], Jerusa Simone Garcia[c], Gustavo Henrique Martins Ferreira de Souza[c,d], Marcos Nogueira Eberlin[c], Fábio César Gozzo[e], Marco Aurélio Zezzi Arruda[a,b,*]

[a] Group of Spectrometry, Sample Preparation and Mechanization (GEPAM), Institute of Chemistry, PO Box 6154, University of Campinas, UNICAMP, 13084-862, Campinas, SP, Brazil
[b] National Institute of Science and Technology for Bioanalytics, Institute of Chemistry, University of Campinas, UNICAMP, PO Box 6154, 13083-970, Campinas, SP, Brazil
[c] ThoMSon Mass Spectrometry Laboratory, Institute of Chemistry, PO Box 6154, University of Campinas, UNICAMP, 13084-862, Campinas, SP, Brazil
[d] Department of Pharmacology, Faculty of Medical Sciences, PO Box 6111, University of Campinas, UNICAMP, 13083-887, Campinas, SP, Brazil
[e] Department of Organic Chemistry, Institute of Chemistry, PO Box 6154, University of Campinas, UNICAMP, 13084-862, Campinas, SP, Brazil

ARTICLE INFO

Article history:
Available online 12 June 2009

Keywords:
2D electrophoresis
Sunflower
Sample preparation
MALDI-Q-TOF MS
Cross species identification

ABSTRACT

Six protocols for extraction of proteins from sunflower (*Helianthus annuus* L.) leaves were evaluated for their abilities in both removing interferents and attaining the best resolution in two-dimensional gel electrophoresis. "Classical" phenol extraction followed by precipitation with ammonium acetate in methanol displayed the most efficient protocol, which allowed the detection of 244 protein spots with *ca.* 485 μg of protein in gel electrophoresis. Tandem mass spectrometry was performed to identify proteins in 61 spots, and cross species identification was used for this task. Proteins from twenty two spots were identified, and 12 of these proteins are up to now not included into the ExPASy sunflower protein databank.

© 2009 Elsevier B.V. All rights reserved.

1. Introduction

Proteomics is currently one of the most preeminent areas in science [1,2]. To explore and fully understand each aspect involved in proteomic studies is a hard and complex task, but a myriad of case studies have put in evidence a profitably synergism that places proteomics as an important multidisciplinary and interdisciplinary area with many applications [3,4]. Despite all efforts and developments achieved recently in protein separation, purification, characterization and quantification [5–8], sample preparation is the first and perhaps most fundamental step in protein analysis. Proteins are variable in their physicochemical properties and relatively unstable molecules, being located in every one of the many compartments of a cell, and in a variety of forms with different masses and pIs. When dealing with plants tissues, these molecules are commonly purified in the presence of interferents such as polyphenols, pigments, terpenes, and lignins. A general sample preparation protocol for protein extractions and clean-up is therefore nearly unfeasible. Customized sample preparation protocols must therefore be developed to achieve reliable proteomic profiles, particularly when most complex matrices [9,10] are handled as now widely recognized in the proteomic field [11,12].

In plant materials, when the targets are the leaf tissue proteins, sample handling is particularly laborious and therefore crucial owing to both lower protein content (as compared to bacterial or animal tissues), and the presence of large amounts of non-protein components [13]. The presence of these interferents can compromise two-dimensional gel electrophoresis (2-DE) separations, requiring customized experimental strategies for each plant [11,14]. Sample preparation for 2-DE protein separation usually takes several steps and reagents. Protein solubilization requires normally three major steps: (1) extraction of proteins from biological sample, (2) removal of interferents, and (3) preservation of proteins in solution until the separation process is finished [11].

Several sample preparation protocols applied to leaves from different species have been reported [15,16]. However, an evaluation of different protein extraction protocols from sunflower (*Helianthus annuus* L.) leaves, and their 2-DE separations, is apparently not available. Sunflower is of strategic importance owing to its high protein content and wide use in oil production and remediation processes [17–19]. Herein we report on a study aimed to evaluate some protocols for sunflower protein extraction for optimal proteomic analysis.

* Corresponding author at: Group of Spectrometry, Sample Preparation and Mechanization (GEPAM), Institute of Chemistry, PO Box 6154, University of Campinas, UNICAMP, 13084-862, Campinas, SP, Brazil. Tel.: +55 19 3521 3089; fax: +55 19 3521 3023.
E-mail address: zezzi@iqm.unicamp.br (M.A.Z. Arruda).

0039-9140/$ – see front matter © 2009 Elsevier B.V. All rights reserved.
doi:10.1016/j.talanta.2009.06.016

2. Materials and methods

2.1. Reagents and sample

Reagents employed in electrophoretic separations (acrylamide, bis acrylamide, DTT, iodoacetamide, urea, thiourea, ampholytes, strips for isoelectric focusing, mineral oil) were from Amersham Biosciences (Uppsala, Sweden). Mass spectrometry grade trypsin was from Promega (Madison, USA). All other chemical (including mineral acids, reagents for buffers preparation and gel stain) were obtained from J.T. Baker (Phillipsburg, NJ, USA) and Merck (Darmstadt, Germany). All solutions were prepared with deionized water ($\geq$18.2 MΩ cm) using a Milli-Q water purification system (Millipore, Bedford, USA).

Sunflower leaves (*Helianthus annuus* L.) were cultivated under ambient conditions (during 40 days as described by Garcia et al. [20]) and using plastic pots containing 400 g of soil at average temperatures from 18 to 24 °C (night and day, respectively). In the specific case of this work, the irrigation was carried out using deionized water only. After harvested, the plants were immediately frozen in liquid nitrogen and stored at −80 °C.

2.2. Protein extraction protocols

For each extraction procedure, 1.0 g of fresh wet leaf was grounded in a mortar with liquid nitrogen and an adequate volume of extraction mixture was then added.

Protocols P1 and P2 were based on Bellato et al. [21] excepting the addition of charged ions, as $MgCl_2$, allowing the isoelectric focusing of the proteins. In this way, 3.0 mL of a solution containing 50 mmol L^{-1} Tris–HCl (pH 8.8), 10 mmol L^{-1} DTT, 10 mmol L^{-1} phenylmethanesulphonylfluoride (PMSF) and 0.1% (w/v) SDS was added to the grounded material and mixed with a vortex for 20 min. The remaining insoluble material was then removed by centrifugation at 8500 × *g* (4 °C) for 5 min in a model Bio-Spin-R ultracentrifuge (BioAgency, São Paulo, Brazil) and then a precipitation step was carried out. Acetone/methanol (3:1, v/v) as well as 100 mmol L^{-1} ammonium acetate in methanol, both solutions at −20 °C, were respectively employed as precipitant agents for P1 and P2 protocols. Mixtures were kept at −20 °C overnight until the pellets formation. Then, supernatants were removed and pellets dissolved in an adequate volume (250 μL) of a typical two-dimensional electrophoresis buffer (2-DE buffer) containing 7 mol L^{-1} urea, 2 mol L^{-1} thiourea, 2% (w/v) CHAPS, 0.002% (w/v) bromophenol blue, 0.5% (v/v) ampholytes (pH from 3 to 10) and 1% (w/v) DTT.

Protocols P3 and P4 were based on that reported by Garcia et al. [20] and Carpentier et al. [22] with a modification in the SDS concentration (50% lower). In these protocols 3.0 mL of a solution containing 125 mmol L^{-1} Tris–HCl (pH 6.8), 1.0% (w/v) SDS, 1.0% (v/v) glycerol and 0.5% (v/v) β-mercaptoethanol was used. The procedure for protein extraction and insoluble material removal was the same as described in P1 and P2 protocols. Then, a clean-up step was carried out. Solutions containing 100 mmol L^{-1} ammonium acetate in cold methanol, as well as 20% (w/v) TCA + 0.2% (w/v) DTT in acetone were respectively used for P3 and P4 protocols. Tubes were kept incubated overnight at −20 °C and then centrifuged at 1800 × *g* for 5 min (4 °C). Supernatants were removed and the pellets were washed three times with cold acetone containing 0.2% (w/v) DTT. The mixtures were incubated at −20 °C for 1 h before centrifugation, employing the same conditions described above, and the pellets were dissolved with 2-DE buffer.

Protocols P5 and P6 can be considered as classical protocols for protein extraction from vegetal tissues [11]. P5 protocol, based on Xie et al. [23] comprises the TCA/acetone extraction. 4.0 mL of extraction buffer containing 10% (w/v) TCA and 0.07% (v/v) β-mercaptoethanol in acetone was added to the sample. The mixture was kept overnight at −20 °C and a 5-min centrifugation was carried out at 8700 × *g* (4 °C). The buffer was removed and the resulting material was 8 times washed with cold acetone and then dried with nitrogen. 250 μL of 2-DE buffer was added to the pellet and the mixture was 5-min vortexed. A 5-min centrifugation at 8500 × *g* was carried out and the supernatant was subsequently employed for electrophoretic separations.

Protocol P6 used a phenol based extraction protocol according to Delaplace et al. procedure [24] with a minor modification: 4.0 mL of protein extraction buffer containing 700 mmol L^{-1} sucrose, 50 mmol L^{-1} EDTA, 100 mmol L^{-1} KCl, 10 mmol L^{-1} thiourea, 50 mmol L^{-1} DTT, 2 mmol L^{-1} PMSF dissolved in 500 mmol L^{-1} Tris–HCl at pH 7.5 was added to the grounded material. This mixture was centrifuged at 6000 × *g* (4 °C) for 10 min. Proteins contained in the supernatant were collected and subsequently extracted using the same protein extraction buffer (at pH 7.5) saturated with phenol. This step consisted in the major difference between our protocol and that one proposed by Delaplace [24]. The phenolic mixture was homogenized and centrifuged at 6000 × *g* (4 °C) for 10 min. Phenolic phase (upper phase) was then collected, and those proteins present in this phase were extracted twice after addition of 5.0 mL of protein extraction buffer. The solutions were homogenized using a vortex mixer and centrifuged again at 6000 × *g* (4 °C) for 10 min. The upper phenolic phase was collected and a protein precipitation step using 10 mL of 100 mmol L^{-1} ammonium acetate in methanol was performed. This mixture was kept overnight and subsequently centrifuged at 8700 × *g* (4 °C) for 5 min. The pellet was washed with 4.0 mL of 100 mmol L^{-1} ammonium acetate in methanol, centrifuged at 8700 × *g* and dissolved with 2-DE buffer.

After application of each protocol, total protein concentrations were determined according to the Bradford method [25] using bovine serum albumin fraction V as standard. In this case, the pellets were solubilized into 100 mmol L^{-1} phosphate buffer at pH 7.2 previously to the measurement.

2.3. Two-dimensional gel electrophoresis separation

IPG strips for isoelectric focusing—IEF (13 cm length, pH 3-10, Immobiline™ DryStrip Amersham Biosciences, Uppsala, Sweden) were rehydrated overnight at room temperature with 250 μL of 2-DE buffer containing adequate mass of protein (ranging from 448 to 485 μg). IEF was performed using a Multiphor II system (Amersham Biosciences, Uppsala, Sweden) as follow: (1) step to 500 V (0.5 kVh); (2) gradient to 1000 V (0.8 kVh); (3) gradient to 10,000 V (11.3 kVh); (4) step to 10,000 V (3.0 kVh). After isoelectric focusing, proteins were reduced with 1.0% (w/v) DTT, dissolved into equilibration buffer (50 mmol L^{-1} Tris–HCl pH 8.8, 6 mol L^{-1} urea, 30% (v/v) glycerol and 2.0% (w/v) SDS) for 15 min, and alkylated with 2.5% (w/v) iodoacetamide in the equilibration buffer for 15 min. SDS-PAGE was carried out employing a 12.5% (w/v) polyacrylamide gel on the Ettan™ DALT system with 1 mm lab cast (Amersham Biosciences, Uppsala, Sweden). Constant voltage of 90 V and 25 mA per gel were applied overnight. Protein spots were visualized after staining with colloidal CBB G-250 [26]. The gels were scanned using an ImageScanner II (Amersham Biosciences, Uppsala, Sweden) with the densitometer operating at 300 dpi resolution and the ImageMaster 2D Platinum 6.0 software (GeneBio, Geneva, Switzerland) was employed to gel image analysis.

2.4. Tandem mass spectrometry (MS/MS) analysis

As accurate protein identification is dependent on the gel resolution, 61 spots from the gel obtained with the best protein extraction protocol (P6) were randomly chosen once that little information is achieved in the sunflower protein databank. For this task, the

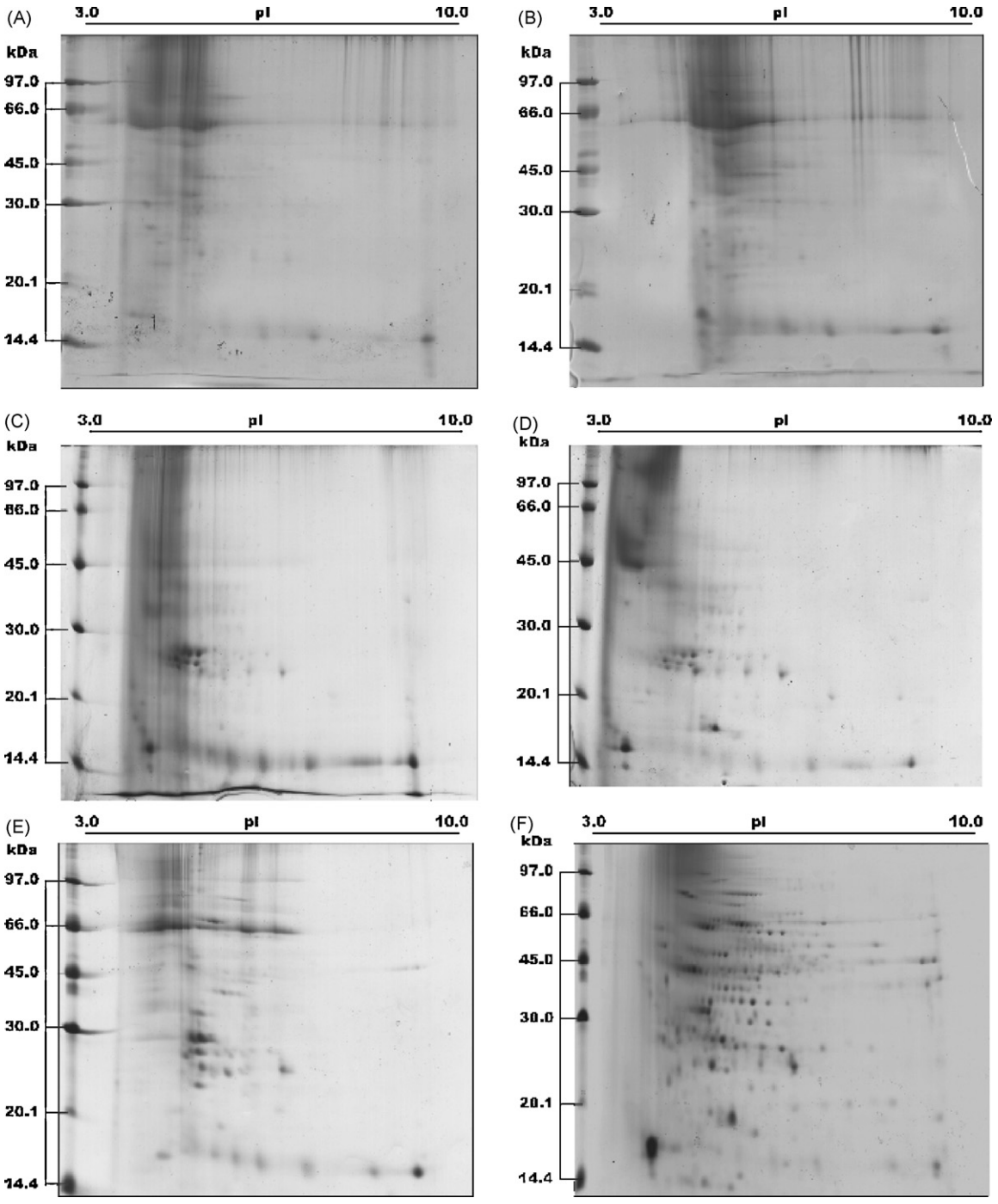


Fig. 1. Gel electrophoresis profiles obtained from P1 (A); P2 (B); P3 (C); P4 (D); P5 (E) and P6 (F) protocols.

spots (*ca*. 2 mm) were manually cut from the gel and placed into a micro-SPE plate containing peptide affinity resin—Montage® In-Gel digest$_{ZP}$ kit (Millipore, MA, USA). The digestion and vacuum elution protocols were performed according to the manufacture's recommendations. Basically, a dye removal step using acetonitrile was firstly employed followed by the tryptic digestion (using *ca*. 166 ng of enzyme for each spot). Then, a clean-up step was carried out using 330 μL of 0.2% TFA solution. Finally, purified peptides were eluted from resin using 20 μL of acetonitrile. For vacuum elution, a Multiscreen® Vacuum Manifold (Millipore, MA, USA) was used.

After tryptic digestion, the resulting peptides were analyzed using the dried droplet method. 1 μL of each sample was mixed with the same volume of MALDI matrix (1% (w/v) α-cyano-4-hydroxycinnamic acid dissolved into 1:1 (v/v) acetonitrile:water solution containing 0.1% (v/v) TFA). The mixture was immediately spotted to the MALDI plate and dried at room temperature until complete solvent evaporation.

Mass spectra were acquired in the positive mode using a MALDI-Q-TOF Premier mass spectrometer (Waters—Micromass, Manchester, UK) and a Nd:YAG laser (337 nm) MALDI source. Lock-Mass correction was performed with PEG 800. The following main parameters were used: laser firing rate of 200 Hz, mass range of 880.0–3000.0 Da, peak detection threshold for MS/MS of 1500.0, mass threshold of 200 Da, scan time of 2 s, Np multiplier set to 0.70, resolution of 10,000 with "V" mode, trigger threshold of 700, signal threshold of 80 and microchannel plate (MCP) set to 2100 V. Spectra

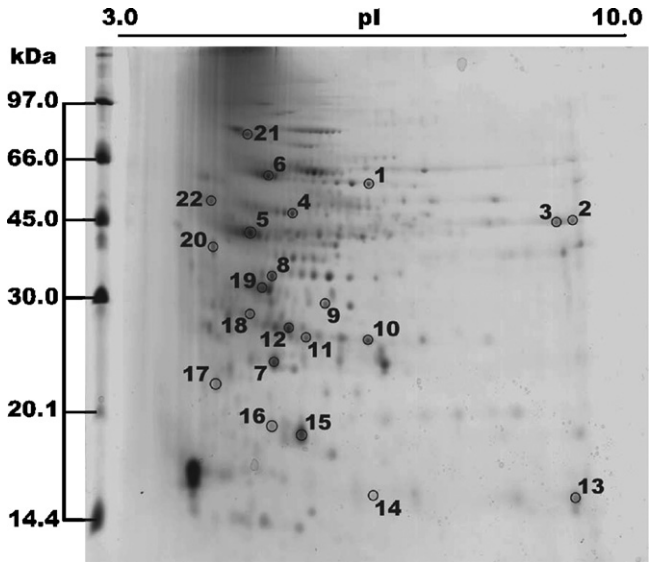


Fig. 2. 2-D gel map of proteins tentatively identified from sunflower leaves by MALDI-Q-TOF MS. Proteins were extracted using the P6 protocol and circled spots were identified.

were collected over 2 s scans, and accumulated over *ca.* 2 min using argon as collision gas. Typical collision energies ranging from 34 to 161 eV were employed. The instrument was controlled by MassLynx 4.1 software and all MS spectra were processed into peak lists files with *.pkl extension using ProteinLynxGlobalServer 2.2.5v (Waters, UK).

Peptides identification was achieved employing MASCOT Distiller software (Matrix Science, London, UK) for improving peak detection by attempting to match an ideal isotopic distribution to the experimental data, followed by MASCOT Server database search engine (Matrix Science, London, UK) [27] using a public sunflower gene databank containing *ca.* 151,000 EST sequences compiled from Plant Genome DataBase [28]. MS/MS search parameters included oxidation of methionine as variable modification, carbamidometylation of cysteine as fixed modification, ±0.1 Da peptide and fragment mass tolerance, and maximum of one missed cleavage. The significance threshold was set at $P < 0.05$, which correspond to a minimum score of 37.

The peptides determined by tandem MS were then used to determine sunflower gene sequences and posterior searching for homologous proteins (cross species identifications) using NCBI's Basic Local Alignment Search Tool (BLAST). Default configurations and no filters were used for BLAST searches.

3. Results and discussion

3.1. Protein extraction methods results

Protocols P1 and P2 were quite inefficient for protein extraction from sunflower leaves. Only 15 protein spots were visualized for P1 protocol, and 24 spots for P2 protocol as showed in the gels (Fig. 1A and B, respectively). In the referred cases, the majority of the extracted proteins presented acidic characteristics.

Protocols P3 and P4 used a lysis buffer comprising β-mercaptoethanol. Although this chemical shows lower efficiency as a reducing agent than DTT, better results (than P1 and P2 protocols) were obtained in terms of variety and quantity of extracted sunflower leaves proteins. This improvement may be attributed to the differences on pH extraction values of P3 and P4 when compared to P1 and P2 protocols. Using P3 protocol, gels with *ca.* 41 detected

Table 1
Spot identification and their comparison with the highest homology protein in NCBI database.

Spot number	Probable protein definition[a]	Homologue protein			Estimated experimental molar mass (kDa)	Peptide coverage of protein (%)
		Genus and specie	ExPASy accession code	Expected molar mass (kDa)		
1	**Putative alanine aminotransferase**	*Vitis labrusca*	CAO16115	53	56	10
2	**Peroxisomal glycolate oxidase**	*Glycine max*	BAG09382	41	45	13
3	**Glycolate oxidase**	*Arabidopsis thaliana*	NP_188059	42	44	18
4	Phosphoglycerate kinase	*Nicotiana tabacum*	Q42961	50	47	20
5	Unnamed protein product	*Vitis vinifera*	CAO17011	42	42	24
6	ATP synthase beta subunit	*Protea cynaroides*	ABO43930	53	59	14
7	**Triose-phosphate isomerase**	*Arabidopsis thaliana*	AAF70259	32	34	13
8	**N-glyceraldehyde-2-phosphotransferase-like**	*Arabidopsis thaliana*	BAA97552	39	33	15
9	Unnamed protein product	*Vitis vinifera*	CAO15661	28	26	13
10	**Ribulose-phosphate-epimerase**	*Solanum tuberosum*	CAA90426	31	26	7
11	**Triose phosphate isomerase cytosolic isoform-like**	*Solanum tuberosum*	ABB02628	27	27	8
12	**Triose-phosphate isomerase**	*Arabidopsis thaliana*	NP_179713	33	24	13
13	Ribulose bisphosphate carboxylase/RuBisCO	*Helianthus annuus*	P08705	20	15	6
14	Nucleoside diphosphate kinase	*Helianthus annuus*	Q96559	16	15	10
15	Cu/Zn superoxide dismutase precursor	*Helianthus annuus*	CAH06449	20	18	9
16	Cu/Zn superoxide dismutase precursor	*Helianthus annuus*	CAH06449	20	19	11
17	**Thioredoxin peroxidase**	*Nicotiana tabacum*	CAC84143	29	22	29
18	**Oxygen evolving complex 33 kDa photosystem II protein**	*Nicotiana tabacum*	AAP03871	35	28	18
19	**Putative peroxidase**	*Zinnia elegans*	CAI54300	34	31	20
20	**Putative peroxidase**	*Zinnia elegans*	CAI54300	34	37	26
21	Chloroplast heat shock protein	*Ipomonea nil*	ABZ04081	74	77	18
22	Chloroplast heat shock protein	*Ipomonea nil*	ABZ04081	74	50	18

[a] Protein in bold denote its absence in the sunflower protein databank.

Table 2
Identified peptides and confidence levels obtained after MASCOT and Blast searches. Scores are based on each software algorithm. Bold highlighted aminoacids indicate identity with the homologue protein sequence; aminoacids succeeded by (*) indicate similarity with their homologue. The columns % identity/similarity (partial) show the correlation percentage between identified peptides sequences and peptides sequences of the homologue proteins; columns of peptides overall identity/similarity (%) show the number of aligned aminoacids in Blast and their correlation percentage (shown in parenthesis).

Spot number	Identified peptides sequences	Sunflower gene accession code	MASCOT scores	Homologue protein match				
				Blast scores–bits (e values)	% identity (partial)	% similarity (partial)	Peptides overall identity (%)	Peptides overall similarity (%)
1	**K.EGVFHLR.T** **K.G**F*L**GECGQR.G** **K.V**P**DVFYCLK.L**	gi|22459149	74	395 (1e−108)	100 82 91	100 91 91	188 (87)	207 (96)
2	**R.VPVFLDGGVR.R** **R.**L*A**I***Q**A***GAAGIIVSNHGAR.Q**	gi|22310690	68	179 (1e−43)	100 85	100 100	90 (93)	96 (100)
3	**R.VPVFLDGGVR.R** **R.**D***HIVTEWDA**PR.**A** **R.**L***AIQAGAAGIIVSNHGAR.Q**	gi|32530022	153	343 (7e−93)	100 77 95	100 85 100	176 (91)	183 (95)
4	**K.YSLAPLVPR.L** **K.RPFAAIVGGSK.V** **K.VILSSHLGRPK.G** **R.ADLNVPLDDNQNITDDTR.I**	gi|90443727	209	404 (3e−111)	100 100 100 100	100 100 100 100	210 (84)	229 (91)
5	**K.MFSPGNLR.A** **K.**M***FSPGNLR.A** **R.FEETLYGSSR.L** **R.DQVAAAMGIYGPR.T** **R.ATFDNPDYDKLINYYVK.E**	gi|22308388	177	355 (7e−97)	100 90 100 100 100	100 100 100 100 100	173 (89)	186 (96)
6	**K.VVDLLAPYR.R** **K.AHGGVSVFGGVGER.T** **K.VALVYGQMNEPPGAR.M**	gi|125406600	94	353 (3e−124)	100 100 100	100 100 100	180 (94)	184 (96)
7	K*.**.FFVGGNWK.C** **K.WVILGHSER.R** K.**VAS***P**E***QAQEVHVAVR.D**	gi|22461563	184	408 (2e−112)	90 100 82	100 100 94	199 (85)	214 (91)
8	**R.YFNYYK.V** **K.VQYGTLC**V***R.E** **R.ENPGCLF**L***ATNR.D** **K.LIDGVPETL**E*L***LR.S**	gi|113176214	164	324 (3e−87)	100 91 93 80	100 100 100 100	178 (80)	186 (86)
9	**K.**S***LF**A***QIT***S***R.F** **R.ELLVGKDDELL**Q***TETR.T** **R.KAEQYLADSGIPYTIIR.A**	gi|90457285	155	432 (2e−119)	64 94 100	100 100 100	211 (85)	232 (93)
10	**K.AGADIVSVHCEQSSTIHLHR.T**	gi|113183739	71	411 (3e−113)	100	100	212 (88)	223 (92)
11	**K.VASPAQAQEVHA**G**LR.K**	gi|90461820	65	440 (5e−122)	94	94	212 (84)	236 (94)
12	**K.FFVGGNWK.C** **K.WVILGHSER.R** **K.VASP**E***QAQEVHVAVR.**D	gi|22461563	196	412 (1e−113)	100 100 88	100 100 94	200 (85)	216 (92)
13	**R.IIGFDNVR.Q** **K.EYPQAWIR.I**	gi|32530202	103	115 (4e−24)	100 100	100 100	53 (100)	53 (100)
14	**R.GDFAIDIGR.N** **K.IIGATNP**A**ESAPGTIR.G**	gi|32532684	77	263 (8e−69)	100 94	100 94	143 (99)	143 (99)
15	**R.ALVVHELADDLGK.G** **K.GGHELSLSTGNAGGR.L**	gi|33130416	87	343 (1e−92)	100 100	100 100	199 (98)	202 (100)
16	**K.GGHELSLSTGNAGGR.L**	gi|33127814	55	70 (4e−11)	100	100	33 (100)	33 (100)
17	**K.**A***F***NVLI**E**DQGIALR.G** **K.EGVIQHSTINNL**A**IGR.S**	gi|22311529	95	174 (2e−42)	81 94	94 94	86 (93)	90 (97)
18	**R.VPFLFTV*K.**E* **K.RLTFDEIQSK.T** **K.DGIDYAAVTVQLPGGER.V** **K.**E***LVA**T***GPPE**N***FSGEFLVPSYR.G**	gi|90444512	160	487 (5e−136)	80 100 100 83	100 100 100 96	245 (85)	264 (91)
19	**R.DASVAVGGPSWTVR.L** **R.EMVALSGSHTLGQAR.C** **K.AAVE**S**VCPGVVSCADILAVAAR.D**	gi|22312177	125	358 (2e−97)	100 100 96	100 100 96	183 (80)	197 (87)
20	**R.DASVAVGGPSWTVR.L** **R.EMVALSGSHTLGQAR.C** **K.**M**SEI**E**VL***TGTSGI**I***R.T** **K.AAVE**S**VCPGVVSCADILAVAAR.D**	gi|32530590	209	358 (2e−97)	100 100 82 96	100 100 94 100	183 (80)	197 (87)

Table 2 (*Continued*)

Spot number	Identified peptides sequences	Sunflower gene accession code	MASCOT scores	Homologue protein match				
				Blast scores–bits (e values)	% identity (partial)	% similarity (partial)	Peptides overall identity (%)	Peptides overall similarity (%)
21	**K.QFAAEEISAQVLR.K** **K.AVVTVPAYFNDSQR.T** **R.IINEPTAASLAYGFER*.K**	gi|22394523	78	454 (3e−126)	100 100 94	100 100 100	231 (96)	234 (99)
22	**K.QFAAEEISAQVLR.K** **K.AVVTVPAYFNDSQR.T** **R.IINEPTAASLAYGFER*.K**	gi|22394523	104	454 (3e−126)	100 100 94	100 100 100	231 (96)	234 (99)

spots were obtained (see Fig. 1C), while P4 protocol resulted in gels with *ca*. 64 spots (see Fig. 1D).

Poor separation obtained with P1, P2, P3 and P4 protocols may be attributed to the high concentration of the SDS during protein extraction steps, making difficult the isoelectric focusing, even with previous precipitation step.

The P5 protocol using TCA/acetone based extraction is classical for the clean-up of complex matrixes such as vegetal samples, and for further protein extraction [11,29] using 2-DE buffer. But despite its wide use, P5 protocol applied to sunflower leaves was found to be quite ineffective to remove secondary metabolites such as phenols, lignins, and pigments. Fig. 1E shows the gel obtained for P5 protocol in which 76 spots were detected, including some groups of protein isoforms (*ca*. 66 kDa) not so well resolved.

Application of P6 protocol resulted in a great improvement in the gel resolution, leading to the identification of 244 spots when *ca*. 485 μg of protein was loaded in the gel. Once that it presented the best result, three independently extractions using the P6 protocol were then carried out, and one gel was obtained from each one. Fig. 1F shows the gel profile obtained using this protocol. As one can see SDS is not applied to the extraction buffer in such case since thiourea as well as ionic substances, such as KCl, were added to increase protein solubility [30]. Unlike those from soy or peanuts, sunflower proteins are highly soluble in electrolytes, more than in pure water, owing to the salting-in effect [22,30]. As conclusion, the absence of SDS in extracting buffer may contribute to improve the gel resolution. Moreover, salt addition was found not to compromise isoelectric focusing steps once that its conductivity was within an acceptable level for an IEF experiment. Additionally, phenol contributes to protein solvation and removal of interferents (such as nucleic acids), since it acts as a dissociating agent for proteins reducing protein aggregation and interfering molecules [22,31]. Moreover, sucrose is used in P6 protocol to change phase densities and thus to ensure that the phenolic rich phases will be the upper phase. When the pH of extraction solution was near to seven, PMSF was employed as a protease inhibitor to minimize formation of degradation products. Additionally, phenol/polyphenol absorbents such as polyvinylpirrolidone (PVP) were not used because they are more effective at low pH values.

3.2. Mass spectrometry protein identification

Considering the small number of entries in the *Helianthus annuus* L. protein database, we expected low identification rate for Sunflower proteins. Cross species identifications were therefore used for identification. mRNA sequences were then correlated with peptides previously identified from MALDI-Q-TOF MS. The correlated mRNA sequences were in turn associated with homologue proteins from another organism providing the identity of the sunflower protein by homology.

Gel obtained from P6 protocol was employed for protein identification due to its best separation resolution. Fig. 2 shows circled spots, which were successfully identified (*ca*. 36% from the total spots randomly selected), as well as Table 1 presents their respective identifications by homology and the correlation with the organism (genus and specie) that presented higher homology. Experimental molar mass (estimated from gel electrophoresis spots), expected molar mass (based on protein homologues), and peptide coverage of protein are also shown. As visualized, experimental molar mass of proteins match with theoretical values except for some evident degradation products such as those from spots 17, 18 or 22. For instance, spot 22, in particular, seems to represent a fragment of protein from spot 21. It was observed that experimental molar masses higher than the theoretical values could be attributed to experimental variations, inherent to electrophoresis technique. In this case, acceptable values do not overcome 10%.

Table 1 highlights, in bold, those proteins not included in the ExPASy Proteomics Server [32], which have been therefore first characterized in this study at the proteomic level for *Helianthus annuus*.

Peptides obtained from MS/MS mass spectra data and used for protein identifications as well as the accession code, obtained from the compiled gene databank for each group of peptides can be observed in Table 2. This table includes the percentage of correlation between the identified peptides and peptides of the homologue protein, and the statistical scores given by MASCOT and Blast algorithms.

4. Conclusion

Six different protocols for protein extraction from sunflower leaves, a high complex vegetal sample, were evaluated. The protocol using phenol extraction was found to provide the best extraction efficiency and best protein separation using two-dimensional gel electrophoresis. Although this protocol is quite time consuming, the use of phenol maximizes the elimination of interferents and minimizes most abundant proteins. From 61 sunflower protein spots investigated, 22 spots (36%) were identified by tandem mass spectrometry, and 12 of them (*ca*. 55%) were found to correspond to new Sunflower proteins not listed yet in the current ExPASy databank. This result illustrates the efficiency of the protocol in terms of improved gel resolution and reliable mass spectrometry characterization. The use of the phenol based extraction protocol described herein for extraction and separation of sunflower proteins followed by gel electrophoresis may therefore facilitate sunflower proteomic studies and guide protocols for other complex plant materials.

Acknowledgements

The authors thank the Fundação de Amparo a Pesquisa do Estado de São Paulo (FAPESP, São Paulo, Brazil), the Conselho Nacional de Desenvolvimento Científico e Tecnológico (CNPq, Brasília, Brazil), the Coordenação de Aperfeiçoamento de Pessoal de Nível Superior (CAPES, Brasília, Brazil) and the Financiadora de Estudos e Projetos (FINEP, Brasília, Brazil) for financial support and fellowships. The authors also thank to the Brazilian Synchrotron Light

Laboratory – Associação Brasileira de Tecnologia de Luz Síncrotron (Proteome Network of the São Paulo State – FAPESP process number 2004/14846-0/and FINEP process number 01.07.0290.00) for using the mass spectrometry facilities.

References

[1] W.A. Dowsey, G. Yang, Proc. IEEE 96 (2008) 1292.
[2] A. Mehta, A.C.M. Brasileiro, D.S.L. Souza, E. Romano, M.A. Campos, M.F. Grossi-de-Sá, M.S. Silva, O.L. Franco, R.R. Fragoso, R. Bevitori, T.L. Rocha, FEBS J. 275 (2008) 3731.
[3] H. Waldmann, Bioorg. Med. Chem. 11 (2003) 3045.
[4] D. Fenyö, R.C. Beavis, Mass Spectrom. Rev. 27 (2008) 1.
[5] A.D. Sarma, N.W. Oehrle, D.W. Emerich, Anal. Biochem. 379 (2008) 192.
[6] B. Cañas, C. Piñeiro, E. Calvo, D. López-Ferrer, J.M. Gallardo, J. Chromatogr. A 1153 (2007) 235.
[7] M. Bantscheff, M. Schirle, G. Sweetman, J. Rick, B. Kuster, Anal. Bioanal. Chem. 389 (2007) 1017.
[8] I. Roy, K. Mondal, M.N. Gupta, J. Chromatogr. B 849 (2007) 32.
[9] E. Jamet, C. Albenne, G. Boudart, M. Irshad, H. Canut, R. Pont-Lezica, Proteomics 8 (2008) 893.
[10] W. Wang, R. Vignani, M. Scali, M. Cresti, Electrophoresis 27 (2006) 2782.
[11] W. Wang, F. Tai, S. Chen, J. Sep. Sci. 31 (2008) 2032.
[12] C.S. Magalhães, M.A.Z. Arruda, Talanta 71 (2007) 1958.
[13] J.S. Garcia, G.M.F. Souza, M.N. Eberlin, M.A.Z. Arruda, Metallomics 1 (2009) 107.
[14] C.S. Magalhães, J.S. Garcia, A.S. Lopes, E.C. Figueiredo, M.A.Z. Arruda, in: M.A.Z. Arruda (Ed.), Trends in Sample Preparation, Nova Science Publishers, New York, 2007, pp. 245–288.
[15] C. Espagne, A. Martinez, B. Valot, T. Meinnel, C. Giglione, Proteomics 7 (2007) 3788.
[16] P. Giavalisco, E. Nordhoff, H. Lehrach, J. Gobom, J. Klose, Electrophoresis 24 (2003) 207.
[17] Z. Gong, K. Alef, B.-M. Wilke, P. Li, Chemosphere 58 (2005) 291.
[18] K.G. Georgogianni, M.G. Kontominas, P.J. Pomonis, D. Avlonitis, V. Gergis, Fuel Process. Technol. 89 (2008) 503.
[19] M.P. Schneider, J. Sci. Food Agric. 86 (2006) 1769.
[20] J.S. Garcia, P.L. Gratão, R.A. Azevedo, M.A.Z. Arruda, J. Agric. Food Chem. 54 (2006) 8623.
[21] C.M. Bellato, A.K.M. Garcia, F. Mestrinelli, S.M. Tsai, M.A. Machado, L.W. Meinhardt, Braz. J. Microbiol. 35 (2004) 235.
[22] S.C. Carpentier, E. Witters, K. Laukens, P. Deckers, R. Swennen, B. Panis, Proteomics 5 (2005) 2497.
[23] H. Xie, S. Pan, S. Liu, K. Ye, K. Huo, Electrophoresis 28 (2007) 871.
[24] P. Delaplace, F. van der Wal, J. Dierick, J.H.G. Cordewener, M. Fauconnier, P. du Jardin, A.H.P. America, Proteomics 6 (2006) 6494.
[25] M.M. Bradford, Anal. Biochem. 72 (1975) 248.
[26] G. Candiano, M. Bruschi, L. Musante, L. Santucci, G.M. Ghiggeri, B. Carnemolla, P. Orecchia, L. Zardi, P.G. Righetti, Electrophoresis 25 (2004) 1327.
[27] D.N. Perkins, D.J.C. Pappin, D.M. Creasy, J.S. Cottrell, Electrophoresis 20 (1999) 3551.
[28] Web site http://www.plantgdb.org/, acessed in September 2008.
[29] C. Vâlcu, K. Schlink, Proteomics 6 (2006) 1599.
[30] M.C. Carrão-Panizzi, J.M.G. Mandarino, in: R.M.V.B.C. Leite, A.M. Brighenti, C. de Castro (Eds.), Girassol no Brasil, Embrapa Soja, Londrina, Brazil, 2005, pp. 62–66.
[31] A. Pusztai, Biochem. J. 99 (1966) 93.
[32] Web site http://br.expasy.org, accessed in September 2008.

Talanta 80 (2010) 1552–1560

Contents lists available at ScienceDirect

Talanta

journal homepage: www.elsevier.com/locate/talanta

Strategies to optimize two-dimensional gel electrophoresis analysis of the human joint proteome

Cristina Ruiz-Romero, Valentina Calamia, Vanessa Carreira, Jesús Mateos, Patricia Fernández, Francisco J. Blanco*

Proteomics Unit and Associated Node to ProteoRed, Osteoarticular and Aging Research Lab, INIBIC-Hospital Universitario A Coruña, A Coruña, Spain

ARTICLE INFO

Article history:
Available online 22 May 2009

Keywords:
Proteomics
2-DE
Joint
Cartilage
Chondrocyte
Synovium
Synovial fluid

ABSTRACT

Due to the complex structure of the articular joint, it requires great effort to fully understand joint disease pathogenesis. The proteomic analysis of articular joint tissues could contribute greatly to our insight into the endogenous control mechanisms of matrix turnover and the unravelling of the molecular and cellular mechanisms involved in the progression of the arthritides. To date, most proteome analysis strategies use the two-dimensional gel electrophoresis (2-DE) technique to separate proteins according to their isoelectric point, molecular mass, solubility and relative abundance. In this work, we describe optimization of human joint sample preparation techniques to obtain high quality 2-DE maps of human joint tissues (cartilage and synovium), cells (chondrocytes and synoviocytes) and synovial fluid. These techniques improve the performance of gel-based differential proteomic analysis, and facilitate the application of proteomics to rheumatology studies.

© 2009 Elsevier B.V. All rights reserved.

1. Introduction

A comprehensive understanding of the protein pathways involved in normal and disease states is required if we are to effectively treat disease. Proteome analyses not only aim to identify changes in protein expression, but also protein interactions, post-translational modifications and protein distribution. Proteomics, therefore, has become a useful technology for gaining an understanding of the complex and unknown processes that participate in joint disease pathogenesis. More efficient strategies are needed to obtain high throughput proteomics analysis of tissues and cells, in order to gain insight into metabolic dysregulations and structural changes that lead to disease development.

Many proteomic research strategies currently employ two-dimensional gel electrophoresis (2-DE) to separate proteins according to their isoelectric point (p*I*), molecular mass, solubility and relative abundance [1]. The gels are then stained with Coomasie brilliant blue [2], silver nitrate [3] or fluorescent dyes such as SYPRO Ruby or ruthenium II tris(bathophenanthroline disulfonate) [4,5] to visualize the protein spots. Digitized gel images are used for analysis and specific proteins to be identified are removed from the gel and digested using a specific protease, usually trypsin. The proteins are subsequently identified using mass spectrometry [6]. The high resolution of this technology makes it suitable for the analysis and parallel quantitative profiling of complex protein mixtures, such as whole cell lysates or tissues. Unlike other proteomic approaches that work with peptides, such as those methods based on liquid chromatography with tandem mass spectrometry (LC–MS/MS), 2-DE provides information about molecular weight and isoelectric point, and delivers a map of intact proteins that reflects changes in isoforms, post-translational modifications and protein expression levels. Early limitations of 2-DE have been largely overcome, not only with respect to reproducibility and handling, but also with the resolution of proteins that are hydrophobic or that exhibit extreme p*I* values. This has been possible mainly with the development of immobilized pH gradients (IPGs) that enable the analysis of very acid or alkaline proteins (IPGs between 2.5 and 12), and also provide increased resolution and allow detection of low abundance proteins using narrow-overlapping IPG strips. Because of this increased resolution, 2-DE can resolve more than 5000 proteins simultaneously using the proper gel size, sample characteristics and pH gradient. 2-DE technology is now able to detect and quantify less than 1 ng of protein per spot.

Joint diseases are the leading cause of disability in people over 55 years old. These diseases include degenerative pathologies such as osteoarthritis (OA), autoimmune diseases such as rheumatoid arthritis (RA) or psoriatic arthritis (PA), and metabolic disorders such as gout. While all these pathologies progress with joint inflammation and pain, the patterns differ depending on the type and

* Corresponding author at: Unidad de Investigación Osteoarticular y del Envejecimiento, Laboratorio de Investigación, INIBIC - Complejo Hospitalario Universitario A Coruña, C/ Xubias, 84, 15006 A Coruña, Spain. Tel.: +34 981 178272; fax: +34 981 178273.
E-mail address: Francisco.Blanco.Garcia@sergas.es (F.J. Blanco).

0039-9140/$ – see front matter © 2009 Elsevier B.V. All rights reserved.
doi:10.1016/j.talanta.2009.05.022

location of the arthritic disease. Considering the complex structure of the articular joint, intensive effort is required to gain an understanding of joint disease pathogenesis. The proteome analysis of articular joints would be very useful to gain insight into the endogenous control mechanisms of matrix turnover in joint tissues, and to unravel molecular and cellular mechanisms that contribute to disease progression. In this paper we describe the sample preparation techniques we have found useful for the study of human joint proteomics using 2-DE for the analysis of joint tissues, cells and fluids.

2. Materials and methods

2.1. Reagents and chemicals

Culture media and fetal calf serum (FCS) were from Gibco BRL (Paisley, UK). Culture flasks were obtained from CoStar (Cambridge, MA, USA). 2-DE electrophoresis materials, including IPG buffer and strips were from GE Healthcare (Uppsala, Sweden). Anti-human serum albumin (HSA) and immunoglobulin G (IgG) resin were from Vivascience (Sartorius, Germany). Unless otherwise indicated, all other chemicals were obtained from Sigma–Aldrich (St. Louis, MO, USA).

2.2. Collection of cartilage, synovial membrane, joint cells and synovial fluid

Fig. 1 shows protocols followed to obtain joint tissue samples for proteomic analysis. Normal human knee and hip samples were obtained from adult donors, either from joint surgery or autopsy, who had no history of joint disease and macroscopically normal articular tissues. All donors or donor families gave written informed consent for the tissue donation. This study was approved by the Ethics Committee of Galicia (Spain).

Synovial membranes were extracted using biopsy forceps, rinsed in sterile phosphate-buffered saline (PBS), weighed, and either frozen at −80 °C or processed for synoviocyte isolation. Cartilage surfaces of femoral condyles were rinsed thoroughly with sterile saline; parallel sections 5 mm apart were then excised using scalpels to cut vertically from the cartilage surface to the subchondral bone. After resection from the subchondral bone, the cartilage strips were weighed and frozen at −80 °C or processed for chondrocyte isolation.

Synovial fluid from OA patients with joint effusion was aseptically aspirated. Normal synovial fluid was obtained from organ and tissue donors who did not have detectable OA. The synovial fluid was centrifuged at 800 × *g* for 15 min, after which the supernatant was divided into 1 mL aliquots and frozen at −80 °C.

2.2.1. Chondrocyte isolation and culture

The cartilage tissue strips obtained as described above were digested with 2.5 mg/mL trypsin in DMEM at 37 °C for 10 min. After removing the trypsin solution, the cartilage slices were incubated for 12–16 h with type IV clostridial collagenase (2 mg/mL) in Dulbecco's modified Eagle's medium (DMEM) with 5% FCS to release the cartilage cells. The chondrocytes were recovered and plated at high density (4×10^6 per 162-cm^2 flask) in DMEM supplemented with 100 U/mL penicillin, 100 μg/mL streptomycin, 1% glutamine and 10% FCS. The cells were incubated at 37 °C in a humidified gas mixture containing 5% CO_2 balanced with air. Confluency was achieved at 2–3 weeks of primary culture. The cells were serum-starved in fresh DMEM with 0.5% FCS for 48 h prior to trypsinization. Cell viability was assessed by trypan blue dye exclusion. Finally, the chondrocytes ($3–5 \times 10^6$) were recovered from the culture flasks by trypsinization, washed twice in a buffer containing 130 mM NaCl, 5 mM KCl, 2.5 mM Tris–HCl (pH 7.5) and 0.7 mM Na_2HPO_4, and transferred to microcentrifuge tubes for protein extraction.

2.2.2. Synoviocyte isolation and culture

Synovial membranes were minced and exposed to enzymatic digestion with 1.25 mg/mL trypsin in PBS 1 h at 37 °C with agitation. Dissociated cells were plated onto 162-cm^2 flasks and cultured overnight in RPMI 1640 medium supplemented with 100 U/mL penicillin, 100 μg/mL streptomycin, 2 μM glutamine and 10% FCS at 37 °C with 5% CO_2. Non-adherent cells were discarded and the adherent cells were cultured further in fresh medium until confluent, when the cells were trypsinized and subcultured. Synoviocytes from passages 4–8 were recovered from the culture

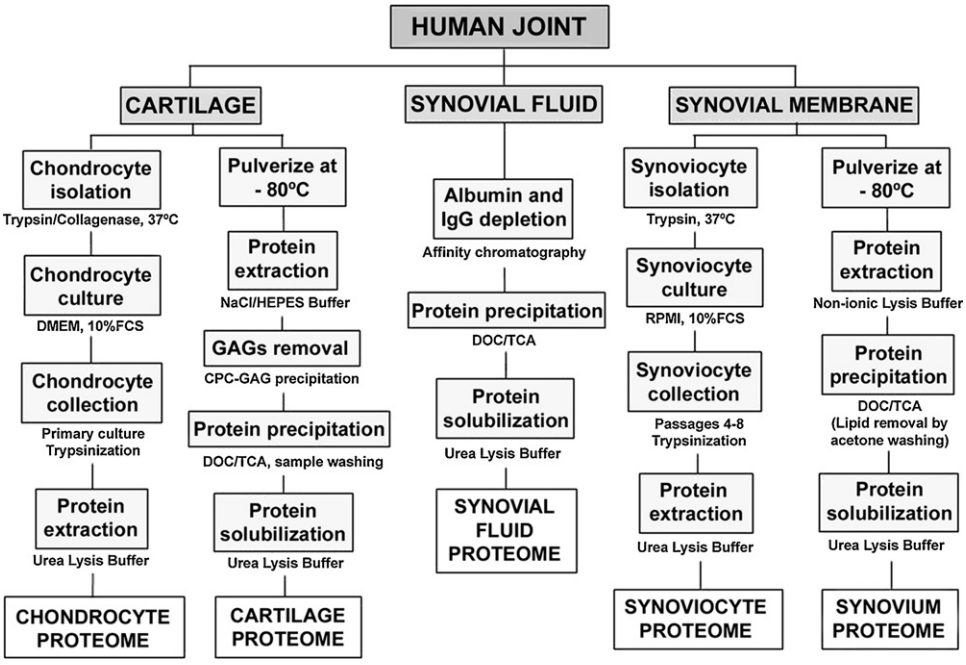


Fig. 1. Schematic workflow for the preparation of different protein samples obtained from human joints for two-dimensional electrophoresis (2-DE) analysis.

flasks, washed twice, and transferred to microfuge tubes for protein extraction.

2.3. Cartilage glycosaminoglycan (GAG) precipitation

We optimized our procedure for 2-DE of cartilage samples by precipitating their GAGs with cetylpyridinium chloride (CPC) with subsequent washing of the sample. Briefly, cartilage samples were pulverized at −80 °C in a tissue grinder, and the resulting powder was transferred to a microfuge tube. The cartilage proteins were extracted using a mild extraction buffer composed of 500 mM NaCl, 50 mM HEPES, pH 7.2, and protease inhibitors. Extraction was carried out for 1 h at room temperature with agitation and occasional vortexing. The samples were cleared by centrifugation at 12,000 × *g* for 10 min; the supernatant was either stored at −80 °C or subjected to proteoglycan (GAG) removal. The removal of GAGs was done using the method of Hermansson et al. [14], with some modifications. Briefly, the GAG content was determined using the dimethylmethylene blue assay [15], and GAGs were precipitated by incubation with 3 mg CPC per mg GAG. After precipitate removal, the proteins in the supernatant were precipitated overnight at 4 °C with 1/10 vol. of 0.2% sodium deoxycholate (NaDOC) and 1/10 vol. of 100% trichloroacetic acid (TCA). The remaining CPC was removed from the precipitate by cationic exchange, washing the pellet with 1 mL 0.4 M sodium acetate in 90% ethanol for 30 min with gentle agitation. The pellets were washed with 1 mL 100% ethanol at −20 °C to remove excess salts, and then with 100% acetone at −20 °C prior to solubilization in ULB as described in the next section.

2.4. General procedures used for two-dimensional electrophoresis (2-DE)

2.4.1. Protein solubilization

Tissue proteins or cell pellets were solubilized by vortexing followed by gentle agitation during a 1 h incubation in 200 μl of an isolectric focusing-compatible lysis buffer (ULB) containing 8.4 M urea, 2.4 M thiourea, 5% cholamidopropyl diethylamoniopropane sulfonate (CHAPS), 1% carrier ampholytes (IPG buffer pH 3–10 nonlinear (NL)), 0.4% Triton X-100 and 2 mM dithiothreitol (DTT).

For protein quantification, 10 μl of the protein extract were diluted 10× with distilled deionized water and precipitated for at least 1 h using 0.02% sodium deoxycholate and 10% trichloroacetic acid. The precipitate was washed once with two volumes of ice-cold acetone, allowed to dry, and solubilized in alkaline sodium dodecyl sulphate (SDS) (5% SDS, 0.1 N NaOH). 5–10 μl of this sample were employed to quantify the proteins in each lysate using the bicinchoninic acid (BCA) technique (Pierce Chemical Company, Rockford, IL, USA).

2.4.2. First dimension: isoelectric focusing

Solubilized protein (100 μg) was incubated for 1 h with gentle agitation in a rehydration buffer (8.4 M urea, 2 M thiourea, 2% CHAPS, 0.5% carrier ampholytes, 1.2% Destreak Reagent (GE healthcare) and 0.002% bromophenol blue). The proteins were then applied to 24 cm, pH 3–10 NL, IPG strips (GE Healthcare) using passive overnight rehydration. Focusing was performed at 20 °C for a total of 64,000 Vhr (IPGphor, GE Healthcare). The strips were stored in tubes at −80 °C.

2.4.3. Second dimension electrophoresis using SDS-PAGE

Second dimension electrophoresis followed equilibration of the strips for 15 min in 6 M urea, 50 mM Tris–HCl (pH 8.8), 30% glycerol, 2% SDS and 1% DTT (reduction step), and 15 min in 6 M urea, 50 mM Tris–HCl (pH 8.8), 30% glycerol, 2% SDS, 0.002% bromophenol blue and 4% iodoacetamide (alkylation step). The strips were first washed with electrophoresis buffer (25 mM Tris–HCl, pH 8.3, 192 mM glycine, 0.1% SDS) then attached to the surface of a 21 cm × 26 cm 10% polyacrylamide gel using 0.5% agarose. Electrophoresis was carried out according to the procedure of Laemmli [7], but using Tris–glycine electrophoresis buffer for the lower (anode) buffer and 2× Tris–glycine for the upper (cathode) buffer. Samples were run at 2.5 W/gel for the first 30 min and then at 17 W/gel until the bromophenol blue dye reached the bottom of the gel.

2.4.4. Gel staining

Gels were stained with either Coomasie Blue or silver nitrate. Coomasie staining used 0.1% Brilliant Blue G-250 (Sigma–Aldrich) in 40% methanol with 10% acetic acid, followed by destaining in 40% methanol with 5% acetic acid.

Silver nitrate staining was performed using standard protocols [8] with modifications. Briefly, gels were fixed overnight at 4 °C in 40% ethanol with 10% acetic acid and washed three times for 10 min with water. Sensitization was carried out for 1 min in 0.02% sodium thiosulphate (Fluka, Buchs, Switzerland). After two consecutive 1-min water washes, the gels were impregnated with 0.2% silver nitrate (Fluka) in 0.075% formalin for 60–90 min. Excess silver nitrate was removed by a few seconds of water rinses, and stain development was carried out in a solution containing 3% potassium carbonate, 12.5 mg/l sodium thiosulphate and 0.025% formalin. Once the bands or spots on the gel reached the desired intensity, the reaction was stopped by transferring gels to 3% Trizma-base (Sigma–Aldrich) in 10% acetic acid. After 30 min in the stop solution, gels were scanned and dried or stored at 4 °C in water.

2.4.5. Image acquisition

Coomasie and silver-stained gels were digitized using a densitometer (ImageScanner, Amersham), and analyzed with PDQuest 7.3.0 computer software (Bio-Rad, Hercules, CA, USA). Utilizing PDQuest tools, protein spots were enumerated, quantified and characterized by their molecular mass and isoelectric point by bilinear interpolation between landmark features of each image previously calibrated with internal 2-DE standards (Bio-Rad).

2.5. Mass spectrometry identification of proteins

2.5.1. Protein in-gel digestion

Selected spots of interest on the gel were excised and transferred to microcentrifuge tubes. Samples selected for analysis were reduced, alkylated and digested with trypsin according to Sechi and Chait [9]. Briefly, spots were washed twice with water, shrunk with 100% acetonitrile and dried in a Savant SpeedVac (Thermo Scientific, Waltham, MA, USA). The samples were then reduced with DTT and subsequently alkylated with iodoacetamide. Finally, samples were digested overnight at 37 °C with 12.5 ng/μl sequencing-grade trypsin (Roche Molecular Biochemicals, Indianapolis, IN, USA).

2.5.2. Mass spectrometry analysis

After digestion, the supernatant was collected and 1 μl was spotted onto a MALDI target plate and allowed to air-dry at room temperature. Subsequently, 0.5 μl of a 3 mg/mL solution of α-cyano-4-hydroxy-trans-cinnamic acid matrix (Sigma–Aldrich) in 0.1% TFA–50% acetonitrile (ACN) was applied to the dried peptide digest spots and again allowed to air-dry. The samples were analyzed using the MALDI-TOF/TOF mass spectrometer 4800 Proteomics Analyzer (Applied Biosystems, Framingham, MA, USA). MALDI-TOF spectra were acquired in reflector positive-ion mode at 1000 laser shots per spectrum. Mass spectra were internally calibrated using autoproteolytic trypsin fragments and externally calibrated using a standard peptide mixture (Sigma–Aldrich). TOF/TOF fragmentation spectra were acquired by selecting the 10

most abundant ions of each MALDI-TOF peptide mass map, excluding trypsin autolytic peptides and other known background ions, at an average of 2000 laser shots per fragmentation spectrum. The parameters used to analyze the data were a signal-to-noise threshold of 20 and resolution higher than 10,000 with a mass accuracy of 20 ppm.

2.5.3. Database search

The monoisotopic peptide mass fingerprinting data obtained from MS and the aminoacidic sequence tag obtained from each peptide fragmentation in MS/MS analyses were used to search for protein candidates using Mascot 1.9 (http://www.matrixscience.com). Tryptic autolytic fragments and other contaminations were removed from the dataset used for the database search. Search parameters for peptide mass fingerprints and tandem MS spectra were set using databases SWISS-PROT/TrEMBL (http://www.expasy.ch/sprot) and NCBI (http://www.ncbi.nlm.nih.gov). Fixed and variable modifications were considered (Cys as the S-carbamidomethyl derivate and Met as oxidized methionine, respectively) allowing one missed cleavage site, a precursor tolerance of 50 ppm and MS/MS fragments tolerance of 0.3 Da. The accepted isoelectric point range was from 3 to 10 and the accepted protein mass range was from 10 to 100 kDa. A positive identification was considered to be the achievement of at least five matching peptides and when at least 20% of the peptide coverage of the theoretical sequences matched, within a mass accuracy of 50 or 25 ppm with internal calibration. In all the positive identifications, the probability scores were greater than the score fixed as significant with a p value <0.05.

3. Results and discussion

3.1. Overview of sample preparation for proteomic analysis

Fig. 1 shows the workflow we designed for the study of joint proteomes using 2-DE. The diverse protein samples were obtained following the procedures described in Section 2.2. Despite the differences between samples described below, the proteins were all extracted using a urea-based lysis buffer and most were cleaned with sodium deoxicholate-trichloroacetic acid precipitation.

For the first dimension of the 2-DE analysis, protein extracts were separated with nonlinear immobilized pH gradient strips covering a wide pH range (3–10) to make possible the study of the complete proteome. In the second dimension, proteins were fractionated on large-format SDS-PAGE gels and visualized with Coomasie blue or mass spectrometry-compatible silver nitrate staining. Selected spots were then excised, destained, in-gel digested with trypsin and analyzed by MALDI-TOF/TOF mass spectrometry. The two-dimensional maps shown in the present work are representative of the results obtained in our laboratory. The proteomic patterns were found to be highly reproducible.

3.2. Pre-treatment and 2-DE of cartilage and synovial membrane samples

3.2.1. Cartilage

Articular cartilage is a tissue with a very low cell density and an extracellular matrix (ECM) composed mainly of water (approximately 75% of tissue weight) and an abundant network of collagen (predominantly type II), proteoglycans and other macromolecules. These features render cartilage proteomic analysis difficult because the relatively few structural proteins are in such abundance that other interesting components may remain masked and undetectable. A number of strategies for enrichment of the less abundant cartilage proteins and removal of contaminants have been developed. These include ultrafiltration [10,11], the use of differential protein solubilization procedures [12,13], and proteoglycan substraction by cetylpyridinium chloride precipitation [12,14] or CsCl gradient ultracentrifugation [13]. Moreover, proteoglycans are strongly anionic, which interferes with isoelectric focusing and makes their removal essential to obtain definitive 2-DE gels. A selective loss or enrichment of some proteins may have occurred due to sample preparation in our studies; this should be considered when interpreting results.

We optimized our procedure for 2-DE of cartilage samples by precipitating their GAGs with cetylpyridinium chloride (CPC) with subsequent washing of the sample (see Section 2.3 and Fig. 1). Fig. 2 shows 2-DE maps of human cartilage proteins obtained prior to (A) and after (B) GAG removal. The differences between the images illustrate the advantage of proteoglycan removal and the efficiency of this approach. The most representative spots from human cartilage maps were excised from the gels to identify the proteins shown in Fig. 3A and listed in Table 1. These included collagen and collagen-associated proteins, such as fibromodulin (FMOD) and cartilage oligomeric matrix protein (COMP). Interestingly, both FMOD and COMP have been proposed as markers for alterations in cartilage metabolism. Degraded fragments of FMOD have been found in RA and OA cartilage [16], increasing with age [17]. Elevated mRNA levels in human OA cartilage and increased total amounts of translated FMOD protein indicate that attempts to repair damaged cartilage

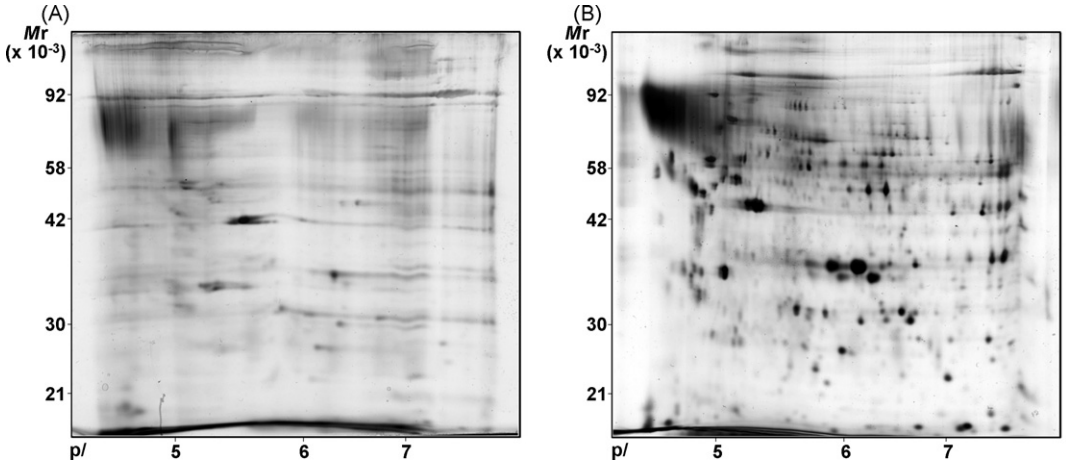


Fig. 2. Effect of glycosaminoglycan (GAG) removal on the proteome of cartilage. Two-dimensional electrophoresis (2-DE) gels of articular cartilage proteins before (A) and after (B) removal of GAGs by cetylpyridinium chloride (CPC) precipitation, showing the improvement in isoelectric focusing obtained after high anionic GAG depletion (IPG strip pH 3–10 NL, 10% T SDS-PAGE, silver staining).

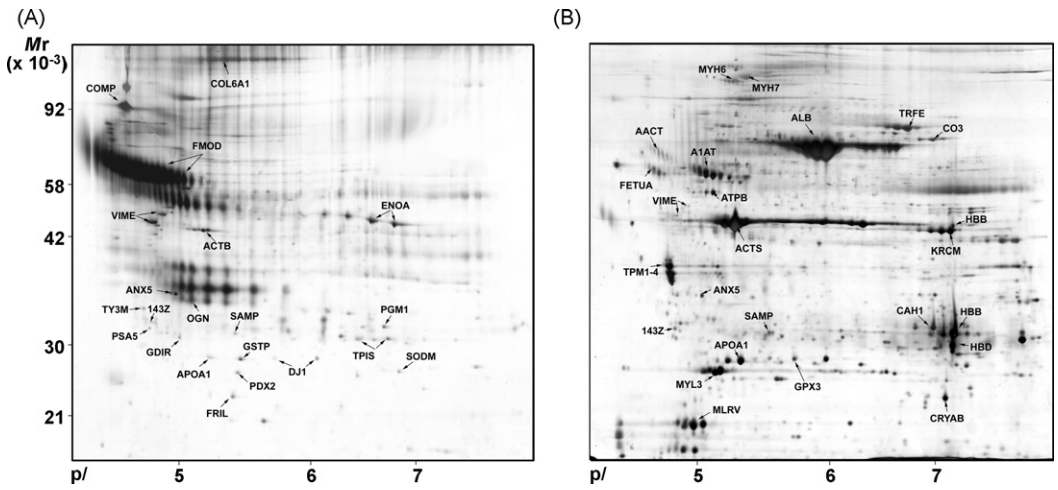


Fig. 3. Two-dimensional electrophoresis (2-DE) map of human articular cartilage (A) and synovial (B) proteins. Proteins are identified by the names used in the SWISS-PROT database (IPG strip pH 3–10 NL, 10% T SDS-PAGE, silver staining). Protein names are listed in Tables 1 and 2.

may be occurring [16,18]. COMP has received great interest in recent years as a biomarker for joint damage, including that resulting from RA [19], OA [20] and other skeletal diseases, as recently reviewed in Ref. [21].

3.2.2. Synovial membrane

The synovial membrane is located within the joint space and maintains normal joint function. Its anatomy can vary, but it often has two layers. The outer layer, or subintima, can be fibrous or fatty, whereas the inner layer, or intima, consists of a sheet of synoviocyte cells of two types, fibroblasts and macrophages. The fibroblast-like synoviocytes manufacture and secrete hyaluronan [22] and lubricin [23] into the synovial fluid, while the macrophages are responsible for the removal of undesirable substances from the synovial fluid.

Following a procedure similar to that used for cartilage samples, synovial membranes from healthy joints were pulverized at −80 °C and synovial proteins were extracted for 1 h using 1 mL of a non-ionic extraction buffer composed of 5 M urea, 1 M thiourea, 2% CHAPS and 2 mM DTT. The samples were then cleared by two successive centrifugations at 12,000 × *g* for 10 min; the supernatants were placed overnight in NaDOC/TCA for protein precipitation, as previously described. Synovial samples are characterized by a high lipid content, requiring that the protein pellet be washed with 500 μl of 100% acetone at −20 °C for 30 min to remove these lipids. The resulting pellet was then dried and solubilized in ULB as described in Section 2. Fig. 3B shows a representative 2-DE map of normal synovial proteins obtained by this technique. Table 2 lists some proteins indentified from this 2D map. In synovial membranes, we found an abundance of proteins related to fibrous structures, such as myosin and tropomyosin, in accordance with the described characteristics of the subintima. Fig. 3 shows the very different proteomic patterns obtained from cartilage and synovium, reflecting the diversity of the structures of the human joint.

Proteomes of degenerative/inflamed synoviums from RA, OA and a chronic arthritic condition, spondyloarthropathy (SpA) were compared using 2-DE followed by tandem mass spectrometry [24]. A similar strategy of separating whole tissue proteins by 2-DE prior to western blotting with sera from RA patients was employed to detect novel citrullinated autoantigens of synovium in RA [25].

Table 1
Sixteen representative proteins from human normal articular joints identified by mass spectrometry of cartilage protein extracts separated by two-dimensional electrophoresis (2-DE).

Spot name[a]	Description	Acces. No.[a]	M_r pre[b] (kDa)	p*I* pre[b]	No. of matched peptides[d]	Seq. cov.[e] (%)
ACTB	Actin beta chain	P60709	41.7	5.29	17	58
APOA1	Apolipoprotein A-I precursor (fragment)	P02647	28.1	5.27	21	64
COL6A1	Collagen, type VI, alpha 1 precursor	Q7Z645	109.6	5.29	18	21
COL6A2	Alpha 2 type VI collagen, isoform 2C2	Q6P0Q1	109.7	5.85	17	18
COMP	Cartilage oligomeric matrix protein	P49747	82.2	4.38	19	34
ENOA	Alpha enolase	P06733	47.4	6.99	18	45
FMOD	Fibromodulin precursor	Q06828	43.5	5.55	10	20
FMOD	Fibromodulin	Q8IV47	43.5	5.66	11	28
FRIL	Ferritin, light chain	P02792	16.4	5.65	7	32
GDIR	Rho gdp dissociation inhib. alpha, chain E	P52565	20.6	6.73	8	35
GSTP1	Glutathione S-transferase P	P09211	23.2	5.44	FQDGDLTLYQSNTILR[f]	
MIME	Mimecan (osteoglycin)	P20774	33.9	5.46	8	30
PA2	Phospholipase A2	P04054	14.7	9.38	7	52
PRDX2	Peroxiredoxin 2 isoform b	P32119	16	6.13	8	39
SAMP	Serum amyloid P component, chain A	P02743	23.4	6.12	10	38
VIME	Vimentin	P08670	53.6	5.06	29	59
VIME	Vimentin	P08670	53.6	5.06	15	37

Experimental M_r and p*I* calculated by analysis of the gel images with PDQuest 7.3.0 software.
[a] Protein name and accession number according to SwissProt and TrEMBL databases.
[b] Predicted M_r and p*I* according to protein sequence and Swiss-2DPAGE database.
[d] Number of peptide masses matching the top hit from MS-Fit PMF.
[e] Aminoacidic sequence coverage for the identified proteins.
[f] Sequence tag identified by tandem mass spectrometry using MALDI-TOF/TOF MS.

Table 2
Twenty-seven representative proteins from human normal articular joints identified by mass spectrometry of synovial membrane two-dimensional electrophoresis (2-DE).

Spot name[a]	Description	Acces. No.[a]	M_r pre[b] (kDa)	pI pre[b]	No. of matched peptides[c]	Seq. cov.[d] (%)
A1AT	Alpha-1-antitrypsin precursor	P01009	46.9	5.37	22	55
AACT	Alpha-1-antichymotrypsin precursor	P01011	47.8	5.33	12	38
ACTC	Actin alpha cardiac	P68032	42.3	5.23	10	36
ACTS	Actin, alpha skeletal muscle	P68133	42.4	5.23	13	42
APOA1	Apolipoprotein A I precursor	P02647	30.8	5.56	26	67
CAH1	Carbonic anhydrase 1	P00915	28.8	6.63	14	67
CO3	Complement C3 precursor	P01024	187.2	6.02	21	18
CRYAB	Alpha crystallin beta chain	P02511	20.1	6.76	15	69
FETUA	α-2-HS-glycoprotein precursor (Fetuin A)	P02765	40.1	5.43	9	29
GPX3	Glutathione peroxidase 3 precursor	P22352	25.8	8.20	11	44
HBB	Hemoglobin beta chain	P68871	16.0	6.81	11	79
HBB	Hemoglobin beta chain	P68871	16.0	6.81	14	84
HBD	Hemoglobin delta chain	P02042	16.0	7.97	6	39
KCRM	Creatine kinase M-type	P06732	43.3	6.77	15	42
MLRV	Myosin regulatory light chain, ventricular/cardiac muscle isoform	P10916	18.6	4.92	10	62
MYH6	Myosin heavy chain, cardiac muscle α	P13533	223.7	5.60	31	17
MYH7	Myosin heavy chain, cardiac muscle β	P12883	223.1	5.63	38	21
MYL3	Myosin light polypeptide 3	P08590	22.0	5.03	15	74
SAMP	Serum amyloid P-component precursor	P02743	25.5	6.10	9	30
TPM1	Tropomyosin 1 alpha chain	P09493	32.7	4.69	9	29
TPM2	Tropomyosin beta chain	P07951	32.9	4.66	14	38
TPM3	Tropomyosin alpha-3 chain	P06753	32.8	4.68	12	30
TPM4	Tropomyosin alpha-4 chain	P67936	28.5	4.67	10	32
TRFE	Serotransferrin precursor	P02787	79.3	6.81	36	47
ZN622	Zinc finger protein 622	Q969S3	54.8	5.80	13	27

Abbreviations as in Table 1.

3.3. Pre-treatment and 2-DE of chondrocyte and synoviocyte samples

A straightforward approach to analyze the human joint is by proteomic analysis of joint cells. Joint cells are responsible for ECM synthesis and turnover; the global study of their proteins may provide valuable information about processes occurring in these tissues in joints. Working directly with cells for proteomic studies is in many ways more straightforward than using samples from other sources because most cellular proteins are easy to extract, their quantitative dynamic range is not extremely high, and they are easily freed from matrix components. Moreover, the culture of joint cells is a widely used method for increasing the quantity of proteins available for extraction. This is particularly useful for cells occurring in low numbers in joint tissue, such as chondrocytes, which represent less than 5% of cartilage weight. Cultures of articular chondrocytes isolated from various animal and human sources currently serve as useful models to study mechanisms controlling responses to growth factors and cytokines. Cultured chondrocytes also shed light on the mechanisms of pathogenesis and degenerative processes of some rheumatic diseases, such as OA. Using cells in primary culture, our group succeeded in partially delineating the proteome of human normal articular chondrocytes [26], generating a chondrocyte 2-DE reference map that at present encompasses almost 200 identified spots that correspond to more than 140 individual proteins. More recently, a similar strategy was used to develop a comparative proteomic analysis of OA chondrocytes employing fluorescent staining of the gels, bioinformatic analysis and identification of proteins varying in abundance [27].

Fibroblast-like synoviocytes, which are the characteristic cell type present in the synovial membrane, have proved to be useful models for the study of joint inflammatory disease, such as RA [28]. Synoviocytes obtained from RA patients have been analyzed by 2-DE, leading to the identification of 192 distinct proteins [29], many of which are known to be involved in cartilage physiology or pathophysiology.

For proteomic analysis, joint cells must be first isolated from their tissues by enzymatic digestion of the ECM with trypsin and, in the case of cartilage, collagenase. Freshly isolated cells can be used for protein extraction and analysis procedures with the caveat that some characteristics of the resulting proteomic profiles may be caused by cellular responses to the enzymatic treatment. Chondrocytes easily de-differentiate into fibroblasts and should be used during the first tissue culture passage while synovial cells are stable during further subculturing and may be trypsin-digested and collected after as many as 12–15 passages. The isolated cells are washed and their proteins extracted in a urea-based lysis buffer. Cellular protein extracts were resolved by 2-DE without need for further cleaning. Chondrocytes (Fig. 4A) and synoviocytes (Fig. 4B) show a marked similarity in their proteomes. The comparison of the synoviocyte map with reference maps allows identification of 82 different proteins involved in a broad range of biological functions. Some of the most abundant proteins appearing in the maps are vimentin, gelsolin or lamin A, filament proteins characteristic of adherent cells. These and 13 other protein forms common to both proteomic maps are depicted in Fig. 4 to illustrate their similarity.

3.4. Pre-treatment for 2-DE of synovial fluid samples

Proteomics shows great promise for discovery of biomarkers to improve the diagnostic capability for a wide range of diseases. Biological markers are needed to better understand and characterize disease types, monitor disease status and progression, and response to current and new therapies. The search for candidates to serve as specific markers of joint damage for early diagnosis of disease is a major aim in rheumatology research. Blood plasma, serum, and other body fluids that come in contact with a variety of tissues are expected to be the best sources of protein biomarkers for proteomic analysis. These circulating fluids have recently been shown to be the most likely carriers of proteins secreted or shed by tissues [30]. The major advantage of serum is its ready availability, but proteins secreted or released from a specific tissue or cell type, i.e. those that hold the highest potential as biomarkers, are so diluted in blood that they are often undetectable by current methods. This has generated great interest in the analysis of "proximal" body fluids, which have been in contact with only one or a few tissues, so less dilution of tissue-derived proteins would be expected. Synovial fluid is one of these "proximal" fluids, being derived directly from the site of joint

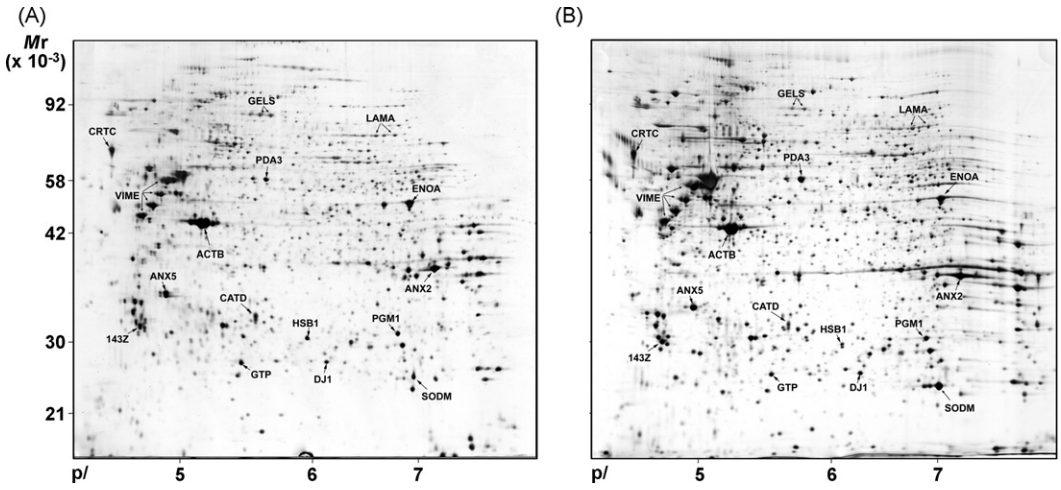


Fig. 4. Two-dimensional electrophoresis (2-DE) maps of human articular chondrocyte (A) and synoviocyte (B) proteins. Representative proteins are identified by the names used in the SWISS-PROT database (IPG strip pH 3–10 NL, 10% T SDS-PAGE, silver staining).

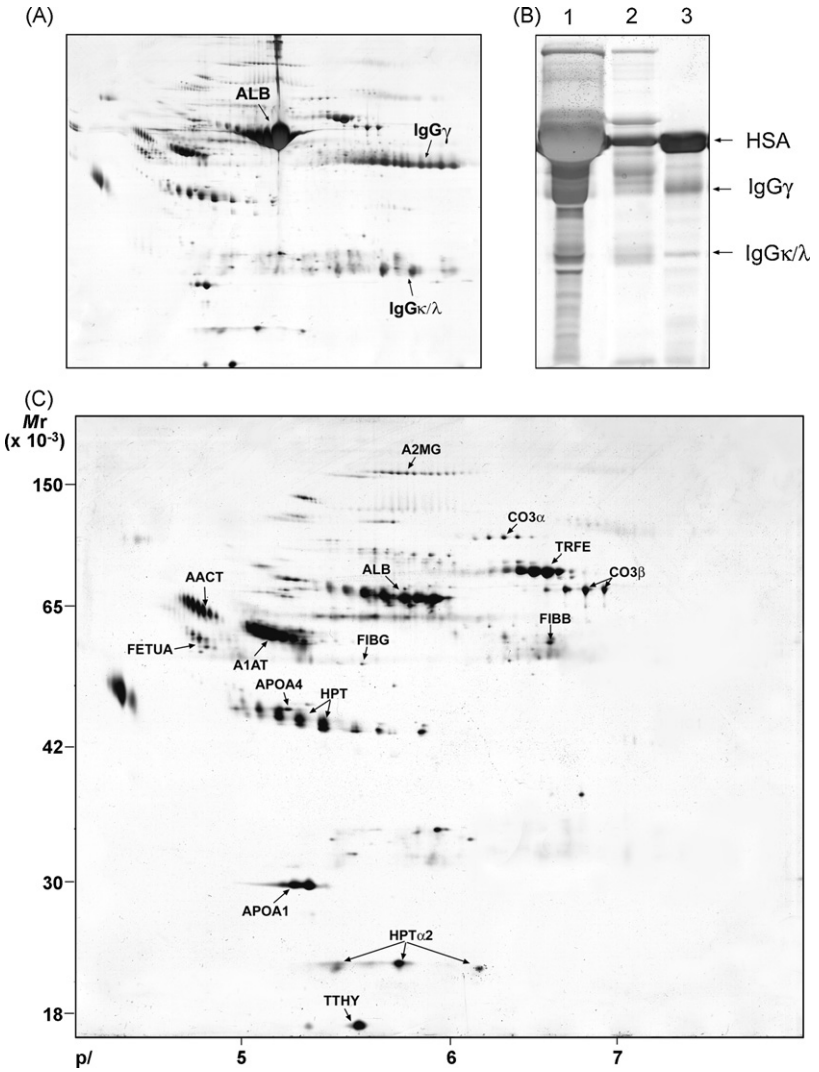


Fig. 5. Effect of albumin and immunoglobulin G (IgG) depletion on the synovial fluid proteome. (A) Whole human synovial fluid two-dimensional electrophoresis (2-DE) map. (B) Silver-stained SDS-PAGE gel showing the effect of depletion on the synovial fluid protein profile. Lane 1: non-depleted synovial fluid; lane 2: depleted synovial fluid; lane 3: protein fraction bound to the affinity resin. (C) 2-DE map of human synovial fluid proteins (IPG strip pH 3–10 NL, 10% T SDS-PAGE, silver staining). The 16 mapped proteins are identified by the names used in the SWISS-PROT database. Protein names are listed in Table 3.

Table 3
Thirteen representative proteins from human osteoarthritic joints identified by mass spectrometry of two-dimensional electrophoresis (2-DE) gels of synovial fluids.

Spot name[a]	Description	Acces. No.[a]	M_r pre[b] (kDa)	pI pre[b]	No. of matched peptides[c]	Seq. cov.[d] (%)
A1AT	Alpha-1-antitrypsin precursor	P01009	46.9	5.37	24	56
A2MG	Alpha-2-macroglobulin precursor	P01023	163.3	6.00	22	21
AACT	Alpha-1-antichymotrypsin precursor	P01011	47.8	5.33	12	38
APOA1	Apolipoprotein A I precursor	P02647	30.8	5.56	26	67
CO3	Complement C3 precursor	P01024	18.9	6.02	20	15
FETUA	α-2-HS-glycoprotein precursor (Fetuin A)	P02765	40.1	5.43	9	29
HBB	Hemoglobin beta chain	P68871	16.0	6.81	14	84
HBD	Hemoglobin delta chain	P02042	16.0	7.97	6	39
HPT	Haptoglobin precursor	P00738	45.9	6.13	14	32
IGHG1	Immunoglobulin gamma 1 chain C	P01857	37.0	8.46	7	33
SAMP	Serum amyloid P-component precursor	P02743	25.5	6.10	9	30
TRFE	Serotransferrin precursor	P02787	79.3	6.81	36	47
TTHY	Transthyretin precursor	P02766	16.0	5.52	7	69

Abbreviations as in Table 1.

disease. Proteomic studies in rheumatology have been designed to identify prospective biomarkers in SF, and attempt to then validate them in serum.

SF is a hyaluronic acid-rich fluid secreted by the synovium. Under normal conditions it lubricates the joint and provides articular cartilage with the nutrients necessary for chondrocyte metabolism. It also serves as the intermediate carrier of proteins shed by articular cartilage and transferred to the systemic circulation. SF sampling is invasive, thus samples need to be centrifuged to remove contaminating cells, such as mononuclear cells before use for proteomics. It is also useful to digest samples with hyaluronidase to remove the HA, which may complicate proteomics analyses [31]. In both serum and SF, large quantitative variability among samples has been reported for a number of proteins when using 2-DE on samples from OA patients. One study found that 41 of 139 spots sampled showed differences of greater than threefold between any two samples, with nine having greater than 100-fold differences [32]. This study illustrates the need to analyze a large number of samples and a clearly defined reference map for normal SF proteins to differentiate between changes due to OA and normal variation between individuals. Variability among samples was also noted in a proteomic study of recurrent joint inflammation in juvenile idiopathic arthritis, where both plasma and synovial fluid were analyzed using 2-DE and cases with single-event knee joint inflammation were compared to a group with recurrent knee disease [33].

The large dynamic range of individual protein concentrations in plasma, serum, and synovial fluid is one of the most challenging issues in body fluid proteomics aimed at biomarker discovery. Disease biomarkers typically appear in low concentrations, making their detection difficult in the presence of proteins appearing in higher abundance. A practical and effective strategy solution for this problem is the removal of diagnostically uninformative high abundant proteins, thus enhancing the detection of low abundance proteins to penetrate deeper into the plasma proteome. Several systems to deplete plasma of the unwanted high concentration proteins have been developed and are commercially available. They use antibody-based resins with specific affinities for as many as 20 of the most abundant proteins in plasma. We employed resins with affinity for HSA, which represents about 65% of total plasma proteins, and IgG, which represents about 15% of total plasma proteins. Because SF and plasma have a similar composition of high abundance proteins this technique is also suitable for depleting SF of these proteins. Fig. 5A is a 2D map of synovial fluid showing the remarkably high concentrations of albumin and IgG. The affinity chromatography protocol to remove these two proteins is illustrated in Fig. 5B. A conventional SDS-PAGE gel was used to evaluate the protein profiles of SF before (lane 1) and after (lane 2) protein depletion, as well as to define the protein fraction bound to the affinity resin (lane 3). Depletion of these two proteins enabled better visualization of other proteins (Fig. 5C), and improved identification of lower abundance proteins. Table 3 shows those less abundant proteins identified using this technique.

Table 4
Principal protocol recommendations.

Joint sample	Protocol modification before 2-DE
Cartilage	Glycosaminoglycan depletion by CPC precipitation.
Synovium	Lipid removal with acetone.
Cells (synoviocytes and chondrocytes)	Follow protocol for chondrocytes [26].
Synovial fluid	Depletion of albumin and IgG by affinity chromatography.

CPC: cetylpyridinium chloride.

4. Conclusions

The proteomic analysis of the articular joint tissues and cells should prove very helpful for increasing our insight into the endogenous control mechanisms of joint matrix turnover and unravelling the molecular and cellular mechanisms that participate in arthritic disease onset and progression. We have described a set of sample pre-treatment protocols that improve 2-DE proteomic analyses of cartilage, synovium, chondrocytes, synoviocytes, and synovial fluid. The main points of the optimized procedures are summarized in Table 4 and should prove useful to increase knowledge about joint pathogenesis. Hopefully, the proteomic analysis of synovial fluid and other body fluids will result in definition of biomarkers valuable for early diagnosis and monitoring of joint disease.

Acknowledgements

We are thankful to Mrs. Pilar Cal for her expert secretarial assistance. The authors express their appreciation to the Pathology Service and to Mrs. Lourdes Sanjurjo, and Mrs. Dolores Velo from the Orthopaedics Department of CHU A Coruña for providing cartilage samples. This work was supported by grants from the Ministerio de Educación y Ciencia, Spain (SAF2005–06211), Fondo Investigación Sanitaria, Spain (CIBER-CB06/01/0040) and Secretaria I+D+i (PGIDIT06PXIB916358PR). C. Ruiz was supported by Programa Parga Pondal, Secretaria Xeral I+D+i, Xunta de Galicia. J. Mateos was supported by Fondo Investigación Sanitaria-Spain (CA07/00243). V. Carreira was supported by Xunta de Galicia (PGEIDIT06PXIC916175PN). Patricia Fernandez was supported by Fondo Investigación Sanitaria, Spain (CIBER-CB06/01/0040).

References

[1] A. Görg, W. Weiss, M.J. Dunn, Proteomics 4 (2004) 3665–3685.
[2] V. Neuhoff, N. Arold, D. Taube, W. Ehrhardt, Electrophoresis 9 (1988) 255–262.
[3] A. Shevchenko, M. Wilm, O. Vorm, M. Mann, Anal. Chem. 68 (1996) 850–858.
[4] I.R. White, R. Pickford, J. Wood, J.M. Skehel, B. Gangadharan, P. Cutler, Electrophoresis 25 (2004) 3048–3054.
[5] K. Berger, D. Wissmann, C. Ihling, S. Kalkhof, A. Beck-Sickinger, A. Sinz, et al., Mol. Cell. Endocrinol. 227 (2004) 21–30.
[6] R. Aebersold, M. Mann, Nature 422 (2003) 198–207.
[7] U.K. Laemmli, Nature 227 (1970) 680–685.
[8] T. Rabilloud, V. Brodard, G. Peltre, P.G. Righetti, C. Ettori, Electrophoresis 13 (1992) 264–266.
[9] S. Sechi, B.T. Chait, Anal. Chem. 70 (1998) 5150–5158.
[10] D. Belluoccio, R. Wilson, D.J. Thornton, T.P. Wallis, J.J. Gorman, J.F. Bateman, Proteomics 6 (2006) 6549–6553.
[11] B.A. Garcia, M.D. Platt, T.L. Born, J. Shabanowitz, N.A. Marcus, D.F. Hunt, Rapid Commun. Mass Spectrom. 20 (2006) 2999–3006.
[12] J.B. Vincourt, F. Lionneton, G. Kratassiouk, F. Guillemin, P. Netter, D. Mainard, et al., Mol. Cell Proteomics 5 (2006) 1984–1995.
[13] J. Wu, W. Liu, A. Bemis, E. Wang, Y. Qiu, E.A. Morris, et al., Arthritis Rheum. 56 (2007) 3675–3684.
[14] M. Hermansson, Y. Sawaji, M. Bolton, S. Alexander, A. Wallace, S. Begum, et al., J. Biol. Chem. 279 (2004) 43514–43521.
[15] R.W. Farndale, C.A. Sayers, A.J. Barrett, Connect. Tissue Res. 9 (1982) 247–248.
[16] G. Cs-Szabo, P.J. Roughley, A.H. Plaas, T.T. Glant, Arthritis Rheum. 38 (1995) 660–668.
[17] P.J. Roughley, R.J. White, G. Cs-Szabo, J.S. Mort, Osteoarthritis Cartilage 4 (1996) 153–161.
[18] G. Cs-Szabo, L.I. Melching, P.J. Roughley, T.T. Glant, Arthritis Rheum. 40 (1997) 1037–1045.
[19] Z. de Jong, M. Munneke, V. Vilim, A.H. Zwinderman, H.M. Kroon, H.K. Ronday, et al., Rheumatology (Oxford) 47 (2008) 868–871.
[20] F.M. Williams, T.D. Spector, Arthritis Res. Ther. 10 (2008) 101.
[21] K.L. Posey, J.T. Hecht, Curr. Drug Targets 9 (2008) 869–877.
[22] Y. Yamanishi, G.S. Firestein, Rheum. Dis. Clin. North Am. 27 (2001) 355–371.
[23] G.D. Jay, U. Tantravahi, D.E. Britt, H.J. Barrach, C.J. Cha, J. Orthop. Res. 19 (2001) 677–687.
[24] K. Tilleman, K. Van Beneden, A. Dhondt, I. Hoffman, F. De Keyser, E. Veys, et al., Proteomics 5 (2005) 2247–2257.
[25] K. Matsuo, Y. Xiang, H. Nakamura, K. Masuko, K. Yudoh, K. Noyori, et al., Arthritis Res. Ther. 8 (2006) R175.
[26] C. Ruiz-Romero, M.J. Lopez-Armada, F.J. Blanco, Proteomics 5 (2005) 3048–3059.
[27] C. Ruiz-Romero, V. Carreira, I. Rego, S. Remeseiro, M.J. Lopez-Armada, F.J. Blanco, Proteomics 8 (2008) 495–507.
[28] I. Kramer, A. Wibulswas, D. Croft, E. Genot, Prog. Cell Cycle Res. 5 (2003) 59–70.
[29] K. Dasuri, M. Antonovici, K. Chen, K. Wong, K. Standing, W. Ens, et al., Arthritis Res. Ther. 6 (2004) R161–R168.
[30] H. Zhang, A.Y. Liu, P. Loriaux, B. Wollscheid, Y. Zhou, J.D. Watts, et al., Mol. Cell Proteomics 6 (2007) 64–71.
[31] H. Liao, J. Wu, E. Kuhn, W. Chin, B. Chang, M. Jones, et al., Arthritis Rheum. 50 (2004) 3792–3803.
[32] H. Yamagiwa, G. Sarkar, M.C. Charlesworth, D.J. McCormick, M.E. Bolander, J. Orthop. Sci. 8 (2003) 482–490.
[33] D.S. Gibson, S. Blelock, S. Brockbank, J. Curry, A. Healy, C. McAllister, et al., J. Proteome Res. 5 (2006) 1988–1995.

Talanta 80 (2010) 1561–1568

Contents lists available at ScienceDirect

Talanta

journal homepage: www.elsevier.com/locate/talanta

Monitoring virus-like particle and viral protein production by intact cell MALDI-TOF mass spectrometry

Catarina F. Franco[b], Maria Cândida M. Mellado[b], Paula M. Alves[a,b], Ana V. Coelho[a,c,*]

[a] Instituto de Tecnologia Química e Biológica, Universidade Nova de Lisboa, Av. da Republica – EAN, 2780-157 Oeiras, Portugal
[b] Instituto de Biologia Experimental e Tecnológica, Oeiras, Portugal
[c] Universidade de Évora, Évora, Portugal

ARTICLE INFO

Article history:
Available online 9 July 2009

Keywords:
Intact cell MALDI-TOF mass spectrometry
Virus-like particles
Monitor protein production
Spectra clustering
Intact insect cell fingerprint

ABSTRACT

A new application of *intact cell MALDI-TOF MS* (*ICM-MS*) methodology is described for monitoring the production of viral proteins and viral like particles using the baculovirus/insect cells expression system. Various MALDI matrices, cell preparation methods, cell/matrix volume ratio and MALDI target application procedures were tested in order to obtain the highest intensity and reproducibility of intact insect cell spectra. The web interface, SPECLUST (http://bioinfo.thep.lu.se/speclust.html), was used to construct dendograms based on MALDI-TOF MS data for evaluation of fingerprint changes.

We demonstrate that insect cell mass spectrum fingerprints are characteristic of each viral protein/particle production. Their changes along the time for each production experiment correlate with the intracellular viral protein content determined by Western blot.

This work shows that this simple, fast and low cost assay, which requires low sample volume, is a powerful analytical tool that complements the most common analytical methods used for monitoring bioprocesses and has potential application in the biotechnological industry namely, in the production of recombinant proteins.

© 2009 Elsevier B.V. All rights reserved.

1. Introduction

Since the late 80's [1,2], matrix-assisted laser-desorption/ionization (MALDI) time-of-flight (TOF) mass spectrometry (MS) has been applied in many scientific research areas, mainly in the proteomics field [3]. More recently, the suitability of MALDI MS approaches for identification and characterization of clinically important microorganisms [4], including bacteria [2,5–10], fungi [11–13], viruses [14] and spores [15–18] has been probed. MALDI-TOF MS profiles have also been used to analyze single cells and tissue samples from animals namely, mollusk, insect neurons [19,20] and mammalian cells [21].

Besides detecting various metabolites or characteristic components of the cell envelopes [2,22,23] in the low mass range, intact cell MALDI (ICM-MS[1]) also provides unique insights into cell biology and chemistry based on the detection of chemicals or in the measurement of chemical changes in response to environmental, temporal or other external influences [8,24,25]. MALDI-TOF MS fingerprint comparisons in the mass range 2–20 kDa are currently considered as a rapid approach for bacterial identification, an application termed phyloproteomics [8,17,26–28]. This strategy is based on the computer-assisted comparison of spectral fingerprints obtained directly from intact cells [29–32] with internet-accessible protein sequence databases [17,33–36], for identification of specific biomarkers based on the molecular masses of proteins.

In the intact cell MALDI-TOF MS (ICM-MS) approach, cells are mixed with an energy-absorbing matrix and irradiated with UV-laser. The matrix promotes laser energy transfer to the cells that results in the ionization of cell-surface macromolecules. The quality of the spectra produced is highly dependent on the choice of matrix, composition of the matrix solvent and sample preparation procedure [37]. Matrix solvent influences the release of macromolecules from the cell and co-crystallization with the matrix compound affects the mass range of the molecules being ionized, allowing enhancing the differential ionization of specific compounds, such as proteins, lipopeptides or nucleotides [8,38].

In this study, a novel application for the ICM-MS method is reported. This methodology was used to monitor the production of viral proteins (VP) and virus-like particles (VLPs) by the insect cells *Spodoptera frugiperda* Sf-9/baculovirus expression system. This is a widely used system for recombinant protein and VLP production

* Corresponding author at: Instituto de Tecnologia Química e Biológica, Universidade Nova de Lisboa, Av. da Republica – EAN, 2780-157 Oeiras, Portugal.
Tel.: +351 21446 9452; fax: +351 21441 1277.
E-mail address: varela@itqb.unl.pt (A.V. Coelho).

[1] Abbreviations: ICM-MS – intact cell MALDI-TOF mass spectrometry; VLP – virus like particle; VP – viral protein; MOI – multiplicity of infection; HPI – hours post-infection; DHB – 2,5-dihydroxybenzoate; SA – sinapinic acid; DHAP – 2,6-dihydroxyacetophenone; *dS* – Dissimilarity Score.

0039-9140/$ – see front matter © 2009 Elsevier B.V. All rights reserved.
doi:10.1016/j.talanta.2009.06.081

as it allows high productivities, it does not contain contaminants from mammalian sources and the baculovirus expression vectors are flexible and easy to handle [39]. In this work, cells involved in real time production of Rotavirus VLP's, were used as a model to follow insect cell fingerprint changes by ICM-MS. These triple layered particles, contain, in the inner shell, 60 dimers of VP2 (102.7 kDa); in the middle shell, 260 trimers of VP6 (44.9 kDa) and in the outer shell, 780 monomers of the glycosylated VP7 (37.2 kDa) [40].

The ICM-MS experimental approach has many advantages, namely: (i) it is compatible with crude samples and sample clean up is minimal; (ii) there is no need for tagging or pre-select proteins or peptides of interest; (iii) uses simple instrumentation; (iv) has high sensitivity; (v) provides complementary information to immunochemical methods; (vi) is compatible with post-translational modifications; (vii) requires low amounts of sample and (viii) is low time consuming due to minimal sample preparation [41]. ICM-MS is therefore, a very interesting alternative to monitor the production of recombinant proteins avoiding high analytical costs, usually associated to immunochemical reagents, large sample volumes and time consuming protocols.

2. Materials and methods

2.1. Cell line and baculovirus

Spodoptera frugiperda Sf-9 and *Sf-21* cell lines were obtained from the American Type Culture Collection (ATCC, USA). Sf-9 cells were used for production of baculovirus and VLPs, Sf-21 cells were used for virus titration. Both cell types were cultured in serum free media SF900II (Gibco, Glasgow, UK) at 27 °C in 250 mL (working volume) Wheaton spinner flasks stirred at 150 rpm or in 500 mL Erlenmeyers with 50 mL (working volume) at 90 rpm.

Autographa californica nucleopolyhedrovirus (AcMNPV) recombinant baculovirus vectors, individually expressing bovine vp2 or vp6 or vp7 gene, under the control of polyhedron promoter, were constructed and kindly provided by Dr. Jean Cohen from Centre National de la Recherche Scientifique-Institut National Recherche Agronomique, Gif-sur-Yvette, France.

The viruses were titrated using the assay described by Mena [42], based on cell viability. Infections were performed at a cell concentration at infection (CCI) of 1×10^6 cell mL^{-1}. The recombinant baculovirus were amplified by infecting Sf-9 cells at a multiplicity of infection (MOI) of 0.1 pfu $cell^{-1}$. Baculovirus were harvested with a cell viability of approximately 70%, corresponding to the 4–5 days post-infection [43], by centrifugation at $200 \times g$ for 10 min. For proteins and VLP production a MOI of 5 pfu $cell^{-1}$ was used. The density of infected cells was determined by haemocytometer cell counts (Brandt, Werthein/Main, Germany) and the viability evaluated by trypan blue exclusion dye (Merck, Darmstadt, Germany) in 0.4% of phosphate-buffered saline (PBS).

2.2. Monitoring kinetics of VPs and VLP production

The following kinetic experiments were carried out in duplicate: (i) *Control* 1, non-infected insect cells; (ii) *Control* 2, insect cells infected with a wild type baculovirus; (iii) *VP production*, insect cells independently infected with monocistronic recombinant baculovirus for VP2, VP6 and VP7 production; and (iv) *VLP production*, insect cells co-infected simultaneously with VP2, VP6 and VP7 monosistronic recombinant baculovirus for VLP2/6/7 production.

Aiming at monitoring VPs production kinetics, samples were collected approximately every 12 h and centrifuged at $200 \times g$ for 10 min. The cell pellet was washed three times with PBS and finally resuspended in 3 μL of 0.9% (w/v) NaCl for insect cell ICM-MS analysis. Total protein content was also assessed using the BCA Protein Assay Kit (Pierce, Rockford, USA).

2.3. VPs quantification

Intracellular viral protein quantification was done by Western blot, according to the protocols previously described [44]. The amount of each protein was normalized using a well characterized VLP standard, produced and purified using a method described elsewhere [45]. Immunochemical staining for recombinant protein detection was carried out with a polyclonal anti-Rotavirus serum (for VP6 and VP7 detection) and a monoclonal antibody produced against VP2, both kindly provided by Dr. Jean Cohen, Gif-sur-Yvette, France. Blots were developed after incubation with an alkaline phosphatase conjugated anti-rabbit IgG antibody (Sigma, St. Louis, USA) and an alkaline phosphatase conjugated anti-mouse IgG antibody (Sigma, St. Louis, USA) using 1-stepTM NBT/BCIP blotting detection reagent (Pierce, Rockford, USA). The product yield was estimated by densitometry analysis of the scanned images (ImageQuant® for Microsoft® WindowsNT®, Molecular Dynamics, Inc., USA, 1998).

2.4. Sample preparation for ICM-MS

The quality of *Spodoptera frugiperda* Sf-9 cell suspension spectra was evaluated using three MALDI matrices. All matrix solutions, 2,5-dihydroxybenzoate (DHB), sinapinic acid (SA) and 2,6-dihydroxyacetophenone (DHAP), were prepared daily in 70% (v/v) acetonitrile 0.1% (v/v) trifluoroacetic acid with the concentration of 20 mg mL^{-1}.

Two sample MALDI target application procedures were tested: direct spotting of the insect cells on the MALDI target plate followed by the matrix solution which were air-dried prior to analysis; or by spotting the previously mixed cell suspension with the matrix solution. Different matrix:cell suspension volume ratios were tested for the direct spotting method 1:1 and 1:0.6. For the mixture spotting a 1:5 volume ratio has been used.

In order to try improving MALDI-TOF spectra intensity [7,46], mechanical disruption of cells was done using glass beads under vigorous agitation for 1 min after the addition of matrix to the cell suspension (1:1). Obtained whole cell lysates were directly spotted on the MALDI plate for further analysis.

2.5. Data acquisition and processing

All mass spectra were obtained using a PerSeptive Biosystems MALDI-time-of-flight (TOF) MS Voyager-DE STR (Framingham, USA) equipped with delayed extraction, and a 337-nm N_2 laser. Mass spectra were acquired in linear delayed extraction mode using an acceleration of 20 kV and a low mass gate of 5000 Da. The laser power was set to just above the threshold of ionization. Spectra for individual samples were accumulated, averaging 150 shots taken across the width of the sample spot for m/z values between 5000 and 25 000.

The individual spectra were initially processed by Data Explorer 4.2 software (Applied Biosystems, Foster City, USA) used for baseline correction, noise removal and peak detection. For each spectra, m/z peaks relative intensities were computed with the most intense peak set to 100%. Peaks with 5% maximum peak area, relative intensity below 5%, and a mass resolution bellow 500 were ignored. From the peak lists obtained as previously described, m/z peaks were deleted if their relative intensity was below 20% for the mass range of 5000–7500 Da; below 10% for the mass range of 7500–10 000 Da; and below 5% for the mass range of 10 000–25 000 Da.

The web interface SPECLUST created by The Computational Biology & Biological Physics Group at Lund University

(http://bioinfo.thep.lu.se/speclust.html) was used to construct dendograms based on MALDI-TOF MS data. To proceed with statistical analysis, the processed mass lists were converted into SPECLUST input format files. This program compares *m*/*z* peak lists by measuring a distance between each pair of lists [50]. A mass tolerance of 10 Da was given to assign peak similarity due to the resolution achieved in the used *m*/*z* range.

3. Results

3.1. Sample preparation and ICM-MS method optimization

Apart from the classical application of MALDI MS in proteomics (e.g. identification of isolated and purified proteins and peptides), it has also been used more recently with intact cells for identification of microbes and monitoring of recombinant protein productions in *E. coli* [25]. It is known that intact cell MALDI spectra profiles can be highly variable [46,47]. Therefore, it is important to investigate the effect of sample preparation procedure on spectra quality and data acquisition reproducibility. Cell treatment (cell suspension or whole cell lysate), appropriate MALDI matrices and several matrix:cell suspension ratios were evaluated. Two MALDI target plate sample application methods were also assessed. In each case, mass spectra were examined for number and relative abundance of *m*/*z* peaks detected. The best condition was direct spotting on the MALDI plate, using 2,6-dihydroxyacetophenone matrix in a matrix:cell suspension volume ratio of 1:1. The number of detectable peaks and their relative intensities were considerably higher when comparing with those detected using sinapinic acid matrix. No peaks were detected when using DHB matrix (Fig. 1).

Different methods for applying samples onto the MALDI target plate and insect cell treatment conditions were also evaluated. The *m*/*z* peaks that passed the acceptance criteria (described under Materials and methods) were listed for each spectrum and both common and new peaks were identified. The number of occurrences was determined for each *m*/*z* peak using *Peaks In Common consensus analysis*, a functionality of SPECLUST. Peaks were considered as *common* when appearing in more than 70% of the spectra and as *new* if fewer occurrences took place. Then, the percentage of *common* and *new* peaks was determined by dividing the number of each occurrence by the total number of peaks per spectra. The mean number of the overall detectable peaks was 23 for the direct application of insect cells onto the MALDI plate, 12 when previously mixing the cell suspension with matrix (1:1 ratio) and 14 for the cell lysate treatment. Fewer peaks were detected when diluting cell suspension in matrix. The higher number of detectable *m*/*z* peaks was obtained by direct spotting the cell suspension onto the MALDI plate (Fig. 2). In this condition, lower inter-spectra variability was also achieved, corresponding to an average of 6 *new* *m*/*z* peaks per spectra (26% of total detectable *m*/*z* peaks). To estimate the reproducibility associated with the selected method, the total number of detectable peaks and the number of peaks assigned as *common* was determined in 6 replicates. The outcome of this analysis revealed an average of 23 detectable peaks in which 15 and 17 of them are common to at least 90% and 70% of the analyzed spectra, respectively.

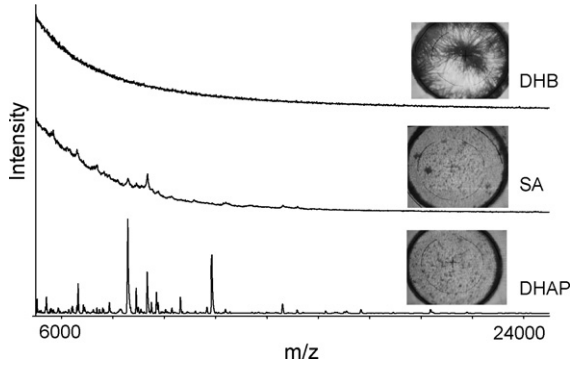


Fig. 1. Effect of matrix on insect cell ICM-MS spectra: Insect cell suspension MALDI-TOF MS spectra using different matrices (DHB, SA and DHAP) and pictures of their co-crystallization are presented. All spectra were collected after direct spotting. A ratio of 1:1 of matrix:insect cell suspension was used. DHAP (20 mg mL^{-1}) in 70% acetonitrile 0.1% trifluoroacetic acid seems to be the optimal matrix since it originates spectra with more detectable peaks.

3.2. S. frugiperda cells fingerprint evaluation and the Dissimilarity Score

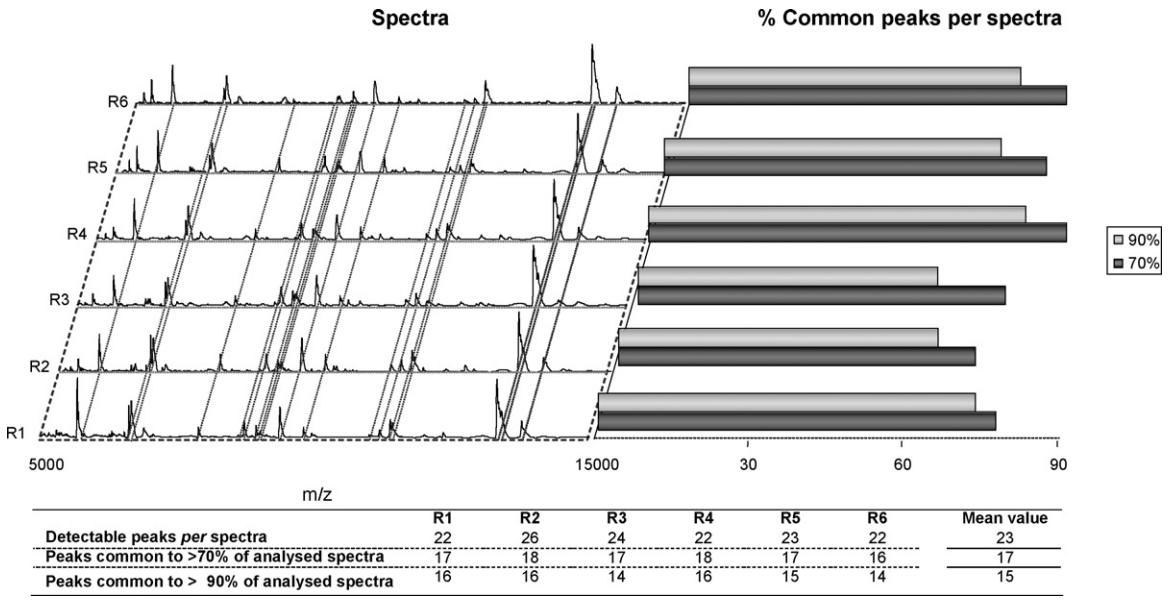
ICM-MS approach was already been used to study regulation of recombinant protein production *in vivo* by monitoring the *m*/*z* peak that corresponds to the molecular mass of the over expressed protein [25]. Similarly, we examined the presence of *m*/*z* peaks corresponding to the molecular masses of the expressed viral proteins in the MALDI-MS fingerprint of the intact insect cells, but no matching peaks were observed. This could be explained by the fact that the viral proteins VP6 and VP7 are secreted from the insect cells into the culture media, being the VP2 protein the only one that accumulates in the cellular cytoplasm. However, VP2 protein has a molecular mass of 102 kDa, making it more difficult to detect since MALDI ionization efficiency is reduced with protein size. Our strategy was then to evaluate if protein production could be indirectly monitored *in vivo* by studying the real-time changes in the MALDI-MS fingerprints of the intact insect cells during the bioreaction events.

For this purpose, some factors such as cell growth phase on bioreactor or cell stress caused by baculovirus infection had to be evaluated, since they can imply changes on the insect cell's fingerprint, independently of the changes imposed by the production of the viral proteins. In order to evaluate the contribution of these factors to the acquired spectra pattern and reproducibility, we have undertaken assays with *S. frugiperda* Sf-9 cells collected from two different experiments. In *Control* 1, insect cells were simply left under optimal growing conditions in the bioreactor for 5 days. In *Control* 2, insect cells were infected with "empty" wild type baculovirus allowing evaluation of the infection impact on insect cell MALDI spectra fingerprint. For both experiments, ICM-MS spectra were acquired using the optimized conditions previously described for the various insect cell pellets, corresponding in total to 11 time checkpoints (approximately 12 h cycles) of the real bioreactor productions.

After MS data acquisition and processing, 11 *m*/*z* peak lists were generated for each control group assay and submitted for consensus analysis. In SPECLUST, a new list is generated per control group containing the *m*/*z* values for the detectable peaks, where the mean *m*/*z* value is included in the *common* peaks. A simple mathematical expression has been developed to estimate the insect cell fingerprint differences between groups of submitted spectra. The Dissimilarity Score, *dS* (Eq. (1)), is the ratio between the total number of *m*/*z* peaks in the list generated by the *consensus analysis*, P|x|, and the mean number of *m*/*z* peaks per spectrum list in the analyzed group, which represents the mean value of the number of detectable peaks per spectra, |Px|; where *n* represents the number of spectra to be compared.

$$dS = \frac{P|x|}{|Px|}, \quad 1 < dS < n \tag{1}$$

Equal spectra have the same number of *m*/*z* peaks as the number of peaks in the list generated by the *consensus analysis* P|x|, and it will be equal to the mean number of detectable *m*/*z* peaks per spectra |Px|. So when comparing equal spectra, the Dissimilarity Score value is 1 ($dS = 1$).



	R1	R2	R3	R4	R5	R6	Mean value
Detectable peaks *per* spectra	22	26	24	22	23	22	23
Peaks common to >70% of analysed spectra	17	18	17	18	17	16	17
Peaks common to > 90% of analysed spectra	16	16	14	16	15	14	15

Fig. 2. Inter-spectra variability inherent to sample preparation method. Six MS spectra (R1–R6) were acquired after direct spotting of cell suspension: DHAP matrix solution (1:1) onto the MALDI plate. An average of 23 *m*/*z* peaks was detected *per* spectrum, 15 and 17 of them are common to at least 90% and 70% of the analyzed spectra, respectively. Vertical lines match common *m*/*z* peaks.

By opposition, if the compared spectra are completely different with no common peaks in the submitted spectra, the Dissimilarity Score will have the maximum value, equivalent to the number of peak lists that were submitted.

The Dissimilarity Score values are only comparable when submitting the same number of MS spectra per group. In the present work, we have analyzed 11 time checkpoints on cell samples collected from each bioreaction run, which allowed comparing *dS* between different kinetic experiments.

Higher *dS* values correspond to stronger differences among *m*/*z* peak lists of the analyzed time checkpoints. This indicates the occurrence of more extensive modifications on the insect cell fingerprint during the kinetic experiment. This becomes obvious when comparing the insect cells fingerprint variation along time in both experiments (Fig. 3). In *Control* 1 group, there are about 20 *m*/*z* peaks common to 70% of the spectra and 10 common to 90% of the spectra. This is within the estimated spectra variability (15 peaks common to 90% of the spectra in a total of 23 detectable peaks), meaning there are no apparent changes in the fingerprint along the time. In contrast, in *Control* 2, the number of common *m*/*z* peaks decreases to 13 when considering 70% of the spectra and 5 when considering 90% (in a total of 34 detectable peaks). These values are considerably lower, and show that after infection, the insect cells fingerprint changes throughout time. This is also

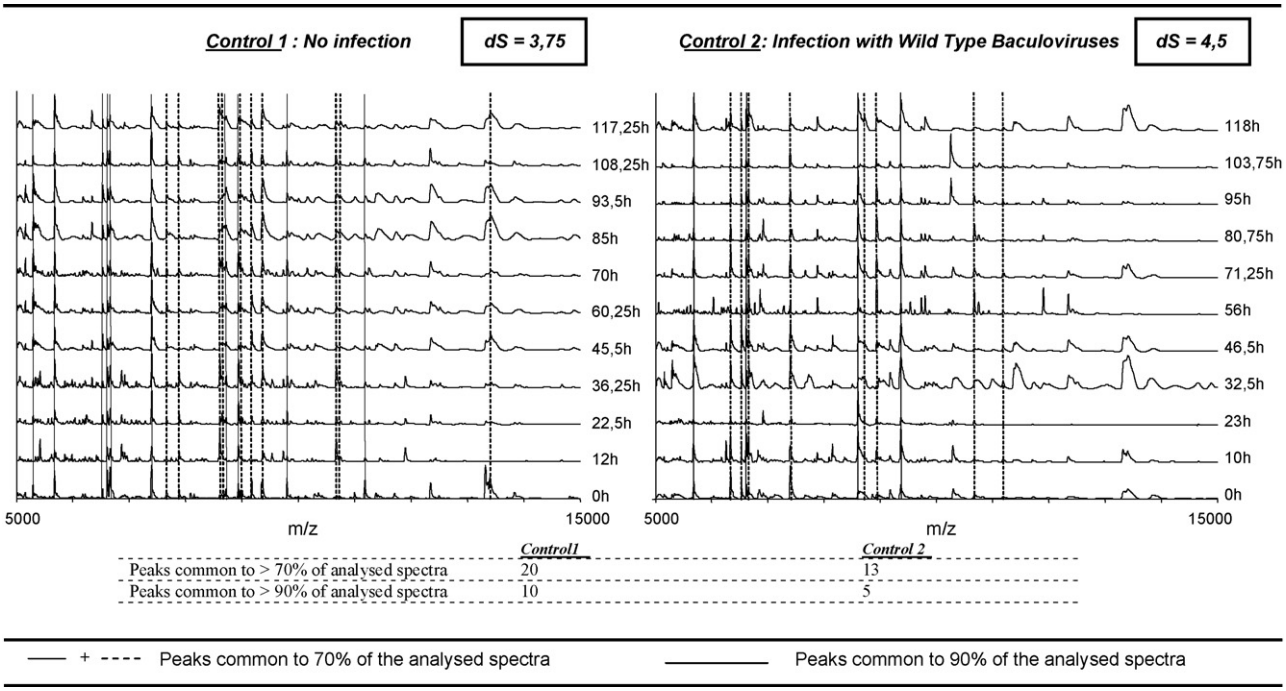


Fig. 3. Sf-9 intact cell fingerprints. Intact cell fingerprints along time for non-infected (*Control* 1) and infected (*Control* 2) are presented in the left and right side, respectively. A strong variation of the fingerprint along the kinetic experiment was observed for the insect cells infected with wild type baculovirus, in accordance with the calculated *dS* values. Vertical lines match common *m*/*z* peaks.

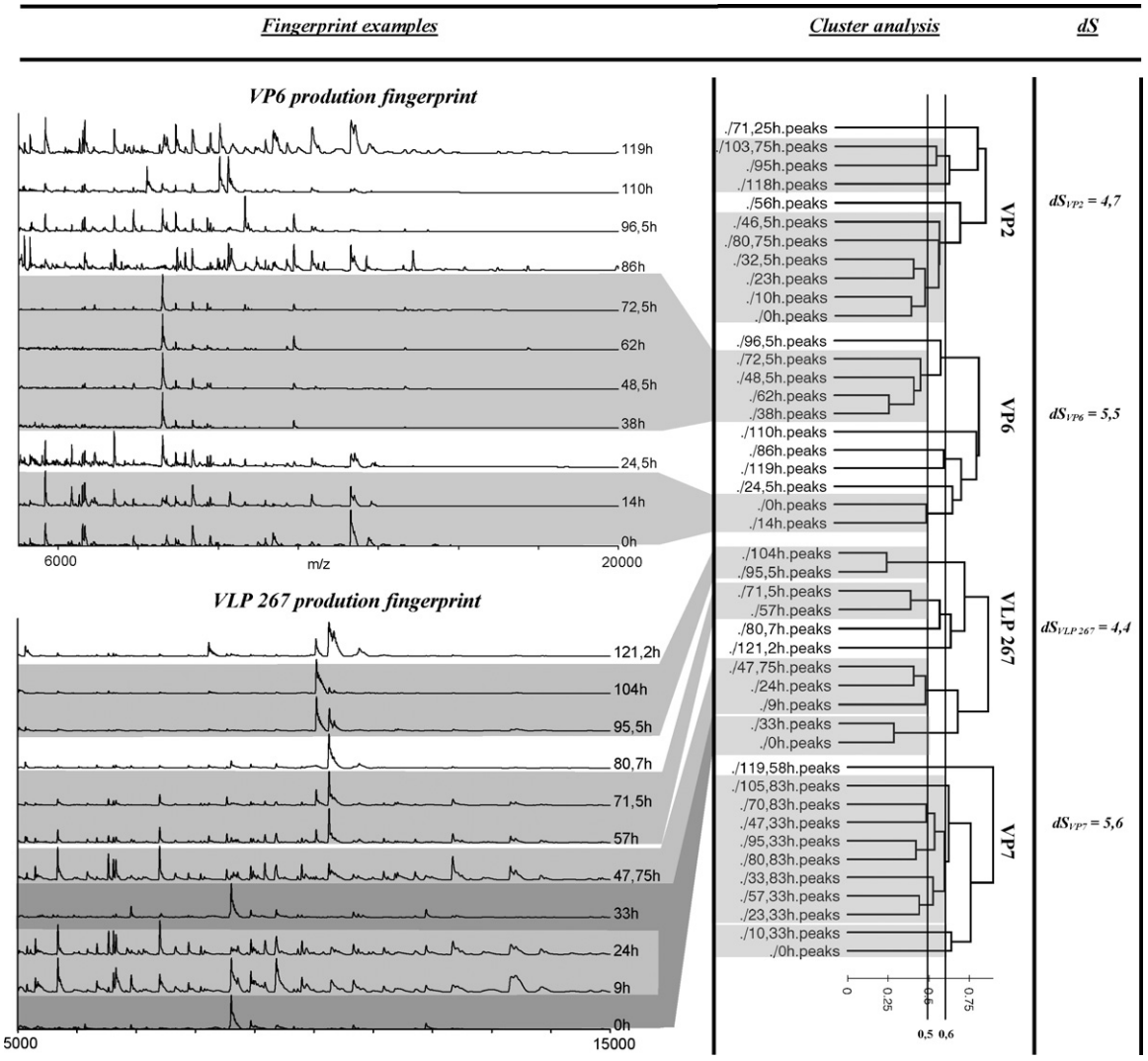


Fig. 4. Fingerprinting the production of VP2, VP6, VP7 and VLP2/6/7 in the Sf-9 cells. Cluster analysis was performed, for each group, using SPECLUST in order to evaluate the changes within time for each production run (middle column) and the Dissimilarity Scores were calculated (right column). Two examples of insect cell fingerprints for individual productions are shown (left column) and the determined similar groups in the correspondent dendograms are highlighted in grey. The grouping of the cluster analysis is consistent with fingerprint changes as judged by visual inspection.

confirmed by the values of the Dissimilarity Score. For both groups the score limits are 1 for ideally equal spectra and 11 for spectra without common peaks. For *Control* 1 $dS = 3.75$ is lower than *Control* 2 $dS = 4.5$, which confirms that insect cells fingerprint in *Control* 2 group suffers more changes along time than in *Control* 1. Apparently, optimal bioreactor working conditions without other external *stimuli* do not cause changes in cells fingerprint. However, significant changes could be detected when infection is induced.

3.3. Fingerprinting the bioproduction of VP2, VP6, VP7 and VLP 267 in insect cells by ICM-MS

So far, it has been proved that the infection process itself induces fingerprint changes on insect cells, but there is still a question left to answer: if fingerprint evolution is affected by the infection mode and assembly of VLP's. Two possibilities were evaluated: infection with baculovirus expressing one recombinant protein and co-infection with three baculovirus for co-expression of three recombinant proteins. To address this question, the groups of fingerprints for each viral protein production were analyzed using two different approaches: (i) the *Dissimilarity Scores* were calculated for each group and (ii) a cluster analysis was performed for each kinetic experiment using SPECLUST.

By comparison of the *Dissimilarity Score* values for the kinetic experiments, it is possible to detect changes in the MS profiles of the insect cells along the production time when the viral proteins are produced separately (VP2 or VP6 or VP7) or when VLP's are produced by co-expression of the three genes (VP2, VP6 and VP7). All the determined values are above the *dS* for *Control* 1 (3.75) where no relevant fingerprint changes occurred. For insect cells producing VP2, VP6, VP7 and VLP 2/6/7, the *dS* are 4.7, 5.5, 5.6 and 4.4, respectively. These values are in accordance with a visual comparison of the spectra, showing fingerprint profile changes for each bioproduction opposed to more stable fingerprints in *Control* 1 (Fig. 4).

In order to analyze these changes in further detail, we performed a *hierarchical clustering* of the mass spectra for each group. The main goal was to compare and correlate results from a Western blot traditional assay with the obtained ICM-MS spectra from insect cells in the various stages of the protein production.

In the SPECLUST cluster analysis, each m/z peak list is initially assigned to its own cluster. Distances are calculated between each pair of m/z peak lists. The closest pair is found and merged to a new cluster. Distances between the new cluster and each of the old

clusters are calculated. This procedure is repeated until there is only one single cluster. Then, a score for matching m/z peaks is created, where the similarity between two m/z peak lists is calculated. This is then translated into a distance measure, which varies between 1 for completely different set of m/z peaks, and zero for a perfect match. This is the starting point in clustering the m/z peak lists and building a dendogram.

To interpret the cluster analysis of the insect cells fingerprints, it was verified that, for distances smaller than 0.6 in the dendograms scale, the grouped spectra were similar [50]. Considering this scale limit, several interesting spectra grouping occurred in each protein/particle production. In detail, for insect cells producing VP2 there are two main spectra groups formed in the dendogram (Fig. 4), one representing times 0–46.5 h and another spectra group that includes the three last time points, collected from 96.5 to 119.0 h.

When comparing with methods routinely used to monitor protein production during bioreaction (e.g. Western blot), in the first group of similar spectra, the turning point in fingerprint change is at 46.5 h, which is consistent with an increase of intracellular protein concentration value related to the initiation of VP2 production (Fig. 5A). The second group of similar spectra (96.5 to 119.0 h) is distinct from the first one, corresponding to the terminus of the bioproduction process. It has been previously reported that VP2 accumulates intracellularly when VP6 is not co-expressed [48]. There are still two time points remaining, 56.0 and 71.2 h, where the spectra are distinct from one and other and from the two formed groups. This is possibly related to a temporary decrease in cell viability (data not shown).

In cells producing VP6, there is also fingerprint grouping which can be related to biological events. Two main groups of similar spectra (Fig. 4) were obtained: the first group includes the time points 0.0 and 14.0 h, which is, in fact, the starting of the protein production (Fig. 5B). In the second group, spectra are similar from the 38.0 to 72.5 h time points, which is consistent with a stable intracellular concentration of VP6 (Fig. 5B). In the last phase of protein production the data do not correlate with each other, which is in accordance with random variation in the intracellular protein concentration, possibly associated with protein excretion events.

VP7 is a glycosylated secreted protein, an interesting correlation with the results obtained in the Western blot analysis is observed. There seems to be two groups of similar spectra: time points 0.0 and 10.3 h, and the rest of the time points. For the first group intracellular VP7 concentration is almost zero, however, after this time period its concentration increases and is maintained constant till the end of the bioreaction (Fig. 5C). This behavior is eventually related to the fact that VP7 is secreted to the extracellular medium early in the bioreaction process, thus, it does not accumulate intracellularly, and it does not trigger major fingerprint changes.

For the VLP 2/6/7 particle production, insect cells undergo even more complex biological processes: infection and replication of three monocistronic baculovirus, the co-expression of three recombinant proteins, and their assembly into VLPs, among other important events. There is a curious phenomenon of spectra grouping, due to similarity between distant time point's fingerprints (Fig. 4). This is observed up to 47.8 h post-infection, where the points 0.0 and 33.0 h group together as so do points 9.0–24.0 h and 47.8 h. These variations in intracellular total protein concentration are eventually related to the several steps involved in the baculovirus replication process, in which baculovirus proteins are expressed (Fig. 5D).

3.4. Infection stress versus viral protein production: distinct specific fingerprints?

Firstly, since it was determined that the infection process itself induces fingerprint changes on the insect cells, it was decided to evaluate if the fingerprint changes of the insect cells producing viral particles and proteins were different and could be correlated with a particular kinetics of viral protein production. Secondly, we tried to understand if the fingerprint changes were specific of each particular recombinant protein being produced with this expression system. To address these questions dendograms were constructed using both the fingerprints of the different protein kinetics and the fingerprints of *Control* 2 (Fig. 6). Taking into account the cluster analysis results, the overall conclusion is that the fingerprint of the first time points of the infection are similar either for infection with wild type baculovirus and for cells producing the different viral proteins. This reveals that in these first time points, fingerprints show only the contribution of the infection processes and infection stress related events. As infection proceeds in time, fingerprints start to differentiate from the initial time point pattern, and no longer are similar with the fingerprint of cells infected with wild type

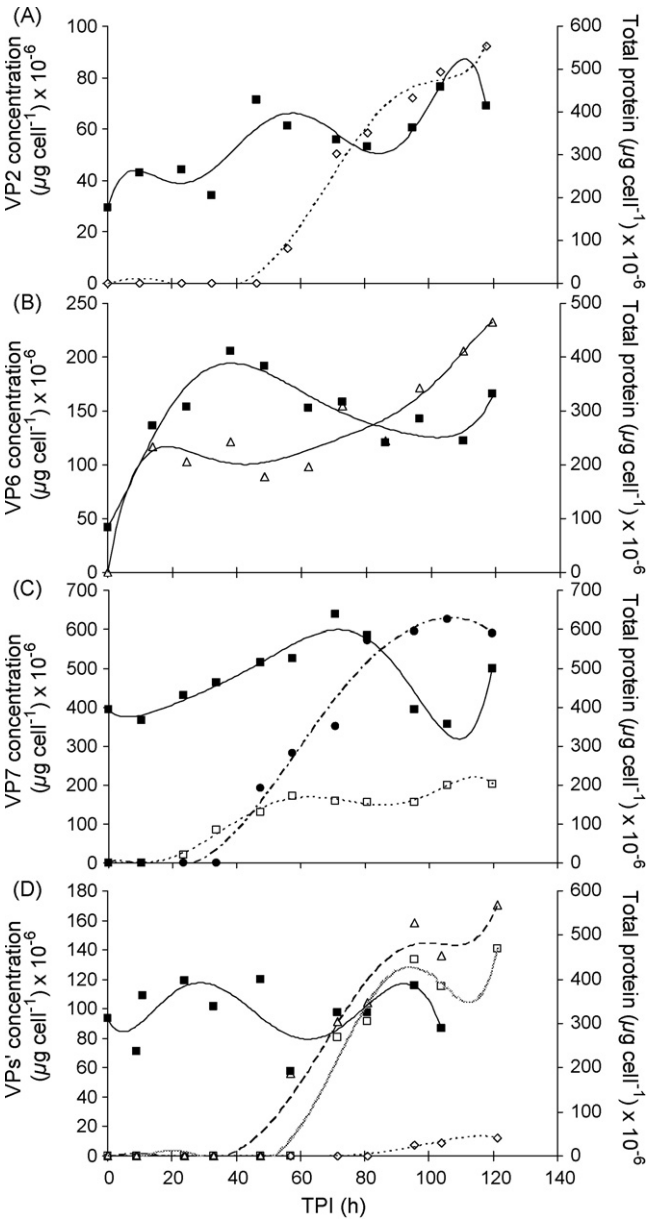


Fig. 5. Kinetics of VP2 (A), VP6 (B), VP7 (C) and VLP 2/6/7 (D) production and total protein concentration. Intracellular VP2 (◊), VP6 (△), VP7 (□) and extracellular VP7 (●) concentration were calculated from densitometry analysis of Western blot bands using a VLP standard for calibration. Intracellular total protein concentration (■) was measured with BCA assay.

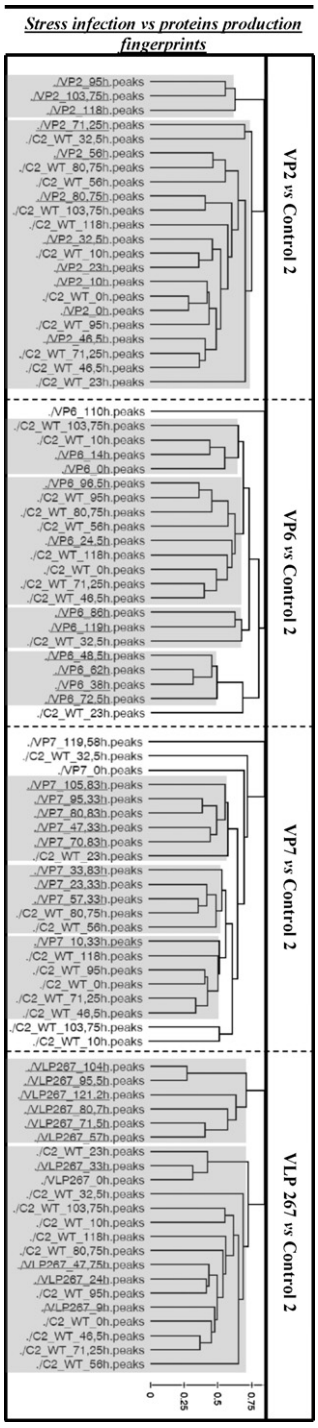


Fig. 6. Comparison of viral protein production with cell stress caused by baculovirus infection. Cluster analysis of insect cells fingerprints of each viral protein production and from infected insect cell (*Control* 2).

baculovirus. This indicates that the production of each viral protein or VLP has an impact on insect cell fingerprint. To determine if each fingerprint change, for the production of a particular viral protein or VLP is specific and unique, cluster analysis was also performed comparing pairs of two of all protein production (data not shown) (VP2 vs. VP6; VP2 vs. VP7; VP2 vs. VLP 2/6/7; VP6 vs. VP7; VP6 vs. VLP 2/6/7; VP7 vs. VLP 2/6/7). This cluster analysis shows that each fingerprint profile depends on the specific protein(s) that is (are) being produced, showing the same cluster behavior as described for the comparison of each protein(s) production(s) with *Control* 2, where only the fingerprints of the first time points are similar.

4. Discussion

The usefulness of mass spectrometry approaches in bioanalysis of recombinant protein from biotechnological production has already been described when using liquid chromatography coupled with a mass spectrometer [49] as being *potentially useful as it may offer rapid development and improved assay specificity*. In this paper we present a new application for the described mass spectrometry method *intact cell MALDI-TOF MS* (*ICM-MS*). This MALDI-MS approach has application in the biotechnological industry allowing monitoring the production of viral proteins and virus-like particles. This technique is presented here as a complementary analytical method to monitor recombinant protein production during bioreaction and using the established pattern for the expression system/recombinant protein produced. Herein this method has been optimized for insect cells/baculovirus expression system and the production of Rotavirus proteins and virus-like particles. The experimental results obtained show that this is a highly reproducible method for each recombinant protein that allows checking if production is in fact occurring, by monitoring fingerprint changes observed when insect cells are producing the viral proteins. Moreover, the proposed method indicates the bioproduction phase allowing monitoring the lag periods. These fingerprint changes are independent of cell stress due to infection and are characteristic of each protein or VLP production.

This very simple, fast (10 min sample preparation) and low cost assay requires low sample volumes and can be used as a complement or even as a substitute of common analytical methods for bioproduction monitoring. However, careful method optimization is still required when applied to other biological samples, since sample preparation procedure can be substantially different.

Acknowledgments

FCT is acknowledged for financial support of the project (POCI/BIO/55975/2004).

We acknowledge Dr. A.L. Simplicio for the English revision.

References

[1] K. Tanaka, H. Waki, Y. Ido, S. Akita, Y. Yoshida, T. Yoshida, Rapid Commun. Mass Spectrom. 2 (1998) 151–153.
[2] M.A. Claydon, S.N. Davey, V. Edwards-Jones, D.B. Gordon, Nat. Biotechnol. 14 (1996) 1584–1586.
[3] M. Mann, R.C. Hendrickson, A. Pandey, Annu. Rev. Biochem. 70 (2001) 437–473.
[4] C. Fenselau, P.A. Demirev, Mass Spectrom. Rev. 20 (2001) 157–171.
[5] T. Krishnamurthy, P.L. Ross, U. Rjamani, Rapid Commun. Mass Spectrom. 10 (1996) 883–888.
[6] R.D. Holland, J.D. Wilkes, F. Raffi, J.B. Sutherland, C.C. Persons, K.J. Voorhes, J.O. Lay, Rapid Commun. Mass Spectrom. 10 (1996) 1227–1232.
[7] S.C. Smole, L.A. King, P.E. Leopold, R.D.J. Arbeit, Microbiol. Methods 48 (2002) 107–115.
[8] J.O. Lay, Mass Spectrom. Rev. 20 (2001) 172–194.
[9] V. Edwards-Jones, M.A. Claydon, D.J. Evason, J. Walker, A.J. Fox, D.B. Gordon, J. Med. Microbiol. 49 (2000) 295–300.
[10] R. Dieckman, R. Helmuth, M. Erhard, B. Malorny, Appl. Environ. Microbiol. 74 (2008) 7767–7778.
[11] K.J. Welham, M.A. Domin, K. Johnson, L. Jones, D.S. Ashton, Rapid Commun. Mass Spectrom. 14 (1999) 307–310.
[12] J.M. Hettick, M.L. Kashon, J.P. Simpson, P.D. Siegel, G.H. Mazurek, D.N. Weissman, Anal. Chem. 76 (2004) 5769–5776.
[13] P. Krader, D. Emerson, Extermophiles 8 (2004) 259–268.
[14] Y.J. Kim, A. Freas, C. Fenselau, Anal. Chem. 73 (2001) 5228–5231.
[15] E. Elhanany, R. Barak, M. Fisher, D. Kobiler, Z. Altoum, Rapid Commun. Mass Spectrom. 15 (2001) 2110–2116.
[16] T.Y. Li, B.H. Lee, Y.C. Chen, Rapid Commun. Mass Spectrom. 14 (2000) 2393–2400.
[17] V. Ryzhov, C. Fenselau, Anal. Chem. 73 (2001) 746–750.
[18] T. Neuhof, R. Dieckmann, I.S. Druzhinina, C.P. Kubicek, T. Nakari-Setala, M. Penttila, D. Von, H. FEBS J. 274 (2007) 841–852.
[19] P.A. Veelen, P.R. Jimenez, K.W. Li, W.C. Wildering, W.P. Geraerts, U.R. Tjaden, V. Greef, Org. Mass Spectrom. 28 (1993) 1542–1546.
[20] S.S. Rubakhin, V.J. Sweedler, Nat. Protoc. 2 (2007) 1987–1997.

[21] Z. Xu, M. Scalf, T.W. Berggren, M.S. Westphall, L.M. Smith, J. Am. Soc. Mass Spectrom. 4 (2006) 490–499.
[22] D.J. Evanson, M.A. Conway, D.B. Gordon, J. Am. Soc. Mass Spectrom. 12 (2001) 49–54.
[23] J.J. Jones, M.J. Stump, R.C. Fleming Jr., J.O. Lay, C.L. Wilkins, J. Am. Soc. Mass Spectrom. 15 (2004) 1665–1674.
[24] M. Erhard, H.V. Döhren, P. Jungblut, Nat. Biotechnol. 15 (1997) 906–909.
[25] M.J. Kulkarni, V.P. Vinod, P.K. Umasankar, M.S. Patole, M. Rao, Rapid Commun. Mass Spectrom. 20 (2006) 2769–2772.
[26] M.A. Conway, S.C. Smole, D.A. Sarracino, R.D. Arveit, P.E. Leopold, J. Mol. Microbiol. Biotechnol. 3 (2001) 103–112.
[27] E. Stackebrandt, O. Päuker, M. Erhard, Curr. Microbiol. 50 (2005) 71–77.
[28] K.L. Wahl, S.C. Wunschel, K.H. Jarman, N.B. Valentine, C.E. Petersen, M.T. Kingsley, T.A. Zartolas, Anal. Chem. 74 (2002) 6191–6199.
[29] R. Arnold, J.P. Reilley, Anal. Chem. 269 (1999) 105–112.
[30] J.J. Bright, M.A. Claydon, M. Soufian, D.B. Gordon, J. Microbiol. Methods 48 (2002) 127–138.
[31] K.H. Jarman, S.T. Cebula, A.J. Saenz, C.E. Petersen, N.E. Valentine, M.T. Kingley, K.L. Wahl, Anal. Chem. 72 (2000) 1217–1223.
[32] M.Z. Vargha, Z. Takáts, A. Konopka, C.H. Nakatsu, J. Microbiol. Methods 66 (2006) 399–409.
[33] P.A. Demirev, Y.P. Ho, V. Ryxhov, C. Fenselau, Anal. Chem. 71 (1999) 2732–2738.
[34] E.C. Lynn, M. Chung, W. Tsai, C. Han, Rapid Commun. Mass Spectrom. 13 (1999) 2022–2027.
[35] F.J. Pineda, M.D. Antoine, P.A. Demirev, A.B. Feldman, J. Jackman, M. Longnecker, J.S. Lin, Anal. Chem. 75 (2003) 3817–3822.
[36] Z. Wang, K. Dunlop, S.R. Long, L. Li, Anal. Chem. 73 (2002) 3174–3182.
[37] M.A. Domin, K.J. Welham, D.S. Ashton, Rapid Commun. Mass Spectrom. 13 (1999) 222–226.
[38] F. Leeders, T.H. Stein, K. Bärbel, P. Franke, J. Vater, Rapid Commun. Mass Spectrom. 13 (1999) 943–949.
[39] L. Maranga, Adv. Biochem. Eng. Biotechnol. 74 (2002) 183–206.
[40] L. Palomares, S. López, O.T. Ramirez, Biotechnol. Bioeng. 78 (2002) 1–9.
[41] L. Lingjun, R.W. Garden, J.V. Sweedler, TibTech 18 (2000) 151–160.
[42] J. Mena, O.T. Ramirez, L. Palomares, Biotechniques 34 (2003) 260–264.
[43] V.L. Petricevich, L. Palomares, M. Gonzalez, O.T. Ramirez, Biotechniques 34 (2001) 260–264.
[44] H.L. Vieira, C. Estêvão, A. Roldão, C.C. Peixoto, M.F. Sousa, M.J.T. Carrondo, P.M. Alves, J. Biotechnol. 120 (2005) 72–82.
[45] C. Peixoto, M.F. Sousa, C. Silva, M.J.T. Carrondo, P.M. Alves, J. Biotechnol. 127 (2007) 452–461.
[46] S.L. Gantt, N.B. Valentine, A.J. Saenz, M.T. Kingsley, K.L. Wahl, J. Am. Soc. Mass Spectrom. 10 (1999) 1131–1137.
[47] T.L. Williams, D. Andrzejewski, J.O. Lay, S.M. Musser, J. Am. Soc. Mass Spectrom. 14 (2003) 342–351.
[48] M. Labbé, A. Charpilienne, S.E. Crawford, M.K. Estes, J. Cohen, J. Virol. 65 (1991) 2946–2952.
[49] E. Ezan, M. Dubois, F. Becher, Pharm. Technol. Eur. (2008) 77–82.
[50] R. Johansson, P. Hjerno, C. Emanuelsson, M. Ringnér, J. Hakkinen, Proteom. Res. 5 (2006) 785–792.

Talanta 80 (2010) 1569–1575

Contents lists available at ScienceDirect

Talanta

journal homepage: www.elsevier.com/locate/talanta

Covalent selection of the thiol proteome on activated thiol sepharose: A robust tool for redox proteomics

Wentao Hu[a,1], Sara Tedesco[a,1], Roberto Faedda[b,1], Goffredo Petrone[c], Santa Olga Cacciola[d], Anne O'Keefe[a], David Sheehan[a,*]

[a] Proteomics Research Group, Dept. of Biochemistry, University College Cork, Cork, Ireland
[b] Dipartimento di Scienze e Tecnologie Fitosanitarie, Università degli Studi di Catania, Via S. Sofia 100, 95123 Catania, Italy
[c] Dipartimento di Scienze Agronomiche, Agrochimiche e delle Produzioni Animali, Università degli Studi di Catania, Via S. Sofia 98, 95123 Catania, Italy
[d] Dipartimento di Chimica Biologica, Chimica Medica e Biologia Molecolare, Università degli Studi di Catania, Viale A. Doria 6, 95125 Catania, Italy

ARTICLE INFO

Article history:
Available online 31 October 2009

Keywords:
Redox proteomics
Activated thiol sepharose
Cysteine
Thiol-containing proteins
Escherichia coli
Trichoderma harzianum
Mytilus edulis
Oxidative stress

ABSTRACT

Protein thiols contribute significantly to antioxidant defence and selective oxidation of cysteines is important in signal transduction even in sub-stress scenarios. However, cysteine is the second rarest residue in proteins and it can be difficult to target low-abundance thiol (–SH)-containing proteins in proteomic separations. Activated thiol sepharose (ATS) allows covalent selection of –SH-containing proteins which can then be recovered by reduction with mercaptoethanol or dithiothreitol. This is a robust method for enriching –SH-containing proteins. We have used ATS to estimate the percentage (by weight) of thiol-containing proteins in cell extracts from a range of biological sources: a bacterium, *Escherichia coli*; a fungus, *Trichoderma harzianum*; and a bivalve mollusc *Mytilus edulis*. –SH-containing proteins account for 2.52% (*E. coli*), 1.4% (*T. harzianum*) and 1.4% (*M. edulis*) of total protein. Exposure to pro-oxidants did not materially alter these values. On removal of low M_r thiols such as glutathione, the values for *M. edulis* did not significantly change but those for *T. harzianum* increased threefold. The two-dimensional electrophoresis profiles of ATS-selected proteins for each organism were compared in control and pro-oxidant-exposed preparations. This revealed that some proteins present in controls were absent in pro-oxidant-treated extracts which we attribute to thiol oxidation. ATS has significant potential in enrichment for –SH-containing proteins in redox proteomics.

© 2009 Elsevier B.V. All rights reserved.

1. Introduction

Since the adoption of aerobic metabolism as the most efficient means to convert food such as glucose into biologically useful energy, cells have been faced with the "oxygen paradox"; oxygen is essential for aerobic metabolism but inevitably produces highly toxic derivatives such as the superoxide radical, H_2O_2 and the hydroxyl radical [1,2]. These and related species, collectively referred to as reactive oxygen species (ROS), can react with cell components at rate constants approaching, in some cases, diffusion-limited values [1]. Cells have evolved impressive defences against ROS such as the antioxidant glutathione (GSH) and enzymes such as peroxidase, superoxide dismutase and catalase [1] and these maintain a state of redox homeostasis in normal cell functioning. However, if these defences are overwhelmed by an over-supply of ROS, or a decrease in antioxidant defence (e.g. on ageing), a state of oxidative stress results [3] which is often a feature of important human pathologies [3–6].

Proteins absorb ~70% of ROS and this causes covalent changes to amino acid side-chains with the potential to complicate the proteome [1–3]. Redox proteomics often focuses on comparisons of protein profiles of control to those of oxidatively stressed cells [7]. Sulphur-containing residues are especially susceptible to oxidation. Methionine is oxidised sequentially to methionine sulphoxide and sulphone and accumulation of oxidised methionine variants in proteins is a marker for ageing [8]. It has been suggested that methionines may contribute to antioxidant defence by buffering transient ROS increases [8]. Cysteine, the second rarest residue in proteins after tryptophan, is often evolutionarily conserved and possesses functional significance [2]. Oxidation of the cysteine sulphydryl group (–SH) can form sulphenic (–SOH), sulphinic ($-SO_2H$), sulphonic/cysteic ($-SO_3H$) acids, inter-/intra-chain disulphide bridges (–S–S–) or thiolsulphinates [1,2]. Oxidation to –SOH and –S–S– is thought to be

* Corresponding author at: Proteomics Research Group, Dept. of Biochemistry, University College Cork, Lee Maltings, Prospect Row, Mardyke, Cork, Ireland. Tel.: +353 21 4904207.
E-mail address: d.sheehan@ucc.ie (D. Sheehan).
[1] These authors contributed equally to this work.

0039-9140/$ – see front matter © 2009 Elsevier B.V. All rights reserved.
doi:10.1016/j.talanta.2009.10.047

reversible *in vivo* whilst oxidation to $-SO_2H$ or $-SO_3H$ is largely irreversible leading to protein degradation [1,2]. In response to oxidative stress, protein thiols form intra-/intermolecular –S–S– or mixed disulphides with GSH [9,10]. It is increasingly thought that, even under sub-stress conditions, protein thiols can be selectively converted to sulphenic acid with a role in redox signalling [11,12]. Some proteins key to triggering/regulating apoptosis (e.g. NEMO, ASK-1, STRAP, GAPDH, SAG) alter their disulphide bridge structure as part of their activation and a similar redox-sensitivity has been found in some microbial proteins [13–19].

A shortcoming of traditional two-dimensional electrophoresis (2DE) approaches is the fact that it can be difficult to detect or identify low-abundance proteins [20]. This can be overcome by enriching for proteins carrying particular structural features such as glycosylation [21] or phosphorylation [22]. Because of their importance as targets in redox proteomics and yet low-abundance, thiol-containing proteins have been tagged or enriched for studies of oxidative stress and redox signalling [13,23–26]. *N*-Ethyl maleimide (NEM)–biotin conjugates react with available –SH groups and can be selected on avidin columns [25]. Similarly, biotin-conjugated iodoacetamide has been used to trap thiol-containing proteins with low thiol pK_a values in competition with hydrogen peroxide [27]. The difficulties raised by non-specificity of reagents and the need for chemical derivatization to visualise reversible oxidations have been reviewed [28]. Because biotin–avidin binding is a non-covalent binding process, it has limitations including variable binding efficiencies and a need to avoid detergents or chaotropic agents which may be necessary to disrupt protein–protein interactions.

Activated thiol sepharose (ATS) is a commercially available, thiol-specific resin with an activated disulphide structure which reacts efficiently with –SH groups to form a covalent mixed disulphide linkage. The resin has previously been used in a column format for protein purification [29] but has only occasionally been used in a batch format suitable for proteomics work [30,31]. Protein thiols represent some 69% of total cell thiols in cultured human cells with the remainder being contributed by GSH [9]. As has previously been suggested for methionine [8], protein thiols act as an active redox buffer which is actually more quantitatively important than GSH [9]. In eukaryotes, protein thiols seem to account for 2–3% of total protein [9,32]. In this paper, we have used ATS-based covalent selection of –SH-containing proteins from three disparate biological extracts (*Escherichia coli, Trichoderma harzianum and Mytilus edulis*) as a means of enriching for SH-containing proteins in redox proteomics studies. We have quantified the percentage by weight of applied proteins trapped by ATS and find generally comparable values for all extracts to those previously reported for eukaryotes [9]. From this we conclude that ATS provides a robust and generally applicable one-pot route to enriching for the thiol proteome.

2. Materials and methods

2.1. Materials and reagents

Culture components for *E. coli*, dithiothreitol (DTT), urea and all other general reagents suitable for electrophoresis were purchased from Sigma (Poole, Dorset, UK). *T. harzianum* (strain IMI 393899) was maintained on potato dextrose agar (PDA, Oxoid Ltd., Basingstoke, UK). ATS was purchased from GE Healthcare, Little Chalfont, Bucks, UK. *M. edulis* was sampled from a previously used intertidal reference site in Cork Harbour, Ireland [33].

2.2. Culturing and handling procedures

2.2.1. E. coli

E. coli strain DH5α available in our laboratory was grown on LB-agar plates. Single colonies were selected for culture in LB broth. Pre-cultures (10 ml) were grown under constant agitation overnight and then added to 250 ml cultures for growth for an 8-h period at 37 °C with constant agitation until OD_{600} reached 0.4. These cultures were grown in control condition and also in the presence of 1 mM menadione. Cells were collected by centrifugation at 10,000 × *g* for 10 min.

2.2.2. T. harzianum

T. harzianum (strain IMI 393899) available in our laboratory was maintained on PDA. Conidia were collected using 10 ml sterile dH_2O and 15×10^6 spores were used to inoculate 150 ml of Czapek-Dox broth supplemented with 10 ppm of $CdCl_2$ in Roux flasks. Control cultures were grown in the same medium but lacking $CdCl_2$. Fungal mycelia were grown at 24 ± 1 °C for 8 days.

2.2.3. M. edulis

M. edulis was sampled from Cork Harbour, Ireland, at low tide, acclimated for a week in 50-l tanks containing natural aerated seawater collected from Bantry Bay, Ireland. They were kept in a 12-h light/dark cycle, at temperature of 15 °C, fed and with regular water changing (48 h intervals; Phytoplex™ phytoplankton feed, Kent Marine Inc., Acworth, GA, USA). There were three groups of five animals for each treatment and these were exposed (24 h) to 10 ppm of $CdCl_2$. Control groups (3 × 5 animals) were treated identically but not exposed to any treatment. Compounds were poured directly into the tank water and no mortality was observed under any of the conditions used.

2.3. Preparation of protein extracts

2.3.1. E. coli

Cell pellets were collected by centrifugation at 10,000 × *g* for 20 min and suspended in HEPES buffer (10 mM HEPES (N-[2-Hydroxyethyl]piperazine-N′-[2-ethanesulphonic acid]), pH 7) for sonication (Soniprep 150) at 14 μm amplitude 10 times for 15 s with a 1 min interval (on ice). Cell debris was collected by centrifugation at 12,000 × *g* for 5 min. Protein extracts were stored at −20 °C until required.

2.3.2. T. harzianum

Mycelia were collected by filtration on Whatman filter paper, washed with 100 ml of sterile dH_2O and immediately chilled on ice. Approximately 3 g of mycelia (wet weight) was ground in a mortar to a fine powder in liquid nitrogen and was suspended in 12 ml of extraction buffer (10 mM Tris–HCl, pH 7.2; 0.5 M sucrose; 0.15 M KCl; 1 mM EDTA; 1 mM PMSF). The suspension was centrifuged at 40,000 × *g* for 40 min (Sorvall RC 5C plus), the supernatant was ultracentrifuged at 100,000 × *g* for 40 min (Beckman-Coulter Optima L-100XP ultracentrifuge) and finally filtered through 0.2 μm filter. All operations were carried out at 4 °C. Total protein content of the samples was quantified.

2.3.3. M. edulis

Digestive glands were dissected, pooled (five animals), frozen in liquid nitrogen and stored at −70 °C until required. Samples were homogenized (10 mM Tris–HCl, pH 7.2; 0.5 M sucrose; 1 mM EDTA; 1 mM PMSF), centrifuged at 20,000 × *g* for 1 h and supernatants were stored at −70 °C.

Table 1
Thiol-containing proteins retained on activated thiol sepharose.

Species	Expt. 1	Expt. 2	Expt. 3	Mean (±SD)
E. coli				
Total protein loaded (μg)	2000	2000	2000	2000
–SH-containing protein (μg)	58	51.6	41.6	50.4 ± 8.26
% Retained	2.9	2.58	2.08	2.52 ± 0.41
T. harzianum				
Total protein loaded (μg)	2000	2000	2000	2000
–SH-containing protein (μg)	27	29	28	28 ± 1
% Retained	1.45	1.4	1.35	1.4 ± 0.05
M. edulis				
Total protein loaded (μg)	2000	2000	2000	2000
–SH-containing protein (μg)	30	13.4	40.8	28.06 ± 13.8
% Retained	1.5	0.67	2.04	1.4 ± 0.69

2.4. Protein estimation

Protein content was calculated by the method of Bradford using bovine serum albumin (BSA) as a standard [34]. Protein estimations were performed in triplicate and the percent protein retained on ATS was calculated from a known amount of total protein applied. Data from three independent experiments are shown for each organism studied.

2.5. ATS selection of thiol-containing proteins

All buffers used during this procedure were first filtered using 0.2 μm nitrocellulose membranes (ProTran, Schleicher & Schuell, Dasel, Germany) and degassed to reduce air oxidation. A detailed description of the method used is described elsewhere [35]. Briefly, extract samples (2 mg protein) were diluted with urea stock solution to 5 M final urea concentration and incubated in Eppendorf tubes for 10 min at room temperature to unfold protein. ATS (20 mg unswollen resin) and 200 μl binding buffer solution (0.1 M Tris–HCl, pH 7.5; 0.5 M NaCl; 1 mM EDTA) were then added, followed by incubation on ice for 1.5 h with gentle shaking every 15 min. Samples were washed 8 times (500 μl binding buffer), centrifuged (11,000 × *g* for 3 min) after each wash, and supernatants discarded to remove unbound proteins. Elution buffer (200 μl; binding buffer containing 25 mM DTT) was added to sample after the final washing step and beads were incubated for 1 h with gentle shaking every 15 min to release SH-containing proteins. Samples were centrifuged briefly and supernatants collected.

2.6. Two-dimensional electrophoresis

Non-protein contaminants were first removed from protein aliquots (200 μg) by precipitation in 10% (w/v) trichloroacetic acid followed by centrifugation (10,000 × *g* for 10 min) and then washed with acetone. The resulting pellet was re-suspended in rehydration buffer containing 5 M urea, 2 M thiourea, 2% (w/v) CHAPS, 4% (w/v) carrier ampholyte (Pharmalyte 3–10, GE Healthcare), 1% (w/v) DeStreak reagent (GE Healthcare) and a trace amount of bromophenol blue. Proteins (20 μg) were loaded on 7 cm pH 3–10 non-linear immobilised pH gradient (IPG) strips (BioRad, Hercules, CA, USA) and rehydrated overnight for at least 15 h. IPG strips were focused on a Protean IEF Cell (BioRad) with linear voltage increases. Following IEF, strips were equilibrated (20 min) in equilibration buffer (6 M urea; 0.375 M Tris, pH 8.8; 2% (w/v) SDS; 20% (v/v) glycerol) containing 2% (w/v) DTT, and then for 20 min in equilibration buffer containing 2.5% (w/v) iodoacetamide. Equilibrated strips were embedded in molten agarose (0.5%; w/v) containing trace bromophenol blue atop 12% (w/v) SDS–polyacrylamide gels, and electrophoresed at a constant voltage (150 V) at 4 °C using an Atto AE-6450 mini PAGE system (Atto, Tokyo, Japan) until the dye front reached the end of the gel. After separation, gels were silver-stained [36] followed by densitometry scanning.

2.7. Removal of low M_r thiols

In the case of *T. harzianum* and *M. edulis*, the effect of removal of low M_r thiols such as GSH was studied. Extracts were concentrated to a final volume of 1 ml and diluted with 5 volumes of extraction buffer followed by desalting on Ultra-15 Centrifugal Filter Devices (3000 NMWL, Amicon). This process was repeated three times. ATS was then added to 2 mg protein aliquots as described in Section 2.5.

2.8. Statistical analysis

Data are shown for three independent experiments and means and standard deviations were calculated. Significance testing was by paired Student's *t*-test.

3. Results

3.1. Activated thiol sepharose capture of –SH-containing proteins

Accurate protein estimations were made of the quantity of –SH-containing proteins retained on ATS from control extracts (Table 1). For the bacterium *E. coli* the average value was 2.6%, for the fungus *T. harzianum*, it was 1.4% whilst for the bivalve mollusc *M. edulis* the value was 1.39%. Despite the fact that there is some variation in total protein concentrations of the differing extracts, there is remarkably good agreement in the percentage of proteins captured both across each preparation experiment and each species studied suggesting that resting cells contain broadly similar percentages of thiols. In redox proteomics, it is often of interest to study effects of pro-oxidants on populations of –SH-containing proteins and ATS has an important potential role in making such comparisons. We therefore subjected each study species to known pro-oxidants; the redox cycling agent menadione in the case of *E. coli* and the metal $CdCl_2$ in the case of *T. harzianum* and *M. edulis* (Fig. 1). This showed no significant difference in percentage of –SH-containing proteins retained on ATS.

3.2. Contribution of low M_r thiols to retention estimate

It is known that GSH is present in cells in high concentrations both in free form and as mixed disulphides with proteins [9]. It was therefore of interest to assess whether low M_r thiols like GSH might influence our estimate of retained thiols. We removed low M_r thiols by repeatedly passing aliquots of total protein extracts of *T. harzianum* and *M. edulis* through centrifugal concentrators with

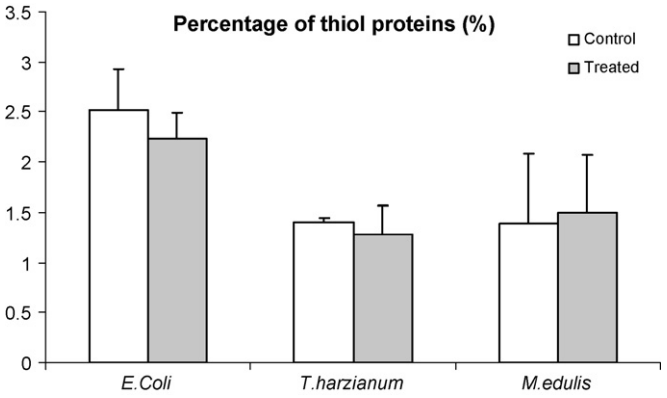


Fig. 1. Percentage of thiol-containing proteins trapped on ATS: mean values of three independent estimates for percentage –SH-containing proteins are shown (±standard deviation) for control (white bars) and pro-oxidant-treated organisms (grey bars).

a size-exclusion of 3 kDa and again capturing –SH-containing proteins on ATS (Fig. 2). This gave a higher estimate of retained thiols in each case with the apparent value for *M. edulis* almost doubling to 2.17% and that for *T. harzianum* almost tripling to 5.08%. The latter increase was statistically significant whilst the former was not. This experiment suggested that it may not always be routinely necessary to remove endogenous GSH from protein preparations as it has a modest effect on the ability of ATS to capture protein thiols. This is generally consistent with recent observations on the proportionately greater contribution of protein thiols than GSH in mammalian cultured cells [9].

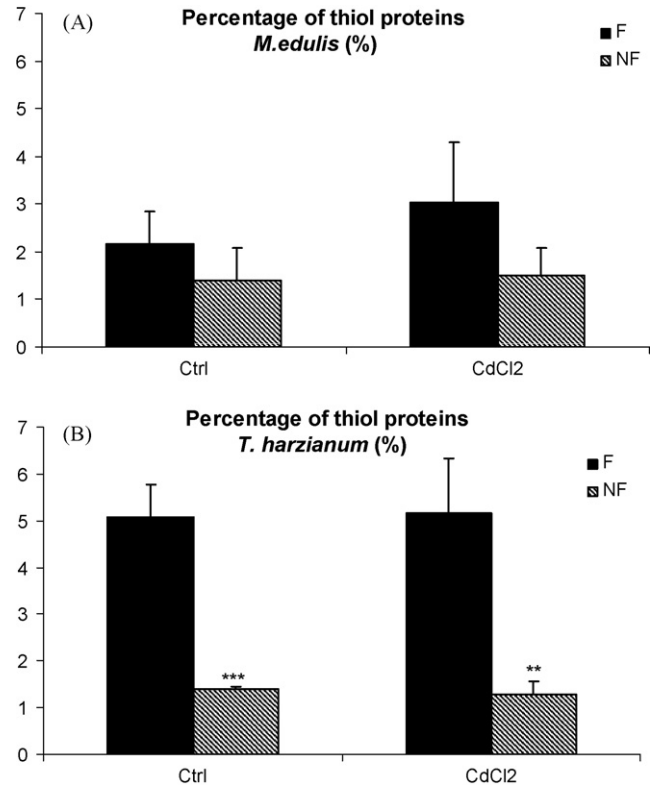


Fig. 2. Effect of removal of low M_r thiols by filtration: (A) *M. edulis* digestive gland. (B) *T. harzianum* mycelia. Samples from control and $CdCl_2$-treated organisms were selected on ATS and filtered through 3 kDa centrifugal concentrators (F, black bars). Percentages of proteins trapped on ATS are compared with non-filtered extracts (NF, hatched bars) (***$p < 0.001$ and **$p < 0.01$).

3.3. Two-dimensional electrophoresis analysis of ATS-retained proteins

One of the principal techniques used in proteomics is 2DE [20]. ATS is a potentially generally useful method for enriching SH-containing proteins to allow their visualisation, quantification or detection in 2DE. A common proteomic comparison often made in redox proteomics is of protein populations exposed to pro-oxidants with non-exposed controls. Pro-oxidants can cause covalent changes to protein structure which are detectable in 2DE [7] and can also cause up- or down-regulated proteomic changes. Comparisons of ATS-selected proteins from test and pro-oxidant-exposed organisms are shown in Fig. 3. These reveal that, whilst most spots are identical in control and pro-oxidant-treated samples, there are subtle differences in which a relatively small number of spots are either weakened or disappear altogether on pro-oxidant treatment. It is known that cysteine is especially susceptible to oxidation, so we interpret this phenomenon as most likely being due to oxidation of –SH groups. It is known that oxidised variants of –SH (like disulphides and sulphenic acids) have very different chemistries and will not bind to thiol-specific reagents or (in the context of the present paper) undergo disulphide exchange to bind to ATS. This resin therefore provides a potentially powerful tool for distinguishing variants in thiol status when comparing proteomes.

4. Discussion

In addition to their potential toxicity at high dose, ROS are now known to be important signalling molecules in biological systems [28,37]. Thus, redox proteomics faces the challenging task of studying large-scale protein oxidation in which gross effects are seen on perhaps very abundant protein targets and more subtle redox effects perhaps involving low-abundance proteins.

4.1. Importance of cysteine as a target in redox proteomics

Cysteines are relatively rare in proteins but they have increased in frequency during evolution and are often conserved in protein families [38]. Some proteins exploit cysteine's redox chemistry in defence against oxidative stress but also in sub-stress redox signalling which makes them especially attractive targets for redox proteomics [9–12,27]. The properties of cysteine's thiol group are crucial in this regard, especially the pK_a for deprotonation. Cysteines normally have a pK_a of approximately 9 but, in some proteins, the surrounding electrostatic field of a thiol can perturb its pK_a to values as low as 4.0 [2]. These are referred to as "active thiols". Although we routinely use a pH value of 7.5 (i.e. similar to that of cytosol), we have observed that ATS binds proteins in a pH-dependent manner with some proteins binding at pH values below 6 whilst maximum binding is observed at pH 9. It is therefore likely that proteins selected at low pH values contain active thiols. These can selectively form oxidised variants such as sulphenic acid, thiolsulphinates and disulphide bridges [2,27,39]. The surrounding structural context of the thiol forms an elegant basis for selectivity whereby only some thiols in only some proteins are oxidised by a given alteration such as a change in redox status. Well-known examples of modifications with relevance to signalling include proteins that trigger apoptosis [13–15], the endogenous inhibition of the Jun N-terminal kinase by disulphide bridged glutathione transferase Pi [40] and reversible coordination to metals in some transcription and replication factors [41].

Cysteines only account for 1–2% of residues in proteins but are predicted in ~27% of tryptic peptides from the human genome allowing coverage of ~96% of proteins by shotgun MS

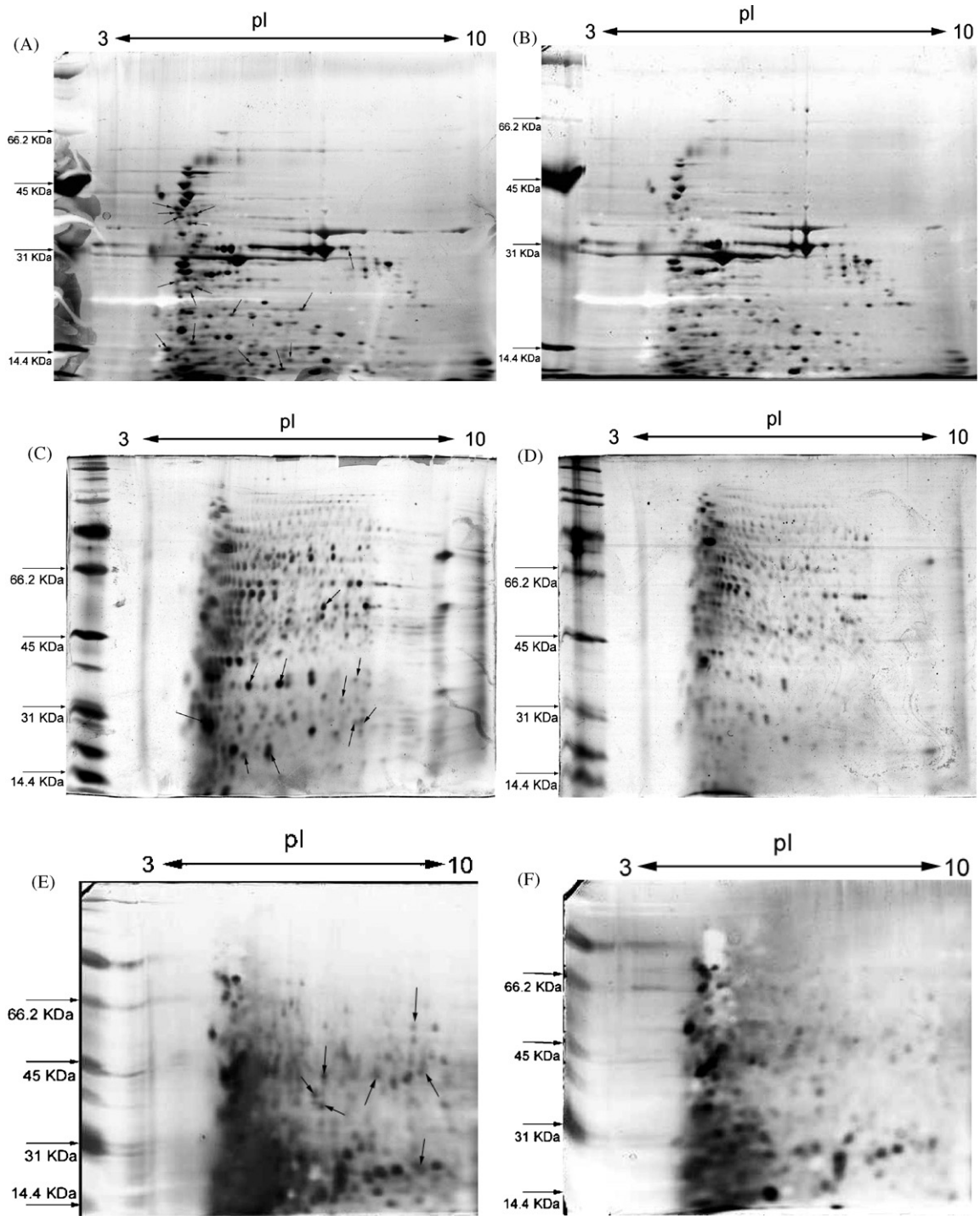


Fig. 3. 2DE profiles of ATS-selected sub-proteomes: thiol-containing proteins were selected on ATS, separated in 2DE and silver-stained. (A) *E. coli* control. (B) *E. coli* grown in menadione. (C) *T. harzianum* control. (D) *T. harzianum* grown in $CdCl_2$. (E) *M. edulis* control. (F) *M. edulis* exposed to $CdCl_2$. Proteins present in control but missing in pro-oxidant-treated profiles are shown with black arrows.

approaches [42]. In 2DE separations, tagging of cysteines has enabled identification of some redox targets [24]. However, these approaches may not detect low-abundance proteins or, even if detectable, there may not be enough material to facilitate detection by MS analysis of excised spots. For this reason, enrichment approaches involving selection of –SH-containing proteins are necessary. Biotin derivatised with –SH-specific groups such as *N*-ethyl maleimide (NEM) or biotin-conjugated iodoacetamide can be trapped on avidin affinity columns [19,27,43] and this general approach has also been applied in shotgun proteomics [44]. Study of protein thiols presents a significant analytical challenge because of the range of redox variants in proteins and difficulties presented by varying reagent specificities [28]. The present paper explores covalent selection of –SH-containing proteins as an alternative to affinity selection. ATS can select proteins under a wide range of experimental circumstances including native and denaturing conditions. Moreover, since beads can be collected by centrifugation and the proteins are covalently attached to the beads, handling losses are kept to a minimum.

4.2. Activated thiol sepharose selection of –SH-containing proteins

Pre-treatment of protein extracts with NEM completely abolishes protein binding to ATS showing high selectivity for –SH-containing proteins [35]. For general applicability, it is important to know that target proteins are being quantitatively captured and are not just a subset of proteins such as those possessing active thiols which might be expected to be more chemically reactive. GSH provides a major category of thiols in cells which both contribute to antioxidant defence and can form mixed disulphides with thiols of certain proteins with functional significance [10]. However, it has recently been shown that protein thiols are even more quantitatively important than GSH and collectively represent an active redox buffer to absorb transient increases in ROS. Thiol-containing proteins represent 2–3% of total protein in cultured human cells [9].

Sequence analyses can provide estimates of the frequency at which residues occur in genomes [38] but are not really predictive of their likely abundance in the proteome since some proteins are present in large amounts whilst others may be expressed at low levels or not at all in some contexts. It is also possible that proteomes may differ from species to species or with growth condition in terms of abundance of –SH-containing proteins. For these reasons, in this study we quantified the percentage of –SH-containing proteins binding to ATS in three widely differing biological sources. Reproducibility was ensured by carrying out a minimum of three independent experiments. Our study revealed percentage values for the three organisms which are closely similar to that reported for cultured human cells (Table 1, Fig. 1) [9]. Using the same experimental protocol, we also found kidney medulla extracts to contain 1.07% –SH-containing proteins (not shown). These observations suggest that ATS can trap essentially all thiol-containing proteins in a single step from a wide range of biological sources. Thus, ATS would have general applicability in redox proteomics studies where there is often a need to trap protein –SH groups quantitatively whilst simultaneously preventing their oxidation during experimental manipulation. This one-step, one-pot approach is complementary to the more traditional multi-step and non-covalent avidin–biotin affinity selection [19,27,43,44].

Since GSH is present in millimolar concentrations in cells, it was possible that it too would bind to ATS, possibly affecting the estimate of percentage –SH-containing proteins. For this reason, in the case of the *M. edulis* and *T. harzianum* extracts, GSH was removed by rapid desalting in centrifugal concentrators and the effect of this on the percentage thiol protein estimate assessed. This gave no effect in the case of *M. edulis* but an increased estimate for *T. harzianum* (Fig. 2). In mammals, GSH levels vary with factors such as disease state, gender and age [45,46]. This ought not to be an important factor in routine use of ATS for 2DE proteomics since most methods remove low M_r contaminants before the IEF step. However, for MS studies, it is possible that co-selection of GSH with protein thiols may lead to unwanted interference and it may be necessary to desalt extracts before ATS capture.

4.3. Use of activated thiol sepharose in redox proteomics

Having established that ATS provided a highly reproducible and quantitative method for the capture of –SH-containing proteins, it was necessary to explore its usefulness in the kinds of studies often performed in redox proteomics. Frequently, this involves comparing preparations from organisms exposed to pro-oxidants with suitable controls and looking for differences. In 2DE [7,20], this might involve analysing spot patterns to look for up- or down-regulated spots. Alternatively, specific redox lesions on proteins such as carbonyl groups might be of interest in 2DE separations [7]. –SH groups are far more readily oxidised than the formally similar –OH group because of a markedly lower bond energy in S–H compared to O–H [47]. This means that protein thiols will readily oxidise if brought into contact with ROS and this is even more likely in the case of active thiols. The reactivity of –SH groups differs markedly from that of their oxidised variants giving a useful means of distinguishing proteins containing –SH from variants containing groups such as –SOH or –S–S–. Binding to ATS involves a disulphide exchange and so is highly selective for thiols and does not bind oxidised variants of thiols. It therefore ought to be possible to compare 2DE profiles from control and oxidised extracts and identify specific spots not present in the oxidised sample due to –SH oxidation. The 2DE profiles obtained here (Fig. 3) confirm that generally similar spot patterns are obtained from matched control and oxidised preparations with hundreds of spots visible. However, close inspection reveals that several spots present in the control pattern are weaker or missing in the oxidised sample. These spots would either be too faint or invisible in 2DE analyses of total proteomes from these sources emphasising the importance of enrichment on ATS.

Further dissection of the thiol proteome is made possible by combining pre-treatment with agents such as NEM to block –SH groups with selective reduction to regenerate –SH groups from oxidised variants. Examples include selective reduction of –S–S– with DTT [24,35], reduction of –SOH with arsenite [26] and reduction of nitrosothiols by ascorbic acid or transition metals as used in the "biotin switch" assay [48]. In such experiments ATS would provide a rapid one-step method with high capacity to enrich for these sub-proteomes in which proteins can be collected by a facile reduction with DTT making them available for analysis by MS or 2DE.

5. Conclusion

ATS selects 1.4–2.52% of the total proteome in diverse microbial and eukaryote extracts. These values agree well with the predicted percentage of thiol-containing proteins observed in mammalian cell culture and are consistent with essentially complete enrichment for the thiol proteome. There is good reproducibility between independent experiments suggesting that this one-step, one-pot approach is sufficiently robust for widespread used in enriching for –SH-containing proteins in redox proteomics. We cannot exclude the possibility that GSH also binds to ATS in some protein sources and this may require inclusion of a desalting step. When combined with selective reduction of oxidised thiol variants, this capture approach could select for sub-proteomes containing disulphides, sulphenic acid and nitrosothiol derivatives of protein thiols.

Acknowledgements

D.S.'s lab is supported by the Higher Education Authority of Ireland, Programme for Research in Third Level institutions. W.H. is funded by *NeuroNano* (European Union Seventh Framework). S.T. is funded by the Irish Research Council for Science Engineering and Technology EMBARK initiative.

References

[1] M.J. Davies, Biochim. Biophys Acta 1703 (2005) 93.
[2] C.C. Winterbourn, Nat. Chem. Biol. 4 (2008) 278.
[3] B. Halliwell, J.M.C. Gutteridge, Free Radicals in Biology and Medicine, fourth edition, Oxford University Press, Oxford, 2007, 851pp.
[4] B. Halliwell, Annu. Rev. Nutr. 16 (1999) 33.
[5] R.J. Castellani, X.W. Zhu, H.G. Lee, M.A. Smith, G. Perry, International, J. Mol. Sci. 10 (2009) 1386.
[6] M. Valko, D. Leibfritz, J. Moncol, M.T.D. Cronin, M. Mazur, J. Telser, Int. J. Biochem. Cell Biol. 39 (2007) 44.
[7] D. Sheehan, Biochem. Biophys. Res. Commun. 349 (2006) 455.
[8] R.L. Levine, J. Moskovitz, E.R. Stadtman, IUBMB Life 50 (2000) 301.

[9] R.E. Hansen, D. Roth, J.R. Winther, Proc. Natl. Acad. Sci. USA 106 (2009) 422.
[10] I. Dalle-Donne, R. Rossi, G. Colombo, D. Giustarini, A. Milzani, Trends Biochem. Sci. 34 (2009) 86.
[11] O.N. Oktyabrsky, G.V. Smirnova, Biochemistry (Moscow) 72 (2007) 132.
[12] P. Chiarugi, F. Buricchi, Antioxidants Redox Signal. 9 (2007) 1.
[13] J.R. Burgoyne, M. Madhani, F. Cuello, R.L. Charles, J.P. Brennan, E. Schroder, D.D. Browning, P. Eaton, Science 317 (2007) 1393.
[14] M. Herscovitch, W. Comb, T. Ennis, K. Coleman, S. Yong, B. Armstead, D. Kalaitzidis, S. Chandani, T.D. Gilmore, Biochem. Biophys. Res. Commun. 367 (2007) 103.
[15] H. Nakajima, W. Amano, A. Fujita, A. Fukuhara, Y.T. Azuma, F. Hata, T. Inui, T. Takeuchi, J. Biol. Chem. 282 (2007) 26562.
[16] M.F. Christman, G. Storz, B.N. Ames, Proc. Natl. Acad. Sci. USA 86 (1989) 3484.
[17] A. Delaunay, D. Pflieger, M.B. Barrault, J. Vinh, M.B. Toledano, Cell 111 (2002) 471.
[18] J.G. Kang, M.S.B. Paget, Y.J. Seok, M.Y. Hahn, J.B. Bae, J.S. Hahn, C. Kleanthous, M.J. Buttner, J.H. Roe, EMBO J. 18 (1999) 4292.
[19] M. Ilbert, J. Horst, S. Ahrens, J. Winter, P.C.F. Graf, H. Lilie, U. Jakob, Nat. Struct. Mol. Biol. 14 (2007) 556.
[20] A. Görg, W. Weiss, M.J. Dunn, Proteomics 4 (2004) 3665.
[21] H. Zhang, X.J. Li, D.B. Martin, R. Aebersold, Nat. Biotechnol. 21 (2003) 660.
[22] S. Morandell, T. Stasyk, K. Grosstessner-Hain, E. Roitinger, K. Mechtler, G.K. Bonn, L.A. Huber, Proteomics 6 (2006) 4047.
[23] T. Liu, W.J. Qian, W.N.U. Chen, J.M. Jacobs, R.J. Moore, D.J. Anderson, M.A. Gritsenko, M.E. Monroe, B.D. Thrall, D.G. Camp, R.D. Smith, Proteomics 5 (2005) 1263.
[24] J.W. Baty, M.B. Hampton, C.C. Winterbourn, Proteomics 2 (2002) 1261.
[25] C. Lind, R. Gerdes, Y. Hamnell, I. Schuppe-Koistinen, H.B. von Lowenhielm, A. Holmgren, I.A. Cotgreave, Arch. Biochem. Biophys. 406 (2002) 229.
[26] A.T. Saurin, H. Neubert, J.P. Brennan, P. Eaton, Proc. Natl Acad. Sci. USA 101 (2004) 17982.
[27] J.R. Kim, H.W. Woon, K.S. Kwon, S.R. Lee, S.G. Rhee, Anal. Biochem. 283 (2000) 214.
[28] Y.M.W. Janssen-Heininger, B.T. Mossman, N.H. Heintz, H.J. Forman, B. Kalvanaraman, T. Finkel, J.S. Stamler, S.G. Rhee, A. van er Vliet, Free Radic. Biol. Chem. 45 (2008) 1–17.
[29] K. Angermann, H.J. Barrach, Anal. Biochem. 94 (1979) 253.
[30] K. Lee, J. Lee, Y. Kim, D. Bae, K.-Y. Kang, D. Lim, Electrophoresis 25 (2004) 532.
[31] C. Lee, Y.M. Lee, R.H. Rice, Chemico-Biol. Interact. 55 (2005) 43.
[32] I. Pe'er, C.E. Felder, O. Man, I. Silman, J.L. Sussman, J.S. Beckmann, Proteins 54 (2004) 20–40.
[33] B. McDonagh, D. Sheehan, Proteomics 7 (2007) 3395.
[34] M.M. Bradford, Anal. Biochem. 72 (1976) 248.
[35] W. Hu, S. Tedesco, B. McDonagh, J.A. Bárcena, C. Keane, D. Sheehan, Anal. Biochem. (2009), in press, doi:10.1016/j.ab.2009.11.002.
[36] T. Rabilloud, Electrophoresis 13 (1992) 429.
[37] M. Zheng, G. Storz, Biochem. Pharmacol. 59 (2000) 1.
[38] D.J. Brooks, J.R. Fresco, Mol. Cell. Proteom. 1 (2002) 125.
[39] A. Claiborne, T.C. Mallett, J.I. Yeh, J. Luba, D. Parsonage, Adv. Prot. Chem. 58 (2001) 215.
[40] V. Adler, Z.M. Yin, S.Y. Fuchs, M. Benezra, L. Rosario, K.D. Tew, M.R. Pincus, M. Sardana, C.J. Henderson, C.R. Wolf, R.J. Davis, Z. Ronai, EMBO J. 18 (1999) 1321.
[41] J.X. Yan, A.T. Devenish, R. Wait, T. Stone, S. Lewis, S. Fowler, Proteomics 2 (2002) 1682.
[42] H. Zhang, W. Yan, R. Aebersold, Curr. Opin. Chem. Biol. 8 (2004) 66.
[43] J. Ying, N. Clavreul, M. Sethuraman, T. Adachi, R.A. Cohen, Free Radic. Biol. Med. 43 (2007) 1099.
[44] B. McDonagh, S. Ogueta, G. Lasarte, C.A. Padilla, J.A. Barcena, J. Proteom. 72 (2009) 677.
[45] M.A. Korolainen, T.A. Nyman, P. Nyyssonen, E.S. Hartikainen, T. Pirttila, Clin. Chem. 53 (2007) 657.
[46] P. Maher, Ageing Res. Rev. 4 (2005) 288.
[47] J.D. Roberts, R. Stewart, M.C. Caserio, Organic Chemistry, W.A. Benjamin Inc., New York, 1971.
[48] L.M. Lopez-Sancha, J. Muntane, M. de la Mata, A. Rodriguez-Ariza, Proteomics 9 (2009) 808.

Talanta 80 (2010) 1576–1585

Contents lists available at ScienceDirect

Talanta

journal homepage: www.elsevier.com/locate/talanta

First complexomic study of alkane-binding protein complexes in the yeast *Yarrowia lipolytica*

Jean-Paul Lasserre[a,b,*], Jean-Marc Nicaud[c], Yves Pagot[c], Raymonde Joubert-Caron[a], Michel Caron[a], Julie Hardouin[a,d]

[a] *Laboratoire de Biochimie des Protéines et Protéomique, UMR CNRS 7033, Université Paris 13, 74 rue Marcel Cachin, F-93017 Bobigny cedex, France*
[b] *Centre de Recherche Public–Gabriel Lippman, Department of Environment and Agro-biotechnologies (EVA), 41 rue du Brill, L-4422 Belvaux, Luxembourg*
[c] *Laboratoire de Microbiologie et de Génétique Moléculaire, CNRS UMR2585, INRA UMR1238 -AgroParisTech, INRA Centre de Versailles-Grignon, BP 01, F-78850 Thiverval-Grignon, France*
[d] *Laboratoire CSPBAT, Equipe C2B, FRE CNRS 3043, Université Paris 13, 74 rue Marcel Cachin, F-93017 Bobigny cedex, France*

ARTICLE INFO

Article history:
Available online 10 July 2009

Keywords:
Complexomic
Yarrowia lipolytica
Two-dimensional blue native/SDS-PAGE
Mass spectrometry
Native protein complex
Heteromultimer
Homomultimer
Alkane

ABSTRACT

The yeast *Yarrowia lipolytica* uses hydrophobic substrates, such as alkanes, fatty acids and oils, for its growth. It has developed a strategy for the use of such substrates, involving the production of hydrophobic binding structures called protrusions on the cell surface. These protrusions are resemble channels connecting the cell wall to the inside of the cell, and are probably involved in transport mechanisms that we do not yet fully understand. The complete genome of the haploid *Y. lipolytica* strain E150 (CLIB99) was sequenced in 2004 by the Génolevures Consortium. The availability of a complete genome sequence for this species has made it possible to carry out proteomic and other investigations, leading to the characterization of lipid bodies (LB) in terms of (i) their lipid composition, (ii) the major LB proteins, as identified by mass spectrometry, and (iii) differences in protein or lipid composition as a function of the carbon source used. Functional analyses would provide insight into the biological processes associated with these bodies and 2D BN/SDS-PAGE is a highly suitable method for the analysis of protein complexes.

This report provides a first description of the analysis and identification of hydrophobic binding protein complexes in *Y. lipolytica*. For this purpose, we used 2D BN/SDS-PAGE for the separation of protein complexes and HPLC-chip-MS for protein identification. We separated and identified 40 protein complexes (11 heteromultimeric and 29 homomultimeric), providing insight into their function. This study represents a major step forward, as most previous studies identified proteins either on the basis of sequence similarity to proteins from other organisms (44% of the proteins identified in this study) or by prediction (50% of proteins identified in this study) alone.

© 2009 Elsevier B.V. All rights reserved.

1. Introduction

Yarrowia lipolytica is a hemiascomycetous yeast that can be isolated from substrates rich in proteins and lipids, such as dairy products (e.g. cheese) and sausages. This species has also been isolated from soil, waste and seawater [1]. This non-conventional yeast is currently used as a model for the study of protein secretion [2,3], peroxisome biogenesis [4], dimorphism transition [1,5], the degradation of hydrophobic substrates (HS) [1] (alkanes, fatty acids, oils) and mitochondrial complex I [6]. Since the recent determination of the complete genomic sequence [7], comparative genomics, proteomics and transcriptomics studies have been initiated. *Y. lipolytica* has a 20.5 Mb genome composed of six chromosomes, for which genome annotation was performed by the Génolevures Consortium [8]. The *Y. lipolytica* genome comprises 6448 genes, 957 of which have at least one intron [9].

Y. lipolytica is well adapted for the utilization of HS as a carbon source, because it can use alkanes, fatty acids and oil. For oil utilization, *Y. lipolytica* produces several lipases, which are secreted either into the medium, as for the extracellular lipase Lip2p [10], or principally into the cell wall, as for Lip7p and Lip8p [11]. Depending on growth conditions, *Y. lipolytica* either breaks down the lipids and uses them for growth through β-oxidation to produce biomass, or stores lipids in lipid bodies (LB) [1]. The water-miscibility of HS is poor. So, when grown on HS, *Y. lipolytica* adapts its physiology and metabolism to facilitate the solubilization of these substrates, together with their transport and degradation. It produces a sur-

Abbreviation: 2D BN/SDS-PAGE, two-dimensional blue native/SDS-PAGE.

* Corresponding author at: Centre de Recherche Public–Gabriel Lippman, Department of Environment and Agro-biotechnologies (EVA), 41 rue du Brill, L-4422 Belvaux, Luxembourg. Tel.: +352 470261 436; fax: +352 470264.
E-mail address: lasserre-jean-paul@orange.fr (J.-P. Lasserre).

0039-9140/$ – see front matter © 2009 Elsevier B.V. All rights reserved.
doi:10.1016/j.talanta.2009.07.016

factant called liposan [12]. Cell surface modifications occur when this yeast is grown on HS. These changes include the induction of "protrusions" enabling HS droplets to dock on the cell surface [13].

Systematic comparisons have been initiated, to compare *Saccharomyces cerevisiae*, *Y. lipolytica* and other organisms. Swennen and Beckerich performed a comparative genomic analysis of the secretion pathway and showed that 40% of the proteins involved in this process in *Y. lipolytica* were very similar to homologous proteins in animals, whereas only 13% of these proteins were found to be similar to proteins in *S. cerevisiae* [3]. A highly representative two-hybrid library for *Y. lipolytica* has been constructed for the analysis of protein–protein interactions [14]. Sequence of the entire genome of this yeast has facilitated –omics approaches, including proteomics investigations, and has led to the characterization of LB in terms of (i) lipid composition, (ii) the major LB proteins present, as identified by mass spectrometry (MS), and (iii) differences in protein or lipid composition as a function of the carbon source used [15].

Our knowledge of the building blocks used to construct protein complexes in this yeast is limited and cannot be substantially improved by genomic techniques. Various methods have been developed for the identification of protein–protein interactions and to improve our understanding of protein complexes. These methods include yeast two-hybrid systems [16–24], protein microarrays [25,26], affinity purification-mass spectrometry [27–34] and two-dimensional blue native/sodium dodecyl sulfate polyacrylamide gel electrophoresis (2D BN/SDS-PAGE) [35–43]. 2D BN/SDS-PAGE is a highly suitable technique for the analysis of protein complexes. This technique is based on the initial separation of proteins as a function of molecular weight and charge in native conditions (BN-PAGE) as a first dimension. Proteins from the same complex are then separated in a second dimension, in denaturing conditions, as a function of molecular weight (SDS-PAGE). Aligned spots of the same shape on the gel are considered to correspond to proteins from the same protein complex. This applies, in particular, to heteromultimeric protein complexes. Homomultimeric protein complexes give rise to a single spot in the second dimension and are less mobile than expected in the first dimension. The spots are excised and digested with a specific endoprotease, generally trypsin. The products of this digestion are then analyzed by nanoliquid chromatography coupled to tandem mass spectrometry (nanoLC-MS/MS). The MS and MS/MS data are used to identify the proteins forming the complex. By integrating all the results obtained with yeast two-hybrid systems, protein microarrays and 2D BN/SDS-PAGE, complexomic databases can be made more comprehensive and a the protein–protein interaction network can be deciphered, increasing our understanding of protein function [44,45].

We present here, for the first time, a study of hydrophobic binding protein complexes in *Y. lipolytica,* providing new insight, validating the annotation, identifying the partners in the complex that could not be identified by genomic comparisons, due to the low level of homology, and providing information about protein function. The protein complexes were separated by 2D BN/SDS-PAGE. The protein spots were excised, digested with trypsin and identified with the HPLC-chip-IT-MS/MS microfluid chromatography system [46,47]. We identified 40 protein complexes with this experimental procedure: 11 heteromultimeric protein complexes and 29 homomultimeric protein complexes.

2. Materials and methods

2.1. Strain and culture conditions

The wild-type German *Y. lipolytica* strain H222 was grown at 28 °C in glucose complete medium (YPD; yeast peptone dextrose) or YNB-derivative (YNBD) minimal medium [48]. The YNB medium contained 1.7 g/l yeast nitrogen base without amino acids and ammonium sulfate (Yeast Nitrogen Base, Difco, Paris, France), 5 g/l NH_4Cl and 50 mM phosphate buffer (pH 6.8). YNBD contained 20 g/l glucose; YNBYC16 contained 1.5 g/l yeast extract and 10 g/l of hexadecane (C16 alkane). For growth on alkane, cells growing exponentially in glucose minimal medium (YNBD) were centrifuged, washed twice with water and resuspended in minimal medium without a carbon source. The resulting cell suspension was used to inoculate 100 ml of YNBYC16 in 500 ml Erlenmeyer.baffled shaking flasks at an optical density OD600 of 0.05.

2.2. Isolation and characterization of hydrophobic (alkane)-binding complexes

After 24 h of growth in YNBYC16, five 200 ml cultures were filtered through an HA filter with 0.45 μm pores (Millipore, St Quentin en Yvelines, France) and the cells on the filters were washed with 50 ml cold phosphate buffer (50 mM, pH 6.8). Cells were resuspended in 5 ml of extraction buffer (50 mM Tris, 0.75 M 6-aminocaproic acid, 1 mM PMSF, EDTA-free protease inhibitors cocktail (Roche Applied Science, Switzerland)) and centrifuged at 3000 × *g* for 5 min. The resulting pellets were resuspended in 7 ml of extraction buffer at an OD_{600} of 2000 (about 5 g wet weight of cells) and cooled on ice. Cells were disrupted with a CellD cell disruptor (CellD, Roquemaure, France). Disrupted cells were centrifuged at 3000 × *g* for 5 min, at 4 °C. Supernatants were collected and centrifuged for 10 min at 6000 × *g*. The pellet was extracted in 4 ml of alkane (decane, C10) for 30 min (fraction E6) and dried under nitrogen flux. The supernatant S6 was extracted with 4 ml of alkane (decane, C10) for 30 min and frozen at −20 °C. The upper organic fraction (alkane phase) was further centrifuged at 100,000 × *g* for 45 min at 4 °C. Pellet (P100) and supernatant S100 were extracted as described above for P6 and S6, generating the P100E and S100E fractions, respectively, which were then dried.

2.3. Extraction of protein complexes

Fraction P100E was resuspended in 200 μl of extraction buffer to which dodecyl-β-D-maltoside was added to a final concentration of 2% (w/v). Samples solubilized with dodecyl-β-D-maltoside were directly centrifuged at 100,000 × *g* for 30 min at 4 °C. The supernatant was used immediately or stored at −20 °C until further analyses.

2.4. 2D BN/SDS-PAGE

Samples were prepared and BN-PAGE was carried out as described by Schägger et al. [39] but with the following modifications. The gel dimensions were 22 cm × 16.5 cm × 0.1 cm. Linear 3 to 18% (w/v) acrylamide gradient gels were used for the first dimension. Anode and cathode buffers contained 50 mM Tris, 75 mM glycine. The cathode buffer was supplemented with 0.002% (w/v) Coomassie Brillant Blue G-250 (Bio-Rad, Hercules, California). Before loading, 1 μl of sample buffer (500 mM 6-amino-n-caproic acid, 5% (w/v) Coomassie Brillant Blue G-250) was added to 20 μl of sample. The gel was run at 4 °C, 1 W, 100 V and 28 mA. Thyroglobulin (669 kDa) and BSA (66 kDa) (Sigma, Saint-Louis, MO) were used as molecular weight size standards for BN-PAGE analysis.

Individual lanes from the BN-PAGE gel were excised and equilibrated in 1% (w/v) SDS, 6 M urea, 0.125 M Tris/HCl pH 6.8 for 5 min. Each individual lane was immersed in equilibrating buffer supplemented with 100 mM DTT for 20 min and was then soaked for 20 min in equilibrating buffer supplemented with 55 mM iodoacetamide. The gel strip was then washed with equilibrating buffer for 5 min.

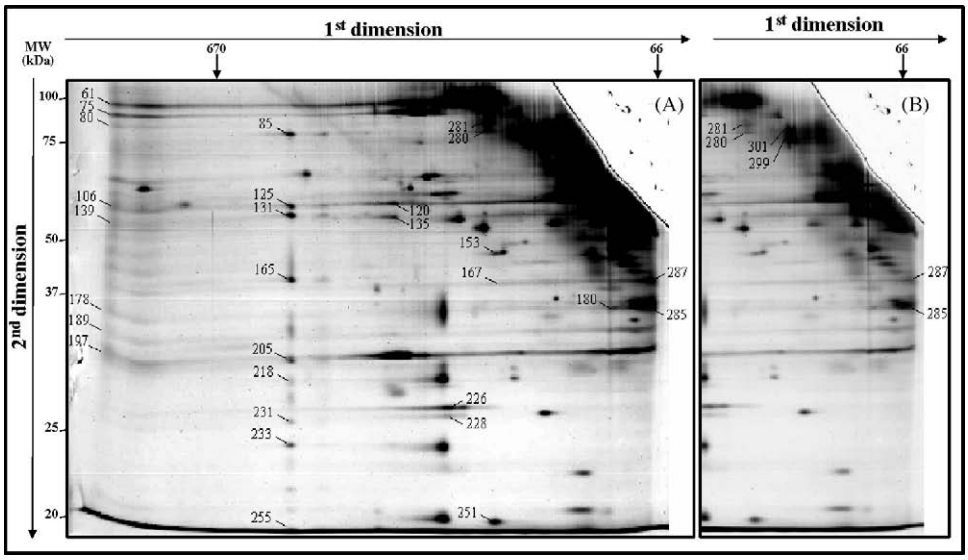


Fig. 1. (A) 2D BN/SDS-PAGE gel showing the heteromultimeric protein complexes of *Y. lipolytica* presenting hydrophobic binding properties. (B) Zoom of the right side of the gel.

The lane was placed on top of the previously poured stacking and separating gels, between the two glass plates. Additional stacking gel mixture was then poured around it.

The gel was then subjected to electrophoresis and, after migration, proteins were visualized by staining the gel with the PROTSIL2 silver staining kit (Sigma–Aldrich, St. Louis, MO), according to the manufacturer's instructions.

2.5. Protein digestion

Silver-stained proteins separated by 2D BN/SDS-PAGE were excised and destained with the PROTSIL2 silver staining kit (Sigma–Aldrich, St. Louis, MO), according to the manufacturer's instructions. Spots were subsequently rinsed twice in ultrapure water for 5 min and dehydrated in 50% ethanol in 50 mM NH_4HCO_3 for 30 min. This step was repeated three times. Spots were also incubated twice with acetonitrile (ACN). After the ACN had been removed, gel pieces were dried at room temperature, covered with the trypsin solution (10 ng/μl in 50 mM NH_4HCO_3) and rehydrated at 4 °C for 45 min. The excess solution was removed and the spots were finally incubated overnight at 37 °C in 50 mM NH_4HCO_3. The supernatant was collected, and an extraction solution (H_2O/ACN/TFA (49.9:50:0.1)) was incubated with the gel slices for 20 min. The supernatant was kept and ACN was incubated with the gel slices for 20 min. Supernatants were pooled and concentrated by drying at 37 °C for 2 h.

2.6. HPLC-Chip-IT-MS/MS

All experiments were carried out with an Agilent 1100 LC/MSD Trap SL series system. Ionization was carried out with the Chip Cube, by HPLC-Chip-MS (Agilent Technologies, Santa Clara, CA, USA). The chip was automatically loaded and placed in the MS nanospray chamber. The chip contained a Zorbax 300SB-C_{18} column (43 mm × 75 μm, 5 μm) and a Zorbax 300SB-C_{18} enrichment column (40 nl, 5 μm). The sample was loaded onto the enrichment column at a flow rate of 4 μl/min, in a 98/2 mixture of H_2O/0.1% FA and ACN/0.1% FA. The liquid chromatography gradient (mobile

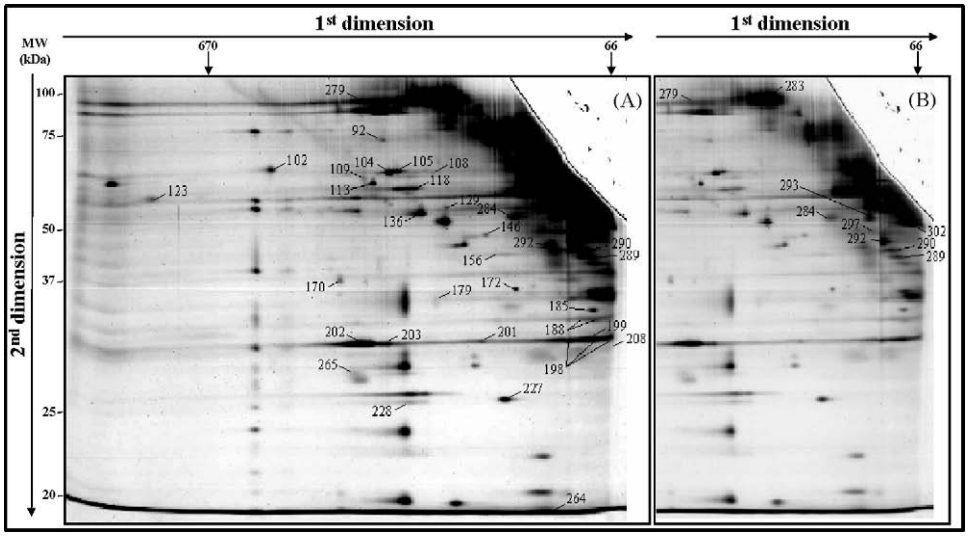


Fig. 2. (A) 2D BN/SDS-PAGE gel showing the homomultimeric protein complexes of *Y. lipolytica* presenting hydrophobic binding properties. (B) Zoom of the right side of the gel.

phase A: H_2O/0.1% FA; mobile phase B: ACN/10% H_2O/0.1% FA) was delivered at a flow rate of 300 nl/min. Tryptic peptides were eluted from the reverse-phase column into the mass spectrometer, using a linear gradient of 15% to 55% B over 30 min. The capillary voltage was set at 1800 V; the flow rate and dry gas temperature were 4 l/min and 280 °C, respectively. The mass range was from m/z 400 to m/z 2200. The MS and MS/MS data were analyzed with Data Analysis software version 3.3. For protein identification, the MS/MS spectra were obtained automatically and Data Analysis software (Agilent Technologies) was used to produce a peak list from raw data: background subtraction with a flatness of 0.8; peak smoothing with the Gauss algorithm, using a smooth width m/z of 0.2 and one cycle; the mass list was generated by the Apex method.

2.7. Protein identification

Database searches were carried out with the Mascot Server software package and the Mascot Daemon client application version 2.0 (Matrix Science, London, UK). Database searches were performed against the *Y. lipolytica* protein sequence database [8]. Many of the 6436 proteins in this database were identified on the basis of similarity to known proteins from other yeasts (particularly *S. cerevisiae*). The parameters used for searches were as follows: one missed trypsin cleavage, mass tolerance of precursor ions and product ions ±0.4 Da, carboxymethylation of cysteine as a fixed modification, oxidation of methionine as a variable modification. Proteins matching at least two peptides were considered to have been identified. Only proteins with a protein score greater than 22 and a p-value less than 0.05 were considered to have been identified.

3. Results and discussion

We used a combination of 2D BN/SDS-PAGE and the HPLC-chip-MS method to analyze protein complexes with alkane-binding properties from the yeast *Y. lipolytica*. We tested different acrylamide gradients with a view to obtaining optimal resolution and repeatable separations during the first dimension for protein complexes. A 3–18% (w/v) acrylamide gradient was chosen for BN/PAGE, as this gave optimal focusing and separation within a given range (Figs. 1 and 2). Proteins from the same complex migrated together in the first dimension, but independently in the second, denaturing dimension. Thus, proteins from the same complex were detected as aligned spots of similar shape on the gel, as previously described [37]. Aligned spots of different shapes were considered to originate from different complexes. Gel analysis led to the identification of 40 different alkane-binding protein complexes in *Y. lipolytica* (Figs. 1 and 2, Tables 1 and 2): 11 heteromultimeric protein complexes (Fig. 1, Table 1) and 29 homomultimeric protein complexes (Fig. 2, Table 2).

3.1. Previously described protein complexes

This technology has been successfully used in the past for protein complex identification [35–43]. Observations of previously described complexes are of interest for the validation of both new technologies and analysis criteria. Heteromultimeric protein complexes # 2, 3 and 11 (Table 1) had already been partially or totally characterized in other studies, and were used here to demonstrate the utility of our approach. For example, protein complex # 3 (Table 1) is an ATPase complex. ATPases catalyze the breakdown of adenosine triphosphate (ATP) into adenosine diphosphate (ADP) and a free phosphate ion. Here, the F-ATPase (Table 1, complex # 3) produces ATP using the proton gradient generated by oxidative phosphorylation. This mitochondrial protein complex has been described as a complex of nine subunits,

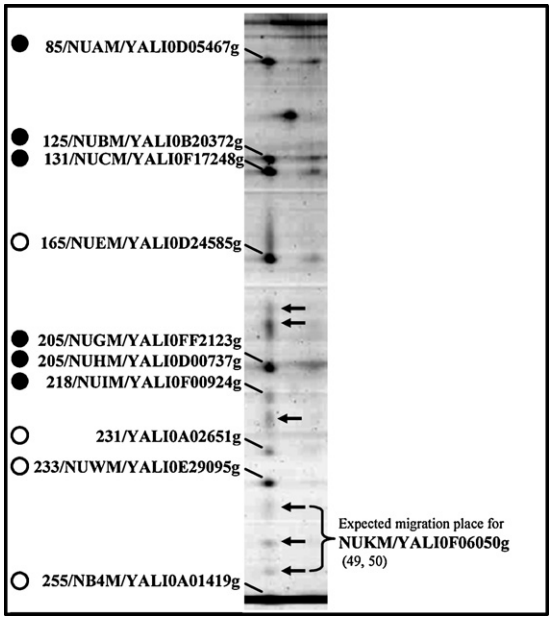


Fig. 3. Zoom on alkane-binding complex # 2 corresponding to respiratory chain complex I. Nuclear-encoded core units (●), and nuclear-encoded accessory subunits (○) of NADH:ubiquinone oxidoreductase identified by MS are indicated. Information is noted as: spot number/gene usual name/accession number. The expected location of the NUKM core subunit is shown on the right. Arrows indicate spots with no identification.

of five different types ($\alpha_3\beta_3\gamma\delta\varepsilon$). However, only two of these subunits α (spot 120, gene ATP1, YALI0F03179g, Table 1) and β (spot 135, gene ATP2, YALI0B03982g, Table 1) were observed on the 2D BN/SDS-PAGE gel. This may be due to the stoichiometry of the different subunits in the complex ($\alpha_3\beta_3\gamma\delta\varepsilon$). However, in this particular case, as previously described in *E. coli* [37], the absence of the γ, δ and ε subunits may also be accounted for by instability of the F-ATPase complex. Furthermore, both the genes identified encode proteins with a potential mitochondrial targeting sequence with a prediction value of 0.99, identified with MITOPROT [48].

3.2. Protein complex # 2: no subunit encoded by the mitochondrial genome

Protein complex # 2 corresponds to the NADH dehydrogenase complex or NADH:quinone oxidoreductase (Table 1). These enzymes are located in the inner mitochondrial membrane and catalyze electron transfer from NADH to coenzyme Q (CoQ). Little is known about these enzymes, despite their importance in biological pathways. For *Y. lipolytica*, Abdrakhmanova et al. [49] described this protein complex as having 14 central subunits: 7 proteins encoded by the nuclear genome and 7 proteins encoded by the mitochondrial genome. Subunit mass fingerprinting analysis of *Y. lipolytica* mitochondrial complex I recently identified 37 subunits [50]. In addition to these the 14 core subunits, this complex contains a large number of accessory subunits in eukaryotes: 32 subunits in bovine heart mitochondrial complex I [51], 21–23 subunits in the fungal enzyme [49,52] and about 16–28 subunits in photosynthetic organisms, such as *Vicia faba L* [53], *Arabidopsis thaliana* and *Chlamydomonas reinhardtii* [54]. We found 10 subunits (Fig. 3). Six of the seven central subunits encoded by the chromosomal genome were identified (NUAM, NUBM, NUCM, NUGM, NUHM, NUIM), while NUKM (YALI0F06050g), was not identified. From the accessory subunits, three proteins were identified (NUEM, NUWM, NB4 M). NUWM was shown to be a specific accessory subunit of *Y. lipolytica* [49] (Table 1, complex

Table 1
List of the heteromultimeric protein complexes of *Y. lipolytica* presenting hydrophobic binding properties.

#	Spot number	Protein name[a]	Gene name[b]	Usual name	Protein function	Score[c]	Peptide[d]	% cov[e]	MW[f] (Da)	Localization[g]
	61	Q6CDQ7	YALI0B22066g		Highly similar to sp|P05030 *S. cerevisiae* YGL008c PMA1 H + -transporting P-type ATPase	94	3	5	99504	Membrane
1	75	Q9P4D9	YALI0E15378g	MFE	*Y. lipolytica* Multifunctional β-oxidation enzyme, hydratase-dehydrogenase-epimerase	622	13	18	97297	PERO
		Q6L8F1	YALI0D04422g	CPR	*Y. lipolytica* NADPH-cytochrome P450 reductase	131	4	7	80298	ER
	80	Q6C9P6	YALI0D09361g	ACO1	Highly similar to sp|P19414 *S. cerevisiae* Aconitate hydratase	34	1	1	85266	MITO/PERO
	106	P41555	YALI0C16885g	ICL1	*Y. lipolytica* Isocitrate lyase	162	4	8	60182	PERO (SKL)
	178	Q6C8V3	YALI0D16753g	MDH1	Highly similar to tr|Q8TG27 *Talaromyces emersonii* Malate dehydrogenase precursor	58	1	4	35853	MITO
	189	Q6C3I0	YALI0E34672g	SFC1	Similar to sp|P33303 *S. cerevisiae* YJR095w ACR1 succinate-fumarate transporter	84	3	11	34848	MITO
	197	Q6CA86	YALI0D04983g		Similar to sp|P38626 *S. cerevisiae* YIL043c CBR1 cytochrome-b5 reductase	94	2	8	32090	MITO/ER
		Q8J0M2	YALI0A10659g		tr|Q8J0M2 *Y. lipolytica* ADP/ATP carrier protein	60	1	3	32967	
	139	EF1A	YALI0C09141g		*Y. lipolytica* Elongation factor 1-alpha (EF-1-alpha)	111	2	6	50508	CYTO
		Q6CBL6	YALI0C17545g		Weakly similar to tr|Q06705 *S. cerevisiae* YLR380w CSR1 weak similarity to SEC14 protein	35	1	3	46787	
	85	Q9UUU3	YALI0D05467g	NUAM	*Y. lipolytica* NUAM protein precursor	267	5	12	79689	MITO
	125	Q9UUU2	YALI0B20372g	NUBM	*Y. lipolytica* NADH:ubiquinone oxidoreductase 51 kDa subunit	241	3	9	54462	MITO
	131	Q9UUU1	YALI0F17248g	NUCM	*Y. lipolytica* NUCM protein precursor	222	7	14	52682	MITO
2		Q6C6I2	YALI0E09306g	LYS5	Weakly similar to sp|P50113 *S. cerevisiae* YGL154c LYS5 L-aminoadipate-semialdehyde dehydrogenase	32	2	7	29011	CYTO
	165	Q6C7X4	YALI0D24585g	NUEM	Similar to tr|Q86ZJ8 *Podospora anserina*, NADH-ubiquinone reductase accessory subunit,(complex I)	283	8	24	42793	MITO
	218	Q9UUT8	YALI0F00924g	NUIM	tr|Q9UUT8 *Y. lipolytica* Subunit NUIM of protein NADH:ubiquinone oxidoreductase (Complex I)	72	2	8	26091	MITO
	205	Q9UUT9	YALI0D00737g	NUHM	tr|Q9UUT9 *Y. lipolytica* Subunit NUHM of protein NADH:ubiquinone oxidoreductase (Complex I)	25	2	8	27598	MITO
		Q9UUU0	YALI0F02123g	NUGM	tr|Q9UUU0 *Y. lipolytica* Subunit NUGM protein precursor	160	4	17	32382	MITO
	231	Q6CI10	YALI0A02651g		Similar to sp|P19968 *Neurospora crassa* NADH:ubiquinone oxidoreductase 21.3 kDa subunit	144	4	25	19794	MITO
	233	Q6ZY23	YALI0E29095g	NUWM	NADH:ubiquinone oxidoreductase accessory subunit (Complex I)	166	3	15	28475	MITO
	255	Q6CI60	YALI0A01419g	NB4M	NADH-ubiquinone oxidoreductase 21.3 kDa accessory subunit	116	2	12	21486	MITO
3	120	Q6C326	YALI0F03179g	ATP1	Highly similar to sp|P07251 *S. cerevisiae* YBL099w ATP1 F1F0-ATPase complex, F1 alpha subunit	812	17	37	58100	MITO (0.99)
	135	Q6CFT7	YALI0B03982g	ATP2	Highly similar to sp|P00830 *S. cerevisiae* ATP synthase beta chain mitochondrial precursor	414	11	26	54616	MITO (0.99)
4	153	Q6L8K7	YALI0E11099g	PAT1	*Y. lipolytica* Acetoacetyl-CoA thiolase (EC 2.3.1.9)	184	3	10	41560	PERO
	251	Q6C2B5	YALI0F09229g		Highly similar to sp|P36010 *S. cerevisiae* YKL067w YNK1 nucleoside diphosphate kinase	64	1	5	17208	
5	280	Q6C800	YALI0D23947g		Some similarities with sp|P25386 *S. cerevisiae* YDL058w USO1 intracellular protein transport	170	3	5	76569	

Table 1 (*Continued*)

#	Spot number	Protein name[a]	Gene name[b]	Usual name	Protein function	Score[c]	Peptide[d]	% cov[e]	MW[f] (Da)	Localization[g]
	281	Q6CCN4	YALI0C07953g		Highly similar to sp|P46598 *Candida albicans* CaHSC82, Heat shock protein 90 homolog	51	1	1	80285	
6	299	O74935	YALI0F10857g	POX2	tr|O74935 *Y. lipolytica* Acyl-CoA oxidase 2	608	14	20	79098	PERO
	301	O74936	YALI0D24750g	POX3	tr|O74936 *Y. lipolytica* Acyl-CoA oxidase 3, peroxisomal, specific toward short chain fatty acid	89	2	2	78645	PERO
		Q6C6T4	YALI0E06479g		Similar to sp|P23254 *S. cerevisiae* YPR074c TKL1 transketolase	291	8	11	76469	
7	167	Q6CGG6	YALI0A19536g		weakly similar to tr|Q873D6 *Neurospora crassa* B17B1.060	301	7	25	39105	
		Q6CC94	YALI0C11341g		Similar to tr|Q12230 *S. cerevisiae* Hypothetical 38.1 kDa protein YPL004C	125	3	12	34617	
8	180	Q6C1Q9	YALI0F14223g		similar to sp|P40035 *S. cerevisiae* YER053c related to mitochondrial phosphate carrier protein 2	123	3	11	39628	Membrane
		Q6CD20	YALI0C04455g		Weakly similar to sp|P53747 *S. cerevisiae*	83	2	11	28872	
9	285	Q6C5X9	YALI0E14190g	MDH2	Similar to sp|P17505 *S. cerevisiae* YKL085w MDH1 malate dehydrogenase precursor	271	6	18	39431	PERO/CYTO
		Q6C1Q9	YALI0F14223g		Similar to sp|P40035 *S. cerevisiae* YER053c related to mitochondrial phosphate carrier protein 2	174	4	13	39628	
10	287	Q6CGG6	YALI0A19536g		Weakly similar to tr|Q873D6 *Neurospora crassa* B17B1.060	239	3	16	39105	
		Q6CC94	YALI0C11341g		Highly similar to tr|Q12230 *S. cerevisiae* Hypothetical 38.1 kDa protein YPL004C	180	4	16	34617	
11	228	Q6CFH9	YALI0B06831g		Highly similar to sp|O13350 *Kluyveromyces lactis* ATP synthase D chain	49	1	5	19808	
	226	Q6C105	YALI0F20306g		Similar to sp|O13349 *Kluyveromyces lactis* ATP synthase subunit 4	150	5	24	23988	

[#] Protein complex spot number.
[a] Swissprot accession number.
[b] Annotation according to Génolevures [8].
[c] Mascot MS protein score.
[d] Number of peptides used for protein identification.
[e] Sequence coverage percentage.
[f] Predicted molecular weight (MW) in Daltons (Da), based on protein sequences.
[g] MITO: Mitochondrial (when a mitochondrial targeting sequence was identified by MITOPROT [49], the prediction value is indicated in parentheses); PERO: Peroxisomal (when a peroxisomal targeting sequence of type I (PST1) was observed at the C-terminus of the protein, the three terminal amino acids are indicated in parentheses); CYTO: Cytoplasmic, when mitochondrial prediction was poor and no obvious PTS1 sequence could be observed; ER: endoplasmic reticulum.

2, spot 233). Spot 231 (YALI0A02651g) displayed similarity to the potential *Candida albicans* mitochondrial complex I 21/29 kDa subunit (Q5AEI1|Q5AEI1_CANAL). No homologs were found in hemiascomycetous yeasts other than *Y. lipolytica* and *Debaryomyces hansenii*. Surprisingly, no subunit encoded by the mitochondrial genome was identified in this protein complex. These results suggest that the NADH:ubiquinone oxidoreductase complex with hydrophobic binding properties contains at least of 10 subunits encoded exclusively by the nuclear genome. The comparison of our complex I purified from whole cells on the basis of alkane-binding properties with that obtained by affinity tag purification [49] shows the relevance of our analysis of protein complexes. Indeed, the exclusive presence of proteins encoded by the nuclear genome in complex I suggests that these seven subunits may be assembled before entry into the mitochondria. These results would be consistent with the identification in this study of a premitochondrial complex I. Further investigation is required to determine the mechanisms involved in the entry of this protein complex into the mitochondria.

The NUKM protein (YALI0F06050g) was not identified, but one of the three spots in Fig. 3 may potentially correspond to the size of the NUKM protein. Other spots from this complex, indicated by arrows in Fig. 3, were unfortunately not identified (problems of detection threshold, or absence of identification after MS analysis etc.).

3.3. Protein complexes # 6 and # 12: complexes containing acyl-CoA oxidase isozymes

The association of five isoforms of acyl-CoA oxidase (Aox) (from Aox1p to Aox5p) was described as a 443-kDa heteropentameric complex containing one polypeptide chain of each isoform within the peroxisomal matrix of the yeast *Y. lipolytica* [55]. The Aox complex is assembled in the cytosol and then imported into peroxisomes [55]. The complete *Y. lipolytica* genome sequence [7] revealed

Table 2
List of the homomultimeric protein complexes of *Y. lipolytica* presenting hydrophobic binding properties.

#	Spot number	Protein name[a]	Gene name[b]	Usual name	Protein function	Score[c]	Peptide[d]	% cov[e]	MW[f] (Da)	Localization[g]
12	92	O74935	YALI0F10857g	POX2	*Y. lipolytica* Acyl-coA oxidase 2	367	8	15	79098	PERO
13	102	Q6C342	YALI0F02805g		Highly similar to sp|P19882 *S. cerevisiae* YLR259c HSP60 heat shock protein	637	12	28	60799	
14	104	P41555	YALI0C16885g	ICL1	*Y. lipolytica* Isocitrate lyase	746	15	37	60182	PERO (SKL)
15	105	Q6BZP5	YALI0F31999g	ICL2	Similar to sp|Q12031 *S. cerevisiae* YPR006c ICL2 non-functional isocitrate lyase	189	4	9	63251	MITO (0,98)
16	108	Q6C812	YALI0D23683g		Similar to sp|P12695 *S. cerevisiae* Dihydrolipoamide acetyltransferase component of pyruvate dehydrogenase complex	306	7	18	45714	
17	109	Q6CF74	YALI0B09647g		Similar to sp|P07275 *S. cerevisiae* Delta-1-pyrroline-5-carboxylate dehydrogenase	518	11	21	63313	
18	113	Q6CDB9	YALI0C01859g		Similar to sp|Q02253 *Rattus norvegicus* Methylmalonate-semialdehyde dehydrogenase (acylating)	307	7	15	56956	
19	118	Q6C7J6	YALI0E00264g		similar to sp|P46367 *S. cerevisiae* YOR374w ALD4 aldehyde dehydrogenase	61	1	2	56830	
20	123	Q6C5L8	YALI0E16929g		Similar to sp|P19262 *S. cerevisiae* YDR148c KDG2 2-oxoglutarate dehydrogenase complex E2	43	1	2	48792	
21	136	Q6CCT2	YALI0C06776g	FUM1	Highly similar to sp|P55250 *Rhizopus oryzae* Fumarate hydratase	204	5	14	53119	MITO (0,98)
22	146	Q6C643	YALI0E12573g		Similar to tr|Q8AW60 *Brachydanio rerio* SI:dZ181P14.1	174	4	11	45116	
23	156	Q6CAF8	YALI0D03135g		Highly similar to sp|P06168 *S. cerevisiae* YLR355c ILV5 ketol-acid reducto-isomerase	99	2	7	44246	
24	170	Q6C1H5	YALI0F16181g		highly similar to sp|P32366 *S. cerevisiae* YLR447c VMA6 H + -ATPase V0 domain 36 KD subunit	84	1	5	39883	
25	172	Q6CDL1	YALI0B23100g		Weakly similar to DEHA0E01430g *D. hansenii* IPF 5716.1	42	1	4	34604	
26	179	Q6CCJ7	YALI0C08811g		Similar to tr|Q9K6C9 *Bacillus halodurans* 3-hydroxybutyryl-CoA dehydrogenase	61	1	5	32925	
27	185	Q6C612	YALI0E13420g		Similar to tr|Q9HZP7 *Pseudomonas aeruginosa* Electron transfer flavoprotein alpha-subunit	215	4	19	34557	
28	188	Q6C338	YALI0F02893g		Similar to sp|P38077 *S. cerevisiae* YBR039w ATP3 F1F0-ATPase complex, F1 gamma subunit	157	4	17	31136	

Table 2 (*Continued*)

#	Spot number	Protein name[a]	Gene name[b]	Usual name	Protein function	Score[c]	Peptide[d]	% cov[e]	MW[f] (Da)	Localization[g]
29	198, 201, 202, 303	Q6C1D2	YALI0F17314g		Similar to sp|P04840 *S. cerevisiae* YNL055c POR1 mitochondrial outer membrane porin	188, 207, 465, 154	5, 5, 9, 4	20, 22, 45, 15	29627	Integral to membrane, mitochondrial outer membrane
30	199	Q6CBA9	YALI0C20449g		Similar to sp|P42940 *S. cerevisiae* YGR207c ETF-beta electron-transferring flavoprotein	64	3	12	27714	
31	208	Q6CBY2	YALI0C14498g		Highly similar to sp|P38988 *S. cerevisiae* Putative mitochondrial carrier protein YHM1/SH	395	8	37	32736	
32	227	Q6CFA1	YALI0B08921g		Similar to sp|O13401 *Candida albicans* Superoxide dismutase [Mn], mitochondrial precursor	64	1	6	25453	
33	264	Q6CAF5	YALI0D03245g		Highly similar to tr|Q6C2W4 *Y. lipolytica* YALI0F04598g	36	1	4	23428	
34	279, 283	Q6CDQ7	YALI0B22066g		Highly similar to sp|P05030 *S. cerevisiae* YGL008c PMA1 H + -transporting P-type ATPase	534, 848	10, 18	13, 19	99540	Integral to membrane
35	284	Q8J0M2	YALI0A10659g		Highly similar to sp|P38720 *S. cerevisiae* YHR183w GND1 6-phosphogluconate dehydrogenase	329	6	16	53895	
36	292	Q05493	YALI0E18568g	THIO1	sp|Q05493 *Y. lipolytica* 3-ketoacyl-CoA thiolase, peroxisomal precursor	417	9	29	43488	PERO
37	293	Q6C7I2	YALI0E00638g	CIT1	Similar to tr|Q9TEM3 *Emericella nidulans* MCSA Methylcitrate synthase precursor	395	11	25	51116	MITO (0,98)
38	297	Q6CA97	YALI0D04741g		Highly similar to sp|Q9P567 *Neurospora crassa* Probable succinyl-CoA ligase (GDP-forming) beta-chain	55	1	3	47280	
39	302	Q6C793	YALI0E02684g	CIT2	Highly similar to sp|P00890 *S. cerevisiae* YNR001c CIT1 citrate (si)-synthase	182	5	11	51734	MITO (0,98) PERO (LKL)
40	289, 290	Q6C2E3	YALI0F08613g	QCR2	Weakly similar to sp|P07257 *S. cerevisiae* YPR191w QCR2 ubiquinol–cytochrome-c reductase	193, 224	5, 5	15, 12	44203	

[#] Protein complex spot number.
[a] Swissprot accession number.
[b] Annotation according to Génolevures [8].
[c] Mascot MS protein score.
[d] Number of peptides used for protein identification.
[e] Sequence coverage percentage.
[f] Predicted molecular weight (MW) in Daltons (Da), based on protein sequences.
[g] MITO: Mitochondrial (when a mitochondrial targeting sequence was identified by MITOPROT [49], the prediction value is indicated in parentheses); PERO: Peroxisomal (when a peroxisomal targeting sequence of type I (PST1) was observed at the C-terminus of the protein, the three terminal amino acids are indicated in parentheses); CYTO: Cytoplasmic when mitochondrial prediction was poor and no obvious PTS1 sequence could be observed.

the existence of another gene encoding an acyl-CoA oxidase (*POX6*, YALI0E06567g). In this study, the Aox complex migrated to two different locations (Table 1, protein complexes # 6 and # 12, Fig. 1). At the first, this complex (complex # 6) was consisted of three proteins: gene product O74935 (Pox 2p, spot 299), gene product Q6C6T4 (spot 301) and gene product O74936 (Pox 3p, spot 301, YALI0D24750g). At the second, the complex (complex # 12) seemed to contain only one protein (Pox2p, spot 92, YALI0F10857). These incomplete AcylCoA oxidase complexes may have different affinities for alkanes (membrane), facilitating their migration from the matrix to the membrane of the peroxisomes. This migration may correspond to the complex shown to be involved in peroxisome division [56].

3.4. β-oxidation and glyoxylate cycle complexes

In yeasts and fungi growing on hydrophobic substrates in minimal medium, the tricarboxylic acid cycle is replenished by the reactions catalyzed by isocitrate lyase (ICL) and malate synthase (MLS), forming the glyoxylate bypass, also known as the glyoxylate bypass or glyoxylate shunt. This replenishing function has been described as "anaplerotic" [57] and probably plays an essential role in the growth of microorganisms on fatty acids.

The glyoxylate cycle is a metabolic pathway occurring in plants, some vertebrates and several microorganisms, such as *E. coli* and yeast, and allowing the synthesis of carbohydrates from fats. Fatty acids from lipids are generally broken down into acetate molecules by β-oxidation, for subsequent use as an energy source. The acetate binds to the active thiol group of coenzyme A and enters the glyoxylate cycle, generating carbohydrates in two ways: (i) the acetyl-CoA is fully oxidized to carbon dioxide. In this case, the acetyl-CoA produced by β-oxidation is channeled to the glyoxylate cycle and converted into malate. The malate is released into cytosol, where it is converted into phosphoenolpyruvate; (ii) the succinate is transferred to the mitochondria and converted there into malate by a partial reaction of the citric cycle. The malate is then released from mitochondria into the cytosol, where it is converted into phosphoenolpyruvate. Phosphoenolpyruvate is a precursor for the synthesis of hexoses by gluconeogenesis. The intermediates of the pentose phosphate pathway can be used for the biosynthesis of other compounds, such as RNA and proteins. For example, the cell wall of growing *Y. lipolytica* cells requires very large amounts of carbohydrates for the biosynthesis of complex structural polysaccharides. In the absence of available carbohydrates (for example, in certain microbial environments, such as in the presence of hydrophobic substrates), the glyoxylate cycle enables this yeast to synthesize glucose from lipids via acetate produced through β-oxidation of fatty acids.

Protein complex # 1 is very interesting because it consists of 11 proteins involved in the glyoxylate cycle (Q6C9P6_spot 80, P41555_spot 106 and Q6C8V3_spot 178), the transport of succinate-fumarate (Q6C3I0_spot 189) or β-oxidation (Q9P4D9_spot 75). The Q6CBL6 protein (spot 139) contains a CRAL-TRIO domain. This domain is a structurally conserved element, of about 170 amino acids in length, which forms a large hydrophobic lipid-binding pocket composed of six β-strands α-helices forming the sides of the cavity [58]. This domain is important for the protein–lipid interactions involved in protein targeting, signal transduction, lipid transport, lipid biosynthesis, lipid metabolism and the maintenance of cellular compartments and membranes [59]. In complex # 1, this protein binds to lipids, leading to the entry of the lipid into the β-oxidation cycle. The multifunctional β-oxidation enzyme Q9P4D9 (protein complex # 1, spot 75, Table 1) then catalyzes the transformation of trans-delta-enoylCoA into 3-ketoacylCoA. Furthermore, complex # 1 contains three proteins involved in the glyoxylate cycle. Aconitate hydratase (Q6C9P6_spot 80) transforms citrate in isocitrate. Isocitrate lyase (P41555_spot 106) is the first enzyme unique to the glyoxylate cycle and catalyzes the reversible cleavage of isocitrate to generate glyoxylate and succinate. This enzyme acts at a branch point in carbon metabolism and diverts isocitrate through a carbon-conserving pathway, the glyoxylate cycle, bypassing the two decarboxylation steps of the tricarboxylic acid cycle, which converts isocitrate to succinyl-CoA. The third enzyme of this complex from the glyoxylate cycle is malate dehydrogenase (Q6C8V3_spot 178), which transforms S-malate into oxaloacetate. Moreover, protein complex # 1 contains the Sfcp succinate-fumarate transporter (Q6C3I0_spot 189), which may be involved in transferring succinate to mitochondria. The *SFC1* and *ICL1* genes have been shown to be required for growth on hydrophobic substrates [60]. Alternatively, complex # 1 may correspond to intracellular vesicles, precursors of the extracellular vesicles recently observed in ascomycetes and containing proteins involved in diverse processes [61].

3.5. First observation of proteins

These results will enrich the complexomic and proteomic databases for *Y. lipolytica*. Most of the proteins identified in this report are described as 'Inferred from homology' or 'Predicted' in the database [62]. Thus, these proteins are probably present because orthologs are found in closely related species, or are thought to exist despite a lack of evidence protein-, transcript- or homology-based evidence. In this study, 44% of the 66 distinct proteins identified had been inferred from homology whereas 50% of the proteins identified had been predicted from the genome sequence alone, with no evidence at protein, transcript or homology levels. These protein complexes were localized on the basis of predictions of targeting sequences (mitochondria, peroxisome) or N-terminal signal peptides for secretion, together with published data concerning their distribution. However, proteins lacking an N-terminal secretion signal were recently found to be located at the yeast cell surface [63]. Some of the alkane-binding complexes we have identified may be located in the cell wall, as part of the "protrusion complex" and may be involved in alkane binding and utilization [13,15].

4. Conclusion

In this study, the combination of 2D BN/SDS-PAGE and HPLC-chip-MS methods made it possible to identify 40 different alkane-binding protein complexes: 11 heteromultimeric and 29 homomultimeric complexes. After validation, this approach led to the identification of mitochondrial complex I, which contained only subunits encoded by the nuclear genome, consistent with the possible assembly of this complex before entry into the mitochondria. We detected two different Aox complexes with potentially different affinities for alkane (membrane), facilitating their migration from the matrix to the membrane of the peroxisome. This strategy also highlighted the role of the glyoxylate cycle in the synthesis of carbohydrates from fats. This replenishing function probably plays an essential role in the growth of microorganisms on fatty acids. Finally, this work has contributed new findings to yeast databases. Indeed, these results confirmed the existence of hypothetical proteins previously inferred purely from homology or predicted from the genome sequence in the absence of evidence at the protein or transcript level.

Acknowledgments

This work was financially supported in part by INRA, CNRS and Oxyrane (grant n° B 05344). We thank Julie Sappa of Alex Edelman

& Associates for her excellent help in correcting the English version of the manuscript.

References

[1] P. Fickers, P.H. Benetti, Y. Wache, A. Marty, S. Mauersberger, M.S. Smit, J.M. Nicaud, FEMS Yeast Res 5 (2005) 527.
[2] J.M. Beckerich, A. Boisrame-Baudevin, C. Gaillardin, Int Microbiol 1 (1998) 123.
[3] D. Swennen, J.M. Beckerich, BMC Evol Biol 7 (2007) 219.
[4] V.I. Titorenko, J.J. Smith, R.K. Szilard, R.A. Rachubinski, Cell Biochem Biophys 32 Spring (2000) 21.
[5] A. Dominguez, E. Ferminan, C. Gaillardin, Contrib Microbiol 5 (2000) 151.
[6] S. Kerscher, S. Drose, K. Zwicker, V. Zickermann, U. Brandt, Biochim Biophys Acta 1555 (2002) 83.
[7] B. Dujon, D. Sherman, G. Fischer, P. Durrens, S. Casaregola, I. Lafontaine, J. De Montigny, C. Marck, C. Neuveglise, E. Talla, N. Goffard, L. Frangeul, M. Aigle, V. Anthouard, A. Babour, V. Barbe, S. Barnay, S. Blanchin, J.M. Beckerich, E. Beyne, C. Bleykasten, A. Boisrame, J. Boyer, L. Cattolico, F. Confanioleri, A. De Daruvar, L. Despons, E. Fabre, C. Fairhead, H. Ferry-Dumazet, A. Groppi, F. Hantraye, C. Hennequin, N. Jauniaux, P. Joyet, R. Kachouri, A. Kerrest, R. Koszul, M. Lemaire, I. Lesur, L. Ma, H. Muller, J.M. Nicaud, M. Nikolski, S. Oztas, O. Ozier-Kalogeropoulos, S. Pellenz, S. Potier, G.F. Richard, M.L. Straub, A. Suleau, D. Swennen, F. Tekaia, M. Wesolowski-Louvel, E. Westhof, B. Wirth, M. Zeniou-Meyer, I. Zivanovic, M. Bolotin-Fukuhara, A. Thierry, C. Bouchier, B. Caudron, C. Scarpelli, C. Gaillardin, J. Weissenbach, P. Wincker, J.L. Souciet, Nature 430 (2004) 35.
[8] http://www.cbi.labri.fr/Genolevures.
[9] C. Neuvèglise, personal communication.
[10] G. Pignede, H. Wang, F. Fudalej, C. Gaillardin, M. Seman, J.M. Nicaud, J Bacteriol 182 (2000) 2802.
[11] P. Fickers, F. Fudalej, M.T. Le Dall, S. Casaregola, C. Gaillardin, P. Thonart, J.M. Nicaud, Fungal Genet Biol 42 (2005) 264.
[12] S.S. Zinjarde, A. Pant, J Basic Microbiol 42 (2002) 67.
[13] K. Mlickova, E. Roux, K. Athenstaedt, S. d'Andrea, G. Daum, T. Chardot, J.M. Nicaud, Appl Environ Microbiol 70 (2004) 3918.
[14] M. Kabani, A. Boisrame, J.M. Beckerich, C. Gaillardin, Gene 241 (2000) 309.
[15] K. Athenstaedt, P. Jolivet, C. Boulard, M. Zivy, L. Negroni, J.M. Nicaud, T. Chardot, Proteomics 6 (2006) 1450.
[16] S. Fields, O. Song, Nature 340 (1989) 245.
[17] M. Fromont-Racine, J.C. Rain, P. Legrain, Nat Genet 16 (1997) 277.
[18] L. Giot, J.S. Bader, C. Brouwer, A. Chaudhuri, B. Kuang, Y. Li, Y.L. Hao, C.E. Ooi, B. Godwin, E. Vitols, G. Vijayadamodar, P. Pochart, H. Machineni, M. Welsh, Y. Kong, B. Zerhusen, R. Malcolm, Z. Varrone, A. Collis, M. Minto, S. Burgess, L. McDaniel, E. Stimpson, F. Spriggs, J. Williams, K. Neurath, N. Ioime, M. Agee, E. Voss, K. Furtak, R. Renzulli, N. Aanensen, S. Carrolla, E. Bickelhaupt, Y. Lazovatsky, A. DaSilva, J. Zhong, C.A. Stanyon, R.L. Finley Jr., K.P. White, M. Braverman, T. Jarvie, S. Gold, M. Leach, J. Knight, R.A. Shimkets, M.P. McKenna, J. Chant, J.M. Rothberg, Science 302 (2003) 1727.
[19] T. Ito, K. Tashiro, T. Kuhara, Tanpakushitsu Kakusan Koso 46 (2001) 2407.
[20] P. Legrain, L. Selig, FEBS Lett 480 (2000) 32.
[21] J.C. Rain, L. Selig, H. De Reuse, V. Battaglia, C. Reverdy, S. Simon, G. Lenzen, F. Petel, J. Wojcik, V. Schachter, Y. Chemama, A. Labigne, P. Legrain, Nature 409 (2001) 211.
[22] J.F. Rual, K. Venkatesan, T. Hao, T. Hirozane-Kishikawa, A. Dricot, N. Li, G.F. Berriz, F.D. Gibbons, M. Dreze, N. Ayivi-Guedehoussou, N. Klitgord, C. Simon, M. Boxem, S. Milstein, J. Rosenberg, D.S. Goldberg, L.V. Zhang, S.L. Wong, G. Franklin, S. Li, J.S. Albala, J. Lim, C. Fraughton, E. Llamosas, S. Cevik, C. Bex, P. Lamesch, R.S. Sikorski, J. Vandenhaute, H.Y. Zoghbi, A. Smolyar, S. Bosak, R. Sequerra, L. Doucette-Stamm, M.E. Cusick, D.E. Hill, F.P. Roth, M. Vidal, Nature 437 (2005) 1173.
[23] U. Stelzl, U. Worm, M. Lalowski, C. Haenig, F.H. Brembeck, H. Goehler, M. Stroedicke, M. Zenkner, A. Schoenherr, S. Koeppen, J. Timm, S. Mintzlaff, C. Abraham, N. Bock, S. Kietzmann, A. Goedde, E. Toksoz, A. Droege, S. Krobitsch, B. Korn, W. Birchmeier, H. Lehrach, E.E. Wanker, Cell 122 (2005) 957.
[24] P. Uetz, R.E. Hughes, Curr Opin Microbiol 3 (2000) 303.
[25] C. Hultschig, J. Kreutzberger, H. Seitz, Z. Konthur, K. Bussow, H. Lehrach, Curr Opin Chem Biol 10 (2006) 4.
[26] G. MacBeath, S.L. Schreiber, Science 289 (2000) 1760.
[27] R. Aebersold, M. Mann, Nature 422 (2003) 198.
[28] G. Butland, J.M. Peregrin-Alvarez, J. Li, W. Yang, X. Yang, V. Canadien, A. Starostine, D. Richards, B. Beattie, N. Krogan, M. Davey, J. Parkinson, J. Greenblatt, A. Emili, Nature 433 (2005) 531.
[29] R.M. Ewing, P. Chu, F. Elisma, H. Li, P. Taylor, S. Climie, L. McBroom-Cerajewski, M.D. Robinson, L. O'Connor, M. Li, R. Taylor, M. Dharsee, Y. Ho, A. Heilbut, L. Moore, S. Zhang, O. Ornatsky, Y.V. Bukhman, M. Ethier, Y. Sheng, J. Vasilescu, M. Abu-Farha, J.P. Lambert, H.S. Duewel, I.I. Stewart, B. Kuehl, K. Hogue, K. Colwill, K. Gladwish, B. Muskat, R. Kinach, S.L. Adams, M.F. Moran, G.B. Morin, T. Topaloglou, D. Figeys, Mol Syst Biol 3 (2007) 89.
[30] A.C. Gavin, P. Aloy, P. Grandi, R. Krause, M. Boesche, M. Marzioch, C. Rau, L.J. Jensen, S. Bastuck, B. Dumpelfeld, A. Edelmann, M.A. Heurtier, V. Hoffman, C. Hoefert, K. Klein, M. Hudak, A.M. Michon, M. Schelder, M. Schirle, M. Remor, T. Rudi, S. Hooper, A. Bauer, T. Bouwmeester, G. Casari, G. Drewes, G. Neubauer, J.M. Rick, B. Kuster, P. Bork, R.B. Russell, G. Superti-Furga, Nature 440 (2006) 631.
[31] Y. Ho, A. Gruhler, A. Heilbut, G.D. Bader, L. Moore, S.L. Adams, A. Millar, P. Taylor, K. Bennett, K. Boutilier, L. Yang, C. Wolting, I. Donaldson, S. Schandorff, J. Shewnarane, M. Vo, J. Taggart, M. Goudreault, B. Muskat, C. Alfarano, D. Dewar, Z. Lin, K. Michalickova, A.R. Willems, H. Sassi, P.A. Nielsen, K.J. Rasmussen, J.R. Andersen, L.E. Johansen, L.H. Hansen, H. Jespersen, A. Podtelejnikov, E. Nielsen, J. Crawford, V. Poulsen, B.D. Sorensen, J. Matthiesen, R.C. Hendrickson, F. Gleeson, T. Pawson, M.F. Moran, D. Durocher, M. Mann, C.W. Hogue, D. Figeys, M. Tyers, Nature 415 (2002) 180.
[32] O. Puig, F. Caspary, G. Rigaut, B. Rutz, E. Bouveret, E. Bragado-Nilsson, M. Wilm, B. Seraphin, Methods 24 (2001) 218.
[33] M. Schuldiner, S.R. Collins, N.J. Thompson, V. Denic, A. Bhamidipati, T. Punna, J. Ihmels, B. Andrews, C. Boone, J.F. Greenblatt, J.S. Weissman, N.J. Krogan, Cell 123 (2005) 507.
[34] J. Vasilescu, D. Figeys, Curr Opin Biotechnol 17 (2006) 394.
[35] M.M. Camacho-Carvajal, B. Wollscheid, R. Aebersold, V. Steimle, W.W. Schamel, Mol Cell Proteomics 3 (2004) 176.
[36] D. Claeys, K. Geering, B.J. Meyer, Electrophoresis 26 (2005) 1189.
[37] J.P. Lasserre, E. Beyne, S. Pyndiah, D. Lapaillerie, S. Claverol, M. Bonneu, Electrophoresis 27 (2006) 3306.
[38] S. Pyndiah, J.P. Lasserre, A. Menard, S. Claverol, V. Prouzet-Mauleon, F. Megraud, F. Zerbib, M. Bonneu, Mol Cell Proteomics 6 (2007) 193.
[39] H. Schagger, W.A. Cramer, G. von, Jagow, Anal Biochem 217 (1994) 220.
[40] H. Schagger, G. von, Jagow, Anal Biochem 166 (1987) 368.
[41] H. Schagger, G. von, Jagow, Anal Biochem 199 (1991) 223.
[42] F. Stenberg, P. Chovanec, S.L. Maslen, C.V. Robinson, L.L. Ilag, G. von Heijne, D.O. Daley, J Biol Chem 280 (2005) 34409.
[43] A. Stroh, O. Anderka, K. Pfeiffer, T. Yagi, M. Finel, B. Ludwig, H. Schagger, J Biol Chem 279 (2004) 5000.
[44] B. Schwikowski, P. Uetz, S. Fields, Nat Biotechnol 18 (2000) 1257.
[45] C. von Mering, R. Krause, B. Snel, M. Cornell, S.G. Oliver, S. Fields, P. Bork, Nature 417 (2002) 399.
[46] J. Hardouin, M. Duchateau, R. Joubert-Caron, M. Caron, Rapid Commun Mass Spectrom 20 (2006) 3236.
[47] J. Hardouin, R. Joubert-Caron, M. Caron, J Sep Sci 30 (2007) 1482.
[48] http://www.ihg2.helmholtz-muenchen.de/ihg/mitoprot.html.
[49] A. Abdrakhmanova, V. Zickermann, M. Bostina, M. Radermacher, H. Schagger, S. Kerscher, U. Brandt, Biochim Biophys Acta 1658 (2004) 148.
[50] N. Morgner, V. Zickermann, S. Kerscher, I. Wittig, A. Abdrakhmanova, H.D. Barth, B. Brutschy, U. Brandt, Biochim Biophys Acta 1777 (2008) 1384.
[51] J. Hirst, J. Carroll, I.M. Fearnley, R.J. Shannon, J.E. Walker, Biochim Biophys Acta 1604 (2003) 135.
[52] A. Videira, M. Duarte, Biochim Biophys Acta 1555 (2002) 187.
[53] S. Leterme, M. Boutry, Plant Physiol 102 (1993) 435.
[54] P. Cardol, F. Vanrobaeys, B. Devreese, J. Van Beeumen, R.F. Matagne, C. Remacle, Biochim Biophys Acta 1658 (2004) 212.
[55] V.I. Titorenko, J.M. Nicaud, H. Wang, H. Chan, R.A. Rachubinski, J Cell Biol 156 (2002) 481.
[56] T. Guo, Y.Y. Kit, J.M. Nicaud, M.T. Le Dall, S.K. Sears, H. Vali, H. Chan, R.A. Rachubinski, V.I. Titorenko, J Cell Biol 162 (2003) 1255.
[57] J.M. Ashworth, H.L. Kornberg, Proc, R Soc Lond B Biol Sci 165 (1966) 179.
[58] B. Sha, S.E. Phillips, V.A. Bankaitis, M. Luo, Nature 391 (1998) 506.
[59] K. Saito, L. Tautz, T. Mustelin, Biochim Biophys Acta 1771 (2007) 719.
[60] F. Thevenieau, M.-T. Le Dall, B. Nthangeni, S. Mauersberger, R. Marchal, J.-M. Nicaud, Fungal Genet Biol 44 (2007) 531.
[61] P.C. Albuquerque, E.S. Nakayasu, M.L. Rodrigues, S. Frases, A. Casadevall, R.M. Zancope-Oliveira, I.C. Almeida, J.D. Nosanchuk, Cell Microbiol 10 (2008) 1695–1710.
[62] http://www.ca.expasy.org/uniprot.
[63] C. Nombela, C. Gil, W.L. Chaffin, Trends Microbiol 14 (2006) 15–21.

Talanta 80 (2010) 1587–1597

Contents lists available at ScienceDirect

Talanta

journal homepage: www.elsevier.com/locate/talanta

Review

An overview on the accumulation, distribution, transformations, toxicity and analytical methods for the monitoring of persistent organic pollutants

M.S. El-Shahawi[a,*], A. Hamza[a], A.S. Bashammakh[b], W.T. Al-Saggaf[a]

[a] Department of Chemistry, Faculty of Science, King Abdulaziz University, P.O. Box 80203, Jeddah 21589, Saudi Arabia
[b] The Centre of Excellence in Environmental Studies, King Abdulaziz University, P.O. Box 80203, Jeddah 21589, Saudi Arabia

ARTICLE INFO

Article history:
Received 22 July 2009
Received in revised form
25 September 2009
Accepted 25 September 2009
Available online 2 October 2009

Keywords:
Persistent organic pollutants
Accumulation
Transformation
Chromatographic determination

ABSTRACT

Recent years have seen an upsurge of interest in developing low cost and reliable methods for the detection and precise determination of ultra-trace concentrations of persistent organic pollutants (POPs), because of their bioaccumulation, transformation and toxicity. Therefore, a comprehensive review with 108 references referring to the distribution, source, accumulation, transformation, types and toxicity of polychlorinated biphenyls (PCBs) and organochlorine pesticides (OCPs) is presented. The review also aims to highlight on the current best practices for the analysis of PCBs and OCPs. Moreover, with the signing of the Stockholm convention on POPs and the development of global monitoring programs, there is an increased need for laboratories in developing countries to determine such class of chemicals. A major focus revealed the need for low cost methods that can be implemented easily in developing countries such as electrochemical techniques.

© 2009 Published by Elsevier B.V.

Contents

1. Historical overview 1587
2. Distribution of POPs 1588
3. Sources of POPs 1588
4. Type of persistent organic pollutants 1590
   4.1. Intentionally POPs 1590
      4.1.1. Organochlorine pesticides (OCPs) 1590
      4.1.2. Industrial chemicals 1592
   4.2. Unintentionally POPs 1593
      4.2.1. Polycyclic aromatic hydrocarbons (PAHs) 1593
      4.2.2. Dioxins and dibenzofurans 1593
5. Properties of POPs 1593
6. Dosage and toxicity of POPs 1594
7. Extraction and analytical techniques 1595
8. Removal and/or minimization of POPs 1595
9. Conclusion 1596
   References 1596

1. Historical overview

After the Second World War, scientists began to recognize that, certain chemical pollutants were capable of persistent in the environment for long time, migrating in air, water, soil and sediments and accumulating to levels that could harm wildlife and human health. These chemical pollutants called persistent organic pollutants (POPs) [1]. These pollutants are organic compounds of natural

* Corresponding author. Permanent address: Department of Chemistry, Faculty of Science at Damiatta, Mansoura University, Mansoura, Egypt.
Tel.: +966 2 6952000x64960; fax: +966 2 6952292.
E-mail addresses: mohammad_el_shahawi@hotmail.com, malsaeed@kau.edu.sa (M.S. El-Shahawi).

0039-9140/$ – see front matter © 2009 Published by Elsevier B.V.
doi:10.1016/j.talanta.2009.09.055

or anthropogenic origin that possess a particular combination of physical and chemical properties such that, once released into the environment, they remain intact for exceptionally long periods of time as they resist photolytic, chemical and biological degradation [2,3]. Compounds of this nature are highly resistant to degradation by biological photolytic and/or chemical means [3].

Recently, POPs are a matter of concern because of their toxicity and tendency to accumulate in food chains [4]. The environmental impact of a particular species becomes more important than a total metal concentration. Thus, metal speciation is of great importance in environmental science. However, due to their low concentrations, pre-concentration (enrichment) step is needed prior to their determination. The pollution by POPs and determination and chemical speciation of toxic trace metal ions will be discussed more in detail below.

The carbon–chlorine bond is very stable toward hydrolysis and the greater the number of chlorine substitution and/or functional group, the greater the resistant to biological and photolytic degradation. Because POPs break down very slowly, they will present in the environment for long time to come, even if all new sources were immediately eliminated [5]. POPs in the environment are transported at low concentrations by movement of fresh and marine waters and, as they are semi-volatile, are transported over long distances in the atmosphere. The result is widespread distribution of POPs across the globe, including regions where they have never been used [2]. The POP's level found in the Arctic of Alaska is surprising to many people. This is because some of these pollutants have been banned from the United State and Canada for many years. POPs travel toward colder area like Alaska and then sink due to the colder temperature. The settled contaminants remain in the area for a long period of time because the temperature does not allow theme to break down very easily. Because of this, they move from the air and water in to soil and plants, then to animals and humans with ease. The persistence of contaminants in the Arctic from distant sources first came to light in the late 1970 when pesticides were found in polar bear fat tissue, then the reality of atmospheric POPs, their effect on wildlife and human health. A well-known story in the Arctic, researches have begun to look for evidence of airborne POPs in other cold ecosystems, our mountain environments [6,7].

2. Distribution of POPs

In 1945, a booming industry launched a new, effective tool for dealing with insect pests: DDT. It held great promise, including the hope of saving crops and eradicating disease-carrying insects. Twenty years later, DDT and other similar chemicals had indeed benefited agriculture and relieved some of the problems associated with insects in many areas of the world. However, these gains came at a price, as DDT is toxic to many more organisms than those it was intended to kill. In particular, birds of prey had trouble to reproduce, and their population declined in many polluted parts of the world. Since, the commercial manufacture of anthropogenically synthesized organic chemicals began in the 1920s. Production, use and trade of these substances rose sharply after World War II, driven by a desire to produce more and better food and cash crops, protect public health, and facilitate industrial development [8,9].

The first public warnings about possible dangers came in relation to local environmental effects in the early 1960s, and grew stronger in the 1970s [7]. During 1960 and 1970 they were extensively utilized in order to protect crops and to prevent health diseases. Some of these compounds such as hexachlorobenzene (HCB), hexachlorocyclohexane (HCH) and Dichlorodiphenyltrichloroethane (DDT) were among the most widely used pesticides in the world during 1970–1980. Nowadays they are banned or restricted in the majority of the industrialized countries, but they still used in Africa, South Asia, Central and South America [7–10].

In the late of 1980s, new scientific discoveries resulted in changing perception, highlighting the transboundary nature of the POPs problem. Many of the discoveries were related to the Arctic region. These discoveries were spurred by both qualitative and quantitative improvements in data samples, measurement and analytical techniques. Also, in August 1989, Canada presented a report on hazardous persistent organic chemicals [8].

In the 1990, research found that the largest lake trout in Bow Lake contain high levels of some of these pollutants such as toxaphene. Since, the lake supports only a small population of large lake trout (2.5 kg) and people do not consume high amounts of fish from the lake, human health is not at risk. However, predators such as osprey feed exclusively on fish [12]. Also in Taiwan, the Danshui consider the largest river in the north, it receives liquid effluents and atmospheric fallout resulting from industrial and municipal emissions which include multiple forms of POP pollutants associated with these emissions, including polychlorinated biphenyls (PCBs), are transported down-river in association with particulates and deposited in river sediments, as well as those in nearby coastal areas. The presence of these pollutants causes a large toxicity on fish and other living organisms in the river [13].

The persistence in the compounds allows them to accumulate in animals and pass on more. When the pollutants progress in to animals, they accumulate in the fat cells, organs and muscles. In Adriatic sea which is an arm of the Mediterranean sea separating Italy from the Balkan peninsula, there are concentrations so low of some of these pollutants such as PCB, HCB, HCH and organochlorine pesticides (OCPs) in the fish liver collected from the Adriatic sea during 1993–2003 such as DDT in order to estimate the long-term changes in residue levels and the present status of contamination of this aquatic zone [14].

In China, many high-yield grain fields have become high-intense by POPs – especially pesticide – application areas in China. It was shown by sampling surveys from 1985 to 1991 that pesticide consumption ranged from 4.65 to 15.75 kg/h m^2 increasing by threefold and 41.8% annually. Pesticide consumption in southeast regions of China including Zhejiang, Shanghai, Fujian, and Guangzhou provinces accounted for 36.7% of the nationwide consumption, while six provinces in the northwest of China, including Qinghai, Ningxia, Gansu, Xinjiang, Heilongjiang, and Inner Mongolia, only accounted for 3.4%. The consumption of pesticides in Zhejiang was about 9.96 kg/h m^2 and 3.7 times that of the national average (2.71 kg/h m^2), and 28 times more than that in Inner Mongolia, which was the lowest user of these chemicals. The distribution pattern of pesticide application in China shown in Fig. 1 was as follows: southeast > central > northwest [15].

In 1999, during the so-called dioxin scandal in Belgium, Polish Veterinary Inspectorate ordered an analysis of food samples of Polish and international origin. The Inspectorate tried not to make the results of those analyses publicly available. This can be seen from the Inspectorate's response to the request of world protection agency (WPA) for allowing access to them. They said that *in the period in question, no such analyses were made in Poland* as seen in Table 1. These data were published in a scientific publication with a limited circulation [16].

3. Sources of POPs

Volcanic activity and vegetation fires are the two possible natural sources of dioxins and dibenzofurans. Some of these volcanoes are located in central Africa. Some attention will be given to sources or uses particular to southern and South Africa. One of these sources is fire, both natural, accidental and managed burning of vegetation [17–20]. POPs, as are apparent from their definition, are very

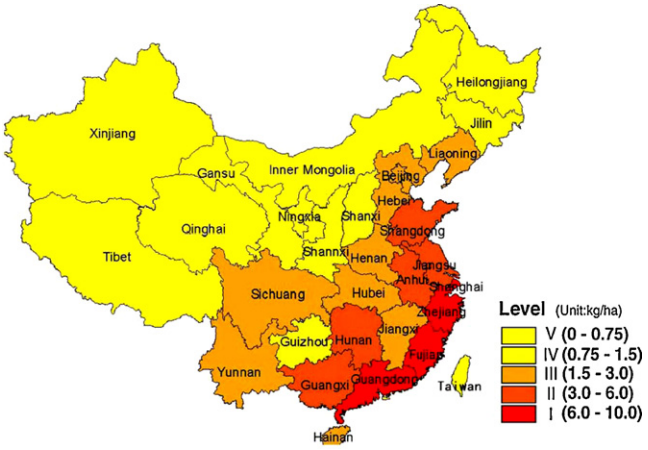


Fig. 1. Distribution of persistent organic pollutants in China in 1996.

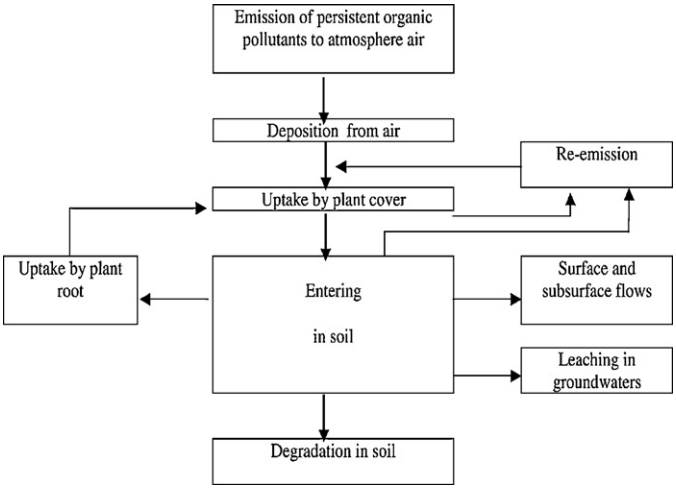


Fig. 2. Conceptual model for the behavior of persistent organic pollutants in the air–plant soil system.

stable in all constituents of the environment. They enter the atmosphere from a number of industrial sources such as power stations, heating stations, incinerating plants as well as from household furnaces, transport, use of agricultural sprays, evaporation from water surfaces, soil, or from the landfills. Other sources for POPs compounds such as the unintentional production can be found by incinerations, chemical facilities, diverse combustions, bushfires and putrefaction and wastes containing PCBs. This class of wastes can be found in many areas and stemming from different activities, e.g. the use of obsolete oil, the repairing and maintenance of equipments, demolition of building, evaporation, cement manufacture, animal carcass incinerator, coal combustion, lixiviation of dumps and recycling operations, incineration-municipal, hazardous, medical waste, sewage sludge, industry-chlor-alkali plants, aluminium secondary plants, organ chlorine pesticide plant and cock plant, landfills-hazardous waste/plastic waste, fly ash storage, and organochlorine pesticide storage [21,22].

The sources of access of the substances, oil, fates, liquid fuels, soil, ash and sediment into the water system are wastewaters from plants producing or using POPs, along with runoffs from fields and roads and from the atmospheric deposition. Their largest reservoirs are oceans and seas, where they gather from river sediments, by the atmospheric deposition, by disposing wastes, and by accidents. They are stored in sediments on the beds of seas, oceans, and large lakes, where they can be released from after a time and then re-enter the atmosphere as shown in Fig. 2 [23,24].

During the last 10 years, a lot of sources of POPs were stopped due to the economical changes in the country. Moreover a lot of new wastewater treatment plants were built during this period. Another reason of the observed decreasing trends in POPs occurrence in waters and sediments is found in the more principal ecological politics of government and local authorities [22]. In Poland, no wide-ranging investigations of dioxin-related environmental contamination, especially the presence of those compounds in human tissues and milk of breastfeeding mothers, have ever been conducted. Any publicly available data is random or based on unreliable estimates. According to the information provided to the Central Statistical Office by the Institute for Environmental Protection, the dioxin and furan emissions in 1998 are estimated at 290.353 g TEQ. According to the Institute, the main sources of dioxin emissions in Poland are given in Fig. 3 [25].

Recently, the Ministry of Environment has undertaken great efforts to provide a basis for estimating the real emission of dioxins and furans. In different regions of Poland, in urbanized areas as well

Table 1
Analysis of dioxin scandal in fat of food samples (pg-TEQ g^{-1}) of Polish and international origin in 1999 for dioxin scandal with a limited circulation [15–17].

Product	Concentration, pg-TEQ g^{-1} fat	Reference data, pg-TEQ g^{-1} fat [15–17]
Fish oil from Baltic fish (imported from Scandinavia)	12.6–50.0	–
Sea Fish (from Baltic Sea)	7.0–40.0	2.4–214.3
Fish oil from Baltic fish	11.2–40.0	–
Pork grilled in open fire	20.0–25.0	–
Fish meal (imported from Scandinavia)	6.5–20.0	–
Poultry	0.6–12.8	0.7–2.2
Freshwater fish	1.2–9.4	2.4
Beef	2.4–8.5	0.1–16.7
Pork	0.05–1.3	0.31
Hard cheese	0.2–7.7	–
Eggs (Yolk)	0.6–7.4	1.2–4.6
Butter	0.6–6.5	0.16–4.8
Powdered milk	0.3–5.0	–
Polish bone meal	0.25–4.25	–
Milk	0.1–4.0	0.5–3.8
Beef fat	3.8	–
Yoghurts with fat content >2%	0.1–1.8	0.18
Used vegetable oil (frying chips)	0.15–0.8	–
Chocolate products	0.05–0.75	–
Fresh vegetable oil	0.02–0.1	0.01–0.2
Low-fat yoghurts	Less than 0.01	–
Meat of Belgian chicken fed on contaminated feed	–	700

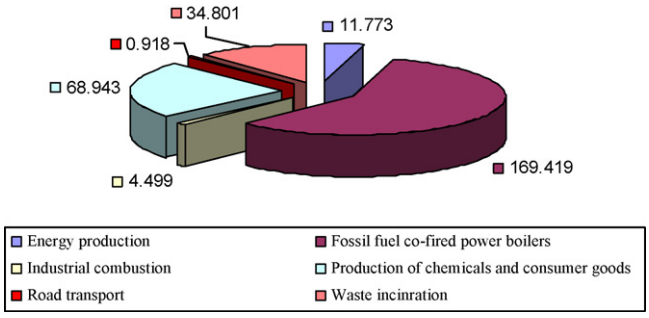


Fig. 3. The main sources of dioxin emissions in Poland.

Table 2
The permissible concentrations (pg-TEQ g^{-1}) of PCBs, DDT and gamma-HCH.

Substance	The permissible dose, pg-TEQ g^{-1} fat
PCBs	2.8
DDT	4.2
Gamma-HCH	13.3

Table 3
Analysis of some selected POPs (mg kg^{-1}) in samples of fatty tissues of patients aged from 10–80 years in one of Warsaw's hospitals.

Substance	mg kg^{-1} of fat		
	Median	Maximum	Mean
PCBs	0.500	36.000	0.856
HCB	0.120	9.020	0.310
Alpha-HCH	0.160		0.016
Beta-HCH	0.120	5.097	0.228
Gamma-HCH	0.030	2.727	0.074
p,p′-DDE	4.382	35.850	5.745
p,p′-DDT	0.478	9.600	0.537

as those potentially free from dioxin contamination, 118 geological samples have been taken. The analysis thereof will allow for determining the so-called background dioxin level. The reference source for monitoring of that compounds in milk of breastfeeding mothers has been reported by Ludwicki et al. [25] to assign the content of other persistent organic pollutants. The investigation covered a group of 462 women from Warsaw and other localities [26]. The permissible concentrations (pg-TEQ g^{-1}) of PCBs, DDT and gamma-HCH are summarized in Table 2. The increased level of persistent organic pollutants was found primarily in older women, aged 30 and more, and those who gave birth to more than four children.

In the years 1989–1992, in one of Warsaw's hospitals, samples of fatty tissues have been undertaken from 277 patients aged from 10 to 80 years and were successfully subjected to analysis for a series of PCBs, HCB, alpha-HCH, beta-HCH, gamma-HCH, *p,p′*-DDE and p,p′-DDT [25]. The results are summarized in Table 3. Higher concentrations of POPs have been found in tissues of older people [25]. In the case of gamma-HCH, only a higher level was noted in the samples that taken from patients aged below 25 years.

4. Type of persistent organic pollutants

In Stockholm 2001, representatives from 92 countries have agreed to sign the Stockholm Convention on POPs to reduce and/or eliminate the release of 12 original POP substances which are namely the dirty dozen. More contaminants have been discovered; the main concern is over the original 12. These contaminants are the 10 intentionally produced chemicals: aldrin, endrin, chlordane, DDT, dieldrin, heptachlor, mirex, toxaphene, hexachlorobenzene (HCB) and polychlorinated biphenyls (PCBs) and the two unintentionally produced substances polychlorinated dibenzo-p-dioxins (PCDDs) and polychlorinated dibenzofurans (PCDFs) [26,27]. Also, polycyclic aromatic hydrocarbons (PAHs) are also classified as persistent organic compounds, and they are formed as unintentionally substances by combustion and burning of organic compounds. Their occurrences are related to anthropogenic processes, and contamination of PAHs in river sediment is especially serious in high-density industrial areas [26]. The chemical structures of the most common persistent pollutants are given in Fig. 4. Moreover, in general POPs can be divided intentionally and unintentionally into two types of POPs as shown in Fig. 5.

4.1. Intentionally POPs

These compounds will be produced as wanted products by different chemical reactions that include chlorine. These types are organic molecules with linked chlorine atoms, high lipophilicity and, usually, high neurotoxicity, and they are called organochlorine compounds (OCs). Examples of OCs are the chlorinated insecticides, such as dichlorodiphenyltrichloroethane (DDT), and polychlorinated biphenyls (PCBs). They have several compounds which can be divided into two types that are industrial chemicals and organochlorine pesticides [28,29].

4.1.1. Organochlorine pesticides (OCPs)

Pesticides are chemicals or biological substances used to kill or control pests. They fall into three major classes: insecticides, fungicides, and herbicides (or weed killers). There are also rodenticides, nematicides, molluscicides, and acaricides. These chemicals are typically man-made synthetic organic compounds, but there are exceptions which occur naturally that are plant derivatives or naturally occurring inorganic minerals. Since, in the seventeenth century the first naturally occurring insecticide, nicotine from extracts of tobacco leaves, was used to control the plum curculio and the lace bug. In the 1940s, many chlorinated hydrocarbon insecticides were developed though they did not come into widespread use until the 1950s. Common examples include aldrin, dieldrin, heptochlor, and endrin. However, in spite of their early promise, these organochlorine insecticides are now much less used because of their environmental pollution impact [30,31].

Pesticides have been widely used throughout the world since middle of the last century. Around 1000 active ingredients have been employed and are currently formulated in thousands of different commercial products. They include a variety of compounds, mainly insecticides, herbicides and fungicides, with very different physico-chemical characteristics, and large differences in polarity, volatility and persistence. Pesticides are employed for many different purposes. About 80% of the pesticides is used in agriculture and moved in the environment by means of volatilization, runoff, infiltration, transport along the food chain, etc. Although the application of OCPs has been forbidden for a considerable period in many countries, the residues continue to induce a significant impact on the environment and its ecosystems [32]. Chemicals used in the control of invertebrates include insecticides, molluscicides for the control of snails and slugs, and nematicides for the control of microscopic roundworms. Vertebrates are controlled by rodenticides which kill rodents, avicides used to repel birds, and pesticides used in fish control. Herbicides are used to kill plants. Plant growth regulators, defoliants, and plant desiccants are used for various purposes in the cultivation of plants. Fungicides are used against fungi, bactericides against bacteria, slimicides against slime-causing organisms in water, and algicides against algae. As of the mid-1990s, U.S. agriculture used about 365 million kg of pesticides per year, whereas about 900 million kg of insecticides were used in non-agricultural applications including forestry, landscaping, gardening, food distribution, and home pest control. Insecticide production has remained about level during

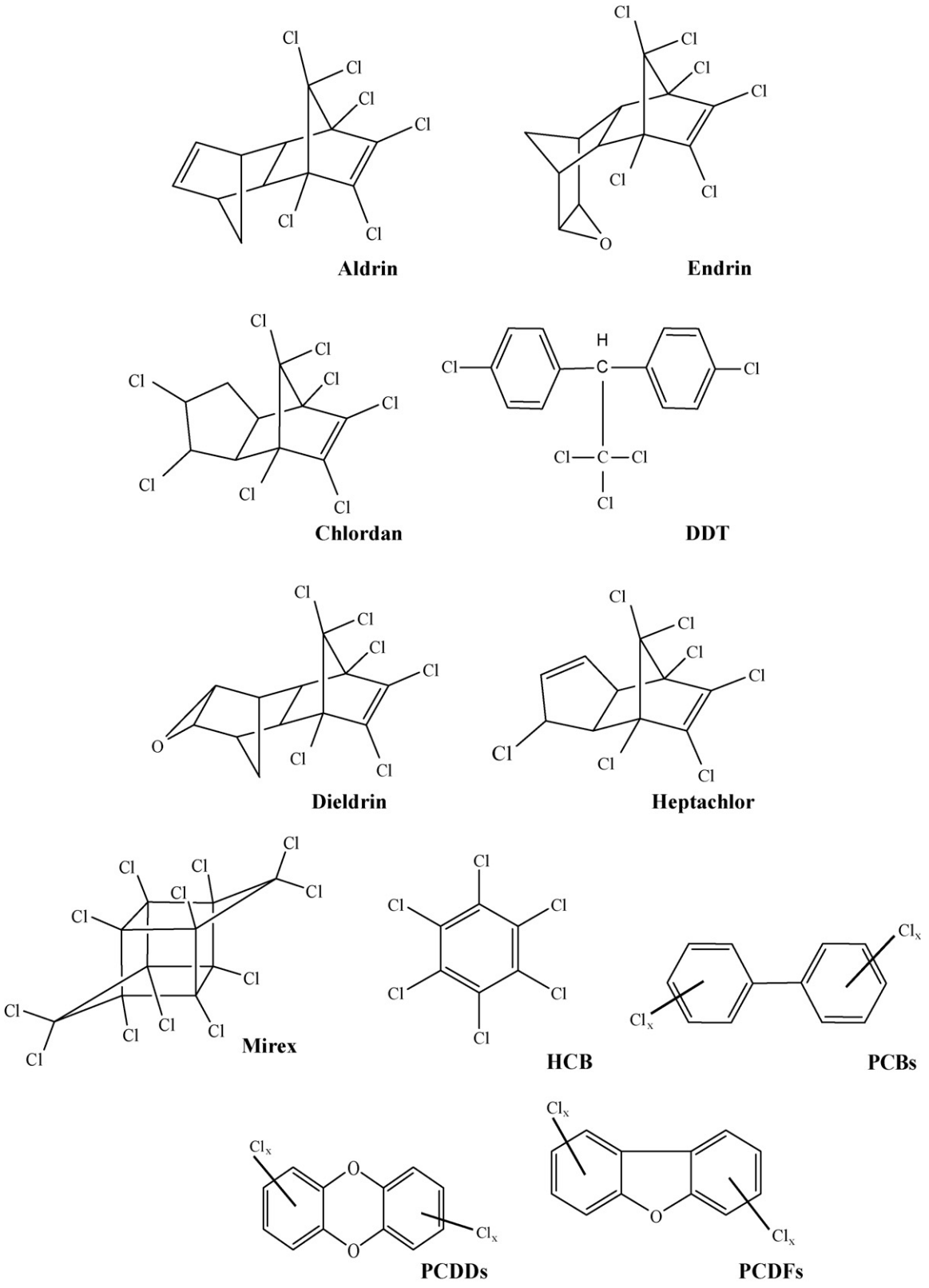


Fig. 4. The chemical structures of the most common persistent pollutants.

the last three or four decades. However, insecticides and fungicides are the most important pesticides with respect to human exposure in food because they are applied shortly before or even after harvesting. Herbicide production has increased as chemicals have increasingly replaced cultivation of land in the control of weeds and now accounts for the majority of agricultural pesticides. The potential exists for large quantities of pesticides to enter water either directly, in applications such as mosquito control or indirectly, primarily from drainage of agricultural lands [33–35].

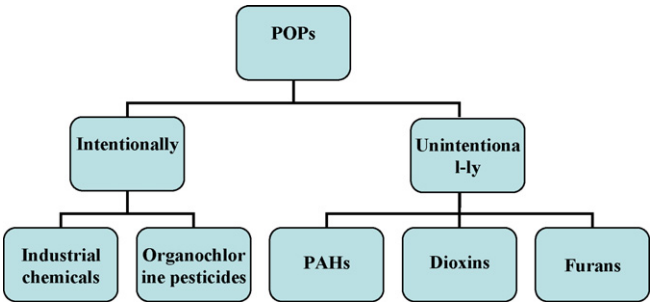


Fig. 5. Classification of POPs.

In the United States in 1993, an approximate percent (75%) of the sold pesticides have been used in agriculture [30]. Government and industry have been used 18%, and home and garden consumption accounts for the remaining 7%. Industrial and commercial users consist of pest control operators, turf and sod producers, floral and scrub nurseries, railroads, highways, utility rights-of-way, and industrial plant site landscape management [31]. The U.S. estimated volume of the conventional pesticides in 1993 is shown in Fig. 6.

Many public health benefits have been gained from the use of synthetic pesticides, but in spite of the obvious advantages, the potential adverse impact on the environment and public health can be substantial. Once in the environment, contemporary pesticides are relatively labile and tend not to persist for long periods of time. However, with the widespread use of pesticides, it is virtually impossible to avoid exposure at some level. Due to the general population's exposure to pesticides, it is important to investigate the concentration levels of pesticides and their metabolites in samples from human origin [29,30].

Before the insidious effects of DDT on humans and wildlife were known, this potent nerve poison was widely used to control mosquitoes, black flies and other vectors that carry diseases such as malaria, typhus and yellow fever. Farmers also used it to control insect damage to their crops. In the 1950s and 1960s, DDT was embraced as a cheap, effective, broad spectrum chemical pesticide. It was used worldwide and applied generously and indiscriminately to communities and crops alike. It did the job, reducing the threat of malaria and the loss of income to the agriculture industry [24]. Residues of PCBs were found in all food samples analyzed. However, their concentrations were many times lower than the permissible limits in place in other countries [24].

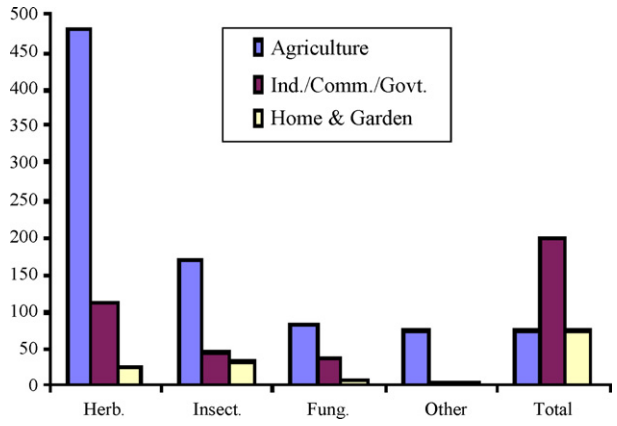


Fig. 6. The U.S. estimated volume for the conventional pesticides in 1993.

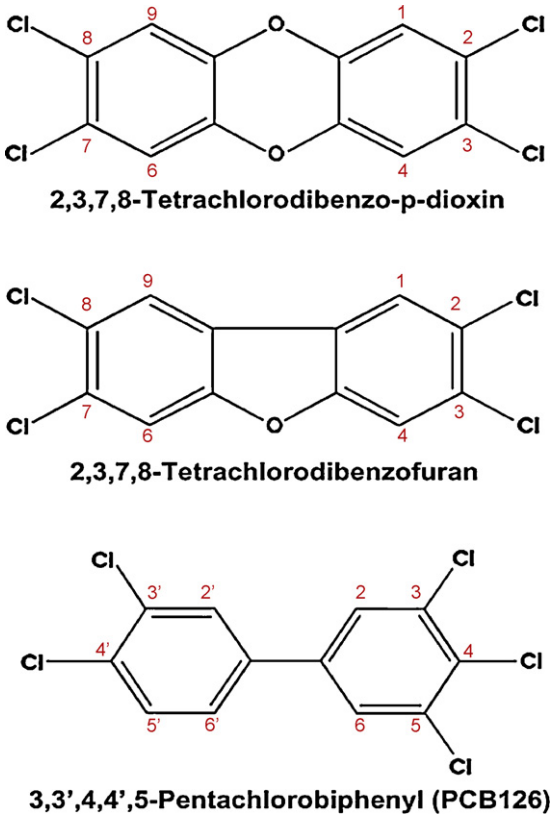


Fig. 7. Basic structures of the chlorinated dibenzo-p-dioxins (dioxins), chlorinated dibenzofurans (furans) and polychlorinated biphenyls (PCBs).

4.1.2. Industrial chemicals

First discovered as environmental pollutants in 1966, polychlorinated biphenyls (PCB compounds) have been found throughout the world in water, sediments, bird tissue, and fish tissue. These compounds constitute an important class of special wastes. PCBs are a class of chemical compounds in which 2–10 chlorine atoms are attached to the biphenyl molecule. Monochlorinated biphenyls (i.e., one chlorine atom attached to the biphenyl molecule) are often included when describing PCBs. The general chemical structure of chlorinated biphenyls is shown in Fig. 7. Theoretically, there are 209 different PCB congeners. Many of them are resistant to degradation, which allows them to persist in the environment for a long time and become widespread via atmospheric and water transport mechanisms [10,36,37].

PCBs are chemicals that were widely used in industrial processes from the 1930s until the late 1970s. Although their production ended in the late 1970s, the majority of the cumulative world production of PCBs are still in the environment. PCBs were used extensively in many industrial applications, including in fire-resistant transformers and insulating condensers. Prior to 1977, they were used as heat exchanger fluids, and in aluminium, copper, iron and steel manufacturing processing [37]. PCBs were also used as plasticizers, in natural and synthetic rubber products, as adhesives, insulating materials, flame retardant, lubricants in the treatment of wood, clothes, paper and asbestos, chemical stabilizers in paints, pigments and as dispersing agents in formulations of aluminium oxide. PCBs are often found both in the effluent and in the sludge of municipal wastewater. Since PCBs were widely used as dielectric fluids from the 1950s, they are present in transformers in several Brazilian cities, despite its prohibition in the 1980s [38,39].

Every year, over 6000 food samples from all over Poland are being analyzed to determine the contents of residues of pesticides,

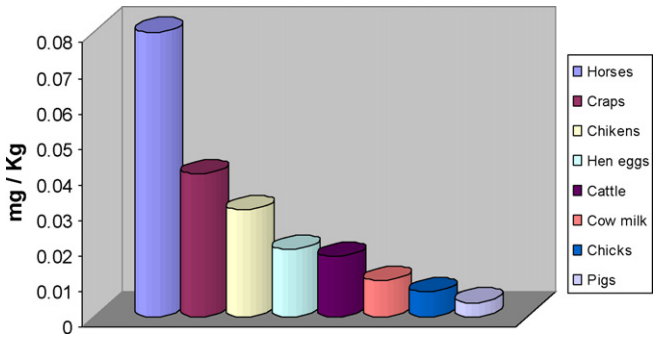


Fig. 8. Distribution of PCBs in food during the years 1995–1999.

polychlorinated biphenyls and other toxic substances in the fatty tissue of various animal species, cow milk and hen eggs. The results are summarized in the diagram given in Fig. 8. This diagram summarizes the results of research in the presence of PCBs in food during the years 1995–1999.

4.2. Unintentionally POPs

They were produced as unwanted by-products of combustion or chemical process that take places in the presence of chlorine compounds. They are divided into three types: polycyclic aromatic hydrocarbons (PAHs), dioxin and furan compounds.

4.2.1. Polycyclic aromatic hydrocarbons (PAHs)

The PAHs consist of two or more fused benzene rings in linear, angular or cluster arrangements, containing only carbon and hydrogen. The central molecular structure is held together by stable carbon–carbon bonds. The United States Environmental Protection Agency (EPA) listed 16 PAHs on a list of priority pollutants since they are considered either possible or probable human carcinogens. Hence, their distribution and the possibility of human exposure to them have been the focus of much attention. The PAHs have been detected in soil, air, and sediments as well as on various consumable products. They can occur naturally in the environment, mainly as a result of synthesis by plants or after forest and prairie fires. However, the greatest amounts of PAHs released into the environment are via anthropogenic processes like fossil fuel combustion and by-products of industrial processing. Agricultural fires as well as cooking may also release PAHs. The distribution of PAHs found in the sediments can give information on precursor sources, that is, if they are pyrogenic or petrogenic [40–42].

4.2.2. Dioxins and dibenzofurans

Chlorinated dibenzo-*p*-dioxins (dioxins) have been of concern for decades because of their toxic properties, as described below. A structurally similar series of compounds, the chlorinated dibenzofurans (furans), have similar chemical properties and toxic effects, and are generally determined as a group with the dioxins. In recent years there has been a growing trend to include a specific subgroup of the polychlorinated biphenyls (PCBs): the so-called dioxin-like PCBs (DLPCBs). This has been added to methods along with the dioxins and furans. Fig. 8 shows the structures of 2,3,7,8-TCDD, 2,3,7,8-TCDF and PCB-126. It is commonly recognized that man-made sources and activities are far greater contributors to the environmental burden of polychlorinated dioxins (PCDDs) and dibenzo furans (PCDFs) than natural processes, especially since the 1930s, from which time there had been a steady increase in environmental levels coinciding with the large-scale production and use of chlorinated chemicals [42,43]. Man-made sources of PCDDs and PCDFs can be divided into three main categories: chemical processes, combustion processes and secondary sources [44]. Municipal waste incinerator, coal combustion, chemical waste incineration plant, clinical waste incinerator, landfill gas combustion, crematoria, animal carcass incinerator and cement manufacture are the main sources of PCDDs and PCDFs in Hong Kong [45]. The dioxins and furans, congeners with chlorine substitution at the 2, 3, 7 and 8 positions are considered toxic. Of the 75 possible dioxin and 135 possible furan structures, only 17 have 2,3,7,8-substitution. The carbon numbering system is marked next to each carbon to indicate substitution positions. Dioxin and furan congeners substituted in the 2, 3, 7 or 8 position are toxic, while PCBs substituted in the 3,3′,4,4′,5 or 5′ position and no or only one 2- or 2′-substitution are considered to be dioxin-like (Table 4). This class of compounds was found able to exhibit dioxin toxicity (see Table 4).

5. Properties of POPs

The behavior and fate of chemicals in the environment are determined by their chemical and physical properties and by the nature of the environment. The chemical and physical properties are determined by the structure of the molecule and the nature of the atoms present in the molecule. The properties of their physico-chemical characteristics that permit these compounds to occur either in vapour phase or adsorbed on atmospheric particles, thereby facilitating their long-range transport through the atmosphere. Some of these properties are: very low solubility, high lipid solubility since, these two properties leading to their bioaccumulation in tissues, high toxic compound, and semi-volatile enabling them to move long distance in the atmosphere before deposition [47,48].

POPs can be present as vapours in the atmosphere or are bound to the surface of solid (dust) particles (particles of soil, of water sediments, of ashes). They are transferred to the ground surface from the atmosphere either by the deposition of the flying ashes (dry deposition) or by rain that absorbs substances present in the gas phase and pulls solid particles (wet deposition). The solubility of most POPs in water is minimal. They are, however, easily captured on solid particles (dust, ash, soil, and sediments). They are also fairly soluble in organic fluids (oils, fats, and liquid fuels). This implies that the more solid particles and polluting organic liquids present in the water, the higher the probability of their higher POPs content [49].

In the atmosphere, POPs undergo a slow decomposition due to of the solar radiation (photolysis) in the presence of water humidity and of other organic and inorganic substances. Their persistence in the atmosphere depends on thermal and reaction conditions of the given place. This durability in the tropical atmosphere is a maximum several days for a number of POPs; however, this can stretch up to several years for the occurrence of the same compound in the polar atmosphere [50].

Their stability in the atmosphere results into their long-distance transport of thousands of kilometers. This allows their transport from locations, where a number of them, namely pesticides, are still in use in significant amounts (Africa, South America) to the proximity of the North Pole. This was confirmed by a number of measurements of their presence in the snow and in the ice around the North Pole, as well as in the North Sea organisms. As these substances have never been used in these polar areas, their presence there is a clear proof of their long-distance transport [7,47].

POPs are anthropogenic compounds that are possessing characteristics toxic, persistent, bioaccumulate (build up in fatty tissues in individual organisms). Also, POPs are prone to long-range transboundary atmospheric transport and deposition, are likely to cause significant adverse human health or environmental effects near to and distant from their sources and concentrate further, or biomagnify up food chain. POPs can be divided into three categories: pesticides such as: aldrin, endrin, merix and chlordane, industrial

Table 4
Maximum WHO toxic equivalent factors (TEFs) for humans/mammals, fish and birds [46].

Congener	Humans/mammals	Fish	Birds
2,3,7,8-Tetrachlorodibenzo-p-dioxin (TCDD)	1	1	1
1,2,3,7,8-Pentachlorodibenzo-p-dioxin (PeCDD)	1	1	1
1,2,3,4,7,8-Hexachlorodibenzo-p-dioxin (HxCDD)	0.1	0.5	0.05
1,2,3,6,7,8-Hexachlorodibenzo-p-dioxin (HxCDD)	0.1	0.1	0.01
1,2,3,7,8,9-Hexachlorodibenzo-p-dioxin (HxCDD)	0.1	0.1	0.1
1,2,3,4,6,7,8-Heptachlorodibenzo-p-dioxin (HpCDD)	0.01	0.001	<0.001
1,2,3,4,5,6,7,8-Octachlorodibenzo-p-dioxin (OCDD)	0.0001	<0.0001	0.001
2,3,7,8-Tetrachlorodibenzofuran (TCDF)	0.1	0.05	1
1,2,3,7,8-Pentachlorodibenzofuran (PeCDF)	0.05	0.05	0.1
2,3,4,7,8-Pentachlorodibenzofuran (PeCDF)	0.5	0.5	1
1,2,3,4,7,8-Hexachlorodibenzofuran (HxCDF)	0.1	0.1	0.1
1,2,3,6,7,8-Hexachlorodibenzofuran (HxCDF)	0.1	0.1	0.1
1,2,3,7,8,9-Hexachlorodibenzofuran (HxCDF)	0.1	0.1	0.1
2,3,4,6,7,8-Hexachlorodibenzofuran (HxCDF)	0.1	0.1	0.1
1,2,3,4,6,7,8-Heptachlorodibenzofuran (HpCDF)	0.01	0.01	0.01
1,2,3,4,7,8,9-Heptachlorodibenzofuran (HpCDF)	0.01	0.01	0.01
1,2,3,4,5,6,7,8-Octachlorodibenzofuran (OCDF)	0.0001	<0.0001	0.001
3,4,4′,5-Tetrachlorobiphenyl (PCB 81)	0.0001	0.0005	0.1
3,3′,4′,4′-Tetrachlorobiphenyl (PCB 77)	0.0001	0.0001	0.05
2′,3,4,4′,5-Pentachlorobiphenyl (PCB 123)	0.0001	0.000005	0.00001
2,3′,4,4′,5-Pentachlorobiphenyl (PCB 118)	0.0001	<0.000005	0.00001
2,3,4,4′,5-Pentachlorobiphenyl (PCB 114)	0.0005	<0.000005	0.0001
2,3,3′,4,4′-Pentachlorobiphenyl (PCB 105)	0.0001	<0.000005	0.0001
3,3′,4,4′,5-Pentachlorobiphenyl (PCB 126)	0.1	0.005	0.1
2,3′,4,4′,5,5′-Hexachlorobiphenyl (PCB 167)	0.00001	<0.000005	0.00001
2,3,3′,4,4′,5-Hexachlorobiphenyl (PCB 156)	0.0005	<0.000005	0.0001
2,3,3′,4,4′,5′-Hexachlorobiphenyl (PCB 157)	0.0005	<0.000005	0.0001
3,3′,4,4′,5,5′-Hexachlorobiphenyl (PCB 169)	0.01	0.00005	0.001
2,3,3′,4,4′,5,5′-Heptachlorobiphenyl (PCB 189)	0.0001	<0.000005	0.00001
	0.0001	<0.000005	0.00001

chemicals such as: PCB, PCP and HCB, and unintentionally produced by-product like polycyclic aromatic hydrocarbons (PAHs), dioxins and furans compounds. Long-range transport via the atmosphere is the most likely source of these persistent organic pollutants in the Arctic. However, efforts to quantify the amount of POPs transported in this way and to determine source regions are quite limited. POPs have been associated with a number of environmental risks. These risks include oestrogenic effects, disruption of endocrine function with observed impairments of immune system function, generation of functional and physiological effects on reproduction capabilities and reduced survival and growth of offspring [26,51].

6. Dosage and toxicity of POPs

POPs so including are significant concern due to their potential toxicity and prevalence in arrangement of environmental media, even at remote geographical location. The ecotoxicological effects of POPs in the environment have caused much concern in recent years, and this has led to the control or complete ban on the use of these chemicals in many countries. Among the wide range of organic substances contaminating the aquatic environment a major concern has so far focused on PCBs and (OCPs). High persistence and biological degradation resistance of these toxic organic pollutants make them continue to be yet largely present in the marine environment. POPs are found not only in living organism as animals and plants, but also in humans [26,52].

Public concern about contamination by POPs increased recently because several of these compounds are identified as hormone disrupters which can alter normal function of endocrine and reproductive systems in humans and wildlife. There are many risks and effects of having these chemicals in our environment and none of them are a benefit to the earth. After these pollutants are put into the environment, they are able to stay in the system for decades causing problems such as cancer, birth defects, learning disabilities, immunological, behavioral, neurological and reproductive discrepancies in human and other animal species [52].

POPs contaminate food, water and accumulate in the food chain such as eagles, polar bears, killer whales and human being. There is evidence that many people worldwide may now carry enough POPs in their body fat where POPs accumulate to cause serious health effects, including illness and death. Laboratory investigations and environmental impact studies in the wild have implicated POPs in endocrine disruption, reproductive and immune dysfunction, neurobehavioral and disorder and cancer [53,49].

More recently some POPs have also been implicated in reduced immunity in infants and children, and the concomitant increase in infection, also with developmental abnormalities, neurobehavioral impairment and cancer and tumor induction or promotion. Some POPs are also being considered as potentially important risk factor in the etiology of human breast cancer by some authors [54]. Human exposure to POPs is carried through the food chain. Because the animals are subsisting in water contaminated with these pollutants, they are affected as well when the humans consume these animals, they have also consumed the pollutant which then is accumulated in the body [49].

Because children are still developing, they are much more susceptible to the effects of pollutants. Their developing cells are sensitive to contaminants and are more likely to be affected by exposure of POPs. The brain is apparently in the greatest concern because some studies have shown that children exposed to POPs during infancy had remarkably lower scores on assessments determining intelligence and ability to shut out distractions [19,55].

At a young POPs can have serious consequences side effects such any of the following: birth defects, certain cancer and tumors at multiple sites, immune system disorders, reproductive problems, reduced ability toward off diseases, stunted growth and permanent impairment of brain function, POPs are a suspected carcinogen, diseases such as endometriosis (a painful, chronic gynecological disorder in which uterine tissues are affected), increased incidence of diabetes and others and Neurobehavioral impairment including learning disorders, reduced performance on standard tests and changes in temperament [55]. Commonly used analytical methods

Table 5
Analytical methods for determination POPs in different matrices.

Methods	Analyte	Environmental matrix	References
GC/ECD	PCBs; OCPs; HCH; HCB; PAHs; DDT	Sediments, soil, liver and fat of birds, water, fungal, human hair, plants, adipose tissue	[56,4,58,61,62,66,69,73,78,81,52,85,5]
GC/MS	PCBs; OCPs; PBDEs; HCH; HCB; PAHs; OPPs; DDT	Dolphins, river water and sediment, livers and fat of birds, human adipose tissue, ice	[57,63,9,72,75,77,60,21,81–83,88–90,11]
HRGC/ECD	HCH; HCB; PCBs	Livers of code fish, eggs	[4,58]
HRGC/LRMS	Pesticides, PCBs, PAHs	Water, plant	[64,91]
HRGC/MSD	PCBs; OCPs	Water, liver and muscle of tuna	[65]
HPLC-DAD	Pesticides	Ground water	[66]
RH-GC-FPD	OPPs	Fruit and vegetables	[67]
HRGC/HRMS	PCDD/Fs; OCPs; PCBs; HCB; HCH	Flue gas, livers, eggs of birds, river water, sediment, atmosphere, gastropods	[6,68,80,92–94]
GC/NPD	Pesticides	Bananas	[70]
GC-MS-MS	Pesticides	Rain water	[71]
GC-ECNI-MS	Toxaphene	Bird eggs	[74]
LC-MS-MS	Pesticides	Grain sample	[75]
SPE-HPLC	PCBs	Endogenous hormones	[76]
RP-LC-FLD	PAHs	Marin biota	[79]
HPLC/FLD	PAHs	Food sample, soil, air	[21]
PLVI-CC/ECNI-qMS	OCPs; HCB; HCH	Fish tissue	[84]
GC/FID	HCB	Soil	[87]

for POPs monitoring and surveillance are summarized in Table 5. Numerous methods have been published over the past 30 years related to specific analytical techniques for the determination of PCBs and OCPs in food and environmental matrices.

7. Extraction and analytical techniques

Classical extraction techniques like liquid/liquid extraction and Soxhlet extraction are described in detail in the methods listed in Table 6. A number of alternative extraction techniques are summarized in Table 3. Supercritical fluid extraction (SFE) uses a gas above the critical point (the combination of temperature and pressure where the gas has liquid-like properties enabling enhanced extraction capability) to extract analytes from the matrix. The main advantage with SFE is that the extracting gas can be evaporated and so solvent disposal is not required. SFE behaves significantly differently to classical solvent extraction and recoveries can be reduced or enhanced. Pressurized liquid extraction (PLE), also known as accelerated solvent extraction (ASE) evolved from SFE. Solvents were added to SFE extractions as modifiers in order to mimic classical liquid extractions. SFE without extraction gas and only solvent modifier best matched classical extraction recoveries. This led to the development of PLE. Microwave-assisted extraction (MAE or MASE) uses closed vessels to increase pressure and extraction efficiency. Polar solvents like acetone or water are required to supply heat for extraction. San et al. [95] reported the analysis of wet samples by MAE, indicating that significant time was saved by the reduced sample drying requirements. Solid-phase extraction can significantly reduce analysis times and solvent usage for the extraction of water and wastewater samples, even with significant particulate loadings [95]. Particles collected on C18 extraction disks can be extracted quantitatively without Soxhlet or PLE extraction. Water samples have also been analyzed using semi-permeable membrane devices (SPMDs). SPMD sampling is a form of passive sampling that can be used for water, air or sediments [86,96].

Recently, Namiesnik et al. [97] have reviewed passive sampling techniques in environmental samples. Passive sampling is based on the free flow of analytes from the sampling medium to the collecting medium. This technique eliminates the requirement for power, and is a composite sampling procedure that can reduce analysis cost because of reduced sampling events and analyte loss during shipping and storage as the analyte is on a trapping medium. Swipe tests of biofilms on surfaces can also be used to monitor ambient conditions, especially after fires or from fugitive emissions.

8. Removal and/or minimization of POPs

Environmentally relevant polar persistent organic pollutants (pharmaceuticals and diagnostic agents) have been chosen according to human consumption and occurrence in the aquatic environment (sewage plant effluents, rivers and groundwater) to investigate their behavior during photo catalytic oxidation. From

Table 6
Extraction techniques of POPs in various matrices at different regions.

Sample matrix	Extraction technique.	Region/country	Analyte	References
Sediment	SE, LSE, LLE, SFE, MASE	Argentine, Singapore, China, Germany, Italy, Canada	PCBs, OCPs, PAHs, HCB, HCH, DDT, PBDEs, PCDD/Fs	[56,60,63,77,82,90,93,97,98]
Soil	SE, SPE, PLE, LLE, sonication	Singapore, Australia, Europe, Brazil, China	PAHs, OCPs, HCB, PCBs	[60,78,21,87,89,99,100]
Fruit and vegetable	GPC, SE, SPE, PLE, passive sampling	Europe, Sweden, China	OPPs, OCPs, DDT, PCBs, PAHs	[67,70,72,73,21,89,91]
Water (marine, fresh, ground rain and wastewater)	Sonication process, SPMD, LLE, filter DOC	Europe, Zambia, Indonesia, Italy, Spain, Turkey	HCH, HCB, PCBs, PAHs, OCPs	[59,64–66,69,71,79,80,85,88]
Fish (liver, tissue, egg and muscle)	SE, LLE	Pakistan, Japan, Philippines, Brazil, China	HCB, HCH, PCBs, OCPs	[4,58,65,84,5]
Dolphin	GPC	India	PBDEs, PCBs, OCPs	[57]
Bird (tissue, egg, liver and fat)	LLE, SE	Greece, USA, Japan	OCPs, PCBs, toxaphene	[62,74,6]
Air	Swipe/biofilms, passive sample	Italy	PCDD/F, HCB	[80,101–103]
Ice and snow core	LLE	Italy	OCPs, PCBs	[9]
Human (hormone, hair, tissue and adipose tissue)	LLE, SPE, SE, LSE, hot SE	China, USA, Romania, Belgium	PCBs, HCH, OCPs, HCB, DDT	[63,76,81,52]

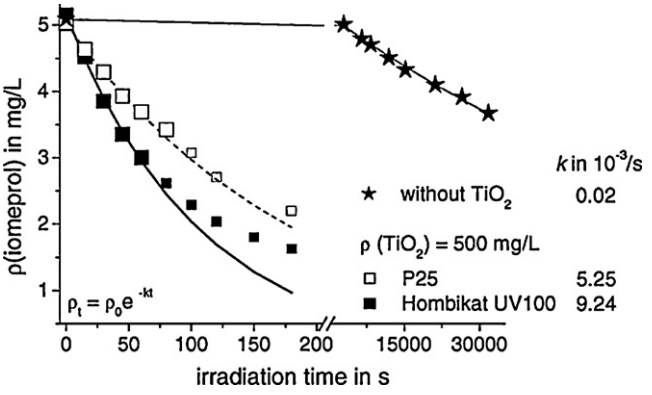


Fig. 9. Changes of iomeprol concentrations (2 mg L^{-1}, pH 6.5) during irradiation with and without suspended TiO_2 (Hombikat UV100 or P25 (TiO_2) = 0.5 mg L^{-1}).

the data compilation in the literature, the active metabolite clofibric acid of some lipid lowering agents, the antiepileptic drug carbamazepine and the X-ray contrast media imperils were selected. The degradation of the persistent pollutant was monitored by HPLC/DAD/FLD. The study has been focused also on the identification and quantification of possible degradation products by HPLC/DAD/FLD and HPLC/MS/MS. The degradation process has also been monitored the determination of sum parameters and inorganic ions. Various aromatic and aliphatic degradation products have been identified and quantified [104,105]. Since, the photochemical degradation (irradiation without TiO_2) of the persistent organic pollutants was studied [106]. It turned out to be negligible compared to their photocatalytic degradation. For example the photocatalytic degradation rate constant (k) of iomeprol with Hombikat UV100 was about 500 times higher than the photochemical degradation rate constant of iomeprol (Fig. 9). For the determination of the first order rate constant (k) only the concentration values with rt/r0—0.5 (large symbols) were used. The fitting was done by the least squares method [106]. Moreover, the stabilized nanoparticles of FeS have showed excellent degradation (over 94%) of lindane pesticide in its hexane extract to 1,2,4-trichlorobenzene or TCB, a key intermediate of lindane degradation pathway. The non-stabilized FeS could degrade merely 25% lindane in the same period clearly indicated that these nanoparticles catalyzed a rapid reductive dehalogenation reaction [107,108].

9. Conclusion

The determination of POPs in various matrices is characterized by instrumental complexity and highly cost. The electrochemical techniques in particular stripping analysis have no contribution on the analysis of such class of chemicals. Thus, the use of voltammetric techniques for the analysis of such class of compounds will provide an efficient and excellent alternative approach for the determination of POPs in different matrices because of its low cost, sensitively and selectivity for trace and ultra-trace concentration of the POPs in complicated matrices. However, further work is still continuing for the possible application of the on-line voltammetric stripping analysis of the pesticides in serum, routine and various environmental samples.

References

[1] S. Manahan, Environmental Chemistry, 7th edn, Lewis Publishers/CRC Press LLC, London, 2000.
[2] J. Buccini, The development of a global treaty on persistent organic pollutants (POPs), in: H. Fiedler (Ed.), The Hand Book of Environmental Chemistry, Persistent Organic Pollutants, 3rd edn, Springer-Verlag, Berlin/Heidelberg, 2003, Chapter 2.
[3] M. Wang, A. Leung, J. Chan, M. Choi, Chemosphere 60 (2005) 740.
[4] F. Mason, N. Barak, Chemosphere 21 (1990) 659.
[5] W. Chu, M. Wong, J. Zhang, Environ. Geochem. Health 28 (2006) 169.
[6] G. Zhao, Y. Ying, G. Han, B. Ling, Environ. Geochem. Health 28 (2006) 341.
[7] K. Kumar, K. Watanable, H. Takemori, N. Iseki, S. Masunaga, T. Takasaga, Arch. Environ. Contam. Toxicol. 48 (2005) 538.
[8] H. Selin, N. Eckley, Politics Low Econ. 3 (2003) 1.
[9] J. Krueger, H. Selin, Governance for sound chemicals management: the need for a more comprehensive global strategy, global governance, in press.
[10] S. Villa, A. Finizio, R. Diazdiaz, N. Vighi, Water Air Soil Pollut. 146 (2003) 335.
[11] J. Lyche, J. Skaare, H. Larsen, E. Ropstad, Chemosphere 55 (2004) 621.
[12] C. Hunge, G. Gang, K. Jiann, K. Yeager, P. Santsch, T. Wade, J. Sericans, H. Hsien, Chemosphere 65 (2006) 1452.
[13] M. Storelli, R. Addabboad, G. Marcotrigiano, Environ. Int. 30 (2004) 343.
[14] X. Song, B. Chen, Environ. Prot. 2 (2001) 9.
[15] A. Grochowalski, B. Oznaczaniem, Polychlorinated Dibenzodioxin, Taylor and Francis, Ltd, Dibenzofuran, Krakow, 2000.
[16] Compilation of EU Dioxin Exposure and Health Data, Summary Report, European Commission DG Environment, 1999.
[17] Exposure and Health Assessment for 2,3,7,8-Tetrachlorobenzo-p-dioxine (TCDD) and Related Compounds, Part 3 Integrated Summary and Risk Characterization for 2,3,7,8-Tetrachlorobenzo-p-dioxin (TCDD) and Related Compounds, US EPA, 2000.
[18] R. Santillo, L. Stringer, P. Johnston, The Global Distribution of PCBs, Organochlorine Pesticides, Polychlorinated Dibenzo-p-dioxins and Polychlorinated Dibenzofurans Using Butter as an Interactive Matrix, Green Peace, 2000.
[19] H. Bouwman, POPs in Southern Africa, in: H. Fiedler (Ed.), The Hand Book of Environmental Chemistry, Persistent Organic Pollutants, 3rd edn, Springer-Verlag, Berlin/Heidelberg, 2003, Chapter 11.
[20] M. Wong, B. Poon, Sources, fates and effects of persistent organic pollutants in China, with emphasis on the Pearl River Delta, in: H. Fiedler (Ed.), The Hand Book of Environmental Chemistry, Persistent Organic Pollutants, 3rd edn, Springer-Verlag, Berlin/Heidelberg, 2003, Chapter 13.
[21] Y. Ying, Y. Yong, R. Dawson, S. Yajuan, H. Zhang, T. Wong, W. Liu, H. Ren, Chemosphere 60 (2005) 731.
[22] T. Wenzl, R. Simon, J. Kleiner, E. Auklam, Trends Anal. Chem. 25 (2006) 716.
[23] R. Galiulin, V. Bashkin, R. Galiulina, Water Air Soil Pollut. 137 (2002) 179.
[24] J. Petrlik, D. Zeme, H. Stiftung, Persistent Organic Pollutants in Poland, Waste Prevention Association "3R", Krakòw, 2001.
[25] J. Ludwicki, K. Goralczyk, K. Czaja, in: H. Mareriaxach (Ed.), HCH Isomers in Human Tissues in Poland, 4th edn, Forum HCH and Unwanted Pesticides, Poznan, 1999.
[26] Presented at the ICS, UNIDO Workshop on Contamination of Food and Agro Products, 2000, Croatia.
[27] H. Fiedler, The Hand Book of Environmental Chemistry, Persistent Organic Pollutants, 3rd edn, Springer-Verlag, Berlin/Heidelberg, 2003, Chapter 1.
[28] T. Harner, K. Pozo, T. Gouin, A. Macdonald, H. Hung, I. Cieny, A. Peters, Environ. Pollut. 144 (2006) 445.
[29] Kelce, C. Stone, S. Laws, G. Earl, J. Kemppalnen, E. Wilson, Nature 375 (1995) 581.
[30] Strompl, J. Thiele, Arch. Environ. Contam. Toxicol. 33 (1997) 350.
[31] A. Aspelin, Pesticide Industry Sales and Usage: 1992 and 1993 Market Estimates, U.S. Environmental Protection Agency, 1994.
[32] Chen, L. Shi, Z. Shan, Q. Hu, Food Chem. 104 (2007) 1315.
[33] J. Weinbe, An Overview of POPs Treaty-Public Forum on Persistent Organic Pollutants—the International POPs, Elimination Network, 1998.
[34] J. Junior, N. Poppi, Talanta 72 (2007) 1833.
[35] M. Espinosa, A. Granada, J. Carreno, M. Salvatierra, F. Serrano, N. Olea, Placenta 28 (2007) 631.
[36] O. Panic, T. Gorecki, Anal. Bioanal. Chem. 384 (2006) 1366.
[37] D. Korytar, P. Leonards, J. Bore, U. Brikmoan, J. Chromatogr. A 958 (2002) 203.
[38] D. Amato, J. Torres, Quim 25 (2002) 995.
[39] A. Amador, Buried pesticides waste hazard to Poland, Waste Manage. Res. 10 (1992).
[40] T. Aboul-Kassim, B. Simueit, Environ. Sci. Technol. 29 (1995) 247.
[41] Agency for Toxic Substance and Disease Registry (ATSDR) Toxicology Profile for Polycyclic Aromatic Hydrocarbons US Department of Health and Human Services, Public Health Service, Atlanta, GA, 1995.
[42] B. Zielinska, S. Samy, Anal. Bioanal. Chem. 384 (2006) 1383.
[43] C. Fortin, D. Caldbick, Organochlor. Compd. 32 (1997) 417.
[44] R. Alcock, R. Gemmill, K. Joues, Chemosphere 38 (1998) 759.
[45] H. Fiedler, Organochlor. Compd. 11 (1993) 221.
[46] Environmental Protection Department, Assessment of Dioxin Emission in Hong Kong: Final Report, Air Policy and Planning Group, Environmental Protection Department, Hong Kong SAR Government, 2000.
[47] M. Berg, L. Birnbaum, A. Bosveld, B. Brunstrom, P. Cook, M. Feeley, J. Giesy, A. Hanverg, R. Hasegawa, S. Kennedy, T. Kubiak, J. Larsen, F. Leeuwen, A. Liem, C. Nolt, R. Peterson, L. Poellinger, S. Safe, D. Schrenk, D. Tillit, M. Tysklind, M. Younes, F. Waern, T. Zacharewski, Environ. Health Perspect. 106 (1998) 775.
[48] L. Guzella, C. Rscioli, L. Vigano, S. Sarkar, A. Bhaltacharya, Environ. Int. 31 (2005) 523.
[49] A. Katsoyiannis, C. Samara, Environ. Res. 97 (2005) 245.
[50] X. Huang, L. Lessner, D. Carpenter, Environ. Res. 102 (2006) 101.

[51] B. Wahlstrom, Criteria for additional POPs, in: H. Fiedler (Ed.), The Hand Book of Environmental Chemistry, 3rd edn, Springer-Verlag, Berlin/Heidberg, 2003.
[52] A. Sweetman, M. Vall, K. Predouros, K. Tones, Chemosphere 60 (2005) 959.
[53] A. Pauwels, A. Covaci, J. Weyler, L. Delbek, M. Dhont, P. Sutter, T. Haoghe, P. Schepens, Arch. Environ. Contam. Toxicol. 49 (2000) 265.
[54] O. Roots, V. Zitko, A. Roos, Chemosphere 60 (2005) 914.
[55] H. Bolt, G. Degen, Arch. Environ. Contam. Toxicol. 76 (2002) 187.
[56] H. Fiedler, Dioxins and furans (PCDD/PCDF), in: The Handbook of Environmental Chemistry, Persistent Organic Pollutants, 3rd edn, Springer-Verlag, Berlin/Heidelberg, 2003.
[57] M. Menone, J. Moreno, V. Moreno, A. Lanfranchi, T. Metcalfe, C. Metcafe, Arch. Environ. Contam. Toxicol. 40 (2001) 335.
[58] K. Kannan, K. Ramu, N. Kajiwara, R. Sinha, T. Tanabe, Arch. Environ. Contam. Toxicol. 49 (2005) 415.
[59] C. Sanpera, X. Ruiz, L. Jover, G. Liorente, R. Jabeen, A. Muhammad, E. Boncompagni, M. Fasola, Arch. Environ. Contam. Toxicol. 44 (2003) 360.
[60] P. Fernandez, G. Carrera, J. Grimalt, Aquat. Sci. 67 (2005) 263.
[61] C. Basheer, J. Obbard, H. Lee, Water Air Soil Pollut. 149 (2003) 315.
[62] A. Barakat, Bull. Environ. Contam. Toxicol. 50 (2003) 174.
[63] D. Hela, I. Konstantinou, T. Sakellarides, D. Lambropoulou, T. Akriotis, T. Albanis, Arch. Environ. Contam. Toxicol. 50 (2006) 603.
[64] B. Poon, C. Leung, C. Wong, M. Wong, Arch. Environ. Contam. Toxicol. 49 (2005) 274.
[65] L. Norrgren, U. Pettersson, S. Orn, P. Beggvist, Arch. Environ. Contam. Toxicol. 38 (2000) 334.
[66] D. Uneo, S. Takahashi, H. Tanaka, A. Subramanian, G. Fillman, H. Nakata, P. Lam, J. Zheng, M. Muchtar, M. Prudente, K. Chung, S. Tanabe, Arch. Environ. Contam. Toxicol. 45 (2003) 378.
[67] M. Cuesta, R. Boque, F. Rius, J. Vidal, A. Frenich, Chemometr. Intell. Lab. Sys. 77 (2005) 251.
[68] K. Patel, R. Fussell, R. Macarthur, D. Goodall, B. Keely, J. Chromatogr. A 1046 (2004) 225.
[69] J. Wang, C. Hung, C. Hsuang, G. Chien, J. Hazard. Mater. 161 (2009) 800.
[70] K. Cailleaud, J. Leray, L. Peluhet, K. Lemenach, S. Souissi, H. Budzinski, Environ. Pollut. 157 (2009) 64.
[71] J. Borges, J. Cabrera, M. Delgado, E. Suarez, V. Sauco, Food Chem. 113 (2009) 313.
[72] A. Scheyer, S. Morville, P. Mirabel, M. Millet, Atmos. Environ. 41 (2007) 7241.
[73] J. Ramos, R. Otero, L. Ramos, J. Capelo, J. Chromatogr. A 1212 (2008) 145.
[74] H. Gao, X. Jiang, F. Wang, D. Wang, Y. Bian, Bull. Environ. Contam. Toxicol. 74 (2005) 673.
[75] K. Maruya, K. Smalling, M. Mora, Arch. Environ. Contam. Toxicol. 48 (2005) 567.
[76] G. Pang, Y. Liu, C. Fan, J. Zhang, Y. Cao, X. Li, Z. Li, Y. Wa, T. Guo, Anal. Bioanal. Chem. 384 (2006) 1366.
[77] P. Hjelmborg, M. Ghisari, E. Jorgensen, Anal. Bioanal. Chem. 385 (2006) 875.
[78] S. Heim, J. Schwarzbauer, A. Kronimus, R. Littke, A. Herger, Environ. Chem. Lett. 1 (2003) 169.
[79] A. Juhasz, E. Smith, J. Smith, R. Naidu, Water Air Soil Pollut.: Focus 3 (2003) 233.
[80] J. Landaluze, L. Bartolome, O. Zuloaga, L. Gouzalez, C. Dietz, C. Camara, Anal. Bioanal. Chem. 384 (2006) 1331.
[81] C. Bettiol, F. Collavini, S. Guerzoni, E. Molinaroli, D. Rossiui, L. Zaggia, R. Zonta, Hydrobiologia 550 (2005) 151.
[82] A. Covaci, P. Schepens, Chromatographia 53 (2001) 366.
[83] A. Cicero, M. Finoia, M. Gabelini, E. Veschetti, Environ. Monit. Assess. 64 (2000) 607.
[84] I. Corsi, M. Mariottini, A. Badesso, T. Caruso, N. Borghesi, S. Bonacci, A. Iacacca, S. Facardi, Hydrobiologia 550 (2005) 237.
[85] Y. Zhao, L. Yang, Q. Wang, J. Am. Soc. Mass Spectrom. 18 (2007) 1375.
[86] A. Katsoyiannis, C. Samara, Chemosphere 67 (2007) 1375.
[87] X. Zhao, M. Zheng, l. Ilang, Q. Zhang, Y. Wang, G. Jiang, Arch. Environ. Contam. Toxicol. 49 (2005) 178.
[88] D. Matheus, V. Bononi, K. Machado, World J. Microbiol. Biotechnol. 16 (2000) 415.
[89] C. Guitart, N. Flor, J. Dachs, J. Bayona, J. Albaiges, Mar. Pollut. Bull. 48 (2004) 961.
[90] Y. Chen, C. Wang, Z. Wang, Environ. Int. 31 (2005) 778.
[91] R. Bettinetti, C. Giarei, A. Provini, Arch. Environ. Contam. Toxicol. 45 (2003) 72.
[92] P. Bergquist, L. Augulyte, V. Jurjaniene, Water Air Soil Pollut. 175 (2006) 291.
[93] M. Ekmekci, Environ. Geol. 49 (2005) 19.
[94] P. Sathe, M. Ikonomou, K. Haya, Aquaculture 254 (2006) 234.
[95] Y. San, M. Takaoka, N. Takeda, T. Matsumato, K. Osnita, J. Sep. Sci. 28 (2005) 585.
[96] K. Taylor, D. Waddell, E. Reiner, K. Macpherson, Anal. Chem. 67 (1995) 1186.
[97] J. Namiesnik, B. Zabigala, A. Kat-Wasik, M. Partyaka, A. Wasik, Anal. Bioanal. 381 (2005) 279.
[98] M. Mannila, J. Koistinen, T. Vartianinen, J. Chromatogr. A 975 (2002) 189.
[99] A. Vanbeuzekekom, W. Hijman, C. Berkhoff, B. Stoffessen, A. Denboer, G. Groenemeijer, D. Mooibroek, R. Hoogerbrugge, M. Broekman, R. Baumann, E. Hogendoorn, Talanta 63 (2003) 1183.
[100] Method 1668, Revision A, Chlorinated Biphenyl Congeners in Water, Soil, Sediment and Tissue by HRGC/HRMS, US Environmental Protection Agency (1999), Office of Water, Washington, DC.
[101] International Organization for Standardization Soil Quality Determination of Organochlorine Pesticides and Polychlorinated Biphenyles, in: Gas Chromatographic Method with Electron Capture Detection, ISO, Geneva, Switzerland, 2002.
[102] S. Rayne, M. Ikonomou, C. Butt, M. Diamond, J. Troung, Environ. Sci. Technol. 39 (2005) 1995.
[103] C. Lucaciu, L. Fayez, E. Reiner, T. Kolic, A. Boden, K. Macpherson, P. Crozier, F. Wania, R. Emerson, Organohalog. Compd. 66 (2004) 153.
[104] N. Hanari, Y. Horii, T. Okazawa, J. Falandysz, I. Bochentin, A. Orlikowska, T. Puzyn, B. Wyrzykowska, N. Yamashita, J. Environ. Monit. 6 (2004) 305.
[105] T. Dol, F. Frimmel, Catalysis Today 101 (2005) 195.
[106] T. Doll, F. Frimmel, Chemosphere 52 (2003) 1757.
[107] N. Assaf-Anid, L. Kun-Yu, J. Environ. Eng. 128 (2002) 94.
[108] K. Paknikar, V. Nagpat, A. Pethkar, J. Rajwade, Sci. Technol. Adv. Mater. 6 (2005) 370.

Talanta 80 (2010) 1598–1605

Contents lists available at ScienceDirect

Talanta

journal homepage: www.elsevier.com/locate/talanta

Review

Application of porphyrins in flow-injection analysis: A review

Jacobus F. van Staden*, Raluca I. Stefan-van Staden

Process Analytical Technology Laboratory (PATLAB) and Laboratory of Electrochemistry, National Institute of Research and Development for Electrochemistry and Condensed Matter (INCDEMC), 202 Splaiul Independentei Str., Bucharest 060021, Romania

ARTICLE INFO

Article history:
Received 22 June 2009
Received in revised form
23 September 2009
Accepted 8 October 2009
Available online 17 October 2009

Keywords:
Porphyrins
Metalloporphyrins
FIA
Optical and electrochemical sensors

ABSTRACT

Porphyrins and metalloporphyrins fulfil a very important role in the metabolism of living organisms through biological pigments or biochromes and are therefore also employed in numerous applications in analytical chemistry. In flow-injection analysis the role of porphyrins and metalloporphyrins are centered as either that of analyte or that of a reagent or modifier in the determination of other species. This paper covers the attributes of porphyrin and metallophorphyrin complexes as enhancements in chemical analysis in flow-injection systems and points out the advantages and disadvantages in the implementation thereof.

© 2009 Elsevier B.V. All rights reserved.

Contents

1. Introduction 1598
2. Fast screening of porphyrins in biological samples 1599
3. Normal photometric detection 1600
4. Multicomponent analysis with diode array detection 1602
5. Waveguide optical metalloporphyrin-based sensors 1602
6. On-line enrichment with FAAS/ICP-AES detection 1602
7. Luminescent detection with porphyrins 1603
8. Electrochemical detection involving porphyrins 1603
9. Conclusions 1604
Acknowledgements 1605
References 1605

1. Introduction

Porphyrins are a large class of natural occurring intensely colored, red or purple, macrocyclic pigmented compounds with the name originated from the ancient Greek word porphura that was used to describe the color purple (or royal purple) [1]. Porphyrins play a very important role in the metabolism of living organisms through biological pigments or biochromes that include plant and flower pigments. Through heme, an iron porphyrin, they are intimately associated with blood, and many of the redox enzymes involved in metabolic processes. Through chlorophyll, a reduced magnesium porphyrin, they orchestrate photosynthesis, without which life would be impossible [1]. The importance of porphyrins is not limited to their participation in oxygen transport as hemo proteins and essential biological photosynthetic activities alone. In fact they also do have valuable contributions and are applied in various fields, such as liquid crystalline materials [2] due to their remarkable electro-optical properties, measurements of oxygen *in vivo* using EPR techniques [3,4], photodynamic therapy [5,6], malaria treatment [7], molecular wires [8–11], light-energy conversion like solar cells [12–14] and fluorescence switches [15]. As a result porphyrins increasingly have found a place in numerous applications in chemical analysis [16] such as the design of electrochemical and optical sensors [17,18], modification of voltammetric electrodes [19,20], as spectrophotometric reagents [21–23], as

* Corresponding author. Tel.: +40 74 169 5743.
E-mail address: koosvanstaden@yahoo.com (J.F. van Staden).

0039-9140/$ – see front matter © 2009 Elsevier B.V. All rights reserved.
doi:10.1016/j.talanta.2009.10.016

stationary phases in HPLC [24,25] and as modifiers in open tubular electrochromatography [26].

The basic structure of the porphyrin molecule has in common a substituted aromatic macrocyclic ring consisting of four pyrrole-type rings linked together by four methine bridges [1,16,27] with an extensive system of delocalized π electrons that gave the highest degree of bond equalisation [4,28], and thus with an enhancement of the aromatic character and stability of the porphyrin ring system. Porphyrins can also be modified by adding different peripheral substitutes, incorporation of metal ions into the porphyrin ring, changing the central metal or expanding the size of the macromolecule [4]. Formation reactions of metalloporphyrins are very important processes from both analytical and bioinorganic points of view and therefore the large molar absorption coefficient (molar absorptivities of the order of 10^5 often found in the Soret band from 400 to 500 nm) and very high stability of metalloporphyrins (e.g. the stability constant for ZnTPP, TPP = tetraphenylporphyrin, is 10^{29} [27]) are very useful for the analysis of metal ions. A covalently linked porphyrin, 5,10,15,20-tetrakis(phenoxy acetic acid) porphyrin (PAAP), to Merrifield chloromethylated resin was used as sorbent for the separation and enrichment of the *d*-electron metals such as Mn(II), Co(II), Ni(II), Cu(II) and Zn(II) at pH 6–8 and of the *f*-electron metals such as U(VI) and Th(IV) at pH 4–5 with a concentration factor range of 115–215 [29]. However, a disadvantage is that the incorporation reaction of metal ions into the porphyrin ring is very slow with the rate of incorporation of metal ions typically around 10^9 times slower than that of the complex formation of metal ions with noncyclic ligands [30]. An account of this behavior has been given in a dynamic study of metal ion incorporation into porphyrins based on the dynamic characterization of metal ions and on sitting-atop complex formation [31]. To enhance the reaction rate, several procedures have been implemented. Acceleration of the rate of incorporation of the Fe(II) ion *in vivo* into the protoporphyrin IX is catalyzed by enzymes with the catalytic function of the enzyme proposed as the porphyrin distortion caused by steric and electronic interactions with amino acid residues at the enzyme active site. The incorporation of the fourth-row metal (II) ions, such as Mn(II), Cu(II), and Zn(II) ions are accelerated by the presence of a small amount of metal (II) ions having a larger ionic radius, such as Cd(II), Pb(II), and Hg(II) ions [31] and of metal ions incorporation into a cationic water-soluble porphyrin by 5-sulfo-8-quinolinol [32].

The systematic nomenclature of porphyrins, metalloporphyrins and related molecules is detailed by IUPAC [33] and a World Wide Web version [34], while Fisher numeration [33], trivial names [33] and abbreviations [16] are also found in literature.

Flow-injection analysis (FIA), introduced in 1975 [35], marked an important breakthrough in unsegmented automatic continuous flow analysis and has developed over three decades as a simple, convenient, feasible analytical technique with the capability of a high sample frequency and degree of automation [36–46]. FIA is an analytical technique that is based on injecting a known volume of sample, with a well-defined shape, into a moving, unidirectional unsegmented carrier or reagent stream (Fig. 1). In this moving stream, the sample is physically and chemically transformed into a detectable specie that causes a detector response downstream of the injection point. If all critical parameters (reproducible injection, controlled reaction time, and controlled dispersion) are held within certain tolerance levels, the result will be reproducible [36,40]. The basic instrumentation needed for an FIA system are a multichannel pump, an injection valve, a flow-through detector, and a signal output device (originally a recorder, lately a computer). With the establishment and advances inherent in FIA, the scope and potential of the technique caught the eyes of many analytical chemists and these features make the technique very suitable over the years for satisfying the increasing demand in various fields for control

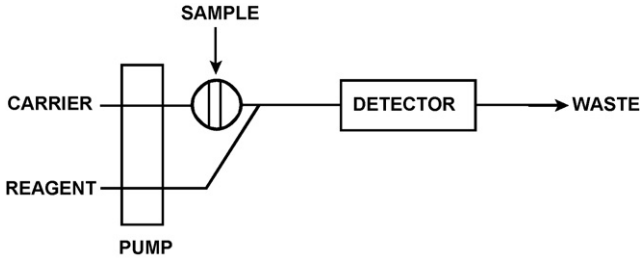


Fig. 1. Schematic diagram of a basic FIA system.

and routine analysis of analytical chemistry. With their pioneering innovation Ruzicka and Hansen [35] brought an entirely new concept to analytical chemistry by creating a concentration profile (gradient) of the sample, thus, allowing any point along the gradient to be used as a potential read-out, thus exploiting transient signals. As a result of this, the kinetic nature is one of the fundamental properties of FIA. Because of the inherent dynamic nature of FIA, measurements are always performed under non-equilibrium conditions, while the system is still in its kinetic phase; it is, therefore, properly classified as a kinetic system [36,41–50]. In addition to the reaction and/or dispersion rate, kinetic aspects of FIA can be further exploited by incorporation into the system strategies which rely on controlled kinetic processes such as catalysis, stopped-flow, rate of absorption and desorption, extraction, separation, diffusion of ions or gases through membranes or packed reactors, and enzymatic reactions [35,47–51].

There are basic two roles that porphyrins fulfilled in flow-injection analysis, that of an analyte or that of a reagent or modifier in the determination of other species.

2. Fast screening of porphyrins in biological samples

Although the fluorescence of metal-free porphyrins is most efficiently excited at the major absorption band, the Soret band, centered at about 400 nm with an UV light source, significant gain in selectivity can be achieved by performing fluorimetric excitation at one of the minor absorption bands located at the blue-green or yellow-red region of the visible spectrum since only a small number of organic substances present in biological materials actually absorb a photon efficiently and yield detectable fluorescence in these longer wavelength regions [52,53]. This information was used by Huie et al. [54] for the fast measurement of fluorescence from microtrace amounts of total porphyrins in biological fluids using FIA and visible laser fluorimetry. A high sample throughput was obtained by the fast sample introduction of diluted urine and serum samples without prior extraction directly into the FIA system. Urine and serum were diluted with 0.15 mol/l cetyltrimethylammonium bromide (CTAB) in a 0.01 mol/phosphate buffer at a pH 7.4 and the sample solutions were injected into a carrier stream of the same buffer. The fluorescence of the compounds was measured at an emission wavelength of ca. 620 nm with an excitation wavelength at 488 nm provided by an Argon-ion laser with a power of 1.0 W. The authors found that urine spiked with 0.02, 0.04 and 0.06 μmol/l of total porphyrin standard (corresponding to 0.15, 0.3 and 0.45 mg/l in undiluted urine) was clearly distinguishable from the urine blank; these concentrations representing the lower range for abnormal urine. With serum the limit of detection was around 0.015 μmol/l (ca. 0.05 mg/l in undiluted serum).

Lin and Huie [55] developed a flow-injection chemiluminescence (CL) method for the determination of porphyrins in biological fluids based on the reaction of bis-(2,4-dinitrophenyl) oxalate (DNPO) with H_2O_2 and porphyrin. The design of a proper detection flow-cell played a very important role in obtaining the highest

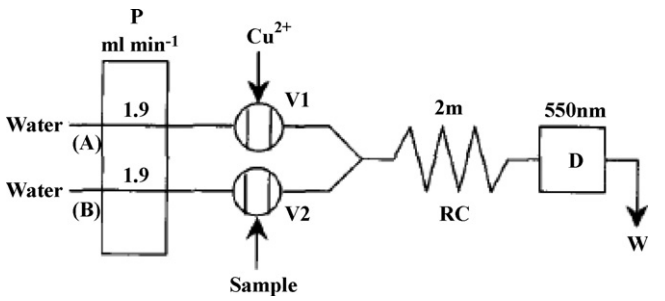


Fig. 2. Manifold used for determination of ascorbic acid with an FIA merging zone manifold. Reproduced from Ref. [56].

signal and this was achieved with a detection flow-cell that allowed the DNPO reagent to the carrier stream containing H_2O_2 and porphyrin at a position of approximately 1 cm from the detection window. The chemiluminescence emission was detected with a photomultiplier tube via a 570 nm cut-off filter. The effects of experimental parameters such as pH, solvents, flow-rate, and reagent concentrations on CL kinetics and intensity were investigated and optimized, resulting in optimum conditions with a flow-rate of 1.25 ml/min, concentrations of DNPO of 1.5 mmol/l and H_2O_2 of 3% and pH 6. Calibration graphs for porphyrins were linear up to 1000 μg/ml, recoveries for coproporphyrin from spiked urine were 97–98.2%, detection limit for urinary coproporphyrin was about 0.1 μg/l (S/N = 3) and the average precision was about 1.5%. The method was applied to determine coproporphyrin in urine samples from healthy adults.

3. Normal photometric detection

Tabata and Morita [56] used the accelerating catalytic effect of nanomolar levels of ascorbic acid on the formation rate of 5,10,15,20-tetrakis(1-methylpyridium-4-yl)porphyrincopper(II), $Cu^{II}(tmpyp)^{4+}$ with the subsequent increase in absorbance of the Cu(II) porphyrin to develop a simple, fast and sensitive flow-injection system for the determination of nanomolar amounts of ascorbic acid in tea, urine and blood. Ascorbic acid reduces Cu(II) to Cu(I) and the Cu(I) formed catalyzes the rate of incorporation of Cu(II) into the porphyrin core of H_2tmpyp^{4+} by deforming the porphyrin plane favorably for the attack of Cu(II) from underneath to form $Cu^{II}(tmpyp)^{4+}$. In this FIA procedure (Fig. 2) two solutions (each with a sample volume of 120 μl), one containing ascorbic acid and H_2tmpyp^{4+} and the other containing Cu(II) and acetate buffer (pH 5.0) were injected into two separate water carrier streams with equal flow rates of 1.9 ml/min. The two merging zones was allowed to react in a 2 m × 0.5 mm i.d. reaction coil and the colored solution of $Cu^{II}(tmpyp)^{4+}$ was monitored at 550 nm ($\varepsilon = 2.01 \times 10^4\,l\,mol^{-1}\,cm^{-1}$). The spectral changes during the course of the reaction were the disappearance of the characteristic absorption bands of H_2tmpyp^{4+} (Q bands at 520, 558 and 647 nm) and the growth of the characteristic band of $Cu^{II}(tmpyp)^{4+}$ (Q band at 550 nm). The isosbestic points were observed at 490, 534 and 577 nm. The change in absorbance was therefore monitored at 550 nm. The calibration graph was linear for 5.0×10^{-7} to 1.2×10^{-7} mol/l ascorbic acid and the RSD was 2.8% for the determination of 1.0×10^{-8} mol/l ascorbic acid. No detection limit or recoveries are given. Reducing agents such as sugars and vitamin B compounds did not interfere seriously.

The same concept was exploited by Lui and Itoh for the FIA kinetic determination of cysteine [57] in pharmaceutical injections and a permanent wave agent and ascorbic acid [58] in soft drinks by utilizing the catalytic complexation reaction of Cu(II) with 5,10,15,20-tetrakis(4-N-trimethyl-aminophenyl)porphyrin (TTMAPP). The absorbance increase belonging to the formed Cu(II)-TTMAPP was measured at the Soret band of 411 nm as the FIA signal for cysteine [57] as well as for the FIA system for ascorbic acid [58]. For cysteine [57] a RSD of 0.73% ($n = 10$) for 0.1 μg/ml cysteine at a throughput of $30\,h^{-1}$ was obtained, the detection limit (S/N = 3) was 15 ng/ml and the working dynamic range was 25 ng/ml to 1 μg/ml. Organic species like sugar, organic acids and amino acids could be tolerated at high concentration levels except for ascorbic acid that interfered seriously due to a similar catalytic effect. For ascorbic acid [58] a RSD of 0.11% ($n = 10$) for 0.1 μg/ml ascorbic acid at a throughput of $35\,h^{-1}$ was obtained, the detection limit (S/N = 3) was 5 ng/ml, broad dynamic range was 0.1–1000 μg/ml and at trace level between 20 and 100 ng/ml. Substances like amino acids, vitamins, sugars, organic acids and metal ions, showed no or little interference.

Merging zones FIA was also used for the spectrophotometric determination (absorbance of lead–porphyrin complex measured at 480 nm) of lead in tap water with 5,10,15,20-tetra (4-N-sulfoethylpyridinium)porphyrin [59], while a FIA system was also used for the differential-kinetic determination of lead in the soaking extract of pottery and porcelain, and human hair with *meso*-tetrakis (4-trimethylammoniumphenyl)porphyrin measuring the absorbance of the lead–porphyrin at 465 nm [60]. A kinetic method, based on the measurement of the absorbance due to the formation of Zn-*meso*-tetra(4-sulphophenyl)porphyrin(I) complex using imidazole(II) as catalyst, was also reported [61] for the determination of traces of Zn in hair, tap water and peach leaves.

The advances of water-soluble and difference in stability of metallo-water-soluble porphyrin complexes was used by Igarashi et al. [62] for the flow-injection spectrophotometric determination of ng/ml levels of cobalt(II). The cadmium(II) complex (CdL) of 5,10,15,20-tetrakis(4-sulfophenyl)porphine (TSPP) {Soret band: maximum wavelength (λ_{max}) = 432 nm, molar absorptivity ($\varepsilon = 4.8 \times 10^5\,l\,mol^{-1}\,cm^{-1}$} was found to be uniquely decomposed by irradiation with blue light around 432 nm. However, the cobalt complex of the same ligand ($\lambda_{max} = 432$ nm, $\varepsilon = 2.8 \times 10^5\,l\,mol^{-1}\,cm^{-1}$) was stable to visible light. The authors also confirmed that the composition of CdL and $Co^{III}L$ to be [M]:[L] = 1:1 by the mole ratio method. The authors used the photochemical properties mentioned above for the elimination of the absorbance blank of the chromogenic reagent CdL in the spectrophotometric detection of Co(II) following the exchange and oxidation reaction $CdL + Co^{2+} \rightarrow Co(III)L + Cd^{2+}$ for the FIA determination of cobalt(II) ions. A linear calibration graph was obtained in the range 1×10^{-7} to 1×10^{-6} mol/l, the detection limit (S/N = 3) was 3.45×10^{-8} mol/l (2 ng/ml) and the RSD ($n = 10$) for 6.8×10^{-7} mol/l cobalt was 0.6%. Mn(II), Cu(II), Zn(II) and Cr(II) interfered, masking agents for these metals were discussed.

The incorporation of the corresponding immobilized oxidase enzyme columns to yield hydrogen peroxide enhanced the selectivity of the respective FIA procedures for the corresponding compounds with spectrophotometric detection by a titanium(IV)–porphyrin reagent. Matsubara et al. [63,64] developed an acidic aqueous solution of oxo[5,10,15,20-tetra(4-pyridyl)porphyrinato]titanium(IV) complex, $[TiO(tpypH_4)^{4+}]$, (denoted as the Ti–TPyP reagent) as a highly sensitive spectrophotometric reagent for the determination of trace amounts of hydrogen peroxide. Following the addition of hydrogen peroxide to the Ti–TPyP reagent, the absorbance at 432 nm decreased and a new peak appeared at 450 nm (the Soret band) accompanied by the consumption of the $[TiO(tpypH_4)^{4+}]$ complex and the formation of the monoperoxo complex, $[TiO_2(tpypH_4)^{4+}]$ [65]. The degrees of the absorbance changes were found to be proportional to the hydrogen peroxide concentration with the apparent molar absorptivities of 1.9×10^5 (432 nm) and 1.1×10^5 (450 nm) $l\,mol^{-1}\,cm^1$. Both values are much larger than those obtained by conventional

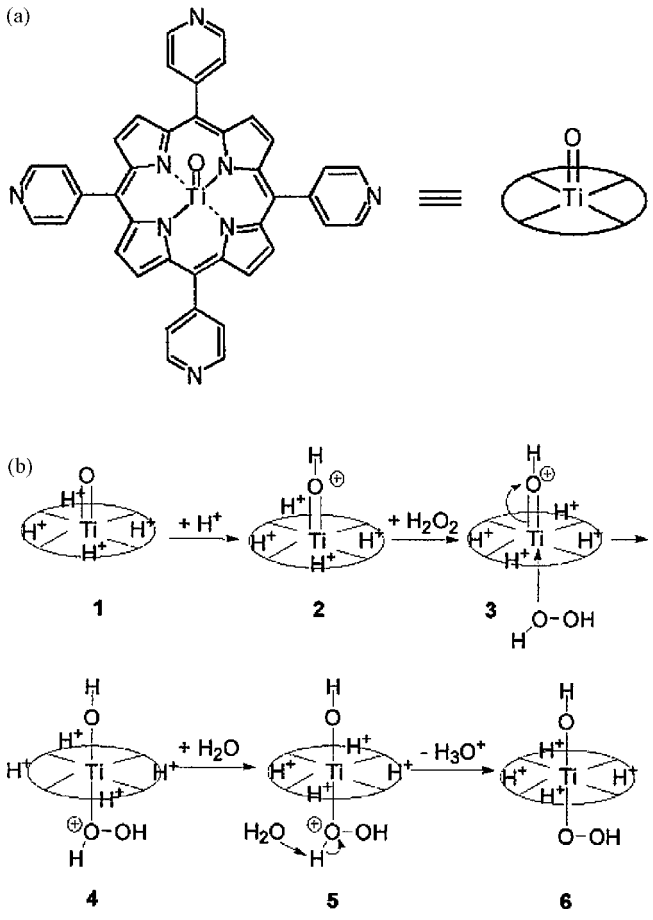


Fig. 3. (a) TiO(tpyp) complex and its simplified representation. (b) Proposed mechanism for the reaction of the $[TiO(tpypH_4)^{4+}]$ complex 1 with hydrogen peroxide under acidic conditions. Reproduced from Ref. [66].

analysis methods. However, a substantial account for the reaction specificity of the $[TiO(tpypH_4)^{4+}]$ complex to hydrogen peroxide should be quite important to secure the reliability of analysis using the Ti–TPyP reagent. Therefore, to ensure that the high specificity is free from the effects of interfering substances, Takamura et al. [66–68] studied the relationship between the $[TiO(tpypH_4)^{4+}]$ complex and hydrogen peroxide from the viewpoint of reaction mechanisms and theoretical calculations and reported a proposed mechanism (Fig. 3), in which assignment of the absorption peaks and the verification of the reaction mechanism (slightly revised) were made based on the spectral simulations [68]. Based on these facts, a FIA system was reported for the determination of hydrogen peroxide (Fig. 4) in rainwater [69], yielding a linear response from 10 nmol/l to 10 μmol/l for H_2O_2 (detection limit 5 nmol/l), with a coefficient of variation ($n = 10$) of 1% for 1 μmol/l of H_2O_2. The

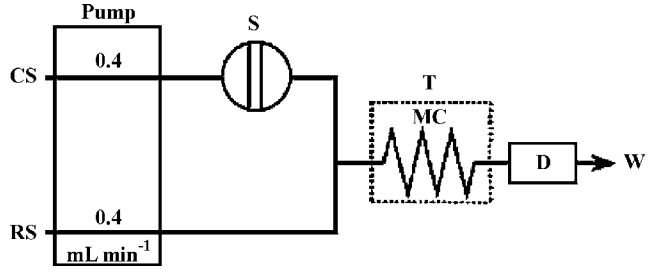


Fig. 4. Schematic diagram of the FIA system for the determination of hydrogen peroxide. Reproduced from Ref. [69].

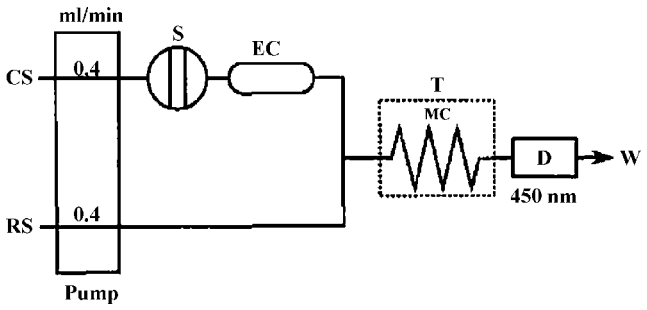


Fig. 5. Flow diagram for the determination of oxalate using an immobilized oxalate oxidase column reactor. Reproduced from Ref. [70].

same facts was used to develop also a rapid and sensitive FIA system for the spectrophotometric determination of oxalate in beverages, milled jelly, homogenized (details given in reference) fruit and vegetables using an immobilized oxidase reactor to yield hydrogen peroxide [70]. The flow-injection manifold comprised of a two-channel system with an immobilized oxalate oxidase column (Fig. 5). The calibration graph was linear between an oxalate concentration range of 5×10^{-7} and 2.5×10^{-4} mol/l ($r = 0.999$) with a sampling rate of 25 h^{-1}. The RSD was 0.48% ($n = 10$) at 2.5×10^{-5} mol/l (500 pmol/20 μl injection). The authors [71] used the same concept for the determination of trace components of physiological significance in human serum. The method was assessed for the determination of glucose, urate and galactose levels in human serum using the corresponding oxidase enzyme columns incorporated into the FIA system. Small sample volumes, 0.05 μl serum for glucose and 0.5 μl serum for urate, were used and the response was linear against concentrations ranging from 1 to about 1000 and 0.5 to about 600 μmol/l (5 to about 5000 and 2.5 to about 3000 pmol/test) for glucose respectively with a sample throughput of 40 samples per hour. No sample pretreatment such as deproteinization or preconcentration was necessary. For the determination of galactose in serum a 20 μl of deproteinized serum was, however, used. Response was linear for a galactose concentration range between 0.5 to about 500 μmol/l (10 to about 10 000 pmol/test).

Metalloporphyrins can also serve as modified artificial solid-catalysts in catalytic columns inside a FIA system for the determination of ascorbic acid [72]. In the FIA system (Fig. 6) a sample solution containing ascorbic acid is injected into an acetate buffer (pH 5.0) and oxidized in a pre-column, containing silica gels modified with Co-tetrakis(carboxyphenyl)porphine with the formation of hydrogen peroxide. The resulting hydrogen peroxide reacts with a chromogen solution containing phenol, 4-aminoantipyrine and borate buffer (pH 8.5) under catalyzed conditions in a main column, containing glass beads modified with Mn-tetrakis(carboxyphenyl)porphine to form a quinoid dye that was detected spectrophotometrically at 505 nm. The calibration graph was linear for ascorbic acid concentrations between 0.20 and 10.0 μmol/ml and the coefficient of variation ($n = 10$) was 4.1% for 8.0 μmol/ml. Ascorbic acid was determined in vitamin compounds and soft drinks and the results obtained compared favorably with an official phenol method.

Lead and cadmium from injected synthetic soil sample extracts and certified river water samples were separated by an in-line cation-exchange column with a carrier of malic acid, pH 5.5, as eluent solution in an FIA system before merging with TMPyP [5,10,15,20-tetrakis (N-methyl-pyridynium-4-yl)-21H,23H-porphine, tetrakis(*p*-toluenesulfonate)] in a basic medium (pH 10.1) to form water-soluble lead–TMPyP and cadmium–TMPyP complexes, respectively, before photometric detection at 476 nm [73]. The detection limits are 0.001 mg/l for

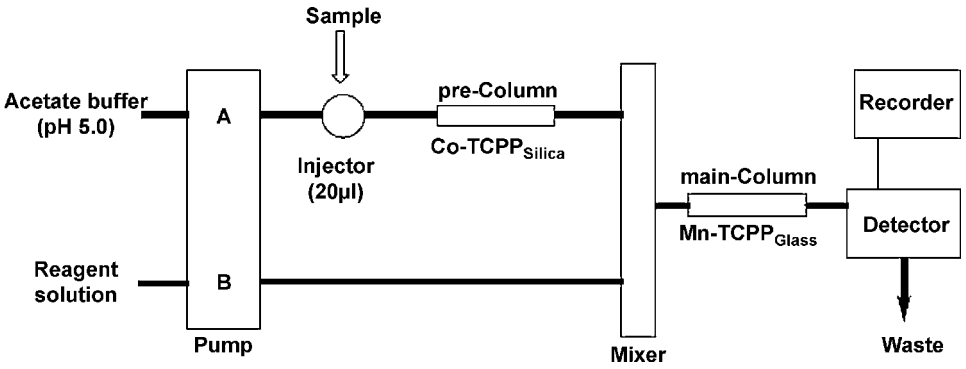


Fig. 6. FIA system for the determination of ascorbic acid. Reproduced from Ref. [72].

lead and 0.002 mg/l for cadmium. A novel indirect substitution spectrophotometric methodology using porphyrin was also developed [74] for the determination of some metals that do not react with porphyrin directly. This methodology was verified and further developed into an automatic procedure on a HPLC post-column FIA system that first separate the lanthanides before a multistep reaction system for the individual lanthanides is employed. The multistep reaction system consists of three complexation reactions that occur in sequence of EDTA with metal, EDTA with Cu(II) and porphyrin with Cu(II). The complexation reaction of Cu(II) with a cationic porphyrin, *meso*-tetrakis (4-N-trimethyl-aminophenyl)-porphine (ttmapp), which has a high molar absorptivity of about 5×10^5 l mol^{-1} cm^{-1}, serves for spectrophotometric detection as the signal from the absorbance decrease at 433 nm.

4. Multicomponent analysis with diode array detection

Metal ions of zinc, lead and cadmium frequently exist together in many real environmental and food samples and it is necessary to determine these metal ions simultaneously in most instances. Li et al. [75] developed a multicomponent analysis system with flow-injection diode array detection-absorption spectrophotometry using a partial least squares (PLS) calibration model for the simultaneous determination of zinc, cadmium and lead in a water standard reference material and samples of beverage, powdered corn and powder milk. The spectrophotometric determination is based on the reaction of the metallic ions and *meso*-tetra(4-trimethylammonium phenyl) porphyrin (TAPP) forming colored complexes. The overlapped spectra of these complexes are collected by charge coupled device (CCD)-diode array detector and the multi-wavelength absorbance data are processed using PLS algorithm. The results of environmental and food samples of the reported FIA method were in good agreement with a standard AAS procedure. Average spiked recoveries were 89.6–103.2% with an RSD of 2.8–7.1% at a sampling rate of 30 samples/h.

5. Waveguide optical metalloporphyrin-based sensors

Metalloporphyrin is not only useful as anion-selective ionophores, but can also be utilized as chromophores that exhibit optical changes upon binding with target anions. A very good example reported in literature is an optical chloride sensor based on a monomer–dimer equilibrium of indium(III) porphyrin where a hydroxo-bridged dimer of indium(III) octaethyl porphyrin, In(III)OEP, is broken into corresponding monomeric species as chloride replaces hydroxide as an axial ligand of the metalloporphyrin that results in a simultaneous optical shift of the Soret absorption band [76]. Scandium(III) porphyrins also form dimers that exhibit a hypsochromic shift of the Soret band from scandium(III) porphyrins [77]. These properties were used by the group of Meyerhof [78] to develop waveguide optical metalloporphyrin-based sensors with fast response times (1–2 s) towards solution phase chloride species in flow-through analytical systems like FIA. The sensors (Fig. 7) are based on the incorporation of In(III)OEP within ultrathin polymeric films (<0.5 µm) deposited via spin coating on a planar fused silica waveguide. In the FIA arrangement (Fig. 7 outlined in Ref. [78]) 50 µl sample solutions containing various levels of chloride prepared in 0.05 mol/l phosphate buffer (pH 3.0) were injected while the spectral change was recorded at 392 nm (dimer) and 408 nm (monomer) as well as 450 and 700 nm (background), simultaneously. The background shift originating from bubbles and osmolarity changes of sample solution [79,80] was corrected by using the absorbance changes at 450 and 700 nm. The response due to $[Cl^-] = 1.0 \times 10^{-3}$ mol/l for the FIA system was given. No calibration curve with chloride concentration range, no detection limit and no recoveries are given. A disadvantage is the leaching of membrane components that must be overcome to ensure more stable sensor response over longer time periods. The group of Meyerhof [81] reported also an optical fluoride sensor based on the monomer–dimer equilibrium of scandium(III)-octaethylporphyrin in a plasticized polymeric film for FIA measurements. Fast and reversible fluoride response over the range 10^{-4} to 10^{-2} mol/l was observed and the selectivity for fluoride over ClO_4^-, SCN^-, NO_3^-, Br^-, Cl^- is quite high. Only organic salicylate is a major interference.

6. On-line enrichment with FAAS/ICP-AES detection

Chelating of metal ions with porphyrin forms the bases for on-line enrichment FIA systems. The group of Pyrzynska investigated the suitability of 5,10,15,20-tetrakis(4-carboxyphenyl)porphine, TCPP, as a complexing agent for the on-line preconcentration of cadmium [82] and manganese [83] using an anion exchanger (Amberlite IRA-904) in a microcolumn. In the preconcentration

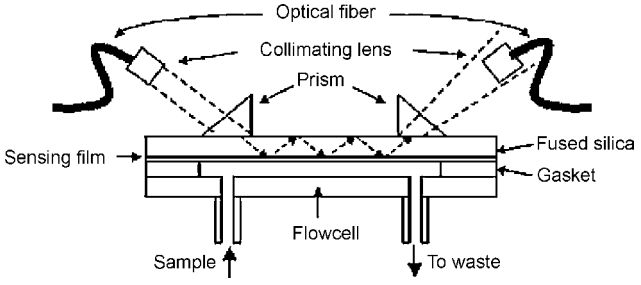


Fig. 7. Schematic diagram of the planar waveguide type optical sensor based on thin polymeric film containing In(III)[OEP] within the low volume flow-cell. Reproduced from Ref. [78].

step, a premixed cadmium [82] sample and TCPP solution, at 5×10^{-4} mol/l for TCPP in 0.05 mol/l borate buffer, pH 9, were pumped continuously through the manifold at a flow rate of 3.5 ml/min for 2 min. Cd–TCPP complex was retained on the microcolumn, and the sample matrix was sent to the waste system. A first injection valve was switched to its other position and a 2 mol/l nitric acid solution was injected by means of a second injection valve in order to release cadmium directly into the nebulizer of the spectrometer. Finally, a blank carrier (deionized water) was passed through the microcolumn for 30 s in order to condition it for the following sample introduction. A good precision (2.1% RSD for 40 μg/l cadmium) and a high enrichment factor (36) with detection limit (3σ) of 1.4 μg/l were obtained. The achieved analytical results for a standard reference material (SRM 1643d) were in good agreement with the certified values. In the preconcentration step for the determination of manganese [83], a 10^{-5} mol/l TCPP reagent was mixed on-line with an aqueous manganese sample solution and transported through the microcolumn packed with anion-exchange resin (Amberlite IRA-904) for 5 min. After the preconcentration step, the first injection valve was switched to its other position and a 0.5 ml of 2 mol/l nitric acid solution was injected by means of a second injected valve to release manganese directly into the nebulizer of the spectrometer. A good precision (2.2–3.1% RSD for 50 μg/l manganese) and good enrichment factor of 30 were obtained with a detection limit of 12 μg/l for a loading time of 5 min. Results obtained for the determination of manganese in natural water by the FI-FAAS system and ETAAS were in good agreement with differences between the results of the two methods not significant at the 5% level.

7. Luminescent detection with porphyrins

The use of metalloporphyrin complexes as a substitute for peroxidase has been applied in a number of analytical applications and various metalloporphyrins have been used as mimetic peroxidase in fluorescence and chemiluminescence analysis. Ci et al. [84] used the observation, that the catalytic activity of mimetic peroxidase (metalloporphyrin) in the chemiluminescence reaction between luminol and hydrogen peroxide is inhibited in the presence of an amino acid, to develop a FIA system for the detection of four amino acids. Only L-cysteine, L-tyrosine, L-tryptophan and L-cystine quenched the chemiluminescence intensity significantly giving detection limits (S/N = 3) of 6.8×10^{-8}, 1.3×10^{-7}, 8.5×10^{-6} and 2.2×10^{-5} mol/l, respectively. In a later publication Ci et al. [85] reported that the presence of DNA significantly enhanced the catalytic activity of the manganese *meso*-tetrakis(4-N-methylpyridinyl)porphyrin, Mn-TMPyP, on the luminol-H_2O_2 chemiluminescence reaction. They used a previously described [84] FIA chemiluminescence manifold for the determination of calf thymus DNA. A calibration graph was obtained between 20 and 200 ng/ml of DNA with a fixed concentration of Mn-TMPyP of 2×10^{-8} mol/l, the RSD ($n = 11$) was 2.6% at 10 ng/ml and the detection limit was 0.20 ng/ml. The on-line monitoring of NO complexed with porphyrin ring-bearing (PRB) materials using the chemiluminescence emission generated by the oxidation of luminol with H_2O_2 as detection system was employed [86] in a FIA manifold incorporating a UV-sensitive photomultiplier tube. The protein hemoglobin (Hb) and the enzymes horseradish peroxidase (HRP) and catalase (CAT) were used as PRB agents in complexes with NO. The method is quite sensitive, simple, rapid and precise with a sensitivity of 2.63×10^5 mV/mol NO, a range of 2.0×10^{-5} up to 1.0×10^{-2} mol NO (under the conditions used), a reproducibility of 1.0% over the range 1.0×10^{-3} up to 1.0×10^{-2} mol NO, a frequency of about five samples per minute and a detection limit of 1.0×10^{-5} mol NO.

Rana and Tamake [87–89] studied the formation of ferryl porphyrin, induced by the electrochemical reduction of iron(III)tetrakis-5,10,15,20-(N-methyl-4-pyridyl)porphyrin, Fe^{III}TMPyP, with FIA by measuring luminol chemiluminescence and recording the absorption spectrum. They found that both the anodic oxidation and cathodic reduction of iron(III) porphyrin induced the formation of a ferryl species, which is widely accepted to be responsible for stimulating luminol chemiluminescence. Emission was observed both below the reduction potential of Fe^{III}TMPyP (−0.08 V at pH 11, −0.02 V at pH 7 and 0.15 V at pH 3) and above the oxidation potential (0.6 V at pH 11, 0.75 V at pH 7 and 1.1 V at pH 3) [88,89]. The emission was relatively greater below the reduction potential than in the oxidative region. It was significantly higher especially at lower pH (<pH 4). The cathodic emission was largely dependent on the concentration of dissolved molecular oxygen while the anodic emission was not. Emission on both sides was inhibited significantly by the addition of alkene solutions downstream of the working electrode. The spectra on both the positive and negative potential sides were shifted to longer wavelengths (>424 nm) compared to the original spectrum of Fe^{III}TMPyP (422 nm). Computer analysis also showed that the spectra on both sides were perfectly reproduced by a combination of two spectra, those of Fe^{III}TMPyP and O = Fe^{IV}TMPyP (436 nm at pH 11). The authors [90] described a similar FIA chemiluminescence system for the detection of electrochemically generated H_2O_2 and ferryl porphyrin.

Vong et al. [91] developed a FIA system for the non-specific determination of iron–porphyrin-like complexes in natural waters that also allowed the direct injection of seawater with a detection limit of 0.11 nmol/l of equivalent hemin (Fe-protoporphyrin IX). Papkovsky et al. [92] reported a FIA system for the determination of sulfite based on the spectral-luminescent properties and quenching behavior of the covalent conjugate of the platinum(II) complex of coproporphyrin-I and bovine serum albumin (PtCP-BSA). The sensor membrane was excited with green light (535 nm) and the phosphorescence monitored at 650 nm.

8. Electrochemical detection involving porphyrins

Porphyrin-modified electrodes have received considerable attention in analytical and bioanalytical chemistry for the enhancement of selectivity in electrochemical detection of samples with complex matrices in biological fields. The group of Toma in Sao Paulo, Brazil [93–96] reported the properties and analytical application of a new polymetallic species containing four $[Ru(bipy)_2Cl]^+$ (bipy = 2,2′-bipyridine) groups coordinated to the pyridine residues of the *meso*-tetra(pyridyl)porphynate cobalt(III) complex in a series of publications. The electrochemistry of the polymetallated porphyrins is very rich owing to the presence of many electroactive groups in the supermolecules. It is well known that the complexes of ruthenium(II) 2,2′-bipyridine can be oxidized to the corresponding ruthenium(III) complexes, and each bipy ligand can be reduced by successive addition of electrons. Likewise, the porphyrin ring can either be oxidized or reduced generating the cation-radical and its corresponding dication, or the anion-radical and its corresponding dianion, respectively. The central metal ion is also electrochemically active. Araki et al. [93] reported, that in the range −1.8 to 1.6 V, it is possible to add up to twelve electrons and to remove up to four electrons from the tetraruthenated cobalt porphyrin complex, $[CoTPyP\{Ru^{II}(bipy)_2Cl\}_4]^{5+}$ complex (structure given in Ref. [93]). The cyclic voltammograms (given in Ref. [93]) of the tetraruthenated cobalt porphyrin, in DMF solution, exhibit an intense reversible wave at $E_{1/2} = 0.93$ V associated with the $Ru^{III/II}$ redox couple, and two irreversible cathodic waves at $E_{pc} = -1.37$

and −1.63 V, involving the stepwise reduction of the bipyridine ligands in each peripheral ruthenium complex. Three successive reductions of the cobalt porphyrin center were detected in the range between −0.5 and −0.7 V, using spectroelectrochemical techniques (given in Ref. [93]). The authors [93] also found that stable, homogeneous films of the polymetallic porphyrin was generated by dip-coating on to electrode surfaces, exhibiting pronounced electrochemical activity. They then successfully applied the modified electrodes as amperometric sensors in FIA systems for the determination of reducing analytes, such as nitrite and sulphite ions. A good linearity was obtained for nitrite in the range 2×10^{-7} to 8×10^{-7} mol/l with a slope of 0.48 A mol^{-1} cm^{-2} and for sulphite in the range 2×10^{-6} to 8×10^{-6} mol/l with a slope of 0.15 A mol^{-1} cm^{-2}.

Angnes et al. [94] employed modified electrodes with molecular films of the tetraruthenated cobalt–porphyrin complex in a FIA system for the determination of NADH and dopamine with amperometric detection. The electrochemical oxidation of these bioanalytes was monitored at the onset of the $Ru^{III/II}$ redox wave (E° = 0.70 V vs. Ag/AgCl), exhibiting a very sharp peak consistent with a rapid and efficient electron transfer process. Flow amperometric responses of glassy carbon electrodes modified with tetraruthenated cobalt porphyrin, at E = 0.85 V, to consecutive injections of NADH revealed a linearity between 2×10^{-6} and 8×10^{-6} mol/l with a slope of 0.114 and for amperometric responses of glassy carbon electrodes modified with tetraruthenated cobalt porphyrin, at E = 0.9 V, to consecutive injections of dopamine a linearity between 2×10^{-7} and 8×10^{-7} mol/l with a slope of 0.219. Azevedo et al. [95] reported a method for the determination of sulfur dioxide in wines by gas-diffusion flow-injection analysis utilizing modified electrodes with electrostatically assembled films of tetraruthenated porphyrin. The amperometric measurements were done using an applied potential of +0.90 V (vs. $Ag/AgCl_{KCl}$). The FIA system was implemented for the determination of free SO_2 (12.0–44.7 mol/l) and total SO_2 (62.6–83.7 mol/l) in wines with a typical frequency of injection of 30 injections/h. The RSD was 1.9% (i = 750.9 ± 14.3 nA) obtained for repetitive injections of a 1×10^{-3} mol/l sulfite solution (n = 10). The results demonstrate a good accuracy, comparable with those obtained using the conventional method. In addition, the method can be readily applied to red, white and rose wines, other compounds in wine do not interfere, it consumes small amounts of sample and is faster than the iodometric method. The continuous use of the same sensor indicates a small decrease (14%) on the signal after 5 days of use.

The modification of a glassy carbon surface by coating with an electrostatically assembled film of tetraruthenated cobalt porphyrin/*meso*-tetra(4-sulphonatephenyl) porphyrinate zinc(II) yields an indicator electrode that allows the determination of nitrite to be performed with a limit of detection of 0.1 μmol/l in a flow-injection configuration [96] with amperometric detection. The dynamic range extended up to 1000 μmol/l, the RSD (n = 20) was 1.5% for 5 μmol/l nitrite solutions and the analytical frequency was 50 samples/h. The efficiency of the bilayered film to mediate the electron transfer allows the determination to be performed at a less positive potential (+0.75 V) with enhanced sensitivity of about 15-fold current enhancement compared with results obtained with a bare electrode. The coating also prevents surface poisoning and its stability is maintained over several weeks. By incorporating a copper–cadmium reductor column into the FIA manifold, nitrate analysis was also achievable, both analytes being determined in several samples. Analytical characteristics for pure nitrate samples determinations were found to be a linear dynamic range of 5–100 μmol/l, an RSD (n = 20) of 1.5% and limit of detection of 1 μmol/l. The method was used for the determination of nitrate and nitrite in mineral water, saliva and cured meats and the results obtained were in good agreement with certified values and standard spectrophotometry.

Guerra et al. [97] described a FIA system for the determination of hydrazine using a carbon paste electrode modified with copper porphyrin occluded into a zeolite cavity. They used a sampling volume of 50 μl, applied potential of 270 mV vs. SCE and a flow rate of 1 ml/min. Operational range was between 5 and 60 μmol/l and the analytical frequency was 70 determinations/h. The recovery test carried out with the system presented good results; 97 ± 2% for a solution concentration of 5 μmol/l. The detection limit considering the signal to noise ratio as 3:1 was 1.0 μmol/l and the operational limit was 5.0 μmol/l. The authors reported that the system was stable for at least 3 months in continuous use and the response kept 76% of the initial response.

Li et al. [98] developed an amperometric biosensor based on the immobilization of acetylcholinesterase on a manganese(III) *meso*-tetraphenylporphyrin nanoparticles-modified glassy carbon electrode for the detection of trichlorfon, an organophosphate pesticide, with a FIA system. A wide linear inhibition response for trichlorfon was observed in the range of 1.0 nmol/l to 1.0 mmol/l corresponding to a 10–83% inhibition for acetylcholinesterase with a detection limit of 0.5 nmol/l.

Hassan et al. [99] described two novel potentiometric membrane sensors based on the use of manganese(III) porphyrin and cobalt(II) phthalocyanine ionophores dispersed in plasticized poly(vinyl chloride) PVC matrix membranes for the FIA determination of azide. The intrinsic characteristics of the manganese(III) porphyrin and cobalt(II) phthalocyanine-based detectors in a low dispersion manifold showed calibration slopes of −51.2 and −33.5 mV per decade for the concentration ranges of 1.0×10^{-5} to 1.0×10^{-2} and 1.0×10^{-4} to 1.0×10^{-2} mol/l azide and the detection limits are 1.0×10^{-5} and 3.1×10^{-5}, respectively. The detectors were used for the determination of azide in FIA at an input rate of 40–60 samples per hour. The responses of the sensors were stable within ±0.9 mV for at least 8 weeks and were pH independent in the range of 3.9–6.5.

9. Conclusions

The importance and successful implementation of rapid screening FIA systems for porphyrins in biological samples is marked by the efficiency with which metal-free porphyrins can be excited at the Soret band with measurement of fluorescence at an emission wavelength above 600 nm or the chemiluminescence reaction with detection of chemiluminescence emission with a photomultiplier tube via a 570 nm cut-off filter.

In normal photometric detection, the accelerating catalytic effect of ascorbic acid was applied to develop numerous simple, fast, sensitive and selective FIA systems with 5,10,15,20-tetrakis(macromolecular) methallated porphyrins as important part of the system. The solubility of porphyrins is a major drawback for employment in FIA systems, but the advances of water-soluble and difference in stability of metallo-water-soluble porphyrin complexes is clearly an asset.

The incorporation of the corresponding immobilized oxidase enzyme columns to yield hydrogen peroxide enhanced the selectivity of FIA procedures with the spectrophotometric detection with an oxo[5,10,15,20-tetra(4-pyridyl)porphinato] titanium(IV) complex and this FIA–Ti(IV)–porphyrin system was intensively studied in various papers and successfully implemented.

Porphyrins and metalloporphyrins also found a place in FIA systems for multicomponent analysis of metal ions with diode array detection-absorption spectrophotometry using PLS calibration for simultaneous determination in complex sample matrices,

as waveguide optical metalloporphyrin-based sensors, on-line enrichment with FAAS/ICP-AES detection and luminescent detection.

Porphyrin-modified electrodes have received considerable attention in analytical and bioanalytical chemistry for the enhancement of selectivity in electrochemical detection of samples with complex matrices in biological field. Although there were a number of successful applications of FIA-electrochemical detection systems, there is a large scope for improvement on validation with real samples.

Any new future exploitation of porphyrins lies in the way the characteristics of these macromolecules will be changed and adapted in multidisciplinary research and development to satisfy applications in process analytical technology (recently even more so for micro- and nanoprocess analytical technology) with roots in health sciences and energy sources. Of the current available variety of macromolecules, the colorful and other properties of porphyrins make it the most suitable for new developments of interdisciplinary significance. Looking at properties such as light-energy conversion in solar cells and fluorescence switches in the energy environment as well as photodynamic therapy and malaria treatment in health sciences a correct diversion of porphyrins structures for sure has a bright future. Among some of the disadvantages of porphyrins are the slow reaction rates for incorporation of species into the porphyrin ring and water solubility for process streams, but there are ways to change these properties to faster reaction rates by for example suitable catalysts and soluble substances by conversion to water-soluble salts. However, the low water solubility and stability are among some of the advances for use in electrochemical sensors.

Acknowledgements

The authors would like to acknowledge the financial support received from projects financed by contract 120 CP/I/14.09.2007 from PN II, Capacity, Module 1 and contract D1 1055/2007-PORFSENS from PN II, Partnership

References

[1] L.R. Milgrom, The Colours of Life. An Introduction to the Chemistry of Porphyrins and Related Compounds, Oxford University Press, 1997.
[2] J. Li, T. Tang, F. Li, M. Li, Dyes Pigments 77 (2008) 395.
[3] H.M. Swartz, R.B. Clarkson, Phys. Med. Biol. 43 (1998) 1957.
[4] W. Zheng, N. Shan, L. Xu, X. Wang, Dyes Pigments 77 (2008) 153.
[5] I.J. MacDonald, T.J. Dougherty, J. Porphyr. Phthalocya. 5 (2001) 105.
[6] A. Dudkowiak, E. Teslak, J. Habdas, J. Mol. Struct. 792–793 (2006) 93.
[7] A. Robert, F. Benoit-Vical, O. Dechy-Cabaret, B. Meunier, Pure Appl. Chem. 73 (2001) 1173.
[8] M.J. Crossley, P.L. Burn, J. Chem. Soc. Chem. Commun. 21 (1991) 1569.
[9] J.S. Lindsey, R.W. Wagner, J. Am. Chem. Soc. 116 (1994) 9759.
[10] M. Kawao, H. Ozawa, H. Tanaka, T. Ogawa, Thin Solid Films 499 (2006) 23.
[11] T. Ishida, Y. Morisaki, Y. Chujo, Tetrahedron Lett. 47 (2006) 5265.
[12] D. Wrobel, J. Lukasiewicz, J. Goc, A. Waszkowiak, R. Ion, J. Mol. Struct. 555 (2000) 407.
[13] D.M. Guldi, J. Phys. Chem. B 109 (2005) 11432.
[14] K. Takechi, T. Shiga, T. Motohiro, T. Akiyama, S. Yamada, H. Nakayama, et al., Solar Energy Mater. Solar Cells 90 (2006) 1322.
[15] L. Yang, C. Lifeng, T. He, J. Org. Chem. 71 (2006) 8279.
[16] M. Biesaga, K. Pyrzynska, M. Trojanowicz, Talanta 51 (2000) 209.
[17] Y. Itagaki, K. Deki, S.I. Nagashima, Y. Sadaoka, Sens. Actuators B-Chem. 117 (2006) 302.
[18] G. Di Marco, M. Lanza, Sens. Actuators B-Chem. 63 (2000) 42.
[19] D.J. Dobson, S. Saini, Anal. Chem. 69 (1997) 3532.
[20] S.V. Guerra, C.R. Xavier, S. Nagagaki, L.T. Kubota, Electroanalysis 10 (1998) 465.
[21] K. Kilian, K. Pyrzynska, Talanta 60 (2003) 669.
[22] R. Giovannetti, V. Bartocci, F. Pucciarelli, M. Ricciutelli, Talanta 63 (2004) 857.
[23] M. Tabata, H. Morito, Talanta 44 (1997) 151.
[24] Y. Kitamura, K. Kawata, K. Tanaka, Y. Furuyasshiki, M. Mifune, I. Tsukamoto, M. Saito, J. Haginaka, Y. Saito, Talanta 69 (2006) 1260.
[25] Q.F. Hu, G.Y. Yang, J.Y. Yin, Y. Yao, Talanta 57 (2002) 751.
[26] Z. Deyl, I. Mitsik, A. Eckhardt, V. Kasicka, V. Kral, Curr. Anal. Chem. 1 (2005) 103.
[27] J.E. Falk, Porphyrins and Metalloporphyrins, Elsevier, New York, 1975.
[28] J.H. Kim, J.Y. Jaung, Dyes Pigments 77 (2008) 474.
[29] S. Seyan, M. Merdivan, N. Demirel, H. Hosgoren, Microchim. Acta 161 (2008) 87.
[30] P. Hambright, P.B. Chock, J. Am. Chem. Soc. 96 (1974) 3123.
[31] S. Funahashi, Y. Inada, M. Inamo, Anal. Sci. 17 (2001) 917.
[32] K. Kawamura, S. Igarashi, T. Yotsuyanagi, Microchim. Acta 153 (2006) 145.
[33] G.P. Moss, Pure Appl. Chem. 59 (1987) 779.
[34] http://www.chem.qmul.ac.uk/iupac/tetrapyrrole/.
[35] J. Ruzicka, E.H. Hansen, Anal. Chim. Acta 78 (1975) 145.
[36] J. Ruzicka, E.H. Hansen, Flow Injection Analysis, 2nd edition, Wiley, New York, 1988.
[37] J.L. Burguera (Ed.), Flow Injection Atomic Spectroscopy, Marcel Dekker, New York, 1989.
[38] Z. Fang, Flow Injection Atomic Absorption Spectrometry, Wiley, Chicester, 1995.
[39] M. Trojanowicz, Flow Injection Analysis: Instrumentation and Applications, World Scientific, River Edge, NJ, 1999.
[40] R.E. Taljaard, J.F. van Staden, Lab. Robot. Automat. 10 (1998) 325.
[41] J. Saurina, S. Hernandez-Cassou, Anal. Chim. Acta 438 (2001) 335.
[42] E.A.G. Zagatto, J.F. van Staden, N. Maniasso, R.I. Stefan, G.D. Marshall, Pure Appl. Chem. 74 (2002) 585.
[43] J.F. van Staden, Anal. Chim. Acta 467 (2002) 61.
[44] J.F. van Staden, R.I. Stefan, Anal. Bioanal. Chem. 374 (2002) 3.
[45] B. Karlberg, R. Torgrip, Anal. Chim. Acta 500 (2003) 299.
[46] J. Ruzicka, E.H. Hansen, Trends Anal. Chem. 27 (2008) 390.
[47] H.L. Pardue, Anal. Chim. Acta 216 (1989) 69.
[48] E.H. Hansen, Anal. Chim. Acta 261 (1992) 125.
[49] J.F. van Staden, Curr. Trends Anal. Chem. 1 (1998) 89.
[50] J.F. van Staden, Pure Appl. Chem. 71 (1999) 2303.
[51] M.D. Luque de Castro, M. Valcarcel, Trends Anal. Chem. 8 (1989) 172.
[52] C.W. Huie, W.R. Williams, Anal. Chem. 61 (1989) 2288.
[53] M.J.P. Leiner, M.R. Hubmann, O.S. Wolfbeis, Anal. Chim. Acta 98 (1987) 13.
[54] C.W. Huie, J.H. Aiken, W.R. Williams, Anal. Chim. Acta 254 (1991) 189.
[55] M. Lin, C.W. Huie, Anal. Chim. Acta 339 (1997) 131.
[56] M. Tabata, H. Morita, Talanta 44 (1997) 151.
[57] J. Liu, J. Itoh, Talanta 70 (2006) 791.
[58] J. Liu, J. Itoh, Spectrochim. Acta A 67 (2007) 455.
[59] J.A. Schneider, J.F. Hornig, Analyst {London} 118 (1993) 933.
[60] Q. Mao, C. Zhang, J. Cheng, Fenxi-Huaxue 18 (1990) 952.
[61] X. Peng, Q. Mao, J. Cheng, Lihua-Jianyan,-Huaxue-Fence 28 (1992) 170.
[62] S. Igarashi, T. Aihara, T. Yotsuyanagi, Anal. Chim. Acta 323 (1996) 63.
[63] C. Matsubara, N. Kawamoto, K. Takamura, Analyst {London} 117 (1992) 1781.
[64] K. Takamura, C. Matsubara, Bull. Chem. Soc. Jpn. 76 (2003) 1873.
[65] M. Inamo, S. Funahashi, M. Tanaka, Inorg. Chem. 22 (1983) 3734.
[66] K. Takamura, C. Matsubara, T. Matsumoto, Anal. Sci. 24 (2008) 401.
[67] K. Takamura, T. Matsumoto, Anal. Bioanal. Chem. 391 (2008) 951.
[68] K. Takamura, T. Matsumoto, Appl. Spectrosc. 63 (2009) 579.
[69] C. Matsubara, N. Nakamichi, N. Kawamoto, K. Takamura, Bunseki Kagaku 42 (1993) 363.
[70] C. Matsubara, Y. Yokoi, M. Tsuji, K. Takamura, Anal. Sci. 11 (1995) 245.
[71] K. Takamura, N. Nakamichi, C. Matsubara, Bunseki Kagaku 53 (2004) 315.
[72] A. Iwado, M. Mifune, H. Akizawa, N. Motohashi, Y. Saito, J. Pharm. Biomed. Anal. 30 (2003) 1923.
[73] T. Yamane, T. Tsuchimoto, H. Yoshikawa, Bunseki Kagaku 53 (2004) 297.
[74] J. Itoh, J. Liu, M. Komato, Talanta 69 (2006) 61.
[75] Y. Li, J. Hu, J. Yang, B. Zheng, Y. Ha, Anal. Chim. Acta 461 (2002) 181.
[76] W. Zhang, E. Roznieka, E. Malinowska, P. Parzuchowski, M.E. Meyehoff, Anal. Chem. 74 (2002) 4548.
[77] M. Gouterman, D. Holten, E. Lieberman, Chem. Phys. 25 (1977) 139.
[78] Y. Kang, M.E. Meyerhof, Anal. Chim. Acta 565 (2006) 1.
[79] Z. Li, X. Li, M. Rothmaier, D.J. Harrison, Anal. Chem. 68 (1996) 1726.
[80] Z. Li, X. Li, S. Petrovic, D.J. Harrison, Anal. Chem. 68 (1996) 1717.
[81] Y. Kang, J.W. Kampf, M.E. Meyerhof, Anal. Chim. Acta 598 (2007) 295.
[82] K. Kilian, K. Pyrzynska, Anal. Sci. 18 (2002) 571.
[83] M. Knap, K. Kilian, K. Pyrzynska, Talanta 71 (2007) 406.
[84] Y.X. Ci, J.K. Tie, Q.W. Wang, W.B. Chang, Anal. Chim. Acta 269 (1992) 109.
[85] Y.X. Ci, Y.G. Zheng, J.K. Tie, W.B. Chang, Anal. Chim. Acta 282 (1993) 695.
[86] D. Yao, A.G. Vlessidis, N.P. Evmiridis, Anal. Chim. Acta 435 (2001) 273.
[87] S. Rana, Saudi Pharm. J. 13 (2005) 97.
[88] M.S. Rana, K. Tamagake, J. Electroanal. Chem. 581 (2005) 145.
[89] M.S. Rana, K. Tamake, Chem. Pharm. Bull. 53 (2005) 604.
[90] S. Rana, K. Tamake, Bioelectrochemistry 68 (2006) 31.
[91] L. Vong, A. Laes, S. Blain, Anal. Chim. Acta 588 (2007) 237.
[92] D. Papkovski, M.A. Uskova, G.V. Ponomarev, T. Korpela, S. Kulmala, G.G. Guilbault, Anal. Chim. Acta 374 (1998) 1.
[93] K. Araki, L. Angnes, C.M.N. Azevedo, H.E. Toma, J. Electroanal. Chem. 397 (1995) 205.
[94] L. Angnes, C.M.N. Azevedo, K. Araki, H.E. Toma, Anal. Chim. Acta 329 (1996) 91.
[95] C.M.N. Azevedo, K. Araki, H.E. Toma, L. Angnes, Anal. Chim. Acta 387 (1999) 175.
[96] J.R.C. da Rocha, L. Angnes, M. Bertotti, K. Araki, H.E. Toma, Anal. Chim. Acta 452 (2002) 23.
[97] S.V. Guerra, L.T. Kubota, C.R. Xavier, S. Nakagaki, Anal. Sci. 15 (1999) 1231.
[98] X.H. Li, Z.H. Xie, H. Min, Y.Z. Zian, L.T. Jin, Electroanalysis 19 (2007) 2551.
[99] S.S.M. Hassan, A.E. Kelany, S.S. Al-Mehrezi, Electroanalysis 20 (2008) 438.

Talanta 80 (2010) 1606–1610

Contents lists available at ScienceDirect

Talanta

journal homepage: www.elsevier.com/locate/talanta

Determination of colloidal and dissolved silver in water samples using colorimetric solid-phase extraction

April A. Hill[a,b], Robert J. Lipert[a,b], Marc D. Porter[c,*]

[a] Iowa State University, Institute for Combinatorial Discovery, Departments of Chemistry and of Chemical and Biological Engineering, Ames, IA 50011, United States
[b] Ames Laboratory – U.S. DOE, Ames, IA 50011-3020, United States
[c] Departments of Chemistry, Chemical Engineering, Bioengineering, and Pathology, University of Utah, Salt Lake City, UT 84108, United States

ARTICLE INFO

Article history:
Received 9 July 2009
Received in revised form
24 September 2009
Accepted 25 September 2009
Available online 3 October 2009

Keywords:
Solid-phase extraction
Diffuse reflectance spectroscopy
Colloidal silver
Silver(I)

ABSTRACT

The increase in bacterial resistance to antibiotics has led to resurgence in the use of silver as a biocidal agent in applications ranging from washing machine additives to the drinking water treatment system on the International Space Station (ISS). However, growing concerns about the possible toxicity of colloidal silver to bacteria, aquatic organisms and humans have led to recently issued regulations by the US EPA and FDA regarding the usage of silver. As part of an ongoing project, we have developed a rapid, simple method for determining total silver, both ionic (silver(I)) and colloidal, in 0.1–1 mg/L aqueous samples, which spans the ISS potable water target of 0.3–0.5 mg/L (total silver) and meets the US EPA limit of 0.1 mg/L in drinking water. The method is based on colorimetric solid-phase extraction (C-SPE) and involves the extraction of silver(I) from water samples by passage through a solid-phase membrane impregnated with the colorimetric reagent DMABR (5-[4-(dimethylamino)benzylidene]rhodanine). Silver(I) exhaustively reacts with impregnated DMABR to form a colored compound, which is quantified using a handheld diffuse reflectance spectrophotometer. Total silver is determined by first passing the sample through a cartridge containing Oxone, which exhaustively oxidizes colloidal silver to dissolved silver(I). The method, which takes less than 2 min to complete and requires only ~1 mL of sample, has been validated through a series of tests, including a comparison with the ICP-MS analysis of a water sample from ISS that contained both silver(I) and colloidal silver. Potential earth-bound applications are also briefly discussed.
© 2009 Elsevier B.V. All rights reserved.

1. Introduction

The increased antibiotic resistance of many bacteria has led to a renewed interest in silver as a biocidal agent. Silver has been used for its antimicrobial properties at least since the ancient Romans used silver coins to treat drinking water [1]. Indeed, antimicrobial coatings of colloidal silver are present in a wide variety of applications, including deodorizing shoe inserts, washing machines, and wound dressings [1,2]. There are, however, risks associated with its use. High levels of silver are toxic to human cells, which can slow healing in the case of wound care. Other problems associated with silver include argyria, which is a condition characterized by a permanent blue-gray discoloration of the skin [3].

In light of these issues, the FDA ruled that over-the-counter products containing silver colloids or its salts are not generally recognized as safe for human use [2,4]. Moreover, the US EPA has been petitioned to regulate colloidal silver as a pesticide [5]. These dictates highlight the need for rapid, simple, field-deployable methods for determining colloidal silver concentrations in liquid samples. Test kits for the determination of silver(I) are available, most of which are based on colorimetric reagents that are "read-out" by a visual color matching of test strips or liquid samples. These methods, however, typically require large sample volumes (e.g., 10–100 mL), deliver only semi-quantitative results, and often use potentially hazardous, highly acidic reaction conditions [6–8]. Furthermore, none of these methods can be applied to the detection of colloidal silver.

This paper details the development and testing of a method capable of determining both colloidal and ionic silver (silver(I)) in water samples in under 2 min. Though clearly useful in many earth-bound applications, this method was created as part of an effort to monitor total silver concentrations in the potable water supply on the International Space Station (ISS), which employs electrolytically generated silver (i.e., colloidal silver and silver(I)) as a biocidal agent [9]. ISS documentation lists a target level for total silver of 0.3–0.5 mg/L to ensure effective biocidal activity while limiting exposure to ISS crewmembers [9]. At present, the approach to monitoring ISS water quality relies on samples returned to Earth for analysis by techniques like ICP-MS [10]. Unfortunately, the gap between sample collection and analysis can span several months, preventing the timely implementation of correction scenarios. The development of rapid, on-board methods for monitoring trace lev-

* Corresponding author. Tel.: +1 801 587 1505; fax: +1 801 585 0575.
E-mail address: marc.porter@utah.edu (M.D. Porter).

0039-9140/$ – see front matter © 2009 Elsevier B.V. All rights reserved.
doi:10.1016/j.talanta.2009.09.056

els of critical components in spacecraft drinking water is therefore a priority for NASA. Importantly, these methods must have sufficient selectivity and sensitivity to detect analytes at low concentrations, be user-friendly, compact, lightweight, capable of operation in microgravity, and employ non-toxic materials. Recent reports from our laboratory have demonstrated that colorimetric solid-phase extraction (C-SPE) meets many of these requirements [11–26]. Indeed, a 6-month validation test of C-SPE on ISS (see below) is scheduled to begin before the end of 2009.

C-SPE typically involves the extraction of an analyte from a water sample by its passage through a solid-phase membrane impregnated with a colorimetric reagent. Using diffuse reflectance spectroscopy (DRS), quantification of the analyte after reaction with the colorimetric reagent is accomplished via a calibration plot of the Kubelka–Munk function [27,28]. The complete procedure usually requires less than 2 min per analysis. Note that impregnating the extraction membranes with colorimetric reagents eliminates the need to handle solvents and chemicals throughout sample workup, minimizing the exposure of crewmembers to hazardous materials. The use of a solid-phase extraction membrane also results in concentration factors on the order of 1000, leading to low limits of detection [29].

To date, our laboratory has developed C-SPE methods for the NASA-based biocides iodine (I_2) [11,20,30], silver(I) [12,20], the heavy metals nickel(II) [16,22], chromium(VI) [22], copper(II) [22], iron(III) [22], and formaldehyde [26]. We have also assessed the performance of C-SPE in microgravity flight simulations [15,20,23], which in tests to date have shown excellent agreement between flight and ground-based analyses of iodine and silver(I) [24,25].

The existing C-SPE method for silver(I) employs the colorimetric reagent DMABR (5-[4-(dimethylamino)benzylidene]rhodanine) [12,20], which is both sensitive and selective for silver(I), even in the presence of many common interferents [20]. However, as DMABR is unreactive to colloidal silver, we examined the use of an oxidizing agent as an additive to the collected water sample to exhaustively convert colloidal silver to silver(I). This paper presents the development and testing of a C-SPE method for determining the total silver content (i.e., colloidal silver and silver(I)) in drinking water using the well-known oxidizing agent Oxone.

Oxone, a potassium triple salt ($2KHSO_5 + KHSO_4 + K_2SO_4$), was selected for a number of reasons. It is: (1) readily dissolved in water, but very stable in powder form; (2) non-toxic, as evidenced by its popularity as an ingredient in denture cleansers and swimming pool disinfectant [31]; and (3) already approved for use on-board NASA spacecraft, being employed to pre-treat urine before its storage in the waste collection system [32]. The active ingredient in Oxone is potassium monopersulfate ($KHSO_5$), a neutralization salt of peroxymonosulfuric acid. Oxone solutions are slightly acidic, and are often buffered when used in cleansers to near-neutral pH by alkaline salts like sodium carbonate [31]. Our technique also uses sodium carbonate to raise the pH of the solution following oxidation of the silver. This step prevents Oxone from oxidizing, and hence decolorizing, the colorimetric reagent DMABR. The resulting C-SPE method determines the total concentration of colloidal and dissolved silver in the range of 0.1–1 mg/L in less than 2 min and, when combined with the existing C-SPE method for silver(I), provides the capability to determine colloidal silver in the presence of dissolved silver.

2. Experimental

2.1. Reagents

All solutions were made daily with deionized water prepared with Millipore Milli-Q water purification system.

2.1.1. Silver(I) sample solutions

Solutions with dissolved silver concentrations between 0.25 and 1.0 mg/L were prepared by diluting the appropriate mass of a 996 mg/L silver atomic absorption standard (Sigma–Aldrich) with deionized water.

2.1.2. Colloidal silver samples

Silver nanoparticle (20, 40, 60, and 80 nm in diameter) suspensions were purchased from Ted Pella at respective concentrations of 7.0×10^{11}, 9.0×10^{10}, 2.6×10^{10}, and 1.1×10^{10} particles/mL. These sizes were chosen to mimic the range found in ISS water, which is "silverized" by an electrolytic technique [10]. The actual concentration of silver, when converted to silver(I) in each suspension was determined by ICP-MS, and equaled (within 2.55% or less) 6.05, 5.91, 5.96, and 5.77 mg/L for the 20, 40, 60, and 80-nm particles, respectively. Colloidal silver samples were prepared by diluting either the 80 nm colloidal suspension or a mixture containing equal volumes of all four colloidal suspensions. The amount of silver, given as silver(I), in each sample solution was verified by ICP-MS.

2.1.3. Extraction cartridges

Two solutions were used for disk impregnation. The colorimetric reagent for silver(I) was prepared by dissolving 0.060 g DMABR (Aldrich) in 20 mL of dimethyl formamide in a 100 mL volumetric flask. After sonicating for ~5 min to dissolve DMABR, the solution was brought to volume using methanol. A second solution was prepared by pipetting 3.0 g of Brij 30 surfactant (Aldrich) into a Nalgene bottle and bringing the total mass to 100 g with deionized water.

These solutions were used to impregnate 3M Empore SDB-XC (polystyrene-divinylbenzene) 47 mm extraction membranes. Each membrane was placed into an all-glass filter holder assembly (Millipore), and 10.0 mL of the DMABR solution was pipetted into the funnel. Using a vacuum pump, a pressure differential of ~1 in. of Hg was applied to drive the solution through the membrane. After the DMABR solution had passed through the membrane, the pressure differential was maintained for another 10 s to remove residual liquid. The vacuum was then removed, the funnel on the glass filter holder was replaced with a second funnel, and 5.0 mL of the Brij 30 solution was added via a pipette. A vacuum-derived pressure difference of ~3.5 in. Hg was applied to pass the Brij 30 solution through the membrane. This pressure differential was subsequently increased to ~20 in. Hg for 30 s to dry the membrane. The addition of Brij 30 markedly enhances the uptake of water by the membrane, which we believe creates a microenvironment conducive to the rapid reaction of silver(I) with impregnated DMABR; there is no detectable complexation in the absence of this additive [12].

After impregnation, the membranes were fully dried by storage in the dark for ~16 h, cut into 13 mm disks, and placed on the support screen in the bottom portion of a Swinnex polypropylene filter holder (Millipore). The holder was assembled by sealing against a silicone gasket (11 mm inner diameter), which also defines the area of the disk exposed to the water sample.

2.1.4. Oxone cartridges

Oxidant-impregnated disks were prepared by pipetting a 1.0 mL aliquot of 300 mg/mL Oxone (Aldrich) in deionized water onto a 47 mm diameter glass fiber filter (Millipore). These filters were dried in an oven at 110 °C for ~1 h before being cut into 13 mm disks and loaded into Swinnex filter holders as described in Section 2.1.3. These holders contained ~25 mg Oxone.

2.1.5. Sodium carbonate cartridges

A 2.0 mL aliquot of 200 mg/mL sodium carbonate in deionized water was pipetted onto a 45 mm diameter media pad (Millipore) in a Petri dish. The pad was heated for ~20 min (110 °C) until excess

liquid had evaporated, leaving a saturated pad, and then cut into 9 mm disks. These disks, which contained ~16 mg sodium carbonate, were dried again at 110 °C for ~2 h, and then loaded into Swinnex filter holders.

2.2. Instrumentation

A BYK-Gardner color-guide sphere (d/8°) diffuse reflectance spectrophotometer (Model LCB-6830) was used to analyze the disks. This handheld spectrophotometer is small, lightweight, and battery-powered, and can collect reflectance data from 400 to 700 nm in 20 nm intervals in under 2 s [15]. The diffuse reflection spectra were used to calculate the Kubelka–Munk function ($F(R)$), which is given by Eq. (1) [27]:

$$F(R) = \frac{(1-R)^2}{2R} \quad (1)$$

where R is the diffuse reflectance measured relative to a reflectance standard. Note that the $F(R)$ at a given wavelength is directly related to the concentration of the complex in the membrane, C, by Eq. (2):

$$F(R) = \frac{2.303\varepsilon C}{s} \quad (2)$$

where ε is the molar absorptivity of the colorimetric product and s is the scattering coefficient of the sample surface, both of which are assumed constants [28].

3. Results and discussion

3.1. Overview of C-SPE method for silver(I)

Fig. 1a summarizes key components of the existing C-SPE method for silver(I). In Step 1, a 1.0 mL aqueous sample is collected in a 1 mL polypropylene syringe and passed through an extraction cartridge containing a DMABR reagent disk in Step 2. A second syringe is then used to pass ~60 mL of air through the cartridge to dry the disk. The cartridge is opened and the diffuse reflection spectrum of the reagent disk is acquired in Step 3.

Representative DRS data for the C-SPE analysis of silver(I) are presented in Fig. 1b. The reflectance at 580 nm is used to calculate $F(R)$ which, when used to prepare a calibration plot, yields a detection limit of 0.1 mg/L silver(I). Earlier tests of this method, which included interference studies, validated its effectiveness in measuring silver(I) levels in a wide range of ISS water samples [12,20].

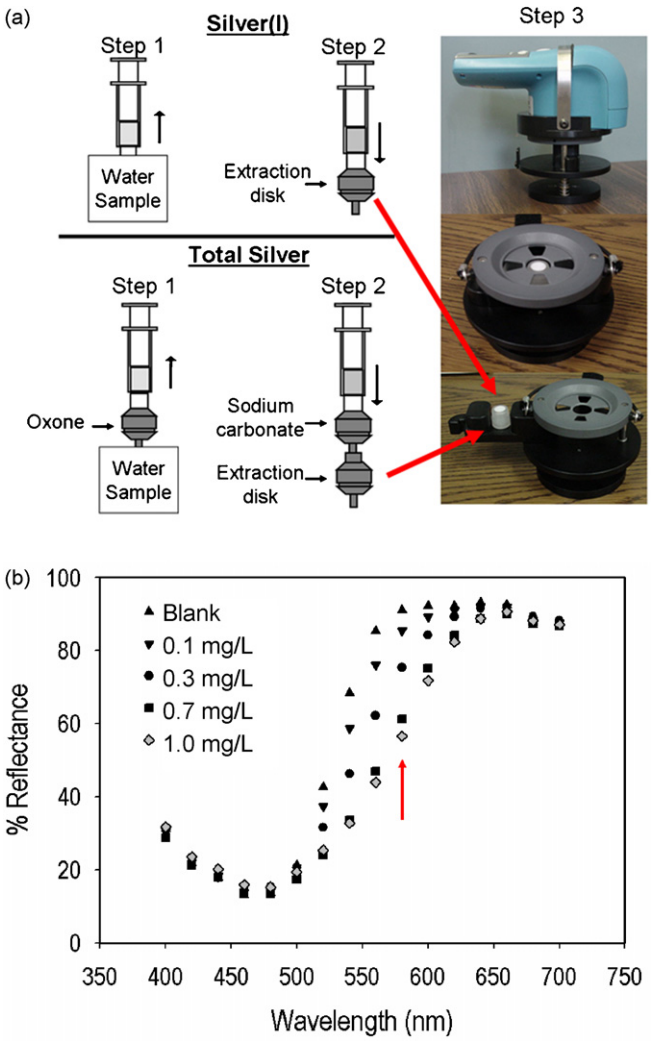


Fig. 1. (a) Schematic of the procedures for determining silver(I) and total silver by C-SPE. For both methods, Step 1 is sample collection, Step 2 is analyte extraction, and Step 3 is membrane interrogation using the handheld DRS instrument and sample holder. (b) Representative DRS data from an analysis of silver(I). The $F(R)$ value calculated from the reflectance at 580 nm is used for analyte quantification.

3.2. Assessment of Oxone as an oxidizing agent

To determine the efficiency of Oxone as an oxidizing agent for colloidal silver, various amounts of this reagent were added to separate suspensions (1.0 mL) of 0.57 mg/L colloidal silver (80 nm). After stirring, the reaction was allowed to proceed for 1 h, and the concentration of silver(I) was determined by C-SPE and ICP-MS. These results indicated that the optimum amount of Oxone needed to exhaustively convert colloidal silver to silver(I) is ~6 mg/mL. Moreover, higher levels of Oxone induced a rapid fading of impregnated DMABR from orange-yellow to white.

To determine the time required for Oxone to dissolve colloidal silver, a second set of the same test suspensions was prepared, vigorously mixed with Oxone (~6 mg) for 20 s, allowed to react for different lengths of time, and analyzed by C-SPE. The results, plotted in Fig. 2, indicate that the method requires ~1 h to fully dissolve the collected particles in the suspension, which is not only much too long in view of the time demands of crew members on ISS but also likely to be problematic for field-deployment on earth.

As mentioned, Oxone solutions are slightly acidic and often modified with alkaline salts to maintain a neutral pH. One example

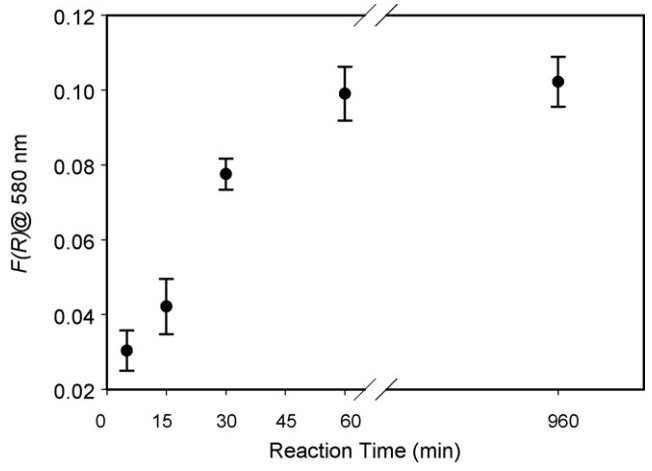


Fig. 2. Plot of KM function ($n = 3$) vs. reaction time for the C-SPE determination of total silver using ~6 mg/mL Oxone as an oxidizing agent and a sample containing 80 nm colloidal silver at a concentration of 0.57 mg/L.

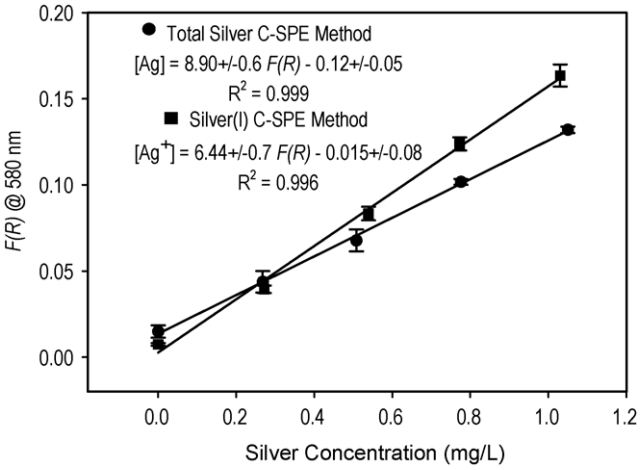


Fig. 3. Calibration plot of the C-SPE method for total silver, which uses ~25 mg/mL Oxone as an oxidizing agent and sodium carbonate to neutralize the excess Oxone before the extraction step. A calibration plot for the silver(I) C-SPE method is provided for comparison. Each plot was generated by carrying out the corresponding procedure in triplicate on samples prepared by diluting a silver atomic absorption standard. The uncertainties in the coefficients represent 95% confidence intervals.

mixes sodium carbonate and Oxone in a 1:4 mass ratio to create a pool disinfectant at neutral pH [31]. Initial tests of the effectiveness of combining sodium carbonate and Oxone (using another set of the same colloidal suspensions) showed that: (1) much higher concentrations of Oxone can be employed without any visible deterioration of the impregnated DMABR and (2) the conversion rate of colloidal silver to silver(I) increased with the Oxone concentration.

We also found that adding sodium carbonate before the Oxone notably reduced the amount of silver(I) produced at short reaction times. This situation can be explained by the fact that Oxone relies on peracid chemistry for colloidal silver oxidation, and therefore has a strong pH dependence, as shown by the reaction in Eq. (3) [31]. As such, sodium carbonate affects the sample in two ways. It neutralizes the hydrogen ions in the sample and decreases the oxidation strength of residual Oxone, both of which affect the color of impregnated DMABR.

$$HSO_5^- + 2H^+ + 2e^- \rightarrow HSO_4^- + H_2O, \quad E^\circ = +1.85\,V\,(NHE) \qquad (3)$$

3.3. C-SPE method for total silver using Oxone and sodium carbonate

Based on these initial assessments, a procedure for the C-SPE determination of total silver using the Oxone/sodium carbonate method, illustrated in Fig. 1a, was developed and tested. In Step 1, an Oxone cartridge is connected to a 3 mL Luer Lock polypropylene syringe and an aqueous sample containing colloidal silver is drawn into the syringe, passing through the cartridge and dissolving the ~25 mg of Oxone. Roughly 1.1 mL of sample is pulled into the syringe, along with air (~1 mL) from the dead volume of the cartridge. The Oxone cartridge is removed and the syringe capped and shaken by hand for ~20 s. The air and excess liquid are then expelled from the syringe to yield a 1.0 mL sample volume. In Step 2, the metered sample is passed through a sodium carbonate cartridge and then an extraction cartridge. These two cartridges are connected in series. Next, the sample syringe is separated from the cartridge assembly and replaced by a 60 mL syringe. About 60 mL of air are passed through the two-cartridge assembly to drive any sample remaining in the cartridge through the extraction disk and to dry the disk. Finally, the holder is disassembled and the diffuse reflectance spectrum of the reagent disk is acquired. The entire process requires less than 2 min to complete.

Table 1
Validation data of the C-SPE method for total silver using colloid silver suspensions. The three colloidal silver samples were prepared by mixing equal volumes of the 20, 40, 60, and 80 nm silver colloid solutions (such that each particle size accounts for ~25% of the total silver concentration) and diluting with deionized water.

Colloidal sample[a]	Total silver concentration (mg/L) by ICP-MS	Total silver concentration (mg/L) by C-SPE
1	0.95 ± 0.05	1.03 ± 0.09
2	0.42 ± 0.02	0.42 ± 0.01
3	0.12 ± 0.01	0.12 ± 0.01

[a] See Section 3.3 for additional information on sample preparation.

The calibration plot shown in Fig. 3 was obtained by performing this procedure in triplicate on solutions containing silver(I) at concentrations from 0 to 1.0 mg/L. For comparison, a plot of the response obtained from the C-SPE method for silver(I) (i.e., no Oxone or sodium carbonate) over this concentration range is also presented. The small differences between the two plots are an indication of the effects of Oxone and sodium carbonate on the membranes (see below). In spite of the slight deviation, the new method gives a linear response over the concentration range of importance to NASA, with a calculated limit of detection (using three times the standard deviation of the blank) of 0.1 mg/L silver. This value is comparable to the LOD of our silver(I) method (0.06 mg/L silver(I)), and is at the EPA limit set for silver(I) levels in drinking water.

To evaluate the developed method for use with samples containing colloidal silver, three samples were created by first mixing 2.0 mL aliquots of each silver colloid suspension (20, 40, 60, and 80 nm), and diluting the mixture with deionized water to give three sample solutions with approximate concentrations of 1, 0.5, and 0.15 mg/L silver. These samples were analyzed by ICP-MS and by the total silver C-SPE method. Using the calibration plot in Fig. 3, the concentration of total silver detected by C-SPE in each sample was calculated from the average $F(R)$ value at 580 nm ($n = 3$). As evident in Table 1, all the values given by the C-SPE method match those given by ICP-MS to within 10% (or better), demonstrating the validity of the new total silver method.

Interestingly, the data in Table 1 show that the error in the C-SPE measurement is the largest at the highest concentration of colloidal silver. Coupled with the deviation found in Fig. 3, we attribute this finding to the fact that samples with higher concentrations of colloidal silver reduce more of the Oxone present in the sample, leading to a relative excess of sodium carbonate. The result is a slight increase in the alkalinity of the sample, which causes a small change in the color of the membrane. This is a minor issue, however, since the accuracy of these determinations is on a level comparable to that for other C-SPE methods.

To assess the effect of colloidal silver on the analysis of silver(I) by C-SPE, suspensions containing 80-nm silver colloids at concentrations between 0 and 1.0 ppm Ag were analyzed by the C-SPE method for silver(I). The average $F(R)$ at 580-nm ($n = 3$) for all concentrations tested fell within two standard deviations of the $F(R)$ for the blank. Therefore, we can conclude that the presence of colloidal silver has a negligible effect on the silver(I)-sensitive membranes. These results indicate that C-SPE can be used to determine the concentration of colloidal silver in the presence of silver(I) by simply subtracting the concentration given by the silver(I) method from that given by the total silver method.

As a further validation of the C-SPE method for total silver, a sample of potable water from ISS, which was returned to Earth by the shuttle Endeavour (Mission STS-97) on December 11, 2000 and stored at ~5 °C, was analyzed by ICP-MS ($n = 10$) and by the silver(I) and total silver C-SPE methods ($n = 3$). The results of this analysis, presented in Table 2, demonstrate that (a) the total silver method can rapidly detect all of the silver present in the potable

Table 2
Validation data of the C-SPE method for total silver using an ISS potable water sample containing electrolytically generated silver.

	Method			
	ICP-MS	Total silver C-SPE	Silver(I) C-SPE	Colloidal silver[a]
Silver (mg/L)	0.45 ± 0.02	0.45 ± 0.05	0.32 ± 0.03	0.13 ± 0.06

[a] Colloidal silver concentration calculated by subtracting silver(I) concentration from total silver concentration.

water supplies of ISS and (b) the combination of the silver(I) and total silver methods allows for the determination of colloidal silver in the presence of silver(I).

4. Conclusions

A rapid, simple method for reliably determining total silver has been developed. This method uses Oxone, a relatively safe and readily available oxidizing agent, to convert colloidal silver to silver(I), which is then detected using C-SPE. The entire procedure requires less than 2 min to complete, making this method an attractive option for a wide variety of applications. Moreover, by combining this new method with our C-SPE analysis of silver(I), colloidal silver concentrations can be determined in the presence of silver(I), thus enabling a rapid determination of silver speciation in aqueous samples.

This work has also presented preliminary data validating the potential utility of the total silver C-SPE method for determining the biocidal silver present in spacecraft water supplies. Present plans call for performance tests of this method in microgravity aboard NASA's C-9 aircraft, and we hope to report on results from an upcoming 6-month test on ISS of our C-SPE methods for biocidal silver and iodine in the near future. There is also considerable potential for earth-bound applications of this method, based on the widespread growth in the use of colloidal silver as a biocidal agent in recent years, particularly in view of the fact that this method is a viable alternative to the more expensive (ICP-MS) and less effective (test strip) methods currently available. Work to this end is also underway.

Acknowledgements

The authors would like to acknowledge Jeff Rutz, Dan Gazda and John Schultz of Wyle Laboratories for insightful discussions and for providing the ISS water sample. The expert input and assistance of Lorraine Siperko of the University of Utah is also noted. This work was supported by NASA contract NAG91510. The Ames Laboratory is operated by Iowa State University under U.S. Department of Energy contract DE-AC02-07CH11358.

References

[1] B. Halford, Chem. Eng. News 84 (16) (2006) 35–36.
[2] S. Morrissey, Chem. Eng. News 84 (49) (2006) 14.
[3] D. Brandt, B. Park, M. Hoang, H.T. Jacobe, J. Am. Acad. Dermatol. 53 (2005) S105–S107.
[4] Department of Health and Human Services, Food and Drug Administration, Federal Register 1999, 64, pp. 44653–44658.
[5] United States Environmental Protection Agency 1993, EPA-738-F-93-005.
[6] LaMotte Silver Test Kit Information, http://www.lamotte.com/pages/common/pdf/instruct/3617.pdf, 2007.
[7] Hach RapidSilver Visual Silver Test Kit Manual, http://www.hach.com/fmmimghach?/CODE%3A2674588912%7C1, 2007.
[8] HMT Silver Test Kit: How to Test, http://www.heavymetalstest.com/_agtest.php, 2007.
[9] Technical Requirements Specification Document for the ISS Water Transfer Hardware, JSC-39223, NASA-JSC, June 1999.
[10] D.K. Plumlee, 32nd International Conference on Environmental Systems, San Antonio, TX, 2002 (SAE Technical Paper #2002-01-2537).
[11] M.P. Arena, M.D. Porter, J.S. Fritz, Anal. Chem. 74 (2002) 185–190.
[12] M.P. Arena, M.D. Porter, J.S. Fritz, Anal. Chim. Acta 482 (2003) 197–207.
[13] N.C. Dias, J.S. Fritz, M.D. Porter, 35th International Conference on Environmental Systems, Rome, Italy, 2005 (SAE Technical Paper #2005-01-3065).
[14] N.C. Dias, D.B. Gazda, J.S. Fritz, M.D. Porter, 34th International Conference on Environmental Systems, Colorado Springs, CO, 2004 (SAE Technical Paper #2004-01-2539).
[15] D.B. Gazda, R.J. Lipert, J.S. Fritz, M.D. Porter, J. Rutz, P. Mudgett, J. Schultz, 33rd International Conference on Environmental Systems, Vancouver, B.C., Canada, 2003 (SAE Technical Paper #2003-01-2406).
[16] D.B. Gazda, J.S. Fritz, M.D. Porter, Anal. Chim. Acta 508 (2004) 53–59.
[17] D.B. Gazda, J.S. Fritz, M.D. Porter, Anal. Chem. 76 (2004) 4881–4887.
[18] J. Nordling, R.J. Lipert, M.D. Porter, D.B. Gazda, 35th International Conference on Environmental Systems, Rome, Italy, 2005 (SAE Technical Paper #2005-01-2891).
[19] C.J. Shih, N.C. Dias, M.D. Porter, 35th International Conference on Environmental Systems, Rome, Italy, 2005 (SAE Technical Paper #2005-01-2890).
[20] M.P. Arena, M.D. Porter, J.S. Fritz, P. Mudgett, J. Rutz, J. Schultz, 32nd International Conference on Environmental Systems, San Antonio, TX, 2002 (SAE Technical Paper #2002-01-2535).
[21] N.C. Dias, M.D. Porter, J.S. Fritz, Anal. Chim. Acta 558 (2006) 230–236.
[22] J.S. Fritz, M.P. Arena, S.A. Steiner, M.D. Porter, J. Chromatogr. A 997 (2003) 41–50.
[23] L.M. Ponton, D.B. Gazda, R.J. Lipert, J.S. Fritz, M.D. Porter, J. Rutz, P. Mudgett, D. Dungan, J. Schultz, 33rd International Conference on Environmental Systems, Vancouver, B.C., Canada, 2003 (SAE Technical Paper #2003-01-2408).
[24] M. Porter, M. Arena, D. Weisshaar, P. Mudgett, J. Rutz, M. Benoit, Colorimetric solid phase extraction measurements of spacecraft drinking water contaminants, in: KC-135 Postflight Report, 2004.
[25] M.D. Porter, J.T. McCoy, A.A. Hazen-Bosveld, R.J. Lipert, J. Nordling, C.J. Shih, D.B. Gazda, J. Rutz, J. Straub, J. Schultz, J. Alverson, Colorimetric solid phase extraction measurements of spacecraft drinking water contaminants, in: C-9 Postflight Report, 2006.
[26] A.A. Hill, R.J. Lipert, J.S. Fritz, M.D. Porter, Talanta 77 (2009) 1405–1408.
[27] G. Kortum, Reflectance Spectroscopy: Principles, Methods, Applications, Springer, New York, 1969.
[28] J.P. Blitz, in: F.M. Mirabella (Ed.), Modern Techniques in Applied Molecular Spectroscopy, John Wiley & Sons, Inc., New York, 1998, pp. 185–217.
[29] J.S. Fritz, Analytical Solid-Phase Extraction, John Wiley & Sons, Inc., New York, 1999.
[30] D.B. Gazda, R.J. Lipert, J.S. Fritz, M.D. Porter, Anal. Chim. Acta 510 (2004) 241–247.
[31] DuPont Oxone Monopersulfate Compound Technical Information, http://www.dupont.com/oxone/techinfo/index.html, 1998.
[32] S.G. Howard, C.F. Hutchens, D.W. Rethke, V.L. Swartley, R.W. Marsh, 28th International Conference on Environmental Systems, Danvers, MA, USA, 1998 (SAE Technical Paper #981620).

Talanta 80 (2010) 1611–1618

Contents lists available at ScienceDirect

Talanta

journal homepage: www.elsevier.com/locate/talanta

Dispersive liquid–liquid microextraction versus single-drop microextraction for the determination of several endocrine-disrupting phenols from seawaters

Jessica López-Darias [1], Mónica Germán-Hernández [1], Verónica Pino *, Ana M. Afonso

Departamento de Química Analítica, Nutrición y Bromatología, Universidad de La Laguna (ULL), avda. Astrofísico Francisco Sánchez s/n, 38206 La Laguna (Tenerife), Spain

ARTICLE INFO

Article history:
Received 28 April 2009
Received in revised form
21 September 2009
Accepted 25 September 2009
Available online 4 October 2009

Keywords:
Single-drop microextraction
Dispersive liquid–liquid microextraction
Endocrine-disrupting phenols
Seawater analysis

ABSTRACT

Two liquid-phase microextraction procedures: single-drop microextraction (SDME) and dispersive liquid–liquid microextraction (DLLME), have been developed for the determination of several endocrine-disrupting phenols (EDPs) in seawaters, in combination with high-performance liquid chromatography (HPLC) with UV detection. The EDPs studied were bisphenol-A, 4-cumylphenol, 4-tertbutylphenol, 4-octylphenol and 4-*n*-nonylphenol. The optimized SDME method used 2.5 μL of decanol suspended at the tip of a micro-syringe immersed in 5 mL of seawater sample, and 60 min for the extraction time. The performance of the SDME is characterized for average relative recoveries of 102 ± 11%, precision values (RSD) < 9.4% (spiked level of 50 ng mL^{-1}), and detection limits between 4 and 9 ng mL^{-1}. The optimized DLLME method used 150 μL of a mixture acetonitrile:decanol (ratio 15.7, v/v), which is quickly added to 5 mL of seawater sample, then subjected to vortex during 4 min and centrifuged at 2000 rpm for another 5 min. The performance of the DLLME is characterized for average relative recoveries of 98.7 ± 3.7%, precision values (RSD) < 7.2% (spiked level of 20 ng mL^{-1}), and detection limits between 0.2 and 1.6 ng mL^{-1}. The efficiencies of both methods have also been compared with spiked real seawater samples. The DLLME method has shown to be a more efficient approach for the determination of EDPs in seawater matrices, presenting enrichment factors ranging from 123 to 275, average relative recoveries of 110 ± 11%, and precision values (RSD) < 14%, when using a real seawaters (spiked level of 3.5 ng mL^{-1}).

© 2009 Elsevier B.V. All rights reserved.

1. Introduction

Several environmental contaminants, termed as endocrine disrupting chemicals (EDCs), can interfere with the function of the endocrine system in living organisms [1,2]. Chemical exposure to EDCs has been linked to neurological and reproductive effects on fish and wildlife [1,3], and may also affect human fertility [4]. These findings have raised public concern over their environmental and human health effects. Sewage treatment plants (STP) effluent outfalls constitute significant sources of EDCs to the receiving surface, coastal waters and regional environments [5,6], thus increasing the risk of exposure. Among the increasing list of substances classified as EDCs, an important attention has been paid to a selected group of endocrine-disrupting phenols (EDPs), alkylphenols (APs), including nonylphenol (NP) and bisphenol-A (BPA), due to their wide presence in household and industrial processes [5].

A number of analytical methods have been employed to determine EDPs in the aquatic environment, including drinking water, river water and wastewater [7–10]. Limited data are present in the literature about EDC determinations in marine water [11–13], due to the complexity of the salty matrix. Many conventional methods used to obtain quantitative extractions for APs are characterized as being labor-intensive and time-consuming, because in most cases derivatization and/or solvent-exchange steps are needed [6,13,14]. The conventional extraction methods are also hazardous to human health as they often use large amounts of organic solvents, which are known for being hazardous, flammable, and damaging to the environment. These disadvantages have been the basis of a trend to develop analytical methods aimed at eliminating, or at least minimizing, the organic solvent consumption in sample preparation [15]. Solid-phase microextraction (SPME) [16] and liquid-phase microextraction (LPME) [17,18] can be highlighted among them.

Single-drop microextraction (SDME) [18–20] is a liquid-phase microextraction technique which consists of the suspension of a drop of a solvent (typically few micro-liters of an organic solvent) at the tip of a micro-syringe. The drop, in which analytes suffer partitioning, is exposed to the sample, then retracted into the syringe and transferred to an appropriate analytical system. SDME can be conducted in headspace or in direct immersion mode, and it includes many advantages such as low cost and little sample and solvent consumption. It combines extraction, preconcentration and sample introduction in one step. In addition to this, the possibility of carry over between analyses is negligible.

* Corresponding author. Tel.: +34 922 318012; fax: +34 922 318090.
E-mail addresses: veropino@ull.es, vero_pino@terra.es (V. Pino).
[1] These authors contributed equally to this work.

0039-9140/$ – see front matter © 2009 Elsevier B.V. All rights reserved.
doi:10.1016/j.talanta.2009.09.057

Dispersive liquid–liquid microextraction (DLLME) is another recent microextraction technique [21,22] which employs a mixture of a non-water-miscible extraction solvent and a water miscible polar disperser solvent. Analytes experience enrichment in the low volume of extraction solvent which is dispersed into the bulk aqueous solution, and separated by centrifugation. DLLME is a successful extraction technique due to the high contact surface of fine droplets of extraction solvent and analytes, which speeds up the mass transferring processes of analytes from aquatic phase to the extractant organic phase. DLLME presents characteristics of homogeneous liquid–liquid extraction and cloud-point extraction. Some advantages of DLLME are simplicity of operation, rapidity, low sample volume, low cost and high enrichment factor.

Main analytical applications of these two liquid-phase microextraction techniques, SDME and DLLME, have been conducted in combination with GC, HPLC and AAS [20–28].

The main purpose of this work was to carry out a comparison of the two liquid-phase microextraction techniques: single-drop microextraction and dispersive liquid–liquid microextraction, for the determination of a group of endocrine-disrupting phenols in seawaters close to a STP plant. To our knowledge, this is the first report in which both microextraction procedures are used in the analysis of this group of EDPs from seawaters.

2. Experimental

2.1. Reagents

The endocrine-disrupting phenols (EDPs) used in this study were bisphenol-A (BPA), 4-cumylphenol (4-CP), 4-tertbutylphenol (*t*-BP), 4-octylphenol (OP), and 4-*n*-nonylphenol (NP). They were all supplied by Sigma–Aldrich Chemie GmBH (Steinheim, Germany) except for NP, which was supplied by Alfa-Aesar (Karlsruhe, Germany). Individual standard solutions of these EDPs were prepared in acetonitrile of HPLC gradient quality (Merck, Darmstadt, Germany), with individual concentrations of 400 mg L^{-1}. Working standard solutions were prepared by adequate dilutions of these individual standards. 1-Decanol of 99% purity was obtained from Sigma–Aldrich.

Preparation of the artificial seawater was carried out by dissolving the following salts in 1 L of deionized water: NaF (3 mg), KBr (100 mg), $Na_2SiO_3{\cdot}9H_2O$ (20 mg), $SrCl_2{\cdot}H_2O$ (20 mg), KCl (3 mg), $MgCl_2{\cdot}6H_2O$ (10.780 g), $NaHCO_3$ (200 mg), H_3BO_3 (30 mg), $CaCl_2{\cdot}2H_2O$ (1.470 g) and NaCl (23.500 g) [29]. All of these pro-analysis salts were supplied by Merck. Deionized water was obtained from a Milli-Q gradient A10 system (Millipore, Watford, UK).

Real seawater samples came from two quite different sampling areas in Tenerife Island: the coasts of Candelaria and the surroundings of a petroleum refinery, where effluent waters are discharged from a STP. Amber glass bottles 100 mL in volume were used for sampling. Seawaters from Candelaria characteristically presented a content of 3.8 mg L^{-1} in suspended solids, a pH of 8.1, a content of dissolved oxygen of 8.0 mg L^{-1}, and a salinity value of 36.2 g L^{-1}. Seawaters close to the refinery had a variable content in terms of suspended solids, from 3.4 to 5.6 mg L^{-1}, salinity values, from 36.3 to 36.7 g L^{-1}, and dissolved oxygen, from 7.1 to 8.3 mg L^{-1} (depending on the sample location), and an average pH of 8.2.

Acetonitrile of gradient quality (Merck) and deionized water were used for HPLC analysis.

2.2. Instrumentation

The HPLC equipment consisted of a gradient system L-2130 Merck Hitachi Pump (supplied by Merck) and a Rheodyne valve (Supelco, Bellefonte, PA, USA) with a 20 μL loop. The detection of EDPs was carried out using a Waters Lambda Max 481 UV detector (Milford, MA, USA). The analytical column was a C18 Res Elut HPLC Column (5 μm, 150 mm × 4.6 mm) supplied by Varian (Harbor City, CA, USA), and protected by a Pelliguard LC-18 guard column (Supelco). Data were acquired with the Autoanalysis 2.4 software (Sciware, victor.cerda@uib.es). The HPLC method used for the separation and determination of the EDPs consists of a gradient elution procedure with a UV detector operating at 228 nm. For the mobile phase, a mixture of acetonitrile and water was used at a flow-rate of 1 mL min^{-1}. A linear gradient was employed from 50 to 80% of acetonitrile over 8 min, and then 80% of acetonitrile was maintained for 9 min.

A vortex model reax-control from Heidolph Instruments GmbH (Schwabach, Germany) and a centrifuge model EBA3 S from Hettich-Zentrifugen (Tuttlingen, Germany) were used in all DLLME experiments. A magnetic stirrer model Ikamag RCT basic (IKA Werke GmbH, Staufen, Germany) was used in all SDME experiments.

The Statgraphic (Statistical Graphics, Rockville) software package Version 5.1 was used for the statistical treatment.

2.3. Procedures

The syringe used for single-drop microextraction experiments, dispersive liquid–liquid microextraction experiments, and sample injection, was 25 μL in volume and from Hamilton (Bonaduz, Switzerland).

In SDME experiments, the vial was placed on the magnetic stirrer. The optimized technique is performed by suspending a 2.5 μL drop of decanol at the tip of the 25 μL micro-syringe immersed in the 5 mL of aqueous solution (7 mL vial) stirred at 100 rpm. The aqueous solution was a real seawater sample (spiked or not) or an artificial seawater sample (spiked). Following sample extraction, the magnetic stirrer was switched off and the drop was withdrawn into the syringe. Then, acetonitrile (Scharlau) was withdrawn into the syringe to complete around 20 μL. After the needle tip was carefully cleaned with a tissue, the content of the syringe was injected into the HPLC for analysis. The overall SDME method calibration was performed using artificial seawater calibration solutions submitted to the same SDME procedure described above. The agitation for the SDME extractions was performed by using PTFE stir bars. Sorption of EDPs can take place on PTFE stir bars, and so they were carefully rinsed after use with acetone, then methanol, then acetonitrile and finally with deionized water to avoid memory effects. The stir bars were also daily sonicated for 10 min with acetonitrile.

In DLLME experiments, 5 mL of real seawater samples (spiked or not) or artificial seawater samples (spiked) are placed in a glass tube of 8 mL. Then, 150 μL of an adequate mixture acetonitrile:decanol is rapidly injected to the sample. The optimum ratio acetonitrile:decanol was 15.7 (v/v). Under the optimized procedure, the mixture is vigorously shaken during 4 min using the vortex at 2000 rpm. Following extraction, the tube is subjected to centrifugation during 5 min at 3600 rpm. Afterwards, the upper phase of 1-decanol containing the extracted EDPs (~19 μL) is removed using the Hamilton syringe. The overall DLLME method calibration was performed using artificial seawater calibration solutions submitted to the same DLLME procedure described above.

3. Results and discussion

3.1. Optimization of the SDME method

Several considerations must be taken into account to select an adequate extractant solvent for a SDME application in direct

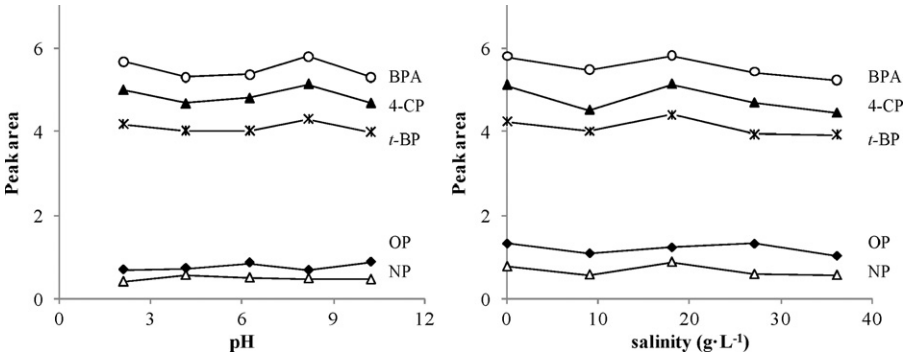


Fig. 1. Extraction efficiency of the SDME method when modifying the pH or the salinity of the water matrices (5 mL spiked with 50 ng mL^{-1} of each EDP).

immersion mode. The application is intended for a group of endocrine-disrupting phenols in seawater matrices. Therefore, the selected solvent must be immiscible with water. It must also be miscible with the mobile phase composition further used in HPLC and it should not absorb at the selected wavelength in the UV detector (228 nm), or at least should not co-elute with any of the EDPs studied. Furthermore, the solvent should ensure drop stability during long periods of time while stirring. Several solvents were initially selected to develop the SDME application: 1-octanol, dichloromethane, 1-decanol, and the ionic liquid 1-butyl-3-methylimidazolium hexafluorophosphate (BMIm-PF_6). The drop of dichloromethane, given its volatility, practically disappeared at extraction times of 15 min. The BMIm-PF_6 drop did not resist long extraction times either, and moreover its absorption signal in UV interfered with the identification of OP and NP. It has been described the difficulty to carry out SDME with ILs in direct immersion due to the fact that even hydrophobic ILs have some solubility in water resulting in a continual decrease in the drop volume with longer extraction times. This justifies the high number of applications of ILs in headspace compared to those in direct immersion mode [30,31]. The drop of octanol resisted long extraction times but its maximum size was smaller than the corresponding to 1-decanol. Given these results, 1-decanol was the solvent selected.

The drop size volume of 1-decanol was optimized by maximizing its size while ensuring its stability during stirring for long time (up to 2 h), being 2.5 μL the size of the drop finally selected. The stirring rate was fixed at 100 rpm to avoid drop instability.

The microextraction procedures for a number of phenols have been described to improve when utilizing low pH media and high ionic strengths, mainly in headspace applications [32]. The optimized SDME method is going to be applied in direct immersion mode for real seawater samples; therefore, high ionic strengths are going to be found in the matrices. Two different studies were conducted, one fixing the ionic strength to a salinity value of 36.1 g L^{-1} (artificial seawater matrices) and varying the pH of the aqueous solution from 2 to 10. The second one was performed without controlling the pH (pH 8.5 at room temperature) and varying the salinity of the aqueous solution from 0 to 36.1 g L^{-1}. The aqueous solution was spiked with a EDPs content of 50 ng mL^{-1} in these experiments. SDME was performed using 60 min of extraction time. In all cases, there were no significant variations in the obtained extraction efficiencies for the EDPs studied when the pH or the salinity were modified, as it can be observed in Fig. 1. Hence, no control of the pH or the ionic strength was carried out in further experiments, and the optimization was directly carried out in artificial seawater matrices.

SDME is an equilibrium extraction method rather than an exhaustive extraction method [19,20]. The amount of analyte extracted at a given time depends upon the mass transfer of analyte from the aqueous phase to the extractant drop. The equilibrium time determines the maximum amount of analyte that can be extracted by the drop, which controls the sensitivity of the method. The sorption time profiles were studied by monitoring the peak area as a function of extraction time, as can be seen in Fig. 2. Experiments were conducted in standard solutions of 100 ng mL^{-1} for the studied EDPs in artificial seawater samples, with stirring at room temperature for a time period that was increased from 15 to 80 min. It can be observed that the equilibration was not attained for any of the EDPs, and that efficiencies greatly increase when increasing the extraction time. For quantitative analysis, it is not necessary for the analytes to reach equilibrium, as long as the extraction time is carefully controlled.

3.2. Quality parameters of the SDME method

The overall SDME calibration method was carried out at two different extraction times, 20 and 60 min, with artificial seawater matrices. The purpose was to evaluate the sensitivity of the overall method as a function of the extraction time. Table 1 includes the quality parameters for these calibrations. Lower times are beneficial for achieving rapid analyses, but the sensitivity is compromised. Therefore, an extraction time of 60 min was considered adequate to reach acceptable sensitivity.

The limits of detection (LODs) were calculated as three times the signal to noise ratio, and were verified by injection of artificial seawater samples spiked at such levels and subjected to the overall optimized procedure. At the optimum extraction conditions (60 min for 5 mL aqueous samples) the detection limits oscillate from 4 ng mL^{-1} for BPA and 4-CP to 9 ng mL^{-1} for OP and NP. To our knowledge, only one SDME work has been reported for the determination of two endocrine-disrupting phenols, NP and 4-*t*-

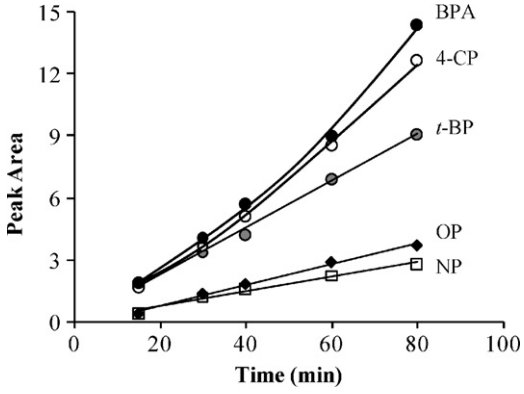


Fig. 2. Sorption time profiles for the SDME method obtained when utilizing artificial seawater samples (5 mL) spiked with 100 ng mL^{-1} of each EDP.

Table 1
Quality parameters of the overall SDME calibration method, using different extraction times.

Analyte	Extraction time (min)	Calibration range (ng mL^{-1})	Slope ± SD[a]	Error of the estimate	R	LOD (ng mL^{-1})
BPA	20	30–150	0.032 ± 0.002	0.253	0.989	15
t-BP	20	30–150	0.017 ± 0.001	0.077	0.995	19
4-CP	20	30–150	0.030 ± 0.002	0.236	0.989	18
OP	20	50–200	0.013 ± 0.002	0.089	0.988	39
NP	20	50–200	0.010 ± 0.001	0.056	0.993	32
BPA	60	15–125	0.110 ± 0.006	0.711	0.993	4
t-BP	60	15–125	0.071 ± 0.004	0.512	0.991	6
4-CP	60	15–125	0.090 ± 0.004	0.457	0.996	4
OP	60	20–125	0.037 ± 0.002	0.291	0.990	9
NP	60	20–125	0.025 ± 0.001	0.105	0.997	9

[a] Error of the slope for $n = 6$ calibration levels.

OP, in waters (tap, river and wastewaters) [25]. Such work was conducted with HPLC-fluorescence detection (FD) using the ionic liquid hexylmethylimidazolium hexafluorophosphate as extractant (10 μL microdrop in 15 mL aqueous samples) [25]. The work reports detection limits of 0.3 and 0.7 ng mL^{-1} for NP and *t*-OP, respectively, using a 40 min extraction time, with dynamic linear ranges of 10–100 ng mL^{-1}. These detection limits, obtained with HPLC-FD, are better than the ones reported with our SDME method, but it must be considered that our work uses HPLC-UV. The utilization of SDME in direct immersion mode in combination with HPLC-UV presents detection limits around 5 ng mL^{-1} for polar compounds such as formaldehyde using 30 min for the extraction time [33].

The precision of the SDME method was determined by performing five consecutive extractions from artificial seawater solutions with EDPs concentrations of 50 ng mL^{-1}. At the optimum extraction conditions, the relative standard deviation values oscillate from 4.1% for BPA to 9.4% for 4-CP, as can be observed in Table 2. The reported precision is comparable to common applications in SDME [30,34]. Precision values up to 7.8% (RSD) have been reported for NP (spiked level: 25 ng mL^{-1}) in waters using a SDME-HPLC-FD method [25].

Given the fact that SDME is not an exhaustive extraction method, there are several ways to evaluate its performance, by means of the enrichment factor or by means of the relative recovery. The enrichment factor (E_F) was calculated according to the following equation:

$$E_F = \frac{C_{drop}}{C_{initial}} \quad (1)$$

where C_{drop} is the concentration of the EDPs in the drop after extraction, and $C_{initial}$ is its initial concentration in the seawater solution. Table 2 shows the obtained E_F values for a spiked level of 50 ng mL^{-1}, which oscillate from 49 to 195. E_F values ranging from 130 to 163 have been described for a spiked level of 25 ng mL^{-1} for NP and *t*-OP using SDME-HPLC-FD [25]. Typical E_F values of 42–166 [30], 4–178 [35], and 83–157 [36], are described in regular direct mode-SDME applications.

The relative recovery (RR) was calculated according to the following equation:

$$RR\ (\%) = 100 \cdot \frac{C_{found}}{C_{initial}} \quad (2)$$

where C_{found} is obtained from the overall SDME calibration method. Table 2 shows the calculated relative recoveries for a spiked level of 50 ng mL^{-1}. Average relative recoveries of 102 ± 11% have been obtained with artificial seawater matrices. Relative recoveries around 100% are commonly described in SDME applications.

3.3. Optimization of the DLLME method

The primary requirements of an adequate extraction solvent in DLLME must be: low water solubility and high extraction capability for the analytes of interest. The choice of dispersive solvent in DLLME depends on the miscibility in the organic extraction solvent and in the aqueous sample, with the purpose to disperse the extraction solvent into very fine droplets in to the aqueous sample.

The DLLME method for determining EDPs in seawater matrices was carried out selecting 1-decanol as the extraction solvent in order to compare with SDME. The selected dispersive solvent was acetonitrile, avoiding in all cases water:acetonitrile ratios higher than 1:1 (v/v) to prevent the solubilization of 1-decanol. The aqueous sample volume was also fixed to 5 mL to make an appropriate comparison with SDME. Furthermore, 5 mL is the most common aqueous sample volume to perform a DLLME application [21,22,26–28].

Some authors have also pointed out the necessity of utilizing extraction solvents with higher density than water, to facilitate a fast mixing favored by gravity [27,37]. The selected extraction solvent for this application, 1-decanol, has a lower density than water. Therefore, the ability of the dispersive solvent to mix 1-decanol with water must be improved. It has been recently described that the utilization of ultrasounds improves the extraction efficiencies in DLLME [38]. Therefore, a comparison between ultrasound-assisted DLLME and vortex-assisted DLLME was conducted using 5 mL of artificial seawater samples containing 125 ng mL^{-1} of EDPs. 150 μL of the mixture acetonitrile:decanol were quickly added to the aqueous sample. Two different ratios of the mixture acetonitrile:decanol

Table 2
Extraction efficiency and precision of the optimized SDME and DLLME methods when utilized with artificial seawater matrices.

Analyte	SDME—spiked amount: 50 ng mL^{-1}			DLLME—spiked amount: 3.5 ng mL^{-1}			DLLME—spiked amount: 20 ng mL^{-1}		
	RR[a] (%)	RSD (%)	E_F	RR[a] (%)	RSD (%)	E_F	RR[a] (%)	RSD (%)	E_F
BPA	91.1	4.1	143	121	9.2	126	105	7.2	89
t-BP	101	8.7	195	96.4	11	183	98.3	3.1	131
4-CP	92.5	9.4	179	89.9	5.9	257	97.1	3.6	151
OP	112	6.5	70	99.6	14	201	96.5	3.8	163
NP	114	5.7	49	105	16	120	96.3	4.3	116

[a] Average relative recovery for $n = 5$.

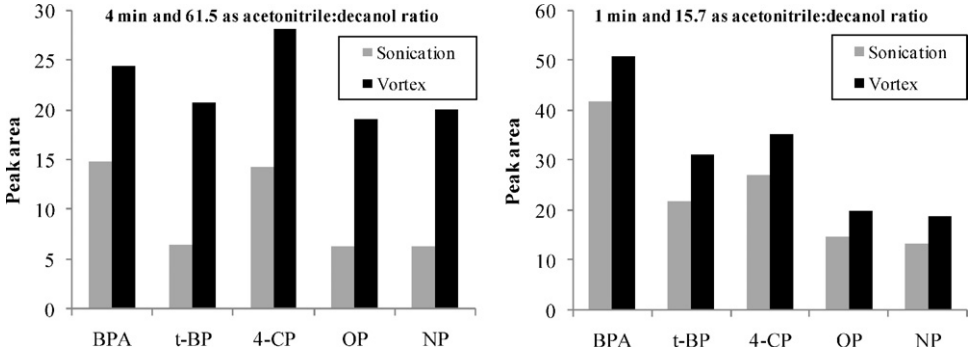


Fig. 3. Extraction efficiency of the DLLME method when using vortex or ultrasounds at different extraction times and mixture ratios. Artificial seawater samples (5 mL spiked with 125 ng mL^{-1} of each EDP) were subjected to the overall procedure.

Table 3
Design matrix and obtained results for the response surface design used in the optimization of the DLLME procedure.

Run	Design matrix		Response: peak area				
	Mixture ratio[a]	Extraction time (min)	BPA	*t*-BP	4-CP	OP	NP
1	61.5	4.0	1.218	1.226	4.134	2.246	2.044
2	15.7	4.0	2.805	3.583	6.885	5.638	4.746
3	15.7	2.5	3.109	3.309	5.909	3.863	2.905
4	25.3	2.5	2.539	2.400	5.174	2.941	2.837
5	61.5	2.5	1.556	1.152	2.823	1.696	1.374
6	25.3	4.0	2.511	2.536	4.569	3.403	3.165
7	15.7	1.0	2.920	3.287	5.740	4.508	3.187
8	61.5	1.0	1.359	1.381	3.115	1.959	2.024
9	25.3	1.0	2.281	2.609	4.793	2.743	2.652
10	25.3	2.5	2.423	2.450	4.467	2.524	2.551
11	25.3	2.5	2.551	2.645	4.727	2.250	2.051

[a] Mixture formed by acetonitrile:decanol.

were tried: 15.7 and 61.5 (v/v). Then, vortex agitation or ultrasounds were applied during two different extraction times: 1 and 4 min. In DLLME, extraction time is defined as the time interval after injecting the extraction solution (mixture of dispersive solvent and extraction solvent) and before centrifugation. Following centrifugation, the final extractant phase containing EDPs was subjected to chromatographic analysis. The obtained extraction efficiencies, expressed as peak areas, can be observed in Fig. 3. In all cases, it can be observed that the vortex agitation is more efficient than ultrasounds for the extraction of EDPs from seawaters at any extraction time or any acetonitrile:decanol ratio used. Hence, it was decided to use vortex to assist the DLLME method rather than ultrasounds.

In DLLME, unlike other liquid-phase microextraction techniques, the extraction efficiency depends not only on the extractant, but also on the type and volume of the dispersive solvent. Given the fact that the variation of the dispersive solvent volume would result in the change of the volume of the final extractant phase, it is not possible to directly assess the effect of the volume of dispersive solvent on the extraction efficiency. It becomes much more convenient to evaluate the effect of the dispersive solvent:extractant solvent ratio (acetonitrile:decanol ratio), fixing the spiked volume of such mixture. In addition to this, it is also necessary to optimize the extraction time. An experimental design was then conducted in order to obtain the optimum conditions for the mixture ratio and extraction time. The variables investigated were evaluated at two levels using a response surface methodology, based on a factorial design with a two replicate center point. The peak area of each analyte was selected as the response variable. This design involved a total of 11 randomized runs. The levels selected for ratio of the mixture (acetonitrile:decanol) were 15.7 and 61.5, using 150 μL

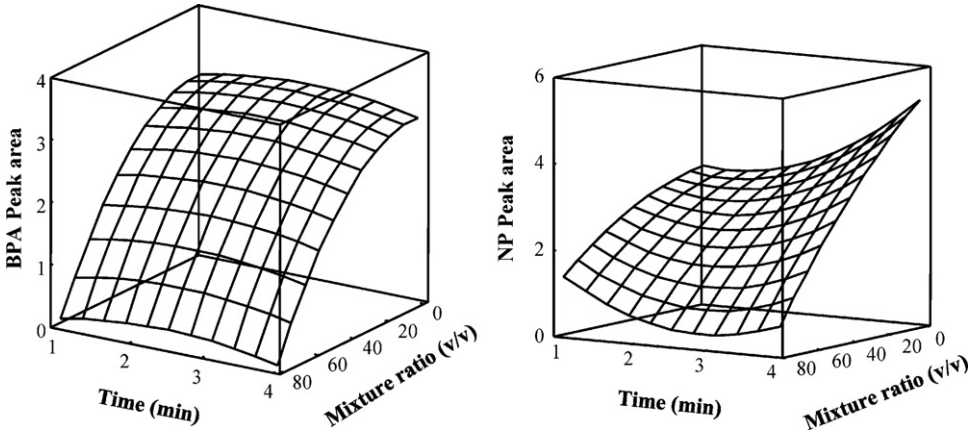


Fig. 4. Response surfaces estimated from the design for bisphenol-A (left) and nonylphenol (right) in the DLLME optimization.

Table 4
Quality parameters of the overall DLLME calibration method.

Analyte	Calibration range (ng mL^{-1})	Slope ± SD[a]	Error of the estimate	R	LOD (ng mL^{-1})
BPA	2–20	0.54 ± 0.03	0.371	0.996	0.7
t-BP	3–20	0.36 ± 0.01	0.188	0.997	0.8
4-CP	2–20	0.54 ± 0.02	0.267	0.998	0.2
OP	3–20	0.43 ± 0.02	0.256	0.997	0.8
NP	3–20	0.31 ± 0.01	0.137	0.998	1.6

[a] Error of the slope for $n = 6$ calibration levels.

as the fixed spiked volume of the mixture for 5 mL of aqueous sample. Higher ratios make difficult the obtaining of a final drop with enough size volume to be easily handled. Lower ratios generate a final drop of more than 20 μL, which is not convenient for HPLC requirements of sensitivity. With respect to the extraction time, the levels studied were 1 and 4 min, given the fact that higher times are rarely necessary in DLLME procedures, and in order to develop a fast procedure. The concentration of the analytes in the artificial seawater samples was kept constant at 7.5 ng mL^{-1} (5 ng mL^{-1} for BPA) during these experiments. Table 3 summarizes the experimental design matrix altogether with the obtained peak areas for each EDP. The chronological listing of the experimental design parameters represents the statistical randomized order in which the experimental runs were undertaken.

Fig. 4 shows representative response surfaces estimated from the design. For all EDPs studied, the maximum was observed in the region of low acetonitrile:decanol ratios (15.7). The maximum was attained at 4 min for all EDPs except for BPA, for which the extraction time was not a significant variable. Given these results, 4 min for the extraction time and 15.7 for the mixture ratio were the conditions selected to perform an adequate DLLME procedure.

3.4. Quality parameters of the DLLME method

The overall DLLME calibration method was carried out under the optimized conditions using artificial seawater matrices. Table 4 shows the quality parameters of the calibrations obtained. Detection limits were calculated as three times the signal to noise ratio, and were verified by injection of artificial seawater samples spiked at such levels and subjected to the overall optimized procedure. LODs oscillate from 0.2 ng mL^{-1} for 4-CP to 1.6 ng mL^{-1} for NP using this DLLME-HPLC-UV method. It must be highlighted that these LODs are comparable to others obtained with SDME-HPLC-FD [25], SPME-HPLC-FD [39] or GC-MS [40]. To the best of our knowledge, this group of EDPs has not been determined by DLLME in seawaters. DLLME applications conducted in combination with HPLC-UV (using aqueous samples of 5 mL) report LOD values of 1 ng mL^{-1} for the insecticide methomyl [41], of 3–7 ng mL^{-1} for several antioxidants [42], of 0.5–1.3 ng mL^{-1} for four insecticides [43], or of 0.4–1 ng mL^{-1} for several carbamate pesticides [44], among others.

The precision of the DLLME method was determined by performing five consecutive extractions from artificial seawater solutions spiked at two different levels (low and high) of EDPs contents, 3.5 and 20 ng mL^{-1}, respectively. Table 2 shows the obtained results, where it can be observed lower precision values for higher spiked levels, with RSD values ranging from 3.1 to 7.2% of RSD, than for lower spiked levels, with RSD values ranging from 5.9 to 16% of RSD, which is a logical trend. The reported precision is comparable to common applications in DLLME [28,37,43,45].

The performance of the method was also evaluated calculating the relative recovery (obtaining in this case C_{found} from the overall DLLME method) with these spiked artificial seawater samples. Average relative recoveries of 102 ± 12% for lower spiked levels and of 98.7 ± 3.7% for higher spiked levels were obtained, which also reflects the accuracy of the method. Relative recoveries around 100% are commonly described in DLLME applications.

The obtained enrichment factor values have also been included in Table 2, oscillating between 89 for BPA when spiked at 20 ng mL^{-1} and 257 for 4-CP when spiked at 3.5 ng mL^{-1}. For each spiked level, the higher E_F values are obtained for 4-CP and OP, and the lower E_F values for BPA and NP. Different DLLME-HPLC-UV applications (for 5 mL aqueous samples) report comparable E_F values: 71 for the insecticide methomyl [41], 168–220 for three antioxidants [42], 209–273 for four insecticides [43], 41–94 for several amines [46], or 101–145 for four carbamate pesticides [44], among many others.

3.5. Influence of real seawater matrices on SDME and DLLME

The applicability of both optimized extraction methods to real seawater samples was investigated to evaluate the matrix effects.

Table 5
Analytical performance of the optimized DLLME and SDME procedures when extracting real seawater samples spiked at different levels.

Analyte	SDME low spiked level: 15 ng mL^{-1}			DLLME low spiked level: 3.5 ng mL^{-1}		
	RSD (%)	RR[a] (%)	E_F	RSD (%)	RR[a] (%)	E_F
BPA	11	118	158	14	118	123
t-BP	9.7	112	227	7.5	94.1	178
4-CP	8.9	104	199	5.2	104	275
OP	7.0	104	74	12	116	220
NP	9.7	116	52	10	119	137
Analyte	SDME high spiked level: 125 ng mL^{-1}			DLLME high spiked level: 20 ng mL^{-1}		
	RSD (%)	RR[a] (%)	E_F	RSD (%)	RR[a] (%)	E_F
BPA	5.9	103	114	3.1	92.9	79
t-BP	3.8	99.2	149	5.8	98.3	130
4-CP	5.4	97.6	140	2.7	87.8	137
OP	4.7	101	68	7.3	93.1	163
NP	6.7	96.0	44	9.9	85.5	100

[a] Average relative recovery for $n = 5$.

Seawaters from Candelaria (Tenerife Island) are known for presenting low contamination levels, and are usually employed as blanks in performing recovery studies. To avoid carry over problems, non-spiked seawater samples from Candelaria were subjected for the overall optimized procedures with both SDME and DLLME, and the presence of EDPs was not observed. The precision of both optimized procedures, SDME and DLLME, was then evaluated by performing five consecutive extractions from real seawaters from Candelaria spiked at two different levels (low and high EDPs contents, depending on the specific method). Table 5 shows the obtained analytical performance.

Average relative recoveries of $110 \pm 11\%$ at low spiked levels ($3.5\ ng\ mL^{-1}$) and $91.5 \pm 5.0\%$ at high spiked levels ($20\ ng\ mL^{-1}$) have been obtained when applying the DLLME method to real seawater samples. These efficiencies are totally comparable to the ones obtained with artificial seawater samples (Table 2) and so the matrix effect is not significantly affecting the extraction process in DLLME. With respect to the precision of the DLLME method, better precision is obtained at higher spiked levels, as it happened with artificial seawater samples. The overall precision of the DLLME method with real samples oscillates between 2.7 and 14% (RSD), being also comparable to the one obtained with artificial seawaters. It must be highlighted here the similarities in the E_F values obtained with artificial and real seawater samples when spiked at the same levels using the DLLME method (Tables 2 and 5), which reflects the robustness of the method.

The utilization of SDME with real seawater matrices presents average relative recoveries of $111 \pm 7\%$ at low spiked levels ($15\ ng\ mL^{-1}$) and $99.4 \pm 2.8\%$ at higher spiked levels ($125\ ng\ mL^{-1}$). These efficiencies are also comparable to the ones obtained with artificial seawater samples (Table 2). The overall precision of the SDME method oscillate between 3.8% and 11% (RSD), whereas the enrichment factor values range from 44 to 227.

The comparison between E_F values for SDME and DLLME must be conducted considering that a final drop of 2.5 μL is obtained in SDME, being of 19 μL in DLLME. In this sense, it results more convenient to carry out the comparison using the relative enrichment factor (RE_F). The relative enrichment factor, also known as real extraction recovery (E_R), can be calculated according to the following equation:

$$E_R\ (\%) = RE_F\ (\%) = 100 \cdot \frac{E_F}{E_{Fmax}} \quad (3)$$

where E_{Fmax} is the maximum preconcentration achieved if all analytes are effectively concentrated in the final drop (in both SDME and DLLME). E_{Fmax} can be calculated from the ratio $V_{initial}/V_{drop}$, being $V_{initial}$ the aqueous volume (5 mL). Therefore, E_R (%) is a measure of the real extraction efficiency of the method. At the lowest spiked level with real seawater matrices, E_R values oscillate from 3 to 11% in SDME, and from 49 to 108% in DLLME. In other words, the extraction is more efficient with DLLME. In fact, the extraction is quantitative, or practically quantitative, in DLLME for *t*-BP (72%), OP (88%) and 4-CP (108%). Few works report real extraction efficiencies, being more common to report relative recoveries. E_R values of 29–91% [22], 24–116% [45], 60–111% [21], or 55–74% [28], have been reported in DLLME applications for different analytes, being totally comparable to the values obtained in this work for the EDPs studied. Real extraction efficiencies are also rarely reported in SDME works. E_R calculated values of 1–3% [30], 11–21% [36], or 0.2–9% [35] can be observed in SDME applications for different types of analytes, with values of 9–11% for NP and *t*-OP in a SDME-HPLC-FD application [25]. These values are in agreement with the real extraction efficiencies obtained in this SDME application.

Finally, non-spiked seawaters coming from three different sampling points, all close to an oil-petroleum refinery and to a STP discharge outfall, were subjected to the overall optimized SDME and DLLME procedures. EDPs were not detected when applying SDME in any of the three samples studied. When using DLLME, *t*-BP was detected in two of these samples, but it could not be quantified ($\sim 0.8\ ng\ mL^{-1}$), and NP was also detected in one of the samples, but it could not be quantified either ($\sim 1.6\ ng\ mL^{-1}$).

4. Conclusions

Two liquid-phase microextraction procedures, single-drop microextraction and dispersive liquid–liquid microextraction, have successfully been developed for the determination of five endocrine-disrupting phenols in seawaters. Both optimized liquid-phase microextraction methods have shown comparable relative recoveries and precision in the developed application. Both methods are also environmental-friendly due to the low organic solvent consumption requirements (20 μL at most) and low sample volume (5 mL). The DLLME method has shown to be much more efficient than SDME to carry out the determination of EDPs, presenting better detection limits (down to $0.2\ ng\ mL^{-1}$) and better real extraction recoveries (from 49 to 108%). In addition, the DLLME method is rapid: around 10 min for the overall process compared to the necessity of 60 min in SDME.

Acknowledgements

Funding from the Spanish Ministry of Innovation and Science project ref. CTQ2008-06253/BQU is acknowledged. The authors also acknowledge the Servicio de Medioambiente de la Universidad de La Laguna (SEMALL) for providing the seawater samples.

References

[1] L.J. Mills, C. Chichester, Sci. Total Environ. 343 (2005) 1–34.
[2] B. Kudak, J. Namienik, Crit. Rev. Anal. Chem. 38 (2008) 242–258.
[3] S. Gimeno, H. Komen, P.W.M. Venderbosch, T. Bowmer, Environ. Sci. Technol. 31 (1997) 2884–2890.
[4] V.A. Baker, Toxicol. In Vitro 15 (2001) 413–419.
[5] G.G. Ying, B. Williams, R. Kookana, Environ. Int. 28 (2002) 215–226.
[6] A. Arditsoglou, D. Voutsa, Environ. Sci. Pollut. Res. 15 (2008) 228–236.
[7] P. López-Roldan, M.J. López de Alda, D. Barceló, Anal. Bioanal. Chem. 378 (2004) 599–609.
[8] M.D. Hernando, M. Mezcua, M.J. Gómez, O. Malato, A. Agüera, A.R. Fernández-Alba, J. Chromatogr. A 1047 (2004) 129–135.
[9] M. Kawaguchi, N. Sakui, N. Okanouchi, R. Ito, K. Saito, H. Nakazawa, J. Chromatogr. A 1062 (2005) 23–29.
[10] A. Gentili, S. Marchese, D. Perret, Trends Anal. Chem. 27 (2008) 888–903.
[11] G. Famiglini, P. Palma, A. Siviero, M.A. Rezai, A. Cappiello, Anal. Chem. 77 (2005) 7654–7661.
[12] J. López-Darias, V. Pino, J.H. Ayala, V. González, A.M. Afonso, Anal. Bioanal. Chem. 391 (2008) 735–744.
[13] C. Basheer, H.K. Lee, K.S. Tan, Mar. Pollut. Bull. 48 (2004) 1161–1167.
[14] R. Liu, J.L. Zhou, A. Wilding, J. Chromatogr. A 1022 (2004) 179–189.
[15] C. Nerín, J. Salafranca, M. Aznar, R. Batlle, Anal. Bioanal. Chem. 393 (2009) 809–833.
[16] S. Risticevic, V.H. Niri, D. Vuckovic, J. Pawliszyn, Anal. Bioanal. Chem. 393 (2009) 781–795.
[17] J. Lee, H.K. Lee, K.E. Rasmussen, S. Pedersen-Bjergaard, Anal. Chim. Acta 624 (2008) 253–268.
[18] L. Xu, C. Basheer, H.K. Lee, J. Chromatogr. A 1152 (2007) 184–192.
[19] H. Liu, P.K. Dasgupta, Anal. Chem. 68 (1996) 1817–1821.
[20] M.A. Jeannot, F.F. Cantwell, Anal. Chem. 68 (1996) 2236–2240.
[21] M. Rezaee, Y. Assadi, M.R.M. Hosseini, E. Aghaee, F. Ahmadi, S. Berijani, J. Chromatogr. A 1116 (2006) 1–9.
[22] N. Fattahi, Y. Assadi, M.R.M. Hosseini, E.Z. Jahromi, J. Chromatogr. A 1157 (2007) 23–29.
[23] Y.C. Fiamegos, A.P. Kefala, C.D. Stalikas, J. Chromatogr. A 1190 (2008) 44–51.
[24] A. Tor, J. Chromatogr. A 1125 (2006) 129–132.
[25] J.F. Liu, Y.G. Chi, G.B. Jiang, C. Tai, J.F. Peng, J.T. Hu, J. Chromatogr. A 1026 (2004) 143–147.
[26] Y. Li, J. Hu, X. Liu, L. Fu, X. Zhang, X. Wang, J. Sep. Sci. 31 (2008) 2371–2376.
[27] R.S. Zhao, C.P. Diao, X. Wang, T. Jiang, J.P. Yuan, Anal. Bioanal. Chem. 391 (2008) 2915–2921.
[28] A.S. Yazdi, N. Razavi, S.R. Yazdinejad, Talanta 75 (2008) 1293–1299.
[29] APHA, AWWA, WPCF, Métodos normalizados de análisis de aguas potables y residuales, Díaz de Santos, Madrid, 1992, p. 8.
[30] J. Liu, G. Jiang, Y. Chi, Y. Cai, Q. Zhou, J.T. Hu, Anal. Chem. 75 (2003) 5870–5876.

[31] E. Aguilera-Herrador, R. Lucena, S. Cárdenas, M. Valcárcel, J. Chromatogr. A 1209 (2008) 76–82.
[32] M.F. Alpendurada, J. Chromatogr. A 889 (2000) 3–14.
[33] J.F. Liu, J.F. Peng, Y.G. Chia, G.B. Jiang, Talanta 65 (2005) 705–709.
[34] Q. Zhou, C. Ye, Microchim. Acta 162 (2008) 153–159.
[35] J.-F. Liu, Y.-G. Chi, G.-B. Jiang, J. Sep. Sci. 28 (2005) 87–91.
[36] M. Saraji, B. Farajmand, J. Chromatogr. A 1178 (2008) 17–23.
[37] Y. Li, G. Wei, J. Hu, X. Liu, X. Zhao, X. Wang, Anal. Chim. Acta 615 (2008) 96–103.
[38] Q. Zhou, X. Zhanga, J. Xiao, J. Chromatogr. A 1216 (2009) 4361–4365.
[39] Y. Fan, M. Zhang, S.L. Da, Y.Q. Feng, Analyst 130 (2005) 1065–1069.
[40] G. Gatidou, N.S. Thomaidis, A.S. Stasinakis, T.D. Lekkas, J. Chromatogr. A 1138 (2007) 32–41.
[41] G. Wei, Y. Li, X. Wang, J. Sep. Sci. 30 (2007) 3262–3267.
[42] M.A. Farajzadeh, M. Bahrama, J. Jönsson, Anal. Chim. Acta 591 (2007) 69–79.
[43] Y. Liu, E. Zhao, W. Zhu, H. Gao, Z. Zhou, J. Chromatogr. A 1216 (2009) 885–891.
[44] Q. Wu, X. Zhou, Y. Li, X. Zang, C. Wang, Z. Wang, Anal. Bioanal. Chem. 393 (2009) 1755–1761.
[45] D. Nagaraju, S.-D. Huang, J. Chromatogr. A 1161 (2007) 89–97.
[46] X. Wang, L. Fu, G. Wei, J. Hu, X. Zhao, X. Liu, Y. Li, J. Sep. Sci. 31 (2008) 2932–2938.

Talanta 80 (2010) 1619–1625

Contents lists available at ScienceDirect

Talanta

journal homepage: www.elsevier.com/locate/talanta

Analysis of ammonia and aliphatic amines in environmental water by micellar electrokinetic chromatography and QSPR modeling of electrophoretic migration time

Yang Hui, Lei Zhou, Xing-Guo Chen*

Department of Chemistry, Lanzhou University, Lanzhou, 730000, PR China

ARTICLE INFO

Article history:
Received 25 May 2009
Received in revised form
23 September 2009
Accepted 26 September 2009
Available online 3 October 2009

Keywords:
Aliphatic amine
Environmental water sample
MEKC
LIF
QSPR
CODESSA

ABSTRACT

In this paper, a rapid and sensitive method for the determination of ammonia and 22 aliphatic amines derivatized was established by cyclodextrin (CD) modified micellar electrokinetic chromatography with laser-induced fluorescence detection using 4-chloro-7-nitrobenzo-2-oxa-1,3-diazole as a derived reagent. By a series of unvaried studies, the best conditions were selected using 20 mM tetraborate (pH 9.70) containing 25 mM SDS, 7 mM β-CD, 10% acetonitrile, 0.5 M urea, and applied voltage 25 kV. Under the optimum conditions, ammonia and 22 aliphatic amines were separated successfully in 19 min. The signal response was linear over three-order of concentrations. The intra-day and inter-day relative standard deviations (RSD) were less than 0.81% and 1.00% for migration times, 1.76% and 2.01% for peak areas. Limits of detection (LOD) for the analytes was (S/N = 3) approximate 10^{-9}–10^{-12} M. The method was applied to the determination of ammonia and aliphatic amines in environmental water with recoveries in the range of 90.2–110.8%. In addition, a quantitative structure–property relationship (QSPR) model for the estimation of the electrophoretic migration time was established with the comprehensive descriptors for structural and statistical analysis (CODESSA) program for the first time. The multilinear regression (MLR) equation contained two theoretical descriptors and had the following statistical indices: $R^2 = 0.9668$, $F = 290.7839$, $R^2_{cv} = 0.9576$ and $S^2 = 0.8149$.

© 2009 Elsevier B.V. All rights reserved.

1. Introduction

Aliphatic amines are a group of low-molecular-mass active organic bases that usually act as an important class of environmental pollutants due to their odorous and toxic characteristic [1]. They are emitted into the environment from anthropogenic sources such as cattle feedlot operations, waste incineration, sewage treatment, automobile exhausts and various industries [2]. A natural background level of aliphatic amines can also be assumed to originate from animal waste and microbiological activities [3]. The many commercial uses and natural occurrences of aliphatic amines suggest that ultimately they will appear in the environment as pollutants which can be found in biological fluid, environmental samples and industrial process streams at trace levels. Furthermore, aliphatic amines, through nitrosation by nitrite as a reagent in conditions of defined pH and in other conditions similar to those in the mammalian stomach or small intestine [4,5], and some of nitrosamines products have strong mutagenic and oncogenic activities [6–8]. It is well known that nitrite is widely present in nature and is also produced in human saliva, and the possibility that nitrosation may occur in vivo, particularly in the gastrointestinal trace, upon ingestion of foods or water containing aliphatic amines has been reported [9]. The U.S. Environmental Protection Agency (U.S. EPA) maintains a continuing interest in analytical method for aliphatic amines because of their wide occurrences and toxicities.

In order to deeply understand the role of aliphatic amines in biological processes and their effects on human health, it is essential to develop simple and sensitive analytical techniques for quantifying these compounds in environmental samples. So far, some analytical methods have been exploited for the determination of some aliphatic amines in various matrices, including water, aerosol and beverages, such as GC [10,11], HPLC [12–16], RP-HPLC [17], CE [18–25] and ion chromatography [26]. By these methods only a few short chain aliphatic amines were examined. Furthermore, they cannot meet the requirement of the high sensitivity in analyzing real environmental sample matrix with low concentration. Thus, it is necessary to develop a rapid and sensitive method to determine ammonia and aliphatic amines derivatized.

Migration time is an apparent manifestation of material's separation in electrophoresis. Material can be separated in the electrophoresis was reflected in their different migration times.

* Corresponding author. Tel.: +86 931 891 2763; fax: +86 931 891 2582.
E-mail address: chenxg@lzu.edu.cn (X.-G. Chen).

0039-9140/$ – see front matter © 2009 Elsevier B.V. All rights reserved.
doi:10.1016/j.talanta.2009.09.047

Therefore, migration time is a very important qualitative indicator in electrophoresis. We tried to establish the structure–activity relationship between the physical structure and electrophoretic migration time. QSPR provides a promising method for the estimation of compounds' electrophoretic behavior based on the descriptors derived solely from the molecular structure. CODESSA program is a comprehensive program for developing QSAR/QSPR models. It has been successfully employed in QSPR studies concerning the prediction of diverse physical properties and of chemical reactivity [27,28]. It also has shown promising results in medicinal chemistry applications [29]. To sum up, by dint of the chemical informatics to predict electrophoresis behaviors of compounds based on their chemical structures is important and necessary for developing new CE systems.

In this work, we report the first attempt to use MEKC-LIF for the rapid and selective determinations of ammonia and 22 aliphatic amines. The study included an extensive evaluation of different variables that affect derivatization, including the buffer concentration, pH, derived reagent concentration, reaction time and temperature. We also investigate the variables in separation, including pH, buffer concentration and various modifiers. Then the system was successfully applied in the analysis of ammonia and aliphatic amines in lake water, aquarium water, and the Yellow River water. Comparing with other chromatography methods reported previously, this developing method could provide bigger peak capacity with superior resolution in shorter analytical time. In addition, a multilinear regression (MLR) equation contained two theoretical descriptors were established for the estimation of the electrophoretic migration time.

2. Experimental

2.1. Instrumentation

CE was carried out on a Beckman P/ACE 5510 CE system (Beckman Coulter, Fullerton, CA, USA), equipped with a LIF detector. The excitation light from an argon ion laser (3 mW) was focused on the capillary window by means of a fiber-optic connection. The excitation was performed at 488 nm and a 520 nm bandpass filter was used for emission. The system was controlled by P/ACE Station software. The separation was carried out on a 57 cm (50 cm to the detector) × 75 mm ID fused-silica capillary (Yongnian Photoconductive Fiber Factory, Hebei, China). The samples were hydrodynamic injected by applying a pressure of 0.5 psi for 3 s. The separations were carried out at a constant voltage of 25 kV. The capillary was pre-treated with methanol, 0.1 M NaOH and water for 30 min sequentially. Each day before starting analysis and between two runs, the capillary was rinsed with 0.1 M NaOH for 5 min and water for 5 min and preconditioned with running buffer for 5 min. The capillary was maintained at 25 °C.

2.2. Materials and sample preparation

The aliphatic amine standards were all purchased from Sigma (Steinheim, Germany). The derived reagent, 4-chloro-7-nitrobenzo-2-oxa-1,3-diazole (NBD-Cl), was obtained from Acros Organics Company (Geel, Belgium). Analytical reagent grade chemicals were used along with distilled water to prepare solutions. Standard solutions of aliphatic amines were prepared individually in methanol (200 μg/mL each), stored at 4 °C and used after dilution to required concentration. A stock solution of derived reagent was prepared by mixing of 60 mg NBD-Cl with 10 mL acetonitrile and used as required. A PHS-10A acidity meter (Xiaoshan Science Instrumentation Factory, Zhejiang Province, China) was used for the pH measurement. The pH of buffer was adjusted using 1.0 M sodium hydroxide. Buffer solutions were freshly prepared for each experiment followed by filtration through a membrane filter of 0.45 μm pore size.

Water samples were collected in polypropylene bottles from aquarium, South-lake and the Yellow River, Lanzhou, China, respectively. The water samples were centrifuged to remove solid particles and then the supernatant was filtered through a 0.45 μm pore size membrane filter before analysis.

2.3. Derivatization procedure

20 μL of a mixture solution of ammonia and standard aliphatic amines, 200 μL of 30 mM tetraborate buffer (pH 9.0), and 80 μL of 1.5 mM NBD-Cl dissolved in acetonitrile were added into a 1.5 mL plastic tubes sequentially and thoroughly mixed. Then the mixture was heated at 70 °C for 20 min under dark. After cooling to room temperature, the mixture was diluted with 500 μL running electrolyte and then applied to injection for CE. The water samples and reagent blanks were treated in the same manner.

2.4. Computational methods

All molecules were drawn and pre-optimized using (MM+) encoded in the HyperChem 4.0 program (Hypercube, 1994). A more precise optimization was done with the semi-empirical PM3 method in HyperChem. The output files were transferred into the Microsoft Windows version of the CODESSA program version 2.6.3 (University of Florida, Gainesville, FL, 1994) developed by Katritzky et al. to calculate molecular descriptors. Then, a feature selection step was carried out to reduce the large set of descriptors to a suitable number without losing any important information. The HM in CODESSA was employed to select the suitable descriptors combinations to build the linear QSPR model. The lack of fit for the regression model was performed in the Minitab 15 program.

3. Results and discussion

3.1. Derivatization conditions studied

In order to achieve optimization derivatization efficiency, the effects of reaction variables were investigated: buffer pH (8.0–10.0), reaction temperature (25–70 °C), reaction time (3–60 min), NBD-Cl concentration (1–10 mM) and sodium tetraborate buffer concentration (10–50 mM). In our original experiment, we found that the buffer capacity of lower concentration buffer was not sufficient, whereas higher concentration buffer would result in the dismatch between higher concentration sample zone and lower concentration separation buffer. Therefore, a proper buffer concentration (30 mM sodium tetraborate) was applied as the derivatization buffer. The result implied that this value of 30 mM sodium tetraborate could enhance fluorescence intensity and meanwhile improve peak symmetry of the derivatives. In the experiment, in order to avoid the effect of delay time on fluorescence intensity, we injected immediately after derivative, and a fixed time interval from the end of derivative reaction to injection was strictly controlled.

3.1.1. Effect of buffer pH on derivatization

As the derivatization reaction of aliphatic amines with NBD-Cl is a typical nucleophilic reaction, basic reaction conditions were expected to be beneficial. The pH ranges of sodium tetraborate buffer from 8.0 to 10.0 were studied, respectively. Generally, NBD-Cl derivatization should be carried out at a higher pH (>8.4) to make the primary amine deprotonated [30,12], which is consistent with the results of aliphatic amine in our experiment. However, the fluorescence intensity of aliphatic amine derivatives decreased with

the increasing of buffer pH beyond pH 9.0. So the derivatization reaction at pH 9.0 was applied.

3.1.2. Effect of reaction temperature and time on derivatization

The effect of reaction temperature on the fluorescence intensity was investigated at 25, 50, 60, 70, 80 and 90 °C. The derivatization reaction was found to be rapid even at room temperature (25 °C), readily observed as a color change to yellow of the reaction mixture within a few seconds of the addition of NBD-Cl, while the reagent blank color changed to yellow only slowly (NBD-Cl hydrolysis reaction). However, there was a significant increase on the yield of fluorescent derivatives when the reaction temperature increased from 25 to 70 °C. But the fluorescence intensity at temperature above 70 °C was much smaller than that at 70 °C. It can be seen that the higher reaction temperature could provide higher derivatization efficiency, but the derivatives of aliphatic amines were not stable at temperature above 70 °C.

The influence of reaction time on the fluorescence intensity was investigated in the range of 3–60 min at 70 °C. The results showed that the fluorescence intensity increased with increasing reaction time, but the response of aliphatic amine derivatives exhibited a decreased tendency with prolonged reaction time exceeding 20 min. This maybe attributed to the fact that the derivatives of aliphatic amines were not very stable at 70 °C over a long time. So the derivatization reaction at 70 °C for 20 min was applied.

3.1.3. Effect of NBD-Cl concentration on derivatization

In addition, the fluorescence signal intensity depends also on NBD-Cl concentration investigated in the range of 1–10 mM. We observed that, for simple aqueous solutions of the aliphatic amines, concentrations of NBD-Cl as low as 1 mM could be used without sacrificing the yields. Considering that the method may be applied to a biological matrix which will contain other compounds capable of reacting with NBD-Cl, 1.5 mM was chosen as the optimal reagent concentration in the reaction mixture.

Based on the optimization studies, the derivatization conditions for further studies were chosen as a reaction medium consisting of NBD-Cl solution of 1.5 mM, 30 mM sodium tetraborate buffer with pH of 9.0, a reaction temperature of 70 °C for 20 min. In order to obtain high reproducibility, the derivatization mixture prepared freshly for each run was recommended.

3.2. Separation conditions studied

3.2.1. Effect of buffer concentration on the separation

In preliminary studies, CZE separation mode was chosen for the simultaneous separation of 24 compounds. A sodium tetraborate buffer was chosen as the background electrolyte. The effect of sodium tetraborate buffer concentration was investigated in the range of 5–30 mM. The result indicated that aliphatic amine derivatives could not achieve baseline separation at lower buffer concentration (5–10 mM). Higher concentration (30 mM) buffer would generally bring two results: (i) higher electric current resulting in generation of excessive Joule heat, thereby increasing the extent of diffusion for analytes and then causing poor peak shapes, and (ii) suppressing of EOF leading to longer analysis time, which can also cause poor peak shapes. In order to obtain high sensitivity and keep good peak shape, a buffer of 20 mM sodium tetraborate was selected for all further experiments.

3.2.2. Effect of buffer pH on the separation

The running buffer pH was noted to affect the separation efficiency and fluorescence quantum yields of the derivatives. The pH of running buffer was then examined from 9.5 to 10.1. It was observed that the resolutions increased dramatically with the increasing of buffer pH in the range of 9.5–9.7. But, some aliphatic amine derivatives still could not be separated absolutely. In addition, a significant influence of buffer pH on the fluorescence signal intensity was founded, which was accounted for the fact that derivatives were not stable at higher buffer pH. As a compromise of resolution and fluorescence signal intensity, pH 9.70 was chosen in subsequent experiments.

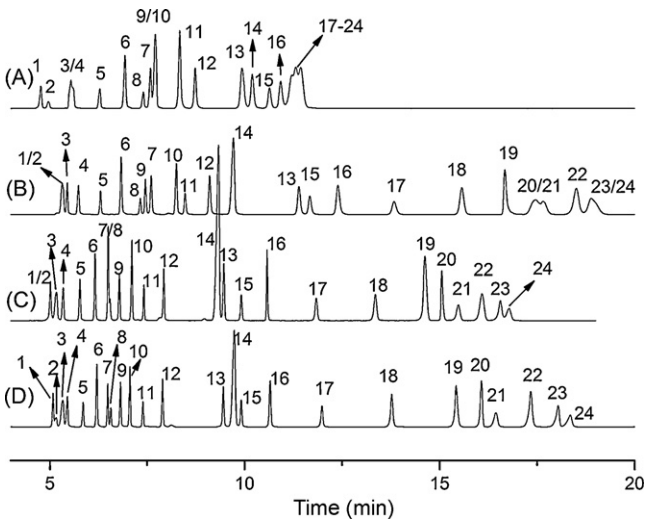


Fig. 1. Effect of the components of running buffer on the separation of ammonia and aliphatic amines. (A) Sodium tetraborate 20 mM, SDS 25 mM: peaks 3/4, 9/10, 17–24 overlapped; (B) sodium tetraborate 20 mM, SDS 25 mM, 10% acetonitrile: peaks 1/2, 20/21, 23/24 overlapped; (C) sodium tetraborate 20 mM, SDS 25 mM, 10% acetonitrile, 7 mM β-CD: peaks 1/2, 7/8 overlapped; (D) sodium tetraborate 20 mM, SDS 25 mM, 10% acetonitrile, β-CD 7 mM, urea 0.5 M: accepted resolution is obtained for all compounds. Analyte identities No. as in Table 1.

3.2.3. Effect of SDS concentration on the separation

Due to the pseudo-stationary phase effect of surfactant, SDS concentration showed a notable effect on the separation. In order to further improve the separation efficiency, the effect of SDS concentration (10–40 mM) was studied. It was found that the appropriate addition of SDS (25 mM) could improve separation efficiency and the peak shape. At the same time, the increasing of SDS concentration led to the delay of migration time with peak broadening. However, with sodium tetraborate and SDS as running buffer the 24 analytes involving ammonia, 22 aliphatic amines and NBD-Cl could not be completely separated (see Fig. 1A). It can be seen that only 15 peaks were obtained, due to that some of them have similar mobilities and comigrated.

3.2.4. Effect of modifier on the separation

Under normal MEKC conditions, these analytes cannot be separated completely, so efforts were shifted towards the use of modifiers. The addition of organic solvents to the buffer can improve the selectivity, efficiency and resolution of CE as they modify the partition coefficient, viscosity, and polarity of the mobile phase and electroosmotic flow. Here, acetonitrile was introduced into the running buffer and the effect in the concentration range of 0–20% (v/v) on the separation was tested based on the optimum conditions mentioned above. The result showed the resolution and analysis time increased with the increasing of acetonitrile concentration. Meanwhile, longer analysis time revealed severe tailed peaks. This could be explained by the change of the solubility of the derivatives in the water-acetonitrile mobile phase, which resulted in the change of the partition behavior of the derivatives between the mobile phase and the SDS pseudo-stationary phase. On the other hand, extension of time maybe due to the decreasing of the electroosmotic flow. Hence, the 10% (v/v) acetonitrile

was applied as a compromise consideration between resolution and migration time. However, the analytes could not be well separated in a shorter analysis time with higher separation efficiency when acetonitrile was applied (see Fig. 1B, nonyl-/decylamine and *t*-butyl-/cyclopropylamine both comigrated).

Then, β-CD as another modifier was introduced in the subsequent experiments and the effect in the concentration range of 5–12 mM on the separation was studied. The result showed that higher concentration (above 8 mM) was not beneficial to the separation of short chain aliphatic amines, but the lower concentration (below 6 mM) led to bad resolution of long chain aliphatic amines. Take care of two aspects, 7 mM was chosen in the subsequent experiments but separation was still incomplete with ammonia continuing to comigrate with methylamine, and same problem was also existed in the separation of heptyl-/dibutylamine (Fig. 1C). Urea was then added to the buffer to enhance the resolution and was tested in the concentration range of 0.2–1.4 M. As demonstrated in the literature [20], the addition of urea in MEKC allowed the reduction of the distribution of the solutes between the background electrolyte and the pseudo-stationary phase by increasing the solubility of the hydrophobic compounds in aqueous media. Finally, addition of 0.5 M urea led to the completely separation of all of the analytes. It is noted that the resolution was improved at the expense of analysis time as migration is finished within 19 min (Fig. 1D). This can be explained by the change of the solubility of the analytes in the water–acetonitrile mobile phase, which resulted in the change of the partition behavior of the analytes between the mobile phase and micellar pseudo-stationary phase, this is also the explanation to migration order change of the analytes with the addition of various modifiers.

According to the factors mentioned above, the best separation was obtained with running buffer containing 20 mM sodium tetraborate, 25 mM SDS buffer with 7 mM β-CD and 10% acetonitrile, 0.5 M urea at pH 9.70 and an applied voltage of 25 kV. Under the optimized condition, 24 compounds were well separated within 19 min. This results in the separation of the most aliphatic amines in the shortest analysis time ever reported in CE. The typical electropherogram for a standard mixture of MEKC system was shown in Fig. 2.

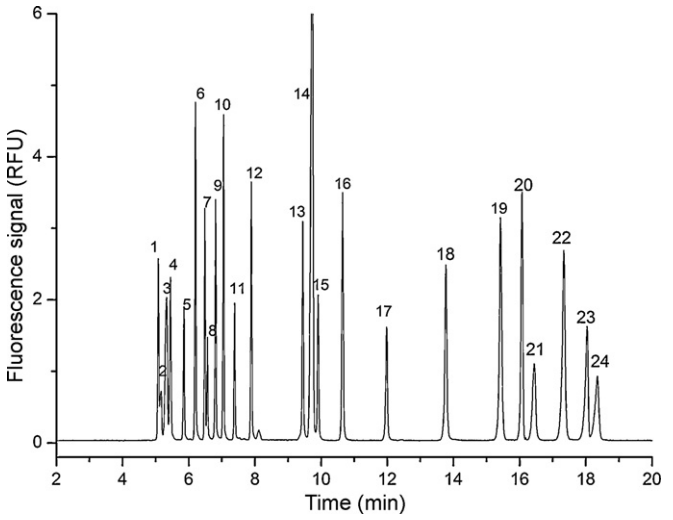


Fig. 2. Electropherogram of optimized MEKC separation of standard mixture of ammonia and aliphatic amines. MEKC system: 20 mM sodium tetraborate, 25 mM SDS buffer with 10% acetonitrile and 7 mM β-CD, 0.5 M urea at pH 9.7. Analyte identities No. as in Table 1.

3.3. Analytical calibration

The method validation including linearity, detection limits and precision was carried out using standard solutions under the optimized derivatization and separation conditions. Figures of merit are summarized in Table 1. The linear relationship between the peak area and the concentration of analytes was obtained by using the corresponding peak area (y) of the analytes versus their concen-

Table 1
Analytical figures of merit of the proposed MEKC method for the determination of aliphatic amines.

Peak No.	Analyte	Regression equation		Correlation coefficient	Linearity (μg/mL)	RSD (%, $n = 5$)[a]				LOD[b] (ng/mL)	LOQ[c] (ng/mL)
		Slope	Intercept			Intra-day		Inter-day			
						MT	PA	MT	PA		
1	Ammonia	3.17×10^7	3.16×10^5	0.9975	0.15–60.0	0.35	1.02	0.45	1.21	1	3.3
2	Methylamine	2.16×10^7	2.77×10^4	0.9986	0.03–6.0	0.81	1.73	1	1.88	0.2	0.7
3	Ethanolamine	6.41×10^7	7.48×10^4	0.9999	0.01–6.0	0.23	0.89	0.25	1	0.1	0.3
4	Ethylamine	3.47×10^7	9.80×10^4	0.9993	0.015–6.0	0.67	1.33	0.7	1.41	0.1	0.3
5	Isopropylamine	2.61×10^7	1.05×10^4	0.9999	0.015–6.0	0.63	1.42	0.77	1.55	0.1	0.3
6	Propylamine	7.32×10^7	2.54×10^4	0.9996	0.008–6.0	0.72	1.66	0.82	1.87	0.06	0.2
7	*t*-Butylamine	7.67×10^8	9.28×10^3	0.9999	0.0001–0.20	0.25	0.93	0.34	1.15	0.006	0.02
8	Cyclopropylamine	1.16×10^7	2.42×10^4	0.9997	0.03–12.0	0.52	1.34	0.6	1.41	0.4	1.3
9	Cyclobutylamine	1.72×10^8	-4.20×10^4	0.9998	0.001–2.0	0.72	1.76	0.79	1.82	0.03	0.1
10	Diethylamine	4.09×10^7	3.14×10^5	0.9976	0.01–12.0	0.52	1.32	0.61	1.41	0.1	0.3
11	Isobutylamine	6.60×10^8	-3.45×10^3	0.9993	0.002–2.0	0.47	1.02	0.51	1.33	0.007	0.02
12	Butylamine	1.49×10^8	-1.88×10^4	0.9996	0.002–2.0	0.57	1.35	0.62	1.45	0.03	0.1
13	Cyclohexylamine	8.47×10^7	4.57×10^3	0.9998	0.01–6.0	0.72	1.87	0.82	2.01	0.05	0.2
15	Isoamylamine	9.04×10^7	7.55×10^4	0.9995	0.005–2.0	0.56	1.33	0.71	1.42	0.05	0.2
16	Amylamine	5.25×10^8	4.12×10^4	0.9997	0.0002–0.40	0.46	1.21	0.52	1.34	0.008	0.03
17	Dipropylamine	2.30×10^7	1.25×10^5	0.9989	0.02–12.0	0.51	1.53	0.63	1.61	0.2	0.7
18	Hexylamine	1.88×10^8	2.91×10^5	0.9951	0.005–2.0	0.47	1.42	0.49	1.56	0.02	0.07
19	Diisobutylamine	2.03×10^7	-2.94×10^5	0.9994	0.14–28.0	0.56	1.38	0.71	1.5	0.2	0.7
20	Heptylamine	3.66×10^8	-7.78×10^4	0.9991	0.005–2.0	0.26	0.92	0.32	1.01	0.01	0.03
21	Dibutylamine	2.48×10^8	2.21×10^4	0.999	0.005–2.0	0.52	1.72	0.61	1.87	0.02	0.07
22	Octylamine	4.90×10^8	-3.22×10^5	0.9992	0.005–2.0	0.46	1.47	0.49	1.6	0.009	0.03
23	Nonylamine	3.62×10^8	-5.67×10^5	0.9975	0.005–2.0	0.33	1.11	0.54	1.25	0.01	0.03
24	Decylamine	2.44×10^8	-5.00×10^4	0.9998	0.005–2.0	0.52	1.51	0.67	1.73	0.02	0.07

[a] MT, migration time; PA, peak area.
[b] The limit of detection was estimated based on three-time ratio of signal to noise.
[c] The limit of quantitation was estimated based on ten-time ratio of signal to noise.

Table 2
Comparison of the analytes number, separation time and detection limits reported for aliphatic amines.

Separation method	Derivatized reagent	Detection method	Analytes number	Separation time (min)	Detection limit (*M*)	Refs.
GC	SIBA[a]	FID	7	28	10^{-9}	[11]
	2,4-BSC[b]	MS	7	21	10^{-8}	[10]
	2,4-DNFB[c]	MS	7	21	10^{-8}	[10]
HPLC	NBD-Cl	UV	5	50	10^{-7}–10^{-8}	[12]
	–	UV	11	40	10^{-7}–10^{-8}	[14]
	PITC[d]	UV	5	22	10^{-7}	[15]
	SIFA[e]	Fluorescence	8	18	10^{-7}	[16]
RP-HPLC	NPA-OSu[f]	Fluorescence	8	15	10^{-11}–10^{-12}	[17]
CE	FITC[g]	LIF	4	25	10^{-9}	[18]
	–	Indirect UV	7	-	10^{-5}	[19]
	FITC[g]	LIF	4	9.3	10^{-9}	[20]
	NBD-Cl	LIF	4	12	10^{-5}–10^{-6}	[21]
	OPA[h]	LIF	14	17	10^{-7}	[23]
	SAMF[i]	LIF	7	15	10^{-10}–10^{-11}	[24]
	SIFA[e]	LIF	5	8.5	10^{-10}–10^{-11}	[25]
	NBD-Cl	LIF	23	19	10^{-9}–10^{-12}	This work

[a] *N*-Succinimidyl benzoate.
[b] Benzenesulfonyl chloride.
[c] 2,4-Dinitrofluorobenzene.
[d] Phenyl isothiocyanate.
[e] *N*-Hydroxysuccinimidyl fluorescein-*O*-acetate.
[f] *N*-Hydroxysuccinimidyl 4,3,2′-naphthapyrone-4-acetate.
[g] Fluorescein isothiocyanate.
[h] *O*-Phthalaldehyde.
[i] 6-Oxy-(N-succinimidylacetate)-9-(2-methoxycarbonyl)fluorescein.

tration (c). The results indicated that excellent linear relationship is attainable over the concentration range studied with satisfactory correlation coefficients. The detection limits, calculated for an S/N of 3, and quantitation limits, calculated for an S/N of 10 were both listed in Table 1, indicating higher sensitivity than that of the previously reported method (see Table 2). The precision of the method, including intra-day and inter-day relative standard deviations (RSD) were also listed in Table 1, indicating good precision.

3.4. Application

The applicability of the proposed method was tested by determining ammonia and aliphatic amines in various environmental water samples (see Fig. 3). All peaks in water samples were identified by comparing the migration times and spiking the standards to the sample solutions. The results were given in Table 3. From the recovery results, there is no significant matrix effect. The RSD can be considered as generally acceptable, although – as might be expected – the errors (as a percentage) increased for lower concentrations of the analytes.

3.5. QSPR model

To predict the migration times of analytes, QSPR model was used and described by the following equation:

$$\mathrm{MT\ (min)} = 6.6573 + 2.4205 \times \mathrm{IC2} - 3.2347 \times \mathrm{AIC2} \quad (1)$$

MT: migration time; IC2: information content (order 2); AIC2: average information content (order 2)

According to the *t*-test, the most important descriptor for the model is the information content (order 2): IC2, which is equal to average information content (AIC2) multiplied by the total number of atoms, defined as [31,32]:

$$\mathrm{IC2} = \mathrm{AIC2} \times n \quad (2)$$

$$\mathrm{IC2} = -\sum_{i=1}^{k} \frac{n_i}{n} \log_2 \frac{n_i}{n} \quad (3)$$

n_i: number of atoms in the ith class; n: the total number of atoms in the molecule; k: number of atomic layers in the coordination sphere around a given atom that are accounted for.

By interpreting the descriptors in the regression model, it is possible to gain some insight into the factors that are likely to govern the electrophoretic migration of the compounds. The two information-theoretic descriptors take into account different aspects of the molecular structure. IC describes the information content or complexity of a hydrogen-filled graph, considered the ordering of the atoms relative to one another within a molecule and AIC encodes the connectivity and molecule branching, so it

Table 3
Analysis of real environmental water samples by the proposed MEKC method.

Peak No.	Analyte	Concentration (ng/mL)	Recovery (%)	RSD (%)	
				MT	PA
Aquarium water					
1	Ammonia	198	100.5	0.17	0.43
7	*t*-Butylamine	0.6	90.2	0.72	3.14
9	Cyclobutylamine	2.4	105.7	0.94	2.24
11	Isobutylamine	3.5	93.5	1.06	2.11
13	Cyclohexylamine	21.4	105.8	0.42	0.92
South-lake water					
1	Ammonia	420	102.2	0.19	0.54
3	Ethanolamine	22.5	104.6	0.23	0.61
7	*t*-Butylamine	0.3	106.5	0.73	2.84
9	Cyclobutylamine	2.5	97.6	0.86	1.53
11	Isobutylamine	2.5	95.1	0.91	1.82
12	Butylamine	3.5	93.2	0.48	1.32
16	Amylamine	0.2	110.8	1.14	3.34
Yellow River water					
1	Ammonia	288	96	0.25	0.71
3	Ethanolamine	13.5	95.5	0.23	0.83
6	Propylamine	8.8	96.7	1.27	2.52
7	*t*-Butylamine	0.8	92.1	0.51	1.71
9	Cyclobutylamine	3.6	104.8	0.87	1.84
10	Diethylamine	41.3	94.2	0.74	1.92
11	Isobutylamine	5.5	109	0.93	2.12
13	Cyclohexylamine	11.4	90.8	0.98	2.24
17	Dipropylamine	20	106.1	0.63	1.87

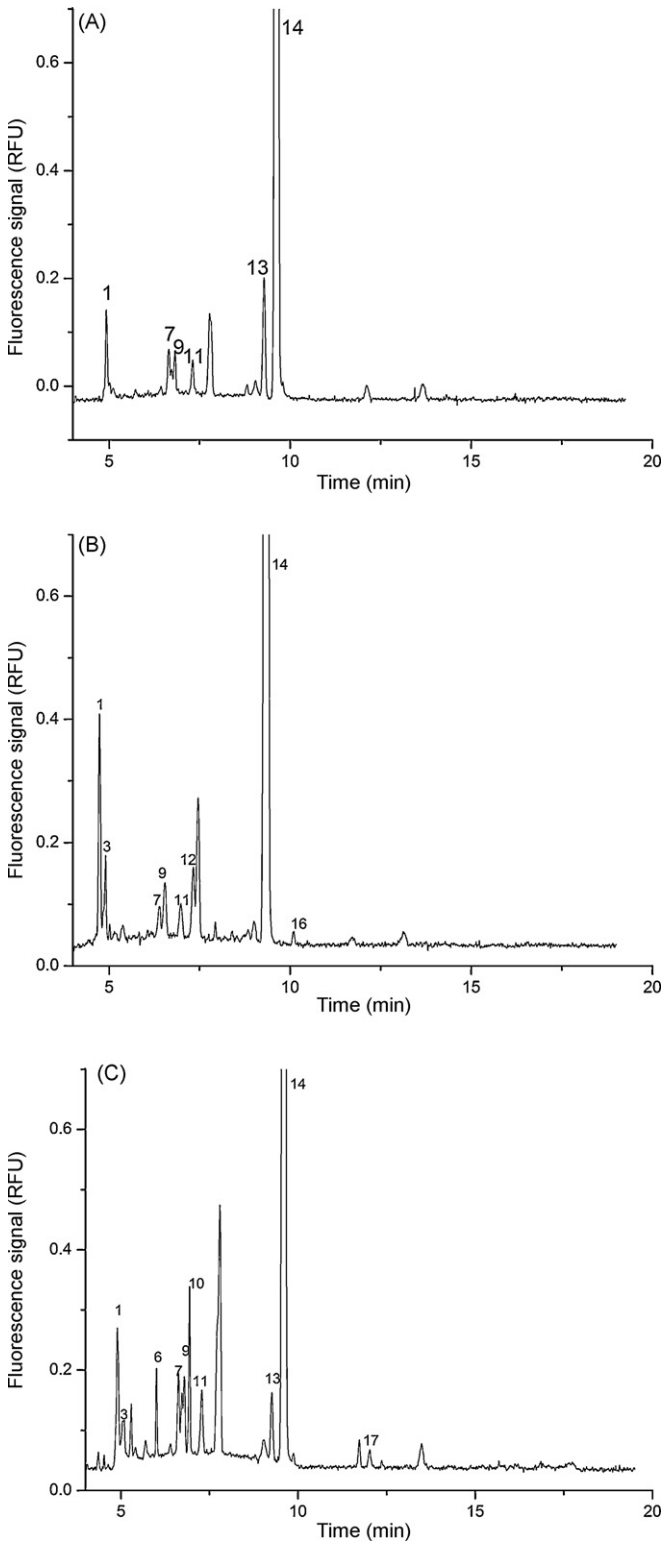


Fig. 3. Electropherograms obtained for ammonia and aliphatic amines in different environmental water matrices. (A) Aquarium water; (B) South-lake water; (C) Yellow River water. Analyte identities No. as in Table 1.

is related to the molecular shape and symmetry. The molecule structures play an important role in the migration process, so the two topological descriptors have high correlation with the MTs. The model may be explained by the fact that the magnitude of intermolecular interaction between the compounds and the pseudo-stationary phase is directly related to the degree of branching and molecular size.

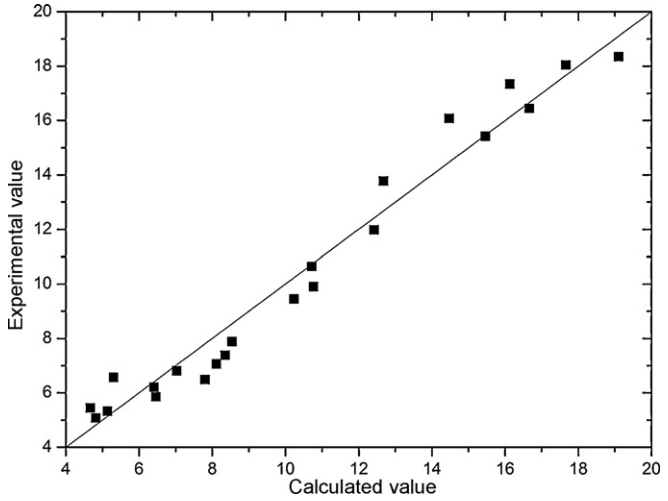


Fig. 4. Scatter plot of the calculated electrophoretic migration times vs. the experimental electrophoretic migration times.

Table 4
The linear model and the statistical characteristics of the regression model.

System		X^a	DX^b	*t*-Test	Descriptors
MEKC	0	6.6573e+00	1.0305e+00	6.4602	Intercept
	1	2.4205e−01	1.1072e−02	21.8611	IC (order 2)
	2	−3.2347e+00	5.1226e−01	−6.3145	AIC2 (order 2)

$R^2 = 0.9668$; $F = 290.7839$; $R^2_{cv} = 0.9576$; $S^2 = 0.8149$; lack of fit test, $P = 0.006$; X^a: regression coefficient; DX^b: regression coefficient mean square error; R^2: squared correlation coefficient; F: Fisher ratio; R^2_{cv}: cross-validated correlation coefficient; S^2: squared standard deviation;

In Fig. 4, the scatter graph represents the predicting migration times (MTs) versus experiment MTs for all of the analytes studied in MEKC system. The statistical characteristics of the regression model were presented in detail in Table 4. The cross-validated correlation coefficient R^2_{cv}, as compared with the correlation coefficient R^2, indicated the stability of the regression equation. And the P value of the lack of fit test indicated that the chance of lack of fit of the regression model is very little. All of the results suggested that the model possessed promising predictive ability for describing the migration times of analytes.

4. Conclusions

In conclusion, a rapid and sensitive MEKC-LIF method was developed for the separation and detection of ammonia and aliphatic amines after NBD-Cl derivatization. Compared with previous reported methods, this approach provided bigger peak capacity with superior resolution in shorter analytical time. So the proposed method displays great potential for the determination or confirmation of ammonia and aliphatic amines in various complex environmental samples. Furthermore, QSPR model was used to describe the relationship between migration time and molecule structure, which was an alternatively choice for the simplification of design and optimization CE system. The method can be extended to the analysis of carcinogenic N-nitrosamines upon their electrochemical reduction. It would be of great significance that allows the bulk of experimental work to be performed with innocuous aliphatic amines rather than the carcinogenic nitrosamines.

Acknowledgments

This work was supported by the National Natural Science Foundation of China (Grant No. 20275014, 20875040). The authors would like to express thanks for Dr. Xiaoyun Zhang's assistance (Department of Chemistry, Lanzhou University, Lanzhou, China).

References

[1] J.I. Korschwitz, Kirk-Othmer Encyclopedia of Chemical Technology, vol. 2, 4th ed., Wiley-Interscience, New York, 1991.
[2] S.E. Mnahan, Environmental Chemistry, 4th ed., Lewis, Chelsea, 1990.
[3] B.J. Finlayson-Pitts, J.N. Pitts Jr, Atmospheric Chemistry, Wiley-Interscience, New York, 1986.
[4] S.S. Miruish, Toxicol. Appl. Pharm. 31 (1975) 325.
[5] B. Speigelhalder, R. Preussmann, Carcinogenesis 6 (1985) 545.
[6] J.N. Pitts, D. Grojean, K.V. Cauwenberghe, J.P. Schmid, D.R. Fitz, Environ. Sci. Technol. 12 (1978) 946.
[7] R.C. Shank, Toxicol. Appl. Pharm. 31 (1975) 361.
[8] A.R. Tricker, R. Preussman, Mutat. Res. 259 (1991) 277.
[9] B. Pfundstein, A.R. Tricker, Food Chem. Toxicol. 29 (1991) 733.
[10] F. Sacher, S. Lenz, H. Brauch, J. Chromatogr. A 764 (1997) 85.
[11] Y.Y. Zhao, L.S. Cai, H. Wang, H.S. Zhang, J. Chromatogr. A 1021 (2003) 175.
[12] F. Hao, T. Lwin, W.J. Bruckard, J.T. Woodcock, J. Chromatogr. A 1055 (2004) 77.
[13] G.M. Murray, M.J. Sepaniak, J. Liq. Chromatogr. 6 (1983) 931.
[14] K. Ohta, A. Towata, M. Ohashi, T. Takeuchi, J. Chromatogr. A 1039 (2004) 161.
[15] B. Sahasrabuddhey, A. Jain, K.K. Verma, Analyst 124 (1999) 1017.
[16] H. Wang, J. Li, X. Liu, H.S. Zhang, Anal. Chim. Acta 423 (2000) 77.
[17] X. Liu, H. Wang, S.C. Liang, H.S. Zhang, Anal. Chim. Acta 441 (2001) 45.
[18] W.C. Brumley, V. Kelliher, J. Liq. Chromatogr. Relat. Technol. 20 (1997) 2193.
[19] W.H. Matchett, W.C. Brumley, J. Liq. Chromatogr. Relat. Technol. 20 (1997) 79.
[20] W. Maruszak, J. High Resol. Chromatogr. 22 (1999) 126.
[21] L.M. Preston, M.L. Weber, G.M. Murray, J. Chromatogr. B 695 (1997) 175.
[22] B. Santos, B.M. Simonet, Electrophoresis 25 (2004) 3231.
[23] E.D. Zlotrzynska, W. Maruszak, J. Chromatogr. B 714 (1998) 77.
[24] L.W. Cao, H. Wang, H.S. Zhang, Electrophoresis 26 (2005) 1954.
[25] Y.H. Deng, H. Wang, L. Zhong, H.S. Zhang, Talanta 77 (2009) 1337.
[26] I.H. Chang, C.G. Lee, D.S. Lee, Anal. Chem. 75 (2003) 6141.
[27] A.R. Katritzky, U. Maran, V.S. Lobanov, M. Karelson, J. Chem. Inf. Comput. Sci. 40 (2000) 1.
[28] A.R. Katritzky, R. Petrukhin, D. Tatham, S. Basak, E. Benfenati, M. Karelson, U. Maran, J. Chem. Inf. Comput. Sci. 41 (2001) 679.
[29] A.R. Katritzky, D.C. Fara, R.O. Petrukhin, D.B. Tatham, U. Maran, A. Lomaka, M. Karelson, Curr. Top. Med. Chem. 2 (2002) 1333.
[30] M. Yigit, L. Ersoy, J. Pharm. Biomed. Anal. 31 (2003) 1223.
[31] A.R. Katritzky, S.H. Slavov, D.A. Dobchev, J. Comput. Aided Mol. Des. 21 (2007) 371.
[32] L.B. Kier, J. Pharm. Sci. 69 (1980) 807–811, http://www.codessa-pro.com/descriptors/topo/mici.htm.

Talanta 80 (2010) 1626–1631

Contents lists available at ScienceDirect

Talanta

journal homepage: www.elsevier.com/locate/talanta

Gold nanoparticle-based colorimetric sensor for studying the interactions of β-amyloid peptide with metallic ions

Chengke Wang[a,b], Jine Wang[a,b], Dianjun Liu[a], Zhenxin Wang[a,*]

[a] State Key Laboratory of Electroanalytical Chemistry, Changchun Institute of Applied Chemistry, Chinese Academy of Sciences, Changchun 130022, China
[b] Graduate School of the Chinese Academy of Sciences, Beijing 100039, China

ARTICLE INFO

Article history:
Received 25 July 2009
Received in revised form
24 September 2009
Accepted 26 September 2009
Available online 3 October 2009

Keywords:
β-Amyloid1–16
Gold nanoparticle probes
Metallic ions
SHG-44 cell

ABSTRACT

In this paper, a kind of β-amyloid peptide (Aβ1–16) conjugated gold nanoparticles (Aβ1–16@GNPs) are prepared and employed as colorimetric indicator for studying the interaction of β-amyloid peptide with metallic ions (e.g. Zn^{2+} and Ca^{2+}). In the presence of Zn^{2+}, mono-dispersing Aβ1–16@GNPs enable to form aggregates or attach on the SHG-44 (human glioma cell) cellular surface which results in significant color change of the solution. The experimental results indicate that Zn^{2+} can interact with Aβ1–16 and form Zn^{2+}–β-amyloid peptide complexes. In particular, in the presence of Zn^{2+}, a time-dependent interaction of cells with Aβ1–16@GNPs has been observed that may suggest different expression levels of β-amyloid peptide related proteins in various cell cycles. In addition, the aggregating/binding process can be easily reversed by adding EDTA, a good chelated ligand of Zn^{2+}, which gives further proof of the interaction mechanism.

© 2009 Elsevier B.V. All rights reserved.

1. Introduction

A variety of human diseases are suspected to be directly linked to protein misfolding and assembling because highly organized protein aggregates, called amyloid fibrils, and aggregation intermediates are observed in these processes [1]. In particular, neurodegenerative pathologies, such as Alzheimer's disease, are account for a major part of these protein misfolding diseases [2]. β-Amyloid (Aβ) 1–42 is an Alzheimer's disease related peptide consists of 42 amino acids, which is the predominant species found in plaque deposits. The Aβ1–42 peptide can change its conformation and lead to form amyloid-like aggregates or fibrils when it is exposed to some metallic ions, such as Zn^{2+} [3–7]. There is a general consensus that protein aggregate is the major element of cell toxicity [2], especially when the Aβ exposed to Zn^{2+}, the rate of aggregate process was increased dramatically [3]. The coordination and/or reactions of the amino acid residues (i.e. histidines at position 6, 13, 14 and tyrosine at position 10) in the chain of the peptide Aβ1–42 with Zn^{2+} is assumed as main reason for causing this consequence [6].

Although many biophysical and biochemical methods (e.g. circular dichroism (CD) spectroscopy, thioflavin T (ThT) fluorescence spectroscopy, electron paramagnetic resonance (EPR) spectroscopy and transmission electron microscopy (TEM)) have been employed to successfully study the details of Aβ conformation and aggregate morphology in the presence of metallic ions [5–9], there are problems associated with cost-consuming and complicated operation. There is a highly demand motive to develop a novel method requiring simple or no instrumentation yet still providing great sensitivity and accuracy of analysis in vivo. In this regard, colorimetric methods based on functionalized gold nanoparticles (GNPs) are convenient and attractive, and can satisfy to meet these requirements. As versatile optical probes, gold nanoparticles have been extensively applied in analytical and biomedical researches [10–20] since the surface plasmon resonance (SPR) absorption of GNPs are not only dependent on their shape and size, but also very sensitive to their local environments.

Here, a kind of Aβ1–16 (the core fragment of Aβ1–42 which consists of 16 amino acids (sequence: DAEFR HDSGY EVHHQ K)) conjugated gold nanoparticles (named as Aβ1–16@GNPs) are prepared and used to study the interaction of Aβ1–16 with metallic ions. The stability and functionality of the GNPs are achieved by surface modification with the biotinylated peptide, CALNN GK(biotin)G, and the Aβ1–16 is linked with the CALNN GK(biotin)G functionalized GNPs by standard biotin–streptavidin chemistry. The interactions of the Aβ1–16@GNPs with two metallic ions (Zn^{2+}, Ca^{2+}) with or without cells have been carefully studied by UV–visible spectroscopy and TEM. We demonstrate that the GNP-based approach is possible to (i) identify metallic ion inducing Aβ peptide misfolding/aggregation, and (ii) develop a simple assay for screening amyloid-like aggregate inhibitors.

* Corresponding author. Fax: +86 431 85262243.
E-mail address: wangzx@ciac.jl.cn (Z. Wang).

0039-9140/$ – see front matter © 2009 Elsevier B.V. All rights reserved.
doi:10.1016/j.talanta.2009.09.052

2. Materials and methods

2.1. Materials and reagents

Peptides (CALNN), (CALNN GK(biotin)G), (GK(biotin)G DAEFR HDSGY EVHHQ K) were purchased from Scilight Biotechnology Ltd. (Beijing, China). Tetrachloroaurate ($HAuCl_4$) was purchased from Sigma–Aldrich Co. (USA). Streptavidin was purchased from Amresco Co. (USA). Other chemicals were analytical grade and used as received. Milli-Q water (18.2 MΩ cm) was used in all experimental processes.

2.2. Preparation of peptide-functionalized nanoparticles

The citrate stabilized 13 nm GNPs were synthesized by traditional Turkevich–Frens method [21,22]. Peptide-stabilized nanoparticles were prepared by previously reported peptide capping procedure [23,24]. Generally, an aqueous solution of peptide mixture (CALNN:CALNN GK(biotin)G) was added to the solution of 1 mL 13 nm GNPs (5 nM) to give a final concentration of total peptide of 1.5 mM. The ratio of CALNN and CALNN GK(biotin)G in the mixture is 9:1. After 1 h incubation, excess peptides were removed by repeated centrifugation at 8600 rpm (∼6900 × *g*, 3×) using an Eppendorf centrifuge (Eppendorf, Germany). The purified GNPs were resuspended in 1 mL water. Then a 30 μL streptavidin (2 mg/mL) aqueous solution was added to the peptide-capped GNPs solution. After 1 h incubation, excess streptavidin was removed by repeated centrifugation at 8600 rpm (∼6900 × *g*, 3×). The purified streptavidin-conjugated GNPs were resuspended in 1 mL HEPES buffer (pH 7.4, 10 mM HEPES, 0.8% NaCl), which were named as streptavidin@GNPs. Following a 50 μL GK(biotin)G Aβ1–16 (1 mg/mL) aqueous solution was added to the streptavidin@GNPs solution. After 1 h incubation, excess GK(biotin)G Aβ1–16 peptide was removed by repeated centrifugation at 8600 rpm (∼6900 × *g*, 3×). The purified Aβ1–16 decorated GNPs (named as Aβ1–16@GNPs) were then resuspended in HEPES buffer (pH 7.4, 10 mM HEPES, 0.8% NaCl) and stored at 4 °C. The CALNN GK(biotin)G conjugated GNPs (named as CALNN@GNPs) were also prepared under the similar procedure of Aβ1–16@GNPs synthesis except using CALNN GK(biotin)G replaces GK(biotin)G Aβ1–16. All experiments were carried out at room temperature and the HEPES buffer was used in the washing steps.

2.3. General chelation procedure

Aqueous solutions of Zn^{2+} and Ca^{2+} were prepared from their chloride salts. A series of aliquots with a desired amount of metallic ions were added to Aβ1–16@GNPs solution by a syringe and mixed thoroughly. After 30 min of incubation, the samples were ready for detection.

2.4. Reversibility study

For the reversibility experiment, equal molar of EDTA disodium solution was added to Aβ1–16@GNPs solution containing 50 μM Zn^{2+} by a syringe and mixed thoroughly. After 30 min of incubation, the samples were ready for detection.

2.5. Interaction of cells with functionalized GNPs

Before being treated with GNPs, SHG-44 cell line was grown with fresh medium (Dulbecco's Modified Eagle's medium, supplemented with 10% fetal bovine serum) in a humidified 5% CO_2 incubator at 37 °C. Then the cells were washed with HEPES buffer (three times) for the following studies. SHG-44 cell line was obtained from Chinese Academy of Sciences Cell Bank, which derived from a case of frontal lobe astrocytoma (grades II–III). This cell line contains S-100 protein specific for the nerve system and GFA protein specific for the astrocyte.

Firstly, the cells were incubated with CALNN@GNPs, streptavidin@GNPs or Aβ1–16@GNPs with the concentration of 2.4 nM in 150 μL of HEPES buffer with or without Zn^{2+} or Ca^{2+} for 2 h at 37 °C, respectively. Then, the cells were washed with HEPES buffer (three times) and imaged by an XSP-11CE optical microscope (Changfang Optical Instruments Ltd., China) equipped with a S5 IS digital camera (Canon, Japan).

2.6. Cell viability determination

The viability of cells was determined by a hemacytometer under a microscope. Generally, after being incubated with Aβ1–16@GNPs and/or Zn^{2+} as previously described, the cells were rinsed with HEPES buffer, detached by trypsin, and dispersed in the HEPES buffer; then the cell suspensions (50 μL) were incubated with 50 μL of trypan blue (0.4% w/v) for 5 min at room temperature. Experiments were repeated three times.

2.7. UV–visible absorption of stained cells measurements

After being incubated with functionalized GNPs in the absence or presence of metallic ions as mentioned above, GNPs stained cells were washed with HEPES buffer (three times), detached from the culture plates and dispersed in 150 μL HEPES buffer with a concentration of 2.3×10^4 cells/mL, then the spectrum of each cell sample was recorded, respectively. In the spectroscopic assay, corresponding streptavidin@GNPs stained cells (2.3×10^4 cells/mL in HEPES buffer) were employed as background.

2.8. Instruments

UV–visible spectra of all solutions were recorded on a UV–visible spectrophotometer (UV mini1240, Shimadzu Instruments, Japan).

TEM micrographs of all samples were obtained by a JEOL 2000FX (JEOL, Japan) operated at an accelerating voltage of 200 kV. Specimens for inspection by TEM were prepared by evaporating a droplet of sample solution onto a carbon-coated copper mesh grid.

3. Results and discussion

3.1. Metallic ions induced Aβ1–16@GNPs aggregation

UV–visible spectra of the Aβ1–16@GNPs with different amounts of ions (e.g. Zn^{2+} and Ca^{2+}) in solution are shown in Fig. 1. In the presence of Zn^{2+}, the SPR band of Aβ1–16@GNPs is gradually red-shifted from 527 nm to 537 nm with increasing the concentration of Zn^{2+} from 10 to 100 μM, corresponding to the color change of the solution from red to red-purple. The evolution of the UV–visible spectra reflects the decrease of free GNPs and the formation of nanoparticle aggregates in the solution. The interactions of Aβ1–16@GNPs with Ca^{2+} are relatively poor because the SPR band of Aβ1–16@GNPs does not change under same experimental conditions. As a control experiment, no significant change of the SPR band of CALNN@GNPs has been observed while Zn^{2+} is introduced into the solution below 100 μM. The experimental results indicate that Zn^{2+} is able to interact with Aβ1–16 which leads to form GNPs aggregates. This phenomenon agrees with previous reports on that Zn^{2+} can induce aggregation of Alzheimer's disease related β-amyloid peptides and forming fibrils [3,25].

The dependence of the maximum SPR band of Aβ1–16@GNPs solution on time is shown in Fig. 1. In the presence of 50 μM Zn^{2+}, the shift of the maximum wavelength of SPR band of Aβ1–16@GNPs takes place immediately and terminated in 30 min.

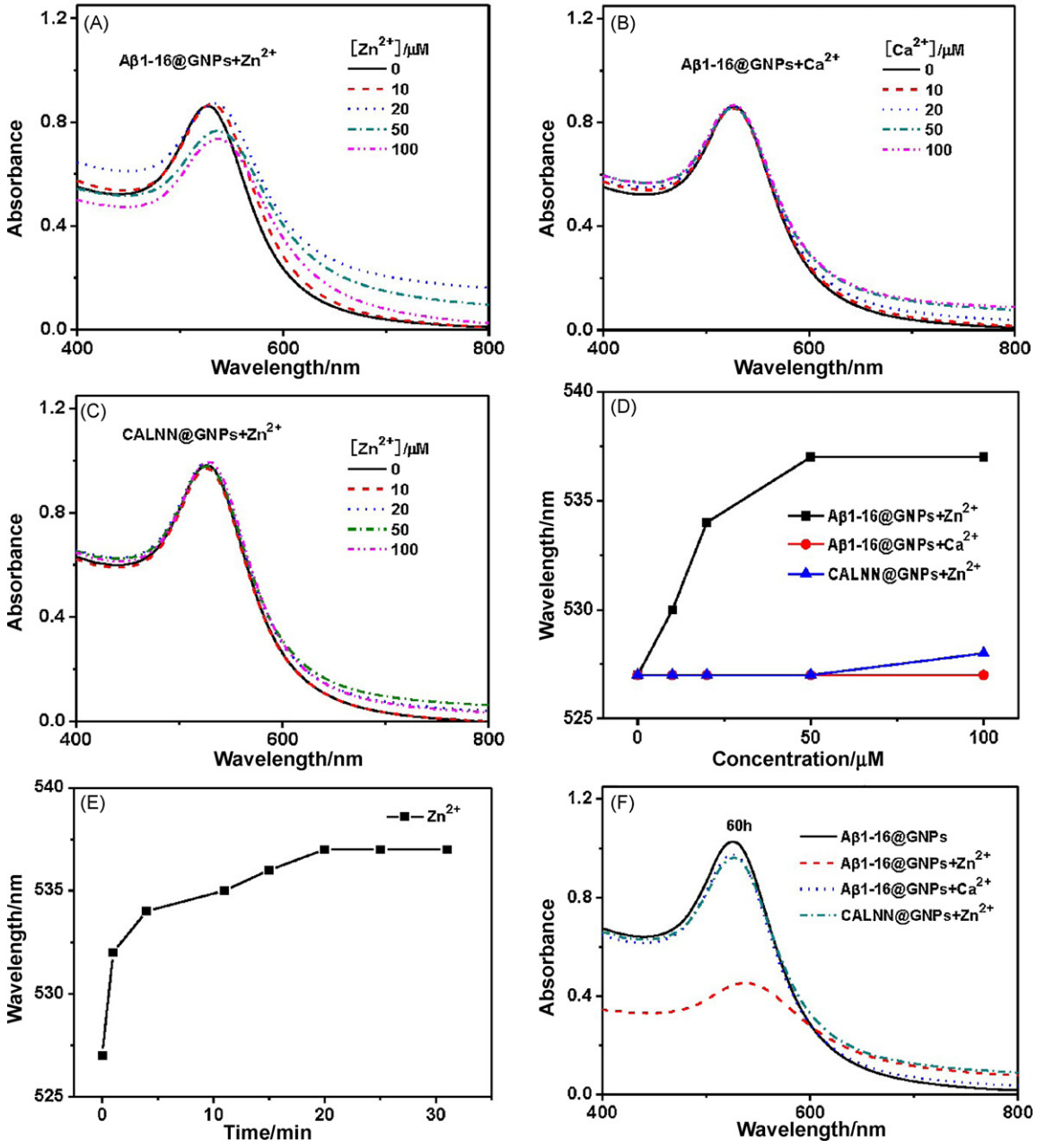


Fig. 1. The UV–visible spectra of Aβ1–16@GNPs and CALNN@GNPs versus different ion concentrations after 30 min incubation. The figures represent Aβ1–16@GNPs solutions with Zn^{2+} (A), Ca^{2+} (B), CALNN@GNPs solutions with Zn^{2+} (C) and the changes of maximum wavelength (λ_{max}) of GNPs solutions with metallic ions (D). Changes of λ_{max} as a function of time of Aβ1–16@GNPs with 50 μM Zn^{2+} (E), UV–visible spectra of Aβ1–16@GNPs or CALNN@GNPs after incubation with 50 μM metallic ions for 60 h (F).

However, the maximum absorption of Aβ1–16@GNPs is gradually decreased and the absorption peak becomes broaden with increasing the incubation time. This phenomenon indicates that large scale Aβ1–16@GNPs aggregation/polymerization is formed. On the contrary, no significant spectral change is observed in series of control experiments (i.e. Aβ1–16@GNPs without ions or with 50 μM Ca^{2+}, and CALNN@GNPs with Zn^{2+} under same condition). This result gives a further spectral evidence that the changes of Aβ1–16@GNPs were caused by the interaction of Aβ1–16 with Zn^{2+}.

To further confirm that the observed phenomenon is GNPs-based reaction, the system is examined by TEM. The TEM micrographs show that Aβ1–16@GNPs are stable and able to keep well mono-disperse in solution even after 60 h (as shown in Fig. 2A and D). In the presence of Zn^{2+}, large scale of Aβ1–16@GNPs aggregation has been observed (as shown in Fig. 2B and E). However, no significant aggregation of Aβ1–16@GNPs has been observed after being incubated with Ca^{2+} under same condition (as shown in Fig. 2C and F). This experimental result agrees with previous reports on that Aβ1–16 alone can hardly self-assemble into fibrils in water without metallic ions (e.g. Zn^{2+}) [3] and consistent with our UV–visible study.

3.2. Reversibility of aggregation of Aβ1–16@GNPs

In addition, the aggregation process can be reversed by the addition of EDTA, a good chelation agent of Zn^{2+}, resulting in a blue shift of the SPR peak of Aβ1–16@GNPs from 537 nm back to the initial position (527 nm), and the change can be cycled by the alternating addition of Zn^{2+} or EDTA (as shown in Fig. 3A and B), respectively. Furthermore, the process has also been examined by TEM (as shown in Fig. 3C and D). The TEM experimental result is consistent with UV–visible study.

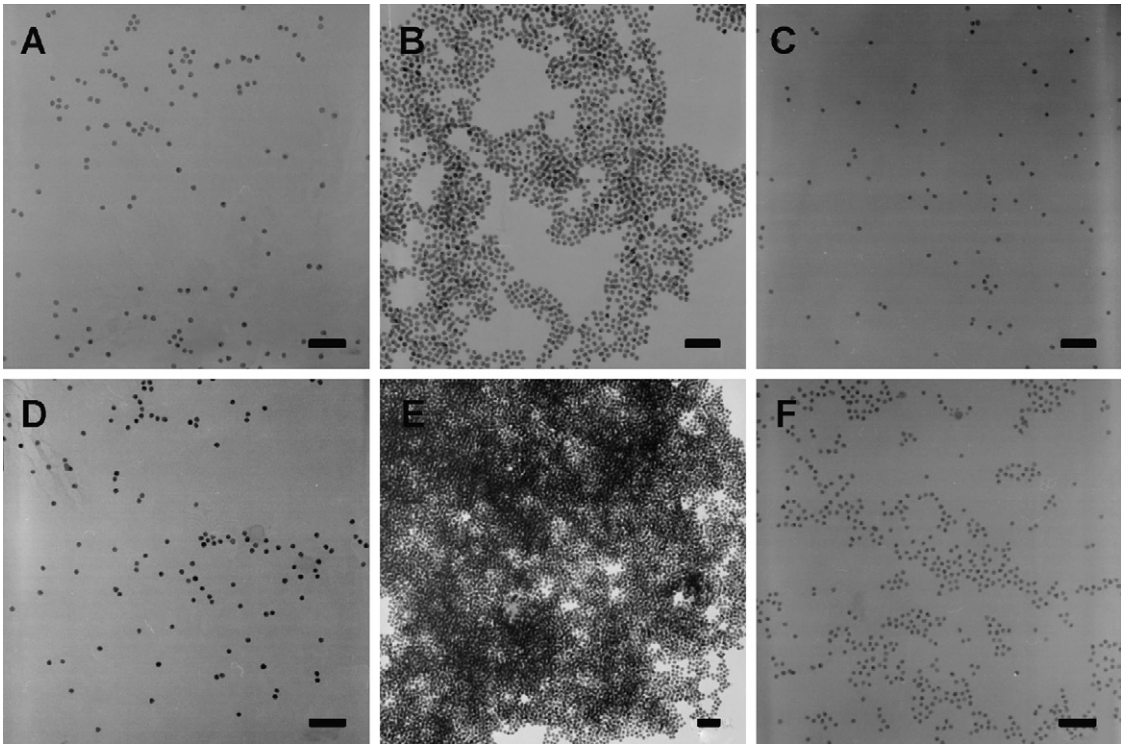


Fig. 2. TEM micrographs of Aβ1–16@GNPs without (A and D) and with 50 μM Zn^{2+} (B and E), 50 μM Ca^{2+} (C and F), respectively. The reaction times are 30 min (A–C) and 60 h (D–F). The scale bars indicate 100 nm.

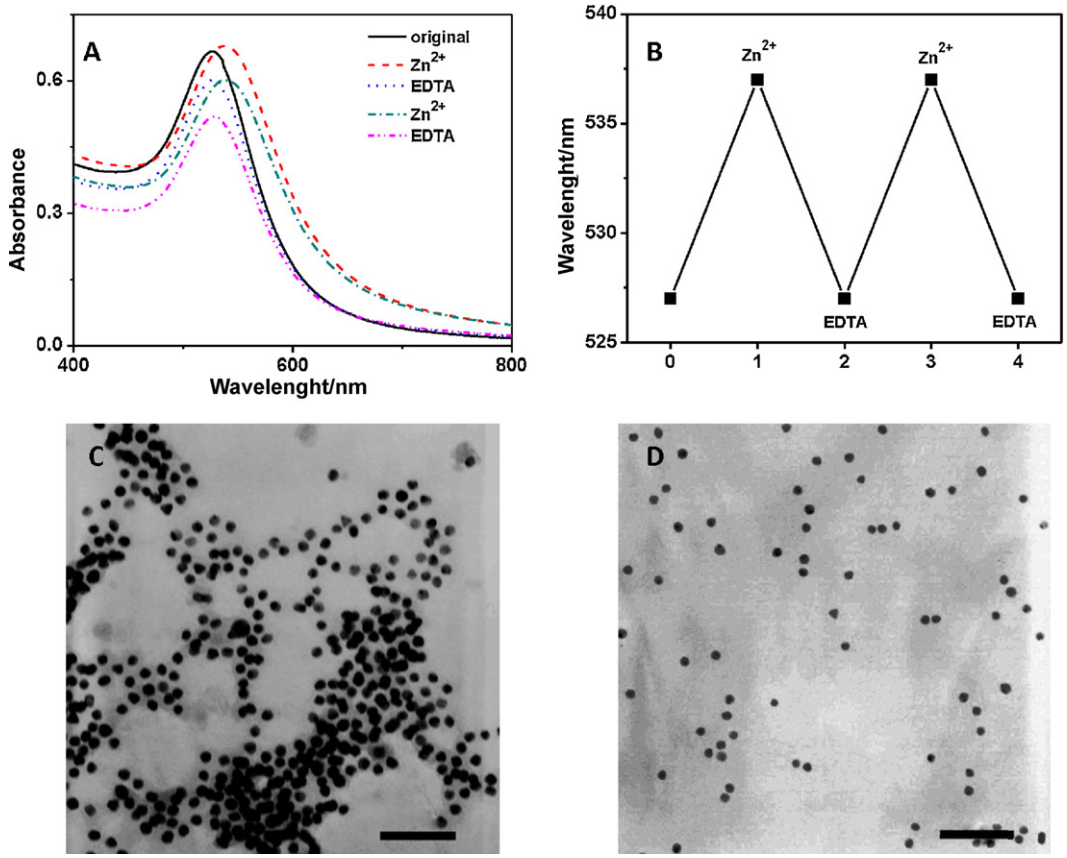


Fig. 3. The UV–visible spectra of Aβ1–16@GNPs after the addition of Zn^{2+} and EDTA (A), changes of λ_{max} in the presence of Zn^{2+} and EDTA (B), TEM micrographs of Aβ1–16@GNPs after the addition of 50 μM Zn^{2+} (C), 50 μM Zn^{2+} with 50 μM EDTA (D), respectively. The scale bars indicate 100 nm.

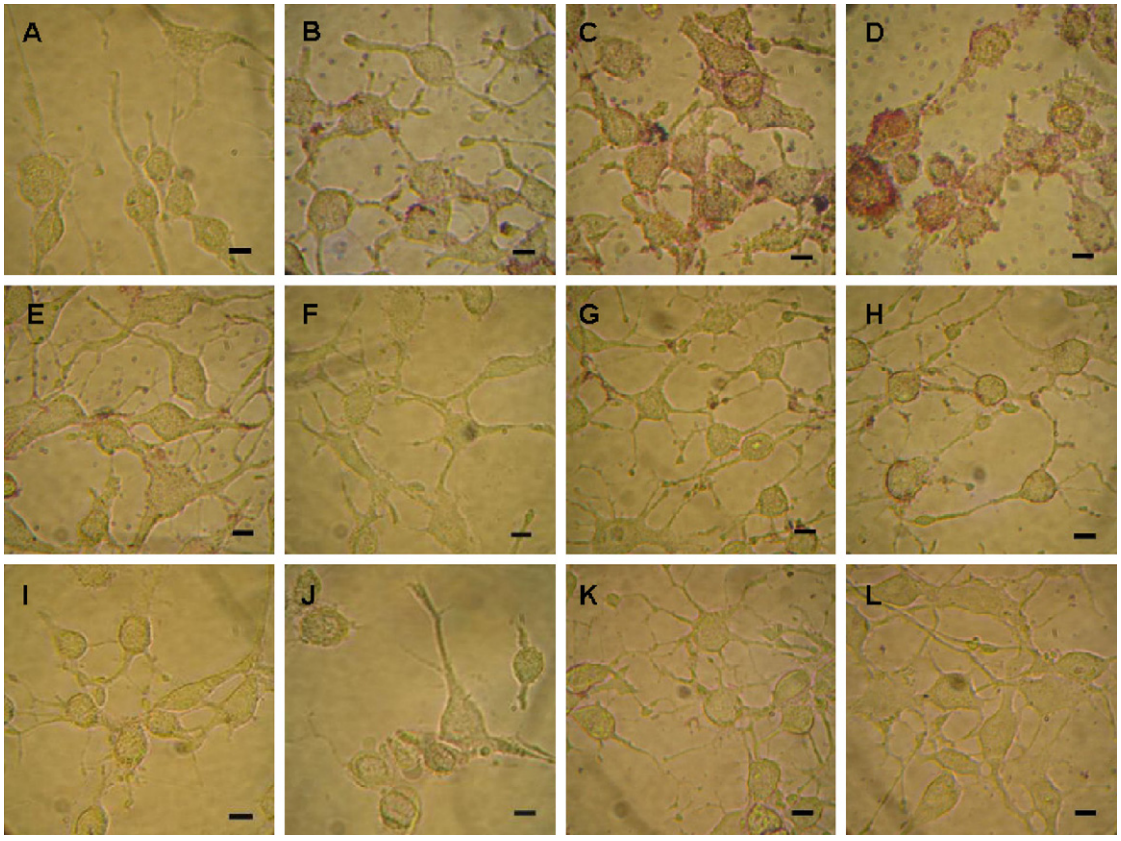


Fig. 4. Co-culturing of SHG-44 cells with GNPs. The figures represent cells alone (A). Cells co-cultured with Aβ1–16@GNPs and 20 (B), 50 (C), 100 μM (D) Zn^{2+} and 50 μM Zn^{2+} with 100 μM EDTA (E), respectively. Cells co-cultured with 50 μM Zn^{2+} (F) or Aβ1–16@GNPs (G). Cells co-cultured with Aβ1–16@GNPs and 50 μM Ca^{2+} (H). Cells incubated with streptavidin@GNPs without ions (I), with 50 μM Zn^{2+} (J) and cells incubated with CALNN@GNPs without ions (K), with 50 μM Zn^{2+} (L), respectively. The scale bars indicate 10 μm.

3.3. Interactions of Aβ1–16@GNPs with SHG-44 cells

SHG-44 cell line was chosen here to investigate the interaction of Aβ1–16@GNPs, living cells and Zn^{2+} since SHG-44 cell was derived from human frontal lobe astrocytoma which relates to some severe brain diseases. A clear Zn^{2+}-induced binding of Aβ1–16@GNPs with living SHG-44 cells has been observed. In the presence of Zn^{2+} in the culture medium, SHG-44 cell line exhibits a high level of Aβ1–16@GNPs binding. The phenomena were able to be observed by a conventional microscope and the amount of cellular binding particles was increased with increasing the concentration of Zn^{2+} (as shown in Fig. 4A–D). In addition, the Aβ1–16@GNPs staining cells can be reversed from bright red to colorless by the addition of EDTA (as shown in Fig. 4E). The experimental result is consistent with previous reports on that strongly metal chelating agents are able to reverse the aggregation of synthetic Aβ peptide and dissolve amyloid in postmortem human brain specimens [26–28]. In the control experiments, no significant cellular binding behavior of particles has been observed (as shown in Fig. 4F–L). The results indicate that it is possible to devolop a assay without complex instrumentation to identify metallic ion inducing Aβ peptide misfolding/aggregation and screening amyloid-like aggregate inhibitors in vivo.

3.4. Cytotoxicity of Aβ1–16@GNPs

Cellular cytotoxic effect is a critical issue of the protein aggregates/fibers. To determine cytotoxicity of Zn^{2+}, Aβ1–16@GNPs on SHG-44 cells, cell viability is investigated by classic trypan blue exclusion. As shown in Fig. 5, in the presence of Zn^{2+}, the Aβ1–16@GNPs reveal strongly cytotoxic effects on the cells, only half of the cells survived after co-culturing with Zn^{2+} and the Aβ1–16@GNPs for 2 h. The experimental results indicate that Zn^{2+} can induce Aβ1–16@GNPs binding on the cellular surface and inhibit cell viability. This phenomenon agrees with literature reports on the cytotoxicity of protein aggregates/fibers [29,30].

3.5. Time-dependent effect of Aβ1–16@GNPs on cells

When SHG-44 cells are co-cultured with Aβ1–16@GNPs and 50 μM Zn^{2+}, a time-dependent binding behavior is observed (as shown in Fig. 6A–E). The amount of cellular binding of

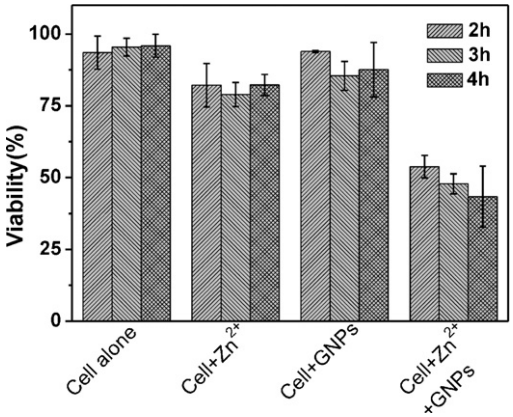


Fig. 5. Cell viability study after being co-cultured with 50 μM Zn^{2+} and/or 2.4 nM Aβ1–16@GNPs.

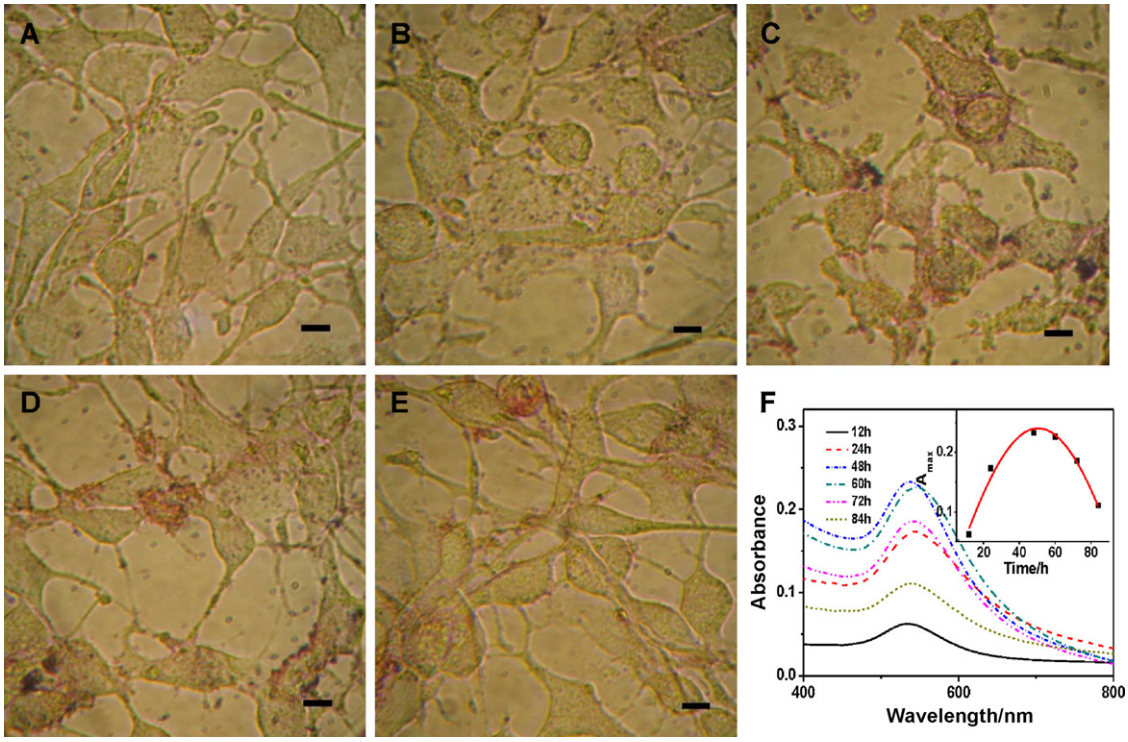


Fig. 6. Time-dependent study of SHG-44 cells co-cultured with Aβ1–16@GNPs and 50 μM Zn^{2+} after 12 h (A), 24 h (B), 48 h (C), 60 h (D), 84 h (E), respectively; the UV–visible spectra of cell solutions after co-cultured with Aβ1–16@GNPs and Zn^{2+} in the different time (F). Inset of (F) shows the maximum absorbance changes with time increasing. The scale bars indicate 10 μm.

Aβ1–16@GNPs is increased by increasing incubation time from 0 h to 48 h and reach saturation at 48 h. Then, binding amount of the particles on cellular surface was gradually decreased from 48 h to 84 h. This result may indicate changes in cellular membrane composition (i.e. amyloid precursor protein or tau protein expressing level) during progression of cells. Initial evidence has been obtained by the cellular DNA isolating experiment (data not shown) and further studies on the mechanism of this phenomenon are currently in progress.

4. Conclusions

In summary, benefit on the unique optical properties of GNPs, a simple colorimetric approach for studying the interaction of Aβ1–16 with metallic ions is developed. As proof-of-principle experiments, the interaction of two metallic ions (Zn^{2+} and Ca^{2+}) with Aβ1–16 functionalized GNPs in solution and co-culturing with SHG-44 cells have been carefully studied. The experiment results suggest that the Aβ1–16 conjugated GNPs could be used as an optical nanosensor to detect Aβ1–16 aggregation/polymerization induced by metallic ions both in solution and different cell circle phases. Therefore, this new type of GNP-based assay could open up a new possibility to develop simple biosensors for biological or biomedical applications, such as amyloid-like aggregate inhibitors screening and the aggregate process study of the peptide in vivo.

Acknowledgments

The authors would like to thank the NSFC (Grant No. 20675080), Chinese Academy of Sciences (Grant No. KJCX2-YW-H11) and CAS-Bayer Start-up Fund (2008) for financial supports.

References

[1] C. Ross, M. Poirier, Nat. Med. 10 (2004) S10.
[2] B. Bulic, M. Pickhardt, B. Schmidt, E.-M. Mandelkow, H. Waldmann, E. Mandelkow, Angew. Chem. Int. Ed. 48 (2009) 1740.
[3] S.A. Kozin, S. Zirah, S. Rebuffat, G. Hui Bon Hoa, P. Debey, Biochem. Biophys. Res. Commun. 285 (2001) 959.
[4] J. Dong, C.G. Atwood, V.E. Anderson, S.L. Siedlak, M.A. Smith, G. Perry, P.R. Carey, Biochemistry 42 (2003) 2768.
[5] K. Pagel, T. Seri, H. v. Berlepsch, J. Griebel, R. Kirmse, C. Böttcher, B. Koksch, ChemBioChem 9 (2008) 531.
[6] T. Miura, K. Suzuki, N. Kohata, H. Takeuchi, Biochemistry 39 (2000) 7024.
[7] H. Yu, J. Ren, X. Qu, ChemBioChem 9 (2008) 879.
[8] H. LeVine, Protein Sci. 2 (1993) 404.
[9] M.J. Kogan, N.G. Bastus, R. Amigo, D. Grillo-Bosch, E. Araya, A. Turiel, A. Labarta, E. Giralt, V.F. Puntes, Nano Lett. 6 (2006) 110.
[10] M.C. Daniel, D. Astruc, Chem. Rev. 104 (2004) 293.
[11] Y. Zhou, S. Wang, K. Zhang, X. Jiang, Angew. Chem. Int. Ed. 47 (2008) 7454.
[12] K.L. Kelly, E. Coronado, L.L. Zhao, G.C. Schatz, J. Phys. Chem. B 107 (2003) 668.
[13] D. Zhou, L. Yang, R. Yang, W. Song, S. Peng, Y. Wang, Talanta (2009), doi:10.1016/j.talanta.2009.06.048.
[14] Z. Wang, L. Ma, Coord. Chem. Rev. 253 (2009) 1607.
[15] Mrinmoy De, P.S. Ghosh, V.M. Rotello, Adv. Mater. 20 (2008) 4225.
[16] M.R. Satyabrata Si, T.K. Paira, T.K. Mandal, ChemPhysChem 9 (2008) 1578.
[17] B. Sepulveda, C. Angelome Paula, L.M. Lechuga, L.M. Liz-Marzan, Nano Today 4 (2009) 244.
[18] H. Wang, Y. Wang, J. Jin, R. Yang, Anal. Chem. 80 (2008) 9021.
[19] D. Aili, K. Enander, J. Rydberg, I. Nesterenko, F. Björefors, L. Baltzer, B. Liedberg, J. Am. Chem. Soc. 130 (2008) 5780.
[20] F. He, Q. Shen, H. Jiang, J. Zhou, J. Cheng, D. Guo, Q. Li, X. Wang, D. Fu, B. Chen, Talanta 77 (2009) 1009.
[21] J. Turkevich, P.C. Stevenson, J. Hillier, Discuss. Faraday Soc. 11 (1951) 55.
[22] G. Frens, Nat. Phys. Sci. 241 (1973) 20.
[23] Z. Wang, R. Levy, D.G. Fernig, M. Brust, Bioconjug. Chem. 16 (2005) 497.
[24] R. Levy, N.T.K. Thanh, R.C. Doty, I. Hussain, R.J. Nichols, D.J. Schiffrin, M. Brust, D.G. Fernig, J. Am. Chem. Soc. 126 (2004) 10076.
[25] D. Noy, I. Solomonov, O. Sinkevich, T. Arad, K. Kjaer, I. Sagi, J. Am. Chem. Soc. 130 (2008) 1376.
[26] R.A. Cherny, J.T. Legg, C.A. McLean, D.P. Fairlie, X. Huang, C.S. Atwood, K. Beyreuther, R.E. Tanzi, C.L. Masters, A.I. Bush, Biol. Chem. 274 (1999) 23223.
[27] C.J. Maynard, A.I. Bush, C.L. Masters, R. Cappai, Q.-X. Li, Int. J. Exp. Pathol. 86 (2005) 147.
[28] C.S. Atwood, R.D. Moir, X. Huang, R.C. Scarpa, N.M. Bacarra, D.M. Romano, M.A. Hartshorn, R.E. Tanzi, A.I. Bush, J. Biol. Chem. 273 (1998) 12817.
[29] N. Arispe, E. Rojas, H. Pollard, Proc. Natl. Acad. Sci. U.S.A. 90 (1993) 567.
[30] M. Lin, T. Mirzabekov, B. Kagan, J. Biol. Chem. 272 (1997) 44.

Talanta 80 (2010) 1632–1637

Contents lists available at ScienceDirect

Talanta

journal homepage: www.elsevier.com/locate/talanta

A sensitive and highly stable electrochemical impedance immunosensor based on the formation of silica gel–ionic liquid biocompatible film on the glassy carbon electrode for the determination of aflatoxin B_1 in bee pollen

Li Zaijun[a,*], Wang Zhongyun[a], Sun Xiulan[b], Fang Yinjun[c], Chen Peipei[a]

[a] School of Chemical and Material Engineering, Jiangnan University, 1800 Lihu Dadao, Wuxi 214122, China
[b] School of Food Science and Technology, Jiangnan University, Wuxi 214122, China
[c] Zhejiang Zanyu Technology Co., LTD., Hangzhou 310009, China

ARTICLE INFO

Article history:
Received 13 August 2009
Received in revised form
24 September 2009
Accepted 28 September 2009
Available online 4 October 2009

Keywords:
Ionic liquid
Silica gel
Immunosensor
Aflatoxin B_1
Bee pollen

ABSTRACT

The paper describes a sensitive and highly stable label-free electrochemical impedance immunosensor for the determination of aflatoxin B_1 (AFB_1), which is based on the formation of silica gel–ionic liquid biocompatible film on the glassy carbon electrode. The electrochemical performances of the sensor were investigated by electrochemical impedance spectroscopy using a $Fe(CN)_6^{3-/4-}$ phosphate buffer solution as base solution for test. As new ionic liquid, 1-amyl-2,3-dimethylimidazolium hexafluorophosphate, offers a very biocompatible microenvironment for AFB_1 antibody, the sensor exhibits good repeatability (RSD = 1.2%), sensitive electrochemical impedance response to AFB_1 in the range of 0.1–10 ng ml^{-1} and lowers the detection limit of AFB_1 (0.01 ng ml^{-1}). The electron-transfer resistance change of the sensor after and before incubation with AFB_1 of 2.0 ng ml^{-1} can retain 95% over a 180-day storage period at 4 °C. The results present a remarkable improvement of sensitivity (2-fold) and long-term stability (190-fold) when compared to classical silica gel sensor. Moreover, proposed sensor has a high selectivity to AFB_1 alone with no significant response to AFB_2, AFG_1, AFG_2 and AFM_1 as single substrates, it has been successfully applied to the determination of trace AFB_1 in bee pollen samples with a spiked recovery in the range of 96.0–102.5%.

© 2009 Elsevier B.V. All rights reserved.

1. Introduction

Bee pollen has been widely used as food in human diets, providing a well-being sensation and contributing to functional and harmonious balance of the body [1]. However, during collecting, treating and storing bee pollen may be contaminated by aflatoxins (AFs) [1,2]. AFs are highly oxygenated polyketides produced as secondary metabolites by the fungi *Aspergillus flavus* and *Aspergillus parasiticus* [3]. Naturally, occurring AFs are composed of AFB_1, AFB_2, AFG_1, and AFG_2. AFB_1, which is the most abundant and carcinogenic, was classified as a carcinogenic substance of group 1 by the International Agency for Research on Cancer [4]. AFB_1 is of good thermal stability, it is hard to destroy them once they are formed [5]. Thus, the determination of AFB_1 in bee pollen is of very importance.

Some modern analytical methods have been developed for the determination of AFB_1 such as thin-layer chromatography (TLC) [6], high performance liquid chromatography (HPLC) [7–10], enzyme-linked immunosorbant assay (ELISA) [11] and spectrofluorimetry [12]. TLC, HPLC and spectrofluorimetry typically require skilled operators, extensive sample pretreatment and expensive equipment. ELISA is simple and rapid and was mainly used for screening purposes. To increase the selectivity, the antibody was widely used to clean up samples prior to measurement with a concomitant increase in assay sensitivity by LC, HPLC [13], electrochemical [14] and fluorescence spectroscopy [15]. Recently, various electrochemical sensors were given special attention due to their fast, simple, and low-cost. Some novel technologies were also employed for fabrication of the sensors to improve sensitivity, selectivity or stability, including biocatalytic amplification of enzyme labels [16], biocatalyzed precipitation [17], silver-enhanced gold nanoparticle label [18], biocatalytic deposition of silver nanoparticles [19,20], and biocatalytic metal deposition [19]. However, present electrochemical sensors are difficult to be widely applied to routine analysis due to the lack of enough stability.

Ionic liquids are compounds consisting entirely of ions that exist in liquid state around room temperature. The investigation of ionic liquids has gained increasing attention because of their unique chemical and physical properties, such as negligible vapor pressure, low toxicity, wide potential window, high ionic conductivity and good solubility. Although ionic liquids have been extensively used

* Corresponding author. Tel.: +86 5105811863; fax: +86 5105811863.
E-mail address: zaijunli@263.net (L. Zaijun).

0039-9140/$ – see front matter © 2009 Elsevier B.V. All rights reserved.
doi:10.1016/j.talanta.2009.09.058

as biocompatible materials for the fabrication of biosensor [21–23] and non-aqueous biocatalysts [24,25], there is no report, in which ionic liquid was directly used for the fabrication of electrochemical immunosensor.

In this work, we present preliminary studies to establish a novel label-free electrochemical impedance immunosensor as a tool for AFB_1 detection. The sensor uniquely incorporates excellent biocompatibility of ionic liquid with highly efficient antibody immobility of silica gel. A new ionic liquid, 1-amyl-2,3-dimethylimidazolium hexafluorophosphate, was employed for improving electrochemical performance of the sensor. The main parameters governing the impedance responses were optimized, including operating pH and incubation time. Proposed immunoassay was overall proofed with simple, selective, sensitive and highly stable analysis feature by real bee pollen and spiked sample with known AFB_1 concentration.

2. Experimental

2.1. Materials and reagents

Tetraethoxysilane (TEOS), AFs and Triton X-100 were purchased from Sigma. Polyclonal antibody (Ab) was generated in rabbits in the laboratory by immunizing the animals with AFB_1-BSA [26,27]. 1-Bromopentane was purchased from Yixing Cheng Yuan Chemical Co., Ltd. (Yixing, China) and 1,2-dimethylimidazole was provided by Linhai Kaile Chemical Co., Ltd. (Linhai, China). Phosphate-buffered saline (PBS, pH 7.5, Na_2HPO_4–KH_2PO_4–NaCl–KCl, 0.01 mol l^{-1}) was prepared. All other reagents employed were of analytical reagent grade or with highest quality and were purchased from Shanghai Chemical Company (Shanghai, China), and ultra pure water (18.2 ΩM cm) purified from a Milli-Q purification system was used throughout the experiment.

2.2. Apparatus

Electrochemical experiments were performed with an IM6e electrochemical system (ZAHNER Elektrik, German). A conventional three electrode system was used with Ag/AgCl (saturated KCl) electrode as the reference electrode, platinum wire as the counter electrode, and a modified glassy carbon electrode (GCE, 2 mm in diameter) as working electrode. If not mentioned, all potentials given below were relative to Ag/AgCl (saturated KCl) electrode.

2.3. Preparation of the ionic liquid

Transfer equal amounts (0.5 mol) of 1-bromopentane and 1,2-dimethylimidazole (distilled freshly) to 500 ml of the round bottom flask, which is fitted with reflux condenser and nitrogen protecting facilities. Add 100 ml of toluene to the flask as solvent. After the mixture was stirred for 48 h at 40 °C, a transparent viscous product 1,2-dimethyl-3-amylimidazolium bromide was formed. The liquid was cooled and transferred to a 2000 ml of the beaker. And then 400 ml of potassium hexafluorophosphate (0.5 mol) was added to the well stirred mixture. After the addition of the reagent, the mixture was continuously stirred for 4 h. And then the water phase was discarded and the formed 1-amyl-2,3-dimethylimidazolium hexafluorophosphate was washed with distilled water until bromide ion was wiped off completely using a silver nitrate test. The collected ionic liquid was heated to 110 °C under vacuum to remove water for 30 min, the solvent and unreacted reactant, total yield was about to 95%. The ^1H NMR data of the product were listed in the following (400 MHz, CD_3OCD_3): 0.9 (t, 3H), 1.3(m, 4H), 1.8 (m, 2H), 2.6 (s, 3H), 3.8 (s, 3H), 4.0 (t, 2H), 7.15 (s, 1H), 7.2 (s, 1H).

2.4. Electrodes preparation

Procedure of the electrode preparation includes four assemble processes, i.e. pretreatment of GCE, preparation of silica gel/ionic liquid (SGIL), immobilization of Ab on the electrodes surface and immunity of the sensor (shown in Fig. 1). (1) GCE was polished successively with 1.0, 0.3, and 0.05 μm alumina powder, and sonicated in a 6.0 mol l^{-1} nitric acid/doubly distilled water and ethanol/doubly distilled water for 20 min, respectively. Then, the GCE electrode as working electrode was subjected to cyclic scanning in 0.5 mol l^{-1} H_2SO_4 solution in a potential range from −0.1 to 1.0 V. When the cyclic voltammogram was almost unchanged, the electrode was taken out, cleaned with water and dried under a stream of nitrogen. (2) The sol cocktail was prepared by mixing TEOS and acidified water (HCI, pH 2). In order to avoid occurring crack on the final composite film, a non-ionic surfactant Triton X-100 was added for the purpose. The volume ratio 10% (v/v) Triton X-100:TEOS:H_2O equal to 1:40:40 was held. The mixture initially comprising of two phases is made uniform by stirring vigorously under magnetic stirring at room temperature until SiO_2 was distributed evenly in the aqueous solution while the hydrolysis reaction occurs. After 10 h, the opaque silica sol was obtained. The silica sol/ionic liquid was prepared by mixing a 0.9 ml of the silica sol and 0.1 ml of the ionic liquid with a magnetic stirring for 1 h at room temperature. (3) After 1.0 ml of the silica sol gel/the ionic liquid mixed with 1.0 ml of the Ab solution containing 0.66 mg of the Ab under magnetic stirring for 0.5 h, immobilization of the Ab was completed by dropping a 0.7 μl of above mixture on the electrode surface, and it was then stored in a refrigerator at 4 °C overnight. (4) For immunity of the sensor, the modified electrode was incubated in the 20 ml of PBS (pH 7.5) containing different concentrations of AFB_1 at 37 °C under magnetic stirring for 25 min.

2.5. Electrochemical measurements

Prior to each experiment, the buffer solutions were purged with highly purified nitrogen for at least 30 min and a nitrogen atmosphere environment was kept in electrochemical measurements. Electrochemical experiments were performed with IM6e electrochemical system. Cyclic voltammetry (CV) and impedance measurements were performed in 10 ml of a pH 7.5 PBS containing 1.0 mmol l^{-1} $K_3[Fe(CN)_6]$/$K_4[Fe(CN)_6]$ (1:1 mixture as redox probe). The impedance spectra were measured in the frequency range from 10^5 to 1 Hz in a potential of 0.20 V versus Ag/AgCl (saturated KCl), with a voltage amplitude of 5 mV. The impedance Z was expressed in terms of a real (Z') and an imaginary (Z'') component. Impedance signals were recorded after reaction between the electrodes and the unstirred substrate solution for 5 min.

2.6. Sample preparation

Bee pollen samples were purchased from China market in Wuxi city. 5.0 g of the sample was extracted with 25 ml of extraction solvent (85% methanol in PBS) by shaking for 45 min. Then the extract was separated from the insoluble materials by centrifugation for 10 min at 6000 rpm. A 2 ml of the extract was diluted five times with PBS. The suspension was then hand shaken for 10 min. After the separation of the two layers, the aqueous layer was used for AFB_1 detection by the procedure described in Section 2.5.

3. Results and discussions

3.1. Cyclic voltammetry characterization

The cyclic voltammetric studies of pretreated bare GCE and modified GCE fabricated based on the silica gel–ionic liquid com-

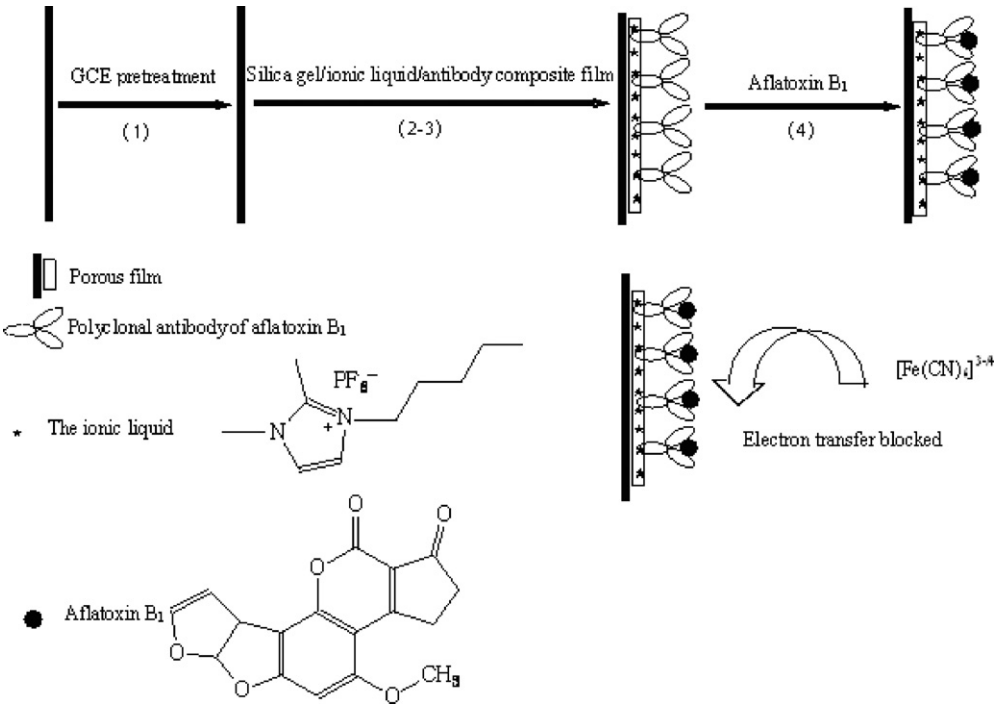


Fig. 1. Procedure of the immunosensor preparation.

posite film incubated in PBS (at pH 7.5) containing AFB_1 of 0.0, 1.0 and 7.0 ng ml^{-1} in 1.0 mmol l^{-1} $[Fe(CN)_6]^{3-/4-}$ at scan rate of 100 mV s^{-1} have been conducted to understand the nature of the bond between the ionic liquid and Ab as well and the effect of ionic liquid (Fig. 2). The cyclic voltammetric of pretreated bare GCE (curve a) shows well-defined reversible redox behavior attributed to highly electron-transfer between $[Fe(CN)_6]^{3-/4-}$ solution and the electrode. After attachment of Ab–SGIL film on the surface of the electrode, magnitude of current decreases (curve b) due to complex between –OH and –OH (or $-O^-$ and 1,2-dimethyl-3-amylimidazolium) partially block the electron-transfer between $[Fe(CN)_6]^{3-/4-}$ solution and the electrode, and the reduction potential is shifted towards the lower side at 0.24 V as compared to that of bare GCE (0.34 V). It appears the ionic liquid enhances electron conduction pathway due to its good

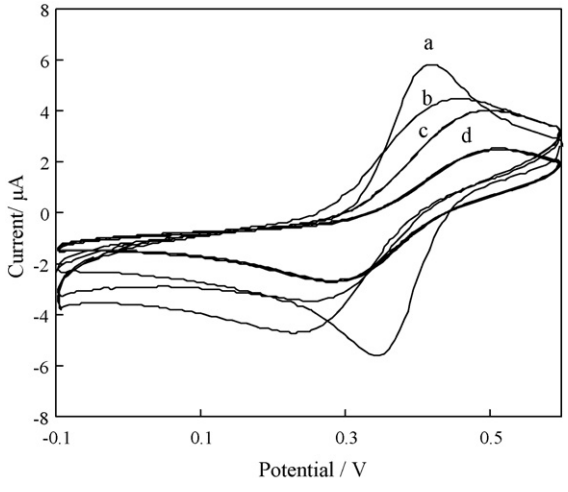


Fig. 2. Cyclic voltammograms for bare GCE (a) and modified GCE fabricated based on the silica gel/the ionic liquid composite films incubated in PBS (at pH 7.5) containing AFB_1 of 0.0 ng ml^{-1} (b), 1.0 ng ml^{-1} (c) and 7.0 ng ml^{-1} (d) for 25 min in 1.0 mmol l^{-1} $[Fe(CN)_6]^{3-/4-}$. The scan rate was 100 mV s^{-1}.

conductivity. After modified electrode was incubated in PBS containing AFB_1, the more decrease of magnitude of current was observed (curves c and d). The formation of Ab–AFB_1 complex on surface of Ab–SGIL–GCE results in an increasing block performance of electron-transfer between $[Fe(CN)_6]^{3-/4-}$ solution and the electrode, this lead to decrease of magnitude of current of Ab–AFB_1–SGIL–GCE.

3.2. Impedance spectroscopy characterization

The detailed electron-transfer behaviors of Ab–SG–GCE and Ab–SGIL–GCE electrode were also performed by electrochemical impedance spectroscopy. The clear semicircle portions were recorded in Nyquist plots of electrochemical impedance spectra for the bare GCE electrode (Fig. 3(a, EIS)), Ab–SG–GCE electrode (Fig. 3(b, EIS)) and Ab–SGIL–GCE electrode (Fig. 3(c and d, EIS)), indicating they are the electron-transfer limited process. From Fig. 3(EIS) it can be seen the electron-transfer resistances of the redox (R_{et}) for Ab–SG–GCE and Ab–SGIL–GCE electrodes increased obviously when incubated with AFB_1. The increase of R_{et} is caused by electrically insulating bioconjugates produced from specific interaction of AFB_1 and Ab, which will block the electron-transfer of $[Fe(CN)_6]^{3-/4-}$ solution to the electrode. Moreover, Fig. 3(EIS) indicated also Warburg impedance value (Z_w) of the Ab–SGIL–GCE electrode was obviously bigger than that of Ab–SG–GCE electrode, this was ascribed to diffusivity of the ionic liquid. Since taking into account the effect of the roughness of electrode surfaces, constant phase element (CPE), expressed as $Z_{cpz} = K\omega^{-\alpha}$, was chosen to replace the ideal element, i.e. capacitance or resistance. The deviation of frequency exponent α from ideal values was attributed to the homogeneities of the analyzed layer, like roughness or defects. Randles model was used as an equivalent circuit to fit all the data of electrochemical impedance measurement (Fig. 3(EC)) Here, R_s, R_{et}, Q and Z_w represented ohmic resistance of electrolyte solution, the electron-transfer resistance of the redox, constant phase element and Warburg impedance, respectively. It was found that all the square of standard derivations between original and simulated

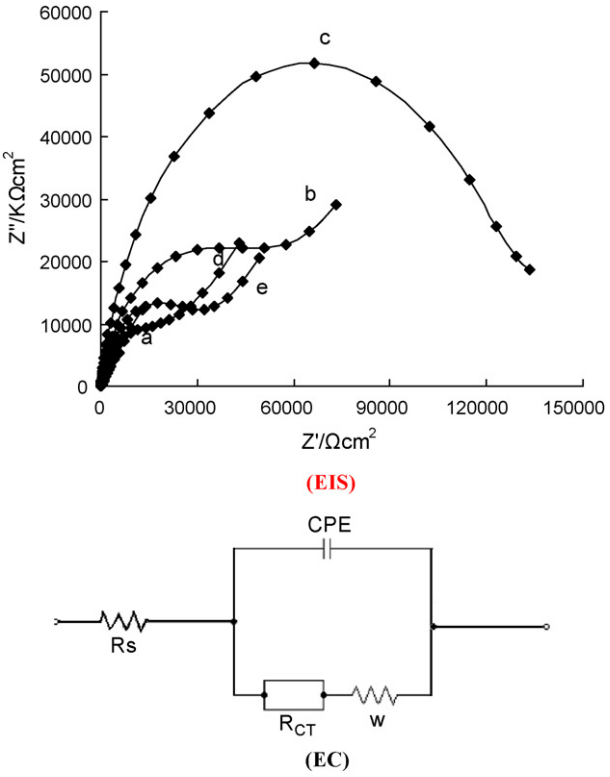


Fig. 3. Faradaic impendence spectra that corresponded to bare GCE in 1.0 mmol l^{-1} $[Fe(CN)_6]^{3-/4-}$ solution (a), the modified electrode based on normal silica gel technology before (b) and after (c) incubating with 2.0 ng ml^{-1} of AFB_1 in PBS (pH 7.5) solution in 1.0 mmol l^{-1} $[Fe(CN)_6]^{3-/4-}$, and the modified electrode based on silica gel/the ionic liquid composite film before (d) and after (e) incubating with 2.0 ng ml^{-1} of AFB_1 in PBS (pH 7.5) in 1.0 mmol l^{-1} $[Fe(CN)_6]^{3-/4-}$ solution, respectively. Symbols represented the measured data, while solid lines were the theoretical spectra of equivalent circuit, and equivalent circuit (EC).

Table 1
The electron-transfer resistance and other electrical parameters for different electrodes measured by electrochemical calculated by Randle electrical circuit.

Electrodes	R_s (Ω)	R_{et} (Ω)	Q (μF)	Z_w
Ab–SG–GCE	213.6	34930	2.782	2.54×10^{-5}
Ab–SGIL–GCE	202.3	18730	1.317	3.528×10^{-5}

data for the immunosensors which based on SGIL composite film were in the range from 0.0023 to 0.0034.

The detailed data of electrochemical impedance spectroscopy for two immunosensors were calculated. The results clearly indicated the electron-transfer resistance for Ab–SGIL–GCE electrode was obviously lower than that of Ab–SGIL–GCE electrode (see Table 1). Lower electron-transfer resistance for Ab–SGIL–GCE electrode is mainly ascribed to good conductibility of the ionic liquid.

To the compare effect of different ionic liquids on the electrochemical performance of the sensor, another similar ionic liquid, 1-butyl-2,3-dimethylimidazolium hexafluorophosphate was used to fabricate the immunosensor with a similar procedure in Section 2.4. The R_{et} of the sensor incubated in blank PBS solution (pH 7.5) and in PBS solution containing 3 ng ml^{-1} of AFB_1 were measured

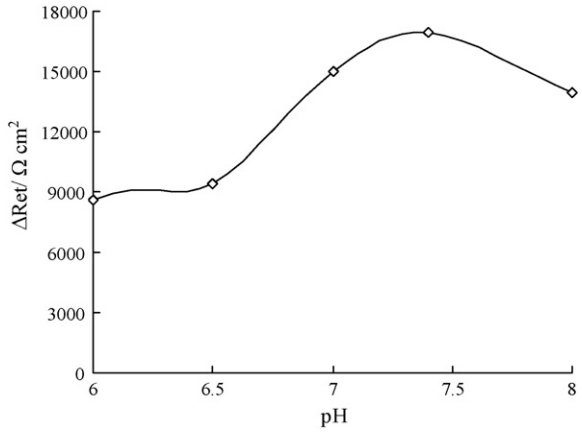


Fig. 4. Effect of pH of PHS on the specific binding of AFB_1 and the Ab immobilized on the surface of the immunosensor. The concentration of AFB_1 was 3.0 ng ml^{-1} and the interaction time 25 min.

and calculated, the results exhibited in Table 2. Table 2 clearly indicates the sensor with ionic liquid 1-amyl-2,3-dimethylimidazolium hexafluorophosphate provides a lower R_{et} in blank PBS solution and more sensitive the R_{et} response to AFB_1 than that with ionic liquid 1-butyl-2,3-dimethylimidazolium hexafluorophosphate, indicating 1-amyl-2,3-dimethylimidazolium hexafluorophosphate offers better conductivity and microenvironment to maintain activity of the Ab than 1-butyl-2,3-dimethylimidazolium hexafluorophosphate.

3.3. Optimization of the assay conditions

In order to optimize assay conditions, effects of the operating pH and incubation time were investigated well. The relationship of the relative changes of ΔR_{et} for Ab–AFB_1–SGIL–GCE electrode was evaluated over a pH range from 6.0 to 8.0 (shown in Fig. 4), in which the modified electrode was incubated in different PBS solutions containing 3.0 ng ml^{-1} of AFB_1 for 25 min. As shown in Fig. 4, the changes of ΔR_{et} for the sensor increased with the increase of pH value in value in range of pH 6–7.5, attained maximum value at about pH 7.5, and then reduced with increasing pH of buffer solution. This exhibited that specific interaction between AFB_1 and the antibody takes place more effectively at pH 7.5.

The incubation time also played an important role in the detection of AFB_1. Fig. 5 indicated with the increase of the incubation time electron-transfer resistance of the modified electrode rapidly increased until the incubation time reached 25 min. When the incubation time exceeds 25 min, the electron-transfer resistance reached maximum and remained almost unchanged. To obtain good sensitivity and rapidity, the operating pH 7.5 and the incubation time of 25 min were adopted in all the following experiments.

3.4. Analytical characteristics

A Nyquist diagram of the electrochemical impedance spectrum is an effective way to measure the electron-transfer resistance. Fig. 6 shows the representative Nyquist diagrams of proposed

Table 2
Comparison of the electron-transfer resistance (R_{et}) of the sensor with different ionic liquids.

The ionic liquid for fabrication of the sensor	R_{et} of the sensor before incubated AFB_1 (Ω)	R_{et} of the sensor after incubated AFB_1 (Ω)	ΔR_{et} of the sensor after and before incubated AFB_1 (time)
1-Butyl-2,3-dimethylimidazolium hexafluorophosphate	21,720	31,180	1.44
1-Amyl-2,3-dimethylimidazolium hexafluorophosphate	18,730	35,670	1.90

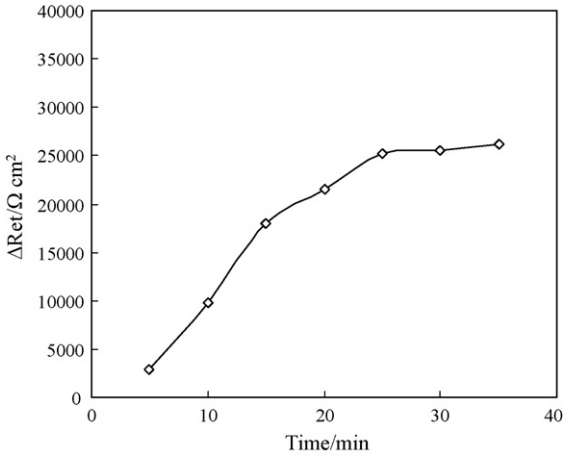


Fig. 5. Effect of the incubation time on the specific binding of AFB_1 and the antibody immobilized on the surface of the immunosensor. The concentration of AFB_1 was 7.0 ng ml^{-1} and the incubation process was performed in PBS solution (pH 7.5).

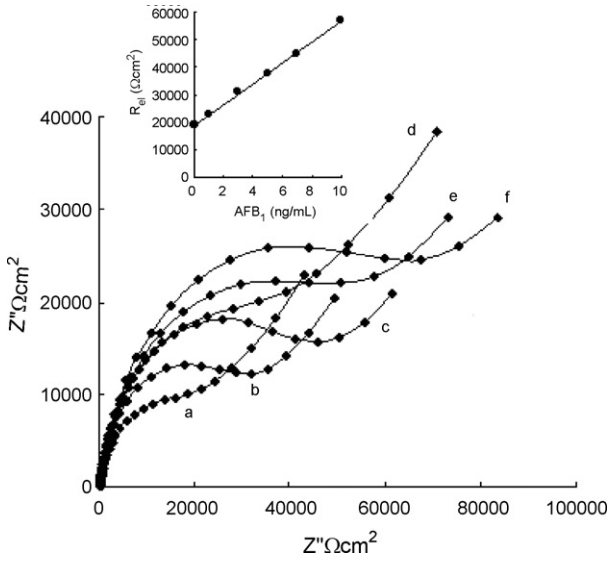


Fig. 6. Faradaic impendence spectra that corresponded to the immunosensor after incubating with different concentrations of AFB_1 in PBS (pH 7.5) containing 1.0 mmol l^{-1} $[Fe(CN)_6]^{3-/4-}$. (a), (b), (c), (d), (e) and (f) represented 0.1, 1.0, 3.0, 5.0, 7.0 and 10.0 ng ml^{-1} of AFB_1, respectively. Symbols represented the measured data, while solid lines were the theoretical spectra of equivalent circuit. The insertion: calibration curve for AFB_1.

sensor in 1.0 mmol l^{-1} $[Fe(CN)_6]^{3-/4-}$ after incubation for 25 min in PBS solution (pH 7.5) containing different concentrations of AFB_1. The electron-transfer resistance increased along with the increase of AFB_1 as shown in curves a–f. The insertion in Fig. 6 indicated the relationship of the electron-transfer resistance with AFB_1 concentrations. A linear relationship between the electron-transfer resistance and AFB_1 concentration value was found in an AFB_1 concentration range of 0.1–10 ng ml^{-1}. The linear equation was R_{et} = 3788.5C + 18,959, with a statistically significant correlation coefficient of 0.9996. The detection limit of label-free impedance detection assay was 0.01 ng ml^{-1} for Ab–SGIL–GCE electrode and 0.02 ng ml^{-1} for Ab–SG–GCE electrode that was obtained from the signal-to-noise characteristics of these data (S/N = 3). This indicated the sensitivity of Ab–SGIL–GCE electrode is 2-fold as same as that of Ab–SG–GCE electrode.

The long-term stability of both Ab–SGIL–GCE and Ab–SG–GCE sensors was examined. The electron-transfer resistance changes (ΔR_{et}) of the sensor after and before incubation with AFB_1 of 2.0 ng ml^{-1} retains 95% for Ab–SGIL–ECE electrode (from 77,577 to 7199 Ω) and 0.5% for Ab–SG–GCE electrode (from 6062 to 303 Ω) over a 180-day storage period at 4 °C. These present remarkable improvement of long-term stability (190-fold) when compared to classical silica gel sensor. We think good sensitivity and stability of Ab–SGIL–GCE electrode ascribe to relatively stable spatial configuration of the Ab, in which the ionic liquid provides favorable microenvironment for the Ab.

The precision was evaluated by successive determinations of 3.0 ng ml^{-1} AFB_1 for six times using the same Ab–SGIL–GCE electrode and experimental conditions. The relative standard deviation was calculated to be 1.2%. The fabrication reproducibility was estimated by the measurements of 3.0 ng ml^{-1} AFB_1, in duplicate, with six different electrodes made at the same GCE electrode independently. The relative standard deviation was 1.7%, showing a good reproducibility and acceptable precision.

3.5. Nonspecific interactions

Since selectivity is a very important characteristic, it was necessary to check it for Ab–SGIL–GCE electrode. Among 18 different types of AFs identified, the major ones are AFB_1, AFB_2, AFG_1, AFG_2 and AFM_1. The International Agency for Research on Cancer has classified all four AFs as Group 1 carcinogens. We, therefore, examined the proposed sensor response to AFB_1 and AFG_1, AFB_2, AFG_2, AFM_1. The results indicated proposed sensor has a high selectivity to AFB_1 alone with no significant response to AFB_2, AFG_1, AFG_2 and AFM_1 as single substrates.

3.6. Regeneration of the electrode

The regeneration of Ab–SGIL–GCE electrode was investigated by repeatedly monitoring the binding of 2.0 ng ml^{-1} AFB_1 under

Table 3
The results for the determination of real and spiked bee pollen samples (n = 5).

Samples	Added AFB_1 (ng g^{-1})	Found AFB_1 by proposed method (ng g^{-1})	Found AFB_1 by HPLC method (ng g^{-1}) [28]	Recovery (%)
Bee pollen 1	0.0	0.52 ± 0.011	0.50 ± 0.018	
	2.0	2.57 ± 0.030		102.5
Bee pollen 2	0.0	0.16 ± 0.046	0.13 ± 0.013	
	2.0	2.08 ± 0.055		96.0
Bee pollen 3	0.0	0.00 ± 0.002	0.00 ± 0.011	
	2.0	1.96 ± 0.019		98.0
Bee pollen 4	0.0	0.39 ± 0.11	0.32 ± 0.17	
	2.0	2.42 ± 0.23		101.5
Bee pollen 5	0.0	0.22 ± 0.006	0.23 ± 0.009	
	2.0	2.15 ± 0.030		96.5

same experimental conditions. Following each binding event, the electrode was regenerated for 30 min in 0.1 mol l^{-1} glycine buffer solution (pH 2) to desorb the combined Ab. The relative standard deviation of the changes of electron-transfer resistances for twenty binding and regeneration cycles was found to be 1.2%. The fact has demonstrated the method using the sensor for AFB_1 detection was of excellent reproducibility.

3.7. Analysis of real samples

The feasibility of the newly developed method for possible applications was investigated by analyzing real bee pollen samples. The preparation of sample was described in Section 2.6. The sample and the spiked sample with different amounts of AFB_1 were testified. The sample was used for the analysis to replace the PBS solution of AFB_1 as mentioned above. The concentration of AFB_1 in bee pollen sample was determined from the calibration curve and the value can be used to calculate the concentration in the original sample. The mean ± SD of each sample and recovery of each spiked sample were calculated, and the values are reported in Table 3. The analytical data for various samples given in Table 3 indicate a high degree of correlation between the results of HPLC and proposed sensor. The recovery of AFB_1 for spiked samples analysis is in the range from 96.0% to 102.5%. These indicated proposed method has a good accuracy and precision.

4. Conclusion

In this paper, a highly sensitive and stable impedance sensor based on silica gel/ionic liquid composite film was developed for AFB_1 detection in bee pollen. Because of good biocompatibility and conductibility of the ionic liquid, the resulting proposed sensor exhibited high sensitivity and stability, indicating the composite film can retain antibody activity. The sensor showed good precision, reproducibility, regeneration and storage stability, and acceptable accuracy for sample determination, which exhibited promising application prospect as novel sensor.

Acknowledgements

The authors acknowledge the financial support from the National Natural Science Foundation of China (Nos. 20771045 and 20676052), the National High Technique Development Plan of 863 (2007AA10Z428), sponsored by Qing Lan Project and the Natural Science Foundation of Zhejiang Province (No. Y4080404).

References

[1] L.B. Almeida-Muradian, L.C. Pamplona, S. Coimbra, O. Monika Barth, J. Food Compos. Anal. 18 (2005) 105–111.
[2] M.J. O'Riordan, M.G. Wilkinson, Food Chem. 107 (2008) 1429–1435.
[3] R.R.M. Paterson, Food Control 18 (2007) 817–820.
[4] J.W. Bennett, M. Klich, Clin. Microbiol. Rev. 16 (2003) 497–513.
[5] A.Y. Kolosova, W.B. Shim, Z.Y. Yang, S.A. Eremin, D.H. Chung, Anal. Bioanal. Chem. 384 (2006) 286–294.
[6] B.B. Jarvis, J.D. Miller, Appl. Microbiol. Biotechnol. 66 (2005) 367–372.
[7] I. Var, B. Kabak, F. Gok, Food Control 18 (2007) 59–62.
[8] M. Alcaide-Molina, J. Ruiz-Jimenez, J.M. Mata-Granados, M.D.L. Luque de Castro, J. Chromatogr. A 1216 (2009) 1115–1125.
[9] L.E. Edinboro, H.T. Karnes, J. Chromatogr. A 1083 (2005) 127–132.
[10] G. Tavcar-Kalcher, K. Vrtac, U. Pestevsek, A. Vengust, Food Control 18 (2007) 333–337.
[11] A. Radoi, M. Targa, B. Prieto-Simon, J.L. Marty, Talanta 77 (2008) 138–143.
[12] J. Hashemi, G.A. Kram, N. Alizadeh, Talanta 75 (2008) 1075–1081.
[13] P.W. Li, Q. Zhang, W. Zhang, J.Y. Zhang, X.M. Chen, J. Jiang, L.H. Xie, D.H. Zhang, Food Chem. 115 (2009) 313–317.
[14] E. Calleri, G. Marrubini, G. Brusotti, G. Massolini, G. Caccialanza, J. Pharm. Biomed. 44 (2007) 396–403.
[15] X.Y. Jin, X.F. Jin, L.G. Chen, J.H. Jiang, G.L. Shen, R.Q. Yu, Biosens. Bioelectron. 24 (2009) 2580–2586.
[16] Y. Wang, J. Dostalek, W. Knoll, Biosens. Bioelectron. 24 (2009) 2264–2267.
[17] Z.P. Chen, Z.F. Peng, Y. Luo, B. Qu, J.H. Jiang, X.B. Zhang, G.L. Shen, R.Q. Yu, Biosens. Bioelectron. 23 (2007) 485–491.
[18] E. Katz, L. Alfonta, I. Willner, Sens. Actuat. B 76 (2001) 134–141.
[19] X. Chu, X. Fu, K. Chen, G.L. Shen, R.Q. Yu, Biosens. Bioelectron. 20 (2005) 1805–1812.
[20] Z.P. Chen, Z.F. Peng, J.H. Jiang, X.B. Zhang, G.L. Shen, R.Q. Yu, Sens. Actuat. B 129 (2008) 146–151.
[21] H.S. Wang, E. Kim, J. Kwak, Anal. Chem. 77 (2005) 579–584.
[22] X.D. Shangguan, H.F. Zhang, J.B. Zheng, Electrochem. Commun. 10 (2008) 1140–1143.
[23] W. Sun, Z.Q. Zhai, D.D. Wang, S.F. Liu, K. Jiao, Bioelectrochemistry 74 (2009) 295–300.
[24] W.W. Tu, J.P. Lei, H.X. Ju, Chemistry 15 (2009) 779–784.
[25] H.X. Shan, Z.J. Li, M. Li, G.X. Ren, Y.J. Fang, J. Chem. Technol. Biotechnol. 83 (2008) 886–891.
[26] F.S. Chu, I. Ueno, Appl. Environ. Microbiol. 33 (1977) 1125–1231.
[27] L. Zhu, X. Chen, Experimental Methods of Immunology, Public of Army Press of China, Beijing, 2000.
[28] M. Muscarella, S.L. Magro, C. Palermo, Anal. Chim. Acta 594 (2007) 257–264.

Talanta 80 (2010) 1638–1642

Contents lists available at ScienceDirect

Talanta

journal homepage: www.elsevier.com/locate/talanta

Temperature-controlled ionic liquid–liquid-phase microextraction for the pre-concentration of lead from environmental samples prior to flame atomic absorption spectrometry

Huahua Bai[a], Qingxiang Zhou[a,*], Guohong Xie[b], Junping Xiao[c]

[a] School of Chemistry and Environmental Sciences, Henan Normal University, Henan Key Laboratory for Environmental Pollution Control, Key Laboratory for Yellow River and Huaihe River Water Environment and Pollution Control, Ministry of Education, Xinxiang 453007, China
[b] College of Resources and Environment, Henan Institute of Science and Technology, Xinxiang 453003, China
[c] Department of Chemistry, University of Science and Technology Beijing, Beijing 100083, China

ARTICLE INFO

Article history:
Received 2 July 2009
Received in revised form
25 September 2009
Accepted 28 September 2009
Available online 4 October 2009

Keywords:
Temperature-controlled ionic liquid–liquid-phase microextraction
Lead
Flame atomic absorption spectrometry

ABSTRACT

Hydrophobic ionic liquid could be dispersed into infinite droplets under driving of high temperature, and then they can aggregate as big droplets at low temperature. Based on this phenomenon a new liquid-phase microextraction for the pre-concentration of lead was developed. In this experiment, lead was transferred into its complex using dithizone as chelating agent, and then entered into the infinite ionic liquid drops at high temperature. After cooled with ice-water bath and centrifuged, lead complex was enriched in the ionic liquid droplets. Important parameters affected the extraction efficiency had been investigated including the pH of working solution, amount of chelating agent, volume of ionic liquid, extraction time, centrifugation time, and temperature, etc. The results showed that the usually coexisting ions containing in water samples had no obvious negative effect on the recovery of lead. The experimental results indicated that the proposed method had a good linearity ($R = 0.9951$) from 10 ng mL^{-1} to 200 ng mL^{-1}. The precision was 4.4% (RSD, $n = 6$) and the detection limit was 9.5 ng mL^{-1}. This novel method was validated by determination of lead in four real environmental samples for the applicability and the results showed that the proposed method was excellent for the future use and the recoveries were in the range of 94.8–104.1%.

© 2009 Elsevier B.V. All rights reserved.

1. Introduction

Along with the development of industry, the environmental pollution induced by lead became more and more serious and threw a threat on the human health. Reports have indicated that lead had neurotoxicity [1], nephrotoxicity [2] and carcinogenicity [3,4]. Therefore, the environmental pollution of lead resulted in a public health problem and the monitoring of lead in environment was very important.

Nowadays, a variety of techniques are developed for the trace and ultra-trace determination of lead. Erta et al. [5] has established a hydride generation atom trapping flame atomic absorption spectrometry method for the determination of lead and the detection limits are in the range of 0.028–0.075 ng mL^{-1}. When an induction-heating electrothermal vaporizer (IH-ETV) ICP–MS was applied for use, the detection limit of lead reached to 0.04 μg g^{-1} [6]. A direct determination of lead in solid samples had been developed based on high-resolution continuum source graphite furnace atomic absorption spectrometry, and its detection limit was 0.01 μg g^{-1} [7].

In general, the low concentration of analyte and complex sample matrix would influence the sensitivity and accuracy of the developed method. Hence the enrichment or cleanup step is very necessary in the analytical procedure. Up to date, a variety of methods have been reported for the pre-concentration and separation of lead including solid phase extraction [8,9], cloud point extraction [10], capillary microextraction [11], solid phase microextraction [12], and single-drop microextraction [13], etc. Among them, solid phase extraction is the most widely used one due to the merits such as simplicity, low consumption of organic solvents, and stable extraction performance. Solid phase microextraction is a good sample pretreatment method, but it suffers from sample carryout and a decline in performance with the reuse of the fiber. As the determination of lead was concerned, a derivatization step is needed when solid phase microextraction is used [10]. Recently, dispersive liquid–liquid microextraction has been developed as a new mode of liquid-phase microextraction and attracted increasing attention for its simple operation, rapidness, and high extraction efficiency. In this extraction procedure, two organic solvents having different characteristics are involved in use, one is

* Corresponding author. Tel.: +86 373 3325971; fax: +86 373 3326336.
E-mail address: zhouqx@henannu.edu.cn (Q. Zhou).

0039-9140/$ – see front matter © 2009 Elsevier B.V. All rights reserved.
doi:10.1016/j.talanta.2009.09.059

hydrophilic which performs as dispersive solvent such as methanol [14] and acetone [15] etc., and the other is hydrophobic which performs as extraction solvent such as chlorobenzene [16] and carbon tetrachloride [17]. The extraction solvent would form innumerable infinite small droplets, when it was rapidly injected into the sample solution. These droplets limitlessly enlarge the contact area between extraction solvent and analytes. So far, this method has been successfully applied to the enrichment of heavy metals [18,19], metallo-organic compound [17], polychorinated biphenyls [20], polycyclic aromatic hydrocarbons [21], polyphenol-like compounds [22–24], polybrominated diphenyl ethers [25], pesticides [26] and herbicides [27].

On the basis of traditional dispersive liquid–liquid microextraction, Zhou [28,29] established a better extraction mode termed temperature-controlled ionic liquid dispersive liquid-phase microextraction. This method used ionic liquid to substitute for the conventional organic solvents and utilized the change of temperature to realize the enrichment of the organophosphorus pesticides and pyrethroid pesticides. Ionic liquids (ILs), which have been considered as green solvent, and have been used as extraction solvent in solvent extraction [30] and single-drop microextraction [31] for the enrichment of nickel in water, rice flour, and black tea [32], mercury [33], and aromatic hydrocarbons [34]. However, ionic liquids have not been often used in dispersive liquid-phase microextraction. The goal of present work is to establish a new method for the trace determination of lead using temperature-controlled ionic liquid dispersive liquid-phase microextraction coupled with flame atomic absorption spectrometry. The effect of various experiment conditions on the extraction of lead is investigated and discussed in detail.

2. Experimental

2.1. Reagents and standard solution

1-Hexyl-3-methylimidazolium hexafluorophosphate [C_6MIM][PF_6] was purchased from Acros Organics and used as obtained. Stock standard solution of lead with a concentration of 1000 μg mL^{-1} was obtained by dissolving appropriate amount of lead acetate (Kermel Chemistry Reagent Company, Tianjin, China) in double-distilled water. Working standard solution was obtained by appropriate dilution of the stock standard solution. The solution of dithizone was prepared by dissolving an appropriate amount of dithizone (Shanghai Reagent Factory, Shanghai, China) in ethanol. The double-distilled water was prepared in the lab using quartz-glass vaporization purchased from Ya-rong (Shanghai, China) and all the other solvents were analytical reagent grade unless otherwise stated. 0.5 mol L^{-1} of sodium hydroxide and concentrated hydrochloric acid were used for adjusting the pH value of the water samples. All glassware used in the experiments were cleaned with pure water, then soaked in 6 mol L^{-1} nitric acid for 24 h and then washed with purified water.

2.2. Apparatus

A Z-5000 Polarized Zeeman Atomic Absorption Spectrophotometer (Hitachi, Ltd. Tokyo. Japan) fitted with lead hollow cathode lamp was used. This apparatus was equipped with Zeeman effect background correction. The main instrument parameters were listed as below, lamp current, wavelength, slit, burner height, flame, oxidant gas pressure and fuel gas flow rate are 9 mA, 283.3 nm, 1.3 nm, 7.5 mm, 160 kPa, and 2.2 L min^{-1}, respectively. Centrifuger (Shanghai Surgery Machinery Factory, Shanghai, China) was used to achieve the phase separation. 81-2 thermostatic magnetic stirring apparatus (Si-le Instrumental Company, Shanghai, China) was used for heating in water bath.

2.3. Temperature-controlled ionic liquid–liquid-phase microextraction

In the pre-concentration procedure of lead, 50 μL [C_6MIM][PF_6] was used as extraction solvent and added into a 10 mL glass marked conical tube. 50 μL dithizone was used as chelating agent and the working solution was spiked with a lead concentration of 200 ng mL^{-1}. Then the sample solutions were heated in a water bath with the temperature controlled at 80 °C. The IL was dissolved completely and would entirely mix with the working solutions in order to make the chelate complex migrate into the IL phase. The tube was thereafter cooled with ice water and the solution became turbid. Then the solution was centrifuged for 15 min. The upper aqueous phase was removed with a syringe, and the residue was dissolved in 150 μL methanol and 1.5 M nitric acid to 0.8 mL. The final solution was determined by flame atomic absorption spectrometry (FAAS).

2.4. Real water sample analysis

Four environmental samples were used to investigate the applicability of this proposed method. These samples included river water, groundwater, reservoir water and rainwater. River water was collected from Anyang River, Anyang City, Henan province, China. Groundwater was obtained from Henan Normal University, Xinxiang City, Henan province, China. Reservoir water was collected form Shi-men reservoir in Xinxiang City, Henan province, China. Rainwater was obtained from Henan Normal University. Before use all the environmental water samples were filtered through 0.45 μm micro-pore membranes and stored in brown glass containers under low temperature.

3. Results and discussion

Temperature-controlled ionic liquid–liquid-phase microextraction is a new process, but it has some similarities with the dispersive liquid-phase microextraction. Compared with a conventional liquid-phase microextraction carried out in a single solvent drop, these two extraction modes infinitely enlarge the surface area of the extraction solvent and the contact area between extraction solvent and analytes which significantly enhance recoveries of analytes. In addition, compared with dispersive liquid-phase microextraction, ionic liquid is used as a substitute for toxic organic reagents in temperature-controlled ionic liquid–liquid-phase microextraction. Some important parameters that would influence the enrichment performance had been investigated in detail, in order to obtain the maximal extraction efficiency.

3.1. Effect of sample pH

The acidity of sample solution plays an important role in an extraction procedure, because it determines the present state of analytes in most cases. In general, analytes would be preferably extracted in most of the extraction procedure as molecular state. Hence in this experiment lead ion should be converted into molecular form to make the extraction procedure available. For this propose, the effect of sample acidity was investigated systematically between pH 2 and pH 11 with dithizone as chelating reagent, which ensured that lead ion could be extracted as chelate complex. The results exhibited in Fig. 1 and it showed that the recovery of lead increased significantly as the sample acidity increased from 2 to 7 and decreased between 9 and 11. When pH was between 7 and 9, the recoveries of lead were up to 92.3–111.7% and the maximum recovery was achieved at 8. Thus, a sample pH of pH 8 was selected for use in the following experiments.

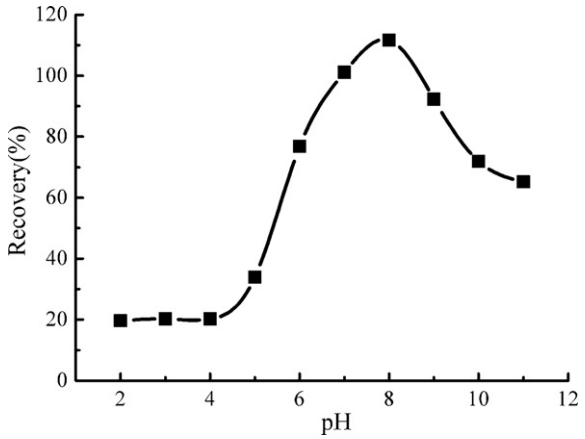


Fig. 1. Effect of samples pH. Concentration: 200 ng mL^{-1}; volume of ionic liquid: 50 μL; volume of dithizone: 40 μL; extraction time: 30 min; centrifugation time: 15 min; dissolve temperature: 50 °C; centrifugation rate: 4000 rpm.

3.2. Effect of the volume of dithizone

Dithizone was a better chelating agent for lead extraction and its chelating ratio was 2:1. Enough dithizone was needed to assure the lead would be extracted completely. Therefore, the volume of dithizone was investigated over the range of 15–50 μL with a concentration of 1×10^{-3} mol L^{-1} and using a standard solution of 200 ng mL^{-1}. Fig. 2 exhibited that when the volume of dithizone was up to 20 μL, the lead would be extracted completely. However, 50 μL of dithizone was used in the subsequent research to avoid the competitive chelation of coexisting ions in real samples.

3.3. Effect of volume of ionic liquid

In conventional liquid-phase extraction and microextraction, the volume of extractant was a crucial parameter, which significantly influences extraction efficiency of analytes. Theoretically, the larger the volume of extractant is, the higher recoveries of analytes would be. In practice, the volume of extractant of single-drop liquid-phase microextraction was limited to several microliters, as for the hollow fiber based liquid-phase microextraction, the extractant volume was not beyond to 20 μL, which seriously influences the absolute recoveries of analytes. In this experiment [C_6MIM][PF_6] was selected as extraction solvent because of its hydrophobicity. The volume of ionic liquid was optimized between 35 and 50 μL and the results were exhibited in Fig. 3. As can be seen,

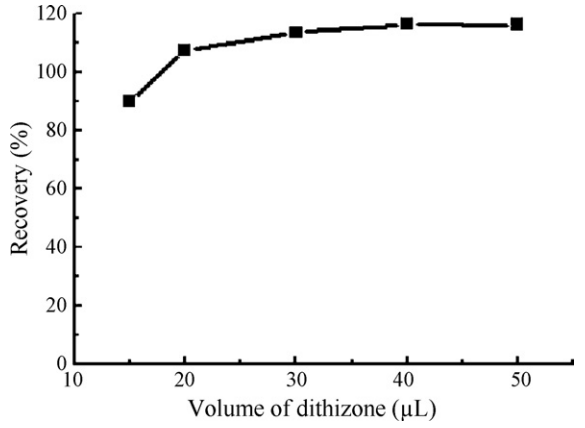


Fig. 2. Effect of volume of dithizone. Concentration: 200 ng mL^{-1}; volume of ionic liquid: 50 μL; pH: 8; extraction time: 30 min; centrifugation time: 15 min; dissolve temperature: 50 °C; centrifugation rate: 4000 rpm.

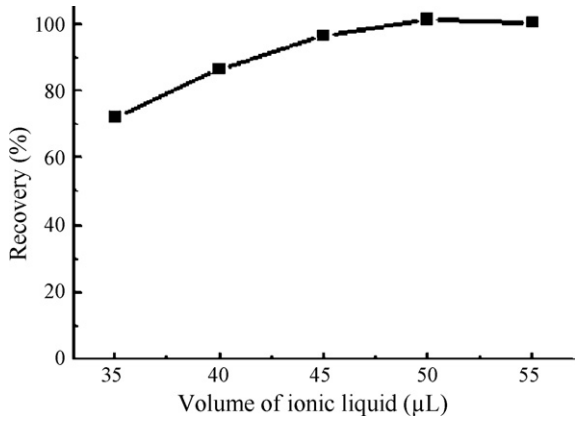


Fig. 3. Effect of volume of ionic liquid. Concentration: 200 ng mL^{-1}; pH 8; volume of dithizone: 50 μL; extraction time: 30 min; centrifugation time: 15 min; dissolve temperature: 50 °C; centrifugation rate: 4000 rpm.

the recovery of lead increased along with the increase of volume of ionic liquid from 35 μL to 45 μL, and kept stable between 45 μL and 50 μL. This was because of the fact that the fine IL droplets increased along with the increase of the [C_6MIM][PF_6] volume and more chelate complex were transferred into the IL droplets, which leaded to the higher enrichment performance. On the basis of these facts, 50 μL ionic liquid was selected in order to achieve the perfect analytical performance.

3.4. Effect of extraction time

In this experiment, extraction time was defined as the time from the moment that the solution started to be cooled to the moment that it was put in the centrifuger. This process was very important because it was the phase separation procedure. The effect of extraction time was examined over 5–45 min and the results indicated that the recovery of lead increased slowly when the extraction time was changed from 5 to 15 min and the recovery of lead had no obvious change when the extraction time was longer than 15 min. According to these, 15 min was chosen in the following study in order to reduce the analytical time of this experiment.

3.5. Effect of centrifugation time and centrifugation rate

Centrifugation time and centrifugation rate were important parameters that influenced the separation of ionic liquid from water phase. And the centrifugation time was optimized between 5 and 25 min. The results exhibited that when the centrifugation time was up to 15 min, the recovery of lead was over 95%. When the centrifugation time was shorter or longer, the recoveries were both lower than 95%. The short centrifugation time could not insure the preferable phase separation, and longer centrifugation time would induce the ionic liquid dissolved in water phase again. In addition, the centrifugation rate was optimized between 500 and 4000 rpm. When the centrifugation rate was at 500 rpm, the recovery was about 84.6%. When the centrifugation rate was over 500 rpm, the recovery was increased slowly and achieved the most value at 4000 rpm. So 15 min and 4000 rpm were selected for further use.

3.6. Effect of temperature

In the conventional dispersive liquid–liquid-phase microextraction, the dispersing of extractant was achieved with the help of hydrosoluble solvent such as acetone and methanol. In this experiment, temperature has been used as the driving power to make ionic liquid dissolved in aqueous solution. Therefore, temperature

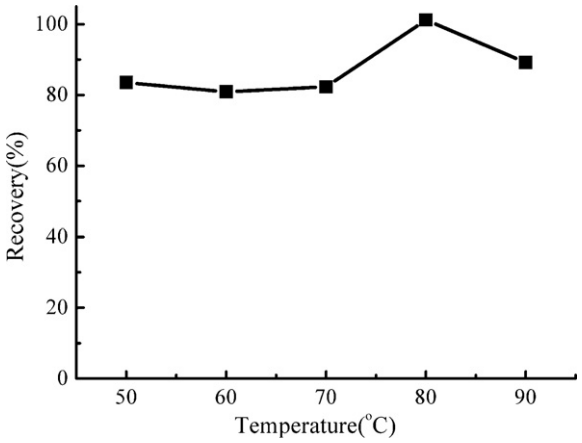


Fig. 4. Effect of dissolve temperature. Concentration: 200 ng mL^{-1}; volume of ionic liquid: 50 μL; pH 8; volume of dithizone: 50 μL; extraction time: 25 min; centrifugation time: 15 min; centrifugation rate: 4000 rpm.

became much more important because it significantly influenced the dispersive performance of ionic liquid in water solution. The effect of temperature was optimized in the range of 50–90 °C and the results were showed in Fig. 4. It was obviously that the recoveries were all lower than 85% when the temperature was between 50–70 °C due to that the lower temperature could not realize the complete dispersion. On the hand a higher temperature make the chelation of lead and dithizone difficult. So 80 °C was reasonable for the application in the following experiments.

3.7. Effect of coexisting ion

It has been documented that many metal ions existing in environmental waters would form stable chelating complexes with dithizone within a wide pH range and may be co-extracted along with the analytes. Moreover, this competitive chelating effect coupled with co-extracted effect would influence the chelating degree between lead and dithizone and make the extraction efficiency of lead decrease. Therefore, a series of experiments have been designed using a standard solution of 200 ng mL^{-1} of lead under the above-optimized conditions. The results were given in Table 1. The obtained results indicated that the presence of large amounts of cation and anion including Na^+, K^+, Mg^{2+}, and SO_4^{2-}, etc. had no obvious influence on the recovery of lead within a ±5% error range except for Fe^{3+}.

Table 1
Effect if coexisting ion (Pb^{2+}: 200 ng mL^{-1}).

Coexisting ion	Concentration of coexisting ion (μg mL^{-1})	Recoveries of Pb (%)
Na^+	400	97.4
Ca^{2+}	130	98.1
K^+	160	97.3
Mg^{2+}	100	103.0
Zn^{2+}	30	98.8
Cu^{2+}	30	96.8
Fe^{3+}	30	92.9
Cd^{2+}	25	99.4
Cr^{3+}	15	96.5
SO_4^{2-}	160	100.1
Cl^-	400	97.4

3.8. Analytical performance

The analytical performance of temperature-controlled ionic liquid–liquid-phase microextraction coupled with FAAS for the pre-concentration and determination of lead from environmental samples was systematically investigated under optimized experimental conditions. The results exhibited that there was an excellent linear correlation between ABS and the concentration of lead from 10 to 200 ng mL^{-1} and good correlation coefficient of 0.9995. The precision of this method was 4.4% (RSD, $n = 6$) at the spiked concentration of 50 ng mL^{-1}. And the detection limit (calculated as the concentration corresponding to three times the standard deviation of 11 runs of the blank samples) of proposed method for lead was 9.5 ng mL^{-1}. The proposed method was also validated with certified reference water sample (GSB 07-1183-2000). The standard value is 0.593 μg mL^{-1} and the mean determined value is 0.579 μg mL^{-1} ($n = 6$). The recovery and precision are 97.6% and 1.5%, respectively. This result indicated that the proposed method is very reliable. Compared to the developed method for the lead determination, present method was not the best sensitive method (see Table 2). The reason was that the small sample volume and the instrument with low sensitivity. If the proposed method could be in combination with ICP–MS or atomic fluoresce spectrometry, the detection limit of the method would be significantly improved.

Table 2
Comparison of proposed method with the reported methods.

Enrichment method	Materials	Instrument	Detection Limits (ng mL^{-1})	References
SPE	Iminodiacetate chelating resin	AFS	0.004	[35]
SPE	PTFE beads	ICP–MS	0.006	[36]
Knotted reactor	PTFE	FAAS	0.43	[37]
SPE	Polyurethane foam column modified by addition of 2-(2-benzothiazolylazo)-p-cresol	FAAS	1	[38]
SPE	DBQ embedded benzophenone	FAAS	2	[39]
SPE	Rice husks	FAAS	14.1	[40]
Cloud poing extraction	Triton X-114	FAAS	4.5	[41]
SPE	Activated carbon loaded with xylenol orange dithiocarbamate immobilized/functionalized merrifield chloromethylated resin	FAAS	1.3	[42]
SPE	Beads diethylammonium dithiocarbamate (DDTC) sorbed merrifield chloromethylated resin beads	FAAS	3	[43]
SPE	PTFE turnings	FAAS	0.8	[44]
SPE	Silica gel chemically modified with zirconium (IV) phosphate	FAAS	6.1	[45]
SPE	Amberlite XAD-2000 resin	FAAS	0.51	[46]
SPE	Polyuethane foam	FAAS	1.8	[47]
cloud point extraction	Triton X-114	FAAS	1.6	[48]
SPE	Polyurethane foam (PUF) with 2-(6-methy1-2-benzothiazolylazo) chromotropic acid	FAAs	3.75	[49]
LPME	Ionic liquid	FAAS	9.5	Present work

Table 3
Spiked recoveries of four real water samples (Pb: 50 ng mL^{-1}).

Samples	Blank (ng mL^{-1})	Spiked recoveries(%)
Anyang river	–	94.9 ± 3.6
Shimen reservoir	–	101.8 ± 6.8
Rain water	–	94.8 ± 6.3
Ground water	–	104.1 ± 6.9

3.9. Analysis of real water samples

In order to demonstrate the applicability and reliability of the proposed method for realworld samples, four environmental samples, including river water, reservoir water, ground water and rainwater were collected. Three spiked and two blank experiments for each real water sample were carried out according to the above-mentioned procedure. There found no lead in blank solutions of four samples. Subsequently extraction of four samples spiked with lead at 50 ng mL^{-1} were processed as the described above. The concentration of lead was determination by FAAS and the results were given in Table 3. The recoveries of lead were in the range of 94.8–104.1%.

4. Conclusions

A novel and simple method temperature-controlled ionic liquid–liquid-phase microextraction was developed for the pre-concentration of lead in water samples. The experimental results demonstrated that this new extraction technique coupled with FAAS for the pre-concentration and determination of lead exhibited many merits such as excellent enrichment performance, sensitive, simple operation, cost-effective and no consumption of organic toxic solvents. However it could not reach the reported sensitivity level of SPE-FAAS, etc., it still offered a new procedure for the enrichment of lead in water samples and it would achieve much better detection sensitivity if ICP–MS, GFAAS and atomic fluoresce spectrometry could be used as the detector. Its high tolerance to coexisting ions and perfect analytical performance indicated that this proposed method was a well alternative for the determination of lead in environmental samples.

Acknowledgements

This work was supported by High-Tech Research & Development Planning (863 Plan) of P.R. China (2006AA06Z424), the Natural Science Foundation of China (020877022), the Natural Science Foundation of Henan Province (082102350022), the Personal Innovation Foundation of Universities in Henan Province ([2005]126), the fund of Henan Normal University (no. 2006PL06), and the funds from the Henan Key Laboratory for environmental pollution control.

References

[1] M.G. Zurich, C. Eskes, P. Honegger, M. Berode, F. Monnet-Tschudi, J. Neurosci. Res. 70 (2002) 108.
[2] E.B. Ekong, B.G. Jaar, V.M. Weaver, Kidney Int. 70 (2006) 2074.
[3] K. Steenland, P. Boffetfa, Am. J. Ind. Med. 38 (2000) 295.
[4] E.K. Silbergeld, M. Waalkes, J.M. Rice, Am. J. Ind. Med. 38 (2000) 316.
[5] N. Erta, Z. Arslan, J.F. Tyson, J. Anal. At. Spectrom. 23 (2008) 223.
[6] R. Lam, E.D. Salin, J. Anal. At. Spectrom. 22 (2007) 1430.
[7] D.L.G. Borges, A.F. Silva, B. Welz, A.J. Curtius, U. Heitmann, J. Anal. At. Spectrom. 21 (2006) 763.
[8] X.H. Shang, X.P. Yan, J. Anal. At. Spectrom. 22 (2007) 1284.
[9] J.S. Suleiman, B. Hu, H.Y. Peng, C.Z. Huang, Talanta 77 (2009) 1579.
[10] E.L. Silva, P.D. Roldan, J. Hazard. Mater. 161 (2009) 142.
[11] B. Hu, F. Zheng, Talanta 73 (2007) 372.
[12] T. Gorecki, J. Pawliszyn, Anal. Chem. 68 (1996) 3008.
[13] X.J. Liu, Z.F. Fan, At. Spectrosc. 28 (2007) 215.
[14] R. Montes, I. Rodríguez, E. Rubí, R. Cela, J. Chromatogr. A 1216 (2009) 205.
[15] H. Farahani, P. Norouzi, R. Dinarvand, M.R. Ganjali, J. Chromatogr. A 1172 (2007) 105.
[16] E. Zhao, W. Zhao, L. Han, S. Jiang, Z. Zhou, J. Chromatogr. A 1175 (2007) 137.
[17] A.P. Birjandi, A. Bidari, F. Rezaei, M.R.M. Hosseini, Y. Assadi, J. Chromatogr. A 1193 (2008) 19.
[18] P. Liang, E. Zhao, F. Li, Talanta 77 (2009) 1854.
[19] M.T. Naseri, P. Hemmatkhah, M.R.M. Hosseini, Y. Assadi, Anal. Chem. Acta 610 (2008) 135.
[20] F. Rezaei, A. Bidari, A.P. Birjandi, M.R.M. Hosseini, Y. Assadi, J. Hazard. Mater. 158 (2008) 621.
[21] M. Rezaee, Y. Assadi, M.M. Hosseini, E. Aghaee, F. Ahmadi, S. Berijani, J. Chromatogr. A 1116 (2006) 1.
[22] M. Rezaee, Y. Yamini, S. Shariati, A. Esrafili, M. Shamsipur, J. Chromatogr. A 1216 (2009) 1511.
[23] N. Fattahi, Y. Assadi, M.R.M. Hosseini, E.Z. Jahromi, J. Chromatogr. A 1157 (2007) 23.
[24] L. Fariña, E. Boido, F. Carrau, E. Dellacassa, J. Chromatogr. A 1157 (2007) 46.
[25] Y.Y. Li, G.H. Wei, J. Hu, X.J. Liu, X.N. Zhao, X.D. Wang, Anal. Chim. Acta 615 (2008) 96.
[26] Y. Liu, E. Zhao, W. Zhao, H. Gao, Z. Zhou, J. Chromatogr. A 1216 (2009) 885.
[27] D. Nagaraju, S.D. Huang, J. Chromatogr. A 1161 (2007) 89.
[28] Q.X. Zhou, H.H. Bai, G.H. Xie, J.P. Xiao, J. Chromatogr. A 1177 (2008) 43.
[29] Q.X. Zhou, H.H. Bai, G.H. Xie, J.P. Xiao, J. Chromatogr. A 1188 (2008) 148.
[30] A.B. Pereiro, A. Rodriguez, Ind. Eng. Chem. Res. 48 (2009) 1579.
[31] E. Aguilera-Heirador, R. Lucena, S. Cardenas, M. Valcarcel, Anal. Chem. 80 (2008) 793.
[32] S. Dadfarnia, A.M.H. Shabani, M.S. Bidabadi, A.A. Jafari, J. Hazard. Mater., in press.
[33] R. Germani, M.V. Mancini, G. Savellia, N. Spreti, Tetrahedron Lett. 48 (2007) 1767.
[34] G.W. Meindersma, A.J.G. Podt, A.B. de Haan, Fuel Process. Technol. 87 (2005) 59.
[35] Z. Wan, Z. Xu, J.H. Wang, Analyst 131 (2006) 141.
[36] J.H. Wang, E.H. Hansen, J. Anal. At. Spectrom. 17 (2002) 1278.
[37] A.S. Souza, G.C. Brandao, W.N.L. dos Santos, V.A. Lemos, E.M. Ganzarolli, R.E. Bruns, S.L.C. Ferreira, J. Hazard. Mater. 141 (2007) 540.
[38] V.A. Lemos, M. de la Guardia, S.L.C. Ferreira, Talanta 58 (2002) 475.
[39] K. Prasad, P. Gopikrishna, R. Kala, T. Prasada Rao, G.R.K. Naidu, Talanta 69 (2006) 938.
[40] C. Ricardo, T. Tarley, S.L.C. Ferreira, M.A.Z. Arruda, Microchem. J. 77 (2004) 163.
[41] E.L. Silva, P. dos, S. Roldan, J. Hazard. Mater. 161 (2009) 142.
[42] A.A. Ensafi, A.Z. Shiraz, J. Hazard. Mater. 150 (2008) 554.
[43] R.S. Praveen, G.R.K. Naidub, T.P. Rao, Anal. Chim. Acta 600 (2007) 205.
[44] G.A. Zachariadis, A.N. Anthemidis, P.G. Bettas, J.A. Stratis, Talanta 57 (2002) 919.
[45] E. Matoso, L.T. Kubota, S. Cadore, Talanta 60 (2003) 1105.
[46] L. Elci, A.A. Kartal, M. Soylak, J. Hazard. Mater. 153 (2008) 454.
[47] A.N. Anthemidis, G.A. Zachariadis, J.A. Stratis, Talanta 58 (2002) 831.
[48] M. Ghaedi, A. Shokrollahi, K. Niknam, E. Niknam, A. Najibi, M. Soylak, J. Hazard. Mater. 168 (2009) 1022.
[49] E.M. Gama, A. da, S. Lima, V.A. Lemos, J. Hazard. Mater. B 136 (2006) 757.

Talanta 80 (2010) 1643–1647

Contents lists available at ScienceDirect

Talanta

journal homepage: www.elsevier.com/locate/talanta

Detection of T4 DNA ligase using a solid-state electrochemiluminescence biosensing switch based on ferrocene-labeled molecular beacon

Xiaoying Wang[a,b], Ping Dong[a], Wen Yun[a], Ying Xu[a], Pingang He[a,*], Yuzhi Fang[a,*]

[a] Department of Chemistry, East China Normal University, Shanghai 200062, China
[b] School of Public Health, Southeast University, Nanjing 210009, China

ARTICLE INFO

Article history:
Received 12 July 2009
Received in revised form
24 September 2009
Accepted 28 September 2009
Available online 4 October 2009

Keywords:
Solid-state electrochemiluminescence
biosensing switch
Molecular beacon
T4 DNA ligase
Ferrocene
Quenching effect

ABSTRACT

A solid-state electrochemiluminescence (ECL) biosensing switch based on special ferrocene-labeled molecular beacon (Fc-MB) has been successfully developed for T4 DNA ligase detection. Such special switch system consisted of two main parts, an ECL substrate and an ECL intensity switch. The ECL substrate was made by modifying the complex of Au nanoparticle and Ruthenium (II) tris-(bipyridine) ($Ru(bpy)_3^{2+}$-AuNPs) onto Au electrode. A molecular beacon labeled by ferrocene as the ECL intensity switch. The molecular beacon is designed with special base sequence, which could combine with its target biomolecule *via* the reaction of the repair and recombination of nucleic acids by DNA ligase. During the reaction, the molecular beacon opened its stem–loop, and the labeled Fc was consequently kept away from the ECL substrate. Such structural change resulted in an obvious increment in ECL intensity due to the decreased Fc quenching effect to the ECL substrate. The analysis results are sensitive and specific.
© 2009 Elsevier B.V. All rights reserved.

1. Introduction

Nucleic acid ligation is one vital process in the repair, replication and recombination of nucleic acids and also an important tool for editing DNA both *in vivo* and *in vitro* [1–3]. Therein, DNA ligase plays an indispensable role in catalyzing the formation of phosphodiester bonds at single strand nick between adjacent 3′-hydroxyl and 5′-phosphate ends in double strand DNA [4–7]. Therefore, specific recognition and quantitative detection of DNA ligase are crucial to fundamental research as well as clinical practice. Currently, the ligation process is usually assayed by radial P labeling, denaturing gel electrophoresis, autoradiography and fluorescence [4]. But these methods are time consuming and not sensitive [8–11].

Molecular beacon (MB), a stem–loop structure oligonucleotide, was initially described in 1996 as a switch able to undergo spontaneous conformational change following hybridization with the complementary nucleic acid target [12,13]. It possesses high selectivity, fast speed, convenience and excellent sensitivity. MB has been used in the investigation of genetic disease, the studies of DNA–protein interactions, the monitoring of the nucleic acids ligation process and the detection of DNA/RNA hybridization in living cells [14–19]. Tang et al. have used MB to monitor the nucleic acid ligation process in real-time, the sequence of which is designed to be complementary with the product of the ligation [9]. However, the MB, ligation substrate, nucleic acid hybridization complex and DNA ligase are all in solution. MB can only be used to detected DNA ligase in homogeneous solution.

In our recently studies, a solid-state electrochemiluminescence biosensing switch was developed successfully [20,21]. The biosensing system employed $Ru(bpy)_3^{2+}$-AuNPs modified Au electrode to emit ECL, and the ferrocene-labeled molecular beacon (Fc-MB) to control the ECL intensity with consideration of the high ECL quenching efficiency of Fc to $Ru(bpy)_3^{2+}$. It has been found that the ECL intensity of the $Ru(bpy)_3^{2+}$-AuNPs modified Au electrode was correlated to the conformation of the Fc-MB. The Fc-MB was designed with special base sequence, which could be combined with its target biomolecule *via* the reaction of DNA hybridization or aptamer–protein combination. Therefore, the system can be applied to recognize the relevant biomolecules selectively.

Based on these studies, we attempt to combine the solid-state electrochemiluminescence biosensing switch with the template of nucleic acids ligation as well as the repair and recombination of nucleic acids by DNA ligase to detect DNA ligase. The Fc-MB is not only a probe for the detection of the ligation process, but also a template for the two oligos in the ligation process. Using this method, an efficient bioassay for monitoring the activity of T4 DNA ligase has been developed. In this protocol, the MB, ligation substrate, nucleic acid hybridization complex and DNA ligase were all captured to the surface of the electrode to avoid the interference by the target

* Corresponding authors. Tel.: +86 21 62233508/798; fax: +86 21 62233508.
E-mail addresses: pghe@chem.ecnu.edu.cn (P. He), yzfang@chem.ecnu.edu.cn (Y. Fang).

0039-9140/$ – see front matter © 2009 Elsevier B.V. All rights reserved.
doi:10.1016/j.talanta.2009.09.060

oligos and basal solution in detection. The method can be used to quantitate the T4 DNA ligase rapidly, sensitively and selectively.

2. Experimental

2.1. Reagents and apparatus

Oligonucleotides were purchased from Shenggong Bioengineering Ltd Company (Shanghai, China). The sequence of molecular beacon (MB): 5′-NH_2-$(CH_2)_6$-GGGCGTTGA*TGGTTCCACTTCTCGTGCGT* TCAACG-$(CH_2)_6$-SH-3′ (the underlined and italic sequences indicate the stem and loop of the MB), Fragment N1: 5′-CGCACGAGAAGTGGAACC-3′ (18-nt oligo matching the loop of the MB), N2: 5′-CGCACGAGA-3′ (9-nt oligo matching 3′ half part of the loop of the MB), N3: 5′-AGTGGAACC-3′ (9-nt oligo matching 5′ half part of the loop of the MB), N4: 5′-pAGTGGAACC-3′ (9-nt oligo matching 5′ half part of MB's loop and was phosphorylated at its 5′ end). T4 DNA ligase (5 U μL^{-1}) and diluted buffer (66 mM Tris–HCl containing 50% glycerol, 10 mM 2-mercaptoethanol, 0.1 mM EDTA and 50 mM KCl, pH 7.5) were purchased from Dingguo Biological Technology Corporation of Shanghai. $Ru(bpy)_3^{2+}$ (99.95%), $HAuCl_4$, 6-mercapto-1-hexanol (SH-$(CH_2)_6$-OH, >97.0%), cysteamine (SH-$(CH_2)_2$-NH_2) and 1-ethyl-3-[(3-dimethylamino)propyl]carbodiimide (EDC) were purchased from Sigma (USA). Ferrocenecarboxylic acid (FCA), dithiothreitol (DTT), horseradish peroxidase (HRP) and glucose oxidase (GOD) were purchased from Maoji Bioengineering Ltd Company of Shanghai. The following buffers were used: 66 mM Tris–HCl containing 0.8 M NaCl and 100 mM $LiClO_4$ (pH 7.5), 66 mM Tris–HCl containing 50 μM ATP, 20 mM $MgCl_2$, 10 mM DTT and 100 mM $LiClO_4$ (pH 7.5). 66 mM Tris–HCl containing 1.0 mM tri-*n*-propylamine (TPrA) and 5.0 mM $LiClO_4$ (pH 8.7) was used as the detecting solution. Other reagents were of analytical reagent grade. All of the solutions were prepared with ultrapure water from a Millipore Milli-Q system.

ECL was recorded with MPI-E electrogenerated chemiluminescence analyzer (Xi'an Remax Electronic Science Tech., Co. Ltd), a CHI 660A electrochemical analyzer (CHI instruments Inc., USA) was used to carry out impedance measurements.

2.2. Preparation of Fc-MB–$Ru(bpy)_3^{2+}$-AuNPs electrode

The Fc-MB–$Ru(bpy)_3^{2+}$-AuNPs electrode was prepared according to previously published protocols [20]. Briefly, a self-assembled monolayer of cysteamine is prepared onto Au electrode firstly (cysteamine-derivated Au electrode), then, the $Ru(bpy)_3^{2+}$-AuNPs composite is assembled onto the cysteamine-derivated Au electrode to form the luminescent substrate. The as-prepared electrode was $Ru(bpy)_3^{2+}$-AuNPs electrode. The Fc-MB is attached onto the above electrode *via* Au–S interaction, and the electrode was then treated with SH-$(CH_2)_6$-OH solution to occupy the unassembled surface of $Ru(bpy)_3^{2+}$-AuNPs as well as adjust the Fc-MB distribution on the electrode surface. Thus, the Fc-MB–$Ru(bpy)_3^{2+}$-AuNPs electrode was obtained which has a solid-state electrochemiluminescence biosensing switch of Fc-MB–$Ru(bpy)_3^{2+}$-AuNPs.

2.3. The specific recognition of T4 DNA ligase onto Fc-MB–$Ru(bpy)_3^{2+}$-AuNPs electrode

The Fc-MB–$Ru(bpy)_3^{2+}$-AuNPs electrode was incubated in 500 μL of 66 mM Tris–HCl (pH 7.5) containing 0.8 M NaCl, 100 mM $LiClO_4$ and the two short complementary DNA at room temperature for 2 h to form a DNA complex with a nick. By this way, the dsDNA with a nick electrode was formed.

The resultant electrode was incubated with T4 DNA ligase in 66 mM Tris–HCl (pH 7.5) containing 50 μM ATP, 20 mM T4 DNA ligase $MgCl_2$, 10 mM DTT and 100 mM $LiClO_4$ for 15 min. Then the electrode was washed with the same buffer to decrease the non-specific binding at most, and the dsDNA electrode was obtained.

2.4. Electrogenerated chemiluminescence detection

A three-electrode system was used with the modified Au electrode (2 mm in diameter) as the working electrode, an Ag/AgCl (sat.) as the reference electrode and a platinum wire as the counter electrode. Cyclic voltammetry mode with continuous potential scanning from 0.0 to 1.2 V and scanning rate of 0.1 V s^{-1} was applied to achieve ECL signal in 66 mM Tris–HCl containing 1.0 mM TPrA and 5.0 mM $LiClO_4$ (pH 8.7) at room temperature. A high voltage of −800 V was supplied to the photomultiplier for luminescence intensity determination.

3. Results and discussion

3.1. Recognition of T4 DNA ligase using the solid-state electrochemiluminescence biosensing switch

The ligation system is composed of a DNA ligase, two oligos to be ligated and a ferrocene-labeled molecular beacon (Fc-MB), in which the combined sequences of the two oligos are complementary to the loop sequence of the Fc-MB. Fig. 1 presents an illustration of the ligation process. In the beginning, each oligo is hybridized to one-half of the loop of the Fc-MB to form a DNA complex with a nick as shown in step a in Fig. 1. It cannot open the Fc-MB stem completely, but can slightly destabilize the stem. Once ligase is added, the ligation reaction closes the nick to form a longer DNA strand which is complementary to the Fc-MB, resulting in the Fc-MB opening completely and the Fc being pulled away from the electrode (step b).

The corresponding ECL intensity–potential curves of the electrodes are presented in Fig. 2. As shown in the figure, compared to the ECL signal of Fc-MB–$Ru(bpy)_3^{2+}$-AuNPs electrode without hybridization with any DNA (curve a), the ECL signal should be a slight increase for the slight torsion of the stem of Fc-MB and part of Fc being shifted from original position after the process of hybridization with the two short complementary DNA (curve b). The ligation reaction closes the nick to form a longer DNA strand which is complementary to the MB, resulting in the stem of Fc-MB being separated and Fc being pulled away from the electrode. So a remarkable increase of ECL signal was presented simultaneity (curve c). Thus, the difference of ECL intensity before and after the ligation (ΔI_{ECL}) can be used to quantify the T4 DNA ligase.

3.2. The characterization of solid-state electrochemiluminescence biosensing electrode

The fabrication processes of solid-state electrochemiluminescence biosensing electrode and the interaction between fabricated biosensing electrode and T4 DNA ligase were characterized by electrochemical impedance spectroscopy (EIS). For EIS measurements, $[Fe(CN)_6]^{3-/4-}$ was employed as the redox probe and Nyquist plots were used to calculate the R_{et} for modified electrodes. As shown in Fig. 3, the R_{et} for bare Au electrode was 246.4 Ω, and increased to 469.7 Ω for the cysteamine-derivated Au electrode, then declined to 327.9 Ω for the $Ru(bpy)_3^{2+}$-AuNPs electrode. It is attributed to the electronic conductive capacity of Au nanoparticles. The results showed that 10 μM Fc-MB was self-assembled onto the $Ru(bpy)_3^{2+}$-AuNPs electrode, the R_{et} increased to 737.6 Ω. This is attributed to fact that self-assembled biosensing switch of the Fc-MB having negative charges on its phosphate backbone makes an electrostatic repulsive force to $[Fe(CN)_6]^{3-/4-}$. The R_{et} of dsDNA with a nick electrode and dsDNA electrode was 1164.3 Ω and 2069.2 Ω, respectively. The successive increase in

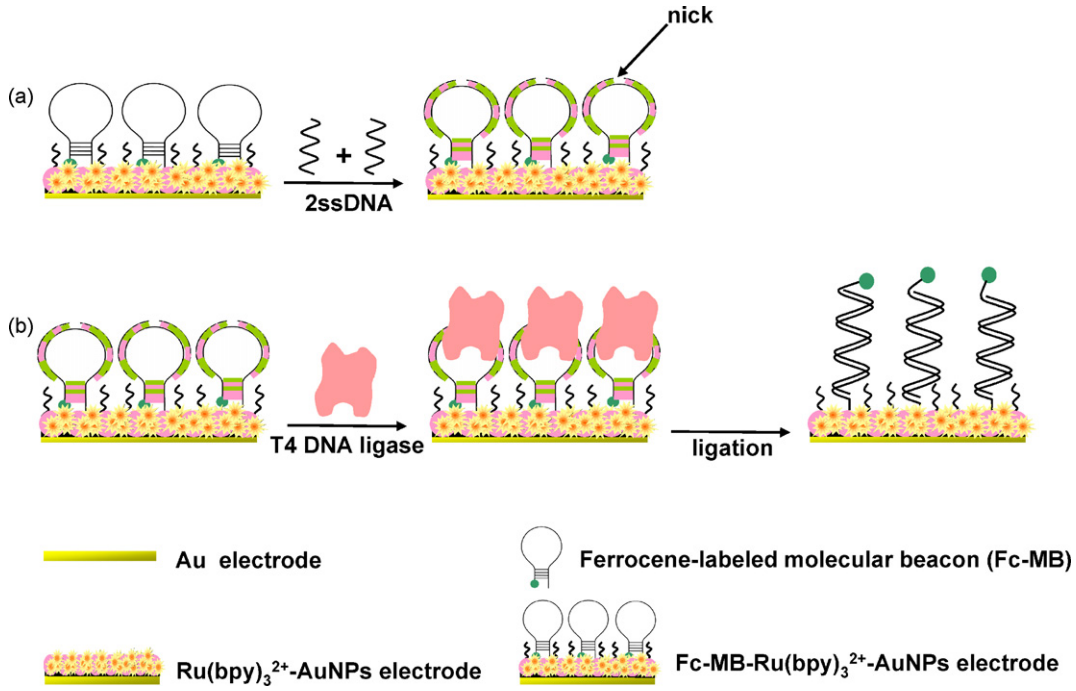


Fig. 1. The specific recognition of T4 DNA ligase by using the Fc-MB–$Ru(bpy)_3^{2+}$-AuNPs electrode. (a) The two half-matching oligos hybridize with the Fc-MB to form a nick. (b) The T4 DNA ligase binds to the nick and catalyzes the ligation of two short oligos to form a longer oligo.

the R_{et} illustrates the successful modification of the biomolecules onto Fc-MB–$Ru(bpy)_3^{2+}$-AuNPs electrode. It also indicates that the interactions between immobilized Fc-MB and the two short complementary DNA, dsDNA with a nick and T4 DNA ligase arise successively.

3.3. *The selectivity of solid-state electrochemiluminescence biosensing switch*

Two control experiments were performed for evaluating the selectivity of solid-state electrochemiluminescence biosensing switch. In order to confirm the repair and recombination specificity of T4 DNA ligase to target nucleic acids, ECL experiments were performed for different samples, such as Fc-MB with N1 (sample a), Fc-MB with N2 and N4 (sample b), Fc-MB with N2 and N3 (sample c) and Fc-MB only (sample d). The difference between N3 and N4 is that whether the 5′ end of DNA fragment was modified with a phosphate group or not, and it is a necessary condition for repair and recombination nucleic acids in DNA ligation reaction [5–7]. As presented in Fig. 4, there was no ECL change for samples a, c and d. It implied that there was no significant change in Fc-MB stem–loop structure after the addition of T4 DNA ligase into these sample solutions. However, the ECL of sample b increased rapidly and reached a plateau after 15 min, which is contributed to the ligation reaction of T4 DNA ligase to link N2 and N4 into one long DNA strand that is complementary to Fc-MB (displayed in Fig. 1). As a result, the Fc-MB opened completely, and ferrocene molecule was away from the $Ru(bpy)_3^{2+}$-AuNPs electrode, which finally led to the increase of the ECL intensity. An almost complete ligation reached after 15 min.

Another control experiment was carried out by using 5 U mL^{-1} T4 DNA ligase, horseradish peroxidase (HRP), glucose oxidase (GOD) or mixed sample to react with N2 and N4. It could be found

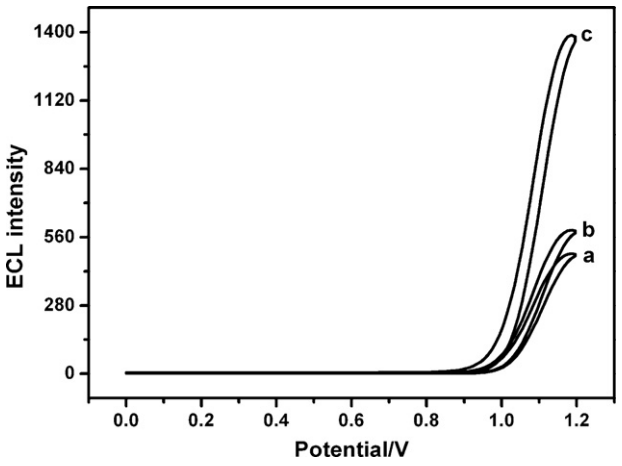


Fig. 2. ECL intensity–potential curves for various electrodes: (a) Fc-MB–$Ru(bpy)_3^{2+}$-AuNPs electrode, (b) dsDNA with a nick electrode and (c) dsDNA electrode.

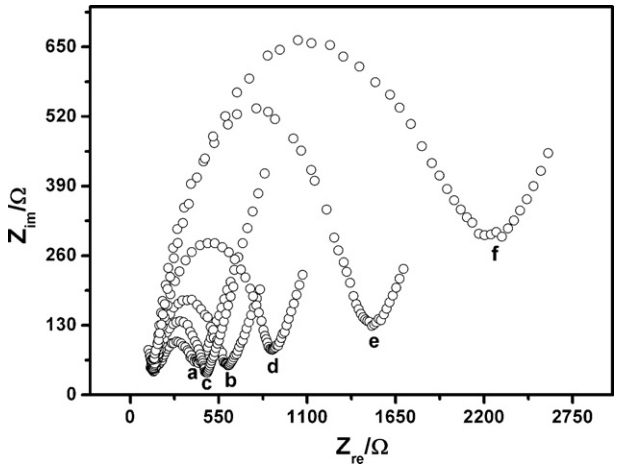


Fig. 3. Nyquist plots for the impedance measurement in 10 mM $[Fe(CN)_6]^{3-/4-}$ solution for the bare Au electrode (a), cysteamine-derivated Au electrode (b), $Ru(bpy)_3^{2+}$-AuNPs electrode (c), Fc-MB–$Ru(bpy)_3^{2+}$-AuNPs electrode (d), dsDNA with a nick electrode (e) and dsDNA electrode (f).

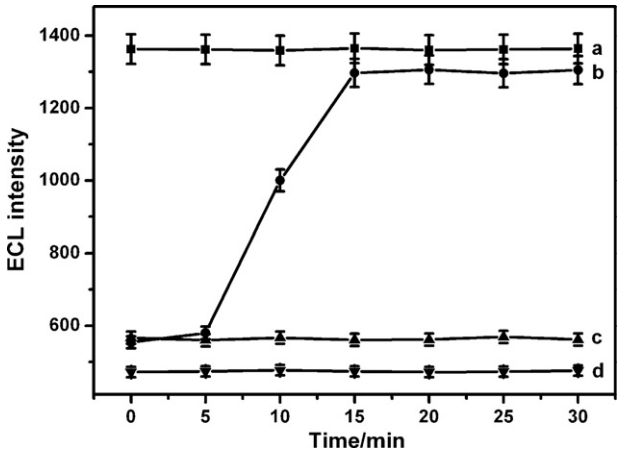


Fig. 4. ECL measurements for the repair and recombination specificity of T4 DNA ligase to target nucleic acids. The Fc-MB–$Ru(bpy)_3^{2+}$-AuNPs electrode incubated with N1 and T4 DNA ligase (a), N2, N4 and T4 DNA ligase (b), N2, N3 and T4 DNA ligase (c), and T4 DNA ligase (d).

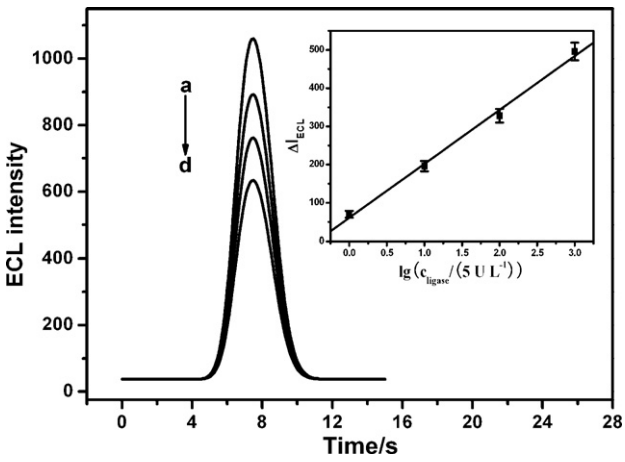


Fig. 6. ECL intensity–time curves for various dsDNA electrodes. The concentrations of T4 DNA ligase were 5×10^{-3} U μL^{-1} (a), 5×10^{-4} U μL^{-1} (b), 5×10^{-5} U μL^{-1} (c) and 5×10^{-6} U μL^{-1} (d), respectively. Inset: the calibration curve of T4 DNA ligase detection. ECL curves were measured in 66 mmol/L Tris–HCl containing 1.0 mM TPrA and 5.0 mM $LiClO_4$ (pH 8.7). Scan rate: 0.1 V s^{-1}, scan range: 0.0–1.2 V.

that only the samples containing T4 DNA ligase showed an obvious increase of ECL intensity as shown in Fig. 5. However, the change of the ECL intensity for the dsDNA with a nick electrode reacting with HRP or GOD can be neglected. It is therefore can be concluded that the ECL intensity increase is caused by the T4 DNA ligase combining with the nick as showed in Fig. 1, which suggested the unique repair and recombination specificity of the T4 DNA ligase to the nick between Fc-MB and the two short complementary DNA, N2 and N4. Above results also indicate that the solid-state electrochemiluminescence biosensing switch has a good selectivity for discriminating the two short DNA to other complementary DNA and T4 DNA ligase from other enzyme.

3.4. Optimization of experimental conditions

The ligation process can be affected by many molecular species including biomolecules and metal ions. The effect of four molecular species, including ATP, Mg^{2+}, K^+ and Na^+ was studied. The experimental results show that the ligation did not take place unless ATP or Mg^{2+} was added to the ligation mixtures. The ligation reached its maximum rate at 50 μM of ATP or at 20 mM of Mg^{2+}, respectively. The high concentration of K^+ and Na^+ obviously hindered the ligation process. The initial ligation velocity decreased proportionally to the concentrations of K^+ or Na^+, and the velocity was close to 0 when the concentrations were ~300 mM. In addition, the activity of T4 DNA ligase has been maintained by dithiothreitol (DTT). Therefore, the 66 mM Tris–HCl buffer solution (pH 7.5) containing 50 μM ATP, 20 mM $MgCl_2$ and 10 mM DTT was selected as the ligation buffer solution.

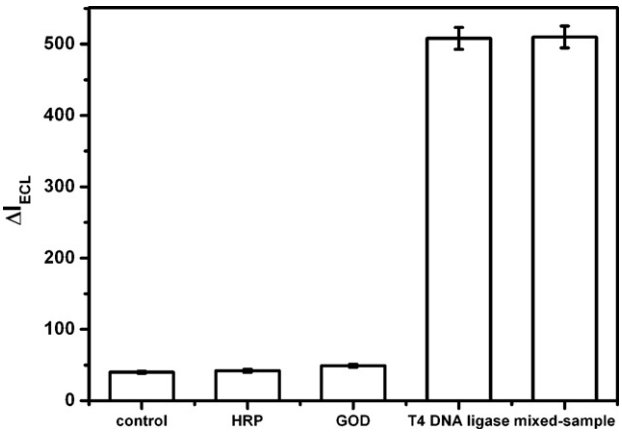


Fig. 5. Comparison of the ΔI_{ECL} of the dsDNA with a nick electrode when incubated with T4 DNA ligase, HRP, GOD and mixed sample (T4 DNA ligase/HRP/GOD).

The efficiency of the ligation, which effects on the ECL intensity of the second ECL determination, is in correlation with ligation time and ligation temperature. The ECL intensity increased with the increment the ligation time, and reached its plateau regions at the ligation time of 15 min. Thus, the optimal ligation time was chosen at 15 min. The influence of the hybridization temperature on the response is investigated, the ECL signal increased rapidly from 5 to 30 °C, then changed slowly from 35 to 40 °C, and reduced notably after 50 °C. So, 37 °C was chosen as the hybridization temperature at the following experiment.

3.5. The calibration curve of T4 DNA ligase detection

According to the Michaelis–Menten equation, the initial reaction rate catalyzed by enzymes is directly proportional to the concentration of the enzyme within a certain concentration range [22]. When the initial reaction rate of the T4 DNA ligation reaction was expressed as the increased rate of the ECL intensity, it was namely the increased value of the ECL intensity (ΔI_{ECL}) in a certain period of time. The sensitivity of the solid-state electrochemiluminescence biosensing switch was investigated. Fig. 6 shows the ECL profiles of the different concentration of T4 DNA ligase after binding with dsDNA electrode. The ECL intensity was enhanced when the T4 DNA ligase concentration increased, and the change of the ECL intensity, ΔI_{ECL}, was found to be linear with the logarithm of T4 DNA ligase concentration in the range from 5×10^{-6} U μL^{-1} to 5×10^{-3} U μL^{-1} (as shown in the inset). The equation for the resulting calibration plot was $y = 141 \lg x + 14$ (x: the concentration of T4 DNA ligase divide 5 U L^{-1}, y: ΔI_{ECL}) with correlation coefficient of 0.9975 and detection limit of 2.5×10^{-6} U μL^{-1}.

4. Conclusions

An efficient bioassay for monitoring the T4 DNA ligase has been developed using a solid-state electrochemiluminescence biosensing switch based on Fc-MB. The Fc-MB is not only a probe for the detection of the ligation process, but also a template for the two oligos in the ligation process. The conformation change information of the Fc-MB before or after the ligation was a reflection of the ECL

signal changes of the whole modified electrode. Thus, the ECL signal changes of the modified electrode can be detected once the nucleic acids were ligated. By this way, the ligation process can be monitored simultaneously and accurately. This method provides a new and effective platform for studying a wide variety of nucleic acids ligation processes and interactions between protein (enzyme) and nucleic acid. Furthermore, it is meaningful to the deeply study the dynamics of them.

Acknowledgment

We thank the National Nature Science Foundation of China (Grant No. 20675031) for financial support of this work.

References

[1] D.M. Wilson III, L.H. Thompson, Proc. Natl. Acad. Sci. U.S.A. 94 (1997) 12754–12757.
[2] T. Lindahl, R.D. Wood, Science 286 (1999) 1897–1905.
[3] R.C. Alexander, A.K. Johnson, J.A. Thorpe, T. Gevedon, S.M. Testa, Nucleic Acids Res. 31 (2003) 3208–3216.
[4] M. Odell, L. Malinina, V. Sriskanda, M. Teplova, S. Shuman, Nucleic Acids Res. 31 (2003) 5090–5100.
[5] A.J. Doherty, S.W. Suh, Nucleic Acids Res. 28 (2000) 4051–4058.
[6] I.R. Lehman, Science 186 (1974) 790–797.
[7] M. Zirvi, T. Nakayama, G. Newman, T. McCaffrey, P. Paty, F. Barany, Nucleic Acids Res. 27 (1999) e40.
[8] A.J. Doherty, T.R. Dafforn, J. Mol. Biol. 296 (2000) 43–56.
[9] Z. Tang, K. Wang, W. Tan, J. Li, L. Liu, Q. Guo, X. Meng, C. Ma, S. Huang, Nucleic Acids Res. 31 (2003) e148.
[10] J. Li, X. Chu, Y. Liu, J.H. Jiang, Z. He, Z. Zhang, G. Shen, R.Q. Yu, Nucleic Acids Res. 33 (2005) e168.
[11] C. Yuan, X.W. Lou, E. Rhoades, H. Chen, L.A. Archer, Nucleic Acids Res. 35 (2007) 5294–5302.
[12] S. Tyagi, F.R. Kramer, Nat. Biotechnol. 14 (1996) 303–308.
[13] S. Tyagi, D.P. Bratu, F.R. Kramer, Nat. Biotechnol. 16 (1998) 49–53.
[14] P.V. Riccelli, F. Merante, K.T. Leung, S. Bortolin, R.L. Zastawny, R. Janeczko, A.S. Benight, Nucleic Acids Res. 29 (2001) 996–1004.
[15] M.B. Wabuyele, H. Farquar, W. Stryjewski, R.P. Hammer, S.A. Soper, Y.W. Cheng, F. Barany, J. Am. Chem. Soc. 125 (2003) 6937–6945.
[16] A. Bourdoncle, A. Estevez Torres, C. Gosse, L. Lacroix, P. Vekhoff, T. Le Saux, L. Jullien, J.L. Mergny, J. Am. Chem. Soc. 128 (2006) 11094–11105.
[17] D.M. Jenkins, B. Chami, M. Kreuzer, G. Presting, A.M. Alvarez, B.Y. Liaw, Anal. Chem. 78 (2006) 2314–2318.
[18] R. Miranda-Castro, P. de-Los-Santos-Alvarez, M.J. Lobo-Castanon, A.J. Miranda-Ordieres, P. Tunon-Blanco, Anal. Chem. 79 (2007) 4050–4055.
[19] Y. Li, H. Qi, Y. Peng, Q. Gao, C. Zhang, Electrochem. Commun. 10 (2008) 1322–1325.
[20] X. Wang, W. Yun, P. Dong, J. Zhou, P. He, Y. Fang, Langmuir 24 (2008) 2200–2205.
[21] X. Wang, P. Dong, W. Yun, Y. Xu, P. He, Y. Fang, Biosens. Bioelectron. 24 (2009) 3288–3292.
[22] A.L. Lehninger, D.L. Nelson, M.M. Cox, Principles of Biochemistry, Worth Publishers, New York, 1993.

Talanta 80 (2010) 1648–1652

Contents lists available at ScienceDirect

Talanta

journal homepage: www.elsevier.com/locate/talanta

Non-enzymatic electrochemical CuO nanoflowers sensor for hydrogen peroxide detection

Min-Jung Song[a,b], Sung Woo Hwang[a,b,*], Dongmok Whang[a,c,**]

[a] Research Center for Time-Domain Nano-Functional Devices, Korea University, Seoul 136-701, Republic of Korea
[b] School of Electrical Engineering, Korea University, Seoul 136-701, Republic of Korea
[c] SKKU Advanced Institute of Nanotechnology and School of Advanced Materials Science & Engineering, Sungkyunkwan University, 300 Cheoncheon-Dong, Suwon 440-746, Republic of Korea

ARTICLE INFO

Article history:
Received 17 August 2009
Accepted 29 September 2009
Available online 7 October 2009

Keywords:
Electrochemical sensor
Hydrogen peroxide sensor
Non-enzymatic sensor
Copper oxide nanoflower
Effective surface area

ABSTRACT

The electrocatalytic activity of a CuO flower-like nanostructured electrode was investigated in terms of its application to enzyme-less amperometric H_2O_2 sensors. The CuO nanoflowers film was directly formed by chemical oxidation of copper foil under hydrothermal condition and then used as active electrode material of non-enzymatic electrochemical sensors for H_2O_2 detection under alkaline conditions. The sensitivity of the sensor with CuO nanoflowers electrode was 88.4 μA/mM cm^2 with a linear response in the range from 4.25×10^{-5} to 4×10^{-2} M and a detection limit of 0.167 μM ($S/N = 3$). Excellent electrocatalytic activity, large surface-to-volume ratio and efficient electron transport property of CuO nanoflowers electrode have enabled stable and highly sensitive performance for the non-enzymatic H_2O_2 sensor.
© 2009 Elsevier B.V. All rights reserved.

1. Introduction

Rapid and accurate determination of hydrogen peroxide (H_2O_2) is of practical importance in various fields such as food, clinical and environmental analyses. To date, H_2O_2 detection has been mainly studied using spectrometry [1], fluorescence [2], chemiluminscence [3,4] and electrochemistry [5,6]. In particular, the electrochemical technique using an electrode modified with the redox active enzyme, horseradish peroxidase (HRP), has been extensively applied due to its simple, accurate, and fast analytical process [7,8]. The sensitivity of these sensors depends on the activity of the immobilized enzymes. However, one common drawback of enzyme-based sensors is insufficient stability originating from the nature of the enzymes, because enzymes are easy to deform thermally and chemically during fabrication, storage or use. In addition, the responses of most enzyme-based electrodes are not completely free from oxygen effects because the electron-mediating sites compete with oxygen dissolved in the solution [9].

Recently, it is of great interest to develop an enzyme-less electrochemical sensor with high sensitivity, fast response time, and long-term stability. In particular, electrochemically active nanomaterials consisting of metals [10–12], metallic carbon nanotubes [13–15], transition metal oxides [16,17], or conducting polymers [18,19] have been extensively studied for non-enzymatic electrochemical sensors, because they have large surface-to-volume ratio and increased catalytic activities.

Of these, CuO nanomaterials are one of the promising candidates for the active electrode material of non-enzymatic electrochemical sensors. Semiconducting CuO is a *p*-type semiconductor having a band gap of 1.2 eV and has shown its potential for applications in various fields, such as superconductors, magnetic storage media, solar energy transformation, electronics, batteries, sensors and catalysis [20,21]. Different synthetic methods have been developed for the fabrication of CuO nanostructures with various morphologies, including nanowire and nanosheet [22–24].

Although most of metallic Cu(0) nanomaterials are not stable enough to be used for electroanalysis because they are easily oxidized in air or aqueous solution, chemically more stable CuO nanomaterials have been studied for various applications including electrochemical H_2O_2 sensors [17,25].

For example, electrochemical H_2O_2 sensor based on Nafion and CuO nanoparticle modified Pt electrode was reported [17]. As another example, Jia et al. demonstrated the simple and convenient detection of H_2O_2 using vertically aligned CuO nanowires [25]. The nanowires-modified electrode has benefit for increase

* Corresponding author at: School of Electrical Engineering, Korea University, Seoul 136-701, Republic of Korea. Tel.: +82 2 32903241.
** Corresponding author at: SKKU Advanced Institute of Nanotechnology and School of Advanced Materials Science & Engineering, Sungkyunkwan University, 300 Cheoncheon-Dong, Suwon 440-746, Republic of Korea.
Tel.: +82 31 2907399; fax: +82 31 2907410.
E-mail addresses: swhwang@korea.ac.kr (S.W. Hwang), dwhang@skku.edu (D. Whang).

0039-9140/$ – see front matter © 2009 Elsevier B.V. All rights reserved.
doi:10.1016/j.talanta.2009.09.061

of sensor performance. However efficient use of the high surface area of the structure may be limited by undesirable effects including the internal electrical resistance due to high aspect ratio of the semiconductor nanowires. The electrochemical properties of CuO nanomaterials are strongly dependent on its structural features such as crystal sizes, orientations, stacking manners, aspect ratios, and crystalline densities, which promote the study in this paper.

Herein, we describe a facile approach for developing an enzymeless H_2O_2 sensor based on CuO nanoflowers. The electrochemically active CuO nanostructure was grown from the substrate in a single step, and they can be directly used as sensor electrodes without additional processes such as surface modification or immobilization of expensive enzymes. Moreover, we achieve extremely large surface-to-volume ratio and efficient electron transport property due to the high-density single crystalline nano-petals in the electrode.

2. Experimental

2.1. Chemicals

$(NH_4)_2S_2O_8$ and H_2O_2 were purchased from Sigma Chemical (St. Louis, USA). High-purity copper foils (Cu, 99.99%) were obtained from Nilaco Co. (Tokyo, Japan). Sodium hydroxide (NaOH) and potassium ferricyanide ($K_3Fe(CN)_6$) were obtained from Duksan Pure Chemicals (Gyeonggi-do, Korea). All reagents were of analytical grade, and doubly distilled water was used throughout the experiments.

2.2. Preparation and characterization of CuO nanoflower and CuO nanowire electrodes

CuO nanoflowers were grown on a copper foil by a simple solution-based method [21]. Briefly, a piece of copper foil (5 mm × 5 mm × 0.2 mm) was immersed in 5 ml of 10 M NaOH solution and 13 ml of H_2O in a Teflon-lined stainless steel autoclave and then 2 ml of 1 M $(NH_4)_2S_2O_8$ solution was added. The autoclave was sealed and maintained at 100 °C for 12 h and was then cooled in tap water. The product was obtained in the form of a black thin film covering the copper foil. The product was washed with distilled water and ethanol, and then dried in air. As a comparative electrode, nanostructured electrode decorated with highly dense CuO nanowires was also prepared by previously reported method [26]. In short, a piece of copper foil was cleaned in 1.0 M HCl solution and distilled water. After drying it under N_2 gas flow, it was treated in air for 4 h at 500 °C using a muffle furnace.

The morphologies and structures of the nanostructures were determined using transmission electron microscopy (TEM), high-resolution TEM (HR-TEM) equipped with selected area electron diffraction (SAED) and field emission scanning electron microscopy (FE-SEM). The images were taken with a JEM 2100F TEM (JEOL Ltd., Japan) operating at an accelerating voltage of 200 kV and a JSM 7000F SEM (JEOL Ltd., Japan). The samples for HR-TEM were prepared by placing a drop of precipitate on a carbon-coated copper grid and allowing it to dry in air. The phase purity of the CuO nanoflowers on the Cu substrates was characterized by powder X-ray diffraction (XRD) using a D8 DISCOVER powder X-ray diffractometer (Bruker AXS, USA) with Cu Kα radiation.

2.3. Electrochemical measurement

The electrochemical measurements were performed on a micro Autolab III potentiostat (Eco Chemie, Netherlands). A series of electrochemical experiments was conducted using a standard cell with three electrodes: a modified Cu electrode as the working electrode, a Pt counter electrode, and a saturated calomel electrode (SCE) used as a reference electrode. A 0.1 M NaOH solution was used as the supporting electrolyte because H_2O_2 is reduced in an alkaline medium. The active surface area was estimated by cyclic voltammetry in 3 M KCl solution harboring 10 mM $K_3Fe(CN)_6$ at a variety of scan rates. The applied potential ranged from −0.4 to 0.2 V versus SCE with a Pt counter electrode.

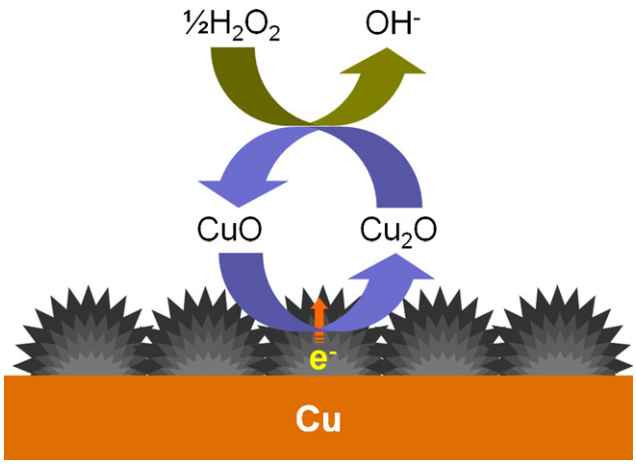


Fig. 1. A schematic view of the electrocatalytic mechanism of CuO nanoflowers for the reduction of H_2O_2.

2.4. Mechanisms for the formation of CuO nanoflowers and electron transfer in the modified electrode

The formation mechanism of the CuO nanoflowers film is as follows [23]:

$$Cu + 2NaOH + (NH_4)_2S_2O_8 \rightarrow Cu(OH)_2 + Na_2SO_4 + (NH_4)_2SO_4 \quad (1)$$

$$Cu(OH)_2 + 2OH^- \rightarrow [Cu(OH)_4]^{2-} \quad (2)$$

$$[Cu(OH)_4]^{2-} \rightarrow CuO + 2OH^- + H_2O \quad (3)$$

When metallic Cu foils were immersed in a basic solution with $(NH_4)_2S_2O_8$ oxidants, the foil surface quickly turned blue. Cu tends to dissolve in solutions that produce Cu complexes [27].

As shown in Eq. (3), $[Cu(OH)_4]^{2-}$ anions are produced as a precursor entity for the formation of CuO in a NaOH aqueous solution with a high concentration. Then, CuO is formed along with two hydroxyl ions and one water molecule. These CuO nuclei coalesce in order to decrease the total surface energy of the system and grow larger to form many CuO nanosheets with flower-like structures [24,27].

The electron-transfer mechanism in the modified electrode is shown in Fig. 1. In the catalytic mechanism for the reduction of H_2O_2, Cu(II) is reduced electrochemically to Cu(I), and H_2O_2 is simultaneously reverted to OH^- along with the regeneration of the catalyst [17].

3. Results and discussion

3.1. CuO nanoflowers film

CuO nanoflowers film was directly fabricated by the oxidation reaction of copper foil under hydrothermal conditions [21]. As shown in Fig. 2, a nanostructured film with high density, flower-shaped CuO nanocrystals were produced on the copper foil. The CuO flowers consist of many thin CuO single crystalline petals with

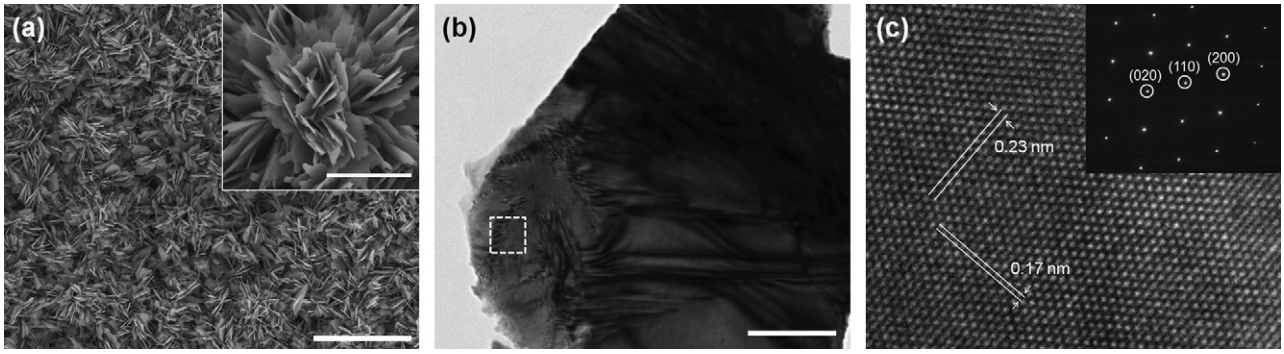


Fig. 2. (a) A SEM image showing high-density CuO nanoflowers grown out of a Cu foil. Scale bar, 5 μm. (Inset of a) A higher magnification SEM image of a CuO nanoflower, scale bar, 1 μm. (b) A TEM image of a single crystalline petal of the CuO nanoflowers. Scale bar, 200 nm. (c) A lattice-resolved TEM image taken at the marked region of (b). Scale bar, 5 nm. (Inset of c) A SAED pattern of the CuO single crystalline petal shown in (c).

an edge length of 100–500 nm and a thickness of ~50 nm. The CuO petals rooted in the center are connected to each other through their wider bases.

Typical TEM images and the corresponding selected area electron diffraction (SAED) patterns of the CuO petals clearly reveal that the petals are single crystals (Figs. 2(b) and (c)). The plane spacings of 0.17 and 0.23 nm correspond to the {0 2 0} and {2 0 0} planes of the CuO structure, respectively (Fig. 2(c)). The sharp diffraction spots in Fig. 2(c) can be indexed as the (0 2 0), (1 1 0), and (2 0 0) reflections of the CuO structure with the [0 0 1] zone axis, which further indicates that the [2 0 0] and [0 2 0] directions are perpendicular to the edges of a petal.

SEM images of in Fig. 3(a) shows highly dense CuO nanowires were also grown on a Cu substrate, which is quite similar to previously reported nanowires. Fig. 3(b) shows typical XRD spectra of the as-prepared CuO nanoflowers and CuO nanowires on the Cu surfaces. Two broad diffraction peaks of CuO nanoflowers located at $2\theta = 35.6$ and 38.8 are well indexed as $(\bar{1}11)$–(0 0 2) and (1 1 1)–(2 0 0) planes of monoclinic CuO structure (JCPDS Card No. 05-0661), respectively. There are no additional peaks except for the peaks (marked with an asterisk) from the Cu substrate. However, diffraction patterns of the as-synthesized CuO nanowire/Cu sample are more complex and have addition peaks which are corresponding to the Cu_2O structure. It has been known, when copper is oxidized in air, the initial product is Cu_2O, and CuO is formed slowly only through a second step of oxidation in which Cu_2O served as a precursor to CuO [26].

3.2. Determination of effective surface area of the CuO-nanoflower-modified electrode

The electroactive surface area of the nanostructured electrode was estimated by cyclic voltammetry using ferricyanide as a redox probe. Fig. 4 displays a series of cyclic voltammograms (CVs) on the CuO nanostructured electrodes as a function of different scan rates in 5 mM $K_3Fe(CN)_6$ solution with 3 M KCl as supporting electrolyte and the dependence of the peak current on the square root of the scan rate. At both of the nanostructured electrodes, the peak current (I_p) increases linearly with the increasing of the square root of the potential scan rate ($\nu^{1/2}$), which suggests that the reactions occurring on the modified electrode were nearly reversible, since the Randles' slope would be nonlinear if the redox reactions were either quasi-reversible or irreversible. This result also means that the mass transfer phenomenon in the double layer region of the electrodes is mainly diffusion controlled [27].

Under semi-infinite linear diffusion conditions and 25 °C, the dependence of peak current I_p on the scan rate ν is described by the Randles–Sevcik equation:

$$I_p = (2.69 \times 10^5) n^{3/2} A D_0^{1/2} C_0^* \nu^{1/2} \quad (4)$$

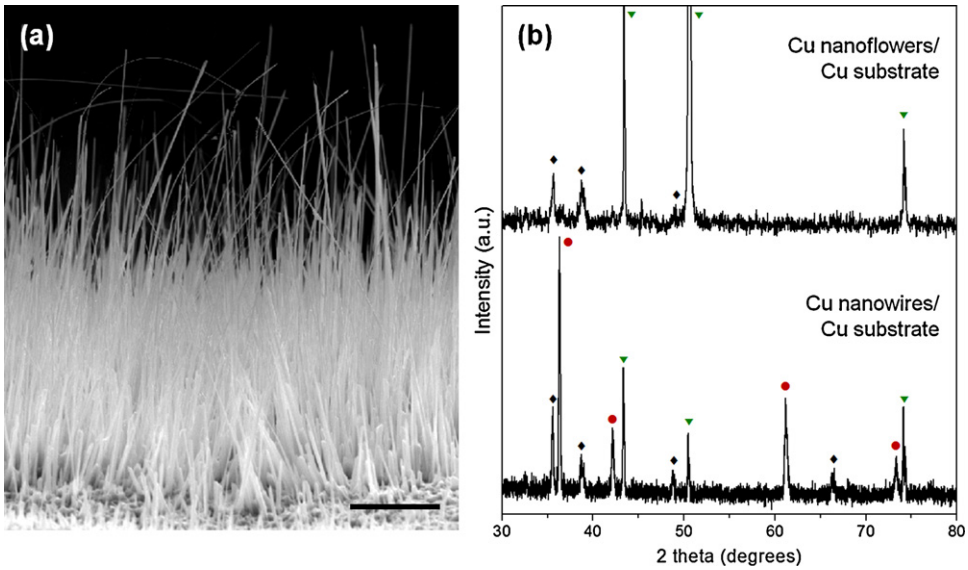


Fig. 3. (a) A typical SEM image of the CuO nanowires on the Cu substrate. (b) XRD patterns of the as-prepared CuO nanoflowers and CuO nanowires on Cu substrates. Diffraction peaks correspond to metallic Cu, cupric oxide (CuO) and Cuprous oxide (Cu_2O) are marked with ▼ (green), ♦ (black), and ● (red), respectively.

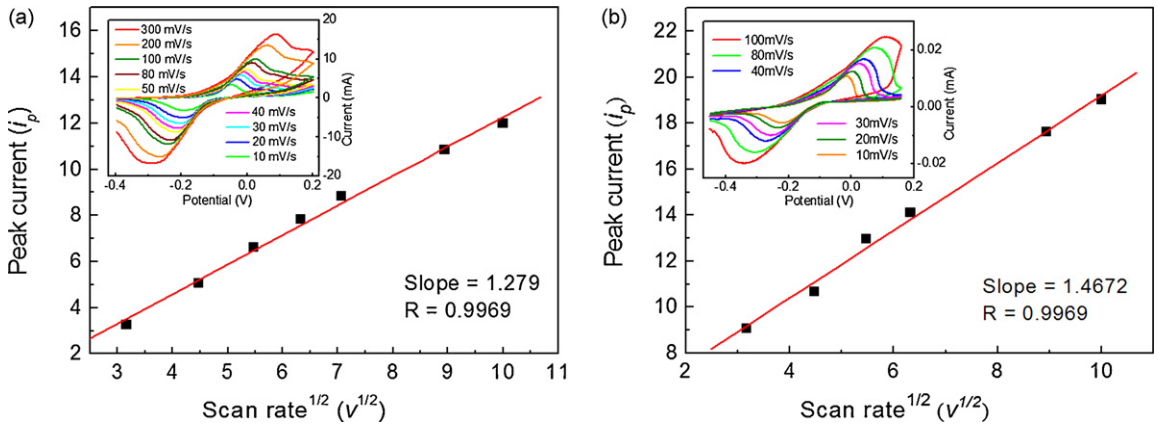


Fig. 4. Peak currents as a function of scan rate for the determination of the effective working surface area on (a) the CuO-nanoflower-modified electrode and (b) the CuO nanowire-decorated electrode. Insets: CV diagram of the modified electrodes in a 3 M KCl solution containing 10 mM ferricyanide at the different scan rates.

where n represents the number of electrons participating in the redox reaction, v is the scan rate of the potential perturbation (V/s), A is the area of the electrode (cm^2), D is the diffusion coefficient of the molecules in the solution (cm^2/s), C^* is the concentration of the probe molecule in the bulk solution (mol/cm^3), and I_p is the peak current of the redox couple illustrated in Fig. 1. In the equation, the effective surface area (A) can be calculated from the value of $I_p/v^{1/2}$ since D, n and C^* are constant values. As shown in Fig. 4(a), slope was 1.467 (R = 0.9969) as the value of $I_p/v^{1/2}$ and the calculated effective working area of the CuO nanoflowers electrode was 6.26 cm^2, which is ~25 times larger than the area of the equivalent bare Cu electrode (5 mm × 5 mm). The effective working area of CuO nanowires electrode was 5.46 cm^2, which are quite similar to that of CuO nanoflowers electrode.

3.3. Electrochemical characterization of the sensor

As previously mentioned, CuO displays excellent catalytic activity and can facilitate electron-transfer process. Here, the electrochemical process of the CuO nanostructured electrodes was examined for its amperometric response toward hydrogen peroxide. Fig. 5(a) shows that the CV of the CuO nanoflowers electrode has two pairs of oxidation and reduction peaks in the potential region from −0.9 to 0.8 V in an alkaline solution. The anodic peaks at −0.4 and −0.05 V represent the oxidation from Cu(0) to Cu(I) and from Cu(I) to Cu(II), respectively, while the cathodic peaks at −0.67 and −0.74 V correspond to the reductions from Cu(II) to Cu(I) and from Cu(I) to Cu(0), respectively.

As shown in Fig. 5(b), upon the addition of H_2O_2 to 5 mL of NaOH solution (0.1 M), the CV currents of the modified electrode changed dramatically with an increase of the reduction peak current and a decrease of the oxidation peak current, which is characteristic of electrochemical catalysis to H_2O_2.

Fig. 6 shows a typical amperometric response curve of H_2O_2 at the CuO nanostructured electrode. Well-defined, stable, and fast amperometric responses were observed at an applied potential of −0.3 V with successive step additions of H_2O_2 in the stirred 0.1 M NaOH solution. The addition of H_2O_2 is marked by arrows at the concentrations mentioned. It is clear that the response current of

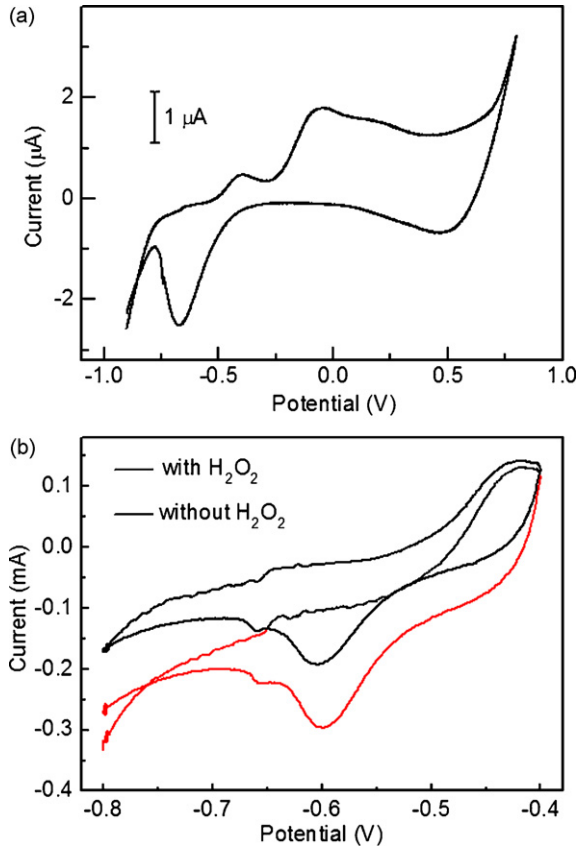


Fig. 5. (a) Cyclic voltammograms (CVs) of CuO-nanoflower-modified electrode in a NaOH solution (0.1 M) at a scan rate of 50 mV/s. (b) Cyclic voltammograms of CuO-nanoflower-modified electrode in a NaOH solution (0.1 M) at a scan rate of 50 mV/s with and without H_2O_2.

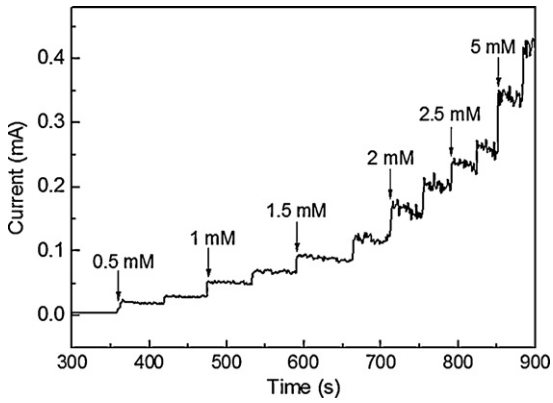


Fig. 6. Steady-state current time responses of H_2O_2 to various concentrations of H_2O_2 in a stirred 0.1 M NaOH solution at the CuO-nanoflower-modified electrode under an applied potential of -0.3 V.

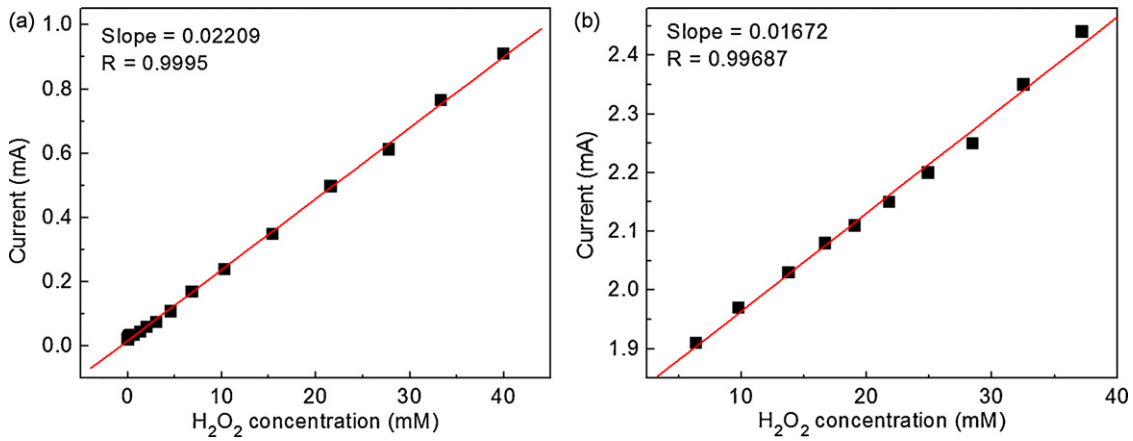


Fig. 7. Calibration curves of (a) the CuO-nanoflower modified and (b) the CuO nanowire-decorated electrodes in a NaOH solution (0.1 M) containing various H_2O_2 concentrations under an applied potential of −0.3 V.

the modified electrode abruptly increases to steady-state values upon the addition of H_2O_2. This sensor shows a very fast response, as the response reaches 95% of the steady-state value within 10 s.

Fig. 7 shows the calibration curves for nanoflowers and nanowires electrodes. The amperometric sensitivity of the nanoflowers sensor was 88.4 μA/mM cm^2 (R = 0.9995) with the linear range of 42.5 μM to 40 mM. And that of the nanowires sensor was 66.88 μA/mM cm^2 (R = 0.9969) with the linear range between 6.4 mM and 37.2 mM. The CuO nanoflowers sensor is 1.3-fold larger than that of the sensor based on the CuO nanowires electrode. And, it is ca. 3 times larger than that of the previously reported sensor based on a vertically aligned CuO nanowires-modified electrode, in which response of the sensor was linear up to 28.87 mM with a sensitivity of 30.11 μA/mM cm^2 [25].

The enhanced sensitivity of nanoflowers sensor compared to that of nanowires case may be explained by the difference in electron transport efficiency of the nanostructured electrodes, though CuO purity in the electrodes could be another source of the sensitivity difference. If the electrode is composed of semiconductor nanowires, the internal resistance contribution due to the electrodes with high aspect ratio can be significant, which may limit increase of sensitivity with increase of nanowire length. Therefore, the high sensitivity and fast response time of the sensor in the present study can be attributed to the fact that high-density nanoscale petals in the CuO nanostructured electrode can greatly increase the electrocatalytic active areas and also promote electron transfer in the reduction of H_2O_2, since plate-like structures have larger cross-section area than thin nanowires [14].

The good reproducibility and long-term stability of the electrodes are also critically important in the context of practical applications. In general, the insufficient stability of enzyme electrodes is the result of the loss and deactivation of enzymes [9,11]. Because the sensor fabricated in this study was enzyme-less, the long-term stability of the sensor was evaluated by measuring its sensitivity to H_2O_2 with the sensor stored in air at ambient conditions. The electrodes were not poisoned by the reduction product and can be used repeatedly for the detection of H_2O_2.

4. Conclusions

We demonstrated a sensitive non-enzymatic H_2O_2 sensor based on flower-shaped CuO nanocrystalline films. The CuO nanoflowers electrode was directly fabricated in a single step by the simple surface oxidation of Cu foil. The CuO nanomaterial as the cathode material exhibited remarkable electrocatalytic activity for the reduction of H_2O_2 under alkaline conditions. In addition, this non-enzymatic sensor has demonstrated both long-term stability and high sensitivity due to enzyme-less detection and the large surface area of the CuO nanostructure. The proposed electrochemical sensing technology is thus expected to generate new opportunities for the development of reliable and miniaturized sensor devices for monitoring H_2O_2 concentrations in food industry and clinical and environmental analyses fields.

Acknowledgments

This work was supported by Creative Research Initiatives (Research Center for Time-domain Nano-functional Devices, R16-2007-007-01001-0(2009)) of MEST/KOSEF and by the second stage of the Brain Korea 21 Project in 2009.

References

[1] R. Santucci, E. Laurenti, F. Sinibaldi, R.P. Ferrari, Biochim. Biophys. Acta 1596 (2002) 225.
[2] Z. Rosenzweig, R. Kopelman, Anal. Chem. 68 (1996) 1408.
[3] L. Luo, Z. Zhang, Anal. Chim. Acta 580 (2006) 14.
[4] U. Spohn, F. Preuschoff, G. Blankenstein, D. Janasek, M.R. Kula, A. Hacker, Anal. Chim. Acta 303 (1995) 109.
[5] Y. Lin, X. Cui, L. Li, Electrochem. Commun. 7 (2005) 166.
[6] G. Shi, J. Lu, F. Xu, H.G. Zhou, L. Jin, J. Jin, Anal. Chim. Acta 413 (2000) 131.
[7] Y. Xiao, H.-X. Ju, H.-Y. Chen, Anal. Chim. Acta 391 (1999) 73.
[8] C.-X. Lei, S.-Q. Hu, G.-L. Shen, R.-Q. Yu, Talanta 59 (2003) 981.
[9] S. Park, H. Boo, T.D. Chung, Anal. Chim. Acta 556 (2006) 46.
[10] S. Park, T.D. Chung, H.C. Kim, Anal. Chem. 75 (2003) 3046.
[11] B.K. Jena, C.R. Raj, Chem. Eur. J. 12 (2006) 2702.
[12] Y. Li, Y.Y. Song, C. Yang, X.H. Xia, Electrochem. Commun. 9 (2007) 981.
[13] J.S. Ye, Y. Wen, W.D. Zhang, L.M. Gan, G.Q. Xu, F.S. Shen, Electrochem. Commun. 6 (2004) 66.
[14] X. Kang, Z. Mai, X. Zou, P. Cai, J. Mo, Anal. Biochem. 363 (2007) 143.
[15] L.Q. Rong, C. Yang, Q.Y. Qian, X.H. Xia, Talanta 72 (2007) 819.
[16] Z. Zhuang, X. Su, H. Yuan, Q. Sun, D. Xiao, M.M.F. Choi, The Analyst 133 (2008) 126.
[17] X.M. Miao, R. Yuan, Y.Q. Chai, Y.T. Shi, Y.Y. Yuan, J. Electroanal. Chem. 612 (2008) 157.
[18] S.T. Farrell, C.B. Breslin, Electrochim. Acta 49 (2004) 4497.
[19] M.R. Guascito, P. Boffi, C. Malitesta, L. Sabbatini, P.G. Zambonin, Mater. Chem. Phys. 44 (1996) 17.
[20] B. Liao, Q. Wei, K.Y. Wang, Y.X. Liu, Sens. Actuators B: Chem. 80 (2001) 208.
[21] W. Zhang, S. Ding, Z. Yang, A. Liu, Y. Qian, S. Tang, S. Yang, J. Cryst. Growth 291 (2006) 479.
[22] K. Zhou, R. Wang, B. Xu, Y. Li, Nanotechnology 17 (2006) 3939.
[23] Y. Liu, Y. Chu, Y. Zhuo, M. Li, L. Li, L. Dong, Cryst. Growth Des. 7 (2007) 467.
[24] Z. Yang, J. Xu, W. Zhang, A. Liu, S. Tang, J. Solid State Chem. 180 (2007) 1390.
[25] W. Jia, M. Guo, Z. Zheng, T. Yu, Y. Wang, E.G. Rodriguez, Y. Lei, Electroanalysis 20 (2008) 2153.
[26] X. Jiang, T. Herricks, Y. Xia, Nano Lett. 2 (2002) 1333.
[27] L. Yu, G. Zhang, Y. Wu, X. Bai, D. Guo, J. Cryst. Growth 310 (2008) 3125.

Talanta 80 (2010) 1653–1656

Contents lists available at ScienceDirect

Talanta

journal homepage: www.elsevier.com/locate/talanta

Au nanoparticle decorated silicate network for the amperometric sensing of isoniazid

Bikash Kumar Jena, C. Retna Raj*

Department of Chemistry, Indian Institute of Technology, Kharagpur, West Bengal, India

ARTICLE INFO

Article history:
Received 28 August 2009
Received in revised form 1 October 2009
Accepted 3 October 2009
Available online 12 October 2009

Keywords:
Au nanoparticle ensemble
Sol–gel network
Amperometric sensor
Isoniazid

ABSTRACT

Au nanoparticle (nAu) based electrochemical platform for the amperometric sensing of isoniazid at sub-nanomolar level is developed. The sol–gel derived 3-dimensional silicate network pre-assembled on a conducting substrate is chemically decorated with nAu of 70–100 nm by seed-mediated growth approach. The Au nanoseeds are first chemisorbed onto the thiol functional groups of the silicate network and their size was enlarged by hydroxylamine seeding. The nanoparticles efficiently catalyze the oxidation of isoniazid at less positive potential. Large decrease in the overpotential and significant enhancement in the anodic peak current with respect to the polycrystalline Au electrode are observed. The nanoparticle based platform is highly sensitive (4.03 ± 0.01 nA/nM) and it linearly responds to isoniazid up to the concentration of 1 mM. It could detect as low as 0.1 nM (S/N = 5) of isoniazid at the potential of 10 mV in aqueous solution without any redox mediator. The catalytic response of the sensing platform depends on the amount of nanoparticles loaded onto the silicate network. Very interestingly, the sensing platform could simultaneously detect isoniazid and hydrazine in their coexistence without compromising the sensitivity. Well separated individual voltammetric response is obtained for both analytes. The sensing platform is highly stable and it can be repeatedly used for 7 days.

© 2009 Elsevier B.V. All rights reserved.

1. Introduction

Isoniazid is an important drug used in the clinical practice for the treatment of tuberculosis. It can cause hepatotoxicity in patient with an inflammatory response [1] and it is known to induce tumors in mice and cause chromosome aberrations [2]. It has been demonstrated further that long-term therapy of isoniazid can trigger systemic lupus erythematosus [3]. Various analytical methods based on spectral and electrochemical techniques have been developed for the quantitative determination of isoniazid [4–16]. The electrochemical methods are interesting as they require low cost equipment and isoniazid can be quantified without any special reagents [8–14]. However, the high overpotential required for the oxidation of isoniazid with unmodified electrode is a major concern with the electrochemical techniques. Traditionally, mediator and polymer based electrodes have been used to decrease the overpotential [8,10,12,14,15]. The lack of long-term stability due to the leaching of mediator is one of the disadvantages with the mediator modified electrodes. Liu et al. have utilized the palladium-modified microdisk array electrode for the electrocatalytic oxidation of isoniazid [4]. Although this microdisk array electrode has good sensitivity, it requires high overpotential as large as 1 V for the oxidation of isoniazid and the voltammetric response was not well-defined. Gao et al. used ferrocene derivative for the mediated oxidation of isoniazid [15]. Recently, carbon nanotube based electrode has been used for the detection of isoniazid in mild acid pH at the potential of 0.8 V [11]. Development of a highly sensitive and stable electrode for the sensing of isoniazid at less positive potential is desired for the accurate measurement of isonizid.

Tailoring of electrode surface with nanoscale metal particles is of significant interest in the recent years owing to the fact that the nanomaterials have excellent catalytic properties. The catalytic properties of nanomaterials depend on their shape, size and morphology; the catalytic activity is ascribed to the large surface-to-volume ratio and the existence of special binding site on their surface. Electrodes based on arrays or ensembles of micro/nanoparticles are of great interest in the development of electrochemical sensing platform. It has been shown theoretically and experimentally that the electrochemical platforms based on arrays or ensembles of nanoparticles have high sensitivity with respect to the macroelectrodes of same geometrical surface area [17]. In principle, very low detection limit can be achieved in array or ensemble based electrodes. The high sensitivity and low detection limit is ascribed to the enhancement in the signal-to-noise ratio (S/N) and high mass transport to the electrode surface [18]. Various methodologies have been used for the development of electrochemical interface based arrays/ensemble [17–22]. Bard and

* Corresponding author. Tel.: +91 3222 283348; fax: +91 3222 282252.
E-mail address: crraj@chem.iitkgp.ernet.in (C.R. Raj).

0039-9140/$ – see front matter © 2009 Elsevier B.V. All rights reserved.
doi:10.1016/j.talanta.2009.10.002

co-workers have first explored the colloidal chemical approach for the development of ultramicroelectrode [22]. This approach has been extensively used in the recent past in the development of nanoparticle ensemble based electrodes for various electroanalytical studies [23,24]. We have recently developed nAu based ensemble electrode for the sensing of NADH, glucose, hydrazine, metal ions etc. and for the fabrication of biosensors [25–28]. In continuation of earlier efforts in the development of electrochemical sensors, herein for the first time we report the amperometric sensing of isoniazid and simultaneous electroanalysis of isoniazid and hydrazine using nAu based platform.

2. Experimental

2.1. Materials

(3-Mercaptopropyl)trimethoxysilane (MPTS), $HAuCl_4$, isoniazid and hydrazine were obtained from Sigma–Aldrich and used as received. All other chemicals used in this investigation were of analytical grade unless mentioned otherwise. All the solutions were prepared with Millipore water.

2.2. Instrumentation

Electrochemical measurements were performed with computer controlled CHI643B electrochemical analyzer according to procedures reported elsewhere [25,26]. X-ray diffraction analysis of nanoparticles was carried out with Phillips X'pert. PRO X-ray diffraction unit using Ni filtered CuKα ($\lambda = 1.54$ Å) radiation. Scanning electron microscopic measurements were performed with Jeol JEM 6700F field emission scanning electron microscope (FESEM).

2.3. Development of sensing platform

The electrode used for the detection of isoniazid was prepared according to our earlier procedures [26]. Briefly, a cleaned polycrystalline Au electrode was first modified with a 3D silicate network containing thiol functional groups. This silicate modified electrode was soaked in colloidal nanoseeds for 18 h. The colloidal Au nanoseeds chemisorb onto the thiol functional groups of the 3D sol–gel network. The Au nanoseeds on the silicate network have been enlarged by seed-mediated growth approach using hydroxylamine [29]. For FESEM measurements, the gold-coated cover slip was first modified with the MPTS sol to get the sol–gel network and the self-assembling of Au nanoseeds and hydroxylamine seeding were performed as described earlier. Hereafter, the nanoseed modified and hydroxylamine seeded electrodes will be referred as AuS and AuE, respectively.

3. Results and discussion

3.1. Characterization of nanoparticles on the sensing platform

The nanoparticles on the silicate network (Fig. 1) have been characterized according to our earlier procedures [26]. The nanoparticles have a size distribution between 70 nm and 100 nm. The nanoparticles are randomly distributed throughout the network and the interparticle distance is less than the particle diameter (Supporting information). XRD profile obtained for AuE show four peaks corresponding to (1 1 1), (2 0 0), (2 2 0) and (3 1 1) planes (Supporting information). The absorption spectral measurement shows characteristic spectral signature for nanosized Au particles [26]. The nanoparticle on the silicate network can be considered as ensembles of nanoelectrode. The electrochemically accessible area of the nanoparticles were obtained by chronoamperometric measurement using $Fe(CN)_6^{3-/4-}$ as a redox probe. The electrochemically active area of the AuS and AuE electrodes was calculated to be 0.03 cm^2 and 0.07 cm^2, respectively.

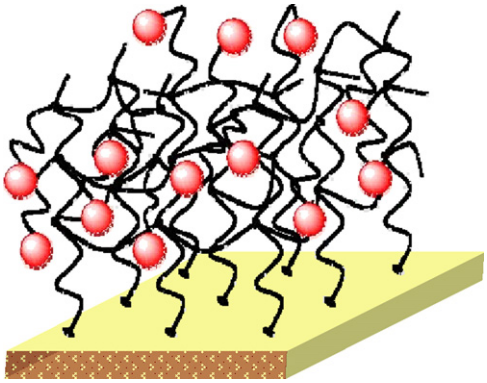


Fig. 1. Au nanoparticle decorated silicate network.

3.2. Electrocatalytic oxidation of isoniazid

Fig. 2 represents the voltammograms obtained for the oxidation of isoniazid at MPTS, AuS and AuE electrodes. The MPTS network modified electrode does not show any characteristic response for the oxidation of isoniazid in the potential window used. However, as can be readily seen from Fig. 2, well-defined voltammetric response at less positive potential was obtained for the oxidation of isoniazid on the nanoparticle modified electrodes. Interestingly, the isoniazid oxidation on AuE electrode occurs at 10 mV, which is 450 mV less positive than that on polycrystalline Au electrode. The onset potential for the oxidation of isoniazid on AuE electrode is much negative (~−100 mV) than the actual oxidation potential. The polycrystalline Au electrode shows a broad oxidation peak (Fig. 2 inset) at more positive potential (>450 mV), presumably due to sluggish electron transfer kinetics. The decrease in the overpotential associated with an enhancement in the peak current evidences the high catalytic activity of the nanoparticles. The peak current linearly increases with square root of sweep rate, supporting that the electron transfer involves a diffusion controlled process. The oxidation peak on the AuS electrode appears at the potential of 130 mV; the peak current on this electrode is significantly lower than the AuE electrode, suggesting that the surface area and particle coverage has great control over the oxidation process (vide

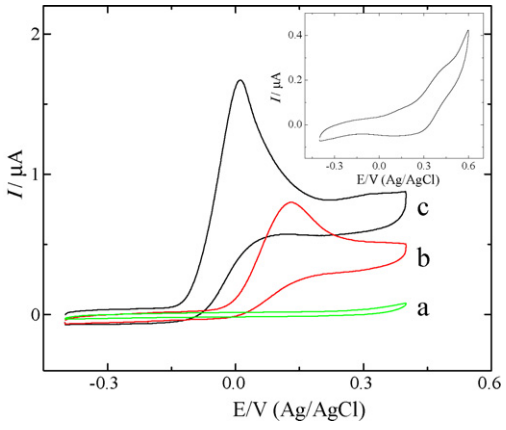


Fig. 2. Voltammetric profile obtained for the oxidation of isoniazid (0.1 mM) on (a) MPTS sol–gel network (b) AuS and (c) AuE electrodes in 0.1 M PBS (pH 9.2). Scan rate: 10 mV/s. Inset shows the voltammogram obtained for isoniazide on polycrystalline Au electrode.

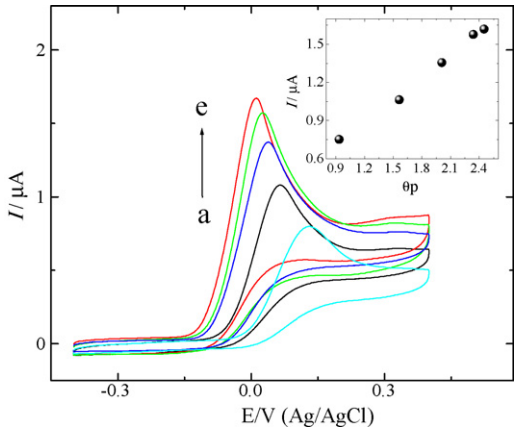


Fig. 3. Cyclic voltammograms obtained for the oxidation of isoniazid (0.1 mM) at different θ_p; other experimental conditions are same as in Fig. 2.

infra). The pH of the supporting electrolyte solution strongly influence the voltammetric peak potential and peak current (Supporting information). As expected, the peak potential shifts to more positive side as the solution pH was decreased. As the magnitude of peak current in alkaline pH is significantly high, amperometric sensing of isoniazid was performed at the pH of 9.2.

The particle coverage (θ_p) [30] on the electrode surface have great control over the catalytic activity of nanoparticles. In order to examine the influence of θ_p of the nanoparticle on the electrocatalytic oxidation of isoniazid, electrodes have been prepared by changing the hydroxylamine seeding time. Fig. 3 illustrates the effect of particle coverage on the electrocatalytic oxidation of isoniazid. Negative shift (120 mV) in the oxidation potential and enhancement in the peak current were noticed while increasing the particle coverage from 0.93 to 2.45. The negative shift in the peak potential evidence the facilitated electron transfer kinetics at the electrode surface. These results are in accordance with the theory of micro/nanoelectrode ensembles [17–21]. On such electrodes, sweep rate and interparticle distance dictate the voltammetric profile [17–21]. The negative shift in the oxidation potential while increasing the particle coverage can be ascribed to the change in the diffusion pattern [31]. The diffusion pattern would change from mixed non-linear and linear diffusion to a mostly linear diffusion while increasing the particle coverage.

3.3. Amperometric sensing of isoniazid

Fig. 4 is the amperometric *i–t* curve obtained for the sensing of isoniazid on AuE electrode at pH 9.2. The potential of the electrode was held at 10 mV and isoniazid was injected at regular time intervals. Steady and rapid increase in the amperometric current for the oxidation of isoniazid was noticed upon every injection. Steady state response was attained within 4 s. The sensitivity of the electrode was obtained from the calibration plot and was 4.03 ± 0.01 nA/nM. This electrode could detect as low as 0.1 nM (S/N = 5) of isoniazid. To the best of our knowledge this is the lowest detection limit achieved with electrochemical methods. The electrode offers linear response (0.1–1 mM) towards isoniazid. Table 1 compares the analytical performance of AuE electrode with the existing electrochemical sensors for isoniazid. Polycrystalline Au electrode has been used for the pulse voltammetric determination of isoniazid and the limit of detection (from the calibration plot) was 96 nM in strongly alkaline solution [9]. The stability of the electrode was not evaluated in this study. The polymer based electrodes could detect isoniazid in the range of 3–100 μM in neutral/alkaline pH [10,12]. Recently, carbon nanotube based electrode has been used for the voltammetric sensing of isoniazid at the potential of

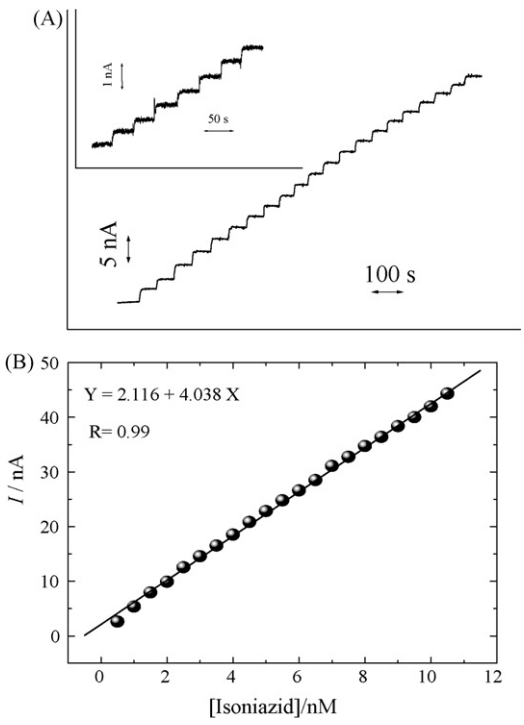


Fig. 4. (A) Amperometric *i–t* curve for the detection of isoniazid at AuE electrode. 0.5 nM of isoniazid was injected at regular time intervals. (B) Corresponding calibration plot. Inset shows the *i–t* curve for 0.1 nM.

0.85 V and it detects isoniazid at sub-micromolar level [11]. It is apparent from Table 1 that the present Au nanoparticle based electrode is superior to the existing sensors; it is highly sensitive, stable and it could detect isoniazid at sub-nanomolar level without any redox mediators.

3.4. Simultaneous electrochemical detection of isoniazid and hydrazine

Simultaneous voltammetric sensing of hydrazine and isoniazid is a challenging task, as both the analytes are expected to undergo oxidation almost at the same potential. We observed earlier that the oxidation of hydrazine on Au nanoparticle based electrode occurs at the potential of ∼−140 mV [27]. Fig. 5 displays the linear sweep voltammogram obtained for the oxidation of hydrazine and isoniazid in their coexistence. The voltammetric peak for the oxidation of hydrazine appears at the potential of ∼−140 mV whereas the oxidation peak for isoniazid appears at 10 mV. As the separation between the voltammetric peaks is >150 mV, the simultaneous detection of both analytes using the nanoparticle based platform is feasible. Linear increase in the peak current was obtained while increasing the concentration of isoniazid and hydrazine simulta-

Table 1
Electrochemical detection of isoniazid using different electrodes.

Electrode	Detection/peak potential	LOD (nM)	Reference
Au[a]	−300 mV (SCE)	96	[9]
Polypyrrole-GC[b]	105 mV (SCE)	3150	[10]
Polymer-GC[c]	550 mV (SCE)	10	[12]
CNT[d]	849 mV (Ag/AgCl)	500	[11]
Au nanoparticle	10 mV (Ag/AgCl)	0.1	Present work

[a] In pH 13.68; LOD obtained from the calibration plot.
[b] pH 9.
[c] pH 6.5; accumulation potential −200 mV.
[d] pH 4.

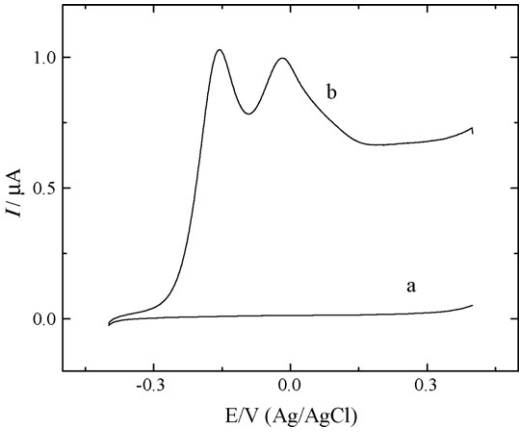


Fig. 5. Linear sweep wave voltammogram obtained for (a) MPTS sol–gel network and (b) AuE electrodes towards isoniazid and hydrazine (50 μM each) in their coexistence. Scan rate 10 mV/s.

neously (Supporting information). However, slight positive shift (~20 mV) in the peak corresponding to isoniazid was observed while simultaneously increasing the concentration of the hydrazine and isoniazid.

3.5. Stability

The stability of the nanoparticle based platform was evaluated using the same electrode for 20 repeated measurements with 50 μM of isoniazid. The same electrode was again utilized for a set of another 20 measurements after one day. The peak potential and peak current remained almost same in both sets of experiments; the coefficient of variation in the peak current was 0.2%, indicating the high stability of the electrode. To examine the long-term storage stability, the same electrode was used for a period of 7 days (Supporting information). The electrode was stored in phosphate buffer solution after the everyday's measurement. No significant change in the peak current and peak potential was noticed for 4 days; 8% decrease in the peak current was noticed after 7 days, demonstrating the long-term stability of the electrode.

4. Conclusions

We have demonstrated the electrocatalytic sensing of isoniazid using the nanoparticle based sensing platform. Au nanoparticles efficiently catalyze the oxidation of isoniazid. The electrocatalytic property of the sensing platform strongly depends on the particle coverage on the electrode surface. Large decrease in the overpotential and enhancement in the peak current without any redox mediator was obtained. The sensing platform is highly sensitive and it could sense as low as 0.1 nM of isoniazid. Simultaneous sensing of hydrazine and isoniazid is achieved with the Au nanoparticle based platform for the first time. Well separated voltammetric peaks for the oxidation of both analytes were observed. This electrode is very stable and it offers linear response for a wide concentration range.

Acknowledgement

This work was supported by grants from Department of Science and Technology New Delhi (No. SR/S5/NM-80/2006).

Appendix A. Supplementary data

Supplementary data associated with this article can be found, in the online version, at doi:10.1016/j.talanta.2009.10.002.

References

[1] S. Tafazoli, M. Mashregi, P.J. O'Brien, Toxicol. Appl. Pharmacol. 229 (2008) 94–101.
[2] R.L. Rubin, Toxicology 209 (2005) 135–147.
[3] G.B. Maru, S.V. Bhide, Cancer Lett. 17 (1982) 75–80.
[4] J. Liu, W.H. Zhou, T.Y. You, F.L. Li, E.K. Wang, S.J. Dong, Anal. Chem. 68 (1996) 3350–3353.
[5] Y. Xiong, H. Zhou, Z. Zhang, D. He, C. He, Spectrochim. Acta A: Mol. Biomol. Spectrosc. 66 (2007) 341–346.
[6] Z.H. Song, J.H. Lu, T.Z. Zhao, Talanta 53 (2001) 1171–1177.
[7] N.M.A. Mahfouz, K.M. Emara, Talanta 40 (1993) 1023–1029.
[8] J. Tong, X.J. Dang, H.L. Li, Electroanalysis 9 (1997) 165–168.
[9] H.Y. Xia, X.Y. Hu, Anal. Lett. 38 (2005) 1405–1414.
[10] M.R. Majidi, A. Jouyban, K. Asadpour-Zeynali, J. Electroanal. Chem. 589 (2006) 32–37.
[11] S. Shahrokhian, M. Amiri, Microchim. Acta 157 (2007) 149–158.
[12] G. Yang, C. Wang, R. Zhang, C. Wang, Q. Qu, X. Hu, Bioelectrochem 73 (2008) 37–42.
[13] M.M. Ghoneim, K.Y. ElBaradie, A. Tawfik, J. Pharm. Biomed. Anal. 33 (2003) 673–685.
[14] J. Tong, X.J. Dang, H.L. Li, Electroanal 9 (1997) 165–168.
[15] Z.-N. Gao, X.-X. Han, H.-Q. Yao, B. Liang, W.-Y. Liu, Anal. Bioanal. Chem. 385 (2006) 1324–1329.
[16] M.R. Majidi, A. Jouyban, K. Asadpour-Zeynali, Electroanal 17 (2005) 915–918.
[17] V.P. Menon, C.R. Martin, Anal. Chem. 67 (1995) 1920–1928.
[18] Y. Kobayashi, C.R. Martin, Anal. Chem. 71 (1999) 3665–3672.
[19] W.S. Baker, R.M. Crooks, J. Phys. Chem. B 102 (1998) 10041–10046.
[20] E. Jeoung, T.H. Galow, J. Schotter, M. Bal, A. Ursache, M.T. Tuominen, C.M. Stafford, T.P. Russell, V.M. Rotello, Langmuir 17 (2001) 6396–6398.
[21] R.M. Penner, C.R. Martin, Anal. Chem. 59 (1987) 2625–2630.
[22] C. Demaille, M. Brust, M. Tsionsky, A.J. Bard, Anal. Chem. 69 (1997) 2323–2328.
[23] K.C. Grabar, K.R. Brown, C.D. Keating, S.J. Stranick, S.-L. Tang, M.J. Natan, Anal. Chem. 69 (1997) 471–477.
[24] W. Cheng, S. Dong, E. Wang, Anal. Chem. 74 (2002) 3599–3604.
[25] B.K. Jena, C.R. Raj, Chem. Eur. J. 12 (2006) 2702–2708.
[26] B.K. Jena, C.R. Raj, Anal. Chem. 78 (2006) 6332–6339.
[27] B.K. Jena, C.R. Raj, J. Phys. Chem. C 111 (2007) 6228–6232.
[28] B.K. Jena, C.R. Raj, Talanta 76 (2008) 161–165.
[29] K.R. Brown, M.J. Natan, Langmuir 14 (1998) 726–728.
[30] S. Kumar, S. Zou, Particle coverage is the ratio of the surface area of nanoparticles on the network to the geometrical surface area of the under lying electrode surface, J. Phys. Chem. B 109 (2005) 15707–15713.
[31] S. Kumar, S. Zou, J. Phys. Chem. B 109 (2005), 15707–15713 and the references cited therein.

Talanta 80 (2010) 1657–1664

Contents lists available at ScienceDirect

Talanta

journal homepage: www.elsevier.com/locate/talanta

Preparation of silver hexacyanoferrate nanoparticles and its application for the simultaneous determination of ascorbic acid, dopamine and uric acid

Meissam Noroozifar[a,*], Mozhgan Khorasani-Motlagh[b], Aboozar Taheri[a]

[a] Analytical Research Laboratory, Department of Chemistry, University of Sistan & Baluchestan, P.O. Box: 98155-147, Zahedan, Iran
[b] Inorganic Research Laboratory, Department of Chemistry, University of Sistan & Baluchestan, Zahedan, Iran

ARTICLE INFO

Article history:
Received 6 July 2009
Received in revised form 1 October 2009
Accepted 3 October 2009
Available online 12 October 2009

Keywords:
Silver hexacyanoferrate nanoparticles
Carbon nanotube
Ascorbic acid
Dopamine
Uric acid
Simultaneous determination

ABSTRACT

A silver hexacyanoferrate nanoparticles/carbon nanotubes modified glassy carbon electrode was fabricated and then successfully used for the simultaneous determination of ascorbic acid, dopamine and uric acid by cyclic voltammetry. A detailed investigation by transmission electron microscopy (TEM) and electrochemistry was performed in order to elucidate the preparation process and properties of the nanocomposites. The size of silver hexacyanoferrate nanoparticles was examined by TEM around 27 nm. Linear calibration plots were obtained over the range of 4.0×10^{-6}–7.8×10^{-5}, 2.4×10^{-6}–1.3×10^{-4} and 2.0×10^{-6}–1.5×10^{-4} mol L^{-1} with detection limits of 4.2×10^{-7}, 1.4×10^{-7} and 6.0×10^{-8} mol L^{-1} for ascorbic acid, dopamine and uric acid, respectively. The practical analytical utilities of the modified electrode were demonstrated by the determination of ascorbic acid, dopamine and uric acid in urine and human blood serum samples.

© 2009 Elsevier B.V. All rights reserved.

1. Introduction

Dopamine (DA) is a chemical messenger produced within the nerve cells that is essential for the transmission of the nerve impulse and hence involved in a wide range of important functions, including movement, cognition and behavior. Dysfunctions in the central nervous dopamine system can lead to diseases such as Parkinson's and Schizophrenia [1]. Therefore, the determination of DA has attracted much attention of researchers. Similarly, ascorbic acid (AA) functions as a redox cofactor and catalyst in a broad array of biochemical reactions and processes. In humans, vitamin C cures and prevents scurvy, hence the designation ascorbic acid [2]. AA is present in mammalian brain in the presence of several neurotransmitter amines including DA. Uric acid (UA) is produced from the cellular breakdown products of the purine nucleosides, adenosine and guanosine [3]. As DA, UA and AA are copresent in biological fluids such as blood and urine, it is important to develop a technique to selectively detect DA and UA in the presence of AA conveniently in routine assay. Therefore, the selective detection of DA, UA and AA in the presence of other two species or their simultaneous determination has been a major goal of much research. For this purpose, various chemically modified electrodes have been constructed [4].

Metal hexacyanoferrate (MHCF) modified electrodes have been investigated intensively for a variety of application areas including electrocatalysis [5–11], ion selectivity [12], electrochromism [13,14], photoresponse [15] and solid state batteries [16,17]. Among these MHCF, Prussian blue is more used as sensors and biosensors, so far as Koncki [18] published a review about it. Some MHCF were used for determination of AA, DA or UA such as; lanthanum [19], palladium [20], tin [21], cobalt [22], nickel [23], copper [24] hexacyanoferrates and Prussian blue [7,11,25,26]. Recently, the use of nanoparticles has been reported [27] claiming that a better separation between individual signals, AA and DA, has been achieved. Based on our best knowledge, there is no report on the application of silver hexacyanoferrate nanoparticles (AgHCFNPs) for simultaneous determination of ascorbic acid, dopamine and uric acid.

Here we report for the first time a simultaneous voltammetric determination of AA, DA and UA using a glassy carbon electrode modified with a mixture of AgHCFNPs and multi-walled carbon nanotubes (CNT). Compared with the existing reports about simultaneous determination of AA, DA and UA, the proposed method is much more convenient to prepare the GC/CNT-AgHCFNPs modified electrode.

2. Experimental

2.1. Chemicals

Multi-walled carbon nanotubes (10–15 nm in diameter) were obtained from Aldrich and used without any pretreatment. All other chemicals used were of analytical reagent grade from

* Corresponding author. Tel.: +98 541 244 6565; fax: +98 541 244 6888.
E-mail address: mnoroozifar@chem.usb.ac.ir (M. Noroozifar).

0039-9140/$ – see front matter © 2009 Elsevier B.V. All rights reserved.
doi:10.1016/j.talanta.2009.10.005

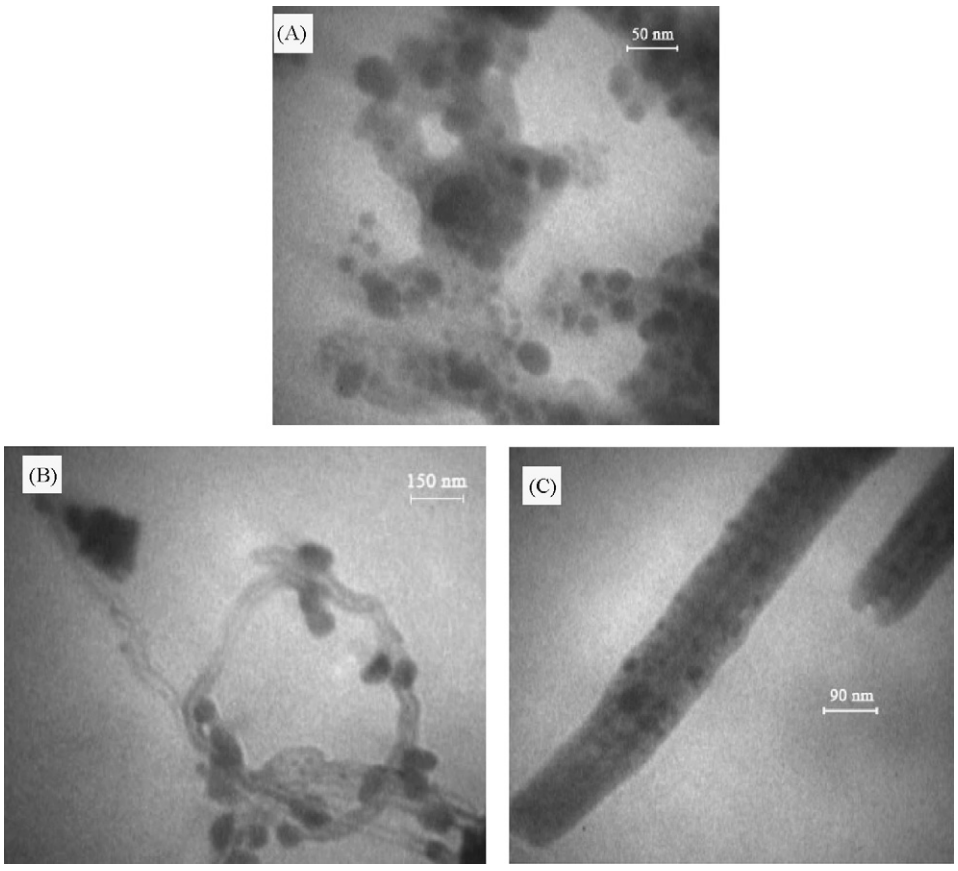


Fig. 1. A typical TEM images of the prepared AgHCFNPs with accelerating voltage, (A) 140 kV and CNT-AgHCFNPs nanocomposite with accelerating voltage, (B) 50 kV and (C) 140 kV.

Merck. Aqueous solutions were prepared with doubly distilled water (DDW). The stock solutions of dopamine (0.01 mol L^{-1}) and ascorbic acid (0.01 mol L^{-1}) were freshly prepared by dissolving dopamine hydrochloride and ascorbic acid in DDW, purged with pure nitrogen gas (99.999%) before investigations. Uric acid solution (0.01 mol L^{-1}) was prepared by dissolving the solid in a small volume of 0.1 mol L^{-1} NaOH solution and diluted to reach desired concentration. Dichloroacetic acid (pK_a = 1.26) was used for preparation of buffer solutions between pH 1.0 and 1.8, it was prepared by adjusting it to desire pH with 0.1 mol L^{-1} NaOH solution. In a same way, chloroacetic acid (pK_a = 2.87) for pH between 1.8 and 3.8 and acetic acid (pK_a = 4.76) for pH between 3.8 and 5.6 were used.

Fresh urine and serum samples were obtained from the Omid Clinical Laboratory (Zahedan, Iran) and passed through a filter with suitable porosity.

2.2. Apparatus

Cyclic voltammetric experiments were performed using a SAMA500 Electroanalyser (SAMA Research Center, Iran). All experiments were carried out using a conventional three-electrode system with the glassy carbon (GC) electrode with 2.0 mm diameter as the working electrode, a platinum wire as the auxiliary electrode, and a saturated calomel electrode (SCE) as the reference electrode. Cyclic voltammetric experiments were performed in quiescent solution. Electrolyte solutions were purged with high-purity nitrogen prior to electrochemical experiments. All the measurements were performed at room temperature.

The nanoparticles size and distribution of AgHCFNPs assembled on CNT were investigated using a JEOL TEM-2010 transmission electron microscopy.

2.3. Preparation of AgHCFNPs

Silver hexacyanoferrate nanoparticles ($Ag_4[Fe(CN)_6]$) were synthesized according to following reaction [28]:

$$[Fe(CN)_6]^{4-} + 4Ag^+ \rightarrow Ag_4[Fe(CN)_6] \quad (1)$$

All glassware was thoroughly cleaned in aqua regain (3 HCl:1 HNO_3, v/v), rinsed in distilled water and air-dried prior use. In a typical synthesis, 25.0 mL 4.0×10^{-3} mol L^{-1} $AgNO_3$ was drop wised added (2 drops per second) to 25.0 mL 1.0×10^{-3} mol L^{-1} $K_4[Fe(CN)_6]$ solution (which was purged with pure nitrogen gas prior to use), in a ultrasonic bath and under dark condition. After the addition, the reaction mixture was turned milky immediately. The mixture was sonicated further for 30 min. The solid was isolated by centrifugation and washed five times by water to remove any unreacted impurities. At the end, the solid was dispersed in 10 ml water with the aid of sonication. The concentration of nanoparticles in resulted suspension was 2.5×10^{-3} mol L^{-1}. The suspension was stored at 4 °C and prevented from light. This suspension was stable at least for 3 weeks.

2.4. Electrode modification

The GC electrode was polished with 0.05-μm alumina slurry. After rinsing with double-distilled water, it was sonicated in water and absolute ethanol for about 1 min each. Next, the GC electrode was transferred to the electrochemical cell for further cleaning by using cyclic voltammetry between −0.5 and +1.5 V at a scan rate of 100 mV s^{-1} in freshly prepared deoxygenated 0.5 mol L^{-1} H_2SO_4 until a stable cyclic voltammetric profile was obtained. The treated electrode was dried under a nitrogen stream and used immediately

for modification. With the help of ultrasonic agitation, 2 mg CNT was dispersed into 5 mL *N*,*N*-dimethylformamide (DMF) containing 0.5 mL of AgHCFNPs for 1 h. This mixture was denoted as CNT-AgHCFNPs. The clean GC electrode was coated by casting 5.0 μL of the CNT-AgHCFNPs suspension and dried under infrared radiation to form the CNT-AgHCFNPs adsorbed GC electrode, denoted as GC/CNT-AgHCFNPs. When not in use, the modified electrode was stored in DDW.

3. Results and discussion

3.1. TEM characterization of AgHCFNPs

Silver hexacyanoferrate nanoparticles were successfully prepared by sonication method, which exhibits a milk-white turbidity due to the light scattering of the nanoparticles. Fig. 1A shows the TEM images of prepared AgHCFNPs, with an average diameter of around 27 nm based on the TEM measurement out of 200 nanoparticles. As shown in Fig. 1B and C, the attachment of nanoparticles onto multi-walled carbon nanotube were successful, and the carbon nanotube was surrounded with abundant nanoparticles.

3.2. Electrochemical characteristics of modified electrode

Fig. 2 showed the cyclic voltammograms (CVs) of the resulting electrode obtained in chloroacetate buffered solution (CABS) with pH 2.0 (0.1 mol L^{-1}) and in various potential sweep rates. The electrochemical response of AgHCFNPs exhibited a pair of well-defined redox peaks at 0.034 and −0.058 V, in CABS which can be attributed to the electron transformations between Fe(II) and Fe(III) in the nanoparticles. The electrochemical properties of modified GC electrode with CNT-AgHCFNPs (GC/CNT-AgHCFNPs) were studied by cyclic voltammetry in pure buffered aqueous solution (pH 2.0) at various scan rates.

Fig. 2A shows the cyclic voltammograms of GC/CNT-AgHCFNPs at various scan rates. The reaction of these voltammograms is as following:

$$Ag_4[Fe^{II}(CN)_6] \rightleftarrows Ag_3[Fe^{III}(CN)_6] + e^- + Ag^+ \quad (2)$$

The Eq. (2) includes the oxidation and reduction of $Ag_4[Fe(CN)_6]$ and production of $Ag_3[Fe(CN)_6]$ with loss of one electron in anodic sweep.

As can be seen, the peak separation potential, ΔEp ($\Delta Ep = E_{pa} - E_{pc}$), is greater than the $59/n$ mV expected for a reversible system; this result suggests that AgHCFNP does not act as a reversible system in the carbon nanotube paste matrix. These cyclic voltammograms were used to examine the variation of peak current versus sweep rate. Fig. 2A shows that the modified

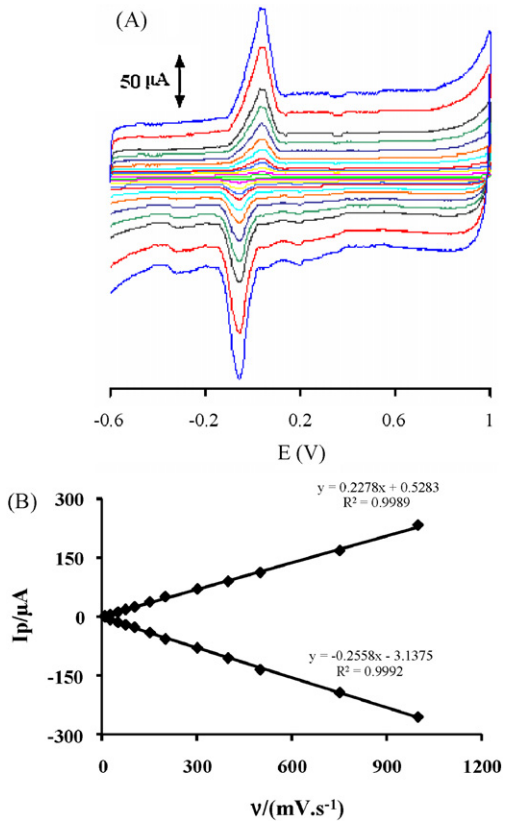


Fig. 2. (A) Cyclic voltammograms of the GC/CNT-AgHCFNPs electrode in CABS with pH 2.0 (0.1 mol L^{-1}) and at various scan rates (from inner to outer curve): 10, 25, 50, 75, 100, 150, 200, 300, 400, 500, 750, and 1000 mV s^{-1}. (B) Plots of peak currents versus scan rates.

electrode had a chemically reversible redox couple in pH 2.0) solution and the peak currents were increased due to the cyclic voltammetric scan rate. As shown in Fig. 2B, I_{pa} and I_{pc} were linearly dependent on scan rate, as expected for surface confined redox process. And the ratio of the anodic peak current to the cathodic peak current I_{pc}:I_{pa}, is almost equal to unity. These behaviors are consistent with a diffusionless system, reversible electron transfer process [29]. It suggested that the modified electrode reaction could be a one electron transfer process ($n = 1$).

An approximate amount of the electroactive species can be estimated by the method suggested by Sharp et al. [30]. According to this method, the peak current is related to the surface concentration

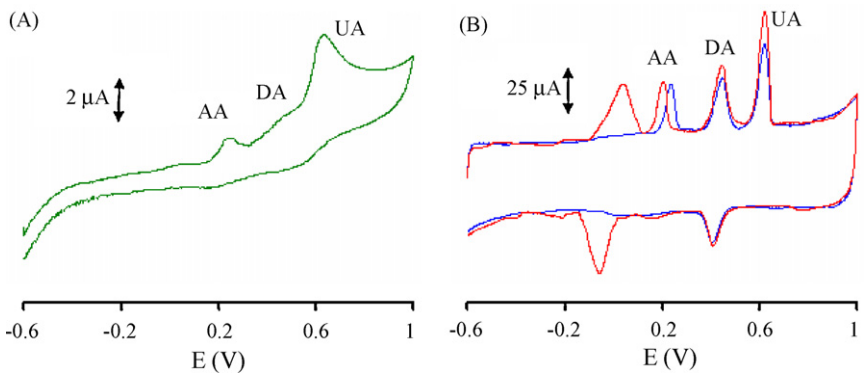


Fig. 3. CVs of 4.0×10^{-5} mol L^{-1} AA, DA and UA at the surface of (A) bare GC and (B) GC/CNT (blue line) and GC/CNT-AgHCFNPs (red line) electrode, in 0.1 mol L^{-1} CABS (pH 2.0). Scan rate: 100 mV s^{-1}. (For interpretation of the references to color in this figure legend, the reader is referred to the web version of the article.)

Table 1
Comparison of E_{pa} and I_{pa} at the surface of different electrodes in CABS (pH 2.0) containing 4.0×10^{-5} mol L^{-1} AA, DA and UA. Scan rate, 100 mV s^{-1}.

Electrode	E_{pa}/V			I_{pa}/μA		
	AA	DA	UA	AA	DA	UA
Bare GC	0.263	0.482	0.643	0.48	0.85	2.07
GC/CNT	0.246	0.448	0.624	37.09	42.77	58.22
GC/CNT-AgHCFNPs	0.19307	0.444	0.622	41.38	48.47	73.66

of electroactive species, Γ, by the following equation:

$$I_p = \frac{n^2F^2A\Gamma\nu}{4RT} \quad (3)$$

where n represents the number of electrons involved in the reaction, A is the geometric surface area of the electrode (0.0314 cm^2), Γ (mol cm^{-2}) is the surface coverage and other symbols have their usual meanings ν is the scan rate; R, F and T have their normal meanings. From the slope (0.2278 from Fig. 2b) of anodic peak currents versus scan rate (Fig. 1B) the calculated surface concentration of AgHCFNP is 7.72×10^{-9} mol cm^{-2} for $n = 1$.

3.3. Electrocatalytic oxidation of DA, UA and AA

The voltammetric behaviors of a mixture of AA, DA and UA on a bare GC electrode, GC/CNT and GC/CNT-AgHCFNPs, were studied, and a comparison of the CV results is shown in Fig. 3.

DA showed broad oxidation peak and could not be discriminated from AA and UA when a bare GC electrode was used (Fig. 3A). For DA, the anodic and cathodic peaks appear at 0.482 V and 0.552 V, respectively, and the separation of peak potential is about 0.070 V. Moreover, the cathodic peak current is much smaller than the anodic peak current. It is clear that the electrochemical reaction of DA at the bare GC is irreversible, indicating the sluggish electron transfer kinetic of DA at the bare GC, which may be related to the electrode fouling caused by the deposition of this compound and its oxidation product on the electrode surface [31]. When GC/CNT or GC/CNT-AgHCFNPs was used as the working electrode, the detection sensitivity was improved significantly and effective separation of the anodic peaks of AA, DA and UA was obtained (Fig. 3B). The large peak separation of the anodic peaks for these three compounds allows us to simultaneously determine them in the mixture solutions. Also, Fig. 3B compares the catalytic effect of CNT and CNT-AgHCFNPs for detection of these compounds. It can be seen from the Fig. 3, CNT-AgHCFNPs has more electrocatalytic effect toward the oxidation of AA, DA and UA. The results in Fig. 3B clearly show that the electrochemical responses of AA, DA and UA on the CNT-AgHCFNPs electrode occurred at different potential windows, which means that the electrochemistry of these three compounds can be well resolved from their mixed solutions. For better comparison, oxidation peak potentials and peak currents of AA, DA and UA on bare GC electrode, GC/CNT and GC/CNT-AgHCFNPs modified electrode are shown in Table 1.

The results in Table 1 indicate that in comparison with bare GC electrode, both GC/CNT and GC/CNT-AgHCFNPs electrodes reduce anodic overpotential of the analytes. Meanwhile, the enhancement of the anodic peak currents is most predominant at GC/CNT-AgHCFNPs than other electrodes. In addition, dopamine gives a more reversible redox behavior at the GC/CNT-AgHCFNPs and GC/CNT than at bare GC electrode. Having catalytically active surface and very high aspect ratio (length versus diameter), CNT can increase the surface area of the electrode, so the background voltammetric response for the CNT-coated surface is stronger than that for the bare surface [32].

Table 2
Cyclic voltammetric data of compositions with different ratios mg CNT mL^{-1} AgHCFNPs in CABS (pH 2.0) containing 4.0×10^{-5} mol L^{-1} AA, DA and UA. Scan rate, 100 mV s^{-1}.

mg CNT mL^{-1} AgHCFNPs	E_{pa}/V			I_{pa}/μA		
	AA	DA	UA	AA	DA	UA
1.0/0.50	0.200	0.444	0.628	34.54	40.82	61.49
2.0/0.00	0.246	0.448	0.624	37.09	42.77	58.22
2.0/0.25	0.219	0.446	0.624	40.51	45.20	68.23
2.0/0.50	0.19307	0.444	0.622	41.38	48.47	73.66
2.0/1.0	0.205	0.444	0.624	41.16	47.60	72.32
3.0/0.5	0.224	0.446	0.624	41.73	46.52	70.27

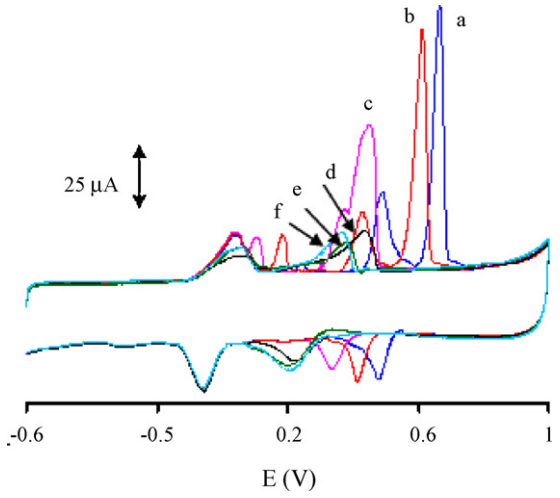


Fig. 4. Effect of pH on the peak separation and peak current for the oxidation of AA (2.0×10^{-5} mol L^{-1}), DA (4.0×10^{-5} mol L^{-1}) and UA (8.0×10^{-5} mol L^{-1}); pH= (a) 1.0, (b) 2.0, (c) 3.1, (d) 4.0, (e) 5.1 and (f) 5.6. Scan rate, 100 mV s^{-1}.

3.4. The effect of CNT-AgHCFNPs composition

The composition of the modified electrode was optimized by comparing the voltammetric response of different amounts of CNT to different volumes of AgHCFNPs suspension in CABS 0.1 mol L^{-1} (pH 2.0) containing 4.0×10^{-5} mol L^{-1} AA, DA and UA. The best composition is defined as the composition that by which maximum oxidation peaks separation and maximum anodic peak currents is achieved. For this purpose a series of experiments were carried out at above-mentioned conditions. The results are shown in Table 2.

According to table, when glassy carbon electrode was coated with 5 μL of a mixture containing 2 mg CNT and 0.5 ml AgHCFNPs suspension in 5 mL DMF, maximum peak separation and peak current was obtained. If the CNT content in the modificative mixture was too high (>3 mg) or too low (<1 mg), then the sensitivity was low due to the presence of a large background current or insufficient

Table 3
Analytical characteristics for simultaneous determination of AA, DA and UA by proposed method.

Analyte	Linear range (mol L^{-1})	Linear regression equation (I: μA, C: $\times 10^6$ mol L^{-1})	Correlation coefficient	Detection limit (mol L^{-1})
AA	4.0×10^{-6}–7.8×10^{-5}	$I = 14.637 + 0.1522C$	0.9924	4.2×10^{-7}
DA	2.4×10^{-6}–1.3×10^{-5}	$I = 18.457 + 0.4541C$	0.9960	1.4×10^{-7}
UA	2.0×10^{-6}–1.5×10^{-5}	$I = 21.253 + 1.2241C$	0.9963	6.0×10^{-8}

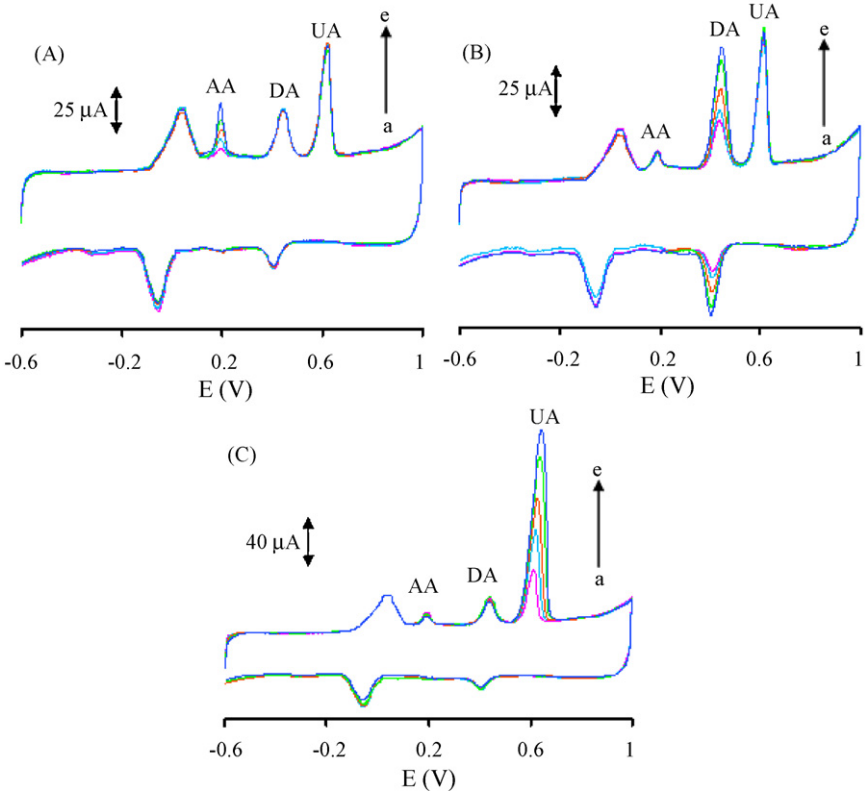


Fig. 5. CVs for the mixture containing AA, DA and UA with different concentrations in CABS (pH 2.0) at the GC/CNT-AgHCFNPs modified electrode. (A) DA (1.6×10^{-5} mol L^{-1}), UA (7.9×10^{-5} mol L^{-1}) and AA (a–e: 4.0×10^{-6}, 1.0×10^{-5}, $2.0 \times 10^{-}$, 4.0×10^{-5}, 6.3×10^{-5} mol L^{-1}); (B) AA (2.0×10^{-5} mol L^{-1}), UA (9.9×10^{-5} mol L^{-1}) and DA (a–e: 2.4×10^{-6}, 12.0×10^{-5}, 30.0×10^{-5}, $7.8, \times 10^{-5}$, 1.0×10^{-4} mol L^{-1}); (C) AA (2.0×10^{-5} mol L^{-1}), DA (1.6×10^{-5} mol L^{-1}) and UA (a–e: 8.0×10^{-6}, 3.0×10^{-5}, 5.2×10^{-5}, 7.9×10^{-5}, 1.0×10^{-4} mol L^{-1}).

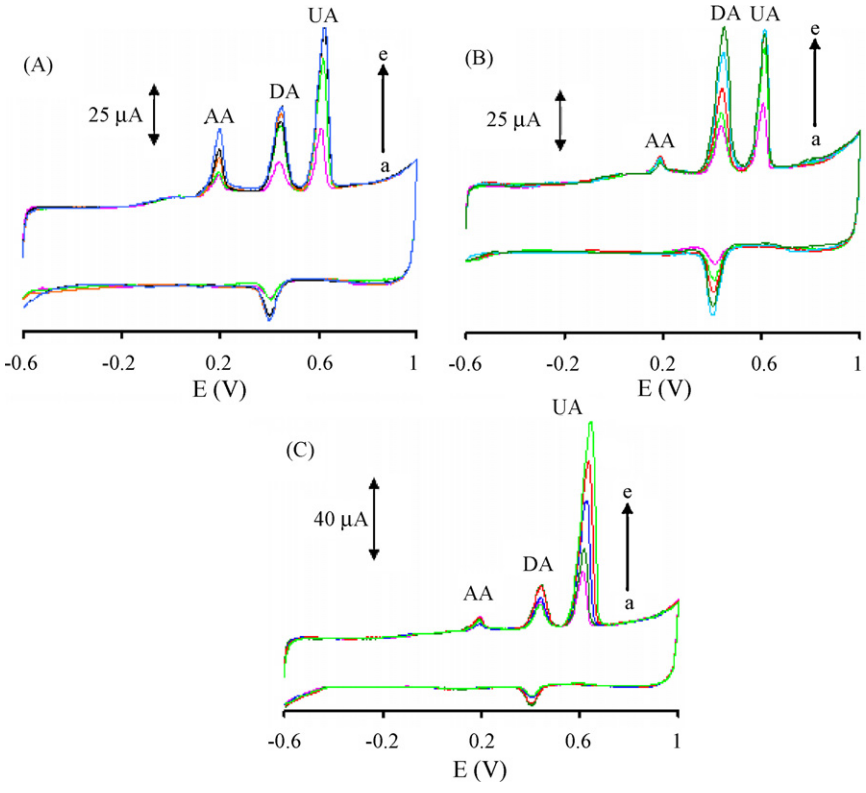


Fig. 6. CVs for the mixture containing AA, DA and UA with different concentrations in CABS (pH 2.0) at the GC/CNT modified electrode. (A) DA (1.6×10^{-5} mol L^{-1}), UA (7.9×10^{-5} mol L^{-1}) and AA (a–e: $4.0, \times 10^{-6}$ 1.0×10^{-5}, 2.0×10^{-5}, 4.0×10^{-5}, 6.3×10^{-5} mol L^{-1}); (B) AA (2.0×10^{-5} mol L^{-1}), UA (9.9×10^{-5} mol L^{-1}) and DA (a–e: 2.4×10^{-6}, 1.2×10^{-5}, 3.0×10^{-5}, 7.8×10^{-5}, 1.0×10^{-4} mol L^{-1}); (C) AA (2.0×10^{-5} mol L^{-1}), DA (1.6×10^{-5} mol L^{-1}) and UA (a–e: 8.0×10^{-6}, 3.0×10^{-5}, 5.2×10^{-5}, 7.9×10^{-5}, 1.0×10^{-4} mol L^{-1}).

Table 4
Determination of AA, DA and UA in real samples using GC/CNT-AgHCFNPs electrode.

Sample	Analyte	Detected[a] ($\times10^{-6}$ mol L^{-1})	Added ($\times10^{-6}$ mol L^{-1})	Found[a] ($\times10^{-6}$ mol L^{-1})	Recovery (%)	Total value[b] ($\times10^{-6}$ mol L^{-1})
Serum 1	AA	–	25.0	24.2 (±0.7)	96.8	–
	DA	2.4 (±1.0)	50.0	52.7 (±1.8)	100.6	0.12 (±1.62)
	UA	8.5 (±0.4)	100.0	110.9 (±2.5)	102.4	0.43 (±0.85)
Serum 2	AA	–	45.0	43.8 (±0.5)	97.3	–
	DA	–	25.0	25.6 (±1.7)	102.4	–
	UA	22.1 (±1.3)	50.0	73.0 (±1.5)	101.8	1.13 (±1.05)
Urine 1	AA	–	10.0	9.7 (±2.4)	97.0	–
	DA	–	100.0	103.1 (±1.2)	103.1	–
	UA	33.7 (±2.2)	25.0	59.2 (±2.7)	102.0	4.25 (±2.18)
Urine 2	AA	–	60.0	58.6 (±0.5)	97.7	–
	DA	–	125.0	126.8 (±1.9)	101.4	–
	UA	18.8 (±0.9)	80.0	100.3 (±1.3)	101.9	2.37 (±1.53)

[a] Average of three replicates ± standard deviation.
[b] Total value was obtained by multiplying the detected value by the appropriate dilution factor (51 for serum and 126 for urine samples).

amount of the CNT for adhesion nanoparticles to the glassy carbon electrode surface, respectively. In the later case, modificative film was easily removed from the electrode's surface.

3.5. Effect of pH on the oxidation of AA, DA and UA in a ternary mixture

The effect of solution pH on the electrochemical response of the GC/CNT-AgHCFNPs towards the simultaneous determination of AA, DA and UA was studied. A series of buffer solutions including phosphate buffer (0.1 mol L^{-1} H_3PO_4/KH_2PO_4 and KH_2PO_4/K_2HPO_4), universal buffer (0.1 mol L^{-1} CH_3COOH, 0.1 M H_3PO_4, and 0.1 mol L^{-1} H_3BO_3) and acetate-based buffer (0.1 mol L^{-1} CH_3COOH/CH_3COONa, $CClH_2COOH/CClH_2COONa$ and $CCl_2HCOOH/CCl_2HCOONa$, CCl_3COOH/CCl_3COONa) were prepared and tested as supporting electrolyte. In phosphate and universal buffers, modified electrode showed unstable responses for a certain concentration of AA, DA and UA. Therefore, future studies were carried out in the acetate based buffer solutions. The variations of peak separation and peak current with respect to the change in the pH of the electrolyte in the pH range from 1.0 to 5.8 are shown in Fig. 4.

It can be seen from Fig. 4 that except AA, the anodic peak current of DA and UA decreases slightly with an increase in the solution pH until it reaches 5.8; that of AA increases with increasing pH until pH reaches 2.0, and then it decreases when the pH exceeds 2.0. Hence, for AA, DA and UA, the highest anodic peak current was obtained at pH 2.0, 1.0 and 1.0, respectively. In addition, all the anodic peak potentials for the oxidation of AA, DA and UA shifted towards negative direction with increasing pH, showing that protons have taken part in their electrode processes. Its must be noted, that from pH 2.0 to higher pH the anodic peak potentials of DA and UA were broader and overlap together. Because of having most peaks separation and satisfactory peak currents and negatively shifts, a chloroacetate buffer solution with pH 2.0 was chosen as optimal pH.

3.6. Simultaneous determination of AA, DA and UA

The electro-oxidation processes of AA, DA and UA at the GC/CNT-AgHCFNPs in the mixture have also been investigated when the concentration of one species changed, whereas those of other two species are kept constant and the results are shown in Fig. 5.

Examination of Fig. 5A shows that the peak current of AA increased with an increase in AA concentration when the concentrations of DA and UA were kept constant. Although the charge current was enhanced after AA was oxidized, the peak currents of DA and UA did not change. Similarly and obviously, as shown in Fig. 5B and C, keeping the concentrations of other two compounds constant, the oxidation peak current of DA or UA was positively proportional to its concentration, while those of other two compounds did not change. Similar experiments were repeated at the GC/CNT and the results are shown in Fig. 6.

From our experimental results described above, it was known that in the ternary mixture containing AA, DA and UA when a GC/CNT-AgHCFNPs was used the oxidation peaks of these three compounds were clearly separated from each other, but when a GC/CNT was used as working electrode these species could not be determined simultaneously. If the concentrations of AA, DA and UA increased synchronously, on increasing the concentrations of the three compounds, the peak currents at the modified electrode increase accordingly as shown in Fig. 7. It can be seen that the peak currents for the three analytes increase linearly with their concentrations.

The voltammetric responses of the modified electrode (GC/CNT-AgHCFNPs) towards the simultaneous determination of AA, DA and UA are listed in Table 3. The relative standard deviations of the determination of 1.2×10^{-5} mol L^{-1} AA, 8.0×10^{-5} mol L^{-1} DA and 4.6×10^{-5} mol L^{-1} UA repeated seven times were 2.5%, 1.70% and 3.0%, respectively.

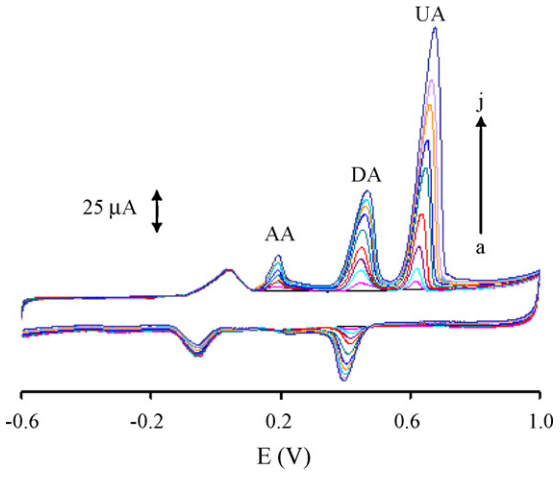


Fig. 7. CVs of the mixture containing AA, DA and UA at the GC/CNT-AgHCFNPs electrode in CABS (pH 2.0) at the scan rate of 100 mV s^{-1}. Concentrations of the three compounds (from a to j): 0.0, 4.0×10^{-6}, 8.0×10^{-6}, 12.0×10^{-5}, 2.0×10^{-5}, 3.0×10^{-5}, 4.9×10^{-5} and 7.8×10^{-5} mol L^{-1} for AA; 0.0, 2.4×10^{-6}, 8.0×10^{-6}, 1.2×10^{-5}, 2.0×10^{-5}, 3.0×10^{-5}, 4.9×10^{-5}, 7.8×10^{-5}, 9.7×10^{-5} and 1.3×10^{-4} mol L^{-1} for DA; 0.0, 2.0×10^{-6}, 8.0×10^{-6}, 2.0×10^{-5}, 4.0×10^{-5}, 6.9×10^{-5}, 9.7×10^{-5}, $1.1.\times10^{-4}$, 1.3×10^{-4} and 1.5×10^{-4} mol L^{-1} for UA.

Table 5
Comparison the proposed method with other electroanalytical methods with modified GC electrodes for the simultaneous determination of ascorbic acid, dopamine and uric acid.

Electrochemical method	Modification method	Analyte	Sample	Linear range (mol L^{-1})	Detection limit (mol L^{-1})	R.S.D.%	Reference
CV	Oxidation in mild acidic media	AA DA UA	Not reported	$1.97–9.88 \times 10^{-4}$ $1.97–9.88 \times 10^{-6}$ $1.97–9.88 \times 10^{-5}$	–	<1.5	[33]
DPV	Poly (3-(5-chloro-2-hydroxyphenylazo)-4,5-dihydroxynaphthalene-2,7-disulfonic acid) film	AA DA UA	Vitamin C tablets human urine samples Food	$5.0–240 \times 10^{-6}$ $5.0–280 \times 10^{-6}$ $0.1–18.0 \times 10^{-6}$	1.43×10^{-6} 2.9×10^{-6} 1.6×10^{-7}	1.7 1.3 1.4	[34]
DPV	PtAu hybrid film	AA DA UA	Injection solution, vitamin C tablets and human urine samples	$0.103–1.65 \times 10^{-3}$ $0.024–0.384 \times 10^{-3}$ $0.021–0.336 \times 10^{-3}$	1.03×10^{-4} 2.4×10^{-5} 2.1×10^{-5}	<2.0	[35]
DPV	Carbon-nanofiber	AA DA UA	Not reported	$2–64 \times 10^{-6}$ $0.04–5.6 \times 10^{-6}$ $0.8–16.8 \times 10^{-6}$	2×10^{-6} 0.04×10^{-6} 0.2×10^{-6}	Not reported	[36]
DPV	Mesoporous carbon/Nafion composite film	AA DA UA	Standard and real samples	$40–800 \times 10^{-6}$ $1–90 \times 10^{-6}$ $5–80 \times 10^{-6}$	0.5×10^{-6} 20×10^{-6} 4.0×10^{-6}	Not reported	[37]
DPV	Poly (vinyl alcohol)	AA DA UA	Human urine	$10.0–250.0 \times 10^{-6}$ $2.0–70.0 \times 10^{-6}$ $2.0–50.0 \times 10^{-6}$	7.6×10^{-6} 1.4×10^{-6} 6.0×10^{-7}	Not reported <3.0 Not reported	[38]
DPV	Dopamine solutions-phosphate buffer	AA DA UA	Human urine, serum and blood	$2.5 \times 10^{-5}–5.0 \times 10^{-4}$ $1.0 \times 10^{-6}–2.0 \times 10^{-5}$ $2.5 \times 10^{-6}–2.0 \times 10^{-5}$	1.3×10^{-5} 1.1×10^{-7} 1.4×10^{-6}	Not reported	[39]
CV	Silver hexacyanoferrate nanoparticles	AA DA UA	Urine and human blood serum	$4.0 \times 10^{-6}–7.8 \times 10^{-5}$ $2.4 \times 10^{-6}–1.3 \times 10^{-4}$ $2.0 \times 10^{-6}–1.5 \times 10^{-4}$	4.2×10^{-7} 1.4×10^{-7} 6.0×10^{-8}	<2.5 <1.70 <3.0	This work

3.7. Interference study

To evaluate the selectivity of the GC/CNT-AgHCFNPs modified electrode, the interference effects were investigated by detecting the response of the modified electrode to 2.0×10^{-5} mol L^{-1} AA, 8.0×10^{-5} mol L^{-1} DA and 4.0×10^{-5} mol L^{-1} UA in the presence of glucose and fructose, each in concentration 250 times of that of three analytes, 80 times of citric acid, 400 times of K^+ and Na^+, 150 times of Mg^{2+} and Zn^{2+}, 200 times of Ca^{2+} and chloride each. The results showed that the aforementioned species did not cause observable interference at the concentrations given.

3.8. Sample analysis

Human serum and urine samples were selected as real samples for analysis by the proposed method using the standard addition method. In order to avoid from the interferences of the real samples matrix and to fit into the linear range of AA, DA and UA, only 0.2 mL of urine samples and 0.5 mL serum samples were added to the electrochemical cell containing 25 mL of CABS. The results are presented in Table 4.

The recovery of the spiked samples ranged between 97.9% and 102.2%, indicating the detection procedures are free from interferences of the urine and serum samples matrix.

4. Conclusions

The modification of the GC electrode surface by CNT-AgHCFNPs not only improves the electrochemical catalytic activities towards the oxidation of AA, DA and UA, but also resolves the overlapped oxidation peaks of AA, DA and UA into three well-defined peaks at potentials 0.193 V, 0.444 V and 0.620 V in CV, respectively. Comparison between GC/CNT and GC/CNT-AgHCFNPs demonstrates that GC/CNT-AgHCFNPs more facilitates the simultaneous determination of AA, DA and UA with good stability, sensitivity and selectivity. In comparison with other electroanalytical methods that reported for the simultaneous determination of ascorbic acid, dopamine and uric acid, this method has better figures of merit (Table 5). The proposed method can be applied to the simultaneous determination of AA, DA and UA concentrations in real samples with satisfactory results.

Acknowledgments

We gratefully acknowledge the financial support of the University of Sistan & Baluchestan (USB) Research Vice Chancellery (Grant No. 87g09) and the Laboratory of Electron Microscopy of College of Science, University of Tehran.

References

[1] B. Larijani, C.A. Rosser, R. Woscholski, Chemical Biology, John Wiley & Sons Ltd, England, 2006.
[2] R.B. Rucker, J.W. Suttie, D.B. McCormick Lawrence, J. Machlin, Handbook of Vitamins, third ed., Marcel Dekker, New York, 2001.
[3] W. Arneson, J. Brickell, Clinical Chemistry: A Laboratory Perspective, F.A. Davis Company, Philadelphia, 2007.
[4] J. Huang, Y. Liu, H. Hou, T. You, Biosens. Bioelectron. 24 (2008) 632.
[5] J. Wang, X. Zhang, M. Prakash, Anal. Chim. Acta 395 (1999) 11.
[6] R. Garjonyte, A. Malinauskas, Sens. Actuators B 63 (2000) 122.
[7] S. Lupu, C. a Lete, M. Marin, N. Totir, P.C. Balaure, Electrochim. Acta 54 (2009) 1932.
[8] N. Adhoum, L. Monser, Sens. Actuators B 133 (2008) 588.
[9] Y. Liu, Z. Chu, W. Jin, Electrochem. Commun. 11 (2009) 484.
[10] A. Abbaspour, M. Ayatollahi Mehrgardi, Anal. Chem. 76 (2004) 5690.
[11] J. Bai, B. Qi, J.C. Ndamanisha, L.-p. Guo, Micropor. Mesopor. Mater. 119 (2009) 193.
[12] H. Düssel, A. Dostal, F. Scholz, Fresenius J. Anal. Chem. 355 (1996) 21.
[13] B. Petter Jelle, G. Hagen, Sol. Energy Mater. Sol. Cells 58 (1999) 277.
[14] P. Somani, S. Radhakrishnan, Chem. Phys. Lett. 292 (1998) 218.
[15] M. Kaneko, S. Hara, A. Yamada, J. Electroanal. Chem. 194 (1985) 165.
[16] V.D. Neff, J. Electrochem. Soc. 131 (1985) 1382.
[17] M. Kaneko, T. Okada, J. Electroanal. Chem. 255 (1988) 45.
[18] R. Koncki, Crit. Rev. Anal. Chem. 32 (2002) 79.
[19] G. Wang, J. Meng, H. Liu, S. Jiao, W. Zhang, D. i Chen, B. Fang, Electrochim. Acta 53 (2008) 2837.
[20] H. Razmi, A. Azadbakht, Electrochim. Acta 50 (2005) 2193.
[21] R. Hosseinzadeh, R.E. Sabzi, K. Ghasemlu, Colloids Surf. B: Biointerf. 68 (2009) 213.
[22] Z.Y. Xun, C.X. Cai, W. Xing, T.H. Lu, J. Electroanal. Chem. 545 (2003) 19.
[23] D.M. Zhou, H.X. Ju, H.Y. Chen, J. Electroanal. Chem. 408 (1996) 219.
[24] R. Pauliukaite, M.E. Ghica, C.M.A. Brett, Anal. Bioanal. Chem. 381 (2005) 972.
[25] M.J. Ruedas Rama, A. Ruiz Medina, A. Molina Díaz, Microchem. J. 78 (2004) 157.
[26] T. Lenarczuk, I. Roszczyk, R. Koncki, Anal. Lett. 33 (2000) 137.
[27] L. Zhang, X. Jiang, J. Electroanal. Chem. 583 (2005) 292.
[28] R.L. Richard, Inorganic Reactions in Water, first ed., Springer-Verlag, Berlin/Heidelberg, 2007.
[29] A.P. Brown, F.C. Anson, Anal. Chem. 49 (1977) 1589.
[30] M. Sharp, M. Petersson, K. Edstrom, J. Electroanal. Chem. 95 (1979) 123.
[31] A. Salimi, H. Mam-Khezri, R. Hallaj, Talanta 70 (2006) 823.
[32] J. Wang, M. Li, Z. Shi, N. Li, Z. Gu, Electroanalysis 14 (2002) 225.
[33] S. Thiagarajan, T.-H. Tsai, S.-M. g Chen, Biosens. Bioelectron. 24 (2009) 2712.
[34] A.A. Ensafi, M. Taei, T. Khayamian, J. Electroanal. Chem. 633 (2009) 212.
[35] S. Thiagarajan, S.-M. Chen, Talanta 74 (2007) 212.
[36] Y. Liu, J. Huang, H. Hou, T. You, Electrochem. Commun. 10 (2008) 1431.
[37] D. Zheng, J. Ye, L. Zhou, Y. Zhang, C. Yu, J. Electroanal. Chem. 625 (2009) 82.
[38] Y. Li, X. Lin, Sens. Actuators B 115 (2006) 134.
[39] R.P. da Silva, A.W.O. Lima, S.H.P. Serrano, Anal. Chim. Acta 612 (2008) 89.

Talanta 80 (2010) 1665–1671

Contents lists available at ScienceDirect

Talanta

journal homepage: www.elsevier.com/locate/talanta

Detection of bio-constituents in complex biological tissue using Raman microscopy. Application to human nail clippings

Effendi Widjaja*, Marc Garland

*Process Science and Modeling, Institute of Chemical and Engineering Sciences, Agency for Science, Technology and Research (A*STAR), 1 Pesek Rd, Jurong Island 627833, Singapore*

ARTICLE INFO

Article history:
Received 31 July 2009
Received in revised form 1 October 2009
Accepted 3 October 2009
Available online 13 October 2009

Keywords:
Raman microscopy
Human nail clippings
Band-target entropy minimization
Bio-constituents
Biological tissue
Pure component spectral estimates

ABSTRACT

Raman spectra of human nail clippings from various sources were collected and then deconvoluted to obtain the pure component spectra of the underlying constituents present. This blind-deconvolution was performed using a self-modeling curve resolution technique, namely band-target entropy minimization (BTEM). The aim was to simplify the complexity of the Raman spectra and hence to identify the underlying biological molecules in more detail. BTEM analysis could recover 13 pure component Raman spectral estimates from the collected 438 spectra measured from 113 nail samples. Six recovered pure component spectral estimates correspond to proteins or polypeptides that contain various amino acids such as phenylalanine, tyrosine, tryptophan, and cysteine. Two are associated with the secondary structures of proteins, and five are associated with two carotenoid species, lipid, ferulic acid, and calcium phosphate. Subsequently, the relative concentrations of these bio-constituents were calculated from the measured mixture spectra and the pure component BTEM estimates. These profiles indicated that the concentrations of some bio-constituents are correlated while others are not. A further analysis using target transformation factor analysis (TTFA) revealed the possible presence of curcumin in the human nails. Since the present approach and analysis is rather general, it might be extended to many other biological tissues in a rather straightforward and similar manner, thus revealing more detailed underlying biochemical information such as biomarkers that may be useful for diagnostic purposes.

© 2009 Elsevier B.V. All rights reserved.

1. Introduction

Raman spectroscopy has been used repeatedly to characterize the molecular structures of keratotic tissues, such as skin, callus, hair, and nail [1]. Barry et al. [2] and Williams et al. [1] were the first to assign the Raman spectral bands of these keratotic materials to specific vibrational modes of the chemical bonds. They also found that the principal differences in the Raman spectra of these samples were mainly due to variations in the sulphur content, as shown by the relative intensities of the C–S and S–S stretching modes [1,2]. Raman characterization of human nail, in particular, has also received greater attention lately in forensic studies. In forensic science, Raman spectroscopy and multivariate classification have been used for the differentiation of finger nails and toe nails and for human gender classification [3,4]. Edwards et al. have also applied Raman confocal microscopy to detect explosives and drugs of abuse as well as other substances on human nails, which were present due to contact and handling [5,6].

Human nail is a complex biological tissue, whose main structural component consists of hard α-keratins [1]. Besides Raman spectroscopy, previous analyses of human nail have included the use of Fourier-transform infrared spectroscopy [7], gas–liquid chromatography (GLC) [8], gas chromatography–mass spectrometry [9], X-ray diffraction [10], etc. Typically, relatively simple analyses were performed with these measurements. For example, with FT-IR and Raman, the presence of different functional groups were determined by the observed spectral band positions and with GLC, comparisons of retention times with standards were used.

In the present contribution, the collected Raman data are analyzed together in order to determine the underlying spectral patterns. In this regard, a multivariate spectral processing approach based on self-modeling curve resolution (SMCR) method can be used [11]. More specifically, in the current analysis, band-target entropy minimization (BTEM) [12] is used to reconstruct the pure component spectra of the underlying biological constituents without recourse to any a priori information, particularly spectral libraries. BTEM method was developed for analyzing large sets of multicomponent spectroscopic measurements (FTIR [13–15], Raman [16,17], MS [18], UV–vis [19], NMR [20]). It has now been extended to various applications, including the analysis of spectral data collected from biomedical [21], pharmaceutical [17,22], commercial [23] and other samples [24]. Various biological molecules are identified in the present analysis and as such the complexity of human nail spectra can be considerably simplified. The identifica-

* Corresponding author. Tel.: +65 6796 3943; fax: +65 6316 6185.
E-mail address: effendi_widjaja@ices.a-star.edu.sg (E. Widjaja).

0039-9140/$ – see front matter © 2009 Elsevier B.V. All rights reserved.
doi:10.1016/j.talanta.2009.10.006

tion of these bio-constituents may facilitate better understanding of nail chemistry and its relationship to diet, disease, chemical exposure, etc. Furthermore, since the present approach is rather general, it can probably be extended to many other biological tissues, thus revealing more detailed underlying biochemical information such as certain biomarkers that may be useful for diagnostic purposes.

2. Materials and methods

2.1. Experimental

A total of 113 samples of both fingernail and toenail clippings were kindly donated, on a volunteer basis, by 55 adult people (27 males and 28 females) from the Institute of Chemical and Engineering Sciences. These volunteers were aware that no identification would be made between the donor and the samples (anonymity of donor). In addition, the volunteers were informed of the type of study undertaken, i.e. Raman measurements for the purpose of deconvoluting biomarkers. This multiracial group of individuals ranged in age from 20 to 50 years and consisted of both vegetarians and non-vegetarians. On average, nail clippings were stored for a few days before Raman measurements were performed. No rigorous sample pretreatment of any kind was performed, with the exception of simple cleaning using acetone to remove dirt or contaminants on the nail samples after clipping. Raman spectra of nail clippings were collected using a Renishaw InVia Reflex dispersive Raman microscope. The Raman scattering was excited with a 785 nm near-infrared diode laser. From each nail clipping, three or four Raman spectra were measured on three or four different spots, and thus altogether 438 measurements were taken. All measurements were carried out using a 20× objective lens. The acquisition time for each Raman spectrum was circa 25 seconds with laser power on the sample of circa 20 mW. The Raman shift range acquired was 400–1800 cm^{-1}. In general, these Raman measurements exhibited some intra-nail spectral variations, but considerably more inter-nail spectral variations.

2.2. Data analysis

The raw spectra acquired from the nail clippings were only despiked. No further preprocessing of any kind, such as noise filtering, baseline correction, or spectral normalization was used. The aim was to preserve all of the chemically relevant spectral information for subsequent BTEM analysis. BTEM is a self-modeling curve resolution technique, which was developed to recover the pure component spectra of underlying constituents from a set of mixture spectra without recourse to any a priori known spectral libraries. This type of analysis in the signal processing area is also known as blind-source separation.

Unlike most self-modeling curve resolution (SMCR) algorithms, BTEM was especially developed to reconstruct one pure component spectrum at a time from a set of mixture spectra. The first step in the analysis is the use of singular value decomposition (SVD) to extract the singular vectors that describe the variance of the original mixture data set. With the present data set, in order to extract an estimate of a pure Raman scattering coefficient, a selected band in the non-noise right singular vectors is targeted. The BTEM algorithm then retains this feature and, at the same time, returns an entire full-length spectrum containing this band and all correlated bands, which have minimum entropy. This routine is repeated for all important observable physical features in the selected right singular vectors.

The criterion for selecting the band-targets is quite simple. A user can first set a tolerance for accepting/rejecting a feature. Then, all the observed spectral features in the first few right singular vectors with intensity above this threshold are selected as band-targets for BTEM. After applying BTEM to all of these band-targets, a superset of reconstructed pure component Raman scattering coefficients is obtained, and this set can be reduced to eliminate redundancies. This results in an enumeration of all observable pure component spectra. As mentioned, the targeted bands are retained during the reconstruction. As part of the process, the resulting pure spectral patterns are returned in a normalized form. When all normalized observable pure component spectra have been reconstructed, relative contributions of these signals can be calculated by projecting them onto the original data set. For a detailed description of the BTEM algorithm, readers are referred to refs. [12–15].

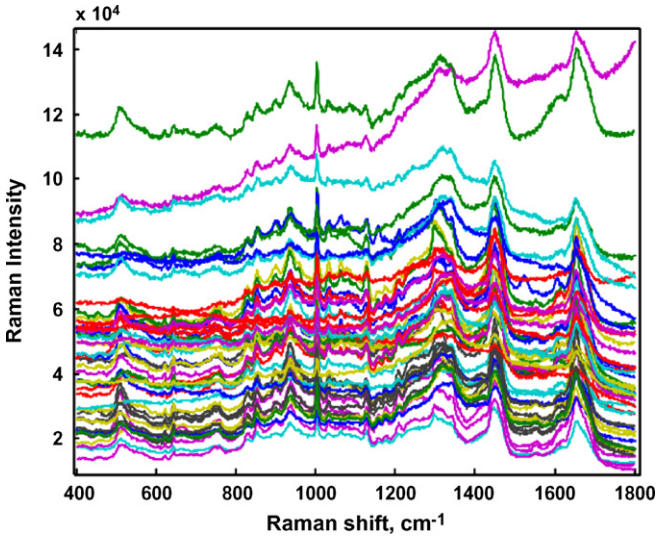


Fig. 1. The 48 despiked Raman spectra of human nail clippings.

All data analyses were performed in MATLAB 7.1 (The Mathworks Inc., Natick, MA). A personal computer with dual 3 GHz Pentium IV processors and 2 GB of RAM was used for all computations. In-house programs written in MATLAB were used for BTEM as well as other analyses.

3. Results and discussion

Fig. 1 shows the stacked-plot of 48 of the 438 acquired Raman spectra of human nails. Although broad autofluorescence signals are present, despite the use of a near-infrared 785 nm laser as the scattering source, clear Raman spectral features measured from all samples can still be observed. Relative peak intensities and small differences in Raman spectral features among different samples are also seen, which shows that biomolecular variations in human nails are quite high. These variations may be due to differences in race, gender, age, dietary habits, etc. of the individuals from whom nail samples were obtained.

Without any further spectral baseline correction or normalization, the collected 438 Raman spectra were subjected to SVD. The first 20 right singular vectors are shown in Fig. 2. There are many identifiable Raman bands (extrema) in the first twenty right singular vectors, and these peaks were subsequently used as the band-targets for the BTEM analysis. The entire set of data was analyzed together since larger variability in the original set of signals assists the analysis.

Exhaustive band-targeting was performed on all significant peaks and a superset of reconstructed pure component spectra was obtained. After eliminating the redundancies to reduce the number of BTEM estimates, 13 pure component Raman spectral estimates

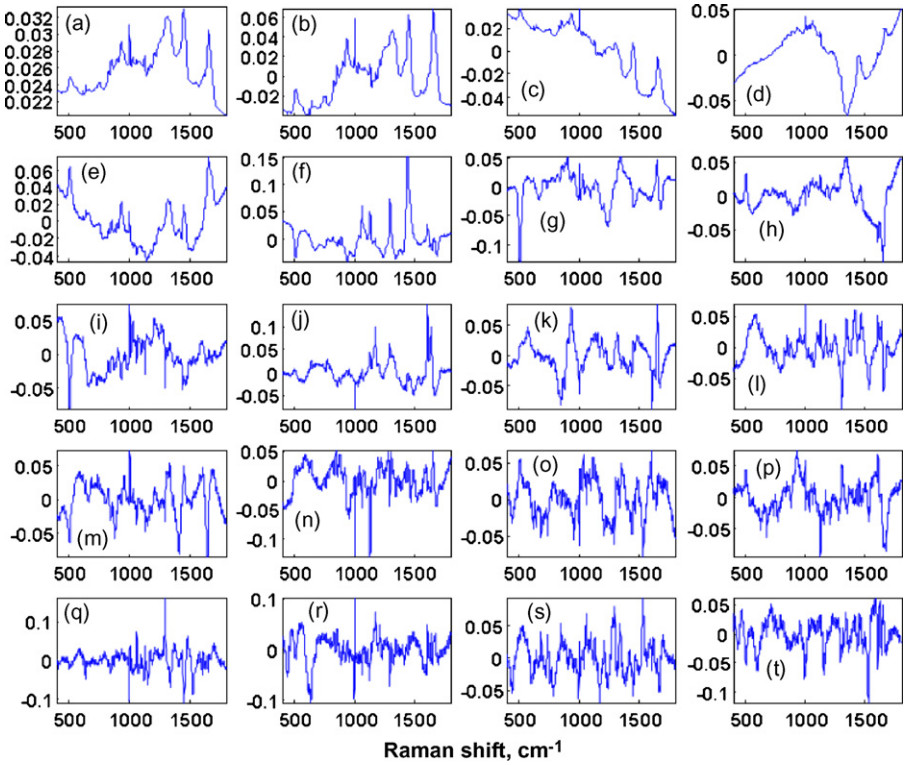


Fig. 2. The first 20 right singular vectors obtained from SVD decomposition, (a) 1st vector, (b) 2nd vector, (c) 3rd vector. . ., (t) 20th vector.

were obtained and these are shown in Figs. 3–5. Six of these estimates correspond to proteins and polypeptides that contain various amino acids such as phenylalanine, tyrosine, tryptophan, and cystine. Two estimates are associated with the secondary structures of proteins, and five estimates are associated with fatty acid, two carotenoid species, ferulic acid, and calcium phosphate (details are provided in the next section).

3.1. Pure component spectral estimates of proteins and polypeptides

The BTEM pure component spectra estimate in Fig. 3(a) shows a prominent Raman band centered at 508 cm^{-1}, which can be assigned to the S–S stretching mode of cystine and cysteine residues. This prominent band at 508 cm^{-1} also verifies that the conformation of the group C–C–S–S–C–C is gauche–gauche–gauche, which is the most stable form [25]. For other conformations, such as gauche–gauche–trans and trans–gauche–trans, S–S stretching modes commonly appear at 525 and 540–550 cm^{-1}, which are not observed in the present study. These other types of conformations are known to be more common in other types of tissue such as skin [25]. The relatively weak Raman bands at 638 and 663 cm^{-1} can be assigned to the C–S

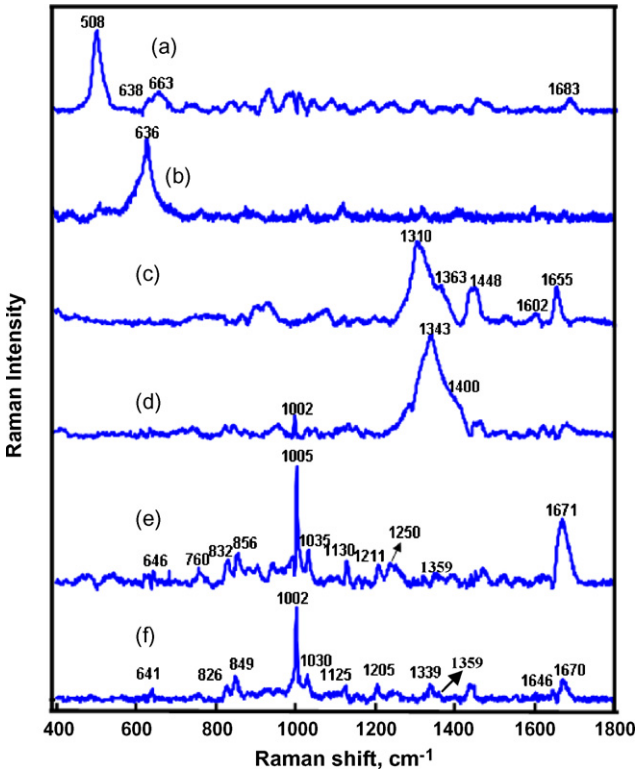


Fig. 3. Six BTEM pure component spectral estimates of various proteins and polypeptides.

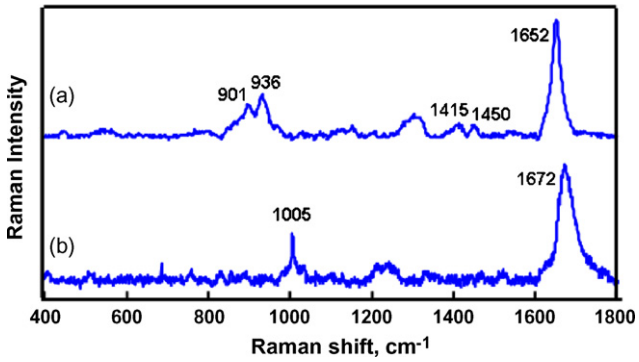


Fig. 4. BTEM pure component spectral estimates of secondary structures of proteins, (a) α-helix conformation, and (b) β-sheet conformation.

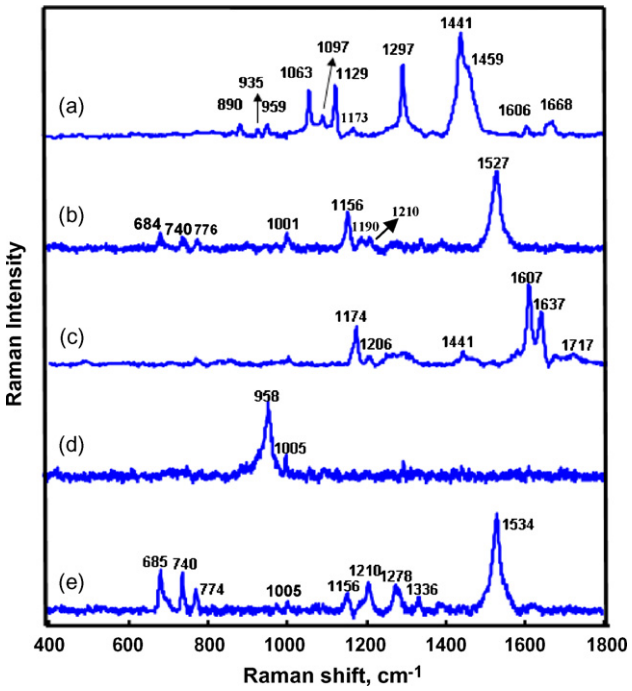


Fig. 5. BTEM pure component spectral estimates of other constituents found in human nails, (a) lipid, (b) 1st carotenoid species, (c) ferulic acid, (d) calcium phosphate like species, (e) 2nd carotenoid species.

stretching vibration of cystine and cysteine residues and the weak band at 1683 cm^{-1} corresponds to the amide I stretching vibration (although it is shifted to slightly higher wavenumber, see Section 3.2 for further details). From Fig. 3(b), another pure component spectrum associated with cystine and cysteine residues is resolved with a prominent Raman band at 636 cm^{-1}. This band can again be assigned to a C–S stretching mode [26].

The pure component spectral estimates in Fig. 3(c) and (d) show broad bands at 1250–1425 cm^{-1}, which may arise from the overlapping Raman signals of the C–H deformation and amide III [26]. The intensities of the methylene (CH_2) deformation, C_α–H stretching, and tryptophan appears at 1343, 1310, and 1304 cm^{-1}, and the intensity of the amide III band for α-helix structure appears around 1260–1300 cm^{-1}. Since all these bands are highly overlapping, broad bands arise as shown in Fig. 3(c) and (d). Additional bands at 1448, 1602, and 1655 cm^{-1} also appear in Fig. 3(c) and they can be assigned to CH_2 bending, C=C in-plane bending mode of phenylalanine and tyrosine, and amide I α-helix modes. The weak Raman band at 1002 cm^{-1} seen in Fig. 3(d) is associated with the symmetric breathing mode of the aromatic ring of phenylalanine.

Fig. 3(e) and (f) are two rather similar pure component spectral estimates which were recovered using BTEM analysis. However, these two estimates are certainly different species, as closer inspection shows that the peak maxima are significantly different. Fig. 3(e) exhibits Raman bands at 646, 832, 856, 1005, 1035, 1130, 1211 cm^{-1} whereas Fig. 3(f) shows bands at 641, 826, 849, 1002, 1030, 1125, 1205 cm^{-1}. With regard to their primary structures, these two spectral estimates certainly belong to proteins, as several amino acid residues can be clearly observed. The Raman bands of phenylalanine residues are clearly shown at 1005, 1035, 1211 cm^{-1} in Fig. 3(e) and at 1002, 1030, 1205 cm^{-1} in Fig. 3(f). Both sets of three Raman bands are associated with the breathing mode of the aromatic ring, δ(CH) in-plane and $\nu(C_6H_5–C)$, respectively [27]. Raman signals of tyrosine residues are also seen at the Raman vibration frequencies 646, 832, and 856 cm^{-1} in Fig. 3(e) and 641, 826, 849 cm^{-1} in Fig. 3(f). These sets of vibrations can be attributed to the aromatic ring and Fermi resonance doublet, respectively. The tyrosine doublets observed at 832/856 and 826/849 cm^{-1} in the current study have been well investigated and are due to the Fermi resonance between the ring-breathing vibration and the overtone of an out-of-plane ring-bending vibration of the para-substituted benzenes [28]. As the peak-height intensity of the band at 856 and 849 cm^{-1} is higher than the peak-height intensity of the band at 832 and 826 cm^{-1}, it is suggested that the tyrosine residues in human nails are mostly exposed and are likely to form intermolecular bonds with other amino acids [29,30]. Tryptophan residues are seen at the Raman vibrational frequencies 760 and 1359 cm^{-1} in Fig. 3(e) and at 1339 and 1359 cm^{-1} in Fig. 3(f). The band at 760 cm^{-1} can be attributed to indole ring-breathing and the bands at 1339 and 1359 cm^{-1} can be assigned to the Fermi resonance doublet of tryptophan, which has been used as an indicator of hydrophobicity. Higher intensity ratios of the doublet, I_{1339}/I_{1359} suggest that a hydrophobic environment is present, whereas lower intensity ratios suggest that the tryptophan is involved in the hydrogen bonding of a hydrophilic environment [31]. In Fig. 3(f), the peak-height Raman intensity of 1339 cm^{-1} is higher than 1359 cm^{-1}, which indicates that a hydrophobic environment may exist in some parts of human nails. On the other hand, in Fig. 3(e), it can be seen that the Raman band centered at 1359 cm^{-1} is weak and the corresponding Fermi resonance peak commonly observed at 1339 cm^{-1} is missing. The lack of this peak indicates that the tryptophan is exposed and linked to other amino acids [32]. In the two spectral estimates shown in Fig. 3(e) and (f), amide I bands are also recovered at 1671 cm^{-1} (Fig. 3(e)) and 1670 cm^{-1} (Fig. 3(f)). The position of these two amide I bands indicated that these two proteins have primarily β-sheet secondary structures [25,26].

3.2. Pure component spectral estimates of secondary structures of protein

Fig. 4 presents BTEM pure component spectral estimates of two different protein structures. The first estimate as shown in Fig. 4(a) has a strong and prominent band centered at 1652 cm^{-1} and some additional bands at 901, 936, 1415, and 1450 cm^{-1}. The band at 1652 cm^{-1} is unambiguously assigned to the amide I vibrational mode, which involves mainly C=O stretching vibrations, but also C–N stretching, C_α–C–N bending, and N–H in-plane bending of peptide groups [25,26]. This band at 1652 cm^{-1} also indicates that this estimate possesses a α-helix conformation, which is further confirmed by the presence of skeletal C–C stretching vibrations at 901 and 936 cm^{-1} [33]. The bands at 1415 and 1450 cm^{-1} correspond to methylene deformation and bending modes, respectively. The second estimate as shown in Fig. 4(b) has a strong band centered at 1672 cm^{-1} and relatively weaker bands at 1005 and 1180–1280 cm^{-1}, which correspond to the amide I stretching vibration of a β-sheet conformation, ring-breathing mode of phenylalanine, and amide III stretching vibration, respectively. The recovery of these two secondary structures of protein via BTEM analysis, α-helix and β-sheet, indicates that human nail specimens contain two protein conformations. As observed in Fig. 4, the recovered spectral estimate of β-sheet conformation has a lower signal-to-noise ratio compared to the recovered spectral estimate of α-helix conformation. This suggests that proteins in human nails contain predominantly α-helix structures and a lower content of β-sheet structures. The reliability of BTEM analysis in recovering pure component spectral estimate of minor constituents has been repeatedly shown in other studies [17,34].

3.3. Pure component spectral estimates of other constituents

As shown in Fig. 5, pure component spectral estimates of five other constituents are also recovered using BTEM analysis. The

first estimate as presented in Fig. 5(a) shows prominent and sharp Raman bands between 1050 and 1300 cm^{-1} that have typical characteristics consistent with palmitic saturated fatty acid [35]. Thus, this estimate can be assigned as a lipid constituent of human nail. Raman bands at 1063, 1097, 1129, and 1173 can be assigned to (C–C) skeletal stretching. The band at 1297 and a group of bands between 1400 and 1500 cm^{-1} can be assigned to $\delta(CH_2)$ twisting vibrations and $\delta(CH_3)$ or $\delta(CH_2)$ deformations, respectively. However, as shown in Fig. 5(a), there is an absence of the ester band commonly found near 1740 cm^{-1}, which is replaced by an amide-like band at 1668 cm^{-1}. Such an amide band can be assigned to the C=O stretching vibration coupled to a N–H bending vibration [36]. This amide band indicates that this lipid constituent belongs to the group called sphingolipids. Sphingolipids are a group of lipid constituents, which are composed of a sphingoid base backbone to which a fatty acid may be attached through an amide bond and/or a head group at the primary hydroxyl [37]. These may be associated, in part, with the hydrophobic regions mentioned earlier (Section 3.1).

The second estimate as shown in Fig. 5(b) has prominent Raman bands of carotenoid species at 1001, 1156, and 1527 cm^{-1}, which can be attributed to the δ(C=CH) methyl in-plane rocking vibrations, ν_2(C–C) in-plane single bond stretching, and ν_1(C=C) stretching mode respectively [38]. In addition, two smaller bands of carotenoid species appearing at 1190 and 1210 cm^{-1} are also recovered by BTEM analysis as seen in this estimate. These two bands can be assigned to $\nu(C–CH_3)$ stretching and combination of CH_3 deformation and in-plane CH methine vibrations, respectively [39]. The other three smaller bands found between 650 and 800 cm^{-1} are probably Raman bands associated with amino acid signals from cysteine and tryptophan. The presence of these three bands may indicate that this carotenoid species is bound with proteins.

The third spectral estimate shown in Fig. 5(c) has some prominent Raman bands centered at 1174, 1206, 1441, 1607, 1637, and 1717 cm^{-1}. This recovered spectral estimate may correspond to ferulic acid, a phenolic compound that is commonly found in leaves, seeds of many plants and especially grains such as brown rice, whole wheat and oats. Ferulic acid is normally bound to cell wall polymers. The pure ferulic acid Raman spectrum is characterized by a vibration at 1178 cm^{-1} and by the doublet stretching vibration C=C of the phenolic ring at 1603 and 1630 cm^{-1} [32,40]. However in the present estimate, the recovered pure component spectral estimate of ferulic acid has slightly shifted peak positions. The recovered spectral Raman bands at 1174 and 1206 cm^{-1} can be assigned to C–C stretching and C–O stretching vibrations. The recovered peak at 1441 cm^{-1} can be assigned to both symmetrically and asymmetrically CH_3 deformations and the recovered peaks at 1607 and 1637 cm^{-1} can be assigned to the C=C stretching vibration of the benzene or a phenolic ring [32]. The identification of ferulic acid in nail specimens via Raman microscopy and BTEM analysis is somewhat surprising. Since ferulic acid is known as a potent anti-oxidant, it has been added to skin and nail healthcare products, as it can neutralize free radicals that can cause oxidative damage of cell membranes and DNA. Ferulic acid is also added to some healthcare supplements to prevent damage to cells caused by ultraviolet light. In addition, adding ferulic acid to vitamins C and E also appears to increase protection from UV-induced skin damage. The long-term usage of skin and nail care products containing ferulic acid may have caused some incorporation of ferulic acid component into the nail plate. Simple nail cleaning using acetone prior to Raman measurements ultimately does not help to remove this anti-oxidant species and as such ferulic acid can still be identified in the present analysis.

The fourth spectral estimate shown in Fig. 5(d) shows one major band centered at around 958 cm^{-1} and one small band at around 1005 cm^{-1}. This spectral estimate may be associated with calcium phosphate found in human nails. As the amount of calcium phosphate in human nail is very small, the recovered pure spectral estimate via BTEM analysis has lower signal-to-noise ratio, and therefore, other peaks correlated with the main peak (958 cm^{-1}) are imbedded in the noise [41]. The two recovered peaks, 958 and 1005 cm^{-1}, can be attributed to the stretching vibration of PO_4 mineral and P–O stretching of monohydrogen phosphate and/or the phenyl breathing modes that might be present in human nails.

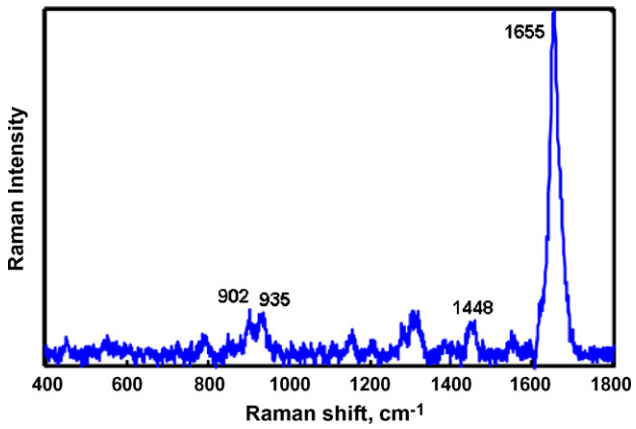


Fig. 6. Another spectral pattern estimate obtained from BTEM analysis—similar to an α-helix secondary structure.

As shown in Fig. 5(e), the recovered fifth spectral estimate looks quite similar to the second spectral estimate. This high degree of similarity indicates that this estimate is another carotenoid species found in human nail. The most prominent Raman band in this estimate, which can be assigned to a ν_1(C=C) stretching mode, is centered at 1534 cm^{-1}. This peak position is higher than the second estimate which is centered at 1527 cm^{-1}. A relationship between the peak position of the ν_1(C=C) stretching mode and the number of conjugated double bonds in the carotenoid chain has been previously studied [42]. It was found that the wavenumber of the ν_1(C=C) band decreases with the increasing number of conjugated double bonds in the carotenoid chain due to an electron–phonon coupling. Accordingly, the present estimates may suggest that the first species with ν_1(C=C) band at 1527 cm^{-1} is the nine-double bond conjugated carotenoid, whereas the second species with ν_1(C=C) band at 1534 cm^{-1} is the seven-double bond conjugated carotenoid. Additional Raman bands for the fifth spectral estimate were also recovered at 675, 740, 774, 1005, 1156, 1210, 1278, 1336, and 1534 cm^{-1}, in which the first three bands correspond to cysteine and tryptophan (675, 740, and 774 cm^{-1}). The Raman peaks at 1005, 1156, and 1210 cm^{-1} correspond to the other carotenoid signals, which can be attributed to δ(C=CH) methyl in-plane rocking vibrations, ν_2(C–C) in-plane stretching, and a combination of CH_3 deformation and in-plane CH methine vibrations. The Raman peaks at 1278 and 1336 cm^{-1} correspond to amide III and a methylene bending vibration. The presence of amino acids and an amide vibration again indicate that this estimate is a carotenoid species bound to protein, similar to the second estimate shown in Fig. 5(b).

3.4. Other spectral patterns

A few additional spectral patterns were obtained by BTEM analysis. However, these additional spectral patterns are all very similar to pure patterns already presented in Figs. 3–5. Fig. 6 shows one of these patterns. This spectrum surely represents an α-helix but the main peak maximum is shifted just slightly, and the relative intensities of the other bands are slightly lower. Mathematically, this high degree of similarity means that the inner product of Fig. 4(a) and the Fig. 6 will approach unity, and hence further analysis to determine

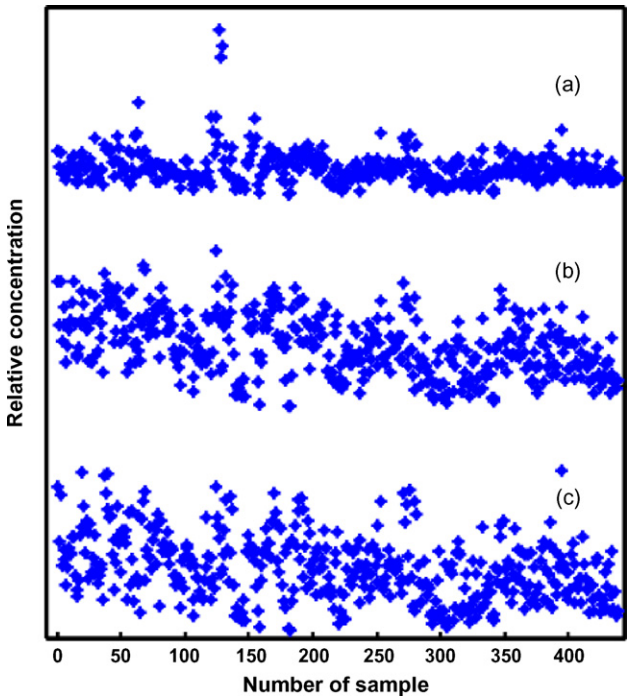


Fig. 7. The relative concentration profiles, (a) ferulic acid in Fig. 5(c), (b) polypeptide in Fig. 3(e), (c) an α-helix conformation structure in Fig. 4(a).

their individual signal contributions will be problematic. Accordingly, in the following section, only the 13 original BTEM estimates (Figs. 3–5) will be used, in order to facilitate further analyses.

3.5. Relative concentrations

A least squared fit of the 13 primary pure component spectra (Figs. 3–5) onto the baseline corrected nail spectra generally resulted in less than circa 2% mismatch. This indicates that most of the information content of the experimental measurements was captured by the above 13 pure component spectra. Accordingly, the relative concentrations of the previously identified components can be readily obtained. Fig. 7 shows the relative concentration profiles of 3 components, namely the ferulic acid in Fig. 5(c), polypeptide in Fig. 3(e), and an α-helix in Fig. 4(a). These were chosen to illustrate the wide range of concentration profile behaviors observed. For example, the concentration profile of ferulic acid Fig. 7(a) shows pronounced person-to-person variation. Indeed, the 3 concentrations associated with samples 127–129 (the 3 concentration outliers) all belong to one individual.

The issue of correlations between concentration profiles was also investigated. The inner product between the concentrations of ferulic acid in Fig. 7(a) and of polypeptide Fig. 7(b) was 0.60. A relatively low value is expected since there is no obvious correlation between ferulic acid and a polypeptide. In contrast, the inner product between the concentrations of polypeptide Fig. 7(b) and of an alpha-helix in Fig. 7(c) was 0.91. This relatively high value is not entirely unexpected since some polypeptides should exhibit an α-helical structure.

3.6. Potential of target transformation factor analysis (TTFA) in further analysis

Target transformation factor analysis is an established method for evaluating a set of 1D data for the presence of a test vector [43]. After consideration of the widely varying diets of the individuals from whom the nails were acquired, curcumin was chosen as the test constituent. It is well known that tuber turmeric/curcumin is a major constituent of some Southeast Asian foods [44]. It is also well known that the polyphenolic compound curcumin is rather hydrophobic [45]. A Raman spectrum was measured of an authentic sample of curcumin. Subsequently, the experimental data set was tested. Fig. 8 shows the experimentally measured Raman spectrum of curcumin as well as the predicted spectrum from the test. As can be seen, there is considerable similarity between the curcumin spectrum and the predicted spectrum (even though the latter has relatively low S/N). This suggests that curcumin (or closely related metabolites) are present in minute spectroscopic quantities in at least a few of the nail samples. Attempts at reconstructing a curcumin spectrum using BTEM were unsuccessful, probably due to the very low signal contribution.

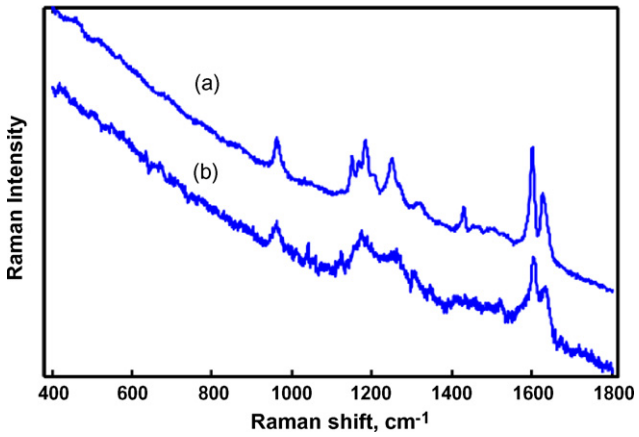


Fig. 8. Raman spectrum of curcumin, (a) experimental measured from authentic sample, (b) predicted spectrum via TTFA using 50 right singular vectors.

3.7. Limitations and extensions

Raman microscopy was used as the spectroscopic method throughout the present study. The primary limitation of the present approach is associated with the specificity of this spectroscopy. Reasonably good Raman scatter is an important pre-requisite to the subsequent signal processing, i.e. deconvolution and TTFA. Hence, molecules like water and functional groups such as OH may not be easily identifiable. A complementary vibrational measurement, such as FTIR microscopy might be able to fill this gap. As an extension of the present method, a laser change from near-infrared to UV, might dramatically increase the sensitivity for some molecules due to resonance enhancement. Indeed, the general increase in signal-to-noise afforded by the short wavelength excitation source could also possibly enhance the subsequent signal processing steps, and additional components may be detectable.

4. Conclusions

The present results have shown that combined Raman spectroscopy and BTEM analysis of human nail clippings can result in the reconstruction of the underlying pure component spectra of various constituents present in this complex biological tissue. This has subsequently allowed identification of some proteins and their secondary structures in greater detail. As shown in Fig. 3(e) and (f), the Fermi resonance doublet of tyrosine and tryptophan could be well resolved, and as such it was found that the tyrosine and tryptophan residues in human nails are mostly exposed and not buried and that they form intermolecular bonds with other amino acids. BTEM analysis has also helped to verify that the protein secondary structures in human nails are predomi-

nantly α-helix conformations but that β-sheet conformations are also present. Pure component spectra of minor constituents, i.e. lipid, carotenoid species, ferulic acid, and calcium phosphate like species, have also been recovered from some of the human nail clippings. The recovered pure spectrum of lipid without an ester band but with an amide-like band indicates that the lipid constituent in human nail plate mainly consists of sphingolipids. The two recovered carotenoid species with different ν_1(C=C) peak positions suggest that these two carotenoid species have a different number of conjugated double bonds in the carotenoid chain. The identification of carotenoid species and ferulic acid in the present study from some nail clippings is somewhat unexpected, since the presence of these components in human nails has not been reported before. Carotenoid species and ferulic acid are popular anti-oxidants, which are added into healthcare products particularly for skin and nails. Long-term usage of such healthcare products, and subsequent incorporation into nail, may be responsible for the observations made in this study.

The combination of Raman spectroscopy and BTEM analysis as shown in the present study can probably be extended to other complex biological tissues. This type of approach may help to identify certain bio-constituents in other biological tissues, or even identify biomarkers of disease or chemical exposure.

Acknowledgements

This work was supported by Agency for Science, Technology, and Research (A*STAR), Singapore.

References

[1] A.C. Williams, H.G.M. Edwards, B.W. Barry, J. Raman Spectrosc. 25 (1994) 95–98.
[2] B.W. Barry, H.G.M. Edwards, A.C. Williams, J. Raman Spectrosc. 23 (1992) 641–645.
[3] E. Widjaja, R.K.H. Seah, Appl. Spectrosc. 60 (2006) 343–345.
[4] E. Widjaja, G.H. Lim, A. An, Analyst 133 (2008) 493–498.
[5] E.M.A. Ali, H.G.M. Edwards, M.D. Hargreaves, I.J. Scowen, J. Raman Spectrosc. 40 (2009) 144–149.
[6] E.M.A. Ali, H.G.M. Edwards, M.D. Hargreaves, I.J. Scowen, Anal. Bioanal. Chem. 390 (2008) 1159–1166.
[7] A. Sakudo, H. Kuratsune, Y.H. Kato, K. Ikuta, Clin. Chim. Acta 402 (2009) 75–78.
[8] M.S. Greaves, J.M.H. Moll, Clin. Chem. 22 (1976) 1608–1613.
[9] M.H. Choi, Y.S. Yoo, B.C.J. Chung, Chromatogr. B. Biomed. Sci. Appl. 754 (2001) 495–501.
[10] H.P.J. Baden, Invest. Dermatol. 55 (1970) 115–122.
[11] J.-H. Jiang, Y. Ozaki, Appl. Spectrosc. Rev. 37 (2002) 321–345.
[12] E. Widjaja, Development of band-target entropy minimization (BTEM) and associated software tools, PhD Thesis, National University of Singapore. Singapore, 2002.
[13] E. Widjaja, C.Z. Li, M. Garland, Organometallics 21 (2002) 1991–1997.
[14] W. Chew, E. Widjaja, M. Garland, Organometallics 21 (2002) 1982–1990.
[15] E. Widjaja, C.Z. Li, W. Chew, M. Garland, Anal. Chem. 75 (2003) 4499–4507.
[16] E. Widjaja, N. Crane, T.S. Chen, M.D. Morris, M.A. Ignelzi Jr., B.R. McCreadie, Appl. Spectrosc. 57 (2003) 1353–1362.
[17] E. Widjaja, R.K.H. Seah, J. Pharma. Biomed. Anal. 46 (2008) 274–281.
[18] H.J. Zhang, M. Garland, Y.Z. Zeng, P. Wu, J. Am. Soc. Mass Spectrosc. 14 (2003) 1295–1305.
[19] S.Y. Cheng, F. Gao, K.I. Krummel, M. Garland, Talanta 74 (2008) 1132–1140.
[20] L.F. Guo, A. Wiesmath, P. Sprenger, M. Garland, Anal. Chem. 77 (2005) 1655–1662.
[21] N.J. Crane, V. Popescu, M.D. Morris, P. Steenhuis, M.A. Ignelzi, Bone 39 (2006) 434–442.
[22] T.S. Chen, M.J. Lee, Y.S. Kim, S.M. Lee, S. Kummar, M. Gutierrez, S.M. Hewitt, J.B. Trepel, I.W. Levin, Anal. Chem. 80 (2008) 6390–6396.
[23] E. Widjaja, M. Garland, Anal. Chem. 80 (2008) 729–733.
[24] N.A. Macleod, A. Goodship, A.W. Parker, P. Matousek, Anal. Chem. 80 (2008) 8146–8152.
[25] H.G.M. Edwards, D.E. Hunt, M.G. Sibley, Spectrochim. Acta Part A 54 (1998) 745–757.
[26] W. Akhtar, H.G.M. Edwards, Spectrochim. Acta Part A 53 (1997) 81–90.
[27] R.C. Lord, N.T. Yu, J. Mol. Biol. 50 (1970) 509–524.
[28] M.N. Siamwiza, R.C. Lord, M.C. Chen, T. Takamatsu, I. Harada, H. Matsuura, T. Shimanouchi, Biochemistry 14 (1975) 4870–4876.
[29] A.T. Tu, in: R.J.H. Clark, R.E. Hester (Eds.), Spectroscopy of Biological Systems, John Wiley and Sons, New York, 1986, pp. 47–112.
[30] G.J. Thomas Jr., Biopolymers 67 (2002) 214–225.
[31] A.M. Herrero, Crit. Rev. Food Sci. Nutri. 48 (2008) 512–523.
[32] O. Piot, J.-C. Autran, M.J. Manfait, Cereal Sci. 32 (2000) 57–71.
[33] B.G. Frushour, J.L. Koenig, Biopolymers 14 (1975) 379–391.
[34] C.Z. Li, E. Widjaja, W. Chew, M. Garland, Angew. Chem. 41 (2002) 3784–3789.
[35] J. De Gelder, K. De Gussem, P. Vandenabeele, L. Moens, J. Raman Spectrosc. 38 (2009) 1133–1147.
[36] C. Krafft, L. Neudert, T. Simat, R. Salzer, Spectrochim. Acta Part A 61 (2005) 1529–1535.
[37] A.H. Merrill Jr., in: D.E. Vance, J.E. Vance (Eds.), Biochemistry of Lipids, Lipoproteins and Membranes, 5th ed., Elsevier, St. Louis, 2008, pp. 364–396.
[38] N. Tschirner, M. Schenderlein, K. Brose, E. Schlodder, M.A. Mroginski, P. Hildebrandt, C. Thomsen, Phys. Stat. Sol. B 245 (2008) 2225–2228.
[39] C. Arcangeli, S. Cannistraro, Biopolymers 57 (2000) 179–186.
[40] M.S. Ram, F.E. Dowell, L.M. Seitz, Cereal Chem. 80 (2003) 188–192.
[41] J.S. Cheah, E. Jacob, P.P.B. Yeo, H.M. Gwee, P. Lim, Singapore Med. J. 23 (1982) 273–274.
[42] W. Barnard, D. de Waal, J. Raman Spectrosc. 37 (2006) 342–352.
[43] E.R. Malinowski, Factor Analysis in Chemistry, 3rd ed., Wiley, New York, 2002.
[44] R. Hanif, L. Qiao, S. Shiff, B.J. Rigas, Lab. Clin. Med. 130 (1997) 576–584.
[45] F. Yang, G.P. Lim, A.N. Begum, O.J. Ubeda, M.R. Simmons, S.S. Ambegaokar, P.P. Chen, R. Kayed, C.G. Glabe, S.A. Frautschy, G.M. Cole, J. Biol. Chem. 280 (2005) 5892–5901.

Talanta 80 (2010) 1672–1680

Contents lists available at ScienceDirect

Talanta

journal homepage: www.elsevier.com/locate/talanta

Rapid determination of aristolochic acids I and II in herbal products and biological samples by ultra-high-pressure liquid chromatography–tandem mass spectrometry

Ching-Hua Kuo[a,b,*], Chia-Wen Lee[a], Shu-Chiao Lin[a], I-Lin Tsai[a], Shoei-Sheng Lee[a,c], Y. Jane Tseng[a,d], Jaw-Jou Kang[c,e], Fu-Chuo Peng[e], Li Wei-Chu[f]

[a] School of Pharmacy, College of Medicine, National Taiwan University, Taipei, Taiwan
[b] Department of Pharmacy, National Taiwan University Hospital, Taipei, Taiwan
[c] Drug Research Center, College of Medicine, National Taiwan University, Taipei, Taiwan
[d] Graduate Institute of Biomedical Electronic and Bioinformatics, National Taiwan University, Taipei, Taiwan
[e] Institute of Toxicology, College of Medicine, National Taiwan University, Taipei, Taiwan
[f] Sheng Chang Pharmaceutical Co., Ltd., Jung-Li, Taiwan

ARTICLE INFO

Article history:
Received 19 June 2009
Received in revised form 2 October 2009
Accepted 5 October 2009
Available online 12 October 2009

Keywords:
Aristolochic acid
Herbal products
Aristolochic acid nephropathy
UHPLC–MS/MS
Biological samples

ABSTRACT

Aristolochic acids (AAs) are a mixture of structural-related compounds, in which aristolochic acid I (AA I) and aristolochic acid II (AA II) are reported to be correlated with Aristolochic acid nephropathy (AAN). In this work, a rapid and sensitive ultra-high-pressure liquid chromatography–tandem mass spectrometry (UHPLC–MS/MS) method was developed to determine AA I and AA II in herbal products and biological fluids. By using gradient elution with a mobile phase composed of a mixture of 10 mM ammonium formate buffer (pH 3.0) and acetonitrile, AAs could be determined within 10 min. Under optimum UHPLC–MS/MS conditions, the limit of detections was 0.14 and 0.26 ng mL^{-1} for AA I and AA II, respectively. Run-to-run repeatability and intermediate precision of peak area for AA I and AA II were less than 5.74% relative standard deviation (RSD). Accuracy was tested by spiking 10, 100 and 1000 ng mL^{-1} in rat serum and the recoveries were within 76.5–92.9%. Matrix effects were within 78.8–127.7%. The developed method was successfully applied to determine AA I and AA II in several herbal products and to investigate their pharmacokinetic behavior in female Wister rats. The result shows that the developed UHPLC–MS/MS method is efficient, sensitive, and accurate for the determination of AA I and AA II in herbal products and biological samples.

© 2009 Elsevier B.V. All rights reserved.

1. Introduction

Aristolochic acids (AAs) are found primarily in the plant genera *Aristolochia* and *Asarum* [1]. Pharmacological properties of AAs are anti-inflammatory, antitussive, antiplatelet aggregation. And they are also used as pain-relievers [2–4]. Inadvertent replacement of the plant *Stephania tetrandra* with *Aristolochia fangchi* in Chinese herbal medicines has caused many renal fibrosis problems, named Aristolochic acid nephropathy (AAN), in young women on a sliming regimen [5]. AAs were proved to be the major components that caused such toxicity [6]. Due to the serious side effect, USA, UK, Canada, Australia, and Germany government agencies have banned the use of a range of species of plants that contain AAs. For similar reasons, several Chinese herbal medicines, including *Aristolochia fangchi* (Guangfangji), *A. debilis* (Qingmuxiang), *A. manshuriensis* (Guanmuton), and *A. contorta* (Madouling), have been prohibited to be imported or manufactured in Taiwan since 2003.

Despite the warning and import alert issued by the US Food and Drug Administration that herbal products containing AAs are unsafe [7], 19 products containing AAs and 95 products suspected to contain AAs were found to be sold on the Web in 2003 [8,9]. A recent study used capillary electrophoresis with laser-induced fluorescence to analyze 61 herbal products, and found that 24 samples suspected to contain AAs [10]. One way to reduce the incidence is by controlling the quality of herbal preparation via regular checking. Therefore, it is essential to develop sensitive and efficient analytical methods for the determination of AAs.

AAs are a mixture of structural-related 10-nitrophenanthrene 1-carboxylic acids [11], where AA I, the 8-methoxy-3,4-

* Corresponding author at: School of Pharmacy, College of Medicine, National Taiwan University, 1, Section 1, Jen-Ai Road, Taipei 100, Taiwan.
Tel.: +886 2 23123456x88394; fax: +886 2 23919098.
E-mail address: kuoch@ntu.edu.tw (C.-H. Kuo).

0039-9140/$ – see front matter © 2009 Elsevier B.V. All rights reserved.
doi:10.1016/j.talanta.2009.10.003

methylenedioxy derivative, and AA II, the 3,4-methylenedioxy derivative, are the major components in the *Aristolochia* species [12]. Thin layer chromatography [13], high performance liquid chromatography (HPLC) with UV absorption detection [14–16] and capillary electrophoresis (CE) with UV detection [17,18] had been developed to analyze AA I and AA II in herbal products. Recently, HPLC coupled with fluorescence detection [19–21], CE coupled with laser-induced fluorescence detection [10], electrochemical detection [22], and on-line concentration technique [23] were developed to improve the sensitivity in detection.

HPLC and mass spectrometry hyphenated technique (HPLC–MS) has been proven to be a powerful tool in determining AAs in herbal products [24–29]. Due to the complexity in sample constituents, matrix effect is found to be remarkably significant in herbal extracts. The importance of eliminating matrix effect and ion suppressions during the development of quantitative methods based on HPLC–MS has been demonstrated in [30]. Various approaches have been used to eliminate matrix effect, including: (1) changing and improving sample extraction procedure by eliminating undetected matrix interferences, (2) performing the assay under more efficient chromatographic conditions to separate analytes of interest from other components, and (3) evaluating and changing the HPLC–MS interface [31]. The first two approaches, however, dramatically increase the analytical time, while the third approach may sacrifice sensitivity. In general, using the HPLC–MS/MS method to determine AAs in herbal products normally takes 20–60 min for an analysis [24–29].

Ultra-high-pressure liquid chromatography (UHPLC) is a recently developed technique which shows great advantages in providing better efficiency, sensitivity, and speed over ordinary HPLC. UHPLC columns packed with sub-2-μm particles can significantly increase the theoretical plate. Also, the increase in flow rate does not have negative impact on efficiency [32–34]. With sharper peaks and improved chromatographic resolution, matrix effect could be minimized without increasing the separation time [35]. There was one work which uses UHPLC–MS to analyze AAs, in which UHPLC–MS was applied to fingerprint analysis of AAs-containing preparations [36]. It used principal components analysis (PCA) and partial least square-discriminate analysis (PLS-DA) to identify the existence of AAs in pharmaceutical preparations. Due to the lack of selectivity and sensitivity consideration in that work, it is impractical to use the proposed method to quantitatively determine AAs in herbal preparations and biological samples. And the applicability to analyze biological samples is essential for the evaluation of nephrotoxicity. Up to now, there have been only two studies which investigated pharmacokinetic properties of AAI and AAII *in vivo*. Both of them used rabbits as their study animals because their analytical methods require a large sample volume [37,38]. The restriction of applying those methods to analyze rat serum limits the applicability of their approaches. Several studies revealed that AAs nephrotoxicity could be regulated by enzyme activity [39,40]. Since the pharmacokinetic properties of AAs are still unclear, it is necessary to develop a sensitive analytical method to facilitate these studies.

The primary goal of our research is to develop a sensitive and efficient UHPLC–MS/MS method to satisfy the demands on the aspects described earlier. To reach this goal, UHPLC–MS/MS conditions were systemically optimized for fast separation and sensitive detection. We used various herbal products, plasma samples, microsome incubation samples to demonstrate the practicability of the developed method. To the best of our knowledge, this is the first study using UHPLC–MS/MS to quantitatively analyze AA I and AA II in herbal products and biological samples.

2. Experimental

2.1. Chemicals

An AAs standard containing 90.9% of AA I and 5.7% of AA II was obtained from Acros (Geel, Belgium). Ammonium formate and ammonium acetate were obtained from Fluka Chemicals (Buchs, Switzerland). Methanol (MeOH) and acetonitrile (ACN) of chromatography grade were obtained from Mallinckrodt (Phillipsburg, NJ, USA). MeOH, ACN, and water of LC–MS grade were obtained from J.T. baker (Philipsburg, NJ). Dried fruits of *A. contorta* was collection from Liaoning, China in 2007. Dried roots of *A. debilis* was collected from Guangdong, China in 2007 and dried roots of *A. fangchi* were collected from Guangdong, China in 2007. The herbal samples were authenticated by Dr. Wei-Chu Li (Sheng Chang Pharmaceutical Corporation, Jhongli City, Taoyuan Country, Taiwan). The identification lab has laboratory accreditation issued by Taiwan accreditation foundation. Voucher specimens were stored at the Sheng Chang Pharmaceutical Corporation Herbarium. The concentrated powders of the decoction Bu-fei-a-jiau-tang was provided by Sheng Chang pharmaceutical co. (Chung-Li, Taiwan) under a research project contract (CCMP96-RD-044). Hsiao-Ching-Lung-Tang, Chuan-Chiong-Char-Tiao-San and Shin-Yi-San were obtained in the Taipei market (Taipei, Taiwan).

All solutions were filtered through 0.2-μm GH Polypro filters before use. All samples were filtered through 0.22-μm PVDF filters before use (Millipore, Bedford, MA, USA).

2.2. Isolation of AA I and AA II from AAs standard mixture

AA I and AA II standards were separated by semi-preparative RP-HPLC. The mobile phase was an ammonium acetate buffer–ACN mixture (72:28, v/v). The buffer was prepared by adjusting 10 mM ammonium acetate to pH 3.0 with acetic acid. The flow rate was 2 mL min^{-1}, and the detection wavelength was 254 nm. The AAs standard mixture was dissolved in tetrahydrofuran at a concentration of 10 mg mL^{-1}. The injection amount was 100 μL.

The equipments consisted of a Hitachi UV Pump L-7100 (Kyoto, Japan), a Rheodyne 7725i 5-mL manual injector (Cotati, CA, USA) and a Hitachi L-7400 UV detector. Separations were carried out on a Hibar Purospher RP-18 column (250 mm × 10 mm, 5 μm) (Merck, Darmstadt, Germany).

Stock solution (1000 μg mL^{-1}) was prepared by dissolving 1 mg AA I and 1 mg AA II in 1 mL MeOH separately. Adequate amounts of the stock solution were diluted with MeOH to prepare for the standard solutions for the respective experiment.

2.3. Apparatus

2.3.1. UHPLC–DAD

The equipments consisted of a Waters Acquity UPLC autosampler, column manager and thermostat, binary solvent manager, and an Acquity UPLC diode array detector (Waters, Milford, MA). The UV detection range was 200–400 nm. Separations were carried out on a Waters Acquity UPLC BEH C18 column (100 mm × 2.1 mm, 1.7 μm).

2.3.2. UHPLC–MS/MS

The Acquity UPLC system consisted of an autosampler, column manager with thermostat, a degasser, and a binary solvent manager (Waters, Milford, MA).

A Quatro Micro triple-quadrupole mass spectrometer (Micromass, Manchester, UK) equipped with an electrospray ionization (ESI) source was used. The mass spectrometer was operated in the positive ion electrospray mode with selective reaction monitoring (SRM). The analyses were performed in positive mode with a cone voltage of 20 V for AA I and 20 V for AA II, extractor voltage of 3.0 V,

RF lens voltage of 0.0 V, capillary voltage of 3.0 kV, ion source temperature of 80 °C, and desolvation temperature of 450 °C. A cone gas flow of 50 L h^{-1} and desolvation gas flow of 1100 L h^{-1} were used. Argon (99.999%) was used as a collision gas. Gas flow rate was kept at 0.13 nL min^{-1} in the collision cell. The collision energy was 12 eV for AA I and 10 eV for AA II. MassLynx 4.1 software was used for data analysis.

Chromatographic separation was performed by using an Acquity BEH C18 column (100 mm × 2.1 mm, 1.7 μm) (Waters, Milford, MA). The mobile phase was composed of 10 mM ammonium formate (pH 3.0) (solvent A) and ACN (solvent B). The gradient profile was: 0–2 min: 34% B; 2–10.5 min: linear from 34% to 36% B; 10.5–10.6 min: linear from 36% to 34% B and then re-equilibrium of the column. The flow rate was kept at 0.3 mL min^{-1} The column oven was set at 40 °C and the auto-injection system was set at 4 °C. Partial loop with needle overfill mode was used for sample injection, and the injection volume was 5 μL.

2.4. Pharmacokinetic study of AA I in rat

2.4.1. Drug administration and sample collection

AAs standard powder (90.9% of AA I and 5.7% of AA II) was dissolved in corn oil at a concentration of 0.5 mg mL^{-1}. The AA standard solution was administered to female Wistar rats at a dose of 10 mg kg^{-1} through an intragastric tube. Blood samples (0.2 mL) were taken from the femoral vein at 15, 30, 45, 60, 90, 120, 240, 360, 480, 600 min after oral treatment. The blood samples were centrifuged and the serum was taken and stored at −80 °C until analyzed by the UHPLC–MS/MS method.

2.4.2. Preparation of liver microsomes

Two adult male ICR mice were injected with β-naphthoflavone at a dose of 50 mg kg^{-1} for three consecutive days to induce liver CYP1A enzyme activities. Mice were sacrificed by cervical dislocation, and their livers were removed immediately on ice for further microsomes preparation.

Livers were homogenized in 1.15% KCl buffer, and the mixture was centrifuged at 8000 rpm for 20 min at 4 °C. The supernatant was further subjected to ultracentrifuge at 39,000 rpm (Beckman, Fullerton, CA) for 60 min. The pellet was rinsed with 1.15% KCl buffer and then ultracentrifuged again. The pellet was collected and dissolved in equal amount of 100 mM K_2HPO_4 (pH 7.4).

The microsomal protein concentration was determined by BCA protein assay (Thermo Fisher Scientific, Rockford, IL).

The animal study presented in this paper was approved by National Taiwan University, College of Medicine, and College of Public Health Institutional Animal Care and Use Committee (IACUC Approval No: 20070151).

2.5. Sample preparation

2.5.1. Extraction of plant material

Aristolochia plants and their pharmaceutical preparations were grounded to powder. Two grams of each powder were ultrasonically extracted with 10 mL of MeOH for 10 min and followed by centrifugation at 8000 rpm for 5 min. The extraction was repeated for three times and the supernantants were combined and concentrated under reduced pressure until dry. Suitable amount of the residue was re-dissolved with MeOH for the respective experiment.

2.5.2. Serum sample pretreatment

One hundred and sixty microliters of ACN was added to 80 μL serum for deproteination. After 15 min, the mixture was centrifuged at 12,000 rpm for another 15 min to remove proteins. Two hundred microliter of supernatant was evaporated to dryness under nitrogen flow, and then reconstituted in MeOH. The reconstituted solution was subjected to UHPLC–MS/MS analysis.

2.5.3. Microsome incubation sample

The incubation mixture (final volume 0.75 mL) contained 0.75 mg mice liver microsomes, 0.19 mM NADPH, 1.56 mM $MgCl_2$, 0.1 M sodium phosphate buffer (pH 7.4) and 0.3 mM AAI standard. The 0.3 mM of AAI standard was replaced with Bu-fei-a-jiau-tang in the study of herbals mixture study. The mixture was shaken (100 oscillations/min) for 5 min at 37 °C. Then the substrate was added to trigger the reaction. After 30 min of incubation with shaking at 37 °C, the reaction was stopped by adding 0.2 mL of methanol and the mixture was centrifuged at 39,000 rpm for 25 min at 4 °C. Part of the supernatant (100 μL) was mixed with 100 μL ACN. After 15 min, the mixture was centrifuged at 3000 rpm for 5 min to separate precipitated proteins. The supernatant was then transferred into a 1.5-mL tube containing 50–60 mg sodium chloride. The suspension was vortex-mixed briefly and incubated at room temperature for 20 min and vortex-mixing again. Finally, the mixture was centrifuged at 3000 rpm for 5 min, and then was subjected to UHPLC–MS/MS analysis.

3. Results and discussion

Parameters affecting UHPLC–MS/MS performance were systemically optimized in this study.

3.1. Optimization of UHPLC–MS/MS conditions

AA I and AA II tends to form ammonia adduct in the mobile phase [24]. The precursor ion were set at m/z 359 $[AA\ I + NH_4]^+$ and m/z 329 $[AA\ II + NH_4]^+$ to provide the best detection sensitivity. The most intense precursor–product transitions were selected as the quantification transitions in the multiple reaction monitoring (MRM) mode. The fragmentation mass spectra of the ion $[M + NH_4]^+$ derived from AA I and AA II are shown in Fig. 1. As depicted in the figures $[M + H\text{-}CO_2]^+$ was the base peak for both analytes. The fragment ions at m/z 298 $[AA\ I + H\text{-}CO_2]^+$ and m/z 268 $[AA\ II + H\text{-}CO_2]^+$ were therefore selected as the product ions. Both APCI (+) and ESI (+) (−) modes have been reported as the LC–MS ionization source in AAs analysis [21–26]. APCI with a mobile phase flow rate at 0.5 mL min^{-1} and ESI with a mobile phase flow rate at 0.3 mL min^{-1} were tested for their ionization efficiency. Signal intensity obtained under ESI (+) was found to be higher than that under APCI (+) over ten fold. Thus, ESI (+) was used as the ionization source in our study.

The UHPLC mobile phase was optimized to provide the best selectivity and the highest signal intensity in this study. The structures of both AA I and AA II contain one carboxylic acid group with a pK_a value being 3.2–3.4 and 3.3–3.5, respectively [41]. Due to the acidic properties of AA I and AA II, the acidic mobile phase gave better retention and chromatographic separation in the reversed phase column. The addition of buffer also assisted the ESI analysis. The influence of the buffer type and the pH value of the mobile phase on selectivity and sensitivity were further investigated.

3.1.1. Optimization of UHPLC mobile phase

Kite et al. had studied the effect of the LC buffer type on MS signal intensities of AAs [24]. In their study, 0.1% ammonium acetate gave the best results. The buffer type investigation presented by Chan showed that the addition of 1.0 mM ammonium acetate in 0.2% acetic acid dramatically increases the signal of the ammonium adduct [26]. In this study, mobile phase with the use of 10 mM ammonium acetate and 10 mM ammonium formate as buffer solution were compared to see their effect on MS peak intensity. The intensities of MS signals were shown in Fig. 2. It was found that peak intensity obtained under ammonium formate system was more

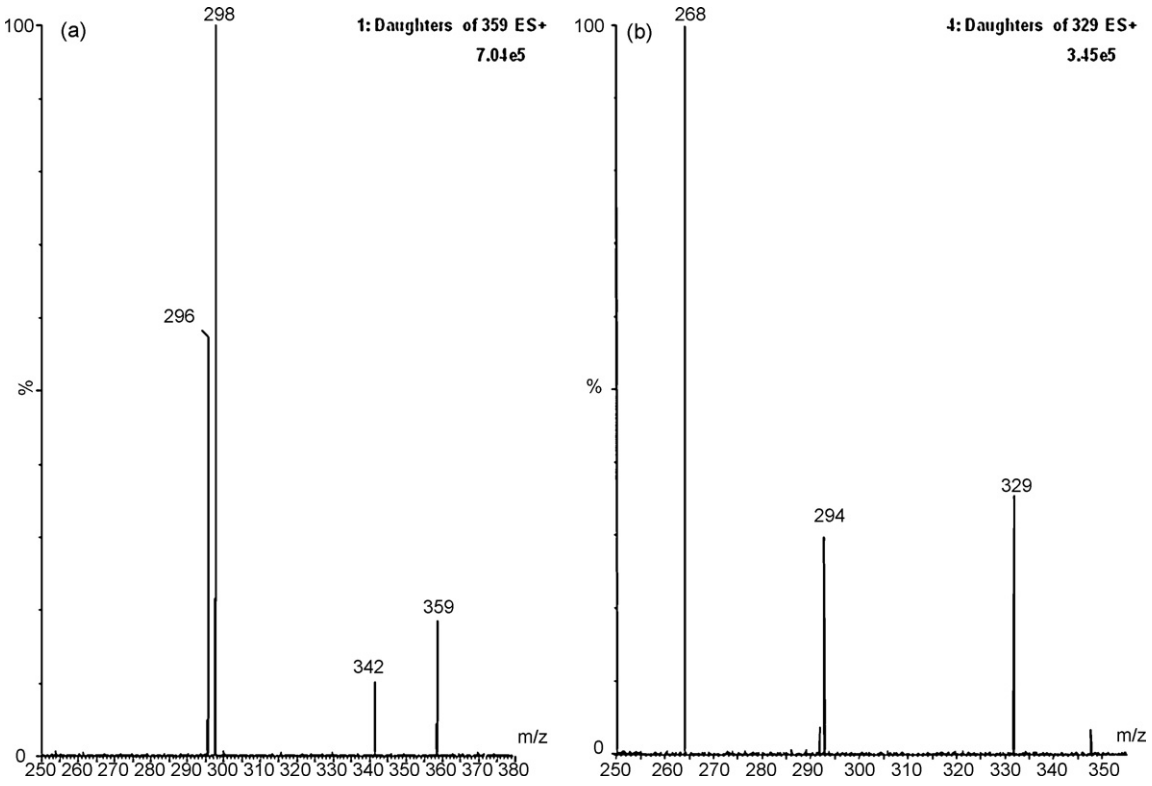


Fig. 1. MS/MS spectra of AA I (a) and AA II (b).

than two fold higher than that under ammonium acetate system. Therefore, 10 mM ammonium formate was selected to be the buffer system. The influence of organic solvent on the peak intensity was also investigated. Peak efficiencies were better when ACN instead of MeOH was used as the organic solvent in the mobile phase. Moreover, signal intensities obtained under the ACN system was higher than those under the MeOH system for more than five fold. ACN was therefore chosen as the organic solvent in the mobile phase.

Because radioactive isotope-labeled internal standards of AA I and AA II were not commercially available, the higher resolution provided by UHPLC played an important role in reducing the matrix effect. This is especially important for complicated samples such as herbal products. The pK_a value of AA I is between 3.2 and 3.4, and that of AA II is between 3.3 and 3.5. It was expected that in the mobile phase, various pH values from 3 to 5 would show significant effect on their retention. Several herbals containing AAs were tested in this experiment to evaluate the resolution of AA I and AA II from the complicated plant constituents. In order to test the selectivity of the developed conditions to herbals mixture, we used Bu-fei-a-jiau-tang as the tested formula. It was observed that the retention time of AA I and AA II increased while the pH value was decreased because AAs tend to be in their free form in more acidic conditions. The best resolution was obtained at pH 3.0. Gradient shape, gradient steepness and gradient range of the mobile phase were subsequently studied for the optimum separation conditions. The optimum gradient profile was: 0–2 min: 34% ACN; 2–10.5 min: linear from 34% to 36% ACN and then re-equilibrium of the column. UHPLC–UV and UHPLC–MS/MS chromatograms of the herbal extracts obtained under the optimum separation conditions are shown in Fig. 3. The results show that AA I and AA II could be baseline-separated from other herbal constituents within 10 min under optimum UHPLC conditions.

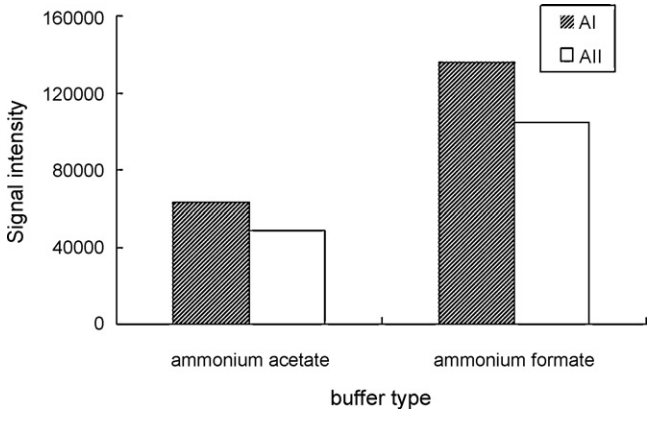


Fig. 2. Effect of buffer type on peak intensity of AAI and AAII in UHPLC–MS/MS system.

3.1.2. Optimization of ESI interface and mass spectrometry conditions

In the ESI mode, the distance from the emitter to the inlet has significant effect on mass sensitivity; at shorter distances, more of the ES plume will be sampled into the instrument. However, droplet evaporation time also reduces at smaller distances, resulting in lower ionization efficiency [42]. In this study, we found that the signals of AA I and AA II were intensified when the distance was increased from 3 to 4 mm, but dramatically weakened when the distance was further increased up to 5 mm, which was due to the low transmitted ES current. The value of 4 mm was consequently selected as the distance from the emitter to the inlet.

Cone voltage was shown to have the most profound effect on the signal intensity among all of the mass parameters. Signal intensity of AA I was increased more than four fold when the voltage was increased from 15 to 20 V, but decreased significantly if the voltage was further increased. This was attributed to the disappearance of ammonia in the mixture at the high voltage. The phenomenon is

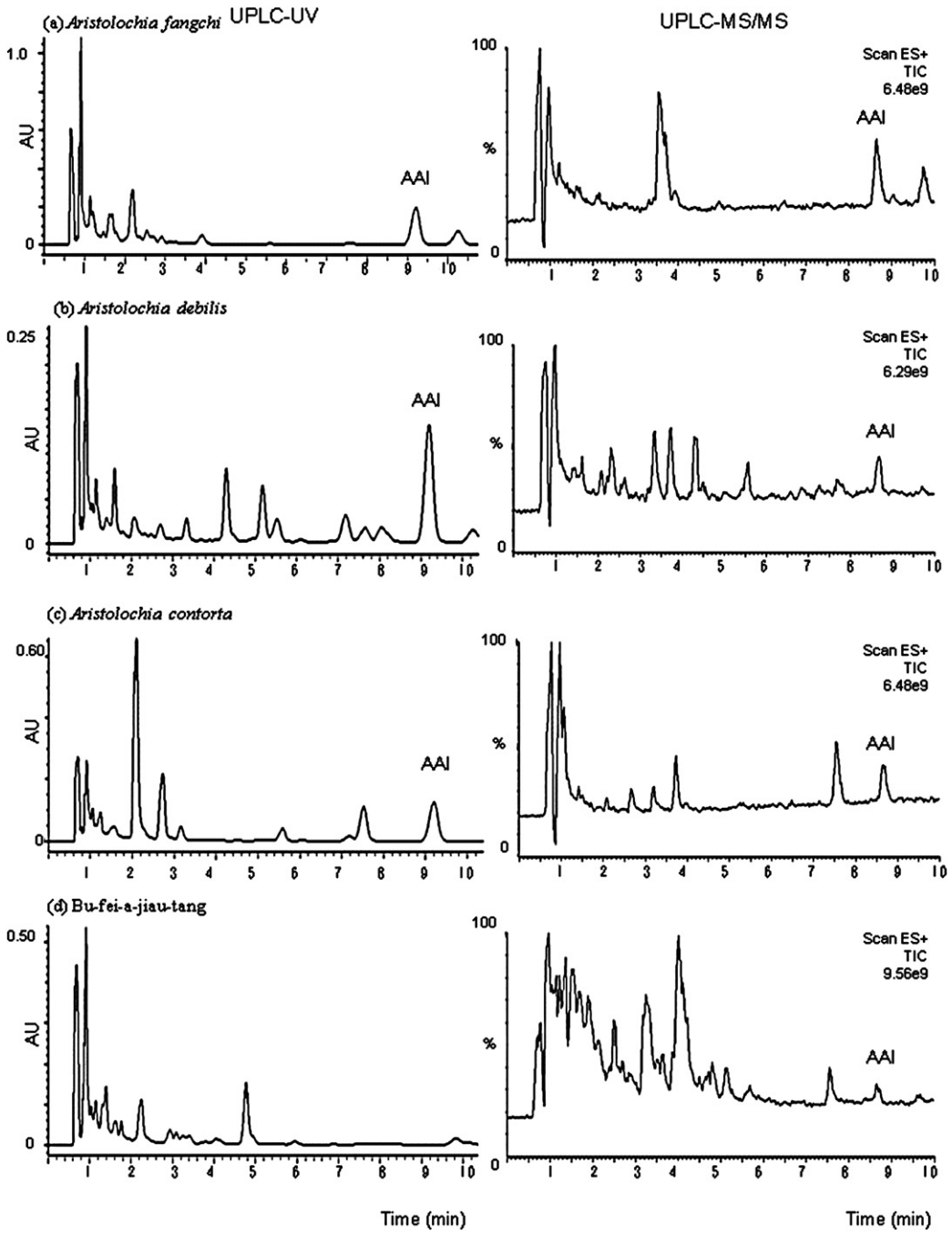


Fig. 3. UHPLC–UV and total ion scan (m/z = 200–1000) of UHPLC–MS/MS chromatograms of the crude extract of (a) *Aristolochia fangchi* 2000 μg mL^{-1}, (b) *A. debilis* 5000 μg mL^{-1}, (c) *A. contorta* 2000 μg mL^{-1} and (d) Bu-fei-a-jiau-tang 3000 μg mL^{-1} obtained under optimized conditions. UHPLC chromatographic conditions: solvent A: pH 3.0, 10 mM ammonium formate; solvent B: ACN. Gradient profile: 0–2 min: 34% B, 2–10.5 min: 34–36% B, 10.5–10.6 min: 36 –100% B, 10.6–16.9 min: 100% B, 16.9–17.0 min: 100–34% B, 17.0–20.0 min: 34% B. Flow rate: 0.3 mL min^{-1}. Injection volume: 5.0 μL. UV: 254 nm. MS conditions: cone voltage, 20 V; capillary voltage, 3.0 kV; collision energy for AA I, 12 eV; collision energy for AA II, 10 eV; ion source temperature, 80 °C; desolvation temperature, 450 °C; desolvation gas flow, 1100 L h^{-1}; cone gas flow, 50 L h^{-1}; probe distance, 4 mm.

consistent with what is reported by Kasai et al. [43]. Higher cone voltage should decrease the amount of ammonium-cation adduct. The value of 20 V was selected as the cone voltage for AA I and AA II analysis.

Since raising desolvation temperature would improve solvent evaporation and increase the amount of gas-phase ions and clusters, the desolvation temperature varied from 350 to 500 °C was investigated. Signal intensities of AA I and AA II were found to be increasing with the rise of desolvation temperature up to the highest applicable 500 °C, which was therefore selected as the desolvation temperature in this study. Collision energy larger than 20 eV resulted in higher degree of fragmentation which led to lower signal intensity. Values of 12 and 10 eV were selected for AA I and AA II, respectively. Other mass parameters (ion source voltage, temperature of the heated capillary, and flow rate of nitrogen gas) had minor influence on the mass sensitivity. Optimum values of these parameters are listed in the Section 2. Multiple reaction monitoring (MRM) chromatogram of AA I and AA II at 1 μg mL^{-1} obtained under the optimum conditions is shown in Fig. 4.

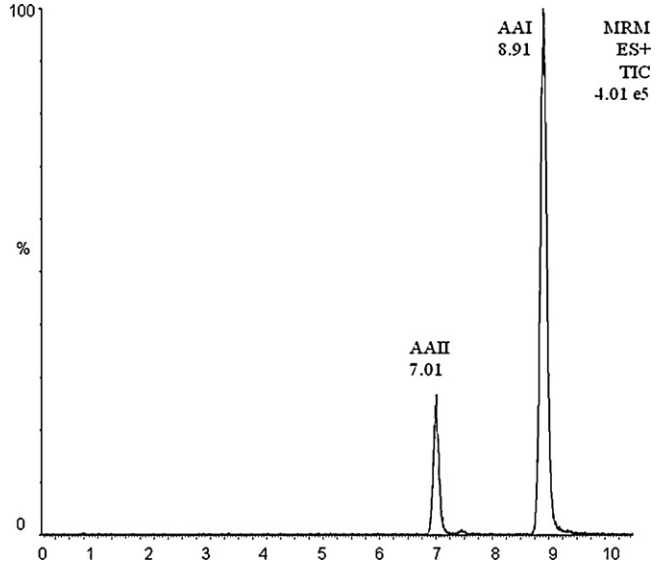


Fig. 4. UHPLC–MS/MS chromatogram (MRM) of AA I and AA II obtained under optimum conditions. UHPLC–MS/MS conditions are the same with those described in Fig. 3.

3.2. Method validation

3.2.1. Precision and accuracy

Run-to-run repeatability (intraday, $n = 3$) and intermediate precision (interday, $n = 3$) of migration time and peak area were tested. Both repeatability and intermediate precision of AA I and AA II in terms of migration time were within 1.25% relative standard deviation (RSD). The precision of peak areas of AA I and AA II were tested at 10, 100 and 3000 ng mL^{-1}. Repeatability ($n = 3$) and intermediate precision ($n = 3$) were within 3.99% and 5.74% RSD, respectively.

The accuracy of the method was studied by spiking AA I and AA II at 10, 100 and 3000 ng mL^{-1} in blank rat serum. The recoveries were within 76.5 ± 0.6% and 92.9 ± 1.1%, and the detailed data were shown in Table 1.

3.2.2. Linearity

Linearity of the method was tested with eight standard solutions of AA I and AA II at concentrations ranging from 10 to 3000 ng mL^{-1}. Each solution was tested for three times. The regression equation is $y = 84.501x - 99.882$ ($r^2 = 0.9999$) for AA I, and $y = 36.363x - 207.87$ ($r^2 = 0.9999$) for AA II.

3.2.3. Limit of detection (LOD) and limit of quantification (LOQ)

LOD of the method was defined as the concentration of AA I and AA II detected at S/N = 3. It was found to be 0.14 ng mL^{-1} for AA I and 0.26 ng mL^{-1} for AA II. LOQ of this method was determined with a concentration of AA I and AA II at S/N = 10. Its value was found to be 0.5 ng mL^{-1} for AA I and 0.7 ng mL^{-1} for AA II.

3.2.4. Matrix effect

Matrix effects may cause ion suppression or ion enhancement. Their magnitude may vary between sample components. Standard solutions of 10, 100 and 1000 ng mL^{-1} of AA I and AA II were added to the sample solutions of *A. debilis* and rat serum. Area of post-extraction spike was calculated against area of standard in order to study the matrix effect. The test results are shown in Table 2. Matrix effects of AA I and AA II in *A. debilis* and rat serum were within 127.7 ± 10.5% to 78.8 ± 3.9%.

Table 1
Recovery of AAI and AAII in rat serum.

Concentration (ng mL^{-1})	Recovery (%)	
	AAI	AAII
10	76.5 ± 0.6	80.4 ± 1.8
100	83.6 ± 3.5	80.4 ± 3.4
1000	92.9 ± 1.1	89.7 ± 1.1

Table 2
Matrix effects of AA I and AA II in *Aristolochia debilis* and rat serum.

Concentration (ng mL^{-1})	Matrix effect (%)			
	Aristolochia debilis		Rat serum	
	AA I	AA II	AA I	AA II
10	127.7 ± 10.5	120.0 ± 7.7	78.8 ± 3.9	83.5 ± 4.1
100	104.3 ± 5.9	95.6 ± 3.0	87.0 ± 2.2	88.0 ± 3.2
1000	93.8 ± 1.3	95.8 ± 1.9	115.6 ± 0.7	113.0 ± 2.6

3.3. Application

3.3.1. Herbal medicines

Herbal products were generally given as mixtures of herbs. Therefore, both plants of *Aristolochia*-genius and traditional Chinese medicines containing plants with AAs were included to investigate the applicability of our developed method to real samples. The UHPLC–MS/MS method validated above was applied to analyze the crude extract of *A. contorta* (dried fruits), *A. debilis* (dried roots), *A. fangchi* (dried roots), *A. heterotropoides* (dried roots), Bu-fei-a-jiau-tang, Hsiao-Ching-Lung-Tang, Chuan-Chiong-Char-Tiao-San and Shin-Yi-San. Bu-fei-a-jiau-tang is an antitussives preparation which has been banned in Taiwan since 2003, Hsiao-Ching-Lung-Tang and Shin-Yi-San are used to relieve cold symptoms, and Chuan-Chiong-Char-Tiao-San is used for migraine. And these preparations are still available in the market. Total ion scan and MRM chromatograms of the four of the herbal products were shown in Figs. 3 and 5, respectively, The constituents in Bu-fei-a-jiau-tang were the most complicated among them. The contents of AA I and AA II are shown in Table 3. AAI, the compound predominantly responsible for the nephropathy and urothelial cancer of AAN [39], is much higher than AAII in all tested herbal products. Among the tested herbal products, *A. debilis* contains the highest amount of AAs. With the high sensitivity of the developed method, several herbal products which are still available in the market were detected to contain small amount of AAI. It is worthwhile to investigate the safety of long-term exposure to these products.

3.3.2. Pharmacokinetics of AA

With the high sensitivity of the developed UHPLC–MS/MS method, the pharmacokinetic parameters of AA I and AA II in rats can be investigated. AAs standard containing 90.9% of AA I and 5.7% of AA II was dissolved in corn oil and intragastrically administered to a female Wister rat at a dose of 10 mg kg^{-1}. Blood samples were taken from femoral vein at the designed time intervals. Serum samples were subjected to protein denaturation and then analyzed by UHPLC–MS/MS. The serum concentration–time curves of AA I and AA II after oral administration of AAs are shown in Fig. 6. Table 4 presents the pharmacokinetics parameters of AA I and AA II calculated by WinNolin. The data revealed that AAs could be quickly absorbed in gastro-intestinal tract, and their T_{max} was within 1 h.

The role of biotransformation enzymes in the development of renal injury caused by AAs remains unclear. Xiao et al. had performed *in vivo* and *in vitro* studies to investigate the correlation between hepatic cytochrom P450 (P450) enzyme activity and AAI toxicity. The conclusion was that hepatic P450 1A1 and 1A2 could detoxify AAI through the metabolism of AAI into less toxic metabolites aristolactam I (AL I) [39]. In this study, we tested

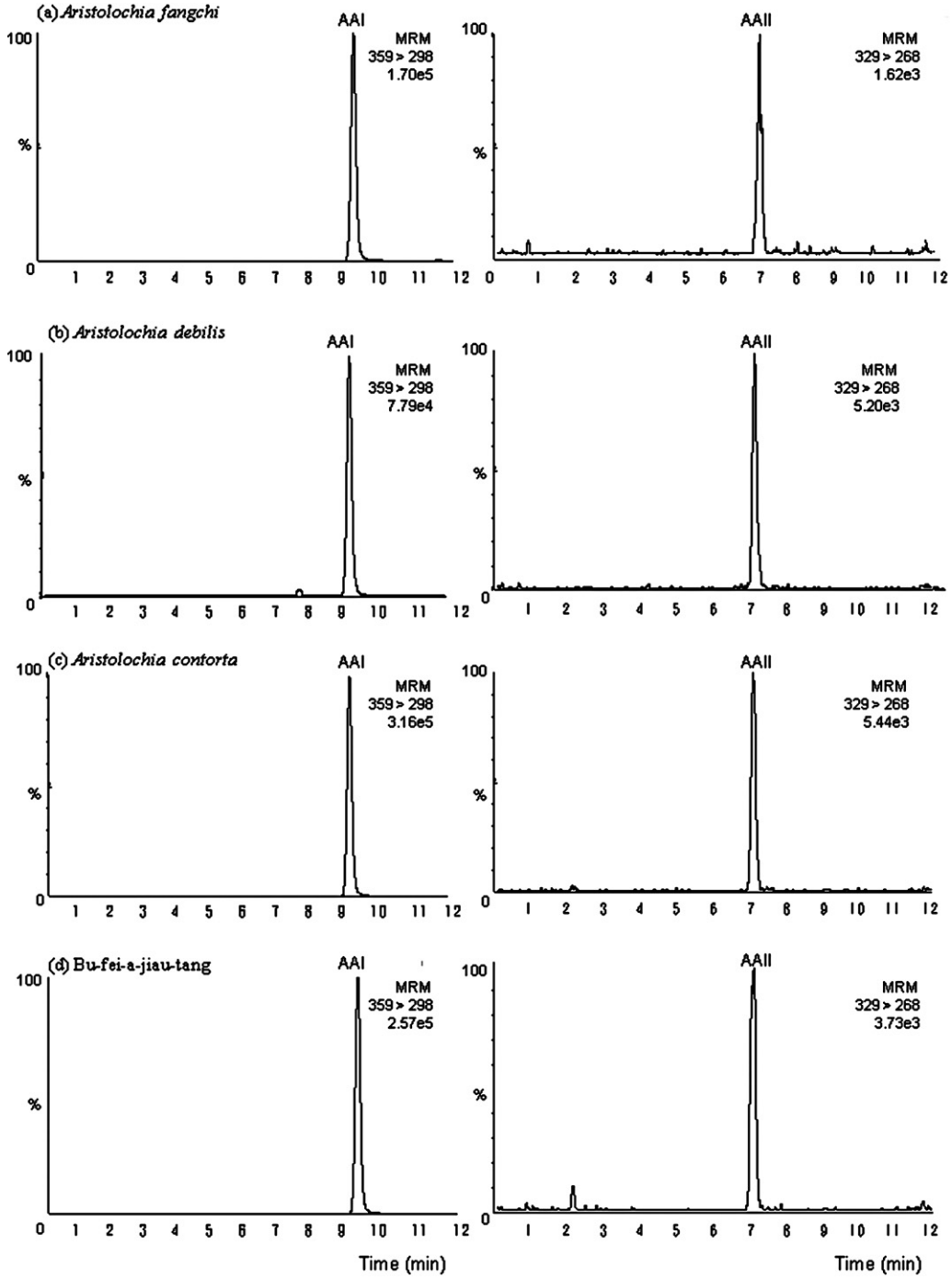


Fig. 5. MRM chromatograms of the crude extract of (a) *Aristolochia fangchi*, (b) *A. debilis*, (c) *A. contorta* and (d) Bu-fei-a-jiau-tang. UHPLC–MS/MS conditions are the same with those described in Fig. 3.

Table 3
Contents of AAI and AAII in herbal products.

Content	AA I ($\mu g\,g^{-1}$)	AA II ($\mu g\,g^{-1}$)
Aristolochia fangchi (fruits)	944.569 ± 36.206	50.078 ± 1.845
Aristolochia debilis (roots)	802.565 ± 38.238	148.687 ± 8.038
Aristolochia contorta (roots)	511.478 ± 19.275	29.386 ± 1.143
Asarum heterotropoides (roots)	7.572 ± 0.043	–[a]
Bu-fei-a-jiau-tang	119.674 ± 3.298	6.802 ± 0.289
Hsiao-Ching-Lung-Teng	0.194 ± 0.001	–
Chuan-Chiong-Char-Tiao-San	0.384 ± 0.012	–
Shin-Yi-San	0.525 ± 0.001	–

[a] Below detection limit.

the applicability of our developed method in the investigation of AAI metabolism. Both AA I standard and Bu-fei-a-jiau-tang were incubated with liver microsome. The microsome incubated samples were subjected to protein denaturation and then analyzed by UHPLC–MS/MS. The MRM chromatograms were shown in Fig. 7. AL I only appeared in sample treated with Bu-fei-a-jiau-tang. Since toxicity between AA I and AL I, are different, our finding showed that the toxicity of AA I standard and herbal mixtures containing AA I might be different. Although more experiments should be preformed to explain this phenomenon, our study showed that the developed UHPLC–MS/MS is a powerful tool to investigate the pharmacokinetic properties of AAs.

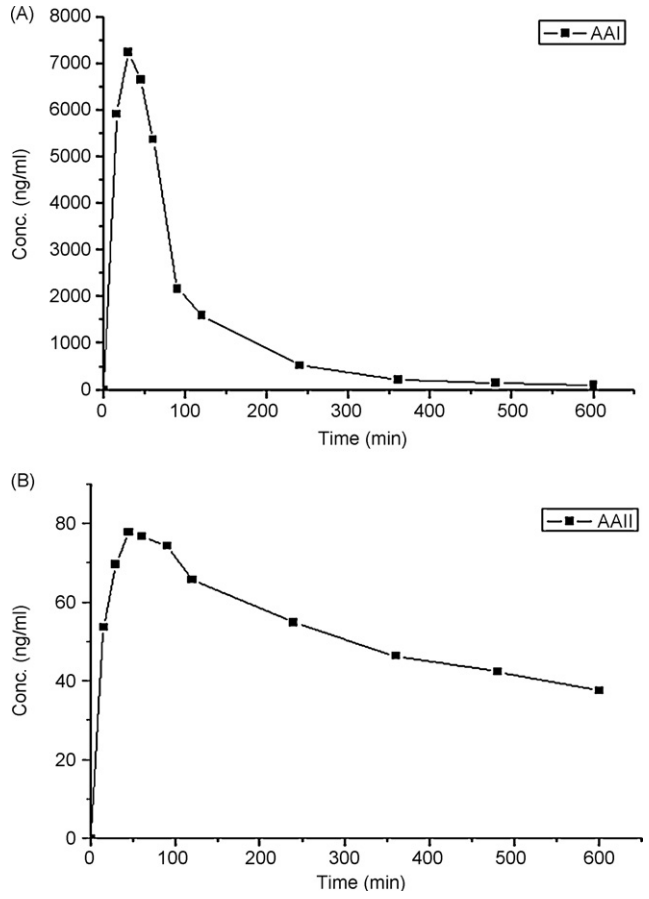


Fig. 6. Serum concentration–time plots of AA I (A) and AA II (B) after oral administration of AAs at a dose of 10 mg kg^{-1} in female Wister rats.

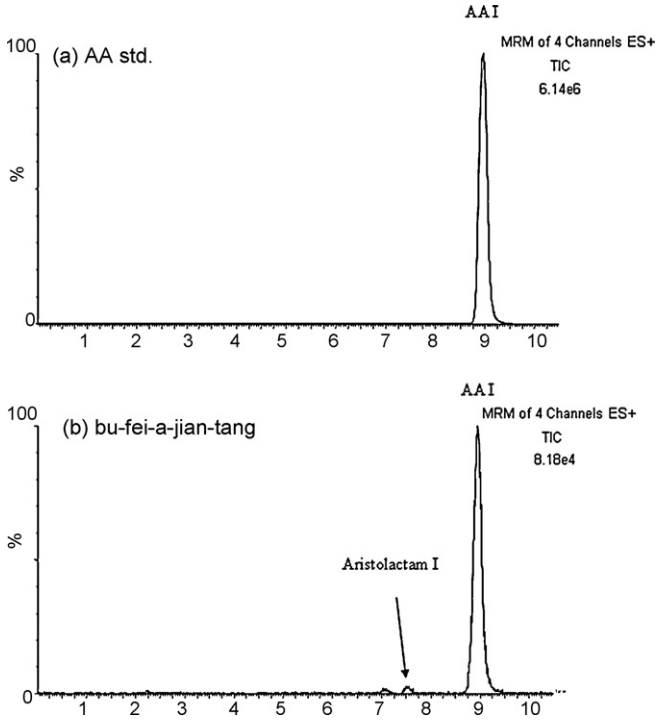


Fig. 7. UHPLC–MS/MS chromatogram (MRM) of liver microsome treated with (a) AA I standard; (b) Bu-fei-a-jiau-tang for 30 min. UHPLC–MS/MS conditions are the same with that described in Fig. 3.

3.4. Performance of UHPLC–MS/MS

Several HPLC–UV methods have been applied to analyze AAs in plants similar to this study [14–16,19,25]. The analytical time of those studies were all longer than 15 min. Other studies used the HPLC–MS methods and their analytical time were higher than 12 min. Also the LODs of these methods were higher than 3.99 ng mL^{-1} for AAI and 3.71 ng mL^{-1} for AAII [26,28,29]. By using the presented UHPLC–MS/MS method, AAI and AAII could be determined within 10 min, and the LODs were 0.14 ng mL^{-1} for AA I and 0.26 ng mL^{-1} for AA II. Our developed UHPLC–MS/MS shows advantages in both the analytical time and sensitivity. Jacob et al. used UHPLC–MS for the detection of AAs [34]. Their analytical time is close to our study. They used the chemometrics approach for AAs detection. Since quantitation work was not included in their study, they did not evaluate the accuracy and matrix effect of their system. They also did not optimize their conditions for the best sensitivity. The applicability of their method to quantitatively analyze AAs in herbal products and biological samples was unknown. Comparing to their method, the high selectivity of the presented UHPLC–MS/MS conditions significantly minimized the matrix effect, which allows this method to be applied to analyze complex samples. Recently, capillary electrophoresis and HPLC coupled with fluorescence detector have been used for sensitive detection of AAs in herbal products [10,19,22]. Although the LODs could reach the sub-ppb levels when coupling with fluorescence detection, chemical reaction should be preformed before analysis. The proposed UHPLC–MS/MS method is superior to those methods in its simplicity in sample preparation.

Table 4
Pharmacokinetic parameters after single oral administration of 10 mg/kg standard in female Wister rats.

	AAI	AAII
T_{max} (min)	30	45.0
C_{max} (ng mL^{-1})	7249.3	77.7
AUC (ng mL^{-1} min)	716,936.3	31,344.8
$T_{1/2}$ (min)	234.6	800.7
k (min^{-1})	0.003	0.0009
Oral clearance (mL min^{-1})	2.9	66.0

4. Conclusion

A fast, sensitive and reliable UHPLC–MS/MS method for the determination of AA I and AA II was established in this study. By using a mixture of 10 mM ammonium formate buffer (pH 3.0) and acetonitrile as mobile phase with gradient elution, AAs could be determined within 10 min. The LODs was 0.14 ng mL^{-1} for AA I and 0.26 ng mL^{-1} for AA II. Due to its high selectivity and sensitivity, the developed method could be directly used to analyze crude herbal extracts as well as biological samples without solid phase extraction or liquid/liquid extractions. The applicability of the method was demonstrated by applying the developed method to analyze various herbal products, rat serum and liver microsome incubation samples. The results revealed that the developed approach is powerful for quality control of herbal products and pharmacokinetic study of AAs.

Acknowledgements

This study was supported by a research grant (CCMP96-RD-044) from the Committee on Chinese Medicine and Pharmacy, Department of Health, Executive Yuan, Taiwan. We thank Waters Asia Ltd., Taiwan Branch for technical support. We also acknowledge Dr. Shao-Wen Sun for editing this manuscript.

References

[1] K. Hashimoto, M. Higuchi, B. Makino, I. Sakakibara, M. Kubo, Y. Komatsu, M. Maruno, M. Okada, J. Ethnopharmacol. 64 (1999) 185–189.
[2] M.Y. Shen, C.L. Liu, G. Hsiao, C.Y. Liu, K.H. Lin, D.S. Chou, J.R. Sheu, Planta Med. 74 (2008) 1240–1245.
[3] J.J. Moreno, Immunopharmacology 26 (1993) 1–9.
[4] B.S. Vishwanath, A.A. Fawzy, R.C. Franson, Inflammation 12 (1988) 549–561.
[5] J.L. Vanherweghem, M. Depierreux, C. Tielemans, D. Abramowicz, M. Dratwa, M. Jadoul, C. Richard, D. Vandervelde, D. Verbeelen, R. Vanhaelen-Fastre, et al., Lancet 341 (1993) 387–391.
[6] J.L. Nortier, M.C. Martinez, H.H. Schmeiser, V.M. Arlt, C.A. Bieler, M. Petein, M.F. Depierreux, L. De Pauw, D. Abramowicz, P. Vereerstraeten, J.L. Vanherweghem, N. Engl. J. Med. 342 (2000) 1686–1692.
[7] Available: U.S. Food and Drug Administration, Dietary supplements: aristolochic acid, http://www.cfsan.fda.gov/~dms/ds-bot.html.
[8] L.S. Gold, T.H. Slone, N. Engl. J. Med. 349 (2003) 1576–1577.
[9] F.D. Debelle, J.L. Vanherweghem, J.L. Nortier, Kidney Int. 74 (2008) 158–169.
[10] S.C. Hsieh, M.F. Huang, B.S. Lin, H.T. Chang, J. Chromatogr. A 1105 (2006) 127–134.
[11] M.L. Pailer, L. Belohlav, E. Simonitsch, Angew. Chem. 68 (1955) 386.
[12] V.M. Arlt, M. Stiborova, H.H. Schmeiser, Mutagenesis 17 (2002) 265–277.
[13] J.R. Ioset, G.E. Raoelison, K. Hostettmann, Food Chem. Toxicol. 41 (2003) 29–36.
[14] W. Chan, K.M. Hui, W.T. Poon, K.C. Lee, Z. Cai, Anal. Chim. Acta 576 (2006) 112–116.
[15] L. Wei, R.K. Li, T. Bo, H.W. Liu, X.F. Feng, S.L. Hu, Chromatographia 59 (2004) 233–236.
[16] J. Yuan, L. Nie, D. Zeng, X. Luo, F. Tang, L. Ding, Q. Liu, M. Guo, S. Yao, Talanta 73 (2007) 644–650.
[17] W. Li, S. Gong, D. Wen, B. Che, Y. Liao, H. Liu, X. Feng, S. Hu, J. Chromatogr. A 1049 (2004) 211–217.
[18] W. Li, Z. Chen, Y. Liao, H. Liu, Electrophoresis 27 (2006) 837–841.
[19] J. Yuan, Q. Liu, W. Zhu, L. Ding, F. Tang, S. Yao, J Chromatogr. A 1182 (2008) 85–92.
[20] H. Yue, W. Chan, L. Guo, Z. Cai, J. Chromatogr. B 877 (2009) 995–999.
[21] J. Yuan, X. Luo, M. Guo, J. Wu, W. Yang, R. Yu, S. Yao, Talanta 78 (2009) 1141–1147.
[22] X. Zhou, C. Zheng, J. Sun, T. You, J. Chromatogr. A 1109 (2006) 152–159.
[23] F. Wei, Y.Q. Feng, Talanta 74 (2008) 619–624.
[24] G.C. Kite, M.A. Yule, C. Leon, M.S. Simmonds, Rapid Commun. Mass Spectrom. 16 (2002) 585–590.
[25] M.C. Lee, C.H. Tsao, S.C. Iou, W.C. Chuang, S.J. Sheu, J. Sep. Sci. 26 (2003) 818–822.
[26] S.A. Chan, M.J. Chen, T.Y. Liu, M.R. Fuh, J.F. Deng, M.L. Wu, S.J. Hsieh, Talanta 60 (2003) 679–685.
[27] C.Y. Huang, M.C. Tseng, J.H. Lin, J. Food Drug Anal. 13 (2005) 125–131.
[28] J. Yuan, Q. Liu, G. Wei, F. Tang, L. Ding, S. Yao, Rapid Commun. Mass Spectrom. 21 (2007) 2332–2342.
[29] T.T. Jong, M.R. Lee, S.S. Hsiao, J.L. Hsai, T.S. Wu, S.T. Chiang, S.Q. Cai, J. Pharm. Biomed. Anal. 33 (2003) 831–837.
[30] B.K. Matuszewski, M.L. Constanzer, C.M. Chavez-Eng, Anal. Chem. 70 (1998) 882–889.
[31] B.K. Matuszewski, M.L. Constanzer, C.M. Chavez-Eng, Anal. Chem. 75 (2003) 3019–3030.
[32] L. Novakova, L. Matysova, P. Solich, Talanta 68 (2006) 908–918.
[33] S.A. Wren, P. Tchelitcheff, J. Chromatogr. A 1119 (2006) 140–146.
[34] J.M. Cunliffe, S.B. Adams-Hall, T.D. Maloney, J. Sep. Sci. 30 (2007) 1214–1223.
[35] J.C. Van De Steene, W.E. Lambert, J. Am. Soc. Mass Spectrom. 19 (2008) 713–718.
[36] S.S. Jacob, N.W. Smith, C. Legido-Quigley, J. Sep. Sci. 30 (2007) 1200–1206.
[37] S.M. Chen, M.Y. Fan, C.C. Tseng, Y. Ho, K.Y. Hsu, Toxicon 50 (2007) 180–188.
[38] T.H. Tsai, C.J. Chou, L.C. Lin, W.J. Tsai, C.F. Chen, J. Liq. Chromatogr. 16 (1993) 1173–1182.
[39] Y. Xiao, M. Ge, X. Xue, C. Wang, H. Wang, X. Wu, L. Li, L. Liu, X. Qi, Y. Zhang, Y. Li, H. Luo, T. Xie, J. Gu, J. Ren, Kidney Int. 73 (2008) 1231–1239.
[40] M. Stiborova, B. Sopko, P. Hodek, E. Frei, H.H. Schmeiser, J. Hudecek, Cancer Lett. 229 (2005) 193–204.
[41] X. Fu, Y. Liu, W. Li, Y. Liao, M. Zhai, H. Liu, Proceedings of the 22nd International Symposium on Microscale Bioseparations and Methods for Systems Biology, 2008.
[42] J.S. Page, R.T. Kelly, K. Tang, R.D. Smith, J. Am. Soc. Mass Spectrom. 18 (2007) 1582–1590.
[43] H.F. Kasai, M. Tsubuki, S. Matsuo, T. Honda, Rapid Commun. Mass Spectrom. 21 (2007) 1100–1114.

Talanta 80 (2010) 1681–1685

Contents lists available at ScienceDirect

Talanta

journal homepage: www.elsevier.com/locate/talanta

A new and facile method for measurement of apparent density of monodisperse polymer beads

Qi Zhang[a,b], Balasubramanian Srinivasan[c], Yuanpeng Li[a], Ying Jing[a], Chengguo Xing[c], Jin Chang[b,*], Jian-Ping Wang[a,*]

[a] Department of Electrical and Computer Engineering, University of Minnesota, Minneapolis, MN 55455, USA
[b] School of Materials Science & Engineering, Tianjin University, Tianjin 300072, PR China
[c] Department of Medicinal Chemistry, College of Pharmacy, University of Minnesota, Minneapolis, MN 55455, USA

ARTICLE INFO

Article history:
Received 28 July 2009
Received in revised form 2 October 2009
Accepted 5 October 2009
Available online 12 October 2009

Keywords:
Apparent density
Viscosity
Hybrid beads
Polymer beads
Micro-total analysis systems
Suspension stability

ABSTRACT

The apparent density, an intrinsic physical property of polymer beads, plays an important role in the application of beads in micro-total analysis systems and separation. Here we have developed a new, facile and milligram-scale method to describe the motion of beads in aqueous solution and further detect the apparent density of beads. The motion of beads in solutions is determined by the viscosity of solutions and the density difference between beads and solutions. In this study, using various glycerol aqueous solutions with certain viscosities and densities, the motion time (i.e. floating or sedimentation time) of hybrid polymer beads was experimentally measured and theoretically deduced, and consequently, the apparent density of monodisperse beads can be quickly and easily calculated. The results indicated that the present method provided a more precise way to predict the movement of hybrid beads in aqueous solution compared with the approach for commercial use. This new method can be potentially employed in flow cytometry, suspension stability, and particle analysis systems.

© 2009 Elsevier B.V. All rights reserved.

1. Introduction

In micro-total analysis systems (μTAS), monodisperse hybrid polymer beads have been widely used in many fields of biological analysis, high-throughput screening, and immunoassay and among others [1–3]. However, due to the unmatched densities of hybrid polymer beads and aqueous solutions [4], a well suspension of polymer beads in aqueous solutions cannot be achieved, resulting in a higher measurement error and lower signal-to-noise ratio [5]. Obviously, a feasible solution is adjusting either the densities of polymer beads [4] or those of aqueous solutions (e.g. an addition of glycerol or sucrose [6]). Although, the densities of polymer beads can be measured by a density meter (ASTM D4052) [7], the measurement of apparent densities of hybrid beads is still a grand challenge due to hybridization of nanoparticles, surface hydrophilic liquid layer [8] and inner nano-scale pores [9]. Here a simple and robust method that can precisely describe the movement of hybrid polymer beads in glycerol aqueous solution, was demonstrated, and further applied to the measurement of apparent density. And it also has potential use in flow cytometry, microfluidics chips, bead suspensions, and particle analysis systems.

2. Materials and methods

2.1. Materials

Monodisperse polymer beads (PC06N/6182, with carboxyl group, size 9.77 μm) were purchased from Bangs Laboratories, Inc. Uniform magnetic beads were obtained from Micromod (micromod Partikeltechnologie GmbH, Micromer®-M, Prod.-No. 08-01-104, with amine group, size 10 μm). The densities of polymer beads and magnetic beads provided by vendor are 1.062 and 1.1 g/cm^3, respectively. Sodium dodecyl sulfate (SDS) and glycerol (≥99% (GC)) was procured from Sigma. The water used in all experiments was de-ionized water.

2.2. Motion of beads in glycerol–water mixtures

0.5 mg of polymer beads or commercial magnetic beads was dried under air at room temperature and re-dispersed in a 1.5 mL vial containing 0.5 mL of glycerol–water mixtures. Owing to the lower or higher densities of beads compared with those of glycerol solutions, the beads were buoyed up or sunk down in the

* Corresponding authors.
E-mail addresses: jinchang@tju.edu.cn (J. Chang), jpwang@umn.edu (J.-P. Wang).

0039-9140/$ – see front matter © 2009 Elsevier B.V. All rights reserved.
doi:10.1016/j.talanta.2009.10.004

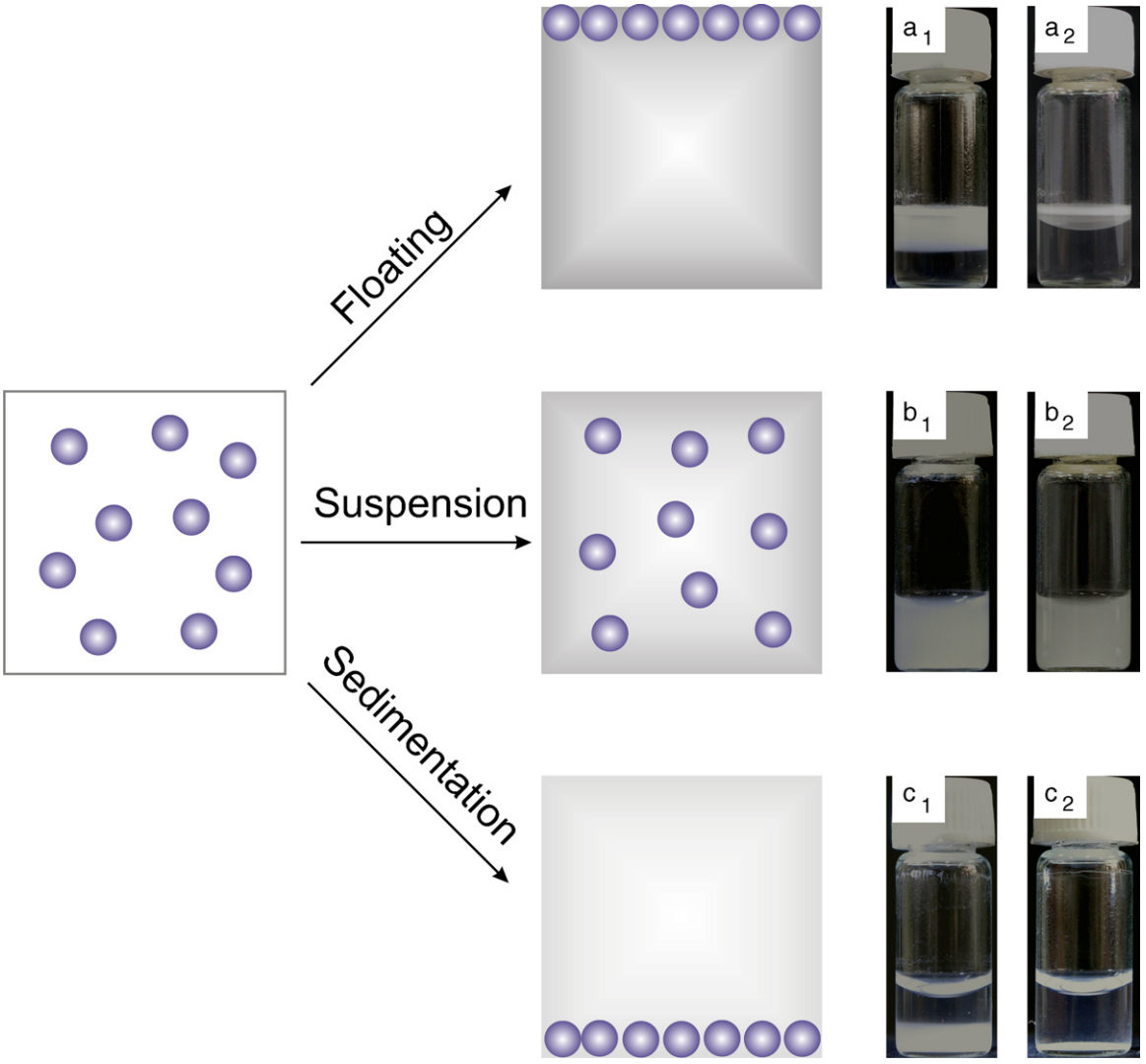


Fig. 1. Schematic description of bead motion in various glycerol–water mixtures (the darker color means higher mass fraction of glycerol in mixture); (a) 50 wt% glycerol solution, the digital pictures of a_1 and a_2 were taken at 1.2 and 2.7 h, respectively. (b) 23 wt% glycerol solution, b_1 and b_2 at 3.5 and 7.5 h, respectively. (c) 10 wt% glycerol solution, c_1 and c_2 at 0.7 and 1.4 h, respectively. The beads were obtained from Bangs Laboratories, Inc.

solution. The total time taken for entire-bead floating to the surface or sedimentation to the bottom of glycerol solutions was defined as floating or sedimentation time of beads. The accuracy of the measurements was evaluated from 5 repetitive determinations (repeatability) of the motion time of polymer beads in the same glycerol aqueous solution, and the relative standard deviations (*RSD*) were also calculated. The schematic process and digital photos are shown in Fig. 1. We have included more digital photos taken at different time in supporting information (see Fig. S1).

2.3. Characterization

The images of beads were taken using a microscope (Olympus, IX 51). Flow cytometry (Coulter, Epics XL) was utilized to measure the bead's relative size (forward light scatter, FS signal), relative granularity or internal complexity (side light scatter, SS signal). Flow cytometry was set up according to the standard operating procedure. During detection, a total of 20000 events were recorded for each time point, and the beads dispersed in water or glycerol solutions were detected at the low flow rate with a concentration of 1 mg/mL. The populations of single beads and doublet beads were selected based on forward and side scatter. The *mean* and *RSD* of these populations were also measured. All flow cytometric data were performed using FlowJo 5.7 software (Tree Star, San Carlos, CA, USA).

3. Results and discussions

3.1. Densities and viscosities of glycerol–water mixtures

The densities of glycerol–water mixtures were measured by comparing their mass to their volume. The viscosities were calculated using the following empirical equation [10].

$$\frac{\ln \nu_m - \ln \nu_w}{\ln \nu_g - \ln \nu_w} = C_m[1 + (1 - C_m)\{a + bC_m + cC_m^2 + \cdots\}] \quad (1)$$

where ν is kinematic viscosity ($\nu = \mu/\rho$), μ is dynamic viscosity, ρ is the density, C_m is the mass fraction of glycerol in the mixture, and subscripts m, g and w denote the glycerol–water mixtures, glycerol and water, respectively. The constants a, b and c at 20 °C are assigned to −0.76728, 0.12153 and −1.41519, respectively. As shown in Table 1, the detected densities are close to those provided by the vendor, and the interpolated viscosities are in accordance

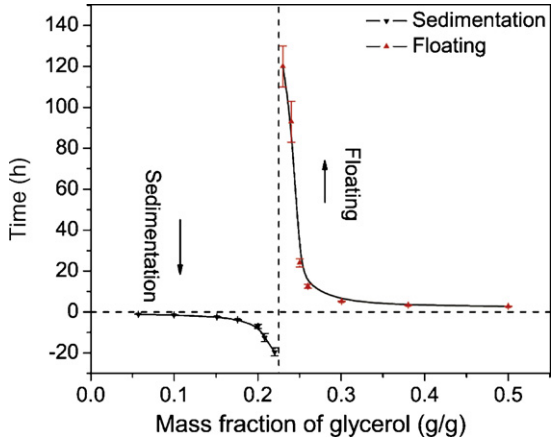


Fig. 2. The floating and sedimentation time of polymer beads in various glycerol–water mixtures, the positive and negative values indicate that the beads are floating and sedimentating, respectively.

Table 1
The density and viscosity of glycerol–water mixtures.

Mass fraction [g/g]	Density [g/mL]	μ viscosity [mPa s]
0.0000	0.9984	1.0085
0.0996	1.0218	1.2804
0.1510	1.0323	1.4920
0.1758	1.0392	1.6178
0.2002	1.0449	1.7546
0.2084	1.0512	1.8123
0.2202	1.0537	1.8868
0.2301	1.0558	1.9527
0.2402	1.0594	2.0260
0.2502	1.0606	2.0974
0.2601	1.0634	2.1744
0.3006	1.0727	2.5252
0.3802	1.0925	3.4571
0.5000	1.1251	5.9486

with those published [10] (the comparison between the densities and viscosities in the present study and those published were shown in Tables S1 and S2 in supporting information, respectively).

3.2. Theory of bead movement in aqueous solution

The net force, ΔF_b, of a bead in aqueous solution is composed of following two contributions,

$$\Delta F_b = F_{b,1} - F_{b,2} \tag{2}$$

where $F_{b,1}$ and $F_{b,2}$ are the sum of the buoyant force and the bead's weight, and the force of movement resistance (Stokes' drag force), respectively.

According to Archimedes' principle, the $F_{b,1}$ is given by,

$$F_{b,1} = V_b \times (\rho_m - \rho_b) \times g \tag{3}$$

where V_b is the volume of a bead, ρ_m and ρ_b are the density of the aqueous solution and hybrid polymer beads (or magnetic beads), respectively, and g is the gravitational acceleration.

The force of the movement resistance (Stokes' drag force [11]) $F_{b,2}$ is obtained by the following equation.

$$F_{b,2} = 6\pi\mu R v \tag{4}$$

where μ is the viscosity of aqueous solution, R is the radius of a bead, and v is the velocity.

Hence, the ΔF_b is deduced by,

$$\Delta F_b = F_{b,1} - F_{b,2} = V_b \times (\rho_m - \rho_b) \times g - 6\pi\mu R v$$
$$= \frac{4}{3}\pi R^3 \times (\rho_m - \rho_b) \times g - 6\pi\mu R v \tag{5}$$

Based on Eq. (5), the suspended bead has a tendency to rise or sink in the glycerol–water mixture if ρ_b is not equal to ρ_m. The beads were buoyed up in aqueous solutions when their densities were less than those of the mixture (Fig. 1a). The beads were stably suspended in solutions as their densities were accurately equal to those of the

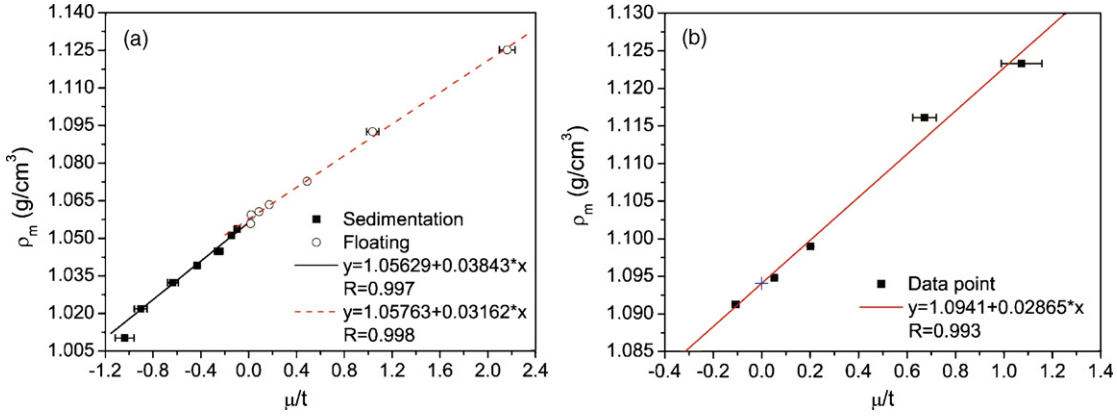


Fig. 3. Estimation of the density of (a) polymer beads and (b) commercial magnetic beads by Eq. (8), the apparent density of beads, ρ_b is equal to the ρ_m of the point where the fitted linear curve intercepts the line $x = 0$.

Table 2
The flow cytometric data of polymer beads shown in Fig. 4.

Mass fraction of glycerol [wt%]		FS in R1		SS in R1		The proportion of beads in		The ratio of doublet beads (in R2) to singlet beads (in R1) [%]
		Mean	*RSD* [%]	Mean	*RSD* [%]	R1 [%]	R2 [%]	
4a	0	436.22	6.28	427.33	13.57	81.48	15.78	19.4
4b	10	458.66	5.53	423.74	13.33	89.42	7.36	8.2
4c	20	483.35	7.38	430.75	13.22	89.52	2.97	3.3
4d	24	541.42	9.71	425.56	13.71	–	–	–
4e	30	746.31	20.9	445.70	25.42	–	–	–

mixture (Fig. 1b), and the beads were sunk to the bottom of the vial while their densities were larger than those of the mixture (Fig. 1c).

3.3. Estimation of bead density

The floating velocity is defined as positive, and sedimentation velocity as negative. As shown in Eq. (5), the velocity (floating or sedimentation) of beads reaches the maximum at equilibrium states ($\Delta F_b = 0$), and the equation of equilibrated floating or sedimentation velocity is given as follows (transformation of Eq. (5)),

$$v = \frac{2R^2 g(\rho_m - \rho_b)}{9\mu} \tag{6}$$

Since t is equal to d/v, the time (t) of floating or sedimentation is derived by,

$$t = \frac{9\mu d}{2R^2 g(\rho_m - \rho_b)} = k \cdot \frac{\mu}{\rho_m - \rho_b} \quad \left(k = \frac{9d}{2R^2 g}\right) \tag{7}$$

where the distance (d) of floating or sedimentation is a constant, and consequently, k is a constant.

According to Eq. (7), the floating or sedimentation time depends on the viscosities of aqueous glycerol solutions and the densities difference between the beads and the solutions [8]. Fig. 2 showed that the detected floating or sedimentation time of polymer beads is in accordance with Eq. (7).

Moreover, the density of polymer beads can be obtained by using the floating or sedimentation time. Changing the expression of Eqs. (7) and (8), the result is represented as follows,

$$\rho_m - \rho_b = k \times \frac{\mu}{t} \Rightarrow \rho_m = \rho_b + k \times \frac{\mu}{t} \tag{8}$$

where the ρ_m and μ are shown in Table 1, and the motion time (t) is illustrated in Fig. 2.

The density, ρ_m and the μ/t are illustrated in Fig. 3a. The ρ_b fitted by linear least square method is 1.0570 g/cm^3 ((1.0563 + 1.0576)/2). The calculated *RSD* was 0.07%. As shown in Table 1, the densities of 25 and 26 wt% glycerol solutions were 1.0606 and 1.0634 g/cm^3, respectively. The bead density provided by the vendor ($\rho_{b,\text{vendor}} = 1.062$ g/cm^3) stands between the densities of 25 wt% ($\rho_{b,\text{vendor}} > \rho_{m,25\%}$) and 26 wt% glycerol solutions ($\rho_{b,\text{vendor}} < \rho_{m,26\%}$). However, in experiments, the bead were buoyed up in both 25 wt% and 26 wt% glycerol solutions (see Fig. 2), which indicated that the density (apparent) of beads was lower than those ($\rho_{b,\text{apparent}} < \rho_{m,25\%} < \rho_{b,\text{vendor}} < \rho_{m,26\%}$, see Eq. (5)). In other words, by adopting the vendor-provided density, the movement of beads in aqueous solution cannot be precisely predicted. In contrast, the motion of hybrid beads in solution can be more accurately estimated by using the detected apparent density (see Eqs. (6) and (7) and Fig. 2).

Similarly, as shown in Fig. 3b, the detected density of magnetic beads, 1.0941 g/cm^3, is a little bit smaller than that provided by vendor. The *RSD* obtained was 0.11%. The smaller measured densities are probably due to surface hydrophilic liquid layer [8] and inner nano-scale porous [9].

3.4. Influence of the motion of beads on flow cytometric analysis

The motion of beads plays a crucial role in the flow cytometric analysis. As illustrated in Fig. 4 and Table 2, the *mean* of forward light scatter (FS) signals are increased with increasing of glycerol mass fraction. In the mean time, those of side light scatter (SS) signals are close to a constant. The light signals are generated as beads pass through the laser beam in a fluid stream. And the FS signal is proportional to the projected spot area or size which is related to the size of beads and the distance between the beads and the sensor [5b]. When the motion tendency of beads was changed from

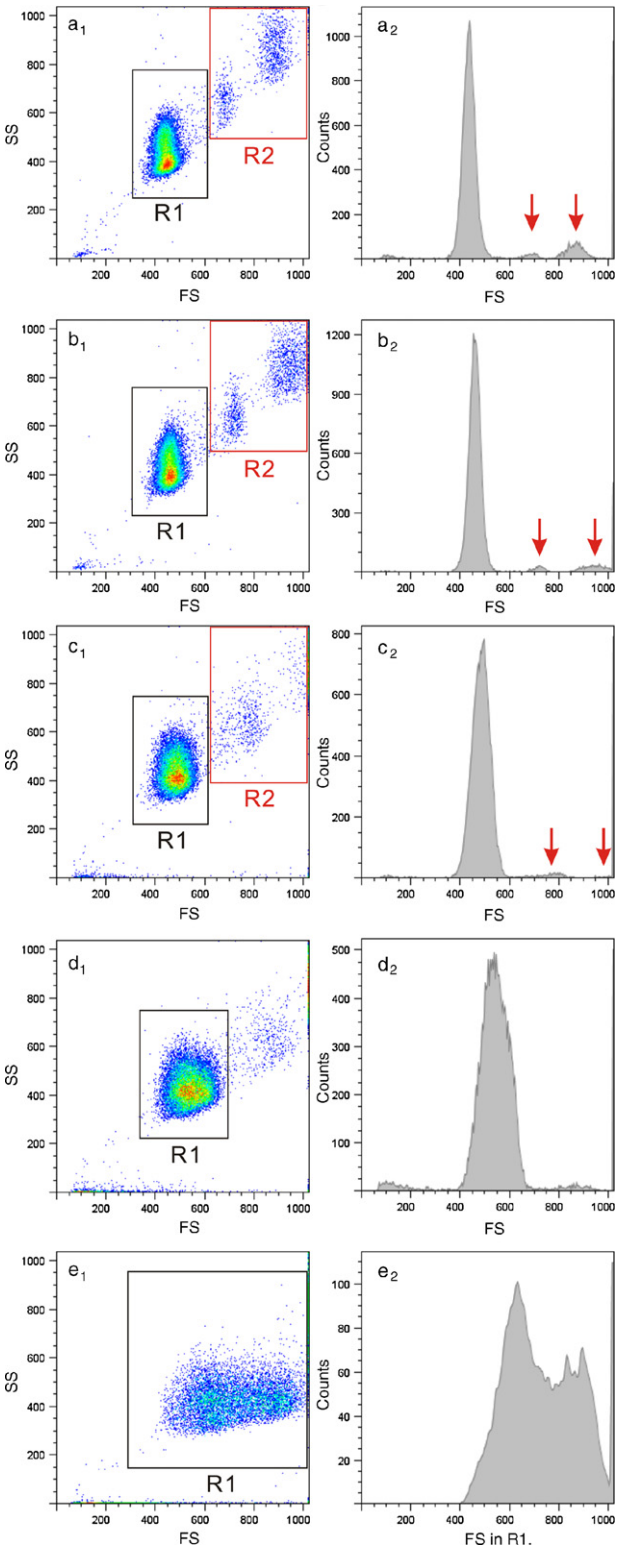


Fig. 4. Flow cytometry analysis of polymer beads. The dispersion solutions of a–e are pure water, 10, 20, 24 and 30 wt% glycerol solutions, respectively. (a_1–e_1) The bead subpopulations based on side light scatter (SS) vs. forward light scatter (FS); (a_2–e_2), the histogram of size distribution. The singlet beads were counted in the region 1 (R1, a_1–e_1), the doublet beads were recorded in the red region 2 (R2, a_1–c_1) and marked by red arrows in the diagrams a_2–c_2. (For interpretation of the references to color in this figure legend, the reader is referred to the web version of the article.)

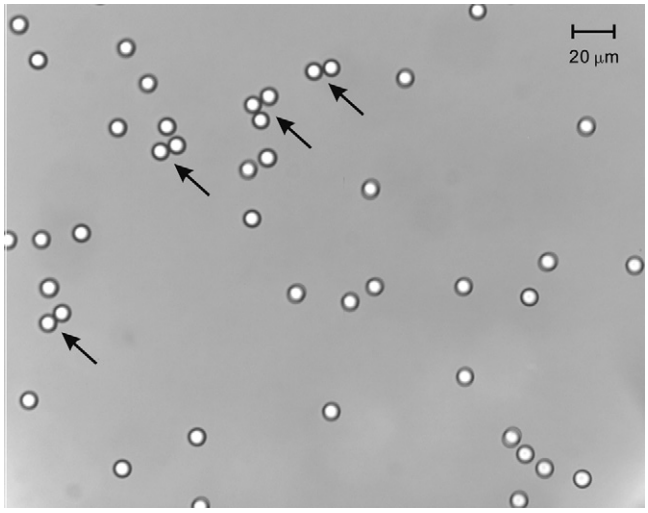


Fig. 5. The microphotograph of polymer beads dispersed in a solution containing 5 wt% glycerol and 0.05 wt% SDS, and the doublet beads were marked by arrows.

sedimentation to floating (Fig. 4a–e), the distance was increased, resulting in a larger FS signal. In addition, the increase of FS signals is not mainly due to the diffusion of glycerol from the core flow to the sheath flow [12], otherwise, the *mean* and *RSD* of SS signals should be also changed (see Table 2).

Moreover, the proportion of doublet beads is decreased with the prolongation of suspension time (Fig. 4a–c). The doublet beads suspended in a liquid are shown in Fig. 5. Their signals might affect the accuracy of flow cytometry detection [13]. The numbers of doublet beads depend on previous treatment of the suspension (e.g., sonication and vortex), age, and solvent [14]. Since all the samples were performed with the same operations, the proportion of doublet beads can be reduced by extension of their suspension time.

4. Conclusions

Theoretical description for the motion, including floating or sedimentation of polymer bead in aqueous solution was deduced by analysis of the net force of a liquid-suspended bead. Furthermore, the apparent density of beads can be easily calculated by using the measured floating or sedimentation time. For polymer beads and commercial magnetic beads, the detected apparent densities in the present study were 1.0570 and 1.0941 g/cm^3, respectively. The analysis showed that this milligram-scale method provided a more facile and precise approach to predict the movement of hybrid beads in aqueous solution than the general method. This work is beneficial to micro-total analysis systems, separation, suspension stability [15], particle analysis systems and so forth.

Acknowledgment

This work was supported by the Center for Nanostructured Application and Nanobiotechnology Initiative at the University of Minnesota and by the NSF BME 0730825.

Appendix A. Supplementary data

Supplementary data associated with this article can be found, in the online version, at doi:10.1016/j.talanta.2009.10.004.

References

[1] G.M. Whitesides, Nature 442 (2006) 367.
[2] (a) C.-Y. Chang, Y. Takahashi, T. Murata, H. Shiku, H.-C. Chang, T. Matsue, Lab. Chip 9 (2009) 1185;
(b) J.G. Kralj, A. Player, H. Sedrick, M.S. Munson, D. Petersen, S.P. Forry, et al., Lab. Chip 9 (2009) 917;
(c) D.H. Yoon, J.B. Ha, Y.K. Bahk, T. Arakawa, S. Shoji, J.S. Go, Lab. Chip 9 (2009) 87.
[3] (a) X. Llopis, M. Pumera, S. Alegret, A. Merkoçi, Lab. Chip 9 (2009) 213;
(b) N. Pamme, Lab. Chip 6 (2006) 24;
(c) K.S. Kim, J.-K. Park, Lab. Chip 5 (2005) 657.
[4] (a) A. Funfak, M. Fischlechner, E. Donath, J.M. Köhler, The 2007 Spring National Meeting Houston, 2007, p. T1011;
(b) K.D. Vorlop, D. Estapé, F. Gòdia, Biotechnol. Tech. 7 (1993) 287.
[5] (a) B. Srinivasan, Y. Li, Y. Jing, Y. Xu, X. Yao, C. Xing, et al., Angew. Chem. Int. Ed. 48 (2009) 2764;
(b) Introduction to Flow Cytometry: A Learning Guide, BD Biosciences, Manual Part Number: 11-11032-01, 2000. http://www.cancer.umn.edu/exfiles/research/fcintro.pdf (accessed Oct 27, 2009).
[6] T.W. Work, E. Work, Laboratory Techniques in Biochemistry and Molecular Biology, North Holland Publ. Comp., Amsterdam, 1976.
[7] Test Method for Density and Relative Density of Liquids by Digital Density Meter, ASTM D 4052, 2002.
[8] X.M. Sun, S.M. Tabakman, W.-S. Seo, L. Zhang, G.Y. Zhang, S. Sherlock, et al., Angew. Chem. Int. Ed. 48 (2009) 939.
[9] X. Gao, S. Nie, Anal. Chem. 76 (2004) 2406.
[10] P.N. Shankar, M. Kumar, Proc. R. Soc. Lond. A 444 (1994) 573.
[11] V.G. Zarnitsyn, A.G. Fedorov, Langmuir 23 (2007) 6245.
[12] C. Wang, Y. Gao, N.-T. Nguyen, T.N. Wong, C. Yang, K.T. Ooi, J. Micromech. Microeng. 15 (2005) 2289.
[13] (a) S. Hansen, R. Dahl, H.J. Hoffmann, J. Immunol. Meth. 338 (2008) 58;
(b) A.G. Schrum, D. Gil, E.P. Dopfer, D.L. Wiest, L.A. Turka, et al., Sci. STKE 389 (2007) pl2. [doi:10.1126/stke.3892007pl2];
(c) S.E. Weigum, P.N. Floriano, N. Christodoulides, J.T. McDevitt, Lab. Chip 7 (2007) 995;
(d) N.K.Christensen, J. Laursen, L. Winther, USP 2008/0194508 A1 (2006).
[14] A.K. Gaigalas, L. Wang, Springer Ser. Fluoresc. 6 (2008) 371.
[15] J. Chang, Q. Zhang, W. Wang, Y. Han, P. Wang, X. Dong, CN Patent CN101109689 (2007) (in Chinese).

Talanta 80 (2010) 1686–1691

Contents lists available at ScienceDirect

Talanta

journal homepage: www.elsevier.com/locate/talanta

Simultaneous determination of ascorbic acid, dopamine, uric acid and xanthine using a nanostructured polymer film modified electrode

Palraj Kalimuthu, S. Abraham John*

Department of Chemistry, Gandhigram Rural University, Gandhigram 624 302, Dindigul, India

ARTICLE INFO

Article history:
Received 31 July 2009
Received in revised form 2 October 2009
Accepted 5 October 2009
Available online 12 October 2009

Keywords:
Electropolymerization
2-Amino-1,3,4-thiadiazole
Ascorbic acid
Dopamine
Xanthine
Uric acid

ABSTRACT

This paper describes the simultaneous determination of ascorbic acid (AA), dopamine (DA), uric acid (UA) and xanthine (XN) using an ultrathin electropolymerized film of 2-amino-1,3,4-thiadiazole (p-ATD) modified glassy carbon (GC) electrode in 0.20 M phosphate buffer solution (pH 5.0). Bare GC electrode failed to resolve the voltammetric signals of AA, DA, UA and XN in a mixture. On the other hand, the p-ATD modified electrode separated the voltammetric signals of AA, DA, UA and XN with potential differences of 110, 152 and 392 mV between AA–DA, DA–UA and UA–XN, respectively and also enhanced their oxidation peak currents. The modified electrode could sense 5 μM DA and 10 μM each UA and XN even in the presence of 200 μM AA. The oxidation currents were increased from 30 to 300 μM for AA, 5 to 50 μM for DA and 10 to 100 μM for each UA and XN, and the lowest detection limit was found to be 2.01, 0.33, 0.19 and 0.59 μM for AA, DA, UA and XN, respectively (S/N = 3). The practical application of the present modified electrode was demonstrated by the determination of AA, UA and XN in human urine samples.
© 2009 Elsevier B.V. All rights reserved.

1. Introduction

Dopamine (DA) is an important neurotransmitter molecule present in our body and it plays a significant role in the functioning of central nervous, renal, hormonal and cardiovascular systems [1]. Low level of DA is related to neurological disorders such as Parkinson's disease, schizophrenia and to HIV infection [2–4]. Uric acid (UA) is another important compound in our body and its abnormal concentration levels lead to several diseases such as hyperuricaemia, gout, leukemia and pneumonia [5,6]. Xanthine (XN) is an intermediate of the purine metabolism and is produced after adenosine triphosphate decomposition [7]. The concentration level of XN in blood plasma and urine may provide sensitive indicators of certain pathologic states, especially for xanthinuria. It is a rare genetic disorder where the lack of xanthine oxidase leads to high concentration of XN in body fluids and can cause health problems such as renal failure. The physiological conversion of XN by xanthine oxidase is of great interest in medical because this reaction is related to the formation of superoxide one of the reactive oxygen species involved in inflammation and cancer [7–9]. Ascorbic acid (AA) is used for the prevention of scurvy and treatment of common cold, mental illness, infertility, cancer and AIDS [10]. Usually AA, DA, UA and XN are coexisting in our body fluids. Therefore, it is very important to develop simple and rapid methods for their selective determination in routine analysis.

Various techniques have been utilized to determine these biomolecules including fluorimetry [11], chemiluminescence [12], ion-exchange column chromatography [13], ultraviolet–visible spectroscopy [14] and capillary electrophoresis [15]. However, such methods of detection are often complicated, very expensive, suffered from sensitivity, selectivity and reproducibility. To overcome these problems, several researchers have employed electrochemical method for the determination of biomolecules. In electrochemical method, electrodes modified with gold nanoparticles [16], self-assembled monolayers [17], carbon nanotube [18] and polymer film [19–26] were employed for the determination of AA, DA, UA and XN. Among them, polymer modified electrodes prepared by electropolymerization method have received extensive interest because chemically stable homogeneous film with controlled thickness can be prepared by this method. It has been demonstrated that electropolymerized films showed excellent selectivity and sensitivity with stable voltammetric response towards several biomolecules. For example, poly(*N*,*N*′-dimethylaniline) [19], poly(3,4-ethylenedioxy)thiophene [22], poly(methylene blue) [23], poly(eriochrome black T) [24], poly(3,4-ethylenedioxythiophene-co-(5-amino-2-napthalenesulfonic acid)) [25] and poly(5-amino-2-mercapto-1,3,4-thiadiazole) [26] modified electrodes have been used for the determination of DA and UA in the presence of main interferent AA. However, to the best of our knowledge, no report has been published for the simultaneous determination of AA, DA, UA and XN.

* Corresponding author. Tel.: +91 451 245 2371; fax: +91 451 245 3031.
E-mail address: abrajohn@yahoo.co.in (S.A. John).

0039-9140/$ – see front matter © 2009 Elsevier B.V. All rights reserved.
doi:10.1016/j.talanta.2009.10.007

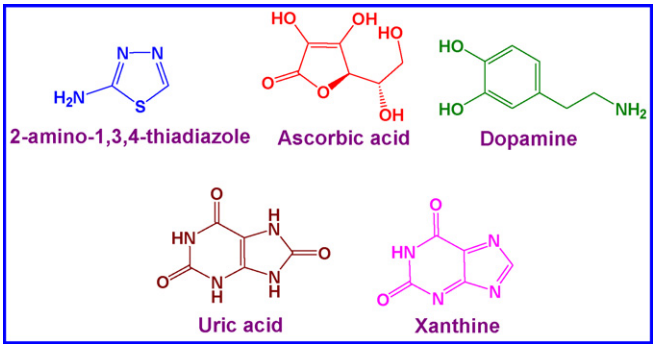


Chart 1. Structure of a monomer and biomolecules.

Very recently, we have prepared an ultrathin polymer film of 5-amino-2-mercapto-1,3,4-thiadiazole (p-AMT) on GC electrode by potentiodynamic polymerization and successfully used this film for the determination of dopamine [26], L-cysteine [27], folic acid [28], epinephrine [29] and nitrite ion [30]. In the present study, we have examined the utility of another ultrathin polymer film, 2-amino-1,3,4,thiadiazole (p-ATD) for the simultaneous determination of AA, DA, UA and XA in 0.20 M phosphate buffer (PB) solution (pH 5.0) for the first time (Chart 1). It was found that the p-ATD modified electrode not only separated the voltammetric signals of DA, AA, UA and XA but also enhanced their oxidation currents when compared to bare GC electrode. Further, the present modified electrode is successfully applied to determine AA, UA and XN in human urine samples.

2. Experimental

2.1. Chemicals

2-Amino-1,3,4-thiadiazole (ATD), ascorbic acid (AA), dopamine (DA), uric acid (UA) and xanthine (XN) were purchased from Aldrich and were used as received. Dopamine hydrochloride injections were purchased from Neon Laboratory Limited, India and were used as received. All other chemicals used in this investigation were of analytical grade. The PB solution was prepared using Na_2HPO_4 and NaH_2PO_4. Double distilled water was used to prepare the solutions used in the present study.

2.2. Instrumentation

Electrochemical measurements were performed in a conventional two compartment three electrode cell with a mirror polished 3 mm glassy carbon (GC) as the working electrode, Pt wire as counter electrode and a NaCl saturated Ag/AgCl as reference electrode. The electrochemical measurements were carried out with CHI Model 643B (Austin, TX, USA) Electrochemical Workstation. All the experiments were carried out under nitrogen atmosphere at room temperature. Tapping mode AFM image was recorded by using a Nanoscope (IV) instrument (Vecco).

2.3. Fabrication of p-ATD modified GC electrode

Prior to modification, the GC electrode was polished with 0.50 and 0.05 μm alumina slurries and then rinsed thoroughly with water. Then, the electrode was sonicated in water for 5 min to remove adsorbed alumina particles on the electrode surface. Electropolymerization of ATD on GC electrode was carried out by 15 successive potential sweeps between −0.20 and +1.70 V at a scan rate of 50 mV s^{-1} in 1 mM ATD containing 0.10 M H_2SO_4 [31].

3. Results and discussion

3.1. Atomic force microscopic studies of p-ATD film on ITO electrode

AFM was used to find the morphology and thickness of the p-ATD film. Fig. 1 displays the tapping mode AFM images of p-ATD film deposited on ITO electrode by 15 cycles. The p-ATD film deposited on ITO plate showed a spherical like structure with a thickness of ~25 nm. The diameter of each spherical was found to be 30–50 nm.

3.2. Electrochemical behavior of AA, DA, UA and XN at bare and p-ATD modified GC electrodes

The electrochemical impedance spectroscopy was used to investigate the conductivity of p-ATD film deposited by different cycles. The impedance measurements were performed in the presence of 1 mM $K_3[Fe(CN)_6]$ in 0.1 M KCl at scanning frequencies from 0.01 to 100,000 Hz. It was found that the radius of the semicircle in the Nyquist plot decreased when the deposition cycles increases. It indicated that the charge transfer resistance decreases when the

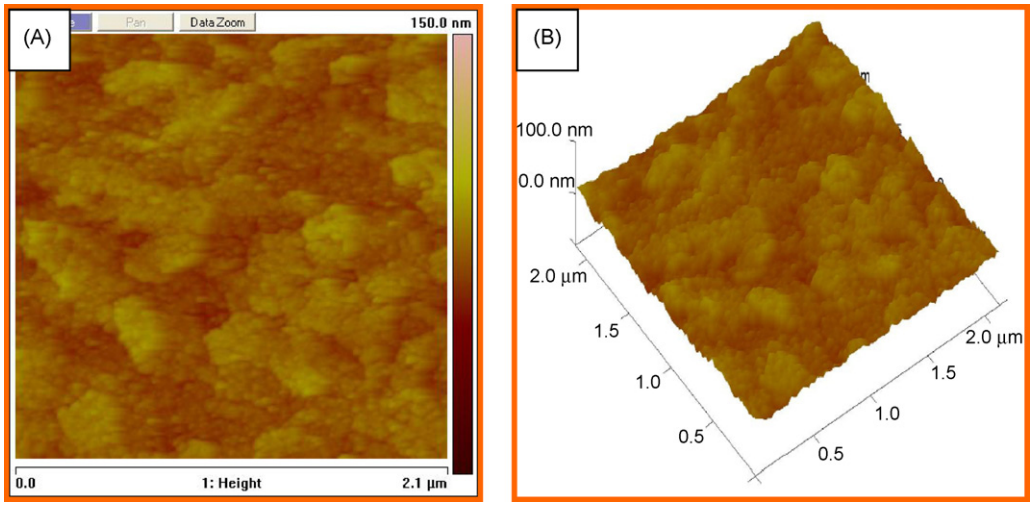


Fig. 1. (A) 2D and (B) 3D tapping mode AFM images of p-ATD film deposited on ITO plate by 15 cycles in 1 mM ATD containing 0.10 M H_2SO_4.

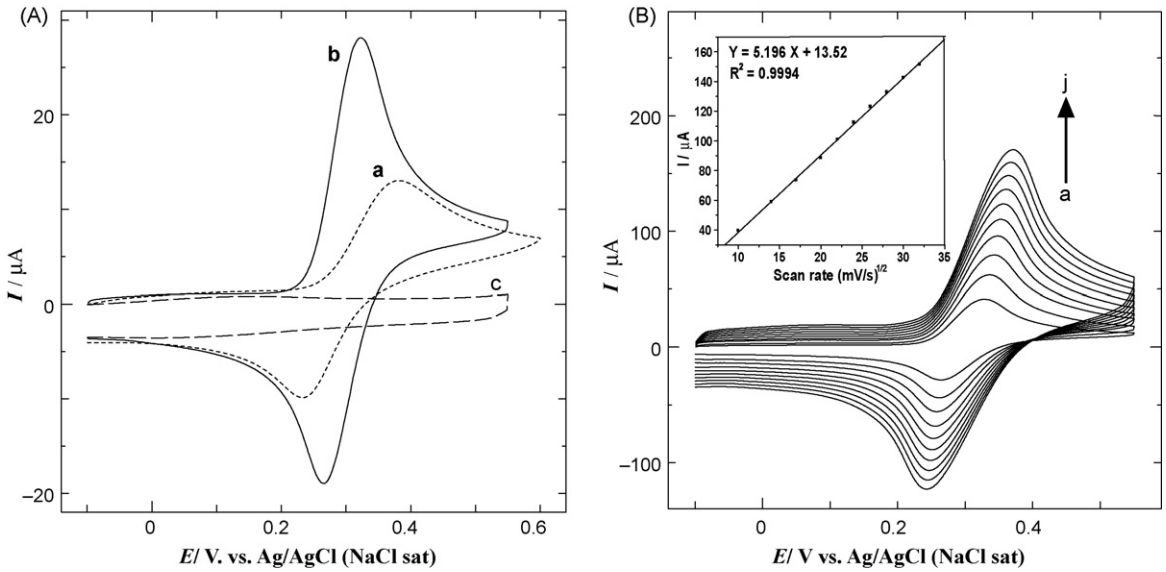


Fig. 2. (A) CVs obtained for 0.50 mM DA at (a) bare GC and (b) p-ATD modified electrodes at a scan rate of 50 mV s^{-1}. (c) p-ATD modified electrode in the absence of DA in 0.20 M PB solution (pH 5.0). (B) CVs for the oxidation of DA at p-ATD modified electrode in 0.20 M PB solution at different scan rates: (a) 100 mV s^{-1}, (b) 200 mV s^{-1}, (c) 300 mV s^{-1}, (d) 400 mV s^{-1}, (e) 500 mV s^{-1}, (f) 600 mV s^{-1}, (g) 700 mV s^{-1}, (h) 800 mV s^{-1}, (i) 900 mV s^{-1} and (j) 1000 mV s^{-1}. Inset: Plot of the anodic peak current vs square root of scan rate.

deposition cycles increases. We have calculated the charge transfer resistance (R_{ct}) for p-ATD film deposited by 15, 50 and 100 cycles using the equation $R_{ct} = RT/nFi_0$. Where R_{ct} is the charge transfer resistance due to electron transferring at the p-ATD film/solution interface, R is the gas constant, T is the experimental temperature, n is the electron transfer number of the redox process, as one for $[Fe(CN)_6]^{4-}/[Fe(CN)_6]^{3-}$, F is the Faraday constant, i_0 is the exchange current of the redox couple. The p-ATD film deposited by 15, 50 and 100 cycles showed the R_{ct} of 23.93, 14.39 and 11.63 Ω, respectively. The impedance measurements revealed that the resistance of the p-ATD film was decreased when the deposition cycles were increased. However, the double layer charging current increases while increasing the deposition cycles from 15 to 100 cycles. Thus, the sensitivity of p-ATD film was decreased towards AA, DA, UA and XN as the deposition cycles increased from 15 to 100 cycles. Thus, we have used p-ATD film deposited by 15 cycles for the determination of AA, DA, UA and XN in the present work. Further, we have performed the redox reaction of DA and oxidations of AA, UA and XN at different pH using p-ATD film. We obtained higher oxidation current, less positive oxidation potential for AA, DA, UA and XN at pH 5.0. Thus, p-ATD film deposited by 15 cycles and 0.20 M PB solution (pH 5.0) were chosen for all the electrochemical measurements.

Before carrying out the simultaneous determination of AA, DA, UA and XN, we have studied their electrochemical behavior individually at bare and p-ATD modified GC electrodes in 0.20 M PB solution (pH 5.0). Fig. 2A shows the cyclic voltammograms (CVs) of 0.50 mM DA in pH 5.0 PB solution at bare GC and p-ATD modified electrodes. At bare GC electrode, a broad redox wave was observed for DA with a peak separation of 140 mV (curve a). However, a well-defined redox peak as well as nearly two-fold higher oxidation current with 50 mV less positive potential and a peak separation of 56 mV were observed for DA at p-ATD modified electrode when compared to bare GC electrode (curve b). The observed redox peak corresponds to two-electron oxidation of DA to dopaminequinone and the subsequent reduction of dopaminequinone to DA [32,33]. The p-ATD film showed a redox wave at 0.11 V in 0.20 M PB solution (pH 5.0) (curve c) and it was attributed to a proton and electron addition/elimination reaction at the –NH– sites [31]. The effect of scan rate on the redox reaction of DA was studied at p-ATD modified electrode (Fig. 2B). Both anodic and cathodic peak currents were increased while increasing the scan rate. A good linearity between the anodic peak current and square root of scan rate with a correlation coefficient of 0.9994 was obtained within the range of 100–1000 mV s^{-1} (inset of Fig. 2B). This indicated that the electrode reaction process is controlled by the diffusion of DA. Further, at bare GC electrode, AA, UA and XN oxidations were occurred at 0.22, 0.52 and 0.89 V, respectively (figure not shown). On the other hand, p-ATD modified electrode oxidized them at 0.11, 0.46 and 0.83 V, respectively with 110, 60 and 60 mV less positive potential when compared to bare GC electrode. The oxidation currents obtained for AA and UA were nearly two-fold higher whereas three-fold higher for XN at p-ATD modified electrode in contrast to bare GC electrode.

3.3. Electrochemical behavior of ascorbic acid (AA), dopamine (DA), uric acid (UA) and xanthine (XN) in a mixture at p-ATD modified electrode

Fig. 3A displays the CVs of 0.50 mM of AA, DA, UA and XN in 0.20 M PB solution (pH 5.0) at bare GC and p-ATD modified electrodes. Bare GC electrode showed oxidation peaks for AA, UA and XN at 0.24, 0.47 and 0.88 V, respectively in a mixture (curve a). It is difficult to locate the oxidation potential of DA from Fig. 3a. It was almost merged with the oxidation potential of UA. Further, in the subsequent cycles, the oxidation peaks of AA, UA and XN were shifted to more positive potential and after eight cycles, oxidation peaks were observed for them at 0.31, 0.49 and 0.93 V, respectively with decreased peak currents (curve b). This revealed that bare GC electrode is not suitable for the stable determination of AA, DA, UA and XN. In contrast to bare GC electrode, p-ATD modified electrode oxidized AA, DA, UA and XN at 0.20, 0.33, 0.49 and 0.86 V, respectively with enhanced current response in a mixture (curve c). Oxidation of AA and XN was observed at p-ATD modified electrode with 110 and 70 mV less positive potentials, respectively than that at bare GC electrode. Further, the oxidation peaks of AA, DA, UA and XN were more stable at p-ATD modified electrode in the subsequent cycles (curve d). The separations of oxidation peak potentials of AA–DA, DA–UA and UA–XN were of 130,

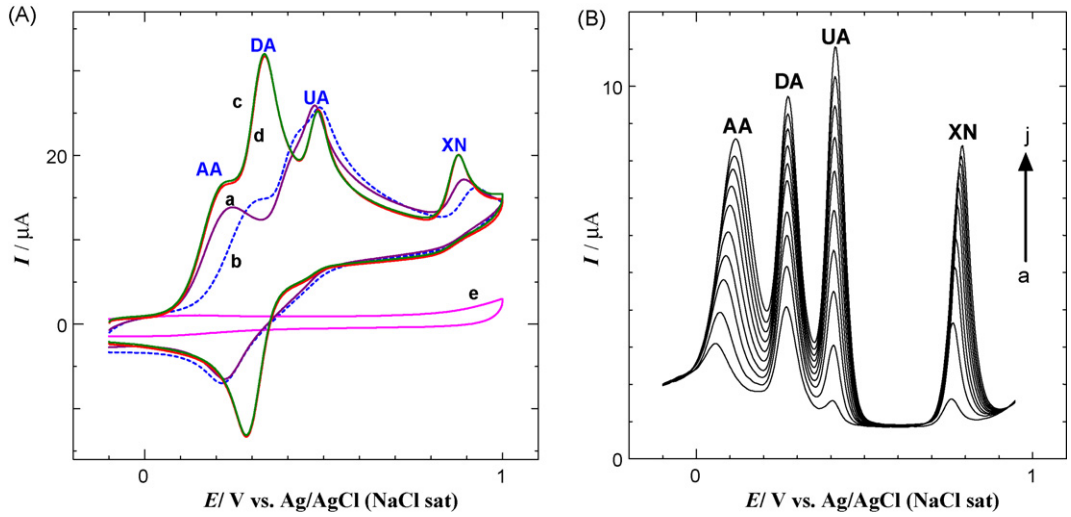


Fig. 3. (A) CVs for the oxidation of 0.50 mM AA, DA, UA and XN at bare GC electrode (a) 1st cycle and (b) 8th cycles and p-ATD modified electrode (c) 1st cycle and (d) 8th cycles at a scan rate of 50 mV s^{-1}. (e) p-ATD modified electrode in the absence of AA, DA, UA and XN in 0.20 M PB solution. (B) DPVs for the simultaneous oxidation of each addition of 30 μM AA, 5 μM DA, 10 μM each UA and XN at p-ATD modified electrode in 0.20 M PB solution. Pulse width = 0.06 s, amplitude = 0.05 V, sample period = 0.02 s and pulse period = 0.2 s.

160 and 370 mV, respectively which were enough for the simultaneous determination of them in a mixture. The observed clearly distinguished stable oxidation peaks for AA, DA, UA and XN at p-ATD modified electrode indicated that the oxidation processes of them at this electrode are independent. Thus, simultaneous or independent measurements of the four analytes are possible without any interference. The p-ATD film showed a redox wave at 0.11 V (curve e).

It is well known that AA (pK_a = 4.10), UA (pK_a = 5.7) and XN (pK_a = 7.4) exist as anionic forms whereas DA (pK_a = 8.87) exists as cationic form in pH 5.0 [25,34]. It is expected that anionic form of the AA, UA and XN were attracted by the positively charged backbone of p-ATD film [31] while positively charged DA was attracted by the hetero atoms (N and S) of the p-ATD film. Thus, enhanced oxidation peak currents were observed for anionic and cationic forms of the analytes at p-ATD modified electrode. This indicated that p-ATD film is very much suitable for the determination of both anionic and cationic forms of the analytes. Fig. 3B shows the differential pulse voltammograms (DPVs) for the simultaneous determination of AA, DA, UA and XN at p-ATD modified electrode. It showed the oxidation peaks at 0.06, 0.27, 0.41 and 0.76 V for 30 μM AA, 5 μM DA and 10 μM each UA and XN, respectively. The oxidation peaks remained same for DA, UA and XN whereas a slight shift in the oxidation potential of AA was observed for further addition of respective analytes. When the concentration was increased from 30 to 300 μM for AA, 5 to 50 μM for DA and 10 to 100 μM for each UA and XN, the peak currents of them were increased with correlation coefficient of 0.9992, 0.9994, 0.9998 and 0.9988, respectively. The lowest detection limit was found to be 2.01, 0.33, 0.19 and 0.59 μM for AA, DA, UA and XN, respectively (S/N = 3).

Further, we have compared sensitivity of p-ATD film towards the detection of DA with other polymer modified electrodes. The lowest detection limit of 1.5 and 0.38 μM (S/N = 3) was reported for DA at poly(cresol red) [35] and overoxidized polypyrrole/single-walled carbon nanotubes [36] modified GC electrodes. When compared to these electrodes p-ATD showed the lowest detection limit of 0.33 μM (S/N = 3) for DA. Furthermore, we have also compared the sensitivity of p-ATD film towards the detection of AA, DA, UA and XN individually with the p-AMT film electrode, recently reported from our laboratory [27]. Both p-AMT and p-ATD modified electrodes showed almost same sensitivity towards the detection of aforesaid analytes.

3.4. Simultaneous determination of DA, UA and XN in the presence of AA using p-ATD modified electrode

The main objective of the present study is to determine DA, UA and XN simultaneously in the presence of AA using p-ATD modified electrode. It is well known that AA coexists with DA, UA and XN in our body fluids and further its concentration is much higher than that of DA, UA and XN [37]. Therefore, determination of DA, UA and XN in the presence of higher concentration of AA is very important for the clinical point of view. Fig. 4 shows the DPVs obtained from the different concentration of DA (5 μM), UA (10 μM) and XN (10 μM) in the presence of very high concentration of AA (200 μM). The concentration of DA varied from 5 to 45 μM and UA and XN varied from 10 to 90 μM, respectively while the peak current of AA remains unchanged. The oxidation currents of DA, UA and XN were linearly increased with correlation coefficient of 0.9998, 09997 and 0.9993, respectively. These results showed that p-ATD modified

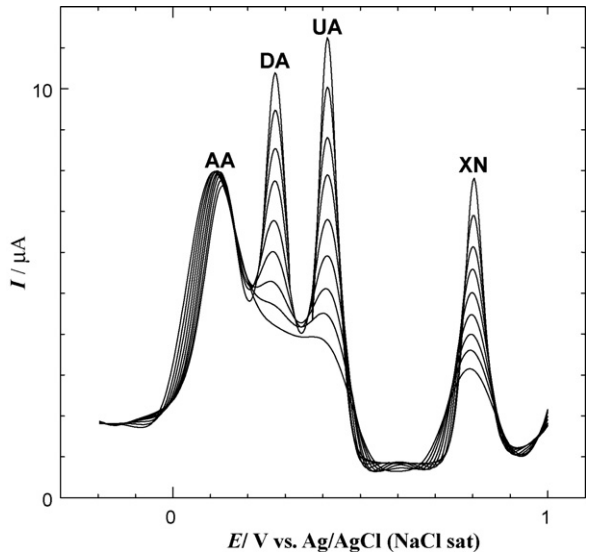


Fig. 4. DPVs obtained for the simultaneous increment of 5 μM DA and 10 μM each UA and XN to the 200 μM AA at p-ATD modified electrode in 0.20 M PB solution. Pulse width = 0.06 s, amplitude = 0.05 V, sample period = 0.02 s and pulse period = 0.2 s.

Table 1
Simultaneous determination of AA, UA and XN in human urine samples.

Samples	Original (μM/mL)			Added (μM/mL)			Found (μM/mL)			Recoveries (%)		
	AA	UA	XN	AA	UA	XN	AA	UA	XN	AA	UA	XN
Urine 1	2.12	15.20	5.60	5	5	5	7.12	20.18	10.60	100	99.9	100
Urine 2	1.43	14.50	6.20	10	10	10	11.42	24.40	16.14	99.9	99.6	99.6

Three replicate measurements were made on each sample.

electrode is more selective towards DA, UA and XN even in the presence of high concentration of AA.

3.5. Stability of the p-ATD film

In order to investigate the stability of the p-ATD modified electrode, the DPVs for 0.10 mM DA in 0.20 M PB (pH 5.0) solution were recorded for every 10 min interval. It was found that both anodic and cathodic peak currents remained same with a relative standard deviation of 2.4% for 20 times repetitive measurements indicating that this electrode has a good reproducibility and does not undergo surface fouling during the voltammetric measurements. After measurements the electrode was kept in pH 5.0 PB solution at room temperature. The current response decreased about 2% in 1 week and 5.1% in 2 weeks.

3.6. Anti-interference ability of the p-ATD film

The anti-interference ability of the p-ATD film was tested towards the detection of AA, DA, UA and XN from common physiological interferents such as glucose, urea, oxalate, Na^+, Ca^{2+} and Mg^{2+} by DPV. No change in the current response was observed for 10 μM each AA, DA, UA and XN in the presence of 10 mM of these interferents indicating that the present modified electrode is highly selective towards the determination of these analytes even in the presence of 1000-fold excess of common physiological interferents (figure not shown).

3.7. Determination of AA, UA and XN in human urine samples

The practical application of p-ATD modified electrode was tested by measuring the concentrations of AA, UA and XN in human urine samples. The standard addition technique was used for the determination of these biomolecules. The human urine samples were collected from laboratory co-workers and were diluted to 50 times with pH 5.0 PB solution without any treatment. The DPV of AA, UA and XN showed oxidation peaks at 0.15, 0.42 and 0.78 V, respectively (Fig. 5, curve a). The oxidation wave appeared at 0.05 V was due to the oxidation of p-ATD film. To confirm the observed oxidation peaks are due to AA, UA and XN, the urine sample is spiked with known concentrations of commercial AA, UA and XN (Fig. 5, curve b). The increasing peak currents at 0.15, 0.42 and 0.78 V after the addition of AA, UA and XN confirmed that the observed oxidation peaks are due to the oxidations of AA, UA and XN, respectively. The results obtained for the urine samples were summarized in Table 1. The present method showed better recoveries of spiked DA in injection and AA, UA and XN in urine samples indicating that this method could be efficiently used for the determination of these biomolecules in real samples.

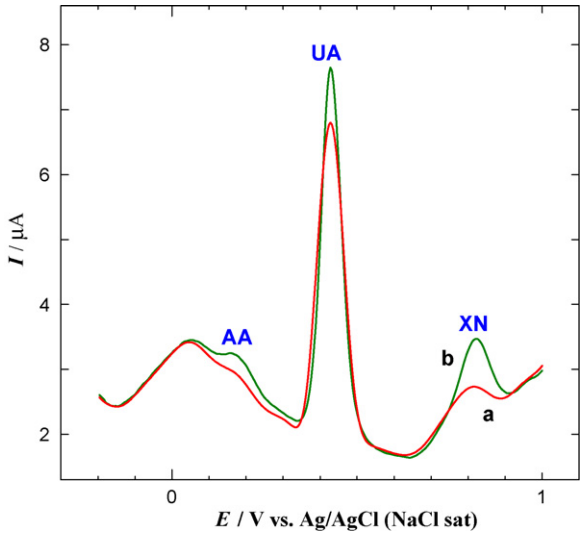


Fig. 5. DPVs obtained for (a) human urine (b) after the addition of 5 μM each AA, UA and XN to human urine at p-ATD modified electrode in 0.20 M PB solution. Pulse width = 0.06 s, amplitude = 0.05 V, sample period = 0.02 s and pulse period = 0.2 s.

4. Conclusions

In the present study, we have demonstrated the simultaneous determination of AA, DA, UA and XN using p-ATD modified GC electrode in 0.20 M PB solution (pH 5.0) for the first time. AFM image showed that the deposited p-ATD film having a homogeneous spherical structure with a thickness of ~25 nm. The bare GC electrode failed to distinguish the voltammetric signals of AA, DA, UA and XN whereas p-ATD modified electrode separated the voltammetric signals of them with potential differences of 110, 152 and 392 mV between AA–DA, DA–UA and UA-XN, respectively. It is expected that anionic forms of AA, UA and XN were attracted by positively charged backbone of the p-ATD film whereas positively charged DA was attracted by heteroatom of the p-ATD film. Thus, enhanced peak currents were observed for these analytes at p-ATD modified electrode. The oxidation currents were increased from 30 to 300 μM for AA, 5 to 50 μM for DA and 10 to 100 μM for each UA and XN, and the lowest detection limit was found to be 2.01, 0.33, 0.19 and 0.59 μM for AA, DA, UA and XN, respectively (S/N = 3). The present method was successfully applied for the determination of AA, UA and XN in human urine samples.

Acknowledgements

Palraj Kalimuthu thanks the Council of Scientific and Industrial Research (CSIR), New Delhi, for the award of Senior Research Fellowship (09/715(0008)/2008/EMR-I). Financial support from the Department of Science and Technology, New Delhi under Nanomission (No. SR/NM/NS-28/2008) is gratefully acknowledged.

References

[1] P. Demier, E.C. Hirsch, Y. Agid, A.M. Graybiel, Brain 122 (1999) 1437.
[2] C. Martin, Chem. Br. 34 (1998) 40.
[3] H. Heinz, G. Przuntek, A. Winterer, A. Pietzeker, Nervenarzt 66 (1995) 662.
[4] R.M. Wightman, L.J. May, A.C. Michael, Anal. Chem. 60 (1988) 769A.
[5] H.A. Harper, Review of Physiological Chemistry, 13th ed., Lange Medical Publications, Los Altos, CA, 1977.
[6] G.G. Guilbault, Analytical Uses of Immobilized Enzymes, Marcel Dekker, New York, 1984.
[7] D.E. Metzler, Biochemistry: The Chemical Reactions of Living Cells, Academic Press, New York, 1997.

[8] V. Venugopal, Biosens. Bioelectron. 17 (2001) 147.
[9] J.M. Amigo, J. Coello, S. Maspoch, Anal. Bioanal. Chem. 382 (2005) 1380.
[10] O. Arrigoni, C.D. Tullio, Biochim. Biophys. Acta 11569 (2002) 1.
[11] H.Y. Wang, Q.S. Hu, L.X. Xu, J.G. Jiang, Y. Sun, Anal. Chim. Acta 497 (2003) 93.
[12] Y. Hu, X. Li, Z. Pang, J. Chromatogr. A 1091 (2005) 194.
[13] X. Dai, X. Fang, C. Zhang, R. Xu, B. Xu, J. Chromatagr. B 857 (2007) 287.
[14] L. Fraisse, M.C. Bonnet, J.P.d. Farcy, C. Agut, D. Dersigny, A. Bayolb, Anal. Biochem. 309 (2002) 173.
[15] E. Causse1, A. Pradelles, B. Dirat, A.N. Salvayre, R. Salvayre, F. Couderc, Electrophoresis 28 (2007) 381.
[16] C.R. Raj, T. Okajima, T. Ohsaka, J. Electroanal. Chem. 543 (2003) 127.
[17] P. Kalimuthu, S.A. John, Anal. Biochem. 357 (2006) 188.
[18] H.-S. Wang, T.-H. Li, W.-L. Jia, H.-Y. Xu, Biosens. Bioelectron. 22 (2006) 664.
[19] P.R. Roy, T. Okajima, T. Ohasaka, Bioelectrochemistry 59 (2003) 11.
[20] S. Cosnier, Anal. Bioanal. Chem. 377 (2003) 507.
[21] L. Xu, W. Chen, A. Mulehandani, Y. Yan, Angew. Chem. Int. Ed. 44 (2005) 6009.
[22] V.S. Vasantha, S.-M. Chen, J. Electroanal. Chem. 592 (2006) 77.
[23] U. Yogeswaran, S.-M. Chen, Sens. Actuators B 130 (2008) 739.
[24] H. Yao, S. Yuanyuan, X. Lin, Y. Tang, L. Huang, Electrochim. Acta 52 (2007) 6165.
[25] A. Balamurugan, S.–M. Chen, Anal. Chim. Acta 596 (2007) 92.
[26] P. Kalimuthu, S.A. John, Bioelectrochemistry 77 (2009) 13.
[27] P. Kalimuthu, S.A. John, Electrochem. Commun. 11 (2009) 367.
[28] P. Kalimuthu, S.A. John, Biosens. Bioelectron. 24 (2009) 3575.
[29] P. Kalimuthu, S.A. John, Anal. Chim. Acta 647 (2009) 97.
[30] P. Kalimuthu, S.A. John, Electrochem. Commun. 11 (2009) 1065.
[31] P. Kalimuthu, S.A. John, Electrochim. Acta 55 (2009) 183.
[32] X.-L. Wen, Y.-H. Jia, Z.-L. Liu, Talanta 50 (1999) 1027.
[33] S.-M. Chen, K.-T. Peng, J. Electroanal. Chem. 547 (2003) 179.
[34] H. Zhao, Y. Zhang, Z. Yuan, Anal. Chim. Acta 441 (2001) 117.
[35] W. Chen, X. Lin, L. Huang, H. Luo, Microchim. Acta 151 (2005) 101.
[36] Y. Li, P. Wang, L. Wang, X. Lin, Biosens. Bioelectron. 22 (2007) 3120.
[37] T. Zetterstrom, T. Sharp, C.A. Marsden, U.J. Ungerstedt, Neurochemistry 41 (1983) 1769.

Talanta 80 (2010) 1692–1697

Contents lists available at ScienceDirect

Talanta

journal homepage: www.elsevier.com/locate/talanta

Multi-walled carbon nanotubes and $Ru(bpy)_3^{2+}$/nano-Au nano-sphere as efficient matrixes for a novel solid-state electrochemiluminescence sensor

Li Mao [a,b], Ruo Yuan [a,*], Yaqin Chai [a], Ying Zhuo [a], Xia Yang [a], Shirong Yuan [a]

[a] Education Ministry Key Laboratory on Luminescence and Real-Time Analysis, College of Chemistry and Chemical Engineering, Southwest University, Chongqing 400715, PR China
[b] College of Chemistry and Chemical Engineering, China West Normal University, Nanchong 637002, PR China

ARTICLE INFO

Article history:
Received 12 June 2009
Received in revised form
27 September 2009
Accepted 7 October 2009
Available online 13 October 2009

Keywords:
Electrochemiluminescence
$Ru(bpy)_3^{2+}$
Ru-AuNPs
Multi-walled carbon nanotubes (MWCNTs)
Tripropylamine (TPA)
Electro-active surface area
Matrine

ABSTRACT

An effective method for immobilization of $Ru(bpy)_3^{2+}$ on glassy carbon electrode surface (GCE) is developed for the preparation of a novel electrochemiluminescence sensor. First of all, the positively charged $Ru(bpy)_3^{2+}$ is modified on the surface of negatively charged gold nanoparticles (nano-Au) via the electrostatic interactions to obtain the $Ru(bpy)_3^{2+}$/nano-Au nano-sphere (abbreviate as Ru-AuNPs). Subsequently, the large amount of Ru-AuNPs are immobilized on the multi-wall carbon nanotubes (MWCNTs)-Nafion homogeneous composite coated GCE by dual interaction: firstly, the Nafion, a kind of typical cation-exchange membrane, can absorb the Ru-AuNPs as the enrichment of cation $Ru(bpy)_3^{2+}$ on the Ru-AuNPs surface; secondly, the employment of carboxylic MWCNTs in the Nafion film can also chemosorb the $Ru(bpy)_3^{2+}$ cation on the Ru-AuNPs surface to increase the carrier content. At the same time, the experiment confirms that the enhancement of the ECL intensity on the sensor is attributed to following reasons. One hand, the employment of MWCNTs in the Nafion film enlarged the electro-active surface areas to benefit the contact between the signal probe on the composite film and coreactant used as reinforcing agent. On the other hand, the nano-materials of MWCNTs and nano-Au also improve the conductivity of the assembled film to increase the quantity of excited state of $Ru(bpy)_3^{2+}$ in the unit time under the electrochemical condition and finally cause better properties in luminescence. In the experiment, the influence of the coreactant tripropylamine (TPA) on proposed ECL sensor is investigated. The logarithm of ECL intensity is proportional to the logarithm of TPA concentration on the range of 4×10^{-10} M to 2.8×10^{-6} M and 2.8×10^{-6} M to 0.71×10^{-3} M. After optimizing these conditions, the ECL sensor with TPA as coreactant is employed to detect a kind of alkaloid medicine, Matrine, for evaluating the practical application in the medicine analysis. The present sensor with TPA as coreactant shows the good response to the medicine concentration of the Matrine from 2.0×10^{-6} M to 6.0×10^{-3} M, which is used to detect the Matrine concentration in the Matrine injection.

© 2009 Elsevier B.V. All rights reserved.

1. Introduction

Electrogenerated chemiluminescence (ECL) of tris(2,2′-bipyridyl) ruthenium has been a long history since Rubinstein and Bard demonstrated light emission triggered from $Ru(bpy)_3^{2+}$ and postulated the oxidation-reduction reaction mechanism for $Ru(bpy)_3^{2+}$ ECL [1]. Since many researches show that solid-state ECL system of $Ru(bpy)_3^{2+}$ is better than the solution-phase ECL system due to the advantages of low consumption, simple operation and reproducing property, extensive efforts have been made to create a solid-state sensor [2]. However, the leakage of $Ru(bpy)_3^{2+}$ as its inherent water-solubility is always a bottleneck to gain the stable ECL sensor. Therefore, the immobilization of $Ru(bpy)_3^{2+}$ on a solid electrode surface has been extensively focus over the past several decades.

Today many different methods for the immobilization of $Ru(bpy)_3^{2+}$ have been widely developed, such as Langmuir–Blodgett film [3], self-assembly monolayer [4] and sol–gel technology [5]. It is worth to be mentioned that the immobilizing $Ru(bpy)_3^{2+}$ technology with the help of the nanoparticles make the ECL sensor have a good perform on faster response and better stability. Among these methods, nanoparticles, such as Au [6], Ag [7], TiO_2 [8], ZrO_2 [9] and SiO_2 [10], exhibit unique physical and chemical properties because of their size, morphology and large surface area. Especially, citrate-capped gold nanoparticles have negative charges on the surface and some research indicates the treatment of citrate-capped AuNPs with cationic molecules in aqueous medium, such as $Ru(bpy)_3^{2+}$, can result in their aggregation and precipitate to form multiple nano-sphere with $Ru(bpy)_3^{2+}$ on the surface [11]. This method can be employed

* Corresponding author. Tel.: +86 23 68252277; fax: +86 23 68252277.
E-mail address: yuanruo@swu.edu.cn (R. Yuan).

0039-9140/$ – see front matter © 2009 Elsevier B.V. All rights reserved.
doi:10.1016/j.talanta.2009.10.008

to immobilize $Ru(bpy)_3^{2+}$ with the sharp increase of the carrier content of $Ru(bpy)_3^{2+}$ due to the nano size and morphology of nano-Au.

Nafion, a kind of ion-exchange polymer, contain a phase composed of fluorocarbon skeleton and an ionized sulfonate group [12]. Though the fluorocarbon skeleton is very resistant to chemical attack, the unique ion-exchange property can make the cation $Ru(bpy)_3^{2+}$ to be easily incorporated into the composite films via an ion-exchange process [13]. In pure Nafion film, the rate of charge transfer is relative slow due to the nearly insulated Nafion film which was a barrier of the electron propagation [14]. But after dispersing multi-walled carbon nanotubes (MWCNTs) into the Nafion film, the specific surface area of the composite film and the charge transport in the composite film should be enhanced, which is attributed to the characteristic of MWCNTs including good mechanical strength, high-aspect ratio, excellent electrical conductivity, favorable chemical stability and the ability to promote electron-transfer reaction [15]. And it is more important that the negatively charged carboxylic MWCNTs also can chemosorb the cation on their surface [16]. Thus the composite film also can increase the carrier content of $Ru(bpy)_3^{2+}$.

Tripropylamine (TPA) is an organic amine coreactant reported earliestly and used most widely, which can replace the organic acid, such as oxalate or pyruvate, to form the oxidative-reduction-type ECL reaction with $Ru(bpy)_3^{2+}$ [17]. One advantage of using the $Ru(bpy)_3^{2+}$/TPA reaction system is that a single $Ru(bpy)_3^{2+}$ molecule may participate in multiple ECL reaction cycles to produce multiple photons due to the formation of the luminescent excited state and its ground state near the electrode surface, thereby increasing sensitivity and lowering detection limits can be obtained [18]. And another advantage is that the $Ru(bpy)_3^{2+}$/TPA reaction sequence usually operate in the optimum pH value of 7–8 [19], which is applicable for the biological system. These advantages make TPA used as the preferred detected model to evaluate the capability of the sensor fabricated with $Ru(bpy)_3^{2+}$ [14,20], and make the coreactant system used widely in the biological diagnostic assays [18].

Considering above properties, we present a stable and efficient method for immobilizing $Ru(bpy)_3^{2+}$ by assembling the Ru-AuNPs nano-sphere on the MWCNTs-Nafion modified GC electrode surface, design an experiment to compare quantificationally the electro-active surface area of different nano-materials modified electrodes and evaluate the influence of MWCNTs and the nano-Au on the capability of the ECL sensor. The $Ru(bpy)_3^{2+}$–TPA reaction system is constructed by the $Ru(bpy)_3^{2+}$ immobilized on the sensor and the coreactant TPA in the base solution. Under the optimized condition of the $Ru(bpy)_3^{2+}$–TPA system, the present ECL sensor also has been employed in the determination of real world sample. Matrine, which is a kind of alkaloid found in the Chinese herb of *Sophora* and employed to treat with the cancer and hepatitis in the clinic [21], is the aliphatic amine. The structure of Matrine is shown in Fig. 1. In the experiment, we found the ECL intensity of the proposed sensor in the $Ru(bpy)_3^{2+}$–TPA system could increase with the adding of Matrine. Therefore, the ECL sensor could be employed in the medicine analysis of Matrine. As a result, the ECL sensor presents linear answers with the concentration of Matrine, exhibits low detection limit and good stability. Comparing with previous methods of immobilizing $Ru(bpy)_3^{2+}$ in Nafion film [13], these matrixes of MWCNTs-Nafion and the Ru-AuNPs could simplify the assembling operation, increase synchronously the immobilization quantity of gold nanoparticle and $Ru(bpy)_3^{2+}$ as the aggregation of $Ru(bpy)_3^{2+}$ and nano-Au, enlarge the electro-active surface areas and improve the conductivity, which finally benefit to enhance the intensity of ECL and increase the sensitivity of sensor.

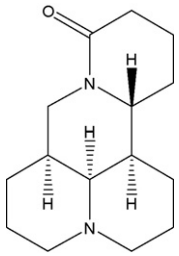


Fig. 1. The structure of Matrine.

2. Experimental

2.1. Materials

Nafion (5 wt%), $Ru(bpy)_3Cl_2{\cdot}6H_2O$, tripropylamine (TPA), gold chloride ($HAuCl_4$) and sodium citrate are purchased from Sigma–Aldrich Co. (St. Louis, MO, USA). Matrine (>98% purity) is purchased from Angsheng Biological Reagent Co. Ltd (Shaanxi, China). Matrine injection (50 mg:5 mL) is bought from the Ninth People's Hospital (Chongqing, China). MWCNTs (>95% purity) are purchased from Chengdu Organic Chemicals Co. Ltd., of the Chinese Academy of Science. And carboxylic MWCNTs are prepared as the literature method [22]. Nafion is diluted to 2 wt% with ethanol solution. All chemicals and solvents used are of analytical grade and are used as received. Double-distilled water is used throughout this study. Phosphate buffered solutions (PBS) (pH 7.4) are prepared using 0.1 M Na_2HPO_4, 0.1 M KH_2PO_4 and 0.1 M KCl. Gold nanoparticles with a diameter of 16 nm are produced by reducing gold chloride tetrahydrate with citric acid at 100 °C for half an hour [23]. Prepared solutions are kept at 4 °C before use.

2.2. Apparatus

Cyclic voltammetric (CV) measurements are carried out with a CHI 600B electrochemistry workstation (Shanghai CH Instruments, China). The ECL emission is monitored with a model MPI-A electrochemiluminescence analyzer (Xi'An Remax Electronic Science & Technology Co. Ltd., Xi'An, China) with the voltage of the photomultiplier tube (PMT) set at 800 V in the process of detection. All experiments are performed with a conventional three-electrode system. The three-compartment electrochemical cell contain a platinum wire auxiliary electrode, an Ag/AgCl (saturated KCl) reference electrode and Ru-AuNPs/MWCNTs-Nafion modified glassy carbon electrode ($\Phi = 4$ mm) as working electrode. The size of Au colloid is estimated from transmission electron microscopy (TEM) (H600, Hitachi Instrument, Japan) at an accelerating voltage of 200 kV. And the process of assembling working electrode is tracked by a scanning electron microscope (SEM, S-4800, Hitachi, Tokyo, Japan) at an acceleration voltage of 20 kV. The pH measurements are made with a pH meter (MP 230, Mettler-Toledo, Switzerland) and a digital ion analyzer (Model PHS-3C, Dazhong Instruments, Shanghai, China).

2.3. Fabrication of the electrochemiluminescence sensor

The nano-spheres of Ru-AuNPs are prepared according to the following method [11]. 300 μL of 50 mM $Ru(bpy)_3Cl_2$ aqueous solution is added into 20 mL of nano-Au (16 nm, citrate-capped) solution under vigorous stirring at room temperature. Several minutes later, a large amount of black precipitate (Ru-AuNPs) appear. Resulting precipitates are collected by centrifugation and suspension. Just as the TEM image of Ru-AuNPs shown in Fig. 2A, these nanoparticles are dispersed in the solution as the form

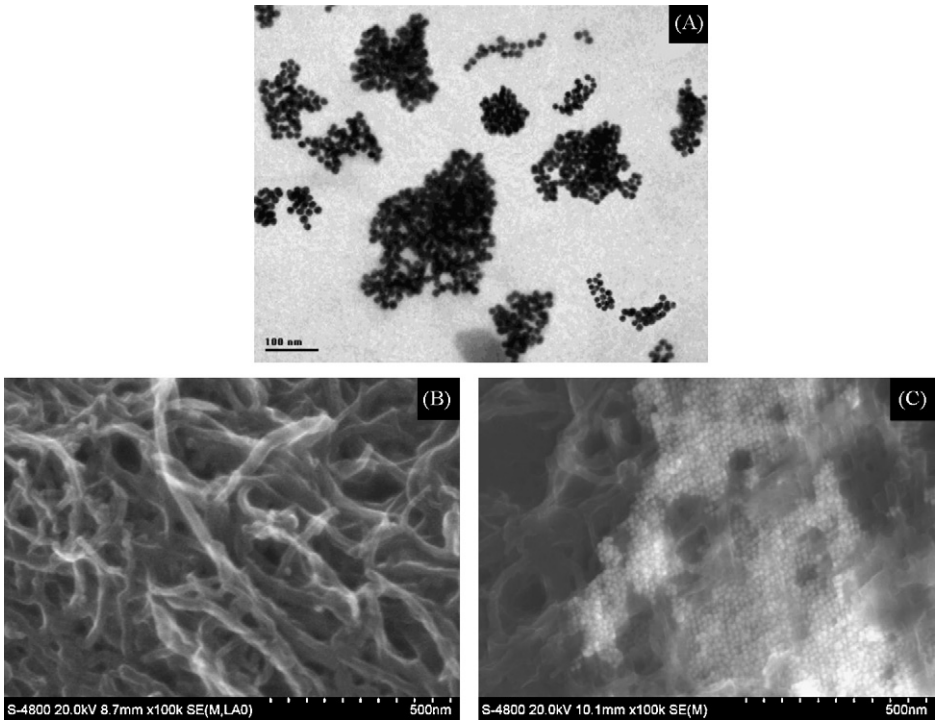


Fig. 2. TEM image of the resulting Ru-AuNPs precipitate (A); SEM images of assembling films on MWCNTs-Nafion modified electrode (B) and on Ru-AuNPs/MWCNTs-Nafion modified electrode (C).

of agglomeration because the charges lie on the particle surface. The phenomenon of aggregation can be attributed to the fact that the treatment of citrate-capped AuNPs with the cationic $Ru(bpy)_3^{2+}$ in aqueous medium results in their aggregation and precipitation, where the cationic molecules cause the cross-linking of the nanoparticles as a consequence of electrostatic interactions between the positive charges of cationic molecules and the negatively charged citrate coating on the nano-Au [24].

Before each modification, the GC electrode ($\Phi = 4$ mm) is polished with 0.3, 0.05 μm alumina slurry, successively sonicate in ethanol and double-distilled water for 5 min and dried in air. The resulting GC electrode is firstly coated with MWCNTs-Nafion suspension (3 μL, 1 mg/mL) and allowed to evaporate at room temperature. Then 5 μL suspensions of Ru-AuNPs is cast onto the modified electrode surface and dried in air. The finished sensor is stored at 4 °C when not in use. The schematic illustration of the stepwise self-assemble procedure of the sensor is shown in Fig. 3. The morphologies and microstructures of the prepared different modified films are studied by means of SEM. As shown in the SEM profiles (Fig. 2B), the homogeneous dispersion MWCNTs can be observed, which would benefit the sensor performance [25]. Fig. 2C show the treatment of above electrode with Ru-AuNPs. The nano-sphere of Ru-AuNPs are immobilized on the MWCNTs-Nafion modified electrode via the ion-exchange and electrostatic interaction between negatively charged MWCNTs-Nafion and positively charged Ru-AuNPs to assemble a novel ECL sensor.

In order to compare the ECL intensity without MWCNTs or AuNPs modified electrode, two kind of modified electrodes are fabricated. One is modified with the same volume and concentration of MWCNTs-Nafion suspensions and pure $Ru(bpy)_3^{2+}$ solution, another is assembled with pure Nafion and Ru-AuNPs suspensions.

3. Results and discussion

3.1. Electrochemistry and electrochemiluminescence of the sensor

Fig. 4 shows the cyclic voltammetry and ECL process of a bare GC electrode (a), a MWCNTs-Nafion composite film modified electrode (b) and Ru-AuNPs assembled successively on the electrode surface (c) in phosphate buffer solution (pH 7.4). All these results are recorded until the electrode has reached a steady-state response after scanning ~10 cycles. Comparing with the bare GC electrode, the background current at the MWCNTs-Nafion composite film modified electrode increase because of the strong background current of MWCNTs [16,26]. And at this step the ECL intensity weaken. Then, after modified with Ru-AuNPs, a distinguished response appears in the cyclic voltammogram and ECL in the absence of TPA. Because $Ru(bpy)_3^{2+}$ is the only electro-active and luminescent probe in the Ru-AuNPs, one broad anodic peak and one cathodic peak near 1.1 V in the cyclic voltammogram are characteristic redox waves of $Ru(bpy)_3^{2+}$. And in the ECL graph the strong luminescence at 1.15 V is the result of emission, which was caused by

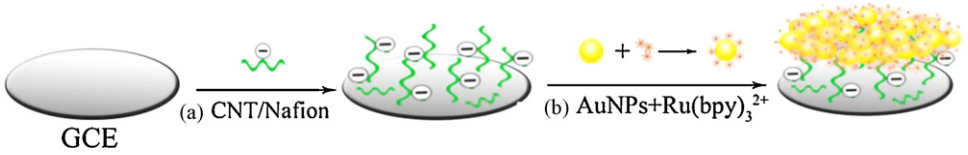


Fig. 3. Formation of Ru-AuNPs/MWCNTs-Nafion modified GCE. The process of MWCNTs-Nafion modified on the GC electrode (a); the nano-sphere formation of Ru-AuNPs due to electrostatic interaction between $Ru(bpy)_3^{2+}$ and citrate-capped AuNPs and the immobilization of Ru-AuNPs on MWCNTs-Nafion modified GC electrode (b).

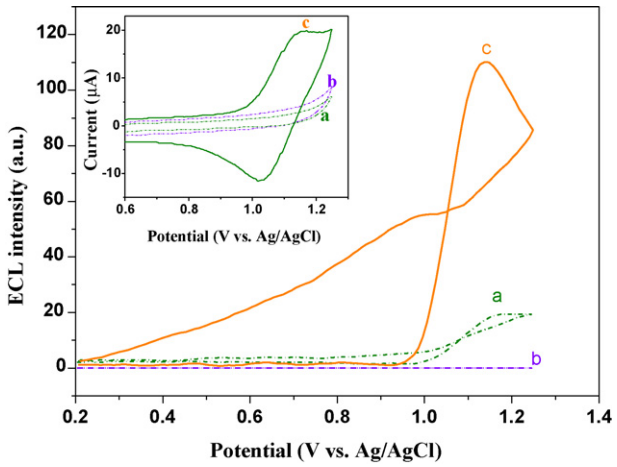


Fig. 4. The ECL intensity–potential curve and CV (inset) of bare electrode (a), MWCNTs-Nafion modified electrode (b) and Ru-AuNPs/MWCNTs-Nafion modified electrode (c) in PBS (pH 7.4) without TPA. *Inset*: the CVs of the immobilized process of $Ru(bpy)_3^{2+}$.

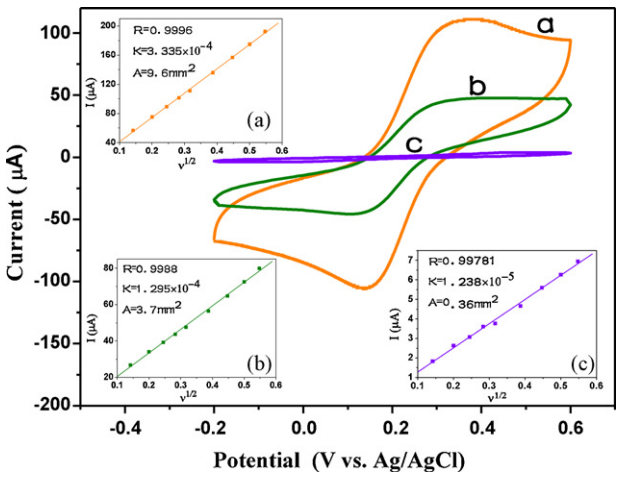


Fig. 5. The CVs of Ru-AuNPs/MWCNTs-Nafion modified electrode (a), the electrode of absent AuNPs (b) and the electrode of absent MWCNTs (c) in 5.0 mM $Fe(CN)_6^{3-/4-}$ containing 4.0 mM TPA at scan rate of 100 mV/s. *Inset*: linear relations with the anodic peak current against the square root of scan rate.

the transition from the excited state to ground state of $Ru(bpy)_3^{2+}$ [27].

3.2. The influence of nanoparticles on the capability of the sensor

As many reports mentioned, $Ru(bpy)_3^{2+}$–TPA can give ~10-fold higher ECL compared to other commonly used reductant such as oxalate [28]. TPA acting as coreactant has the same aggrandizement operation to the sensor in our works. With addition of TPA into the PBS solution (pH 7.4), the ECL intensity enhance distinctly. The ECL at the higher potential is attributed to direct oxidization of $Ru(bpy)_3^{2+}$ on the electrode to form $Ru(bpy)_3^{3+}$, which further reacts with the $TPA^{\bullet}$ radical species to generate $Ru(bpy)_3^{2+*}$. And the transition from the excited state to ground state of $Ru(bpy)_3^{2+}$ causes the luminescence [27,17].

Since Bard's research group reported the electrogenerated chemiluminescence of nano-crystals in organic solvents, the study on the function of nanoparticles assembled electrode in ECL has received considerable attention [29]. The nanoparticle assembled electrode has different properties from conventional electrodes, which can lead to new ECL properties and new ECL reactions [30]. An enormous surface area-to-volume ratio, which is highly susceptible to heterogeneous redox chemistry with surrounding environment, is pivotal factor [31]. Bard and Faulkner mentioned in their book that the electro-active surface area of these electrodes can be estimated for a reversible process according to the Randles–Sevcik equation [32].

$$I_p = 2.69 \times 10^5\ A \times D^{1/2}\, n^{3/2}\, n^{1/2}\, C$$

I_p refers to the redox peak current; n and C represent the transferring electron number and the concentration (mol cm^{-3}) of the ferricyanide; A is the area of the electrode (cm^2), D is the diffusion coefficient of the molecule in solution ($cm^2\ s^{-1}$), and ν is the scan rate of the potential perturbation ($V\ s^{-1}$). D, C and n are constants. If the electrochemical behavior of the electrode surface is controlled by diffusion, the slope that is gained by plotting the picture of the peak current against the square root of scan rate and fitting linearly is the function of the electro-active surface area (A). According to the Randles–Sevcik equation, we can get the approximate value of A.

So we design this experiment to compare quantificationally the electro-active surface area of different electrodes and confirm the influence of nanoparticles on the sensor by mensurating steady-state CVs for proposed electrode (a), the electrode of absent AuNPs (b) and the electrode of absent MWCNTs (c) at a series of scan rates in 5.0 mM $Fe(CN)_6^{3-/4-}$ and 0.1 M KCl. The $Fe(CN)_6^{3-/4-}$ redox system used in this study is one of the most extensively studied redox couples in electrochemistry and exhibits a heterogeneous one-electron transfer ($n = 1$). The diffusion coefficient (D) at 25 °C is $6.70 \pm 0.02 \times 10^{-6}\ cm^2\ s^{-1}$.

In Fig. 5, the main graph is the CVs responses of three detected electrodes in the same 5.0 mM $Fe(CN)_6^{3-/4-}$ work solution containing 4.0 mM TPA (pH 7.4). And the inset graphs are respectively linear relations with the anodic peak current of electrode (a), (b) and (c) against the square root of scan rate. As Fig. 5 shown, the peak currents of three electrodes all present good linearity with the square root of scan rates, which indicate that their electrochemical behavior of the electrode surface are controlled by diffusion. According to above equation, the values of the electro-active surface area are respectively 9.6 mm^2, 3.7 mm^2 and 0.36 mm^2. And the CVs of three electrodes in the main graph show that the proposed electrode (a) has higher conductivity than other electrodes at scan rate of 100 mV/s. Comparing the luminescence of these electrodes, as Fig. 6 shown, the proposed electrode (a) has more strong ECL

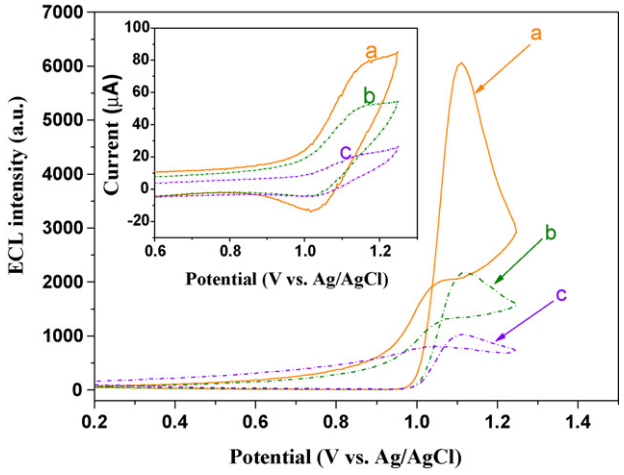


Fig. 6. The ECL intensity–potential curve of Ru-AuNPs/MWCNTs-Nafion modified electrode surface (a), MWCNTs-Nafion/$Ru(bpy)_3^{2+}$ modified electrode surface (b) and Nafion/Ru-AuNPs modified electrode surface (c) in PBS (pH 7.4) containing 4.0 mM TPA. *Inset*: the CVs of $Ru(bpy)_3^{2+}$ on three different electrodes.

intensity than other two electrodes. This trend is consistent with the electro-active surface area and the peak current. Thus it can be seen that firstly, MWCNTs and nano-Au with nanometer diameters can authentically increase the electro-active surface area, which benefit the contact between the signal probe $Ru(bpy)_3^{2+}$ on the composite film and coreactant of TPA. Secondly, the nano-materials of MWCNTs and nano-Au also can improve the conductivity of the assembled film to increase the quantity of excited state of $Ru(bpy)_3^{2+}$ in the unit time under the electrochemical condition and finally cause better properties in luminescence.

3.3. Capability of the presented sensor and ECL analytical performances of the proposed ECL sensor for Matrine

The $Ru(bpy)_3^{2+}$–TPA couple is a typical ECL system. The potential interferences on the system have been researched very extensively and deeply. The concomitant halide anion in solution, the pH value of solution and the scan rate during the detection process are main potential interferences on the ECL intensity of $Ru(bpy)_3^{2+}$–TPA system. Because the chemical adsorption of halide happened at platinum and gold electrodes can retard the formation of surface oxides and finally result a lower rate of the direct oxidation of TPA to weaken the ECL intensity [19,30], the glass carbon electrode (GCE) is chosen to fabricate the proposed sensor. The ECL system of $Ru(bpy)_3^{2+}$–TPA is sensitive to the solution pH value [33]. And the suitable pH value of the TPA buffer solution to the $Ru(bpy)_3^{2+}$ ECL analysis is usually about 7–8 [19]. Considering the application of the proposed sensor in the detection of medicine or biomolecule existed in the humoral environment, the pH value of 7.4 has been chosen [27]. The scan rate also has important influence on the ECL signal in the $Ru(bpy)_3^{2+}$–TPA system [13]. The effect of the scan rate on ECL signal of the Ru-AuNPs/MWCNTs-Nafion modified sensor is presented in Fig. 7. When the scan rate is below 100 mV/s, ECL intensity decreases faintly with the increasing of the scan rate. As the scan rate increased from 100 mV/s to 250 mV/s, ECL intensity decrease sharply. Therefore, the influence of the coreactant TPA on the ECL intensity of proposed sensor was investigated (Fig. 8A) at a scan rate of 100 mV/s. Each point on the calibration curve was the average of five ECL values obtained by consecutive cyclic potential scans at a rate of 100 mV/s in PBS solution (pH 7.4). The logarithm of ECL intensity is proportional to the logarithm of TPA concentration. The relation presented two linear sections. One linear range is from 4×10^{-10} M to 2.8×10^{-6} M, another is from 2.8×10^{-6} M to 0.71×10^{-3} M. Furthermore, with the increasing of TPA concentration, the change of ECL intensity is inconspicuous in the lower concentration range and obvious in higher concentration range. The lowest detection limit (S/N = 3) is 0.2 nM. Compared with previous results of $Ru(bpy)_3^{2+}$/MWCNT-Nafion composite films [13], the improvement of sensitivity could be attributed to the MWCNTs and Ru-AuNPs matrix, which aggrandize the contact surface of the sensor with co-reagent and make the transfer of electrons more easy on the solid modified electrode surface.

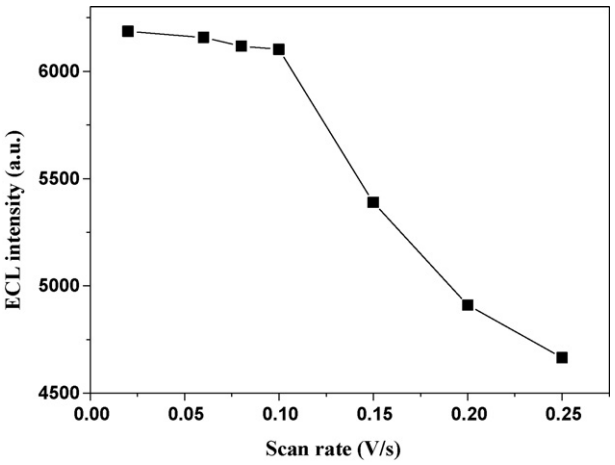


Fig. 7. Effect of scan rate on ECL intensity of Ru-AuNPs/MWCNTs-Nafion modified sensor in PBS (pH 7.4) containing 4.0 mM TPA.

In addition, with increasing the concentration of Matrine, the ECL intensity of proposed sensor enhances in $Ru(bpy)_3^{2+}$–TPA system. The ECL sensor presents linear response to the concentration of Matrine in the PBS (pH 7.4) buffer containing 0.01 mM TPA (shown in Fig. 8B), which can be employed to perform the determination of Matrine in pharmaceutical preparations. Because the enhancement ECL response of the sensor to the concentration of Matrine could not be found in same PBS buffer without TPA, the ECL response to the concentration of Matrine in the PBS buffer with TPA can attribute to the change of pH resulted by the Matrine. Each point on the calibration curve of Matrine was obtained by scanning consecutively at same scan rate of 100 mV/s and noting the ECL intensity after scanning for 14 cycles. The curve shows that the ECL intensity of present sensor is directly proportional to the concentration of Matrine from 2.0×10^{-6} M to 6.0×10^{-3} M (496.7 ng/mL to 1.5 mg/mL). And the lowest detection limit (S/N = 3) is 0.7 μM (165.6 ng/mL, Mr = 248.36). We employed the proposed ECL sensor to detect the concentration of Matrine in the Matrine injection bought from the Ninth People's Hospital in Chongqing. The Matrine injection (10 mg/mL) is diluted tenfold before the sample is detected. The obtained concentration of the diluted sample is 0.991 ± 0.052 mg/mL. Therefore, the detection concentration of Matrine in the Matrine injection is 9.91 ± 0.52 mg/mL, which is approximately equal to the label concentration of the Matrine injection (10 mg/mL).

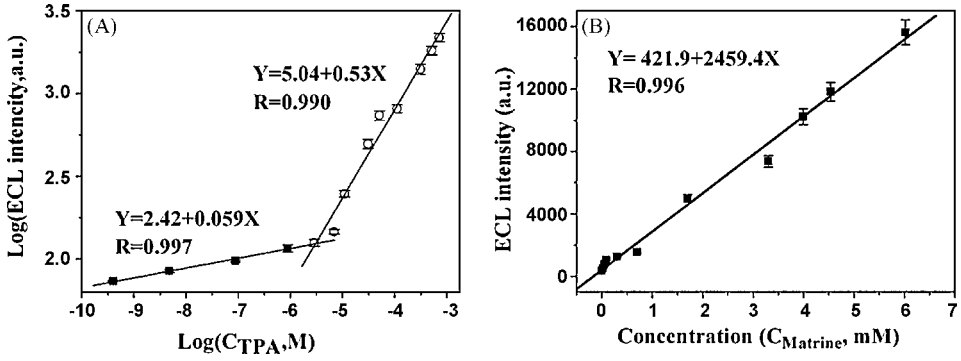


Fig. 8. (A) Calibration curve of TPA with the proposed sensor in PBS (pH 7.4); scan rate 100 mV/s. (B) Calibration curve of Matrine with the sensor in PBS (pH 7.4) buffer containing 0.01 mM TPA at same scan rate.

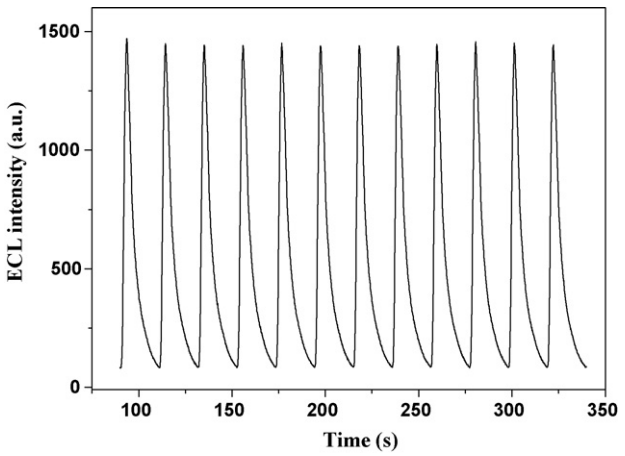


Fig. 9. ECL intensity–potential curve of Ru-AuNPs/MWCNTs-Nafion modified electrode in PBS (pH 7.4) containing 0.3 mM TPA under continuous cyclic potential scans for 12 cycles.

Fig. 9 shows the good stability of the working electrode under the present conditions. Under consecutive cyclic potential scans for 12 cycles at a scan rate of 100 mV/s, the relative standard deviation of the ECL is less than 0.8%. The mechanical stability of the sensor is due to enhanced ion-exchange and electrostatic interactions by MWCNTs and nano-Au particles.

4. Conclusions

A new method of ECL sensor assembling is constructed using the MWCNTs and nano-Au. After optimization of the influencing factors on the ECL signal, a well-performed ECL sensor with high sensitivity and good stability is obtained. Comparing with the previous assembled layer-by-layer method, the assembling method simplifies the operation, increases the immobilized quantity of nano-Au and $Ru(bpy)_3^{2+}$ as the aggregation of Ru-AuNPs nano-sphere, and makes the sensor have better performance on bio-compatibility and sensitivity due to the using of composite nano-sphere of Ru-AuNPs and composite MWCNTs-Nafion. It is more important that the experiment that can quantificationally evaluate the effect of nanoparticle on the capability of the proposed sensor has been designed. And the quantificational counting also successfully testifies that the nanostructure can increase the electro-active surface area, facilitate the electron-transfer processor, which benefit the contact between the $Ru(bpy)_3^{2+}$ and TPA, increase the quantity of excited state of $Ru(bpy)_3^{2+}$ in the unit time under the electrochemical condition and finally promote the ECL properties of the proposed sensor. Moreover, the present sensor is employed to detect the medicine of Matrine, show good stability and good response. Therefore, the ECL sensor also has great potentials in medicine analysis application combined with capillary electrophoresis and microfluidics.

Acknowledgments

This work was supported by the NNSF of China (20675064), the Ministry of Education of China (Project 708073) and High Technology Project Foundation of Southwest University (XSGX02), China.

References

[1] I. Rubinstein, A.J. Bard, J. Am. Chem. Soc. 103 (1981) 5007.
[2] K.A. Fähnrich, M. Pravada, G.G. Guilbault, Talanta 54 (2001) 531.
[3] C.J. Miller, P. Mecord, A.J. Bard, Langmuir 7 (1991) 2781.
[4] W. Yun, Y. Xu, P. Dong, X.X. Ma, P.G. He, Y.Z. Fang, Anal. Chim. Acta 635 (2009) 58.
[5] P. Kalimuthu, S. Abraham John, J. Electroanal. Chem. 617 (2008) 164.
[6] H. Tsyunoyama, H. Sakurai, Y. Negishi, T. Tsukuda, J. Am. Chem. Soc. 127 (2005) 9374.
[7] D.P. Tang, R. Yuan, Y.Q. Chai, J. Phys. Chem. B 110 (2006) 11640.
[8] H.N. Choi, S.H. Cho, W.Y. Lee, Anal. Chem. 75 (2003) 4250.
[9] S.N. Ding, J.J. Xu, H.Y. Chen, Electrophoresis 26 (2005) 1737.
[10] A.N. Khramov, M.M. Collinson, Anal. Chem. 72 (2000) 2943.
[11] X.P. Sun, Y. Du, S.J. Dong, E.K. Wang, Anal. Chem. 77 (2005) 8166.
[12] P.C. Lee, D.J. Meisel, J. Am. Chem. Soc. 102 (1980) 5477.
[13] Z.H. Guo, S.J. Dong, Anal. Chem. 76 (2004) 2683.
[14] W. Gao, X.H. Xia, J.J. Xu, H.Y. Chen, J. Phys. Chem. C 111 (2007) 12213.
[15] J. Wang, M. Musameh, Y. Lin, J. Am. Chem. Soc. 125 (2003) 2408.
[16] N. Li, R. Yuan, Y.Q. Chai, S.H. Chen, H.Z. An, W.J. Li, J. Phys. Chem. C 111 (2007) 8443.
[17] J.K. Leland, M.J. Powell, J. Electrochem. Soc. 137 (1990) 3127.
[18] M.M. Richter, Chem. Rev. 104 (2004) 3003.
[19] Y.B. Zu, A.J. Bard, Anal. Chem. 72 (2000) 3223.
[20] J. Li, Y.H. Xu, H. Wei, T. Huo, E.K. Wang, Anal. Chem. 79 (2007) 5439.
[21] L.J. Zhang, T.T. Wang, X.M. Wen, Y. Wei, X.C. Peng, H. Li, L. Wei, Eur. J. Pharmacol. 563 (2007) 69.
[22] M.L. Guo, J.H. Chen, L.H. Nie, S.Z. Yao, Electrochim. Acta 49 (2004) 2637.
[23] Y. Zhuo, R. Yuan, Y.Q. Chai, et al., Sens. Actuators, B 114 (2006) 631.
[24] A.N. Shipway, M. Lahav, R. Gabai, I. Willner, Langmuir 16 (2000) 8789.
[25] M.N. Zhang, K.P. Gong, H.W. Zhang, L.Q. Mao, Biosens. Bioelectron. 20 (2005) 1270.
[26] L.Y. Zhao, H.Y. Liu, N.F. Hu, J. Colloid Interface Sci. 296 (2006) 204.
[27] W.D. Cao, P.F. Jerome, D. James, P.L. James, J. Am. Chem. Soc. 128 (2006) 7572.
[28] W.Y. Lee, T.A. Nieman, Anal. Chem. 67 (1995) 1789.
[29] N. Myung, Z.F. Ding, A.J. Bard, Nano. Lett. 2 (2002) 1315.
[30] H. Cui, Y. Xu, Z.F. Zhang, Anal. Chem. 76 (2004) 4002.
[31] Z.F. Ding, B.M. Quinn, S.K. Haram, L.E. Pell, B.A. Korgel, A.J. Bard, Science 296 (2002) 1293.
[32] A.J. Bard, L.R. Faulkner, Electrochemical Methods: Fundamentals and Applications, 2nd ed. 2001, Wiley, New York, 1980, p. 231.
[33] X.H. Xu, R.B. Jeffers, J. Gao, B. Logan, Analyst 126 (2001) 1285.

Talanta 80 (2010) 1698–1701

Contents lists available at ScienceDirect

Talanta

journal homepage: www.elsevier.com/locate/talanta

Variable-weighted least-squares support vector machine for multivariate spectral analysis

Hong-Yan Zou, Hai-Long Wu*, Hai-Yan Fu, Li-Juan Tang, Lu Xu, Jin-Fang Nie, Ru-Qin Yu

State Key Laboratory of Chemo/Biosensing and Chemometrics, College of Chemistry and Chemical Engineering, Hunan University, Changsha 410082, PR China

ARTICLE INFO

Article history:
Received 28 June 2009
Received in revised form 3 October 2009
Accepted 7 October 2009
Available online 13 October 2009

Keywords:
Multivariate regression
Variable selection
LS-SVM
Particle swarm optimization
PLS

ABSTRACT

Multivariate spectral analysis has been widely applied in chemistry and other fields. Spectral data consisting of measurements at hundreds and even thousands of analytical channels can now be obtained in a few seconds. It is widely accepted that before a multivariate regression model is built, a well-performed variable selection can be helpful to improve the predictive ability of the model. In this paper, the concept of traditional wavelength variable selection has been extended and the idea of variable weighting is incorporated into least-squares support vector machine (LS-SVM). A recently proposed global optimization method, particle swarm optimization (PSO) algorithm is used to search for the weights of variables and the hyper-parameters involved in LS-SVM optimizing the training of a calibration set and the prediction of an independent validation set. All the computation process of this method is automatic. Two real data sets are investigated and the results are compared those of PLS, uninformative variable elimination-PLS (UVE-PLS) and LS-SVM models to demonstrate the advantages of the proposed method.

© 2009 Published by Elsevier B.V.

1. Introduction

With the development of modern spectrometers, nowadays spectral data consisting of measurements at hundreds and even thousands of analytical channels can be obtained in a few seconds. The practical need for fast and reliable quantification of sought-for components in complex samples is increasing. Least-squares support vector machine (LS-SVM) [1,2], a relatively new algorithm from the machine learning community, has the capability of dealing with linear and nonlinear multivariate calibration. The superiority of LS-SVM to traditional support vector machine (SVM) [3,4] is that it requires solving a set of only linear equations (linear programming) instead of a set of nonlinear equations (quadratic programming) which is much easier and computationally very simple. It has been introduced into multivariate calibration by many investigators for its attractive features and promising empirical performance [5–9]. One problem in LS-SVM multivariate calibration is whether the whole wavelength range should be used or only a proper subset of the spectra would be enough. Theoretically, some variables of these full spectrum data may contain useless or irrelevant information for calibration model like noise and background, which can worsen the predictive ability of the calibration model. Recently, variable selection [10–20] or uninformative variable elimination [21–24] has attracted more and more attention for the development of multivariate calibrations. These variable selection methods could improve the predictive ability of the calibration models. But some wavelengths might represent similar data structure when kept together [25,26], selection of a few individual wavelengths from them would cause a loss of useful information. And for the spectra with heteroscedastic noises, wavelength ranges with comparatively high noise might carry useful relevant information for prediction and simply deleting such wavelengths would lead to a model with much less variables, which would spoil the multi-channel advantage of the model to some extent. So it is important for us to have a general view of variable selection. This paper addresses this significant issue of introducing the wavelength variable weighting to LS-SVM model. Unlike in ordinary variable selection methods, where the wavelengths selected are weighted 1.0 and the wavelengths deleted are weighted 0, we have introduced wavelength sampling with continuous nonnegative values.

Like SVM, the conventional LS-SVM is performed first by adjusting the parameters in regularization item and kernel function called hyper-parameters, which play an important role to the algorithm performance. The existing techniques for adjusting the hyper-parameters in LS-SVM can be summarized into two kinds: one is based on analytical techniques which are computationally intolerable to optimize these parameters [27,28]. The other is based on heuristic searches including genetic algorithms (GA), simulated annealing algorithms (EA) and other evolutionary strategies [29–32], which are the tricky tasks since a suitable sampling step varies from kernel to kernel and the grid interval may not be easy to locate without prior knowledge of the problem. Moreover, when

* Corresponding author. Fax: +86 731 88821818.
E-mail address: hlwu@hnu.cn (H.-L. Wu).

0039-9140/$ – see front matter © 2009 Published by Elsevier B.V.
doi:10.1016/j.talanta.2009.10.009

there are more than two hyper-parameters, the manual model selection may become intractable. The particle swarm optimization (PSO) method [33,34], a new optimization technique, developed by Eberhart and Kennedy in 1995, is a stochastic global optimization technique inspired by social behavior of bird flocking. Compared with GA and EA, PSO has no evolution operators and does not need any priori knowledge on the analytic property of the generalization performance measure and can be used to determine multiple hyper-parameters at the same time.

In this paper the idea of wavelength variable weighting is incorporated into LS-SVM for multivariate calibration. A global optimization algorithm, particle swarm optimization is used to automatically search for the variable weights and the hyper-parameters involved in LS-SVM simultaneously optimizing the training of calibration set and the prediction of an independent validation set. The details of this method will be described in the following part.

2. Theory

2.1.1. Optimized wavelength-weighted least-squares support vector machine (VWLS-SVM)

The least-squares support vector machine (LS-SVM), a relatively new algorithm from the machine learning community, has been described in detail by Suykens et al. [1,2]. It has attracted great attention and gained extensive application in pattern recognition and regression problems for its remarkable generalization performance. Typically, one solves a convex quadratic programming (QP) problem in dual space in order to determine the SVM model [3,4]. But in these LS-SVM formulations one works with equality instead of inequality constraints and a sum squared error (SSE) cost function as it is frequently used. This reformulation greatly makes the problem simpler in such a way that the solution is characterized by a linear system.

Consider an $n \times p$ matrix $\boldsymbol{X}$ including p predictor variables for n samples and an $n \times 1$ vector $\boldsymbol{y}$ including the corresponding dependent variable for the n samples. For simplicity and without loss of generality, both $\boldsymbol{X}$ and $\boldsymbol{y}$ is column centered. Not like in an ordinary LS-SVM model, where variables in $\boldsymbol{X}$ are considered as making the same contribution to the LS-SVM model, in VWLS-SVM, $\boldsymbol{X}$ is right multiplied by a diagonal matrix diag($\boldsymbol{w}$), which makes:

$$\boldsymbol{X_w} = \boldsymbol{X}\,\mathrm{diag}(\boldsymbol{w}) \tag{1}$$

where $\boldsymbol{w}$ is a $p \times 1$ variable weighting vector with all the elements being non-negative values and diag($\boldsymbol{w}$) is a $p \times p$ matrix whose diagonals are the elements of $\boldsymbol{w}$. A LS-SVM model is built between $\boldsymbol{X}_w$ and $\boldsymbol{y}$.

$$\boldsymbol{y} = \boldsymbol{X}_{\boldsymbol{w}}^{T}\boldsymbol{t_w} + \boldsymbol{b_w} \tag{2}$$

For prediction, the dependent variable $\mathbf{y}_\mathrm{u}$ of unknown samples with measurement matrix $\boldsymbol{X}_\mathrm{u}$ is predicted as:

$$y_\mathrm{u} = \boldsymbol{X}_\mathrm{u}^{T}\,\mathrm{diag}(\boldsymbol{w})\boldsymbol{t_w} + \boldsymbol{b_w} \tag{3}$$

It can be seen from Eq. (1) that when $\boldsymbol{w}$ is a vector with all the elements being 1, the above model is the same as a LS-SVM model built with the whole wavelength range. If the elements of $\boldsymbol{w}$ just consist of 0 and 1, a LS-SVM model with variable selection is obtained, where the variables in $\boldsymbol{X}$ corresponding to 1 s in $\boldsymbol{w}$ are selected variables and those corresponding to 0 s are deleted.

From the above analysis, a LS-SVM model with full wavelength range or variable selection are just special cases of variable weighting, so VWLS-SVM is expected to be more flexible and rational. The problem is how to determine the variable weighting vector $\boldsymbol{w}$. The PSO algorithm is simultaneously implemented for the sample weights and hyper-parameters training.

Since the present method is oriented to improve the predictive ability of LS-SVM, the weights and hyper-parameters are automatically configured that the training of calibration set and prediction of an independent validation set are optimized. The following objective function is minimized:

$$Re = \sqrt{\frac{(\mathrm{RSSC} + \mathrm{RSSV})}{(n + n_\mathrm{v})}} \tag{4}$$

where RSSC is the sum of squared residual of the original calibration set and RSSV the sum of squared residual of the independent validation set, n and n_v is the size of calibration set and validation set, respectively.

The steps of VWLS-SVM can be described as follows:

Step 1. With the 100 initial feasible solutions of variable weighting vector w and two hyper-parameters (kernel widths and the relative weight of the error term) in LS-SVM. A LS-SVM model between predictor matrix $\boldsymbol{X}_w = \boldsymbol{X}\,\mathrm{diag}(\boldsymbol{w})$ and dependent variable $\boldsymbol{y}$ is built.
Step 2. For different numbers of generations, PSO is used to search for w and two hyper-parameters that minimize Re defined in Eq. (4).
Step 3. With the best optimized variable weighting vector w and hyper-parameters determined in Step 2, an LS-SVM model is built and then applied to unknown samples

3. Data sets

The following two real data sets are investigated:

3.1. Meat data [35]

The experimental data set consists of NIR spectra of 240 samples of ground pork meat with corresponding wet-chemistry results on fat, water, and protein contents. These spectra are recorded on a Tecator Infratec spectrometer that measures the absorbance at 100 wavelengths with the region 850–1050 nm at intervals of 2 nm by the near-infrared transmission (NIT) principle. A Soxhlet method was used as the laboratory reference for the fat determination. Soxhlet values ranged from 2% to 59% fat content of pork meat.

3.2. Diesel fuels data [36]

The diesel database can be downloaded from http://software.eigenvector.com/Data/index.html. The research was conducted to develop instrumentation for fuel quality assessment on battle fields. The database contains only summer fuels, and outliers were removed. It consists of scans of approximately 250 diesel fuel samples. All spectra range from 750 to 1550 nm, has been discretized into 401 wavelength values. The total 256 samples include 20 high leverage samples. The spectra have been preprocessed by the original author and the wavelengths are not released.

4. Results and discussion

For the meat data, standard normal variate (SNV) is used to preprocess the spectra. The total 240 samples are split into a calibration set with 120 samples, a validation set with 60 samples and a prediction set with 60 samples by DUPLEX method [37]. The number of variable selected and root mean square error of prediction (RMSEP) of the prediction set by ordinary PLS with total wavelength, uninformative variable elimination-PLS (UVE-PLS), LS-SVM models with total wavelength, LS-SVM models with selected wavelength by UVE-PLS and VWLS-SVM models are listed in the Table 1. The PLS model is built on 180 samples containing the calibration

Table 1
A comparison of the results obtained by PLS, UVE-PLS, LS-SVM and VWLS-SVM.

Models	Number of variables	RMSEP
Meat data		
PLS	100 (total wavelength)	5.10
UVE-PLS	43	2.58
LS-SVM	100 (total wavelength)	2.78
LS-SVM[a]	43	2.58
VWLS-SVM	100 (total wavelength)	1.31
Diesel fuels data		
PLS	401(total wavelength)	0.86
UVE-PLS	227	0.79
LS-SVM	401(total wavelength)	0.83
LS-SVM[a]	227	0.81
VWLS-SVM	401(total wavelength)	0.78

[a] LS-SAM model is performed with the variables selected by UVE-PLS model.

set and the validation set. The number of latent variables is determined to be 10 by the Monte Carlo cross-validation (MCCV) [38]. As to LS-SVM, 60 samples picked are used as the monitoring set for training hyper-meters in LS-SVM model by PSO algorithms to mitigate the probability of overfitting the training data. It is obvious that LS-SVM obtains much better prediction ability than PLS model with total wavelength. It may result from the presence of the complex or unknown nonlinearity in the data set. The uninformative variable elimination-PLS (UVE-PLS) [21] as a popular wavelength selection method is carried out on the calibration set and it gets better results than PLS and LS-SVM models with total wavelength. When LS-SVM model is performed with the variables selected by UVE-PLS, it gets even better results than ordinary LS-SVM model with total wavelength and UVE-PLS models. For VWLS-SVM, an 800-cycle PSO is carried out to search for the variable weights and hyper-parameters minimizing the objective function defined in Eq. (4) and the corresponding wavelength weights are shown in Fig. 1. It can be seen that the VWLS-SVM model obtains the best precise prediction when wavelength weighting is introduced. It can be seen from Fig. 1 the wavelength ranges are differently weighted. A few of the wavelengths are highly weighted and much more wavelengths have smaller weights. Compared with traditional variable selection methods, much more wavelengths are included into the calibration model and thus useful information carried by the spectra would be retained for prediction.

For diesel fuels data, the total 256 samples are split into a calibration set with 128 samples, a validation set with 64 samples and a prediction set with 64 samples by DUPLEX method [37]. The number of PLS latent variables is determined to be 12 by MCCV. As to LS-SVM, 64 samples picked are used as the monitoring set for training the LS-SVM model. For VWLS-SVM, a 350-cycle PSO is carried out to search for the variable weights and hyper-parameters minimizing the objective function defined in Eq. (4). The corresponding variable weights are shown in Fig. 2. It can be seen that most of the variables are high weighted, and useful information carried by these variables would be retained for prediction. The results of all the models are also listed in Table 1. It can be seen VWLS-SVM can slightly improve the performance of other models in selecting wavelength weighting.

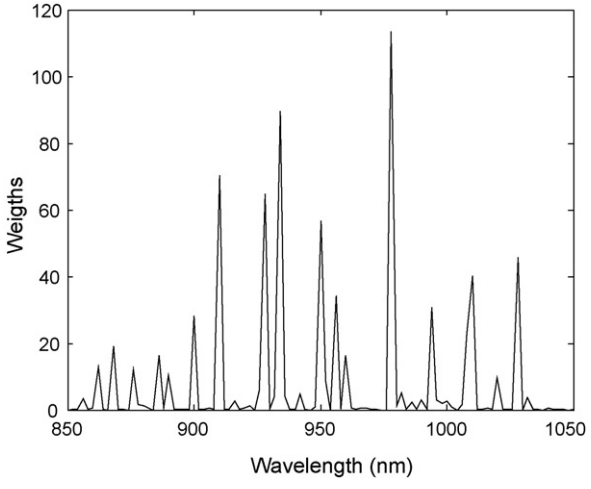


Fig. 1. Wavelength variable weights after an 800-cycle PSO search for the meat data by VWLS-SVM.

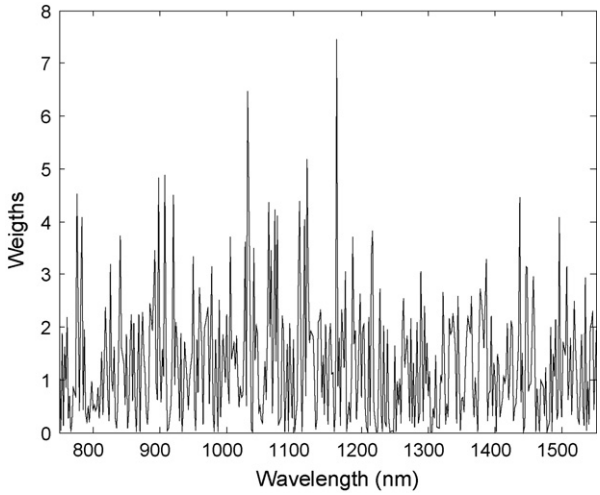


Fig. 2. Wavelength variable weights after a 350-cycle PSO search for the diesel fuels data by VWLS-SVM.

5. Conclusions

In this paper, we have extended the concept of wavelength variable selection and introduced the variable weighting to LS-SVM for multivariate calibration. A global optimization algorithm, particle swarm optimization is used to simultaneously search for the variable weights and the hyper-parameters involved optimizing the training of calibration set and the prediction of an independent validation set. From the results of real data sets, much more variables are included into VWLS-SVM than traditional variables selection methods and thus prevent the possible spoiling of multi-channel advantage. VWLS-SVM can provide better prediction ability comparing with PLS, LS-SVM with total wavelength and UVE-PLS models. The overall conclusion is that VWLS-SVM is a useful method for multivariate calibration, especially when the spectra data contains wavelengths with undesirable qualities like serous noise, nonlinearity and poor information.

Acknowledgements

The authors wish to thank the National Nature Science Foundation of China (Grant Nos. 20775025 and 20435010) and the National 973 Project (2007CB216404) for financial support.

References

[1] J.A.K. Suykens, J. Vandewalle, Neural Process. Lett. 9 (1999) 293–300.
[2] J.A.K. Suykens, T. Van Gestel, J. De Brabanter, B. De Moor, J. Vandewalle, Least-Squares Support Vector Machines, World Scientific, Singapore, 2002.
[3] V.N. Vapnik, The Nature of Statistical Learning Theory, Springer, New York, 1995.
[4] V.N. Vapnik, Statistical Learning Theory, John Wiley &Sons, New York, 1998.
[5] F. Chauchard, R. Cogdill, S. Roussel, J.M. Roger, V. Bellon-Maurel, Chemom. Intell. Lab. Syst. 71 (2004) 141–150.

[6] A. Borin, M.F. Ferrão, C. Mello, D.A. Maretto, R.J. Poppi, Anal. Chim. Acta 579 (2006) 25–32.
[7] M.F. Ferrão, S.C. Godoy, A.E. Gerbase, C. Mello, J.C. Furtado, C.L. Petzhold, R.J. Poppi, Anal. Chim. Acta 595 (2007) 114–119.
[8] A. Niazi, J. Ghasemi, M. Zendehdel, Talanta 74 (2007) 247–254.
[9] F. Liu, F. Zhang, Z.L. Jin, Y. He, H. Fang, Q.F. Ye, W.J. Zhou, Anal. Chim. Acta 629 (2008) 56–65.
[10] J.H. Jiang, R.J. Berry, H.W. Siesler, Y. Ozaki, Anal. Chem. 74 (2002) 3555–3565.
[11] H. Swierenga, E. Wülfert, O.E. de Noord, A.P. de Weijer, A.K. Smilde, L.M.C. Buydens, Anal. Chim. Acta 411 (2000) 121–135.
[12] H.C. Goicoechea, A.C. Olivieri, J. Chem. Inf. Comput. Sci. 42 (2002) 1146–1153.
[13] M. Khanmohammadi, M.A. Karimi, K. Ghasemi, M. Jabbari, A. Bagheri Garmarudi, Talanta 72 (2007) 620–625.
[14] A. Höskuldsson, Chemom. Intell. Lab. Syst. 55 (2001) 23–38.
[15] L. Xu, W.J. Zhang, Anal. Chim. Acta 446 (2001) 477–483.
[16] K.H. Esbensen, Multivariate Data Analysis in Practice, 5th ed., CAMO Process As, Oslo, 2002.
[17] V.G. Franco, J.C. Perín, V.E. Mantovani, H.C. Goicoechea, Talanta 68 (2006) 1005–1012.
[18] B. Hemmateenejad, R. Ghavami, R. Miri, M. Shamsipur, Talanta 68 (2006) 1222–1229.
[19] L. Xu, J.H. Jiang, Y.P. Zhou, H.L. Wu, G.L. Shen, R.Q. Yu, Chemom. Intell. Lab. Syst. 87 (2007) 226–230.
[20] H. Xu, Z.C. Liu, W.S. Cai, X.G. Shao, Chemom. Intell. Lab. Syst. 97 (2009) 189–193.
[21] V. Centner, D.L. Massart, O.E. de Noord, S. de Jong, B.M. Vandeginste, C. Sterna, Anal. Chem. 68 (1996) 3851–3858.
[22] J. Koshoubu, T. Iwata, S. Minami, Anal. Sci. 17 (2001) 319–322.
[23] W.S. Cai, Y.K. Li, X.G. Shao, Chemom. Intell. Lab. Syst. 90 (2008) 188–194.
[24] Q.J. Han, H.L. Wu, C.B. Cai, L. Xu, R.Q. Yu, Anal. Chim. Acta 612 (2008) 121–125.
[25] R.W. Gerlach, B.R. Kowalsky, H.O.A. Wold, Anal. Chim. Acta 112 (1979) 417–421.
[26] H. Martens, T. Naes, Multivariate Calibration, Wiley, Chichester, UK, 1989.
[27] S.J. An, W.Q. Liu, S. Venkatesh, Pattern Recognit. 40 (2007) 2154–2162.
[28] M. Adankon, M. Cheriet, Pattern Recognit. 42 (2009) 3264–3270.
[29] J. Caballero, L. Fernández, M. Garriga, J.I. Abreu, S. Collina, M. Fernández, J. Mol. Graphics Modell. 26 (2007) 166–178.
[30] D.R. Eads, D. Hill, S. Davis, S.J. Perkins, J. Ma, R.B. Porter, J.P. Theiler, in: B. Bosacchi, D.B. Fogel, J.C. Bezdek (Eds.), Applications and Science of Neural Networks, Fuzzy Systems, and Evolutionary Computation V. Proceedings of the SPIE 4787, 2002, pp. 74–85.
[31] F. Friedrichs, C. Igel, Neurocomputing 64 (2005) 107–117.
[32] H. Frohlich, O. Chapelle, B. Scholkopf, Proceedings of the 15th IEEE International Conference on Tools with AI (ICTAI 2003), IEEE Computer Society Institute of Electrical and Electronics Engineers Inc., USA, 2003, pp. 142–148.
[33] J. Kennedy, R. Eberhart, Proceedings of the IEEE International Conference on Neural Networks, Perth, Australia, IEEE Service Center, Piscataway, NJ, 4, 1995, pp. 1942–1948.
[34] Q. Shen, J.H. Jiang, C.X. Jiao, S.Y. Huan, G.L. Shen, R.Q. Yu, J. Chem. Inf. Comput. Sci. 44 (2004) 2027–2031.
[35] C. Borggaard, H.H. Thodberg, Anal. Chem. 64 (1992) 545–551.
[36] http://software.eigenvector.com/Data/index.html.
[37] R.D. Snee, Technometrics 19 (1977) 415–428.
[38] Q.S. Xu, Y.Z. Liang, Chemom. Intell. Lab. Syst. 56 (2001) 1–11.

Talanta 80 (2010) 1702–1712

Contents lists available at ScienceDirect

Talanta

journal homepage: www.elsevier.com/locate/talanta

Simultaneous determination of angiotensins II and 1-7 by capillary zone electrophoresis in plasma and urine from hypertensive rats

Fermín Alejandro Tenorio-López[a,1], Gabriela Zarco-Olvera[a], Alicia Sánchez-Mendoza[a], Martín Rosas-Peralta[b], Gustavo Pastelín-Hernández[a], Leonardo del Valle-Mondragón[a,*]

[a] Departamento de Farmacología, Instituto Nacional de Cardiología "Ignacio Chávez", Juan Badiano No. 1, Col. Sección XVI, 14080 Tlalpan, México D.F., Mexico
[b] Departamento de Cardiología Adultos III, Instituto Nacional de Cardiología "Ignacio Chávez", Juan Badiano No. 1, Col. Sección XVI, 14080 Tlalpan, México D.F., Mexico

ARTICLE INFO

Article history:
Received 30 June 2009
Received in revised form 5 October 2009
Accepted 7 October 2009
Available online 13 October 2009

Keywords:
Angiotensin II
Angiotensin-(1-7)
Capillary zone electrophoresis
Hypertension

ABSTRACT

We describe the procedure developed for the simultaneous detection and quantification of angiotensin II and angiotensin-(1-7), by capillary zone electrophoresis with UV detection by photodiode-array, at a wavelength of 200 nm, in the plasma and urine from hypertensive rats. Optimal separation was achieved with a 100 mM boric acid + 3 mM tartaric acid + 10 fM gold (III) chloride electrolyte solution at pH 9.80. The applied voltage was 30 kV and the capillary temperature was kept constant at 20 °C. The method was over the concentration range of 0.01–500 pmol/mL. All determination coefficients were higher or equal to 0.9985. Limits of detection and quantification for angiotensin II were 0.0110 pmol/mL (S/N = 3) and 0.0195 pmol/mL (S/N = 5), respectively. While for angiotensin-(1-7), the limits were 0.0112 pmol/mL (S/N = 3) and 0.0193 pmol/mL (S/N = 5), respectively. The present method offers a time-saving way to simultaneous determination of angiotensin II and angiotensin-(1-7), since it can be completed in 10 min, compared to other methodologies reported in the literature for capillary electrophoresis and liquid chromatography, which require more than 1 h for analysis of complex matrices, such as plasma and urine. The procedure is illustrated by experiments that quantify simultaneously angiotensin II and angiotensin-(1-7) in plasma and urine from hypertensive and normotensive rats, with and without antihypertensive treatment. The levels of angiotensin II and angiotensin-(1-7) detected in the experimental model, resulted in a recovery of 99.00–106.01% and a reproducibility of less than 10%. The proposed analytical method is a use full tool for the simultaneous detection of angiotensin II and angiotensin-(1-7) implicated in vascular remodeling in pathologies such as hypertension.

© 2009 Elsevier B.V. All rights reserved.

1. Introduction

Essential arterial hypertension is the most frequent chronic disease in the world and one of the main cardiovascular risk factors [1–4]. Over the past 60 years, studies have been carried out to elucidate its genesis and they show that this disease results from a syndrome of metabolic and structural abnormalities from genetic and acquired nature, in which the direct participation of the renin–angiotensin system has been evidenced. This system has been and still is one of the most studied mechanisms in relation to the physiopathology of arterial hypertension [1,3]. Angiotensin II, the main effector molecule of the renin–angiotensin system, is a potent vasoconstrictor that exerts diverse effects on multiple target organs that cause the increase in arterial blood pressure, this can be achieved by either an increase in vascular resistance or an increase in the extracellular fluid volume. Angiotensin II, exerts its actions by binding to AT1 and AT2 receptors G protein-coupled located in the heart, kidneys, arteries, etc. AT1 receptor mediates the vasoconstriction and cardiac and arterial hypertrophy, whereas AT2 receptor exerts an opposite effect [5–8]. For this reason, the inhibition of ACE with drugs such as captopril, enalapril, lisinopril and ramipril, among others, has been relevant for the antihypertensive treatment [1,3,6,8]. The angiotensin-(1-7) has different cellular functions from those established for angiotensin II. Angiotensin-(1-7) is neither dipsogenic nor aldosterone secretagogue, but it favors vasopressin, prostaglandins, and nitric oxide secretion [9–11].

The most commonly used methods to determine independent angiotensin II and angiotensin-(1-7) in biological fluids are radioimmunoassay (RIA), high performance liquid chromatography (HPLC), and capillary electrophoresis (CE) [12–14]. RIA requires the use and elimination of radioactive material and is relatively long and tedious, because peptides must be previously separated through liquid chromatography, then concentrated and analyzed

* Corresponding author. Tel.: +52 55 5573 2911x1317.
E-mail addresses: leonardodvm65@hotmail.com, ldvm.pharm.cardiol.mx@gmail.com (L. del Valle-Mondragón).

[1] In memory of a friend, colleague and excellent researcher ... Forever in our heart.

0039-9140/$ – see front matter © 2009 Elsevier B.V. All rights reserved.
doi:10.1016/j.talanta.2009.10.010

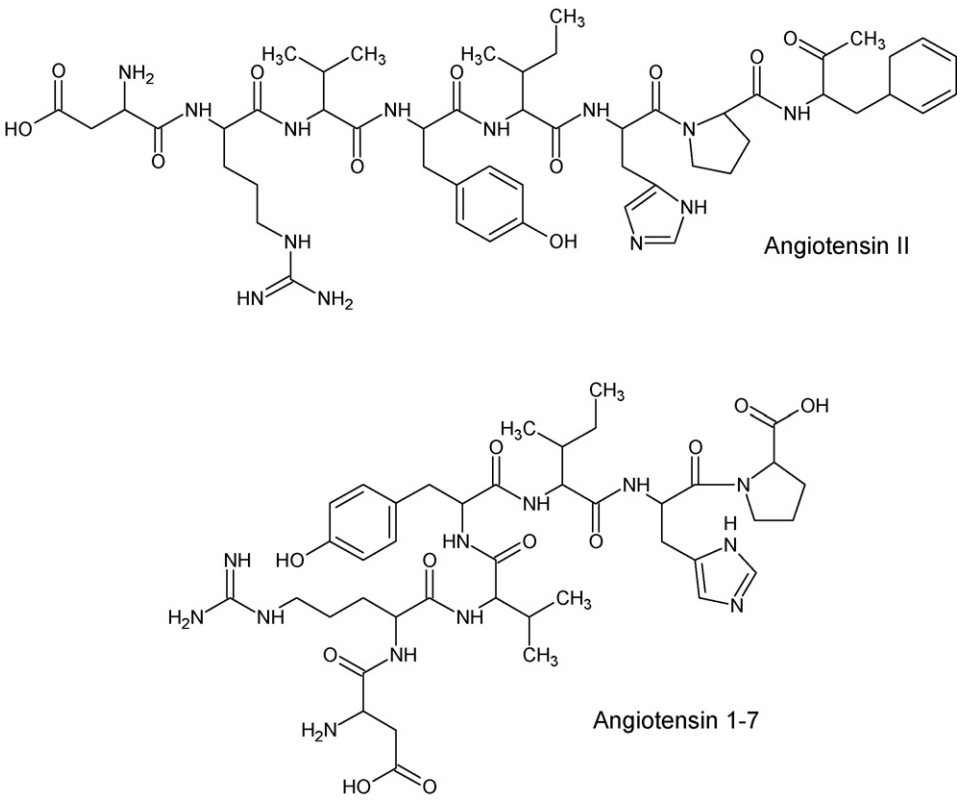


Fig. 1. Molecular structure of angiotensin II and angiotensin-(1-7).

by RIA. For this reason, alternative approaches have been oriented toward HPLC and CE studies for the detection of diverse peptides derived from angiotensinogen in blood [15–17].

Although angiotensin II and angiotensin-(1-7) (Fig. 1) according to the nature of the dispersion medium, are molecules that can be detected in the ultraviolet region (UV) at a 190–230 nm range, the detection is not very sensitive. Therefore, the techniques have included the use of fluorescence and electrochemical detectors coupled to HPLC and CE [11–13]. Later on, mass spectrometry detection systems were incorporated, which lowered the level of quantification in industrial and pharmaceutical samples, complicating and limiting severely the analysis of biological fluid studies, because of the complexity of a biological matrix. It has been seen that when highly pure reagents are used and extreme care is given to the management and treatment of the samples, detection through photodiode-array (PDA) in the UV region offers a versatile and low cost alternative for the quantification of a large range of analytes of biological interest, susceptible to be detected in that spectral region in matrices as complex as the blood [12].

There are additional complications in measure real angiotensin II and angiotensin-(1-7) concentrations in a biological sample. Angiotensin II and angiotensin-(1-7) are susceptible to degradation by proteases; therefore, the use of protease inhibitors becomes mandatory, but it sometimes is self-defeating in CE studies because they interfere with the resolution of peaks, complicating the separation and quantification of the peptides [18]. However, the use of protease inhibitors can be omitted if the physicochemical properties that inhibit the proteases are known. Likewise, a pH lower than 3.5 or higher than 9.0 inactivates them; the handling of biological samples at a temperature below 25 °C or above 45 °C, as well as the addition of methanol or acetonitrile, also inhibit their activity [19].

Regarding the quantitative analysis of angiotensinogen derivates with HPLC, a large variety of techniques have been published. The most employed includes the use of monolithic columns coupled to fast protein liquid chromatography (FPLC) [20], as well as the use of reverse phase C18 columns [21] and HPLC with hydroorganic phase systems (water/acetonitrile 1:2 with a 0.1% trifluoroacetic acid gradient) [22]. Another HPLC study, performed by Matsui et al. [23], used RP-C4 columns with fluorometric detection for quantitative analysis of angiotensin II and angiotensin-(1-7) contained in human plasma samples. Sakamoto et al. [24] used cationic exchange liquid chromatography for the analysis of angiotensinogen derivates, using a TSK-sulfopropyl column, which separates nitrated products through a linear ammonium acetate gradient (pH 9.0) at 210 nm in 50 min. Another analytical approach includes the use of western blot and ELISA methods, which are time-consuming and inconvenient procedures for the treatment of multiple samples, additionally the results are not accurate [25,26]. Nowadays, CE techniques are employed to separate molecules with a high resolution and the method has been extended to a large diversity of chemical compounds, as it contemplates the separation based on the number of theoretical plates, which improves considerably its efficiency with respect to HPLC. Other advantages of CE are its low consumption of samples and reagents, use of aqueous disolutions, compatibility with auto-samplers, easy cleaning and conditioning of capillaries, as well as the different modes of electrophoretic separation that can be coupled to diverse detection methods in the same equipment. These latter methods include UV detection, laser-induced fluorescence (LIF) excitation, electrochemical detection and mass spectrometry [18]. Several studies designed for the separation and quantification of angiotensinogen derivates through CE have been published, standing out the use of monolithic capillaries [27], molecular reconditioning through derivatization with macrocyclic polyamine [28], use of capillary isotachophoresis [29], monolithic microextraction using metacrylate-derived polymers [30], immunodetection [31], and by capillary zone electrophoresis

(CZE). This late study involves pre-treatment methodologies that increase the risk of losing the analyte of interest, as well as complex detection systems that focus on the independent quantitative determination of angiotensin II, or angiotensin-(1-7), or any other angiotensinogen derivate in biological samples, mainly urine. Some methodologies have been reported for blood samples in studies related to hypertension [32], endothelial function [33], hypothalamic effect on aortic coarctation [34], and preeclampsia [35], among others. Hence, it is convenient to establish a simple, fast, and robust procedure for simultaneous analysis of angiotensin II and angiotensin-(1-7) in both plasma and urine.

In this study, we developed a methodology through CZE–PDA, with UV detection, for the simultaneous quantification of angiotensin II and angiotensin-(1-7) in biological samples. The parameters assessed for optimization of the separation of the peptides under study were: pH, concentration of the background electrolyte (BGE), applied voltage, injection time and temperature, as well as conditions for PDA detection. For the applicability and optimization of the developed method, the levels of angiotensin II and angiotensin-(1-7) were assessed in the plasma and urine of normotensive and hypertensive rats.

2. Experimental

2.1. Chemicals

Acetic acid, boric acid, chlorhidric acid, ethylenediaminetetraacetic acid, tartaric acid, trichloroacetic acid, angiotensin II, angiotensin-(1-7), cyclosporine A, gold (III) chloride, enalapril, dibasic sodium phosphate, monobasic sodium phosphate, sodium hydroxide and polyvinylpirrolidone were obtained from Sigma Chemical Co. (St. Louis, MO, USA). Methanol was from Mallinckrodt Baker (Xalostoc, Estado de México, México). Angiotensin II (100 μM) and angiotensin-(1-7) (100 μM) stock solutions were prepared in 100 mM phosphate buffer at pH 10, and stored at −70 °C until use. The working standard solutions were prepared daily by dilution of the stock solution with 100 mM phosphate buffer at pH 10. Deionized water (≥18.2 MΩ cm) used throughout the study was obtained with a Simplicity System (Millipore SAS, Molsheim, Alsace, France).

2.2. Apparatus

All experiments were performed with a Beckman Coulter (Fullerton, CA, USA) P/ACE^{TM} MDQ Capillary Electrophoresis System equipped with PDA and controlled by means of the P/ACE MDQ Capillary Electrophoresis System software, version 7.0 (Beckman Coulter Inc., Fullerton, CA, USA). The fused-silica capillary of 57 cm (50 cm to the detector) × 75 μm i.d., manufactured by Polymicro Technologies (Phoenix, AZ, USA) was maintained at 20 °C in a cartridge with a 100 μm × 800 μm detection window. The use of a PDA allowed us to confirm the identity of the peaks, not only by their migration time, but also by the overlay of the UV–vis spectra of the samples with an angiotensin II and angiotensin-(1-7) standards solution. PDA was set at an acquisition range from 190 to 600 nm (bandwidth of 6 nm) at a spectral acquisition rate of 1.25 scans s^{-1} (peak width 0.2 min). A Corning pH/ion analyzer 350 (Corning Inc., Corning, NY, USA) with Hanna HI 1230B combined pH/ORP electrodes (Hanna Instruments, Woonsocket, RI, USA), calibrated with Sigma (St. Louis, MO, USA) reference standard buffers (pH 4.00 ± 0.01, 7.00 ± 0.01, and 10.00 ± 0.01, respectively), was employed for the pH measurement. Mean blood pressure was recorded using a pressure monitor for veterinary use (SurgiVet V60046 NIBP, Smiths Medical PM, Inc., Veterinary, Waukesha, WI, USA), equipped with a pneumatic bracelet (Vetronics VT-1201, VASi Vetronics, Bioanalytical Systems, Inc., West Lafayette, IN, USA).

2.3. Capillary conditioning and electrophoretic separation conditions

To activate a new capillary it was rinsed with 1 M NaOH for 60 min, deionized water for 60 min and finally with the BGE for 60 min, to ensure a clean capillary surface [13]. Daily, before the first sample injection, the capillary was flushed with 1 M NaOH for 2 min, followed by deionized water for 2 min and finally with the BGE for 4 min. Samples were introduced from the anodic end of the capillary by hydrodynamic injection for 10 s at 0.5 psi. PDA was set at an acquisition range from 190 to 600 nm (bandwidth of 6 nm) at a spectral acquisition rate of 1.25 scans s^{-1} (peak width 0.2 min). As BGEs, several solutions were prepared as follows: a 100 mM phosphates buffer at pH 2.05 was prepared by mixing equal volumes of a 55.73 mM H_3PO_4 solution and a 44.27 mM $NaH_2PO_4{\cdot}H_2O$ solution, and then the volume of the mixture was adjusted to 100 mL with deionized water; a 100 mM borates buffer at pH 9.00 was prepared by mixing equal volumes of a 68.57 mM H_3BO_3 solution and a 31.43 mM $Na_2B_4O_7{\cdot}10H_2O$ solution. Then, the volume of the mixture was adjusted to 100 mL with deionized water; a mixed buffer of boric acid, tartaric acid and gold chloride (III) at pH 9.80 was prepared by mixing equal volumes of a 100 mM H_3BO_3 solution, 3 mM $HO_2CCH(OH)CH(OH)CO_2H$ solution and 10 fM $AuCl_3$ solution. Then the volume of the mixture was adjusted to 100 mL with deionized water. Before use, BGEs based on borates were adjusted accurately to the desired pH value with either 0.1 M HCl or 0.1 M NaOH, whereas BGE based on phosphates was adjusted to the desired pH value with the addition of 0.1 M H_3PO_4. All BGEs were degassed by sonication (T490DH instrument, Elma, Singen, Germany), and filtered through 0.22 μm mixed cellulose ester filters (Millipore, Billerica, MA, USA). Unless otherwise stated, no more than 100 μL of 0.1 M HCl, 0.1 M NaOH or 0.1 M H_3PO_4 were required for pH adjustment. All operations were performed at 25 ± 0.5 °C. To avoid BGE and sample evaporation, BGE and sample reservoirs were capped. The migration times corresponding to the electroosmotic flow (EOF) were determined conventionally by injecting DMSO as the EOF marker. Between runs, a rinse cycle was performed by flushing the capillary with 1 M NaOH for 2 min followed by deionized water for 2 min, and then with BGE for 4 min. Data acquisition was achieved with a ThinkCentre (IBM Corporation, White Plains, NY, USA) workstation.

2.4. Animals

For this study, male Wistar rats (500–550 g) normotensive and hypertensive, maintained at the animal facility of the Instituto Nacional de Cardiología "Ignacio Chávez" were used. They were housed under standard conditions of temperature and light (12-h light:12-h dark cycle) and fed standard diet (Labdiet 5008, PMI International Nutrition, Richmond, IN, USA) and tap water *ad libitum*. All animal procedures were conducted in accordance with our Federal Regulations for Animal Experimentation and Care (Ministry of Agriculture, SAGARPA, NOM-062-ZOO-1999, Mexico), which follows the Guidelines for Care and Use of Laboratory Animals, and were approved by the Institutional Animal Care and Use Committee. During the experiments, all efforts were made to minimize animal suffering.

2.5. Induction of hypertension

Normotensive rats (200 ± 5 g), were made hypertensive through the chronic administration of cyclosporine A (10 mg/kg/day) dissolved in polyvinylpirrolidone (45% in H_2O, $M_r \approx 160{,}000$) and subcutaneously administered (400 μL/day) for 60 days (until animals reached 500–550 g body weight), according to Bartholomeusz et al. [36] and Phillips et al. [37]. Research started once animals were

confirmed to be hypertensive, by monitoring their mean arterial pressure.

2.6. Antihypertensive treatment

Enalapril, an angiotensin converting enzyme (ACE) inhibitor, was used for the antihypertensive treatment, at a 20 mg/kg/day dose, administered in the drinking water during 12 weeks. Animals were divided in four study groups: (1) normotensive control; (2) hypertensive control; (3) normotensive + enalapril; and (4) hypertensive + enalapril.

2.7. Measurement of mean arterial pressure

Mean arterial pressure of rats was monitored through a non-invasive technique by using a veterinary-use device, connected to a pneumatic bracelet at 0.5 cm from the base of the tail. Animals were placed in a smoked-acrylic box. Before starting arterial pressure measurements, animals were familiarized with the equipment and the personnel in charge of their handling to minimize stress. The adaptation period for each animal was of 5 min before starting the readings.

2.8. Preparation of biological samples

Blood samples, anticoagulated with ethylenediaminetetraacetic acid (1 mg/mL of blood), were centrifuged at 3500 rpm for 5 min at 10 °C (Sorvall RT 6000D, DuPont, Newtown, CT, USA). The obtained plasmas were preserved at −70 °C in cryogenic tubes (SARSTEDT AG & Co., Rommelsdorfer, Nümbrecht, Germany) until use. Samples were gradually thawed and maintained at a temperature of 10–15 °C. The plasma was deproteinized with methanol at a 10:1 proportion, homogenized and centrifuged at 16,000 × *g* for 15 min at 4 °C (Sorvall RC-28S, rotor SS34, DuPont, Newtown, CT, USA). Pellet was discarded and supernatant was deproteinized by the addition of 20% trichloroacetic acid, homogenized and centrifuged at 16,000 × *g* for 15 min at 4 °C. Supernatant was filtered through 0.22 μm nitrocellulose membrane filters (Millipore, Billerica, MA, USA), diluted 1:10 with 0.1 M NaOH, the sample (2 mL) was passed through a Sep-Pak Classic C-18 cartridge (Waters Corporation, Milford, MA, USA). A volume of 100 μL was employed for the CZE–PDA analysis. Urine preserved with 4% acetic acid (120 μL of the acid/2 mL of urine) was centrifuged at 6000 × *g* for 10 min at 4 °C. Supernatant was filtered through 0.22 μm nitrocellulose membrane filters, diluted 1:10 with 0.1 M NaOH and passed (2 mL) through a Sep-Pak Classic C-18 cartridge. 100 μL were employed for the CZE–PDA analysis.

2.9. Statistical analysis

Data analysis was carried out using SPSS 12.0.1 for Windows software (SPSS Inc., Chicago, IL, USA) with one-way analysis of variance (ANOVA) followed by a Student's *t*-test for independent samples. All results are expressed as the mean ± standard deviation of 10 independent determinations. A value of $p < 0.05$ was considered as statistically significant.

3. Results and discussion

3.1. Optimization of the test electrophoretic procedure

To optimize the CZE–PDA separation of angiotensins II and 1-7 from other compounds present in the analyzed matrix (plasma and urine), the effect of several variables was systematically explored: pH of the BGE (2.05, 9.00, and 9.80), BGE concentration (20–150 mM), applied voltage (5–30 kV), injection time (4–12 s), temperature (15–25 °C), as well as PDA conditions.

3.1.1. Effect of pH

It has been repeatedly demonstrated that the inner wall of the fused-silica capillary is a potential site for interactions among the separated analytes [18], because it controls the electroosmotic speed and provides active centers for adsorption of multiple charged molecules as are proteins [18]. This effect not only fosters loss but also decreases reproducibility and efficiency of the system. In CE, proteins can adsorb to the capillary wall causing alterations of the EOF and band broadening. The use of non-coated fused-silica capillaries the adsorption of proteins in the capillary wall can lead to a very poor migration time and low plate number. In order to minimize such effects, the separation of protein mixtures is run at extreme pH values, by which either the dissociation of the silanol groups of the capillary wall is minimized (at acid pH) or the dissociation of free amino groups of the proteinous solutes is decreased (at high pH values) [18]. On the other hand, pH regulation is an important purpose of the BGE in order to keep the migration velocity of the analytes and the velocity of EOF constant. In this way, a stable and reproducible migration behavior of the sample components can be obtained [18].

In CZE, the whole system is filled with a BGE, whose main purposes are to transport the electrical current if a voltage is applied over the system, to provide an electrical field strength and to facilitate the separation of the analytes. Optimization of the CE system started by selecting the BGE for the analysis of angiotensins II and 1-7 contents on biological samples (plasma and urine). For this purpose, the following buffer solutions were selected as BGEs: a 100 mM phosphate buffer at pH 2.05 (which may favor positive mobility since the net charge of the angiotensin II and angiotensin-(1-7) is positive at pH 2.05) [38], a 100 mM borate buffer at pH 9.00 (chosen because of its ability to generate an increase in the silanol groups charge, which intensifies the EOF, allowing thereby to mobilize rapidly molecules with high negative charge, as are proteins. It was also selected because borate can chelate the analytes to form more soluble complex anions) [38], and finally, a mixed buffer containing 100 mM boric acid + 3 mM tartaric acid + 10 fM gold (III) chloride at pH 9.80 (chosen due to the capacity of boric and tartaric acids to form stable chelates in a pH range from 9 to 10 with the analytes of interest) resulting in more soluble anionic complexes that can generate alterations in the charge arrangement of silanol groups that, in turn, alter EOFs intensity; the latter is minimized by the addition of small ionic molecules, such as Cu^{2+} and Au^{3+} to the BGE [39], or by inverting the EOF direction by the addition of cetyltrimethylammonium [40]. Under the experimental conditions, a 10 pmol/mL standard solution of angiotensin II and, separately, a 10 pmol/mL standard solution of angiotensin-(1-7), prepared in 100 mM phosphate buffer at a pH 10.0 showed an adequate behavior with all chosen BGEs. However, to explore whether each BGE showed an adequate performance when real samples were analyzed, it was decided to analyze plasma and urine samples of both normotensive and hypertensive animals, and were either unspiked or spiked with a angiotensin II (1, 150, and 400 pmol/mL) and angiotensin-(1-7) (1, 150, and 400 pmol/mL) standard solution prepared in 100 mM phosphate buffer at a pH 10.0. Then, performance parameters such as resolution, peak area and plate number were calculated for unspiked or spiked samples. Under this scheme, we found that at a low pH, resolution decreases (Fig. 2A). In order to achieve an adequate separation, the peak area and the plate number were calculated. It was observed that the best resolution (Fig. 2A), plate number (Fig. 2B) and peak area (Fig. 2C) were obtained when employing as BGE a 100 mM boric acid + 3 mM tartaric acid + 10 fM gold (III) chloride buffer at pH 9.8. Although a more convenient migration time (Fig. 2D) was

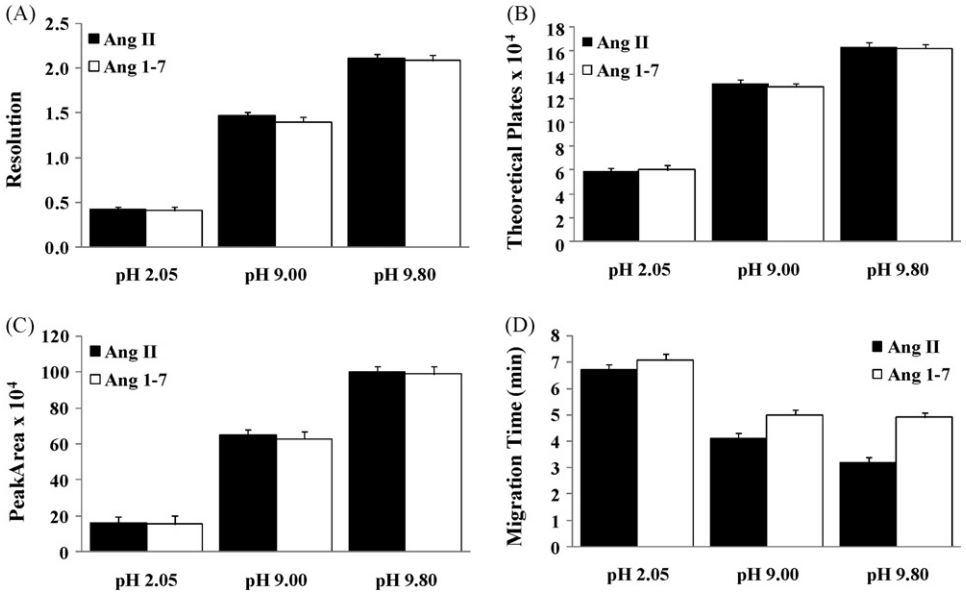


Fig. 2. Influence of the BGE pH on resolution (A), plate number (B), peak area (C) and migration time (D) of angiotensin II (Ang II) and angiotensin-(1-7) (Ang 1-7). Mean and standard deviation of 10 experiments are depicted.

obtained at pH 9.8, based on results obtained with respect to resolution, plate number and peak area, respectively, it was decided to employ a 100 mM boric acid + 3 mM tartaric acid + 10 fM gold (III) chloride buffer (pH 9.8) for further experiments. In addition, it was observed that with BGEs based on 100 mM phosphate buffer at pH 2.05 or on 100 mM borate buffer at pH 9.00, angiotensins (II and 1-7) and its coexisting interferences could not be separated well in these electrolyte solutions. Moreover, at high pH values, the analyte could be more susceptible to oxidation, this can be minimized by reducing the temperature of the disolution medium [39,41]. However, although it was initially hypothesized that angiotensins II and 1-7 may display a negative mobility because of their peptide nature, calculation of its effective electrophoretic mobility (μ, expressed in $m^2\,v^{-1}\,s^{-1}$), showed that angiotensin II μ was not opposite to the EOF ($\mu = 320.11\,m^2\,v^{-1}\,s^{-1}$). The same occurred for angiotensin-(1-7) ($\mu = 146.41\,m^2\,v^{-1}\,s^{-1}$). EOF effective electrophoretic mobility (μ_{EOF}) was calculated as $175.96\,m^2\,v^{-1}\,s^{-1}$ [42,43].

3.1.2. Effect of BGE concentration

The concentration of the BGE plays an important role in separation resolution in electrophoresis. If a constant voltage is applied over the capillary, the electric current will increase at higher BGE concentrations and this can cause extra peak broadening due to a strong increase in Joule heat. Provided that the generated Joule heat is not too high to affect peak efficiency, a higher buffer concentration can produce better peak shapes at high analytic concentrations and will lead to improved peak reproducibility [44]. Our previous experiments showed that the most adequate pH analyzed to study biological samples was 9.80 [44,45]. Therefore, the next step was to study the influence of BGE concentration, in the range 20–120 mM, on the separation of angiotensin II and angiotensin-(1-7). At BGE concentrations above 100 nM boric acid, keeping constant the tartaric acid concentration (3 mM) and that of gold (III) chloride (10 fM), unacceptably high currents were observed (data not shown). As the BGE concentration increased, both the resolution (Fig. 3A) and plate number (Fig. 3B) increased, achieving a resolution of 2.11 and a plate number of approximately 163,000 for angiotensin II. For angiotensin-(1-7) a resolution of 2.09 and a plate number of 162,100 was observed when 100 mM boric acid + 3 mM tartaric acid + 10 fM gold (III) chloride buffer at pH 9.8 was employed. The increase of the plate number observed for the positively charged angiotensin II and angiotensin-(1-7) is probably due to a reduced interaction with the capillary wall and not to a stacking, which is more apparent when the difference of conductivity between the BGE and the injection zone is very large.

3.1.3. Effect of the applied voltage

Ideal separation in CZE is usually obtained by using a voltage as high as possible in order to obtain the best separation in the shortest time with the best efficiency. However, high voltage lead to difficult heat dissipation during the electrophoretic separation due to Joule heat, which is known to affect the EOF, diffusion of analytes, and therefore, the efficiency and reproducibility of the separation.

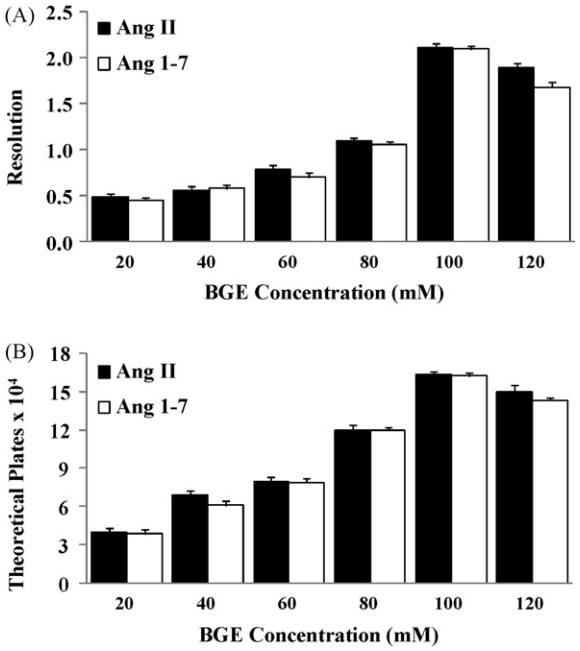


Fig. 3. Effect of BGE concentration on resolution (A) and plate number (B) of angiotensin II (Ang II) and angiotensin-(1-7) (Ang 1-7) of plasma and urine. Mean and standard deviation of 10 experiments are depicted.

For this reason, it is important to control this phenomenon [44]. To choose the most appropriate voltage in the electrophoretic separation, the effect of the voltage applied from 5 to 30 kV (steps of 5 kV) was investigated. A voltage of 30 kV of positive polarity, yielded the best compromise in terms of lower migration times and higher areas and resolutions.

3.1.4. Optimization of the injection time

In order to decrease the limit of detection, the injection time was varied between 4 and 12 s (steps of 2 s). As expected, when the injection time increased, the peak area of all compounds also increased, but for injection times lower than 10 s, a loss of resolution between peaks was observed. For this reason, a 10 s injection time was chosen as optimal value, while the separation efficiency remained largely unchanged. In all cases, the injection pressure was kept constant at 0.5 psi.

3.1.5. Effect of temperature

Changes in capillary temperature can cause variations in efficiency, viscosity, migration time, injection volumes and detector response. Temperature variations and corresponding changes in viscosity have been determined to be detrimental to obtain reproducible results [41,44]. The effect of temperature on the separation was investigated in the range 15–30 ± 0.5 °C (steps of 5 ± 0.5 °C). As temperature increases, the viscosity of the buffer decreases, so the resistance of the buffer decreases [41]. The decrease in the migration times of angiotensin II and angiotensin-(1-7) results in poor resolution, which might be caused by the direct effect of temperature on the rate of EOF, that might be increased, and buffer depletion occurs more rapidly. More directly, changes in viscosity alter the injected amount when using hydrodynamic injection. Therefore, the selected temperature was 20 ± 0.5 °C because it resulted in the best resolution.

3.1.6. Selection of optimal wavelength

Maximal absorption for angiotensin II and angiotensin-(1-7) lies in the range from 190 to 230 nm, at a pH of 2–12, this variation depends on the nature of the analytes dissociation medium [19]. We performed a spectral scan with a mixture of the standard solutions, in a 190–600 nm range, dissociated in 100 mM phosphate buffer at pH 10.0 [19]. The maximal absorption for the mixture of angiotensin II more angiotensin-(1-7) was 200 nm (Fig. 4A). A similar analysis of biological samples (plasma and urine) for the quantitative analysis of angiotensin II and angiotensin-(1-7), revealed that these molecules was best detected at 200 nm (Fig. 4B and C). Therefore, this wavelength was selected for the quantitative analysis of angiotensin II and angiotensin-(1-7) in plasma and urine.

The above results revealed that optimal separation conditions were: 100 mM boric acid + 3 mM tartaric acid + 10 fM of gold (III) chloride buffer, pH 9.80, applied voltage 30 kV, hydrodynamic injection mode at 0.5 psi for 10 s, capillary cartridge temperature maintained at 20 ± 0.5 °C and PDA operating at 200 nm (bandwidth 6 nm). Fig. 5 shows the electropherograms obtained for plasma and urine samples from normotensive and hypertensive animals, which were employed for the quantitative determination of angiotensin II and angiotensin-(1-7) release under the proposed experimental conditions.

3.2. Validation of the electrophoretic procedure

The protocol for the validation of the method encompassed stability, linearity, precision, specificity, limit of detection, limit of quantitation, recovery and robustness.

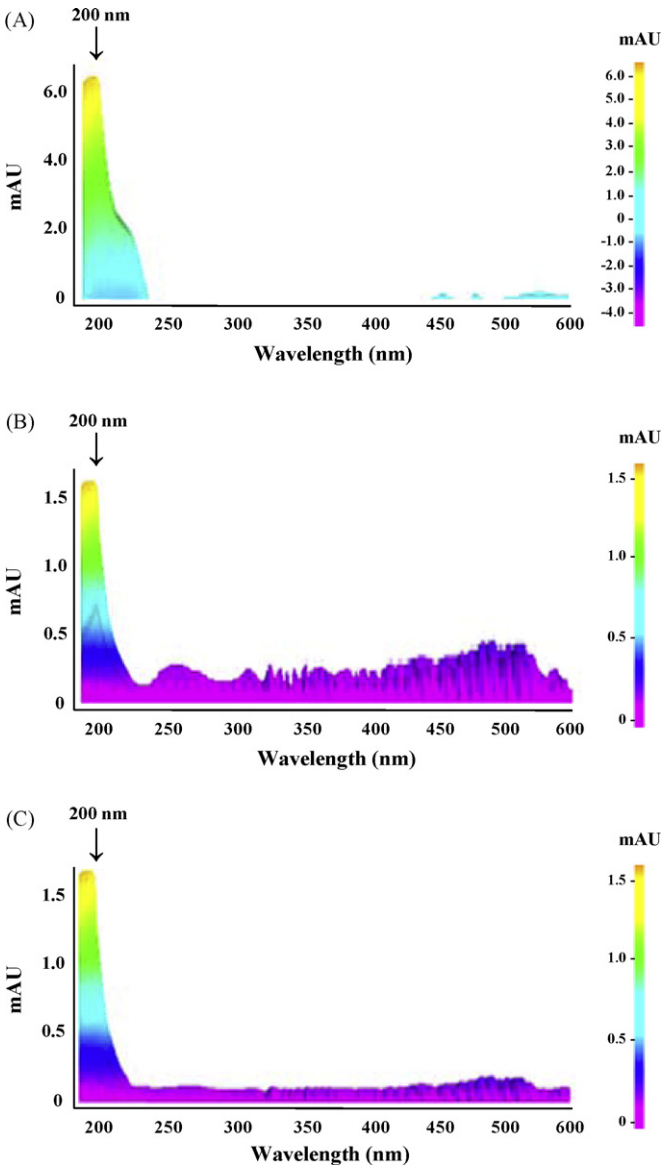


Fig. 4. UV–vis spectrum for a mixture of angiotensin II (10 pmol/mL) and angiotensin-(1-7) (10 pmol/mL) standards solution prepared in phosphate buffer (A). UV–vis spectrum for a plasma sample (B) and urine sample (C) from normotensive animals, were employed for the quantitative analysis of angiotensin II and angiotensin-(1-7).

3.2.1. Stability of the solutions

The stability of the standards and test solutions of angiotensin II and angiotensin-(1-7) was determined by comparing the response factors (concentration/average peak areas) of triplicate solutions stored at 4 °C, in darkness, with those of freshly prepared triplicate solutions. A concentration difference greater than 2% was found between the freshly prepared standard solutions and the solutions prepared 10 days before. For this reason, it is advisable to employ freshly prepared angiotensin II and angiotensin-(1-7) solutions (Table 1A).

The stability of unspiked and spiked biological samples (plasma and urine) was evaluated by comparing the relation peak areas obtained at different time intervals with those of freshly prepared biological samples. It was found that the biological samples were stable for at least 8 h (Table 1B). For this reason, we recommended that CZE–PDA analysis must be carried out within this period of time after the preparatory of such biological samples.

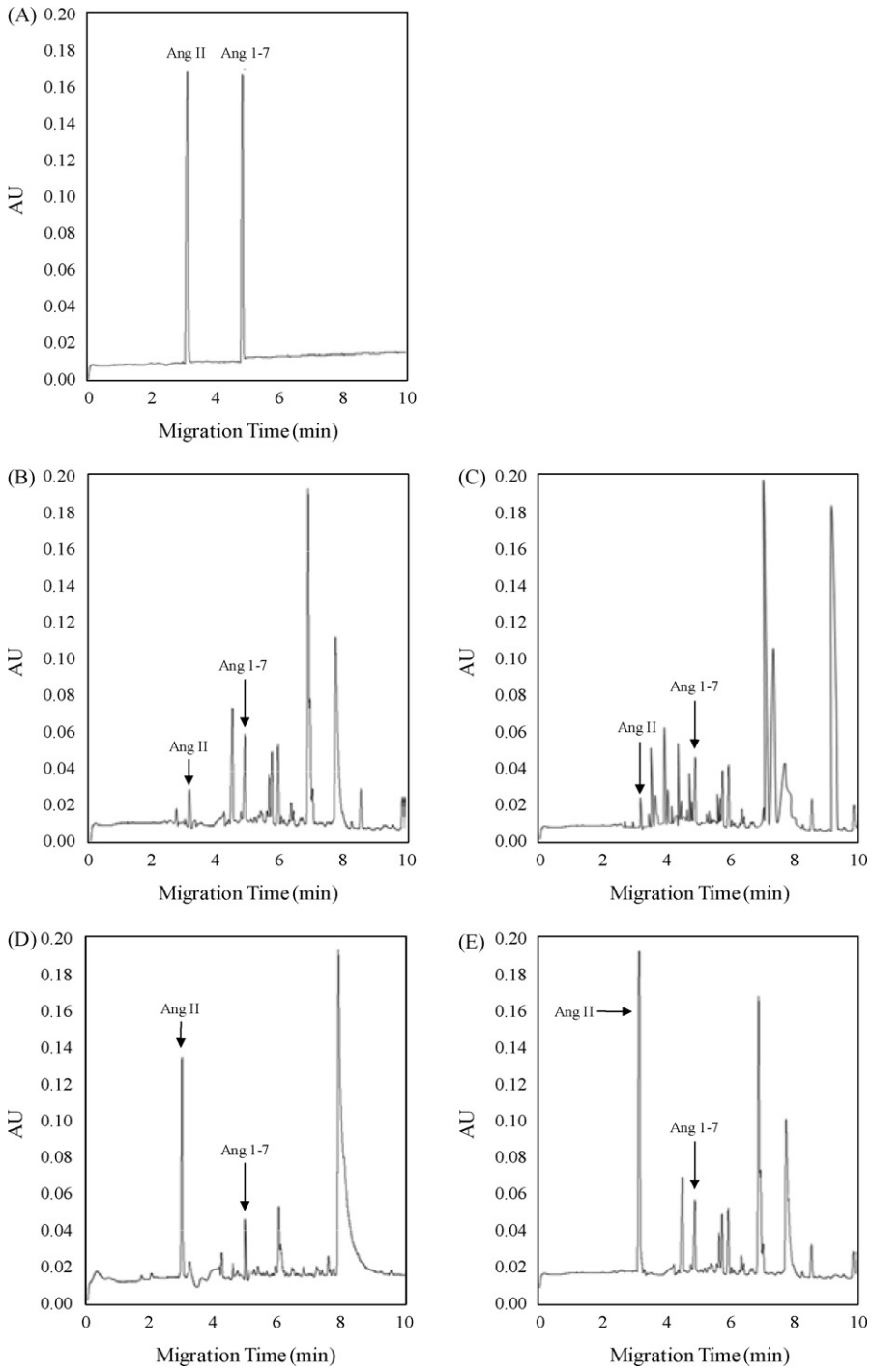


Fig. 5. Electropherogram obtained for a mixture of 10 pmol/mL angiotensin II (And II) and 10 pmol/mL angiotensin-(1-7) (Ang 1-7) standards solution prepared in phosphate buffer (A). Electropherograms obtained from a urine sample (B) and a plasma sample (C) of normotensive animals; of a urine sample (D) and a plasma sample (E) of hypertensive animals are also shown.

3.2.2. Linearity

Linearity is the ability to show that the results are directly proportional to the analytes concentrations in samples within a given range. The sample matrix can affect the area and migration rate of angiotensin II and angiotensin-(1-7) when real samples are analyzed in the CZE system, causing deviations from those of pure standards. Therefore, the quantitation of angiotensin II and angiotensin-(1-7) was performed by applying standards addition technique for plasma and urine. However, according to our experience, the conventional quantitation based on a calibration curve created by prepared standard solutions can be applied as well. To assess the linearity of the proposed CZE–PDA method, six independent calibration plots, analyzed per triplicate, were constructed over the calibration range of 0.1–800 pmol/mL. The curves were prepared on five different days, and linear regression was evaluated. Analytical figures of merit are shown in Table 2.

3.2.3. Precision

The precision of a method is determined by the extent to which the test results of multiple injections of standards agree. The precision of the proposed method is expressed in terms of relative standard deviation (RSD). In order to test the precision of the over-

Table 1A
Stability of the solutions.

Stored	Analyte solution	Time after preparation (days)	Analyte content (pmol/mL)
At 4 °C	Ang II	0	20.00 ± 0.02
		10	17.53 ± 2.52
	Ang 1-7	0	20.00 ± 0.03
		10	16.99 ± 3.69
In darkness	Ang II	0	20.00 ± 0.03
		10	17.87 ± 3.07
	Ang 1-7	0	20.00 ± 0.03
		10	16.49 ± 343
Freshly prepared	Ang II	0	20.00 ± 0.02
	Ang 1-7	0	20.00 ± 0.03

The optimal conditions were used. Results are expressed as mean ± standard deviation of three independent measurements. Ang II: angiotensin II; Ang 1-7: angiotensin-(1-7).

all process, five different samples of plasma and urine spiked with angiotensin II and angiotensin-(1-7) were carried out sequentially. The precision of the migration times and relative peak area were good with a RSD between 0.20% and 0.24% for migration times and between 1.18% and 2.05% for relative peak areas.

3.2.4. Specificity

Specificity can also be determined by measurement of peak homogeneity. Because there are different techniques available for PDA and they vary for the detection of possible impurities or interferences in an electrophoretic peak, the use of several techniques is recommended [45]. In this work, the techniques used to validate the peak purity of angiotensin II and angiotensin-(1-7) present in the plasma and urine were [46]: (a) normalization and comparison of spectra from different peak sections; and (b) absorbance at 200 nm. Both techniques revealed a high level of purity of the peaks corresponding to the studied compounds in the samples.

3.2.5. Limits of detection (LOD) and quantitation (LOQ)

The limit of detection (LOD), defined as the lowest concentration of an analyte that the analytical procedure can reliably differentiate from background noise; was evaluated based on a signal-to-noise ratio (S/N) of 5 (S/N = 5) [46]. The limit of quantification (LOQ), is defined as the level at, or above, in which the measurement precision is satisfactory for quantitative analysis. In our case, the LOQ was evaluated based on an S/N = 5 [46]. Results are shown in Table 2.

3.2.6. Recovery

Recovery is reported as the extraction efficiency of an analytical process, reported in percentage. It should be emphasized that the lack of suitable internal standards requires finding alternative ways to evaluate the recovery of angiotensin II and angiotensin-(1-7). In order to test the accuracy of the proposed method, several aliquots of angiotensin II and angiotensin-(1-7) standard solutions were added into the plasma and the urine. As can be observed in Table 3, good results were obtained. Recoveries of an added amount were calculated by using the calibration curves, taking into account the endogenous angiotensin II and angiotensin-(1-7) concentrations.

3.2.7. Robustness

Robustness is an important feature in the development of analytical methods since it evaluates the influence of small changes in the operating conditions of the analytical procedure on measured or calculated responses. Since variables such as BGE, pH, as well as its concentration, proved to be crucial in early stage of method development, it was decided to explore whether deliberate changes in these parameters could affect the CZE–PDA separation. Results showed that selectivity was good enough for all the responses in

Table 1B
Stability of the biological samples.

Sample	Analyte	Time after preparation (h)	Analyte content (pmol/mL)
PNR	Ang II	0	0.79 ± 0.01
		1	0.79 ± 0.02
		2	0.78 ± 0.02
		4	0.79 ± 0.03
		6	0.79 ± 0.02
		8	0.79 ± 0.05
		10	0.75 ± 0.08
		12	0.62 ± 0.12
	Ang 1-7	0	3.28 ± 0.03
		1	3.28 ± 0.04
		2	3.27 ± 0.01
		4	3.27 ± 0.02
		6	3.28 ± 0.02
		8	3.28 ± 0.04
		10	2.78 ± 0.11
		12	2.39 ± 0.33
PHR	Ang II	0	2.06 ± 0.01
		1	2.06 ± 0.02
		2	2.06 ± 0.02
		4	2.05 ± 0.03
		6	2.06 ± 0.01
		8	2.05 ± 0.04
		10	1.73 ± 0.23
		12	1.15 ± 0.51
	Ang 1-7	0	1.03 ± 0.02
		1	1.03 ± 0.03
		2	1.03 ± 0.02
		4	1.02 ± 0.03
		6	1.03 ± 0.04
		8	1.03 ± 0.03
		10	0.86 ± 0.10
		12	0.79 ± 0.37
UNR	Ang II	0	0.33 ± 0.01
		1	0.33 ± 0.01
		2	0.33 ± 0.02
		4	0.34 ± 0.03
		6	0.33 ± 0.03
		8	0.33 ± 0.02
		10	0.28 ± 0.11
		12	0.26 ± 0.28
	Ang 1-7	0	2.66 ± 0.02
		1	2.66 ± 0.02
		2	2.66 ± 0.04
		4	2.64 ± 0.03
		6	2.66 ± 0.04
		8	2.66 ± 0.05
		10	2.42 ± 0.19
		12	2.11 ± 0.48
UHR	Ang II	0	1.40 ± 0.04
		1	1.41 ± 0.04
		2	1.41 ± 0.03
		4	1.40 ± 0.05
		6	1.40 ± 0.02
		8	1.40 ± 0.08
		10	1.21 ± 0.12
		12	1.10 ± 0.67
	Ang 1-7	0	1.85 ± 0.03
		1	1.85 ± 0.02
		2	1.87 ± 0.04
		4	1.85 ± 0.04
		6	1.85 ± 0.03
		8	1.84 ± 0.03
		10	1.63 ± 0.15
		12	1.32 ± 0.33

The optimal conditions were used. Results are expressed as mean ± standard deviation of three independent measurements. PNR: plasma of normotensive rats; PRH: plasma of hypertensive rats; UNR: urine of normotensive rats; UHR: urine of hypertensive rats.

Table 2
Linearity and sensitivity.

Analyte	t_m (min) RSD ($n = 10$)	Linear range (pmol/mL)	Linear regression ($y = mx + b$)	Coefficient of determination (R^2)	Area RSD ($n = 10$)[a]	LOD (pmol/mL)[b]	LOQ (pmol/mL)[c]
Angiotensin II	3.20 ± 0.09	0.02–500	$y = (9.422 \times 10^3)x + 2.657 \times 10^4$	0.9985	1.4398×10^6	0.0110	0.0195
Angiotensin-(1-7)	4.91 ± 0.04	0.02–500	$y = (9.392 \times 10^3)x + 2.768 \times 10^4$	0.9991	1.4364×10^6	0.0112	0.0193

The optimal conditions were used; x, analyte concentration (pmol/mL); y, peak area; t_m, migration time; RSD, relative standard deviation.
[a] Calculated from peak areas for 150 pmol/mL of angiotensin II and 150 pmol/mL of angiotensin-(1-7) in phosphate buffer (pH 10).
[b] LOD is calculated based on S/N = 3.
[c] LOQ is calculated based on S/N = 5.

Table 3
Analytical results and recovery of angiotensins II and 1-7 in plasma and urine from normotensive and hypertensive animals with or without enalapril treatment.

Sample	Analyte	Analyte content (pmol/mL)[a]	RSD (%, $n = 10$)	Added (pmol/mL)	Total found (pmol/mL)[a]	Recovery (%)[b]
PNR (control)	Ang II	0.80 ± 0.10	1.82	1	1.9 ± 0.1	106.1 ± 0.5
				150	150.8 ± 0.2	100.0 ± 1.0
				400	400.5 ± 0.5	100.0 ± 1.2
	Ang 1-7	3.51 ± 0.20	1.78	1	4.5 ± 0.3	102.0 ± 0.9
				150	153.4 ± 0.7	100.0 ± 1.1
				400	403.3 ± 0.5	100.0 ± 1.3
PHR	Ang II	2.10 ± 0.28[c]	1.09	1	3.0 ± 0.8	99.0 ± 0.8
				150	152.1 ± 0.2	100.1 ± 1.2
				400	402.0 ± 0.6	99.9 ± 1.6
	Ang 1-7	1.20 ± 0.16[c]	1.34	1	2.2 ± 0.2	101.0 ± 0.7
				150	151.3 ± 1.1	100.1 ± 1.5
				400	401.2 ± 0.4	100.0 ± 0.8
PNR + enalapril (control)	Ang II	0.08 ± 0.02	2.01	1	1.0 ± 0.1	101.2 ± 1.2
				150	150.1 ± 0.7	100.0 ± 0.9
				400	400.0 ± 1.0	100.2 ± 1.1
	Ang 1-7	2.81 ± 0.15	1.92	1	3.9 ± 0.1	102.9 ± 0.8
				150	152.7 ± 0.5	100.0 ± 1.4
				400	402.8 ± 1.0	99.9 ± 1.1
PHR + enalapril	Ang II	0.30 ± 0.11[c]	0.90	1	1.2 ± 0.3	99.3 ± 0.5
				150	150.3 ± 0.7	100.0 ± 1.0
				400	400.3 ± 0.9	100.1 ± 1.7
	Ang 1-7	2.30 ± 0.18[c]	1.22	1	3.3 ± 0.2	101.0 ± 0.2
				150	152.4 ± 0.8	100.1 ± 0.6
				400	402.3 ± 0.4	100.0 ± 1.0
UNR (control)	Ang II	0.31 ± 0.03	2.51	1	1.2 ± 0.1	100.9 ± 0.8
				150	150.3 ± 0.3	100.0 ± 1.0
				400	400.3 ± 1.2	100.2 ± 0.5
	Ang 1-7	2.57 ± 0.30	0.89	1	3.6 ± 0.2	104.1 ± 1.1
				150	152.5 ± 0.1	99.9 ± 0.9
				400	402.5 ± 0.4	100.0 ± 1.0
UHR	Ang II	1.51 ± 0.28[c]	1.11	1	2.5 ± 0.1	101.1 ± 0.3
				150	151.5 ± 0.3	99.9 ± 0.4
				400	401.4 ± 0.5	100.0 ± 0.8
	Ang 1-7	1.87 ± 0.19[c]	0.83	1	2.9 ± 0.3	103.0 ± 0.9
				150	151.8 ± 0.4	99.9 ± 1.1
				400	401.8 ± 0.6	100.2 ± 0.5
UHR + enalapril (control)	Ang II	0.05 ± 0.02	2.00	1	1.0 ± 0.1	102.3 ± 0.7
				150	150.0 ± 1.0	100.0 ± 0.2
				400	400.0 ± 0.8	100.0 ± 1.6
	Ang 1-7	2.55 ± 0.12	1.34	1	3.6 ± 0.2	101.1 ± 0.4
				150	152.5 ± 0.8	100.0 ± 0.3
				400	402.5 ± 0.6	99.7 ± 1.0
UHR + enalapril	Ang II	0.25 ± 0.01[c]	1.18	1	1.2 ± 0.1	99.9 ± 0.2
				150	150.2 ± 1.2	100.0 ± 0.5
				400	400.2 ± 0.7	99.9 ± 0.7
	Ang 1-7	1.87 ± 0.19[c]	2.31	1	2.8 ± 0.3	101.0 ± 0.8
				150	151.8 ± 0.5	100.1 ± 1.0
				400	401.9 ± 0.9	100.0 ± 0.9

The optimal conditions were used; PNR: plasma of normotensive rats; PRH: plasma of hypertensive rats; UNR: urine of normotensive rats; UHR: urine of hypertensive rats; RSD: relative standard deviation.
[a] Results are expressed as mean ± standard deviation of 10 independent measurements.
[b] Recovery = (total found − found in the sample)/added (%). Results are expressed as mean ± standard deviation of 10 independent measurements.
[c] $p < 0.05$ *vs.* control, one-way ANOVA followed by a Student's t-test.

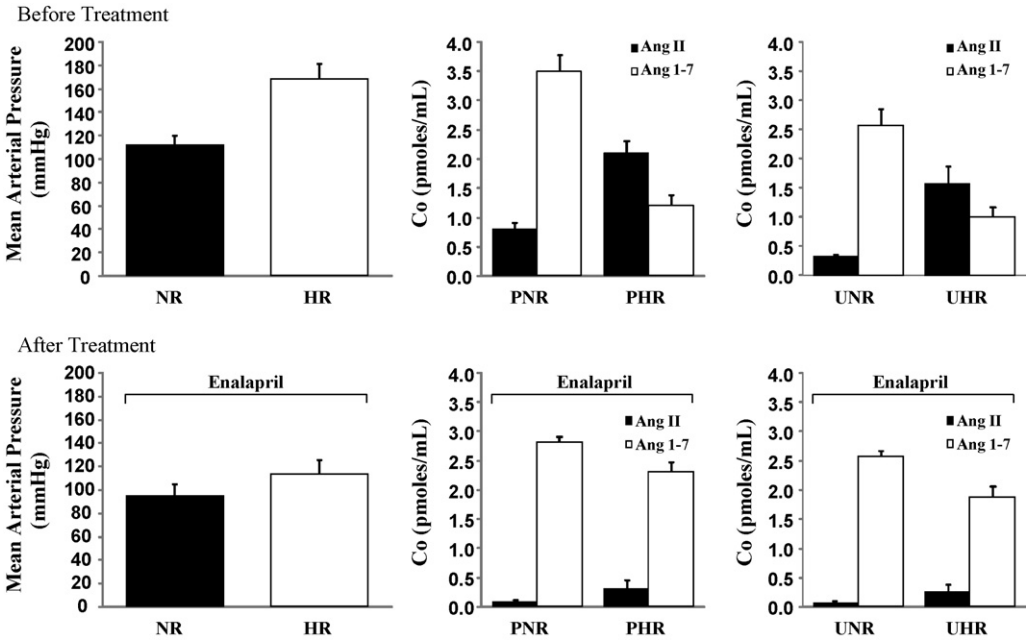


Fig. 6. Mean arterial pressure measurements of normotensive and hypertensive animals, before and after enalapril treatment. Results of angiotensin II (Ang II) and angiotensin-(1-7) (Ang 1-7) levels measured in plasma and urine of normotensive and hypertensive animals, before and after enalapril treatment. Results correspond to the mean ± SD of 10 experiments per study group. NR: Normotensive rats; HR: Hypertensive rats; UNR: Urine of normotensive rats; UHR: Urine of hypertensive rats; PNR: Plasma of normotensive rats; PHR: Plasma of hypertensive rats.

the buffer pH range from 9.00 to 10.00. Boric acid concentration is restricted from 95 to 105 mM in order to have a resolution greater or equal to 2.0. It means that the method is robust within this range.

3.3. Applications

3.3.1. Hypertension induction study

In order to test the applicability of the method, a hypertensive study was performed during 60 days and samples from plasma and urine from normotensive and hypertensive animals were analyzed with the developed CZE–PDA method. Under the optimized conditions, angiotensin II, angiotensin-(1-7) and unknown compounds, were all successfully separated. Angiotensin II and angiotensin-(1-7) produced, respectively, a single peak and was sufficiently resolved from other unknown endogenous compounds to permit accurate determination (Fig. 5). The concentration of angiotensin II and angiotensin-(1-7) (expressed as mean ± standard deviation) found in these samples, using the proposed method, as well as results from recovery experiments, are shown in Table 3. It has been repeatedly demonstrated that angiotensin II and angiotensin-(1-7) derive from the renin–angiotensin system. The renin secreted by the juxtaglomerular apparatus of the kidney acts upon a precursor, angiotensinogen, to generate angiotensin I, which has few pressor effects and is converted by ACE, during its lung passage, into angiotensin II that is a potent vasopressor that acts together with the G protein by coupling to receptors AT1 and AT2. Stimulation of AT1 receptors induces deleterious effects, such as vasoconstriction, myocardial hypertrophy, vascular cell proliferation, release of catecholamines, antidiuretic hormone, and stimulates thirst. To counteract these effects, the angiotensin converting enzyme inhibitor (ACEI) decrease arterial pressure rapidly by avoiding the transformation of angiotensin I in angiotensin II. In consequence, ACEI induce prolonged hypotensive responses. Although, at the beginning it was thought that ACEIs would only be efficacious in patients with high activity of the renin–angiotensin system, it has been observed that ACEIs are also efficacious in patients with a normal or even scarce activity of the renin–angiotensin system [10,11]. This fact suggested that, aside from the inhibition in angiotensin II production, there might be other mechanisms that would explain the hypotensive action of ACEIs. In this regard, inhibition of ACE increases angiotensin-(1-7) levels, because angiotensin I, by not being degraded to angiotensin II by ACE, which is inhibited, is degraded by neutral endopeptidases (NEP 24.11, NEP 24.15, and NEP 24.26) to angiotensin-(1-7) [7]. The prototype drug of the ACEIs group is captopril, a dipeptide that binds to the active site of ACE through a sulfhydril group (–SH) and acts as a competitive inhibitor of ACE. Another ACEI, the dipeptide enalapril, is administered orally as a pro-drug and it has to be transformed in the liver to its active metabolite, enalaprilate, hence, its antihypertensive effects start more slowly than those of captopril, although it is more potent and has a longer half life, it lacks the –SH group. In this *in vivo* study in which we used enalapril to control the induced hypertension, and measured angiotensin II and angiotensin-(1-7) in both plasma and urine of normotensive and hypertensive rats by means of the CZE–PDA, we observed that in hypertensive animals, as verified by monitoring the mean arterial pressure, the levels of angiotensin II were considerably elevated, whereas angiotensin-(1-7) was decreased compared with normotensive animals and before enalapril treatment (Fig. 6). After enalapril treatment at a dose of 20 mg/kg per day during 12 weeks, the mean arterial tension of the hypertensive rats decreased substantially as a consequence of a decrement in angiotensin II levels and an increment in angiotensin-(1-7) levels (Fig. 6). On other side, we were able to confirm that the primary pharmacological effect of ACEIs (reduction of arterial pressure) is also exerted on normotensive rats, as their mean arterial pressure was also decreased (Fig. 6), this is due to the reduction in angiotensin II levels by the blocking effect of enalapril by hindering the conversion of angiotensin I into angiotensin II, allowing for conversion of angiotensin I into angiotensin-(1-7), increasing levels of the latter in normotensive rats (Fig. 6).

4. Conclusion

The determination of angiotensin II and angiotensin-(1-7) in complex biological samples is an analytical challenge. Therefore,

a simple, rapid and sensitive capillary electrophoresis method has been developed for the simultaneous quantitative analysis of angiotensin II and angiotensin-(1-7) in both plasma and urine from rats. Although these analytes have been previously analyzed by HPLC with PDA using 190 and 230 nm detection, this is the first report, to our best knowledge, that deals with the simultaneous determination of angiotensin II and angiotensin-(1-7) in plasma and urine obtained from normotensive and hypertensive rats in an *in vivo* model. Compared to previous HPLC [23,24] and CE [30,41,47,48] methods, this method obtains comparable LOD (angiotensin II, 0.0110 pmol/mL; angiotensin-(1-7), 0.0112 pmol/mL) and LOQ (angiotensin II, 0.0195 pmol/mL; angiotensin-(1-7), 0.0193 pmol/mL) for these analytes. However, in previously reported methods, a non-linear response between peaks area and amount of angiotensin II and angiotensin-(1-7) below 0.011 pmol/mL has been observed (Table 2). The proposed CZE–PDA method has been validated and the reliability of the electrophoretic procedure for its desired application was demonstrated by means of the experimental results regarding linearity, accuracy, specificity, sensitivity and precision. Major advantages of the present CE method are the use of PDA detection and that no sample pretreatment other than filtration is needed, as well as no need to use coating and previous derivatization of the capillary, compared to previous CE methods with UV absorbance detection. The proposed CZE–PDA provides similar results regarding analysis time and recovery, with advantage of simultaneous detection of both analytes in complex matrices like plasma and urine. In addition, this method may be useful to elucidate the role of renin–angiotensin system, in particular in cases of hypertension, which is a fact that has attracted considerable attention as a potentially reversible cause of cardiac and systemic functional deterioration.

Acknowledgements

The authors are grateful to Fundación Río Arronte for the donation of a Beckman Coulter P/ACE™ MDQ Capillary Electrophoresis System and to Dr. Ingrid Mascher for her English Language editorial review. This work was partially supported by a CONACYT (Mexico) grant 44173-M (Dr. A. Sánchez-Mendoza) and Dr. Martín Rosas-Peralta (Departamento de Cardiología Adultos III, INCICH, México).

References

[1] M. Rosas, G. Pastelín, G. Vargas-Alarcón, J. Martínez-Reding, C. Lomelí, C. Mendoza-González, J.A. Lorenzo, A. Méndez, M. Franco, L.G. Sánchez-Lozada, J. Verdejo, N. Sánchez, R. Ruiz, S.M. Férez-Santander, F. Attie, Arch. Cardiol. Mex. 78 (2008) 5–57.
[2] J.K. Cruickshank, J. Hypertens. 22 (2004) 21–24.
[3] O. Velázquez-Monroy, M. Rosas-Peralta, A. Lara-Esqueda, G. Pastelín-Hernández, F. Attie, R. Tapia-Conyer, Grupo ENSA 2000, Arch. Cardiol. Mex. 72 (2002) 71–84.
[4] D.M. Lloyd-Jones, J.C. Evans, M.G. Laron, D. Levy, Hypertension 40 (2002) 640–646.
[5] M.A. Crackower, R. Sarao, G.Y. Oudit, C. Yagil, I. Kozieradzki, S.E. Scanga, Nature 417 (2002) 822–828.
[6] M. Donoghue, F. Hsieh, E. Baronas, K. Godbout, M. Gosselin, N. Stagliano, Circ. Res. 87 (2000) E1–E9.
[7] R.A. Skidgel, E.G. Erdos, Peptides 25 (2004) 521–525.
[8] C. Vickers, P. Hales, V. Kaushik, L. Dick, J. Gavin, J. Tang, J. Biol. Chem. 277 (2002) 14838–14843.
[9] C.M. Ferrario, Circulation 105 (2002) 1523–1525.
[10] C.M. Ferrario, M.C. Chappell, E.A. Tallant, K.B. Brosnihan, D.I. Diz, Hypertension 30 (1997) 535–541.
[11] C.M. Ferrario, M.C. Chappell, Cell. Mol. Life Sci. 61 (2004) 2720–2727.
[12] D.M. Osbourn, D.J. Weiss, C.E. Lunte, Electrophoresis 21 (2000) 2768–2779.
[13] K.D. Altria, M.M. Rogan, in: C. Beckman (Ed.), Introduction to Quantitative Applications of Capillary Electrophoresis in Pharmaceutical Analysis, Beckman Coulter Publication, Fullerton, 1999, pp. 27–52.
[14] L. González, J.A. López, R.M. Alonso, R.M. Jiménez, J. Chromatogr. A 949 (2002) 49–60.
[15] M. Hanssens, M.J.N.C. Keirse, P.J. Lijnen, M.J. Kucharski, C. Luyten, F.A.V. Assche, J. Biochem. Biophys. Methods 21 (1990) 103–113.
[16] K. Hermann, J. Ring, M.I. Phillips, J. Chromatogr. Sci. 28 (1990) 524–528.
[17] Q.C. Meng, J. Durand, Y.F. Chen, S. Oparil, J. Chromatogr. 614 (1993) 19–25.
[18] S. Terabe, M.R.N. Monton, T.L. Saux, K. Imami, Pure Appl. Chem. 78 (2006) 1057–1067.
[19] D.W. Margerum, G.D. Owens, in: D. Marcel (Ed.), Biological Systems, Marcel Dekker Publication, New York, 1981, pp. 77–128.
[20] I. Gusev, X. Huang, C. Horváth, J. Chromatogr. A 855 (1999) 273–290.
[21] T. Seki, K. Yamazaki, M. Kayano, J. Chromatogr. B Biomed. Sci. Appl. 688 (1997) 101–106.
[22] S. Zheng, Z. Li, Y.X. Wang, Z.Q. Xiang, Zhonghua Nan Ke Xue 9 (2003) 669–672.
[23] T. Matsui, K. Tamaya, T. Kawasaki, Y. Osajima, J. Chromatogr. B Biomed. Sci. Appl. 729 (1999) 89–95.
[24] Y. Sakamoto, T. Miyazaki, M. Kai, Y. Ohkura, J. Chromatogr. 380 (1986) 313–320.
[25] G. Sun, K. Haginoya, H. Dai, Y. Chiba, M. Uematsu, N. Hino-Fukuyo, A. Onuma, K. Iinuma, S. Tsuchiya, J. Neurol. Sci. 280 (2009) 40–48.
[26] N. Ide, T. Hirase, A. Nishimoto-Hazuku, Y. Ikeda, K. Node, Hypertens. Res. 31 (2008) 1257–1267.
[27] Y. Li, R. Xiang, C. Horváth, J.A. Wilkins, Electrophoresis 25 (2004) 545–553.
[28] T.H. Chen, T.K. Misra, Ch.Y. Liu, Electrophoresis 29 (2008) 1651–1657.
[29] J.C.M. Waterval, C.J.L. la Porte, R. van't Hof, J. Teeuwsen, A. Bult, H. Lingeman, W.J.M. Underberg, Electrophoresis 19 (1998) 3171–13171.
[30] M. Zhang, F. Wei, Y.F. Zhang, J. Nie, Y.Q. Feng, J. Chromatogr. A 1102 (2006) 294–301.
[31] F.T.A. Chen, in: C. Beckman (Ed.), Quantitation of Bioactive Peptides in Serum by Capillary Electrophoresis with Laser-induced Fluorescence Immunodetection (CE-LIF-ID), Beckman Coulter Publication, Fullerton, 1995, pp. 1–12.
[32] J.E. Jalil, C. Palomera, M.P. Ocaranza, I. Godoy, M. Román, M. Chiong, S. Lavandero, Am. J. Cardiol. 92 (2003) 749–751.
[33] H. Heitsch, S. Brovkovych, T. Malinski, G. Wiemer, Hypertension 37 (2001) 72–76.
[34] C. Höcht, J.A.W. Opezzo, M. Gironacci, C. Peña, C.A. Taira, Rev. Arg. Cardiol. 73 (2005) 346–351.
[35] E.P. Velloso, R. Vieira, A.C. Cabral, E. Kalapothakis, R.A.S. Santos, Braz. J. Med. Biol. Res. 40 (2007) 583–590.
[36] B. Bartholomeusz, K.J. Hardy, A.S. Nelson, P.A. Phillips, J. Hum. Hypertens. 12 (1998) 839–844.
[37] P.A. Phillips, K.A. Rolls, L.M. Burrell, D. Casley, K.L. Aldred, K.J. Hardy, Clin. Exp. Pharmacol. Physiol. 21 (1994) 223–226.
[38] T. Rodemann, C. Johns, W.S. Yang, P.R. Haddad, M. Macka, Anal. Chem. 77 (2005) 120–125.
[39] D.W. Margerum, L.F. Wong, F.P. Bossu, K.L. Chellapa, J.J. Czarnecki, D.T. Kirksey Jr., T.A. Neubecker, in: K.N. Raymond (Ed.), Bioinorganic Chemistry II, American Chemical Society, Washington, 1977, pp. 281–303.
[40] N. Smith, in: C. Beckman (Ed.), Capillary ElectroChromatography, Beckman Coulter Publication, Fullerton, 1999, pp. 33–36.
[41] S. Zhang, J. Zhang, C. Horváth, J. Chromatogr. A 914 (2001) 189–200.
[42] A. Jouyban, A. Batish, S.J. Rumbelowb, B.J. Clarka, Analyst 26 (2001) 1958–1962.
[43] M. Wang, F. Qu, X. Shan, J. Lin, J. Chromatogr. A 989 (2003) 285–292.
[44] X. Xuan, G. Hu, D. Li, Electrophoresis 27 (2006) 3171–3180.
[45] L. Huberm, Applications of Diode-Array Experience, 12, Hewlett-Packard Publication, Urbana, 1989.
[46] D.B. Hibbert, Analyst 131 (2006) 1273–1278.
[47] M. Erbanová, M. Thumová, Z. Husková, I. Vanecková, Z. Vanourková, J.J. Mullins, H.J. Kramer, M. Bürgelová, D. Rakusan, L. Cervenka, J. Hypertens. 27 (2009) 575–586.
[48] N.A. Lacher, K.E. Garrison, S.M. Lunt, Electrophoresis 23 (2002) 1577–1584.

Talanta 80 (2010) 1713–1718

Contents lists available at ScienceDirect

Talanta

journal homepage: www.elsevier.com/locate/talanta

Monodispersed, molecularly imprinted polymers for cinchonidine by precipitation polymerization

Yueqi Liu, Kaori Hoshina, Jun Haginaka*

Faculty of Pharmaceutical Sciences, Mukogawa Women's University, 11-68, Koshien Kyuban-cho, Nishinomiya 663-8179, Japan

ARTICLE INFO

Article history:
Received 14 July 2009
Received in revised form 5 October 2009
Accepted 7 October 2009
Available online 14 October 2009

Keywords:
Molecularly imprinted polymer
Cinchonidine
Precipitation polymerization
Core–shell polymer
Stereoisomer separation

ABSTRACT

Three monodispersed, molecularly imprinted polymers (MIPs) for cinchonidine (CD) have been synthesized by precipitation polymerization. MIP1 was prepared using methacrylic acid (MAA) as a functional monomer and divinylbenzene (DVB) as a cross-linker and MIP2 was prepared with further addition of 2-hydroxyethyl methacrylate (HEMA) as a co-monomer. For the preparation of MIP3, core–shell type MIP, monodispersed DVB homopolymers, which are prepared by precipitation polymerization, were used as a core and CD-imprinted MAA–DVB copolymer phases were coated onto the core. Three MIPs synthesized gave monodispersed, spherical beads in micrometer sizes. The binding characteristics and molecular recognition properties of MIP1–3 were examined by Scatchard analysis and chromatographic studies. The association constant of CD with MIP1 was the highest among MIPs prepared, while that with MIP3 was the lowest. The template molecule, CD, was more retained than its stereoisomer, cinchonine, on the three MIPs, and the stereoseparation factor of 38 was obtained with MIP3.

© 2009 Elsevier B.V. All rights reserved.

1. Introduction

Typically, molecularly imprinted polymers (MIPs) were prepared by a bulk polymerization method, where the resultant monoliths had to be crushed, ground and sieved to produce microparticles for their applications [1]. In recent years, monodispersed MIPs as selective stationary phases for a given target analyte in HPLC have gained significant interests due to their high column efficiencies [2]. Several synthetic strategies such as multi-step swelling and polymerization [3,4], precipitation polymerization [5,6] and grafting or coating thin films of MIP phases onto the surfaces of spherical materials [7–9] have been reported for the preparation of monodispersed MIP beads. Precipitation polymerization seems to be an attractive and straightforward method. This method involves dissolution of prepolymerization mixtures (functional monomer, template molecule, cross-linker and initiator) in a suitable solvent and their polymerization. Monodispersed MIP microspheres for theophyllin [6], thiabendazole [10], (*S*)-nicotine [11], 17β-estradiol [12] and propranolol [13] have been prepared by this method. Recently, Li and Stöver [14] reported to prepare monodispersed, core–shell microspheres by precipitation polymerization. We were hence interested in preparing monodispersed, core–shell type MIPs by precipitation polymerization.

Cinchonidine (CD) and its stereoisomer, cinchonine (CN), are cinchona alkaloids, which have antimalarial activities. The presence of rigid structures, bulky groups and hetero-atom functionalities in their molecules could give the possibility of forming a good molecularly imprinting site [15]. MIPs for CD and CN have been prepared using methacrylic acid (MAA) as a functional monomer and ethylene glycol dimethacrylate (EDMA) as a cross-linker by bulk polymerization [15], *in situ* polymerization [16], and multi-step swelling and polymerization [17] methods. The MIPs prepared by the three methods gave high stereoseparation factors for CD and CN [15–17]. In this study, three monodispersed MIPs for CD have been synthesized by precipitation polymerization. MIP1 was prepared using methacrylic acid (MAA) as a functional monomer and divinylbenzene (DVB) as a cross-linker and MIP2 was prepared with further addition of 2-hydroxyethyl methacrylate (HEMA) as a co-monomer. For the preparation of MIP3, core–shell type MIP, monodispersed DVB homopolymers, which are prepared by precipitation polymerization, were used as a core and CD-imprinted MAA–DVB copolymer phases were coated onto the core. The binding characteristics and molecular recognition properties of the three MIPs were examined by Scatchard analysis and chromatographic studies.

2. Experimental

2.1. Materials

MAA, DVB (a mixture of *m*- and *p*-DVB), HEMA and 2,2′-azobis(isobutyronitrile) (AIBN) were purchased from Wako (Osaka, Japan). CD and CN were purchased from Tokyo Kasei (Tokyo, Japan). Other reagents and solvents of an analytical-reagent grade were

* Corresponding author. Tel.: +81 798 45 9949; fax: +81 798 41 2792.
E-mail address: haginaka@mukogawa-u.ac.jp (J. Haginaka).

0039-9140/$ – see front matter © 2009 Elsevier B.V. All rights reserved.
doi:10.1016/j.talanta.2009.10.011

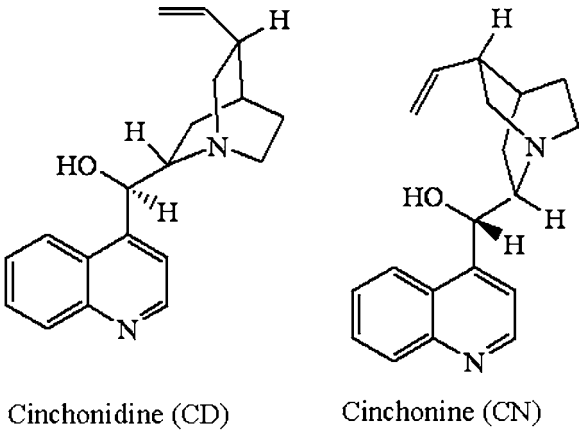


Fig. 1. Structures of compounds used in this study.

used without further purification. Water purified with a Purelab ultra (Organo, Tokyo, Japan) was used to prepare mobile phases and sample solutions. The structures of CD and CN are illustrated in Fig. 1.

2.2. Preparation of MIPs by a precipitation polymerization method

Table 1 shows the molar amounts of a template molecule, functional monomer and cross-linker used for the preparation of MIP1–3. Non-imprinted polymers (NIPs) were prepared similarly without a template molecule. MIP1 and MIP2 were prepared by one-step precipitation polymerization. For the preparation of MIP1, CD, MAA and DVB were dissolved with 0.475 mmol of AIBN in 32 mL of acetonitrile–toluene (3:1, v/v). In the case of MIP2, HEMA was further added as a co-monomer. The mixture was degassed with an argon gas for 15 min and then rotated slowly at 16 rpm using a Shellspin VS-60 rotor (Taitec, Tokyo, Japan). Reaction temperature was raised from 25 to 60 °C for 2 h and then kept at 60 °C for 15 h.

MIP3 was prepared in two successive precipitation polymerization processes. In the first reaction stage, 3.35 mmol of DVB were dissolved with 0.061 mmol of AIBN in 25 mL of acetonitrile and were polymerized at 70 °C for 6 h, resulting in the formation of monodispersed DVB homopolymers [poly(DVB)] used as a core. For the second reaction stage, CD, MAA, DVB and 0.061 mmol of AIBN dissolved in 25 mL of acetonitrile–toluene (1:1, v/v) were introduced into the same reaction vessel and the mixture was polymerized at 70 °C for 12 h, resulting in the formation of the imprinted shell. For each reaction period, the mixture was degassed with an argon gas for 15 min and then rotated slowly at 16 rpm using a Shellspin VS-60 rotor (Taitec). Reaction temperature was raised from 25 to 70 °C for 2 h and then kept at 70 °C for time intervals described above.

After polymerization, a dispersion of polymerized particles was poured into 200 mL of methanol and the supernatant was discarded after sedimentation of the particles. The obtained polymers were redispersed into methanol, and this procedure was repeated three times in methanol, once in water, and twice in tetrahydrofuran. The resulting μm-sized polymer particles were collected using a membrane filter, washed with tetrahydrofuran and dried at room temperature.

2.3. Porosity measurements

Surface areas and porosity of MIPs, NIPs and poly(DVB) were measured by nitrogen sorption porosimetry using a TriStar surface area and porosity analyzer (Micrometrics Instrument, Norcross, GA, USA). Prior to measurement, 200 mg of the particles were heated at 80 °C for 5 h in vacuo. The specific surface areas were calculated using the BET method, and the specific pore volumes and average pore diameters were calculated according to the BJH method.

2.4. Scanning electron micrographs

Scanning electron micrographs (SEMs) were performed on MIP1–3, NIPs and poly(DVB) using a Mighty-8 instrument (Technex, Machida, Tokyo, Japan).

2.5. Scatchard analysis

A 10 mg weight of MIP, NIP or poly(DVB) was added to 1 mL of acetonitrile including 0.09–1.2 mmol L^{-1} CD. After shaken at 25 °C for 24 h, an aliquot of each sample was taken and filtrated with a 0.45-μm membrane filter. The concentration of free CD, [CD], in the supernatant was determined by HPLC under the following conditions: column, Cosmosil $5C_{18}$-MS-II (150 mm × 4.6 mm ID, Nacalai Tesque, Kyoto, Japan); column temperature, 25 °C; mobile phase, 20 mmol L^{-1} sodium phosphate buffer (pH 3.2)–CH_3CN (85:15, v/v); flow rate, 0.5 mL min^{-1}; detection, 235 nm. The amount of CD bound to MIPs, n, was calculated by the subtraction of [CD] from the initial CD concentration. The association constant (K_a) and apparent maximum number of binding sites (N) are determined according to the Scatchard plot and Scatchard equation, $n/[CD] = (N - n)K_a$.

2.6. Chromatographic evaluation of MIPs

The obtained polymers were packed into a stainless-steel column by a slurry packing technique using methanol–2-propanol (2:1, v/v) as the slurry solvent and methanol as the packing solvent to evaluate their chromatographic characteristics.

The HPLC system used was composed of a PU-980 pump, a UV-970 spectrophotometer (both from Jasco, Tokyo, Japan), a C-R6A integrator (Shimadzu, Kyoto, Japan), a Rheodyne 7125 injector with a 20-μL loop (Rheodyne, Cotati, CA, USA) and a CO-1093C column oven (Uniflows, Tokyo, Japan). The HPLC conditions used are specified in the legends of a table and figures.

The retention factor (k) was calculated from the equation $k = (t_R - t_0)/t_0$, where t_R and t_0 are retention times of retained and unretained solutes, respectively. The retention time of unretained solute, t_0, was measured by injecting acetone. The stereoseparation

Table 1
The molar amount of template molecule, functional monomer and cross-linker used for the preparation of MIP1–3, NIP1–3 and poly(DVB), and their physical properties.

Entry	Template molecule (mmol)	Functional monomer (mmol)	Cross-linker (mmol)	Surface area (m^2 g^{-1})	Pore volume (cm^3 g^{-1})	Average pore diameter (nm)
MIP1	CD (0.375)	MAA (1.5)	DVB (7.2)	460	0.16	3.3
NIP1	–	MAA (1.5)	DVB (7.2)	600	0.26	3.2
MIP2	CD (0.375)	MAA (1.5) + HEMA (0.72)	DVB (6.48)	540	0.20	3.2
NIP2	–	MAA (1.5) + HEMA (0.72)	DVB (6.48)	610	0.34	3.5
MIP3	CD (0.375)	MAA (0.59)	DVB (3.01)	570	0.21	3.2
NIP3	–	MAA (0.59)	DVB (3.01)	650	0.26	3.0
Poly(DVB)	–	–	DVB (3.35)	8.36	0.03	7.8

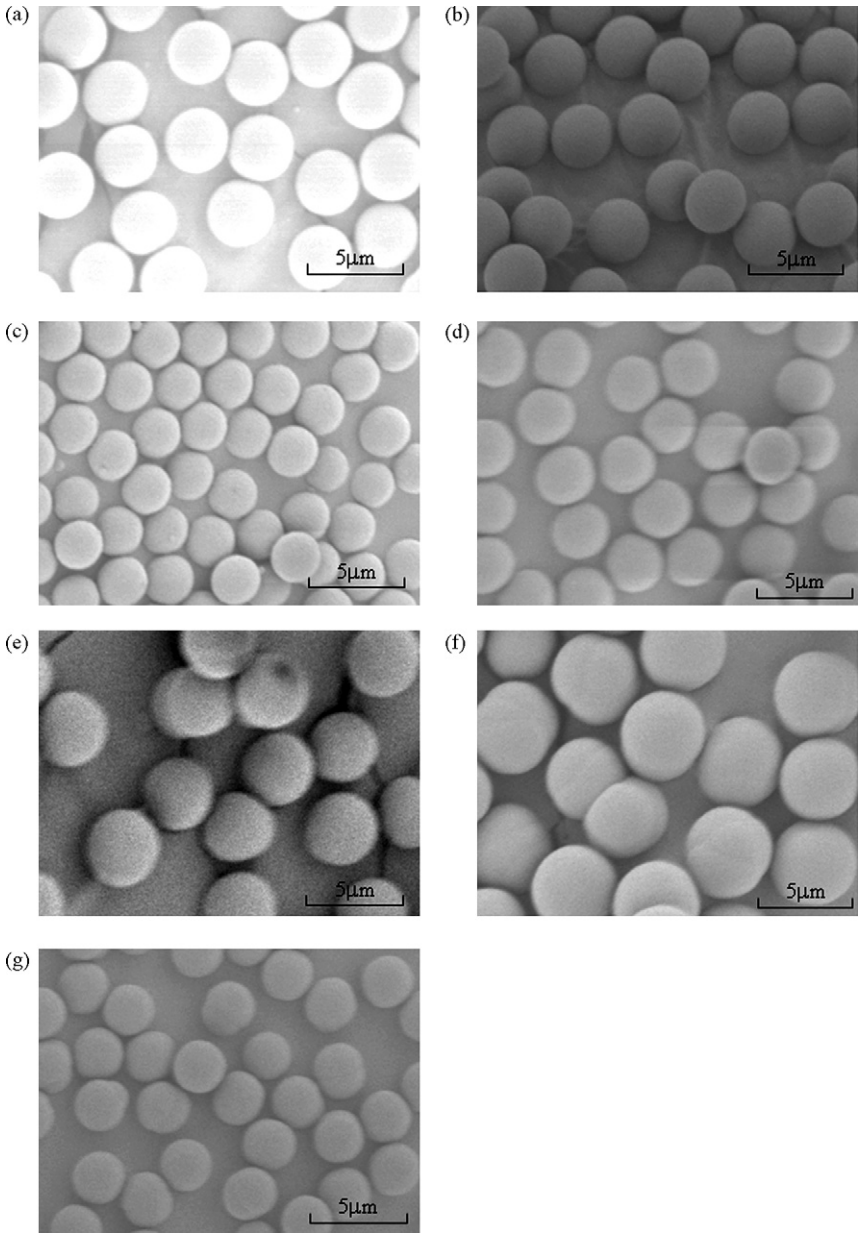


Fig. 2. SEMs of (a) MIP1, (b) NIP1, (c) MIP2, (d) NIP2, (e) MIP3, (f) NIP3 and (g) poly(DVB).

factor (α) was calculated from the equation $\alpha = k_{CD}/k_{CN}$, where k_{CD} and k_{CN}, respectively, are the retention factors of CD and CN on the MIP, NIP or poly(DVB) columns.

3. Results and discussion

3.1. Preparation of MIPs by a precipitation polymerization method

Previously, we prepared MIPs for (*S*)-nicotine using MAA as a functional monomer and DVB as a cross-linker by a precipitation polymerization method. The (*S*)-nicotine-imprinted MAA–DVB copolymers gave monodispersed microspheres of 3.5 μm in diameter and showed a high imprinting effect for (*S*)-nicotine [11]. Similarly, we tried to prepare MIPs for CD by a precipitation polymerization method using MAA as a functional monomer and DVB as a cross-linker. MIP1, CD-imprinted MAA–DVB copolymer, gave microspheres of 3.7 ± 0.07 (standard deviation) μm in diameter together with microspheres of a few hundred μm in diameter. The latter ones could be removed by repeated sedimentation and decantation. However, non-imprinted MAA–DVB copolymers gave only monodispersed microspheres of 3.5 ± 0.07 μm. This result suggests that the template molecule affected growth of microspheres during precipitation polymerization.

MIP2, CD-imprinted MAA–HEMA–DVB terpolymer, was also prepared by precipitation polymerization. MIP2 gave microspheres having two different particle sizes, 2.8 ± 0.11 μm and a few hundred μm in diameter, while non-imprinted MAA–HEMA–DVB terpolymers gave microspheres of 3.2 ± 0.09 μm and a few hundred μm in diameter. The particle sizes of these polymers prepared with addition of HEMA were smaller than those prepared without HEMA, suggesting that the co-monomer HEMA could have a profound influence on growth of microspheres during precipitation polymerization.

MIP3, core–shell type MIP, was prepared in two successive precipitation polymerization processes. In the first reaction stage,

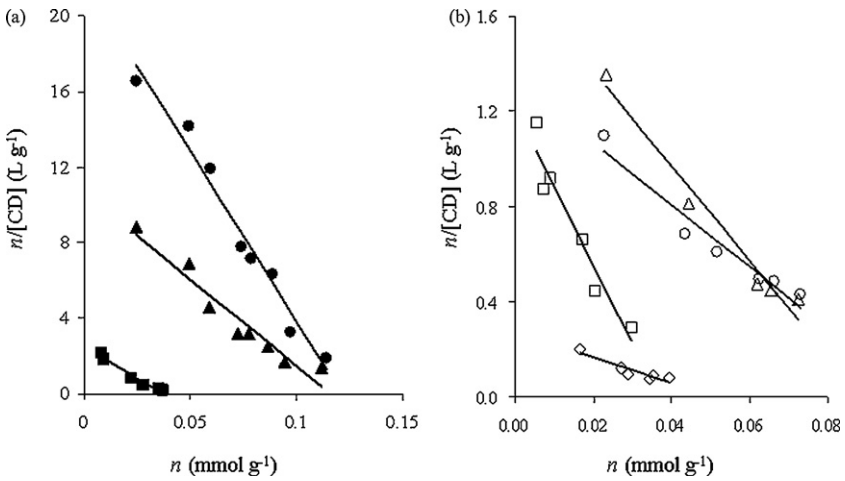


Fig. 3. Scatchard plots of (●) MIP1, (▲) MIP2 and (■) MIP3 (a), and (○) NIP1, (△) NIP2, (□) NIP3 and (◊) poly(DVB) (b). These plots were obtained based on the following equation: $n/[CD] = (N - n)K_a$, where K_a is the association constant and N is the apparent maximum number of binding sites.

Table 2
The association constant (K_a) of CD with MIP1–3, NIP1–3 and poly(DVB) and the apparent maximum number of binding sites (N).

	$K_a \times 10^5$ [L mol^{-1}]	N (mmol g^{-1})
MIP 1	1.8	0.12
NIP 1	0.13	0.10
MIP 2	0.92	0.12
NIP 2	0.19	0.087
MIP 3	0.67	0.037
NIP 3	0.27	0.040
Poly(DVB)	0.054	0.050

monodispersed poly(DVB) was obtained, and in the second reaction stage, *in situ* addition of CD, MAA, DVB and AIBN was followed by polymerization. Poly(DVB), MIP3 and NIP3, respectively, gave monodispersed microspheres of 2.8 ± 0.09, 4.1 ± 0.14 and 4.9 ± 0.08 μm in diameter, indicating that thickness of the imprinted and non-imprinted shells are about 0.65 and 1.1 μm, respectively. Fig. 2 shows SEMs of MIP1–3, NIP1–3 and poly(DVB). The good size uniformity was obtained with MIP1–3, NIP1–3 and poly(DVB).

Table 1 shows the physical properties (specific surface area, specific pore volume and average pore diameter) of MIP1–3, NIP1–3 and poly(DVB), measured using nitrogen sorption porosimetry. These data indicate that the obtained MIPs and NIPs have high specific surface areas associated with microporous structures and that MIP1–3 and NIP1–3 has similar morphology. On the other hand, poly(DVB) is non-porous polymer beads.

3.2. Scatchard analysis

To investigate their binding properties, Scatchard analysis of MIP1–3, NIP1–3 and poly(DVB) was carried out. The Scatchard plots shown in Fig. 3a and b gave straight lines, indicating that the affinities of the binding sites in MIP1–3, NIP1–3 and poly(DVB) are homogeneous among the concentrations tested. Similar Scatchard plots were obtained with the case of bisphenol A-imprinted polymers prepared by a precipitation polymerization method [18]. Table 2 shows the association constant (K_a) of CD with MIP1–3, NIP1–3 and poly(DVB) and the apparent maximum number of binding sites (N). The association constant of CD with MIP1 was larger

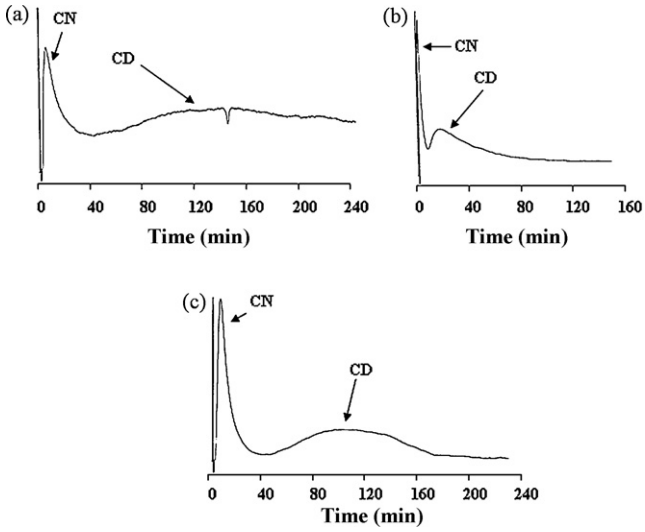


Fig. 4. Chromatograms of CN and CD on (a) MIP1, (b) MIP2 and (c) MIP3. HPLC conditions: column size, 50 mm × 2.0 mm ID; mobile phase, 50 mmol L^{-1} potassium phosphate buffer–CH_3CN (30:70, v/v) (final pH 4.5 for (a), and final pH 4.8 for (b) and (c)); flow rate, 0.2 mL min^{-1}; detection, 220 nm; column temperature, 25 °C; loaded amount, 500 ng.

Table 3
Effects of mobile phase pH on the retention factors of CN and CD and their stereoseparation factors on MIP1–3, NIP1–3 and poly(DVB).

Mobile phase pH	MIP1			NIP1			MIP2			NIP2			MIP3			NIP3			Poly(DVB)		
	k_{CN}	k_{CD}	α	k_{CN}	k_{CD}	α	k_{CN}	k_{CD}	α	k_{CN}	k_{CD}	α	k_{CN}	k_{CD}	α	k_{CN}	k_{CD}	α	k_{CN}	k_{CD}	α
3.7	0.33	8.5	26	0.0	0.0	1.0	0.14	1.00	7.3	0.0	0.0	1.0	0.10	1.7	17	0.0	0.0	1.0	0.0	0.0	1.0
4.2	1.1	32	28	0.03	0.03	1.0	0.27	3.3	12	0.07	0.06	0.80	0.50	15	30	0.0	0.0	1.0	0.0	0.0	1.0
4.5	2.9	84	29	0.21	0.19	0.87	0.36	7.1	20	0.23	0.20	0.88	1.3	41	32	0.0	0.0	1.0	0.0	0.0	1.0
4.8	–	–	–	0.54	0.50	0.93	0.81	19	23	0.46	0.44	0.94	2.9	100	36	0.10	0.09	0.86	0.06	0.04	0.76
5.1	–	–	–	1.07	1.03	0.96	1.9	52	27	0.85	0.79	0.93	5.4	200	38	0.27	0.24	0.90	0.16	0.15	0.91

HPLC conditions: column size, 50 mm × 2.0 mm ID; mobile phase, 50 mmol L^{-1} potassium phosphate buffer–CH_3CN (30:70, v/v); flow rate, 0.2 mL min^{-1}; detection, 220 nm; column temperature, 25 °C; loaded amount, 500 ng.

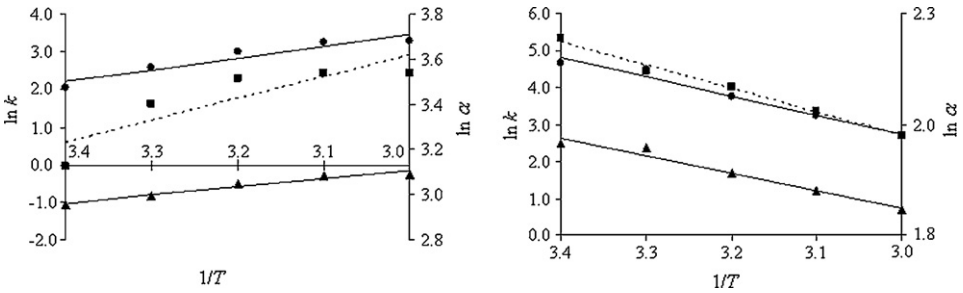


Fig. 5. van't Hoff plots of CN and CD on MIP3 in mobile phases of (a) pH 4.2 and (b) pH 11.7. Keys: (●) k_{CD}; (▲) k_{CN}; (■) α. HPLC conditions: column size, 50 mm × 2.0 mm ID; mobile phase, 50 mmol L^{-1} potassium phosphate buffer (pH 2.9)–CH_3CN (30:70, v/v) (final pH 4.2) for (a), and 50 mmol L^{-1} potassium phosphate buffer (pH 11.0)–CH_3CN (30:70, v/v) (final pH 11.7) for (b); flow rate, 0.2 mL min^{-1}; detection, 220 nm; loaded amount, 1000 ng.

than that with MIP2 despite the similar apparent maximum number of binding sites in both MIPs, suggesting that hydrophilic HEMA had a negative influence on the CD binding. On the other hand, the association constant and apparent maximum number of binding sites for MIP3 was lower than those for MIP1 and MIP2. This could be due to that only the shell of MIP3 contributes to recognition of CD. Furthermore, the association constants of CD with MIP1–3 were larger than those with NIP1–3, respectively, and that with poly(DVB) is extremely small. These results indicate that MIP1–3 has complementary binding sites for CD.

3.3. HPLC separation of CN and CD on MIPs for CD

The retention and molecular recognition properties of MIP1–3, NIP1–3 and poly(DVB) were evaluated in HPLC using a mixture of phosphate buffer and acetonitrile as the mobile phase. Table 3 shows the effects of mobile phase pH on the retention factors of CN and CD and their stereoseparation factors on MIP1–3, NIP1–3 and poly(DVB). Extremely low retentions for CN and CD on NIP1-3 and poly(DVB) were observed, resulting in earlier elution of CD than CN, while the retention factor of CD was much larger than that of CN on MIP1–3, suggesting that stereoselective binding sites were formed in these imprinted polymers. With an increase in the mobile phase pH, the retention factors of CN and CD and their stereoseparation factors increased due to ionic interactions of their nitrogen atoms with negatively charged MAA in the imprinted polymers. On the other hand, the retention factors of CN and CD and their stereoseparation factors decreased with an increase in the acetonitrile content (data not shown). These results indicated that in aqueous media, the hydrophobic and ionic interactions between the analytes and polymers are dominant for the retention and molecular recognition process. Among the MIPs prepared, MIP1 gave the highest retention factor for CD, while MIP2 showed the lowest retention factor for CD. This might be due to a decrease in hydrophobicity of MIP2 by introduction of hydrophilic HEMA. It is interesting that MIP3 having imprinting sites only on its surface showed the highest stereoseparation factor among the MIPs prepared, whose value is estimated to be 38. The shorter diffusion paths of MIP3, compared to those of MIP1, could likely reduce the band broadening and give the higher column efficiency. It is apparent that resolution of CD and CN on MIP3 is superior to that on MIP1 (Fig. 4). MIP1 and MIP2 could be useful for preparative chromatography because of larger association constant and apparent maximum number of binding sites, while MIP3 could be useful for analytical applications.

In our previous study [17], we prepared the MIP for CD by multi-step swelling and polymerization. Under the same mobile phase condition with in Fig. 3a, the retention factors of CN and CD were 0.81 and 8.9, respectively, resulting in the stereoseparation factor of 11. This indicates that MIP1–3 prepared by precipitation polymerization gives higher recognition abilities for CD than the MIP prepared by multi-step swelling and polymerization. The MIP for CD prepared by bulk polymerization gave the stereoseparation factor of 31 in an organic mobile phase [15]. The advantage of precipitation polymerization is that higher stereoseparation factor of CD could be obtained without tedious preparation steps.

3.4. Effect of column temperature

Fig. 5 shows van't Hoff plots of CD and CN on MIP3, where the mobile phases used were 50 mmol L^{-1} potassium phosphate buffer containing 70 (v/v%) acetonitrile (final pH 4.2 and 11.7, respectively). It is interesting that the retention factors of CN and CD, and their stereoseparation factors increased with an increase in column temperature in a mobile phase of pH 4.2, while those decreased with an increase in column temperature in a mobile phase of pH 11.7. Thus, the stereoseparation process is entropy-driven in the former mobile phase, while the enthalpy-driven interactions seem to be dominant in the latter mobile phase. Similar results were observed with the MIP for CD prepared by a multi-step swelling and polymerization method [17].

4. Conclusions

Three monodispersed MIPs for CD have been synthesized by precipitation polymerization. MIP1 was prepared using MAA as a functional monomer and DVB as a cross-linker and MIP2 was prepared with further addition of HEMA as a co-monomer. For the preparation of MIP3, core–shell type MIP, monodispersed DVB homopolymers, which are prepared by precipitation polymerization, were used as a core and CD-imprinted MAA–DVB copolymer phases were coated onto the core. Three MIPs synthesized gave monodispersed, spherical beads in micrometer sizes. Scatchard analysis of MIPs revealed that the association constant of CD with MIP1 was the highest among MIPs prepared, while that with MIP3 was the lowest. The template molecule, CD, was more retained than its stereoisomer, CN, on the three MIPs, and the stereoseparation factor of 38 was obtained with MIP3. Thermodynamic studies suggested that the retention of CD and CN on MIP3 was entropy- and enthalpy-driven, respectively, in acidic and basic mobile phases.

Acknowledgment

This work has been supported in part by the Grant-in-Aid for Scientific Research (B) (No. 19390013) from the Ministry of Education, Culture, Sports, Science and Technology, Japan.

References

[1] B. Sellergren (Ed.), Molecularly Imprinted Polymers: Man-made Mimics of Antibodies and their Applications in Analytical Chemistry, Elsevier, Amsterdam, 2001.
[2] J. Haginaka, J. Chromatogr. B 866 (2008) 3–13.

[3] J. Haginaka, H. Takehira, K. Hosoya, N. Tanaka, J. Chromatogr. A 816 (1998) 113–121.
[4] Q. Fu, H. Sambe, C. Kagawa, K.-K. Kunimoto, J. Haginaka, Anal. Chem. 75 (2003) 191–198.
[5] L. Ye, P.A.G. Cormack, K. Mosbach, Anal. Commun. 36 (1999) 35–38.
[6] J. Wang, P.A.G. Cormack, D.C. Sherrington, E. Khoshdel, Angew. Chem. Int. Ed. 42 (2003) 5336–5338.
[7] T.H. Kim, C.D. Ki, H. Cho, T. Chang, J.Y. Chang, Macromolecules 38 (2005) 6423–6428.
[8] N. Pérez-Moral, A.G. Mayes, Macromol. Rapid Commun. 28 (2007) 2170–2175.
[9] Y. Lu, C.-L. Yan, S.-Y. Gao, Appl. Surf. Sci. 255 (2009) 6061–6066.
[10] E. Turiel, J.L. Tadeo, P.A.G. Cormack, A. Martin-Esteban, Analyst 130 (2005) 1601–1607.
[11] H. Sambe, K. Hoshina, R. Moaddel, I.W. Wainer, J. Haginaka, J. Chromatogr. A 1134 (2006) 88–94.
[12] S. Wei, A. Molinelli, B. Mizaikoff, Biosens. Bioelectron. 21 (2006) 1943–1951.
[13] K. Yoshimatsu, K. Reimhult, A. Krozer, K. Mosbach, K. Sode, L. Ye, Anal. Chim. Acta 584 (2007) 112–121.
[14] W.-H. Li, H.D.H. Stöver, Macromolecules 33 (2000) 4354–4360.
[15] J. Matsui, I.A. Nicholls, T. Takeuchi, Tetrahedron Asymmetr. 7 (1996) 1357–1361.
[16] X. Huang, H. Zou, X. Chen, Q. Luo, L. Kong, J. Chromatogr. A 984 (2003) 273–282.
[17] J. Haginaka, C. Kagawa, Anal. Sci. 19 (2003) 39–42.
[18] M. Jiang, J.-H. Zhang, S.-R. Mei, Y. Shi, L.-J. Zou, Y.-X. Zhu, K. Dai, B. Lu, J. Chromatogr. A 1110 (2006) 27–34.

Talanta 80 (2010) 1719–1724

Contents lists available at ScienceDirect

Talanta

journal homepage: www.elsevier.com/locate/talanta

Polymerized ionic liquid-wrapped carbon nanotubes: The promising composites for direct electrochemistry and biosensing of redox protein

Chunhui Xiao, Xiaochen Chu, Bohua Wu, Haili Pang, Xiaohua Zhang, Jinhua Chen*

State Key Laboratory of Chemo/Biosensing and Chemometrics, College of Chemistry and Chemical Engineering, Hunan University, Lushan Road, Changsha 410082, PR China

ARTICLE INFO

Article history:
Received 16 July 2009
Received in revised form
28 September 2009
Accepted 7 October 2009
Available online 14 October 2009

Keywords:
Polymerized ionic liquid
Carbon nanotubes
Glucose oxidase
Direct electrochemistry
Biosensing

ABSTRACT

Polymerized ionic liquid-wrapped carbon nanotubes (PIL-CNTs) were firstly designed for direct electrochemistry and biosensing of redox proteins. The CNTs were coated successfully with polymerized ionic liquid (PIL) layer, as verified by transmission electron microscopy (TEM), thermogravimetric analysis (TGA) and Fourier transform infrared (FT-IR) spectroscopy. The PIL-CNTs were dispersed better in water and showed superior electrocatalysis toward O_2 and H_2O_2 comparing to pristine CNTs and the mixture of IL monomer and CNTs. With glucose oxidase (GOD) as a protein model, the direct electrochemistry of the redox protein was investigated on the PIL-CNTs modified glassy carbon (GC) electrode and excellent direct electrochemical performance of GOD molecules was observed. The proposed biosensor (GOD/PIL-CNTs/GC electrode) displayed good analytical performance for glucose with linear response up to 6 mM, response sensitivity of 0.853 μA mM^{-1}, good stability and selectivity.

© 2009 Elsevier B.V. All rights reserved.

1. Introduction

The design of new biocompatible materials with good conductivity [1], large surface area [2], and good biocompatibility [3] for biosensors has been paid considerate attention over the last decade. Several classes of materials have been investigated including carbon [4–6], polymer [7,8], silicate [9], and metal nanoparticles [10]. Among these materials, carbon nanotubes (CNTs) are leading the development of the biosensor materials because of their outstanding physical and electronic properties (such as high conductivity, specific surface area and electrocatalytic activity) [11,12]. CNTs modified electrodes have been illustrated to improve electrochemical behavior of important biochemical matters such as hydrogen peroxide [13], NADH [14], catecholamine [15], dopamine, uric acid [16], 3,4-dihydroxyphenylacetic acid [17], hydrazine [18], and nucleic acid [19]. On the other hand, many redox proteins such as hemoglobin [20], myoglobin [21], horseradish peroxide [22], cytochrome c [23], and GOD [24,25] showed direct electron transfer in a series of CNTs modified electrodes.

On the other hand, room temperature ionic liquids (ILs), are composed of two asymmetrical ions with opposite charges that only loosely fit together with low melting point (<100 °C), high ionic conductivity and a wide electrochemical window. Due to the excellent physicochemical properties, ionic liquids have been extensively used as the modifiers for the CNT-based electrode to fabricate the biosensors with fast electron transfer rate and good enzyme stability [26–29]. Although the general method of physically mixing into composite matrix to immobilize ionic liquid units on the CNT-based electrode is facilitated, the quantity of IL unit binding on the surface of CNTs is limited and IL components leak easily from the electrode due to their wide solubility in the solutions, especially during the electrochemical measurements. Strategies in which ionic liquid monomer is directly polymerized on the surface of CNTs to form stable ionic liquid functionalized composites offer a solution to this problem. Recently, our group developed an approach to obtain high dispersion and narrow size distribution of metal nanoparticles on the surface of CNTs functionalized by polymerized ionic liquid (PIL) and the metallic nanoparticles/PIL-CNTs nanohybrids showed excellent electrocatalytic properties toward methanol oxidation [30]. However, according to our best knowledge, no works applied polymerized ionic liquid-wrapped carbon nanotubes (PIL-CNTs) to construct biosensors.

In this paper, with GOD as a protein model, we have developed a new biosensor based on the PIL-CNTs for the first time, which combined the excellent physicochemical properties of CNTs with the good biocompatibility and unique ionic properties of ILs. The immobilized GOD on the PIL-CNTs modified electrode shows excellent direct electrochemical response. This new bionanocomposite may offer an efficient strategy and a promising platform for the further study of direct electron transfer of the redox proteins and the development of biosensors.

* Corresponding author. Tel.: +86 731 8821818; fax: +86 731 8821818.
E-mail addresses: chenjinhua@hnu.cn, chenjh001@hotmail.com (J. Chen).

0039-9140/$ – see front matter © 2009 Elsevier B.V. All rights reserved.
doi:10.1016/j.talanta.2009.10.012

2. Experimental

2.1. Reagents and apparatus

Multi-walled carbon nanotubes (CNTs, >95%, diameter 20–60 nm, length 5–15 μm) prepared by chemical vapor deposition (CVD) were purchased from Shenzhen Nanotech Port Ltd., and used without any purification. 1-Vinylimidazole was purchased from Alfa Aesar. Glucose oxidase (E.C. 1.1.3.4, Type X-S, 136100 U/G from *Aspergillus niger*), 5 wt.% Nafion 117 solution was purchased from Sigma–Aldrich (USA). Glucose stock solution was stored overnight at room temperature before use. All other chemicals were of analytical grade. Aqueous solutions used throughout were prepared with double-distilled water obtained from a Millipore system (>18 MΩ cm).

Micrographs of transmission electron microscopy (TEM) were obtained on a JEOL 3010 transmission electron microscope operating at 200 kV. The characterization of PIL-CNTs analyzed by the thermogravimetric analysis (TGA) was measured by Luxx STA 409 PC with 10 °C/min heating rate in the nitrogen flow and the FT-IR spectroscopy was carried on Nicolet 6700. All electrochemical measurements were performed on a IM6ex Electrochemical Workstation (Zahner-elektrik Gmbh & Co. KG, Germany) with a conventional three-electrode cell. A platinum wire was used as the counter electrode and a saturated calomel electrode (SCE) as the reference electrode. Except the specific statement, the electrochemical measurements were carried out in a phosphate buffer solution (PBS, 0.1 M, pH 7.0) at room temperature (25 ± 2 °C). All the potentials in this paper were referred to SCE.

2.2. Preparation of the PIL-CNTs

1-Vinyl-3-ethyl imidazolium bromide ([VEIM]Br) was synthesized according to the literature [31]. In brief, the mixture of 6.54 g bromoethane and 5.00 g 1-vinylimidazole was refluxed for 3 h at 70 °C under vigorous stirring. Then the excess bromoethane was removed on a Rotavapor for 2 h at 60 °C to obtain ILs. The PIL-CNTs were fabricated by the thermal initiation free radical polymerization of IL monomer ([VEIM]Br) to form ionic liquid polymer (PIL) on the CNT surface: a mixture of [VEIM]Br (1.56 g) and CNT powder (200 mg) was mixed and ground in an agate mortar for 30 min, subsequently mixed with 2,2′-azobisisobutyronitrile (AIBN 76 mg) as an initiator. The mixture was then placed in a flask and heated at 80 °C under nitrogen protection for 12 h. The formed black polymeric gel was then washed by ethanol to remove AIBN and unreacted monomer of [VEIM]Br. Finally the polymeric bucky gel was dried in vacuum at 60 °C for 12 h after centrifugation.

2.3. Preparation of PIL-CNTs modified electrode

Prior to use, glassy carbon electrodes (GC, 3 mm in diameter) were carefully polished to a mirror-like plane with 0.5- and 0.05-μm alumina slurries successively, followed by rinsing thoroughly with double-distilled water and dried in nitrogen atmosphere.

The PIL-CNTs modified electrode was prepared by casting 8 μL of uniform PIL-CNTs suspension (1.5 mg/mL) on the GC surface and dried under an infrared lamp. In control experiments, the CNTs (or ILs-CNTs) modified GC electrode was prepared by casting pristine CNTs (or ILs-CNTs) on the GC electrode according to the above procedure. Pristine CNTs was dispersed in DMF for better solubility and ILs-CNTs sample was prepared by dispersing ILs monomer and pristine CNTs (w/w = 35:65) in water.

For fabricating GOD biosensor, a 5 μL of GOD solution (10 mg mL^{-1} GOD in PBS, pH 7.0) was dropped on the PIL-CNTs modified GC electrode and dried at less than 4 °C, the obtained GOD/PIL-CNTs modified electrode was then washed carefully with double-distilled water and dried, followed by coating 1.5 μL of Nafion ethanol solution (1 wt.%) onto the electrode surface to avoid the leak of the GOD. The Nafion/GOD/PIL-CNTs electrode was washed thoroughly with double-distilled water. For comparison, CNTs modified electrode was also used to immobilize GOD via same procedure.

3. Results and discussion

3.1. Characterization of the PIL-CNTs nanocomposite

During the polymerization process, oligomeric 1-vinyl-3-ethyl imidazolium ion-base ionic liquid radicals, because of the strong π–π stacking interaction between the imidazolium ion moieties and CNTs, would attach to the surface of nanotubes, leading to the formation of PIL layer on the CNT surface [32,33]. Fig. 1A and B shows the TEM images of the PIL-CNTs. It can be observed that a PIL layer with the thickness of 7–8 nm presents on the outside wall of CNTs. Noteworthy is that the PIL layer is distributed uniformly along the whole tubes, which would create a uniform distribution of ionic species with positive charge that prevents aggregation of CNTs and induces stable nanotube suspensions in water.

The modification of CNTs by PIL has also been characterized by TGA and FT-IR. Fig. 1C shows the TGA spectra of the CNTs and PIL-CNTs. Comparing to the CNTs sample, the PIL-CNTs sample shows a significant weight loss in the range of 500–700 K, which confirms the PIL functionalization of CNTs. A ratio of PIL:CNTs in the as-prepared PIL-CNTs sample is also obtained to be about 35:65 (w/w). In addition, both of the PIL-CNTs and CNTs have been characterized by FT-IR spectroscopy (Fig. 1D), which shows a C=N stretch at 1500–1600 cm^{-1}. The peak of 1200 and 1258 cm^{-1} is strengthened by the modification of PIL, which may be due to increased C–N functional group from PIL.

3.2. Electrocatalysis of O_2 and H_2O_2 at the PIL-CNTs modified GC electrode

Fig. 2A shows the cyclic voltammograms (CVs) of bare GC, CNTs/GC, ILs-CNTs/GC and PIL-CNTs/GC electrodes in 0.1 M PBS (pH = 7.0) saturated with O_2 (or degassed with N_2). For the CNTs/GC, ILs-CNTs/GC and PIL-CNTs/GC electrodes, an obvious reduction wave of O_2 starts at about −0.16 V. However, for the bare GC electrode, the onset potential for O_2 reduction is about −0.32 V. It is further noted that the reduction current of O_2 on the PIL-CNTs/GC is obviously higher than that on the ILs-CNTs/GC, CNTs/GC, and bare GC electrodes and the following order can be obtained: PIL-CNTs/GC ≫ CNTs/GC ≅ ILs-CNTs/GC ≫ bare GC. This implies that the PIL-CNTs/GC electrode has the highest electrocatalytic activity for O_2 reduction, which should be beneficial to the third generation enzyme biosensors. In addition, H_2O_2 is an intermediate in most oxidase-based enzymatic reaction. Therefore, the electrocatalytic properties of the PIL-CNTs composite for the redox of H_2O_2 have also been investigated. Fig. 2B shows the background-subtracted CVs of the bare GC, CNTs/GC, ILs-CNTs/GC and PIL-CNTs/GC electrodes in 0.1 M PBS with 5 mM H_2O_2. The following order of the oxidation (or reduction) current of H_2O_2 at different electrodes can be observed: PIL-CNTs/GC ≫ ILs-CNTs/GC ≅ CNTs/GC ≫ bare GC. It is also noted that the PIL-CNTs/GC electrode has the highest electrocatalytic activity for H_2O_2 oxidation and reduction. The superior electrocatalytic activity toward O_2 reduction and H_2O_2 oxidation (reduction) of the PIL-CNTs/GC electrode might originate from the synergistic effect between the CNTs and PIL. Such excellent electrocatalytic activities for O_2 reduction and H_2O_2 oxidation (reduction) should lead to good properties of the PIL-CNT-based biosensors.

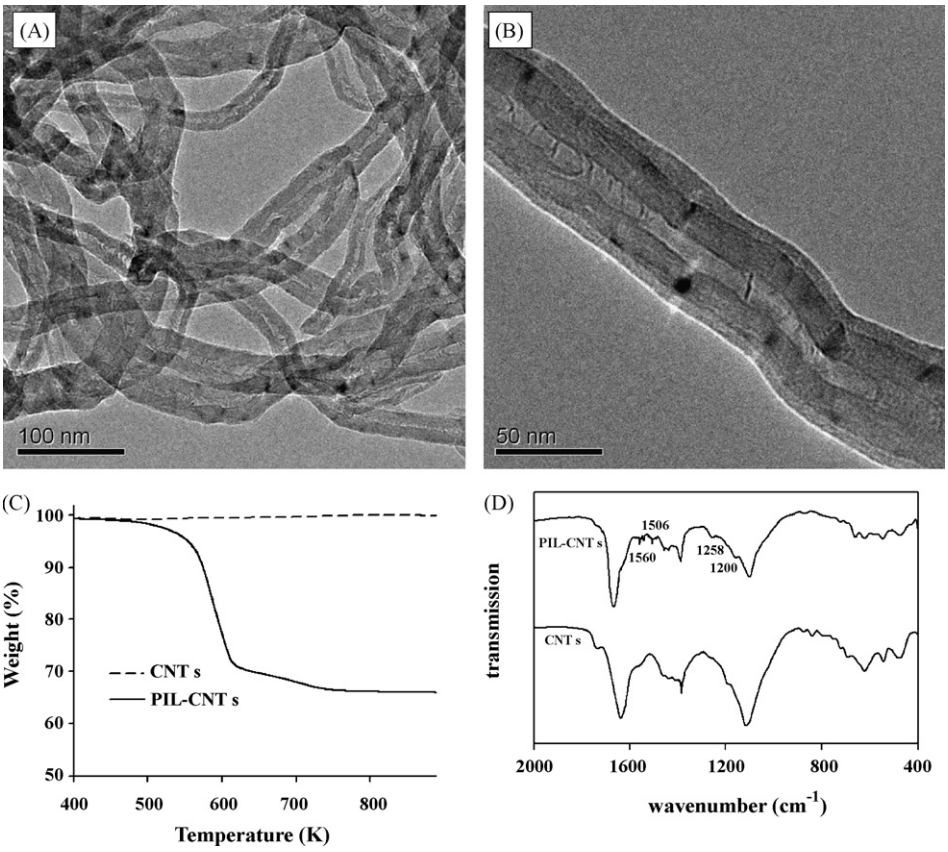


Fig. 1. TEM images of the PIL-CNTs at different magnifications (A and B) and TGA (C), FT-IR (D) spectra of PIL-CNTs and CNTs.

3.3. Direct electrochemistry of the Nafion/GOD/PIL-CNTs/GC electrode

In order to explore the application of PIL-CNTs composite in biosensors, GOD was selected as the model and the direct electrochemistry of the immobilized GOD on the PIL-CNTs/GC electrode has been investigated. Fig. 3 shows the cyclic voltammograms of the different electrodes in 0.1 M nitrogen-saturated PBS (pH 7.0) at 50 mV s^{-1}. A pair of well-defined and nearly symmetric redox peaks is observed on both of CNTs (solid) and PIL-CNTs modified electrodes (dashed) with immobilized GOD, while the related electrodes without GOD do not show such redox waves in the control experiments. This indicates that the redox waves are ascribed only to GOD redox. These features are the characteristics of the nearly reversible electron transfer process of the redox active centre (flavin adenine dinucleotide, FAD) in GOD biomolecules, suggesting that the direct electron transfer of GOD can be achieved on both CNTs and PIL-CNTs modified electrodes. From the integration of the reduction peak of GOD, the surface coverage of GOD on the Nafion/GOD/CNTs/GC and Nafion/GOD/PIL-CNTs/GC electrodes can be calculated to be 1.84 and 4.30×10^{-9} mol cm^{-2}, respectively. It is noted that GOD immobilized on the PIL-CNTs/GC electrode is much larger than that on the CNTs/GC electrode, demonstrating that the PIL-CNTs modified electrode is more beneficial to the immobilization of GOD than the CNTs modified electrode. All those may ascribe to the uniform distribution of ionic species with positive

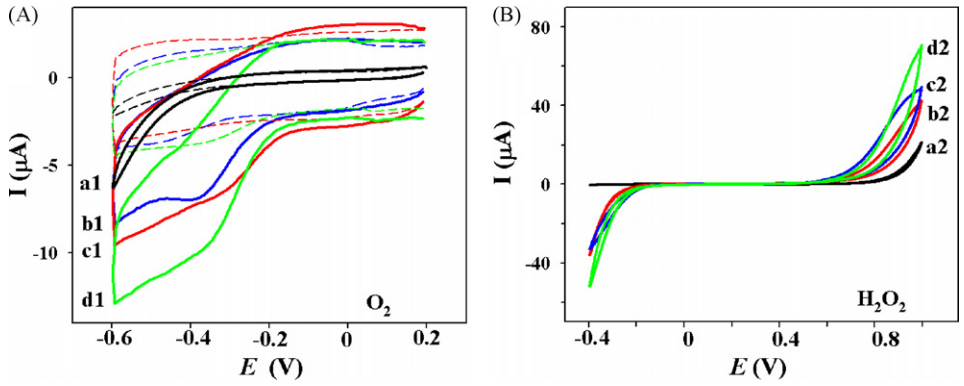


Fig. 2. (A) Cyclic voltammograms of the GC (black), CNTs/GC (red), ILs-CNTs/GC (blue) and PILs-CNTs/GC (green) electrodes in 0.1 M PBS solution saturated with O_2 (solid) or degassed with pure N_2 (dotted). Scan rate: 50 mV s^{-1}. (B) Background-subtracted CVs for 5 mM H_2O_2 at GC (black), CNTs/GC (red), ILs-CNTs/GC (blue) and PILs-CNTs/GC (green) electrodes in 0.1 M PBS solution. Scan rate: 50 mV s^{-1}. (For interpretation of the references to color in this figure legend, the reader is referred to the web version of the article.)

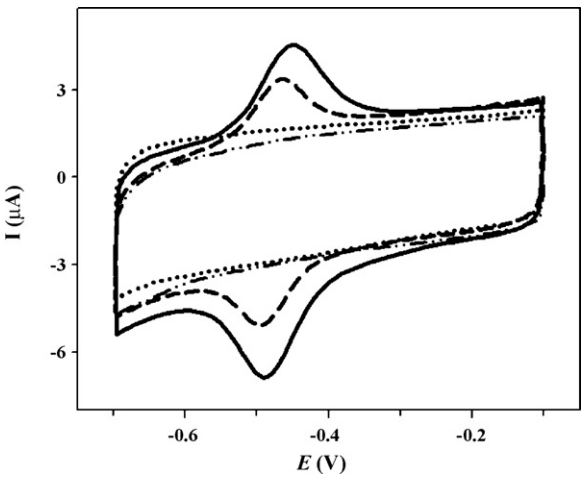


Fig. 3. Cyclic voltammograms of the Nafion/GOD/PIL-CNTs (solid), PIL-CNTs (dotted), Nafion/GOD/CNTs (dashed), CNTs (dashed-dotted) modified GCE in 0.1 M deoxygenated PBS (pH 7.0) at the scan rate of 50 mV s^{-1}.

charge present on the PIL-CNTs, resulting in more GOD molecules to be immobilized on the PIL-CNTs through electrostatic interaction between GOD (net negatively charged in the pH 7.0 PBS solution) and PIL-CNTs (positively charged). The more GOD molecules immobilized on the electrode imply that the Nafion/GOD/PIL-CNTs/GC electrode should have better analytical performance. On the other hand, for the Nafion/GOD/PIL-CNTs/GC electrode, the formal potential (E^0) was calculated by averaging the cathodic and anodic peak potentials and is ca. −0.471 V, which is close to the values reported previously [34,35]. The related anodic peak potential ($E_{p,a}$) and cathodic peak potential ($E_{p,c}$) are −0.455 and −0.487 V, respectively and the peak-to-peak potential separation is about 32 mV. The small peak-to-peak potential separation value indicates that GOD immobilized on the PIL-CNTs/GC electrode has a fast electron transfer rate, due to the strong interaction of GOD with the PIL-CNTs and the high conductivity of the PIL-CNTs [35].

The effect of the scan rate on the cyclic voltammetric response of the Nafion/GOD/PIL-CNTs/GC is shown in Fig. 4A and B. The anodic and cathodic peak currents increase linearly with the increase of the scan rate from 25 to 225 mV s^{-1}, indicating that the GOD immobilized on the PIL-CNTs/GC electrode demonstrates a surface-controlled process, not a diffusion-controlled process. It is well known that the direct electrochemistry of GOD is a two-electron coupled with two-proton reaction, which undergoes a redox reaction as follows [36]:

$$\text{GOD-FAD} + 2e^- + 2H^+ \leftrightarrow \text{GOD-FADH}_2 \quad (1)$$

Based on Eq. (1), the direct electron transfer process of GOD will be affected by the solution pH value. Fig. 4C shows the cyclic voltammograms of the Nafion/GOD/PIL-CNTs/GC electrode in the PBS with different pH values. From Fig. 4C, stable and well-defined cyclic voltammograms can be observed in the pH range of 5.0–8.0. The increase of the solution pH value causes a negative shift of both cathodic and anodic peak potentials. Fig. 4D shows the effect of the solution pH value on the formal potential (E^0) of the Nafion/GOD/PIL-CNTs/GC electrode. It can be seen that the formal potential depends linearly on the pH value in the range of 5.0–8.0 with a slop of −52.7 mV/pH (r = 0.9971), which is close to the theoretical value of −58.6 mV/pH according to the reaction shown in Eq. (1).

3.4. Biosensing application of the Nafion/GOD/PIL-CNTs modified GC electrode

On the basis of the high electrocatalytic activity of the PIL-CNTs nanocomposite toward O_2 reduction and good direct electrochemical behavior of GOD on the PIL-CNTs/GC electrode, a third

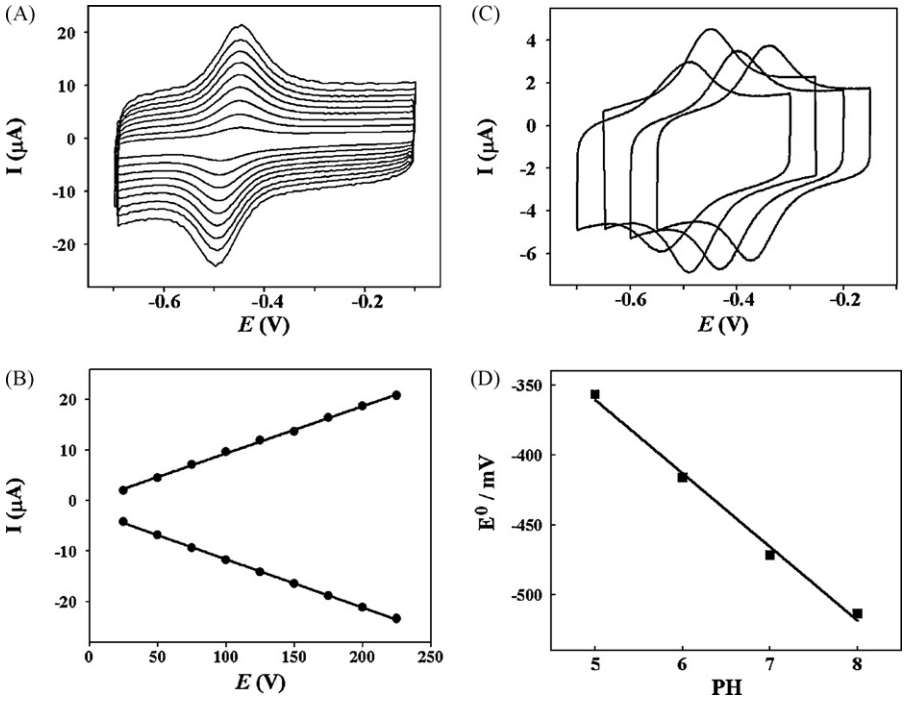


Fig. 4. (A) Cyclic voltammograms of the Nafion/GOD/PIL-CNTs modified GC electrode in 0.1 M deoxygenated PBS (pH 7.0) at scan rates of 25, 50, 75, 100, 125, 150, 175, 200, 225 mV s^{-1} (from inner to outer). (B) The dependence of the anodic and cathodic peak currents versus the scan rate. (C) Cyclic voltammograms of the Nafion/GOD/PIL-CNTs modified GC electrode in 0.1 M deoxygenated PBS with pH values of 5.0, 6.0, 7.0, and 8.0. Scan rate, 50 mV s^{-1}. (D) The dependence of the formal potential of the Nafion/GOD/PIL-CNTs modified GC electrode on the pH value.

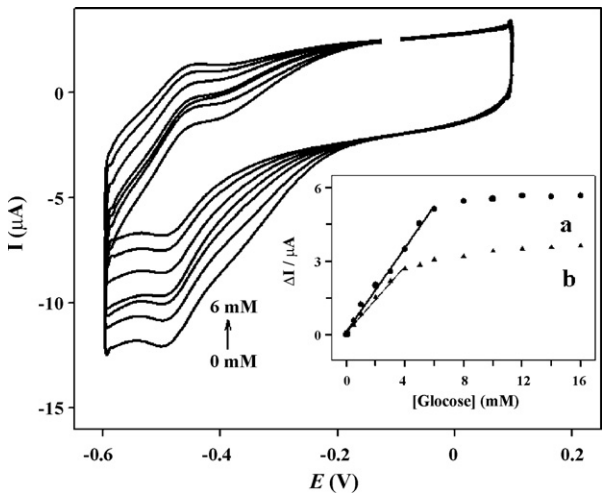


Fig. 5. Cyclic voltammograms of the Nafion/GOD/PIL-CNTs modified GC electrode in 0.1 M air-saturated PBS (pH 7.0) containing 0, 1, 2, 3, 4, 5 and 6 mM of glucose (from bottom to top) at the scan rate of 50 mV s^{-1}. The insert plot shows the dependence of the decreased reduction peak current of the Nafion/GOD/PIL-CNTs modified GC electrode (a) and Nafion/GOD/CNTs modified GC electrode (b) on the concentration of glucose in 0.1 M air-saturated PBS (pH 7.0).

generation glucose biosensor was developed further. Fig. 5 shows cyclic voltammograms of the Nafion/GOD/PIL-CNTs/GC electrode in 0.1 M air-saturated PBS (pH 7.0) with different concentrations of glucose (0.05–6 mM). The reduction current becomes smaller and smaller with the increase of the glucose concentration because of the consumption of dissolved oxygen. The insert plot in Fig. 5 shows the relationship between the decrease of the reduction peak current and the glucose concentration at the Nafion/GOD/PIL-CNTs/GC (a) and Nafion/GOD/CNTs/GC (b) electrodes. The linear response ranges for the Nafion/GOD/PIL-CNTs/GC and Nafion/GOD/CNTs/GC electrodes are 0.05–6 mM (R = 0.9946) and 0.05–4 mM (R = 0.9955), respectively. It is noted that the Nafion/GOD/PIL-CNTs/GC electrode has wider linear range than Nafion/GOD/CNTs/GC electrode. Furthermore, the sensitivity of the Nafion/GOD/PIL-CNTs/GC electrode is calculated to be 0.853 μA mM^{-1}, which is higher than that of Nafion/GOD/CNTs/GC electrode (0.676 μA mM^{-1}) and other third generation glucose biosensors reported in literatures [37–39].

To evaluate the stability of the electrode, the cyclic voltammetry measurements were carried out continuously in a 0.1 M PBS (pH 7.0). The decrease in the peak currents can be observed on both Nafion/GOD/PIL-CNTs and Nafion/GOD/CNTs electrodes. However, after 40 cycles, the decrease in the peak currents is less than 6% for the Nafion/GOD/PIL-CNTs/GC electrode and more than 20% for the Nafion/GOD/CNTs/GC electrode. It is noted further that more than 90% of peak current on Nafion/GOD/PIL-CNTs/GC electrode is retained even after 100 cycles successively scan in 0.1 PBS (pH 7.0). This implies that the Nafion/GOD/PIL-CNTs/GC electrode has better stability than the Nafion/GOD/CNTs/GC electrode, which may result from the additional electrostatic interaction between the positive sites on the PIL and negative charges in the GOD (FAD). Additionally, when the Nafion/GOD/PIL-CNTs/GC electrode was stored in 0.1 M PBS at 4 °C, it retains 94% of its initial current response toward glucose after intermittent use over a 2-week period, further corroborating the good stability of the biosensor and high efficiency of PIL-CNTs for retaining the activity of the enzyme.

Because of the low detection potential, the biosensor also shows good selectivity for glucose. In an air-saturated and stirred 0.1 M PBS solution (pH 7.0) containing 0.5 mM glucose, the response arising from 0.01 mM uric acid (UA) and 0.01 M ascorbic acid (AA) is negligible. The reproducibility of the glucose biosensor was also investigated by detecting the current response at −0.49 V to 2 mM glucose in the PBS for six successive times, the relative standard deviation (RSD) is 3.3%, demonstrating a good reproducibility of the biosensor.

4. Conclusion

In this work, we demonstrated the PIL-CNTs bionanocomposite for direct electrochemistry and biosensing application of redox protein. Due to the uniform distribution of ionic species layer and good stability of IL units, the PIL-CNTs show superior electrocatalytic activity for O_2 reduction and H_2O_2 oxidation (reduction) and provide a promising platform for direct electrochemistry of GOD. The immobilized GOD on the PIL-CNTs modified GC electrode shows good direct electrochemical response and biosensing performance for glucose. All these characteristics suggest that PIL-CNTs nanocomposite provides a potential material for direct electrochemistry and biosensing of redox proteins.

Acknowledgments

This work was financially supported by NSFC (20675027, 20975033) and the Program for Fu-Rong Scholar in Hunan Province, China.

References

[1] S. Sampath, O. Lev, Anal. Chem. 68 (1996) 2015–2021.
[2] Z.H. Dai, S.Q. Liu, H.X. Ju, H.Y. Chen, Biosens. Bioelectron. 19 (2004) 861–867.
[3] P. Roach, D. Farrar, C.C. Perry, J. Am. Chem. Soc. 127 (2005) 8168–8173.
[4] J.J. Gooding, R. Wibowo, J.Q. Liu, W.R. Yang, D. Losic, S. Orbons, F.J. Mearns, J.G. Shapter, D.B. Hibbert, J. Am. Chem. Soc. 125 (2003) 9006–9007.
[5] M. Hartmann, A. Vinu, Chem. Mater. 17 (2005) 829–833.
[6] A. Vinu, M. Miyahara, K.J. Ariga, Phys. Chem. B 109 (2005) 6436–6441.
[7] B.S. Lele, H. Murata, K. Matyjaszewski, A.J. Russell, Biomacromolecules 6 (2005) 3380–3387.
[8] A. Lewis, Y.Q. Tang, S. Brocchini, J.W. Choi, A. Godwin, Bioconjug. Chem. 19 (2008) 2144–2155.
[9] Y. Han, S. Lee, J. Ying, Chem. Mater. 18 (2006) 643–649.
[10] I. Lynch, K.A. Dawson, Nano Today 3 (2008) 40–47.
[11] Y.D. Zhao, W.D. Zhang, H. Chen, Q.M. Luo, Talanta 58 (2002) 529–534.
[12] J. Zhong, L. Song, J. Meng, B. Gao, W.S. Chu, H.Y. Xu, Y. Luo, J.H. Guo, A. Marcelli, S.S. Xie, Z.Y. Wu, Carbon 47 (2009) 967–973.
[13] J. Wang, M. Musameh, Y.H. Lin, J. Am. Chem. Soc. 125 (2003) 2408–2409.
[14] M. Musameh, J. Wang, A. Merkoci, Y.H. Lin, Electrochem. Commun. 4 (2002) 743–746.
[15] J. Wang, M. Li, Z. Shi, N. Li, Z. Gu, Electroanalysis 14 (2002) 225–230.
[16] Z.H. Wang, J. Liu, Q.L. Liang, Y.M. Wang, G. Luo, Analyst 127 (2002) 653–658.
[17] J.X. Wang, M.X. Li, Z.J. Shi, N.Q. Li, Z.N. Gu, Electrochim. Acta 47 (2001) 651–657.
[18] H.T. Zhao, H.X. Ju, Anal. Biochem. 350 (2006) 138–144.
[19] C.V. Nguyen, L. Delzeit, A.M. Cassell, J. Han, M. Meyyappan, Nano Lett. 2 (2002) 1079–1081.
[20] H.Y. Zhao, W. Zheng, Z.X. Meng, H.M. Zhou, X.X. Xu, Z. Lia, Y.F. Zheng, Biosens. Bioelectron. 24 (2009) 2352–2357.
[21] C.Y. Liu, J.M. Hu, Biosens. Bioelectron. 24 (2009) 2149–2154.
[22] Z.J. Cao, X.Q. Jiang, Q.J. Xie, S.Z. Yao, Biosens. Bioelectron. 24 (2008) 222–227.
[23] C.L. Xiang, Y.J. Zou, L.X. Sun, F. Xu, Electrochem. Commun. 10 (2008) 38–41.
[24] Q. Liu, X.B. Lu, J. Li, X. Yao, J.H. Li, Biosens. Bioelectron. 22 (2007) 3203–3209.
[25] P.P. Joshi, S.A. Merchant, Y.D. Wang, D.W. Schmidtke, Anal. Chem. 77 (2005) 3183–3188.
[26] Y.J. Zhang, Y.F. Shen, D.X. Han, Z.J. Wang, J.X. Song, F. Li, L. Niu, Biosens. Bioelectron. 23 (2007) 438–443.
[27] F. Jia, C.S. Shan, F.H. Li, L. Niu, Biosens. Bioelectron. 24 (2008) 945–950.
[28] R.T. Kachoosangi, M.M. Musameh, I. Abu-Yousef, J.M. Yousef, S.M. Kanan, L. Xiao, S.G. Davies, A. Russell, R.G. Compton, Anal. Chem. 81 (2009) 435–442.
[29] Y. Liu, L.J. Huang, S.J. Dong, Biosens. Bioelectron. 23 (2007) 35–41.
[30] B.H. Wu, D. Hu, Y.J. Kuang, B. Liu, X.H. Zhang, J.H. Chen, Angew. Chem. Int. Ed. 48 (2009) 4751–4754.
[31] X.D. Mu, J.Q. Meng, Z.C. Li, Y. Kou, J. Am. Chem. Soc. 127 (2005) 9694–9695.
[32] R. Marcilla, M.L. Curri, P.D. Cozzoli, M.T. Martinez, I. Loinaz, H. Grande, J.A. Pomposo, D. Mecerreyes, Small 2 (2006) 507–512.
[33] T. Fukushima, T. Aida, Chem. Eur. 13 (2007) 5048–5058.

[34] I. Tinoco, K. Kauer, J.C. Wang, Physical Chemistry—Principles and Applications in Biological Sciences, Prentice-Hall, Englewood Cliffs, NJ, 1978.
[35] S. Wu, H.X. Ju, Adv. Funct. Mater. 17 (2007) 585–592.
[36] C.Y. Deng, J.H. Chen, X.L. Chen, C.H. Xiao, L.H. Nie, S.Z. Yao, Biosens. Bioelectron. 23 (2008) 1272–1277.
[37] C.S. Shan, H.F. Yang, J.F. Song, D.X. Han, A. Ivaska, L. Niu, Anal. Chem. 81 (2009) 2378–2382.
[38] X.D. Shangguan, H.F. Zhang, J.B. Zheng, Electrochem. Commun. 10 (2008) 1140–1143.
[39] L.D. Zhu, R.L. Yang, J.G. Zhai, C.Y. Tian, Biosens. Bioelectron. 23 (2007) 528–535.

Talanta 80 (2010) 1725–1729

Contents lists available at ScienceDirect

Talanta

journal homepage: www.elsevier.com/locate/talanta

Direct fluorescence detection of point mutations in human genomic DNA using microbead-based ligase chain reaction

Xiangxian Meng[a], Xiaohai Yang[a], Kemin Wang[a,*], Qiuping Guo[a], Yongjun Tan[a], Qiuhua Mo[b], Xiangmin Xu[b]

[a] State Key Laboratory of Chemo/Biosensing and Chemometrics, College of Chemistry and Chemical Engineering, Biomedical Engineering Center, Key Laboratory for Bio-Nanotechnology and Molecular Engineering of Hunan Province, Hunan University, Changsha 410082, PR China
[b] Department of Medical Genetics, Southern Medical University, Guangzhou 510515, PR China

ARTICLE INFO

Article history:
Received 16 July 2009
Received in revised form
30 September 2009
Accepted 7 October 2009
Available online 14 October 2009

Keywords:
Genotyping
Point mutation
Ligase chain reaction
Microbead-enrichment
Thalassemia

ABSTRACT

This report has described a convenient genotyping method capable of detecting point mutations directly in human genomic DNA based on the combination of ligase chain reaction (LCR) and microbead-enrichment technique. LCR primers, including a biotin-labeled common primer and two fluorescence-labeled allele-specific primers, are designed for two alleles of a mutated site. When genomic DNA carries the mutated site, the common primer and allele-specific primer are ligated to form exponential amplified biotin-labeled fluorescence ligation products. These ligated products are enriched by streptavidin-coated microbeads, and genotypes are identified conveniently according to the fluorescence color of microbeads using fluorescent microscopy. Due to amplification of LCR process and enrichment of microbeads, the detection limit of the proposed method is as low as 10^{-15} mol/L templates. The method provides a convenient and simple strategy to detect point mutation directly in human genome. We have confirmed the efficiency of this approach with the identification of β-globin gene point mutation, which results in the reduced production of globin in an inherited hemoglobin disorder *thalassemia* disease.

© 2009 Elsevier B.V. All rights reserved.

1. Introduction

Single nucleotide polymorphisms (SNPs) are the prevalent genetic variations and there are more than three million SNPs in the human genome [1,2]. Many pathogenic or genetic diseases are associated with single-base mutations of particular genes [3–5]. Identification of these single-base mutations offers the possibility of improved therapeutic and prophylactic measures of these diseases [6]. Many techniques have been developed for point mutation detection [7–14]. Overcoming the complexity of 10^9 bp in human genome remains one of the principal challenges for mutation detection [8]. Typical assays for reducing this complexity to detect point mutations usually come from preamplification of genomic DNA via PCR [9], such as ligase-mediated colorimetric method [10], specific primer extension [11], allele-specific PCR [12], molecular beacon assay [13]. Recently, we established a fidelity genotyping method for point mutation detection by enhancing the melting point difference among genotypes using PCR preamplification [14]. PCR-based methods provide high sensitivity in detection, but easy cross-contamination in PCR process results in rigorous and complicated operations [9]. Several strategies have been developed to detect point mutations directly in human genomic DNA without PCR [15–18]. For example, Wabuyele et al. [9] used ligase detection reaction (LDR) and fluorescence resonance energy transfer (FRET) to identify point mutations in Kras oncogenes. Yeh et al. [17] used ligation reaction and quantum dot-mediated two-color fluorescence coincidence analysis to detect point mutation in Kras gene. Bao et al. [7] employed gold nanoparticle probes to identify gene mutations in thrombotic disorders. These methods are highly specific and sensitive, however, expensive laser detection systems or rigorous design procedures cause great limitation to their applications.

In this paper, we report a convenient method to detect point mutation directly in genomic DNA. We combine ligase chain reaction (LCR) and microbead-enrichment technique to increase sensitivity, and employ fluorescence ligation products to allow identifying analysis. According to a point mutation site, a biotin-labeled common LCR primer and two fluorescence-labeled allele-specific LCR primers are designed. When genomic DNA carries the mutation site, ligation reaction occurs and forms exponential amplified biotin-labeled fluorescence ligation products. Then streptavidin-coated microbeads capture these fluorescence ligation products. Detection is performed according to fluorescence color of microbeads using fluorescent microscopy. The method has been demonstrated as convenient point mutation detection in human genome with the genotyping of the CD17 (A → T)

* Corresponding author. Tel.: +86 731 88821566; fax: +86 731 88821566.
E-mail address: kmwang@hnu.cn (K. Wang).

0039-9140/$ – see front matter © 2009 Elsevier B.V. All rights reserved.
doi:10.1016/j.talanta.2009.10.013

point mutation of β-globin gene associated with *thalassemia* disease.

2. Materials and methods

2.1. Materials

The point mutation CD17 (A → T) of β-globin gene associated with *thalassemia* disease [19] was investigated. A series of oligos were commercially synthesized by TaKaRa Bio Inc. (Dalian, China). Sequences of these oligos are listed in Table 1. N1 and N2 were 39-nt oligos, representing two alleles of the CD17 mutated site (N1 for mutated template and N2 for wildtype template); a 50/50 mixture of N1 and N2 symbolized the heterozygous [20]. pr1–6 (Primer1, 2, 3, 4, 5, 6) was LCR primers for two alleles of the CD17 mutated site (pr1, 2, 4, 6 for mutated template; pr1, 3, 5, 6 for wildtype template). Streptavidin-coated microbeads were purchased from Sigma–Aldrich (MO, USA) and TaqDNA ligase was obtained from New England Biolabs (MA, USA). Other reagents were of analytical reagent grade. Deionized water was obtained through a Nanopure Infinity™ ultrapure water system (Barnstead/Thermolyne Corp., IA, USA).

2.2. LCR amplification

LCR was performed on a GeneAmp™ PCR System 2700 (Applied Biosystems, CA, USA). Extracted genomic DNA or synthesized templates were used as LCR template. Each LCR reaction contained 50 μL reaction volumes: 5 μL of 10× Taq ligase buffer; 4 units TaqDNA ligase; 200 nmol/L pr1–6 probes; template (10^{-10} mol/L synthesized template or 20 ng genomic DNA). The conditions of LCR were the following: initial denaturation at 94 °C for 5 min, followed by 30 cycles of denaturation at 94 °C for 30 s, then 65 °C for 5 min. The reaction was terminated in addition of 0.5 nmol/L EDTA in reaction solution. In sensitivity experiments, the concentration of template N1 was adjusted.

2.3. Coupling LCR ligated products

The proposed method employed microbeads to capture fluorescence ligation products through biotin–streptavidin interaction. Firstly, microbeads were washed twice in PBS solution. Then the washed microbeads were resuspended in PBS solution and stored at 4 °C. The capturing process involved two major steps: (1) capturing fluorescence ligation products using streptavidin-coated microbeads; (2) removal of non-specific absorption components on the surface of microbeads using washing buffer as described before [21]. We optimized the capturing time and the concentration of formamide, an important component in washing buffer. All optimization assays were run in three sample replicates.

Experiments for the optimal capturing time were performed at room temperature. Microbeads were incubated with LCR reaction solution with end-to-end shaking. Then equal volume of incubated samples was drawn at different incubating times. Here, incubating times of 20, 45, 60, 75 and 90 min were chosen.

Microbeads captured fluorescence ligation products and all other components should be washed by washing buffer in order to eliminate background signal. The washing buffer was 10 mmol/L PBS (pH 7.6) containing 150 mmol/L NaCl, 0.1% Tween 20 and 80% formamide. After incubating process ended, the drawn samples were kept quietly for 3 min and then the supernatant was removed. The deposited microbeads were incubated with the washing buffer for 5 min with end-to-end shaking and then the supernatant was removed. Finally, some deposited microbeads were resuspended in 10 μL PBS (10 mmol/L, pH 7.6) to wait for detection. The concentration of formamide in the washing buffer was adjusted while its influence was investigated.

Table 1
Oligos*.

Name	Sequence (5 → 3)
N1	CGT TAC TGC CCT GTG GGG CTA GGT GAA CGT GGA TGA AGT
N2	CGT TAC TGC CCT GTG GGG CAA GGT GAA CGT GGA TGA AGT
pr1	p-GCC CCA CAG GGC AGT AAC GTT TTT TTT TT-biotin
pr2	ROX-ACT TCA TCC ACG TTC AC CTA
pr3	FAM-ACT TCA TCC ACG TTC ACC TT
pr4	CGT TAC TGC CCT GTG GGG CT
pr5	CGT TAC TGC CCT GTG GGG CA
pr6	p-AGG TGA ACG TGG ATG AAG T
Random M0	GGT GGT GAG GCC CTG GGC AGG TTG GTA TCA AGG TTA CAA G

* Templates and probes used in this paper were designed according to Ref. [24] with some modifications. These designed sequences were used to detect CD17 (A → T) point mutation of β-globin in *thalassemia* disease. pr1 and pr2 were forward primers for mutated template, pr4 and pr6 for reverse primer. pr1 and pr3 were forward primers for wildtype template, pr5 and pr6 for reverse primer. ROX was 6-carboxy-X-rhodamine. FAM was 6-carboxy-fluorescein. p represented 5′-phosphorylation.

2.4. Fluorescent detection by fluorescent microscopy

Fluorescence ligation products on the surface of microbeads were detected by the cool CCD system in the Leica Inverted fluorescence microscopy and the corresponding quantitative values were obtained by calculating the gray scale of fluorescent particles with the software Image J as described before [22].

2.5. DNA extraction and determination genotypes by reverse dot-blot assay (RDB)

Patients, who originated from Guangzhou city, Guangdong province, South China, had classic β-*thalassemia* trait. Their genotypes were investigated using RDB method established in the laboratory of Department of Medical Genetics, Southern Medical University, China [19]. Genomic DNA was isolated from leucocytes in peripheral blood of normal subjects and patients using standard DNA extraction method [23].

3. Results and discussion

3.1. Assay principle

Schematic representation of the assay method is shown in Fig. 1. According to a mutated site, LCR primers are designed for two alleles of a mutated site (Table 1). Among these oligos, three label probes are needed for each biallelic marker. A 3′-biotin, 5′-phosphorylated common probe (pr1) is designed to terminate one base immediately upstream from the mutated site. Two fluorescence-labeled allele-specific probes are designed and have the allelic base at the 3′-end, respectively. In this study, pr2 (ROX-labeled) is the allele probe of mutated template N1 and pr3 (FAM-labeled) is the allele probe of wildtype template N2. Ligation reaction performs between two adjacent labeled probes when their hybridization is complementary to template. In contrast, in the presence of a mismatch between two adjacent probes and template, ligation will not occur. During LCR process, 3′-biotin, 5′ROX-labeled ligation product (ROX-LP) for mutated template is amplified and 3′-biotin, 5′-FAM-labeled ligation product (FAM-LP) for wildtype template is amplified. These fluorescence ligation products are captured by streptavidin-coated microbeads through biotin–streptavidin interaction, while other non-special absorption components on microbeads are washed away by washing buffer. Genotypes are determined by

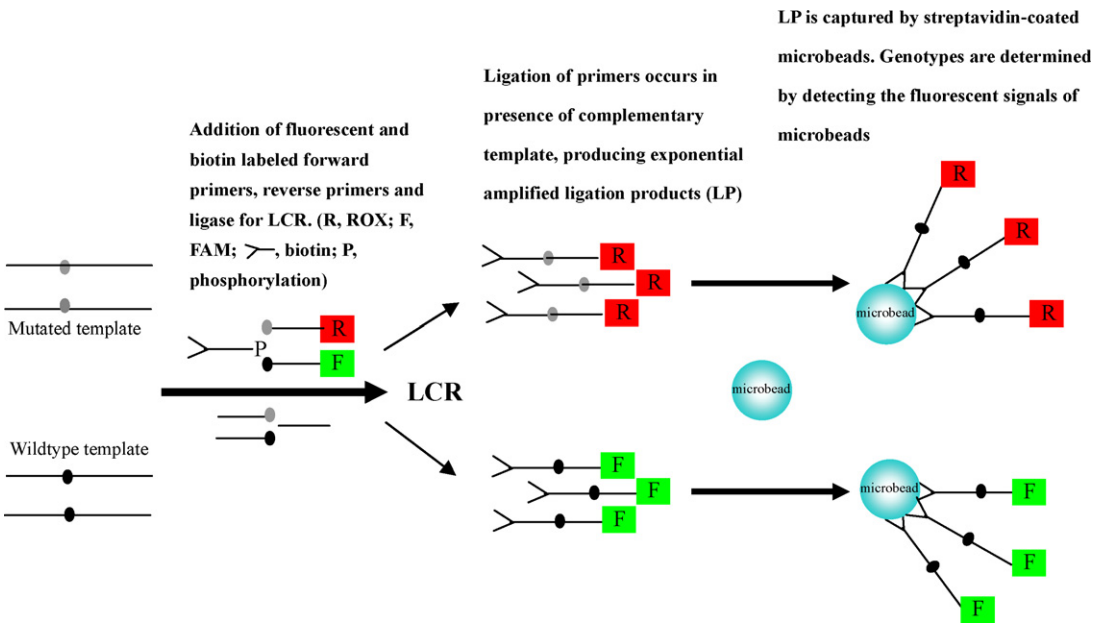


Fig. 1. Schematic diagram of the assay. Taq DNA ligase joins two adjacent primers when these primers perfectly match to the template. In this study, 3′-biotin, 5′-ROX-labeled ligation products (ROX-LP) for mutated templates are amplified and 3′-biotin, 5′-FAM-labeled ligation products (FAM-LP) for wildtype templates are amplified. These fluorescence ligation products are captured by streptavidin-coated microbeads. Genotypes are determined by detecting the fluorescence color of microbeads using fluorescent microscopy. Only three fluorescence ligation products are shown aligning in a microbead. In reality, large numbers are formed on it. R: ROX; F: FAM; P: phosphorylation; ⟩— : biotin; LP: ligation products.

detecting the fluorescence color of microbeads using fluorescent microscopy.

3.2. Detection of single-base mutations in oligos target

In evaluation of the assay, we began by analyzing single-base mutations in synthesized mock templates (Table 1). Mock template DNA (N1 for mutated template and N2 for wildtype template) and a 50/50 mixture of N1 and N2 (to mimic the heterozygous template) were detected [20]. The detection results are shown in Fig. 2. In the presence of template N1, there was only red fluorescent signal (Fig. 2A). This indicated the formation of ROX-LP, but not FAM-LP; in the presence of template N2, it occurred green fluorescent signal (Fig. 2B), which indicated the formation of FAM-LP and not

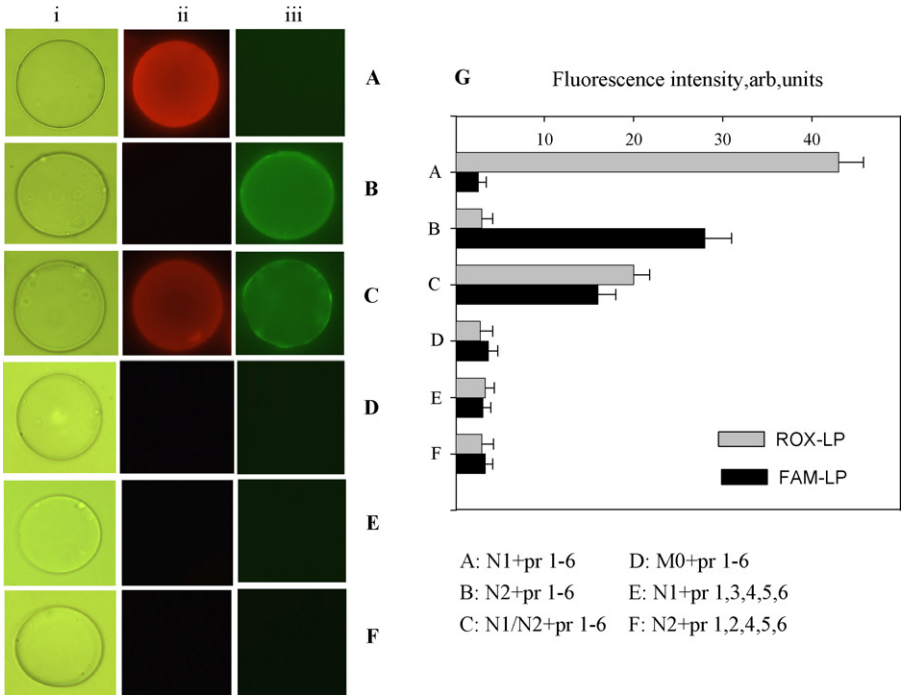


Fig. 2. Detection of point mutations in synthesized oligos target. A–F are images of samples on the fluorescent microscopy [(i) is optic images, (ii) is fluorescent images from ROX-LP (red) and (iii) is fluorescent images from FAM-LP (green)]. G was the corresponding fluorescence strength column blots of A–F. ROX-LP represented ROX-labeled ligation products; FAM-LP represented FAM-labeled ligation products. (For interpretation of the references to color in this figure caption, the reader is referred to the web version of the article.)

ROX-LP. While in the presence of a 50/50 mixture of N1/N2, it had red and green two fluorescent signals (Fig. 2C). This indicated the formation of FAM-LP and ROX-LP. By observing fluorescence color, three genotypes were identified conveniently and quickly.

In order to validate the fluorescent signal of microbeads resulting from ligation products, three control experiments were designed. One used random template M0; one used template N1 and pr3, but the corresponding ROX-labeled allele probe (pr2) was not added; another was template N2 and pr2, but the corresponding FAM-labeled allele probe (pr3) was not added. Detection results are shown in Fig. 2D–F. There was no obvious fluorescence as shown in Fig. 2D–F. This indicated that a mismatched duplex between template and allele-specific probes did not produced fluorescence ligation products. In order to quantify the fluorescence signal, the corresponding fluorescent volume blots of Fig. 2A–F are shown in Fig. 2G.

3.3. Assay refinement

It is shown clearly in Fig. 1 that this proposed method employed microbeads to enrich fluorescence ligation products through biotin–streptavidin interaction. Enhancement of the capturing number of fluorescence ligation products and reduction of the non-specific absorption on the surface of microbeads were very important to establish the method. Therefore, some experiments were performed to optimize the capturing time and the washing buffer components.

Fig. 3 displays the detection signal for template N1 at various capturing times. It showed that there was weak fluorescence strength at 20 min capturing time; however, there was strong and similar fluorescence strength at capturing times for 45, 60, 75, and 90 min, respectively. This indicated that capturing time in range from 45 to 90 min could capture effectively fluorescence ligation products. To ensure efficient capturing for fluorescence ligation products, 60 min was chosen as capturing time in experiments.

In this study, fluorescence ligation products were captured by microbeads through biotin–streptavidin interaction while all other components were washed using washing buffer. Therefore, appropriate washing buffer was important to the sensitivity and specificity of this method. We investigated the effect of formamide, an important component of the washing buffer in this method [21]. Fig. 4 shows the detection fluorescent signal for two alleles at various concentrations of formamide. It showed that there was strong fluorescent signal for mutated template N1 at various concentrations of formamide. For wildtype template N2, strong fluorescent signals was found at 30% formamide, but there was no obvious fluorescent background signal when the concentration of formamide in range from 60 to 85%. It was indicated that a wide concentration of formamide in range from 60 to 85% was very effective to remove non-specific absorption components. To eliminate efficiently non-specific absorption fluorescent signal, 80% formamide in washing buffer was chosen in experiments.

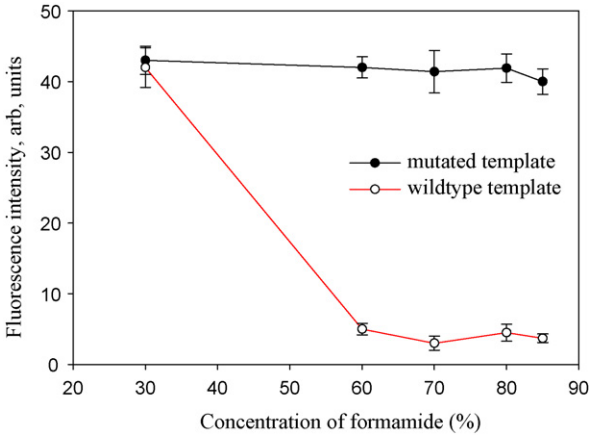


Fig. 4. The fluorescent signal of at various concentrations of formamide (30, 60, 70, 80, 85%) in washing buffer. pr1, 2, 4, 6, template N1 or N2 was used in LCR.

3.4. Detection sensitivity

The sensitivity of the system was investigated under the afore-mentioned optimized conditions. Various concentrations of template N1 were detected. It is shown in Fig. 5 that the fluorescent signal kept was rising with the enhancement of the concentration of N1. It was also found that there was obvious fluorescent signal when the concentration of N1 was low to 10^{-15} mol/L. The detection limit of the proposed method achieved to 10^{-15} mol/L templates, which made it possible to detect point mutations directly in human genomic DNA.

3.5. CD17 mutation detection in human genomic DNA

Here, genomic DNAs, isolated from leucocytes in peripheral blood of normal subjects and patients with CD17 (A → T) mutated site, were investigated. Their genotypes have been investigated using RDB method in clinic before [19]. We used the proposed method to detect these samples. Table 2 is the discrimination results of these samples. As expected, the mutated homozygosity

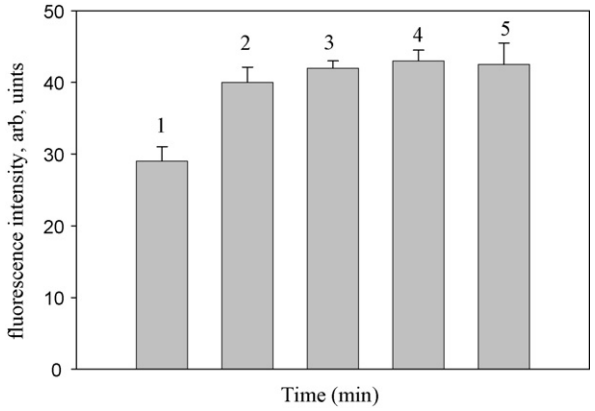


Fig. 3. The fluorescent signal at various capturing times. The capturing times of columns 1, 2, 3, 4 and 5 are 20, 45, 60, 75 and 90 min, respectively. Template N1, pr1, 2, 4, 6 were used in LCR.

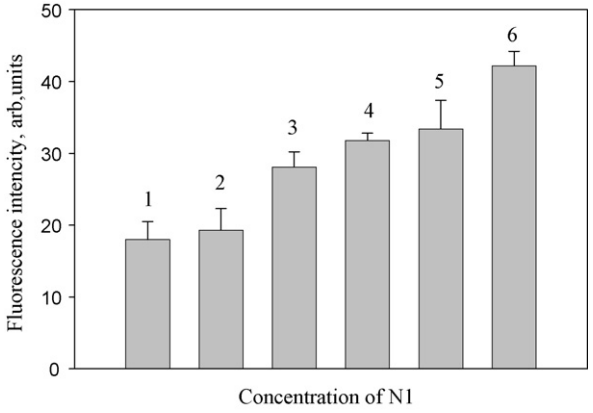


Fig. 5. The fluorescent signal at various concentrations of template N1. The concentrations of columns 1, 2, 3, 4, 5 and 6 are 1×10^{-15}, 1×10^{-14}, 1×10^{-13}, 1×10^{-12}, 1×10^{-11} and 1×10^{-10} mol/L. Template N1, pr1, 2, 4, 6 were used in LCR.

Table 2
Detection CD 17 point mutation of β-globin in *thalassemia* disease in human genomic DNA.

Sample	ROX-LP	FAM-LP	Detection resulting	RDB resulting
Sample 107			Mutant type	Mutant type
Sample 108			Mutant type	Mutant type
Sample 109			Wildtype	Wildtype
Sample 110			Mutant type	Mutant type
Sample 111			Heterozygote	Heterozygote
Sample 112			Mutant type	Mutant type
Sample 113			Wildtype	Wildtype
Sample 114			Wildtype	Wildtype
Sample 115			Heterozygote	Heterozygote
Sample 116			Mutant type	Mutant type

produced red fluorescent signal, but not green signal; the wildtype produced green fluorescent signal, but not red signal; the heterozygosity produced red and green two fluorescent signals. We found that the genotypes of these samples were all in agreement with the results of RDB. This method provides a convenient and efficient assay to detect point mutations directly in total genomic DNA. This could bring faster and cheaper genotyping possibilities in the nearest future.

4. Conclusions

In this paper, we describe a microbead-based LCR technique that could detect directly point mutations in human genomic DNA. The success of the system depends on three components: (1) accuracy of the allele discrimination reaction by thermal DNA ligase, which has been well-established, (2) specificity biotin–streptavidin interaction between microbeads and fluorescence ligation products, (3) the sensitive detection resulting from amplification of fluorescence ligation product during LCR and enrichment of streptavidin-coated microbeads.

Acknowledgements

This work was supported by the Key Project of Natural Science Foundation of China (90606003), Natural Science Foundation of China (20505007), Key Technologies Research and Development Program of China (2005EP090026), and Hunan Provincial Natural Science Foundation of China (08JJ1002).

References

[1] D.N. Cooper, B.A. Smith, H.J. Cooke, S. Niemann, J. Schmidtke, Hum. Genet. 69 (1985) 201–205.
[2] R. Sachidanandam, D. Weissman, S.C. Schmidt, J.M. Kakol, L.D. Stein, G. Marth, S. Sherry, J.C. Mullikin, B.J. Mortimore, D.L. Willey, Nature 409 (2001) 928–933.
[3] N.J. Christie, I.J. Christopher, D.G. William, F.A. Paul, L. Linda, J. Biol. Chem. 283 (2008) 34445–34456.
[4] A.D. Roses, Nature 405 (2000) 857–865.
[5] D.P. Maurizia, M. Susan, J.S. Domchek, E. Julie, D.S. Jill, Cancer Res. 68 (2008) 7006–7014.
[6] B.W. Kirk, M. Feinsod, R. Favis, R.M. Kliman, F. Barany, Nucleic Acids Res. 30 (2002) 3295–3311.
[7] Y.P. Bao, H. Martin, T.F. Wei, S.S. Marla, J.J. Storhoff, U.R. Muller, Nucleic Acids Res. 33 (2005) e15.
[8] G.C. Kennedy, H. Matsuzaki, S.L. Dong, W.M. Liu, J. Huang, G.Y. Liu, X. Xu, M.Q. Cao, W.W. Chen, J. Zhang, Nat. Biotechnol. 21 (2003) 1233–1237.
[9] M.B. Wabuyele, H. Farquar, W. Stryjewski, R.P. Hammer, S.A. Soper, Y. Cheng, F. Barany, JACS 125 (2003) 6937–6945.
[10] J.S. Li, X. Chu, Y.L. Liu, J.H. Jiang, Z.M. He, Z.W. Zhang, G.L. Shen, R.Q. Yu, Nucleic Acids Res. 33 (2005) e168.
[11] B.A. Cornell, V.L. Maksvytis, L.G. King, P.D. Osman, Nature 387 (1997) 580–583.
[12] P. Ross, L. Hall, I. Smirnov, L. Haff, Nat. Biotechnol. 16 (1998) 1347–1351.
[13] K. Takatsu, T. Yokomaku, S. Kurata, T. Kanagawa, Nucleic Acids Res. 32 (2004) e60.
[14] X.X. Meng, H.M. Li, K.M. Wang, W.H. Tan, J. Li, Q.P. Guo, X.H. Yang, Q.H. Mo, X.M. Xu, Talanta 73 (2007) 23–29.
[15] P.M. Lizardi, X.C. Huang, Z. Zhu, W.P. Bray, D.C. Thomas, D.C. Ward, Nat. Genet. 19 (1998) 225–232.
[16] P. Hardenbol, J. Baner, M. Jain, M. Nilsson, E.A. Namsaraev, G.A. Karlin, H. Fakhrai, M. Ronaghi, T.D. Willis, U. Landegren, Nat. Biotechnol. 21 (2003) 673–678.
[17] H.C. Yeh, Y.P. Ho, L.M. Shih, T.H. Wang, Nucleic Acids Res. 34 (2006) e35.
[18] D.L. Barker, M.S. Hansen, A.F. Faruqi, D. Giannola, O.R. Irsula, R.S. Lasken, M. Latterich, V. Makarov, A. Oliphant, J.H. Pinter, Genome Res. 14 (2004) 901–907.
[19] Q.H. Mo, H.L. Zhu, Y. Li, X.M. Xu, Genet. Test. 8 (2004) 257–262.
[20] W.M. Howell, M. Jobs, U. Gyllensten, A.J. Brookes, Nat. Biotechnol. 17 (1999) 87–88.
[21] H. Zhang, X.H. Yang, K.M. Wang, W.H. Tan, L.J. Zhou, X.B. Zuo, J.H. Wen, Y.Q. Chen, Electrophoresis 28 (2007) 4668–4678.
[22] X.B. Zuo, X.H. Yang, K.M. Wang, W.H. Tan, H.M. Li, L.J. Zhou, J.H. Wen, H. Zhang, Anal. Chim. Acta 567 (2006) 173–178.
[23] J. Sambrook, D.W. Russell, Molecular Cloning: A Laboratory Manual, 3rd ed., Science Press, Beijing, 2002.
[24] G. Wu, L. Hua, J. Zhu, Q.H. Mo, X.M. Xu, Br. J. Hematol. 122 (2003) 311–316.

Talanta 80 (2010) 1730–1736

Contents lists available at ScienceDirect

Talanta

journal homepage: www.elsevier.com/locate/talanta

Square wave voltammetric determination of nitrofurantoin in pharmaceutical formulations on highly boron-doped diamond electrodes at different boron-doping contents

Pedro de Lima-Neto[a,*], Adriana N. Correia[a], Rafael R. Portela[a], Murilo da Silva Julião[b], Gilberto F. Linhares-Junior[c], Janete E.S. de Lima[c]

[a] Departamento de Química Analítica e Físico-Química, Centro de Ciências, Universidade Federal do Ceará, Bloco 940, Campus do Pici, 60455-970 Fortaleza, CE, Brazil
[b] Centro de Ciências Exatas e Tecnologia, Universidade Estadual Vale do Acaraú, Av. da Universidade, 850, 62040-370 Sobral, CE, Brazil
[c] Departamento de Farmácia, Faculdade de Farmácia, Odontologia e Enfermagem, Universidade Federal do Ceará, Rua Capitão Francisco Pedro 1210, 60430-370 Fortaleza, CE, Brazil

ARTICLE INFO

Article history:
Received 21 July 2009
Received in revised form 5 October 2009
Accepted 7 October 2009
Available online 14 October 2009

Keywords:
Boron-doped diamond film electrode
Nitrofurantoin
Cyclic voltammetry
Square wave voltammetry
Electroanalytical determination

ABSTRACT

The influence of the boron-doping levels in boron-doped diamond film electrodes on the electrochemical response of nitrofurantoin (NFT) and the development of an electroanalytical procedure for NFT determination were investigated. The investigations were carried out using the techniques of cyclic voltammetry and square wave voltammetry on diamond film electrodes with different boron-doping levels (i.e., 5000, 10,000 and 20,000 mg L^{-1}). The level of boron-doping in the diamond film electrodes influenced the electrochemical reduction of NFT. The appropriate cyclic voltammetric response of NFT was obtained with Britton–Robinson buffer at pH 4 and for diamond films doped with 10,000 and 20,000 mg L^{-1} of boron. These two films were selected for the development of the electroanalytical procedure. The use of square wave voltammetry with the optimized parameters demonstrated a good linear relationship between the peak current and the NFT concentration for a wide range of concentration. The lower limit of detection for the electrodes doped with 10,000 and 20,000 mg L^{-1} of boron were 2.69×10^{-8} mol L^{-1} (6.40 μg L^{-1}) and 8.15×10^{-9} mol L^{-1} (1.94 μg L^{-1}), respectively, while the lower limits of quantification were 8.96×10^{-8} mol L^{-1} (21.33 μg L^{-1}) and 2.72×10^{-8} mol L^{-1} (6.47 μg L^{-1}), respectively. The applicability of the proposed procedure was tested using a commercial pharmaceutical formulation of NFT, and the results were compared with the procedure recommended by the British Pharmacopeia. The proposed procedure was sensitive, accurate and precise for analysis of NFT and did not require complex preparations or renovations of the electrode surface. This presents the advantage of eliminating mercury waste and minimizing the adsorptive problems related to the use of other electrodic solid surfaces.

© 2009 Elsevier B.V. All rights reserved.

1. Introduction

The replacement of mercury electrodes with solid electrodes is difficult due to the poisoning of the electrode surface, which is caused by the adsorption of compounds, analytical solution constituents or redox reaction products. This results in a loss of sensitivity and reproducibility. The search for non-toxic solid materials to be used as electrodes for the electroanalytical determination of organic compounds has risen in the last two decades. This pursuit falls into the newly developed field of green electroanalytical chemistry.

Several materials have been tested toward this aim, including solid amalgam electrodes (SAE), carbon paste electrodes (CPE), nanotube carbon paste electrodes (NTCPE), glassy carbon electrodes (GCE), solid composite electrodes (SCE) and boron-doped diamond film electrodes (BDDFE). Several reviews illustrating the use of these materials in the electroanalytical field have been published in recent years [1–11].

Among these materials, BDDFE has attracted the attention of electroanalytical researchers as a candidate for the electrochemical determination of pharmaceutical compounds, since BDDFE presents a stable background current, wide potential window for aqueous and non-aqueous electrolytes, high thermal conductivity, high hardness, high electrochemical stability, low organic molecule adsorption and high sensitivity for analytical purposes [5,8,9,12–14]. However, little attention has been given in the literature concerning the influence of different boron-doping levels

* Corresponding author. Fax: +55 85 3366 9956.
E-mail addresses: pln@ufc.br, plimaneto@yahoo.com.br (P. de Lima-Neto).

0039-9140/$ – see front matter © 2009 Elsevier B.V. All rights reserved.
doi:10.1016/j.talanta.2009.10.014

on the electrochemical response of the pharmaceutical compounds.

In addition, some reports have been published showing that nitrofurazone, which is in the group of nitrofuran antibacterial agents, has a good electrochemical response on the BDDFE [15,16]. This enables the application of this electrode for the electrochemical detection and quantification of compounds belonging to the nitrofuran group. Among them, nitrofurantoin [NFT; 1-((5-nitro-2-furfurylidene)-1-amino)hydantoin] is a drug synthesized from nitrofuran that is very useful in the treatment of urinary tract diseases. Depending on its concentration at the inflammation site, this drug may act as a bacteriostatic or bactericidal agent [17]. As pointed out by Hamman [17], this drug can act against various gram-negative bacteria, as well as some gram-positive bacteria, including *Citrobacter*, *Corynebacterium*, *Enterobacter*, *Escherichia coli*, *Klebsiella*, *Neisseria*, *Salmonella*, *Staphylococcus aureus* and *Enterococcus faecalis*. It is efficient against these bacterias in the concentration range of 1–32 $\mu g\,mL^{-1}$. However, this drug is partially metabolized, and 24 h after the application of a single oral dose, 30–50% of this drug is excreted in its original form and 1% is excreted as aminofurantoin in the urine [17]. Thus, this drug can become a water contaminant, which can be dangerous for human health.

Several non-electrochemical techniques have been reported in the literature for the detection of NFT. Colorimetric and spectrophotometric methods have been used since the 1960s [18–20], and the use of high performance liquid chromatography (HPLC) began in the 1970s [21,22]. However, according to Jain et al. [23], the colorimetric and spectrophotometric techniques do not offer a satisfactory quantification limit for the determination of this drug. In addition, the chromatographic methods require pre-treatment and extraction stages for the sample, which demand a great amount of time and increase the cost of the analysis. These stages also increase the exposure time of the drug to light, which can promote the partial photochemical degradation of the compound.

On the other hand, electroanalytical techniques are increasingly used to detect organic compounds. These techniques have several advantages, including that they are quick and reproducible, present low limits of detection and quantification and have relatively low cost compared with the more traditional techniques [8]. The two initial reports about the use of electroanalytical techniques to determine NFT came from the sixties and seventies years, when Jones et al. [24] and Mason and Sandmann [25] reported the use of the polarographic method and the reductive voltammetric method using a rotating platinum electrode, respectively. Recently, three reports have been published that demonstrate the use of square wave cathodic adsorptive stripping voltammetry for the detection on mercury electrodes [17,23] and on activated carbon fiber microelectrodes [26]. In these works, this technique was shown to be a very sensitive and selective methodology for NFT analysis [17,23,26].

A literature survey revealed that no electrochemical studies have been published concerning the electrochemical behavior of NFT on BDDFE. Thus, the aim of this work was to investigate the electrochemical behavior of NFT and develop an electroanalytical procedure to quantify this compound in commercial formulations. This was performed using BDDFE with different boron-doping levels combined with the square wave voltammetry technique.

2. Experimental

2.1. Reagents and equipment

All voltammetric measurements were taken with a potentiostat (Autolab PGSTAT 30, Metrohm-Eco Chemie), which was controlled by a computer using the General Purpose Electrochemical System software, Version 4.9 (GPES; Metrohm—Eco Chemie). A Beckman Coulter model DU 640 spectrophotometer with 1.00 cm quartz cells was used for the ultraviolet–visible (UV–vis) measurements. A Micronal B474 pH meter equipped with a 3.0 $mol\,L^{-1}$ Ag/AgCl/KCl-glass combined electrode was used to adjust the pH values. All solutions were prepared with water purified by a Milli-Q system (Millipore Corporation). A conventional cell with a three-electrode system was used in all electrochemical experiments. The cell consisted of a saturated KCl Ag/AgCl/Cl^- electrode as the reference electrode, platinum wire as the auxiliary electrode and BDDFE with different boron-doping levels as the working electrode. Prior to the electrochemical measurements, N_2 gas was bubbled through the solution to eliminate any dissolved oxygen. The BDDFE employed as the working electrode was produced by LAS-INPE (São Paulo, SP, Brazil). The BDDFE were grown on planar silicon substrates by chemical vapor deposition, using previously described conditions [14]. Three boron-doping contents were used in this work: 1.9×10^{19}, 7.6×10^{20} and 1.5×10^{21} atoms cm^{-3}, corresponding to about 5000, 10,000 and 20,000 mg L^{-1}, respectively, for the ratio of boron to carbon dissolved in methanol. The working electrodes were built following the procedure described by Julião et al. [15,16]. In this procedure, the silicon substrate with the boron-doped diamond film was attached to a brass plate with silver paste for electrical contact, and it was further insulated with Teflon to protect areas other than the planar surface from contact with solutions. A stock solution of 1.0×10^{-3} mol L^{-1} USP-grade NFT dissolved in methanol (P.A.) was prepared daily. This was stored in a dark flask and kept in a refrigerator to prevent degradation. The stock solution was used as the supporting electrolyte in 0.1 mol L^{-1} Britton–Robinson (BR) buffer, which was prepared as described in the literature [27]. Solution pH was adjusted to the desired value by adding appropriate amounts of 2.0 mol L^{-1} NaOH stock solution. Prior to the voltammetric NFT experiments, the active electrode surfaces were determined by cyclic voltammetry of the $Fe(CN)_6^{4-}/Fe(CN)_6^{3-}$ in 0.1 mol L^{-1} KCl.

2.2. Working procedure

In this work, all electrochemical measurements were taken under ambient conditions. Prior to the experiments, the BDDFE was submitted to an anodic pre-treatment, which was carried out in 0.5 mol L^{-1} H_2SO_4 by applying a current of 500 mA cm^{-2} for 3 min, followed by a cathodic treatment, which was performed by applying −500 mA cm^{-2} for 10 min. Afterwards, the cyclic voltammetry (CV) experiments were conducted at 100 mV s^{-1} using the potential interval of +1.3 to −0.8 V in a cell containing 0.5 mol L^{-1} H_2SO_4 to provide the stabilized electrochemical profile of the working electrode. After each measurement with NFT, the solution was stirred thoroughly for 1 min to remove any possible residues adsorbed on the electrodic surface, thus ensuring experimental reproducibility. The cyclic voltammograms were recorded between −0.75 V and 0.0 V to evaluate the influence of different boron-doping levels on the electrochemical response of NFT on the BDDFE and also to determine the best electrolyte pH for electroanalytical purposes. Square wave voltammetry (SWV) was used for the electroanalytical determination of NFT. The following parameters were investigated to obtain the best analytical signal: peak current (I_p), peak potential (E_p), frequency of pulse potential (f), pulse amplitude (E_{sw}) and scan increment (ΔE_s). All parameters were duly optimized, as their values strongly affect the sensitivity of the voltammetry. After the optimization of the voltammetric parameters, analytical curves were obtained in pure electrolyte using the standard addition method. The standard deviation of the mean current, measured at the oxidation potential of NFT for 10 blank voltammograms in pure electrolyte (S_b), and the slope of the straight line from the analytical curves (s) were employed for the determinations of the detection

limit (DL) and of the quantification limit (QL), using $DL = 3S_b/s$ and $QL = 10S_b/s$ [28,29]. The proposed procedure was compared to the UV–vis spectrophotometric measurements, according to the procedure recommended by the British Pharmacopeia [30]. Thus, the spectrum and characteristic absorbance of NFT were evaluated at 368 nm. Analytical curves were also constructed, and the DL and QL values were calculated using the same relations employed for the voltammetric measurements. On the other hand, the S_b values were determined by the standard deviation of the y-intercept of the analytical curves. Recovery experiments were carried out using the voltammetry and spectrophotometry procedures. For this purpose, a known amount of a pharmaceutical formulation was added to the supporting electrolytes, followed by standard additions of the NFT stock solutions. The resulting analytical curves were plotted, and all measurements were taken in triplicate. The recovery efficiencies were calculated using the relationship between the determined NFT concentration, which was obtained by extrapolating the analytical curves of the corresponding spiked samples, and the NFT concentration added value, which corresponded to the nominal concentration of the samples, multiplied by 100. The precision of the proposed procedure was evaluated based on the reproducibility experiments, which were realized with different standard NFT solutions on different days (intra-day). The experimental accuracy was evaluated using the repeatability obtained in 10 replicated determinations with the same NFT solution (inter-day). The relative standard deviations (RSD) were calculated for the reproducibility and repeatability measurements, using the relationships between the standard deviation and the mean of the peak current values obtained.

2.3. Analysis of the commercial formulation

After calculating the DL and QL for the NFT determination in the supporting electrolyte, the accuracy, reproducibility, procedure precision and interference from excipients present in a commercial NFT formulation were studied. This was done by means of recovery experiments with a commercial product purchased locally. The commercial formulation chosen was Macrodantina (capsule form), which contained 100 mg of NFT. The content of 10 capsules was weighed, and the average mass of each capsule was calculated. The content was homogenized and the amount of NFT, required for the preparation of a solution with a final concentration of 1.0×10^{-3} mol L^{-1} NFT, was calculated based on the pharmaceutical product. This amount was then weighed and dissolved in methanol using an ultrasonic bath for 20 min. From this stock solution, a solution of 1.0×10^{-4} mol dm^{-3} was prepared in BR buffer. All solutions were used immediately after their preparation to prevent decomposition by light or heat.

3. Results and discussion

3.1. Cyclic voltammetry experiments

Fig. 1 shows the cyclic voltammograms of NFT in BR buffer at various pHs and the cyclic voltammograms obtained on the BDDFE containing different boron-doping levels. In these cyclic voltammograms, an irreversible reduction peak (C_1) can be observed in the cathodic scan. This cyclic voltammetric behavior was similar to that in previous reports in the literature that used other electrodic surfaces and other antibacterial nitro compounds [15–17,23,26]. The peak C_1 was shifted to more negative potential values with increasing pH, indicating the involvement of hydrogen ions in the electrode reaction. This dependence of the cathodic potential on pH is in agreement with other reports in the literature [15–17,23,26]. Experimental evidences indicate that the electrochemical reduction mechanism of the nitro group in the NFT molecule to the corresponding hydroxylamine involves four electrons and four protons [31].

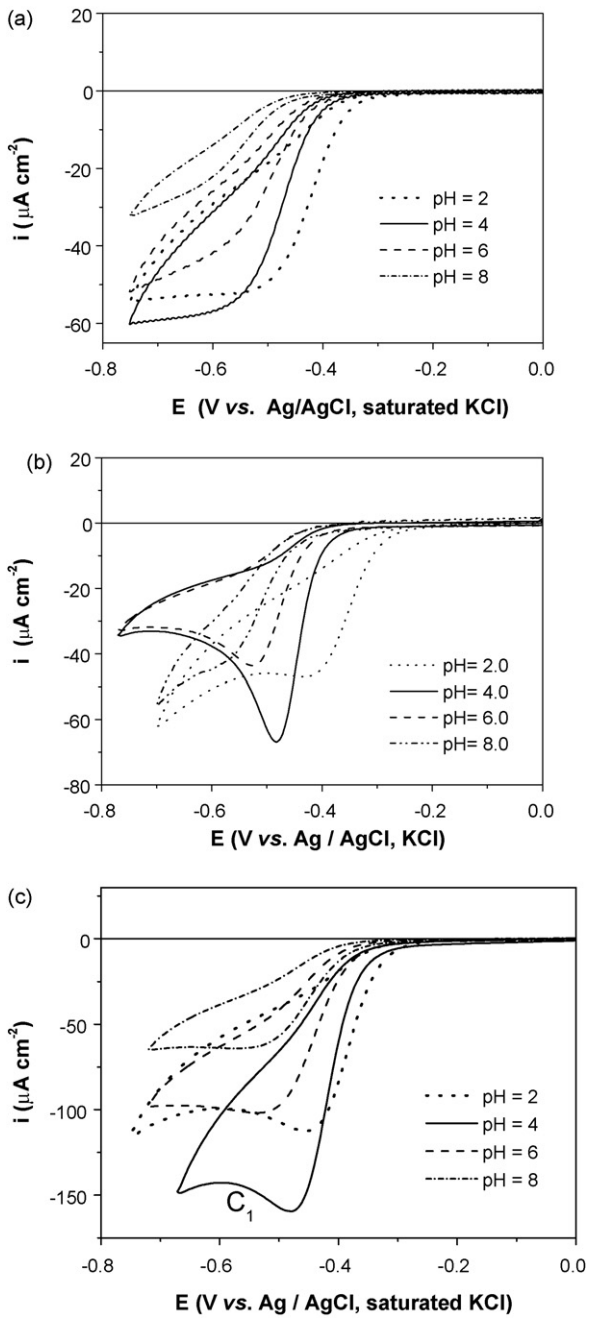


Fig. 1. Cyclic voltammograms for 1×10^{-4} mol L^{-1} NFT in BR buffer, at different pHs and at 100 mV s^{-1}, on the BDDFE with different levels of boron-doping: (a) 5000 mg L^{-1}; (b) 10,000 mg L^{-1}; (c) 20,000 mg L^{-1}.

Fig. 1 also shows that the boron-doping level affects the shape and the I_p of the peak C_1. For the electrode doped with 5000 mg L^{-1}, the peak was not well defined due to the competition between the NFT reduction and the hydrogen evolution reaction (HER). This suggests that this is not a suitable electrodic surface for the electroanalytical determination of NFT. For the electrodes with higher boron-doping contents, the peak C_1 was better defined in acidic pH because the hydrogen evolution reaction shifts to a more negative value, indicating that the increase in the boron-doping content in the diamond film decreased the electrocatalytic properties of this electrodic material for the HER. On the other hand, the peak C_1 was not well defined at pH 8.

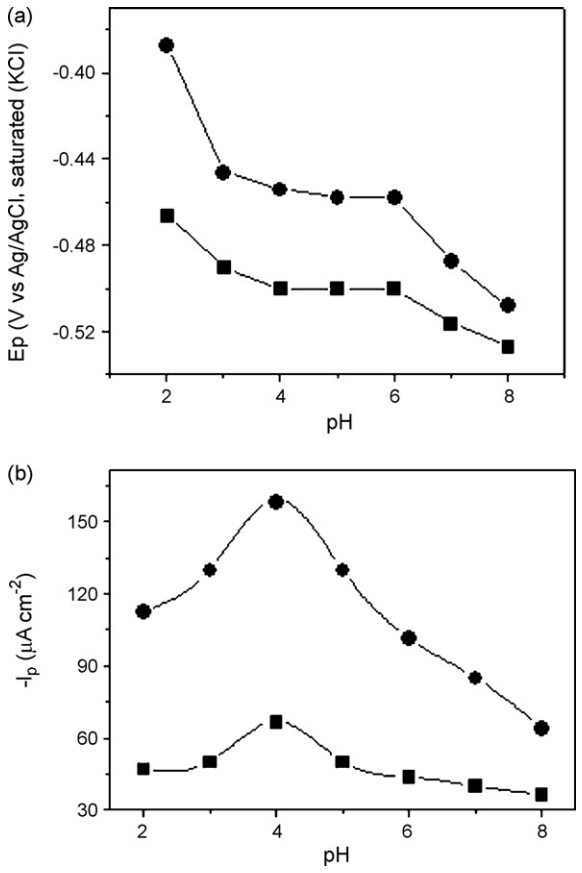


Fig. 2. Variation of E_p (a) and I_p (b) with pH for the electrochemical reduction of nitrofurantoin on the BDDFE doped with 10,000 mg L^{-1} (■) and 20,000 mg L^{-1} (●) of boron.

In order to better understand the influence of the pH in the electrochemical response of the nitrofurantoin, the variations of E_p and I_p with pH for the electrodes doped with 10,000 and 20,000 mg L^{-1} of boron are shown in Fig. 2. The E_p versus pH plot (Fig. 2a) shows three regions for both electrodes. Initially, a shift to more negative potentials was observed in the pH range from 2 to 4. For the pH range between 4 and 6, the E_p values remained approximately constant, followed by a shift to more negative potentials for higher pH values. Fig. 2a also shows that the E_p values obtained for the electrode doped with 10,000 mg L^{-1} of boron were slightly more negative than those obtained for the electrode doped with 20,000 mg L^{-1} of boron, suggesting that the increase in the amount of boron-doping favors the electrochemical reduction of the nitrofurantoin. Furthermore, the I_p versus pH plot (Fig. 2b) showed a maximum at pH 4, which indicates this pH as the optimum for electroanalytical purposes. In addition, comparing the electrodes doped with 10,000 and 20,000 mg L^{-1}, it can be observed that I_p increases about 2.4 times with twice the boron-doping level in the BDDFE. Zhang et al. [32] showed that the resistivity of the boron-doped diamond films decrease linearly with the increase in the amount of boron in the diamond film. Accordingly, the observed increase in I_p can be associated with the increase in the conductivity of the diamond film when the amount of boron is doubled. Unfortunately, a similar comparison cannot be done with the 5000 mg L^{-1} BDDFE because the current shown in the cathodic branch of Fig. 1a also has the contribution of the current related the hydrogen evolution reaction and well defined peaks were not observed. Morales et al. [33] used the polarographic technique to study the electrochemical reduction of nitrofurantoin on the Hg electrode; they observed three linear portions in the $E_{1/2}$ versus pH plot, and they found that the diffusion-limited current was also pH dependent. From the present authors [33], the decreases in the I_p for pH below 4 can be associated with an acid–base equilibrium. For pH higher than 4, the decrease in the I_p can be explained as due to the fact that the hydroxylamine intermediate in the reduction of the nitro group is no longer protonated and it is not easily reduced. Finally, the cyclic voltammetry studies at pH 4 showed a linear dependence between the peak current and the square root of the scan rate, indicating that the electrochemical reduction of NFT was controlled by diffusion. This is also in close agreement with the reports previously published in the literature for other nitro compounds [15–17,23,26].

Thus, to develop an electroanalytical procedure for the NFT determination on a BDDFE, a BR buffer solution with pH adjusted to 4.0 and electrodes doped with 10,000 and 20,000 mg L^{-1} boron were selected.

3.2. Square wave voltammetry experiments

Typical square wave voltammograms (SWV) for 1×10^{-4} mol L^{-1} NFT in BR buffer (pH 4) on the BDDFE are shown in Fig. 3. This figure shows a well-defined cathodic square wave voltammetric peak, which was observed for the two selected electrodes. The SWV parameters (f, E_{sw} and ΔE_s) were evaluated to determine the optimal values for obtaining the best analytical signal. The correlations between the peak current and the frequency of the pulse potential, the pulse amplitude and the scan increment are shown in Fig. 4.

The frequency was optimized in the range of 10–100 Hz, using an increment of 2 mV and a pulse amplitude of 50 mV. The variation of I_p with frequency for both selected electrodes is shown in Fig. 4a. A linear relationship was observed between the peak current and the frequency (f) for both selected electrodes, which yielded similar slopes. The increase in I_p with f suggests that the NFT was weakly absorbed on the electrode surfaces [34–36]. This was corroborated by the experimental evidence, as the voltammetric profile of NFT on the BDDFE surface was obtained again following agitation of the solution. For the BDDFE doped with 10,000 mg L^{-1} of boron, linearity was maintained up to 80 Hz. However, for the electrode doped with 20,000 mg L^{-1} boron, linearity was observed over the entire analyzed frequency range. In addition, the electrode doped with 20,000 mg L^{-1} boron presented higher I_p values, while the E_p values were approximately independent of frequency.

The influence of E_{sw} on the I_p intensities was evaluated for values of E_{sw} from 10 to 80 mV, and the results are shown in Fig. 4b.

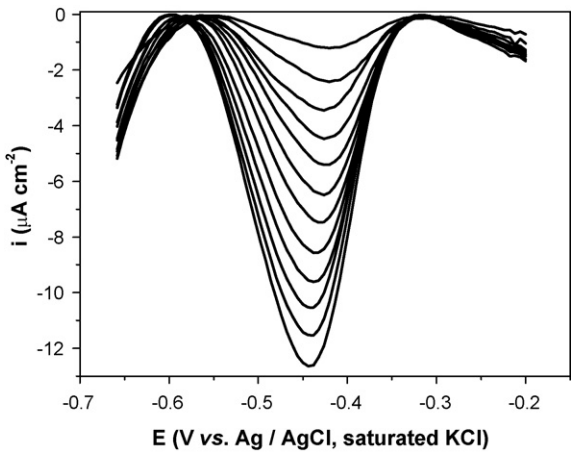


Fig. 3. Typical square wave voltammograms obtained for the NFT in BR buffer at pH 4 in the concentration range of 4.97–56.6 × 10^{-7} mol L^{-1} NFT on the BDDFE. In this case, the BDDFE electrode was doped with 10,000 mg L^{-1} boron.

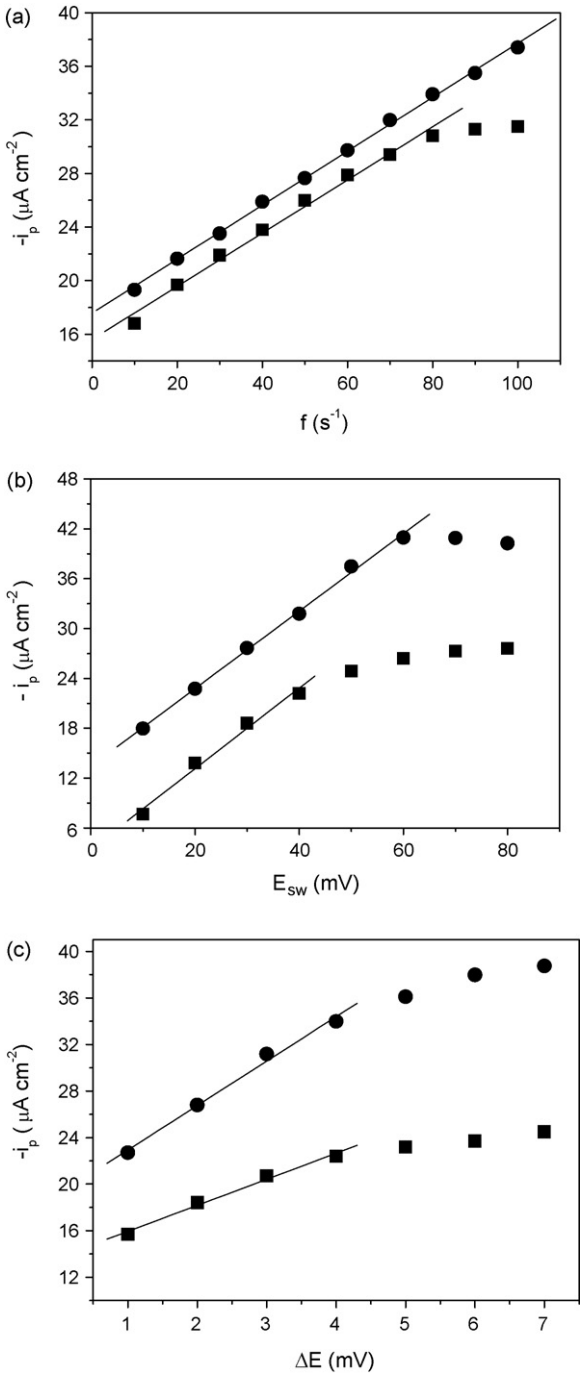


Fig. 4. Variation of the peak current with the frequency of the pulse potential (a), pulse amplitude (b) and scan increment (c) obtained from the square wave voltammograms of 1×10^{-4} mol L^{-1} NFT in BR buffer at pH 4 on the BDDFE doped with 10,000 mg L^{-1} (■) and 20,000 mg L^{-1} (●) of boron.

For both electrodes, the increase of E_{sw} led to an increase in I_p. For the 10,000 mg L^{-1} boron electrode, a linear relationship was observed up to 40 mV, while for higher E_{sw}, the I_p tended to reach a plateau. For the 20,000 mg L^{-1} boron electrode, a linear relationship between E_{sw} and I_p was observed up to 60 mV, and for E_{sw} higher than 60 mV, the I_p remained approximately constant. For the higher boron-doping contents, the I_p values were higher than those obtained for 10,000 mg L^{-1} of boron. Additionally, the E_p value showed no variation with E_{sw}.

The response of I_p with ΔE_s is shown in Fig. 4c. These results show that I_p increased with increasing ΔE_s. Additionally, a linear relationship between I_p and ΔE_s was observed from 1 mV to 4 mV, and the slopes were similar. For ΔE_s higher than 4 mV, the increase in the I_p values with ΔE_s was not linear.

Therefore, for investigations concerning the influence of the boron-doping content of the BDDFE on the electroanalytical NFT determination, the discussion presented in the previous paragraphs indicates that the optimized experimental conditions are as follows: f = 80 Hz, E_{sw} = 40 mV and ΔE_s = 4 mV for the electrode doped with 10,000 mg L^{-1} boron, and f = 100 Hz, E_{sw} = 60 mV and ΔE_s = 4 mV for the electrode doped with 20,000 mg L^{-1} boron.

3.3. Analytical curves

The optimized parameters were employed to draw the analytical curves for NFT reduction on the BDDFE in BR buffer solution. These parameters were also used to evaluate the influence of the boron-doping content on the sensitivity of the proposed procedure and for the applications of the commercial pharmaceutical formulation.

The NFT analytical curves were obtained, as described in Section 2, for the concentration range of 4.97–56.6 × 10^{-7} mol L^{-1}. Aliquots from the NFT stock solution were added consecutively to the electrochemical cell, and the voltammetric responses were recorded and are presented in Fig. 5. A linear relationship can be observed between the peak current and the added concentration of NFT for both BDDFE. The linear behavior was maintained for the electrode doped with 20,000 mg L^{-1} of boron for all studied NFT concentrations. However, for the electrode doped with 10,000 mg L^{-1}, the I_p values slightly deviated from colinearity for the higher concentrations of NFT.

Table 1 presents the analytical parameters obtained for the NFT determination using the SWV and UV–vis spectrophotometry procedures. These include the linearity range (LR), analytical curve equations, correlation coefficients (r; determined by the degree of linearity for the correlation between NFT concentration and peak currents), standard error of the intercept (SE_a), standard error of the slope (SE_b), standard deviation of the arithmetic mean of 10 blank solutions (S_b), detection limits (DL), quantification limits (QL), repeatability and reproducibility. All data shown in this table were obtained in triplicate, and the results reported here represent the average of the values obtained.

The results for the regression equation associated with the analytical curves exhibited good linearity, as shown in Table 1, indicating the validation of the proposed procedure. In addition, the electrode doped with 20,000 mg L^{-1} presented a higher slope

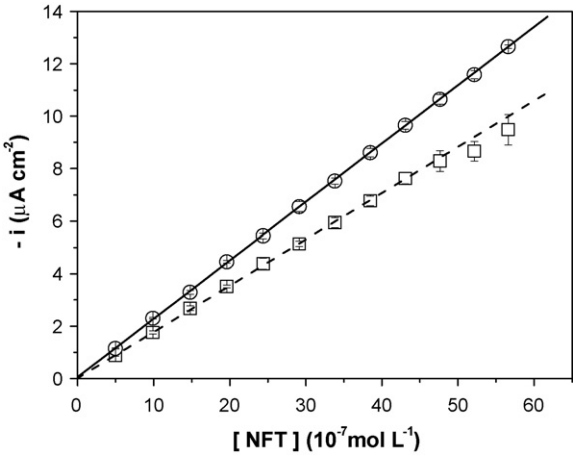


Fig. 5. Analytical curves obtained for the BDDFE with boron-doping levels of 10,000 mg L^{-1} (□) and 20,000 mg L^{-1} (○).

Table 1
Analytical parameters obtained for the NFT determination using SWV and UV–vis spectrophotometry procedures. LR: linearity range; r: correlation coefficient; SE_a: standard error of the intercept; SE_b: standard error of the slope; S_b: standard deviation of the arithmetic mean of 10 blank solutions; DL: detection limit; QL: quantification limit; RSD: relative standard deviation.

Parameters	BDDFE-SWV		UV–vis spectrophotometry
	10,000 mg L^{-1}	20,000 mg L^{-1}	
LR	$4.97–47.62 \times 10^{-7}$	$4.97–56.6 \times 10^{-7}$	$4.90–51.9 \times 10^{-7}$
Equation curve	$I_{pc} = 7.35 \times 10^{-7} + 1.74$ [NFT]	$I_{pc} = 5.74 \times 10^{-7} + 2.22$ [NFT]	ABS = $5.23 \times 10^{-3} + 1.78 \times 10^{4}$ [NFT]
R	0.9997	0.9998	0.9957
SE_a	3.5×10^{-7} A	1.1×10^{-7} A	2.59×10^{-3}
S_b	1.56×10^{-8}	6.03×10^{-9}	3.29×10^{-3}
SE_b	0.357 A mol^{-1} L	0.147 A mol^{-1} L	51.4 mol^{-1} L
DL (mol L^{-1})	2.69×10^{-8} (6.40 μg L^{-1})	8.15×10^{-9} (1.94 μg L^{-1})	5.56×10^{-7} (132 μg L^{-1})
QL (mol L^{-1})	8.96×10^{-8} (21.33 μg L^{-1})	2.72×10^{-8} (6.47 μg L^{-1})	1.85×10^{-6} (440 μg L^{-1})
Repeatability (%)	1.20% (n = 10)	0.95% (n = 10)	4.37% (n = 13)
Reproducibility	3.40% (n = 5)	1.19% (n = 5)	7.22% (n = 9)

Table 2
Results obtained from the recovery curve of NFT for the commercial formulation and using the two analytical procedures employed here.

Parameters	BDDFE-SWV		UV–vis
	10,000 mg L^{-1}	20,000 mg L^{-1}	
$[NFT]_{added}$ (mol L^{-1})	9.9×10^{-7}	9.9×10^{-7}	10.15×10^{-7}
$[NFT]_{found}$ (mol L^{-1})	$(10.36 \pm 0.2) \times 10^{-7}$	$(10.23 \pm 0.2) \times 10^{-7}$	$(10.87 \pm 0.7) \times 10^{-7}$
Recovery (%)	105 ± 3	103 ± 2	107 ± 4

for the calibration curve, indicating that the increase in the boron-doping content led to an increase in the sensibility of the proposed procedure.

The validation of the procedure was also examined by evaluating the DL and QL, as described in Section 2 and as recommended by the IUPAC [28]. These values were compared to similar results obtained using UV–vis spectrophotometry, as recommended in the British Pharmacopeia [30]. As shown in Table 1, the more highly boron-doped electrodes presented lower DL and QL calculated values. The DL and QL values for both selected electrodes, as calculated by the proposed procedure, were very close to the values reported in the literature for NFT determination using SWV, with previous cathodic adsorptive stripping that utilized a mercury electrode [17,23] and a carbon fiber microelectrode [26]. The DL and QL of the proposed procedure were lower than those presented by the recommended procedure, indicating that the BDDFE combined with SWV is a suitable tool for the NFT determination. Furthermore, the BDDFE proved to be suitable electrodic surfaces for the NFT determination, as it was possible to perform the NFT determination without modification of the electrode surface or complex electrochemical pre-treatments. This enables the simplification of the analytical procedure, thus lowering the cost and providing reliable sensitivity for analytical purposes.

The precision and accuracy were also evaluated using the proposed SWV procedures, considering the two selected electrodes and using the recommended UV–vis spectrophotometry procedure. The precision was evaluated from reproducibility experiments in which five different measurements, performed on different days, were carried out employing a standard solution containing 9.9×10^{-7} mol L^{-1} NFT and using the procedure described earlier. The measurement accuracy was also evaluated from 10 repetitive determinations (repeatability) of the same standard solution.

From the obtained results (Table 1), it is apparent that the BDDFE with 20,000 mg L^{-1} boron as the doping level presented better reproducibility and repeatability compared to the BDDFE with 10,000 mg L^{-1} boron. However, the reproducibility and repeatability of the NFT electrochemical reduction process on both selected BDDFE were very good.

These results indicate that both electrodes are excellent electrodic materials for the NFT determination. They can replace other electrodic surfaces, such as mercury electrodes. Also, the proposed procedure using BDDFE with the SWV technique can be a substitute for the UV–vis spectrophotometry procedure.

3.4. Application of the proposed procedure to a commercial formulation

The determination of NFT in its pharmaceutical formulation was carried out to evaluate the applicability of the proposed procedure toward complex samples. There was no need for an extraction step prior to the drug assay. The experiments were carried out in triplicate with both the SWV and UV–vis procedures. The recovery curves were built by the standard addition method, and the recovery percentage was identified graphically, with the abscissa axis referring to the NFT concentration in the electrochemical cell. Extrapolating the curve along this axis yielded the sample concentration, allowing for the calculation of the recovery values. Table 2 shows the results obtained from the NFT recovery curve for the commercial formulation and using the two analytical procedures employed here. The calculated values are shown to be in a suitable range for analytical purposes (i.e., from 70% to 130%) [37,38], indicating that the proposed procedure is appropriate for NFT quantification in complex samples, such as pharmaceutical formulations. In addition, the recovery values for both selected electrodes were similar to those reported in the literature for the NFT determination on mercury electrodes using square wave cathodic adsorptive stripping voltammetry. These recovery values were 101.49 [18] and 99.87 [23]. Finally, the boron-doping content did not influence the recovery value.

4. Conclusions

The electrochemical reduction of NFT is influenced by the level of boron-doping in diamond film electrodes. The appropriate cyclic voltammetric response of NFT was obtained with a BR buffer at pH 4 on diamond films doped with 10,000 and 20,000 mg L^{-1} boron. The use of square wave voltammetry with the optimized parameters showed a good linear relationship between the peak current and the NFT concentration over a wide concentration range. The proposed procedure proved to be sensitive, accurate and precise for the

analysis of NFT and did not require complex preparations or renovation of the electrode surface. Finally, boron-doped diamond film electrodes can be considered as environmentally friendly alternatives for the electroanalytical determination of NFT. This presents the advantage of eliminating mercury waste and minimizing the adsorptive problems related to the use of other electrodic solid surfaces.

Acknowledgments

The authors gratefully acknowledge funding provided by the following Brazilian agencies: CNPq, CAPES, FINEP (Brazil).

References

[1] R. Baron, G.G. Wildgoose, R.G. Compton, J. Nanosci. Nanotechnol. 9 (2009) 2274.
[2] I. Švancara, K. Vytras, K. Kalcher, A. Walcarius, J. Wang, Electroanalysis 21 (2009) 7.
[3] L. Agüí, P. Yáñez-Sedeño, J.M. Pingarrón, Anal. Chim. Acta 622 (2008) 11.
[4] O. Mikkelsen, K. Strasunskiene, S.M. Skogvold, K.H. Schroder, H. Knut, Curr. Anal. Chem. 4 (2008) 202.
[5] S.H.P. Serrano, R.C.M. de Barros, M.S.S. Julião, F.R. Paula, in: J.A. Squella, S. Bollo (Eds.), Electroanalytical Aspects of Biological Significance Compounds, Transworld Research Network, Kerala, India, 2006, p. 51.
[6] B. Uslu, S.A. Ozkan, Anal. Lett. 40 (2007) 817.
[7] B. Uslu, S.A. Ozkan, Comb. Chem. High Throughput Screening 10 (2007) 495.
[8] J. Barek, J. Fischer, T. Navrátil, K. Pecková, B. Yosypchuk, J. Zima, Electroanalysis 19 (2007) 2003.
[9] G. Chen, Talanta 74 (2007) 326.
[10] K.P. Gong, Y.M. Yan, M.N. Zhang, L. Su, S.X. Xiong, L.Q. Mao, Anal. Sci. 21 (2005) 1383.
[11] B. Yosypchuk, L. Novotny, Crit. Rev. Anal. Chem. 32 (2002) 141.
[12] B. Dogan, S. Tuncel, B. Uslu, S.A. Özkan, Diamond Relat. Mater. 16 (2007) 1695–1704.
[13] H. Girard, N. Simon, D. Ballutaud, M. Herlem, A. Etcheberry, Diamond Relat. Mater. 16 (2007) 316.
[14] N.G. Ferreira, L.L.G. Silva, E.J. Corat, V.J. Trava-Airoldi, Diamond Relat. Mater. 11 (2002) 1523.
[15] M.S.S. Julião, E.I. Ferreira, N.G. Ferreira, S.H.P. Serrano, Electrochim. Acta 51 (2006) 5080.
[16] M.S.S. Julião, E.C. Almeida, N.G. Ferreira, R.G. Compton, S.H.P. Serrano, Electroanalysis 17 (2005) 269.
[17] E. Hammam, J. Pharm. Biomed. Anal. 30 (2002) 651.
[18] J.D. Conklin, R.D. Hollifield, Clin. Chem. 11 (1965) 925.
[19] J.D. Conkin, R.D. Hollifield, Clin. Chem. 12 (1966) 690.
[20] J.D. Conklin, R.D. Hollifield, Clin. Chem. 12 (1966) 632.
[21] M.B. Aufrère, B.A. Hoener, M.E. Vore, Clin. Chem. 23 (1977) 2207.
[22] T.B. Vree, Y.A. Hekster, A.M. Baars, J.E. Damsma, E. van der Kleijn, J. Chromatogr. 162 (1979) 110.
[23] R. Jain, A. Dwivedi, R. Mishra, J. Hazard. Mater. 169 (2009) 667.
[24] B.M. Jones, R.J.M. Ratcliffe, S.G.E. Stevens, J. Pharm. Pharmacol. Suppl. 17 (1965) 52.
[25] W.D. Mason, B. Sandmann, J. Pharm. Sci. 65 (1976) 599.
[26] A. Guzmán, L. Agüí, M. Pedrero, P. Yáñez-Sedeño, J.M. Pingarron, Electroanalysis 16 (2004) 1763.
[27] H.T.S. Britton, R.A. Robinson, J. Chem. Soc. 458 (1931) 1456.
[28] J. Mocak, A.M. Bond, S. Mitchel, G. Scollary, Pure Appl. Chem. 69 (1997) 297.
[29] Analytical Methods Committee, Analyst 112 (1987) 199.
[30] J.E.F. Reynolds (Ed.), Martindale. The Extra Pharmacopoeia, 31st ed., Royal Pharmaceutical Society, London, 1996.
[31] L.J. Núnez-Vergara, J.C. Sutrm, C. Olea-Azar, P. Navarrete-Encina, S. Bollo, J.A. Squella, Free Radical Res. 32 (2000) 399.
[32] R.J. Zhang, S.T. Lee, Y.W. Lam, Diamond Relat. Mater. 5 (1996) 1288.
[33] A. Morales, M.I. Toral, P. Richter, Analyst 109 (1984) 633.
[34] V. Mirceski, S. Komorsky-Lovric, M. Lovric, in: F. Sholz (Ed.), Square Wave Voltammetry—Theory and Application, Springer, Berlin, 2007.
[35] S. Komorsky-Lovrid, M. Lovrid, J. Electroanal. Chem. 384 (1995) 115.
[36] B.A. Brookes, R.G. Compton, J. Phys. Chem. B 103 (1999) 9020.
[37] ICH-Q2Bn, International Conference on Harmonization of Technical Requirements for Registration of Pharmaceuticals for Human Use, Geneva, Switzerland, November, 1996.
[38] J.N. Miller, J.C. Miller, Statistics and Chemometrics for Analytical Chemistry, Pearson Prentice Hall, UK, 2005.

Talanta 80 (2010) 1737–1743

Contents lists available at ScienceDirect

Talanta

journal homepage: www.elsevier.com/locate/talanta

Electrochemiluminescence of CdTe quantum dots as labels at nanoporous gold leaf electrodes for ultrasensitive DNA analysis

Xiaofei Hu, Rongyue Wang, Yi Ding, Xiaoli Zhang*, Wenrui Jin*

School of Chemistry and Chemical Engineering, Shandong University, Jinan 250100, China

ARTICLE INFO

Article history:
Received 10 August 2009
Received in revised form 3 October 2009
Accepted 7 October 2009
Available online 11 November 2009

Keywords:
Electrochemiluminescence
Quantum dots
DNA analysis
Nanoporous gold leaf electrode

ABSTRACT

A new electrochemiluminescence (ECL) DNA assay is developed using quantum dots (QDs) as DNA labels. When nanoporous gold leaf (NPGL) electrodes are used, sensitivity of the ECL assay is remarkably increased due to ultra-thin nanopores. In this assay, target DNA (t-DNA) is hybridized with capture DNA (c-DNA) bound on the NPGL electrode, which is fabricated by conjugating amino-modified c-DNA to thioglycolic acid (TGA) modified at the activated NPGL electrode. Following that, amino-modified probe DNA is hybridized with the t-DNA, yielding sandwich hybrids on the NPGL electrode. Then, mercaptopropionic acid-capped CdTe QDs are labeled to the amino group end of the sandwich hybrids. Finally, in the presence of $S_2O_8^{2-}$ as coreactant, ECL emission of the QD-labeled DNA hybrids on the NPGL electrode is measured by scanning the potential from 0 to −2 V to record the curve of ECL intensity versus potential. The maximum ECL intensity ($I_{m,ECL}$) on the curve is proportional to t-DNA concentration with a linear range of 5×10^{-15} to 1×10^{-11} mol/L. The ECL DNA assay can be used to determine DNA corresponding to mRNA in cell extracts in this study.

© 2009 Elsevier B.V. All rights reserved.

1. Introduction

As an analytical technique, electrochemiluminescence (ECL) assays possess several advantages such as low background noise, high sensitivity and selectivity, as well as high versatility [1]. A variety of ECL luminophores, including inorganic and organic luminophores, have been discovered and extensively applied in bioanalysis. Recently, quantum dots (QDs) as a new kind of ECL luminophores have been developed. However, analytical applications of QD ECL are still limited. It is noted that all reported analytical methods relying on ECL of QDs can be divided into two kinds based on relationship between signal and concentration. In the first kind, detected signal is proportional to concentration of target molecules. These methods are suitable only for coreactants such as H_2O_2 [2–5] and 2-(dibutylamino)ethanol [6]. In the second kind, ECL signal decreases with increasing concentration of target compounds. Some of the target compounds react with ECL coreactants (glucose [7]) or with their products in ECL pathways of QDs (thiol compounds [8–10]). Other target compounds are quenchers (proteins [11,12]) or products of their chemical (tyrosine [13]) or electrochemical reaction (catechol derivatives [14]) are quenchers. In conventional and commercial biological assays based on ECL of inorganic and organic luminophores, the luminophores are most commonly used as labels [1,15]. If QDs can serve as ECL labels of biomolecules, a variety of ECL bioassays will be developed.

Recently, Ding et al. reported a simple dealloying route to make ultra-thin nanoporous gold leaves (NPGLs) that are free-standing, highly conductive with tunable nanoporosity and very high surface area [16–18]. NPGLs can float on aqueous solution and be easily attached to a variety of substrates. Importantly, NPGLs are nearly transparent, an essential character for ECL applications. In this paper, we realize the new ECL assay mode at NPGL electrodes using CdTe QDs as the ECL label. DNA is chosen as the model biomolecule because of its importance in the study of genetic basis of diseases, clinical diagnosis and gene therapy. Indeed, our results show extraordinary and reproducible DNA detection at a concentration down to 5×10^{-15} mol/L. In order to verify the method, the DNA synthesized corresponding to cellular osteopontin (OPN) mRNA is quantified.

2. Materials and methods

2.1. Materials

Tellurium powder and sodium borohydride from Sinopharm Chemical Reagent Co., Ltd. (Shanghai, China), cadmium chloride from Alfa Aesar China Ltd. (Tianjin, China), Bovine serum albumin (BSA), thioglycolic acid (TGA) and mercaptopropionic acid (MPA, 99%) from Sigma (St. Louis, MO, USA), *N*-hydroxysuccinimide (NHS) from Huifeng Chemical Industry Ltd. (Weinan, China), L-cysteine

* Corresponding authors. Fax: +86 531 8856 5167.
E-mail address: jwr@sdu.edu.cn (W. Jin).

0039-9140/$ – see front matter © 2009 Elsevier B.V. All rights reserved.
doi:10.1016/j.talanta.2009.10.015

from KangDa Amino Acids Co. (Shanghai, China), 1-ethyl-3-(3-dimethylaminopropyl) carbodiimide hydrochloride (EDC) from Shanghai Medpep Co., Ltd. (Shanghai, China), $K_2S_2O_8$ from Tianjin Dongfang Chemical Plant (Tianjin, China), RNase H (60 U/μL) and 5× hybrid RNA degeneration buffer from TaKaRa Biotechnology Co., Ltd. (Dalian, China) and diethypyrocarbonate (DEPC) from Bio Basic Inc. (Ontario, Canada) were used in this work. Other chemicals (analytical grade) were obtained from standard reagent suppliers. The phosphate buffer (PB) (pH 7.4) consisted of 7.6×10^{-3} mol/L NaH_2PO_4, and 2.4×10^{-3} mol/L Na_2HPO_4. The physiological buffer saline (PBS) consisted of 0.15 mol/L NaCl, 7.6×10^{-3} mol/L NaH_2PO_4 and 2.4×10^{-3} mol/L Na_2HPO_4 (pH 7.4). The borate buffer consisted of 0.2 mol/L H_3BO_3 and 0.05 mol/L $Na_2B_4O_7$ (pH 7.4). DEPC water was prepared by incubating 1 L of doubly distilled water with 1 mL of DEPC for 4 h.

Single-stranded DNAs (sequences shown in Table 1) were purchased from SBS Genetech Co., Ltd. (Beijing, China). 1.00×10^{-4} mol/L stock solutions for each DNA were prepared by centrifuging for 1 min at 1000 rpm and dissolving in an appropriate volume of borate buffer and stored at −20 °C. Dilute DNA solutions were obtained by a serial dilution with borate buffer. Preparation of the DNA solutions was performed in a clean bench. To prevent the contamination from the possible repeat sampling, aliquots of DNA stock solutions were stored in sterile plastic tubes. The DNA sample synthesized from intracellular OPN mRNA and its standard solutions were provided by School of Life Science, Shandong University. All aqueous solutions were prepared with doubly distilled water. Extra care was taken to minimize contamination accordingly to our previous description [19].

2.2. Apparatus

The voltammetric and ECL measurements were performed using a CHI832 electrochemical analyzer (CH Instruments, Austin, TX, USA). A PMT (model H9305-04, Hamamatsu Photonics K. K., Japan) with a spectral width of 185–830 nm was used to measure ECL emission. A TU-1901 UV–vis spectrophotometer (Beijing Purkinje General Instrument Co., Ltd., Peking, China) and an FL-4500 spectrofluorimeter (Hitachi, Japan) were used to acquire UV–vis absorption spectra and photoluminescence spectra, respectively.

2.3. Preparation of water-soluble CdTe QDs

MPA-capped CdTe QDs were synthesized using a slightly modified procedure reported in Ref. [9]. First, NaHTe solution was synthesized. After 0.024 g of Te powder, 0.032 g of $NaBH_4$ and 5 mL of H_2O were mixed in a 50-mL three-necked pear-shaped flask, the mixture was bubbled with highly pure N_2 for 60 min at room temperature to obtain NaHTe solution (supernatant) for use. In a 100-mL three-necked flask with 50 mL oxygen-free water, 1 mL of 0.1 mol/L $CdCl_2$ and 30 μL of MPA were added and the pH value of the solution was adjusted to 9–10 using 1 mol/L NaOH. After bubbling with highly pure N_2 for 30 min, 800 μL of NaHTe solution was slowly added into the vigorously stirred oxygen-free solution. The solution was refluxed for 6 h under open-air conditions to obtain a yellow brown solution containing ~2.5-nm CdTe QDs. The mixture was dialyzed against doubly distilled water for 5 h to purify QDs. The CdTe QD solution is stable for more than 3 months at 4 °C.

2.4. Preparation of NPGLs

NPGLs were prepared by floating 12 carat white-gold leaves (Ag/Au, 1:1 by weight, Sepp Leaf Products, New York, USA) onto concentrated HNO_3 solution for 60 min [18], which were subsequently rinsed with doubly distilled water for a couple of times. During this process, nearly all Ag atoms were dissolved away, leaving behind a bicontinuous porous Au membrane structure with a thickness around 100 nm.

2.5. Voltammetric and ECL measurements

Voltammetric and ECL measurements were carried out using a three-electrode system consisted of an Au disk or a NPGL working electrode, a saturated calomel reference electrode and a Pt auxiliary electrode. The NPGL working electrode was fabricated by attaching an NPGL sample onto a 6-mm diameter Au disk electrode, which was then cured for 20 min at 120 °C in an oven. Before use, the Au disk electrode was polished with 0.05 μm γ-Al_2O_3 and cleaned with ethyl alcohol and doubly distilled water, respectively, in an ultrasonicator. Before measurements, the Au disk and NPGL electrodes were activated by performing repetitive cyclic scans between 0.0 and 1.5 V at 50 mV/s in 0.5 mol/L H_2SO_4 until stable voltammograms were obtained, followed by washing with doubly distilled water. In ECL measurements, the electrochemical cell with the three electrodes and the PMT were placed in a dark box in order to prevent any light from external sources. The Au disk or NPGL electrode faced the observation window of the PMT and was directly connected to the first working electrode port of the electrochemical analyzer. The output end of the PMT was connected to the second working electrode port of the electrochemical analyzer to record ECL intensity (I_{ECL}). ECL measurements were performed in PB-$K_2S_2O_8$ solution (0.1 mol/L PB (pH 7.4) containing 0.1 mol/L $K_2S_2O_8$ and 0.1 mol/L KNO_3). The curve of I_{ECL} versus applied potential (E) was recorded by scanning the potential from 0.0 to −2 V.

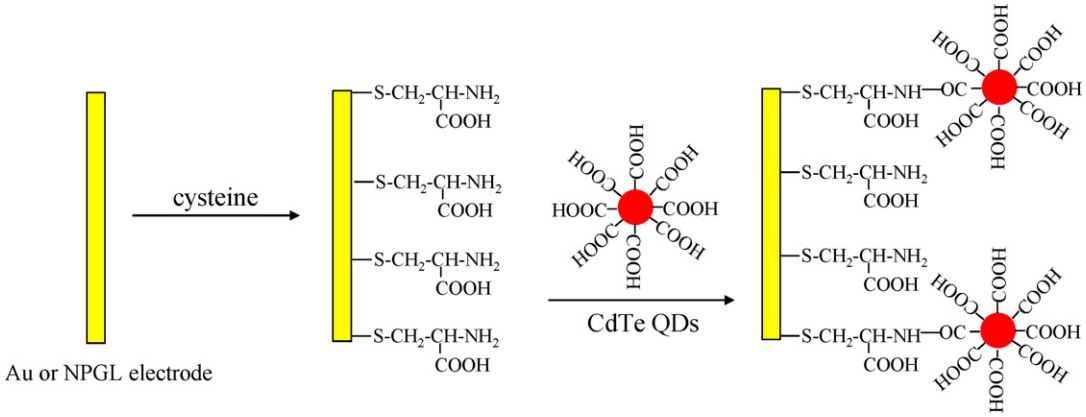
2.6. MPA-capped CdTe QDs immobilization on Au disk electrode and NPGL electrode

The procedure of immobilizing MPA-capped CdTe QDs onto the Au disk electrode or NPGL electrode was illustrated in Scheme 1. First, cysteine was self-assembled on the activated electrode described above by immersing the electrode in 0.02 mol/L cysteine

Table 1
Sequence of synthesized single-stranded used in this work.

Single-stranded DNA	Sequences
c-DNA for method investigation	NH_2-5′-T_{20} TTA TCC TTA TCA ATA TT-3′
c-DNA for determination of DNA sample corresponding to cellular OPN mRNA	NH_2-5′-T_{10}GGACCTGCCAGCAACCGA-3′
t-DNA for method investigation	5′-GGA TTA TTG TTA AAT ATT GAT AAG GAT-3′
p-DNA for method investigation	5′-TAA CAA TAA TCC T-3′-NH_2
p-DNA for determination of DNA sample corresponding to cellular OPN mRNA	5′-TTTTCACTCCAGTTGTCCCCAT-3′-NH_2
Single base mismatched DNA in the interference test	5′-GGA T**A**A TTG TTA AAT ATT GAT AAG GAT-3′[a]
Noncomplementary DNA in the interference test	5′-TAG CCT CCA GAC TCA CAA ATA CTT ATG-3′
	5′-CTC CAA ATG TAG GAG CTA TCG TT-3′
	5′-TCA TTG GAG CCA CTA TCG ACT ACG C-3′
	5′-AAG CCA TGA AGC GGC TTA TGA TTC TTA CCG CCC ACT-3′
	5′-GCG AGG ATT TGA CGA AAG CGC ACC TTA AAG-3′

[a] The boldface portion is the mutation base.



Scheme 1. Steps for immobilizing CdTe QDs onto Au disk electrode or NPGL electrode.

solution (5 mL) for 10 h. After washing twice with doubly distilled water, carboxyl group of the MPA-capped CdTe QDs was covalently conjugated to amino group of the cysteine on the electrode through EDC and NHS [20]. To do so, 25 μL of a solution containing 100 mg/mL EDC and 100 mg/mL NHS and 25 μL of 2×10^{-4} mol/L MPA-capped CdTe QD solution were dropped onto the Au disk or NPGL electrode and the assembly was incubated for 3 h for the Au disk electrode and 6 h for the NPGL electrode in a constant-humidity chamber as described in our previous work [21], followed by washing twice with doubly distilled water.

2.7. DNA determination using CdTe QDs as ECL labels

The activated NPGL electrode was immersed in 0.01 mol/L TGA solution (5 mL) for 10 h, followed by washing with doubly distilled water. Then, the NPGL electrode was incubated for 10 h with a solution consisted of 20 μL of EDC (100 mg/mL) and NHS (100 mg/mL), 10 μL of 1.0×10^{-5} mol/L amino-modified capture DNA (c-DNA) in borate buffer (pH 7.4) and 50 μL of 1 mol/L NaCl and for 3 h with 2% BSA solution (20 μL), respectively, in the constant-humidity chamber. After that, the NPGL electrode was incubated for 10 h with 2 mL of different concentrations target DNA (t-DNA) in 0.5 mol/L NaCl, for 10 h with 2 mL of 5×10^{-10} mol/L probe DNA (p-DNA) in 0.5 mol/L NaCl and for 10 h with 2 mL of 1×10^{-4} mol/L MPA-capped CdTe QD solution containing 50 mg/mL EDC and 50 mg/mL NHS, respectively. In the incubation steps, the solutions were shaken gently at 72 rpm. After each incubation, the electrode was washed five times with PBS (pH 7.4) and 1 mol/L NaCl, respectively. Finally, ECL emission of the CdTe QDs labeled on the sandwich DNA hybrids immobilized on the NPGL electrode was detected.

2.8. Quantification of DNA synthesized corresponding to intracellular OPN mRNA

The DNA sample contained the hybrid of OPN mRNA and its complementary DNA, which was synthesized from cellular OPN mRNA template in the cell extract using reverse transcription. In order to obtain single-stranded DNA, the mRNA in the RNA-DNA hybrid was digested by mixing 15 μL of the sample solution, 1 μL of RNase H, 15 μL of 5× hybrid RNA degeneration buffer and 44 μL of DEPC water, and incubating at 30 °C for 1 h. For purification of the single-stranded DNA, 7.5 μL of 3 mol/L NaOAC (pH 5.2) and 187.5 μL of 100% ethanol were added, followed by placing it at −20 °C for 1 h. Then, the DNA was collected by centrifuging for 10 min at 12,000 rpm. After washing with 70% ethanol, the DNA was dried in air. The resulting DNA was dissolved in 15 μL of DEPC water. After that, 1 μL of the DNA solution was diluted to 20 mL of 0.5 mol/L NaCl. Finally, the 2 mL of the diluted solution was used to determine DNA using the ECL method according to the procedure described above. In this case, the sequences of c-DNA and p-DNA are shown in Table 1. The maximum ECL intensity ($I_{m,ECL}$) on the I_{ECL}–E curves was used for quantification using the calibration curve method.

3. Results and discussion

3.1. Cathodic ECL behavior of CdTe QDs on NPGL electrodes

NPGLs are large scale, crack-free, large surface area, corrosion resistive and conductive electrode materials that can be easily transferred from various solutions to substrates. Because of the intrinsic hydrophilic nature of Au and the capillary force of nanopores, solutions and molecules can be readily pulled into the nanopores for electrode reactions. The scanning electron microscopy (SEM) image of NPGL in Fig. 1 displays a uniform pore size distribution centered around ~20 nm. The active surface area of the NPGL electrode can be estimated by cyclic voltammetry in 0.5 mol/L H_2SO_4 [22]. Based on the specific charge value of 386 μC/cm^2 for gold oxide reduction [23] and the area of the reduction peak on the voltammogram (Fig. 2, curve 1), we can calculate the active area to be 198 mm^2, whereas the active area of a flat Au disk electrode with the same geometric area, calculated from its voltammogram, is 26 mm^2 (Fig. 2, curve 2). This indicates a ~7.6-fold area enhancement for NPGL electrodes.

In this work, the as-prepared MPA-capped CdTe QDs in 0.1 mol/L PB (pH 7.4) can be characterized by its photoluminescence (PL) and UV–vis absorption spectra. The maximum absorption appears at 375 nm. When the QDs are exited at 385 nm, the PL maximum

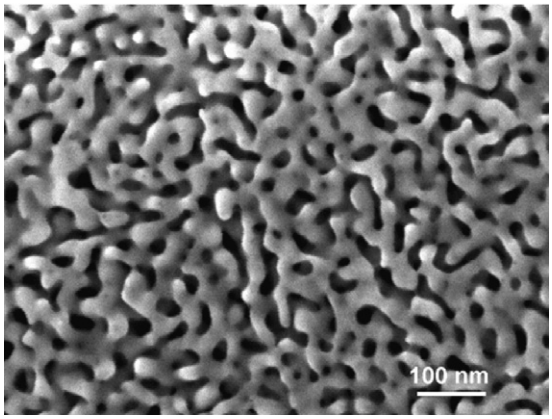


Fig. 1. Plan-view SEM image of NPGL.

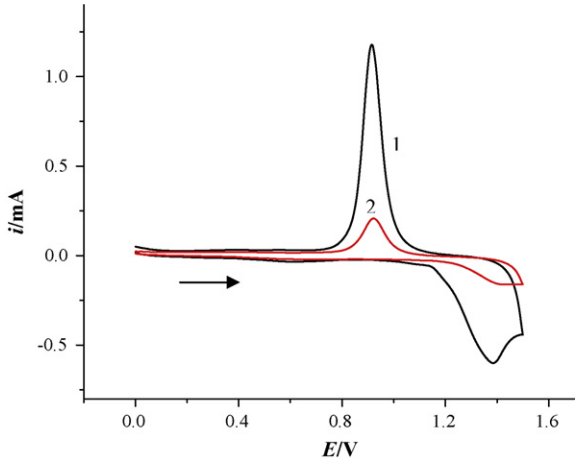


Fig. 2. Cyclic voltammograms of (1) NPGL electrode and (2) Au disk electrode with a geometric area of 28.3 mm^2 in 0.5 mol/L H_2SO_4. Scan rate: 50 mV/s.

wavelength (530 nm) is shifted to the red light direction, indicating quantum confinement [23]. The size of CdTe QDs is calculated to be ~2.5 nm based on the absorption peak on the UV–vis spectrum using the empirical equations [24].

Anodic ECL behavior and mechanism of MPA-capped CdTe QDs with O_2 [9] or sulfite/O_2 [7] as coreactant at an indium tin electrode [9] or at a paraffin-impregnated graphite electrode [7] and MPA-capped CdTe QDs with amines as coreactant at a glassy carbon electrode [14] have been investigated. Here we compare the cathodic ECL behavior of MPA-capped CdTe QDs with O_2, H_2O_2 and $S_2O_8^{2-}$ as coreactant at the Au disk electrode and NPGL electrode. The CdTe QDs were immobilized on the Au disk electrode and NPGL electrode according to the procedure described in Section 2. In this case, maximum coverage of CdTe QDs on both electrodes was obtained. Fig. 3 shows the I_{ECL}–E curves of MPA-capped CdTe QDs in air-saturated 0.1 mol/L PB (pH 7.4) containing 0.1 mol/L KNO_3 with and without H_2O_2 or $S_2O_8^{2-}$. MPA-capped CdTe QDs can emit light in all three solutions. The maximum ECL intensity ($I_{m,ECL}$) for $S_2O_8^{2-}$ is higher than that in the air-saturated solution with and without H_2O_2. Additionally, $I_{m,ECL}$ measured at the NPGL electrode is 5.7-fold higher than those at the Au disk electrode. A possible reason is that the amount of the CdTe QD immobilized on the NPGL electrode is more than that on the Au disk electrode due to its nanoporous structure with a large surface area, which results in the occurrence of ECL signal not only at the surface but also inside the nanopores of the NPGL electrode. The relationships between $I_{m,ECL}$ and the concentration of H_2O_2 or $S_2O_8^{2-}$ is shown in Fig. 4. When the concentration of H_2O_2 or $S_2O_8^{2-}$ is higher than 0.04 or 0.1 mol/L, $I_{m,ECL}$ hardly changes. The maximum value of $I_{m,ECL}$ using $S_2O_8^{2-}$ as coreactant is ~2.7-fold higher than that using H_2O_2. Therefore, ECL of CdTe QDs immobilized on the NPGL electrode coupled with $S_2O_8^{2-}$ as coreactant was used in our work.

3.2. Cathodic ECL mechanism of CdTe QDs with $S_2O_8^{2-}$ as coreactant at Au electrode

In order to investigate cathodic ECL mechanism of CdTe QDs/$S_2O_8^{2-}$ system in 0.1 mol/L PB (pH 7.4) containing 0.1 mol/L KNO_3, dissolved oxygen was removed from the solution by bubbling high-purity nitrogen, as oxygen can be reduced and catalyze ECL emission of QDs [5]. The cyclic voltammograms and I_{ECL}–E curves of PB (pH 7.4) containing 0.1 mol/L KNO_3 with and without $S_2O_8^{2-}$ at the Au disk electrode are shown in Fig. 5. In the solution without $S_2O_8^{2-}$, neither cathodic/anodic peak nor ECL was observed (curve 1 in Fig. 5A). In the presence of $S_2O_8^{2-}$, one cathodic

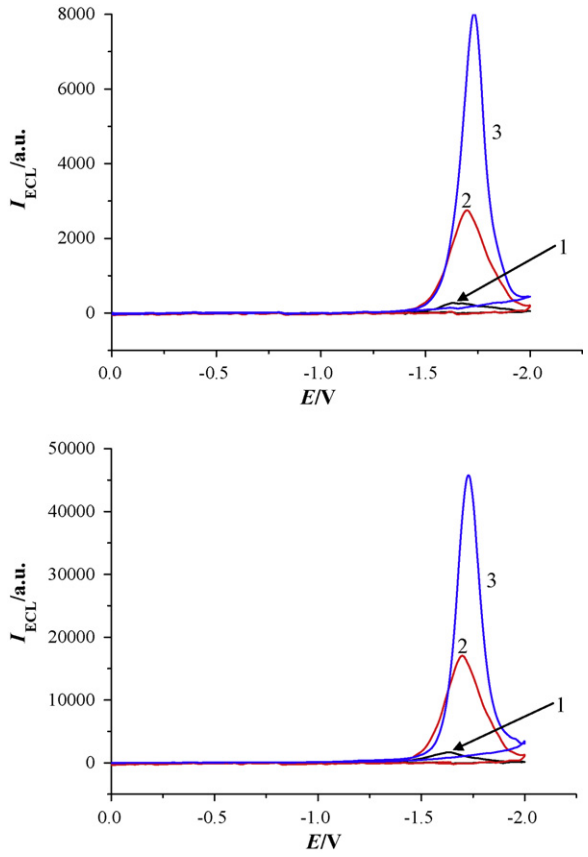


Fig. 3. I_{ECL}–E curves of MPA-CdTe QDs immobilized on (A) Au disk electrode and (B) NPGL electrode in air-saturated 0.1 mol/L PB (pH 7.4) containing 0.1 mol/L KNO_3 (1) without and with (2) 0.1 mol/L H_2O_2 or (3) 0.1 mol/L $S_2O_8^{2-}$ as the coreactant. Scan rate: 50 mV/s.

peak appears on the cyclic voltammogram (curve 2 in Fig. 5A), which corresponds to the reduction of $S_2O_8^{2-}$ to anion sulfate radical $SO_4^{\bullet-}$ according to reaction (1). In this case, no ECL emission was observed (curve 2 in Fig. 5D). The cyclic voltammograms and I_{ECL}–E curves of CdTe QDs at the Au disk electrode with and without $S_2O_8^{2-}$ in the same solution are also shown in Fig. 5. In the absence of $S_2O_8^{2-}$, a cathodic reduction peak is displayed on the voltammogram (curve 3 in Fig. 5B) and a very low ECL signal was observed (curve 3 in Fig. 5D). The cathodic peak attributes to electrochemical

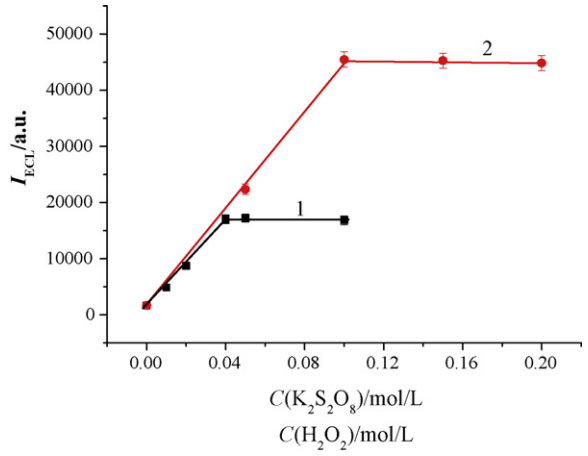


Fig. 4. Relationships between $I_{m,ECL}$ of MPA-CdTe QDs immobilized on Au disk electrode and coreactant concentration of (1) H_2O_2 and (2) $K_2S_2O_8$. 0.1 mol/L PB (pH 7.4).

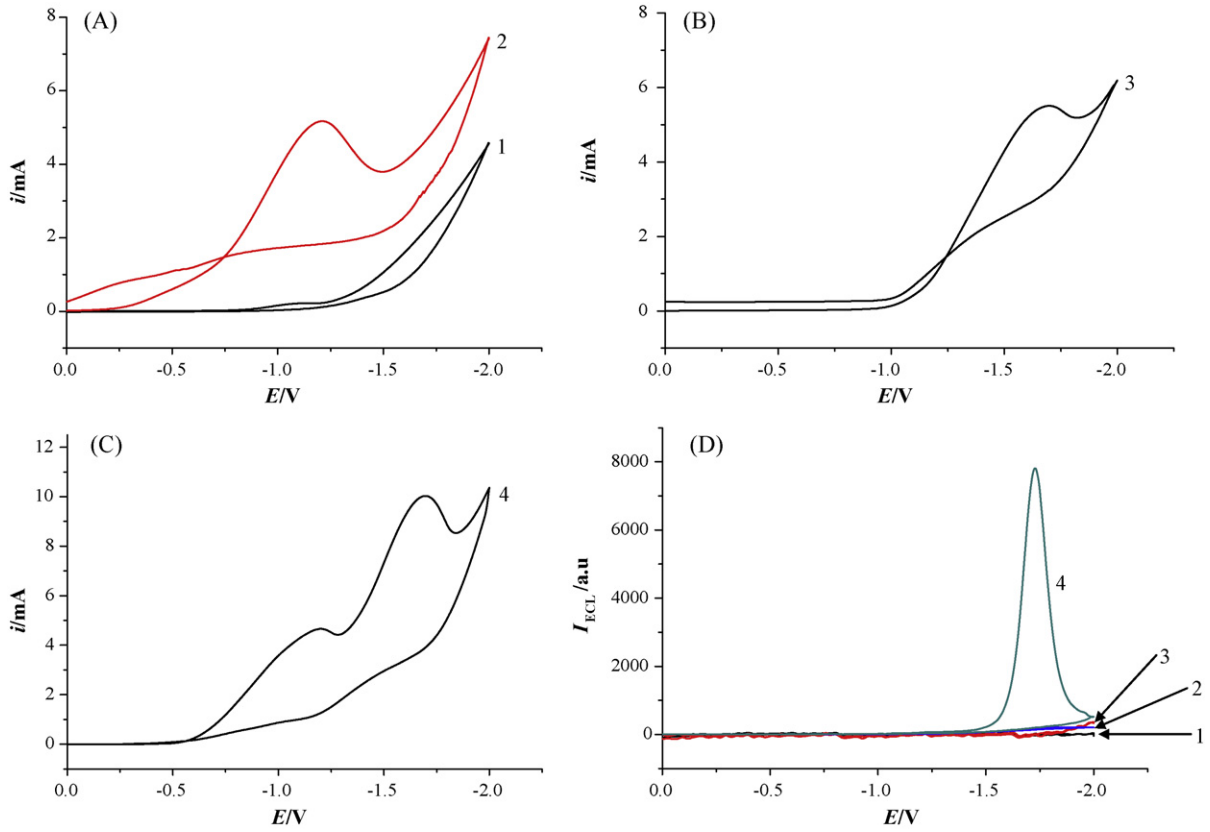


Fig. 5. (A–C) Cyclic voltammograms and (D) I_{ECL}–E curves at Au disk electrode. (1) PB (pH 7.4) containing 0.1 mol/L KNO_3 bubbled with nitrogen for 15 min, (2) (1) + 0.1 mol/L $K_2S_2O_8$, (3) (1) + MPA-CdTe QDs, and (4) (1) + MPA-CdTe QDs and 0.1 mol/L $K_2S_2O_8$. Scan rate: 50 mV/s.

reduction of the CdTe QDs, producing negatively charged radicals ($CdTe^{\bullet -}$). The electrochemical process can be expressed in reaction (2). In the presence of $S_2O_8^{2-}$, two cathodic peaks corresponding to the reduction of $S_2O_8^{2-}$ and CdTe QDs were still observed and no new peak was found (curve 4 in Fig. 5C), implying that no new electrochemical reaction occurs. In this system, a very strong ECL emission was observed with a peak potential of ~−1.75 V as indicated in curve 4 (Fig. 5D). According to the mechanism of other QDs such as Si [25], CdSe [11,26], CdS [12,27], Bi_2Te_3 [28], and ZnS QDs [29], the possible ECL mechanism of the CdTe QDs/$S_2O_8^{2-}$ system can be expressed as reactions (1)–(4): CdTe QDs and $S_2O_8^{2-}$ are electrochemically reduced to $CdTe^{\bullet -}$ and $SO_4^{\bullet -}$, respectively. The formed $SO_4^{\bullet -}$ reacts with $CdTe^{\bullet -}$ generated at the electrode by injecting a hole (h^+) into the highest occupied molecular orbital (HOMO) to produce the excited state CdTe*, which emits light.

$$S_2O_8^{2-} + e^- \rightarrow SO_4^{2-} + SO_4^{\bullet -} \quad (1)$$

$$CdTe + e^- \rightarrow CdTe^{\bullet -} \quad (2)$$

$$SO_4^{\bullet -} + CdTe^{\bullet -} \rightarrow CdTe* + SO_4^{2-} \quad (3)$$

$$CdTe* \rightarrow CdTe + h\nu \quad (4)$$

In the air-saturated 0.1 mol/L PB (pH 7.4) containing 0.1 mol/L KNO_3, the cyclic voltammogram and I_{ECL}–E curve of CdTe QDs at the Au disk electrode are similar to those reported in Ref. [5]. Thus, in the air-saturated solution, the following reactions [5] should be involved in the ECL emission of CdTe QDs immobilized on the Au electrode.

$$CdTe + e^- \rightarrow CdTe^{\bullet -} \quad (5)$$

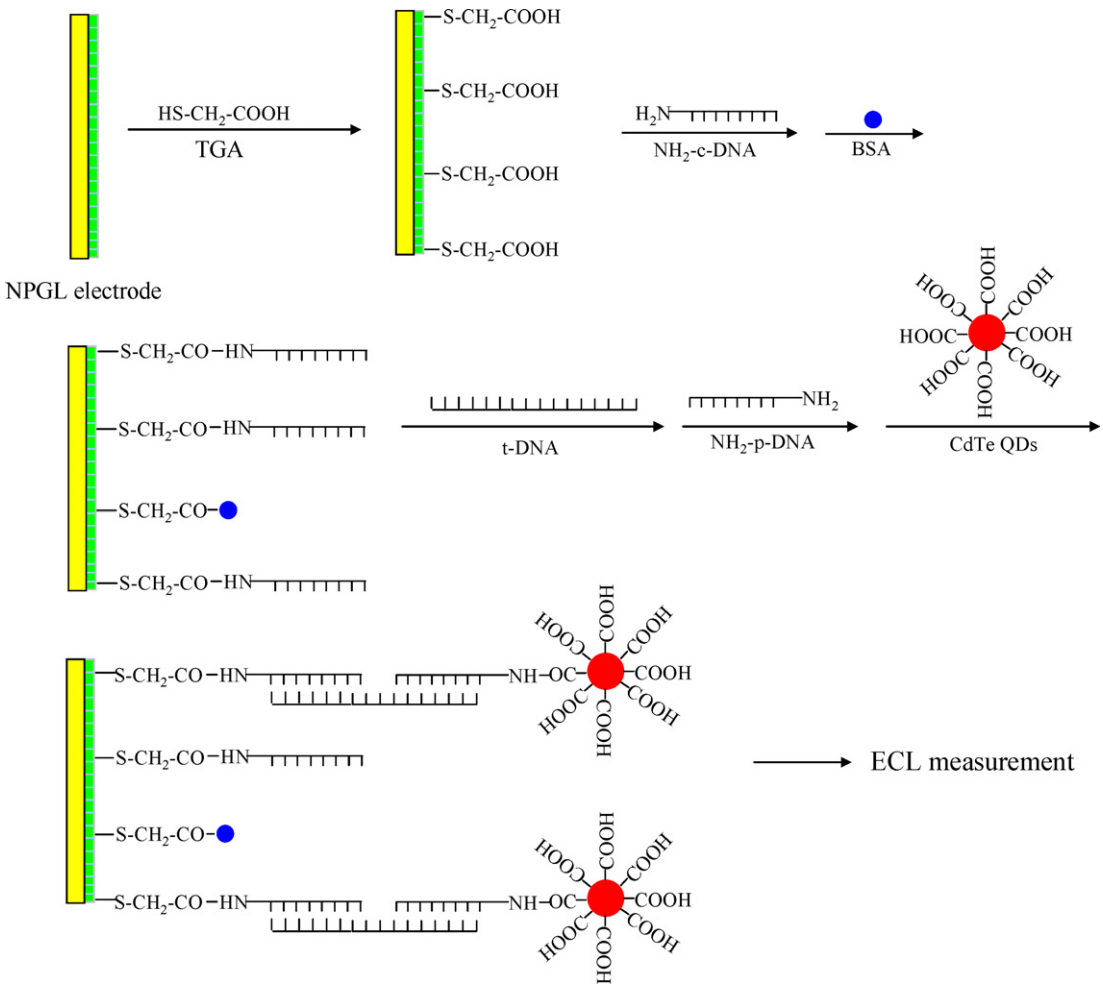
$$O_2 + H_2O + 2e^- \rightarrow OOH^- + OH^- \quad (6)$$

$$2CdTe^{\bullet -} + OOH^- + H_2O \rightarrow 3OH^- + 2CdTe* \quad (7)$$

$$CdTe* \rightarrow CdTe + h\nu \quad (8)$$

3.3. DNA determination using CdTe QDs as ECL labels

The basic protocol for DNA quantification is illustrated in Scheme 2. First, TGA was conjugated onto the surface of the activated NPGL electrode, followed by binding amino-modified c-DNA to it. The unbound TGA was blocked with BSA to prevent nonspecific binding. Then, t-DNA as the analyte, containing complementary sequence to both c-DNA and p-DNA, was hybridized with the c-DNA. Following that, the amino-modified p-DNA was hybridized with the t-DNA, forming the sandwich hybrid on the substrate. Subsequently, MPA-capped CdTe QDs were labeled to the amino group end of the sandwich hybrids. The DNA sequences used in our experiments are listed in Table 1. Finally, the ECL emission of the QDs labeled to the DNA hybrids on the NPGL electrode in the presence of $S_2O_8^{2-}$ was measured by scanning potential from 0 to −2 V with a scan rate of 50 mV/s. The I_{ECL}–E curves of the CdTe QD-labeled DNA hybrids fabricated using 1.0×10^{-11} mol/L t-DNA for seven consecutive cyclic potential scans shown in Fig. 6 indicates fine repeatability of the ECL signal. In order to evaluate the reproducibility of the method, the I_{ECL}–E curves of nine CdTe QD-labeled DNA hybrids fabricated using 1.0×10^{-11} mol/L t-DNA were measured. The relative standard deviation (RSD) of $I_{m,ECL}$ on the I_{ECL}–E curves is 4.3%. The reproducible $I_{m,ECL}$ suggests that this method is suitable for DNA determination. Fig. 7 shows the typical I_{ECL}–E curves of the CdTe QD-labeled DNA hybrids obtained from different concentrations of t-DNA in the range of 5.0×10^{-15} to 1.0×10^{-11} mol/L. The logarithmic relationship between $I_{m,ECL}$ and the concentration of t-DNA ($n = 3$) is displayed in Fig. 7 (Insert). A straight line with a slope of 1.03 and a correlation coefficient of 0.9996 in the concentration range was obtained. The limit of detection (LOD) was



Scheme 2. Schematic representation of the process of DNA determination.

4.7×10^{-15} mol/L according to LOD = $3\sigma/S$ where σ and S were the standard deviation for a series of nine measurements of the blank solution and the slop of the calibration curve.

To explore the selectivity of the method, in the interference test, the single base mismatched DNA sequence (1b-m-DNA) and a mixture consisting of five random noncomplementary DNA sequences as the interfere DNAs (their sequences are shown in Table 1) were detected using the ECL method described here. For 1.0×10^{-11} mol/L t-DNA and 1b-m-DNA, as well as the noncomplementary DNA mixture with a total concentration of 1.0×10^{-11} mol/L (2.0×10^{-12} mol/L for each DNA), $I_{m,ECL}$ detected from the 1b-m-DNA and the noncomplementary DNA mixture was 3.9% and 3.8% of that obtained from the t-DNA, demonstrating the high selectivity of the ECL DNA assay.

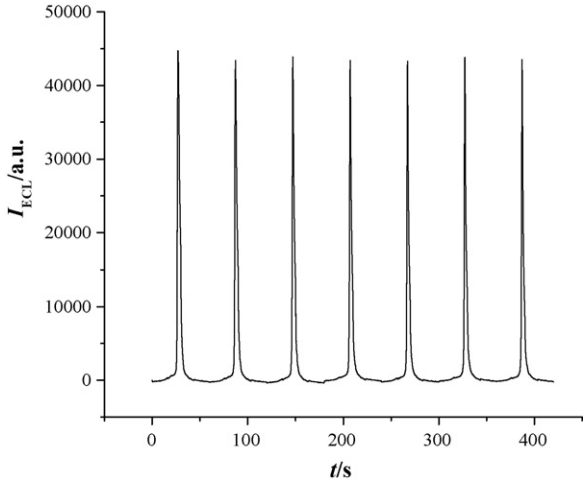


Fig. 6. ECL emission of the CdTe QD-labeled DNA hybrids fabricated using 1.0×10^{-11} mol/L t-DNA for seven consecutive cyclic potential scan with a scan rate of 50 mV/s. PB (pH 7.4) containing 0.1 mol/L $K_2S_2O_8$ and 0.1 mol/L KNO_3.

3.4. Quantification of DNA synthesized corresponding to intracellular OPN mRNA

In order to obtain information about specific gene expression levels in cells, the most widely used method is determination of DNA synthesized from a cellular mRNA template using RNA-dependent DNA polymerase reverse transcriptase (RT) coupled to the polymerase chain reaction (PCR). Here, we used the current ultrasensitive ECL assay to quantify the synthesized DNA without PCR amplification.

Osteopontin (OPN) is a glycophosphoprotein cytokine. Analysis of its contribution to immune responses suggests that OPN is essential for efficient development of Th1 immune responses. Therefore, determination of OPN mRNA in decidual stromal cells is selected as a model system. The synthesized DNA sample from cellular OPN mRNA contains the hybrid of OPN mRNA and its complementary DNA. Before detecting the DNA, the hybrid is dehybridized

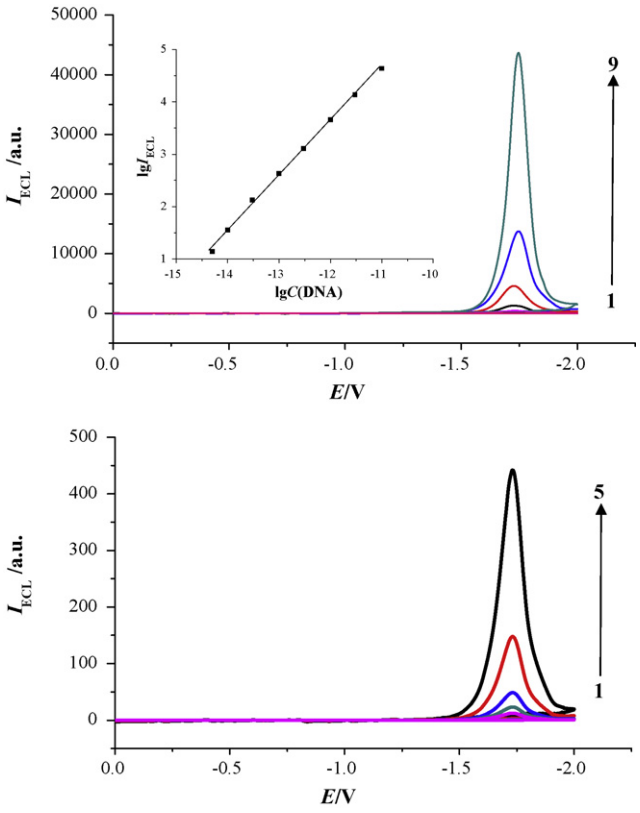


Fig. 7. (A) I_{ECL}–E curves of CdTe QD-labeled DNA hybrids immobilized on NPGL electrode in PB (pH 7.4) containing 0.1 mol/L $K_2S_2O_8$ and 0.1 mol/L KNO_3 for different t-DNA concentrations (10^{-15} mol/L): (1) 0, (2) 5.0, (3) 10, (4) 30, (5) 100, (6) 500, (7) 1000, (8) 2000, (9) 4000, (10) 6000, (11) 8000 and (12) 10,000. (B) Magnification of the I_{ECL}–E curves indicated in (1–5). Insert: Relationship between $I_{m,ECL}$ on I_{ECL}–E curves and t-DNA concentration.

in the presence of RNase H to remove the mRNA. After purification according to the procedure described in Section 2, the purified single-stranded DNA solution is analyzed using the present ECL method. In this assay, the sequences of the c-DNA and p-DNA are listed in Table 1. The profile of the recorded I_{ECL}–E curves is similar to that indicated in Fig. 7. Using the $I_{m,ECL}$ values on the I_{ECL}–E curves and the calibration curve, the DNA concentrations in the determined solutions are obtained. From the DNA concentrations, the average DNA concentration in the original DNA sample is calculated to be 5.6×10^{-10} mol/L with an RSD of 4.5% ($n = 10$). The value is in agreement with that (6.1×10^{-10} mol/L, provided by School of Life Science, Shandong Universite) determined using real-time quantitative PCR, suggesting that the ECL method proposed here is suitable to DNA assay.

4. Conclusion

The success of the application of QDs as ECL labels in bioanalysis may extend QD applications in chemical analysis, especially in bioassays. NPGL is a perfect electrode material and can be applied in ECL techniques to enhance the ECL intensity due to its unique features such as high conductivity, transparency and nanoporous structure. Although the strategy described here is used for DNA quantification, the same technique can be applied in many other assays, e.g., immunoassay.

Acknowledgments

This project was supported by the National Natural Science Foundation of China (Grant Nos. 20675047, 90713016 and 20705016), the National Basic Research Program of China (Grant No. 2007CB936602), the Natural Science Foundation of Shandong Province in China (Grant No. Y2008B20) and the SEM-NCET, SRF-ROCS Programs, the Shandong Natural Science Fund for Distinguished Young Scholars. We are grateful to Professor Jinxing Wang (School of Life Science, Shandong University) for providing the DNA sample synthesized from intracellular OPN mRNA and its standard solutions.

References

[1] W. Miao, Chem. Rev. 108 (2008) 2506.
[2] G. Zou, H. Ju, Anal. Chem. 76 (2004) 6871.
[3] G. Jie, B. Liu, J. Miao, J. Zhu, Talanta 71 (2007) 1476.
[4] Z. Dai, J. Zhang, J. Bao, X. Huang, X. Mo, J. Mater. Chem. 17 (2007) 1087.
[5] H. Han, Z. Sheng, J. Liang, Anal. Chim. Acta 596 (2007) 73.
[6] L. Zhang, X. Zou, E. Ying, S. Dong, J. Phys. Chem. C 112 (2008) 4451.
[7] H. Jiang, H. Ju, Chem. Commun. (2007) 404.
[8] H. Jiang, H. Ju, Anal. Chem. 79 (2007) 6690.
[9] L. Hua, H. Han, H. Chen, Electrochim. Acta 54 (2009) 1389.
[10] L. Hua, H. Han, X. Zhang, Talanta 77 (2009) 1654.
[11] G. Jie, J. Zhang, D. Wang, C. Cheng, H. Chen, J. Zhu, Anal. Chem. 80 (2008) 4033.
[12] G. Jie, B. Liu, H. Pan, J. Zhu, H. Chen, Anal. Chem. 79 (2007) 5574.
[13] X. Liu, H. Ju, Anal. Chem. 80 (2008) 5377.
[14] X. Liu, H. Jiang, J. Lei, H. Ju, Anal. Chem. 79 (2007) 8055.
[15] M.M. Richter, Chem. Rev. 104 (2004) 3003.
[16] Y. Ding, J.J. Erlebacher, Am. Chem. Soc. 125 (2003) 7772.
[17] Y. Ding, M. Chen, J.J. Erlebacher, Am. Chem. Soc. 126 (2004) 6876.
[18] Y. Ding, Y. Kim, J.J. Erlebacher, J. Adv. Mater. 16 (2004) 1897.
[19] X. Sun, W. Jin, Anal. Chem. 75 (2003) 6050.
[20] K. Jiang, L.S. Schadler, R.W. Siegel, X. Zhang, H. Zhang, M. Terrones, J. Mater. Chem. 14 (2004) 37.
[21] N. Gao, M. Zhao, X. Zhang, W. Jin, Anal. Chem. 78 (2006) 231.
[22] R. Szamocki, A. Velichko, C. Holzapfel, F. Mucklich, S. Ravaine, P. Garrigue, N. Sojic, R. Hempelmann, A. Kuhn, Anal. Chem. 79 (2007) 533.
[23] S. Ben-Ali, D.A. Cook, S.A.G. Evans, A. Thienpont, P.N. Bartlett, A. Kuhn, Electrochem. Commun. 5 (2003) 747.
[24] W. Yu, L. Qu, W. Guo, X. Peng, Chem. Mater. 15 (2003) 28540.
[25] Z. Ding, B.M. Quinn, S.K. Haram, L.E. Pell, B.A. Korgel, A.J. Bard, Science 296 (2002) 1293.
[26] S.K. Poznyak, D.V. Talapin, E.V. Shevchenko, H. Weller, Nano Lett. 4 (2004) 693.
[27] J. Miao, T. Ren, L. Dong, J. Zhu, H. Chen, Small 1 (2005) 802.
[28] B. Zhou, B. Liu, L. Jiang, J. Zhu, Ultrason. Sonochem. 14 (2007) 229.
[29] L. Shen, X. Cui, H. Qi, C. Zhang, J. Phys. Chem. C 111 (2007) 8172.

Talanta 80 (2010) 1744–1749

Contents lists available at ScienceDirect

Talanta

journal homepage: www.elsevier.com/locate/talanta

Determination of rare-earth elements in uranium-bearing materials by inductively coupled plasma mass spectrometry

Zsolt Varga[a,*], Róbert Katona[b], Zsolt Stefánka[b], Maria Wallenius[a], Klaus Mayer[a], Adrian Nicholl[a]

[a] European Commission, Joint Research Centre, Institute for Transuranium Elements, P.O. Box 2340, 76125 Karlsruhe, Germany
[b] Institute of Isotopes, Hungarian Academy of Sciences, Konkoly-Thege M. ut 29-33, H-1121 Budapest, Hungary

ARTICLE INFO

Article history:
Received 10 August 2009
Received in revised form
28 September 2009
Accepted 8 October 2009
Available online 14 November 2009

Keywords:
Inductively coupled plasma mass spectrometry
Lanthanides
Uranium ores
Nuclear forensics
Extraction chromatography

ABSTRACT

A novel and simple analytical procedure has been developed for the trace-level determination of lanthanides (rare-earth elements) in uranium-bearing materials by inductively coupled plasma sector-field mass spectrometry (ICP-SFMS). The method involves a selective extraction chromatographic separation of lanthanides using TRU™ resin followed by ICP-SFMS analysis. The limits of detection of the method proposed is in the low pg g^{-1} range, which are approximately two orders of magnitude better than that of without chemical separation. The method was validated by the measurement of reference material and applied for the analysis of uranium ore concentrates (yellow cakes) for nuclear forensic purposes, as a potential application of the methodology.

© 2009 Elsevier B.V. All rights reserved.

1. Introduction

Lanthanide or rare-earth elements (REE) are present in nuclear materials (uranium and plutonium) in widely variable concentrations. Certain lanthanides may be added intentionally to the nuclear materials. For instance, burnable poisons, such as erbium or gadolinium, are added to nuclear fuel in order to control the reactivity of the fuel in nuclear reactors. REE are also formed in the reactor as a result of nuclear fission. Lanthanides can also be present in nuclear materials in trace-level amounts either as residues from the raw material or as a contamination of the process.

There are several important applications of lanthanide determination in nuclear materials. Their measurements are used for the quality control and development of the nuclear fuel material [1], burn-up determination (e.g. via the isotopic analysis of neodymium) [2,3] or for the nuclear forensic investigation of found or confiscated illicit nuclear materials [4–6]. Therefore, accurate determination of these elements is of high importance.

Several analytical techniques can be applied for such purposes with or without prior chemical separation of the analytes [7]. Direct-current plasma emission spectrometry [8], atomic absorption spectrometry [1] or inductively coupled plasma atomic emission spectrometry (ICP-AES) [3,9,10] can be used for the lanthanide analysis if the analyte is present at a concentration close to or above μg g^{-1}. Because of the complex emission spectrum of uranium and the lanthanides, removal of uranium is usually necessary before the measurement. Recently mainly mass spectrometric techniques, such as inductively coupled plasma mass spectrometry (ICP-MS) or thermal ionisation mass spectrometry (TIMS) are used for the isotopic and elementary measurements of the lanthanides in nuclear matrices [2,11–13]. Very low detection limits and high precision can be achieved by mass spectrometry, however, the presence of molecular isobaric interferences and matrix suppression of signal intensity due to considerable amounts of matrix elements often hinder the low-level lanthanide determinations. The spectral interferences in the m/z = 146–170 mass region were generally caused by oxide and hydroxide molecular ions of barium [14,15]. As Ba is usually present in high amount compared to lanthanides in most investigated materials and the oxide production rate is relatively high in ICP-MS for most sample introduction systems (typically 1–2% of the parent ion), the isobaric interferences can cause erroneous results. Spectral interferences can be eliminated by the use of higher instrumental mass resolution or by the measurement of the doubly charged ions [14,16–18], however, these approaches also imply the strong decrease in the sensitivity (high increase in the detection limit). The mass resolution required for the separation of the interfering oxide ions from lanthanides are typically between 7000 and 10,000 [18].

* Corresponding author. Tel.: +49 7247 951 491; fax: +49 7247 951 99491.
E-mail address: zsolt.varga@ec.europa.eu (Z. Varga).

0039-9140/$ – see front matter © 2009 Elsevier B.V. All rights reserved.
doi:10.1016/j.talanta.2009.10.018

Chemical separation of lanthanides from the matrix is another option to reduce spectral interferences and matrix-induced signal suppression. It also enables to pre-concentrate the analyte to a higher degree and to protect the instrument from a contamination of e.g. uranium or, if present, of different radioactive activation or fission products other than lanthanides. Most frequently precipitation (*i.e.* co-precipitation with carriers), solvent extraction, ion exchange or extraction chromatographic methods are used to separate and pre-concentrate the lanthanides. Co-precipitation is rarely used as the carrier has to be removed prior to the analysis, thus requiring an additional step [10,19]. Ion exchange offers a rapid possibility for the separation of the trivalent lanthanides, although it is less selective and robust to matrix effects compared to solvent extraction [3,8,19,20]. Various extractants, such as TBP (tri-n-butylphosphate), TBP–TOPO (tri-n-octylphosphine-oxide) or TOPO alone (in CCl_4, xylene or dodecane) are most often used for the solvent extraction of rare-earths [3,9,10,19]. Although high selectivity can be achieved and the methods do not require special instrumentation, the cumbersome separation, the high amount of generated organic and/or radioactive waste makes its routine use less attractive. Extraction chromatography, on the other hand, offers a possibility to combine the selectivity of solvent extraction method with the ease of use of column separation [3,21]. Extraction chromatography has already been used for the separation of trace-level activation products, such as Pu and Am from uranium materials [22–24].

The aim of this study is the development of a straightforward and simple extraction chromatographic method followed by inductively coupled plasma sector-field mass spectrometric analysis for the determination of lanthanide elements from uranium-bearing nuclear materials. Measurement of a certified reference material was used to validate the procedure. The method was applied for the measurement of lanthanide composition in uranium ore concentrates (yellow cakes) for nuclear forensic investigation. The sample preparation, elimination of possible interferences and figures of merit of the developed method are discussed.

2. Experimental

2.1. Instrumentation

The mass spectrometric analysis was carried out using a double-focusing magnetic sector inductively coupled plasma sector-field mass spectrometer (ICP-SFMS) equipped with a single electron multiplier (ELEMENT2, Thermo Electron Corp., Bremen, Germany). All measurements were carried out in low resolution mode ($R = 300$) to keep on sensitivity using a low-flow microconcentric nebulizer operated in a self-aspirating mode (flow rate was 60 μL min^{-1}). Optimized operating parameters are summarized in Table 1. Prior to the sample analysis the instrument was tuned using a 1 ng g^{-1} multielement solution (Merck, Darmstadt, Germany). The optimization was carried out with respect to maximum uranium sensitivity and low UO^+/U^+ ratio. The sensitivity was approximately 1.4×10^6 cps for 1 ng g^{-1} ^{238}U and the UO^+/U^+ ratio $\sim 3.5 \times 10^{-2}$.

2.2. Reagents and materials

For the lanthanide measurements external calibration standard solutions and spike solution used for the optimization of the separation were prepared from a 10 μg g^{-1} lanthanide standard solution (Spex, Metuchen, NJ, USA) by gravimetric dilution. Uranium and rhodium monoelemental standard solutions were purchased from Alfa Aesar (Karlsruhe, Germany). The TRU^{TM} extraction chromatographic column (100–150 μm particle size, active component: octylphenyl-N,N-di-isobutyl carbamoylphosphine oxide dissolved in tri-n-butyl phosphate) were supplied by Eichrom (Eichrom Europe Laboratories, Bruz, France). For the preparation of columns, 1.6 mL of the resin was placed in plastic Bio-Rad holders (diameter: 8 mm) and plugged with porous Teflon frit (Reichelt Chemietechnik Heidelberg, Germany) on the top of the resin to avoid mixing. The free-column volume (FCV) of the column is approximately 1.05 mL. For dilution high-purity water was used (UHQ System, USF Elga, Germany). Hydrochloric acid used for the sample preparation was of Suprapur grade (Merck, Darmstadt, Germany). Suprapur grade nitric acid was further purified by subboiling distillation in quartz equipment. Analytical grade phosphoric acid and sulphuric acid used for the robustness tests were purchased from Merck (Darmstadt, Germany). The U_3O_8 certified reference material, Morille, (Cetama, France) used for the validation of the method is certified for four lanthanide content (Dy, Gd, Eu and Sm). Uranium ore concentrates (yellow cakes) analysed in this study originate from three different milling facilities (Beverley in Australia; Cluff Lake and Stanrock in Canada).

Table 1
Optimized ICP-MS operating parameters.

Forward power (W)	1350
Cooling gas flow rate (L min^{-1})	16.0
Auxiliary gas flow rate (L min^{-1})	0.92
Nebulizer gas flow rate (L min^{-1})	1.240
Solution uptake rate (μL min^{-1})	∼100
Data acquisition	
Resolution	300
Runs and passes	5 × 5
Mass window (%)	120
Sampling time (s)	0.01
Samples per peak	20
Search window (%)	80
Integration window (%)	60
Sampling time (s)	0.1
Integration type	Average
Scan type	E-scan
Measured isotopes	^{103}Rh (internal standard), ^{137}Ba, ^{139}La, ^{140}Ce, ^{141}Pr, ^{146}Nd, ^{147}Sm, ^{153}Eu, ^{157}Gd, ^{159}Tb, ^{163}Dy, ^{165}Ho, ^{167}Er, ^{169}Tm, ^{172}Yb, ^{175}Lu, ^{235}U

2.3. Sample preparation for ICP-SFMS analysis

Approximately 300–500 mg of sample was weighed into a Teflon vial and dissolved in 9 ml 10 M ultra-pure nitric acid while heating to 90 °C on a hot-plate for 6 h. After cooling to room temperature, the weight of the solution was calculated as the difference of the weight of the vial containing the solution and the vial weight (M_{stock}). Approximately 300 μL of this stock solution was weighed gravimetrically into a polyethylene vial (M_{load}) and diluted four-fold using ultra-pure water in order to adjust the proper HNO_3 concentration. This aliquot was used for the lanthanide separation, corresponding to about 13 mg of sample (approximately 10 mg of uranium). The lanthanide content of the sample aliquots was separated using extraction chromatography by the selective retention of trivalent lanthanides and actinides on the TRU^{TM} resin in 3 M nitric acid medium. After conditioning of the resin with 10 mL 2 M HNO_3 the sample aliquot was loaded on the column. After washing the column and removal of the non-retaining matrix components with 2 mL of 2 M HNO_3, the lanthanides were stripped from the column into a Teflon beaker using 1 mL concentrated HCl followed by 4 mL of 4 M HCl. After the addition of 200 μL ultra-pure HNO_3 to the final fractions, the samples were evaporated to almost complete

dryness on a hot-plate in order to destroy the organic resin residuals. The residue was dissolved in 1 mL of 2% (m/m) ultra-pure nitric acid while heating slightly. After the gravimetric weighing of the final fraction and the gravimetric addition of Rh internal standard (m_{finfr}), the samples were analysed by ICP-SFMS using external calibration, *i.e.* the lanthanide concentrations were determined using a calibration curve established by analysis of separately measured (uranium free) standards.

For comparison purpose and to validate the separation procedure, the lanthanide content of the samples was also measured without chemical separation. In this case the dissolved sample solution was diluted to a uranium concentration of approximately 100 μg g^{-1}. After adding Rh internal standard, the lanthanide concentration was measured in the sample by ICP-SFMS using external calibration with matrix-matched standards. The matrix-matched standards were prepared by dilution of the monoelemental U standard to 100 μg g^{-1} U concentration and addition of diluted lanthanide standard mixture. All dilutions were performed gravimetrically.

2.4. Data evaluation

The concentration of the lanthanide elements in the starting sample material was calculated as follows:

$$c_{Ln} = \frac{m_{finfr} c_{finfr} M_{stock}}{M_{sample} M_{load} R} \quad (1)$$

where c_{Ln} is the concentration of the lanthanide element in the starting material, c_{finfr} is the concentration of the lanthanide element in the final fraction measured by ICP-SFMS, m_{finfr} is the weight of the final fraction, M_{stock} is the weight of the stock solution obtained after the dissolution of the material, M_{load} is the weight of the stock solution aliquot used for the separation, M_{sample} is the weight of the dissolved sample, R is the chemical recovery estimated by the measurement of certified reference material. The overall uncertainty of the result was calculated taking into account the uncertainties of the measured concentration values, weight measurements and chemical recovery.

3. Results and discussion

3.1. Optimization of the separation scheme

Relatively few commercially available extraction chromatographic resins retain lanthanides in nitric acid medium. For our work we chose TRU™ resin because of the following reasons: highly retains uranium (its distribution coefficient is typically higher than 900 at nitric acid concentrations in excess of 2 M [21]), relatively high retention of lanthanide in nitric acid medium, no retention of alkali metals, alkali earth elements and most transition metals. The lanthanides show relatively high retention in the range of 1–5 M nitric acid concentration and they can be stripped from the column using HCl [21]. In order to optimize the separation scheme, a laboratory-prepared standard solution containing 100 μg g^{-1} U and 1 ng g^{-1} of lanthanides was prepared and its elution behaviour on TRU™ column was investigated. The test solution was loaded on the columns in 2 M HNO_3 and eluted with HNO_3 followed by HCl. After loading, 8 mL of 2 M HNO_3 was added to the column in 1 mL portions, thereafter the resin was converted to chloride-form with 1 mL of concentrated HCl. Finally, the lanthanides were stripped with eight times of 1 mL of 4 M HCl. The aliquots were collected separately and their uranium and lanthanide contents were analysed by ICP-SFMS. The elution profile of the elements is shown in Fig. 1. We observed uranium visibly formed a yellow band on the upper part of the column, since under such circumstances uranium highly retains on the column (only a very small portion appears in the load fraction). As shown in Fig. 1, all lanthanides can be quantitatively recovered using the HNO_3 elution and the first two HCl strip steps (total chemical recovery was between 95 and 102%).

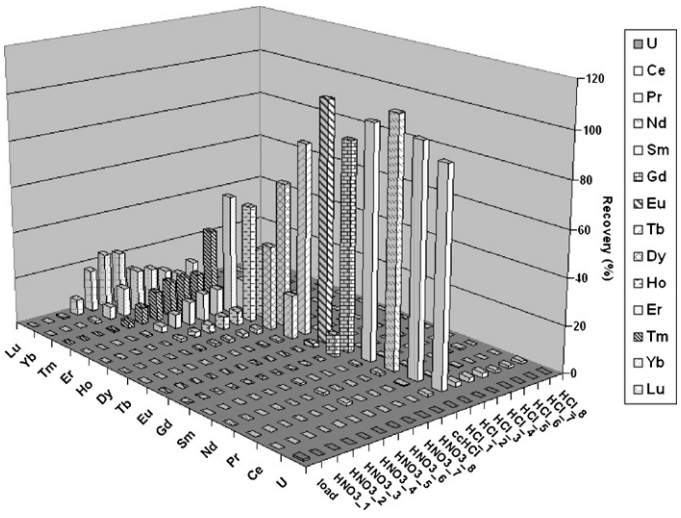


Fig. 1. Elution profile of lanthanides and uranium on TRU™ column. Column: 1.6 mL TRU™, diameter: 8 mm. Elution after load: 8 × 1 mL 2 M HNO_3, 1 mL *cc*HCl, 8 × 1 mL 4 M HCl.

Lanthanides sequentially elute from the column: the less-retaining heavy lanthanides start to elute from the column after about 2 mL 2 M HNO_3. As our aim was to measure all lanthanides simultaneously, in our final method described in Fig. 2 we used only 2 mL of 2 M HNO_3 in order to avoid any chemical fractionation of lanthanides (partial elution of heavy lanthanides), followed by the stripping using HCl. Using this scheme all the lanthanides can be collected in a single fraction, while uranium and most metal ions, which can cause interference or matrix effects, are separated from the analytes. Uranium content in the HCl fractions was very low (typically <50 pg g^{-1}), due to the high retention of U (VI) on the column in both HNO_3 and HCl media.

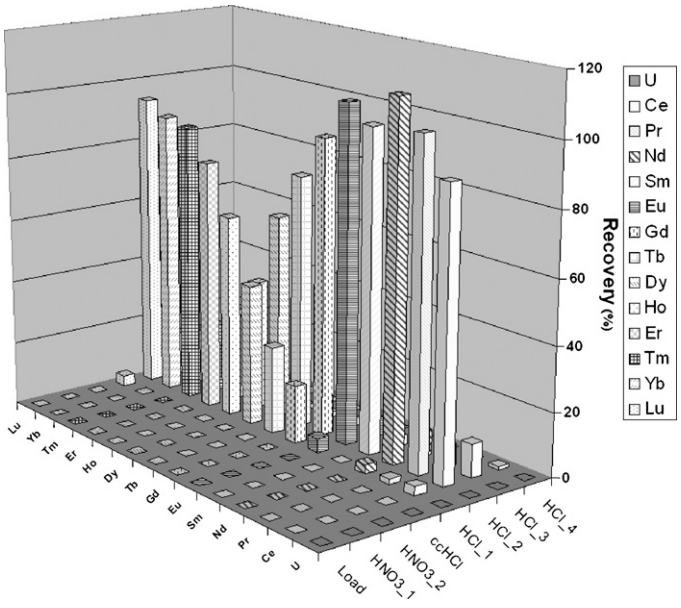


Fig. 2. Elution profile of the final method used for the separation of lanthanides. Column: 1.6 mL TRU™, diameter: 8 mm. Elution after load: 2 × 1 mL 2 M HNO_3, 1 mL *cc*HCl, 4 × 1 mL 4 M HCl.

Table 2
Limits of detection (LOD) of the method developed in comparison with the direct measurement using external matrix-matched calibration (in ng g^{-1} of the original material).

Element	LOD using external matrix-matched calibration (ng g^{-1})	LOD of the developed method with chemical separation (ng g^{-1})
La	37.6	0.080
Ce	12.7	0.082
Pr	2.3	0.014
Nd	3.5	0.14
Sm	3.5	0.20
Eu	1.4	0.021
Gd	1.3	0.048
Tb	0.12	0.0087
Dy	7.5	0.025
Ho	1.55	0.0066
Er	2.2	0.039
Tm	0.51	0.0024
Yb	8.2	0.12
Lu	0.58	0.0039

3.2. Figures of merit

The calculation of the limit of detection (LOD) was based on three times the standard deviation of the method blank (3σ *criterium*). The detection limits of the method developed in comparison with the direct measurement of the sample after dilution using external matrix-matched calibration are shown in Table 2. The detection limit of the developed method is approximately two orders of magnitude better than that of without chemical separation. This is due to the higher pre-concentration (less dilution) and the lack of signal suppression due to the removal of the uranium matrix. Considering that approximately 13 mg of the sample was used for the analysis, the absolute detection limit corresponds to approximately 0.02–2 pg. Another advantage of the developed method is that the components of the possibly interfering molecular ions, such as barium, which would cause barium-oxide and hydroxide molecular ion interferences in the m/z = 146–170 region, are removed. This is often a serious problem with samples having complex matrixes, like uranium ores and spent nuclear fuels. The typical intensity of $^{137}Ba^{+}$ at m/z = 137 for these samples was less than 10^4 cps, thus the estimated level of oxides and other molecular ions are negligible taking into account the applied oxide formation rate. By the separation scheme the possible oxide interferences of the lighter rare-earth oxides on the heavier rare-earth intensities cannot be avoided, as they are co-separated. For samples with elevated light rare-earth content either mathematical correction of the oxide interference or proper modification of the sample preparation method by the separation of light and heavy rare-earth elements can be a possible option (Fig. 1).

3.3. Validation of the method

For the validation of the method, Morille certified reference material (CRM) was analysed by the method developed. In addition, the lanthanide concentrations were also determined in the dissolved CRM after only diluting the sample to approximately 100 μg g^{-1} U concentration without chemical separation. In this case, external calibration with matrix-matched standards was used for the quantification. The measured concentrations of the four certified lanthanides together with the certified contents are shown in Table 3. The concentrations presented are given relative to the uranium content, which was determined in an independent measurement. The measured values agree well with each other and also with the reference values. The chemical recovery of the chemical separation (calculated by the measurement of the reference material in the same batch) was 94 ± 6% for all the lanthanides. The overall uncertainty of the concentration measurement is slightly higher than that of the direct measurement (Table 3), which is due to the additional uncertainty of the chemical recovery (Eq. (1)). The overall uncertainties of the lanthanide determinations with and without chemical separation for the Morille reference material are ranged in 7.1–8.9% and 2.4–6.6% relative standard deviation, respectively. It is noteworthy that the precision of the chemical recovery can be further improved if any of the lanthanides can be measured just by the dilution of the sample. The replicate analysis of the Morille reference material yielded an analytical precision of 3.2–8.6% relative standard deviation for all the four certified lanthanide elements. The procedural blanks of the method proposed are 0.1–3 pg. The decontamination factor for uranium (defined as the ratio of uranium amount before and after the chemical separation) is approximately 2×10^6, thus the uranium concentration in the final fraction (typically 1–10 ng g^{-1}) is low enough to avoid any matrix effect and to protect the instrument from contamination. The concentration of uranium in the final fraction is also low enough to avoid the decrease in the sensitivity due to matrix effects.

3.4. Robustness test of the method

The robustness of the method was tested by the measurement of a dissolved uranium ore concentrate sample from Cluff Lake mine spiked with increasing amount of sulphate and phosphate, which are reported to be possible interferences during the extraction chromatographic separation [21]. The uranium content in the load was approximately 10 mg. Aliquots of the load solution were spiked with known amounts of sulphate and phos-

Table 3
Analysis results of Morille reference material measured using the two methods and their comparison to the certified values.

Element	Developed method with chemical separation		Matrix-matched method	Certified concentration (ng g^{-1} U)
	Measured concentration (ng g^{-1} U)	Chemical recovery (%)	Measured concentration (ng g^{-1} U)	
Sm	482 ± 31	94 ± 3	492 ± 18	500 ± 120
Eu	499 ± 26	97 ± 4	507 ± 14	520 ± 30
Gd	503 ± 33	92 ± 4	487 ± 21	560 ± 60
Dy	525 ± 35	95 ± 3	514 ± 16	500 ± 120

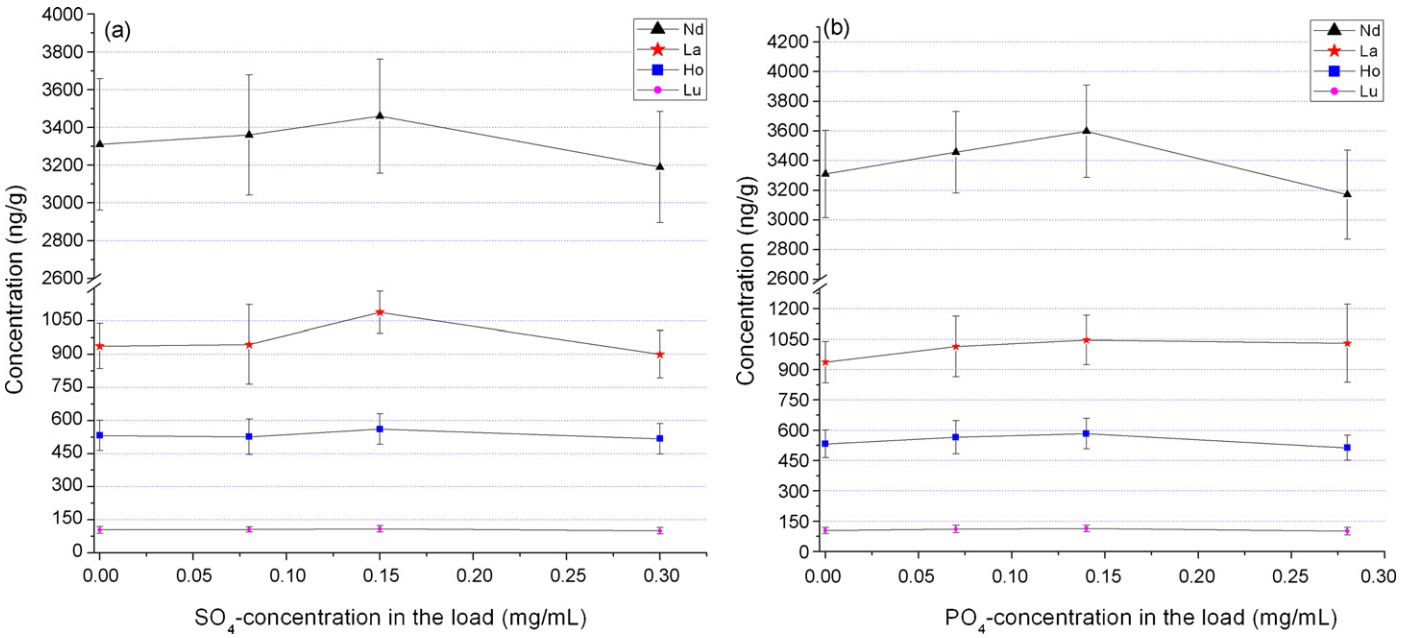


Fig. 3. Effect of sulphate (a) and phosphate (b) as possible interfering anions on the lanthanides separation method.

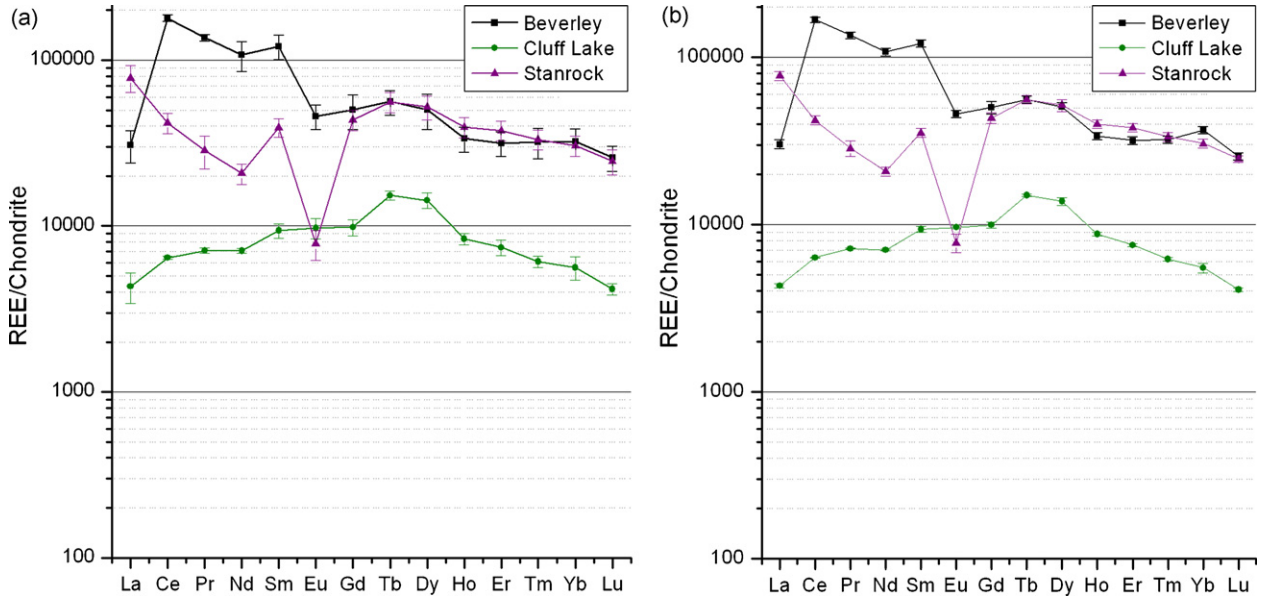


Fig. 4. Lanthanide pattern of three uranium ore concentrates of different origin. The lanthanide concentrations were measured with the method developed (a) and after only dilutions with matrix-matched calibration (b). The lanthanide concentrations are normalized to chondritic values [25].

phate prepared from diluted H_2SO_4 and H_3PO_4, respectively. The sample was then subjected to the chemical separation described above. The effect of sulphate and phosphate on the measured concentration of selected lanthanides is shown in Fig. 3a and b, respectively. As seen, the polyatomic anions have no adverse effect on the lanthanides retention even in case of Ho and Lu, which have the lowest retention coefficients to the resin and which are most prone to matrix constituents during the chemical separation. The lanthanide content of the sample was also determined without chemical separation performing only dilution of the sample and matrix-matched measurement by ICP-SFMS. The La, Nd, Ho and Lu concentrations were $963 \pm 48\ ng\ g^{-1}$, $3178 \pm 201\ ng\ g^{-1}$, $504 \pm 8\ ng\ g^{-1}$ and $102 \pm 4\ ng\ g^{-1}$, respectively. The values obtained are in good agreement with the results measured for the robustness test samples.

3.5. Application of the method

The method developed was applied for the analysis of three uranium ore concentrates (yellow cakes) originating from different mills in order to compare their lanthanide profiles (also called *rare-earth pattern*) for nuclear forensic studies. The measured lanthanide concentrations presented were normalized to chondrite values as a general practice in geochemistry in order to eliminate effects related to nuclear stability [25]. This normalization produces a smooth pattern. The lanthanide patterns of the samples after chemical separation are shown in Fig. 4a. For these samples the lanthanide content was high enough to determine it also after only diluting the sample (Fig. 4b). Moreover, as the samples are relatively pure intermediate products of uranium production, the level of possibly occurring interfer-

ents (especially barium) is relatively low. The Ba/La ratios in the samples investigated are between 0.2 and 16, thus the effect of isobaric interferences on the measured isotopes is negligible in this case even without chemical separation of the analytes. The measured values agree well using the two different methods. The lanthanide profile obtained for the yellow cake samples can be used to verify the origin of the material, as the rare-earth element pattern reflects the formation conditions of the uranium deposits [26].

4. Conclusions

A novel analytical method for the determination of lanthanides in uranium-bearing materials has been developed. The method, involving a rapid chemical separation of lanthanides by TRU™ extraction chromatography resin followed by ICP-MS analysis, has great advantage over direct measurement of the analyte especially when analysing lanthanides in difficult matrixes at trace-level (containing rare-earth at pg g^{-1} concentration level). For instance, if possible interferents are present at high level or in radioactive materials (e.g. U ores, spent fuels). The method also allows the reduction of the sample size due to the pre-concentration. The method described in the present paper separates lanthanides without any chemical fractionation and with good chemical recovery (above 94%) from uranium matrices and interfering elements. The amount of chemicals consumed for the separation and thus the waste generated is much less (only a few mL per sample) compared to other separation methods, e.g. ion exchange or solvent extraction, which is of vital importance for radioactive and nuclear materials. This also allows decreasing the background originating from the chemicals. As the TRU™ resin used in this study strongly retains Th and Pu, the method can be extended for the lanthanide determination from other types of nuclear materials and fuels. The method has potential application also in the field of nuclear forensics, where rare-earth element pattern can be used for the origin assessment of unknown samples.

References

[1] M.V. Ramaniah, Pure Appl. Chem. 54 (1981) 889–908.
[2] J.M. Barrero Moreno, J.I. Garcia Alonso, P. Arbore, G. Nicolaou, L. Koch, J. Anal. At. Spectrom. 11 (1996) 929–935.
[3] C.H. Lee, M.Y. Suh, K.S. Choi, J.S. Kim, B.C. Song, K.Y. Jee, W.H. Kim, Anal. Chim. Acta 428 (2001) 133–142.
[4] K. Mayer, M. Wallenius, I. Ray, Analyst 130 (2005) 433–441.
[5] M. Wallenius, K. Mayer, I. Ray, Forensic Sci. Int. 156 (2006) 55–62.
[6] M.E. Ketterer, S.C. Szechenyi, Spectrochim. Acta B 63 (2008) 719–737.
[7] X. Hou, W. Chen, Y. He, B.T. Jones, Appl. Spectosc. Rev. 40 (2005) 245–267.
[8] F. Flavelle, A.D. Westland, Talanta 33 (1986) 445–447.
[9] R.K. Malhotra, K. Satyanarayana, Talanta 50 (1999) 601–608.
[10] A. Premadas, P.K. Srivastava, J. Radioanal. Nucl. Chem. 251 (2002) 233–239.
[11] S. Röllin, Z. Kopatjtic, B. Wernli, B. Magyar, J. Chromatogr. A 739 (1996) 139–149.
[12] A. Pitois, L.A.d.L. Heras, M. Betti, Int. J. Mass Spectrom. 270 (2008) 118–126.
[13] R. Brennetot, A.L. Becquet, H. Isnard, C. Caussignac, D. Vailhen, F. Chartier, J. Anal. At. Spectrom. 20 (2005) 500–507.
[14] K.E. Jarvis, A.L. Gray, E. McCurdy, J. Anal. At. Spectrom. 4 (1989) 743–747.
[15] A.J.R. Kent, C.A. Ungerer, J. Anal. At. Spectrom. 20 (2005) 1256–1262.
[16] Y. Takaku, K. Masuda, T. Takahashi, T. Shimamura, J. Anal. At. Spectrom. 8 (1993) 687–690.
[17] W. Pretorius, D. Weis, G. Williams, D. Hanano, B. Kieffer, J. Scoates, Geostand. Geoanal. Res. 30 (2006) 39–54.
[18] J.S. Becker, H.-J. Dietze, J. Anal. At. Spectrom. 12 (1997) 881–889.
[19] J.E. Gindler, The Radiochemistry of Uranium, National Academy of Sciences, National Research Council, U. S. Atomic Energy Commission, Los Alamos Scientific Laboratory, 1978.
[20] X. Cao, G. Zhao, M. Yin, J. Li, Analyst 123 (1998) 1115–1119.
[21] E.P. Horwitz, M. Dietz, R. Chiarizia, H. Diamond, S.L. Maxwell, M. Nelson, Anal. Chim. Acta 310 (1995) 63–78.
[22] D. Desideri, M.A. Meli, C. Roselli, C. Testa, Int. J. Environ. Anal. Chem. 84 (2004) 331–339.
[23] M. Bertaux, A. Hanssens, C. Madic, Radiochim. Acta 84 (1999) 11–19.
[24] Z. Varga, G. Surányi, Appl. Radiat. Isot. 67 (2009) 516–522.
[25] E. Anders, N. Grevesse, Geochim. Cosmochim. Acta 53 (1989) 197–214.
[26] Z. Varga, M. Wallenius, K. Mayer, Appl. Radiat. Isot., submitted.

Talanta 80 (2010) 1750–1757

Contents lists available at ScienceDirect

Talanta

journal homepage: www.elsevier.com/locate/talanta

Active content determination of non-coated pharmaceutical pellets by near infrared spectroscopy: Method development, validation and reliability evaluation

J. Mantanus[a,*,1], E. Ziémons[a,1], P. Lebrun[a], E. Rozet[a], R. Klinkenberg[b], B. Streel[b], B. Evrard[c], Ph. Hubert[a]

[a] Laboratory of Analytical Chemistry, CIRM, University of Liège, 1 Avenue de l'Hôpital, 4000 Liège, Belgium
[b] Galéphar Research Center M/F, 39 rue du Parc Industriel, 6900 Marche en Famenne, Belgium
[c] Laboratory of Pharmaceutical Technology, CIRM, University of Liège, 1 Avenue de l'Hôpital, 4000 Liège, Belgium

ARTICLE INFO

Article history:
Received 19 April 2009
Received in revised form
26 September 2009
Accepted 8 October 2009
Available online 17 October 2009

Keywords:
Near infrared spectroscopy
Process Analytical Technology
Pharmaceutical pellets
Active content
Validation
Accuracy profile
Multivariate analysis

ABSTRACT

A robust near infrared (NIR) method able to quantify the active content of pilot non-coated pharmaceutical pellets was developed. A protocol of calibration was followed, involving 2 operators, independent pilot batches of non-coated pharmaceutical pellets and two different NIR acquisition temperatures. Prediction models based on Partial Least Squares (PLS) regression were then carried out. Afterwards, the NIR method was fully validated for an active content ranging from 80 to 120% of the usual active content using new independent pilot batches to evaluate the adequacy of the method to its final purpose. Conventional criteria such as the R^2, the Root Mean Square Error of Calibration (RMSEC), the Root Mean Square Error of Prediction (RMSEP) and the number of PLS factors enabled the selection of models with good predictive potential. However, such criteria sometimes fail to choose the most fitted for purpose model. Therefore, a novel approach based on accuracy profiles of the validation results was used, providing a visual representation of the actual and future performances of the models. Following this approach, the prediction model using signal pre-treatment Multiplicative Scatter Correction (MSC) was chosen as it showed the best ability to quantify accurately the active content over the 80–120% active content range. The reliability of the NIR method was tested with new pilot batches of non-coated pharmaceutical pellets containing 90 and 110% of the usual active content, with blends of validation batches and industrial batches. All those batches were also analyzed by the HPLC reference method and relative errors were calculated: the results showed low relative errors in full accordance with the results obtained during the validation of the method, indicating the reliability of the NIR method and its interchangeability with the HPLC reference method.

© 2009 Elsevier B.V. All rights reserved.

1. Introduction

Near infrared (NIR) spectroscopy belongs to vibrational spectroscopy and covers a region between 14,000 and 4000 cm^{-1}. Vibrations like overtones and combination of fundamental vibration of hydrogen bonds such as C–H, N–H, O–H and S–H give birth to the NIR spectrum. Such vibrations lead to large overlapping bands which contain both physical and chemical information. Therefore, chemo-metrical tools such as mathematical pre-treatments and regression methods are required to extract the significant information [1–3].

FDA's Process Analytical Technology (PAT) is an analytical concept which focuses on the real time monitoring of each critical step of a manufacturing process leading to a better understanding of the process itself. Consequently, as the process understanding improves, PAT gives the opportunity to detect the endpoints inherent in a process and so to optimize it in order to lower the risk of losing batches. PAT may also reduce the batch release time as most of the conformity analyses are realized during the manufacturing process itself [4,5].

An analytical tool such as PAT requires analyzers able to perform fast data acquisition without any sample preparation and compatible with the use of optical fibers. Thanks to its own features, NIR spectroscopy matches the PAT requirements: it has already been used many times in this concept [6–10]. Indeed, once you overcome the calibration phase which takes into account a reference method as well as environmental constrains, near infrared spectroscopy offers many advantages such as suppression of sample

* Corresponding author. Tel.: +32 04 366 43 24; fax: +32 04 366 43 17.
E-mail address: jmantanus@ulg.ac.be (J. Mantanus).
[1] These authors contributed equally to this work.

0039-9140/$ – see front matter © 2009 Elsevier B.V. All rights reserved.
doi:10.1016/j.talanta.2009.10.019

preparation and/or destruction and the use of optical fibers allows online analyses [1–3]. Moreover, the calibration set does not need to be updated or rebuilt as long as there is an agreement between the validation results and the Quality Controls (QCs) results.

The more complex is a manufacturing process, the more interesting becomes the PAT approach. An example of a complex manufacturing process associated with PAT can be found in the pellets manufacturing field [11,12]. Indeed, pellets fabrication can be split into plenty of crucial steps, including successively: weighting, blending, extrusion, spheronization, drying, coating, and a last drying step. For such a complex process, it would be interesting to evaluate the active content of the non-coated pellets before beginning the coating and final drying steps. The active determination is usually performed using time consuming and sample destructive HPLC methods. NIR spectroscopy can replace those tedious methods: it has already been used in different fields such as the pharmaceutical [9,13–15], the food [16,17] and the fuel industries [18].

To give laboratories guarantees about the accuracy of a new method, validation must be carried out, as defined by the ICH Q2 R1 regulatory documents [19]. Based on β-expectation tolerance intervals, the accuracy profile makes possible a visual and reliable representation of the actual and future performances of the analytical method [20–22]. This novel approach facilitates the analytical interpretation and enables a better risk management [23–29]. In addition, the accuracy profile integrates all the useful required validation criteria, such as accuracy, trueness, precision, quantitative limits and linearity [20–22].

The aim of the present study was first to develop a reliable near infrared method able to determine the active content of non-coated pilot pharmaceutical pellets. The second aim was to fully validate the method for an active content ranging from 80 to 120% of the usual active content. The final aim was to test the method reliability with new pilot batches containing 90 and 110% of the usual active content, blends of pilot batches used for the validation and industrial batches.

2. Materials and methods

2.1. Chemicals

2.1.1. Calibration samples

Pilot batches of non-coated pharmaceutical pellets were manufactured at Galephar Research Center M/F. The usual targeted formulation contains 57% w/w of Active Pharmaceutical Ingredient (API) T200999, this formulation will be further considered as the 100% active content formulation. For the calibration set, pilot batches containing 46 and 69% w/w of API were also manufactured (80 and 120% API formulations). Three independent batches were manufactured per formulation type.

2.1.2. External validation samples

New pilot batches of non-coated pharmaceutical pellets were manufactured at Galephar Research Center M/F. The same formulations as for the calibration samples were manufactured: 80, 100 and 120% API formulations, three batches per formulation type.

2.1.3. Reliability evaluation samples

To evaluate the reliability of the developed NIR method, new pilot batches containing 52 and 63% w/w of API were also manufactured at Galephar Research Center M/F (90 and 110% API formulations, 3 batches per formulation type). Industrials batches of non-coated pellets were also provided by Galephar. Besides, blends of batches belonging to the validation sets were made to obtain active content formulations between 80 and 120%.

2.2. FT-NIR equipment and software

Non-coated pharmaceutical pellets were analyzed with a multipurpose analyzer Fourier transform near infrared spectrometer (MPA, Bruker Optics, Ettlingen, Germany) equipped with a semiconductor room temperature sulfide lead (RT-PbS) detector. The NIR spectra of the samples put in vials were acquired using the integrating sphere module of the spectrometer which allows reflectance measurement of an 18 mm diameter sample area. An internal computer-controlled reference wheel enables an automatic background spectrum acquisition without the need to remove the sample from the integrating sphere window. The spectra were collected with the Opus software 6.5 (Bruker Optics). Each spectrum was the average of 32 scans and the resolution was 8 cm^{-1} over the range from 12,500 to 3600 cm^{-1}.

2.3. Reference method

A confidential HPLC method previously developed and validated by Galephar was used to determine the amount of API in batches of non-coated pharmaceutical pellets.

2.4. Near infrared method: calibration and validation protocol

An experimental protocol was followed for the calibration and validation steps to develop and to validate a robust near infrared model. This protocol included batches, operators, days and temperature conditions as sources of variability for the calibration as well as for the validation steps. Three concentration levels of active ingredients were evaluated.

NIR spectra of the pellets samples were first recorded before performing one active content measurement per vial using the reference method. Three different NIR measurements (*i.e.* replicates) of the same sample were performed. After each NIR acquisition, the vial was gently shaken to completely evaluate the sample.

2.5. Data treatment

The Opus software 6.5 (Bruker Optics) has been used to carry out the signal processing of the near infrared spectra.

Using the QUANT package of the Opus 6.5 software, prediction models based on PLS (Partial Least Squares) regression using stratified cross-validation were carried out with the calibration set and tested with the validation set. Each cross-validation fold contains the six spectra associated with a sample.

In PLS methods the regressions are computed with least squares algorithms. The goal of the PLS is to establish a linear link between two matrices, the spectral data X and the reference values Y (which can be of dimension above one). This technique works both on X and Y in order to find out the variables in the X matrix that will best describe the Y matrix through linear combinations of wavelengths, called factors, which describe best the studied properties [2].

Cross-validation is a classical way of building a model [30]. The first step consists in removing a group of samples from the calibration set. If the group of samples contains only one sample, the cross-validation is called leave-one-out cross-validation. Based on the remaining samples, a model is then built and tested with the removed samples. Afterwards, the removed samples are put back in the calibration set while a new group of samples is removed. A new model is then calculated and tested. The operations described above are repeated until all the samples from the calibration set have been removed once [3].

Two different types of data pre-treatment were used in our study: Standard Normal Variate (SNV) and Multiplicative Scatter Correction (MSC) pre-treatments. The first reduces mathematically the differences between the baselines of the spectra and then nor-

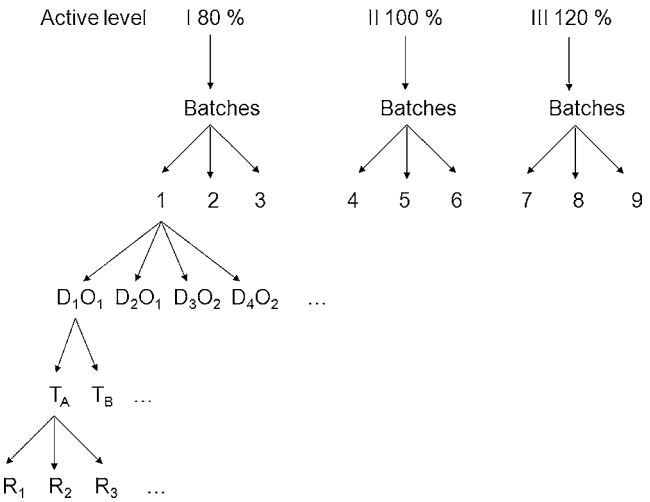


Fig. 1. Schematic illustration of the calibration protocol. D means *day*, O means *operator*. T_A: the sample is measured under ambient temperature conditions (25 °C). T_B: the sample is measured under high temperature conditions (35 °C). R_1, R_2 and R_3 represent different NIR measurements of the same sample.

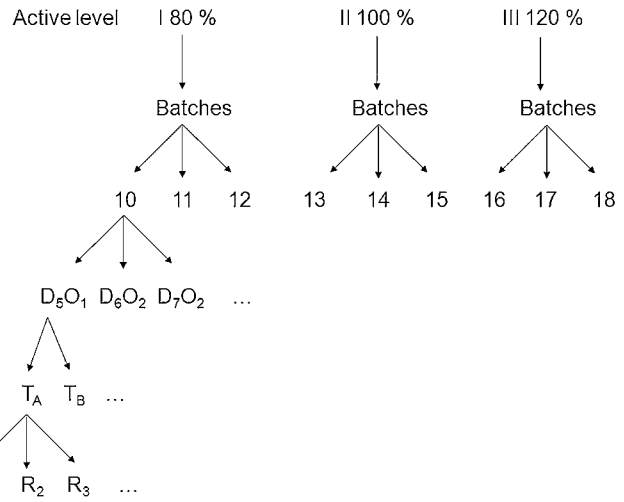


Fig. 2. Schematic illustration of the validation protocol. D means *day*, O means *operator*. T_A: the sample is measured under ambient temperature conditions (25 °C). T_B: the sample is measured under high temperature conditions (35 °C). R_1, R_2 and R_3 represent different NIR measurements of the same sample.

malizes them while the second reduces the effect of scattered light on diffuse reflection NIR spectra [3].

The calculation of the accuracy profiles based on the validation set results were realized with e.noval V2.1 (Arlenda, Liège, Belgium).

3. Results and discussion

3.1. Calibration

In order to meet the requirements of routine analyses and to guarantee the robustness of the NIR method, the calibration was designed focusing on different parameters. First, prediction models were built using independent pilot batches of non-coated pharmaceutical pellets. Indeed, once a batch of pharmaceutical pellets was manufactured, the mixer-extruder and the spheronizer were successively dismantled, cleaned and put together again before the manufacturing of a new batch. As it is difficult to restore the exact manufacturing conditions of the previous batch, each batch is an independent batch. Secondly, as different operators are likely to use the NIR method, the calibration protocol was designed for two operators. In addition, as temperature changes can induce variations in the spectral response, samples were scanned under two different temperature conditions (25 and 35 °C).

As shown in Fig. 1, the calibration was designed using three different active content formulations: 80, 100 and 120% formulations. There are 3 independent pilot batches of non-coated pharmaceutical pellets per formulation type. All the calibration batches were analyzed by NIR spectroscopy and the reference method by the two operators two times: *operator 1* and *2* made their own series on *day 1*, *day 2* and *day 3*, *day 4*, respectively. The NIR measurements were realized under two different temperature conditions (25 and 35 °C) and in triplicate. For example, on *day 1*, operator 1 took a sample from the 9 batches of non-coated pharmaceutical belonging to the calibration set. Those samples were analyzed two times in triplicate by NIR spectroscopy: one first triple measurement when the sample was thermostated at 25 °C and one second triple measurement when the sample was the sample was thermostated at 35 °C. Afterwards, all the samples were analyzed once by the HPLC reference method. For one series, a total number of 54 NIR spectra were recorded and 9 reference measurements were carried out. As the calibration is built with 4 independent series of measurements, the entire calibration set contains a total of 216 NIR spectra and 36 reference measurements.

3.2. Validation

Fig. 2 illustrates the validation protocol that comprises the same type of formulations as in the calibration protocol: 80, 100 and 120% active content formulations. There are also 3 independent batches of non-coated pharmaceutical pellets per formulation type. All the validation batches were analyzed by NIR spectroscopy and the reference method by the two operators: one time by *operator 1* on *day 5* and 2 times by *operator 2* on *day 6* and *day 7*. The NIR measurements were realized under two different temperature conditions (25 and 35 °C) and in triplicate. For example, on *day 5*, operator 1 took a sample from the 9 batches of non-coated pharmaceutical belonging to the validation set. In the same way as for the calibration set, those samples were analyzed two times in triplicate by NIR spectroscopy: one first triple measurement when the sample was thermostated at 25 °C and one second triple measurement when the sample was the sample was thermostated at 35 °C.

Table 1
Type of spectral pre-treatment, R^2, spectral range selected, number of PLS factors, RMSEC and RMSEP of different models.

Model	(a)	(b)	(c)
Pre-treatment	None	SNV	MSC
R^2	0.991	0.994	0.994
Spectral range selected (cm^{-1})	7502.2–6098.2 5450.2–4597.7	12493.3–7498.3 6102–5774.2 4601.6–4246.7	12493.3–7494.5 6102–5774.2 4917.9–4543.7
Number of PLS factors	7	4	3
RMSEC (%)	1.18	0.95	1.02
RMSEP (%)	2.15	1.37	1.28

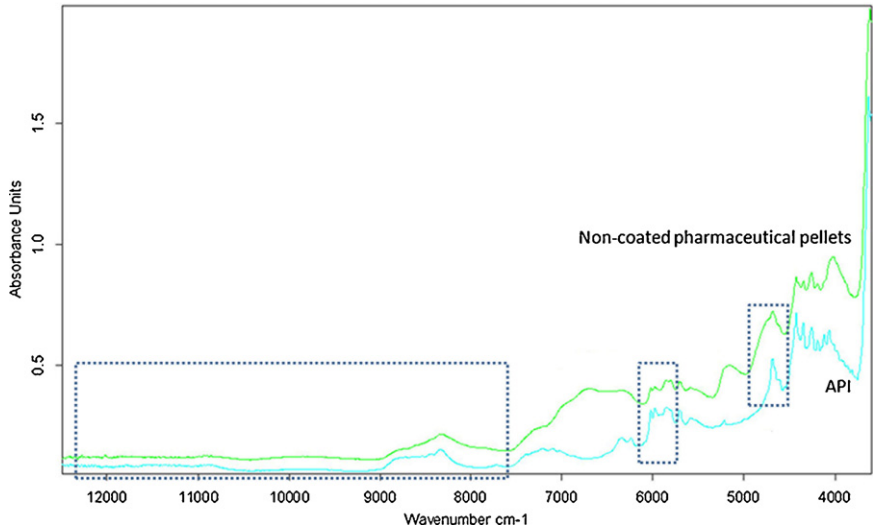


Fig. 3. NIR spectra of the non-coated pharmaceutical pellets and the API. The spectral areas selected for the (c) model are highlighted.

Afterwards, all the samples were analyzed one time by the HPLC reference method. For one series, a total of 54 NIR spectra were recorded and 9 reference measurements were taken. Consequently, as the validation is built with 3 series of measurements, the entire validation set contains a total of 162 NIR spectra and 27 reference measurements.

3.3. Validation results of the NIR method

Depending on the type of mathematical pre-treatment applied, the spectral range selected and the number of PLS factors chosen, a large amount of models can be generated. Classically, the models with the biggest predictive potential can be selected according to conventional criteria such as the R^2, the number of PLS factors, the Root Mean Square Error of Calibration (RMSEC) and the Root Mean Square Error of Prediction (RMSEP). Table 1 shows the conventional parameters of three potentially interesting models.

As the R^2 of the three models are very close, it does not allow any clear differentiation between the models.

Concerning the spectral regions selected, it can be seen from Fig. 3 that the spectral regions selected for the 3 models are related to the pellets active content.

Regarding the number of PLS factors, the bigger the number of PLS factors selected is, the more important is the risk to overfit the model. Hence, the (a) model seems to use too many factors to predict the active content with a good robustness.

Considering RMSEC and RMSEP, the (b) and (c) model seem to be slightly better than the (a) model: their RMSEC and RMSEP are

Table 2
ICH Q2R1 validation criteria of the (c) model.

	Concentration level (% active)	Mean introduced concentration (% active)	Relative bias (%)
Trueness	80	80.7	−0.25
	100	100.9	0.00
	120	122.0	0.05

	Concentration level (% active)	Mean introduced concentration (% active)	Repeatability (RSD %)	Intermediate precision (RSD %)
Precision	80	80.7	1.4	1.6
	100	100.9	1.0	1.2
	120	122.0	1.0	1.2

	Concentration level (% active)	Mean introduced concentration (% active)	Relative β-expectation tolerance limits (%)
Accuracy	80	80.7	[−3.65, 3.14]
	100	100.9	[−2.70, 2.71]
	120	122.0	[−2.59, 2.68]

Limits of quantification (LOQ)	
Lower LOQ (% active)	Upper LOQ (% active)
80.7	122.0

Table 3
Uncertainty of measurements of the (c) model.

Concentration level (% active)	Mean introduced concentration (% active)	Uncertainty of the bias (% active)	Uncertainty (% active)	Expanded uncertainty (% active)	Relative expanded uncertainty (%)
80	80.7	0.35	1.33	2.7	3.3
100	100.9	0.40	1.30	2.6	2.6
120	122.0	0.46	1.53	3.1	2.5

the smallest. However, it is impossible to select the model which is the most fitted for purpose. Moreover, those criteria do not allow the assessment of the model ability to quantify accurately over the investigated active content range.

Consequently, accuracy profiles based on tolerance intervals were used as a complementary decision tool to evaluate the models predictive performances. Tolerance intervals have the advantage to convey a predictive ability to the accuracy profile: for example, 95% of the future results will be included within a 95% tolerance interval. In opposition to a confidence interval which only takes into consideration the existing results but does not guarantee that the future results (routine results for example) will be situated within the interval.

Hubert et al. [20–22] showed that the accuracy profile which uses the total error concept meets the ICH Q2 (R1) guideline requirements. Facing the confusion found between accuracy and trueness in the ICH document, it seems important to remind that accuracy represents the total error concept which is the sum of the trueness (systematic error) and precision (random error).

Fig. 4 shows accuracy profiles based on the validation results obtained with the (a), (b) and (c) model, respectively. From this figure, it can be observed that the active content of validation samples belonging to the same concentration level is identical: it is caused by the alignment on the mean concentration, which is necessary to calculate a variance (for repeatability and intermediate precision estimates).

As this study focuses on the determination of the active content in a pharmaceutical formulation, the acceptance limits were set at ±5% for the validation of the NIR method while the maximum risk $(1-\beta)$ to obtain results outside the tolerance interval was set at 5%.

The lower and upper limits of quantification (LLOQ and ULOQ) define the range where an analytical method is able to quantify accurately. They are located where the β-expectation tolerance interval is included within the acceptance limits. If the β-expectation tolerance interval never crosses the acceptance limits, then the LLOQ and ULOQ are located at the beginning and at the end of the active content range investigated.

As can be seen in Fig. 4, the (b) and (c) models are able to quantify accurately over all the chosen active content range [80–122%]. However, the (a) model has a LLOQ of 95% making this model inaccurate for the 80% active content level. Moreover, of the 3 models, the (a) model has the most important bias.

Regarding the (b) and (c) models, although 95% of the future results will be included within the β-expectation tolerance interval which fall in the acceptance limits over the entire active content range, the (c) model is the best fitted for purpose. Indeed, the (b) model β-expectations tolerance limits are closer to the acceptance limits over the entire active content range than those of the (c) model. Consequently, the NIR method will use the (c) model to determine the active content of the non-coated pharmaceutical pellets.

Fig. 5 shows the evolution of the (c) model RMSECV according to the number of PLS factors chosen: as there is no significant change of the RMSECV value from 3 PLS factors, this number of PLS factors was selected for the (c) model.

The comparison of Fig. 3 and the first loadings of the (c) model displayed on Fig. 6 confirms that the spectral area selected are relevant for the determination of the active content.

Table 2 shows the ICH Q2R1 validation criteria of the (c) model. As seen in the accuracy profile, the bias is stable and points towards zero: the relative bias does not exceed [−0.25%, 0.05%].

The precision of the method was estimated by measuring repeatability and intermediate precision at the three active content levels shown in the validation protocol. The repeatability and intermediate precision are both good for the three levels of active content. As can be observed in the accuracy profile, the 80% active

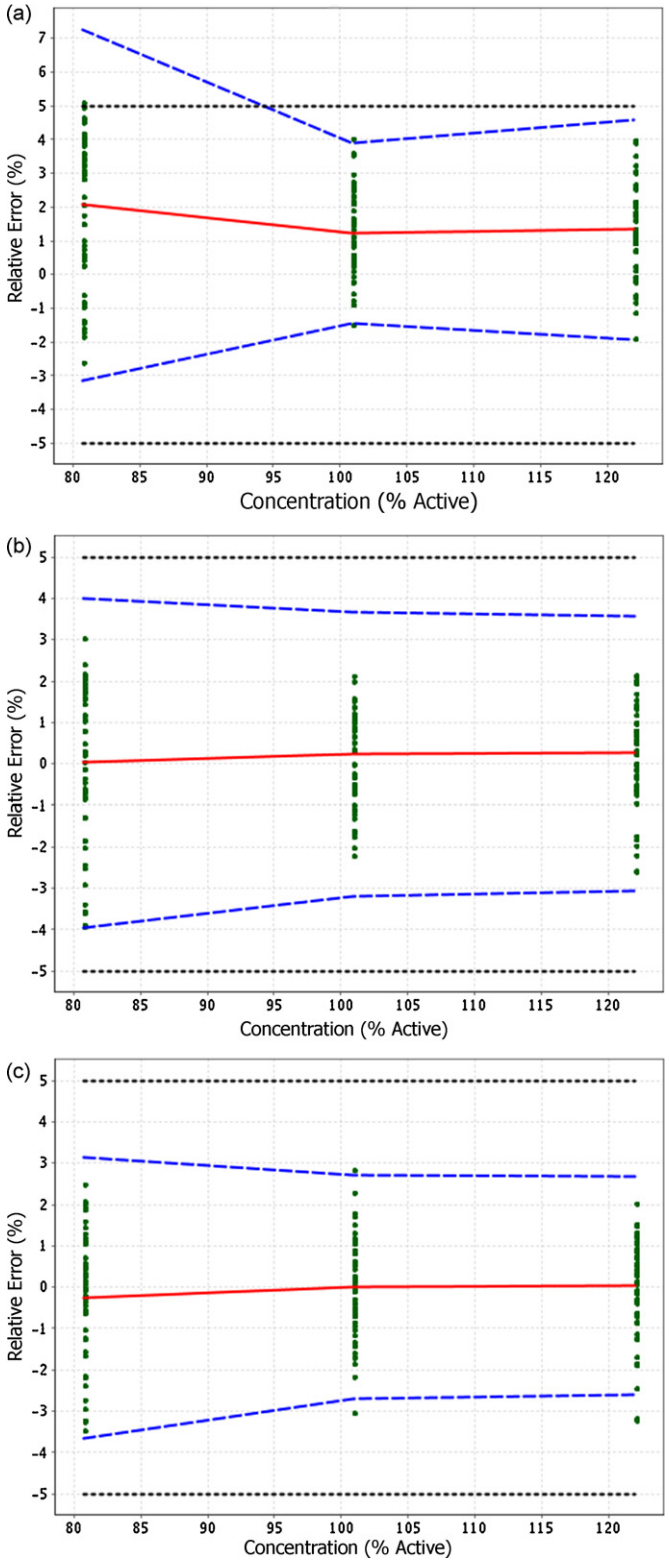


Fig. 4. (a), (b) and (c) Accuracy profiles based on the validation results of the (a), (b) and (c) models. The plain line is the relative bias, the dashed lines are the β-expectations tolerance limits (β = 95%) and the dotted lines represent the acceptance limits (±5%).

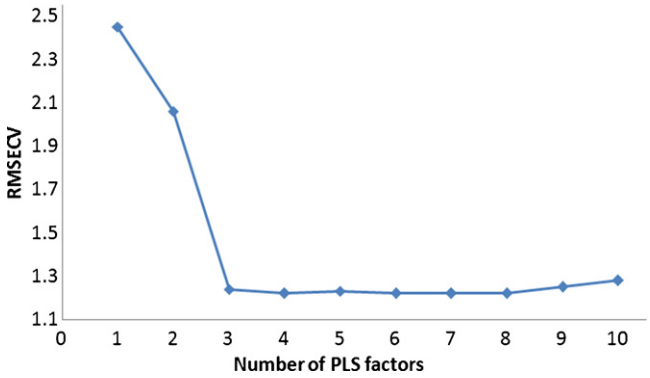


Fig. 5. (c) model: RMSECV versus the number of PLS factors.

content level is the worst level for the repeatability and the intermediate precision but this is still very satisfactory.

As shown with the accuracy profile, the accuracy is very good for the entire active content range as the values of the relative β-expectation tolerance limit never exceed [−3.65%, 3.14%].

Fig. 7 is showing the linear profile of the (c) model. A linear model was fitted on the calculated concentrations of the validation standards for all series as a function of the introduced concentrations. The intercept, the slope and the R^2 values are also presented in Fig. 7. The slope and intercept are close to 1and 0 respectively confirming the absence of proportional and constant systematic error of the (c) model. The linearity of the method for the 80–120% active content range is demonstrated since the β-expectation tolerance limits were included in the absolute acceptance limits. Further, the (c) model reliability was tested with 90 and 110% active content formulations, providing two additional active content levels to evaluate the NIR method linearity. As can be seen from Fig. 8, the linearity was confirmed as the slope and intercept are still close to 1 and 0, respectively.

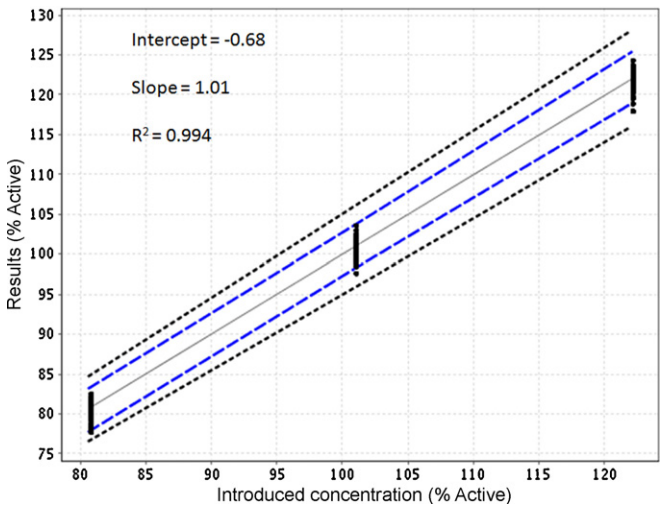


Fig. 7. Linear profile of the (c) model. The dashed limits on this graph correspond to the accuracy profile, *i.e.* the β-expectation tolerance limits expressed in absolute values. The dotted curves represent the acceptance limits at ±5% expressed in the concentration unit. The continuous line is the identity line $y = x$.

3.4. Uncertainty assessment of the NIR method (c model)

The uncertainty characterizes the dispersion of the values that could reasonably be attributed to the measurand [31,32]. Several uncertainty results were generated and are presented in Table 3: the uncertainty of bias of the method at each concentration level of the validation standard, the uncertainty which combines the uncertainty of the bias with the uncertainty of the method obtained during the validation step, *i.e.* the intermediate precision standard deviation, and the expanded uncertainty which equals to the uncertainty multiplied by a coverage factor $k = 2$ representing an interval around the results where the unknown true value can be observed with a confidence level of 95% [33,34]. In addition, the relative expanded uncertainties (%) for active content obtained by dividing the corresponding expanded uncertainties with the corresponding introduced concentrations (Table 3) are not higher than 3.3%, which means that with a confidence level of 95%, the unknown true value is located at a maximum of ±3.3% around the measured result.

3.5. Reliability evaluation of the NIR method

Method validation is the first step to evaluate the fitness of purpose and the reliability of a newly developed analytical method. In order to increase and further guarantee the reliability of the NIR method (c model), a three steps additional reliability evaluation

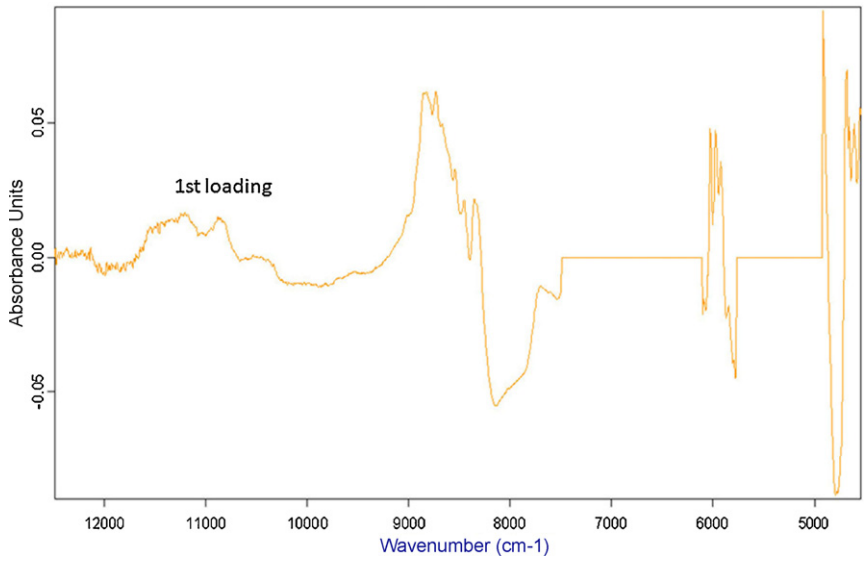


Fig. 6. (c) model: first loading factor.

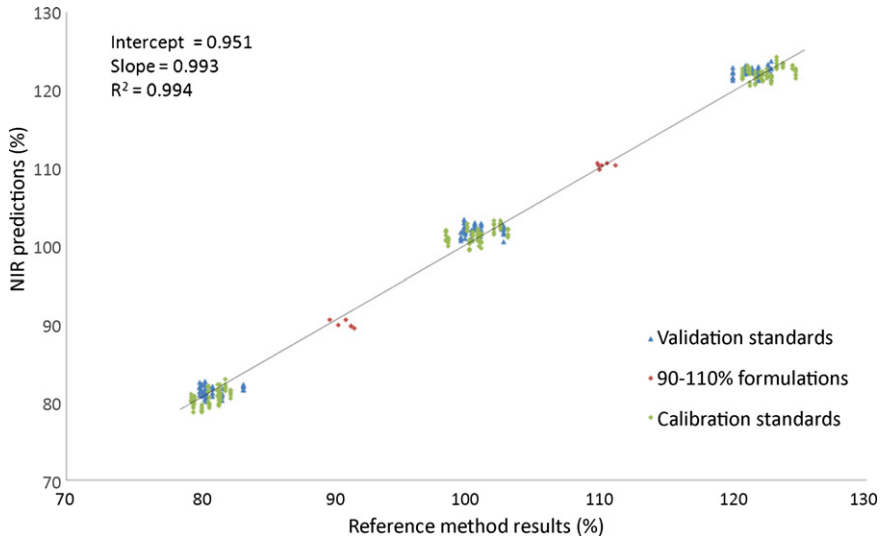


Fig. 8. (c) model: calibration set, validation set and 90/110% formulations NIR predictions versus the reference method predictions.

of the analytical method was performed. The aim of this evaluation is to check the robustness of the NIR method and to ensure its interchangeability with its HPLC reference method.

First, 90 and 110% active content formulations were manufactured. Those batches were analyzed by two operators using both the HPLC reference method and the NIR method (c model), relative errors were calculated. The aim was here to verify that the predictions of the accuracy profile at concentration levels not investigated during the validation step were reliable. Fig. 9 plots the relative error versus the active content level, 95% prediction intervals limits were defined for each level of active content. These prediction intervals define the area containing 95% of the relative errors. Regarding the 90% active content level, 95% of the future results are likely to show a relative error not exceeding [−2.44%, 0.44%]. Besides, 95% of the future results are expected to have a relative error within [−0.62%, 0.72%] for the 110% active content level. All those results indicate that the NIR method is able to quantify accurately 90 and 110% active content formulations. Fig. 8 summarizes the predictions of the (c) model versus the references measurements of the calibration and validation sets as well as for the 90 and 110% active content batches.

Secondly, using batches belonging to the validation set, blends containing different amounts of active content were realized by two operators to obtain between 80 and 120% active content formulations. The results of the reference HPLC method were used to calculate a theoretical active content for each blend. The average between the NIR results (c model) and the HPLC reference results and relative errors were calculated. A Bland and Altman plot is shown in Fig. 10. This plot represents the relative errors against mean (NIR + HPLC)/2 results. Regarding this plot, 95% of the relative errors between the two methods do not exceed [−2.25%, 1.74%].

Finally, the NIR method (c model) was also tested with 10 industrial batches of non-coated pharmaceutical pellets (100% active content formulations) belonging to 2 different production campaigns. Those batches were analyzed by the two operators. The average between the NIR results (c model) and the HPLC reference results and relative errors were calculated. Fig. 11 shows a Bland Altman plot of those results: 95% of the relative errors between the two methods are expected to have relative errors within [−2.32%, 3.40%].

As the results shown in this section are all in full accordance with the validation results, it can be concluded that the NIR method using (c) model was reliable and robust enough to quantify with good accuracy samples with an active content not included in the calibration set (90 and 110% active content formulations). Therefore, it was not necessary to include those levels of active content in the calibration set. Besides, the (c) model also gave accurate predictions for blends of validation batches, which were independent from the model calibration batches. Further, the predictive ability of the (c) model was also adequate to quantify the active content of 100% formulation industrial batches of non-coated pharmaceutical. Therefore, the NIR method can replace the HPLC reference method for the accurate quantification of the API in non-coated pharmaceutical pellets.

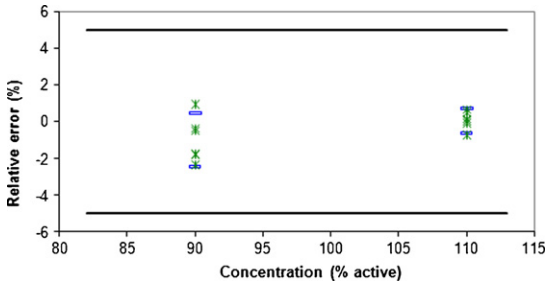


Fig. 9. Relative errors (100 × ((NIR − HPLC)/HPLC)) versus the active content level of batches containing 90 and 110% of the usual active content. The continuous lines are the ±5 acceptance limits. The boxes define the 95% prediction interval limits.

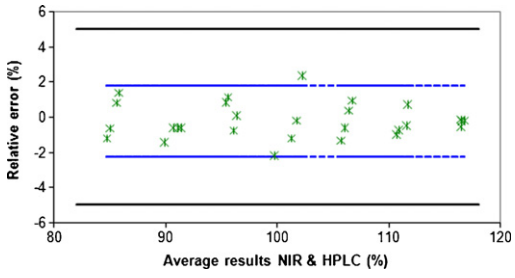


Fig. 10. Blends of batches of pharmaceutical pellets belonging to the validation set: Bland and Altman's plot: Relative errors (100 × ((NIR − HPLC)/HPLC)) against mean ((NIR + HPLC)/2) for different concentration levels. The continuous lines are the ±5 acceptance limits. The dashed lines define the 95% tolerance interval limits.

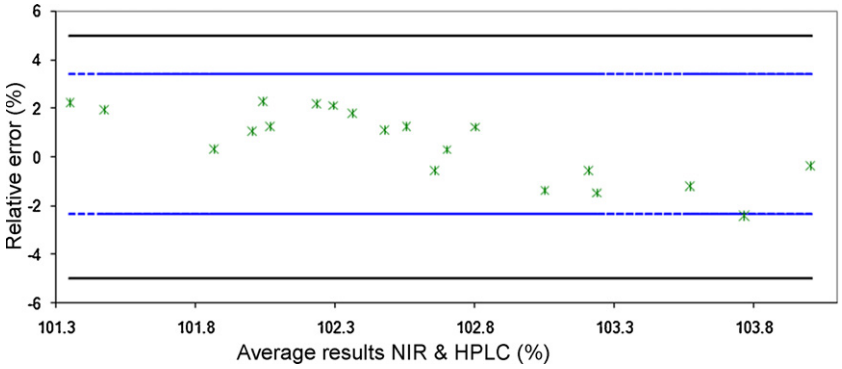


Fig. 11. Industrial batches of pharmaceutical pellets: Bland and Altman's plot: Relative errors ($100 \times ((NIR - HPLC)/HPLC)$) against mean ($(NIR + HPLC)/2$) for different concentration levels. The continuous lines are the ±5 acceptance limits. The dashed lines define the 95% tolerance interval limits.

4. Conclusion

A near infrared method was developed for the determination of the active content of non-coated pharmaceutical pellets. The method was fully validated and showed very good precision, trueness and accuracy for the determination of an active content ranging from 80 to 120% of the usual active content confirming the potential of near infrared spectroscopy in the PAT concept.

As the conventional criteria failed to select the most accurate model because of a lack of interpretation, a novel approach based on accuracy profiles was chosen, which translates the results of the validation set in an effective visual manner, showing the models ability to quantify the active content over the chosen active content range. As it is based on β-expectation tolerance interval, the accuracy profile also gives a representation of the future performances of the analytical method. Consequently, this approach has finally enabled to choose the best model in full accordance with the very final goal of the developed near infrared method: to quantify accurately an active content of non-coated pharmaceutical pellets ranging from 80 to 120%.

The validated near infrared method was successfully tested with pilot batches of non- coated pharmaceutical pellets containing 90 and 110% of the usual active content, with blends of validation batches and industrial batches of non-coated pharmaceutical pellets. The results were in full accordance with the validation results, demonstrating the reliability of the NIR method and its interchangeability with the HPLC reference method.

Acknowledgements

Thanks are due to the Walloon region and Galéphar research center M/F for a research grant provided to Jérôme Mantanus. A research grant from the Belgium National Fund for Scientific Research (FRS-FNRS) to E. Rozet is also gratefully acknowledged.

References

[1] J. Luypaert, D.L. Massart, Y. Vander Heyden, Talanta 72 (2007) 865.
[2] Y. Roggo, P. Chalus, L. Maurer, C. Lema-Martinez, A. Edmond, N. Jent, J. Pharm. Biomed. Anal. 44 (2007) 683.
[3] D.A. Burns, E.W. Ciurczak, Handbook of Near-Infrared Analysis, vol. 35, 3rd ed., CRC Press, New York, 2008.
[4] American Food and Drug Administration (FDA), Guidance for Industry PAT-A Framework for Innovative Pharmaceutical Manufacturing and Quality Assurance, FDA, 2004.
[5] International Conference on Harmonisation (ICH) of technical requirements for registration of pharmaceuticals for human use, Topic Q8: Pharmaceutical Development, Geneva, 2005.
[6] J.A. Lopes, P.F. Costa, T.P. Alves, J.C. Menezes, Chemo. Intel. Lab. Syst. 74 (2004) 269.
[7] J.J. Moes, M.M. Ruijken, E. Gout, H.W. Frijlink, M.I. Ugwoke, Int. J. Pharm. 357 (2008) 108.
[8] C. Bodson, W. Dewé, Ph. Hubert, L. Delattre, J. Pharm. Biomed. Anal. 41 (2006) 783.
[9] C. Bodson, E. Rozet, E. Ziémons, B. Evrard, Ph. Hubert, L. Delattre, J. Pharm. Biomed. Anal. 45 (2007) 356.
[10] J. Mantanus, et al., Anal. Chim. Acta (2008), doi:10.1016/j.aca.2008.12.031.
[11] J. Rantanen, E. Räsänen, O. Antikainen, J.-P. Mannermaa, J. Yliruusi, Chemo. Intel. Lab. Syst. 56 (2001) 51.
[12] N. Sandler, J. Rantanen, J. Heinämäki, M. Römer, M. Marvola, J. Yliruusi, AAPS PharmSciTech. 6 (2) (2005) Article 26.
[13] M. Ito, T. Suzuki, S. Yada, A. Kusai, H. Nakagami, E. Yonemochi, K. Terada, J. Pharm. Biomed. Anal. 47 (2008) 819.
[14] L.O. Rodrigues, J.P. Cardoso, J.C. Menezes, Talanta 75 (2008) 1203.
[15] S.S. Rosa, P.A. Barata, J.M. Martins, J.C. Menezes, Talanta 75 (2008) 725.
[16] H. Huang, H. Yu, H. Xu, Y. Ying, J. Food Eng. 87 (2008) 303.
[17] Q. Chen, J. Zhao, S. Chaitep, Z. Guo, Food Chem. 113 (2009) 1272.
[18] M.R. Monteiro, A.R.P. Ambrozin, L.M. Liao, A.G. Ferreira, Talanta 77 (2008) 593.
[19] International Conference on Harmonization (ICH) of Technical Requirements for registration of Pharmaceuticals for human use, Topic Q2 (R1): Validation of Analytical Procedures: Text and Methodology, Geneva, 2005.
[20] Ph. Hubert, J.J. Nguyen-Huu, B. Boulanger, E. Chapuzet, P. Chiap, N. Cohen, P.A. Compagnon, W. Dewé, M. Feinberg, M. Lallier, M. Laurentie, N. Mercier, G. Muzard, C. Nivet, L. Valat, J. Pharm. Biomed. Anal. 36 (2004) 579.
[21] Ph. Hubert, J.J. Nguyen-Huu, B. Boulanger, E. Chapuzet, P. Chiap, N. Cohen, P.A. Compagnon, W. Dewé, M. Feinberg, M. Lallier, M. Laurentie, N. Mercier, G. Muzard, C. Nivet, L. Valat, E. Rozet, J. Pharm. Biomed. Anal. 45 (2007) 70.
[22] Ph. Hubert, J.J. Nguyen-Huu, B. Boulanger, E. Chapuzet, N. Cohen, P.-A. Compagnon, W. Dewé, M. Feinberg, M. Laurentie, N. Mercier, G. Muzard, L. Valat, E. Rozet, J. Pharm. Biomed. Anal. 45 (2007) 82.
[23] Ph. Hubert, P. Chiap, J. Crommen, B. Boulanger, E. Chapuzet, N. Mercier, S. Bervoas-Martin, P. Chevalier, D. Grandjean, P. Lagorce, M. Lallier, M.C. Laparra, M. Laurentie, J.C. Nivet, Anal. Chim. Acta 391 (1999) 135.
[24] E. Rozet, A. Ceccato, C. Hubert, E. Ziémons, R. Oprean, S. Rudaz, B. Boulanger, P. Hubert, J. Chromatogr. A 1158 (2007) 111.
[25] E. Rozet, R. Morello, F. Lecomte, G.B. Martin, P. Chiap, J. Crommen, K.S. Boos, P. Hubert, J. Chromatogr. B 844 (2006) 251.
[26] E. Rozet, V. Wascotte, N. Lecouturier, V. Préat, W. Dewé, B. Boulanger, Ph. Hubert, Anal. Chim. Acta 591 (2007) 239.
[27] E. Rozet, C. Hubert, A. Ceccato, W. Dewé, E. Ziemons, F. Moonen, K. Michail, R. Wintersteiger, B. Streel, B. Boulanger, Ph. Hubert, J. Chromatogr. A 1158 (2007) 126.
[28] M. Feinberg, B. Boulanger, W. Dewé, Ph. Hubert, Anal. Bioanal. Chem. 380 (2004) 502.
[29] International Conference on Harmonisation (ICH) of technical requirements for registration of pharmaceuticals for human use, Topic Q9: Quality Risk Management, Geneva, 2005.
[30] European Medicines Agency, draft: guideline on the use of near infrared spectroscopy by the pharmaceutical industry and the data requirements for new submissions and variations, EMEA/CHMP/CVMP/QWP/17760/2009 Rev 1.
[31] Analytical Methods Committee, Analyst 120 (1995) 2303.
[32] Eurachem/Citac guide quantifying the uncertainty in analytical measurement, second ed., 2000.
[33] CB EA-4/16, EA Guidelines on the Expression of Uncertainty in Quantitative Testing, 2004, http://www.european-accreditation.org.
[34] R.D. Marini, P. Chiap, B. Boulanger, S. Rudaz, E. Rozet, J. Crommen, Ph. Hubert, Talanta 68 (2006) 1166.

Talanta 80 (2010) 1758–1770

Contents lists available at ScienceDirect

Talanta

journal homepage: www.elsevier.com/locate/talanta

Whole-cell spectroscopy is a convenient tool to assist molecular identification of cultivatable marine bacteria and to investigate their adaptive metabolism

Stéphanie Salaün[a,b,c], Nelly Kervarec[d], Philippe Potin[a,b], Dominique Haras[c], Martial Piotto[e], Stéphane La Barre[a,b,*]

[a] Université Pierre et Marie Curie-Paris 6, UMR 7139 Végétaux marins et Biomolécules, Station Biologique F-29682, Roscoff, France
[b] CNRS, UMR 7139 Végétaux marins et Biomolécules, Station Biologique F-29682, Roscoff, France
[c] Université de Bretagne-Sud, Laboratoire de Biotechnologie et de Chimie Marines, EA3884, BP 92116, 5632 Lorient, France
[d] Service Commun de Résonance Magnétique Nucléaire, Université de Bretagne Occidentale, UFR Sciences et Techniques, 6 avenue Le Gorgeu, BP 809 29285, Brest, France
[e] Institut de Chimie, FRE 2446, 4 rue Blaise Pascal, Université Louis Pasteur, 67084 Strasbourg, France

ARTICLE INFO

Article history:
Received 1 July 2009
Received in revised form
29 September 2009
Accepted 8 October 2009
Available online 11 November 2009

Keywords:
Marine bacteria
MALDI-TOF MS
HR-MAS NMR
16S rDNA taxonomy
Physiological adaptation
Brown algae

ABSTRACT

Recent developments in whole-cell spectroscopic methods allow rapid characterization of microorganisms of interest to human health, but have yet to be widely applied to marine microbiological studies. In this study of bacteria associated with the kelp *Laminaria digitata*, we have isolated 18 epiphytic bacterial strains from several thalli, sequenced their 16S rDNA, built corresponding phylogenetic trees, and characterized them using spectroscopic methods. Molecular taxonomy revealed Gram$^+$ *Actinobacteria* and Gram$^-$ *Alphaproteobacteria*, *Gammaproteobacteria* and *Bacteroidetes*. Twelve marine reference strains (Gram$^+$ *Firmicutes*, and Gram$^-$ *Alphaproteobacteria*, *Gammaproteobacteria* and *Bacteroidetes*) were treated accordingly. Whole-cell MALDI-TOF MS spectral profiles of 29 of the 30 strains were built into a database against which 16 replicate spectra of each strain were compared and categorized into groups. The proton HR-MAS NMR stack plots allowed visual delineation into taxonomic groups according to their most common peaks, in agreement with identifiable compounds from corresponding D_2O solution spectra. With both methods, these groups corresponded to taxa identified by 16S rDNA sequences, MALDI-TOF MS being more discriminative than HR-MAS NMR. Culture age did not influence the spectral signatures in both approaches. Most cells grown under minimal conditions (VNSS medium) afforded HR-MAS NMR profiles markedly different to those grown in enriched conditions (ZoBell medium), indicating different adaptive metabolic responses between the two media. Spectral signatures obtained under strictly controlled conditions can be used as rapid and reliable tools for taxonomic purposes and as markers of physiological status.

© 2009 Elsevier B.V. All rights reserved.

1. Introduction

The study of marine biofilms associated with living organisms or developing on inert surfaces under immersion requires the isolation of cultivatable bacterial strains in order to study surface interactions [1,2]. Similar to the studies of microorganisms of medical or food safety importance, the taxonomy of bacterial consortia associated with a specific aquatic niche is fundamental to any scientific investigation [3,4]. Characterizations through traditional bacteriological techniques such as culture on selective media and biochemical activity tests are prerequisite for identification of novel species [5], but are time-consuming and labour-intensive for routine checking. Molecular taxonomy using DNA–DNA re-association, PCR fingerprinting and DNA sequencing of reference organisms are generally more discriminatory than methods based on phenotypic characters. Currently employed for routine bacterial identification, molecular methods can be tedious and costly for applications such as contamination checks, strain selection, presence of new species, etc. Mass spectrometry (MS) and nuclear magnetic resonance spectroscopy (NMR) provide attractive alternative methods for routine bacterial differentiation. As a rapid and sensitive method, MS has been widely used for identification and typing of microorganisms during the last 30 years [6]. However, due to some limitations in ionization techniques, access to MS equipment or tedious sample preparation prior to analysis, these methods were not developed for chemotyping of bacteria. MALDI-TOF MS has been used since the 1980s for the determination of proteins within the 2000–20,000 Da range as molecular taxonomic biomarkers in microorganisms, and

* Corresponding author at: Université Pierre et Marie Curie-Paris 6, UMR 7139 Végétaux marins et Biomolécules, Station Biologique F-29682, Roscoff, France. Tel.: +33 0 298292361; fax: +33 0 298292385.
E-mail address: labarre@sb-roscoff.fr (S. La Barre).

0039-9140/$ – see front matter © 2009 Elsevier B.V. All rights reserved.
doi:10.1016/j.talanta.2009.10.020

a useful user guide for optimizing the technique on whole cells was subsequently published by its pioneers [7]. Recent studies have demonstrated that bacteria from different species and strains could be rapidly identified and distinguished by matrix-assisted laser desorption/ionization—time-of-flight mass spectrometry (MALDI-TOF MS) in microbial mixtures with automated data analysis algorithms [6,8]. MALDI-TOF MS fingerprinting requires very small sample amounts and is relatively fast as product separation is not required. As illustrated by its routine use in proteomic studies, MALDI-TOF MS has proven very useful for the fingerprinting of peptidic masses [9]. Molecular signatures sorted out by mass to charge ratio (m/z) can be compared and matched with referenced proteins which are deposited online in protein databanks. However, not only whole cells or tissue proteome but also secreted biopolymers and membrane-associated components (proteins, carbohydrates, glycoconjugates and lipoconjugates) representing the secretome can be analyzed with the MALDI-TOF technique [10,11]. MALDI-TOF MS proteome analysis has a recognized taxonomic value [12], which has yet to be fully exploited in marine bacteria taxonomy [13]. Original metabolites produced by microorganisms, including bacteria and fungi, have proven useful to establish the chemo-type of microorganisms and are conveniently studied using NMR spectroscopy techniques. In addition, determination of bacterial types associated with pus [14] or from cell extracts [15], or metabolic studies [16], has validated the use of proton NMR for broad taxonomic use in medical microbiology. Delpassand et al. [17] have pioneered high resolution NMR (δ 0.5–4.5 ppm) for fingerprinting of bacterial extracts and found that identification of strains is straightforward and spectra are consistent within strains. NMR offers a high-throughput, rapid, polyphasic approach by providing information simultaneously on a large range of metabolites, and by unraveling bacterial amino acid biosynthesis from labeled precursors. ^{1}H NMR spectra of cell suspensions acquired in static mode provide an overview of mobile hydrogen-containing compounds which can be better identified by multidimensional NMR correlation spectroscopy on corresponding cell extracts. Water soluble metabolites typically include mono and oligomers of carbohydrates, amino acids and some of their derivatives, and organic ions involved in substrate-dependant metabolic pathways. Significant patterns emerge upon applying multivariate statistics on signals (peaks) most representative of a selected spectral window [18], often using the dedicated software developed by the instrument manufacturer. Bourne et al. [19] introduced PCA analysis to simplify classification of the spectra since significantly different metabolite pool sizes would be detected as differences between the ^{1}H NMR spectra of the different bacterial groups. In an effort to reduce handling and increase efficiency in preparation procedures, Motta et al. [20] successfully applied NMR directly to bacterial suspension media of marine strains in order to quantify the various released water solubles. A particularly interesting variant of whole-cell NMR is High Resolution Magic Angle Spin NMR (HR-MAS NMR) now extensively used in *in vivo* and *ex vivo* studies of biological tissues and of whole organisms by pathologists, environmental chemists [21,22], plant physiologists [23–25] and microbiologists [26]. HR-MAS NMR spectroscopy on live tissues, e.g. [27,28] and body fluids [18,29] was primarily used in clinical investigations of biomarkers of cancer and neurological dysfunctions and also proved useful in marine applications, e.g. for macroalgae [23] and for phytoplankton [24]. Bacteriological applications included some technical refinements, e.g. 2D ^{1}H–^{13}C HSQC on ^{13}C labeled cells to study membrane components [26]. The idea behind the MAS method is the tilting of the solid sample by an angle of 54.7° (the "magic angle") to the axis of the static magnetic field, and by rotating the sample at great speed (usually 5–15 kHz) about its own axis, the line broadening of signals is corrected due to a reduction of the anisotropic interactions in the tissue. Lengthy extraction procedures are thus avoided, and time series snapshot spectra can even be taken to monitor metabolic changes in live cells or whole organisms exposed to an experimental disturbance. As a rule, most small water soluble analytes can be observed with HR-MAS preparations, albeit with a lesser resolution than with preparations from extracts. As for MALDI-TOF MS, NMR spectroscopy has been applied to the study of only few marine prokaryotes, and to our knowledge, HR-MAS NMR has never been used as an analytical tool by marine microbiologists.

In this study, we have selected 30 cultivatable bacterial strains (18 regularly found on the thalli of the temperate brown kelp *Laminaria digitata*, 12 environmental isolates some of which are referenced) and we have matched their metabolic and their whole-cell proteomic fingerprints obtained by spectroscopic methods, to the 16S rDNA-based identifications. The aim is to evaluate each spectroscopic method as complementary or substitutive taxonomic tool to gene sequencing, and as a metabolomic (proton HR-MAS NMR) or proteomic (MALDI-TOF MS) tool, with databases constructed directly from whole cells grown under controlled conditions.

2. Materials and methods

2.1. Sample collection

Adult thalli of the brown kelp *L. digitata* Lamouroux were collected seasonally in 2006 on the upper subtidal portions of Bloscon harbour (48°43′19″N; 3°58′15″W) at Roscoff (France). Laboratory sampling of bacterial epiphytes at the holdfast, stipe, meristem and blade portions of the thalli was performed as follows: (i) 3 min sonication of (2–3 cm^2) of tissue coupons in filtered and sterile seawater in 50 ml Falcon tubes, followed by vacuum filtrations (60 μm, then 8 μm mesh, Millipore, France). The filtrates were then seeded in Petri dishes containing agar-enriched ZoBell culture medium [30]. Alternatively (ii) was used: fresh coupons of algae from various portions of algae (<1 cm^2) were placed directly on the surface of the medium. After suitable development, CFU (Colony Forming Units) were selected and each was spread on individual sterile plates to obtain monospecific clonal cultures. Only 18 maintainable strains within the Ld1 to Ld20 series were studied among the numerous strains originally obtained (Ld is used hereafter as shorthand notation for *L. digitata*—associated bacterial consortia). Reference bacterial strains previously isolated from inert or biological surfaces were obtained from various sources. Strains *Vibrio* sp. D01 [31] and *Pseudoalteromonas* sp. D41 were obtained from DERT at Ifremer (Plouzané, France); *Cytophaga* sp. 1M6 [32], *Paracoccus* sp. 4M6 [32], *Pseudoalteromonas* sp. 3J3 [32], *Pseudoalteromonas* sp. 3J6 [32] and *Pseudoalteromonas* sp. 3J6GFP (a plasmid transform of 3J6) and *Bacillus* sp. 4J6 [32] from LBCM at Université de Bretagne-Sud (Lorient, France); *Pseudoalteromonas carrageenovora* ATCC 43555^{T}, *Pseudoalteromonas haloplanktis* ATCC 14393, *Cobetia marina* ATCC 25374^{T} and *Zobellia galactanivorans* Dsij^{T} from Station Biologique de Roscoff (Roscoff, France). All strains are kept at −80 °C in 15% glycerol—ZoBell medium. All bacteria were cultivated on plates with ZoBell—agar medium or VNSS (Väätänen nine-salt solution)—agar medium [33] at 13 °C (±1 °C), during 6, 10 and 18 days (±1 day). Standard seawater (filtered and sterilized natural, 35‰ total salinity) was used for preparation to obtain equivalent final salt concentrations in both media.

2.2. Molecular taxonomy

2.2.1. Amplification of 16S rDNA genes

A small amount of CFU (1–2 μg) of all strains was directly diluted in 200 μl of sterile water MilliQ. Nearly full-length 16S rDNA genes were amplified by PCR with *Taq* polymerase (Promega), and two bacteria-specific primers: forward primer 8F (5′-AGAGTTTGATCCTGGCTCAG-3′) [34] and reverse primer 1492R

(5′-GGTTACCTTGTTACGACTT-3′) [35]. PCR amplifications were performed using reaction mixtures (final volume of 25 μl) containing 1.5 mM $MgCl_2$, 0.2 μM of each primer, 0.2 mM of each dNTP, 0.5 U of Taq polymerase, 1× GoTaq Buffer (Promega), and 1 μl of bacteria-water mixture. Reactions without DNA were used as negative controls. PCR reactions were performed using a thermal cycler (GeneAmp® PCR System 2700, Applied Biosystems) under the following conditions: initial denaturation at 95 °C for 10 min, 35 cycles consisting of 95 °C for 30 s, 53 °C for 30 s and 72 °C for 1 min 30 s, and a final extension at 72 °C for 4 min. Amplified PCR products were analyzed by electrophoresis on 0.8% (w/v) agarose (Eurogentec) in 0.5× TAE (40 mM Tris–acetate, 1 mM EDTA pH 8). Smart Ladder (Eurogentec) was used as the molecular weight standard.

2.2.2. 16S ribosomal DNA sequencing and phylogenetic analysis

PCR products were purified by using Montage™ μPCR96 Cleanup kit (Millipore, France). Full-length sequences were obtained using the primers 8F and 1492R and the ABI v. 3.1 BigDye kit (Applied Biosystems). After purification, sequencing reaction products were run using an ABI 3130xl capillary sequencer (Applied Biosystems) on the sequencing technological platform of the Marine Station Biologique de Roscoff, Genopôle Ouest. The sequencing strategy generated 16S rDNA gene fragments in-between positions 34 and 1404 corresponding to the numbering of nucleotides in the *E. coli* 16S rDNA molecule [36].

The 16S rDNA sequences were edited using the DNAMAN v. 4.15 software, and compared to public nucleotide databases using the advanced Basic Local Alignment Search (BLAST) program (www.ncbi.nlm.nih.gov/BLAST). The resulting sequences were aligned to currently available 16S rRNA gene sequences which showed significant identity to those in EMBL, GenBank and RDP databases, using the SINA Webaligner interface which considers to both their primary and secondary structures ([37], www.arb-silva.de/aligner/). The multiple sequence alignment, including both conserved and variable domains of the 16S rRNA primary structure, was used to generate pairwise similarities and genetic distances between Ld strains and related bacteria. The final alignment was edited using MEGA v. 4.0.2 software [38] and further curated using less stringent parameters of GBlocks freeware [39] available at: www.phylogeny.fr [40]. Phylogenetic analyses were carried out on 62 sequences and 948 nucleotide positions using two reconstructing methods: (i) the Maximum Likelihood (ML) using the PhyML software at www.atgc-montpellier.fr/phyml [41] and (ii) the neighbour joining (NJ) approach using the PHYLIP software package [42], both with F84 models. Other phylogenetic reconstructions with both methods were also conducted using HKY85, Jukes and Cantor and GTR, leading to highly similar topologies and bootstrap supports. For both methods, the input order of sequences into the various phylogenetic programs and the selection of outgroups were also varied in this study. Statistical evaluation of the genetic divergences was performed by bootstrap re-sampling of the sequence data (100 replicates) to provide confidence estimates for the phylogenetic tree topologies.

The partial 16S rRNA gene sequences fully sequenced in this study have been deposited in the GenBank database under the accession numbers FJ966928–FJ966945, for the sequences obtained from *L. digitata* of Roscoff and FJ966946–FJ966951 for the sequences of the other reference bacterial strains used.

2.3. MALDI-TOF mass spectrometry

For each sample with the exception of Ld1, approximately 1–2 μg of live bacteria was carefully collected from a single CFU, directly spotted onto a MALDI target plate (MSP 96 ground S/N, Bruker) as a thin bacterial film and allowed to air dry. Each spot was overlaid with 1 μl of a fresh solution of saturated α-cyano-4-hydroxycinnanic acid matrix solution in 50% acetonitrile/50% water acidified with 2.5% trifluoroacetic acid, and then air dried at room temperature. MALDI spectra were acquired on Microflex Bruker Daltonics «time-of-flight» instrument (Bruker Daltonics GmbH, Leipzig, Germany) in linear positive mode with an accelerating voltage of ±20 kV, a time allowed to 300 ns and an emission wavelength of 337 nm. A total of 200 consecutive laser shots were accumulated from each sample. The instrument was calibrated with the following 11 reference masses from *E. coli* CIP53.126 from CGI-IPL Bretagne (Lorient, France): RL36 4364,33; RS32 5095,82; RS34 5380,39; RS33 Meth 6254,39; RL32 6315,19; RL30 6410,60; RL35 7157,74; RL29 7273,45; RL31 7871,06; RS15 8476,74; RS19 10137,57. All spectra were smoothed with the *Savitzky-Golay* centroid algorithm and a TopHat baseline subtraction. Mass spectra were acquired with FlexControl v. 3.0 and worked with FlexAnalysis v. 3.0 (software provided with the instrument). Post acquisition Biotyper v.1.0 software was used to classify all 464 database matrix spectra using a PCA (principal component analysis) approach. First, 29 strains were analyzed with an acquisition of 16 individual spectra (replicate spectra) per strain, that had intensity signals between 2000 and 6000, in order to build a database of 29 "consensus" spectra, based on averaging of the 16 replicate spectra, i.e. 29 consensus spectra × 16 replicate spectra amounting to 464 individual spectra. Second, each of the 464 individual spectra was compared for consistency against the 29 consensus spectra, and an averaged identity score was assigned to the five most resembling strains. Once validated, the database was used to classify samples from two experiments: 29 strains were grown on both ZoBell and VNSS media, each with 4 different culture replicates, yielding (i) 116 new ZoBell individual spectra and (ii) 116 new VNSS individual spectra.

2.4. NMR spectroscopy

Whole-cell samples were obtained from individual monocultures by collecting isolated live CFU which were introduced in a 4 mm zircon oxide rotor. Samples were homogenized with D_2O (Euriso-top, Saclay, France) and after sealing, the rotor was spun at 5000 Hz at 298 K in a HR-MAS SB BL4 $^1H/^{31}P$ probe which equipped a 500 MHz DRX Bruker supraconductive magnet at Service Commun de RMN at Université de Bretagne Occidentale, Brest. Recordings were made using a standard protocol for presaturation of the residual water peak. For all ZoBell grown strains, three sets of HR-MAS spectra were recorded corresponding to day 6, day 11 and day 18 plates. D_2O extracts from 8 day cultures were made from whole plate surface scrapings of CFU which were homogenized in a French press (1.5 bar pressure). High resolution solution one and two dimensional ^1H and ^{13}C spectra were obtained using the 5 mm triple resonance TBI $^1H/\{BB\}/^{13}C$ probe head. Standard pulse sequences were used for COSY (^1H–^1H correlation spectroscopy), HMQC experiments (^1H detected ^1H–^{13}C heteronuclear multiple quantum coherence), and HMBC (heteronuclear multiple bond correlation). Using the same protocol, HR-MAS profiles of 16 strains cultured on VNSS medium were acquired for comparison to the HR-MAS profiles of same strains grown on ZoBell medium.

HR-MAS data preprocessing (normalization) included: (i) baseline corrections on all spectra using Bruker's XWIN standard baseline correction algorithms, (ii) referencing of all spectra according to most common identified peaks (glycine betaine methyl singlets at $\delta = 3.90$ and 3.26 ppm, or alanine at $\delta = 1.47$ ppm, respectively) and (iii) scaling. Spectra were first stacked using MestReNova v. 5.2.5 software (MestRec, Santiago, Spain), compared and grouped visually. Automated PCA analysis: spectra were processed with AMIX v. 3.8 software (Bruker Biospin, Rheinstetten, Germany) using the $\delta = 0.5$–4.5 ppm spectral region deemed the most representative, with a matrix comprising rectangular bucket sizes of 0.04 ppm.

Table 1
Bacteria used for comparative strain identification between molecular taxonomy (16S rDNA) using 1492R and 8F primers.

Code	Source	Genus/species	Family	Order	Class	Phylum	Gram type
Ld1	*L. digitata* Holdfast	*Pseudoalteromonas*	*Pseudoalteromonadaceae*	*Alteromonadales*	*γ-Proteobacteria*	*Proteobacteria*	G− obl. Aerobic
Ld4	*L. digitata* Holdfast	*Curtobacterium*	*Microbacteriaceae*	*Actinomycetales*	*Actinobacteria*	*Actinobacteria*	G+ obl.aerobic cocci
Ld5	*L. digitata* Holdfast	*Arthrobacter*	*Micrococcaceae*	*Actinomycetales*	*Actinobacteria*	*Actinobacteria*	G+ obl.aerobic cocci
Ld6	*L. digitata* all parts	*Pseudomonas*	*Pseudomonadaceae*	*Pseudomonadales*	*γ-Proteobacteria*	*Proteobacteria*	G− rods aerobic
Ld7	*L. digitata* Holdfast	*Agrococcus*	*Microbacteriaceae*	*Actinomycetales*	*Actinobacteria*	*Actinobacteria*	G+ aerobic
Ld8	*L. digitata* Holdfast	*Cobetia*	*Halomonadaceae*	*Oceanospirillales*	*γ-Proteobacteria*	*Proteobacteria*	G− rods aerobic
Ld9	*L. digitata* Blade prox.	*Pseudoalteromonas*	*Pseudoalteromonadaceae*	*Alteromonadales*	*γ-Proteobacteria*	*Proteobacteria*	G− obl. aerobic
Ld10	*L. digitata* Holdfast	*Paracoccus*	*Rhodobacteraceae*	*Rhodobacterales*	*α-Proteobacteria*	*Proteobacteria*	G− rods aerobic
Ld11	*L. digitata* Holdfast	*Algibacter*	*Flavobacteriaceae*	*Flavobacteriales*	*Flavobacteria*	*Bacteroidetes*	G− rods aerobic
Ld12	*L. digitata* Holdfast	*Cellulophaga*	*Flavobacteriaceae*	*Flavobacteriales*	*Flavobacteria*	*Bacteroidetes*	G− rods aerobic
Ld13	*L. digitata* Holdfast	*Algibacter*	*Flavobacteriaceae*	*Flavobacteriales*	*Flavobacteria*	*Bacteroidetes*	G− rods aerobic
Ld14	*L. digitata* Holdfast	*Curtobacterium*	*Microbacteriaceae*	*Actinomycetales*	*Actinobacteria*	*Actinobacteria*	G+ obl. aerobic cocci
Ld15	*L. digitata* Holdfast	*Kocuria*	*Micrococcaceae*	*Actinomycetales*	*Actinobacteria*	*Actinobacteria*	G+ obl.aerobic cocci
Ld16	*L. digitata* Stipe	*Paracoccus*	*Rhodobacteraceae*	*Rhodobacterales*	*α-Proteobacteria*	*Proteobacteria*	G− rods aerobic
Ld17	*L. digitata* Holdfast	*Rhodococcus*	*Nocardiaceae*	*Actinomycetales*	*Actinobacteria*	*Actinobacteria*	G+ rods aerobic
Ld18	*L. digitata* Holdfast and blade	*Pseudoalteromonas*	*Pseudoalteromonadaceae*	*Alteromonadales*	*γ-Proteobacteria*	*Proteobacteria*	G− obl. aerobic
Ld19	*L. digitata* Blade prox.	*Pseudoalteromonas*	*Pseudoalteromonadaceae*	*Alteromonadales*	*γ-Proteobacteria*	*Proteobacteria*	G− obl. aerobic
Ld20	*L. digitata* Blade prox.	*Pseudoalteromonas*	*Pseudoalteromonadaceae*	*Alteromonadales*	*γ-Proteobacteria*	*Proteobacteria*	G− obl. aerobic
D41	*t* = 24 h Teflon chip	*Pseudoalteromonas* sp. nov.	*Pseudoalteromonadaceae*	*Pseudomonadales*	*γ-Proteobacteria*	*Proteobacteria*	G− rods aerobic
D01	*t* = 6 h glass chip	*Vibrio*	*Vibrionaceae*	*Vibrionales*	*γ-Proteobacteria*	*Proteobacteria*	G− aerobic
1M6	*t* = 6 h	*Algibacter*	*Flavobacteriaceae*	*Flavobacteriales*	*Flavobacteria*	*Bacteroidetes*	G− rods aerobic
4M6	*t* = 6 h glass chip	*Paracoccus*	*Rhodobacteraceae*	*Rhodobacterales*	*α-Proteobacteria*	*Proteobacteria*	G− rods aerobic
4J6	*t* = 6 h glass chip	*Bacillus*	*Bacillaceae*	*Bacillales*	*Bacilli*	*Firmicutes*	G+ aerobic
3J6GFP	bactérie modifiée	*Pseudoalteromonas*	*Pseudoalteromonadaceae*	*Alteromonadales*	*γ-Proteobacteria*	*Proteobacteria*	G− obl. aerobic
3J6	*t* = 6 h glass chip	*Pseudoalteromonas*	*Pseudoalteromonadaceae*	*Alteromonadales*	*γ-Proteobacteria*	*Proteobacteria*	G− obl. aerobic
3J3	*t* = 3 h glass chip	*Pseudoalteromonas*	*Pseudoalteromonadaceae*	*Alteromonadales*	*γ-Proteobacteria*	*Proteobacteria*	G− obl. aerobic
Pc	ATCC 43555, algal source	*P. carrageenovora*	*Pseudoalteromonadaceae*	*Alteromonadales*	*γ-Proteobacteria*	*Proteobacteria*	G− rods obl. aerobic
Ph	ATCC 14393	*Pseudoalteromonas haloplanktis*	*Pseudoalteromonadaceae*	*Alteromonadales*	*γ-Proteobacteria*	*Proteobacteria*	G− obl. aerobic
Cm	ATCC 25374, seawater	*Cobetia marina*	*Halomonadaceae*	*Oceanospirillales*	*γ-Proteobacteria*	*Proteobacteria*	G− rods aerobic
Zg	*Delesseria sanguinea*, red alga	*Zobellia galactanivorans*	*Flavobacteriaceae*	*Flavobacteriales*	*Flavobacteria*	*Bacteroidetes*	G− rods aerobic

Series Ld was isolated from various parts (holdfast, stipe, proximal and distal areas of blade) of the brown kelp *Laminaria digitata*; strains *Pseudoalteromonas* sp. D41^T and *Vibrio* sp. D01 are from IFREMER culture collection; *Algibacter* sp. 1M6, *Paracoccus* sp. 4M6, *Bacillus* sp. 4J6, *Pseudoalteromonas* sp. 3J6 and a plastid transform *Pseudoalteromonas* sp. 3J6GFP, and *Pseudoalteromonas* sp. 3J3 are from LBCM culture collection; *P. carrageenovora*, *P. haloplanktis* and *C. marina* are from the DMSZ culture collection; *Z. galactanivorans* is from the Roscoff culture collection. Nomenclature follows NCBI recommendations: http://www.ncbi.nlm.nih.gov/Taxonomy/Browser/wwwtax.cgi?name=Eubacteria.
Note: Identification of strain 4M6 as *Paracoccus* sp. was made on the basis of (i) indications from supplier (LBCM) and (ii) spectroscopic profile resemblance, i.e. intact cell ^{1}H HR-MAS NMR metabolomes (Table 3) and whole-cell MALDI-TOF MS proteomic profiles (Table 2), but not on 16S rDNA sequencing.

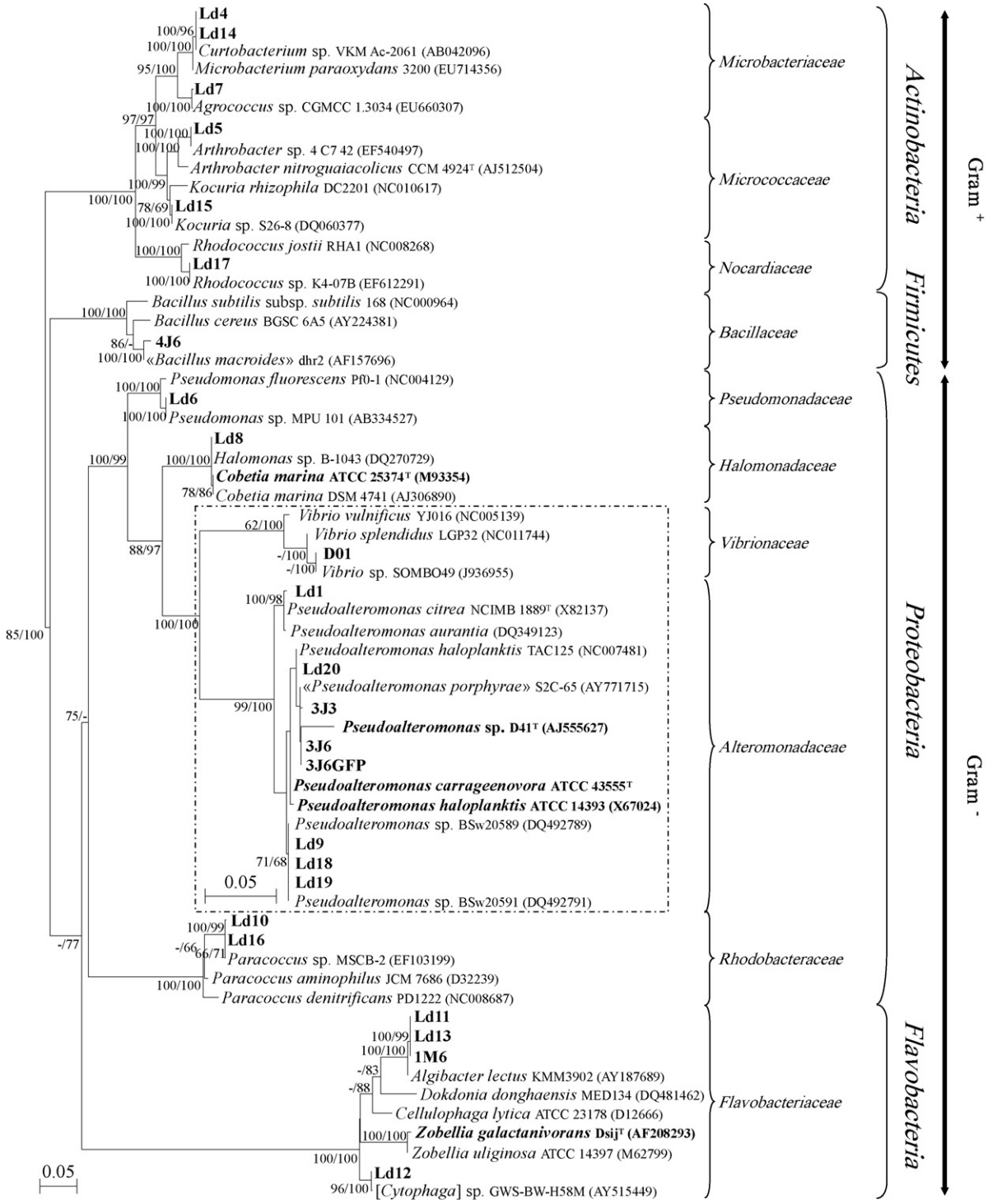


Fig. 1. Maximum likelihood tree of 68 *Laminaria digitata*—associated and reference bacteria sequences based on 16S ribosomal DNA genes. Neighbour joining and PHYML trees were constructed from 948 nucleotides sites. If above 65, bootstrap values (100 replicates) are provided for neighbour-joining (first value) and PHYML (second value) analyses. Dotted line box represents an enlargement of the subtree of *Vibrionaceae* and *Pseudoalteromonadaceae*. Bolding of strains indicates that the 16S rDNA was sequenced in this study whereas other sequences were retrieved from databases. The scale represents the expected number of changes per sequence position

3. Results

3.1. Molecular taxonomy of a selection of the cultivatable microbial epiflora of L. digitata

Eighteen strains isolated from *L. digitata* and cultivatable on ZoBell medium were each assigned a code number (Ld series, Table 1). Most 16S rDNA sequences of about 1370 bases were identified to genus level (up to 99% identity or better), using available Genbank databases. The tree topology shown in Fig. 1 is identical to other statistical representations of the sequence data, including parsimony, maximum likelihood and neighbour joining.

The twelve exogenous reference strains were identified to genus level exactly as expected, except for *Cytophaga* sp. 1M6. We confirmed that the Gram$^+$ *Bacillus* sp. 4J6 belongs to the *Bacillaceae* family (phylum *Firmicutes*). Accordingly, the Gram$^-$ include

Vibrio sp. D01 (phylum *Proteobacteria*; class *Gammaproteobacteria*; family *Vibrionaceae*), and *P. carrageenovora* ATCC 43555^T, *Pseudoalteromonas* sp. 3J3, 3J6 and 3J6GFP with 97% between *P. carrageenovora* and 3J6 and 100% between 3J6 and 3J6GFP. Finally, *Cytophaga* sp. 1M6 (phylum *Bacteroidetes*, family *Flavobacteriaceae*) presenting 100% identity with *Algibacter* sp. Ld11 and Ld13, which means that *Cytophaga* sp. 1M6 is in fact an *Algibacter* sp. 1M6. Additional data was merely retrieved from the NCBI site http://www.ncbi.nlm.nih.gov/sites/entrez. It included *C. marina* ATCC 25374^T, GenBank M93354 (class *Gammaproteobacteria*, family *Halomonadaceae*) presenting 99% identity with *Cobetia* sp. Ld8, *Pseudoalteromonas* sp. D41, GenBank AJ555627 (class *Gammaproteobacteria*, family *Pseudoalteromonadaceae*) presenting a 98% identity with *Pseudoalteromonas* sp. 3J6, *P. haloplanktis* ATCC 14393, GenBank X67024 (class *Gammaproteobacteria*, family *Pseudoalteromonadaceae*), presenting 97% identity with 3J6, and finally *Z. galactanivorans* Dsij^T, GenBank AF208293 (phylum *Bacteroidetes*, family *Flavobacteriaceae*).

3.2. Bacterial identification by MALDI-TOF MS

Table 2 summarizes all experiments undertaken on 29 strains (only 17 *L. digitata* isolates since Ld1 was not used in this experiment, and 12 environmental isolates from our marine culture collection), grown on ZoBell—agar (enriched medium) and on VNSS—agar (minimal medium) for approximately 7 days, and using a 2–18 kDa spectral window. The top block represents the comparison between the 464 individual spectra and the database of 29 consensus spectra (averaged by MALDI BioTyper software), in order to test the database for consistency. Scores over 50 are considered valid, i.e. there are enough similarities between each individual spectrum and the consensus spectrum to consider the corresponding strain as taxonomically related. In all cases, the consensus spectra (up to five) that are PCA selected as best matches include the same strain as the corresponding individual spectrum (highest self scores, up to 410), indicating a sound choice of spectral window and a good experimental reproducibility throughout. The other matching profiles may be taxonomically identical or related, as determined by 16S rDNA analyses (q.v. Table 1), and as suggested by neighbour scores above 50. With Gram$^+$ members, Ld4 and Ld14 which both belong to the genus *Curtobacterium* displayed scores of 264 and 122, respectively, strongly suggesting they are conspecific. On the other hand, the Gram$^+$ *Kocuria* sp. Ld15, *Arthrobacter* sp. Ld5, and *Agrococcus* sp. Ld7 are not related with any other strains because they are recognized only by their own consensus profile, confirming distinct genera within the family *Micrococcaceae*. Similarly, *Rhodococcus* sp. Ld17 from the family *Nocardiaceae* and *Bacillus* sp. 4J6 from class *Bacilli* do not match with any other strains. Within Gram$^-$ members, the *Alphaproteobacteria* 4M6, Ld10 and Ld16 are *Paracoccus*, the high neighbour scores between 4M6 and Ld10 (between 220 and 248) suggest conspecificity. However, Ld16 (low neighbour scores between 14 and 30) is very likely a distinct species. The *Gammaproteobacteria* includes the major genus *Pseudoalteromonas* which appears quite heterogenous. Ld9, Ld18 and Ld19 form a separate subgroup to other *Pseudoalteromonas*, Ld18 being quite distinct from Ld9 and Ld19 which are very similar. *P. haloplanktis* ATCC 14393 and *Pseudoalteromonas* sp. 3J6 and 3J6GFP appear to form another coherent subgroup. *P. carrageenovora* ATCC 43555^T is poorly related with only 3J6GFP with an insignificant score of 7, and finally *Pseudoalteromonas* strains Ld20, 3J3 and D41 which have very high self scores (296–410 level) do not match with any other strains. *Vibrio* sp. D01 (self score 236) and *Pseudomonas* sp. Ld6 (self score 214) do not match with any other strains, as expected. *Cobetia* sp. Ld8 and *C. marina* ATCC 25374^T both belong to the family *Halomonadaceae*, yet they are significantly different taxa with scores of 3. Within the *Flavobacteriaceae,* Ld11, Ld13 and 1M6 are *Algibacter* sp. display high neighbour scores suggesting conspecificity, whereas Ld12 (identified as *Cellulophaga* sp.) and *Z. galactanivorans* Dsij^T do not match with any other strains within the phylum *Bacteroidetes*.

The second block of Table 2 represents a classification of 116 individual spectra (4 individual spectra per strain, i.e. 4 × 29 strains) of ZoBell—newly grown bacteria, against the database of 29 consensus spectra (ZoBell profiles). In all cases (with the exception of Ld18 and Ld19) the new set of 116 spectra matches the consensus database, with scores above 50.

The third block represents a classification of individual spectra × 29 strains, i.e. 116 spectra of VNSS—grown bacteria, against the database. There is a total match of all 116 individual spectra with the corresponding consensus database, with scores comparable to those obtained with the top block, i.e. above 50.

3.3. Bacterial studies by NMR spectroscopy

3.3.1. Similarities in metabolic profiling

Stack plots of ^{1}H HR-MAS 6–11 day CFU's of ZoBell grown bacteria shown in Fig. 2 clearly delineate bacterial groups sharing similarities in their 0.5–4.5 ppm proton profiles. Some Gram$^-$ phyla, e.g. *Bacteroidetes* (Fig. 2D) and the Gram$^+$ phyla *Actinobacteria* and *Firmicutes* (class *Bacilli*) in Fig. 2A have visually characteristic spectral profiles while other groups, e.g. genus *Pseudoalteromonas* in Fig. 2B are somewhat less homogeneous in appearance, forming groups of more or less strongly resembling spectra. PCA analysis of NMR signals by the AMIX software on all normalized spectra (q.v. Supplementary Figure S2) could discriminate between different strains of a given age, but concluded that differences between cultures of different ages were not significant, despite visually important qualitative and quantitative changes in profiles in a number of strains. Out of the 16 strains analyzed by NMR on both ZoBell and VNSS media, (i) four pairs of spectra showed no significant qualitative difference, (ii) six pairs presented major differences to totally different spectra, and (iii) the remaining six pairs presented highly similar spectra, with few visible differences in the expression of one or more minor metabolites in one medium and not (or much less) in the other. Fig. 2E compares 6–10 day ^{1}H HR-MAS spectra of 3 selected strains grown on both media: *Pseudomonas* sp. Ld6 illustrating (i), *Pseudoalteromonas* sp. 3J3 illustrating (ii) and *Arthrobacter* sp. Ld5 illustrating (iii). The expression of several aliphatic amino acids and of glycine betaine in one medium and not in the other occurs in VNSS in some cases and in ZoBell in other cases. Other metabolites are medium-specific in our spectra: proline shows up in three VNSS spectra and not in corresponding ZoBell grown strains, whereas acetate and succinate ions appear in ZoBell grown strains and not in corresponding VNSS grown strains.

3.3.2. Compound identification by solution NMR

D_2O solution samples of all bacteria evidence the presence of medium to highly polar metabolites. All identifiable molecules are listed in Table 3 with their indicative chemical shifts. Their presence and abundance can be correlated to 16S rDNA determinations, as we order all strains according to the phylogenetic tree of Fig. 1., and clustering patterns of black (= dominant metabolite) and grey (= minor metabolite) boxes follow taxonomic distribution. Thus, some multi-species genera (*Curtobacterium*, *Paracoccus*, *Algibacter*) are homogenous, i.e. all compounds present in the poorest spectrum of a genus are found in all congeneric species. Other genera have a less coherent metabolite distribution, e.g. *Cobetia* and *Pseudoalteromonas*, with sometimes only half of the compounds shared between their members. Within the genus *Pseudoalteromonas*, the Ld9–Ld18–Ld19 cluster is fairly homogenous, forming a discrete subgroup (as in the MALDI-TOF MS analysis); the same is observed with the 3J6–3J6GFP–3J3–D41–*P. carrageenovora* and *P. haloplank-*

Table 2
MALDI-TOF profiling of macromolecules (essentially ribosomal proteins) from MW ca. 2,000–18,000 Da from cultured strains.

Zobell database (16 replicates)

Matrix ZoBell strains	Ld4		Ld5	Ld6	Ld7	Ld8		Ld9		Ld10			Ld11			Ld12		Ld13		Ld14		Ld15		Ld16			Ld17	Ld19	
Matching ZoBell standards	Ld4	Ld14	Ld5	Ld6	Ld7	Ld8	Cm	Ld9	Ld19	Ld10	4M6	Ld16	Ld11	Ld13	1M6	Ld12	Ld13	Ld11	1M6	Ld14	Ld4	Ld15	Ld16	Ld10	4M6	Ld17	Ld19	Ld9
% times ranking first	37,5	62,5	100	100	100	100	0	100	0	87,5	12,5	0	100	0	0	100	100	0	0	100	0	100	100	0	0	100	100	0
Average Biotyper score	216	264	237	214	166	345	3	234	101	275	220	14	297	171	147	179	234	151	147	399	122	309	308	25	30	211	91	40
Matrix ZoBell strains	Ld18			Ld20	Ph			PC		Cm		Zg	1M6			4M6			4J6	3J3	3J6			3J6GFP			D01	D41	
Matching ZoBell standards	Ld18	Ld19	Ld19	Ld20	Ph	3J6gfp	3J6	PC	3J6gfp	Cm	Ld8	Zg	1M6	Ld13	Ld11	4M6	Ld10	Ld16	4J6	3J3	3J6	3J6gfp	Ph	3J6gfp	3J6	Ph	D01	D41	
% times ranking first	100	3J6	0	100	100	0	0	100	0	100	0	100	93.7	6.3	0	81.2	18.8	0	100	100	33.3	66.7	0	93.7	0	6.3	100	100	
Average Biotyper score	172	15	4	296	319	103	3	377	7	138	3	303	262	178	145	280	248	21	329	410	113	142	32	401	89	92	236	325	

Zobell (4 replicates)

Matrix ZoBell strains	Ld4		Ld5	Ld6		Ld7	Ld8	Ld9		Ld10		Ld11				Ld12	Ld13			Ld14		Ld15	Ld16	Ld17		Ld19		Ld18	
Matching ZoBell standards	Ld4	Ld14	Ld5	Ld6		Ld7	Ld8	Ld9	Ld19	Ld10	4M6	Ld11	Ld13	1M6		Ld12	Ld13	Ld11	1M6	Ld14	Ld4	Ld15	Ld16	Ld17	Ld9	Ld19	Ld18	Ld9	Ld19
% times ranking first	0	100	100	100		100	100	50	50	33.3	66.7	25	25	50		100	25	75	0	100	0	100	100	100	100	0	0	100	0
Average Biotyper score	58	272	134	263		261	274	60	68	148	159	169	158	169		68	120	112	98	272	68	224	113	54	62	39	9	56	39
Matrix ZoBell strains	Ph		Pc					Zg	1M6			4M6		4J6	3J3	3J6				3J6GFP			D01	D41					
Matching ZoBell standards	Ph	3J6gfp	Pc	3J6gfp	Cm	Ld8	Zg	1M6	Ld13	Ld11	4M6	Ld10	4J6	3J3	3J6	Ph	3J6gfp	3J6gfp	3J6	Ph	D01	D41								
% times ranking first	100	0	100	0	100	0	100	0	75	25	50	50	100	100	50	0	50	100	0	0	100	100								
Average Biotyper score	212	69	267	13	109	42	166	84	116	105	68	76	118	150	201	55	204	247	108	92	172	143								

VNSS (4 replicates)

Matrix ZoBell strains	Ld4		Ld5	Ld6	Ld7	Ld8			Ld9			Ld10		Ld11			Ld12	Ld13			Ld14		Ld15	Ld16		Ld17	Ld19	
Matching VNSS standards	Ld4	Ld14	Ld5	Ld6	Ld7	Ld8	Cm	Ld9	Ld19	Ld18	4M6	Ld10	Ld16	Ld11	Ld13	1M6	Ld12	Ld13	Ld11	1M6	Ld14	Ld4	Ld15	Ld16	4M6	Ld17	Ld19	Ld9
% times ranking first	0	100	100	100	100	100	0	100	0	0	50	0	0	100	0	0	100	100	0	0	100	0	100	100	0	100	0	100
Average Biotyper score	147	399	79	84	230	240	5	122	74	6	194	174	19	166	142	114	74	91	68	56	488	169	210	144	17	100	80	125
Matrix ZoBell strains	Ld18			Ld20	Ph			Pc		Cm	Zg	1M6			4M6		4J6	3J3	3J6			3J6gfp			D01	D41			
Matching VNSS standards	Ld18	Ld9	Ld19	Ld20	Ph	3J6gfp	3J6	Pc	3J6gfp	Cm	Zg	1M6	Ld13	Ld11	4M6	Ld10	4J6	3J3	3J6	3J6gfp	Ph	3J6	Ph	3J6gfp	D01	D41			
% times ranking first	100	0	0	100	100	0	0	100	0	100	100	0	75	25	25	75	100	100	0	100	0	0	0	100	100	100			
Average Biotyper score	137	30	25	209	255	102	14	407	5	98	73	65	101	82	123	129	123	363	82	296	61	71	61	296	67	237			

Top block: comparison of the 464 individual spectra against database of bacteria grown on ZoBell medium (see text). Top line: represents the 16 replicate spectra × 29 strains (with code names of the 29 strains), i.e. 464 individual spectra, which are individually compared to the 29 consensus spectra of the database (obtained by MALDI Biotyper averaging of the same 16 replicate spectra). Line 2: outcome of the comparison of the 464 individual spectra against the database, indicating up to three best matches. Line 3: entries represent the percentages of occurrence as top match. Line 4: average score based on spectral similarities of each of the 16 replicates of each strain against database. Self scores are highest (e.g. 4M6 vs 4M6 score 280), high neighbour scores suggest same or very closely related strain (e.g. 4M6 vs Ld10 score 248), and scores under 50 are not significant (e.g. 4M6 vs Ld16 score 21) whereas 16S rDNA taxonomy unambiguously assigns 4M6, Ld10 and Ld16 as *Paracoccus* sp. Intermediate block: new series of four individual spectra per strain grown on ZoBell medium compared with the database. Bottom block: series of four spectra per strain grown on VNSS medium compared with the database.

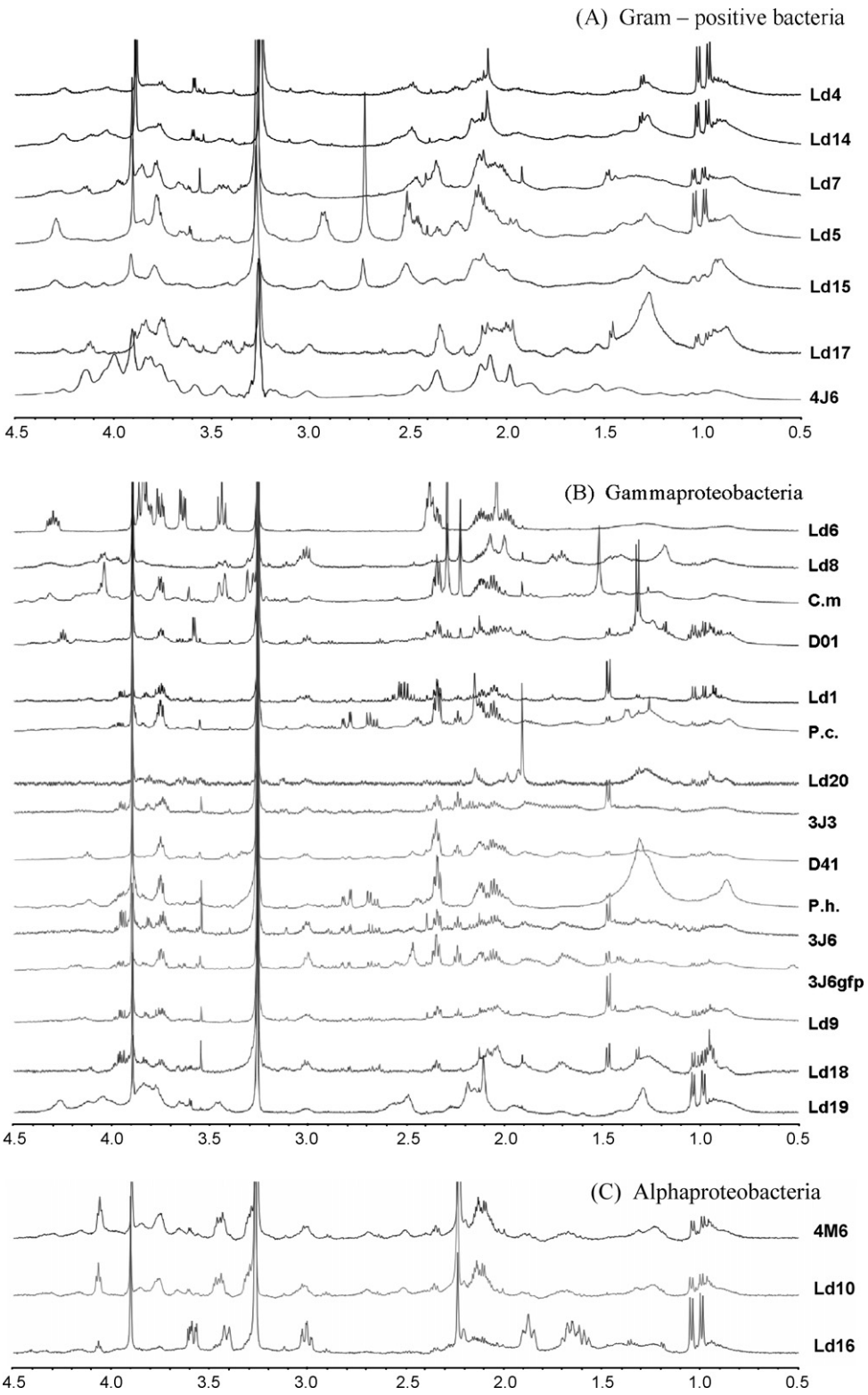


Fig. 2. Stackplots of HR-MAS NMR (δ = 0.5–4.5 ppm) profiles of bacteria isolated from *L. digitata* thalli or from environmental samples, arranged according to tree of Fig. 1. (A) Gram$^+$ (i) phylum and class *Actinobacteria*. Families are *Microbacteriaceae* (*Curtobacterium* sp. Ld4 and *Curtobacterium* sp. Ld14; *Agrococcus* sp. Ld7), *Micrococcaceae* (*Arthrobacter* sp. Ld5; *Kocuria* sp. Ld15 and *Nocardiaceae* (*Rhodococcus* sp. Ld17), and (ii) phylum *Firmicutes*. Only represented genus is *Bacillus* (*Bacillus* sp. 4J6). (B) Gram$^-$ class *Gammaproteobacteria*. Families are *Pseudomonadaceae* (*Pseudomonas* sp. Ld6), *Halomonadaceae* (*Cobetia* sp. Cm and Ld8), *Pseudoalteromonadaceae* (3J6, 3J6GFP, Pc, Ph, D41, 3J3, Ld20, Ld19, Ld18, Ld9, Ld1, all *Pseudoalteromonas* species) and *Vibrionaceae* (*Vibrio* sp. D01). (C) Gram$^-$ class *Alphaproteobacteria*. Family is *Rhodobacteraceae* (Ld16, Ld10, 4M6, all *Paracoccus* species). (D) Gram$^-$ phylum *Bacteroidetes*. Family is *Flavobacteriaceae* (*Algibacter* sp. Ld11, Ld13 and 1M6; *Cytophaga* sp. Ld12 and *Zobellia galactanivorans* Zg). (E) Examples of VNSS vs ZoBell fingerprints of metabolites (i) presenting no differences, e.g. in *Pseudomonas* sp. Ld6, (ii) with no signals in common, e.g. in *Pseudoalteromonas* sp. 3J3, and (iii) with few differences, e.g. in *Arthrobacter* sp. Ld5. Note: scaling represents chemical shifts in the F1 dimension ($4.5 < \delta < 0.5$ ppm) and was added to each original stackplot spectra.

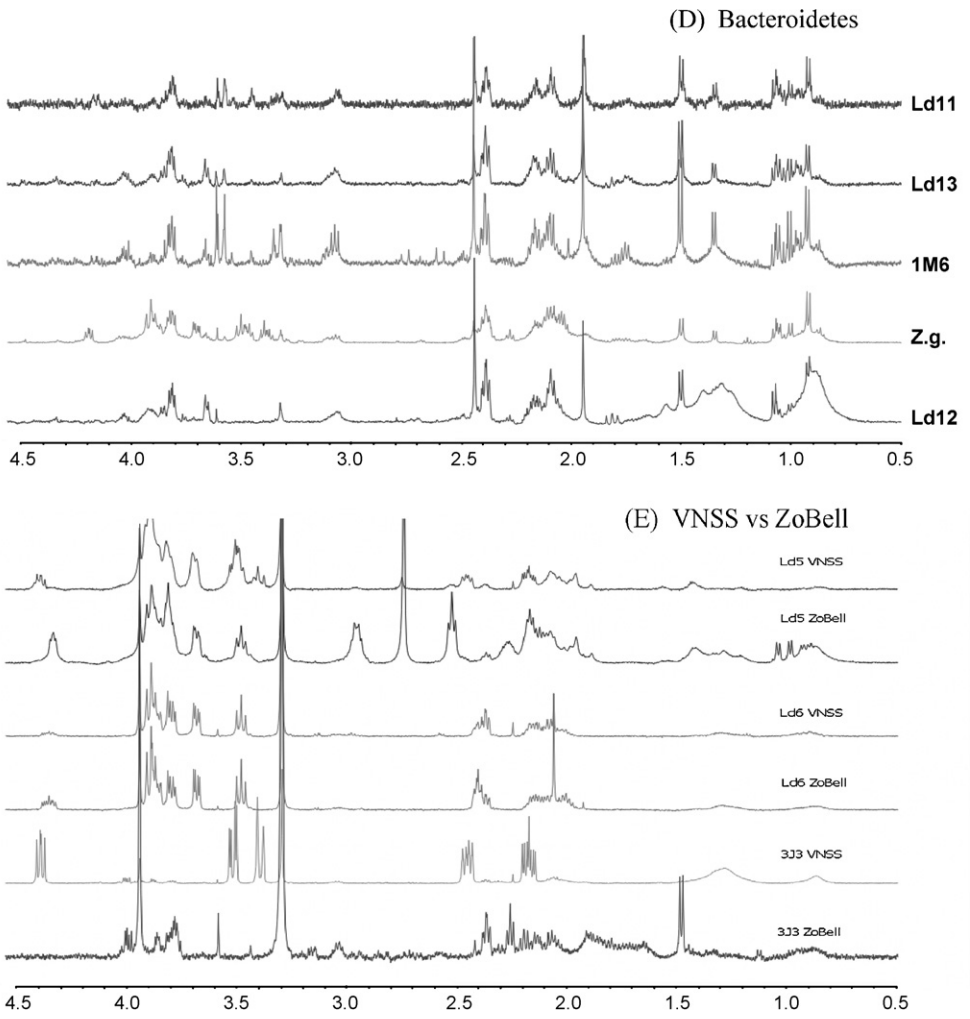


Fig. 2. (*Continued*).

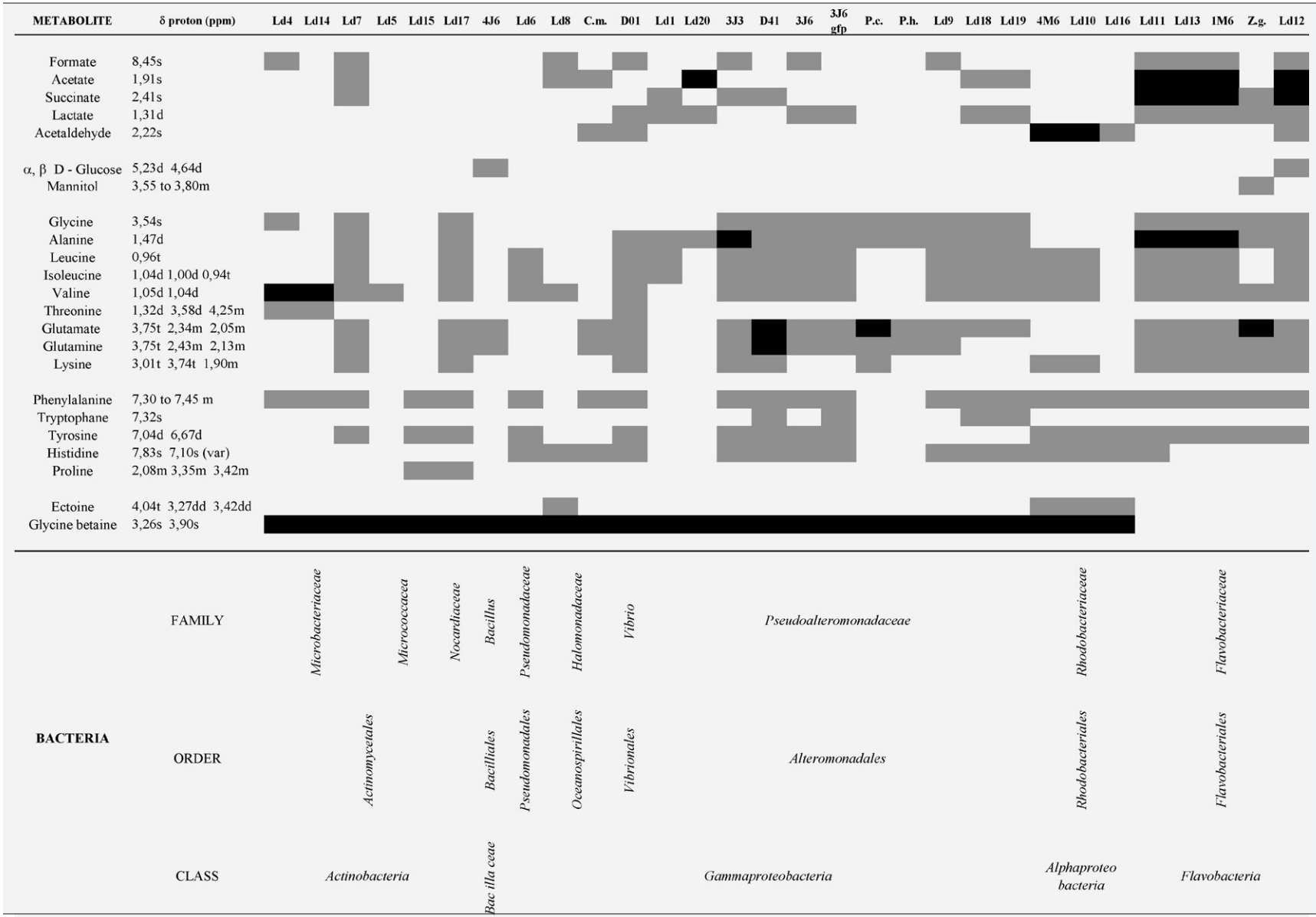
tis subgroup of the phylogenetic tree of Fig. 1. The molecules are conveniently organized in three categories in Table 3: easily ionizable molecules (salts) and aminated compounds, simple carbohydrates (carbon sources), non-cyclic and cyclized amino acids. Among the polyaminated compounds, glycine betaine is the most prevalent compound (present in all Gram$^+$ and in most Gram$^-$ strains except for the phylum *Bacteroidetes*), and ectoine was tentatively identified almost exclusively in class *Alphaproteobacteria*. Regular amino acids are better identified in solution spectra than in HR-MAS NMR spectra, especially for species that are less soluble or present in very small concentrations. Alanine was present in most Gram$^-$ samples (except class *Alphaproteobacteria*) but was less frequent in the Gram$^+$ strains and was the dominant compound in the two *Curtobacterium* sp. (Ld 4 and Ld14), in the phylum *Bacteroidetes* (Ld11, Ld12, Ld13, 1M6 and Zg) and in *Pseudoalteromonas* sp. 3J3. Likewise, the other aliphatic amino acids leucine, isoleucine and valine had similar distributions across both Gram$^+$ and Gram$^-$ taxa. Glycine was also represented in all groups, and was the dominant metabolite in *Pseudoalteromonas* sp. Ld19 and the long chained lysine was just detectable in 40% of all samples. Glutamate and glutamine were also widely found in both Gram$^-$ and Gram$^+$ samples, except again in class *Alphaproteobacteria*, and it was the dominant compound in two *Pseudoalteromonas* sp. (D41 and *P. carrageenovora*) and in *Z. galactanivorans* (phylum *Bacteroidetes*, class *Flavobacteria*). Proline was only found in two Gram$^+$ *Actinobacteria* (*Kocuria* sp. Ld15 and *Rhodococcus* sp. Ld17). Other compounds included mannitol only found in *Z. galactanivorans*, and all *Bacteroidetes* were conspicuously lacking glycine betaine, present in all other strains. Glucose (or related species, e.g. trehalose) was identified only on the basis of their alpha and beta anomeric protons, in low amounts and in very few strains: *Bacillus* sp. 4J6 (Gram$^+$) and *Cellulophaga* sp. Ld12 (Phylum *Bacteroidetes*). Lactate resulting from carbohydrate fermentation was found in all *Bacteroidetes* and in several *Gammaproteobacteria* (all *Pseudoalteromonas* sp.). Organic ions appearing as sharp singlets on proton spectra may be useful taxonomic markers, e.g. formate, acetate and succinate were well represented in all five *Bacteroidetes*. Acetate and succinate occasionally dominated the proton spectra as possible products of carbohydrate catabolism (*Flavobacteriaceae* Ld11, Ld12 and Ld13). Finally, aldehydes which are considered volatile were found in all studied *Alphaproteobacteria* (*Paracoccus* sp. Ld10, Ld16 and 4M6) where they occasionally dominated the spectrum (*Paracoccus* sp. Ld10 and 4M6), but also in the *Gammaproteobacteria Vibrio* sp. D01 and *C. marina* and in the *Bacteroidetes Cellulophaga* sp. Ld12.

4. Discussion

4.1. MALDI-TOF MS spectrometry provides a useful technique for rapid identification of marine bacteria

This study demonstrates that MALDI-TOF MS of CFU of marine bacteria provides reliable and strain-specific profiles in the 2–18 kDa range, which appeared here to consist mostly of peptides

Table 3
Compounds from HR-MAS NMR spectra, using corresponding solution spectra for tentative identification, and their distribution according to 16S phylogeny.



From right to left: metabolites are arranged by type: simple salts, sugars, non cyclic amino acids, cyclised amino acids, aminated osmolytes, chemical shifts (δ in ppm) of protons that characterize the above metabolites in HR-MAS spectra and in solution spectra, bacterial strains arranged in taxonomic categories as defined in tree of Fig. 1. All extracts are from 10 to 11-day-old CFUs grown on ZoBell enriched medium. Black blocks represent metabolites present in major concentrations from corresponding proton signals, grey blocks represent metabolites in minor concentrations, and white blocks correspond to traces or no metabolite. Block clusters follow a phyletic distribution thus confirming visual inspection of HR-MAS NMR spectra (Fig. 2), the presence in specific taxa of some of the listed metabolites being characteristic of their known osmoregulatory pathways.

and small proteins. MALDI-TOF MS is now considered as the main tool in the analysis of proteome signatures in response to changing environmental conditions [9]. For example, Arnold et al. [43] have shown that culture age makes the MALDI proteomic profile of *E. coli* strain K-12 present considerable quantitative variations between 2 and 84 h of incubation in liquid medium. Interestingly, we found that CFU grown on solid media did not vary significantly with age (according to Biotyper analysis), and we may attribute this fact to different gene expressions relating to different lifestyles, one planktonic and the other as microcolonies. The fact that MALDI-TOF MS profiles obtained from colonies grown on VNSS (minimal medium) were not found to vary significantly from same grown on ZoBell medium (enriched medium) in the present study is more puzzling, inasmuch as the profiles established by proton HR-MAS NMR can be visually very different. In this respect, MALDI-TOF MS spectra are not as responsive as physiological markers as HR-MAS NMR spectra on whole cells (see below). Our findings agree with [44] who have used MALDI-TOF MS to discriminate between Gram$^+$ *Arthrobacter* sp. isolates at strain level with 100% agreement with 16S rDNA gene sequences. They found that age differences between agar-plated *Arthrobacter* sp. strains appear less important than when the same are grown in liquid medium. This could be due to changes in protein profiles in the growth phase in liquid medium. In the same study, *Arthrobacter* sp. profiles from enriched vs minimal culture media did not present significant differences, in agreement with our own observations, indicating no major changes in biopolymer expression between the two media. Unwanted variability requires that a reference database be constructed from of spectral profiles using strains grown under strictly controlled conditions. The full taxonomic potential of a reliable reference database is indeed only revealed against samples series grown under identical conditions [8] and in our case it could discriminate *Pseudoalteromonas* sp. D41 (probably a new species, C. Compère, pers. com.) from *P. haloplanktis* as tentatively attributed by 16S rDNA sequence analysis with 98% sequence identity! The metabolomic potential of individual strains can thence be exploited by changing selected parameters one at a time, e.g. different culture medium, salinity, temperature, etc., and compare the profiles against the consensus database. Bacterial proteomics is an actively growing field with great medical and biotechnological importance, e.g. in adhesion studies in which both membrane proteins and EPS (extrapolymeric substances) are involved.

In this study, the cultivatable *Gammaproteobacteria* are dominated by the recently revised [45] genus *Pseudoalteromonas*, which is ecologically diverse [46] and often associated with algal surfaces. This genus has provided several useful models for adhesion and quorum-sensing studies [47]. Among the several *Pseudoalteromonas* "control" (environmental) strains used in our study, MALDI-TOF MS was expectedly capable of discriminating between strain 3J6 and its plasmid transform 3J6GFP, indicating major changes in the proteome expression of the transformants. Thomas et al. [48] compared several genomes and secretomes of *Pseudoalteromonas* sp. and related *Alteromonas* sp. genomes, and singled out the "antifouling subgroup" among which *P. tunicata* is a superior competitor [49]. Our MALDI-TOF MS data on Ld series rather agrees with this analysis (no 16S rDNA matching with *P. tunicata* and several subgroups among which *P. haloplanktis*, *P. carrageenovora* and *Pseudoalteromonas* sp. D41. Our study indicates only two *Alphaproteobacteria* (*Paracoccus* sp.) out of 18 ZoBell cultured strains, but this may not reflect the overall natural biodiversity of this class in association with *L. digitata*. In fact, in a culture-independent experiment, it was found that planktonic *Alphaproteobacteria* strains are not as efficiently eliminated by *Laminaria* allelopathic exudates as planktonic *Roseobacter*, i.e. they may be differentially selected for [50]. This culture-based bias may also explain the absence in our isolates of *Vibrio*, a prominent planktonic *Gammaproteobacteria* taxon. Specific primers and especially formulated growth media were not investigated, the purpose of this study being to validate the use of spectral fingerprints as taxonomic, proteomic and metabolomic aids rather than to optimize the corpus of cultivatable bacteria.

4.2. NMR spectroscopy, a powerful complementary tool for chemotaxonomy and physiological studies

The combination of HR-MAS and solution (D_2O) proton NMR on whole bacterial cells proved very useful both as a rapid chemotaxonomic indicator and as a metabolomic tool for compounds most of which are known to have an important role in bacterial environmental adaptation [20,51,52]. The spectral database we constructed from 30 strains of bacteria associated with *L. digitata* (Ld series) and isolated from inert surfaces and grown under strictly controlled conditions on ZoBell medium can be visually analyzed and strains segregated into taxonomic groups that agree with assignments from 16S rDNA sequence analyses and MALDI-TOF MS spectral groups, down to genus or family level. High resolution solution NMR (δ 0.5–4.5 ppm) has been successfully applied for fingerprinting of bacterial extracts, with good reproducibility [17]. During the course of our study, using the ^{1}H HR-MAS NMR method, we have indeed been able to evidence one hitherto unsuspected label error on two accidentally swapped strains in the reference collection. The present study indicates its potential use in investigations on marine strains. The distribution of the metabolites tentatively identified in our 30 strains and presented correlates with the HR-MAS (δ = 0–4.5 ppm) profiles grouped by visual resemblance. They are small molecules that are generally involved in medium adaptation and chemical communication, and their distribution into different taxonomic groups as presented in the results section above is consistent with information found in textbooks on microbial physiology and biochemistry, and in specialized reviews [e.g. [51]]. NMR has been usefully applied to the elucidation of bacterial amino acid biosynthesis from labeled precursors [e.g. [53]]. The fact that some taxa utilize different regulatory pathways may confer some value to individual molecules as biomarkers, e.g. the *Flavobacteriaceae* examined here do not use glycine betaine but present high levels of ions such as succinate or acetate, in contrast to other groups. Likewise, the *Rhodobacteriaceae* identified here (*Alphaproteobacteria*) do not contain alanine, glutamine and glutamate, all prevalent transient metabolites in many bacteria, and seem in turn to produce large amounts of aldehydes which are rarely encountered in other taxa. In practice, the NMR informations provided on individual strains grown on a given medium under controlled conditions can be useful to evaluate in each case the biochemical suitability and the limitations of this medium, or to follow enzyme kinetic studies on live bacteria and other applications beyond the aims of this study. Furthermore, Motta et al. [20] successfully applied NMR directly to bacterial suspension media of marine strains in order to quantify the various released water solubles, a feature which cannot be achieved with HR-MAS analysis.

HR-MAS NMR thus represents a useful chemotaxonomic tool for rapid characterization of unknown bacteria, as one proton acquisition takes less than 10 min per CFU. The requirement is that all bacteria be grown under conditions identical to database samples, a restriction already noted on ^{1}H NMR of bacterial extracts [15]. In some cases, physiological adaptation to a different culture medium must be achieved by activation of different regulatory pathways if the precursor is not present in the minimal medium, i.e. if the default carbon sources are different, overall salinity levels being equivalent. Our comparative analysis of spectra of bacteria grown on minimal (VNSS) and complete (ZoBell) media shows examples of major qualitative differences in NMR spectral profiles of CFU of same age, which can be attributed to differential adaptive capabilities between the different strains (e.g. strain *Pseudoalteromonas*

sp. 3J3 in Fig. 2). Other strains are capable of growing on both media with no visible change in adaptive responses (e.g. strain *Pseudomonas* sp. Ld6 in Fig. 2E). Finally, over one third of our strains presented profile modifications of varying extent, sometimes more complex on the VNSS medium, sometimes on the ZoBell medium (e.g. strain *Arthrobacter* sp. Ld5 in Fig. 2E). The ability to rapidly monitor such sensitive physiological responses on live cells by HR-MAS NMR spectroscopy may indeed help in improving specific growth media targeted to VBNC (viable but not cultivatable) bacterial species, which represent over an estimated 98% of the bacterial diversity found on natural algal samples. The fact that PCA-based AMIX analysis was not capable of globally discriminating between the ZoBell vs VNSS profiles may be attributed to an insufficient dataset, to inadequate spectra preparation or simply to the inability of establishing a trend of significance with such highly diverse responses (q.v. S2 as Supplementary data). Exometabolome responses as reflected by amino acid and by other regulatory metabolites is in fact quite very complex, both medium and age-dependant, and can escape PCA-based signal treatment discrimination. Again, using CFU grown under strictly identical conditions on medium-agar cultures, and profiled (either by HR-MAS NMR spectroscopy or in solution NMR) at the same incubation stage limits signal variability in the fingerprinting and appear as essential procedures for constructing a reliable comparative fingerprint database. For single-strain investigations, the use of HR-MAS NMR can be extended as a rapid method to monitor the metabolic responses at different growth stages, and hence to compare the kinetics of appearance and disappearance of metabolites between different media, as proposed by [54] who successfully monitored and compared in particular the exometabolome of *E. coli* on two liquid media at different growth stages, using NMR on cell extracts.

4.3. Combining molecular taxonomy, MALDI-TOF MS spectrometry and NMR spectroscopy

Earlier approaches to studies of eukaryote and associate microflora often involved tedious physico-chemical and visual characterizations, e.g. on brown algal kelp microepiphytes [55–57]. These are progressively replaced by global diversity studies on environmental samples using molecular taxonomy, e.g. on *Laminaria saccharina* [58] and by more specific studies using cultivatable strains to investigate allelopathy between competing epiphytes [48,50] and host-related defense responses [59–61] in *L. digitata*. Addressing community-level investigations, our study indicates that rapid, informative and reliable spectroscopic techniques can not only provide useful chemotaxonomic fingerprints, but also evidence adaptive responses at proteome and at metabolome level, thus offering a dynamic dimension to former physico-chemical characterization. To this end, spectral databases must be constructed from strains under strictly controlled culture parameters. Pursuing at single-strain level, we believe that MALDI-TOF MS and HR-MAS NMR can complement genomic and transcriptomic investigations, by varying selectively key parameters, e.g. time-resolved metabolic footprinting [54].

5. Conclusion

We show for the first time that two different spectroscopic techniques can usefully be associated with molecular taxonomy on cultivatable marine bacterial populations. Rapid identification can be achieved directly on entire cells by providing metabolic fingerprints that can be checked against a customized database of profiles of bacteria that are cultivated under strictly identical conditions, and previously characterized by their 16S rDNA sequences. MALDI-TOF MS profiles have a definite taxonomic interest with fingerprints that are highly reproducible irrespective of culture age and even culture conditions (within the limitations of the present study). In addition, MALDI-TOF fingerprints can be of assistance in proteomic studies and glycopolymer expression in adhesion studies. HR-MAS NMR spectra have an indicative taxonomic value if cultures are carried out under controlled conditions, but they are of great interest in monitoring specific adaptive responses of bacterial strains to different conditions. We suggest that the combination of molecular and spectroscopic methods has a great potential in studying the biology of cultivatable bacteria.

Acknowledgments

The authors would like to thank L. Delage for helping with PCR work, T. Barbeyron and C. Leblanc for helping construct the phylogenetic tree from 16S rDNA sequences, and X. Pennanec for introducing S. Salaün to MALDI-TOF whole-cell spectrometry. *Pseudoalteromonas* sp. strain D41 and *Vibrio* sp. strain D01 were kindly provided by C. Compère (IFREMER at Brest, France). S. Salaün benefits from a 3-yr student living allowance by Région de Bretagne (ARED 2842). This study was also partially funded by GIS EUROPOLE-Mer Project “Biofilms”.

Appendix A. Supplementary data

Supplementary data associated with this article can be found, in the online version, at doi:10.1016/j.talanta.2009.10.020.

References

[1] D. Rao, J.S. Webb, S. Kjelleberg, Appl. Environ. Microbiol. 71 (2005) 1729–1736.
[2] D. Rao, J.S. Webb, S. Kjelleberg, Appl. Environ. Microbiol. 72 (2006) 5547–5555.
[3] S. La Barre, D. Haras, J. Soc. Biol. 201 (2007) 281–289.
[4] P. Patel, M.E. Callow, I. Joint, J.A. Callow, Environ. Microbiol. 5 (2003) 338–349.
[5] N.R. Krieg, J.G. Holt (Eds.), Bergey's Manual of Systematic Bacteriology, Williams and Wilkins, Baltimore, London, 1984, p. 964.
[6] H. Liu, Z. Du, J. Wang, R. Yang, Appl. Environ. Microbiol. 73 (2007) 1899–1907.
[7] C. Fenselau, P.A. Demirev, Mass Spectrom. Rev. 20 (2001) 157–171.
[8] V. Ruelle, B. El Moualij, W. Zorzi, P. Ledent, E. De Pauw, Rapid Commun. Mass Spectrom. 18 (2004) 2013–2019.
[9] T. Schweder, S. Markert, M. Hecker, Electrophoresis 29 (2008) 2603–2616.
[10] T. Hindré, S. Didelot, J.-P. Le Pennec, D. Haras, A. Dufour, K. Vallée-Réhel, Appl. Environ. Microbiol. 69 (2003) 1051–1058.
[11] J. Vater, B. Kablitz, C. Wilde, P. Franke, N. Mehta, S.S. Cameotra, Appl. Environ. Microbiol. 68 (2002) 6210–6219.
[12] A. Claydon, S.N. Davey, V. Edward-Jones, D.B. Gordon, Nat. Biotechnol. 14 (1996) 1584–1586.
[13] R. Dieckmann, I. Graeber, I. Kaesler, U. Szewzyk, H. von Döhren, Appl. Microbiol. Biotechnol. 67 (2005) 539–548.
[14] M. Garg, M.K. Misra, S. Chawla, K.N. Prasad, R. Roy, R.K. Gupta, Eur. J. Clin. Invest. 33 (2003) 518–524.
[15] J.G. Bundy, T.L. Willey, R.S. Castell, D.J. Ellar, K.M. Brindle, FEMS Microbiol. Lett. 242 (2005) 127–136.
[16] J.B. Aguayo, M.P. Gamsick, J.D. Dick, J. Biol. Chem. 263 (1988) 19552–19557.
[17] E.S. Delpassand, M.V. Chari, C.E. Stager, J.D. Morisett, J.J. Ford, M. Romazi, J. Clin. Microbiol. 33 (1995) 1258–1262.
[18] M. Fujiwara, K. Arifuku, I. Ando, T. Nemoto, Anal. Sci. Rapid Commun. 21 (2005) 1259–1262.
[19] R. Bourne, U. Himmelreich, A. Sharma, C. Mountford, T. Sorrell, J. Clin. Microbiol. 39 (2001) 2916–2923.
[20] A. Motta, I. Romano, A. Gambacorta, J. Microbiol. Met. 58 (2004) 289–294.
[21] B. Combourieu, J. Inacio, A.-M. Delort, C. Forano, Chem. Commun. (2001) 2214–2215.
[22] M.J. Simpson, Soil Sci. Soc. Am. J. 70 (2006) 95–1004.
[23] A. Broberg, Planta 206 (1998) 300–307.
[24] M.S. Chauton, O.I. Optun, T.F. Bathen, Z. Volent, I.S. Gribbestad, G. Johnsen, Mar. Ecol. Prog. Ser. 256 (2003) 57–62.
[25] P. Krishnan, N.J. Kruger, R.G. Ratcliffe, J. Exp. Bot. 56 (2005) 255–265.
[26] W. Li, Analyst 131 (2006) 777–781.
[27] M.E. Bollard, S. Garrod, E. Holmes, J.C. Lindon, E. Humpfer, M. Spraul, J.K. Nicholson, Magn. Reson. Med. 44 (2000) 201–207.
[28] B. Sitter, S. Lundgren, T.F. Bathen, J. Halgunset, H.E. Fjosne, I.S. Gribbestad, NMR Biomed. 19 (2006) 30–40.
[29] E.M. Lenz, J. Bright, I.D. Wilson, S.R. Morgan, A.F.P. Nash, J. Pharm. Biomed. Anal. 33 (2003) 1103–1115.
[30] C.E. ZoBell, J. Mar. Res. 4 (1941) 41–75.

[31] C.M. Pradier, C. Rubio, C. Poleunis, P. Bertrand, P. Marcus, C. Compère, J. Phys. Chem. B 109 (2005) 9540–9549.
[32] B. Grasland, J. Mitalane, R. Briandet, E. Quemener, T. Meylheuc, I. Linossier, K. Vallee-Rehel, D. Haras, Biofouling 19 (2003) (2003) 307–313.
[33] P. Marden, A. Tunlid, K. Malmcrona-Friberg, G. Odham, S. Kjelleberg, Arch. Microbiol. 142 (1985) 326–332.
[34] R.E. Hicks, R.I. Amann, D.A. Stahl, Appl. Environ. Microbiol. 58 (1992) 2158–2163.
[35] W.G. Weisburg, S.M. Barns, D.A. Pelletier, D.J. Lane, J. Bacteriol. 173 (2) (1991) 697–703.
[36] J. Brosius, T.J. Dull, D.D. Sleeter, H.F. Noller, J. Mol. Biol. 148 (1981) 107–127.
[37] E. Pruesse, C. Quast, K. Knittel, K. Fuchs, W. Ludwig, W. Peplies, F.O. Glockner, Nucleic Acids Res. 35 (2007) 7188–7196.
[38] K. Tamura, J. Dudley, N. Masatoshi, S. Kumar, Mol. Biol. Evol. 24 (2007) 1596–1599, doi:10.1093/molbev/msm092.
[39] J. Castresana, Mol. Biol. Evol. 17 (2000) 540–552.
[40] A.V. Dereeper, V. Guignon, G. Blanc, S. Audic, S. Buffet, F. Chevenet, J.-F. Dufayard, S. Guindon, V. Lefort, M. Lescot, J.-M. Claverie, O. Gascuel, Nucleic Acids Res. 36 (2008) W465–W469, doi:10.1093/nar/gkn180.
[41] S. Guindon, O. Gascuel, Syst. Biol. 52 (2003) 696–704.
[42] J. Felsenstein, Cladistics 5 (1989) 164–166.
[43] R.J. Arnold, J.A. Karty, A.D. Ellington, J.P. Reilly, Anal. Chem. 71 (1999) 1990–1996.
[44] M. Vargha, Z. Takáts, A. Konopka, C.H. Nakatsu, J. Microbiol. Met. 66 (2006) 399–409.
[45] E.P. Ivanova, S. Flavier, R. Christen, Int. J. Syst. Evol. Microbiol. 54 (2004) 1773–1788.
[46] J.P. Bowman, Mar. Drugs 5 (2007) 220–241.
[47] A. Mai-Prochnow, J.S. Webb, B.C. Ferrari, S. Kjelleberg, Appl. Environ. Microbiol. 72 (2006) 5414–5420.
[48] T. Thomas, F.F. Evans, D. Schleheck, A. Mai-Prochnow, C. Burke, A. Peneysian, D.S. Dalisay, S. Stelzer-Braid, N. Saunder, J. Johnson, S. Ferriera, S. Kjelleberg, S. Egan, PLoS ONE 3 (9) (2008) e252.
[49] T.L. Skovhus, C. Holmström, S. Kjelleberg, I. Dallhöff, FEMS Microbiol. Ecol. 61 (2007) 348–361.
[50] C. Lam, A. Stang, T. Harder, FEMS Microbiol. Ecol. 63 (2008) 283–291.
[51] L.N. Csonka, A.D. Hanson, Annu. Rev. Microbiol. 45 (1991) 569–606.
[52] N. Empadinhas, M.S. da Costa, Int. Microbiol. 11 (2008) 151–161 (review article).
[53] N.A. Cornick, B. Yan, S. Bank, M.J. Allison, Can. J. Microbiol. 42 (1996) 1219–1224.
[54] V. Behrends, T.M.D. Ebbels, H.D. Williams, J.G. Bundy, Appl. Environ. Microbiol. 75 (2009) 2453–2463.
[55] S. Corre, D. Prieur, Bot. Mar. 33 (1990) 515–524.
[56] R.A. Laycock, Mar. Biol. 25 (1974) 223–231.
[57] J.H. Sieburth, R.D. Brooks, R.V. Gessner, C.D. Thomas, J.L. Tootle, in: R.R. Colwell, R.Y. Morita (Eds.), Effects of the Ocean Environment on Microbial Activities, University Park Press, Baltimore, MD, 1974, pp. 418–432.
[58] T. Staufenberger, V. Thiel, J. Wiese, J.F. Imhoff, FEMS Microbiol. Ecol. 64 (2008) 65–77.
[59] S.A. Borchardt, E.J. Allain, J.J. Michiels, G.W. Stearns, R.F. Kelly, W.F. Mc Coy, Appl. Environ. Microbiol. 67 (2001) 3174–3179.
[60] A. Cosse, C. Leblanc, P. Potin, Adv. Bot. Res. 46 (2008) 222–266.
[61] C. Leblanc, C. Colin, A. Cosse, L. Delage, S. La Barre, P. Morin, B. Fiévet, C. Voiseux, Y. Ambroise, E. Verhaeghe, D. Amouroux, O. Donard, E. Tessier, P. Potin, Biochimie 88 (2006) 1773–1785.

Talanta 80 (2010) 1771–1776

Contents lists available at ScienceDirect

Talanta

journal homepage: www.elsevier.com/locate/talanta

Application of point-to-point matching algorithms for background correction in on-line liquid chromatography–Fourier transform infrared spectrometry (LC–FTIR)

J. Kuligowski, G. Quintás, S. Garrigues, M. de la Guardia*

Department of Analytical Chemistry, Universitat de València, Edificio Jeroni Muñoz, 50th Dr. Moliner, 46100 Burjassot, Spain

ARTICLE INFO

Article history:
Received 7 July 2009
Received in revised form
23 September 2009
Accepted 8 October 2009
Available online 6 November 2009

Keywords:
On-line liquid chromatography–Fourier transform infrared spectrometry
Reference spectra matrix background correction
Point-to-point matching algorithm

ABSTRACT

A new background correction method for the on-line coupling of gradient liquid chromatography and Fourier transform infrared spectrometry has been developed. It is based on the use of a point-to-point matching algorithm that compares the absorption spectra of the sample data set with those of a previously recorded reference data set in order to select an appropriate reference spectrum. The spectral range used for the point-to-point comparison is selected with minimal user-interaction, thus facilitating considerably the application of the whole method. The background correction method has been successfully tested on a chromatographic separation of four nitrophenols running acetonitrile (0.08%, v/v TFA):water (0.08%, v/v TFA) gradients with compositions ranging from 35 to 85% (v/v) acetonitrile, giving accurate results for both, baseline resolved and overlapped peaks.

© 2009 Elsevier B.V. All rights reserved.

1. Introduction

Infrared (IR) spectrometry has been extensively used as a general research tool for the identification and quantification of analytes in a variety of fields of application. The potential of coupling liquid chromatography (LC) to IR spectrometry combines the high resolution provided by LC with the molecular specific information extracted from the IR spectra. LC–IR methods can be clustered in two groups: those that perform an off-line IR detection after eluent elimination using solvent removal interfaces, and those that use flow-through cells for the continuous on-line measurement of the LC eluate.

On-line detection presents a series of advantages over the off-line approach: (i) from a technical viewpoint the on-line coupling is less complicated, (ii) it can be implemented applying flow through cells, (iii) non-volatile buffer systems can be used, (iv) there exists the possibility of further hyphenation with additional detectors and (v) it also allows the measurement of IR spectra without any orientation, crystallization or degradation occurring during the solvent elimination in the off-line measurement [1].

Nevertheless, it is worth paying some attention to the main drawbacks of the on-line approach: (i) the limited concentration sensitivity of IR detection and (ii) existing difficulties in on-line measurements arising from the dominating absorption of most of the commonly used mobile phase components [2]. Concerning the lack of sensitivity, it is reasonable to expect that recent advances in instrumentation will help to overcome the low sensitivity of the IR detection. Laser sources emitting more intense IR radiation that can be tuned across 275 wavenumbers (24% of the laser's center wavelength at 8.8 μm) [3], room temperature mercury–cadmium–telluride (MCT) detectors with improved sensitivity [4] and miniaturized flow cells with nL volumes and capillary-LC systems [5], are among the most relevant developments of special significance that could be highlighted. However, to increase the use of on-line LC–IR the combination of the aforementioned instrumental advances, with chemometric techniques allowing for an efficient compensation of the eluent absorption, would permit a significant extension of the usefulness of on-line LC–IR in many areas including industrial and biochemical analysis. Therefore, there is an interest in the development of chemometric methods for background correction in on-line LC–FTIR.

Basics of the on-line detection approach are well known: if there are k absorbing species in the reaction system, according to the Lambert–Beer's law the recorded absorbance at each wavelength (A_r) is assumed to be the sum of contributions of all components. This can be extended to the whole spectrum and written in a matrix notation as:

$$D = CS^{T} + E \quad (1)$$

* Corresponding author. Tel.: +34 96 3544838; fax: +34 96 3544845.
E-mail address: miguel.delaguardia@uv.es (M. de la Guardia).

0039-9140/$ – see front matter © 2009 Elsevier B.V. All rights reserved.
doi:10.1016/j.talanta.2009.10.021

where D ($z \times c$) is the original raw LC–FTIR data matrix with the overall spectral information of all absorbing species present in the system, C ($z \times k$) is the vector of the concentration profiles of the species, S ($k \times c$) is matrix containing the pure spectra of the k compounds, E ($z \times c$) is the error-related matrix and k, c and z are the number of absorbing species, variables (wavenumbers) and spectra, respectively. Under isocratic conditions, the eluent composition and hence its spectrum is known and theoretically constant. Therefore, direct subtraction of the solvent spectrum in the raw data matrix D allows a reduction of the systems complexity as the IR active eluting analytes are the only remaining components in the background corrected data matrix. Of course, this approach has its limitations. For example, minor changes in the mobile phase delivered by the LC pump can lead to strong changes in both, intensity and shape of the eluent absorbance spectrum. Thus, a direct subtraction of a reference spectrum might lead to inaccurate background compensation obtaining noisy chromatograms and distorted spectra of analytes. In spite of that, the overall simplicity of this approach has proven to be very useful in on-line isocratic LC–FTIR methods [1,6–10].

Under gradient conditions, the background correction process is not as straightforward as under isocratic conditions. A common mobile phase system in LC composed by acetonitrile and water can be used as an example: increasing the acetonitrile concentration of aqueous solutions, the composition of the mixture progressively shifts from pure H_2O to the $(CH_3CN)\cdot(H_2O)$ complexes and to pure (CH_3CN). Different species with characteristic infrared absorptions have been identified [11] including: $(CH_3CN)\cdot(H_2O)_5$, $(CH_3CN)_2\cdot(H_2O)_4$ and $(CH_3CN)_2\cdot(H_2O)$. Therefore, the IR absorption during the LC run raises due to the presence of the eluting sample components and to a variable number of IR absorbing solvent complexes difficult to estimate.

Recently a straightforward strategy was developed to overcome the problems of background absorbance elimination in on-line LC–FTIR systems. This chemometric approach is based on the use of the information content of a set of spectra of different eluent compositions named '*reference spectra matrix*' *(RSM)*. The *RSM* acquisition is carried out in practice measuring a blank LC gradient with eluent compositions falling within known limits. Besides, the *Sample Matrix (SM)* corresponding to the measurement of the injection of a sample into the LC–FTIR system is viewed as a series of independent spectra with different unknown solvent compositions. Then for each spectrum included in the *SM* an appropriate reference spectrum is selected or calculated from data included in the *RSM* matrix. Afterwards, background correction is accomplished subtracting the selected or calculated reference spectrum from the *SM* spectrum. Detailed descriptions of the procedure and examples of its application can be found in previous works [5,12–15].

In spite of the promising results obtained till now, the selection of the optimum parameters used to find an appropriate reference spectrum might become troublesome and time consuming when a gradient covering a wide range of eluent compositions is used for the LC analysis. In order to overcome this limitation, this paper reports a new approach for the selection of appropriate *RSM* spectra based on the direct comparison of characteristic absorption bands of the eluent during the chromatographic run with those of a reference data set in a point-to-point way. Following previous results, this paper focuses on the development of a new background correction approach paying attention to features that facilitate its use reducing the number of user-defined variables which increases the applicability of the background correction approach. Different alternatives are presented and discussed on real LC–FTIR data sets obtained from the analysis of a solution of four nitrophenols as a model system using an acetonitrile (0.08%, v/v TFA):water (0.08%, v/v TFA) gradient with compositions ranging from 35 to 85% (v/v) acetonitrile.

2. Proposed background correction procedure

As indicated above, a new criterion for the selection of appropriate reference spectra from the *RSM* is introduced. The proposed procedure compares characteristic absorption bands of the eluent during the chromatographic run of a sample injection with those of a reference data set using a point-to-point matching method (point-to-point – univariate background correction – reference spectra matrix, p2p-UBC-RSM). Similarity or distance methods based on point-to-point matching are methods in which equal-length vectors describing two spectra are compared point by point, and a single statistic is obtained [16,17]. Thereby, the usefulness of a matching method relies on the ability of the selected statistic to discriminate subtle differences in similar spectra. There are a number of different similarity indices that can be used [17]. As an example, in this work the performance of the correlation coefficient on the mean centered absorbances (COR) was evaluated.

The spectral similarity index COR between two spectra, S_A ($1 \times c$) and S_B ($1 \times c$), is calculated as described in Eq. (2) from the mean centered vectors (z_A and z_B), where $\bar{S}_n$ is the arithmetic mean absorbance in spectrum S_n (n = A, B):

$$COR = \frac{z_A^T z_B}{||z_A|| \cdot ||z_B||} \tag{2}$$

where $Z_n = S_n - \bar{S}_n$.

The background correction process of each spectrum S_i ($i = 1, \ldots, z$) included in the *SM* ($z \times c$) can be described in two steps:

1. Using the absorbance values in a defined spectral interval, r similarity indices for the set of spectra included in the *RSM* ($r \times c$) with the sample spectrum S_i are calculated. Then, the *RSM* spectrum showing the highest similarity value is selected as the corresponding reference of spectrum i (RS_i).
2. The background corrected spectrum (CS_i) is calculated by direct subtraction of the selected or calculated eluent spectra:

$$CS_i = S_i - RS_i \tag{3}$$

The process is repeated for each *SM* spectrum until the whole LC chromatogram has been corrected.

This simple background correction strategy presents a series of requirements and conditions of applicability, equal to those in previously published RSM-based approaches: (i) very good instrument stability and performance (e.g. apart from spectral noise, spectral drifts have a very strong negative effect on the accuracy of RSM-based background corrections); (ii) appropriate measurement of the *RSM* and *SM* data sets; (iii) the mobile phase spectra should present a spectral region characteristic of its composition and free from interferences from the eluting compounds.

It must be emphasized that slight drifts in the experimental conditions (T or pH, for example) might affect the spectrum of a defined mobile phase composition and thus, changes in these parameters must be minimized. From our experience with real (i.e. not simulated) data sets, we recommend to use RSM spectra measured during the re-equilibration of the LC–FTIR system after each gradient run. This straightforward approach can minimize some instrumental effects such as T changes, detector drifts or water vapor interferences, for example, which strongly affect the background correction.

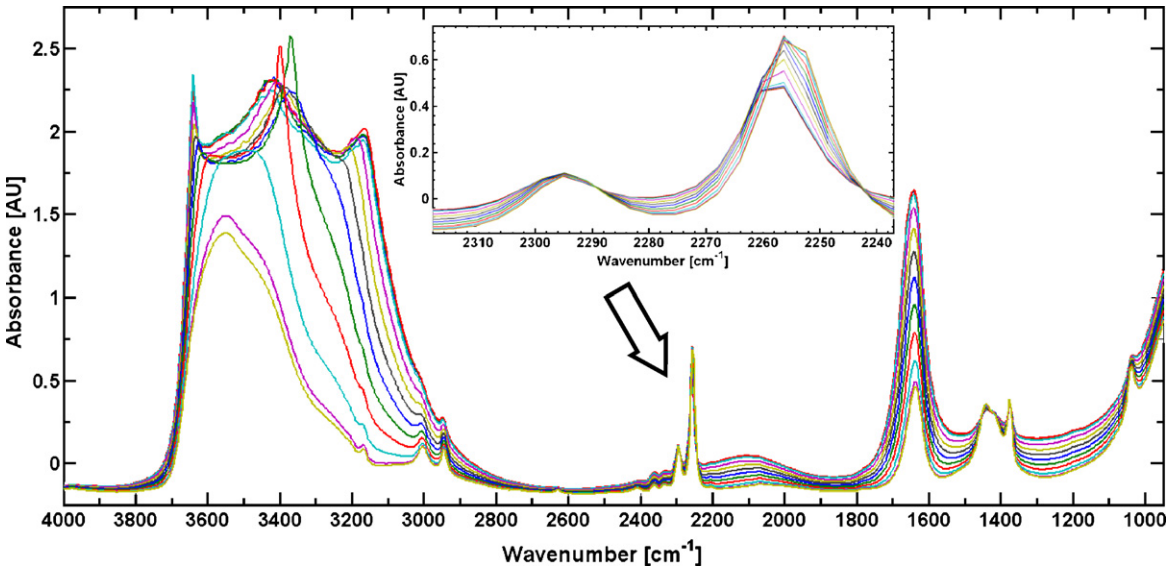


Fig. 1. On-line FTIR spectra measured during a LC gradient with mobile phase compositions ranging from 35:65 (v/v) to 85:15 (v/v) acetonitrile (0.08%, v/v TFA):water (0.08%, v/v TFA).

3. Experimental

3.1. Apparatus and reagents

4-Nitrophenol (4-NP), 2,4-dinitrophenol (2,4-dNP), 2-nitrophenol (2-NP) PESTANAL grade (Fluka, Buchs, Switzerland) and 3-methyl-4-nitrophenol (3m4-NP) (98%, Sigma–Aldrich, Switzerland) standard solutions were prepared by dissolving an appropriate amount of each compound in a 85:15 (v/v) water (0.08%, v/v TFA):acetonitrile (0.08%, v/v TFA) solution. Solutions were filtered (0.22 μm) prior to injection. HPLC grade acetonitrile and trifluoroacetic acid (TFA) were obtained from Scharlau (Barcelona, Spain) and Sigma–Aldrich, respectively. De-ionized water was purified with a Millipore system.

A Dionex (Sunnyvale, CA, USA) P680 high performance liquid chromatography system, equipped with a C_{18} column (150 mm × 2.0 mm, 5 μm) at 22 °C was employed using a sample injection loop of 20 μl. Mobile phase gradients were run from 65:35 (v/v) water (0.08%, v/v TFA):acetonitrile (0.08%, v/v TFA) to 15:85 (v/v) water (0.08%, v/v TFA):acetonitrile (0.08%, v/v TFA) in 20 min (recording of the *SM*), re-equilibrating the system in 7 min (recording of the *RSM*). Reference spectra were recorded in stopped-flow mode filling the flow cell with standard solutions of each analyte using a 85:15 (v/v) water (0.08%, v/v TFA):acetonitrile (0.08%, v/v TFA) solution as reference background.

An IR transparent flow cell was constructed using CaF_2 windows and an aluminium spacer with a channel of 2.5 mm width and a pathlength of 16.5 μm. For FTIR spectra acquisition a Bruker (Bremen, Germany) IFS 66/v FTIR spectrometer equipped with a liquid nitrogen refrigerated mercury–cadmium–telluride (MCT) detector, a vacuum system and a dry air purged sample compartment was used. The scanner for the interferometer was operated at a HeNe laser modulation frequency of 100 kHz. Spectra were recorded in the range between 4000 and 950 cm^{-1} using the spectrum of the empty sample compartment as background, with a resolution of 8 cm^{-1} and a zerofilling factor of 2. An aperture of 3 mm and a grating to attenuate the intensity of the irradiating light on the detector element were used to achieve optimum signal intensity. During gradient experiments, 25 scans per spectrum were averaged, providing a spectra acquisition frequency of 15 spectra min^{-1}. For instrumental and measurement control as well as for data acquisition, the OPUS program (version 6.5) from Bruker was employed. Background correction was run under Matlab 7.7.0 from Mathworks (Natick, USA) using an in-house written Matlab function available from the authors.

4. Results and discussion

4.1. Selection of the spectral interval used for the calculation of the similarity index

Fig. 1 shows FTIR spectra measured during an on-line LC–FTIR gradient as described in the experimental section. The spectra show clearly the strong change in both, intensity and shape of the background absorption spectrum due to the acetonitrile and water bands in the 4000–950 cm^{-1} region. It can also be seen in the detailed view of the spectral region between 2318 and 2237 cm^{-1}. Detailed description of these bands can be found elsewhere [18]. The need for an accurate background correction technique is evident if we consider on the one side, that the absorption of the

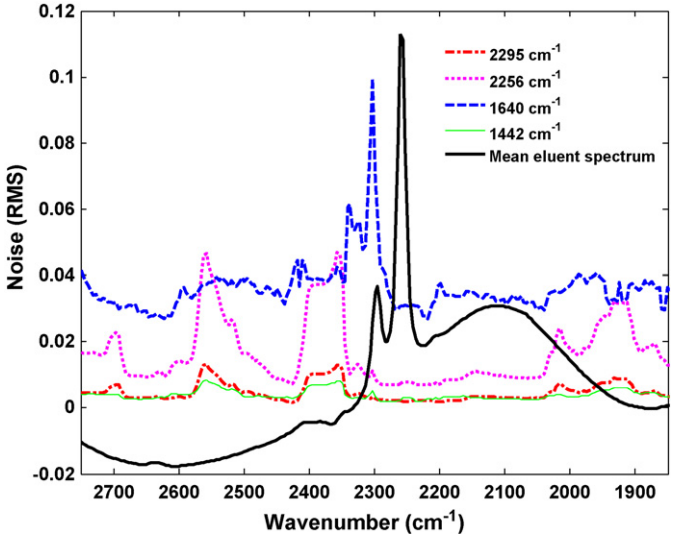


Fig. 2. Chromatographic noise values in a background corrected chromatogram calculated at four mobile phase characteristic wavenumbers, found during the selection process of the spectral interval. *Note*: see the text for details.

analytes rarely lies above 10×10^{-3} AU due to the reduced path-length of the flow cell and because of the inherent low absorptivity of mid-IR bands. On the other side, changes in the eluent absorbance in the studied mobile phase composition interval ranged between 0.32 AU at 2252 cm^{-1} and −1.82 AU at 1658 cm^{-1}.

The selection of an appropriate spectral interval is a critical step of any point-to-point comparison approach which can be time consuming. The number of selected variables should be kept as low as possible to reduce the effect of spectral interferences from the eluting compounds but it must include an adequate number of variables capable to discriminate minor differences between eluent spectra with very close compositions. Taking into account the chemical and spectroscopic information about the studied mobile phase system, some regions of the absorbance spectrum can be excluded of further considerations. The very intense water absorbance band at about 3500 cm^{-1} leads to spectral saturation affecting a large part of the spectrum and therefore the region above ~2750 cm^{-1} cannot be used. Furthermore, in the evaluation of nitrophenols the region below 1800 cm^{-1} was not considered because of spectral overlapping of the mobile phase spectrum with the spectra of the sample constituents.

In this work, an intuitive 'moving window' approach is proposed for the selection of an adequate spectral interval for background correction in the present mobile phase system and concentration interval. Briefly, in this approach, a spectral window starting at the variable t and ending at the spectral variable $(t + ws - 1)$, where ws is the window size, is selected. The spectral window is moved through a predetermined spectral range. At each position, the background eluent spectra are selected comparing the absorption spectra of the sample LC data set with those of the reference data set using the calculated spectral similarity index, as described in Section 2. Therefore, for each tested variable window, a background corrected chromatogram is obtained. Then, the noise level in the corrected chromatograms is calculated and plotted at wavenumbers where

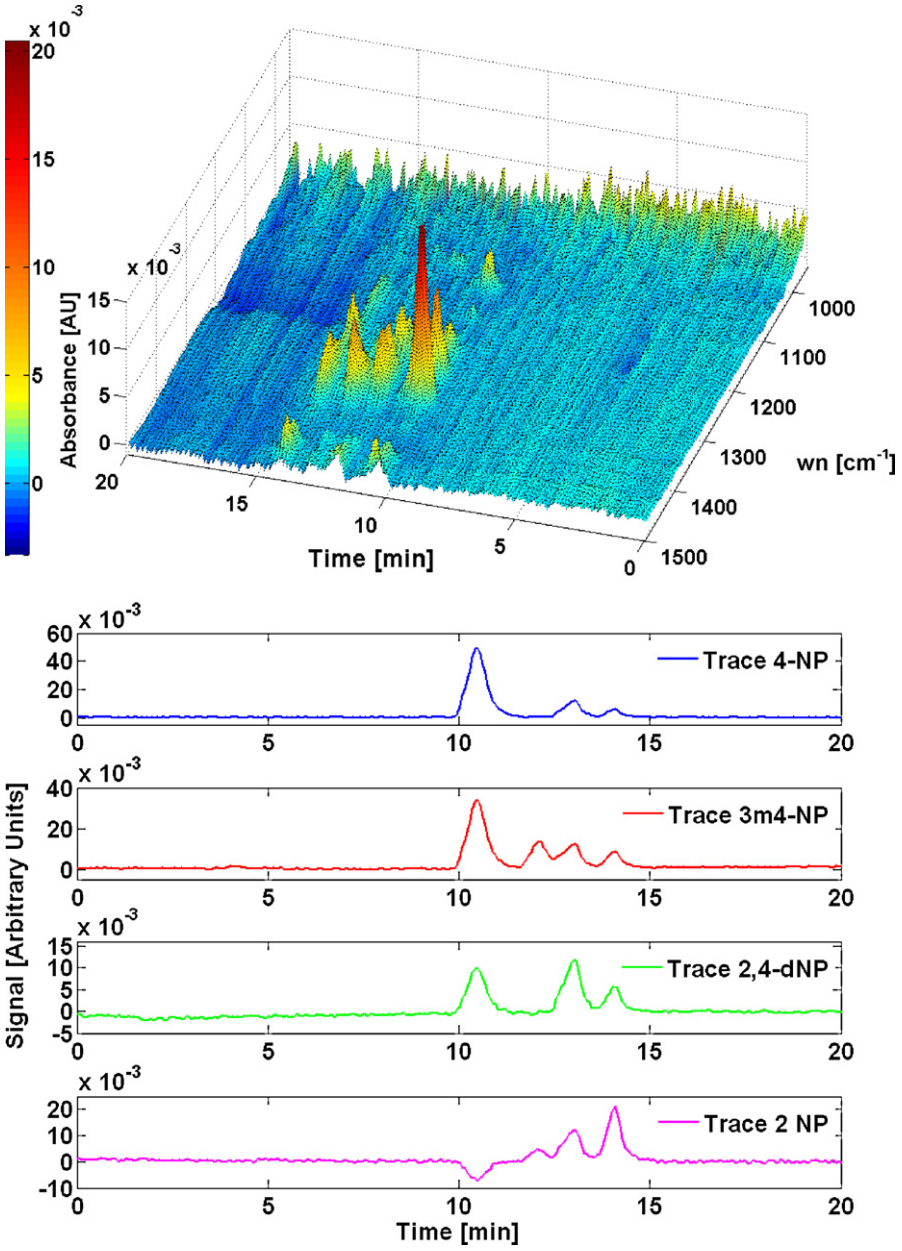


Fig. 3. (A) 3D spectral plot of background corrected spectra measured upon injection of a standard nitrophenols mixture containing 3 mg ml^{-1} 4-NP, 3.5 mg ml^{-1} 3m4-NP, 6 mg ml^{-1} of 2,4-dNP and 5 mg ml^{-1} of 2-NP. (B) Chromatograms extracted from the background corrected chromatogarm. *Note*: chromatograms were extracted as described in Table 1.

Table 1
Linear regression curves of 4-NP, 3m4-NP, 2,4-dNP and 2-NP using height values of the background corrected LC–FTIR chromatographic peaks.

Trace	Analytical signal[a] (y)		Retention time [min]	$y^a = (k \pm s_k) \times C\ [\mathrm{mg\,ml^{-1}}] + (d \pm s_d)$	R^2	Concentration range [mg ml^{-1}]
	Absorbance (wavenumber) [cm^{-1}]	Baseline correction [cm^{-1}]				
4-NP	$A(1335)+A(1338)+A(1342)$	$A(1311)$	10.4	$(9.8 \pm 0.7)C+(-3 \pm 1)$	0.97	0.4–5
3m4-NP	$A(1335)+A(1338)$	$A(1215)$	12.1	$(2.2 \pm 0.1)C+(-0.3 \pm 0.3)$	0.990	0.6–4
2,4-dNP	$A(1346)+A(1350)$	$A(1512)$	13.0	$(1.24 \pm 0.01)C+(0 \pm 0.1)$	0.9993	1–10
2-NP	$A(1324)+A(1327)+A(1531)+A(1535)$	$A(1500)$	14.1	$(2.8 \pm 0.1)C+(-0.3 \pm 0.2)$	0.997	0.6–8

[a] The analytical signal (y) is the sum of single point baseline corrected absorbance values (A) at the wavenumbers indicated between brackets.

the eluent present intense absorption bands, giving a quick and easy indication about the regions which provide accurate results. Visual inspection of this plot is used afterwards to select a combination of contiguous or non-contiguous variables to define the optimal spectral window used for the background correction.

In this work the chromatographic noise in the corrected chromatogram was measured as root mean square (RMS) at the wavenumbers 2295, 2256, 1640 and 1442 cm^{-1}, corresponding to characteristic acetonitrile and water vibrations. Results obtained for the considered similarity for an evaluated spectral interval between 2750 and 1800 cm^{-1}, using a window size of 21 variables and no correction factor, are shown in Fig. 2. From this figure it can be seen that the best results for the studied similarity index COR were obtained when the selection was made according to the changes in the CN stretching band. From the information obtained by the 'moving window' approach applied to the present mobile phase system, the use of the spectral interval between 2318 and 2237 cm^{-1} centered at 2280 cm^{-1} was selected for the background correction of further LC–FTIR runs.

4.2. On-line LC–FTIR injection of nitrophenols standard solutions

On-line LC–FTIR chromatograms obtained from injections of standard solutions of four nitrophenols were background corrected using the point to point matching algorithm COR and the region selected in the previous section. The experiments shown in Fig. 3 were carried out using a gradient of water (0.08%, v/v TFA):acetonitrile (0.08%, v/v TFA) from 65:35 (v/v) to 15:85 (v/v) in 20 min. It can be seen that peaks are not baseline resolved using a rapid gradient of 20 min. However, as illustrated in this figure, the overlapping of chromatographic peaks does not affect the accuracy of RSM-based background correction approaches. Even when peak overlapping occurs, the background correction algorithm works well resulting in a low noise in the background corrected spectra over the whole mid-IR region where the spectra are not saturated. Peaks of the four analytes could be identified from the depicted chromatograms measured in 20 min at 10.4, 12.1 and 13.0 and 14.1 min corresponding to 4-NP, 3m4-NP, 2,4-dNP and 2-NP, respectively (see Table 1). The negative peak which can be observed at 10.4 min in the 2-NP chromatogram in Fig. 3 is due to the baseline correction used for the extraction of the trace.

Table 1 summarizes the main analytical figures of merit considering the whole process and the background correction method. Appropriate values for linearity were achieved resulting in R^2 between 0.97 and 0.9993, injecting a series of five independent standards solutions with different concentrations of each analyte. The applied concentration ranges of the injected solutions as well as on column mass ranges are listed for all four analytes in Table 1.

In a previous work Quintás et al. [5] evaluated the on-line hyphenation of FTIR spectrometry and a capillary LC system with

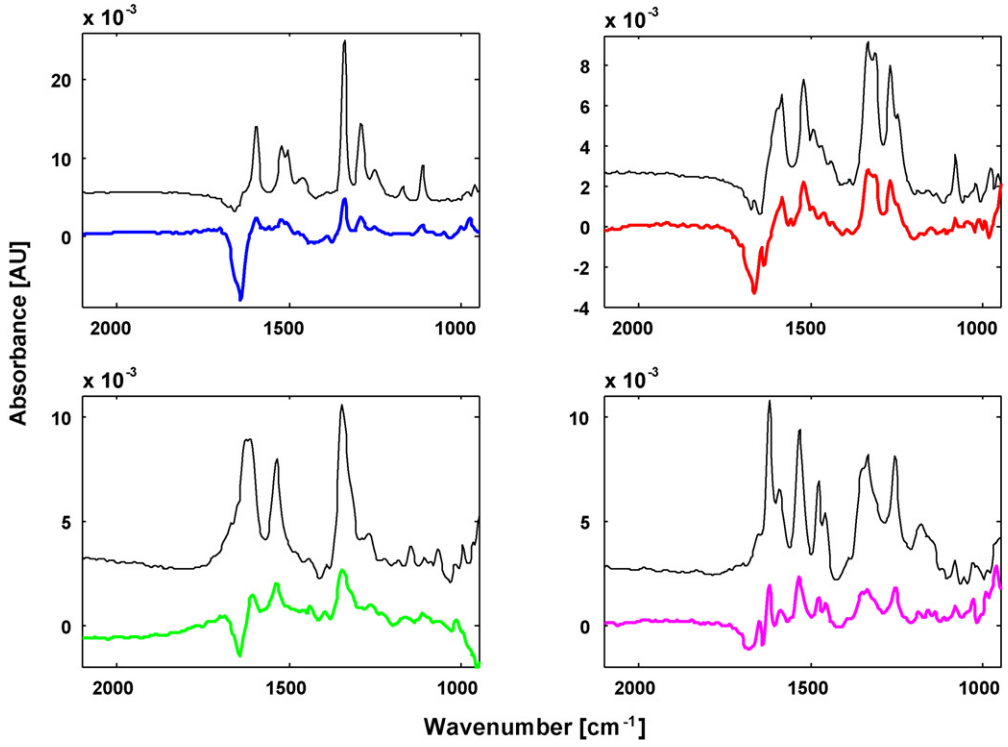


Fig. 4. Background corrected spectra of the four nitrophenols at the peak apex extracted from the injection of a solution containing 1.25 mg ml^{-1} 4-NP (A), 2 mg ml^{-1} 3m4-NP (B), 2.25 mg ml^{-1} 2,4-dNP (C) and 4.5 mg ml^{-1} of 2-NP (D). Reference spectra (black fine lines) measured in stopped-flow are included for comparison.

a mobile phase composed by acetonitrile (0.05%, v/v TFA) and water (0.05%, v/v TFA) within a composition range between 50 and 65% (v/v) acetonitrile, for the separation of the set of analytes used in this work. In the aforementioned study, accurate results were obtained using a RSM-based background correction approach which used the difference in absorbance (relative absorbance – univariate background correction – reference spectra matrix, RW-UBC-RSM) between 2256 and 2260 cm^{-1} and a correction factor established at 2260 cm^{-1} to improve the obtained results. To allow comparison of the aforementioned RW-UBC-RSM background correction method with the p2p-UBC-RSM approach, both procedures were applied to the same gradient measured between 35 and 85% (v/v) acetonitrile in 20 min injecting a standard solution. Whereas both approaches provided comparable results (data not shown), the selection of the conditions for the background correction in p2p-UBC-RSM was significantly simpler as compared to that required for the RW-UBC-RSM previous procedure.

One of the biggest advantages of FTIR detection in LC, compared to other detection methods like for example UV, is its potential for identification of the analytes, which obviously depends on an accurate background correction. Fig. 4 shows recovered spectra from the peak maxima for all analytes obtained from a standard injection after applying the p2p-UBC-RSM background correction method and the corresponding reference spectra previously obtained. For evaluation of the spectral accuracy, the correlation coefficient between each pair of spectra was calculated. The spectra extracted at the peak apex from the background corrected gradient chromatograms correlate well with the reference spectra using the region between 1200 and 1550 cm^{-1} where all analytes show typical absorption bands. The calculated spectral correlations were 91.7, 98.6, 97.8 and 98.4% for 4-NP, 3m4-NP, 2,4-dNP and 2-NP, respectively. These results evidenced that the selected conditions of measurement and background correction were appropriate for the identification and quantification of the considered analytes.

5. Conclusions

The proposed background correction process has been used in on-line LC–FTIR using acetonitrile (0.08%, v/v TFA):water (0.08%, v/v TFA) gradients between 35 and 85% acetonitrile for the determination of nitrophenols as model compounds, obtaining accurate results. Comparing the p2p-UBC-RSM method to a previously published approach (RW-UBC-RSM), similar results were obtained with both procedures. However, the selection of the parameters for background correction was facilitated considerably as the user-interaction was reduced to the selection of the spectral interval and the window size used for the point-to-point spectral comparison. On the other hand, it could be shown that the background correction process is not influenced by the chromatographic resolution as it works not only with baseline resolved peaks but also with overlapping peaks.

In short, the main features of the proposed point-to-point selection criterion for RSM-based background correction approaches in on-line LC–FTIR are: (i) simplified and fast initial selection of the RSM-BGC parameters (window size, variable interval and correlation coefficient), and (ii) the use of a single criterion for the selection of appropriate RSM reference spectra through a gradient elution with a wide range of the mobile phase compositions.

Whereas the present work only shows results obtained from an acetonitrile:water mobile phase system, further work is in due course to investigate the applicability of the proposed strategy to other common solvent systems in both normal and reversed phase LC including THF, methanol and hexane.

Acknowledgements

Authors acknowledge the financial support of Ministerio de Educación y Ciencia (Project CTQ2008-05719) and Generalitat Valenciana (Project GVA-PRE-2008-301). JK acknowledges the "V Segles" grant provided by the University of Valencia to carry out this study.

References

[1] R. Schulte-Ladbeck, A. Edelmann, G. Quintás, B. Lendl, U. Karst, Anal. Chem. 78 (2006) 8150.
[2] P.R. Griffiths, J.A. de Haseth, Fourier Transform Infrared Spectrometry, 2nd edition, Wiley, 2008.
[3] http://www.daylightsolutions.com/.
[4] http://www.vigo.com.
[5] G. Quintás, J. Kuligowski, B. Lendl, Anal. Chem. 81 (2009) 3746.
[6] B.M. Patterson, N.D. Danielson, A.J. Sommer, Anal. Chem. 76 (2004) 3826.
[7] B.M. Patterson, N.D. Danielson, A.J. Sommer, Anal. Chem. 75 (2003) 1418.
[8] A. Edelmanm, J. Diewok, J. Rodríguez-Baeza, B. Lendl, Anal. Bioanal. Chem. 376 (2003) 92.
[9] A. Edelmann, I. Ruzicka, J. Frank, B. Lendl, W. Schrenk, E. Gornik, G. Strasser, J. Chromatogr. A 934 (2001) 123.
[10] J. Kuligowski, A. Breivogel, G. Quintás, S. Garrigues, M. de la Guardia, Anal. Bioanal. Chem. 392 (2008) 1383.
[11] J.J. Max, C. Chapados, Can. J. Anal. Sci. Spectrosc. 47 (2002) 72.
[12] G. Quintás, B. Lendl, S. Garrigues, M. de la Guardia, J. Chromatogr. A 1190 (2008) 102.
[13] J. Kuligowski, G. Quintás, S. Garrigues, M. de la Guardia, Talanta 77 (2008) 779.
[14] J. Kuligowski, G. Quintás, S. Garrigues, M. de la Guardia, Anal. Chim. Acta 624 (2008) 278.
[15] G. Quintás, J. Kuligowski, B. Lendl, Appl. Spectrosc., in press.
[16] J. Li, D. Brynn Hibbert, S. Fuller, G. Vaughn, Chem. Int. Lab. Syst. 82 (2006) 50.
[17] K. Varmuza, M. Karlovits, W. Demuth, Anal. Chim. Acta 490 (2003) 313.
[18] T. Takamuku, M. Tanata, A. Yamaguchi, J. Nishimoto, J. Phys. Chem. B 102 (1998) 8880.

Talanta 80 (2010) 1777–1781

Contents lists available at ScienceDirect

Talanta

journal homepage: www.elsevier.com/locate/talanta

Contribution to vapor generation-inductively coupled plasma spectrometric techniques for determination of sulfide in water samples

Jiří Čmelík[a], Jiří Machát[b,*], Vítězslav Otruba[a], Viktor Kanický[a]

[a] Department of Chemistry, Faculty of Science, Masaryk University, Kotlářská 2, Brno, Czech Republic
[b] Research Centre for Environmental Chemistry and Ecotoxicology, Faculty of Science, Masaryk University, Kamenice 3, Brno, Czech Republic

ARTICLE INFO

Article history:
Received 9 July 2009
Received in revised form
23 September 2009
Accepted 8 October 2009
Available online 5 November 2009

Keywords:
Hydrogen sulfide
Sulfide
Vapor generation
ICP-OES
Chemical interference

ABSTRACT

Vapor generation-inductively coupled plasma-optical emission spectrometry was used for the determination of sulfide in water samples preserved by the addition of a zinc acetate and sodium hydroxide solution. Hydrogen sulfide and acid-volatile sulfides were transformed, by acidification, to a gaseous phase in a vapor generator and subsequently detected by inductively coupled plasma optical emission spectrometry. Compounds interfering with iodometric titration and spectrophotometric determination were examined as potential chemical interferents. The proposed method provides results comparable to iodometric titration in the tested concentration range 0.06–22.0 mg L^{-1}. Limit of detection for the determination of hydrogen sulfide by this method is 0.03 mg L^{-1}.

© 2009 Elsevier B.V. All rights reserved.

1. Introduction

Sulfide concentration in a water sample is an important parameter for the assessment of spring, surface or waste water pollution [1]. There are several established methods for the determination of sulfide and/or hydrogen sulfide such as iodometric titration, spectrophotometric determination, potentiometry or ion chromatography [2–5]. Some drawbacks of these methods (insufficient limit of detection and their laboriousness) led to the development of their modification and to the establishment of completely new methods. The application of inductively coupled plasma (ICP) spectrometry hyphenated to a vapor generator (VG) for sulfide determination is one such innovative approach.

Inductively coupled plasma-mass spectrometry hyphenated to vapor generation (VG-ICP-QMS) was used for the determination of sulfide in water samples in ref. [6]. The quadrupole analyzer of the mass spectrometer suffers from insufficient spectral resolution hence the measurement of sulfur is strongly interfered by polyatomic ions mainly from molecular ion O_2^+. Oxygen forming these interfering ions arises particularly from water when nebulizing aqueous solutions. Generation of water-free gaseous hydrogen sulfide into the ICP results in the suppression of polyatomic interference. Further elimination of O_2^+ can be achieved by using a collision-reaction cell (CRC) in mixed H_2/He mode. In this work, optimization of the CRC parameters was primarily solved to obtain a satisfactory LOD. The LOD obtained for VG-ICP-MS determination of sulfide in water was 2 μg L^{-1}.

Inductively coupled plasma-optical emission spectrometry (ICP-OES) can also be used for sulfur detection. Measurement of the main sulfur analytical emission lines in vacuum UV range are not usually subject to spectral interference as the ICP emission spectrum in this region is relatively low in emission lines. In the case of ICP-OES, two techniques of sample introduction, both taking full advantage of vapor generation, can be used. A vapor generator with a gas/liquid phase separator enables introduction of the gaseous phase and thus only volatilized sulfide is detected [7]. The advantage of this technique is the elimination of spectral and non-spectral interferences in the ICP resulting from matrix separation. Nebulization of the reaction mixture (sample and acid) is another concept for the introduction of a volatile analyte allowing sensitive determination of sulfide as well as sulfate, latter being introduced into the ICP as an aerosol. Both these techniques were applied by [7,8]. Limits of detection for sulfide using VG and aerosol were 6 and 5 μg L^{-1}, respectively, with an axially-viewed ICP.

Hydrogen sulfide and sulfide concentration in water can be influenced by volatilization and/or oxidation; hence preservation of the samples is necessary in the sampling step. Preservation can be provided, for example, by adjustment of the pH to 8.5–9 with sodium hydroxide and ascorbic acid [9], or by zinc or cadmium acetate with subsequent alkalinization [10] and storage at a low

* Corresponding author. Tel.: +420 549 495 684; fax: +420 549 492 840.
E-mail address: machat@chemi.muni.cz (J. Machát).

0039-9140/$ – see front matter © 2009 Elsevier B.V. All rights reserved.
doi:10.1016/j.talanta.2009.10.022

temperature (1–5 °C). Sodium hydroxide solution (2 mol L^{-1}) and ascorbic acid (0.2 mol L^{-1}) was used in ref. [6] for sample treatment by mixing the same volumes of both water sample and buffer. Separation of the gaseous analyte from liquid waste is achieved in a vapor-generator, thus high concentrations of sodium in a sample does not present a problem. In the case of nebulization of a reaction mixture [7,8] into the ICP, high Na concentrations in the solution lead to plasma instability. In this case an ammonium/ammonium chloride buffer was successfully used for alkalinization. Both ICP methods were successfully applied to spiked and natural water samples [6–8] and to the determination of acid volatile sulfide in marine sediment [6]. Results of these techniques were compared to those of a potentiometric method.

A vapor generator with a phase separation – ICP-OES method was also applied in our work for the determination of sulfide in water samples. The addition of zinc acetate/sodium hydroxide was used for the sample preservation with subsequent dissolution of the precipitate by adding EDTA prior to the measurement. Considering the lack of study of chemical interference in the above-mentioned works [6–8], we have dealt with the effect of some ions in the vapor generation of hydrogen sulfide. Our method was applied to real spring water samples with sulfide concentrations in the range 0.06–22 mg L^{-1} and the results were compared with the results from iodometric titration following distillation separation of hydrogen sulfide from the sample.

2. Experimental

2.1. Instrumentation

An optical emission spectrometer with inductively coupled plasma Jobin-Yvon 170 Ultrace (JY-Horiba, Longjumeau, France) and hydride generator HG-1 (Labtech Ltd., Brno, Czech Republic) were used in this work. The schematic of the vapor generation system can be found in [11]. Operating conditions are shown in Table 1. Standard alumina injector (i.d. 2.5 mm) in the JY demountable plasma torch was replaced by a quartz injector because of the significant memory effects with the alumina injector. Similar effects were observed with iodine vapor generation as presented by Niedobova et al. [11].

2.2. Chemicals

Chemicals of reagent grade quality (Lach-Ner, Neratovice, Czech Republic) and deionized water were used throughout the experiments. Zinc acetate, sodium hydroxide, di-sodium EDTA (dihydrate) and hydrochloric acid (6 mol L^{-1}) were used for the preservation of the samples and following the generation of hydrogen sulfide. Chemical interferences were examined using the following chemicals: sodium nitrite, nitrate, sulfate, sulfite, bicarbonate, copper (II) sulfate pentahydrate, iron (II) sulfate heptahydrate, and iron (III) chloride hexahydrate.

Standard sulfide solutions were prepared by dissolving an appropriate amount of sodium sulfide (nonahydrate) in sodium hydroxide solution (0.1 mol L^{-1}) and by subsequent dilution. These calibration solutions were standardized by iodometric titration because of the poorly defined content of sulfide in sodium sulfide and its instability. In the case of distillation separation of hydrogen sulfide from the real samples, glycerol was used in a trap solution of sodium hydroxide [2]. Iodine volumetric solution (0.01 mol L^{-1}) was prepared by precisely weighing potassium iodate and the excess of potassium iodide after acidification by sulfuric acid. Sodium thiosulfate solution (0.01 mol L^{-1}, prepared from sodium thiosulfate pentahydrate) was standardized by titration of an iodine solution using starch as an indicator.

Table 1
Operation conditions of ICP spectrometer and vapor generator.

ICP spectrometer	
Forward power ICP (W)	1200
Plasma gas flow (L min^{-1})	12.0
Carrier gas flow (L min^{-1})	0.5
Sheath gas flow (L min^{-1})	0.5
Monochromator purging (Ar) (L min^{-1})	3.0
Plasma viewing	Radial
Vapor generator	
Carrier gas flow (L min^{-1})	0.5
Sample flow rate (mL min^{-1})	1.0
Acid flow rate (mL min^{-1})	0.5

2.3. Samples

The proposed method was applied to spring water samples with different concentrations of sulfide which were preserved immediately after sampling. The preservation was performed by adding of 1 mL 10% (m/m) zinc acetate and 0.5 mL 4 mol L^{-1} sodium hydroxide to 100 mL of water sample. For VG-ICP-OES determination powdered $Na_2EDTA{\cdot}2H_2O$ (about 200 mg) was added to each sample and mixed thoroughly to dissolve the precipitate in the sample prior to the analysis. The amount of $Na_2EDTA{\cdot}2H_2O$ depends on the amount of the precipitate formed by the preservation.

The preservation was performed in the laboratory during the development of the method and during the investigation of chemical interferences. Real samples were preserved immediately after the sampling procedure. Real samples of spring waters (100 mL) were sampled from the inspection wells in the region around Hodonín city (Southern Moravia, Czech Republic). The inspection wells are located near petroleum and exploratory wells where a high concentration of sulfate and variable concentrations of hydrogen sulfide can be found, probably as a result of microbial reduction of sulfate. Reference values of sulfide concentration in the samples were obtained by iodometric titration with a separation step [2].

Concentration of potential interferents was determined by an outside analytical laboratory. Sulfate in samples A, B and G was found to be in range 450–500 mg L^{-1} and for other samples 60–100 mg L^{-1}. Concentrations of other ions in all samples was as follows: NO_3^- < 5 mg L^{-1}, NO_2^- < 0.1 mg L^{-1}, Fe (total) < 1 mg L^{-1}, Cu < 5 μg L^{-1}. The following pH values of original samples were measured: samples A, B and G (6.9), C (8.2), D, E, F (7.4), and H (7.1).

2.4. Determination of sulfide by VG-ICP-OES method

Determination of sulfide in water samples was realized by the continuous generation of gaseous hydrogen sulfide to the ICP source. Generation and separation of hydrogen sulfide from a sample has been performed in a hydride generator HG-1 with siphon gas/liquid separator. Hydrochloric acid (6 mol L^{-1}) was applied for acidification and releasing of hydrogen sulfide from the sample. An ICP spectrometer was used for measuring the emission intensity of S(*I*) 180.676 nm line in radial mode. Linearity of the calibration curve was checked in the concentration range of sulfide 4–40 000 μg L^{-1}.

Interference effects of some potential interferents were checked for the VG-ICP-OES method. The compounds (ions) which interfere with iodometric and spectrophotometric determination (based on methylene blue reaction) were selected as potential interferents. Ions were added to model samples with a constant concentration of sulfide (100 μg L^{-1}) at the following concentration levels: 10, 100 and 1000 mg L^{-1} (for sulfate and bicarbonate), 1, 10 and 100 mg L^{-1}

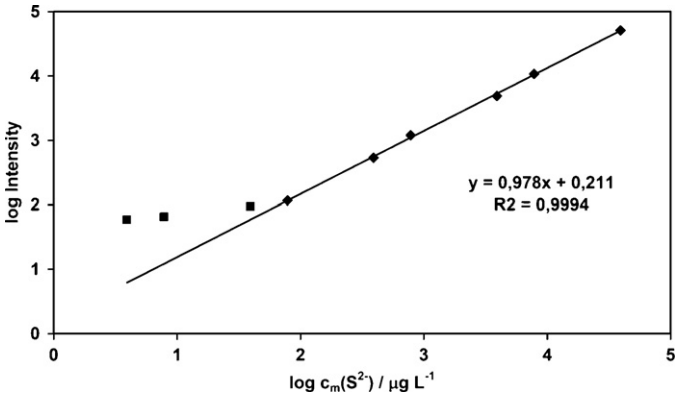


Fig. 1. Logarithmic form of calibration graph (sulfur emission line S(*I*) 180.676 nm) for the determination of S^{2-} in the concentration range 4–40 000 µg L^{-1}. Values below 80 µg L^{-1} (black squares) are not included in linear regression.

(for nitrite, nitrate, sulfite, Fe^{3+}, Fe^{2+}) and 0.1, 1 and 10 mg L^{-1} for Cu^{2+}. The concentration range for the interferents was selected with respect to their concentration in the real spring, surface or waste water samples.

3. Results and discussion

3.1. Method development

Determination of hydrogen sulfide and sulfide in water samples through vapor generation ICP optical emission spectrometry is based on the separation of hydrogen sulfide and the detection of sulfur. Hydrogen sulfide dissolved and/or fixed in sulfides is released from a sample by acidification. Separation of hydrogen sulfide from the liquid phase is provided by a gas/liquid phase separator and then the gaseous phase is introduced to plasma where the atomization and excitation of sulfur atoms is performed. Subsequently optical emission is registered by optical emission spectrometry. The intensity of emission is proportional to the concentration of sulfidic sulfur in the sample.

Linearity of the calibration curve with our VG system was tested in the concentration range 4–40 000 µg L^{-1} S^{2-} for two sulfur emission lines S(*I*) 180.676 nm and S(*I*) 181.978 nm. Sensitivities of both sulfur emission lines were comparable thus only emission line S(*I*) 180.676 nm was used for further measurements. The calibration curve was found to be linear in the range 80–40 000 µg L^{-1} (Fig. 1). Determination of concentration below about 80 µg L^{-1} was found to be influenced by a non-zero blank value which is caused by the presence of impurities, such as hydrogen sulfide or sulfur dioxide, in argon, the atmosphere and probably in the chemicals. Limit of detection for sulfide, calculated as 3σ of blank measurement ($n = 10$), was 30 µg L^{-1}. The blank samples were prepared with deionized water by the preservation method described below. LOD value of our configuration is about five-times higher when compared to other works [7,8] as axially-viewed ICP was also applied in these works.

3.2. Sample preservation and treatment

The real samples have to be preserved immediately after sampling otherwise changes in sulfide concentration caused by oxidation or vaporization can be observed. For the preservation, alkalinization with a reducing agent [9] or the addition of a heavy metal salt (Zn, Cd) with subsequent alkalinization [10] can be used. Hydrogen sulfide and sulfides are precipitated as ZnS or CdS and hence are protected from oxidation and/or vaporization. Excess of a heavy metal cation is precipitated as hydroxide. When pumping such a sample for analysis by continuous flow vapor generation, vigorous mixing of this mixture is necessary to ensure a constant input of sample and, as a result, constant analyte signal.

Dissolution of the formed precipitate by di-sodium EDTA salt was used as an alternative technique. The amount of EDTA must be sufficient for dissolution of all the sulfide and hydroxide precipitate and depends on its amount. In our case 200 mg of $Na_2EDTA{\cdot}2H_2O$ was sufficient for 100 mL of water sample preserved with 1 mL 10% (m/m) zinc acetate followed by mixing the contents for 5 min. Dissolution of the precipitate results in a homogenous solution or very fine dispersed colloid particles and, as a consequence, repeatability (RSD) of the measurement is significantly improved. Results of analysis of two different samples by both methods, with and without dissolution of the precipitate, are shown in Table 2. Results of both methods are comparable in terms of accuracy. However, repeatability of the measurement is improved in the case of precipitate dissolution and there is no need for sample mixing during analysis.

3.3. Interference study

Spectrophotometric determination of sulfide, iodometric titration and other methods can be interfered by a family of compounds. Therefore the effect of known interferents and some major anions in natural waters on the vapor generation technique was investigated. The influence of the following ions was tested: nitrite, nitrate, sulfate, bicarbonate, sulfite and the effect of Fe^{2+}, Fe^{3+} and Cu^{2+} cation. The effect of the interferents was tested with preserved samples of sulfide with subsequent dissolution of precipitate by Na_2EDTA.

Sulfate does not interfere with sulfide determination as it does not form volatile species after acidification and thus is separated in a gas/liquid separator as liquid waste (see Table 3). Nitrate in the sample does not interfere in the investigated range (up to 100 mg L^{-1}). A weak suppression of the sulfide signal could be observed with a higher bicarbonate concentration. Concentration of bicarbonate over 100 mg L^{-1} can frequently be found in natural water and, moreover, the concentration of dissolved free carbon dioxide must be taken into account since it forms (bi)carbonate with an alkaline reagent (hydroxide) used for the sample preservation. The mechanism of this effect was not investigated in this study. Significant positive interference was observed in the case of sulfite. Even the lowest concentration 1 mg L^{-1} caused a significant increase of the sulfur signal. The signal appearing at 1 and 100 mg L^{-1} of sulfite corresponds to 0.09 and 16.4 mg L^{-1} of sulfide, respectively. This positive interference is induced by volatilization of sulfur dioxide formed by acidification of the sulfite. Hydrogen sulfide and sulfur dioxide cannot be distinguished in the detector as ICP-OES is an element-specific detector. On the other hand, this fact can be employed in the determination of sulfur dioxide and/or sulfite, for example, in wine samples [12]. Conversely, the determination of sulfide at lower concentrations of sulfite can be influenced by a mutual reaction of both gases (ions in acidic solution) producing elemental sulfur as described in [13]. Due to this fact we can

Table 2
Influence of precipitate dissolution on repeatability of results.

Sample	Dissolution[a]	Sulfide concentration (mg L^{-1})	RSD (%)
B	+	1.14 ± 0.02	2
	–	1.2 ± 0.2	13
D	+	3.5 ± 0.1	3
	–	3.4 ± 0.4	11

The value ± denotes standard deviation of measured concentration ($n = 3$), RSD = relative standard deviation

[a] +: Determination with precipitate dissolution, –: determination without precipitate dissolution.

Table 3
Relative VG-ICP-OES signal of sulfide (100 μg L^{-1}) in the presence of potential chemical interferents.

$c_{interferent}$ (mg L^{-1})	Relative S signal (%)							
	SO_4^{2-}	HCO_3^-	NO_3^-	NO_2^-	SO_3^{2-}	Fe^{3+}	Fe^{2+}	Cu^{2+}
0.1	–	–	–	–	–	–	–	86 ± 3
1	–	–	102 ± 3	103 ± 3	190 ± 3	99 ± 3	105 ± 3	40 ± 3
10	104 ± 3	98 ± 3	104 ± 3	75 ± 3	1760 ± 60	101 ± 3	94 ± 3	10 ± 3
100	102 ± 3	95 ± 4	101 ± 3	19 ± 3	16400 ± 800	90 ± 3	68 ± 4	–
1000	102 ± 3	88 ± 3	–	–	–	–	–	–

The value ± denotes standard deviation of relative signal (n = 3).

speculate that, in such cases, the ICP signal of the volatile sulfur species would decrease as elemental sulfur is not vaporized under these conditions. The amount of volatile sulfur species entering the plasma will depend on the molar ratio of sulfide and sulfite and, in the case of an equimolar ratio (2 mol sulfide + 1 mol sulfite), the signal should reach the minimum. The excess of sulfite will result in production of sulfur dioxide and a subsequent increase in the emission signal. However, interferences of sulfite at the equimolar sulfide to sulfite ratio and below were not investigated. This interference can be significant in the case of waste water from the pulp and paper industry where both sulfite and sulfide can be found. Their mixture is however stable only in an alkaline environment for the reasons given above.

Negative interference was also observed for nitrite at concentrations over 1 mg L^{-1}. Oxidative properties of nitrite in acidic solution result in an oxidation of sulfide to elemental sulfur and signal suppression. However, nitrite concentration in spring water should be far below this limit which is not the case of waste water. For Fe^{2+} and Fe^{3+} ions, the signal suppression can be observed at Fe concentrations over 10 mg L^{-1}. For Fe^{3+} at 100 mg L^{-1} signal suppression is about 10% which is an acceptable measure of error. The same concentration of Fe^{2+} results in 40% decrease in signal. In the case of Cu^{2+} only 0.1 mg L^{-1} results in 10% decrease of signal, 1 mg L^{-1} Cu^{2+} results in even more than 50% decrease. Formation of insoluble sulfides causes signal suppression in the cases of Fe and Cu as these sulfides do not react with hydrochloric acid quantitatively in the hydrogen sulfide generation step. Other cations forming stable, acid resistant sulfides can be expected as interfering ions for this technique. On the other hand, the proportion of sulfur related to metallic insoluble sulfides is considered to be non-toxic in an aquatic environment. The distillation separation step for the determination of this type of sulfide requires a reaction performed at higher temperatures with over a prolonged time sufficient for almost the complete sulfide decomposition. The same technique can be used for determination of acid-volatile sulfide (AVS) in sediments [6].

3.4. Application to real samples

The VG-ICP-OES method was applied to a series of spring water samples from the inspection wells in the region Hodonín (South Moravia, Czech Republic). Results from the VG-ICP-OES method and iodometric titration with distillation separation step are presented in Table 4. Results of both methods were tested by the Student's t-test (α = 0.05, critical value t_α = 4.303). Because of the low power of this test (due to low n = 3), results were also tested using the pair t-test with t = 0.988 (α = 0.05, critical value t_α = 2.365). Both these tests revealed non-significant statistical differences between the values from LOD to 22 mg L^{-1}.

Routine elemental analysis of samples indicated that concentrations of Fe and Cu, as the main cationic interferents, were below maximal acceptable limits resulting from the study in Section 3.3. These limits can be determined as 10 and 0.1 mg L^{-1} for total Fe and Cu, respectively. Hence concentrations of both these elements in real samples did not affect the accuracy of sulfide determination.

Table 4
Results of the real samples of water with different concentration analyzed by VG-ICP-OES method and iodometric titration with distillation step.

Sample	Iodometric titration (mg L^{-1})	VG-ICP-OES (mg L^{-1})	t-test
A	0.06 ± 0.01	0.06 ± 0.01	0
B	1.05 ± 0.07	1.14 ± 0.02	1.748
C	3.10 ± 0.05	3.18 ± 0.05	1.600
D	3.7 ± 0.1	3.5 ± 0.1	1.500
E	6.2 ± 0.1	6.2 ± 0.1	0.571
F	6.5 ± 0.2	6.4 ± 0.3	0.513
G	7.2 ± 0.1	7.26 ± 0.08	0.588
H	20.3 ± 0.8	22 ± 2	1.070

The value ± denotes standard deviation of measured concentration (n = 3).

4. Conclusion

The applicability and reliability of the vapor generation technique with ICP detection for sulfide determination has been demonstrated in previous works and in our recent work. These methodologies have certain advantages compared to the methods usually applied for the determination of sulfide, including better LOD, lower time and chemical consumption and higher sample throughput, especially when compared to iodometric titration following distillation separation. The main disadvantage of these instrumental methods is the need for standardized calibration solutions resulting from the inaccessibility of defined chemicals and the instability of sulfide solution. In our work, applicability of sulfide preservation by co-precipitation with zinc hydroxide was demonstrated. Dissolution of precipitate by EDTA prior to VG-ICP-OES analysis results in a homogenous mixture and improves measurement repeatability.

As a chemical reaction is involved in the vapor generation step, chemical interferences can be expected with this method. Generally, three groups of chemical interferents can be mentioned:

1. Sulfur-containing species forming volatile compounds in acidic conditions (sulfite demonstrated here, predictably thiosulfate, dithionate and volatile organic sulfur-containing species).
2. Oxidants oxidizing sulfide to non-volatile sulfur.
3. Heavy metal ions forming insoluble sulfides.

These interferences will definitely be observed in the VG technique with experimental setups, gas-phase separation or reaction mixture nebulization, and ICP-OES or ICP-MS detection.

Acknowledgement

Authors would like to thank the Ministry of Education, Youth and Sports of the Czech Republic for financial support in project registration number MSM0021622412 and also Dr. L. Ďurd'ová (Academy of Sciences of the Czech Republic) for providing samples and information on their composition.

References

[1] P. Patnaik, A Comprehensive Guide to the Hazardous Properties of Chemical Substances, Wiley, New York, 1999.
[2] Czech National Regulation 830530/31, Chemical and physical analysis of surface water, Determination of sulfide and hydrogen sulfide.
[3] N. Gilboa-Garber, Anal. Biochem. 43 (1971) 129–133.
[4] E. Schmidt, A. Marton, J. Hlavay, Talanta 41 (1994) 1219–1224.
[5] S-H. Ohira, K. Toda, J. Chromatogr. A 1121 (2006) 280–284.
[6] M. Colon, M. Iglesias, M. Hidalgo, Spectrochim. Acta B 62 (2007) 470–475.
[7] M. Colon, M. Iglesias, M. Hidalgo, J.L. Todoli, J. Anal. At. Spectrom. 23 (2008) 416–418.
[8] M. Colon, J.L. Todoli, M. Hidalgo, M. Iglesias, Anal. Chim. Acta 609 (2008) 160–168.
[9] US EPA, SW-846, Test Methods for Evaluating Solid Waste, Physical/Chemical Methods, Method 9215 Potentiometric Determination of Sulfide in Aqueous Samples and Distillates with Ion-Selective Electrode, 1996.
[10] US EPA, SW-846, Test Methods for Evaluating Solid Waste, Physical/Chemical Methods, Method 9030b – Acid-Soluble and Acid-Insoluble Sulfides: Distillation, 1996.
[11] E. Niedobova, J. Machat, V. Otruba, V. Kanicky, J. Anal. At. Spectrom. 20 (2005) 945–949.
[12] J. Cmelik, J. Machat, E. Niedobova, V. Otruba, V. Kanicky, Anal. Bioanal. Chem. 383 (2005) 483–488.
[13] C. Chambers, A.K. Holliday, Modern Inorganic Chemistry, Butterworth & Co., London, 1975.

Talanta 80 (2010) 1782–1788

Contents lists available at ScienceDirect

Talanta

journal homepage: www.elsevier.com/locate/talanta

Molecularly imprinted polymer for the extraction of parabens from environmental solid samples prior to their determination by high performance liquid chromatography–ultraviolet detection

L. Núñez, E. Turiel*, A. Martin-Esteban, J.L. Tadeo

Departamento de Medio Ambiente, INIA, Ctra. de La Coruña Km 7, 28040 Madrid, Spain

ARTICLE INFO

Article history:
Received 23 July 2009
Received in revised form
28 September 2009
Accepted 8 October 2009
Available online 11 December 2009

Keywords:
Environmental solid samples
Molecularly imprinted polymer
Parabens
HPCL–UV

ABSTRACT

An analytical methodology incorporating a molecularly imprinted solid-phase extraction procedure (MISPE) has been developed for the determination of parabens in environmental solid samples. Four different polymers were prepared combining the use of acetonitrile or toluene as porogen, and 4-vinylpyridine (VP) or methacrylic acid (MAA) as monomer, using benzylparaben (BzP) as a template molecule. Although all the polymers were able to recognize the template in rebinding experiments, the MIP prepared in toluene using MAA showed better performance. This polymer was also capable of recognizing other parabens (methyl, ethyl, isopropyl, propyl, isobutyl, butyl and benzylparaben) allowing to develop an appropriated MISPE procedure for this family of compounds. The extraction of the parabens from environmental solid samples was performed by ultrasonic assisted extraction in small columns (SAESC), and this procedure next to MISPE as clean-up step followed by HPLC–UV determination was successfully used for the determination of parabens in soil and sediment samples of different locations. Recoveries ranging from 80% to 90% have been achieved depending on the compound and the samples, and limits of detection (LODs) were under 1 ng g^{-1} for all the compounds, making this method suitable for the determination of parabens in environmental solid matrices. The method was further applied to the determination of paraben contents in real samples, founding levels up to 11.5 ng g^{-1} in sea sediments.

© 2009 Elsevier B.V. All rights reserved.

1. Introduction

Parabens are a group of synthetic compounds used worldwide as preservative and antimicrobial agents in different products because of their broad antimicrobial spectra, good stability and non-volatility [1–4]. They are esters of 4-hydroxybenzoic acid (Fig. 1) and their antimicrobial activity increases when increasing ramification of the esteric chain. Although they were considered to have low toxicity, recent studies have demonstrated the endocrine disruption activity of parabens [5,6], have reported allergic contact dermatitis [7], and a relation with male infertility [8]. Moreover some studies suggest a connection between parabens and the risk of breast cancer [9], in fact, MeP in human breast tumours has been found with an overall mean value of 12.8 ng g^{-1}. Due to this fact, various companies are trying to produce products free of these classical preservatives and different patents have been registered in the last year for Givaudan S.A. and L'oréal S.A. [10,11]. Moreover, The European Community with The Council Directive 76/768/EC have restricted paraben contents up to concentration of 0.4% (w/w) for a single ester or 0.8% (w/w) for ester mixtures, expressed as p-hydroxybenzoic acid content [12].

Parabens, however, can still be found nowadays in a high number of pharmaceutical preparations, cosmetics, medications, personal care products, as well as in food and beverages. Among them, methylparaben (MeP) and propylparaben (EtP) are the parabens most commonly used in cosmetics, since they are added together and have synergistic effects. Due to that, concentrations as high as 5 mg g^{-1} have been found in these products [13,14]. On the other hand, and as a consequence of continuous dispatching of urban waste waters, the presence of parabens in the environment has been confirmed in different environmental compartments (water, air, dust, soil and sediments) using different techniques of extraction (accelerated solvent extraction (ASE), solid-phase extraction (SPE), matrix solid-phase dispersion MSPE, ultrasonic assisted extraction) and separation and determination (specially GC–MS with derivatization). Concentrations of 21 ng m^{-3} of MeP in indoor air [15], and 2.92 ng ml^{-1} in water from sewage treatment plants [16] have been reported, the highest concentration corresponding to methyl paraben. In a previous work of our group [17], an extraction procedure for the determination of parabens in solid

* Corresponding author. Tel.: +34 91 34738700; fax: +34 91 3572293.
E-mail address: turiel@inia.es (E. Turiel).

0039-9140/$ – see front matter © 2009 Elsevier B.V. All rights reserved.
doi:10.1016/j.talanta.2009.10.023

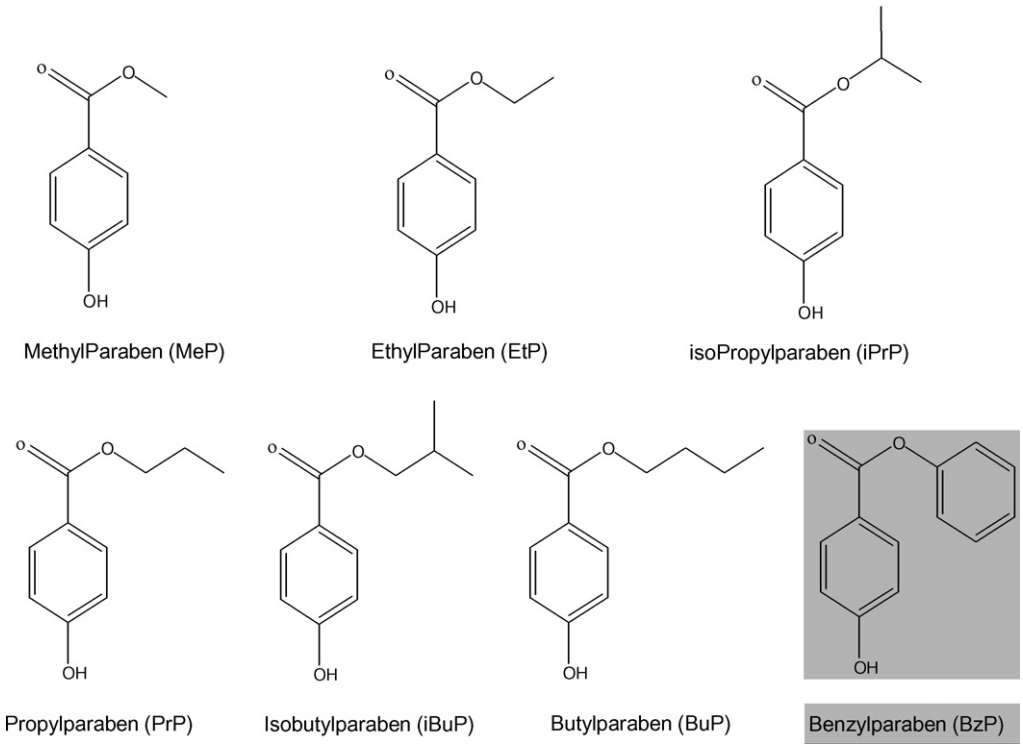


Fig. 1. Chemical structures of parabens. BzP, used as template, is highlighted.

environmental samples was for first time reported, and paraben contents up to 6 ng g^{-1} were found in soil and sediment samples. Due to the complexity of the samples and the lack of selectivity of the extraction, final analysis by HPLC–UV was not possible, and determinations required the use of MS–MS in tandem, which considerably increases the cost per sample preventing its use in routine analysis, this technique has been also used for the determination of parabens in sludge samples [18].

Molecular imprinting allows preparing polymeric sorbents with high selectivity for predetermined analytes, to be used in multiple areas of analytical chemistry. One of the most promising technical applications has been the use of molecularly imprinted polymers in SPE procedures (MISPE) for the selective extraction of organic compounds from complex sample extracts, such as biological and environmental samples, food, plants and tobacco [19]. Molecularly imprinted polymers (MIPs) preparation involves the interaction of a template molecule with an appropriate functional monomer to establish specific interactions. Later, removal of the template molecule from the resultant polymer leaves behind specific recognition sites for template and closely related compounds. Thus, the present work is focused on the synthesis of a MIP sorbent and further development of a selective MISPE procedure to permit HPLC–UV multiresidue analysis of parabens in solid environmental samples.

2. Experimental

2.1. Reagents

Methacrylic acid (MMA), 2,2′-azobis-2-metylbutyronitrile (AIMN) and divinylbenzene (80) (DVB) were obtained from Sigma–Aldrich Química (Madrid, Spain). Methylparaben (MeP) (CAS N° 99-76-3), ethylparaben (EtP) (CAS N° 120-47-8), isopropylparaben (iPrP) (CAS N° 4191-73-5), propylparaben (PrP) (CAS N° 94-13-3), benzylparaben (BzP) (CAS N° 94-18-8) and butylparaben (BuP) (CAS N° 94-26-8) were obtained from Sigma–Aldrich (St Louis, MO, USA) and HPLC grade organic solvents were supplied by Scharlab S.L. (Barcelona, Spain). Stock solutions of 1000, 100 and 10 μg ml^{-1} were prepared in acetonitrile and stored at −18 °C.

2.2. Instruments and materials

2.2.1. Extraction equipment

Glass columns (10 cm × 2 cm i.d.) were obtained from Scharlab S.L (Barcelona, Spain). Polyethylene frits (20 ml) were purchased from Supelco (Bellefonte, USA). The ultrasonic water bath (290 W, 50/60 Hz, S 40 H Elmasonic) was supplied by Elma (Singem, Germany). A vacuum manifold (Supelco Visiprep, Madrid, Spain) was employed to collect the extracts.

2.2.2. Polymer preparation and MISPE

The polymer preparation was carried out in a STR1 Roller Mixer located inside an incubator from Stuart (USA). Empty glass SPE cartridges with one teflon frit (6 ml) were obtained from Supelco (Bellefonte, PA, USA). Nylon filters (0.45 μm) were supplied by Jasco Analitica S.L (Madrid, Spain). A vacuum manifold (Supelco Visiprep, Madrid, Spain) was employed to collect the elution solvent.

2.2.3. HPLC–UV analysis

All measurements were performed using an Agilent 1100 LC instrument equipped with gradient pump, autosampler and programmable ultraviolet (UV) detector from Agilent Technologies (Wilmington, DE, USA). The chromatographic separation was carried out with Zorbax Eclipse XDB-C_8 HPLC column (4.6 mm × 150 mm, 5 μm) column from Agilent Technologies.

2.2.4. LC–MS/MS analysis

The confirmation measurements were carried out in a LC–MS/MS system from Agilent Technologies consisting of a 1200 LC instrument coupled to a triple quadrupole mass spectrometer (6410 TripleQuad). The chromatographic separation was carried

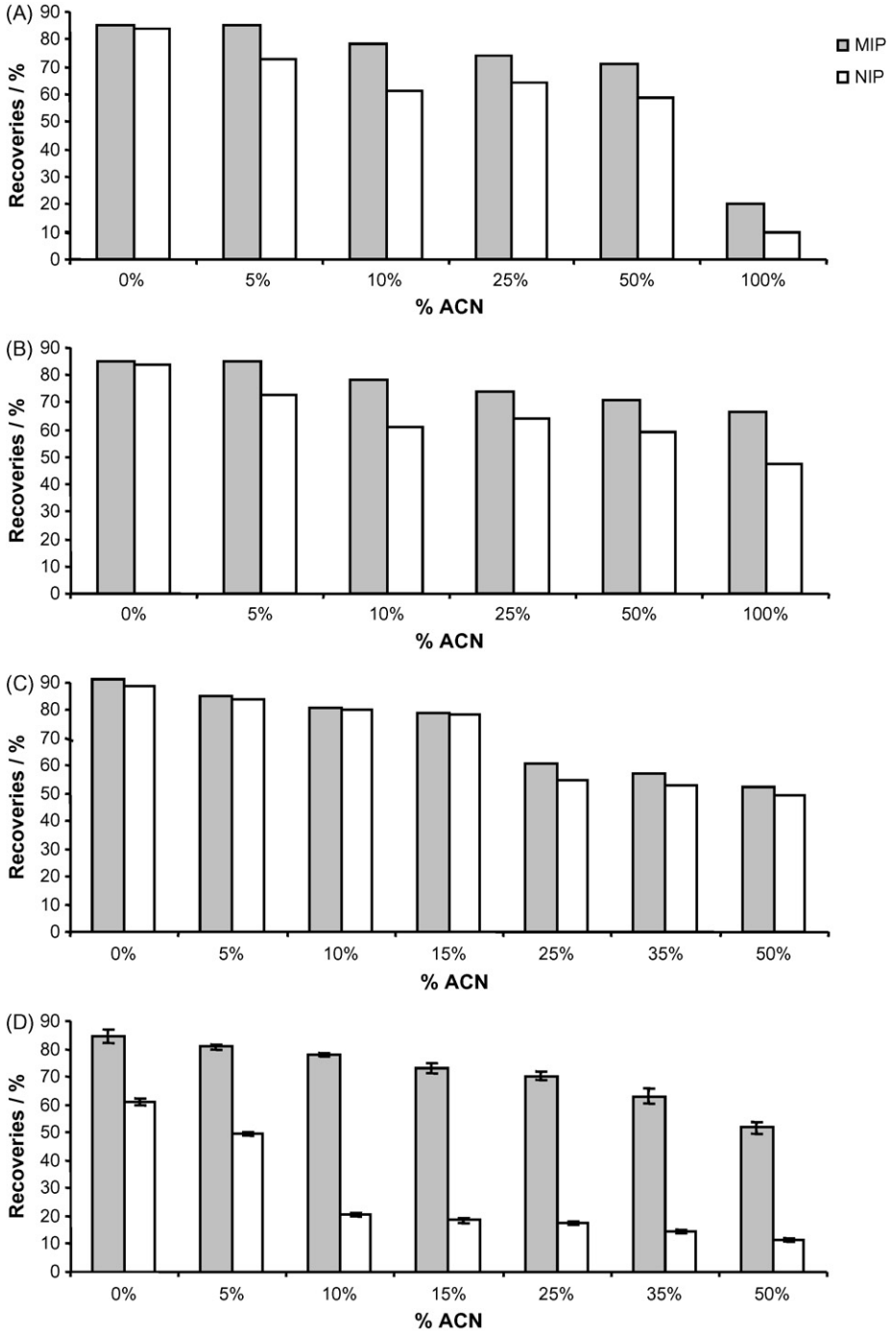


Fig. 2. MISPE optimization using A: P1 (VP and mixture 75:25 Tol:AcN), B: P2 (MAA and mixture 75:25 Tol:AcN), C: P3 (VP and Tol) and D: P4 (MAA and Tol).

out with a Zorbax Eclipse XDB-C_8 HPLC column (4.6 mm × 150 mm, 5 μm) column from Agilent Technologies.

2.3. Procedures

2.3.1. Polymer preparation

Different molecularly imprinted polymers were prepared by precipitation polymerization as follows: 0.14 mmol of template (BzP), 0.54 mmol of monomer (MAA or 4-VP), and 10 ml of different porogen (toluene and mixtures acetonitrile/toluene) were placed in a 15 ml glass tube (Table 1). The mixture was left in contact for 5 min and then 2.71 mmol of DVB and 0.2 mmol of AIMN were added. The tube was placed in a rotor oven at 60 °C to start the polymerization process. After 24 h the polymer particles obtained were air dried and the template was removed by Soxhlet extraction with a methanol: acetic acid mixture (1:1) for 12 h. After that procedure, no template leaking was detected in any of the polymers used in this work. Non-imprinted polymers (NIPs) were prepared following the same procedure but without the addition of the template molecule. All polymers have been prepared with the molar relation of 1:4:20 between template: monomer: cross-linker, which has been proved to be the best for the polymerization.

2.3.2. Sample preparation

Forest and agricultural soil samples were collected from different locations of Spain (Madrid and Badajoz). Sediments were

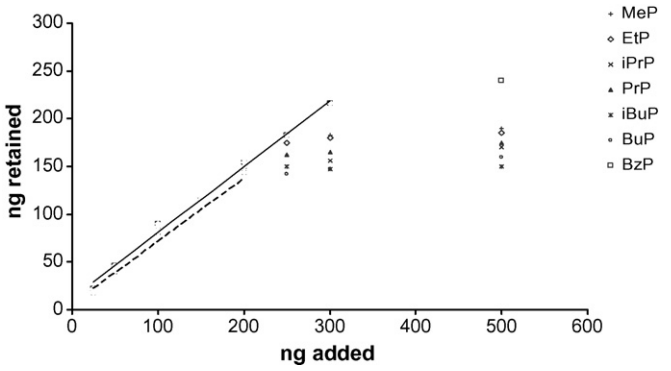


Fig. 3. Capacity study of P4 for selected parabens. Solid line: linear regression for template (BzP), dotted line: linear regression for BuP.

obtained from Ria Arousa and Ria Pontevedra (Galicia, Spain) and from Mediterranean Sea (Piles, Valencia, Spain).

Extraction of samples was carried out by ultrasonic assisted extraction in small columns following a procedure used in this laboratory for the analysis of parabens and other contaminants [17,20]. Polyethylene frits were placed at the end of each glass column and 15 g of sample was added. Subsequently, 8 ml of acetonitrile was added and the columns were immersed in the ultrasonic water bath to perform two consecutive extraction cycles of 15 min. After extraction, the columns were placed in a vacuum manifold and the extracts were collected.

2.3.3. MISPE

An amount (200 mg) of molecularly imprinted polymer was placed in a SPE cartridge and conditioned with 50 ml of methanol, 50 ml of acetonitrile and 50 ml of toluene. The conditioning step used between samples consisted of 2 × 6 ml of methanol (MeOH), 2 × 6 ml of acetonitrile (AcN), 2 × 6 ml of toluene (Tol) and 2 × 1 ml Tol. Next, sample was loaded in toluene (1 ml), and cartridges were washed with 1 × 1 ml of toluene and 1 × 1 ml of a mixture of Tol:AcN 90:10. The elution was achieved with 1 × 1 ml of AcN, 1 × 1 ml of MeOH and 5 × 1 ml of methanol containing 2.5% of acetic acid. The obtained extract was evaporated under nitrogen stream to dryness and redissolved in 0.5 ml of AcN:H_2O 50:50 for HPLC analysis.

2.3.4. High pressure liquid chromatography

HPLC separations were performed using a Zorbax Eclipse XDB-C_8 HPLC column (4.6 mm × 150 mm, 5 μm), injection volumes of 50 μl and an elution program as follows: (1) 60% A (water), 25% B (AcN) and 15% C (MeOH) during 10 min; (2) increase organic content up to 40% AcN and 30% MeOH in 10 min and (3) return to initial conditions in 3 min. For real samples it was necessary to add an extra step to clean the column with 80% B and 10% C. Flow rate was always 1.5 ml min^{-1} and the selected analytes were monitored at λ = 254 nm.

2.3.5. LC–MS

The confirmation with mass-spectroscopy was performed using a method with a Zorbax Eclipse XDB-C_8 HPLC column (4.6 mm × 150 mm, 5 μm) column, injection volumes of 10 μl and a gradient elution program with 5 mM ammonium formate in methanol (B) and 5 mM ammonium formate in water (A), 40–85% B in 10 min maintained 2 min, reduced to 80% in another 2 min, and to 78% in 1 min. LC–MS/MS was operated in the negative ionization mode and nitrogen was used as drying gas and was pumped into the interface at 9 l/min with a temperature of 350 °C. Nitrogen was also used as nebulizer gas at 50 p.s.i.

For each compound the optimized settings for fragmentor (cone voltage) and collision energy were adjusted by flow injection analysis. The deprotonated molecular ion (M-1) was chosen as parent ion and collision energy was optimized by selecting the more intensive ion as quantifier. A dwell time of 882 s $scan^{-1}$ was chosen for all compounds. The main MS/MS parameters for these compounds appear in a previous article [17].

Table 1
Conditions for the preparation of different BzP-molecularly imprinted polymers.

Polymer no.	Monomer	Porogen	Volume (ml)
Polymer 1	4-VP	ACN/Tol 75/25	10
Polymer 2	MAA	ACN/Tol 75/25	10
Polymer 3	4-VP	Tol	10
Polymer 4	MAA	Tol	10

3. Results and discussion

3.1. Polymer selection and MISPE

Precipitation polymerization is one of the most attractive and reliable methods available that allows the preparation of polymer particles [21–23]. Apart from the inherent advantage of avoiding crushing and sieving steps, this technique leads to a more homogeneous binding site distribution and higher performance in comparison to bulk polymerization. This method involves carrying out polymerization under high dilution conditions (<5%, w/v monomers/porogen) in a suitable solvent, therefore parameters such as monomers, solvents, cross-linking agent, temperature and stirring conditions have an important effect on particle morphology.

The mixture acetonitrile/toluene (75:25) has proven to be useful for the synthesis of DVB-80 based polymers with good performance [23]. On the other hand, both MAA and 4-VP monomers are expected to interact with the selected template (BzP) by hydrogen bonds. Thus, in a first approach, two different polymers were prepared using MAA (P1) or 4-VP (P2) and 75/25 acetonitrile/toluene porogenic mixture, as well as the corresponding non-imprinted polymers. Next, and in order to evaluate the presence of specific binding sites, rebinding experiments were carried out over 200 mg of each polymer in empty solid-phase extraction cartridges.

The mixture acetonitrile/toluene 75/25 was firstly tested as loading solvent, since specific interactions in MIPs use to be maximised in the solvent that has been used as porogen. However, in this case, the template molecule was poorly retained, and more than 60% of added BzP was recovered in the breakthrough fraction for both in P1 and P2. In contrast, quantitative retention (higher than 80%) could be achieved by performing loading in pure toluene, although in this case non-specific interactions were also very high in both cases. Subsequently, in order to disrupt non-specific interactions, various washing conditions with acetonitrile and mixtures of acetonitrile and methanol, with toluene were assayed, and relevant results are plotted in Fig. 2. The best results were obtained using AcN/Tol mixtures, where some differences between the MIPs and the corresponding NIPs could be observed, confirming the creation of selective binding sites for both MAA and VP based MIPs. However, such low differences were not useful for MISPE applications and thus P1 and P2 were finally discarded.

The use of toluene as porogen has proven to produce MIPs with improved selectivity for low polarity analytes [24]. Accordingly, polymers 3 (P3) and 4 (P4) were synthesized using 4-VP and MAA monomers, respectively, in pure toluene, and the success of the imprint effect was evaluated in the same way as P1 and P2. Fig. 2C and D shows the results obtained after loading 1 ml of 0.5 mg ml^{-1} of BzP in toluene and subsequent washing with toluene/acetonitrile mixtures in different percentages. As can be observed, the behaviour of P3 was quite similar to P1 and P2.

Although BzP was quantitative retained in the VP-MIP, it was not possible to ensure the presence of selective binding sites on it, since the washing conditions needed to remove non-specific interactions also disturbed selective recognition. In contrast, very satisfactory results were obtained in the evaluation of the MAA based polymer, in which a clear imprint effect could be observed. As can be seen in Fig. 2D, increasing the content of acetonitrile in the washing solution drastically reduced recoveries in the non-imprinted polymer, whereas BzP was selectively retained in the MIP, demonstrating the success of the imprinting process. Thus, Polymer 4 was selected for further development of a selective MISPE procedure for parabens.

According to data plotted in Fig. 2, the mixture Tol/AcN 90/10 was selected as optimum washing solution, and the volume was fixed in 1 ml. Washing steps consisting in 2×1 ml and 3×1 ml of this solution were also assayed, but a decrease in MIP recovery was observed. Concerning elution, quantitative elution was easily achieved with 1 ml methanol followed by 5×1 ml of 2.5% acetic acid in methanol.

The recognition of other parabens (MeP, EtP, iPrP, PrP, iBuP, BuP) in the optimized MISPE conditions was then evaluated. In a first study, aliquots of 1 ml of toluene containing 0.5 mg l^{-1} of each analyte were independently extracted both onto MIP and NIP cartridges. All the selected parabens were quantitatively recovered from the MIP while the non-specific interactions were lower than 30% in all cases. These results confirmed that the imprinted polymer was able to recognize the common structure of parabens (class selective), making in principle this material suitable for multiresidual analysis of parabens. In this sense, a second study focused on the determination of the capacity of the MIP was performed. Mixtures of all the studied parabens in concentrations ranging from 25 to 500 ng ml^{-1} were extracted onto the MIP and the corresponding binding curve for each analyte was obtained. Results are shown in Fig. 3. A linear relationship was obtained for all the analytes under study up to 200 ng ml^{-1}, with correlation coefficients higher than 0.994 in all cases. Regression curves of BuP and BzP are plotted as an example in that figure. In the case of the template, the linearity range is extended up to 300 ng ml^{-1}. Although the obtained capacity of the polymer was not very high, it is enough to be used in environmental solid sample analysis (soils and sediments) where, as it was previously reported, the concentration of parabens is in the low ng g^{-1} level [17].

3.2. Analytical performance in real samples

To determine the potential of this polymer for environmental applications, it was evaluated for the clean-up of soil and sediment extracts containing all the studied parabens at concentration levels in the range of those found in real samples. Extracts were obtained by ultrasonic assisted extraction as described in Section 2. Both non-spiked and spiked samples at 0.5 and 5 ng g^{-1} concentration levels were prepared and analysed by HPLC–UV with and without performing MISPE, and the results obtained for soils and sediments are illustrated in Figs. 4 and 5, respectively. As can be seen, analysis

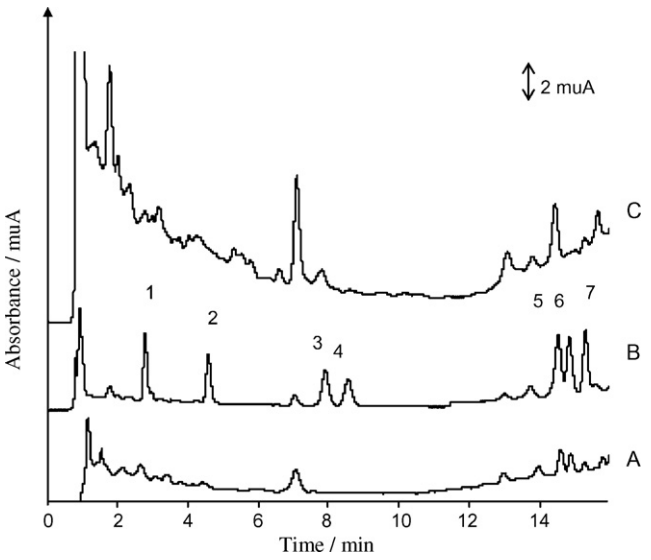


Fig. 4. Chromatograms obtained in the analysis of soil samples. A: MISPE of a non-spiked sample; B: MISPE of a sample spiked with 5 ng g^{-1} of each compound; C: Non-spiked sample without MISPE. Chromatographic conditions: see Section 2. Peak identification: (1) MeP, (2) EtP, (3) iPrP, (4) PrP, (5) iBuP, (6) BuP and (7) BzP.

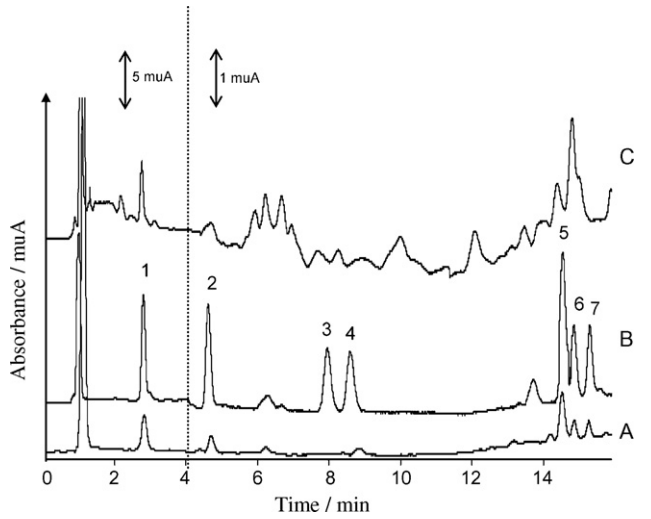


Fig. 5. Chromatograms obtained in the analysis of sediments samples. A: MISPE of a non-spiked sample; B: MISPE of a sample spiked with 25 ng g^{-1} of MeP and 5 ng g^{-1} of EtP, iPrP, PrP, iBuP, BuP and BzP; C: Non-spiked sample without MISPE. Chromatographic conditions: see Section 2. Peak identification: (1) MeP, (2) EtP, (3) iPrP, (4) PrP, (5) iBuP, (6) BuP and (7) BzP.

of selected parabens without MISPE was almost impossible, especially in the case of soil samples. In fact, the different parabens that were found in these samples could only be detected after MISPE. The developed procedure allows to selectively retain parabens in

Table 2
Range of linearity, R^2, recoveries (%R), detection limits (LOD) and quantification limits (LOQ) of parabens after MISPE of soil sample extracts on BzP-imprinted polymer.

	Linearity (ng g^{-1})	R^2	%R^a	RSD	%R^b	RSD	LOD (ng g^{-1})	LOQ (ng g^{-1})
MeP	0.5–25	0.996	83.2	5.3	85.3	4.2	0.33	1.12
EtP	0.5–25	0.995	86.8	5.2	88.1	3.2	0.21	0.69
iPrP	0.5–25	0.996	85.5	2.9	89.2	1.2	0.16	0.53
PrP	0.5–25	0.999	84.5	2.5	86.2	2.4	0.17	0.54
iBuP	0.5–25	0.995	82	3.4	84.1	2.1	0.27	0.89
BuP	0.5–25	0.999	86.4	7.2	90.7	5.2	0.30	1.02
BzP	0.5–25	0.993	80.2	2.4	89.8	1.7	0.29	0.95

[a] Spiked concentration of 0.5 ng g^{-1} for each compound.
[b] Spiked concentration of 5 ng g^{-1} for each compound.

Table 3
Range of linearity, R^2, recoveries (%R), detection limits (LOD) and quantification limits (LOQ) of parabens after MISPE of sediment sample extracts on BzP-imprinted polymer.

	Linearity (ng g^{-1})	R^2	%R[a]	RSD	%R[b]	RSD	LOD (ng g^{-1})	LOQ (ng g^{-1})
MeP	0.5–25	0.998	88.0	3.2	93.3	2.1	0.27	0.89
EtP	0.5–25	0.998	85.5	4.1	97.1	5.0	0.20	0.65
iPrP	0.5–25	0.999	87.5	2.4	92.0	3.7	0.24	0.81
PrP	0.5–25	0.995	87.4	2.2	95.5	3.2	0.23	0.77
iBuP	0.5–25	0.997	87.2	3.7	91.4	2.3	0.24	0.79
BuP	0.5–25	0.996	85.6	2.5	85.3	3.7	0.16	0.53
BzP	0.5–25	0.996	88.1	3.2	90.2	3.0	0.18	0.61

[a] Spiked concentration of 0.5 ng g^{-1} for each compound.
[b] Spiked concentration of 5 ng g^{-1} for each compound.

Table 4
Levels of MeP, EtP, iPrP, PrP, iBuP, BuP and BuP determined in forest and agricultural soils and in sediments.

	MeP		EtP		iPrP		PrP		iBuP		BuP		BzP	
	ng g^{-1}	*SD*	ng g^{-1}	*SD*	ng g^{-1}	*SD*	ng g^{-1}	*SD*	ng g^{-1}	*SD*	ng g^{-1}	*SD*	ng g^{-1}	*SD*
1	11.50	0.57	0.90	0.05	<LOQ		0.67	0.05	2.68	0.09	0.97	0.12	0.66	0.08
2	6.05	0.49	0.80	0.06	<LOQ		0.63	0.04	0.87	0.04	1.40	0.12	2.12	0.16
3	10.85	0.21	6.70	0.42	<LOQ		<LOQ		2.80	0.28	1.85	0.21	<LOQ	
4	2.55	0.35	1.80	0.28	0.85	0.21	1.95	0.49	0.70	0.09	1.10	0.08	<LOQ	
5	1.60	0.21	<LOQ		<LOQ		<LOQ		2.30	0.10	1.87	0.19	0.80	0.05
6	<LOQ		<LOQ		<LOQ		<LOQ		<LOQ		1.55	0.11	<LOQ	
7	2.01	0.06	1.00	0.13	<LOQ		1.97	0.09	<LOQ		<LOQ		<LOQ	
8	1.51	0.04	<LOQ		<LOQ		1.27	0.07	<LOQ		<LOQ		1.21	0.06
9	<LOQ		<LOQ		<LOQ		<LOQ		1.04	0.11	<LOQ		<LOQ	

1—Sediments from The Mediterranean sea at Piles (Valencia, Spain); 2—sediments from Ria Arousa (Galicia, Spain); 3—sediments from Ria Pontevedra (Galicia, Spain); 4–8—agricultural soils from Madrid (Spain); 9—forest soil from Badajoz (Extremadura, Spain).

the MIP, whereas matrix compounds were washed out from the cartridge. In that way, the obtained chromatograms were almost free of interferences allowing to detect the studied analytes in these samples. The UV spectra of the obtained peaks were recorded and compared with the corresponding standards and match factors higher than 950 confirming the presence of parabens in the studied soil and sediment samples.

Tables 2 and 3 summarize the results obtained in the analysis of spiked samples together with data derived from the analytical performance study. As can be seen, mean quantitative recoveries were obtained for both levels of concentration studied with RSDs values lower than 8% in al cases. Internal calibrations curves with matrix matched standards were also obtained for the range 0.5–25 ng g^{-1} for each analyte using the selected soil and sediment samples. All calibrations were linear with regression coefficients higher than 0.993. Also, comparison of the obtained results with those of an external calibration in pure solvents proved the absence of matrix effect for all the analytes studied. The LODs and LOQs were calculated as 3 and 10 times respectively the standard deviation of the lowest point of the internal calibration curve and are also included in Tables 2 and 3. The obtained values were low enough to determine the selected compounds at concentration levels required for environmental studies, and they were one order of magnitude lower than those obtained without the MISPE procedure.

3.3. Analysis of soil and sediments samples

Finally, the developed procedure was applied to the determination of paraben contents in soil and sediment samples from different locations. Table 4 summarizes the analysed samples and the concentrations encountered for the different parabens. As can be seen, residues of parabens were found in all the analysed samples, and sediment samples had in general higher contents of parabens than soil samples. Among them, it is remarkable the highest content for MeP that was found in sediments collected in Piles (Valencia) beach of the Mediterranean coast of Spain. This result can be attributed to the intensive use of sun creams in this area, which, as mentioned in Section 1, usually contain parabens and MeP is the most frequently used additive.

It is important to stress that all samples were further analysed by a LC–MS–MS confirmatory method previously developed in our laboratory [17]. Confirmation of the results obtained by HPLC–UV could be done in all cases, proving the selectivity of the MIP for extraction of parabens in sediment and soil samples. Therefore, the developed MISPE–HPLC–UV method can be considered a clear low cost alternative to LC–MS–MS for multiresidue monitoring of parabens in the selected environmental solid samples.

4. Conclusions

In this work, a selective MISPE procedure for multiresidue analysis of parabens in solid environmental samples has been successfully developed. The optimized MISPE protocol allows the quantitative determination of parabens in soil and sediment samples at the concentration levels that have been found in the environment.

Several soil and sediments samples from different parts of Spain were analysed and parabens were detected in all of the samples but in general, at trace levels. The highest concentration found belongs to MeP in sediments from the Mediterranean coast, which is not really strange because this preservative appears in the composition of the majority of the sun lotions.

Acknowledgements

Authors wish to thank J. Otero-Román from University of Santiago de Compostela for providing sediment samples, INIA for a predoctoral fellowship (L. Núñez) and Spanish Ministry of Science and Innovation (RTA 2008-00040) for financial support.

References

[1] L. Labat, E. Kummer, P. Dallet, J.P. Dubost, J. Pharm. Biomed. Anal. 23 (2000) 763.
[2] J.K. Lokhnauth, N.H. Snow, Anal. Chem. 77 (2005) 5938.

[3] B. Saad, M.F. Bari, M.I. Saleh, K. Ahmad, M.K.M. Talib, J. Chromatogr. A 1073 (2005) 393.
[4] F.F. Cantwell, Anal. Chem. 48 (1976) 1854.
[5] E.J. Routledge, J. Parker, J. Odum, J. Ashby, J.P. Sumpter, Toxicol. Appl. Pharmacol. 153 (1998) 12.
[6] R. Golden, J. Gandy, G. Vollmer, Crit. Rev. Toxicol. 35 (2005) 435.
[7] M. Zirwas, J. Moennich, Dermatitis 20 (2009) 106.
[8] R.S. Tavares, F.C. Martins, P.J. Oliveira, J. Ramalho-Santos, F.P. Peixoto, Reprod. Toxicol. 27 (2009) 1.
[9] P.D. Darbre, A. Aljarrah, W.R. Miller, N.G. Coldham, M.J. Sauer, G.S. Pope, J. Appl. Toxicol. 24 (2004) 5.
[10] A. Natsch, Personal care product composition e.g. creams, salves, lotions, soaps, shampoos, balm, comprises benzaldehyde or benzaldehyde-derivative compound, fragrant acid and a cosmetically-acceptable base, patent number: WO2009000097-A2, Patent Assignee(s) and Codes(s): GIVAUDAN SA. (GIVA-C).
[11] A. Themens, Cosmetic composition in water-in-oil emulsion form, useful for make-up/care of keratinous fiber, preferably skin, comprises water, hydrocarbon surfactant, charge, and hydroxy compound comprising e.g. propylene glycol, patent number: FR2917609-A1, Patent Assignee(s) and Codes(s): L'OREAL SA. (OREA-C).
[12] The Council Directive 76/768/EC, 1976, http://www.leffingwell.com/cosmetic/vol_1en.pdf.
[13] Q. Zhang, M. Lian, L. Liu, H. Cui, Anal. Chim. Acta 537 (2005) 31.
[14] H.-Y. Shen, H.-L. Jiang, H.-L. Mao, G. Pan, L. Zhou, Y.-F. Cao, J. Sep. Sci. 30 (2007) 48.
[15] R.A. Rudel, D.E. Camann, J.D. Spengler, L.R. Korn, J.G. Brody, Environ. Sci. Technol. 37 (2003) 4543.
[16] P. Canosa, I. Rodríguez, E. Rubí, M.H. Bollaín, R. Cela, J. Chromatogr. A 1124 (2006) 3.
[17] L. Nuñez, J.L. Tadeo, A.I.G. Valcarcel, E. Turiel, J. Chromatogr. A 1214 (2008) 178.
[18] A. Nieto, F. Borrull, R.M. Marcé, E. Pocurull, J. Chromatogr. A 1216 (2009) 5619.
[19] S.-P. Wang, C.-L. Chang, Anal. Chim. Acta 377 (1998) 85.
[20] L. Nuñez, E. Turiel, J.L. Tadeo, J. Chromatogr. A 1146 (2007) 157.
[21] L. Ye, P.A.G. Cormack, K. Mosbach, Anal. Commun. 36 (1999) 35.
[22] F.G. Tamayo, J.L. Casillas, A. Martín-Esteban, Anal. Chim. Acta 482 (2003) 165.
[23] J. Wang, P.A.G. Cormack, D.C. Sherrington, E. Khoshdel, Angew. Chem. 115 (2003) 5494.
[24] L. Nuñez, E. Turiel, A. Martín-Esteban, J.L. Tadeo, J. Sep. Sci. 31 (2008) 2492.

Talanta 80 (2010) 1789–1798

Contents lists available at ScienceDirect

Talanta

journal homepage: www.elsevier.com/locate/talanta

A Wireless Sensor Network approach for distributed in-line chemical analysis of water

J.V. Capella [b], A. Bonastre [b], R. Ors [b], M. Peris [a,*]

[a] Departamento de Química, Universidad Politécnica de Valencia, 46071 Valencia, Spain
[b] Departamento de Informática de Sistemas y Computadores, Universidad Politécnica de Valencia, 46071 Valencia, Spain

ARTICLE INFO

Article history:
Received 10 June 2009
Received in revised form
26 September 2009
Accepted 8 October 2009
Available online 14 October 2009

Keywords:
Wireless Sensor Networks
In-line chemical analysis
Water
Distributed system

ABSTRACT

In this work we propose the implementation of a distributed system based on a Wireless Sensor Network for the control of a chemical analysis system for fresh water. This implementation is presented by describing the nodes that form the distributed system, the communication system by wireless networks, control strategies, and so on.

Nitrate, ammonium, and chloride are measured in-line using appropriate ion selective electrodes (ISEs), the results obtained being compared with those provided by the corresponding reference methods. Recovery analyses with ISEs and standard methods, study of interferences, and evaluation of major sensor features have also been carried out.

The communication among the nodes that form the distributed system is implemented by means of the utilization of proprietary wireless networks, and secondary data transmission services (GSM or GPRS) provided by a mobile telephone operator. The information is processed, integrated and stored in a control center. These data can be retrieved – through the Internet – so as to know the real-time system status and its evolution.

© 2009 Elsevier B.V. All rights reserved.

1. Introduction

Water quality monitoring is usually carried out off-line in the laboratory. This is a cumbersome process and often does not provide the required spatial discrimination and/or the large sets of data necessary to describe the temporal evolution of the parameters of interest. It is also known that during storage the integrity of the sample may not be preserved, due to a number of effects that include biological activity and matrix effects, even when correct sample handling protocols are strictly followed. An alternative approach consists in performing the measurements at the location of interest (in-line analysis), since this is probably the best way to overcome a major problem facing aquatic analytical chemists, i.e., how to maintain the sample in its original state during sampling and handling, without stimulating any of the very dynamic chemical, biological and physical processes which may continue after sample collection [1].

The major advantages of in-line analysis compared with the classical off-line procedures are the following: (a) elimination of contaminants due to sample handling, i.e., no or minimum sample transformation; (b) minimization of the overall cost of data acquisition (in particular, due to a reduction of time for sampling, handling and analysis of the sample); (c) possibility of real-time analysis, allowing the rapid detection of pollutants (e.g., monitoring of industrial wastewater or water quality in water treatment plants); (d) ability to obtain detailed spatial and temporal data sets of complete ecosystems (lakes, aquifers, etc.) and (e) possibility of performing measurements in locations which are difficult to access (deep lakes or oceans).

There has been an extensive effort to design chemical sensors and analyzers that are capable of operating *in situ*. Much of this work has been summarized in a monograph on chemical sensor systems for aquatic sciences, which describes a variety of continuous flow analyzers, electrochemical sensors and optical sensors for in-line measurements of dissolved chemical species [2]. In this sense, the constant development of new sensors with increasingly better features undoubtedly permits to minimize the sometimes unavoidable problem of interferences from other species occurring in the analyzed water.

Among the *in situ* chemical sensors, ion selective electrodes (ISEs) are able to continuously monitor a system [3]; this is invaluable when it is necessary to use large sets of data to calibrate mathematical models that describe the behavior of complex ecosystems and when the sample matrix can be altered by sampling and storage and/or by inflow of nutrients or elements from various sources (such as, for example, wastewater and agricul-

* Corresponding author.
E-mail address: mperist@qim.upv.es (M. Peris).

0039-9140/$ – see front matter © 2009 Elsevier B.V. All rights reserved.
doi:10.1016/j.talanta.2009.10.025

ture). In this work, we analyze nitrate, ammonium, and chloride concentration using the corresponding ion selective electrodes (described in Section 3.1) placed *in situ* in a suitable analysis probe.

Nitrate and ammonium are important because they are the major forms of nitrogen which are directly assimilated by plants and organisms, the former being one of the most common contaminants of groundwater, originating mainly from agricultural fertilizer application and release of sewage. Chloride is one of the major inorganic anions in water and wastewater. A high value of chloride may indicate the inflow of wastewater or industrial effluents into the river. The chloride concentration is higher in wastewater than in raw water because sodium chloride is a common constituent of the diet and passes unchanged through the digestive system.

The monitoring of these three chemical species is therefore very important in rivers, lakes, etc. In this sense, nowadays there are commercial systems based on great-size buoys that are able to carry out in-line measurements in aquatic systems, although they are somewhat expensive and have a limited communication capability [4].

Nevertheless, the present work represents a step forward in in-line chemical monitoring of water and wastewater, since it proposes an automatic system, based on Wireless Sensor Networks, that allows a real-time, economic and efficient monitoring of the wastewater generated by any type of use [5,6].

In our case this system arises from the need at both institutional and private level of controlling the quality of the water spilt into Lake Albufera, which is located a few kilometers away from the city of Valencia (eastern Spain), due to the presence of many potential sources of pollution in the surroundings.

For this purpose, an automatic distributed system [7] of chemical analysis is proposed that replaces the current system [8] of analysis and control that usually operates in a manual and decentralized way, so that it could obtain a faster and more effective response against the different problems of pollution that may occur. However, the fact that the sampling points are physically distributed implies the need to place a set of devices, called 'sensor nodes' from now on, at each of these points. The set of these nodes, interconnected by means of a communication network and supervised from a 'control center', can be considered a distributed system of acquisition of information.

Among the most important requirements of this system it can be remarked the need that the functioning of the nodes [9] be as automatic and intelligent as possible, which will allow us to obtain two significant advantages. First of all, the possibility of self-diagnosis will permit to reduce the visits of maintenance of the nodes, then being reducing to a minimum. The information monitored by each node is sent to the control node for its storage and handling. In this sense, the utilization of a private communications network allows to establish an optimal system for the information exchange among all the system elements without any additional expense, a Wireless Sensor Network being used for this purpose [10]. Only in case of emergency or upon user's request, a public telephone network will be employed, thus drastically reducing the use, and therefore the investment, of the system operation.

The aforementioned self-diagnosis does not exclude the possibility of performing a centralized diagnosis, which can be carried out by means of analyses of the obtained data. This would further improve the reliability of the results.

We try to achieve this intelligent and robust functioning without excessively increasing the cost of the nodes; another purpose is also to keep the simplicity in their design, but with the possibility of automatically updating the program depending on the need of the moment. Additionally, the nodes should be as autonomous as possible [11].

2. Why a Wireless Sensor Network?

In the last few years, huge advances have taken place in the field of electronic circuits, as well as in that of wireless communications [5]. They have opened an interesting research line with the development of low-energy, cheap electronic devices that are able to carry out data acquisition tasks; these data are then processed and the results transmitted to a process center for their storage and further study. This research field is the so-called Wireless Sensor Networks (WSNs) [5,12], which makes low consumption prevail over bandwidth and coverage, hence achieving to cover long distances thanks to the application of multi-hop communications [13,14]. Moreover, these networks offer a greater fault tolerance and provide interesting features in terms of real-time, composability, and scalability [15].

On the other hand, important advances have also been obtained in the field of transducers [16], which allows for the development of new devices for the detection and measurement of chemical and physical properties in an easy and inexpensive way. Therefore, they replace the traditional techniques since they are usually slower, more expensive, and more difficult to be automated. These new transducers, mainly in solid state (ion selective electrodes, ISEs) have provided important advantages such as easiness, lower size, precision, easy automation, and low-cost. ISEs are membrane electrodes that respond selectively to ions in solution in the presence of others. The nature of the membrane determines the selectivity of the electrode.

In this paper, and taking into account the aforementioned advances, a new approach in the field of Chemical Wireless Sensor Networks (CWSNs) is proposed. Although this is an important topic that inherits the benefits from WSN technology (it being able to be used as in-line chemical tool for gathering sensor data in real-time with an spatio-temporal resolution), currently there is still limited amount of work describing fully operational CWSNs. Anyway, some interesting contributions have been described in the monograph edited by Ilyas and Mahgoub [17]. Special mention should also be made to the recent work of Okolisa [18], who has created an integrated wireless network of sensors for measuring the concentration of several chemical species in water and wastewater. However, our present work provides additional, interesting features such as the possibility of real-time analysis of different space points; for each one of them, the spatial distribution of the analyzed parameters, as well as its variation with the passing of time, is obtained. In many cases, this information is as important as the own value of the parameters.

Given the low price of the sensor nodes, it is possible – with no heavy expenses – to display a great amount of nodes to cover wide areas and/or decrease the distance among them, thus increasing the precision of the spatial distribution function of the analyzed parameters. Furthermore, unlike in the case of other solutions based on phone systems, the cost of the communications disappears-except in the case of long distances and warnings to cell phones-due to the use of private wireless networks.

Finally, we believe that the proposed model has a promising future thanks to the continuous improving of WSN technologies as well as those of transducers, which opens a wide way of new applications.

3. System description

The system architecture, as shown in Fig. 1, consists of three major subsystems:

(a) Data acquisition subsystem. It is formed by a set of transducers that are in charge of getting information on the different parameters to be analyzed.

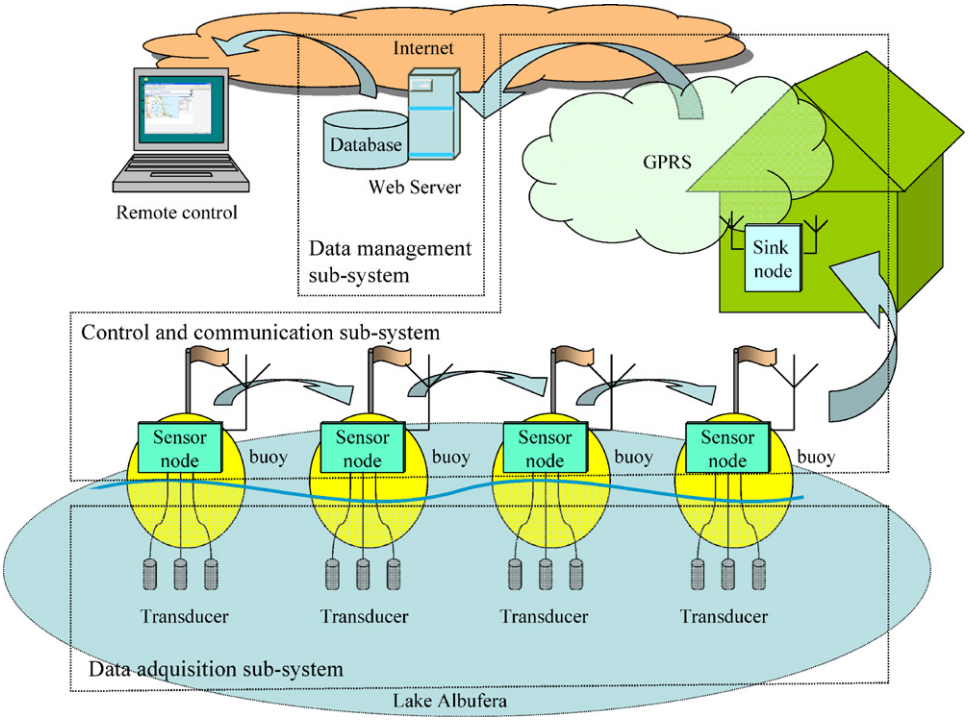


Fig. 1. System architecture.

(b) Control and communication subsystem. It is the sensor network itself, which controls the chemical analysis subsystem, collects the information that it provides, and carries it to the data management subsystem.
(c) Data management subsystem. It is in charge of receiving the information from the control and communication subsystem, which is then handled and stored. This information can be accessed through the Internet, and it can generate the appropriate warnings.

3.1. Data acquisition subsystem

Nitrate, ammonium, and chloride are monitored in-line. They are measured using three homemade ISEs incorporated in a probe (the sensor node). These ISEs were prepared and conditioned following some of the guidelines provided by the literature [16].

The probe nitrate ISE employs a silver/silver chloride wire electrode in a custom filling solution. The internal solution is separated from the sample medium by a polyvinylchloride (PVC) membrane, which selectively interacts with NO_3^- ions. The probe ammonium ISE makes use of a silver/silver chloride (Ag/AgCl) wire electrode in a custom filling solution. A nonactin membrane separates the internal solution from the sample medium and this membrane selectively interacts with ammonium ions. Finally, the probe chloride ISE utilizes a solid state poly-crystalline membrane attached to a conductive wire. Details of membrane preparation are given in Section 5.5.

For all three ions, when the probe is immersed in water, a potential is established across the membrane that depends on the relative amounts of analyte in the medium, this potential being read relative to the reference electrode of the probe. Double-junction reference electrodes have been used in all instances, each sensor having its own reference electrode.

It should be remarked that the control of all transducers is carried out through the microcontroller node itself, their tension values being measured through analog inputs; the acquired value is then interpreted and so are the suitable calibration mechanisms.

3.2. Control and communication subsystem

Fig. 1 shows that this subsystem is formed by a set of sensor nodes and a sink node, all of them interconnected by means of a private wireless network. On the other hand, the sink node is communicated with the data management system through a public network.

3.2.1. Sensor node

Each one of these nodes, as shown in Fig. 2, is based on a microcontroller that (a) controls the different aforementioned transducers, and (b) has a communication module and a power

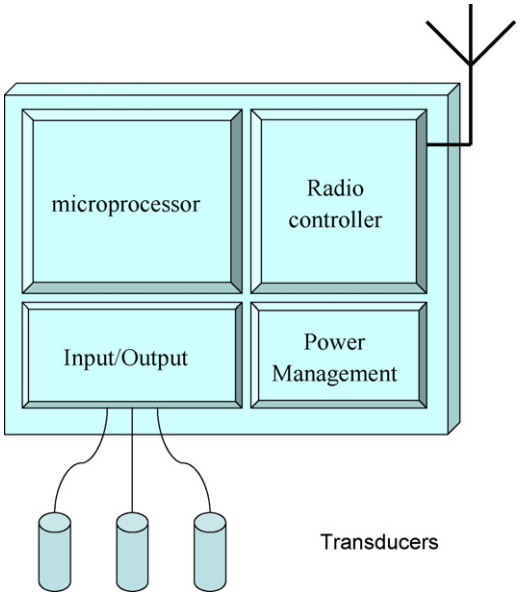


Fig. 2. Sensor node structure.

mode. Everything is located inside a small-size, inexpensive buoy.

We have chosen the CC1110 microcontroller system (Texas Instruments, Inc., TX, USA) – based on I'8051 (Intel Corporation, CA, USA) – due to their excellent features for WSN implementation, namely: low price and consumption, and the availability of a chip-integrated radio circuit for communications in the ISM 800/900 MHz band, as well as a suitable number of I/O lines for the interconnection of the utilized transducers. On the other hand, the potential is (after the appropriate amplification) being measured through analog inputs that the microcontroller has to connect with its own internal A/D converter. Finally, a typical differential amplifier has been used, whose input impedance is similar to that of the electrode in order to achieve a correct impedance adaptation.

It should be remarked that these nodes have an autonomous power supply. A set of rechargeable batteries along with a specific, intelligent system of charge control and management make them able to provide with enough power to ensure a nearly perpetual supply. Energy management is complemented with an RTC (real-time clock), which allows the sensor to work in a low-energy mode during a certain period of time, thus saving energy in a significant way [10].

The power supply of the node is then based on the use – among other components – of lithium-ion batteries, which are capable of storing 10 W. Since the processor consumption is negligible, that of each electrode is around 0.2 W per measurement. Thus, taking into account the number of electrodes utilized and the number of measurements taken every day, the whole network could be working for 16 days without power supply. If a longer working time is required, each buoy has been equipped with a 50 mm × 70 mm solar panel that can provide up to 0.75 W/h. It can be noticed that, in most cases, nodes work by directly using the energy captured by the solar panel; nevertheless, under no-sun conditions batteries are employed to ensure an uninterrupted service. On the other hand, if the level of these batteries falls below a certain threshold (in our case when the charge is less than 90%), batteries are recharged provided that the environmental conditions allow for it. It is important to remark that this recharging process should not begin if the intensity provided by the panel is not enough, since it could result in battery malfunction.

Thanks to this mechanism, and considering the possibility of 10,000 battery recharging processes and an average of 65% sunny days (usual in the region of Lake Albufera), the operational lifetime of the system could exceed 10 years. In the absence of solar panels we estimate that this figure could decrease 10,000 times, although we have not been able to check it for obvious reasons.

3.2.2. Sink node

This node is in charge of receiving data from all the sensor nodes of the network, performing an intelligent processing of them, and resending them to the data management subsystem. Furthermore, it carries out key tasks in the wireless network management, such as the creation of its topology, the diagnosis on the status of the sensor nodes, and the recovery mechanisms in case of malfunctions. Finally, from the point of view of the data, it is an interesting passing route between local and remote communications, since it can carry out different treatments (filtration, compression, summary, and aggregation) on the data received before resending them.

As shown in Fig. 3, an ARM9 microcontroller has been used for its implementation, to which the following devices have been connected:

- An RF module in the ISM 800/900 MHz band: it is based on a CC1101 chip, and connected by SPI.
- A GSM/GPRS [19] communication module based on an integrated TELIT GM 862 [20] connected to the microcontroller by means of an RS232 link. Nowadays, a new WiMax communication system is being set up to replace the GSM/GPRS, which will provide a communication system without any cost for amount of data nor for connection time [21].
- A supply module, capable of getting the energy from either the mains supply or solar panels (when the former is not available).

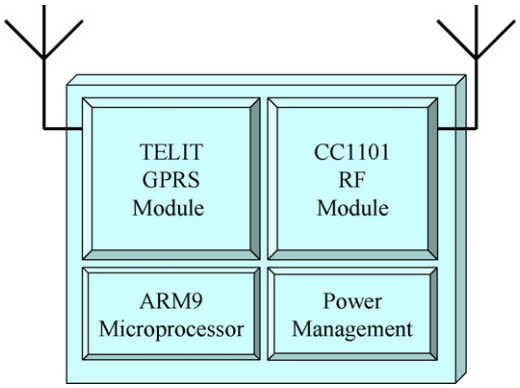


Fig. 3. Sink node structure.

Finally, this sink node is located in a small hut securely anchored on the floor.

3.3. Data management subsystem

The data management subsystem is based on a server with a PC-architecture equipped with an uninterruptible power supply (UPS), and is located at our university (Polytechnic University of Valencia, Valencia, Spain) and connected to the Internet. The following software is then run:

- A web server. It is based on a GNU software (Apache). This server has two major functions: on one hand, it permits the sink node to introduce the data on the database, but it also contains the reference pages that allows for getting (from this database) reports, statistics, and graphics. With the appropriate permissions, these pages can be accessed from any device (PC, Laptop, PDA, SmartPhone, and so on) connected to the Internet, by using a standard web browser. Furthermore, it is also possible – by means of these pages – to modify the working parameters of the system.
- Database manager system. It is also based on GNU (MySQL) software; it contains all acquired data recorded so far.
- Program of management and supervision of the information. This homemade software is in charge of analyzing the data received and checking their coherence, as well as of warning generation if necessary.

A detailed description of the functioning of the system is shown in the following section.

4. How the system works

In order to carry out the distributed analysis of the water, the system periodically takes measurements at the different points where the sensor nodes are located, this information being led to the sink node, which introduces it in the remote database. The different data can then be consulted in real-time as well as those coming from previous times. The process of all these information flow will now be described.

4.1. System initialization

In the establishment phase, when a node is connected for the first time, it looks for all other nodes within reach. If in this search the sink node is found, an association between each other is established; otherwise, the association occurs with that closest to the sink node. In this way, from the beginning this association gives rise to a tree structure (routing tree) [9] whose bottom part is the sink node, which provides the node sensors with the working parameters, thus making the nodes enter the normal operation mode (low consumption) until the timer begins to work. The sink node remains waiting for the data transmission from the sensor nodes.

4.2. Data gathering

Each sensor node – when its timer shows it – gets the data from the transducers, and builds a frame that contains the obtained measurements, a node identifier, and a time stamp. This frame is transmitted towards its parent node and then retransmitted again following the routing tree until the sink node is reached. This one, after handling the information, introduces it in the server database by means of the GPRS link. These mechanisms will be described now.

4.2.1. Functioning at node level

Timing is in charge of scheduling the chemical analyses, following the established guidelines, which can be configured by the user in advance as well as in running time in a remote way. This timing is achieved thanks to the real-time clock (RTC) included in the microcontroller, which also permits synchronization functions among nodes. It should be remarked that this scheduling can be modified by the same node according to the data interpretation.

As regards data acquisition, an ion selective electrode measures the potential against a stable reference electrode of constant potential. The potential difference between the two electrodes will depend upon the activity of the specific ion in solution. This potential difference is conveniently amplified and read by means of an internal A/D converter (12 bits, with an impedance of 192 kΩ, and a time conversion of 132 μs for 12 bits). This value provides the concentration of the ion in solution, i.e. the analyzed parameter.

Once the measurement is obtained, the sensor node will interpret it, considering – in a logical way – if the value is as expected. This interpretation is based on predetermined values, for instance, (a) the working range of the sensor in previous values of the parameter, (b) the evaluation of the variation from the last measurements, and (c) the values from other sensors with which a known relationship exists.

In case the obtained measurements do not comply with the aforementioned logical checking, the node may decide to repeat the measurement (if enough energy is available); if the result obtained is confirmed, it is sent to the sink node.

This process is carried out for each one of the parameters to be analyzed by the sensor node. After taking all the measurements, they are communicated.

4.2.2. Communications in the WSN

For the data transmission to the sink node, we have implemented a routing-tree-based protocol. In this algorithm, each node sends data (either of its own or from its sons) towards the sink node through its parent node, and the process goes on in this way until the data reach the sink node. The communications from the sink node to the sensor nodes follow the opposite direction. In this protocol, and for the tree maintenance, the necessary mechanisms have been implemented, nodes with malfunction problems being detected; in such cases, the corresponding data are re-sent through another alternative parent node.

Another feature of the developed protocol is that, most of the time, nodes remain in a stand-by mode, thus ensuring a longer system working although it is supplied by solar panels, even in cloudy days or at night. For this purpose, a reliable system based on RTC has been required so as to allow for the nodes to return to their normal activity in a controlled way.

4.2.3. Sink node working

Once the information from a sensor node has reached the sink node, this one manages a first data evaluation; in this way, and according to the parameters, threshold values, and methods provided by the user (all of them modifiable in a remote way at run time, a data management is carried out before the transmission). Although several treatments (filtration, compression, addition, and so on) can be performed on the received data before being re-sent, in this application we have chosen a single aggregation in order to minimize the number of GPRS messages.

Finally, the sink node utilizes TCP/IP to transfer – through the GPRS module – the data to the server, so that this one stores them in the database. The protocol used is HTTPS, specifically, the POST command, calling for a PHP page [22] available in the server.

4.2.4. Database update

The last step in the data gathering is their introduction into the database. For this purpose, the recalled PHP page opens a link with the SQL (structured query language) server and inserts the data contained in the POST method into the corresponding fields of the SQL database, which is managed by the MySQL software. This architecture, in spite of giving rise to a certain delay in the data flow, permits the possibility of locating the database in a server other than the web server. In the case of our implementation, both Apache [23] and MySQL are situated in the same computer.

4.3. Data management

The previous PHP program also performs a continuous monitoring on the received data by applying the user's guidelines. If necessary, an alarm must be generated. This may be reported (a) through the Internet (e-mail, Microsoft Network—MSN, etc.), (b) by using mobile phones (SMS's, phone calls), or (c) visually on the web pages, by means of color codes.

The information introduced in the database may also be used upon request to consult – through the suitable permissions – the system status and guidelines configuration from any Internet-connected device. This function is carried out by the so-called Management and Supervision Program.

For both the access to the data stored in the database and guideline changes, a graphic user's interface based on web technologies has been developed. It is intuitive, customizable, and powerful, and allows for the total monitoring of the system in an easy way, as shown in Fig. 4.

The advantages of utilizing a standard web browser are obvious. These applications are familiar to all types of users and, as it is standard, non-specific software, allows for accessing the information from a PC or laptop as well as from a cell phone or a PDA. In all cases, it is carried out after the correct identification of the user by means of digital certificates or a password.

The aforementioned interface helps to display the sensor network in the lake by showing us – at every moment – the connected, running nodes, as well those having malfunctions. Furthermore, it permits their geographical location by means of a GIS (geographical information system), informing us about the situation and status of the nodes on a map.

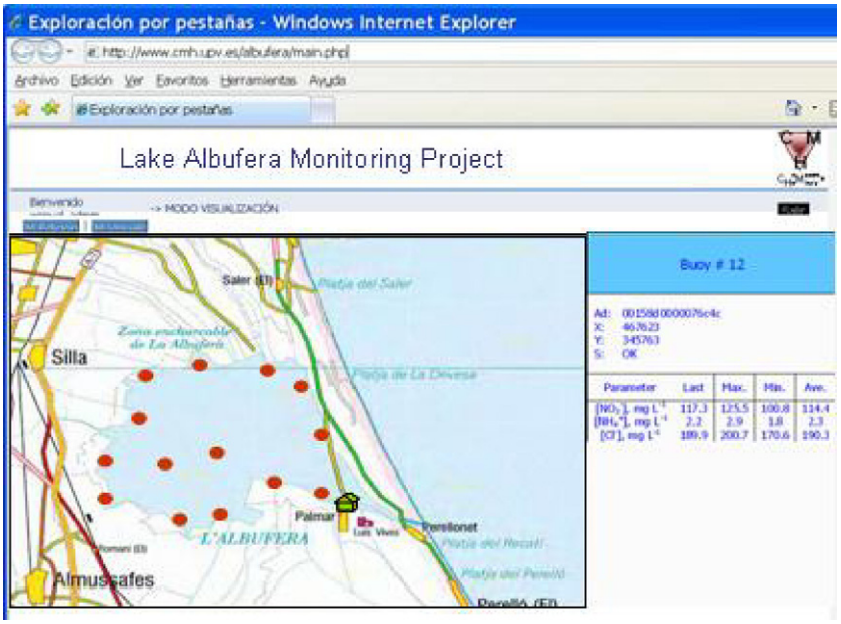


Fig. 4. Web interface.

On the other hand, by means of this interface we can know the concentration of the specified pollutants at any time, at any point, and from anywhere (only a connection to the Internet is required); this can be achieved by simply clicking on the desired node or looping at the data tables and graphics provided, which also permit to carry out searches according to different criteria. Moreover, the system can inform about risk situations or warnings, for instance, in the case that a determined pollutant exceeds the maximum value permitted. From this interface, it is possible to configure the warnings, as well as the way of sending them (e-mail, SMS, and so on).

The flexibility of the system is also an outstanding feature, since it is very easy to implement new treatments on the stored data through the edition of consulting PHP pages.

This web interface also offers the possibility of customizing the system on nearly every aspect of functioning, be it acquisition (interval between measurements, calibration parameters, etc.), warning generation (threshold values), working parameters of the wireless network (routing parameter selection, node reprogramming, etc.), or database management (maximum number of samples, safety permissions).

The access control mechanism of the Apache web server has been used for modifying the input parameters of the control system, three functioning profiles being established: (a) consult only; the reception of parameters from the browser is not implemented (b) modification of references; only the variables defined as web inputs can be modified, and (c) total control; the user can alter (under his/her own responsibility) any variable of the system. This access control is carried out through user and password validation. It is also possible to perform an IP address filtration to allow the connection only for certain machines, as well as to use digital certificates to authenticate the user's identity. Furthermore, the safe HTTPS protocol (based on public key cryptography) has been used, and it also implements the Apache server. On the other hand, the server keeps a log of all the events occurring in the system, such as user authentication, start/end of session, control instructions sent, and so on; each one of them is recorded along with the user identification, remote IP address, date, and time. This also ensures that the information cannot be altered (accidentally or intentionally) during its transmission.

All these security procedures are compliant with international regulations such as CFR 21 part 11 [24].

5. Experimental

5.1. Sampling and storage for reference measurements

Water samples were regularly collected at the study site between 9 and 10 a.m., maintained at 4 °C during transportation and filtered through 0.47 μm glass fibre filters (Schleicher & Schuell) immediately at the arrival in the laboratory. Sample conservation was suitably carried out.

5.2. Probe procedure

The probe containing the ISEs was cleaned with distilled water (and soft paper) and calibrated for all parameters (see Section 5.6) before being placed in the lake, inside a metal structure for security reasons.

5.3. Reference methods

The reference methods used in the laboratory for comparison with the in-line measurements were the cadmium reduction for nitrate, the phenate method for ammonium, and the argentometric method for chloride [25]. In the cadmium reduction method, nitrate is reduced almost quantitatively to nitrite in the presence of cadmium treated with copper sulfate and packed in a glass column. The nitrite thus produced is determined by diazotizing with sulfanilamide and coupling with *N*-(1-naphthyl)-ethylenediamine dihydrochloride to form a highly colored azo dye that is measured colorimetrically at 540 nm. A correction may be made for any nitrite present in the sample by analyzing without the reduction step. As for the phenate method, it is based on the formation of indophenol, an intensely blue compound (spectrophotometrically monitored at 640 nm), that results from the reaction of ammonia, hypochlorite and phenol, which is catalyzed by sodium nitroprusside. Finally, the argentometric method consists of the precipitation of silver chloride, which is indicated by the formation of red silver chromate

(potassium chromate is used as indicator). Three replicates were done for all the methods.

5.4. Chemicals and apparatus

All standard and reagent solutions were prepared from analytical reagent grade chemicals using distilled and deionized water from a Milli-Q water purification system. The deionized water had a specific conductivity less than 0.1 $\mu s\,cm^{-1}$.

A Shimadzu UV/Vis spectrophotometer was used for all reference measurements of nitrate and ammonium with the cadmium reduction method and the phenate method, respectively.

5.5. Membrane preparation

A mixture of 45 mg tridodecylammonium nitrate for nitrate electrodes, 45 mg nonactin for ammonium electrodes, and 45 mg poly(3,4-ethylenedioxythiophene) doped with chloride for chloride electrodes, 370 mg dibutylphthalate as plasticizer and 160 mg PVC is thoroughly dissolved in 7 mL tetrahydrofuran. The resulting solution is then poured into small glass rings and the organic solvent is evaporated, thus obtaining homogeneous membrane layers with a thickness ranging between 450 and 500 μm.

5.6. Probe calibration

Nitrate standard solutions of 100 and 200 $mg\,L^{-1}$, ammonium standard solutions of 1 and 5 $mg\,L^{-1}$, and chloride standard solutions of 100 and 300 $mg\,L^{-1}$ were used for probe calibration. For all three ions, a two-point calibration was performed everyday at noon.

6. Results

6.1. Analysis of real samples with the probe and the respective standard methods. Comparison with standard solutions

To establish the validity of our procedure, before using the multi-parametric probe in real samples we compare the ISE results with the standard methods, using standard solutions. In each case, three replicates were measured, Figs. 5–7 showing the corresponding average values obtained.

For nitrate, the probe ISE was compared with the cadmium reduction method. Fig. 5 depicts the results obtained with these methods in a standard solution and in real samples. It can be seen that in a solution with a known concentration of nitrate (126.2 $mg\,L^{-1}$ NO_3^-) the values obtained are in close agreement for both methods, considering the experimental errors associated with each method. For real samples, the values obtained with the cadmium reduction method showed to be lower than those yielded by the probe ISE.

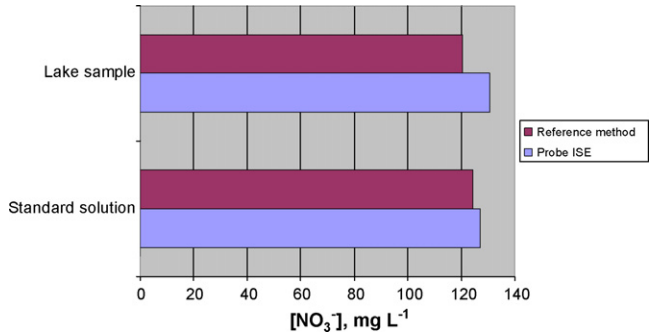


Fig. 5. An example of nitrate determinations in standard solutions and lake samples using the probe ISE and the reference method (cadmium reduction method).

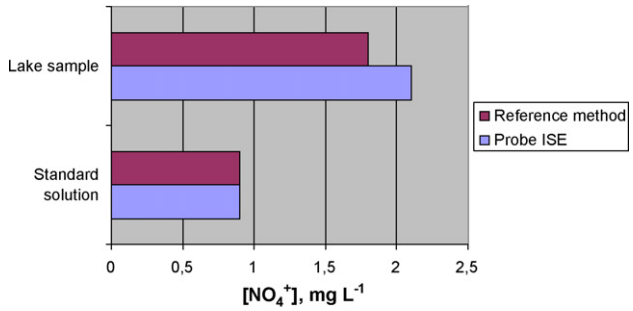


Fig. 6. An example of ammonium determinations in standard solutions and lake samples using the probe ISE and the reference method (phenate method).

The results obtained with the probe and the phenate method on a standard ammonium solution (0.9 $mg\,L^{-1}$ NH_4^+) agreed, within experimental error (Fig. 6). On the other hand, in real samples, the values obtained with the probe ISE were higher than the values obtained with the phenate method.

Finally, Fig. 7 shows that the values obtained for chloride using a standard solution of 167.4 $mg\,L^{-1}$ Cl^-, were almost the same for the probe ISE and for the argentometric method, within the experimental errors. Nevertheless when the chloride concentration was determined in real samples the probe ISE results were higher than those obtained with the argentometric method.

6.2. Recovery analysis with probe and standard methods

We have studied the response of the probe and of the adopted standard methods using field samples. For nitrate the recovery values obtained with the probe were 103% ($n = 3$; R.S.D. = 4.2%), whereas with the cadmium reduction method they were 97% ($n = 3$; R.S.D. = 3.1%). For ammonium the values obtained were 82% ($n = 3$; R.S.D. = 0.6%) with the probe and 98% ($n = 3$; R.S.D. = 2.1%) with the phenate method. For chloride the recovery obtained in real samples was 99% ($n = 3$; R.S.D. = 3.8%) using the probe and 97% ($n = 3$; R.S.D. = 0.3%) using the argentometric method. The recoveries obtained were therefore good, with the exception of the one obtained for ammonium using the probe, which can only be considered as acceptable.

6.3. Study of interferences

The effect of potential interfering ions normally found in association with NO_3^- (chloride and hydrogen carbonate), and Cl^- (hydrogen carbonate) was studied. It should be taken into account that a given ion was considered to significantly interfere with the

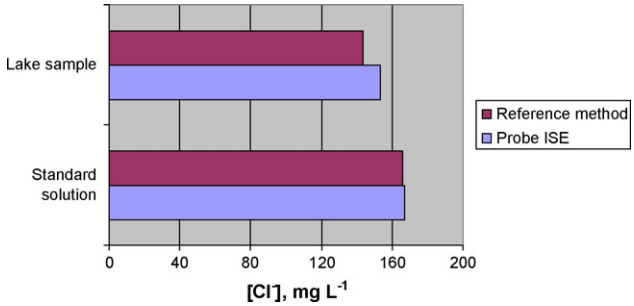


Fig. 7. An example of chloride determinations in standard solutions and lake samples using the probe ISE and the reference method (argentometric method).

determination when a mean change was observed in the results that reached at least 5%.

6.3.1. Chloride interference

In order to study the influence of Cl^- in the determination of nitrate, we measured nitrate using standard solutions of 100 mg L^{-1} (NO_3^-) in the absence and presence of several chloride concentrations (50, 100, 150, and 200 mg L^{-1} Cl^-). All these concentrations were chosen according to the range of concentrations likely to be expected from our previous knowledge of nitrate and chloride measurements in Lake Albufera samples. It was observed that the presence of chloride in such concentrations enhances the nitrate measured values by 8–12.5% for both methods used (cadmium reduction and ISE), 10% being an approximate average value. It can be concluded that chloride indeed interferes with the measurement of nitrate by such methods, but because such interference goes in the same sense and is of the same range for both methods, it may be not particularly relevant if our goal is the determination of trends in the concentration variation in the course of time.

6.3.2. Hydrogen carbonate interference

To test the possible interference of HCO_3^- on the determination of nitrate we measured nitrate, by both the reference and the ISE methods, using standard solutions of 1 mg L^{-1} (NO_3^-) in the absence and in the presence of hydrogen carbonate ion, with known concentrations (100 and 200 mg L^{-1}). These hydrogen carbonate ion concentrations were chosen according to the range found in previous field sample analysis.

For the cadmium reduction method the changes observed were lower than 5%. However, the hydrogen carbonate ion contributed to increase the values given for the concentration of nitrate when using the probe ISE, by a relative change of 17%. Furthermore, the probe ISE measurements were more affected by the increase in the hydrogen carbonate concentration.

In order to study the influence of hydrogen carbonate ion on the determination of chloride we determined chloride using standard solutions with 70 mg L^{-1} (Cl^-) in the absence and presence of hydrogen carbonate ions in two concentrations (100 and 200 mg L^{-1}). The HCO_3^- ion does not interfere with the determination of chloride, the relative error associated being lower than 2%, both for the probe and the reference (argentometric) methods.

6.4. Sensor features

The efficiency of the electrodes was evaluated on the basis of their limits of detection, slopes, dependence of interfering ions (see the preceding section), response times, and long-term stability behavior. Calibrations were carried out as stated in Section 5.6; based on the respective calibration graphs, the lowest limit of detection (LLD) were (a) 0.3 mg L^{-1} for the probe nitrate ISE, (b) 0.1 mg L^{-1} for the probe ammonium ISE, and (c) 0.5 mg L^{-1} for the probe chloride ISE. The slope in the linear range amounts to 60 mV/decade for all three electrodes. The potential response for all of them was linear in the range over which the concentrations of nitrate, ammonium, and chloride varied in Lake Albufera. All three ISEs were previously tested for long-term stability by continuous immersion in the lake over 3 days. The potential drift was less than 1 mV h^{-1}. It was not a monotonic drift, and after 24 h we observed a drift of about 1.5 mV. It was also found that the electrodes had response times of less than 20 s to changes in ion concentration (it far exceeds our needs, since no significant changes in analyte concentrations are expected to occur in the lake in seconds range). The responses were determined by rapidly changing the concentration of standard ion solutions with short rinsing time between the measurements. The time required to obtain a 90% response to a stepwise change from 10 to 100 mg L^{-1} of the ions in a stirred solution was 15 and 10 s in the opposite direction. And last but by no means least, the half lifetimes of the electrodes turned out to be >3 months, when stored in solutions of 0.8 g L^{-1} potassium nitrate or 0.8 g L^{-1} ammonium chloride.

6.5. In-line measurements

A series of 14 buoys, each one of them containing a sensor node as the one mentioned above, have suitably been placed at several points of the lake, according to a spatial distribution shown in Fig. 4. As mentioned in the preceding section, the ISEs were exposed to the lake water at all times along the whole monitoring process (i.e. there is no system that drives the sample to the electrodes at certain times). The results obtained in the in-line continuous monitoring of nitrate, ammonium, and chloride for 7 days are summarized in Table 1. It should be noted that – for each buoy – the average value was obtained from ten consecutive measurements (every hour, 9 a.m. to 6 p.m.). The temperature of the water at the different points of the lake where the probes were located was measured during the whole week, the obtained values varying between 21 and 23 °C. This is quite normal, since Lake Albufera is a shallow lake, with an average depth of 1 m. Furthermore, its geographical location (39° north) and the proximity (less than 500 m on average) to the Mediterranean Sea, allow for the lake to enjoy a mild weather throughout the year. Taking into account this small temperature variation, a very scarce influence of this parameter is to be expected on ISEs measurements, without a significant relationship between system drift and temperature changes.

On the other hand, a test of reliability was also carried out by comparing the results obtained by the probe with those provided by the corresponding reference methods. Buoy No. 9 was chosen as an example and, in this case, measurements were taken daily at noon for 7 consecutive days. Reference analysis was performed simultaneously following the previous steps shown in Section 5.1. The results are summarized in Table 2. In general, a satisfactory agreement between both procedures was achieved.

Moreover, the sensor nodes have shown a correct behavior regarding the supply system as well as the electrode control system and the wireless transmission of the results. The reliability observed in the system as a whole can then be considered satisfactory.

Finally, it should also be remarked that the data management system has allowed for studying the concentrations of all monitored parameters at any time, as well as their evolution. Another interesting achievement has been the possibility of knowing the node status, with a low rate of communication failures and no con-

Table 1
Results obtained for nitrate, ammonium, and chloride, in the different buoys[a].

Buoy No.	$[NO_3^-]$, mg L^{-1}			$[NH_4^+]$, mg L^{-1}			$[Cl^-]$, mg L^{-1}		
	Max.	Min.	Ave.	Max.	Min.	Ave.	Max.	Min.	Ave.
1	102.8	99.3	100.5	1.3	0.2	0.4	202.8	170.4	180.6
2	117.6	115.3	115.8	0.8	0.1	0.5	206.4	162.7	174.8
3	127.3	120.0	125.0	2.4	2.0	2.1	223.3	179.9	185.1
4	122.6	110.9	131.5	1.3	0.0	0.5	184.4	118.3	159.0
5	147.7	130.7	132.3	1.1	0.2	0.4	207.7	145.5	166.0
6	136.4	125.5	130.9	0.6	0.0	0.1	186.0	160.2	173.2
7	134.8	128.5	130.1	0.2	0.0	0.0	198.9	170.1	183.2
8	134.9	130.4	131.2	1.0	0.3	0.7	205.2	198.8	203.8
9	135.1	115.6	120.4	0.4	0.0	0.1	156.8	130.6	137.2
10	120.7	112.6	117.4	0.4	0.0	0.2	179.5	148.8	168.0
11	126.4	98.4	105.0	0.3	0.0	0.1	202.9	179.4	194.1
12	125.5	100.8	114.4	2.9	1.8	2.3	200.7	170.6	190.3
13	127.5	121.1	126.3	3.7	1.9	2.5	203.6	196.2	201.1
14	139.0	127.2	133.8	3.5	2.2	2.4	162.2	147.2	154.7

[a] Max. = maximum value; Min. = minimum value; Ave. = average value (from ten measurements)

Table 2
Results obtained in the determination of nitrate, ammonium, and chloride, in buoy No. 9 along a whole week[a].

Day	$[NO_3^-]$, mg L^{-1}		$[NH_4^+]$, mg L^{-1}		$[Cl^-]$, mg L^{-1}	
	Probe	Reference method	Probe	Reference method	Probe	Reference method
1	127.3	125.6	0.2	0.2	135.8	131.7
2	126.2	126.0	0.3	0.2	139.8	136.0
3	128.9	124.3	0.3	0.3	143.2	140.7
4	130.4	127.4	0.1	0.1	137.6	131.0
5	132.7	127.5	0.2	0.2	136.0	134.6
6	125.7	120.9	0.2	0.2	130.7	128.8
7	134.3	133.9	0.4	0.3	134.3	130.9

[a] Measurements using both the probe and the reference methods were taken everyday at noon, right before the calibration procedure. See Section 5.1 for details concerning the reference measurements.

trol errors at all. Additionally, several parameter sets have been evaluated in terms of measurement schedule, working cycle (time on/off), and warning thresholds; in this way, a fine tunning of the system has been achieved, thus obtaining a highly efficient energy management. The main drawback to be taken into account is that we have 'suffered' some faults in the functioning of the GPRS public network, which reinforces our trend towards the use of the WiMax technology.

As regards the obtained values themselves, the following aspects are to be highlighted:

(a) The content in nitrates is relatively high, probably due to the fertilizers used in the surrounding cultivated areas. Since these cultivars are widespread all around the lake, no determined sequence may be inferred from the values obtained at the different sampling points (buoys), higher and lower values occurring somewhat at random. A serious problem may be deduced from the nitrate concentrations obtained, as all of them far exceed 50 mg L^{-1}, which make Lake Albufera waters unsafe for human consumption according to Spanish regulations.
(b) In the case of chloride ions, their high values can be attributed to the special characteristics of Lake Albufera, which is linked to the Mediterranean Sea through three natural channels (none of them exceeding 200 m). No relationship can be established between the concentrations found and the locations at which they were measured.
(c) The concentration of ammonium ions found is rather low. These are good news for fishes since high values of this parameter can be toxic for them. However, further complications may arise if the content of organic matter in the lake increases, since it can reduce nitrate ions to ammonium, thus increasing its concentration.

7. Conclusions and future works

A new model has been proposed based on WSN and IES transducers that allows for the implementation of flexible, low-cost, high-performance chemical analysis systems, which are suitable for a distributed monitoring of processes undergoing variations of chemical parameters in the course of time.

These systems are straightforward with (a) a low maintenance thanks to the use of suitable ISEs and low consumption nodes with endless supply, and (b) a high flexibility, which permits their application to different situations as well as the remote configuration of the working parameters.

Our proposal has been applied to carry out the implementation of a distributed system for in-line chemical analysis of wastewater based on WSN. In comparison with the results obtained in previous works, it can be observed that, owing to the introduction of WSN, a considerable decrease in the price of both the nodes and the communications has been achieved; this offers the possibility of increasing the number of nodes (higher spatial precision) and decreasing the time between measurements (higher time precision).

Nevertheless, a certain amount of work is still needed in the calibration step. The aforementioned accumulated drift of about 1.5 mV during a day could be acceptable for a small-scale CWSN and the manual calibration used in this work could also be suitable for a 1-week monitoring period, but larger networks and/or longer monitoring processes will undoubtedly require a somewhat automated calibration procedure, for example the one proposed by the authors of this work [8] which we are currently trying to couple to the CWSN before being tested. If this implementation succeeds, a more frequent re-calibration will be carried out, which will undoubtedly yield even more accurate and reliable results, with a better correlation between the measured values and those obtained by the reference methods.

All in all, we can finally conclude that the proposed approach has a promising future, since the constant development of the technologies on which it is based will result in lower expenses and, at the same time, higher performances.

Acknowledgements

The authors gratefully acknowledge financial support from the CICYT (research projects DPI2007-66796-C03-01 and TRA2006-15620-C02-01).

References

[1] D. Kaelin, K. Rottermann, H. Siegrist, L. Rieger, C. Banninger, J. Eugster, Water Science and Technology 58 (2008) 629–637.
[2] J. Buffle, G. Horvai (Eds.), In Situ Monitoring of Aquatic Systems: Chemical Analysis and Speciation, Wiley, New York, 2000.
[3] J. Wang, Analytical Electrochemistry, Wiley-VCH, New York, 2006.
[4] K. Nittis, C. Tziavos, R. Bozzano, V. Cardin, Y. Thanos, G. Petihakis, M.E. Schiano, F. Zanon, Ocean Science Discussion 3 (2006) 1399–1440.
[5] F. Akyildiz, W. Su, Y. Sankarasubramaniam, E. Cayirci, Computer Networks 38 (2002) 393–422.
[6] A. Bonastre, R. Ors, J.V. Capella, M. Peris, Journal of Process Analytical Chemistry 10 (2008) 50–56.
[7] A. Bonastre, R. Ors, M. Peris, Trends in Analytical Chemistry 20 (2001) 263–270.
[8] A. Bonastre, R. Ors, J.V. Capella, M.J. Fabra, M. Peris, Trends in Analytical Chemistry 24 (2005) 128–137.
[9] D. Remondo, I.G. Niemegeers, Computer Communications 26 (2003) 36–40.
[10] Y. Yu, R. Govindan, D. Estrin, UCLA Computer Science Department Technical Report UCLA/CSD-TR-01-0023, May 2001.
[11] I. Chlamtac, M. Conti, J. Liu, Ad Hoc Network Journal 1 (January–March (1)) (2003).
[12] G. Lu, B. Krishnamachari, C. Raghavendra, Workshop on Energy-Efficient Wireless Communications and Networks (EWCN), Held in Conjunction With the IEEE International Performance Computing and Communications Conference (IPCCC), 2004.
[13] M. Abolhasan, T.A. Wysocki, E. Dutkiewicz, Elsevier Journal of Ad hoc Networks 2 (2004) 1–22.
[14] J.N. Al-Karaki, A.E. Kamal, IEEE Wireless Communications 11 (December (6)) (2004).
[15] C. Perkins, E. Royer, S. Das, M. Marina, IEEE Personal Communications (February) (2001) 16–28.
[16] E. Pretsch, Trends in Analytical Chemistry 26 (2007) 46–51.
[17] M. Ilyas, I. Mahgoub (Eds.), Handbook of Sensor Networks: Compact Wireless and Wired Sensing Systems, CRC Press, Boca Raton, 2004.
[18] Z. Okolisa, Gradevinar 61 (2009) 205–208.
[19] M. Brand, H. Aghvami, Multiple Access Protocols for Mobile Communications GPRS, UMTS, and Beyond, John Wiley & Sons, Chichester, 2002.
[20] http://www.telit.com/en/products/gsm-gprs.php?p_id=12&p_ac=show&p=4, (accessed September, 2008).
[21] http://www.wimaxforum.org/ (accessed September, 2008).
[22] http://www.php.net/, (accessed September, 2008).
[23] http://www.apache.org/, (accessed September, 2008).
[24] Risk-Based Approach to 21 CFR Part 11, http://www.ispe.org (accessed January, 2008).
[25] American Public Health Association, Standard Methods for Examination of Water and Wastewater, 20th ed., American Public Health Association, Washington, D.C., USA, 1998.

Juan V. Capella received the Eng. degree in Computer Science from the Universidad Politecnica de Valencia (UPV), Spain, in 1998. He joined the Fault-Tolerant Systems Research Group (GSTF) at UPV, where he received the M.Sc. degree in Computer Engineering in 2000. He has been an Assistant Professor of the Department of Computer Engineering, UPV, since 2002. His main research interests are distributed control systems design and Wireless Sensor Networks. He has published 4 books and more than 20 papers in international journals and conferences about his research projects. He is a member of the editorial committee of the IEEE RITA Journal, and has been both reviewer and member of the program committee of several international conferences organized by IEEE.

Alberto Bonastre is Associate Professor at the Universidad Politecnica de Valencia (UPV), Spain, and member of the Fault-Tolerant Systems Research Group (GSTF). He obtained the M.Sc. degree in Computer Engineering at the UPV in 1991, and the Ph.D. degree in 2001. He is currently teaching Computer Networks and Wireless Sensor Networks. His research is centered on Wireless Sensor Networks, it being especially devoted to Fault-Tolerance in chemical analysis systems.

Rafael Ors is Professor at the Department of Computer Engineering (DISCA), Universidad Politecnica de Valencia (UPV). Professor Ors teaches Computer Engineering, Computer Networks, and Fault-Tolerant Systems. He is co-director of the Fault-Tolerant Systems Research Group (GSTF). His research focuses on the development of real-time reliable distributed systems and its applications in the control of several industrial processes. He has published more than sixty research papers on these subjects, and has taken part in several projects on industrial applications.

Miguel Peris is Associate Professor at the Universidad Politecnica de Valencia (UPV), Spain, and member of the Department of Chemistry. He obtained a M.Sc. in Chemistry at the Universidad de Valencia (Spain) in 1984 and the Ph.D. degree in 1994. He is currently teaching Chemical Fundamentals of Engineering, and Food Analysis. His research is centered on advanced automation of chemical analysis systems. He has published more than 40 scientific papers and several chapters of books in this field.

Talanta 80 (2010) 1799–1804

Contents lists available at ScienceDirect

Talanta

journal homepage: www.elsevier.com/locate/talanta

Development and validation of a cellular biosensor detecting pesticide residues in tomatoes

Kelly Flampouri[a,b], Sophie Mavrikou[a,b], Spiridon Kintzios[a,b,*], George Miliadis[c], Pipina Aplada-Sarlis[c]

[a] Laboratory of Plant Physiology, Faculty of Agricultural Biotechnology, Agricultural University of Athens, Athens, Greece
[b] EMBIO Diagnostics Project, Nicosia, Cyprus
[c] National Reference Laboratory of Pesticides Residues, Benaki Phytopathological Institute, Athens, Greece

ARTICLE INFO

Article history:
Received 15 June 2009
Received in revised form
22 September 2009
Accepted 8 October 2009
Available online 5 November 2009

Keywords:
Bioelectric Recognition Assay (BERA)
Dithiocarbamates
N2a cells
Organophosphates
Tomato
Vero cells

ABSTRACT

Two of the most important categories of pesticides used in agricultural practice are organophosphates and dithiocarbamates. Their extensive and inappropriate use has rendered their reliable monitoring at trace levels more and more necessary. This study presents the construction of a rapid and sensitive cellular biosensor test based on the measurement of changes of the cell membrane potential of immobilized cells, according to the working principle of the Bioelectric Recognition Assay (BERA). The cells were immobilized by entrapment in a sodium alginate bead and directly applied in different pesticide dilutions and agricultural samples. The pesticides used were the organophosphate insecticide diazinon and the dithiocarbamate fungicide propineb. Two different cell types, N2a (neuroblastoma) and Vero (fibroblast) were used as the biosensory elements in order to investigate their differential response against the pesticides. In this way, we hoped to increase the selectivity of the assay. Based on the observed patterns of response, we demonstrate that the sensor can be used for the qualitative and, in some concentrations, quantitative detection of the pesticides with a high degree of reproducibility. The lowest detected concentration was 3 nM. Finally, for the investigation of the effects of different pesticides on the accumulation of cytosolic Ca^{2+}, we conducted a fluorescent assay on N2a cells treated with tomato sample extracts, which were replicates of the E.U. proficiency test sample. The tomato samples were either organically grown or contained 14 different pesticides. The experimental results showed a higher increase of the intracellular Ca^{2+} concentration in cells treated with non-organic samples compared to the cells treated with organic samples.

© 2009 Elsevier B.V. All rights reserved.

1. Introduction

During the last two decades there have been growing societal concerns over issues related to public health, environmental quality, and food safety. One of the major controversies inciting these concerns involves the production and consumption of fresh fruits and vegetables [1]. It is well known that the level of risk is closely related to the daily intake of chemically contaminated food and that for certain products which are frequently consumed the risk is higher than others [2]. Tomato (*Lycopersicon esculentum*) is one of the most widely grown vegetables in the world and a basic component of the Mediterranean diet and is used almost daily in several European countries, raw, home-cooked or processed as a canned product, juice or paste [3].

In environmental pollution monitoring, it is becoming a general opinion that chemical analysis by itself does not provide sufficient information to assess the ecological risk of polluted waters and wastewaters [4]. Although conventional techniques such as HPLC/MS and GC/MS give satisfactory analytical results for pesticide determination, new assays and sensors for cheaper and faster on-site analysis are being developed.

Biosensors are being developed for different applications, including environmental and bioprocess control, quality control of food, agriculture, military, and, particularly, medical applications. In fact, most of the commercially available biosensor systems are applied in the clinical and pharmaceutical markets. Accordingly, most research and development has been devoted to this area. In the food industry, the detection of contaminants, verification of product content, monitoring of raw materials conversion and product freshness [5] are areas of potential biosensor application.

Based on the inhibition of acetylcholinesterase (AChE) and choline oxidase, many biosensors have been developed for the detection of organophosphorous and carbamate pesticides such as those described by Andres and Narayanaswamy [6], Choi et

* Corresponding author at: Laboratory of Plant Physiology, Faculty of Agricultural Biotechnology, Agricultural University of Athens, Athens, Greece.
Tel.: +30 210 529 429; fax: +30 210 529 4286.
E-mail address: skin@aua.gr (S. Kintzios).

0039-9140/$ – see front matter © 2009 Elsevier B.V. All rights reserved.
doi:10.1016/j.talanta.2009.10.026

al. [7], Andreou and Clonis [8] and Mavrikou et al. [9]. The biological effects of organophosphorous (OPs) insecticides such as diazinon are exerted by reversible or irreversible inhibition of acetylcholinesterase (AChE), which results in decreased catalysed hydrolysis and excessive accumulation of extracellular acetylcholine (ACh). The ensuing hyperactivation of ACh receptors results in various toxic effects including hypersecretions, convulsions, respiratory distress, coma, and ultimately death [10,11].

Propineb is a fungicide with the propylene-bis-dithiocarbamate structure. It is widely used in fruit and vegetable horticulture. Dithiocarbamates (DTCs) form lipophilic complexes with di- and trivalent metallic cations, bonding through the sulfur atoms. In the case of propineb, a zinc ion is chelated. It was shown that Zn^{2+} concentration is dose-dependently accumulated in liver and kidney tissue [12]. In addition, DTCs-induced neurobehavioral and extrapyramidal symptoms have been related to the impairment of central neurotransmitter release mechanism; alteration of dopamine [13–15], noradrenaline, and acetylcholine (ACh) [16] levels were mainly observed in rat and mouse brain areas after DTCs administration.

Interactions of mammalian cells with pesticides are frequently associated with changes in cell membrane functions: in the case of neuronal cells these changes are associated with altered responses to neurotransmitters, such as ACh. The presence of pesticidal compounds is directly associated with changes of the immobilized cell membrane potential. Even changes associated with non-membrane effects, such as the cytoplasmic induction of apoptotic pathways will frequently involve changes in calcium ion (Ca^{2+}) concentrations that could be eventually translated in changes of the membrane potential [17]. In this way, a pesticide assay could be based on electrically active cells, interfaced with microelectrodes which allow the capture of extracellular spikes or impedance changes associated with cellular response against the pesticide under detection. An example is the Bioelectric Recognition Assay (BERA) which has been originally developed for the detection of viruses on the basis of their specific interaction with appropriately immobilized, mammalian cells and the measurement of the change of the electric potential that is caused by the aforementioned interaction [18,19]. It has been recently demonstrated that the assay could be used for the detection of the organophosphate pesticide chlorpyriphos and the carbamate carbaryl in a concentration-dependent pattern [9]. According to the working principle of the method, the presence of the pesticides is detected by the degree of inhibition of cellular AChE, which is inversely associated with ACh concentration. Inhibition of AChE lead in increased excitatory ACh transmission and depolarization of the cell membrane, which was measured as a change of the sensor's potential, due to changes in the concentration of electrolytes in the immediate vicinity of the working electrode. This methodological approach displays many advantages over other biosensor techniques, such as high speed (assay time = 3 min), sensitivity (1 ppt to 1 ppb, depending on the pesticide), reproducibility and low cost. However, the selectivity of the assay is questionable, because a given cell type can react in roughly the same manner against a large number of different pesticides (a common problem in cell-based toxicity assays).

One method to increase the selectivity of the assay could be the use of different cell types having a different response pattern to the assayed pesticides. Therefore, in the present study we report the development of a cellular biosensor utilizing the BERA working principle and based on neuroblastoma N2a or Vero cells, two cell types quite different in their physiology. The novel sensor was tested against standard solutions of the organophosphate insecticide diazinon and the dithiocarbamate fungicide propineb and validated against tomato samples containing a mixture of pesticides.

2. Experimental

2.1. Materials

Mouse neuroblastoma (N2a) and monkey African green kidney (Vero) cell cultures were originally provided from LGC promochem (UK). Diazinon (diethoxy-[(2-isopropyl-6-methyl-4-pyrimidinyl)oxy]-thioxophosphorane; CAS [333–41–5]; Mw = 304.35; Sigma–Aldrich, USA) was used as a standard organophosphate insecticide and propineb ([[2-[(dithiocarboxy) amino]-1-methylethyl]carbamodithioato]](2-)-k*S*,k*S*′] zinc; CAS [235–134–0]; Mw = 289.80; Bayer Cropscience, Germany) as a standard dithiocarbamate fungicide. Pesticide mixtures which contained 10 μM of each pesticide, were prepared daily in acetone solution. All other reagents were purchased from Fluka (Switzerland).

2.2. Cell culture and sensor fabrication from N2a and Vero cells

Cells were cultured in Dulbecco's medium with 10% heat-inactivated fetal calf serum (FCS), 10% antibiotics (streptomycin) and 10% L-glutamine. After cell detachment from the culture vessel by adding trypsine/EDTA for 10 min at 37 °C and cell concentration by centrifugation (6 min, 1200 rpm, 25 °C), 1 ml of cells (at a density of 2.5×10^6/ml) were mixed with 2 ml of 4% (w/v) sodium alginate solution and then the mixture was added drop wise, by means of a 22G syringe, in 0.8 M $CaCl_2$. Each of the resulting calcium alginate beads had an approximate diameter of 2 mm and contained approximately 5×10^4 cells.

The sensors were storable at room temperature in culture medium, under normal atmospheric conditions (i.e. non-CO_2 enriched) for at least three weeks without any loss of performance.

2.3. Sample preparation

Thirteen blended tomato samples were analysed. Five of them were replicates of a control sample derived from strictly organically grown tomatoes, free of pesticide residues while the rest of them were replicates of the E.U. proficiency test sample containing a mixture of fourteen pesticides at concentrations ranging from 0.05 to 3.955 mg/kg (Table 1).

Standard aqueous solutions of either diazinon or propineb were prepared in the range of concentrations 0.003, 0.016, 0.03, 0.16, 0.33, 1.65 and 3.30 μM in water. The concentrations 1.65 and 3.30 μM of the pesticides had to be dissolved in a small amount of ethanol and diluted with water (5%, v/v) because of their insolubility in water.

2.4. Assay principle

According to the working principle of the method, the presence of organophosphate compounds is detected by the degree of inhibition of cellular AChE, which is inversely associated with ACh concentration. ACh is an excitatory neurotransmitter [20], the activity of which is regulated by AChE. Therefore, inhibition of AChE can lead in increased excitatory ACh transmission, which can be measured by the depolarization of the cell membrane. In other words, inhibition of AChE by pesticide residues in the sample will result to excessive stimulation of N2a cells by ACh, which will further lead to membrane depolarization above a pre-determined threshold. The presence of DTCs is also detected by the increase of ACh concentration: it has been previously reported that propineb (0.001–100 nM) dose-dependently increases ACh release from PC12 differentiated by NGF [21]. In addition, previous data obtained from Marinovich et al. [22] indicated a possible involvement of nicotinic

Table 1
Fourteen pesticides contained in E.U. proficiency test tomato samples.

Acrinathrin0.284 mg/kg	Azoxystrobin 0.225 mg/kg	Bromopropylate 0.490 mg/kg	Chlorothalonil 1.626 mg/kg	Diazinon 3.955 mg/kg
Dimethoate0.132 mg/kg	Endosulfan 0.344 mg/kg	Imazalil 0.167 mg/kg	Imidacloprid 0.232 mg/kg	Dithiocarbamates 0.810 (as CS_2)
Metalaxyl 0.050 mg/kg	Oxydemeton methyl 0.199 mg/kg	Procymidone 0.412 mg/kg	Thiabendazole 0.314 mg/kg	

receptors present on nerve terminals in propineb-induced ACh release.

Correspondingly Vero cells were used as a non-responsive biosensory element for the case of organophosphates. On the other hand propineb may exert a high sensitivity response in kidney-derived Vero cells due to its Zn-containing molecule: zinc concentration varies widely in different tissues, but Zn is known to accumulate in two particular organs, namely the liver and kidney, where it may cause biochemical and histopathological changes [23,24]. According to Davies et al. [25] and Houtani et al. [26] zinc-activated ion channel (ZAC) is a mammalian protein, expressed in prostate, thyroid, trachea, lung, brain (adult and fetal), spinal cord, skeletal muscle, heart, placenta, pancreas, liver, kidney and stomach. The L2 sequence of ZAC gene is conserved among species including human, chimpanzee, dog, cow, and opossum [26]. Membrane depolarization events and associated electrolyte influx/efflux will reflect themselves on the sensor's response as a change of the sensor's potential, due to changes in the concentration of electrolytes in the immediate vicinity of the working electrode.

2.5. Assay procedure

Each cell-bearing bead (cell sensor) was manually connected to a working electrode (the electrode was inserted through the entire length of the sensor without extruding from the opposite end) made from pure silver, electrochemically coated with an Ag/AgCl layer and having a diameter of 0.75 mm. The distance between working and reference electrode was 3 cm. Electrodes were connected to the recording device, which comprised the PMD-1608FS A/D card (Measurement Computing, Middleboro, MA). The software responsible for recording the signal and data processing was InstaCal (Measurement Computing).

For each assay, the sensor system, comprising of the bead attached to the working electrode and a reference electrode, was immersed into each sample solution (200 μl). The response of each sensor was estimated by recording the average change of the sensor potential for a period of 180 s after sample application.

2.6. Fluorescence assays of pesticide–cell interaction

Changes in cytoplasmic Ca^{2+} concentration in N2a cells were measured microscopically, after the addition of pesticide-free tomato samples and tomato samples containing 14 different pesticides were monitored by the uptake of the acetomethyl ester of Fluo-3 [27]. After application of 5 μl of the dye, the fluorescence of the specimens was recorded for 5 min at 10 s intervals. Slides with stained cells were mounted on a Zeiss Axiolab fluorescent microscope equipped with a BP-546 excitation filter and an FT-580 chromatic beam splitter. A digital camera (SONY S75 digital still camera) was attached to the microscope with adjustable BP-546/FT-580 excitation filter/chromatic beam splitter combinations. In order to control photobleaching, we kept specimen exposure times at a minimum level.

In addition, a fluorescence assay was conducted spectrophotometrically. Cells were plated on special optics 96-well plates (black, clear-bottom; Greiner) coated with poly-L-lysine (100 μg/ml) at a density of 2×10^4 cells per well. After 3 days in culture, Fluo-3 AM (10 μM) was added to the cell suspension of each well, which was subsequently incubated for 60 min at 37 °C. The cells were then washed two times with sterile deionized water. The cells were incubated with either tomato samples or with K^+ (70 mM) in a standard medium (containing 140 mM NaCl, 5 mM KCl, 1 mM $MgCl_2$, 5.6 mM glucose, 1.5 mM $CaCl_2$, and 20 mm HEPES-Na (final pH 7.4)), which was used for loading and for the subsequent fluorescence measurements. The fluorescence intensity of Fluo-3 was quantified by a fluorescence spectrophotometer (Molecular Devices Spectramax M2e microplate reader), with a single excitation wavelength set at 492 nm and an emission wavelength monitored at 520 nm. All data points were done in triplicates, and experiments were repeated at least three times with different batches of N2a cells.

2.7. Data analysis and experimental design

Both biosensor and conventional sample analysis were conducted according to a double-blind protocol. Experiments were set up in a completely randomized design and each experiment was repeated four times. Results were assessed by a standard analysis of variance. In each application, a set of five biosensors was tested against each individual sample. Data means among different days were compared using Duncan's multiple range test (with significance at $p < 0.05$).

3. Results

3.1. Response of the sensor to standard pesticide solutions

The results of the assay of standard propineb solutions at different concentrations with neuroblastoma and Vero biosensors are shown in Fig. 1A, while the results of assaying standard diazinon solutions with neuroblastoma and Vero biosensors are shown in Fig. 1B. In the case of Vero cells, when no pesticide was present in the sample (control sample), a constant sensor response of -70 ± 5 mV was observed. The sensors responded to propineb by considerable positive increase of the sensor's potential (Fig. 1A). This response was concentration-depended in the range of 0.03–0.33 μM ($r^2 = 0.9816$, $y = 7.788x - 37.758$), so that both the qualitative and the quantitative detection of the pesticide was possible, at least at concentrations lower or close to either 0.33 μM (Vero cells) or 1.65 μM (N2a cells). The biosensor based on N2a cells gave also a concentration-depended response in the range of 0–0.16 μM ($r^2 = 0.9527$, $y = 15.5x - 68.386$).

A similar, concentration-dependent pattern ($r^2 = 0.9046$, $y = 6.4788x - 59.268$) was observed in the N2a sensor's response against diazinon (Fig. 1B), in the range of 0–0.33 μM. In contrast, the Vero cell biosensor's response did not follow a concentration-depended pattern.

Depending on the concentration of each pesticide, representative recovery rates ranged from 51 to 93% for diazinon and from 52 to 122% for propineb (Table 2).

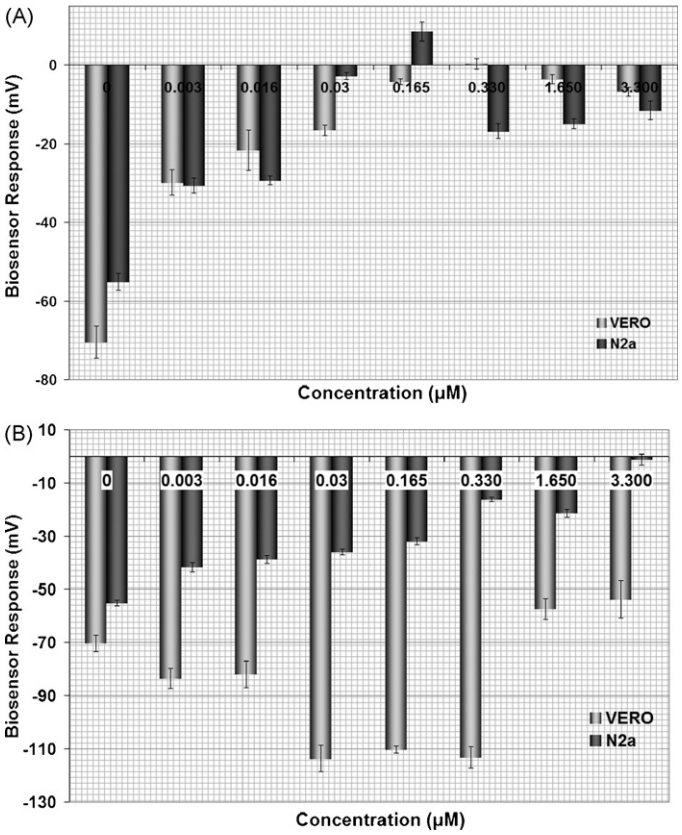


Fig. 1. Biosensor response against standard solutions containing propineb (A) or diazinon (B) at various concentrations. Sensor response is expressed as a change in the membrane potential of immobilized cells. ($n = 15$ replications (different sensors) for each sample and error bars represent standard errors of the average value of all replications with each sample.) The white columns represent Vero cells and the gray columns N2a cells. With each different colour, columns marked with different letters indicate statistically different values ($p < 0.01$).

3.2. Residue profile by conventional analysis of tomato samples

Eight of the thirteen tomato samples contained a mixture of fourteen pesticides which are presented in Table 1, while the biosensor responses for the thirteen tomato samples are presented in the *y* axis of Fig. 2. The white columns represent organic tomato samples and the gray columns represent tomato samples containing the fourteen pesticides in various concentrations. Pesticide residues in tomato samples caused a considerable cell membrane depolarization on neuroblastoma cells immobilized in the sensor, as indicated by the decrease of the negative sensor potential, which was clearly distinguishable from the sensor's response against pesticide-free control samples. There were no false-negative measurements.

Differences in responses between replicates of the control sample may be due to enhanced matrix effect of the tomato samples on the neuroblastoma cells immobilized in the sensor. Tomato is rich in carotenoids, such as lycopene. It has been previously shown that carotenoids and their oxidation products promote gap junctional communication [28]. It is, therefore, quite possible, that differences in the oxidation rate of lycopene and other carotenoids between individual samples resulted in the observed differences in responses between replicates of the control sample.

Table 2
Recovery rates for diazinon and propineb with the novel cell biosensor assay.

Pesticide	Concentration (μM)	Recovery rate (%)
Diazinon	0.01	51.01
	0.05	92.81
Propineb	0.01	121.93
	0.05	51.62

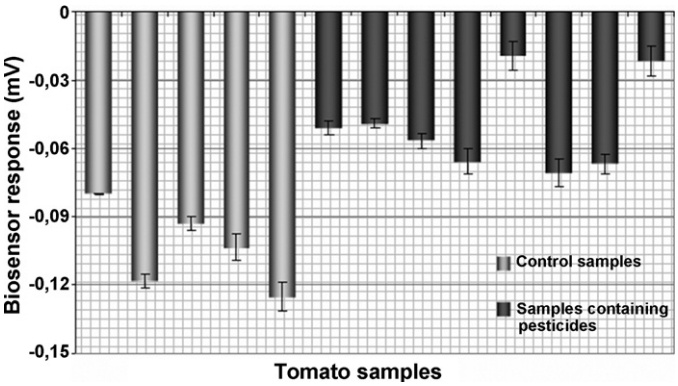


Fig. 2. Biosensor response against thirteen different tomato samples. The sensor was based on neuroblasoma N2a cells. The white columns represent pesticide free tomato samples and the gray columns represent tomato samples containing fourteen pesticides in various concentrations. Sensor response is expressed as a change in the membrane potential of immobilized cells. ($n = 15$ replications for each samples and error bars represent standard errors of the average value of all replications with each sample.)

3.3. Fluorescence assays on calcium uptake by N2a cells after treatment with various tomato samples

Neuroblastoma cells responded to the presence of tomato samples containing 14 different pesticides in various concentrations, by a rapid and very considerable increase of their intracellular Ca^{2+} concentration (Fig. 3), compared to cells treated with pesticide free tomato samples. The spectrophotometric assay gave similar results in the fluorescence intensity (Fig. 4). The pesticide free samples indicated a significant difference compared with the samples containing pesticides. Cells incubated with a Krebs HEPES buffer containing a high concentration of K^+ (70 mM) were used as a positive control, while cells incubated with Krebs HEPES buffer were used as a control. The purpose of the microscopy fluorescence assay was to investigate the participation of Ca^{2+} traffic through the cell membrane as a possible mechanism underlying the observed changes in cell membrane potential, as measured with the biosensor. This measurement was not meant to include a complete fluorescence-based assay for pesticide detection, therefore different pesticide concentrations were not tested.

4. Discussion

Cell-based biosensors constitute a promising field that has numerous applications ranging from pharmaceutical screening to environmental monitoring. Cells provide an array of naturally evolved receptors and pathways that can respond to an analyte in a physiologically relevant manner. Enzymes, receptors, channels, and other signalling proteins that may be targets of an analyte are maintained and, as necessary, regenerated by the molecular machinery present in cells [29].

The results of the present study clearly demonstrate that detection of different pesticide substances with BERA, was primarily based on the specificity of the cell line used in the biosensor. The biosensor presented in this study belongs to a new category of pesticide residue detectors based on mammalian cell lines. Previous studies report the use of genetically modified bacteria for the detection of toxic and especially mutagenic compounds [30]. Even though the biosensor development is at an early stage the biosen-

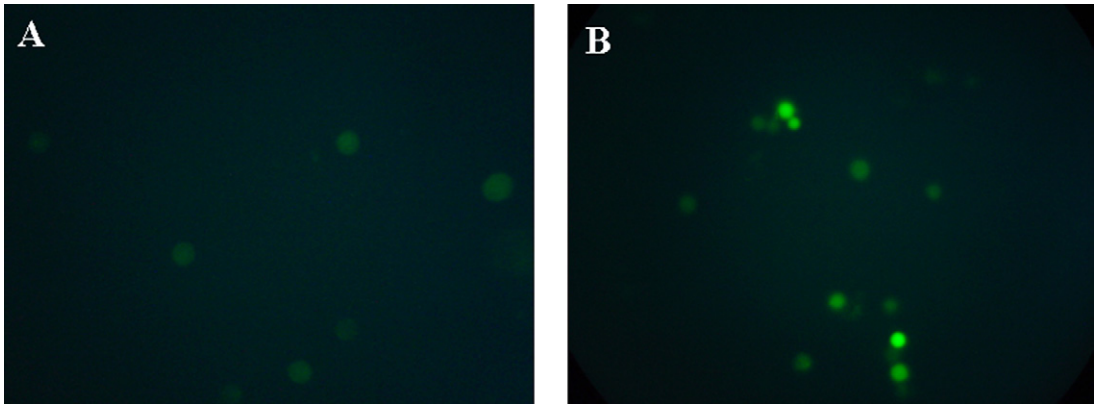


Fig. 3. Changes (expressed as differences in fluorescence intensity) of the cytoplasmic calcium ion concentration in N2a cells treated with pesticide free tomato samples (A) and tomato samples containing 14 different pesticides (B).

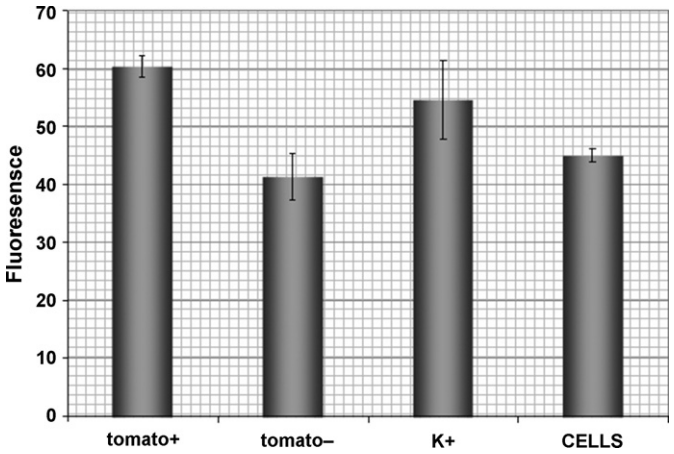


Fig. 4. N2a cells were treated with pesticide-free tomato samples (tomato −), tomato samples containing 14 different pesticides (tomato +) or K^+ solution (70 mM) (K^+). Cells treated with buffer were used as control (CELLS). Calcium mobilization was determined using a fluorometric imaging plate reader. Shown are average values ± standard deviations of triplicate determinations of endpoint measurements. These graphs are representative of four similar experiments.

sor gave satisfactory results due to the high reproducibility and the differentiation between control and positive samples.

Vero cells are widely used in studies of in vitro cytotoxicity [31]. The results of the present study, as expected, indicate that Vero cells present higher specificity to the dithiocarbamate fungicide, propineb than to the organophosphate insecticide diazinon. These results provide an indication that the zinc organometallic fungicide propineb, reacts with the zinc receptors on the kidney cells [26]. Furthermore, N2a cells, as expected due to their membrane-bound AChE [32], demonstrate higher selectivity to the organophosphate diazinon in contrast to propineb (Fig. 1A). However, propineb resulted in a satisfactory response between the concentrations 173 nM and 3 nM (the latest being the lower detectable concentration). In previous studies using rat pheochromocytoma cells differentiated by NGF (PC12), propineb (0.001–100 nM) dose-dependently increased ACh release from PC12. At concentrations between 0.001 and 1 nM propineb-induced ACh release reached a maximal effect (~50%) while at higher concentrations (10–100 nM), propineb caused a progressive disappearance of the effect [21]. It seems that pesticide concentrations above a limit caused cellular toxicity or otherwise major, non-reproducible biochemical changes that could not fit in a linear response pattern. This effect was cell line- and pesticide-dependent, as observed by the results presented in Fig. 1, whereas cells responded to the applied pesticides in a linear pattern only within a certain range of concentrations.

The results of the present study showed a higher fluorescence intensity of the samples containing pesticides compared to pesticide-free samples. Calcium ions (Ca^{2+}) are universal secondary messengers that are key players in many cellular signal transduction pathways [17]. Cell damage induced by environmental insults or by overstimulation of physiological pathways results in pathological Ca^{2+} signals, which trigger necrotic or apoptotic cellular death [33]. Increased Ca^{2+} influx through voltage-operated calcium channels (VOCCs) is implicated in many forms of both apoptotic and necrotic cell death [34]. Wang and Xu [35] report a possible involvement of Ca^{2+} signalling in rotenone-induced apoptosis in human neuroblastoma SH-SY5Y cells.

There are several areas of future work that would improve the utility of cell-based biosensors. Numerous applications would benefit from the development of parallel systems that allow for simultaneous measurements on multiple cell lines. The development of a system utilizing multiple cell types will offer improvements to both the breadth of sensitivity and the ability to discriminate or classify analytes.

Acknowledgements

The research project was funded by the EMBIO Project of the Cypriot Ministry of Industry, Commerce and Tourism. The authors thank Dr. Olga Magana (Ministry of Agriculture, Centre of Athens Veterinary Institutions, Institute of Infectious and Parasitic Diseases) for the provision of Vero cell cultures.

References

[1] T. Stevens, R. Kilmer, IFAS Extension 331 (1999) 1–22.
[2] C. Mestres, P. Colonna, A. Buleon, J. Food Sci. 53 (1988) 1809–1812.
[3] Tomato products situation & outlook, production and trade in selected tomato products for selected countries, United Sates Department of Agriculture, Washington, DC, 2004. http://www.fas.usda.gov/htp/Hort_Circular/2004.
[4] M. Castillo, M.C. Alonso, J. Riu, M. Reinke, G. Klöter, H. Dizer, B. Fischer, P.D. Hansen, D. Barceló, Anal. Chim. Acta 426 (2001) 265–277.
[5] A.F. Collings, F. Caruso, Rep. Prog. Phys. 60 (1997) 1145–1397.
[6] R.T. Andres, R. Narayanaswamy, Talanta 44 (1997) 1335–1352.
[7] J.W. Choi, Y.K. Kim, I.H. Lee, J. Min, W.H. Lee, Biosens. Bioelectron. 16 (2001) 937–943.
[8] V.G. Andreou, Y.D. Clonis, Biosens. Bioelectron. 17 (2002) 61–69.
[9] S. Mavrikou, K. Flampouri, G. Moschopoulou, O. Mangana, A. Michaelides, S. Kintzios, Sensors 8 (2008) 2818–2832.
[10] C.P. Holstege, M. Kirk, F.R. Sidell, Crit. Care Clin. 13 (1997) 923–942.
[11] C.A. Broomfield, S.D. Kirby, J. Appl. Toxicol. 21 (2001) 43–46.
[12] K. Güven, E. Deveci, D. Pomerai, Turk. J. Biol. 23 (1999) 413–422.
[13] A. Vaccari, P.L. Saba, S. Ruiu, M. Collu, P. Devoto, Toxicol. Appl. Pharmacol. 139 (1996) 102–108.

[14] B.K. Barlow, M.J. Thiruchelvam, L. Bennice, D.A. Cory-Slechta, N. Ballatori, E.K. Richfield, J. Neurochem. 85 (2003) 1075–1086.
[15] J. Zhang, V.A. Fitsanakis, G. Gu, D. Jing, M. Ao, V. Amarnath, T.J. Montine, J. Neurochem. 84 (2003) 336–346.
[16] L. Molinengo, L. Oggero, P. Ghi, M. Orsetti, Brain Res. 551 (1991) 72–77.
[17] M.J. Berridge, Neuron 21 (1998) 13–26.
[18] S. Kintzios, E. Pistola, P. Panagiotopoulos, M. Bomsel, N. A$lexandropoulos, F. Bem, C. Varveri, G. Ekonomou, J. Biselis, R. Levin, Biosens. Bioelectron. 16 (2001) 325–336.
[19] S. Kintzios, F. Bem, O. Mangana, K. Nomikou, P. Markoulatos, N. Alexandropoulos, C. Fasseas, V. Arakelyan, A.-L. Petrou, K. Soukouli, G. Moschopoulou, C. Yialouris, A. Simonian, Biosens. Bioelectron. 20 (2004) 906–916.
[20] B.X. Hoang, D. Graeme Shaw, P. Pham, S.A. Levine, Med. Hypothes. 68 (2007) 832–843.
[21] B. Viviani, S. Bartesaghi, M. Binaglia, E. Corsini, M. Boraso, E. Grazi, C.L. Galli, M. Marinovich, Toxicol. Lett. 182 (2008) 63–68.
[22] M. Marinovich, B. Viviani, V. Capra, E. Corsini, L. Anselmi, G. D'Agostino, A. Di Nucci, M. Binaglia, M. Tonini, C.L. Galli, Chem. Res. Toxicol. 15 (2002) 26–32.
[23] R.A. Goyer, in: M.O. Amdur, J. Doull, C.D. Klaassen (Eds.), Toxicology: The Basic Science of Poisons, Pergamon Press, New York, 1986, pp. 623–680.
[24] T. Wlostowski, Biochem. Physiol. 103C (1992) 35–41.
[25] P.A. Davies, W. Wang, T.G. Hales, E.F. Kirkness, J. Biol. Chem. 278 (2003) 712–717.
[26] T. Houtani, Y. Munemoto, M. Kase, S. Sakuma, T. Tsutsumi, T. Sugimoto, Biochem. Biophys. Res. Commun. 335 (2005) 277–285.
[27] R.J. Whelan, R.N. Zare, Biosens. Bioelectron. 18 (2003) 1065–1072.
[28] O. Aust, N. Ale-Agha, L. Zhang, H. Wollersen, H. Sies, W. Stahl, Food Chem. Toxicol. 41 (2003) 1399–1407.
[29] J.J. Pancrazio, J.P. Whelan, D.A. Borkholder, W. Ma, D.A. Stenger, Ann. Biomed. Eng. 27 (1999) 697–711.
[30] S. Daunert, G. Barrett, J.S. Feliciano, R.S. Shetty, S. Shrestha, W. Smith-Spencer, Chem. Rev. 100 (2000) 2705–2738.
[31] ISO 10993-5: Biological evaluation of medical devices, Part 5: Tests for in vitro cytotoxicity, International Standardization Organization, Switzerland, 1999.
[32] J. Flaskos, W.G. McLean, M.J. Fowler, A.J. Hargreaves, Neurosci. Lett. 242 (1998) 101–104.
[33] A. Verkhrastky, Calcium signalling and disease: molecular pathology of calcium, in: E. Carafoli, M. Brini (Eds.), Subcell. Biochem. (2007) 465–480.
[34] F. Barone, S. Aguanno, A. D'Alessio, A. D'Agostino, FASEB J. 18 (2004) 353–354.
[35] X.J. Wang, J.X. Xu, Neurosci. Lett. 376 (2005) 127–132.

Talanta 80 (2010) 1805–1808

Contents lists available at ScienceDirect

Talanta

journal homepage: www.elsevier.com/locate/talanta

Sonogel–carbon electrode based on hemin for detection of superoxide

Hanane Zejli[a,b,c,*], Jose Luis Hidalgo-Hidalgo de Cisneros[b], Ignacio Naranjo-Rodríguez[b], Khalid Riffi Temsamani[c], Jean-Louis Marty[a]

[a] Centre de Phytopharmacie, Université de Perpignan-Biomem, Perpignan Cedex, France
[b] Department of Analytical Chemistry, Faculty of Sciences, University of Cádiz, Cádiz, Spain
[c] Equipe de Recherche Bioelectrochemie et Systèmes Interfaciaux, University Abdelmalek Essaadi, Tétouan, Morocco

ARTICLE INFO

Article history:
Received 10 May 2009
Received in revised form
30 September 2009
Accepted 9 October 2009
Available online 14 November 2009

Keywords:
Superoxide
Superoxide sensor
Hemin
Hemin-modified electrode
Antioxidant

ABSTRACT

The Sonogel electrode was immersed in hemin solution to obtain the hemin–Sonogel-modified electrode by cyclic voltammetry (CV). It was applied to detect superoxide radicals produced by xanthine oxidase catalyzed hypoxanthine oxidation. The characterization of hemin–Sonogel was modified by impedance and CV.

© 2009 Elsevier B.V. All rights reserved.

1. Introduction

Hemin–iron protoporphyrin is the active center of the family of heme-proteins, such as cytochromes, peroxidase, myoglobin, and hemoglobin. In 1968, the electrochemical behaviour of hemin at a platinum electrode was already studied in a homogeneous solution by means of the coulostatic method [1]. Furthermore, the adsorption characteristics of hemin or hemin derivatives on carbon and mercury electrodes have been evaluated [2–6]. Hemin adsorbs strongly on the carbon electrode, especially on a pyrolytic graphite (PG) electrode. The adsorbed hemin remains fast electron transfer to the electrode surface. The adsorption of hemin on PG electrode can exceed the monolayer coverage, and thus, a higher amount of active species can be obtained [4,5]. The application of hemin electrodes in catalysis and the reduction of hydrogen peroxide and oxygen were also reported.

Superoxide is an oxygen-derived, potentially cytotoxic specie. Recently, there has been increasing evidence that superoxide is implicated in the pathology of many human diseases. The determination of superoxide has become a major interest to scientists from many fields. The electrochemical assay of superoxide has caused considerable attention during the past decade. There are two main types of electrochemical superoxide sensors. The work principle of the first type is based on the specific dismutation of superoxide by superoxide dismutase (SOD) [7–9]. In this case, hydrogen peroxide, the product of superoxide dismutation, is determined at the electrode surface. However, at the high electrode potential −0.5 V vs. Ag/AgCl, serious interferences appear from other substances in the medium. The selectivity of the electrode can be improved by using a superoxide permeable membrane, such as Teflon. However, the sensitivity and the response rate are decreased. The second group is based on the reduction of cytochrome *c* (cyt *c*) by superoxide. The reoxidation of cyt *c* on an electrode surface led to a current proportional to superoxide concentration. In order to establish electrochemical communication between the redox protein and the electrode, mediator-based configurations as well as configurations without mediator were used. Analytical application of cyt *c* for electrochemical assay of superoxide in a homogeneous solution was demonstrated with a promotor-modified electrode [10,11]. In the investigations carried out by Campanella et al. [12], hemin contained in a carbon paste electrode was used as electron mediator between cyt *c* and the carbon electrode in the detection of superoxide. Other attempts involved covalently immobilized cyt *c* on a 3,3-dithiobis-sulfosuccinimidylpropionate-modified gold electrode for the determination of superoxide [13]. Recently, the in vivo measurements have been successfully performed with cyt *c* covalently bound to an alkane thiol modified gold electrode [14,15].

The Sonogel–carbon electrode constitutes the novelty of the paper. The relative stability of these biosensors can be attributed to

* Corresponding author at: Centre de Phytopharmacie, Université de Perpignan-Biomem, Perpignan Cedex, France.
E-mail address: zejlih@yahoo.fr (H. Zejli).

0039-9140/$ – see front matter © 2009 Elsevier B.V. All rights reserved.
doi:10.1016/j.talanta.2009.10.017

two factors. The first of them is the biocompatibility of the Sonogel electrode with hemin, probably because of the inorganic–organic structure of the Sonogel. The second is the inertness of this material. The shrinking phenomenon was avoided, thanks to the exclusion of the use of organic solvent in the sonogeling process, and the porosity and dry at room temperature. In this paper, a hemin-modified Sonogel–carbon electrode and its application for the electrochemical determination of superoxide is reported.

2. Experimental

2.1. Reagents

Xanthine oxidase (XOD) from cow milk (EC 1.1.3.22) was supplied by Boehringer-Mannheim. Hypoxanthine, catalase, and superoxide dismutase (SOD) were purchased from Sigma. All other products were of reagent grade and were used as received. Water purified by a Milli-Q system was used to prepare all the solutions. Stock solutions of 20 U XOD were prepared. The concentration of the hypoxanthine stock solution was 4 mM. The stock solution of hemin was prepared by dissolving hemin in 0.1 ml, 1 M NaOH, then diluted with 4.9 ml phosphate buffer solution (PBS) to acquire a final pH value of 7.5. A 0.1 M PBS containing 0.1 mM EDTA was prepared by mixing Na_2HPO_4, NaH_2PO_4, and EDTA with distilled water; the pH value was 7.5.

2.2. Apparatus

The measurements were performed in a stirred electrochemical cell. The three electrodes system consisted of Sonogel–carbon modified electrode as working electrode, an Ag/AgCl (3 M KCl) as reference electrode and a platinum wire as auxiliary electrodes. The formal potential values of hemin adsorbed on the electrode surface reported in the literature were recalculated vs. Ag/AgCl in 1 M KCl solution at pH 7.5. Cyclic voltammetry (CV) was performed using an Autolab system, Eco Chemie, the Netherlands.

2.3. Electrode preparation

The unmodified Sonogel–carbon electrode was prepared as described previously [16,17]. Before modification, the electrodes were polished with emery paper No. 1200 to remove extra composite material, wiped gently with weighing paper, thoroughly washed with deionised water and allowed to dry at room temperature. The prepared electrode was then immersed in 0.05 mM hemin solution to obtain the hemin-modified electrode by CV.

2.4. Superoxide measurement

In the electrochemical measurements, superoxide is generated by the reaction of hypoxanthine with XOD in the presence of dioxygen in PBS at room temperature. The reaction is:

$$\text{Hypoxanthine} + O_2 \xrightarrow{\text{XOD}} \text{uric acid} + O_2 + H_2O \quad (1)$$

$$H_2O_2 \xrightarrow{\text{catalase}} \frac{1}{2}O_2 + H_2O \quad (2)$$

The PBS containing hypoxanthine and 40 U ml^{-1} catalase was added to the electrochemical cell. The function of catalase was to remove the co-product H_2O_2. The reaction was started by adding XOD in the activity range of 10–90 mU ml^{-1}. The concentration of hypoxanthine in the electrochemical cell was 100 mM.

To test the effect of SOD, superoxide was generated by the use of 30 mU ml^{-1} XOD. The relative current decrease compared to the measurement without SOD was evaluated as the sensor signal.

2.5. Electrochemical Impedance Spectroscopy measurements

Electrochemical Impedance Spectroscopy (EIS) measurements were performed with a Voltalab 10 type PGZ 100 from Radiometer. The impedance spectra were recorded using the same three-electrode-cell setup described before. The initial frequency used was 100 KHz and the final one was 10 mHz with an AC amplitude of 5–10 mV. In order to insure the inert effect of hemin during the experiment, the potential of 0.15 V was chosen in the presence or in the absence of hemin.

3. Results and discussion

3.1. The effect of hemin concentration, scan rate, and number of scan cycles on the characteristics of the modified electrode

It was found that hemin concentration, scan rate, and number of scan cycles affect the formation of the electropolymerizate membrane. For low hemin concentration, the catalytic current decreased due to the lower degree of polymerization. The catalytic current increased with increasing hemin concentration due to the higher degree of polymerization. However, when the concentration of hemin reached 1×10^{-4} mol l^{-1}, the catalytic current became lower; therefore, 5×10^{-5} mol l^{-1} hemin concentration was used for subsequent experiments. The effect of scan rate is related to the hemin concentration and number of scan cycles. When the number of scan cycles is constant, the catalytic current increases with scan rate. The peak current was proportional to the potential scan rates, in the range of 10–700 mV s^{-1} (Fig. 1), as expected for a diffusion-controlled process.

When scan rate is constant, the catalytic current also increases with increasing number of scan cycles. However, when the scan rate or the number of cycles was too high, the catalytic current decreased slightly. This is because the electrochemical characteristics of the modified electrode are closely related to the thickness of the membrane at the surface of the modified electrode. When the membrane is thicker, more electro-active groups are linked to the membrane so the catalytic current is higher, but at the same time the resistance-to-charge transfer in the membrane also increases, which decrease the catalytic current to sum up. The optimum conditions for preparation of the hemin/Sonogel electrode used in subsequent studies are as follows: hemin concentration: 5×10^{-5} mol l^{-1}; scan rate: 50 m Vs^{-1}; number of scans: 60 cycles.

3.2. The selection of supporting electrolyte

For an organic system the proton is always involved in the electrode reaction, so a buffer solution is often used as the supporting

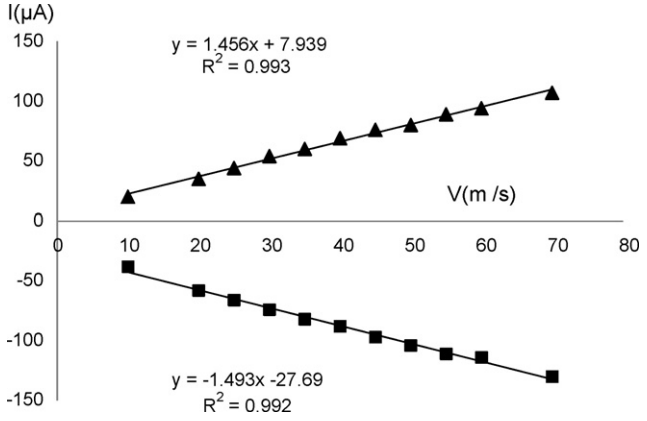


Fig. 1. Plots of cathodic (triangular) and anodic (square) current at the electrode as a function of scan rates in 0.2 M BR buffer, pH 6.

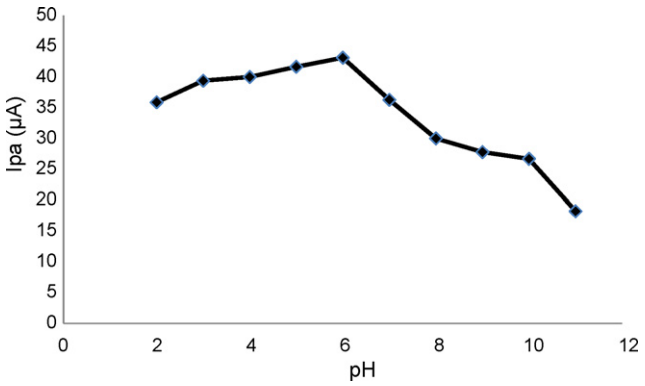


Fig. 2. Effect of pH, 0.2 M BR buffer.

electrolyte, and the peak shape and $E_{1/2}$ are closely related to the pH of the buffer solution. Therefore, selection of a suitable buffer solution is very important. The cyclic voltammetric behaviour of hemin in different media: HCl (pH 1.0–2.0) Britton–Robinson (BR) buffer solution (pH 2.0–10.0), HAc–NaAc buffer solution (pH 3.6–5.7), Michlaelis buffer solution (pH 5.2–8.3), and NH_3–NH_4Cl buffer solution (pH 7.5–11.0) were investigated. The results showed that the electrochemical responses of hemin were better in the acidic and neutral media. In NH_3–NH_4Cl buffer, the oxidation peaks of hemin were unsymmetrical, and their peak current was lesser. Symmetrical oxidation peaks were obtained in HCl, BR buffer, HAc–NaAc buffer and Michlaelis buffer, but the sensitivity is better for BR buffer, so it was used for subsequent experiments.

3.3. Effect of pH supporting electrolyte on hemin matrix

The pH of the supporting electrolyte affects directly the performance of the enzyme sensor due to the accumulation of protons. Fig. 2 shows the effect of pH on the anodic peak current of hemin. The best response is obtained at pH 6. All subsequent experiments were performed at pH 6.

3.4. Adsorption of hemin on Sonogel–carbon electrode

The preparation of hemin-modified Sonogel–carbon electrode is carried out by CV in a hemin solution; Fig. 3 shows the CV curve obtained. The formal potential estimated by $E^{\circ\prime} = (E_{pa} + E_{pc})/2$ is −0.34 V at pH 6. It is almost the same as that obtained with a hemin-modified basal plane PG [3], glassy carbon [2], and PG electrode [4]. It is about 20 mV more positive than the formal potential of hemin adsorbed on an edge plane PG electrode [5]. This shows that the formal potential of hemin is only slightly dependent on the characteristics of the electrode surface.

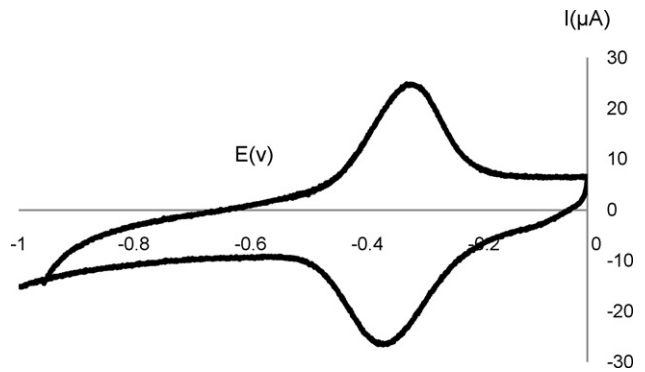


Fig. 3. Cyclic voltammograms of hemin/Sonogel–carbon electrode in 0.2 M BR buffer, pH 6.

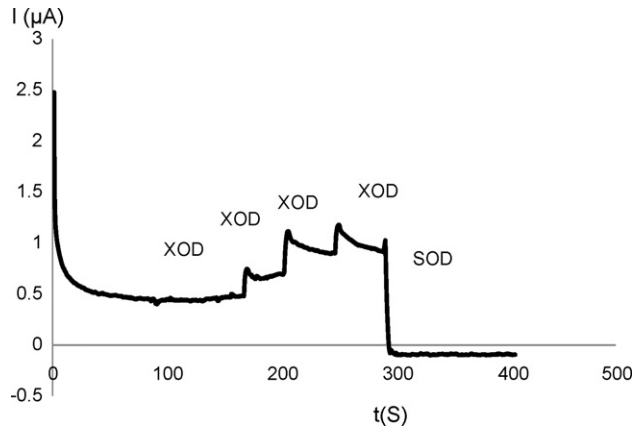


Fig. 4. Amperometric response of the hemin/Sonogel–carbon electrode on 30 mU ml^{-1} addition to a 100 mM hypoxanthine containing BR buffer and the effect of 2 U SOD, detection potential 0.15 V.

3.5. Oxidation of superoxide obtained with hemin–Sonogel–carbon electrode

For amperometric measurements of superoxide, the electrode was operated at a constant potential of 0.15 V [18]. The response of the hemin-modified Sonogel electrode to superoxide is shown in Fig. 4. Under the reaction conditions described here, a plateau response current was attained a few seconds after the addition of XOD in solution, i.e. at the start of the superoxide generation. The steady-state response current resulted from the counter balance between the enzymatic generation and the spontaneous dismutation of superoxide. It is a function of XOD concentration added in the solution. XOD obviously did not induce response in the absence

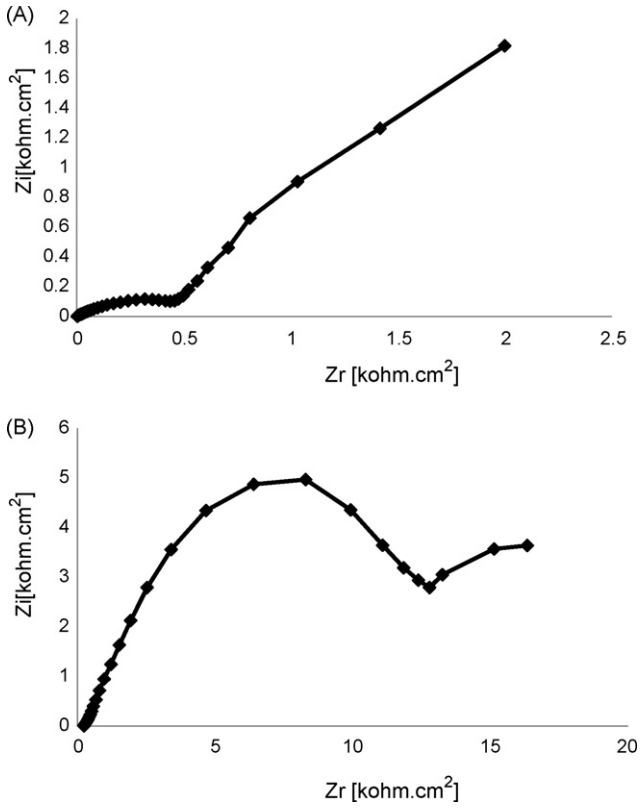


Fig. 5. Nyquist plot for (A) Sonogel–carbon electrode and (B) hemin/Sonogel–carbon.

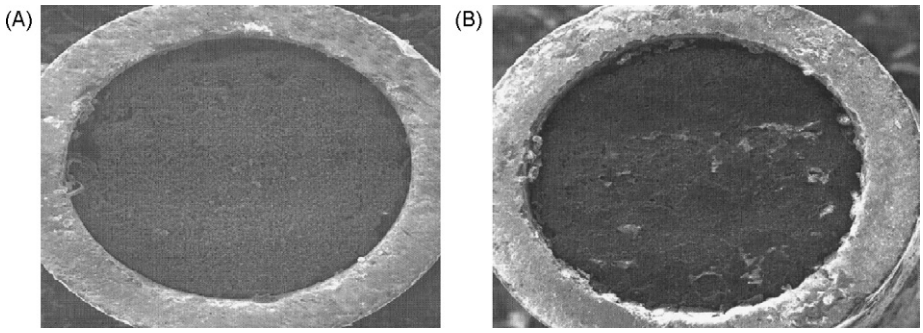


Fig. 6. SEM measurements obtained at 25.0 KV with a 500× zoom. (A) Sonogel–carbon electrode and (B) Hemin/Sonogel–carbon electrode.

of hypoxanthine. It is important to note that the response current could be eliminated immediately on the addition of SOD.

3.6. EIS measurements

In order to confirm the mechanisms suggested in the voltammetric part of this work regarding the hemin/Sonogel–carbon electrode interaction, we have performed EIS measurements. The impedance spectra in Fig. 5 were collected at 150 mV in a frequency range from 100 KHz to 10 mHz with an AC amplitude of 5 mV. Fig. 5A shows the Nyquist plot for the hemin-modified electrode. The high-frequency arc observed may be associated to charge transfer at the hemin–Sonogel–carbon electrode/solution interface. If we admit the randle equivalent circuit model, the calculated (Voltamaster® 4.0 software) charge transfer resistance (Rct) and the double layer capacitance Cd are, respectively: Rct = 14.22 kohm cm^2 and Cd = 27.97 $\mu F\,cm^{-2}$.

On the other hand, Fig. 5B also exhibited an arc like Nyquist plot for the Sonogel system; the electrical parameters calculated were: Rct = 619.2 kohm cm^2 and Cd = 25.68 $\mu F\,cm^{-2}$. It appears clearly from these data that the capacitance at the interface increases when the Sonogel–carbon electrode is modified with hemin. This observation is in agreement with literature. The observed decrease of the charge transfer resistance means also that Sonogel–Carbon/hemin system favors the electron transfer reaction at the electrode surface.

3.6.1. Reproducibility and stability

The reproducibility of the biosensors was evaluated by mean of 11 repetitive measurements with each electrode in 0.2 mol/l BR buffer, pH 7, 30 mU ml^{-1} XOD, 100 mM hypoxanthine. Relative standard deviation is 4.5%.

The hemin electrode responded quickly to superoxide, the hemin–Sonogel electrode could work stably for more than 22 h. The reproducibility of the hemin–Sonogel electrode is acceptable. The mean error of the amperometrie response of the amperometrie response of the hemin–Sonogel is within 5% for 10 measurements during more than 1 h.

3.6.1.1. SEM measurements. The results of morphological studies conducted on hemin/Sonogel–carbon are shown in Fig. 6. The SEM of Sonogel–carbon indicates that the film is uniform. The SEM of hemin/Sonogel–carbon shows the particle on the Sonogel carbon confirms the presence of hemin.

4. Conclusion

In this work, we have prepared a new modified Sonogel–carbon electrode based on the incorporation of hemin for detection of superoxide in aqueous solution. This method is very simple and offers a relative short analysis time. It is inexpensive and presents easy operability; and could be applicable for field-analysis use.

Acknowledgements

Support of this study by the Agence Universitaire de la Francophonie and Mr. Marty are gratefully acknowledged.

References

[1] R.F. Martin, D.G. Davis, Biochemistry 7 (1968) 3906–3912.
[2] Z.Q. Feng, T. Sagara, K. Niki, Anal. Chem. 67 (1995) 3564–3570.
[3] T. Sagara, S. Takagi, K. Niki, J. Electroanal. Chem. 349 (1993) 159–171.
[4] P. Bianco, J. Haladjian, K. Draoui, J. Electroanal. Chem. 279 (1990) 305–314.
[5] T. Sagara, S. Takeuchi, K. Kumazaki, N. Nakashima, J. Electroanal. Chem. 396 (1995) 525–533.
[6] C.F. Kolpin, H.S. Swofford Jr., Anal. Chem. 50 (1978) 916–920.
[7] S. Mesaros, Z. Vankova, S. Grunfeld, A. Mesarosova, T. Malinski, Anal. Chim. Acta 358 (1998) 27–33.
[8] V. Lvovich, A. Scheeline, Anal. Chem. 69 (1997) 454–462.
[9] M.I. Song, F.F. Bier, F.W. Scheller, Bioelectrochem. Bioenerg. 38 (1995) 419–422.
[10] C.J. McNeil, K.A. Smith, P. Bellavite, J.V. Bannister, Free Radic. Res. Commun. 7 (1989) 89–96.
[11] F. Matsumoto, K. Tokuda, T. Ohsaka, Denki Kagaku 63 (1995) 1205–1208.
[12] L. Campanella, G. Favero, M. Tomassetti, Sens. Actuators B44 (1997) 559–565.
[13] K. Tammeveski, T.T. Tenno, A.A. Mashirin, E.W. Hillhouse, P. Manning, C.J. McNeil, Free Radic. Biol. Med. 25 (1998) 973–978.
[14] W. Scheller, W. Jin, E. Ehrentreich-Fo¨rster, B. Ge, F. Lisdat, R. Bu¨ttemeier, U. Wollenberger, F.W. Scheller, Electroanalysis 11 (1999) 703–706.
[15] F. Lisdat, B. Ge, E. Ehrentreich-Fo¨rster, R. Reszka, F.W. Scheller, Anal. Chem. 71 (1999) 1359–1365.
[16] M.M. Cordero-Rando, J.L. Hidalgo-Hidalgo de Cisneros, E. Blanco, I. Naranjo-Rodríguez, Anal. Chem. 74 (2002) 2423.
[17] J.L. Hidalgo-Hidalgo de Cisneros, M.M. Cordero-Rando, I. Naranjo-Rodríguez, E. Blanco, L. Esquivias, Patent P200100556, Spain, March 2001.
[18] J. Chen, U. Wollenberger, F. Lisdat, B. Ge, F.W. Scheller, Sens. Actuators B 70 (2000) 115–120.

Talanta 80 (2010) 1809–1815

Contents lists available at ScienceDirect

Talanta

journal homepage: www.elsevier.com/locate/talanta

A sensor based on electrodes supported on ion-exchange membranes for the flow-injection monitoring of sulphur dioxide in wines and grape juices

Rosanna Toniolo, Andrea Pizzariello, Sabina Susmel, Nicolò Dossi, Gino Bontempelli*

Department of Chemical Science and Technology, University of Udine, via Cotonificio 108, I-33100 Udine, Italy

ARTICLE INFO

Article history:
Received 6 August 2009
Received in revised form
29 September 2009
Accepted 9 October 2009
Available online 8 November 2009

Keywords:
Sulphur dioxide
Wines and grape juices
Solid polymer electrolyte (SPE) electrodes
Gold electrodes supported on ion-exchange membranes
Flow-injection analysis

ABSTRACT

A sensitive and fast responding electrochemical sensor is described for the determination of free and total sulphur dioxide in wines and grape juices which prevents interferences coming from ethanol and other natural components. It consists of a cell provided with a porous gold working electrode supported on one face of an ion-exchange membrane, acting as a solid polymer electrolyte (SPE), which allows gaseous electroactive analytes to be detected. This sensor was used as an amperometric detector for a flow injection system in which controlled volumes of headspace equilibrated with samples were injected. This approach was adopted to make also possible the determination of total SO_2, avoiding drawbacks caused by the high relative humidity generated by the sample heating resulting from the neutralization reaction of excess NaOH, whose addition was required to release sulphur dioxide from its combined forms. Factors affecting the detection process were examined and optimised. Under the identified optimal conditions, SO_2 detection resulted in sharp peaks which allowed to infer detection limits for a signal-to-noise ratio of 3, referred to liquid samples, of 0.04 and 0.02 mg L^{-1} for free and total SO_2 which were determined at 20 and 35 °C, respectively. Moreover, the responses were found to be characterized by good repeatability (±2% and ±4%, respectively) and linear dependence on the SO_2 concentration over a wide range (0.2–500 mg L^{-1} for both free and total SO_2). Finally, the long-term stability of the sensor turned out to be totally satisfactory in that responses changed of ±9% alone even after long periods of continuous use. The application to some commercial wines and grape juices is also presented.

© 2009 Elsevier B.V. All rights reserved.

1. Introduction

Sulphur dioxide is extensively used in food and beverage making, not only in view of its profitable antioxidant properties but also because it displays a selective inhibitor effect on enzymatic and microbial activity. In particular, this compound is largely employed in grape processing for both selecting yeast strains in wines and preventing oxidative and fermentative processes in the storage of grape juices (as well as of other fruit juices) intended for the direct consumption. At a certain level, sulphur dioxide is toxic for human health since it can cause asthmatic attacks and allergic reactions [1,2], so that the excess added must be removed and its residual content must be controlled carefully.

In wine and grape juices, as well as in other several food products, the unremoved SO_2 can occur as both free and bound sulphur dioxide. Free SO_2, the actual active fraction, includes all unreacted species (typically HSO_3^- and SO_2) present at the specific pH, whereas bound SO_2 corresponds to its combined forms with different functional groups displayed by some of the constituents (mainly carbonyl groups, e.g. acetaldehyde, and pigments, e.g. anthocyanins). Such a combined sulphur dioxide can be released by promoting hydrolysis of its derivatives in basic media.

Residual sulphur dioxide represents a potential hazard, so that both the World Health Organization (WHO) and the Food and Agriculture Organization (FAO) have recommended a maximum daily intake (ADI) for adults of 0.7 mg kg^{-1} body weight, including all species containing S(IV) [3]. Moreover, in the European Community the presence of total sulphur dioxide is regulated by strict provisions which set legal limits for their maximum content in several foods, including wines (ranging from 160 to 400 mg L^{-1}, depending on wine quality) [4] and grape juices (10 mg L^{-1}) [5].

The standard method recommended for the determination of free SO_2 in wines or grape juices involves its transfer (with N_2 as a sweeping gas or with air aspiration) from acidified samples into a hydrogen peroxide trap where it is oxidized to H_2SO_4, which is then titrated with NaOH [6]. Total SO_2 is recommended to be determined by the same procedure, but after addition of NaOH and subsequent heating, so as to allow bound SO_2 to be released by hydrolysis of the relevant compounds [6]. This approach is tedious, time consuming, not easy to be automatized and suffers moreover from many possible interferences. This is the reason why several alternative methods have been proposed, mainly based on spectrophotometric

* Corresponding author. Tel.: +39 0432 558842; fax: +39 0432 558803.
E-mail address: gino.bontempelli@dstc.uniud.it (G. Bontempelli).

0039-9140/$ – see front matter © 2009 Elsevier B.V. All rights reserved.
doi:10.1016/j.talanta.2009.10.024

[7,8], chromatographic [9] electrophoresis [10], electroanalytical [11–13] and enzymatic [14,15] approaches. Even though some of these approaches are characterized by good selectivity and quite low detection limits, they are in general unsuitable for on-line and in situ monitoring. The sole exception is given by electroanalytical methods that, in principle, make possible in situ and instantaneous multicomponent measurements with on-line capabilities and low-cost instrumentation.

Unfortunately, conventional electroanalytical measurements performed directly in wines or grape juices are expected to be markedly interfered from other several reducing species present in these matrices (such as ascorbate ions and polyphenolics). Improved accuracy could certainly be attained by headspace analysis, by profiting of SO_2 volatility, but usual electroanalytical procedures cannot be directly applied to gaseous samples in which no supporting electrolyte is present and none can be added.

To overcome this obstacle, gas-permeable membrane electrodes have been developed, based on the diffusion of gaseous analytes through a membrane, so as to dissolve in an internal electrolyte solution where they diffuse to the working electrode. The performance of these devices is just conditioned by these diffusion steps which proves to be critical because they affect unfavourably sensitivity and response time [16,17].

A considerable amount of work has been performed in the last two decades on amperometric gas sensors of last generation which allow electroanalytical measurements to be performed in gas phase, without suffering from the drawbacks above. They are based on the use of moist ion-exchange membranes as solid polymer electrolytes (SPEs) [16–29] which are usually coated on one side (facing the analyte sample) with a porous conductive film (working electrode), while the other side contacts an electrolyte solution containing counter and reference electrodes. In these devices any membrane-permeation step is avoided since the membrane separating the sample from the internal electrolyte is not permeated by gaseous analytes but serves to ensure the transfer of charged species from the working to the counter electrode, thus playing the role usually played by supporting electrolytes [16].

In this paper we propose just the use of a SPE sensor allowing the selective detection of sulphur dioxide in the head-space in equilibrium with samples involved in grape processing, thanks to the appropriate choice of electrode material and internal electrolyte, as well as of the applied electrode potential. In particular, it prevents interferences coming from other volatile species (mainly ethanol) present in these real samples. Moreover, the optimised conditions of its use as a detector for a flow-injection system make possible very good performance to be achieved for the determination of both free and bound SO_2.

2. Experimental

2.1. Chemicals and instrumentation

All chemicals used were of analytical reagent grade quality and were employed without further purification. In all instances, high purity deionized water (resistivity $\geq$18 MΩ cm), purified with an Elgastat® UHQ-PS system ("Elgastat water"), was used as the solvent.

Stock standard solutions (0.05 M) of sodium sulphite were prepared daily by dissolving weighed amounts of the pure compound in Elgastat water and immediately deaerated by bubbling nitrogen, so as to minimize oxidation to sulphate caused by dissolved oxygen. Their standardization was conducted by the conventional iodimetric procedure involving slow addition of a controlled aliquot of sulphite sample to an acidified standard iodine solution, whose excess was back titrated with standard thiosulphate.

Synthetic samples were usually prepared by adding known amounts of sodium sulphite to Elgastat water containing or not 12% (v/v) ethanol for mimicking wine and grape juice samples, respectively. In some cases, to mimic better real samples, home-made musts were used, prepared by manual squeezing of different types of red and white table-grapes. They were filtered through sterilized gauzes and stored at 0 °C after addition of sodium benzoate, to inhibit bacterial growth. Soon before their use, either known amounts of sodium sulphite alone or Na_2SO_3 plus 12% (v/v) ethanol were added to these musts to mimic grape juices and wines, respectively. Sulphur dioxide was released from all these synthetic samples by addition of 85% (w/w) phosphoric acid, so as to achieve a 3 M final acid concentration.

Real grape juice and wine samples were purchased from local supermarkets and were used without preliminary treatments.

All voltammetric and amperometric experiments were performed by an EG&G PARC Model 273 potentiostat driven by an EG&G PARC Model 270 software installed on a Pentium IV computer. Flow-injection analyses were carried out by using nitrogen as carrier gas, whose rate was controlled in the range 70–200 mL min^{-1} by a micrometric valve Viton SS-22RS2.

2.2. Electrode assembly

The design of the SPE electrode used throughout this investigation is sketched in Fig. 1. Its core was the ion-exchange membrane, one surface of which (that facing the sample) was covered with a porous Au layer acting as the working electrode. The ion-exchange material used as SPE was a Nafion® 117 cationic perfluorinated membrane, 0.175 mm thick, supplied by Sigma–Aldrich, which was preliminarily cleaned by boiling in concentrated HNO_3 for 1 h and then in high purity deionized water for 1 h.

Au composite electrodes were prepared by pressing mechanically a close-mesh Au net (wire diameter 0.06 mm) onto one surface of a Nafion membrane, preliminarily coated with a very thin film of Nafion formed by droplet evaporation of a 5% (w/w) Nafion alcoholic solution (Aldrich). Au net and membrane were then placed one on another and tightened between two aluminium blocks suitably heated at 50 °C for 1.5 h.

Coated membranes were then cut into discs 1 cm in diameter, which were used to assemble SPE electrodes. To this end, one of the desired disc-shaped composites was clamped, with the conductive layer directed downward, at the bottom of a Pyrex cylinder, the end of which was threaded for connection to a drilled Teflon holder sealing the assembly by means of an elastic O-ring resistant to acids and bases. Electrical contact with the porous working electrode was made by inserting a thin Au ring in the shallow recession on the bottom of the inner side of the drilled holder, onto which the border of the electrode was pressed. A metallic wire contacting this ring and piercing through the holder permitted electrical connection. Such an assembly allowed ca. 0.5 cm^2 of covered membrane to be exposed to external media.

The uncoated side of the membrane was brought into contact with an aqueous electrolyte solution (1 M $HClO_4$) contained in an internal compartment which was equipped with a platinum counter electrode and an $Ag/AgCl,Cl^-_{sat}$ reference electrode, connected by a salt bridge containing 1 M $HClO_4$ either. This internal compartment was made out of the extension of the Pyrex cylinder which was sealed to the bottom of a suitable standardized hollow glass stopper, so as to can be used as a gas-tight stopper for containers in which measurements were conducted.

When the working electrode was held at an appropriate potential, sulphur dioxide oxidation became possible (see reaction (1)) just as SO_2 molecules from the gaseous sample reached the

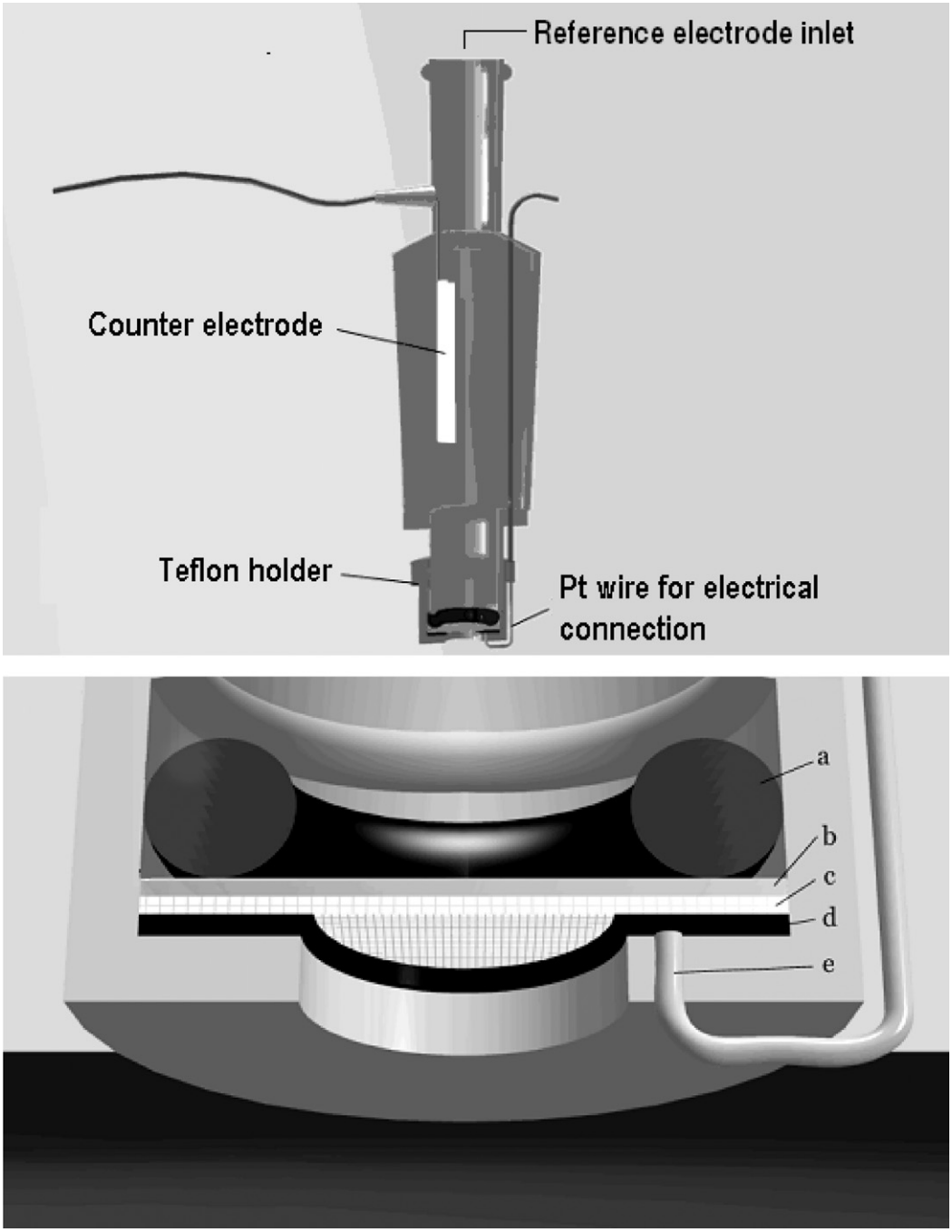


Fig. 1. Schematic view of the electrode assembly. Upper view: electrode seen as a whole. Lower view: enlargement of the electrode bottom; (a) elastic O-ring resistant to acids and bases; (b) Nafion membrane; (c) gold net; (d) gold ring; (e) copper wire for electrical connection.

metal/Nafion interphase.

$$SO_2 + 2H_2O \rightarrow {SO_4}^{2-} + 4H^+ + 2e^- \quad (1)$$

Hydrogen ions released by this anodic reaction were trapped in the membrane, coupled with an ionic migration through the membrane to maintain electroneutrality. Concurrently, hydrogen ions in the internal electrolyte were reduced at the counter electrode, thus restoring its ionic content.

2.3. Apparatus

Voltammetric and amperometric measurements by electroanalytical sensors described above were performed in gas phase under both static and flowing conditions.

Static measurements, were conducted by using SPE electrodes as gas-tight stoppers for a glass cell (ca. 110 mL) filled with 50 mL of either real or synthetic sample, this last containing variable but controlled Na_2SO_3 amounts, and provided with two additional holes and a thermostatic jacket connected to a Haake F3 thermostatic bath. One of the additional holes served for the addition of H_3PO_4 aimed at releasing SO_2, while in the other a thermometer was inserted. Electrodes were exposed to the headspace (ca. 50 mL) equilibrated with sulphur dioxide (and/or ethanol) released from the sample, by keeping it at controlled temperature (20–35 °C) in a thermostatic bath under stirring at a constant rate (100 rev min^{-1}) by an Amel (Milan, I) 291 Mast magnetic stirrer.

Flow-injection analyses were instead performed by employing the apparatus sketched in Fig. 2(A). It consisted of a glass cell, whose

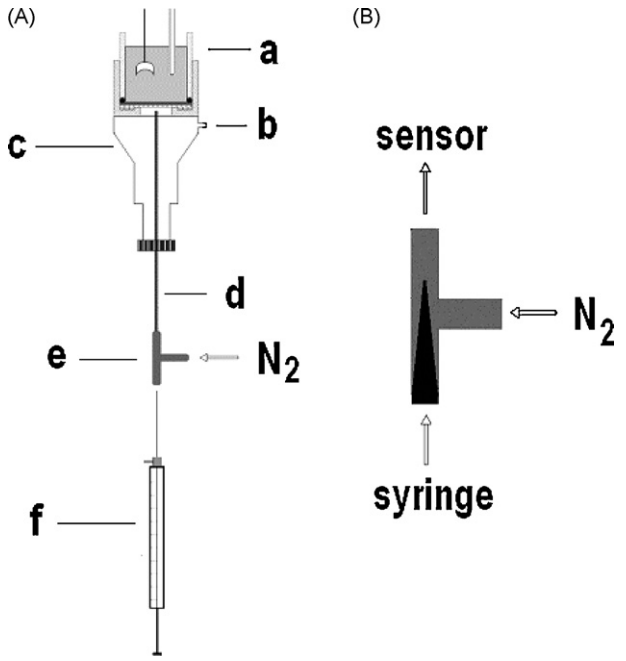


Fig. 2. (A) schematic view of the flow apparatus: (a) SPE sensor; (b) side exit for the carrier gas; (c) glass cell; (d) glass tube; (e) three-way injection device; (f) gas-tight syringe. (B) Enlarged view of the three-way injection device.

top was once again sealed by the SPE electrode acting as a gas-tight stopper, which was provided with a side exit for the carrier gas. The lower hole in the cell was sealed by a drilled stopper through which a thin glass tube (internal diameter 1.5 mm) was pierced, so as to allow flowing gas to be conveyed perpendicularly to the metal-covered Nafion surface (wall-jet configuration). The distance of the outlet of this tube from the sensing surface could be controlled by a Mitutoyo collimator microscope (Narishige, Japan). A suitable three-way connection (enlarged in Fig. 2(B)) was applied to the opposite end of the glass tube, for the carrier gas (nitrogen) supply and sample injection (by gas-tight microsyringes, through the septum covering the input opening).

An Eppendorf pipette tip was inserted into the arm for sample injection of this three-way connector (10 mm arm length; 4 mm internal diameter), to allow samples to be introduced in the same direction as that acquired by the carrier gas when its laminar flow is restored, after entrance in the connector and subsequent direction change. In such a way, a satisfactory flat baseline and well defined narrow peaks were recorded in a wide SO_2 concentration range.

All potentials are quoted versus an aqueous Ag/AgCl, $NaCl_{sat}$ reference electrode.

2.4. Analytical procedure

Free SO_2 determinations under static conditions were conducted by exposing SPE electrodes to the headspace (ca. 50 mL) in equilibrium with real or synthetic samples (50 mL) introduced in a glass cell (ca. 110 mL) thermostated at 20 °C and added with 10.2 mL of 85% (w/w) H_3PO_4 (3 M final acid concentration). After 5 min of equilibration under vigorous stirring, to attain phase distribution of released SO_2, a potential of 0.8 V versus Ag/AgCl,Cl^-_{sat} was imposed to the Au–Nafion composite electrode. Steady-state currents, recorded by keeping solutions stirred at constant rate (100 rev min^{-1}), were used to infer SO_2 contents by comparison with a calibration plot constructed for standard samples.

Total SO_2 under static conditions was instead determined after release from its combined forms by basic hydrolysis. With this aim, small amounts of a concentrated NaOH solution (19 M) were added to 50 mL of sample introduced in the thermostated glass cell, so as to achieve a 2 M final hydroxide concentration. After 7 min equilibration, 85% (w/w) H_3PO_4 was added to neutralize excess hydroxide and to achieve also in this case a 3 M final acid concentration. This neutralization caused a considerable solution heating (up to 45–50 °C) which was not counteracted quickly by water circulating into the cell jacket. Consequently, amperometric detection of total SO_2 was performed after a longer equilibration time (10 min, once again under vigorous stirring) which allowed the sample to attain a temperature of about 35 °C. The effect caused on current signals by small temperature fluctuations was accounted for by using a correction factor inferred by plotting the current signal recorded for standard SO_2 solutions against the temperature (about 3.5% signal increase per °C). The analysis was then conducted by following the procedure above for free SO_2.

Free and total sulphur dioxide determinations under flow conditions were performed on synthetic and real samples introduced once again into the 110 mL thermostated glass cell where they were subjected to all treatments described above. After equilibration, controlled headspace volumes (0.2–1.0 mL) were drawn by gas-tight syringes and injected in the flow apparatus sketched in Fig. 2(A). By applying at the Au–Nafion composite electrode a potential of 0.8 V versus Ag/AgCl,Cl^-_{sat}, narrow peaks were recorded, whose heights were related to SO_2 contents by exploiting calibration plots constructed by using standard samples.

3. Results and discussion

3.1. Voltammetric behaviour of SO_2 and C_2H_5OH at Au covered Nafion electrodes

In order to individuate the optimum operative potential for the amperometric detection of sulphur dioxide, preliminary voltammetric investigations were performed at gold covered Nafion electrodes, with 1 M aqueous perchloric acid as the internal electrolyte. They were conducted on headspaces in equilibrium with stirred aqueous solutions containing controlled amounts of sodium sulphite and/or ethanol introduced in the thermostated glass cell mentioned above and added with suitable amounts of H_3PO_4 (see above).

A single well formed and reproducible anodic wave was observed for SO_2, whose limiting current extended in a fairly wide potential range, as shown in Fig. 3. The height of this wave increased linearly with sulphur dioxide concentration and was located at potentials (ca. 0.45 V versus Ag/AgCl, Cl^-_{sat}) in full agreement with previous findings at SPE electrodes [28,30] and resembling closely those found at conventional Au electrodes for the oxidation of SO_2 dissolved in aqueous perchloric acid [31], i.e. the medium used as the internal electrolyte wetting the rear side of the Nafion membrane. When the 1 M $HClO_4$ internal electrolyte was replaced by solutions buffered at increasing pH up to 7, no appreciable potential shift could be detected, thus suggesting that the oxidation process is mediated by the low-coverage hydrous gold oxide species formed at potentials below those required to initiate regular monolayer gold oxide (or OH_{ads}) formation [32]. However, no progressive wave decrease was observed in the second and subsequent voltammetric scans, contrary to the results found at conventional electrodes for SO_2 dissolved in aqueous solutions [33], probably thanks to the ability of ion-exchange membranes of preventing electrode passivation, which was indeed observed previously [34].

Conversely, no signal for the oxidation of ethanol (up to contents of 20% (v/v) in the aqueous solutions assayed) could be detected at Au–Nafion electrodes with an acid internal electrolyte (see Fig. 3), while this process turned out to occur at about 0.2 V versus Ag/AgCl,Cl^-_{sat} only with strongly basic internal electrolytes. These

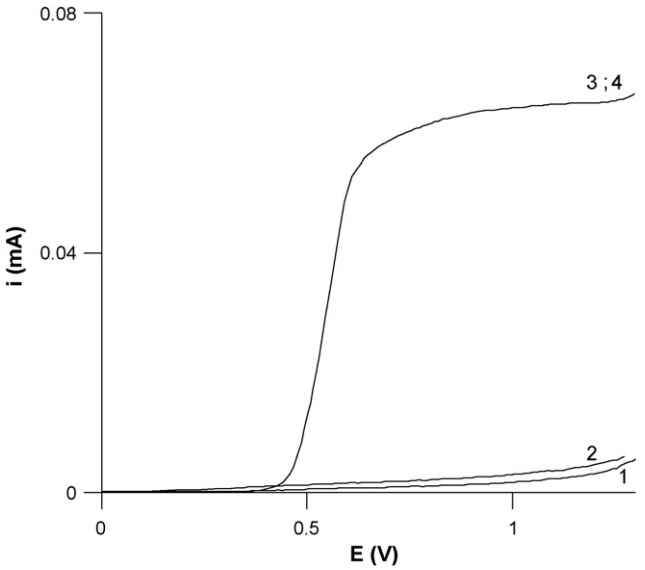


Fig. 3. Linear sweep voltammograms recorded at Au-SPE electrodes with aqueous 1 M $HClO_4$ internal electrolyte on the headspace in equilibrium with stirred: (1) Elgastat water (background profile); (2) Elgastat water containing 10% (v/v) ethanol; (3) aqueous 10^{-3} M Na_2SO_3 solution (126 mg L^{-1}, equivalent to 64 mg L^{-1} of SO_2) acidified with 85% (w/w) H_3PO_4 to achieve a 3 M final acid concentration; (4) as in (3), after addition of 10% (v/v) ethanol. Scan rate: 20 mV s^{-1}.

results agree well with previous reports on the anodic behaviour of this species at gold anodes for fuel cells [35], at gold microelectrodes [11] and at Au supported on Nafion membranes [36].

Consequently, an acid internal electrolyte was always used in the following because it proved to be suitable for the selective detection of sulphur dioxide even in the presence of ethanol, i.e. in environments like those present in the headspace of wines and grape juices.

3.2. Amperometric detection of SO_2 under static conditions

Amperometric measurements of SO_2 released by synthetic samples, consisting of either aqueous solutions or homemade musts with controlled concentrations of Na_2SO_3 and acidified with excess H_3PO_4, were first performed under static conditions. After 5 min of equilibration under vigorous stirring, the sulphur dioxide content was monitored by sampling for 2 min steady-state anodic currents recorded by applying a potential of 0.8 V to the Au working electrode. Recorded currents attained satisfactorily constant values in a fairly short time (about 15 s) and were reproducible within ±4% in replicate measurements. By plotting current signals versus SO_2 concentrations in acidified samples, a linear dependence over a wide range was found (from 0.5 to 100 mg L^{-1}) with a correlation coefficient of 0.998. From this plot, a detection limit of approximately 0.1 mg L^{-1} could be inferred for a signal-to-noise ratio of 3. Moreover, when these measurements were repeated after addition of increasing amounts of ethanol up to 20% (v/v) to synthetic sulphite samples, no appreciable change of the recorded signals was observed, thus proving that good selectivity could be achieved. Finally, when SPE electrodes were transferred from the cell to air, a rather rapid current decrease to the residual value was observed, as expected in the absence of memory effects.

Nevertheless, quite unsatisfactory results were found for the determination of total sulphur dioxide because anodic currents recorded after the equilibration time (10 min) attained acceptably constant values only after very longer times (ca. further 10 min). Moreover, these nearly constant currents turned out to be scarcely reproducible in replicate measurements (even ±25% relative standard deviations) and lacked accuracy (even – 30% recoveries were found in some cases). These very bad findings were due conceivably to the high relative humidity generated inside the cell by the solution heating caused by the neutralization reaction with H_3PO_4 of excess NaOH, required to release sulphur dioxide from its combined forms. In fact, as it could be visually observed, such a very moist atmosphere caused water condensation onto cold walls, including the Au net supported on the Nafion membrane acting as sensor probe, thus troubling markedly its basic operating mechanism. SPE electrodes are indeed effective fast-responding sensors, unlike conventional membrane electrodes, thanks to the fact that gaseous analytes undergo electrochemical reaction just as they reach directly the three-phase sites where the electrode, ion-exchange membrane and gas meet [16]. Instead, when a thick layer of condensed water is formed onto the sensor probe, the electrochemical reaction can occur only after two additional quite slow steps consisting in the dissolution of gaseous analytes into this water layer and their subsequent diffusion to the sensing surface. Consequently, under these conditions a lengthening of the response time, together with a decrease in sensitivity and a lack of signal constancy (owing to fluctuations with time of the water layer thickness) have to be expected. Moreover, changes with time of the swelling degree of the Nafion membrane are conceivably involved, which cause modifications of its area contacted by the Au net and hence of the effective electrode surface.

To overcome this drawback caused by the high humidity of the detection environment, the sensor was used as a flow-injection detector in a device separated from the vessel where hydrolysis and neutralization were let to occur, so as to minimize water condensation onto the sensor surface thanks to the use of small aliquots of the sample headspace.

3.3. Amperometric detection of SO_2 under flow-injection conditions

The performance of this detection approach is expected to be affected significantly by some important parameters, such as sample size, carrier gas flow rate and distance from the sensing surface of the outlet of glass tubing conveying gaseous samples (see Fig. 2(A)).

Sample size was first considered by injecting volumes ranging from 0.2 to 1.0 mL and keeping constant both carrier gas flow rate (150 mL min^{-1}) and distance between sample outlet and sensing surface (1 mm). As expected, the progressive increase of headspace volume injected caused improvement of sensitivity (a higher number of electroactive molecules reached the sensor surface), but also a concomitant shortening of the dynamic range (a progressively decreasing fractions of whole SO_2 molecules injected hit indeed the electrode surface, so as to undergo oxidation). The results found in these tests, which are summarized in Table 1, led to conclude that the most profitable performance was achieved by injecting 0.5 mL of sample, because this volume allows a satisfactory detection limit to be achieved concomitantly with a so wide linear range as to include even the maximum SO_2 legal limit set in wines (400 mg L^{-1}).

As to the effect of the carrier gas flow rate, which was evaluated in the range 50–200 mL min^{-1}, Table 2 compares some of the most

Table 1
Comparison of dynamic ranges and detection limits found by injecting different volumes of headspace in equilibrium with synthetic samples containing different SO_2 contents. Carrier gas flow rate: 150 mL min^{-1}; distance of the tube outlet from the sensing surface: 1 mm.

Sample volume (mL)	Dynamic range (mg L^{-1})	Detection limit (mg L^{-1})
0.2	0.5–700	0.10
0.5	0.2–450	0.05
1.0	0.2–200	0.03

Table 2
Comparison of peak width, dynamic range and detection limit found by using different carrier gas flow rates. Injected volume of headspace in equilibrium with synthetic samples containing different SO_2 contents: 0.5 mL; distance of the tube outlet from the sensing surface: 1 mm.

Flow rate ($mL\,min^{-1}$)	Base peak width (s)	Dynamic range ($mg\,L^{-1}$)	Detection limit ($mg\,L^{-1}$)
50	8	0.5–400	0.08
70	6	0.4–450	0.06
100	4	0.2–500	0.04
150	3	0.2–450	0.05
200	2	0.3–250	0.07

significant results found. These results suggested the use of a flow rate of 100 mL min^{-1}, in that higher rates led to lower sensitivities (because increasing fractions of analyte molecules are removed by the carrier gas before they find time to be oxidized), while lower rates led to progressively broader peaks whose height depended linearly on SO_2 concentration in progressively narrower ranges.

Finally, the distance between sample outlet and sensing surface, when varied in the range 0.5–2.0 mm, turned out to have a minimal effect upon stability of background currents, sensitivity and repeatability. Consequently, a distance of 1 mm was chosen arbitrarily and always adopted in further determinations.

It must be remarked that strictly similar results were found when all tests above were conducted on synthetic samples also containing increasing amounts of ethanol up to 20% (v/v), thus pointing out that also for this detection approach no interference was caused by this volatile component of wines and grape juices.

As shown in Fig. 4, which reports some typical signals recorded under the optimised conditions thus identified and reported in the relevant caption, detection of SO_2 by flow injection resulted in sharp peak readouts with rapid increases and decreases of the current that reflect the passage of the sample zone over the working electrode. On the basis of the results found for replicate measurements performed within about six months of continuous use on samples with different SO_2 contents, a very favourable performance was estimated (detection limit: 0.04 $mg\,L^{-1}$; dynamic range: 0.2–500 $mg\,L^{-1}$; regression equation: $i(\mu A) = 2.75\,C_{SO_2}(mg\,L^{-1}) + 1.03$; correlation coefficient: 0.998; repeatability: ±2% relative standard deviation; long-term stability: ±9%).

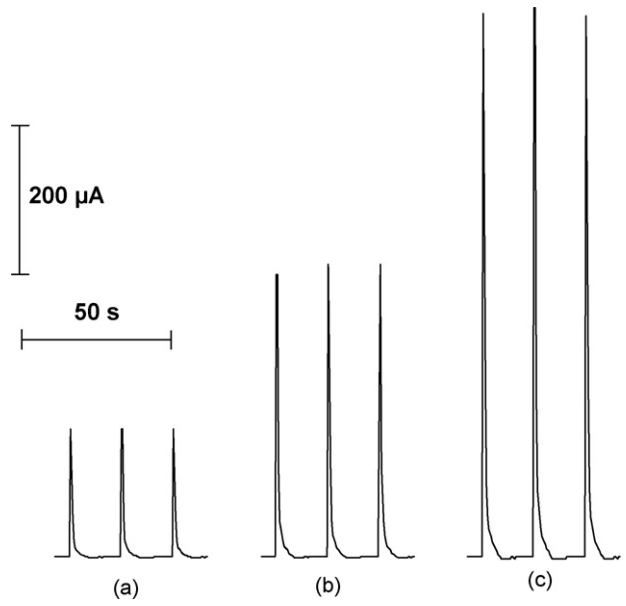


Fig. 4. Flow-injection peaks recorded at a gold–Nafion electrode with aqueous 1 M $HClO_4$ internal electrolyte for headspaces in equilibrium with aqueous Na_2SO_3 solutions reacted with 85% (w/w) H_3PO_4, so as to achieve SO_2 concentrations of: (a) 59 $mg\,L^{-1}$; (b) 142 $mg\,L^{-1}$; (c) 265 $mg\,L^{-1}$. Electrode potential: 0.8 V versus Ag/AgCl, Cl^-_{sat}; carrier gas flow rate: 100 mL min^{-1}; sample volume: 0.5 mL; distance of sample outlet from sensing surface: 1 mm.

This flow-injection approach, totally satisfactory for the selective determination of free SO_2, was subsequently also tested for the detection of total SO_2. Thus, known amounts of sodium sulphite and ethanol were added to synthetic samples consisting of home made musts, in order to verify whether sample heating caused by the mentioned neutralization of excess NaOH with H_3PO_4 allowed some possible interfering natural components of wines and/or grape juices to be transferred in the vapour phase.

Headspace samples to be injected in the flow apparatus were drawn from the reaction vessel after an equilibration time of 10 min, when the temperature (however always measured carefully) decreased to about 35 °C. Consequently, as expected on the basis of the Henry's law, higher SO_2 fractions were transferred in the vapour phase in comparison with those involved at 20 °C for free SO_2 measurements, so that a quite higher sensitivity became available. In agreement with our calibration displaying a ca. 3.5% signal increase per °C, about a 54% sensitivity increase was found, which allowed a lower detection limit (0.02 $mg\,L^{-1}$) to be inferred. Also for samples equilibrated just at 35 °C, the calibration plot was highly linear in a wide SO_2 concentration range which extended once again from 0.2 to 500 $mg\,L^{-1}$, with a good correlation coefficient (0.997). At times, after 10 min equilibration the temperature achieved in the reaction vessel differed from 35 °C, even though in a small range (±2 °C). In these cases, the current signal recorded was again referred to the calibration plot relative to 35 °C, but after correction by the suitable factor inferred from the plot of current signals against temperature (complying with the Henry's law).

No appreciable interference caused by components present in the homemade musts was observed and repeatability turned out to be satisfactory also at this temperature. In fact, replicate measurements allowed to estimate a repeatability of ±3% when performed within the same day and of ±8% when performed within one month of continuous use.

As expected, under these operative conditions no trouble was caused by the high humidity degree characterizing the headspace injected. This was because the small volume of moist atmosphere conveyed to the sensor surface was unable to cause appreciable condensation, also in view of the drying effect provided by the flowing carrier gas.

3.4. Analysis of real samples

The flow-injection apparatus above was also assayed for the determination of free and total SO_2 content in some real grape juice and red or white wine samples, all purchased from local supermarkets. These real samples were directly subjected to the analytical procedure above, without any sample pre-treatment.

Quantitative determinations of free and total SO_2 were performed by exploiting calibration plots constructed by using synthetic samples, since no appreciable matrix effect was observed for all drink samples analysed. This was checked by supplementing sulphite in each matrix considered and comparing the results found with those gained by using the mentioned calibration plots. The data obtained by these two approaches differed from each other by about ±6% at the most, thus indicating that a satisfactory recovery (and hence good accuracy) was achieved by the procedure adopted.

Table 3
Results found in the determination of free and total SO_2 contents in real samples, together with the recoveries achieved when they were spiked with 9.8 mg L^{-1} of sodium sulphite.

Real sample	Free SO_2 (mg L^{-1})[a]	Total SO_2 (mg L^{-1})[a]	Recovery (%)[a]	
			20 °C	35 °C
Red wine 1	13.1 ± 0.5	44.8 ± 1.4	98.6 ± 2.1	100.8 ± 0.7
Red wine 2	24.3 ± 0.9	81.2 ± 2.6	96.9 ± 3.6	99.7 ± 0.8
White wine 1	16.4 ± 0.6	55.6 ± 1.7	103.2 ± 3.8	102.3 ± 2.8
White wine 2	37.7 ± 1.2	122.6 ± 3.8	99.7 ± 0.8	102.4 ± 2.2
Grape juice 1	1.0 ± 0.0	3.2 ± 0.1	99.1 ± 3.8	101.8 ± 0.8
Grape juice 2	1.9 ± 0.1	5.5 ± 0.2	100.8 ± 3.1	98.9 ± 1.2
Grape juice 3	1.2 ± 0.0	4.1 ± 0.1	98.4 ± 2.7	100.2 ± 3.1

[a] Mean values calculated for five replicate measurements. The reported standard deviations were calculated accordingly.

In particular, sulphur dioxide recovery was evaluated in all cases from quintuplicate measurements performed on samples spiked with about 9.8 mg L^{-1} of sulphite (equivalent to about 5 mg L^{-1} of SO_2). The relevant results are summarized in Table 3.

We have preferred to check the reliability of these determinations by the recovery approach, instead of comparing our results with those found by the standard method [6] or other methods proposed previously [7–15]. This was because the standard method is characterized by a very poor repeatability (even standard deviations of ±15 mg L^{-1} are usually found), since it is affected by many drawbacks, such as interferences from reducing species frequently present in real samples and difficulties encountered both to recognize indicator colour changes in coloured media and to conduct some of the required experimental steps under standardized conditions. Similarly, also other methods proposed previously suffer in turn from some drawbacks making their findings scarcely reliable.

4. Concluding remarks

The results of this investigation point out that SPE electrodes make possible the selective detection of free and total SO_2 in wines and grape juices, thanks to the appropriate choice of electrode material and supporting electrolyte, as well as of the applied electrode potential. In particular, their use as detectors for flow-injection analysis performed under suitably optimised conditions leads to a very good performance, coming from quite attractive features such as: (i) high sensitivity; (ii) low detection limits; (iii) wide dynamic range; (iv) good repeatability; (v) long-term stability; (vi) absence of interferences. Moreover, it is worth highlighting that they are well suited for SO_2 on-line and in situ monitoring applications, since no real preliminary sample manipulation is involved and requires light weight, low cost and real-time instrumentation which also is simple compared to usual laboratory equipments. This approach appears to be particularly attractive when the acquirement of real-time analytical data are essential for the management of production plants, such as those designed for the removal of sulphur dioxide from stored fruit juices.

The detection of free and total SO_2 in wines and grape juices by SPE electrodes appears to be a very effective alternative not only to the standard method [6], requiring a complicated procedure unsuitable to be automatized and providing scarcely repeatable results, but also to other methods conventionally adopted as reference methods for sulphite determination in food. Thus, detection limits, repeatability and dynamic range found in our measurements (0.04 mg L^{-1}; ±2%; 0.2–500 mg L^{-1} for free SO_2 and 0.02 mg L^{-1}; ±4%; 0.2–500 mg L^{-1} for total SO_2, respectively) are undoubtedly better than those proper for the ion chromatographic method (0.05 mg L^{-1}; ±5%; 0.1–100 mg L^{-1}) which is one of the official methods for sulphite determination in food [37]. Moreover, they turn out to be advantageous even when compared with the same characteristics (0.05 mg L^{-1}; ±2%; 1–5 mg L^{-1}) of the conventional para-rosaniline-formaldehyde spectrophotometric method [38], whose advantageous application to food samples was recently proved [39].

Acknowledgement

Financial aid from the Italian Ministry of University and Scientific Research is gratefully acknowledged.

References

[1] D.H. Allen, Food Technol. Aust. 37 (1985) 506.
[2] A. Isaac, C. Livingstone, A.J. Wain, R.G. Compton, J. Davis, Trends Anal. Chem. 25 (2006) 589.
[3] Seventeenth Report of the Joint FAO/WHO Expert Committee on Food Additives, World Health Organization, Technical Report Series no. 539, Geneva, 1974, p. 35.
[4] Official Journal of European Community, Council Directive 95/2/EC, 20th February 1995.
[5] Official Journal of European Community, Council Directive 93/77/EC, 21st September 1993.
[6] Official Journal of European Community, Council Directive 90/2676/EC, 17th September 1990.
[7] S. Sasaki, Y. Arikawa, M. Shimomura, K. Ikebukuro, I. Karube, Anal. Commun. 34 (1997) 299.
[8] M.A. Sagundo, A.O.S.S. Rangel, A. Cladera, V. Cerdà, Analyst 125 (2000) 1501.
[9] M.B. Wygant, J.A. Statler, A. Henshall, J. AOAC Int. 80 (1997) 1374.
[10] M. Masar, M. Dankova, E. Olvecka, A. Stachurovà, D. Kaniansky, B. Stanislawski, J. Chromatogr. A 1084 (2005) 101.
[11] M.A. Baldo, S. Daniele, G.A. Mazzocchin, Analyst 119 (1994) 1239.
[12] J. Svitel, M. Stredansky, A. Pizzariello, S. Miertus, Electroanalysis 10 (1998) 591.
[13] R. Carballo, V. Campo Dall'Orto, A. Lo Balbo, I. Rezzano, Sens. Actuators B: Chem. 88 (2003) 155.
[14] J.P. Hart, A.K. Abass, D. Cowell, Biosens. Bioelectron. 17 (2002) 389.
[15] M.K. Sezginturk, E. Dinckaya, Talanta 65 (2005) 998.
[16] G. Bontempelli, N. Comisso, R. Toniolo, G. Schiavon, Electroanalysis 9 (1997) 433.
[17] R. Knake, P. Jaquinot, A.W.E. Hodgson, P.C. Hauser, Anal. Chim. Acta 549 (2005) 1.
[18] G. Schiavon, G. Zotti, R. Toniolo, G. Bontempelli, Electroanalysis 3 (1991) 527.
[19] L. Loub, F. Opekar, V. Pacakova, K. Stulik, Electroanalysis 4 (1992) 447.
[20] R. Toniolo, N. Comisso, G. Bontempelli, G. Schiavon, Talanta 41 (1994) 473.
[21] G. Schiavon, G. Zotti, R. Toniolo, G. Bontempelli, Anal. Chem. 67 (1995) 318.
[22] L.R. Jordan, P.C. Hauser, G.A. Dawson, Anal. Chem. 69 (1997) 558.
[23] L.R. Jordan, P.C. Hauser, Anal. Chem. 69 (1997) 2669.
[24] R. Toniolo, N. Comisso, G. Bontempelli, G. Schiavon, S. Sitran, Electroanalysis 10 (1998) 942.
[25] F. Opekar, K. Stulik, Anal. Chim. Acta 385 (1999) 151.
[26] R. Toniolo, P. Geatti, G. Bontempelli, G. Schiavon, J. Electroanal. Chem. 514 (2001) 123.
[27] R. Knake, P. Jacquinot, P.C. Hauser, Analyst 127 (2002) 114.
[28] R. Knake, R. Guchardi, P.C. Hauser, Anal. Chim. Acta 475 (2003) 17.
[29] R. Toniolo, N. Comisso, G. Schiavon, G. Bontempelli, Anal. Chem. 76 (2004) 2133.
[30] C.-Y. Chiou, T.-C. Chou, Sens. Actuators B 87 (2002) 1.
[31] D.T. Sawyer, A. Sobkowiak, J.L. Roberts Jr., Electrochemistry for Chemists, second ed., Wiley, New York, 1995, p. 425.
[32] L.D. Burke, J.F. O'Sullivan, Electrochim. Acta 37 (1992) 385.
[33] R.M. Spotnitz, J.A. Colucci, S.H. Langer, Electrochim. Acta 28 (1983) 1053.
[34] O. Enea, J. Electroanal. Chem. 235 (1987) 393.
[35] R. Parsons, T.J. VanderNoot, J. Electroanal. Chem. 257 (1988) 9.
[36] G. Schiavon, N. Comisso, R. Toniolo, G. Bontempelli, Electroanalysis 8 (1996) 544.
[37] H.J. Kim, Y.K. Kim, J. Food Sci. 51 (1986) 1360.
[38] P.K. Dasgupta, K. DeCesare, J.C. Ulrey, Anal. Chem. 52 (1980) 1912.
[39] Y. Li, M. Zhao, Food Control 17 (2006) 975.

Talanta 80 (2010) 1816–1822

Contents lists available at ScienceDirect

Talanta

journal homepage: www.elsevier.com/locate/talanta

Headspace single-drop microextraction and fibre optics-based cuvetteless micro-spectrophotometry for the determination of chloride involving oxidation with permanganate

Aradhana K.K.V. Pillai, Archana Jain, Krishna K. Verma*

Department of Chemistry, Rani Durgavati University, Pachpedi, Jabalpur 482001, Madhya Pradesh, India

ARTICLE INFO

Article history:
Received 10 August 2009
Received in revised form 12 October 2009
Accepted 14 October 2009
Available online 23 October 2009

Keywords:
Micro-spectrophotometry
Fibre optics
Charged couple device-array
Headspace single-drop microextraction
Chloride
Oxidation
Permanganate

ABSTRACT

Headspace single-drop microextraction has been investigated for the determination of chloride in conjunction with fibre optic-based cuvetteless micro-spectrophotometry which accommodates sample volume of 1 μL placed between the two ends of optical fibres. Method has been evolved for the determination of 0.025–4 mg L^{-1} of chloride involving its oxidation with permanganate in sulphuric acid medium, and reaction of chlorine with 2 μL drop of starch-iodide reagent suspended at the tip of microsyringe needle in the headspace of the reaction mixture. The limit of detection was found to be 2.8 μg L^{-1} of chloride which was better than obtained by existing methods. The method was highly selective and a number of ions which interfered severely in other methods did not affect the results. The method has been used to analyze water samples, inorganic compounds and cement when the overall recovery of chloride was 94.9% with a relative standard deviation of 3.9%.

© 2009 Elsevier B.V. All rights reserved.

1. Introduction

Miniaturization of analytical methods and instrumentation has resulted in precisely controlled trace level analyses, and their high environmental compatibility owing to insignificant amount of solvent and reagent consumption, low waste production, and low operational cost. Most of the current analytical procedures consist of a sample preparation step, and quantitation by chromatography and spectrometry.

Solvent extraction has been most widely used method for sample preparation. However, the classical mode of solvent extraction performed in a separatory funnel has inconveniences of unfavourable partition equilibria, formation of emulsions, necessity to use large volume of hazardous and ozone depleting organic solvents and difficulty in waste disposal. Miniaturization of extraction process by using microlitre volumes of the organic solvent has avoided many of these problems, allowed new ways in which the sample pre-treatment can be performed [1–3], and resulted in high sample throughput [4]. Thus, 50 or 200 μL portion of toluene, hexane or cyclohexane was used to extract the organic derivatives of nitrite, iodide, iodate and bromate in the standard flask, and a portion of extract settled in the neck of the flask was analyzed by gas chromatography [5–8]. Dispersive liquid–liquid microextraction in 70 μL of 1,2-dichlorobenzene of complexes of palladium and cobalt formed with 1-(2-pyridylazo)-2-naphthol (PAN) [9], or cloud point extraction of cobalt and nickel complexes with PAN [10] have been used along with fibre optic-linear array detection spectrophotometry that employed a 50-μL cylindrical cell of 1-cm pathlength. Extraction with microvolumes of ionic-liquids and dilution of extract with ethanol allowed the use of conventional 1-cm sample cell [11], but at the cost of sensitivity. A simple and robust microextraction method used 2–25 μL of solvent placed in the lumen of a hollow fibre that was previously impregnated with an organic solvent, and the device was placed in the sample solution [12–14]. Use of solvent drop represents further miniaturization of extraction, the early attempts were for ammonia and sulphur dioxide in air [15]. Methods involving use of microlitre drop at the tip of a capillary [16,17] or placed in a drop sized aqueous sample [18,19] or held at the end of polytetrafluoroethylene rod [20] had operational characteristics and theoretical background that appeared in a much simplified manner in the technique called single-drop microextraction (SDME) which used a 1–3 μL extraction solvent drop suspended from the tip of a microsyringe needle and held in the aqueous sample [21]. Since then, SDME has found extensive acceptance and applications in a wide variety of analyses [1–3].

* Corresponding author. Tel.: +91 761 2605103.
E-mail address: arichna@sancharnet.in (K.K. Verma).

0039-9140/$ – see front matter © 2009 Elsevier B.V. All rights reserved.
doi:10.1016/j.talanta.2009.10.027

Single-drop microextraction customarily results in high enrichment factor due to a large ratio (V_{aq}/V_o) of the volume of aqueous sample (V_{aq}) to that of organic phase (V_o), and this technique has mostly been used in conjunction with gas chromatography [22–25], high performance liquid chromatography [26], atomic absorption spectrometry [27–29], inductively coupled plasma mass spectrometry [30] and capillary electrophoresis [31]. However, the extracted volume is so small that SDME was not amenable to conventional UV–visible spectrophotometry. Advances in array detectors, fibre optic wave guides and high speed electronics has enabled the introduction of new generations of spectrometers that use charged couple device (CCD) or photodiode arrays as replacement to photomultipliers of classical spectrometers. NanoDrop® is a new generation of fibre optic-linear array detection spectrophotometer that is equipped to accommodate sample volumes as small as 1 μL for absorbance measurement with high accuracy and reproducibility. Utilizing the principle of surface tension, it holds the test solution in place between the two ends of optical fibres giving a sample path length of 0.2 and 1 mm. So far, only a few applications of NanoDrop® microspectrophotometry have been reported. Iodide was oxidized with hydrogen peroxide and the iodine liberated in the headspace (HS) was preconcentrated in a microdrop of dimethylformamide and its absorbance measured [32]. Hydrogen sulphide liberated by acid treatment of labile sulphide was absorbed in sodium zincate drop held in the headspace, and measured by turbidimetry [33]. Recently, a combination of HS-SDME and cuvetteless microspectrophotometry has been used for the determination of trimethylamine in fish [34]. The decreased path length (1 mm) used in cuvetteless NanoDrop® microspectrophotometry diminishes the sensitivity, however, methods for circumventing this inherent problem were illustrated for a number of analytes by using suitable reaction chemistry and enrichment of measurable species by liquid phase microextraction [35]. In this work further application of NanoDrop® microspectrophotometry is demonstrated for the simple and rapid determination of chloride in a variety of matrices.

For monitoring of water quality some components of water are controlled by non-enforceable regulations as they only cause cosmetic or aesthetic effects. One of aesthetic contaminants is chloride as it imparts a salty taste to water. The concentration of chloride in water is variable, normally low for ground water than for surface water, and quite elevated in wastewaters. Flow based methods using different detection systems are the most common procedures for the determination of chloride. Reaction between mercury thiocyanate and chloride leading to the displacement of thiocyanate, and thereafter, formation of an intensely coloured Fe(III)-thiocyanate complex and its spectrophotometry [36–39] is far more popular than the other methods that use displacement of chloranilate, and its spectrophotometry, by reaction of chloride with silver chloranilate [40]; reaction with silver(I) and measurement of turbidity caused by silver chloride precipitation [41]; or ion selective electrode based on Ag/AgCl [42,43]. The silver ion based methods principally aim to avoid the use of toxic mercury thiocyanate. The multi-syringe flow injection system was also proposed to minimize the consumption of mercury thiocyanate [39]. In using both reaction chemistries, ions which can interfere are several, and include bromide, iodide, sulphide, thiocyanate, cyanide, etc.; though the concentration level of these ions may be very low in natural waters. For analysis of such samples, ion chromatography is more versatile than spectrophotometric methods [44]. The features of diverse analytical methods for chloride are presented in Table 1. The limit of detection (LOD) of spectrophotometric methods is better (range 0.2–0.5 mg L^{-1}) than of potentiometric or turbidimetric methods (range 0.4–2 mg L^{-1}). Precipitation of chloride as silver chloride, and determination after its filtration by dispersive X-ray fluorescence [45], or oxidation of chloride to chlorine, air extraction and its chemiluminescence detection by reaction with luminol [46] give LOD of 25 μg L^{-1} and 4 μg L^{-1}, respectively. However, both methods are cumbersome to perform.

NanoDrop® microspectrophotometer allowed measurement of absorbance of a few microlitres of solvent, a volume that is commonly used for SDME. Headspace SDME (HS-SDME) is an efficient variation of the technique that is based on the transfer of volatile analytes from the sample matrix into the headspace, and thence into the solvent drop held in the headspace of the sample. In the proposed method chloride was oxidized to free chlorine using potassium permanganate in sulphuric acid medium which was then extracted into an aqueous drop of starch-iodide held in the headspace to form blue coloured starch-iodine complex. Finally, absorbance of the drop was measured at 553 nm using NanoDrop® microspectrophotometer. This simple and sensitive method, LOD of 2.8 μg L^{-1}, not only utilizes preferred reagents in terms of toxicity and cost but also has freedom from a number of potentially interfering materials.

2. Experimental

2.1. Equipment

All spectrophotometric measurements were made with a NanoDrop® ND 1000 full spectrum (220–750 nm) spectrophotometer (NanoDrop Technologies, Wilmington, DE, USA). It utilized surface tension of liquid sample to hold it in place between the two ends of optical fibres. This eliminated the need for cuvettes or other sample containment devices and allowed clean up by wiping. For absorbance measurement, a 1 μL sample was placed on to the one end of a fibre optic cable (the receiving fibre) and the second fibre optic cable (source fibre) was then brought into contact with liquid sample causing the liquid to bridge the gap between the two ends of optical fibres. The gap was controlled to both 1 mm and

Table 1
Comparison of figures of merit of diverse methods for the determination of chloride.

Method[a]	Principle	Sample	Linear range, mg L^{-1}	LOD, μg L^{-1}	Ref.
FI potentiometry	Ag/AgCl ion selective electrode	Cement	10–100	2000	[42]
FI potentiometry	Ag/AgCl ion selective electrode	Milk	4–1000	400	[43]
Pyrohydrolysis	Ion chromatography	Nuclear fuel	0.05–10	25	[44]
MSFI spectrophotometry	Cl^-–$Hg(SCN)_2$–Fe^{3+}	Water	1–40	200	[39]
CFI spectrophotometry	Immobilized Ag chloranilate	Water	0.5–100	300	[40]
FI spectrophotometry	Immobilized $Hg(SCN)_2$	Water	2.0–7.8	500	[38]
Chemiluminescence	Oxidation to chlorine; luminol reaction	Water	?	4	[46]
SI turbidimetry	AgCl precipitation	Water	2–400	2000	[41]
EDXRF	AgCl precipitation	Ethanol fuel	0.05–2	25	[45]
HS-SDME-ND	Oxidation to chlorine; KI-starch reaction	Water; salts	0.025–4	2.8	This work

The '?' refers to data not quoted in the original paper.

[a] FI, flow injection; MSFI, multi-syringe flow injection; CFI, commuted flow injection; SI, sequential injection; EDXRF, energy dispersive X-ray fluorescence; HS-SDME, headspace single-drop microextraction; and ND, NanoDrop® microspectrophotometry.

0.2 mm paths, the former was used for absorbance measurement in the present work. The light source was a pulsed Xenon flash lamp, and the spectrophotometer utilized a 2048-element linear silicon CCD array detector to analyze the light after passing through the sample. The instrument was controlled by a software run from a PC.

Four millilitres vials, sealed by screw cap with PTFE-faced silicon septum (Supelco, New Delhi, India), were used for all HS-SDME measurements. A 10 μL Hamilton microsyringe (Supelco, New Delhi, India) with bevel tip was used for SDME. Thermostated magnetic heating plate (Kumars Equipments, Mumbai, India) was used for heating.

2.2. Reagents and samples

All aqueous solutions were prepared in HPLC grade water (Millipore-India, Mumbai, India). Potassium permanganate (Reanal, Hungary), 1 g was dissolved in 50 mL of HPLC grade water and mixed with 25 mL of 9 mol L^{-1} sulphuric acid. This solution was purged with nitrogen at the flow rate of 5 mL min^{-1} for 10 min to remove any chlorine that is formed from trace chloride impurity in the reagent, and finally diluted to 100 mL with HPLC grade water. Aqueous starch-iodide reagent was prepared freshly by dissolving 10 mg of potassium iodide (Qualigens, Mumbai, India) in 10 mL of 0.5% starch solution. Chloride solution, 1 g L^{-1} Cl was prepared by dissolving 210.0 mg of analytical reagent grade potassium chloride (Qualigens, Mumbai, India) in 100 ml of HPLC grade water. Less concentrated solutions were made by sequential dilution with water. All reagents and standards were kept refrigerated when not in use.

River water samples (the Ganga river, Kolkata, West Bengal, India; and the Narmada river, Jabalpur, Madhya Pradesh, India); Jabalpur city tap water; a Jabalpur city lake water were collected in amber glass bottles with polypropylene screw caps having PTFE septum. Commercial table salt and cement samples were purchased from local market. All aqueous samples were centrifuged (4000 rpm) to remove particulate matter, and stored at 4 °C before analysis. Solid samples were used without any treatment.

2.3. Determination of chloride

A 10 μL – 1 mL portion of sample solution containing 25 μg – 4 mg L^{-1} of chloride was placed in a 4 mL vial and capped. All subsequent additions were made by microsyringe through the septum in the vial cap. A 200 μL portion of potassium permanganate reagent solution, 500 μL of 9 mol L^{-1} sulphuric acid were added, and the total volume was made up to 2 mL by adding HPLC water. The reaction mixture was placed on a hot plate pre-heated to 50 °C (±5 °C). The needle of a 10 μL Hamilton syringe, containing 2 μL of starch-iodide reagent, was penetrated through the septum of the vial until the tip protruded 1 cm above the meniscus of the solution. The plunger was depressed to form a drop of the reagent at the tip which was then kept exposed in the headspace. After 15 min, the plunger was retracted back into the syringe, moved twice back and forth for uniform mixing of liquid, and the coloured drop was immediately transferred to the lower pedestal of the NanoDrop® spectrophotometer for absorbance measurement at 553 nm against the reagent blank. All steps of procedure are illustrated in Fig. 1.

3. Results and discussion

The basis of headspace in-drop reaction and NanoDrop® spectrophotometry for the determination of chloride was a set of oxidation reactions; first, the oxidation of chloride by potassium

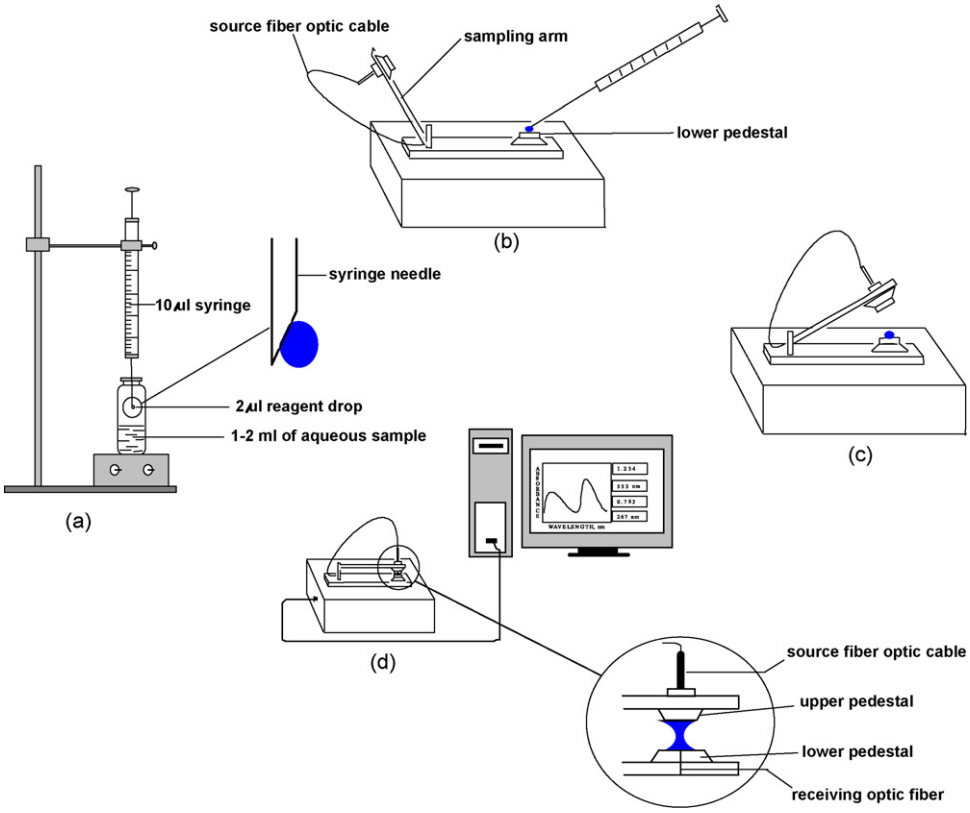


Fig. 1. Schematic representation of different steps involved in the determination of chloride by headspace in-drop extraction/reaction and absorbance measurement by NanoDrop® spectrophotometer. (a) Headspace single-drop microextraction and reaction of chlorine, showing 2 μL aqueous drop of starch-iodide suspended at the tip of a 10 μL microsyringe needle; (b) placement of drop on to the lower pedestal; (c) closing the sampling arm; and (d) spectral measurement using the operating software on the PC.

permanganate in sulphuric acid medium to form chlorine which was later released into the headspace of the reaction mixture, and secondly, oxidation of iodide to iodine by chlorine in the starch-iodide reagent drop held in the headspace. Immediately the drop acquired a blue colour due to the formation of starch-iodine complex. The uniformity of retracted extraction phase, that occurs due to parabolic flow profile, be ascertained by once or twice repeating drop formation and retraction. Headspace sampling has been found to have the benefit of preconcentration of measurable coloured species in the reagent drop, and freedom from interference of involatile oxidizing agents that happened to be present in the environmental and salt samples.

3.1. The oxidizing agent

The standard reduction potential (E°) [47] of chlorine-chloride system is 1.36 V, and many oxidizing agents (E° given in parentheses) that could be used in acid medium to oxidize chloride include peroxydisulphate (2.01 V), hydrogen peroxide (1.77 V), cerium(IV) (1.61 V) and permanganate (1.51 V). The higher reduction potential of peroxydisulphate may partly release chlorine from organo-chlorine compounds [48]. Hydrogen peroxide on heating was found to oxidize iodide in headspace reagent drop. Permanganate is a versatile and eco-friendly oxidizing agent [49,50]. A little higher reduction potential over chlorine-chloride system, non-volatility and ability to oxidize a large number of substances to give products which do not interfere in the present method made permanganate a reagent of choice for chloride oxidation.

To optimize the volume of the reagent, the variation in absorbance for the blue starch-iodine complex versus the volume of potassium permanganate was investigated. The absorbance reached optimum when the overall concentration of permanganate was 3.16 mmol L^{-1} in the reaction mixture, and then remained unaffected on further addition of reagent (Fig. 2). In the optimized method 0.2 mL of 63.2 mmol L^{-1} (1%) permanganate was used for 2 mL of reaction mixture giving 6.32 mmol L^{-1} of reagent concentration.

3.2. The headspace drop reagent

For the spectrophotometric detection of chlorine the three recommended standard methods are based on the oxidation of *N*,*N*-diethyl-*p*-phenylenediamine (also named as 4-*N*,*N*-diethylaminoaniline) (DPD), leuco crystal violet, and syringaldazine [51]. The stability of the coloured product of DPD was poor, the fading commencing almost immediately unless an excess of

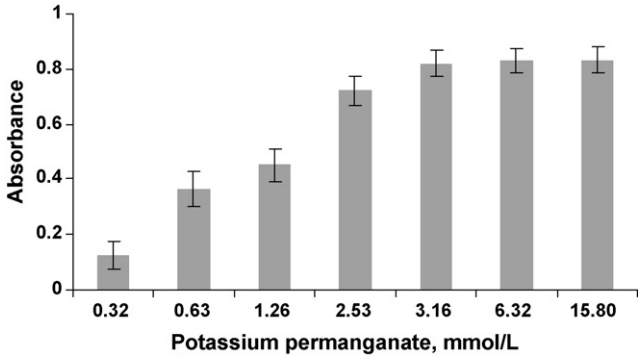


Fig. 2. Effect of permanganate concentration in the determination of 1.25 mg L^{-1} chloride. Other conditions include 0.2 mL of 9 mol L^{-1} sulphuric acid, reaction temperature 50 °C, equilibrium time 15 min, and 2 μL aqueous drop containing 6.0 mmol L^{-1} iodide in 0.5% starch. Absorbance measurement at 553 nm. The results are averages of 5 determinations. Error bars denote the standard error values.

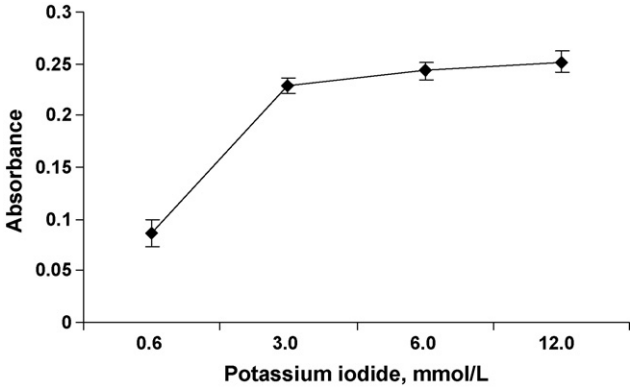


Fig. 3. Effect of iodide concentration in the headspace extraction/reaction drop in the determination of 0.125 mg L^{-1} chloride. Other conditions include 0.2 mL of 63.2 mmol L^{-1} permanganate, 0.2 mL of 9 mol L^{-1} sulphuric acid, reaction temperature 50 °C, equilibrium time 15 min, and 2 μL aqueous drop containing different concentrations of iodide in 0.5% starch. Absorbance measurement at 553 nm. The results are averages of 5 determinations. Error bars denote the standard error values.

reagent is used [52]. Other methods were found to be unsuitable since the coloured products were extremely unstable [53]. The other reagents which have been used are 4-nitrophenylhydrazine [54] or phenylhydrazine-4-sulphonic acid [55] together with *N*-(1-naphthyl)ethylenediamine dihydrochloride; *o*-dianisidine and *o*-tolidine [56]. However, the use of these reagents is restricted due to their carcinogenic nature. Aqueous starch-iodide reagent was selected in this work as it was eco-friendly and cost effective, and produced stable starch-iodine blue complex.

There were two equilibria in operation involving partitioning of chlorine. First, transfer of chlorine from aqueous sample to the headspace and, second, from headspace to aqueous drop. For the favourable position of first equilibrium, high temperature and excess of permanganate oxidized any traces of chloride to release molecular chlorine into the headspace. In the second equilibrium, the driving force for transfer of molecular chlorine from headspace to aqueous reagent was oxidation reaction giving tri-iodide anion and then starch-iodine complex within the drop. The concentration of iodide was very important parameter in the development of starch-iodine blue colour. A range of iodide concentrations from 0.60–30.0 mmol L^{-1} in 0.5% starch solution were studied. The absorbance increased till 6.0 mmol L^{-1} of potassium iodide was used and thereafter practically remained unaffected (Fig. 3). On increasing the iodide concentration beyond 12 mmol L^{-1}, the colour of the starch-iodine complex changed from blue to bluish brown, and some brownish precipitate appeared in the drop which impaired the analysis. Starch concentration did not play crucial role, and it was convenient to use its 0.5% aqueous solution. Thus, a 6.0 mmol L^{-1} (0.1%) iodide in 0.5% starch was used as reagent in subsequent studies.

3.3. Optimization of conditions

Since the extraction of analytes in headspace SDME is based on an equilibrium distribution process, the amount of analyte extracted at a given time depends on the mass transfer of the analytes from the headspace to the single-drop of extractant. One of the most important criteria of choosing the solvent for headspace extraction while heating is that the solvent drop must not evaporate during the process. Moreover, NanoDrop® spectrophotometer, which is based on the surface tension of the drop [57], imposes certain restrictions on the solvent that can be used for absorbance measurement. Solvent should be viscous enough so that it does not flow out of the pedestal, and should not be too volatile as to evaporate before measurement is completed. Hence, there should be a fair

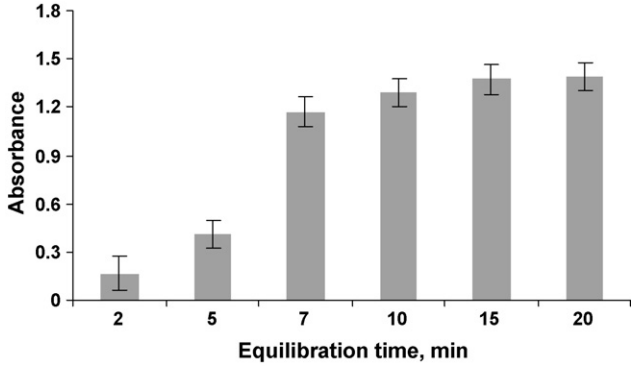


Fig. 4. Effect of equilibrium time for the extraction/reaction efficiency in the determination of 2.5 mg L^{-1} chloride. Other conditions include 0.2 mL of 63.2 mmol L^{-1} permanganate, 0.2 mL of 9 mol L^{-1} sulphuric acid, reaction temperature 50 °C, and 2 μL aqueous drop containing 6.0 mmol L^{-1} iodide in 0.5% starch. Absorbance measurement at 553 nm. The results are averages of 5 determinations. Error bars denote the standard error values.

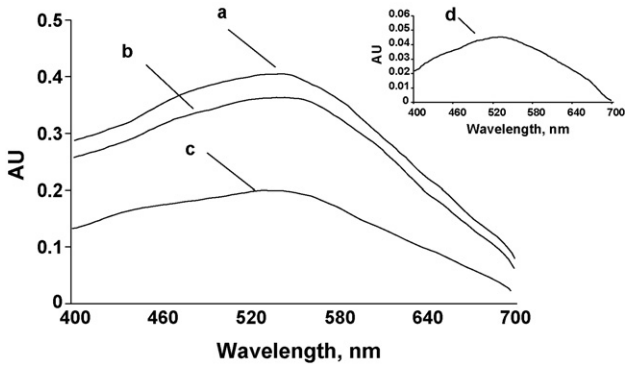


Fig. 6. Effect of drop volume in the determination of 0.25 mg L^{-1} chloride; (a) 3 μL drop (absorbance 0.401), (b) 2 μL drop (absorbance 0.373), and (c) 1 μL drop (absorbance 0.194). (d) Absorption spectrum for 0.025 mg L^{-1} chloride; 2 μL drop (absorbance 0.042). Other conditions include 0.2 mL of 63.2 mmol L^{-1} permanganate, 0.2 mL of 9 mol L^{-1} sulphuric acid, reaction temperature 50 °C, equilibrium time 15 min, and aqueous drop containing 6.0 mmol L^{-1} iodide in 0.5% starch. Absorbance measurement at 553 nm.

compromise in solvent selection for SDME and cuvetteless spectrophotometry. Water was indeed a good choice in present system as a medium for headspace extraction of chlorine, and its in-drop reaction with iodide leading to the formation of blue complex with starch.

The microdrop was kept exposed in the headspace of the reaction mixture for 2–20 min. A graph of extraction time versus absorbance of starch-iodine complex is shown in Fig. 4, which showed that the absorbance levelled at 15 min. Hence, 15 min was selected as the optimal extraction–complexation period.

For headspace SDME, the effect of sample temperature in range 30–90 °C was investigated. As shown in Fig. 5, the absorbance for the product was found dependent on the temperature. Generally, increasing the temperature would increase diffusion coefficient, so the vapour pressure and the concentration of analyte in the headspace increase [58]. As a result, the mass transfer of the analytes into the microdrop was also improved, and the equilibrium time would be shorter [59]. But, on increasing the temperature above 50 °C, the absorbance decreased significantly. Absorption of analytes in the microdrop is an exothermic process [60]. Thus, the depressive effect at higher temperature was due to decreased partition in the heated microdrop. All later experiments were conducted at 50 °C.

The effect of microdrop volume was investigated in the range 1–3 μL. The absorbance for the starch-iodine blue complex increased significantly with increase in the drop volume (Fig. 6) but drop bigger than 2 μL was more often prone to fall. Thus, the reagent drop of 2 μL was used.

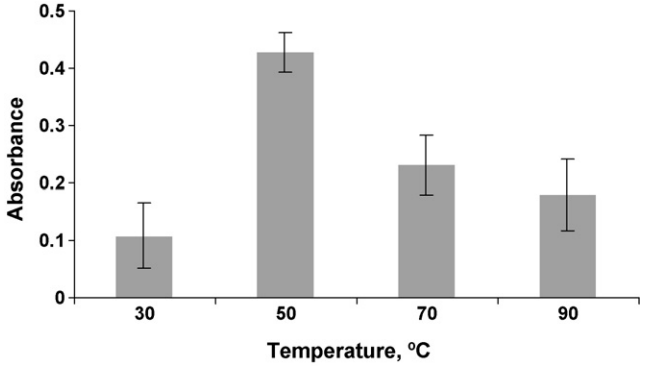


Fig. 5. Effect of reaction temperature in the determination of 0.5 mg L^{-1} chloride. Other conditions include 0.2 mL of 63.2 mmol L^{-1} permanganate, 0.2 mL of 9 mol L^{-1} sulphuric acid, equilibrium time 15 min, and 2 μL aqueous drop containing 6.0 mmol L^{-1} iodide in 0.5% starch. Absorbance measurement at 553 nm. The results are averages of 5 determinations. Error bars denote the standard error values.

Equilibrium between the aqueous and vapour phases can be achieved more rapidly by stirring the aqueous sample. For studying this effect, the aqueous reaction mixture was continuously agitated at 50 °C with stirring rates in range 200–500 rpm but this produced no significant increment in absorbance. Since the system without stirring was found to have adequate sensitivity, no attempts were made at higher stirring rate. All subsequent experiments were performed without stirring.

3.4. The interferences

In order to investigate the selectivity of the proposed method, the effect of diverse anions that are usually present in environmental aqueous samples was studied. The interferences were examined on 0.1 mg L^{-1} chloride standard spiked with 1–3 mg L^{-1} of each interferences. There was no influence of ions such as sulphate, nitrate, phosphate, iodate, bromate, chlorate, chromate, calcium(II), mercury(II), copper(II), iron(II) and nickel(II). Silver(I) precipitated with chloride and interfered. Lead(II) and thallium(I) also precipitated chloride, however, lead chloride was soluble at the reaction temperature (50 °C), and thallium(I) chloride was oxidized by permanganate in acidic medium to thallium(III) and chlorine. The tested reducing anions were iodide, bromide, thiocyanate, nitrite, sulphite, thiosulphate and sulphide. Except bromide, which produced a positive error, no other anion showed any interference. It was important to use excess of permanganate so that enough reagent was left for chloride oxidation. This was visually indicated by appreciable decolourization of the purple colour of permanganate. A 5% permanganate could be used for samples with high content of reducing ions.

Though iodide was smoothly oxidized to iodic acid (E° for iodic acid-iodine system, 1.20 V), bromide was oxidized mainly to bromine since oxidation to bromic acid was difficult using permanganate (E° for bromine–bromide system, 1.06 V; and for bromic acid-bromine system, 1.52 V). Bromine thus formed also behaved similar to chlorine in the present method. The only way to avoid the interference of bromide was to scavenge bromine by acetanilide, which showed rapid bromination reaction to form 4-bromoacetanilide [61], and had practically no reaction with permanganate in the present method. Chlorination of acetanilide was observed to be too slow in acidic medium. A 50 mg L^{-1} acetanilide was used along with other reagents for chloride determination in the presence of bromide.

Table 2
Determination of chloride in water samples.

Sample	Chloride found[a], mg L^{-1}	RSD (%)	Recovery[b] (%) at spiking level			
			1 mg L^{-1}	RSD (%)	2 mgL^{-1}	RSD (%)
Lake water	40.5	2.5	95	3.1	96	2.9
Ganga river water	37.3	1.8	92	4.5	97	5.2
Tap water	2.9	4.8	95	3.6	94	4.0
Narmada river water	1.7	2.4	98	3.2	96	3.8

[a] The results are the averages of 5 determinations.
[b] The results are the averages of 3 determination. The recovery has taken into account the chloride already present in the sample.

Table 3
Determination of chloride in inorganic compounds and cement.

Sample	Cl found[a] mg kg^{-1}	RSD (%)	Cl spiked, mg kg^{-1}	Cl recovery[b] (%)	RSD (%)
Lead nitrate	<LOD[c]		2.50	82	5.4
			1.25	90	4.3
			0.25	94	5.0
			0.125	89	4.6
Nickel sulphate	<LOD		1.25	106	3.5
			1.0	99	4.9
			0.50	102	4.2
Copper(II) sulphate	<LOD		1.0	98	3.6
			0.70	94	4.5
			0.125	99	5.8
Potassium dichromate	69.2	3.8	0.50	104	3.5
			0.25	85	4.6
			0.125	99	5.2
Potassium sulphate	0.88	4.2	1.25	100	3.6
			0.50	90	2.3
			0.150	92	2.9
Vanadium pentoxide	9.3	5.1	1.00	98	4.5
			0.50	91	4.1
			0.125	86	3.5
Potassium permanganate	133.0	3.9	0.70	93	3.5
			0.25	101	4.0
			0.125	89	3.7
Potassium permanganate	61.5	3.2	2.5	92	2.7
			0.7	93	3.1
			0.5	86	2.9
Potassium bromide[d]	<LOD		0.80	97	4.3
			0.50	93	4.8
			0.125	98	5.5
Cement	106.0	5.5	0.50	90	3.7
			0.25	103	4.5
			0.125	96	4.9

[a] Results are the averages of 3 determinations.
[b] Results are the averages of 3 determinations. The recovery has taken into account the chloride already present in the sample.
[c] Below the limit of detection.
[d] Chloride oxidation in the presence of 50 mg L^{-1} acetanilide.

3.5. Method validation

A rectilinear calibration graph was obtained for 0.025–4 mg L^{-1} of chloride, the correlation coefficient and limit of detection (LOD) were respectively 0.998 and 2.8 μg L^{-1}. The regression equation found was, $A = 0.6464C + 0.0673$, where A = absorbance, and C = concentration (mg L^{-1}) of chloride. The RSD in six replicate analyses of 0.025, 1.25 and 4 mg L^{-1} of chloride by the present method was 3.8%, 2.1% and 4.9%, respectively.

In order to investigate the applicability of the present method to real samples, chloride was determined in river, lake and tap waters (Table 2), inorganic compounds and cement (Table 3). Standard addition method was used to validate the method. In the analysis of spiked water samples, an average recovery of 95.4% (range 92–98%) was obtained with the average RSD of 3.8% (range 2.9–5.2%). An average recovery of 94.5% (range 82–106%) was obtained with the average RSD of 4.1% (range 2.3–5.8%) in the analysis of spiked inorganic compounds and cement.

The present method has distinct advantages over many of those reported in literature (Table 1) in terms of simplicity, sensitivity and selectivity. Methods based on mercury(II) thiocyanate [38,39], silver chloranilate [40] and silver chloride precipitation [41,45] are interfered by a number of anions. Some methods, such as based on energy dispersive X-ray fluorescence [45], make use of specialized instrumentation.

4. Conclusions

The proposed method for the determination of chloride is simple, sensitive, selective, eco-friendly and cost effective. The inherent drawbacks of low sensitivity of NanoDrop® spectrophotometry using cuvetteless 1 mm sample path length has been

avoided by headspace SDME leading to the enrichment of measurable species starch-iodine blue complex. The method requires low reagent consumption and produces minimal waste. Comparison of features of merit suggests that the proposed method has better sensitivity than conventional spectrophotometry, and flow injection analysis, and has less sensitivity to interferences.

Acknowledgements

The authors are very much thankful to reviewers for their kind suggestions to improve the manuscript. Thanks are due to the University Grants Commission, New Delhi, for financial support to this work.

References

[1] F. Pena-Pereira, I. Lavilla, C. Bendicho, Spectrochim. Acta B 64 (2009) 1.
[2] L. Xu, C. Basheer, H.K. Lee, J. Chromatogr. A 1152 (2007) 184.
[3] L. Xu, C. Basheer, H.K. Lee, J. Chromatogr. A 1216 (2009) 701.
[4] J. Jakmunee, L. Patimapornlert, S. Suteerapataranon, N. Lenghor, K. Grudpan, Talanta 65 (2005) 789.
[5] A. Jain, R.M. Smith, K.K. Verma, J. Chromatogr. A 760 (1997) 319.
[6] S. Mishra, V. Singh, A. Jain, K.K. Verma, Analyst 125 (2000) 459.
[7] K. Reddy-Noone, A. Jain, K.K. Verma, J. Chromatogr. A 1148 (2007) 145.
[8] K. Reddy-Noone, A. Jain, K.K. Verma, Talanta 73 (2007) 684.
[9] N. Shokoufi, F. Shemirani, Y. Assadi, Anal. Chim. Acta 597 (2007) 349.
[10] N. Shokoufi, F. Shemirani, F. Memarzadeh, Anal. Chim. Acta 601 (2007) 204.
[11] M. Baghdadi, F. Shemirani, Anal. Chim. Acta 613 (2008) 56.
[12] S. Pedersen-Bjergaard, K.E. Rasmussen, Anal. Chem. 71 (1999) 2650.
[13] K.E. Rasmussen, S. Pedersen-Bjergaard, Trends Anal. Chem. 23 (2004) 1.
[14] E. Psillakis, N. Kalogerakis, Trends Anal. Chem. 22 (2003) 565.
[15] S. Liu, P.K. Dasgupta, Anal. Chem. 67 (1995) 2042.
[16] E.A. Pereira, P.K. Dasgupta, Int. J. Environ. Anal. Chem. 66 (1997) 201.
[17] A. Pretto, M.R. Milani, A.A. Cardoso, J. Environ. Monit. 2 (2000) 566.
[18] H. Liu, P.K. Dasgupta, Anal. Chem. 68 (1996) 1817.
[19] H.-F. Wu, J.-H. Yen, C.-C. Chin, Anal. Chem. 78 (2006) 1707.
[20] M.A. Jeannot, F.F. Cantwell, Anal. Chem. 68 (1996) 2236.
[21] M.A. Jeannot, F.F. Cantwell, Anal. Chem. 69 (1997) 235.
[22] E. Aguilera-Herrador, R. Lucena, S. Cardenas, M. Valcarcel, J. Chromatogr. A 1201 (2008) 106.
[23] Y.C. Fiamegos, C.D. Stalikas, Anal. Chim. Acta 609 (2008) 175.
[24] M. Saraji, B. Farajmand, J. Chromatogr. A 1178 (2008) 17.
[25] P. Das, M. Gupta, A. Jain, K.K. Verma, J. Chromatogr. A 1023 (2004) 33.
[26] A.K.K.V. Pillai, K. Gautam, A. Jain, K.K. Verma, Anal. Chim. Acta 618 (2009) 61.
[27] S. Fragueiro, I. Lavilla, C. Bendicho, Talanta 68 (2006) 1196.
[28] H. Jiang, B. Hu, Microchim. Acta 161 (2008) 101.
[29] F. Pena, I. Lavilla, C. Bendicho, Spectrochim, Acta Part B 63 (2008) 498.
[30] S. Gil, M.T.C. de Loos-Vollebregt, C. Bendicho, Spectrochim. Acta Part B 64 (2009) 208.
[31] K. Choi, Y.G. Jin, D.S. Chung, J. Chromatogr. A 1216 (2009) 6466.
[32] F. Pena-Pereira, I. Lavilla, C. Bendicho, Anal. Chim. Acta 631 (2009) 223.
[33] I. Lavilla, F. Pena-Pereira, S. Gil, M. Costas, C. Bendicho, Anal. Chim. Acta 647 (2009) 112.
[34] F. Pena-Pereira, I. Lavilla, C. Bendicho, Food Chem. (2009), doi:10.1016/j.foodchem.2009.07.038.
[35] N. Sharma, A.K.K.V. Pillai, N. Pathak, A. Jain, K.K. Verma, Anal. Chim. Acta 648 (2009) 183.
[36] J. Ruzicka, J.W.B. Stewart, E.A.G. Zagatto, Anal. Chim. Acta 81 (1976) 387.
[37] F.J. Krug, L.C.R. Pessenda, E.A.G. Zagatto, A.O. Jacinto, B.F. Reis, Anal. Chim. Acta 130 (1981) 409.
[38] C.R. Silva, H.J. Vieira, L.S. Canaes, J.A. Nobrega, O. Fatibello-Filho, Talanta 65 (2005) 965.
[39] F. Maya, J.M. Estela, V. Cerda, Talanta 74 (2008) 1534.
[40] V.G. Bonifacio, L.C. Figueiredo-Filho, L.H. Marcolino, O. Fatibello-Filho, Talanta 72 (2007) 663.
[41] R.B.R. Mesquita, S.M.V. Fernandes, A.O.S.S. Rangel, J. Environ. Monit. 4 (2002) 458.
[42] J. Junsomboon, J. Jakmunee, Talanta 76 (2008) 365.
[43] I.S. da Silva, E.M. Richter, C.L. do Lago, I.G.R. Gutz, A.A. Tanaka, L. Angnes, Talanta 67 (2005) 651.
[44] S. Jeyakumar, V.V. Raut, K.L. Ramakumar, Talanta 76 (2008) 1246.
[45] L.S.G. Teixeira, T.J. Chaves, P.R.B. Guimaraes, L.A.M. Pontes, Anal. Chim. Acta 640 (2009) 29.
[46] O.V. Zui, Fresenius' J. Anal. Chem. 351 (1995) 209.
[47] G.D. Christian, Analytical Chemistry, John Wiley & Sons, New York, 2001, p. 779.
[48] US Patent 6096283, Integrated system for the destruction of organics by hydrolysis and oxidation with peroxydisulfate, Issued on August 1, 2000.
[49] J.L. Adcock, P.S. Francis, N.W. Barnett, Anal. Chim. Acta 601 (2007) 36.
[50] S. Dash, S. Patel, B.K. Mishra, Tetrahedron 65 (2009) 707.
[51] American Public Health Association, American Water Works Association and Water Pollution Control Federation, Standard Methods for the Examination of Water and Wastewater, American Public Health Association, Washington, DC, 16th ed., 1985, pp.298–320.
[52] G. Gordon, D.L. Sweetin, K. Smith, G.E. Pacey, Talanta 38 (1991) 145.
[53] B. Chriswell, K.R. O'Halloran, Anal. Chim. Acta 249 (1991) 519.
[54] K.K. Verma, A. Jain, A. Townshend, Anal. Chim. Acta 261 (1992) 233.
[55] M. Pandey, S. Gosain, B. Sahasrabuddhey, K.K. Verma, Analyst 123 (1998) 2319.
[56] B. Saad, W.T. Wai, M.S. Jab, W.S.W. Ngah, M.I. Saleh, J.M. Salater, Anal. Chim. Acta 537 (2005) 197.
[57] http://www.nanodrop.com/Library/nd-1000-v3.7-users-manual-8.5×11.pdf.
[58] L. Hou, H.K. Lee, J. Chromatogr. A 976 (2002) 377.
[59] S. Shariati-Feizabadi, Y. Yamini, N. Bahramifar, Anal. Chim. Acta 489 (2003) 21.
[60] A. Przyjazny, J.M. Kokosa, J. Chromatogr. A 977 (2002) 143.
[61] J. Clayden, N. Greeves, S. Warren, P. Wothers, Organic Chemistry, Oxford University Press, Oxford, 2005, pp. 559–560.

Talanta 80 (2010) 1823–1826

Contents lists available at ScienceDirect

Talanta

journal homepage: www.elsevier.com/locate/talanta

A simplified UV spectrometric method for determination of peroxide value in thermally oxidized canola oil

M. Younis Talpur, S.T.H. Sherazi*, S.A. Mahesar, Aijaz A. Bhutto

National Center of Excellence in Analytical Chemistry, University of Sindh, Jamshoro 76080, Pakistan

ARTICLE INFO

Article history:
Received 11 September 2009
Received in revised form 8 October 2009
Accepted 14 October 2009
Available online 23 October 2009

Keywords:
Peroxide value
Ultraviolet spectroscopy
Canola oil
Thermal oxidation

ABSTRACT

The aim of present study was to develop a simple method on UV spectrometer for the determination of peroxide value (PV) of the frying oil. The basis of the PV determination was the stoichiometric reaction of triphenylphosphine (TPP) with the hydroperoxides present in frying oil to produce triphenylphosphine oxide (TPPO), which exhibits a readily measurable absorption band at 240 nm by ultraviolet region. The PV ranged between 0.15 and 11.66 meq. of active oxygen per kilogram of oil as the canola oil was heated from 0 to 12 h in the fryer at 180 °C. The proposed method was correlated with official AOCS titration method and best correlation coefficient (R^2 = 0.99525) was achieved, proving that there is no significant difference in the results. Therefore, developed method could serve as an alternative to the titration method, for the determination of PV in frying oils.

© 2009 Elsevier B.V. All rights reserved.

1. Introduction

Basically frying is a cooking method in which food is submerged in hot oil. During frying thermo-oxidative or lipid oxidation and hydrolytic reactions take place that results in deterioration of the frying oil [1–3]. The primary oxidation products that develop in triacylglycerols are hydroperoxides, which may later break down to produce lower molecular weight compounds, such as free fatty acids, alcohols, aldehydes, and ketones, eventually leading to rancid product [4]. Lipid oxidation is a main deteriorative process which has an important implication in stipulations of the quality and value of fats and oils, particularly in relation to the off-flavors that develop as an outcome of autoxidation [5]. The level of hydroperoxides is commonly determined by using well-established standard AOCS iodometric procedure [6], and the resulting peroxide value (PV) is expressed as milliequivalents (meq.) of peroxide oxygen per kilogram of oil. Besides the sensitivity and reproducibility, the titrimetric methods are laborious and need a lot of chemicals and solvents, hence are associated with environmental issues. In the literature some other methods have been reported for PV determination that were based on both direct and indirect measurement of hydroperoxides by spectrophotometery [7,8] and infrared spectroscopy [9,10,11,5]. The common spectrophotometric method is very complex and involves numerous steps with the use of several chemicals and reagents [12]. Subsequently, a very useful and more accurate method was developed by Xiuzhu Yu et al. [5] on FT-IR spectroscopy using an established stoichiometric reaction of triphenylphosphine (TPP) with hydroperoxides developed in oil to form triphenylphosphine oxide (TPPO). Our present work was focused on to develop an effective UV spectrometric method based on a stoichiometric reaction involving hydroperoxides. According to well-recognized reaction (Fig. 1), hydroperoxides present in the oil react stoichiometrically with TPP to form TPPO and their respective alcohols.

2. Experimental

2.1. Reagents, standards and samples

All chemicals and reagents used were of analytical grade. Chloroform was purchased from Fischer scientific UK Ltd. Triphenylphosphine (TPP), Triphenylphosphine oxide (TPPO), potassium iodide, sodium thiosulphate and acetic acid were obtained from Sigma–Aldrich Chemie GmbH (Buchs, Germany). The concentrated stock solution for working standards was prepared by dissolving TPPO in the chloroform (40%). Fresh refined, bleached and deodorized canola oil was obtained from the local edible oil industry in Karachi, Pakistan.

2.2. Determination of peroxide value

Peroxide value, expressed in milliequivalents of active oxygen per kilogram of oil (meq./kg), was determined by standard procedure by a mixture of oil and chloroform/acetic acid which was

* Corresponding author. Tel.: +92 22 771379; fax: +92 22 771560.
E-mail address: tufail.sherazi@yahoo.com (S.T.H. Sherazi).

0039-9140/$ – see front matter © 2009 Elsevier B.V. All rights reserved.
doi:10.1016/j.talanta.2009.10.028

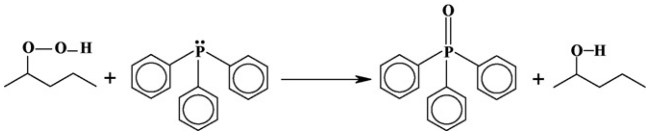


Fig. 1. Reaction of hydroperoxides with triphenylphosphine (TPP) to form triphenylphosphine oxide (TPPO) and alcohol.

left to react with a solution of potassium iodide in darkness; and then free iodine was titrated with a sodium thiosulfate solution [13].

2.3. Standard and sample preparation

Stock solutions (0.7 g) of TPPO (40% in chloroform) were mixed into 100 g of zero-PV canola oil to produce base oils which contained 50 PV equivalents of TPPO [9]. Calibration standards ranging from 0.5 to 50 PV were then prepared by gravimetrically mixing various amounts of stock oils of 30 PV in the chloroform. Just for 30 s, all the standard solutions were heated in the microwave oven to dissolve the TPPO completely. Furthermore, the PV values of standards were also confirmed by standard AOCS titration method. Similarly the preparation of oil samples involved the mixing of thermally oxidized canola oil (0.7 g) with TPP (40% in chloroform) in stoppered Erlenmeyer flask and kept in microwave oven for 30 s to complete reaction of peroxide of oil with TPP to form TPPO.

2.4. Instrumentation

2.4.1. UV–visible spectrophotometer

UV–vis spectra were recorded the respective absorbance value at specific wavelength on a PerkinElmer Lambda 35 UV/visible spectrophotometer, using standard 1.00 cm quartz cells.

2.4.2. Domestic microwave oven

A domestic microwave oven, Pell-PM 023 (Japan) with power settings range from 100 to 900 W was used in the present study. All standards of TPPO in canola oil and chloroform as well as samples with TPP in chloroform containing glass vial were subjected to full power (900 W) of microwave irradiation. After 30 s microwave heating the vial was taken out and shaken vigorously to cool. Then the UV spectra of each standard and sample were taken.

2.4.3. Heating procedure

The west point deep fryer (E-2016) was used for carrying out the thermal oxidation of canola oil at frying temperature. The capacity of fryer was 3 L with thermostatic temperature control up to 180 °C. 2 L pure canola oil was initially heated to about 180 °C, then kept at constant frying temperature i.e. 180 °C for 12 h. After each hour heating interval, about 10 mL of the heated canola oil was filtered into a screw cap vial and stored at 4 °C until analysis. The volume of oil was not refilled during the heating process.

2.4.4. Calculations and statistical analyses

Each standard and sample was analyzed twice. The data obtained were put into OriginPro 7.5 program and reported as mean ($n = 1 \times 2 \pm$ SD).

3. Result and discussion

3.1. General spectroscopy

The UV spectral characteristics of TPPO in canola oil at various concentrations were investigated by adding the TPPO to zero-PV canola oil. The recorded UV spectra of the standards for the calibration with 0, 0.5, 1, 2, 4, 6, 8, 10, 15, 20, 25, 30, 35, 40, 45 and 50 PV are shown in Fig. 2. Sophisticated chemometric technique i.e. PLS was used to achieve the regression equation for the quantification of PV in the thermally oxidized canola oil.

3.2. PLS calibration

A PLS calibration model was developed to predict PV based on the quantitation of TPPO using the absorbance at 240 nm. Excellent correlation coefficient of 0.99885 was achieved which proves the good accuracy of proposed method as shown in Fig. 3. Following regression equation was achieved from the plot of various PV of the standards versus UV absorbance at 240 nm (Fig. 3) by using OriginPro 7.5 program to predict the unknown PV in thermally oxidized canola oil.

$$Y = 0.03193 + 0.01385X$$

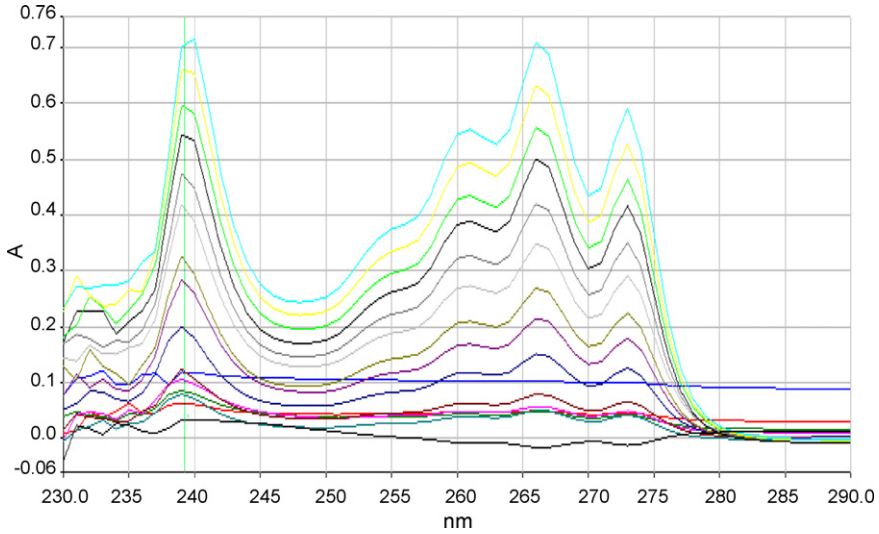


Fig. 2. Spectra showed the calibration range of TPPO concentration in canola oil vs absorbance for PV from 0, 1, 2, 4, 10, 15, 20, 25, 30, 35, 40, 45 and 50 PV.

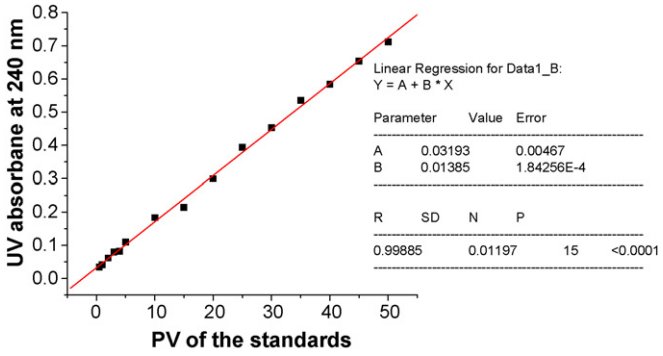


Fig. 3. Plot illustrating the various concentrations of TPPO calibration standards versus UV absorbance at 240 nm in the partial least squares calibration standards.

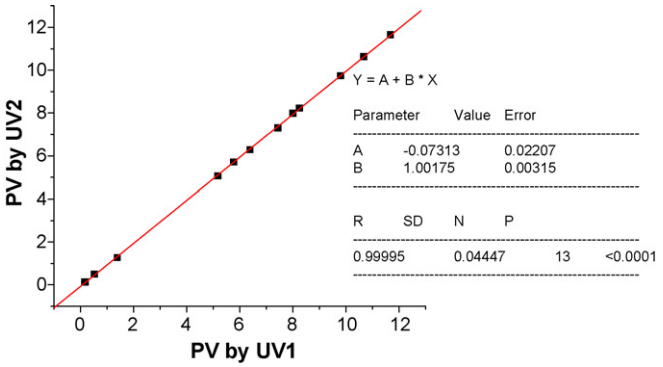


Fig. 6. Plot of PV data obtained from duplicate analysis by UV method.

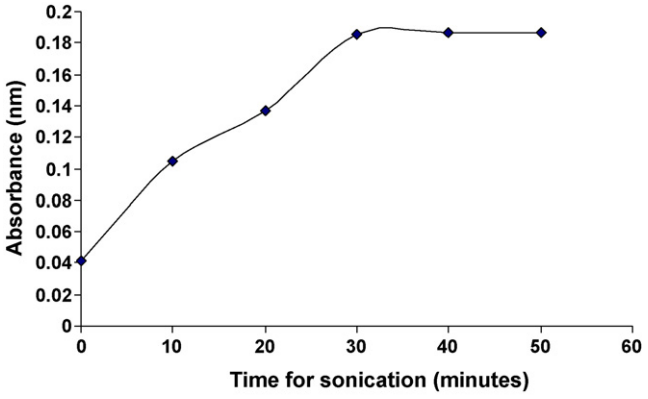


Fig. 4. Response of absorbance on reaction stability of TPP and oil at different sonication time.

3.3. Reaction stability of TPP and hydroperoxide of oil to form TPPO

The reaction stability between TPP and hydroperoxide in oil to form TPPO is very important for accurate determination of the PV content in thermally oxidized canola oil. The reaction was carried out by different methods such as ultrasonic waves, microwaves, hand shaking and electrical shaking on 12 h thermally oxidized canola oil samples. Each method was performed at different time intervals, to get the maximum response by conversion of TPP to TPPO in oil, each method has its own significance, but interestingly the only method that gave good results was the microwaves method through which we get the excellent response i.e. maximum UV absorbance with in only 30 s. As the sonication time increased the reaction between TPP and oil also increased, but it reached to plateau after 30 min as shown in Fig. 4. As there was no any significant change after 30 min reaction time, this time was considered for the complete reaction between the oil and TPP. Hand shaking and electrical shaking gave poor results as compared to ultrasonic and microwave method to determine the response of absorbance on reaction stability of TPPO. Therefore, domestic microwave oven was selected for all other samples due to quick reaction (30 s) and save enough time.

3.4. Validation

The PLS calibration model was validated by analyzing a series of thermally oxidized canola samples obtained after each hour heating from 0 to 12 h. 0.7 g of TPP was added to each sample and kept for 30 s in domestic microwave oven for a complete reaction between TPP and hydroperoxide of canola oil to form TPPO. UV spectra of

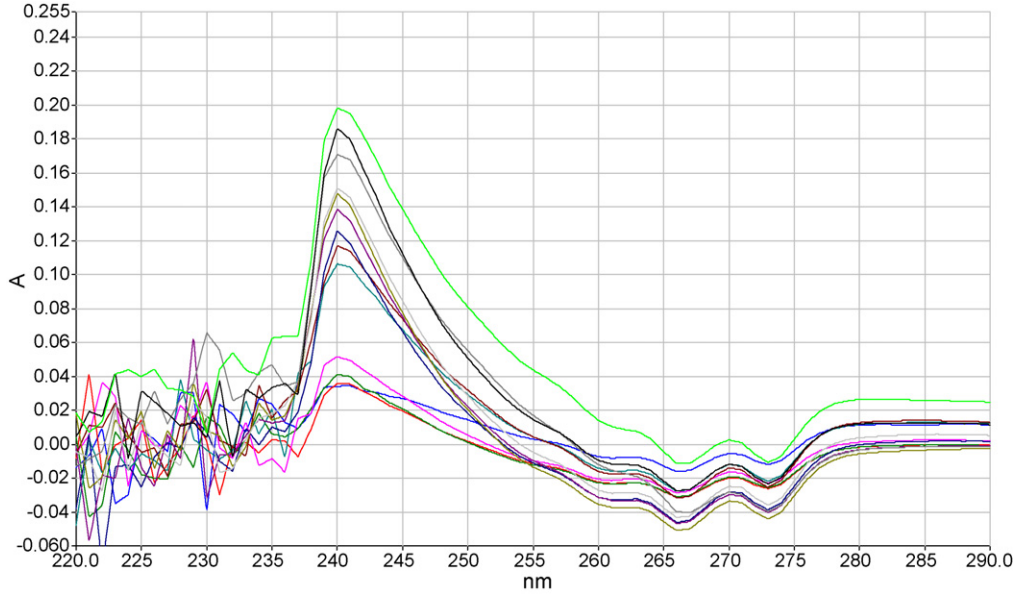


Fig. 5. UV spectra of the sample from 0 to 12 h thermally oxidized canola oil.

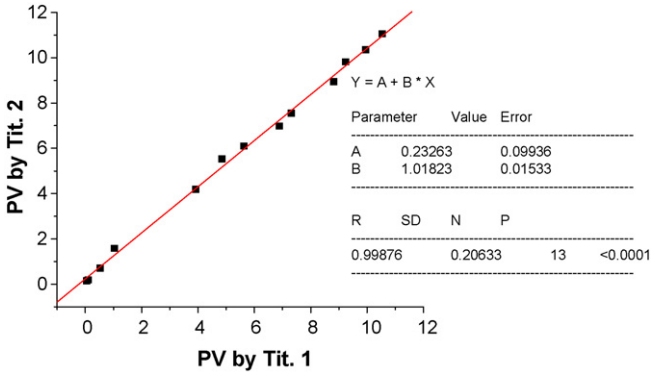


Fig. 7. Plot of PV data obtained from duplicate analysis by titration method.

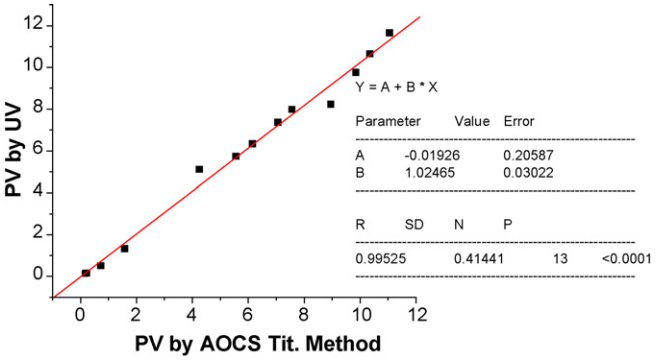


Fig. 8. Plot of mean UV-predicted PV versus mean titration PV values.

samples were recorded. The UV spectra of the sample (0–12 h) are shown in Fig. 5.

Duplicate analyses were performed and the mean difference for reproducibility (MD*r*) and the SD of the differences (SDD*r*) for the UV duplicate predictions were 0.06 PV and ± 0.04 PV units, respectively as shown in Fig. 6. These validation samples were also chemically analyzed by the AOCS PV method (Cd 86-90) (1).

A careful assessment of duplicate analyses by the AOCS chemical method indicated that the reproducibility of the chemical method was good but comparatively less from the proposed UV method, producing a mean difference for reproducibility (MD*r*) of 0.33 PV and SDD*r* of ± 0.21 PV. A plot of the duplicates against each other (Fig. 7) was linear ($r = 0.9986$), had a slope close to 1 (1.01823) and intercept close to zero (0.23263 PV).

Fig. 8 illustrates the validation plot of the mean UV-predicted PV values versus their mean AOCS titration PV values. The linear regression equation for the plot was $Y = A + BX$, with a correlation coefficient of 0.99525. The mean difference for accuracy (MD*a*) and the SD of the differences (SDD*a*) for the UV duplicate predictions were −0.12 PV and ± 0.41 PV units, respectively. The data of study clearly indicate that one can routinely reproduce PV results within SD ±0.50.

Although standard AOCS titration method is quite simple and reproducible but proved to be relatively insensitive at lower PV values as compare to UV method. Table 1 presents comparative results of mean PV values obtained from duplicate analyses by the AOCS titrimetric and UV method. No significant variation was observed in the results of PV values for all analyzed samples. The following equation deduced from the Fig. 8 could be used to match PV values

Table 1
Peroxide value (meq. of O_2/kg oil) obtained from duplicate analysis of a fresh and 12 thermally oxidized canola oil samples by spectrometer and titration and methods.

Frying oil samples	Method UV–vis	Titration method
Fresh	0.15 ± 0.02	0.17 ± 0.12
FO-1	0.16 ± 0.03	0.22 ± 0.11
FO-2	0.51 ± 0.01	0.72 ± 0.19
FO-3	1.33 ± 0.06	1.58 ± 0.54
FO-4	5.12 ± 0.06	4.25 ± 0.33
FO-5	5.74 ± 0.03	5.56 ± 0.71
FO-6	6.34 ± 0.05	6.15 ± 0.52
FO-7	7.37 ± 0.07	7.06 ± 0.17
FO-8	7.99 ± 0.01	7.56 ± 0.25
FO-9	8.24 ± 0.01	8.95 ± 0.14
FO-10	9.77 ± 0.03	9.85 ± 0.61
FO-11	10.65 ± 0.02	10.35 ± 0.40
FO-12	11.66 ± 0.01	11.05 ± 0.51

FO: indicates the frying oil.

of UV and standard AOCS titration method.

$$\mathrm{PV(UV)} = -0.01926 + 1.02465 \times \mathrm{PVAOCS},$$

$$R = 0.99525; \quad \mathrm{SD} = 0.41$$

4. Conclusion

Due to a simple and rapid stiochometric reaction and excellent association to the AOCS titration method, the UV method could provide a simple and alternative means of measuring PV values in the edible oils. Also the instrumental method could provide UV spectra as a solid document for the PV results in contrast to AOCS titration method. The UV method has a major advancement over titration method in terms of reducing solvent and reagent, which not only cuts the cost but also avoids disposal and environmental problems associated with the toxic chemicals. Furthermore, the proposed UV method would reduce labor requirements in routine quality control analysis of edible fats and oils.

Acknowledgments

The authors would like to thank the management of Shujabad Agro Industries (Pvt.) Limited, Karachi, Pakistan for providing the oil samples and the National Centre of Excellence in Analytical Chemistry, University of Sindh, Jamshoro, Pakistan for the financial support to carry out this research work.

References

[1] A. Romero, C. Cuesta, F.J. Saĭnchez-Muniz, J. Am. Oil Chem. Soc. 77 (2000) 1169.
[2] A. Romero, C. Cuesta, F.J. Saĭnchez-Muniz, J. Am. Oil Chem. Soc. 80 (2003) 437.
[3] S. Paul, G.S. Mittal, Crit. Rev. Food Sci. Nutr. 37 (1997) 632.
[4] G. Barthel, W. Grosch, J. Am. Oil Chem. Soc. 51 (1974) 540.
[5] F.R. Xiuzhu Yu, J. van de Voort, Sedman, Talanta 74 (2007) 241.
[6] American Oil Chemists' Society, Official Methods and Recommended Practices of the American Oil Chemists' Society, fourth edn., American Oil Chemists' Society, Champaign, IL, 1989 (Method Cd 8b-90).
[7] J. Nourooz-Zadeh, J. Tajaddini-Sarmadi, I. Birlouez-hagon, S.P. Wolff, J. Agric. Food Chem. 43 (1995) 17.
[8] D. Hornero-Méndez, A. Pérez-Gálvez, M.I. Mínguez-Mosquera, J. Am. Oil Chem. Soc. 78 (2001) 1151.
[9] H. Li, F.R. van de Voort, A.A. Ismail, R. Cox, J. Am. Oil Chem. Soc. 77 (2000) 137.
[10] G. Yildiz, R.L. Wehling, S.L. Cuppett, J. Am. Oil Chem. Soc. 78 (2001) 495.
[11] F.R. Van de Voort, A.A. Ismail, J. Sedman, J. Dubois, T. Nicodemo, J. Am. Oil Chem. Soc. 71 (1994) 921.
[12] E. Lovaas, J. Am. Oil Chem. Soc. 69 (1992) 777.
[13] AOCS, Official Methods and Recommended Practices, The American Oil Chemists' Society, Champaign, IL, 1997.

Talanta 80 (2010) 1827–1831

Contents lists available at ScienceDirect

Talanta

journal homepage: www.elsevier.com/locate/talanta

Preparation of a carbon ceramic electrode modified by 4-(2-pyridylazo)-resorcinol for determination of trace amounts of silver

Tahereh Rohani*, Mohammad Ali Taher

Department of Chemistry, Shahid Bahonar University of Kerman, P.O. Box 76175-133, 22th Bahman Blvd, Kerman, Iran

ARTICLE INFO

Article history:
Received 15 September 2009
Accepted 14 October 2009
Available online 23 October 2009

Keywords:
Modified carbon ceramic electrode
Sol–gel
Differential pulse anodic stripping voltammetry
Silver(I)

ABSTRACT

A 4-(2-pyridylazo)-resorcinol (PAR)-modified carbon ceramic electrode (CCE) prepared by the sol–gel technique has been reported for the first time in this paper. By immersing the CCE in aqueous solution of PAR (0.001 mol L^{-1}), after a short period of time, a thin film of PAR was rapidly formed on the surface of the electrode due to its strong adsorption properties. A differential pulse anodic stripping voltammetric (DPASV) method was developed for determination of Ag(I) at the modified carbon ceramic electrode. The analysis procedure consisted of an open circuit accumulation step in a sample solution which was continuously stirred for 12 min. This was followed by replacing the medium with a clean solution where the accumulated Ag(I) was reduced for 15 s in −0.6 V. Then, the potential was scanned from −0.2 to +0.2 V to obtain the voltammetric peak. The detection limit of silver(I) was 0.123 μg L^{-1}, and for seven successive determinations of 10, 100 and 200 μg L^{-1} Ag(I), the relative standard deviations were 2.1, 1.4 and 1.03%, respectively. The calibration curve was linear for 0.5–300 μg L^{-1} silver(I). The procedure was applied to determine silver(I) in X-ray photographic films and super-alloy samples.

© 2009 Elsevier B.V. All rights reserved.

1. Introduction

Silver is a metal of commercial importance for use in high-strength and corrosion resistance alloys, and jewellery. For example, because of the marked antibacterial properties of silver, its compounds and alloys have been widely used in dental and pharmaceutical preparations, and in implanted prosthesis. In addition, for the increase in the use of highly pure materials [1–3], and as silver has enough potential to become a highly pure metal, it is one the most widely used metals in electronic devices. Also, it is extensively utilized in the photographic and imaging industry. Considering the wide use of silver, it can be discharged in to the environment from its industrial applications, and this may cause the aquatic and terrestrial organisms to be exposed to silver. The toxicity of silver ranges between several orders of magnitude depending on the silver forms. While the ionic form of silver has been shown to be toxic to a variety of aquatic organisms, the forms of silver other than ionic silver are significantly less toxic [4]. With due attention to the above, silver(I) determination in industrial and environmental samples is very important.

Several analytical techniques including flame atomic absorption spectrometry [5,6], spectrophotometry [7–9], ion chromatography [10], colorimetric solid-phase extraction [11] and discontinuous flow analysis (DFA) [12] were applied for the determination of silver(I) ion in food, water and real samples.

The above techniques, which are commonly used for trace measurement of silver(I) ion in laboratories, are not suitable for in situ testing and monitoring. Electrochemical methods are the most favorable techniques to determine metal ions due to their low cost, high sensitivity, easy operation and the ability to carry out speciation analysis.

A group of ion-selective electrodes have been used for Ag^+ measurements based on different ionophores including tetrakis (4-*n*-dodecylphenyl) porphyrin [13], 2,6-bis-methylsulfanyl-[1,3,5]-thiadiazine-4-thione [14], hexathia-18-crown-6 [15], *p*-*tert*butylcalix[4]arene derivatives [16], octahydroxy-calix[4]arene derivative [17] and trialkyl phosphorothioates [18].

These ion-selective electrodes are not sensitive enough for direct determination of trace amounts of silver. Stripping voltammetric analysis is one of the most sensitive methods to determine ion metals [19]. A number of articles discuss the determination of silver by stripping analysis at modified carbon paste electrodes. There are carbon paste electrodes modified by alizarin violet [20], Dowex 50 W-12 [21], EDTA [22], S_2O_2-donor dopant [23], vermiculite clay mineral [24], keratin [25], 2,3-dicyano-1,4-naphthoquinone (CYNQ) [26], 2-mercaptoimidazole [27], *N*,*N*-diphenyl oxamide [28], zeolites [29] and *N*-benzoyl-*N*,*N*-di-butylthiourea [30].

* Corresponding author. Tel.: +98 341 3220041; fax: +98 341 3643853.
E-mail address: th_rohani@yahoo.com (T. Rohani).

0039-9140/$ – see front matter © 2009 Elsevier B.V. All rights reserved.
doi:10.1016/j.talanta.2009.10.029

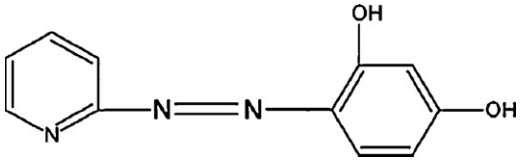


Fig. 1. Molecular structure of 4-(2-pyridylazo)-resorcinol (PAR).

In recent years, modification methods by adsorption have attracted considerable amount of attention because of their unique advantages such as surface renewal, easier preparation, low cost and high stability.

Sol–gel technology involves the fabrication of a material through the low temperature hydrolysis of a suitable monomeric precursor, followed by condensation and polycondensation to yield a polymeric oxo-bridged SiO_2 network. In 1994, Lev et al. [31] introduced the sol–gel derived carbon ceramic electrodes (CCEs) which are comprised of dispersion of carbon powder into the starting sol–gel solution. And, this new kind of electrode had been largely utilized to design electrochemical devices whose surfaces could be renewed by a simple polishing step [32,33]. Other than carbon (graphite) particles, gold [34] or glassy carbon particles [35] can also be incorporated into the sol–gel solution to construct new ceramic composite materials.

Zhu et al. [36] fabricated a MB-intercalated zirconium phosphate-modified CCE. This type of electrode has several advantages, including the convenience of surface renewal, preparation and bulk modification as well as the ability to control the surface wetness in aqueous solution, especially the high capacity for adsorption without any activation. Salimi et al. fabricated a surface-modified CCE by chlorogenic acid, and the resulting modified electrode was used for amperometric detection of NADH [37] and hydrazine [38].

The possibility of sol–gel method to prepare glassy materials at room temperature, which can support the immobilization of different reagents, was investigated earlier for electrochemical application [39]. The sol–gel method as a simple-handled method is well suited for thin-film fabrication in electrochemical studies since it provides excellent physical and chemical stability for the sensors [40–42]. The species embedded in the inert and stable solid matrices usually preserve their functional characteristics with no significant leaching in case an appropriate entrapment procedure is used. These properties will contribute to the long-term operational stability of the sol–gel-doping materials under storage conditions. The isolation of reagents from their surrounding by the bottle-neck structure of the pores makes their stability comparable to those of covalently bonded species but superior to adsorbed ones [40]. An interesting feature of the carbon ceramic electrodes, due to the brittleness of the sol–gel silicate backbone, is that the active section of the electrodes is not clogged upon successive mechanical polishing of its surface. The modified CCEs containing ruthenium metallodendrimer, manganese and nickel hexacyanoferrate were fabricated by the sol–gel technique and used for voltammetric and amperometric detection of insulin, l-methionine, l-cysteine, thiosulfate, sulfide and sulfur oxoanions [43–45].

4-(2-Pyridylazo)-resorcinol (PAR), with the structure shown in Fig. 1, is a sensitive and selective azo dye, widely used as a colorimetric reagent for metal ions as it forms very stable and highly colored complexes with some of transition metals [46–48]. Silver(I) reacts with PAR and gives an orange red chelate. The complex is stable and is not affected by light. The composition of the complex was found to be 1:1 by Job's and mole ratio methods [49].

The aim of the present investigation is to develop a new CCE modified by PAR, for selective preconcentration and determination of Ag(I) by differential pulse anodic stripping voltammetry. In addition, the PAR-modified CCE exhibited several advantages such as simple preparation, reproducibility of surface renewal by simple polishing, good stability and excellent ability to determine trace amounts of silver(I) in super-alloy samples and X-ray photographic films.

2. Experimental

2.1. Reagents

Methyltrimethoxysilane (MTMOS) and highly pure graphite powder were purchased from Fluka. PAR, of analytical grade, and methanol were purchased from Merck. Silver nitrate solutions were prepared in triply distilled deionized water and their concentrations were checked by an atomic absorption spectrometer (PerkinElmer model 2380). The silver solutions were placed in the dark and protected against light in amber bottles. The accumulation solution for silver(I) was a buffer solution containing sodium bicarbonate (0.1 mol L^{-1}) and NaOH (0.1 mol L^{-1}) (pH 9.5). Highly pure nitrogen was used for deaeration. PAR solutions (1 mmol L^{-1}) were freshly prepared just prior to use.

2.2. Apparatus

Voltammetric experiments were performed using a Metrohm electroanalyzer (Model 757 VA Computrace). The measurements were recorded using VA computrace version 2.0 (Metrohm) run under windows 98 operating system. All voltammograms were recorded with a three-electrode system consisting of an Ag/AgCl electrode as the reference electrode, a platinum wire as the auxiliary electrode, and the CCEs (modified or unmodified) as the working electrode. A Metrohm 710 pH meter was used for pH adjustments. All the electrochemical experiments were carried out under pure nitrogen atmosphere at room temperature.

2.3. Preparation of bare and PAR-modified CCEs

The bare CCEs were prepared according to the procedure described by the Lev et al. [31]. The real fabrication procedures were as follows: a mixture of 0.75 mL CH_3OH, 0.5 mL MTMOS and 0.05 mL HCl (11 mol L^{-1}) was prepared and sonicated for 2 min. Then, 1.20 g of graphite powder was added and the mixture was sonicated for another 2 min, until a homogeneous gel solution was obtained. Next, the mixture was packed into one end of the glass tubes (with 3 mm inner diameter and 5 cm length, the composite material in the tube was about 0.3 cm high), and the resulting electrode was dried for 48 h at room temperature. Electric contacts of the electrodes were made by a copper wire inserted from the other end of the electrodes. The prepared carbon ceramic electrode was polished with some polishing paper to remove any extra composite material. By immersing the bare CCE in 1.0 mmol L^{-1} aqueous solution of PAR for 1–15 s, a stable film of PAR was adsorbed on the surface of the electrode. The electrode was rinsed with ultra pure water and used for electrochemical experiments.

3. Results and discussion

3.1. The effect of the immersing time on voltammograms

Cyclic voltammograms of the modified electrode with different surface concentrations of PAR were recorded by immersing the bare electrode in 1.0 mmol L^{-1} PAR solution for different lengths of time (1–15 s). Results showed that a stable thin film of PAR adsorbed on the surface of the CCE had no well-defined voltammetric wave within the applied potential window. Further experiments showed

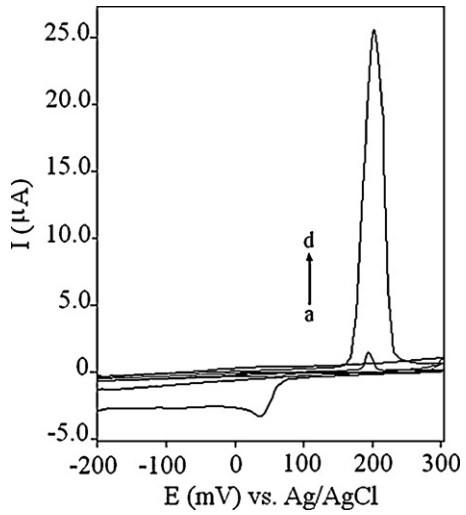


Fig. 2. Cyclic voltammograms in 0.1 mol L^{-1} HCl after open circuit accumulation in buffer solution (pH 9.5): (a) unmodified CCE, no Ag(I) in accumulation medium, (b) CCE, with 100 μg L^{-1} Ag(I) in accumulation medium, (c) PAR-MCCE, no Ag(I) in accumulation medium and (d) PAR-MCCE, with 100 μg L^{-1} Ag(I) in accumulation medium. Other conditions: accumulation time = 12 min and scan rate was 50 mV s^{-1}.

that the back current of the modified electrode increased with an increase in immersing time. A thin film of PAR was adsorbed on the electrode surface after immersing the bare CCE in 1.0 mmol L^{-1} PAR solution for only 2 s. Therefore, the 2 s length of time was selected as the optimum immersing time in all the following experiments.

3.2. General procedure

Cyclic voltammograms (CVs) were recorded after purging the solutions for at least 5 min with ultra pure nitrogen gas. After a 12 min preconcentration in open circuit condition the CVs were recorded within the potential window of −0.2 to +0.3 V (with a 50 mV s^{-1} scan rate). For differential pulse anodic stripping voltammetric experiments, the modified carbon ceramic electrode was immersed in a 10 mL of sample solution (pH 9.5) containing a known amount of Ag(I) and the solution was stirred for 12 min. This was followed by replacing the medium with a 0.1 mol L^{-1} HCl solution, where the accumulated silver(I) was reduced for 15 s in −0.6 V. Finally the differential pulse voltammogram was recorded from −0.2 to +0.2 V (with 30 mV s^{-1} scan rate, 100 mV pulse amplitude, and 4 ms pulse period). All the measurements were carried out at room temperature (23 ± 1°C).

3.3. Voltammetric behavior of silver(I) at PAR-MCCE

The ability of the PAR-MCCE to preconcentrate Ag(I) was investigated. Fig. 2(a) and (c) shows the CVs of CCE and PAR-MCCE in 0.1 mol L^{-1} HCl after preconcentration in the buffer solution as the accumulation medium. In the applied potential range only residual current was observed. Fig. 2(b) and (d) shows the CVs obtained from the same procedure at the CCE and PAR-MCCE, but with 100 μg L^{-1} Ag(I), in the accumulation medium. In CCE case, a small anodic peak at about +0.18 V indicates that some adsorption of Ag(I) occurred at the CCE surface. However, this miniscale peak provided an evidence for the absence of a significant preconcentration of Ag(I) at the unmodified electrode. In contrast, when PAR-MCCE was applied, a well-defined anodic stripping peak at +0.20 V appeared after accumulation in the medium containing 100 μg L^{-1} Ag(I). This peak was due to the reoxidation of elemental silver, produced by the reduction of accumulated Ag(I) at the negative potentials. On the reverse scan, a smaller cathodic peak with a peak potential at 0.03 V was also observed due to the reduction of Ag(I) (Fig. 2d). As it can be seen, the anodic peak current of silver at PAR-MCCE is several times larger than that of the unmodified electrode. A substantial enhancement in silver oxidation peak current was observed when the modified carbon ceramic electrode was applied. Hence, the anodic peak of silver(I) was systematically studied by differential pulse anodic stripping voltammetry for analytical applications.

3.4. Principle of the method

Regarding the above-discussed observations, and under the experimental conditions, the possible pathways for analysis cycle, from accumulation step to voltammetric scan, can be presented as follows:

Accumulation step via complex formation:

$$Ag^{+}_{aq} + PAR^{-}{}_{sur} \rightarrow [Ag\text{-}PAR]_{sur} \quad (1)$$

Reduction step in negative potentials:

$$[Ag\text{-}PAR]_{sur} + e + H^{+} \rightarrow Ag^{0}{}_{sur} + PARH_{sur} \quad (2)$$

Stripping step via positive scan:

$$Ag^{0}{}_{sur} \rightarrow Ag^{+}_{aq} + e \quad (3)$$

3.5. pH of accumulation medium

No voltammetric peaks were observed when acidic or neutral media were used to accumulate Ag(I). This can also be understood from the structure of PAR. When the pH decreases, PAR is protonated in the nitrogen and oxygen atoms reducing the complexing ability of the PAR. Therefore, we can expect that the most favorable conditions for complexation can be those with higher pHs. The influence of pH on the stripping peak current and potential was studied in buffer solutions (pH range 7.5–11). It was found that the greatest peak current was in the pH range of 9–10.5. As a result, pH 9.5 was used in all the measurements.

3.6. Stripping medium

0.1 mol L^{-1} of HCl, HNO_3, H_3PO_4, H_2SO_4 and CH_3COOH solutions were used as the stripping medium. The best solution, by which we achieved the most ideal shape and the highest current, was HCl. The effect of HCl concentration on the shape of voltammograms was also investigated, a small current was observed in 0.001 mol L^{-1} HCl, which gradually increased up to 0.1 mol L^{-1} HCl and then decreased at higher concentrations. Anodic peak also shifts to negative potentials due to the effect of H^{+} concentration which shown in Eq. (2). So the concentration, 0.1 mol L^{-1}, was used in all the measurements.

3.7. Accumulation time

The dependence of anodic peak current on the accumulation time for 100 μg L^{-1} Ag(I) was also investigated. The anodic peak current increases with the increase of accumulation time between 0 and 11 min above which it becomes nearly constant. Hence, for all the subsequent measurements accumulation time of 12 min was applied.

3.8. Reduction potential and reduction time

The influence of reduction potential on the anodic peak current of silver(I) was studied by varying the reduction potential from 0 to −1.6 V. When the potential was increased to −0.5 V, a well-defined peak with the highest peak current was obtained. Further

Table 1
The effect of co-existing metal ions.

Co-existing ion	Recovery (%)
Ni(II)	100
Pb(II)	97
Zn(II)	98
Mn(II)	100
Co(II)	98
Au(III)	98
Na(I)	100
Bi(III)	99
Fe(II)	98
K(I)	100
Cd(II)	95
Hg(II)	88
Cu(II)	86

Table 2
Determination of Ag(I) in super-alloy samples and X-ray photographic films ($n = 5$).

Sample	Serial no.	Certified ($\mu g\,g^{-1}$)	Found by this method ($\mu g\,g^{-1}$)	Found by AAS
Super-alloy	GBW01621	5.4	5.45 ± 1.8	–
Super-alloy	GBW01619	3.7	3.64 ± 1.5	–
X-ray film	–	–	4.5 ± 2.1	4.3 ± 1.5

increases in the reduction potential from −0.8 to −1.6 V led to a decrease in peak currents. This is mainly due to the cohydrogen evolution at such high potentials. Therefore, −0.6 V was applied as an optimum reduction potential for further studies. The effect of reduction time was also examined. The peak current of silver(I) was found to increase linearly by increasing the reduction time up to 15 s. So a time of 15 s was consequently used for all the measurements.

3.9. Calibration curve, detection limit and reproducibility

Standard solutions containing different amounts of Ag(I) were prepared in pH 9.5. And the general procedure was applied to these solutions. Voltammograms at these concentrations are shown in Fig. 3a. A linear calibration graph was obtained in the concentration range of 0.5–300 $\mu g\,L^{-1}$ (Fig. 3b). The detection limit was found to be 0.123 $\mu g\,L^{-1}$ Ag(I), and for seven successive determinations of 10, 100 and 200 $\mu g\,L^{-1}$ Ag(I), the relative standard deviations were 2.1, 1.4 and 1.03%, respectively.

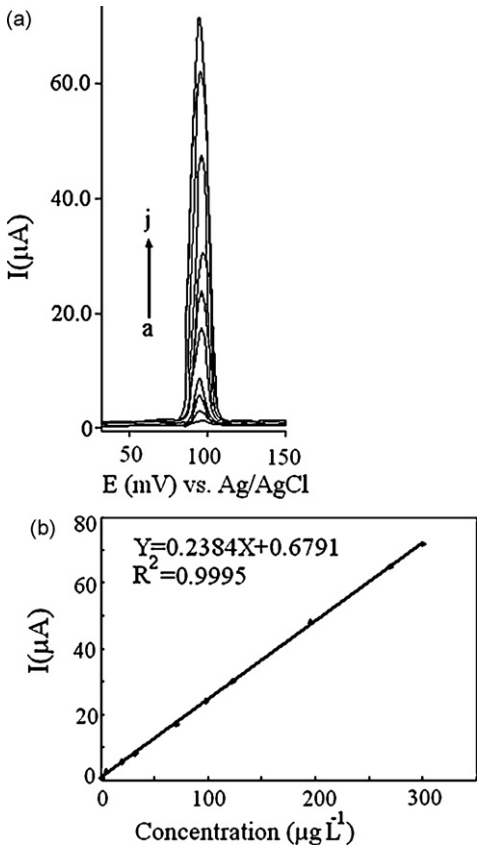


Fig. 3. (a) Differential pulse anodic stripping voltammograms of silver(I) accumulated on the PAR-modified carbon ceramic electrode. Silver(I) concentrations ($\mu g\,L^{-1}$). (a–i): 0.5, 5.0, 20.0, 32.0, 70.0, 98.0, 123.0, 196.0, 270.0, 300.0. (b) The calibration graph of Ag(I) according to data in (a). Other conditions: accumulation time = 12 min, reduction potential = – 0.6 V, reduction time = 15 s and scan rate was 30 mV s^{-1}.

3.10. Interferences

The presence of other metal ions can interfere with Ag(I) determination if they compete for complexation in the PAR complexing sites. When the developed procedure was employed for the determination of 100 $\mu g\,L^{-1}$ Ag(I) in optimum conditions, no interference was seen for adding 10 mg L^{-1} of each of Ni(II), Pb(II), Zn(II), Mn(II), Co(II), Au(III), Na(I), Bi(III), Fe(II) and K(I). However,

Table 3
Comparison of some properties of the present work with other studies.

Modifier	DL (nmol L^{-1})[a]	LR (nmol L^{-1})[b]	Procedure	Ref.
3-Amino-2-mercapto quinazolin-4(3H)-one	3.7	8.3–2780	Differential pulse anodic stripping voltammetric method at a modified CPE.	[50]
Ion-exchanger Dowex	2.5	15–7400	Square-wave anodic stripping at a modified CPE.	[21]
DL-Dithiothreitol	–	600–2400	Stripping voltammetric method at a self-assembled monolayer-modified gold electrodes.	[51]
Polythiophene	560	650–9260	Differential pulse stripping voltammetric method at modified platinum electrode.	[52]
S_2O_2-Donor dopant	200	500–1500	Anodic stripping voltammetric method at a modified CPE.	[23]
Vermiculite clay mineral	62.1	203.9–8010.4	Anodic stripping square-wave voltammetric at a modified CPE.	[24]
2-Mercaptobenzoxazole	5	5–1000	Flow injection stripping voltammetric method at a bulk-modified graphite tube electrode.	[27]
Zeolites	741.7	–	Anodic stripping voltammetric measurement at a chemically modified CPE.	[29]
4-(2-Pyridylazo)-resorcinol	1.14	4.64–2781	Differential pulse anodic stripping method at a modified CCE.	This work

[a] Detection limit.
[b] Linear range.

the presence of 10 mg L^{-1} Cu(II), Hg(II) and Cd(II) caused a 14%, 12% and 5%—decrease in the Ag(I) peak, respectively (Table 1).

3.11. Analytical application

In order to evaluate the performance of the PAR-modified carbon ceramic electrode in practical analytical applications, determination of silver(I) in super-alloy samples and X-ray photographic films was attempted. The results are given in Table 2.

For X-ray photographic films analyses, the used films were washed with distilled water and were cut into small pieces after drying in an oven at 40 °C for 20 min. 20 mL of aqueous nitric acid (5 mol L^{-1}) was added to 2.0 g of the film. The mixture was filtered, and the solution was diluted to 500 mL and pH was adjusted to 7 by NaOH solution (2 mol L^{-1}). 100 μL of the solution was added to 10 mL of the buffer solution (pH 9.5), and the general procedure was applied to the resultant solution. Samples were also analyzed using an independent technique, atomic absorption spectrometry (AAS). The measured values are in agreement with the certified values or those obtained by atomic absorption spectrometry, as shown in Table 2.

4. Conclusions

We have demonstrated that carbon ceramic electrode modified by 4-(2-pyridylazo)-resorcinol can be used to determine trace amounts of silver(I). The ability of the PAR to extract silver(I) into the carbon ceramic leads to fabrication of an electrode that is precise and accurate. The analyte ion may be preconcentrated by chemical interaction with the electrode at open circuit potential. This method showed a high selectivity because of the complexation and the exchange of the medium. The calibration graph of Ag(I) showed an ideal linear relationship from 0.5 to 300 μg L^{-1}, with a slope factor of 0.2384 μA(μg L^{-1})$^{-1}$ and the correlation coefficient, R^2, of 0.9995.

The limit of detections for some modified electrodes to determine Ag based on 3-amino-2-mercapto quinazolin-4(3H)-one [50], ion-exchanger Dowex [21], DL-dithiothreitol [51], polythiophene [52], S_2O_2-donor podand [23], vermiculite clay mineral [24], 2-mercaptobenzoxazole [27] and zeolites [29] together with their reported linear ranges are also included in Table 3 for comparison. The data given in Table 3 indicate that the LOD associated with the proposed modified electrode for Ag(I) ion determination is undoubtedly superior to that of all the other modified electrodes. In addition, the PAR-modified CCE exhibited some advantages such as simple preparation, surface renewal, good stability, reproducibility and finally excellent ability towards the determination of trace amounts of silver(I) in X-ray photographic films and super-alloy samples with acceptable results.

Acknowledgements

We are grateful to the anonymous reviewers for the careful reading of the manuscript. We are also thankful to Ehsan Mehrabi Kermani for editing the English text.

References

[1] I. Kojima, A. Takayanagi, J. Anal. Atom. Spectrom. 11 (1996) 607.
[2] E. Vassileva, S. Arpadjan, Analyst 115 (1990) 399.
[3] K. Chiba, I. Inamoto, M. Saeki, J. Anal. Atom. Spectrom. 7 (1992) 115.
[4] T.W. Purcell, J.J. Peters, Environ. Toxicol. Chem. 17 (1998) 539.
[5] S. Zhang, Q. Pu, P. Liu, Q. Sun, Z. Su, Anal. Chim. Acta 452 (2002) 223.
[6] A. Tunceli, A.R. Türker, Talanta 51 (2000) 889.
[7] Q. Hu, Y. Guangyu, Z. Huang, J. Yin, Talanta 58 (2002) 467.
[8] S.C. Hung, C.L. Qu, S.S. Wu, Talanta 29 (1982) 85.
[9] K. Ohshita, H. Wada, G. Nakasawa, Anal. Chim. Acta 182 (1986) 157.
[10] P. Jones, H.G. Beere, Anal. Proc. 32 (1995) 169.
[11] M.P. Arena, M.D. Porter, J.S. Fritz, Anal. Chim. Acta 482 (2003) 197.
[12] A.J. Dole, T.J. Cardwell, R.W. Cattrall, R. Giacomo, C.G. Rodrigues, G.R. Scollary, Electroanalysis 10 (1998) 21.
[13] T. Moriuchi-Kawakami, H. Nishimura, K. Fujimori, Y. Shibutani, T. Sugino, Y. Shimizu, Chem. Lett. 33 (2004) 1474.
[14] R.K. Mahajan, P. Sood, M.P. Mahajan, P. Singh, Anal. Sci. 20 (2004) 1423.
[15] M.H. Mashhadizadeh, M. Shamsipur, Anal. Chim. Acta 381 (1999) 111.
[16] R.K. Mahajan, I. Kaur, M. Kumar, Sens. Actuators B 91 (2003) 26.
[17] M.M. Ardakani, A.A. Ensafi, M.S. Niasari, H. Mirhoseini, Anal. Sci. 19 (2003) 1187.
[18] D. Xu, T. Katsu, Anal. Chim. Acta 443 (2001) 235.
[19] J. Wang, Analytical Electrochemistry, John Wiley, New York, 2000.
[20] Y.H. Li, H.Q. Xie, F.Q. Zhou, Talanta 67 (2005) 28.
[21] H. Gellon, P.S. Gonzalez, C.A. Fontal, Anal. Lett. 36 (2003) 2749.
[22] S.B. Zhang, X.J. Zhang, X.Q. Lin, Chin. J. Anal. Chem. 30 (2002) 745.
[23] K.S. Ha, J.H. Kim, Y.S. Ha, S.S. Lee, M.L. Seo, Anal. Lett. 34 (2001) 675.
[24] I.G. Svegl, M. Kolar, B. Ogorevc, B. Pihlar, Fresenius J. Anal. Chem. 361 (1998) 358.
[25] K. Sugawara, H. Matsui, S. Hoshi, K. Akatsuka, Analyst 123 (1998) 2013.
[26] M. Khodari, M.M. Abou-Krish, R. Fandy, Talanta 41 (1994) 2179.
[27] R. Ye, S.B. Khoo, Electroanalysis 9 (1991) 481.
[28] M.S. Won, J.S. Yeom, J.H. Yoon, E.D. Jeong, Y.B. Shim, Bull. Korean Chem. Soc. 24 (2003) 948.
[29] J. Wang, T. Martinez, Anal. Chim. Acta 207 (1988) 95.
[30] M. Guttmann, K.H. Lubert, L. Beyer, Fresenius J. Anal. Chem. 356 (1996) 263.
[31] O. Lev, M. Tsionsky, J. Gun, V. Glezer, Anal. Chem. 66 (1994) 1747.
[32] J. Gun, O. Lev, Anal. Chim. Acta 336 (1996) 95.
[33] J. Wang, Anal. Chim. Acta 399 (1999) 21.
[34] J. Wang, P.V. Pamidi, Anal. Chem. 69 (1997) 4490.
[35] D.Z. Sun, L.D. Zhu, G.Y. Zhu, Anal. Chim. Acta 564 (2006) 243.
[36] G.Y. Zhu, P. Wang, Y. Yuan, J. Electroanal. Chem. 519 (2002) 130.
[37] A. Salimi, R. Hallaj, M. Ghadermazi, Talanta 65 (2005) 888.
[38] A. Salimi, R. Hallaj, Electroanalysis 16 (2004) 1964.
[39] O. Lev, M. Tsionsky, L. Rabinovich, V. Glezer, S. Sampath, I. Pankratov, J. Gun, Anal. Chem. 67 (1995) 22.
[40] D.H. Scott, J.A. Cox, Anal. Chem. 72 (2000) 3191.
[41] P. Wang, Y. Yuan, X. Jing, G. Zhu, Talanta 53 (2001) 863.
[42] A. Abbaspour, L. Baramakeh, S.M. Nabavizadeh, Electrochim. Acta 52 (2007) 4798.
[43] L. Cheng, G.E. Pacey, J.A. Cox, Anal. Chem. 73 (2001) 5607.
[44] P. Wang, X. Jing, W. Zhang, J. Zhn, J. Solid State Electrochem. 5 (2001) 369.
[45] J.A. Cox, T.J. Gary, Anal. Chem. 62 (1990) 2742.
[46] J. Dolezal, L. Sommer, Collect. Czech. Chem. Commun. 59 (1994) 2209.
[47] J. Ghasemi, H. Peyman, M. Meloun, J. Chem. Eng. Data 52 (2007) 1171.
[48] M.F. Molima, J.M. Bosque-Sendra, M. Nechar, R. El Bergmi, Anal. Chim. Acta 389 (1999) 281.
[49] M.C. Eshwar, B. Subrahmanyam, Z. Anal. Chem. 1 (1974) 272.
[50] A.R. Mohadesi, M.A. Taher, Talanta 71 (2007) 615.
[51] B. Zeng, X. Ding, D. Pan, F. Zhao, Talanta 59 (2003) 501.
[52] H. Zejli, J.L. Hidalgo-Hidalgo de Cisneros, I. Naranjo-Rodriguez, K.R. Temsamani, Talanta 71 (2007) 1594.

Talanta 80 (2010) 1832–1837

Contents lists available at ScienceDirect

Talanta

journal homepage: www.elsevier.com/locate/talanta

Chemometrical strategies for feature selection and data compression applied to NIR and MIR spectra of extra virgin olive oils for cultivar identification

Monica Casale[a,*], Nicoletta Sinelli[b], Paolo Oliveri[a], Valentina Di Egidio[b], Silvia Lanteri[a]

[a] University of Genoa, Department of Drug and Food Chemistry and Technology, Via Brigata Salerno 13, I-16147 Genoa, Italy
[b] University of Milan, Department of Food Science and Technology, Via Celoria 2, I-20133 Milan, Italy

ARTICLE INFO

Article history:
Received 15 April 2009
Received in revised form 5 October 2009
Accepted 15 October 2009
Available online 24 October 2009

Keywords:
Infrared
Near infrared
Data fusion
Olive cultivar
Variable selection
Wavelet compression

ABSTRACT

The possibility provided by Chemometrics to extract and combine (fusion) information contained in NIR and MIR spectra in order to discriminate monovarietal extra virgin olive oils according to olive cultivar (Casaliva, Leccino, Frantoio) has been investigated.

Linear discriminant analysis (LDA) was applied as a classification technique on these multivariate and non-specific spectral data both separately and jointly (NIR and MIR data together).

In order to ensure a more appropriate ratio between the number of objects (samples) and number of variables (absorbance at different wavenumbers), LDA was preceded either by feature selection or variable compression. For feature selection, the SELECT algorithm was used while a wavelet transform was applied for data compression.

Correct classification rates obtained by cross-validation varied between 60% and 90% depending on the followed procedure. Most accurate results were obtained using the fused NIR and MIR data, with either feature selection or data compression.

Chemometrical strategies applied to fused NIR and MIR spectra represent an effective method for classification of extra virgin olive oils on the basis of the olive cultivar.

© 2009 Elsevier B.V. All rights reserved.

1. Introduction

Nowadays, one of the major issues regarding food products is to develop objective tools to determine the origin of raw materials as well as finished products in order to ensure their traceability. The application of spectroscopy which includes IR and Raman techniques combined with chemometric methods is a relatively new approach in food characterisation studies [1,2].

Extra virgin (e.v) olive oils come from many olive varieties which are generally grown on a specific soil type: both these factors (olive variety and soil type) confer specific sensory [3] and chemical properties on an oil. Often, olive cultivar and olive oil production area are linked together, but the main varieties are cultivated in many different geographical areas.

Recently, many applications of NIR and MIR spectroscopy for composition studies [4,5] and geographical characterisation (authenticity) have been reported [6–11].

In particular, there have been many studies attempting to elucidate the link between composition and geographical origin using NIR and MIR spectroscopy coupled with multivariate analysis.

For example, the results obtained by Downey et al. [6], Bertran et al. [7], Carazzolo et al. [8], Galtier et al. [9], Casale et al. [10] and Woodcock et al. [11] have suggested that near infrared spectroscopy has the potential to separate virgin olive oils coming from adjacent geographic regions with a high degree of accuracy and to discriminate olive oils bearing different denominations of origin.

With respect to MIR, Tapp et al. [12] investigated whether Fourier transform infrared spectroscopy (FTIR), in combination with multivariate analysis, could distinguish extra virgin olive oils from different producing countries. Both MIR and NIR spectra were considered for the characterisation and classification of Italian virgin olive oils by Sinelli et al. [13].

In this work, it is mainly the identification of the olive cultivar used for the oil production which is of interest.

Since the spectroscopic techniques provide multivariate and non-specific signals, Chemometrics is necessary to filter out the most relevant information from the data sets.

In this work, the data collected from a NIR and a MIR spectrometer, have been processed both separately and jointly, using chemometrical techniques, to demonstrate the synergistic effect of information obtained from the two instruments. In the literature, some examples of data fusion in food authentication problems are reported [14,15].

* Corresponding author. Tel.: +39 010 3532648; fax: +39 010 3532684.
E-mail address: monica@dictfa.unige.it (M. Casale).

0039-9140/$ – see front matter © 2009 Elsevier B.V. All rights reserved.
doi:10.1016/j.talanta.2009.10.030

Linear discriminant analysis (LDA) [16] has been used as a classification technique in order to discriminate oil samples on the basis of the olive cultivar.

Because the number of variables (wavenumbers) was much greater than the number of training set objects in our data set, LDA was applied after feature selection or data compression.

Application of methods for variable selection or data compression is important since they enable variables with low information content to be discarded; inclusion of such variables may results in an overestimation of prediction ability during classification. Despite this advantage, the use of variable selection methods is still limited in practice. Most of the chemometrical software integrated into the commercial NIR and MIR instruments contains chemometrical modules for the development of classification models, which only permit that part of the spectrum without any significant absorption signal to be removed. In fact these software do not normally contain any tool able to discard the non-informative variables on the basis of a mathematical analysis.

This paper contains the results of a study designed to illustrate the advantage of using, first, such pre-treatment tools and, second, using fused spectroscopic data sets for a classification problem. For variable selection, the SELECT algorithm [17] has been used while for data compression, a wavelet transform [18] has been deployed.

2. Experimental

2.1. Oil sampling

A total of 82 monovarietal extra virgin olive oils were analysed. This sample set comprised oils from the cultivars Casaliva, Leccino and Frantoio (27 from Casaliva, 28 from Leccino and 27 from Frantoio). Each cultivar was grown in three different sites (Puegnago, Follonica and Mirto) representative of Italian olive growing regions. In particular, Puegnago is representative of the "Garda Bresciano" area (western shore of Lake Garda) in Lombardy (northern Italy); Follonica, of the "Tyrrhenian cost" area in Tuscany (central Italy) and Mirto of the "Ionian cost" area in Calabria (southern Italy).

The monovarietal extra virgin olive oil samples were obtained from 6 kg to 10 kg of olives, harvested in the harvest period of 2005–2006: a standard continuous procedure in a mini oil mill (Toscana Enologica Mori, mod. Mini 50 modified - Tavarnelle Val Di Pesa) was used within three days of picking the olives. Olives, collected at commercial maturity, were crushed with an hammer mill and the crushed olive pasta was then submitted to a malaxation (20 °C for 30 min) to allow the microscopic oil droplets to coalesce into larger globules. Oil was then extracted by hydraulic press (maximum 20 MPa) and separated by centrifugation for 10 min at 3000 rpm.

2.2. Instruments and procedures

2.2.1. NIR spectroscopy

NIR spectral data were collected in transmission mode using vials of 8 mm path length with an FT-NIR spectrometer (MPA, Bruker Optics, Ettlingen, Germany). Data were collected over the range 12,500–4500 cm^{-1} (resolution: 8 cm^{-1}, scanner velocity: 10 kHz, background: 64 scans, sample: 64 scans) at room temperature. Instrument control and initial data processing were performed using Opus software (v. 6 Bruker Optics, Milan, Italy).

2.2.2. MIR spectroscopy

ATR FT-IR experiments were performed on a spectrometer (VERTEX 70, Bruker Optics, Ettlingen, Germany) equipped with a deuterated triglycine sulfate (DTGS) detector.

For both background and sample, 16 cm^{-1} asymmetric interferograms with a spatial resolution of 4 cm^{-1} were co-added and Fourier transformed. Oil samples were spread out on a horizontal germanium crystal ATR plate with 11 internal reflections (Pike Technologies, Inc., Madison, USA) in order to cover the entire crystal. For each sample, spectral data were collected in the range 4000–700 cm^{-1} at 20 °C and stored as $\log(1/R)$ files. Opus software (v. 6, Bruker Optics, Ettlingen, Germany) was used for spectral acquisition, instrument control and preliminary file manipulation. In order to eliminate disturbing H_2O and/or CO_2 bands in the ratio spectra, the spectra were compensated with the Atmospheric Compensation command, using Opus software.

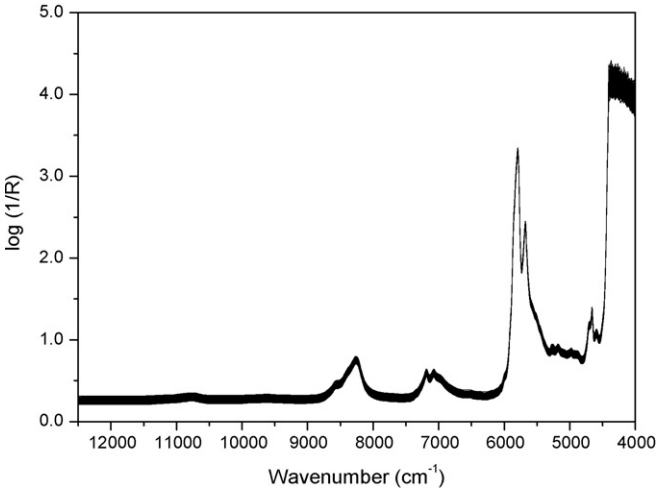


Fig. 1. Raw NIR spectra.

2.3. Data analysis

Figs. 1 and 2 show the raw NIR and MIR spectra respectively. As far as the NIR spectra are concerned, four segments of the signal without absorption were removed: 12,493–8650 cm^{-1}, 8000–7400 cm^{-1}, 6700–6000 cm^{-1}, 4400–4000 cm^{-1}. Therefore, the final NIR data matrix contained 82 rows (samples, olive oils obtained by different cultivars) and 766 columns (variables, absorbance at different wavenumbers). This data matrix will be identified by the notation $N_{82,766}$.

As far as the MIR spectra are concerned, three segments without absorption were removed: 3996–3040 cm^{-1}, 2650–1870 cm^{-1}, 1600–1490 cm^{-1}. So, the final MIR data matrix had 82 rows (sam-

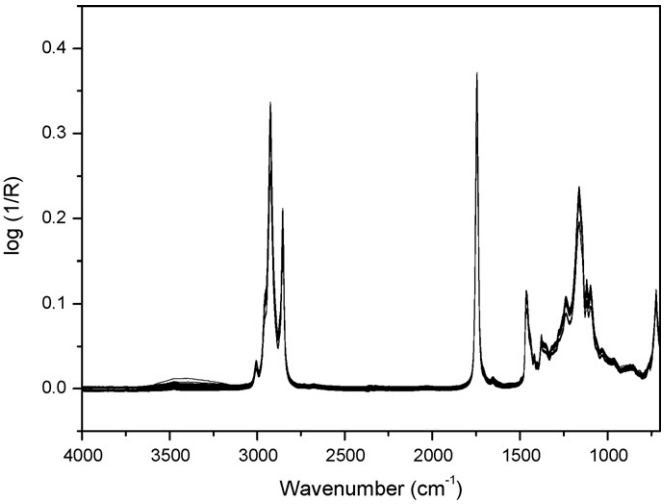


Fig. 2. Raw MIR spectra.

ples) and 753 columns. This data matrix will be identified by the notation $M_{82,753}$.

Subsequently, as first step, the NIR and MIR spectra were pre-treated separately, in order to eliminate differences due to base-line shift and scatter effects. A standard normal variate (SNV) transformation [19] and a first derivative were performed: the method of Savitzky and Golay [20] with third-order smoothing polynomials through eleven points was used to compute the first derivatives of the spectra that were used for all the data analysis.

These pre-treated matrices were as $Nt_{82,766}$ and $Mt_{82,753}$.

At the beginning, $Nt_{82,766}$ and $Mt_{82,753}$ were processed separately. After which the two matrices were joined to evaluate the synergistic effect of data recorded by these techniques. This unified matrix was called $U_{82,1519}$. In this case, the use of autoscaling was necessary to standardize the variable scale.

Linear discriminant analysis (LDA) was used as a classification technique in order to classify oil samples on the basis of olive cultivar. For classification analysis, the Casaliva olive oils were ascribed to class 1, the Leccino olive oils to class 2 and Frantoio olive oils to class 3.

LDA is a probabilistic classification technique which searches for directions (canonical variables) with maximum separation among categories; the first canonical variable is the direction of the maximum ratio between inter-class and intra-class variances. Although the transformation from the original variables to the canonical variables is non-orthogonal, nevertheless, the plots on the first canonical variables are useful display methods, widely applied in classification studies. An important restriction in the application of LDA concerns the ratio between the number of objects in the sample training set and the number of variables. From a strictly mathematical point of view, it is sufficient that the number of objects is one more than the number of variables. But, in practice, for a significant result, a total number of objects equal to at least three times, preferably five times, the number of variables is suggested. Thus, collecting a number of samples which is both reasonable and satisfactory for the above requirement could be very difficult or impossible when the number of variables is very large: in such cases, LDA should be applied after a reduction in the number of variables, performed either by means of feature selection or data compression.

Therefore, in this work, LDA was carried out, initially, after application of an algorithm for stepwise decorrelation of the variables (SELECT) as a feature selection techniques.

SELECT, introduced by Kowalski and Bender [21] is based on stepwise decorrelation of variables. In the application of this algorithm to classification problems, the first variable to be decorrelated, the first Z, is the predictor with the maximum Fisher weight (a measure of the between-class and within class variance ratio) [22]. Z_1 is copied as the first column of the matrix P of selected predictors and then it is decorrelated from all the other predictors. The second selected predictor, Z_2, will be that, from the non-selected predictors, with the maximum Fisher weight. It will be copied as the second column of the matrix P, and it will be decorrelated from all predictors. Decorrelation continues until the Fisher weight is lower than a fixed value or a fixed number of variables to retain is reached. The models obtained contain a minimum number of relevant predictors, and as a consequence of the stepwise decorrelation, these predictors are orthogonal. The algorithm permits the retention of either the decorrelated variables or the original ones.

In a second approach, LDA was applied after a data compression performed by means of the wavelet transform.

Wavelet transform is the name of a technique developed to study, as the Fourier transform, the frequency components of a signal with the main objective of compression. The compression is realized by replacing the original variables with a series of wavelet coefficients, the "basis", and discarding the irrelevant variables.

The problem studied in this paper involved not single independent signals, but matrices of signals, characterised by having as many rows as samples analysed and as many columns as variables measured (e.g., absorbance at different wavenumbers). For this reason, the compression of all signals was performed by keeping, for each of them, the same number of corresponding coefficients: the so-called "common basis" [23]. Many criteria to choose the best common basis exist: in this study, the cut-off value criteria was used [24].

Wavelets are based on the repeated use of low-pass and high-pass filters and there are many types of filters, constituting the families of wavelets. The Daubechies filters are the best known; they work progressively on an even number of points (windows).

In this study, the Wavelet Packet Transform (WPT) algorithm was applied using Daubechies filters working on eight points windows (D8).

In the case of both feature selection and data compression, the classification rules were evaluated on the basis of the predictive ability in cross-validation groups.

In order to obtain reliable classification rules, a rigid validation is necessary, but in this case the number of objects was too low to create an external test set; for this reason, we used a cross-validation procedure. In cross-validation, with N objects, the number of cancellation groups can range from 3 to N. Cross-validation with N cancellation groups is generally known as a leave-one-out procedure (LOO). LOO produces, in each validation cycle, a very small change in the training set and this small perturbation has the consequence that the measure of the predictive ability can be overly optimistic. On the contrary, with a small number of cancellation groups, the resulting training sets are very different, and the measure of the predictive ability is not optimistic, possibly pessimistic. So, we performed cross-validation many times, with a different number of cancellation groups, specifically with LOO, seven (7CV) and five (5CV) cancellation groups. Such a validation procedure required a little additional time, but it ensured a significant measure of the predictive ability.

All the above mentioned chemometrical techniques are implemented in the package V-PARVUS that was used for the data analysis [25].

3. Results and discussion

3.1. Feature selection by SELECT algorithm

The same processing strategy was performed on the three data sets $Nt_{82,766}$, $Mt_{82,753}$ and $U_{82,1519}$.

The stepwise decorrelation of the variables (SELECT) was applied on these three matrices in order to retain 15 variables. In both NIR and MIR regions the 15 wavenumbers selected are associated with the absorption bands of the most important compounds of olive oil, like fatty acids, phenols, triglycerides and tocopherols. In particular, regarding near infrared region, the principal wavenumbers selected are in the range 8500–6800 cm^{-1} and 5500–4900 cm^{-1} where there are the absorption bands of C–H (second overtone and combination bands) and C–H and C=O (first overtone and combination bands of stretching vibration), respectively. In the mid region the main variables selected (1330–1380 cm^{-1} and 1630–1811 cm^{-1}) correspond to CH_3 bending and C=O stretching vibration.

LDA was then performed on the three reduced data matrices. The results, reported in Table 1, show the ability of NIR and MIR spectroscopy to classify extra virgin olive oils on the basis of the olive cultivar. The prediction ability obtained using the MIR data ($Mt_{82,753}$) was better (overall rate of about 86%) than that obtained

Table 1
LDA results after feature selection (15 variables retained).

	Mean classification ability (%)	Mean prediction ability (%)	Prediction ability for class 1 (%)	Prediction ability for class 2 (%)	Prediction ability for class 3 (%)
$Nt_{82,766}$					
SELECT_LDA 5CV	94.6	82.9	77.8	82.1	88.9
SELECT_LDA 7CV	94.2	80.5	77.8	92.9	70.4
SELECT_LDA LOO	94.5	81.7	77.8	89.3	77.8
$Mt_{82,753}$					
SELECT_LDA 5CV	94.6	85.4	88.9	85.7	81.5
SELECT_LDA 7CV	93.7	86.6	92.6	85.7	81.5
SELECT_LDA LOO	93.6	86.6	92.6	89.3	77.8
$U_{82,1519}$					
SELECT_LDA 5CV	96.6	87.8	88.9	92.9	81.5
SELECT_LDA 7CV	96.6	87.8	88.9	92.9	81.5
SELECT_LDA LOO	96.2	90.2	92.6	92.9	85.2

Cross-validation performed with 5, 7 and 82 (LOO) cancellation groups.

using the NIR data ($Nt_{82,766}$). The best results were obtained by combining information from NIR and MIR spectra: the mean rate of samples correctly predicted was about 88%.

Generally, the classification results are considered acceptable when the prediction rate is significantly larger than the null-model rate that is the probability of correct predictions only by chance. For three categories, the null-model rate is 33.3%, and its confidence interval with 82 objects is 22.9–44.2% [26]; the upper limit of the null-model rate confidence interval differed a lot from the lower limit of the confidence interval of the prediction rate.

Moreover, taking into account the chemical and physical nature of the samples of this study, the classification task was not easy, in effect the NIR and MIR spectra showed a high degree of overlap among the three categories and in this view, the results obtained were very satisfactory.

For both NIR and MIR spectroscopy, the Casaliva (class 1) and Leccino (class 2) olive oils were classified more accurately than the oils belonging to class 3 (Frantoio). In fact, in all cross-validation models performed with five, seven and LOO cancellation groups (CV), the prediction rates for categories 1 and 2 were higher than for class 3.

In particular, the LDA results obtained by joining NIR and MIR spectra ($U_{82,1519}$) showed the best prediction ability for category 2 (Leccino cultivar), with an overall rate of 93%: a graphical display of these results is shown in Fig. 3, in which samples are projected on the first two canonical variables of LDA. The figure highlights the ability of spectroscopic techniques to discriminate extra virgin olive oils on the basis of the olive cultivar.

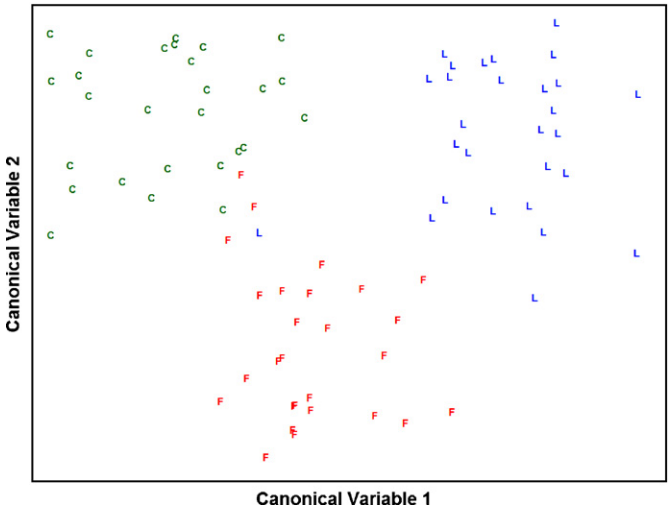


Fig. 3. NIR and MIR spectra fused. Projection on the first two canonical variables of LDA computed on 15 selected variables by SELECT. Samples are shown by their class symbol: C (Casaliva), L (Leccino) and F (Frantoio).

3.2. Data compression with wavelets transform

As above, the same processing strategy was performed on the three data sets $Nt_{82,766}$, $Mt_{82,753}$ and $U_{82,1519}$.

The WPT algorithm with Daubechies filters D8 was applied on the signals and the best common basis was obtained with the cut-off value criterion.

A number of wavelet coefficients corresponding to 75% of the total variance was retained and the LDA was performed on these selected coefficients.

To evaluate the prediction rate, the leave-one-out (LOO) and the usual cross-validation procedure with five and seven cancellation groups, were performed; the detailed results are listed in Table 2, with prediction rates reported for the three categories. Even though the results were worst than those obtained above by feature selection, data compression was helpful in extracting useful information from the NIR and MIR spectra and allowing a partial discrimination among cultivars. The prediction results for the compressed data were in agreement with the results obtained by SELECT algorithm, in fact they showed how the performances of the classification rules computed after the fusion of the NIR and MIR variables were better than those obtained using the separate data sets and how the samples of class 2 (Leccino) were better discriminated than the other two cultivars.

Fig. 4 shows the sample scores plot on the first two canonical variables of LDA for fused NIR and MIR spectra, after data compression using the wavelet transform.

In order to provide a benchmark against which to evaluate the merits of variable reduction and data compression with regard to classification performance, LDA was also performed using the complete NIR and MIR spectra, that is without reduction of the number of original variables. Since the high number of variables prevented the use of LDA, this classification method was performed working on the Principal Components. These results, listed in Table 3, were compared with those obtained after feature selection or data compression; they demonstrated that the application of strategies for discarding the not informative variables improved the classification performances.

Summarising, the LDA results showed that it is possible to discriminate the olive oils on the basis of the olive cultivar using NIR and MIR spectroscopy, in fact the prediction rates were generally satisfactory especially for category 2, the oils from cultivar 'Leccino'. The better classification of 'Leccino' cultivar could be due to its antioxidant profile. As demonstrated by Tura et al. [27], the olive

Table 2
LDA results after data compression (75% retained variance).

	Mean classification ability (%)	Mean prediction ability (%)	Prediction ability for class 1 (%)	Prediction ability for class 2 (%)	Prediction ability for class 3 (%)
$Nt_{82,766}$					
WPT_D8 5CV	80.2	67.1	59.3	85.7	55.6
WPT_D8 7CV	81.2	57.3	55.6	82.1	33.3
WPT_D8 LOO	78.6	56.1	44.4	82.1	40.7
$Mt_{82,753}$					
WPT_D8 5CV	97.1	62.2	55.6	71.4	59.3
WPT_D8 7CV	96.7	65.8	66.7	78.6	51.8
WPT_D8 LOO	96.2	64.6	59.3	78.6	55.6
$U_{82,1519}$					
WPT_D8 5CV	98.8	71.9	78.6	81.5	55.6
WPT_D8 7CV	99.0	70.7	75.0	85.2	51.8
WPT_D8 LOO	97.5	67.1	59.3	78.6	63.0

Cross-validation performed with 5, 7 and 82 (LOO) cancellation groups.

Table 3
LDA results obtained without feature selection or data compression.

	Mean classification ability (%)	Mean prediction ability (%)	Prediction ability for class 1 (%)	Prediction ability for class 2 (%)	Prediction ability for class 3 (%)
$Nt_{82,766}$					
LDA 5CV	55.6	45.1	40.7	71.4	22.2
LDA 7CV	56.4	45.1	44.4	71.4	18.5
LDA LOO	55.7	50.0	59.3	71.4	18.5
$Mt_{82,753}$					
LDA 5CV	60.2	57.3	63.0	71.4	37.0
LDA 7CV	59.7	58.5	70.4	75.0	29.6
LDA LOO	60.7	52.4	55.6	67.9	33.3
$U_{82,1519}$					
LDA 5CV	75.6	65.8	59.3	92.9	44.4
LDA 7CV	75.9	61.0	63.0	89.3	29.6
LDA LOO	73.1	61.0	59.3	89.3	33.3

Cross-validation performed with 5, 7 and 82 (LOO) cancellation groups.

oil of this cultivar is characterised by an antioxidant pattern that differs from those of the other two cultivars. The authors showed that 'Leccino' had higher tocopherol content and higher ratio of saturated to polyunsaturated fatty acids in comparison to the two cultivars 'Casaliva' and 'Frantoio'.

Variable selection was more efficient than data compression in the elimination of useless information and the best LDA results were obtained after having used SELECT as a feature selection technique.

Moreover, there was a positive effect of the fusion of NIR and MIR spectra, in fact the prediction abilities always increased after coupling the two types of information, using either feature selection or data compression.

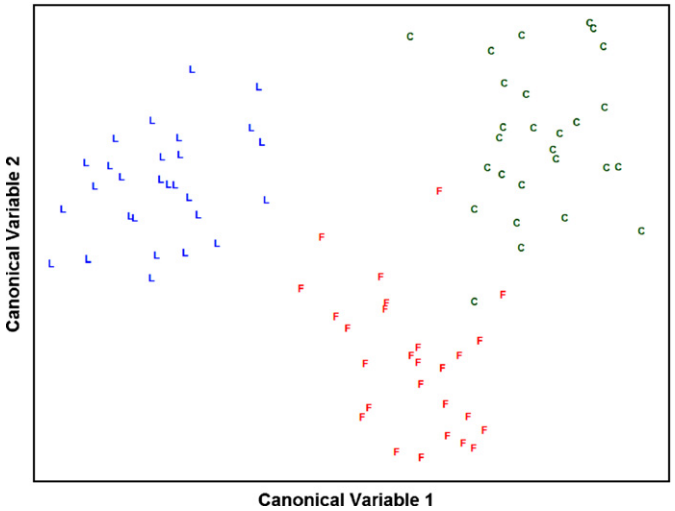


Fig. 4. NIR and MIR spectra fused. Projection on the first two canonical variables of LDA computed on the wavelet coefficients. Samples are shown by their class symbol: C (Casaliva), L (Leccino) and F (Frantoio).

4. Conclusion

In this paper, in order to discriminate extra virgin olive oils according to the olive cultivar, the "fusion" of NIR and MIR variables was performed.

For high resolution methods such as MIR–NIR spectroscopy, a common problem is that the data are over determined in that there are more variables than objects. This case presents a problem for all supervised chemometrical methods in that models exist for fitting the data perfectly by modeling insignificant variations in the data (i.e., noise). Therefore, variable selection or data compression are important to extract the maximum useful information enclosed in the data.

In this study, an algorithm for variable selection (SELECT) and a method for data compression (wavelet transform) were applied on NIR and MIR spectra, both separately and after fusion.

The results of the classification analysis were acceptable and showed the potential of fused NIR and MIR spectra for the classification of extra virgin olive oils on the basis of the olive cultivar. LDA prediction abilities always increased after coupling the data obtained by the two analytical techniques.

However, this study presents some limitations and some work has still to be done: a higher amount of samples from many different

harvesting years and geographical areas should be analysed, aiming to obtain more robust classification rules, able to account in a better way both for the regional and for the time variability of the different classes. It could be surely useful and interesting to extend the study in this direction, considering not only Italian olive cultivars, but for example, cultivars coming from different Mediterranean areas.

Acknowledgements

The authors wish to thank Prof. Daniele Bassi, Dr. Tura Debora (Di.Pro.Ve., University of Milano), Dr. Antonio Cimato (Istituto per la Valorizzazione del Legno e delle Specie Arboree, CNR) and Dr. Enzo Perri (Istituto Sperimentale per l'Olivicoltura, CRA) for supplying olive oil samples. Study developed with funds of National Ministry of University and Research and funds of the University of Genoa.

References

[1] V. Baeten, J.A.F. Pierna, P. Dardenne, M. Meurens, D.L. García-González, R. Aparicio-Ruiz, J. Agric. Food Chem. 53 (2005) 6201–6206.
[2] H. Yang, J. Irudayaraj, M.M. Paradkar, Food Chem. 93 (2005) 25–32.
[3] M.J. Tovar, M.P. Romero, S. Alegre, J. Girona, M.J. Motilva, J. Sci. Food Agric. 82 (2002) 1755–1763.
[4] R.M. Maggio, T.S. Kaufman, M. Del Carlo, L. Cerretani, A. Bendini, A. Cichelli, D. Compagnone, Food Chem. 114 (2009) 1549–1554.
[5] L. Lagardère, H. Lechat, F. Lacoste, OCL 11 (2004) 70–75.
[6] G. Downey, P. McIntyre, A.N. Davies, Appl. Spectrosc. 57 (2003) 158–165.
[7] E. Bertran, M. Blanco, J. Coello, H. Iturriaga, S. Maspoch, I. Montoliu, J. Near Infrared Spectrosc. 8 (2000) 45–52.
[8] A. Carazzolo, L. Conte, O. Pavan, P. Tonutti, L'Informatore Agrario 4 (1999) 115–122.
[9] O. Galtier, N. Dupuy, Y. Le Dréau, D. Ollivier, C. Pinatel, J. Kister, J. Artaud, Anal. Chim. Acta 595 (2007) 136–144.
[10] M. Casale, C. Casolino, G. Ferrari, M. Forina, J. Near Infrared Spectrosc. 16 (2009) 39–47.
[11] T. Woodcock, G. Downey, C. O'Donnell, J. Agric. Food Chem. 56 (2008) 11520–11525.
[12] H.S. Tapp, M. Defernez, E.K. Kemsley, J. Agric. Food Chem. 51 (2003) 6110–6115.
[13] N. Sinelli, E. Casiraghi, D. Tura, G. Downey, J. Near Infrared Spectrosc. 16 (2008) 335–342.
[14] G. Downey, R. Briandet, R.H. Wilson, E.K. Kemsley, J. Agric. Food. Chem. 45 (11) (1997) 4357–4361.
[15] M. Casale, C. Casolino, P. Oliveri, M. Forina, Food Chem. 118 (2010) 163–170.
[16] D.L. Massart, B.G.M. Vandeginste, L.M.C. Buydens, S. De Jong, P.L. Lewi, J. Smeyers-Verbeke, Handbook of Chemometrics and Qualimetrics: Part B, Elsevier, Amsterdam, 1998, 213.
[17] M. Forina, S. Lanteri, M. Casale, M.C. Cerrato Oliveros, Chemometrics Intell. Lab. Syst. 87 (2007) 252–261.
[18] Y. Mallet, D. Coomans, O. de Vel, in: B. Walczak (Ed.), Wavelet Packet Transforms and Best Base Algorithms. Wavelets in Chemistry, Elsevier, Amsterdam, 2000, pp. 151–164 (Chapter 6).
[19] R.J. Barnes, M.S. Dhanoa, S.J. Lister, Appl. Spectrosc. 43 (1989) 772–777.
[20] A. Savitzky, M.J.E. Golay, Anal. Chem. 36 (1964) 1627–1639.
[21] B.R. Kowalski, C.F. Bender, J. Pattern Recogn. 8 (1976) 1–4.
[22] A.M. Harper, D.L. Duewer, B.R. Kowalski, J.L. Fashing, in: B.R. Kowalski (Ed.), ARTHUR and Experimental Data Analysis, Chemometrics: Theory and Applications. ACS Symposium Series 52, Am. Chem. Soc. Publ., 1977, p. 43.
[23] B. Walczak, D.L. Massart, Chemometrics Intell. Lab. Syst. 38 (1997) 39–50.
[24] B. Walczak, D.L. Massart, in: B. Walczak (Ed.), Joint Basis and Joint Best-basis for Data Sets. Wavelets in Chemistry, Elsevier, Amsterdam, 2000, pp. 165–176 (Chapter 7).
[25] M. Forina, S. Lanteri, C. Armanino, C. Casolino, M. Casale, P. Oliveri, V-PARVUS, Dip. Chimica e Tecnologie Farmaceutiche ed Alimentari, University of Genova, 2008 (free available at http://www.parvus.unige.it).
[26] M. Forina, S. Lanteri, S. Rosso, Chemometrics Intell. Lab. Syst. 57 (2001) 121–132.
[27] D. Tura, C. Gigliotti, S. Pedò, O. Failla, D. Bassi, A. Serraiocco, Sci. Hortic. 112 (2007) 108–119.

Talanta 80 (2010) 1838–1845

Contents lists available at ScienceDirect

Talanta

journal homepage: www.elsevier.com/locate/talanta

11-Molybdobismuthophosphate—A new reagent for the determination of ascorbic acid in batch and sequential injection systems

Andriy B. Vishnikin[a,b,*], Tatyana Ye. Svinarenko[a], Hana Sklenářová[b], Petr Solich[b], Yaroslav R. Bazel[c,d], Vasil Andruch[d]

[a] Department of Analytical Chemistry, Faculty of Chemistry, Dnipropetrovsk National University, Gagarina 72, Dnipropetrovsk 49050, Ukraine
[b] Department of Analytical Chemistry, Faculty of Pharmacy, Charles University, Heyrovského 1203, Hradec Králové 50005, Czech Republic
[c] Department of Analytical Chemistry, Faculty of Chemistry, Užhorod National University, Pidhirna 46, Užhorod 88000, Ukraine
[d] Department of Analytical Chemistry, P.J. Šafárik University, Moyzesova 11, SK-01454 Košice, Slovak Republic

ARTICLE INFO

Article history:
Received 1 May 2009
Received in revised form 3 October 2009
Accepted 15 October 2009
Available online 24 October 2009

Keywords:
Sequential injection analysis
Spectrophotometry
Ascorbic acid determination
Heteropolymolybdate
Molybdenum blue reaction

ABSTRACT

The guanidinium salt of the new heteropolymolybdate 11-molybdobismuthophosphate $Gua_6PBiMo_{11}O_{40}$ (11-MBP) was synthesized, characterized and used as a reagent for batch spectrophotometric (SP) and sequential injection determination of ascorbic acid (AsA). When compared to other Keggin's heteropolyanions, the reduction of 11-MBP with AsA is both fast and maximal within a pH range of 1.6–2.0. The stoichiometry of the reaction was determined using molar ratio and continuous variation methods and was shown to be 1:1. The molar absorptivity of the reduced form of 11-MBP was 6.0×10^3 L mol^{-1} cm^{-1} at 720 nm. The reaction is also specific for AsA. Only cysteine, hydroquinone and hydroxyacids were found to interfere with the reaction, while no interference was observed with the common reducing agents, including reducing sugars, catecholamines, nitrite, sulfite and iron(II) ions. Batch SP and sequential injection analysis (SIA) systems were developed for the determination of AsA, with calibration ranges of the SP methods at 2×10^{-6}–8×10^{-5} M for a 10 mm cell and 5×10^{-7}–3×10^{-5} M for a 50 mm cell and a limit of detection at 3×10^{-7} M. The linear range of the SIA method was 6×10^{-6}–5×10^{-4} M, with a detection limit of 2×10^{-6} M and a sample throughput of 15 h^{-1}. The proposed methods were successfully used for the determination of AsA in both pharmaceuticals and fruit juices, and the results were consistent with those provided by the 2,6-dichlorophenolindophenol method.

© 2009 Elsevier B.V. All rights reserved.

1. Introduction

The widespread use of L-ascorbic acid (AsA) in medicine and the food industry is the reason why so many determination methods have been developed for this substance. The importance of AsA (vitamin C) for the human immune system and its use in the prevention of numerous diseases is well known. AsA is therefore a common ingredient of multivitamin preparations, food additives and pharmaceuticals, and because of its antioxidant properties, it is commonly added to foods, juices and beverages.

Due to its simplicity of use and low cost, spectrophotometry is considered one of the most effective and appropriate method for routine analysis of AsA. In addition, a great many colorimetric methods have been designed for determining AsA [1–3], based primarily on its oxidation–reduction properties or on its ability to couple with diazotized aniline derivatives. Some of these methods are quite time-consuming and lack either specificity or sensitivity, particularly when used for the analysis of beverages, fruits and certain pharmaceutical substances.

Most batch spectrophotometric (SP) and flow injection methods rely on AsA's ability to reduce Fe(III) or Cu(II) and the reaction of the resulting Fe(II) with 1,10-phenanthroline [4–6], ferrozine [7,8] or 2,2′-bipyridyl [9], or the reaction of Cu(I) with neocuproine [10,11]. Interference from PO_4^{3-}, SO_3^{2-} and S^{2-} is particularly strong due to their complexation or oxidation with Fe(III). However, most of these methods have either a limited range for upper determination [7,9,11,12], a prohibitively low sensitivity [4,13,14] or potential interferences have simply not been reported [6,13,14]. In addition, a washing step between sample injections is usually included in order to avoid the absorption of Fe(III) or Prussian blue [12] on the Teflon tubing and the walls of the flow cell. The reaction of AsA with hexacyanoferrate [1] or 2,2′-bipyridyl [15,16] requires a 10–60 min waiting period before measuring absorbance, while in the case of ferrozine and o-phenanthroline complex formation with Fe(II), the reaction is relatively fast but not selective enough [10,17]. These methods also have another disadvantage: the interference of

* Corresponding author at: Department of Analytical Chemistry, Faculty of Chemistry, Dnipropetrovsk National University, Gagarina 72, Dnipropetrovsk 49050, Ukraine. Tel.: +380 56 2361864; fax: +380 56 3749841.
E-mail address: vishnikin@hotmail.com (A.B. Vishnikin).

0039-9140/$ – see front matter © 2009 Elsevier B.V. All rights reserved.
doi:10.1016/j.talanta.2009.10.031

metal ions such as Co(II), Ni(II), Cu(II) and Fe(II), as well as interference from polyphenols, hydroxyacids, cysteine, nitrite, sulfite, thiosulfate, riboflavin and oxidants.

Heteropolycomplexes have long been known as useful reagents for the determination of organic reducing substances due to their ability to form highly colored reduction products, their stability, the reversibility of the reduction processes, as well as their low cost and easy availability. The substitution of Mo atoms in heteropolyanions (HPA) with a Keggin structure of $XMo_{12}O_{40}^{q-}$ (X = P(V), As(V), Si(IV), Ge(IV), Ga(III)) on the W or V atoms [18,19] leads to a continuous change in their oxidation–reduction properties. One of the molybdenum atoms in 12-HPA can be substituted by a metal ion, thus forming metal-substituted HPA $XMeMo_{11}O_{40}^{p-}$, which can also lead to valuable changes in the chemical–analytical properties.

A variety of reagents based on iso- or heteropolyanions have been reported for the determination of AsA. These include isopolymolybdate, 12-molybdophosphate, 12-molybdosilicate HPA in addition to others. The molybdate system requires 1 h for complete color development with AsA [20]. The method based on the reaction of AsA with Folin–Ciocalteu reagent [21] is almost equally time-consuming, requiring some 40–50 min to obtain full color intensity. In addition, these methods are not sufficiently sensitive and serious interferences caused by phenolic compounds, such as catechins, gallic acid, pyrogallol and gallotannins as well as thiosulfate ions and thiourea, are observed.

AsA [22] was determined, along with cystine or cysteine, using 18-tungsto-2-phosphate HPA $P_2W_{18}O_{62}^{6-}$ [23]. It can be determined by this reagent in mixtures with cysteine using the inhibition of color production of thiol compounds with $HgCl_2$, or, even better, formaldehyde. The reaction is fast and reproducible, but polyphenols and many inorganic reducers, including Fe(II), Cu(II), Sn(II) and SO_3^{2-}, interfere with it.

12-Molybdophosphate and 18-molybdo-2-phosphate HPA doped on xerogels were used for the determination of hydrazine and Sn(II), whereas reaction with AsA was very slow and required more than an hour of analysis [24]. The reaction was accelerated in the presence of Cu(II), however, finishing in 10–15 min. This method was therefore used for the development of the solid-phase SP and visual determination of AsA [25]. Molybdosilicate and molybdophosphate HPAs immobilized on polyurethane foam have been proposed for the sorption-photometric determination of AsA, but the reaction took 18–20 h to complete [26]. Intensification of the reduction process by microwave irradiation was used in another paper from the same authors [27], a process that complicated the procedure but shortened the reaction time to 6 min.

A procedure based on the reduction of AsA with the ternary Mo(VI)–Sb(III)–P(V) HPA was described [1,28]. The color in this case ($\varepsilon_{710} = 3.68 \times 10^3$ L mol^{-1} cm^{-1}) was produced in 35 min, and the linearity of the calibration plot remained within the limits of 6×10^{-6}–3×10^{-5} M. AsA was determined in the flow injection system using the reduction of vanadotungstophosphoric acid [29], with a detection limit of 6×10^{-6} M. Although the influence of many reducing agents was not evaluated, the peak did show a 67% increase at 100-fold weight excess of semicarbazide and an 8% decrease with an excess of sulfite. Molar absorptivity was estimated for this heteropolyblue (HPB) as 1×10^3 L mol^{-1} cm^{-1} [18].

In general, a number of shortcomings limit the broader application of HPAs to the determination of reducing agents. Such reactions, especially those involving Keggin-type HPAs, are usually slow and are sometimes not sufficiently sensitive or selective enough. As a result, overcoming such problems in a search for new HPAs and the investigation of their properties seems a potentially promising task.

Among the various detection techniques used in flow injection analysis (FIA), visible spectrophotometry has been the most predominant. FIA provides high sample throughput, high repeatability and easily automated operation. It is widely used for the determination of pharmaceuticals [30–32]. Sequential injection analysis (SIA) based on principles similar to FIA, but with the possibility of universal flow manipulation, was introduced in 1990 [33]. Among the major benefits of SIA systems are reduced consumption of reagents by at least one order of magnitude, robust hardware and flexible control software which enables the convenient optimization and operation of the system. Few papers have been published that used the SIA method for the determination of AsA [6,31,34–38], and these have shown few advantageous analytical parameters when compared to FIA procedures. SIA has allowed for the use of titrimetry [35,36] and kinetics study [6] as well as the simultaneous determination of AsA and other active substances [37].

It is clear from the preceding short description that the application of reactions between HPAs and AsA in flow analytical methods has, until now, been restricted by its limited selectivity and in particular by its prolonged reaction time. The purpose of this work was to develop a sufficiently sensitive, rapid, simple, selective batch SP and SIA method for the determination of AsA using the recently synthesized 11-molybdobismuthophosphate HPA.

2. Materials and methods

2.1. Reagents

All reagents used were of analytical-reagent grade, and deionized water (Millipore, USA) was used throughout. An AsA solution was prepared daily by dissolving 0.176 g of L-AsA (Fluka, Germany) in methanol and filling the flask up to the 100 mL mark. Pure grade $Na_2MoO_4 \times 2H_2O$ (Alfarus, Ukraine) was additionally re-crystallized from a water–alcohol solution, while 0.4 M bismuth nitrate solution was prepared by dissolving 2.5 g $Bi(NO_3)_3 \times 5H_2O$ in 2.5 mL of 5 M aqueous H_2SO_4 and diluting it to 25 mL with water. The guanidinium (Gua) nitrate (Applichem, Germany), potassium dihydrogen phosphate (Sigma–Aldrich, Ireland) and sulfuric acid (Alfarus, Ukraine) were used as purchased. A 2×10^{-3} M solution of 11-molybdobismuthophosphate HPA (11-MBP) was prepared by dissolving 0.230 g of re-crystallized $(Gua)_6PBiMo_{11}O_{40}$ in 50 mL of water. The 11-MBP solution is stable for at least one month after preparation but should be preserved from contact with reducing substances contained in water or air. Working solutions of samples and reagents were prepared by appropriate dilution with water.

2.2. Apparatus

2.2.1. Batchwise method

Absorbance measurements were made using SF-26 (LOMO, Sankt-Petersburg, Russia) and SPECORD M-40 (Carl Zeiss, Jena, Germany) spectrophotometers with 10 and 50 mm light-path cells. The IR spectra of the samples (2% sample in KBr) were recorded as KBr discs on a Nicolet Impact 410 FT-IR spectrophotometer (Thermo-Nicolet, Madison, WI, USA). The pH of the solutions was monitored using an EV-74 pH-meter with glass and silver/silver chloride reference electrodes. The ^{31}P NMR spectra were recorded with a Bruker Avance 300 spectrometer (Bruker Biospin, Rheinstetten, Germany) operating at 121.5 MHz. 7.55 s pulse (90°), pulse level on ^{31}P channel 0 dB, relaxation delay time of 2.0 s, an acquisition time of 0.8979s (AQ) were used. Chemical shifts are given on the δ-scale and were referenced to an external standard (phosphoric acid, 300 K).

2.2.2. SIA method

The commercially available FIAlab 3000 system (FIAlab Instruments, USA) having a microsyringe pump (syringe reservoir 5.0 mL) and an 8-port selection Cheminert valve (Valco Instrument Co.,

USA) was used. The manifold was equipped with a fibre optic UV–vis CCD detector USB 2000 (Ocean Optics Inc., USA) having an LS-1 tungsten lamp (Ocean Optics Inc., USA). The entire SIA system was controlled by the latest version of the FIAlab program for Windows 5.0. The SIA system was made of PTFE tubing 0.75 mm in diameter, and a 10 mm FIAlab fiber optic SMA-Z flow cell was used.

2.3. Synthesis of $(Gua)_6PBiMo_{11}O_{40}$

The guanidinium salt of 11-MBP was prepared and purified as follows: a solution of 2.662 g (11 mmol) $Na_2MoO_4 \times 2H_2O$ in 25 mL of water was prepared and 2 mL of 0.5 M KH_2PO_4 along with 2 mL of 5 M H_2SO_4 were added. Then 4 mL of a 0.4 M solution of $Bi(NO_3)_3$ in 0.5 M H_2SO_4 was added drop-wise. The pH of the yellow-orange solution was maintained at 1.5–1.8 by the addition of 1 M sodium acetate or 1 M H_2SO_4. For precipitation, 40 mL of a 0.2 M Gua nitrate was used. The resulting $(Gua)_6PBiMo_{11}O_{40}$ was filtered off, carefully washed with a small quantity of water, dried in air and purified by re-crystallizing from hot water at 80–90 °C.

2.4. Procedures for AsA determination

2.4.1. Batchwise procedure

Calibration solutions for batch SP determination of AsA were prepared as follows: 1 mL of 10^{-3} M 11-MBP, 3 mL of 0.05 M H_2SO_4 (pH 1.7 ± 0.1) and the required amount of AsA were mixed in a 25 mL volumetric flask. The flask was then filled with water to the mark. Absorbance was measured after 5 min at 720 nm against water in a 10 or 50 mm glass cell.

2.4.2. SIA procedure

The SIA manifold configuration employed for the determination of AsA is depicted in Fig. 1. The analytical cycle began by filling the piston pump syringe with 800 μL of the carrier solution (water acidified with sulfuric acid to pH 1.7 ± 0.1), which was drawn into the syringe at a flow rate of 50 $\mu L\,s^{-1}$. This was followed by 60 μL of reagent (2×10^{-3} M solution of 11-MBP) and 140 μL sample or AsA standard aspirated sequentially into the holding coil at 50 $\mu L\,s^{-1}$ through separate ports (ports no. 4 and no. 5, respectively) of the selection valve (Fig. 1). The end of the holding coil was filled through valve port no. 2 with 120 μL of carrier solution, used as a spacer. To achieve better mixing, the reaction mixture was moved back and forth in 40 μL steps. A delay of 90 s was used to prolong the reduction time of 11-MBP. Using port no. 6, the entire volume was then propelled at 20 $\mu L\,s^{-1}$ through the Z flow cell. The spectrometer reference scan was made after 2 s and then absorbance scanning began.

2.4.3. Determination of AsA in pharmaceuticals

The following three commercial ascorbic acid formulations available from local sources were subjected to the proposed analytical procedures: (1) tablets containing AsA (250 mg) as a single component (Celascon, producer «Zentiva», Praha, Czech republic); (2) tablets containing AsA (60 mg) together with ferrous sulfate (320 mg) (Durules, producer «Egis», Budapest, Hungary); (3) multivitamin tablets containing nicotinamide (18 mg), vitamin E (10 mg), vitamin A (0.8 mg), pantothenic acid (6.6 mg), vitamin B_1 (1.4 mg), vitamin B_2 (1.6 mg), vitamin B_6 (2 mg), vitamin D (5 μg) (Spofavit, producer « Zentiva », Praha, Czech republic). The tablets also contained inactive ingredients. Ten tablets were accurately weighed and crushed into a powder. An amount equivalent to one tablet was weighed, dissolved in water, transferred to a 100 mL volumetric flask and sonicated for 10 min. The solution was then filtered through a Whatman no. 41 paper filter to separate the insoluble sample matrix. The solution was then filled up with water. A known volume containing the appropriate weight needed to give approximately 2.5×10^{-4} M of AsA was further diluted to 20 mL and analyzed as described above.

2.4.4. Determination of AsA in fruit juices

Commercially available fruit juices were centrifuged at 3500 rpm for 4 min at 4 °C. The solution obtained was filtered through a Whatman no. 42 paper filter and diluted to an appropriate volume. Suitable aliquots (1–2 mL) of the clear juices were then immediately analyzed as described above.

3. Results and discussion

3.1. Synthesis and identification of $(Gua)_6PBiMo_{11}O_{40}$

11-Molybdobismuthophosphate HPA could be easily synthesized by the careful addition of a bismuth nitrate solution to an acidified mixture of sodium molybdate and potassium dihydrogen phosphate. Quantitative formation of 11-MBP in a dilute solution was observed in a pH range from 1.7 to 3.5 [39]. In order to prevent hydrolysis of BiO^+ cations during synthesis, the acidity of the solution must be maintained at pH < 1.8, or sometimes more acidic, using 1 M sodium acetate. For completion of the reaction, a small excess up to 1.6-fold of the Bi(III) nitrate should be used. The 11-MBP can also be obtained in an excess of molybdate ions [39], but this method is less suitable from a synthetic standpoint considering the very similar conditions needed for the precipitation of iso- and heteropolymolybdate ions.

The selective precipitation of 11-MBP occurred with a number of tetraalkylammonium or pyridinium salts, but the use of Gua nitrate was preferable because its salt was more soluble in water, making it easy to obtain a concentration of up to approximately 5×10^{-3} M. The Gua salt could also be easily purified by re-crystallization from hot water. The purity and composition of the 11-MBP obtained was confirmed by elemental analysis, vis–near-IR, FT-IR and ^{31}P NMR spectroscopy.

It is well known that no more than one molybdenum or tungsten atom in a Keggin HPA can be substituted by a metal ion [40,41]. Nevertheless, in most published papers, the HPA formed during the reduction of 12-molybdophosphate (12-MPA) with AsA in the presence of Sb(III) or Bi(III) was considered to have a formula of $PSb_2Mo_{10}O_{40}$ [42,43] or $PBi_2Mo_{10}O_{40}$ [44], respectively. Consequently, a series of syntheses altering the Bi(III):Mo(VI) ratio from 1:1 to 3:1 was undertaken. In all studies, the analysis of the Gua salt was consistent with the same composition, that is, close to the ratio P:Bi:Mo = 1:1:11. Thus, along with the results of CHN analysis, the formula of the heteropolycomplex as $(Gua)_6PBiMo_{11}O_{40}$ was confirmed. In addition, potentiometric titration of the heteropolyacid obtained from Gua salt by exchange on an ion-exchange resin in the form of H^+ confirmed a basicity equal to six.

The IR spectrum of the Gua salt of 11-MBP (Fig. 2) was similar to the spectrum of 12-molybdophosphate HPA, which is evidence of the structural identity of the anions. In general, four characteristic IR bands appeared in the spectra of the Keggin HPAs [45,46]. For the 11-MBP reported here, three bands were readily assigned upon comparison with values in the literature: Mo=O terminal, 937 cm^{-1}; Mo–O–Mo corner-sharing, 869 cm^{-1}; Mo–O–Mo edge-sharing, 789 cm^{-1}. The fourth band is associated with a stretching mode of the central PO_4 moiety. This band was split into two new bands at 1071 and 1032 cm^{-1} as the symmetry of the HPA decreased from T_d to C_s due to substitution of one of the molybdenum atoms in 12-MPA on the large Bi atom [47]. This part of the IR spectrum was thus useful for checking the purity of the obtained compound.

The structure and purity of the synthesized heteropolycomplex was confirmed by ^{31}P NMR spectroscopy. In the spectrum of

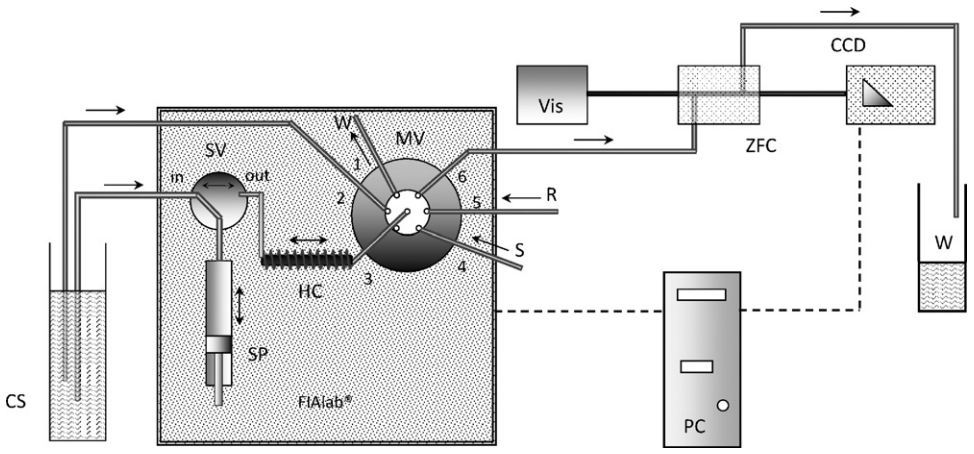


Fig. 1. Scheme of SIA manifold for the determination of ascorbic acid. CCD: charge-coupled detector; ZFC: Z-flow cell; Vis–tungsten lump; MV: 6-port multi-position valve; HC: holding coil; SP: syringe pump; SV: syringe valve; PC: computer; CS: carrier solution; W: waste; R: reagent; S: sample.

the 0.05 M solution of $(Gua)_6PBiMo_{11}O_{40}$ in dimethylformamide, only one signal, at −2.05 ppm, was observed with a chemical shift aside from the signals from the 12-molybdophosphate ($\delta = -3.79$ ppm), 18-molybdo-2-phosphate ($\delta = -3.01$ ppm) and 11-molybdophosphate ($\delta = -1.49$ ppm) HPAs. The formation and coexistence of 12-MPA and 11-MPA with mixed HPAs of Bi(III) and Fe(III) in the water solution had been found earlier using ^{31}P NMR spectroscopy [39,48].

3.2. Relation between the 11-MBP and HPB formed by the reduction of 12-molybdophosphate with AsA in the presence of Bi(III) ions. Optimization of the conditions for the batch SP method

Batch SP methods based on the reduction of 12-molybdophosphate by AsA in the presence of As(III), Sb(III) or Bi(III) were among the most widely used in procedures for the determination of phosphorus(V). The reaction was accelerated through the use of VA Group elements, resulting in a fast reduction at room temperature. In contrast, it had been reported that 24 h were required to complete the reaction in the absence of Bi(III) at room temperature [49]. Data concerning the nature of HPB and its spectrum, as well as the mechanism of the reaction in the P(V)–Mo(VI)–Bi(III)–H^+ system, are rare and conflicting [42,44,50–52]. Several quite different hypotheses concerning the position of Bi(III) in the complex formed were explored. It was supposed that Bi(III) takes a position in the center of the HPA [50], substitutes one [51] or two [43,44] of the Mo atoms in the polymeric ligand, or even forms an ion association complex [53].

In the system being investigated, reduction of the synthesized 11-MBP with AsA provided a much faster reaction than for the parent 12-MPA. The reaction rate was dependent on the temperature, and the reduction took about 5–7 min at 20–25 °C. The HPB obtained remained stable for at least 1 h.

Complete HPB formation was observed in a narrow pH range between 1.55 and 1.80 (Fig. 3). The mixed HPA was stable at pH > 1.80, but in this case the difference in redox potential between AsA and HPA was not large enough to shift the reaction to the HPB side. The decrease in absorbance at pH < 1.55 could be explained by the destruction of 11-MBP.

Stoichiometry for the 11-MBP-AsA reduction reaction was determined using the mole-ratio method and Job's method of continuous variation. In both cases, the intersection point of the extrapolated lines corresponded to the interaction of one mole of AsA with one mole of HPA. It was seen also from the plots that even in the big excess of AsA only one complex was formed. It could be concluded that two of the eleven Mo(VI) atoms present in the HPA were reduced to the five-valent state. If so, the equation of the reaction between 11-MBP and AsA could be presented as

$$P\mathrm{Bi}^{\mathrm{III}}\mathrm{Mo}^{\mathrm{VI}}{}_{11}O_{40}{}^{6-} + H_2AsA = H_2P\mathrm{Bi}^{\mathrm{III}}\mathrm{Mo}_2{}^{\mathrm{V}}\mathrm{Mo}_9{}^{\mathrm{VI}}O_{40}{}^{6-} + 2AsA$$

At the same time, the reduction of 11-MBP in a more acidic solution and other conditions typical to the standard method for phosphorus(V) determination leads to the formation of a more intensely colored HPB. In this case, stoichiometry of the reaction

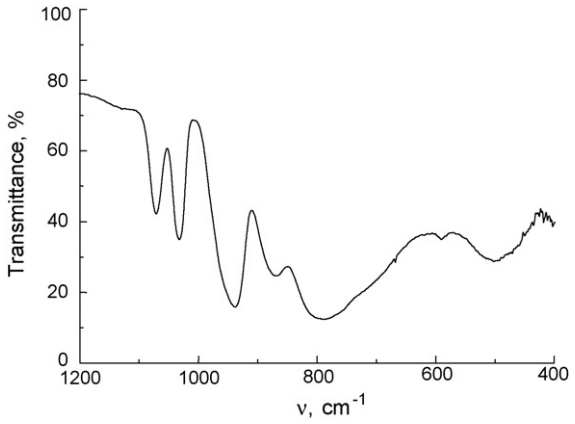


Fig. 2. IR spectrum of $(Gua)_6PBiMo_{11}O_{40}$.

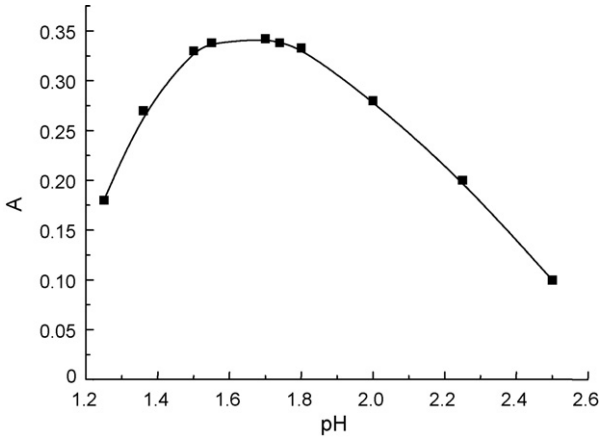


Fig. 3. Influence of medium acidity on the absorbance of reduced 11-MBP. C(11-MBP) = 4×10^{-5} M, λ = 720 nm, l = 10 mm, C(AsA) = 10^{-5} M.

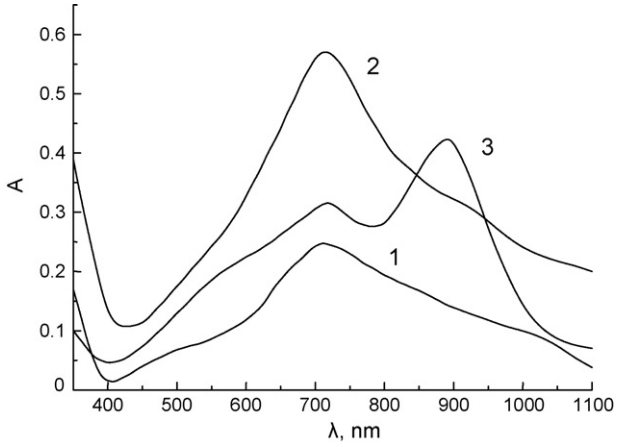


Fig. 4. Absorption spectra of metal-substituted HPBs prepared by reduction with AsA from synthesized 11-MBP (1) or obtained from components in the excess of molybdate and Bi(III) (2) or Sb(III) (3). 1–$C_{11\text{-MBP}} = 4 \times 10^{-5}$ M, $C_{AsA} = 4 \times 10^{-5}$ M, $C_{Sulfuric\ acid} = 7.0 \times 10^{-3}$ M; 2–$C_{P(V)} = 4 \times 10^{-5}$ M, $C_{AsA} = 8 \times 10^{-4}$ M, $C_{Sulfuric\ acid} = 0.1$ M, $C_{Mo(VI)} = 2.8 \times 10^{-3}$ M, $C_{Bi(III)} = 1.4 \times 10^{-4}$ M; 3–$C_{P(V)} = 2 \times 10^{-5}$ M, $C_{AsA} = 8 \times 10^{-4}$ M, $C_{Sulfuric\ acid} = 0.1$ M, $C_{Mo(VI)} = 2.8 \times 10^{-3}$ M, $C_{Sb(III)} = 1.6 \times 10^{-4}$ M, $l = 10$ mm.

between AsA and 11-MBP is equal to 2:1. Consequently, four-electron reduced specie was formed from 11-MBP in the excess of the AsA and Bi(III) ions.

Several intensive overlapping bands were present in the visible region in the absorption spectra of the two- and four-electron reduction products formed by the reaction of 11-MPB with AsA (Fig. 4). The most characteristic feature of each spectrum was the presence of a band with an absorption maximum near 720 nm. As was earlier pointed out [54], the band close to this wavelength appeared in the spectra of other metal-substituted HPBs with Sb(III), Ti(IV) and Sn(II). Unlike the behavior of other molybdenum HPBs, the position of the band did not actually depend on a change in pH [18]. Two absorption maxima appeared in the spectrum of the blue derived from the Sb(III) mixed complex, with the more intense band occurring at 890 nm [42]. The same feature also appeared in the spectrum of the blue formed in the presence of As(III) [53].

The four-electron reduced species obtained from 11-MBP in the excess of AsA, molybdate and Bi(III) had the same spectrum and molar absorptivity as the blue formed in the reaction used in the standard method for the determination of phosphate [53,55]. The identical character of the reduction process means the following can be suggested. When 12-MPA reacted with AsA in the presence of the Bi(III) or Sb(III) ions, mixed HPA was primarily formed. In the second step, a metal-substituted complex was quickly reduced with AsA. It is well known that both the three- and pentavalent states are stable in the case of VA Group elements. This feature, in addition to the ability of Bi(III) or Sb(III) to form complexes with AsA, could be responsible for facilitating the electron transfer in the reaction between AsA and the metal-substituted HPAs. It has often been claimed in the literature that Bi(III) or Sb(III) acts as a catalyst in the reaction discussed above. However, an excess of the metal ions was used in the formation of the intermediate complex, so we cannot consider their catalytic character.

The determination of AsA could be performed using mixed HPA obtained directly from the components in the solution, as was suggested for the analogous complex with Sb(III) [1]. However, in this case, high molybdate and acid concentrations should be used to ensure the complete formation of the complex. Therefore, the oxidation of AsA could not be carried out at the optimal pH. In addition, the use of synthesized compounds was well-suited for the development of different methods based on impregnated species, such as spot test determination. Their use in flow methods simplified the configuration of the system and the choice of optimal conditions.

3.3. Batch procedure. Calibration

Two calibration curves were obtained in the optimal conditions found for the determination of AsA. The two curves differed in the path lengths used. The concentration of 11-MBP should be increased to 8×10^{-5} M to extend the analytical range. In this case, absorbance was measured in a 10 mm cell. A linear relationship was observed over a range of 2×10^{-6}–8×10^{-5} M of AsA using a 10 mm cell and over a range of 5×10^{-7}–3×10^{-5} M using a 50 mm cell, respectively. The corresponding linear regression equations of the calibration plots were $A_{720} = [(6.0 \pm 0.2) \times 10^3]C_{AsA}$ ($R^2 = 0.9983$) and $A_{720} = (0.025 \pm 0.003) + [(2.71 \pm 0.05) \times 10^4]C_{AsA}$ ($R^2 = 0.9982$), where A is the absorbance, and C_{AsA} is the concentration of AsA in mol L^{-1}. The standard deviations of the intercept and slope are given in parentheses. The relative standard deviation (RSD) for five runs of 2×10^{-5} M AsA was 1.4%. The limit of detection (LOD), calculated using the equation LOD = $3 \times S_a/b$, where S_a is the standard deviation of the intercept a, was found to be 3×10^{-7} M.

3.4. SIA procedure. Optimization of the manifold parameters

As is shown above, 11-MBP was slowly reduced by AsA. Therefore, the use of this reaction for the development of a method using an FIA configuration would require a long flow line resulting in a high dispersion of the colored zone and a prolonged residence time. In an SIA manifold, the mixing of reagents and sample in the holding coil could be carried out by gentle flow manipulation.

In order to develop the final system, the SIA variables were studied using the above-mentioned optimal chemical variables. The concentration of the 11-MBP was kept at a value of 2×10^{-3} M, close to the maximum value needed to extend the analytical concentration range. The effect of pH changes on product absorbance was low in the range from 1.4 to 2.1, while in the pH range of 1.6–1.8, in direct relation to the results obtained in the batch method, absorbance was found to be independent of pH. Thus, a pH of 1.7 was selected as the optimal value.

Simple mixing of the reagents in the holding coil led to distorted or double peaks. Thus, additional moving of the reaction mixture back and forth through the holding coil was found to be sufficient to obtain symmetric signals with common shapes.

Compared to the batch method, SIA measurements were made under non-equilibrium conditions, when the signal has not yet reached its maximum value. This was the reason for the shorter delay time in comparison with the batch method. Investigation of the influence of the delay time on the absorbance of the HPB formed showed that the response reached a plateau at 90 s, and the decrease in the absorbance due to dispersion became significant after 200 s.

The effect of variation in the flow rate during the measurement stage with respect to the shape and intensity of the recorded peak was investigated. The signal intensity was independent of the flow rate in the range from 5 to 20 μL s^{-1}. Absorbance was slightly decreased when using faster flow rates. Thus, a flow rate of 20 μL s^{-1} was chosen as optimal to ensure a higher throughput value.

Under the above SIA optimized conditions, the effect of the volume of 2×10^{-3} M 11-MBP was studied in the range of 5–140 μL. As can be seen in Fig. 5, increasing the concentration of the reagent increased the signal intensity, which reached a plateau at a volume of 60 μL of 11-MBP. No difference was further observed; hence a 60 μL sample was selected as the most appropriate volume. The influence of the sample volume was investigated by injecting volumes in the range of 20–200 μL. A sample volume of 140 μL was

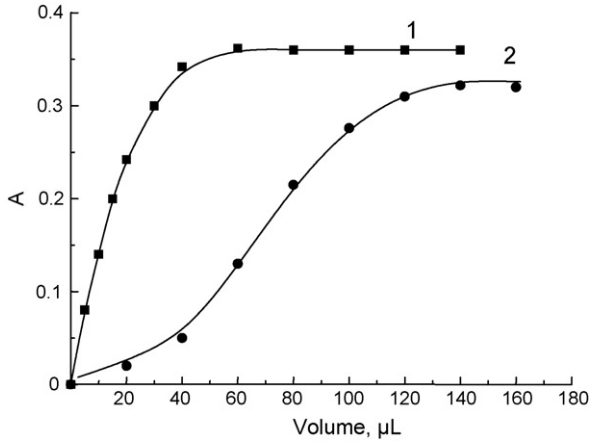


Fig. 5. Influence of reagent (1) and sample (2) injected volume on product absorbance.

then chosen as optimal, considering sample consumption and the fact that maximum absorbance was achieved at this value.

Aspiration of a series of standard AsA solutions resulted in the flow signals shown in Fig. 6. The equation of the calibration plot in the AsA concentration range from 6×10^{-6} to 5×10^{-4} M was as follows: $A_{720} = (-0.009 \pm 0.016) + [(1.49 \pm 0.08) \times 10^3] C_{AsA}$, ($R^2 = 0.998$). The precision of the proposed method was checked by repeated aspiration of the same standard AsA solutions. The relative standard deviations (R.S.D.) of 20 aspirations of each solution containing 12.5, 50, and 250 μM of AsA were 4.8%, 3.6% and 2.7%, respectively. The limit of detection obtained with a peak height by three-times of the signal-to-noise ratio (S/N = 3) was 2×10^{-6} M. Under the SIA optimized conditions, the throughput was calculated as 15 h^{-1}, with negligible carryover.

3.5. Interference study

In order to assess the possible analytical applications of the batch SP and SIA methods described above, the effect of interfering species on the determination of AsA in real samples was studied by analyzing a model sample solution containing AsA and various excess amounts of common interferents. The tolerance limit was set as the maximum amount causing an error of ≤± 5% in the absorbance.

It is easily seen in Table 1 that the reaction of 11-MBP with AsA was found to be highly selective. This could be explained by the optimal difference of the redox potentials and by favorable kinetic factors. The E^0_{red} for [Fe(III,II)-(phen)$_3$] (1.06 V in 1.0 M H_2SO_4 solution) and the E^0_{red} for [Cu(II,I)-(Nc)$_2$] (0.603 V, pH 7.0) [10] are higher than the E^0_{red} for 11-MBP$_{ox}$/11-MBP$_{red}$ (0.52 V, pH 2.0). The reaction rates of 12-MPA and 11-MBP with AsA differed greatly. At the same time, the reduction potentials of these HPAs were close to one another. Consequently, an additional factor—the presence of Bi atom in HPA—influenced the studied reaction. The 11-MBP reacted very slowly even with strong reducing agents, and a large excess of such compounds did not seriously interfere with the reaction. Thus, most organic and inorganic reducing agents did not influence the reduction of 11-MBP, including high concentrations of species such as the reducing sugars, norepinephrine, methyldopa, uric acid, sodium sulfite, hydrazine and ferrous sulfate.

In addition, no interferences were found for saccharose, acetylsalicylic acid, paracetamol, nicotinic acid, caffeine and other excipients at ratios [interferent]/[AsA] much higher than those found commonly in pharmaceuticals. A large excess of vitamins could be tolerated, excepting vitamin B_1. Sulfide as well as thiamine formed brown complexes with Bi atom in 11-MBP, and cysteine slowly reduced the 11-MBP. Cu(II) ions, in contrast to Fe(III) ions, were unable to oxidize the HPB. As for other HPAs, hydroxyacids were able to induce their destruction. For example, with citric acid at a concentration of 5×10^{-4} M, the color produced by the reaction between AsA and 11-MBP began to disappear, while increasing the concentration of citric acid to 2×10^{-3} M completely prevented the development of color. Hydroquinone appreciably interfered with the determination of AsA, resulting in a relative error of 8% at a 10-fold excess and 24% at a 50-fold excess.

Table 1
Influence of some interfering species on the determination of AsA ($C_{AsA} = 8 \times 10^{-6}$ M).

Species	Tolerable concentration (mol L^{-1})
Na^+, K^+, Mg^{2+}, Ca^{2+}	0.1[a]
NO_3^-, SO_4^{2-}, PO_4^{3-}, Cl^-	0.1[a]
Al^{3+}, Zn^{2+}	0.01[a]
Cu^{2+}, Fe^{2+}	1×10^{-3}[a]
Fe^{3+}	1×10^{-5}
$NaNO_2$	4.0×10^{-3}
Na_2SO_3	5.0×10^{-3}[a]
Na_2S	2×10^{-4}
Thiosulfate	4×10^{-4}
Hydrazine	2.0×10^{-3}
Saccharose, glucose, galactose	0.02[a]
Thiourea	1.2×10^{-3}
Tannin	2.0×10^{-3}
Paracetamol, nicotinic acid, acetylsalicylic acid, caffeine	4×10^{-3}
Uric acid	1.1×10^{-4}[a]
Vitamins B_1, B_2, B_6, B_{12}, D, E	1×10^{-3}[a]
Norepinephrine, methyldopa	4×10^{-3}
Tartaric, oxalic acid	2.0×10^{-3}
Citric acid	5.0×10^{-4}
Hydroquinone, thiamine	1×10^{-5}
Cysteine	8×10^{-6}

[a] Highest studied concentration of the interferent.

3.6. Application

The determination results of the AsA content in some pharmaceuticals obtained by the proposed and standard titrimetric

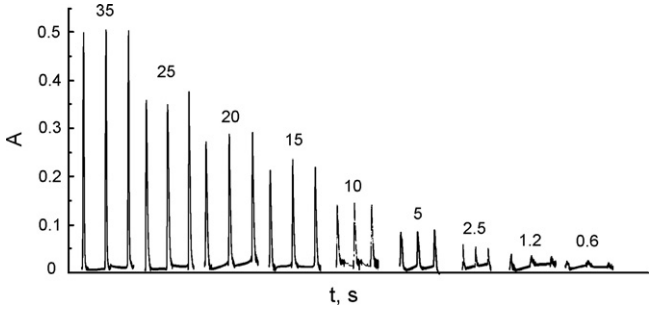


Fig. 6. Typical SIA signals obtained by construction of the calibration graph for the determination of AsA using standards in the range from 0.6×10^{-5} to 35×10^{-5} M.

Table 2
Results of the determination of AsA in pharmaceutical preparations by the proposed and reference methods (mg/tablet ± confidence intervals of the method for $n = 5$ and 95% confidence level).

Sample	Proposed method		Reference method [56]	Claimed value
	SIA	SP		
Celascon	247 ± 5	251 ± 2	251 ± 1	250
Durules	61 ± 2	59.5 ± 0.6	–	60
Spofavit	60.5 ± 0.7	60.3 ± 0.3	60.1 ± 0.3	60

Table 3
Results of the determination of AsA in juices (mg/100 mL ± confidence intervals for $n = 5$ and 95% confidence level).

Sample	Proposed batch SP method	Reference method [56]
Orange juice "Parmalat"	41 ± 2	40 ± 1
Orange juice "Sandora"	40 ± 1	40.2 ± 0.4
Pineapple juice "Parmalat"	12.5 ± 0.4	12.5 ± 0.1
Orange juice "FMG"	92 ± 2	90 ± 2

method based on the colorimetric titration of AsA with 2,6-dichlorophenolindophenol [56] are presented in Table 2 and were in good agreement with each other. The results of analyses of pharmaceuticals obtained using the proposed methods also agreed well with the claimed value of producers in all instances, thus confirming the accuracy of the developed methods. In addition, the developed procedures were easy to apply to the analysis of pharmaceuticals containing ferrous sulfate, which usually interferes strongly with AsA determination in other batch SP and FIA methods. Based on these results, it could be concluded that no interference was found in the presence of complex matrices such as multivitamin pharmaceutical formulations, common excipients and additives used in pharmaceutical preparations. It is thus possible to use this method for the direct determination of AsA in pharmaceuticals without separating potentially interfering materials.

The developed batch SP method was used for the determination of AsA in orange and pineapple juices produced by "Parmalat" (Belgorod, Russia), and orange juices from the "Frout Master Group" (Beregovo, Ukraine) and "Sandora" (Mykolayvske, Ukraine). Table 3 shows the AsA content in some of the analyzed fruit juices. No interference was found even in the presence of a very complex matrix of the samples. Fruit juices could be analyzed without any prior chemical treatment except dilution. The potential interference of iron(II) and hydrogensulfite, which could be present in fruit juices, was excluded using a selective reagent. Accuracy was assessed by comparing results with those obtained by the reference method [56]. No significant differences at 95% confidence level were observed.

4. Conclusions

The developed batch SP and SIA methods for the determination of AsA proved to be more rapid, more selective and sufficiently sensitive when compared with most of the reported methods. The reaction of AsA with 11-MBP is simple and direct. Unlike electrochemical procedures, the proposed methods are robust and relatively low cost in terms of equipment and operations when compared with methods involving enzymes and chromatography. Furthermore, the method eliminates many of the disadvantages of previously reported methods for batch SP and FIA/SIA determination of AsA, in particular those involving heteropolycomplexes. There is no need to use laborious and time-consuming washing or background correction steps. The reagent solution is stable and does not need to be standardized before use. The SIA procedure is characterized by small reagent consumption of just 0.08 mL, a good sampling frequency of 15 h^{-1} and a broad calibration range of 6×10^{-6}–5×10^{-4} M. In addition, 11-MBP is a milder, and therefore more selective, oxidant than Fe(III)-phenantroline or Cu(II)-neocuproine. The significant interference from catecholamines, polyphenols, vitamins, nitrite, sulfite, ferrous(II) and copper(II), frequently mentioned in many papers, is eliminated by using the proposed reagent.

The investigation of pure synthesized complex allowed us to elucidate its structure, its formula, its chemical properties, the extent of the reduction, and the spectrum of the HPB. The accelerating effect of Bi(III) on the reaction between AsA and 12-molybdophosphate has been explained by the intermediate formation of the mixed HPA, which is reduced by AsA much faster than 12-MPA. Due to the presence of a Bi atom, mixed HPA can coordinate AsA, thus facilitating a transfer of the electrons. The same behavior is proposed when using mixed complex containing Sb(III). A general feature of all the investigated molybdenum metal-substituted HPBs is the presence of the absorption band at approximately 720 nm. With a single exception—the analysis of beverages with very high citric acid content—the proposed methods have been successfully applied to the determination of AsA in complex matrices such as multivitamins, pharmaceutical formulations and fruit juices.

Acknowledgements

P.S. and H.S. gratefully acknowledge financial support of the Czech Ministry of Education, MSM 0021620822. V.A.B. wishes to thank the Slovak Academic Information Agency for its financial support. Ya.B. is grateful to the Scientific Grant Agency of the Ministry of Education of the Slovak Republic and the Slovak Academy of Sciences for supporting by Grant No. 1/4450/07.

References

[1] S.P. Arya, M. Mahajan, P. Jain, Anal. Sci. 14 (1998) 889.
[2] M.C. Yebra-Biurrun, Talanta 52 (2000) 367.
[3] O.A. Zaporozhets, E.A. Krushinskaya, J. Anal. Chem. 57 (2002) 286.
[4] S.M. Sultan, A.M. Abdennabi, F.E.O. Suliman, Talanta 41 (1994) 125.
[5] A. Besada, Talanta 34 (1987) 731.
[6] S.M. Sultan, N.I. Desai, Talanta 45 (1998) 1061.
[7] A. Molina-Diaz, I. Ortega-Carmona, M.I. Pascual-Reguera, Talanta 47 (1998) 531.
[8] B. Jaselskis, Anal. Chem. 44 (1972) 379.
[9] T. Kleszczewski, E. Kleszczewska, J. Pharm. Biomed. Anal. 25 (2001) 477.
[10] K. Güçlü, K. Sözgen, E. Tütem, M. Özyürek, R. Apak, Talanta 65 (2005) 1226.
[11] A.V. Pereira, O. Fatibelo-Filho, Anal. Chim. Acta 366 (1998) 55.
[12] J.A. Nobrega, G.S. Lopes, Talanta 43 (1996) 971.
[13] J.M. Alamo, A. Maquieira, R. Puchades, S. Sagrado, Fresenius J. Anal. Chem. 347 (1993) 293.
[14] K. Grudpan, K. Kamfoo, J. Jakmunee, Talanta 49 (1999) 1023.
[15] M. Okamura, Clin. Chim. Acta 103 (1980) 259.
[16] M. Okamura, Clin. Chim. Acta 115 (1981) 393.
[17] N. Teshima, T. Nibuta, T. Sakai, Anal. Chim. Acta 438 (2001) 21.
[18] M.T. Pope, Heteropoly and Isopoly Oxometalates, Springer-Verlag, New York, 1983.
[19] L.P. Tsiganok, A.B. Vishnikin, Peculiarities of Formation and Reduction Reactions of Heteropolycomplexes of IIIA Group Elements of Periodic Table, Dnipropetrovsk, DNU, 1996.
[20] E.S. Elnenaey, R. Soliman, Talanta 28 (1979) 1164.
[21] V.K.S. Shukla, C.K. Kokate, K.C. Srivastava, Microchem. J. 24 (1979) 124.
[22] M. Rutkowski, K. Grzegorczyk, J. Greger, Z. Naturforschung, Sect. C 59 (2004) 762.
[23] K. Shinohara, K.E. Padis, J. Biol. Chem. 118 (1935) 697.
[24] E.I. Morosanova, A.A. Velikorodnyi, E.A. Reznikova, N.M. Kuz'min, J. Anal. Chem. 55 (2000) 378.
[25] E.I. Morosanova, E.A. Reznikova, A.A. Velikorodnyi, J. Anal. Chem. 56 (2001) 173.
[26] S.G. Dmitrienko, L.V. Goncharova, B.K. Runov, Zh. Anal. Khim. 53 (1998) 800.
[27] S.G. Dmitrienko, L.V. Goncharova, A.V. Zhigulev, R.E. Nosov, N.M. Kuzmin, Yu.A. Zolotov, Anal. Chim. Acta 373 (1998) 131.
[28] B. Chen, Q. Guo, Z. Guo, X. Wang, Tsinghua Sci. Technol. 8 (2003) 422.
[29] D. Thorburn Burns, N. Chimplaee, D. Chimplaee, S. Rattanariderom, Anal. Chim. Acta 243 (1991) 187.
[30] J.M. Calatayud, Flow Injection Analysis of Pharmaceuticals, Taylor Francis, London, UK, 1996.
[31] P. Solich, M. Polášek, J. Klimundova, J. Ruzicka, Trends. Anal. Chem. 22 (2003) 116.
[32] P. Solich, H. Sklenarova, M. Polasek, R. Karlicek, J. Flow. Injection Anal. 18 (2001) 13.
[33] J. Ruzicka, G.D. Marshall, Anal. Chim. Acta 237 (1990) 329.
[34] N. Anastos, N.W. Barnett, B.J. Hindson, C.E. Lenehan, S.W. Lewis, Talanta 64 (2004) 130.
[35] N. Lenghor, J. Jalmunee, M. Vilen, R. Sara, G.D. Christian, K. Grudpan, Talanta 58 (2002) 1139.
[36] S.M. Sultan, Y.A.M. Hassan, K.E.E. Ibrahim, Analyst 124 (1999) 917.

[37] Z. Legnerova, D. Šatinsky, P. Solich, Anal. Chim. Acta 497 (2003) 165.
[38] D.T. Newcombe, T.J. Cardwell, R.W. Cattrall, S.D. Kolev, Lab. Robot. Automation 12 (2000) 200.
[39] O.M. Trokhimenko, V.V. Trachevskii, Ukr. Khim. Zh. 62 (1996) 46.
[40] G.M. Maksimov, R.I. Maksimovskaya, I.V. Kozhevnikov, Russ. J. Inorg. Chem. 37 (1992) 2279.
[41] G.M. Maksimov, Russ. Chem. Rev. 64 (1995) 480.
[42] H. Kobayashi, E. Nakamura, Bunseki Kagaku 53 (2004) 119.
[43] L. Drummond, W. Maher, Anal. Chim. Acta 302 (1995) 69.
[44] H. Kobayashi, E. Nakamura, Bunseki Kagaku 56 (2007) 561.
[45] C. Rocchiccioli-Deltcheff, R. Thouvenot, R. Frank, Spectrochim. Acta 32A (1976) 587.
[46] C. Rocchiccioli-Deltcheff, M. Fournier, R. Thouvenot, R. Frank, Inorg. Chem. 22 (1983) 207.
[47] G.M. Maksimov, G.N. Kustova, K.I. Matveev, T.P. Lazarenko, Koord. Khim. 15 (1989) 788.
[48] O.M. Trokhimenko, N.F. Falendish, Zh. Anal. Khim. 53 (1998) 475.
[49] J.-Z. Zhang, C.J. Fischer, P.B. Ortner, Talanta 49 (1999) 293.
[50] L.G. Hargis, Anal. Chem. 41 (1969) 597.
[51] L.V. Tumurova, L.A. Lyalyulina, S.A. Morosanova, I.P. Alimarin, Zh. Anal. Khim. 26 (1971) 2155.
[52] H.D. Goldman, L.G. Hargis, Anal. Chem. 41 (1969) 490.
[53] L. Cariani, L. Thomas, J. Brito, J.R. del Castillo, Anal. Biochem. 324 (2004) 79.
[54] T.E. Svinarenko, A.B. Vishnikin, M.N. Timofeeva, Russ. J. Inorg. Chem. 53 (2008) 1359.
[55] R.P. Mihajlovic, N.R. Ignjatovic, M.R. Todorovic, I. Hoclajtner-Antunovic, V.M. Kaljevic, J. Serb. Chem. Soc. 68 (2003) 65.
[56] P. Cunniff, Official Methods of Analysis of the AOAC, 16th ed., AOAC International, Maryland, MA, 1999, p. 16.

Talanta 80 (2010) 1846–1848

Contents lists available at ScienceDirect

Talanta

journal homepage: www.elsevier.com/locate/talanta

Determination of NTBC in serum samples from patients with hereditary tyrosinemia type I by capillary electrophoresis☆

M. Şerif Cansever[a,b], A. Çiğdem Aktuğlu-Zeybek[a], F. Bedia Erim[b,*]

[a] Department of Pediatrics, Division of Metabolism, Cerrahpaşa Medical School, University of Istanbul, Cerrahpaşa 3430, Istanbul, Turkey
[b] Department of Chemistry, Istanbul Technical University, Maslak 34469, Istanbul, Turkey

ARTICLE INFO

Article history:
Received 21 May 2009
Received in revised form 8 October 2009
Accepted 15 October 2009
Available online 24 October 2009

Keywords:
NTBC
Tyrosinemia
MEKC
Capillary electrophoresis
Metabolic disorder

ABSTRACT

Hereditary tyrosinemia type I is a serious metabolic disorder leading to liver failure. 2-(2-Nitro-4-trifluoromethylbenzoyl)-1,3-cyclohexanedione (NTBC) is a relatively new drug which is used to prevent the accumulation of toxic metabolites in patients with hereditary tyrosinemia type I. In the present study, we have developed a new, simple, fast, and cost-effective capillary electrophoresis method for the quantitative monitoring of this drug in serum samples. Micellar electrochromatographic separation of NTBC was performed using 20 mmol/L phosphate and 40 mmol/L sodium dodecylsulfate (SDS) at pH 12 as running electrolyte. Separation of NTBC was achieved in around 4 min. Reproducibilities of migration times and corrected peak areas of NTBC (as R.S.D.%) were found as 0.73 and 1.99, respectively. The detection limit was 3.17 and the quantification limit was 10.6 μmol/L for NTBC using UV detection at 278 nm. The utility of the method was demonstrated by the detection of NTBC in serum samples from patients with hereditary tyrosinemia type I using this drug.

© 2009 Elsevier B.V. All rights reserved.

1. Introduction

Tyrosinemia type I is a metabolic disorder caused by enzyme deficiency in tyrosine catabolism pathway, leading to liver failure [1]. Diagnosis is confirmed by increased tyrosine serum levels and large amounts of succinylacetone (SA) in urine. As the liver transplantation had been the only option, the introduction of NTBC in the treatment of tyrosinemia in 1992 [2] has reduced the need of liver transplantation and gave a good outlook for children with this disorder [3,4]. The use of NTBC is still under study. The clinical studies on the NTBC treatment have been steadily reported in different hospitals and in different countries. Every year, the European Medicines Agency (EMEA) reviews any new information on NTBC treatments. The current recommended starting dose is 1 mg/kg body weight/day and the dose is adjusted to the patient. In patients with poor response to NTBC treatment, the NTBC dose is increased to prevent the production of hepatotoxic metabolites, but keeping the serum NTBC concentration within the desired range of 40–50 μmol/l to prevent possible secondary NTBC effects [3,5–7]. A column liquid chromatographic method [8] and a LC–MS/MS method [9] were reported by now for the analysis of NTBC in plasma. Individual dose adjustment is based on the biochemical response and the plasma NTBC concentration. However, the analysis of plasma NTBC level is not routinely available for many laboratories. Following our first study on the rapid and easy capillary electrophoresis (CE) method for the determination of succinylacetone in urine samples from patients with hereditary tyrosinemia type I [10], the aim of present study is to develop an inexpensive and trustable capillary electrophoretic method for the detection and quantitative determination of NTBC in serum samples.

2. Experimental

2.1. Chemicals, standards and serum samples

Sodium dodecyl sulfate (SDS), and phosphoric acid were obtained from Merck (Darmstadt, Germany). Acetonitrile is from J.T. Baker (Deventer, Holland). All solutions were prepared with distilled water purified in an Elgacan C114 filtration system.

NTBC as Orfadin capsules with a purity of 99.8% (w/w) was supplied by Swedish Orphan AB, Stockholm, Sweden. Orfadin is a hard white-opaque capsule, marked as 2, 5, or 10 mg NTBC, plus pregelatinized starch. Orfadin capsules with a known amount of NTBC were dissolved in 5 mol/L NaOH. Starch was separated by centrifugation. After dilution to the desired concentration, solutions were filtered using 0.45 μm microfilter and injected directly to the capillary column.

☆ Presented at the "Annual Symposium of the Society for the Study of Inborn Errors of Metabolism" (SSIEM) in Lisbon, Portugal, 2–5 September 2008.

* Corresponding author. Tel.: +90 212 285 3151.
E-mail address: erim@itu.edu.tr (F.B. Erim).

0039-9140/$ – see front matter © 2009 Elsevier B.V. All rights reserved.
doi:10.1016/j.talanta.2009.10.032

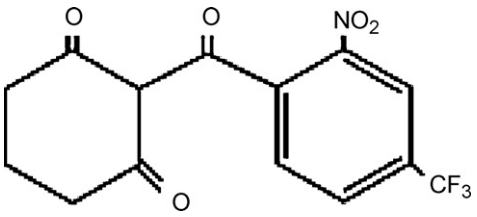


Fig. 1. Chemical structure of NTBC.

Serum samples were prepared by diluting the serum with acetonitrile (1/1.5, v/v) [11]. The solution was shaken for 5 min and centrifuged for 10 min. Before injection, the supernatant solutions were filtered using microfilter with a pore size of 0.45 μm. Buffer solution was prepared from H_3PO_4 stock solution by diluting it to 20 mmol/L by water and adjusting its pH with 0.1 M NaOH solution.

2.2. Apparatus and operating condition

Separations were performed with an Agilent capillary electrophoresis system (Germany) equipped with a diode-array detector. The data processing was carried out with the Agilent ChemStation software. The wavelength was set at 278 nm. The separation was performed at 28 kV. The fused silica capillaries used for the separation experiments were 75 μm i.d. and were obtained from Agilent. The total length of the capillary was 65 cm and the length to the detector was 56.5 cm. The new fused silica capillary was conditioned prior to use by rinsing with 1 mol/L NaOH for 30 min and with water for 10 min. The capillary was flushed by 0.1 mmol/L NaOH and water for 5 min each, in the beginning of every working day, and then the capillary was washed with buffer for 5 min. 5 min of flushing with buffer was performed between runs. Injections were made at 5×10^{-3} MPa for 5 s.

3. Results and discussion

NTBC is a triketone. The structure of molecule shown in Fig. 1 suggests that it could not be charged and separated in capillary zone electrophoretic conditions. In order to separate nonionic compounds in CE, an interaction with a charged carrier in the buffer must be provided. The most common technique to separate nonionic compounds is MEKC. By including a surfactant in the mobile phase, neutral molecules can be separated on the basis of their interaction with the micelles. The concentrations between 20 and 50 mmol/L in phosphate were tried as buffer and between 20 and 50 mol/L as surfactant. The optimal mixture was selected as 20 mmol/L phosphate and 40 mmol/L SDS. NTBC migrated in only 4 min with a good sensitivity using this buffer composition at pH 12. Fig. 2 A and B show the electropherograms of a serum sample and serum sample spiked with NTBC, respectively.

3.1. Method validation

3.1.1. Reproducibility

The precision of the method was checked by 5 successive injections of 100 μmol/L NTBC solution. The precision values for migration times and corrected peak areas (A/t) were 0.73 and 1.99% R.S.D., respectively. Between days precision values for peak areas ($n = 3$) were found as 2.43% R.S.D.

3.1.2. Linear range, LOD and LOQ

The calibration solutions were performed with NTBC solutions obtained by diluting standard NTBC solution with water. The calibration curve was plotted according to the corrected peak areas (A/t) between 25 and 200 μmol/L concentration ranges. The regression equation between this range was $y = 0.00101585x - 0.0006789$ and the correlation coefficients was found to be 0.99611 (r).

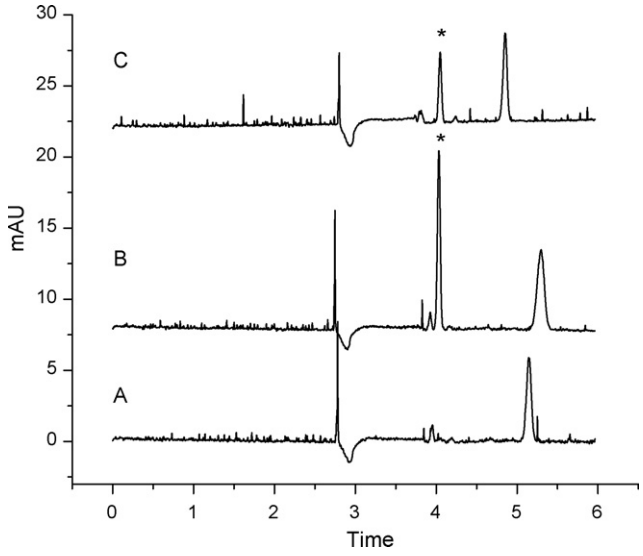


Fig. 2. Electropherogram of a serum sample (A); serum sample spiked with NTBC (B); serum sample from a patient with hereditary tyrosinemia type I (C), who was administrated NTBC. Injections: 5×10^{-3} MPa for 5 s. Running voltage: 28 kV. Capillary: 65 × 56.5 cm and 75 μm i.d. Detection: 278 nm. Separation electrolyte: 20 mmol/L phosphate and 40 mmol/L SDS at pH 12. *Shows NTBC peak, second peak is an unknown coming from serum.

The limit of detection was calculated as 3 times of the average noise taken for three different baseline areas and found to be 3.17 μmol/L for NTBC using UV detection at 278 nm. The limit of quantification is 10.6 μmol/L as 10 times of the average noise.

3.1.3. Accuracy of the method

Accuracy of the method was checked with the addition of NTBC to the serum samples for six measurements at three concentration levels, i.e., 50, 100, and 150 μmol/L NTBC. The recovery values were found between 74 and 84%.

Validation values are given all together in Table 1.

3.2. Application

The utility of the method was demonstrated by the detection of NTBC in serum samples from patients with hereditary tyrosinemia type I using this drug**.** The NTBC peak was identified by spiking with standard solution. Fig. 2C shows the electropherogram of a serum sample from a patient taken 1 mg NTBC/kg daily. The plasma concentration of this patient was found as 38.43 μmol/L NTBC.

Table 1
Validation values.

Run to run ($n = 5$) precision		
Corrected area (A/t)	1.99	
Day to day ($n = 5 \times$ 3 days) precision		
Corrected area (A/t)	2.43	
LOD (μmol/L)	3.17	
LOQ (μmol/L)	10.6	
Spiked to serum sample (μmol/L)		Recovery (%)
50		74 ± 7
100		84 ± 5
150		84 ± 4

4. Conclusion

In conclusion, NTBC level that is considered adequate in the treatment of tyrosinemia, is much higher than the LOD value in our developed method. Thus, capillary electrophoresis is highly recommended for the simultaneous control of both NTBC and succinylacetone, the latter with the use of the method that we have developed earlier [10] as an economic method both in time and money.

References

[1] P.A. Russo, G.A. Mitchell, R.M. Tanguay, Pediatr. Dev. Pathol. 4 (2001) 212.
[2] S. Lindstedt, E. Holme, E.A. Lock, O. Hjalmarson, B. Strandvik, Lancet 340 (1992) 813.
[3] E. Holme, S. Lindstedt, J. Inherit. Metab. Dis. 21 (1998), 507 139.
[4] A. Masurel-Paulet, J. Poggi-Bach, O. Bernard, N. Guffon, D. Dobbelaere, H. Ogier de Baulny, G. Touati, J. Inherit. Metab. Dis. 31 (2008) 81.
[5] S. Santra, U. Baumann, Expert Opin. Pharmacother. 9 (2008) 1229.
[6] S. Pitkanen, M.K. Salo, K. Vettenranta, K. Nanto-Salonen, M. Heikinheimo, J. Pediatr. Gastr. Nutr. 29 (1999) 38.
[7] J. Crone, D. Moslinger, O.A. Bodamer, W. Schima, W.D. Huber, E. Holme, S.S. Ipsiroglu, Acta Paediatr. 92 (2003) 625.
[8] M. Bielenstein, L. Astner, S. Ekberg, J. Chromatogr. B 730 (1999) 177.
[9] D. Herebian, U. Spiekerkötter, M. Lamshöft, E. Thimm, M. Laryea, E. Mayatepek, J. Chromatogr. B 877 (2009) 1453.
[10] M.Ş. Cansever, F.B. Erim, J. Chromatogr. B 818 (2005) 309.
[11] R. vanholder, N. Hoefliger, R. De Smet, S. Ringoir, Kindey Int. 41 (1992) 1707.

Talanta 80 (2010) 1849–1855

Contents lists available at ScienceDirect

Talanta

journal homepage: www.elsevier.com/locate/talanta

Separation of PCBs by liquid chromatography on reversed phase sub-2-micron particle columns

Jana Olšovská, Zdena Křesinová, Miroslav Flieger, Tomáš Cajthaml*

Institute of Microbiology, Academy of Sciences of the Czech Republic, v.v.i., Vídeňská 1083, CZ-142 20 Prague 4, Czech Republic

ARTICLE INFO

Article history:
Received 26 May 2009
Received in revised form 7 October 2009
Accepted 15 October 2009
Available online 24 October 2009

Keywords:
Ultra high-performance liquid chromatography
PCB
Congener analysis
GC–MS

ABSTRACT

A new ultra high-performance liquid chromatography method with UV detection was examined for detection and separation of polychlorinated biphenyls. This included optimization of separation conditions for two model mixtures containing seven and fifteen most relevant congeners, comparison of three types of reversed phase sub-2-micron particle sized columns and assessment of system suitability under the optimized conditions. Calibration curves determined in the range from 0.5 to 50.0 μg/mL exhibited correlation coefficients ranging from 0.997 to 0.999. Lower limits of detection ranged from 0.1 to 0.5 ppm. The most efficient Grace C18 column filled with 1.5 μm particles was then tested to separate the complex commercial mixture Delor 103, where the elution order was confirmed by GC–MS. 13 individual congeners were separated and some of the other co-eluting congeners could be resolved using another separation dimension performed with a mass spectrometry detector. The developed method could be directly applied to the separation of less complex mixtures in aqueous sample matrixes, which are used in general for enzyme degradation studies.

© 2009 Elsevier B.V. All rights reserved.

1. Introduction

Although the industrial use and production of polychlorinated biphenyls (PCBs) has long been banned, the persistency of these compounds means they still represent a serious environmental problem. It has been widely reported that determination of PCBs in environmental samples is a difficult task [1,2].

The complexity of the chromatographic separation of PCBs consists in the number of possible congeners (209) and their physico-chemical similarities, together with the complexity of environmental matrices harboring the PCBs. For this reason, gas chromatography (GC) has always been the method of choice for determination of these compounds [3,4], since it allows the congener-specific analysis of PCBs and the routinely used detectors, ECD, MS and HRMS, to exhibit high sensitivity.

Two-dimensional gas chromatography [5,6] has been investigated by a number of researchers in order to solve certain co-elution problems inherent in single-column analysis. A number of GC column combinations have been used to resolve the co-elution of PCBs [7]. Several authors used two-dimensional chromatography with HPLC as the first separation dimension for fractionation. PCB atropisomers were partially separated using chiral stationary phases (beta-cyclodextrin derivatized silica) [8] and dioxin-like PCBs were fractionated on an activated carbon-based column [9,10], porous graphitic carbon [11], or (2-(1-pyrenyl)ethyl)dimethylsilylated silica [12]. Other applications of column liquid chromatography described in the literature include the use of various systems for PCB separations from the matrix or other compounds [13,14]. A limited number of publications are available on application of the HPLC technique for determination of PCBs. Andersson and Kaiser [15] tested several modified stationary phases including octadecylsilica for separation of commercial mixture Aroclor. A partial improvement of separation was observed with phenyl butano sulfide stationary phase [15].

Another new technique, ultra high-performance liquid chromatography (UHPLC), which has been introduced into practice, is based on the HPLC principle but provides separation efficiency attaining GC parameters. According to the Van Deemter equation, when the particle size of the chromatographic sorbent is decreased, the efficiency of the separation process increases and the efficiency does not diminish at higher flow rates or linear velocities [16]. The separation speed, resolution, sensitivity and peak capacity can be improved by using smaller particles. UHPLC technique offers both a high throughput of the analyzed samples and separation of complex mixtures like PCBs. The latter feature is caused by the large peak capacity mentioned above. Another advantage over common HPLC consists in the reduced time of analysis and solvent consumption. Sub-2-micron particle columns provide maximum efficiency, leading to back-pressures of more than 60 MPa, which cannot be achieved by using conventional liquid chromatographic systems or

* Corresponding author. Tel.: +420 241062498; fax: +420 241062384.
E-mail address: cajthaml@biomed.cas.cz (T. Cajthaml).

0039-9140/$ – see front matter © 2009 Elsevier B.V. All rights reserved.
doi:10.1016/j.talanta.2009.10.033

columns [17]. UHPLC systems can work at extreme pressures up to 100 MPa [18] due to hardware adjustments. While the separation of PCB derivatives using HPLC is probably not sufficient, the UHPLC application on special columns with sub-2-micron particle could lead to better separation. A number of producers currently offer reversed phase columns with sub-2-micron particle size sorbents with different properties that are suitable for UHPLC applications. In addition to the original columns provided by Waters that use octadecyl silica Bridged Ethyl Hybrid (BEH) particles with diameter of 1.7 μm, several other producers manufacture UHPLC columns e.g. Zorbax Rapid Resolution High Throughput 1.8 μm from Agilent or C18 Grace 1.5 μm from Alltech.

The aim of this study was to test the ability of liquid chromatography on reversed phase sub-2-micron particle columns, viz. BEH C18 (1.7 μm), Waters; BEH Phenyl (1.7 μm), Waters; Vision HT C18 Grace (1.5 μm), Alltech, for the separation of the most often monitored PCB congeners in two premixed mixtures and for the separation of the commercial mixture Delor 103.

2. Experimental

2.1. PCB model mixtures and other chemicals

Two model mixtures of PCBs were used to test the retention behavior and for a quantitative study. Mix A consisted of PCBs 18, 28, 52, 101, 153, 138, 180 (Dr. Ehrenstorfer GmbH, Augsburg, Germany). Mix B included the most toxic PCB congeners supplemented with several other congeners with three, four and five mainly ortho-chlorine substituents: 18, 28, 37, 45, 77, 81, 91, 101, 105, 114, 118, 123, 126, 156 and 169. The individual PCB congeners used for the preparation of this mixture were also obtained from Dr. Ehrenstorfer GmbH (Augsburg, Germany). Both of the mixtures contain the most relevant congeners that are commonly monitored [19,20]. The PCB commercial mixture used for the investigation, Delor 103, with an average of 3 chloro substituents, was obtained from a former Czechoslovak producer (Chemko Strážské, Slovakia). The congener composition of Delor 103 has been described in detail in previous investigations [21]. Acetonitrile (Biosolve) and water (Biosolve) used for UHPLC mobile phase preparation were of UHPLC–MS grade and were purchased from Chromservis (Prague, Czech Republic).

2.2. UHPLC analysis conditions

An Acquity UHPLC system (Waters, Milford, MA, USA), equipped with a 2996 photodiode-array detection (DAD) system detector operating at 202 nm, was used for PCB analysis. The data were processed with Empower 2 software (Waters). For elucidation of the UHPLC elution order and identification of the PCB congeners, the mobile phase of the best chromatographic run was collected (4 times per minute) using an automated fraction collector (Labio, Prague, Czech Republic). These fractions were subsequently analyzed using GC–MS to confirm the structures of the individual congeners.

For simplicity, PCBs were monitored at the same wavelength of 202 nm, where all of them display significant absorbance.

Three sub-2micron particle UHPLC analytical columns were compared for their efficiency in PCB separation: BEH C18 (50 mm × 2.1 mm I.D., particle size 1.7 μm), Waters; BEH Phenyl (50 mm × 2.1 mm I.D., particle size 1.7 μm), Waters; Vision HT C18 Grace (50 mm × 2.0 mm I.D., particle size 1.5 μm), Alltech.

The binary mobile phase consisted of solvent A, 100% acetonitrile, and solvent B, 10% acetonitrile in water was employed under the following linear gradient program (min/%A) 0/15, 6/40, 14/40, 20/45, 30/95, 35/95. This program was used for column comparison and later also for separation of Delor 103.

Each analysis was followed by a column equilibration step (5 min). The column temperature was maintained at 35 °C, and the flow rate was set at 0.4 mL/min. Sample volumes of 5 μL were injected. The total analysis time was 30 min, the data were collected at 20 Hz sample rate and the filter constant was set at 0.5.

2.3. UHPLC partial validation (calibration curves, LLOQ, LOD)

Calibration curves obtained with UHPLC technique were determined over a linear range from 0.5 to 50.0 μg/mL for the selected PCBs (Nos. 18, 28, 37, 45, 52, 77, 81, 91, 101, 105, 114, 118, 123, 126, 138, 153, 156, 169 and 180). Accurately weighted portions of each solid congener were dissolved in acetonitrile to prepare 50 μg/mL stock solutions. Then each stock solution was diluted stepwise with acetonitrile to prepare a series of standard solutions, with concentrations of 50.0, 25.0, 10.0, 5.0, 1.0, 0.5 and 0.1 μg/mL.

The lower limit of quantification (LLOQ) was determined as the lowest concentrations of PCBs quantified with precision (RSD) and accuracy lower than 20% [22]. For quality control (QC), six replicates of all the quantified PCB standards with the concentration 0.5 μg/mL (0.1 μg/mL in the case of PCB 101) were measured. At this concentration level, the signal-to-noise ratio was found to be greater than 10.

The limit of detection (LOD) was calculated as follows: LOD = LLOQ/0.33.

2.4. UHPLC system suitability

Both model mixtures (Mix A and Mix B) were injected 6 times into a UHPLC system under optimized conditions (Grace column, for chromatographic conditions see Section 2.2, UHPLC analysis conditions). The mean values and RSD (%) of the peak retention times and peak areas of the monitored congeners were calculated to obtain the repeatability. The other parameters to be determined included the peak symmetry, resolution and EP plate count.

2.5. GC–MS analysis conditions

The GC–MS system 450-GC with an ion trap 240-MS (Varian, Walnut Creek, CA, USA) was used for a qualitative PCB analysis. The Varian MS workstation 6.9.1. was used as data processing software.

The column used was a 30 m DB-5MS capillary column of 0.25 mm I.D. and 0.25 μm film thickness (C&W). One microliter of each sample was splitless injected at 240 °C. Helium was used as a carrier gas with a constant flow rate of 1 mL/min. The GC oven temperature program started at 60 °C, was held for 1 min and then increased at 25 °C/min to 120 °C. Further heating followed at 2.5 °C/min to 240 °C, which was finally maintained for 19 min. The transfer line, manifold and ion chamber temperatures were set at 240, 220 and 240 °C, respectively. The mass spectrometer operated under an external ionization mode and mass spectra were recorded under electron impact at 70 eV.

2.6. HPLC analysis conditions

In order to compare the efficiency of the HPLC technique an HPLC system was used for separation of D103, as well. Separation was tested on two conventional reversed phase columns: Xbridge C18 (250 mm × 4.6 mm I.D., particle size 3.5 μm), Waters and Synergy Polar RP (250 mm × 4.6 mm I.D., particle size 4 μm), Phenomenex. The HPLC system consisted of binary gradient pump 522, autosampler 465, and diode-array detector 540+, (Bio-tek Instruments, Italy). The binary mobile phase consisted of solvent A, 100% acetonitrile, and solvent B, 10% acetonitrile in water, was employed under the following linear gradient programs: Xbridge column (min/%A) 0/65; 30/100; 50/100 and Synergi column 0/65; 60/100; 70/100

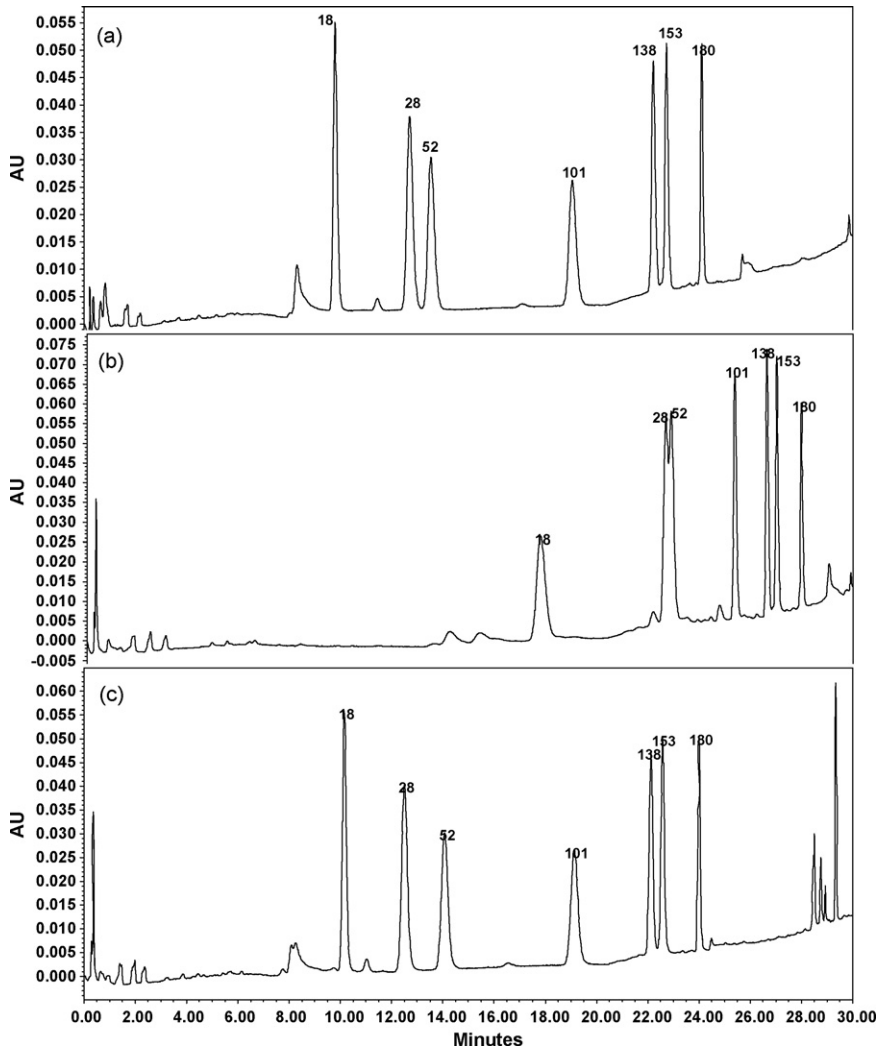


Fig. 1. Comparison of Mix A (4 μg/mL of each congener) separation with three various columns: Vision HT C18 Grace column (a), BEH C18 column (b), BEH Phenyl column (c). Chromatographic conditions: solvent A, 100% acetonitrile, solvent B, 10% acetonitrile, gradient program (min/%A) 0/15; 6/40; 14/40; 20/45; 30/95; 35/95, equilibration step (5 min), column temperature 35 °C, flow rate 0.4 mL/min, sample volume 5 μL.

Table 1
Verified values of LLOQ and LOD of the tested PCB congeners separated on the C18 Grace column.

PCB No.	LLOQ (μg/mL)	Accuracy (%)	RSD (%)	LOD (μg/mL)	Regression equations	R^2
18	0.5	104.1 ± 0.3	0.3	0.15	$y = 1.40 \times 10^5 x - 7.26 \times 10^3$	0.999
28	0.5	113.4 ± 2.4	2.1	0.15	$y = 1.11 \times 10^5 x - 1.33 \times 10^4$	0.999
37	0.5	114.3 ± 0.4	0.3	0.15	$y = 7.74 \times 10^4 x - 2.36 \times 10^3$	0.999
45	0.5	108.0 ± 1.0	1.0	0.15	$y = 8.69 \times 10^4 x - 8.90 \times 10^2$	0.999
52	0.5	106.3 ± 2.9	2.8	0.15	$y = 1.24 \times 10^5 x + 2.47 \times 10^2$	0.998
77	0.5	115.9 ± 4.2	3.6	0.15	$y = 5.65 \times 10^4 x - 2.06 \times 10^3$	0.997
81	0.5	117.9 ± 1.7	1.4	0.15	$y = 6.53 \times 10^4 x - 2.65 \times 10^3$	0.998
91	0.5	109.7 ± 3.3	3.1	0.15	$y = 1.08 \times 10^5 x - 5.09 \times 10^3$	0.998
101	0.1	107.3 ± 2.1	1.9	0.03	$y = 1.06 \times 10^5 x - 5.23 \times 10^3$	0.999
105	0.5	114.2 ± 1.7	1.5	0.15	$y = 7.51 \times 10^4 x - 1.06 \times 10^4$	0.999
114	0.5	92.0 ± 1.6	1.7	0.15	$y = 5.57 \times 10^4 x + 4.18 \times 10^3$	0.999
118	0.5	110.0 ± 2.9	2.6	0.15	$y = 6.34 \times 10^4 x - 9.48 \times 10^3$	0.999
123	0.5	114.0 ± 4.5	4.0	0.15	$y = 8.18 \times 10^4 x - 6.75 \times 10^3$	0.999
126	0.5	102.6 ± 5.3	5.1	0.15	$y = 4.19 \times 10^4 x - 5.55 \times 10^2$	0.999
138	0.5	91.4 ± 3.3	3.6	0.15	$y = 1.04 \times 10^5 x + 9.15 \times 10^3$	0.999
153	0.5	101.6 ± 3.3	3.4	0.15	$y = 1.01 \times 10^5 x + 3.44 \times 10^3$	0.999
156	0.5	109.5 ± 6.2	5.7	0.15	$y = 5.25 \times 10^4 x - 3.31 \times 10^3$	0.999
169	0.5	116.4 ± 4.0	2.9	0.15	$y = 3.12 \times 10^4 x - 9.20 \times 10^2$	0.997
180	0.5	105.7 ± 1.1	1.0	0.15	$y = 7.23 \times 10^4 x + 3.76 \times 10^3$	0.999

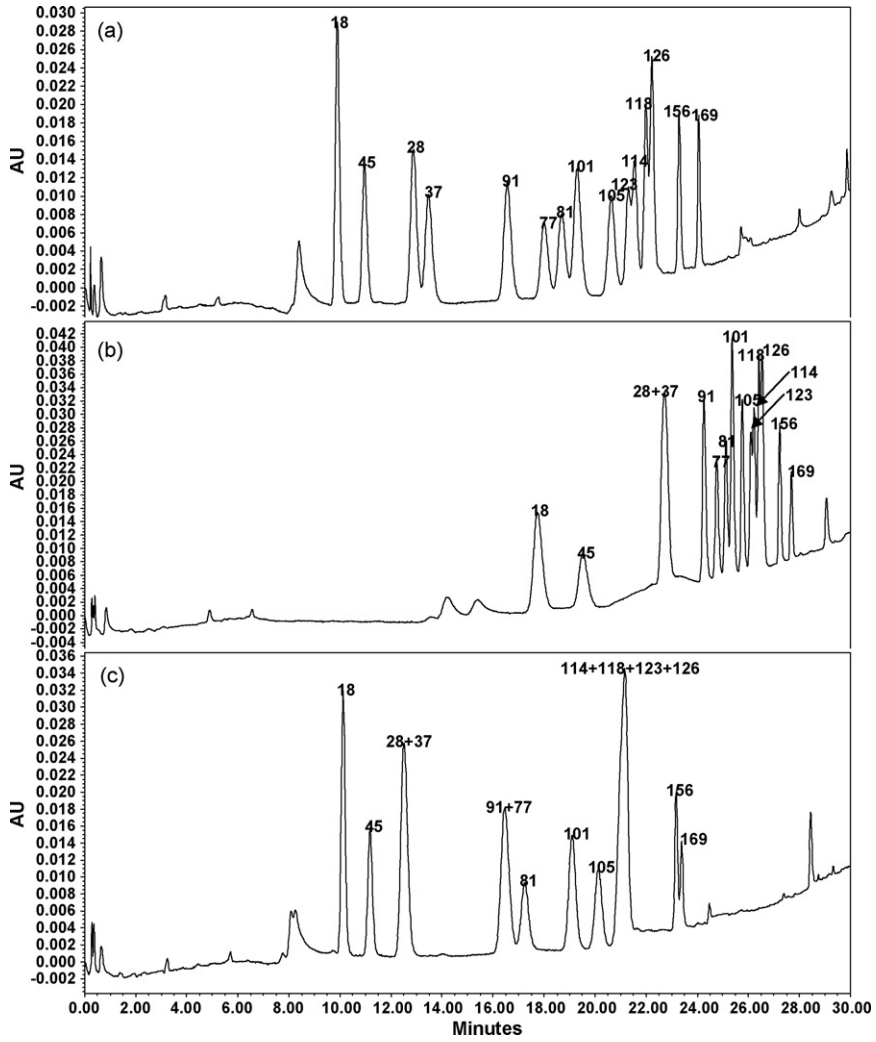


Fig. 2. Comparison of Mix B (2.5 μg/mL of each congener) separation with three different columns: Vision HT C18 Grace column (a), BEH C18 column (b), BEH Phenyl column (c). For chromatographic conditions see Fig. 1.

Table 2
System suitability data for congeners in Mixture A and Mixture B separated on the C18 Grace column.

PCB No.	RT (min)	Resolution	EP plate count	Symmetry factor	RT repeatability (RSD %)	Area repeatability (RSD %)
Mix A						
18	9.90		15 900	1.16	0.0	2.6
28	12.89	7.70	12 431	1.13	0.1	2.4
52	13.73	1.77	12 239	1.11	0.1	3.4
101	19.30	10.09	21 791	1.15	0.0	4.8
138	22.34	7.74	113 887	1.18	0.0	3.6
153	22.84	2.03	156 303	1.09	0.0	4.2
180	24.18	6.62	305 328	1.19	0.0	1.1
Mix B						
18	9.90		6 209	1.15	0.0	2.5
45	10.96	3.18	14 778	1.14	0.0	1.1
28	12.88	4.67	12 452	1.12	0.1	2.3
37	13.47	1.22	11 245	1.11	0.0	0.4
91	16.56	5.97	15 757	1.12	0.1	4.0
77	18.00	2.69	17 259	1.10	0.0	4.5
81	18.69	1.25	17 994	1.10	0.1	4.3
101	19.29	1.11	20 992	1.11	0.0	4.4
105	20.63	2.61	27 363	1.09	0.1	3.3
123	21.30	1.72	100 293	0.85	0.1	4.9
114	21.54	0.97	90 381	1.23	0.0	5.0
118	21.99	1.65	145 100	0.89	0.0	4.8
126	22.22	1.06	133 244	1.27	0.0	4.9
156	23.29	4.06	201 826	1.13	0.0	3.2
169	24.06	3.97	274 867	1.15	0.0	3.7

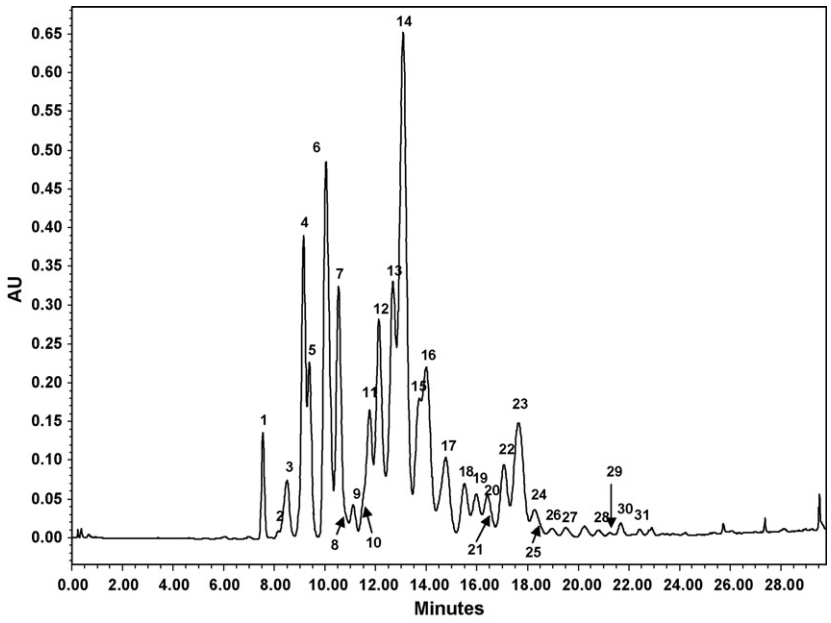


Fig. 3. Chromatogram of Delor 103 (100 μg/mL) UHPLC separation with the C18 Grace column. For peak identification see Table 3, for chromatographic conditions see Fig. 1.

(min/%A). The column temperature was maintained at 35 °C, and the flow rate was set at 1 mL/min. Sample volumes of 5 μL were injected and PCBs were monitored at the wavelength of 202 nm.

3. Results and discussion

3.1. UHPLC

Several gradient programs (approximately 20 for each column, data not shown) based on a multiple, stepwise increase of the acetonitrile ratio were applied to all of the three tested sub-2-micron particle columns in order to obtain the separation of the congeners in the premixed mixtures. All of the three columns yielded sufficient separation of Mixture A (Fig. 1). However, only the C18 Grace column exhibited the ability to separate more complex Mixture B (Fig. 2), while some congeners showed poor or no tendency to separate on columns BEH C18 (1.7 μm), and BEH Phenyl (1.7 μm) (Waters). The optimized gradient program (see Section 2.2) for the C18 Grace column was therefore used with the other columns to demonstrate their selectivity for the PCB congeners in the mixtures. The chromatograms presented in Figs. 1 and 2 show that, under these conditions, the Phenyl BEH column appeared to be almost as efficient in the separation of Mix A as the C18 Grace column while, in Mixture B, it was not able to separate the congeners 28 from 37, 91 from 77 and especially the later-eluting congeners (Nos. 114, 118, 123, 126) (see Fig. 1c). The C18 BEH column, which was the first one routinely used for UHPLC separations [23,24], yielded good separation of most of the peaks in the mixtures (Fig. 1b). However, it was necessary to substantially extend the chromatographic run to attain sufficient separation of congeners Nos. 123, 114, 118 and 126. Also in this case, the early eluting congeners Nos. 28 and 37 were not separated under any of the tested conditions.

The results in Fig. 1 also suggest that, in addition to different analyte–sorbent interactions among phenyl and the octadecylsilica columns, the size of the particles can probably play an important role in the efficacy of the separation [16]. Another explanation for the different selectivity of both C18 columns could be the silica end-capping technology used. Residual silica hydroxyl groups in the Grace column might probably cause higher specificity of this stationary phase for PCB congeners due to a different solute–sorbent interaction.

3.2. Calibration curves

The PCB (except for the congener No. 101) calibration curves were prepared over a linear range from 0.5 to 50.0 μg/mL at six concentration levels, 0.5, 1.0, 5.0, 10.0, 25.0, 50.0 with the C18 Grace column. The calibration curve of congener No. 101 was prepared in the range from 0.1 to 50.0 μg/mL at seven concentration levels, 0.1, 0.5, 1.0, 5.0, 10.0, 25.0, and 50.0. The relevant regression equations and determination coefficients R^2, which range from 0.997 to 0.999, are given in Table 1.

3.3. LOD, LLOQ

The LLOQ of the quantified congeners, except for congener No. 101, was 0.5 μg/mL with a precision (RSD) ranging from 0.3 to 5.7% and accuracy from 91.4 ± 3.3 to 117.9 ± 1.7% (n = 6). The LOD for these congeners were 0.15 μg/mL. The LLOQ of congener No. 101 was determined as 0.1 μg/mL with a precision (RSD) of 1.9% and accuracy of 107.3 ± 2.1%. The calculated LOD of congener No. 101 was 0.03 μg/mL.

3.4. System suitability

System suitability data are listed in Table 2. The retention time repeatability (RSD) is excellent (maximum of 0.01%). The peak area repeatability ranges from 0.4 to 5.0%. The maximal RSD values were observed for peaks that were not sufficiently separated. Part of this error can be attributed to use of the partial loop injection mode, which was discussed by other authors [25].

The peak symmetry, resolution and EP plate count were calculated for sufficiently separated peaks. Since the mixtures contain PCB congeners without any significant interferences, the resolutions were calculated only between the nearest congeners. The column efficiency expressed as the EP plate counts increases for compounds with higher retention times. This fact corresponds with the band broadening theory. As the content of acetonitrile is higher during the gradient, the later-eluting peaks are sharper since they are focused in a narrower zone. This phenomenon is also visible in the chromatograms depicted in Fig. 1. All the peaks had symmetrical shape with a symmetry factor ranging from 1.09 to 1.18.

Table 3
Delor 103 peak identification after separation on the C18 Grace column.

Peak No.	Retention time (min)	Congener No.	Peak No.	Retention time (min)	Congener No.
1	7.6	4	17	14.8	47,49, 84, 89, 92
2	8.2	19	18	15.6	48
3	8.6	5+8	19	16.0	56
4	9.2	Unknown	20	16.5	55, 60, 91
5	9.4	32	21	16.8	70
6	10.0	18, 24, 27	22	17.1	63, 66, 67, 82
7	10.6	17, 16	23	17.7	74, 76, 83, 148
8	10.8	46	24	18.3	77, 87, 110
9	11.2	45	25	18.4	97, 111
10	11.5	53	26	19.0	101
11	11.8	22	27	19.6	99, 113
12	12.1	33, 40	28	20.8	105
13	12.7	25, 26	29	21.3	123
14	13.1	28, 31, 44	30	21.7	118
15	13.8	37, 42	31	22.47	138, 163
16	14.1	52, 71, 64, 41,72			

3.5. Comparison of HPLC and UHPLC for the separation of Delor 103

The UHPLC C18 Grace column was subsequently tested for the separation of PCB congeners in the commercial mixture Delor 103. The chromatogram is depicted in Fig. 3 and the peak identification is given in Table 3. The results show that the UHPLC method was able to separate 13 individual congeners in the D103 mixture. Other compounds were co-eluted in clusters, but some of these co-eluting congeners could be resolved using another separation dimension performed with a mass spectrometry detector e.g. Nos. 37-42, 41, 91, 83, 148. Generally, the elution order of UHPLC is comparable with that of GC, suggesting participation of a similar hydrophobic retention mechanism.

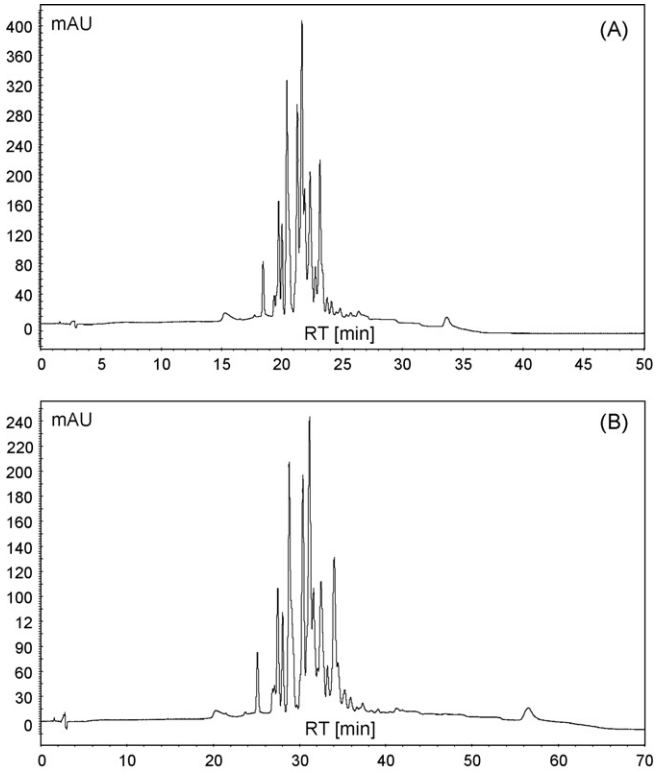


Fig. 4. Chromatogram of Delor 103 (100 μg/mL) HPLC separation with the C18 Xbridge (A) and Synergi (B) columns. For chromatographic conditions see Section 2.6.

In order to show the reasonability of this study of the UHPLC application we also briefly tested two conventional HPLC packed with 3.5 and 4.0 μm particles, respectively. Several various gradients were also applied in this case and the selected ones (see Section 2.6) were applied to separation of D103 mixture. The chromatograms are shown in Fig. 4. The figure documents substantially lower separation efficiency of the HPLC stationary phases comparing to sub-2-micron particle columns. This is mainly evident for the dominant trichloro congeners. The later-eluting tetra chlorinated representatives that are only partially separated from the main peak cluster.

The outcomes of this study imply that UHPLC separation of PCB mixtures cannot be for the meantime a real alternative to the classical GC determination. However, the results show that the technique could be used for specific experiments like biodegradation studies that are carried out with less complex mixtures of PCBs [26]. Another aspect to be pointed out is that the study was performed with commercial UHPLC columns and development of taylor made stationary phases for the separation of chlorinated aromatics could lead to further improvement of PCB separation.

4. Conclusion

In this article, three columns were compared under chromatographic conditions optimal for the most efficient column. Two premixed mixtures of PCBs often monitored for their abundance or high toxicity were successfully separated with the Grace C18 column filled with 1.5 μm particles. The fact that the best column was filled with the smallest particles indicates the importance of the sorbent particle size. The newly developed UHPLC method was partially validated and exhibited a linear range of detector response for quantification of PCBs with acceptable correlation coefficients. LLOQ was determined and verified at sub μg/mL concentrations. An attempt was made to separate the commercial PCB mixture Delor 103 under the selected conditions and the mixture was separated with some success. Individual PCB congeners were identified using comparison with standard retentions and also using GC–MS of collected UHPLC fractions.

To our knowledge, this is the first article dealing with UHPLC reversed phase separation of complex PCB mixtures suggesting a new potential direction in UHPLC applications. The combination of high throughput and efficiency of the UHPLC technique with the selectivity and sensitivity of mass spectrometry would be a promising way to enlarge the number of UHPLC applications in the environmental analysis.

The advantage of PCB determination with the liquid chromatography alternative to GC should be not only an enlargement of applications for UHPLC, but also it could be useful for specific sit-

uations such as performing PCB biodegradation experiments. For example enzymatic studies are carried out in liquid water systems and direct analyses of such samples allow to measure kinetics directly from one experimental sample avoiding extraction and purification steps that are necessary for GC and lead to termination of the particular sample [26].

Acknowledgments

This work was supported by grants no. 2B06156 of the Ministry of Education, Youth and Sports of the Czech Republic, no. 525/09/1058 Grant Agency of the Czech Republic and by Institutional Research Concept No. AV0Z50200510.

References

[1] S.P.J. van Leeuwen, J. de Boer Source, J. Chromatogr. A 1186 (2008) 161.
[2] J.W. Cochran, G.M. Frame, J. Chromatogr. A 843 (1991) 323.
[3] D. Muir, E. Sverko, Anal. Bioanal. Chem. 386 (2006) 769.
[4] R. Montes, M. Ramil, I. Rodríguez, E. Rubí, R. Cela, J. Chromatogr. A 1124 (2006) 43.
[5] J.F. Focant, E.J. Reiner, K. MacPherson, T. Kolic, A. Sjodin, D.G. Patterson Jr., S.L. Reese, F.L. Dorman, J. Cochran, Talanta 63 (2004) 1231.
[6] J. van Loco, S.P.J. van Leeuwen, P. Roos, S. Carbonnelle, J. de Boer, L. Goeyens, H. Beernaert, Talanta 63 (2004) 1169.
[7] J.F. Focant, A. Sjodin, D.G. Patterson Jr., J. Chromatogr. A 1040 (2004) 227.
[8] P. Haglund, J. Chromatogr. A 724 (1996) 219.
[9] K. Lundgren, B. van Bavel, M. Tysklind, J. Chromatogr. A 962 (2002) 75.
[10] A. Trost, W. Kleibohmer, K. Cammann, Fresen. J. Anal. Chem. 359 (1997) 249.
[11] M.C. Pietrogrande, M. Michi, M.N. Plasencia, F. Dondi, Chromatographia 55 (2002) 189.
[12] A. Jaouen-Madoulet, A. Abarnou, A.M. Le Guellec, V. Loizeau, F. Leboulenger, J. Chromatogr. A 886 (2000) 153.
[13] M. Numata, T. Kaneko, Q.D. Mi, M. Ye, S. Kawamata, M. Matsuo, T.J. Yarita, J. Chromatogr. A 1210 (2008) 68.
[14] M. Numata, Y. Aoyagi, M. Matsuo, K. Ishikawa, N. Hanari, S. Otsuka, Y. Tsuda, T. Yarita, Anal. Bioanal. Chem. 391 (2008) 1985.
[15] J.T. Andersson, G. Kaiser, Anal. Chem. 69 (1997) 636.
[16] J.J. van Deemter, F.J. Zuiderweg, A. Klingengerg, J. Chem. Eng. Sci. 5 (1956) 272.
[17] D.T.T. Nguyen, D. Guillarme, S. Rudaz, J.L. Veuthey, J. Chromatogr. A 1128 (2006) 105.
[18] S.A.C. Wren, J. Pharmaceut. Biomed. 38 (2005) 337.
[19] M. van den Berg, L. Birnbaum, A.T.C. Bosveld, B. Brunström, P. Cook, M. Feeley, J.P. Giesy, A. Hanberg, R. Hasegawa, S.W. Kennedy, T. Kubiak, J.Ch. Larsen, F.X.R. van Leeuwen, A.K.D. Liem, C. Nolt, R.E. Peterson, L. Poellinger, S. Safe, D. Schrenk, D. Tillitt, M. Tysklind, M. Younes, F. Wærn, T. Zacharewski, Environ. Health Perspect. 106 (1998) 775.
[20] European Standard EN 15308:2008.
[21] A. Kubátová, M. Matucha, J.G.K. Ševčík, J. Chromatogr. A 752 (1996) 197.
[22] CDER/CBER, Guidance for industry: Bioanalytical Method Validation, US Department of Health and Human Services, Food and Drug Administration, Center for Drug Evaluation and Research, Center for Biologics Evaluation and Research, 2001 (May).
[23] R. Plumb, J. Castro-Perez, J.H. Granger, I. Beattie, K. Joncour, A. Wright, Rapid Commun. Mass Spectrom. 18 (2004) 2331.
[24] J. Castro-Perez, R. Plumb, J.H. Granger, I. Beattie, K. Joncour, A. Wright, Rapid Commun. Mass Spectrom. 19 (2005) 843.
[25] L. Nováková, L. Matysová, P. Solich, Talanta 68 (2006) 908.
[26] L. Chromá, M. Macková, P. Kučerová, C.I. Wiesche, C. Burkhard, T. Macek, Acta Biotechnol. 22 (2002) 35.

Talanta 80 (2010) 1856–1861

Contents lists available at ScienceDirect

Talanta

journal homepage: www.elsevier.com/locate/talanta

Determination of dimethylselenide and dimethyldiselenide in milk and milk by-products by solid-phase microextraction and gas chromatography with atomic emission detection

Natalia Campillo, Rosa Peñalver, Manuel Hernández-Córdoba*

Department of Analytical Chemistry, Faculty of Chemistry, University of Murcia, E-30071 Murcia, Spain

ARTICLE INFO

Article history:
Received 28 May 2009
Received in revised form 2 October 2009
Accepted 15 October 2009
Available online 24 October 2009

Keywords:
Dimethylselenide
Dimethyldiselenide
Milk
Milk by-products
Solid-phase microextraction
Gas chromatography–atomic emission detection

ABSTRACT

A method based on solid-phase microextraction (SPME) followed by gas chromatography with microwave-induced plasma atomic emission detection for determining dimethylselenide (DMSe) and dimethyldiselenide (DMDSe) in milk and milk by-products is proposed. Parameters affecting the SPME, such as sample volume or mass, ionic strength, adsorption and desorption times and temperatures were optimized in the headspace mode. The matrix effect was evaluated for the different samples studied, concluding that standard additions calibration was required for quantification purposes. The detection limits ranged from 70 to 110 pg mL^{-1} for DMSe and from 80 to 400 pg mL^{-1} for DMDSe, depending on the sample under analysis. None of the twenty-three samples analyzed contained the studied compounds at concentrations above the corresponding detection limits.

© 2009 Elsevier B.V. All rights reserved.

1. Introduction

The selenium content in the milk of dairy cows from different countries has been reported to be in the 2–1270 $\mu g\,L^{-1}$ range [1], these values being directly related with the cow origin and feed, the amount of selenium in the soil and the season. Because of the role that selenium plays in cancer prevention, the supplementation of foods (including milk) has been gaining ground in the recent years, and it has been found that supplementing the cows' diet with selenium-enriched yeast is generally more effective than with inorganic selenium [2]. Selenoaminoacids and selenoproteins are the main forms in which this element appears in milk [3], whereas the appearance of alkyl volatile compounds dimethylselenide (DMSe) and dimethyldiselenide (DMDSe) in this sample matrix has not been reported in the literature. It is widely known that they are the most abundant organoselenium compounds in environmental and biological samples [4], and are considered to be 500 times less toxic than selenite. The production of both compounds by the biomethylation of inorganic selenium by microorganisms, as well as by the conversion of selenocystine and selenomethionine by various organisms, is well documented [4–6]. Bacteria cultures are used in milk fermentation to produce yogurt, *Lactobacillus bulgaricus* being the most widely used and sometimes others *Lactobacillus* like *acidophilus* or *casei* and *Streptococcus salivarius*. Since several milk by-products are enriched with lactic bacteria, the question of a possible appearance of volatile selenium compounds in these enriched dairy products could be posed.

Volatile organic selenium compounds are traditionally determined by gas chromatography because of its high sensitivity and the fact that no derivatization step has to be included in the whole procedure [6–19]. Plasma spectrometry has proved to be an interesting detection system to gas chromatography [4], with microwave induced plasma coupled to atomic emission detection (MIP-AED) [7,15–19] considered as a good alternative to the expensive detector based on inductively coupled plasma with mass spectrometry (ICP-MS) [10,13]; other detection techniques used in selenium speciation are atomic fluorescence spectrometry (AFS) [9], electrothermal atomic absorption spectrometry (ETAAS) [6,11], mass spectrometry (MS) [5,8] and photoionization detection (PID) [14].

The low concentration of the analytes here aborded and the complexity of the milk matrix make it necessary to include extraction and preconcentration steps in the analysis procedure. Solid-phase microextraction (SPME) is a simple and efficient alternative to the analysis of the organic substances present at trace concentration levels in complex matrices [20]. SPME, which brings together all the conditions necessary to be considered as a sample preparation technique in green analytical chemistry, since it avoids

* Corresponding author. Tel.: +34 86 8887406; fax: +34 86 8884148.
E-mail address: hcordoba@um.es (M. Hernández-Córdoba).

0039-9140/$ – see front matter © 2009 Elsevier B.V. All rights reserved.
doi:10.1016/j.talanta.2009.10.034

the use or generation of substances harmful to human health and the environment [21], has been used to preconcentrate alkylselenium compounds from different matrices [13,15–17,19,22].

The present work focuses on the determination of the low-molecular-weight volatile selenium compounds, DMSe and DMDSe, by means of SPME in headspace mode and GC–MIP–AED. The possibility of that organic or inorganic selenium compounds may be converted into DMSe and/or DMDSe in milk and milk by-products matrices is also considered.

2. Experimental

2.1. Chemicals

Dimethylselenide [$(CH_3)_2Se$, DMSe; 99% purity] and dimethyldiselenide [$(CH_3)_2Se_2$, DMDSe; 98% purity] were obtained from Fluka (Buchs, Switzerland) and Aldrich (Steinheim, Germany), respectively. Standard solutions of 1000 μg mL^{-1} of the volatile compounds were prepared by appropriate dilution in methanol and stored at 4 °C. Lower concentration stock solutions of the organocompounds were prepared daily in methanol and stored in the refrigerator. Working standard solutions of both analytes were prepared immediately before use by diluting with water obtained from a Milli-Q water purification system (Millipore, Bedford, MA, USA). Sodium chloride, casein powder from bovine milk and lactalbumin were provided by Sigma (St. Louis, MO, USA).

The plasma gas and carrier gas used for GC was helium. The reagent gas for the AED was hydrogen. Nitrogen was used for purging the AED system. All the gases (99.999% purity) were supplied by Air Liquide (Madrid, Spain).

It should be noted that DMSe and DMDSe have the following risk (R) [23] and safety (S) [24] notes: R23/25-33-50;S20/21-28-45-60-61, and should be handled with the appropriate caution.

2.2. Instrumentation

The SPME device for manual sampling consisted of a holder assembly and several replaceable fibers, all obtained from Supelco (Bellefonte, PA, USA). SPME fibers coated with non-bonded polydimethylsiloxane (PDMS) of 100 μm thickness, bonded polydimethylsiloxane/divinylbenzene (PDMS/DVB) of 65 μm, bonded stableFlex divinylbenzene/Carboxen/polydimethylsiloxane (DVB/CAR/PDMS) of 50/30 μm, bonded Carboxen/polydimethylsiloxane (CAR/PDMS) of 75 μm and bonded polyacrylate (PA) of 85 μm, were obtained from Supelco. The fibers were conditioned prior to use by heating in the injection port of the chromatographic system under the conditions recommended by the manufacturer for each fiber coating. Whenever needed, the conditioning step was repeated for fiber cleanup. All analyses were performed in 15 mL clear glass sealed vials. An RH-KT/C magnetic stirrer (IKA, Staufen, Germany) and a home-made heating system consisting of a drilled block provided with an electronic temperature control system were used for stirring and heating, respectively, during the extraction step. PTFE-coated magnetic stir bars (10 mm × 6 mm O.D.) were used for stirring the samples. The SPME experimental conditions appear in Table 1.

An Agilent 6890 gas chromatograph was directly coupled by a transfer line to a G2350A microwave-induced plasma atomic emission detector (Agilent, Waldbronn, Germany). The updated G2070AA ChemStation application with G2360AA GC–AED software was used to control the GC and AED systems, and for data acquisition and treatment. The experimental conditions for chromatographic separation and the detection system are summarized in Table 1. A SPME liner (Supelco) of 0.75 mm I.D. was used. The helium make-up flow-rate was set at 180 mL min^{-1}, and was measured with the window purge gas flow on. Filter and backamount adjustment in the AED were set according to Agilent default specifications.

2.3. Samples. SPME procedure

The twenty-three dairy products analyzed (four whole milk samples, four partially skimmed milk samples, four skimmed milk samples, two infant formula samples, one probiotic infant formula sample, three yogurt samples, two probiotic yogurt samples and three probiotic liquid yogurt samples enriched with bifidobacteries) were obtained from a local supermarket.

The infant formula samples were prepared by dissolving 12 g of sample in 100 mL of water, according to the manufacturer's recommendations. The yogurt was prepared by adding 1 mL of water to 2 g of the solid sample previously weighed; the rest of the samples were analyzed as received.

To carry out the extractions, 2 mL of sample were placed into a 15 mL SPME–vial, into which 0.6 g NaCl had been previously weighed. The vial was immediately sealed with the cap after introducing the magnetic stir bar and the mixture was homogenized for 0.5 min by inserting the vial in the home-made heating module previously programmed at 40 °C and setting the stirring speed at 1300 rpm. The SPME fiber was exposed for 5 min to the headspace sample solution. Next the fiber was placed into the GC injector, thermally desorbed for 1 min and then removed. Each sample was performed in duplicate. Table 1 shows the experimental conditions of the SPME–GC–AED system.

2.4. Recovery assays

Since no reference materials are available for the validation of the method, spiked samples were prepared. Samples were spiked by adding 25 and 50 μL of a working solution, containing DMSe and DMDSe at concentration levels of 100 and 250 ng mL^{-1} to 2 mL of milk sample and 2 g of yogurt, respectively, previously weighed in 15 mL SPME vials, these concentration levels corresponding to about 5 and 10-fold the corresponding quantitation limits. The spiked samples were set aside for 60 min in the closed vessels and analyzed as described above. The fortification procedure was applied to four different samples.

3. Results and discussion

3.1. Chromatographic and AED parameters

To proceed with the optimization of the chromatographic separation and detection steps, 0.2 μL of a methanolic standard solution containing the analytes at a concentration level of 250 ng mL^{-1} were injected in the splitless mode. With the polar-stationary phase DB-624 and the program finally selected (summarized in Table 1), the most volatile compound was eluted at about 90 °C and DMDSe at the beginning of the ramp from 140 to 300 °C. Separation was carried out at a 4 mL min^{-1} constant flow-rate, since this value reduced the analysis time needed and increased the sensitivity compared with lower flow-rates. Higher helium flow-rate values are not recommended by the manufacturer to preserve the stationary phase. The chromatographic conditions finally adopted elute DMSe and DMDSe at retention times of 3.03 and 4.96 min, respectively.

Hydrogen is the only reagent gas required for monitoring the selenium wavelength emission line. When hydrogen pressure was varied between 5 and 30 psi, the peak area of both compounds was maximum at 10 psi, so this value was selected. To study the supplementary helium required, a standard solution was injected using different make-up gas-flow rates ranging from 140

Table 1
Experimental conditions of the SPME–GC–AED system.

SPME conditions	Adsorption step	5 min at 40 °C (Headspace mode)
	Desorption step	1 min at 310 °C (splitless)
	Fiber material	CAR/PDMS, 75 μm
GC conditions	Capillary column	DB-624 (30 m × 0.32 mm I.D. × 1.8 μm)
	Carrier gas	Helium, 4 mL min^{-1}
	Oven program	40 °C (2 min)–140 °C at 50 °C min^{-1}, 140–300 °C at 60 °C min^{-1} (1 min)
GC–AED interface	Transfer line	DB-624
	Transfer line temperature	325 °C
AED conditions	Reagent gas	H_2 at 10 psi
	Spectrometer purge flow	Nitrogen, 2.5 L min^{-1}
	Helium make-up flow	180 mL min^{-1}
	Cavity temperature	325 °C
	Se wavelength	196.018 nm

to 200 mL min^{-1}. Maximum sensitivity was obtained for both analytes at 180 mL min^{-1}, which was selected. The transfer line and the cavity temperatures were optimized between 250 and 350 °C and best results were obtained at 325 °C.

3.2. Optimization of the SPME procedure

To optimize the SPME procedure a fortified sample was used considering the possibility that the sample matrix influences the extraction parameters. Seven mililiters of a partially skimmed milk fortified at a concentration level of 10 ng mL^{-1} for both analytes were used. All experiments were carried out in duplicate and, unless specified, in the headspace mode, considering the volatility of the studied compounds.

3.2.1. Selection of the fiber coating and the extraction mode

Five different fiber-coating materials were tested in order to obtain maximum sensitivity and repeatability by exposing the fiber to the sample for 20 min at 40 °C. Neither analyte was extracted when the polar polyacrylate and the non-polar polydimethylsiloxane materials were used. As can be observed in Fig. 1, the 65 μm PDMS/DVB extracted the compounds but to a very low extent. As regards the partially crosslinked 50/30 μm divinylbenzene/Carboxen/polydimethylsiloxane (DVB/CAR/PDMS) and the 75 μm Carboxen/polydimethylsiloxane (CAR/PDMS) fiber materials, although no significant sensitivity-related differences were obtained in the case of DMDSe, the CAR/PDMS fiber provided higher sensitivity for DMSe and higher repeatability in both cases, as can be observed in Fig. 1. Both immersion and headspace extraction modes were checked for each fiber coating, headspace providing higher sensitivity in all cases except for the preconcentration of DMDSe when using PDMS/DVB. The results obtained are in accordance with those previously reported by Dietz et al. [22].

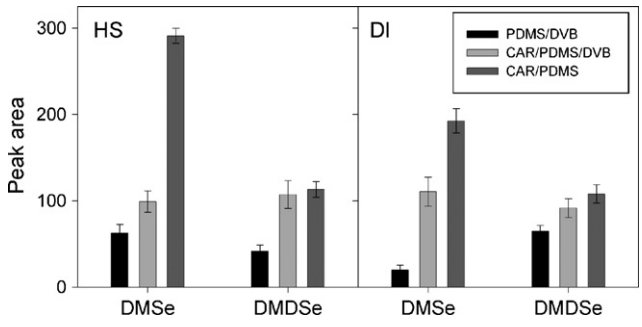


Fig. 1. SPME-extraction efficiencies for DMSe and DMDSe obtained using different fiber coating materials in the headspace (HS) and direct immersion (DI) mode, with temperatures of 40 and 300 °C and times of 20 and 2 min for the extraction and desorption steps, respectively. Vertical bars indicate the corresponding standard deviations ($n = 5$).

The influence of the ionic strength of the extraction solution was studied by incorporating different percentages from 0 to 30% (w/v) of sodium chloride to the extraction vial, and extracting the mixture for 20 min at 40 °C. The presence of salt in the sample matrix did not change the sensitivity in the case of DMDSe, while a 30% (w/v) salt concentration resulted in much higher sensitivity for DMSe. The addition of NaCl at this concentration level was therefore adopted.

3.2.2. Adsorption temperature and time

The adsorption temperature was varied between ambient and 98 °C for 7 mL of partially skimmed milk fortified with 2.5 and 5 ng mL^{-1} of DMSe and DMDSe, respectively, with an adsorption time of 20 min and the results are shown in Fig. 2A. Temperatures higher than 60 °C provided a decrease of sensitivity for both compounds probably due to a decrease in the partition coefficients between the fiber coating material and the sample headspace. A temperature of 40 °C was finally selected. The adsorption time was studied from 2 to 20 min, maintaining the vial at 40 °C. As can be observed in Fig. 2B, 5 min were enough to reach equilibrium, and this extraction time was adopted.

3.2.3. Extraction solution volume and stirring speed

The sample volume was studied in 15 mL SPME vials using volumes ranging between 1 and 10 mL of a fortified partially skimmed milk sample. Higher volumes were not assayed because they led to partial immersion of the fiber in the sample solution. The sensitivity of both selenium compounds was maximum for 2 mL, decreasing at higher volumes, especially in the case of DMDSe (Fig. 2C). Taking into account that sample dilution may lead to higher sensitivity [25,26], a study was carried out by diluting the fortified sample. The lowest detection limits were obtained by preconcentrating the analytes from 2 mL of non-diluted milk sample. In the case of solid samples, such as yogurts, different sample mass to water volume ratios were assayed, and best results were obtained for 2 g sample mass homogenized with 1 mL of water.

Stirring of the sample solution enhanced the sensitivity for both analytes, and when the effect of this parameter was studied by varying the stirring speed between 0 and 2000 rpm, maximum sensitivity for both alkyl selenium compounds was observed at 1300 rpm, which was selected.

3.2.4. Desorption parameters

The CAR/PDMS fiber was submitted to different temperatures in the injection port of the GC ranging from 250 °C and the highest temperature permitted by the coating, 310 °C, for 1 min. The sensitivity increased with temperature, 310 °C providing the best results for both compounds. The desorption time was varied at the temperature value selected, with 0.3 min being sufficient to desorb the analytes. 1 min was finally selected in order to ensure the des-

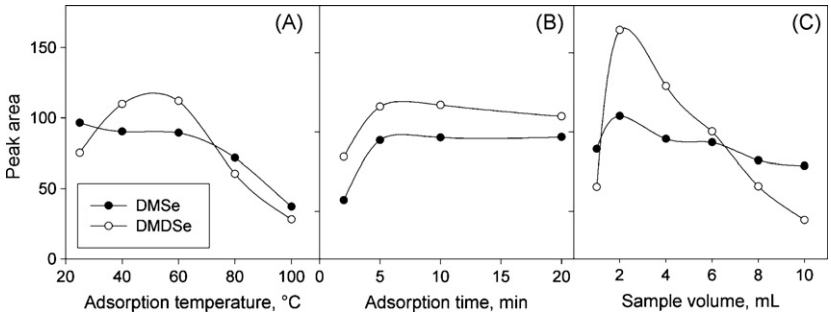


Fig. 2. Influence of (A) adsorption time, (B) adsorption temperature and (C) sample volume on the analytical signal of a partially skimmed milk sample fortified with 2.5 and 5 ng mL^{-1} of DMSe and DMDSe, respectively, by using a CAR/PDMS fiber in the HS mode.

orption of higher analyte concentrations and to remove possible carryover effects.

3.3. Analytical characteristics of the method

Different values for the calibration slopes were obtained when standard additions calibration graphs were constructed, the values depending on the sample. The calibration data obtained for five different samples under the optimized conditions, as well as those obtained with aqueous standards, are shown in Table 2. In all cases, six concentration spiking levels were used and two replicates for each level were measured. Correlation coefficients higher than 0.99 were obtained in all cases. When comparing the slopes for DMSe and DMDSe obtained by using aqueous standards, the sensitivity for each analyte depended not only on the number of the heteroatoms contained in the molecular formula, but also (and to a greater extent) on the volatility and the affinity of the compound for the CAR/DVB fiber material. Moreover, the influence of the sample matrix may lead to greater sensitivity to the analyte which contains only one heteroatom, although this effect was not observed in liquid yogurts. On the other hand, as expected, the sensitivity for both analytes decreased when the fat content in the milk samples increased, this effect being more pronounced in the case of DMDSe. Consequently, according to the obtained results, the use of the standard additions method is required for quantification.

In order to investigate other components of milk and milk by-products, in addition to fat, which could affect the sensitivity of the analytes under study, the effect of casein and lactalbumin concentrations was studied. Different percentages ranging between 0 and 10% (w/v) of casein and lactalbumin were added to aqueous DMSe and DMDSe standards. As shown in Fig. 3, the signal of DMSe was not affected by either of the two proteins. However, the sensitivity for DMDSe decreased with increasing concentration of both proteins, concluding that the less volatile and more heavy analyte is affected by the sample matrix in a higher extent than DMSe. The slopes of the calibration graphs obtained from aqueous standards in the absence of lactalbumin and casein were compared with those corresponding obtained of standards prepared in the presence of 2.7 and 3.5% (w/v) casein and lactalbumin, respectively, values which correspond to the average concentration of these proteins in real milk samples. As expected, the presence of the proteins did not change the slope value for DMSe, but decreased in the presence of lactalbumin and casein in the case of DMDSe (Table 2).

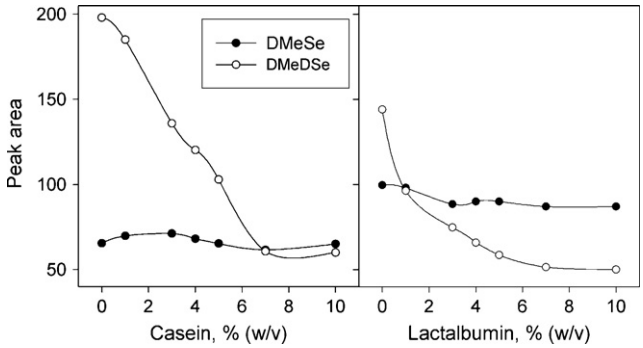


Fig. 3. Effect of the addition of casein and lactalbumin on the peak area obtained from aqueous standard solutions.

The detection limits calculated using a signal-to-noise ratio of three and considering the slopes of the standard additions calibration graphs obtained for skimmed-milk sample are shown in Table 3. Detection limits ranged from 70 to 110 pg mL^{-1} for DMSe, corresponding to a skimmed-milk sample and a liquid yogurt sample, respectively. For DMDSe, detection limits between 80 and 400 pg mL^{-1} were obtained, which corresponded to a skimmed milk sample and a whole milk sample, respectively. The quantification limits were calculated for the same milk sample using a signal-to-noise ratio of ten. These values must be considered as orientative as they are dependent on the sample matrix. The repeatability, calculated using the relative standard deviation for 10 successive injections of a fortified sample at 6 ng mL^{-1}, were 2.85 and 3.03% for DMSe and DMDSe, respectively. The analytical characteristics calculated for a yogurt sample also appear in Table 3. Detection limits obtained for the two other yogurts analyzed were similar.

3.4. Real samples and recovery studies

None of the samples analyzed contained the studied selenium compounds, at least above the stated detection limits. As no reference materials are available, recovery studies were carried out

Table 2
Comparison of the slopes of the standard addition method for different samples.

Analyte	Slopes[a] (mL ng^{-1})								
	Aqueous standard	Skimmed-milk	Partially skimmed milk	Whole milk	Yogurt[b]	Liquid yogurt 1	Liquid yogurt 2	3.5% (w/v) Lactalbumin	2.7% (w/v) Casein
DMSe	77 ± 8	70 ± 2	62.1 ± 0.4	50 ± 2	68 ± 8	42 ± 4	46 ± 2	73 ± 7	72 ± 6
DMDSe	98 ± 2	37 ± 2	26.6 ± 0.4	15 ± 3	47 ± 3	78 ± 2	68 ± 2	65 ± 8	56 ± 5.

[a] Mean value ± standard deviation (n = 6).
[b] Slopes given in g ng^{-1}.

Table 3
Analytical characteristics of the proposed method.

Compound	Liquid samples				Yogurt samples			
	Detection(pg mL^{-1}) limit[a]	Quantification limit[b] (ng mL^{-1})	R.S.D.[c] (%)	Linearity range (ng mL^{-1})	Detection (pg g^{-1}) limit[a]	Quantification limit[b] (pg g^{-1})	R.S.D.[c] (%)	Linearity range (ng g^{-1})
DMSe	70	0.23	2.85	0.12–10	40	130	3.45	0.1–10
DMDSe	170	0.57	3.03	0.20–25	95	315	5.72	0.15–15

[a] Corresponding to S/N = 3.
[b] Corresponding to S/N = 10.
[c] Calculated for concentrations of about 20-times the corresponding quantification limits.

in order to verify the accuracy of the proposed method, fortifying four samples at two different concentration levels. An average recovery ± S.D. (n = 48) of 89.5 ± 15.5% was obtained.

On the other hand, a study on the stability of DMSe and DMDSe in different fortified sample matrices was carried out. Liquid yogurt and partially skimmed milk were fortified at concentration levels of 2.5 ng mL^{-1} for both analytes, and stored in the fridge and at 25 °C in open vessels. Fig. 4 shows the results obtained. As can be observed higher recovery values were obtained for both compounds when samples were stored at 4 °C, especially in the case of DMDSe.

Finally, 5 μg mL^{-1} of inorganic selenium were incorporated to a probiotic liquid yogurt enriched with bifidobacteria and a partially skimmed milk sample to check its possible methylation to produce DMSe and/or DMDSe, being the samples maintained in closed vessels. The analytical signals obtained after different storage intervals of time ranging between 0 and 36 h at the temperature values of 25 and 40 °C, showed no differences in the absence or in the presence of inorganic selenium.

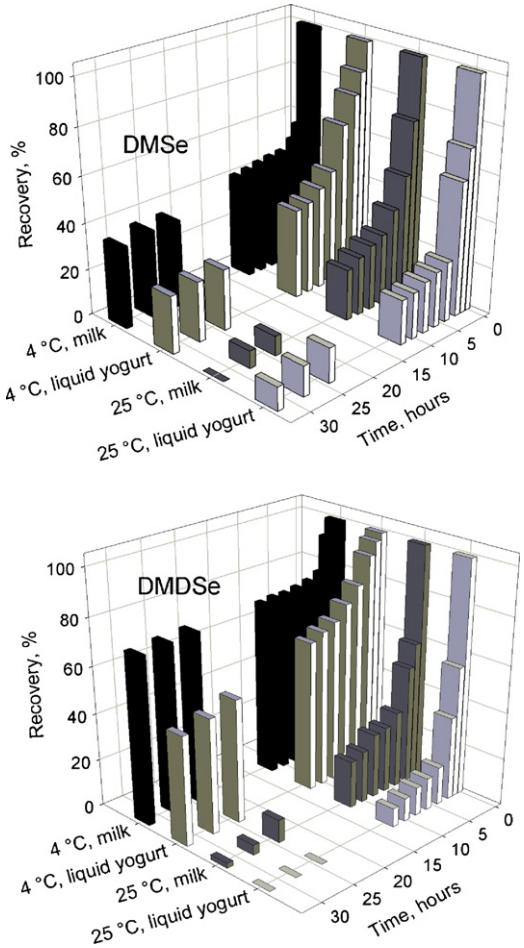


Fig. 4. Stability with time of DMSe and DMDSe incorporated in different sample matrices stored at different temperatures and analyzed using the finally selected SPME–GC–AED conditions.

4. Conclusion

DMSe and DMDSe can be preconcentrated from the sample headspace in only 5 min, an extraction mode that minimizes the coextraction of undissolved particles and non-volatile components from the sample matrix; it also prolongs the life time of the fibers. The analytical characteristics of the proposed method make it a useful tool for the monitoring of selenium volatile compounds in milk and milk by-products. Nevertheless, the complexity of this type of matrix makes it necessary to quantify the analytes using the standard additions method. No methylation of inorganic selenium was observed in the storage conditions assayed.

Acknowledgments

Financial support from the Spanish MEC (Project CTQ2006-08037/BQU) is gratefully acknowledged. R. Peñalver acknowledges a fellowship of Cajamurcia.

References

[1] P.C. Aleixo, J.A. Nóbrega, Food Chem. 83 (2003) 457.
[2] M.P. Rayman, Br. J. Nutr. 92 (2004) 557.
[3] E. Dumont, F. Vanhaecke, R. Cornelis, Anal. Bioanal. Chem. 385 (2006) 1304.
[4] J.C.A. Wuilloud, R.G. Wuilloud, A.P. Vonderheide, J.A. Caruso, Spectrochim. Acta Part B 59 (2004) 755.
[5] A. Chatterjee, Y. Shibata, M. Yoneda, R. Banerjee, M. Uchida, H. Kon, M. Morita, Anal. Chem. 73 (2001) 3181.
[6] J. Gui-bin, N. Zhe-ming, Z. Li, L. Ang, H. Heng-bin, S. Xiao-quan, J. Anal. At. Spectrom. 7 (1992) 447.
[7] M.B. de la Calle Guntiñas, M. Ceulemans, C. Witte, R. Łobiński, F.C. Adams, Mikrochim. Acta 120 (1995) 73.
[8] J.H. Tsai, R.D. Hiserodt, C. Ho, T.G. Hartman, R.T. Rosen, J. Agric. Food Chem. 46 (1998) 2541.
[9] C. Pécheyran, D. Amouroux, O.F.X. Donard, J. Anal. At. Spectrom. 13 (1998) 615.
[10] D. Amouroux, E. Tessier, C. Pécheyran, O.F.X. Donard, Anal. Chim. Acta 377 (1998) 241.
[11] M.B. de la Calle-Guntiñas, F. Laturnus, F.C. Adams, Fresenius J. Anal. Chem. 364 (1999) 147.
[12] P.C. Uden, Anal. Bioanal. Chem. 373 (2002) 422.
[13] J. Meija, J.M. Bryson, A.P. Vonderheide, M. Montes-Bayón, J.A. Caruso, J. Agric. Food Chem. 51 (2003) 5116.
[14] W.J. Hunter, L.D. Kuykendall, J. Chromatogr. A 1038 (2004) 295.
[15] C. Dietz, J. Sanz Landaluze, P. Ximénez-Embún, Y. Madrid-Albarran, C. Cámara, Anal. Chim. Acta 501 (2004) 157.
[16] J. Sanz Landaluze, C. Dietz, Y. Madrid, C. Cámara, Appl. Organomet. Chem. 18 (2004) 606.
[17] C. Dietz, J. Sanz Landaluze, P. Ximénez-Embún, Y. Madrid-Albarrán, C. Cámara, J. Anal. At. Spectrom. 19 (2004) 260.
[18] N. Campillo, N. Aguinaga, P. Viñas, I. López-García, M. Hernández-Córdoba, J. Chromatogr. A 1095 (2005) 138.
[19] N. Campillo, R. Peñalver, M. Hernández-Córdoba, C. Pérez-Sirvent, M.J. Martínez-Sánchez, J. Chromatogr. A 1165 (2007) 191.
[20] S. Risticevic, V.H. Niri, D. Vuckovic, J. Pawliszyn, Anal. Bioanal. Chem. 393 (2009) 781.
[21] C. Nerín, J. Salafranca, M. Aznar, R. Batlle, Anal. Bioanal. Chem. 393 (2009) 809.
[22] C. Dietz, T. Pérez-Corona, Y. Madrid-Albarrán, C. Cámara, J. Anal. At. Spectrom. 18 (2003) 467.

[23] http://www.ilo.org/public/English/protection/safework/cis/products/ics/dtasht/riskphrs/index.htm, accessed in March 2009.
[24] http://www.ilo.org/public/English/protection/safework/cis/products/ics/dtasht/sftyphrs/index.htm, accessed in March 2009.
[25] N. Campillo, R. Peñalver, M. Hernández-Córdoba, Talanta 71 (2007) 1417.
[26] N. Campillo, R. Peñalver, M. Hernández-Córdoba, J. Chromatogr. A 1210 (2008) 222.

Talanta 80 (2010) 1862–1867

Contents lists available at ScienceDirect

Talanta

journal homepage: www.elsevier.com/locate/talanta

Tungsten carbide precursors as an example for influence of a binder on the particle formation in the nanosecond laser ablation of powdered materials

Markéta Holá [a,*], Pavel Mikuška [b], Renáta Hanzlíková [c], Jozef Kaiser [d], Viktor Kanický [a]

[a] Department of Chemistry, Faculty of Science, Masaryk University, Kotlářská 2, 611 37 Brno, Czech Republic
[b] Institute of Analytical Chemistry, Academy of Sciences of the Czech Republic v.v.i., Veveří 97, 602 00 Brno, Czech Republic
[c] Institute of Scientific Instruments, Academy of Sciences of the Czech Republic v.v.i, Královopolská 147, 612 64 Brno, Czech Republic
[d] Institute of Physical Engineering, Faculty of Mechanical Engineering, Brno University of Technology, Technická 2896/2, 616 69 Brno, Czech Republic

ARTICLE INFO

Article history:
Received 19 June 2009
Received in revised form 7 October 2009
Accepted 15 October 2009
Available online 24 October 2009

Keywords:
Laser ablation (LA)
Inductively coupled plasma mass spectrometry (ICP-MS)
Powder
Matrix effect
Fractionation
Binder
Particle size distribution

ABSTRACT

A study of LA–ICP-MS analysis of pressed powdered tungsten carbide precursors was performed to show the advantages and problems of nanosecond laser ablation of matrix-unified samples. Five samples with different compositions were pressed into pellets both with silver powder as a binder serving to keep the matrix unified, and without any binder. The laser ablation was performed by nanosecond Nd:YAG laser working at 213 nm.

The particle formation during ablation of both sets of pellets was studied using an optical aerosol spectrometer allowing the measurement of particle concentration in two size ranges (10–250 nm and 0.25–17 μm) and particle size distribution in the range of 0.25–17 μm. Additionally, the structure of the laser-generated particles was studied after their collection on a filter using a scanning electron microscope (SEM) and the particle chemical composition was determined by an energy dispersive X-ray spectroscope (EDS).

The matrix effect was proved to be reduced using the same silver powdered binder for pellet preparation in the case of the laser ablation of powdered materials.

The LA–ICP-MS signal dependence on the element content present in the material showed an improved correlation for Co, Ti, Ta and Nb of the matrix-unified samples compared to the non-matrix-unified pellets. In the case of W, the ICP-MS signal of matrix-unified pellets was influenced by the changes in the particle formation.

© 2009 Elsevier B.V. All rights reserved.

1. Introduction

Laser ablation inductively coupled plasma mass spectrometry (LA–ICP-MS) has become a method commonly used for the direct analysis and microanalysis of solid samples with a very wide field of application. The main problems that still hinder LA–ICP-MS as an ideal method for any kind of direct analysis are fractionation and quantification [1].

The common term "fractionation" comprises non-stoichiometric effects observed with the LA–ICP-MS. A lot of works describe the influence of the laser parameters on the particle formation and consequently various "suggestions" on how to reduce the fractionation effects using an appropriate laser wavelength [2–6], pulse duration [7–15] or energy density [15–17] have been proposed. However most of these parameters are dictated by the construction of the ablation laser used and so their variability becomes strongly dependent on the available experimental setup.

Besides the ablation process itself, the transport of aerosol particles to the ICP [18–22,4,23] and vaporization and ionization in the ICP [24] are important and also contribute to the fractionation manifesting itself as matrix interference of the ICP-MS signal. During transportation, diffusion of the particles smaller than 2 nm and gravitational settling of particles in micrometric range (contingent on the particle density) takes place and, depending on the small and large particle representation, the mentioned factors occur [10]. In the ICP itself the main problem is that large particles cannot be completely vaporized and ionized. Some works determine 0.5 μm as a critical size for the particle vaporization [24,25], however the volatility of particles influences the limit of the maximum diameter of the particle evaporated in the ICP.

The "matrix effect" is another frequent and permanent problem arising during the LA–ICP-MS quantitative analysis. The "matrix effect" is a term for the variable ablation mechanism of materials in different matrices causing changes in volume and composition of the generated particles during the laser beam interaction with the various sample surfaces. To overcome the "matrix effect", it is necessary to create a suitable calibration strategy for the LA–ICP-MS quantitative analysis. To compensate for the matrix effect, matrix

* Corresponding author.
E-mail address: mhola@sci.muni.cz (M. Holá).

0039-9140/$ – see front matter © 2009 Elsevier B.V. All rights reserved.
doi:10.1016/j.talanta.2009.10.035

matched calibration has become the most common quantification technique relying on the use of a reference material with the same matrix as the analysed sample [1,26].

The analysis of powdered materials by LA–ICP-MS requires a preparative procedure resulting in a target with sufficient homogeneity, cohesion and stability during laser ablation. Plenty of different methods have been described for the target preparation such as melting with lithium borate [27–31], casting with a glue [32,33] or pressing into pellets [34–39]. The choice of a suitable method depends on the sample properties and laboratory facilities. Possible resulting problems must be taken into consideration like sample contamination, loss of volatile elements or sample dilution.

To press the powder into a pellet is the most common way because of its speed and simplicity. The pellets are pressed with or without other additives serving as a binder, matrix unifier or internal standard. The possibility of the matrix unification by using diverse powdered samples offers the LA–ICP-MS a great advantage in comparison to the analysis of naturally compacted samples where matrix unification is impossible. On the other hand, the presence of any kind of additive influences the ablation process. Therefore the choice of the additive should conform not only to the pellet's physical properties, but also to the suitability of the ablation mechanism providing successful quantitative analysis.

The purpose of this study is to show the effect of adding a matrix unifier into the powdered samples on the particle formation and the ICP-MS signals. Five powdered Co-cemented ceramic samples containing tungsten carbide (WC) as the main constituent were chosen as samples belonging to the same sort. The sample set selection gives a great opportunity to study particle formation behaviour of real samples with similar matrices but different main components giving the specific properties of each sample. Detailed description of the Co-cemented ceramic is made in work studying the particle formation of cemented WC samples [40]. As a matrix unifier powdered silver meeting also the criteria of the suitable binder such as easy homogenization with the sample, proper binding effect and positive price was used on the basis of previous experience with the silver as a binding material for the pellet preparation [36,38,39].

2. Experimental

2.1. Samples

2.1.1. Tungsten carbide precursors

The powdered precursors (WC/Co) for cemented carbides were obtained from Pramet Tools, L.L.C., Šumperk, Czech Republic, a subsidiary of Seco Tools AB, Fagersta, Sweden. Co-cemented carbide, or hardmetal as it is often called, is a material containing ceramic non-conductive constituent (tungsten carbide (WC)) and metal cobalt which plays the role of a binder during the sintering process, so the physical properties of both main constituents are very different (WC m.p. 2870 °C, b.p. 6000 °C, density 15.8 g cm^3; Co m.p. 1495 °C, b.p. 2877 °C, density 8.9 g cm^3). To obtain a hardmetal with specific properties, other constituents such as Ti, Ta, Nb or V are added in the form of carbides before sintering. By the addition of titanium carbide and tantalum carbide, the high temperature wear resistance, the hot hardness and the oxidation stability of hardmetals have been considerably improved, and the WC–TiC–(Ta,Nb)C–Co hardmetals are excellent cutting tools for the machining of steel [41]. The physical properties of TiC and TaC as the additives with the highest content in the final product are: TiC m.p. 3160 °C, b.p. 4820 °C, density 4.9 g cm^3; TaC m.p. 3880 °C, b.p. 5500 °C, density 13.9 g cm^3.

Five powdered precursors of hardmetals with a varied content of their main constituents were selected as representatives of a larger set of miscellaneous samples. Their properties were expected to vary over the whole sample collection. Samples were routinely analysed using XRF spectrometry in the laboratory of the Research Institute of Inorganic Chemistry, J.S.C., (VÚAnCh) Ústí nad Labem, Czech Republic. Details on the XRF instrumentation and analysis have already been described by Kanický et al. [42–44]. The composition of studied powdered tungsten carbide precursors is shown in Table 1.

Table 1
The chemical composition of the tungsten carbide precursor samples (wt%).

Sample	Co	Ti	Ta	Nb	W
3152	8.06 ± 0.41	14.4 ± 0.70	8.00 ± 0.36	3.10 ± 0.24	57.7 ± 1.5
4795	6.00 ± 0.25	3.24 ± 0.25	3.86 ± 0.21	1.59 ± 0.11	78.5 ± 1.7
5046	9.88 ± 0.44	2.48 ± 0.22	3.17 ± 0.14	1.31 ± 0.08	76.7 ± 1.2
5120	8.09 ± 0.36	6.37 ± 0.41	3.84 ± 0.19	1.58 ± 0.12	72.6 ± 0.9
5124	22.5 ± 0.8	0.04 ± 0.01	–	–	72.3 ± 1.0

2.1.2. Sample preparation for LA–ICP-MS

The powdered samples were employed for the analysis as pressed pellets with and without the binder. In both cases, the first preparation step consisted of sample grinding to obtain a fine powder. The particle size distribution, measured by laser diffractometry, showed diameter values not exceeding 5 μm after 5 min of sample grinding in a ball mill (Planetary Micro Mill Pulverisette 7, FRITSCH, Germany). The 25 ml mortars as well as milling balls (Ø 12 mm) were from Sialon material (90% Si_3N_4). To obtain binderless pellets, ground samples were pressed without any additional material, while the binder-containing ones were prepared in the ratio of 1:1 ground sample (3 g) and the silver powder (3 g, 99.99% purity, particle size <15 μm; Safina Vestec Company, Czech Republic), which was homogenized in the ball mill for 10 min. Pellets of both types were made by pressing with a hydraulic press (Mobiko Company, Czech Republic) at 1.3 GPa for 30 s. The pellet diameter and thickness was 12 mm and 1–1.5 mm, respectively. The weight of the binderless pellets was in the range of 1.3–1.7 g whilst binder-containing pellets had a weight between 1.2 and 1.5 g.

2.2. Laser ablation system

The laser ablation was realized by a pulsed Nd:YAG laser operating at a wavelength of 213 nm with a pulse duration of 4.2 ns (UP 213, New Wave Research, Inc., Fremont, CA, USA). In order to generate a sufficient number of particles within the whole particle size range studied for all examined sample types, several optimization experiments were undertaken. Based on these experiments, the following parameters of the ablation laser system were employed: a laser spot diameter of 100 μm, a laser pulse repetition rate of 10 Hz and a fluence of 13 J cm^{-2}. Higher fluences (30 and 40 J cm^{-2}) were also tested for the experiments, but with the increasing fluence the reproducibility of the particle concentration measurements rapidly decreased (13 J cm^{-2} with 7% RSD, 40 J cm^{-2} with 23% RSD). Because the particle size distribution diagrams have the same shape differing only with the particle number, the fluency of 13 J cm^{-2} was employed for the rest of the experiments. The laser spot of 100 μm diameter was used because of its suitability for the bulk analysis of powdered material where the representative sampling is very important and so larger laser spot is required. The 33 cm^3 sample chamber (SuperCell, New Wave Research, USA) of the ablation system was specifically designed to enable rapid eluting of the aerosol in a large format cell. Using helium as a carrier gas under normal operating conditions with a flow rate of 1.0 l min^{-1}, the ablation-generated aerosol was transported from the chamber through a 1-m long polyurethane transport tube (i.d. 4 mm) to either an ICP-MS system or an aerosol spectrometer.

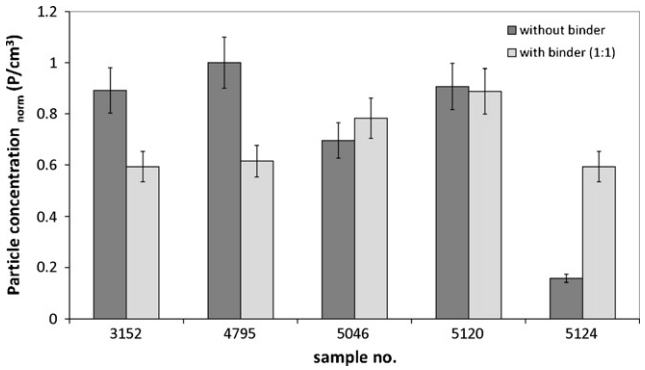


Fig. 1. Total concentration of particles (10 nm–17 μm) formed during the laser ablation of non-matrix-unified (without binder) and matrix-unified (with Ag binder) samples. The error-bars signify the standard deviation of three parallel measurements of each sample.

2.3. Inductively coupled plasma mass spectrometry

The aerosol was transported to the ICP discharge of the quadrupole mass spectrometer (ICP-MS Agilent 7500ce, Agilent Technologies, Santa Clara, CA, USA). The following isotopes were selected and used for the LA–ICP-MS analyses: ^{48}Ti, ^{51}V, ^{59}Co, ^{93}Nb, ^{181}Ta and ^{184}W.

2.4. Measurement of aerosol particles

The particle size and concentration of the laser produced aerosol particles was measured and evaluated on-line with an optical Aerosol Spectrometer Welas® 3000 Series (Palas, Germany). The Welas® operates on the principle of the single particle scattering of white light. The Welas® sensor 2200 provides a direct measurement of size distribution of particles in the size range 0.25–17 μm with a maximum concentration of 10^4 particles cm^{-3}. The particles are classified into 60 size channels on the basis of polystyrene-latex-equivalent diameters. Particles smaller than 250 nm are below the size limit for the detection by the Welas® sensors. To detect these small particles, their size is first increased by condensing 2-propanol vapor onto the small particles in the Condensation Nucleus Counter (CNC), to μm-sized particles that can be on-line detected with the Welas® sensor 2100. However, as a result of 2-propanol condensation, the former size distribution of small particles is lost and we can only count the total concentration of all particles larger than 10 nm up to 17 μm with a maximum concentration of up to 10^5 particles cm^{-3}. The number concentration of small particles (the size range 0.01–0.25 μm) was calculated as a difference between the total number concentration of all particles (measured with sensor 2100 as a result of 2-propanol condensation in the CNC; the size range 0.01–17 μm) and the number concentration of large particles (measured with sensor 2200; the size range 0.25–17 μm).

To avoid coincidence error of Welas sensors, high concentration of particles produced during the laser ablation was diluted at the output from LAS by mixing with stream of argon (5–15 l min^{-1}), part of formed mixture (5 l min^{-1}) was analysed in Welas and rest was wasted. Measuring of particles by CNC required higher dilution coefficient (12–15) than in case of sensor 2200 (dilution factor 5–7). Because of non-linear dependence of the dilution factor on the absolute particle concentration value for two types of sensors we prefer to demonstrate normalized values instead of absolute values of PC in Figs. 1 and 4. Dilution factor for PC measured by CNC was 15 (Fig. 1) while sensor 2200 used for the large particles determination worked with the dilution factor of 6 (Fig. 4).

2.5. Scanning electron microscopy and energy dispersive X-ray spectrometry

The structure and chemical composition of the laser-generated particles was studied *off-line* after their collection on a polycarbonate membrane filter (25 mm diameter, 0.2 μm pores, Cyclopore, Whatman). To collect a sufficient number of particles, the ablation was performed over a 5 min time period. The filter was placed behind the ablation cell at a distance equal to the ablated particle measurements conducted on the Welas® (0.5 m). The particles collected on the filter as well as the laser ablated craters were studied using an EDS instrument (INCA x-sight, Oxford Instruments Ltd., UK) of field emission SEM (JSM-6700F, JEOL, Japan). A secondary electron detector providing the topographical contrast was used. The acceleration voltage was 5 kV. The EDS analyses were performed at the electron acceleration voltage of 15 kV. A liquid nitrogen cooled Si(Li) detector of the INCA x-sight analyser guaranteed a stable output with a count rate.

The EDS allows analysis of W and Co as matrix elements. Method of EDS did not detect other elements as Ti, Ta and Nb due to the thickness of carbon coating used for sample conductivity that was approximately 30 nm. The carbon layer decreases the intensity of X-ray that leaves the sample for the reason of decreasing the primary electron flux and its own absorption of an output signal.

2.6. Optical profilometry

The ablation crater shape and volume was measured with 1-μm lateral and 3-nm vertical resolution by an optical profilometer MicroProf (FRT, Germany) [40]. In this device white light from a halogen lamp passes through the CHR 150 N lens with a high chromatic aberration. Different monochromatic light components are focused at different heights from a reference plane at the output of the optical fibre. The same optical fibre collects scattered light from the surface under study. This light is analysed by means of a spectrometer. The height of the surface irregularities is deduced by means of a calibration table from the wavelength of the spectral intensity distribution maximum.

3. Results and discussion

3.1. Matrix unification of different powdered samples

The real function of the silver binder as a matrix unifier was proved by two ways – by the particle concentration measurements and by the ablation crater studies. In both cases we presumed more similar results (smaller RSD) in the particle formation (measuring the particle concentration (PC)) as well as in the formation of ablation craters (more similar ablation rates and crater structure) – for samples prepared as matrix-unified pellets than for non-matrix-unified samples. The measurement of each pellet was done three times and the repeatability did not reach deviation of 10%. The RSD value used in the text as a criterion for the "level of unification" was calculated from mean values of the three repeated measurements of different samples. The matrix-unified samples represented pellets prepared by pressing of the sample and silver powder mixture as described in 2.1.2.

The total concentration of generated particles was monitored during the laser ablation of either non-matrix-unified or matrix-unified samples. The particle concentration of the five non-matrix-unified pellets differed from sample to sample very distinctly with a relative standard deviation (RSD) of 46%. It signifies a high influence of the sample composition on the particle production during laser ablation. Even if the tungsten content varies from sample to sample, the most important changes in elemental composition occur in the

Table 2
The coefficients of determination of the LA–ICP-MS signals dependent on the element concentration for the non-matrix-unified and the matrix-unified samples.

R^2	Without binder	WC + Ag (1:1)
Ti	0.9571	0.9860
Nb	0.9388	0.9782
Ta	0.9698	0.9862
Co	0.9356	0.9822
W	0.6976	0.0391

case other components such as Co, Ti and Ta (see Table 1). The RSD value, calculated from the PC values of all five samples, decreased to the value of 19% using the binder for the matrix unification. The results of PC measurements for both sets of samples are displayed in Fig. 1.

The observation of different ablation craters can also outline the similarity or difference in the laser ablation processes – the shape, structure and volume of the ablation crater can be used to explain the ablation process behaviour. One of the parameters that can be estimated from the crater depth is the ablation rate. Here the ablation crater depths were measured using the optical profilometer after 100 laser pulses. The crater depths on the non-matrix-unified samples fell in the range of 45–116 μm with the mean value of 93 μm and RSD of 36%. This result indicates the differences in the ablation rates for the samples with different compositions. The preparation of samples as matrix-unified matrix pellets caused a reduction in ablation rate differences – the depths of the ablation craters varied from 58 to 87 μm with a mean value of 70 μm. The RSD value decreased to 16%. The comparison of crater depths thus proved the results of particle formation. Both data sets confirmed our expectations that the binder unifies sample properties and consequently the ablation process.

3.2. LA–ICP-MS

The suitability of the matrix unification of the powdered hardmetal precursor for the LA–ICP-MS analysis was tested for Co, Ti, Ta, Nb and W using the conditions described above. On the basis of the LA–ICP-MS measurements, the appropriate isotope intensity (cps–count per second) dependence on the element content in the sample (simulated calibration curve) was created for each element and the regression lines were constructed. The following isotopes were used for analysis: ^{48}Ti, ^{51}V, ^{59}Co, ^{93}Nb, ^{181}Ta and ^{184}W. The measurements were done on both sets of pellets – (non)/matrix-unified samples. The coefficients of determination of the regression lines pertaining to the same element but different pellets (with or without binder) were compared.

For the matrix-unified samples, the results obtained show improved correlation of regression lines for all elements except W. It means that the Ag powder additive helps to unify the LA–ICP-MS conditions for Co, Ta, Ti and Nd while the possibility of the W quantification in the matrix-unified samples is unsatisfactory. The improvement of correlation is shown in Fig. 2, where the regression lines for Ti are displayed.

Coefficients of determination for all elements are summarized in Table 2.

3.3. Particle structure and composition

The information about the particle chemical composition can explain the behavior of the particle formation and consequently the estimation of the elemental fractionation degree during the ablation. The particle formation and elemental fractionation of Co-cemented tungsten carbides during ns laser ablation has already been described in detail elsewhere [40]. Single spherical particles with diameters in the size range of 0.25–2 μm and agglomerates

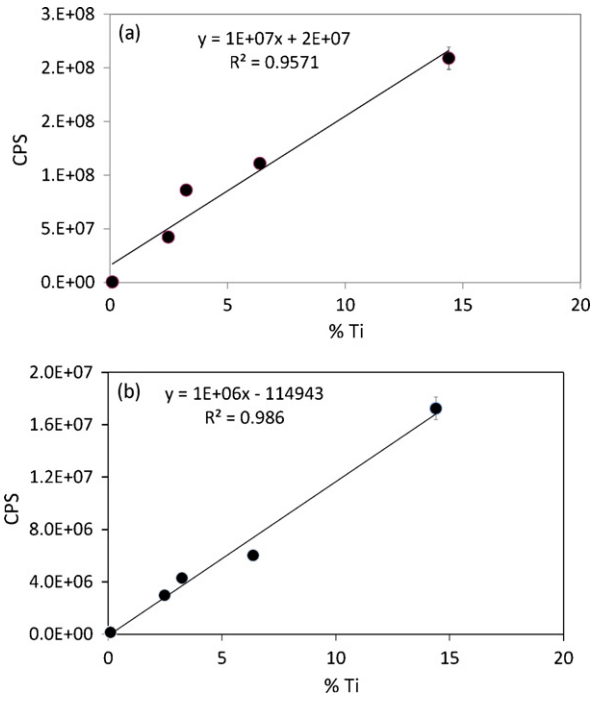


Fig. 2. The LA–ICP-MS signal dependence on the element content for 5 samples: (a) ^{48}Ti for non-matrix-unified samples and (b) ^{48}Ti for matrix-unified samples. The error-bars signify the standard deviation of three parallel measurements of each sample.

composed of primary particles of diameters ranging from tens to hundreds of nanometers were observed on the filter. The presence of tungsten (representing a low volatile element) entirely in the large spherical particles and the strong cobalt enrichment of the small particles proved the theory of particle formation: small particles, enriched with a more volatile constituent, can be formed by nucleation and condensation from the vapor, whereas larger particles rich in lowly volatile elements are ejected from the melted liquid due to hydrodynamic instability of the surface recoil pressure from the expanding vapor plume [45–47]. The elemental fractionation during ns ablation of non-matrix-unified powdered tungsten carbide precursors was identical with the above described Co-cemented samples. In the case of the matrix-unified samples, the influence of silver on the particle composition was studied. The particles were collected on the polycarbonate membrane filter during the 5 min ablation-time period. The particle structure and composition were then studied using SEM and EDS, respectively. The SEM images show, on the first sight, typical structures including single spherical particles and smaller agglomerates creating fibres and adhered to the large particle surface (Fig. 3a). With a higher magnification we can observe that the surface of the large spherical (tungsten) particle is covered by a non-homogenous layer (Fig. 3b). This is the layer where the agglomerates are bound. The EDS analysis showed the preferential presence of silver in the layer – the Ag/W mass ratio increased to the value of 25 from the declared 1.4. This finding clarifies the "destiny" of silver during ablation – the silver vapor condenses on the tungsten particle surface, which results from the much higher silver volatility than the volatility of other sample constituents (Ag melting point is 960 °C, boiling point is 2212 °C).

The EDS analysis did not allow the analysis of other elements such as Ti, Ta and Nb. On the base of the LA–ICP-MS results we can presume homogenous distribution of these elements in smaller particles. The agglomeration with the large tungsten particles seems to be logical especially for tantalum as an element with

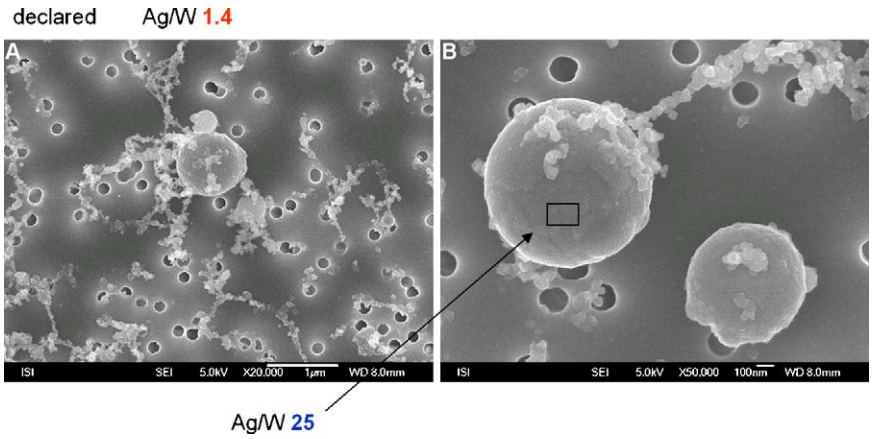


Fig. 3. The SEM images of laser-generated particles from matrix-unified sample no. 5124 after their collection on a polycarbonate membrane filter; (a) overall view, (b) detailed view with large spherical particles and surrounding clusters; a square label defines the area analysed by the EDS, the results of the EDS analysis are pasted together with the declared values.

similar physical properties to tungsten but no dependence of the analytical results on the particle formation was observed.

3.4. Particle size distribution

Silver condensation on the spherical tungsten particles leads to the growth of these particles. This fact was proved by the particle size measurements using the Welas spectrometer. The particle sizes were measured in the diameter range of 0.25–17 μm for the sample 3152 pressed in to 4 various pellets with differing amounts of the silver binder: without any added binder, 33%, 50% and 66% of the binder in the silver–sample mixture. The particle size distribution diagrams show changes in particle concentration with the increasing amount of Ag binder in the pellet (Fig. 4). For those particles with a diameter smaller than 0.31 μm the difference in the particle concentration is not significant, but the particles larger than 0.31 μm in diameter were formed in higher concentrations from the binder pellets. The dependence of particle concentration on the amount of added binder is also evident and the largest difference between the particle distribution diagrams was observed between the pellet without any binder and the pellet with the highest studied amount of added binder (i.e., 66% Ag).

Even if the analytical results of tungsten are surely influenced by the fractionation caused by the gravitational settling of the particles in the ablation cell and the transporting tube (because of the high density of W), the growth in volume of the tungsten particles caused by the Ag condensation most probably leads to another fractionation of laser formed particles inside the ICP. The incomplete particle vaporization/ionization in the inductively coupled plasma then results in problems with the tungsten quantitative analysis. The particle distribution graphs (Fig. 4) show that the concentration of the particles with a diameter larger than 0.5 μm (which can be the critical value for the particle vaporization [24,25]) increase very significantly.

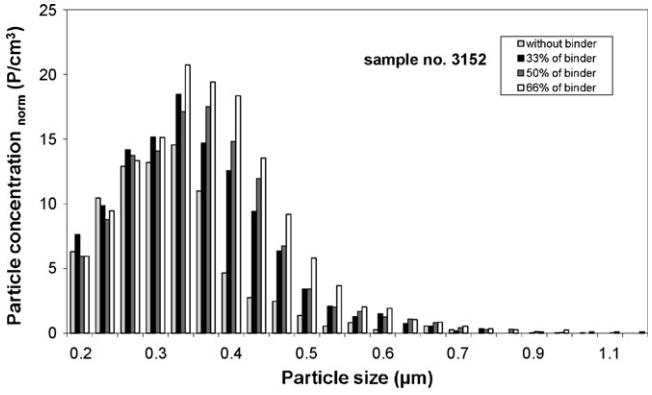


Fig. 4. Particle size distribution of the large particles (0.25–17 μm) for the sample 3152 prepared by pressing different amounts of binder. Histograms are based on a single measurement.

4. Conclusion

The reduction of the "matrix effect" by using a binder for the pellet preparation of powdered materials was investigated. Five samples representing Co-tungsten carbide precursors were prepared for ns laser ablation as pressed pellets without any binder and with the powdered silver serving as the binder and matrix unifier. The study of particle and ablation crater formation clearly demonstrated the function of the matrix unifier - the differences between studied samples in the particle concentration were reduced (RSD decreased from 46% to 19%) as well as the differences in the volumes of the ablation craters (the RSD decreased from 36% to 16%). The effect of the binder utilization on the LA–ICP-MS signals shows an improvement correlation of different samples in simulated calibration curve (increasing of the correlation coefficients of the isotope intensity *vs.* elemental content in the sample) for all elements of interest (Co, Ti, Ta, Nb) except W. In order to find a solution for the deterioration of the tungsten analytical response in the case of binder pellets, the structure and chemical composition of the particles formed during the laser ablation was investigated. The particle size distribution measurements showed an increase in the number of particles for the size range from 0.31 to 1.2 μm with the increasing binder content in the pellet. This effect was assigned to the condensation of vapor enriched by silver as a highly volatile component on the surface of the larger particles created from the melted material. It resulted in the production of large tungsten particles covered with a silver layer which was further proved by the SEM and the EDS measurements. Because the particle diameter is a critical parameter for the fractionation in the ICP, the increasing diameter of the silver-covered tungsten particle leads to their incomplete atomisation and ionization. The important role plays also the gravitational settling of W particles because of their extreme high density. Consequently, the W quantification in the matrix-unified samples is unsatisfactory.

This study shows that matrix unification can be a useful tool for the LA–ICP-MS quantitative analysis of powdered materials, but it can also cause changes in the particle formation during the ablation process leading to fractionation. The matrix unification of the Co-

tungsten carbide samples using the silver binder markedly reduced differences in the crater volumes as well as the evenly balanced concentration of generated particles during the laser ablation of different samples. On the other hand the matrix unification did not lead to complex improvement of analytical results. In general, the choice of the matrix unifier (binder) must therefore be done very carefully depending on the sample to be analysed and the ablation conditions.

Acknowledgements

M.H. gratefully acknowledges the Czech Science Foundation for bestowing the project 203/07/P439. V.K. acknowledge the Ministry of Education, Youth and Sports of the Czech Republic for the research project MSM0021622412 and MSM0021622410, respectively. P.M. acknowledges an institutional research plan of the Institute of Analytical Chemistry of the Academy of Sciences of the Czech Republic No. AV0 Z40310501. J.K. acknowledges the Ministry of Education, Youth and Sports of the Czech Republic for the research project MSM 0021630508.

References

[1] S.F. Durrant, J. Anal. Atom. Spectrom. 14 (1999) 1385.
[2] R.E. Russo, X.L. Mao, O.V. Borisov, H. Liu, J. Anal. Atom. Spectrom. 9 (2000) 1115.
[3] D. Bleiner, D. Günther, J. Anal. Atom. Spectrom. 16 (2001) 449.
[4] M. Guillong, I. Horn, D. Günther, J. Anal. Atom. Spectrom. 18 (2003) 1224.
[5] J. Gonzáles, C. Liu, X. Mao, R.E. Russo, J. Anal. Atom. Spectrom. 19 (2004) 1165.
[6] J. Koch, M. Wälle, J. Pisonero, D. Günther, J. Anal. Atom. Spectrom. 21 (2006) 932.
[7] R.E. Russo, X. Mao, J.J. Gonzales, S.S. Mao, J. Anal. Atom. Spectrom. 17 (2002) 1072.
[8] F. Poitrasson, X. Mao, S.S. Mao, R. Freydier, R.E. Russo, Anal. Chem. 75 (2003) 6184.
[9] C. Liu, X.L. Mao, S.S. Mao, X. Zeng, R. Greif, R.E. Russo, Anal. Chem. 76 (2004) 379.
[10] J. Koch, A. von Bohlen, R. Hergenröder, K. Niemax, J. Anal. Atom. Spectrom. 19 (2004) 267.
[11] J. Gonzáles, S.H. Dundas, C.Y. Liu, X. Mao, R.E. Russo, J. Anal. Atom. Spectrom. 21 (2006) 778.
[12] V. Možná, J. Pisonero, M. Holá, V. Kanický, D. Günther, J. Anal. Atom. Spectrom. 21 (2006) 1194.
[13] N.J. Seatveit, S.J. Bajic, D.P. Baldwin, R.S. Houk, J. Anal. Atom. Spectrom. 23 (2008) 54.
[14] J. Koch, D. Günther, Anal. Bioanal. Chem. 387 (2007) 149.
[15] C.C. Garcia, H. Lindner, A. von Bohlen, C. Vadla, K. Niemax, J. Anal. Atom. Spectrom. 19 (2008) 470.
[16] S.H. Jeong, O.V. Borisov, J.H. Yoo, X.L. Mao, R.E. Russo, Anal. Chem. 71 (1999) 5123.
[17] J.H. Yoo, O.V. Borisov, X. Mao, R.E. Russo, Anal. Chem. 73 (2001) 2288.
[18] D. Bleiner, P. Lienemann, H. Vonmont, Talanta 65 (2005) 1286.
[19] J. Koch, I. Feldmann, N. Jakubowski, K. Niemax, Spectrochim. Acta B 57 (2002) 975.
[20] I. Horn, D. Günther, Appl. Surf. Sci. 207 (2003) 144.
[21] D.B. Aeschliman, S.J. Bajic, D.P. Baldwin, R.S. Houk, J. Anal. Atom. Spectrom. 18 (2003) 1008.
[22] H.R. Kuhn, D. Günther, Anal. Bioanal. Chem. 383 (2005) 434.
[23] J. Koch, M. Wälle, R. Dietiker, D. Günther, Anal. Chem. 80 (2008) 915.
[24] M. Guillong, D. Günther, J. Anal. Atom. Spectrom. 17 (2002) 831.
[25] H.-R. Kuhn, D. Günther, J. Anal. Atom. Spectrom. 19 (2004) 1158.
[26] D. Günther, H. Cousin, B. Magyar, I. Leopold, J. Anal. Atom. Spectrom. 12 (1997) 165.
[27] F.E. Lichte, Anal Chem. 67 (1995) 2479.
[28] M. Odegard, S.H. Dundas, B. Flem, A. Grimstvedt, Fresenius J. Anal. Chem. 362 (1998) 477.
[29] J.S. Becker, H.-J. Dietze, Fresenius J. Anal. Chem. 365 (1999) 429.
[30] S. Nam, W.R.L. Masamba, A. Montaser, Anal. Chem. 65 (1993) 2784.
[31] C. Prokisch, A.M. Bilgic, E. Voges, J.A.C. Broeckaert, Spectrochim. Acta B 54 (1999) 1253.
[32] W. Klemm, G. Bombach, Fresenius J. Anal. Chem. 370 (2001) 641.
[33] M. Holá, P. Krásenský, V. Otruba, V. Kanický, J. Anal. Atom. Spectrom. 21 (2006) 974.
[34] J.S. Becker, Spectrochim. Acta B 57 (2002) 1805.
[35] T. Li, Q. Lou, Y. Wei, F. Huang, J. Dong, J. Liu, Appl. Surf. Sci. 181 (2001) 225.
[36] P. Musil, V. Otruba, V. Kanicky, J.-M. Mermet, Spectrochim. Acta B 55 (2000) 1747.
[37] O.V. Borisov, C.J. Bannochie, R.E. Russo, Appl. Spectrosc. 55 (2001) 1304.
[38] J. Mikolas, P. Musil, V. Stuchlikova, K. Novotny, V. Otruba, V. Kanicky, Anal. Bioanal. Chem. 374 (2002) 244.
[39] M. Holá, V. Otruba, V. Kanický, Spectrochim. Acta B 61 (2006) 515.
[40] M. Holá, V. Konečná, P. Mikuška, J. Kaiser, K. Páleníková, S. Průša, R. Hanzlíková, V. Kanický, J. Anal. Atom. Spectrom. 23 (2008) 1341.
[41] G.S. Upadhyaya, Cemented Tungsten Carbides: Production, Properties, and Testing, Noyes publications, New Jersey, USA, 1998.
[42] V. Kanický, V. Otruba, J.-M. Mermet, Spectrochim. Acta B 55 (2000) 575.
[43] V. Kanický, V. Otruba, J.-M. Mermet, Spectrochim. Acta B 55 (2000) 1601.
[44] V. Kanický, V. Otruba, J.-M. Mermet, Fresenius J. Anal. Chem. 371 (2001) 934.
[45] R. Jaworski, E. Hoffmann, H. Stephanowitz, Int. J. Mass Spectrom. 219 (2002) 373.
[46] H.R. Kuhn, D. Günther, Anal. Chem. 75 (2003) 747.
[47] C. Liu, X. Mao, S.S. Mao, R. Greif, R.E. Russo, Anal. Chem. 77 (2005) 6687.

Talanta 80 (2010) 1868–1872

Contents lists available at ScienceDirect

Talanta

journal homepage: www.elsevier.com/locate/talanta

An aptamer-based assay for thrombin via structure switch based on gold nanoparticles and magnetic nanoparticles

Jing Zheng[a,b,*], Gui-Fang Cheng[a], Pin-Gang He[a,**], Yu-Zhi Fang[a]

[a] Department of Chemistry, East China Normal University, Shanghai 200062, China
[b] Department of Chemical Engineering, Shanghai University of Engineering Science, Shanghai 201620, China

ARTICLE INFO

Article history:
Received 2 February 2009
Received in revised form 8 October 2009
Accepted 18 October 2009
Available online 28 October 2009

Keywords:
Aptamer
Gold nanoparticle
Magnetic nanoparticle
Thrombin

ABSTRACT

An aptamer-based assay for thrombin with high specificity and sensitivity was presented. In the protocol, the aptamer for thrombin was immobilized on magnetic nanoparticle, and its complementary oligonucleotide was labeled with gold nanoparticles, then the aptamer was hybridized with the complementary oligonucleotide to form the duplex structure as a probe, this probe could be used for the specific recognition for thrombin. In the presence of thrombin, the aptamer prefer to form the G-quarter structure with thrombin, resulting in the dissociation of the duplex of the probe and the release of the gold labeled oligonucleotide. Upon this, we were able to detect thrombin through the detection of the electrochemical signal of gold nanoparticles. The strategy combines with the high specificity of aptamer and the excellent characteristics of nanoparticles. This assay is simple, rapid, sensitive and highly specific, it does not require labeling of thrombin, and it could be applied to detect thrombin in complex real sample. The method shows great potential in other protein analysis and in disease diagnosis.

© 2009 Elsevier B.V. All rights reserved.

1. Introduction

The detection of protein is of central importance for diagnosis and treatment of diseases and attracts increasing attention in the biomedical fields [1,2]. In most diagnosis application, specific protein recognition is often accomplished by antibodies [3–4]. Aptamers, the synthetic DNA/RNA selected from combinatorial libraries by SELEX, promise to replace antibodies for their small size, chemical simplicity and flexibility [5–7] and they are considered promising recognition elements for biosensor application. Aptamer-based protein detections have been illustrated such as colorimetric [8], fluorescence [9], quartz crystal microbalance [10] and electrochemical detection [11–13].

In the paper, human thrombin was chosen as the target analyte of interest. Thrombin (activated Factor II) is a specific serine protease involved in the coagulation cascade, which converts soluble fibrinogen into insoluble strands of fibrin and catalyzes many other coagulation-related reactions [14]. The concentration of thrombin in blood during the coagulation progress varies from nM to low μM levels [15], while the detection of thrombin is important for related diagnoses [16]. Therefore, it is necessary to develop an assay for thrombin with high sensitivity, selectivity, and simplicity. Recently, electrochemical [17,18] and optical techniques [19–21] were widely applied in the field of thrombin detection. However, the reliability, selectivity and the sensitivity of the assay should be improved. We show here an analytical strategy based on gold nanoparticles and magnetic nanoparticles that achieves both high specificity and the enhanced sensitivity.

Nanoparticles can be used as scaffolds for assembling nanoparticle-based biosensors [22]. Gold nanoparticles are excellent candidate for bioconjugation, owing to the fact that they are compatible, and bind readily to a range of biomolecules such as amino acids, protein, enzymes and DNA [23–25]. Gold nanoparticle-based DNA electrochemical detections have been reported due to the sensitivity and excellent electrochemical signal [26,27]. In addition, magnetic nanoparticles have been widely used in bioanalysis and pharmaceutical detection for the particular properties and magnetism [28].

An electrochemical protocol for detection of thrombin based on the gold nanoparticles and magnetic nanoparticles was proposed. As shown in Fig. 1, the aptamer for thrombin was immobilized on magnetic nanoparticles, and its complementary oligonucleotides was labeled with gold nanoparticles, and then the aptamer was hybridized with the complementary oligonucleotide to form the duplex structure as a probe (A). In the presence of thrombin, the aptamer prefers to bind with thrombin and cause the dissociation of the probe, liberating the gold nanoparticle-labeled complemen-

* Corresponding author at: Department of Chemical Engineering, Shanghai University of Engineering Science, Shanghai 201620, China. Tel.: +86 21 67791214.
** Corresponding author. Tel.: +86 21 62233798.
E-mail addresses: kkzhengjing707@163.com (J. Zheng), pghe@chem.ecnu.edu.cn (P.-G. He).

0039-9140/$ – see front matter © 2009 Elsevier B.V. All rights reserved.
doi:10.1016/j.talanta.2009.10.036

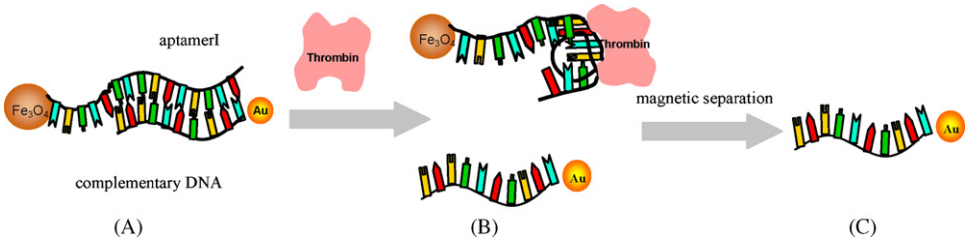


Fig. 1. Schematic representation of the assay. (A) The duplex structure of magnetic nanoparticle-aptamer/gold nanoparticle-oligonucleotide. (B) In the presence of thrombin, the dissociation of the duplex structure and the liberating of the gold nanoparticles labeled complementary oligonucleotides. (C) After the magnetic separation, the released gold nanoparticle-labeled complementary oligonucleotide to produce an electrochemical signal.

tary oligonucleotide (B). The basic principle for the strategy is that aptamers could form defined tertiary structure when binding to target protein, and also able to bind to complementary DNA sequence to form a duplex structure. Therefore, when the target protein and the complementary oligonucleotide are introduced, the aptamer is in a conformational equilibrium between the duplex structure and the tertiary structure [29,30]. It prefers to bind to the target protein and thus resulting in the specific recognition of the target [31,32]. Then after magnetic separation, high specific and sensitive detection of thrombin was achieved in connection to measurement of the electrochemical signal of the released gold nanoparticle-labeled complementary oligonucleotide (C). The electrochemical signal of gold is proportional to the amount of thrombin and the quantitative assay of thrombin was accomplished by using this proposed electrochemical sensor. In this strategy, gold nanoparticle offered excellent electrochemical signal and magnetic nanoparticle was used for separation. The assay responds rapidly and specifically to thrombin, which shows extensive application in protein monitoring, in disease diagnosis as well as other research fields.

2. Experimental

2.1. Apparatus and reagents

Differential pulse voltammetry (DPV) was performed using a CHI Instruments model 832 Electrochemical Analyzer (CHI Instrument Inc., USA). The electrochemical system comprised of a working electrode of glassy carbon electrode, an Ag/AgCl reference electrode, and a platinum wire counter electrode. SEM data were recorded using a JEOL JSM-6700F Field Emission Scanning Electron Microscope (JEOL, Japan).

The oligonucleotides used in this study were purchased from Sangon Biotechnology Inc. (Shanghai, China) with the following sequences: the oligonucleotide with amino-group at 5′ end (aptamer) : 5′ H_2N-$(CH_2)_6$–ATAGGTTGGTGTGGTTGG; complementary oligonucleotide with mercapto-group at 5′ end: (5′SH-$(CH_2)_6$CCAACCACACCAACC); thrombin, bovine plasma albumin (BSA) and lysozyme were purchased from Sigma–Aldrich. Magnetic nanoparticle (50 mg/mL, carboxyl functionalized, average diameter 100 nm) was purchased from Chemicell Inc. (Berlin, Germany). Sodium citrate, $AuCl_3HCl{\cdot}4H_2O$, ethyl-3-(dimethylaminopropyl)-carbodiimide hydrochloride (EDAC), imidazole, PBS (0.1 M, pH 7.3), Tris–HCl buffer and other reagents were commercially available and were all of analytical reagents grade, and ultrapure water was used from Aquapro system (specific resistance is 13 MΩ cm).

2.2. Immobilization of the aptamer onto magnetic nanoparticles

The immobilization of the aptamer onto magnetic nanoparticles was carried out on, briefly, magnetic nanoparticles were washed three times with PBS buffer (pH 7.3) and resuspended in 500 μL of PBS buffer, then ultrasonicated for 30 min after 4.3 mg imidazole was added. After 2.0 OD of aptamer was dissolved in 100 μL of PBS buffer solution and 4.6 mg of EDAC was added. The resulting mixture was stirred for 8 h for the amidation between amino aptamer and carboxyl functionalized magnetic nanoparticles. After magnetic separation, the magnetic nanoparticles with immobilized aptamer was washed three times with 500 μL of PBS, unbounded aptamer was removed by using a magnet, the resulting solution was resuspended in 500 μL of PBS buffer and stored at 4 °C.

2.3. Preparation of the gold nanoparticles

Gold nanoparticles were prepared according to the literature [33]. All glassware used in the following procedure was cleaned in a bath of freshly prepared 3:1 HNO_3–HCl, rinsed thoroughly in twice-distilled water and dried in air. $HAuCl_4$ and sodium citrate solution needs to be filtered through a 0.22 μm microporous membrane filter prior to use. Gold nanoparticles were prepared by adding 2.5 mL of sodium citrate solution to 100 mL of boiling aqueous solution containing 1 mL of 1% (w/w) $HAuCl_4$, and stirred for 30 min; within the time, the color of the solution changed from grey, blue, purple, to wine red. The mixture continued to stir for 10 min after removal from the heater. The preparation was stored in dark glass bottles at 4 °C for further use.

2.4. Preparation of gold nanoparticle-labeled oligonucleotide

Gold nanoparticle-labeled oligonucleotide was prepared as literature [23], briefly, gold nanoparticle solution was mixed with 1 OD of mercapto-oligonucleotide for 16 h, and the solution was centrifugated for at least 25 min at 16,128 × *g* to remove the excess oligonucleotide. The wine red precipitate was washed with 0.1 M PBS and redispersed in 0.1 M PBS. Then, the resulting solution was stored in the refrigerator for further use.

2.5. Preparation of the probe of magnetic nanoparticle-aptamer/gold nanoparticle-oligonucleotide

The probe of magnetic nanoparticle-aptamer/gold nanoparticle-oligonucleotide was prepared as follows, after 600 μL of the gold nanoparticle-labeled oligonucleotides were added in the solution containing 40 μL of magnetic nanoparticle-aptamer in PBS buffer, then 0.585 g of NaCl was added to retain a certain salinity for hybridization, and the volume was adjusted to 1000 μL by adding PBS buffer. The hybridization was carried out for 1 h at 37 °C. The final magnetic nanoparticle-aptamer/gold nanoparticle-oligonucleotide were washed five times with 200 μL of PBS buffer and resuspended in 300 μL of PBS buffer for further use.

2.6. Experimental method for the recognition of thrombin

The specific recognition for thrombin was carried out in an electrochemical cell containing 15 μL of the probe, adding 10 μL of definite concentration of thrombin and the volume was adjusted

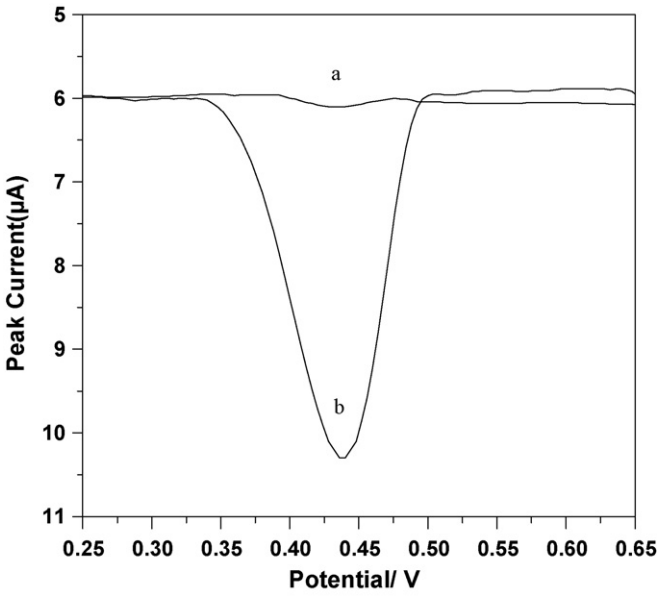


Fig. 2. DPV response of (a) in the absence of thrombin; (b) in the presence of 3.36×10^{-11} M thrombin.

to 100 μL by adding PBS buffer (pH 7.3) containing Mg^{2+} (1 mM Mg^{2+}). The incubation was carried out for 20 min at 37 °C, after the magnetic separation, the supernatant fluid was dissolved in 0.1 M HCl solution for detection.

2.7. Electrochemical measurements

All electrochemical experiments were directly performed in an electrochemical cell, with a glassy carbon working electrode (diameter = 5.0 mm), an Ag/AgCl (saturated KCl) reference electrode and a platinum auxiliary electrode. The supernatant fluid was dissolved in 1 mL of 0.1 MHCl solution and the electrochemical oxidation of gold was performed at +1.25 V for 120 s in the solution. Immediately after the electrochemical oxidation, differential pulse voltammetry was performed with the scan range from +0.65 V to 0.25 V (scan rate 20 mV/s, pulse width 0.05), resulting in an analytical signal due to the reduction of $AuCl_4^-$, which relates to the amount of the gold nanoparticle-oligonucleotide released upon the target protein. The DPV peak height at a potential of +0.43 V of the reduction of $AuCl_4^-$ was used in all of the measurements.

3. Results and discussion

3.1. The recognition for thrombin

Upon the presence of the target protein, the probe of magnetic nanoparticle-aptamer/gold nanoparticle-oligonucleotide dissociated and cause the release of the gold nanoparticle-labeled oligonucleotide, which can be investigated by the DPV responses of the gold nanoparticles. As shown in Fig. 2(a), without thrombin for incubation, the peak current of DPV at +0.43 V (vs Ag/AgCl) could be neglected. For that without thrombin, gold nanoparticle-oligonucleotide would not dissociate from the duplex structure, therefore no DPV response of gold was observed. When 3.36×10^{-11} M of thrombin was added, 4.2340 μA of peak current of DPV was observed (Fig. 2(b)). Because the aptamer is in a conformational equilibrium between duplex structure and the G-quarter structure, it prefers to bind with thrombin to form the G-quarter structure, and liberate the gold nanoparticle-labeled oligonucleotide.

3.2. The SEM identification for the displacement assay

Two samples were prepared according to the protocol, sample a contains thrombin, sample b contains no thrombin as a control experiment. After the incubation, wash, the samples were diluted by 600 μL distilled water respectively. 30 μL of the resultant solution was used for SEM. Fig. 3(b) shows apparently that gold nanoparticle adhered on the magnetic nanoparticles, owing to the fact that the magnetic nanoparticle-aptamer bind to the gold nanoparticle-oligonucleotide through the hybridization. While no gold nanoparticles was observed in sample a (Fig. 3 (a)), which has identified that in the present of the target protein, the aptamer prefers to bind to thrombin, and therefore the gold nanoparticle-labeled oligonucleotide released from the duplex structure.

3.3. Optimization for the assay

3.3.1. Effect of the temperature and time

The temperature of the incubation has an influence on the dissociation of the probe of magnetic nanoparticle-aptamer/gold nanoparticle-oligonucleotide and the displacement reaction in the presence of thrombin. According to the experimental scheme, two samples were prepared, one contained 1.12×10^{-11} M of thrombin, another contained no thrombin as control. The effect of the temperature was investigated in the range of 17–57 °C and the interval is 5 °C. The experimental results were shown that in the absence of thrombin (Fig. 4A (curve a)), the peak current could be neglected in the range of 17–42 °C, for the probe would not dissociate during the range of 17–42 °C, and it began to dissociate at 45 °C. While in the presence of thrombin (Fig. 4A (curve b)), during the range of 17–37 °C, the peak current gradually increased with the increase of the temperature, and a higher response was obtained at 37 °C, thus 37 °C was chosen in the experiment for the determination. Afterwards, the peak current increased swiftly with the increase of the temperature, owing to the fact that the probe may dissociate after 45 °C, resulting in the rapid increase of the peak current. These experimental results showed that the specific recognition for thrombin at 37 °C was induced by thrombin, not by the dissociation of the complex.

The time dependence of the assay was also studied in the range of 5–30 min at 37 °C (Fig. 4B), the electrochemical signal we obtained increased swiftly with the time increased, reached at a platinum at 20 min, then decreased after 25 min. We deduced from the experiments that 20 min will assure the fully dissociation of the duplex and the formation of the G-quarter structure. The probable reason of the signal decreased after 25 min is that the activity of thrombin may decreased after 25 min, therefore affect the binding affinity toward aptamer. Therefore 20 min was chosen in the experiment.

3.3.2. Effect of the buffer

The effect of buffer in the assay was compared by carrying out the assay in Tris–HCl, PBS and PBS containing MgCl. The experimental results revealed that the signal obtained in PBS buffer was significantly higher than in Tris–HCl, which indicates that PBS buffer was more favorable for the incubation. This is consistent with the report that PBS buffer is suitable for the incubation of thrombin [34]. The results also showed that the signal achieved in PBS containing MgCl was higher than in PBS because Mg^{2+} could stabilize the G-quarter structure of the aptamer-protein. It was reported that Mg^{2+}, Ca^{2+}, Na^+, K^+ have a great influence on the formation of the G-quarter structure of the aptamer [35], thus PBS containing 0.001 M Mg^{2+} was chosen as the reaction buffer.

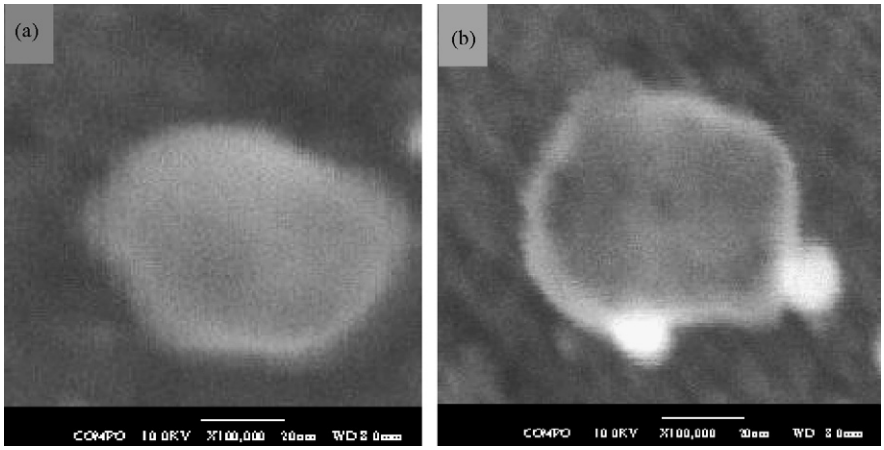


Fig. 3. SEM of the specific recognition for thrombin. (a) In the presence of thrombin; (b) in the absence of thrombin.

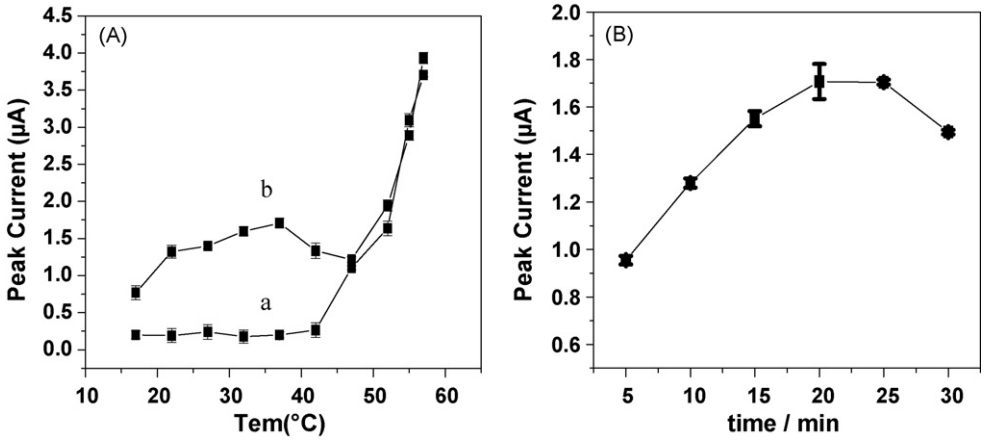


Fig. 4. (A) Effect of the temperature (a) on the dissociation of the probe, (b) on the displacement assay in the presence of thrombin; (B) effect of the time on the displacement assay, the temperature applied in the experiments is 37 °C. The error bar indicates the RSD of five independent experiments, the concentration of thrombin applied in the experiments is 1.12×10^{-11} M.

3.4. Specificity of the assay

As signaling is based on a specific, binding-induced conformational change, the sensor should be relatively insensitive to nonspecific binding, such as adsorption. In order to test this, we have shown that 1.49×10^{-6} M of BSA and 3.13×10^{-6} M of lysozyme did not exhibit any measurable signal (Fig. 5(a) and (b)). Similarly, when thrombin coexisted with other protein, 1.49×10^{-6} M of BSA (Fig. 5(d)) or 3.13×10^{-6} M of lysozyme (Fig. 5(e)), did not exhibit any apparent signal change compared with thrombin (Fig. 5(c)). These results imply that the dissociation of the duplex, and the subsequent increase of the peak current require the formation of a specific aptamer–thrombin complex. Therefore the sensor is highly selective, quite affinity toward the target protein. It is quite insensitive to nonspecific binding and thus readily detects physiological thrombin levels, even in complex sample such as blood serum.

3.5. Quantitative detection of thrombin

The illustrated error bars represent the RSD of five measurements conducted at each thrombin concentration.

To assess the sensitivity and the linear range of the optimized assay, the target thrombin was serially diluted and analyzed. In Fig. 6, the increased electric current generated by gold was observed depending on the increased concentration of thrombin.

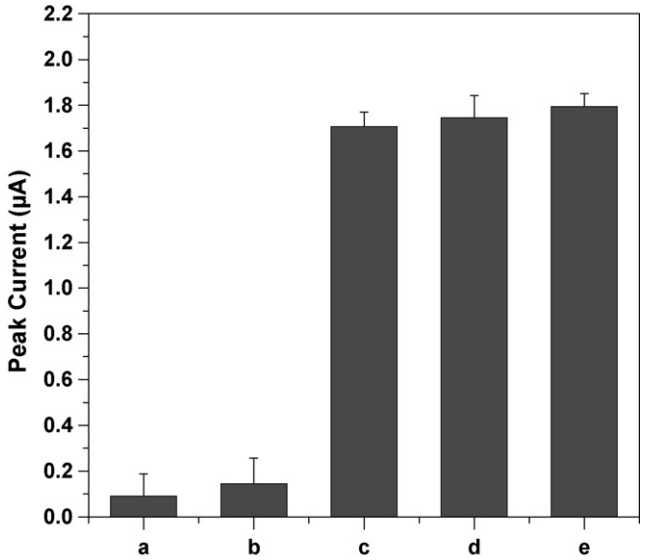


Fig. 5. Specificity of the assay (a) with 1.49×10^{-6} M BSA (b) with 3.13×10^{-6} M lysozyme (c) with 1.12×10^{-11} M thrombin (d) with 1.12×10^{-11} M thrombin and 1.49×10^{-6} M of BSA coexisted (e) with 1.12×10^{-11} M thrombin and 3.13×10^{-6} M lysozyme coexisted. The error bars indicates the RSD of five independent experiments.

Table 1
Assay results of thrombin in plasma.

Sample	Thrombin amount found after dilution (M)	Added amount (M)	Found amount (M)	Recovery (%)	Thrombin amount in plasma (M)
1	7.47×10^{-12}	5.60×10^{-12}	13.45×10^{-12}	106.8	
2	7.48×10^{-12}	5.60×10^{-12}	12.58×10^{-12}	91.07	7.76×10^{-7}
3	8.33×10^{-12}	5.60×10^{-12}	13.52×10^{-12}	92.70	

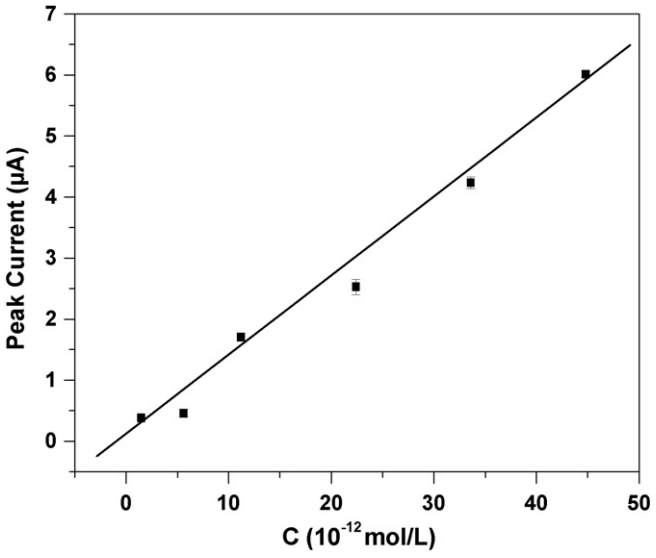


Fig. 6. Dependence of the peak current on the concentration of target thrombin, the concentration of the thrombin is 1.47×10^{-12} M to 4.48×10^{-11} M. The illustrated error bars represent the RSD of five measurements conducted at each thrombin concentration.

The dynamic range of the assay covers physiologically relevant concentrations, which range from 1.47×10^{-12} M to 4.48×10^{-11} M. The resulting linear regression is $Y = 0.12427 + 0.12958X$ (X stands for the value of the 10^{-12} M, and Y is the value of the DPV current, unit: μA), with a correlation coefficient of 0.997. As low as 6.616×10^{-13} M of the target thrombin can be detected with a signal-to-background ratio of 2.7 with the proposed assay. The reproducibility of the assay assessed by analyzing samples containing 4.48×10^{-11} M of target thrombin was 4.87% ($n = 5$).

The amount of thrombin in real plasma sample was detected. Thrombin is a plasma protein, and all of the thrombin in plasma is present in the form of its precursor, prothrombin. Trypsin was added in 100 μL of the plasma to convert the prothrombin to thrombin. Calcium ion was added to retain 1 M. After proper dilution, the electrochemical detection were carried out as the procedure mentioned above. Three different plasma samples were detected, the amount of thrombin found in plasma and the recovery were presented in Table 1. Data show that the concentration of thrombin in plasma is 7.76×10^{-7} M.

4. Conclusion

In conclusion, the present study described a novel and efficient detection procedure for thrombin. In the sensing system, the electrochemical signals with the concentration of thrombin over a range from 1.47×10^{-12} M to 4.48×10^{-11} M were detected and the detection limit obtained was 6.616×10^{-13} M. This aptamer-based assay demonstrated several advantages. Gold nanoparticles and magnetic nanoparticles exhibit excellent electrochemical characteristics to assure the high sensitivity. The simplicity and the selectivity were achieved by the aptamer-based structure switch system. On the other hand, it is fit for the detection of real sample, as a result of the high specificity to human thrombin, even in a complex blood serum.

The assay provides a new platform for the specific recognition of other proteins. It is also believed that the facile method developed will find more potential biological applications due to its simple, fast, specificity and stability.

Acknowledgment

This research was supported by grants from the NSFC (Grant No. 20675031), and from Shanghai Science and Technology Committee (Grant No. 06PJ14032).

References

[1] S. Fields, Science 291 (2001) 1221–1224.
[2] R.F. Service, Science 294 (2001) 2080–2082.
[3] A. Abbott, Nature 402 (1999) 715–720.
[4] G. Blobel, R.W. Wozniak, Nature 403 (2000) 835–836.
[5] A.D. Ellington, J.W. Szostak, Nature 346 (1990) 818–822.
[6] C. Tuerk, L. Gold, Science 249 (1990) 505–510.
[7] I. German, D.D. Buchanan, R.T. Kennedy, Anal. Chem. 70 (1998) 4540–4545.
[8] M.N. Stojanovic, D.W. Landry, J. Am. Chem. Soc. 124 (2002) 9678–9679.
[9] E.J. Merino, K.M. Weeks, J. Am. Chem. Soc. 125 (2003) 12370–12371.
[10] M. Liss, B. Petersen, H. Wolf, E. Prohaska, Anal. Chem. 74 (2002) 4488–4495.
[11] D. Xu, D. Xu, X. Yu, Z. Liu, W. He, Z. Ma, Anal. Chem. 77 (2005) 5107–5113.
[12] I. Kazunori, K. Chiharu, S. Koji, Biosens. Bioelectron. 20 (2005) 2168–2172.
[13] A.E. Radi, J.L.A. Sanchez, E. Baldrich, C.K. O'Sullivan, Anal. Chem. 77 (2005) 6320–6323.
[14] C.A. Holland, A.T. Henry, H.C. Whinna, F.C. Church, FEBS Lett. 484 (2000) 87–91.
[15] M.A. Shuman, P.W. Majerus, J. Clin. Invest. 58 (1976) 1249–1258.
[16] J. Bichler, J.A. Heit, W.G. Owen, Thromb. Res. 84 (1996) 289–294.
[17] H. Yang, J. Ji, Y. Liu, J. Kong, B. Liu, Electrochem. Commun. 11 (2009) 38–40.
[18] E. Suprun, V. Shumyantseva, T. Bulko, S. Rachmetova, Biosens. Bioelectron. 24 (2008) 825–830.
[19] J. Hu, P.C. Zheng, J.H. Jiang, G.L. Shen, R.Q. Yu, G.K. Liu, Anal. Chem. 81 (2009) 87–93.
[20] Y. Wang, H. Wei, B. Li, W. Ren, S. Guo, S. Dong, E. Wang, Chem. Commun. 28 (2007) 5220–5222.
[21] L. Fang, Z. Lü, H. Wei, E. Wang, Anal. Chim. Acta 628 (2008) 80–86.
[22] C.M. Niemeyer, B. Ceyhan, Angew. Chem., Int. Ed. 113 (2001) 3798–3801.
[23] R. Elghanian, J.J. Storhoff, R.C. Mucic, R.L. Letsinger, C.A. Mirkin, Science 277 (1997) 1078–1080.
[24] D.J. Maxwell, J.R. Taylor, S. Nie, J. Am. Chem. Soc. 124 (2002) 9606–9612.
[25] C.A. Mirkin, R.L. Letsinger, R.C. Mucic, Nature 382 (1996) 607–609.
[26] H. Cai, Y. Xu, P.G. He, Y.Z. Fang, J. Electroanal. Chem. 510 (2001) 78–85.
[27] J. Zheng, L. Lin, G. Cheng, A. Wang, X. Tan, P. He, Y. Fang, Sci. Chin., Ser. B: Chem. 36 (2006) 485–492.
[28] J. Wang, A. Kawade, Electrochem. Commun. 4 (2002) 349–352.
[29] N. Hamaguchi, A. Ellington, M. Stanton, Anal. Biochem. 294 (2001) 126–131.
[30] R. Nutiu, Y. Li, J. Am. Chem. Soc. 125 (2003) 4771–4778.
[31] W.U. Dittmer, A. Reuter, F.C. Simmel, Angew. Chem., Int. Ed. 43 (2004) 3550–3553.
[32] Y. Xiao, B.D. Piorek, K.W. Plaxco, A.J. Heeger, J. Am. Chem. Soc. 127 (2005) 17990–17991.
[33] A. Doron, E. Katz, I. Willner, Langmuir 11 (1995) 1313–1317.
[34] H.A. Ho, M. Leclerc, J. Am. Chem. Soc. 126 (2004) 1384–1387.
[35] C. Kneuer, M. Sameti, U. Bakowsky, T. Schiestel, H. Schirra, H. Schmidt, C. Lehr, Bioconjugate Chem. 11 (2000) 926–932.

Talanta 80 (2010) 1873–1880

Contents lists available at ScienceDirect

Talanta

journal homepage: www.elsevier.com/locate/talanta

Mixed hemimicelles SPE based on CTAB-coated Fe_3O_4/SiO_2 NPs for the determination of herbal bioactive constituents from biological samples

Li Zhu, Di Pan, Li Ding, Fei Tang, Qianli Zhang, Qian Liu, Shouzhuo Yao*

College of Chemistry and Chemical Engineering, Hunan University, Changsha 410082, PR China

ARTICLE INFO

Article history:
Received 28 May 2009
Received in revised form 15 October 2009
Accepted 18 October 2009
Available online 30 October 2009

Keywords:
Mixed hemimicelles
Silica-coated magnetic nanoparticles
Solid-phase extraction
Biological samples
Rhubarb

ABSTRACT

In this paper, a solid-phase extraction (SPE) method based on mixed hemimicelles of cetyltrimethyl ammonium bromide (CTAB) on silica-coated magnetic nanoparticles (MNPs) is developed for extraction and preconcentration of compounds from the biological samples. We selected rhein and emodin which are the major active anthraquinones of rhubarb as model analytes. A high performance liquid chromatography–fluorescence detection (HPLC/FLD) method was developed for the determination of rhein and emodin in urine and serum samples. The main factors influencing the extraction efficiency including the amount of surfactant, the concentration of MNPs, the shaking time and the desorption ability of organic solvents were investigated and optimized. No interferences were caused by proteins or endogenous compounds in urine and serum samples. Good linearities ($r^2 > 0.9995$) for all calibration curves were obtained, and the limits of detection (LODs) for rhein and emodin were 0.2 and 0.5 ng/mL in urine samples and 7 and 10 ng/mL in serum samples, respectively. Satisfactory recoveries (92.76–109.90% and 97.53–107.72% for rhein and emodin) in the biological matrices were achieved.

© 2009 Published by Elsevier B.V.

1. Introduction

Rhei Rhizoma (rhubarb) is a well-known traditional Chinese herbal medicine. Anthraquinone components are the main effective ingredients of rhubarb, which have many pharmacological activities including anti-bacterial [1,2], anticancer [3,4], antifungal [5], antioxidative actions [6,7] and protection of the damaged liver [8,9]. Therefore, it is necessary to determine the content of anthraquinones in biological samples for their pharmacological studies. Rhein and emodin are the major active anthraquinones [10,11]. Several analytical methods have been reported for the quantification of them in biological matrices, such as TLC [12], HPLC/UV [1], LC/MS [12], etc. Generally, for chromatographic analysis of pharmaceutical compounds in biological matrices such as urine, serum and plasma, sample pretreatment is required to clean up the sample before injection. A literature survey reveals that there have been a number of pretreatment methods for analysis of bioactive components in rhubarb, e.g., protein precipitation [12–14], liquid–liquid phase extraction (LLE) [10,15], column-switching [16], etc. However, these methods still have some limitations or shortcomings, for example, need of sample dilution, incomplete protein precipitation, drug co-precipitation, etc. Compared with LLE, solid-phase extraction (SPE) has many obvious advantages including high preconcentration factors, low consumption of organic solvents and ease to operate.

The absorption of ionic surfactants on metal oxides such as alumina, silica, titanium dioxide and ferric oxyhydroxides can form hemimicelles and admicelles [17–21]. Recently, new SPE methods based on mixed hemimicelles assembles has been proposed for the extraction and preconcentration of ionic [19], non-ionic [22,23], amphiphilic [18] compounds. In these methods, the sorbents were produced by the adsorption of ionic surfactants such as sodium dodecyl sulfate (SDS) or cetyltrimethyl ammonium bromide (CTAB) on the surface of mineral oxides [24]. Compared with the normal sorbents, one feature of these sorbents is that the outer surface of hemimicelles is hydrophobic and the admicelles is ionic, which offers different mechanisms for extraction. Moreover, the number of commercially available surfactants is very large, hence the degree of hydrophobicity and the charge of the sorbent can be easily modified according to the nature of analytes. Therefore, using mixed hemimicelles in SPE has many advantages, such as high extraction yields, high breakthrough volumes, and rapid elution of analytes. However, to our knowledge, mixed hemimicelles have not yet been applied in the analysis of biological samples.

Recently, many research groups have explored the application of several nanosized SPE adsorbents such as nanoparticles (NPs) and nanotubes. Magnetic nanoparticles are one of the most popular materials in analytical biochemistry, medicine, and biotechnology, and they have been increasingly applied to immobilize proteins, enzymes, and other bioactive agents [25]. Fe_3O_4 nanoparticles have

* Corresponding author. Tel.: +86 731 8821968; fax: +86 731 8821848.
E-mail address: szyao@hnu.cn (S. Yao).

0039-9140/$ – see front matter © 2009 Published by Elsevier B.V.
doi:10.1016/j.talanta.2009.10.037

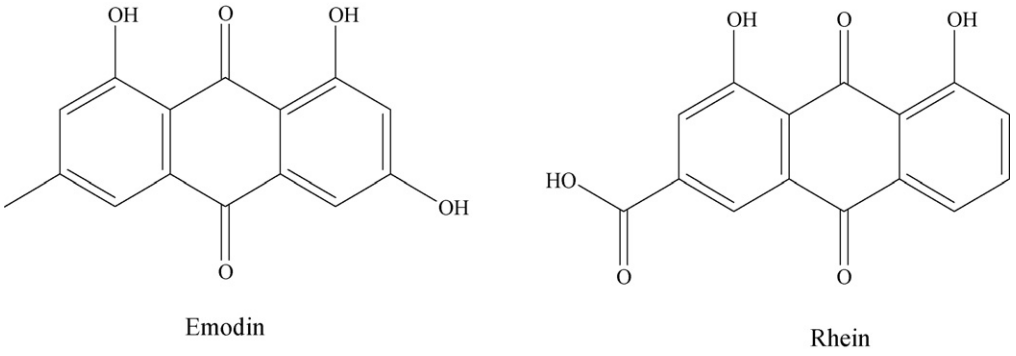


Fig. 1. The chemical structures of rhein and emodin.

attracted particular interest in separation science, for they can be easily isolated by using an external magnetic field placed outside of the extraction container. However, pure magnetic particles are prone to form aggregates and their magnetic properties can be altered in complex environmental and biological systems. To solve the above problems, a suitable protective coating on a magnetic core is often used. The core–shell magnetic nanoparticles have high surface areas. Silica has been considered as one of the most ideal shell materials due to its reliable chemical stability, biocompatibility and versatility in surface modification [26]. Hence, silica-coated Fe_3O_4 nanoparticles could be used for rapid separation. Mixed hemimicelles based silica-coated magnetic nanoparticles were proposed to preconcentrate phenolic compounds from environmental samples [27].

In this work, we combine the advantages of both mixed hemimicelles and silica-coated magnetic nanoparticles, and a mixed hemimicelles based nanosized SPE sorbent is proposed for the extraction and preconcentration of the two active components (rhein and emodin) of rhubarb from the serum and urine samples. We synthesized the Fe_3O_4/SiO_2 core/shell nanoparticles and modified them by coating with cationic surfactants (CTAB) to form the nanosized SPE sorbents. The factors influencing the formation of mixed hemimicelles and the recoveries of the analytes in biological samples were investigated. We found that, for the analysis of rhein and emodin in biological samples, the proposed mixed hemimicelle based nanosized SPE method is more sensitive than the conventional method.

2. Experimental

2.1. Instrumentation and chromatographic conditions

Liquid chromatographic system (Shimadzu, Kyoto, Japan) was consisted of two LC-20AT pumps, a CTO-10AS VP column oven and a RF-10A XL FLD system. They were connected via a communication bus module (Model CBM-20A), and controlled by a Shimadzu LC Solution workstation. A Shimadzu Shim-pack vp-ODS column (5 μm, 4.6 mm × 150 mm) was utilized. When methanol or acetonitrile/water was used as the mobile phase, the peaks of analytes showed band broadening and tailing. In order to improve the peak shape, acetic acid was used to modify the mobile phase. Acetic acid solution (0.1%, 0.3%, 0.5%, 0.8%)–methanol was tested as mobile phases. When the concentration of acetic acid solution was increased to 0.5%, narrow peaks, good symmetry and smooth baselines were obtained. So the mobile phase was composed of A (0.5% acetic acid, v/v)–B (methanol) with the gradient elution (0–5 min, isocratic conditions with 65% of methanol; 5–20 min, linear gradient from 65% to 90% of methanol). The other analysis

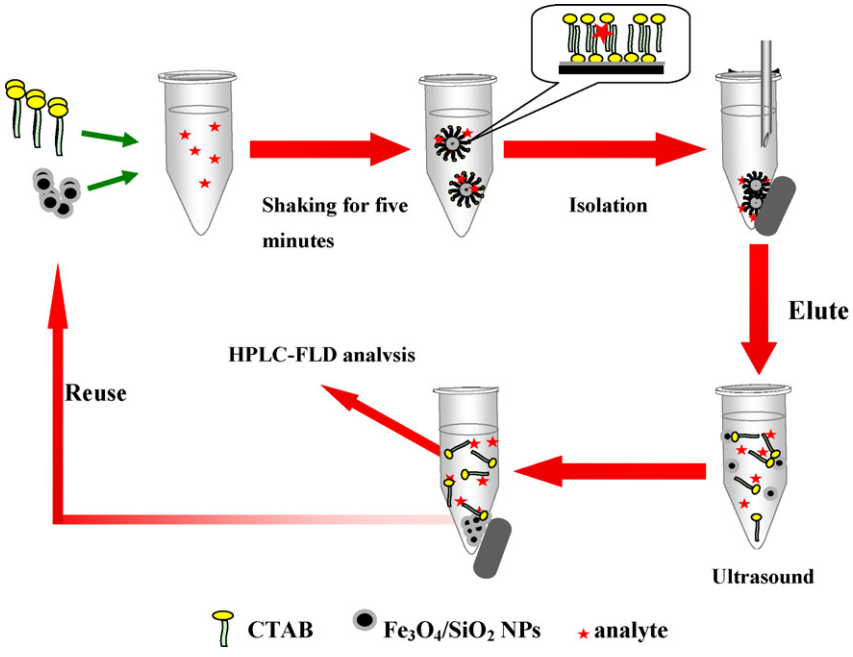


Fig. 2. Schematic illustration of the preparation of surfactants coated Fe_3O_4/SiO_2 MNPs and its application for enriching the active compounds as SPE sorbents.

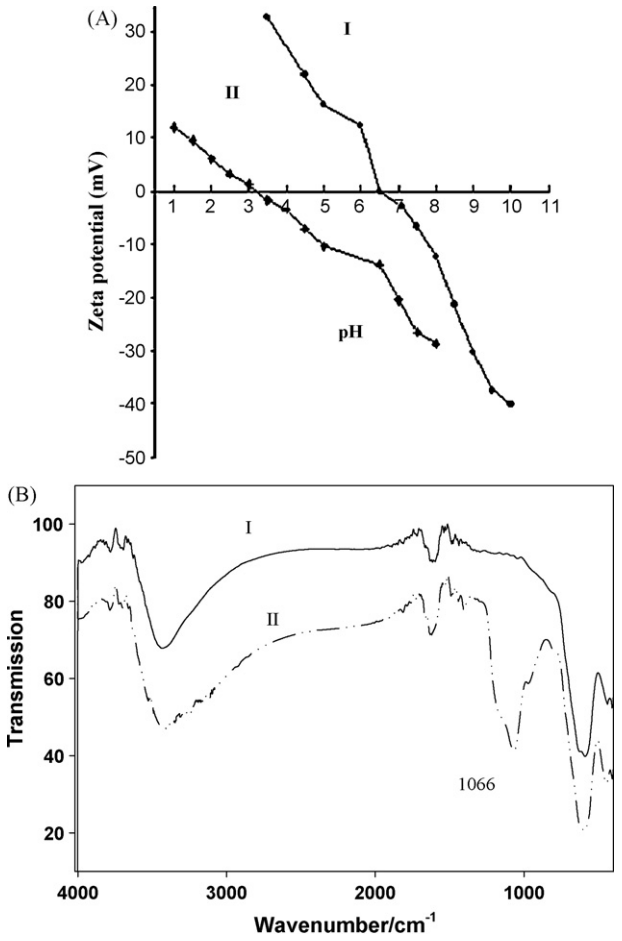


Fig. 3. Zeta-potential at different pH (A) and the infra-red spectrogram (B) of Fe_3O_4 MNps (I) and Fe_3O_4/SiO_2 MNPs (II).

conditions were as follows: column temperature, 30 °C; flow rate, 1.0 mL/min; injection volume, 20 μL. The detection wavelengths were selected at 435 and 515 nm for excitation and emission, respectively. Samples were filtered through 0.45 μm membrane prior to injection.

Zeta-potential measurements of Fe_3O_4 NPs and Fe_3O_4/SiO_2 NPs were performed with Zetasizer 3000 HAS apparatus (Malvern, United Kingdom).

2.2. Chemicals and reagents

The standards of emodin and rhein were purchased from Herbwide Scientific and Technical Development Center (Beijing, China). Their structures are shown in Fig. 1. HPLC-grade methanol (E. Merck, Darmstadt, Germany) was used for HPLC analysis. Ultrapure water was prepared using an Aike purification system (Chengdu, China). Other reagents were of analytical grade, including CTAB, ferric chloride ($FeCl_3{\cdot}6H_2O$), ferrous chloride ($FeCl_2{\cdot}4H_2O$), hydrochloric acid (HCl), aqueous ammonia and tetraethyl orthosilicate (TEOS).

2.3. Preparation of silica-coated magnetite nanoparticles

Fe_3O_4 magnetite was prepared by the coprecipitation method [28]. 1.08 g $FeCl_3{\cdot}6H_2O$ and 0.376 g $FeCl_2{\cdot}4H_2O$ were dissolved in 6 mL 1 mol/L hydrochloric acid. The resulted clear yellowish green solution was then added into 50 mL (5%, v/v) ammonia solution. Upon addition, the solution turned black and was then stirred magnetically at 1000 rpm for 1 h. The Fe_3O_4 magnetite was then washed three times with ethanol and suspended in the ethanol.

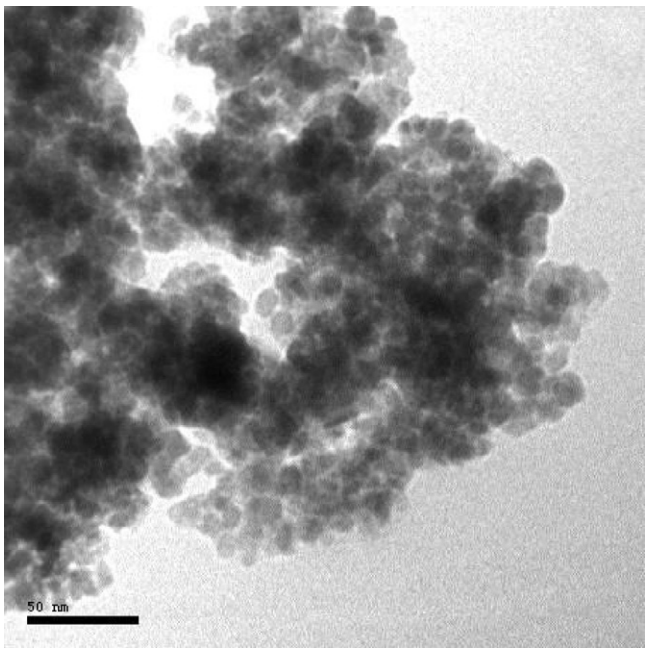


Fig. 4. TEM image of Fe_3O_4/SiO_2 MNPs.

The Fe_3O_4 nanoparticles (0.2 g) were suspended in ethanol (40 mL) under sonication for 1 h. Aqueous ammonia (4.5 mL), deionized water (3.75 mL) and TEOS (0.1 mL) were added in sequence to the suspension. The mixture was sonicated for 1 h followed by vortex mixing for another 8 h. The silica-modified nanoparticles were isolated by magnetic separation and were rinsed with deionized water three times and then resuspended in deionized water (10 mL). The concentration of the generated nanoparticles was estimated to be 20 mg/mL.

2.4. Serum and urine sampling

A mixed stock solution containing rhein (50 μg/mL) and emodin (100 μg/mL) was prepared in methanol. Blank serum and urine samples were collected from volunteers in the Hospital of Hunan University (Changsha, China) and stored at 4 °C. Appropriate milliliters of stock solution of rhein and emodin were added to the blank urine and human serum solutions. The urine samples were prepared with 0.5–250 ng/mL of rhein and 1–500 ng/mL of emodin, respectively. While the serum solutions were prepared with 5–2500 ng/mL of rhein and 10–5000 ng/mL of emodin, respectively.

2.5. Solid-phase extraction procedure

For the extraction and preconcentration of analytes in urine samples, 10 μL MNPs solution (10 mg/mL), 10 μL CTAB solution (4 mg/mL) and 1 mL urine samples were added into a 2 mL centrifuge tube in sequence. For serum samples, 80 μL MNPs solution (10 mg/mL), 70 μL CTAB solution (4 mg/mL) and 100 μL serum samples were added into a 2 mL centrifuge tube, and then was diluted by ultrapure water to 1 mL. To form CTAB-coating on magnetic particles and to trap the targets completely, the above-mentioned centrifuge tube was equilibrated for 5 min in an oscillator. After equilibrium, the MNPs were isolated by placing a strong magnet at the side of the tube and the supernatant

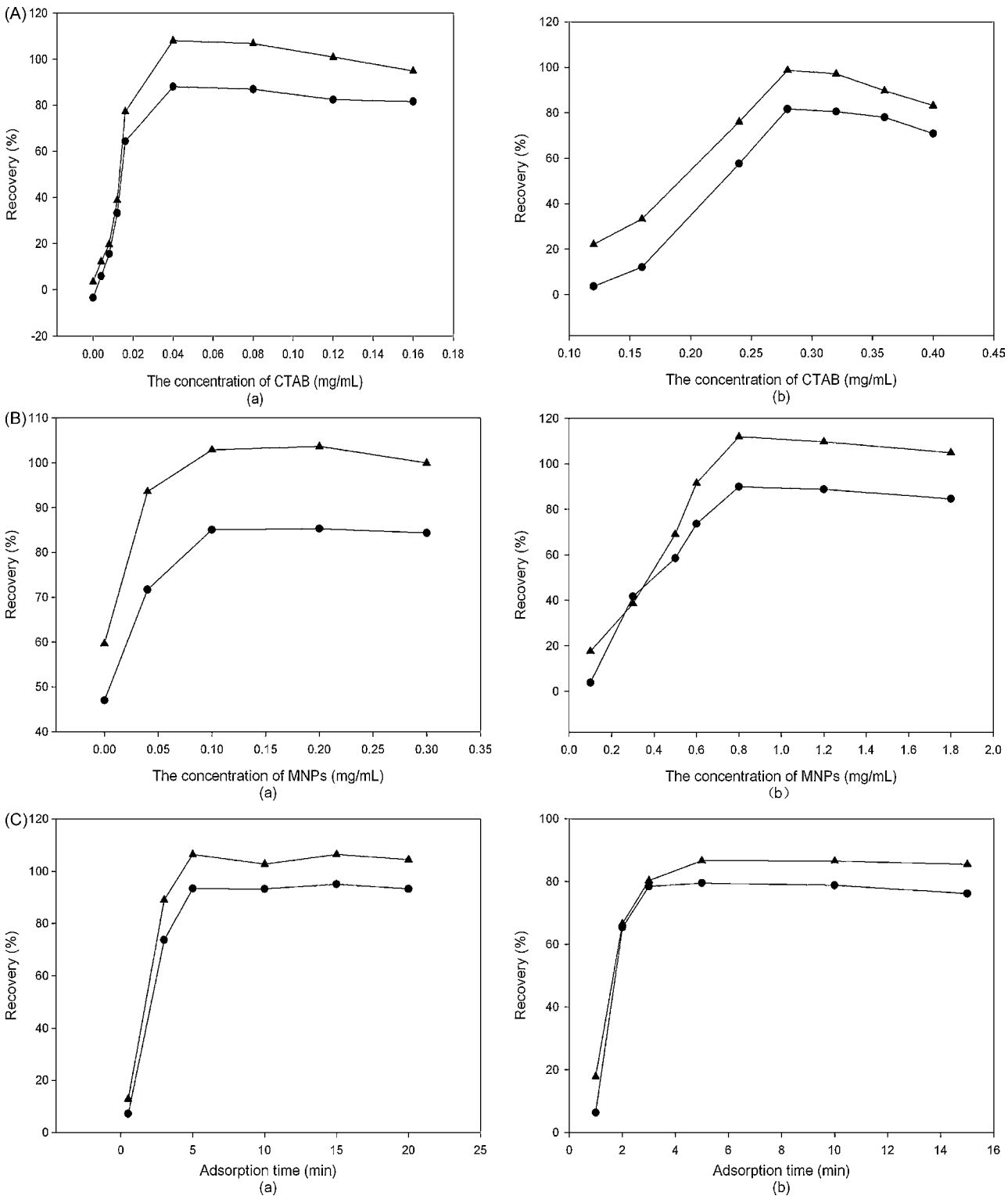


Fig. 5. Effects of the amount of CTAB (A), the concentration of MNPs (B), and the shaking time (C) on the adsorption of rhein (●) and emodin (▲) performed in urine samples (a) and serum samples (b). Performed in batch mode. Concentrations of analytes: 25 ng/mL for rhein and 50 ng/mL for emodin, respectively. (A) The concentration of MNPs was 15 mg/mL. (B) The concentration of CTAB was 4 mg/mL. (C) The concentration of MNPs was 10 mg/mL and the concentration of CTAB was 4 mg/mL.

was discarded. To the isolated NPs, acetonitrile containing 1% acetate acid was added to desorb the analytes (washed twice, 0.5 mL each time). The acetonitrile solution was collected and then dried under a stream of nitrogen at 60 °C and redissolved in 100 μL methanol. After filtration through 0.45 μm membrane, 20 μL of this solution was injected into the HPLC system for analysis. After the nanoparticles were totally isolated by strong magnet, we proved that the nanoparticles can be reused at least for three times, with recoveries of analytes around 90% for each time, and the RSD of the recoveries were 4.98% and 2.56% for rhein and emodin, respectively. Fig. 2 shows the procedure of such a SPE.

3. Results and discussion

3.1. Characterization of CTAB-coated Fe_3O_4/SiO_2 NPs

3.1.1. Characterization of Fe_3O_4/SiO_2 NPs

The isoelectric point (iep) is an important characteristics of metal oxides. In this study, the iep was determined by zeta-potential of NPs under different pH (Fig. 3A). The iep of Fe_3O_4 NPs is consistent with the reported value at pH 6.5. The iep of silica-coated magentic NPs was 3.23, and it approached to the reported value of natural silica which is 3 [29,30]. The infra-red spectrogram of the silica-coated magentic NPs is shown in Fig. 3B. The characteristic band of Si—O is at 1066 cm^{-1}. Therefore, the results confirm that the Fe_3O_4 NPs were protected by silica coating.

Fig. 4 shows the TEM image of the nanoparticles. We can see that the diameters of most particles are around 10 nm, and most of the particles are quasi-spherical in shape. Besides, we made nitrogen adsorption experiments using Autosorb-6 of Quantachrome and found that the specific area was 157.33 m^2/g when p/p_0 was 0.25897 and the total pore volume was 0.1625 cm^3/g when p/p_0 was 0.99513.

3.1.2. Evaluation of magnetic ability of the sorbent

For practical application of MCT (magnetic carrier technology), it is important that the CTAB-coated Fe_3O_4/SiO_2 NPs should possess sufficient magnetic attraction. We have tested three different cases, using three vials each containing 0.01 mg/mL Fe_3O_4 MNPs (a), 0.01 mg/mL Fe_3O_4/SiO_2 MNPs (b) and 0.01 mmol/L CTAB and 0.01 mg/mL Fe_3O_4/SiO_2 MNPs (c), respectively. It is found, when the magnet was placed beside the three vials, all NPs were quickly attracted to the walls of the vials within a few seconds, leaving the solution transparent. The results indicate that the CTAB-coated Fe_3O_4/SiO_2 nanoparticles as sorbents can be completely aggregated by an external magnetic field.

3.2. Mixed hemimicelle-based SPE

As we know that when the micelles concentration is less than critical micelle concentration (CMC), the micelles will form hemimicelles and admicelles spontaneously on the surface of the metal or non-metal. So the absorption of ionic surfactants on metal oxides such as alumina, silica, titanium dioxide and ferric oxyhydroxides can form hemimicelles and admicelles which is used as sorbents for the SPE of organic compounds. In this study, we tested CTAB-coated Fe_3O_4/SiO_2 NPs, where the analyte retention mechanism is mainly based on electrostatic interaction and lipophilic interaction. The predominant factors affecting the SPE of bioactive analyte with CTAB-coated NPs were investigated.

3.2.1. Influence of the amount of CTAB on the adsorption of the analytes

The influence of CTAB concentration on the adsorption of the analytes from the urine and serum samples was studied in batch mode. The experimental results are shown in Fig. 5A. It can be seen that, without CTAB, the analytes hardly adsorb onto the surface of Fe_3O_4/SiO_2 NPs. However, with the increase in CTAB concentration, the adsorption amount of targets increases remarkably. While surfactant concentration is above the CMC, the adsorption of analytes decreases gradually. The increase in adsorption can be explained by the gradual formation of hydrophobic mixed hemimicelles and admicelles on the surface of NPs. And the adsorption amount decreased when micelles were formed in the bulk aqueous solution, because the micelles caused the analytes to redistribute into the solution again. Comparing Fig. 5A a and b, more CTAB is needed for serum samples than urine samples because more protein or endogenous compound is presented in the former. Therefore, 0.04 and 0.28 mg/mL of CTAB were used for extraction of the analytes from urine and serum samples, respectively.

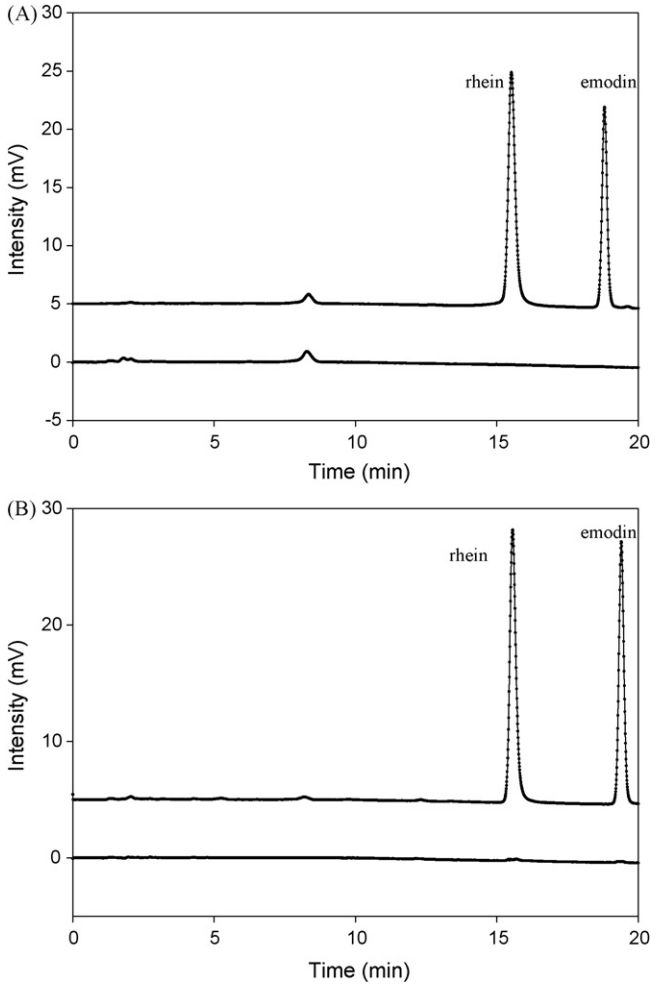


Fig. 6. (A) Comparison of chromatogram of blank urine sample and chromatogram of spiked urine sample for rhein (250 ng/mL) and emodin (500 ng/mL), respectively. (B) Comparison of chromatogram of blank serum sample and chromatogram of spiked serum sample for rhein (2.5 μg/mL) and emodin (5 μg/mL), respectively.

3.2.2. Effect of the concentration of Fe_3O_4/SiO_2 NPs

Nanoparticles have been used as better sorbents for their high surface areas than conventional sorbents. Therefore, fewer amounts of nanoparticle sorbents can achieve satisfactory results. In this work, we found that 0.1 and 0.8 mg/mL were adequate for extracting the analytes from urine and serum, respectively. The results are shown in Fig. 5B.

3.2.3. Shaking time for adsorption

In the SPE process, the shaking time is one of the prime factors influencing the target analytes extraction. As shown in Fig. 5C, when the NPs were isolated immediately without a shaking process into the urine or serum samples, the analytes were hardly adsorbed. However, when the samples were shaken for 5 min, as shown in Fig. 5C, the peak areas of analytes all achieve their maximums both in urine and serum samples. Therefore, a short shaking time of 5 min was selected for adsorption, which enables the targets to be completely absorbed on the CTAB-coated Fe_3O_4/SiO_2 NPs.

3.2.4. Desorption conditions

Organic solvents can rapidly and completely disrupt the mixed hemimicelles. In this paper, acetonitrile and methanol were stud-

Table 1
Linear range, slope, intercept, correlation coefficients (r^2) and limits of detection (LOD) of the investigated compounds.

Compound (n = 6)	Linear range (ng/mL)	Slope	Intercept	r^2	LOD (ng/mL)
Rhein					
Urine	0.5–2500	1366.1	1193.6	0.9999	0.2
Serum	10–2500	148.48	1859.6	0.9997	7
Emodin					
Urine	1–5000	427.37	−746.58	0.9997	0.5
Serum	20–5000	52.24	−3399	0.9996	10

ied for the desorption of analytes from the CTAB-coated Fe_3O_4/SiO_2 NPs. We found that the desorption ability of acetonitrile was superior to that of methanol. Furthermore, while acetic acid was added into the organic solvent, the recoveries of the targets were improved. We studied acetonitrile containing 0.5%, 0.8%, 1%, 1.2% acetic acid as the solvent. When acetonitrile containing 1% acetic acid was used, the analytes can be fully desorbed (washed twice, 0.5 mL each time).

3.3. Method validation

Based on the above results, the conditions of the SPE were as follows: 0.04 mg/mL CTAB and 0.1 mg/mL NPs were added into the urine samples while 0.28 mg/mL CTAB and 0.8 mg/mL of NPs were added into the serum samples, shaking time was 5 min, and acetonitrile containing 1% acetic acid was used for the desorption. Fig. 6A shows the chromatograms of blank and the spiked urine samples, respectively. Fig. 6B shows the chromatograms of blank and the spiked and serum samples. All the samples were dealed with the proposed SPE method before injection. The urine samples can be preconcentrated by ten times. The retention times of rhein and emodin were 15.56 and 19.12 min, respectively. No interferences from the proteins and endogenous components of the urine and serum samples were observed, which shows the excellent specificity for the determination of rhein and emodin with this mixed hemimicelles coated MNPs SPE method.

3.3.1. Linearity, limit of detection and comparison with other methods

The linearities of the analytes were studied in urine and serum samples, respectively. Three injections were examined at each level. Limits of detection (LODs) of the investigated compounds were estimated as the minimum concentration determined with a signal-to-noise ratio of 3. The linear range, slope, intercept, correlation coefficients (r^2) and LODs are listed in Table 1. The results show good linearity ($r^2 > 0.9995$) of the calibration curves. The LODs of rhein and emodin were 0.2 and 0.5 ng/mL in urine samples and 7 and 10 ng/mL in serum samples, respectively.

The extraction efficiency of this proposed method was compared with the protein precipitation method. 1 mL Sample (with spiked given concentration analytes) was added to 3 mL acetonitrile. After vortex-mixing for 1 min, the solution were centrifuged

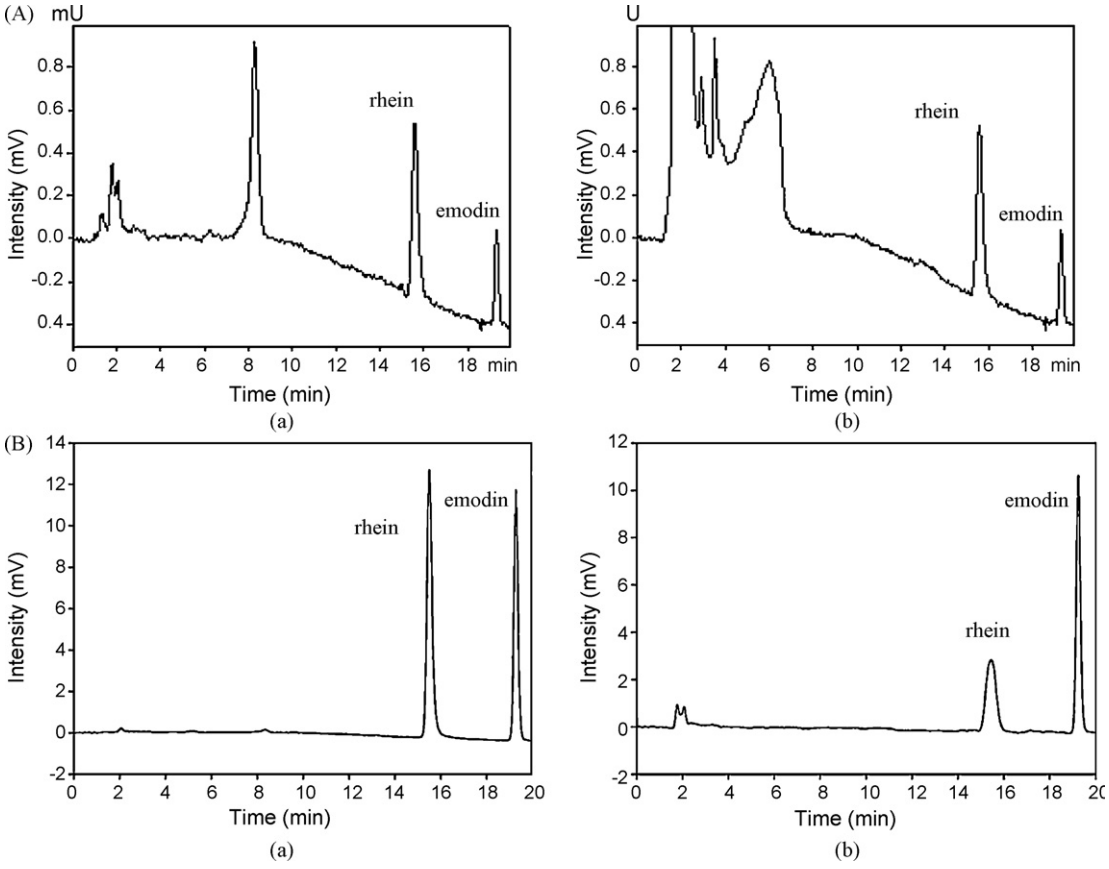


Fig. 7. The chromatograms of the urine (A) and serum (B) samples with the proposed sample pretreatment method (a) and protein precipitation method (b). The concentrations in urine sample are 10 ng/mL for rhein and 20 ng/mL for emodin, and that in serum sample are 2.5 and 5 μg/mL, respectively.

Table 2
Comparison of the reported work with the present work.

Instrument	The method of urine sample pretreatment	Rhein		Emodin		Recovery (%)
		Linear range (ng/mL)	LOD (ng/mL)	Linear range (ng/mL)	LOD (ng/mL)	
HPLC–UV [10]	Protein precipitation	100–2000	33.3	No data were reported		80.8–83.5
This work	The proposed method	0.5–2500	0.2	1–5000	0.5	92.76–109.90

Table 3
Precision and accuracy for detection of rhein and emodin in serum and urine samples.

	Rhein			Emodin		
	Conc. (ng/mL)	Mean accuracy (%)	RSD (%)	Conc. (ng/mL)	Mean accuracy (%)	RSD (%)
Inter-day ($n = 5$)						
Urine	5	96.43	4.37	10	97.91	3.15
	20	96.08	4.58	40	98.03	4.56
	200	98.15	3.45	400	97.18	3.81
Serum	20	95.86	4.18	40	96.49	4.13
	200	97.76	5.27	400	96.27	5.38
	2000	96.86	3.65	4000	95.89	4.59
Intra-day ($n = 5$)						
Urine	5	97.42	4.03	10	95.73	3.93
	20	96.88	2.46	40	96.46	4.59
	200	96.23	3.68	400	95.69	6.73
Serum	20	97.51	5.01	40	97.42	4.58
	200	97.93	5.49	400	97.16	3.27
	2000	96.82	5.82	4000	96.12	4.17

Table 4
Recovery for CT and TS from blank serum, urine samples ($n = 5$).

Matrix	Rhein			Emodin		
	Conc. (ng/mL)	Mean recovery (%)	RSD (%)	Conc. (ng/mL)	Mean recovery (%)	RSD (%)
Urine	5	107.93	4.17	10	103.06	2.92
	20	109.90	2.65	40	107.45	5.27
	200	92.76	4.83	400	97.53	3.35
Serum	20	106.87	3.76	40	107.72	3.48
	200	103.91	3.82	400	104.83	4.76
	2000	108.49	5.36	4000	103.36	3.55

at 5000 rpm for 10 min, the supernatants were evaporated to dryness under a stream of nitrogen flow at 60 °C, then the residue was treated with 100 μL methanol solution. An aliquot (20 μL) was injected into the LC system for analysis. Fig. 7 shows the chromatograms of the samples with the proposed method (left) and the classical method (right). It can be seen from Fig. 7 that no interference was caused in both methods, but while using the mixed hemimicelles coated MNPs method, the background noise was less.

Compared with the previously reported method, wider linear ranges, lower LODs and better recoveries were obtained for rhein (no data were reported for emodin in [10]). The comparison result is given in Table 2.

3.3.2. Precision and accuracy

The intra-day and inter-day precision and accuracy of the method were evaluated by assaying five replicate spiked urine and serum samples at three different concentration levels (low, middle and high quantification concentrations) of the targets in the same day and in three consecutive days, respectively. The relative standard deviations (RSDs) of the intra-day and inter-day precision and accuracy values for spiked biological samples are summarized in Table 3. The RSDs of the intra-daily tests are less than 5.5%, and the RSDs of inter-daily tests (three consecutive days) are less than 6.8%. These results indicate that the present method has good accuracy and precision.

3.3.3. Recovery

The recovery of the method was studied using the standard addition method. The reference standards were added at three different concentration levels (low, middle and high concentrations of the matrix) with five parallels at each level. The recoveries of rhein and emodin in urine and serum samples are shown in Table 4. It can be seen that satisfactory recovery (92.8–109.9%) was obtained using the proposed method. Thus it is suitable for analyzing the biological samples.

4. Conclusion

A rapid, sensitive and simple SPE method which combined the advantages of mixed hemimicelles and silica-coated magnetic nanoparticles was applied in extraction and preconcentration of the active compounds in biological samples firstly. Rhein and emodin which are the major active anthraquinones of rhubarb were selected as the example. This method was proved to be feasible. The analytes were extracted and preconcentrated by this SPE method before HPLC/FLD analysis. Compared with the classical pretreatment method (protein precipitation), the amount of the analytes found in the biological samples are superior. Also we obtained good linearities and recoveries with serum and urine samples, which indicates that this proposed method can be successfully applied in the sample preparation of biological samples.

Acknowledgements

This work was financially supported by the National Basic Research Program (also called 973 Program) (No. 2006CB504701 and No. 2009CB421601) and the Innovation Foundation of Graduate Student of Hunan Province.

References

[1] B. Subhalakshmi, G. Abhijit, H. Banasri, Phytother. Res. 19 (2005) 888.
[2] C.H. Chang, C.C. Lin, J.J. Yang, Am. J. Chin. Med. 24 (1996) 139.
[3] S.G. Lin, M. Fujii, D.X. Hou, Arch. Biochem. Biophys. 418 (2003) 99.
[4] J. Koyamaa, I. Morita, K. Tagahara, Y. Nobukuni, T. Mukainaka, M. Kuchide, H. Tokuda, H. Nishino, Cancer Lett. 182 (2002) 135.
[5] S.K. Agarwal, S.S. Singh, S. Verma, S. Kumar, J. Ethnopharmacol. 72 (2000) 43.
[6] A. Iizuka, O.T. Iijima, K. Kondo, H. Itakura, F. Yoshie, H. Miyamoto, M. Kubo, M. Higuchi, H. Takeda, T. Matsumiy, J. Ethnopharmacol. 91 (2004) 89.
[7] G.C. Yen, P.D. Duh, D.Y. Chuang, Food Chem. 70 (2000) 437.
[8] M. Koyama, T.R. Kelly, K.A. Watanabe, J. Med. Chem. 31 (1988) 283.
[9] H.C. Huang, S.H. Chu, P.D. Lee-Chao, Eur. J. Pharmacol. 198 (1991) 211.
[10] W.F. Tang, X. Huang, Q. Yu, F. Qin, M.H. Wan, Y.G. Wang, M.Z. Liang, Biomed. Chromatogr. 21 (2007) 1186.
[11] W.F. Tang, Q. Yu, M.H. Wan, F. Qin, Y.G. Wang, G.Y. Chen, M.Z. Liang, X. Huang, Biomed. Chromatogr. 21 (2007) 701.
[12] J.H. Lee, J.M. Kim, C.S. Kim, J. Ethnopharmacol. 84 (2003) 5.
[13] F.G. Xu, Y. Liu, Z.J. Zhang, R. Song, H.J. Dong, Y. Tian, J. Pharm. Biomed. Anal. 47 (2008) 586.
[14] V. Springolo, G. Coppi, J. Chromatogr. 428 (1988) 173.
[15] U. Katsuyoshi, Y. Yoshikanzu, S. Yukiya, N. Fujio, J. Chromatogr. 380 (1986) 462.
[16] Y. Li, J.P. Gao, X. Xu, L.X. Dai, J. Chromatogr. B 838 (2006) 50.
[17] R. Atkin, V.S.J. Craig, E.J. Wanless, S. Biggs, Adv. Colloid Interface Sci. 103 (2003) 219.
[18] F. Merino, S. Rubio, D.P. rez-Bendito, Anal. Chem. 75 (2003) 6799.
[19] F. Merino, S. Rubio, D.P. rez-Bendito, Anal. Chem. 76 (2004) 3878.
[20] M.R. Bohmer, L.K. Koopal, Langmuir 8 (1992) 2649.
[21] M.R. Bohmer, L.K. Koopal, Langmuir 8 (1992) 2660.
[22] M. Cantero, S. Rubio, D. Pérez-Bendito, J. Chromatogr. A 1067 (2005) 161.
[23] M. Cantero, S. Rubio, D. Pérez-Bendito, J. Chromatogr. A 1046 (2004) 147.
[24] J.D. Li, X.L. Zhao, Y.S. Cai, S.F. Mou, G.B. Jiang, J. Chromatogr. A 1180 (2008) 24.
[25] X.L. Zhao, Y.L. Shi, Y.Q. Cai, S.F. Mou, Environ. Sci. Technol. 42 (2008) 1201.
[26] Z.C. Zhang, L.M. Zhang, L. Chen, L.G. Chen, Q.H. Wan, Biotechnol. Prog. 22 (2006) 514.
[27] X.L. Zhao, Y.L. Shi, T. Wang, Y.Q. Cai, G.B. Jiang, J. Chromatogr. A 1188 (2008) 140.
[28] W.J. Chen, P.J. Tsai, Y.C. Chen, Small 4 (2008) 485.
[29] Q. Wang, J.S. Jiang, Z.F. Gan, Chem. Bull. 3 (2006) 52.
[30] A. Moral, M.D. Sicilia, S. Rubio, D. Pérez-Bendito, J. Chromatogr. A 1100 (2005) 8.

Talanta 80 (2010) 1881–1887

Contents lists available at ScienceDirect

Talanta

journal homepage: www.elsevier.com/locate/talanta

Evaluation of thin mercury film rotating disk electrode to perform absence of gradients and Nernstian equilibrium stripping (AGNES) measurements

Luciana S. Rocha[a,*], Encarnació Companys[b], Josep Galceran[b], Helena M. Carapuça[a], José Paulo Pinheiro[c]

[a] Department of Chemistry/CICECO, University of Aveiro, 3810-193 Aveiro, Portugal
[b] Department of Chemistry, University of Lleida, Rovira Roure 191, 25198 Lleida, Spain
[c] IBB/CBME, Department of Chemistry, Biochemistry and Pharmacy, Faculty of Sciences and Technology, University of Algarve, 8005-139 Faro, Portugal

ARTICLE INFO

Article history:
Received 9 June 2009
Received in revised form 13 October 2009
Accepted 18 October 2009
Available online 24 October 2009

This work is dedicated to the memory of Professor Helena Maria Carapuça, acknowledging her inspiration, her limitless support and especially her constant friendship always demonstrated.

Keywords:
Thin mercury film rotating disk electrode (TMF-RDE)
Absence of gradients and Nernstian equilibrium stripping (AGNES)
Heavy metals speciation

ABSTRACT

In the present work, the applicability of thin mercury film on a rotating disk electrode (TMF-RDE), to assess the free metal ion concentration by the absence of gradients and Nernstian equilibrium stripping (AGNES), is evaluated. The thickness of the mercury film and several AGNES parameters has been optimized. A nominal 16 nm film is chosen due to the higher signal (faradaic current) relative to the value of the noise (capacitive current). Due to the smaller volume to area ratio, the deposition time needed to reach a certain preconcentration factor (Y) is much shorter than in larger electrodes, like the HMDE. The limit of detection (3σ) for lead(II) is 7.4×10^{-9} M and 7.2×10^{-8} M for a Y of 5000 (deposition time of 150 s) and 1000 (deposition time of 100 s), respectively. A specific mathematical treatment is developed in order to subtract a corrected blank taking into account the degradation of the thin film (presumably, falling down of drops). The couple TMF-RDE/AGNES is successfully applied for speciation purposes in the systems Pb(II)–latex nanospheres and Pb(II)–IDA (iminodiacetic acid), where the stability constants calculated for both systems agree with values reported in the literature.

© 2009 Elsevier B.V. All rights reserved.

1. Introduction

Absence of gradients and Nernstian equilibrium stripping (AGNES) was recently proposed for the determination of the free metal ion concentration of amalgamating elements [1]. The key idea in this technique is that during the deposition step the metal within the mercury electrode is allowed to proceed until reaching Nernstian equilibrium without concentration gradients. Therefore, the concentrations of amalgamated metal and the faradaic stripping current are proportional to the free metal ion concentration in the bulk solution [1,2].

Recently, instead of using the conventional HMDE, AGNES was applied with Hg–Ir microelectrodes. Due to a reduction of the drop size in the latter case, the amount of deposited metal for a given preconcentration is much less and the deposition time can be reduced. Because of the larger ratio of the accessible area over the volume of the amalgam, shorter times will be required to attain the target conditions (Nernst equilibrium). Despite of these advantages, the preparation procedure of the microelectrode is time consuming and the mechanical resistance of this electrode still needs to be improved. Moreover, the large capacitive current only allowed a modest decrease in the limit of detection [3].

In a previous work, the thin mercury film rotating disk electrode (TMF-RDE) proved to be suitable in stripping chronopotentiometry and scanning stripping chronopotentiometry (SCP/SSCP) studies of metal cations, due to the high sensitivity and resolution attained [4]. A relatively stable, homogeneous and reproducible *ex situ* thin mercury film (TMF) could be easily plated, with a single electrodeposition step of high overpotential, in acidic solutions [4,5].

The aim of the present work is to evaluate the TMF-RDE to perform AGNES. For that, the evolution of the film electrode is taken into account by means of a mathematical treatment. The TMF-RDE thickness is optimized in order to obtain a stable film coating that could be used for one day, without recasting the electrode. The key parameters of the technique, such as deposition time, deposition potential and also the rotation speed applied to the rotating disk electrode (RDE) are also investigated. The main goal is to shorten the time of analysis while obtaining a low detection limit.

* Corresponding author. Tel.: +351 234 370732; fax: +351 234 370084.
E-mail address: lrocha@ua.pt (L.S. Rocha).

0039-9140/$ – see front matter © 2009 Elsevier B.V. All rights reserved.
doi:10.1016/j.talanta.2009.10.038

Additionally, the speciation capability of the TMF-RDE coupled with AGNES is assessed, evaluating the interaction of lead(II) cation with two ligands: (i) iminodiacetic acid (IDA) and (ii) 40.0 nm radius carboxylated latex nanospheres (P(S/V–COOH)).

2. Theoretical background

We now summarize the principles of AGNES and its application with non-evolving electrodes (fixed area and fixed volume).

AGNES consists of two conceptual steps or stages: deposition or first stage, and stripping or second stage. The aim of the deposition step is to attain a special situation without concentration gradients (both inside the mercury film electrode and in the solution in contact with the electrode), while a constant ratio is kept between the concentrations of the electroactive couple due to the Nernstian equilibrium [1]. This ratio is called gain or preconcentration factor Y, and depends on the applied potential, E_1:

$$Y = \frac{c^*_{M^0}}{c^*_M} = \exp\left[\frac{-nF(E_1 - E^{0'})}{RT}\right] \quad (1)$$

where $E^{0'}$ stands for the standard formal potential of the redox couple of the metal M and $c^*_{M^0}$ and c^*_M correspond to the final homogeneous metal concentrations inside the mercury electrode and the bulk solutions, respectively. The duration of the deposition stage is denoted as t_1. The gain Y for a given applied potential E_1 is determined from the peak potential of a differential pulse polarography (DPP) experiment, E_{peak} [6]:

$$Y = \sqrt{\frac{D_M}{D_{M^0}}}\exp\left[-\frac{nF}{RT}\left(E_1 - E_{peak} - \frac{\Delta E_{DPP}}{2}\right)\right] \quad (2)$$

where D_{M^0} is the diffusion coefficient of the reduced metal, and ΔE_{DPP} is the modulation amplitude of the DPP experiment.

In the second (or quantification) step, a sufficiently less negative potential, E_2, is applied in order to produce a stripping current under diffusion limited conditions. The measured response function is the current I at a certain time t_2. The faradaic component of this current is linearly related with $c^*_{M^0}$, due to the linear features of the metal diffusion inside the mercury film. So, the free metal ion concentration is directly proportional to the faradaic current with a proportionality factor h (which can be obtained from the calibration), since, according to Eq. (1) [1], $c^*_{M^0}$ is Yc^*_M. So

$$I_f = hc^*_M \quad (3)$$

The measured current contains other components apart from the faradaic current; therefore it is necessary to subtract a blank from the total current.

3. Experimental

3.1. Reagents

All chemicals were of analytical reagent grade and all solutions were prepared with ultra-pure water (18.3 MΩ cm, Milli-Q systems, Millipore-waters). Sodium nitrate, potassium chloride, nitric acid 65% (Merck, suprapur), hydrochloric acid 37% (trace select, Fluka) and 1000 ppm Hg and Pb AA-Spectrosol metal ion standards (Merck) were also used. Ferricyanide standard solution (1.929×10^{-3} mol dm^{-3}) in 1.0 mol dm^{-3} KCl was used for chronoamperometry. Nitric acid (1 M) and sodium hydroxide solutions (1 M) were used for pH adjustments. Stock solution of MES 2-(N-morpholino-ethanesulfonic acid) buffer (0.1 M) was prepared from the solid (Merck). Solutions of ammonium acetate (NH_4Ac 1.0 M/0.5 M HCl) pH buffer and ammonium thiocyanate 1.0 M were prepared monthly and used without further purification. Biohit Proline pipettes equipped with disposable tips were used for appropriate dilutions. All measurements were carried out at room temperature (20 °C).

3.2. Apparatus

An EcoChemie Autolab PGSTAT12 potentiostat (controlled by GPES 4.9 software from EcoChemie, the Netherlands) was used in conjunction with a Metrohm 663 VA stand (Metrohm, Switzerland). The three electrode configuration was used comprising a TMF plated onto a rotating glassy carbon (GC) disk (1.9 mm diameter, Metrohm) as the working electrode, a GC rod counter electrode and a double junction $Hg|Hg_2Cl_2|KCl$ (3 M) encased in a 0.1 M $NaNO_3$ solution, as the reference electrode. The electrochemically active surface area of the glassy carbon electrode (3.098 ± 0.015) mm^2, was measured by chronoamperometry (in 1.929×10^{-3} M ferricyanide/1.0 M KCl solution; two polishing experiments, each with four replicate determinations).

A combined glass electrode (Radiometer Analytical pHC3006-9) connected to a pH meter (Thermo Electron Corporation, Model Orion 3-Start) was used for pH measurements.

The microscope examinations were carried out with an optical inverted microscope Zeiss Axiovert 40 MAT connected to a digital camera Cannon Powershot A620 and an AxioVision LE Canon Module software.

3.3. Preparation of the thin mercury film electrode

Prior to coating, the GCE was conditioned following a reported polishing/cleaning procedure [7]. The GCE was polished with an alumina slurry (grain size 0.3 μm, Metrohm) and sonicated in pure water for 60 s, to obtain a renewed electrode surface. Then, an electrochemical pre-treatment was carried out with a multicycle voltammetric scanning (50×) between −0.8 and +0.8 V at 0.1 V s^{-1}, in NH_4Ac–HCl solution. These polishing and electrochemical pretreatments were repeated daily.

The thin mercury film was then *ex situ* prepared in 0.12 mM mercury(II) nitrate and adjusted to pH ~ 1.9, with a 1 M nitric acid solution, by electrodeposition at −1.3 V for different deposition times (240 s and 480 s) and a rotation rate of 1000 rpm [5,8].

The charge associated to the deposited mercury (Q_{Hg}) was calculated by electronic integration of the linear sweep stripping peak of mercury, for $\nu = 0.005$ V s^{-1}. The electrolyte solution was ammonium thiocyanate 5 mM (pH 3.4). The stripping step began at −0.15 V and ended at +0.6 V [8]. All charges quoted are mean values of 6 replicate measurements (RDS < 7%). The thickness of the TMF-RDE was estimated using this mean value of Q_{Hg} and assuming a uniform spread of the mercury on top of the entire disk surface [5,8]. Assuming a thin-film condition, the volume of the mercury electrode, $V_{Hg,dep}$, can be estimated from the amount of deposited mercury measured as the charge, Q_{Hg}, using the Faraday law and assuming the Hg atomic radius (r_{Hg}) as 1.44×10^{-10} m [7]. For the thin mercury film used in this work, the Q_{Hg} was 1.28×10^{-3} C (mean value of 6 replicate measurements with an RDS < 7%), leading to a $V_{Hg,dep}$ 5.01×10^{-14} m^3.

When not in use, the GCE was stored dry in a clean atmosphere [5].

3.4. AGNES procedures

AGNES experiments for optimization of parameters and for calibration were carried out in 20 mL 0.01 M $NaNO_3$ solutions spiked with lead(II) at pH of *ca.* 4. The potential program used consists in applying one potential step along the first stage ("1 pulse" or "1P" strategy) [6].

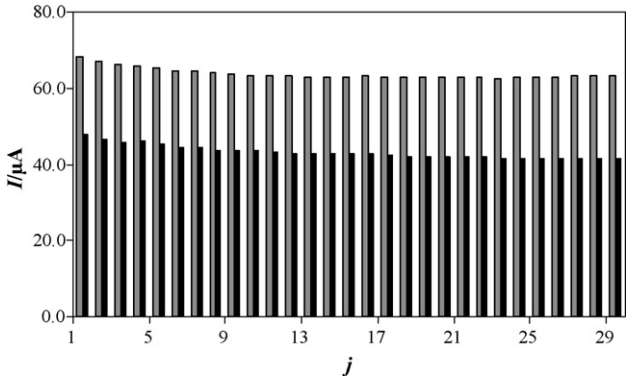


Fig. 1. Evolution of the measured current I (grey bars) and the current of the shifted blank I_{sb} (black bars) over 29 consecutive measurements. Parameters $t_2 = 2$ ms, $Y = 2000$ and $t_1 = 150$ s. The experiments were performed in 0.01 M $NaNO_3$ media, at a pH *ca.* 4 and for a total concentration of lead(II) of 3.96×10^{-7} M. The RDE was rotated at 500 rpm.

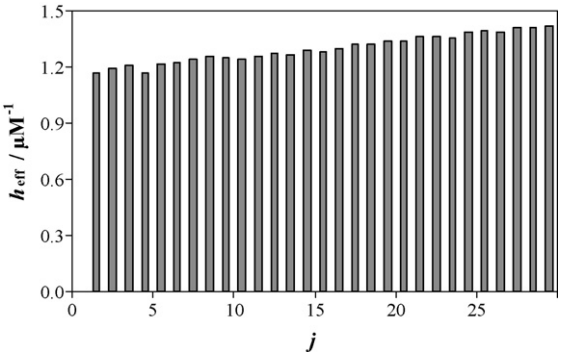


Fig. 2. Variation of the h_{eff} throughout 29 consecutive measurements. The current was measured at t_2 of 2 ms and the other experimental parameters used were: $Y = 2000$ and $t_1 = 150$ s. The experiments were performed in 0.01 M $NaNO_3$ media, at a pH *ca.* 4 and for a total concentration of lead(II) of 3.96×10^{-7} M. The RDE was rotated at 500 rpm.

The measured response is the current I at a certain time t_2. To this current we have to subtract a blank to remove the contributions other than the faradaic one. The synthetic blank [1,2,9] (obtained applying the same potential program in a solution with the same composition of the sample but no metal) is not suitable in case of presence of traces of contaminants or when dealing with natural samples with complex matrices. So, we developed a new kind of blank, the "shifted blank" [3,6,10–12]. The "shifted blank" is applied to the solution containing the metal but with a potential program shifted with respect to the main measurement; the deposition potential $E_{1,sb}$ corresponds to a very low gain ($Y_{sb} = 0.01$) and a $E_{2,sb}$ is applied keeping the same potential jump ($\Delta E = E_{1,sb} - E_{2,sb}$) of the main measurement. To avoid the effects caused by the presence of residual oxygen in the test solution, all of the current values (of the main and the shifted blank measurements) are corrected with the residual current (I_∞), which is obtained at very large stripping time (usually 20 s) [3].

All solutions were purged for 60 min at the beginning of each series of AGNES experiments and 60 s (assisted by mechanical stirring of the rotating GCE for the experiments performed using the rotation of the electrode) after each measurement.

Prior to the addition of the ligand (latex nanospheres or IDA) for the speciation assays, a calibration plot was performed using the optimized experimental parameters (t_1, t_2, Y and rotation speed of the rotating disk electrode).

4. Results and discussion

4.1. AGNES with evolving electrodes

4.1.1. Mechanical stability of the TMF-RDE

One of the problems reported with the use of the TMFE, especially when applied in the rotating mode of the electrode, is its mechanical degradation due to the coalescence or falling of the small drops of Hg. The stability of the mercury coating was assessed by evaluating the repeatability of the current measured at t_2 of 2 ms and for a Y of 2000. A set of 29 consecutive AGNES measurements, each of them immediately followed by a measurement of the shifted blank (a total of 58 measurements in 29 pairs of main measurement and shifted blank), is shown in Fig. 1. A "synthetic blank" with just background electrolyte ($NaNO_3$ 0.01 M solution, pH *ca.* 4) in the solution was run prior to the addition of the metal to the electrolyte solution.

Despite of this slight drift, we accept that this electrode can be used for a maximum of 58 AGNES experiments. A strategy (not essayed here) could be to discard the first few AGNES measurements, since the highest current deviations occur along these initial values.

4.1.2. Mathematical treatment

One interpretation of the observed decrease of the main measurements and blank currents is the falling down of some of the small drops that make up the film. Up to date, AGNES technique has only been used with electrodes whose area and volume remained fixed during the experimental course. Given that the shifted blanks could not be used because of their anomalously high values, we develop next a new mathematical treatment for this electrode with non-fixed area and volume.

We assume that AGNES principles apply to each individual drop, so that the *faradaic* current of a drop ($I_{f,j}^{drop}$) is proportional to the free metal concentration c_j at that moment or addition. j denotes a given configuration in the life of the evolving film, e.g. the electrode situation for a pair of main measurement and shifted blank in Fig. 2. So,

$$I_{f,j}^{drop} = h^{drop} c_j \tag{4}$$

where h^{drop} depends on the area of the drop. For the sake of simplicity, we assume that all drops are identical.

Assuming that the capacitive current (e.g. via the area) is proportional to the number of drops:

$$I_{sb,j} = n_j I_{sb,j}^{drop} \tag{5}$$

we can divide the previous equation applied to a general j with respect to a fixed (selected) "reference" moment or addition:

$$\frac{I_{sb,j}}{I_{sb,ref}} = \frac{n_j I_{sb,j}^{drop}}{n_{ref} I_{sb,ref}^{drop}} = \frac{n_j}{n_{ref}} \tag{6}$$

We assume that, for each j, we can use a certain synthetic blank, which denoted $I_{NaNO_3,j}$. This value cannot be experimentally measured for each moment j, but rather is estimated from the initial measurement $I_{NaNO_3,0}$ (synthetic blank with just background electrolyte):

$$\frac{I_{NaNO_3,j}}{I_{NaNO_3,0}} = \frac{n_j}{n_0} \Rightarrow I_{NaNO_3,j} = \frac{n_j}{n_0} I_{NaNO_3,0} = \frac{I_{sb,j}}{I_{sb,0}} I_{NaNO_3,0} \tag{7}$$

Thus, the faradaic component of one main measurement is:

$$I_{f,j} = I_j - I_{NaNO_3,j} = I_j - \frac{I_{sb,j}}{I_{sb,0}} I_{NaNO_3,0} = n_j I_j^{drop} = n_j h^{drop} c_j \tag{8}$$

where I_j is the total current of the main measurement.

Let us divide the previous equation applied to a general moment or addition j with respect to a fixed (selected) "reference" moment or addition:

$$\frac{I_j - (I_{sb,j}/I_{sb,0})I_{NaNO_3,0}}{I_{ref} - (I_{sb,ref}/I_{sb,0})I_{NaNO_3,0}} = \frac{n_j \bar{h}^{drop} c_j}{n_{ref} \bar{h}^{drop} c_{ref}} = \frac{n_j c_j}{n_{ref} c_{ref}} \quad (9)$$

We can isolate the faradaic component as

$$I_{f,j} = I_j - \frac{I_{sb,j}}{I_{sb,0}} I_{NaNO_3,0} = \left(I_{ref} - \frac{I_{sb,ref}}{I_{sb,0}} I_{NaNO_3,0} \right) \frac{I_{sb,j}}{I_{sb,ref}} \frac{c_j}{c_{ref}} \quad (10)$$

which, by defining a dimensionless or normalized current as

$$I_{norm,j} \equiv \frac{I_j - (I_{sb,j}/I_{sb,0})I_{NaNO_3,0}}{I_{sb,j}} = \frac{I_j}{I_{sb,j}} - \frac{I_{NaNO_3,0}}{I_{sb,0}} \quad (11)$$

the relationship can be simply written as

$$I_{norm,j} = h_{eff} c_j \quad (12)$$

with h_{eff} being the "effective" proportionality between concentration and the ratio between the faradaic and the shift blank currents:

$$h_{eff} \equiv \frac{(I_j/I_{sb,j}) - (I_{NaNO_3,0}/I_{sb,0})}{c_j} \quad (13)$$

From the calibrations, we compute h_{eff} as the slope of $(I_j/I_{sb,j}) - (I_{NaNO_3,0}/I_{sb,0})$ *vs* c_j and then we use this h_{eff} in Eq. (12) to determine the free metal concentration in a speciation experiment.

As a simple verification of this proposal, we have computed h_{eff} with Eq. (13) for the experiments shown in Fig. 1 and plot the results in Fig. 2. The variation of h_{eff} is around 20% from $j = 1$ to $j = 29$, but is around 10% if we go from $j = 1$ to $j = 15$ (30 experiments). This variation in h_{eff} is reasonably acceptable for the small number of experiments performed by us in one day (e.g. in the speciation experiments). We speculate (with the support of a simple model based on the proportionality between capacitive current with area and the functional dependence for h given in Eq. (A9) of ref. [1]) that the increase with time of h_{eff} could be due to the falling down of the smallest droplets, while the largest ones would remain attached.

4.2. Selection of the mercury film thickness in AGNES

The TMF-RDE is subject to mechanical deterioration of the electrode surface during the experimental course. To improve the electrode stability, the electrodeposition of mercury was performed in very acidic solutions (pH *ca.* 1.9) as in [5]. The result was the formation of highly reproducible thin mercury films, consisting of a collection of very small radius mercury droplets, as can be seen in the optical microphotographs (Fig. 3). The performance, i.e. reproducibility, stability/durability, of the TMF-RDE prepared by this procedure is similar to that achieved for the mercury films, *ex situ* prepared in thiocyanate media [7], as reported in a previous work [4].

The capacitive currents exhibited by microelectrodes [3] and by the TMF-RDE (probed in this work) are relatively large (i.e. of the same order of magnitude as the main measurement, so that the faradaic component is less well-defined). Here, the thickness of the mercury coating has revealed as key to reduce the charging currents [3]. Indeed, for the TMF-RDE of 9.1 nm the current obtained in the main experiment was practically the same as the capacitive current (provided by the shifted blank and for a concentration of lead(II) of 2.0×10^{-7} M) and so, a thicker, of *ca.* 16 nm, TMF-RDE was used in this work.

4.3. Optimization of AGNES parameters

Now we evaluate the impact of the different AGNES experimentally controlled parameters, such as the interval time used to measure the current (t_2) during the stripping step, the deposition time (t_1) and the rotation speed applied to the disk electrode, on the performance of the TMF-RDE.

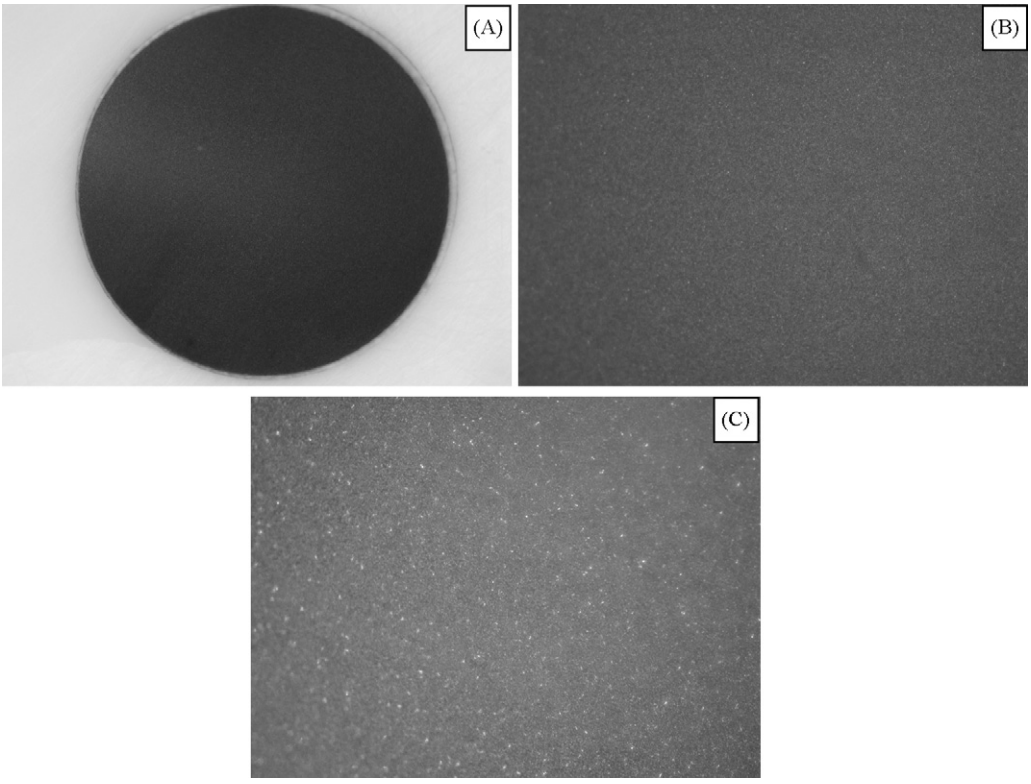


Fig. 3. Optical micrographs: ×50 (A), ×100 (B) and ×500 (C) of a TMFE (16 nm of nominal thickness), plated on a glassy carbon electrode.

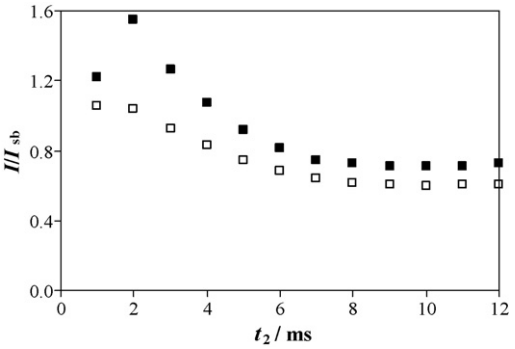


Fig. 4. Ratio between the measured current and the current of the shifted blank along the second stage of AGNES, within the t_2 interval 1–12 ms, in a given moment of the life of the evolving electrode (i.e. same *j*). The experiments were performed in 0.01 M $NaNO_3$ medium at a pH *ca.* 4 and for a total concentration of lead(II) of: (□) 1.99×10^{-7} M and (■) 5.99×10^{-7} M. Other experimental conditions: $Y = 2000$ and $t_1 = 150$ s; no rotation speed of the RDE was used.

4.3.1. Selection of t_2

The new mathematical treatment for evolving electrodes relies on the application of Eq. (12). The faradaic current $I_{f,j}$ (see Eq. (10)) is obtained by subtraction of the corrected synthetic blank Eq. (7)) from the main measurement of the current, being all currents measured at the same fixed t_2.

The selection of the measuring time t_2 stems from the idea of minimizing the relative importance of the capacitive current (estimated with the corrected synthetic blank) in the total current, which can be reformulated as obtaining larger values for the normalized current). In order to look for the ideal t_2, the ratio of the measured current over the shifted blank was plotted (Fig. 4) within the time interval of 1–10 ms, for a *Y* of 2000 and for two concentrations of lead(II).

The results point out that the suitable t_2 values are within the interval of 1–3 ms, where the I/I_{sb} ratio goes through a maximum around 2 ms. Therefore, 2 ms was the time chosen as the standard t_2 for the present work, representing a time neither too short (where large initial capacitive current arise) nor too long (where the gradual extinction of the faradaic current proceeds). Of course that, depending on the experimental set-ups, the optimum t_2 might suffer slight variations, but they can be easily followed given that the stripping current is recorded for a large number of t_2 values.

4.3.2. Effect of the deposition time, t_1

The deposition time is a key parameter in AGNES experiments. Higher t_1 values will favour the approach to the Nernst equilibrium, although too long deposition times would render the technique less useful. Therefore, using a one pulse strategy (i.e. the simplest potential program, that consists in applying only one deposition potential), the effect of the deposition time t_1 on the reaching of the sought equilibrium was evaluated. The deposition gain (*Y*) used in this experiment was 5000 and the total lead(II) concentration selected was 1.49×10^{-7} M. In the first stage (see Fig. 5A), no rotation was applied to the rotating disk electrode during the deposition step. The results reveal that for a gain (or preconcentration factor) of 5000, deposition times (t_1) longer than *ca.* 1600 s at the AGNES first stage, are required to reach the equilibration with flat profile.

Previous works of AGNES with the HMDE have systematically used stirring as a means of improving the efficiency of the mass transport, this resulting in a reduction of the required deposition time (t_1) [1]. This feature is particularly relevant to measure trace levels of free metal ions, where high preconcentration factors are frequently required. Therefore, the effect of the rotation speed in the experimental time of AGNES first stage under the same experimental conditions, i.e. using a *Y* of 5000, was evaluated (Fig. 5B).

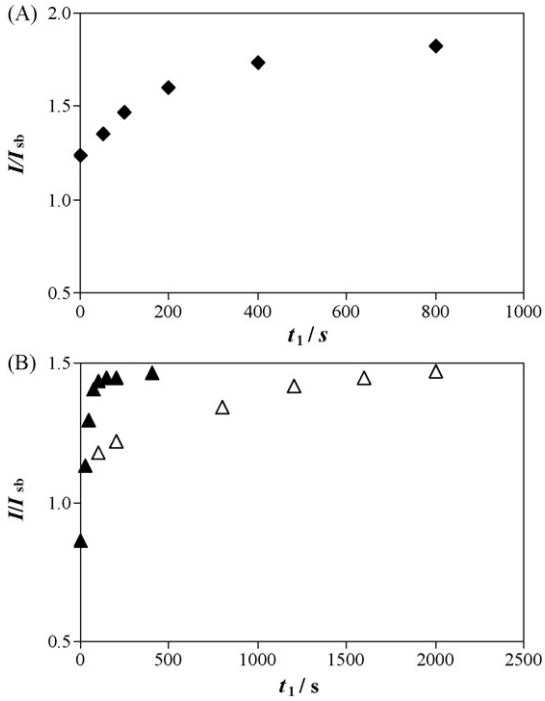


Fig. 5. Variation of the normalized current (I/I_{sb}) as a function of the deposition time (t_1), measured at t_2 of 2 ms and for: *Y* of 2000 for a rotation speed of the RDE of 0 rpm (A) and *Y* of 5000 for a rotation speed of the RDE of 0 rpm (white triangles) and 500 rpm (black triangles), respectively (B). The experiments were performed in 0.01 M $NaNO_3$ media, at a pH *ca.* 4 and for a total concentration of lead(II) of 4.99×10^{-7} M (A) and 1.49×10^{-7} M (B).

As expected, Nernst equilibrium is attained much faster with the rotation of the electrode, during the application of the potential deposition E_1. For the *Y* of 5000 used in this experiment, the plateau is reached for a deposition time of 100 s with a rotation speed of 500 rpm, which is sixteen times less the time needed without the rotation of the RDE (1600 s). In both cases, a stabilized faradaic current of *ca.* 2×10^{-5} A is achieved. The small t_1 values needed to reach the equilibrium at the TMF-RDE allow the use of higher preconcentration factors, thus lowering the limit of detection (LOD) of the technique.

Comparing the performance of the TMF-RDE with that of the Hg–Ir microelectrode [3], apart from the differences in the composition of the test solution used in the set-ups of experiments (the measurements using the microelectrode were made in 0.1 M KNO_3 media, at a pH 6.1), the results reveal that shorter t_1 values are required for the film electrode to reach AGNES conditions. For a gain of 5000, the microelectrode requires a t_1 of 400 s and reaches a LOD of 3.43×10^{-8} M, while the TMF-RDE for the same *Y*, reaches a lower LOD of 7.20×10^{-9} M with a shorter t_1 (150 s) for a rotation speed of 500 rpm.

The thin mercury film electrode is considered to be morphologically characterized not as a true film, but as a collection of small mercury droplets (*cf.* Fig. 3). The increased efficiency of the TMF-RDE with respect to the Hg–Ir microelectrode is a combination of a favourable ratio accessible area over volume and to the possibility of enhancing the mass transport via rotation [1,3,13].

In this work, other experiments were performed using a rotation speed of the RDE of 1000 rpm. The results were quite similar to the ones obtained with a rotation of 500 rpm, i.e. the time needed to obtain the plateau was basically the same. Since higher rotation speeds promote the faster mechanical degradation of the TMFE, the rotation speed of 500 rpm was selected as the more adequate, being applied in the subsequent studies.

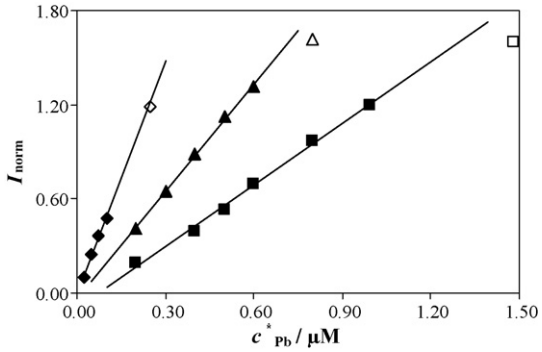


Fig. 6. Plot of I_{norm} (see Eq. (11)) *vs* the free metal concentration of lead(II) (c^*_{Pb}), for different *Y* values: 1000 (■ and □), 2000 (▲ and △) and 5000 (♦ and ◊). Full markers are related to the linear interval of concentrations and the open markers to the concentration range where the TMF-RDE stripping current deviates from the linear behaviour. The experiments were performed in 0.01 M $NaNO_3$ media, at a pH *ca.* 4. The current was measured at a t_2 of 2 ms and the deposition times used were: t_1 = 150 s for a *Y* of 5000 and t_1 = 100 s for a *Y* of 1000 and 2000. The RDE was rotated at 500 rpm.

4.4. Determination of the working concentration range for AGNES at the TMF-RDE

The proportionality between I_{norm} and c^*_{Pb} (given by Eq. (12)) on the TMF-RDE of 16 nm of thickness was evaluated. The calibration curves for three *Y* values (1000, 2000 and 5000) are displayed in Fig. 6. Before the additions of the metal to the electrolyte solution ($NaNO_3$ 0.01 M solution, pH *ca.* 4), a "synthetic blank" was made.

The interval of linearity between the faradaic current and the concentration of the free lead(II) ion clearly depends on the gain applied in the experiment. A higher gain produces higher faradaic current and as a result, the deviation to the linearity occurs at lower metal ion concentrations. Fig. 7 shows the chronoamperograms obtained in the second stage of AGNES for several concentrations of the total lead(II) and for a *Y* of 5000. The distortion in the AGNES signals for a concentration of the total lead(II) above 5×10^{-7} M is clearly seen. The anomalous stripping behaviour of Zn and Cd in AGNES experiments has been recently described in [14] and mostly attributed to a low ratio of the electroactive to background electrolyte concentrations [15]. One strategy, to avoid these distortions in the current values consists in increasing the ionic strength (provided this change or selection is allowed in the specific study undertaken, e.g. in many titrations of humic acids with metals). Alternatively, one can use the stripped charge (by integration of the stripping current all along the second stage) as response function, thus, increasing the range of linearity of the response function with the reduced metal concentration quite close to the saturation conditions.

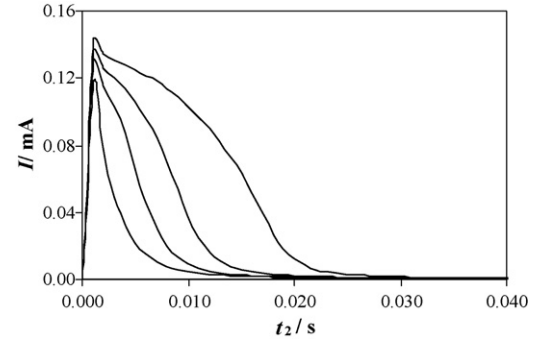


Fig. 7. Stripping signals along the first 40 ms of the AGNES second stage after reaching a *Y* of 5000. The concentrations of the total lead(II) used are (from lower curves to upper curves): 1.0×10^{-7} M, 5.0×10^{-7} M, 9.9×10^{-7} M and 20×10^{-7} M.

Table 1
Maximum workable concentration ($c_{Pb\,max}$) values and the corresponding LOD and calibration data (h_{eff} and *r*) for three gains at the 16 nm thick TMFE (plots presented in Fig. 6) for a rotation speed of 500 rpm.

Y	$c_{Pb\,max}$ (M)	Calibration data		LOD (M)
		h_{eff} (M^{-1})	*r*	
1000	1.0×10^{-6}	1.32×10^{6}	$0.995_{(N=5)}$	7.4×10^{-8}
2000	6.0×10^{-7}	2.28×10^{6}	$0.999_{(N=6)}$	2.1×10^{-8}
5000	2.0×10^{-7}	4.97×10^{6}	$0.998_{(N=4)}$	7.2×10^{-9}

Table 1 presents the interval of operational concentration values (expressed by the total lead(II) concentration) at this ionic strength, the limit of detection (LOD) and the calibration data, i.e. the slope (the proportionality factor, h_{eff}) and the correlation coefficient (*r*).

By applying a *Y* of 1000 it is possible to work with higher concentrations, but impossible to go below 7.4×10^{-8} M of lead(II), since the metal current is mainly capacitive current. The analytical window can be lowered applying a *Y* of 5000. Though, at this preconcentration factor it is not possible to go above a total lead(II) concentration of 2.0×10^{-7} M, due to the anomalous behaviour of the stripping currents at high reduced metal concentrations (for this ionic strength), but further work could take advantage of the wider analytical window available with the charge as response function [14]. The limit of detection (LOD) of this technique at the TMFE was 7.4×10^{-8} M and 7.2×10^{-9} M for a *Y* of 1000 and 5000, respectively. Lower LOD can – in principle – be achieved increasing the preconcentration factor applied in the experiment, though – in practice – the degradation with the required increased deposition times might pose restrictions. AGNES with the TMF-RDE and the essayed selection of the preconcentration gains, has measured the free metal concentration within a wide range of metal concentrations, i.e. from 7.2×10^{-9} M to 1×10^{-6} M, depending on the chosen conditions.

The factor h_{eff}, that represents the direct proportionality between the normalized current measured and the free metal concentration (Eq. (3)), when plotted as a function of the preconcentration factor *Y*, confirms the direct proportionality between these two parameters by the linearity attained (slope = 9.13×10^2 and correlation factor: 0.9999).

4.5. AGNES for metal speciation studies

4.5.1. Labile system

Monodisperse carboxylated latex nanospheres (P(S/VCOOH)) with 40.0 nm radius constitute a good model for macromolecular and particulate binding. The interaction of lead(II) with the latex nanospheres was studied with AGNES and the values obtained were compared with the experimental values obtained at the HMDE [11]. The experiments were performed for a total concentration of lead(II) of 6.0×10^{-7} M, at ionic strength 0.01 M in $NaNO_3$, and a MES 2-(N-morpholino-ethanesulfonic acid) buffer concentration of 2.0×10^{-3} M to fix the value of the pH to 5.5 and 6.1. The experiment at the TMF-RDE was carried out using a *Y* of 5000 and 2000, a deposition time of 150 s and a rotation speed of 500 rpm. Prior to the addition of the ligand to the test solution, the calibration plots for both preconcentration factors were obtained (pH *ca.* 4), see Table 2.

To compare with existing literature, we have computed the conditional stability constant as

$$K = \frac{c_{ML}}{c_M c_L} = \frac{c_{M,t} - c_M}{c_M(c_{L,t} - c_{M,t} + c_M)} \quad (14)$$

(i.e. by assuming that M only forms the complex ML with L, and neglecting other forms of species M and L, such as $PbNO_3^+$). We include these retrieved values of *K* in the last column of Table 2.

Table 2
Values of the logarithm of the free metal ion concentration and bulk stability constant value obtained for two measurements for the lead(II)–latex nanospheres (40 nm radius latex and 0.08 and 0.1%, w/w) at the TMF-RDE. Total concentration of lead(II) 6.0×10^{-7} M.

pH	Y	c_L (M)	$\log c_M^*$	$\log K$
5.51	5000	1.6×10^{-5}	−6.56	4.77
6.12	5000	1.6×10^{-5}	−7.06	5.46
5.50	2000	1.8×10^{-5}	−6.59	4.87
6.12	5000	1.8×10^{-5}	−7.00	5.37

Table 3
Values of the logarithm of the free metal ion concentration and bulk stability constant value obtained for the lead(II)–IDA system for N measurements at the TMF-RDE. Total concentration of lead(II) 2.49×10^{-7} M.

c_L (M)	N	$\log c_M^*$	$\log K$
2.5×10^{-5}	2	−6.75	8.63
4.9×10^{-5}	2	−6.86	8.62
9.8×10^{-5}	2	−7.00	8.58
2.5×10^{-4}	1	−7.54	8.63

The calculated values perfectly agree with the values of [4.9–5.0] and [5.3–5.6] for pH 5.6 and 6.1, respectively, obtained with the HMDE by Domingos et al. [11].

4.5.2. Quasi-labile system

The interaction of lead(II) with iminodiacetic acid (IDA) was studied with AGNES at the TMFE. In order to assess this, a titration was performed by adding different concentrations of IDA to a test solution, containing a total concentration of lead(II) of 2.49×10^{-7} M and a MES 2-(N-morpholino-ethanesulfonic acid) buffer concentration of 2.0×10^{-3} M to fix the value of the pH to 5.5. The experiment was performed using a Y of 5000 and the other AGNES parameters (deposition time and rotation speed of the RDE) were the same as in Section 4.5.1. The results are presented in Table 3.

For the Pb–IDA system, the values obtained for $\log K$, mean value of 8.61 ± 0.06 for 0.01 mol dm^{-3} ionic strength, are in reasonable agreement with the $\log K$ value of 8.48 dm^3 mol^{-1} computed with Davies correction from the reported value in references [16,17]. However, one obtains an average $\log K$ value 8.1 from works reported in MiniSCD where Davies correction [18–20] is applicable.

5. Conclusions

The free metal determination with AGNES using a TMF-RDE has been implemented. The thickness of the film (16 nm) and the rotation of the electrode (500 rpm) have been optimized, as well as the parameters of AGNES technique (deposition time, gain and reoxidation measuring time). A specific mathematical treatment (*cf.* Section 4.1.2 and Eq. (12)) has also been developed to take into account the degradation suffered with time and stirring with this kind of film electrodes.

Lower LOD, in comparison with the conventional dropping mercury electrode or the Ir–Hg microelectrode, can be attained with this electrode for comparable times. Special care has to be taken to avoid anomalous stripping currents for higher metal ion concentrations (relative to the background electrolyte) which lead to a loss of linearity in the calibration plot. The measurement of the charge is expected, in further work, to allow access to higher concentrations.

Good results have also been obtained with TMF-RDE when performing speciation determinations. The free metal concentration, and, thus, the conditional stability constants, determined with AGNES for the two systems considered (the complexation of Pb(II) with monodisperse carboxylated latex nanospheres and the complexation of Pb(II) with iminodiacetic acid (IDA), are in reasonable agreement with values reported previously.

Acknowledgments

Thanks are due to University of Aveiro and Fundacão para a Ciência e a Tecnologia (FCT) project POCI/AMB/55939/2004. Luciana Rocha acknowledges FCT, for a PhD grant. Financial support by the Spanish Ministry of Education and Science (Projects CTQ2006-14385) and from the "Comissionat per a Universitats i Recerca del Departament d'Innovació, Universitats i Empresa de la Generalitat de Catalunya" is acknowledged. JPP acknowledges financial support from IBB/CBME, LA, FEDER/POCI 2010.

References

[1] J. Galceran, E. Companys, J. Puy, J. Cecilia, J.L. Garces, J. Electroanal. Chem. 566 (2004) 95–109.
[2] E. Companys, J. Cecília, G. Codina, J. Puy, J. Galceran, J. Electroanal. Chem. 576 (2005) 21–32.
[3] C. Huidobro, E. Companys, J. Puy, J. Galceran, J.P. Pinheiro, J. Electroanal. Chem. (2007) 134–140.
[4] L.S. Rocha, H.M. Carapuça, J.P. Pinheiro, J. Electroanal. Chem. 610 (2007) 37–45.
[5] S.C.C. Monterroso, H.M. Carapuça, A.C. Duarte, Electroanalysis 15 (2003) 1878–1883.
[6] J. Galceran, C. Huidobro, E. Companys, G. Alberti, Talanta 71 (2007) 1795–1803.
[7] S.C.C. Monterroso, H.M. Carapuça, J.E.J. Simões, A.C. Duarte, Anal. Chim. Acta 503 (2004) 203.
[8] L.S. Rocha, H.M. Carapuça, J.P. Pinheiro, Langmuir 22 (2006) 8241–8247.
[9] E. Companys, J. Puy, J. Galceran, J. Environ. Chem. 4 (2007) 347–354.
[10] G. Alberti, R. Biesuz, C. Huidobro, E. Companys, J. Puy, J. Galceran, Anal. Chim. Acta 599 (2007) 41–50.
[11] R.F. Domingos, C. Huidobro, E. Companys, J. Galceran, J. Puy, J.P. Pinheiro, J. Electroanal. Chem. 617 (2008) 141–148.
[12] E. Companys, M. Naval-Sánchez, N. Martínez-Micaelo, J. Puy, J. Galceran, J. Agric. Food Chem. 56 (2008) 8296–8302.
[13] A.J. Bard, L.R. Faulkner, Electrochemical Methods—Fundamental and Applications, second ed., Wiley, 2001 (Chapter 11–12).
[14] J. Galceran, et al., J. Electroanal. Chem. (2009), doi:10.1016/j.jelechem.2009.10.008.
[15] J.G. Limon-Petersen, I. Streeter, N.V. Rees, R.G. Compton, J. Phys. Chem. C 112/44 (2008) 17175–17182.
[16] J. Ambrose, A. Covington, H. Thirsk, Trans. Faraday Soc. 65 (1969) 1897–1905.
[17] Academic Software, K.J. Poweel, Mini-SCDatabase, Academic Software, UK, 2005.
[18] J. Felcman, J.J.R. Fraústo da Silva, Talanta 30 (1983) 565–570.
[19] J. Ambrose, A.K. Covington, H.R. Thirsk, Trans. Faraday Soc. 65 (1969) 1897–1905.
[20] G. Atkinson, J.E. Bauman Jr., Inorg. Chem. 2 (1963) 64–67.

Talanta 80 (2010) 1888–1893

Contents lists available at ScienceDirect

Talanta

journal homepage: www.elsevier.com/locate/talanta

Improving detection limits for organotin compounds in several matrix water samples by derivatization-headspace-solid-phase microextraction and GC–MS

L. Segovia-Martínez[a], A. Bouzas-Blanco[a], P. Campíns-Falcó[b,*], A. Seco-Torrecillas[a]

[a] Dpto. Ingeniería Química, Universidad de Valencia, Doctor Moliner 50, 46100 Burjassot, Valencia, Spain
[b] Dpto. Química Analítica, Universidad de Valencia, Doctor Moliner 50, 46100 Burjassot, Valencia, Spain

ARTICLE INFO

Article history:
Received 26 June 2009
Received in revised form 14 October 2009
Accepted 18 October 2009
Available online 24 October 2009

Keywords:
Gas chromatography
Mass detection
Headspace solid-phase-microextraction
Ethylation
Organotin compounds

ABSTRACT

Triethyltin, tributyltin, diphenyltin and triphenyltin were selected as model compounds. The method is based on in situ ethylation and simultaneous headspace-solid-phase microextraction (HS-SPME) and gas chromatographic-mass spectrometry analysis (GC–MS). The extraction procedure was optimized studying some variables such as reaction time, salinity, sample volume and headspace volume. SPME–GC–MS and SPME–GC–FID techniques were compared; quality assurance parameters such as sensitivity, selectivity and precision were established. The proposed procedure showed limits of detection between 0.025 and 1 ng/L. The linearity was in the 0.025–5000 ng/L range. The precision expressed as relative standard deviations (RSD), were below 20%. Real wastewaters and seawaters were analyzed. The method permits controlling legislated annual average values.

© 2009 Elsevier B.V. All rights reserved.

1. Introduction

In the 1980s, organotin compounds were recognized for the first time as being responsible of very serious environmental contamination, and consequently the European Union listed them as priority pollutants. The Directive 2000/60/EC (Water Framework Directive, WFD) is probably the most significant international legislation to be introduced in the field of water from many years [1]. WFD includes and protects different kinds of water in Europe (surface water, subterranean, transitional and coastal) with the aim to achieve and ensure a good quality for all of them. WFD includes as a priority and hazardous substance the tributyl compounds among others substances. Furthermore, Directive 2008/105/EC lays down environmental quality standards (EQS) for priority substances and certain other pollutants as provided for in WFD. The Directive 2008/105/EC establishes the extent permitted of tributyl compounds (tributyltin-cation) in inland and other surface waters, expressed as an annual average value (0.0002 μg/L) or as maximum allowable concentration (0.0015 μg/L).

Organotin compounds have been extensively used in recent decades. Several monoalkyl tins have been used as PVC stabilizers, catalysts, water repellents and fire retardants. Some dialkyl tins have been used as catalysts, stabilizers against heat and light effects in construction industry, anthelmintics in poultry management, insecticides for sheep and cattle and for packaging of food, beverages, pharmaceuticals and cosmetics. Trialkyl tins have been used as biocides in marine antifouling paints, fungicides, insecticides, mosquito larvicides, wood preservatives and industrial circulation water disinfectant [1,2].

Organotins toxicity is dependent on the size and number of organic groups attached to the tin atom. Trialkyltins are generally more toxic than the corresponding dialkyl or monoalkyl derivatives. Within the trialkyltin compounds, the lower homologues, triethyltin and trimethyltin, have the greatest acute toxicity. Various dialkyltin and trialkyltin compounds have an immunotoxic effect. Tributyltin is particularly toxic in gastropods and molluscs. It can produce chronic toxic effects on oysters (shell deformation), mussels (growth inhibition) and marine gastropods (sterilization of females) [3,4].

Analytical methods for organotin compounds determination wearing in mind WFD must be highly sensitive. Determination of trace organotins in water requires the combination of a separation method, usually gas chromatography (GC) or liquid chromatography (LC), coupled with highly selective and sensitive detectors, such as mass spectrometry [5–9], atomic absorption spectrometry [10], flame photometry [11–13] and flame ionization detection [14,15].

Solid phase microextraction (SPME) was developed as a useful alternative to liquid–liquid extraction (LLE) [16,17] or solid phase extraction (SPE), as it reduces extraction time, and no organic solvent is necessary. This technique is based on equilibrium between

* Corresponding author.
E-mail addresses: laura.segovia@uv.es (L. Segovia-Martínez), alberto.bouzas@uv.es (A. Bouzas-Blanco), pilar.campins@uv.es (P. Campíns-Falcó), aurora.seco@uv.es (A. Seco-Torrecillas).

0039-9140/$ – see front matter © 2009 Elsevier B.V. All rights reserved.
doi:10.1016/j.talanta.2009.10.039

Table 1
Selected methods for speciation of organotin compounds in water.

Compound	LOD (ng/L)	Pre-treated procedure	Technique	Derivatizing reagent	Total analysis time (min)[a]	Sample volume (mL)	Reference
TET	48.8	SPME	GC–FID	STEB	30	20	16
TBT	0.5	SPME	GC–MS	STEB	45	5	6
	7–29	LLE	GC–HRMS	STEB	90	100	8
	4	SPME	GC–FPD	STEB	60	100	12
	4	SPME	GC–FPD	STEB	60	100	12
	17.5	HS-SPME	GC–PFPD	STEB	50	80	14
	2500	SPME	GC–FID	STEB	30	18	16
	0.525	HS-SPME	GC–AED	STEB	40	40	23
	0.55	HS-SPME	GC–AED	STPB	40	40	23
DPT	7–29	LLE	GC–HRMS	STEB	90	100	8
	2	SPME	GC–FPD	STEB	60	100	12
	7	SPME	GC–FPD	STEB	60	100	12
	26.37	HS-SPME	GC–PFPD	STEB	50	80	14
	0.465	HS-SPME	GC–AED	STEB	40	40	23
	0.44	HS-SPME	GC–AED	STPB	40	40	23
TPT	7–29	SPME	GC–MS	STEB	45	5	6
	4.6	LLE	GC–HRMS	STEB	90	100	8
	3	SPME	GC–FPD	STEB	60	100	12
	11	SPME	GC–FPD	STEB	60	100	12
	0.125	SPME	GC–ICPMS	STEB	45	40	21
	0.63	HS-SPME	GC–AED	STEB	40	40	23
	0.39	HS-SPME	GC–AED	STPB	40	40	23

[a] Estimated value. STEB: sodium tetraethyl borate. STPB: sodium tetrapropyl borate.

the analyte concentration in the solution matrix and that in the solid-phase fibre; the fibre is coated generally with a polymeric organic stationary phase. SPME has been used to extract organotins from water samples [18] and from sediments [19]. The SPME sampling can be carried out in direct mode, immersed in liquid or in the headspace mode [13].

Organotins due to its low volatility need to be derivatized before being injected into the gas chromatograph. The methods of derivatization used include hydride generation with sodium borohydrate [12] or alkylation by Grignard reagent [20]. These methods have been used for long time, however, requires a strictly aprotic medium for the derivatization [21]. In the last years sodium tetraethylborate [11,13] or sodium tetrapropylborate (STPB) [21–23] have been used. These compounds can be used directly in aqueous phase. Derivatization with sodium tetraethylborate (STEB) converts ionic organotins compound into non-polar volatile derivates in situ, removing the problems associated with extracting ionic compounds into an organic solvent from an aqueous matrix. In Table 1 several analytical studies about organotins analysis by using STEB and STPB are compared, any method used HS-SPME–GC–MS for water analysis. Any method could detect TBT at the legislated annual average concentration.

The aim of this work was to develop a cost-effective method to detect in several water matrices the organotins compounds at the levels required by the legislation. HS-SPME–GC–MS is the best option as this manuscript demonstrates. Figures of merit were established and some samples of wastewater and seawaters were analyzed by the optimized HS-SPME–GC–MS procedure to test the reliability of the method.

2. Experimental

2.1. Reagents and solutions

All the reagents were of analytical grade, Triethyltin bromide (TET, 97% purity), tributyltin chloride (TBT, 96% purity), diphenyltin dichloride (DPT, 96% purity), triphenyltin chloride (TPT, 97% purity) and sodium tetraethylborate (STEB, 97% purity) were purchased from Sigma–Aldrich (Steinheim, Germany). Sodium chloride and sodium acetate were obtained from VWR International Eurolab (Barcelona, Spain).

Individual standard solutions of the organotins (200 mg/L) were prepared in methanol and more diluted aqueous solutions were prepared from the most concentrated solutions. Methanol was of spectrophotometric grade (Sigma–Aldrich, St. Louis, MO, USA) and pure water was obtained by means of a Milli-Q water purification system (Millipore).

A 2% (w/v) aqueous solution of STEB was used for derivatization. STEB was kept in desiccators into a glove bag under dry nitrogen and was always manipulated in the glove bag inside of an extractor hood. The STEB solution was prepared every day taking certain amount of reagent and adding the necessary volume of pure water into a dark and sealed vial.

Sodium chloride solutions and sodium acetate buffer solution were used to adjust the salinity and the pH in the derivatization process. The buffer solution was prepared by dissolving the necessary amount of sodium acetate in pure water to get 0.1 M concentration and then adding acetic acid (98% purity) to adjust the pH to 5. Solutions were kept in darkness at 5 °C.

2.2. Apparatus and chromatographic conditions

Analysis by GC–FID was performed with a gas chromatographic system (Agilent Tecnologies 6890N, Palo Alto, CA, USA) coupled with a flame ionization detector and operated by the Chemstation Software (Agilent Tecnologies).

Analysis by GC–MS was conducted using a mass spectrometer (Agilent Tecnologies 5973 inert), a gas chromatograph (Agilent Tecnologies 6890N) and a split/splitless injection port and operated by MSD Chemstation Software (Agilent Tecnologies).

A 30 m × 0.250 mm i.d. capillary column HP-5MS (Agilent Tecnologies) with a stationary phase with a thickness of 0.25 μm was used for analytes separation in both systems. The carrier gas was helium.

Both gas chromatographs were operated in splitless mode and the injection port temperature was held isothermally at 260 °C. The temperature program used was as follows: initial temperature of 50 °C, 15 °C/min to 190 °C, 10 °C/min to 240 °C, 30 °C/min to 290 °C, held for 4 min, for a total run time of 19 min.

A SPME holder with replaceable extraction fibres was used for extraction of organotin compounds from water samples. The fibre used in the study was coated with 100 μm thickness polydimethyl-

siloxane (PDMS). The SPME holder and the fibres were obtained from Supelco (Bellefonte, PA, USA). A magnetic stirrer and stir bars (VWR International Eurolab) were used for the extraction.

2.3. Extraction procedures

The GC–FID system was used for optimizing variables. In all assays, the fibre was introduced in the headspace of a glass vial containing the standard samples of the organotins. Afterwards, the SPME device was placed into the GC interface and the organotins were desorbed from the fibre under static mode during 2 min.

Sodium chloride concentration was changed from 0% to 7% (w/v) of salt. The volume of STEB 2% (w/v) solution assayed was 0.3 mL and 1 mL. The derivatization time (i.e., time since the STEB was added until the fibre was introduced in the chromatograph inlet port) was varied between 15 and 60 min. 30 and 45 min were also assayed by using MS detection.

The sample volume was optimized testing both miniaturized (2.54 mL) and normal volumes (12.7 mL) using different total volumes (2.8 and 14 mL, respectively) and different vial sizes (5 mL and 22 mL, respectively). The headspace volume was tested for 22 mL vial size employing 14 mL and 7 mL of mixture solution. Higher volumes of mixture solution cannot be tested considering the SPME device.

All the experiments were performed in duplicate at ambient temperature.

2.4. Analytical performance

The retention times of all organotins were determined using aqueous standard solutions up to 150 μg/L of each organotin for the SPME–GC–FID system and aqueous standard solutions up to 50 ng/L of each organotin for the SPME–GC–MS system. The mass spectrums were obtained at a mass ratio scan range from 100 to 400 m/z to determine the appropriate masses for selected ion monitoring (SIM). SIM mode was used for quantification.

Solutions of 1, 2 and 5 μg/L for TPT; 0.1, 0.5, 1, 2 and 5 μg/L for TET, TBT and DPT were prepared for detection limits determination in the SPME–GC–FID system. Solutions of 0.5, 1, 2, and 5 ng/L for TET and TPT; 0.025, 0.05, 0.1, 0.25, and 0.5 ng/L for TBT and DPT were prepared to calculate detection limits in the SPME–GC–MS system.

Linearity and precision were determined in SPME–GC–FID system using solutions of 1, 5, 10 and 15 μg/L of TET, TBT and DPT, and solutions of 10, 15, 30 and 40 μg/L of TPT. Moreover, in SPME–GC–MS system, linearity and precision were determined using solutions between 5 and 5000 ng/L for TET and TPT and solutions between 1 and 5000 ng/L for TBT and TPT.

2.5. Analysis of real water samples

Wastewater samples and seawater samples were use to validate the developed methods. Grab wastewater samples were collected at 7 wastewater treatment plants effluents located in close proximity to the Comunidad Valenciana coast (East of Spain). Seawater samples were collected at 24 different geographical sites along the Comunidad Valenciana coast. Samples were introduced into amber bottles and kept in the fridge at 4 °C till the analysis. Each sample was analyzed in duplicate at all assays were carried out at ambient temperature.

Real sample analysis was carried out with 12.7 mL of water sample in a 22 mL vial. Then, 1 mL of acetate buffer and 0.3 mL of STEB were added into the vial and finally the sample was extracted in headspace for 45 min with constant stirring. Wastewater and seawater samples were analyzed by SPME–GC–MS. The found concentration is always characterized by the expanded uncertainty ($K = 2$) estimated with EURACHEM/CITAC Guide Quantifying Uncertainty in Analytical Measurement [24].

3. Results and discussion

3.1. Optimization of the extraction process

Fig. 1 shows the salinity effect employing normalized chromatographic signals for each compound. For all organotins studied, the signal percentage steeply decreases with salt concentration increase. The sodium chloride addition in the standard solution, within the 0–7% (w/v) range, revealed that the salinity negatively affects the analyte extraction efficiency. Therefore, the salt addition is not advisable. However, a final sodium chloride concentration of 3.3% (w/v), similar to that of Mediterranean waters, was used in the standards when this kind of samples was processed.

The variation of the STEB volume added did not produce any improvement in the extraction efficiency (data not shown), achieving the same results for the two volumes studied (a t-test was applied and no significant value was obtained at 95% confidence level). Therefore, it seems more suitable to work with the lower amount in order to optimize the cost of the procedure (see experimental section). The use of STEB could generate tetraethyltin, affecting on the analysis of TET [22]. Nevertheless, this possible interference in TET analysis was not observed in this study.

Standard solutions containing a mixture of the organotins evaluated (15 μg/L of each compound, wearing in mind that the detector used was FID) were prepared in a 22 mL vial as follows: 12.7 mL of water, 1 mL of acetate buffer, 0.3 mL of STEB, 0.5 g of sodium chloride for sea water and the necessary amount of the organotin concentrated solutions (no correction volume was necessary). Samples were extracted during 15, 30, 45 and 60 min in order to get the optimum reaction time. The extraction started in headspace just after adding the STEB and with constant stirring (750 rpm) due to liquid sample agitation improves the kinetics of the derivatizing reaction and the analytes transport towards the fibre [19]. As Fig. 2 shows, the optimum reaction time changes for each compound. The signal increases with the reaction time for TET, DPT and TPT but not for TBT, for which the signal drops off after reaching an optimum at 30 min. The same pattern was obtained for all derivatives by employing smaller concentrations by use of MS detection (30 and 45 min were tested). The reasons for TBT-derivative behaviour could be mainly explained by its affinity by the fibre and its stability. Finally, within the time range considered, a 45 min value was considered as optimum reaction time for further work.

Other sample volume was assayed in order to minimize reagents and sample consumptions: in a 5 mL vial were placed 2.54 mL of water, 0.2 mL of acetate buffer, 0.06 mL of STEB, and the necessary

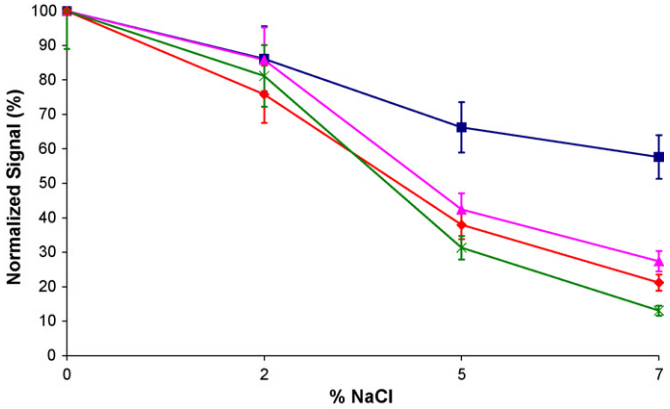


Fig. 1. Effect of salinity in the GC–FID system. TET (■), TBT (▲), DPT (♦) and TPT (×).

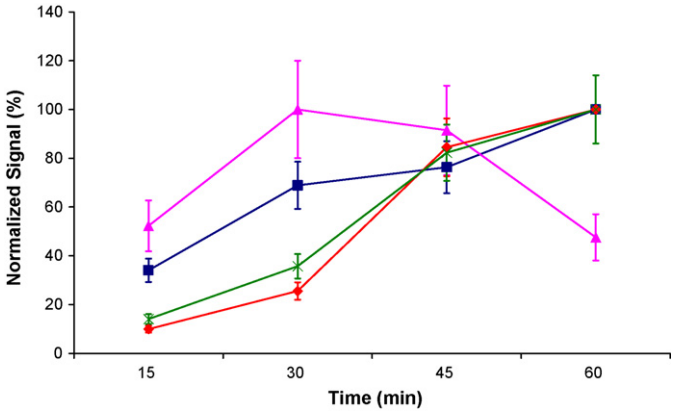


Fig. 2. Effect of reaction time between analytes and STEB. TET (■), TBT (▲), DPT (♦) and TPT (×).

amount of standard solution (no correction volume was necessary) in order to get 15 μg/L concentration for each organotin being the final volume 2.8 mL. Similar signals than those obtained with 22 mL vials were achieved. Then, if necessary less volume of sample could be used.

Regarding headspace volume optimization, two solutions volumes were prepared in a 22 mL vial size: a 14 mL solution (maximum volume of mixture solution permitted considering SPME device and consequently minimum headspace volume) was prepared adding, 12.7 mL of water, 1 mL of acetate buffer, 0.3 mL of STEB and the necessary amount of standard solution in order to get a concentration of 15 μg/L (of each organotin); and a 7 mL solution adding, 6.35 mL of water, 0.5 mL of acetate buffer, 0.15 mL of STEB, 0.2 g of sodium chloride for sea water and the necessary standard solution so to get 15 μg/L concentration (of each organotin). Once the solutions were prepared, the fibre was exposed in the headspace solution during 45 min. Higher analytical signals were obtained with the smallest headspace volume of 8 mL assayed

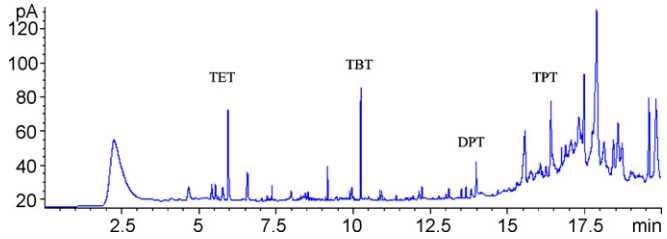


Fig. 3. FID chromatogram for a solution containing 15 μg/L of each organotin.

considering the response for all organotins tested, being the preconcentration factor the highest one.

3.2. Analytical parameters

Fig. 3 shows an organotins chromatogram in the optimized conditions by use FID detection. Figures of merit achieved from this detector are given in Table 2. The detection and quantification limits were determined experimentally as the lowest concentration giving a chromatographic peak three times the signal/noise ratio and ten times the signal/noise ratio, respectively. The detection limits in the GC–FID system are above the environmental quality standards established for TBT by Directive 2008/105/EC.

The first study undertook with the GC–MS system was in full scan mode in order to find the characteristic ions and the abundance of each organotin (Fig. 4). The mass spectra obtained were similar to mass spectra showed by NIST library [25]. Each organotin had different number of characteristic ions depending on its structure. TBT showed more fragmentation than TET since its molecule is bigger and it is more easily fragmented than DPT or TPT.

Selected quantification ions were chosen for each organotin and other characteristic ions were also selected in order to identify each compound. Table 3 shows quantification and identification ions used for the studied organotins.

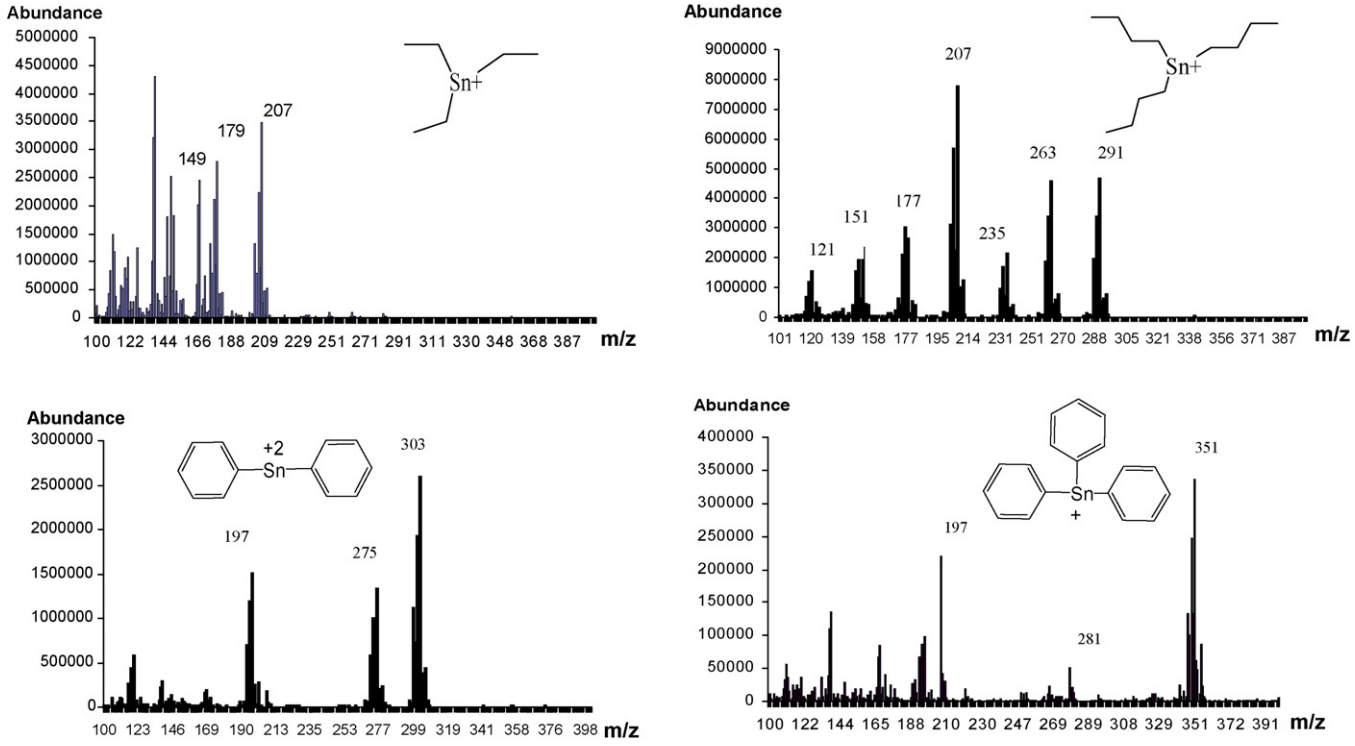


Fig. 4. Mass spectra for TET, TBT, DPT and TPT in scan mode at 10 μg/L.

Table 2
SPME–GC–FID analytical parameters.

Compound	LODs (μg/L)	$b_0 \pm s_0$ (μg/L)	$b_1 \pm s_1$ (μg/L)	r^2	RSD (%)
TET	0.1	7 ± 7	6.9 ± 0.8	0.9756	8
TBT	0.1	4 ± 9	11.2 ± 0.9	0.9860	9
DPT	0.1	−4 ± 9	5.1 ± 0.3	0.9918	4
TPT	1	−6 ± 8	6.1 ± 0.5	0.9961	12

LOD: detection limits. b_0 and b_1: parameters of calibration curve *peak area* vs *concentration*. r^2: determination coefficient. RSD: relative standard deviation for 10 μg/L ($n = 3$).

Table 3
Quantification and characteristics ions of the analyzed compounds.

Compound	Quantification ion	Chemical formula	Characteristic ions	Chemical formula
TET	179	$SnEt_2H$	149	$SnEtH_2$
			207	$SnEt_3$
TBT	291	$SnBu_3$	121	SnH_3
			151	$SnEtH_2$
			177	$SnBuH_2$
			207	SnEtBuH
			235	$SnEt_2Bu$
			263	$SnEtBu_2$
DPT	303	$SnEtPh_2$	197	SnPhH
			275	$SnPh_2H$
TPT	351	$SnPh_3$	197	SnPhH
			281	$SnEt_3Ph$

Table 4
SPME–GC–MS analytical parameters.

Compound	LODs (ng/L)	$b_0 \pm s_0$ (μg/L)	$b_1 \pm s_1$ (μg/L)	r^2	RSD (%)
TET	1	$(3 \pm 3) \times 10^5$	$(5.6 \pm 0.1) \times 10^6$	0.9967	11
TBT	0.025	$(4 \pm 4) \times 10^4$	$(2.3 \pm 0.1) \times 10^6$	0.9940	9
DPT	0.025	$(3 \pm 5) \times 10^4$	$(1.0 \pm 0.1) \times 10^6$	0.9831	20
TPT	0.5	$(1 \pm 1) \times 10^4$	$(0.5 \pm 0.1) \times 10^6$	0.9971	12

LOD: detection limits. b_0 and b_1: parameters of calibration curve *peak area* vs *concentration*. r^2: determination coefficient. RSD: relative standard deviation for 5 ng/L ($n = 3$).

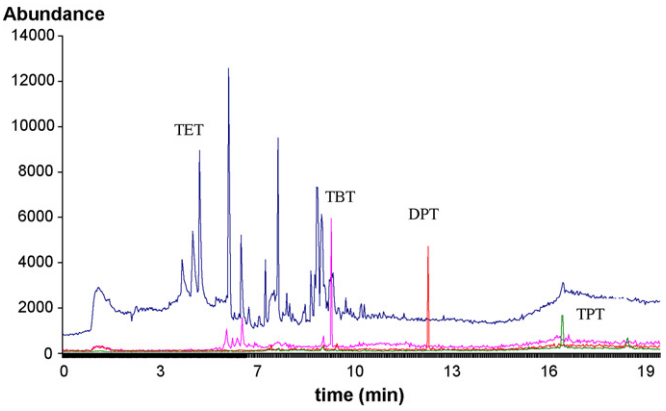


Fig. 5. Selected ion monitoring for studied organotins at 5 ng/L for TET, TBT and DPT and at 10 ng/L for TPT. See Table 3.

The SIM mode analysis was used to determine the quality assurance parameters such as detection and quantification limits, precision and linearity. All determinations were carried out in the optimized conditions: 3.3% of salinity (for sea water), 0.3 mL of STEB, 45 min for extraction, 14 mL of solution and 22 mL total volume vials. Fig. 5 shows the chromatograms obtained in the SIM mode for each compound and Table 4 the figures of merit obtained.

The detection and quantification limits were determined as described for the GC–FID. The detection limits in the GC–MS system are quite lower than the environmental quality standards established for TBT by Directive 2008/105/EC.

3.3. Real samples

The accuracy of method was evaluated by analyzing fortified seawater and wastewater samples. The obtained recoveries were 90 ± 20 ($n = 12$) being independent of the organotin assayed.

Wastewater sample analysis revealed the presence of DPT at detection limit level in two samples. Detection of DPT in wastewater could be derived from its use as plasticizer.

The analysis of seawater samples revealed the presence of DPT and TBT. DPT was detected and quantified in one sample, reaching a concentration of 0.14 ± 0.04 ng/L. TBT was found at detection limit level in 11 samples. Moreover, TBT was detected and quantified in a sample grabbed in close proximity to a harbour. The TBT concentration in this sample was 1.3 ± 0.3 ng/L. This value is below the maximum allowable concentration permitted by Directive 2008/105/EC but is above the annual average value permitted. Hence, periodical sampling campaigns should be needed in order to evaluate, in the long term, the water chemical status regarding TBT.

4. Conclusions

The HS-SPME–GC–MS method is a cost-effective method with adequate figures of merit for the study of the presence of organotins in environmental water samples. The detection limits achieved with the proposed method are far below of concentration levels established in Application of EU Water Framework Directive (DMA 2000/60/EC).

The proposed method allows detect organotin compounds in water samples at concentration of pg/L with low sample volume (12.7 or even 2.54 mL) compared with those required by other methods (see Table 1). The method also avoids the use of organic solvents for the treatment of the sample. Table 1 shows that this method offers the best detection limits with the less time and volume for all studied organotins.

Acknowledgments

This research was financially supported by The Government of the Region of Valencia (Generalitat Valenciana), within the research project "Application of EU Water Framework Directive 2000/60/EC on endocrine disrupters and other priority substances in coastal areas in the Region of Valencia". Also the project CTQ2008-01329/BQU financially supported by Ministerio de Educación y Ciencia of the Spanish Government has contributed.

References

[1] M. Coquery, A. Morin, A. Bécue, B. Lepot, TRAC 24 (2005) 117.
[2] K.M. Attar, Appl. Organometal. Chem. 10 (1996) 317.
[3] D.S. Forsyth, B. Jay, Appl. Organometal. Chem. 11 (1997) 551.
[4] B. Atinzar-Ladislao, Environ. Int. 34 (2008) 292.
[5] R.M. Cristòfol, S. Gassó, Toxicol. Lett. 152 (2004) 35.
[6] Chi-Chi Chou, Maw-Rong Lee, J. Chromatogr. A 1064 (2005) 1.
[7] S. White, T. Catterick, B. Fairman, K. Webb, J. Chromatogr. A 794 (1998) 211.
[8] M.G. Ikonomou, M.P. Fernández, T. He, D. Cullon, J. Chromatogr. A 975 (2002) 319.
[9] G. Lawson, R.H. Dahm, N. Oslah, E.D. Woodland, Appl. Organometal. Chem. 10 (1996) 125.
[10] V. Kaur, A.K. Malik, N. Verma, J. Sep. Sci. 29 (2006) 333.
[11] G. Lespes, V. Desauziers, C. Montigny, M. Potin-Gautier, J. Chromatogr. A 826 (1998) 67.
[12] G.B. Jiang, F.Z. Xu, Fresenius J. Anal. Chem. 363 (1999) 256.
[13] M. Le Gac, G. Lespes, M. Potin-Gautier, J. Chromatogr. A 999 (2003) 123.
[14] I. Arambarri, R. Garcia, E. Millan, Chemosphere 51 (2003) 643.
[15] E. Millán, J. Pawliszyn, J. Chromatogr. A 873 (2000) 63.
[16] M. Bravo, G. Lespes, I. De Gregori, H. Pinochet, M. Potin-Gautier, J. Chromatogr. A 1046 (2004) 217.
[17] E. Cukrowska, L. Chimuka, H. Nsengimana, V. Kwaramba, Anal. Chim. Acta 523 (2004) 141.
[18] M. Guidotti, M. Vitali, Ann. Chim. 87 (1997) 497.
[19] P.N. Carvalho, L.F. Pinto, M.C.P. Basto, M.T.S.D. Vasconcelos, Microchem. J 87 (2007) 147.
[20] S. Rapsomanikis, Analyst 119 (1994) 1429.
[21] M. Crnoja, C. Haberhauer-Troyer, E. Rosenberg, M. Grasserbauer, J. Anal. At. Spectrom. 16 (2001) 1160.
[22] P. Schubert, E. Rosenberg, Fresenius J. Anal. Chem. 366 (2000) 356.
[23] T. Gorecki, J. Pawliszyn, Anal. Chem. 68 (1996) 3008.
[24] S.L.R. Ellison, M. Rösslein, A. Williams, Guide Quantifying Uncertainty in Analytical Measurement, second ed., EURACHEM/CITA, Berlin, 2000.
[25] M.A. Belkin, L.K. Olson, J.A. Caruso, J. Anal. At. Spectrom. 12 (1997) 1255.

Talanta 80 (2010) 1894–1898

Contents lists available at ScienceDirect

Talanta

journal homepage: www.elsevier.com/locate/talanta

Sample cleanup-free determination of mycophenolic acid and its glucuronide in serum and plasma using the novel technology of ultra-performance liquid chromatography–electrospray ionization tandem mass spectrometry

Joachim Kuhn*, Christian Götting, Knut Kleesiek

Institut für Laboratoriums- und Transfusionsmedizin, Herz- und Diabeteszentrum Nordrhein-Westfalen, Universitätsklinik der Ruhr-Universität Bochum, Georgstraße 11, 32545 Bad Oeynhausen, Germany

ARTICLE INFO

Article history:
Received 29 June 2009
Received in revised form 7 October 2009
Accepted 18 October 2009
Available online 24 October 2009

Keywords:
Mycophenolic acid
Mycophenolic acid glucuronide
Ultra-performance liquid chromatography
Electrospray ionization tandem mass spectrometry

ABSTRACT

Mycophenolic acid (MPA) is an immunosuppressant drug which powerfully inhibits lymphocyte proliferation. Since the early 1990s it has been used to prevent rejection in organ transplantation. The requirement of therapeutic drug monitoring shown in previous studies raises the necessity of acquiring accurate and sensitive methods to measure MPA and its major metabolite mycophenolic acid glucuronide (MPAG).

The authors developed a sample cleanup-free, rapid, and highly specific method for simultaneous measurement of MPA and MPAG in human plasma and serum using the novel technology of ultra-performance liquid chromatography–electrospray ionization tandem mass spectrometry. MPA- and MPAG-determinations were performed during a 2.0-min run time. Multiple calibration curves for the analysis of MPA and MPAG exhibited consistent linearity and reproducibility in the range of 0.05–100 ($r > 0.999$) mg L^{-1} and 4–4000 mg L^{-1} ($r > 0.999$), respectively. Limits of Detection were 0.014 mg L^{-1} for MPA and 1.85 mg L^{-1} for MPAG. Lower Limits of Quantification were 0.05 mg L^{-1} for MPA and 2.30 mg L^{-1} for MPAG. Interassay imprecision was <10% for both substances. Mean recovery was 103.6% (range 78.1–129.7%) for MPA and 111.1% (range 73.0–139.6%) for MPAG. Agreement was good for MPA and MPAG between the presented method and a validated HPLC-MS/MS method. The Passing-Bablok regression line for MPA and MPAG was HPLC-MS/MS = 1.14 UPLC-MS/MS—0.14 [mg L^{-1}], $r = 0.96$, and HPLC-MS/MS = 0.77 UPLC-MS/MS + 0.50 [mg L^{-1}], $r = 0.97$, respectively. This sample cleanup-free and robust LC-MS/MS assay facilitates the rapid, accurate and simultaneous determination of MPA and MPAG in human body fluids.

© 2009 Elsevier B.V. All rights reserved.

1. Introduction

Mycophenolic acid (MPA) is an immunosuppressant drug which is derived from the fungus *Penicillium stoloniferum*. The pharmacological effect of MPA is based on the selective inhibition of the inosine-monophosphate dehydrogenase, the enzyme that controls the synthesis rate of guanine monophosphate in the *de novo* pathway of purine synthesis used in the proliferation of T- and B-lymphocytes [1]. Therefore, MPA was used as an immunosuppressive drug after organ transplantation to prevent acute rejection of the transplant. Furthermore, MPA was increasingly used as part of a multiple-drug regime to prevent acute rejection of the transplant because the mode of action of MPA differs from that of cyclosporine, tacrolimus, and sirolimus. The large interindividual variation in the pharmacokinetic profiles for MPA, as well as the effort to achieve both increase efficacy and decrease toxicity, has promoted the monitoring of MPA concentrations [2–5]. In general, 97% of MPA is bound to albumin and more than 90% of MPA is metabolized in the liver by glucuronidation to mycophenolic acid glucuronide (MPAG), an inactive compound that is excreted in the urine and feces [5].

For the purpose of therapeutic drug monitoring (TDM) different routine assays like enzyme-multiplied immunoassay technique (EMIT), HPLC with UV-detection and liquid chromatography–tandem mass spectrometry (LC-MS/MS) have been developed to measure total MPA in blood serum or plasma [6–26]. The EMIT assay for MPA, which shows some cross-reactivity

Abbreviations: CI, confidence interval; EMIT, enzyme-multiplied immunoassay technique; ESI-MS, electrospray ionization mass spectrometry; LC-MS/MS, liquid chromatography–tandem mass spectrometry; MMF, mycophenolate mofetil; MPA, mycophenolic acid; MPAG, mycophenolic acid glucuronide; LOD, limit of detection; LLOQ, lower limit of quantification; PBR, Passing-Bablok regression; PPA, N-phthaloyl-L-phenylalanine; PPG, phenolphthalein-β-glucuronic acid; RT, room temperature; TDM, therapeutic drug monitoring; UPLC, ultra-performance liquid chromatography.

* Corresponding author. Tel.: +49 5731 971390; fax: +49 5731 972013.
E-mail address: jkuhn@hdz-nrw.de (J. Kuhn).

0039-9140/$ – see front matter © 2009 Elsevier B.V. All rights reserved.
doi:10.1016/j.talanta.2009.10.040

with acyl-MPAG and used expensive antibodies, has the advantage of being less laborious and time-consuming than chromatography technology and was therefore often used for routine drug monitoring. Using ultra-performance liquid chromatography–electrospray ionization tandem mass spectrometry (UPLC-ESI-MS/MS), we combined the advantage of both technologies and developed an assay for MPA and MPAG which not only shows high analytical sensitivity and specificity and which uses inexpensive reagents, but which also needs nearly no sample preparation and is very fast.

2. Materials and methods

2.1. Reagents, internal standards, calibrators, and quality-control samples

HPLC-grade water and methanol were purchased from Fisher Scientific GmbH (Schwerte, Germany). MPA, ammonium acetate, sodium acetate and formic acid were obtained from Sigma–Aldrich (Deisenhofen, Germany). MPAG was obtained from Analytical Services International Limited (London, UK).

To identify appropriate internal standards, eligible compounds like ascomycin, cyclosporine D, indomethacin, indole-3-butric acid, indole-3-propionic acid, napropamide, naphthalane, naproxen, N-phthaloyl-L-phenylalanine (PPA), phthalide, and phenolphthalein-β-glucuronic acid (PPG), which were obtained from Fluka (Taufkirchen, Germany), were tested.

Stock solutions of MPA, MPAG, PPA, and PPG, each at a concentration of 10 g L^{-1}, were prepared separately in acetonitrile/water (90:10) and stored at −20 °C. Internal standard solution including 5 mg L^{-1} PPA and 25 mg L^{-1} PPG was prepared by mixing 50 μL PPA stock solution, 250 μL PPG stock solution and 99.7 mL methanol/water (5:95) containing 0.1% formic acid and 2 mmol L^{-1} ammonium acetate.

Using drug-free serum or EDTA plasma, we prepared several calibrators and in-house quality-control samples as described previously [25]. In addition, commercially available calibrators and quality-control samples for MPA purchased from Chromsystems (Munich, Germany), as well as from Siemens Medicals Solutions Diagnostics (Tarrytown, NY), were used.

2.2. Serum samples

Venous blood samples from blood donors and patients were collected in EDTA sample tubes, as well as in serum monovettes from KABE Labortechnik GmbH (Nümbrecht-Elsenroth, Germany). All samples were anonymized prior to inclusion within the study.

2.3. Sample preparation for UPLC-MS/MS

Sample preparation was performed in a 1.5-mL polypropylene microcentrifuge tube. 10 μL each of EDTA plasma, serum, calibrator or quality-control sample were added to 990 μL internal standard solution (see above). After vortex-mixing for 10 s, the final solution was transferred to the autosampler vessel and 1.5 μL were injected into the UPLC-MS/MS system.

2.4. UPLC-MS/MS analysis

For measurement of MPA and MPAG, a 2.1 × 50-mm reverse phase column (Waters, Acquity UPLC BEH C8, 1.7 μm) maintained at 55 °C was used for separation by an UPLC system (Waters Acquity UPLC Basissystem) directly coupled to a Waters TQ tandem mass spectrometer fitted with Z Spray ion source. A 1.5-μL sample was injected at a flow rate of 0.35 mL min^{-1}. The gradient program was 95%/5% water/methanol containing 0.1% formic acid and 2 mmol L^{-1} ammonium acetate for 0.70 min, followed by a step gradient of 5%/95% water/methanol containing 0.1% formic acid and 2 mmol L^{-1} ammonium acetate. After additional 1.1 min, the mobile phase was reverted to the initial state, and the run was terminated at 2.0 min. The mass spectrometer was operated in electrospray positive ionization mode, and the system control and data acquisition were performed using MassLynx NT 4.1 software, with automated data processing by the MassLynx QuanLynx program provided with the instrument. Nitrogen was used as the nebulizing gas. Argon was used as the collision gas. Instrument settings were as follows: capillary voltage, 3.8 kV; source temperature, 120 °C; desolvation temperature, 400 °C; sample cone energy for MPA ammonium adduct, MPAG ammonium adduct, PPA, and PPG, 13, 20, 29, and 38 eV, respectively; and collision energy for MPA ammonium adduct, MPAG ammonium adduct, PPA, and PPG, 23, 34, 13, and 16 eV, respectively. The collision gas pressure was 3.4×10^{-3} mbar. Sample analysis was performed in the multiple reaction monitoring mode (MRM) of the instrument, with a dwell time of 0.10 s for all compounds and the mass transitions for MPA ammonium adduct, MPAG ammonium adduct, PPA, and PPG m/z 338.0 → 207.1, m/z 514.2 → 207.1, m/z 296.1 → 250.1, and m/z 495.1 → 319.1, respectively.

2.5. Ion suppression

Ion suppression was investigated by a post column infusion experiment as described previously [25].

2.6. Validation

2.6.1. Linearity studies

A matrix-based calibration curve for MPA, as well as MPAG using drug-free serum, was constructed as described elsewhere [25]. In addition, commercially available calibrators for MPA were used for linearity studies.

2.6.2. Limit of Detection (LOD) and Lower Limit of Quantification (LLOQ)

The minimum of detectable concentration was assessed as 3 SD_0, where SD_0 is the value of the standard deviation as the concentration of the analyte approaches 0. The LOD was determined by performing 25 replicates measurements in a single UPLC-MS/MS assay with drug-free serum as a sample. LLOQ was the value for which the interassay CV reached <20%.

2.6.3. Imprecision

The intraassay imprecision was determined by analyzing 20 replicates of a low (0.53/48.5 mg L^{-1}), medium (3.28/96.5 mg L^{-1}), and high (6.31/255 mg L^{-1}) MPA and MPAG sample, respectively, on the same day. The interassay precision was also obtained by measurement of a low (0.79/55.9 mg L^{-1}), medium (3.36/114 mg L^{-1}), and high (6.44/230 mg L^{-1}) MPA and MPAG sample, respectively, on 20 different days over 1 month.

2.6.4. Stability

The stability of MPA, as well as MPAG in serum, was investigated by measurement of these compounds in a freshly collected patient sample and the measurement of the same sample at RT after 1 day, 1 week and 1 month.

2.6.5. Recovery

The recovery efficiency of the assay was established by measuring the MPA, as well as MPAG concentration in serum, before and after enrichment with different amounts of MPA and MPAG, respectively. Analytical recoveries were calculated as the mea-

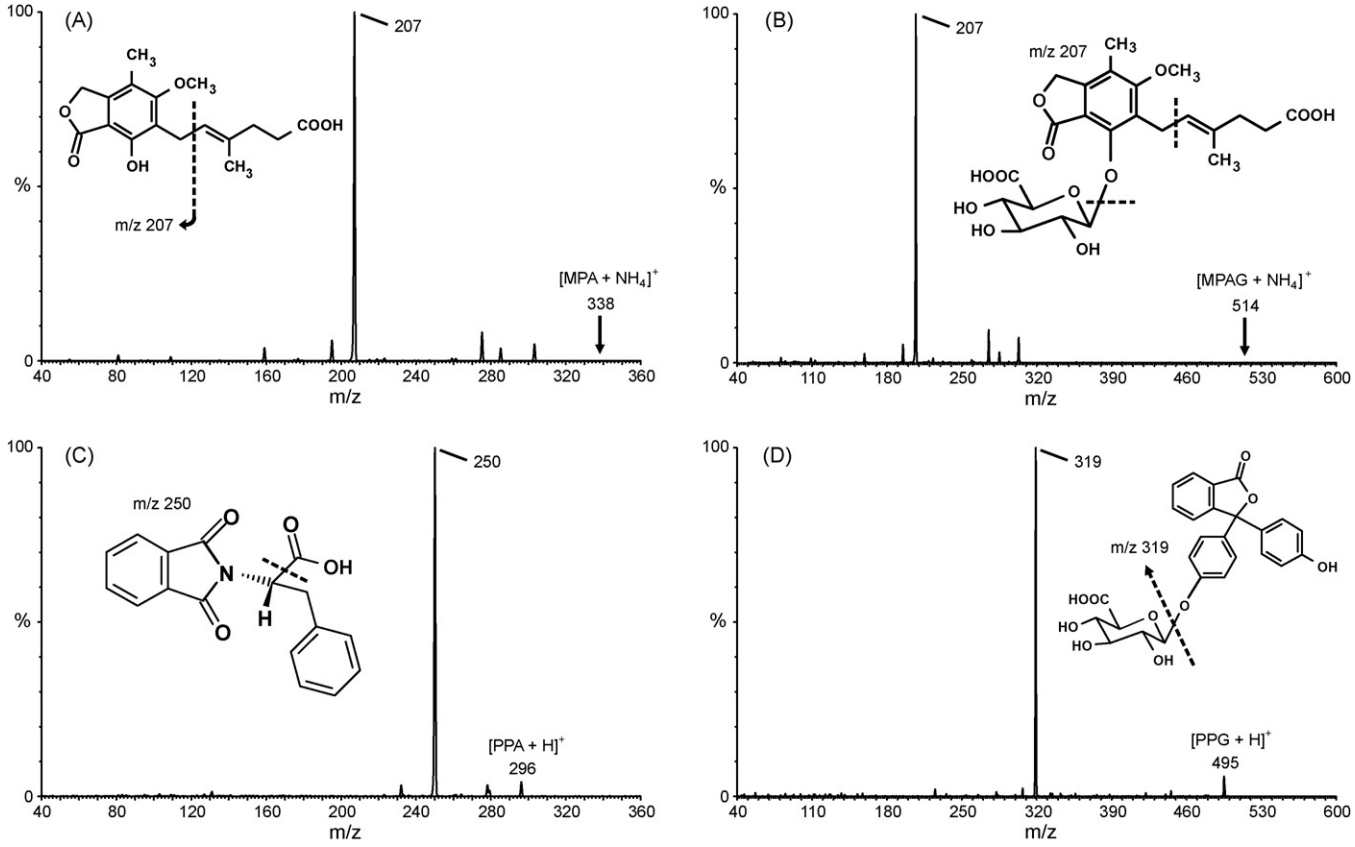


Fig. 1. Product ion spectrum of MPA (A) and MPAG (B), as well as its internal standards PPA (C) and PPG (D). The arrow at *m/z* 338 and *m/z* 514 shows the position of the $[MPA+NH_4]^+$ and the $[MPAG+NH_4]^+$ precursor ion, respectively (A and B). Both precursor ions were not detected in the product ion spectra because the ions were completely fragmented under experimental conditions. The other precursor ions $[PPA+H]^+$ and $[PPG+H]^+$ at *m/z* 296 and 495, as well as the fragment ions of MPA ammonium adduct, MPAG ammonium adduct, PPA and PPG at *m/z* 207, 207, 250, and 319 are shown. The chemical structures of the molecules are depicted and the fragmentation positions are shown (dotted arrows and dotted lines).

sured concentrations divided by the expected concentrations and expressed as a percentage.

2.6.6. Comparison of MPA and MPAG concentrations in EDTA plasma and serum

We used 96 serum and 96 EDTA plasma samples from the same patient from routine MPA monitoring to compare the MPA and MPAG concentrations in the different materials.

2.7. Method comparison

The UPLC-MS/MS method proposed here was compared with a validated LC-MS/MS assay described previously [25] using the same set of clinical samples. The resulting data were analyzed by Passing-Bablok regression.

3. Results

3.1. General approaches of the UPLC-ESI-MS method

N-phthaloyl-L-phenylalanine (PPA) and phenolphthalein-β-glucuronic acid (PPG) were detected as appropriate internal standards for MPA and MPAG, respectively, as a result of intensive investigation of potential compounds like ascomycin, cyclosporine D, indomethacin, indole-3-butric acid, indole-3-propionic acid, napropamide, naphthalane, naproxen, PPA, phthalide, and PPG. As shown in Fig. 1, MPA and the referable internal standard PPA, as well as MPAG and the referable internal standard PPG, have not only same structure similarities but also as shown in Fig. 2 nearly the same retention time. Therefore, quantitative errors of both MPA and MPAG resulting from potential ion suppression during measurement will be compensated via its internal standards PPA and PPG, respectively.

In-source fragmentation of MPAG was detected by measuring $[MPA+H]^+$, but not by measuring the MPA ammonium adduct $[MPA+NH_4]^+$ (Fig. 2). Thus, determination of MPA concentration in blood samples by measuring $[MPA+NH_4]^+$ was not interfered with in-source fragmentation of MPAG. Furthermore, the MPA peak resulting from in-source fragmentation of MPAG was clearly separated from the original MPA peak, which was apparent by measuring $[MPA+H^+]$ (Fig. 2). Maximum sensitivity was achieved by monitoring the fragmentation of single-charged molecule ions $[MPAG+NH_4]^+$, $[PPA+H]^+$, $[PPG+H]^+$, and the MPA ammonium adduct $[MPA+NH_4]^+$, respectively. 1.5 μL of 100-fold diluted sample (see sample preparation) gave clean chromatograms with no interfering components present (Fig. 2). All compounds were clearly separated from the void volume (0.3 min) and elute in <2 min, allowing an injection-to-injection cycle time of <3 min. Loss of sensitivity resulting from the contamination of the sample cone of the mass spectrometer was tested by 100 repeated injections of 1.5 μL of a pooled sample. No systematic loss in sensitivity was observed in the absolute peak areas measured, and the CV for peak-area ratio (analyte/internal standard) was 3.7%.

3.2. Validation

The MPA calibration curve was linear between 0.05 and 100 mg L^{-1} ($r > 0.999$), and the MPAG calibration curve was linear

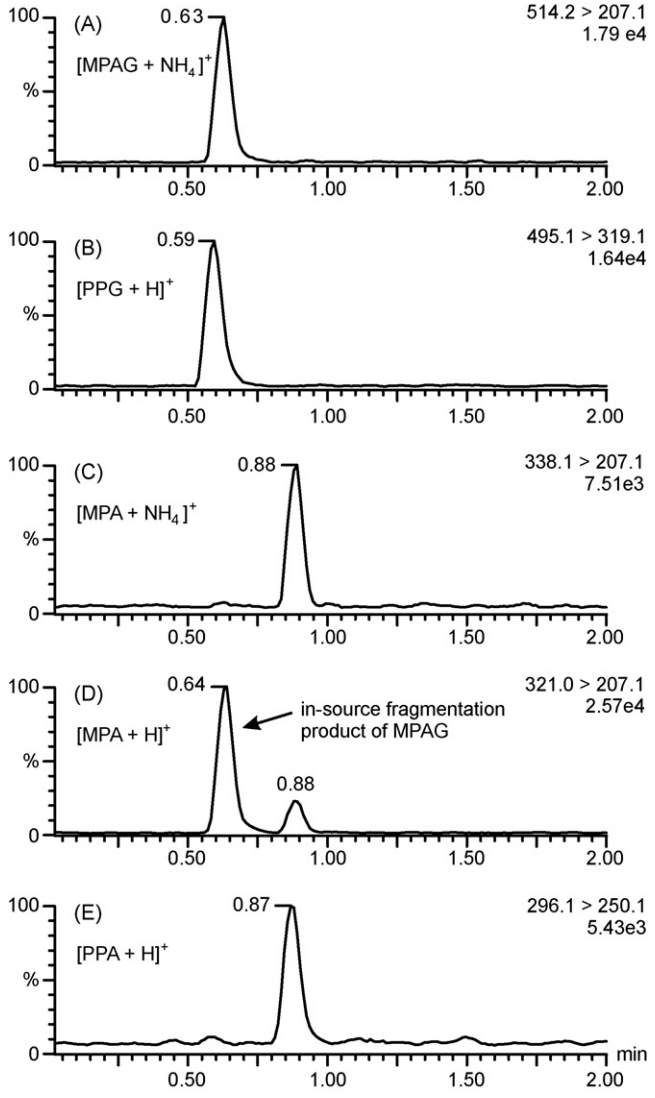


Fig. 2. MRM chromatograms of a serum sample diluted 100-fold with internal standard solution from a patient under treatment with MMF. (A) MRM transitions for the ammonium adduct of MPAG, m/z 514.2 > 207.1, (B) MRM transitions for the internal standard of MPAG which is the protonated adduct of PPG, m/z 495.1 > 319.1, (C) MRM transitions for the ammonium adduct of MPA, m/z 338.1 > 207.1, (D) MRM transitions for the protonated adduct of MPA, m/z 321.0 > 207.1, and (E) MRM transitions for the internal standard of MPA which is the protonated adduct of PPA, m/z 296.1 > 250.1.

between 4 and 4000 mg L^{-1} (r = 0.999). The LODs were 0.014 mg L^{-1} for MPA and 1.85 mg L^{-1} for MPAG, using an injection volume of 1.5 μL. The LLOQ were 0.05 mg L^{-1} for MPA and 2.30 mg L^{-1} for MPAG which is comparable with other MPA-, MPAG-assays [25]. The within-run and between-run CVs which were measured for different concentrations of MPA and MPAG, respectively, were all <10% (Table 1). The mean recovery for MPA at a concentration of 0.4–10.0 mg L^{-1} was 103.6% (range: 78.1–129.7%) and that for MPAG at a concentration of 10–100 mg L^{-1} was 111.1% (range: 73.0–139.6%). MPA and MPAG were stable in EDTA plasma or serum at 4 °C for at least 21 days, as well as RT which was found by systematical testing over a period of 1 month.

To estimate the importance of sample material, we compared the MPA, as well as the MPAG measurements of serum and EDTA plasma samples, each from the same patients (n = 96), in a side-by-side assay on the same day and analyzed them by least-square linear regression. The resulting regression line was y (plasma) = 0.92 (serum) + 0.05 [mg L^{-1}]; r = 0.99 for MPA and y (plasma) = 0.95 (serum) + 1.32 [mg L^{-1}]; r = 0.99 for MPAG, respectively.

Table 1
Analytical imprecision of LC-MS/MS assay.

Concentration	Intraassay (n = 20)		Interassay (n = 20)	
	Mean ± SD, mg/L	CV, %	Mean ± SD, mg/L	CV, %
MPA				
Low	0.53 ± 0.03	5.4	0.79 ± 0.08	9.6
Medium	3.28 ± 0.16	4.9	3.36 ± 0.27	7.9
High	6.31 ± 0.23	3.7	6.44 ± 0.44	6.6
MPAG				
Low	48.5 ± 2.3	4.7	55.9 ± 2.8	5.1
Medium	96.5 ± 3.0	3.1	114 ± 4.7	4.1
High	255 ± 9.7	3.8	230 ± 14.2	6.1

3.3. Method comparison

Method comparison analysis was performed using samples from 121 heart transplantation patients who used MMF as part of a multiple-drug regime to prevent acute rejection of the transplant. As shown in Fig. 3 the correlation between the validated LC-MS/MS assay and our novel UPLC-MS/MS assay was good.

4. Discussion

Recent developments in high performance liquid chromatography using columns packed with smaller particles with superior resolution and sensitivity have yielded an improved technology, termed ultra-performance liquid chromatography, or UPLC [26]. Here we could demonstrate that the combination of UPLC technology with the sensitivity of mass spectrometry facilitates a direct measurement of MPA, as well as MPAG in human serum or plasma. Apart from a simple dilution step with the internal standard solution, no sample preparation was necessary. Therefore, the method was less labor-intensive and the need of chemicals was limited. In addition, the application of the small sample size used in the method should prove useful when monitoring pediatric patients and will spare expensive calibrators and quality-control materials. Furthermore, it might be possible to validate MPA- and MPAG-determination in capillary blood finger prick collection.

The use of ammoniated MPA, as well as MPAG species increases the assay sensitivity by effectively concentrating all the usual fragment ions resulted from the fragmentation of the precursor ion into a single product ion species. Both $[MPA+NH_4]^+$ and $[MPAG+NH_4]^+$ ions produced the major product ion species at m/z 207 whereas both precursor ions were not detected in the product ion spectra because the ions were completely fragmented under experimental conditions (Fig. 1). PPA, the internal standard of MPA, and PPG, the internal standard of MPAG, produced, in contrast to the mycophenolate compounds, no ammonium adducts and show high sensitivity as single ion species which effectively fragmented to a major product ion at m/z 250 and 495, respectively. Our method conception in combination with the sensitivity and the specificity of the MS/MS detector makes lengthy sample preparation such as solid-phase or liquid–liquid extraction unnecessary and is, therefore, eminently suitable for the measurement of MPA and MPAG in routine samples.

The method was very fast in comparison to other MPA assays [16–19]. The run time was only 2 min which limited on the one hand solvent consumption and made the assay on the other hand much more suitable for the analysis of large number of clinical samples, where a fast turnaround time is required. Loss of sensitivity as a result of a potential contamination of the sample cone of the mass

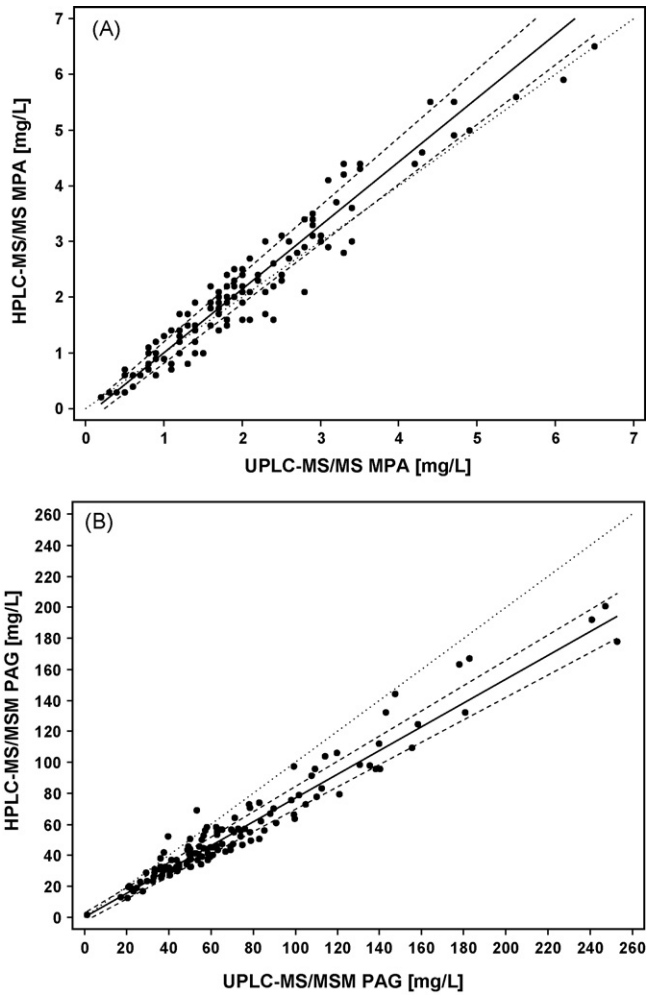


Fig. 3. (A) Comparison of MPA results obtained by UPLC-MS/MS assay and a validated LC-MS/MS assay by Passing-Bablok regression. HPLC-MS/MS = 1.14 UPLC-MS/MS—0.14 [mg L^{-1}] (r = 0.96; n = 121; 95% CI for slop, 1.07–1.22; 95% CI for intercept, −0.26 to −0.03). (—), PBR; (- - -), 95% CI; (···), line of equality. (B) Comparison of MPAG results obtained by UPLC-MS/MS assay and a validated LC-MS/MS assay by Passing-Bablok regression. HPLC-MS/MS = 0.77 UPLC-MS/MS + 0.50 [mg L^{-1}] (r = 0.97; n = 125; 95% CI for slop, 0.72–0.82; 95% CI for intercept, −2.60 to 2.71). (—), PBR; (- - -), 95% CI; (···), line of equality.

spectrometer was not detected even after 100 repeated injections of a pooled sample.

The LOD and the LLOQ were, at 0.014 and 0.050 mg L^{-1} for MPA and 1.85 and 2.30 mg L^{-1} for MPAG, comparable with other MPA-, MPAG-assays [25]. The intra- and inter-assay imprecision for MPA and MPAG, respectively, was, at <10% for all CVs, very good. MPA and MPAG were measured in parallel from the same injection in 2 min. The comparison between our UPLC-MS/MS and a validated LC-MS/MS assay [25] was good which is shown in Fig. 3.

Ion suppression will be compensated via the internal standards PPA and PPG for MPA and MPAG, respectively, showing certain structural similarity and having nearly the same retention time as its corresponding analyte. In-source fragmentation of MPAG was clearly detected as a single-charged molecule ion $[MPA+H]^+$ (Fig. 2D), but not as an MPA ammonium adduct $[MPA+NH_4]^+$ (Fig. 2C) which we used for quantification of MPA in our assay. In addition, MPA was chromatographically separated from MPAG, which prevented interfering effects of MPAG (Fig. 2D).

In summary, the advantages of this method over existing LC-MS/MS methods, including a direct measurement of MPA and MPAG from a diluted serum or plasma sample without any other sample preparation step, couplet with a shorter analysis time on the UPLC-MS/MS which allow a faster throughput of samples.

5. Conclusion

The combination of UPLC and MS/MS with an ESI interface facilitates a rapid method for measuring MPA, as well as MPAG in serum and plasma, with minimum sample consumption and without the need for sample cleanup or other purification steps.

Acknowledgments

We thank Annika Wolf for her excellent technical assistance and Sarah Kirkby for her linguistic advice.

References

[1] T.J. Franklin, J.M. Cook, Biochem. J. 113 (1969) 515.
[2] L.M. Shaw, B. Kaplan, D. DeNofrio, M. Korecka, K.L. Brayman, Ther. Drug Monitor. 22 (2000) 14.
[3] M. Oellerich, M. Shipkova, E. Schütz, E. Wieland, L. Weber, B. Tönshoff, V.W. Armstrong, Ther. Drug Monitor. 22 (2000) 20.
[4] M. Mourad, P. Wallemacq, M. De Meyer, J. Malaise, L. De Pauw, D.C. Eddour, E. Goffin, J. Lerut, V. Haufroid, Transplantations 85 (2008) 19.
[5] R.E. Bullingham, A.J. Nicholls, B.R. Kamm, Clin. Pharmacokinet. 34 (1998) 429.
[6] M. Vogl, G. Weigel, G. Seebacher, A. Griesmacher, G. Laufer, M.M. Müller, Ther. Drug Monitor. 21 (1999) 638.
[7] M. Shipkova, E. Schütz, V.W. Armstrong, P.D. Niedmann, E. Wieland, M. Oellerich, Transplant. Proc. 31 (1999) 1135.
[8] J.L. Beal, C.E. Jones, P.J. Taylor, S.E. Tett, Ther. Drug Monitor. 20 (1998) 685.
[9] A. Premaud, A. Rousseau, Y. Le Meur, G. Lachatre, P. Marquet, Ther. Drug Monitor. 26 (2004) 609.
[10] N. Sugioka, H. Odani, T. Ohta, H. Kishimoto, T. Yasumura, K. Takada, J. Chromatogr. B: Biomed. Appl. 654 (1994) 249.
[11] I. Tsina, F. Chu, K. Hama, M. Kaloostian, Y.L. Tam, T. Tarnowski, B. Wong, J. Chromatogr. B: Biomed. Appl. 675 (1996) 119.
[12] J.J.Z. Huang, H. Kiang, T.L. Tarnowski, J. Chromatogr. B 698 (1997) 293.
[13] K. Na-Bangchang, O. Supasyndh, T. Supaporn, V. Banmairuroi, J. Karbwang, J. Chromatogr. B 738 (2000) 169.
[14] R.W. Sparidans, R.M.W. Hoetelmans, J.H. Beijnen, J. Chromatogr. B 750 (2001) 155.
[15] K. Wiwattanawongsa, E.L. Heinzen, D.C. Kemp, R.E. Dupuis, P.C. Smith, J. Chromatogr. B 763 (2001) 35.
[16] C. Willis, P.J. Taylor, P. Salm, S.E. Tett, P.I. Pillans, J. Chromatogr. B 748 (2000) 151.
[17] M. Plätzer, K. Jahn, J. Wohlrab, R.H. Neubert, J. Chromatogr. B 755 (2001) 355.
[18] F. Streit, M. Shipkova, V.W. Armstrong, M. Oellerich, Clin. Chem. 50 (2004) 152.
[19] T.M. Annesley, L.T. Clayton, Clin. Chem. 51 (2005) 872.
[20] E. Schütz, M. Shipkova, V.W. Armstrong, P.D. Niedmann, L. Weber, B. Tönshoff, K. Pethig, T. Wahlers, F. Braun, B. Ringe, M. Oellerich, Transplant. Proc. 30 (1998) 1185.
[21] J.F. Gummert, U. Christians, M. Barten, H. Silva, R.E. Morris, J. Chromatogr. B: Biomed. Sci. Appl. 721 (1999) 321.
[22] H. Hosotsubo, S. Takahara, Y. Kokado, S. Permpongkosol, J.D. Wang, T. Tanaka, K. Matsumiya, M. Kitamura, A. Okuyama, H. Sugimoto, J. Chromatogr. B: Biomed. Sci. Appl. 753 (2001) 315.
[23] C.G. Patel, A.E. Mendonza, F. Akhlaghi, O. Majid, A.K. Trull, T. Lee, D.W. Holt, J. Chromatogr. B: Anal. Technol. Biomed. Life Sci. 813 (2004) 287.
[24] B. Atcheson, P.J. Taylor, D.W. Mudge, D.W. Johnson, P.I. Pillans, S.E. Tett, J. Chromatogr. B: Anal. Technol. Biomed. Life Sci. 799 (2004) 157.
[25] J. Kuhn, C. Prante, K. Kleesiek, C. Götting, Clin. Biochem. 42 (2009) 83.
[26] F.T. Musuamba, V. Di Fazio, R. Vanbinst, P. Wallemarcq, Ther. Drug Monitor. 31 (2009) 110.

Talanta 80 (2010) 1899–1906

Contents lists available at ScienceDirect

Talanta

journal homepage: www.elsevier.com/locate/talanta

Threshold detection of aromatic compounds in wine with an electronic nose and a human sensory panel

José Pedro Santos[a,*], Jesús Lozano[b], Manuel Aleixandre[a], Teresa Arroyo[c], Juan Mariano Cabellos[c], Mar Gil[c], Maria del Carmen Horrillo[a]

[a] Instituto de Física Aplicada (CSIC), Madrid, Spain
[b] Grupo de Investigación en Sistemas Sensoriales, Universidad de Extremadura, Badajoz, Spain
[c] Department Agroalimentación, Instituto Madrileño de Investigación y Desarrollo Rural, Agrario y Alimentario, Madrid, Spain

ARTICLE INFO

Article history:
Received 1 July 2009
Received in revised form 9 October 2009
Accepted 18 October 2009
Available online 28 October 2009

Keywords:
Electronic nose
Sensory panel
Wine compounds thresholds

ABSTRACT

An electronic nose (e-nose) based on thin film semiconductor sensors has been developed in order to compare the performance in threshold detection and concentration quantification with a trained human sensory panel in order to demonstrate the use of an e-nose to assess the enologists in an early detection of some chemical compounds in order to prevent wine defects. The panel had 25 members and was trained to detect concentration thresholds of some compounds of interest present in wine. Typical red wine compounds such as whiskeylactone and white wine compounds such as 3-methyl butanol were measured at different concentrations starting from the detection threshold found in literature (in the nanograms to milligrams per liter range). Pattern recognition methods (principal component analysis (PCA) and neural networks) were used to process the data. The results showed that the performance of the e-nose for threshold detection was much better than the human panel. The compounds were detected by the e-nose at concentrations up to 10 times lower than the panel. Moreover the e-nose was able to identify correctly each concentration level therefore quantitative applications are devised for this system.

© 2009 Elsevier B.V. All rights reserved.

1. Introduction

Electronic noses have aroused in last years as a powerful tool in many applications mainly in food [1–3]. Their performances are usually compared with respect to analytical methods as gas chromatography–mass spectrometry or human sensory panels. Comparison with human panels has been performed mostly in food quality applications [4–6] with a qualitative approach. There are few examples of quantitative applications [7] and are outside this field. Electronic noses have been applied to wine related measurements since last decade for several purposes: varietal origin [8], oak toasting levels [9], regional characterization [10–12], ageing [13], defects detection [14–16] and sensory properties prediction [17,18] among others.

A sensory panel can provide information about the sensory properties of consumer products that is far richer than can be provided by instrumental devices alone, but significant training is required before the panel becomes a reliable sensory instrument [19] specially dealing with wine, a very complex product.

In the present work a sensory panel and an electronic nose (e-nose) based on semiconductor oxide sensors have been trained in parallel with several aromatic compounds present in wine in order to compare their performances in threshold detection and concentration quantification. This threshold is the minimum concentration of an aroma in water perceived for at least 50% of the members of a sensory panel. Other term related to the olfactory threshold detection is the difference threshold detection, the minimum amount of an aroma that has to be added to a product already containing this aroma in order to produce an appreciable sensory change. This concept is especially useful in dealing with compounds in wine. Usually this threshold is evaluated in an artificial wine [20] but in the present case we used real wines.

The great influence of water and ethanol in the response of semiconductor oxide sensors is known [21,22]. We have employed two sampling methods, headspace and purge and trap in order to elucidate the influence of these interferents in the e-nose performance.

The aim of this work is to assess if the sensory panel can be substituted by an electronic nose for some specific tasks such as threshold detection. This experimental method may eventually replace current sensory evaluation techniques, with a simpler qualitative and quantitative technique, offering better reliability and reproducibility of results, faster operation and lower cost.

* Corresponding author.
E-mail address: josepe@ifa.cetef.csic.es (J.P. Santos).

0039-9140/$ – see front matter © 2009 Elsevier B.V. All rights reserved.
doi:10.1016/j.talanta.2009.10.041

2. Materials and methods

2.1. Aromatic compounds

Thirty-eight aromatics compounds of white and red wines belonging to different chemical families and grouped under nine aromatic descriptors of wine quality were used in the training and initial selection of the members of a sensorial panel. These descriptors were: fruity-like, herbaceous, spicy, phenolic, microbiologic, oxidation, chemical, woody-like and off-flavours (Table 1). Standard solutions were diluted with water and/or ethanol (adjusting final ethanol content to 12%, v/v) at concentrations typically found in wine. All solutions were added with 5 g/l tartaric acid and the pH was adjusted at 3.2 with 1 M NaOH [23].

Last, a set of eight typical compounds of white and red wines have been measured at increasing levels from the olfactory detection threshold. The compounds chosen were whiskeylactone, nonalactone, decalactone and diacetyl for red wines and 3-methyl butanol, 4-vinyl guaiacol, butyric acid and damascenone for white wines. Table 2 shows these volatile compounds with their odor descriptors and their threshold values (*T*) found in literature [24–26]. These threshold values were used in the initial phases of the training of the panel, in which solutions of pure chemical compounds at different concentrations were presented to the panel.

Table 1
Aromatics compounds used in the training and selection of members of the sensorial panel.

Descriptor	Pure standard compounds
Fruity-like	Ethyl octanoate Isoamyl acetate Hexyl acetate Ethyl cinnamate Ethyl-isobutyrate Ethyl hexanoate Ethyl isovalerate 2-Methylethyl butyrate
Herbaceous	1-Hexanol c-3-Hexenol Benzaldehyde
Spicy	Eugenol 2-Methyl-3-methoxy-pyracine
Phenolic	Guaiacol 4-Vinylguaiacol 4-Ethylguaiacol Vanillin
Microbiologic	Diacetyl Butyric acid Isovaleric acid Octanoic acid Acetoine Acetic acid
Oxidation	Acetaldehyde
Chemical	Isoamyl-alcohol 3-Methyl butanol Decanoic acid Sulphur dioxide Ethanol
Woody-like	β-Damascenone γ-Octolactone γ-Nonalactone δ-Decanolactone (E)-whiskeylactone 2-Furan-methanothiol
Off-flavour	Ethyl acetate Ethanethiol 2,4,6-Trichloroanisol (TCA)

Table 2
Odor thresholds, odor descriptions and concentrations in the test wines of the studied compounds.

Compound	Odor threshold (μg/l)	Odor description	Concentration (μg/l)
Whiskeylactone	67	Wood, sweet fruit	8.5
Nonalactone	30	Coconut	16.2
Decalactone	88	Sweet fruit	0.5
Diacetyl	100	Creamy, milk	350
3-Methyl butanol	29,930	Oil	185,000
4-Vinyl guaiacol	1,146	Phenolic	900
Butiric acid	173	Cheese	500
Damascenone	0.05	Fruit, mulberry	1.8

Sample sets with the aromatics compounds were prepared at three different concentrations: *T*, 2*T* and 4*T*. When the panel did not perceive the 4*T* concentration, 6*T* and 8*T* and 10*T* concentrations were used in the next session of training. All compounds were of analytical quality and were provided by Sigma–Aldrich and Merck.

2.2. Sensory panel

Initially 36 voluntary subjects from both investigation groups IMIDRA, IFA and staff cellars took part in the training program during several months. Sensory evaluations were realized under ISO standards related to methodology (ISO 3972:1991), sensory analysis vocabulary (ISO 5492:1992), tasting room (ISO 8589:1988), selection and formation of tasters (ISO 8586-1 and 2: 1993). Sample sets of synthetic wines added with the 38 aromatic compounds (Table 1) were given to the panellist at threshold concentration (*T*). 30 subjects that were able to correctly classify the 80% of the compounds continued with the training. In a second stage an experimental young white wine from Airén variety and a young red wine of Tempranillo variety were used as control wine. Vinyl guaiacol, butyric acid, 3-methyl butanol and damascenone, typical of white wines, were added one to one to the Airén wine. Whiskeylactone decanolactone, nonalactone and diacetyl generally more characteristic of red wines, were presented in the Tempranillo wine. First, the original concentration of the aromatic compounds in these wines was quantified by CG–MS [27]. The results showed that all compounds were under threshold human detection with the exception of 3-methyl-butanol that presented an odor activity value (OAV) > 1. Finally, four experimental white wine sample sets and four experimental red wine sample sets were obtained and the only difference with their corresponding test wine was the concentration of one aromatic compound. Each sample set was made of six levels of concentration *T*, 2*T*, 4*T*, 6*T* 8*T* and 10*T*. These concentrations correspond to 1, 2, 4, 6, 8 and 10 times the threshold value of detection of the volatile compounds.

In a second selection operation ANOVA analysis ($p < 0.05$) was applied to the rate of the correct panellist responses after they arranged the six levels of concentration of diacetyl and β-

Table 3
Percentage of panel members that recognized the compounds at each concentration level.

Compound	*T*	2 × *T*	4 × *T*	10 × *T*
Whiskeylactone	16.7	25	41.7	45.8
Nonalactone	29.2	33.3	45.8	41.7
Decalactone	8.3	41.7	45.8	62.5
Diacetyl	22.2	44.4	55.6	81.5
3-Methyl butanol	11.1	14.8	29.6	77.8
4-Vinyl guaiacol	10.7	32.1	60.7	75
Butiric acid	3.6	17.9	35.7	56.5
Damascenone	25	39.3	46.4	53.6

T: odor threshold concentration (see Table 2).

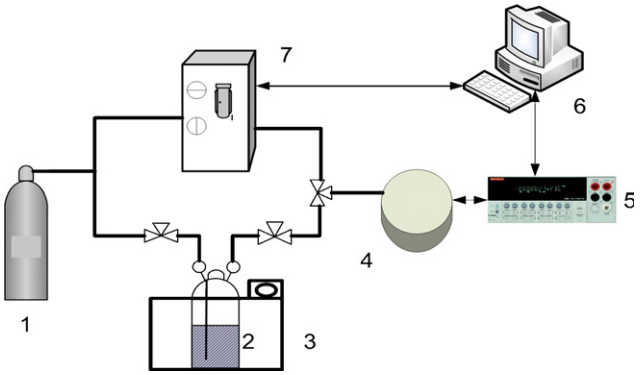


Fig. 1. Measurement setup: (1) nitrogen bottle, (2) Dreschell bottle with sample, (3) thermostatic bath, (4) sensors cell, (5) multiplexer and DMM, (6) personal computer, (7) purge and trap.

damascenone sample sets and 25 people were selected to take part in the human sensory panel.

The trial of the selected sensory panel consisted in the determination of the perception threshold by triangular probe (ISO 4120:1983) of each aroma when it was added to experimental wines. To avoid a saturation effect in tasters, the training was carried out along four sessions in different days. Six concentration levels of two different aromas were evaluated in each session.

2.3. Electronic nose

An electronic nose based on a tin oxide array has been employed. The array was composed by 16 thin film tin oxide sensors with thickness between 200 and 800 nm doped with small amounts of chromium and indium (both as surface or intermediate layer) to increase their selectivity. Sensors were deposited by reactive sputtering onto an alumina substrate. Details of the preparation can be found elsewhere [28]. The array was place in a 20 cm^3 stainless steel cell kept at 300 °C.

Two sampling methods were used: headspace and purge and trap. In the first case 10 ml of sample was kept in a Dreschell bottle at 30 °C for 20 min. The headspace was carried by an inert gas for 10 min to the sensor cell. The carrier used gas was nitrogen 99.998% purity at a constant flow of 200 ml/min. We used an inert, no oxidizing gas to ensure the stability of the wines during the experiments. With the purge and trap method 1 ml of sample were placed in the vessel of a Tekmark 3000 purge and trap concentrator. The sample was purged with pure helium into a Tenax trap for 10 min and then desorbed at 250 °C with a nitrogen flux. With this adsorbent water and ethanol content of the sample are minimized.

The resistance of the sensors were measured with a Keithley 2001 digital multimeter (DMM) connected to a Keithley 7001 multiplexer controlled by a personal computer. The sensor responses were calculated as the relation between the equilibrium resistance value in pure nitrogen, R_N, and the equilibrium resistance value in

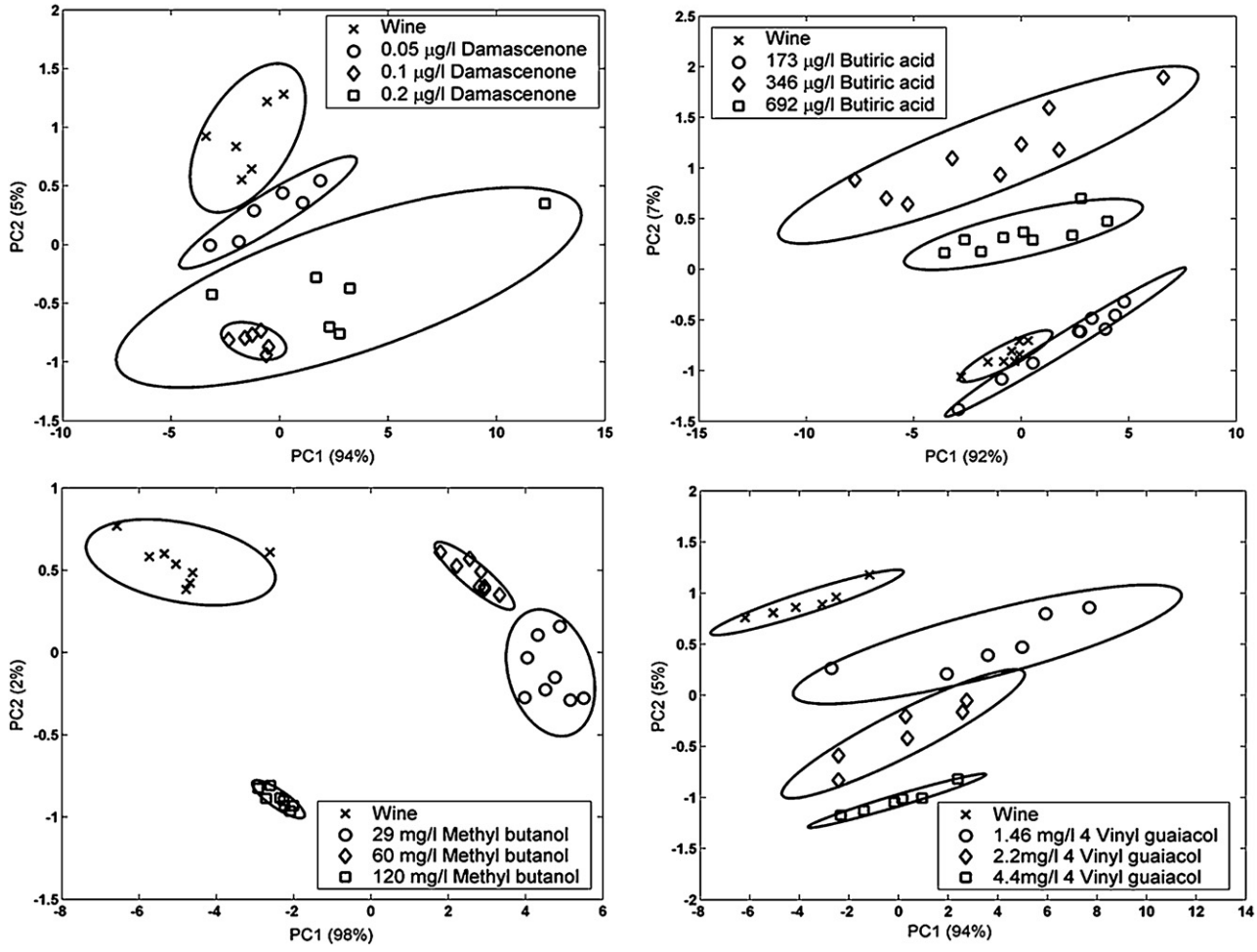


Fig. 2. PCA score plot for white wine compounds with headspace sampling.

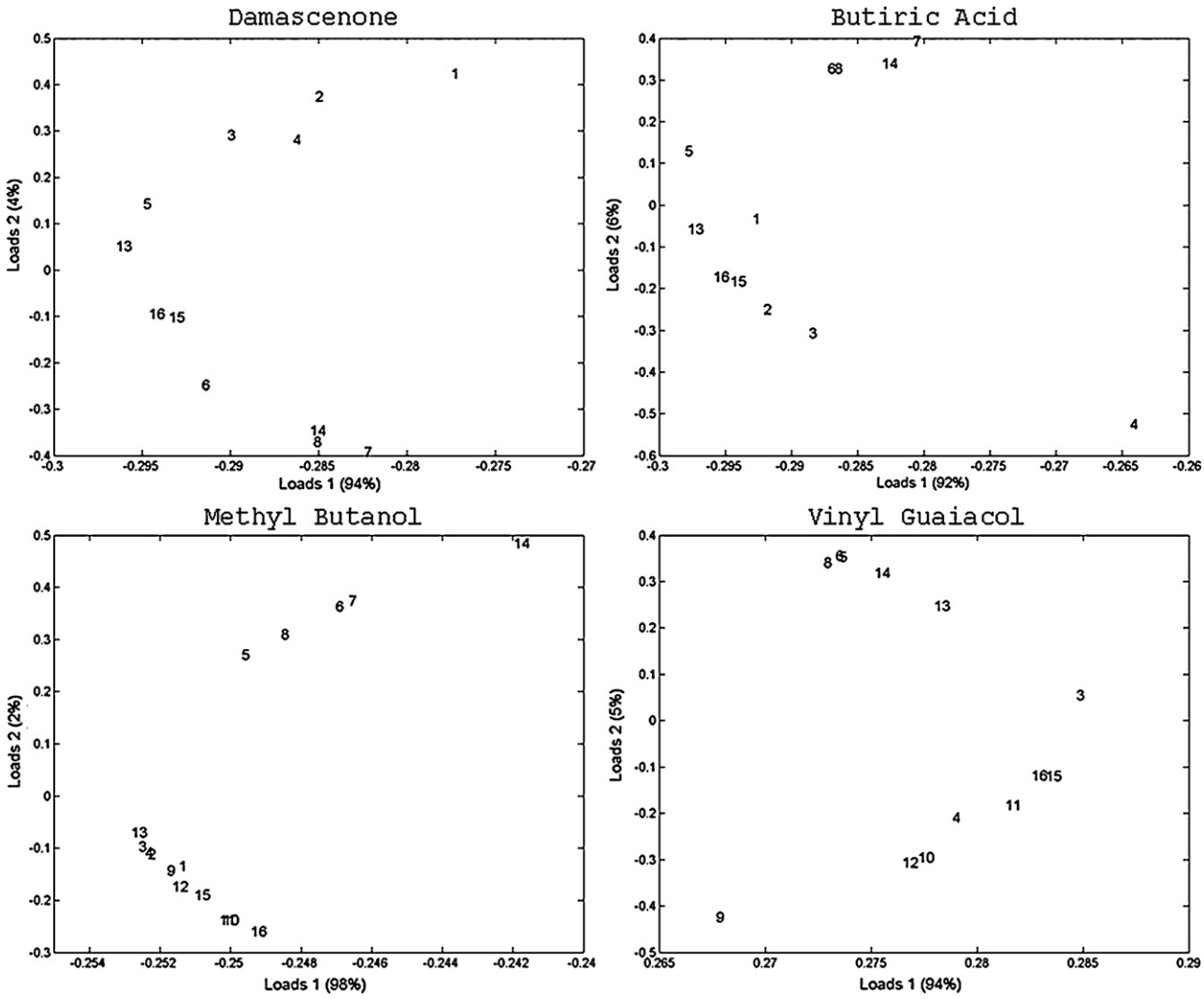


Fig. 3. PCA loadings plot for white wine compounds with headspace sampling.

the presence of the sample R_S:

$$r = \frac{R_N}{R_S} \quad (1)$$

The sensors were calibrated with ethanol in a weekly basis to compensate for drift. The experimental setup is shown in Fig. 1.

2.4. Data analysis

Two multivariate data processing techniques have been used: a linear unsupervised one, principal component analysis (PCA) and a nonlinear supervised one, a probabilistic neural network (PNN) [29].

Principal component analysis (PCA) is a chemometric linear, unsupervised and pattern recognition technique used for analyzing and reducing the dimensionality of numerical datasets in a multivariate problem. This method extracts the features from a data matrix in terms of a complementary set of scores (coordinates of the data in the new base) and loadings (contribution of the sensors to the components) plots. This method applies a linear transformation to the data and result in a new space of variables called principal components. The scores plot is usually used for studying the distribution of the data clusters. In the loading plot sensors with similar contributions will be close together. Sensors close to the origin have comparably small contribution.

The scores of the three first principal components were used in the training of the neural network.

The PNN was used for classification purposes. This network was composed by three layers. In the input layer there were three elements that corresponded with the first three components of the PCA. The hidden layer had the same number of neurons as the number of training vectors with radial basis transfer functions. The purpose of this layer is to measure and weight with a radial function the distance of the input layer vector with each training set element. The output layer was a competitive one with four neurons, one for the test wine and the others for the samples with added compounds (T, $2T$ and $4T$). In this third layer we add up the weighed distances for each class and the neural network select the highest one as the classification result. As we did not have many measurements leave one out cross validation was applied to check the performance of the network [30]. This method consists of training N distinct nets (in this case, N is number of measurements) by using $N-1$ training vectors, while the validation of the trained net is carried out by using the remaining vector, excluded from the training set. This procedure is repeated N times until all vectors are validated. Both PCA and PNN were performed in Matlab (version 6.1, Mathworks Inc., Natick, MA, USA).

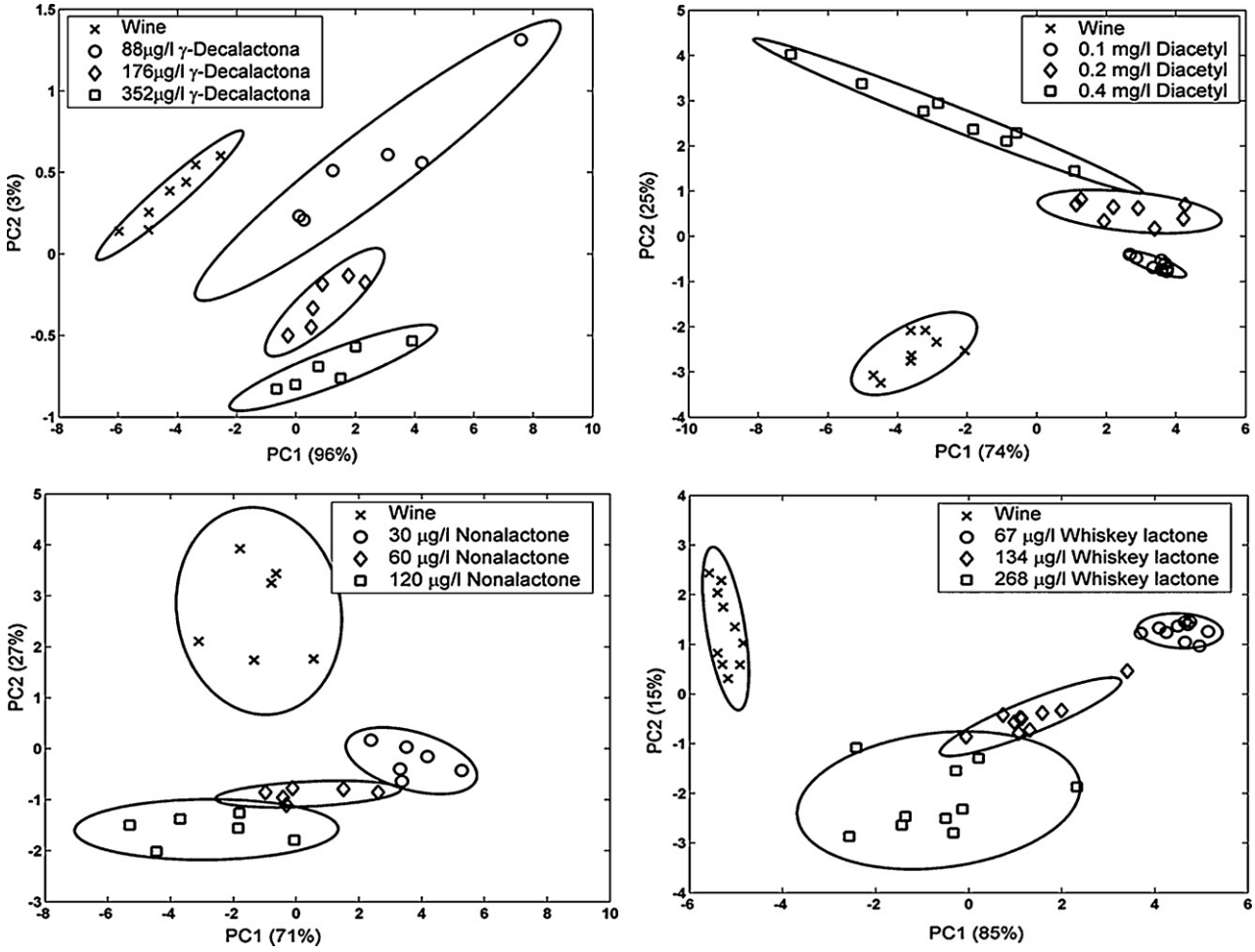


Fig. 4. PCA score plot for red wine compounds with headspace sampling.

3. Results

3.1. Sensory panel

The analysis of the sensory panel is summarized in Table 3. The table gives the percentage of panel members that detects each compound at each concentration. No compound was detected at the olfactory detection threshold. Only two compounds (diacetyl and 4-vinyl guaiacol) were detected by at least 50% of the panel at four times the threshold although more than 40% of the panelists recognized the rest of the compounds except 3-methyl butanol and butiric acid. The other compounds were detected at or above 10 times the threshold.

3.2. Electronic nose

After feature extraction using equation 1 data were preprocessed before PCA analysis. The preprocessing involved autoscaling and centering:

$$r_i = \frac{(r - \bar{r}_i)}{\sigma_i} \quad (2)$$

where $\bar{r}_i$ is the mean and σ_i is the standard deviation of sensor i response over the input data. The distribution of values for each sensor across the entire database is set to have zero mean and unit standard deviation.

The first three principal components accounted for more than 98% of the cumulative variance. Ellipsoids in the score plots are drawn assuming a Gaussian data distribution and represent the curve with a 90% probability.

3.3. Headspace

The PCA score plot for compounds in white wine is shown in Fig. 2. The variance explained by each principal component is in brackets. Only the datasets corresponding to methyl butanol are clearly separated. For the other compounds datasets showed partial overlapping. The corresponding PCA loadings plot is shown in Fig. 3. Sensors are well distributed around the loadings plane although there are some sensors close to each other for several compounds such as sensors 15 and 16 (indium doped sensors) for damascenone, butyric acid and vinyl guaiacol. This implies colinearity and redundancy of these two sensors. However their contribution to methyl butanol are more differentiated. For this last compound sensors 2, 3, 4 (undoped sensors), 8 and 13 (chromium doped sensors) are redundant and also 10 and 11 (indium intermediate layer doped sensors) are very close.

The PCA score plot for compounds in red wine is shown in Fig. 4. Although there is overlapping between datasets corresponding to nonalactone and whiskeylactone the wine datasets are clearly separated for every compound. The loadings plot showed a similar distribution than in the previous case. There was as well colinearity for some sensors but not for the same ones. For example sensors 7 and 8 (chromium intermediate layer doped sensors) gave similar information for decalactone, but differentiated contributions for the other three compounds. As in the previous

Table 4
Success rates of the PNN for headspace sampling for white wine compounds.

Compound	Qualitative	Quantitative
3-Methyl butanol	100	100
4-Vinyl guaiacol	96	83
Butiric acid	89	74
Damascenone	92	83

Table 5
Success rates of the PNN for headspace sampling for red wine compounds.

Compound	Qualitative	Quantitative
Whiskeylactone	100	100
Nonalactone	100	96
Decalactone	100	75
Diacetyl	100	83

case no sensor appears to be redundant for the whole compound dataset.

In general the output of the neural network is given as a confusion matrix. From the confusion matrix a success rate is defined as the number of correct classified measures in each class over the total number of measures in this class. In our case we have two success rates: a qualitative success rate and a quantitative success rate. In the quantitative case each compound concentration is considered a separated class. In the qualitative case we have only two classes: test wine and wine plus added compound. For headspace sampling the success rates are shown in Table 4 for white wine and Table 5 for red wine. For white wine compounds qualitative success rates are near 100% but only for 3-methyl butanol the neural network is able to classify correctly all classes both qualitatively and quantitatively. For red wine compounds test wine are correctly separated from wine added compounds measurements. A 100% quantitative success rate is achieved for whiskeylactone samples.

3.4. Purge and trap

The PCA score plot for compounds in white wine is shown in Fig. 5. Datasets for all compounds appear clearly separated except for the high concentration levels of damascenone. The PCA loadings plot showed similar trend tan in the headspace case except for damascenone. For this compound most sensors contributed in a similar way to PC1 and there was more variation in the contributions to PC2. For the other compounds the loadings of the sensors are more separated although there is a similar contribution from the sensors 2, 4 and 5.

The PCA score plot for compounds in red wine is shown in Fig. 6. In this case the separation between datasets is less clear but the test wine dataset is always separated from the wine with added compounds datasets. Datasets are better separated for compounds in white wine than for compounds in red wine as in the case of headspace extraction. The PCA loadings plot showed two group of sensors with similar contribution to the first principal component for nonalactone: sensors 9–12 (indium doped in an intermediate layer sensors) and the rest of the array. For the rest of the com-

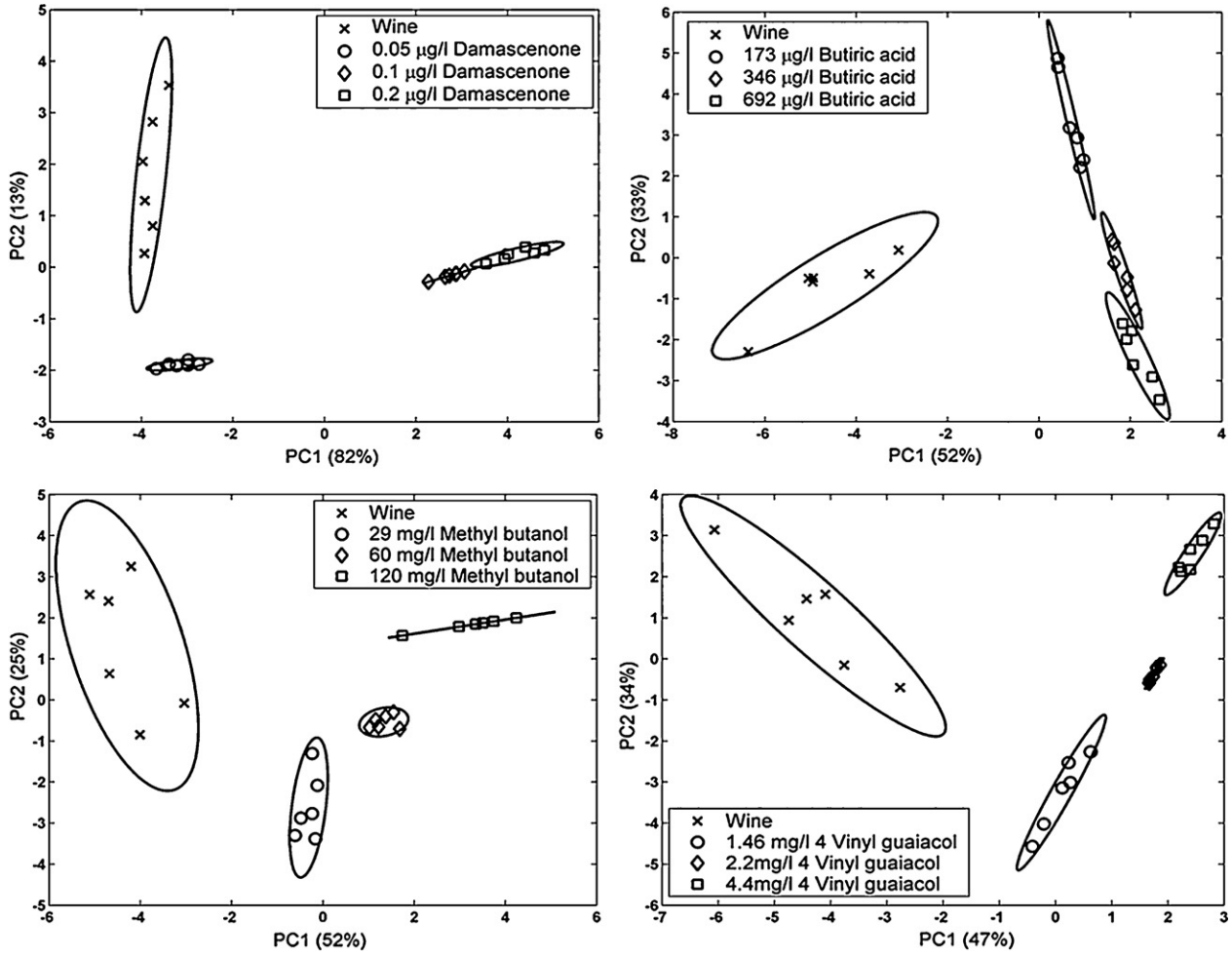


Fig. 5. PCA score plot for white wine compounds with purge and trap sampling.

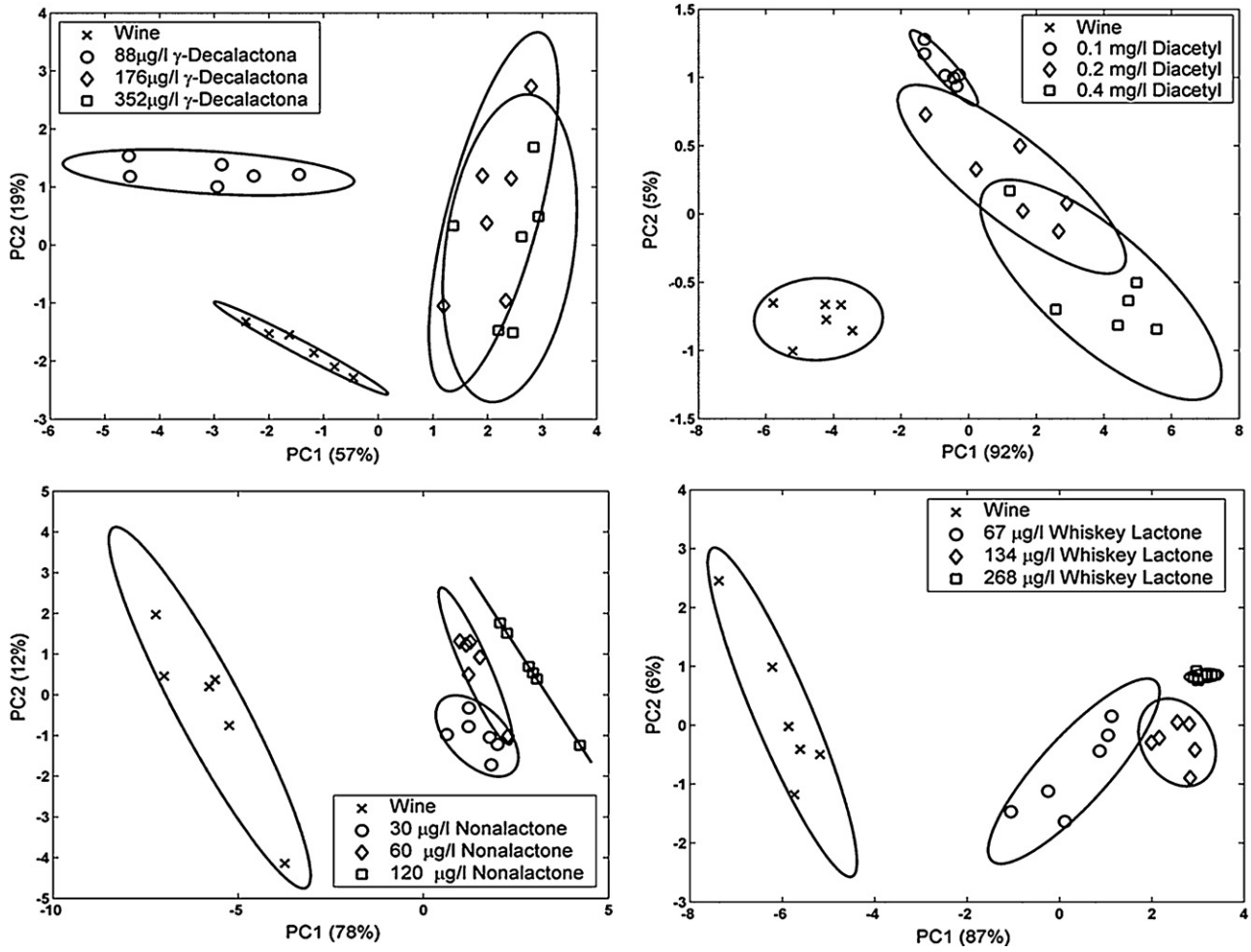


Fig. 6. PCA score plot for red wine compounds with purge and trap sampling.

Table 6
Success rates of the PNN for purge and trap sampling for white wine compounds.

Compound	Qualitative	Quantitative
3-Methyl butanol	100	100
4-Vinyl guaiacol	100	100
Butiric acid	100	96
Damascenone	100	100

pounds the sensor loadings are more separated. It can be noted that sensors 13 and 14 (chromium surface doped sensors) have the greatest contribution to PC2 for all compounds.

The success rates of the probabilistic neural network are shown in Table 6 for white wine compounds and Table 7 for red wine compounds. Success rates are 100% qualitative both for white and red wine compound. We obtain better quantitative success rates for the compounds in white wine just as in the PCA analysis.

The separation is better for purge and trap sampling method than for headspace as expected. Purge and trap is especially successful for the compounds in white wine with a minimum of 96% correct quantitative classifications.

Table 7
Success rates of the PNN for purge and trap sampling for red wine compounds.

Compound	Qualitative	Quantitative
Whiskeylactone	100	93
Nonalactone	100	92
Decalactone	100	80
Diacetyl	100	96

4. Discussion and conclusions

In every case the electronic nose exhibited a better performance than the human sensory panel in the discrimination of aromatic compounds. The first threshold data are correctly separated from wine data for all compounds with purge and trap method. Higher concentration datasets are separated as well but in most cases there is confusion between the different concentrations tested. In the case of the sensory panel the compounds are detected only at concentrations four times higher than the threshold for diacetyl and 4-vinyl guaiacol and 10 times higher than the threshold for decalactone, 3-methyl butanol and butiric acid.

Whiskeylactone and nonalactone are not recognized even at the maximum concentration. The electronic nose, however, performed very well with a 100% quantitative success rate with purge and trap extraction for white wine compounds. On the other hand decalactone gave the poorest response. In the case of the damascenone only detected by the panel even at 10 times the threshold, the electronic nose performed well both qualitative and quantitative despite the low concentrations involved (the first odor threshold is only 0.05 μg/l). It appears evident that the performance of the electronic nose is not directly related either to the odor threshold concentration of a compound or to the ratio of its real concentration in wine to its threshold concentration. From the loading plots we

can conclude that none of the 16 sensors appears to be redundant for the whole compound dataset for both sampling methods.

On the other hand, despite the strong ethanol and water interference the electronic nose performs well with headspace sampling method due to the saturation of the sensors to low levels of ethanol although purge and trap gives better results. This result confirms previous results in compounds discrimination in wine and ethanol [31].

We can conclude that the use of electronic noses in the determination of compound thresholds is advantageous over the human sensory panel in terms of training time and accuracy.

Acknowledgement

This work was supported by Comunidad de Madrid under the project OLFACTOSENSE (S-SEM-0255-2006) into the Bioscience activities program.

References

[1] S. Esposto, G. Montedoro, R. Selvaggini, I. Riccò, A. Taticchi, S. Urbani, M. Servili, Food Chem. 113 (2009) 345–350.
[2] D.M.A.M. Luykx, S.M. van Ruth, Food Chem. 107 (2008) 897–911.
[3] J.P. Santos, M.J. Fernández, J.L. Fontecha, J. Lozano, M. Aleixandre, M. García, J. Gutiérrez, M.C. Horrillo, Sens. Actuators, B 107 (2005) 291–295.
[4] C. Di Natale, R. Paolesse, M. Burgio, E. Martinelli, G. Pennazza, A. D'Amico, Anal. Chim. Acta 513 (2004) 49–56.
[5] E.Z. Panagou, N. Sahgal, N. Magan, G.J.E. Nychas, Sens. Actuators, B 134 (2008) 902–907.
[6] D.A. Luzuriaga, F. Korel, M.Ö. Balaban, J. Aquat. Food Prod. Technol. 16 (2007) 57–75.
[7] J. Poprawski, P. Boilot, F. Tetelin, Sens. Actuators, B 116 (2006) 156–160.
[8] C. Di Natale, F.A.M. Davide, A. D'Amico, P. Nelli, S. Groppelli, G. Sberveglieri, Sens. Actuators, B: Chem. 33 (1–3) (1996) 83–88.
[9] P. Chatonnet, D. Dubourdieu, J. Agric. Food Chem. 47 (10) (1999) 4319–4322.
[10] J.P. Santos, T. Arroyo, M. Aleixandre, J. Lozano, I. Sayago, M. García, M.J. Fernandez, L. Ares, J. Gutierrez, J.M. Cabellos, M. Gil, M.C. Horrillo, Sens. Actuators, B: Chem. 102 (2) (2004) 299–307.
[11] S. Buratti, S. Benedetti, M. Scampicchio, E.C. Pangerod, Anal. Chim. Acta 525 (1) (2004) 133–139.
[12] D. Cozzolino, H.E. Smyth, K.A. Lattey, W. Cynkar, L. Janik, R.G. Dambergs, I.L. Francis, M. Gishen, Anal. Chim. Acta 563 (1–2) (2006) 319–324.
[13] M. García, M.J. Fernández, J.L. Fontecha, J. Lozano, J.P. Santos, M. Aleixandre, I. Sayago, J. Gutiérrez, M.C. Horrillo, Talanta 68 (2006) 1162–1165.
[14] A.Z. Berna, S. Trowell, W. Cynkar, D. Cozzolino, J. Agric. Food Chem. 56 (9) (2008) 3238–3244.
[15] J.A. Ragazzo-Sanchez, P. Chalier, C. Ghommidh, Sens. Actuators, B: Chem. 106 (1) (2005) 253–257.
[16] M.P. Martí, R. Boqué, M. Riu, O. Busto, J. Guasch, Anal. Bioanal. Chem. 376 (4) (2003) 497–501.
[17] S. Buratti, D. Ballabio, S. Benedetti, M.S. Cosio, Food Chem. 100 (1) (2007) 211–218.
[18] J. Lozano, J.P. Santos, T. Arroyo, M. Aznar, J.M. Cabellos, M. Gil, M.d.C. Horrillo, Sens. Actuators, B: Chem. 127 (1) (2007) 267–276.
[19] C.J. Findlaya, J.C. Castura, P. Schlich, I. Lesschaeve, Food Qual. Prefer. 17 (2006) 266–276.
[20] T. Yong-Sheng, L. Yong-qiang, L. Hua, Food Chem. 114 (2009) 565–569.
[21] T. Schäfer, M.B. Serrano-Santos, S. Rocchi, R. Fuoco, Anal. Bioanal. Chem. (2006) 860–866.
[22] A. Fort, M. Gregorkiewitz, N. Machetti, S. Rocchi, B. Serrano, L. Tondi, N. Ulivieri, V. Vignoli, G. Faglia, E. Comini, Thin Solid Films 418 (1) (2002) 2–8.
[23] C. Ortega, R. López, J. Cacho, V. Ferreira, J. Chromatogr. A 923 (2001) 205–214.
[24] M. Aznar, R. López, J. Cacho, V. Ferreira, J. Agric. Food Chem. 51 (2003) 2700–2707.
[25] H. Guth, in: A.L. Waterhouse, S.E. Ebeler (Eds.), Chemistry of Wine Flavor, American Chemical Society, Washington, DC, 1998.
[26] V. Ferreira, R. Lopez, J.F. Cacho, J. Sci. Food Agric. 80 (2000) 1659–1667.
[27] M. Gil-Díaz, J.M. Cabellos, T. Arroyo, M. Prodanov, Anal. Chim. Acta 563 (2006) 145–153.
[28] M.C. Horrillo, I. Sayago, M.J. Fenández, R. Gómez-Espinosa, A. Blanco, in: L.O. tero, M. García, L. Arés, J. Gutiérrez (Eds.), Electronic Noses and Olfaction 2000, Institute of Physics Publishing, Bristol, Philadelphia, 2000, pp. 75–80.
[29] P.D. Wasserman, Advanced Methods in Neural Computing, Van Nostrand Reinhold, New York, 1993.
[30] E.P.P.A. Derks, M.L.M. Beckers, W.J. Melssen, L.M.C. Buydens, Comput. Chem. 20 (1995) 439–448.
[31] J.P. Santos, J. Lozano, M. Aleixandre, I. Sayago, M.J. Fernández, L. Arés, J. Gutiérrez, M.d.C. Horrillo, Sens. Actuators, B 103 (1–2) (2004) 98–103.

Talanta 80 (2010) 1907–1912

Contents lists available at ScienceDirect

Talanta

journal homepage: www.elsevier.com/locate/talanta

Eggshell membrane-based solid-phase extraction combined with hydride generation atomic fluorescence spectrometry for trace arsenic(V) in environmental water samples

Yongjiang Zhang [a], Weidong Wang [a], Lu Li [a], Yuming Huang [a,*], Jia Cao [b]

[a] The Key Laboratory of Luminescence and Realtime Analysis, Ministry of Education, College of Chemistry and Chemical Engineering, Southwest University, No. 2 Road Tiansheng, Beibei, Chongqing 400715, China
[b] Department of Hygienic Toxicology, Preventive Medicine College, Third Military Medical University, Chongqing 400038, China

ARTICLE INFO

Article history:
Received 27 July 2009
Received in revised form 13 October 2009
Accepted 18 October 2009
Available online 24 October 2009

Keywords:
Arsenic
Eggshell membrane
Solid-phase extraction
Hydride generation atomic fluorescence spectrometry

ABSTRACT

The eggshell membrane (ESM) contains several surface functional groups such as amines, amides and carboxylic groups with potential as SPE adsorbent for the retention of target species of interest. In this paper, the potential use of ESM, a typical biomaterial, as solid-phase extraction (SPE) adsorbent is evaluated for analysis of trace arsenic(V) in environmental water samples in combination with hydride generation atomic fluorescence spectrometry (HG-AFS). In order to obtain the satisfactory recovery of arsenic(V), various parameters including the desorption and enrichment conditions such as pH, the flow rate and the volume of sample solution, the amount of ESM and the content of sodium chloride were systematically optimized and the effects of co-existed ions were also investigated in detail. Under the optimal conditions, arsenic(V) could be easily extracted by the ESM packed cartridge and the breakthrough adsorption capacity was found to be 3.9 $\mu g\,g^{-1}$. The favorable limit of detection (LOD) for arsenic(V) was found to be 0.001 $\mu g\,L^{-1}$ with an enrichment factor of 33.3, and the relative standard deviations (R.S.Ds) was 2.1% for 0.6 $\mu g\,L^{-1}$ arsenic ($n = 11$). The reproducibility among columns was satisfactory (R.S.D. among columns is less than 5%). The proposed method has been successfully applied to analysis of arsenic(V) in aqueous environmental samples, which suggests the ESM can be an excellent SPE adsorbent for arsenic(V) pretreatment and enrichment from real water samples.

© 2009 Elsevier B.V. All rights reserved.

1. Introduction

Up to now, the world-wide consumption of arsenic compounds in pesticides, wood preservatives, glassware production, electronics industries, waste incineration and the amounts derived from volcanic emissions, fossil fuels have made arsenic be one of the abundant elements in environment [1–3]. Thus, the arsenic was inevitably brought into the environment [4] and accumulated especially via food chains in vegetables, milk and rice [5]. Arsenic is a highly toxic pollutant. In general, the inorganic forms of arsenic are more toxic than its organic ones; the toxicity of trivalent forms of arsenic is greater than that of pentavalent forms [6]. Arsenic have caused a potential threat for environment safety, human health owing to its carcinogenic effects on hematopoietic system, lungs, kidneys, liver, bladder and the central nervous system, cardiovascular diseases, and dermal changes [7–10]. Recently, the contamination incidents of arsenic were reported in groundwater [11,12]. Therefore, the residual level of arsenic in drinking water is restricted by some the major world governments' health policies. For example, the United States Environment Protection Agency (US EPA) regulates arsenic maximum contaminant level (MCL) of 10 $\mu g\,L^{-1}$ [13], the World Health Organization (WHO) and Japanese restrict it to be 10 $\mu g\,L^{-1}$ [3]. Meanwhile, the European Community has limited the concentrations of arsenic in superficial waters to be 1.6 and 1.4 $\mu g\,L^{-1}$ from 2008 to 2015 [14]. Hence, it is particularly important to develop effective and reliable analytical techniques for arsenic determination.

In recent years, many analytical methods have been developed to determine arsenic in surface water, ground water and wastewater including hydride generation atomic absorption spectrometry (HG-AAS) [15], inductively coupled plasma atomic emission spectrometry (ICP-AES) [16], inductively coupled plasma mass spectrometry (ICP-MS) [17], hydride generation atomic fluorescence spectrometry (HG-AFS) [18], etc. Among above-mentioned methods, HG-AFS was widely used as a routine method for arsenic analysis due to its adequate sensitivity and selectivity, wide linear dynamic range and easy operation [19–21].

* Corresponding author. Tel.: +86 23 68254843; fax: +86 23 68367675.
E-mail address: yuminghuang2000@yahoo.com (Y. Huang).

0039-9140/$ – see front matter © 2009 Elsevier B.V. All rights reserved.
doi:10.1016/j.talanta.2009.10.042

Due to low concentration level of arsenic in natural water, preconcentration is necessary piror to determination. Among various pretreatment methods, SPE has several merits of short extraction time, high enrichment factor, low consumption of eluent, easy automation and has been used for arsenic preconcentration. Literature survey demonstrated that some new materials including ion exchange resins [16,22], carbon nanofibers [17], surfactant modified silica [23], nanometer titanium dioxide [24], the PTFE turnings for retention of As(III)–PDC (pyrrolidine dithiocarbamate) complex [25], activated alumina [26], etc., have been adopted as SPE adsorbent for preconcentration of arsenic from water samples. Recently, our group has induced a novel SPE format based on MWCNTS functionalized with CTAC hemimicelle as adsorbent for arsenic in environmental waters [27].

Due to having abundant of functional groups such as carboxyl, hydroxyl, sulfhydryl and amino groups, the exploitations of biomaterials or cells as solid substrates for solid-phase extraction of analytes have attracted extensive attentions recently [28–31]. ESM is a cheap, green and easily achieved biological material. It is mainly composed of a thin inner and a thick outer membrane including typical collagen protein, amino acids, saccharides and lipids [32,33] with a complex lattice network composed of stable and water-insoluble protein fibers. So, it could be considered as a promising candidate for SPE adsorbent due to attractive features such as the high specific surface area, excellent chemical stability and high density of surface functional groups including amines, amides and carboxylic [34]. In the previous research, the ESM which has been applied as an effective adsorbent for removing various heavy metals including Au, Pt, Cu, Cr, Pd [33–35] and the textile dyes [36]. In the study by Ishikawa et al., eggshell membrane and broiler chicken feathers were evaluated for the removal of the oxyanions selenium [Se(IV) and Se(VI)] and arsenic [As(III) and As(V)] from aqueous solutions in batch mode [37]. Recently, the batch removal of arsenic from aqueous solution using powdered eggshell was also reported [38]. However, to the best of our knowledge, there is no report on natural biomaterial ESM-based adsorbent for arsenic enrichment as SPE format. The goal of this study is to develop an analytical method for the determination of arsenic(V) by using ESM as SPE adsorbents to enrich arsenic(V) from water samples. The off-line SPE followed by HG-AFS method were chosen for monitoring arsenic in aqueous environmental samples.

2. Experimental

2.1. Chemicals and reagents

The stock standard solution of 1000 mg L^{-1} arsenic(V) was purchased from the national standard material center (National Center for Standard Material, Beijing, China). Working standard solutions of arsenic(V) (100 μg L^{-1}) were further prepared by serial dilution of the arsenic(V) stock standard solution with ultrapure water. All reagents used in the experiments were of analytical-reagent grade, except that the hydrochloric acid was guarantee reagent. 0.01 mol L^{-1} HCl and 0.01 mol L^{-1} NaOH solutions were prepared by adequate dilution of concentrated HCl and adequate amount of NaOH, respectively. The 2% (m/v) of sodium borohydride ($NaBH_4$) was freshly prepared by dissolving the sodium borohydride (Tianjin Institute of Chemical Reagents, Tianjin, China) in 0.5% (m/v) NaOH solution. The 5% (m/v) ascorbic acid and 5% (m/v) sulfocarbamide mixture solution were freshly prepared daily. The water used in this study is ultrapure water. All the glassware and polyethylene bottles used in experiments were firstly soaked with 10% (v/v) nitric acid for at least 24 h and cleaned with ultrapure. The glassware and polyethylene bottles were dried in a clean oven before use.

Table 1
Parameters and operating condition of AFS-230E.

Parameters	Settings
Lamp current	60 mA
Auxiliary lamp current	30 mA
Atomizer height	8 mm
Atomization temperature	250 °C
High negative voltage of photomultiplier	300 V
Carrier argon flow rate	400 ml min^{-1}
Shield gas flow rate	1000 ml min^{-1}
HCl carrier solution	5 (%, v/v)

Fresh eggs were purchased form the Chongqing local supermarket, and the ESM of hen eggs was obtained by opening the eggshell, then emptying the albumen and yolk and thoroughly washed with ultrapure water. The ESM was carefully peeled off the emptied fresh eggshell by hand. The cleaned ESM was finally immersed in 1 mol L^{-1} nitric acid for 12 h and rinsed with ultrapure water several times. Then the membrane was placed in a clean beaker, and dried at 80 °C for 2 h and cut into a small piece (about 0.5 mm × 0.5 mm). The as-treated ESM was used as SPE adsorbent material.

2.2. Instrumentation

A model AFS-230E hydride generation, double-channel atomic fluorescence spectrometer (Beijing Haiguang Instrument Ltd., Beijing, China) was used throughout for arsenic determination. The arsenic high-intensity hollow cathode lamp (General Research Institute of Non-Ferrous Metals, Beijing) was employed as the radiation sources. The working conditions of HG-AFS were listed in Table 1.

2.3. SPE procedure

An ESM packed cartridge was organized by modifying a C18 cartridge (1 g, 6 mL, popropylene) purchased from SUPELCO Cooperation, USA. The C18 packing material was evacuated and a proper amount of ESM was packed into the cartridge. The popropylene upper frit was reset at the upper end of the column to prevent the ESM leaching. Then the outlet tip of the column was connected to a model SHZ-3 (III) vacuum pump (Yuhua Instrument Co. Ltd., Zhengzhou, Henan), and the inlet end of column was connected to PTFE suction tube whose other end was inserted into sample solution. In order to reduce the possible interferences of metal ions, the entire SPE assembly needed to be preconditioned by washing with 5 mL of 2 mol L^{-1} nitric acid and 150 mL of ultrapure water before the pretreatment procedure. Next, sample solution was passed through cartridge at a flow rate of 3 mL min^{-1} by a vacuum pump. After the cartridge was washed with 5 mL of ultrapure water and dried under a certain negative pressure (20 mmHg) for 5 min, then arsenic(V) retained on the ESM column was eluted with an optimal volume of nitric acid. Finally, the eluent was used for arsenic(V) analysis. After finishing the elution process, 5 mL of 2 mol L^{-1} HNO_3 were employed to pass through the mini-column to regenerate the column for the next run and then washed with water until neutral pH was reached. The recovery was used as criterion to optimize the parameters for ESM-based SPE. The recovery was calculated as the ratio of the amount of arsenic(V) with and without preconcentration.

2.4. Analytical application

In this work, several types of environment water samples were selected for investigation the potential of ESM-based SPE for arsenic(V) enrichment. Tap water sample was collected from our laboratory after flowing for 10 min. River water sample was

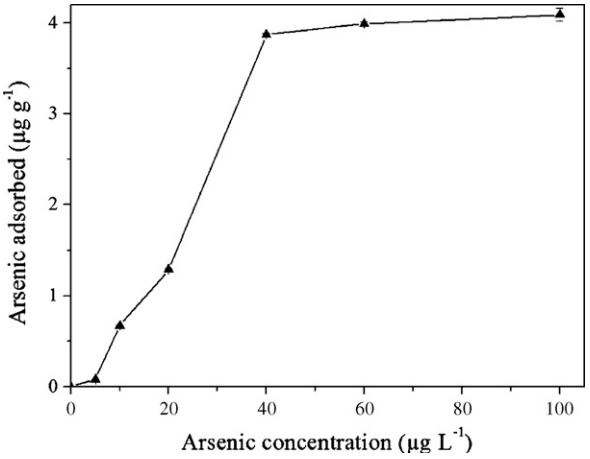


Fig. 1. The breakthrough curve of arsenic on the ESM. Sample volume: 40 mL; pH: 11. ESM: 500 mg, flow rate: 3 mL min^{-1}. Error bars represent one standard deviation for three measurements.

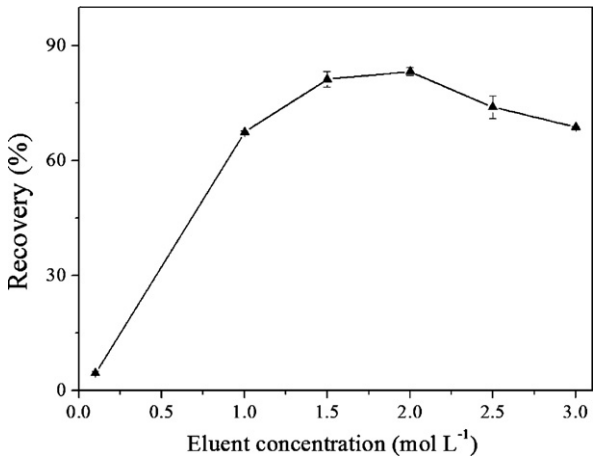


Fig. 2. Effect of nitric acid concentration on recoveries of arsenic. Arsenic(V) concentration in sample solution: 0.5 μg L^{-1}; volume of sample solution: 40 mL; the amount of ESM: 500 mg; sample flow rate: 3 mL min^{-1}; sample pH: 6.0. Error bars represent one standard deviation for three measurements.

collected from Jialingjiang River water. Lake water was collected from ChongDe Lake located in Southwest University. Wastewater samples were from sewage and effluent of the constructed wetland system. Before analysis, all the water samples were filtered through 0.45 μm membrane filters to remove suspended solids and stored in acid-cleaned polyethylene bottles at 4 °C in refrigerator. For real water sample analysis, 8 mL of 0.5 mol L^{-1} sodium fluoride as masking agent was added to 200 mL (adjusted to pH 11) of the environmental water samples for eliminating the interference of metal ions. Note that if the precipitation takes place after addition of sodium fluoride, the sample should be filtered through 0.45 μm membrane filters, then used for arsenic analysis.

3. Results and discussion

3.1. Adsorption capacity of eggshell membrane

In order to study the adsorption capacity of ESM-based SPE column for arsenic(V), according to the method by Maquieira et al. [39], 40 mL of sample solutions containing different concentrations (0–100 μg L^{-1}) of arsenic(V) were extracted by the SPE. Then, the amount of arsenic(V) adsorbed by ESM packed cartridge at the each concentration level was calculated. The dynamic adsorption curve for arsenic(V) was obtained by plotting the concentration (μg L^{-1}) of sample solution versus the microgrammes of arsenic(V) adsorbed on per gram of the ESM (μg g^{-1}), and shown in Fig. 1. As can be seen that the breakthrough capacity of the ESM biosorbent materials for arsenic(V) was found to be 3.9 μg g^{-1}. So, ESM shows good retention ability for arsenic(V) and can be used as adsorbent for arsenic(V) enrichment.

3.2. Optimization for the solid-phase extraction

3.2.1. Effects of the desorption reagent

Desorption of arsenic(V) from the ESM packed cartridge was investigated using different concentrations of nitric acid between 0.1 and 3 mol L^{-1}. The results presented in Fig. 2 indicated that the recoveries increased with the increase of nitric acid concentration to 2.0 mol L^{-1}, above which the recovery decreased. Then, the volume of nitric acid for desorption of arsenic(V) from the ESM was also investigated in the range of 2–10 mL. The experimental results shown that 6 mL of nitric acid was enough to desorb arsenic(V) from the ESM column. In order to obtain a higher preconcentration factor and satisfactory recovery, 6 mL of 2 mol L^{-1} nitric acid was selected for further experiments.

3.2.2. Effect of pH

The effect of pH on recovery was investigated in the range of 4–12. Results shown in Fig. 3 revealed that the recoveries of arsenic(V) were not significantly affected by the pH value from 5 to 9. It was worth noticing that the maximum recoveries were obtained between pH 10 and 11, above which, it decreased. Hence, a pH value of sample solution adjusted to 10–11 was adopted as the optimum pH value for in the present study. The pH effect was somewhat similar to that by Ishikawa et al. [37] who discovered that the adsorption efficiency of arsenic on the ESM increased gradually with the increase of pH from 8 to 11, and the maximum adsorption amount was generally found at pH 11. The adsorption of metal ions such as Cr(VI) and As(V) onto the surface of organic substrates such as eggshell membrane is a complicated process. It has been demonstrated by Zou et al. [35] that ESM shows good retention ability for Cr(VI) due to the presence of the positively charged functional groups such as $-NH_3^+$ and $-CO\text{-}NH_2^+-$. Therefore, the adsorption processes of As(V) onto the ESM surface might be similar to that of Cr(VI), which is electrostatic interaction between the As(V) and ESM surface due to the fact that As(V) is in the forms of oxyanions in surface water [40]. According to Zou et al., the N-acetyl group might contribute to the bio-sorption of As(V) on the surface of ESM [35]. When performing arsenic analysis, pH adjustment should be

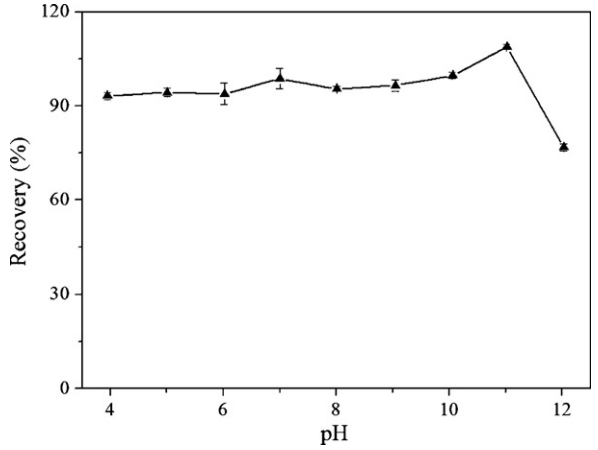


Fig. 3. Effect of sample pH on recoveries of arsenic. Arsenic(V) concentration in sample solution: 0.5 μg L^{-1}; volume of sample solution: 40 mL; the amount of ESM: 500 mg; sample flow rate: 3 mL min^{-1}; eluent: 6 mL of 2.0 mol L^{-1} nitric acid. Error bars represent one standard deviation for three measurements.

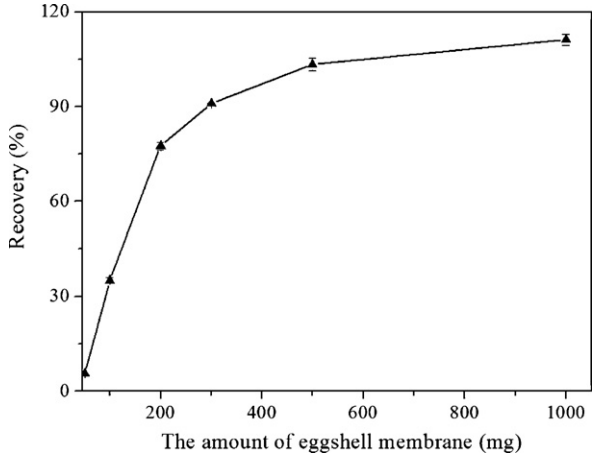


Fig. 4. Effect of amount of the ESM on the recoveries of arsenic. Arsenic(V) concentration in sample solution: 0.5 μg L^{-1}; volume of sample solution: 40 mL; sample flow rate: 3 mL min^{-1}; sample pH: 11; eluent: 6 ml of 2.0 mol L^{-1} nitric acid. Error bars represent one standard deviation for three measurements.

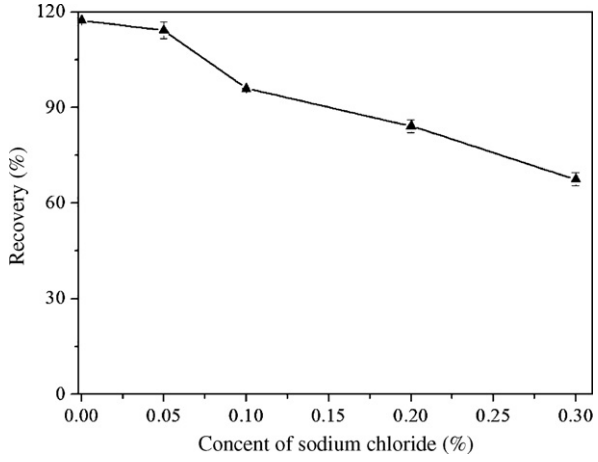


Fig. 5. Effect of the content of sodium chloride on the recoveries of arsenic. Arsenic(V) concentration in sample solution: 0.5 μg L^{-1}; volume of sample solution: 40 mL; the amount of ESM: 1000 mg; sample flow rate: 3 mL min^{-1}; sample pH: 11; eluent: 6 ml of 2.0 mol L^{-1} nitric acid. Error bars represent one standard deviation for three measurements.

an important step to ensure quantitative retention of As(V) onto ESM due to the fact that it not only determined the present state of analytes in solution as ionic or molecular state, but also the sorbent surface properties [35]. The effect of solution pH can be tentatively explained by considering the surface charge of the ESM and the distribution of As(V) species. As indicated previously, the adsorption processes of As(V) onto the ESM surface might be the electrostatic interaction between the As(V) and ESM surface due to the presence of the positively charged functional groups such as $–NH_3^+$ and $–CO\text{-}NH_2^+$–. The majority of As(V) is present in neutral molecular H_3AsO_4 at pH below 2, the lower adsorption of arsenic can be obtained. At pH values of 2.24–6.76, and 6.76–11.60, the major forms of As(V) are $H_2AsO_4^-$ and $HAsO_4^{2-}$, respectively [40], the arsenic adsorption tends to increase, suggesting that ESM can more easily adsorb $H_2AsO_4^-$ and $HAsO_4^{2-}$. However, the competition phenomena with hydroxides could tend to reduce the arsenic adsorption at higher pH (pH 12).

3.2.3. Effect of sample solution flow rate and volume

The effect of flow rate on retention of arsenic(V) was studied from 1.0 to 8.0 mL min^{-1} (the maximum flow rate of the vacuum pump). The experimental results demonstrated that the recoveries decreased with the increase of the flow rate. Finally, 3 mL min^{-1} was chosen as the flow rate for subsequent experiments. The effect of sample solution volume was determined for achieving higher enrichment factor by using different volume of sample solution (100, 150, 200, 300 and 500 mL) through the ESM packed cartridge. The results exhibited that the satisfactory recovery of arsenic(V) was obtained from 100 to 200 mL. Further increase of the solution volume led to significantly decrease for the recovery of arsenic(V). When 200 mL was selected, an enhancement of 33.3 based on calculation of preconcentration factor (PF) was obtained for arsenic(V) because 6 mL of 2.0 mol L^{-1} nitric acid was chosen as optimal eluent. Therefore, 200 mL of sample volume was selected as the optimal sample volume for further investigation.

3.2.4. Effects of ESM amount

Effect of the ESM amount on SPE efficiency of arsenic(V) was shown in Fig. 4. As can be seen that the recovery of arsenic(V) increased remarkably with increase of the amount of ESM when packed ESM was lower than 300 mg. The recovery of arsenic(V) increased gradually with increase of the ESM amount in the range from 300 to 1000 mg. To gain high enrichment efficiency and provide more adsorption sites, 1000 mg of ESM was selected as the optimal amount of ESM for the subsequent works.

3.3. Effect of sodium chloride and other co-existing substances

In this study, the content of sodium chloride ranging from 0 to 0.3% (w/v) was evaluated. The experimental results shown in Fig. 5 indicated that addition of sodium chloride would lead to decrease of arsenic(V) retention. It should be easily observed that the recovery of arsenic(V) was lower than 95% at the sodium chloride concentration above 0.1% (w/v), corresponding to 393 and 607 mg L^{-1} for Na^+ and Cl^-, respectively. A previous study reported that the electrolytes (e.g. sodium chloride) caused the adsorption capacity of arsenic decrease on an activated carbon with an increase of sodium chloride concentration [14]. This phenomenon may be caused by the competitive adsorption between chloride anion and the oxyanions of arsenic at the same active sites on the ESM surface. In order to evaluate the analytical applications of developed method, the effect of other co-existing substances were investigated under the optimized conditions. The effect of foreign substances was tested by enrichment a standard solution of As(V) (0.5 μg L^{-1}) according to SPE procedure described in experimental section to which increasing amounts of interfering substances was added. The tolerable concentration ratios with respect to 0.5 μg L^{-1} arsenic(V) for interference at less than 10% level were listed in Table 2. As can be seen that Fe, Mn and Pb are the main interferences for arsenic(V) retention. In fact, less than 5% recoveries were obtained when performing direct arsenic preconcentration without considering the elimination of cation ions. In order to eliminate the interferences derived from Fe, Mn, Pb and other co-existing transient metals, different chelate reagents such as EDTA, triethanolamine, 8-hydroxyquinoline and NaF were tested. Experimental results indicate that quantitative recoveries of arsenic(V) were obtained when NaF was added to the water samples. Hence, for real sample analysis for arsenic(V), NaF was selected.

3.4. Analytical performance

Analytical parameters for the quantitative analysis of arsenic(V) such as linear range, limit of detection (LOD), correlation coefficient (R^2), and the relative standard deviation (R.S.D.) were evaluated under the optimal conditions. According to experimental results, the calibration curves were in the range of

Table 2
Recoveries of arsenic(V) sorbed onto the ESM surface in the presence of foreign species (arsenic concentration: 0.5 μg L^{-1}).

Co-existing ions	At concentration	Recovery (%)[a]
NO_3^-	100 mg L^{-1}	91.38 ± 0.41
SO_4^{2-}	100 mg L^{-1}	90.80 ± 0.89
K^+	130 mg L^{-1}	101.83 ± 1.94
Na^+	393 mg L^{-1}	94.18 ± 0.92
Cl^-	607 mg L^{-1}	95.98 ± 1.94
Ca^{2+}	72 mg L^{-1}	96.13 ± 0.69
CO_3^{2-}	10 mg L^{-1}	93.01 ± 1.25
NH_4^+	2.5 mg L^{-1}	97.74 ± 0.97
Mg^{2+}	1 mg L^{-1}	92.21 ± 1.18
PO_4^{3-}	1 mg L^{-1}	96.68 ± 1.16
Co^{2+}	1 mg L^{-1}	99.37 ± 2.27
SO_3^{2-}	500 μg L^{-1}	97.96 ± 2.81
NO_2^-	500 μg L^{-1}	103.23 ± 0.65
I^-	250 μg L^{-1}	101.90 ± 0.53
Cd^{2+}	250 μg L^{-1}	95.01 ± 0.84
Cu^{2+}	200 μg L^{-1}	95.17 ± 1.21
Ni^{2+}	190 μg L^{-1}	90.61 ± 0.70
Al^{3+}	100 μg L^{-1}	109.83 ± 0.87
Mn^{2+}	50 μg L^{-1}	100.34 ± 1.33
Fe^{3+}	50 μg L^{-1}	91.69 ± 1.08
Pb^{2+}	20 μg L^{-1}	97.64 ± 0.64

[a] Mean value ± standard deviation (n = 3).

0.005–2.0 μg L^{-1} arsenic(V) standards by HG-AFS detection. The calibration equation was $\Delta I = 2611.5c + 190$ with a correlation coefficient of 0.9947 (n = 11), where ΔI being the net fluorescence intensity, c being the arsenic(V) concentration (μg L^{-1}). The linear calibration plot for arsenic(V) was shown in Fig. 6. The LOD (3σ) and limit of quantitation (LOQ) (10σ) was found to be 0.001 and 0.0033 μg L^{-1}, respectively. The present method was compared to the analytical methods previously published in literatures [16–20,22,23,25,27,41–43] using solid-phase extraction for arsenic analysis in terms of the detection limits (LODs). And the LODs were listed in Table 3. As can be seen, the LOD of this work was at least one order of magnitude lower than the reported SPE-ICP method [16,17,41,42], showing high sensitivity of the proposed method. Also, the LOD of this method was comparable with that obtained by functionalized MWCNTS and cigarette filter-based SPE methods [27,43]. The R.S.D. was 2.1% for 0.6 μg L^{-1} arsenic level (n = 11), indicating favorable precision of the proposed method.

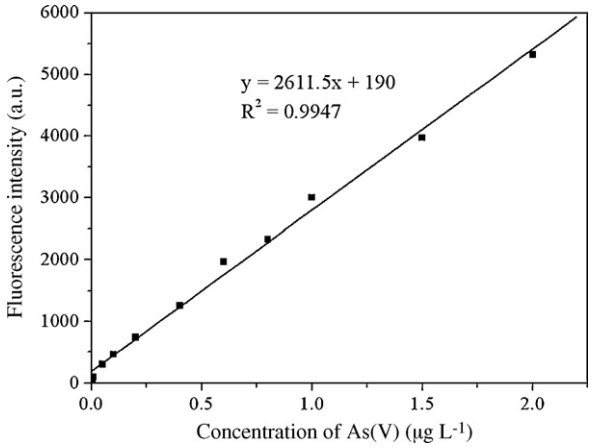


Fig. 6. The linear calibration plot for arsenic(V).

Three replicate determinations at 0.5 μg L^{-1} As(V) concentration level were carried out to test the reproducibility among

Table 3
Comparison LOD of this work with some established methods using solid-phase extraction for arsenic.

Sorbent material/complexing reagent	Analytical method	Detection limit (ng L^{-1})	Reference
Anion exchange resin Muromac®[a]	ICP-AES	100	[16]
Carbon nanofibers[b]	ICP-MS	240	[17]
Octadecyl modified silica/APDC for As(III)[a]; 717 anion exchange resin for As(V)[a]	HG-AFS	20 for As(III) 30 for As(V)	[18]
Knotted reactor/APDC[a]	HG-AFS	23	[19]
Anion exchanger Q-Sepharose[a]	HG-AFS	20	[20]
Amberlite IRA-410[a]	HG-AFS	20	[22]
CTAB-modified alkyl silica[a]	ICP-OES	15	[23]
PTFE turnings/APDC[a]	HG-AAS	20	[25]
CTAC hemimicelle functionalized MWCNTS[b]	HG-AFS	2	[27]
Amine resin LC-SAX	ICP-MS	36–94	[41]
Modified mesoporous TiO_2[b]	ICP-OES	100	[42]
Cigarette filter[a]	HG-AFS	7.4	[43]
ESM[b]	HG-AFS	1	This method

[a] On-line
[b] Off-line.

Table 4
Analytical results of arsenic(V) in various samples by the proposed method.

Samples	Certified (mg L^{-1})	Found (mg L^{-1})[a]	Added (μg L^{-1})	Found (μg L^{-1})	Recovery (%)[a]
CRM GBW (E) 080391[a]	4.0 ± 0.3	3.9 ± 0.1	/	/	/
Tap water	/	/	/	0.597	/
	/	/	0.2	0.822	112.67 ± 5.97
Jialing river water	/	/	/	0.611	/
	/	/	0.2	0.818	103.67 ± 5.92
Living sewage	/	/	/	0.890	/
	/	/	0.2	1.099	104.72 ± 4.24
Lake water	/	/	/	1.169	/
	/	/	0.2	1.375	102.95 ± 6.35
Wetland water	/	/	/	0.957	/
	/	/	0.2	1.153	98.00 ± 11.02

[a] Mean value ± standard deviation (n = 3).

three columns. The R.S.Ds were 2.6 and 4.3% for day-to-day and column-to-column, respectively. As can be seen, R.S.D. (precision) of day-to-day and column-to-column is less than 5%, suggesting the reproducibility among columns is satisfactory.

3.5. Application to environmental water samples

In order to validate the proposed method, a certified reference material was analyzed for arsenic(V) concentration (CRM GBW(E) 080391, environmental water sample) (Institute of Reference Materials, Beijing, PR China). The result was listed in Table 4. As can be seen, the analytical result of the certified reference was satisfactorily in agreement with the certified value.

The developed method was also applied to arsenic determination in several environmental water samples. In order to eliminate the possible interferences from metal ions, NaF was used as masking reagent. As can be seen from Table 4 that the recoveries of arsenic(V) in the spiked environmental water samples ranged from 98 to 113%, which demonstrated that the proposed method was satisfactory for arsenic analysis. It should be indicated that the extraction recoveries above 100% for some water samples were probably caused by the experimental errors and matrix effects.

4. Conclusion

In summary, we propose a natural biomaterial ESM-based adsorbent for arsenic(V) enrichment as SPE format coupled with HG-AFS in this study. The current investigation has demonstrated well the potential of ESM as SPE adsorbent for enriching of arsenic(V) in environmental aqueous samples by adsorption capacity test, desorption test and real sample application. The proposed method promises high sensitivity and good reproducibility for arsenic(V) determination. In addition, the ESM-based adsorbent promises to be cheap, environmentally benign and biodegradable. It is believed that the eggshell membrane may be useful a SPE adsorbent for other pollutants.

Acknowledgements

The authors thank the Key Technologies R&D Programme from Chongqing Science and Technology Commission (No. 2006AA7003), the Natural Science Foundation of Chongqing (No. 2004BA7019) and Key Laboratory of Luminescence and Realtime Analysis (Ministry of Education) for their financial supports.

References

[1] J. Matschullat, Sci. Total Environ. 249 (2000) 297.
[2] M. Berg, H.C. Tran, T.C. Nguyen, H.V. Pham, R. Schertenleib, W. Giger, Environ. Sci. Technol. 35 (2001) 2621.
[3] P.L. Smedley, D.G. Kinniburgh, Appl. Geochem. 17 (2002) 517.
[4] D.K. Nordstrom, Science 296 (2002) 2143.
[5] A. Masotti, L.D. Sacco, G.F. Bottazzo, E. Sturchio, Environ. Pollut. 157 (2009) 1771.
[6] J.K. Yang, M.O. Barnett, J. Zhuang, S.E. Fendorf, P.M. Jardine, Environ. Sci. Technol. 39 (2005) 7102.
[7] W.F. Chen, R. Parette, J.Y. Zou, F.S. Cannon, B.A. Dempsey, Water Res. 41 (2007) 1851.
[8] D. Mishra, A. Mehta, S.J. Flora, Chem. Res. Toxicol. 21 (2008) 400.
[9] B.K. Mandal, K.T. Suzuki, Talanta 58 (2002) 201.
[10] J.D. Ayotte, D.L. Montgomery, S.M. Flanagan, K.W. Robinson, Environ. Sci. Technol. 37 (2003) 2075.
[11] A.J. Signes-Pastor, K. Mitra, S. Sarkhel, M. Hobbes, F. Burlo, W.T. de Groot, A.A. Carbonell-Barrachina, J. Agric. Food Chem. 56 (2008) 9469.
[12] H. Kondo, Y. Ishiguro, K. Ohno, M. Nagase, M. Toba, M. Takagi, Water Res. 33 (1999) 1967.
[13] US Environmental Protection Agency, 2002. Office of Ground water and Drinking Water, http://www.epa.gov//safewater/arsenic.html.
[14] F. Di Natale, A. Erto, A. Lancia, D. Musmarra, Water Res. 42 (2008) 2007.
[15] M. Tuzen, D. Citak, D. Mendil, M. Soylak, Talanta 78 (2009) 52.
[16] K. Jitmanee, M. Oshima, S. Motomizu, Talanta 66 (2005) 529.
[17] S.Z. Chen, X.L. Zhan, D.B. Lu, C. Liu, L. Zhu, Anal. Chim. Acta 634 (2009) 192.
[18] M.L. Chen, Y.M. Huo, J.H. Wang, Talanta 78 (2009) 88.
[19] X.P. Yan, X.B. Yin, X.W. He, Y. Jiang, Anal. Chem. 74 (2002) 2162.
[20] X. Long, M. Miró, E.H. Hansen, J.M. Estela, V. Cerdà, Anal. Chem. 78 (2006) 8290.
[21] M.L. Chen, A.M. Zou, Y.L. Yu, R.H. He, Talanta 73 (2007) 599.
[22] L.O. Leal, N.V. Semenova, R. Forteza, V. Cerda, Talanta 64 (2004) 1335.
[23] C. Xiong, M. He, B. Hu, Talanta 76 (2008) 772.
[24] P. Liang, R. Liu, Anal. Chim. Acta 602 (2007) 32.
[25] A.N. Anthemidis, E.K. Martavaltzoglou, Anal. Chim. Acta 573 (2006) 413.
[26] S. Karthikeyan, T. Prasada Rao, C.S. Iyer, Talanta 49 (1999) 523.
[27] L. Li, Y.M. Huang, Y. Wang, W.D. Wang, Anal. Chim. Acta 631 (2009) 182.
[28] X.W. Chen, L.L. Huang, R.H. He, Talanta 78 (2009) 71.
[29] A.M. Zou, M.L. Chen, Y. Shu, M. Yang, J.H. Wang, J. Anal. Atom. Spectrom. 22 (2007) 392.
[30] A.M. Zou, M.L. Chen, X.W. Chen, J.H. Wang, Anal. Chim. Acta 598 (2007) 74.
[31] X.W. Chen, A.M. Zou, M.L. Chen, J.H. Wang, P.K. Dasgupta, Anal. Chem. 81 (2009) 1291.
[32] M.S. Fernandez, A. Moya, L. Lopez, J.L. Arias, Matrix Biol. 19 (2001) 793.
[33] K. Suyama, Y. Fukazawa, Y. Umetsu, Appl. Biochem. Biotechnol. 45–46 (1994) 871.
[34] S. Ishikawa, K. Suyama, K. Arihara, M. Itoh, Bioresour. Technol. 81 (2002) 201.
[35] A.M. Zou, X.W. Chen, M.L. Chen, J.H. Wang, J. Anal. Atom. Spectrom. 23 (2008) 412.
[36] M. Arami, N. Yousefi Limaee, N.M. Mahmoodi, Chemosphere 65 (2006) 1999.
[37] S. Ishikawa, S. Sekine, N. Miura, K. Suyama, K. Arihara, M. Itoh, Biol. Trace Elem. Res. 102 (2004) 113.
[38] I.A. Oke, N.O. Olarinoye, S.R.A. Adewusi, Adsorption 14 (2008) 73.
[39] A. Maquieira, H.A.M. Elmahadi, R. Puchades, Anal. Chem. 66 (1994) 3632.
[40] P.J. Swedlund, J.G. Webster, Water Res. 33 (1999) 3413.
[41] A.P. Packer, V.S.T. Ciminelli, Atom. Spectrosc. 26 (2005) 131.
[42] C.Z. Huang, B. Hu, Z.C. Jiang, Spectroc. Acta B 62 (2007) 454.
[43] N. Li, G. Fang, H. Zhu, Z. Gao, S. Wang, Microchim. Acta 165 (2009) 135.

Talanta 80 (2010) 1913–1918

Contents lists available at ScienceDirect

Talanta

journal homepage: www.elsevier.com/locate/talanta

Analysis of ultratrace triorganotin compounds in aquatic organisms by using capillary electrophoresis–inductively coupled plasma mass spectrometry

GuiDi Yang[a,b], JinHua Xu[a], LiangJun Xu[a], GuoNan Chen[a], FengFu Fu[a,*]

[a] Key Laboratory of Analysis and Detection Technology for Food Safety of Ministry of Education, Department of Chemistry, Fuzhou University, Fuzhou, Fujian 350108, China
[b] College of Life Sciences, Fujian Agriculture and Forestry University, Fuzhou 350002, China

ARTICLE INFO

Article history:
Received 16 August 2009
Received in revised form 8 October 2009
Accepted 18 October 2009
Available online 24 October 2009

Keywords:
Organotin
Aquatic organisms
Mya arenaria Linnaeus
Corbicula fluminea
CE–ICP-MS

ABSTRACT

A microwave-assisted extraction used to extract trace triorganotin from aquatic organisms and a sensitive analytical method for the determination of ultratrace triorganotin (namely trimethyltin, triethyltin, tripropyltin and tributyltin) with capillary electrophoresis–inductively coupled plasma mass spectrometry were firstly described in this study. The extraction method is simple, effective and can be used to extract trace triorganotin in aquatic organisms within several min. The analytical method has a much lower detection limit of 0.2–0.7 ng Sn/mL for triorganotin compounds, and can be used to determine trace triorganotin in aquatic organisms directly without any derivatization and preconcentration. Using above methods, we have successfully determined trimethyltin, triethyltin, tripropyltin and tributyltin in dried *Mya arenaria Linnaeus* and *Corbicula fluminea* within 17 min with a recovery of 93–104% and a RSD (relative standard deviation, $n = 6$) of 2–5%. Our results showed that dried *M. arenaria Linnaeus* contained an extremely high tributyltin of 5.1 μg Sn/g dried weight, indicating that it may be a good biomarker for the organotin pollution in ocean.

© 2009 Elsevier B.V. All rights reserved.

1. Introduction

For environmental studies, speciation is of major interest in organotin analysis, since the organotin's toxicity is strongly dependent on the species [1]. Especially, environmental concern about organotin compounds (OTCs) has increased considerably in recent years owing to the extensive use of these compounds as active components in antifouling paints (mainly tributyltin, TBT) and in pesticide formulations (mainly triphenyltin, TPhT) [2]. It is well known that TBT and TPhT are one of the endocrine disruptors and have a harmful influence on "non-target" marine organisms even at the ng/L level [3]. Their direct introduction into the marine environment has caused environmental and economic damage [4]. Therefore, in many countries, the use of triorganotin compounds such as TBT and TPhT has been prohibited or restricted by law. In order to control the effectiveness of these legal provisions and to evaluate the distribution and the fate of triorganotin compounds in the marine environment, it is very important to develop a sensitive and accurate analytical method for the quantification of ultratrace triorganotin compounds in aquatic organisms including *Mya arenaria Linnaeus* and *Corbicula fluminea*.

So far, main techniques employed to the speciation analysis of OTCs are based on the combination of separation techniques such as gas chromatography (GC) or liquid chromatography (LC) and sensitive, element-selective detectors such as flame photometric detection (FPD) [5–7], atomic absorption spectrometry (AAS) [8], atomic emission spectrometry (AES) [9,10], mass spectrometry (MS) [11–13] and inductively coupled plasma mass spectrometry (ICP-MS), etc. [14–18]. However, GC-based techniques require a previous derivatization step due to the low volatility of OTCs, and the derivatization is one of the most critical steps in organotin analysis. Low yield as well as degradation phenomena in derivatization can heavily affect the quality of the results [2]. LC-based methods do not require previous derivatization, however, LC-based techniques often suffer from one or more of the following deficiencies: lower resolution, poor sensitivity (combined with UV, AES, AAS and so on), inadequate stability due to much organic solvent (combined with ICP-MS) and so on [19].

In comparison with GC and LC, capillary electrophoresis (CE) offers higher separation efficiency, requires much smaller sample and has various separation modes [20]. Combined with different detectors such as UV-spectrometry, atomic fluorescence spectrometry (AFS) and so on, CE has been used in the analysis of various OTCs [21–24]. However, the combination of CE and UV or AFS has obvious limitations such as lower sensitivity, poorer stability

* Corresponding author at: Department of Chemistry, Fuzhou University, Qi-Shan Campus, Xue-Yuan Road 2, Fuzhou, Fujian 350108, China. Tel.: +86 591 28306608; fax: +86 591 28306608.
E-mail address: fengfu@fzu.edu.cn (F. Fu).

0039-9140/$ – see front matter © 2009 Elsevier B.V. All rights reserved.
doi:10.1016/j.talanta.2009.10.043

and so on. On the other hand, ICP-MS possesses several inherent advantages such as extremely high sensitivity for metallic ions, wide linear dynamic range, high speed analysis and the ability to perform isotopic analysis. These advantages make it an attractive CE detector for elemental speciation analysis [25]. Therefore, the coupling of CE and ICP-MS has received considerable attention due to the potential benefits offered by the combination of these two methodologies [26], and has been used in the speciation analysis of some elements [27]. However, the simultaneous determination of trimethyltin (TMT), triethyltin (TET), tripropyltin (TPT) and tributyltin (TBT) with CE–ICP-MS has not been reported up to date, because these four triorganotin compounds have very similar chemical structure and are difficult to be separated by CE.

The main aim of the present study is to develop a novel method for the simultaneous determination of ultratrace level of TMT, TET, TPT and TBT by using CE–ICP-MS, in hope of providing a realistic approach for the evaluation of organotin pollution in aquatic organisms.

2. Materials and methods

2.1. Reagents

The analytical grade of four triorganotin compounds including TMT, TET, TPT and TBT were purchased from Tianjin Alfa Aesar Co. Ltd. (Tianjin, China). The 1000 μg/mL stock standard solutions of TMT, TET, TPT and TPT were prepared by dissolving appropriate amounts of above drugs in methanol (HPLC grade, Shanghai Reagents Co. Ltd., Shanghai, China). The stock standard solutions were stored at 4 °C, and the working standard solutions were prepared by diluting stock standard solutions to the desired concentration with buffer solution just before use.

The super-pure sodium dodecyl sulfate (SDS) was obtained from Sigma company (USA), analytical grade sodium tetraborate ($Na_2B_4O_7{\cdot}10H_2O$) and boric acid (H_3BO_3), super-pure nitric acid and sodium hydroxide were purchased from Shanghai Reagents Co. Ltd. (Shanghai, China). The running buffer solution of 50 mmol/L H_3BO_3–12.5 mmol/L $Na_2B_4O_7$–20 mmol/L SDS was prepared by dissolving above reagents in Milli-Q water. All solutions were treated with ultrasonic agitation and filtered through a 0.22 μm membrane filter before use. All experiments were performed at room in which the temperature was regulated in 23–25 °C by air conditioners, and water used in this experiment is Milli-Q water (18.2 MΩ).

Dried *M. arenaria Linnaeus* sample, a marine bivalve molluscs, was offered by The Research Center for Eco-Environmental Sciences, Chinese Academy of Sciences. Dried *C. fluminea* sample, a species of fresh water clam, was purchased in local market. All samples were lyophilized and grinded into powder, and then were stored in a desiccator.

2.2. CE–ICP-MS system

The CE–ICP-MS system used in this study is the same as that reported in our previous paper, which consists of a home-made CE unit and an Agilent 7500ce ICP-MS system (Agilent Technologies, USA) [28]. The home-made CE was coupled to ICP-MS with a home-made interface. Sample solution was injected into CE–ICP-MS for determination with electro-migration injection. The CE capillary was conditioned daily by purging with Milli-Q water for 10 min, 0.1 mol/L NaOH solution for 10 min, Milli-Q water for 10 min and running buffer solution for 10 min, respectively. Between each run, the CE capillary was flushed with Milli-Q water and running buffer solution for 2 min, respectively.

2.3. Determination of TMT, TET, TPT and TBT in dried M. arenaria Linnaeus and C. fluminea

OTCs in dried *M. arenaria Linnaeus* and *C. fluminea* was extracted with the modified method of Wang et al. [11]. Firstly, about 0.2 g sample was accurately weighed and put into a 15 mL polyethylene centrifuge tubes, and 4.0 mL of methanol solution was added. Then, the tube was put into a 250 mL beaker in which has 100 mL water and the beaker was put into microwave digester (Sineo Microwave Chemical Technology Co. Ltd., Shanghai, China). The microwave system was programmed to heat the whole at 90 °C for 3 min under 500 W power. After the whole in the centrifuge tube was cooled to room temperature, the extract was separated by filtering it through a 0.22 μm membrane filter. Then, the extract was evaporated to near dryness using moderate N_2 stream and the residue was diluted to the appropriate volume (12.0 mL for *M. arenaria Linnaeus* and 2.0 mL for *C. fluminea*) with buffer solution again. The final solution was used for the CE–ICP-MS analysis with continuous sample-introduction mode.

3. Results and discussion

3.1. The optimum CE–ICP-MS conditions for the separation and detection of TMT, TET, TPT and TBT

In CE-based analysis, the buffer solution including its chemical components, pH and concentration greatly affected the separation of analytes by affecting the electroosmosis flow (EOF). In this study, we firstly try to separate TMT, TET, TPT and TBT with CZE (capillary zone electrophoresis), and several different buffer solutions including HAc–NaAc, H_3PO_4–NaH_2PO_4, NaH_2PO_4–$Na_2B_4O_7$, H_3BO_3–$Na_2B_4O_7$, strong inorganic acid and tartaric acid were used to separate TMT, TET, TPT and TBT. The experimental results showed that TET, TPT and TBT can not be completely separated under each of above buffer solution by CZE. It was reported that micelle capillary electrophoresis has many advantages for the separation of OTCs [29]. In this study, we also try to separate TMT, TET, TPT and TBT with micelle capillary electrophoresis by adding different surfactant such as SDS and sodium cholate into each of above buffer solution. The experimental results showed that TMT, TET, TPT and TBT can be completely separated when the H_3BO_3–$Na_2B_4O_7$ solution ($H_3BO_3/Na_2B_4O_7$ = 4/1, mole concentration) containing a 10 mmol/L SDS (critical micellar concentration of SDS) was used as buffer solution. Therefore, the H_3BO_3–$Na_2B_4O_7$ solution (4:1, mole concentration) containing a certain concentration of SDS was chosen as running buffer solution in this study.

The effect of the concentration of SDS on the separation and migration time of TMT, TET, TPT and TBT was studied in range of 10–40 mmol/L at 50 mmol/L H_3BO_3–12.50 mmol/L $Na_2B_4O_7$ buffer solution (pH 8.0) in detail, and the results indicated that higher concentration of SDS is favorable to prolong the migration time of all four triorganotin compounds and improve the electrophoretic resolution (see Fig. 1), however, higher concentration also increased background. Considered all of analytical time, background and resolution, 20 mmol/L was selected as the optimal SDS concentration.

The pH of the running buffer solution strongly affects the electrophoretic resolution and sensitivity. The relationship between migration time/resolution and pH was studied in detail with a 50 mmol/L H_3BO_3–12.5 mmol/L $Na_2B_4O_7$–20 mmol/L SDS buffer solution in the range of 7.50–8.50, and the results are shown in Fig. 2. From Fig. 2, we found that higher pH is favorable to improve the separation of TPT and TBT, TPT and TBT can be base line separated when pH is higher than 7.75. However, when pH is higher than 8.5, TMT and TET can not be completely separated. The electropherogram shown in Fig. 2 indicated that all four triorganotin

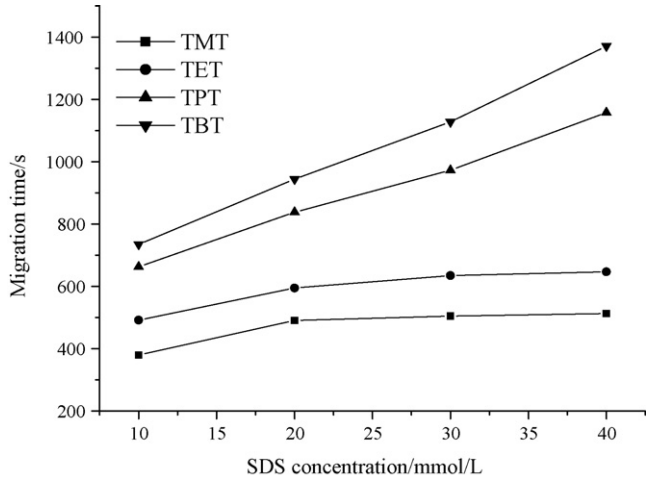


Fig. 1. The effect of SDS concentration on the separation of TMT, TET, TPT and TBT. The data was obtained by determining a 100 ng/mL mixed solution of TMT, TET, TPT and TBT with CE–ICP-MS under conditions of Table 1 except SDS concentration.

compounds can be base line separated with symmetrical peak shape when pH was in range of 7.75–8.25. Finally we chose pH 8.00 as the optimum pH for the separation of TMT, TET, TPT and TBT.

The effect of the concentration of running buffer solution on the separation and migration time was studied by using different concentration of H_3BO_3–$Na_2B_4O_7$ solution (H_3BO_3:$Na_2B_4O_7$ = 25.0:6.25, 37.5:9.38, 50:12.50, 75:18.75 and 100:25.00 mmol/L) containing 20 mmol/L SDS at pH 8.00 and +15 kV voltage, and the results are shown in Fig. 3A. From Fig. 3A, we found that the migration times of all four triorganotin compounds became longer with the increase of the concentration of H_3BO_3–$Na_2B_4O_7$ solution, however, higher concentration also led to a higher current and finally resulted in a bigger noise and a poorer reproducibility. The experimental results showed that when 50 mmol/L H_3BO_3–12.50 mmol/L $Na_2B_4O_7$ containing 20 mmol/L SDS (pH 8.00) was used as running buffer solution, the resolution and the peak shapes of four triorganotin compounds were the best. Therefore, 50 mmol/L H_3BO_3–12.50mmol/L $Na_2B_4O_7$ containing 20 mmol/L SDS (pH 8.00) was selected as the running buffer solution.

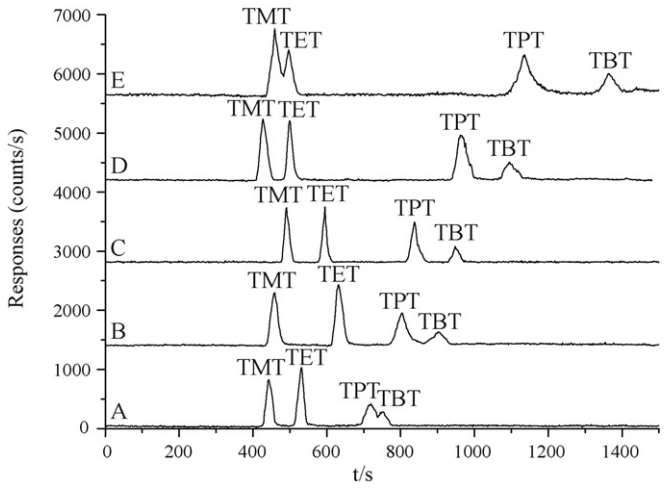


Fig. 2. The electropherograms of TMT, TET, TPT and TBT under different pH. The data was obtained by determining a 100 ng/mL mixed solution of TMT, TET, TPT and TBT with CE–ICP-MS under conditions of Table 1 except pH. (A) pH 7.50; (B) pH 7.75; (C) pH 8.00; (D) pH 8.25; and (E) pH 8.50.

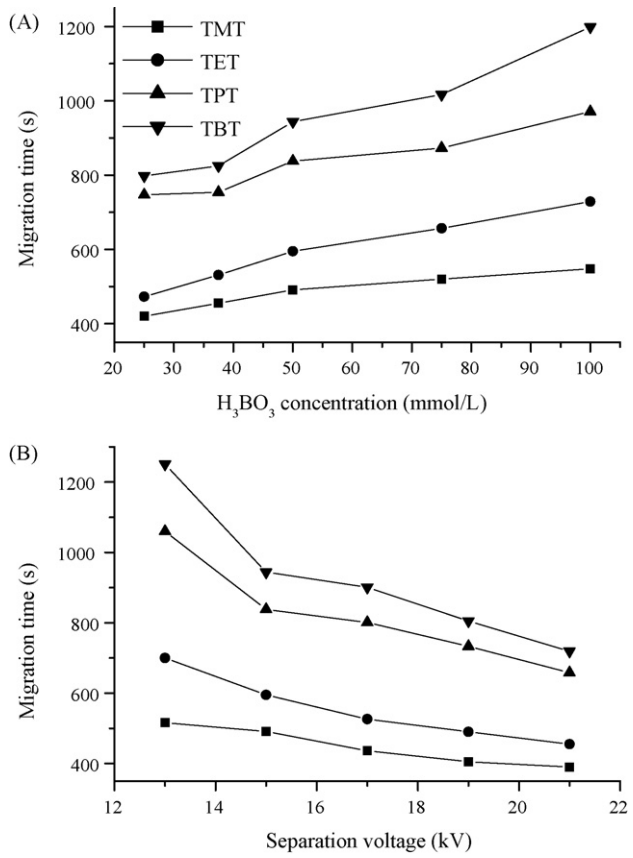


Fig. 3. The effect of buffer solution concentration and separation voltage on the separation of TMT, TET, TPT and TBT. The data was obtained by determining a 100 ng/mL mixed solution of TMT, TET, TPT and TBT with CE–ICP-MS under conditions of Table 1 except buffer solution concentration (A) and separation voltage (B). (A) Buffer solution concentration and (B) separation voltage.

The effect of the separation voltage on the migration time and electrophoretic resolution was investigated in the range of 13–21 kV, the results indicated that higher voltage is favorable to shorten the migration time, improve the sensitivities and the peak shapes (especially for TPT and TBT) (see Fig. 3B). However, higher voltage led to poorer reproducibility due to Joule heating effect. Considered all of reproducibility, analytical time and peak shape, +15 kV was selected as the separation voltage.

Different injection times (5, 10, 15, 20 and 25 s) were tested in this experiment, and the results showed that the sensitivities of four triorganotin compounds become higher with the increase of injection time. However, longer injection time will degrade electrophoretic resolution and broaden the peaks. Considering both sensitivity and separation efficiency, we selected 10 s as sample's injection time.

As we mentioned in our previous paper [28], the flow rate of pump 1, which was used to transport the analyte solution eluted out of the CE capillary to three-way PEEK and introduce a tiny sheath-flow into the outlet of CE capillary, will influence the peak shape and the sensitivity. By change the rate of pump 1 from 1.5 rpm (3 μL/min) to 7.5 rpm (15 μL/min), we found that 6.0 rpm of pump 1 (12 μL/min) provide a better peak shapes and sensitivity. The optimum rate of pump 2, which was used to pump Milli-Q water to ICP-MS nebulizer in order to achieve stable atomization and ionization efficiency, was selected by change the rate from 0 rpm (0 μL/min) to 10.0 rpm (400 μL/min), and the results showed that the flow rate of pump 2 = 5.0 rpm (200 μL/min) is the best choice.

At above optimum CE–ICP-MS conditions (see Table 1), four triorganotin compounds were completely separated within 17 min,

Table 1
Optimal running parameters of CE–ICP-MS.

Parameter	Value
CE voltage	+15 kV
Sample injection time	10 s
CE capillary	i.d. 75 μm; o.d. 365 μm; 60 cm long
Lab temperature	23–25 °C
Running buffer solution	50 mmol/L H_3BO_3–12.5 mmol/L $Na_2B_4O_7$ (pH 8.0) containing 20 mmol/L SDS
Flow rate of pump 1	12 μL/min
Flow rate of pump 2	200 μL/min
RF power	1300 W
Outer plasma gas	15 L/min
Intermediate plasma gas	0.90 L/min
Carrier gas	0.75 L/min
Makeup gas	0.30 L/min
Monitored isotope (m/z)	^{118}Sn, ^{120}Sn
Nebulizer type	MCN (optimum flow is 50–200 μL/min)

and their electropherograms are shown in Fig. 4 together with the electropherogram of reagent blank.

3.2. Reproducibility, linear relationship and detection limits

At the optimal CE–ICP-MS conditions shown in Table 1, the determination of 100 ng/mL mixed standard solution was repeated for six times in order to investigate the reproducibility of our method. The RSD ($n = 6$) of migration time was calculated to be 1.3%, 2.1%, 2.2% and 3.2% for TMT, TET, TPT and TBT, respectively, and that of peak area is 3.4%, 4.2%, 4.4% and 5.8% for TMT, TET, TPT and TBT, respectively. A series of different concentrations of mixed standard solutions (10, 20, 30, 50, 75, and 100 ng/mL) were determined in order to obtain calibration curves. The linear correlation coefficients between counts (peak area) and concentrations were better than 0.995 for all TMT, TET, TPT and TBT in the concentration range of 10–100 ng/mL (see Table 2). The instrument detection limits ($3\sigma/S$, the concentration necessary to yield a net signal equal to three times the standard deviation of the background) were calculated to be 0.2, 0.2, 0.3 and 0.7 ng/mL for TMT, TET, TPT and TBT, respectively, much lower than those obtained with other CE-based techniques [22,24].

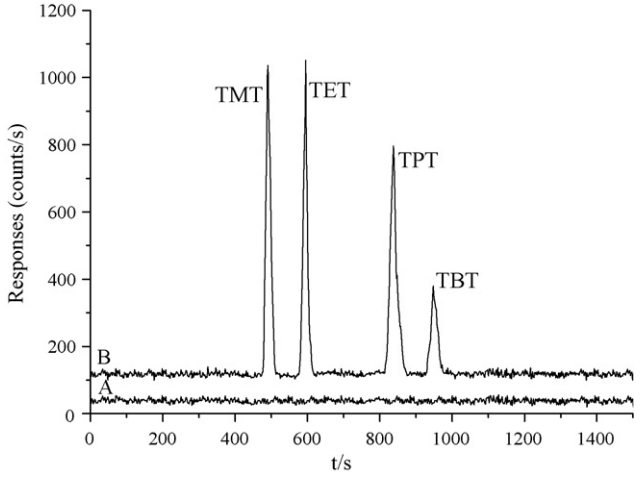


Fig. 4. The electropherograms of TMT, TET, TPT, TBT under the optimal CE–ICP-MS conditions shown in Table 1. The data was obtained by determining a 100 ng/mL mixed solution of TMT, TET, TPT and TBT and a reagent blank with CE–ICP-MS, respectively. (A) Blank and (B) mixed standard solution.

Table 2
Linear relationship and detection limits of our method.

Analyte	Regression equation[a]	Correlation coefficient	Liner range (ng/mL)	Detection limit[b] (ng/mL)
TMT	$y = 1133x + 301$	0.998	10–100	0.2
TET	$y = 1080x + 251$	0.997	10–100	0.2
TPT	$y = 923x + 337$	0.995	10–100	0.3
TBT	$y = 380x + 272$	0.996	10–100	0.7

[a] x = concentration (ng/mL), y = counts.
[b] Instrument detection limit.

3.3. The extraction of triorganotin compounds in M. arenaria Linnaeus and C. fluminea samples

To perform the speciation analysis of triorganotin compounds in aquatic organisms, the extraction of each triorganotin is another key point. The extraction method must be capable of quantitatively extracting each triorganotin species from samples without altering the individual organotin species during extraction process. So far, several kinds of organic solvent such as toluene, acetic acid–methanol, methanol–water have been used to extract OTCs in environmental and biological materials [11,30,31] and microwave-assisted extraction was reported to be an effective method for element species in marine plant and animal tissues [11,32]. Considering that methanol has a good solubility for all of TMT, TET, TPT and TBT and has a lower toxicity than toluene, in this study, a microwave-assisted extraction with methanol as solvent was used to extract triorganotin compounds in *M. arenaria Linnaeus* and *C. fluminea*. The effect of extracting temperature on the extracting efficiency was also investigated in 70–100 °C with *M. arenaria Linnaeus* as target, and the results showed that microwave-assisted extraction have a highest and most stable extracting efficiency in 90–100 °C (see Fig. 5). In this study, we selected 90 °C as the optimum temperature.

The power of microwave digester, ratio of extracting solvent volume to the mass of sample and extracting time are also important factors for the extraction of OTCs. In our experiments, a 500 W microwave digester was used for the extraction, and the effect of power on the extracting efficiency was not studied in detail since the power of microwave digester cannot be adjusted. The ratio of extracting solvent volume to the mass of sample was also optimized in this study, and the experimental result showed that the best ratio was 20. Higher ratio will increase the background of reagent blank and harm the detection limit of the method, whereas, lower

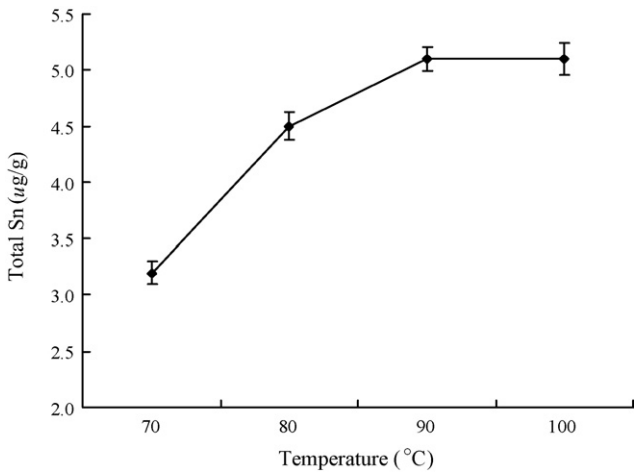


Fig. 5. The effect of extracting temperature on the extracting efficiency (the total concentration of tin) in *Mya arenaria Linnaeus*. 0.2 g of dried *Mya arenaria Linnaeus* sample was extracted with 4.0 mL of methanol.

Table 3
The analytical results of dried *Mya arenaria Linnaeus* and *Corbicula fluminea* samples.

Total con.[a]	*Mya arenaria Linnaeus*					*Corbicula fluminea*				
	5.2 ± 0.1					0.45 ± 0.02				
	DL[b]	Added con.[c]	Detected con.[c]	RSD[d] (%)	Rec. (%)	DL[b]	Added con.[c]	Detected con.[c]	RSD[d] (%)	Rec. (%)
TMT	2.0	0	<DL			2.0	0	0.43	2	
		3.0	2.9	2	97		0.50	0.92	3	98
TET	2.0	0	<DL			2.0	0	<DL		
		3.0	2.8	3	93		0.50	0.48	4	96
TPT	3.0	0	<DL			3.0	0	<DL		
		3.0	2.9	2	97		0.50	0.48	3	96
TRT	7.0	0	5.1	5		7.0	0	<DL		
		3.0	8.2	4	103		0.50	0.52	5	104

[a] The concentrations determined with ICP-MS after samples were completely decomposed with 7 mol/L HNO_3, unit is μg Sn/g dried weight.
[b] The detection limits of analyte in samples, unit is ng Sn/g dried weight.
[c] Unit is μg Sn/g dried weight.
[d] $n = 6$.

ratio will decrease the extracting efficiency of TMT, TET, TPT and TBT. Under 90 °C, 500 W and 20 times of solvent, OCTs in the dried *M. arenaria Linnaeus* and *C. fluminea* can be completely extracted within 3 min.

3.4. Determination of TMT, TET, TPT and TBT in dried M. arenaria Linnaeus and C. fluminea samples

In order to verify the reliability of our methods, the TMT, TET, TPT and TBT in dried *M. arenaria Linnaeus* and *C. fluminea* were extracted by the above method and their concentrations were determined with CE–ICP-MS under the conditions of Table 1. The analytical results are shown in Table 3 and their electropherograms are shown in Fig. 6.

The recoveries were also obtained by determining dried *M. arenaria Linnaeus* samples spiked with 3.0 μg Sn/g dried weight of TMT, TET, TPT and TBT and dried *C. fluminea* samples spiked with 0.50 μg Sn/g dried weight of TMT, TET, TPT and TBT with the same procedure described as above. The recoveries are also shown in Table 3 together with RSD. From Table 3, we found that the recovery is 93–104% and RSD ($n = 6$) is smaller than 5% for all four triorganotin compounds.

It was well known, if all OTCs in samples were completely extracted and if each triorganotin species keep no change during extraction process are two key points to the speciation analysis of triorganotin. From the results shown in Table 3, we found that the sum of the concentrations of each triorganotin species is consistent with the total concentration of tin (the concentration determined with ICP-MS after sample was completely decomposed with 7 mol/L HNO_3), indicated that all tin had been completely extracted using our method. The approximately 100% of recovery for all TMT, TET, TPT and TBT obviously indicated that each triorganotin species kept no change during extracting and analytical process, since the recovery of at least one triorganotin species should excessively deviated from 100% if any triorganotin species was changed during extracting and analytical process. The detection limits of analytes in samples can be calculated according to the detection limits of instrument and the preconcentration times of sample. In the case of dried *M. arenaria Linnaeus* and *C. fluminea*, 2 mL extracting solution of 0.2 g sample can be directly analyzed using our method without any pretreatment, therefore the method detection limits of each triorganotin in dried *M. arenaria Linnaeus* and *C. fluminea* were calculated to be 2.0, 2.0, 3.0 and 7.0 ng Sn/g dried weight (or 0.2, 0.2, 0.3 and 0.7 ng Sn/g fresh weight) for TMT, TET, TPT and TBT, respectively, equal to those obtained with GC-based technique [33]

From the electropherograms shown in Fig. 6, it was clearly found that TBT was detected in dried *M. arenaria Linnaeus*, and TMT was detected in dried *C. fluminea*. It was well known that TBT was deadly toxic to bivalve molluscs [34]. Zhou et al. reported that *M. arenaria Linnaeus* may have stronger ability to accumulate or lower rate to metabolize TBT than other marine organisms, and can become a more sensitive bio-monitor to effectively evaluate tributyltin con-

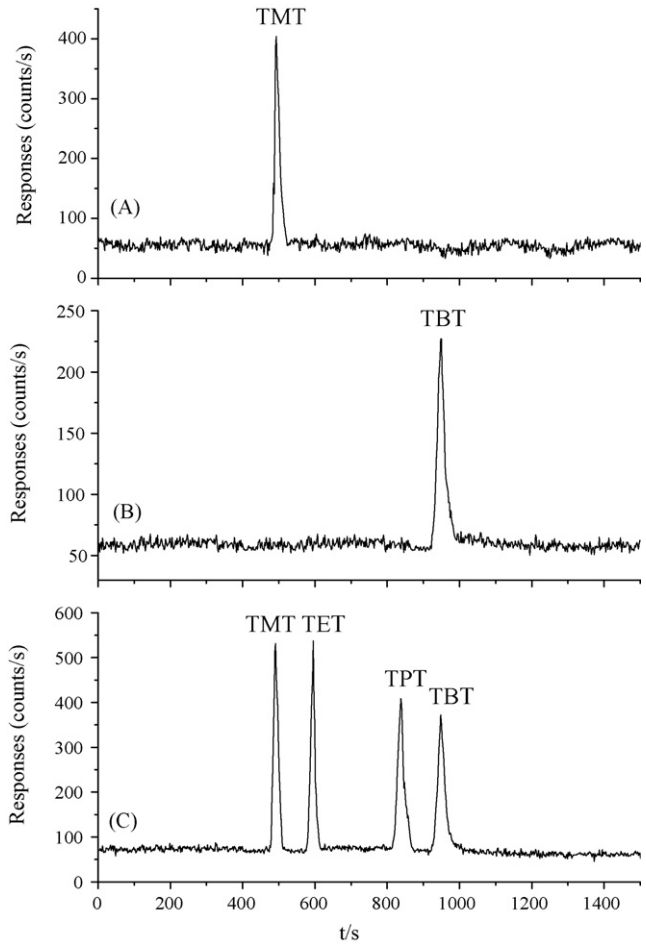


Fig. 6. The electropherograms of TMT, TET, TPT and TBT under the optimal CE–ICP-MS conditions shown in Table 1. (A) *Corbicula fluminea*; (B) *Mya arenaria Linnaeus*; and (C) *Mya arenaria Linnaeus* spiked with 3.0 μg Sn/g dried weight of TMT, TET, TPT and TBT.

tamination in ocean [35]. Our results also verified that *M. arenaria Linnaeus* had a much higher accumulation for TBT, the concentration of TBT in dried *M. arenaria Linnaeus* up to 5.1 μg Sn/g dried weight or 510 ng Sn/g fresh weight. While, no TBT was detected in *C. fluminea*, the major triorganotin species in *C. fluminea* was TMT and the concentration of TMT in dried *C. fluminea* was about 0.43 μg Sn/g dried weight or 43 ng Sn/g fresh weight.

According to the average seafood consumption (68.8 g/day, FAO, 1997–1999), the tolerable average residue level (TARL) for TBT in Chinese seafood was estimated to be 90.8 ng Sn/g for a common person with a weight of 60 kg [36]. The 510 ng Sn/g fresh weight of TBT in *M. arenaria Linnaeus* was much higher than TARL, implied that some people with *M. arenaria Linnaeus* preference may be at a high risk to organotin exposure. As for *C. fluminea*, the content of OTCs is much lower than TARL, and its predominant OTC was TMT. The potential danger of *C. fluminea* to the consumers should be further investigated.

4. Conclusion

An effective microwave-assisted extraction used to extract trace triorganotin compounds in aquatic organisms and a sensitive analytical method for the determination of ultratrace TMT, TET, TPT and TBT with CE–ICP-MS were firstly described in the study. The extraction method is simple, effective and can be used to extract trace triorganotin compounds in aquatic organisms with a satisfactory recovery within several minutes. The CE–ICP-MS analytical method have a much lower detection limit of 0.2–0.7 ng Sn/mL for TMT, TET, TPT and TBT, and can be used to simultaneously determine trace TMT, TET, TPT and TBT in aquatic organisms directly without any derivatization and preconcentration. With the help of above extraction and analytical method, we have successfully determined TMT, TET, TPT and TBT in dried *M. arenaria Linnaeus* and *C. fluminea* with detection limits of 2–7 ng Sn/g dried weight, RSD ($n = 6$) of 2–5% and recovery of 93–104%. About 5.1 μg Sn/g dried weight of TBT was detected in dried *M. arenaria Linnaeus*, whereas only about 0.43 μg Sn/g dried weight of TMT was detected in dried *C. fluminea*, indicating that *M. arenaria Linnaeus* is a good biomarker for TBT.

Acknowledgements

This work was supported by Fujian Provincial Department of Science and Technology (2009J01026, 2008Y0034), National Nature Sciences Funding of China (20735002, 40875087) and Fuzhou University (XSJRC2007-03). We also thank Prof. GuiBin Jiang (The Research Center for Eco-Environmental Sciences, Chinese Academy of Sciences) who provided us with dried *M. arenaria Linnaeus* samples.

References

[1] G.B. Jiang, Q.F. Zhou, B. He, Environ. Sci. Technol. 34 (2000) 2697.
[2] R. Morabito, P. Massanisso, Trends Anal. Chem. 19 (2000) 113.
[3] K. Fent, Crit. Rev. Toxicol. 26 (1996) 1.
[4] D.W. Evans, R.B. Laughlin, Chemosphere 13 (1984) 213.
[5] T. Zuliani, G. Lespes, R. Milacic, J. Scancar, M. Potin-Gautier, J. Chromatogr. A 1188 (2008) 281.
[6] J. Heroult, T. Zuliani, M. Bueno, L. Denaix, G. Lespes, Talanta 75 (2008) 486.
[7] A. Wasik, T. Ciesielski, Anal. Bioanal. Chem. 378 (2004) 1357.
[8] H. Narasaki, H.B. Hou, Y.C. Morimura, Anal. Sci. 16 (2000) 855.
[9] N. Campillo, N. Aguinaga, P. Viñas, I. López-García, M. Hernández-Córdoba, Anal. Chim. Acta 525 (2004) 273.
[10] A. Sadiki, D.T. Williams, Chemosphere 32 (1996) 1983.
[11] X.P. Wang, H.Y. Jin, L. Ding, H.R. Zhang, H.Q. Zhang, C.L. Qu, A.M. Yu, Talanta 75 (2008) 556.
[12] C.C. Chou, M.R. Lee, J. Chromatogr. A 1064 (2005) 1.
[13] G. O'Connor, R. Wahlen, B. Fairman, K.S. Webb, Adv. Mass Spectrom. 15 (2001) 965.
[14] H. Tao, C.R. Quetel, T. Nakazeto, M. Tominaga, A. Miyazaki, R.B. Rajendran, Anal. Chem. 71 (1999) 4208.
[15] F. Bianchi, M. Careri, M. Maffini, A. Mangia, C. Mucchino, J. Anal. Atom. Spectrom. 21 (2006) 970.
[16] R. Wahlen, T. Catterick, J. Chromatogr. B 783 (2003) 221.
[17] G.S. Zhai, J.F. Liu, L. Li, L. Cui, B. He, Q.F. Zhou, G.B. Jiang, Talanta 77 (2009) 1273.
[18] A. Ugarte, N. Unceta, C.M. Sampedro, M.A. Goicolea, A. Gomez-Caballero, R.J. Barrio, J. Anal. Atom. Spectrom. 24 (2009) 347.
[19] E. González-Toledo, R. Compañó, M. Granados, M.D. Prat, Trends Anal. Chem. 22 (2003) 26.
[20] J. Li, T. Umemura, T. Odake, K. Tsunoda, Anal. Chem. 73 (2001) 5992.
[21] E. Pobo˙zy, B. Głód, J. Kaniewska, M. Trojanowicz, J. Chromatogr. A 718 (1995) 329.
[22] K.S. Whang, C.W. Whang, Electrophoresis 18 (1997) 241.
[23] F. Han, J.L. Fasching, P.R. Brown, J. Chromatogr. B 669 (1995) 103.
[24] L.P. Yu, Anal. Lett. 40 (2007) 1879.
[25] A.L. Rosen, G.M. Hieftje, Spectrochim. Acta B 59 (2004) 135.
[26] J.W. Olesik, J.A. Kinzer, S.V. Olesik, Anal. Chem. 67 (1995) 1.
[27] G. Alvarez-Llamas, F. Lacampa, A. Sanz-Medel, Trends Anal. Chem. 24 (2005) 28.
[28] G.D. Yang, J.H. Xu, J.P. Zheng, X.Q. Xu, W. Wang, L.J. Xu, G.N. Chen, F.F. Fu, Talanta 78 (2009) 471.
[29] K. Li, S.F.Y. Li, H.K. Lee, J. Liq. Chromatogr. 18 (1995) 1325.
[30] G.B. Jiang, P.S. Maxwell, K.W.M. Siu, V.T. Luong, S.S. Berman, Anal. Chem. 63 (1991) 1506.
[31] S. Tsunoi, T. Matoba, H. Shioji, L.T.H. Giang, H. Harino, M. Tanaka, J. Chromatogr. A 962 (2002) 197.
[32] S. Foster, W. Maher, F. Krikowa, S. Apte, Talanta 71 (2007) 537.
[33] M.M. Santos, P. Enes, M.A. Reis-Henriques, J. Kuballa, L. Filipe, C. Castro, M.N. Vieira, Chemosphere 75 (2009) 661.
[34] R.B. Laughlin, J.W. French, H.E. Guard, Environ. Sci. Technol. 20 (1986) 884.
[35] Q.F. Zhou, Z.Y. Li, G.B. Jiang, R.Q. Yang, Environ. Pollut. 125 (2003) 301.
[36] R.Q. Yang, Q.F. Zhou, J.Y. Liu, G.B. Jiang, Food Chem. 97 (2006) 637.

Talanta 80 (2010) 1919–1925

Contents lists available at ScienceDirect

Talanta

journal homepage: www.elsevier.com/locate/talanta

Electrochemical oxidation of dopamine and ascorbic acid at a palladium electrode modified with in situ fabricated iodine-adlayer in alkaline solution

Emad A. Khudaish*, Aysha A. Al Farsi

Sultan Qaboos University, College of Science, Department of Chemistry, P O Box 36, P C 123, Muscat, Oman

ARTICLE INFO

Article history:
Received 9 September 2009
Received in revised form 17 October 2009
Accepted 19 October 2009
Available online 28 October 2009

Keywords:
Dopamine
Ascorbic acid
Iodine-adlayer
Palladium modified electrode
Anodic stripping

ABSTRACT

The self-assembled iodine-adlayer was fabricated at the palladium (Pd) electrode surface throughout a spontaneous oxidative chemisorption of iodide ions contained in an alkaline supporting electrolyte. It enhances the electron transfer kinetics for the oxidation of dopamine (DA) and ascorbic acid (AA) and was important to separate the peak current of both species with a practical potential difference compared with that occurred at the unmodified electrode. The anodic peak currents of both species were linearly increased with their respective concentrations using linear square stripping voltammetry. The activity of the electrode system was further investigated applying chronoamperometry method. The steady–state amperometric signal for the oxidation of DA in the presence of iodide ions was five times greater than that in its absence. The current–time response was also used to evaluate the diffusion coefficient of DA based on Cottrell plot that results with a value of 4.19×10^{-8} m^2 s^{-1}. The proposed method was successfully applied to detect DA and AA in human serum.

© 2009 Elsevier B.V. All rights reserved.

1. Introduction

The determination of DA and AA in biological fluids of humans is important in clinical analysis. The concentration of DA in the fluids of brain tissues is in the range of 10–1000 nmol L^{-1} [1,2], while the concentration of AA in biological systems is as high as 100 μmol L^{-1} [3]. Both species are vitally related to the diagnosis of various kinds of diseases. For instance, abnormal levels of DA are diagnostic to Parkinson's disease, Schizophrenia and neuroendocrine disorder [4–6]. Similarly, the content of AA in biological samples has been taken as an index for oxidative stress in human metabolism [7,8] which is related to cancer and hepatic disease.

Electrochemically, both compounds are active and known to be oxidized at very close potentials at most unmodified electrodes causing a great interference, unselective identification and poor current peak separation [9,10]. In order to address such a problem, considerable efforts have been devoted including surface modification of electrode substrates with conducting polymeric films [11–15], self-assembled monolayer films [16–18], electrodes based on ion exchange membrane coated film [4,19–22] and composite electrode based on methylene blue entrapped in a sol–gel matrix film [23,24]. Also, nanomaterials have received considerable interest due to their remarkable physical and chemical properties. Therefore, many approaches were based on the fabrication of metal or metal oxide nanoparticles modified electrodes as biochemical sensors [25–30]. Others combined conducting organic polymers and inorganic porous metal oxides to form nanocomposite materials that showed unique mechanical and electrical properties [31,32] and used successfully for the above important applications.

Another area of interest concerning electrode modification is the formation of anion adlayer by oxidative chemisorptions. Of the various systems studied, halide adsorption (mostly bromide and iodide) on metal electrodes [33–36] has been of central significance in surface electrochemistry. The structure and the composition of the adsorbed layer were thoroughly characterized by many ex situ and in situ techniques such as low-energy electron diffraction (LEED) [37,38], scanning tunneling microscopy (STM) [39–42] and surface X-ray scattering (SXRS) [43,44]. Iodide is chemically stable anion forming a compact iodine-adlayer on electrode surface due to its strong adsorption affinity. Iodine-adlayer modified electrodes were employed successfully for numerous applications and studies such as catalytic anodic stripping of metallic films [45,46], catalytic oxidation of hydrogen peroxide [36] and uric acid [47], and test of the catalytic activity by active site blocking method [48].

In this work, the in situ fabrication of potentially dependent iodine-adlayer at Pd-electrode surface in alkaline solution assigned as (I_{ad}/Pd-modified electrode) is described and tested for electrochemical measurements of DA and AA.

* Corresponding author. Tel.: +968 2414 1474; fax: +968 2414 1469.
E-mail address: ejoudi@squ.edu.om (E.A. Khudaish).

0039-9140/$ – see front matter © 2009 Elsevier B.V. All rights reserved.
doi:10.1016/j.talanta.2009.10.044

2. Experimental

2.1. Reagents

All solutions were made from high purity chemicals prepared in Millipore water. A phosphate buffer solution (PBS) of 0.100 mol L^{-1} (pH = 7.28) was used to prepare the standard solutions of DA and AA (Aldrich–Chemie) as well as the serum sample. All electrochemical measurements were carried out in 0.100 mol L^{-1} sodium hydroxide (NaOH) solution at ambient temperature in the presence of 10 mM KI (BDH Limited Poole England). The electrolyte was degassed with stirring by purging oxygen-free nitrogen gas for 10 min and blanketed throughout the experiment.

2.2. Electrodes

The electrochemical measurements including cyclic voltammetry (CV), chronoamperometry (CA) and linear square stripping voltammetry (LSSV) experiments were conducted using a BAS 50W work station (Bioanalytical System, West Lafayette, IN, USA). The three electrode cell consisting of a Pd-electrode with geometric area of 0.0707 cm^2, a platinum coil with geometric area of 1.90 cm^2 and an $Ag/AgCl/KCl_{(sat.)}$ (Bioanalytical System, West Lafayette, IN, USA) were used as the working, counter and reference electrodes, respectively.

Prior to each experiment, the working electrode was polished using a polishing cloth and alumina slurry (5.0 and 1.0 μm), rinsed thoroughly with distilled water, ultrasonicated for 5 min using (JAC Ultra Sonic, 1505, LABKOREA INC, Korea) and finally rinsed with distilled water. The electrode was then pretreated electrochemically by scanning the potential reversibly between −400 mV and +1000 mV for 25 cycles at 100 mV s^{-1} and terminating at the anodic potential limit in PBS to establish a reproducible electrode surface and avoid any previous fouling effect.

The CV experiments were utilized mainly to study the electrode behavior in iodide containing solution and characterize the adsorption/desorption of iodine-adlayer by scanning the potential reversibly between +800 mV and −1000 mV at particular scan rates.

CA measurements were made by stepping the electrode potential from −500 mV to 0 mV over a range of pulse widths (2000–30,000) in milliseconds (ms). The last 50 digitized data points were averaged for each experiment and the mean value and standard deviation were also verified. In other separate experiments, the above anodic potential step was held for 20,000 ms at which the current had approached the steady-state value, averaged as above and collected as a function of [DA] in the presence and absence of KI solution.

For LSSV experiments, the electrode potential is scanned in one direction from −800 mV to +200 mV at 100 mV s^{-1} and the deposition time at the initial electrode potential was 60 s.

2.3. Treatment of the serum sample

The serum was obtained form the University Hospital. A 1.0 mL of the sample was mixed with 5.0 mL of methanol and then centrifuged (Centaur 2, MSE, UK) at 1500 rpm for 20 min. The supernatant was diluted for 4 times with 0.100 mol L^{-1} of PBS (pH = 7.28) before analysis. The contents of DA and AA in the serum were evaluated using the regression data obtained from the calibration plots (current density vs. concentration) of artificial samples.

3. Results and discussion

3.1. Chemisorption of iodide ions at palladium electrode

Fig. 1 shows the cyclic voltammograms obtained at Pd-electrode in alkaline solution in the absence (dotted line, scan rate = 100 mV s^{-1}) and the presence of 10 mmol L^{-1} KI solution (solid lines for a range of scan rates). The voltammogram in the absence of KI is characterized by the potential induced partial oxidative adsorption and reductive desorption of hydroxyl ions (OH^-) [49,50] observed at −450 and −380 mV vs. Ag/AgCl, respectively.

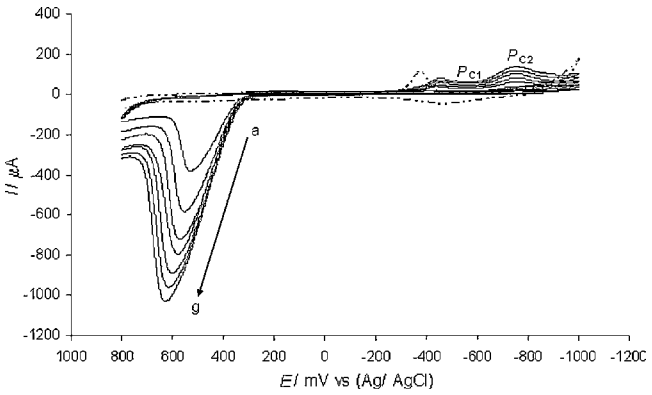


Fig. 1. Cyclic voltammograms at the unmodified electrode (dotted line, ν = 100 mV s^{-1}) and at the I_{ad}/Pd-modified electrode (solid lines) for a range of scan rates; (a) 25, (b) 50, (c) 75, (d) 100, (e) 150, (f) 200, and (g) 300 mV s^{-1}.

The presence of 10 mmol L^{-1} KI generates quite significant change in the cyclic voltammogram obtained in which a significant suppression of OH^- adsorption due to blocking of the Pd-electrode surface by preferential chemisorption of I^- ions [51]. Instead, a couple well-defined cathodic peaks assigned as P_{C1} and P_{C2} appeared at −430 and −770 mV vs. Ag/AgCl, respectively, corresponding to reductive desorption of iodine-adlayer that previously produced due to oxidative adsorption of strongly adsorbed I^- ions characterized by a sharp anodic peak obtained at +530 mV vs. Ag/AgCl (ν = 25 mV s^{-1} and shift to a more positive potential with increasing ν). It should be noted, that the structure and surface coverage of the iodine-adlayer were studied and characterized using different techniques and all agrees that it is potential dependent [34,48,52].

The position and less intensity of the reductive desorption peaks were obtained at extremely negative potential compared with that of the oxidative adsorption peak. This difference may be attributed to (i) reconstruction of the electrode surface structure since the surface coverage of adsorbed OH^- ions manipulate this kind of kinetic transition [53,54], and (ii) the presence of a competitive adsorption between OH^- and I^- species since the surface coverage of iodine-adlayer is pH-independent (because H^+ and OH^- ions are not involved in the adsorption step of I^-), while the adsorption of OH^- is pH− dependent. Accordingly, the kinetics of reductive desorption of iodine is expected to be sluggish and its peak potential shifted to a more negative value.

The couple reductive desorption peaks and the oxidative adsorption peak increases with ν as demonstrated in Fig. 1. The cathodic peak currents (P_{C1} and P_{C2}) were increased linearly with ν and extrapolated to the origin as shown in Fig. 2A indicating a surface confined process at which the cathodic reaction is associated with iodine-adlayer desorption. Similarly, a linear relationship was obtained for the plot of the anodic peak current as a function of the square root of scan rates ($\nu^{1/2}$) which also extrapolated to the origin as shown in Fig. 2B. Therefore, stepping the electrode potential to more positive value enhances the formation of iodine-adlayer (I^- ions adsorbed and potentially oxidized) where the electrode reaction is controlled mainly by mass transport process.

The deposition charge density, σ, in μC cm^{-2} of the adsorbed iodide ions was determined by integrating the area under the

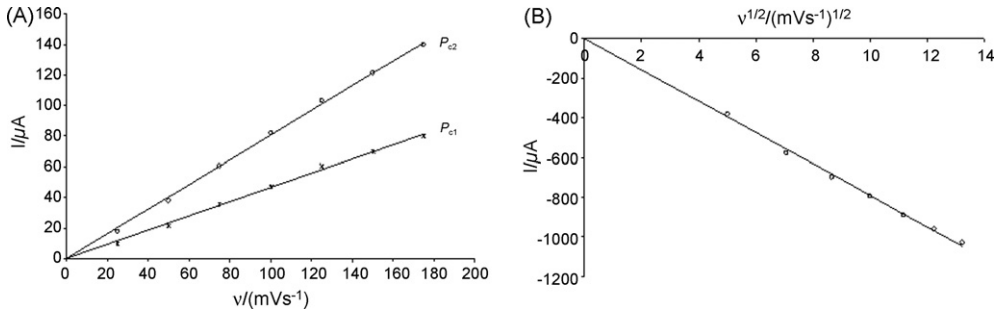


Fig. 2. (A) The cathodic peak currents (P_{C1} and P_{C2}) as a function of scan rate and (B) the dependence of anodic peak current on the square root of scan rates. Data collected from Fig. 1.

oxidative adsorption peak current, while the surface coverage of iodine-adlayer, Γ, was estimated to be 5.69×10^{-8} mol cm^{-2} applying the following equation:

$$\sigma = nF\Gamma \quad (1)$$

The number of electrons transferred during the deposition of iodine-adlayer was 1.96 calculated from the slope of the peak current (I_p) vs. (ν) (for the data presented in Fig. 1) using Eq. (2) [55,56].

$$I_p = \left(\frac{n^2F^2A\nu}{4RT}\right)\Gamma \quad (2)$$

The surface coverage of iodine-adlayer mean value was equal to 5.91×10^{-8} mol cm^{-2} applying Eq. (2) at different (ν) and considering (n = 2).

It should be noted that the present system was tested for electrolyte composition dependency, i.e. pH and the amount of KI. In acidic and neutral media, a deep yellow color was observed during the progress of catalysis which may be related to a partial solubilization (much faster in acidic medium) of iodine-adlayer in excess iodide ions to form tri-iodide ion (I_3^-). Also, it was found that the LSSV voltammetric signal for the oxidation of DA and AA increases with [KI] in the range 2–10 mmol L^{-1}, but approximately attains a steady value up to 16 mmol L^{-1}. Therefore, the electrode system for the present work is defined experimentally by dipping Pd-electrode in alkaline solution containing 10 mmol L^{-1} of KI as described above in Section 2.1.

3.2. Electrochemical oxidation of DA and AA at I_{ad}/Pd-modified electrode

Electrochemical measurements based on LSSV have been conducted instead of differential pulse voltammetry (DPV) for simultaneous determination of DA and AA. For the present system, DPV technique was found to posses a weak separation capability particularly at concentration lower than 10 μmol L^{-1}. At higher concentration levels, the voltammetric peak of AA splits as a peak shoulder on DA, thus the system demonstrating less sensitivity and weak resolution facility that can be utilized for analytical applications. Therefore, LSSV was selected as an alternative and sensitive technique for better resolution and deprive concurrent peak overlapping.

Fig. 3 demonstrates the electrochemical oxidation of an equivalent concentration (25 μmol L^{-1}) of both DA and AA at bare Pd-electrode in 0.100 mol L^{-1} NaOH solution using LSSV method. The anodic peak of both species appeared at approximately similar potential, viz. E_{DA} = −60 mV and E_{AA} = −83 mV, indicating a poor selective property at which the simultaneous determination of these species is prohibited. The narrow peak-to-peak separation as well as low current responses are practically referred to a weak and inactive electrochemical system. Apparently, the electrocatalytic surface of the unmodified system suffers interference process and slow electron transfer reaction. The nature of the electrode system and the electroactive species undergoes surface reaction may play the major role for such a trend. It should be noted that the oxidation of DA and AA is associated with the coadsorption of OH$^-$ ions which occurred at more negative potential (about −450 mV as shown in Fig. 1). Also, the surface coverage of the oxidative adsorption of OH$^-$ ions at the electrode surface is known to be potential dependent [57] which may promote a negatively charged film. It excludes and weaken the adsorption of negatively charged ascorbate ions (pK_a = 4.30) and hence the oxidation of AA occurs at a potential more positive than expected.

On the other hand, the cationic DA species (pK_a = 8.91) may experience a larger electrostatic attraction with the hydroxyl layer and hence produce a greater electrical signal. Apparently, the strong adsorption of cationic DA at the electrode surface may play a significant role in the inhibition process in addition to that caused by the adsorption of oxidation products.

Fig. 4A shows LSSV anodic current density in (μA cm^{-2}) for a range of [AA] at the I_{ad}/Pd-modified electrode. The peak current arises at about −168 mV vs. Ag/AgCl is linearly related to [AA] in the range 1.0×10^{-6} to 1.0×10^{-4} mol L^{-1}, resulting with the following regression data; slope = 6706.2 (±108.9) A cm mol^{-1}, intercept = 1.7760 (±0.5814) μA cm^{-2}, and R^2 = 0.9979. As can be seen from Fig. 4A, the anodic peak of AA increases significantly and shifts to a more negative potential, ca. 85 mV, compared with that typically obtained at the unmodified electrode. The electrode sensitivity and selectivity were improved with the simple modification of the electrode surface provided by the compact iodine layer. Increasing the current response of AA is associated with electrode kinetics in which the electron transfer process becomes more favored at the modified surface [27]. Also, the electrode surface modification decreases the chemisorption of OH$^-$ ions and hence eliminates electrostatic repulsion with anionic AA

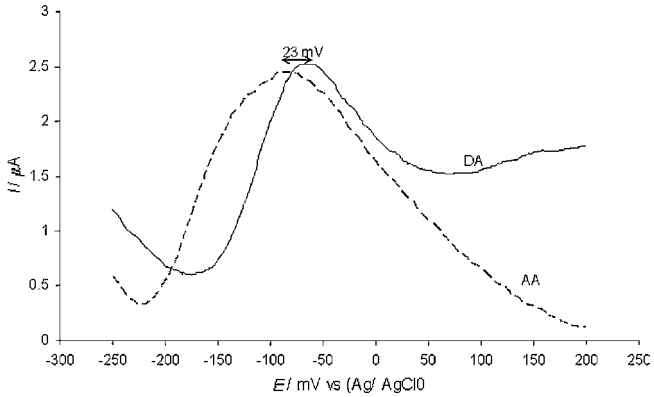


Fig. 3. LSSV curves of equivalent [DA] and [AA] at the unmodified Pd-electrode in (0.100 mol L^{-1}) NaOH solution (ν = 100 mV s^{-1}).

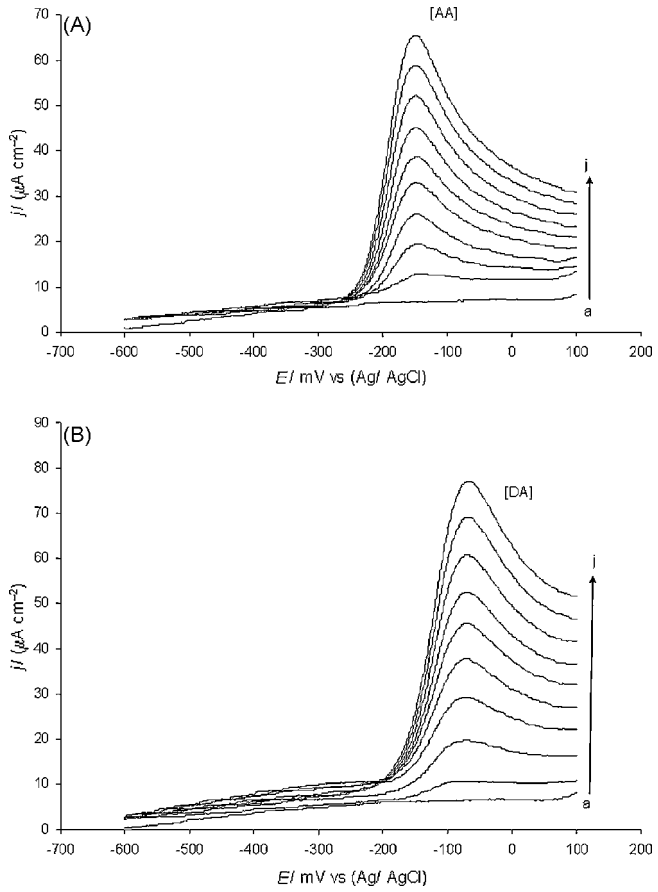


Fig. 4. LSSV curves for (A) AA and (B) DA at the I_{ad}/Pd-modified electrode as a function of their concentrations from (a to j); (0 μmol L^{-1}), (1 μmol L^{-1}), (2 μmol L^{-1}), (3 μmol L^{-1}), (4 μmol L^{-1}), (5 μmol L^{-1}), (6 μmol L^{-1}), (7 μmol L^{-1}), (8 μmol L^{-1}) and (9 μmol L^{-1}).

species that has been shown to occur at the unmodified electrode surface.

Similarly, Fig. 4B shows LSSV signals for the oxidation of DA at the modified electrode where the anodic peak current occurred at about −68 mV increases significantly and linearly with [DA] in the range 1.0×10^{-7} to 1.0×10^{-4} mol L^{-1}. The regression data for the linear relationship of the peak current as a function of [DA] are given by; slope = 8855.4 (±186.7) A cm mol^{-1}, intercept = − 1.6059 (±0.5719) μA cm^{-2}, and R^2 = 0.9955. The estimated slope ratio of DA to AA (S_{DA}/S_{AA} = 1.32) suggests that the modified electrode is relatively much sensitive towards DA than AA. The above trend can be attributed to the nature of iodine-adlayer during oxidative chemisorption which may present as atomic iodine bearing a partial negative charge [57]. The applied negative potential (relevant to the deposition potential conducted in this work by LSSV) promotes and stabilizes the negative charge of iodine-adlayer which has greater affinity for cationic DA and repels anionic AA species. When the electrode potential is stepped linearly to the positive region (typical for DA and AA oxidation), the iodine-adlayer may be considered as a neutral bearing no charge diminishing electrostatic attractions or/and repulsions with DA and AA. Therefore, the anionic AA species, which apparently has less adsorption affinity during the deposition time, becomes more accessible and adsorptive at the modified electrode surface resulting with a reasonable negative potential difference.

Moreover, the remarkable enhancement of the electrode activity towards the oxidation of DA and AA indicates that the electron transfer process is faster and much feasible at the modified electrode surface. It is important to elucidate that the electron transfer

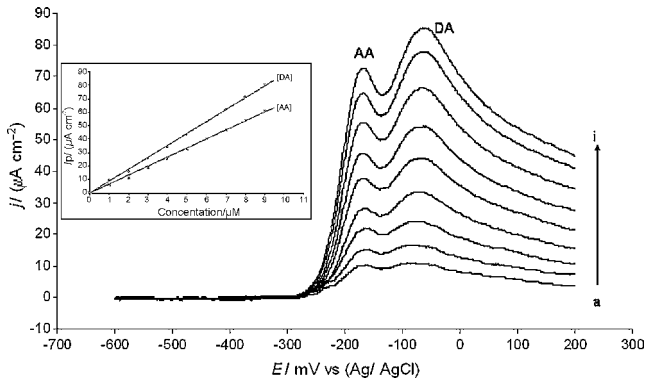


Fig. 5. LSSV curves for a binary mixture containing equal concentrations of DA and AA at the I_{ad}/Pd-modified electrode. Concentrations from (a to i); (1 μmol L^{-1}), (2 μmol L^{-1}), (3 μmol L^{-1}), (4 μmol L^{-1}), (5 μmol L^{-1}), (6 μmol L^{-1}), (7 μmol L^{-1}), (8 μmol L^{-1}) and (9 μmol L^{-1}). Insert shows the calibration curves for DA and AA.

process is occurred at the iodine-adlayer/electrolyte interface rather than at the electrode substrate surface for the following reasons; (i) the formation of a stable and compact iodine-adlayer at relatively large anodic potentials in the presence of high [I^-], (ii) the iodine-adlayer is very thin and free of pinhole [36], thus not accessible by the large cationic DA (or anionic AA) species. Therefore, the mutual electron transfer kinetics is believed to take place by the electron tunneling through the iodine-adlayer to the Pd surface [58]. Accordingly, the most feasible active site for the present electrochemical system is characterized mainly by the iodine-adlayer/electrolyte interface.

3.3. Simultaneous determination of DA and AA

To further investigate the applicability of the system for simultaneous determination of both analytes in a mixture, LSSV was employed to record the anodic peak under conditions similar to those described above. Fig. 5 depicts the simultaneous determination of a binary solution containing equal concentrations of DA and AA species at the I_{ad}/Pd-modified electrode. A well-defined two voltammetric peaks at potentials −170 and −65 mV, corresponding to the oxidation of AA and DA, respectively, are resolved and increased simultaneously as a function of species concentration. The anodic peak current of DA and AA arises at potentials fairly similar to those observed in the individual analysis indicating that the electron transfer process incorporated with the oxidation of each species is not altered by the presence of the other. Moreover, the electrode fouling due to adsorption of oxidation products such as DA-semiquinone from DA or/and dehydroascorbate from AA [59] was negligible and has no major effect on the activity of the modified electrode even at relatively high concentrations of DA and AA.

The regression data of the linear relationship between the peak current as a function of species concentration along with the estimated detection limit (DL) were collected and presented in Table 1. The system maintained the same sensitivity towards DA even in the presence of AA which can be evaluated by means of the slope

Table 1
Analytical parameters and regression data obtained from the plot of peak current against [DA] and [AA] in their binary mixtures.

Species	Slope (A cm mol^{-1})	Intercept (μA cm^{-2})	R^2	DL (3σ) (μmol L^{-1})
DA[a]	9613.1	−1.8292	0.9934	0.57
AA[b]	7258.1	−1.6664	0.9947	0.69

[a] Linear range between 1.0×10^{-6} and 5.0×10^{-5} mol L^{-1}.
[b] Linear range between 1.0×10^{-6} and 1.0×10^{-4} mol L^{-1}.

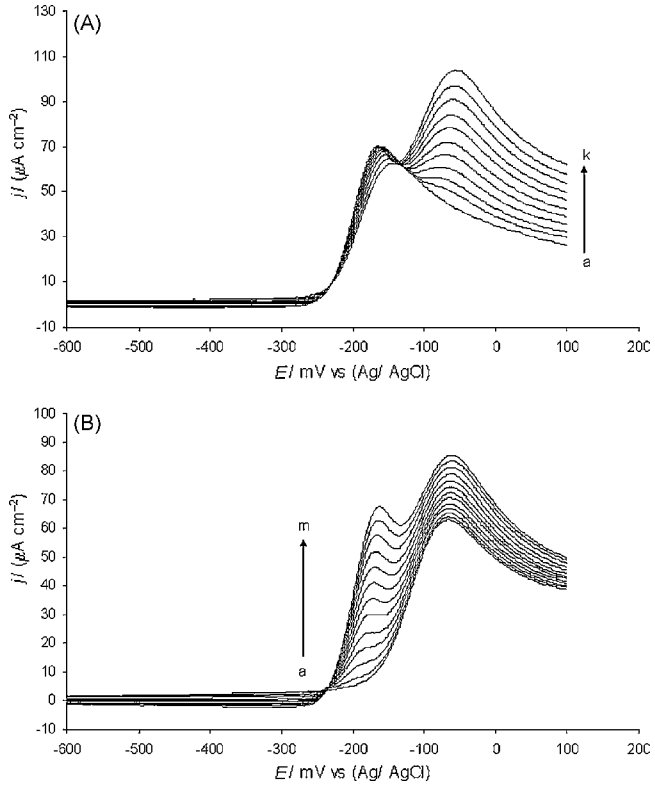


Fig. 6. LSSV curves for the selective determination of (A) DA in the presence of (100 μmol L^{-1}) of AA as a function of [DA]; (a) (0 μmol L^{-1}) increases by (1 μmol L^{-1}) each time to a final (k) (10 μmol L^{-1}). (B) AA in the presence of (100 μmol L^{-1}) of DA as a function of [AA]; (a) (0 μmol L^{-1}) increases by (1 μmol L^{-1}) each time to a final (m) (12 μmol L^{-1}).

value differences of both species. Moreover the slope ratio (DA/AA) obtained by this experiment is equal to 1.32 similar to that evaluated by experiments of individual samples given above. This may reveal a high sensitivity, selectivity and stability of the present system at the above applied concentration range. In a similar electrolytic system using poly crystalline gold electrode, it was found that the peak potentials of uric acid (UA) and AA were well separated. The current responses of both species were also highly reproducible and the system was greatly stable due to the presence of the compact iodine-adlayer.

The stability of the electrode was checked by repeating the electrolysis of sample containing 50 μmol L^{-1} of both species for 12 times at 5 min interval. The peak-to-peak separation was successfully maintained indicating a good stability of the iodine-adlayer. The current variation was estimated mathematically and found to be 4.3% suggesting that the electrode reactivity is not affected critically by the adsorption of analytes or their oxidation products.

3.4. Selective determination of individual component in the presence of a fixed concentration of the other

Fig. 6A depicts the determination of DA in the presence of 100 μmol L^{-1} AA at I_{ad}/Pd-modified electrode using LSSV method. The current response for the oxidation of DA increases with increasing [DA] disregard of interfering tendency that may come up by the presence of large [AA]. Furthermore, the peak current of DA is well separated and occurred as close as to −60 mV, while the peak current for the oxidation of AA arose with no significant change in its intensity. The above experimental data indicates that the working system is able to measure selectively DA at sub-micro-molar levels in the presence of high [AA], mimicking situation in biological fluids.

Table 2
Analytical parameters and recovery percentage (n = 3) for AA and DA species in the serum sample using standard addition method and regression data obtained by Fig. 4A and B, respectively.

	(j) (μA cm^{-2})	[Actual] (μmol L^{-1})	[Found] (μmol L^{-1})	Recovery (%)
AA				
(1)	15.3	2.50	2.55	102
(2)	31.5	5.00	4.96	99
(3)	48.0	7.50	7.42	99
DA				
(1)	16.8	2.00	2.08	104
(2)	34.6	4.00	4.09	102
(3)	52.5	6.00	6.11	102

The same trend can be seen also in Fig. 6B, where the peak current of AA increases with increasing [AA] in the presence of 100 μmol L^{-1} DA. The peak potential of both species unchanged and occurs at the same potential for the one of pure solution containing only AA or DA shown in Fig. 4A and B, respectively. One important point to be addressed here is the slight increase in the current response of DA with increasing [AA]. It might be explained due to convolution of DA peak current with the electrical signal obtained by AA oxidation which occurred at potential more negative than that of DA. Therefore, deconvolution process would be imperative to correct the peak intensity and gain much accurate analysis [60].

For the present electrolytic system, the presence of AA has no major interference property that may catalyze DA oxidation to some extent as described for other modified systems [61,62] since the electrode sensitivity, i.e. the slope ratio, sustained approximately a similar value as that obtained in the individual and mixture analysis described above. Also, such an assumption should be associated with a decrease in the anodic current of AA (which is not observed here) as long as some of AA is consumed to reduce the oxidized form of DA (DA-semiquinone) into DA.

According to the above results, it is believed that the I_{ad}/Pd-modified electrode can be effectively employed for the electrochemical measurements of trace amounts of either DA or AA in the presence of high concentrations of the other species.

3.5. Determination of individual component in real samples

The electrode system was applied for the determination of AA and DA in real samples such as human serum. The pretreated sample was injected in the alkaline iodide solution contained in an electrochemical cell with a dilution ratio of 100 times. The LSSV voltammogram show nil detection for AA and DA species. A standard addition method was applied to measure the [AA] and [DA] using the above method while the regression data obtained in Fig. 4A and B were used to calculate the recovery percentage of both species, respectively.

The electrode system recovers excellently all spikes of both species as described in Table 2 achieving a higher sensitivity and selectivity.

3.6. Amperometric analysis

The catalytic activity of the electrode system towards the oxidation of DA was further investigated using CA technique. The steady-state current responses recorded as a function of [DA] or pulse width has been achieved according to the experimental conditions described above in Section 2.2. Fig. 7 shows the anodic current responses for the oxidation of 50 μmol L^{-1} DA

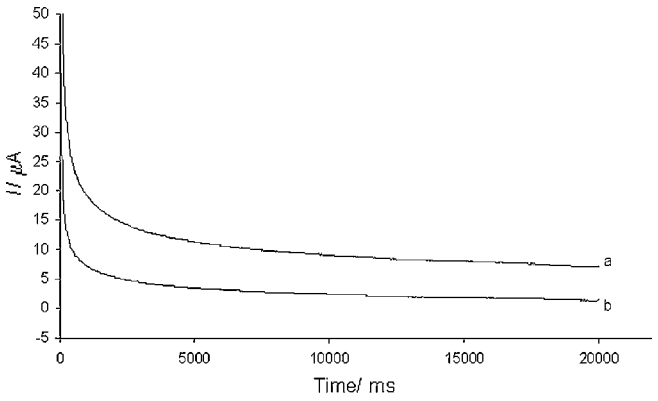


Fig. 7. The current–time responses for the oxidation of (50 μmol L^{-1}) DA obtained at 0.0 mV in the presence (a) and absence (b) of (10 mmol L^{-1}) KI solution.

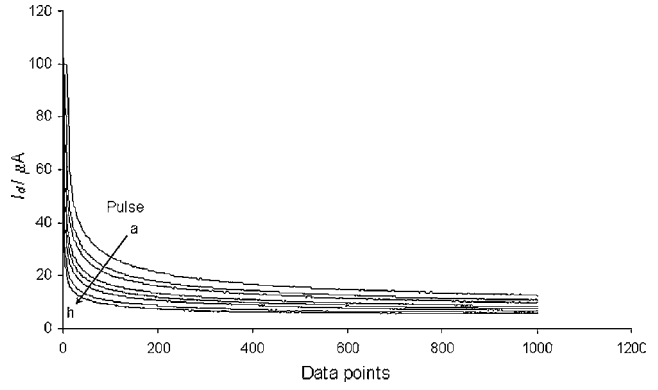


Fig. 8. The steady-state diffusion currents obtained at the I_{ad}/Pd-modified electrode in the presence of (50 μmol L^{-1}) DA as a function of pulse widths: (a) 2, (b) 4, (c) 6, (d) 8, (e) 10, (f) 12, (g) 20 and (h) 30 s.

in 0.100 mol L^{-1} NaOH in the presence (a) and absence (b) of 10 mmol L^{-1} KI solution. The observed current in the presence of iodide ions is significantly five times greater than in its absence. This suggests that the formation of iodine-adlayer at the electrode surface enhances the catalytic oxidation of DA. Moreover, the above method is used successfully to study the electrode reaction under diffusion control process by recording the current–time response for a range of pulse widths at constant species concentration.

The diffusion current (I_d) given by Eq. (3) as a function of electrolysis time can be used to evaluate the diffusion coefficient of DA (D_{DA}).

$$I_d = \frac{nFD^{1/2}C}{\pi^{1/2}t^{1/2}} \quad (3)$$

Equation (3) is known as the Cottrell equation [55] where the plot of (I_d vs. $t^{-1/2}$) must be linear and extrapolated to the origin. Fig. 8 demonstrates the current–time response in the presence of 50 μmol L^{-1} DA, where the anodic diffusion current decays to a lower value with electrolysis time consistent with the form of Cottrell equation. The Cottrell plot was linear with a positive slope resulting with D_{DA} value equals to 4.19×10^{-8} m^2 s^{-1}.

4. Conclusions

A chemically modified electrode was fabricated via the in situ formation of iodine-adlayer at the Pd-electrode surface in alkaline solution containing iodide ions. The modified electrode exhibited a high electrocatalytic activity towards the oxidation of DA and AA. The anodic peak currents of both species in their (1:1), (100:1) or/and (1:100) mixtures were well separated and increased linearly with the respective concentration of each species. Interference effect due the presence of one species at concentration 100 times greater than the other was not practically observed. Also, electrode fouling due to the accumulation of oxidation products was not identified as the electrode system sustain good activity and stability even at high initial concentrations of both species. The present system may be utilized for developing biological sensors to detect DA at sub-nano-molar levels in the presence of other physiological species using microelectrodes. Moreover, the construction of bromine-adlayer modified electrode is another area of research that may produce advantageous results for the above task.

Acknowledgement

The author would like to thank Sultan Qaboos University for supporting this work by the research grant fund number (IG/SCI/CHEM/02/05).

References

[1] L.H. Parsons, J.B. Justice Jr., J. Neurochem. 58 (1992) 212.
[2] C. Amatore, R.S. Kelly, E.W. Kristensen, W.G. Kuhr, R.M. Wightman, J. Electroanal. Chem. 213 (1986) 31.
[3] T. Zetterstrom, T. Sharp, C.A. Marsden, U. Ungersteadt, J. Neurochem. 41 (1983) 1769.
[4] J.W. Mo, B. Ogorevc, Anal. Chem. 73 (2001) 1196.
[5] A. Inoue, Y. Nakata, Jpn. J. Pharm. 86 (2001) 376.
[6] R.M. Wightman, L.J. May, A.C. Michael, Anal. Chem. 60 (1988) 769A.
[7] I. Koshiishi, T. Imanari, Anal. Chem. 69 (1997) 216.
[8] G.N. Bijur, M.E. Ariza, C.L. Hitchcock, M.V. Williams, Environ. Mol. Mutagen. 30 (1997) 339.
[9] R.D. O'Neil, Analyst 119 (1994) 767.
[10] A. Liu, M. Wei, I. Honma, H. Zhou, Adv. Funct. Mater. 16 (2006) 371.
[11] J.B. Raoof, R. Ojani, S. Rashid-Nadimi, Electrochim. Acta 50 (2005) 4694.
[12] V.S. Vasantha, S.-M. Chen, J. Electroanal. Chem. 592 (2006) 77.
[13] I.G. Casella, M.R. Guascito, Electroanalysis 9 (1997) 1381.
[14] P.R. Roy, M.S. Saha, T. Okajima, S.G. Park, A. Fujishima, T. Ohsaka, Electroanalysis 16 (2004) 1777.
[15] J.-M. Zen, I.-L. Shen, Electroanalysis 9 (1997) 537.
[16] U.E. Majewska, K. Chmurski, K. Biesiada, A.R. Olszyna, R. Bilewicz, Electroanalysis 18 (2006) 1463.
[17] R.K. Shervedani, M. Bagherzadeh, S.A. Mozaaffari, Sens. Actuators B 115 (2006) 614.
[18] L. Zhang, J.B. Jai, X.Q. Zou, S.J. Dong, Electroanalysis 16 (2004) 1413.
[19] M.J. Giz, B. Duong, N.J. Tao, J. Electroanal. Chem. 465 (1999) 72.
[20] C.R. Raj, K. Tokuda, T. Ohsaka, Bioelectrochemistry 53 (2001) 183.
[21] C.R. Raj, T. Ohsaka, J. Electroanal. Chem. 496 (2001) 44.
[22] C.R. Raj, T. Okajima, T. Ohsaka, J. Electroanal. Chem. 543 (2003) 127.
[23] S.B. Khoo, F. Chen, Anal. Chem. 74 (2002) 5734.
[24] J. Argüello, V.L. Leidens, H.A. Magosso, R.R. Ramos, T. Gushikem, Electrochim. Acta 54 (2008) 560.
[25] L. Fernández, H. Carrero, Electrochim. Acta 50 (2005) 1233.
[26] R.N. Goyal, V.K. Gupta, A. Sangal, N. Bachheti, Electroanalysis 17 (2005) 2217.
[27] L. Zhang, X. Jiang, J. Electroanal. Chem. 583 (2005) 292.
[28] W. Ren, H.Q. Luo, N.B. Li, Biosens. Bioelectron. 21 (2006) 1086.
[29] R.N. Goyal, V.K. Gupta, M. Oyama, N. Bachheti, Talanta 72 (2007) 976.
[30] P. Shakkthivel, S.-M. Chen, Biosens. Bioelectron 22 (2007) 1680.
[31] S. Senthilkumar, J. Mathiyarasu, P. Lakshminarashimha, J. Electroanal. Chem. 578 (2005) 95.
[32] S. Thiagarajan, S.-M. Chen, Talanta 74 (2007) 212.
[33] O.M. Magnussen, Chem. Rev. 102 (2002) 679.
[34] Ch.-M. Yang, K. Kaneko, J. Colloid Interface Sci. 246 (2002) 34.
[35] U. Hasse, F. Scholz, Electrochem. Commun. 6 (2004) 409.
[36] Md.R. Miah, T. Ohsaka, Anal. Chem. 78 (2006) 1200.
[37] J. Clavilier, D. Armand, S.G. Sun, M. Petit, J. Electroanal. Chem. 205 (1987) 267.
[38] J. Albers, H. Baltruschat, I. Kamphausen, J. Electroanal. Chem. 395 (1995) 99.
[39] A.M. Bittner, J. Wintterlin, G. Ertl, J. Electroanal. Chem. 388 (1995) 225.
[40] A.M. Bittner, J. Wintterlin, B. Beran, G. Ertl, Surf. Sci. 335 (1995) 291.
[41] S. Tanaka, S.L. Yau, K. Itaya, J. Electroanal. Chem. 396 (1996) 125.
[42] J.M. Orts, R. Gomez, J.M. Feliu, A. Aldaz, J. Clavilier, Langmuir 13 (1997) 3016.
[43] B.M. Ocko, G.M. Watson, J. Wang, J. Phys. Chem. 98 (1994) 897.
[44] C.A. Lucas, N.M. Markovic, P.N. Ross, Phys. Rev. B 55 (1997) 7964.
[45] E.A. Lafferty, Y.-G. Kim, M.P. Soriaga, Electrochim. Acta 44 (1998) 1031.
[46] K. Sashikata, Y. Matsui, K. Itaya, M.P. Soriaga, J. Phys. Chem. 100 (1996) 20027.
[47] Md.R. Miah, J. Masud, T. Ohsaka, Electrochim. Acta 54 (2008) 316.
[48] S.-J. Hsieh, A.A. Gewirth, Surf. Sci. 498 (2002) 147.
[49] F. Matsumoto, S. Uesugi, N. Koura, T. Ohsaka, J. Electroanal. Chem. 549 (2003) 71.
[50] B. Blizanac, C. Lucas, M. Gallagher, M. Arenz, P.N. Ross, N.M. Markovic, J. Phys. Chem. B 108 (2004) 625.

[51] R.R. Adžić, J.X. Wang, Electrochim. Acta 45 (2000) 4203.
[52] B.G. Bravo, S.L. Michelhaugh, M.P. Soriaga, D.W. Suggs, J.L. Stickney, J. Phys. Chem. 95 (1991) 5245.
[53] G.J. Edens, X. Gao, M.J. Weaver, N.M. Markovic, P.N. Ross, Surf. Sci. Lett. 302 (1994) L275.
[54] B.E. Conway, Prog. Surf. Sci. 49 (1995) 331.
[55] A.J. Bard, L.R. Faulkner, Electrochemical Methods Fundamentals and Applications, 2nd edition, NY, Wiley, 2001.
[56] A.S. Kumar, J.-M. Zen, Electroanalysis 16 (2004) 1211.
[57] S. Nakanishi, Y. Mukouyama, Y. Nakato, J. Phys. Chem. B 105 (2001) 5751.
[58] C. Vericat, F.R. Lenicov, S. Tonco, G. Andreasen, M.E. Vela, R.C. Salvarezza, J. Phys. Chem. B 106 (2002) 9114.
[59] S.A. Kumar, C.-F. Tang, S.-M. Chen, Talanta 76 (2008) 997.
[60] T. O'Haver (Professor Emeritus), An Introduction to Signal Processing in Chemical Analysis, http://terpconnect.umd.edu/~toh/spectrum/TOC.html, visited on 15/07/2009.
[61] D. Sopchak, B. Miller, R. Kalish, Y. Avyigal, X. Shi, Electroanalysis 14 (2002) 473.
[62] T. Kondo, Y. Niwano, A. Tamura, J. Imai, K. Honda, Y. Einaga, D.A. Tryk, A. Fujishima, T. Kawai, Electrochim. Acta 54 (2009) 2312.

Talanta 80 (2010) 1926–1931

Contents lists available at ScienceDirect

Talanta

journal homepage: www.elsevier.com/locate/talanta

Reversed-phase dispersive liquid–liquid microextraction with central composite design optimization for preconcentration and HPLC determination of oleuropein

Payman Hashemi*, Fatemeh Raeisi, Ali Reza Ghiasvand, Akram Rahimi

Department of Chemistry, Faculty of Science, Lorestan University, Khoramabad, Iran

ARTICLE INFO

Article history:
Received 18 June 2009
Received in revised form 20 October 2009
Accepted 22 October 2009
Available online 31 October 2009

Keywords:
Reversed-phase DLLME
Oleuropein
Olive
HPLC
Multivariate optimization

ABSTRACT

A reversed-phase dispersive liquid–liquid microextraction (RP-DLLME) method was developed for the preconcentration and direct HPLC determination of oleuropein in olive's processing wastewater (OPW) and olive leaves extracts. In conventional DLLME, the sedimented phase is a micro-drop of a chlorinated organic solvent that is not compatible with RP-HPLC. Therefore, solvent evaporation and reconstitution with an appropriate solvent is often required. In RP-DLLME, this problem was overcome by overturning the solvent polarity in the ordinary DLLME and replacing the organic solvent with water. A central composite chemometrics design was used for multivariate optimization of the effects of five different parameters influencing the extraction efficiency of the method. In the optimized conditions, a mixture of 1.4 mL of an ethyl acetate extract of sample and 40 μL water (pH 5.0) was rapidly injected into 5.3 mL of cyclohexane. After centrifugation of the formed cloudy mixture, a micro-drop of the aqueous phase was sedimented at the conical bottom of the centrifuge tube. This phase, that contained the preconcentrated and partially purified analyte, was directly injected into an RP-HPLC column for analysis. A mean extraction recovery of 102.5 (±4.5) % with enrichment factors exceeding 38, was obtained for five replicated analysis. The detection limit of the method (3σ) for OE was 0.02 $\mu g\,L^{-1}$ for OPW and 2×10^{-3} $mg\,kg^{-1}$ for olive leaves samples. The results showed that, RP-DLLME is a promising technique which is quick, easily operated and can be directly coupled to HPLC.

© 2009 Elsevier B.V. All rights reserved.

1. Introduction

Oleuropein (OE) is the main glycoside in olive and is responsible for the bitter taste of olive products [1,2]. OE is known as a strong antioxidant and it has shown to have important human health benefits [3–6]. Olive leaves are whilst and cheap sources of OE. The OE level in olive leaves varies with olive variety, time of collection, climate, etc. [7]. Therefore, the development of simple and effective extraction methods for the preconcentration and accurate determination of OE is of great importance.

Ordinary solvent extraction, solvent extraction assisted by ultrasound [7,8] or microwave [9] energies and extraction with superheated solvents [10] are among the methods extensively used for the extraction of OE and related compounds from olive leaves before their GC or HPLC analysis. Methanol, ethanol, water and ethyl acetate have been among the most commonly used solvents for this purpose. Washing the extracts with non-polar solvents such as hexane [11], cyclohexane [12] and petroleum ether [13] for removing the heavy lipids has been sometimes recommended.

In the production process of table olives, a large quantity of wastewater is produced. The main purpose of this procedure is partial removal of the natural bitterness of the fruit that is mainly related to OE. However, OE is essentially hydrolyzed in the alkaline treatment stages of this procedure [14,16]. Extraction of OE and other biophenols from olive's processing wastewater (OPW) and olive mill wastewater has been performed by different organic solvents such as *tert*-butyl methyl ether, diethyl ether and ethyl acetate, with the last one being the most efficient [14–16].

Microextraction methods have attracted much attention in recent years as alternatives for classic extraction procedures [17]. These techniques are simple and fast, miniaturize sample pretreatment processes and minimize the use of organic solvents. A microextraction method can often be directly coupled to an analytical instrument. Dispersive liquid–liquid microextraction (DLLME) is a promising alternative to the classic liquid-liquid extraction (LLE) and was recently pioneered by Assadi and coworkers [18]. DLLME is simple, rapid and inexpensive and provides high enrichment factors. This method has been used for the extraction of several biochemicals and organic and inorganic compounds

* Corresponding author. Tel.: +98 6612202782; fax: +98 6612200185.
E-mail addresses: payman_hashemi@yahoo.com, hashemi.p@lu.ac.ir (P. Hashemi).

0039-9140/$ – see front matter © 2009 Elsevier B.V. All rights reserved.
doi:10.1016/j.talanta.2009.10.051

followed by their determination with GC [18,19], AAS [20,21] and HPLC [22–24] techniques. DLLME is based on a ternary component solvent system. In this method, generally, a small volume of a chlorinated, heavier than water organic solvent (e.g. carbon tetrachloride and chlorophenol) is dispersed into fine droplets in the sample solution by the aid of a water miscible solvent as disperser. After phase separation followed by centrifugation, the organic solvent is sedimented at the conical bottom of centrifuge tube as a micro-drop that can be withdrawn by a microsyringe. However, the organic solvent used in this procedure is not directly compatible with HPLC or AAS techniques. Therefore, evaporation of the organic solvent in a concentrator and reconstitution by an appropriate solvent is often required before analysis [20–24].

In this paper, a new generation of DLLME, termed as reversed-phase DLLME is presented that is directly compatible with HPLC. The proposed RP-DLLME method overturns the solvent polarity in the ordinary (normal-phase) DLLME and replaces the chlorinated, toxic solvents with water. In this technique, a small volume of water (or aqueous buffer solution) is dispersed in a lighter than water organic solvent with the aim of a moderately polar solvent as disperser. Therefore, the sedimented phase will be an aqueous micro-drop that can be directly injected into an RP-HPLC column. In this way, the time required for the solvent evaporation and reconstitution is saved. The capability of the method is demonstrated by its application to the preconcentration of oleuropein from OPW and olive leaves extracts.

A central composite design (response surface) is used for efficient optimization of the microextraction conditions. This method is a multivariate optimization technique that produces a detailed quantitative model for the response(s). The model can predict how a response relates to the values of various factors and it usually requires less number of experiments compared to a one-at-a-time procedure [25].

2. Experimental

2.1. Reagents and materials

Oleuropein (OE) was purchased from Indofine Chemical Company (Hillsbrough) and Hydroxytyrosol was prepared from Extrasynthesise (Genay, France). HPLC grade acetonitrile, ethyl acetate, cyclohexane and other chemicals were purchased from Merck (Darmstadt, Germany) and used as received. Double-distilled water was used throughout. A solution of 540 μg mL^{-1} OE in ethyl acetate was prepared and used as stock solution for the preparation of working standard solutions.

2.2. Apparatus

HPLC analysis of the samples was conducted using a Shimadzu (model L-10AD) instrument consisting of two reciprocating pumps, a DGU-14A in-line degasser, a model CT10-10AC oven, a high pressure manual injection valve (20 μL injection loop) and a UV/VIS (model SPD-10A) detector. The software used for the data acquirement and processing was Class-vp v.R 6.1. The analytical column was a 25 cm × 4.6 mm i.d. RP-8 column (Shim-Pack CLC-C8) packed with 5 μm particles and equipped with a 1 cm guard column (C8-B197) packed with 10 μm particles of the same type.

A 25 μL HPLC microsyringe (F-LC, SGE, Australia) was used for the sample withdrawal and injection. A variable automatic pipette (ISOLAB, Gmbts) was used for the RP-DLLME procedure.

A totally glass Fisons (UK) double distiller was used for preparation of doubly distilled water.

For ultrasonic irradiation of the samples, an ultrasonic water bath (22 kHz, model 5RS, Sonica, Italy) was used. An Eppendorf AG centrifuge (model 5810, Hamburg) was used for centrifugation of the extracts.

2.3. Field samples

Olive leaves of *Mary Zeitoon, Sevillana* and *Amphisis* varieties were collected from T-57 Agricultural Research Garden, Khoramabad, Iran, in July 2008. The leaves were dried in shadow and ground into approximately 1 mm pieces before analysis.

OPW was obtained from a green olive production plant in Khoramabad, Iran.

2.4. Procedures

For the preliminary extraction of OE from olive leaves, a static ultrasound assisted solvent extraction method was used [7]. To 0.10 g portion of the ground sample, 10 mL ethyl acetate was added in a glass test tube. The test tube was capped, thermostated at 40 °C, and sonicated for 30 min in the ultrasonic water bath. The supernant solution was decantated and filtered through 0.45 μm membrane filter and stored at 4 °C before further extraction by the RP-DLLME method. This extract was also directly injected into the HPLC column after 5 times dilution by ethanol.

For the preliminary extraction of OE from OPW a known LLE method [16] was used with some modifications. To 5 mL of acidified sample (pH 2), 5 mL ethyl acetate was added and the mixture was sonicated for 10 min. After the phase separation, the supernatant solution was decantated and the aqueous phase was extracted with a second 5 mL portion of ethyl acetate and the two extracts were added together.

The RP-DLLME method was performed as follows: A 1.4 mL portion of the ethyl acetate extract of the sample was mixed with 40 μL of water (pH 5.0). This mixture was rapidly injected into 5.3 mL cyclohexane in a centrifuge test tube using a variable pipette. A cloudy solution was formed that was centrifuged at 4000 rpm for 5 min. The sedimented aqueous tiny droplet at the conical bottom of the test tube was carefully withdrawn by a 25 μL syringe and directly injected into the HPLC column for analysis.

For HPLC separation of OE and other co-extracted compounds, a gradient elution with a mixture of solvents A (0.05 mol L^{-1} acetate buffer pH 5.0 in water) and B (acetonitrile) with a flow rate of 1.0 mL min^{-1} was used. The elution program was as follows: 0–8 min, 20–80% B; 8–11 min, 50–70% B; 11–13 min 70% B and 13–15 min, 70–20% B. The chromatograms were acquired at 240 nm.

Optimization of the effects of different parameters affecting the extraction by the RP-DLLME method was performed by a half-fraction central composite design (response surface method) using Minitab statistical software [26]. Table 1 depicts the abbreviation and levels of each factor included in the design.

Extraction recovery (ER%) was calculated from 100 times of the initial amount (μg) of OE in the sample, divided by its amount extracted into the aqueous phase. For calculation of the enrichment factor (EF), the OE concentration in the receiving phase was divided by its initial concentration in the sample.

Table 1
The factors included in the central composite design and the levels for each of them.

Parameter	Abbreviation	Factors' levels	
		Low	High
Cyclohexane volume (mL)	CV	5	3
Ethyl acetate volume (mL)	EV	1.5	0.5
Water volume (μL)	WV	70	50
Water pH	pH	8	6
Centrifuge time (min)	CT	6	4

3. Results and discussion

Preliminary extraction of OE and related compounds into an appropriate solvent for the RP-DLLME method was a critical requirement. Since, methanol, ethanol and ethyl acetate have been the most frequently used solvents for the extraction of OE from olive products [7–13], the possibility of using them as the disperser phase in the RP-DLLME procedure was examined. By using cyclohexane as the bulk organic solvent, it was found that methanol and ethanol tend to sediment together with water and this increases, drastically, the volume of the sedimented phase. Furthermore, the volume of the sedimented micro-drop was quite sensitive to the initial water volume. In an experiment, increasing the water volume from 40 to 45 μL, increased the sedimented aqueous phase volume from zero to about 430 μL. This may be explained by the high tendency of the alcohols to water that causes co-sedimentation of them with water. The volumes of cyclohexane and the dispersers were 5.0 and 1.0 mL, respectively, in these experiments. Ethyl acetate, on the other hand, was found to be quite an appropriate disperser as it produced reasonable and repeatable sedimented phase volumes, and stable cloudy solutions. Therefore, ethyl acetate was selected as an appropriate solvent for the preliminary extraction of OE from olive samples, and an appropriate disperser for the subsequent RP-DLLME procedure.

Using ethyl acetate as the disperser, cyclohexane, petroleum ether, diethyl ether and a 1:1 mixture of cyclohexane and petroleum ether were examined as the organic solvent for the RP-DLLME system. In comparison with the toxic chlorinated solvents usually used in DLLME, these solvents are relatively non-toxic, cheap and have been commonly used for the removal of heavy lipids from olive extracts before their HPLC analysis [11–13]. No considerable differences were observed in the extraction efficiencies of the studied solvents. However, since more stable cloudy solutions and more reproducible volumes of the sedimented phase was obtained by using cyclohexane, this solvent was selected in subsequent experiments. By using cyclohexane, the extraction recoveries were in the range of 91–99%, depending upon the experimental conditions. The mean volume of the sedimented micro-drop was 31.7 (±1.5) μL for three replicates.

3.1. Optimization by the central composite design

After performing some preliminary experiments, optimization of the extraction conditions by the proposed RP-DLLME method was conducted using a half-fraction central composite design. Five factors of cyclohexane (organic solvent) volume, ethyl acetate (disperser) volume, water (extraction solvent) volume, pH of the aqueous phase and centrifugation time (with 3000 rpm) were included in the design (see Table 1). Two dependent variables of extraction recovery (ER%) and enrichment factor (EF) were optimized with the model.

In each experiment, a mixture of the extracting solvent (water with an adjusted pH) and ethylacetate (containing 0.1 mg L^{-1} OE) was rapidly injected into the organic phase. The formed cloudy solution was then centrifuged and the sedimented aqueous phase was directly injected into the HPLC column for subsequent analysis.

The data given in Table 2 show the ER% and EF responses obtained for 28 experiments designed by using the MINITAB software [26]. Table 3 contains the regression coefficients for each term in the model and the analysis of variance (ANOVA) of the effects. The *R*-squared statistic indicated that the model explains 94.25% and 98.83% of the variability in ER% and EF, respectively. The adjusted *R*-squared statistic was 0.7782 for ER% and 0.9549% for EF. The standard error of the estimate showed the standard deviation of the residuals to be 4.27 and 2.13 for the dependent variables, respectively. The Durbin–Watson (DW) statistic showed that there is probably not any serious autocorrelation in the residuals.

Table 2
The conditions of the central composite design experiments and the responses.

No	Parameter*					ER%	EF
	CV	EV	WV	pH	CT		
1	3	0.5	70	6	4	83	7.6
2	5	1.5	70	6	4	106	28.5
3	5	1.5	70	8	6	102	27.3
4	3	1.5	70	8	4	99	26.1
5	4	1.0	60	7	5	103	21.5
6	4	1.0	40	7	5	100	31.3
7	4	1.0	60	9	5	92	18.5
8	6	1.0	60	7	5	92	19.3
9	3	1.5	50	8	6	87	35.0
10	5	0.5	50	6	4	102	12.4
11	3	0.5	50	6	6	90	11.8
12	3	0.5	70	8	6	79	7.6
13	5	0.5	70	8	4	79	7.0
14	3	1.5	70	6	6	91	23.0
15	4	2.0	60	7	5	95	40.4
16	3	1.5	50	6	4	96	25.2
17	2	1.0	60	7	5	88	19.1
18	4	1.0	80	7	5	96	13.7
19	5	0.5	70	6	6	97	8.3
20	4	1.0	60	7	5	110	21.2
21	4	1.0	60	5	5	106	20.5
22	5	1.5	50	8	4	92	38.6
23	4	1.0	60	7	7	94	20.4
24	3	0.5	50	8	4	83	10.4
25	4	1.0	60	7	3	101	22.0
26	5	1.5	50	6	6	112	41.3
27	5	0.5	50	8	6	83	10.4
28	4	1.0	60	7	5	101	22.0

* For the full names of the parameters, see Table 1.

A *p*-value less than 0.05 in the ANOVA table, indicates the statistical significance of an effect at 95% confidence level. The data in Table 3 indicate that ethyl acetate (EV) and cyclohexane (CV) volumes have significant effects on both ER% and EF, but pH influences only ER%. Water's volume, on the other hand, has considerable effect only on EF. The centrifuge time (CT) did not show any significant influence on the responses. The interactions of EV with both CV and WV are significant. As shown in Table 3, quadratic terms of EV^2 and CV^2 also show significant effects on ER%.

Table 3
Estimated regression coefficients and analysis of variance of the predicted model for ER% and EF.

Term	ER%			EF		
	Coefficient	*F*-ratio	*p*	Coefficient	*F*-ratio	*p*
Constant	−32.901	–	0.000	−128.019	–	0.000
CV	42.758	12.180	0.010	18.272	6.960	0.034
EV	1.086	26.630	0.001	11.921	419.110	0.000
WV	−0.257	0.660	0.443	0.576	66.330	0.000
pH	11.388	23.310	0.002	15.418	0.000	0.978
CT	10.635	0.390	0.554	13.198	0.300	0.602
CV^2	−3.574	16.440	0.005	−0.602	1.880	0.213
EV^2	−19.186	19.480	0.003	−2.370	1.200	0.310
WV^2	−0.016	3.190	0.117	0.002	0.260	0.627
pH^2	−1.324	2.260	0.177	−0.527	1.440	0.270
CT^2	−1.699	3.710	0.095	−0.102	0.050	0.824
CV × EV	1.625	0.540	0.471	3.213	9.120	0.019
CV × WV	−0.006	0.000	0.955	−0.084	2.520	0.157
CV × pH	−3.063	8.230	0.024	−1.169	4.830	0.064
CV × CT	1.813	2.880	0.133	−0.456	0.740	0.419
EV × WV	0.388	3.290	0.112	−0.259	5.910	0.045
EV × pH	2.875	1.810	0.220	1.713	2.590	0.152
EV × CT	−0.375	0.030	0.866	0.938	0.780	0.407
WV × pH	0.231	4.690	0.067	−0.019	0.130	0.726
WV × CT	0.019	0.030	0.866	−0.093	3.060	0.124
pH × CT	−0.313	0.090	0.778	−0.781	2.160	0.185

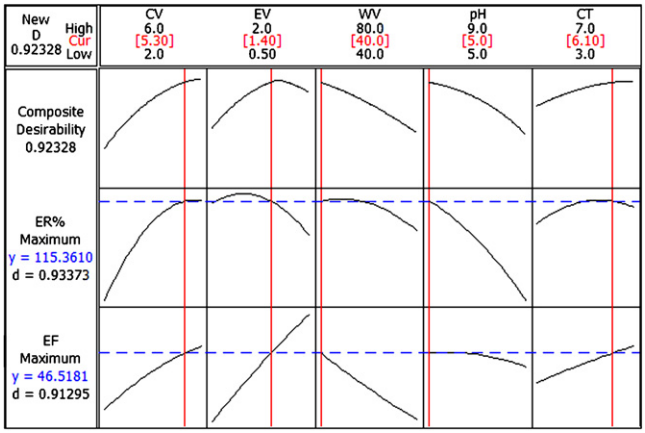


Fig. 1. The optimization plot for the central composite design, including five independent and two dependent variables.

The response surface model with the estimated regression coefficients (see Table 3) was used for the response optimization, including all the factors. The optimization plot (Fig. 1) indicates the predicted conditions for the optimum point and the desirability of the prediction. Each individual plot in the figure shows the way each factor influences the ER%, EF and their composition. Decreasing the extraction efficiency with pH is evident. It is expected that increasing EV should increase the recovery, but in higher EV values no stable cloudy solution is formed and the solution approaches a uniphase at too high ethyl acetate volumes.

Fig. 2 depicts the response surface plots of extraction recovery modeling for some of the significant factors. The curvatures of the plots indicate the interaction between the factors.

3.2. Analytical performances

Five replicated experiments were performed at the predicted optimum conditions by the response surface model (i.e. 1.4 mL ethyl acetate, 5.3 mL cyclohexane, 40 μL water at pH 5.0 and 6.1 min centrifugation time). The extraction of 0.1 mg L^{-1} OE under the optimal conditions resulted in an extraction recovery of 102.5% with a relative standard deviation of 4.5% and an enrichment factor of 38. It can be concluded that the prediction of the model is desirable and the recovery is quantitative. The calibration curve was linear over a range of 0.07–4 mg L^{-1} of OE, with a R^2 of 0.999. The detection limit of the method for OE determination was calculated from 3σ to be 0.02 μg L^{-1} for OPW samples and 2×10^{-3} mg kg^{-1} for olive leaves samples.

3.3. The RP-DLLME of olive leaves samples

The RP-DLLME method was applied for extraction of OE from the ethyl acetate extracts of olive leaves from three different olive varieties. Table 4 indicates the more or less quantitative extraction recoveries for the samples. Fig. 3 compares the chromatograms of *Mary Zeitoon* variety, before (a) and after (b) preconcentration by the proposed method. In Fig. 3(a) only a small peak is observed for

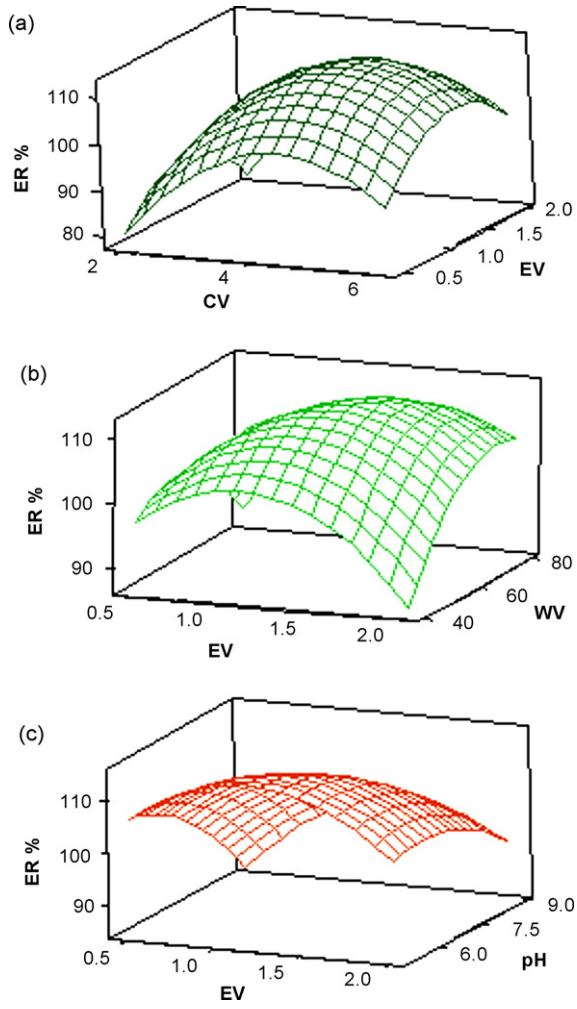


Fig. 2. The response surface plots for extraction recovery (ER%) as a function of CV and EV (a), EV and WV (b) and EV and pH (c).

OE with a signal height of only about 0.03 absorbance units. On the other hand, a sharp OE peak with a height of about 2.4 absorbance units is observed in Fig. 3(b). For direct injection of the ethyl acetate extracts, they were diluted, five times, by ethanol. Evidently, the RP-DLLME method has not only preconcentrated, but also purified the analyte in a considerable extent. Evidently, the system shows a high selectivity towards the extraction and preconcentration of OE into fine droplets of the aqueous phase. Furthermore, the role of the organic phase for removal of heavy lipids and high molecular weight phenolic compounds should not be forgotten [11–13].

3.4. The RP-DLLME of spiked OPW samples

Separation and preconcentration of OPW by the RP-DLLME method resulted in no detectable signal for OE. It has been reported that during the alkaline treatment of olive, OE is essentially hydrolyzed to hydroxytyrosol and other metabolites [14,16].

Table 4
The results of the RP-DLLME-HPLC analysis of the extracts of three olive leaves under the optimized experimental conditions.

Olive variety	OE (mg g^{-1}), direct injection	OE (mg g^{-1}), RP-DLLME	ER%	EF
Mary Zeitoon	126.5 (2.8)	138.0 (1.8)	109.2	39
Sevillana	161.0 (4.4)	167.0 (1.2)	103.5	42
Amphysis	56.0 (2.5)	57.4 (0.9)	102.0	32

Table 5
The results of the RP-DLLME-HPLC analysis of OPW, before and after spiking with different amounts of OE.

Sample	OE (mg L^{-1}), added	OE (mg L^{-1}), found	ER%	EF
OPW	–	n.d.[a]	–	–
Spiked OPW (1)	0.054	0.052 (0.002)	96.2	24
Spiked OPW (2)	0.108	0.107 (0.004)	99.0	23

[a] Not detected.

Table 6
Comparison of the proposed RP-DLLME and some other OE extraction methods.

Extraction method	Sample	LOD[a]	RSD (%)	Extrn. time (min)	Extrn. vol. (mL)	EF	Ref.
Ultrasound assisted	Olive leaves	11.04	5.49	25	15	–	[8]
Microwave assisted	Olive leaves	11.04	3	8	24	–	[9]
Superheated liquid	Olive leaves	11.56	6.89	13	11	–	[10]
RP-DLLME	Olive leaves	2×10^{-3}	4.5	30 + 5	0.040	38	This work
LLE (multiple stages)	OPW	4	5	Long[b]	>150	–	[14]
LLE (multiple stages)	OPW	NR[c]	NR	Long	40	3.3	[16]
RP-DLLME	OPW	0.02	4.5	10 + 5	0.040	38	This work

[a] Limit of detection, in mg Kg^{-1} (for olive leaves) or μg L^{-1} (for OPW samples).
[b] Long = The time is longer than 1 h (the exact time is not reported).
[c] NR = Not reported.

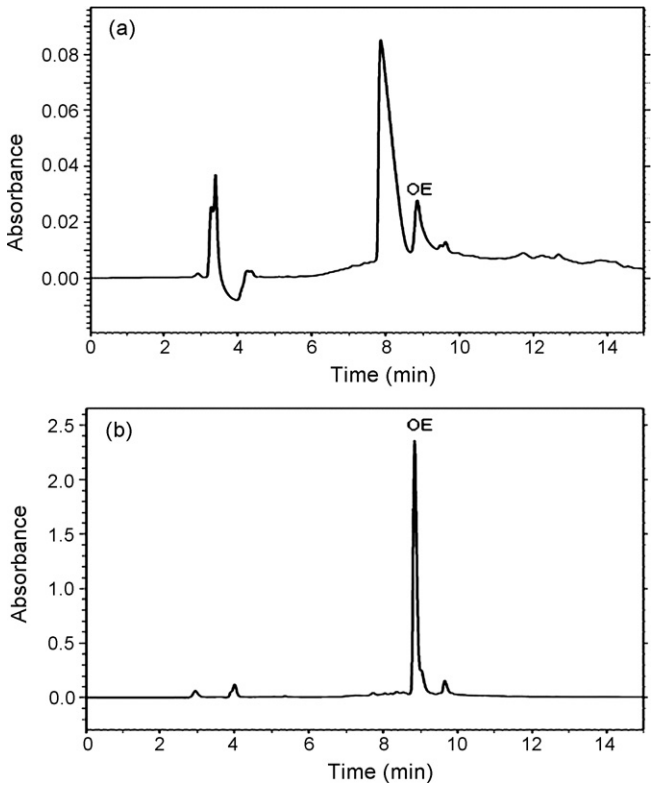


Fig. 3. The chromatograms of the extract of *Mary zetoon* leaves before (a) and after (b) preconcentration by the RP-DLLME method, under the optimized conditions.

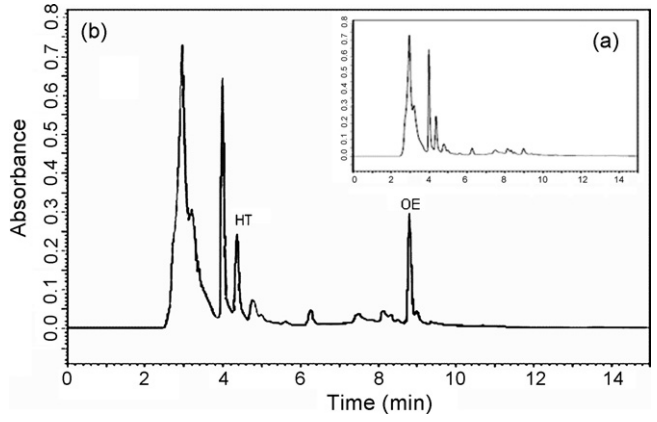


Fig. 4. The chromatograms of non-spiked (a) and spiked (b) OPW by 0.054 mg L^{-1} OE after undergoing the RP-DLLME, under the optimized conditions.

Therefore, the wastewater sample was spiked by OE before the extraction. The results shown in Table 5 indicate a good agreement between the added and found OE which indicates that the proposed method is appropriate for quantitative extraction of OE from such complicated matrices. Fig. 4 shows a chromatogram for one of the spiked samples. The higher area peaks at the beginning of the chromatogram indicate that hydroxytyrosol (HT) and some other biophenols may also be extracted and preconcentrated by the method. Optimization of the RP-DLLME method for the extraction of these compounds will be the subject of our research group future studies.

4. Conclusion

RP-DLLME is a simple and rapid extraction technique with large enrichment factors and low detection limits. In contrast to the conventional DLLME, the extraction phase in the proposed method is a micro-drop of water or an aqueous solution that can be directly injected to HPLC for analysis. The organic phase in this method is lighter than water and is used as the bulk solvent. The solutes distribute between this phase and the aqueous phase and therefore, macromolecules and heavy lipids are removed from the sample. The only disadvantage of RP-DLLME is the relatively high volume of organic solvent used in this method. However, this volume is still far beyond the volumes used in classic LLE techniques. Table 6 compares the proposed method with some other extraction techniques used for the extraction of OE from olive leaves or olive processing wastewater. The much lower detection limits of the RP-DLLME and its small extraction volumes and high enrichment factors are evident.

References

[1] P. Andrews, J.L.H.C. Busch, T.D. Joode, A. Groenewegen, H. Alexandre, J. Agric. Food Chem. 51 (2003) 1415.
[2] H.W. Tan, K.L. Tuck, I. Stupans, P.J. Hayball, J. Chromatogr. B 785 (2003) 187.
[3] C. Manna, S. D'Angelo, V. Migliardi, E. Loffredi, O. Mazzoni, P. Morrica, P. Galletti, V. Zappia, J. Agric. Food Chem. 50 (2002) 6521.
[4] M. Bonoli, A. Bendini, L. Cerretani, G. Lercker, T.G. Toschi, J. Agric. Food Chem. 52 (2004) 7026.
[5] I. Andreadou, F. Sigala, E.K. Iliodromitis, K.M. Papaefthimiou, C. Sigalas, N. Aligiannis, P. Savvari, V. Gorgoulis, E. Papalabros, D.T. Kremastinos, J. Mol. Cell. Cardiol. 42 (2007) 549.
[6] L. Lipworth, M.E. Martinez, J. Angell, C.C. Hsieh, D. Trichopoulos, Prev. Med. 26 (1997) 181.
[7] P. Hashemi, B. Delfan, A.R. Ghiasvand, M. Alborzi, F. Raeisi, Acta Chromatogr. in press.
[8] R. Japon-Lujan, J.M. Luque-Rodriguez, M.D. Luque de Castro, J. Chromatogr. A 1108 (2006) 76.
[9] R. Japon-Lujan, J.M. Luque-Rodriguez, Anal. Bioanal. Chem. 385 (2006) 753.
[10] R. Japon-Lujan, M.D. Luque de Castro, J. Chromatogr. A 1136 (2006) 185.
[11] M. Brenes, A. Garcia, P. Garcia, J.J. Rios, A. Garrido, J. Agric. Food Chem. 47 (1999) 3535.
[12] F.M. Pirisi, P. Cabras, C. Falquicao, M. Migliorini, M. Muggelli, J. Agric. Food Chem. 48 (2000) 1191.
[13] A. Tsarbopoulos, E. Gikas, N. Papadopoulos, N. Aligiannis, A. Kafatos, J. Chromatogr. B 785 (2003) 157.

[14] C.S. Parinos, C.D. Stalikas, T.S. Giannopoulos, G.A. Pilidis, J. Hazard. Mater. 145 (2007) 339.
[15] M. Brenes, L. Rejano, P. Garcia, A.H. Sanchez, A. Garrido, J. Agric. Food Chem. 43 (1995) 2702.
[16] E. De Marco, M. Savarese, A. Paduano, R. Sacchi, Food Chem. 104 (2007) 858.
[17] H. Lord, J. Pawliszyn, J. Chromatogr. A 902 (2000) 17.
[18] M. Rezaee, Y. Assadi, M.R. Milani, E. Aghaee, F. Ahmadi, S. Berijani, J. Chromatogr. A 1116 (2006) 1.
[19] E. Zhao, W. Zhao, L. Han, S. Jiang, Z. Zhou, J. Chromatogr. A 1175 (2007) 137.
[20] M.A. Farajzadeh, M. Bahram, B. Ghorbani Mehr, J.A. Jonsson, Talanta 75 (2008) 832.
[21] A.N. Anthemidis, K.I.G. Ioannou, Talanta 79 (2009) 86.
[22] A. Daneshfar, T. Khezeli, H.J. Lotfi, J. Chromatogr. B 877 (2009) 456.
[23] L. Fu, X. Liu, J. Hu, X. Zhao, H. Wang, X. Wang, Anal. Chim. Acta 632 (2009) 289.
[24] M.B. Melwanki, W.S. Chen, H.Y. Bai, T.Y. Lin, M.R. Fuh, Talanta 78 (2009) 618.
[25] R.G. Breretton, Chemometrics, Data Analysis for the Laboratory and Chemical Plant, John Wiley & Sons Ltd, England, 2003.
[26] Minitab Inc. Minitab Statistical Software, Release 15 for Windows, State College, Pennsylvania, 2006.

Talanta 80 (2010) 1932–1938

Contents lists available at ScienceDirect

Talanta

journal homepage: www.elsevier.com/locate/talanta

Wavelength encoded analytical imaging and fiber optic sensing with pH sensitive CdTe quantum dots

César Maule[a,b,c], Helena Gonçalves[a], Conceição Mendonça[a], Paula Sampaio[d], Joaquim C.G. Esteves da Silva[a,*], Pedro Jorge[b]

[a] Centro de Investigação em Química, Departamento de Química, Faculdade de Ciências da Universidade do Porto, Rua Campo Alegre 687, 4169-007 Porto, Portugal
[b] Optoelectronics Unit, INESC Porto, Rua Campo Alegre 687, 4169-007 Porto, Portugal
[c] Departamento de Física, Faculdade de Ciências da Universidade do Porto, Rua Campo Alegre 687, 4169-007 Porto, Portugal
[d] Instituto de Biologia Molecular e Celular (IBMC), Rua Campo Alegre 823, 4150-180 Porto, Portugal

ARTICLE INFO

Article history:
Received 24 July 2009
Received in revised form 14 October 2009
Accepted 23 October 2009
Available online 29 October 2009

Keywords:
Imaging sensors
Fiber optic sensing
Quantum dots
pH sensing
Wavelength encoded

ABSTRACT

CdTe quantum dots (QDs), capped with mercaptopropionic acid (MPA), were synthesized and the variation of their fluorescence properties (steady state and lifetime) with pH was assessed in solution and when immobilized in a sol–gel host. Three different sizes of CdTe QDs with excited state lifetimes ranging from 42 to 48 ns and with emission maximum at 540 nm (QD_{540}), 580 nm (QD_{580}) and 625 nm (QD_{625}) were selected. The solution pH affects the maximum emission wavelength (shifts to higher wavelengths of 23, 24 and 27 nm for QD_{540}, QD_{580} and QD_{625}, respectively), the excited state lifetime and the fluorescence intensity in a reversible way. Linearization of the maximum emission wavelength variation with the pH allows the estimation of an apparent ionization constant (pK_a) for each QD: 6.5 ± 0.1 (QD_{540}), 6.1 ± 0.5 (QD_{580}) and 5.4 ± 0.3 (QD_{625}). The variation of the QDs fluorescence properties was further explored using confocal laser scanning microscopy allowing the implementation of a new calibration method for pH imaging in solution. QDs were successfully immobilized on the tip of an optical fiber by dip-coating using sol–gel procedure. The immobilized QDs showed a similar pH behaviour to the one observed in solution and an apparent lifetime of 80, 68 and 99 ns, respectively. The proposed QDs based methodology can be successfully used to monitor pH using wavelength encoded data in imaging and fiber optic sensing applications.

© 2009 Elsevier B.V. All rights reserved.

1. Introduction

Semiconductor nanoparticles, or quantum dots (QDs), are presently a widely used tool in the field of biomedical imaging. In addition, their outstanding luminescent properties make them a very appealing alternative to organic dyes in traditional fluorescence based analytical techniques. Their high photostability and quantum yields, together with the ability to tune their absorption and emission properties, simply by changing the size or composition of the nanoparticles, give them superior performance in many applications [1–3]. For these reasons, in the last few years the use of QDs has been demonstrated in a growing range of chemical and biosensing applications [4–6]. While the majority of these applications has been demonstrated in solution assays, the use of quantum dots in combination with optical fibers and other waveguide platforms is a promising emerging field and an essential step towards the implementation of advanced analytical tools [7].

A necessary condition towards the applications of QDs in biological media is the ability to make them stable in aqueous media. The most common strategies to obtain QDs water soluble involve the modifications of their surface with hydrophilic capping ligands [8,9]. Further functionalization of the QD surface with a given ligand can enable its use as a specific indicator for a variety of analytes [10]. A great diversity of sensing applications has been reported where different capping strategies have been used to detect widely different analytes from a diversity of metallic and non-metallic ions [11,12], gases [13] or explosive molecules [14].

Functionalization of the dots surface with ligands containing ionizable groups can render nanoparticles sensitive to pH. The functionalization of CdSe/ZnS QD with a chromophore whose absorption spectrum shifted according to the surrounding pH has been reported [15]. The absorption shift changed the relative overlap with the QD emission, modulating the fluorescence resonance energy transfer (FRET) efficiency according to the pH. Using this method the authors demonstrated an approximately linear variation of the QD luminescence intensity within the pH range 3–11. A potential problem of this strategy lies in the fact that purely intensity based measurements are prone to be affected by

* Corresponding author.
E-mail address: jcsilva@fc.up.pt (J.C.G. Esteves da Silva).

0039-9140/$ – see front matter © 2009 Elsevier B.V. All rights reserved.
doi:10.1016/j.talanta.2009.10.048

several sources of optical power drift. Although the QD luminescence lifetime was shown to be pH dependent, average values in the order of 15 ns were reported. Therefore the implementation of intensity independent lifetime or frequency domain interrogation techniques would require very fast optoelectronic devices. Other authors implementing similar strategies have used pH sensitive QDs to detect glucose or an avian influenza virus [16,17]. Although the pH sensitivity of CdTe QDs has been studied by many authors [18], in most of the reported applications detection was based in simple intensity quenching measurements, few observations were made on QDs wavelength behaviour.

In a more elaborated approach, a QD based ratiometric probe has been designed [19]. This was achieved by conjugating CdSe/ZnS TOPO overcoated with a NIR luminescent squaraine dye. pH modulated FRET resulted in a luminescent emission displaying an isobestic point at 640 nm, which allowed the implementation of ratiometric detection schemes. The generalization of this approach to sensing different biochemical species is possible because the narrow, size-tunable emission spectrum of QD, acting as donors, can be matched with the acceptor absorption features of an analyte sensitive dye, thereby maximizing FRET efficiency.

In this work, the synthesis of thioglycolate capped CdTe QDs is described and their luminescence properties (excitation and emission wavelengths and lifetimes) obtained as function of the reaction time, concentration and pH presented. It is shown, in a confocal microscopy application, that the spectral behaviour of the QDs with pH enables ratiometric pH imaging without the need of combination with organic indicators. Furthermore, the CdTe QDs were immobilized in sol–gel and their pH sensing properties in fiber optic probes assessed.

2. Experimental

2.1. Reagents

Reagents and the respective percentages of purity were the following: tellurium powder (99.997%); cadmium chloride (99.99%); sodium tetrahydroborate (96%); MPA (99%). Deionized and deoxygenated water was used during the synthesis. Water deoxygenating was accomplished by boiling followed by cooling under nitrogen. An inert nitrogen atmosphere was maintained during the synthesis.

A diluted solution of each QD was prepared in a proportion of 1:25 mL in water. The pH of this diluted solution was reversibly changed in the pH range 4–9 with sodium hydroxide (0.1 M) and hydrogen chloride (0.1 M).

TEOS (tetraethoxysilane) (≥99%), TMOS (tetramethyl orthosilicate) and Ph-TriEOS (phenyltriethoxysilane) were obtained from Sigma–Aldrich Química S.A. (Spain).

2.2. Synthesis of CdTe QD

The QDs synthesis was based on well known previously described work [20–22] with the following particular method: (i) 50 mg of sodium tetrahydroborate were mixed with 2 mL of water followed by 75 mg of tellurium—this solution was left to stabilized for about 24 h; this solution was carefully decanted into 100 mL of water; (ii) 230 mg of cadmium chloride was dissolved in 500 mL of water and mixed with 250 μL of MPA—the pH of this solution was rigorously fixed to 6.5 by the addition of sodium hydroxide 1 M; (iii) the tellurium solution was transferred quickly and vigorously into the cadmium solution and the mixture was refluxed up to 27 h. 50 mL samples were removed at selected reaction times (15, 30, 45, 60, 90, 120 and 180 min, 11, 19 and 27 h) for analysis.

By this method the CdTe nanoparticles were capped with mercaptopropionic acid (MPA) becoming water soluble and pH sensitive. One end of the hydrophilic capping ligands contains a thiol group that binds with the QDs surface. The other polar end contains a carboxylic group that makes them water soluble. Because the carboxylic acid group has acid–base properties the optical fluorescence properties of these QDs can be used as pH sensitive indicators.

To evaluate the behaviour of the QDs when submitted to pH changes, three sets of nanoparticles were selected with peak emission at 540 nm (QD_{540}), 580 nm (QD_{580}) and 625 nm (QD_{625}). The fluorescence measurements were performed during the pH titration of the QDs solution. The titration started at pH 6.3 and small amounts of NaOH (0.1 M) were added until the following pH was achieved. After pH 9, small amounts of HCl (0.1 M) were then added to obtain more acidic solutions down to pH 3.0.

2.3. Preparation of optical fiber probes

Silica optical fibers with core/cladding diameters of respectively 550 and 600 μm were purchased from Thorlabs. The fiber tips were carefully polished and their protective coating removed with acetone followed by rinsing with deionized water. To enhance the efficiencies of excitation and collection of luminescence the fiber tips were reshaped by chemical etching. By slow and controlled immersion (using a step motor) of the tip in 40% HF tapered probes with conical shape were obtained (in a 2 cm fiber length the diameter was reduced from 600 μm to approximately 200 μm). To obtain the luminescent probes the fibers were then dip-coated with the QD-doped sol–gel solutions and left to dry in a clean environment at ambient temperature.

2.4. Immobilization of QD in sol–gel matrix and optical fibers

Two sol–gel preparations were tested for the immobilization of the QDs, one based on TMOS and the other, a hybrid sol–gel, based on TEOS and Ph-TriEOS.

(Sol–gel A—TMOS) TMOS was partially hydrolyzed by mixing with an equal amount of HCl (0.1 M), with vigorous stirring for 2 h at room temperature. The resulting solution became a clear and homogeneous sol–gel. At this point equal amounts of the sol–gel was thoroughly mixed with a water solution of the QD, and poured into 1 cm plastic cells. The sol–gel was left in the dark at room temperature for a day and left to dry in a form of a parallelepiped before making the measurements.

(sol–gel B—TEOS/Ph-TriEOS) 1 mL of TEOS and 50 μL Ph-TriEOS were mixed with 250 μL of hydrogen chloride 0.1 M and shaken for 20 min. 2.50 mL of the raw QD solution was added and the mixture shaken for 5 min. Films were immobilized in glass plates and optical fibers by dip-coating [23].

2.5. Instrumentation

A Spex 3D Spectrofluorimeter with a 75 W xenon lamp and a CCD detector was used. Excitation emission matrices of fluorescence (EEM) were acquired, in an excitation wavelength range from 250 to 550 nm, and in an emission wavelength range from 250 to 710 nm, with a resolution of 5 nm. UV–vis spectra were acquired with a Hewlett-Packard HP8452A diode-array spectrophotometer using 1 cm quartz cells in a wavelength range from 240 to 800 nm with a 2 nm interval and an integration time 0.5 s.

The apparent lifetimes of QD doped solutions and sol–gel membranes were estimated using a frequency domain interrogation set-up. The excitation source was a violet LED, and its current modulated with a function generator (Wavetek) and a voltage/current converter (Analog Modules 775). Silica optical fiber bundles were used to guide the excitation radiation to the samples and also to collect the luminescent emission back to detection which was made

using a silicon photodiode (PDA36A). A lock-in amplifier (SRS844) was then used to evaluate the phase difference between the LED emission and the luminescent signals. By performing a phase scan as function of frequency and fitting the acquired data to well known analytical relations between the phase shift and the modulation frequency [24], the samples average lifetime could be estimated.

Using the same excitation source/fiber bundle combination, the spectral characterization of the solutions and of the sol–gel samples was made using a CCD spectrometer (OceanOptics USB4000).

Confocal microscope images were acquired with a Leica SP2 AOBS SE (Leica Microsystems, Germany). The excitation of QDs was made with the Ar laser lines of 458 and 476 nm. A filter-free prism spectrophotometer head with a set of 3 photomultiplier tubes (PMT) allowed the addressing of distinct detection channels in three user-defined spectral ranges. All the image processing operations were done with MATLAB and ImageJ software [25].

3. Results and discussion

3.1. QD fluorescence properties

Table 1 resumes the photophysical properties of the synthesized QDs. These results show that, considering the relative positions of the absorption and emission peaks, all QDs have relatively large apparent Stokes shifts ranging between 230 and 310 nm. It was also observed that the maximum of the excitation wavelength shows a blue shift of about 30 nm when the concentration of the QDs aqueous solution decreases about ten times—at small dilutions the wavelength is kept almost constant and a marked decrease in the excitation wavelength is observed for dilutions higher than 40% the raw concentration. This result may be explained by the aggregation/disaggregation of the QD or a filter effect.

The emission band and the apparent Stokes shift are sensitive to the reaction time, suffering a deviation for the red and an increase, respectively. The increase in the reaction time leads to a shift of the emission wavelength of the CdTe QDs to longer wavelengths (from yellow/green up to red). Longer reaction times result in bigger nanoparticles and, consequently, to a decrease in the carriers' confinement energy and an increase in emission wavelength. The size of the nanoparticles was estimated using the simple model of Bawendi et al. [26], considering a bandgap energy for bulk CdTe of 1.56 eV [27]. The results shown in Table 1, confirm the increasing size of QD_{540}, QD_{580} and QD_{630} which was approximately 6, 7 and 8 nm, respectively. Therefore, by changing the reaction time the size of the nanoparticles can be adjusted and their emission wavelength tuned. Once the reaction is stopped, the resulting nanoparticles are stabilized in water solutions, showing no significant changes in their spectral properties. Therefore, stable nanoparticles can be obtained with different emission characteristics. In addition, by choosing an appropriate wavelength range, all the nanoparticles can be excited using a single excitation source. The full width of half maximum (FWHM) increases with reaction time (from 42 to 62 nm in the range tested), indicating an increase in the dispersion of the size distribution of the nanoparticles.

Table 1
Photophysical and acid–base properties of CdTe QD.

Property	QD_{540}	QD_{580}	QD_{625}
Excitation wavelength (nm)	307	309	316
Emission wavelength (nm)	540	580	625
Estimated size (nm) [26]	6	7	8
FWHM (nm)	42	44	62
pH sensitivity range (ΔpH)	5.7–8.0	4.6–7.5	3.5–8.1
Variation of the emission wavelength with the pH ($\Delta\lambda_{acid/base}$) (nm)	23	24	27
$\Delta\lambda/\Delta$pH (nm)	9.6	8.3	5.9
pK_a	6.5 ± 0.1	6.1 ± 0.5	5.4 ± 0.3
Variation of the lifetime with the pH ($\Delta\tau_{acid/base}$) (ns)		30–90	
τ_{water} (ns)	42	48	44
$\tau_{sol-gel\ based\ TMOS}$ (ns)	80	68	99

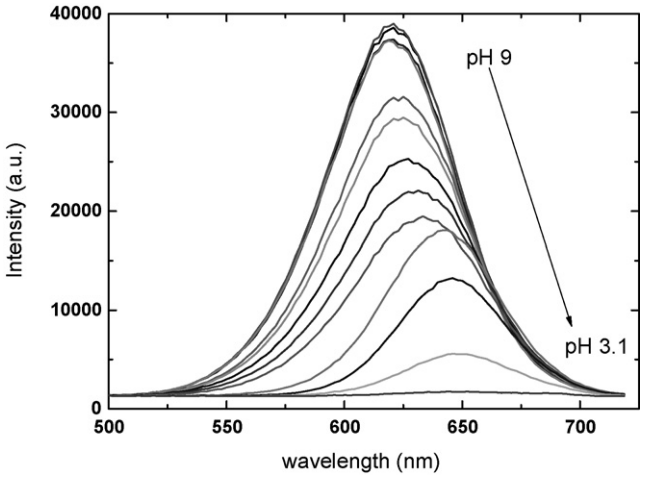


Fig. 1. Emission spectra as function of the pH for QD_{625}.

The emission wavelength of the QDs could be easily tuned between 520 and 630 nm, by increasing the reaction time from 15 min to 27 h. Longer reactions times could result in longer emission wavelengths; however, as the particles grow the effect of quantum confinement starts to decrease, strongly impacting the quantum yield. For smaller nanoparticles the emission efficiency increases with reaction time, however, for reaction times longer than 12 h, the quantum yield decreases. The bandgap energy of bulk CdTe is 1.56 eV [27], which corresponds to an emission wavelength of approximately 795 nm, therefore, to obtain QDs with, longer emission wavelengths different semiconductor materials with smaller bandgap energy must be used (e.g., PbS, PbSe or InAs [28,29]).

The lifetime of the different QDs was also evaluated in water solutions by frequency domain spectroscopy. The decay dynamics of CdTe QD is known to be complex and most often dual or multi-exponential behaviours have been observed. Nevertheless, it is always possible to estimate an average apparent lifetime. The apparent lifetimes of the three QDs were very similar ranging from 42 to 48 ns (Table 1). These values are in agreement with those reported in literature where values ranging from 6 to 125 ns were observed, depending on the QD microenvironment [30,31].

3.2. pH effect on the QD fluorescence properties

The QDs fluorescence intensity, emission spectrum and excited state lifetime in the pH range from 3 to 9 were measured. All QDs exhibited similar behaviour, i.e. as the solution pH was increased, the luminescence intensity increased, the lifetimes decreased and the emission peak was shifted towards shorter wavelengths. The titration procedure was repeated several times, going up and down on the pH scale, and it was observed the changes in the emission peak, the luminescence intensity and the lifetime, were all fully reversible with no observable hysteresis.

Fig. 1 shows an example of the emission spectra variation with the pH of QD_{625}. From this data it can be estimated a wavelength shift of 25 nm for a pH change of 6 units. In the same range the luminescence intensity was quenched by 89%. Similar features were obtained for QD_{540} and QD_{580} and the results are summarized in Table 1.

The presence of a pH dependent wavelength shift suggests that the protonation/deprotonation of the carboxylic ligands of the MPA may influence the QDs bandgap energy. As the pH is increased and the carboxylic ligands ionize, a negatively charged shell builds up in the dots surface that increases the confinement of the charge carriers in the semiconductor core. The increased confinement results in a higher bandgap energy, shorter emission wavelengths and higher quantum yields.

A closer analysis of the data presented in Table 1 reveals that depending on their size, each set of nanoparticles was sensitive to a different pH range. The range of pH sensitivity is 5.7–8.0 for QD_{540}, 4.0–7.0 for QD_{580} and 3.0–8.0 for QD_{625}. The pH dependence of the peak wavelength for the three sets of QDs can be observed in Fig. 2a–c, respectively. Each of the curves obtained are the result of three independent measurements (standard deviation of the average wavelength in each measurement was less than 0.1%), further confirming the reversibility of the changes in the luminescence properties. In addition, these results show that bigger nanoparticles have a pH dependence in an extend range. This happens because, as the average size of particles grows, so does the number of carboxylic ligands on the nanoparticles surface, thereby increasing the number of possible ionization states.

On the other hand, it can also be observed that the shift induced in the emission wavelength is more pronounced for smaller particles. In fact, although the absolute wavelength change increases with particle size, the relative change by pH unit, considering the corresponding sensitive ranges, decreases with growing particle size. This happens because a given change in acidity corresponds to a certain number of ionized carboxylic ligands and the relative change is more pronounced in smaller QDs. In addition, the solutions containing larger nanoparticles have a wider size distribution. This results in a sharper pH response for smaller dots, corresponding to a well defined pK_a and a more broad response for larger QDs, corresponding to a wider pH sensitivity range.

The lifetime of each sample was determined as a function of pH and the corresponding graphical representation is shown in Fig. 3. The analysis of this figure shows that different QDs have different lifetimes, that the lifetime change is relatively small and that this variation occurs in different pH ranges. It can be seen that the lifetime change with pH of bigger QDs has a broader sigmoidal response. This correlates well with the behaviour observed for the wavelength response. In addition, it is also observed that the apparent lifetime decreases as the pH increases. QDs are known to have complex decay dynamics with multi-exponential behaviours. Typically, the shorter lifetime contributions can be attributed to intrinsic recombination of populated core states. Long lived contributions on the other can be associated with the involvement of surface states in the carrier recombination process [32]. Therefore, the behaviour observed could be explained by the increased confinement that enhances the recombination dynamics of surface states. Nevertheless, a more detailed study of the decay dynamics is necessary to better understand the mechanisms involved.

3.3. Confocal microscope imaging

Obtaining analytical information from fluorescent images is a very powerful tool in many applications from biomedical to environmental fields. In particular, self-referenced techniques where the influences of different sources of signal drift are compensated are highly attractive [19,33,34]. If different probes are available, the identification of multiple analytes can be made simultaneously [35]. However, the multiplexing ability of broad emitting organic dyes is quite limited. Therefore, the possibility to use ratiometric analytical imaging methods with the readily multiplexable QDs is highly attractive. To assess the possibility to use these pH sensitive QDs as ratiometric pH probes in imaging applications, different

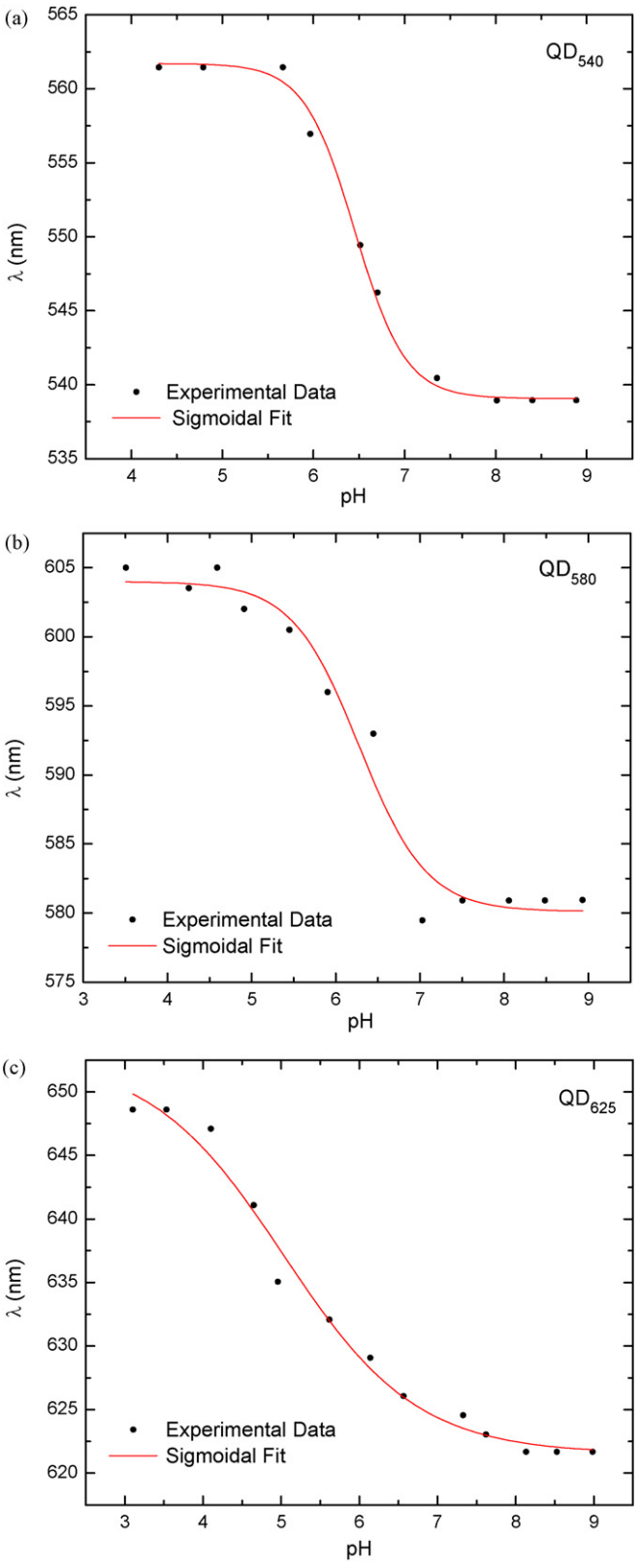


Fig. 2. Variation of the maximum emission wavelength with the solution pH for: (a) QD_{540}; (b) QD_{580}; and (c) QD_{625}. Each curve results from three independent measurements. Standard deviation of measurements is smaller than 0.1%.

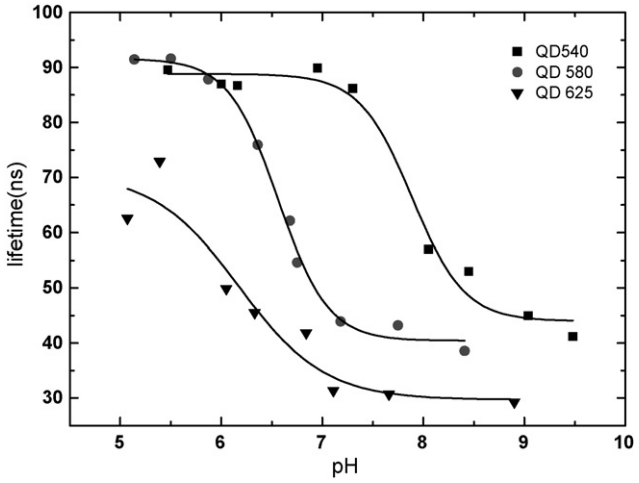


Fig. 3. Dependence of the excited state lifetime with the solution pH.

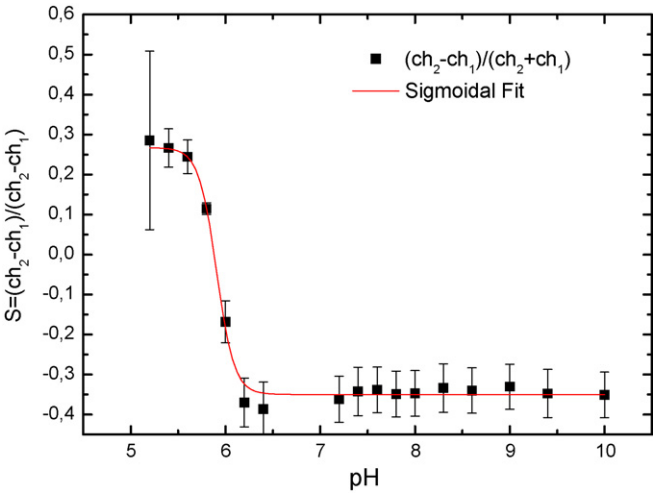


Fig. 4. Ratiometric calibration curve.

buffer solutions doped with pH sensitive QD580 were analysed by confocal laser scanning microscopy.

Using the possibility of the confocal microscope to simultaneously address independent spectral channels a ratiometric detection scheme can be implemented. In particular, if the integrated intensity of two narrow wavelength ranges (channels Ch_1 and Ch_2), chosen in opposite sides of the QDs emission band are recorded, the ratio calculated by $S = (Ch_1 - Ch_2)/(Ch_1 + Ch_2)$ is independent of the intensity and proportional to the wavelength of the emission peak which, in this particular case, is proportional to pH.

This scheme was previously applied for temperature sensing using CdSe–ZnS QDs immobilized in non-hydrolytic sol–gel hosts [36]. This technique can be applied to microscopy by acquiring simultaneously two images of each sample, one through acquisition Ch_1 and another through acquisition Ch_2, each corresponding to the integral of distinct spectral intervals [Ch_1 (540–560 nm) and Ch_2 (620–640 nm)]. By performing the ratiometric scheme described (pixel by pixel), a matrix can then be obtained where each pixel yields a numerical value, given by S, proportional to pH. A false colour scheme can then be applied to obtain images with analytical information.

To calibrate this imaging procedure, several samples corresponding to different pH buffers doped with QDs (ranging from pH 3.2 to 10.0), were analysed. In the pH range between 3.2 and 4.7 the QDs coagulated and precipitated as an orange solid and the images obtained in this pH range were discarded. For the remaining pH range, for each sample, two images with uniform grey level were obtained (one per acquisition channel). The mean value of the grey level intensity (16 bit) of the images was computed, yielding numerical values corresponding to Ch_1 and Ch_2 and ratio S was then calculated. From these operations a sigmoidal calibration curve could be obtained as shown in Fig. 4. In the figure, each data point corresponds to the calculated value of S. The errors bars were calculated considering the standard deviation associated to the values of Ch_1 and Ch_2 and considering error propagation in the calculation of S. The experimental data could be fitted by a four parameter sigmoidal curve with adjusted $R^2 = 0.997$. In the range, pH 5.6–6.2, a linear fit could be obtained with $R^2 = 0.919$.

To demonstrate the feasibility of this method, samples with QDs in different pH buffers were mixed. In particular, a microemulsion was obtained by mixing a few microliters of a QD solution in pH 5.6 and 8 into a drop of silicon oil. Hand shaking of the mixture resulted in a micro-bubbles containing QD solution inside the silica oil droplet.

In Fig. 5, two separate micro-droplets with pH 5.6 (left) and pH 8 (right) are shown. All the images were pre-processed in order to reduce noise (3×3 median filter) and eliminate the non-luminescent background by defining a threshold. The ratiometric scheme and the application of a false colour map using the sigmoidal calibration resulted in images that can be used to estimate the pH. The false colour palette was set between 5 and 6.2 which is the pH range where the wavelength variation took place (all image points with pH higher than 6.2 are represented by the same colour—dark red).

The different stages of the mixing process of two droplets with distinct pH are shown in Fig. 6. The processed images allow seeing clearly that, as the droplets mix, intermediate pH values (between the two extremes 5.4 and 6.2) start to appear. This demonstrates the ability of the ratiometric processing scheme to yield images where a pH value can be ascribe to each pixel.

This technique is therefore promising for pH mapping in bioimaging applications. Similar techniques have been reported using organic dye molecules such as SNARF or phorphyrins (see Ref. [37] and references therein). However, the possibility to implement such analytical imaging techniques using QD introduce several advantages such as increased photostability, narrow emission and tunability of emission wavelength. Such characteristics opens the possibility of using multiple QD probes, each sensitive to a specific analyte (e.g., heavy metals [38,39]), all excited by the same optical source, enabling multianalyte imaging and sensing.

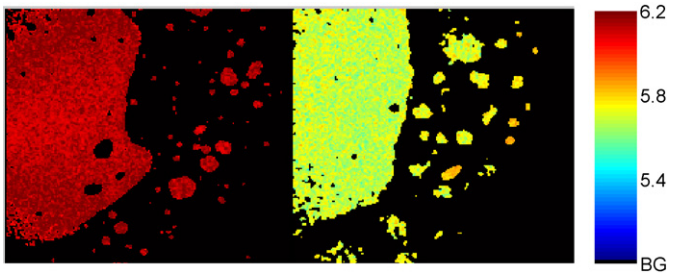


Fig. 5. Image of QDs in pH buffer 5.6 (right) and 8 (left). pH information is given by false colour scale (obtained by application of ratiometric processing and sigmoidal calibration to the original images). Black pixels correspond to background (BG).

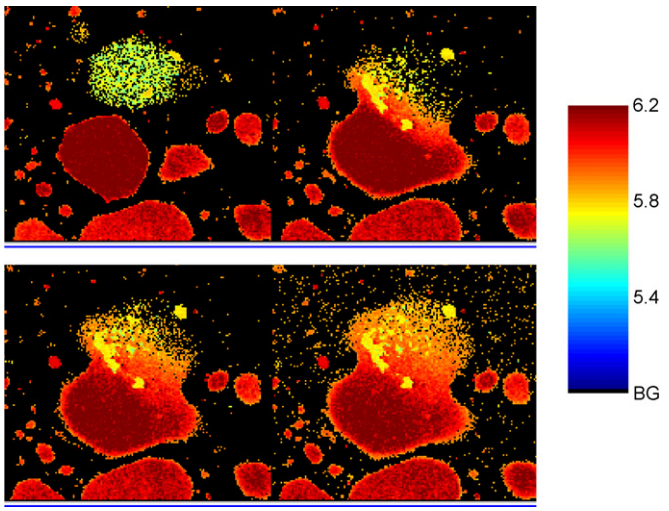


Fig. 6. Sequence of images (from left to right and top to down) showing the mixing process of two droplets with pH values at extremes of the sigmoidal response (8 and 5.6). Black pixels correspond to background (BG).

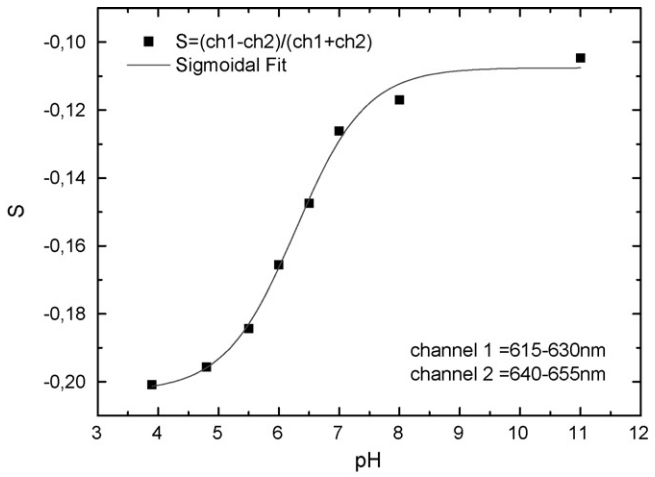


Fig. 7. Ratiometric output of the QD doped fiber probe as function of the solution pH.

3.4. Immobilization of QDs in sol–gel

The QDs were successfully immobilized in TMOS based sol–gel and highly luminescent glass parallelepiped could easily be obtained. The analysis of the emission properties of the monoliths show that the fluorescence intensity of the QDs in the sol–gel based TMOS matrix is enhanced when compared to the one in solutions. This is mostly due to the increase in QDs concentration as a consequence of a volume reduction due to shrinking. Also, the fluorescence emission bands of the different samples are changed from water to sol–gel. All the immobilized QDs showed a shift in their emission peak towards the red, of approximately 14 nm. The immobilization of QDs, introduces changes in their surrounding microenvironment. This is bound to impact mostly their surface states. In particular, the red shift observed indicates that the confinement potential of the immobilized nanoparticles was reduced.

The effect of confinement is also observed in the lifetime behaviour of the QDs. This can be seen in Table 1 where the lifetimes of the QDs in aqueous solutions and in sol–gel matrixes can be compared. In sol–gel the observed lifetimes are higher, by roughly a factor of 2, than those measured in aqueous solutions. The increased lifetimes indicate that the surrounding microenvironment is more favourable to radiative recombination of the long lived surface states when the QDs are immobilized in a sol–gel host. This shows that, while the nanoparticles are very stable in aqueous environments, water may be responsible by partially quenching their luminescence.

When the luminescent glass monoliths entered into contact with different pH aqueous solutions the lifetime and steady state properties of the immobilized QDs did not change significantly and, consequently this sol–gel host was not considered as suitable for sensor applications.

A different immobilization strategy was followed by doping TEOS with Ph-TriEOS. The resulting sol–gel films successfully immobilized the QDs in glass plates and in the tip of optical fibers showing good response to the solution pH. A red shift of approximately 12 nm was observed in the immobilized QDs emission. In this particular case the lifetime was not measured due to reduced signal to noise ratio of the probes obtained. Nevertheless, wavelength ratiometric measurement could be made with the CCD spectrometer.

3.5. Optical fiber probes

The optical fiber probes coated with the TEOS/Ph-TriEOS based films, doped with QD with emission peak at ~635 nm, were tested. When in contact to different pH buffers it could be observed that both luminescence intensity and wavelength were pH dependent, with similar behaviours to the ones observed in solution (Sections 3.2 and 3.3). However, the changes were much smaller indicating that the host matrix had still a significant interference on the QDs behaviour.

In order to evaluate the possibility of using the fiber probes as pH sensors a ratiometric detection scheme, similar to that used above in Section 3.3, was implemented. This scheme was applied to an optical fiber probe doped with QD_{580} setting Ch_1 and Ch_2 for the wavelength intervals of [615, 630 nm], and [640, 655 nm], respectively.

While the wavelength shift observed when the fiber was immersed in pH buffers ranging from pH 4.8 to 11 was barely observable in the spectrometer, it could be easily quantified using the ratiometric scheme. The results obtained are shown in Fig. 7, where the processed output of the fiber probe displays a sigmoidal dependence with pH that is in agreement with the behaviour observed in solution.

These results show the feasibility of pH sensitive QD based optical fiber sensors. However, it was observed that the sensing layer had poor long term stability. The thin film was slowly degrading losing its physical integrity and luminescent capability. This way, although the reversibility of the wavelength response could be observed, a relatively fast degradation of the luminescent intensity was taking place that limited the usefulness of the probes to a small number of essays. Further work is in progress to understand the causes of degradation and to optimize the immobilization procedures.

4. Conclusions

CdTe QDs synthesized and functionalized with MPA were shown to be pH sensitive. The nanoparticles displayed a reversible variation of their peak emission wavelength, emission intensity and lifetime with the pH. The results showed that the emission wavelength changes are more pronounced for smaller particles, which are thus more sensitive to pH. However, it was seen that increasing the particle size lead to sensitivity in a wider range spanning into more acidic pH.

A practical application of these QDs was performed using confocal laser scanning microscopy. A ratiometric scheme was successfully applied to acquired images enabling analytical imaging where pH values could be estimated.

The synthesized QDs were immobilized in different sol–gel hosts. The pH fluorescence behaviour of the nanoparticles immobilized in a TEOS/Ph-TriEOS sol–gel matrix was similar to the one observed in solution. Nevertheless, increased lifetimes and luminescence emission intensities were observed in the solid phase. Also the variations in wavelength and luminescence intensity induced by pH changes were less pronounced in the sol–gel. Nevertheless, it was shown that applying a ratiometric signal processing it was possible to measure pH using a QDs doped optical fiber probe. Work is in progress to improve the long term stability of the fiber probes.

Overall the results obtained show QD as promising labels with analytical capabilities without the need for intermediate indicator dyes and with strong potential for the development of chemically sensitive fluorescent fiber probes. Further functionalization of the quantum dots will enable to apply the same techniques to perform optical fiber sensing or analytical imaging of different chemical analytes, e.g., heavy metals. The use of QDs with different sensitivities together with their multiplexing ability will allow the application of the results obtained in this work in multipoint/multiparameter biochemical sensing and imaging techniques.

Acknowledgements

Financial support from Fundação para a Ciência e Tecnologia (FCT) (Lisboa) (FSE-FEDER) (Projects PTDC/QUI/71001/2006 and POCTI/QUI/44614/2002) is acknowledged. César Maule acknowledges the support from the Marie Curie Early stage research training network, funded by European Commission under the contract MEST-CT-2005-020353. A Ph.D. grant to Helena Gonçalves SFRH/BD/46406/2008 is acknowledged to Fundação para a Ciência e Tecnologia (Lisboa).

References

[1] X.Y. Wu, H.J. Liu, J.Q. Liu, K.N. Haley, J.A. Treadway, J.P. Larson, N.F. Ge, F. Peale, M.P. Bruchez, Nat. Biotechnol. 21 (2003) 41–46.
[2] J.K. Jaiswal, S.M. Simon, Trends Cell Biol. 14 (2004) 497–504.
[3] X. Gao, L. Yang, J.A. Petros, F.F. Marshall, J.W. Simons, S. Nie, Curr. Opin. Biotechnol. 16 (2005) 63–72.
[4] J.M. Costa-Fernandez, R. Pereiro, A. Sanz-Medel, Trac 25 (2006) 207–218.
[5] R.C. Somers, M.G. Bawendi, D.G. Nocera, Chem. Soc. Rev. 36 (2007) 579– 591.
[6] X.X. Wang, M.J. Ruedas-Rama, E.A.H. Hall, Anal. Lett. 40 (2007) 1497–1520.
[7] P. Jorge, M.A. Martins, T. Trindade, J.L. Santos, F. Farahi, Sensors 7 (2007) 3488–3534.
[8] M. Green, H. Harwood, C. Barrowman, P. Rahman, A. Eggeman, F. Festry, P. Dobson, T. Ng, J. Mat. Chem. 17 (2007) 1989–1994.
[9] D. Gerion, F. Pinaud, S.C. Williams, W.J. Parak, D. Zanchet, S. Weiss, A.P. Alivisatos, J. Phys. Chem. B 105 (2001) 8861–8871.
[10] C.J. Murphy, Anal. Chem. 74 (2002) 520A–526A.
[11] Y. Chen, Z. Rosenzweig, Anal. Chem. 74 (2002) 5132–5138.
[12] W.J. Jin, J.M. Costa-Fernandez, R. Pereiro, A. Sanz-Medel, Anal. Chim. Acta 522 (2004) 1–8.
[13] A.Y. Nazzal, L. Qu, X. Peng, M. Xiao, Nano Lett. 3 (2003) 819–822.
[14] G.H. Shi, Z.B. Shang, Y. Wanga, W.J. Jin, T.C. Zhang, Spectrochim. Acta A 70 (2007) 247–252.
[15] M. Tomasulo, I. Yildiz, S.L. Kaanumalle, F.M. Raymo, Langmuir 22 (2006) 10284–10290.
[16] D.B. Cordes, S. Gamsey, B. Singaram, Angew. Chem. Int. Ed. 45 (2006) 3829–3832.
[17] Z. Yun, D. Zhengtao, Y. Jiachang, T. Fangqiong, W. Qun, Anal. Biochem. 364 (2007) 122–127.
[18] A.S. Susha, A.M. Javier, W.J. Parak, A.L. Rogach, Colloids Surf. A 281 (2006) 40–43.
[19] P.T.P.T. Snee, R.C. Somers, G. Nair, J.P. Zimmer, M.G. Bawendi, D.G. Nocera, J. Am. Chem. Soc. 128 (2006) 13320–13321.
[20] J. Huang, K. Sooklal, C.J. Murphy, Chem. Mater. 11 (1999) 3595–3601.
[21] L. Li, H.F. Qian, N.H. Fang, H.C. Ren, J. Lumin. 116 (2006) 59–66.
[22] Z. Deng, Y. Zhang, J. Yue, F. Tang, Q. Wei, J. Phys. Chem. B 111 (2007) 12024–12031.
[23] E.J.E.J. Wang, K.F. Chow, V. Kwan, T. Chin, C. Wong, A. Bocarsly, Anal. Chim. Acta 495 (2003) 45–50.
[24] J.R. Lakowicz, Frequency-Domain Lifetime Measurements in Principles of Fluorescence Spectroscopy, Kluwer-Plenum, New York, 1999, pp. 142–184.
[25] J.B. Sheffield, Microsc. Microanal. 13 (2007) 200–201.
[26] M.G. Bawendi, M.L. Steigerwald, L.E. Brus, Annu. Rev. Phys. Chem. 41 (1990) 477–496.
[27] T. Rajh, O.I. Micic, A.J. Nozik, J. Phys. Chem. 97 (1993) 11999–12003.
[28] E.H. Sargent, Adv. Mater. 17 (2005) 515–522.
[29] L. Levina, W. Sukhovatkin, S. Musikhin, S. Cauchi, R. Nisman, D.P. Bazett-Jones, E.H. Sargent, Adv. Mater. 17 (2005) 1854.
[30] A.M. Kapitonov, A.P. Stupak, S.V. Gaponenko, E.P. Petrov, A.L. Rogach, A. Eychmuller, J. Phys. Chem. B 103 (1999) 10109–10113.
[31] S.F. Wuister, I. Swart, F. van Driel, S.G. Hickey, C.D. Donega, Nano Lett. 3 (2003) 503–507.
[32] S.J. Byrne, S.A. Corr, T.Y. Rakovich, Y.K. Gun'ko, Y.P. Rakovich, J.F. Donegan, S. Mitchell, Y. Volkov, J. Mater. Chem. 16 (2006) 2896–2902.
[33] A. Hakonen, S. Hulth, Anal. Chim. Acta 606 (2008) 63–71.
[34] N. Stromberg, S. Hulth, Anal. Chim. Acta 550 (2005) 61–68.
[35] H.W. Ai, K.L. Hazelwood, M.W. Davidson, R.E. Campbell, Nat. Methods 5 (2008) 401–403.
[36] P.A.S. Jorge, M. Mayeh, R. Benrashid, P. Caldas, J.L. Santos, F. Farahi, Meas. Sci. Technol. 17 (2006) 1032–1038.
[37] T. Leiding, K. Gorecki, T. Kjellman, S.A. Vinogradov, C. Hagerhall, S.P. Arskold, Anal. Biochem. 388 (2009) 296–305.
[38] H.M.R. Gonçalves, C. Mendonça, J.C.G. Esteves da Silva, J. Fluoresc. 19 (2009) 141–149.
[39] J.M.M. Leitão, H.M.R. Gonçalves, C. Mendonça, J.C.G. Esteves da Silva, Anal. Chim. Acta 628 (2008) 143–154.

Talanta 80 (2010) 1939–1944

Contents lists available at ScienceDirect

Talanta

journal homepage: www.elsevier.com/locate/talanta

Supramolecular interaction of cucurbit[*n*]urils and coptisine by spectrofluorimetry and its analytical application

Chang-Feng Li[a,b], Li-Ming Du[a,*], Wen-Ying Wu[a], Ai-Zhuo Sheng[a]

[a] Analytical and Testing Center, Shanxi Normal University, Shanxi Linfen 041004, PR China
[b] School of Chemistry and Materials Science, Shanxi Normal University, Linfen 041004, PR China

ARTICLE INFO

Article history:
Received 10 July 2009
Received in revised form 19 October 2009
Accepted 23 October 2009
Available online 29 October 2009

Keywords:
Coptisine
Cucurbit[*n*]uril
Spectrofluorimetry
Supramolecular interaction

ABSTRACT

The supramolecular interaction of a homologous series of cucurbit[*n*]uril (CB[*n*], *n* = 5, 6, 7, 8) hosts and coptisine (COP) was studied by spectrofluorimetry. All of the CB[*n*]s were found to react with COP to form 1:1 host–guest stable complexes and the fluorescence intensity of the complexes was greatly enhanced. The apparent association constants of the complexes were 1.44×10^4, 1.28×10^4, 1.86×10^4 and 1.26×10^4 L mol^{-1} for CB[5], CB[6], CB[7] and CB[8], respectively. In addition, CB[5] and CB[7] exhibited a higher fluorescence signal than CB[6] and CB[8]. The fluorescence intensity of the complex with CB[7] was enhanced 70-fold compared to that of the studied drug itself. Based on the significant enhancement of fluorescence intensity of supramolecular complex, a simple, rapid, highly sensitive, and selective spectrofluorimetric method was developed for the determination of COP in aqueous solution in the presence of CB[7]. At the optimum reaction conditions, a linear relationship was obtained in the range from 0.05 to 1700 ng mL^{-1} with a detection limit of 0.012 ng mL^{-1}. The proposed method was successfully applied for the determination of the drug in urine and serum samples.

© 2009 Elsevier B.V. All rights reserved.

1. Introduction

The cucurbit[*n*]urils (CB[*n*], *n* = 5, 6, 7, or 8) are a relatively new family of pumpkin-like macrocyclic host molecules comprised of five, six, seven, or eight methylene-bridged glycoluril units, which possess a hydrophobic cavity accessible through portals surrounded by polar carbonyl groups capable of including a variety of hydrophobic or/and positively charged guest molecules [1–5]. Confinement in the cucurbituril macrocycle can alter the chemical and spectroscopic properties of guest molecules [6,7], enhance photostability [8,9] or facilitate stereoselective photodimerization [10,11]. Despite CB[*n*]s (Scheme 1) have become widely used in studies of general inclusion phenomena of guest molecules, little attention has been devoted to their fluorescence properties.

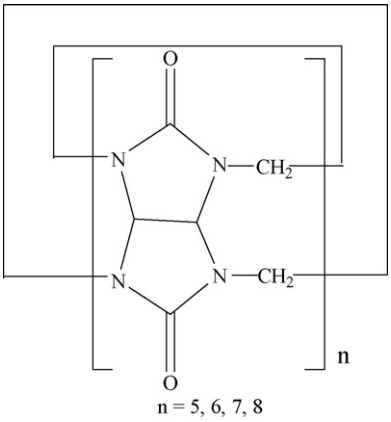
Coptisine (COP) (Scheme 2), an isoquinoline alkaloid originally isolated from rhizome of *Coptis japonica*, has extensive pharmacological actions, including anti-bacterial activity towards antimicrobial, anti-diarrhoea, anti-diabetic, and anti-cancer [12–15]. It also inhibits proliferation of vascular smooth muscle cells [16]. Several methods have been reported for the determination of COP including high performance liquid chromatography (HPLC) [17–20] and capillary electrophoresis (CE) [21–24]. However, most of these methods require the use of organic solvents, complicated extraction processes, expensive instruments, strictly controlled reaction conditions and time-consuming operating steps.

Spectrofluorimetry is a highly sensitive, selective, easily operated, and economical method that is widely used in the determination of pharmaceutical compounds [25–29]. COP possesses a low fluorescence emission in aqueous solution, which means that it cannot be determined directly by normal fluorimetric methods. To the best of our knowledge, fluorimetric determination of COP has not been reported. Therefore, the development of a rapid, simple, highly sensitive, and selective spectrofluorimetric method for the determination of COP in aqueous solution is highly desirable.

In this report, a comparative study of the inclusion interactions of CB[*n*] (*n* = 5, 6, 7, 8) with COP has been carried out on the basis of results obtained by spectrofluorimetry. A significant increase in the fluorescence intensity was observed when CB[*n*] was added to an aqueous solution of COP. In particular, CB[7] exhibited strong binding ability compared with the other CB[*n*]s tested. Based on the significant enhancement of fluorescence intensity of the supramolecular complexes, a spectrofluorimetric method with high sensitivity and selectivity was developed for the determination of COP in aqueous solution in the presence of CB[7]. The method is simple, accurate, and practical. Its detection limit is 0.012 ng mL^{-1}, which is lower than any other method reported thus far in the literature. The proposed method had been applied to the determination of COP in human urine and plasma samples

* Corresponding author.
E-mail address: lmd@dns.sxnu.edu.cn (L.-M. Du).

0039-9140/$ – see front matter © 2009 Elsevier B.V. All rights reserved.
doi:10.1016/j.talanta.2009.10.049



Scheme 1. The structure of the different cucurbit[*n*]urils (*n* = 5, 6, 7, 8).

with satisfactory results. This method shows promising potential for therapeutic drug monitoring, pharmacokinetics, and clinical applications.

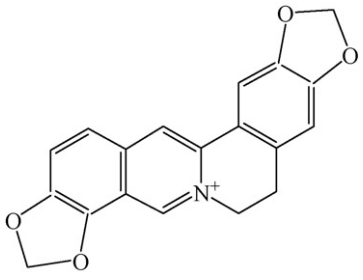
2. Experimental

2.1. Instruments

Fluorescence spectra and intensity measurements were obtained with a Hitachi F-4500 spectrofluorimeter equipped with a 150 W xenon lamp (Tokyo, Japan). All measurements were performed at 25 ± 0.5 °C using a thermostated cell holder and a thermostatically controlled water bath. Values of pH were measured with a pHS-3C digital precision pH meter (Shanghai, China).

2.2. Reagents

All chemicals were of analytical reagent grade and doubly distilled water was used throughout. COP was obtained from China Chengdu Scholar Bio-Tech Co. Ltd. A standard stock solution of 1.0×10^5 ng mL^{-1} was prepared with ethanol. Working solutions were obtained by appropriate dilution of the stock solution with doubly distilled water. CB[*n*] (*n* = 5, 6, 7, or 8) was prepared and characterized according to reported procedures [2]. CB[*n*] (*n* = 5, 6, or 7) stock solutions of 1.25×10^{-3} mol L^{-1} were prepared by dissolving CB[5, 6, or 7] in 3.0 mL hydrochloric acid and diluting to the mark in a 100 mL volumetric flask with doubly distilled water. CB[8] stock solution of 1.25×10^{-3} mol L^{-1} was prepared by dissolving CB[8] in 60 mL formic acid and diluting to the mark in a 100 mL volumetric flask with doubly distilled water. Working solutions were obtained by dilution of the stock solution. All four types of stock standard solutions were stable for several weeks at room temperature. Britton–Robinson buffer solution of pH 1.80 was prepared by mixing 100 mL of 0.04 mol L^{-1} acid (3.92 g of H_3PO_4 + 2.40 g of HAc + 2.47 g of H_3BO_3) with appropriate volumes of 0.2 mol L^{-1} NaOH, and adjusting to pH 2.0.



Scheme 2. The structure of coptisine.

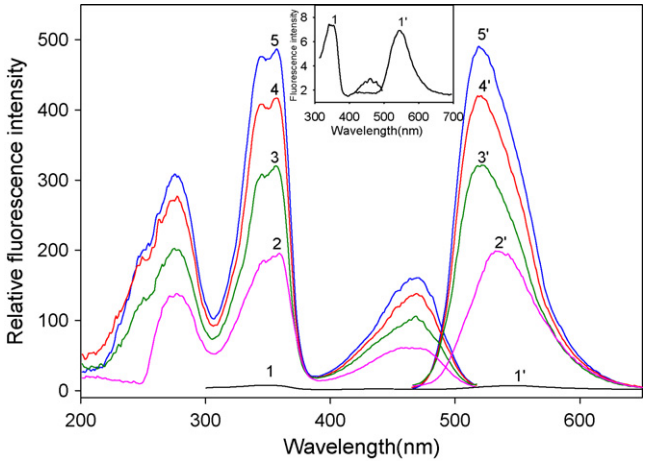


Fig. 1. Excitation and emission spectra. Excitation and emission spectra of: (1, 1′) COP (1.0×10^3 ng mL^{-1}) with $\lambda_{ex}/\lambda_{em}$ = 342/544 nm; (2, 2′) CB[8] (4.375×10^{-4} mol L^{-1})–COP (1.0×10^3 ng mL^{-1}) with $\lambda_{ex}/\lambda_{em}$ = 359/533 nm; (3, 3′) CB[6] (4.5×10^{-4} mol L^{-1})–COP (1.0×10^3 ng mL^{-1}) with $\lambda_{ex}/\lambda_{em}$ = 357/523 nm; (4, 4′) CB[5] (3.0×10^{-4} mol L^{-1})–COP (1.0×10^3 ng mL^{-1}) with $\lambda_{ex}/\lambda_{em}$ = 357/521 nm; (5, 5′) CB[7] (4.6875×10^{-5} mol L^{-1})–COP (1.0×10^3 ng mL^{-1}) with $\lambda_{ex}/\lambda_{em}$ = 358/520 nm; (1, 2, 3, 4, and 5) excitation spectra; (1′, 2′, 3′, 4′, and 5′) emission spectra.

2.3. Procedure

2.3.1. General procedure

A suitable amount of COP solution was transferred into a 10 mL volumetric flask and 2.0 mL of 1.25×10^{-3} or 3.125×10^{-4} mol L^{-1} CB[*n*] solution was added, followed by 5.0 mL of Britton–Robinson buffer of pH 2.0. After dilution to the mark with doubly distilled water, the mixture was shaken and equilibrated at room temperature for 10 min. The relative fluorescence intensity of the solution of the drug with CB[5], CB[6], CB[7] and CB[8] was then measured at 521, 523, 520 and 533 nm with excitation at 357, 357, 358 and 359 nm against a reagent blank, respectively. All measurements were performed using 1.0 cm quartz cells. Both excitation and emission slit widths were set at 2.5 nm. The fluorescence spectra were recorded at scan rate of 1200 nm min^{-1}.

2.3.2. Analysis of plasma and urine samples

5.0 mL of plasma was deproteinized by the addition of 10 mL acetonitrile and centrifuging at 4000 rpm for 5 min. 3 mL volume of the clear supernatant was pipetted into a 50 mL volumetric flask, then 2.0 mL of the drug stock solution was added. The mixture was diluted to the mark with doubly distilled water and the general analytical procedure was followed.

Urine samples were centrifuged at 4000 rpm for 5 min, then 1 mL of the clear supernatant was pipetted into a 50 mL volumetric flask, then 2.0 mL of the drug stock solution was added. The mixture was diluted to the mark with doubly distilled water. The standard additions method was used in the sample analysis procedure.

3. Results and discussion

3.1. Excitation spectra and emission spectra

The spectral characteristics of COP and its complexes were studied. As shown in Fig. 1, an aqueous solution of COP had a weak native fluorescence and the maximum excitation and emission wave-

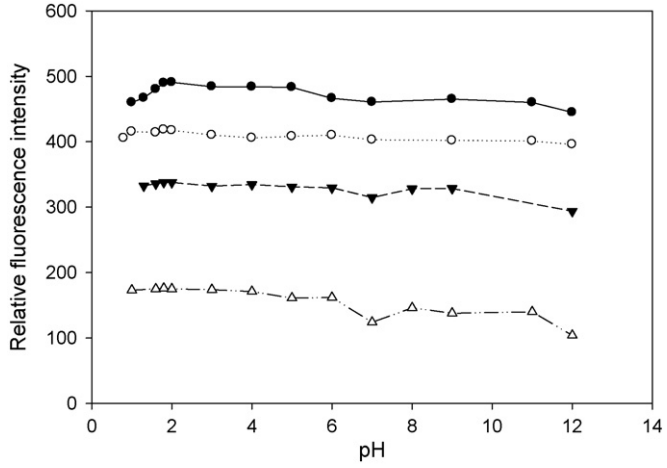


Fig. 2. Influence of pH on the fluorescence intensity. Experiment conditions: COP: 1.0×10^3 ng mL^{-1}; CB[5] (○): 3.0×10^{-4} mol L^{-1}; CB[6] (▼): 4.5×10^{-4} mol L^{-1}; CB[7] (●): 4.6875×10^{-5} mol L^{-1}; CB[8] (△): 4.375×10^{-4} mol L^{-1}.

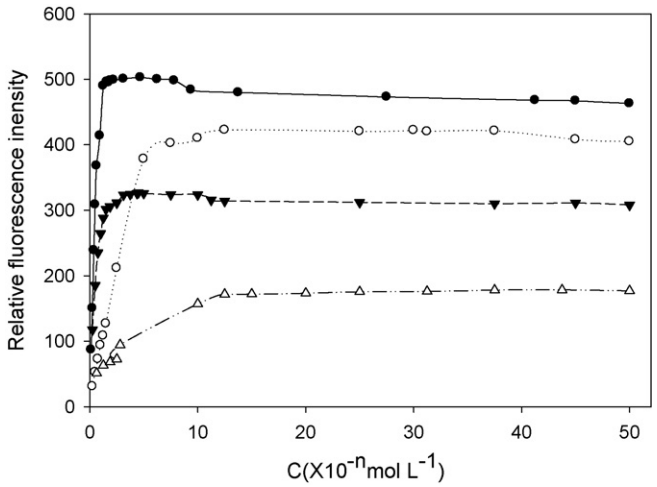


Fig. 3. Influence of CB[n] on the fluorescence intensity. Experiment conditions: COP: 1.0×10^3 ng mL^{-1}, pH 2.0; CB[5] (○): ($C \times 10^{-5}$ mol L^{-1}); CB[6] (▼): ($C \times 10^{-4}$ mol L^{-1}); CB[7] (●): ($C \times 10^{-5}$ mol L^{-1}); CB[8] (△): ($C \times 10^{-5}$ mol L^{-1}).

lengths were located at 342 and 544 nm, respectively. However, significant increases in the fluorescence intensity were observed when CB[5], CB[6], CB[7], or CB[8] were added to the aqueous solution of COP. In addition, the excitation and emission wavelengths of their complexes moved to wavelengths of 357, 357, 358, 359 nm and of 521, 523, 520 and 533 nm, respectively. These modifications of the features of the fluorescence spectra were considered to be a result of inclusion complex formation between the investigated drug and CB[n]. This is most probably due to the combination of ion–dipole interactions and hydrophobic effect contributes to the binding forces. There is coulomb attraction between the positive charge of the heterocyclic nitrogen of the guest and the high electron density of the carbonyl oxygen of the CB[n] (Scheme 1), whereas the apolar part of COP enters the interior of CB[n], displacing solvent water molecules from within the CB[n] and from the solvation sheath of the guest, thereby contributing a hydrophobic effect to the stability of the complex [6,30,31]. In addition, CB[5] and CB[7] exhibited higher signals than CB[6] or CB[8]. The fluorescence intensity of the drug was enhanced 70-fold in the presence of CB[7]. For this reason, further studies used CB[7] as the host for drug determination.

3.2. Influence of pH

The influence of pH on the relative fluorescence intensity of formed CB[n]–COP inclusion complex was therefore studied at their respective maxima using buffer solutions in the pH range of 1.0–12.0 in order to establish an optimal experimental condition. As shown in Fig. 2, the fluorescence intensity was maximal and almost constant over the pH range of 1.0–4.0 for all the studied CB[n]s tested with COP. The fluorescence intensity decreased with any further increases in pH. This behavior was probably attributable to CB[n] preferentially binding cations. Therefore, a pH of 2.0, prepared in the form of aqueous Britton–Robinson buffer solutions, was used for all subsequent experiments.

3.3. Influence of CB[n] concentration

The effect of CB[n] concentration on the fluorescence intensity of COP was examined in the range from 1.25×10^{-6} to 5×10^{-4} mol L^{-1}. As shown in Fig. 3, the fluorescence intensity of COP was rapidly enhanced as the amount of CB[n] was increased. When the concentration of CB[5], CB[6], CB[7] or CB[8] was increased up to 1.25×10^{-4}, 3.75×10^{-4}, 1.56×10^{-5} and 2.5×10^{-4} mol L^{-1}, respectively, the fluorescence intensities were maximal and leveled off at higher concentrations. Thus, the final CB[5], CB[6], CB[7] or CB[8] concentration used in further experiments was 3.0×10^{-4}, 4.5×10^{-4}, 4.6875×10^{-5} or 4.375×10^{-4} mol L^{-1}, respectively.

3.4. Influence of temperature and reaction time

The effect of temperature on the formed complexes was investigated in the range of 5–90 °C as shown in Fig. 4. All of the formed complexes were stable up to 40 °C. At temperature higher than 40 °C, the fluorescence intensity greatly decreased due to dissociation of the complexes at high temperatures. Based on these findings, all further measurements were performed at room temperature.

The fluorescence intensity reached a maximum within 10 min after the reagents had been added and remained constant for at least 5 h as shown in Fig. 5. For this reason, room temperature for 10 min was selected as a standard reaction condition.

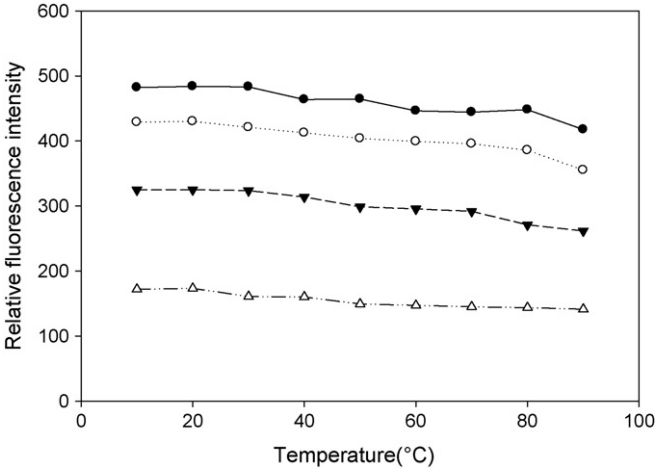


Fig. 4. Influence of temperature on the fluorescence intensity. Experiment conditions: COP: 1.0×10^3 ng mL^{-1}, pH 2.0; CB[5] (○): 3.0×10^{-4} mol L^{-1}; CB[6] (▼): 4.5×10^{-4} mol L^{-1}; CB[7] (●): 4.6875×10^{-5} mol L^{-1}; CB[8] (△): 4.375×10^{-4} mol L^{-1}.

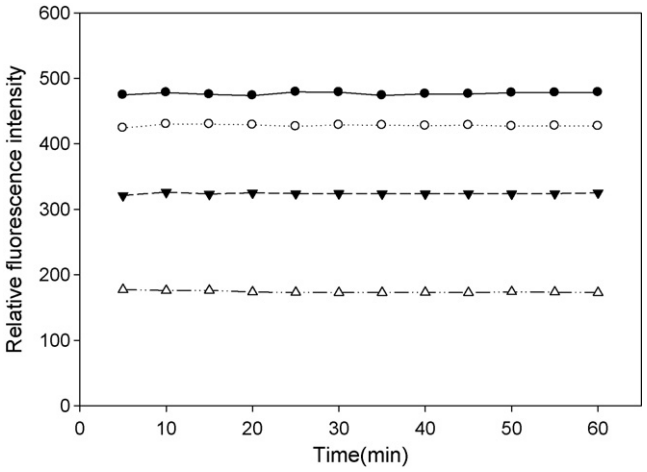


Fig. 5. Effect of reaction time on fluorescence intensity. Experiment conditions: COP: 1.0×10^3 ng mL^{-1}, pH 2.0; CB[5] (○): 3.0×10^{-4} mol L^{-1}; CB[6] (▼): 4.5×10^{-4} mol L^{-1}; CB[7] (●): 4.6875×10^{-5} mol L^{-1}; CB[8] (△): 4.375×10^{-4} mol L^{-1}.

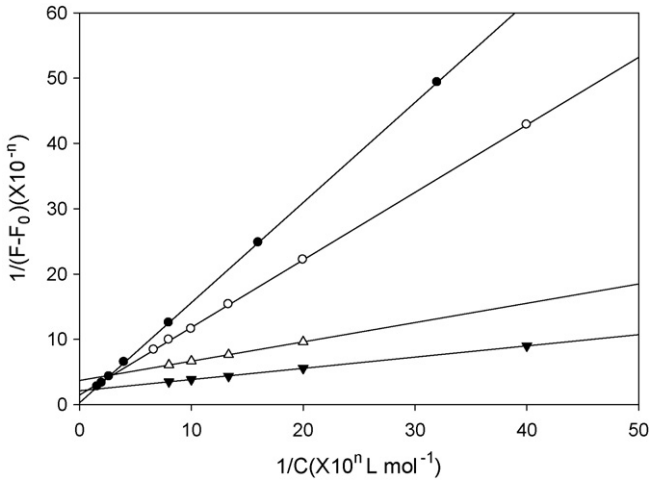


Fig. 6. Plot of $1/(F-F_0)$ vs. $1/C_{CB[n]}$. Experiment conditions: COP: 1.0×10^3 ng mL^{-1}, pH 2.0; CB[5] (○): $(1/C \times 10^4\ \mathrm{L\,mol^{-1}},\ 1/(F-F_0) \times 10^{-4})$; CB[6] (▼): $(1/C \times 10^3\ \mathrm{L\,mol^{-1}},\ 1/(F-F_0) \times 10^{-4})$; CB[7] (●): $(1/C \times 10^5\ \mathrm{L\,mol^{-1}},\ 1/(F-F_0) \times 10^{-4})$; CB[8] (△): $(1/C \times 10^3\ \mathrm{L\,mol^{-1}},\ 1/(F-F_0) \times 10^{-4})$.

3.5. Stoichiometry and association constant of the inclusion complex

The magnitude of the association constant is usually taken as a measure of the strength of the interaction between the two molecules forming the complex. For this study, 1000 ng mL^{-1} of COP solution and varying amounts of 1.25×10^{-3} mol L^{-1} CB[n] solution were prepared. Aliquots of each solution were added in different ratios to a series of 10 mL calibrated flasks, then the general procedure was followed for determination of the association constant.

The stoichiometry and association constant of the inclusion complex were studied under the established experimental conditions by the following method:

Assuming that the composition of the complex was 1:1, the expression can be written as follows:

$$\mathrm{COP} + \mathrm{CB}[n] \leftrightarrow \mathrm{CB}[n]\text{–}\mathrm{COP} \quad (1)$$

The apparent constant of the complex (K) is given by

$$K = \frac{C_{\mathrm{CB}[n]\text{–}\mathrm{COP}}}{C_{\mathrm{COP}} \times C_{\mathrm{CB}[n]}} \quad (2)$$

where C_{COP}, $C_{\mathrm{CB}[n]}$, and $C_{\mathrm{CB}[n]\text{–}\mathrm{COP}}$ are equilibrium concentrations. The association constant value for the inclusion complex can be determined by the typical double reciprocal (or Benesi–Hildebrand) plots:

$$\frac{1}{F - F_0} = \frac{1}{(F_\infty - F_0)KC_{\mathrm{CB}[n]}} + \frac{1}{F_\infty - F_0} \quad (3)$$

where F_0 is the fluorescence intensity of COP in the absence of CB[n], F_∞ is the fluorescence intensity when all of the COP molecules are essentially complexed with CB[n], and F is the observed fluorescence intensity at each CB[n] concentration tested.

A good linear relationship was obtained when $1/(F-F_0)$ was plotted against $1/C_{\mathrm{CB}[n]}$, which supported the existence of a 1:1 complex (R = 0.9998, Fig. 6). The apparent association constants for these 1:1 complexes were determined to be 1.44×10^4, 1.28×10^4, 1.86×10^4 and 1.26×10^4 L mol^{-1} in the presence of CB[5], CB[6], CB[7] and CB[8], respectively. These values were determined by dividing the intercept by the slope of the corresponding lines. It is evident that both CB[5] and CB[7] exhibited stronger binding ability than did CB[6] and CB[8].

3.6. Calibration graph and sensitivity

Under the experimental conditions described, standard calibration curves of the complexes for four CB[n]s with COP were constructed by plotting fluorescence intensity vs. concentration. The linear regression equation for each method is listed in Table 1. The correlation coefficients ranged from 0.9997 to 0.9999, indicating good linearity. The small value for the variance confirmed the small degree of scatter in the experimental data points around the regression line.

The increase in sensitivity obtained with the proposed method, compared with other methods, is very substantial. This comparison (Table 2) showed an improvement of about three orders of magnitude vs. a previous HPLC method [17]. Spectrofluorimetry through supramolecular interaction, as performed in the present study, had the main advantages over HPLC methods [17] of rapidity and sim-

Table 1
Characteristic parameters for the complexes of four CB[n] with COP.

Parameters	COP–CB[5]	COP–CB[6]	COP–CB[7]	COP–CB[8]
Linear relationship (ng mL^{-1})	0.1–1700	0.3–1600	0.05–1700	1.0–1600
LOD (ng mL^{-1})	0.0305	0.093	0.012	0.34
LOQ (ng mL^{-1})	0.1	0.3	0.05	1.0
Slope (b)	0.4175	0.3074	0.4787	0.1903
S.D. of slope (Sb)	0.0085	0.0230	0.0082	0.0150
Intercept (a)	5.1352	9.5007	5.6510	8.8600
S.D. of intercept (Sa)	0.003922	0.008663	0.001741	0.01961
Correlation coefficient (r)	0.9997	0.9997	0.9999	0.9999
S.D. of reagent blanks (S_0)	0.004244	0.009532	0.001924	0.0213

IF = $a + bC$, where IF is the fluorescence intensity of the inclusion complex and C is the concentration of COP in ng mL^{-1}.

Table 2
Comparison with other proposed methods for the determination of COP.

Technique	Linear dynamic range (ng mL^{-1})	LOD (ng mL^{-1})	Application	Reference
HPLC	480–36,000	160	*Coptis-evodia* herb couple	[17]
HPLC-DAD	13,500–270,000	143	*Qinhuanghouzheng* capsule *Xiaoerqingre* tablet	[18]
HPLC-DAD–ESI-MS	4200–84,000	1400	*Zanthoxylum nitidum*	[19]
HPLC–ESI-MS	0.31–20.0	0.1	*Coptidis Rhizoma*	[20]
MEKC-CE	31,000–187,000	10,333	*Scute-coptis* herb couple	[21]
MEKC-CE	10,000–30,000	650	*Coptidis Rhizoma*	[22]
FASI-CE	20–100	5	*Coptidis Rhizoma* alkaloids	[23]
Sweeping-CE	10–50	2.5	*Coptidis Rhizoma* alkaloids	[24]
Spectrofluorimetry				
CB[5]	0.1–1700	0.0305		This work
CB[6]	0.3–1600	0.0930		This work
CB[7]	0.05–1700	0.0120	Plasma and urine	This work
CB[8]	1.0–1600	0.3400		This work

Table 3
Effect of interference on the determination of 1.0×10^3 ng mL^{-1} COP (tolerance error ± 5.0%).

Interferences	Tolerance (ng mL^{-1})	Relative error (%)
Boracic acid	4000	3.3
Sucrose	3000	1.6
Glucose	3000	2.7
Polyethylene glycol	3000	3.0
Gelatin	2000	−2.4
Casein	2000	−3.6
Mg^{2+}	1500	4.3
K^+	1000	−2.4
Na^+	1000	2.1
PO_4^{3-}	1000	2.1
Tryptophan	1000	−3.6
Sorbitol	1000	3.8
Mannitol	1000	2.4
Methyl cellulose	1000	3.7
Lactose	500	2.2
Gum acacia power	500	4.0
Sodium carboxymethyl cellulose	500	4.1
Ca^{2+}	500	−4.2
Sodium acetate	300	2.4
Cl^-	300	2.6
Starch	300	−3.0

plicity. The proposed method was highly sensitive when compared with spectrophotometric methods.

3.7. Effects of interferences

A systematic study of interference by the usual excipients and the main constituents of plasma and urine in the determination of COP were carried out. A 3000-fold mass excess of these over 1.0×10^3 ng mL^{-1} of COP was first tested. If interference occurred, the ratio was reduced gradually until the interference ceased. The criterion for interference was fixed at a ±5% variation in the average fluorescence intensity calculated for the established level of COP. As shown in Table 3, this method had high selectivity and it was obvious that the determination of COP was free from interference due to substances in plasma and urine samples. The emission wavelength of COP itself was 544 nm, however, in the presence of CB[*n*], the emission wavelengths of resultant complexes moved to wavelengths of 521, 523, 520 and 533 nm for CB[5], CB[6], CB[7], or CB[8], respectively. This effectively removed the interference for the determination of COP at pharmaceutical dosages in plasma and urine samples.

4. Analytical application

4.1. Analysis of spiked human plasma and urine

The high sensitivity of the proposed method allows the determination of COP in biological fluids. Therefore, spiked samples of

Table 4
Fluorimetric determination of COP in spiked urine ($n = 5$, $p = 95\%$).

Samples	Spiked urine			Spiked plasma		
	Amount added (ng mL^{-1})	Amount found (ng mL^{-1})	Recovery (%) ± S.D.[a]	Amount added (ng mL^{-1})	Amount found (ng mL^{-1})	Recovery (%) ± S.D.[a]
Urine 1 plasma 1	4.0	4.15	103.8 ± 0.47	4.0	4.16	104.0 ± 0.71
Urine 2 plasma 2	20.0	20.14	100.7 ± 0.28	20.0	20.12	100.6 ± 0.21
Urine 3 plasma 3	100.0	100.6	100.6 ± 0.38	100.0	101.4	101.4 ± 0.51
Urine 4 plasma 4	200.0	199.68	99.84 ± 0.84	200.0	195.7	97.85 ± 1.54
Urine 5 plasma 5	300.0	289.12	96.37 ± 1.9.0	300.0	286.1	95.4 ± 1.58

[a] Average of five determinations.

human urine and plasma were also analyzed, as shown in Table 4. The accuracy was assessed by calculating the recovery of COP at five concentration levels covering the specified range (five replicates at each concentration). Excellent recoveries with S.D. less than 2.0% were obtained, indicating both good accuracy and precision.

5. Conclusion

The proposed method is rapid, simple, reproducible, economical, highly sensitive, and selective. It can be used for determination of COP in its corresponding dosage forms, without interference from commonly used excipients. The proposed procedure is so sensitive that 0.012 ng mL^{-1} of COP could be determined with satisfactory accuracy and precision. The method also permits the determination of the studied drug in biological fluids.

Acknowledgment

This research was supported by the Natural Science Foundation of Shanxi (No. 2007011027).

References

[1] W.A. Freeman, W.L. Mock, N.Y. Shih, J. Am. Chem. Soc. 103 (1981) 7367–7368.
[2] J. Kim, I.S. Jung, S.Y. Kim, E. Lee, J.K. Kang, S. Sakamoto, K. Yamaguchi, K. Kim, J. Am. Chem. Soc. 122 (2000) 540–541.
[3] J.W. Lee, S. Samal, N. Selvapalam, H.J. Kim, K. Kim, Acc. Chem. Res. 36 (2003) 621–630.
[4] J. Lagona, P. Mukhopadhyay, S. Chakrabarti, L. Isaacs, Angew. Chem. Int. Ed. 44 (2005) 4844–4870.
[5] S. Liu, P.Y. Zavalij, L. Isaacs, J. Am. Chem. Soc. 127 (2005) 16798–16799.
[6] M. Megyesi, L. Biczo'k, I. Jablonkai, J. Chem. Phys. C 112 (2008) 3410–3416.
[7] Y.P. Li, H. Wu, L.M. Du, Chin. Chem. Lett. 20 (2009) 322–325.
[8] J. Mohanty, H. Pal, A.K. Ray, S. Kumar, W.M. Nau, ChemPhysChem 8 (2007) 54–56.
[9] J. Mohanty, W.M. Nau, Angew. Chem. Int. Ed. 44 (2005) 3750–3754.
[10] R. Wang, L. Yuan, D.H. Macartney, J. Org. Chem. 71 (2006) 1237–1239.
[11] M. Pattabiraman, L.S. Kaanumalle, A. Natarajan, V. Ramamurthy, Langmuir 22 (2006) 7605–7609.
[12] R. Marek, P. Seckarova, D. Hulova, J. Marek, J. Dostal, V. Sklenar, J. Nat. Prod. 66 (2003) 481–486.
[13] A.H. Gilani, B. Samra, K.H. Janbaz, A. Khan, J. Ethnopharmacol. 96 (2005) 585–589.
[14] C.L. Kuo, C.W. Chi, T.Y. Liu, Cancer Lett. 203 (2004) 127–137.
[15] B.S. Ko, S.B. Choi, S.K. Park, J.S. Jang, Y.E. Kim, S. Park, Biol. Pharm. Bull. 28 (8) (2005) 1431–1437.
[16] H. Tanabe, H. Suzuki, H. Mizukami, M. Inoue, Biochem. Pharmacol. 70 (2005) 1176–1184.
[17] C.Y. Chu, S.J. Sheu, J. Chromatogr. A 756 (1996) 137–144.
[18] L.H. Yin, B.N. Lu, Y. Qi, L.N. Xu, X. Han, Y.W. Xu, J.Y. Peng, C.K. Sun, J. Pharm. Biomed. Anal. 49 (2009) 1101–1108.
[19] M.J. Liang, W.D. Zhang, J. Hu, R.H. Liu, C. Zhang, J. Pharm. Biomed. Anal. 42 (2006) 178–183.
[20] S. Yu, X.Y. Pang, Y.X. Deng, L. Liu, Y. Liang, X.D. Liu, L. Xie, G.J. Wang, X.T. Wang, Int. J. Mass Spectrom. 268 (2007) 30–37.
[21] K.L. Li, S.J. Sheu, Anal. Chim. Acta 313 (1995) 113–120.
[22] L.C. Chang, S.W. Sun, J. Pharm. Biomed. Anal. 40 (2006) 62–67.
[23] S.W. Sun, H.M. Tseng, J. Pharm. Biomed. Anal. 36 (2004) 43–48.
[24] S.W. Sun, H.M. Tseng, J. Pharm. Biomed. Anal. 37 (2005) 39–45.
[25] X.S. Zhu, J. Sun, J. Wu, Talanta 72 (2007) 237–242.
[26] L.A. Hergert, G.M. Escandar, Talanta 60 (2003) 235–246.
[27] Q.J. Gong, J.L. Qiao, L.M. Du, C. Dong, W.J. Jin, Talanta 53 (2000) 359–365.
[28] F. Liu, H.L. Liang, K.H. Xu, L.L. Tong, B. Tang, Talanta 74 (2007) 140–145.
[29] B. Tang, X. Wang, G.L. Wang, C.G. Yu, Z.Z. Chen, Talanta 69 (2006) 113–120.
[30] W.L. Mock, N.Y. Shih, J. Am. Chem. Soc. 110 (1988) 4706–4710.
[31] W.L. Mock, N.Y. Shih, J. Am. Chem. Soc. 111 (1989) 2697–2699.

Talanta 80 (2010) 1945–1951

Contents lists available at ScienceDirect

Talanta

journal homepage: www.elsevier.com/locate/talanta

Development of the extraction method for the simultaneous determination of butyl-, phenyl- and octyltin compounds in sewage sludge

Tea Zuliani[a,b,*], Gaetane Lespes[b], Radmila Milačič[a], Janez Ščančar[a]

[a] Department of Environmental Sciences, Jožef Stefan Institute, Jamova 39, 1000 Ljubljana, Slovenia
[b] Laboratoire de Chimie Analytique, UMR 5254, Université de Pau, BP 1155, F-64013 PAU Cedex, France

ARTICLE INFO

Article history:
Received 6 July 2009
Received in revised form 9 October 2009
Accepted 23 October 2009
Available online 10 November 2009

Keywords:
Organotin compounds
Sewage sludge
Extraction procedures
GC–MS

ABSTRACT

The toxicity and bioaccumulation of organotin compounds (OTCs) led to the development of sensitive and selective analytical methods for their determination. In the past much attention was assigned to the study of OTCs in biological samples, water and sediments, coming mostly from marine environment. Little information about OTCs pollution of terrestrial ecosystems is available. In order to optimise the extraction method for simultaneous determination of butyl-, phenyl- and octyltin compounds in sewage sludge five different extractants (tetramethylammonium hydroxide, HCl in methanol, glacial acetic acid, mixture of acetic acid and methanol (3:1), and mixture of acetic acid, methanol and water (1:1:1)), the presence or not of a complexing agent (tropolone), and the use of different modes of extraction (mechanical stirring, microwave and ultrasonic assisted extraction) were tested. Extracted OTCs were derivatised with sodium tetraethylborate and determined by gas chromatography coupled with mass spectrometer. Quantitative extraction of butyl-, phenyl- and octyltin compounds was obtained by the use of glacial acetic acid as extractant and mechanical stirring for 16 h or sonication for 30 min. The limits of detection and quantification for OTCs investigated in sewage sludge were in the ng Sn g^{-1} range.
© 2009 Elsevier B.V. All rights reserved.

1. Introduction

Organotin compounds (OTCs) are organometallic derivatives of tin that have the highest number of commercial applications than any other element [1]. Mostly they have been used as stabilizers and catalysts in the production of poly(vinyl chloride) (PVC), polyurethanes and silicones, as antifouling paints for ship hulls, and as agricultural and wood preservative fungicides [2–4]. Due to their widespread use, OTCs may be found in different ecosystems. Today, their high toxicity for aquatic and terrestrial organisms is well documented [3,4]. Moreover, because of their toxicity and bioaccumulation potential, OTCs have been registered as priority pollutants by the European Union in the Pollutant Emission Register (2000/479/EC) and in the Water Framework Directive (2000/60/EC).

During last decades, a variety of analytical methods for the speciation of OTCs has been developed. Analytical procedures for OTCs speciation generally attempt to preserve only the organic radical during extraction, whereas the counterion and other tin heteroatomic bonds are cleaved during extraction or derivatisation [5]. Sample preparation techniques for speciation analyses of OTCs in solid samples consist of several steps: solid–liquid extraction, simultaneous derivatisation and extraction into an organic solvent, separation and detection. One of the most difficult parts of the analysis of OTCs in sewage sludge is their extraction from the complex matrix. Extraction of OTCs from solid matrices keeping their speciation preserved is not straightforward because the binding forces between OTCs and matrices are species and matrices dependant [6,7]. In addition, some OTCs are not stable during extraction. Species transformation can be considered to be one of the most serious problems during phenyltin speciation analysis [8–10].

From the discovery of the toxicity of OTCs towards numerous marine species in late 1970s, most efforts have been devoted to the development of analytical methods for their determination in marine environments (seawater, sediments and biota) [5,11,12]. There are few studies concerning tin speciation in samples from terrestrial ecosystem [10,13,14]. OTCs are entering the terrestrial environment via the leaching from products made of PVC and silicone, by the use of pesticides and the amendment of cultivated soil with contaminated sewage sludge [15,16]. OTCs were also found in leachates from landfills [17,18].

Sewage sludge is an important source of OTCs in the terrestrial ecosystems [15,16]. Thus, reliable analytical methods are needed in order to evaluate the contribution of contaminated sewage sludge to the OTCs pollution of terrestrial environment. The aim

* Corresponding author at: Department of Environmental Sciences, Jožef Stefan Institute, Jamova 39, 1000 Ljubljana, Slovenia. Tel.: +386 1 4773900; fax: +386 1 2519385.
E-mail address: tea.zuliani@ijs.si (T. Zuliani).

0039-9140/$ – see front matter © 2009 Elsevier B.V. All rights reserved.
doi:10.1016/j.talanta.2009.10.050

Table 1
Mass/charge (m/z) ratios and retention times for studied OTCs.

OTCs	Retention time (min)	m/z
MBT	6.7	235, **179**, 149
DBT	8.9	**263**, 179, 151
TBT	10.8	291, **263**, 179
MPhT	10.1	255, **197**
DPhT	15.0	303, 275, **197**
TPhT	17.9	**351**, 197
MOcT	11.9	291, **179**, 151
DOcT	16.6	375, **263**, 151
TOcT	19.9	375, 263, **151**
TPrT	7.6	249, 235, **193**

Ions used for quantification are reported in bold.

of our investigation was to set up an analytical procedure for the speciation of OTCs in sewage sludge by gas chromatography mass spectrometry (GC–MS). The influence of the extractant, extraction technique and the presence of complexing agent on the extraction efficiency of butyl-, phenyl- and octyltin compounds from sewage sludge have been studied. The selected methods encompass five different extractants (tetramethylammonium hydroxide (TMAH), hydrochloric acid (HCl) in methanol, glacial acetic acid, mixture of acetic acid and methanol (3:1), and mixture of acetic acid, methanol and water (1:1:1)), the presence or not of a complexing agent (tropolone), and the use of different modes of extraction (mechanical stirring, microwave and ultrasonic assisted extraction). Extracted OTCs were derivatised with sodium tetraethylborate ($NaBEt_4$) and determined by GC–MS.

2. Experimental

2.1. Instrumentation

For the separation and detection a Hewlett-Packard 6890 gas chromatograph (GC) (Hewlett-Packard, Waldbronn, Germany) coupled to a Hewlett-Packard 5972A mass spectrometer (MS) was used. The GC was equipped with a 30 m × 25 mm HP-MS5 polydimethylsiloxane capillary column (film thickness 0.25 μm). The following temperature program was applied for the separation of OTCs: the column temperature was held at 80 °C for the first 4 min, raised to 180 °C at the heating rate of 10 °C min^{-1}, then to 220 °C at 20 °C min^{-1}, and to 270 °C at 30 °C min^{-1} (held at this temperature for 6 min). The splitless injector port was kept at a temperature of 240 °C and the transfer line at 280 °C. Helium (He) was used as a carrier gas (1 mL min^{-1}). The volume of injected sample was 1 μL. The MS operated with the electronic impact (70 eV) ion source at a temperature of 180 °C in the total ionization mode. Selected Ion Monitoring signals (SIM) were recorded. In Table 1 are presented the mass/charge (m/z) ratios of OTCs and their retention times. For the quantification the most abundant ions were used.

Mechanical shaking during the extraction procedure was performed on an elliptical table Vibramax 40 (Tehtnica, Železniki, Slovenia). Microwave assisted extraction was performed with a CEM MARS 5 Microwave Acceleration Reaction System, CEM Corporation (Matthews, NC, USA). Ultrasonic-assisted extraction of samples was performed with an ultrasonic bath Model 550D, VWR International (West Chester, PA, USA). Centrifugation of sample extracts was performed on a Heraeus (Osterode, Germany) Model 17S Sepatech Biofuge centrifuge and on a LC 320 centrifuge (Tehtnica, Železniki, Slovenia).

2.2. Reagents

Monobutyltin trichloride (MBT, 95%), monophenyltin trichloride (MPhT, 98%) and diphenyltin dichloride (DPhT, 96%) were purchased from Aldrich (Milwaukee, WI, USA). Dibutyltin dichloride (DBT, 97%), tributyltin chloride (TBT, 96%), triphenyltin chloride (TPhT, 95%) and tripropyltin chloride (TPrT, 98%) were obtained from Merck (Darmstadt, Germany). Monooctyltin trichloride (MOcT, 98%), dioctyltin dichloride (DOcT, 98%) were obtained from LGC Promochem (Wesel, Germany) and trioctyltin chloride (TOcT, 95%) from Fluka (Buchs, Switzerland). Organotin standard stock solutions (1000 mg Sn L^{-1}) were prepared in methanol. Working standard solutions (10 mg Sn L^{-1}) were prepared weekly from stock standard solutions by dilution in Milli-Q water (18.2 MΩ cm) (Millipore, Bedford, MA, USA). Standard solutions of 100 μg Sn L^{-1} were prepared daily. All the standards were stored in the dark at 4 °C.

Glacial acetic acid, ammonia solution and nitric acid were obtained from J.T. Baker (Phillipsburg, NJ, USA). Methanol was purchased from Merck (Darmstadt, Germany). Sodium tetraethylborate ($NaBEt_4$) was purchased from Strem Chemicals (Newburyport, MA, USA). $NaBEt_4$ was dissolved in Milli-Q water to provide a 2% (m/v) ethylating solution.

2.3. Sample preparation

Sewage sludge samples were dried at 50 °C in the dark for 3 days, homogenised and sieved through a 0.2 mm sieve. The samples were then frozen at −20 °C.

2.4. Analytical procedure

2.4.1. Extraction from the sample

Approximately 1 g of dried sewage sludge was weighted in a polyethylene (PE) extraction tube. Based on our previous experiences 0.2 μg of TPrT in methanol was added as internal standard [19]. After 15 min the samples were subjected to different extraction methods.

2.4.1.1. Method 1. 20 mL of tetramethylammonium hydroxide (TMAH) was added to the sample. The tubes were subjected to ultrasound assisted extraction for 2 h and centrifuged for 15 min at 4200 rpm.

2.4.1.2. Method 2. Samples were supplemented with 15 mL of 0.1 mol L^{-1} HCl in methanol. The closed tubes were firstly mechanically shaken on an elliptic table for 2 h and then subjected to ultrasonic assisted extraction for 1 h and centrifuged for 15 min at 4200 rpm.

2.4.1.3. Method 3. Samples were supplemented with 20 mL of glacial acetic acid. The tubes were subjected to closed vessel microwave assisted extraction for 4, 7 and 16 min. Microwave extraction conditions were as follows: 1200 W, 1 min ramp to 50 °C, hold at that temperature for 3, 6 and 15 min. After the extraction, the suspension was centrifuged for 15 min at 4200 rpm.

2.4.1.4. Method 4. To the solid sample 5 mL of methanol and 15 mL of glacial acetic acid were added. The tubes were subjected to closed vessel microwave assisted extraction for 7 min. The microwave extraction conditions were as described in Section 2.4.1.3. After the extraction, the suspension was centrifuged for 15 min at 4200 rpm.

2.4.1.5. Method 5. Samples were supplemented with 20 mL mixture of acetic acid, methanol and water (1:1:1). The tubes were subjected to closed vessel microwave assisted extraction for 7 min. The microwave extraction conditions were as described in Section 2.4.1.3. After the extraction, the suspension was centrifuged for 15 min at 4200 rpm.

2.4.1.6. Method 6. To the solid sample 5 mL of 0.02% (w/v) tropolone in methanol and 15 mL of glacial acetic acid were added. The tubes were subjected to closed vessel microwave assisted extraction for 7 min. The microwave extraction conditions were as described in Section 2.4.1.3. After the extraction, the suspension was centrifuged for 15 min at 4200 rpm.

2.4.1.7. Method 7. Samples were supplemented with 20 mL of glacial acetic acid. The closed tubes were subjected to ultrasound assisted extraction for 5, 10, 20, 30 and 60 min. After the extraction, the suspension was centrifuged for 15 min at 4200 rpm.

2.4.1.8. Method 8. As Method 7. Acetic acid–methanol mixture (3:1) instead of glacial acetic acid as extractant was applied to the samples.

2.4.1.9. Method 9. To the solid sample 20 mL of glacial acetic acid was added. The closed tubes were mechanically shaken on an elliptic table for 1, 5, 15 and 24 h in the dark. Then, the suspension was centrifuged for 15 min at 4200 rpm.

2.4.2. Derivatisation and extraction

Aliquots (1–4 mL) of the extract described above, 0.5 mL 2% (w/v) solution of $NaBEt_4$ for the derivatisation and 1 mL of isooctane for the extraction of ethylated organotin species were added to 20 mL of sodium acetate-acetic acid buffer (pH 4.8). The mixture was shaken for 45 min at 300 rpm. The same procedure, with the exception that no sample was added, was applied to determine blanks. All the analyses were made in triplicate.

2.4.3. Spiking protocol

The recovery of the studied OTCs from sewage sludge was investigated by spiking known amount of OTCs into samples of relatively low OTCs contents. For spiking of sewage sludge samples OTCs as chlorides dissolved in methanol were used. The equilibration step was carried out by shaking (350 rpm) the samples for 30 min.

For each extraction three different spikes were prepared. One aliquot of the sewage sludge was spiked with 1000 ng Sn g^{-1} of monosubstituted butyl-, phenyl- and octyltin compounds (MBT, MPhT, MOcT). The second one was spiked with 1000 ng Sn g^{-1} of disubstituted butyl-, phenyl- and octyltin compounds (DBT, DPhT, DOcT) and the third with 1000 ng Sn g^{-1} of trisubstituted butyl-, phenyl- and octyltin compounds (TBT, TPhT, TOcT). The differences between recoveries depend only on the differences in extraction procedure, as the post-extraction steps of the analytical method remained the same.

3. Results and discussion

Sewage sludge consists of a complex matrix. In order to release the molecular and ionic OTCs from organic matter in sewage sludge an appropriate digestion/extraction must be applied. In any speciation procedure, the extraction procedure must be carefully chosen so as to destroy the matrix but not to affect the authentic forms of the analyte molecules [20].

The removal of OTCs in wastewater treatment plants takes place in two steps. First, in the primary treatment mostly by sorption onto particulate matter of the wastewater [21]. Second, in the secondary biological treatment by sorption onto particulate organic sludge material and by assimilation of carbon from OTCs by microorganisms [15]. In bio-tissue the OTCs are strongly bound to the cellular structure [9]. Usually, for the extraction of OTCs from bio-tissues 25% water solution of TMAH or 0.1 mol L^{-1} HCl in methanol are applied [5,22,23]. Since sewage sludge from wastewater treatment plant is mostly composed of organic matter (dead biomass), those two extractants (Methods 1 and 2) were considered. On the other hand, the bonds between OTCs and particulate organic matter are strong. So, extraction solvents that are usually applied to sediment samples were also verified. As glacial acetic acid and mixtures of acetic acid and methanol have been the most widely reported in the literature for the extraction of OTCs from sediments and soil [12,14,24], their performance on sewage sludge was examined (Methods 3–9). All the tested methods (1–9) are precisely described in Section 2. In Table 2 a schematic description of the selected methods is presented.

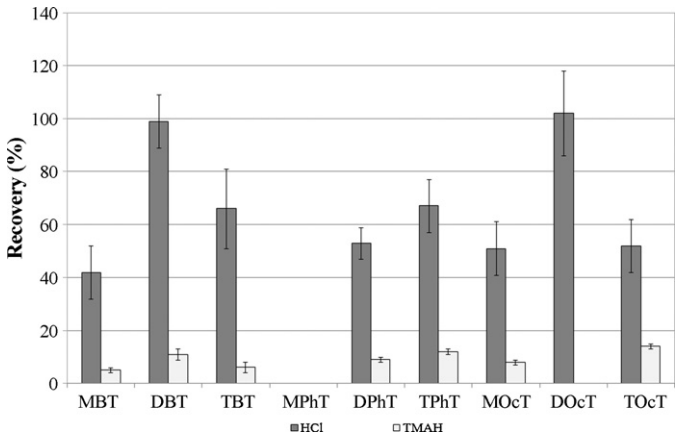


Fig. 1. Extraction recoveries of butyl-, phenyl- and octyltin compounds from spiked sewage sludge sample (1000 ng Sn g^{-1}) applying the extraction with 25% water solution of TMAH and 0.1 mol L^{-1} HCl in methanol.

3.1. Methods 1 and 2

25% water solution of TMAH and 0.1 mol L^{-1} HCl in methanol are the most frequently applied solvents for the extraction of OTCs from biological samples [5,24]. As sewage sludge is mostly composed by organic matter, the extraction efficiency of those two solvents for the extraction of OTCs from sewage sludge was tested. In Fig. 1 the extraction recoveries of both solvents are presented.

When TMAH was applied as extractant, an emulsion disturbing the analytical process during the derivatisation was formed. 25% water solution of TMAH was not efficient for the extraction of butly-, phenyl- and octyltin compounds from sewage sludge. The recoveries for all OTCs were around 10% (Fig. 1). As can be also seen from Fig. 1, when 0.1 mol L^{-1} HCl in methanol was used, the recoveries for butyltins, octyltins, DPhT and TPhT were between 40 and 60%, while MPhT was not extracted at all. High recovery values for DBT and DOcT, 100 and 105%, respectively, were observed.

If OTCs in sewage sludge is bound to the cellular structure of the biomass TMAH would efficiently solubilise the matrix in order to release OTCs (as in fish and mussel tissue). From the results it may be deduced that OTCs present in the sewage sludge are not bound to the cellular structure of the biomass but are sorbed onto the particulate organic matter. Since the binding to particulate organic matter is stronger than that to biological tissue, TMAH was too weak for the extraction of OTCs from the complex matrix of sewage sludge.

As highly polar mono- and disubstituted OTCs need acidification to increase the efficiency of extraction from the sample [7], the use of 0.1 mol L^{-1} HCl in methanol would favour their extraction. The results in Fig. 1 did not confirm that. It can be seen that monosubstituted OTCs were not efficiently extracted most probably due to too low acid concentration. Contrary, 0.1 mol L^{-1} HCl turned out to be too strong for trisubstituted OTCs provoking their degradation.

Table 2
Schematic description of tested extraction methods.

Method	Extractant	Complexing agent	Mode of extraction
1	25% water solution TMAH	–	Ultrasound assisted extraction
2	0.1 mol L^{-1} HCl in methanol	–	Mechanical stirring and ultrasonication
3	Glacial acetic acid	–	Microwave assisted extraction
4	Glacial acetic acid:methanol (3:1)	–	Microwave assisted extraction
5	Glacial acetic acid:methanol:water (1:1:1)	–	Microwave assisted extraction
6	Glacial acetic acid:methanol (3:1)	Tropolone	Microwave assisted extraction
7	Glacial acetic acid	–	Ultrasound assisted extraction
8	Glacial acetic acid:methanol (3:1)	–	Ultrasound assisted extraction
9	Glacial acetic acid	–	Mechanical stirring

Table 3
Extraction recoveries (%) of butyl-, phenyl- and octyltin compounds for spiked sewage sludge (1000 ng Sn g^{-1}) applying MWAE with glacial acetic acid.

OTCs	Extraction times		
	4 min	7 min	16 min
MBT	99 ± 6	107 ± 5	44 ± 5
DBT	105 ± 6	105 ± 6	81 ± 9
TBT	102 ± 6	97 ± 4	78 ± 7
MPhT	81 ± 8	100 ± 11	101 ± 10
DPhT	20 ± 3	10 ± 2	13 ± 2
TPhT	27 ± 4	10 ± 2	11 ± 2
MOcT	86 ± 8	105 ± 5	100 ± 7
DOcT	92 ± 9	107 ± 6	87 ± 5
TOcT	90 ± 7	100 ± 4	98 ± 6

3.2. Methods from 3 to 6

Microwave assisted extraction (MWAE) was investigated in order to substantially reduce the extraction time for the determination of OTCs in sewage sludge. Extraction times of 4, 7 and 16 min were tested. Glacial acetic acid was used as extractant (Method 3). The results are presented in Table 3.

It is evident from Table 3 that butyltin compounds were efficiently extracted with acetic acid after 4 and 7 min of MWAE. At longer extraction time the extraction efficiency of butyltin compounds was appreciably reduced. In order to find out whether the degradation of butyltin compounds took place, an additional experiment was done. Two sewage sludge samples were spiked with DBT and TBT (1000 ng Sn g^{-1}), respectively, and subjected to MWAE with glacial acetic acid for 16 min. Results are presented in Fig. 2(A) and (B).

Data from Fig. 2(A) and (B) indicate that no degradation processess occured during the course of the experiment. In addition, no increase of the Sn(IV) peak was observed. Therefore, the degradation of MBT or DBT and TBT direct to Sn(IV) may be excluded. From the results, it may be presumed that lower extraction efficiencies of butyltin compounds after 16 min of MWAE are most probably related to more efficient extraction of the organic matter from sewage sludge. The co-extracted organic matter inhibits ethylation/extraction steps, resulting in poor butyltin compounds recoveries.

It can be seen from Table 3 that MPhT was efficiently extracted after 7 min. The recoveries for DPhT and TPhT were about 20% after 4 min and below 10% at longer extraction times.

To check if the degradation of phenyltin compounds occurred, two aliquots of sewage sludge were spiked with DPhT and TPhT (1000 ng Sn g^{-1}), respectively, and subjected to MWAE with glacial acetic acid for 4 min, Fig. 3(A) and (B).

From data of Fig. 3, it is obvious that TPhT was almost completely degraded via DPhT to MPhT. Also 90% of DPhT was degraded to MPhT.

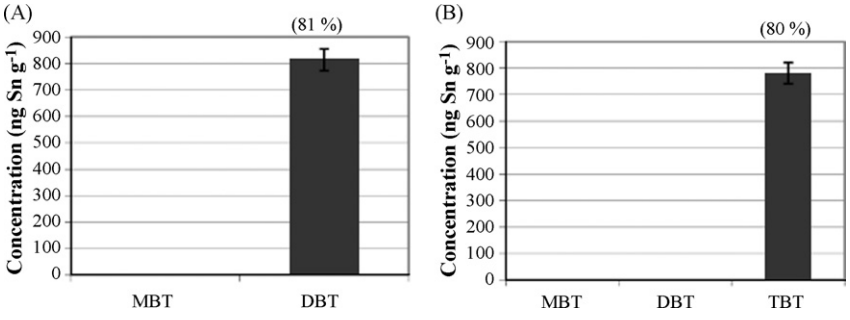


Fig. 2. Degradation of (A) TBT and (B) DBT in spiked sewage sludge (1000 ng Sn g^{-1} of TBT and/or DBT) during MWAE with glacial acetic acid (16 min).

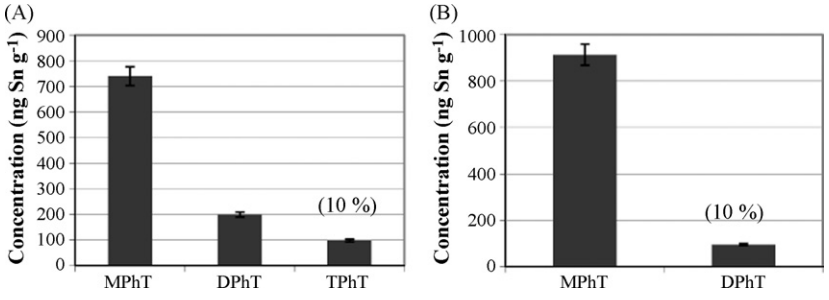


Fig. 3. Degradation of (A) TPhT and (B) DPhT in spiked sewage sludge (1000 ng Sn g^{-1} of TPhT and/or DPhT) during MWAE with glacial acetic acid (4 min).

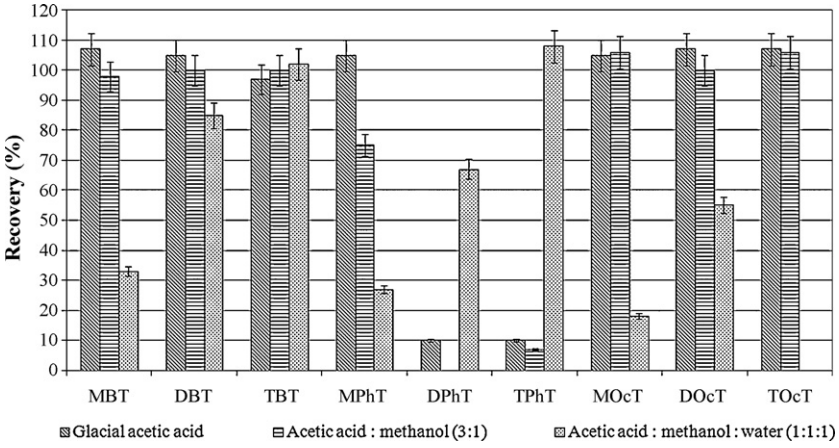


Fig. 4. Extraction recoveries for spiked sewage sludge with OTCs (1000 ng Sn g^{-1}) applying MWAE with glacial acetic acid, acetic acid and methanol (3:1), and acetic acid, methanol and water (1:1:1).

Organometallic degradation during MWAE has been previously reported by Abalos et al. [5] and Huang et al. [10]. The fast temperature increase of extracting solution induces dealkylation and dearylation of analytes [14], especially the most thermolabile, i.e. trisubstituted ones, which is in agreement with the presented data.

Octyltin compounds were efficiently extracted after 7 min (Table 3). When subjected to longer extraction times only DOcT exhibits slightly lower extraction efficiency. Since there was no evidence of the degradation of DOcT, the lower extraction efficiency for DOcT after 16 min of MWAE may be related to the influence of the co-extracted organic matter.

Based on results from Table 3 and Figs. 2 and 3, the optimal extraction time for butyl- and octyltin compounds applying MWAE and glacial acetic acid as extractant was found to be 7 min. The exceptions were phenyltin compounds, for which MWAE was not applicable.

To examine the potential of other extractants, mixtures of acetic acid and methanol (3:1) as well as acetic acid, methanol and water (1:1:1), were subjected to MWAE for 7 min. The comparison between extraction efficiencies of OTCs from spiked sewage sludge samples (1000 ng Sn g^{-1}) of the above-mentioned extractants is given in Fig. 4.

Namely, the addition of methanol to the glacial acetic acid should enhance the extraction efficiency for TBT [6], while the extraction efficiency of phenyltin and octyltin compounds should not be affected [14,25]. From comparison of results (Fig. 4) it can be seen that, as expected, the extraction recovery of TBT using acetic acid–methanol (3:1) was slightly higher than with glacial acetic acid. For MBT, DBT and octyltin compounds the addition of methanol had no great influence on the extraction efficiency, while the extraction efficiency for phenyltin compounds was even worse.

When water was added to glacial acetic acid and methanol quantitative extraction efficiency for TBT and moderate (85%) for DBT was obtained. The addition of water seemed to severely reduce the extraction efficiency of MBT, MPhT and octyltin compounds, most probably due to lower extractant strength. The most beneficial influence of water addition was observed for TPhT, where the extraction recovery raised to 100%. The addition of water and methanol to glacial acetic acid decreased the strength of the acid. This resulted in optimal condition for the extraction of TPhT, while for the efficient extraction of DPhT and MPhT the acid strength was too low.

It was experimentally proven that MWAE using 0.02% tropolone as a component of the extractant solution (Method 6) was not appropriate for OTCs analyses. Tropolone enhanced the extraction of organic matter that resulted in significant increase of the background signal during the chromatographic separation of OTCs (see data from Fig. 5).

3.3. Methods 7 and 8

Ultrasound assisted extraction (USAE) has become a widely used extraction technique. In combination with glacial acetic acid and acetic acid and methanol, high recoveries for sediment and soil samples were obtained [12,14].

For the simultaneous extraction of butyl-, phenyl- and octyltin compounds from sewage sludge sample glacial acetic acid USAE was applied for 5, 10, 20, 30 and 60 min. In Table 4 the obtained extraction efficiencies are presented.

It can be observed from Table 4 that the time of sonication has a great influence on the extraction efficiency. MBT and DBT were quantitatively extracted after 30 min, while for TBT 20 min of sonication gave quantitative recoveries. Longer extraction times did not have significant influence on the recovery of butyltin compounds.

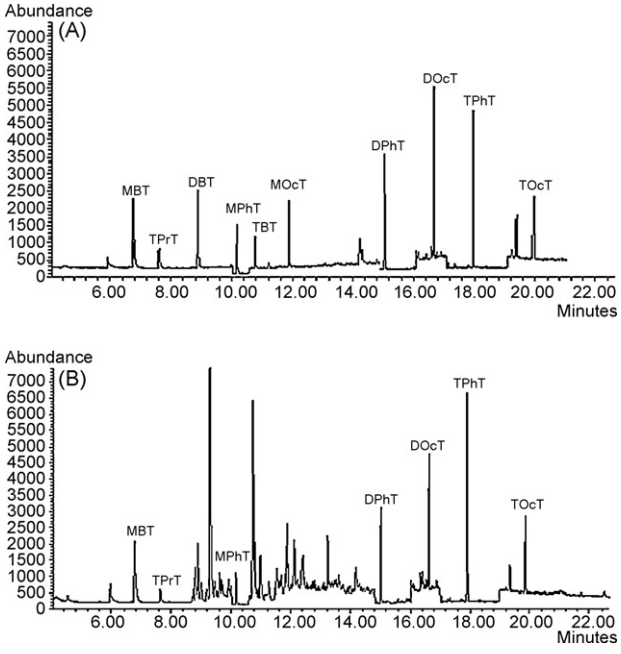


Fig. 5. Chromatograms of butyl-, phenyl- and octyltin compounds from spiked sewage sludge sample (1000 ng Sn g^{-1}) using MWAE with (A) methanol and acetic acid and (B) 0.02% (w/v) tropolone in methanol and acetic acid.

Table 4
Extraction recoveries of butyl-, phenyl- and octyltin compounds for spiked sewage sludge sample (1000 ng Sn g^{-1}) applying USAE with glacial acetic acid.

OTCs	Extraction time				
	5 min	10 min	20 min	30 min	60 min
MBT	31 ± 6	80 ± 7	63 ± 6	100 ± 5	98 ± 9
DBT	86 ± 8	83 ± 6	85 ± 9	97 ± 4	101 ± 10
TBT	89 ± 7	99 ± 10	100 ± 10	100 ± 7	99 ± 10
MPhT	44 ± 10	67 ± 12	63 ± 5	93 ± 5	86 ± 12
DPhT	72 ± 9	81 ± 8	82 ± 7	92 ± 4	88 ± 10
TPhT	90 ± 10	81 ± 9	85 ± 7	100 ± 7	97 ± 15
MOcT	54 ± 8	82 ± 7	80 ± 8	92 ± 5	102 ± 17
DOcT	83 ± 7	83 ± 6	108 ± 10	99 ± 4	100 ± 15
TOcT	89 ± 9	100 ± 9	99 ± 9	96 ± 5	100 ± 16

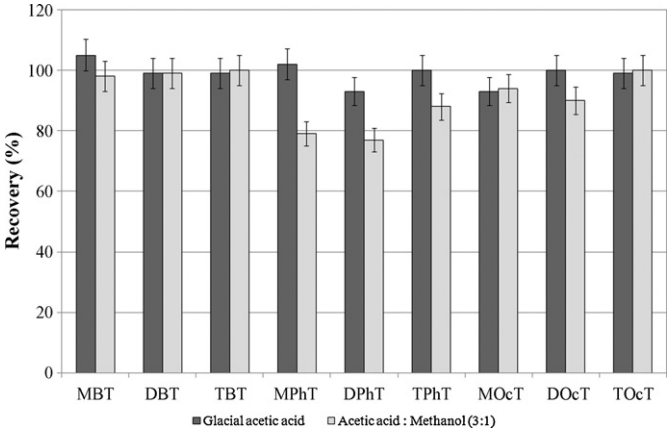


Fig. 6. Extraction recoveries of butyl-, phenyl- and octyltin compounds from spiked sewage sludge sample (1000 ng Sn g^{-1}) applying USAE with acetic acid and methanol (3:1).

Phenyltins are also efficiently extracted after 30 min of USAE. The extraction recoveries for phenyltin compounds remained constant after 30 min of sonication. MOcT showed the same behaviour as phenyltin compounds, while DOcT was efficiently extracted after 20 and TOcT after 10 min. The extending of extraction time did not significantly influence the recoveries of these two octyltin compounds.

The studied OTCs in the spiked sewage sludge sample were extracted also with a mixture of acetic acid and methanol (3:1) and subjected to USAE. The results are presented in Fig. 6.

As it was the case of MWAE, the mixture of acetic acid and methanol lowered the extraction efficiencies for phenyltin compounds by USAE, while it did not have significant influence on the extraction of butyl- and octyltin compounds.

Table 5
Extraction recoveries (%) of butyl-, phenyl- and octyltin compounds from spiked sewage sludge sample (1000 ng Sn g^{-1}) applying MSAE with glacial acetic acid.

OTCs	Extraction time			
	1 h	5 h	16 h	24 h
MBT	67 ± 7	74 ± 7	97 ± 5	82 ± 8
DBT	68 ± 10	79 ± 1	92 ± 4	80 ± 4
TBT	71 ± 8	75 ± 4	109 ± 5	75 ± 3
MPhT	59 ± 6	67 ± 7	100 ± 6	40 ± 3
DPhT	58 ± 7	74 ± 6	98 ± 5	28 ± 4
TPhT	74 ± 10	78 ± 4	97 ± 6	62 ± 6
MOcT	72 ± 7	84 ± 8	104 ± 4	90 ± 9
DOcT	75 ± 15	80 ± 2	97 ± 3	87 ± 2
TOcT	72 ± 10	80 ± 3	95 ± 5	85 ± 3

3.4. Method 9

The most frequently used extraction mode for OTCs determination in solid samples is mechanical stirring (MSAE). For the simultaneous extraction of butyl-, phenyl- and octyltin compounds from sewage sludge sample MSAE using glacial acetic acid as extractant was applied for 1, 5, 16 and 24 h. In Table 5 the obtained extraction efficiencies are presented.

As can be seen from Table 5 the extraction time has a significant influence on the extraction efficiency of MSAE. It is evident that butyl-, phenyl- and octyltin compounds are quantitatively extracted after 16 h and no degradation occurred. At longer extraction time (24 h) lower extraction efficiencies of butyl- and octyltin compounds are observed. Additional experiments where sewage sludge sample was spiked either with TBT and TOcT or with DBT and DOcT confirmed that no degradation occurred. Therefore, lower extraction efficiencies are related most probably to re-adsorption on particulate matter and/or highest amount of co-extracted matter from the sample. From Table 5, it is further evident that poor extraction recoveries after 24 h are obtained for phenyltin compounds. In the additional experiment sewage sludge sample was spiked with either TPhT or DPhT. Under these conditions important degradation of TPhT and DPhT occurred. In addition, no increase of the Sn(IV) peak was observed. Therefore, the degradation of MPhT to Sn(IV) may be excluded. Lower extraction recovery for MPhT after 24 h of MSAE with glacial acetic acid may be due to the influence of the co-extracted matter from the sample and re-adsorption on particulate matter.

Since glacial acetic acid applying MSAE for 16 h quantitatively extracted butyl-, phenyl- and octyltin compounds from sewage sludge other extracting agents (acetic acid and methanol (3:1), and acetic acid, methanol and water (1:1:1)) were not tested.

Table 6
Limits of detection (LOD), quantification (LOQ) and repeatability (as RSD) for MSAE and USAE of butyl-, phenyl- and octyltin compounds in sewage sludge.

OTCs	MSAE			USAE		
	LOD[a] (ng Sn g^{-1})	LOQ[b] (ng Sn g^{-1})	RSD (%)	LOD (ng Sn g^{-1})	LOQ (ng Sn g^{-1})	RSD (%)
MBT	27	53	8	24	49	6
DBT	28	54	3	26	53	5
TBT	40	73	4	39	71	3
MPhT	42	82	5	43	83	5
DPhT	9	18	2	11	23	3
TPhT	5	12	3	7	15	3
MOcT	19	39	3	17	35	9
DOcT	13	25	4	12	24	7
TOcT	16	31	2	17	32	4

Concentrations are expressed in ng Sn g^{-1} (dry mass basis).
[a] Limits of detection.
[b] Limits of quantification.

3.5. Analytical performances of MSAE and USAE

Limits of detection (LOD) and quantification (LOQ) for MSAE and USEA were calculated on the basis of the standard addition method calibration curves [26]. The results for LOD, LOQ and repeatability (as relative standard deviation, RSD) for both methods are presented in Table 6.

Based on results from Tables 4 and 5 it can be concluded that quantitative extraction of butyltin compounds (MBT, DBT, TBT), phenyltin compounds (MPhT, DPhT, TPhT) and octyltin compounds (MOcT, DOcT, TOcT) is obtained by the use of glacial acetic acid as extractant and MSAE for 16 h or USAE for 30 min. As can be seen from Table 6, LOD and LOQ for the two methods are similar. Therefore, the choice of the extraction mode depends on the availability of the laboratory equipment. The experiment also confirmed that MWAE and extractants as TMAH, 0.1 mol L^{-1} HCl in methanol, mixtures of acetic acid and methanol (3:1) and acetic acid, methanol and water (1:1:1) were not applicable for the simultaneous determination of butyl-, phenyl- and octyltin compounds in sewage sludge.

4. Conclusions

For the extraction of OTCs from sewage sludge five extraction solvents (TMAH, HCl diluted with methanol, glacial acetic acid, acetic acid with methanol (3:1), and acetic acid, methanol and water (1:1:1)), the use of complexing agent (tropolone), and three extraction modes (MSAE, USAE and MWAE) were tested. Regardless of extractants applied, MWAE was not appropriate for simultaneous determination of butyl-, phenyl- and octyltin compounds in sewage sludge. Quantitative extraction of butyl-, phenyl- and octyltin compounds was obtained by the use of glacial acetic acid as extractant and MSAE for 16 h or sonication for 30 min. Both extraction procedures represent reliable analytical tool for the determination of the content of OTCs in sewage sludge.

Acknowledgements

The authors would like to acknowledge the financial support of the Ministry of Higher Education, Science and Technology of the Republic of Slovenia within the research programme P1-0143, French Ministry of Education and PROTEUS bilateral project: “Organotin compounds in the Slovenian and French environment”.

References

[1] A. Chapman, S.J. Blunden, in: P.J. Craig (Ed.), Organometallic Compounds in the Environment: Principles and Reactions, Longman, Essex, 1986, pp. 111–150.
[2] L.A. Hobbs, S.J. Blunden, P.J. Smith, in: H.J. Bowen (Ed.), Environmental Chemistry, The Royal Society of Chemistry, London, 1984, pp. 49–77.
[3] M. Hoch, Appl. Geochem. 16 (2001) 719–743.
[4] H. Rüdel, Ecotox. Environ. Safe. 56 (2003) 180–189.
[5] M. Abalos, J.M. Bayona, R. Compano, M. Granados, C. Leal, M.D. Prat, J. Chromatogr. A 788 (1997) 1–49.
[6] C. Brunori, I. Ipolyi, P. Massanisso, R. Morabito, Handbook of Environmental Chemistry. Water Pollution, vol. 5, 2006, pp. 51–70.
[7] F. Smedes, A.S. De Jong, I.M. Davies, J. Environ. Monitor. 2 (2000) 541–549.
[8] R.B. Rajendran, H. Tao, T. Nakazato, A. Miyazaki, Analyst (2000) 1757–1763.
[9] M. Abalos, J.M. Bayona, P. Quevauviller, Appl. Organomet. Chem. 12 (1998) 541–549.
[10] J.H. Huang, G. Ilgen, E. Matzner, Anal. Chim. Acta 493 (2003) 23–34.
[11] Y. Cai, S. Rapsomanikis, M.O. Andreae, Anal. Chim. Acta 274 (1993) 243–251.
[12] T.M. Nemanič, R. Milačič, J. Ščančar, Int. J. Environ. Anal. Chem. 87 (2007) 615–625.
[13] C. Marcic, I. Le Hecho, L. Denaix, G. Lespes, Chemosphere 65 (2006) 2322–2332.
[14] J. Heroult, T. Zuliani, M. Bueno, L. Denaix, G. Lespes, Talanta 75 (2008) 486–493.
[15] K. Fent, Sci. Total Environ. 185 (1996) 151–159.
[16] I. Heninger, M. Potin-Gautier, M. Astruc, L. Galvez, V. Vignier, Chem. Spec. Bioavailab. 10 (1998) 1–10.
[17] P. Pinel-Raffaitin, D. Amouroux, I. LeHecho, P. Rodriguez-Gonzalez, M. Potin-Gautier, Water Res. 42 (2008) 987–996.
[18] P. Pinel-Raffaitin, P. Rodriguez-Gonzalez, M. Ponthieu, D. Amouroux, I. Le Hecho, L. Mazeas, O.F.X. Donard, M. Potin-Gautier, J. Anal. Atom. Spectrom. 22 (2007) 258–266.
[19] T. Zuliani, G. Lespes, R. Milacic, J. Scancar, M. Potin-Gautier, J. Chromatogr. A 1188 (2008) 281–285.
[20] R. Morabito, P. Massanisso, P. Quevauviller, TrAC—Trends Anal. Chem. 19 (2000) 113–119.
[21] O.F.X. Donard, P. Quevauviller, A. Bruchet, Water Res. 27 (1993) 1085–1089.
[22] I. Rodriguez, M. Santamarina, M.H. Bollain, M.C. Mejuto, R. Cela, J. Chromatogr. A 774 (1997) 379–387.
[23] T.M. Nemanič, L. Zupančič-Kralj, R. Milačič, J. Ščančar, Acta Chim. Slov. 54 (2007) 40–48.
[24] B. Radke, L. Leczynski, A. Wasik, J. Namiesnik, J. Bolalek, Chemosphere 73 (2008) 407–414.
[25] C. Montigny, G. Lespes, M. Potin-Gautier, J. Chromatogr. A 819 (1998) 221–230.
[26] J. Mocak, A.M. Bond, S. Mitchell, G. Scollary, Pure Appl. Chem. 69 (1997) 298–320.

Talanta 80 (2010) 1952–1958

Contents lists available at ScienceDirect

Talanta

journal homepage: www.elsevier.com/locate/talanta

Facile, sensitive and selective fluorescence turn-on detection of HSA/BSA in aqueous solution utilizing 2,4-dihydroxyl-3-iodo salicylaldehyde azine

Xiao-tong Chen, Yu Xiang, Ai-jun Tong*

Key Laboratory of Bioorganic Phosphorus Chemistry & Chemical Biology (Ministry of Education), Department of Chemistry, Tsinghua University, Beijing 100084, PR China

ARTICLE INFO

Article history:
Received 15 July 2009
Received in revised form 16 October 2009
Accepted 23 October 2009
Available online 1 November 2009

Keywords:
Hydrophobic interaction
Fluorescence turn-on
Human serum albumin
Bovine serum albumin

ABSTRACT

A novel fluorescence turn-on detection method of human serum albumin (HSA) and bovine serum albumin (BSA) in aqueous solution is investigated using 2,4-dihydroxyl-3-iodo salicylaldehyde azine (DISA). Upon the addition of DISA to HSA/BSA solution, a fluorescence turn-on effect at 529 nm can be observed with a large stokes shift of ~129 nm based on hydrophobic binding-mode between protein and dye. Under the optimal condition, the linear ranges of fluorescence intensity for HSA and BSA are 0.1–30 μg mL^{-1} with the relative correlation coefficient of R^2 = 0.991 (n = 10) and 0.3–50 μg mL^{-1} with R^2 = 0.997 (n = 10); and the detection limits for HSA and BSA based on IUPAC ($C_{DL} = 3S_b/m$) are 20 ng mL^{-1} and 50 ng mL^{-1}, respectively.

© 2009 Elsevier B.V. All rights reserved.

1. Introduction

Protein detection is of profound importance in a wide range of investigations such as biochemistry and immunodiagnostics. Traditional ways of detecting proteins are generally based on absorption spectrometry, such as Bradford method [1], Lowry method [2] and Biuret method [3]. However, these detecting methods usually suffered limitations like complicated steps, limited sensitivity and narrow linear range.

As a conventional and highly sensitive analytical method, fluorometric detection of proteins [4] depending on covalent and noncovalent-labeling has attracted increasing interests [5]. The covalent-labeling fluorescent methods are generally of high sensitivity through the reaction between the fluorophore and the primary amine in proteins [6–8]. Nevertheless, disadvantages such as multi-steps, inefficiency and rigorous conditions-needing have blocked further applications of these measurements. Compared to covalent-labeling, low-cost and fast noncovalent-labeling methods treated with relative facile manipulations are attracting more focuses [9,4,10–15].

Notably, most fluorometric detection of proteins via noncovalent-labeling are based on electrostatic interaction between proteins and dyes [16–19], which might be probably interfered by electrolyte in body fluid when actual sample measurements are processed, or fluorescence-quenching effect of protein endogenous fluorescence by the addition of organic molecules, which would have a negative effect on the detection sensitivity. In this paper, we report a novel fluorescence turn-on bioprobe, 2,4-dihydroxyl-3-iodo salicylaldehyde azine (DISA, Scheme 1), which can facilely, sensitively and selectively detect human serum albumin (HSA) and bovine serum albumin (BSA) in aqueous solution through hydrophobic binding-mode. The application of the proposed method in actual sample detection is also studied.

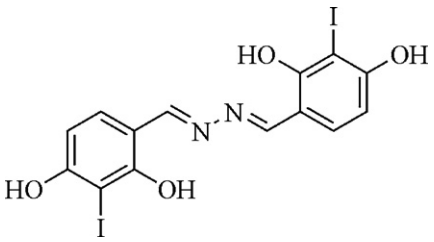
2. Experimental

2.1. Materials, methods, and instrumentation

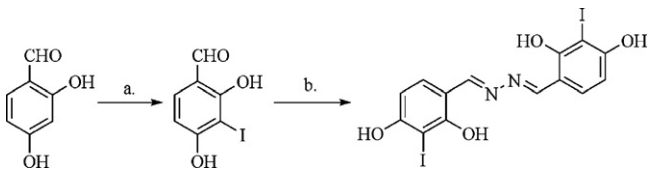
Unless otherwise noted, all reagents and solvents used in this paper are analytical grade without further purification. Proteins (BSA, HSA, ·γ-globulin, ovalbumin and lysozymn) are purchased from Sigma Chemical Co., USA. The stock solutions of proteins are 0.1, 1, and 10 mg mL^{-1}, prepared by dissolving proteins in aqueous phosphate buffer (PB) at pH 6.0 and stored at 4 °C. Other reagents are purchased from Alfa Aesar Co., Tianjin, China. Doubly distilled deionized water is used throughout the experiment. PB solutions with different pH values are prepared by mixing appropriate volumes of Na_2HPO_4 and NaH_2PO_4 to obtain 20 mM stock solution. 1 mM stock solution of DISA is prepared by dissolving appropriate product in ethanol. The determinations of cmc (critical micelle concentration) of SDS, CTAB and Triton X-100 are conducted by plotting the conductivity against the concentration of surfactants in 1:9 ethanol/water buffered by 10 mmol L^{-1} PB at pH 6.0. The curve shows two good linear regions, and cmc is the intersection point obtained by extrapolating the linear region of plots. Samples

* Corresponding author. Tel.: +86 10 62787682; fax: +86 10 62782485.
E-mail address: tongaj@mail.tsinghua.edu.cn (A.-j. Tong).

0039-9140/$ – see front matter © 2009 Elsevier B.V. All rights reserved.
doi:10.1016/j.talanta.2009.10.053



Scheme 1. Molecular structure of DISA.



Scheme 2. Synthesis procedures of DISA. (a) K_2CO_3, I_2; (b) NH_2NH_2, EtOH.

of people serum and bovine serum are bought from Beijing Solarbio Science & Technology Co. Ltd.

Absorption spectra are carried on JASCO V-550 UV–vis spectrophotometer. Fluorescence spectra and intensities are recorded on JASCO FP-6500 spectrofluorimeter equipped with a xenon discharge lamp, 1 cm quartz cells. All pH measurements are performed with a pHS-3C pH meter (Shanghai Precision & Scientific Instrument Co. Ltd., Shanghai, China). ^{1}H and ^{13}C NMR spectra are measured using a JOEL JNM-ECA300 spectrometer operated at 300 MHz. ESI-MS spectra are operated on a HP 1100 LC–MS spectrometer. Elemental analyses are performed on an Elementar Vario EL (Germany). X-ray crystal structure data collection is controlled by XSCANS program. Computations are performed using the SHELXTL NT ver. 5.10 program package on an IBM PC 586 computer. Analytic expressions of atomic scattering factors are employed, and anomalous dispersion corrections are incorporated. Crystal drawing is produced with Windows XP. Unless otherwise mentioned, all measurements are operated at room temperature of about 293 K.

2.2. Synthesis of DISA

As shown in Scheme 2, the synthesis of DISA begins with 3-iodation of 2,4-dihydroxylbenzaldehyde [20], in which K_2CO_3 (1.7 g, 12.5 mM) and I_2 (3.2 g, 25.0 mM) are added to a solution of 2,4-dihydroxylbenzaldehyde in CH_3CN (25.0 mL) and react for 24 h at 50 °C. Above synthetic route affords iodated compounds with a yield of 21% after purification by flash chromatography (petroleum ether:ethyl acetate = 1:1). Immediate product is then reacted with hydrazine hydrate (85%) at molar ratio of 2:1 in ethanol at room temperature overnight to precipitate [21–23]. After that, the resulting precipitations are filtered and washed by 30.0 mL cold ethanol/water (1:1, v/v) for three times. After drying in vacuo and recrystallization in DMSO/ethanol (1:1, v/v), DISA is obtained with a high yield of 80%.

2.3. Characterization

DISA is characterized by ^{1}H, ^{13}C NMR, ESI-MS and elemental analysis. ESI mass spectrometry for DISA: m/z 522.83 ([M−H]$^-$); M$^-$ calculated: 523.87. ^{1}H NMR (DMSO-d_6), δ (ppm): 6.59 (d, 2H, Ar-H, J = 8.4 Hz), 7.38 (d, 2H, Ar-H, J = 8.4 Hz), 8.85 (s, 2H, –CH=N), 11.18 (s, 2H, Ar-OH), 12.65 (s, 2H, Ar-OH). ^{13}C NMR (DMSO-d_6) δ (ppm): 75.8, 107.8, 110.3, 134.4, 160.8, 162.1, 163.5. Elemental analysis: C 32.02%, H 1.99%, I 48.47%, N 5.39%, O 12.13%, calculated for $C_{14}H_{10}I_2N_2O_4$: C 32.09%, H 1.92%, I 48.43%, N 5.35%, O 12.21%. From the crystal structures of DISA in Fig. 1, intramolecular hydrogen bonds of salicylaldamine moieties and stacking of molecules can be clearly observed, which are accordant with analogous compounds in our previous work [21].

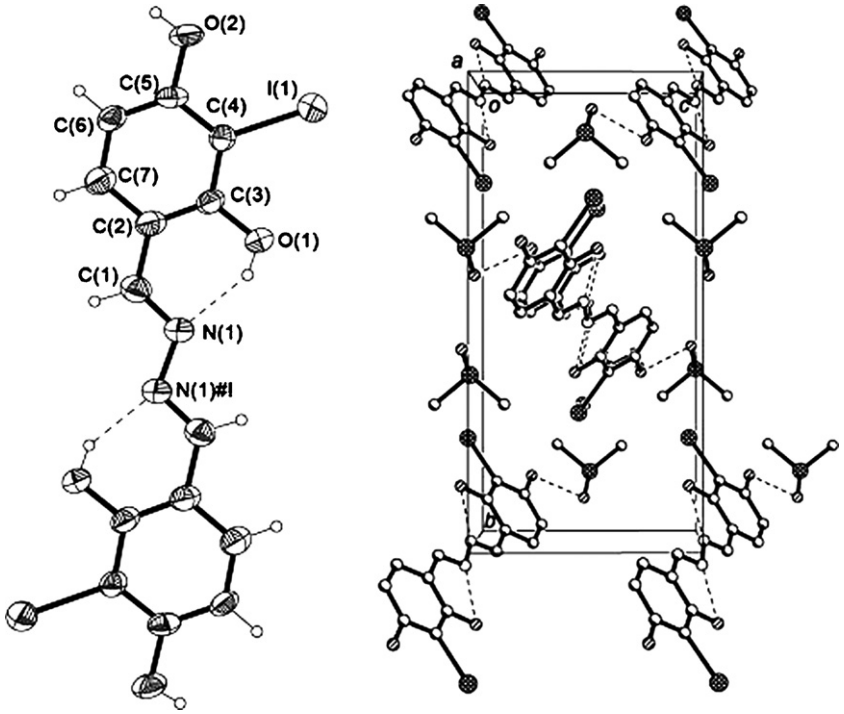


Fig. 1. Crystal structure of compound DISA. Left: ORTEP drawing with 35% probability ellipsoids. Right: A packing view along the *a* direction. The crystal structure is obtained as $C_{14}H_{10}I_2N_2O_4 \cdot 1.5(CH_3)_2SO$ to get reasonable thermal parameters as the mixed solvents of 9:1 ethanol/DMSO is used.

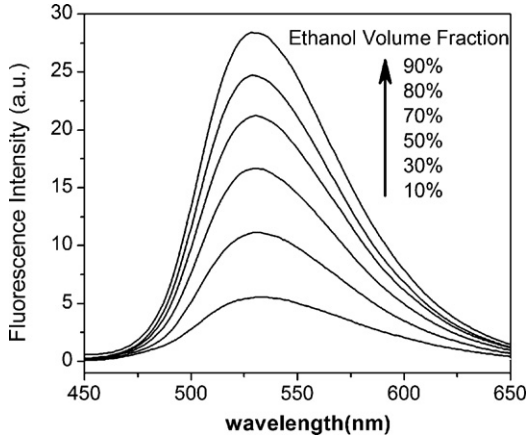


Fig. 2. Fluorescence spectra of DISA (10 μM) with the increasing of ethanol volume fraction from 10% to 90% buffered by 10 mM PB at pH 6.0. Excitation is performed at 400 nm.

3. Results and discussions

3.1. Fluorescence turn-on detection of DISA·HSA and DISA·BSA

For HSA and BSA, these two proteins have been virtually proved to be with very similar protein structure [24], which are mainly composed of α-helices lined with several hydrophobic pockets [25–27]. The presence of surface hydrophobicities in serum albumin underlies effective binding sites with a number of organic and inorganic molecules, especially those compounds with aromatic and heterocyclic ligands [28–31]. As shown in Fig. 2, the fluorescence intensity of DISA increases with the increasing of the solution hydrophobicity as the ethanol volume fraction is from 10% to 90%, predicting the application of DISA in the detection of HSA and BSA [32,33].

Interactions between DISA and proteins are first investigated by fluorescence spectra in aqueous PB (pH 6.0) at room temperature. Fluorescence spectra are performed at λ_{em}(DISA·HSA/BSA) = 529 nm with λ_{ex}(DISA·HSA/BSA) = 400 nm. As shown in Fig. 3, DISA shows little fluorescence in 10 mM PB solution at pH 6.0, while the fluorescence intensity of DISA is greatly enhanced by interacting with HSA and BSA.

In this study, interactions between DISA and HSA/BSA are greatly influenced by pH of the solution. The effect of pH on the fluorescence intensity of DISA·HSA/BSA is investigated in 10 mM PB at pH 5.5–8.0. As illustrated in Table 1, both fluorescence intensity ratio of $I_{HSA·DISA}/I_{DISA}$ and $I_{BSA·DISA}/I_{DISA}$ reach maxima around pH 5.5–6.0 and significantly decline after pH further increasing. That is because DISA might undergo deprotonation at high pH (observed from Fig. 4, pK_a values of DISA are 6.2 and 8.1, respectively) and negatively charged ions of DISA would weaken the hydrophobic force between DISA and proteins. Considering pH 6.0 is closer to physical environment pH, it is set as the optimum pH to detect proteins in this paper.

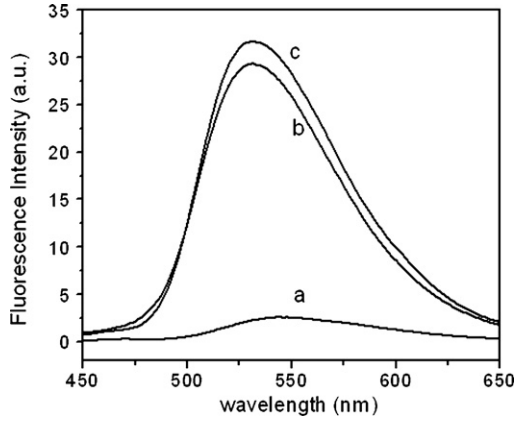


Fig. 3. Fluorescence spectra of DISA·HSA and DISA·BSA. (a) 10 μM DISA; (b) DISA + 0.1 mg mL^{-1} BSA; (c) DISA + 0.1 mg mL^{-1} HSA in 10 mM PB at pH 6.0. Excitation is performed at 400 nm.

Table 1
The pH effect on the fluorescence intensity ratio of $I_{DISA·HSA}/I_{DISA}$ and $I_{DISA·BSA}/I_{DISA}$.

pH	5.5	6.0	6.5	7.0	7.5	8.0
$I_{DISA·HSA}/I_{DISA}$	21.0	21.4	15.9	6.9	3.4	2.8
$I_{DISA·BSA}/I_{DISA}$	15.4	18.3	13.5	7.5	4.3	3.5

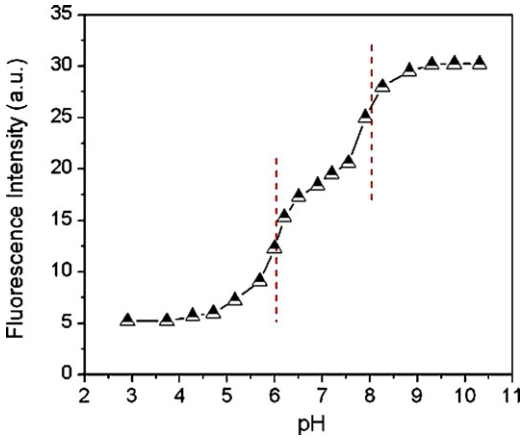


Fig. 4. pH effect on the fluorescence intensity of DISA (10 μM) in 1:9 ethanol/water buffered by 10 mM PB. Excitation is performed at 400 nm.

The dynamics of the reaction between DISA and HSA/BSA is investigated by operating time-dependent fluorescence spectra. As shown in Fig. 5, it takes about 5 min to produce more than 95% of the total fluorescence intensity. Therefore, each sample is laid for 5 min before analyzing procedures.

3.2. The binding modes of DISA·HSA and DISA·BSA

According to previous literatures, iodo-compounds can react with proteins by covalent binding of iodine atom and active residues on proteins, such as thiolate of cyc-34 residues in HSA and BSA [34,35]. To further investigate the interaction between DISA and serum albumin, the possibility of the covalent binding

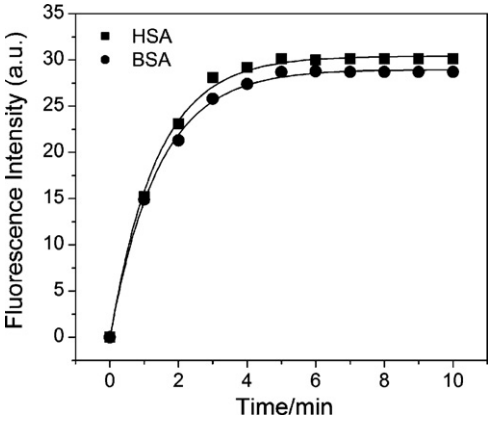


Fig. 5. Kinetic behavior of the fluorescence of DISA·HSA and DISA·BSA in 10 mM PB at pH 6.0. Excitation is performed at 400 nm.

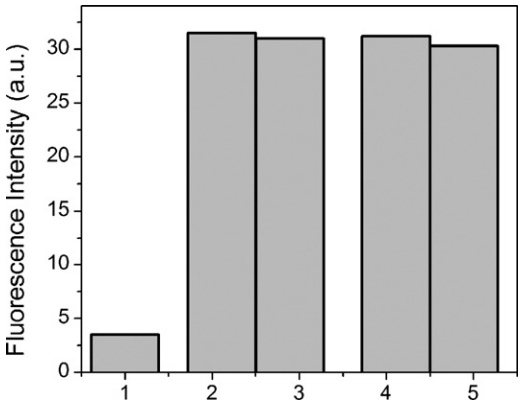


Fig. 6. Comparison between DISA·HSA/BSA and DISA·blocked HSA/BSA in 10 mM PB at pH 6.0. Column 1: DISA; Column 2: DISA·HSA; Column 3: DISA·BSA; Column 4: DISA·blocked HSA; Column 5: DISA·blocked BSA. Excitation is performed at 400 nm.

should firstly be eliminated as there are two iodine atoms on DISA. Hence, HSA and BSA (1 mg mL^{-1}) in 10 mM PB are incubated with a 100-fold molar excess of iodoacetamide for 20 h in the dark [36,37] to block active residues. As demonstrated in Fig. 6, fluorescence intensity of DISA·blocked HSA/BSA show almost no difference from DISA·HSA/BSA, eliminating the possibility of the covalent binding between DISA and HSA/BSA.

To further confirm the noncovalent interaction between DISA and HSA/BSA, several protein-unfolding agents like surfactants and urea are utilized. The protein-structure-unfolding ability for different surfactants below cmc follow the order of anionic > cationic > non-ionic surfactant [38–40]. As shown in Fig. 7, the fluorescence intensities of DISA·HSA and DISA·BSA are dramatically weakened by adding 0.1 mM sodium dodecyl sulphate (SDS, cmc = 0.3 mM), 0.1 mM cetyltrimethyl ammonium bromide (CTAB, cmc = 0.9 mM) and 0.1 mM Triton X-100 (cmc = 8.1 mM) [41] following the order of $I_{\text{DISA·HSA/BSA+SDS}} < I_{\text{DISA·HSA/BSA+CTAB}} < I_{\text{DISA·HSA/BSA+Triton X-100}}$. In the study of urea-induced unfolding of HSA and BSA [42], the fluorescence intensity of DISA·HSA/BSA is also stepwisely weakened by the addition of urea (Fig. 8). These two results both explicate the folding-structure-sensitive interaction between DISA and HSA/BSA; in other words, DISA is confirmed to serve as a noncovalent-labeling bioprobe in protein detection.

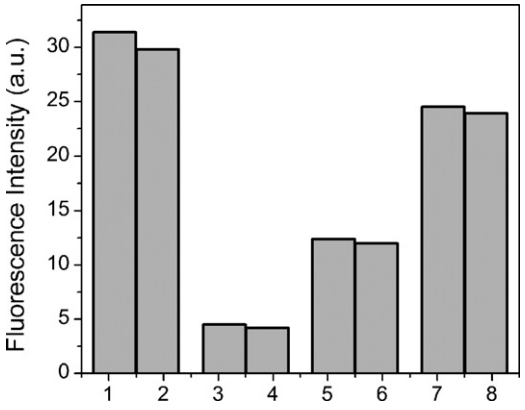


Fig. 7. The effect of different surfactants on the fluorescence intensity of DISA·HSA/BSA in 10 mM PB at pH 6.0. Column 1: DISA·HSA; Column 2. DISA·BSA; Column 3: DISA·HSA + SDS; Column 4: DISA·BSA + SDS; Column 5: DISA·HSA + CTAB; Column 6: DISA·BSA + CTAB; Column 7: DISA·HSA + Triton X-100; Column 8: DISA·BSA + Triton X-100. The concentrations of added surfactant are all 0.1 mM, below the cmc of 8.1, 0.9 and 0.3 mM for SDS, CTAB and Triton X-100, respectively. Excitation is performed at 400 nm.

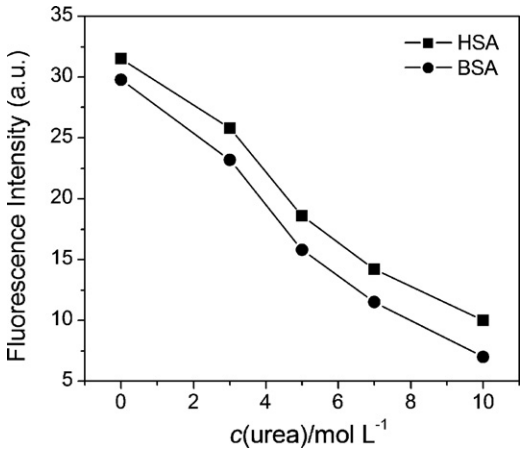


Fig. 8. The effects of different concentrations of urea on the fluorescence intensity of DISA·HSA/BSA in 1:9 ethanol/water buffered by 10 mM PB at pH 6.0. Excitation is performed at 400 nm.

To determine the maximum binding site number of DISA·HSA/BSA, job's plot [43] is constructed by utilizing fluorescence enhancement characteristics of DISA·HSA/BSA while maintaining the total concentration of DISA plus HSA/BSA at a constant value of 10 μM. There are three structurally homologous domains (I–III) in HSA/BSA molecules, each containing two subdomains (A and B) stabilized by disulfide bonds. Particularly, subdomains IIA and IIIA (also called as Sudlow site I and Sudlow site II) are termed to be the predominant binding sites with the foreign compounds [44–47]. This is indeed the case as shown in Fig. 9. The inflection points of job's plot give the value of 0.63 and 0.65 for DISA·HSA and DISA·BSA respectively, indicating a stoichiometric ratio of 2:1 and two noncovalent binding sites for each protein.

Taking into consideration of binding mode for the complex formation, the determination for thermodynamic parameters of enthalpy change (ΔH) and entropy change (ΔS) are carried out. Generally for the noncovalent interactions of DISA·HSA/BSA, hydrogen bonds ($\Delta H < 0$, $\Delta S < 0$), van der Waals forces ($\Delta H < 0$, $\Delta S < 0$), hydrophobic ($\Delta H > 0$, $\Delta S > 0$) and electrostatic interactions ($\Delta H < 0$, $\Delta S > 0$) all play potential roles [48–51]. To obtain these thermodynamic parameters, the temperature dependence of binding constant K is studied by fluorimetric tritration of DISA with

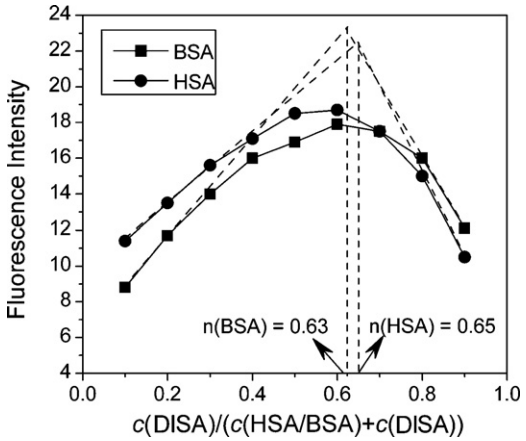


Fig. 9. Job's plots of fluorescence intensities as functions of the molar fraction of HSA/BSA in 10 mM PB at pH 6.0. The total concentration c(HSA/BSA) + c(DISA) is kept constant at 10 μM. The inflection points of job's plot give a value of 0.65 (for HSA) and 0.63 (for BSA) respectively, which correspond to the stoichiometric ratio of n(DISA:HSA/BSA) = 2:1. Excitation is performed at 400 nm.

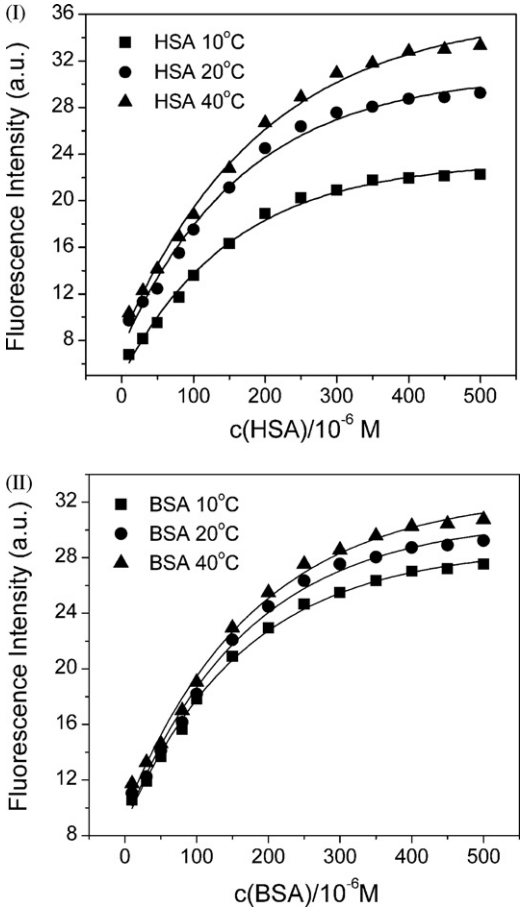


Fig. 10. The binding curve of DISA·HSA (10-I) and DISA·BSA (10-II) at different temperatures of 10 °C, 20 °C and 40 °C in buffered 10 mM PB at pH 6.0. Excitation is performed at 400 nm.

HSA/BSA at three different temperatures, 10 °C, 20 °C and 40 °C, under which HSA and BSA are structure-stable (Fig. 10). The binding constants K for DISA·HSA and DISA·BSA complexes are determined according to the following equation:

$$\Delta I_s = \frac{C[\mathrm{P}](K_1[\mathrm{DISA}] + K_1K_2[\mathrm{DISA}]^2)}{(1 + K_1[\mathrm{DISA}] + K_1K_2[\mathrm{DISA}]^2)}$$

where ΔI_s is the margin of fluorescence intensity ($\Delta I_s = I_s - I_{\mathrm{DISA}}$); [P] is the concentration of protein; K_1 and K_2 are the first and second binding constants, respectively; C is the constant of the equation. Calculations are refined through nonlinear least-squares analysis by origin program. After obtaining fitting K values (Table 2), ΔG, ΔH and ΔS are acquired according to the van't Hoff equation and thermodynamic formulas. As shown in Table 3, the binding reaction of DISA·HSA and DISA·BSA are both spontaneous accompanied by positive ΔH and ΔS values, generally revealing the hydrophobic binding modes mechanism. Consequently, the hydrophobic interaction should probably be the main binding force for DISA·HSA and DISA·BSA complexes.

For comparison, ovalbumin, γ-globulin, and lysozymn are selected, which are of different hydrophobicities following the order HSA > BSA > γ-globulin > lysozymn > ovalbumin (if the hydrophobicity of ovalbumin is set as 1, those of lysozymn, γ-globulin, BSA and HSA are 1.7, 5.5, 181.9 and 182.1, respectively) [52,53]. As demonstrated in Column 1–6 of Fig. 11, the fluorescence intensity of DISA·proteins follow the similar order to that of hydrophobicity: DISA·HSA > DISA·BSA > DISA·γ-globulin > DISA·lysozymn > DISA·ovalbumin, demonstrating selective detection of HSA/BSA due to stronger hydrophobic interactions between DISA and HSA/BSA than other proteins accordant with previous literature [52]. To investigate the potential application of this method to other hydrophobic protein, the fluorescence intensity of gluten (a very hydrophobic protein) [54] upon the addition of DISA is also measured as shown in column 7 of Fig. 11, which is nearly as strong as HSA and BSA. The difference between gluten and HSA/BSA is that HSA/BSA are basically hydrophilic with several hydrophobic pockets in them, while the surface of gluten is mostly composed by hydrophobic amino acids, which can interact with DISA by hydrophobic interaction. Therefore, this method can also be applied in the detection of other hydrophobic proteins.

Table 2
The binding constants for DISA·HSA and DISA·BSA through nonlinear fitting.

Compd.	Stoichiometry	$K_1/10^{-5}$			$K_2/10^{-5}$		
		283 K	293 K	313 K	283 K	293 K	313 K
DISA·HSA	2:1	1.65	1.89	2.13	0.14	0.15	0.17
DISA·BSA	2:1	1.72	1.93	2.18	0.18	0.19	0.20

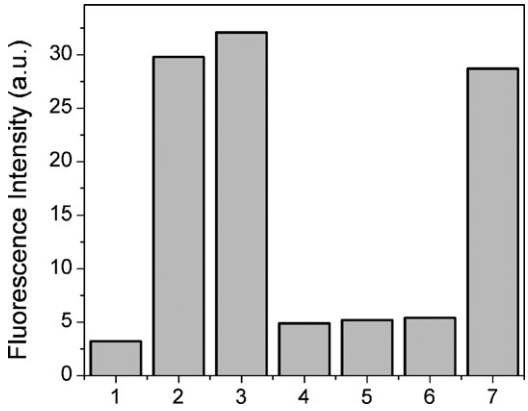


Fig. 11. Comparison of the fluorescence intensity of DISA (10 μM) in the presence of 0.1 mg mL^{-1} proteins. Column 1: without protein; Column 2: BSA; Column 3: HSA; Column 4: ovalbumin; Column 5: lysozymn; Column 6: γ-globulin; Column 7: gluten. Excitation is performed at 400 nm.

3.3. Effect of foreign substances

Interference of foreign substances is carefully tested and demonstrated in Table 4. It is found that most of metal ions, amino acids or nucleic acid displayed no or little interference on HSA/BSA detection.

Table 3
Thermodynamic parameters of DISA·HSA and DISA·BSA at 20 °C[a].

	ΔG_1 (kJ/mol)	ΔH_1 (kJ/mol)	ΔS_1 (J/K mol)	ΔG_2 (kJ/mol)	ΔH_2 (kJ/mol)	ΔS_2 (J/K mol)
DISA·HSA	−6.9	15.2	75.3	−4.9	1.3	21.2
DISA·BSA	−7.5	12.8	69.4	−5.0	0.7	19.5

[a] $\ln K = -\Delta H/RT + \text{constant}$; $\Delta G = -RT\ln K$; $\Delta G = \Delta H - T\Delta S$.

Table 4
Interference of foreign substances.

Foreign substances	Concentration coexisting ($\times 10^{-6}$ M)	Change of $I_{DISA\text{-}HSA/BSA}$
NaCl, $CaCl_2$, KCl	100	<±2.8%
NH_4Cl, $MnSO_4$, $BaCl_2$, $MgCl_2$, $ZnCl_2$, $AgNO_3$, $Al(NO_3)_3$	10	<±2.1%
$CuSO_4$, $FeCl_3$, $FeCl_2$, $CoCl_2$, $Hg(NO_3)_3$, $CdCl_2$	0.1	<±3.5%
L-Asp, DL-Glu, L-His, DL-Lys, L-Phe, Pro, Cys, DL-Thr	10	<±1.8%
ctDNA, yRNA (μg mL^{-1})	100	<±2.3%

Conditions: 20 μg mL^{-1} HSA/BSA, 10 μM DISA, 10 mM PB solution at pH = 6.0, 30 min reaction time at room temperature. Excitation/emission is performed at 400/529 nm.

Table 5
Analytical application of the proposed method.

Sample	HSA/BSA added (mg mL^{-1})	Proposed method[a]			UV detection[b]		
		Found (mg mL^{-1})	Recovery (%)	R.S.D. (%)	Found (mg mL^{-1})	Recovery (%)	R.S.D (%)
Human serum	0	52.1	–	1.2	52.9	–	1.3
	20.0	73.8	102.3	1.4	75.3	103.2	1.1
Bovine serum	0	48.3	–	1.1	49.5	–	0.8
	20.0	69.8	102.2	0.9	71.5	102.8	1.2

[a] Conditions: 20 μg mL^{-1} HSA/BSA, 10 μM DISA, 10 mM PB solution at pH 6.0, 30 min reaction time at room temperature. Excitation/emission is performed at 400/529 nm.
[b] Determination of protein in solution by the absorption of Tyr and Trp at 280 nm; and 1 mg mL^{-1} BSA is set as a protein standard of $A_{280\,nm}$ = 0.66. In analytical procedures, 5.0 mL PB stock solution at pH 6.0 is transferred to a 10.0 mL flask; then 200 μL of a sample solution are subsequently added. The solution is diluted to the mark with water and well mixed in the shaking bed (120 rpm^{-1}, 298 K) for 5 min and then absorbance at 280 nm was recorded.

4. Analytical applications

4.1. Calibration curve and detection limits

Calibration curve is studied for the determination of HSA and BSA. Under optimum conditions (10 mM PB at pH 6.0, 10 μM DISA, 5 min reaction time, $\lambda_{ex}/\lambda_{em}$ at 400/529 nm at room temperature), the linear range for HSA and BSA are 0.1–30 μg mL^{-1} with a relative correlation coefficient of R^2 = 0.991 (n = 10) and 0.3–50 μg mL^{-1} with R^2 = 0.997 (n = 10), respectively. The detection limits for HSA and BSA based on IUPAC ($C_{DL} = 3S_b/m$) are 20 ng mL^{-1} and 50 ng mL^{-1} according to 10 black measurements. The relative standard deviation (R.S.D.) for five repeated measurements of 10 μg mL^{-1} HSA and BSA are 1.3% and 1.5%, respectively.

4.2. Application in real sample detection

This proposed method is applied for detecting HSA in human serum and BSA in bovine serum. In analytical procedures, 50.0 mL PB stock solution at pH 6.0 is transferred to a 100.0 mL flask; then 1.0 mL 0.1 mol L^{-1} DISA stock solution and 50 μL of sample solutions are subsequently added. The solution are diluted to the mark with water and well mixed in the shaking bed (120 rpm, 298 K) for 5 min. Afterwards, the fluorescence spectra are examined at excitation/emission wavelength of 400/529 nm. As shown in Table 5, satisfactory recovery and R.S.D. values are both achieved. Furthermore, a comparison method using UV detection is also applied, which is commonly utilized for analyzing serum album in blood; and experimental results of the proposed method are valid and effective as illustrated in Table 5.

5. Conclusion

In conclusion, we described a novel fluorescence turn-on method for protein detection with facility, selectivity, wide linear range and good sensitivity. A large Stokes shift of ~129 nm is observed for DISA, which serves as a noncovalent fluorescence bioprobe, compared to traditional molecular bioprobes after the addition of HSA/BSA. The binding mode between protein and DISA is proved to be hydrophobic interaction. In addition, the detection of other hydrophobic proteins by DISA is also workable. This method can be successfully used for the determination of HSA in people serum and BSA in bovine serum; and further biological applications for DISA are still in progress in our laboratories.

Acknowledgement

We are very grateful for the financial support from the National Natural Science Foundation of China (NSFC, No. 20875054 and 90813014).

References

[1] M.M. Bradford, Anal. Biochem. 72 (1976) 248.
[2] O.H. Lowry, N.J. Rosebrough, A.L. Farr, R.J. Randall, J. Biol. Chem. 193 (1951) 265.
[3] F. Joseph, Biochem. J. 29 (1935) 799.
[4] C.A. Royer, Chem. Rev. 106 (2006) 1769.
[5] A.P. deSilva, H.Q.N. Gunaratne, T. Gunnlaugsson, A.J.M. Huxley, C.P. McCoy, J.T. Rademacher, T.E. Rice, Chem. Rev. 97 (1997) 1515.
[6] T.K. Kerppola, Nat. Rev. Mol. Cell. Biol. 7 (2006) 449.
[7] W.F. Patton, Biotechniques 28 (2000) 944.
[8] B.K. Hoefelschweiger, A. Duerkop, O.S. Wolfbeis, Anal. Biochem. 344 (2005) 122.
[9] Y. Suzuki, K. Yokoyama, J. Am. Chem. Soc. 127 (2005) 17799.
[10] D.L. Sackett, J. Wolff, Anal. Biochem. 167 (1987) 228.
[11] J.R. Daban, M. Samso, S. Bartolome, Anal. Biochem. 199 (1991) 162.
[12] J.R. Daban, S. Bartolome, M. Samso, Anal. Biochem. 199 (1991) 169.
[13] S.M. Yarmoluk, D.V. Kryvorotenko, A.O. Balanda, M.Y. Losytskyy, V.B. Kovalska, Dyes Pigm. 51 (2001) 41.
[14] A.S. Bhown, T.W. Cornelius, J.E. Volanakis, J.C. Bennett, Anal. Biochem. 131 (1983) 337.
[15] V.S. Jisha, K.T. Arun, M. Hariharan, D. Ramaiah, J. Am. Chem. Soc. 128 (2006) 6024.
[16] T.H. Steinberg, L.J. Jones, R.P. Haugland, V.L. Singer, Anal. Biochem. 239 (1996) 223.
[17] A. Granzhan, H. Ihmels, Org. Lett. 7 (2005) 5119.
[18] L.J. Jones, R.P. Haugland, V.L. Singer, Biol. Techn. 34 (2003) 850.
[19] K. Berggren, T.H. Steinberg, W.M. Lauber, J.A. Carroll, M.F. Lopez, E. Chernokalskaya, L. Zieske, Z. Diwu, R.P. Haugland, W.F. Patton, Anal. Biochem. 276 (1999) 129.
[20] E. Bui, J.P. Bayle, F. Perez, L. Liebert, J. Courtieu, Liq. Cryst. 8 (1990) 513.
[21] W.X. Tang, Y. Xiang, A.J. Tong, J. Org. Chem. 74 (2009) 2163.
[22] X.T. Chen, Y. Xiang, Z.F. Li, A.J. Tong, Anal. Chim. Acta 625 (2008) 41.
[23] H. Görner, S. Khanra, T. Weyhermüller, P. Chaudhuri, J. Phys. Chem. A 110 (2006) 2587.
[24] J. Steinhardt, J. Krijn, J.G. Leidy, Biochemistry 10 (1971) 4005.
[25] U. Kragh-Hansen, Dan. Med. Bull. 37 (1990) 57.
[26] X.M. He, D.C. Carter, Nature 358 (1992) 209.
[27] D.C. Carter, J.X. Ho, Adv. Protein Chem. 45 (1994) 153.

[28] D.P. Cistola, D.M. Small, J.A. Hamilton, J. Biol. Chem. 262 (1987) 10980.
[29] S. Curry, H. Mandelkow, P. Brick, N.P. Franks, Nat. Struct. Biol. 5 (1998) 827.
[30] U. Kragh-Hansen, Mol. Pharmacol. 34 (1988) 160.
[31] A. Ray, J.A. Reynolds, H. Polet, J. Steinhardt, Biochemistry 5 (1966) 2606.
[32] L.A. Sklar, B.S. Hudson, R.D. Simoni, Biochemistry 16 (1977) 5100.
[33] C. Tanford, Protein Sci. 6 (1997) 1358.
[34] H. Yasui, Y. Kunori, H. Sakurai, Chem. Lett. 32 (2003) 1032.
[35] S.Y.C. Wong, G.R. Guile, R.A. Dwek, G. Arsequell, Biochem. J. 300 (1994) 843.
[36] J.F. Stab, S.D. Bradway, P.L. Fidel, P. Sundstrom, Science 283 (1999) 1535.
[37] S. Shimomura, H. Beevers, Plant Physiol. 71 (1983) 742.
[38] W.W. Sukow, H.E. Sandberg, E.A. Lewis, D.J. Eatough, L.D. Hauser, Biochemistry 19 (1980) 912.
[39] J. Lasch, Biochim. Biophys. Acta 1241 (1995) 269.
[40] U. Kragh-Hansen, M. le Maire, J.V. Møller, Biophys. J. 75 (1998) 2932.
[41] D.J. Shaw, Introduction to Colloid and Surface Chemistry, 4th ed., Butterworth/Heineman, Oxford, 1992.
[42] A.K. Bhuyan, Biochemistry 41 (2002) 13386.
[43] W.C. Vosburgh, G.R. Cooper, J. Am. Chem. Soc. 63 (1941) 437.
[44] G. Sudlow, D.J. Birkett, D.N. Wade, Mol. Pharmacol. 11 (1975) 824.
[45] G. Sudlow, D.J. Birkett, D.N. Wade, Mol. Pharmacol. 12 (1976) 1052.
[46] K. Yamasaki, T. Maruyama, U. Kragh-Hansen, M. Otagiri, Biochim. Biophys. Acta 1295 (1996) 147.
[47] K. Yamasaki, T. Miyoshi, T. Maruyama, A. Takadate, M. Otagiri, Biol. Pharm. Bull. 17 (1994) 1656.
[48] G. Nemethy, H.A. Scheraga, J. Phys. Chem. 66 (1962) 1773.
[49] S.N. Timasheff, H. Peeters, Proteins of Biological FluDIS, Pergamon Press, Oxford, 1972.
[50] P.D. Ross, S. Subramanian, Biochemistry 20 (1981) 3096.
[51] B. Lee, G. Graziano, J. Am. Chem. Soc. 118 (1996) 5163.
[52] A. kato, T. Matsuda, N. Matsudomi, K. Kobayashi, J. Agric. Food Chem. 32 (1984) 284.
[53] U. Kragh-Hansen, F. Hellec, B. de Foresta, M. le Maire, J.V. Møller, Biophys. J. 80 (2001) 2898.
[54] P. Torres, L. Vazquez-Moreno, A. Ledesma-Osuna, C. Medina-Rodriguez, Cereal Chem. 77 (2000) 2000.

Talanta 80 (2010) 1959–1963

Contents lists available at ScienceDirect

Talanta

journal homepage: www.elsevier.com/locate/talanta

Determination of cadmium with a sequential injection lab-on-valve by anodic stripping voltammetry using a nafion coated bismuth film electrode

Yang Wang[a,b], Zaiqing Liu[a,b], Guojun Yao[a,b], Peihua Zhu[a,b], Xiaoya Hu[a,*], Qin Xu[a], Chun Yang[a]

[a] College of Chemistry and Chemical Engineering, Yangzhou University, Yangzhou 225002, China
[b] The Key Laboratory of Environmental Material and Engineering of Jiangsu Province, Yangzhou University, Yangzhou 225002, China

ARTICLE INFO

Article history:
Received 22 August 2009
Received in revised form 16 October 2009
Accepted 23 October 2009
Available online 4 November 2009

Keywords:
Sequential injection
Lab-on-valve
Cadmium
Anodic stripping voltammetry
Bismuth film electrode

ABSTRACT

This work exploited a sequential injection lab-on-valve (LOV) system for the determination of cadmium by anodic stripping voltammetry (ASV). A miniaturized electrochemical flow cell (EFC) was fabricated in LOV, in which a nafion coated bismuth film electrode was used as working electrode. The cadmium was electrodeposited on the electrode surface in bismuth solution, and measured with the subsequential stripping scan. Under optimal conditions, the proposed system responded linearly to cadmium concentrations in a range 2.0–100.0 $\mu g\,L^{-1}$. The detection limit of this method was found to be 0.88 $\mu g\,L^{-1}$. By loading a sample volume of 800 μL, a sampling frequency of 22 determinations h^{-1} was achieved. The repeatability expressed as relative standard derivation (R.S.D.) was 3.65% for 20 $\mu g\,L^{-1}$ cadmium ($n = 11$). The established method was applied to analysis of trace cadmium in environmental water samples and the spiked recoveries were satisfactory.

© 2009 Published by Elsevier B.V.

1. Introduction

Cadmium is one of the most dangerous elements in environmental and biological system. Cadmium can accumulate in the bones, liver and kidneys of human body, where it damages the immune system and the central nervous system, and causes psychological disorders. Besides, it takes a very long time for cadmium to be excreted from there. Therefore, accurate determinations for cadmium in environmental and biological samples are highly demanded [1–3].

Anodic stripping voltammetric methods have been widely developed for the determination of trace metals owing to its high sensitivity, relatively inexpensive instrument and multi-element detection ability [4,5]. In traditional stripping voltammetry analysis, mercury film and hanging mercury drop have been used as electrode materials [6,7], because of its favored analytical properties in the negative potential range. However, the environmental regulations and health considerations restrict its continuous application. Bismuth, regarded as an 'environmentally friendly' material, is considered as a substitute for the mercury. The bismuth film electrodes have been applied for anodic stripping voltammetric analysis of metal ions [8–10] and their electrochemical properties were further enhanced by using modified electrode with polymeric materials. Especially, the bismuth film electrode coated with nafion not only exhibited high sensitivity for metals detection, but also alleviated the influence of the surface-active compounds [11,12].

The increasing need to develop more rapid and automatic analytical systems with minimal sample volume for metals determination is of high interest to date. Flow injection (FI) and sequential injection (SI) systems coupled with voltammetric techniques have been developed as an advantageous alternative to the traditional electrochemical analytical systems working in batch mode [13–15], among which, bismuth film electrodes were used as working electrodes for stripping voltammetric determination. These on-line schemes exhibited excellent stripping performance with the features of rapidity, accuracy, low sample and reagents cost in the analysis. SI lab-on-valve (SI–LOV), the third generation of flow injection, has unique sample handing potential due to the combined use of a LOV unit and a dual-directional propulsion system [16–19]. The LOV unit, integrating a set of microchannels and all necessary laboratory facilities for different analytical schemes, such as sampling conduit and flow cell, was placed atop a conventional multiposition valve. The central channel was connected with the syringe pump for precise sample and reagent arrangement. All the manipulations were carried out in a closed system, and the fluidic manipulation in the LOV was at the level of microlitre range. These characteristics were especially beneficial for downscaling the level of sample cost and avoiding solutions contaminations. In previous work, using SI–LOV manifold coupled with stripping voltammetry has been firstly reported for the on-line determination of Pb [20], which was based on the measurement of the stripping current intensity generated on the mercury film

* Corresponding author. Tel.: +86 514 87975587; fax: +86 514 87975587.
E-mail address: xyhu@yzu.edu.cn (X. Hu).

0039-9140/$ – see front matter © 2009 Published by Elsevier B.V.
doi:10.1016/j.talanta.2009.10.054

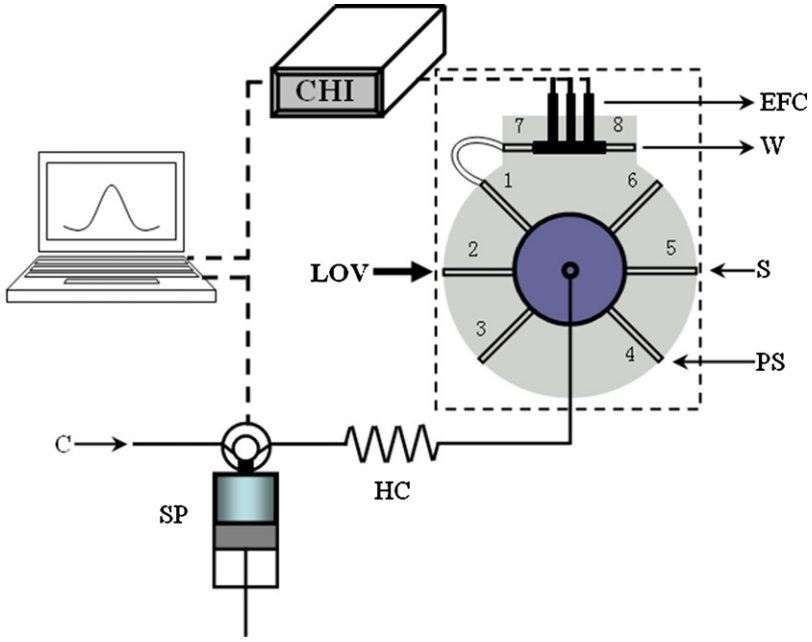


Fig. 1. Configuration of the SI–LOV manifold used for determination of cadmium by ASV method. C, carrier, SP, syringe pump; HC, holding coil; EFC, electrochemical flow cell; W, waste; S, sample; PS, plating solution.

coated glassy carbon electrode. This investigation has highlighted the advantages of electrochemical detection technique with SI–LOV system.

Taking into account the excellent electrochemical activity of bismuth film, the analytical performance and device stability provided by the SI–LOV system, this work described the development of a nafion coated bismuth electrode for the determination of cadmium in a SI–LOV system. To the best of our knowledge, currently there was only a few related work dealing with SIA, and mainly LOV methods with electrochemical detection techniques in literatures. The method involved the formation of the bismuth film and its subsequent application to heavy metal analysis. We further validated the feasibility of the proposed method for its applications in different environmental water samples.

2. Experimental

2.1. Apparatus

The SI–LOV electrochemical analytical system consisted of the following components: a FIAlab-3000 sequential injection system (FIAlab Instruments, Bellevue, WA, USA), a home-made LOV unit, and a CHI660A electrochemical workstation (Chenhua Instrument, Shanghai, China), as shown in Fig. 1. The sequential injection system equipped with a 2.5 mL syringe pump (Cavro, Sunnyvale, CA, USA) was employed for sample and reagent delivery. FIA software for Windows 5.0 was used to control the instrument. The LOV unit, incorporating an electrochemical flow cell (EFC) with a volume of 200 μL, was mounted on the multiport valve. The EFC comprised a three-electrode system with a 2 mm i.d. nafion–bismuth film coated glassy carbon as working electrode, a 0.5 mm platinum wire as counter electrode and a 1.0 mm Ag/AgCl as reference electrode. The three-electrode system was assembled into the LOV unit and the working electrode was placed in the middle. All measurements were carried out using the differential pulse technique and the signals were recorded in the peak height mode. All externally used tubes were made of 0.8 mm i.d. PTFE tubing (Upchurch Scientific, OakHarbor, WA, USA).

2.2. Reagents and chemicals

All the reagents used were at least of analytical reagent grade and purchased from Sinopharm Chemical Reagent Co., Ltd. (Shanghai, China) unless otherwise stated. Double de-ionized water (18 MΩ) was used throughout the experiments.

The bismuth (III) standard stock solutions were prepared by dissolving $Bi(NO_3)_3$ (Sinopharm Chemical Reagent Co., Ltd., Shanghai, China) in 0.1 mol L^{-1} acetate buffer solution (pH 4.5). The working standard solutions served as the plating solutions were obtained by step-wise dilution in the same medium. The cadmium working solution was prepared by dilution commercial standard solution (1000 mg L^{-1}). Nafion (5%, w/v solution in a mixture of water and lower alcohols) was purchased from Aldrich (St. Louis, MO). The dilution nafion solutions were prepared with absolute ethanol. Triton X-100, CTAB, SDS were used as surface-active compounds. Acetate buffer solution (0.1 mol L^{-1}, pH 4.5) was employed as carrier stream. All the experiments were carried out at room temperature without removing the oxygen.

2.3. Preparation of the nafion coated glassy carbon electrode

The glassy carbon electrode surface was polished manually to obtain a fresh surface, then, a drop of the nafion solution (1%, approximate 10 μL) was placed on the surface of electrode. Prior to assembling into the EFC, the coated membrane was left to evaporate at room temperature for 10 min and cured with a hot air stream for 1 min and then left to cool at room temperature.

2.4. Operating procedure

Cadmium solution from port 5 and bismuth plating solution from port 4 were sequential aspirated by syringe pump and stored in the holding coil, where they were subject to overlap (steps 1–2 in Table 1). Then the solution was reversed, and dispensed into the electrochemical flow cell at a flow rate of 17 μL s^{-1} from port 6 while a potential of −1.3 V was subsequently applied to the nafion coated glassy carbon electrode for 100 s to form alloys (step 3 in Table 1). After a rest period of 5 s, the cadmium-bismuth deposits

Table 1
Protocol for the determination of cadmium by SI–LOV–ASV.

Step	Valve position	Electrode potential (V)	Flow rate ($\mu L\,s^{-1}$)	Volume (μL)	Command	Commentary
1	5	–	50	800	Aspirate cadmium solution into HC	Sample loading
2	4	–	50	900	Aspirate bismuth plating solution into HC	Plating solution loading
3	6	−1.3	17	1700	Dispense mixed solution to EFC	Deposition preconcentration
4	6	−1.3	–	–	Stop-flow delay of 5 s	Equilibration
5	6	−1.1 to −0.6	–	–	Stop-flow delay of 10 s	Stripping and recording of voltammogram
6	6	0.3	–	–	Stop-flow delay of 10 s	Cleaning the electrode surface

were stripped from −1.1 to −0.6 V (steps 4–5 in Table 1). Finally, the electrode was directly to be electrochemically cleaned for 10 s at a potential of 0.3 V for the next run (step 6 in Table 1). The completely operational sequence was listed in Table 1.

3. Results and discussion

3.1. Optimization of experimental parameters

Nafion coated electrode was widely employed to enhance sensitivity in ASV determination, which exhibited ideal properties for electrochemical analysis and increased the resistance of electrode against fouling by co-existing surface-active compounds compared with the bare electrode [12]. Fig. 2 illustrated the typical cadmium stripping voltammetric signals at the nafion/bismuth film electrode (a), bismuth film electrode (b), and bare glassy carbon electrode (c). It can be seen that a much narrower and higher peak was obtained at the nafion/bismuth film electrode compared with the bare glassy carbon electrode and the bismuth film electrode. At the same time, the peak potential shifted in the negative direction, which was similar to the previous investigation [14,21]. In this experiment, nafion concentration in a range from 0.1 to 2% was carefully investigated in order to obtain more insights in the cadmium analysis procedure and the experimental results were shown in Fig. 3. The peak current considerably increased with the nafion concentration increased from 0.1 to 1%. This can be attributed to the fact that the polymer film helps confine the stripped species close to the electrode surface where repetitive replating—stripping cycling to cause the signal to amplify. However, with further increasing the nafion concentration up to 2%, the mass transport and charge transfer rate maybe conversely decrease, leading to the current intensity declined. Thus, a nafion concentration of 1% was selected as the optimum condition in the subsequential experiments.

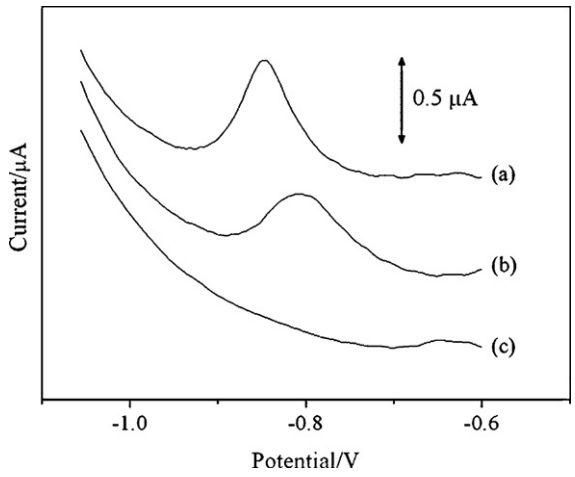


Fig. 2. Stripping voltammetric signals of 20 $\mu g\,L^{-1}$ cadmium at the bismuth/nafion film electrode (a), the bismuth coated electrode (b), the bare glassy carbon electrode (c) in acetate buffer solution (0.1 $mol\,L^{-1}$, pH 4.5).

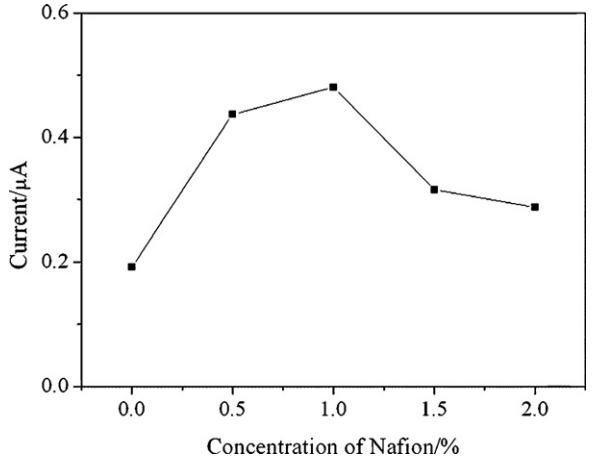


Fig. 3. Effect of the nafion concentration on cadmium stripping signals.

In this work, bismuth solution was utilized for the in situ formation of bismuth film on the nafion modified electrode with target metal ions [22]. The bismuth and cadmium solution were aspirated into the holding coil in sequence and delivered to the EFC for cadmium preconcentration with a potential of −1.3 V, then the stripping signals were recorded with potential scan from −1.1 to −0.6 V. The thickness of bismuth film had a significant effect on the cadmium stripping signals, which were controlled by the bismuth solution concentration. Fig. 4 demonstrated the influence of the bismuth solution concentration on the cadmium stripping signals in the range from 0.25 to 4.0 mg L^{-1}. As can be clearly seen, the signal became narrower and higher gradually with the concentration up to 1.0 mg L^{-1} while the peak position did not shift in the whole concentration range. Such phenomenon may be contributed to the fact that lower concentration cannot form multi-component "fusing" alloys with cadmium completely. When the concentration

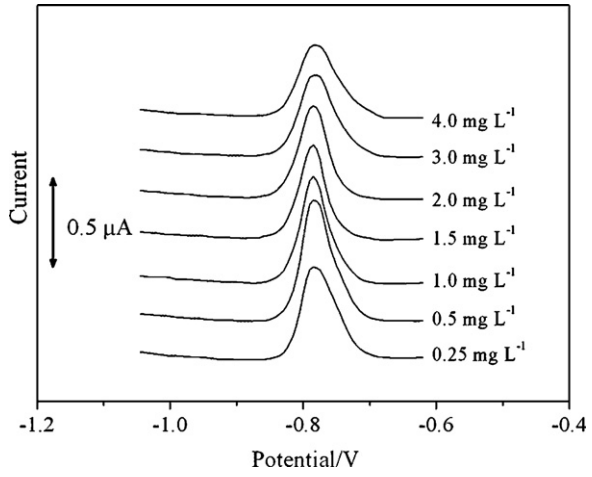


Fig. 4. Effect of the bismuth concentration on cadmium stripping signals.

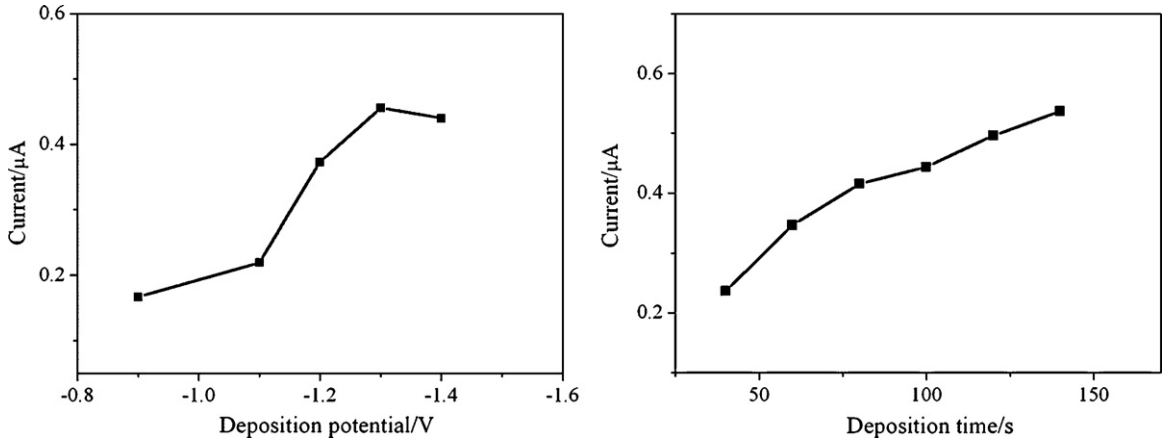


Fig. 5. Effects of the deposition potential (a) and deposition time (b) on cadmium stripping signals.

of bismuth solution varied from 1.0 to 2.0 mg L^{-1}, a thicker bismuth film would be obtained, which would hold back the target metals, with the result that the peak currents decreased and the peak shape became broad [23,24]. Hence, a bismuth concentration of 1.0 mg L^{-1} was employed due to the good sensitivity and well defined peak shape. The formation procedure of bismuth film was finished in the acetate buffer supporting electrolyte, and the effect of acetate buffer concentration on the stripping signals was also investigated in the presence of 1.0 mg L^{-1} bismuth solution. The peak currents increased rapidly with increasing the concentration of buffer solution within the range from 0.01 to 0.1 mol L^{-1}, while higher concentration would keep the signal intensity unchanged. Subsequently, 0.1 mol L^{-1} acetate buffer solution was selected.

Deposition variables, including deposition potential and deposition time, have significant influence on the cadmium stripping performance. In this work, the effect of deposition potential on the stripping peak current was investigated in the range from −0.9 to −1.4 V. As shown in Fig. 5(a), when more negative deposition potential was employed, the current intensity became lower slightly and the stability of peak current was deteriorated, owing to some reduced procedures arose by some other chemicals in the solution. On the contrary, when the more positive deposition potential was employed, the peak current decreased and the background current became higher. This phenomenon can be explained that the applied potential was not sufficient for cadmium to be reduced. Therefore, the deposition potential of −1.3 V was selected for further determinations due to sensitivity and reproducibility. The influence of the deposition time on the peak current was studied at a fixed deposition potential of −1.3 V. As can be seen from Fig. 5(b), the peak current intensity was systematically improved with the increasing of deposition time within the range of 40–140 s. Although a good sensitivity could be achieved with much longer deposition time, the analytical frequency would decrease. From this point of view, 100 s was selected for the ensuing experiments as a compromise between analysis frequency and signal intensity.

The influence of the flow rate on the analytical signal was evaluated with various solution volumes when the sample solution passed through the EFC. It was found that the stripping signals were enhanced with the flow rate increased in a range from 7 to 17 μL s^{-1}. Afterwards, peak current gradually decreased with increasing flow rate. It is probably because higher flow rate may destroy the bismuth film on the electrode surface. Consequently, 17 μL s^{-1} was selected as the optimal flow rate in the following experiments, corresponding to the 1700 μL sample and bismuth mixed solution.

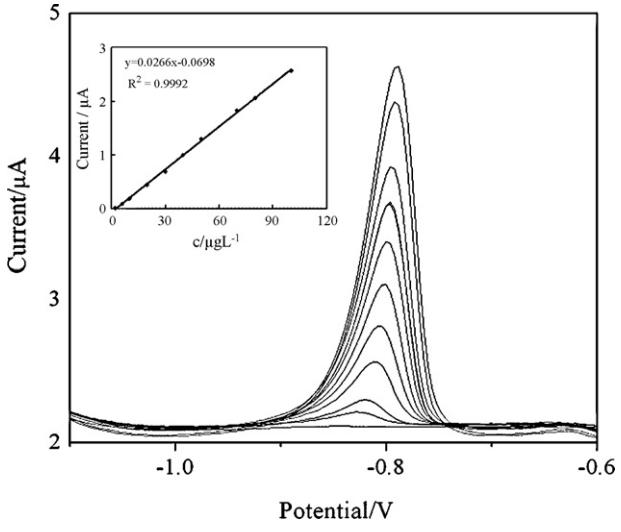


Fig. 6. Voltammograms for the determination of cadmium in the range 2–100 μg L^{-1} using nafion coated bismuth film electrode coupled with SI–LOV system (inset calibration curve). Nafion concentration: 1%; bismuth concentration: 1.0 mg L^{-1}; deposition potential: −1.3 V; deposition time: 100 s; flow rate: 17 μL s^{-1}.

3.2. Interferences

The common existing interferences of various foreign metal ions were investigated to test for sensitivity, as well as the influence of some other surface-active compounds [25,26]. They were added to the sample alone with a cadmium concentration of 20 μg L^{-1}, and the tolerable limit of the foreign substance was defined as the relative error produced by concomitant species not higher than ±5%. No changing of the cadmium voltammetric signals occurred in excess of the following ions: Na^+, K^+, Mg^{2+}, Ca^{2+}, Co^{2+} and Ba^{2+}. The tolerated ration of the other foreign substances were 100-fold for Fe^{3+} and Zn^{2+}, 20-fold for Pb^{2+}, 4-fold for Cu^{2+}. The results showed that most of the metal ions studied had no interference for the determination of cadmium except for Cu^{2+}, which suppressed the peak current intensity down to 50% at a 6-fold excess. The reason for Cu^{2+} interference could be that there was the competition between the bismuth ions and copper ions at the active sites of the nafion coated electrode surface. The surface-active compounds of Triton X-100, CTAB, SDS were also studied as the model compounds to study the potential interferences, which can cause the bismuth film to deactivate by fouling the electrode surface. They exhibited an obviously depressed effect on the cadmium determination and the stripping peak current was decreased drastically with the enhancement of surface-active compounds concentration. If the sample solution

Table 2
Results for the determination of cadmium in water samples.

Sample	Original ($\mu g L^{-1}$)	Added ($\mu g L^{-1}$)	Found ($\mu g L^{-1}$)	Recovery (%)	R.S.D.[a] (%)
1	4.32 ± 0.27	5.00	9.49 ± 0.31	103.4	1.31
		10.00	14.66 ± 0.86	103.4	2.35
		15.00	19.19 ± 1.54	99.1	3.24
2	3.83 ± 0.13	5.00	8.84 ± 0.34	100.2	1.57
		10.00	13.54 ± 0.86	97.1	3.48
		15.00	19.12 ± 1.44	101.9	3.03

[a] Means of three determinations.

contained more than 2.0 mg L^{-1} Triton X-100, 0.5 mg L^{-1} CTAB, and 1.0 mg L^{-1} SDS, respectively, the signal intensity would be declined to 50%. The similar result has been reported for cadmium by ASV quantification. Fortunately, the interferences caused by Cu^{2+}, Triton X-100, CTAB and SDS could be negligible in the real environmental samples analysis, because their concentration was low.

3.3. Analytical figures of merit

Under the optimal conditions, the analytical characteristics of the established sequential injection LOV–ASV system were evaluated by examining the linear range, precision, detection limit and sampling frequency. A series of voltammograms for the determination of cadmium at nafion coated bismuth electrode with increasing concentrations were illustrated in Fig. 6. A linear range 2.0–100 $\mu g L^{-1}$ was obtained with the regression equation $i_p = 0.0266C_{Cd} - 0.0698$ (i_p: 10^{-6} A, C: $\mu g L^{-1}$) and the correlation coefficient of 0.9992. The detection limit, defined as the concentration of the analyte giving signals equivalent to three-time the standard deviation of the blank signals, was 0.88 $\mu g L^{-1}$, which was compatible with those of the published values [27–30]. The R.S.D., evaluated by eleven repetitive determinations of 20 $\mu g L^{-1}$ cadmium solution, was 3.65%. A sampling frequency of 22 determinations h^{-1} was achieved with low solutions consumption.

3.4. Application to water samples

In order to demonstrate the applicability of the proposed method for the direct determination of cadmium, the proposed method was validated by analyzing environmental water samples. Prior to being introduced in the LOV–ASV system, the samples were filtered through a 0.45 μm membrane filter after collection. The results were summarized in Table 2, and the accuracy was checked by analyzing the samples spiked with different cadmium concentration levels in the range of 5.0–15.0 $\mu g L^{-1}$. Higher recoveries, in the range of 97.1–103.4% were obtained.

4. Conclusions

The stripping voltammetric technique using bismuth glassy carbon electrode implemented in a SI–LOV system was successfully carried out for cadmium analysis. The system not only provided sufficient stability and reliability for long term operation under the well-controlled conditions, but also offered high sensitivity and anti-interference ability with the use of nafion coated electrode. More importantly, the unused ports in the LOV unit may serve as micro-column to perform beads renewable on-line matrix elimination manipulation, through which the complicated sample solution could be purified and enriched before dispensed into EFC for stripping voltammetric detection. The practical analysis was applied to the rapid measurement of cadmium at low levels in water samples.

Acknowledgements

This work was supported by the National Natural Science Foundation of China (20675071, 20875081), Postdoctoral Science Foundation of China (20080431125), Postdoctoral Science Foundation of Jiangsu Province (0801056B) and the Innovative Project of Graduate Student in Jiangsu Province (CX09S_050Z).

References

[1] M.P. Waalkes, J. Inorg. Biochem. 79 (2000) 241.
[2] C. Mena, C. Cabrera, M.L. Lorenzo, M.C. López, Sci. Total Environ. 181 (1996) 201.
[3] P. Przybylowski, A. Wilczinska, Food Chem. 74 (2001) 289.
[4] M.R. Gushman, B.G. Bennett, C.W. Anderson, Anal. Chim. Acta 130 (1981) 323.
[5] K.R. Wehmeyer, R.M. Wightman, Anal. Chem. 57 (1985) 1989.
[6] E. Reichart, D. Obendorf, Anal. Chim. Acta 360 (1998) 179.
[7] T.H. Lu, H.Y. Yang, I.W. Sun, Anal. Chim. Acta 454 (2002) 93.
[8] J. Wang, J. Lu, S.B. Hocevar, P.A.M. Farias, B. Ogorevc, Anal. Chem. 72 (2000) 3218.
[9] D. Du, J.W. Ding, Y. Tao, H.B. Li, X. Chen, Biosens. Bioelectron. 24 (2008) 863.
[10] G. Kefala, A. Economou, M. Sofoniou, Talanta 68 (2006) 1013.
[11] J. Li, S.J. Guo, Y.M. Zhai, E.K. Wang, Anal. Chim. Acta 649 (2009) 196.
[12] S. Legeai, O. Vittori, Anal. Chim. Acta 560 (2006) 184.
[13] S. Chuanuwatanakul, W. Dungchai, O. Chailapakul, S. Motomizu, Anal. Sci. 24 (2008) 589.
[14] G. Kefala, A. Economou, Anal. Chim. Acta 576 (2006) 283.
[15] W. Siriangkhawut, S. Pencharee, K. Grudpan, J. Jakmunee, Talanta 79 (2009) 1118.
[16] X.W. Chen, J.H. Wang, Anal. Chim. Acta 602 (2007) 173.
[17] M. Miró, E.H. Hansen, Anal. Chim. Acta 600 (2007) 46.
[18] J.H. Wang, E.H. Hansen, Trends Anal. Chem. 22 (2003) 225.
[19] M. Yang, Y. Xu, J.H. Wang, Anal. Chem. 78 (2006) 5900.
[20] Y. Wang, Z.Q. Liu, X.Y. Hu, J.L. Cao, F. Wang, Q. Xu, C. Yang, Talanta 77 (2009) 1203.
[21] B. Hoyer, T.M. Florence, G.E. Batley, Anal. Chem. 59 (1987) 1608.
[22] A. Economou, Trends Anal. Chem. 24 (2005) 334.
[23] L. Baldrianova, I. Svancara, M. Vlcek, A. Economou, S. Sotiropoulos, Electrochim. Acta 52 (2006) 481.
[24] L.Y. Cao, J.B. Jia, Z.H. Wang, Electrochim. Acta 53 (2008) 2177.
[25] J. Wang, R.P. Deo, S. Thongngamdee, B. Ogorevc, Electroanalysis 13 (2001) 1153.
[26] G. Kefala, A. Economou, A. Voulgaropoulos, M. Sofoniou, Talanta 61 (2003) 603.
[27] H. Xu, L.P. Zeng, D.K. Huang, Y.Z. Xian, L.T. Jin, Food Chem. 109 (2008) 834.
[28] C. Kokkinos, A. Economou, I. Raptis, C.E. Efstathiou, Microchim. Acta 53 (2008) 5294.
[29] G.J. Lee, H.M. Lee, C.K. Rhee, Electrochem. Commun. 9 (2007) 2514.
[30] Y. Wu, N.B. Li, H.Q. Luo, Sens. Actuator B: Chem. 133 (2008) 677.

Talanta 80 (2010) 1964–1969

Contents lists available at ScienceDirect

Talanta

journal homepage: www.elsevier.com/locate/talanta

A high-performance fluorosensor for pH measurements between 6 and 9

Aron Hakonen*, Stefan Hulth

Department of Chemistry, University of Gothenburg, SE-412 96 Göteborg, Sweden

ARTICLE INFO

Article history:
Received 21 August 2009
Received in revised form 16 October 2009
Accepted 23 October 2009
Available online 5 November 2009

Keywords:
pH
Optode
6,8-Dihydroxypyrene-1,3-disulfonic acid
DHPDS
Photoacidity
Fluorescence ratio

ABSTRACT

This study presents a high-performance ratiometric pH optode based on the fluorophore 6,8-dihydroxypyrene-1,3-disulfonic acid (DHPDS). The two pH-sensitive terminal hydroxy groups of DHPDS facilitated dual excitation/dual emission (F_1: $\lambda_{1,ex}$ = 420 nm, $\lambda_{1,em}$ = 462 nm; F_2: $\lambda_{2,ex}$ = 470 nm, $\lambda_{2,em}$ = 498 nm) properties for ratiometric ($R_{F1,F2} = F_1/F_2$) normalization of sensor signal. The sensor demonstrated an exponentially decreasing ratiometric response with increasing pH, with a linear correlation (R^2 = 0.9936) between $^{10}\log(R_{F1,F2})$ and pH within the pH interval 6–9. Precision determined as the IUPAC pooled standard deviation for the pH values 6.00, 7.01 and 9.01, was 0.0057 pH units for the fluorosensor and 0.0054 for a commercially available pH electrode used for comparison. Between the end-points of calibration at pH 7.01, the precision of the sensor was 0.0037 pH units. Effects from changes in ionic strength (I_{tot}, 10–700 mM) were more pronounced for the electrode, with a linear (R^2 = 0.9976) increase in response ($\delta E/\delta pH$) with increasing I_{tot}. The DHPDS-based fluorosensor, however, retained sensitivity ($\delta^{10}\log(R_{F1,F2})/\delta pH = 0.8024 \pm 0.0145$), though with an overall increase in ratiometric signal with increasing I_{tot}. The preserved sensitivity despite changes in ionic strength was possibly a consequence from the dual photo-acidic properties of DHPDS. Analytical characteristics of immobilized DHPDS therefore not only facilitated high-performance measurements over a wide pH range, but also opened for straightforward simultaneous measurements of pH and ionic strength.

© 2009 Elsevier B.V. All rights reserved.

1. Introduction

The activity of hydrogen ions is a master analytical parameter to understand and predict electron transfer and general dynamics during multiple reactions in natural environments [1]. Consequences and feedbacks from changes in pH may have local, regional and global importance. For example, pH of seawater has received particular attention in current characterizations of the oceanic response to anthropogenic emissions of CO_2, in part due to the recently demonstrated acidification of the world's oceans [2]. Although ion-selective electrodes are commonly used for pH measurements [3,4], optical sensors (optodes) have since 1980 frequently been used for pH measurements [5–9]. Optodes are also suitable for high-resolution imaging of pH distributions in complex environments such as aquatic sediments [5,10,11], and there are exciting possibilities for multi-parameter and multi-analyte sensing [9,12–14].

The dynamic range for quantification using optical sensors is normally set by the dependence between the associated and dissociated form of the indicator, and restrictions inherent to the optical instrumentation used during measurements (e.g. [15,16]). For conjugate pairs of acid–base compounds, one compound is often considered undetectable in the presence of the other when relative color intensity is less than ~one-tenth. These traditional limits also tend to fix the dynamic range of fluorescence based sensors to ±1 pH units surrounding the apparent pK_a (pK_a') of the acid–base indicator [17]. In response to biological activities such as intense photosynthesis, bioturbation and organic matter mineralization, pH of natural environments frequently varies by several pH units even on short time-scales [3,18,19]. Such large variation (>2 pH units) in pH is likely to hamper the analytical performance of acid–base indicators and optical sensors in general. Further, an often conveyed limitation of optical sensors is the sensitivity to changes in ionic strength (I_{tot}) of the sample matrix [20]. According to the Debye–Hückel theory, optical sensors for pH normally suffer from a decreased pK_a' with increasing I_{tot} [21]. Despite theoretical and model predictions, there are few, if any, investigations specifically designed to experimentally verify and quantitatively compare the relative dependence to changes in I_{tot} between optodes and ion-selective electrodes available for pH measurements. Overall, the analytical performance of optical pH sensors is due to progressive improvements considered comparable to that of pH electrodes (e.g. [22,23]).

8-Hydroxypyrene-1,3,6-trisulfonate (HPTS; Fig. 1) is one of the most widely used fluorescence indicators for pH measurements in near-neutral samples [8,24,25]. HPTS is a fluorophore used not only

* Corresponding author. Tel.: +46 31 772 2878; fax: +46 31 772 2785.
E-mail address: hakonen@chem.gu.se (A. Hakonen).

0039-9140/$ – see front matter © 2009 Elsevier B.V. All rights reserved.
doi:10.1016/j.talanta.2009.10.055

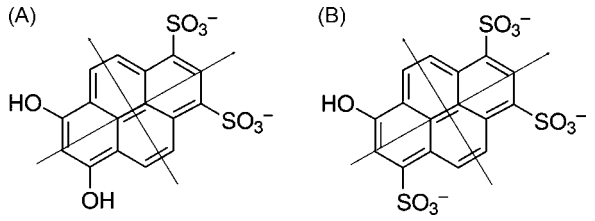


Fig. 1. Chemical structures of (A) 6,8-dihydroxypyrene-1,3-disulfonic acid (DHPDS) and (B) 8-hydroxypyrene-1,3,6-trisulfonate (HPTS) (pH > pK_a of the sulfonate groups, i.e. pH > 1). The arrows represent through atom (excited energy state ^1L_a, arrow through atoms) and through bond (^1L_b) excitation light directions.

to quantify pH in various solutions, but also in more sophisticated applications such as cellular imaging [26] and imaging optodes for both microscopic [23] and macroscopic use [5,11]. General patterns of HPTS fluorescence are essentially governed by the protonation/deprotonation equilibrium of the hydroxyl hydrogen and the photo-acidic properties of HPTS [22]. HPTS is normally considered highly photo-acidic, i.e. the fluorophore is more acidic in the electronically excited state (HPTS*; Fig. 1) than in the ground state [27]. Frequently, pK_a' of excited photo-acidic compounds is 6–7 pH units lower than in the ground state. For example, pK_a' of HPTS in solution is ~7.3 while in excited state it can be as low as 1.0 [28]. Photo-acidic properties therefore govern the dual excitation (~405 and 450 nm) single emission (~520 nm) ratiometric sensing scheme observed for HPTS in solution. Further, HPTS have intrinsic ratiometric properties that provides signal normalization and amplification. The ratiometric approach has been demonstrated to be as effective as lifetime measurements to reduce artifacts [29].

In contrast to the wide range of pH measurements that include HPTS, there are only few studies that have utilized the di-hydroxylated analogue 6,8-dihydroxypyrene-1,3-disulfonate (DHPDS; Fig. 1) [30,31]. DHPDS shares most of the advantageous properties of HPTS, such as high quantum yield, excellent water solubility, ratiometric properties and lack of toxicity. The objective of this study was to reassess the suitability of DHPDS as a fluorophore for pH measurements and to experimentally evaluate fluorescence properties of DHPDS immobilized in a sensing membrane. As the structure of DHPDS includes two hydroxyl groups with overlapping (within 2 pH units) pK_a'-values (7.33 and 8.53; [24]), we hypothesize that, while retaining essential spectroscopic signatures, the analytical characteristics of the two acidic protons provide the basis for a significantly improved sensor dynamic range compared to, for example, HPTS-based sensors.

2. Experimental

2.1. Materials

The sensing film was prepared in a similar manner as was originally described in [10]. A prefabricated transparency film (Hewlett Packard, HP C3835A) consisting of a 100 μm thick polyester foil with a 10 μm cellulose acetate coating was used for the immobilization of DHPDS. In brief, the sensing foil was immersed over night in a high ionic strength (NaCl 1.0 M) solution with 75 μM of the fluorophore 6,8-dihydroxypyrene-1,3-disulfonic acid (DHPDS; >98%, Fluka). The high ionic strength is intended to provide thin double layers, which allows short range fluorophore–foil interactions. These close interactions are the basis for the immobilization mechanism through, e.g. hydrogen bonds, ion-dipole and hydrophobic interactions. The cellulose acetate provides a convenient platform for DHPDS association by these interactions as the ζ-potential is close to zero for ionic strength above 3 mM [32]. Before use, the sensor film was treated in Milli-Q water (deionized water further purified by a Milli-Q system, Millipore Corp., to a resistivity of >18 MΩ cm^{-1}) for 12 h and finally immersed in a sample-like matrix for 12 h. Phosphate buffers ($[H_3PO_4]_{tot}$ = 4 mM) were prepared from appropriate amounts of 40 mM NaH_2PO_4 and Na_2HPO_4 (p.a., Merck) stock solutions in Milli-Q water. Total ionic strength of solutions was adjusted by proper additions of NaCl (p.a., Merck). Buffer solutions for calibration were certified traceable to NIST Standard Reference Material (pH 6.00, 7.01 and 9.01 at 20 °C, Merck).

2.2. Instrumentation

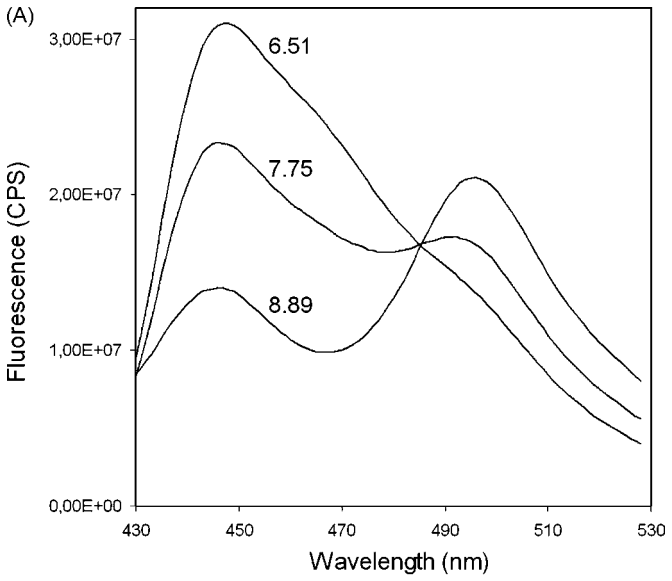
The sensor with immobilized DHPDS was mounted onto a plexiglass support and secured in a plastic cuvette (3 mL), placed in the spectrofluorometer (Fluoromax-3, SPEX Instruments Int., Inc.). To minimize background noise and reflection from incident light, the angle of incidence for the excitation light was set to 30°. Excitation and emission scans were performed at 1.00 nm resolution, 0.25 s time of integration and slit widths corresponding to 2.00 nm bandpass. Matrix scans (Fluoromax-3, SPEX Instruments Int., Inc.) at pH 9.01 and 6.00 were prior to experiments divided to determine the optimum pairs of ratiometric wavelengths for this particular setup. Here, F_1 ($\lambda_{1,ex}$ = 420 nm, $\lambda_{1,em}$ = 462 nm) and F_2 ($\lambda_{2,ex}$ = 470 nm, $\lambda_{2,em}$ = 498 nm) were used for ratiometric ($R_{F1,F2} = F_1/F_2$) detection of fluorescence. The pH electrode (model 6.0232.100, 780 pH meter; Metrohm Ltd.) was calibrated in NIST buffers by a two-point calibration procedure (pH 6.00 and 9.01). Temperature was kept constant (20 ± 1 °C) during all experiments.

2.3. Procedures

Repeatability of the DHPDS-based sensor was analytically evaluated to obtain a quantitative measure of sensor precision within the pH interval 6–9. The repeatability experiment was designed to include four replicates at the end-points of calibration (i.e. two replicates at pH 6.00 and two at pH 9.01) and four at the intermediate pH 7.01 (i.e. n_{tot} = 8). Calibrations were performed before and again repeated after sample measurements (i.e. two-point calibrations were performed at pH 6.00 and 9.01). The ratiometric signal, $R_{F1,F2}$, was linearized ($^{10}\log(R_{F1,F2})$) for visualization purposes and to simplify quantifications. Time-dependent calibration functions were applied on the linearized response function to provide a unique set of calibrations for each individual repetition [22,33]. Replicate measurements were analytically evaluated for repeatability according to IUPAC's definition of pooled standard deviation [34]. The repeatability experiment encompassed 11 consecutive ratiometric measurements, including calibrations and replicate samples. Measurements were performed using NIST traceable standards, 5 min equilibrium time, 0.5 s time of integration.

To evaluate the sensitivity towards changes in ionic strength, the response from the DHPDS-based optical sensor was compared to that of a commercially available pH electrode (model 6.0232.100, 780 pH meter; Metrohm Ltd.). Comparisons were made at pH 6.246 and 8.026 in phosphate buffers ($[H_3PO_4]_{tot}$ = 4 mM) in which the ionic strength was adjusted to 10, 355 and 700 mM with appropriate additions of NaCl (p.a., Merck).

For comparison, the fluorescence response of dissolved DHPDS and HPTS was individually evaluated by titrating 3 μM of each fluorophore in 0.0667 M phosphoric acid with 2 M NaOH. Photobleaching of DHPDS and HPTS was assessed using 3 μM of each fluorophore in NIST buffer (pH 7.00). The experiment was performed in the mode of constant illumination (excitation at 420 and 470 nm for DHPDS, and at 405 and 455 nm for HPTS) for 2 h.



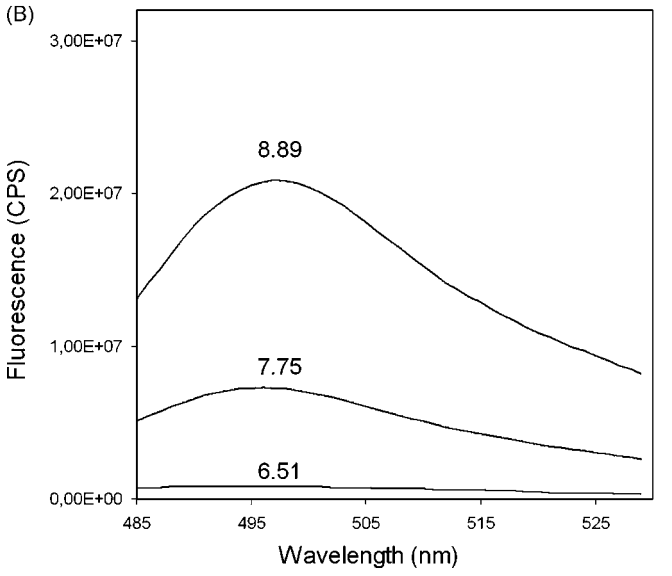


Fig. 2. Emission spectra of DHPDS immobilized in the sensor film at pH 6.51, 7.75 and 8.89 (I_{tot} = 700 mM). Excitation was performed at 420 nm (A) and 470 nm (B). Excitation at 420 nm demonstrated an isosbestic point at ~485 nm.

3. Results and discussion

3.1. General sensor characteristics and sensor response

Fluorescence matrix scans (excitation and emission) were divided to evaluate and optimize pairs of wavelengths for maximum relative response in fluorescence with changing pH. Within the excitation range 340–480 nm and the corresponding emission range 430–550 nm, F_1 ($\lambda_{1,ex}$ = 420 nm, $\lambda_{1,em}$ = 462 nm) and F_2 ($\lambda_{2,ex}$ = 470 nm, $\lambda_{2,em}$ = 498 nm) were associated with the largest relative response. These pairs of excitation and emission wavelengths (F_1 and F_2) were therefore consecutively used for ratiometric ($R_{F1,F2} = F_1/F_2$) normalization of sensor signal (Fig. 2). Procedures of dual excitation and dual emission were used to significantly increase the dynamic range and sensitivity of measurements. Immobilized DHPDS demonstrated double emission maxima at ~450 and ~500 nm (excitation at 420 nm), and a single emission at ~500 nm as a response to the excitation at 470 nm (Fig. 2). The fluorescence observed at 450 nm (excitation

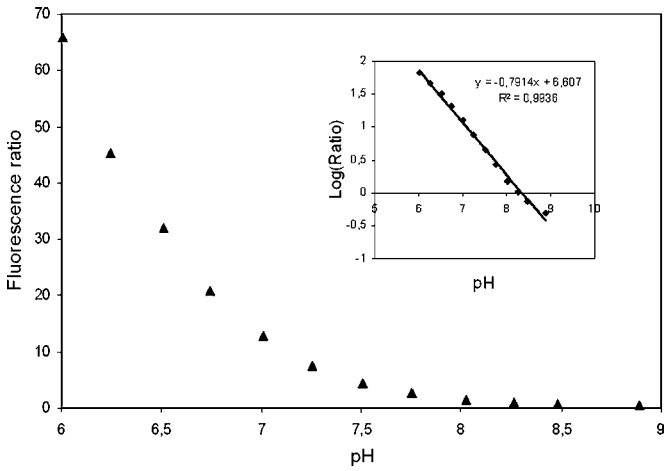


Fig. 3. The ratiometric response ($R_{F1F2} = F_1/F_2$) of immobilized DHPDS as a function of pH. Inserted is the logarithmic response from pH 6 to 9. I_{tot} = 700 mM.

at 420 nm; F_1) decreased, while the fluorescence at 500 nm (excitation 470 nm; F_2) increased with increasing pH. Maximum relative response used for quantification of pH (from the matrix scans) did not exactly match the maximum fluorescence obtained following single-wavelength excitation at 420 nm ($\lambda_{max,em1}$ = 447 nm) and 470 nm ($\lambda_{max,em2}$ = 495 nm; Fig. 2), which is not uncommon during fluorescence detection [35]. The relatively large shift observed for excitation at 420 nm ($\lambda_{1,em}$ = 462 nm rather than 447 nm; Fig. 2) may be caused by a broad overlap of energy levels associated with the fluorescence measured. The ratiometric response ($R_{F1,F2}$; I_{tot} = 700 mM) decreased exponentially from pH ~ 6 ($R_{F1,F2} \approx 65$) to pH ~ 8.9 ($R_{F1,F2} \approx 0.5$) (Fig. 3), with a significant linear correlation between the logarithmic signal ($\delta^{10}\log(R_{F1,F2})$) and pH ($(\delta^{10}\log(R_{F1,F2})/\delta\text{pH}) = -0.7914$; $R^2 = 0.9936$; $n = 12$). Similarly, as was also observed for immobilized DHPDS, the ratiometric response of dissolved DHPDS followed a decreasing exponential function with pH (Fig. 4). The logarithmic ($\delta^{10}\log(R_{F1,F2})$) response of dissolved DHPDS from three independent titrations followed a linear function ($(\delta^{10}\log(R_{F1,F2})/\delta\text{pH}) = -1.01$; $R^2 = 0.9974$; $n = 22$) between pH ~ 5 and pH ~ 10. For comparison, the logarithmic response from a similar titration of HPTS in solution was linear between pH 5 and 8, with a slope ($\delta^{10}\log(R_{F1,F2})/\delta$pH) of −0.82

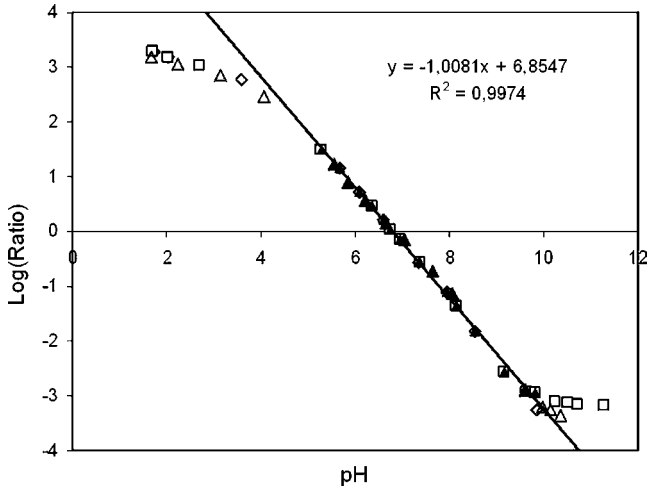


Fig. 4. Logarithmic sensor response ($\delta^{10}\log(R_{F1,F2})$) as a function of pH for 3 μM DHPDS in 0.067 M phosphoric acid titrated with 2 M NaOH (three independent titrations; n_{tot} = 41). Black triangles denote data points used to calculate the linear correlation (n = 22).

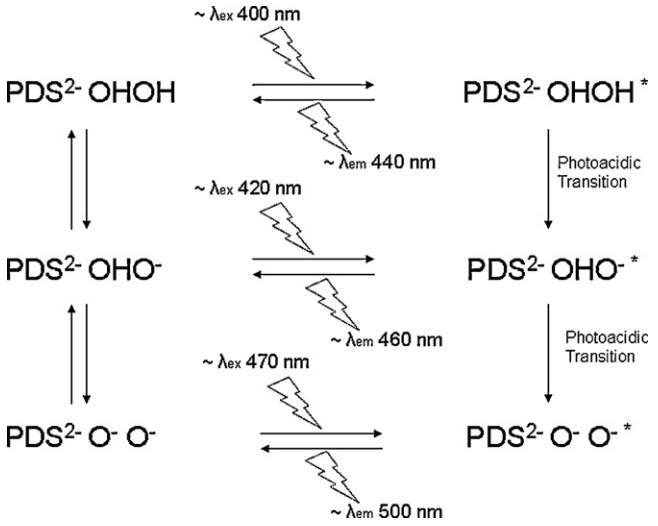


Fig. 5. Suggested proton dynamics for DHPDS. PDS^{2-} denotes the pyrene-disulfonate group to which the hydroxyl groups with the two acidic protons are attached. (*) Indicates electronically excited DHPDS.

($R^2 = 0.9974$; $n = 7$) (not shown). The response of dissolved HPTS and DHPDS not only indicated a significantly larger (close to 2 pH units) dynamic range of DHPDS compared to HPTS. The steeper slope of the response function also suggested an improved sensitivity (>20%) for DHPDS.

Overall, the response of an optical pH sensor is determined by the acid–base equilibria of the immobilized dye, with a classical sigmoidal calibration having an inflection point that corresponds to the pK_a' of the immobilized indicator [10]. The analytical sensitivity is most pronounced close to this pK_a' where the derivative (δ(signal)/δ(pH)) is maximized. An apparent dissociation constant of $10^{-6.4}$ (i.e. $pK_a' = 6.4$) was observed for HPTS immobilized onto cellulose acetate in seawater [10]. As the pH of open seawater is slightly above 8, and even higher in environments of intense primary production (e.g. [19]), the analytical performance of HPTS-based sensors is normally hampered for use in such systems (e.g. [5]). The large dynamic range of DHPDS-based sensors observed in this study, including pH values up to ~9, support the preferential use of DHPDS rather than HPTS for pH measurements in e.g. seawater.

Based on the obtained fluorescence response, a simplified scheme for proton and excited state dynamics of DHPDS is presented (Fig. 5). Fluorescence transitions are not infinitely narrow and there are often significant overlaps between excitation and emission bands. The closely coupled energy levels corresponding to excitations at 400 and 420 nm are particularly likely to be associated. At 500 nm (excitation at 420 nm), the fluorescence of DHPDS in solution was more pronounced (not shown) compared to that observed for DHPDS immobilized onto the sensor film (Fig. 2A). This observation indicated that immobilization of DHPDS onto the sensor support caused a reduced photoacidity by obstructing proton dynamics. The effect following immobilization was, however, not as pronounced as previously demonstrated for HPTS where the complete photoacidity was removed upon immobilized in ethyl-cellulose [22]. Excitation and emission properties for DHPDS demonstrated in this study also support that excited state dynamics of DHPDS may include a double deprotonation (Fig. 5), as 400 nm excitation at pH < 6.5 resulted in a substantial fluorescence at 500 nm (data not shown).

The photobleaching experiment demonstrated that upon constant illumination for 2 h, the emission decreased by 8.5% for DHPDS and 1.5% for HPTS. The corresponding ratiometric signals changed by 0.4% for both DHPDS and HPTS. The combination of ratiometric normalization and time-correlated calibration protocols would thus completely cancel out this potential artifact as well as the plausible leaching of the fluorophore.

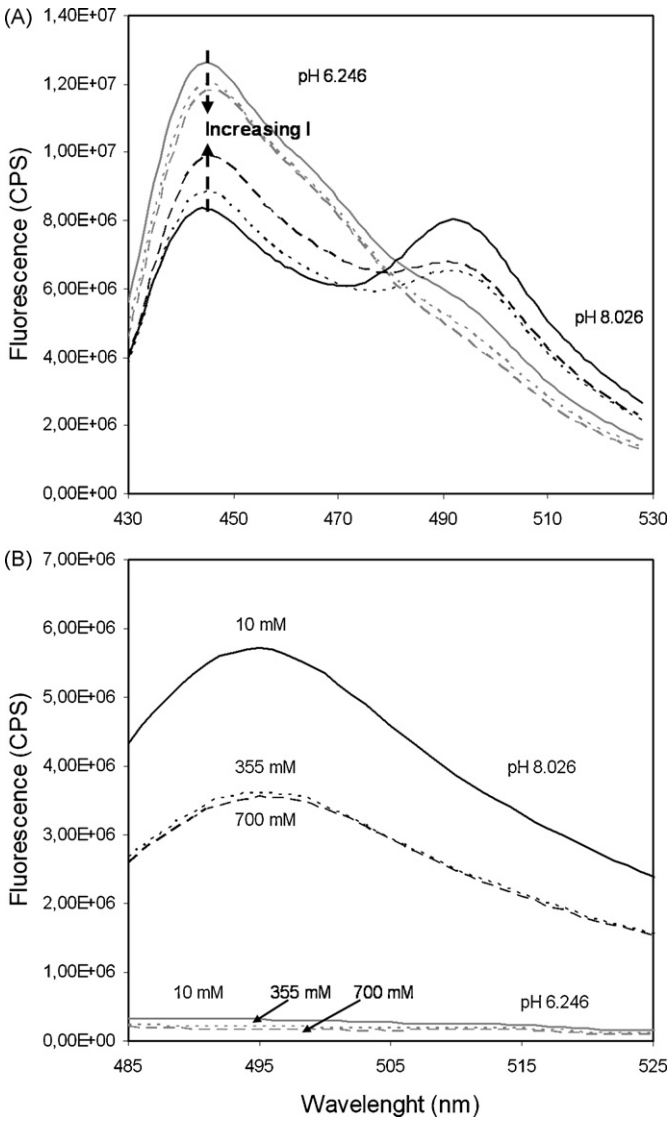


Fig. 6. Emission spectra of immobilized DHPDS at 10 mM (solid), 355 mM (dotted) and 700 mM (dashed) ionic strength. Measurements were performed at pH 8.026 (black) and 6.246 (grey) using excitation at 420 nm (A) or 470 nm (B).

3.2. Effects of ionic strength

Fluorescence spectra for the sensor exposed to pH 6.246 and 8.026 in solutions of 10, 355 and 700 mM total ionic strength (I_{tot}) are shown in Fig. 6. Fluorescence intensity at 450 nm (excitation at 420 nm) was shifted in opposite directions at low and high pH with increasing ionic strength (Fig. 6A). At pH 6.246, the fluorescence decreased, while at pH 8.026 measured fluorescence increased with increasing I_{tot}. In contrast, emission at 500 nm (excitation at 420 nm) decreased progressively with increasing I_{tot} for both pH values. This experimental observation is quite opposite to the Debye–Hückel theory that under conditions of high pH would predict a decrease in pK_a'. As a consequence, fluorescence emission would be significantly reduced with increasing I_{tot} [21]. We suggest that a decreased solvent acceptance of protons, with a subsequent reduction in photoacidity, caused the increase in flu-

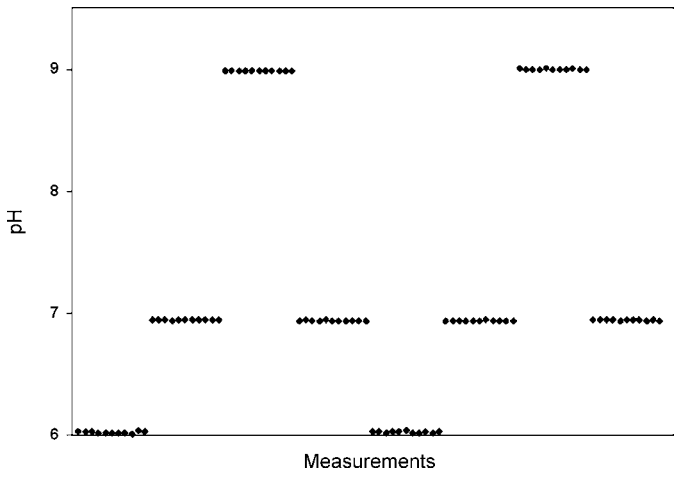


Fig. 7. Repeatability of the DHPDS-based sensor at pH 6.00, 7,01 and 9.01 ($n = 11$). The pooled standard deviation (IUPAC) was 0.0057 ($n = 8$). Time between each data point was 5 s, and the time between sampling occasions was 5 min.

orescence observed at ~450 nm with increasing I_{tot}. A reduced photoacidity may also explain the decrease in F_1 ($\lambda_{1,ex} = 420$ nm, $\lambda_{1,em} = 462$ nm) with increasing I_{tot} observed at pH 6.246. The overlap in energies associated with the excitation at 420 and 400 nm is likely more decoupled as photoacidity decreases, i.e. the reduction of fluorescence observed at 462 nm (excitation at 420 nm; Fig. 6) is generated by the first photo-acidic transition of DHPDS (Fig. 5).

Optodes are normally considered highly sensitive to changes in I_{tot} as the solute activity coefficient of the indicator and the surface potential are partly controlled by changes in I_{tot} (e.g. [20,21]). Further, properties of the surface itself are vital for local fluorescence via acid-base characteristics and changes in the ζ-potential [20]. In this study, samples of variable ionic strength ($I_{tot} = 10$, 355 and 700 mM) demonstrated that the DHPDS-based pH fluorosensor was significantly less sensitive to changes in I_{tot} than the commercially available electrode used for comparison. While the optode seemed to maintain the sensitivity of the ratiometric signal ($\delta^{10}\log(R_{F1,F2})/\delta\text{pH} = 0.8024 \pm 0.0145$) within the pH interval 6.246–8.026, there was a positive linear correlation in electrode response to I_{tot} ($R^2 = 0.9976$; $n = 6$). For comparison, the linear correlation (R^2) between I_{tot} and pH was 0.065 ($n = 6$) for the optode. The quantitative errors related to changes in I_{tot} (10–700 mM) rather than pH correspond to 0.322–0.338 pH units for the optode and 0.528–0.725 for the electrode, respectively. However, as a solution of NaCl was used to moderate ionic strength of samples, effects associated with changes in I_{tot} may at least partly be caused by the linear increase in sodium concentration induced by NaCl additions. Nevertheless, the comparably low sensitivity towards changes in I_{tot} demonstrated for the DHPDS-based pH sensor may open up for simultaneous measurements of pH and ionic strength over wide ranges using DHPDS-based optical sensors. Ideally, fluorescence at the isosbestic point ($\lambda_{ex} = 420$ nm, $\lambda_{em} = 485$ nm, Fig. 2) where sensor response is insensitive to pH, could be used for such dual measurements. Unfortunately, there was only a small response to changes in ion strength at the isosbestic point (Fig. 6).

3.3. Analytical performance

The precision (IUPAC's definition of pooled standard deviation; $n = 8$) of the DHPDS-based optical sensor was within the pH interval 6–9 comparable to that of the electrode used for comparison (Fig. 7). With a linear time-dependent two-point calibration, the precision over three pH values (6.00, 7.01 and 9.01) was 0.0057 pH units for the optical sensor, compared to 0.0054 for the electrode. The accuracy, defined as mean systematic deviation (absolute value) from the NIST pH values, was 0.037 for the optode ($n = 8$) and 0.023 for the electrode ($n = 8$), respectively. Between the end-points of calibration at pH 7.01, the precision of the optode was 0.0037 pH units ($n = 4$). Using a similar experimental set-up, a precision of 0.0029 (IUPAC, $n = 8$) was demonstrated for a HPTS-based ratiometric fluorosensor between pH 6.64 and 7.76 [23]. Optode standardizations were made in relation to a commercially available pH electrode using multi-point ($n = 4$–7) time-dependent sigmoidal calibrations. In the present study, however, NIST buffers were exposed directly to the optode for calibrations and measurements to eliminate limitations inherent to the analytical performance of the electrode. Calibrations were made using time-dependent linear functions linked within a two-point calibration. The comparably large systematic errors (0.037) of the optode response were likely explained by insufficient exchange of sample volume during the analytical procedure, and the dead volume associated with sensor configuration.

Further developments of the DHPDS-based sensing scheme are suggested to include metal enhanced fluorescence (MEF) and plasmonics to further enhance fluorescence characteristics [36]. Properly arranged, the sensor system would benefit from surface plasmon enhancement and lossy surface wave quenching as the fluorophore moves toward the plasmon active nanoparticles [35]. Additionally, constructive scattering effects have the potential to further enhance the signal.

4. Conclusions

DHPDS is a double excitation and double emission (F_1: $\lambda_{1,ex} = 420$ nm, $\lambda_{1,em} = 462$ nm; F_2: $\lambda_{2,ex} = 470$ nm, $\lambda_{2,em} = 498$ nm) ratiometric ($R_{F1,F2} = F_1/F_2$) fluorophore with similar analytical characteristics as HPTS. Due to the dual photo-acidic properties of immobilized DHPDS, the fluorescence dynamic range encompassed pH 6–9, i.e. the range for pH measurements was significantly larger for the DHPDS-based sensor than that previously observed for HPTS-based optical sensors. The precision of the DHPDS sensor was 0.0057 over the investigated pH range. The sensitivity to changes in ionic strength was significantly better for the DHPDS sensor than that of a commercially available pH electrode used for comparison. The DHPDS-based sensor retained sensitivity between 10 and 700 mM ionic strength.

Acknowledgements

Financial support was obtained from the Swedish Research Council (VR), the Foundation for Strategic Environmental Research (MISTRA), the Swedish Research Council for Environment, Agricultural Sciences and Spatial Planning (FORMAS), and the Lovén Centre for marine infrastructure (University of Gothenburg). Thanks to Erik Mattsson for his substantial contribution in the rediscovery of DHPDS.

References

[1] S. Sørensen, Biochemische Zeitschrift 21 (1909) 131–200.
[2] K. Caldeira, M.E. Wickett, Nature 425 (2003) 365.
[3] W.J. Cai, C.E. Reimers, Limnology and Oceanography 38 (1993) 1762–1773.
[4] N.P. Revsbech, B.B. Jorgensen, Advances in Microbial Ecology 9 (1986) 293–352.
[5] A. Hakonen, S. Hulth, S. Dufour, Talanta, 2009, submitted for publication.
[6] J.I. Peterson, S.R. Goldstein, R.V. Fitzgerald, D.K. Buckhold, Analytical Chemistry 52 (1980) 864–869.
[7] L.A. Saari, W.R. Seitz, Analytical Chemistry 54 (1982) 821–823.
[8] Z. Zhujun, W.R. Seitz, Analytica Chimica Acta 160 (1984) 47–55.
[9] D.A. Nivens, M.V. Schiza, S.M. Angel, Talanta 58 (2002) 543–550.
[10] S. Hulth, R.C. Aller, P. Engstrom, E. Selander, Limnology and Oceanography 47 (2002) 212–220.

[11] Q.Z. Zhu, R.C. Aller, Y.Z. Fan, Environmental Science & Technology 39 (2005) 8906–8911.
[12] S.M. Borisov, O.S. Wolfbeis, Analytical Chemistry 78 (2006) 5094–5101.
[13] S.M. Barnard, D.R. Walt, Nature 353 (1991) 338–340.
[14] J. Ji, Z. Rosenzweig, Analytica Chimica Acta 397 (1999) 93–102.
[15] T.D. Clayton, R.H. Byrne, Deep-Sea Research Part I-Oceanographic Research Papers 40 (1993) 2115–2129.
[16] A.G. Dickson, Marine Chemistry 44 (1993) 131–142.
[17] E. Bishop, in: E. Bishop (Ed.), Indicators, Pergamon, 1972, pp. 13–63.
[18] R.L. Marinelli, B.P. Boudreau, Journal of Marine Research 54 (1996) 939–966.
[19] N.P. Revsbech, B.B. Jorgensen, T.H. Blackburn, Y. Cohen, Limnology and Oceanography 28 (1983) 1062–1074.
[20] J. Janata, Analytical Chemistry 59 (1987) 1351–1356.
[21] O.S. Wolfbeis, H. Offenbacher, Sensors and Actuators 9 (1986) 85–91.
[22] A. Hakonen, S. Hulth, Analytica Chimica Acta 606 (2008) 63–71.
[23] N. Stromberg, E. Mattsson, A. Hakonen, Analytica Chimica Acta 636 (2009) 89–94.
[24] O.S. Wolfbeis, E. Furlinger, H. Kroneis, H. Marsoner, Fresenius Zeitschrift Fur Analytische Chemie 314 (1983) 119–124.
[25] O.S. Wolfbeis, Trac-Trends In Analytical Chemistry 4 (1985) 184–188.
[26] C.C. Overly, K.D. Lee, E. Berthiaume, P.J. Hollenbeck, Proceedings of the National Academy of Sciences of the United States of America 92 (1995) 3156–3160.
[27] T. Forster, Naturwissenschaften 36 (1949) 186–187.
[28] J.R. Lakowicz, Principles of Fluorescence Spectroscopy, 2nd ed., Kluwer Academic and Plenum, New York, 1999.
[29] H. Hochreiner, I. Sanchez-Barragan, J.M. Costa-Fernandez, A. Sanz-Medel, Talanta 66 (2005) 611–618.
[30] F.X. Felberbauer, J. Graf, Pflugers Archiv-European Journal of Physiology 419 (1991) 215–217.
[31] X.D. Ge, M. Hanson, H. Shen, Y. Kostov, K.A. Brorson, D.D. Frey, A.R. Moreira, G. Rao, Journal of Biotechnology 122 (2006) 293–306.
[32] I.H. Huisman, G. Tragardh, Colloids and Surfaces A-Physicochemical and Engineering Aspects 157 (1999) 261–268.
[33] N. Stromberg, S. Hulth, Analytica Chimica Acta 550 (2005) 61–68.
[34] IUPAC Compendium of Chemical Terminology, 2nd ed., International Union of Pure and Applied Chemistry, 1997.
[35] A. Hakonen, Analytical Chemistry 81 (2009) 4555–4559.
[36] J.R. Lakowicz, Analytical Biochemistry 337 (2005) 171–194.

Talanta 80 (2010) 1970–1979

Contents lists available at ScienceDirect

Talanta

journal homepage: www.elsevier.com/locate/talanta

Rapid qualitative and quantitative ultra high performance liquid chromatography method for simultaneous analysis of twenty nine common phenolic compounds of various structures

Lucie Nováková [a,*], Zdeněk Spáčil [a], Marcela Seifrtová [a], Lubomír Opletal [b], Petr Solich [a]

[a] Department of Analytical Chemistry, Faculty of Pharmacy, Charles University in Prague, Heyrovského 1203, 500 05 Hradec Králové, Czech Republic
[b] Department of Pharmaceutical Botany, Faculty of Pharmacy, Charles University in Prague, Heyrovského 1203, 500 05 Hradec Králové, Czech Republic

ARTICLE INFO

Article history:
Received 9 September 2009
Received in revised form 5 October 2009
Accepted 23 October 2009
Available online 31 October 2009

Keywords:
UPLC
UHPLC
Tea
Phenolic compounds
Catechins
Flavonoids
Phenolic acids
Caffeine

ABSTRACT

Twenty nine phenolic compounds comprising nine phenolic acids, sixteen flavonoids (including eight tea catechins, glycosides and aglycones), four coumarins plus caffeine were analysed within 20 min using ultra high performance liquid chromatography (UHPLC) with PDA detection. UHPLC system was equipped with C18 analytical column (100 mm × 2.1 mm, 1.7 μm), utilising 0.1% formic acid and methanol mobile phase in the gradient elution mode. The developed method was tested for the system suitability: resolution, asymmetry factor, peak capacity, retention time repeatability and peak area repeatability. The method was fully validated in the terms of linearity ($r^2 > 0.9990$ for all 30 compounds), range (typically 1–100 mg L^{-1}), LOD, LOQ, inter/intra-day precision (<3% and <9% respectively) and inter/intra-day accuracy (typically 100 ± 10%). Subsequently the method was applied to the identification (spectral information and peak purity calculations were profited) and quantification of phenolic compounds and caffeine present in tea infusions and extracts.

© 2009 Elsevier B.V. All rights reserved.

1. Introduction

Phenolic compounds attract the attention of research laboratories and literature especially due to their biological and physiological importance. They are able to scavenge free radicals [1,2], specifically reactive oxygen species (ROS) and reactive nitrogen species (RNS, e.g. nitric oxide). The oxidative stress, caused by the excess ROS/RNS, can damage cellular lipids, proteins or DNA inhibiting their normal function [3]. In this way it is implicated in various pathological conditions involving cardiovascular disease, cancer, neurological disorders, diabetes, ischemia, aging and other diseases [4]. Flavonoids and phenolic acids are two main groups of phenolic compounds with antioxidant activity.

Flavonoids form a large group of structurally related compounds with a chroman-type skeleton and with a phenyl substituent in the C_2 or C_3 position. They are often hydroxylated in positions 3, 5, 7, 3′, 4′ or 5′ and their hydroxylic groups are frequently modified (methylated, acetylated, prenylated or sulphated). In plants are flavonoids often present as *O*- or *C*-glycosides [5]. They are further divided into classes depending on the oxidation degree of the central pyran ring [6]. More than 6500 different flavonoid products of secondary plant metabolism, mainly responsible for the colour of flowers, fruits and sometime leaves, have been characterized in various plant species, but their real number may exceed 8000 [7].

The *phenolic acids* are secondary plant metabolites derived from either benzoic or cinnamic acid (Fig. 1). For instance gallic acid, caffeic acid, vanilic acid, ferulic acid and chlorogenic acid with esters can be frequently found in tea, wine and herbal infusions [8].

Coumarins are often found in phenolic fraction of plant extracts. Presently over 1000 coumarins have been described in the plant families *Fabaceae* (sweet clover, tonka bean), *Apiaceae* (khella, angelica) and *Rubiaceae* (sweet woodruff). Antioxidant activity of these 2H-1-benzopyran-2-ones (Fig. 1) is in general lower [9,10].

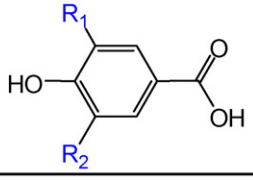
Tea is a rich source of antioxidant phenolic compounds, especially polyphenols, and it is after water the most often consumed beverage worldwide. Therefore it was chosen as matrix for validation in our study. Tea is made by steeping processed leaves, buds, or twigs of *Camellia sinensis* (L.) *Kuntze* (*Theaceae*) in hot water for a few minutes. Tea infusion is a rich natural source of alkaloids (caffeine, theobromine, theophylline, theacrine, adenin, xanthine), phenolic compounds (phenolic acids, flavanols, flavonols), amino acids (L-theanine), metals and vitamins (ascorbic acid) [11,12].

The polyphenolic fraction of tea contains flavanols (catechins), flavonols (myricetin, quercetin, kaempferol) and products

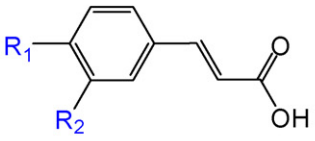
* Corresponding author. Tel.: +420 495067381; fax: +420 495067164.
E-mail address: nol@email.cz (L. Nováková).

0039-9140/$ – see front matter © 2009 Elsevier B.V. All rights reserved.
doi:10.1016/j.talanta.2009.10.056

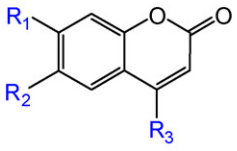
derivatives of benzoic acid	R1	R2
gallic acid	OH	OH
protocatechuic acid	H	OH
vanillic acid	H	OH_3
syringic acid	OCH_3	OCH_3



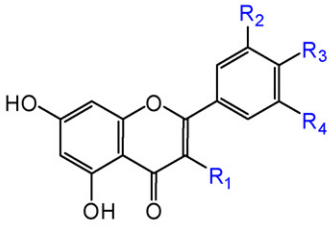
derivatives of cinnamic acid	R1	R2	Rx
caffeic acid	OH	OH	
chlorogenic acid	OH	OH	quinate
ferulic acid	OH	OCH_3	
o-coumaric acid	H	H	2´OH
cinnamic acid	H	H	



coumarins	R1	R2	R3
aesculin	OH	glucose	H
scopoletin	OH	OCH_3	H
4-hydroxycoumarin	H	H	OH
6-methylcoumarin	H	CH_3	H



Flavonoids	R1	R2	R3	R4
rutin	rhamno-glucose	OH	OH	H
myricetin	OH	OH	OH	OH
quercitrin	rhamnose	OH	OH	H
quercetin	OH	OH	OH	H
naringenin*	H	H	OH	H
luteolin	H	OH	OH	H
hesperetin*	H	H	OCH_3	OH
kaempferol	OH	H	OH	H



Catechins	R1	R2
gallocatechin (GC)	OH	OH
epigallocatechin (EGC)	OH	OH
gallocatechin gallate (GCG)	gallate	OH
epigallocatechin gallate (EGCG)	gallate	OH
catechin (C)	OH	H
epicatechin (EC)	OH	H
catechin gallate (CG)	gallate	H
epicatechin gallate (ECG)	gallate	H

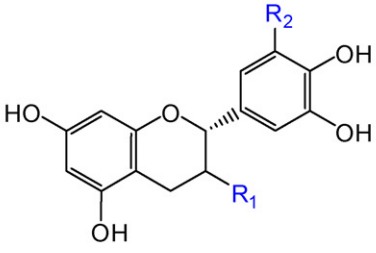


Fig. 1. Structural types of analysed phenolic acids, flavonoids, coumarins and caffeine. *Naringenin and hesperetin have no double bond on benzopyranone ring, they belong among flavanones.

of condensation (proanthocyanidins). Namely (+)-catechin (C), (−)-epicatechin (EC), (−)-epigallocatechin (EGC), (−)-epicatechin gallate (ECg), (−)-epigallocatechin gallate (EGCg) are the most abundant phenols in tea leaves, constituting up to 30% of the dry mass [13]. The representation of particular catechins in the tea infusion is dependent on the processing of tea leaves. EGCg is the major component of unfermented green tea [14], making up to about 10–50% of the total green tea catechins. Its antioxidant activity is 100 times more effective than that of vitamin C and 25 times more effective than that of vitamin E [15]. After the fermentation process the major catechin is GC, while the content of EGCg is decreased approximately 10× [16]. Besides catechins also small amounts of flavonols 3-*O*-glycosides occurs in tea leaves.

Analytical methods employed in analysis of flavonoids and phenolic acids were summarized in recently published review articles [5,17]. Basically all conventional separation methods are used such as capillary electrophoresis and chromatographic methods including HPLC, GC as well as TLC. Although HPLC was a method of choice, none of published works concerning with analysis of phenolic compounds in tea gave satisfactory results for separation of catechins [18–25]. The weak point of all published methods was limited separation efficiency, which press on to compromise separation time or resolution. The methods, which provided sufficient resolution for all peaks were extremely time-consuming, which means analysis time about 25–40 min for typically 7–12 analytes. For instance 15 analytes within 92 min [25] or 24 analytes within

Table 1
Recent LC methods dealing with the analysis of tea flavonoids and phenolic acids.

Ref	Matrix	Analysis		Detection	LOD	Duration [min]
		Qualitative	Quantitative			
(a) UHPLC methods						
[33]	Wine; grapefruit juice; green tea	17 phenolic acids		ESI-MS/MS	0.15–10 pmol/inj	10
[34]	Plant materials; Trifolium pratense; Glycine max; Pisum sativum; Ononis spinosa	(1) Gallic acid, (2) protocatechuic acid, (3) *p*-hydroxybenzoic acid, (4) vanillic acid, (5) caffeic acid, (6) syrinngic acid, (7) *p*-coumaric acid, (8) daidzin, (9) ferulic acid, (10) glycitin, (11) sinapic acid, (12) genistin, (13) ononin, (14) daidzein, (15) glycetin, (16) sissotrin, (17) genistein, (18) formonetin, (19) biochanin A		PDA 270 nm	0.2–0.4 μg L^{-1}	1.9
[35]	*Epimedium*	15 flavonoids – incl. epimedins, icariin, baohuoside, caohuosides and sagittatosides		UV 270 nm	0.05–0.13 ng	13
[36]	Leaves of *Isatis indigotica*	(1) Isoorientin, (2) isoorientin-3-glucoside, (3) isovitexin, (4) isovitexin-3-glucoside, (5) isocoparin, (6) isocoparin-3-glucoside		PDA, ESI-MS	0.8–4.5 μg.L^{-1}	6.5
[37]	Rat plasma	(1) Puerarin, (2) daidzein, (3) baicalin, (4) wogonoside, (5) liquiritin		ESI-MS	2.54–10.2 μg.mL^{-1}	6
[38]	*Rosa damascene*, *Rosa bourboniana*, *Rosa brunonii*	(1) Gallic acid, (2) tetra-O-galloyl hexoside, (3) di-O-galloyl hexoside, (4) galloyl tannin, (5) rutin, (6) quercetin-3-O-hexoside, (7) quercetin-3-O-dipentoside, (8) kempferol-3-O-rutinoside, (9) kaempferol-3-O-rhamnoside, (10) kaempferol-3-O-hexoside, (11) quercitrin, (12) kaempferol-3-0-pentoside, (13) quercetin-3-O-pentoside, (14) flavonol glycoside, (15) myricetin, (16) kempferol-3,7-hexose-rhamnoside, (17) quercetin, (18) kaempferol		ESI-MS/MS, PDA	NA	3
[39]	Tea samples, wine samples	11 phenolic acids, 8 catechins, 6 coumarins, 9 flavonoids – as separated groups		UV 280 nm	NA	3.5, 1.7, 4.0, 6.5
(b) HPLC methods						
[18]	Tea leaves, non-fermented tea dry extracts	(1) Gallic acid, (2) caffeine, (3) theobromine	(4) C, (5) Cg, (6) EC, (7) ECg, (8) EGC, (9) EGCg, (10) GC, (11) GCg	DAD (210 and 280 nm)	0.19–1.16 mg L^{-1}	25
[19]	Non-fermented, decaffeinated non-fermented, partially fermented and fermented tea	(1) Theaflavin, (2) caffeine, (3)C, (4) EC, (5) ECg, (6) EGC, (7) EGCg		DAD (280 nm)	0.02–1.80 mg L^{-1}	10
[20]	Fresh buds and leaves	(1) Theobromine, (2) caffeine, (3) theacrine, (4) C, (5) EC, (6) ECg, (7) EGC, (8) EGCg, (9) GC, (10) GCg		DAD (231 nm)	0.84–2.98 mg L^{-1}	20
[21]	Fresh young shoots of tea	(1) Theogallin, (2) gallic acid, (3) theobromine, (4) isochlorogenic acid, (5) GC, (6) EGC, (7) C, (8) *p*-coumarylquinic acid, (9) chlorogenic acid, (10) caffeine, (11) EGCg, (12) EC, (13) *p*-coumaric acid, (14) 3-(*p*-hydroxyphenyl)propionic acid, (15) GCg, (16) quercetin 3-rhamnosylglucoside, (17) epigallocatechin 3,5-digallate, (18) ECg (19) Cg, (20) quercetin 3-glucoside, (21) quercetin glycoside (22) kaempferol 3-rhamnosylglucoside, (23) kaempferol glycoside, (24) epicatechin 3,5-digallate		DAD (280, 310, 340, 380, 450 and 510 nm)	NA	40
[22]	Non-fermented tea extracts and fermented tea	(1) Theamine, (2) theophylline, (3) theobromine, (4) caffeine, (5) chlorogenic acid (6) C, (7) Cg, (8) EC, (9) ECg, (10) EGC, (11) EGCg, (12) GCG		PDA (200 nm)	0.05–0.20 mg L^{-1}	40
				MS (ESI+/−)	0.01–0.10 mg L^{-1}	
[23]	Non-fermented, partially fermented, fully fermented and post-fermented tea	(1) 3,5-Dihydroxybenzoic acid, (2) *p*-anisic acid, (3) myricetin, (4) 3,4,5-trimethoxycinnamic acid	(5) EC, (6) ECG, (7) EGC, (8) EGCG, (9) CG, (10) gallic acid, (11) caffeine	UV (280 nm)	NA	25
[24]	Non-fermented tea extracts	(1) C, (2) EC, (3) ECg, (4) EGC, (5) EGCg, (6) GC, (7) GCg		DAD (270 nm)	0.40–3.85 mg L^{-1}	18
				MS (ESI+)	0.33–0.71 mg L^{-1}	
[25]	Peanut skin extract	(1) Gallic acid, (2) protocatechuic acid, (3) EGC, (4) C, (5) caffeic acid, (6) procyanidin B2, (7) EC, (8) EGCg, (9) *p*-coumaric acid, (10) ferulic acid, (11) piceid, (12) ECg, (13) Cg, (14) resveratrol, (15) quercetin	PDA 250 nm, 280 nm, 306 nm, 320 nm, 370 nm		0.1–0.9 ppm	92

Table 2
System suitability test, calibration and sensitivity results.

No.	Component	Resolution	Asymmetry factor	Peak Capacity	Retention Time [%RDS]	Peak Area [%RSD]	Range [μg/ml]	Correlation Coefficient	LOD [mg L^{-1}]	LOQ [mg L^{-1}]
1	Gallic acid	–	1.17	122.35	0.22	0.21	0.20–105.88	0.9996	0.06	0.20
2	GC	5.38	1.13	118.26	0.36	0.52	2.70–135.00	0.9998	0.82	2.70
3	Protocatechuic acid	6.20	1.07	71.58	0.26	0.26	0.18–54.31	0.9997	0.05	0.18
4	Esculin	10.92	1.05	75.35	0.35	0.28	0.43–129.20	0.9997	0.13	0.43
5	EGC	6.14	–	73.10	0.52	0.76	1.50–109.95	0.9999	0.45	1.50
6	C	1.34	1.06	55.35	0.51	0.24	0.34–102.24	0.9997	0.10	0.34
7	Chlorogenic acid	5.27	–	37.50	0.33	0.68	0.41–122.44	0.9993	0.12	0.41
8	Vanillic acid	1.37	–	71.85	0.25	0.22	0.19–58.38	0.9998	0.06	0.19
9	Caffeic acid	2.23	0.97	75.77	0.28	0.55	0.04–64.60	0.9995	0.01	0.04
10	Caffeine	1.59	1.04	80.88	0.19	0.20	0.42–125.91	0.9997	0.13	0.42
11	Syringic acid	7.78	1.00	76.39	0.16	0.17	0.23–70.22	0.9997	0.07	0.23
12	EGCg	2.50	1.04	70.98	0.18	0.46	3.20–161.70	0.9997	0.97	3.20
13	EC	5.00	0.97	91.38	0.15	0.20	0.38–112.84	0.9997	0.12	0.38
14	GCg	6.32	1.00	62.83	0.14	0.49	3.00–148.30	0.9995	0.91	3.00
15	Scopoletin	3.97	0.95	85.29	0.10	0.22	0.22–66.59	0.9996	0.07	0.22
16	Ferulic acid	5.26	0.94	80.63	0.11	0.21	0.23–67.87	0.9996	0.07	0.23
17	ECg	2.37	0.99	58.41	0.11	0.83	3.10–156.70	0.9996	0.94	3.10
18	Cg	5.75	0.98	62.80	0.11	0.41	2.90–146.70	0.9994	0.88	2.90
19	o-Coumaric acid	10.85	0.91	69.35	0.10	0.18	0.20–58.58	0.9996	0.06	0.20
20	Rutin	3.40	0.94	57.83	0.12	0.20	0.70–210.75	0.9996	0.21	0.70
21	4-OH-Coumarin	2.14	0.91	65.98	0.09	0.18	0.19–55.54	0.9995	0.06	0.19
22	Myricetin	3.58	0.84	41.09	0.13	0.84	22.98–229.75	0.9992	6.96	22.98
23	Quercitrin	2.98	–	74.08	0.12	0.40	0.24–72.72	0.9994	0.07	0.24
24	6-Me-coumarin	1.30	1.01	56.21	0.07	0.75	0.19–55.56	0.9991	0.06	0.19
25	Cinnamic acid	5.58	0.90	57.36	0.09	0.21	0.17–52.26	0.9993	0.05	0.17
26	Quercetin	5.76	0.88	44.93	0.13	0.91	45.78–228.88	0.9991	13.87	45.78
27	Naringenin	2.01	0.91	54.65	0.11	0.26	1.25–93.81	0.9990	0.38	1.25
28	Luteolin	3.17	0.92	52.94	0.13	0.85	3.66–188.00	0.9994	1.11	3.66
29	Hesperetin	2.63	0.91	49.30	0.10	0.39	1.39–104.46	0.9992	0.42	1.39
30	Kaempferol	5.19	0.89	36.00	0.15	0.73	4.05–202.75	0.9993	1.23	4.05

LOD: limit of detection, LOQ: limit of quantification.

40 min [21]. An overview of HPLC methods used in analysis of phenolics with the emphasis to catechin analysis is displayed in Table 1b.

Recently, Ultra high performance liquid chromatography (UHPLC) has become widely spread technique and new trend in separation sciences. Higher separation efficiency of sub-2-μm particle sorbents allows faster chromatographic separation keeping the same resolution compared to HPLC sorbents with conventional particle size [26]. This is expressed by Knox curves, where lower height equivalent of theoretical plate indicates improved separation efficiency and higher optimum linear velocity, which means decrease in analysis time [27]. Generated back pressure of particle sorbents is inversely related to the cubed particle size, therefore UHPLC system is necessary (back pressures up to 100 MPa). A higher sensitivity is achieved using column with small internal diameter (typically 2.1 mm) and a low volume optical cell for UV detection. UHPLC systems have been demonstrated to be beneficial in the pharmaceutical development [28], drug monitoring [29], metabolite profiling [30], proteomics [31], environmental chemistry [32] or food chemistry [33].

Several new UHPLC methods for the determination of flavonoids and phenolic acids in various matrices have been recently developed [33–39]. An overview is displayed in Table 1a. These methods have typically analytical runs shorter than 10 min, in extremes they are able to separate 19 analytes in 2 min [34]. High applicability is of value especially in work of Gruz et al. [33], who determined 17 common phenolic acids or the work of Klejdus et al. [34], who determined common phenolic acids together with some flavonoids. The main drawback of latter method lays in determination only of vanillic and caffeic acid without chlorogenic acid, as these three phenolic acids typically cause coelutions in real matrices and they are often present together. Kumar et al. developed UHPLC-DAD and UHPLC–ESI-MS/MS method only for determination of phenolic acids and flavonoids [38].

In our previous work four individual methods were developed for four groups of phenolics (catechins, less polar flavonoids, coumarins and phenolic acids) using UHPLC-UV [39]. The aim was to stress the benefit of UHPLC above HPLC analysis in analysis of phenolic compounds. The four newly developed methods used various four completely different gradient elution profiles and temperatures. The convenience of UHPLC was clearly proven in terms of speed of analysis and separation efficiency however previously reported UHPLC methods might be excessively rapid not providing enough peak capacity for separation of all structurally similar compounds. Also selectivity issue was not addressed as single UV detection does not provide sufficient confirmatory results.

The aim of this work was to develop and fully validate fast, efficient routine UHPLC method with PDA detection for the simultaneous qualitative and quantitative analysis of a wide range of the most commonly occurring phenolic compounds of various structures plus caffeine (to exclude the interference) in plant matrices or dietary supplements. Structures have been chosen based upon the occurrence of phenolic compounds in plant material – see Fig. 1, to represent important examples from each group of phenolic compounds of various polarities. Tea infusions and tea extracts were selected in order to demonstrate sufficient separation efficiency, selectivity and sensitivity. The proposed method can be used in other applications, e.g. for the quantification of phenolic compounds in other plant extracts. Notably dietary supplements with contents of phenolic compounds are potential field for application, since their popularity is growing. Manufactures have not been required to demonstrate declared amount of active ingredients of their products so far [40] however, this may change soon. Therefore, commercial dry tea extracts were also included in our study.

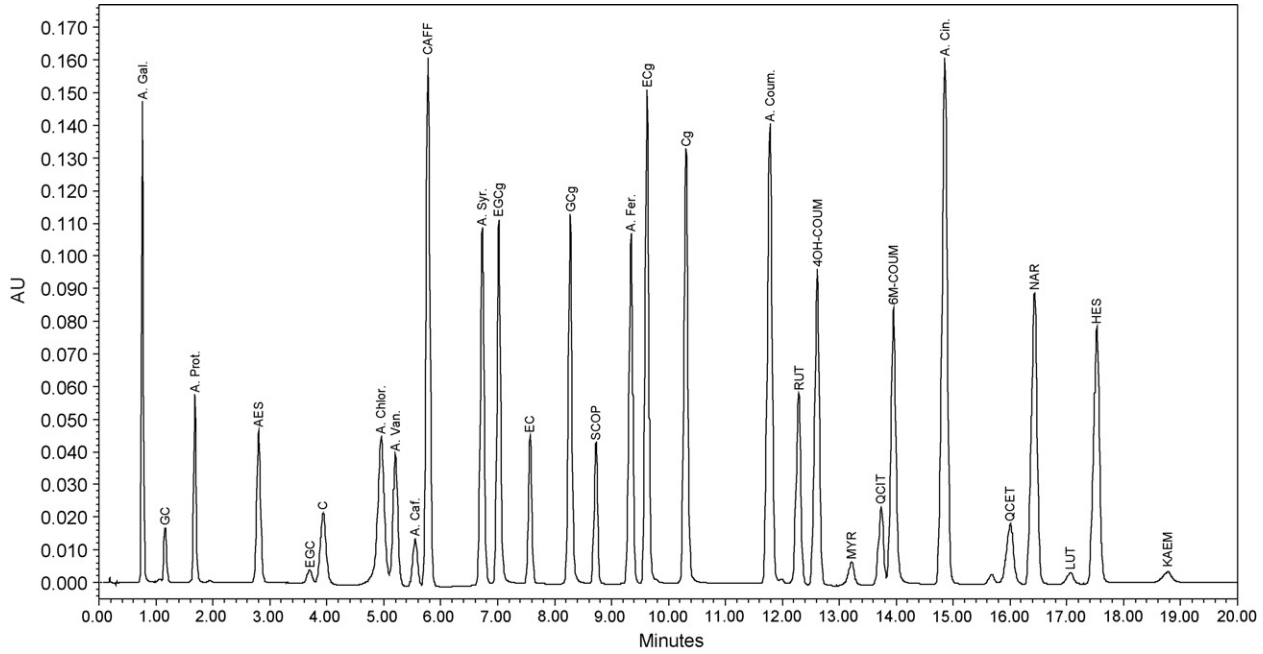


Fig. 2. Chromatogram of a standard mixture of 29 phenolic compounds and caffeine. (UV 280 nm, 0.1% formic acid–methanol from 88.5:11.5 to 50:50 (v/v), 0.45 mL min^{-1}).

2. Experimental

2.1. Chemicals and reagents

Reference standards of phenolic compounds were used in this study. They were purchased from Sigma–Aldrich (Prague, Czech Republic) as follows: phenolic acids: gallic (A. Gal.), protocatechuic (A. Prot.), chlorogenic (A. Chlor.), vanillic (A. Van.), caffeic (A. Caf.), syringic (A. Syr.), ferulic (A. Fer.), o-coumaric (A. Coum.), cinnamic (A. Cin.); flavonoids: catechin (C), catechin gallate (Cg), epicatechin (EC), epicatechin gallate (ECg), epigallocatechin (EGC), epigallocatechin gallate (EGCg), gallocatechin (GC), gallocatechin gallate (GCg), rutin (RUT), myricetin (MYR), quercitrin (QCI), quercetin (QCE), naringenin (NAR), luteolin

Table 3
Spectral data and peak purity calculations. Peak purity criteria are fulfilled when *peak purity angle* is lower than *peak purity threshold*.

Component	t_R	Standard mixture				Formosa gunpowder tea sample			
		λ_{max} 1	λ_{max} 2	Peak purity angle	Peak purity threshold	λ_{max} 1	λ_{max} 2	Peak purity angle	Peak purity threshold
Gallic acid	0.96	216	271	0.436	1.583	216	271	0.860	3.943
GC	1.27	270	335	1.654	12.569	270	–	7.887	32.516
Protocatechuic acid	1.74	260	294	0.344	1.569	260	294	0.632	4.339
Esculin	2.67	334	–	0.176	1.493	335	–	0.280	2.248
EGC	3.24	269	332	2.169	15.980	270	–	3.342	10.448
C	3.46	279	389	2.270	10.522	280	–	5.307	42.763
Chlorogenic acid	4.44	246	324	0.423	2.003	246	323	0.459	3.470
Vanillic acid	4.71	260	292	0.558	2.038	261	292	1.535	7.208
Caffeic acid	4.98	242	323	0.333	0.932	243	323	0.220	1.546
Caffeine	5.45	273	–	0.614	2.506	273	–	0.451	2.989
Syringic acid	6.43	217	274	0.442	1.647	217	274	0.912	5.919
EGCg	6.73	274	–	1.055	3.532	274	–	0.734	2.982
EC	7.31	279	–	2.196	6.782	279	–	3.103	15.093
GCg	8.08	274	–	0.999	2.772	274	–	1.889	8.828
Scopoletin	8.54	228	344	0.137	0.714	228	345	0.168	1.153
Ferulic acid	9.09	235	323	0.151	0.684	236	323	0.633	1.128
ECg	9.46	278	–	0.890	2.297	278	–	1.191	5.098
Cg	10.17	279	–	1.004	2.427	278	–	18.880	7.391
o-Coumaric acid	11.39	277	325	0.216	0.776	277	325	1.154	1.501
Rutin	12.05	256	355	0.318	1.479	256	354	0.930	2.181
4-OH-Coumarin	12.24	281	303	0.588	1.072	281	303	6.485	2.688
Myricetin	12.89	252	373	0.730	1.167	252	371	1.378	1.972
Quercitrin	13.46	256	350	0.274	1.137	256	351	0.327	2.027
6-Me-coumarin	13.70	279	323	0.475	1.286	279	323	0.650	2.859
Cinnamic acid	14.42	217	278	0.346	0.859	217	278	0.622	2.661
Quercetin	15.58	255	370	0.451	1.142	255	370	0.388	1.977
Naringenin	15.96	213	290	0.747	1.603	213	290	0.934	4.070
Luteolin	16.56	254	250	0.223	0.924	254	351	0.231	1.525
Hesperetin	17.09	288	–	0.775	1.572	288	–	0.874	3.808
Kaempferol	18.16	265	365	0.269	1.273	265	366	0.315	2.118

Table 4
Validation results for intra- and inter-day precision.

Method precision [% RSD]							
Component	Concentration level [mg L^{-1}]	Level 1		Level 2		Level 3	
		Intra-day	Inter-day	Intra-day	Inter-day	Intra-day	Inter-day
Gallic acid	25, 50, 100	0.05	2.30	0.11	1.31	0.07	0.63
GC	25, 50, 100	0.08	0.93	0.18	0.59	0.15	0.73
Protocatechuic acid	5, 25, 50	0.42	1.53	0.14	1.31	0.23	1.52
Esculin	5, 25, 50	0.38	0.80	0.31	2.80	0.07	0.26
EGC	25, 50, 100	0.26	1.29	0.28	0.59	1.93	2.14
C	5, 25,50	0.36	0.69	0.86	1.37	0.20	1.94
Chlorogenic acid	1, 5, 25	1.09	8.32	0.45	2.83	0.30	1.37
Vanillic acid	5, 25, 50	0.45	2.68	0.15	2.43	0.04	0.28
Caffeic acid	5, 25, 50	0.20	1.71	0.14	1.15	0.16	1.44
Caffeine	25, 50, 100	0.05	0.39	0.06	0.34	0.02	0.39
Syringic acid	1, 25, 50	0.24	3.51	0.21	2.14	0.10	2.39
EGCg	25, 50, 100	0.10	0.63	0.13	0.70	0.09	0.52
EC	25, 50, 100	0.08	0.67	0.06	0.16	0.04	0.21
GCg	5, 25, 50	0.22	4.88	0.35	3.26	0.28	0.57
Scopoletin	5, 25, 50	0.09	3.33	0.09	2.34	0.10	0.51
Ferulic acid	5, 25, 50	0.19	1.29	0.24	0.93	0.10	1.28
ECg	25, 50, 100	0.08	0.42	0.03	0.28	0.04	0.09
Cg	5, 25, 50	0.17	0.84	0.16	2.15	0.24	1.90
o-Coumaric acid	5, 25, 50	1.31	2.28	0.19	1.49	0.04	1.43
Rutin	25, 50, 100	0.10	0.64	0.07	0.51	0.04	0.47
4-OH-Coumarin	5, 25, 50	0.06	1.51	0.20	1.84	0.25	1.91
Myricetin	1, 25, 50	1.10	5.61	0.25	3.27	0.10	2.37
Quercitrin	1, 25, 50	0.70	3.79	0.37	2.78	0.13	2.04
6-Me-coumarin	5, 25, 50	0.18	2.38	0.16	2.13	0.14	0.48
Cinnamic acid	5, 25, 50	0.16	2.66	0.14	2.38	0.04	0.59
Quercetin	5, 25, 50	0.20	5.87	0.27	4.15	0.10	1.60
Naringenin	1, 25, 50	2.23	3.86	0.11	1.75	0.20	1.97
Luteolin	5, 25, 50	0.27	4.28	0.22	3.79	0.25	1.24
Hesperetin	5, 25, 50	0.12	2.92	0.15	2.63	0.17	0.53
Kaempferol	5, 25, 50	0.21	4.44	0.21	3.82	0.13	1.46

Table 5
Validation results for intra- and inter-day accuracy.

Method accuracy [% of recovery]							
Component	Concentration level [mg L^{-1}]	Level 1		Level 2		Level 3	
		Intra-day	Inter-day	Intra-day	Inter-day	Intra-day	Inter-day
Gallic acid	25, 50, 100	106.11	107.40	112.50	113.10	110.28	111.39
GC	25, 50, 100	100.03	96.84	99.74	98.19	94.38	93.39
Protocatechuic acid	5, 25, 50	93.50	89.17	96.66	93.10	100.03	96.94
Esculin	5, 25, 50	91.11	90.49	101.45	97.42	99.90	100.84
EGC	25, 50, 100	76.89	76.15	92.98	91.82	97.47	96.77
C	5, 25,50	98.72	88.61	97.50	92.70	99.66	96.06
Chlorogenic acid	1, 5, 25	100.67	105.16	95.10	92.15	102.31	104.45
Vanillic acid	5, 25, 50	95.92	93.65	101.36	97.77	100.84	101.29
Caffeic acid	5, 25, 50	92.27	89.01	96.86	92.65	101.62	97.29
Caffeine	25, 50, 100	82.96	82.63	94.35	94.14	95.38	96.77
Syringic acid	1, 25, 50	94.81	93.46	101.85	94.30	100.77	97.84
EGCg	25, 50, 100	87.45	86.54	99.73	99.54	101.14	101.54
EC	25, 50, 100	96.24	95.51	101.06	101.38	95.31	95.00
GCg	5, 25, 50	97.96	92.63	99.12	99.42	105.52	106.87
Scopoletin	5, 25, 50	100.73	97.58	98.85	101.36	101.01	102.17
Ferulic acid	5, 25, 50	96.76	92.00	102.34	96.17	100.28	103.47
ECg	25, 50, 100	99.71	99.56	105.10	105.15	100.68	100.89
Cg	5, 25, 50	100.25	102.13	102.01	96.70	98.53	99.96
o-Coumaric acid	5, 25, 50	93.76	88.05	102.79	96.29	100.50	103.70
Rutin	25, 50, 100	101.11	101.90	104.10	104.75	99.92	100.48
4-OH-Coumarin	5, 25, 50	94.97	89.81	97.36	92.50	100.82	96.17
Myricetin	1, 25, 50	99.82	103.46	103.26	95.38	103.94	107.99
Quercitrin	1, 25, 50	100.20	100.22	103.08	96.06	99.59	99.86
6-Me-coumarin	5, 25, 50	97.39	95.45	102.10	98.89	102.45	102.85
Cinnamic acid	5, 25, 50	97.36	95.26	99.51	102.55	102.55	103.08
Quercetin	5, 25, 50	96.37	92.97	96.94	98.52	106.15	106.88
Naringenin	1, 25, 50	95.12	93.78	95.82	90.22	99.55	94.42
Luteolin	5, 25, 50	96.35	93.64	97.32	101.62	103.13	103.96
Hesperetin	5, 25, 50	97.66	94.97	102.79	98.51	102.42	103.08
Kaempferol	5, 25, 50	97.06	93.99	97.89	102.36	103.79	105.04

(LUT), hesperetin (HES), kaempferol (KAEM); coumarins: aesculin (AES), scopoletin (SCOP), 4-hydroxycoumarin (4OH-COUM), 6-methylcoumarin (6M-COUM) and caffeine (CAFF).

The non-fermented teas Kokaicha and Formosa Gunpowder, the fermented teas Pu-Erh and Nepal SFTGFOP-Maloom, the mixture of non-fermented and fermented tea leaves "Festival", the fruit teas "Messina" and "Cinnamon-Apple" were all obtained from OXALIS (Slušovice, Czech Republic). The non-fermented Vietnam tea with jasmine was purchased from a specialized tea shop. The green tea extracts "GT ex. p." (min. 80% catechins, max 8% caffeine) and "Ethyl Acetate Free Green Tea extract" (80% catechins/50% EGCg) were obtained from PORTA s.r.o (Prague, Czech Republic).

The mobile phase additive formic acid 98% p.a. as well as HPLC grade methanol and acetonitrile were obtained from Sigma–Aldrich. HPLC grade water, prepared by Milli-Q reverse osmosis Millipore (Bedford, MA, USA), was additionally filtrated through a 0.22 μm membrane filter immediately before use.

2.2. Instrumentation

Acquity UPLC system (Waters, Prague, Czech Republic) consisted of Acquity binary solvent manager (BSM), Acquity sample manager (SM), Acquity column manager and Acquity PDA detector. All UPLC analyses were performed on a BEH C18 analytical column (100 mm × 2.1 mm, 1.7 μm, Waters, Czech Republic).

The mobile phase consisted of 0.1% formic acid (solvent A) and methanol (solvent B). The following gradient program was employed: 0–4 min isocratic elution (88.5% A:11.5% B) and 4–20 min linear gradient elution from 88.5% A:11.5% B to 50% A:50% B. The initial flow rate 0.45 mL min^{-1} was reduced to 0.42 mL min^{-1} in the time interval from 4.1 to 20 min. Column oven temperature

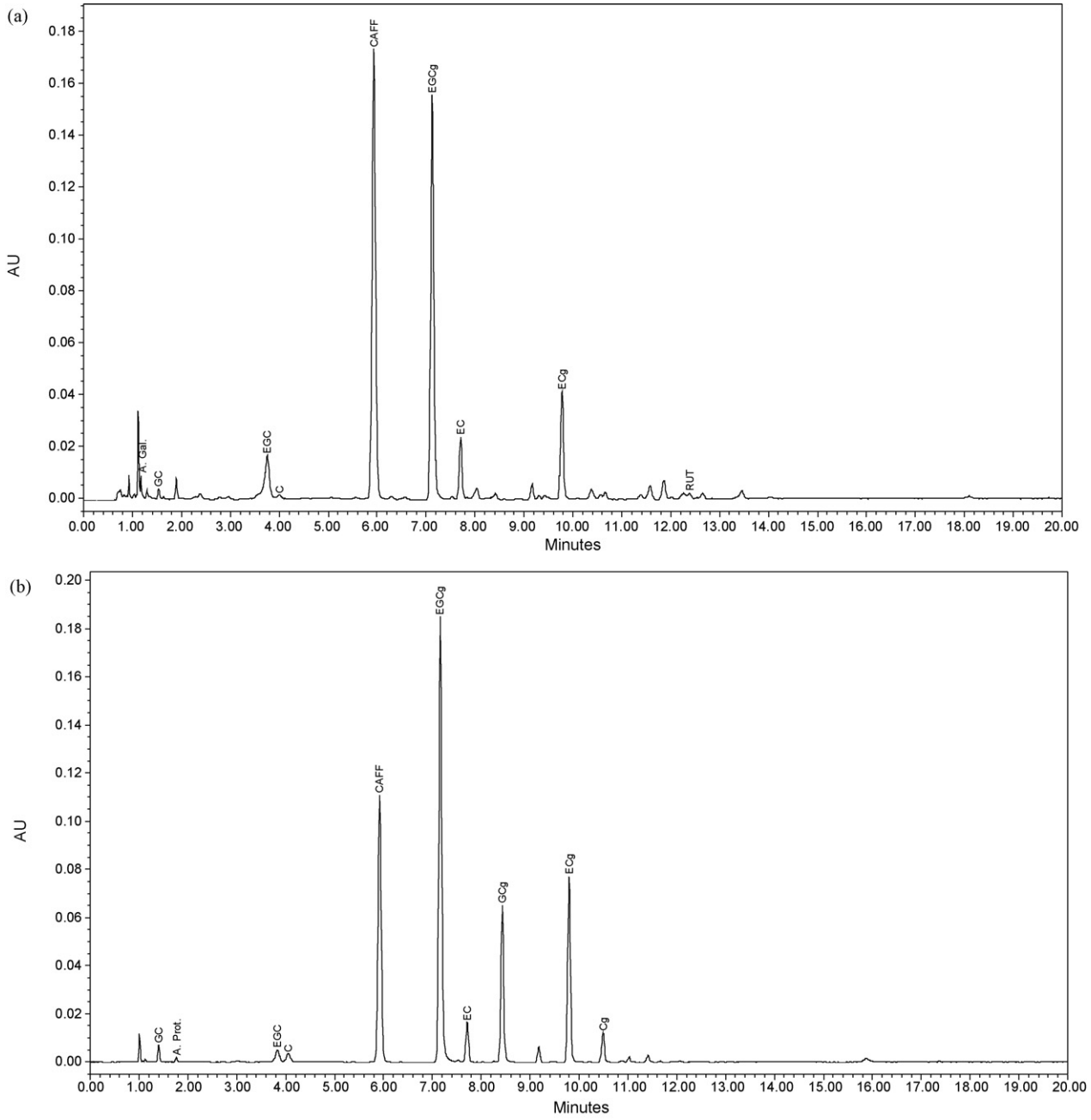


Fig. 3. Chromatograms of Kokaicha (water infusion) (a) and GT ex. p. extract (b).

was set up to 25 °C and the samples were kept at 4 °C in the sample manager. The partial loop injection mode with needle overfill injected a volume of 2.0 μL using 5 μL injection loop. Methanol was used as a strong wash solvent and 20% methanol as a weak wash solvent. The PDA detection was conducted at 280 nm for quantitative purposes with data acquisition rate of 20 Hz. Spectral data and peak purity calculation were used for identity confirmation. Chromatographic software Empower 2 was used for gathering data and processing of the chromatograms. This software enables a calculation of peak purity and operation with spectral data. Two UV absorbance maxima (if available) were used for identity confirmation of all analytes. Peak purity calculations uses two variables – peak purity angle and peak purity threshold. The criteria of peak purity are fulfilled when peak purity angle value is lower than the value of peak purity threshold.

2.3. Stock solutions and tea samples pre-treatment

The *stock solutions* of phenolic acids, flavonoids, catechins, coumarins and caffeine were prepared in methanol at the concentrations ranging from 1 to 5 g L^{-1}, keeping approximately equimolar ratios. All 30 stock solutions were combined into one mixed working solution and further diluted by mobile phase.

The *tea infusions* were prepared by pouring 100 mL of hot water (90 °C) over 1 g of dry tea mixture and 5 min of maceration with mild stirring. Then the cooled down tea infusion was filtrated through 0.20 μm membrane filter and further 2.5 times diluted by the mobile phase. The diluted tea infusions were used for injections immediately.

The *methanolic tea extracts* were prepared by pouring 50 mL of methanol over 1 g of tea mixture and sonication for 20 min. The following steps were the same as in the case of water infusion; the solutions were filtrated and stabilized by low pH of the mobile phase.

The *tea extract samples* prepared from commercially available powder extracts were diluted by methanol, filtrated and further diluted by the mobile phase prior to analysis. Fresh samples prepared daily were used for the analysis.

2.4. System suitability test and validation

A mixed standard solution of all phenolic compounds at the concentration corresponding to the middle of the calibration range was injected in ten replicates for the system suitability test (SST) measurements. Evaluated parameters were the mean values of resolution, asymmetry factor and peak capacity. The repeatability of retention time and peak area expressed as %RSD were checked and they should meet the requirement of RSD < 1%. The rules for measurement and the limits for the acceptance are given by official pharmacopoeias [41,42].

Determined validation parameters were following: range, linearity, LOD, LOQ, precision, accuracy and selectivity. Linearity was established using mixed standard solutions at seven calibration levels for each compound. Method precision was tested at three concentration levels in three replicates using tea samples to calculate RSD of the determination, which describes the closeness of agreement between series of measurements. Tea samples spiked with standard solution at three concentration levels were used for determination of method accuracy and recovery. Spiked samples were run in three replicates and agreement between theoretical and measured value was confronted with appropriate guidelines [43]. Both accuracy and precision were determined as intra-day and inter-day measurements (measurements were performed on three different days). Method selectivity was confirmed by calculation of peak purity and spectral data. Peak purity was calculated using two variables (calculated by software) – peak purity angle and peak purity threshold. The value of peak purity angle must be lower than the value of peak purity threshold. Formosa gunpowder tea was used as tea matrix for precision and accuracy experiments.

3. Results and discussion

3.1. Method development

The different portions of organic modifier present in mobile phase were tested in order to achieve optimal separation. The key issue was to achieve separation between peaks of chlorogenic, vanillic and caffeic acid, due to very similar retention properties. A sufficient separation was obtained eluting 0.1% formic acid and methanol isocratically in the ratio 88.5:11.5 (v/v) for 4 min. Consequently gradient curves of convex and concave profile and several target ratios were tested in order to achieve satisfactory separation of later eluted analytes. The final gradient profile with the target ratio 50:50 (v/v) enabled quick elution of relatively low polar flavonoid aglycons. A less steep gradient profile prolonged the analysis and undesirably affected symmetry of late eluting peaks. Finally the slightly convex gradient curve was performed to optimize the resolution.

The choice of wash liquids and standard/sample dissolution media is of special importance in UHPLC. Concerning wash liquids – weak wash solvent participate on injection procedure, therefore

Table 6
Quantification of tea components in water infusions (mg g^{-1} of dry tea mixture).

	Kokaicha	Vietnam tea with jasmine	Formosa gunpowder	Nepal-Maloom	Pu-Erh	Festival	Messina	Cinnamon-apple
Gallic acid	0.39	0.49	1.05	2.21	3.18	0.94	0.13	0.12
GC	2.53	3.08	3.66	LOD	0.80	LOD	–	–
Protocatechuic acid	–	–	0.18	0.11	–	LOD	0.10	–
EGC	33.82	35.04	37.05	24.71	–	4.88	–	–
C	0.75	1.12	1.69	0.40	–	1.25	–	–
Chlorogenic acid	–	–	0.93	–	–	–	2.20	0.84
Vanillic acid	–	0.47	–	–	–	–	–	–
Caffeic acid	–	–	–	0.05	–	–	–	0.05
Caffeine	14.18	20.72	19.73	24.39	16.04	6.90	–	–
EGCg	22.82	25.90	33.42	12.87	–	4.63	–	–
EC	6.30	5.81	5.94	1.04	0.39	1.25	–	–
GCg	–	0.99	1.02	0.83	–	LOD	–	–
Ferulic acid	–	–	–	0.17	–	0.08	–	–
ECg	4.84	6.21	9.65	5.02	–	1.84	–	–
Cg	–	0.92	0.92	–	–	LOD	–	–
Rutin	1.31	1.15	2.22	0.67	–	–	1.21	0.68
Quercitrin	–	0.49	1.13	0.54	–	–	–	–
Total catechins	71.07	79.06	93.33	45.82	1.19	13.85	0.70	–

Table 7
Quantification of tea components in methanolic tea extracts and in commercial dried tea extracts (mg g^{-1} of dry tea mixture/powder).

	Kokaicha	Vietnam tea with jasmine	Formosa gunpowder	Nepal-Maloom	Pu-Erh	Festival	Messina	Cinnamon-Apple	GT ex. p.	Ethyl acetate free GT extr.
Gallic acid	0.09	0.07	1.85	0.81	0.58	0.97	0.06	0.07	5.57	2.97
GC	0.59	0.92	2.42	LOD	–	0.79	–	–	56.64	13.61
Protocatechuic acid	0.05	–	0.14	–	–	–	0.06	–	–	–
EGC	5.67	7.22	15.13	4.37	–	8.02	–	–	107.67	84.71
C	0.22	0.41	1.27	0.14	–	0.39	–	–	19.63	6.63
Chlorogenic acid	–	–	0.48	–	–	–	0.97	0.30	–	–
Vanillic acid	–	–	–	–	–	–	–	–	–	–
Caffeic acid	–	–	0.04	–	–	0.02	–	–	–	–
Caffeine	3.64	8.01	18.33	13.32	–	13.35	–	–	107.87	49.40
EGCg	7.08	11.90	37.88	13.00	–	14.41	–	–	337.02	524.57
EC	1.53	2.05	5.49	–	–	2.52	–	–	51.47	32.85
GCg	–	0.48	0.69	–	–	0.56	–	–	106.65	26.7
Ferulic acid	–	–	–	–	–	0.09	–	–	–	–
ECg	2.02	3.53	13.27	4.76	–	4.94	–	–	101.57	116.38
Cg	–	0.47	0.52	–	–	0.50	–		23.32	9.86
Rutin	0.40	0.40	1.19	–	–	0.66	1.60	0.42	–	–
Quercitrin	–	–	0.94	0.24	–	–	–	–	–	–
Total catechins	17.11	26.99	76.66	22.27	0	32.12	–	0	803.98	815.31

it was necessary to use one corresponding to initial gradient conditions (20% methanol). The same applied to dissolution media as using narrow diameter columns the choice of dissolution solvent can influence chromatographic separation significantly more than in conventional HPLC analysis.

3.2. System suitability test and validation

SST parameters including resolution – R_s, peak asymmetry, repeatability of retention time and peak area were measured for all 30 compounds. The values of the resolution were in the range specified by pharmacopoeias (>1.5) corresponding to baseline separation, except of the values for the three pairs of substances (EGC and C, chlorogenic and vanillic acid, quercitrin and 6-methylcoumarin, where R_s was around 1.3). The asymmetry factor values varied between 0.84–1.17 fully meeting the criteria for symmetric peaks (0.8–1.5) according to EP [41]. The average peak capacity was 67.7, which is fully acceptable by general recommendations.

RSD for the retention time ranged from 0.09 to 0.52% and for the peak area from 0.17 to 0.91%, respectively. This is again in agreement with the requirements of EP [41]. Details of SST results are given in Table 2 and a typical chromatogram of standard mixture separation is shown in Fig. 2. The developed gradient method met all claims obligatory for SST.

To demonstrate method selectivity, spectral data were acquired and peak purity was calculated – data are displayed in Table 3. Two UV maximum absorbance wavelengths (if available) were compared in measurement of standard mixture and real sample. UV spectra matched for all maximum absorbance wavelengths ± 1 nm. These criteria for the peak purity were met for all 30 compounds in standard mixture, however only for 28 compounds in spiked real tea sample in spite of seeming agreement in UV spectra. Thus it could be concluded, that peak of Cg and 4-hydroxymethylcoumarin probably co-eluted with some interfering compound from matrix and quantitative results will not be reliable.

The calibration curves were measured using mixed standard solutions in a wide concentration range, typically from 1 to 100 mg L^{-1}, details are given in Table 2. The response was linear in tested range with correlation coefficients >0.9990 for all analytes. The last point of calibration curve was considered to be method LOQ (S/N = 10). LOD were calculated by extrapolation (S/N = 3). Typical LOD and LOQ were 0.06 mg L^{-1} or 0.2 mg L^{-1} respectively. Intra-day method precision for all thirty compounds expressed as RSD was less than 3%, while inter-day precision was less than 9%, the results are displayed in Table 4. Intra-day method accuracy expressed as recovery was within the range 77–110%, while inter-day method accuracy within 76–111% with typical values 100 ± 10%. The results are shown in Table 5.

3.3. Quantification of tea samples and extracts

In fact a cup of tea is a simple water infusion. Hence we used the extraction by hot water to study concentrations of polyphenolic tea components available for common tea consumers. Results achieved using the hot water extraction were compared to those achieved by sonication in cold methanol. Although compared to water methanol is theoretically more preferable solvent for polyphenols, the extraction by methanol appeared to be less efficient in case of non-fermented teas than the hot water infusion. Typical chromatogram is given in Fig. 3a. Results of the tea samples quantification can be seen in Tables 6 and 7. The indicated numbers represent the milligram content of tea components in 1 g of dry tea mixture. Excellent sensitivity of proposed UHPLC method allowed quantification of phenolic compounds present even in trace concentrations such as C, Cg, GCg, protocatechuic acid or rutin however, the care must be taken with each sample to verify its selectivity using peak purity calculation and spectral data.

According to the expectations, high content of catechins was found in non-fermented teas, typically ranging from 7 to 9% (w/w). The highest total quantity of catechins at all was found in Formosa gunpowder (93 mg g^{-1}), while very similar quantities were reported by Wang et al. in gunpowder tea [18]. Content of caffeine in the non-fermented teas was around 2% (w/w). Apart from catechins and caffeine also other phenolic compounds were quantified in tea samples. Phenolic acids (gallic, chlorogenic, protocatechuic, vanillic, caffeic and ferulic acid) were present at concentrations around 1 mg g^{-1}. Myricetin, quercetin and kaempferol-3-glycosides were also previously reported in tea infusions [44], although only quercitrin and rutin were found in our samples in detectable concentration. The fermented teas and fruit mixtures contained much lower quantities of monitored phenolic compounds.

The commercially available green tea extracts were tested in order to verify correct quantification of phenolic compounds by UHPLC – see Fig. 3b. Determined quantities were compared to the quantity guaranteed by the producer (>80%) and good agreement between both values was found (Table 7).

4. Conclusions

A newly developed UHPLC method with PDA detection enables simultaneous determination of 29 commonly occurring phenolic compounds and caffeine in tea matrices within only 20 min.

Apart from catechins (the most common antioxidant phenolic compounds abundant in tea and many other plant materials) also other natural phenolic compounds from groups of flavonoids, phenolic acids and coumarins were chosen in order to extend the utilization of this method to a number of various applications. High separation efficiency predestines this analytical method to be, e.g. useful screening tool in pharmaceutical botany or fingerprinting for the quality control of tea and tea extracts. The system suitability test and validation parameters were meeting requirements for all thirty compounds and thus the method was convenient for use in the quantitative analysis. Method selectivity was enhanced using spectral data from PDA detector and peak purity information. Furthermore it is important to highlight the minimal consumption of time and solvents when UHPLC is used contrary to conventional HPLC methods.

Acknowledgements

The authors gratefully acknowledge the financial support of the Czech Ministry of Education, project *MSM 0021620822* and *GAUK No 119308/B/2008*.

References

[1] N. Getoff, Radiat. Phys. Chem. 76 (2007) 1577.
[2] Z. Yang, Y. Tu, H. Xia, G. Jie, X. Chen, P. He, Food Chem. 105 (2007) 1349.
[3] F.L. Muller, M.S. Lustgarten, Y. Jang, Free Radic. Biol. Med. 43 (2007) 477.
[4] M. Valko, D. Leibfritz, J. Moncola, M.T.D. Cronin, M. Mazura, J. Telser, Int. J. Biochem. Cell Biol. 39 (2007) 44.
[5] E. d Rijke, P. Out, W.M.A. Niessen, F. Arbese, C. Gooijer, U.A.T. Brinkman, J. Chromatogr. A 1112 (2006) 31.
[6] J. Brunton, Pharmacognosy, Phytochemistry, Medicinal Plants, 2nd edition, Lavoisier, 1999, pp. 240, 309, 369.
[7] F. Ververidis, E. Trantas, C. Douglas, G. Vollmer, G. Kretzschmar, N. Panopoulos, Biotechnol. J. 2 (2007) 1214.
[8] A.K. Atoui, A. Mansouri, G. Boskou, P. Kefalas, Food Chem. 89 (2005) 27.
[9] R. Torres, F. Faini, B. Modak, F. Urbina, C. Labbe, J. Guerrero, Phytochemistry 67 (2006) 984.
[10] B. Girennavar, G.K. Jayaprakasha, Y. Jadegoud, G.A.N. Gowda, B.S. Patil, Bioorg. Med. Chem. 15 (2007) 3684.
[11] W.T. Chang, Z.H. Shao, J.J. Yin, S. Mehendale, C.Z. Wang, Y. Qin, J. Li, W.J. Chen, C.T. Chien, L.B. Becker, T.L. Vanden Hoek, C.S. Yuan, Eur. J. Pharmacol. 566 (2007) 58.
[12] M.E. Harbowy, D.A. Balentine, Crit. Rev. Plant. Sci. 16 (1997) 415.
[13] A. Wilson, M.N. Clifford, Tea: Cultivation to Consumption, Chapman & Hall, London, 1992, p. 555.
[14] Y. Liang, W. Ma, J. Lu, Y. Wu, Food Chem. 75 (2001) 339.
[15] C. Hu, D.D. Kitts, Mol. Cell. Biochem. 218 (2001) 147.
[16] Y. Liang, J. Lu, L. Zhang, S. Wu, Y. Wu, Food Chem. 80 (2003) 283.
[17] K. Pyrzynska, M. Biesaga, Trends Anal. Chem. 28 (2009) 893.
[18] H. Wang, G.J. Provan, K. Helliwell, Food Chem. 81 (2003) 307.
[19] A.P. Neilson, R.J. Green, K.V. Wood, M.G. Ferruzzi, J. Chromatogr. A 1132 (2006) 132.
[20] X.R. Yang, C.X. Ye, J.K. Xu, Y.M. Jiang, Food Chem. 100 (2007) 1132.
[21] L. Yao, Y. Jiang, N. Datta, R. Singanusong, X. Liu, J. Duan, K. Raymont, A. Lisle, Y. Xu, Food Chem. 84 (2004) 253.
[22] X. Zhu, B. Chen, M. Ma, X. Luo, F. Zhang, S. Yao, Z. Wan, D. Yang, H. Hang, J. Pharm. Biomed. Anal. 34 (2004) 695.
[23] Y. Zuo, H. Chen, Y. Deng, Talanta 57 (2002) 307.
[24] M. Pelillo, M. Bonoli, B. Biguzzi, A. Bendini, T. Gallina Toschi, G. Lercker, Food Chem. 87 (2004) 465.
[25] M.L. dL Francisco, A.V.A. Resurreccion, Food. Chem. 117 (2009) 356.
[26] D. Guillarme, D.T.T. Nguyen, S. Rudaz, J.L. Veuthey, J. Chromatogr. A 1149 (2007) 20.
[27] D.T.-T. Nguyen, D. Guillarme, S. Rudaz, J.L. Veuthey, J. Chromatogr. A 1128 (2006) 105.
[28] S.A.C. Wren, P. Tchelitcheff, J. Chromatogr. A 1119 (2006) 140.
[29] H. Yuan, F. Wang, J. Tu, W. Peng, H. Li, J. Pharm. Biomed. Anal. 46 (2008) 808.
[30] M.C.Y. Wong, W.T.K. Lee, J.S.Y. Wong, G. Frost, J. Lodge, J. Chromatogr. B 871 (2008) 341.
[31] R.A. Everley, T.R. Croley, J. Chromatogr. A 1192 (2008) 239.
[32] G. Gervais, S. Brosillon, A. Laplanche, C. Helen, J. Chromatogr. A 1202 (2008) 163.
[33] J. Gruz, O. Novak, M. Strnad, Food Chem. 111 (2008) 789.
[34] B. Klejdus, J. Vacek, L. Lojková, L. Benešová, V. Kubáň, J. Chromatogr. A 1195 (2008) 52.
[35] X.J. Chen, H. Ji, Q.W. Zhang, P.F. Tu, Y.T. Wang, B.L. Guo, S.P. Li, J. Pharm. Biomed. Anal. 46 (2008) 226.
[36] Y. Deng, G. Gao, S. Zheng, F. Li, J. Pharm. Biomed. Anal. 48 (2008) 562.
[37] Y. Wang, Y. Yao, R. An, L. You, X. Wang, J. Chromatogr. B 877 (2009) 1820.
[38] N. Kumar, P. Bhandari, B. Singh, S.S. Bari, Food Chem. Toxicol. 47 (2009) 361.
[39] Z. Spáčil, L. Nováková, P. Solich, Talanta 76 (2008) 189.
[40] C.L. Brownlee, Mod. Drug Discov. (2002) 39.
[41] European Pharmacopoeia, 6th edition (Ph. Eur. 6), Council of Europe, Strasbourg, 2007.
[42] United States Pharmacopoeia 33, United States Pharmacopoeial Convention, Rockville, MD, 2009.
[43] International Conference on Harmonization (ICH). Q2 (R1): Text on Validation of Analytical Procedures, US FDA Federal Register, 2005.
[44] G.J. Volikakis, C.E. Efstathiou, Anal. Chim. Acta 551 (2005) 124.

Talanta 80 (2010) 1980–1985

Contents lists available at ScienceDirect

Talanta

journal homepage: www.elsevier.com/locate/talanta

Evaluating use of ferricyanide-mediated respiration bioassays to quantify stimulatory and inhibitory effects on *Escherichia coli* populations

Kylie Catterall[a,b], David Robertson[c], Peter R. Teasdale[c,*], David T. Welsh[c], Richard John[b]

[a] Gold Coast Water, PO Box 5042, Gold Coast Mail Centre, QLD 9729, Australia
[b] School of Environment, Griffith University Gold Coast Campus, QLD 4222, Australia
[c] Australian Rivers Institute, Griffith University, QLD 4222, Australia

ARTICLE INFO

Article history:
Received 9 September 2009
Received in revised form 21 October 2009
Accepted 23 October 2009
Available online 31 October 2009

Keywords:
Microbial assay
Biochemical oxygen demand
Toxicity
Wastewater

ABSTRACT

A number of recent studies have utilised ferricyanide as a respiratory mediator for microbial-based assays for determining water quality parameters such as biochemical oxygen demand (BOD) and toxicity. The majority of assays published to date obtain a result by determining the difference in ferrocyanide accumulation between a test sample and one or more control samples. However, a validation of the relationship between ferrocyanide accumulation and standard measures of cell density or viability has not yet been performed. To this end, a rapid microbially catalysed ferricyanide-mediated respiration (FM-RES) assay was compared with standard plate count (SPC) and spectrophotometer (OD_{600}) measurements on a growing batch culture of *Escherichia coli*. Good agreement was observed between all techniques, with predictable deviations noted in different phases of the growth curves. Standardised FM-RES assays showed excellent correlations with the SPC method under controlled conditions, indicating that short-term changes in microbial activity are due to a change in per-cell respiration, rather than changes in cell numbers. The FM-RES assay was then used to observe the changes in the respiration of *E. coli* induced by the addition of a glucose–glutamic acid (GGA) mixture, 3,5-dichlorophenol (3,5-DCP) and Ag^+ in various combinations and concentrations. Stimulation of respiration was pronounced in the presence of GGA while both 3,5-DCP and, in particular, Ag^+ demonstrated inhibitory respiratory effects. The results highlight the validity and suitability of ferricyanide-mediated respiration bioassays, with appropriate modification, to monitor either stimulatory effects on microbial populations, such as occurs with BOD, or inhibitory effects, such as occurs with toxicity assays.

Crown Copyright © 2009 Published by Elsevier B.V. All rights reserved.

1. Introduction

The accurate quantification of microbial populations or microbial respiration is important for the monitoring of water and food supplies, determining the effectiveness of wastewater treatment and for use in rapid microbial-based bioassays. However, due to their microscopic size and large population, direct quantification of the viable micro-organism population in a sample can be difficult and time-consuming. This is especially the case for techniques that involve directly counting bacteria, either via staining or culturing. These include the 4′-6-diamidino-2-phenylindole (DAPI) staining method [1], the standard membrane filtration method and the spread plate count (SPC) methods [2]. Additionally, assays relying on culturing bacteria require suitable growth media upon which the target bacteria are capable of growing rapidly enough in the incubation time to produce a measurable response.

The utility of micro-organisms for a range of rapid bioassays has long been recognised and a variety of techniques that aim to enumerate [3–5] or quantify the activity of [6–8] the microbial population in a sample have been developed. Many of these microbial assays attempt to indirectly measure changes in the activity of a microbial population by quantifying changes to the activity of the micro-organism's electron transport system (ETS), either instantaneously or over a time period. This is useful as the ETS is intrinsically linked to the essential cellular functions of metabolism and respiration and therefore represents an index of the overall integrity of cellular components and functions. Examples of such assays include the quantification of bioluminescence in the Microtox assay [7,9], measurement of respiration inhibition in the OECD 209 activated sludge test [10] or the accumulation of ferrocyanide in rapid, ferricyanide-mediated BOD assays [6,11].

Abbreviations: APHA, American Public Health Association; BOD, biochemical oxygen demand; CFU, colony forming units; ETS, electron transport system; FM-BOD, ferricyanide-mediated biochemical oxygen demand; FM-RES, ferricyanide-mediated respiration; GGA, glucose–glutamic acid; OECD, Organisation for Economic Co-operation and Development; PB, phosphate buffer; SPC, standard plate count.

* Corresponding author.
E-mail address: p.teasdale@griffith.edu.au (P.R. Teasdale).

0039-9140/$ – see front matter. Crown Copyright © 2009 Published by Elsevier B.V. All rights reserved.
doi:10.1016/j.talanta.2009.10.057

Ferricyanide has been used as a redox mediator for studying cellular processes for a considerable time [12], but only recently has research interest into the use of ferricyanide-mediated (FM) microbial reactions focused on rapid analytical bioassays [13–15] or biosensors [11]. Ferricyanide is approximately five orders of magnitude more soluble than oxygen in water and can be used as an alternative terminal electron acceptor by a range of bacterial species, including the commonly studied *Escherichia coli* [6]. This enables the use of high microbial populations in small sample volumes without the electron acceptor limiting the rate of respiration, in turn reducing the incubation time required to achieve a measurable response. An example of this FM approach has been in the development of rapid BOD assays. There are several advantages of this approach over the conventional BOD_5 method, which have been discussed in more detail elsewhere [6]. In short, the FM-BOD assay can be completed in hours rather than days, has a greater linear range and measures the accumulation of the reduced respiration product, ferrocyanide, from a zero background [13]. Minor modification of the assay to quantify the inhibition of FM respiration due to toxicity has also been the subject of several recent studies [16–18].

A number of bacterial species, including *E. coli*, *Pseudomonas putida* and mixed consortia have been investigated as biocatalysts in the FM assays [11,19]. The most recently published versions of the FM-BOD technique have incubation times of 1–4 h [6,20], though some FM biosensors utilising immobilised cells have shorter incubation times [21]. A single FM incubation cannot differentiate changes in overall activity due to individual cell growth, net population size, metabolic activity or substrate availability. However, controlling parameters such as incubation time and the choice of biocatalyst can facilitate investigation into degradation efficiencies of various compounds and provide more insight into the processes occurring during the incubation [19].

All of these studies have assumed that the measured production of ferrocyanide is quantitatively related to cell growth and/or cell activity. In support of this assumption, Morris et al. [13] described the relationship between microbial density and ferrocyanide production, through a dilution process of a homogeneous bacterial culture. However, the ability of an FM bioassay to sensitively monitor changes in a dynamic microbial population has not yet been validated. This study aims to explore the relationship between respiration, as measured by the production of ferrocyanide by a bacterial culture, and quantification by two common, widely used bacterial enumeration methods. The utility of the assay for sensitively describing changes in the activity of bacterial populations will be demonstrated with an example of stimulatory and inhibitory responses to various mixtures of a GGA solution with either 3,5-dichlorophenol (3,5-DCP) or silver ions.

2. Methods

2.1. Bacterial cultures

E. coli K12 was obtained from the University of New South Wales Culture Collection. Cultures were maintained on nutrient agar plates (Oxoid) and re-plated regularly to ensure viability. A 1.5 L solution of autoclaved tryptone soy broth (Gibco) was inoculated with a colony of *E. coli* and grown aerobically at 37 °C for 16–18 h on an orbital shaker.

2.2. Microbial culture growth experiment

At the desired sampling times (either 30 or 60 min intervals), a representative 10 mL subsample was withdrawn from the 1.5 L broth culture and divided into three sub-samples. Each of the sub-samples was analysed concurrently using spectrophotometric analysis of the optical density, the standard spread plate count method and the ferricyanide-mediated respiration rate. For the purposes of this paper, the incubation of bacteria in the presence of ferricyanide is referred to as an FM-RES assay.

For the FM-RES assay, ferricyanide was made up to 600 mM in PB solution comprising 0.08 M K_2HPO_4/0.12 M KH_2PO_4. The ferricyanide-mediated cellular respiration technique consisted of immediately adding 100 μL of freshly prepared ferricyanide to 1 mL aliquots of the batch culture sub-sample, to give a final ferricyanide concentration of 55 mM. The sub-samples were then incubated for 15, 30 and 60 min at 37 °C, after which the biochemical reaction was terminated by centrifugation (13 200 rpm). Determination of microbially produced ferrocyanide in the supernatant was carried out by chronoamperometry using a 25 μm Pt microelectrode, as described in Morris et al. [13].

Optical density measurements of the batch culture sub-samples were taken in 1 mL quartz cuvettes at 600 nm (OD_{600}) using a Shimadzu UV-1601 UV-Vis spectrophotometer. To avoid deviations of linearity in the measurement, when the OD_{600} reached approximately 0.5, the sample was diluted with the remaining reference solution. Reference solution was prepared by centrifuging the remaining sample at 13 200 rpm and then filtering the supernatant through a 0.2 μm cellulose filter. This ensured that, as far as practically possible, the sample and the reference solution were matrix matched.

Standard plate counts were carried out as described by the APHA standard methods [2]. In brief, a serial decimal dilution series was prepared in 3% sterile peptone solution. Following dilution, duplicate 100 μL aliquots were pipetted onto sterile agar plates and spread over the surface of the agar plate using a sterile glass spreader. Following inoculation, the plates were incubated at 37 °C for 24 h and the numbers of colony forming units (CFUs) were counted. As recommended by the APHA standard methods, only dilutions producing counts between 30 and 300 CFUs were considered to be valid to be used in the calculation of population density (CFU/mL).

2.3. Standardised FM-RES and SPC test

An *E. coli* culture was prepared as described above and harvested by centrifugation (4000 rpm) in the late exponential phase of growth, as determined by a growth curve. The cells were washed twice and resuspended in a minimal amount of PB to give a concentrated suspension of cells in their endogenous state.

Serial dilutions (no dilution, 20%, 40%, 60%, 80%, 90%, 98%) of the cell solution were then prepared using PB as the diluent. These solutions were then concurrently analysed employing the SPC and FM-RES techniques described above. As the washed cells contained little exogenous organic substrate, the FM-RES method was slightly altered to supply the bacteria with a carbon source. In this case, 100 μL of the standard GGA mixture (300 mg L^{-1} each of glucose and glutamic acid, giving a BOD_5 equivalent of 396 mg L^{-1}) was added to the FM-RES matrix.

2.4. Microbial response to substrates and toxicants

Cells were harvested as described for the standardised test and resuspended in PB to an OD_{600} of 8.8. Samples were then prepared by adding 1.00 mL of cell suspension, 1.00 mL of test sample, and 0.20 mL of 600 mM potassium ferricyanide solution. Test samples comprised GGA and one of either 3,5-DCP or Ag^+. 3,5-DCP was tested at concentrations of 0, 5, 15 and 40 mg L^{-1}, Ag^+ at concentrations of 0, 2.5, 7.5 and 20 mg L^{-1} and GGA at BOD_5 equivalent concentrations of 0, 25, 100 and 400 mg L^{-1}. Test samples were prepared in a matrix format, in which each toxicant concentration was

tested against each GGA concentration. Each of the three substances was also tested alone at the concentrations described.

Samples were incubated at 37 °C for 15, after which the biochemical reaction was terminated by centrifugation. Samples were then decanted into new sample containers and analysed for ferrocyanide production as described above.

3. Results and discussion

3.1. Batch culture dynamics and effect of FM-RES duration

The growth of an *E. coli* culture was monitored over an 18 h period using three concurrent measurement techniques, the FM-RES assay, the SPC and the spectrophotometric technique. The FM-RES assay, which involves a secondary incubation in the presence of ferricyanide, was carried over three different times to identify whether time exposure to ferricyanide was a significant factor in the FM-RES assay. The net ferrocyanide production at each time point was predictably larger at longer FM-RES assay times (Fig. 1a).

The growth curves shown in Fig. 1 assist in the validation of the FM-RES technique as an indicator of microbial activity for several reasons. First, the curves depict the classic stages of bacterial culture growth, including an initial lag phase, an exponential growth phase, a brief stationary phase and the onset of death phase. Second, the average respiration rate was similar for the three FM-RES incubation times, though the rate in the 60 min incubations peaked lower and dropped more quickly after 14 h than the 15 or 30 min incubations (Fig. 1b). This indicates the respiration rate in a 60 min incubation tapers off in the last 30 min, potentially due to limitation by substrate, electron acceptor or waste product accumulation. The peak rate of ferrocyanide production was highest for 15 min FM-RES assays, which suggests that the 15 min data is the most accurate indicator of the activity of the microbial population at the time the sample is withdrawn from the batch culture. Therefore, data from the 15 min FM-RES assay was used for further comparisons in the study. Most importantly, it is clear that by quantifying cellular respiration with the FM-RES assay, discrete and sensitive changes of the microbial culture population dynamics can be rapidly and readily determined.

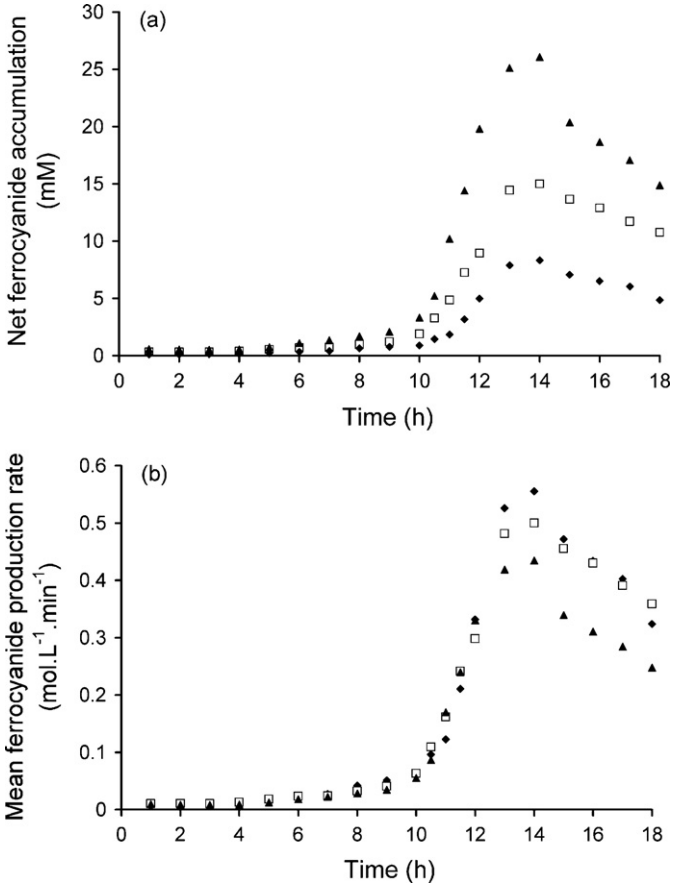


Fig. 1. *E. coli* growth curve as measured by FM-RES incubations of three different durations, 15 min (diamonds), 30 min (open squares) and 60 min (triangles). The data is presented as (a) absolute values of ferrocyanide accumulation and (b) the rate of ferrocyanide accumulation, normalised by assay time.

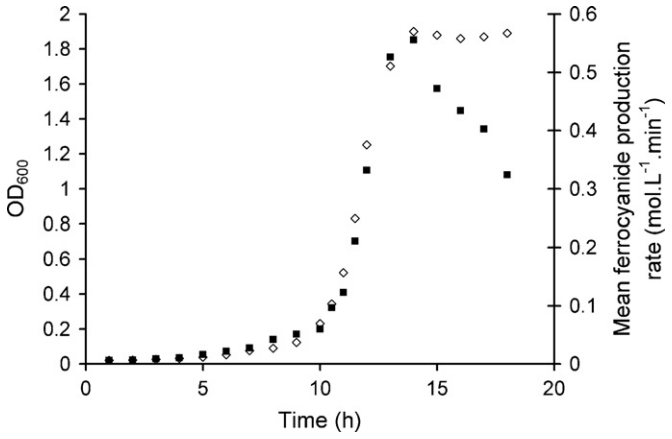


Fig. 2. Comparison of optical density (open diamonds) and FM-RES (squares) measurements across the duration of an 18 h *E. coli* batch culture.

3.2. Comparison of FM-RES, OD_{600} and SPC assays

There was generally close agreement between the spectrophotometric measurement of culture optical density and the FM-RES measured values, as shown in Fig. 2. The largest deviation between the techniques occurred between hours 14 and 18, in which the OD_{600} values remained relatively constant while the FM-RES values dropped substantially, indicating a decrease in cellular activity. This highlights an advantage of the FM-RES method over optical measurements of cell density. The spectrophotometric analysis, while rapid, is not an accurate measure of cell activity, as both living and non-living cells (and potentially other material, such as membrane fragments and extracellular polymers) are part of the analytical signal. Further, attempts to use spectrophotometry as an enumeration method can be confounded by changes in cell size at different growth stages. Therefore, the observed deviation in the OD_{600} and FM-RES curves between 14 and 18 h as the culture passed through stationary phase and into death phase would be expected. The FM-RES assay, by measuring changes in population and per-cell activity directly, avoids problems with optical interferences such as dead cells or debris and provides a more accurate representation of the state of the microbial population.

In contrast to the spectrophotometric technique, the SPC method followed the same general trend as the FM-RES method throughout the growth curve (Fig. 3), including the lag phase, growth phase and death phase. This confirms the previously discussed shortcomings of the spectrophotometric technique, and emphasises the importance of an assay being capable of distinguishing between viable and non-viable cells.

Despite the similarities in the curves between the SPC and FM-RES assay, there are important differences in the nature of the techniques which were evident at different phases of the growth curve. The SPC only measures cells that are capable of growing fast enough on the growth medium to produce a visually identifiable

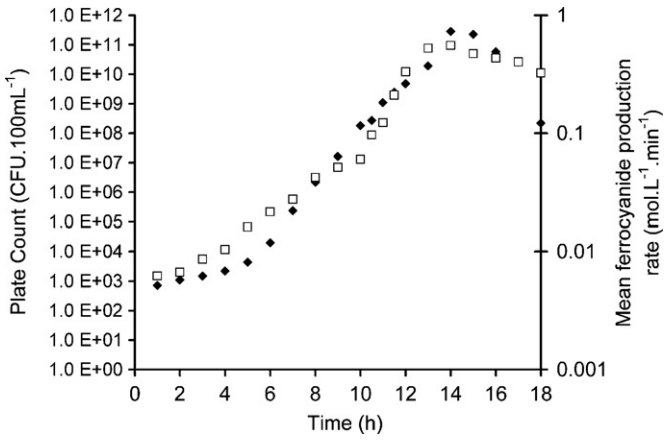


Fig. 3. Plot of growth curve displaying log CFU/mL from the standard SPC (diamonds) and log mean ferrocyanide production rate (open squares) from the FM-RES assay.

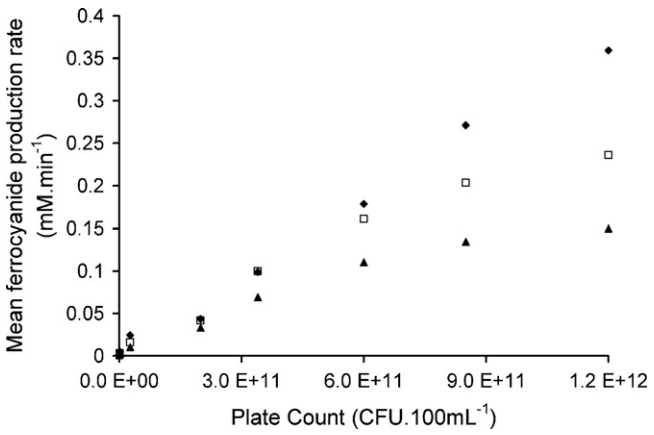


Fig. 4. Linear relationships between the rate of ferrocyanide production and quantity of colony forming units for three FM-RES incubation times, 15 min (diamonds), 30 min (open squares) and 60 min (triangles). Samples comprised *E. coli* harvested from the late exponential phase, standardised at OD_{600} and serially diluted to generate a curve.

colony, which are defined as viable cells. By contrast, the FM-RES signal comprises the net activity of all cells in the population, whether they are respiring at maximal capacity or only a fraction of their potential. This is an important distinction, as microbial activity can change with factors such as the cell size or substrate availability, without necessarily changing the number of viable cells. For example, increasing cell size in the early exponential phase would lead to increasing activity without a proportional increase in viable cell numbers. Conversely, in the death phase, the proportion of cells that are viable may decline rapidly, but these cells may still be respiring and hence contributing to the FM-RES signal. Importantly, the FM-RES assay can provide information about the changing bacterial population in just over 15 min, as opposed to 24 h required for the SPC method.

3.3. Comparison of SPC and standardised FM-RES assay

As there were differences in the growth curves measured by the FM-RES and SPC assays, the final validation experiment standardised the FM-RES and SPC assays for growth stage, by using cells in the late exponential phase of growth, as well as population density, as measured by OD_{600}. In other words, bacteria were harvested at a point when the culture contained the largest number of highly active cells. The cells were then washed to remove exogenous carbon sources and standardised for optical density. Fig. 4 depicts the correlation between the FM-RES and SPC methods for three FM-RES assay incubation times. There was a strong linear trend for all incubation times, most notably the 15 min assay, for which a Pearson product moment correlation analysis gave an r-value of 0.997 ($p < 0.001$, $n = 7$). The 30 and 60 min assays appeared to level off slightly at the highest cell counts, but correlation values of 0.993 for the 30 min assay ($n = 6$) and 0.991 for the 60 min assay ($n = 6$) were achieved by omitting the highest point in each curve.

The excellent correlation between FM-RES and the SPC method when growth phase and optical density were controlled is important for the development of FM bioassays for two reasons. Firstly, it validates the experimental principle behind FM microbial bioassays by showing, for the first time, a strong and significant relationship with a standard viable cell enumeration technique. Second, it has been determined that, under controlled conditions with a standardised biocatalyst and optical density, any change in the analytical response is due to a change in activity per cell. In other words, the control respiration in a 15 min FM-RES assay is directly related to the number of viable cells present. Deviations from this control value in samples exposed to a test substance are therefore due to a change in per-cell respiration, rather than a change in population size or other factors.

However, there were deviations in linearity at higher cell densities for the 30 and 60 min incubations, with values starting to plateau. This result reinforces the previously discussed idea that longer FM-RES incubations may be more susceptible to variability compared to shorter incubations. The deviation in linearity indicates that, above a threshold CFU population, the kinetics of the FM-RES biochemical reaction are limited by factors other than cell population, such as electron acceptor concentration and/or carbon source availability.

For the purposes of a bioassay, standardising the biocatalyst prior to the assay is necessary to ensure the results are comparable and reproducible between assays. While the previous FM-RES tests on a growing bacterial population are promising, it is important to determine if a standardised bacterial population will respond predictably in the presence of different compounds. Washing the bacteria in phosphate buffer solution prior to testing ensures they are suspended in a simple, controlled medium. This will be especially relevant if different biocatalysts are employed in FM assays, as the culture media required to grow the bacteria may differ.

The duration of the FM-RES assay is an important aspect to consider when using the method to assess the activity of a microbial population. FM-BOD assays use longer deployment times, such as 1–4 h [6] to ensure a high percentage of substrate degradation, with the accumulated ferrocyanide used to gauge this value. During the course of such an assay, the rate of accumulation of ferrocyanide can change [20]. Therefore, the information obtained from an FM-RES assay must be interpreted in the context of the incubation time and the presence of other factors, such as exogenous substrates. Non-BOD techniques may require a rapid snapshot of microbial population and/or activity, in which case a shorter incubation is much more desirable, as the result will more closely reflect the activity of the test population at the start of the FM-RES incubation.

3.4. Effect of substrates and toxicants on FM-RES assay

To demonstrate the suitability of the standardised *E. coli* biocatalyst for bioassays, a range of metabolic responses to test samples were studied. Assays were conducted at four fixed GGA levels with varying toxicant concentrations to investigate the interaction between stimulatory and inhibitory influences. Stimulation of respiration in the presence of GGA was pronounced (Fig. 5a), with a rate of ferrocyanide production in the sample

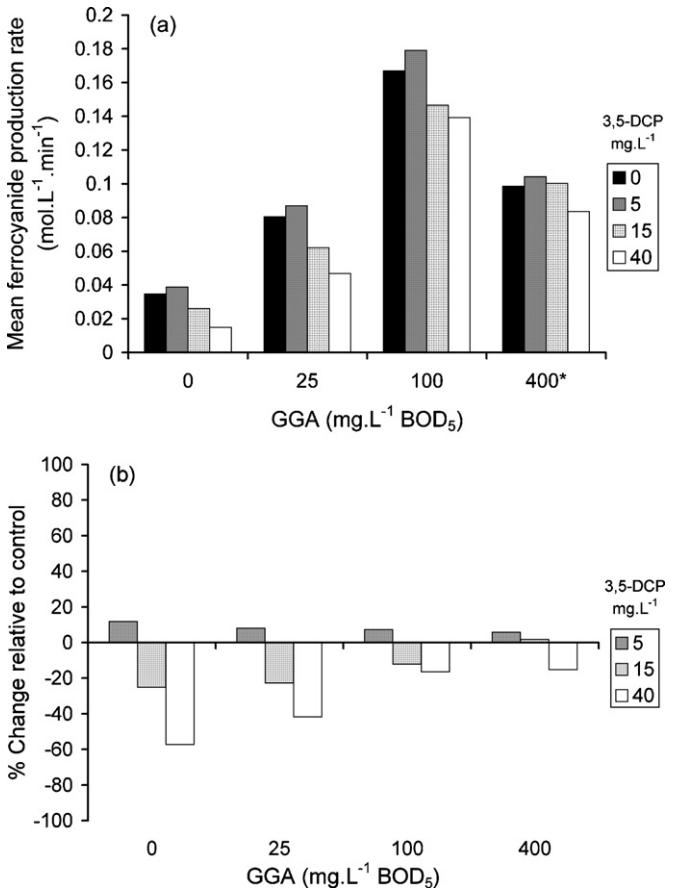


Fig. 5. The (a) rate of ferrocyanide production in samples containing 3,5-DCP at 0, 5, 15 and 40 mg L^{-1} at differing concentrations of GGA (*x*-axis, in terms of mg L^{-1} BOD_5) and (b) the normalised effect of the 3,5-DCP relative to the control (i.e. no 3,5-DCP) samples, as calculated by Eq. (1). **Note*: values for 400 mg L^{-1} GGA were divided by 5 for ease of display in (a).

containing 400 mg L^{-1} BOD_5 (as GGA) an order of magnitude above the endogenous (i.e. no added GGA or toxicant) respiration rate observed. This is in keeping with the observed rapid increase in *E. coli* metabolism with GGA, reported by Morris et al. [13].

In the concentration ranges tested, the stimulatory effect of GGA dominated the inhibitory effect of 3,5-DCP (Fig. 5a). However, despite the differences in magnitude of the control responses (i.e. no toxicant), the effect of the 3,5-DCP can still be measured by normalising the response of each toxicant sample (I_{lim} Sample in Eq. (1)) to the control sample with the corresponding GGA concentration (I_{lim} GGA control in Eq. (1), and the black columns in Fig. 5a). In other words, we can compare the FM-RES response at different toxicant concentrations (5, 15, 40 mg L^{-1} 3,5-DCP) to the FM-RES response at zero toxicant concentration and report the comparison as a percent change in ferricyanide-mediated respiration (Eq. (1)):

$$\%\text{Change} = \left(\frac{I_{\text{lim}}\text{Sample} - I_{\text{lim}}\text{GGA control}}{I_{\text{lim}}\text{GGA control}}\right) \times 100 \quad (1)$$

Therefore, while the production of ferrocyanide was greater in absolute terms for samples with higher GGA, the relative effect on microbial metabolism by the toxicants is still comparable across GGA treatments (Fig. 5b). Change in metabolism, calculated using Eq. (1), can indicate inhibition, as negative percentage values up to −100%, at which point no activity remains in the sample. Conversely, positive percent changes indicate stimulation of respiration, which can be higher than 100%.

The inhibition of respiration by each of the two toxicants tested, when corrected for the effect of added GGA, contrasted strongly

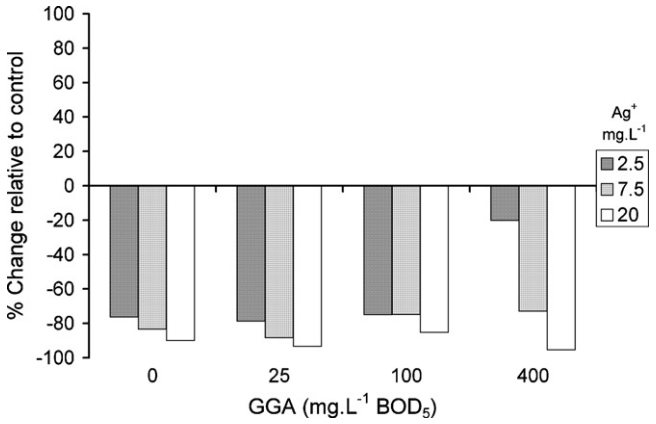


Fig. 6. Changes in ferrocyanide production relative to control samples for three Ag^+ concentrations, as calculated by Eq. (1).

(Fig. 5b vs. Fig. 6). It is apparent that microbial respiration was not completely inhibited by 3,5-DCP in any sample, even at a concentration of 40 mg L^{-1}, which is substantially higher than the EC_{50} values of 3.73 mg L^{-1} for *Vibrio fischeri* in the Microtox test and 13 mg L^{-1} for *E. coli* in the 15 min micredox toxicity assay [16]. This is likely to be due to the experimental conditions, which are not optimised for sensitive toxicity testing.

At low 3,5-DCP concentrations, there was a stimulation of respiration which may be associated with a stress response of the bacteria, as has been reported in other studies [22]. The responses in Figs. 5b and 6 show a range of stimulatory and inhibitory effects on a timescale too small to be detected by either the spectrophotometric method or the SPC technique. This emphasises the importance of measuring cell activity, as opposed to surveying cell numbers or the number of culturable cells in a population, if a rapid, accurate determination of the influence of a test sample on a microbial population is desired.

A key finding from the stimulation and inhibition experiment is that the toxicity of 3,5-DCP was substantially greater when GGA was omitted from the incubation mixture (Fig. 5b). Comparison of the inhibition induced by 40 mg L^{-1} 3,5-DCP on microbial populations shows that the percent change was almost four times greater in the presence of zero GGA (57% inhibition) than with 400 mg L^{-1} BOD_5 GGA added (15% inhibition). Fig. 6, on the other hand, shows that Ag^+ was highly toxic at all concentrations tested irrespective of GGA concentration. All but one sample containing Ag^+ produced ferrocyanide at a rate 75–100% lower than the corresponding controls. The presence of GGA at a concentration of 400 mg L^{-1} BOD appeared to mitigate the inhibitory effect of 2.5 mg L^{-1} Ag^+, as inhibition was only 20%.

The general trend here is relatively simple, in that the presence of exogenous carbon substrate mitigates the inhibitory effect of toxicants. However, the interrelationship between combinations of substrates and toxicants can be highly complex [23]. It is unclear whether the GGA simply allows the cells to metabolise more rapidly despite the inhibition by the toxicants, or whether the presence of the GGA directly interrupts the mode of action of the toxicant, or if a combination of factors is responsible for the changes. Such interpretations are even more difficult if the biocatalyst is capable of metabolising the toxicant, in which case the response induced by a toxicant could change from inhibition to stimulation over the course of an incubation. At a simplistic level, the result in Fig. 5 clearly shows that the addition of exogenous carbon is undesirable if FM-RES methods are to be used in toxicity assays, as toxic effects are more pronounced when there is little or no exogenous carbon. The most recently published ferricyanide-mediated direct toxicity assessment assays include GGA mixture as a substrate, which may

reduce the sensitivity of the assays for some samples and confound comparisons of toxicants [16,18].

Finally, an important consideration for any assay based on the FM-RES technique is that the test sample and the presence of ferricyanide may have time-dependent effects on the microbial population. For example, this study shows that, for a rapid FM-BOD assay, simple substrates such as glucose will have a pronounced effect in a short period of time, whereas recalcitrant substrates will not affect short-term assays but will be a consideration in longer incubations. More thorough investigation of the role of time is required when optimising the FM-RES assay for a particular technique [19]. In the use of FM-BOD assays, clearly a longer incubation time would be desirable, as the microbial population would require a longer period of time to degrade both labile and more recalcitrant organic compounds in the test sample and therefore provide a representative measurement of the potential biochemical oxygen demand. However, in the case of assays which require a rapid assessment of cell activity, such as direct toxicity assays, this study suggests that a shorter time period for incubation in the presence of ferricyanide may be desirable. A 2-step incubation approach, in which the microbial cells are first exposed to a test sample followed by a secondary incubation in the presence of ferricyanide to determine cell activity, may serve to reduce interference by short-term stimulatory stress effects, as observed in Fig. 5b, and the presence of labile carbon compounds. Future development of ferricyanide-mediated direct toxicity assessment assays should proceed with these considerations in mind.

4. Conclusions

The analytical principle of ferricyanide-mediated quantification of the activity of microbial populations has been validated against two commonly used microbial enumeration techniques. The agreement between the FM-RES, OD_{600} and SPC methods was generally very good, with predictable deviations consistent with the nature of each technique. The shortest FM-RES incubation time, 15 min, provided reproducible and sensitive measurements of changing population size and activity across a substantial linear range of cell population. The FM-RES approach is faster and requires fewer resources than the SPC, though the type of information obtained is different. FM-RES also provides much more information than measurements of optical density using a spectrophotometer, as it can distinguish between live and dead cells, as well as changes in per-cell activity, and is less likely to suffer interferences from non-living material in the matrix.

Both stimulation and inhibition of microbial activity was observed in mixtures containing GGA and either 3,5-DCP or silver, varying between almost complete inhibition of ferrocyanide production to a stimulation of approximately fourteen times the endogenous response. This demonstrated the ability of FM-RES methods to sensitively and rapidly investigate changes in the activity of standardised microbial populations in synthetic solutions at a time scale comparable to the fastest available alternatives. Importantly, the addition of exogenous carbon was found to decrease the toxic effect of 3,5-DCP on *E. coli*, which suggests a closer examination of the experimental design of existing rapid, ferricyanide-mediated toxicity assays are required to ensure consistent and sensitive responses across a range of toxicants.

Acknowledgements

This research was supported by an Australian Research Council Linkage Grant (LP0882894) co-funded by Gold Coast Water. Kylie Catterall was supported by a scholarship from the CRC for Water Quality and Treatment.

References

[1] K. Porter, Y. Feig, Limnol. Oceanogr. (1980) 943–948.
[2] APHA, Standard Methods for the Examination of Water and Wastewater, 20th ed., 1998.
[3] K. Gracias, J. McKillip, Can. J. Microbiol. 50 (2004) 883–890.
[4] J. Vives-Rego, P. Lebaron, G. Nebe-von Caron, FEMS Microbiol. Rev. 24 (2000) 429–448.
[5] L. Wegley, P. Mosier-Boss, S. Lieberman, J. Andrews, A. Graff-Baker, F. Rohwer, Environ. Microbiol. 8 (2006) 1775.
[6] K. Morris, H. Zhao, R. John, Aust. J. Chem. 58 (2005) 237–245.
[7] B. Dutka, K. Kwan, Environ. Pollut. Ecol. Biol. 29 (1982) 125–134.
[8] S. Ren, Environ. Int. 30 (2004) 1151–1164.
[9] B. Dutka, N. Nyholm, J. Petersen, Water Res. 17 (1983) 1363–1368.
[10] OECD, Guideline for Testing of Chemicals: Activated Sludge, OECD 209 Respiration Inhibition Test, 1984.
[11] H. Nakamura, K. Suzuki, H. Ishikuro, S. Kinoshita, R. Koizumi, S. Okuma, M. Gotoh, I. Karube, Talanta 72 (2007) 210–216.
[12] C.E. Clifton, J.P. Cleary, J. Bacteriol. 28 (1934) 561–569.
[13] K. Morris, K. Catterall, H. Zhao, N. Pasco, R. John, Anal. Chim. Acta 442 (2001) 129–139.
[14] N. Pasco, K. Baronian, C. Jeffries, J. Hay, Appl. Microbiol. Biotechnol. 53 (2000) 613–618.
[15] K. Morris, H. Zhao, R. John, Water Pollution VII—Modelling, Measuring and Prediction, 2003, pp. 379–390.
[16] N. Pasco, R. Goonerate, R. Daniel, A. Czollner, A. Scott, Int. J. Environ. Anal. Chem. 88 (2008) 1063–1075.
[17] A. Tizzard, J. Webber, R. Gooneratne, R. John, J. Hay, N. Pasco, Anal. Chim. Acta 522 (2004) 197–205.
[18] C. Liu, T. Sun, X. Xu, S. Dong, Anal. Chim. Acta 641 (2009) 59–63.
[19] K. Catterall, H. Zhao, N. Pasco, R. John, Anal. Chem. 75 (2003) 2584–2590.
[20] N. Pasco, K. Baronian, C. Jeffries, J. Webber, J. Hay, Biosens. Bioelectron. 20 (2004) 524–532.
[21] H. Chen, T. Ye, B. Qius, G. Chen, X. Chen, Anal. Chim. Acta 612 (2008) 75–81.
[22] M. Evans, G. Jordinson, D. Rawson, J. Rogerson, Pestic. Sci. 54 (1998) 447–452.
[23] N. Nirmalakhandan, V. Arulgnanendran, M. Mohsin, B. Sun, E. Cadena, Water Res. 28 (1994) 543–552.

Talanta 80 (2010) 1986–1992

Contents lists available at ScienceDirect

Talanta

journal homepage: www.elsevier.com/locate/talanta

Determination of progesterone (P4) from bovine serum samples using a microfluidic immunosensor system

Fernando Javier Arévalo[a], Germán Alejandro Messina[b], Patricia Gabriela Molina[a], María Alicia Zón[a], Julio Raba[b], Héctor Fernández[a,*]

[a] Departamento de Química, Facultad de Ciencias Exactas, Físico-Químicas y Naturales, Universidad Nacional de Río Cuarto, Agencia Postal N° 3 (5800)-Río Cuarto, Argentina
[b] INQUISAL, Departamento de Química, Universidad Nacional de San Luis, CONICET, Chacabuco y Pedernera, D5700BWS San Luis, Argentina

ARTICLE INFO

Article history:
Received 16 August 2009
Received in revised form 22 October 2009
Accepted 23 October 2009
Available online 1 November 2009

Keywords:
Enzyme immunoassays
Progesterone
Amperometric immunosensor
Glassy carbon electrode
Horseradish peroxidase
Flow injection analysis

ABSTRACT

Progesterone (P4) is a steroidal hormone with a vital role in the maintenance of human and animal health. This paper describes the development of an immunosensor coupled to glassy carbon (GC) electrode and integrated to a microfluidic system to quantify P4 from bovine serum samples in a fast and sensitive way. The serum samples spiked with a given P4 concentration and a given P4 concentration bound to horseradish peroxide (HPR) were simultaneously added and, therefore, they competed immunologically with sheep monoclonal anti-P4 antibodies that were immobilized at a rotating disk. HRP in the presence of hydrogen peroxide (H_2O_2) catalyzes the chatecol (H_2Q) oxidation to benzoquinone (Q). Its reverse electrochemical reduction to H_2Q can be detected at a GC electrode surface at −0.15 V by chronoamperometric measurements. These current responses are proportional to the enzyme activity and inversely proportional to the P4 amount present in bovine serum samples. This P4 immunosensor showed a linear working range from 0.5 to 12.5 ng mL^{-1}. The detection (DL) and quantification (QL) limits were 0.2 and 0.5 ng mL^{-1}, respectively. The electrochemical immunosensor had a higher sensitivity than the ELISA method using conventional spectrophotometric detections. However, both methods allowed us to obtain similar detection limits. The immunosensor allowed us to make up to 100 determinations on different samples without any previous pre-treatment. This behavior proved to be suitable to detect P4 in routine veterinary, clinical, biological, physiological, and analytical assays.

© 2009 Elsevier B.V. All rights reserved.

1. Introduction

Nowadays, the use of electrochemical immunosensors as efficient analytical tools in the fields of clinical diagnosis and environmental monitoring is well established [1,2]. These immunosensors have excellent analytical applications, such as higher sensitivity and reproducibility. Their construction and use is very simple. These important advantages allow the electrochemical immunosensors be able to perform immunoreagent immobilizations, be more efficient in transduction events as well as work in a small scale.

Progesterone (P4) (pregn-4-ene-3,20-dione) is an α,β unsaturated ketone, a steroid hormone with a vital role in the maintenance of human and animal health. Its imbalance can cause malformations in the reproductive system as well as infertility problems [3,4]. P4 is secreted by the uterus to prepare it for pregnancy and maintain the pregnancy after conception secretes P4. Therefore, P4 is adequate to diagnose an early pregnancy [5]. P4 levels should be at sufficiently high values in the organism to assure the embryo development [6]. Thus, monitoring of P4 levels is important to reproductive system. A periodic control of P4 level is used to determine the next most fertile ovulation time and to program the animal's service or the artificial insemination, which would help to improve the percentages of pregnancy [7,8].

The most common methods to quantify P4 in animal serum are those based on enzyme-linked immunosorbet assay (ELISA) and radio immuno assay (RIA). These methods are applied using commercial kits [8,9,10]. However, immobilized antibodies have to be discarded immediately after the first use in these assays. HPLC is another technique used to quantify P4, where ethanol–water solvent binary mixtures are employed as the mobile phase and the column should be thermostatized to 40 °C [11]. Hart et al. [12] have designed a carbon paste amperometric biosensor to detect P4 indirectly in milk through determinations of products involved in the enzymatic-substrate reaction. Another biosensor has also been designed by Claycomb et al. [13,14], which uses the same enzymatic immunoassay method to detect P4 in milk. Recently, an amperometric immunosensor was developed using a colloidal gold–graphite–Teflon–tyrosinase composite to determine P4 in milk [15]. Nevertheless, the implementation of sensitive, fast and

* Corresponding author. Tel.: +54 358 467 6440; fax: +54 358 467 6233.
E-mail address: hfernandez@exa.unrc.edu.ar (H. Fernández).

0039-9140/$ – see front matter © 2009 Elsevier B.V. All rights reserved.
doi:10.1016/j.talanta.2009.10.059

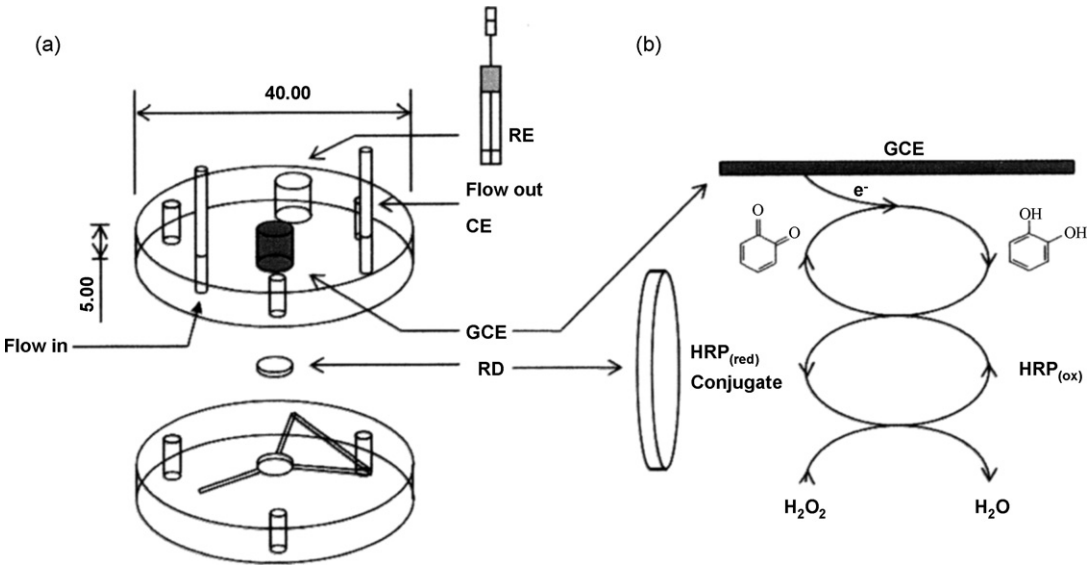


Fig. 1. (a) Schematic representation of the microfluidic sensor cell. (RE) Reference electrode, (CE) counter electrode, (RD) rotating disk. Units of length are given in millimeters. Flow channels i.d.: 0.100 mm. (b) Schematic representation of the reduction wave of the enzymatic process among chatecol (H_2Q), benzoquinone (Q), hydrogen peroxide (H_2O_2), and P4 conjugated with HRP.

low cost methodologies to quantify P4 in bovine serum samples is still a challenge to carry out further studies.

Heterogeneous enzymatic immunoassays, coupled with amperometric detection flow injection (FI) system, represent a powerful analytical tool to determinate low levels of different analytes, such as hormones, antibodies, drugs, tumor markers, and viruses [16]. The amperometric detection offers a good sensitivity combined with a simple and low-cost instrumentation [17,18]. One approach used is to employ a labeled enzyme which generates an electrochemically active product [19–22].

In this paper, we study the development of an immunosensor coupled to a glassy carbon (GC) electrode integrated to a microfluidic system to quantify P4 in bovine serum samples previously spiked with a known P4 concentration. A fast and sensitive method based on the use of a monoclonal antibody (mAb), which was immobilized on a rotating disk. Bovine serum samples containing P4 were added to the reactor with a known concentration of enzyme-labeled antigen (i.e., the "conjugated"). Therefore, labeled and unlabeled antigens compete with antibody binding sites bound at the rotating disk. The enzyme used to label the antigen was horseradish peroxidase (HRP) and chatecol (H_2Q) was the enzymatic redox mediator. HRP in the presence of hydrogen peroxide (H_2O_2) catalyzes the oxidation of H_2Q to benzoquinone (Q). Its reverse electrochemical reduction to chatecol can be detected on the GC electrode surface at −0.15 V through chronoamperometric measurements. These amperometric responses are proportional to the activity of the enzyme and inversely proportional to the amount of P4 in bovine serum samples.

2. Experimental

2.1. Chemicals

All reagents used were of analytical reagent grade. P4, progesterone–3-carboxymethyloxime (P4–3-CMO), 1-ethyl-3-(3-dimethylaminopropyl)carbodiimide (EDAC), sheep monoclonal antibody (mAbP4) and horseradish peroxidase (HRP) were obtained from Sigma Chemical Company and *N*-hydroxysuccinimide (NHS) from Fluka. Anhydrus dimethylformamide (DMF), Glutaraldehyde (25% aqueous solution) and pH 7.00 phosphate buffer solutions (PBS) as well as H_2O_2 were purchased from Aldrich and Merck (Darmstadt, Germany), respectively. H_2Q was obtained from BDH Chemicals Ltd. (Poole, England). All reagents were used as received. 3-Aminopropyl-modified controlled pore glass, 1400 Å mean pore diameter and 24 $m^2\,mg^{-1}$ surface areas, was obtained from Electro Nucleonics (Fairfield, NJ, USA) and contained 48.2 $\mu mol\,g^{-1}$ of amino groups. The School of Agriculture and Veterinary from Universidad Nacional of Río Cuarto gently supplied bovine serum samples. The ELISA test kits for P4 quantitative determination were obtained from Abbott Axsym System®, Reagent Pack, Abbott Japan Co., Ltd. The manufacturer's instructions were taken into account to perform these assays. Aqueous solutions were prepared using purified water from a Milli-Q system.

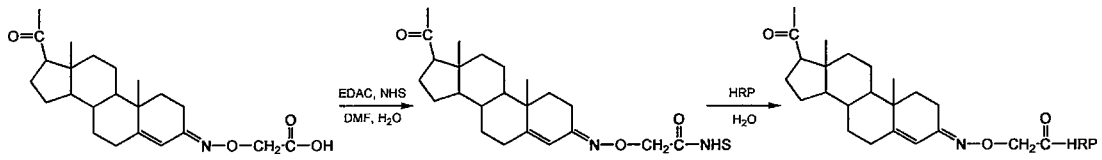
2.2. Apparatus

The main body of the cell was made of Plexiglas. Both the design of the flow through chamber containing the microfluidic immunosensor and its detection system are shown in Fig. 1a.

The volume of the cell was 5 μL. The GC electrode was on the top of the sensor. The rotating reactor was a disk of Teflon (3 mm diameter) where a miniature magnetic stirring bar was incorporated. 0.3 mg of controlled-pore glass is stuck on its surface. The reactor rotation was performed by a magnetic stirrer (Metrohm E649 from Metrohm AG, Herisau, Switzerland) and controlled with a variable transformer of an output between 0 and 250 V and maximum amperage of 7.5 A (Waritrans, Argentina). Chronoamperometry and cyclic voltammetry measurements were performed by using a BAS LC4C and a BAS 100 B (electrochemical analyzer from Bioanalytical Systems, West Lafayette, IN, USA), respectively.

The potential applied to the GC electrode for performing amperometric measurements was −0.15 V *vs* Ag/AgCl, 3.0 $mol\,L^{-1}$ NaCl reference electrode (BAS RE-6). A Pt wire was the counter electrode. A catalytic current was established at this potential. The inner diameter (i.d.) of flow channels was 0.100 mm and the length of flow channels was 10 mm. Pumps (Baby Bee Syringe Pump, Bioanalytical System, West Lafayette, IN) were used for pumping, introducing samples and stopping the flow.

The pH measurements were carried out with an Orion Expandable Ion Analyzer (model EA 940, Orion Research, Cambridge, MA, USA) equipped with a glass combination electrode (Orion



Scheme 1. Synthesis of P4–3-CMO with HRP to form the labeled P4.

Research). Absorbance measurements were performed by Bio-Rad Benchmark microplate readers (Japan) and Hewlett-Packard spectrophotometer, Model 8452A, equipped with a temperature controller.

2.3. Preparation of P4–HRP conjugate

P4 was bound to HRP by following a synthesis of activated ester to generate the P4 labeled. Thus, 7.9 mg of P4–3-CMO were dissolved in 600 μL of DMF containing 400 μL of distilled water and 18 mg of NHS. Then, 33 mg of EDAC were added. Reaction mixture was stirred to 4 °C in the darkness for 5 h to activate the carboxyl group of the steroid. HRP (1 mg) was dissolved in 1 mL of distilled water. Steroid activated solution was added to HRP aqueous solution and then stored and shaken overnight at 4 °C. The solution was then dialyzed in water for 5 days by using a cellulose dialysis membrane (cut-off molecular weight 12 kDa). Finally, it was stored at 4 °C (see Scheme 1).

Concentrations of synthesized P4–HRP conjugated (P4–HRP) were determined spectrophotometrically by measuring absorbance changes at 252 and 402 nm in 0.01 mol L^{-1} PBS (pH 7.0), considering that P4–3-CMO and HRP show absorption maximum at those wavelength, respectively. The synthesized conjugated P4–HRP had 8 mol of P4 per HRP mole as it was determined spectrophotometrically. This ratio showed that there was unbound P4 in the solution. The true synthesized P4–HRP conjugated concentration was unknown. Therefore, different known dilutions were prepared for convenience.

2.4. Progesterone immunoassay

The ELISA test kits with standard series covering the relevant range (0–25 ng mL^{-1}) were supplied by the company, as mentioned before [23]. The manufacturer's protocol was followed to perform standard calibration curves from spectrophotometric measurements. Therefore, P4 concentrations were calculated measuring absorbance changes at 405 nm.

2.5. mAbP4 immobilization

The rotating disk reactor (bottom part, Fig. 1a) was prepared by immobilizing mAbP4 on a controlled pore glass modified by 3-aminopropyl (APCPG), which was smoothly spread on one side of a double-coated tape attached to the disk surface. Then, it was allowed to react with a 5% (w/w) glutaraldehyde aqueous solution of pH 10.0 (0.20 mol L^{-1} carbonate) for 2 h at room temperature. After different washing steps with both purified water and 0.01 mol L^{-1} PBS (pH 7.0), 30 μL of mAbP4 different dilutions were allowed to react with aldehyde residual groups overnight at 5 °C. Then, 30 μL of 0.1 mol L^{-1} glycine solution was added to block the remaining reactive groups for 2 h at room temperature after being thoroughly rinsed with water. Then, these groups were reduced with 30 μL of 0.5% $NaBH_4$ solution for 2 h at room temperature. Finally, the immobilized antibody was washed with 0.01 mol L^{-1} PBS (pH 7.0) and stored in the same buffer at 4 °C between measurements. Immobilized antibody preparations remained stable for at least 1 month.

2.6. Amperometric analysis of P4 in serum bovine samples

The amperometric measurements were applied for P4 determination through a competitive assay in different bovine serum samples, which had been previously spiked with a known P4 concentration. The experimental procedure was performed at a constant rotation speed of 180 rpm and at a flow rate of 50 μL min^{-1}. Unspecific bindings were blocked through a treatment at 37 °C with 3% low-fat milk in a 0.01 mol L^{-1} (pH 7.0) under stopped flow conditions, during 10 min. After that, the immunoreactor was washed with 0.01 mol L^{-1} PBS (pH 7.0) at a flow rate of 50 μL min^{-1} and serum samples and P4–HRP conjugated were then injected into the 0.01 mol L^{-1} PBS (pH 7.0) carrier stream and incubated at 37 °C under stopped flow conditions for 15 min (competitive assay). Then, the immunoreactor was washed by using a 0.01 mol L^{-1} PBS (pH 7.0) at a flow rate of 50 μL min^{-1} in order to eliminate any traces of unbound P4 and P4–HRP. Finally, a substrate solution (10 μL 0.1 mol L^{-1} phosphate–citrate buffer, pH 5.0 + 1×10^{-3} mol L^{-1} H_2O_2 + 1×10^{-3} mol L^{-1} H_2Q) was injected and the enzymatic reaction product was detected through amperometric FI measurements for 2 min under stopped flow conditions.

For the next analysis, the immunoreactor was reconditioned by desorption. First, buffer injections (0.1 mol L^{-1} glycine–HCl, pH 2.0) were applied for 2 min and then, the immunoreactor was washed with 0.01 mol L^{-1} PBS (pH 7.0). The desorption efficiency was checked by the absence of the reduction current of the enzymatic reaction product at GC electrode at −0.15 V after the addition of H_2O_2 and H_2Q, which is a consequence of the absence of P4–HRP.

A standard amperometric curve was generated by employing concentrations which covered the clinically relevant range supplied with ELISA test kits (0–20 ng mL^{-1}). The following protocol was used: amperometric measurements were performed at GC electrode at a potential of −0.15 V at room temperature in 0.1 M phosphate–citrate buffer (pH 5.0) solutions containing 1×10^{-3} mol L^{-1} H_2O_2 + 1×10^{-3} mol L^{-1} H_2Q. The corresponding cathodic peak currents were recorded in the potentiostat meter. The immunoreactor was stored in 0.01 mol L^{-1} PBS (pH 7.0) at 4 °C when it was not used.

3. Results and discussion

3.1. Study of the enzymatic process

Reactions catalyzed by enzymes have been largely used for analytical purposes in determinations of different substrates, inhibitors, etc. Gorton [24] has explained the HRP catalytic mechanism. Therefore, it is well known that in the presence of H_2O_2 the enzyme catalyzes the oxidation of H_2Q to Q [25], which at a potential of −0.15 V can be electrochemically reduced to H_2Q, providing a reduction current peak which can be related to substrate concentration [26]. Fig. 1b shows a schematic representation of this process.

3.2. Optimization of the experimental variables involved on antigen–antibody reaction

mAbP4 concentration is not provided by the Sigma commercial reactive. The synthesized P4–HRP concentration is also unknown,

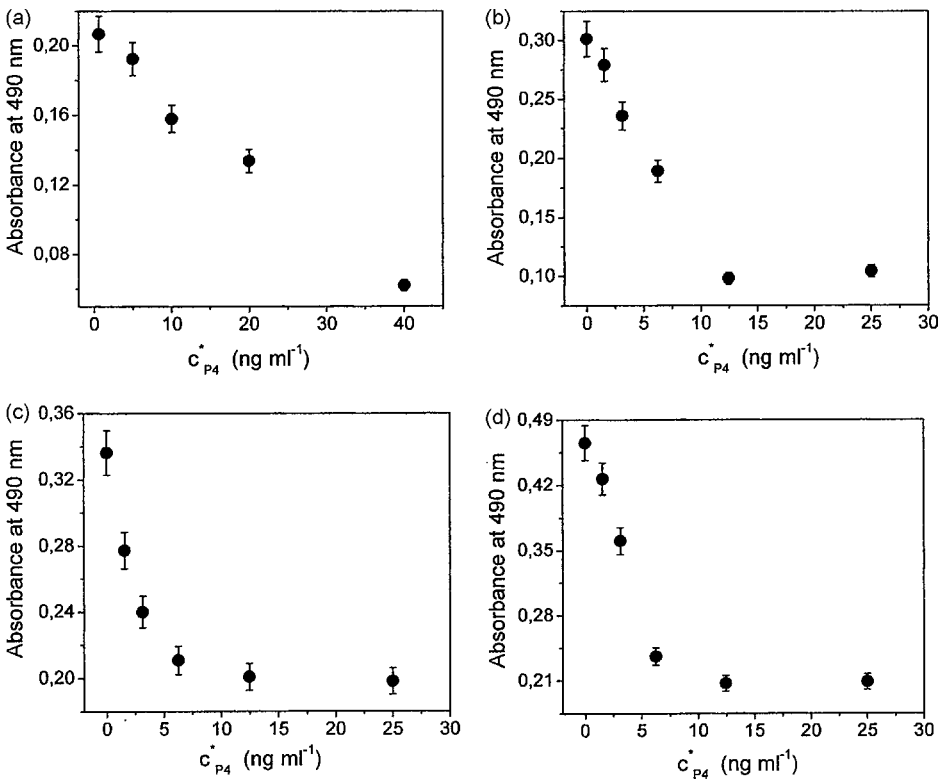


Fig. 2. Optimization of P4–HRP. ELISA assay for different P4–HRP dilution factors. (a) 1/190; (b) 1/100; (c) 1/75 and (d) 1/55. Dilution factor of mAbP4 = 1/50.

so different dilutions were prepared for both. In this study, optimal dilutions for mAb and P4–HRP were studied by using an ELISA test kit. Optimal responses were proved from 1/50 to 1/4000 and 1/10 to 1/1200 dilution ranges for mAb and P4–HRP, respectively.

Curves for each mAbP4 dilution were obtained at different P4–HRP dilutions. It was experimentally observed that the smaller the mAbP4 dilution factor was, the higher the absorbance value was (results not shown). The chosen value for the dilution factor was 1/50 in order to achieve the best sensitivity.

In addition, at a mAbP4 constant dilution factor of 1/50, an increase of P4–HRP concentrations produced also an increase in absorbance values (results not shown). P4–HRP dilution factors smaller than 1/10 produce the saturation of mAbP4 immobilized, since constant absorbance signals were observed when the P4–HRP amount was greater [27]. Different competitive assays between P4–HRP and P4 were carried out in order to know the best dilution factor. Competitive assays for different P4–HRP factor dilutions are shown in Fig. 2.

Absorbance values increased as P4–HRP concentration was increased (lower dilution) but the linear range of P4 concentration decreased due to saturation of mAbP4 adsorbing sites to high P4 concentrations.

The highest linear range with very good responses was obtained by using a 1/100 P4–HRP dilution factor, which coincides with veterinary relevant range (0–15 ng mL^{-1}) [7].

3.3. Effect of reactor rotation and continuous flow/stopped flow operation

The implementation of continuous flow/stopped flow programming was followed by the location of an independent two-phase reactor with two different surfaces, which are facing each other, one is the sensing element itself (GC electrode) and the other is the one where the immune reaction takes place (Teflon disk) (Fig. 1). This design allows for: (I) the use of relatively low immunoreaction loading conditions, (II) an instantaneous operation under high initial rate conditions, (III) the easy detection of accumulated products, and (IV) the reduction of apparent Michaelis–Menten constant K_M'. It is possible to get a complete reagent homogenization because the cell works as a mixing chamber facilitating the arrival of immunoreactants at the specific mAbP4 and enzymatic substrate at active sites as well as the release of products from the same sites [28]. This procedure allows us to obtain higher current values. The main advantages of this system are its simplicity and the convenience to determine P4 in serum samples.

The rotation velocity effect was studied in a range from 60 to 250 rpm under stopped and continuous flow conditions. A linear relationship between the electrical signal and rotation velocity in the range from 60 to 180 rpm under stopped flow conditions was found, showing a response maximum rate for rotation velocities higher than 180 rpm (Fig. 3a). The electrical signal decayed when the reactor operated under continuous flow conditions (Fig. 3b), probably because the reaction product (benzoquinone) escaped from the reactor chamber. When the reactor rotation in the cell stopped, the current response was lower because controlled diffusion reactions were too slow for being detected at the time scale of amperometric measurements, operating under stopped or continuous flow conditions (Fig. 3c and d, respectively). Thus, a rotation velocity of 180 rpm was chosen to be administered to the reactor located at the bottom of the cell under stopped flow conditions (with mAbP4 immobilized and the already formed immunocomplex between P4 of bovine serum samples + the P4–HRP). The sample volume was studied in the range 2–20 μL. Sensitivity was almost tripled in the range between 2 and 10 μL. Insignificant differences were obtained for greater sample size. A sample size of 10 μL had to be injecting in order to minimize convective and dispersive effects that characterize the FI system characteristic as well as to obtain a complete filling of the chamber.

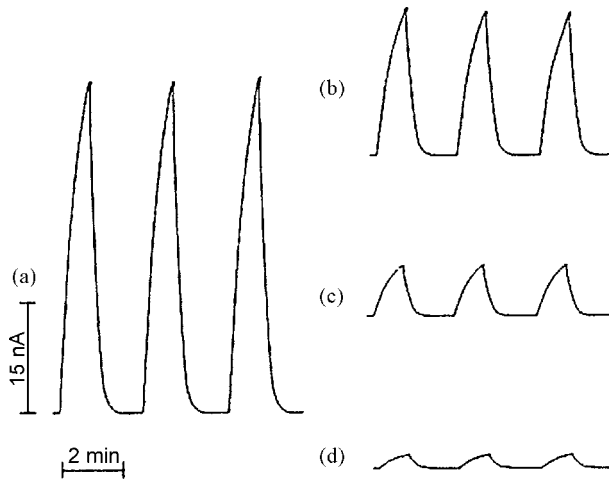


Fig. 3. Effect of reactor's rotation under continuous and stopped flow conditions. (a) Stopped flow with rotation (180 rpm). (b) Continuous flow with rotation (180 rpm). (c) Stopped flow without rotation. (d) Continuous flow without rotation. c^*_{P4} = 3 ng mL^{-1}. Flow rate = 50 μL min^{-1}, cell volume = 5 μL. 0.1 mol L^{-1} phosphate–citrate buffer, pH 5.0 solution containing 1.0×10^{-3} mol L^{-1} H_2O_2 and 1.0×10^{-3} mol L^{-1} H_2Q. The flow was stopped for 2 min during measurement.

3.4. Optimal conditions for the determination of the enzymatic products

The rates of the enzymatic reaction under stopped-flow conditions have been previously studied [28]. These responses showed a maximum value at pH 5.0 in 0.1 mol L^{-1} phosphate–citrate buffer. As it is well known, the optimal temperature of immunoreactions is about 37 °C. Therefore, in this study all experimental measurements were performed at this temperature. The effect of varying H_2O_2 concentration from 7.0×10^{-4} to 5.0×10^{-3} mol L^{-1} at a given H_2Q concentration (1.0×10^{-3} mol L^{-1}) as well as the effect of varying H_2Q concentration from 1.0×10^{-4} to 3.6×10^{-2} mol L^{-1} at a given H_2O_2 concentration (1.0×10^{-3} mol L^{-1}) was evaluated on bioreactor responses. The optimal H_2O_2 and H_2Q concentrations found were 1.0×10^{-3} mol L^{-1} and 1.0×10^{-3} mol L^{-1}, respectively. Those concentrations were, then, used for all experiments.

3.5. Detection and competitive immunoassay on the immunoreactor

Under the previously described selected conditions, amperometric measurements obtained for the reduction of Q in 0.1 mol L^{-1} phosphate–citrate buffer (pH 5.0) were proportional to enzyme conjugated (P4–HRP) activity and, consequently, indirectly proportional to the amount of P4 in serum bovine samples bound to mAbP4 immobilized on the rotating disk. A linear calibration curve for detection of P4 in PBS 0.01 mol L^{-1} (pH 7.0) was obtained. For convenience, sampling times of 2 min at different P4 concentrations were used, considering that longer sampling times than 2 min produced a loss of linear relationship between current responses and P4 concentrations. A good linear calibration curve was found between 0.5 and 12.5 ng mL^{-1} (Fig. 4). For greater concentrations than 12.5 ng mL^{-1}, the saturation of the immobilized mAbP4 took place. The linear regression equation was:

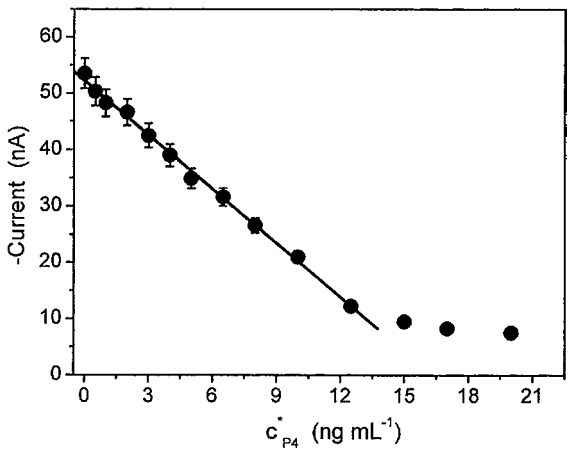


Fig. 4. Calibration curve for P4 determination by amperometric FI immunoassay. Amperometric measurements were performed at −0.15 V *vs* Ag at 37 °C in a 0.1 mol L^{-1} phosphate–citrate buffer (pH 5.0) solution containing 1.0×10^{-3} mol L^{-1} of H_2O_2 and 1.0×10^{-3} mol L^{-1} H_2Q. Current sampling time: 2 min.

$$\text{Current [nA]} = (52.2 \pm 0.9)\,[\text{nA}] - (3.0 \pm 0.1)\,[\text{nA ng}^{-1}\text{ mL}]\,c^*_{P4}\,[\text{ng mL}^{-1}]$$

being the correlation coefficient, $r = 0.998$. Each experimental point shown in Fig. 4 is the average of three replicated measurements.

The precision between the assays of amperometric measurements was tested with three measurements in 5 ng mL^{-1} P4 + 0.01 M PBS (pH 7.0). The percentage variation coefficient (%VC) was 4.5%, showing a good precision. The detection (DL) and the quantification (QL) limits were 0.2 and 0.5 ng mL^{-1}, respectively. The sensitivity was (3.0 ± 0.1) nA ng^{-1} mL in the range from 0.5 to 12.5 ng mL^{-1}.

The determination of P4 was carried out under the best experimental conditions found from bovine serum samples. Considering that serum samples did not contain P4, they were spiked with a known P4 concentration prepared in BPS 0.01 mol L^{-1} (pH 7.0) at a low buffer concentration (≤1%) in order to avoid a dilution effect. Therefore, two samples of serum containing 1 and 5 ng mL^{-1} of P4 were prepared. A given amount of P4–HRP was then added to both serum samples, with a dilution factor of 1/100 for P4 labeled to carry out competitive assays. Serum samples were introduced in the immunoreactor without any previous pretreatment. Obtained results are shown in Table 1, where current values represent an average of three replicated measurements, Recovery percentage values obtained were very good. Concentration values obtained by the ELISA method for the same samples are also shown in Table 1. The results obtained using both methods are very good.

The biosensor stability was tested for nearly 25 days at a P4 constant concentration in the inmunoreactor system. Current responses were practically constant during this period.

Table 1
Statistical analysis of inmunoreactor responses for two samples of serum with different amounts of spiked P4.

c^*_{P4} [a] (ng mL^{-1})	Current[b] (nA)	c^*_{P4} [c] (ng mL^{-1})	%VC[d]	Recovery (%)	c^*_{P4} [e] (ng mL^{-1})
1	50.0	1.03	4.02	103	0.995
5	38.1	5.10	5.80	102	4.86

[a] P4 concentration in samples of bovine serum.
[b] Current values represent an average of three measurements.
[c] Average value of P4 concentration determined by the immunosensor.
[d] Percentage variation coefficient.
[e] Average value of P4 concentration determined by ELISA method.

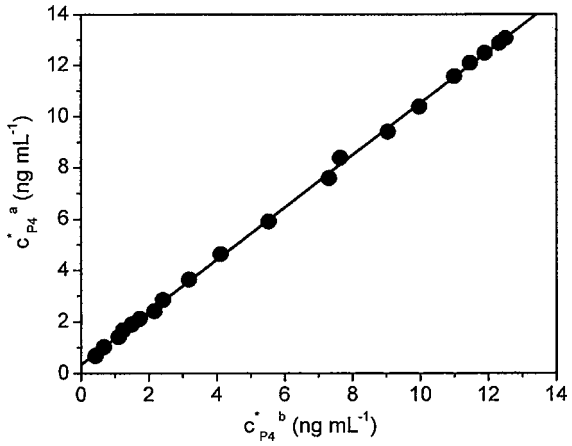


Fig. 5. Correlation between amperometric and commercial photometric assays. Slope = (1.019 ± 0.005), intercept = (0.34 ± 0.04) and r = 0,9997. (a) P4 concentration determined by ELISA method; (b) P4 concentration determined by the electrochemical immunosensor.

The immunoreactor was regenerated by injection of desorption buffer (0.1 mol L^{-1} glycine–HCl, pH 2.0) for 2 min and then washed with 0.01 mol L^{-1} in PBS (pH 7.0), which allowed us to use the reactor with about 100 determinations. For these measurements, P4 standard solutions as well as serum samples were employed alternatively. The reproducible current values that were found showed that the antibody activity loss was not observed. Then, the immunoreactor could be used for performing further analysis.

3.6. Correlations with ELISA assay procedure

The ELISA method was applied in accordance with the manufacturer's protocol. A calibration curve using the absorbance changes was constructed (figure not shown). The expression obtained using a least square procedure was:

$$\text{Absorbance} = (0.993 \pm 0.007) - (0.055 \pm 0.001)\,[\text{ng}^{-1}\,\text{mL}]\,c^{*}_{P4}\,[\text{ng mL}^{-1}] \quad r = 0.995$$

The %VC for the determination of 1 and 5 ng mL^{-1} P4 in bovine serum samples was 4.02 and 5.80% (three replicates), respectively. Results obtained by using the two methods are shown in Fig. 5.

Results of the linear correlation between the two methods render a slope of (1.019 ± 0.005) and an intercept of (0.34 ± 0.04) indicating a very good agreement between both methods (Fig. 5).

P4 ELISA assay kits for in-clinic uses allow P4 concentration to be determined either qualitatively or quantitatively. These results are usually obtainable within 45 to 60 min of sample collection. Most kits are modifications of kits marked for P4 assays used in the dairy industry [9]. The DL obtained for the ELISA procedure is similar to that determined with the electrochemical immunosensor (see Section 3.6). However, the ELISA method requires longer times of analysis. In a conventional ELISA test kit, 96 samples can run simultaneously. We did not compare the number of samples with this electroanalytical method but we just compared the general time of assays. This electroanalytical method could work with more immunosensors simultaneously. The determined number of samples analyzed with this methodology was greater than that obtained with the commercial ELISA test kits. Furthermore, ELISA test kit can be used only for one assay while the immunosensor we described can be used for up to 100 determinations.

Other electrochemical immunosensors to determine P4 in milk have been recently proposed [13–15]. Although the DL is comparable, most of them have higher variation coefficients (6–9%) as well as a longer analysis time. In addition, an important advantage of the immunosensor described in this paper is that it can perform up to 100 determinations before it is regenerated in a very simple way.

4. Conclusions

In this study an electrochemical immunosensor was developed to determine P4 at trace levels in the concentration range of interest in animal sera, particularly of bovine origin. These determinations performed without any pretreatment of samples would indicate the great selectivity of the antibody used. The immunoreactor developed can operate as a fast, selective, and sensitive detector when it is incorporated into a flow injection analysis system. The immunoreactor also minimizes the use of expensive antibodies and other reagents. It also shows physical and chemical stability, a wide working potential range and accuracy. It does not require highly skilled technicians or expensive and dedicated equipments. The electrochemical detection was carried out within 2 min and the total analysis time does not exceed 30 min. Moreover, the bonding between two biological molecules (P4 and HRP) was performed successfully, which allowed us to carry out competitive assays. Immunosensors based on specific reactions between antibodies and antigens seem to be promising alternative tools for the routine veterinary, clinical, biological, physiological assays and analytical practices.

Acknowledgements

Financial support from Consejo Nacional de Investigaciones Científicas y Técnicas (CONICET), Agencia Nacional de Promoción Científica y Tecnológica (FONCYT) and Secretarías de Ciencia y Técnica (SECyT) from the Universidad Nacional de Río Cuarto and Universidad Nacional de San Luis. F.J. Arévalo acknowledges CONICET for research fellowships. We thank to Verónica Muñoz for language assistance.

References

[1] C.A. Vijayavardhara, B. Halsall, W. Heineman, in: A. Brajter-Toth, J.Q. Chambers (Eds.), Electroanalytical Methods for Biological Materials, Marcel Dekker, New York, 2002.
[2] D. Hernández-Santos, M.B. González-García, A. Costa-García, Electroanalysis 14 (2002) 1225.
[3] P.L. Senger, Pathways to Pregnancy and Parturition, Current Conceptions, Inc., Pullman, USA, 1999.
[4] M.S. Christian, R.L. Brent, P. Calda, J. Mat-Fet. Neonat. Med. 20 (2007) 89.
[5] E. Ehrentreich-Forster, F.W. Scheller, F.F. Bier, Biosens. Bioelectron. 18 (2003) 375.
[6] L.E. McDonald (Ed.), Veterinary Endocrinology and Reproduction, 4th ed., Lea & Febinger, Philadelphia, London, 1989.
[7] P.J. Ball, Br. Vet. J. 138 (1982) 546.
[8] G. England, W. Concannon, Recent Advances in Small Animal Reproduction, International Veterinary Information Service, Ithaca, New York, USA, 2002, www.ivis.org.
[9] S.S. Deshpande, Enzyme Immunoassays, from Concept to Product Development, Chapman & Hall, New York, 1996.
[10] A.M.G. Bosch, H. Van Hell, J. Brands, R.H.W.M. Schuurs, in: S.P. Pal (Ed.), Proceedings of the International Symposium on Enzyme Labeled immunoassay of Hormones and Drugs, Walter de Gruyter, Berlin, 1978.
[11] V. Pucci, F. Bugamelli, R. Mandrioli, B. Luppi, M. Raggi, J. Pharm. Biomed. Anal. 30 (2003) 1549.
[12] J.P. Hart, R.M. Pemberton, R. Huxton, R. Wedge, Biosens. Bioelectron. 12 (1997) 1113.
[13] R.W. Claycomb, M.J. Delwiche, C.J. Munro, R.H. Bon Durant, Biosens. Bioelectron. 13 (1998) 1165.
[14] R.W. Claycomb, M.J. Delwiche, Biosens. Bioelectron. 13 (1998) 1173.
[15] V. Carralero, A. González-Cortés, P. Yánez-Seldeño, J.M. Pingarrón, Anal. Chim. Acta 596 (2007) 86.
[16] G. Gubitz, C. Shellum, Anal. Chim. Acta 283 (1993) 421.
[17] W.R. Heineman, H.B. Halsall, Anal. Chem. 57 (1985) 129.
[18] D. Athey, C.J. McNeil, J. Immunol. Methods 176 (1991) 153.
[19] S.S. Babkina, E.P. Medyantseva, H.C. Budnikob, M.P. Tyshlek, Anal. Chem. 68 (1996) 3827.

[20] K.R. Wehmeyer, H.R. Halsall, R. Heineman, C.P. Volle, I.W. Chen, Anal. Chem. 58 (1986) 135.
[21] J. Parellada, A. Narvaes, M.A. Lopez, E. Domínguez, J.J. Fernández, J. Katakis, Anal. Chim. Acta 362 (1998) 47.
[22] T. Lim, Y. Komoda, N. Nakamura, T. Matsunaga, Anal. Chem. 71 (1999) 1298.
[23] ABBOTT Diagnostics, Enzyme Immunoassay for the Quantitative Determination of Progesterone [Instruction Manual], Abbott Laboratories, Abbott Park, IL, U.S.A., 2009.
[24] L. Gorton, Electroanalysis 7 (1995) 23.
[25] C. Ruan, Y. Li, Talanta 54 (2001) 1095.
[26] N. Cénas, J. Rozgaite, A. Pocius, J.J. Kulys, J. Electroanal. Chem. 154 (1983) 121.
[27] L. Gorton (Ed.), Biosensors and Modern Biospecific Analytical Techniques, 44th ed., Elsevier, Amsterdam, Netherlands, 2005.
[28] G.A. Messina, A.J. Torriero, I.E. De Vito, J. Raba, Talanta 64 (2004) 1009.

Talanta 80 (2010) 1993–1998

Contents lists available at ScienceDirect

Talanta

journal homepage: www.elsevier.com/locate/talanta

Serum-protein effects on the detection of the β-blocker propranolol by ion-transfer voltammetry at a micro-ITIES array

Courtney J. Collins, Conor Lyons, Jörg Strutwolf, Damien W.M. Arrigan*

Tyndall National Institute, Lee Maltings, University College Cork, Cork, Ireland

ARTICLE INFO

Article history:
Received 31 July 2009
Received in revised form 8 October 2009
Accepted 23 October 2009
Available online 10 November 2009

Keywords:
Voltammetry
Liquid/liquid interface
Immiscible electrolyte solutions
Bioanalytical
Drug monitoring

ABSTRACT

In this work, the effect of the serum protein, bovine serum albumin (BSA), on the detection of propranolol in artificial serum by ion-transfer voltammetry at an array of micro-interfaces between two immiscible electrolyte solutions (μITIES) is presented. Cyclic voltammetry (CV), differential pulse voltammetry (DPV), and differential pulse stripping voltammetry (DPSV) were examined for the detection of low concentrations of propranolol. Both CV and DPV had an interference effect from BSA, manifested as lower currents in the presence of the protein. DPSV proved to be the most effective technique, enabling the detection of 0.05 μM propranolol in the presence of BSA. The DPSV method employed a preconditioning step as well as a preconcentration step followed by the analytical signal generation step. The latter was based on the back-transfer of the drug across the μITIES. The preconcentration step was crucial to prevention of the adverse effects of BSA on the voltammetric detection. These results demonstrate that serum-protein effects on drug detection at low concentrations can be eliminated by use of DPSV at arrays of μITIES. CVs of propranolol with increasing concentrations of BSA revealed the influence of the drug–protein binding interaction, with decreases in current but no change in transfer potential. Therapeutic concentrations of propranolol were detected, demonstrating the viability of this approach for bioanalytical investigations.

© 2009 Elsevier B.V. All rights reserved.

1. Introduction

Blood and blood-derived samples remain the most investigated physiological matrices for the direct detection of drugs as it provides information on the circulating concentration of the analyte of interest. However, drug detection can be hindered due to drug–protein binding. The most abundant protein in blood is serum albumin, which comprises *ca.* 60% of the total albumin [1], and exhibits a high affinity towards drugs [2–4]. The pharmacological activity of drugs is a function of their free (i.e. non-protein bound) concentration in plasma. One drug with a high affinity for plasma protein binding is propranolol. It has been reported that 90–95% of propranolol, which is the most widely used adrenergic α-receptor blocking agent, binds to plasma proteins [5]. Reports in the literature indicate that propranolol binds to both serum albumin and to α-acid glycoprotein in blood [6–8]. Paxton and Calder [9] investigated the effect of propranolol binding in serum as a function of drug concentration, pH, and temperature using dialysis and ultrafiltration methods and found that an increase in pH and a decrease in temperature reduced the percentage of free (unbound) propranolol. Changes in propranolol concentrations were found to have no effect. It was found that the maximum serum concentration of propranolol (260 ± 80 nM) occurred 1 h after its oral administration (80 mg) [10]. The parameters of propranolol binding to human serum albumin have also been investigated, with a binding constant of $\sim 1000\ M^{-1}$ at 37 °C estimated by capillary electrophoresis [11]. Propranolol has been detected in serum using various analytical techniques, encompassing solid phase microextraction [12,13], capillary electrophoresis [14] and high-performance liquid-chromatography [15]. It is known that interactions between drugs and proteins are extremely important for drug development, with the binding affecting absorption, distribution and metabolism of many common drugs [16,17]. Serum albumin itself is chiefly responsible for the maintenance of blood pH [18]. In this work, bovine serum albumin (BSA) was selected as a model protein because of its abundance, low cost, ease of purification and stability [19,20]. BSA is a water-soluble globular protein comprised of a single 582 amino acid chain containing 17 cystine residues. These cystine residues provide eight disulfide bonds and one free thiol. In contrast to human serum albumin, BSA contains two tryptophan residues, placed in positions 134 and 212 [21]. It has well-known surfactant properties, a molar mass of 69,000 amu, a hydrodynamic radius of *ca.* 3.25 nm [22] and an isoelectric point (p*I*) of 4.7. Shi et al. [23] reported the net charge of BSA at pH 7.4 was

* Corresponding author.
E-mail address: damien.arrigan@gmail.com (D.W.M. Arrigan).

0039-9140/$ – see front matter © 2009 Elsevier B.V. All rights reserved.
doi:10.1016/j.talanta.2009.10.060

−17. This negative charge and the positive charge of propranolol at physiological pH contribute to drug–protein binding.

Electrochemistry at the interface between two immiscible electrolyte solutions (ITIES) [24–27] has been of growing interest over recent decades due to the opportunities it offers for label-free detection of various bioactive substances including peptides, proteins [28,29] and drug molecules [30–33]. Studies have found that proteins adsorb at this liquid–liquid interface [34,35], with some protein behaviours depending on the aqueous phase pH and the nature of the electrolyte anion in the organic phase [28,36,37]. BSA was also found to adsorb at the liquid–liquid interface. Vanysek et al. [22,38] have studied BSA adsorption at the water–nitrobenzene interface using AC impedance measurements and found that adsorption caused the transfer properties of the interface to be altered.

In this paper, the effect of BSA in an artificial serum matrix on the detection of propranolol at an array of miniaturised ITIES was investigated. Such micro-interface (or μITIES) arrays were previously prepared by laser-ablation of holes in thin polymer sheets [39]. These microhole-based ITIES were shown to behave like inlaid microdisc electrodes [40] and had advantages over regularly sized interfaces due to reduced ohmic drop, reduced charging current, enhanced mass transport, and improved sensitivity [41–43]. Liquid–liquid micro-interface arrays have been typically fabricated within thin polymer sheets such as poly(ethylene terephthalate), PET [41,44–48]. Recently, micropore silicon membranes prepared by photolithography and silicon etching processes were introduced [49] and shown to be useful for detection of dopamine and oligopeptides by facilitated ion transfer [28,50,51] and propranolol in an artificial saliva matrix [52].

The aim of the work was to examine the effect of serum protein on the detection of low concentrations of propranolol by voltammetry at the μITIES array. Therefore, propranolol detection in artificial serum with and without BSA was examined and compared using cyclic voltammetry (CV), differential pulse voltammetry (DPV), and differential pulse stripping voltammetry (DPSV).

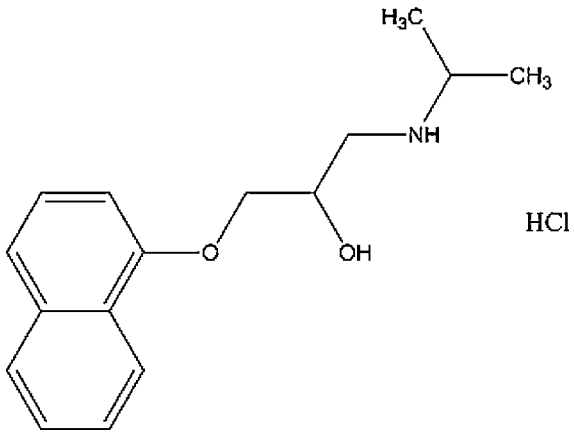
2. Experimental

2.1. Reagents

All chemical reagents were purchased from Sigma–Aldrich and used as received unless indicated otherwise. 1,6-Dichlorohexane (1,6-DCH) (Merck) was purified according to the published procedure [53]. For studies of drug detection at the μITIES array, the aqueous phase was artificial serum [54,55], composed of KCl (1.5 mM), $CaCl_2$ (5 mM), $MgCl_2$ (1.6 mM), D-(+)-glucose (4.7 mM), NaH_2PO_4 (1 mM), KH_2PO_4 (1 mM), urea (2.5 mM, from Qiagen) and bovine serum albumin (0.6 mM). The organogel organic phase was prepared using bis(triphenylphosphoranylidine)ammonium tetrakis(4-chlorophenylborate) (BTPPATCB, 10 mM) in 1,6-DCH and low molecular weight poly(vinyl chloride) (PVC) [28,56]. The BTPPATCB salt was prepared by metathesis [41,57] of bis(triphenylphosphoranylidene)ammonium chloride (BTPPACl) and potassium tetrakis(4-chlorophenyl-borate) (KTCB, Fluka). Propranolol (commercial name: DL-Propranolol hydrochloride, (±)-1-Isopropylamino-3-(1-naphthyloxy)-2-propanol hydrochloride) was purchased from Sigma–Aldrich, relative molecular mass 295.8 g mol^{-1} (see Scheme 1). All aqueous solutions were prepared in purified water from an Elgastat Maxima-HPLC (Elga, UK), with a resistivity of 18 MΩ cm.

2.2. Apparatus

All experiments were performed using a CHI660B electrochemical analyzer (CH Instruments, TX, USA). The micropore arrays were fabricated in silicon using photolithographic patterning and a combination of wet and dry silicon etching [49]. The fabrication procedure provided micropores with hydrophobic walls so that the organic phase filled the pores [49,51]. The micropore array consisted of eight micropores arranged in a hexagonal close-packed arrangement, each with a diameter of 52 μm and a pore center-to-center distance of 500 μm. The microporous silicon membranes were sealed onto the lower orifice of a glass cylinder using a silicone rubber (RS 555-588 silicon rubber compound). The gellified organic phase solution was introduced into the silicon micropores via the glass cylinder, and the organic reference solution was placed on top of the gellified organic phase. The silicon membrane was then immersed into the aqueous phase (artificial serum) and voltammetric experiments performed, as previously described [28,51,52].



Scheme 1. Chemical structure of DL-Propranolol hydrochloride, (±)-1-Isopropylamino-3-(1-naphthyloxy)-2-propanol hydrochloride.

2.3. Electrochemical measurements

The waveform parameters used for DPV and DPSV were as follows: pulse amplitude: 0.05 V; sampling width: 0.055 s; step height: 4 mV. These were applied for all differential pulse voltammetry experiments. For double layer capacitance measurements both a μITIES array and a macro-ITIES electrochemical cell was used. The latter was a four-electrode liquid–liquid cell, with 1,2-dichloroethane containing BTPPATCB (10 mM) as the electrolyte. The interfacial potential difference was applied between a pair of Ag|AgCl reference electrodes. The current was measured by two platinum counter electrodes (one in each phase). The geometric area of the interface in the macro-ITIES cell was 0.95 cm^2.

3. Results and discussion

3.1. Effect of serum albumin on voltammetry at the μITIES array

At physiological pH, BSA bears an overall charge of ∼−17 and propranolol (pK_a 9.23) has a charge of +1. This makes it likely that albumin–propranolol binding will occur, although shielding of the charges by the electrolyte ions will decrease this to some extent. As discussed in Section 1, not only does BSA bind to propranolol [5] but it also adsorbs to the liquid–liquid interface [22,38]. As a result, BSA may hinder the detection of propranolol at the μITIES array by either binding to propranolol and preventing its transfer across the interface or by adsorbing at the μITIES and preventing propranolol transfer. To investigate the effect, two separate artificial serum solutions were prepared: one without BSA and the other containing a physiological concentration of BSA. CV and DPV analyses were carried out on these matrices spiked with 100 μM propranolol (Fig. 1).

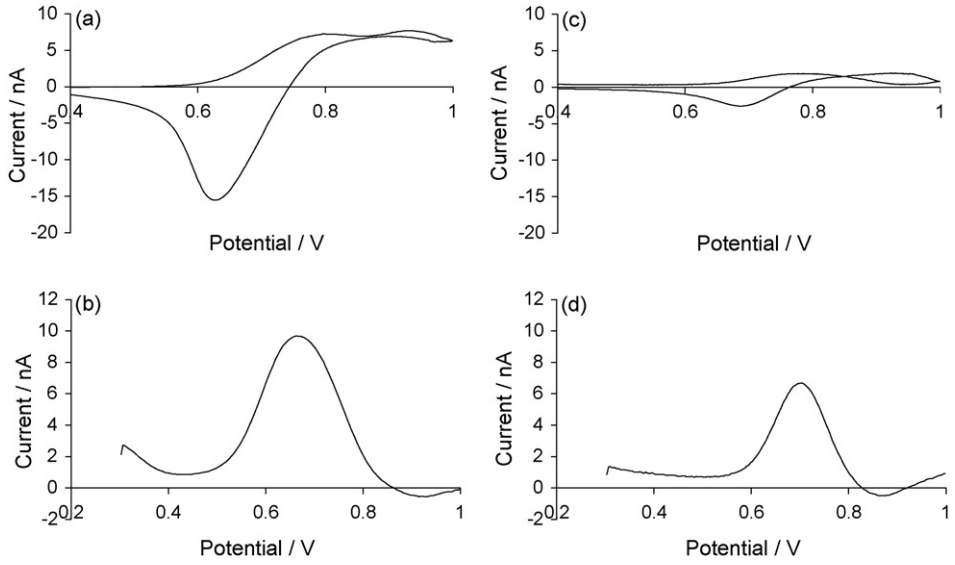


Fig. 1. Electrochemistry of 100 μM propranolol in artificial serum at the μITIES array using (a) cyclic voltammetry (background-subtracted), scan rate, 10 mV s^{-1} (serum without BSA); (b) differential pulse voltammetry (background-subtracted) (serum without BSA); (c) cyclic voltammetry (background-subtracted), scan rate, 10 mV s^{-1} (serum with BSA); (d) differential pulse voltammetry (background-subtracted) (serum with BSA) [the loops in the higher potential regions of (a) and (c) are artifacts of the background subtraction].

The background-subtracted CVs exhibited an asymmetric shape, with an apparent steady-state curve on the forward sweep and a peak-shaped response on the reverse sweep (Fig. 1(a) and (c)). This is due to spherical diffusion of propranolol to the micropores as the controlling mass-transport process occurring on the aqueous side of the interface during the forward sweep. The back-transfer of propranolol from the organogel phase (negative sweep) was controlled by linear diffusion within the micropores, producing a peak-shaped current response, as identified previously by Shao et al. for μITIES formed at micropipettes [58]. It was observed that the peak current magnitudes of the forward and reverse sweeps for propranolol in artificial serum without BSA were almost four times greater than for propranolol in artificial serum with BSA. The forward peak for propranolol transfer from the artificial serum (containing BSA) into the organogel phase was extremely small. This indicated that a lower concentration of free propranolol was present in the aqueous phase, as current signals are proportional to the concentration of the transferring analyte. This reduction in current signal due to the presence of BSA was also seen with background-subtracted DPV (Fig. 1(b) and (d)). For DPV, the potential was scanned in the positive direction only, corresponding to a transfer of the positively charged propranolol from the aqueous phase into the organogel phase. Higher current values were recorded for DPV in comparison to CV values, a feature of its increased sensitivity, thus allowing for better detection of propranolol in artificial serum containing BSA. However, as seen with the CVs, higher peak currents were recorded for propranolol detection in artificial serum without BSA.

These results suggested that BSA has a major influence on the detection of propranolol in artificial serum. Although detection of propranolol in the presence of BSA was possible, peak currents were severely diminished. DPV was shown to provide a more sensitive detection signal for low concentrations of propranolol in the presence of BSA in comparison to CV. As a result, DPV was further investigated.

3.2. Differential pulse voltammetry at the μITIES array

The DPV method consisted of a preconditioning step and a voltammetric step. The preconditioning step may be employed prior to a subsequent voltammetric step in a series of repeated measurements in order to remove any detectable residue of target analyte from the organogel phase remaining after the previous electrochemical measurement step. This ensures that the organogel phase is cleaned. This step is essentially the application of a potential more negative than the transfer potential of the analyte for a given period of time. The optimum preconditioning time for this μITIES arrangement was found to be 90 s [52] and was employed in all DPV experiments at a preconditioning potential of 0.35 V. Increasing concentrations of propranolol were added to two separate artificial serum solutions (without and with BSA) as shown in Fig. 2(a) and (b), respectively. The lowest concentration of propranolol detected when added to serum without BSA was 1 μM; however the lowest concentration detected for propranolol in the presence of BSA was 4 μM.

On examination of both sets of voltammograms it was apparent that BSA caused a reduction in the propranolol detection peak currents. Nevertheless, the currents increased linearly with propranolol concentration both in the absence and in the presence of BSA, as summarized in Table 1. The peak current responses for propranolol were higher in artificial serum without BSA. The precision of the measurements at any single concentration was assessed by the relative standard deviations. These were in the range of 2.8–4.9% and 0.5–23.2% across the concentration ranges studied (as listed in Table 1) for propranolol in artificial serum in the absence and in the presence of BSA, respectively.

Different analytical sensitivities (calibration line slopes) were obtained in the absence and presence of BSA. This may be due to a change in the double layer capacitance upon adsorption of BSA at the interface [22]. When molecular or ion adsorption occurs at the ITIES, both the double layer capacitance and the ion transfer properties will be altered [22]. Since the lowest concentration of propranolol detected in the presence of BSA was 4 μM, an improvement was necessary. DPSV, which has proven to offer improved detection capability [52], was thus investigated.

3.3. Differential pulse stripping voltammetry at the μITIES array

The DPSV method employed consisted of a preconditioning step, a preconcentration step and a voltammetric detection step. The preconditioning step (previously discussed) was employed for 90 s at

Table 1
Linearity data for propranolol in artificial serum in the absence and presence of BSA.

Artificial serum	Slope (±S.D.)[a]/nA μM^{-1}	Intercept (±S.D.)[a]/nA	Concentration range/μM	*n*
Without BSA	0.09 ± 0.01	−0.09 ± 0.24	1–35	8
With BSA	0.07 ± 0.01	−0.11 ± 0.002	4–35	7

[a] S.D., standard deviation.

a potential of 0.35 V. The preconcentration step is crucial in DPSV because it is the factor which enables lower detection limits to be achieved. It was implemented by applying a potential more positive than the transfer potential of the analyte to be detected but at a potential more negative than the transfer potentials of the supporting electrolytes. This ensured only the transfer of the analyte into the organogel phase, where it is preconcentrated prior to the subsequent detection scan. The preconcentrated analyte, in this case propranolol, was then stripped out of the organogel phase using a negative-direction DPV scan. A preconcentration time of 180 s at potentials 0.82 V and 0.88 V was employed for artificial serum with and without BSA, respectively.

As illustrated in Fig. 3(a) and (b), as the concentration of propranolol increased the stripping peak current also increased. The peak currents for propranolol detection in artificial serum with and without BSA were similar, indicating that the presence of albumin did not influence the detection capabilities. In fact a concentration of 0.05 μM was detected for propranolol in the presence of BSA, a vast improvement on the 4 μM detected using DPV. A reason for this may be that the preconcentration step in DPSV was potential-controlled, thus allowing for the selective preconcentration of propranolol and the prevention of BSA interaction at the interface. It may be possible that BSA does not adsorb at the interface, thereby not inhibiting propranolol transfer. As discussed previously, it has been reported that 90–95% of total propranolol in serum is bound to serum albumin [5], however since the peak currents in Fig. 3(a) and (b) are very similar, it seems that the preconcentration step induced the dissociation of propranolol from its complex with BSA and allowed it to transfer across the interface. However, propranolol detection can also be influenced by BSA adsorption at the liquid–liquid interface.

The adsorption of large molecules at the ITIES can lead to a change of its capacitance, which in turn can influence the sensitivity of electroanalytical measurements there. Since adsorption of a protein will effect the charge distribution at an ITIES, a change in the interfacial capacitance is expected. Vanysek and Sun [22] reported that the impedance of the ITIES changed on addition of BSA to the cell, which implied that the interfacial structure had changed, most notably in the capacitance of the interface. It was noted that this was because the amino acid residues of BSA consisted of hydrophobic and hydrophilic regions, making it possible for an adsorbed interfacial layer to form at the interface.

3.4. CV of drug–protein interaction

CV can provide useful information on the kinetics of a reaction, the mass-transport process and the electrochemical reversibility of a reaction. In the present experimental system, the following

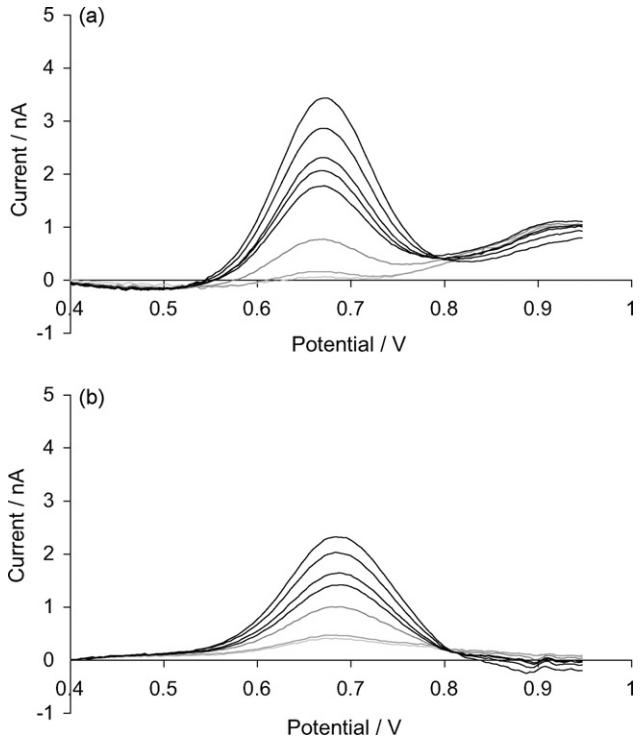


Fig. 2. DPV of increasing propranolol concentrations in artificial serum at the μITIES array. DPV (background-subtracted) (DPV_{bs}) response of (a) artificial serum without BSA for 1 (light gray), 4, 10, 15, 20, 25, 30, and 35 μM (black) and (b) artificial serum with BSA for 4 (light gray), 10, 15, 20, 25, 30, and 35 μM (black) propranolol.

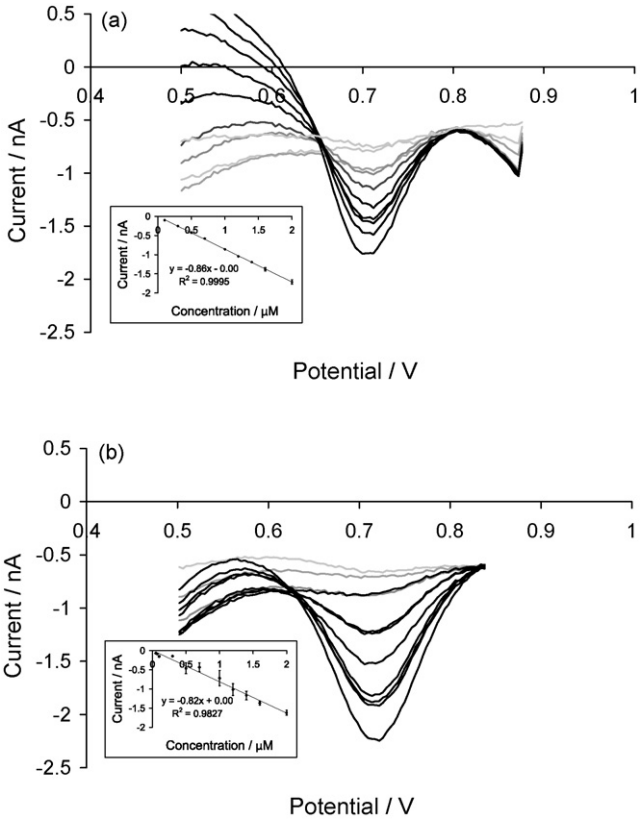


Fig. 3. Electrochemistry of increasing propranolol concentrations in artificial serum at the μITIES using differential pulse stripping voltammetry. DPSV (background-subtracted) (DPV_{bs}) response of (a) artificial serum without BSA and (b) artificial serum with BSA for 0.05 (light gray), 0.1, 0.3, 0.5, 0.7, 1, 1.2, 1.4, 1.6, and 2 μM (black). Inset: calibration curve of current vs concentration.

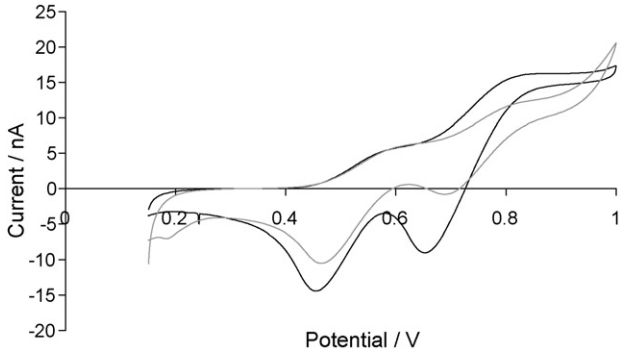


Fig. 4. Cyclic voltammetry of an artificial serum solution of 0.1 mM TPA^+ and 0.2 mM propranolol in the presence of 0 mM BSA (black line) and 1 mM BSA (gray line). Scan rate 10 mV s^{-1}.

reactions occur in solution:

$$[\text{Prop}_{\text{free}}]_{(\text{aq})} + [\text{BSA}_{\text{free}}]_{(\text{aq})} \leftrightarrow [\text{PropBSA}_{\text{complex}}]_{(\text{aq})} \quad (1)$$

$$[\text{Prop}_{\text{free}}]_{(\text{aq})} \rightarrow [\text{Prop}_{\text{free}}]_{(\text{org})} \quad (2)$$

where Prop is propranolol, and the subscripts free and complex refer to non-complexed and complexed propranolol, respectively, and (aq) and (org) refer to locations of the species in the aqueous phase and organic phase, respectively. The binding of drugs to blood plasma is reversible (Reaction (1)) with a rate in the millisecond range [59]. The system is in equilibrium between complexed and free propranolol. To understand the effect of BSA on propranolol transfer, CVs of propranolol transfer at the μITIES array in the absence and presence of different concentrations of BSA were recorded.

CV of these mixtures (Fig. 4) revealed steady-state currents on the forward sweeps, but these were decreased relative to that in the absence of BSA. The relationship between the steady-state current measured on the forward sweep with increasing concentration of BSA was also investigated. The current response for propranolol transfer decreased from ~9.7 nA to ~6.4 nA in the absence and presence (1 mM) of BSA, respectively. Fig. 4 also shows that the half-wave potential for propranolol transfer on the forward sweep was shifted only slightly (Fig. 4). No shift occurred for the reference ion tetrapropylammonium TPA^+ (half-wave potential at ~0.52 V). Neither did a change occur in the transfer current for TPA^+ in the presence of BSA. As BSA concentration increased, the current for propranolol transfer decreased, due to lower concentrations of free drug in solution available for transfer, as expected from Reactions (1) and (2) above. A similar result was obtained for propranolol in the presence of human serum albumin (HSA), with the peak current decreasing from 13 nA (absence) to 8.8 nA in its presence. BSA and HSA have the same effect on propranolol detection. In comparison to BSA, however, the half-wave potential for propranolol transfer on the forward sweep was shifted only slightly, but in the negative direction. No shift occurred in the presence of HSA for the reference ion, TPA^+. These results confirm that complexation of propranolol by serum albumin is an interference mechanism in the detection of propranolol in serum by ion-transfer voltammetry.

4. Conclusions

The effect of BSA on the detection of propranolol by voltammetry at the ITIES was investigated. There was a decrease in the detection signal for propranolol when CV and DPV were employed, however no effect was observed when DPSV was used. As a result, lower concentrations of propranolol were detected with DPSV (0.05 μM) in comparison to DPV (4 μM) in an artificial serum sample matrix. This improvement may be due to the preconcentration step which specifically targets only the transfer of propranolol across the interface. As well as the intended well-known preconcentration effect for stripping voltammetry methods, this option of selectivity may contribute by removing propranolol from its complex with BSA into the organic phases, from where it is subsequently stripped back into the aqueous phase, with this step being seemingly unaffected by complexation with the protein. The interference effect of BSA on propranolol detection is the complexation of the target analyte, making it unavailable for the interfacial charge transfer step.

It was found that propranolol detection at the μITIES array was achievable down to a concentration of 0.05 μM or *ca.* 15 ng mL^{-1}. Blood serum concentrations of propranolol are within the range 46–91 ng mL^{-1}, depending on various health factors [60]. These results demonstrate that propranolol detection in artificial serum in the presence of a globular protein is possible at the μITIES array, with the preconcentration step of DPSV playing a crucial role.

Acknowledgements

This work was supported by Science Foundation Ireland (Grant no. 07/IN.1/B967) and the European Commission's Marie Curie Transfer of Knowledge Programme (Grant no. MTKD-CT-2005-029568). Fabrication facilities employed in this research were supported by the Higher Education Authority's Programme for Research in Third Level Institutions (PRTLI).

References

[1] Y.J. Hu, Y. Liu, T.Q. Sun, A.M. Bai, H.Q. Lu, Z.B. Pi, Int. J. Biol. Macromol. 39 (2006) 280–285.
[2] R. Mallik, M.J. Yoo, S. Chen, D.S. Hage, J. Chromatogr. B 876 (2008) 69–75.
[3] Q.D. Zhang, Y.Y. Huang, R. Zhao, G.Q. Liu, Y. Chen, Biosens. Bioelectron. 24 (2008) 48–54.
[4] P. Zhao, G.J. Zhu, W.B. Zhang, L.H. Zhang, Z. Liang, Y.K. Zhang, Anal. Bioanal. Chem. 393 (2009) 257–261.
[5] R. Zahra, R. Ahmad, M.S. Ali Ashgar, A. Ali, K. Soghra, Indian J. Clin. Biochem. 21 (2006) 121–125.
[6] G.H. Evans, S.A. Nies, D.G. Shand, J. Pharmacol. Exp. Ther. 186 (1973) 114–122.
[7] G. Sager, G. Odd, N. Jacobsen, S. Jacobsen, Biochem. Pharmacol. 28 (1979) 905–911.
[8] K. Ray, W.G. Trawick, R.E. Mullins, Clin. Chem 31 (1985) 131–134.
[9] J.W. Paxton, R.L. Calder, J. Pharmacol. Methods 10 (1983) 1–11.
[10] P. Mahajan, E.D. Grech, R.M. Pearson, E.J. Ridgway, P. Turner, Br. J. Clin. Pharmacol. 18 (1984) 849–852.
[11] Y.S. Ding, X.F. Zhu, B.C. Lin, Chromatographia 49 (1999) 343–346.
[12] W.M. Mullett, P. Martin, J. Pawliszyn, Anal. Chem. 73 (2001) 2383–2389.
[13] H. Kataoka, S. Narimatsu, H.L. Lord, J. Pawliszyn, Anal. Chem. 71 (1999) 4237–4244.
[14] X. Zhu, Y.S. Ding, B. Lin, A. Jakob, B. Koppenhoefer, Electrophoresis 20 (1999) 1869–1877.
[15] I.D. Wainer, T.D. Doyle, K.H. Donn, J.R. Powell, J. Chromatogr. 306 (1984) 405–411.
[16] L.Z. Benet, B. Hoener, Clin. Pharmacol. Ther. 71 (2002) 115–121.
[17] J.R. Simard, P.A. Zunszain, J.A. Hamilton, S. Curry, J. Mol. Biol. 361 (2006) 336–351.
[18] J. Figge, T.H. Rossing, V. Fencl, J. Lab. Clin. Med. 117 (1991) 453–467.
[19] D.C. Carter, J.X. Ho, Adv. Protein Chem. 45 (1994) 153–203.
[20] D.C. Carter, B. Chang, J.X. Ho, K. Keeling, Z. Krishnasami, Eur. J. Biochem. 226 (1994) 1049–1052.
[21] U. Kragh-Hansen, Pharmacol. Rev. 33 (1981) 17–53.
[22] P. Vanysek, Z. Sun, Bioelectrochem. Bioenerg. 23 (1990) 177–194.
[23] Q. Shi, Y. Zhou, Y. Sun, Biotechnol. Prog. 21 (2005) 516–523.
[24] Z. Samec, V. Marecek, J. Weber, J. Electroanal. Chem. 100 (1979) 841–852.
[25] P. Vanysek, R.P. Buck, J. Electrochem. Soc. 131 (1984) 1792–1796.
[26] J.A. Ortuno, J. Hernandez, C.N. Sanchez-Pedreno, Electroanalysis 16 (2004) 827–831.
[27] D.W.M. Arrigan, Anal. Lett. 41 (2008) 1–19.
[28] M.D. Scanlon, G. Herzog, D.W.M. Arrigan, Anal. Chem. 80 (2008) 5743–5749.
[29] G. Herzog, D.W.M. Arrigan, Analyst 41 (2007) 3233–3252.
[30] S. Fantini, J. Clohessy, K. Gorgy, F. Fusalba, C. Johans, K. Kontturi, V.J. Cunnane, Eur. J. Pharm. Sci. 18 (2003) 251–257.
[31] J.A. Ortuno, C. Sanchez-Pedreno, A. Gil, Anal. Chim. Acta 554 (2005) 172–176.
[32] J.A. Ortuno, A. Gil, C. Sanchez-Pedreno, Sens. Actuator B: Chem. 122 (2007) 369–374.
[33] R. Gulaboski, M. Cordeiro, N. Milhazes, J. Garrido, F. Borges, M. Jorge, C.M. Pereira, I. Bogeski, A.H. Morales, B. Naumoski, A.F. Silva, Anal. Biochem. 361 (2007) 236–243.

[34] J. Perrenoud-Rinuy, P.-F. Brevet, H.H. Girault, Phys. Chem. Chem. Phys. 4 (2002) 4774–4781.
[35] D.G. Georganopoulou, D.E. Williams, C.M. Pereira, F. Silva, T.J.S. Su, J.R. Lu, Langmuir 19 (2003) 4977–4984.
[36] G. Herzog, V. Kam, D.W.M. Arrigan, Electrochim. Acta 53 (2008) 7204–7209.
[37] F. Kivlehan, Y.H. Lanyon, D.W.M. Arrigan, Langmuir 24 (2008) 9876–9882.
[38] P. Vanysek, J.D. Reid, M.A. Craven, R.P. Buck, J. Electrochem. Soc. 131 (1984) 1788–1791.
[39] J.A. Campbell, H.H. Girault, J. Electroanal. Chem. 266 (1989) 465–469.
[40] M.C. Osborne, Y. Shao, C.M. Pereira, H.H. Girault, J. Electroanal. Chem. 364 (1994) 155–161.
[41] H.J. Lee, P.D. Beattie, B.J. Seddon, M.D. Osborne, H.H. Girault, J. Electroanal. Chem. 440 (1997) 73–82.
[42] S. Fletcher, M.D. Horne, Electrochem. Commun. 1 (1999) 502–512.
[43] B. Liu, M.V. Mirkin, Electroanalysis 12 (2000) 1433–1446.
[44] S. Wilke, M.D. Osborne, H.H. Girault, J. Electroanal. Chem. 436 (1997) 53–64.
[45] C. Beriet, H.H. Girault, J. Electroanal. Chem. 444 (1998) 219–229.
[46] M.D. Osborne, H.H. Girault, Mikrochim. Acta 117 (1995) 175–185.
[47] Q.S. Qian, G.S. Wilson, K. Bowman-James, H.H. Girault, Anal. Chem. 73 (2001) 497–503.
[48] Q.S. Qian, G.S. Wilson, K. Bowman-James, Electroanalysis 16 (2004) 1343–1350.
[49] R. Zazpe, C. Hibert, J. O'Brien, Y.H. Lanyon, D.W.M. Arrigan, Lab Chip 7 (2007) 1732–1737.
[50] A. Berduque, R. Zazpe, D.W.M. Arrigan, Anal. Chim. Acta 611 (2008) 156–162.
[51] J. Strutwolf, M.D. Scanlon, D.W.M. Arrigan, Analyst 134 (2009) 148–158.
[52] C.J. Collins, D.W.M. Arrigan, Anal. Chem. 81 (2009) 2344–2349.
[53] H. Katano, H. Tatsumi, M. Senda, Talanta 63 (2004) 185–193.
[54] M. Cretin, L. Alerm, J. Bartroli, P. Fabry, Anal. Chim. Acta 350 (1997) 7–14.
[55] S. Makarychev-Mikhailov, A. Shvarev, E. Bakker, Anal. Chem. 78 (2006) 2744–2751.
[56] T. Osakai, T. Kakutani, M. Senda, J. Electrochem. Soc. 134 (1987), C520–C520.
[57] H.J. Lee, H.H. Girault, Anal. Chem. 70 (1998) 4280–4285.
[58] Y. Shao, M.D. Osborne, H.H. Girault, J. Electroanal. Chem. 318 (1991) 101–109.
[59] D.F. Birkett, Aust. Prescip. 15 (1992) 56–57.
[60] J. Wojcicki, V. Sulzyc-Bielicka, J. Kutrzeba, Gawronska-Szklarz, M. Drozdzik, Z. Sterna, J. Clin. Pharmacol. 39 (1999) 826–833.

Talanta 80 (2010) 1999–2006

Contents lists available at ScienceDirect

Talanta

journal homepage: www.elsevier.com/locate/talanta

Electroanalytical determination of estriol hormone using a boron-doped diamond electrode

Keliana D. Santos, Otoniel C. Braga, Iolanda C. Vieira, Almir Spinelli*

Grupo de Estudos de Processos Eletroquímicos e Eletroanalíticos, Universidade Federal de Santa Catarina, Departamento de Química – CFM, 88040-900 Florianópolis, SC, Brazil

ARTICLE INFO

Article history:
Received 12 June 2009
Received in revised form 24 October 2009
Accepted 27 October 2009
Available online 1 November 2009

Keywords:
Hormone
Estriol
Urine
Pharmaceuticals
Electroanalytical method
Boron-doped diamond electrode

ABSTRACT

A boron-doped diamond (BDD) electrode was used for the electroanalytical determination of estriol hormone in a pharmaceutical product and a urine sample taken during pregnancy by square-wave voltammetry. The optimized experimental conditions were: (1) a supporting electrolyte solution of NaOH at a pH of 12.0, and (2) a frequency of 20 Hz, a pulse height of 30 mV and a scan increment of 2 mV (for the square-wave parameters). The analytical curve was linear in the concentration range of 2.0×10^{-7} to 2.0×10^{-5} mol L^{-1} ($r = 0.9994$), with a detection limit of 1.7×10^{-7} mol L^{-1} and quantification limit of 8.5×10^{-7} mol L^{-1}. Recoveries of estriol were in the range of 98.6–101.0%, for the pharmaceutical sample, and 100.2–103.4% for the urine sample, indicating no significant matrix interference effects on the analytical results. The accuracy of the electroanalytical methodology proposed was compared to that of the radioimmunoassay method. The values for the relative error between the proposed and standard methods were −7.29% for the determination of estriol in the commercial product and −4.98% in a urine sample taken during pregnancy. The results obtained suggest a reliable and interesting alternative method for electroanalytical determination of estriol in pharmaceutical products and urine samples taken during pregnancy using a boron-doped diamond electrode.

© 2009 Elsevier B.V. All rights reserved.

1. Introduction

Estriol (1,3,5,(10)-estratriene-3,16α,17β-triol) (Fig. 1) is by far the most abundant estrogen present in pregnant mammals. Estriol is produced by placental syncytiotrophoblasts from dehydroepiandrosterone sulfate and its 16α-derivatives produced by fetal adrenals and the liver, respectively. Since the production of estriol relies on fetal and placental reactions, estriol determinations in blood and urine can be used to monitor the fetus-placental unit and indicate fetal well being. Free estriol is hydrophobic but it is conjugated to hydrosoluble glucuronides and sulfates (70–80% as 16α-glucuronides) by the maternal liver and excreted in the urine [1–2]. The conjugated forms of estriol in urine are quickly hydrolyzed after excretion, leaving estriol in the free form. Oral estriol tablets have been used with good results, primarily for the treatment of local urogenital complaints in postmenopausal women, for over 40 years. One of its product characteristics is that it does not stimulate the endometrium and can, therefore, be used uninterrupted without the cyclical addition of a progestogen to protect the endometrium. Although all available data confirm the endometrial safety of oral estriol tablets, it is considered relevant to update the existing long-term data on this topic [3–4].

Estriol levels in urine, serum and amniotic fluid have been measured by HPLC using various detectors including UV [5,6], fluorescence [7,8] and electrochemical (EC) [9], and different methods such as GC–MS [10,11], micellar electrokinetic chromatography [12], enzyme immunoassay (EIA) [13–15], and radioimmunoassay (RIA) [16]. However, most of these methods require sample preparation steps such as extraction from biological fluids, enzymatic hydrolysis or acidic solvolysis and derivatization. These procedures are tedious and time-consuming, require high-cost equipment and sometimes adversely affect the analytical results. In the case of immunoassays, for example, it is necessary to obtain a specific antibody for this steroid. RIA is currently considered to be the screening method of choice for routine measurements of estriol. Although this method is sensitive and reliable, there are drawbacks associated with the use of radioisotopes, for example, the cost of scintillation fluids, radioactive waste disposal, and its use being restricted to institutes granted permission to handle radioisotopes. Electrochemical studies on alkyl phenols with estrogenic properties have been reported. Vega et al. [17] developed a methodology using a carbon nanotube-modified electrode for amperometric detection of phenolic estrogenic compounds, including estriol, by HPLC. The determination of estriol was obtained in the range of 1.0–100 μmol L^{-1} with a detection limit of 0.340 μmol L^{-1}. The

* Corresponding author at: Universidade Federal de Santa Catarina (UFSC), Centro de Ciências Físicas e Matemáticas (CFM), Departamento de Química, Campus Universitário Trindade, 88040-900 Florianópolis, SC, Brazil. Tel.: +55 48 3721 6844; fax: +55 48 3721 6850.
E-mail address: spin@qmc.ufsc.br (A. Spinelli).

0039-9140/$ – see front matter © 2009 Elsevier B.V. All rights reserved.
doi:10.1016/j.talanta.2009.10.058

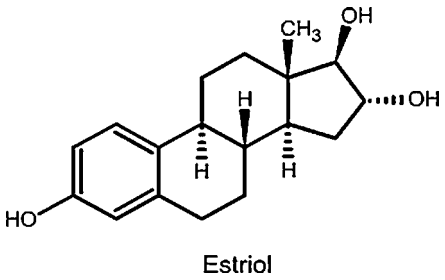


Fig. 1. Chemical structure of estriol.

method was successfully applied to determine estriol in tap water. At the present time, there are no other publications reporting the electrochemical determination or behavior of estriol. Some articles have described the use of chromatographic methods with amperometric detectors to investigate hormones like bisphenol A [18,19], or to develop biosensors for the determination of the hormones 17β-estradiol and estrone [20–24].

In the present study a boron-doped diamond (BDD) electrode was used to develop an electrochemical methodology for determination of estriol. Diamond is an electrical insulator, but conducts heat even more effectively than copper and can withstand very high electric fields. With these physical properties, diamond is an attractive material for electronic applications, particularly when it is rendered conductive through the introduction of charge carriers [25]. Boron has one less electron than carbon and because of its small atomic radius it is relatively easily incorporated into diamond. BDD electrodes have been extensively studied in recent years, in relation of their fundamental electrochemical properties [25] and also in terms of their applications [25,26]. BDD electrodes have high stability and hardness, inert surfaces and very low capacitive background currents. Thus, they have been extensively used in electrosynthesis, electroanalysis, electrochemical combustion, and as electrocatalyst supports [25–27]. Recent reports in the literature have shown that several bio-molecules can be satisfactorily determined using BDD electrodes. Souza et al. [28] quantified sulfonamides in pharmaceutical products and obtained an analytical curve in the concentration range of 8.01×10^{-6} to 1.19×10^{-4} mol L^{-1}. Lourenção et al. [29] developed an electrochemical method for the single or simultaneous determination of paracetamol and caffeine; the calibration curves for the simultaneous determination showed an excellent linear response, ranging from 5.0×10^{-7} to 8.3×10^{-5} mol L^{-1} for both compounds. A methodology to determine perfloxacin in pharmaceuticals and serum presented a linear range for concentrations between 2.0×10^{-6} and 2.0×10^{-4} mol L^{-1} [30]. Many other bio-molecules, including pentachlorophenol, 4-nitrophenol, lincomycin, purine and pyrimidine, dopamine and ascorbic acid, aspartame and cyclamate [31–36], have been determined using BDD electrodes and in all cases the methodologies presented good selectivity, repeatability, reproducibility, precision and accuracy. However, BDD electrodes have not yet been used for the electroanalytical determination of hormones. Thus, the objective of this study is to develop a cost-effective, single-use, feasible, accurate, and reliable method to detect estriol in a complex matrix (urine) and in a drug sample using a boron-doped diamond electrode by square-wave voltammetry.

2. Experimental

2.1. Chemicals and solutions

All reagents used in this study were of analytical grade purchased from Sigma. The solutions were prepared with water purified using a Milli-Q system manufactured by Millipore (Bedford, MA, USA). Sodium hydroxide (pH 12.0) and five buffer solutions were tested as supporting electrolytes: Britton–Robinson (pH 2.0–12.0), acetate (pH 4.5), ammonium (pH 9.4) and Ringer's solution (pH 12.0). All of these solutions had a concentration of 5.0×10^{-3} mol L^{-1}. A solution of 0.1 mol L^{-1} NaOH was used to adjust the pH of the 5.0×10^{-3} mol L^{-1} NaOH supporting electrolyte to 12.0. Progesterone, urea, uric acid, albumin and creatinine were evaluated as potential interferents for estriol determination in urine. The excipients present in the pharmaceutical preparation used in this study (Ovestrion®) are amido, lactose, magnesium stearate and amilopectine. They were tested as potential interferents for estriol determination in the commercial product. Stock solutions of 1.4×10^{-2} mol L^{-1} estriol dissolved in methanol were prepared daily and less concentrated solutions were prepared by dilution. For the recovery studies, standard solutions of the hormone were added to samples of urine and tablets of a commercial product (Ovestrion®). The urine sample was obtained from a woman in the third trimester of pregnancy and no pretreatment was necessary to determine its estriol levels. Commercially available estriol contained 1 mg of estriol. Ten tablets of the medicament were finely macerated in a mortar with a pestle. The powder was weighed in the quantity necessary to prepare the sample solutions, diluted using methanol and mixed for 5 min. The non-dissolved excipients were left to settle and a sample was then withdrawn from the clear supernatant liquor.

2.2. Cell and electrodes

Linear scan, cyclic and square-wave voltammograms were recorded using a 25-mL three-electrode electrochemical cell. The electrochemical detection of estriol was initially tested on five electrodes: copper, platinum, gold, glassy carbon and boron-doped diamond. The electrodes (with the exception of the BDD electrode) were hand-polished before each experiment with 0.05 μm alumina paste and ultrasonically rinsed in deionized water. The BDD working electrode ($A = 0.23$ cm^2) employed for the development of the electroanalytical methodology was a BDD film with around 8000 ppm of boron. A pretreatment procedure was initially applied to the BDD electrode to achieve reproducible results. The procedure consisted of the polarization at −3.0 V of the BDD electrode in 0.5 mol L^{-1} H_2SO_4 for 3 min in a separate cell, as recommended in the literature [27]. Afterwards, the electrode was transferred to the measuring cell containing the supporting electrolyte and estriol, and polarized under stirring at −3.0 V for 30 s between each run. Following this method, excellent electrode response and reproducibility were systematically observed for estriol determination. Platinum wire and Ag/AgCl electrodes were used as auxiliary and reference electrodes, respectively. All potentials were measured versus this reference electrode.

2.3. Instruments

Voltammetric measurements and surface pretreatment of the BDD electrode were performed on a Voltalab PGZ 100 potentiostat/galvanostat interfaced with a computer using the Voltamaster 4.0 software. Linear scan and cyclic voltammmetry were employed for preliminary studies on the electrochemical behavior of the estriol compound. Square-wave voltammetry was used for the development of the electroanalytical methodology and estriol determination in urine and in a commercial drug sample. The accuracy of the proposed method was compared to the standard radioimmunoassay method [37].

3. Results and discussion

3.1. Electrode selection

In order to compare the electrochemical oxidation of estriol, copper, platinum, gold, glassy carbon and BDD were tested as catalyst electrodes. In this study, linear scan voltammetric measurements were carried out from 0.0 to +0.63 V at 50 mV s^{-1} using 2.0×10^{-5} mol L^{-1} estriol in NaOH (pH 12.0) solution. Under these experimental conditions, estriol was electrochemically inactive on copper, platinum and gold electrodes, since no oxidation current was observed. On the other hand, as can be seen in Fig. 2, the voltammograms obtained with the glassy carbon (a and c) and BDD (b and d) electrodes without (a and b) and with (c and d) 2.0×10^{-5} mol L^{-1} estriol solution show that the electrochemical oxidation of estriol produced a good, sensitive and well-defined anodic current peak. However, the current at the BDD electrode was almost 10 times higher than at the glassy carbon electrode. Similar behavior has been systematically observed by other authors for this type of electrode and for other bio-molecules [26,30]. The good performance of BDD electrodes as electrochemical catalysts is due to properties such as low sensitivity to dissolved oxygen and low background currents. The capacitive background current, for example, is ten times lower than that at glassy carbon electrodes [38], making BDD electrodes highly sensitive toward the oxidation/reduction of organic molecules. This study confirms, therefore, that the BDD electrode also offers excellent electrocatalytic properties for the oxidation of hormones, in particular estriol, which is here under study for the first time using this type of electrode surface. Accordingly, the BDD electrode was selected to develop the methodology for the electrochemical determination of estriol.

3.2. Selection of supporting electrolyte

The choice of the supporting electrolyte is an important stage in electroanalytical studies because its composition and pH affect the properties of the solution as well as the electrode–solution interface, modifying the thermodynamics and kinetics of the charge transfer process and the adsorption at the electrode surface [39]. In this study, solutions with different compositions and pH values were tested as the supporting electrolyte to investigate the estriol oxidation at a BDD electrode. Therefore, the buffers Britton–Robinson (pH 2.0–12.0), acetate (pH 4.5), ammonium (pH 9.4) and Ringer's solution (pH 12.0), and the NaOH (pH 12.0) solution, were evaluated. All of these solutions had a concentration of 5.0×10^{-3} mol L^{-1}. Fig. 3A shows the cyclic voltammograms obtained for 5.0×10^{-5} mol L^{-1} estriol in different supporting electrolytes. In all voltammograms, just one oxidation peak was observed when the potential was swept from 0.0 to +1.2 V and back to 0.0 V at a scan rate of 100 mV s^{-1}. As can be seen, estriol oxidized at a high potential of 0.90 V in Britton–Robinson (pH 2.0) solution (Fig. 3A(a)), and a well-defined oxidation peak and analytical signal, i.e. the anodic current density, were observed. In acetate (pH 4.5) buffer (Fig. 3A(b)), the estriol oxidation was observed at 0.75 V with a small current being produced. A very poorly defined current peak was generated at 0.64 V in Britton–Robinson (pH 7.0) buffer (Fig. 3A(c)). The estriol oxidation in ammonium (pH 9.4) (Fig. 3A(d)) and Ringer's solution (pH 12.0) (Fig. 3A(e)) buffers was observed at almost the same potential of 0.45 V. In spite of the well-defined peaks, the analytical signals were also poor. In Britton–Robinson (pH 12.0) solution, a peak with low current and ill-defined peak was observed at 0.40 V (Fig. 3A(f)). The most well-defined oxidation peak and the highest anodic current density were obtained in NaOH (pH 12.0) solution (Fig. 3A(g)). Under this experimental condition the hormone estriol oxidized at 0.38 V, the lowest oxidation potential observed. The relatively high peak current found for estriol oxidation in solutions of pH 12.0 suggests that the electrochemical reaction follows a different mechanism to that in solutions of lower pH and also with a different number of electrons involved. As can be seen in Fig. 3A, the cyclic voltammograms shifted to less positive potentials as the solution pH increased. As a consequence, the water oxidation reaction was anticipated and a narrower cyclic voltammogram was

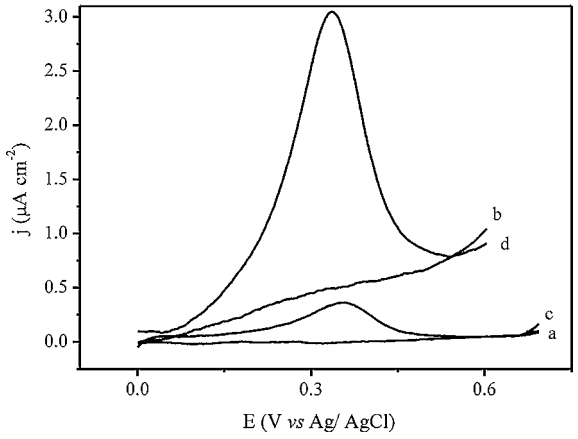


Fig. 2. Linear scan voltammograms for (a) glassy carbon and (b) BDD electrodes in NaOH (pH 12.0) solution and (c and d) in the presence of 2.0×10^{-5} mol L^{-1} estriol, $\nu = 50$ mV s^{-1}.

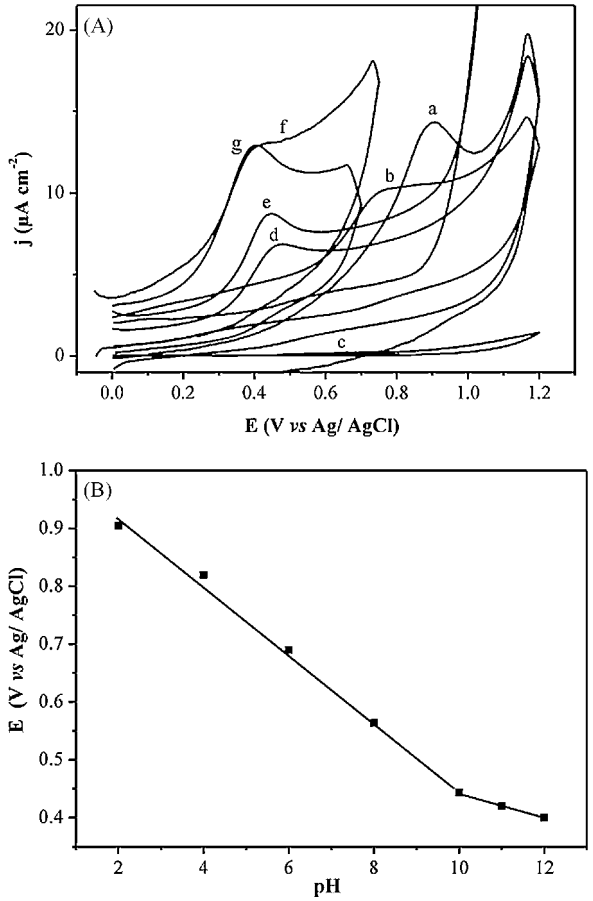


Fig. 3. (A) Cyclic voltammograms for 5.0×10^{-5} mol L^{-1} estriol at a BDD electrode immerse in (a) Britton–Robinson (pH 2.0), (b) acetate (pH 4.5), (c) Britton–Robinson (pH 7.0), (d) ammonium (pH 9.4), (e) Ringer's (pH 12.0), (f) Britton–Robinson (pH 12.0), and (g) NaOH (pH 12.0) solutions, $\nu = 100$ mV s^{-1}. (B) Influence of Britton–Robinson solution pH on the estriol oxidation peak potential.

obtained since the initial potential was the same for all experiments.

The influence of the pH on the oxidation peak of 5.0×10^{-5} mol L^{-1} estriol in Britton–Robinson solutions of pH 2.0–12.0 is shown in Fig. 3B. The increase in pH shifted the estriol oxidation potential to less positive values. This is a typical behavior for the oxidation of phenols and was also observed by Vega et al. [17] for the oxidation of phenolic estrogenic compounds. The intersection of the two straight lines observed in Fig. 3B matches the pK_a of the phenolic group present in the estriol chemical structure. The value found (10.0) is very close to 10.3–10.4, the value reported in the literature [40].

As demonstrated, a good compromise between low detection potential and high peak current was achieved using NaOH (pH 12.0) solution as the supporting electrolyte, which was chosen for further experiments and development of the methodology.

3.3. Electrochemical behavior of estriol at BDD electrode in NaOH (pH 12.0) solution

The cyclic voltammograms shown in Fig. 4 show the electrochemical behavior of 2.0×10^{-5} mol L^{-1} estriol in NaOH (pH 12.0) solution at a BDD electrode. The influence of the potential scan rate on the estriol oxidation was studied over the range of 10–200 mV s^{-1}. The potential was swept from 0.0 to +0.7 V and back to 0.0 V. The cyclic voltammograms are characteristic of an electrochemically irreversible reaction showing just one oxidation peak potential at 0.365 V for a scan rate of 20 mV s^{-1}.

The peak potential shifted to more positive values as the scan rate increased, also in agreement with an irreversible electrochemical behavior. Furthermore, a linear $j \times v^{1/2}$ plot was obtained indicating a diffusion-controlled process of the oxidation reaction. The $\log j \times \log v$ plot showing a slope of 0.64 ($r = 0.999$) confirmed this finding with a small contribution from the adsorption process. Finally, interdependence between the current function ($jv^{-1/2}$) and the potential scan rate indicated that the chemical reaction was coupled to the electrode process, i.e. the reaction followed an EC mechanism. The data collected on the influence of the solution pH and potential scan rate on the electrochemical behavior of estriol at the BDD electrode allow some speculations regarding its oxidation mechanism. The mechanism for the electrochemical oxidation of estriol seems to follow the typical oxidation of phenolic compounds having just one hydroxyl group in their structure [41–43]. Additionally, the cyclic voltammograms of estriol (Fig. 4) are similar to that of β-estradiol [22], a hormone with similar chemical structure.

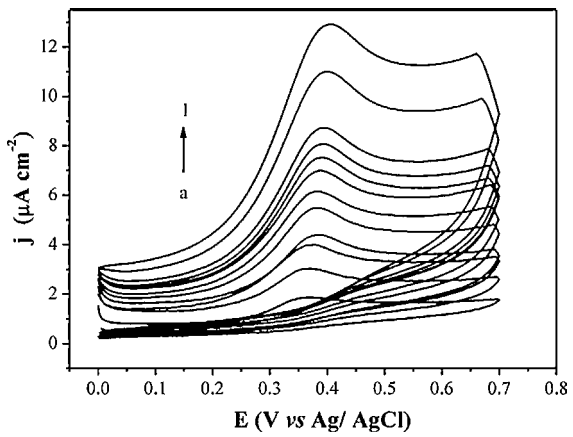


Fig. 4. Cyclic voltammograms for 2.0×10^{-5} mol L^{-1} estriol at a BDD electrode immerse in NaOH (pH 12.0) solution, v (a) 10 mV s^{-1}, (b) 20 mV s^{-1}, (c) 30 mV s^{-1}, (d) 40 mV s^{-1}, (e) 50 mV s^{-1}, (f) 60 mV s^{-1}, (g) 70 mV s^{-1}, (h) 80 mV s^{-1}, (i) 90 mV s^{-1}, (j) 100 mV s^{-1}, (k) 150 mV s^{-1} and (l) 200 mV s^{-1}.

The electrochemical behavior of both hormones shows one oxidation peak and characteristics of an electrochemically irreversible charge transfer.

Hence, we propose that the electrochemical oxidation of estriol forms a phenoxonium ion, the electrochemical step of the EC mechanism, in a two-electron reaction process. Such an oxidation reaction is diffusion-controlled, as indicated by the data obtained at different scan rates. The phenoxonium ion can undergo homogeneous chemical reactions in the sequence, the chemical step of the EC mechanism. The reactions are fast, dependent on the solution pH and irreversible in alkaline media. The resulting products vary according to the rearrangements in the oxidized molecule. In acetonitrile medium, for example, the final identified product was the ketone derivative of β-estradiol [22].

The stability of estriol in NaOH (pH 12.0) solution was initially studied over 6 h by cyclic voltammetry. The cyclic voltammograms obtained over time were reproducible indicating that the estriol solution was stable. The same behavior was observed for a solution studied over 10 days. These experiments indicated that the determination of estriol can be carried out in NaOH (pH 12.0) solution without modifying the composition of the solution containing the analyte.

3.4. Optimization of square-wave voltammetry parameters

Square-wave voltammetry is a pulse technique that offers the advantages of fast speed and good sensitivity for reversible as well as irreversible reactions. The excitation signal is obtained applying a series of forward and reverse pulses superimposed onto a constant-height potential staircase to the working electrode. The current is sampled twice in each wave cycle: once at the end of the forward pulse and once at the end of the reverse pulse. The signal is given by the difference between these two currents. As a consequence, an important step in the development of the electroanalytical methodology is the optimization of the parameters that can influence the voltammetric response. Hence, the dependence of the SWV responses on parameters such as frequency (f), pulse height (PH) and scan increment (ΔE_s) was analyzed in order to optimize the experimental set-up for estriol determination. The SWV parameter optimization was carried out in solutions of 2.0×10^{-5} mol L^{-1} estriol in NaOH (pH 12.0) solution as the supporting electrolyte. The ranges studied were 5–100 Hz for frequency, 10–50 mV for pulse height and 1–5 mV for scan increment. The frequency is one of the most important parameters of SWV since it determines the intensity of the signals and, consequently, the sensitivity of the method. The anodic current density increased with the increase in the frequency at constant PH and ΔE_s values, as shown in Fig. 5A. At higher frequencies, a broadening and a distortion in the voltammograms were observed (data not shown). An excellent compromise between voltammetric profile and sensitivity was obtained at a frequency of 20 Hz. As a consequence, the frequency of 20 Hz was chosen for use in subsequent experiments. For totally irreversible redox systems, analytical sensitivity in the SWV is greatly influenced by variations in the pulse height [44]. It is observed in Fig. 5B that the current density values increased linearly up to 30 mV and for higher values remained almost constant. Thus, a pulse height of 30 mV was selected for further experiments. The scan rate in SWV is the result of the product of the f and ΔE_s. Therefore, a higher ΔE_s can increase the analytical signal and, thus, improve the sensitivity of the method [44]. However, with higher scan increments a broadening of the peak can occur, and thus the resolution of the voltammograms can be affected. Consequently, this is a parameter which also has to be analyzed. In Fig. 5C, it can be seen that the anodic current density remained almost constant for ΔE_s values higher than 2 mV and therefore this ΔE_s value was selected. The optimized values were also used to validate the methodology

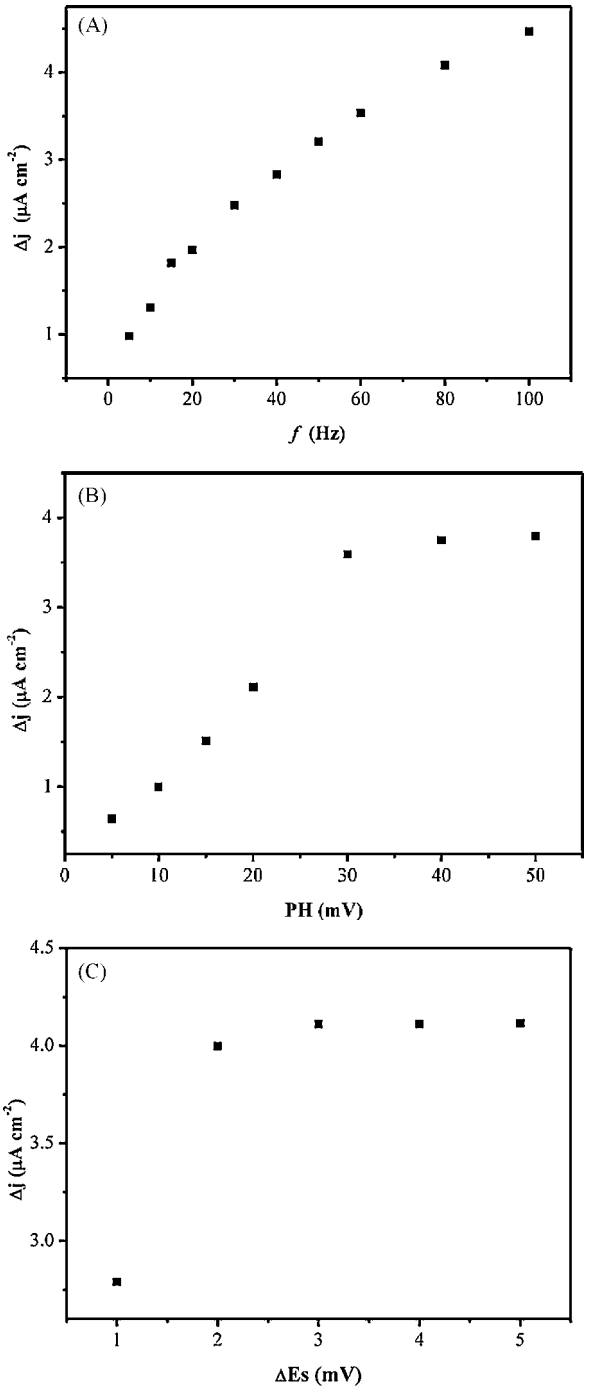


Fig. 5. Dependence of the anodic current density on (A) frequency at PH = 40 mV and ΔE_s = 2 mV, (B) pulse height at f = 60 Hz and ΔE_s = 2 mV and (C) scan increment at PH = 40 mV and f = 60 Hz obtained by square-wave voltammetry for 2.0×10^{-5} mol L^{-1} estriol at a BDD electrode immerse in NaOH (pH 12.0) solution.

proposed as well as for estriol determination in a pharmaceutical product and in urine.

3.5. Analytical curve and validation parameters of the method proposed for estriol determination

The previously optimized SWV parameters were employed to record the analytical curve for estriol in NaOH (pH 12.0) solution as the supporting electrolyte using the BDD electrode. The square-wave voltammograms were collected from 0.0 to 0.7 V and the resultant anodic current density was registered

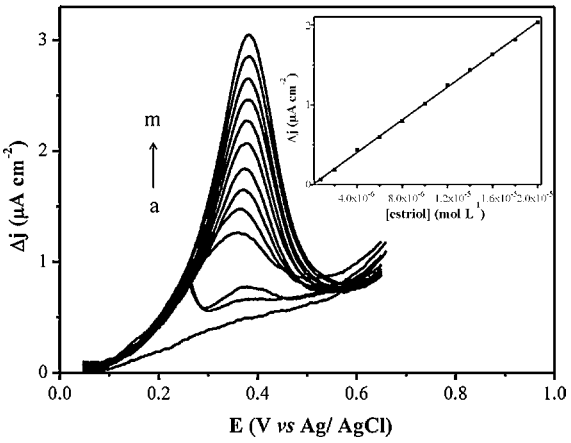


Fig. 6. Square-wave voltammograms for estriol using NaOH (pH 12.0) solution at a BDD electrode: (a) blank; (b) 2.0×10^{-7} mol L^{-1}; (c) 8.0×10^{-7} mol L^{-1}; (d) 2.0×10^{-6} mol L^{-1}; (e) 4.0×10^{-6} mol L^{-1}; (f) 6.0×10^{-6} mol L^{-1}; (g) 8.0×10^{-6} mol L^{-1}; (h) 1.0×10^{-5} mol L^{-1}; (i) 1.2×10^{-5} mol L^{-1}; (j) 1.4×10^{-5} mol L^{-1}; (k) 1.6×10^{-5} mol L^{-1}; (l) 1.8×10^{-5} mol L^{-1}; (m) 2.0×10^{-5} mol L^{-1} (f = 20 Hz; PH = 30 V; ΔE_s = 2.0 mV). Inset: the analytical curve.

at the peak potential. Fig. 6 shows the SWV voltammograms for estriol obtained after successive additions of the respective standard solution and the inset depicts the corresponding analytical curve. For the construction of the analytical curve, the currents shown in the square-wave voltammograms were subtracted from the background current. Table 1 shows some of the validation parameters for the proposed method for estriol determination. As can be seen, a well-defined irreversible oxidation peak was obtained, with the current density increasing proportionally to the estriol concentration. The analytical curve shows a linear response in the range of 2.0×10^{-7} to 2.0×10^{-5} mol L^{-1}. The equation for the straight line can be expressed according to $\Delta j/\mu A\,cm^{-2} = 1.02 \times 10^5$ [estriol]/mol $L^{-1} - 0.0044$. From this plot, the detection limit (DL) was calculated according to the equation: DL = 2 Sb/B, where Sb is the standard deviation of the y-coordinate from the line of best fit (linear coefficient) and B the slope (angular coefficient) of this line. The calculated DL for estriol was 1.7×10^{-7} mol L^{-1}. Additionally, the quantification limit (QL) was calculated using the equation: QL = 10 Sb/B. The calculated QL for estriol was 8.5×10^{-7} mol L^{-1}. The repeatability for five measurements of the current peak for solutions of 5.0×10^{-7} mol L^{-1} estriol, under optimized conditions, was very good, with a relative standard deviation of 0.64%. The reproducibility of the

Table 1
Validation parameters for electroanalytical determination of estriol.

Parameter	Value
Peak potential (V)	0.38
Linear range (mol L^{-1})	2.0×10^{-7} to 2.0×10^{-5}
Correlation coefficient	0.9994
Slope (μA L mol^{-1} cm^{-2}) ($\times 10^5$)	1.02
Standard deviation of slope (μA L mol^{-1} cm^{-2}) ($\times 10^2$)	7.73
Intercept (μA cm^{-2})	−0.0044
Standard deviation of intercept (μA cm^{-2})	0.0088
Detection limit (mol L^{-1})	1.7×10^{-7}
Quantification limit (mol L^{-1})	8.5×10^{-7}
Repeatability of peak current (%)[a,b]	0.64
Reproducibility of peak current (interday) (%)[a,b]	0.98
Reproducibility of peak current (intraday) (%)[a,b]	0.78
Repeatability of peak potential (%)[a,b]	1.05
Reproducibility of peak potential (interday) (%)[a,b]	1.58
Reproducibility of peak potential (intraday) (%)[a,b]	1.23

[a] Relative standard deviation.
[b] n = 5.

Table 2
Estriol determination in commercial pharmaceutical product and in urine sample taken during pregnancy.

Method	Pharmaceutical product		Urine	
	Radioimmunoassay	BDD electrode	Radioimmunoassay	BDD electrode
Labeled values (mg)	1.00	1.00	–	–
Found (mg)[a]	1.03	0.96	–	–
Found (mol L^{-1}) [a]	–	–	8.43×10^{-5}	8.03×10^{-5}
R.S.D. (%)	6.26	1.20	1.37	1.44
Er_1 (%)[b]	2.91	−4.17	–	–
Er_2 (%)[c]	–	−7.29	–	−4.98
t_{value} [d]	0.72	5.5	–	–
F_{value} [e]	0.032	0.032	1.00	1.00

[a] $n = 3$.
[b] Er_1 = relative error between radioimmunoassay or electrochemical methods and labeled values.
[c] Er_2 = relative error between electrochemical method and radioimmunoassay method.
[d] $t_{theoretical} = 5.99$.
[e] $F_{theoretical} = 19$.

current peak was tested using two methodologies: interday, over 5 days using different solutions prepared in the concentration of 5.0×10^{-7} mol L^{-1} and intraday, using five different solutions prepared on the same day and using the same concentration of estriol (5.0×10^{-7} mol L^{-1}). The relative standard deviations ($n = 5$) were 0.98 and 0.78%, respectively. Good data were also obtained for the repeatability and reproducibility of peak potential, as can be seen in Table 1. These results demonstrate that the measurement of the current density and peak potential, as well as of the method proposed, show excellent accuracy, precision, reproducibility, repeatability and sensitivity for estriol determination.

3.6. Estriol determination, recovery and potential interferent studies on a commercial pharmaceutical product

The electroanalytical methodology described above and the standard radioimmunoassay method for estriol determination were applied in pharmaceutical dosage for the hormone quantification. The electroanalytical determination is shown in Fig. 7A. The mean results for three determinations ($n = 3$) of both techniques were very close to the declared value of 1.00 mg; the confidence limits were calculated for a significance level of 0.05. Table 2 summarizes the results obtained. The standard method resulted in a higher value for estriol determination than the value labeled on the commercial pharmaceutical product, while the electroanalytical method resulted in lower values. The relative error between the standard method and the labeled value was 2.91%, while for the method proposed it was −4.17%. The relative error between the method proposed and the radioimmunoassay was −7.29%. The performance of the two methods (proposed and standard) was verified using the Student's *t*- and *F*-tests. The *t*-test was carried out to check the validity of the data obtained using the standard and proposed methods. At the 95% confidence level both results for t_{value} calculated were lower than the result for $t_{theoretical}$ (5.99), indicating no significant differences between the data obtained using the two methods and the true (labeled) values. The precision of the proposed method was compared to that of the standard method through statistical examination of the values obtained from *F*-tests, also at the 95% confidence level. The F_{value} was 0.032, which is lower than the $F_{theoretical}$ (19), indicating excellent performance of the electroanalytical method when compared to the standard method. Taking into consideration that other components of the matrix of the pharmaceutical dosage may interfere with the analysis or accurate quantification of the analyte, potential effects from matrix components must be investigated. If no adequate placebo can be prepared, a known amount of drug substance can also be added to an authentic batch of a drug product (standard addition). In this case, recovery experiments are performed in the presence of the real matrix. The acceptable range of recovery for the analysis of residues is generally between 80 and 120% [45]. As demonstrated in Table 3, the estriol recovery ranged from 98.6 to 101.0%. Furthermore, the slope of 1.09×10^5 μA L mol^{-1} cm^{-2} ($r = 0.9982$) obtained from the curve shown in Fig. 7A, is very close to that obtained from the analytical curve (Table 1), which indicates the excellent selectivity of the method proposed. The results shown in Fig. 7A were converted in order to obtain the same units for the slope of both

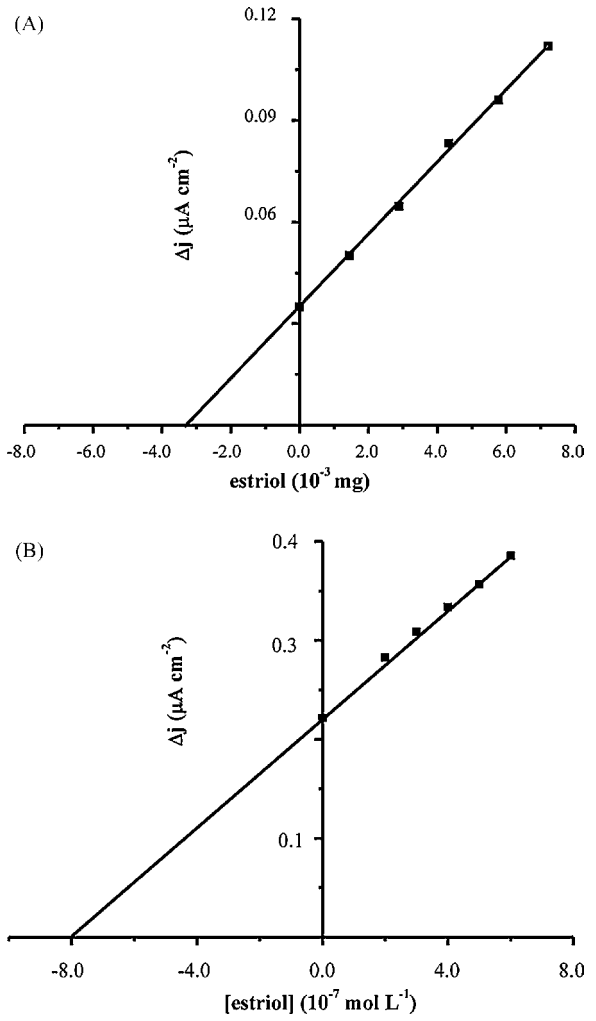


Fig. 7. Electroanalytical determination and recovery studies for estriol in (A) a pharmaceutical product and (B) in urine samples taken during pregnancy using a BDD electrode.

Table 3
Recovery studies for estriol in commercial pharmaceutical drug and in urine sample taken during pregnancy.

Analytes	Added[a]	Found	Recovery (%)
Pharmaceutical	6.00	5.97	99.5
(10^{-7} mol L^{-1})	7.00	6.98	99.7
	8.00	7.89	98.6
	9.00	8.97	99.7
	10.00	10.10	101.0
Urine	2.00	2.07	103.4
(10^{-7} mol L^{-1})	3.00	3.05	101.6
	4.00	4.01	100.2
	5.00	5.08	101.6
	6.00	6.05	100.8

[a] $n = 3$.

curves. Finally, amido, lactose, magnesium stearate and amilopectine (the excipients present in the pharmaceutical preparation used in this study) were also tested as potential interferents. The studies showed that all of them are insoluble in methanol, the solvent used to prepare the solutions. The experiments carried out in the presence of these potential interferents did not change significantly the results described above. These results showed that the proposed method could be applied with great success to assays of estriol in tablet form without any significant matrix interference effects.

3.7. Study of potential interferents for estriol determination in urine

It is well known that urine is a complex matrix and the determination of its components is not an easy task. Urine is composed essentially of water, salts, proteins, principally albumin and creatinine, and uric acid. During pregnancy, it is common for glucose and progesterone concentrations to increase. Most of these compounds could hinder the electrochemical determination of estriol, therefore, studies on interferents were carried out to identify any such influence. The major components of urine, progesterone, urea, uric acid, creatinine and albumin were tested as interferents in a 5.0×10^{-7} mol L^{-1} estriol solution. The estriol:interferent ratios studied were 1:0.01, 1:0.1, 1:1, 1:10 and 1:100. The results for the determination of the anodic current density obtained from the voltammograms recorded for estriol oxidation in the absence and in the presence of the potential interferents are listed in Table 4. As can be seen, the current density generated by the estriol oxidation was almost the same in the absence and presence of the potential interferents. This signifies that progesterone, urea, uric acid, albumin and creatinine did not significantly interfere in the analytical signal produced by the electrochemical oxidation of estriol. Thus, we can extrapolate this observation to a real urine sample and consider that the components of the urine will not significantly interfere in the determination of estriol in urine samples taken during pregnancy.

Table 4
Study of potential interferents for determination of estriol in urine.

	Estriol:interferent ratio					
	(1:0)	(1:0.01)	(1:0.1)	(1:1)	(1:10)	(1:100)
	Anodic current density (μA cm^{-2})[a]					
Progesterone	0.15	0.15	0.16	0.15	0.16	0.16
Urea	0.15	0.15	0.13	0.16	0.15	0.16
Uric acid	0.15	0.16	0.15	0.16	0.15	0.14
Creatinine	0.14	0.14	0.13	0.14	0.14	0.15
Albumin	0.15	0.15	0.16	0.16	0.16	0.17

[a] $n = 3$.

3.8. Estriol determination and recovery studies in urine sample taken during pregnancy

Without any sample preparation, extraction, filtration or evaporation step other than an adequate dilution of the sample, the electroanalytical methodology developed was successfully applied to the determination of estriol in a urine sample taken during pregnancy (Fig. 7B). Table 2 summarizes the results obtained. As can be seen, the value found for estriol determination in urine (8.03×10^{-5} mol L^{-1}, $n = 3$) was lower than that of the comparative radioimmunoassay method (8.43×10^{-5} mol L^{-1}). Both values found were in good agreement with the values published in the pertinent literature [4]. The relative error for the mean of three determinations was −4.98% considering the electroanalytical and radioimmunoassay methods. The precision of the proposed method was compared to the radioimmunoassay method through statistical examination of the values obtained from the *F*-test, considering a 95% confidence level (Table 2). The value for F_{value} (1.0) was lower than that for $F_{theoretical}$ (19.0), indicating excellent performance of the electroanalytical method using the BDD electrode when compared to the radioimmunoassay method. Recovery experiments were performed in the presence of the real matrix in order to check the matrix interference effects. As demonstrated in Table 3, the recovery ranged from 100.2 to 103.4% for estriol, indicating that the composition of the matrix does not significantly interfere in the analytical response of the method proposed. This behavior, i.e. the selectivity of the proposed method, was confirmed by comparing the slopes of the analytical curve (Table 1) and that obtained in Fig. 7B (1.04×10^5 μA L mol^{-1} cm^{-2}, $r = 0.9991$), which were very close. The linearity and slope of the analytical curve and that obtained by the standard addition method, the repeatability and reproducibility of the data and the recovery results obtained for estriol determination using the optimized parameters for SWV and a suitable surface pretreatment for the BDD electrode indicated that the proposed electroanalytical methodology can be successfully applied in control processes and estriol determinations in urine samples taken during pregnancy. The direct determination of estriol in urine here reported is comparable to the existing radioimmunoassay methodology, but with clear advantages, as no preliminary separation steps or pretreatment of the matrix are required.

4. Conclusions

According to the results obtained in this study, it can be concluded that the electroanalytical methodology proposed using a BDD electrode and the SWV technique presented a concentration range and detection limit compatible with the conventional techniques of urine analysis for estriol determination and can also be applied to routine analysis for quality control in the pharmaceutical industry. Another positive aspect observed was the total absence of interferences in the determination of this hormone in a complex sample, in this case urine. The determination of estriol in a urine sample taken during pregnancy was successfully achieved without sample pretreatment. Therefore, this confers credibility and feasibility to the methodology proposed for the determination of estriol in urine samples taken during pregnancy. In addition, due to the simplicity of the preparation procedures, fast routine determinations can also be achieved in the direct electrochemical analysis of estriol and other hormones in pharmaceutical preparations.

Acknowledgements

The authors wish to thank CAPES and CNPq for scholarships and financial support. Prof. Orlando Fatibello-Filho and Prof. Romeu

Costa Rocha-Filho (UFSCar) are gratefully acknowledged for providing the BDD electrode.

References

[1] U. Goebelsmann, R.B. Jaffe, Acta Endocrinol. 66 (1971) 679.
[2] Y. Yaron, M. Cherry, R.L. Kramer, J.E. O'Brien, M. Hallak, M.P. Johnson, M.I. Evans, Am. J. Obstet. Gynecol. 181 (1999) 968.
[3] L.A. Bradley, J.A. Canick, G.E. Palomaki, J.E. Haddow, Am. J. Obstet. Gynecol. 176 (1997) 531.
[4] M.A. Reyes-Romero, Med. Hypotheses 56 (2001) 107.
[5] M.J.L. Alda, S. Díaz-Cruz, D. Barceló, J. Chromatogr. A 1000 (2003) 503.
[6] V. Ingrand, G. Herry, J. Beausse, M. Roubin, J. Chromatogr. A 1020 (2003) 99.
[7] R.W. Reis Filho, J.C. Araújo, E.M. Vieira, Quim. Nova 29 (2006) 817.
[8] X. Huang, D. Yuan, B. Huang, Talanta 75 (2008) 172.
[9] M. Kuster, M.J.L. Alda, M.D. Hernando, M. Petrovic, J. Martín-Alonso, D. Barceló, J. Hydrol. 358 (2008) 112.
[10] N. Tagawa, H. Tsuruta, A. Fujinami, Y. Kobayashi, J. Chromatogr. B 723 (1999) 39.
[11] A. Peñalver, E. Pocurull, F. Borrull, R.M. Marcé, J. Chromatogr. A 964 (2002) 153.
[12] Y.K.K. Koh, T.Y. Chiu, A. Boobis, E. Cartmell, J.N. Lester, M.D. Scrimshaw, J. Chromatogr. A 1173 (2007) 81.
[13] S. Impens, K. Wasch, M. Cornelis, H.F. Brabander, J. Chromatogr. A 970 (2002) 235.
[14] P. Marchand, B. Bizec, C. Gade, F. Monteau, F. André, J. Chromatogr. A 867 (2000) 219.
[15] M.R. Fuh, S.Y. Huang, T.Y. Lin, Talanta 64 (2004) 408.
[16] D. Wu, J. Lin, Z. Li, X. Wang, X. Ying, Fenxi Huaxue 35 (2007) 1241.
[17] D. Vega, L. Agüí, A. González-Cortés, P. Yáñez-Sedeño, J.M. Pingarrón, Talanta 71 (2007) 1031.
[18] M.A. Méndez, M.F. Suárez, M.T. Cortés, J. Electroanal. Chem. 590 (2006) 181.
[19] G.V. Korshin, J. Kim, L. Gan, Water Res. 40 (2006) 1070.
[20] G. Volpe, G. Fares, F. Quadri, R. Draisci, G. Ferretti, C. Marchiafava, D. Moscone, G. Palleschi, Anal. Chim. Acta 572 (2006) 11.
[21] J. Tschmelak, G. Proll, G. Gauglitz, Talanta 65 (2005) 313.
[22] M.M. Ngundi, O.A. Sadik, T. Yamaguchi, S. Suye, Electrochem. Commun. 5 (2003) 61.
[23] K.H.R. Baronian, S. Gurazada, Biosens. Bioelectron. 22 (2007) 2493.
[24] T. Hahn, K. Tag, K. Riedel, S. Uhlig, K. Baronian, G. Gellissen, G. Kunze, Biosens. Bioelectron. 21 (2006) 2078.
[25] F.B. Liu, J.D. Wang, B. Liu, X.M. Li, D.R. Chen, Diam. Relat. Mater. 16 (2007) 454.
[26] L. Codognoto, S.A.S. Machado, L.A. Avaca, Diam. Relat. Mater. 11 (2002) 1670.
[27] G.R. Salazar-Banda, L.S. Andrade, P.A.P. Nascente, P.S. Pizani, R.C. Rocha-Filho, L.A. Avaca, Electrochim. Acta 51 (2006) 4612.
[28] C.D. Souza, O.C. Braga, I.C. Vieira, A. Spinelli, Sens. Actuators B 135 (2008) 66.
[29] B.C. Lourenção, R.A. Medeiros, R.C. Rocha-Filho, L.H. Mazo, O. Fatibello-Filho, Talanta 78 (2009) 748.
[30] B. Uslu, B.D. Topal, S.A. Ozkan, Talanta 74 (2008) 1191.
[31] L. Codognoto, V.G. Zuin, D. Souza, J.H. Yariwake, S.A.S. Machado, L.A. Avaca, Microchem. J. 77 (2004) 177.
[32] V.A. Pedrosa, L. Codognoto, S.A.S. Machado, L.A. Avaca, J. Electroanal. Chem. 573 (2004) 11.
[33] K. Boonsong, S. Chuanuwatanakul, N. Wangfuengkanagul, O. Chailapakul, Sens. Actuators B 108 (2005) 627.
[34] T.A. Ivandini, K. Honda, T.N. Rao, A. Fujishima, Y. Einaga, Talanta 71 (2007) 648.
[35] D.A. Tryk, H. Tachibana, H. Inoue, A. Fujishima, Diam. Relat. Mater. 16 (2007) 881.
[36] R.A. Medeiros, A.E. Carvalho, R.C. Rocha-Filho, O. Fatibello-Filho, Talanta 76 (2008) 685.
[37] E. Diczfaluzy, S. Mancuso, in: A. Kloper, E. Diczfalusy (Eds.), Foetus and Placenta, Blackwell Scientific Publications, Oxford, 1969, pp. 191–248.
[38] I. Duo, P.-A. Michaud, W. Haenni, A. Perret, C. Comninellis, Electrochem. Solid-State Lett. 3 (2000) 325.
[39] S.M.L. Agostinho, R.F.V. Villamil, A. Agostinho Neto, H. Aranha, Quim. Nova 27 (2004) 813.
[40] J.B. Quintana, J. Carpinteiro, I. Rodriguez, R.A. Lorenzo, A.M. Carro, R. Cela, J. Chromatogr. A 1024 (2004) 177.
[41] D. Galato, K. Ckless, M.F. Susin, C. Giacomelli, R.M. Ribeiro-do-Valle, A. Spinelli, Redox Rep. 6 (2001) 243.
[42] C. Giacomelli, K. Ckless, D. Galato, F.S. Miranda, A. Spinelli, J. Braz. Chem. Soc. 13 (2002) 332.
[43] C. Giacomelli, F.S. Miranda, N.S. Gonçalves, A. Spinelli, Redox Rep. 9 (2004) 263.
[44] D. Souza, S.A.S. Machado, L.A. Avaca, Quim. Nova 26 (2003) 81.
[45] M. Ribani, L.F.C. Melo, Quim. Nova 27 (2004) 7.

Talanta 80 (2010) 2007–2015

Contents lists available at ScienceDirect

Talanta

journal homepage: www.elsevier.com/locate/talanta

Quantitative determination of oxybutynin hydrochloride by spectrophotometry, chemometry and HPTLC in presence of its degradation product and additives in different pharmaceutical dosage forms

Nour E. Wagieh[a], Maha A. Hegazy[b,*], M. Abdelkawy[b], Eglal A. Abdelaleem[a,*]

[a] Analytical Chemistry Department, Faculty of Pharmacy, Beni-Suef University, Egypt
[b] Analytical Chemistry Department, Faculty of Pharmacy, Cairo University, Kasr El-Aini St., 11562 Cairo, Egypt

ARTICLE INFO

Article history:
Received 4 August 2009
Received in revised form 15 October 2009
Accepted 2 November 2009
Available online 10 November 2009

Keywords:
Oxybutynin hydrochloride
First derivative of ratio spectra
Principal component regression
Partial least-squares
Chemometrics
Densitometry

ABSTRACT

Simple, accurate, sensitive and validated UV spectrophotometric, chemometric and HPTLC-densitometric methods were developed for determination of oxybutynin hydrochloride (OX) in presence of its degradation product and additives in its pharmaceutical formulations. Method A is the first derivative of ratio spectra (DD^1) which allows the determination of OX in presence of its degradate in pure form and tablets by measuring the peaks amplitude at 216 nm. Method B and C are principal component regression (PCR) and partial least-squares (PLS) for determination of OX in presence of its degradate in pure form, tablets and syrup. While, the developed high performance thin layer chromatography HPTLC-densitometric method was based on the separation of OX from its degradation product, methylparaben and propylparaben followed by densitometric measurement at 220 nm which allows the determination of OX in pure form, tablets and syrup. The separation was achieved using HPTLC silica gel F_{254} plates and chloroform:methanol:ammonia solution:triethylamine (100:3:0.5:0.2, v/v/v/v) as the developing system. The accuracy, precision and linearity ranges of the developed methods were determined. The results obtained were statistically compared with each other and to that of a reported HPLC method, and there was no significant difference between the proposed methods and the reported method regarding both accuracy and precision.

© 2009 Elsevier B.V. All rights reserved.

1. Introduction

Oxybutynin hydrochloride OX, Fig. 1 is an antispasmodic, anticholinergic agent which is commonly indicated for the treatment of overactive bladder with symptoms of urge urinary incontinence and frequency [1]. It is chemically designated as [4-(diethylamino)-2-butynyl (±)-α phenylcyclohexane-glycolate hydrochloride] [2]. The official methods for determination of OX are non-aqueous titration and potentiometric acid–base titration according to USP [3] and BP [4], respectively. A survey of the literature revealed that few methods have been reported for the determination of OX such as UV spectrophotometry [2], RP-HPLC [2,5], HPLC determination of OX in presence of its degradation product [6], an enantioselective method using liquid-phase microextraction (LPME) followed by an HPLC analysis was developed for the determination of OX and its major metabolite N-desethyloxybutynin in rat liver [7], gas chromatography in serum [8], Polymeric matrix membrane sensors were used for stability-indicating potentiometric determination of OX and flavoxate hydrochloride urogenital system drugs [9] and voltammetric technique [1].

So the aim of this work was to develop a comparative study of recent, simple, sensitive, validated stability indicating methods that are of lower cost than the reported HPLC method. Also to develop spectrophotometric methods able to determine the studied drug in presence of methyl and propyl parabens inspite of their high absorptivity. These methods include spectrophotometric, chemometric and HPTLC-densitometric ones for the determination of OX in presence of its degradate in pure form, laboratory prepared mixtures and in its pharmaceutical preparations.

2. Experimental

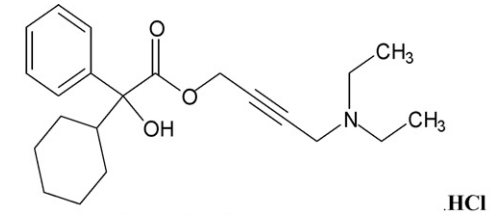
2.1. Samples

2.1.1. Pure samples

Standard oxybutynin hydrochloride OX with claimed purity of 100.02% according to a reported HPLC method [6] was kindly donated by the Egyptian Co. for chemicals and pharmaceuticals, ADWIA, 10th of Ramadan city, Egypt.

* Corresponding authors. Tel.: +202 37802516/+201 12887066.
E-mail address: mahahgazy@yahoo.com (M.A. Hegazy).

0039-9140/$ – see front matter © 2009 Elsevier B.V. All rights reserved.
doi:10.1016/j.talanta.2009.11.002



Mol. Formula $C_{22}H_{31}NO_3$,HCl

Mol. Wt. 393.95

Fig. 1. Chemical structure of oxybutynin hydrochloride.

2.1.2. Pharmaceutical formulations

- Uripan tablets batch no. 0811106, were labeled to contain 5 mg of OX per one tablet, were manufactured by the Egyptian Co. for chemicals and pharmaceuticals, ADWIA, 10th of Ramadan city, Egypt.
- Detronin tablets batch no. 710907, were labeled to contain 5 mg of OX per one tablet, were manufactured by Pharaonia pharmaceuticals, Alexandria, Egypt.
- Uripan syrup batch no. 080470 was labeled to contain 100 mg OX per 100 mL syrup were manufactured by the Egyptian Co. for chemicals and pharmaceuticals, ADWIA, 10th of Ramadan city, Egypt.
- Detronin syrup, batch no. 4038005 and were labeled to contain 100 mg OX, 100 mg methylparaben and 20 mg propylparaben per 100 mL syrup were manufactured by Pharaonia pharmaceuticals, Alexandria, Egypt.

2.2. Chemicals and reagents

- Methanol, ammonia solution, diethylether, ethyl acetate, triethylamine and chloroform (El-Nasr Pharmaceutical Chemicals Co., Abu-Zabaal, Cairo, Egypt).
- HCl and NaOH solutions (0.1N and 1N aqueous solution, respectively). (El-Nasr Pharmaceutical Chemicals Co., Abu-Zabaal, Cairo, Egypt).
- Degraded sample: 0.3 gm of oxybutynin hydrochloride was refluxed with 30 ml of 1N NaOH for three hours. The solution was cooled and then the pH of the solution was adjusted to two pH units for complete precipitation of the degradate then the degradate was extracted with multiple fractions of diethylether (6 mL × 20 mL). The course of the reaction was followed by TLC using plates of silica gel 606F_{254} and using methanol:ethyl acetate:chloroform (1.5.2:7, v/v/v) as a mobile phase. The prepared degradate was subjected to IR and mass spectrometry, where IR spectrum of OX showed a characteristic band at 1741 cm^{-1} indicating the presence of carbonyl group.

2.3. Apparatus

- A double beam UV–vis spectrophotometer (SHIMADZU, Japan) model UV-1601 PC with quartz cell of 1 cm pathlength, connected to IBM compatible computer. The software was UVPC personal spectroscopy software version 3.7.
- Camag TLC scanner 3 S/N 130319 operated with winCATS software.
- Linomat 5 autosampler (Switzerland).
- Camag microsyringe (100 μL).
- Precoated silica gel aluminium Plates 60 F254, ALLUGRAM® SIL G/UV 254 (Machenary-Nagel, Germany) 20 cm × 20 cm with 0.2 mm coating thickness.

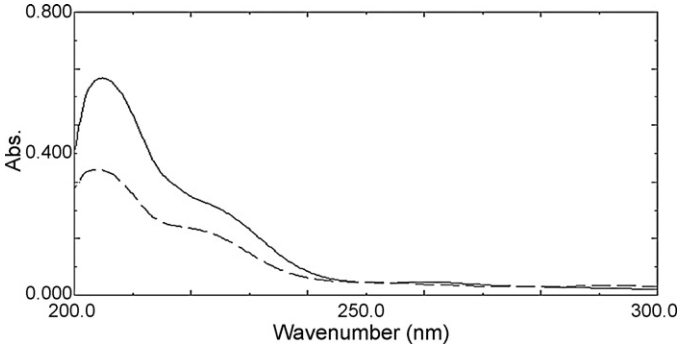


Fig. 2. Zero order absorption spectra of 15 μg/mL of oxybutynin hydrochloride (——) and 15 μg/mL of its degradate (------) using 0.1N HCl as a solvent.

2.4. Software

All computations were performed in Matlab for Windows™ version 6.5 [10]. The PLS procedure was taken from PLS_Toolbox [11] for use with Matlab® 6.5.

2.5. Spectral characteristics

The absorption spectra of OX and its degradate in 0.1N HCl were recorded over the range 200–400 nm using 0.1N HCl as blank, Fig. 2.

2.6. Chromatographic condition

HPTLC was performed using precoated silica 20 cm × 10 cm HPTLC aluminium sheet; the plates were pre-washed with methanol and dried at 60 °C for 15 min prior to sample application. Samples were applied in the form of bands in the length of 4 mm. Linear ascending development was performed in a chromatographic tank previously saturated using chloroform:methanol:ammonia solution:triethylamine (100:3:0.5:0.2, v/v/v/v) as mobile phase for one hour at room temperature.

The mobile phase was allowed to develop 90 mm from the lower edge. The developed plates were air dried and scanned at 220 nm.

Table 1
Concentrations of oxybutynin hydrochloride and the degradate in the calibration and validation set.

Mix. no.	OX (μg/mL)	Degradate (μg/mL)
1	18.00	24.00
2	22.00	20.00
3	18.00	16.00
4	14.00	24.00
5	22.00	24.00
6	22.00	8.00
7	14.00	20.00
8	18.00	20.00
9	18.00	12.00
10	10.00	16.00
11	6.00	8.00
12	6.00	24.00
13	22.00	12.00
14	10.00	24.00
15	22.00	16.00
16	14.00	12.00
17[a]	6.00	20.00
18[a]	18.00	8.00
19[a]	10.00	8.00
20[a]	6.00	12.00
21[a]	14.00	8.00
22[a]	10.00	12.00
23[a]	10.00	20.00

[a] Mixtures of the validation set.

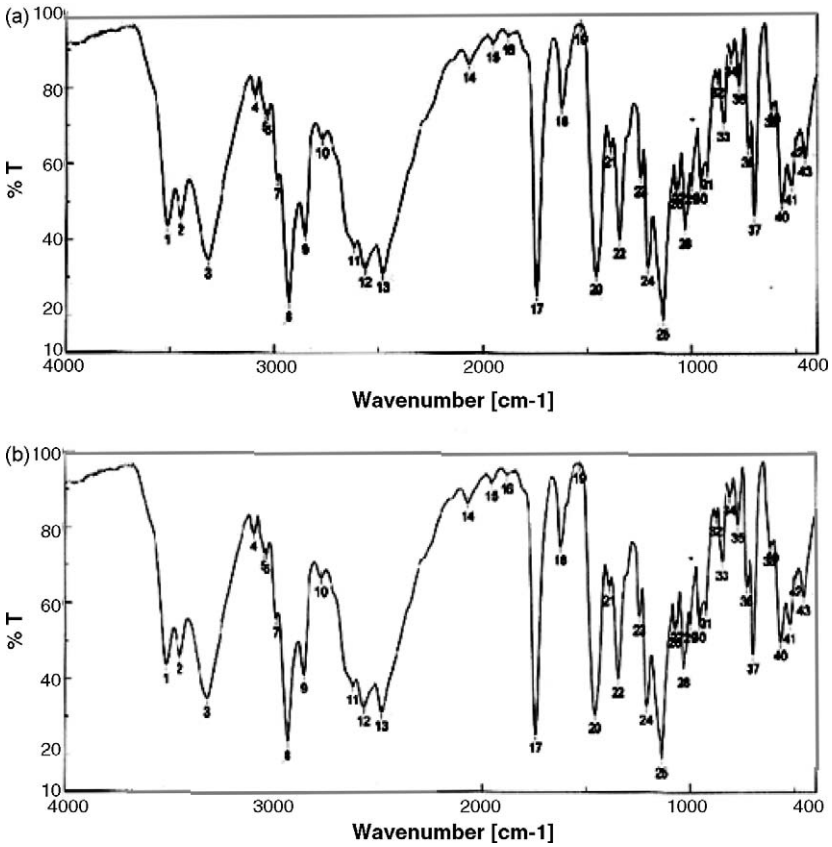


Fig. 3. IR-spectra of oxybutynin hydrochloride (a) and its degradate (b).

2.7. Standard solutions and calibration

For (DD^1) spectrophotometric method

- Stock standard solution of OX and stock solution of the degradate 1 mg/mL were prepared by accurately weighing 100 mg of pure powder of each into two separate 100-mL volumetric flasks dissolved in and diluted to the volume with methanol.
- Working standard solution of OX and working solution of the degradate 100 μg/mL were prepared by transferring 10 mL of stock standard solution of OX and stock solution of the degradate each of 1 mg/mL into two separate 100-mL volumetric flasks dissolved in and diluted to the volume with methanol.

Aliquots equivalent to 60–280 μg OX were accurately transferred from its working standard solution (100 μg/mL) into a series of 10-mL volumetric flasks the volume was completed to the mark with 0.1N HCl to obtain final concentration range of 6–28 μg/mL.

The zero order absorption spectra of the resulting solutions were scanned and divided by the absorption spectrum of 20 μg/mL degradate solution. The peak amplitudes of the first derivative of ratio spectra at 216 nm were differentiated with respect to wavelength with $\Delta\lambda = 4$ and scaling factor = 10) were plotted vs. the corresponding concentration, and regression equation was computed.

2.8. Assay of laboratory prepared mixtures

Solutions containing different ratios of OX and its degradate were prepared to contain 10–90%. The absorption spectra of different laboratory prepared mixtures were divided by the absorption spectrum of 20 μg/mL degradate solution .The DD^1 values were recorded at 216 nm. The concentrations of OX were calculated from the computed regression equation.

For chemometric method

- Stock standard solution of OX and stock solution of the degradate 1 mg/mL were prepared as mentioned previously under (DD^1) spectrophotometric method.
- Working standard solution of OX and working solution of the degradate 100 μg/mL were prepared as mentioned previously under (DD^1) spectrophotometric method.

Multilevel multifactor design was used for the construction of the calibration and validation sets [12]. A five-level, five-factor calibration design was used .The concentrations details are given in Table 1. The absorption spectra of the prepared mixtures were recorded and transferred to Matlab® for subsequent data manipulation. Sixteen mixtures were used for building the calibration model, while seven mixtures were chosen to be used as an external validation set.

For spectrodensitometric method:

Aliquots equivalent to 2–14 mg OX were accurately transferred from its stock standard solution (1 mg/mL) into a series of 10-mLvolumetric flasks dissolved in and diluted to the volume with methanol, 10 μL of each solution was applied on the HPTLC plates. The calibration curve was constructed relating the integrated area under the peak in triplicates to the corresponding concentrations as μg/band.

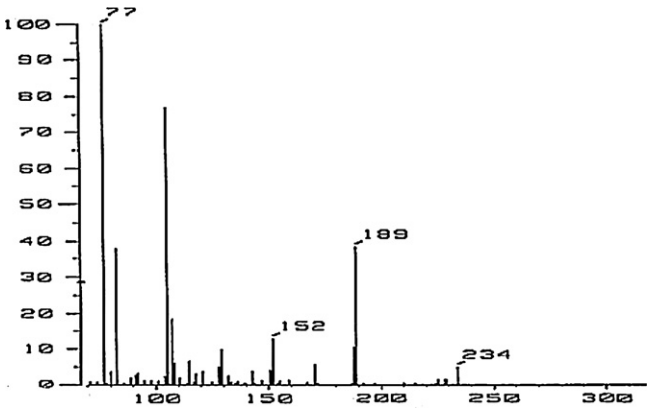


Fig. 4. Mass spectrum of oxybutynin degradate.

2.9. Application to pharmaceutical preparations

The contents twenty tablets were accurately weighted and powdered. An accurate weight of the mixed sample was transferred into a beaker, 50 mL methanol were added with continuous magnetic stirring for about 10 min. The solution was filtered into a 100-mL volumetric flask, and the volume was completed with methanol.

Accurate volume of syrup was transferred, measured and diluted to 100 mL methanol, filtered. Then the procedure detailed under linearity and construction of calibration curve for each method was followed.

3. Results and discussion

The main task of this work was to establish simple, sensitive and accurate analytical methods for the determination of OX in presence of its degradation product in its bulk powder and pharmaceutical dosage forms with satisfactory precision for good analytical practice (GAP). Also, to statistically compare and evaluate the efficiency of the developed methods for determination of the studied compound.

Upon refluxing OX with acid or alkali, the carboxylic acid degradate was obtained, so the determination of OX in presence of its alkaline (or acidic) degradate was essential. The structure of the alkaline (also obtained by acid hydrolysis) degradate was elucidated by IR and mass spectrometry where the IR spectrum of the degradate showed the band of carbonyl group shifted to 1726 cm^{-1} and a new broad band at 3420 cm^{-1} indicating the presence of a hydroxyl group of carboxylic acid resulting from hydrolysis. The mass ion peak of the degradate was at m/z 234 as shown in Figs. 3 and 4. Therefore one can conclude that carrying out the alkaline (or acidic) hydrolysis of OX may proceed as shown in Fig. 5.

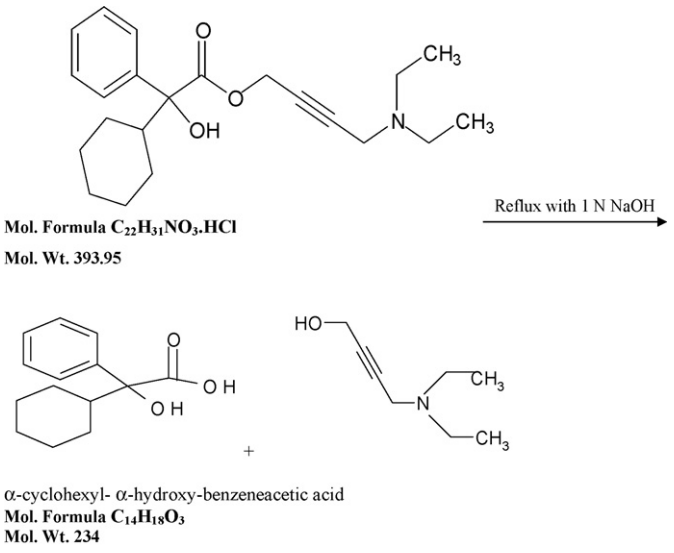


Fig. 5. Scheme of hydrolysis of oxybutynin hydrochloride.

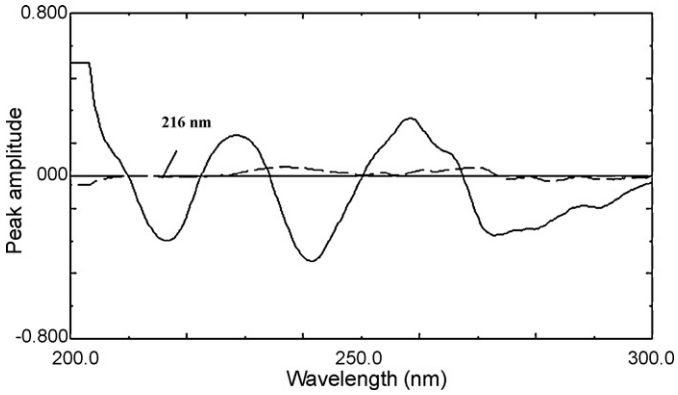


Fig. 6. First derivative of the ratio spectra of 15 μg/mL of oxybutynin hydrochloride (——) and 15 μg/mL of its degradate (------) using 20 μg/mL of the degradate as a divisor and 0.1N HCl as a blank.

3.1. DD^1 spectrophotometric method

OX can be assayed by dividing the absorption spectra of its different concentrations in the range (6–28 μg/mL) by the absorption spectrum of degradate (20 μg/mL), the obtained ratio spectra were differentiated with respect to wavelength ($\Delta\lambda = 4$, scaling factor = 10) (Figs. 6 and 7).

DD^1 values showed good linearity and accuracy at $\lambda = 216$ nm. The linear regression equation was found to be:

$$Y = 0.0196C - 0.0351, \qquad r = 0.9997$$

where Y is the peak amplitude at 216 nm, C is the concentration in μg/mL and r is the correlation coefficient.

To optimize this method, it was necessary to test the influence of variables:

(a) The divisor and its concentration: it was found that the degradate of OX as a divisor could solve the overlap of OX, and give high selectivity. Different concentrations of the degradate were tested, but concentration of (20 μg/mL) gives the best results.

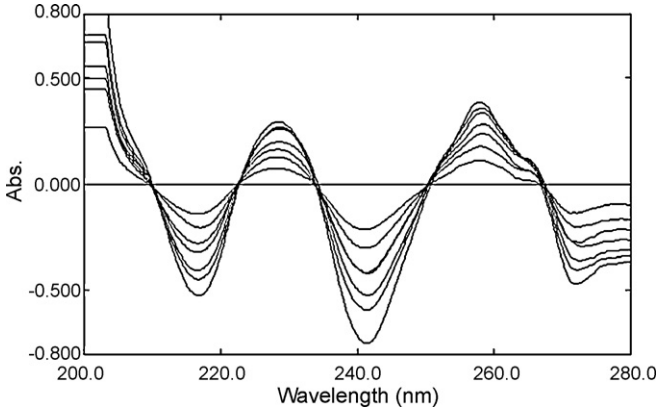


Fig. 7. First derivative of ratio spectra of different concentrations of oxybutynin hydrochloride using 20 μg/mL of its degradate as a divisor.

Table 2
Determination of oxybutynin hydrochloride in presence of its degradate in laboratory prepared mixtures by the DD[1] method.

Degradate %	Recovery[a] % of OX by DD[1] method at 216 nm
10	98.30
20	97.31
30	100.24
40	102.29
50	101.60
60	99.50
70	101.97
80	103.37
Mean ± SD	100.57 ± 2.099

[a] Average of 3 experiments.

(b) Different smoothing factors ($\Delta\lambda$) values were tried where a smoothing factor = 4 showed a suitable signal to noise ratio and the spectra showed good resolution. Different scaling factor values were tried where scaling factor 10 was suitable to enlarge the signal of OX to facilitate its measurement and to diminish error in reading signal.

Different synthetic laboratory prepared mixtures were made to give evidence to this proposal, where OX could be determined in presence of up to 80% of the degradation products without interference with mean percentage recovery100.57 ± 2.099 (Table 2).

The DD[1] spectrophotometric method was applied successfully for the determination of OX in Uripan® tablets and Detronin® tablets and the validity of the method was further assessed by applying the standard addition technique (Table 3). for Uripan® and Detronin® syrup, the preservatives methylparaben and propylparaben were interfered with the determination as they possess high absorbance bands at 256 nm.

3.2. Chemometric methods

3.2.1. Principal component regression (PCR)

The principal component regression method combines the principal component analysis (PCA) with an inverse least square (ILS) regression to create a quantitative model for complex samples. The eigenvectors resulting form the data decomposition represent the spectral variations that are common to all of the spectroscopic calibration data. Therefore, using the new data to calculate a regression model instead of straight spectral responses will produce a robust model for predicting concentrations of the desired constituents in very complex samples [13].

3.3. Partial least-squares (PLS)

Partial least-squares is a quantitative spectral decomposition technique that is closely related to (PCR). However, in PLS, the decomposition is performed in a slightly different fashion. In PCR method only the information in the matrix is used during data decomposition, but in the PLS method, the concentration data matrix is also used in this step. When the decomposition and regression are made at the same time, for all components, the type is named PLS-2, but if the decomposition and regression are made separately for each component the name given is PLS-1. The main advantage of PLS-2 is the higher speed and less complexity, but these advantages have become less important owing to the increase in calculation speed of computers so PLS not only has the advantage of PCR, but also it produces more robust model as it removes noise from both absorbance and concentration data [14,15].

The first step in the determination of the cited drug by multivariate calibration methods involves constructing the calibration matrix for the binary mixture. The calibration set was obtained by using the absorption spectra set of 16 mixtures of OX and its degradate with different ratios of each component. The initial model was

Table 3
Quantitative determination of oxybutynin hydrochloride in Uripan® tablets and Detronin® by the DD[1] method and application of standard addition technique.

	DD[1] method			Pure added μg/mL	DD[1] method	
	Claimed μg/mL	Found μg/mL	Found[a] %		Pure found[b] μg/mL	Recovery %
Uripan® tablets batch no. 0811106	10.00	9.72	97.20 ± 1.470	6.00	5.92	98.67
				8.00	7.91	98.87
				10.00	9.95	99.50
				12.00	12.30	102.50
Mean ± SD						99.88 ± 1.778
Detronin® tablets batch no. 710907	10.00	9.81	98.10 ± 1.298			

[a] Average of 3 experiments.
[b] Average of 6 experiments.

Table 4
Recoveries % of oxybutynin hydrochloride (OX) and the degradate in the validation set by PCR and PLS methods.

OX			The degradate		
True concentration in μg/mL	Recoveries %		True concentration in μg/mL	Recoveries %	
	PCR	PLS		PCR	PLS
6.00	101.83	102.5	20.00	102.20	102.00
18.00	98.27	98.22	8.00	96.25	96.50
10.00	99.50	100.20	8.00	95.50	94.37
6.00	97.17	98.00	12.00	105.17	104.42
14.00	98.71	99.64	8.00	101.37	99.00
10.00	101.10	100.60	12.00	95.00	95.50
10.00	98.70	98.50	20.00	99.75	99.90
Mean	99.32	99.66	Mean	102.20	102.00
SD	1.632	102.5	SD	96.25	96.50

Table 5
Quantitative determination of oxybutynin hydrochloride by the chemometric methods and application of standard addition technique.

	PCR method			PLS method			Pure added µg/mL	PCR method		PLS method	
	claimed µg/mL	Found µg/mL	Found%	Claimed µg/mL	Found µg/mL	Found%		Pure found µg/mL	Recovery %	Pure found µg/mL	Recovery %
Uripan tablets batch no. 0811106	10.00	9.40	94.00 ± 1.060	10.00	9.51	95.10 ± 0.815	6.00	6.08	101.33	5.98	99.67
							8.00	7.96	99.50	8.18	102.25
							10.00	10.16	101.60	10.09	100.90
Mean ± SD									100.81 ± 1.142		100.94 ± 1.290
Detronin tablets batch no. 710907	10.00	9.90	99.00 ± 1.095	10.00	9.93	99.30 ± 1.362					
Uripan syrup batch no. 080470	6.00	5.82	97.00 ± 1.788	6.00	5.88	98.00 ± 1.444					
Detronin syrup batch no. 4038005	10.00	9.69	96.90 ± 1.704	10.00	9.81	98.10 ± 1.678	6.00	5.91	98.50	6.08	101.33
							7.50	7.42	98.93	7.34	97.87
							8.00	7.80	97.50	8.09	101.12
Mean ± SD									98.31 ± 0.734		100.11 ± 1.939

Table 6
Summary of results obtained by applying the diagnostic tools for model validation of the chemometric methods.

Validation parameters	PCR	PLS
(a) Predicted vs. known concentration plot		
1-Slope	0.9762	0.9759
2-Intercept	0.1625	0.1963
3-Correlation coefficient	0.9995	0.9996
(b) Residual vs. actual concentration plot ± error in prediction	0.31	0.32
(c) RMSEP	0.17	0.15

found to give bad results so the regions from 200 to 207 nm and above 340 nm were rejected.

Selection of the optimum number of factors is very important step before constructing the models, because if the number of factors retained is more than the required, more noise will be added to the data. On the other hand, if the number retained is too small meaningful data that could be necessary for the calibration may be discarded. In this study, the data was autoscaled as a pre processing step, leave one out cross validation method was applied and the root mean squared error of calibration RMSEC values of different developed models were compared. The selected model was that with the smallest number of factors such that RMSEC for that model was not significantly greater than RMSEC from model with an additional factor. Five factors were found suitable for both PCR and PLS.

To assess the prediction ability of the suggested models, an external validation set was used. The root mean squared error of prediction (RMSEP) values were calculated and found to be 0.17 for PCR method and 0.15 for PLS method. The percentage recoveries of the validation samples are shown in Table 4.

The two chemometric PCR and PLS methods were successfully applied for the determination of OX in Uripan® tablets, Detronin® tablets.

In order to apply the developed methods for determination of OX in Uripan® syrup and Detronin® syrup, model updating was performed in order to remove the interference of both methylparaben and propylparaben.

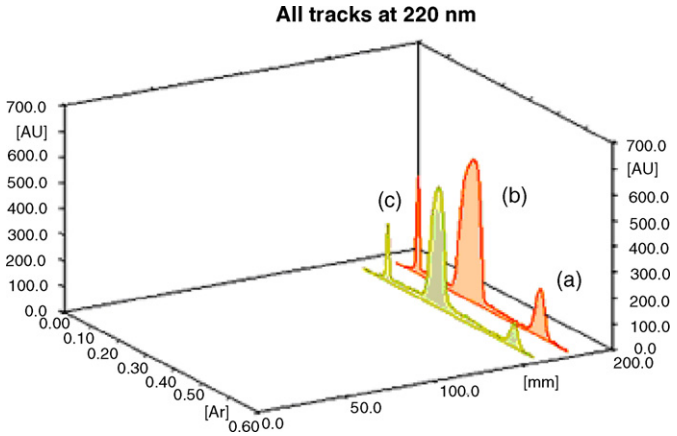


Fig. 8. Thin layer chromatogram of standard oxybutynin hydrochloride (a) (R_f = 0.59), methyl and propyl parabens (b) (R_f = 0.28) and the degradate (c) (R_f = 0.12) using chloroform:methanol:ammonia solution:triethylamine (100:3:0.5:0.2, v/v/v/v) as mobile phase.

Table 7
Quantitative determination of oxybutynin hydrochloride in tablets and syrup by the spectrodensitometric method and application of standard addition technique.

	Claimed taken μg/band	Found μg/band	Found[a] %	Pure added μg/band	Pure found[b] μg/band	Recovery %
Detronin® tablets batch no. 710907	6.00	5.84	97.33 ± 1.648	2.00	2.04	102.00
				4.00	4.03	100.75
				6.00	6.00	100.00
				8.00	7.97	99.62
Mean ± SD						100.59 ± 1.049
Uripan® tablets batch no. 0811106	6.00	6.16	102.68 ± 1.093			
Uripan® syrup batch no. 080470	3.00	2.90	96.67 ± 1.628			
Detronin® syrup batch no. 4038005	3.00	2.94	98.00 ± 1.572	6.00	5.99	99.83
				8.00	8.07	100.87
				9.00	8.85	98.33
Mean ± SD						99.68 ± 1.277

[a] Average of 6 experiments.
[b] Average of 3 experiments.

3.4. Model updating

Multivariate calibration models can be updated by including samples containing the new sources of data variance, $\mathbf{X}_{new}$, to the existing calibration set, **X**, and the concentrations of the new samples $\mathbf{Y}_{new}$ is added to the existing concentration matrix **Y**. This can be represented as follows:

$$\mathbf{X}_{upd} = \begin{bmatrix} \mathbf{X} \\ \mathbf{X}_{new} \end{bmatrix} \qquad \mathbf{Y}_{upd} = \begin{bmatrix} \mathbf{Y} \\ \mathbf{Y}_{new} \end{bmatrix}$$

The updated model was capable of predicting the concentrations of the OX of the syrup with good accuracy and precision without reconstruction of the calibration set, the minimum number of samples necessary to update efficiently the developed model was also studied.

Models updating was applied to predict the concentration of OX in Uripan® and Detronin® syrup formulation which containing different spectral characteristics. The minimal number of samples needed to efficiently update the developed models must be accurately determined. The influence of the number of samples added to the calibration set on RMSEP was studied for each developed multivariate calibration model. One to six samples containing OX in the concentration ranges of 6–18 μg/mL were added to the initial calibration set. The predictive ability of the updated models was checked using external validation samples of syrup dosage form. For Uripan® syrup six samples are necessary to perform an efficient update of the PCR and PLS models while four samples from Detronin® syrup are necessary to perform an efficient update of the PCR and PLS models for Detronin® syrup Table 5.

3.4.1. Validation of PCR and PLS models

The validation of the developed PCR and PLS models was assessed using several diagnostic tools, Table 6. These tools were grouped into two categories in model diagnostic tools that are used to determine the quality of the model and sample diagnostic tools which are used to study the relationship between the samples and to identify unusual samples.

The predicted concentrations of the validation samples were plotted against the true concentration values. This was used to determine whether the model accounted for the concentration variation in the validation set. All plots had a slope of nearly one and an intercept close to zero Table 6.

The RMSEP was another diagnostic tool for examining the errors in the predicted concentrations, it indicates both the precision and accuracy [16]. The results in Table 6 indicating the high predictive abilities of the two models.

3.4.2. HPTLC-densitometric method

The TLC-densitometric method was successfully applied for the determination of OX in pure form, in presence of its degradate and in tablets and syrup. The TLC-densitometric method was characterized by separation OX from methylparaben and propylparaben successfully and efficiently separates from its degradation product. This method offers a simple way to quantify directly on TLC plate by measuring the optical density of the separated bands. The amounts of compounds are determined by comparing to a standard curve from reference materials chromatographed simultaneously under the same condition [17].

Studying the optimum parameters for maximum separation was carried out by trying different developing systems with different ratios but complete separation of the drug, its degradate and parabens was achieved by using chloroform:methanol:ammonia solution:triethylamine (100:3:0.5:0.2, v/v/v/v) as a mobile phase which gave good resolution, sharp and symmetrical peak of OX as shown in Fig. 8.

Table 8
Regression parameters and results of determination of pure samples of OX by DD[1] spectrophotometric and spectrodensitometric methods.

Parameters	DD[1] spectrophotometric method	Spectrodensitometric method
Calibration range	6–28 μg/mL	2–14 μg/band
Slope	0.0196	0.0476
Intercept	−0.0351	0.0782
Mean	100.15	99.77
SD	1.592	1.069
Coefficient of variation	0.016	0.011
Correlation coefficient	0.9997	0.9997
RSD%[a] **	1.279–1.498–1.095	1.157–1.325–0.766
RSD%[b] **	1.184–1.684–1.584	1.417–1.114–1.076
LOD[c]	3.5 μg/mL	0.56 μg/band
LOQ[c]	5.5 μg/mL	1.85 μg/band

RSD%[a] ** and RSD%[b] **; the intra- and inter-day relative standard deviation of concentrations (8, 10, 12 μg/mL) for DD[1] spectrophotometric method and (4, 8, 10 μg/band) for spectrodensitometric method.

[c] Limit of detection and quantitation are determined via calculations [18]. LOD = 3.3 × SD/slope LOQ = 10 × SD/slope. And determined experimentally for spectrodensitometric method.

Table 9
Parameters of system suitability of the TLC-densitometric method.

parameters	OX	Methylparaben	The degradate
Symmetry factor	1.25	1.3	0.98
Resolution (R_s)[a]	1.7	1.5	
Capacity factor (K′)	0.41		
Selectivity (α)[a]	2.107		

[a] The parameters were calculated using OX as reference.

Table 10
Statistical analysis of the proposed methods and the reported method [6] for determination of OX in its pure powdered form.

Items	DD[1] method	Spectrodensitometric method	PCR method	PLS method	Reported method
Mean	100.15	99.77	99.32	99.66	100.02
SD	1.592	1.069	1.632	1.603	2.538
n	11	9	7	7	6
Variance	2.534	1.143	2.663	2.57	6.441
Student's *t*-test (2.23)[a]	0.131	0.02	0.599	0.599	
F-Value (5.05)[a]	2.54	1.033	2.419	2.507	

[a] Figures between parentheses represent the corresponding tabulated values of *t* and *F* at $p = 0.05$.

Table 11
One-way ANOVA testing for the different proposed methods used for the determination of OX.

	Source of variation	DF	Sum of squares	Mean square	*F*-Value
OX	Between exp.	8	3.536	0.442	0.0986
	Within exp.	31	138.888	4.48	

There was no significance difference between the methods using one-way ANOVA (*F*-test), where *F* tabulated = 2.254 at $p < 0.05$.

Different scanning wavelengths were tried; on using 220 nm the separated peaks were more sharp and symmetrical with minimum noise. The R_f values was as follows OX (0.59) parabens (0.28) and the degradate (0.12) as shown in Fig. 8.

The calibration curve was constructed by plotting the integrated peak area $\times 10^{-4}$ versus the corresponding concentration in the concentration range of 2–14 μg/band for OX. The regression equation was calculated and found to be:

$$Y = 0.0476C + 0.0782, \qquad r = 0.9997$$

where, *Y* is the integrated peak area, *C* is the concentration of OX in μg/band and *r* is the correlation coefficient.

The suggested methods are valid and applicable for the analysis of OX in Uripan® tablets, Detronin® tablets, Uripan® and Detronin® syrup. The validity of the proposed methods was assessed by applying the standard addition technique, which showed accurate results and specific for the determination of OX in presence of other excipients as shown in Tables 3, 5 and 7.

Method validation was performed according to USP guidelines [3] for DD1 spectrophotometric and spectrodensitometric methods.

4. Method validation

4.1. Linearity

The linearity of the methods was evaluated by analyzing eleven concentrations of OX ranging between 6–28 μg/mL for DD1 and nine concentrations of OX ranging between 2–14 μg/band for TLC-densitometric. Each concentration was repeated three times. The assay was performed according to the experimental conditions previously mentioned Table 8.

4.2. Accuracy

The accuracy of the results was checked by applying the proposed method for determination of different blind samples of OX. The concentrations were obtained from the corresponding regression equations. From, which the percentage recoveries were calculated with mean percentage recovery 99.75 ± 0.704 for DD1 method and 99.53 ± 1.692 for TLC-densitometric.

Accuracy of the method was further assured by the use of the standard addition technique, it was performed by addition of known amounts of pure OX to known concentrations of the pharmaceutical preparations the resulting mixtures were assayed, and the results obtained were compared with the expected results, Tables 3 and 7. The good recoveries of standard addition technique suggested good accuracy of the proposed methods.

4.3. Precision

4.3.1. Repeatability

Three concentrations of OX (8, 10, 12 μg/mL) for DD1 spectrophotometric method and (4, 8, 10 μg/band) for spectrodensitometric method were analyzed three times intra – daily using the proposed methods. The percentage recoveries and relative standard deviation were calculated, Table 8.

4.3.2. Reproducibility (intermediate precision)

The previous procedures were repeated inter – daily seven times on four different days for the analysis of the three chosen concentrations. The percentage recoveries and relative standard deviation were calculated, Table 8.

4.4. Range

The calibration range was established through considerations of the practical range necessary according to adherence to Beer's law and the concentration of OX present in the pharmaceutical preparations to give accurate precise and linear results Table 8.

4.5. Detection and quantitation limits

According to the ICH recommendations [18], the approach based on the SD of the response and the slope was used for determining the detection and quantitation limits, Table 8.

$$\text{LOD} = 3.3 \times \text{SD/slope} \qquad \text{LOQ} = 10 \times \text{SD/slope}$$

4.6. Selectivity

Selectivity of the methods was achieved by the analysis of different laboratory prepared mixtures of OX and its degradation product for DD1 spectrophotometric within the linearity range. Satisfactory results were shown in Table 2.

4.7. Stability

OX working solution showed no spectrophotometric changes for one week when stored at room temperature (25 °C).

4.8. TLC system suitability

Parameters including resolution (Rs), peak symmetry, capacity factor (K′) and selectivity (α) were calculated (Table 9).

Table 10 shows statistical comparison of the results obtained by the proposed methods and the reported HPLC method [6]. The calculated t and F values are less than the theoretical ones indicating that there is no significant difference between the proposed methods and the reported HPLC method with respect to accuracy and

precision. One-way ANOVA was applied for the purpose of comparison of developed methods Table 11 shows that there was no significant difference between them for the determination of OX.

5. Conclusion

The present work is concerned with the determination OX in presence of its degradate. In this paper simple, sensitive and rapid methods were described for determination of OX in pure form or in pharmaceutical formulations.

DD[1] spectrophotometric method is simple, more convenient, less time consuming and economic stability indicating method compared to other published LC methods.

OX was successfully determined in Uripan® and Detronin® syrup by densitometric and chemometric methods without any interference from excipients.

The suggested methods showed high sensitivity, accuracy, reproducibility and specificity and can be used as stability indicating methods. Moreover, these methods are simple and inexpensive, permitting their application in quality control laboratories.

References

[1] R. Jain, K. Radhapyari, N. Jodon, Journal of Colloid and Interface Science 314 (2007).
[2] V.S. Varma, A.M. Kaushal, S. Garg, Journal of Pharmaceutical and Biomedical Analysis 36 (2004) 669.
[3] The United States Pharmacopeia "The National Formulary USP XXVII NF/XXII", United States Pharmacopeia Convention Inc., 2002.
[4] The British Pharmacopoeia, Her Majesty's Office, London, 2001.
[5] R. Massoud, G. Federici, S. Casciani, S.M. Di-stasi, G. Fucci, A. Giannantoni, C. Cortese, Journal of Chromatography B: Biomedical Applications 734 (1999) 163.
[6] A. El Gindy, IL Farmaco 60 (2005) 689.
[7] P. da Fonseca, L.A.P. de Freitas, L.F.R. Pinto, C.R. Pestana, P.S. Bonato, Journal of Chromatography B: Analytical Technologies in the Biomedical and Life Sciences 875 (2008) 161–167.
[8] B. Lindeke, H. Brotell, B. Karlen, G. Rietz, A. Vietorisz, Acta Pharmaceutica Suecica 18 (1981) 25.
[9] M. Heba, N. Ramadan, M. El-Laithy, Journal of AOAC International 91 (2008) 1318.
[10] Matlab ver. 5.3, Mathworks Inc., 1999.
[11] B.M. Wise, N.B. Gallagher, Version 2.1.1, Eigenvector Research, Inc., 2001.
[12] G.B. Richard, Analyst 122 (1997) 1521.
[13] R. Kramer, Chemometric Techniques for Quantitative analysis, Marcel dekker, New York, 1998.
[14] F. Navarro-Villosalade, L.V. Prez-Arrbas, M.E. Leon-Gonzalez, L.M. Polo-Diez, Analytica Chimica Acta 313 (1995) 93.
[15] A. Garrido Frenich, D. Jouran-Rimbaud, D.L. Massart, S.K. uttatharmmakul, M. Martinez Galera, J.L. Martinez Vidal, Analyst 120 (1995) 2787.
[16] K.R. Beebe, R.J. Pell, M.B. Seashlotz, Chemometrics, A Practical Guide, John Willy and Sons, Inc., 1998.
[17] N. Grinberg, Modern Thin-layer Chromatography, Marcel Dekker Inc., New York, 1990, p. 249.
[18] The European Agency for The evaluation of Medical Products. ICH Topic Q2B Note for Guidance on validation of Analytical Procedures. Methodology GPMP/ICH/ 281/ 95 (1996).

Talanta 80 (2010) 2016–2022

Contents lists available at ScienceDirect

Talanta

journal homepage: www.elsevier.com/locate/talanta

SiO_2 coated Fe_3O_4 magnetic nanoparticle dispersed multiwalled carbon nanotubes based amperometric glucose biosensor

Tessy Theres Baby, S. Ramaprabhu*

Alternative Energy and Nanotechnology Laboratory (AENL), Nano Functional Materials Technology Centre (NFMTC), Department of Physics, Indian Institute of Technology Madras, Chennai, India

ARTICLE INFO

Article history:
Received 22 August 2009
Received in revised form 31 October 2009
Accepted 2 November 2009
Available online 10 November 2009

Keywords:
Amperometric
Vibrating sample magnetometer
Bioelectrode
CNTs
Biosensor

ABSTRACT

A new type of amperometric glucose biosensor based on silicon dioxide coated magnetic nanoparticle decorated multiwalled carbon nanotubes (Fe_3O_4@SiO_2/MWNTs) on a glassy carbon electrode (GCE) has been developed. MWNTs have been synthesized by catalytic chemical vapour decomposition (CCVD) of acetylene over rare earth (RE) based AB_3 alloy hydride catalyst. The as-grown MWNTs have been purified and further functionlized. Functionalized MWNTs have been decorated with magnetic Fe_3O_4 nanoparticles which have been uniformly coated with biocompatible SiO_2 using a simple chemical reduction method. The characterization of magnetic nanoparticle modified MWNTs have been done by X-ray diffraction (XRD), Fourier transform infra red spectroscopy (FT-IR), scanning electron microscope (SEM), transmission electron microscope (TEM), vibrating sample magnetometer (VSM), energy dispersive X-ray analysis (EDX) and UV–vis spectroscopy. Amperometric biosensor has been fabricated by the deposition of glucose oxidase (GOD) over Nafion-solubilized Fe_3O_4@SiO_2/MWNTs electrode. The resultant bioelectrode retains its biocatalytic activity and offers fast and sensitive glucose quantification. The performance of the biosensor has been studied using cyclic voltammetry and amperometry and the results have been discussed. The fabricated glucose biosensor exhibits a linear response from 1 μM to 30 mM with an excellent detection limit of 800 nM indicating the potential applications in food industries.

© 2009 Elsevier B.V. All rights reserved.

1. Introduction

Magnetic core–shell Fe_3O_4@SiO_2 nanoparticles as specially immobilizing carrier of biomolecules have aroused great interest in current researches. The inner iron oxide core with outer shell of silica not only stabilizes the nanoparticles in solution but also provides sites for surface modification with various biomedical ligands in biomedical applications. The coating of silica on the magnetic nanoparticles facilitated the dispersion of nanoparticles [1,2]. Due to their unique physical, chemical, and mechanical properties, superparamagnetic composite nanoparticles (NPs) hold much promise for biosensor applications [3–5]. Superparamagnetic iron oxide core of individual NPs becomes more efficient at dephasing the spins of surrounding water protons, enhancing spin–spin relaxation times (T_2 relaxation times) so that the NPs act as magnetic relaxation switches (MRS) [6]. Carbon nanotubes (CNTs) are one of the most studied nanomaterials for application in biosensor technologies, by immobilizing bioactive molecules on their surfaces through covalent or non-covalent bonds. The nanodimensions of CNTs guarantee a very large active surface area and are especially suited for the conception of miniaturized sensors. In addition to this, high porosity and reactivity makes them ideal candidates for the storage of neutral species as well as electron donors when used as electrodes in electrochemical reactions [7–9].

Compared with the corresponding CNTs-free biosensor, the CNTs-doped counterpart exhibited enhanced stability and sensitivity. Surface functionalization aids CNTs to become biocompatible, improving their solubility in physiological solutions and selective binding to biotargets. CNTs functionalization with biomolecules may occur by adsorption, but covalent tethering provides better stability, accessibility, selectivity and reduced leaching, and usually occurs by an amidation reaction [10]. CNTs are also used for dramatically amplifying enzyme-based bioaffinity electrical sensing of proteins and DNA [11]. Compared with single walled nanotubes (SWNTs), much cheaper multiwalled nanotubes (MWNTs) produced by chemical vapour deposition have more structural defects and thus provide more sites for biomolecule immobilization [8]. Non-covalently functionalized CNTs may also immobilize glucose and small molecules [12].

Nanocomposite materials may play an important role for improving functionalized electrodes envisaging commercial applications. Nanoparticles, especially metal nanoparticles, are an emerging issue in biosensor design, and they have been combined with CNTs to modify a glassy carbon electrode, thus improving the

* Corresponding author. Tel.: +91 44 22574862; fax: +91 44 22570509.
E-mail address: ramp@iitm.ac.in (S. Ramaprabhu).

0039-9140/$ – see front matter © 2009 Elsevier B.V. All rights reserved.
doi:10.1016/j.talanta.2009.11.010

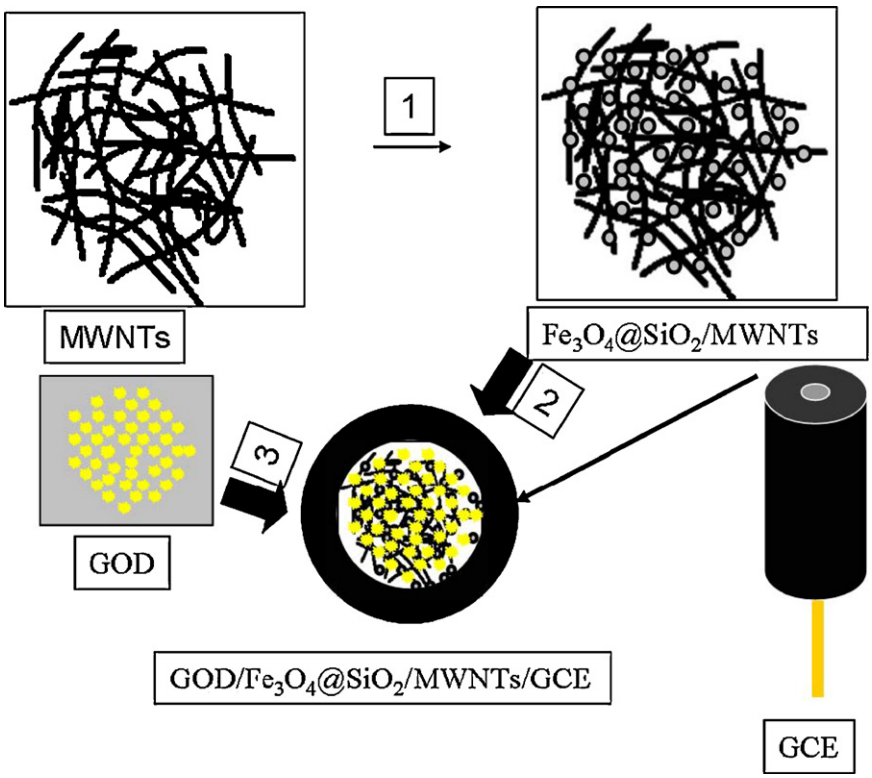


Fig. 1. Schematic of fabricated GOD/Fe_3O_4@SiO_2/MWNTs/GC electrode.

electroactivity and selectivity for glucose [13]. Metal nanoparticles have been applied as catalysts in numerous biosensor applications, due to their superior stability and complete recovery in biochemical redox processes. However, other groups showed that immobilization of the Au nanoparticles (or other metal nanoparticles) on the electrode surface would also cause similar catalytic effect on the electrochemical responses. Amperometric detection of glucose was developed using Au nanoparticles and CNT-multilayer membranes [14].

An electrochemical study with cyclic voltammetry and impedance analysis confirmed that glucose oxidase molecules suffer minimal structure changes after being immobilized on the surface of CNTs, retaining the ability to interact with small biomolecules (e.g., ethidium bromide) [7]. In this present study, MWNTs functionalized with nitric acid, in order to introduce carboxylic acid groups, have been used for the preparation of Fe_3O_4@SiO_2/MWNTs-based electrodes. Prior to immobilization, glucose oxidase (GOD) was physically adsorbed on these modified electrodes. Here, we show a good performance, fast response, nice stability and reproducibility, and a low detection limit of Fe_3O_4@SiO_2/MWNTs nanocomposite based on the reduction of H_2O_2 by immobilizing glucose oxidase on the composite.

2. Experimental

2.1. Materials

Glucose oxidase (GOD, from *Aspergillus niger*), tetraethoxysilane (TEOS) were purchased from Sigma. 0.1 M phosphate buffer solution (PBS, pH 7) prepared using potassium phosphate dibasic anhydrous and potassium dihydrogen orthophosphate. Ferric chloride ($FeCl_3{\cdot}6H_2O$), ferrous sulphate ($FeSO_4{\cdot}7H_2O$), ethanol and ammonium hydroxide (25%) were of analytical grade and deionised (dI) water was used throughout.

2.2. Sample preparation

Carbon nanotubes were synthesized by catalytic chemical vapour deposition over an alloy hydride catalyst. Rare earth based AB_3 alloy hydride was made by arc melting followed by several cycle of hydrogen absorption/desorption process. The catalyst was kept inside a furnace and acetylene (carbon precursor) was allowed at a temperature range 650–750 °C, in an inert atmosphere. Pyrolysis of acetylene was taken place at that temperature and MWNTs start growing. The as-grown MWNTs were purified before using for any applications. The amorphous carbon can be removed by heating the as-grown sample in oxygen atmosphere. Refluxing in concentric acids has been shown to be an

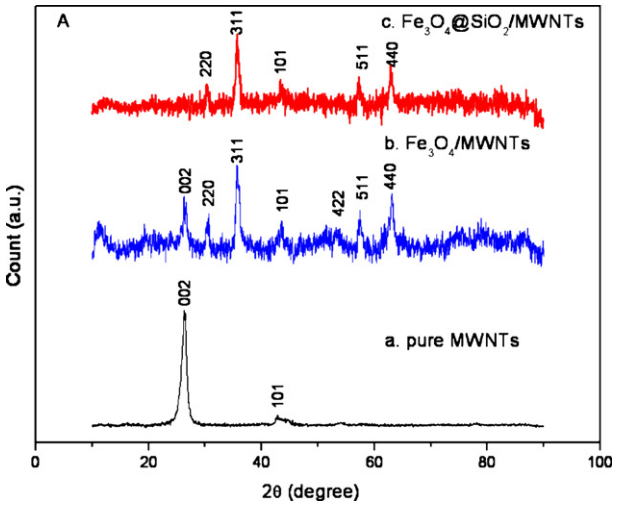


Fig. 2. X-ray diffractograms of (a) pure MWNTs, (b) Fe_3O_4/MWNTs and (c) Fe_3O_4@SiO_2/MWNTs.

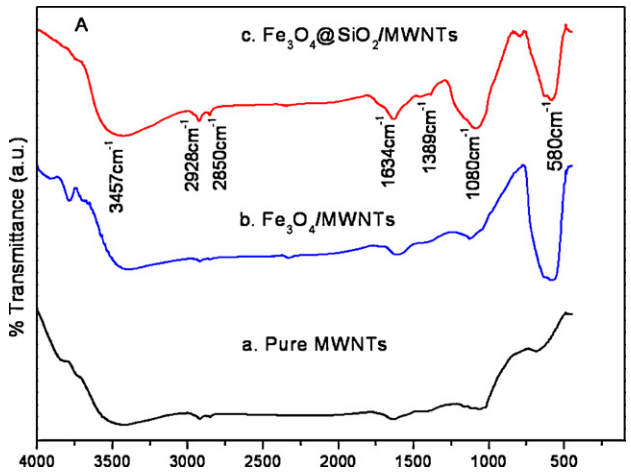


Fig. 3. FT-IR spectrum of (a) pure MWNTs, (b) Fe_3O_4/MWNTs and (c) Fe_3O_4@SiO_2/MWNTs.

effective method for the separation of the catalytic impurities [15].

Hydrated ferric chloride and ferrous sulphate precursors were dissolved in 100 ml water and heated to 90 °C, and then two solutions, 10 ml of ammonium hydroxide (25%) and 0.5 g of functionalized MWNTs dissolved in 50 ml of water, were added rapidly and sequentially. The mixture was stirred at 90 °C for 30 min and then cooled to room temperature. The black precipitate was collected by filtrating and washed to neutral with water. The obtained black precipitate was Fe_3O_4/MWNT nanoparticles and was ready for use.

Core–shell Fe_3O_4@SiO_2/MWNT nanoparticles were prepared by growing silica layers onto the surface of the Fe_3O_4/MWNTs as described by Lu et al. [16]. Twenty-five milliliters of ethanol, 1 ml water, 1 ml ammonium hydroxide and 150 μl of TEOS were added in a 250 ml three neck flask in a 40 °C water bath. Add Fe_3O_4/MWNTs to the above solution under mechanical stirring. Aliquots of the mixture were takes out after 12 h by centrifugation and washed with dI water and vacuum-dried at 50 °C overnight.

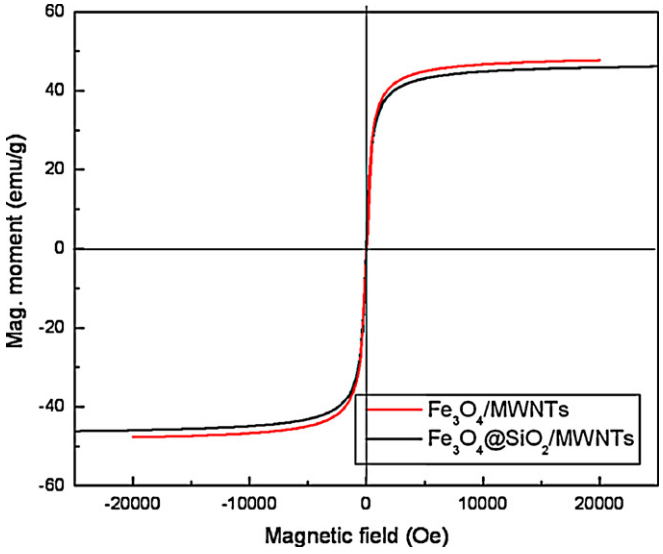


Fig. 4. VSM study of Fe_3O_4/MWNTs (red line) and Fe_3O_4@SiO_2/MWNTs (black line). (For interpretation of the references to color in this figure legend, the reader is referred to the web version of the article.)

2.3. Fabrication of the amperometric immunosensor

The GCE (3-mm diameter) was first polished on chamois leather with 0.05-μm alumina slurry and then washed ultrasonically in doubly distilled water, anhydrous ethanol, and doubly distilled water, respectively. The cleaned GCE was allowed to dry at room temperature.

Fe_3O_4@SiO_2/MWNTs was sonicated in 0.5% Nafion solution to give a concentration of ~1 mg/ml. For example, four microliters of the Fe_3O_4@SiO_2/MWNTs suspension was film-cast onto the surface of the GC electrode and allowed to dry slowly. Films formed from Nafion-solubilized MWNTs are more uniform and stable than those cast from organic solvents. Nafion assists the dispersion of Fe_3O_4@SiO_2/MWNTs, whereby the Fe_3O_4@SiO_2/MWNTs remains well dispersed on prolonged standing. 16 μl of 100 U GOD solution was film-cast onto the surface of the Fe_3O_4@SiO_2/MWNTs/GC electrode and allowed to dry slowly at 4 °C. The obtained Fe_3O_4@SiO_2/MWNTs/GC electrode was washed carefully with DI water and dried at less than 4 °C. Fig. 1 shows the schematic of fabrication of Fe_3O_4@SiO_2/MWNTs/GC electrode. These Fe_3O_4@SiO_2/MWNTs/GC electrodes were coated with an extra 2.5 μl layer of 0.5% Nafion. The electrodes were rinsed with pH 7 phosphate buffer solution (PBS) and stored in the buffer at 4 °C prior to use.

2.4. Characterization methods

The electrochemical measurements were performed with CH Instruments CHI 608C Electrochemical Analyzer/Workstation. A platinum wire counter electrode, Ag/AgCl (3 M KCl) reference electrode and glassy carbon electrode (GCE, diameter 3 mm) were inserted into a modified 5–10 ml glass cell for the measurement. All potentials are referred to the Ag/AgCl reference electrode. The samples were characterized using different techniques. Powder X-ray diffraction studies were carried out using a X'Pert PRO, PANalytical diffractometer with nickel-filtered Cu Kα radiation as the X-ray source. The sample was scanned in steps of 0.016° in the 2θ range 10–90°. Identification and characterization of functional groups were carried out using PerkinElmer FT-IR spectrometer in the range 300–4000 cm^{-1}. The surface morphology of the sample was done by using scanning tunneling microscope (SEM) (FEI; QUANTA scanning electron microscope) with EDX system. The EDX system attached with the SEM enables the elemental analysis of the samples. The TEM images were obtained on a transmission electron microscope (TEM, JEOL JEM-2010F). UV absorption spectra of the samples in deionized water were recorded on JASCO Corp., V-570 spectrophotometer. Magnetic study of the samples had been done by vibrating sample magnetometer (VSM).

3. Results and discussion

3.1. XRD and FT-IR studies of the samples

The XRD pattern in Fig. 2 indicates that the crystal structure of magnetic nanocomposites comprises MWNTs, two phases of cubic Fe_3O_4/MWNTs and Fe_3O_4@SiO_2/MWNTs. Well-resolved diffraction peaks reveal the good crystallinity of the Fe_3O_4 specimens, which are located at 2θ of 30.28°, 35.56°, 43.3°, 53.68°, 57.36° and 62.72°, respectively. These data matched well with the peer Ref. [17]. The peaks in the Fe_3O_4@SiO_2/MWNTs reveal that even after the SiO_2 coating the sample retains its crystallinity [18]. The absence of SiO_2 peak in the XRD pattern in the composite is due to its amorphous structure coated on the Fe_3O_4 nanoparticles. The diffraction peak at 2θ = 26.4° is the typical Bragg peak of pristine MWNTs and can be indexed to the (0 0 2) reflection of graphite. Judging from the pat-

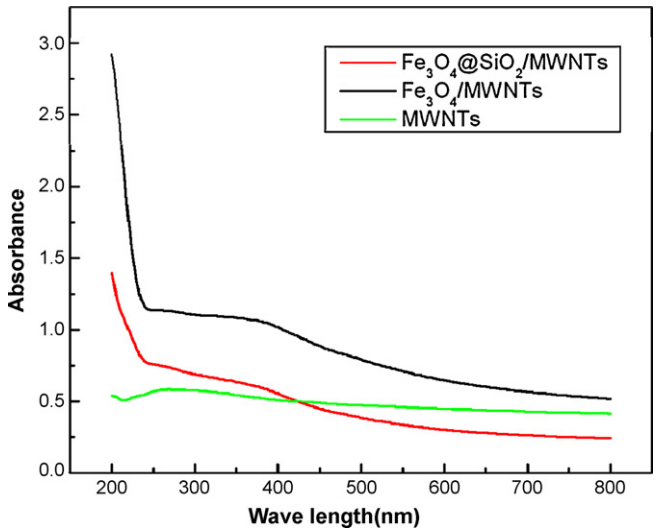


Fig. 5. UV–vis absorbance study of pure MWNTs (green), Fe_3O_4/MWNTs (black) and Fe_3O_4@SiO_2/MWNTs (red). (For interpretation of the references to color in this figure legend, the reader is referred to the web version of the article.)

tern, the third phase does not exist. The average grain size (D) of the Fe_3O_4 particles was calculated using Scherrer's formula described by

$$D = \frac{0.9\lambda}{\beta \cos(\theta)} \quad (1)$$

λ is wave length of X-ray used, β is FWHM of diffraction peak and θ angle corresponding to the peak. The calculated average grain sizes using 35.56° diffraction peak were ~25 nm. Moreover, the diffractive peaks of Fe_3O_4 are broadened, implying that the crystalline size of Fe_3O_4 particles is quite small.

Selectivity of MWNTs-based biosensors may be introduced by anchoring on the MWNTs surface, specific functional groups that selectively bind specific target molecules. All types of MWNTs show peaks between 1300 and 1100 cm^{-1}, which are ascribed to the phenyl-carbonyl C–C stretch bonds (Fig. 3(a)). The peak between 3300–3500 cm^{-1} is normally due to stretching vibration mode of OH and NH group. The peak at 3457 cm^{-1} in curve (a) and curve (b) is due to OH group (due to oxidation with HNO_3) and in curve (c) it is due to both OH and –NH (from ammonia solution). One can see a small broadening of this peak in the case of curve (c). As seen from Fig. 3(b), the peak at 568 cm^{-1} is the stretching vibration due to the interactions of Fe–O–Fe in Fe_3O_4 and the peaks at 1383, 2850 and 2928 cm^{-1} are attributed to the in-plane bending vibration of methyl ($-CH_3$) and the symmetric and asymmetric vibration of methylene ($-CH_2-$). Compared with the two spectra (b and c), the existence of the characteristic Si–O–Si peak at 1080 cm^{-1} in Fig. 3(c) is direct evidence to verify the formation of the silica shell. From Fig. 3(b) and (c), we can also see that the characteristic Fe–O–Fe peak of Fe_3O_4/MWNTs at 568 cm^{-1} shift to 580 cm^{-1} in the spectrum of SiO_2 coated magnetic nanoparticles. It is inferred that the silica shell is linked to the surface of the magnetic nanoparticles by a Fe–O–Si chemical bond [19]. It is generally accepted that the interpretation of surface groups can only be qualitative, as they cannot be expected to behave as isolated functional groups [20].

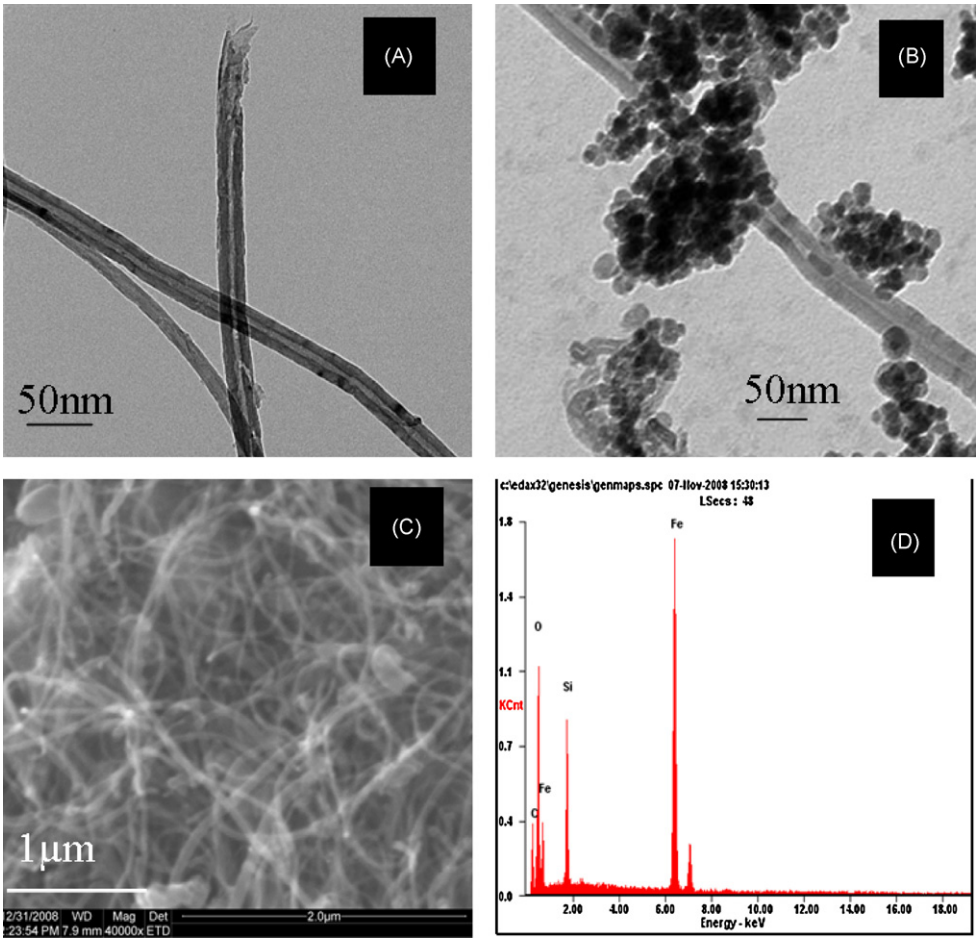


Fig. 6. TEM image of (A) pure MWNTs, (B) Fe_3O_4@SiO_2/MWNTs, (C) SEM image of pure MWNTs and (D) EDX for Fe_3O_4@SiO_2/MWNTs.

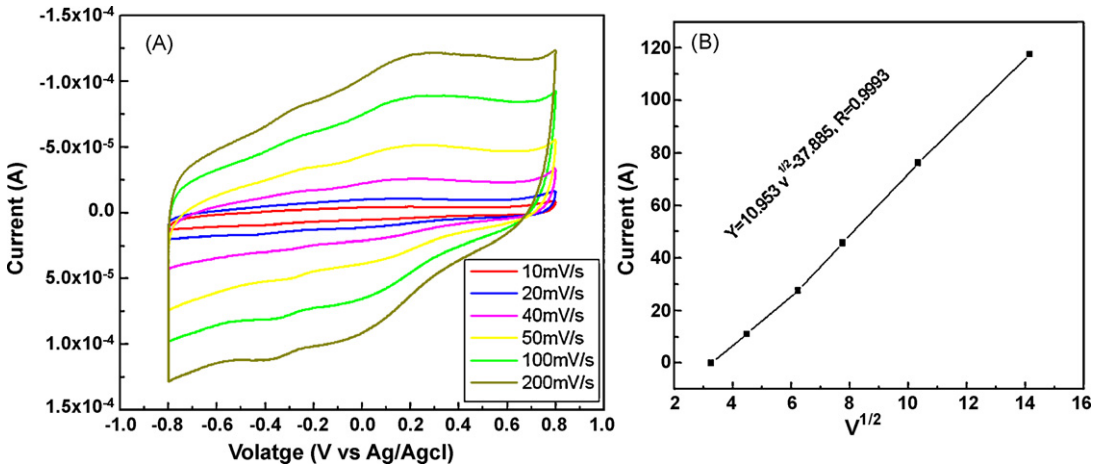


Fig. 7. (A) Fe_3O_4@SiO_2/MWNTs modified electrode at different scan rates in PBS (0.1 M, pH 7) and (B) the plot of peak anodic peak current vs. $v^{1/2}$.

3.2. Magnetic and optical studies of samples

Fig. 4 exhibits the hysteresis loop of the as-prepared sample at room temperature. It can be seen that the saturation magnetization of Fe_3O_4@SiO_2/MWNTs (~44 emu/g) is almost comparable to that of Fe_3O_4/MWNTs (~46 emu/g), which indicates that Fe_3O_4 nanoparticles covered by a silica network can preserve their superparamagnetic properties.

The UV–vis absorption spectrum of different samples in deionized water is illustrated in Fig. 5. A very broad absorption peak appeared at about 267 nm, which originated from the C=C structure of MWNTs [21]. The optical properties of all the magnetic nanoparticles used (with or without silica coating) are dominated by a broad featureless absorption tail characteristic of indirect band gap semiconductors. In the wavelength of >330 nm region, a broad featureless adsorption could be observed in the curves with SiO_2 and without SiO_2 originates primarily from the absorption and scattering of light by magnetic particles, which is in accordance with the previous literatures [22], and is the characteristic of indirect band gap semiconductors [23].

3.3. SEM and TEM analysis of the samples

The morphology of the purified MWNTs is clearly visible from the SEM image shown in Fig. 6(C). Fig. 6(A and B) illustrates the TEM images of the synthesized MWNTs and prepared Fe_3O_4@SiO_2/MWNTs core–shell nanoparticles. The open end of the MWNTs are clearly visible from the TEM image. The diameter of the MWNTs is ~25 nm. With the help of references [24,25] and the TEM and EDX shown in Fig. 6(B and D) we can see that the sample is nearly in core–shell structures, with black color shows Fe_3O_4 and ash color is the SiO_2 shell. This indicates the successful coating on the surface of the magnetic particles with silica. The EDX shown in Fig. 6(D) confirms the presence of iron and silicon in the sample. Inorganic compound functionalized iron oxide NPs can greatly enhance the antioxidation properties for naked iron oxide NPs, and its corresponding scope of application has been greatly extended. Moreover, inorganic compounds functionalized iron oxide NPs are very promising for application in catalysis, biolabeling, and bioseparation [26].

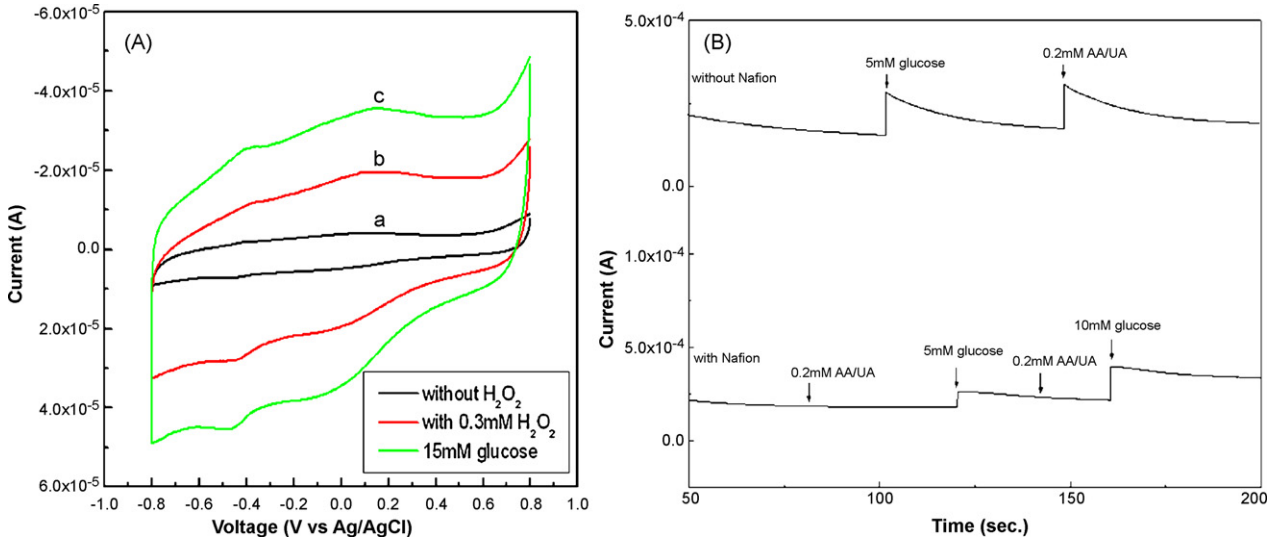


Fig. 8. (A) displays the CV of the Fe_3O_4@SiO_2/MWNTs modified electrode (a) in PBS (b) with 0.3 mM H_2O_2 and (c) 15 mM glucose solution and (B) study of interference due to ascorbic acid and uric acid with and without a selective Nafion film on the GOD/Fe_3O_4 @SiO_2/MWNTs modified electrode.

3.4. Cyclic voltammetry and electrocatalytic properties of the GOD/Fe_3O_4@SiO_2/MWNTs modified electrode toward hydrogen peroxide

Cyclic voltammetry peak currents of the GOD/Fe_3O_4@SiO_2/MWNTs modified electrode increased with scan rate and the peak separation (ΔE_p) was nearly independent of the scan rate (Fig. 7(A)). The anodic peak currents increased linearly with the increase of the square root of scan rate, suggesting that the electrochemical reaction is a diffusion-controlled process (Fig. 7(B)).

Fig. 8(A) shows the cyclic voltammograms of the GOD/Fe_3O_4@SiO_2/MWNTs/GC electrode in the absence (curve a), in the presence of 0.3 mM H_2O_2 (curve b) and in 15 mM glucose solution (curve c). The GOD/Fe_3O_4@SiO_2/MWNTs/GC electrode exhibits significant electrocatalysis to the oxidation and reduction of H_2O_2 starting around 0.1 V, which is even lower than that obtained with the GOD/MWNTs electrode by covalent binding immobilization (0.2 V) [27]. The good performance of the fabricated GOD/Fe_3O_4@SiO_2/MWNTs/GC electrode toward the oxidation of H_2O_2 makes it attractive for glucose sensing applications. When MWNTs were treated with the acid solution, the carboxylic acid functional groups introduced at the end points and surface of MWNTs allow them to adsorb the enzyme of GOD. Since this adsorption was fulfilled through a covalent bond, the link between MWNTs and GOD was more close and stable. Moreover, because the MWNTs have large surface area, they could enhance a large amount of GOD to be immobilized within the nanotubes. The more quantity of GOD made the biosensor possible to engender high response current and expand the detectable range when in a glucose solution.

3.5. Effect of electroactive interferents

The interference of some electroactive compounds to the glucose response was examined. To study this we added 0.2 mM of ascorbic acid (AA) and uric acid (UA) to the solution and checked the GOD/Fe_3O_4@SiO_2/MWNTs/GC electrode with Nafion coating and without Nafion coating. The upper curve in Fig. 8(B) which had been done without Nafion shows the presence of AA and UA. The lower curve in Fig. 8(A) shows the interference study with Nafion coated GOD/Fe_3O_4@SiO_2/MWNTs/GC electrode. There is not much change in the current due to AA and UA. Which clearly shows that 2.5 μl of 0.5 wt% Nafion on the surface of GOD/Fe_3O_4@SiO_2/MWNTs/GC electrode prevent the interference.

3.6. Study of amperometric i–t and calibration curve

The amperometric responses at the GOD/Fe_3O_4@SiO_2/MWNTs/GC electrode for successive addition of different concentration of glucose are presented in Fig. 9 (inset). Well-defined current responses for glucose were obtained at the GOD/Fe_3O_4@SiO_2/MWNTs/GC electrode. The reaction occurring at the biosensor is very fast in reaching a dynamic equilibrium upon each addition of the sample solution, generating a steady-state current signal within 3–6 s. Using the optimum conditions established in the above studies, the calibration of the GOD/Fe_3O_4@SiO_2/MWNTs/GC electrode is depicted in Fig. 9. The steady-state currents gradually increased with increasing concentration of glucose, and exhibited a linear relationship with the concentration of glucose in the range from 1 μM to 30 mM with a detection limit of 800 nM (estimated at S/N = 3) with a correlation coefficient of 0.9994. The performance of GOD/Fe_3O_4@SiO_2/MWNTs/GC electrode is superior than the reported value of GOD/Fe_3O_4@SiO_2/GC electrode which is having

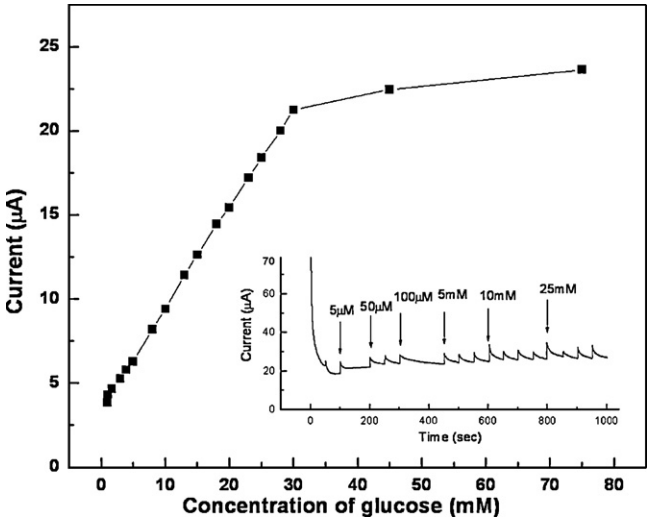


Fig. 9. The calibration curve of the fabricated GOD/Fe_3O_4@SiO_2/MWNTs/GC electrode. Amperometric *i–t* curve with addition of different concentration of glucose solution (inset).

a linear range 1.0×10^{-5} to 4.0×10^{-3} M with a detection limit of 3.2 μM [28].

From Fig. 9, it was observed that the biosensor response gradually deviates from the linear feature as the glucose concentration up to 30 mM. This is the characteristic of a typical Michaelis–Menten kinetics. The apparent Michaelis–Menten constant $K^{app}m$, which depicts the enzyme–substrate kinetics of biosensor, can be calculated from the Line weaver–Burk equation:

$$\frac{1}{I_{ss}} = \left(\frac{K^{app}m}{I_{max}}\right)\left(\frac{1}{C}\right) + \frac{1}{I_{max}} \quad (2)$$

where C is the concentration of substrate, I_{ss} is the steady-state current and I_{max} is the maximum current measured under substrate saturation [29]. Therefore the values of the $K^{app}m$ and I_{max} in this work can be calculated to be 13 mM and 25 μA, respectively. The lower $K^{app}m$ means the higher enzymatic activity of immobilized GOD thus the above result further indicates that the Fe_3O_4@SiO_2/MWNTs modified biosensor possesses a high affinity to glucose [30].

Since MWNTs have excellent electrical conductivity, MWNTs as well as iron oxide dispersed MWNTs attached to the protein shell of enzyme could improve the transfer of electrons between the active redox center of the enzyme. This effect could accelerate the regeneration of GOD and increase the relative activity of the enzyme finally. It is thought to be the mean reason of why the current response of MWNTs and iron oxide dispersed MWNTs modified glucose biosensor was higher than that of the other biosensors.

4. Conclusion

Fe_3O_4 nanoparticles can be successfully stabilized by SiO_2 and Fe_3O_4@SiO_2/MWNTs can be deposited on GCE. GOD can be effectively immobilized on Fe_3O_4@SiO_2/MWNTs/GC electrode to produce a fast direct electron transfer. The immobilized GOD maintains its bioactivity and native structure. Its reduced form can be oxidized by dissolved oxygen to cause an electrocatalytic reaction, which is restrained by glucose due to the reaction between the oxidized form of GOD and glucose. Based on the decrease of electrocatalytic response, a novel glucose sensor has been developed and the resulting sensor displays a high sensitivity (58.9 μA/mM cm^2) and a linear range from 1 μM to 30 mM for glucose determination, and can efficiently exclude the interference of commonly coexisted uric and ascorbic acid. Because of its convenient preparation and

good properties, this biosensor can be used for glucose determination in food industries.

Acknowledgements

The authors acknowledge the funding AOARD, USA and Indian Institute of Technology Madras (IITM).

References

[1] K.H. See, M.E. Mullins, O.P. Mills, P.A. Heiden, Nanotechnology 16 (2005) 1950–1959.
[2] Z.M. Liu, Y.L. Liu, H.F. Yang, Y. Yang, G.L. Shen, R.Q. Yu, Anal. Chim. Acta 533 (2005) 3–9.
[3] J. Heitmann, F. Muller, M. Zacharias, U. Gosele, Adv. Mater. 17 (2005) 795–803.
[4] A.D. Wellman, M.J. Sepaniak, Anal. Chem. 78 (2006) 4450–4456.
[5] X.Y. Zhao, S.A. Shippy, Anal. Chem. 76 (2004) 1871–1876.
[6] L. Josephson, J.M. Perez, R. Weissleder, Angew. Chem. Int. Ed. 40 (2001) 3204–3206.
[7] S. Daniel, T.P. Rao, K.S. Rao, S.U. Rani, G.R.K. Naidu, H.-Y. Lee, T. Kawai, Sens. Actuators B 122 (2007) 672–682.
[8] M. Guo, J. Chen, D. Liu, L. Nie, S. Yao, Bioelectrochemistry 62 (2004) 29–35.
[9] H.Z. Geng, X.B. Zhang, S.H. Mao, A. Kleinhammes, H. Shimoda, Y. Wu, O. Zhou, Chem. Phys. Lett. 399 (2004) 109–113.
[10] K. Jiang, L.S. Schadler, R.W. Siegel, X. Zhang, H. Zhang, M. Terrones, J. Mater. Chem. 14 (2004) 37–39.
[11] Z.M. Tahir, E.C. Alocilja, D.L. Grooms, Biosens. Bioelectron. 20 (2005) 1690–1695.
[12] R.J. Chen, D. Zhang, H.D. Wang, J. Am. Chem. Soc. 123 (2001) 3838–3839.
[13] K.B. Male, S. Harpovic, Y. Liu, D. Wang, J.H.T. Luong, Anal. Chim. Acta 516 (2004) 35–41.
[14] Y. Liu, S. Wu, H. Ju, L. Xu, Electroanalysis (NY) 19 (2007) 986–989.
[15] I.W. Chiang, B.E. Brinson, R.E. Smalley, J.L. Margrave, R.H. Hauge, J. Phys. Chem. B 157 (2001) 1105–1161.
[16] Z. Lu, J. Dai, X. Song, G. Wang, W. Yang, Colloids Surf. A 317 (2008) 450–456.
[17] Q. Lan, C. Liu, F. Yang, S.Y. Liu, J. Xu, D.J. Sun, J. Colloid Interface Sci. 310 (2007) 260–269.
[18] S.L. Tie, C.H. Lee, Y.S. Bae, M.B. Kim, K. Lee, C.H. Lee, Colloid Surf. A 293 (2007) 278–285.
[19] F.H. Chen, Q. Gao, J.Z. Ni, Nanotechnology 19 (2008) 165103.
[20] M.S.P. Shaffer, X. Fan, A.H. Windle, Carbon 36 (1998) 1603–1612.
[21] C.S. Chen, X.H. Chen, B. Yi, T.G. Liu, W.H. Li, L.S. Xu, Z. Yang, H. Zhang, Y.G. Wang, Acta Mater. 54 (2006) 5401–5407.
[22] M.A. Correa-Duarte, M. Giersig, N.A. Kotov, L.M. Liz-Marzán, Langmuir 14 (1998) 6430–6435.
[23] G. Dagan, W.M. Shen, M. Tomkiewicz, J. Electrochem. Soc. 139 (1992) 1855–1861.
[24] G.H. Du, Z.L. Liu, X. Xia, Q. Chu, S.M. Zhang, J. Sol–Gel Sci. Technol. 39 (2006) 285–291.
[25] Z.Z. Xu, C.C. Wang, W.L. Yang, S.K. Fu, J. Mater. Sci. 22 (2005) 4667–4669.
[26] W. Wu, H. Quanguo, C. Jiang, Nanoscale Res. Lett. 3 (2008) 97–415.
[27] C.E. Banks, R.G. Compton, Analyst 130 (2005) 1232–1239.
[28] J. Qiu, H. Peng, R. Liang, Electrochem. Commun. 9 (2007) 2734–2738.
[29] S. Zhang, W. Nü, H. Yu, Y. Niu, C. Sun, Bioelectrochemistry 67 (2005) 15–22.
[30] X. Chu, D. Duan, G. Shen, R. Yu, Talanta 71 (2007) 2040–2047.

Talanta 80 (2010) 2023–2033

Contents lists available at ScienceDirect

Talanta

journal homepage: www.elsevier.com/locate/talanta

Novel fluorimetric bulk optode membrane based on 5,8-bis((5′-chloro-8′-hydroxy-7′-quinolinyl)methyl)-2,11-dithia-5,8-diaza-2,6-pyridinophane for selective detection of lead(II) ions

Mojtaba Shamsipur[a,*], Marzieh Sadeghi[a], Kamal Alizadeh[b], Andrea Bencini[c], Barbara Valtancoli[c], Alessandra Garau[d], Vito Lippolis[d,**]

[a] Department of Chemistry, Razi University, Kermanshah, Iran
[b] Department of Chemistry, Lorestan University, Khorramabad, Iran
[c] Dipartimento di Chimica, Università degli Studi di Firenze, Polo Scientifico, Via della Lastruccia 3, 50019 Sesto Fiorentino (FI), Italy
[d] Dipartimento di Chimica Inorganica ed Analitica, Università degli Studi di Cagliari, S.S. 554 Bivio per Sestu, 09042 Monserrato (CA), Italy

ARTICLE INFO

Article history:
Received 14 September 2009
Received in revised form 31 October 2009
Accepted 2 November 2009
Available online 12 November 2009

Keywords:
Optode membrane
Fluoroionophore
Selective Pb^{2+} determination
Fluorescence quenching

ABSTRACT

A novel fluorescence chemical sensor for the highly sensitive and selective determination of Pb^{2+} ions in aqueous solutions is described. The preliminary potentiometric and spectrofluorimetric complexation studies in solution revealed that the lipophilic ligand 5,8-bis((5′-chloro-8′-hydroxy-7′-quinolinyl)methyl)-2,11-dithia-5,8-diaza-2,6-pyridinophane (**L2**) forms a highly stable and selective $[Pb\mathbf{L2}]^{2+}$ and $[Pb(\mathbf{L2})_2]^{2+}$ complexes which results in a strong fluorescence quenching of the ligand. Thus, a novel fluorescence Pb^{2+} sensing system was prepared by incorporating **L2** as a neutral lead-selective fluoroionophore in the plasticized PVC membrane containing tetrakis(*p*-chlorophenyl) borate as a liphophilic anionic additive. The response of the sensor is based on the strong selective fluorescence quenching of **L2** by Pb^{2+} ions. At pH 5.5, the proposed sensor displays a calibration curve over a wide concentration range of 3.0×10^{-7} to 2.5×10^{-2} M with a relatively fast response time of less than 5 min. In addition to high stability, reversibility and reproducibility, the sensor shows a unique selectivity towards Pb^{2+} ion with respect to common coexisting cations. The proposed fluorescence optode was successfully applied to the determination of lead in plastic toys and tap water samples.

© 2009 Elsevier B.V. All rights reserved.

1. Introduction

Forty years of coordination chemistry of macrocylic ligands, after the first discoveries of crown ethers [1] and cryptands [2], have introduced a large number of macrocylic receptors including metal free ligands and coordinatively unsaturated metal complexes, suitable for selective binding and recognition of a wide variety of cationic, anionic and neutral substrates [3–6]. Many of these interesting macrocylic receptors are still waiting to be engineered via linking to a light emitting fragment to act as luminescent sensors for given ions or molecules of prominent interest in biological, medical, environmental and industrial analyses. Due to their interesting coordination chemistry and wide analytical applications, such conjugated chemosensors consisting of a fluorogenic fragment (signaling unit) covalently linked, via an appropriate spacer, to a platform of a macrocyclic or chelating ligand (receptor unit), have attracted the increasing interest of many research groups throughout the world [7–10].

It is worth mentioning that the development of optical sensors has now become a rapidly expanding area of analytical chemistry, because they offer the advantages of simple preparation, reasonable selectivity and sensitivity and no need for separate reference devices [11–13]. Fluorescence is particularly a suitable optical sensing method for designing these optical sensors. This is mainly due to its inherent sensitivity, its almost complete inertness to turbidity and its flexibility with respect to geometric arrangements [11]. The increasing interest in this field is mainly due to the growing demand for highly selective analytical tools for the detection and monitoring of ions in environmental, biological and industrial effluent samples.

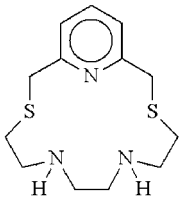
Lead poisoning is one of the most common environmental child health threats which can cause brain and kidney damage, mental retardation, behavior problems, development delays, and other physical and mental problems [14]. Due to increased industrial use of lead on one hand and its serious hazardous effects, on the other [14,15], the preparation of lead ion-selective membrane electrodes by using a wide variety of active materials have been extensively

* Corresponding author. Tel.: +98 21 66908032; fax: +98 21 66908030.
** Corresponding author. Tel.: +39 070 6754467; fax: +39 070 6754456.
E-mail addresses: mshamsipur@yahoo.com (M. Shamsipur), lippolis@unica.it (V. Lippolis).

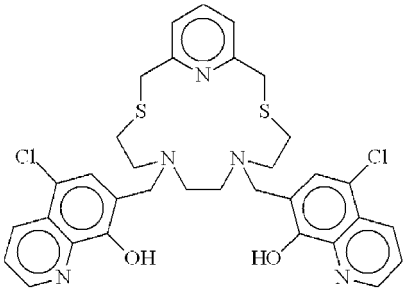
0039-9140/$ – see front matter © 2009 Elsevier B.V. All rights reserved.
doi:10.1016/j.talanta.2009.11.011

studied. Only in the past 5 years, more than 30 lead ion-selective electrodes have been reported in the literature, some of the most sensitive and selective of which are described in Refs. [16–24]. However, compared with Pb^{2+} selective potentiometric sensors, work on ion-selective bulk optodes for lead(II) ion has been quite sparse [25–29].

In recent years, we have been involved in the synthesis and coordination chemistry of mixed thia–aza macrocycles containing heteroaryl moieties [30,31] and their widespread analytical applications as selective ion carriers for transition and heavy metal ions in solid phase extraction, ion transport and ion-selective electrode studies [30,32,33]. We have recently reported the successful use of some thia–aza macrocyclic ligands with different fluorogenic subunits for the preparation of selective fluorescent optical sensors for some heavy metal ions [34–37]. In this work, we found that the strong fluorescence of the new chemosensor 5,8-bis((5′-chloro-8′-hydroxy-7′-quinolinyl)methyl)-2,11-dithia-5,8-diaza-2,6-pyridinophane, **L2**, quenched considerably, and in a selective manner, upon complexation with Pb^{2+} ions. Thus, we decided to probe the fluoroionophore in plasticized PVC-membranes for sensing of traces of lead in aqueous solutions. 2,11-Dithia-5,8-diaza-2,6-pyridinophane, **L1**, is the mother macrocycle of **L2**.



L1



L2

2. Experimental

2.1. Reagents

Reagent-grade *o*-nitrophenyloctylether (NPOE), dioctyl phthalate (DOP), bis(2-ethylhexyl) sebacate (EHS), potassium tetrakis(*p*-chlorophenyl) borate (KTpClPB), high relative molecular weight high molecular weight poly(vinyl chloride) (PVC), tetrahydrofuran (THF) and acetonitrile were purchased from Fluka chemical company and used as received. Reagent-grade nitrate salts of all cations used (all from Merck) where of the highest purity available and used without further purification except for vacuum drying. All other chemicals and solvents needed were of reagent-grade and used as received. Doubly distilled deionized water was used throughout. *N*,*N*′-bis(2-chloroethyl)ethylendiamine hydrochloride and 2,6-dithiomethylpyridine were synthesised according to the literature [38,39].

2.2. Synthesis of *N*,*N*′*(t-butoxycarbonyl)-bis(2-chloroethyl)ethylendiamine*

Bis(2-chloroethyl)ethylendiamine dihydrochloride (6.5 g, 25 mmol) was added to a cooled solution of sodium hydroxide (8 g, 200 mmol) in 120 mL of water. Di-*tert*-butyl dicarbonate (11.8 g, 54 mmol) was carefully added and the reaction mixture was stirred overnight at room temperature. The product was extracted with ethyl acetate (4× 70 mL), dried over Na_2SO_4 and concentrated in vacuo to obtain the protected diamine as a pale yellow oil (8.2 g, 85% yield).

^{1}H NMR (300 MHz, $CDCl_3$), δ_H 1.42 (s, 18H, C(CH_3)$_3$), 3.36–3.41 (4H, m, NCH_2CH_2Cl), 3.47–3.59 (8H, m, $CH_2NCH_2CH_2Cl$). ^{13}C NMR (75 MHz, $CDCl_3$), δ_C 28.2 (C(CH_3)$_3$), 41.5 (NCH_2CH_2Cl), 49.7 (NCH_2CH_2Cl), 52.6 ($CH_2NCH_2CH_2Cl$), 80.3 ($C(CH_3)_3$), 154.9 (C=O).

2.3. Synthesis of *N*,*N*′*-t-butoxycarbonyl-2,11-dithia-5,8-diaza-2,6-pyridinophane*

A solution of *N*,*N*′-(*t*-butoxycarbonyl)-bis-(2-chloroethyl) ethylendiamine (2.1 g, 13.0 mmol) and 2,6-dithiomethylpyridine (4.7 g, 12.0 mmol) in dry DMF (100 mL) was added, under N_2 over 24 h, to a well stirred suspension of Cs_2CO_3 (6.6 g, 20.3 mmol) in dry DMF (300 mL) maintained at 55 °C. The resultant mixture was stirred for 1 h at 55 °C and left for 24 h at room temperature and subsequently concentrated under vacuum. The residue was taken up in CH_2Cl_2 (150 mL) and the organic extract washed with water, dried over Na_2SO_4 and concentrated under vacuum. The resulting brown residue was purified by crystallization from petroleum ether 40–60° to give a pale white product. (1.57 g, 30% yield). mp: 142–144 °C. Elemental analysis: *Anal.* Calc. for $C_{23}H_{37}N_3O_4S_2$: C, 55.3; H, 7.5; N, 8.4; S, 12.8. Found: C, 55.6; H, 7.7; N, 8.7; S, 12.5%. ^{1}H NMR (300 MHz, $CDCl_3$), δ_H 1.41 (18H, s, C(CH_3)$_3$), 2.41–2.60 (12H, m, $SCH_2CH_2NCH_2$), 3.76 (4H, s, $ArCH_2S$), 7.21 (2H, d, J = 6.0 Hz), 7.62 (1H, t, J = 5.7 Hz). ^{13}C NMR (75 MHz, $CDCl_3$), δ_C 28.3 (C(CH_3)$_3$), 29.6 ($ArCH_2S$), 37.1 (SCH_2CH_2N), 46.6 (SCH_2CH_2N), 48.1 ($SCH_2CH_2NCH_2$), 79.1 ($C(CH_3)_3$), 121.4, 137.7, 154.8, 157.8.

2.4. Synthesis of 2,11-dithia-5,8-diaza-2,6-pyridinophane (*L1*)

Trifluoroacetic acid (20 mL) was added to a solution of *N*,*N*′-t-butoxycarbonyl-2,11-dithia-5,8-diaza-2,6-pyridinophane (1.7 g, 3.51 mmol) in CH_2Cl_2 (20 mL) and the resulting solution was stirred at room temperature under N_2 for 2 h. The solvent was removed under reduced pressure and the residue taken up in water. The pH value was adjusted to 14 by adding 6 M NaOH and the product extracted into CH_2Cl_2. The organic layers were dried over Na_2SO_4, filtered and concentrated under reduced pressure to give a white solid. (0.66, 67% yield). mp. 135-138 °C. Elemental analysis: *Anal.* Calc. for $C_{13}H_{21}N_3S_2$: C, 55.1; H, 7.5; N, 14.8; S, 22.6. Found: C, 54.8; H, 7.8; N, 14.5; S, 22.7%. ^{1}H NMR (300 MHz, $CDCl_3$), δ_H 2.26 (2H, s br, NH) 2.64–2.67 (8H, m, SCH_2CH_2N), 2.74–2.78 (4H, m, $SCH_2CH_2NCH_2$), 3.82 (4H, s, $ArCH_2S$), 7.21 (d, 2H, J = 6.0 Hz), 7.61 (1H, t, J = 5.7 Hz). ^{13}C NMR (75 MHz, $CDCl_3$), δ 32.1 ($ArCH_2S$), 38.0 (SCH_2CH_2N), 47.6 ($SCH_2CH_2NCH_2$), 48.2 (CH_2NCH_2), 121.2, 137.3, 158.7 (aromatic carbons).

2.5. Synthesis of 5,8-bis((5′-chloro-8′-hydroxy-7′-quinolinyl) methyl)-2,11-dithia-5,8-diaza-2,6-pyridinophane (*L2*)

5-Chloro-8-hydroxyquinoline (0.47 g, 2.41 mmol) and paraformaldehyde (0.10 g, 3.34 mmol) were added to a mixture of **L1** (0.30 g, 1.06 mmol) in dry benzene (30 mL). The solution was heated to reflux for 12 h under nitrogen. The solution was filtered off and the solvent was evaporated under reduced pressure. The residue was washed with Et_2O to give a light brown solid (0.45 g, yield 64%). mp: 153–155 °C. Elemental analysis: *Anal.* Calc. for $C_{33}H_{33}O_2N_5S_2Cl_2$: C, 59.5; H, 5.0, N, 10.5; S, 9.6. Found: C, 59.3; H, 4.9, N, 10.3; S, 9.4%. ^{1}H NMR (300 MHz, $CDCl_3$): δ_H 2.60–2.65 (8H, m, SCH_2CH_2N), 2.75–2.81 (4H, m, $SCH_2CH_2NCH_2$), 3.80 (4H, s, $ArCH_2S$), 3.85 (4H, s, NCH_2Q), 7.29 (2H, d, J = 7.2 Hz), 7.45–7.48 (2H, m), 7.70 (1H, t, J = 7.6 Hz,), 8.43 (2H, d, J = 8.4 Hz), 8.84 (2H, d, J = 8.0 Hz). ^{13}C NMR (75 MHz, $CDCl_3$): δ_C 27.0 ($ArCH_2S$), 37.0 (SCH_2CH_2N), 51.0 (NCH_2Q), 54.0 (SCH_2CH_2N), 55.3 ($SCH_2CH_2NCH_2$), 119.4 (C–Cl, Q), 121.5 (Py), 121.9 (Q), 122.5 (Q), 125.7 (Q), 127.5 (Q), 133.1 (Q), 137.9 (Py), 139.2 (C–OH, Q), 148.6 (Q), 151.1 (Q), 158.7

(Py); [Py = pyridine framework, Q = 5-chloro-8-hydroxyquinoline framework].

2.6. Apparatus

All melting points are uncorrected. Microanalytical data were obtained using a Fison EA CHNS-O instrument (T = 1000 °C). The ^{1}H and ^{13}C NMR spectra were recorded on a Varian VXR300 spectrometer (operating at 75.4 MHz). All fluorescence measurements were carried out on a JASCO FP 6200 fluorometer. A Jeneway 3345 Ion Meter calibrated against two standard buffer solutions at pH 4.0 and 7.0 was used for the pH measurements.

2.7. Membrane preparation

The membrane solution was prepared by dissolving 3 mg of fluoroionophore **L2**, 30 mg of powdered PVC, 61 mg of plasticizer NPOE and 6 mg of additive KTpClPB in 1.5 mL THF. A volume of 0.1 mL of this solution was pipetted and uniformly spread onto a 24 mm × 13 mm dust-free glass plate by using a spin on device (at a rate of 2000 rpm). The resulting membrane, thickness of ca 2–3 μm, was then placed in a THF saturated desicator for 2 h, and was allowed to stand in ambient air before use.

2.8. Fluorescence measurements

The film was first soaked for more than 20 min in an acetate buffer solution of pH 5.5 until the membrane had a stable fluorescence value before the first lead measurement was made. During its use the membranes were placed diagonally inside the sample cuvette of the instrument containing 2 mL buffer solution of pH 5.5. The fluorescence intensity, at an excitation wavelength of 388 nm was measured at 515 nm. Then the sample was titrated with standardized lead ion solutions and the fluorescence intensity of the system was measured after ~5 min, required to reach the equilibrium.

2.9. Potentiometric measurements

The pH-metric measurements (pH = −log[H$^+$]) employed for the determination of ligand protonation and metal complex stability constants were carried out in the case of ligand **L1** in 0.10 mol L^{-1} NMe_4Cl aqueous solutions and, in the case of **L2** in 0.10 mol L^{-1} NMe_4Cl water–MeCN (1:1, v/v) solution at 298.1 ± 0.1 K by using equipment and procedure described elsewhere [40]. The choice of such solvent mixture was dictated by the low solubility of the complexes with **L2** in pure water. The combined Ingold 405 S7/120 electrode was calibrated as a hydrogen concentration probe by titrating known amounts of HCl with CO_2-free NaOH solutions and determining the equivalent point by Gran's method [41] which allows one to determine the standard potential E^o and the ionic product of water (pK_w = 13.73 in 0.10 mol L^{-1} NMe_4Cl aqueous solutions, pK_w = 14.99 in 0.1 M NMe_4Cl water–MeCN (1:1, v/v) solution). At least three measurements (about 100 data points each one) were performed for each system in the pH ranges 2.5–10.5. In all experiments the ligand concentration was about 1.0×10^{-3} mol L^{-1}. In the complexation experiments the metal ion concentration was varied from 0.3:1 to 0.9:1. The computer program HYPERQUAD [42] was used to calculate the equilibrium constants from e.m.f. data. In the case of Hg^{2+}, under the experimental conditions employed, the formation of metal-chloride complexes is expected to occur. For the determination of the stability constants of the Hg^{2+} complexes with **L1** in aqueous solution, the formation of Hg^{2+} complexes with chloride was taken into account and their stability constants were taken from Ref. [43]. The stability constants of the Hg^{2+} complexes with chloride in 0.10 mol L^{-1} NMe_4Cl water–MeCN (1:1, v/v) solution are not known and the formation of such complexes was not considered in calculations. Hence, the stability constants of Hg^{2+} complexes with **L2** must be referred to the specific composition of the medium employed (0.10 mol L^{-1} NMe_4Cl water–MeCN (1:1, v/v)).

2.10. Procedure for determination of lead content in children plastic toys

About 10.0 g of plastic toy was placed in a crucible and it heated by flame and then kept in a furnace at 700 °C until it changed into white powder. Then 6 mL of HNO_3/HCl, 1:3 (v/v) solution was added. The mixture was heated until dissolution was complete. The sample solution was further heated to reach a volume of 0.5 mL. The solution was then cooled and completely transferred to a calibrated 100.0-mL volumetric flask. The pH was adjusted to 5.5 by acetate buffer and diluted to volume with doubly distilled water. Proper sample solutions were prepared by appropriate dilution of the mother solution. The lead content of sample was determined by the proposed optical sensor, using the calibration method.

3. Results and discussion

3.1. Solution studies

3.1.1. pH-metric studies

In order to obtain a clue about the stoichiometry and stability of the transition metal complexes of some selected metal ions with 5,8-bis((5′-chloro-8′-hydroxy-7′-quinolinyl)methyl)-2,11-dithia-5,8-diaza-2,6-pyridinophane, **L2**, and its mother macrocycle 2,11-dithia-5,8-diaza-2,6-pyridinophane, **L1**, protonation and metal complexation with ligands was studied by means of potentiometric measurements carried out in aqueous solution, in case of **L1** or in acetonitrile/water 1:1 (v/v) solution, in case of **L2**. The use of the latter solvent mixture is due to very scarce solubility of the metal complexes of **L2** in water. Fig. 1 displays the distribution diagrams for the protonated ligands. The calculated stepwise protonation constants of the ligands are also included in the legend of Fig. 1.

Considering ligand protonation, **L1** and **L2** can bind up to three and two acidic protons in solution, respectively. The values of the constants for both the protonation equilibria of **L2** and for the first two of **L1** range between 9.37 and 6.0 log units, accounting for protonation of the aliphatic amine groups of the macrocycles [44]. In fact, pyridine and 5-chloro-8-hydroxyquinoline are featured by lower basicity constant (for instance log K = 5.22 and 4.22 for protonation of pyridine in water and in CH_3CN/H_2O 1:1 (v/v) medium, respectively) [45]. In the case of **L1**, a third protonation step takes place at more acidic pH values, as expected considering that protonation occurs on the weakly basic nitrogen atom of the pyridine unit. Conversely, in the case of **L2** no further protonation step is observed in the pH range investigated (2.5–10.5). On the other hand, **L2** displays also a deprotonation step, with the formation of the anionic species [**L2**(H_{-1})]$^-$ at alkaline pH values; this process can be attributed to deprotonation of one 5-chloro-8-hydroxyquinoline moiety, in agreement with the known ability of 5-chloro-8-hydroxy-quinoline to deprotonate at strongly alkaline pH values (pK_a = 10.64 in water–dioxane 60:40 mixture) [46]. Deprotonation of the second 5-chloro-8-hydroxy-quinoline was instead not observed in our experimental conditions (pH range 2.5–10.5).

Considering metal complexation, in the case of **L1** the potentiometric studies were generally carried out in the pH range 2.5–10.5, with the only exception for Cu^{2+}, where the pH range

Table 1
Stability constants of the Cu^{2+}, Zn^{2+}, Cd^{2+}, Pb^{2+} and Hg^{2+} complexes with **L1** (NMe_4Cl 0.1 mol L^{-1} aqueous solution, 298.1 K) and **L2** (0.1 mol L^{-1} NMe_4Cl water–MeCN (1:1, v/v) solution).

Reaction	log *K*				
	Cu^{2+}	Zn^{2+}	Cd^{2+}	Pb^{2+}	Hg^{2+}
$M + \mathbf{L1} \rightleftharpoons [M\mathbf{L1}]^{2+}$	14.70 (8)	5.7 (1)	5.6 (1)	11.01 (1)	14.95 (1)
$[M\mathbf{L1}]^{2+} + H^+ \rightleftharpoons [M\mathbf{L1}H]^{3+}$	4.86 (3)	8.9 (1)	9.3 (1)	5.73 (1)	3.73 (6)
$[M\mathbf{L1}H]^{3+} + H^+ \rightleftharpoons [M\mathbf{L1}H_2]^{4+}$	–	–	–	4.91 (1)	3.4 (1)
$[M\mathbf{L1}]^{2+} + OH^- \rightleftharpoons [M\mathbf{L1}(OH)]^+$	–	5.5 (1)	3.1 (1)	4.7 (1)	2.8 (1)
$M + \mathbf{L2} \rightleftharpoons [M\mathbf{L2}]^{2+}$	14.5 (1)	10.2 (1)	10.79 (7)	10.87 (3)	11.9 (2)
$[M\mathbf{L2}]^{2+} \rightleftharpoons [M\mathbf{L2}(H_{-1})]^+ + H^+$	3.5 (1)	6.9 (1)	–	–	–
$[M\mathbf{L2}]^{2+} + \mathbf{L2} \rightleftharpoons [M(\mathbf{L2})_2]^{2+}$	–	–	9.5 (1)	7.4 (1)	10.3 (2)

was only 2.0–7.0, due to complex precipitation at alkaline pH values. Similarly, in the case of **L2** the measurements were limited to the pH range 2.0–7.0 for all metal cations, due precipitation of hydroxo-complexes or metal hydroxides in the alkaline region. The formation constants of the complexes are listed in Table 1, while Figs. 2–4 display the distribution diagrams for the complexes with **L1** and **L2**.

Table 1 shows that **L1** forms only 1:1 complexes with all the metal cations investigated. As often found in metal complexation with ligands containing nitrogen atoms, Cu^{2+} and Hg^{2+} form the most stable $[M\mathbf{L1}]^{2+}$ complexes, due to the stabilizing effect of CFSE in the case of Cu^{2+} and to the high affinity of Hg^{2+} for nitrogen donors. The most interesting finding in Table 1, however, is the remarkable higher stability of the $[Pb\mathbf{L1}]^{2+}$ complex with respect to the $[Zn\mathbf{L1}]^{2+}$ and $[Cd\mathbf{L1}]^{2+}$ ones. In fact, it is known that polyamine ligands often form Zn^{2+}, Cd^{2+} and Pb^{2+} complexes with similar stability [47]. In this case, the Pb^{2+} complex is *ca.* 5 orders of magnitude more stable than the Zn^{2+} and Cd^{2+} ones. This selectivity can be interpreted considering the presence of a couple of soft sulfur donors, which generally display a higher binding ability towards the softer Pb^{2+} ion. At the same time, the 15-membered macrocyclic cavity may have the optimal dimensions to host the larger Pb^{2+}.

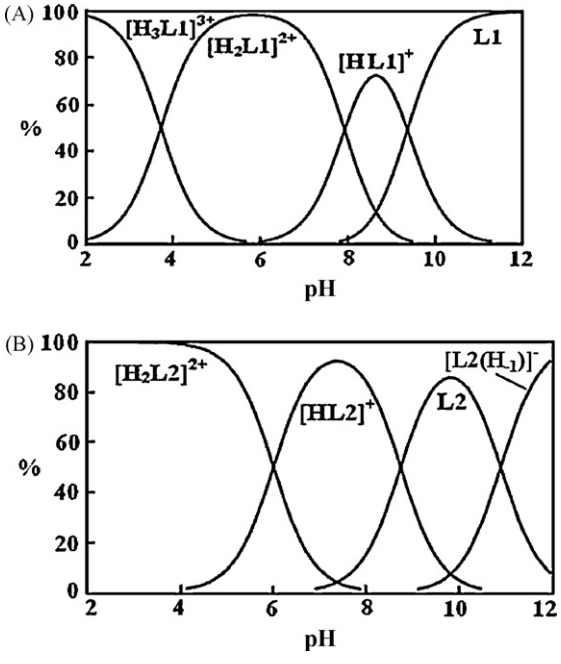


Fig. 1. Distribution diagrams of the protonated species of **L1** (A) and **L2** (B) ($[\mathbf{L1}] = [\mathbf{L2}] = 1.0 \times 10^{-3}$ mol L^{-1}, 298.1 K, 0.1 M NMe_4Cl aqueous solution (**L1**) or 0.1 mol L^{-1} NMe_4Cl water–MeCN (1:1, v/v) solution (**L2**)). In the case of **L1**, the constants (log *K*) for the equilibria $\mathbf{L1} + H^+ = [H\mathbf{L1}]^+$, $[H\mathbf{L1}]^+ + H^+ = H2\mathbf{L1}]^{2+}$ and $[H2\mathbf{L1}]^{2+} + H^+ = [H3\mathbf{L1}]^{3+}$ were respectively 9.37(5), 7.93(9) and 3.7(1), while in the case of **L2** the constants (log *K*) for the equilibria $\mathbf{L2} = [\mathbf{L2}(H^{-1})]^- + H^+$, $\mathbf{L2} + H^+ = [H\mathbf{L2}]^+$ and $[H\mathbf{L2}]^+ + H^+ = [H2\mathbf{L2}]^{2+}$ were respectively 10.9(1), 8.75(9), and 6.00(9).

From this point of view, it can be of interest to compare the stability sequence of the complexes in the present case ($Pb^{2+} > Cd^{2+} \approx Zn^{2+}$) with that previously found in the case of the complexes with macrocycle 2,8-dithia-5-aza-2,6-pyridinophane (**L3**) [47], characterized by an overall structure similar to that of **L1**, but containing a smaller macrocyclic cavity and featuring a N_2S_2 set of donors, instead of the N_3S_2 one of **L1**. Actually **L3** shows a higher affinity for Cd^{2+} over Zn^{2+} and Pb^{2+}. This observation may suggest that the smaller Cd^{2+} cation has the optimal dimension to fit the macrocyclic cavity of **L3**, while the cavity of **L1** is best sized for the larger Pb^{2+} ion.

All the $[M\mathbf{L1}]^{2+}$ complexes show a marked tendency to bind acidic protons affording mono-protonated complexes and, in the case of Pb^{2+} and Hg^{2+}, also diprotonated species (Table 1 and Fig. 2). It is noteworthy that the constants for the addition of the acidic proton to the $[Zn\mathbf{L1}]^{2+}$ and $[Cd\mathbf{L1}]^{2+}$ complexes are remarkably high (log *K* = 8.9 and 9.3 for the equilibrium $[M\mathbf{L1}]^{2+} + H^+ \rightleftharpoons [M\mathbf{L1}H]^{3+}$ with $M = Zn^{2+}$ and Cd^{2+}, respectively). These values are similar to the first protonation constant of the ligand alone (9.37 log units), suggesting that in the $[Zn\mathbf{L1}]^{2+}$ and $[Cd\mathbf{L1}]^{2+}$ complexes protonation occurs on an amine group not involved in metal binding. This observation further supports the hypothesis that the macrocyclic cavity of **L1** is too "large" to optimally host Zn^{2+} and Cd^{2+}.

Finally, deprotonation of a coordinated water molecule affords hydroxo-complexes of the type $[ML(OH)]^+$ at alkaline pH values ($M = Zn^{2+}$, Cd^{2+}, Pb^{2+} and Hg^{2+}; Cu^{2+} coordination was not studied in the alkaline pH region).

The coordination behavior of **L2** is remarkably different with respect to that of **L1**. In fact, while Cu^{2+} and Zn^{2+} forms only 1:1 complexes, at least in the pH range investigated, the larger and softer Cd^{2+}, Pb^{2+} and Hg^{2+} cations give not only 1:1 species, but also complexes featuring a 1:2 metal-to-ligand molar ratio (see Table 1).

Considering Cu^{2+} and Zn^{2+}, metal coordination occurs at acidic pH values (Fig. 3A and B) to give the $[Cu\mathbf{L2}]^{2+}$ or $[Zn\mathbf{L2}]^{2+}$ complexes. Unfortunately, the use of a different solvent in the measurements does not allow reliable comparisons with the stability constants of the corresponding complexes with ligand **L1**. However, the potentiometric titrations also show that the $[Cu\mathbf{L2}]^{2+}$ and $[Zn\mathbf{L2}]^{2+}$ complexes release an acidic proton to form $[Cu\mathbf{L2}(H_{-1})]^+$ and $[Zn\mathbf{L2}(H_{-1})]^+$ species. This process takes place, once again, in the acidic pH region, with pK_a values of 3.5 and 6.9 for the Cu^{2+} and Zn^{2+} complexes, respectively, and it can be reasonably attributed to a metal-assisted deprotonation of the hydroxyl group of one of the 5-chloro-8-hydroxy-quinoline moieties.

Similarly to Cu^{2+} and Zn^{2+} cases, Cd^{2+}, Pb^{2+} and Hg^{2+} form simple $[M\mathbf{L2}]^{2+}$ complexes above pH 2.5 (Figs. 3C–E, 4A–C). In this case, however, this process is followed, at slightly higher pH values by the formation of $[M(\mathbf{L2})_2]^{2+}$ complexes, containing two ligands bound to a single metal. Although the potentiometric data do not allow in this case to infer hypothesis on the structural features of these complexes, it is worth noting that the smaller and more acidic Cu^{2+} and Zn^{2+} ions seem to prefer a binding mode involving deprotonation of the 5-chloro-8-hydroxy-quinoline upon metal coordination, while the larger Cd^{2+}, Pb^{2+} and Hg^{2+} ions appear to be able not only

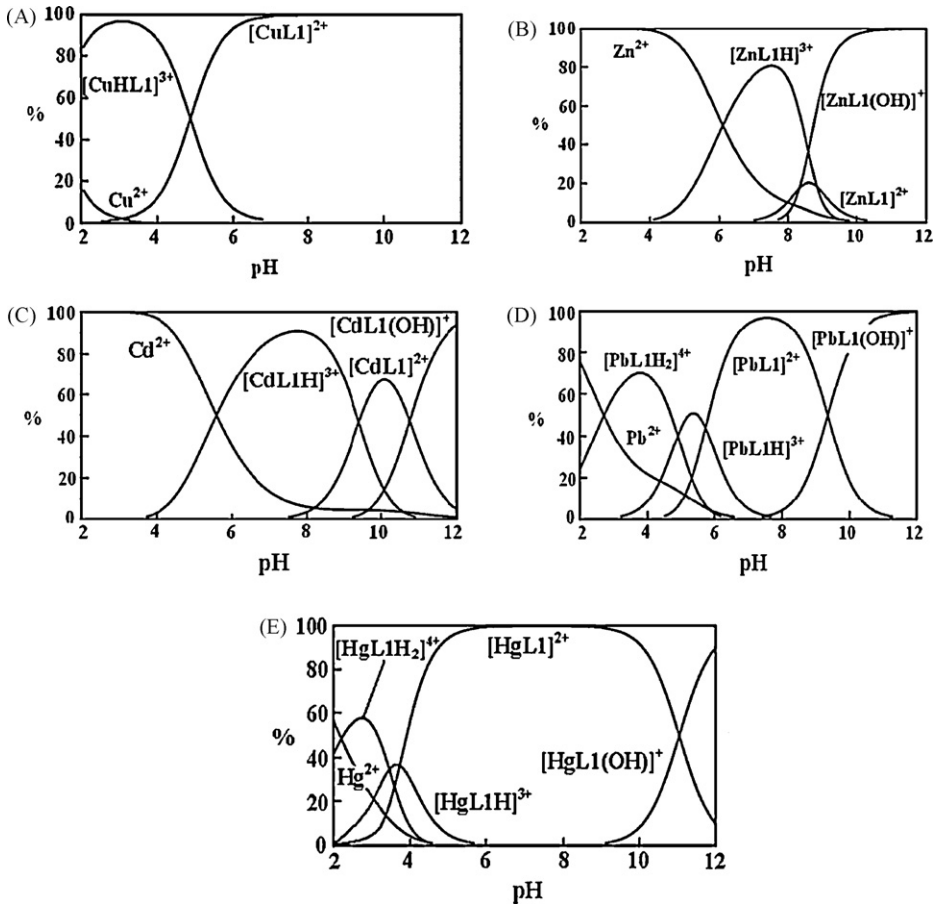


Fig. 2. Distribution of the complexed species of **L1** in the presence of 1 equiv. of Cu^{2+} (A), Zn^{2+} (B), Cd^{2+} (C), Pb^{2+} (D) and Hg^{2+} (E) ([**L1**] = [Cu^{2+}] = [Zn^{2+}] = [Cd^{2+}] = [Pb^{2+}] = [Hg^{2+}] = 1.0×10^{-3} mol L^{-1}, 298.1 K, 0.1 mol L^{-1} NMe_4Cl aqueous solution).

to form "common" 1:1 complexes, but also to arrange two ligand moieties within their coordination sphere.

3.1.2. Fluorescence studies

In order to evaluate whether **L2** could be used as a suitable fluorescent chemosensor for Pb^{2+} ion, we recorded the excitation and emission fluorescence spectra variations that occur upon addition of increasing amount of selected metal cations, and in particular Pb^{2+}, to a MeCN solution of the ligand (8.0×10^{-6} mol L^{-1}) at 25.0 ± 0.1 °C (Fig. 5). As seen from Fig. 5, the excitation and emission spectra of the ligand show sharp bands at 340 nm and 506 nm, respectively, both of which significantly decreased as a function of Pb^{2+}/**L2** molar ratio. The corresponding Pb^{2+}/**L2** plots at maximum excitation (340 nm) and emission (506 nm) wavelengths, shown in Fig. 6, indicate two distinct inflection points at metal ion to ligand mole ratios of 0.5 and 1.0 due to the formation of both [Pb(**L2**)$_2$]$^{2+}$ and [Pb**L2**]$^{2+}$ complexed adducts in solution. It is noteworthy that because of very short fluorescence lifetimes and low concentration conditions used the effect of concentration quenching should be negligible. As is also obvious from Fig. 5, an interesting point about the change in stoichiometry from the 1:2 complex to a 1:1 species upon further addition of the metal is the appearance of new excitation and emission bands at about 375 and 405 nm, respectively, at a Pb^{2+}/**L2** molar ratio of about 0.5 in MeCN solution. These results are nicely in agreement with those obtained from pH-metric study results given in Section 3.1.1.

The resulting fluorescence intensity-molar ratio data for the case of Co^{2+}, Cu^{2+}, Fe^{3+}, Ag^{+}, Hg^{2+}, Y^{3+}, Cd^{2+} and La^{3+} ions are also shown in Fig. 6. As is obvious from Fig. 6, in Y^{3+}, Cd^{2+} and La^{3+} cases, a rather pronounced chelation enhancement of quenching of the fluorescence (CHEQ effect) is observed for **L2** upon addition of increasing quantity of the metal ions, with two more or less pronounced inflection points at metal/**L2** molar ratios of 0.5 and 1.0, similar to that observed for the case of Pb^{2+} ion, but with lower extent of intensity changes. However, in the case of Y^{3+}, Cd^{2+} and La^{3+} ions, a CHEQ effect is observed up to a metal/ligand molar ratio of about 0.5 which is followed by a remarkable enhancement of the fluorescence intensity upon further addition of the metal ions with a more or less pronounced inflection point at a molar ratio of 1.0, clearly indicating the subsequent formation of 1:2 and 1:1 metal-to-ligand complexes. The observed increased fluorescence intensity of the ligand **L2** upon addition of the metal ions should be due to the increased rigidity of the complexed ligand, as already reported [48].

3.2. Ab initio calculations of structure of Pb^{2+} complexes with fluoroionophore *L2*

In order to obtain further information about the optimized structures of the fluoroionophore **L2** and its 1:1 and 1:2 metal-to-ligand complexes with Pb^{2+}, the molecular structures of the uncomplexed ligand and its lead ion complexes were built with the Hyperchem program [49]. The structure of free ligand was optimized using the 6.31 G* basis set at the restricted Hartree-Fock (RHF) level of theory. The optimized structure of the ligand was then used to find out the initial structures of its lead complexes. Finally, the structures of the resulting 1:1 and 1:2 metal-to-ligand complexes were optimized using the Lan12mb basis set at the RHF level of theory. No molecular symmetry constraint was applied; rather, full optimization and frequency option of all bond lengths,

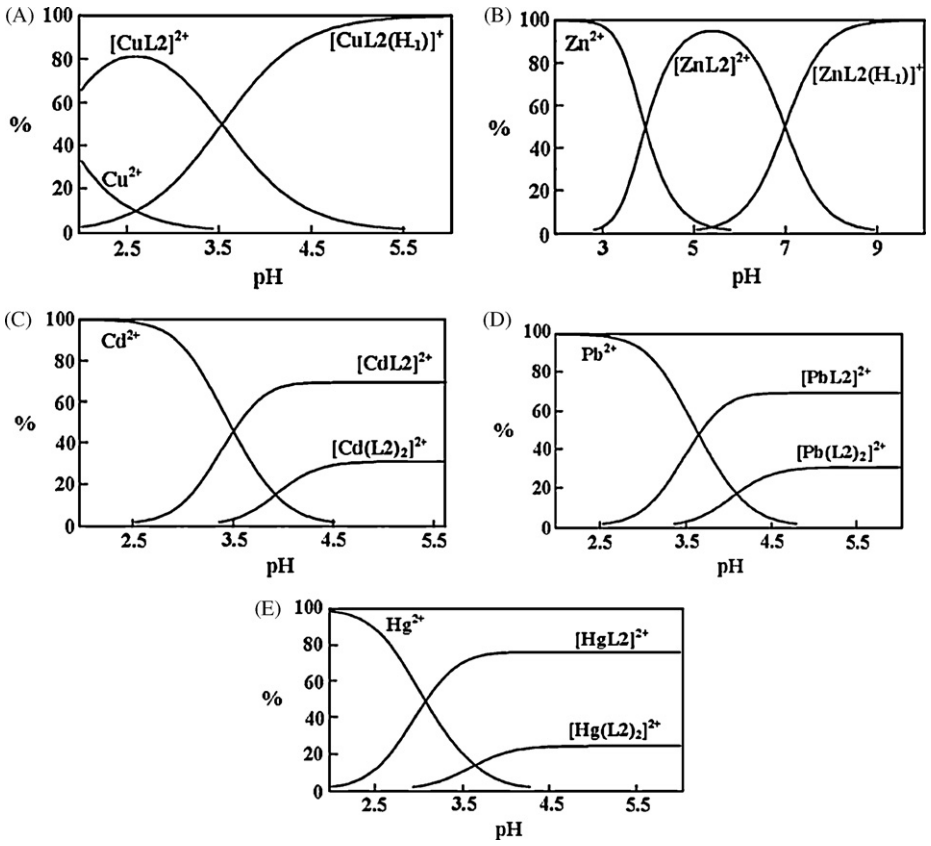


Fig. 3. Distribution of the complexed species of **L2** in the presence of 1 equiv. of Cu^{2+} (A), Zn^{2+} (B), Cd^{2+} (C), Pb^{2+} (D) and Hg^{2+} (E) ([**L2**] = [Cu^{2+}] = [Zn^{2+}] = [Cd^{2+}] = [Pb^{2+}] = [Hg^{2+}] = 1.0×10^{-3} mol L^{-1}, 298 K, 0.1 mol L^{-1} NMe_4Cl water–MeCN (1:1, v/v) solution).

bond angles and torsion angles were carried out using the Gaussian 98 program [50].

The optimized structures of **L2**, [Pb**L2**]$^{2+}$ and [Pb(**L2**)$_2$]$^{2+}$ are shown in Fig. 7. It should be noted that, only real frequency values were observed, indicating that the structural geometries shown in Fig. 7 are quite acceptable [51]. As it is obvious from Fig. 7A, in the case of free ligand, the two (5-chloro-8-hydroxy-7-quinolinyl)methyl groups (as the signaling moieties) are pointing away from plane of the ionophore ring containing a pyridine nitrogen, two donating sulfur atoms and two nitrogens (as the recognition moiety), via proper spatial twisting of the carbon atoms of the ethyl groups, to result in the lowest conformational energy. In this conformation, the ligand benefits from maximum fluorescence intensity. Meanwhile, in the optimized structures of the 1:1 complex (Fig. 7B), the cation is well incorporated inside the twisted ligand cavity and coordinated to all five donor atoms of the ligand molecule, in a more or less square-based pyramidal geometry, as previously reported for the lead(II) complexes with pentadentate ligands, in the corresponding crystal structures [30]. In this case, the two (5-chloro-8-hydroxy-7-quinolinyl)methyl groups are now situated in line with the central lead ion so that it may facilitate the photoinduced electron transfer (PET) from the amino groups to the signaling groups, thus affording a strong fluorescence quenching of the ligand system.

Finally, in the optimized structure of [Pb(**L2**)$_2$]$^{2+}$ complex (Fig. 7C), the Pb^{2+} ion coordinates to one of the amine nitrogens, one of the donating sulfur atoms and the pyridine nitrogen of the ring of each of the two **L2** ligands participating in the complex formation to form an octahedral structure. Here, one of the two (5-chloro-8-hydroxy-7-quinolinyl)methyl groups in each ligand molecule are located too far from the metal centre and, thus, are not able to be involved in any photoinduced electron transfer process in the complexed structure. However, each one of the remaining (5-chloro-8-hydroxy-7-quinolinyl)methyl groups in each ligand molecule are nicely situated in line with the central lead ion to easily facilitate the photoinduced electron transfer (PET) from the amino groups to the signaling groups, thus affording a further fluorescence quenching of the two ligand systems involved. It is interesting to note that the corresponding ΔE values for the resulting lead complexes, i.e., −267.080 kcal mol^{-1} for [Pb**L2**]$^{2+}$ and −283.844 kcal mol^{-1} for [Pb(**L2**)$_2$]$^{2+}$ complexes, clearly revealed that the 1:2 sandwich complex of lead ion is significantly more stable than the 1:1 adduct, and most probably is the one involved in the response mechanism of the lead sensor, as will be discussed later.

Thus, based on the results obtained from preliminary solution studies and from ab initio theoretical calculations discussed above, as well as the high lipophilicity of **L2** and its diminished fluorescence intensity brought about upon complexation with Pb^{2+} (static quenching), the PVC-membrane incorporated **L2** was investigated for low level sensing of lead ion in aqueous solutions.

3.3. Operation principle

The fluorescent optode membrane proposed in this work is based on the incorporation of a lipophilic chromoionophore **L2** in a plasticized PVC containing KTpClPB, as a lipophilic anionic additive. The chromoionophore possesses selective binding properties to Pb^{2+} ions and changes its strong fluorescence intensity as a result of the binding event. Since the chromoionophore is neutral and, therefore, cannot function as an ion-exchanger, the presence of a lipophilic anionic site is necessary to provide the optode membrane with the ion-exchange properties. Under the experimental conditions used and supposing the formation of a 1:2 metal-to-ligand

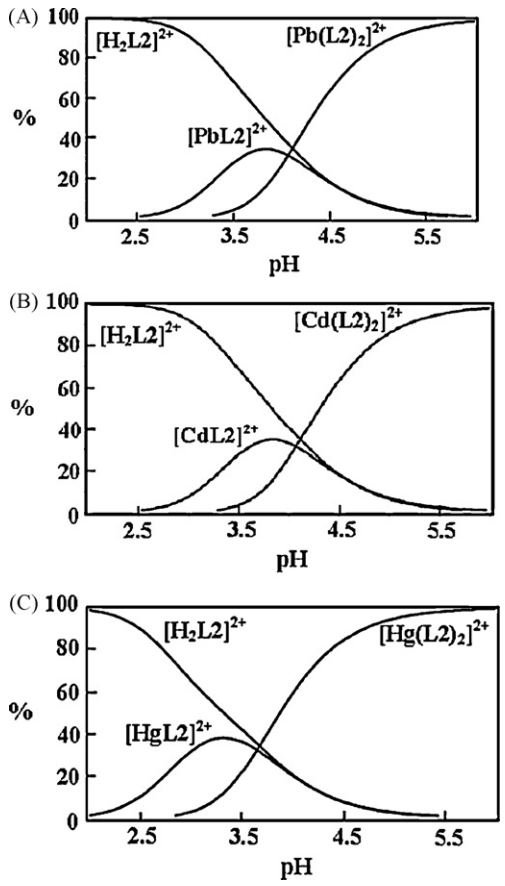


Fig. 4. Distribution of the complexed species of **L2** in the presence of 0.5 equiv. of Pb^{2+} (A), Cd^{2+} (B) and Hg^{2+} (C) ($[\mathbf{L2}] = 1 \times 10^{-3}$ M, $[Pb^{2+}] = [Cd^{2+}] = [Hg^{2+}] = 5.0 \times 10^{-4}$ mol L^{-1} 298.1 K, 0.1 M NMe_4Cl water–MeCN (1:1, v/v) solution).

complex between **L2** and Pb^{2+} ion in the organic phase, the response mechanism of this optical system can be described by the following ion-exchange mechanism [35–37]:

$$2\mathbf{L2}_{(org)} + 2K^{+}_{(org)} + 2TpClPB^{-}_{(org)} + Pb^{2+}_{(aq)} \rightleftharpoons [Pb(\mathbf{L2})_2]^{2+}_{(org)} + 2TpClPB^{-}_{(org)} + 2K^{+}_{(aq)} \quad (1)$$

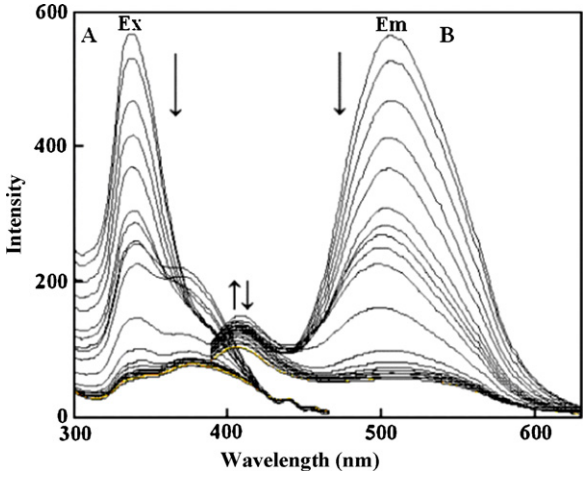


Fig. 5. (A) Excitation, Ex, and (B) emission, Em, spectra of **L2** (8.0×10^{-6} mol L^{-1}) in MeCN in the presence of increasing concentration of Pb^{2+} ion.

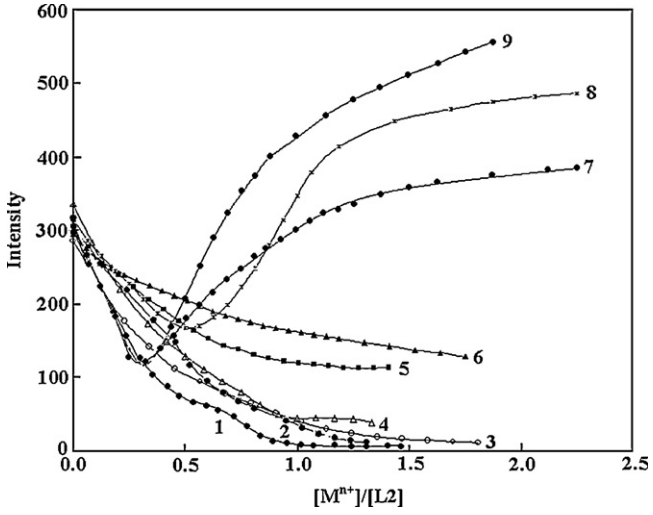


Fig. 6. Fluorescence intensity vs. $[M^{n+}]/[\mathbf{L2}]$ molar ratio plots in MeCN solution for different transition metal ions: (1) Pb^{2+}, (2) Co^{2+}, (3) Cu^{2+}, (4) Fe^{3+}, (5) Ag^{+}, (6) Hg^{2+}, (7) Y^{3+}, (8) Cd^{2+}, and (9) La^{3+}.

The fluorescence excitation and emission spectra of the fluorescent optode membrane in an acetate buffer solution of pH 5.5 and in the presence of increasing concentration of Pb^{2+} ion are shown in Fig. 8. As is obvious, as a result of a strong and selective quenching effect of Pb^{2+}, both the excitation and emission intensities are decreased considerably upon increasing concentration of lead ion in the buffer solution, indicating no measurable spectral position shifts. It is noteworthy that, as expected, the excitation and emission wavelengths observed for the membrane sensor are quite different from those observed in MeCN solution (Section 3.1.2). Here, the maximum intensities for the excitation and emission of **L2** in the membrane are observed at 388 and 515 nm, respectively.

Thus, based on the response mechanism of the proposed fluorescent sensor outlined above, its measuring principle can be explained as follows. Owing to the establishment of a complexation equilibrium between Pb^{2+} ion (M) in the aqueous sample solution and the fluoroionophore **L2** (L) in the organic membrane phase, a M_mL_n complex can be formed as

$$mM_{(aq)} + nL_{(org)} \overset{K}{\rightleftharpoons} M_mL_{n(org)} \quad (2)$$

with

$$K = \frac{[M_mL_n]_{(org)}}{[M]^m_{(aq)}\,[L]^n_{(org)}} \quad (3)$$

where m and n designate the complexing ratio between lead ion and **L2**, and K is the equilibrium constant of the overall reaction.

By definition, the relative fluorescence intensity α, as the ratio of uncomplexed L in the membrane phase, $[L]_{(org)}$, to its total amount, $[L_t]_{(org)}$, is given as

$$\alpha = \frac{[L]_{(org)}}{[L_t]_{(org)}} \quad \text{and} \quad [M_mL_n]_{(org)} = \frac{[L_t]_{(org)}(1-\alpha)}{n} \quad (4)$$

In practice, the α-value during the titration of **L2** with Pb^{2+} ions can be evaluated by measuring the fluorescence intensity of the optical sensor, FI:

$$\alpha = \frac{FI - FI_o}{FI_n - FI_o} \quad (5)$$

where FI_o and FI_n are the limiting fluorescence intensities of the membrane sensor at $\alpha = 0$ (i.e., totally complexed L) and $\alpha = 1$ (i.e., uncomplexed L), respectively. Thus, the relationship between the α-value and the concentration of Pb^{2+} ion in aqueous sample solu-

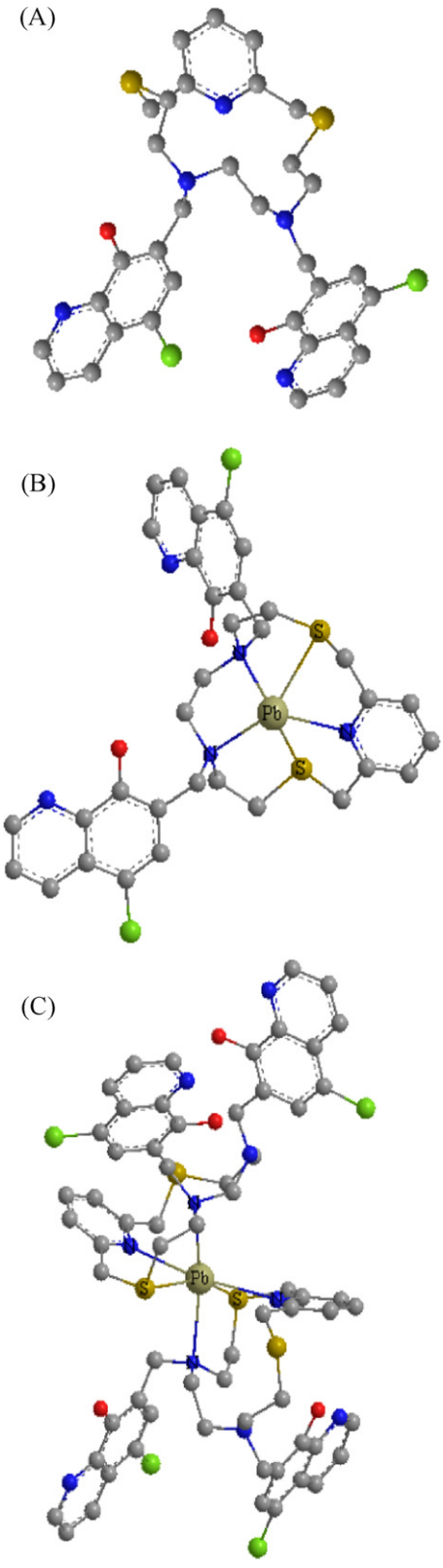


Fig. 7. Optimized structures of free **L2** (A) and its 1:1 $[Pb\mathbf{L2}]^{2+}$ (B) and 1:2 $[Pb(\mathbf{L2})_2]^{2+}$ complexes (C).

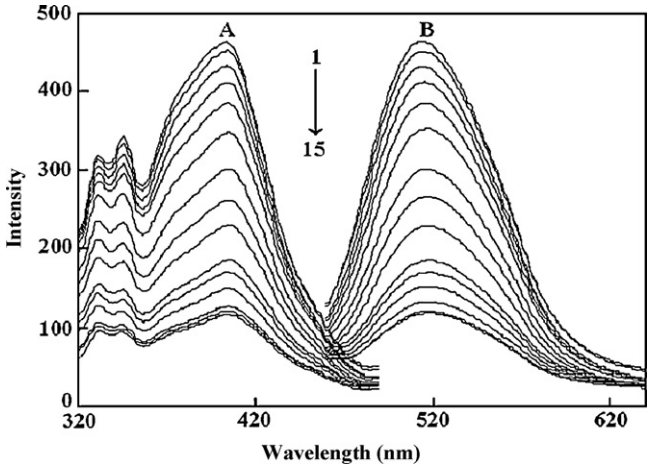


Fig. 8. Excitation (A) and emission (B) spectra of the lead-selective optical sensor in the presence of varying concentrations of Pb^{2+} ion: (1) in acetate buffer of pH 5.5, (2) 5.0×10^{-7} mol L^{-1}, (3) 1.0×10^{-6} mol L^{-1}, (4) 5.0×10^{-6} mol L^{-1}, (5) 1.0×10^{-5} mol L^{-1}, (6) 5.0×10^{-5} mol L^{-1}, (7) 1.0×10^{-4} mol L^{-1}, (8) 2.0×10^{-4} mol L^{-1}, (9) 4.0×10^{-4} mol L^{-1}, (10) 8.0×10^{-4} mol L^{-1}, (11) 1.25×10^{-3} mol L^{-1}, (12) 2.0×10^{-3} mol L^{-1}, (13) 4.0×10^{-3} mol L^{-1}, (14) 8.6×10^{-3} mol L^{-1}, (15) 2.5×10^{-2} mol L^{-1}.

tion, $[M]_{(aq)}$, can be obtained by combining Eqs. (4) and (5), as follows:

$$\frac{\alpha^n}{1-\alpha} = \frac{1}{n\mathrm{K}[\mathrm{L}_t]^{n-1}_{(org)}[\mathrm{M}]^m_{(aq)}} \quad (6)$$

Eq. (6) could be used as a basis for the quantitative determination of lead ions, using the proposed optical membrane sensor.

3.4. Effect of optode membrane composition

It is well documented that the membrane composition may largely influence the response characteristics and working concentration range of the optical sensors [7,52]. Thus, in this work, five PVC-membranes with plasticizer/PVC ratios in the range1.7–2.1, but with varying nature and amount of other ingredients were prepared (Table 2). It is known that the plasticized PVC-membranes used in ion sensors will usually result in the best response membrane characteristics at a plasticizer/PVC ratio of about 2 [52]. As is obvious from Eq. (1), since the bulk membrane optodes must be in thermodynamic equilibrium with the sample, the mass transfer of analyte into the membrane is required [53]. Thus, in the proposed lead-selective optical sensor containing **L2** as a neutral chromoionophore, the presence of a lipophilic additive such as KTpClPB is necessary to facilitate the ion-exchange equilibrium. The absence of KTpClPB was found to affect not only the working concentration range of the sensor (Table 2), but also resulted in the prolonged response time and reduced selectivity of the sensor [54]. The presence of 60–63% plasticizer in the PVC-membranes resulted in optimum physical properties, as well relatively high mobilities of their constituents [55,56]. The nature of plasticizer also influences considerably the measuring range of the solvent polymeric membrane sensors and their selectivity coefficients [57,58]. As is obvious from Table 3, the use of DOS as plasticizer resulted in a large widening of measuring range of the proposed optical sensor (i.e., some two orders of magnitude) over the membrane based on DOP and NPOE. As is seen from Table 2, the presence of 3% chromoionophore **L2** and 6% of additive KTpClPB in the PVC-membrane resulted in the best optical response of the lead-selective sensor. Thus, the membrane number 4 (Table 3) with an optimized PVC:NPOE:KTpClPB:**L2** wt.% ratio of 30:61:6:3 was used for further studies.

Table 2
Optimization of membrane ingredients.

Membrane number	Composition (%)				Working range (mol L^{-1})
	PVC	Plasticizer	KTpClPB	**L2**	
M1	35	60, NPOE	3.5	1.5	1.0×10^{-1} to 7.0×10^{-5}
M2	30	60, NPOE	7.0	3.0	1.0×10^{-1} to 4.0×10^{-5}
M3	31	62, DOP	5.5	1.5	1.0×10^{-3} to 1.0×10^{-4}
M4	30	61, DOS	6.0	3.0	2.5×10^{-2} to 5.0×10^{-7}
M5	30	63, DOS	4.0	2.0	1.0×10^{-2} to 1.0×10^{-6}

Table 3
SSM selectivity coefficients of the optode membranes M4 in acetate buffer of pH 5.5.

Ion	log K^{opt} at $\alpha = 0.5$
Ag^{+}	−1.20
Fe^{3+}	−1.31
Hg^{2+}	−1.23
Mo(VI)	<−4
Mn^{2+}	<−4
Cd^{2+}	−1.95
Cu^{2+}	−0.69
Ni^{2+}	−3.01
Tl^{+}	−3.05
Zn^{2+}	−2.77
Al^{3+}	−2.84
As^{3+}	<−4
Bi^{3+}	−1.50
Sr^{2+}	<−4

3.5. Effect of pH

The influence of pH values on the fluorescence response of the proposed Pb^{2+}-selective optical sensor was studied in the presence of 1.0×10^{-5} mol L^{-1} solution of Pb^{2+}over the range of 1–9, and the results are illustrated in Fig. 9. The pH of solution was adjusted by either HNO_3 or NaOH. As is obvious from Fig. 9, the fluorescence intensity increases with increasing pH of solution and reaches a maximum value at a pH 5.5, and then decreases. The decreased intensity at lower pH might be due to the extraction of H^{+} from the aqueous sample solution into the PVC-membrane, via protonation of the nitrogen atoms of **L2** molecule, which results in an expected change in the mobility of electrons of the system.

On the other hand, the reduced optical response of the sensor at pH >6.0 could be due to a possible slight swelling of the polymeric film under alkaline conditions, as well as the hydroxide formation of lead ions, resulting in decreased concentration of free Pb^{2+} ions in sample solution. Thus, in subsequent experiments, a solution of pH 5.5 adjusted by a 0.05 mol L^{-1} acetate buffer solution, was used for further studies.

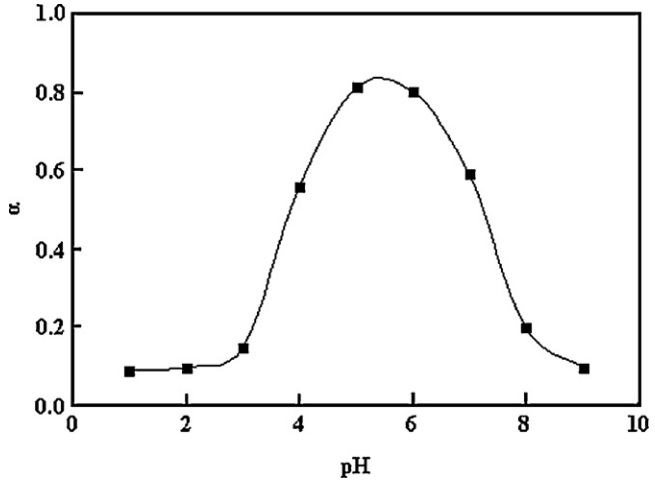


Fig. 9. Effect of pH of the test solution on the optical response of the lead ion-selective sensor in the presence of 1.0×10^{-5} mol L^{-1} Pb^{2+}.

3.6. Measuring range and dynamic response time

Fig. 10 displays the optical response of the proposed Pb^{2+}-selective fluorescent optode to various concentrations of Pb^{2+} ion under optimal experimental conditions at pH 5.5. As is obvious, this curve can be suitably used as a calibration curve for the determination of Pb^{2+} ions in a concentration range of 5.0×10^{-7} to 2.5×10^{-2} mol L^{-1}. The limit of detection (LOD) based on 3σ of the blank was 2.0×10^{-7} mol L^{-1}. The three curves shown in inset of Fig. 10 are calculated based on Eq. (6) with different *m*:*n* ratios. As is quite clear, the curve with *m*:*n* of 1:2 stoichiometric ratio and a reasonable *K* value (2.0×10^{6}) fits the best to the experimental data, while its fitting to other *m*:*n* values of 1:1 and 2:1 was not successful. The results thus obtained further support the formation of a 1:2 $[Pb(\mathbf{L2})_2]^{2+}$ complex in the membrane phase.

The dynamic response time of the present optode, as an important characteristic for any membrane sensor, it is controlled by the time required for the analyte to diffuse from the bulk of the solution toward the membrane interface to associate with ligand. In the case of the proposed fluorescence membrane sensor, the membrane response found to be relatively fast so that the fluorescence intensity of the corresponding signal reached equilibrium within 5 min, over the entire calibration concentration of lead ion.

3.7. Reproducibility, reversibility, short-term stability and life time

The regeneration of the proposed membrane sensor was studied in by the use of different reagents including HCl, HNO_3,

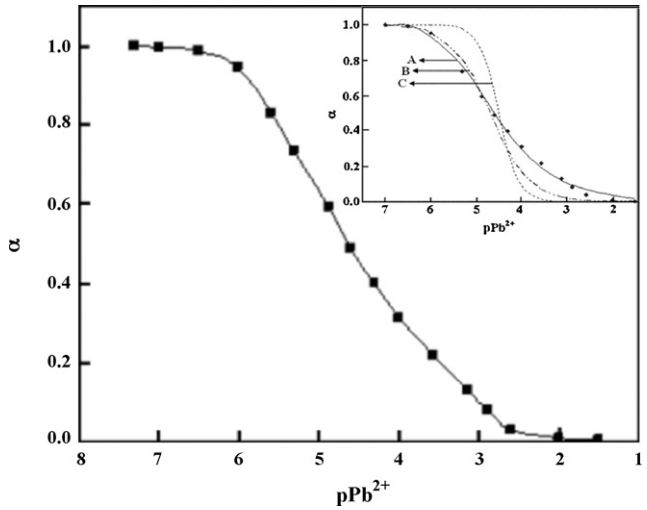


Fig. 10. Relative fluorescence intensity vs. pPb^{2+}. Inset shows the curve fitting of the experimental data based on Eq. (6) for different *m*:*n* and *K* values: (A) *m*:*n* = 1:2, $K = 2.0 \times 10^{6}$; (B) *m*:*n* = 1:1, $K = 5.0 \times 10^{4}$; (C) *m*:*n* = 2:1, $K = 1.0 \times 10^{9}$.

Table 4
Results of three replicate determinations of lead in different real samples.

Sample	Amount of lead		
	Proposed sensor	AAS	Relative error (%)
Toy 1 (China)	37.35 (±1) μg g^{-1}	35.95 (±0.9) μg g^{-1}	3.9
Toy 2 (Iran)	52.65 (±1)	51.50 (±0.9)	2.2
Tap water	Not found	8 ng mL^{-1} [a]	–
Tap water +0.5 μg mL^{-1} Pb^{2+}	0.51 (±0.03) μg mL^{-1}	–	102% recovery

[a] GFAAS was used.

H_3PO_4, NaF, bis(aminoethyl)-glycoether-*N*,*N*,*N*,*N*-tetraacetic acid (EGTA), sodium citrate, nitrilotriacetic acid (NTA), ethylenediaminetetraacetic acid (EDTA), 5-sulfosalicylic acid, thiourea and dithiotritol. It was found that, in the presence of 0.001 mol L^{-1} dithiotritol, the optode membrane will be regenerated completely within a short regeneration time period of 10–20 s. After regeneration and for the next Pb^{2+} ion concentration measurement, the membrane should be kept in a buffer solution of pH 5.5.

The reproducibility and reversibility are two important characteristics in evaluating the suitability of an ion-selective optical sensor for selective determination of ion of interest. These characteristics were studied by fluorescence intensity measurements of the same membrane sensor when it was exposed to repeated concentration step changes between 1.0×10^{-6} and 1.0×10^{-5} mol L^{-1} at pH 5.5. The coefficient of variation of 5 determinations for the 1×10^{-6} and 1.0×10^{-5} mol L^{-1} lead were found to be ±1.5 and ±0.95, respectively. The results indicated that the proposed sensor possess good repeatability and reversibility.

The difference in the response of individual membrane was evaluated by preparing seven membranes from the same mixture and the reproducibility was obtained by determining the fluorescence signal of the membrane to 1.0×10^{-5} mol L^{-1} solution of Pb^{2+}. The standard deviation of response between membranes found to ±0.90. The results show that the reproducibility is satisfactory.

To study the short-term stability of the optode membrane, the fluorescence intensity of the membrane in contact with 1.0×10^{-5} mol L^{-1} Pb^{2+} at pH 5.5 acetate buffer was recorded over a period of 5 h with an interval of 30 min. The membrane exhibited good stability with a relative standard derivation of less than 2.0. In addition, it was found that the membrane sensor could be stored in wet conditions without any measurable change in its fluorescent intensity for at least 2 months, which implies that the fluoroionophore **L2** is quite stable in a membrane contacting with water. The membrane was stable over a period of several months when was not in use (membrane was kept in air) and the signal value of the membrane did not change.

3.8. Selectivity

The selectivity behavior, which is the relative optode response for the primary ion over other ions present in solution, is one of the most important characteristics of an ion-selective optical sensor. The optical selectivity of optical membrane sensor over several interfering ion was investigated by separate solution method (SSM) [36] from the corresponding α vs. pM plots at α value of 0.5, and the results are summarized in Table 3. As it is obvious, the proposed optical sensor possesses good selectivity for Pb^{2+}, so that the disturbance produced by the other cations tested in the functioning of the proposed Pb^{2+} optical sensor is negligible.

3.9. Analytical applications

To test the practical applications of the proposed sensor, it was successfully applied to the determination of lead at micromolar concentration levels in children toys and tap water samples, and the results are summarized in Table 4. Toys samples were prepared as described in Section 2.6. As is obvious from Table 4, the result obtained, for the lead content of the real samples by the proposed sensor correlate well with those from atomic absorption spectrometry (AAS) [19].

4. Conclusions

This work demonstrated that **L2** can be used as a suitable fluoroionophore in the development of a novel optode membrane for Pb^{2+} ion determination at low concentration levels. It is based on the considerable selective quenching of the strong fluorescence of **L2** upon complexation with lead ions. It is fully reversible and can be easily regenerated with 0.001 mol L^{-1} dithiotritol. The sensor is characterized by good response characteristics with respect to stability, reproducibility, reversibility, calibration range detection limit and selectivity. The proposed fluorescent sensor was successfully applied to the direct determination of lead content in different real samples.

Acknowledgements

The authors gratefully acknowledge the support of this work by Iran National Science Foundation (INSF, Grant No. 84123/17). MIUR (Ministero Italiano dell'Istruzione, dell'Università e della Ricerca) is also gratefully acknowledged for financial support (Project PRIN2007C8RW53).

References

[1] C.J. Pedersen, J. Am. Chem. Soc. 89 (1967) 7017.
[2] B. Dietrich, J.M. Lehn, J.P. Sauvage, Tetrahedron Lett. (1969) 2885.
[3] L.F. Lindoy, The Chemistry of Macrocyclic Ligand Complexes, Cambridge University Press, New York, 1989.
[4] Coord. Chem. Rev. (1996) 148, special issue on Macrocyclic Chemistry.
[5] K. Gloe (Ed.), Macrocyclic Chemistry Current Trends and Future Perspectives, Springer, Dordrecht, 2005.
[6] F. Diederich, P. Stang, R.R. Tykwinski (Eds.), Modern Supramolecular Chemistry: Strategy for Macrocycle Synthesis, Wiley-VCH, Weinheim, 2008.
[7] A.P. de Silva, H.Q.N. Gunaratne, T. Gunnlaugsson, A.J.M. Huxley, C.P. McCoy, J.T. Rademacher, T.E. Rice, Chem. Rev. 97 (1997) 1515.
[8] M.V. Alfimov, S.P. Gromov, in: W. Retting, B. Strhmel, S. Schroder, H. Seifert (Eds.), Applied Fluorescence in Chemistry, Biology, and Medicine, Springer-Verlag, Berlin, 1999.
[9] Coord. Chem. Rev. (2000) 205, special issue on Luminescent Sensors.
[10] A. Amendola, L. Fabbrizzi, F. Foti, M. Licchelli, C. Mangano, P. Pallavicini, A. Poggi, D. Sacchi, A. Taglietti, Coord. Chem. Rev. 250 (2006) 273.
[11] J.R. Lakowicz (Ed.), Probe Design and Chemical Sensing, Topics in Fluorescence Spectroscopy, vol. 4, Plenum Press, New York, 1994.
[12] H. Hisamoto, K. Suzuki, Trends Anal. Chem. 18 (1999) 513.
[13] O.S. Wolfbeis, Anal. Chem. 72 (2000) 81R.
[14] I.A. Bergdhal, M. Vahter, S.A. Counter, A. Schutz, L.H. Buchanan, F. Ortega, G. Laurell, S. Skerfring, Environ. Res. Sec. A 80 (1999) 25.
[15] D.R. Lynarn, L.G. Plantanida, J.F. Cole, Environmental Lead, Academic Press, New York, 1975.
[16] M. Puntener, T. Vigassy, E. Baier, A. Ceresa, E. Pretsch, Anal. Chim. Acta 503 (2004) 187.
[17] J. Sutter, E. Lindner, R.E. Gyurcsaïnyi, E. Pretsch, Anal. Bioanal. Chem. 380 (2004) 7.
[18] M. Fouskaki, N.A. Chaniotakis, Anal. Chem. 77 (2005) 1780.
[19] M. Barzegar, M.F. Mousavi, H. Khajehsharifi, M. Shamsipur, H. Sharghi, IEEE Sens. J. 5 (2005) 392.
[20] A.K. Jain, V.K. Gupta, L.P. Singh, J.R. Raisoni, Electrochim. Acta 51 (2006) 2547.

[21] A. Malon, E. Bakker, E. Pretsch, Anal. Chem. 79 (2007) 632.
[22] W. Song, C. Wu, H. Yin, X. Liu, P. Sa, J. Hu, Anal. Lett. 41 (2008) 2844.
[23] G. Lisak, E. Grygolowicz-Pawlak, M. Mazurkiewicz, E. Malinowska, T. Sokalski, J. Bobacka, A. Lewenstam, Microchim. Acta 164 (2009) 293.
[24] X.-G. Li, X.-L. Ma, M.-R. Huang, Talanta 78 (2009) 498.
[25] M. Telting-Diaz, E. Bakker, Anal. Chem. 74 (2002) 5251.
[26] W.-H. Chan, R.-H. Yang, T. Mo, K.-M. Wang, Anal. Chim. Acta 460 (28) (2002) 123.
[27] L. Guo, S. Hong, X. Lin, Z. Xie, G. Chen, Sens. Actuators B130 (2008) 789.
[28] I. Garcés, I. Salinas, J. Alonso, M. Puyol, Sens. Actuators B 137 (2009) 420.
[29] S.S. Bozkurt, S. Ayata, I. Kaynak, Spectrochim. Acta A 72 (2009) 880.
[30] V. Lippolis, M. Shamsipur, J. Iran. Chem. Soc. 3 (2006) 105, and references therein.
[31] M.C. Aragoni, M. Arca, A. Bencini, A.J. Blake, C. Caltagirone, G. De Filippo, F.A. Devillanova, A. Garau, T. Gelbrich, M.B. Hursthouse, F. Isaia, V. Lippolis, M. Mamelli, P. Mariani, B. Valtancoli, C. Wilson, Inorg. Chem. 46 (2007).
[32] M. Shamsipur, O.R. Hashemi, V. Lippolis, J. Membr. Sci. 282 (2006) 221.
[33] M. Shamsipur, M. Hosseini, K. Alizadeh, M.F. Mousavi, A. Garau, V. Lippolis, A. Yari, Anal. Chem. 77 (2005) 276.
[34] M. Shamsipur, M. Mizani, K. Alizadeh, M.F. Mousavi, V. Lippolis, A. Garau, C. Caltagirone, Sens. Actuators B 130 (2008) 300.
[35] M. Shamsipur, M. Hosseini, K. Alizadeh, N. Alizadeh, A. Yari, C. Caltagirone, V. Lippolis, Anal. Chim. Acta 533 (2005) 17.
[36] M. Shamsipur, K. Alizadeh, M. Hosseini, C. Caltagirone, V. Lippolis, Sens. Actuators B 113 (2006) 892.
[37] M. Shamsipur, M. Sadeghi, K. Alizadeh, H. Sharghi, R. Khalifeh, Anal. Chim. Acta 630 (2008) 57.
[38] M. Ishidate, Y. Sakurai, K. Sawatari, Chem. Pharm. Bull. 9 (1961) 679.
[39] I. Jacquet, J.M. Lehn, P. Marsau, H. Adrianatoandro, Y. Barrans, Bull. Soc. Chim. Fr. 133 (1996) 199.
[40] A. Bencini, A. Bianchi, M. Micheloni, P. Paoletti, E. Garcia-España, M.A. Nino, J. Chem. Soc. Dalton Trans. (1991) 1171.
[41] G. Gran, Analyst 77 (1952) 661.
[42] P. Gans, A. Sabatini, V. Vacca, Talanta 43 (1996) 807.
[43] R.M. Smith, A.E. Martell, NIST Stability Constants Database, Version 4.0, National Institute of Standards and Technology, Washington, DC, 1997.
[44] A. Bencini, A. Bianchi, E. Garcia-España, M. Micheloni, J.A. Ramirez, Coord. Chem. Rev. 188 (1999) 97.
[45] S. Espinosa, E. Bosch, M. Roses, Anal. Chim. Acta 454 (2002) 157.
[46] H. Steger, A. Corsini, J. Inorg. Nucl. Chem. 35 (1973) 1621.
[47] A.J. Blake, A. Bencini, C. Caltagirone, G. De Filippo, L.S. Dolci, A. Garau, F. Isaia, V. Lippolis, P. Mariani, L. Prodi, M. Montalti, N. Zaccheroni, C. Wilson, J. Chem. Soc. Dalton. Trans. (2004) 2771.
[48] M.R. Mazieres, F. Wetz, J. Bellan, J.G. Wolf, Dyes Pigments 56 (2003) 231.
[49] Hyperchem, Release 7.0, Hypercube, Inc., Gainesville, 2002.
[50] M.J. Frisch, G.W. Trucks, H.B. Schlegel, G.E. Scuseria, M.A. Robb, J.R. Cheeseman, V.G. Zakrzewski, J.A. Montgomery Jr., R.E. Startmann, J.C. Burant, S. Dapprich, J.M. Millam, A.D. Daniels, K.N. Kudin, M.C. Strain, O. Farkas, J. Tomasi, V. Barone, M. Cossi, R. Cammi, B. Mennucci, C. Pomelli, C. Adamo, S. Clifford, J. Ochterski, G.A. Petersson, P.Y. Ayala, Q. Cui, K. Morokuma, D.K. Malick, A.D. Rabuck, K. Raghavachari, J.B. Foresman, J. Cioslowski, J.V. Ortiz, B.B. Stefanov, G. Liu, A. Liashenko, P. Piskorz, I. Komaromi, R. Gomperts, R.L. Martin, D.J. Fox, T. Keith, M.A. Al-Laham, C.Y. Peng, K. Nanayakkara, C. Gonzalez, M. Challacombe, P.M.W. Gill, B. Johnson, W. Chen, M.W. Wong, J.L. Andres, M. Head-Gordon, E.S. Replogle, J.A. Pople, Gaussian Inc., Pittsburgh, PA, 1998.
[51] M.Z. Kassaee, M. Beigi, S. Arshadi, J. Mol. Struct. (Theochem.) 624 (2003) 69.
[52] E. Bakker, P. Bühlmann, E. Pretsch, Chem. Rev 97 (1997) 3083.
[53] W.E. Morf, K. Seiler, P. Sorensen, E. Pungor (Eds.), Ion-Selective Electrodes, vol. 5, Akadémiai Kiadó, Budapest, 1989, p. 141.
[54] T. Rosatzin, E. Bakker, K. Suzuki, W. Simom, Anal. Chim. Acta 280 (1993) 197.
[55] M.A. Simon, R.P. Kusy, Polymer 34 (1993) 5106.
[56] A.D.C. Chan, D.J. Harrison, Talanta 41 (1994) 849.
[57] P. Anker, E. Wieland, D. Ammann, R.E. Dohner, R. Asper, W. Simon, Anal. Chem. 53 (1981) 1970.
[58] D. Ammann, R. Bissig, M. Guggi, E. Pretsch, W. Simon, I.J. Borwitz, L. Weiss, Helv. Chim. Acta 58 (1975) 1535.

Talanta 80 (2010) 2034–2040

Contents lists available at ScienceDirect

Talanta

journal homepage: www.elsevier.com/locate/talanta

Tetradecyl(trihexyl)phosphonium chloride ionic liquid single-drop microextraction for electrothermal atomic absorption spectrometric determination of lead in water samples

Estefanía M. Martinis[a], Paula Bertón[a], Jorgelina C. Altamirano[a,b], Ullastiina Hakala[c], Rodolfo G. Wuilloud[a,b,*]

[a] Analytical Chemistry Research and Development Group (QUIANID), LISAMEN – CCT – CONICET – Mendoza, Av. Ruiz Leal S/N Parque General San Martín, M 5502 IRA Mendoza, Argentina
[b] Instituto de Ciencias Básicas, Universidad Nacional de Cuyo, Mendoza, Argentina
[c] Finnish Institute for Verification of the Chemical Weapons Convention (VERIFIN), University of Helsinki, Finland

ARTICLE INFO

Article history:
Received 22 June 2009
Received in revised form 30 October 2009
Accepted 2 November 2009
Available online 12 November 2009

Keywords:
Tetradecyl(trihexyl)phosphonium chloride
CYPHOS® IL 101
Ionic liquid
Lead
Single-drop microextraction

ABSTRACT

A highly efficient single-drop microextraction (SDME) procedure using a low-cost room temperature ionic liquid (RTIL), i.e., tetradecyl(trihexyl)phosphonium chloride (CYPHOS® IL 101), for Pb determination at trace levels in real water samples was developed. Lead was chelated with 2-(5-bromo-2-pyridylazo)-5-diethylaminophenol (5-Br-PADAP) reagent and extracted into a 4 μL microdrop of CYPHOS® IL 101. The RTIL drop was directly injected into the graphite furnace of the electrothermal atomic absorption spectrometer (ETAAS). Under optimal microextraction conditions, a preconcentration factor of 32 was achieved with only 1.5 mL of sample resulting in a phase-volume ratio of 375. The limit of detection (LOD) obtained was 3.2 ng L^{-1} and the relative standard deviation (RSD) for 10 replicates at 0.5 μg L^{-1} Pb^{2+} concentration level was 4.9%, calculated at peak heights. The calibration graph was linear from concentration levels near the detection limits up to at least 4.5 μg L^{-1} with a correlation coefficient of 0.9996. The accuracy of the methodology was evaluated by analysis of a certified reference material (CRM). The method was successfully applied to the determination of Pb in tap, mineral, well and river water samples.

© 2009 Elsevier B.V. All rights reserved.

1. Introduction

Lead is one of the metals considered as a major threat to human health. This heavy metal is characterized by its toxic effects on the gastrointestinal tract, renal system and central or peripheral nervous system [1]. The main sources of lead in humans are inhaled air, diet and drinking water [2]. Lead could be present in water due to general environmental contamination. Polluting sources are quite varied, ranging from industrial and traffic emissions to the use of purification mud and agricultural excipients [3]. The World Health Organization (WHO) has established a maximum permissible limit of 10 μg L^{-1} Pb in drinking water [4]. Therefore, evaluation of Pb at levels close to this limit and in presence of relatively high amounts of other ions and organic matter makes straight determination of Pb a difficult task for quality control of waters.

In general, the most widely used techniques for trace determination of Pb are electrothermal atomic absorption spectrometry (ETAAS) [5,6], inductively coupled plasma optical emission spectrometry (ICP-OES) [7,8] and inductively coupled plasma-mass spectrometry (ICP-MS) [9,10]. Among these, ETAAS and ICP-MS are the most sensitive techniques. Despite the great potential of ICP-MS for trace Pb determination, this technique often involves a greater cost, higher sample volume requirements and increased instrumentation complexity, limiting its widespread application to routine analytical work. ETAAS is still being used as it shows several advantages including, fast analysis time, relative simplicity, reduced cost, low sample volume requirements and low detection limits. All of these features have been responsible for its broad application to trace and ultratrace elemental analysis of different samples. However, the low levels of lead in some types of water samples are not compatible with ETAAS detection limits, hence a preconcentration step is needed prior to ETAAS determination [11].

* Corresponding author at: Analytical Chemistry Research and Development Group (QUIANID), LISAMEN – CCT – CONICET – Mendoza, Av. Ruiz Leal S/N Parque General San Martín, M 5502 IRA Mendoza, Argentina. Tel.: +54 261 5244064; fax: +54 261 5244001.
E-mail address: rwuilloud@mendoza-conicet.gov.ar (R.G. Wuilloud).
URL: http://www.mendoza-conicet.gov.ar/lisamen (R.G. Wuilloud).

0039-9140/$ – see front matter © 2009 Elsevier B.V. All rights reserved.
doi:10.1016/j.talanta.2009.11.012

Table 1
Instrumental and experimental conditions for Pb determination.

Instrumental conditions				
Wavelength (nm)	283.3			
Spectral band width (nm)	0.7			
Lamp current (mA)	360			
Modifier volume (μL)	20			
Modifier amount (μg)	50 μg ($NH_4H_2PO_4$) 3 μg $Mg(NO_3)_2$			
Graphite furnace temperature program				
Step	Temperature (°C)	Ramp time (s)	Hold time (s)	Argon flow rate (mL min^{-1})
Drying	110	1	30	300
	150	10	40	300
Pyrolysis	600	10	10	300
	800	5	10	300
Atomization	1600	1	5	0
Cleaning	2400	1	2	300
Extraction conditions				
Working pH	9.0			
Sample volume	1.5 mL			
Pb^{2+} concentration	0.5 μg L^{-1}			
5-Br-PADAP concentration	2.7×10^{-7} mol L^{-1}			
Ethanol concentration	2% (v/v)			
Buffer concentration	4×10^{-2} mol L^{-1}			
RTIL drop volume	4 μL			
Extraction time	15 min			
MeOH volume (washing solution)	20 μL			

Several sample preparation methods such as solid phase extraction [12], liquid–liquid extraction [13], co-precipitation [14] and knotted reactor separation [15] have been employed for traces lead preconcentration. Conventional liquid–liquid extraction (L–L) is a very effective analytical technique to extract and preconcentrate metallic and organometallic species as well as organic compounds from liquid samples [16]. Recently, considerable interest has been appeared in solvent microextraction procedures based on room temperature ionic liquids (RTILs) [17–19], in which the volume of solvent required is significantly reduced while achieving high extraction efficiency. Single-drop microextraction (SDME) is a simple procedure where analytes are extracted into a single-drop of solvent suspended from the tip of a microsyringe needle [20] that can be directly immersed in the aqueous sample (DI-SDME) or in its headspace (HS-SDME). Due to their high viscosity, thermal stability and undetectable volatility in comparison with conventional solvents, ILs are very suitable for single SDME and HS-SDME. Moreover, larger and more reproducible extracting volumes can be used as well as higher stability of the drop and better precision levels are obtained. ILs have been proposed in SDME and HSME for organic compounds determination [21,22]. Very recently, Manzoori et al. have proposed the use of SDME-ETAAS for determining trace amounts of Mn and Pb in water and food samples [23,24].

Ionic liquids (ILs) have been recognized as alternative solvents for a diversity of chemical applications, such as analytical and separation chemistry [25–28]. Among the various IL families, most of the current research has been focused on 1-alkyl-3-methylimidazolium, tetraalkylammonium and alkylpyridinium based ionic liquids [29,30]. Tetraalkylphosphonium-based ILs are also known for their unique solvent properties, and consequently, they have been considered as alternative solvents for separation chemistry in some publications [31–34].

In this work, a phosphonium-containing RTIL tetradecyl(trihexyl)phosphonium chloride (CYPHOS® IL 101) (Fig. 1) is proposed for extraction and preconcentration of Pb with SDME technique. A suitable chelating reagent, such as 2-(5-bromo-2-pyridylazo)-5-diethylaminophenol (5-Br-PADAP), was used to increase extraction efficiency of the metal ion [35]. To our knowledge, the combination of CYPHOS® IL 101 and 5-Br-PADAP chelating agent for developing a SDME and preconcentration procedure to determine Pb has not been reported before. Furthermore, the determination of metals in phosphonium-based ionic media by ETAAS has not been so far studied. The method was applied for evaluating trace levels of Pb in tap, mineral, well and river water samples.

2. Experimental

2.1. Instrumentation

Elemental detection was performed using a Perkin-Elmer 5100 atomic absorption spectrometer (Perkin-Elmer, Norwalk, CT, USA) equipped with a pyrolytic graphite tube (Perkin-Elmer) and a transversely heated graphite atomizer Zeeman-effect background

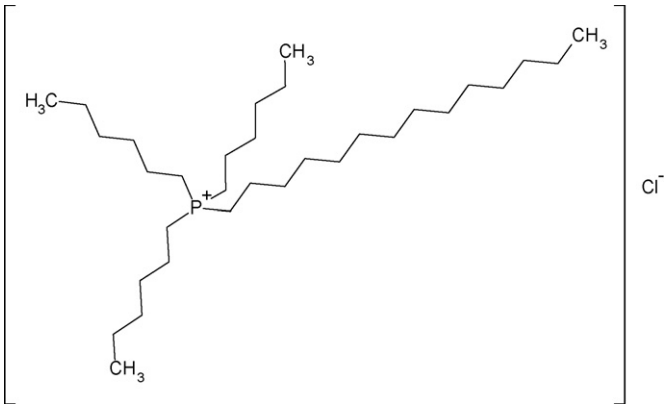


Fig. 1. Molecular structure of the RTIL CYPHOS® IL 101 used in this work.

correction system. A Pb electrodeless discharge lamp (Perkin-Elmer, Norwalk, USA) operated at a current of 360 mA (modulated operation) and a wavelength of 283.3 nm with a spectral band pass of 0.7 nm was used. All measurements were made based on absorbance signals with an integration time of 5 s. The temperature vs. time program for the atomizer is fully depicted in Table 1.

2.2. Reagents

All the reagents were of analytical grade and the presence of Pb was not detected within the working range.

The IL, CYPHOS® IL 101, was provided by CYTEC and molecular structure of this compound is shown in Fig. 1.

A 10^{-2} mol L^{-1} 5-Br-PADAP (Aldrich, Milwaukee, WI, USA) solution was prepared in ethanol (Merck, Darmstadt, Germany). Lower concentrations were prepared by serial dilution with ethanol.

A 1000 mg L^{-1} Pb^{2+} stock standard solution was prepared from $Pb(NO_3)_2$ (Merck) in 0.1 mol L^{-1} nitric acid (Merck). Lower concentrations were prepared by diluting the stock solution with 0.1 mol L^{-1} nitric acid.

The buffer solution was 2.0 mol L^{-1} ammonia (Merck) adjusted to pH 9.0 with hydrochloric acid (Merck).

A 150 mg L^{-1} $Mg(NO_3)_2$ (Merck) and 2500 mg L^{-1} $NH_4H_2PO_4$ (Merck) stock solution was used as chemical modifier. This solution was prepared in 3×10^{-3} mol L^{-1} HNO_3.

A 2 mol L^{-1} $NaNO_3$ (Merck) solution was used to adjust ionic strength.

Ultrapure water (18 MΩ cm) was obtained from a Millipore Continental Water System (Bedford, MA, USA).

2.3. Sample collection and conditioning

For tap water samples collection, domestic water was allowed to run for 20 min and approximately a volume of 1000 mL was collected in a beaker. Tap water samples were analyzed immediately after sampling. Mineral water was a commercial product.

River and well water samples were collected in cleaned bottles rinsed three times with water sample prior to collection. Water samples were conditioned by adding nitric acid until ca. pH 4, filtered through acid cleaned 0.22 μm pore size membrane filters (Millipore Corporation, Bedford, MA, USA) and stored in polypropylene bottles (Nalgene; Nalge, Rochester, NY, USA) at 4 °C [36]. The used sampling material was previously washed overnight with a 1.5 mol L^{-1} HNO_3 water solution and rinsed with ultrapure water.

2.4. General extraction and preconcentration procedure

A 1.5 mL sample volume was placed in a 2 mL glass vial containing a magnetic stirring bar. Then, 30 μL of buffer solution, 30 μL of EtOH and 4 μL of 1×10^{-4} mol L^{-1} 5-Br-PADAP solution were added. A 3 mm long polytetrafluoroethylene (PTFE) tube (0.35 mm I.D.) with a collar of 0.4 mm was fitted to the blunt needle tip of a 50 μL microsyringe (Perkin-Elmer) for maximizing the contact area between the drop and the needle tip. A microsyringe, containing a known volume of CYPHOS® IL 101 as an acceptor phase, was clamped above the vial and its needle was immersed into the sample. The plunger was depressed and a microdrop of the RTIL phase was exposed to the sample under constant stirring at room temperature. After an extraction time of 15 min, the remainder volume of RTIL acceptor phase was retracted into the microsyringe, and then the extract was injected into the graphite furnace of ETAAS instrument. Further washing with 20 μL of MeOH solution served to remove any remaining of analyte still present in the microsyringe. This solution was also injected into graphite furnace followed by 20 μL of chemical modifier mixture ($NH_4H_2PO_4$ + $Mg(NO_3)_2$). ETAAS determination was performed under the conditions showed in Table 1. Calibration was performed against aqueous standards submitted to the same preconcentration procedure. Likewise, blank solutions were analyzed in the same manner as standard and sample solutions.

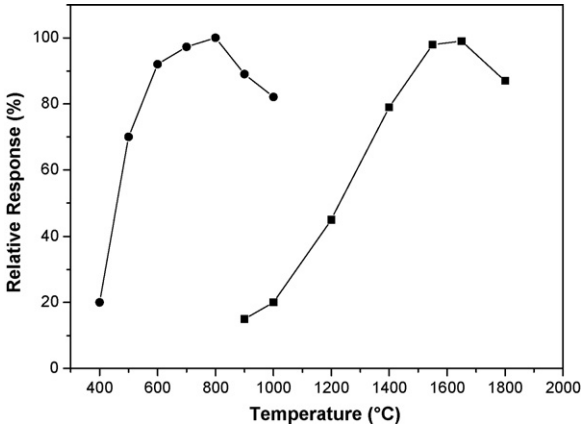


Fig. 2. Pyrolysis (●) and atomization (■) temperature curves for 15 μg L^{-1} of Pb in RTIL-methanol using 50 μg of $NH_4H_2PO_4$ and 3 μg of $Mg(NO_3)_2$ as modifier. Other conditions were as indicated in Table 1.

3. Results and discussion

3.1. RTIL phase analysis by ETAAS

Initial studies were performed for evaluating thermal and spectral behavior of CYPHOS® IL 101 during Pb measurements by ETAAS. With the aim of reducing interferences and increasing accuracy, the use of a chemical modifier or a mixture of modifiers has become indispensable in ETAAS measurements. Two modifiers, $NH_4H_2PO_4$ and $Mg(NO_3)_2$, were investigated. Common used chemical modifiers, such as $NH_4H_2PO_4$ and $Mg(NO_3)_2$, could not be individually used, as high background and poor thermal stabilization were observed. On the other hand, sharp and well-defined signals were obtained with both modifiers. Therefore, a modifier mixture containing 50 μg of $NH_4H_2PO_4$ and 3 μg of $Mg(NO_3)_2$ was injected for each measurement.

An increased background signal was observed during the atomization step in presence of CYPHOS® IL 101 and 5-BrPADAP, due to their organic nature. To eliminate the matrix effect, an *in situ* digestion step was developed by injecting different amounts of HNO_3 and applying diverse temperature ramps during the pyrolysis step [37]. Optimal results, with reduced background, were obtained when 10 μL of 10% (v/v) HNO_3 were injected before the evaporation step. Furthermore, it was very important to select an appropriate pyrolysis temperature for efficient organic matter removal due to RTIL phase while preventing the pyrolysis loss of Pb prior to atomization (Fig. 2). The influence of pyrolysis temperature on the absorbance was studied within a range of 400–1000 °C. The maximum absorbance was observed within a range of 600–800 °C. Therefore, 600 and 800 °C were selected as the working pyrolysis temperature in the two pyrolysis steps. A ramp time of 15 s was chosen as it allowed gradual elimination of organic matrix while avoiding Pb losses. Once selected these pyrolysis conditions, the effect of atomization temperature on Pb absorbance signal was studied within the range of 900–1800 °C. The highest signal was obtained from 1550 °C and remained constant up to 1650 °C. An atomization time and temperature of 5 s and 1600 °C were selected, respectively.

A significant experimental observation was made regarding the injection of the RTIL phase into the graphite furnace of ETAAS. The high viscosity of the resulting RTIL phase compromised quan-

titative and reproducible injection of the RTIL phase. Therefore, the application of an additional injection step using a proper solvent was considered to overwhelm this drawback. After microdrop injection into the furnace, further washing with methanol served to remove any sample still present in the microsyringe. Methanol was assayed in volumes ranging from 5 to 50 μL. A volume of 20 μL was suitable to obtain quantitative elution of the RTIL phase from the syringe. Smaller volumes did not remove completely the RTIL and caused loss of analytical sensitivity. Thus, the resulting alcoholic RTIL phase was successfully analyzed by ETAAS under the conditions showed in Table 1.

3.2. Study of SDME conditions using CYPHOS® IL 101

RTILs are gaining increasing attention due to their promising role as alternative media for developing preconcentration methodologies. The aim of the current work was the evaluation of a new ionic liquid as an efficient and stable media for extraction and preconcentration methods development. Recently, CYPHOS® IL 101 was reported to be chemically stable and remain inert with Grignard reagents such as phenylmagnesium bromide under strongly basic conditions (i.e., the phosphonium cation was not deprotonated to produce the corresponding phosphorane). Several ionic liquids, especially those based on imidazolium ions, such as 1-butyl-3-methylimidazolium ([C_4mim]), have shown to have some degree of chemical reactivity. On the other hand, quaternary phosphonium salts are more stable at high temperatures and longer periods of time than nitrogen-based cations as those present in imidazolium-containing RTILs.

Tetraalkylphosphonium salts do not have such acidic protons or aromatic rings like imidazolium salts, and consequently there is little potential for direct interaction with solutes [31]. Thus, a possible extraction of solutes with phosphonium-ILs would be dominated by polarity affinity. In view of the possibility of Pb chelation with 5-Br-PADAP, this pyridylazo reagent was used to improve affinity of the metal for the RTIL phase. The complexation phenomenon is strongly conditioned by pH value of solutions and it subsequently affects the extraction efficiency of Pb-5-Br-PADAP complex. Therefore, the effect of pH on analyte complexation and extraction of Pb-5-Br-PADAP was studied in the range of 1.5–12. The results illustrated in Fig. 3(a) show that the highest extraction efficiency was achieved between pH 8.1 and 10.5. It has been demonstrated, that this pH region is also the best for optimal Pb chelation with the 5-Br-PADAP reagent. A neutral complex is thus obtained within this pH interval, as it can be deduced from the dissociation constants of 5-Br-PADAP reagent (pK_{a1} = 0.1, pK_{a2} = 2.02, and pK_{a3} = 11.30) [38] and the stoichiometry of Pb-5-BrPADAP complex (1:2) [39]. This finding supports our hypothesis that extraction mechanism involved in this system is based on polarity affinity, as it was early mentioned in this work. A pH value of 9 was chosen for further experiments. This working pH was obtained with a 4×10^{-2} mol L^{-1} ammonia buffer concentration.

Concentration is a critical variable to be optimized in extraction methods based on a chelating agent such as 5-Br-PADAP. Thus, it is highly important to establish the minimal reagent concentration that leads to total complex formation while achieving the highest extraction. The results in Fig. 3(b) show 8×10^{-8} mol L^{-1} 5-Br-PADAP as the minimum concentration required to achieve the highest extraction efficiency, while a drop of extraction performance was observed when 5-Br-PADAP concentration exceeded 3.5×10^{-7} mol L^{-1}. This can be attributed to excessive 5-Br-PADAP concentration in the sample solution, which could be co-extracted along with the complex into CYPHOS® IL 101, thus diminishing extraction efficiency of the proposed method. Thus, a concentration of 2.7×10^{-7} mol L^{-1} was chosen as the optimum.

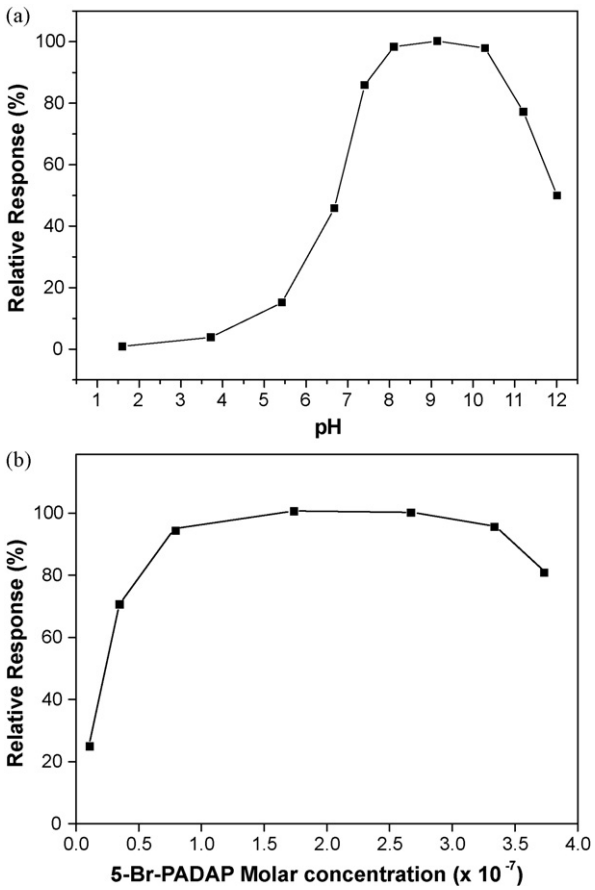


Fig. 3. (a) Effect of pH on Pb preconcentration. Each desired pH was obtained by adding suitable amounts of diluted HCl or NaOH, respectively. (b) Effect of 5-Br-PADAP concentration on Pb preconcentration. Other conditions were as indicated in Table 1.

In order to avoid the precipitation of the complexing agent and Pb-5-Br-PADAP complex in aqueous medium, concentration of ethanol in sample solution was evaluated. The study revealed that both, complexing agent and metal complex remained in solution within an ethanol concentration range of 1.5–5% (v/v). Higher ethanol concentrations led to solubilization of the ionic liquid and hence non-reproducible results. A 2% (v/v) ethanol concentration was chosen for further experiments. No effect on the kinetics of phase separation and extraction was observed with ethanol.

Generally, the addition of a salt in traditional liquid–liquid extraction using conventional organic solvents increases extraction performance due to salting out effect. This effect was investigated using $NaNO_3$ in a concentration range of 0–5% (w/v). As expected, the response was slightly increased by 5% as a result of salting out effect in the range of 0–1% (w/v) of $NaNO_3$. However, background signal was also increased during the atomization step. Since metal determination by ETAAS is more accurate when background absorption is small as compared to atomic absorption, salt addition was not adopted as it would negatively affect to the performance of the system.

One of the most important factors in SDME is the volume of the microdrop as it has deep influence on extraction efficiency. The effect of CYPHOS® IL 101 drop volume on lead signal was investigated in the range of 1–5 μL. The results illustrated in Fig. 4 show an enhancement of the analytical response by increasing the microdrop volume. Obviously, surface area of the microdrop is significantly increased when higher RTIL volumes are used, resulting in higher mass transfer from the bulk aqueous solution to the RTIL drop. However, when volumes larger than 4 μL were used, the

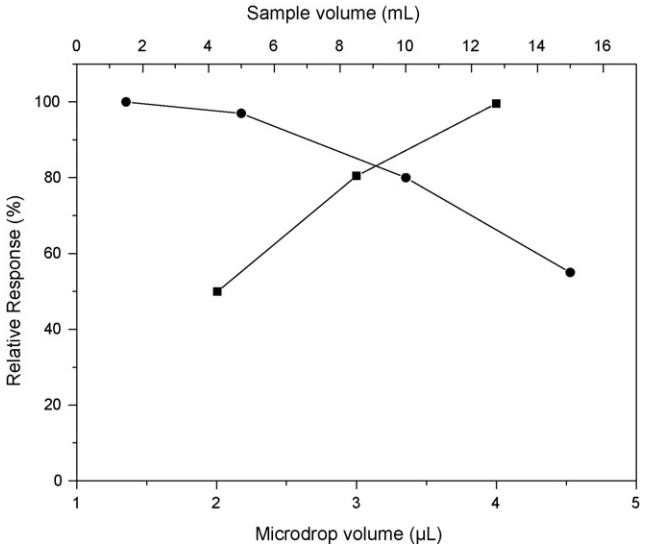


Fig. 4. Effect of the amount of RTIL on the extraction efficiency of the system (■) influence of sample volume on the performance of the extraction system (●) (a microdrop volume of 4 μL was used for this experiment). Other experimental conditions are listed in Table 1.

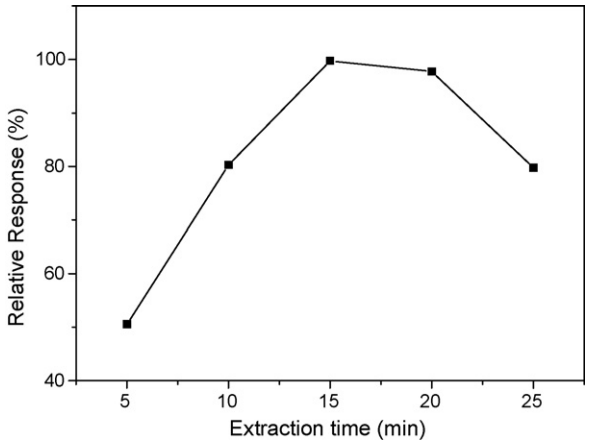


Fig. 5. Effect of the extraction time on the efficiency of the system. Experimental conditions are listed in Table 1.

microdrop became unstable, and it was easily dislodged from the syringe needle tip. Therefore, a 4 μL volume of the RTIL microdrop was selected for next experiments.

Sample volume is critical to be studied, since it strongly conditions the enhancement of analytical sensitivity obtained with preconcentration techniques. The effect of sample volume was examined in a range of 1–15 mL with a 0.5 $\mu g\,L^{-1}$ Pb standard solution (Fig. 4). Due to the minimal volume of the IL microdrop, a high enhancement factor was obtained even with a low sample volume. Thus, a volume of 1.5 mL was sufficient to obtain an appropriate enhancement factor and simplicity in sample treatment. Higher sample volumes negatively affected the extraction efficiency probably due to higher solubility of the RTIL microdrop.

Stirring of the sample is another important parameter which has impact on extraction efficiency and a reduction of the extraction time in SDME. According to film theory, convective–diffusive mass transfer at high stirring rate diminishes the thickness of static solution layer around drop, leading to a better mass transfer between the sample solution and the extracting microdrop [40,41]. Although high stirring rates improve the enrichment factors considerably with SDME technique, the stability of the microdrop at the needle tip could be affected dramatically. This was especially observed for extended stirring times and a microdrop volume of 4 μL were applied. Thus, a stirring rate of 700 rpm was used for all further experiments. Temperature also affects the extraction kinetics. At high temperatures, diffusion coefficient of the analyte increases and viscosity of the organic membrane decreases, therefore the time required to achieve equilibrium decreases [42]. On the other hand, higher temperatures result in some practical difficulties, such as microdrop instability and reduction of its volume due to higher solubility of RTIL in aqueous phase. In order to avoid these drawbacks, all studies were performed at room temperature.

Since analyte mass transfer is a time-dependent process, the effect of extraction time on the analytical signal was investigated and the experimental results are shown in Fig. 5. It can be seen that extraction efficiency of analyte increased within 15 min interval. Extraction time longer than 20 min, led to RTIL microdrop dissolution and thereby to reduce extraction efficiency. An extraction time of 15 min was thus chosen for further studies.

3.3. Potential interfering species

The effect of concomitant ions regularly found in natural water samples was also evaluated in this work. The study was performed by analyzing 1.5 mL of 0.5 $\mu g\,L^{-1}$ Pb solution containing concomitant ions at different concentrations, according to the recommended extraction procedure. A concomitant ion was considered to interfere if it resulted in an analytical signal variation of ±5%. Thus, Cu^{2+}, Zn^{2+}, Ni^{2+}, Co^{2+}, Mn^{2+} and Fe^{3+} could be tolerated up to at least 100 $\mu g\,L^{-1}$. Commonly encountered concomitant ions, such as alkaline and alkaline earth elements, do not form stable complexes with 5-Br-PADAP at working pH. Therefore, they are not extracted from the aqueous solution. Additionally, their contribution to the ionic strength of the system is insignificant and does not affect the extraction efficiency. Analytical signal of the blank was not modified in presence of the concomitant ions assayed. On the other hand, it is expected that humic substances do not produce interference effects on lead extraction with RTILs [43]. In fact, it has been already reported in the literature that stability constants of metal complexes formed with pyridylazo-type reagents [39] are higher than those reported for metal-humates [44].

3.4. Analytical performance and determination of lead in water samples

An extraction efficiency of 45% was achieved when the procedure was developed under optimum experimental conditions (Table 1). It has to be mentioned that, despite the relatively low extraction efficiency obtained with the proposed IL-based SDME method, a sensitivity enhancement factor of 32 was obtained. This was to due to the low volume of CYPHOS® IL 101 phase (4 μL) compared to the sample volume required for the analysis. Thus, significant volume ratio (375) between CYPHOS® IL 101 and sample yielded an acceptable enhancement of the analytical sensitivity. The preconcentration factor was obtained from the ratio of the calibration curve slopes for Pb with and without application of the preconcentration step.

The relative standard deviation (RSD) resulting from the analysis of 10 replicates of 1.5 mL solution containing 0.5 $\mu g\,L^{-1}$ Pb^{2+} was 4.9%. The calibration graph, obtained by analysis of 6 standards with different known concentrations of Pb, was linear with a correlation coefficient of 0.9996 at levels near the detection limits and up to at least 4.5 $\mu g\,L^{-1}$ [$A = 0.0021(\pm 0.002) + 0.25068(\pm 0.0021)C$], where A is the absorbance and C is Pb^{2+} concentration in $\mu g\,L^{-1}$. The limit of detection (LOD), calculated as the concentration of lead required to yield a net peak equal to three times the standard

Table 2
Determination of Pb in water samples and analyte recovery study (95% confidence interval; $n = 6$).

Sample	Base value ($\mu g\,L^{-1}$)	Quantity of Pb^{2+} added ($\mu g\,L^{-1}$)	Quantity of Pb^{2+} found ($\mu g\,L^{-1}$)	Recovery (%)[a]
River water 1	0.53	–	0.53 ± 0.03	–
	0.53	0.5	1.02 ± 0.05	97
	0.53	1	1.54 ± 0.08	101
River water 2	0.42	–	0.42 ± 0.03	–
	0.42	0.5	0.93 ± 0.06	103
	0.42	1	1.42 ± 0.08	100
Well water 1	0.38	–	0.38 ± 0.03	–
	0.38	0.5	0.87 ± 0.06	97
	0.38	1	1.41 ± 0.08	103
Well water 2	0.29	–	0.29 ± 0.02	–
	0.29	0.5	0.77 ± 0.05	97
	0.29	1	1.27 ± 0.06	98
Tap water 1	0.12	–	0.12 ± 0.01	–
	0.12	0.5	0.61 ± 0.04	98
	0.12	1	1.15 ± 0.06	103
Tap water 2	0.18	–	0.18 ± 0.01	–
	0.18	0.5	0.70 ± 0.05	105
	0.18	1	1.15 ± 0.05	97
Mineral water 1	0.05	–	0.05 ± 0.01	–
	0.05	0.5	0.54 ± 0.04	98
	0.05	1	1.05 ± 0.06	100
Mineral water 2	n.d.[b]	–	–	–
	n.d.[b]	0.5	0.48 ± 0.03	97
	n.d.[b]	1	0.98 ± 0.05	98

[a] $100 \times [(\text{found} - \text{base})/\text{added}]$.
[b] Non-detectable.

Table 3
Characteristic performance data obtained by using the proposed method and others reported for Pb determination in water by ETAAS.

Method	LOD ($ng\,L^{-1}$)	RSD (%)	Preconcentration factor	Sample consumption (mL)	Calibration range ($ng\,L^{-1}$)	Analysis frequency (h^{-1})	Ref.
On line [a]SPE	12	3.2	20.5	>3	100–10000	36	[45]
Co-precipitation	500	4.6	20	200	n.r.[b]	2	[46]
Semi on line-activated carbon	7.5	3.1	21	6.75	n.r.[b]	18	[47]
FI-semi online-silica	3.9	5.3	29	3	n.r.[b]	20	[48]
Toluene SDME	90	12.8	90	2	n.r.[b]	n.r.[b]	[49]
PMBP[c] benzene SDME	25	6.1	16	1	0–40000	n.r.[b]	[50]
$CHCl_3$ SDME	200	4	52	2	1000–15000	n.r.[b]	[51]
$[C_4MIM][PF_6]$ SDME	15	5.2	76	1.75	25–800	n.r.[b]	[24]
Cyphos SDME	3.2	4.9	32	1.5	3.2–4500	3	This work

[a] Selective solid phase extraction.
[b] Non-reported.
[c] 1-Phenyl-3-methyl-4-benzoyl-5-pyrazolone.

deviation of the blank signal (3σ), was $3.2\,ng\,L^{-1}$. The calibration graph obtained without the preconcentration method was $A = 6.1 \times 10^{-4} + 0.0078\,C$.

In order to study analyte recovery, 15 mL of tap, mineral, well and river water samples were divided into 10 portions of 1.5 mL each. The proposed method was applied to six portions and the average concentration of Pb^{2+} found was taken as the base value. The remaining aliquots were spiked with increasing quantities of Pb^{2+} and were analyzed by the proposed method. The results are shown in Table 2. The method was applied in different water samples taken from Mendoza province (Argentina). Lead concentrations were 0.42 and $0.53\,\mu g\,L^{-1}$ for river water, 0.29 and $0.38\,\mu g\,L^{-1}$ for well water, 0.12 and $0.18\,\mu g\,L^{-1}$ for tap water and n.d. and $0.05\,\mu g\,L^{-1}$ for mineral water; 95% confidence interval ($n = 6$). Additionally, the accuracy of the proposed methodology was evaluated by analyzing a certified reference material (CRM) described as natural water NIST SRM 1643d, with a Pb^{2+} content of $18.15 \pm 0.64\,\mu g\,L^{-1}$. Using the method developed in this work, the Pb^{2+} content found in the CRM was $18.14 \pm 0.59\,\mu g\,L^{-1}$ (95% confidence interval; $n = 6$).

Finally, a comparison of the proposed method with others reported in the literature for Pb determination in water is shown in Table 3. Our method shows good LOD and a high enhancement factor, considering the low volume of sample required to perform the analysis. Regarding the frequency of analysis, although preconcentration of the analyte for a single sample could take more than 15 min, the extraction procedure can be applied in as many samples as possible at a time, substantially increasing the number of samples analyzed. Considering that CYPHOS® IL 101 is a low-cost ionic liquid, the proposed method could be generally applicable for routine analytical laboratories.

4. Conclusion

In this work, an efficient method for extraction and preconcentration of Pb has been developed based on SDME technique using 4 μL of RTIL tetradecyl(trihexyl)phosphonium chloride prior to ETAAS determination. This methodology combines the advantages of single-drop microextraction (i.e., miniaturization and low solvent consumption) with the use of an ionic liquid as extrac-

tant. SDME technique was particularly useful to overcome those problems associated with separation of low density RTIL, such as CYPHOS® IL 101, from aqueous systems. This work shows that 5-Br-PADAP-CYPHOS® IL 101 system is suitable for trace level determination of Pb. Furthermore, quantitative extraction and a preconcentration factor of 32 were achieved. Direct analysis and accurate determination of Pb by ETAAS is demonstrated even in the presence of complex organic matrix originated from RTIL. The preconcentration method was successfully applied to Pb determination in water samples in the low $\mu g\,L^{-1}$ range, with good accuracy and reproducibility.

Acknowledgements

This work was supported by Consejo Nacional de Investigaciones Científicas y Técnicas (CONICET) and Agencia Nacional de Promoción Científica y Tecnológica (FONCYT) (PICT-BID) (Argentina). The authors of this work would like to thank CYTEC Company for CYPHOS® IL 101 donation.

References

[1] S.V. Verstraeten, L. Aimo, P.I. Oteiza, Arch. Toxicol. 82 (2008) 789.
[2] H.L. Koh, S.O. Woo, Drug Safety 23 (2000) 351.
[3] M.R. Gomez, S. Cerutti, L.L. Sombra, M.F. Silva, L.D. Martinez, Food Chem. Toxicol. 45 (2007) 1060.
[4] W.H. Organization, W.H.O. 2nd ed., vol. 2, 1996, p. 973.
[5] G. Yang, W. Fen, C. Lei, W. Xiao, H. Sun, J. Hazard. Mater. 162 (2009) 44.
[6] Z. Ajtony, N. Szoboszlai, E.K. Suskó, P. Mezei, K. György, L. Bencs, Talanta 76 (2008) 627.
[7] J.S. Suleiman, B. Hu, C. Huang, N. Zhang, J. Hazard. Mater. 157 (2008) 410.
[8] Q. He, X. Chang, X. Huang, Z. Hu, Microchim. Acta 160 (2008) 147.
[9] E.P. Nardi, F.S. Evangelista, L. Tormen, T.D. SaintPierre, A.J. Curtius, S.S.D. Souza, F. Barbosa Jr., Food Chem. 112 (2009) 727.
[10] B.L. Batista, J.L. Rodrigues, J.A. Nunes, L. Tormen, A.J. Curtius, F. Barbosa Jr., Talanta 76 (2008) 575.
[11] M.T. Naseri, M.R. Milani Hosseini, Y. Assadi, A. Kiani, Talanta 75 (2008) 56.
[12] H. Parham, N. Pourreza, N. Rahbar, J. Hazard. Mater. 163 (2009) 588.
[13] A.N. Anthemidis, Talanta 77 (2008) 541.
[14] M. Tuzen, M. Soylak, J. Hazard. Mater. 162 (2009) 724.
[15] J.A. Salonia, R.G. Wuilloud, J.A. Gásquez, R.A. Olsina, L.D. Martinez, J. Anal. At. Spectrom. 14 (1999) 1239.
[16] Y.J. Park, D.J. Fray, J. Hazard. Mater. 163 (2009) 259.
[17] M. Baghdadi, F. Shemirani, Anal. Chim. Acta 634 (2009) 186.
[18] A. Chisvert, I.P. Román, L. Vidal, A. Canals, J. Chromatogr. A 1216 (2009) 1290.
[19] Y. Liu, E. Zhao, W. Zhu, H. Gao, Z. Zhou, J. Chromatogr. A 1216 (2009) 885.
[20] X. Liu, Z. Fan, At. Spectrosc. 28 (2007) 215.
[21] E. Aguilera-Herrador, R. Lucena, S. Cárdenas, M. Valcárcel, J. Chromatogr. A 1209 (2008) 76.
[22] J.F. Liu, G.B. Jiang, Y.G. Chi, Y.Q. Cai, Q.X. Zhou, J.T. Hu, Anal. Chem. 75 (2003) 5870.
[23] J.L. Manzoori, M. Amjadi, J. Abulhassani, Talanta 77 (2009) 1539.
[24] J.L. Manzoori, M. Amjadi, J. Abulhassani, Anal. Chim. Acta 644 (2009) 48.
[25] J.L. Anderson, D.W. Armstrong, G. Wei, Anal. Chem. 78 (2006) 2893.
[26] M.K. Ed, Ionic Liquids in Chemical Analysis, Taylor & Francis Group/CRC Press, 2009.
[27] X. Han, D.W. Armstrong, Acc. Chem. Res. 40 (2007) 1079.
[28] N.V. Plechkova, K.R. Seddon, Chem. Soc. Rev. 37 (2008) 123.
[29] A. Berthod, M.J. Ruiz-Ángel, S. Carda-Broch, J. Chromatogr. A 1184 (2008) 6.
[30] G. Singh, A. Kumar, Indian J. Chem. A: Inorg. Bioinorg. Phys. Theor. Anal. Chem. 47 (2008) 495.
[31] C.J. Bradaric, A. Downard, C. Kennedy, A.J. Robertson, Y. Zhou, Green Chem. 5 (2003) 143.
[32] G.V. Myasoedova, N.P. Molochnikova, O.B. Mokhodoeva, B.F. Myasoedov, Anal. Sci. 24 (2008) 1351.
[33] M. Regel-Rosocka, Sep. Purif. Technol. 66 (2009) 19.
[34] P.G. Rickert, M.R. Antonio, M.A. Firestone, K.A. Kubatko, T. Szreder, J.F. Wishart, M.L. Dietz, J. Phys. Chem. B 111 (2007) 4685.
[35] R.G. Wuilloud, H.A. Acevedo, F.A. Vazquez, L.D. Martinez, Anal. Lett. 35 (2002) 1649.
[36] J.O. Muse, C.N. Carducci, J.D. Stripeikis, M.B. Tudino, F.M. Fernandez, Environ. Pollut. 141 (2006) 126.
[37] P. Berton, E.M. Martinis, L.D. Martinez, R.G. Wuilloud, Anal. Chim. Acta 640 (2009) 40.
[38] D.A. Johnson, T.M. Florence, Talanta 22 (1975) 253.
[39] K.L. Cheng, K. Ueno, T. Imamura, Handbook of Organic Analytical Reagents, CRC Press, Florida, 1982.
[40] M.A. Jeannot, F.F. Cantwell, Anal. Chem. 69 (1997) 235.
[41] E. Psillakis, N. Kalogerakis, TrAC, Trends Anal. Chem. 21 (2002) 53.
[42] H. Ebrahimzadeh, Y. Yamini, A. Gholizade, A. Sedighi, S. Kasraee, Anal. Chim. Acta 626 (2008) 193.
[43] S. Haixia, L. Zaijun, L. Ming, Microchim. Acta 159 (2007) 95.
[44] S. Caroli, Element Speciation in Bioinorganic Chemistry, John Wiley, New York, 1996.
[45] E. Vereda Alonso, M.T. Siles Cordero, A. García De Torres, J.M. Cano Pavón, Anal. Bioanal. Chem. 385 (2006) 1178.
[46] T. Minami, Y. Sohrin, J. Ueda, Anal. Sci. 21 (2005) 1519.
[47] S. Xingguang, W. Meijia, Z. Yihua, Z. Jiahua, Z. Hanqi, J. Qinhan, Talanta 59 (2003) 989.
[48] Q. Jin, X. Su, F. Liang, H. Zhang, Microchem. J. 62 (1999) 316.
[49] H. Jiang, B. Hu, Microchim. Acta 161 (2008) 101.
[50] P. Liang, R. Liu, J. Cao, Microchim. Acta 160 (2008) 135.
[51] H.F. Maltez, D.L.G. Borges, E. Carasek, B. Welz, A.J. Curtius, Talanta 74 (2008) 800.

Talanta 80 (2010) 2041–2048

Contents lists available at ScienceDirect

Talanta

journal homepage: www.elsevier.com/locate/talanta

Determination of volatile organic compounds in contaminated air using semipermeable membrane devices

Saray Ly-Verdú, Francesc A. Esteve-Turrillas*, Agustín Pastor, Miguel de la Guardia

Analytical Chemistry Department, University of Valencia, Edifici Jeroni Muñoz, 50 Dr. Moliner, 46100 Burjassot, Valencia, Spain

ARTICLE INFO

Article history:
Received 3 August 2009
Received in revised form 20 October 2009
Accepted 3 November 2009
Available online 10 November 2009

Keywords:
VOCs
SPMDs
Air passive sampling
Head-space
Radiello®

ABSTRACT

Semipermeable membrane devices (SPMDs) were evaluated as passive samplers for the determination of 26 volatile organic compounds (VOCs) in contaminated air of occupational environments. A direct methodology based on the use of head-space-gas chromatography–mass spectrometry (HS-GC–MS) was developed for VOCs determinations in SPMDs, without any sample pre-treatment and avoiding the use of solvents. A desorption temperature of 150 °C for 10 min was sufficient for a sensitive VOCs determination providing limits of detection in the range of 15 ng SPMD^{-1} for 21 of 26 studied compounds. Linear and equilibrium uptake models were established for each VOC from compound isotherms. Highly volatile compounds were slightly absorbed and moderately volatile compounds were strongly absorbed by SPMDs. This study is the first precedent of the use of SPMDs for the simultaneous sampling of a wide number of VOCs. The use of SPMDs is a simple and low cost alternative to ordinary sampling devices such as Radiello® diffusive samplers or badge-type solid-phase supports.

© 2009 Elsevier B.V. All rights reserved.

1. Introduction

Volatile organic compounds (VOCs) constitute a wide group of chemicals that evaporate easily at room temperature and which are usually found in air. Their sources are numerous and diverse, such as: traffic pollution, paints, cleaning supplies, pesticides, building materials and furnishings, fragrance products or office equipment [1].

Some VOCs can cause sore throats, increase the risk of asthma, or affect the nervous, immune and reproductive systems [2]; other VOCs cannot be considered hazardous to human health in the short-term, but they are mutagenic or carcinogens at long-term exposures [3]. This is the case of benzene and tetrachloroethene that have been recognized by the World Health Organization (WHO) as carcinogenic. Usually, benzene, toluene, ethylbenzene and xylenes (BTEX) are common markers for human exposure to VOCs, but nowadays the monitoring of more compounds are required to obtain an improved evaluation of the risks to human health.

Moreover, the European Commission Regulation No. 1907/2006 established in 2006 the norms for the "Registration, Evaluation, Authorisation and Restriction of Chemicals" (REACH) that are produced in Europe at amounts of more than 1 tonne/year, in order to improve the protection of human health and the environment from the impact of more than 34 millions of chemical substances [4].

The reference procedure, suggested by the U.S. Environmental Protection Agency, for the air measurement of VOCs is based on an active sampling by using sorbent tubes [5] or specially prepared canisters [6]. In spite of this, air pollution measurements with passive samplers have been increased in the last few years due to their simplicity, low prize and ease of use [7]. Passive samplers frequently employed for the sampling of VOCs are: Radiello®, Organic Vapours Monitor (OVM), ORSA passive sorbent sampling badges, PerkinElmer tubes, SKC diffusive samplers, polyurethane foam (PUF), solid-phase microextraction (SPME) or semipermeable membrane devices (SPMD) [8]. In fact, the passive sampling of BTEX compounds [9], polychlorinated biphenyls and polycyclic hydrocarbons [10] and pesticides [11–13] in air by means of SPMDs has been previously studied by our group with excellent results.

A SPMD is made of a low-density polyethylene (LDPE) layflat tube filled with triolein and sealed at both ends. Hydrophobic compounds go easily from air through the LDPE tube and accumulate both in triolein and LDPE. Pollutants bonded to particles will not pass the membrane, so we are only evaluating the time-weighting average (TWA) of pollutants present in the air as gases or vapours and not other sources, such as dust or particulate matter [14].

The uptake kinetics of a pollutant sampled with a SPMD is mediated by its physico-chemical properties and certain environmental factors, mainly temperature and air flow [15]. Thus, if there are not big changes in temperature and air flow, the sampling rate (R_S) can be theoretically calculated by using octanol–water partition coefficient (K_{OW}) and the Henry's law constant (H). Sampler–air partition

* Corresponding author. Tel.: +34 963 543 159; fax: +34 963 544 838.
E-mail address: francesc.a.esteve@uv.es (F.A. Esteve-Turrillas).

0039-9140/$ – see front matter © 2009 Elsevier B.V. All rights reserved.
doi:10.1016/j.talanta.2009.11.001

coefficient (K_{SA}) and sampling rates (R_S) can be also experimentally calculated for each considered compound by the establishment of uptake isotherms, as it was shown in previous studies [9].

The aim of this study was focussed in the evaluation of SPMDs as passive samplers of a wide group of VOCs, commonly found in working environments. Analytical parameters were established for the determination of each studied compound in air. Experimentally calculated R_S values were established for each studied compound, and they were compared with the theoretical ones. Finally, the occupational exposure to VOCs in air of a paint factory was estimated by the use of SPMDs and compared with Radiello® diffusive samplers used as a reference methodology.

2. Experimental

2.1. Apparatus and reagents

VOCs accumulated in SPMDs were determined with the use of an HS2000 head-space (HS) injector from Finnigan (Waltham, MS, USA). A Finnigan Trace gas chromatograph equipped with low bleed column HP-5MS (30 m × 0.32 mm, 0.25 μm) capillary column and Finnigan Polaris Q ion trap mass spectrometer detector were used for VOCs determinations.

Glass vials, with an internal volume of 10 mL, capped with PTFE-butyl rubber seals were employed for HS measurements.

LDPE layflat tubing, 2.9 cm wide, was obtained from Garciplast (Barcelona, Spain). A Rovebloc sealer (Barcelona, Spain) was employed to heat-seal the membranes. Triolein 99% was obtained from Sigma Chemicals Co. (St. Louis, MO, USA).

The Radiello® sampler, provided by Supelco, consists of a microporous polyethylene cylindrical diffusive body (RAD120) that contain a stainless steel coaxial cylindrical cartridge filled with 530 ± 30 mg activated charcoal adsorbent (RAD130), supported by a triangular plate (RAD121).

Studied VOC standards (see Table 1) and hexadecane were obtained from Scharlau (Barcelona, Spain), Fluka Chemie (Steinheim, Germany), Merck (Darmstadt, Germany) and Aldrich (Steinheim, Germany). A 3.85% (w/w) VOCs standard solution was prepared by mixing 1 g of all considered analytes and it was stored at −20 °C. Working standard solutions were prepared by dilution of that in hexadecane. Hexadecane was employed due to its high boiling point. Benzene-free carbon disulphide from Acros organics (Barcelona, Spain) was employed for the extraction of VOCs from Radiello® cartridges.

Glass containers, 2.85 ± 0.01 L volume, were appropriately decontaminated and cleaned-up using a 5 min nitrogen flow before being used to study the absorption isotherms of considered compounds in SPMDs. Several blank studies (sampling the clean containers with SPMDs for 24 h) were performed in order to assure the complete release of VOCs from containers.

2.2. General procedure

2.2.1. Preparation of SPMDs

A standard SPMD is 90 cm long, 2.54 cm wide and contains 1 mL triolein inside, with a surface area–triolein volume ratio of 460 $cm^2\ mL^{-1}$. In this study short SPMDs (10 times smaller) were made with LDPE layflat tubing cut into segments of 10 cm, with one end heat-sealed, then 0.1 mL triolein were introduced into the membrane, squeezing to form a continuous film and the other end was also heat-sealed. The effective length was 8 cm and the obtained surface area–triolein volume ratio was 464 $cm^2\ mL^{-1}$. SPMDs were wrapped in separate aluminum foils and stored in a closed vessel at −20 °C to avoid contamination before in-field deployment. After deployment, the devices were rolled, placed inside 10 mL HS vials, capped hermetically, and stored at −20 °C until the HS-GC–MS measurement.

Calibration curves were prepared with SPMDs spiked by adding 5 μL VOC standards at different concentrations (0.003, 0.015, 0.03, 0.15, 0.3 and 3 $g\ L^{-1}$ of each compound in hexadecane). Standard solutions were directly introduced inside the layflat tube with a glass syringe. The spiked SPMDs were also placed in hermetically capped HS vials and stored at −20 °C or directly measured by HS-GC–MS.

Table 1
GC–MS measurement parameters and physico-chemical properties of the studied VOCs.

	Compound	Retention time (min)	Ions measured (m/z)	Boiling point (°C)	Vapor pressure (mm Hg)	log K_{OA}[a]
1	Carbon disulfide	1.47	76	46	300 (20 °C)	2.28
2	Methylethylketone	1.55[b]	43 + 57	80	78 (20 °C)	2.71
3	Methyl tert-butyl ether	1.56[b]	73 + 177	55	245 (25 °C)	2.58
4	Hexane	1.67[b]	58 + 56	68	130 (20 °C)	2.40
5	Diethyl ether	1.68[b]	43 + 45	35	440 (20 °C)	2.19
6	Ethylacetate	1.77	43	77	76 (20 °C)	2.70
7	Chloroform	1.81	83 + 85	62	159 (20 °C)	2.80
8	Tetrahydrofuran	1.85	71 + 41	66	129 (20 °C)	2.86
9	1,1,1-Trichloroethane	1.97	97 + 99	74	100 (20 °C)	2.70
10	1,2-Dichloroethane	2.02	62 + 64	84	387 (25 °C)	2.78
11	Carbon tetrachloride	2.07[b]	119 + 117	77	91 (20 °C)	2.79
12	Benzene	2.08[b]	78 + 77	80	101 (25 °C)	2.78
13	Cyclohexane	2.10[b]	83 + 57	81	95 (20 °C)	2.74
14	2,2,4-Trimethylpentane	2.29	41 + 57	99	41 (21 °C)	2.00[c]
15	Trichloroethylene	2.46	132 + 130	87	75 (25 °C)	2.99
16	Bromodichloromethane	2.59	85 + 83 + 129	87	50 (20 °C)	3.06[c]
17	Methylisobutylketone	3.04	43 + 85 + 101	117	16 (20 °C)	3.56[c]
18	Toluene	3.53	91 + 92	111	29 (25 °C)	3.31
19	Dibromochloromethane	4.39	127	120	76 (20 °C)	3.59
20	Tetrachloroethene	4.50	166 + 164	121	14 (20 °C)	3.48
21	n-Butylacetate	4.94	43	126	15 (25 °C)	3.65
22	Ethylbenzene	6.73	91 + 106	136	10 (25 °C)	3.74
23	m-Xylene	7.24	91 + 106	139	8 (25 °C)	3.78
24	p-Xylene	7.33	91 + 106	138	9 (25 °C)	3.79
25	Bromoform	8.39[b]	173 + 175 + 171	149	5 (20 °C)	4.06[c]
26	o-Xylene	8.40[b]	91 + 106	144	7 (25 °C)	3.91

[a] Octanol–air partition coefficient (K_{OA}) [16,17].
[b] Overlapped peaks, but well-resolved by MS.
[c] Selected K_{OA} values were estimated with KOAWIN v1.10 software.

2.2.2. Determination of absorption rates

In order to achieve the corresponding calibration parameters (R_S and K_{SA}) for each studied VOC, 5 μL of 3 g L^{-1} VOC standard dissolved in hexadecane was added to a 2 cm^2 piece of filter paper and placed inside closed 2.85 ± 0.01 L glass bottles. After complete VOC evaporation, air concentration of each VOC in the containers was 5.2 mg m^{-3}. Then one SPMD was placed inside each container for variable exposure times of 1–7, 9, 12, 18, 24 and 48 h. These experiments were carried out by triplicate in a clean room with controlled temperature at 25 ± 0.5 °C. SPMDs and the spiked filter papers were placed in 10 mL HS vials and measured by HS-GC–MS.

2.2.3. Field studies

Time weighted average (TWA) concentration of VOCs was measured simultaneously with SPMD and Radiello® devices. Both samplers were deployed in several places of a paint factory, 2 m above the ground during 48 h, to determine the concentration of VOCs in the air. After sampling time both samplers were properly kept, labeled and stored under refrigeration at −20 °C, awaiting their measurement. The corresponding blanks were also analyzed to confirm the absence of contamination in the manufacture, trip or storage of samplers.

2.2.4. HS-GC–MS determination

VOCs vaporization from SPMDs was carried out at 150 °C for 10 min, with a syringe temperature of 150 °C and a constant air flow purge. A volume of 0.1 mL HS fraction was injected in split mode (1:10) at 200 °C, employing 1 mL min^{-1} constant flow of helium as carrier gas. The GC oven temperature program was 40 °C, held for 9 min, increased at a rate of 20 °C min^{-1} up to 200 °C, and finally held for 2 min. The transfer line and source temperatures were 300 and 250 °C, respectively. Electron impact ionization at 70 eV was employed and a mass scanning range from 40 to 180 *m*/*z* was used for full scan acquisitions. The measured *m*/*z* ions employed for each compound are shown in Table 1 together with their chromatographic retention times and their physico-chemical parameters.

2.2.5. VOC determination in Radiello® sampler

Each Radiello® cartridge was extracted as recommended by the supplier, with 2 mL of CS_2 directly in a closed glass tube without drawing out the cartridge, stirring from time to time for 30 min [18]. Then, 1 μL extract was injected employing the same chromatographic and MS conditions than those employed for HS-GC–MS determinations.

3. Results and discussion

3.1. HS-GC–MS measurement

HS desorption has been previously employed for the determination of BTEX compounds from SPMDs [9]. In that study, it was established that longer volatilization times did not increase the obtained recoveries, so a maximum evaporation temperature of 150 °C for 10 min was employed for the determination of BTEX in SPMDs. Thus, the same conditions were assayed for the quantification of VOCs, but a reduced injection volume (100 μL) has been employed in order to improve chromatographic resolution.

To evaluate the use of VOC solutions for external calibrations, signals obtained for SPMDs spiked with different amounts of VOCs were analyzed. As indicated in Fig. 1, slopes of the calibration curves obtained in the presence of the SPMD (LDPE membrane and triolein) varied from 30 to 84% of those found for external calibration. Fig. 1 inset shows the relationship between the obtained relative slope and the boiling point of each VOC. Thus, SPMDs spiked with the correspondent standard were employed to quantify unknown samples.

Fig. 2 shows the HS-GC–MS chromatograms obtained for one SPMD deployed in sampling site number 2 for 48 h and a SPMD spiked with 15 μg $SPMD^{-1}$ VOC standard. As it can be seen the peak

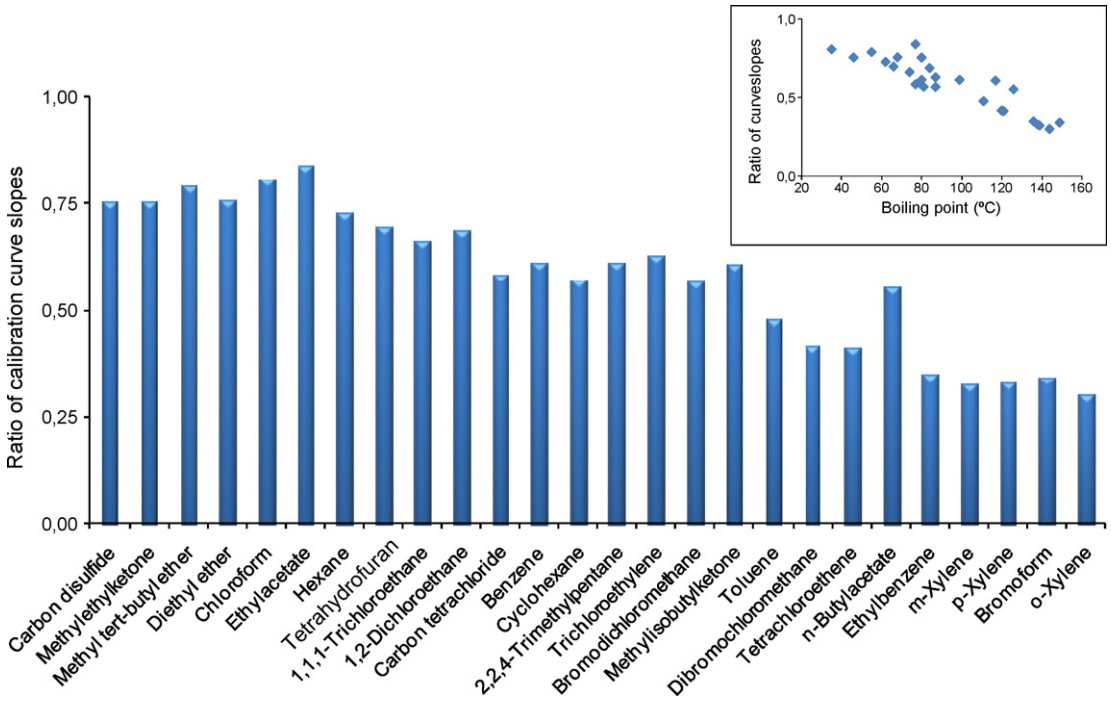


Fig. 1. Relative slope of the VOCs calibration curves obtained in the presence/absence of the SPMD by HS-GC–MS. Inset: relationship between the relative slope and the boiling point of the considered compounds.

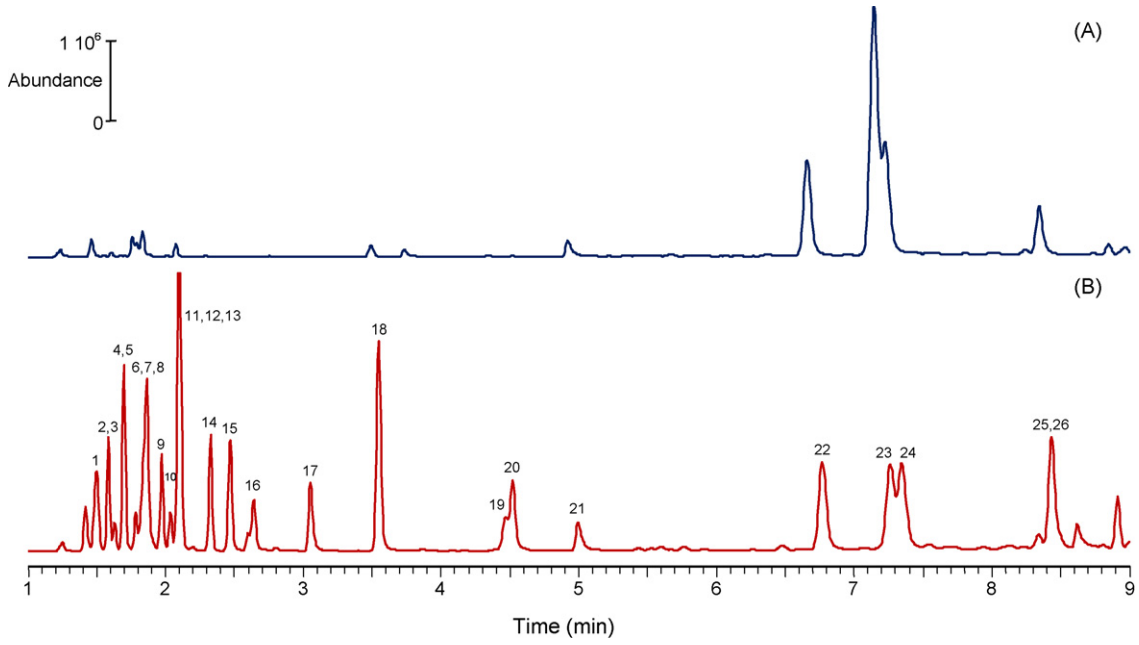


Fig. 2. Total ion chromatogram obtained for SPMD deployed in sampling site 2 for 48 h (A) and a SPMD spiked with 15 μg SPMD^{-1} VOC standard (B). Note: carbon disulfide (1); methylethylketone (2); methyl tert-butyl ether (3); hexane (4); diethyl ether (5); ethylacetate (6); chloroform (7); tetrahydrofuran (8); 1,1,1-trichloroethane (9); 1,2-dichloroethane (10); carbon tetrachloride (11); benzene (12); cyclohexane (13); 2,2,4-trimethylpentane (14); trichloroethylene (15); bromodichloromethane (16); methylisobutylketone (17); toluene (18); dibromochloromethane (19); tetrachloroethene (20); n-butylacetate (21); ethylbenzene (22); m-xylene (23); p-xylene (24); bromoform (25); o-xylene (26).

resolution achieved was adequate to analyze the 26 considered VOCs with enough sensitivity.

3.2. Analytical features

Calibration curves were established with SPMDs spiked with different VOC standards dissolved in hexadecane. Hexadecane was employed for their similarity with triolein (non-polar long-chain alkane) and for its low viscosity. The detector response was linear over a wide concentration range from 0.015 to 15 μg VOCs, with correlation coefficients ranging from 0.9996 to 0.9999.

Limit of detection (LOD) was established as the VOC concentration that provided a signal-to-noise ratio higher than three, which was calculated using Xcalibur software from Thermo-Finnigan. The obtained LOD were 15 ng SPMD^{-1} for most of the compounds, except for carbon disulfide, diethyl ether, chloroform, ethylacetate and n-butylacetate with values of 75 ng SPMD^{-1} (see Table 2).

Precision was established as the relative standard deviation (RSD) of three independent measures of three SPMDs spiked with 750 ng VOCs, each of them in their own HS vial. Repeatability was established as the RSD of 3 and 5 sequential injections of the same spiked SPMD, with 20 min of cooling time between every injection to avoid sample overheating, in order to know the possibility to do replicate analysis of a same sample. It is in fact a great advantage of the HS-GC–MS determination of VOCs in SPMDs, in front of active sampling procedures, that usually involves a total thermal desorption where replicate analysis is not allowed. Precision of the HS-GC–MS method was from 1.6 to 8.6% and repeatability for three sequential injections were satisfactory for all compounds except for some halogenated VOCs, see Table 2. So, triplicate measurements of a same SPMD could be done with the proposed methodology, in the case it was required.

3.3. Experimental estimation of R_S and K_{SA}

The establishment of absorption isotherms with SPMDs allows to calculate the uptake parameters (R_S and K_{SA}) to estimate TWA concentration of VOCs during the sampling of air. The VOCs standard was placed on a paper filter, to increase the volatilization area and to ensure the whole evaporation. SPMDs were placed in the containers and removed after several times and later on the absence of VOCs in the paper filters was checked in order to assure the whole evaporation of the studied compounds.

Fig. 3 shows the VOCs amount absorbed with each SPMD at 25 °C at different uptake times, from air contaminated with 5.2 mg m^{-3} VOCs. As it can be seen, the absorption of dibromochloromethane,

Table 2
Analytical features for the determination of VOCs in SPMDs by HS-GC–MS.

	Compound	LOD (ng SPMD^{-1})	RSD (%, $n=3$)	Repeatability (%)	
				($n=3$)	($n=5$)
1	Carbon disulfide	75	4.9	4.9	5.1
2	Methylethylketone	15	4.9	7.4	9.9
3	Methyl tert-butyl ether	15	3.8	3.8	5.3
4	Diethyl ether	75	7.3	10.7	16.9
5	Chloroform	75	6.8	9.0	13.2
6	Ethylacetate	75	2.9	6.2	6.4
7	Hexane	15	1.6	7.4	7.7
8	Tetrahydrofuran	15	3.2	7.2	7.6
9	1,1,1-Trichloroethane	15	3.5	5.8	6.1
10	1,2-Dichloroethane	15	4.6	5.2	5.9
11	Carbon tetrachloride	15	5.5	2.9	6.6
12	Benzene	15	4.8	4.4	4.9
13	Cyclohexane	15	6.8	5.7	6.5
14	2,2,4-Trimethylpentane	15	6.2	5.6	6.7
15	Trichloroethylene	15	5.9	5.4	5.1
16	Bromodichloromethane	15	6.7	12.7	28.3
17	Methylisobutylketone	15	8.6	7.2	7.9
18	Toluene	15	5.0	5.6	7.0
19	Dibromochloromethane	15	5.2	22.1	45.2
20	Tetrachloroethene	15	4.4	10.2	11.0
21	n-Butylacetate	75	3.4	7.7	9.3
22	Ethylbenzene	15	6.8	8.3	9.7
23	m-Xylene	15	7.9	7.8	11.0
24	p-Xylene	15	7.3	5.2	10.5
25	Bromoform	15	7.7	24.3	48.0
26	o-Xylene	15	8.4	8.3	10.5

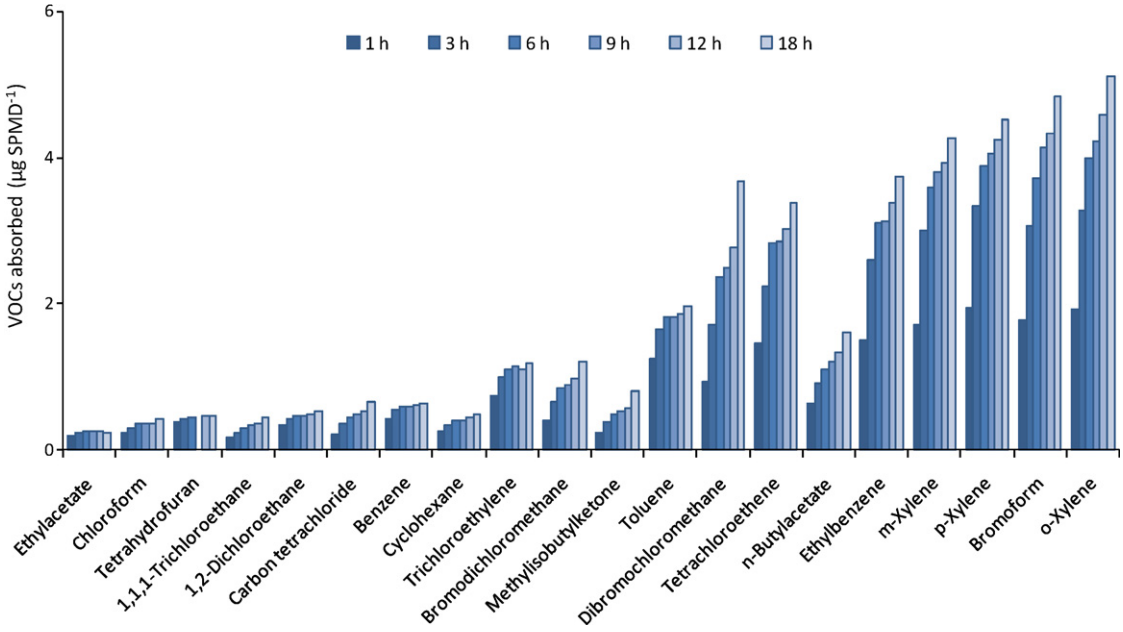


Fig. 3. SPMD absorption isotherms for VOCs at 25 °C in air spiked at 5.2 mg m^{-3} level.

tetrachloroethene, ethylbenzene, xylenes and bromoform was very high, compared with the very volatile compounds evaluated, while toluene and n-butylacetate show an intermediate absorption pattern.

Table 3 shows the time required to reach the equilibrium for each VOC sampled with SPMD in the isotherm study made. This equilibrium time was different for each considered VOC, few hours was enough for most of them, but in the case of 1,1,1-trichloroethane, carbon tetrachloride and n-butylacetate equilibrium was not reached until 18 h. Thus, a specific model was employed for each compound. However, the equilibrium model was used in all cases when a 24 h sampling is performed and linear models were mandatory for 1 h sampling.

As it was well established, the pollutant uptake by the SPMD passive sampler can be explained in three stages: first a linear absorption, later a curvilinear stage, and finally an equilibrium state [19]. Linear and equilibrium models are easy to use with the previous establishment of R_S and K_{SA} parameters, respectively.

For sampling times equal or longer than the equilibrium time (e.g. 24 h), K_{SA} can be used to estimate the TWA concentration of pollutants in air from the amount of VOCs determined in the SPMD, as explained by Eq. (1).

$$C_{AIR} = \frac{N_S}{K_{SA}V_S} = \frac{N_S}{K'_{SA}} \quad (1)$$

where C_{AIR} (mg m^{-3}) is the TWA concentration of a VOC dissolved in air; N_S (mg) is the VOC amount found in SPMD; K_{SA} is the sampler–air partition coefficient; V_S (m^3) is the sampler volume and K'_{SA} (m^3) is the pseudo sampler–air partition coefficient. The K'_{SA} value can be considered as the equivalent volume sampled with SPMD in equilibrium conditions.

In the case of short sampling times (e.g. 1 h), when the VOC amount absorbed by the SPMD is very small and the desorption rate from the SPMD is relatively insignificant, the uptake behavior can be explained by Eq. (2) [20].

$$\frac{dN_{SPMD}}{dt} \approx R_S C_{AIR} \quad (2)$$

where t (days) is exposure time; and R_S (m^3 day^{-1}) is sampling rate. If C_{AIR} is considered to remain constant, it is equivalent to the TWA concentration, then this equation integrates to Eq. (3).

$$N_S = R_S C_{AIR} t \quad (3)$$

Absorption data from laboratory isotherms of SPMDs at 25 °C and Eq. (3) can be used to calculate experimentally R_S values in the linear uptake.

Table 3 shows the corresponding R_S and K'_{SA} values for all the considered VOCs. These values have been expressed as equivalent for standard SPMDs (90 cm × 2.54 cm × 1 mL triolein) in order to be comparable to others found in the literature. As it can be seen R_S values varied from 0.008 to 0.12 m^3 day^{-1} and K'_{SA} values from 0.0003 to 0.0085 m^{-3}. R_S was not calculated for carbon disulfide, methylethylketone, methyl tert-butyl ether, hexane, diethyl ether, hexane and 2,2,4-trimethylpentane because the equilibrium state was reached very fast, in less than 1 h.

There are air R_S values available in the literature for a few number of semi-volatile pollutants. These values varied from 3.6 to 11 m^3 day^{-1} for polychlorinated biphenyls (PCBs) [21], from 0.7 to 15 m^3 day^{-1} for polycyclic aromatic hydrocarbons (PAHs) [20,22] and from 1.5 to 28 m^3 day^{-1} for some pesticides [12,23]. As it can be seen, the above cited R_S values were higher than those obtained for VOCs, but this result is reasonable, taking into account the enormous differences between their physico-chemical properties: such as boiling point, vapor pressure or octanol–air partition coefficient (K_{OA}) (see Table 1).

Sampling LODs were calculated for the determination of VOCs in air, from the LOD values for the SPMD analysis (showed in Table 2), the experimental R_S and K'_{SA} values (Table 3), and a selected sampling time (e.g. 1 and 24 h). Table 3 shows the LOD for each VOC for both considered sampling times and as it can be seen they range between 0.03 and 2.18 mg m^{-3} and between 0.02 and 1.90 mg m^{-3} for 1 and 24 h of sampling time, respectively.

3.4. Theoretical estimation of R_S

A theoretical estimation of R_S values was performed in order to assure the trueness of values that were experimentally calculated. The dependence between the R_S and the K_{OA} of 75 semi-volatile pollutants (over a K_{OA} range from 6 to 12), such as PCBs, PAHs, polychlorinated naphthalenes (PCNs) and several pesticides has been

Table 3
Sampler–air partition coefficients (K_{SA}), sampling rates (R_S) and limits of detection (LOD) for VOCs in sampled air with SPMDs.

	Compound	Experimental data from isotherms			Theoretical R_S[a] ($m^3\ d^{-1}$)		LOD ($mg\ m^{-3}$)	
		Equilibrium time (h)	K'_{SA}[a] (m^3)	R_S[a] ($m^3\ day^{-1}$)	Eq. (4)	Eq. (5)	1 h	24 h
1	Carbon disulfide	<1	0.0007	–[b]	0.36	0.005	–[b]	1.00
2	Methylethylketone	<1	0.0005	–[b]	0.41	0.011	–[b]	0.31
3	Methyl tert-butyl ether	<1	0.0003	–[b]	0.40	0.009	–[b]	0.49
4	Diethyl ether	<1	0.0006	–[b]	0.37	0.006	–[b]	1.30
5	Chloroform	<1	0.0004	–[b]	0.34	0.004	–[b]	1.90
6	Ethylacetate	5	0.0005	0.008	0.41	0.011	2.18	1.60
7	Hexane	<1	0.0007	–[b]	0.43	0.013	–[b]	0.23
8	Tetrahydrofuran	2	0.0008	0.017	0.44	0.014	0.21	0.18
9	1,1,1-Trichloroethane	18	0.0008	0.007	0.41	0.011	0.50	0.25
10	1,2-Dichloroethane	5	0.0009	0.015	0.42	0.012	0.24	0.17
11	Carbon tetrachloride	18	0.0012	0.010	0.43	0.012	0.38	0.13
12	Benzene	5	0.0011	0.019	0.42	0.012	0.19	0.14
13	Cyclohexane	9	0.0008	0.011	0.42	0.011	0.32	0.19
14	2,2,4-Trimethylpentane	<1	0.0024	–[b]	0.32	0.003	–[b]	0.06
15	Trichloroethylene	5	0.0020	0.032	0.46	0.018	0.11	0.07
16	Bromodichloromethane	9	0.0019	0.018	0.47	0.020	0.20	0.08
17	Methylisobutylketone	7	0.0011	0.018	0.56	0.047	0.36	0.13
18	Toluene	5	0.0033	0.054	0.51	0.031	0.07	0.05
19	Dibromochloromethane	6	0.0044	0.057	0.57	0.050	0.06	0.03
20	Tetrachloroethene	6	0.0056	0.049	0.54	0.041	0.07	0.03
21	n-Butylacetate	18	0.0030	0.038	0.58	0.055	0.64	0.25
22	Ethylbenzene	6	0.0061	0.066	0.60	0.065	0.05	0.02
23	m-Xylene	6	0.0071	0.076	0.61	0.069	0.05	0.02
24	p-Xylene	6	0.0075	0.086	0.61	0.071	0.04	0.02
25	Bromoform	6	0.0077	0.124	0.67	0.113	0.03	0.02
26	o-Xylene	7	0.0085	0.084	0.63	0.087	0.04	0.02

[a] K_{SA} and R_S values have been calculated as equivalent for standard SPMDs (90 cm × 2.54 cm × 1 mL triolein).
[b] When equilibrium is reached in less than 1 h, R_S and $LOD_{1\,h}$ were not calculated.

fitted by Huckins et al. as explained in Eq. (4) [20].

$$\log R_S = 0.154 \log K_{OA} - 0.80 \quad (R^2 = 0.64,\ \ n = 75) \tag{4}$$

Experimentally calculated K_{OA} values are easy to be found in the literature for many solvents and volatile compounds [16,17]. Thus, R_S values for the considered VOCs can be easily estimated by substitution of their K_{OA} values (Table 1) in Eq. (4). Table 3 also shows the theoretical R_S for the studied VOC with values ranging between 0.32 and 0.67 $m^3\ day^{-1}$.

Theoretical and experimental R_S values differ considerably, in a factor from 3 to 50 times, depending on the considered compound. This discrepancy can be attributed to the different physico-chemical properties between VOCs and semi-volatile compounds, principally due to the different boiling temperature, vapour pressure and K_{OA} values. Thus, a new mathematical model was proposed to explain the dependence between the R_S and the K_{OA}, equivalent to Eq. (4), but appropriate for very volatile compounds (with K_{OA} values lower than 5), such as those chosen in this study. Fig. 4 shows the linear relationship between the logarithm of experimental R_S and theoretical K_{OA} values (Table 1) and it corresponds to Eq. (5), with a slope of 0.75 ± 0.08 and an intercept of −4.0 ± 0.3.

$$\log R_S = 0.75 \log K_{OA} - 4.0 \quad (R^2 = 0.83,\ \ n = 20) \tag{5}$$

3.5. Comparative study between SPMD and Radiello® samplers

Five sampling sites inside a paint factory were selected to be sampled with SPMDs due to the high use of solvents in the painting industry. A double sampling was performed in each site with one SPMDs and one Radiello® sampler. After a deployment time of 48 h, each sampler was measured by the corresponding methodology: direct HS-GC–MS determinations for SPMDs and CS_2 extraction followed by GC–MS measurement for Radiello® samplers.

Air temperature was monitored in the sampling sites and it ranged from 8 to 19 °C. If we assume that changes in temperature during the sampling step did not affect significantly to the uptake parameters, R_S values could be used together with data of the VOCs amount accumulated in the SPMD to estimate TWA concentration of VOCs in air, as explained in Eq. (3).

Calibration model and other parameters for Radiello® samplers were obtained from the corresponding Technical sheet provided by the supplier, with R_S values ranging between 54 mL min^{-1} for cyclohexane and 75 mL min^{-1} for toluene [18].

Table 4 shows the description of each sampling site and the corresponding air concentration of VOCs sampled with Radiello® and SPMD samplers. Results obtained by both devices were equivalent, taken into account the big differences between the samplers and their corresponding mathematical models used to evaluate the air concentration from the pollutant amount found in each sampler.

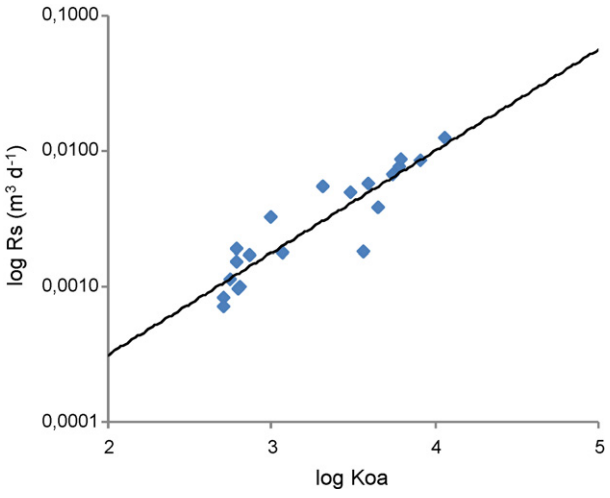


Fig. 4. Dependence between the experimental sampling rates (R_S) and the octanol–air partition coefficient (K_{OA}) of the studied VOCs.

Table 4
Air concentration of VOCs found in different sites of a paint industry by using one SPMD and one Radiello® diffusive sampler in each site.

Sample	Site description	Compounds founded	Air concentration ($mg\,m^{-3}$)	
			Radiello®	SPMD
1	Application laboratory	Methylisobutylketone	7.2	4.1
	Poor ventilation	Ethylbenzene	9.5	2.8
	Temperature range 12–19 °C	(m + p) xylene	14.2	9.8
		o-Xylene	4.4	1.2
2	Colorimetric laboratory	Methylisobutylketone	0.67	1.9
	Poor ventilation	Ethylbenzene	36.8	24.8
	Temperature range 12–19 °C	(m + p) xylene	37.9	41.8
		o-Xylene	16.4	8.0
3	Industry plant (paint mixer)	Methylisobutylketone	12.7	8.6
	Well ventilated	Ethylbenzene	9.7	4.2
	Temperature range 8–18 °C	(m + p) xylene	15.2	15.6
		o-Xylene	4.9	1.7
4	Industry plant (corridor)	Methylisobutylketone	14.6	8.2
	Well ventilated	Ethylbenzene	9.8	3.3
	Temperature range 8–18 °C	(m + p) xylene	15.5	12.9
		o-Xylene	4.8	1.4
5	Industry plant (tin seal)	Methylisobutylketone	10.0	8.8
	Well ventilated	Ethylbenzene	4.0	5.2
	Temperature range 8–18 °C	(m + p) xylene	6.0	19.2
		o-Xylene	1.9	2.0

When concentrations found by SPMDs were correlated with those obtained by Radiello® samplers and adjusted by a least squares regression, the fitted equation was C_{SPMD} ($mg\,m^{-3}$) = (-2 ± 2) + (0.91 ± 0.09)$C_{Radiello}$ ($mg\,m^{-3}$) with a correlation coefficient of $R^2 = 0.86$ ($n = 19$). In this equation, the intercept and slope values were statistically comparable to 0 and 1, respectively, for a probability level of 95%. Thus, it can be concluded that results obtained with SPMDs were statistically comparable with those found using Radiello® samplers.

Concentration of VOCs in indoor air of several places have been reviewed in a recent paper and it ranged from 0.1 to 8.3 $\mu g\,m^{-3}$ in laboratory hospitals; from 0.01 $\mu g\,m^{-3}$ to 4.3 $mg\,m^{-3}$ in social places (restaurant, bar, pub, cinema, theatre, and museum); from 0.01 to 11 $\mu g\,m^{-3}$ in transport environments (car, truck, garage, petrol station, mechanic shop, public transport, station, airport); and from 0.02 $\mu g\,m^{-3}$ to 150 $mg\,m^{-3}$ in other workplaces and indoor environments [7]. In this study, TWA concentration of VOCs found in air of the studied paint industry ranged from 0.7 to 42 $mg\,m^{-3}$. Thus, we can conclude that VOC levels found can be considered as quite high. Lamentably, these results are often found in studies performed in industrial workplaces and indoor environments. So, the VOCs concentration found was reasonable for an industry with intensive use of solvents, but it must be drastically minimized taken into account the today's legal frame.

4. Conclusions

The use of SPMDs for the passive sampling of VOCs has been confirmed as a real alternative to other passive samplers, generally based on solid supports. The HS treatment of SPMDs allowed direct and rapid determinations of VOCs in only 20 min without the use of any extraction solvent, thus providing an environmentally friendly analytical tool [24]. Linear and equilibrium models have been proposed for the passive sampling of the studied VOCs with SPMDs, by using a simple and easy procedure based on the establishment of uptake isotherms in laboratory studies. Finally, a comparative sampling was performed on a paint industry by using SPMD and Radiello® samplers and the obtained results were comparable.

Acknowledgments

Authors acknowledge the financial support of Ministerio de Ciencia e Innovación (CTQ2008-05719/BQU) and project REACH-PACK (PC 2008-132-3-14.2) from the Ministerio de Medio Ambiente.

References

[1] U.S. Environmental Protection Agency, An Introduction to Indoor Air Quality, http://www.epa.gov.
[2] M.R. Ras-Mallorquí, R.M. Marcé-Recasens, F. Borrull-Ballarín, Talanta 72 (2007) 941–950.
[3] O. Baroja, E. Rodríguez, Z. Gomez de Balugera, A. Goicolea, N. Unceta, C. Sampedro, A. Alonso, R.J. Barrio, J. Environ. Sci. Health A 40 (2005) 343–367.
[4] Regulation (EC) No. 1907/2006 of the European Parliament and of the Council of 18 December 2006 concerning the Registration, Evaluation, Authorization and Restriction of Chemicals (REACH), establishing a European Chemicals Agency, amending Directive 1999/45/EC and repealing Council Regulation (EEC) No. 793/93 and Commission Regulation (EC) No. 1488/94 as well as Council Directive 76/769/EEC and Commission Directives 91/155/EEC, 93/67/EEC, 93/105/EC and 2000/21/EC (2006).
[5] E.A. Woolfenden, W.A. McClenny, Compendium Method TO-17. Determination of Volatile Organic Compounds in Ambient Air Using Active Sampling onto Sorbent Tubes, U.S. Environmental Protection Agency, 1999.
[6] L. Drees, Compendium Method TO-14A. Determination of Volatile Organic Compounds (VOCs) in Ambient Air Using Specially Prepared Canisters With Subsequent Analysis By Gas Chromatography, U.S. Environmental Protection Agency, 1999.
[7] R. Barro, J. Regueiro, M. Llompart, C. Garcia-Jares, J. Chromatogr. A 1216 (2009) 540–566.
[8] A. Kot-Wasik, B. Zabiegała, M. Urbanowicz, E. Dominiak, A. Wasik, J. Namieśnik, Anal. Chim. Acta 602 (2007) 141–163.
[9] F.A. Esteve-Turrillas, A. Pastor, M. de la Guardia, Anal. Chim. Acta 593 (2007) 108–116.
[10] A. Zouir, F.A. Esteve-Turrillas, A. Morales-Rubio, T. Chafik, A. Pastor, M. de la Guardia, Int. J. Environ. Anal. Chem. 89 (2009) 917–928.
[11] F.A. Esteve-Turrillas, A. Pastor, M. de la Guardia, Anal. Chim. Acta 560 (2006) 118–127.
[12] F.A. Esteve-Turrillas, A. Pastor, M. de la Guardia, Anal. Chim. Acta 626 (2008) 21–27.
[13] V. Yusà, C. Coscollà, W. Mellouki, A. Pastor, M. de la Guardia, J. Chromatogr. A 1216 (2009) 2972–2983.
[14] F.A. Esteve-Turrillas, V. Yusà, A. Pastor, M. de la Guardia, Talanta 74 (2008) 443–457.
[15] A. Cicenaite, J.N. Huckins, D.A. Alvarez, W.L. Cranor, R.W. Gale, V. Kauneliene, P.A. Bergqvist, Atmos. Environ. 41 (2007) 2844–2850.
[16] W.M. Meylan, P.H. Howa, Estimating Octanol–Air Partition Coefficients with Octanol–Water Partition Coefficients and Henry's Law Constants, SRC Inc., http://srcinc.com.

[17] ChemSpider, Building Community for Chemists. http://www.chemspider.com.
[18] Radiello® Technical Sheet no. 130-01-2006, http://www.radiello.com.
[19] F.A. Esteve-Turrillas, A. Pastor, V. Yusà, M. de la Guardia, TrAC-Trends Anal. Chem. 26 (2007) 703–712.
[20] J.N. Huckins, J.D. Petty, K. Booij, Monitors of Organic Chemicals in the Environment Semipermeable Membrane Devices, Springer, 2006.
[21] W.A. Ockenden, B.P. Corrigan, M. Howsam, K.C. Jones, Environ. Sci. Technol. 35 (2001) 4536–4543.
[22] M.E. Bartkow, J.N. Huckins, J.F. Müller, Atmos. Environ. 38 (2004) 5983–5990.
[23] F.A. Esteve-Turrillas, A. Pastor, M. de la Guardia, J. AOAC Int. 92 (2009) 1557–1565.
[24] S. Armenta, S. Garrigues, M. de la Guardia, TrAC Trends Anal. Chem. 27 (2008) 497–511.

Talanta 80 (2010) 2049–2056

Contents lists available at ScienceDirect

Talanta

journal homepage: www.elsevier.com/locate/talanta

A fast assay of water hardness ions based on alkaline earth metal induced coacervation (HALC)

George Z. Tsogas, Dimosthenis L. Giokas, Athanasios G. Vlessidis*

Laboratory of Analytical Chemistry, Department of Chemistry, University of Ioannina, 45110, Ioannina, Greece

ARTICLE INFO

Article history:
Received 12 August 2009
Received in revised form 23 October 2009
Accepted 3 November 2009
Available online 10 November 2009

Keywords:
Alkaline earth metals
Coacervation
Spectrophotometry
Water hardness

ABSTRACT

In this work, a rapid assay of water hardness is presented based on the formation of a coacervate phase made up of multilamellar vesicles and close bilayers produced upon the reaction of alkaline earth metals with a carboxylate anionic surfactant in the presence of a co-surfactant (methanol). The procedure exploits the light scattering abilities of the coacervate phase which can be logarithmically linked to total hardness as $CaCO_3$ equivalents via spectrophotometric detection at 350 nm. The method, abbreviated as HALC, stemming from hardness by alkaline earth metal coacervation, is straightforwardly applicable overcoming the requirement for regulation of the experimental parameters involved in the determination procedure. In total, 28 water samples with various matrix compositions and hardness contents were analyzed with satisfactory accuracy as evidenced by comparison of the results with EDTA complexometric titration. The method is free from interferences from environmentally significant metal cations and inorganic anions affording detection limits as low as 13.5 mg L^{-1} $CaCO_3$ with the aid of a correction factor, which is determined by the non-linear absorbance properties of the solution mixture, and satisfactory reproducibility (RSD = 4.21–8.08%).

© 2009 Elsevier B.V. All rights reserved.

1. Introduction

Real time monitoring of water quality parameters is of critical importance in environmental and industrial fields, including the water quality control in drinking water treatment plants. Among these parameters, total hardness, defined as the total content of calcium (Ca^{2+}) and magnesium (Mg^{2+}) in water, is one of the most popular indicators of water quality since it is not only related to the deposition of mineral deposits in water pipes but it is also reported to affect the toxicity of certain metal ions in aquatic ecosystems [1]. Furthermore, water hardness contributes to the daily uptake of Ca^{2+} and Mg^{2+} which are physiologically important elements for the human body with significant negative effects encountered in cases of deficiency [2].

The most popular methods for the determination of water harness are those based on complexometric titration [3], flame atomic absorption spectrometry [4] and ion-selective electrodes [5,6]. Complexometric methods are probably the most popular methods due to their simplicity but they are prone to the analysts' efficiency unless an automated system is used that can accurately determine the end point of the titration. On the other hand, flame AAS methods are highly accurate for benchtop analysis but they cannot be used for outdoor studies. Potentiometric ion-selective electrodes (ISEs) are the technique of choice when continuous in situ measurements in an automatic manner are required combining simplicity of operation and low analysis cost. However, the selectivity of measurements is not often sufficient to enable the primary ion to be directly determined; interferences arising from other species with similar size and charge, matrix effects and mediocre day-to-day reproducibility may have serious repercussions in the accuracy of the analysis [5]. To overcome these problems, several techniques have been employed based on physical separation of sample components (i.e., chromatography), modeling the potentiometric response of the analytes in the presence of interferences (Nikolskii–Eisenman equation) or chemometric procedures [5,7].

In the pursue of combining the advantages of the above methods in the determination of water hardness, the phenomenon of coacervation may offer a convenient alternative. By definition, coacervation is the separation of colloidal systems into two liquid phases, a colloid-rich and a colloid-poor phase [8]. In that sense, coacervates can be defined as colloid-rich liquids immiscible with the colloid-poor aqueous equilibrium solution from which it is separated. In this context, if appropriate interactions between the coacervate phase and the analytes of interest can be established, coacervation can be efficiently employed as an alternative to the solvent-free extractions. Up to date, several such systems have appeared in the literature enabling the determination of organic

* Corresponding author. Tel.: +30 26510 08401; fax: +30 26510 08781.
E-mail address: avlessid@cc.uoi.gr (A.G. Vlessidis).

0039-9140/$ – see front matter © 2009 Elsevier B.V. All rights reserved.
doi:10.1016/j.talanta.2009.11.003

and inorganic analytes via hydrophobic, electrostatic and hybrid interactions [9–13].

The coacervation of organic macromolecules induced by metallic ions is a well-known phenomenon and several studies have been devoted to the characterization of the morphological changes induced upon their interaction [14]. In this direction, alkaline earth metals, and especially Ca^{2+}, have received considerable attention due to their high reactivity with anionic surfactants leading either to the formation of well-known lime soaps or to complex vesicle and lamellar phases with interesting properties [14,15]. Nevertheless, the analytical utility of these interactions towards the determination of alkaline earth metals has not been reported despite the fact that vesicle-based extractions of metal ions exploiting their attraction with the anionic head group of anionic surfactants have been described [9,16,17].

Considering the high reactivity of alkaline earth metals with anionic surfactants, this work describes the first analytical application of the phenomenon of coacervation for the determination of water hardness. The proposed method is based on the formation of a lamellar colloid-rich phase induced by alkaline earth metals with sodium dodecanoate in the presence of a co-surfactant (water miscible organic solvent). This reaction results in the formation of a dispersed vesicular phase which scatters visible light in manner related to metal ion concentration. Based on this principle, the absorbance of the coacervate phase formed by Ca^{2+} and Mg^{2+} with sodium dodecanoate was monitored spectrophotometrically yielding a concentration depended response to metal ion concentration. To the best of our knowledge, this is the first time that metal ion induced coacervation is being exploited directly towards the determination of water hardness whish is one of the most popular water quality parameters.

2. Experimental section

2.1. Reagents

All reagents were of analytical-grade and they were used without further purification. Standard metal solutions used for the experiments were prepared by sequential dilution of 1000 mg L^{-1} stock solutions prepared by dissolving appropriate amounts of $Ca(NO_3)_2$ (Merck, Darmstadt, Germany) and $Mg(NO_3)_2{\cdot}6H_2O$ (Fluka, Buchs, Switzerland). Metal standard solutions used for the interference study were prepared by sequential dilution of 1000 mg L^{-1} of Titrisol stock solutions (Merck). Lauric acid in the form of Sodium dodecanoate (Sigma grade, 99–100%, Sigma–Aldrich, Greece) was dissolved in HPLC grade methanol (Labscan, Dublin, Ireland.) to prepare a 5% (w/v) stock solution.

2.2. Instrumentation

Absorbance measurements were performed with matched quartz cells of 1-cm path length in a Jenway 6405 UV–vis spectrophotometer. A pH meter, WTW 552 model glass electrode was employed for the pH measurements for the solutions.

2.3. HALC analytical procedure

In 10 mL of water sample previously equilibrated at room temperature, 1 mL of Lauric acid solution (5% (w/v) in methanol) is added. The mixture is agitated and its absorbance is directly recorded at 350 nm against reagents blank.

2.4. Real samples

In total, 28 water samples of various matrix composition and hardness content were assessed. Bottled waters (9 samples) purchased from local stores, surface waters (6 samples) collected from Acherontas river (N.W. Greece) in various locations from springs to estuary and water samples from six (6) springs used for water supply in Thesprotia region were collected in HNO_3-cleaned glass containers, filtered through a Whatman No. 40 filter (0.45 μm) and stored at room temperature. Tap water was collected directly form the drinking water network supply, filtered and analyzed directly without storage.

A series of samples from underground water aquifers were collected along the coastal line (≤2 km from sea) of north Corfu Island (N.W. Greece) from four (4) different drillings. Infiltration of seawater was qualitatively determined by the addition of $AgNO_3$ leading to the formation of white AgCl precipitate. Two (2) seawater samples were collected from the coastal line of Thesprotia (N.W. Greece). The first sample was collected in the estuaries of Kalamas River and the other by direct sampling of seawater 10 m from the coast.

3. Results and discussion

3.1. Optimization of experimental conditions

The optimization of the experimental conditions that enable the determination of water hardness with the proposed coacervation scheme is not a straightforward objective. That is because Ca^{2+} and Mg^{2+} upon reaction with sodium dodecanoate, in the presence of methanol as a co-surfactant (which affects aggregates size) [18], yield different lamellar structures [17]. According to the SEM micrographs of Fig. 1, Ca^{2+} favours the formation of spongelike phases (Fig. 1b) and Mg^{2+} the formation of bilayer structures (Fig. 1c) while mixtures of alkaline earth metals lead to the formation of a complex network of organized surfactant assemblies containing both multilamellar and bilayer vesicular aggregates (Fig. 1d). From a technical standpoint, these phenomena can be explained taking into consideration the organization phenomena occurring in the oriented molecular layers and the different radii of the hydrated cation condensation [9,17]. However, in the context of the analytical application intended in this study, these structural diversifications of the coacervate phase bring about significant changes in the absorption of each solution. According to the results of the calibration curves of Fig. 2, Ca^{2+} yields a linear response up to a concentration of 100 mg L^{-1} while Mg^{2+} response is rectilinear only up to 15 mg L^{-1}, above which absorbance values gradually reaches a plateau. In the linear range of the calibration curves, the ratio of slopes (Mg^{2+}/Ca^{2+}) is approx. 8 which means that Mg^{2+} induces, on average, 8 times more intense absorption than Ca^{2+} at the same concentration level at 350 nm.

Beyond ion type and concentration, the measured signal strongly depends on other parameters related to the formation and stability of the vesicular (coacervate) phase, like sodium dodecanoate concentration, ionic strength, hydroxyl or hydrogen concentration and temperature [9,10,17]. To this end, we decided to prepare a set of model solutions containing a high variety of Ca^{2+} and Mg^{2+} concentrations and use them as workings solutions for the optimization of the working conditions. The composition of these samples, gathered in Table 1, covers a wide range of Ca^{2+} and Mg^{2+} concentrations (as well as their ratio) so as to provide a representative evaluation of most natural waters. All samples had a total volume of 10 mL and measurements were performed at 350 nm.

3.2. Effect of sodium dodecanoate concentration

The first parameter assessed was sodium dodecanoate concentration in the range of 0.1–2% (w/v). Aqueous solutions (10 mL) were spiked with 0.1–2 mL of 5% (w/v) sodium dodecanoate and the

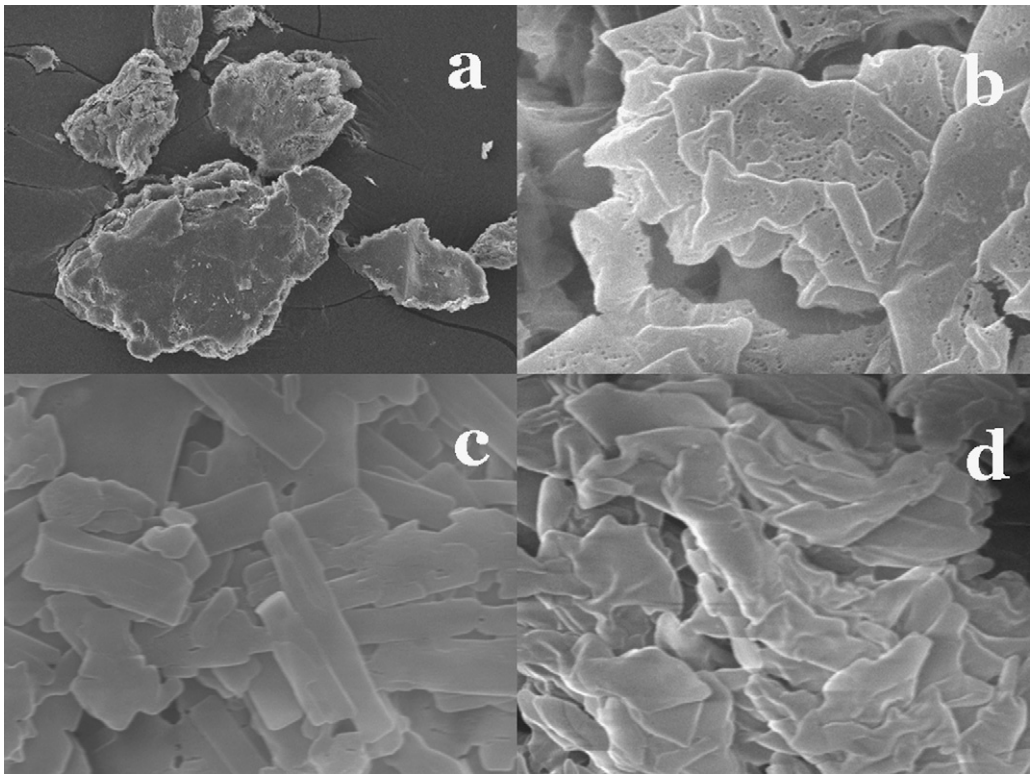


Fig. 1. SEM micrographs of the coacervate phase formed by sodium dodecanoate, methanol and various cations. (a) Na^+ (50 μm at 10 kV), (b) Ca^{2+} (5 μm at 20 kV), (c) Mg^{2+} (5 μm at 20 kV) and (d) Ca^{2+} and Mg^{2+} (1 μm at 20 kV).

absorbance was immediately recorded at 350 nm. According to the data presented in Fig. 3, 0.5% (w/v) sodium dodecanoate provides the optimum absorption for a wide variety of water hardness ranging from soft to very hard water. For lower sodium dodecanoate concentrations, the vesicle's charge was probably counterbalanced due to inadequacy of reactive sites and in combination with the respective low amounts of co-surfactant content did not favour the formation of a lamellar phase. On the other hand, with increasing sodium dodecanoate and co-surfactant concentrations, the precipitate swelled, increasing the absorbance of the solution, either due to transition from vesicles to stacked membranes [17], or due to the increase of surfactant concentration above cmc which complicates solubilization and dispersion of the alkaline earth metal coacervates due to the presence of micellar aggregates. In either case, the analytical signal is deteriorated either due to low UV absorption or due to intense turbidity that reduces the working and measuring range of the method. Therefore, the concentration of 0.5% (w/v) was selected for the remaining work.

It is worth mentioning that at the optimum sodium dodecanoate concentration, sample volume did not have any significant effect on the absorbance of the solutions (±6%). However, to minimize uncertainty it is advisable to maintain a constant sample volume throughout method application.

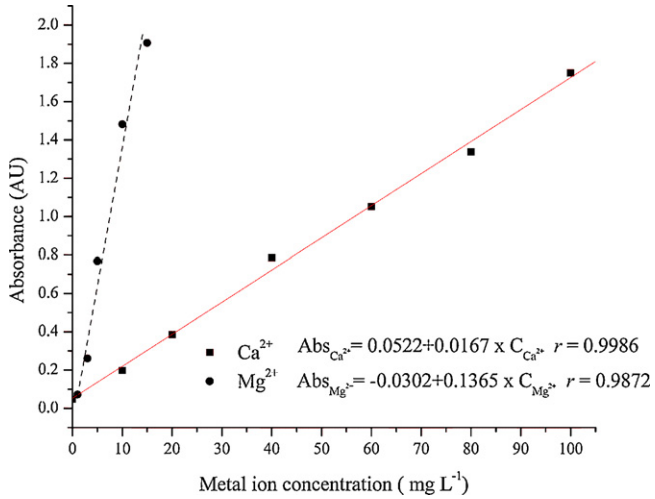


Fig. 2. Absorbance vs. concentration plots for Ca^{2+} and Mg^{2+}.

Table 1
Composition of model solutions used for the optimization study.

Sample	Ca^{2+}	Mg^{2+}	Total hardness (mg L^{-1} $CaCO_3$)	Absorbance (A.U.) at λ = 350 nm
1	5	0	12.5	0.075
2	10	0	25.0	0.215
3	5	5	33.1	0.619
4	10	5	45.6	0.762
5	20	5	70.5	1.141
6	40	5	120.5	1.402
7	60	5	170.4	1.729
8	5	10	53.7	1.043
9	10	10	66.1	1.284
10	20	10	91.1	1.511
11	40	10	141.1	1.660
12	60	10	191.0	2.168
13	5	15	74.2	1.649
14	10	15	86.7	1.740
15	20	15	111.7	1.820
16	40	15	161.6	2.085
17	60	15	211.6	2.340
18	5	20	94.8	1.909
19	10	20	107.3	2.035
20	20	20	132.3	2.136
21	40	20	182.2	2.347
22	60	20	232.2	2.503

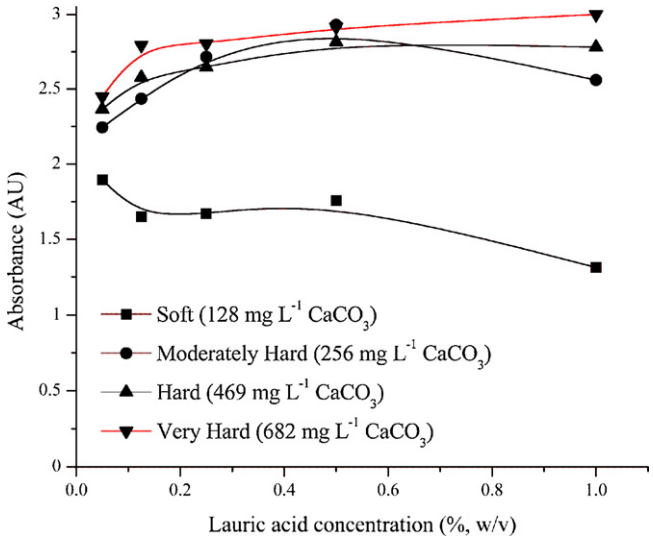


Fig. 3. Effect of sodium dodecanoate concentration in the absorbance of aqueous solutions containing various levels of water hardness.

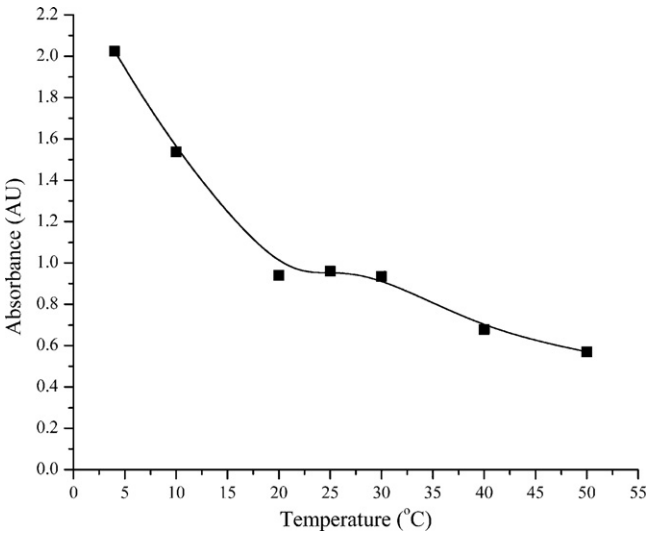


Fig. 5. Absorbance signal as a function of temperature in soft water.

3.3. Reaction kinetics

The incubation time necessary for sodium dodecanoate to react with alkaline earth metals towards the formation of a lamellar structure was the next parameter assessed for its influence on the analytical signal in terms of intensity, measuring range and reproducibility. Absorbance values recorded over the range of 0–240 min showed an increasing absorbance pattern with reaction time. From the data of Fig. 4 it can be inferred that absorbance increases with increasing water hardness gradually limiting the applicability of the method in hard waters since the signal eventually soared up to "out-of-range" absorbance values (not shown). Furthermore, the reproducibility of the measurements was deteriorated probably because vesicle membranes were not homogeneously dispersed in the vial which increases uncertainty. On the other hand, samples analyzed immediately after sodium dodecanoate addition gave the best reproducibility. Based on this observation, samples were measured after addition of sodium dodecanoate followed by vortex agitation to facilitate the reaction of sodium dodecanoate with alkaline earth metals and improve dispersion of the lamellar phase.

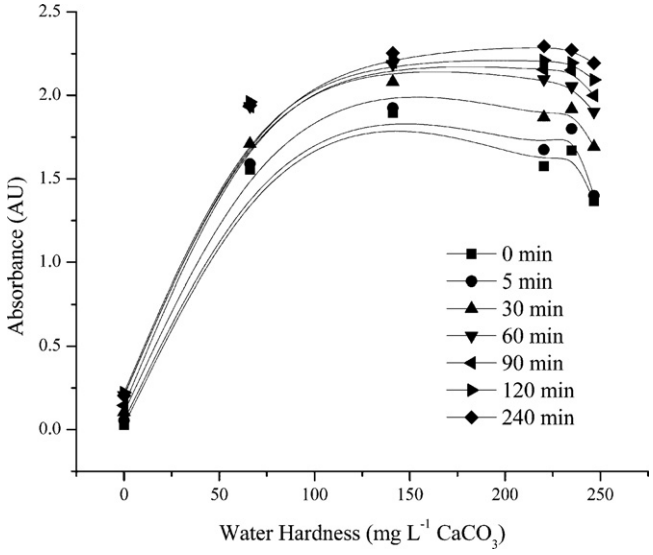


Fig. 4. Effect of incubation time on the absorbance of sodium dodecanoate-alkaline earth cation coacervates.

3.4. Effect of temperature

Temperature was the next parameter assessed for its effect on the analytical response (Fig. 5). Cold conditions (<10 °C) induced significant signal amplification due to the formation of a viscoelastic phase while warm conditions reduced the absorbance due to increased solubility of the lamellar phase and dehydration of the amphiphile head group inducing thermo-sensitive transformations [16,17]. A stable and reproducible response was obtained between 20 and 30 °C, therefore room temperature (approx. 25 °C) was selected for the analysis of real samples.

3.5. Effect of solution pH

The influence of hydrogen or hydroxyl concentration present in the sample was assayed by addition of increasing amounts of dilute HCl or NaOH. At acidic pH values sodium dodecanoate is protonated which increases competition with alkaline earth metals while the opposite is observed in alkaline media where the anionic group of sodium dodecanoate is deprotonated which aids complexation with metal species. In either case, the concentration of Ca^{2+} and Mg^{2+} in the sample was found to be an important factor in the absorbance of the solution as a function of pH. At acidic media higher Ca^{2+} and Mg^{2+} concentrations were necessary to compete for the reactive sites of sodium dodecanoate while in alkaline conditions complexation was favoured with increasing pH and water hardness. In this context, a priori knowledge of total hardness is necessary in order to decide on the appropriate regulation of the solution pH which has no practical meaning since the determination of hardness is of concern. Furthermore, the pH of the solution upon addition of sodium dodecanoate was close to 6.5 which is not far from the usual pH of most natural waters and far less than the solubility limit of both Ca^{2+} and Mg^{2+} in aqueous solutions. Therefore it was decided to apply the method in an unregulated pH environment.

3.6. Calibration procedure

The calibration procedure was performed with a series of model solutions (10 mL sample volume) containing various amounts of water hardness and Ca^{2+}/Mg^{2+} ratios, by extending the

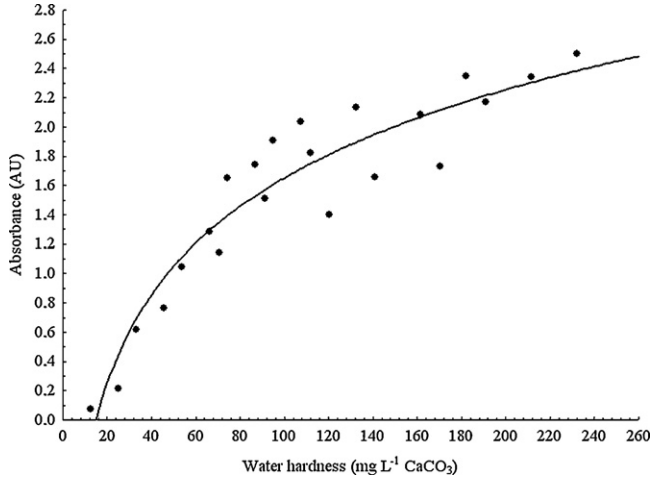


Fig. 6. Logarithmic calibration curve at 350 nm.

experimental data of Table 1, in an unregulated ionic strength environment to simulate the composition of natural waters. The concentration vs. absorbance line plotted in Fig. 6 shows that the absorbance is linearly depended on water hardness up to 60 mg L^{-1} (as $CaCO_3$) but above this value a logarithmic relationship is blatantly observed. This is reasonable since Mg^{2+}-sodium dodecanoate coacervates scavenge the light more intensely than the respective Ca^{2+}-sodium dodecanoate coacervates. As a result, the same absorbance value can be produced by at two combinations, the first involving high Ca^{2+} levels and the second low Mg^{2+} levels. From the concentration curves of Fig. 2 it is inferred that an absorbance value of 1 (a.u.) can be obtained by either 56.7 mg L^{-1} Ca^{2+} or 5 mg L^{-1} Mg^{2+}. In order to account for all occasions (samples with different water hardness giving similar absorbance values analyzed in the same batch) the overall fit to the experimental data was logarithmically expressed as a function of total water hardness. The calibration data were fitted to the expression

$$A = 0.9347 \times \mathrm{Ln}_{(\text{total hardness})} - 2.6626 \quad r = 0.9765 \qquad (1)$$

which was considered satisfactory considering the large number of data points and the high variability in the concentration of the individual data points included in the calibration curve. This equation was therefore applied to the analysis of real samples and the results were evaluated from a qualitative, semi-quantitative and quantitative perspective. It is conceivable that appropriate dilution can bring the sample within the linear range of the calibration curve, provided that an a priori assessment of total hardness has been undertaken.

Starting already from the first attempts to apply HALC method to the analysis of real samples it was revealed that a correction factor (C_f) to the calculated concentration was necessary. This came as no surprise considering the aforementioned discussion regarding the influence of Mg^{2+} in comparison to Ca^{2+}. Despite the fact that in most real samples situations were Ca^{2+} is totally absent or Mg^{2+} significantly surpasses Ca^{2+} concentration are rather scarce, we persisted on accounting for all cases, irrespectively of their scarcity and appearance rate in the natural environment. The calculated values of total hardness were multiplied by a factor of 1.80 ± 0.41 when the absorbance lied within the range $0.31 < Abs_{350} < 2$ and by a factor of 0.70 ± 0.13 when $2 < Abs_{350} < 0.31$. By using this approach the total hardness of real samples was calculated and the results are presented below in more detail. In is conceivable that if another calibration curve equation is used then a re-examination of the correction factors should be applied although no significant differences were observed in model solutions examined for that purpose. The following classification was used according to the level of total hardness: very soft (0–70 mg L^{-1} $CaCO_3$), soft (70–140 mg L^{-1} $CaCO_3$), slightly hard (140–210 mg L^{-1} $CaCO_3$), moderately hard (210–320 mg L^{-1} $CaCO_3$), hard (320–530 mg L^{-1} $CaCO_3$) and very hard (>530 mg L^{-1} $CaCO_3$).

3.7. Analytical characteristics of the method

Due to the lack of linearity of the calibration curve the determination of method detection limit and the quantitation limit as multiples of the signal-to-noise ratio cannot be calculated because of the non-linear properties of the calibration curve which results in variable slope and, as previously discussed, similar responses to more than one combination of Ca^{2+} and Mg^{2+} levels. Therefore, the lower limit of detection (LLD), which is the lowest amount or concentration of analyte which can be distinguished from the blank with a reasonable confidence, was determined by the mean absorbance of the blank sample plus k times the standard deviation of the absorbance obtained on the blank sample, i.e., $A_{LLD} = A_{\text{mean blk}} + k \times A_{SDblk}$, where k is a constant related to the statistical level of confidence [19]. This approach is similar to that proposed in DG SANCO decision were the detection capability (CC_a) is defined "the lowest concentration level at which a method can discriminate with a statistical certainty of $1 - \alpha$ whether the identified analyte is present" [20]. For $k = 3$, the LLD is 19.4 mg L^{-1} $CaCO_3$ and corresponds to the uncorrected concentration determined directly by equation (1). Since the absorbance at this concentration is below 0.31, multiplication by the respective $C_f = 0.70$, results in a final detection limit of 13.5 mg L^{-1} $CaCO_3$.

The reproducibility of the method, expressed by the relative standard deviation (RSD) of repeated assays was 4.21–8.08% ($n = 7$) from very soft to very hard waters, which satisfies the requirements for the application intended in this study.

3.8. Interferences

In view of the low selectivity of the spectrophotometric detector and the competitive reaction ambience where other metallic ions may react with sodium dodecanoate, various metallic cations and inorganic anions were investigated for their effect on the absorbance signal. The tolerance limit of a foreign species was defined as the concentration that causes a relative error greater than ±5%. Trace elements like Pb^{+2}, Cd^{+2}, Sb^{+3}, As^{+3}, Co^{2+}, Ni^{+2} and Cr^{3+} had no effect on the analytical response at concentrations up to 50 μg L^{-1}, which is well above the usual concentration levels. Important elements like Fe^{3+}, Al^{3+} and Zn^{2+} had no effect up to the maximum concentration levels examined (500 μg L^{-1}), while Cu^{2+} could be tolerated up to 200 μg L^{-1}.

Regarding the interference by anions, phosphates (25 mg L^{-1}), chloride (250 mg L^{-1}), nitrates (50 mg L^{-1}), nitrites (0.5 mg L^{-1}), fluoride (1.5 mg L^{-1}) and sulphate (250 mg L^{-1}), which are the indicative values proposed by the 98/83/EC directive, did not interfere with the determination of water hardness. Furthermore, organic matter in the form of humic acids (10 mg L^{-1}) did not exhibit any adverse effects on the analytical response of HALC.

4. Method application

4.1. Qualitative analysis

As previously discussed the reaction of sodium dodecanoate with alkaline earth metals yields a coacervate phase depending on the total water hardness which is further determined by the relative abundance of Ca^{2+} and Mg^{2+}. In most natural waters where Mg^{2+} is less or equal to Ca^{2+} the coacervate phase yields a response similar to that of Fig. 7. As we can observe, although the visual

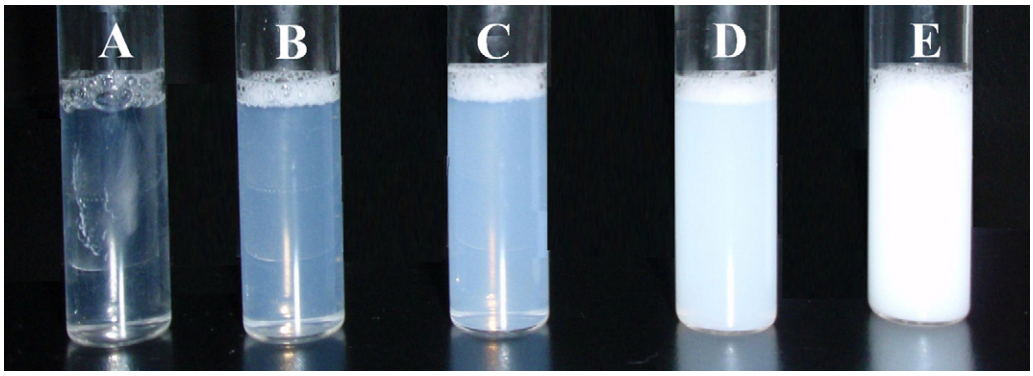


Fig. 7. A photograph of real samples taken after the addition of sodium dodecanoate in the presence of various water hardness content. (A) Very soft water at 35 mg L^{-1} $CaCO_3$, (B) soft water at 105 mg L^{-1} $CaCO_3$, (C) moderately hard water at 265 mg L^{-1} $CaCO_3$, (D) hard water at 425 mg L^{-1} $CaCO_3$ and (E) very hard water at 600 mg L^{-1} $CaCO_3$. Experimental conditions as defined in the text.

differentiation between soft to moderately hard and hard to very hard water requires some degree of familiarization, the classification to soft, moderately hard and hard water can be accomplished by direct visual inspection even without any previous experience in the method. Therefore, the method is directly applicable to the qualitative assay of water hardness by visual inspection which is not offered by any of the usual methods for the determination of water hardness.

4.2. Semi-quantitative analysis

The method was then applied to the classification of water hardness based on the concentration ranges assigned to each type of water adopted in this work (very soft to very hard). The data gathered in Table 2 show that method application successfully assigned almost all samples to the correct concentration range thus providing a good classification of water samples based on the level

Table 2
Determination of water hardness in real samples and comparison with standard methods.

Sample	Total hardness HALC[a]	Total hardness[a,b]	Classification[c]	Relative error (%)	Average relative deviation (ARD)[d]
Bottled waters					
1	218	183	Failed	19.0	
2	158	168	Success	−6.0	
3	285	253	Success	12.5	
4	15	17	Success	−9.5	
5	161	157	Success	2.4	
6	222	241	Success	−7.8	
7	105	149	Success	−29.8	
8	232	246	Success	−5.6	
9	218	233	Success	−6.3	
					0.11%
Tap water	122	134	Success	−8.6	
					–
Acherontas river					
Site 1	103	81	Success	26.3	
Site 2	105	96	Success	8.9	
Site 3	109	93	Success	17.9	
Site 4	255	237	Success	7.7	
Site 5	245	230	Success	6.3	
Site 6	247	233	Success	6.3	
					0.12%
Natural water springs					
Aulotopos	80	103	Success	−22.3	
Ligoneri	88	105	Success	−16.6	
Sikia	201	182	Success	10.4	
Milos	197	179	Success	9.9	
Mboustere	76	96	Success	−20.5	
Mpousmpou	159	184	Success	−13.4	
Kedros	148	150	Success	−1.1	
Frosini	247	222	Success	11.5	
Goura	114	127	Success	−10.3	
					0.13%

[a] Expressed in mg L^{-1} $CaCO_3$.
[b] Based on reported values or measured from the EDTA titration method.
[c] Very soft (0–70 mg L^{-1} $CaCO_3$), soft (70–140 mg L^{-1} $CaCO_3$), slightly hard (140–210 mg L^{-1} $CaCO_3$), moderately hard (210–320 mg L^{-1} $CaCO_3$), hard (320–530 mg L^{-1} $CaCO_3$) and very hard (>530 mg L^{-1} $CaCO_3$).
[d] $\mathrm{ARD} = (1/n)\sum_{i=1}^{n}((X_i^{\mathrm{STD}} - X_i^{\mathrm{HALC}})/X_i^{\mathrm{STD}})$ where n is the number of experimental data points, X_i^{STD} are the measured values of total hardness using a standard method and X_i^{HALC} are the measured values from the proposed (HALC) method.

of total hardness. This is advantageous when a fast estimation of water hardness is of concern, thus minimizing experimental effort.

4.3. Quantitative analysis

The ability of the method to provide an accurate measure of total water hardness is also shown in Table 2. The average relative error ranges, in terms of absolute values, from 0.87 to 29.7% with an average value of $10.7 \pm 7.9\,mg\,L^{-1}$ $CaCO_3$ and a standard error of $1.58\,mg\,L^{-1}$ $CaCO_3$. The distribution of relative experimental error shows that the method affords a satisfactory assessment of water hardness. The relative average deviation (ARD) of all samples, which is a measure of precision, was $0.11 \pm 0.08\%$ to $0.13 \pm 0.1\%$ which is very satisfactory. It is also worth mentioning that the lowest error was observed in bottled waters where the concentrations of both Ca^{2+} and Mg^{2+} were known thus enabling an accurate calculation of total hardness as $CaCO_3$ equivalents, using the equation:

$$[CaCO_3] = 2.497 \times [Ca^{2+}] + 4.117 \times [Mg^{2+}] \quad (2)$$

which derives from the ratio of the molar masses of $CaCO_3$, Ca^{2+} and Mg^{2+}. On the other hand, all other samples were analyzed with the EDTA titration method with visual inspection of the end point of the EDTA titration procedure.

4.4. Analysis of salt containing samples

The analysis of real samples containing inorganic salts was further considered. It is well known that inorganic electrolytes decrease the electrostatic repulsion among adjacent sodium dodecanoate molecules leading to the formation of planar or bent structures (Fig. 1a) while they compete Ca^{2+} and Mg^{2+} for the available reactive sites [9,17]. Therefore the applicability of the method in the presence of NaCl, which is the most common inorganic salt in the environment, was investigated. Considering the competition of Na^+ counter-ions for Ca^{2+} and Mg^{2+} the influence of increasing NaCl was investigated at concentrations from 0 to 0.75 M which is higher than the usual value of seawater (35‰) by direct spiking in salt-free water samples (bottled waters) with variable total hardness content. However, values above 0.5 M could not be employed because the coacervate phase became insoluble forming a thick membrane that remained on the top of the vial especially with increasing total hardness. The analysis of salt containing samples revealed that the absorbance signal soars up to 0.1 M NaCl irrespectively of water hardness, but above this value it descents, increases or reaches a plateau depending on total hardness (Fig. 8), which is attributed to the relative competition of Na^+ with Ca^{2+} and Mg^{2+} for the reactive sites of sodium dodecanoate. From a practical standpoint, the presence of salt deteriorated the relative experimental error between EDTA titration and the proposed method providing no improvement in the measured concentrations. Furthermore, no specific relationship between salt concentration and water hardness could be established. Empirically, it was observed that the influence of ionic strength is related to the relative abundance of individual alkaline earth metals to that of salt counter-ion but the wide distribution of the experimental measurements did not enable the provision of a mathematical expression that could account for these phenomena.

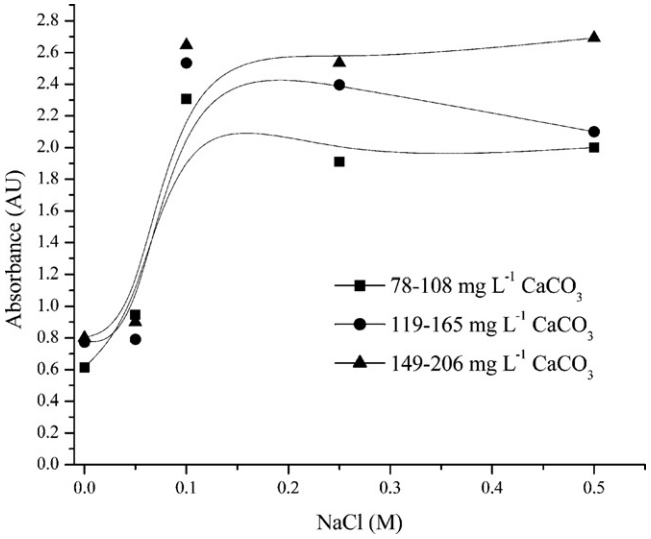


Fig. 8. Influence of ionic strength on the absorbance yield of HALC in variable water hardness.

Since no clear relationship between ionic strength and water hardness was found, it was decided to investigate the influence of NaCl on the analytical response of HALC method empirically by employing real rather than artificial samples. A series of four NaCl-containing samples from different drillings located along the coastal line of north Corfu (<2 km from sea) and two (2) seawater samples from the Thesprotia region were analyzed for that purpose applying various dilution factors (Table 3). The optimum results were obtained at 2-fold dilution of underground water samples and 50-fold for seawater while for higher dilution the relative error deteriorated significantly and was attributed to the high Mg^{2+} content of seawater, compared to Ca^{2+} [21]. Therefore, although the proposed method may provide a fair approximation of water hardness to salt containing samples after appropriate dilution, its application is not a straightforward task and requires the experimental validation of the results before a secure conclusion can be reached. In this sense, samples that contain appreciable amounts of salts should be analyzed in parallel with another method in order to decide on the best dilution factor which enables HALC method to provide an accurate estimate of total hardness. In the same direction, Mg^{2+}-rich waters could be treated in a similar manner in order to reduce the influence of Mg^{2+} in the final measured signal. However, once this is done, the HALC method can be routinely applied to monitor water hardness in salt containing and/or Mg^{2+}-rich samples.

Table 3
Analysis of high ionic strength water samples (calculations and units as in Table 2).

Sample	Total hardness HALC	Total hardness	Classification	Relative error (%)	Average relative deviation (ARD)
Underground water					
Drilling 1	417	570	Failed	26.9	
Drilling 2	438	607	Failed	27.9	
Drilling 3	984	1024	Success	3.9	
Drilling 4	1007	1059	Success	4.9	
					0.16 ± 0.1
Seawater					
Seawater	6520	6856	Success	4.9	
Estuary water	1255	1311	Success	4.3	
					0.02 ± 0.01

4.5. Speciation of water hardness

Despite the non-selective determination of Ca^{2+} and Mg^{2+} ions afforded by HALC, further development towards the individual determination of water hardness components, which may is of interest especially in biological samples, can be pursued. As previously discussed, both Ca^{2+} and Mg^{2+} yield a linear response with increasing concentration suggesting that the method can be conveniently applied to their separate determination. Since most samples of environmental, biological and food origin contain both species, the selective removal or determination of one species must precede the speciation protocol, the other being determined as the difference between total hardness and known ion concentration according to Eq. (2). Ion-selective electrodes or flame atomic absorption spectrometry could be employed towards this direction [4,5,7,22].

5. Conclusions

A rapid and facile method abbreviated as HALC (hardness by alkaline earth metal coacervation) is described in this study for the determination of water hardness exploiting the phenomenon of coacervation of alkaline earth metals in aqueous solution upon their reaction with an anionic surfactant (sodium dodecanoate). Investigation of the experimental conditions that afford the optimum analytical performance was elucidated suggesting that the method is straightforwardly applicable by measuring the absorbance of the solutions at 350 nm, without the need for any adjustment of the usual analytical parameters like pH, ionic strength, temperature and incubation time. Due to the different response of Mg^{2+} and Ca^{2+} in the final absorbance signal, a non-linear calibration curve based on the logarithmic expression of absorbance vs. concentration was constructed and a concentration correction factor was established. The method was successfully applied to various natural water samples yielding a fair estimation of water hardness in terms of qualitative, semi-quantitative and quantitative analysis. The interference from salts (above 0.1 M) or too high Mg^{2+} concentrations can easily be overcome by simple dilution, enabling method application in a wide variety of samples, including seawater.

References

[1] J.H. Yim, K.W. Kim, S.D. Kim, J. Hazard. Mater. 138 (2006) 16.
[2] J. Cotruvo, J. Bartram (Eds.), Calcium and Magnesium in Drinking-water: Public Health significance, World Health Organization, Geneva, 2009.
[3] A.D. Eaton, L.A. Clesceri, A.E. Greenberg (Eds.), APHA-AWWA-WEF, Standard Methods for the Examination of Water and Wastewater, 19th ed., APHA, Washington, 1995.
[4] Official Methods of Analysis, vol. 2, 16th ed., Association of Official Analytical Chemists, Arlington, 1995.
[5] J. Saurina, E. López-Aviles, A. Le Moal, S. Hernández-Cassou, Anal. Chim. Acta 464 (2002) 89.
[6] V.K. Gupta, S. Chandra, R. Mangla, Sens. Actuators B 86 (2002) 235.
[7] P. Kane, D. Diamond, Talanta 44 (1997) 1847.
[8] IUPAC Compendium of Chemical Terminology 31 (1972) 611.
[9] G.Z. Tsogas, D.L. Giokas, E.K. Paleologos, A.G. Vlessidis, N.P. Evmiridis, Anal. Chim. Acta 537 (2004) 239.
[10] G.Z. Tsogas, D.L. Giokas, A.G. Vlessidis, N.P. Evmiridis, Spectrochim. Acta, Part B 59 (2004) 957.
[11] F.J. Ruiz, S. Rubio, D. Perez-Bendito, Anal. Chem. 78 (2006) 7229.
[12] F.J. Ruiz, S. Rubio, D. Perez-Bendito, Anal. Chem. 79 (2007) 7473.
[13] N.I. Kapakoglou, D.L. Giokas, G.Z. Tsogas, A.G. Vlessidis, Anal. Chem. 80 (2008) 9787.
[14] A. Zapf, R. Beck, G. Platz, H. Hoffmann, Adv. Colloid Interface Sci. 100–102 (2003) 349.
[15] D. Grabner, T. Matsuo, E. Hoinkis, C. Thunig, H.J. Hoffmann, Colloid Interface Sci. 236 (2001) 1.
[16] E.K. Paleologos, A.G. Vlessidis, M.I. Karayannis, N.P. Evmiridis, Anal. Chim. Acta 477 (2003) 223.
[17] D.L. Giokas, G.Z. Tsogas, A.G. Vlessidis, M.I. Karayannis, Anal. Chem. 76 (2004) 1302.
[18] M. Mao, J. Huang, B. Zhu, H. Yin, H. Fu, Langmuir 18 (2002) 3380.
[19] J.O. Westgard, Basic Method Validation, third ed., WESTGARD QC Publ, USA, 2008, p. 320.
[20] Commission decision laying down performance criteria for the analytical methods to be used for certain substances and residues there of in live animals and animal products according to Council Directive 96/23/EC, Draft SANCO/1805/2000, 2000, Rev. 1.
[21] M. Sadiq, Toxic Metal Chemistry in Marine Environments, vol. 1, CRC Press, 1992.
[22] D.L. Giokas, E.K. Paleologos, P.G. Veltsistas, M.I. Karayannis, Talanta 56 (2002) 415.

Talanta 80 (2010) 2057–2062

Contents lists available at ScienceDirect

Talanta

journal homepage: www.elsevier.com/locate/talanta

Vortex-assisted liquid–liquid microextraction of octylphenol, nonylphenol and bisphenol-A

Evangelia Yiantzi, Elefteria Psillakis*, Konstantina Tyrovola, Nicolas Kalogerakis

Department of Environmental Engineering, Technical University of Crete, Polytechneioupolis, GR-73100 Chania, Greece

ARTICLE INFO

Article history:
Received 26 June 2009
Received in revised form 21 October 2009
Accepted 3 November 2009
Available online 12 November 2009

Keywords:
Sample preparation
Alkylphenol
Octylphenol
Nonylphenol
Bisphenol-A
VALLME
Water analysis

ABSTRACT

A new and fast equilibrium-based solvent microextraction technique termed vortex-assisted liquid–liquid microextraction (VALLME) has been developed and used for the trace analysis of octylphenol, nonylphenol and bisphenol-A in water and wastewater samples. According to VALLME, dispersion of microvolumes of a low density extractant organic solvent into the aqueous sample is achieved by using for the first time vortex mixing, a mild emulsification procedure. The fine droplets formed could extract target analytes towards equilibrium faster because of the shorter diffusion distance and larger specific surface area. Upon centrifugation the floating extractant acceptor phase restored its initial single microdrop shape and was used for high-performance liquid chromatographic analysis. Different experimental parameters were controlled and the optimum conditions found were: 50 μl of octanol as the extractant phase; 20 ml aqueous donor samples; a 2 min vortex extraction time with the vortex agitator set at a 2500 rpm rotational speed; centrifugation for 2 min at 3500 rpm; no ionic strength or pH adjustment. The calculated calibration curves gave high levels of linearity yielding correlation coefficients (r^2) greater than 0.9935. The repeatability and reproducibility of the proposed method were found to be good and the limits of the detection were calculated in the low $\mu g\,l^{-1}$ level ranging between 0.01 and 0.07 $\mu g\,l^{-1}$. Matrix effects were determined by applying the proposed method to spiked tap, river water and treated municipal wastewater samples. The proposed method was finally applied to the determination of target pollutants in real wastewater effluent samples using the standard addition method.

© 2009 Elsevier B.V. All rights reserved.

1. Introduction

Analytical microextractions represent an important development in the field of sample preparation, addressing issues of simplicity, miniaturization and time efficiency [1]. Although different types of microextraction techniques were initially reported, it was the introduction of solid-phase microextraction (SPME) in 1990 [2] that initiated intensive research efforts in the area. Few years later, solvent microextraction (also known as liquid-phase microextraction or LPME) appeared in the literature [3–6], representing a miniaturization of the traditional liquid–liquid extraction (LLE) procedure whereby the solvent to aqueous phase ratio was greatly reduced. The general requirements for LPME were the use of an acceptor phase immiscible to the aqueous sample donor solution and analytes that were more soluble in the extractant phase than in the sample solution. Hitherto, different methodologies evolved from this approach including amongst others immersion [7] and headspace [8] single-drop microextraction, static and dynamic LPME [9] or even hollow fiber LPME [10,11].

Recently, a new LPME method termed dispersive liquid–liquid microextraction (DLLME), based on a ternary component solvent system similar to the one found in homogeneous liquid–liquid extraction and cloud point extraction, appeared in the literature [12]. For DLLME, a water-immiscible extractant solvent dissolved in a water-miscible dispersive solvent was rapidly injected into an aqueous donor solution leading to the formation of a cloudy solution consisting of fine droplets of the extractant solvent dispersed entirely in the aqueous (continuous) phase. Target analytes were extracted into these fine droplets, which could be subsequently separated by centrifugation and used for analysis. The main drawbacks associated with DLLME were the difficulty to automate and the necessity of using a third component (disperser solvent), which commonly decreased the partition coefficient of analytes into the extractant solvent [13]. Recently, dispersion of the extractant phase into the sample solution was also achieved using the so-called temperature-controlled ionic liquid DLLME method [14]. The method was based on the ability of an ionic liquid drop to disperse in an aqueous phase at higher temperatures, yet return to phase separation upon cooling and centrifugation. Although the method yielded high enrichment factors, analyte losses due to volatilization at higher temperatures were reported. Finally, the possibility of using ultrasound as a mean for dispersing the

* Corresponding author. Tel.: +30 28210 37810; fax: +30 28210 37852.
E-mail address: elia.psillakis@enveng.tuc.gr (E. Psillakis).

0039-9140/$ – see front matter © 2009 Elsevier B.V. All rights reserved.
doi:10.1016/j.talanta.2009.11.005

extractant acceptor phase (organic solvent [13,15] or an organic solvent/ionic liquid mixture [16]) into an aqueous donor phase was recently explored. In general, heterogeneous liquid–liquid systems are known to become uniform when subjected to ultrasonic irradiation. The process is also known as "homogenization" or "emulsification" and has been used as an alternative to the conventional LLE method [17]. Moreover, ultrasound was found to speed up this homogenization/emulsification step given that the formation of submicron size droplets greatly increased the contact surface between the two liquids, yielding fast and efficient analyte transfer. Nevertheless, in many cases analytical chemists have been reluctant to test ultrasound as a mean for improving liquid–liquid extraction given that it most often produces stable emulsions that result in long phase separation times. Problems were also encountered due to the use of cleaning baths as ultrasound irradiation production equipment which are notorious for their tendency to decline in power with time and their lack of uniformity in the transmission of ultrasound irradiation [18]. It should also be mentioned that even at these low frequencies and relatively short application times, analyte degradation may occur through large pressure and temperature gradients, high shear forces, or even by free radicals generation [19,20].

The aim of this research was to introduce a new and fast microextraction method whereby dispersion of the extractant phase into the aqueous is achieved for the first time using vortex mixing, a mild emulsification procedure. The resulting methodology was termed vortex-assisted liquid–liquid microextraction (VALLME) and was used for the extraction of trace amounts of alkylphenols (namely: octylphenol (OP) and nonylphenol (NP)) and bisphenol-A (BPA) used here as model compounds from water and wastewater samples. In general, alkylphenols are considered as degradation products of alkylphenolpolyethoxylates, a widely used class of nonionic surfactants with industrial and household applications [21,22]. OP and NP have been classified as endocrine disruptive compounds by several organizations, and are listed as a priority substance in the Water Framework Directive [23]. BPA on the other hand is commonly used as an intermediate in the production of polycarbonate and epoxy resins, flame retardants and other specialty products [24] and was found to exhibit weakly estrogenic activity as well as antiandrogenic activity [25]. Hitherto, different reports based on SPME or LPME coupled to high-performance liquid chromatography (HPLC) deal with the trace analysis of environmental samples containing these target analytes [21,26–32]. For the purpose of the present investigations, several experimental parameters affecting the extraction process (namely: organic solvent, agitation time, rotational speed of the vortex agitator, acceptor phase volume, aqueous sample volume, pH and salt addition) were initially controlled and optimized and the performance of the proposed method was then assessed. Matrix effects upon extraction were evaluated by analyzing spiked tap and river water as well as effluent water samples taken from a municipal wastewater treatment plant.

2. Experimental

2.1. Chemicals and samples

BPA and OP were purchased from Aldrich (Sigma–Aldrich, Gillingham, Dorset, UK). 1-octanol and NP Pestanal® (94% purity) were purchased from Riedel-de Haën (Seelze, Germany). All organic solvents used here were of pesticide grade. Deionized water was prepared on a water purification system (EASYpure®RF) supplied by Barnstead/Thermolyne Corporation (Dubuque, IO, USA). Stock solutions were prepared in methanol and stored at 4 °C in the dark when not in use. Working standards were prepared daily at the concentration levels of interest.

A 100 μl Hamilton (Bellefonte, BA, USA) HPLC 710 SNR model microsyringe was used to introduce the organic solvent into the aqueous sample and then collect it and inject it into the HPLC system for analysis.

River water samples were collected from the River Koiliaris situated in Chania-Crete (pH 7.5; chemical oxygen demand (COD) = 20 mg/l; total dissolved solids (TDS) = 100 mg/l). Wastewater effluent samples were collected from the municipal wastewater treatment plants of Chania (pH 7.6; COD = 15 mg/l; TDS = 508 mg/l) and Rethymno (pH 8.0; COD = 68 mg/l; TDS = 780 mg/l) situated in the North-West part of Crete, serving approximately 70,000 and 25,000 habitants, respectively. All samples were collected the day before being analyzed and were stored in the dark at 4 °C.

2.2. VALLME

Unless otherwise stated within the text, 20 ml aqueous samples spiked at a known concentration with all target analytes were placed in a round-bottom glass vial (diameter: ~2 cm) and 50 μl of octanol were then slowly introduced acting as the extractant solvent. The mixture was then vigorously shaken using a vortex agitator (Reax Control, Heidolph, Germany) for 2 min at 2500 rpm (maximum setting). As a result fine droplets were formed facilitating mass transfer of the target analytes into the organic acceptor phase. Separation of the two phases occurred upon centrifugation at 3500 rpm for 2 min (Labofuge 400 Heraeus, Kendro Laboratory Products, Germany). The floating octanol phase could thus restore its original single microdrop shape and 30 μl could be easily collected with the help of a microsyringe and used for HPLC analysis. During optimization, all experiments were run at least in duplicate.

2.3. HPLC analysis

Separation and quantification was carried out using an HPLC system, manufactured by Shimadzu (Shimadzu Corporation, Kyoto, Japan), equipped with a fluorescence detector (FLD) and two solvent delivery pumps. A Nucleosil 100-5 C18 (250 mm × 4.6 mm × 5 μm; Macherey-Nagel, Duren, Germany) was used to separate the target analytes at 27 °C. The mobile phase was acetonitrile:water (80:20) with a flow rate of 1.0 ml min^{-1}. The excitation and emission wavelengths of the FLD were set at 277 and 300 nm respectively. The total analysis time was 15 min.

3. Results and discussion

3.1. Optimization of VALLME

Initially, several water immiscible solvents (namely: 1-octanol, toluene, *n*-hexane, octane and cyclohexane) were tested, having densities lower than that of water and differing in polarity and water solubility. Each time, 50 μl of the organic solvent to be tested was slowly added to a 20 ml aqueous sample spiked at 1 μg l^{-1} with BPA and OP and 10 μg l^{-1} with NP. Given that all solvents tested had densities lower than that of water, they resided in the top surface of the water sample in the form of a single microdrop. The mixture was then vigorously agitated using a vortex agitator (2 min; 2500 rpm) leading to drop breakage into fine droplets. In the present studies centrifugation (2 min at 3500 rpm) was chosen as a viable mean for separating the two phases of this liquid–liquid dispersion. Amongst the low density solvents tested, 1-octanol had the ability to "restore" its initial single microdrop shape and as such could be easily collected and used for HPLC analysis. Under the present experimental conditions, coalescence of the fine droplets into a coherent phase did not occur for the rest of the tested solvents which were left scattered on the top surface of the aqueous solution in the form of smaller satellite microdrops hindering thus

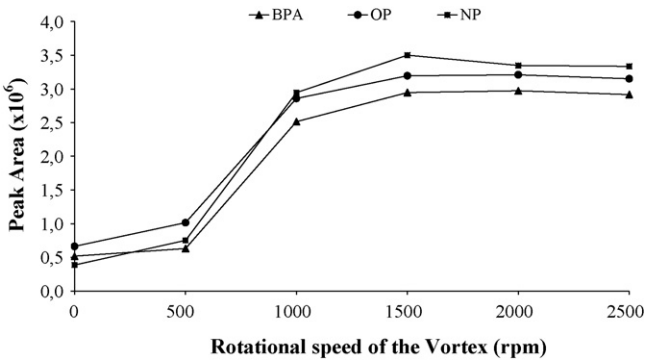


Fig. 1. Effect of the rotational speed of the vortex agitator upon VALLME. Other experimental conditions: 50 μl octanol; 20 ml aqueous samples spiked at 1 μg l^{-1} with BPA and OP and 10 μg l^{-1} with NP; 2 min agitation using a vortex agitator; centrifugation for 2 min at 3500 rpm.

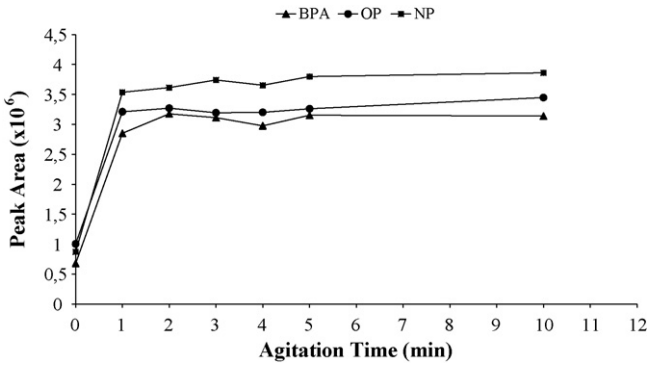


Fig. 2. Effect of vortex extraction time upon VALLME. Other experimental conditions: 50 μl octanol; 20 ml aqueous samples spiked at 1 μg l^{-1} with BPA and OP and 10 μg l^{-1} with NP, vortex agitator set at 2500 rpm rotational speed; centrifugation for 2 min at 3500 rpm.

their collection. Despite the numerous studies in the field separation processes driven by gravity or centrifugal forces are not yet completely understood [33]. In addition the mechanisms involved during drop breakage and formation are rather complex and form part of many ongoing investigations. Nonetheless, they appear to be greatly influenced (amongst others) by the physicochemical properties of the phases involved and the geometry of the apparatus used [34]. It should be mentioned here that the ability of 1-octanol to efficiently extract alkylphenols (NP and 4-*tert*-OP) when compared to ionic liquids and carbon tetrachloride has been demonstrated in the past [27]. Based on the above, 1-octanol was used as the acceptor organic phase for the rest of the experiments.

In general, the effect of a vortex agitator is to swirl the fluids and create a vortex, the size and shape of which depend upon the rotational speed of the rotor. In the case of immiscible liquids and at elevated speeds this generally results into the breakup of one of the two phases into fine droplets. Although such unstable fluid fields would seem unfavorable for operation, solvent microextraction methods are equilibrium methods and mass transfer within the organic acceptor phase is a limit step [6]. These fine droplets could extract analytes towards equilibrium faster because of the shorter diffusion distance and larger specific surface area [35]. Accordingly, in a separate set of experiments, the effect of the rotational speed of the vortex agitator upon VALLME was investigated and the results are depicted in Fig. 1. The "0 rpm" experimental point corresponded to the extraction where the water–octanol mixture was not subjected to vortex agitation and preconcentration of the target analytes was solely due to diffusion during the centrifugation step [36]. Fig. 1 demonstrates the beneficial effect of vortex agitation over centrifugation alone and it appears that the final analyte concentration of the microextract is nearly uniform for speeds greater than 1500 rpm where equilibrium conditions appear to be attained within the 2 min agitation time applied. Based on these observations it was decided to use the maximum speed setting of the vortex agitator (2500 rpm) for all subsequent experiments.

Fig. 2 depicts the results obtained whilst investigating the effect of vortex extraction time upon VALLME. At the experimental point "0 min", samples were only centrifuged and preconcentration was once again solely due to diffusion during centrifugation [36]. As can be seen extraction rates increased for increased vortex extraction times and it appears that equilibrium is attained for all target analytes after only 2 min. Based on the above, a 2 min vortex extraction time was chosen, enabling extraction at equilibrium conditions and resulting in increased precision and sensitivity.

Next, the effect of the acceptor phase volume upon extraction was investigated for volumes ranging between 50 and 80 μl. Octanol volumes lower than 50 μl were avoided, given that final collection of at least 30 μl which could be used for analysis was not always possible. It was assumed that although octanol had the ability to "restore" its initial microdrop shape, the formation of smaller satellite microdrops that could not coalesce with the mother drop was unavoidable. Octanol dissolution into the aqueous phase may have partially contributed to the reduced volumes of the final microdrops used for analysis. In the present investigations an overall 36, 38 and 42% decrease in the response of the instrument was recorded for BPA, OP and NP, respectively, whilst increasing the acceptor phase volume from 50 to 80 μl. This was due to the decreased final concentrations of target analytes in the octanol phase [6]. Thus, for all subsequent extractions, 50 μl octanol volumes were used.

The effect of aqueous sample volume upon VALLME was then investigated. As expected, increasing the volume of the spiked aqueous solution from 5 to 20 ml, increased the total mass of analytes available for extraction [37], resulting in a net increase in the response of the analytical instrument for BPA, OP and NP and the recorded signals were found to be 1.5, 2.4 and 3.4 times higher, respectively. It should be mentioned here that larger volumes were not tested given that the sensitivity of the instrument was found to be satisfactory. Based on the above, 20 ml aqueous samples were used each time for extraction.

It is well known that pH can significantly influence the partitioning of ionizable hydrophobic chemicals to octanol. The pollutants investigated here are considered to be weak acids and are expected to be found mainly in their molecular form for pH values below 8.0 and in their deprotonated form for pH values over 11 [24,27]. During the present studies, a non-significant negative effect of the pH upon VALLME was recorded for pH values ranging from 4 to 8. This is in agreement with a recent report published by Liu et al. [27], who concluded that altering the pH of sample solutions containing 4-*tert*-OP and NP, had a significant effect on the uptake kinetics into the 1-octanol film supported on a hollow fiber, yet no pH effect was observed for the equilibrium distribution, which is the case here. Given that no significant changes in extraction efficiency were observed in the environmentally relevant pH range, it was decided not to alter the pH of the aqueous samples.

Finally, the effect of salt for NaCl concentrations ranging from 0 to 15% (w:v) upon VALLME was investigated and the results are given in Fig. 3. As can be seen the presence of salt restricted the extraction of OP and NP, and was found to be beneficial for BPA. Similar results were obtained by Cai et al. [30], whilst developing an SPME method coupled to HPLC-FLD for the analysis of BPA, NP, and 4-*tert*-OP. In their work, increasing the ionic strength of the samples (up to 20% (w:v) NaCl) resulted in an increase of the extraction efficiency for BPA and a decrease for NP. In the case of 4-

Table 1
Selected method parameters (linear concentration range, r^2 and LOD) and average relative recoveries ($n = 3$) for different samples (namely tap water, river water and wastewater (WW)) spiked at 1 μg l^{-1} with BPA and OP and 10 μg l^{-1} with NP (RSD values given in parentheses).

Compound	Conc. range	r^2	LOD	Relative recoveries (% (RSD))		
				Tap	River	WW effluent
BPA	0.05–100	0.9992	0.02	94 (3)	105 (3)	75 (2)
OP	0.05–100	0.9996	0.01	101 (3)	111 (3)	63 (6)
NP	0.50–100	0.9935	0.07	104 (4)	109 (4)	67 (7)

tert-OP, extraction increased reaching a maximum at 5% (w:v) NaCl and then decreased for increased salt concentrations. Recently, Braun et al. [38] developed a method based on SPME coupled to gas chromatography–mass spectrometry. During optimization the authors reported that the response for 4-*tert*-NP decreased significantly as the salt concentration increased, whereas for BPA a slight increase in extraction yield was recorded for increased NaCl concentrations, which was hardly lowered up to the saturated condition. Finally, Rezaee et al. [31] whilst developing a sample preparation method based on DLLME coupled to HPLC-UV reported a non-significant effect on the extraction recovery of BPA when sodium chloride up to 8% (w:v) was added in the sample solution. The authors in this study took into account for their calculations the increase in volume of the sedimented extractant solvent phase. Given that in the present investigations the presence of salt did not result in significant positive changes in the extraction yields of all target analytes, it was decided not to alter the ionic strength of the aqueous samples destined for analysis.

Overall, the optimized experimental conditions found here were: 50 μl octanol; 20 ml aqueous samples; 2 min vortex extraction time; vortex agitator set at 2500 rpm rotational speed; centrifugation for 2 min at 3500 rpm; no ionic strength or pH adjustment.

3.2. Analytical performance of VALLME

The linearity of the proposed method was determined by extracting under the optimized extraction conditions, aqueous solutions spiked at concentrations ranging from 0.05 to 100 μg/l for BPA and OP and 0.5–100 μg/l for NP. The calculated calibration curves gave a high level of linearity, yielding correlation coefficients (r^2) 0.9992, 0.9996 and 0.9935 ($n = 5$) for BPA, OP and NP, respectively (Table 1). The repeatability of the method, expressed as relative standard deviation (RSD), was evaluated after extracting at two concentration levels five consecutive aqueous samples each time. Spiking aqueous samples at 1 μg l^{-1} with BPA and OP and 10 μg l^{-1} with NP yielded RSD values of the order of 2.4, 2.1 and 2.2%, respectively. For samples containing 0.1 μg l^{-1} BPA and OP and 1 μg l^{-1} NP, the RSD values found were 5.9, 4.6, 8.0%, respectively. The limits of detection (LOD) defined for a signal-to-noise of three (S/N = 3) were found in the low μg l^{-1} level (Table 1), lower or similar to the ones reported when coupling a liquid- or solid-phase microextraction method coupled to HPLC (Table 2). Enrichment factors defined as the ratio between the final analytes concentration in the organic acceptor phase and the initial aqueous sample concentration were found to be approximately for 450, 690 and 150 for BPA, OP and NP, respectively.

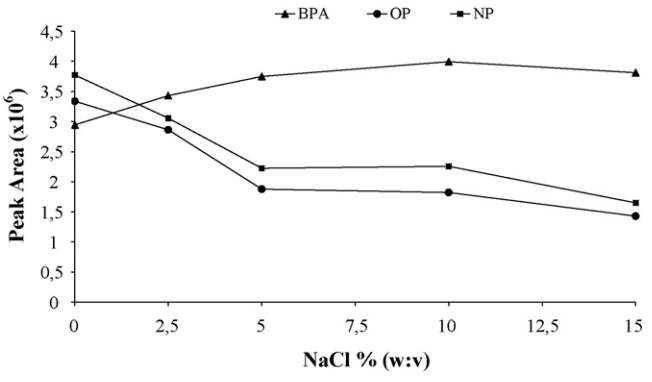


Fig. 3. Effect of ionic strength (% NaCl, w:v) upon VALLME. Other experimental conditions: 50 μl octanol; aqueous samples spiked at 1 μg l^{-1} with BPA and OP and 10 μg l^{-1} with NP; 2 min vortex extraction time; vortex agitator set at 2500 rpm rotational speed; centrifugation for 2 min at 3500 rpm.

It is well known that the efficiency of microextraction methods can be affected by the composition of the sample matrix. Accordingly, tap, river and municipal sewage effluent water samples were spiked at 1 μg l^{-1} with BPA and OP and 10 μg l^{-1} with NP and analyzed under the optimized experimental conditions. The relative recoveries found (defined as the ratio of the concentrations found in environmental and deionized water samples spiked with the same amount of analytes) are given in Table 1. As can be seen, in the case of tap and river water matrix did not affect extraction. However, in the case of effluent wastewater a decrease in extraction yield and as a consequence in sensitivity was observed. A similar observation has been reported in the past [39] and it was decided that for quantification in more complex environmental samples (such as wastewater effluents) the standard addition method should be used. Typical HPLC chromatograms obtained after VALLME of wastewater effluent samples before and after spiking at 1 μg l^{-1} with BPA and OP and 10 μg l^{-1} with NP are given in Fig. 4.

Table 2
Comparison of LOD obtained with VALLME and other published liquid- or solid-phase microextraction methods coupled to HPLC.

Method	LOD (μg l^{-1})	Reference
DLLME coupled to HPLC-UV	BPA: 0.07	[31]
Ionic liquid LPME coupled to HPLC-FLD	4-NP: 0.3 4-*tert*-OP: 0.7	[21]
1-Octanol Thin Film supported on a hollow fiber coupled to HPLC-FLD	4-NP: 0.06 4-*tert*-OP: 0.1	[27]
SPME coupled to HPLC-FLD	BPA: 0.9	[29]
SPME coupled to HPLC-FLD	BPA: 0.43 4-*tert*-OP: 0.16, NP: 0.29	[30]
In-tube SPME coupled to HPLC-UV	BPA: 0.1 OP: 0.8 NP: 0.6	[32]
In-tube SPME coupled to HPLC-UV-FLD	BPA: 2.4	[28]
In-tube SPME coupled to HPLC-FLD	BPA: 0.02	[26]
VALLME coupled to HPLC-FLD	BPA: 0.02 OP: 0.01 NP: 0.07	Present studies

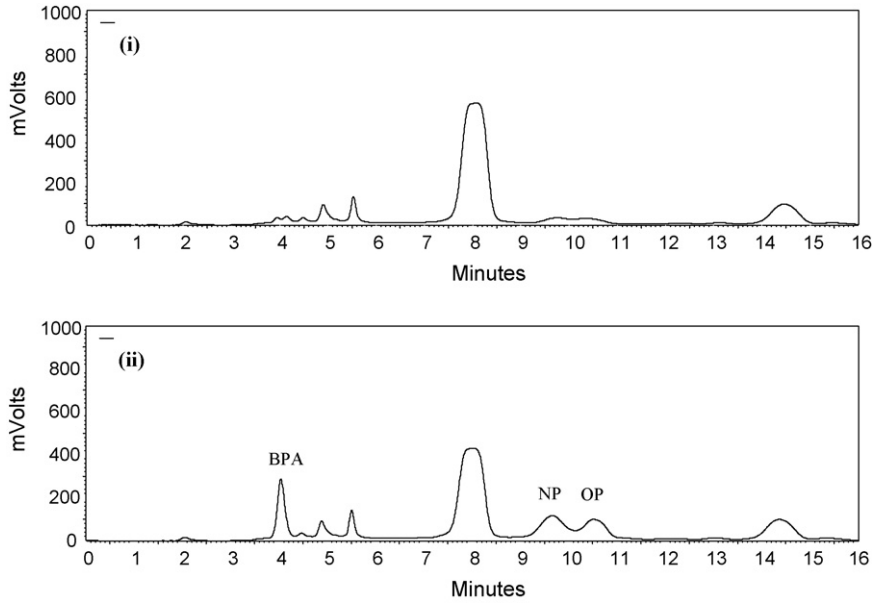


Fig. 4. Typical HPLC chromatograms obtained after VALLME of wastewater effluent samples (i) before and after spiking at 1 $\mu g\,l^{-1}$ with BPA and OP and 10 $\mu g\,l^{-1}$ with NP.

Table 3
Concentrations of target pollutants in wastewater effluent samples originating from two municipal wastewater treatment plants situated in the north part of Crete (Chania and Rethymno). The standard deviations of the measurements are also included.

Compound	WW effluent from Chania ($\mu g\,l^{-1}$)	WW effluent from Rethymno ($\mu g\,l^{-1}$)
BPA	0.14 ± 0.01	0.28 ± 0.03
OP	0.39 ± 0.07	0.21 ± 0.04
NP	3.20 ± 0.25	0.67 ± 0.10

3.3. Analysis of effluent wastewater samples

The presence of BPA, OP and NP in real treated samples taken from two municipal wastewater treatment plants was then quantified using the VALLME. The standard addition method was chosen and samples were multiply extracted. As can be seen (Table 3) the presence of all target pollutants was confirmed, demonstrating the inability of this treatment process to efficiently remove these contaminants [25]. In addition, the contamination levels found in the treated wastewater samples examined here were similar to the ones found in different Mediterranean countries. Gómez et al. studied the contamination levels of effluents samples taken from two municipal wastewater treatment plants located in south-eastern Spain (Almeria), reported a 0.38 $\mu g\,l^{-1}$ mean value for BPA after a 1 year monitoring study [39]. Gonzalez et al., whilst comparing the efficiency of a pilot plant membrane bioreactor working in parallel to a full-scale wastewater treatment plant situated in Rubí (Barcelona-Spain), reported a 2 $\mu g\,l^{-1}$ average value for NP in the effluent samples [40]. Finally, Stasinakis et al. reported 0.18 and 0.15 $\mu g\,l^{-1}$ mean values for NP and BPA respectively for effluent samples taken from six different wastewater treatment plants in Greece [25].

4. Conclusions

A new and fast sample preparation method termed vortex-assisted liquid–liquid microextraction is presented here having the inherent advantage of achieving equilibrium conditions within only a few minutes. For the first time dispersion of the extractant phase into the aqueous was achieved using vortex mixing, a mild emulsification procedure, avoiding thus problems associated with the application of ultrasound. The proposed method was successfully applied to the determination of BPA, OP and NP at trace levels in water samples. For more complicated matrices the standard addition method was found to be suitable for quantification. Overall, this is a promising and fast sample preparation method that can be used for the trace analysis of organic pollutants in aqueous environmental samples.

Acknowledgements

This work was funded by the European Social Fund and National Resources – (EPEAEK-II) "Environment-PYTHAGORAS II: Funding of research groups in Technical University of Crete.- M 2.6-Subcontract 10".

References

[1] J. Pawliszyn, S. Pedersen-Bjergaard, J. Chromatogr. Sci. 44 (2006) 291–307.
[2] C.L. Arthur, J. Pawliszyn, Anal. Chem. 62 (1990) 2145–2148.
[3] H. Liu, P.K. Dasgupta, Anal. Chem. 68 (1996) 1817–1821.
[4] M.A. Jeannot, F.F. Cantwell, Anal Chem. 69 (1997) 235–239.
[5] E. Psillakis, N. Kalogerakis, Trac-Trend Anal. Chem. 22 (2003) 565–574.
[6] E. Psillakis, N. Kalogerakis, Trac-Trend Anal. Chem. 21 (2002) 53–63.
[7] M.A. Jeannot, F.F. Cantwell, Anal. Chem. 69 (1997) 2935–2940.
[8] A. Tankeviciute, R. Kazlauskas, V. Vickackaite, Analyst 126 (2001) 1674–1677.
[9] Y. He, H.K. Lee, Anal. Chem. 69 (1997) 4634–4640.
[10] S. Pedersen-Bjergaard, K.E. Rasmussen, Anal. Chem. 71 (1999) 2650–2656.
[11] L. Zhu, L. Zhu, H.K. Lee, J. Chromatogr. A 924 (2001) 407–414.
[12] M. Rezaee, Y. Assadi, M.-R. Milani Hosseini, E. Aghaee, F. Ahmadi, S. Berijani, J. Chromatogr. A 1116 (2006) 1–9.
[13] J. Regueiro, M. Llompart, C. Garcia-Jares, J.C. Garcia-Monteagudo, R. Cela, J. Chromatogr. A 1190 (2008) 27–38.
[14] Q. Zhou, H. Bai, G. Xie, J. Xiao, J. Chromatogr. A 1177 (2008) 43–49.
[15] J. Regueiro, M. Llompart, E. Psillakis, J.C. Garcia-Monteagudo, C. Garcia-Jares, Talanta 79 (2009) 1387–1397.
[16] Q. Zhou, X. Zhang, J. Xiao, J. Chromatogr. A 1216 (2009) 4361–4365.
[17] J.A. Perez-Serradilla, F. Priego-Capote, M.D. Luque de Castro, Anal. Chem. 79 (2007) 6767–6774.
[18] M.D. Luque de Castro, F. Priego-Capote, Talanta 72 (2007) 321–334.
[19] E. Psillakis, D. Mantzavinos, N. Kalogerakis, Chemosphere 54 (2004) 849–857.
[20] L. Sanchez-Prado, R. Barro, C. Garcia-Jares, M. Llompart, M. Lores, C. Petrakis, N. Kalogerakis, D. Mantzavinos, E. Psillakis, Ultrason. Sonochem. 15 (2008) 689–694.
[21] J.-F. Liu, Y.-G. Chi, G.-B. Jiang, C. Tai, J.-F. Peng, J.-T. Hu, J. Chromatogr. A 1026 (2004) 143–147.
[22] M. Ahel, W. Giger, M. Koch, Water Res. 28 (1994) 1131–1142.

[23] EU, in, Decision no. 2455/2001/EC of the European Parliament and of the council of 20 November 2001 establishing the list of priority substances in the field of water policy and amending directive 2000/60/EC. Off. J. L331, 15/12/2001, 2001.
[24] C.A. Staples, P.B. Dome, G.M. Klecka, S.T. Oblock, L.R. Harris, Chemosphere 36 (1998) 2149–2173.
[25] A.S. Stasinakis, G. Gatidou, D. Mamais, N.S. Thomaidis, T.D. Lekkas, Water Res. 42 (2008) 1796–1804.
[26] Y. Wen, B.-S. Zhou, Y. Xu, S.-W. Jin, Y.-Q. Feng, J. Chromatogr. A 1133 (2006) 21–28.
[27] J.F. Liu, X.L. Hu, J.F. Peng, J.A. Jonsson, P. Mayer, G.B. Jiang, Anal. Chem. 78 (2006) 8526–8534.
[28] Y. Fan, Y.-Q. Feng, Z.-G. Shi, J.-B. Wang, Anal. Chim. Acta 543 (2005) 1–8.
[29] C. Nerin, M.R. Philo, J. Salafranca, L. Castle, J. Chromatogr. A 963 (2002) 375–380.
[30] Y. Cai, G. Jiang, J. Liu, X. Liang, Z. Yao, J. Liu, J. Liu, Q. Zhou, Anal. Lett. 37 (2005) 739–753.
[31] M. Rezaee, Y. Yamini, S. Shariati, A. Esrafili, M. Shamsipur, J. Chromatogr. A 1216 (2009) 1511–1514.
[32] H. Kataoka, M. Ise, S. Narimatsu, J. Sep. Sci. 25 (2002) 77–85.
[33] T. Detloff, D. Lerche, Acta Mech. 201 (2008) 83–94.
[34] A. Hasseine, A.H. Meniai, M.B. Lehocine, H.J. Bart, Chem. Eng. Technol. 28 (2005) 552–560.
[35] L. Yangcheng, L. Quan, L. Guangsheng, D. Youyuan, Anal. Chim. Acta 566 (2006) 259–264.
[36] H. Fang, Z. Zeng, L. Liu, Anal. Chem. 78 (2006) 6043–6049.
[37] L. Vidal, A. Canals, N. Kalogerakis, E. Psillakis, J. Chromatogr. A 1089 (2005) 25–30.
[38] P. Braun, M. Moeder, S. Schrader, P. Popp, P. Kuschk, W. Engewald, J. Chromatogr. A 988 (2003) 41–51.
[39] M.J. Gómez, M. Mezcua, M.J. Martinez, A.R. Fernández-Alba, A. Agüera, Int. J. Environ. Anal. Chem. 86 (2006) 3–13.
[40] S. Gonzalez, M. Petrovic, D. Barcelo, Chemosphere 67 (2007) 335–343.

Talanta 80 (2010) 2063–2067

Contents lists available at ScienceDirect

Talanta

journal homepage: www.elsevier.com/locate/talanta

Influence of the solvent quality on the AhR mediated Procept® assay measurement of dioxin and dioxin-like compounds

Ronan Cariou[a,*], Daniel R. McAlister[b], Philippe Marchand[a], Michael J. Fern[b], Jean-Philippe Antignac[a], Bruno Le Bizec[b]

[a] LABoratoire d'Etude des Résidus et Contaminants dans les Aliments (LABERCA), Ecole Nationale Vétérinaire de Nantes (ENVN), USC INRA 2013, BP 50707, 44307 Nantes Cedex 3, France
[b] Eichrom Technologies LLC, 1955 University Lane, Lisle, IL 60532, United States

ARTICLE INFO

Article history:
Received 2 July 2009
Received in revised form 22 October 2009
Accepted 3 November 2009
Available online 12 November 2009

Keywords:
Dioxin
Screening
AhR
Quantitative PCR
Solvent quality
Toluene

ABSTRACT

Polychlorodibenzo-*p*-dioxins, polychorodibenzofurans and "dioxin-like" polychlorinated biphenyls are widespread persistent organic pollutants sharing a similar toxicological pathway mediated by the aryl-hydrocarbon receptor (AhR). Since the confirmatory method for their measurement at trace levels in complex matrices (using isotopic dilution and gas chromatography–high resolution mass spectrometry) remains time and cost-consuming, growing efforts of the scientific community have been focused on the development of screening approaches, including AhR mediated assays. Unfortunately, AhR ligands are highly diverse and agonistic/antagonistic effects can be observed on procedural blanks and/or sample extracts. In this study, the influence of solvent grade quality on the response of a DNA-binding AhR mediated assay used for screening dioxins has been investigated. Our results demonstrated a very critical impact of this parameter with both strong agonistic and antagonistic effects observed for any tested solvent lot. A small silver nitrate silica column removed partly these interfering compounds and then can be recommended as final purification step. Some preferable grades can be identified and selected in order to guarantee the best possible performances. However, it appears necessary to test every new lot, even if a grade appeared previously compliant.

© 2009 Elsevier B.V. All rights reserved.

1. Introduction

Polychlorodibenzo-*p*-dioxins (PCDD), polychorodibenzofurans (PCDF) and polychlorinated biphenyls (PCB) are widespread persistent organic pollutants. Among these 3 classes of compounds, 29 specific congeners (7 PCDD, 10 PCDF and 12 "dioxin-like" PCB or dl-PCB) are of particular concern for their shared toxic effects at trace level. Most countries have implemented regulations aiming to reduce their impact on public health, which led to appropriate survey control plans and monitoring programs dedicated to environmental matrices as well as foodstuff and biological samples. In this last case, the extremely low residual concentration levels (down to sub-ppt) placed the isotopic dilution method with gas chromatography coupled to high resolution mass spectrometry on electromagnetic sector instruments as the reference analytical method. Since this approach remains time and cost-consuming [1], growing efforts of the scientific community have been focused on the development of analytical alternatives, especially for screening strategies. Various approaches have been described, including the use of (1) alternative GC–MS based instruments [2–5], (2) regression models [6–8], (3) immunoassays [9–11], (4) DNA-binding assays or (5) cell-based bioassays.

All developed cell-based and DNA-binding assays are based on aryl-hydrocarbon receptor (AhR) activation, a ligand-activated transcription factor that mediates the biologic and toxicological effects of 2,3,7,8-tetrachlorodibenzo-*p*-dioxin (TCDD) and the 28 related chemicals [12]. The AhR is a member of the basic-helix–loop–helix (bHLH)–Per-ARNT-Sim (PAS) nuclear receptor superfamily. In dioxin-sensitive organisms, the AhR can be found in the cytosol in a complex with Hsp90 (2 units), XAP2 and p23 proteins. Upon binding to a ligand, the complex translocates to the nucleus and dissociates. Thus, the released ligand/AhR complex forms a heterodimer with the aryl-hydrocarbon receptor nuclear translocator (ARNT), its partner bHLH–PAS protein. The resulting heterodimeric complex shows high affinity to the dioxin response element (DRE), a GCGTG DNA sequence located upstream to the target genes, in the promoter region [13–16].

Cell-based bioassays measure the expression of a marker protein resulting from an exposure to a ligand. One popular example of such test used for routine analysis is the Chemically Activated LUciferase gene eXpression assay (CALUX). The luciferase gene and the DRE have been introduced in the cell line genome. The expres-

* Corresponding author. Tel.: +33 2 40 68 78 80; fax: +33 2 40 68 78 78.
E-mail address: laberca@vet-nantes.fr (R. Cariou).

0039-9140/$ – see front matter © 2009 Elsevier B.V. All rights reserved.
doi:10.1016/j.talanta.2009.11.006

Table 1
Information available from analysis certificate for each tested solvent lot.

	A	B	C	D	E	F
Purity (GC, on anhydrous basis) (%)	99.8	99.8	99.9	99.8	99.8	99.9
Residue after evaporation (ppm, w/w)	<5	<1	1	<5	<5	<0.1
Water (KF) (ppm)	<200	40	30	<50	<100	<100
Color	–	5 APHA	5 APHA	<10 Hazen	<10 Hazen	5 APHA
Acidity (as acetic acid) (ppm)	–	1	1	–	–	–
Acidity (as HCl) (ppm)	–	–	–	10	10	–
GC/ECD dioxins and PCB's (as lindane) (ng/L)	–	<5	–	–	–	–
GC/ECD any pesticide (as lindane) (ng/L)	–	<5	<5	<2	<3	–
GC/ECD any pesticide (as parathion) (ng/L)	–	<10	<10	–	–	–
GC/ECD any pesticide (as heptachlor epoxide) (ng/L)	<10	–	–	–	–	1
GC/FID single impurity peak (as *n*-undecane) (μg/L)	<50	–	–	–	–	–
GC/FID single impurity peak (as hexadecane) (μg/L)	–	–	–	<5	<3	–
GC/FID single impurity peak (as 2-octanol) (μg/L)	–	–	–	–	–	2

sion of luciferase is then measured by recording the emitted light after contact with the luciferine substrate [17–21].

Conversely, DNA-binding assays measure the activated AhR by quantifying the bound DNA *in vitro*. More precisely, a rodent hepatic cytosolic fraction containing AhR, ARNT and co-factors, is mixed with the ligand extract and a synthetic DNA sequence containing the DRE sequence. A first technique, the gel retardation of AhR binding (GRAB), consists in an electrophoretic separation of ^{32}P-labeled DNA complexes, followed by an autoradiography [22]. The GRAB assay is poorly compatible with routine screening analysis. A second technique, namely Procept®, involves quantitative polymerase chain reaction (qPCR), a more suitable technique for high throughput screening. The ligand/AhR/ARNT/DNA complex is trapped on the surface of the qPCR well by a specific antibody. Thus, the bound DNA is amplified after removal of any excess reagents [23–26].

Whatever considered AhR mediated assay, and for regulatory purpose, a TCDD calibration curve allows to express the measured response as a bioanalytical equivalent quotient (BEQ), a TCDD equivalent correlated to the regulatory defined toxic equivalent quotient (TEQ) [12,27,28]. Unfortunately, AhR ligands are highly diverse, including halogenated and polycyclic aromatic hydrocarbons and many other naturally occurring compounds [14]. Consequently, these screening assays still require relatively substantial sample extraction and purification. Indeed, interfering compounds may come from the matrix but also from the analytical procedure itself (*e.g.* stationary phases, glassware and solvents) [21,29]. The volumes of solvents considered are usually in the 10–200 mL range. Working with a cell-based bioassay, Windal et al. [29] reported that in their lab, when just one column of acidic silica is used for the cleanup, the response of a spiked procedural blank is only about half of the expected response, indicating that some inhibitors occur in procedural consumables. Miniaturizing the sample preparation process might be helpful for both saving time/cost and improving performances, but the sensitivity usually achieved with cell-based and DNA-binding assays does not permit such reduction of sample size to a large extend. Consequently, procedural blanks responses are often higher than background level, in the linear range of assays. This impacts negatively on the detection limit by reducing the working range, and necessitates blank correction of the results.

Usually, high attention is paid to the cleanup of glassware and stationary phases, and to the quality of solvents as well. Some laboratories specialized in bioassays usually characterize all solvent lots (toluene, hexane, dichloromethane) since they identified it as a possible source of inhibition and/or signal interference. However, this kind of study has to be conducted for each specific test considered. In the present work, the impact of different toluene grades on the Procept® DNA-binding assay was evaluated, taking into account both agonistic and antagonistic effects, for different target concentration levels.

2. Materials and methods

2.1. Solvents

The six tested toluene grades were: LGC Promochem Picograde lot 811902 (Wesel, Germany), Biosolve Dioxins & PCB's Analysis lot 639871 and Biosolve Pesti-S lot 595921 (Leenderweg, The Netherlands), Carlo Erba Reactifs SDS Atrasol lot D8M052248 M, Carlo Erba Reactifs SDS Pestipur lot D8G002088I (Val de Reuil, France) and JT Baker Ultra Resi-Analyzed lot 0829600025 (Deventer, The Netherlands). Available information regarding these different products, as attested by the joined analysis certificates, is reported in Table 1.

2.2. TCDD dilution series

TCDD was purchased from Wellington Laboratories (Guelph, Canada). For calibration curves, three times TCDD dilution series, from 59,049 down to 27 fg/μL, were prepared in *n*-heptane (Picograde, lot 701228, LGC Promochem) using dedicated syringes.

2.3. Toluene concentration

Each toluene grade was concentrated by a factor of 2000 and re-suspended in *n*-heptane. All used glassware was heated prior to use at 400 °C for 4 h. More precisely, 200 mL of each toluene grade was concentrated to ~2 mL using a Rotavapor®, transferred to a test tube using a Pasteur pipette and then concentrated to 500 μL under a gentle nitrogen stream (Class I, Air Liquide, Paris La Défense, France). The solvent volume was split into 4 equal aliquots in glass vials and evaporated to dryness under a gentle nitrogen stream. Dried extracts remained sealed one night and were re-suspended in 25 μL of *n*-heptane or 25 μL of TCDD solution from the TCDD dilution series (81, 729 or 6561 fg/μL) just prior to AhR contact. These fortification levels corresponded to lower and medium part of linear range, and to a value close to the saturation plateau, respectively. These four toluene extracts with increasing TCDD concentrations can be directly compared to the assay calibration curve plots.

2.4. Silver nitrate treatment

Because a major negative impact of raw toluene extracts was initially observed on the assay, the addition of a purification step applied to the extract was considered, in order to remove most part of these interferences. Indeed, silver nitrate is known to degrade or retain numerous sensitive interfering compounds, including polycyclic aromatic hydrocarbons. Then, alternatively, 200 mL of each toluene grade was concentrated to ~2 mL using a Rotavapor®, transferred to a test tube using a Pasteur pipette and then evap-

orated to dryness under a gentle nitrogen stream. 150 mg of silica gel coated with 10% (w/w) of silver nitrate (Sigma–Aldrich, St Louis, USA) previously activated one night at 200 °C were packed in a glass column (7 mm i.d.) and pre-washed with 10 mL of *n*-hexane. The extract was re-suspended and loaded in 1 mL of *n*-hexane (Picograde, lot 808405, LGC Promochem) and eluted fractions of 6 mL (corresponding to 2,3,7,8-substituted PCDD/F and dl-PCB) were collected and submitted to the same concentration and split than previously described in *n*-heptane.

2.5. Procept® immuno-qPCR assay

The Procept® assay was performed according to the indicated instructions of use. All solution dispensing and measuring was performed using delivery pipets and plastic barrier pipet tips. Plastic 96-well plates for PCR were prepared as follows: (1) washing on a plate washer (ELx50, BioTek, Winooski, USA) using the manufacturer supplied wash solution to remove the protective coating, (2) adding the thawed and diluted antibody solution to each well, (3) equilibrating on a plate shaker (Titramax 100, Heidolph, Schwabach, Germany) for 90 min and (4) washing on the plate washer to remove non-coated excess antibody. While the plastic wells were equilibrating, activation of the AhR was performed in a 96-well plate of glass vials as follows: (1) addition of 25 μL of the manufacturer supplied assay buffer solution, (2) addition of 5 μL of corresponding prepared TCDD standard and/or toluene extract, (3) addition of 25 μL of activation solution diluted by 2 with the assay buffer and containing the AhR, the co-factors, the ARNT and the DNA sequence (stored at −80 °C and thawed immediately prior to use) and (4) equilibration on the plate shaker for 60 min. During the equilibration time, *n*-heptane evaporates and target compounds go to AhR contact in aqueous phase. Following AhR activation, binding of complexed DNA was realized as follows: (1) transfer of 25 μL of complexation solution from each glass vial to corresponding prepared plastic PCR well, (2) equilibrating for 30 min on the plate shaker to bind the ligand/AhR/ARNT/DNA complex to the specific antibody and (3) removal of excess AhR, ARNT, and DNA by washing on the plate washer. The templates included 8 duplicate wells for TCDD standard curve (including assay blank) and 8 duplicate wells for each tested solvent (blank and 3 TCDD spike levels, with/without $AgNO_3$ treatment).

2.6. Quantitative polymerase chain reaction (qPCR)

PCR reagent was prepared according to the manufacturer's instructions by blending 40% Sterile water (Biosolve), 50% TaqMan 2X Universal PCR Master Mix (No AmpErase UNG, Applied Biosystems, Branchburg, USA) and 10% primer/probe solution (included in kit). 40 μL of PCR reagent were added to each well. The plates were sealed using optically clear adhesive film (Applied Biosystems) and placed in the real-time PCR instrument (Gene Amp 5700, Applied Biosystems). The PCR protocol included 2 min at 50 °C, 10 min at

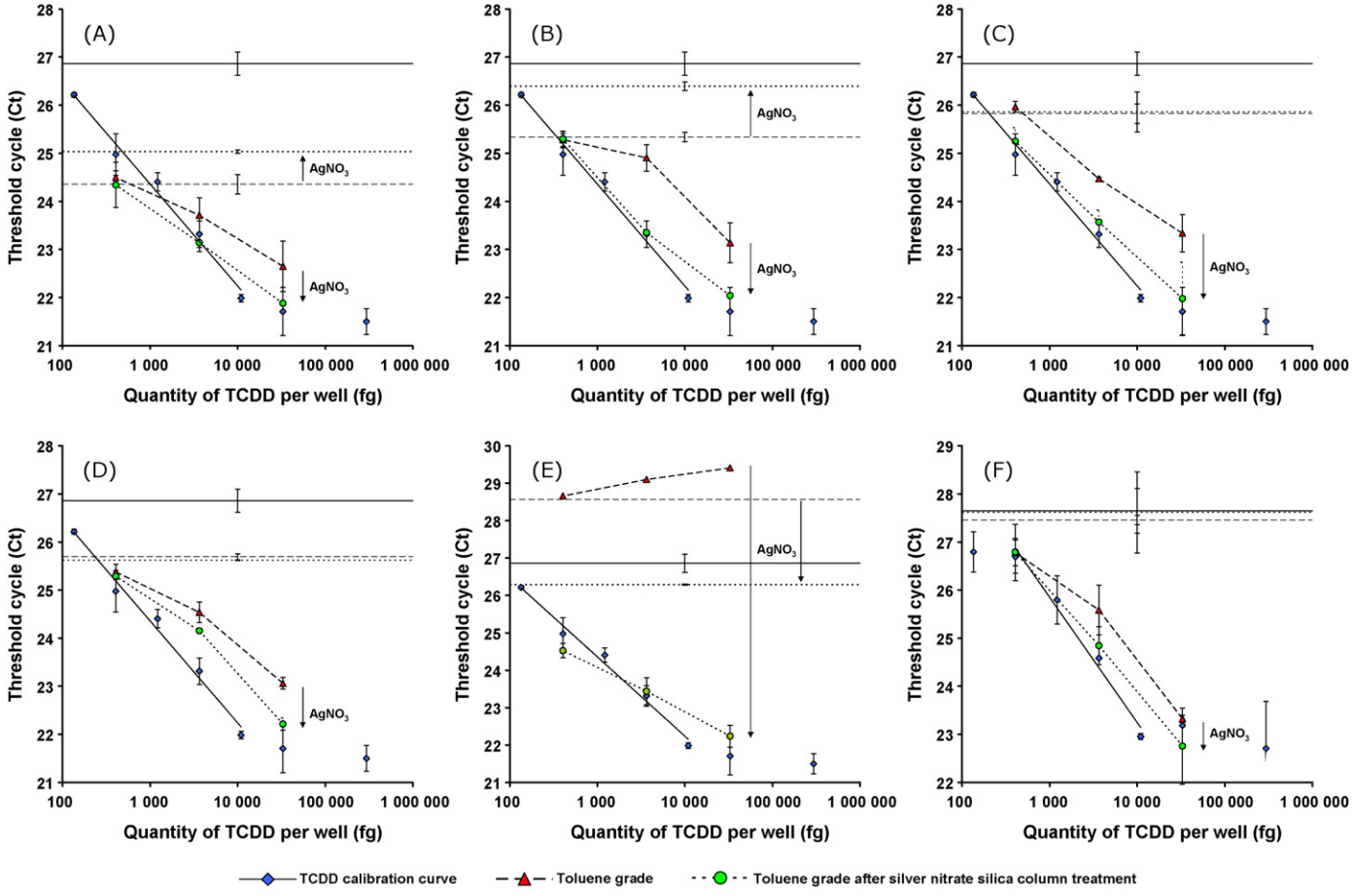


Fig. 1. Threshold cycle obtained for calibration curve (blue diamond, full line) and each tested toluene (A to F), without (red triangle, discontinuous line) or with (green circle, dashed line) silver nitrate silica column purification at background level (no TCDD, symbolic line at corresponding threshold level) and TCDD levels (plots). Standard deviation bars are from 2 assay measurement replicates. Arrows highlight the effect of silver nitrate silica column purification. Nota benne: procedural blanks on silver nitrate silica column showed no significant difference compared to assay TCDD calibration curve. (For interpretation of the references to color in this figure legend, the reader is referred to the web version of the article.)

95 °C and then 40 cycles of 15 s at 95 °C and 60 s at 60 °C. The output from the PCR instrument for each sample is a threshold cycle (Ct). The Ct is the number of real-time PCR temperature cycles at which the fluorescence measurement exceeds a threshold level chosen in the exponential part of amplification curves. *X*-Axis is usually set as logarithmic scale. Indeed, background level Ct appears higher than saturation plateau Ct, leading to a decreasing sigmoid curve.

3. Results and discussion

3.1. TCDD calibration curve

Two 96-well plates were used in this study. Fig. 1 shows results for the 6 toluene grades. Typically, calibration curve has a sigmoid shape. Its three parts correspond to background level, linear or working range and saturation plateau (defined by AhR concentration and well surface binding capacity). The ΔCt between the background level (assay blank) and the saturation plateau (5.36 and 4.95 Ct) were compliant, according to the manufacturer recommendations. The linear parts of the curves ranged from 135 to 10,935 fg/well (5 points, curve 1) or from 405 to 10,935 fg/well (4 points, curve 2). Coefficients of determination (R^2) were higher than 0.98, which appeared compliant with the European guidelines on screening bioassays for PCDD/F and DL-PCB. The obtained EC50 (concentration corresponding to the median response between the background level and saturation plateau) were 1214 and 1811 fg, respectively, these values being considered as usual.

3.2. Background levels

Four of the six toluene extracts (solvents A, B, C and D) gave higher background responses, reducing the Ct range with TCDD calibration saturation plateau by 20–50%. Such a result suggests that these toluene lots bring some agonistic compounds. Then, the sensitivity of the assay significantly decreases when toluene is used for sample preparation. Interestingly, solvent E showed the singularity to give a background level ~1.7 Ct higher than the calibration curve background. This could be interpreted as an inhibitory effect. Since the antibody is specific to the ARNT and that it is suspected that most of the background level is due to some "auto-activated AhR" (e.g. AhR Repressor or naturally occurring agonist in the rodent cytosolic liver extract), this result suggests that it is the antibody binding mechanism which is affected. This hypothesis is supported by the fact that the resulting solvent E background level is corresponding to a response level obtained when no antibody is added in the plastic wells. In such case, the obtained response is coming from unwashed free DNA (adsorption). Finally, solvent F showed the best behavior since no significant deviation was observed.

When concentrated extracts were submitted to a further purification step using a silver nitrate treatment before applying to the assay, the deviations of background levels significantly decreased for 3 of the solvent lots (solvents A, B and E). This purification step appeared to be partially efficient for selected grades only, suggesting that agonistic compounds can differ from a grade to another and that some are not sensitive to $AgNO_3$ treatment.

3.3. TCDD measurements

For each toluene grade, the concentrated extract was resuspended in *n*-heptane with 3 different TCDD concentrations (81, 729 and 6 561 fg/μL). For most of the results, responses were lower, up to −50%, compared to TCDD calibration curve. For lower spike level, solvent A gave a higher response compared to calibration curve, in accordance to the background level (similar signal) which is also higher than the calibration curve for this TCDD level. The singularity of solvent E persisted for spiked levels, with obtained responses also ~1.7 Ct higher than the calibration curve background. This corroborates the fact that there is a negative effect of this grade on the assay response as if no complex with DNA was bound to the antibody and or captured to the surface of the well.

When concentrated extracts were submitted to the silver nitrate purification, the deviations decreased in most of the cases, but not completely. These results suggest that antagonistic compounds occurring in different toluene grades are generally sensitive to $AgNO_3$ treatment but are not completely removed.

3.4. Discussion

The present study investigated the occurrence of both agonistic and antagonistic compounds as impurities in various toluene grades. From this point of view, no toluene grade behaved like the other one, suggesting that each manufacturing process lead to a distinct qualitative and quantitative profile in terms of impurities and interferences. One might suppose that involved compounds and their proportions also differ from one lot to another. Comparing the results with the information available in analysis certificates (Table 1) did not lead to pertinent trend concerning the identification of involved compounds in observed interferences.

Taking into account agonistic and antagonistic effects, the most suitable studied solvent grade appeared to be toluene B (Fig. 1). Starting from 50 mL and without silver nitrate silica column treatment, the working range was significantly reduced and a high inhibitory effect was observed. But after the silver nitrate silica column treatment, the diminution of ΔCt range (agonistic effect) and the inhibition effect on spiked levels appeared to be lower than 10%. This additional purification step appeared to be partially efficient for selected grades and should be adopted as final purification step of sample preparation just prior to assay measurement.

The present work shows that the performances of screening methods are not only depending on extraction/purification strategy but also to given solvent lots. Similar experiments were conducted with *n*-hexane and dichloromethane, with equivalent results and conclusions (data not shown). In order to obtain the best possible analytical performances, the control of each solvent lot before its use on "real" samples is highly recommended. Then, the question is what criteria should one respect to declare a lot compliant. A consensus should be to be defined by all the cell-based/DNA-binding assay and screening method experts.

4. Conclusion

In this study, we clearly demonstrated that the solvent grade has a major impact on the response of an AhR mediated assay. Both strong agonistic and antagonistic effects were observed for any studied lot. A small silver nitrate silica column partly removed these interfering compounds and is recommended as final purification step. Some "better" grades can be identified and selected in order to guaranty the best possible performances. However, it appears necessary to test every new lot, even if a grade previously appeared compliant.

Acknowledgment

The authors want to express their special thanks to the solvent manufacturers who provided free test samples.

References

[1] E.J. Reiner, R.E. Clement, A.B. Okey, C.H. Marvin, Anal. Bioanal. Chem. 386 (2006) 791–806.
[2] B. Aristizabal, A. Quintero, M. Cobo, N. Suarez, E. Hoyos, C. Montes de Correa, M. Avalos, E. Abad, J. Rivera, Organohalogen Compd. 69 (2007) 1269–1271.
[3] E. Dobrzynska, M. Szewczynska, Organohalogen Compd. 69 (2007) 1333–1336.

[4] T. Tagasuga, H. Takemoni, H. Matsukami, T. Inoue, Organohalogen Compd. 69 (2007) 1134–1137.
[5] H. Matsukami, H. Takemoni, S. Takahashi, T. Tagasuka, S. Tanabe, Organohalogen Compd. 70 (2008) 46–49.
[6] S.P. Bhavsar, A. Hayton, E.J. Reiner, D.A. Jackson, Environ. Toxicol. Chem. 26 (8) (2007) 1622–1628.
[7] B. Heinzow, S. Mohr, G. Ostendorp, M. Kerst, W. Körner, Chemosphere 67 (2007) 1746–1753.
[8] S. Hayashi, S. Goto, M. Hirano, K. Ohtsuka, N. Furuno, Organohalogen Compd. 67 (2007) 1002–1005.
[9] M. Nichkova, E.K. Park, M.E. Koivunen, S.G. Kamita, S.J. Gee, J. Chuang, L.M. Van Emon, B.D. Hammock, Talanta 63 (2004) 1213–1223.
[10] M. Nording, M. Nichkova, E. Spinnel, Y. Persson, S.J. Gee, B.D. Hammock, P. Haglund, Anal. Bioanal. Chem. 385 (2006) 357–366.
[11] J.W. Park, S. Kurosawa, H. Aizawa, H. Hamano, Y. Harada, S. Asano, Y. Mizushima, M. Higaki, Biosens. Bioelectron. 22 (2006) 409–414.
[12] M. Van den Berg, L. Birnbaum, A.T.C. Bosveld, B. Brunstrdm, P. Cook, M. Feely, J.P. Giesy, A. Hanberg, R. Hasegawa, S.W. Kennedy, T. Kubiak, J.C. Larsen, F.X.R. van Leeuwen, A.K.D. Liem, C. Nolt, R.E. Peterson, L. Poellinger, S. Safe, D. Schrenk, T. Tillitt, A.O.M. Tysklind, M. Younes, F. Warn, T. Zacharewski, Environ. Health Perspect. 106 (12) (1998) 775–792.
[13] M.E. Hahn, Chem. Biol. Interact. 141 (2002) 131–160.
[14] M.S. Denison, A. Pandini, S.R. Nagy, E.P. Baldwin, L. Bonati, Chem. Biol. Interact. 141 (2002) 3–24.
[15] J.R. Petrulis, G.H. Perdew, Chem. Biol. Interact. 141 (2005) 25–40.
[16] J. Mimura, Y. Fujii-Kuriyama, Biochim. Biophys. Acta 1619 (2003) 263–268.
[17] A.J. Murk, J. Legler, M.S. Denison, J.P. Giesy, C. van de Guchte, A. Brouwer, Fundam. Appl. Toxicol. 33 (1) (1996) 149–160.
[18] M.S. Denison, B. Zhao, D.S. Baston, G.C. Clark, H. Murata, D. Han, Talanta 63 (2004) 1123–1133.
[19] H. Vanderperren, N. Van Wouwe, S. Behets, I. Windal, I. Van Overmeire, A. Fontaine, Talanta 63 (2004) 1277–1280.
[20] N. Van Wouwe, I. Windal, H. Vanderperren, G. Eppe, C. Xhrouet, A.C. Massart, N. Debacker, A. Sasse, W. Baeyens, E. De Pauw, F. Sartor, H. Van Oyen, L. Goeyens, Talanta 63 (2004) 1157–1167.
[21] R. Hoogenboom, T. Bovee, W. Traag, R. Hoogerbrugge, B. Baumann, L. Portier, G. van de Weg, J. de Vries, Mol. Nutr. Food Res. 50 (2006) 945–957.
[22] S.D. Seidel, V. Li, G.M. Winter, W.J. Rogers, E.I. Martinez, M.S. Denison, Toxicol. Sci. 55 (2000) 107–115.
[23] D.R. McAlister, M.J. Fern, R.L. Allen, K. Sakata, B. Le Bizec, P. Marchand, Organohalogen Compd. 68 (2006) 940–943.
[24] D.R. McAlister, M.J. Fern, R.L. Allen, Talanta 74 (2008) 992–997.
[25] R. Cariou, P. Marchand, D.R. McAlister, M.J. Fern, B. Le Bizec, Organohalogen Compd. 69 (2007) 821–824.
[26] R. Cariou, P. Marchand, D.R. McAlister, M.J. Fern, J.-P. Antignac, B. Le Bizec, Organohalogen Compd. 70 (2008) 2094–2097.
[27] Commission Regulation (EC) No 199/2006 of 3 February 2006 amending Regulation (EC) No 466/2001 setting maximum levels for certain contaminants in foodstuffs as regards dioxins and dioxin-like PCBs. Official Journal of the European Union 4.2.2006.
[28] Commission Directive 2006/13/EC of 3 February 2006 amending Annexes I and II to Directive 2002/32/EC of the European Parliament and of the Council on undesirable substances in animal feed as regards dioxins and dioxin-like PCBs. Official Journal of the European Union 4.2.2006.
[29] I. Windal, M.S. Denison, L. Birnbaum, N. Van Wouwe, W. Baeyens, L. Goeyens, Environ. Sci. Technol. 39 (2005) 7357–7364.

Talanta 80 (2010) 2068–2075

Contents lists available at ScienceDirect

Talanta

journal homepage: www.elsevier.com/locate/talanta

Fast multi-element screening of non-digested biological materials by slurry introduction to ICP-AES

Barbro Kollander, Marit Andersson, Jean Pettersson*

Department of Physical and Analytical Chemistry, Uppsala University, Box 599, SE-751 24 Uppsala, Sweden

ARTICLE INFO

Article history:
Received 3 July 2009
Received in revised form 21 October 2009
Accepted 3 November 2009
Available online 12 November 2009

Keywords:
Slurry
Whole blood
Liver
ICP-AES
Internal standards
External calibration

ABSTRACT

A fast method for direct multi-element analysis of non-digested biological samples is presented. The only sample preparation needed is 1 min homogenization with a Polytron mixer in a small volume of neutral phosphate buffer saline solution (PBS). The total time for analysis (sample preparation and measurement) is 4 min only. This "mix and measure" method can handle large sample loads of biological samples and thus minimize dilution of trace elements. For example 100% whole blood was introduced without any clogging of the introduction system or extinguishing of the plasma. In 70% (v/v) whole blood reference material 14 of 16 analytes were quantified within ±10% (Al, B, Ba, Ca, Cu, Fe, Mg, Mn, P, Pb, S, Sr, Ti and Zn) and two semi-quantified within ±20% (Cd and K). Fresh bovine liver was also analyzed with the same method and 7 of 9 analytes were quantified in 5% (w/v) liver slurry. Three different nebulizers were tested, Glass Expansion Concentric (GEC) of Meinhard type, Cross Flow and Burgener T2100 and they performed roughly equally well in giving quantitative results for the slurries but the sensitivity was better with the GEC. The stability of the plasma was studied by evaluating the ratio of Mg 280.270 nm and Mg 285.213 nm lines. When increasing the sample load from 20 to 100% (v/v) of whole blood and from 0.5 to 10% (w/v) of bovine liver the Mg ratio was constant within a few percent for all of the nebulizer tested. The ratio of the sensitivity between GEC and Burgener T2100 was studied and the ratio increased with the energy sum for atomic and ionic lines separately.

© 2009 Elsevier B.V. All rights reserved.

1. Introduction

Fast and accurate analytical methods are the aim for both analytical chemists and the assigners. Therefore a lot of research is performed on reducing the total analysis time needed. In multi-element analysis of different biological materials by inductively coupled plasma-atomic emission spectrometry (ICP-AES) or inductively coupled plasma-mass spectrometry (ICP-MS), like in many other analytical techniques, the most time consuming step is the sample preparation. For ICP-AES and ICP-MS methods there is almost always a digestion or dissolution step involved prior to measurement, which in the worst case could last for several hours or days. By excluding this step not only the time of the total analysis is reduced substantially, but also, it leads to less risk for contamination of the sample from digestion reagents and to reduce consumption of destructive chemicals, which is of concern both environmentally and for occupational health. Moreover, losses of analytes especially volatile ones are minimized by using the slurry technique compared to the more aggressive acid digestion. Analysis of non-dissolved material, i.e. slurries, of both inorganic and organic materials by different plasma techniques, is of great concern due to additional reasons. The limited dilution in slurry analysis is beneficial because it enables analysis of elements present at low concentrations in the sample, which after a digestion procedure would have ended up in concentrations below the detection limit of the instrument. It is also advantageous when the amount of sample is limited, which could be important in analysis of samples with, for example, medical or forensic origin.

The basic concept of slurry analysis is that it is possible to quantify any element as long as the behaviour of the element in the slurry samples resemble the behaviour in the calibration solutions concerning nebulization, transport efficiency, atomization, ionization and excitation. Some of the differences that might occur due to matrix effects from the sample, could however be compensated for by evaluation with internal standard or sometimes with inter element correction (IEC) [1–3].

To bring a solid sample into a sprayable liquid without any tedious digestion there are several options described in the literature, for example, a short semi-digestion procedure including addition of nitric acid [4] and sometimes followed by ultra sonication [5–7]. Also grinding [8–10] or sieving [11] followed by dilution with dilute nitric acid (1–2%) has been tried with varying success on different types of samples. Moreover, carbonisation (ashing) of the organic part of the sample prior to slurry analysis has been

* Corresponding author. Tel.: +46 184713676; fax: +46 184713692.
E-mail address: jean.pettersson@kemi.uu.se (J. Pettersson).

0039-9140/$ – see front matter © 2009 Elsevier B.V. All rights reserved.
doi:10.1016/j.talanta.2009.11.007

reported [7,12]. Most of these methods require a total time of more than 5 min and in some cases hours for successful homogenization to a particle size that is possible to transport to the plasma and to be atomized properly. Ebdon et al. [1] concluded, for example, in their comprehensive review of slurry nebulization in plasmas in 1997, that particles larger than 5 μm do not reach the plasma. In addition, Goodall et al. [12] mention that the maximum size of a particle that reaches the plasma depends on the density.

A crucial point after homogenization of the sample is to keep the slurry homogeneous during introduction into the ICP. In a macro point of view some kind of stirring is used like magnetic stirrer or shaker. In a micro-point of view the particles must be prevented from forming too large aggregates. This is successfull and almost always performed by adding different amounts of the detergent Triton X-100 (0.001–1%) [6,7,9,11,13–15]. However, concern must be taken since using a too large amount of Triton causes foaming in the spray chamber.

When it comes to calibration procedure the calibration solution matrix is in most cases closely matched to the samples. According to the literature published, nitric acid seems to be the preferable choice probably because the slurry samples often are treated or diluted with nitric acid and due to the fact that an acidic matrix prevents precipitation and adsorption of the analytes onto the walls of vessels and tubing. There are however some indications of precipitation of proteins in the slurry sample when using nitric acid [6]. Also some reports are published using alkaline [16] or neutral matrices [14] and then EDTA is added to prevent metal ions to precipitate or to adsorb onto container walls. When working with slurries of organic materials, the general approach seems to be dilution of samples and carrying out quantification without internal standard [5,7–9,12,13,17]. However, internal standards mentioned in the literature when analyzing slurries with ICP-AES are Y [15,18], Sc [6,19] and Lu [14].

For screening purposes, a method including a simple homogenization of cell pellets or biological samples prior to direct measurement by ICP-AES and ICP-MS, has initially been tested in our laboratory for semi-quantification of Gd or B in cultured cells and for determination of Mn in mouse brain [20]. In this method a Polytron mixer was used for fast homogenization of the fresh biological sample followed by dilution by the physiological solution phosphate buffered saline (PBS) to prevent precipitation of proteins. The slurry was then immediately introduced into the ICP-AES and evaluated with aqueous calibration solutions. Total analysis time was only a few minutes.

In this work extremely high sample loads of non-digested biological material were introduced into the plasma. The aim was to investigate the possibilities for a simple "mix and measure" method to accurately quantify some elements of toxic, environmental, and/or physiological concern with the lowest possible dilution. By increasing the sample load, both the inorganic and the organic content are increased at the same time, giving rise to many possible influences on the emission signals of the analytes. The samples also contain fragments of cells that may affect the plasma conditions. The behaviour of the plasma when increasing the sample load was studied by measuring the ratio of Mg 280.270 nm and Mg 285.213 nm lines [21–23] and the effect on emission lines with different ionization and/or excitation energies (energy sum) was investigated [2,22,23]. Also the signal precision [24] of repeated measurements was followed when increasing the sample load. The purpose was to use the equipment most commonly used in ICP-AES with ordinary settings. Three different nebulizers were tested; Glass Expansion Concentric (GEC), Cross Flow and Burgener T2100 and their performance are discussed. As a suitable test sample a whole blood reference material was used since analytical values of the elements of interest are at hand, and the fact that whole blood contains a lot of cells, cell-membranes and other ingredients that are expected in a biological sample. Others have analyzed whole blood by ICP-AES or ICP-MS but for digested [17,25,26] or more diluted samples [27–29]. Since the whole blood reference material is freeze dried and there might be differences concerning cell consistency from fresh biological samples that might affect the behaviour in the ICP, a fresh bovine liver sample was also analyzed.

Table 1
ICP operating conditions.

Rf power/kW	1.4		
Torch, injector	Fassel type, 2.8 mm id		
Auxiliary gas/l min^{-1}	0.9		
Coolant gas/1 min^{-1}	14		
Integration time/s	25		
Number of repetitions	3		
Nebulizer[a]	GEC	CF	B
inner diameter/μm	200	500	750
Nebulizer flow/1 min^{-1}	0.8	0.9	0.9
Sample flow rate/ml min^{-1}	1.8	1.5	1.5

[a] GEC = Glass Expansion Concentric of Meinhard type, CF = Cross Flow, B = Burgener T2100.

2. Experimental

2.1. Chemicals and solutions

All chemicals were of analytical grade and solutions diluted with Milli-Q purified water (Millipore, Billerica, MA, USA). In the following the abbreviation MQ will be used. Multi-element standard stock solution and multi-internal element standard stock solution were obtained by dilution of commercial standards (Teknolab A/S, Drobak, Norway, and Referensmaterial AB, Ulricehamn, Sweden). The phosphate buffered saline, PBS (BioChemika, Fluka, Buchs, Switzerland) was prepared according to instructions from the manufacturer. Nitric acid solutions were obtained by dilution of concentrated nitric acid (Merck, Darmstadt, Germany). A stock solution of 5% (v/v) Triton X-100 was prepared by gentle dilution of Triton (Sigma Aldrich, Steinheim, Germany) to avoid foaming. Triton was added to all solutions and slurries measured by ICP-AES to a final concentration of 0.05% (v/v). Multi-element calibration standards (with sample matched concentrations of the analytes) including internal standards (Sc and Y), were prepared by dilution of stock solutions by either PBS or nitric acid to a final concentration of 10% PBS (13.7 mM NaCl, 2.7 mM KCl and 1 mM phosphate buffer) or 1% nitric acid (0.14 M) respectively. Calibration solutions in PBS were freshly prepared prior to measurement.

The solution added to the slurry samples prior to homogenization was prepared from PBS solution, Triton and appropriate amounts of internal standards. In the following text this solution is referred to as the "mixing solution". The concentration of PBS, Triton and internal standards were in all measurements the same in the samples as in the calibration standards. The concentration of each internal standard was 1 mg/l.

The samples analyzed were one reference material, Seronorm^{TM} Trace Element whole blood L-3 REF 102405, LOT 0512627 (Sero AS, Billingstad, Norway) and a fresh bovine liver from a one year old animal purchased at a supermarket nearby.

2.2. Instrumentation

The ICP-AES instrument used was a Spectro Ciros^{CCD} EOP (Spectro Analytical Instruments, Kleve, Germany), equipped with a Glass Expansion Concentric nebulizer of Meinhard type (Glass Expansion, MA, USA), Burgener T2100 nebulizer (Burgener Research Inc., Ontario, Canada) or Cross Flow nebulizer (supplied by the manufacturer of the ICP instrument) followed by a Scott double-pass spray chamber. The ICP operating conditions are presented in Table 1. The

Table 2
Results from analysis of 40% (v/v) and 70% (v/v) of Seronorm Trace Elements in whole blood L-3 with ICP-AES using Glass Expansion Concentric (GEC) nebulizer of Meinhard type. Results are presented as recoveries of analytical values (%). Yttrium (371.030 nm, II, 9.62 eV) and Sc (361.384 nm, II, 10.03 eV) were used as internal standard (I.S).

Element	ICP-AES line (nm)	[a]	Energy sum[b] (eV)	Analytical value (μg/l)	CL (S.D.) (μg/l)	I.S.	Recovery of analytical value (%) Volume fraction of whole blood in sample (%) (v/v)			
							40% 1[c]	40% 2	70% 1	70% 2
Al	167.08	II	13.47	93.9	5.9	Y	100	100	101	100
						–	88	87	82	81
	396.152	I	3.14			Y	116	112	114	119
						–	103	99	95	98
B	249.773	I	5.93	254	(6)	Sc	103	100	100	95
						Y	98	93	95	91
						–	84	79	76	72
Ba	455.404	II	8	2289	(36)	Sc	100	103	103	103
						Y	94	95	97	98
						–	82	84	79	79
Ca	422.673	I	2.93	74000	2000	Y	100	101	101	101
						–	111	112	98	97
Cd	214.438	II	14.84	8.9	5	Sc	86	88	89	87
						Y	80	81	84	83
						–	70	71	69	67
Cu	324.754	I	3.82	1741	140	Sc	102	102	102	101
						Y	96	95	96	96
						–	83	82	78	77
Fe	259.941	II	12.71	468000	(11000)	Y	106	107	112	109
						–	123	123	111	107
K	766.491	I	1.62	452000	(9000)	Y	203	202	182	185
						–	125	125	114	115
Mg	285.213	I	4.35	21700	(500)	Sc	100	100	98	96
						Y	93	92	93	92
						–	82	81	76	74
Mn	257.611	II	12.25	12.5	1.7	Y	136	129	131	132
						–	112	105	105	105
P	178.287	I	6.95	206000	(5000)	Y	129	126	136	133
						–	108	106	107	104
	213.618	I	6.98			Y	123	123	131	128
						–	104	103	104	100
Pb	220.353	II	14.79	437	25	Y	101	101	109	108
						–	88	88	89	87
S	182.034	I	6.81	1426000	(40000)	Sc	91	91	91	88
						Y	85	84	86	83
						–	75	73	70	67
Sr	407.771	II	8.8	205	(7)	Y	103	103	101	102
						–	91	90	83	82
	460.733	I	2.69			Y	102	102	105	107
						–	90	90	85	86
Ti	334.941	II	10.58	16	4	Y	142	115	101	102
						–	121	97	79	79
Zn	213.856	I	5.8	8032	512	Y	98	99	102	100
						–	86	86	83	81

[a] I = atomic line and II = ionic line.
[b] Energy sum = excitation potential for atomic line and excitation plus ionization potential for ionic line.
[c] The figures after the volume fraction represent replicate 1 and 2.

instrumental settings for each nebulizer were optimized by measuring Mn 257.611 nm in aqueous solution (recommendation from the manufacturer of the instrument). Appropriate background correction for each sample type and element was performed. Lines measured are listed in Tables 2 and 3. The software used was Smart Analyzer Vision (version 2.11) supplied by the manufacturer of the instrument.

A Polytron PT 1200 mixer (Kinematica, AG, Lucerne, Switzerland) was used for homogenization of samples (down to 20 μm particles according to manufacturer) and for the continuously stirring during introduction to the ICP-AES a Heidolph R2R No. 50111 attached with a Teflon tube (1/4″) as stirring tool was used. To increase the stirring efficiency half of the Teflon tube was removed by cutting along the tube at the lower part in contact with the slurry.

For acid digestions stainless steel bombs with Pyrex tubes and Teflon seals were used.

2.3. Sample preparation and measurement procedure

The freeze dried blood (1.21 g) was reconstituted by adding 5.00 ml MQ according to the instructions given by the manufacturer. Different amounts of the reconstituted whole blood were

Table 3
Approximate values of the major matrix components in whole blood and liver.

		Na	K	P	Cl	C	N	S
Whole blood								
Reference Man[a]	g/l	1.9	1.7	0.4	2.9	104	31	1.9
Seronorm TEWB L-3[b]	g/l	4.1	0.4	0.2	–	–	–	1.4
Liver								
Reference Man[a]	mg/g	1.0	2.5	2.6	2.0	144	28	2.9
Bovine liver[c]	mg/g	–	3.4	3.8	–	–	–	2.3
Concentration in representative samples[d]								
70% (v/v) whole blood	g/l	2.9	0.3	0.1	2.0	73	22	1.0
5% (w/v) bovine liver	g/l	0.1	0.2	0.2	0.1	7.2	1.4	0.1
Addition from 10% PBS								
In calibration- and sample solutions	g/l	0.3	0.01	0.03	0.5	–	–	–

[a] Values calculated from Ref. [38].
[b] Seronorm Trace ElementL-3, REF102405, LOT 0512627.
[c] Values from acid digestion of bovine liver.
[d] Values calculated from Seronorm and bovine liver when reference values are available, otherwise from "Reference Man".

weighed directly into 15 ml plastic tubes. A volume of 2.00 ml of mixing solution was added and followed by 3× 15 s homogenization with the Polytron mixer at 14,000 rpm. After mixing, the samples were diluted with MQ to a final volume of 10.00 ml. The procedure was somewhat different when preparing samples of 100% whole blood; 4.00 ml MQ and 1.00 ml mixing solution was directly added to the freeze dried sample for reconstitution, followed by homogenization.

The bovine liver was roughly homogenized with a household mixer and stored in the freezer prior to analysis. Duplicates of different amounts of defrosted liver (50, 100, 200, 500, 750, 1000 mg) were accurately weighed into 15 ml plastic tubes and then treated in the same way as the blood samples.

The measurement sequence was started by aspirating the slurry for 45 s followed by measuring the emission (3× 25 s). After measurement of the slurry the introduction system was washed by aspirating 0.05% Triton for 30 s followed by MQ for at least 1 min. The stability of the emission signals and the possibility of memory effects were checked by frequently measuring the zero calibration solution and one of the multi-element standards.

For the acid digestion about 0.3 g of the bovine liver was weighed into three tubes. 100 μl Yttrium (1000 mg/l) and 4 ml conc. nitric acid was added to each tube and to two empty tubes used as blanks. The tubes were put into bombs and sealed with a Teflon seal, closed with a moment of 32 N m and then heated for 2.5 h at 160 °C. After cooling to room temperature the solutions were transferred to 25 ml volumetric flasks and diluted with MQ. Multi-element standards with sample matched concentrations of the analytes in nitric acid were used for evaluation.

The concentrations were evaluated by calibration with and without internal standards and when necessary, polynomial evaluation (2nd order) was used.

3. Results and discussion

3.1. Whole blood analysis

It is possible to aspirate samples with up to 100% of whole blood into the plasma without clogging of the introduction system or extinguishing the plasma, with GEC, Cross Flow and Burgener nebulizer. This is possible due to the non-acidic matrix, PBS, in the samples. Similar attempts with this high biological sample load in an acidic matrix resulted in immediate precipitation of proteins in the introduction system which has also been reported by others [17]. All three nebulizers gave good recoveries within ±20% for 10–70% (v/v) of whole blood for most elements when evaluated with internal standard (Y 371.030 nm or Sc 361.384 nm), examples shown in Figs. 1 and 2. Without internal standard, the recoveries leveled off at higher sample loads. In Table 2 typical recoveries of analytical values for elements in 40 and 70% (v/v) of whole blood for GEC are shown. The recoveries were evaluated both with and without internal standard. Results in white field are within ±10%, results in light grey field ±20% and dark grey field show results worse than ±20%. Of the 16 analytes measured, 14 could be quantified (±10%) and 2 semi-quantified (±20%) in 70% (v/v) whole blood. Mn and Ti could be quantified despite the low analytical concentration given by the producer; 12.5 and 16 μg/l respectively. Simultaneously with the determination of Mn and Ti in the low μg/l range, Fe, P and S at levels of several hundreds of mg/l could be quantified. With GEC it is also possible to quantify Fe (259.941 nm) in 100% (v/v) whole blood. The too large recovery of K could be explained by signal enhancement caused by the increased amount of easily ionized elements (EIE) in the blood

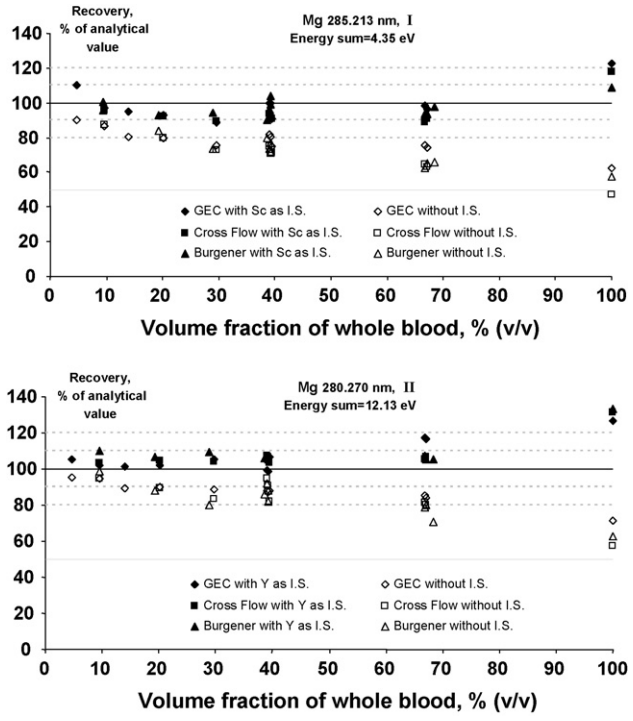


Fig. 1. Recovery of analytical value of Mg (21.7 (±0.6) mg/l) for one atomic and one ionic line in different dilutions of Seronorm Trace Element in whole blood L-3 with Glass Expansion Concentric (GEC), Cross Flow and Burgener T2100 nebulizer respectively.

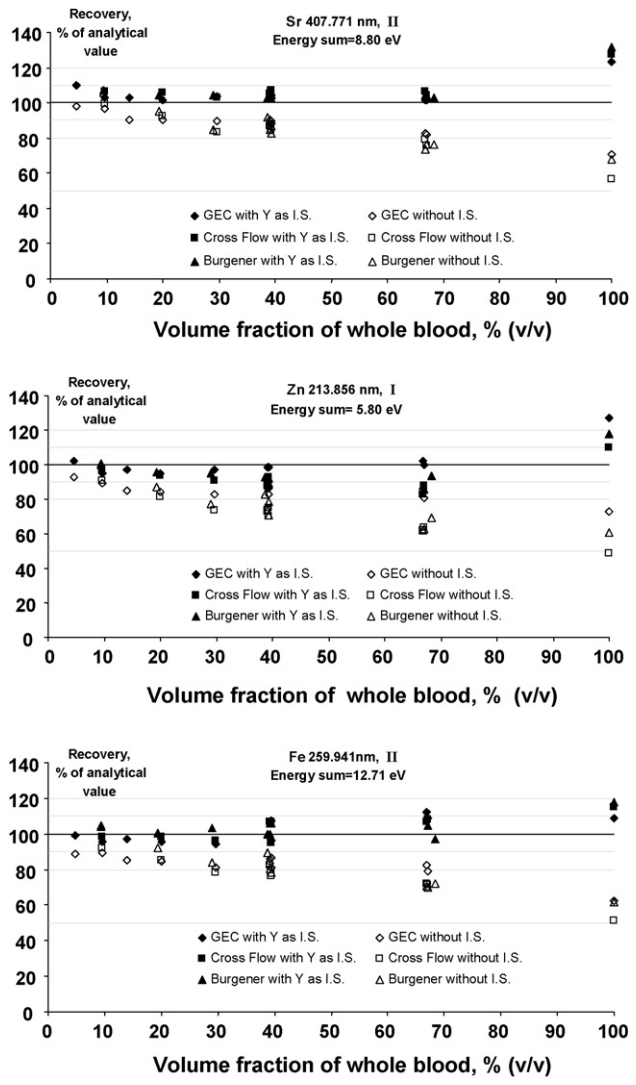


Fig. 2. Recovery (%) of analytical value for Sr (205 (±7) μg/l), Zn (8032 ± 512 μg/l) and Fe (468 (±11) mg/l) in different dilutions of Seronorm Trace Element in whole blood L-3 for Glass Expansion Concentric (GEC), Cross Flow and Burgener T2100 nebulizer respectively. The behaviour is the same for all three elements despite large concentration ranges and differences in energy required for emission.

sample (Table 3). The recoveries with Burgener and Cross Flow nebulizer are both very close to the results with GEC for most elements, which can be seen by the examples given in Figs. 1 and 2. Results with Cross Flow were not as reproducible as GEC and Burgener. Recoveries for Mg with the three nebulizers evaluated with and without internal standard are presented in Fig. 1. The upper diagram shows results for the atomic line (285.213 nm) and the lower for the ionic line (280.270 nm). Using internal standard improved the recoveries generally. Sc gave slightly better results than Y as internal standard for the atomic line but Y was slightly better for the ionic line. The trends were similar for both internal standards giving recoveries <100% for Mg (285.213 nm) and >100% for Mg (280.270 nm), but since most of the recoveries were within ±10% no general conclusions could be drawn from this. In Fig. 2 examples are given for analytes with different concentration levels in the whole blood, as well as different energy sum. The similarity between all the diagrams is striking. It is also clearly demonstrated in the diagrams mentioned above; that the higher the volume percent of whole blood in the sample the more severe are the matrix effects and using internal standard is more important for accurate results. This of course could be expected since both the inorganic and organic contents are increased. For example, Burkowska et al. [23] show similar trends when studying the change in line intensity for several emission lines with increasing Ca + Mg concentration in the matrix and the same trend is also seen in a work by Ioannidou et al. [30] when increasing the carbohydrate concentration. Since the decrease in recovery for all elements (Figs. 1 and 2) are about the same when increasing the blood content in the sample, regardless of their energy sum and/or whether atomic or ionic lines are considered, the decrease could not be explained by reduction of the energy available in the plasma caused by the heavy sample load. This has also been seen by others analyzing dissolved matrices with increasing concentration of NaCl [24]. More likely, decreased nebulization and transport efficiency of the sample to the plasma [2] contribute to the declining recoveries. By using Y or Sc as internal standard the recoveries are improved for all the analytes presented in Figs. 1 and 2 and also for several of the analytes presented in Table 2. Worth notifying is that in 100% (v/v) of whole blood the internal standard is not able to accurately correct for the matrix effects in the same extent as in samples with lower blood content. In this case this is probably due to a too large discrepancy between the physical properties of the 100% (v/v) blood and the calibration solutions, which severely affects the transport efficiency and spray formation. However, even in dissolved matrices it has been verified that the internal standard fail to provide accurate result when the sample matrix is increased [2,31,32] since the analyte and internal standard are differently affected by the matrix (see more detailed discussion about internal standards below).

The stability of the sample introduction system, i.e. transport efficiency and spray formation for a given sample solution could by followed by studying the signal precision [24], i.e. the fluctuations in repeated measurements of the emission signal. When introducing 70% (v/v) whole blood the relative standard deviation (RSD) varied between 0.5 and 2% for triplicate measurements. This is slightly higher than for the calibration solutions which most often gave a RSD below 1%, but still this could be regarded as stable and acceptable values for quantitative analysis.

The conditions in the plasma could be studied by monitoring the ratio between Mg II (280.270 nm) and Mg I (285.213 nm) [21–23]. This ratio gives a measure of the energy available for ionization and excitation in the plasma and a value of eight is reported to indicate a robust plasma [21]. However, the ratio can differ from instrument to instrument due to the type of monochromator and signal collection system. No obvious change in the ratio was seen for any of the three nebulizers tested when 20, 30, 40, 70 and 100% (v/v) of whole blood was introduced into the plasma. For GEC the average ratio (±S.D.) was 8.0 (±0.1), for Cross Flow 6.6 (±0.3), and for Burgener 7.3 (±0.1). Obviously the energy available in the plasma does not change with increased concentration of whole blood. The Mg ratio varied somewhat between different runs but the trend, with no change of the ratio within a run when increasing the blood concentration, was consistent. It should be noted that the emission of Mg at 280.270 nm in 100% blood is close to the upper limit of the linear range. However, the results for Mg, Al and Sr, which all have been evaluated both by an atomic line and an ionic line giving similar results, thus further support that the energy in the plasma is not altered by the sample matrix with the instrumental settings used.

All elements were evaluated both with Y (371.030 nm, II, 9.62 eV) and Sc (361.384 nm, II, 10.03 eV) as internal standards. These lines have been used for analysis of digested [33] or diluted [17,34] serum and digested whole blood [17,35]. In the present study also other emission lines for Y (324.228, 360.073 and 224.306 nm) and Sc (335.374 nm) were studied when increasing the concentration of whole blood. They showed, however, the same behaviour as the commonly used lines mentioned above. In Table 2 results with and without Y as internal standard are presented for all elements. Results evaluated with Sc are only presented for the

elements that gave better recoveries with Sc, namely; B, Ba, Cu, Mg, and S. Elements giving best recoveries with Y were; Al (167.08 nm), Ca, Fe, Pb and Sr. Only Al (396.152 nm), P and Mn yielded best recoveries without internal standard. Since Mn has higher energy sum than both Y and Sc, while Al and P have lower, the failure of the internal standards is not explained by differences in energy sum. Nor is it explained by the different distribution of the elements in either the cellular fraction of the whole blood or in the blood plasma. This could be seen by the quantitative recoveries of Fe evaluated with internal standard. Since Fe almost totally exists in the red blood cells [36] this means that the atomization and excitation is not affected by whether the element exists inside or outside a cell. Further support to this is the quantitative recoveries of Mg, Zn and P, which also predominantly exist in the cellular fraction of whole blood [36]. However, it must be mentioned that in addition to the homogenization of the blood sample by the Polytron, the tested reference blood has been freeze dried, which could contribute to the disruption of the blood cells and thus facilitate the atomization of elements coming from within the cells.

3.2. Analysis of bovine liver

It is possible to aspirate at least up to 10% (w/v) of the fresh bovine liver sample into the plasma without clogging of the introduction system or extinguishing the plasma, both with GEC and with Burgener nebulizer. Cross Flow was not used for the liver analysis due to somewhat more irreproducible performance. Both nebulizers gave recoveries within ±20% for most elements for 0.5–5% (w/v) liver (Table 4). The recovery was calculated by using the analytical value received from analysis of acid digested bovine liver as the true value. Ca, Fe, K, Mg, P and Zn were quantified within ±10% in 10% (w/v) with GEC, and with Burgener Cu and Zn were quantified while Ca, Fe, K, Mg, Mn and P were semi-quantified (±20%). At the lower concentration 5% (w/v) of slurry liver sample it was possible to quantify seven of the nine elements measured with both nebulizers. Most of these elements were quantified with external calibration, and only Cu and Mn gave good and stable recoveries with Y as internal standard. All the examined lines of Y; 371.030, 324.228, 360.073 and 224.306 nm, showed similar behaviour in the liver matrix and thus Y solely is not a good choice as a multi-element internal standard. The fairly good recoveries of elements evaluated with external calibration could probably be improved by using other elements appropriate as internal standards. Since it is shown in this study that quantification is possible with external calibration and the aim was to evaluate the limits for the suggested method no further attempts to improve the recoveries were made.

The liver sample matrix gives a lower sample load than the blood sample, both concerning the total ion concentration and the carbon content (Table 3). This could explain the need of an internal standard for quantitative recoveries in the blood matrix (Table 2) and the fairly good recoveries received without internal standard for the liver samples (Table 4). This also implies that the liver slurries are efficiently nebulized and transported into the plasma, in roughly the same extent as the calibration solutions. The signal precision for 5% (w/v) liver sample varied between 0.5 and 3% for triplicate measurement (average 1.2%) which further verify a quite efficient transport and excitation of the analytes. However, for Y the signal precision was 3.5% and it also varied more between the samples than for the analytes. This could indicate that Y is not uniformly distributed in the liver slurry despite thorough mixing with the Polytron and hence giving erroneous results as an internal standard. In the blood samples the signal precision for Y was equal to the ones for the analytes averaging around 1%.

The condition in the plasma was followed by the Mg ratio mentioned above and there were no change observed when the higher concentrations of liver samples were introduced. The average ratio was 7.6 (±0.1) for both Burgener nebulizer and GEC.

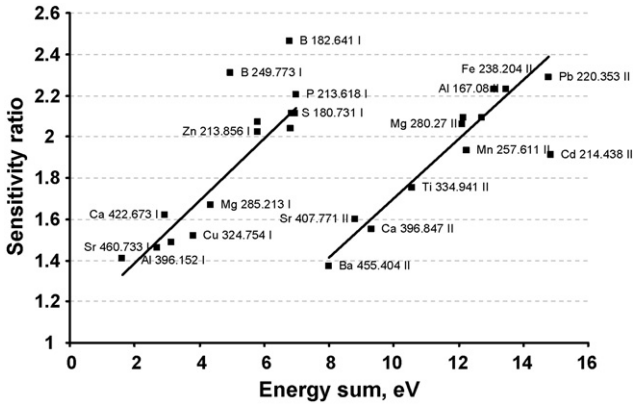


Fig. 3. Sensitivity ratio (slope/slope) for Glass Expansion concentric (GEC) and Burgener T2100 nebulizer from calibration curve as a function of energy sum.

Initially slurry analysis of the reference material NIST SRM 1577a bovine liver (NIST, Boston, MA, USA) was performed. However, the suggested sample preparation method with homogenization by the Polytron mixer did not manage to homogenize some aggregates in the freeze dried liver sample that could be residues of vessel tissue. These aggregates caused frequent clogging in all the sample introduction systems tested and only a few results were obtained. Others have succeeded better with slurry analysis of 1577a probably due to a better homogenization procedure or addition of nitric acid to the freeze dried liver [9] which could disrupt the aggregates properly before introduction to the ICP. Nitric acid is not an option in this work since protein precipitation and leaching from the Polytron mixer must be prevented. Since the method is useful for fresh bovine liver and the aim of this study was not slurry analysis of freeze dried samples, no further effort was made to analyze 1577a.

3.3. Additional comparison of the nebulizers

GEC nebulizer gave superior sensitivity (larger slope from calibration curve) for all elements, while Cross Flow and Burgener T2100 gave about the same with the instrumental settings used. Compared to Burgener, GEC gave from 1.4 to 2.5 times higher sensitivity, Fig. 3. GEC nebulizer is known to create a very fine mist with small droplets while Burgener, due to its wider inner diameter, allows larger droplets to form. These larger droplets are partly filtered by the spray chamber and thus less analyte reaches the plasma which could explain the lower sensitivity in general. In the case of Cross Flow the slightly lower Mg ratio indicates a higher matrix plasma load than for GEC and Burgener. The more heavily loaded plasma has a lower temperature and thus decreased sensitivity due to decreased atomization and excitation. Also the ability of a certain nebulizer to form a well shaped spray of as much sample as possible influences the sensitivity [24] and Cross Flow is not known to give a high sensitivity but for being suitable for slurry analysis [37].

In Fig. 3 the sensitivity ratio between GEC and Burgener for several emission lines, is plotted against the energy sum for each line (values are given in Table 2). There is an obvious trend for atomic lines and for ionic lines separately. In both groups the sensitivity ratio increases with the energy sum. This means that, within each group, the larger the energy sum of an element the larger difference there is in sensitivity between GEC and Burgener nebulizer under the conditions used. However, rather than the energy sum, the wavelength of the emitted radiation seems more important for the difference between the nebulizers. All emission lines that yield

Table 4
Results from analysis of fresh bovine liver ($n = 2$) with ICP-AES using Burgener T2100 (B) or Glass Expansion Concentric (GEC) nebulizer. Results are presented as recovery of analytical value (%). Yttrium 371.030 nm was used as internal standard (I.S).

Element	ICP-AES line (nm)	[a]	Analytical value[b] (μg/g)	SD	Nebulizer	I.S.	Recovery of analytical value (%) Amount of bovine liver in sample (%) (w/v)					
							0.5%	1%	2%	5%	8%	10%
Ca	422.673	I	32	1	B	Y	129	116	105	99	89	89
						–	128	137	128	134	145	136
					GEC	Y	127	126	128	123	142	131
						–	131	113	113	107	97	100
Cu	324.754	I	103	3	B	Y	88	104	95	90	90	91
						–	89	88	78	66	55	60
					GEC	Y	92	104	99	88	92	88
						–	96	96	89	77	64	68
Fe	259.941	II	51	1	B	Y	84	120	111	111	117	111
						–	85	101	91	81	72	73
					GEC	Y	85	117	113	105	119	109
						–	90	107	101	91	81	83
K	766.491	I	3400	140	B	Y	112	135	132	139	159	150
						–	112	111	105	97	88	86
					GEC	Y	128	145	144	129	154	136
						–	129	128	124	107	95	94
Mg	285.213	I	183	6	B	Y	100	121	120	126	139	130
						–	102	103	99	93	85	84
					GEC	Y	101	116	120	116	134	124
						–	106	108	108	101	92	94
Mn	257.611	II	2.77	0.06	B	Y	99	113	103	91	92	88
						–	100	96	84	67	56	57
					GEC	Y	105	115	108	81	88	84
						–	110	106	97	70	61	65
P	213.618	I	3770	120	B	Y	109	130	123	127	135	133
						–	108	106	98	92	82	86
					GEC	Y	116	134	136	128	141	134
						–	116	118	117	108	96	101
S	182.034	I	2260	80	B	Y	102	122	115	115	124	121
						–	104	104	94	82	71	73
					GEC	Y	106	122	119	109	122	117
						–	111	114	107	95	84	89
Zn	213.856	I	31.2	0.9	B	Y	110	156	145	144	153	145
						–	111	131	118	106	93	94
					GEC	Y	112	154	148	137	156	142
						–	118	141	133	120	108	109

[a] I = atomic line and II = ionic line.
[b] Analytical value from acid digestion of triplicate samples of the fresh bovine liver.

a sensitivity ratio higher than 1.8 are in the UV-region from 167 nm for Al up to 280 nm for Mg. Emission lines with a lower ratio range from 285 nm for Mg to 766 nm for K. One explanation could be a higher degree of absorption and/or scattering of these low UV lines and these effects seem to be more severe when using Burgener than GEC. The reason for this is not fully understood but the finer mist from GEC might reduce absorption and scattering and thus contribute to the higher sensitivity.

It should be mentioned that the sensitivity also could be influenced by changing the spray chamber. In this work the same one (Scott double pass) was used in all experiments to focus solely on the nebulizer performance.

More information concerning the change in intensity for different elements as a function of energy sum when altering the plasma power, sample transport efficiency, matrix components, electron density, observation height could be found elsewhere [2,3,21–24,32].

4. Conclusions

By this fast and simple "mix and measure" multi-element method it is possible to quantify macro, micro and trace elements in non-digested biological samples with a total analysis time of 4 min (one for homogenization and three for measurement). In 70% (v/v) whole blood reference material 14 of 16 analytes were quantified within ±10% (Al, B, Ba, Ca, Cu, Fe, Mg, Mn, P, Pb, S, Sr, Ti and Zn) and two semi-quantified within ±20% (Cd and K). In 5% (m/v) fresh bovine liver slurry 7 of 9 elements were quantified; Ca, Cu, K, Mg, Mn, P and Zn, while Fe and S were semi-quantified.

Introduction of these amounts of biological samples do not alter the plasma stability but the analyte signals are frequently suppressed. Evaluation by internal standard is then necessary and both Y (371.030 nm) and Sc (361.384 nm) are suitable for several of the evaluated emission lines.

It is possible to use both GEC and Burgener nebulizers for quantitative analyses in whole blood and liver slurries. Cross Flow could be used for blood analysis but was not tested for liver sample. To obtain highest sensitivity GEC should be used, especially when measuring emission lines in the low UV-region since, according to this study, these lines are more affected by the choice of nebulizer. In sample matrices where there might be residues of larger particles, not sufficiently homogenized by the Polytron, Burgener T2100 could be recommended since the inner diameter is almost four times larger than in GEC and hence problems with clogging would be reduced.

Acknowledgements

The authors gratefully acknowledge Louisa Eriksson and Mattias Brodin for their assistance with the analysis of the fresh liver samples.

References

[1] L. Ebdon, M. Foulkes, K. Sutton, J. Anal. At. Spectrom. 12 (1997) 213–229.
[2] X. Romero, E. Poussel, J.M. Mermet, Spectrochim. Acta Pt. B: At. Spectrosc. 52 (1997) 487–493.
[3] J.L. Todolí, L. Gras, V. Hernandis, J. Mora, J. Anal. At. Spectrom. 17 (2002) 142–169.
[4] G.A. Zachariadis, L.I. Valianou, Appl. Spectrosc. 62 (2008) 716–720.
[5] A. Krejcová, D. Kahoun, T. Cernohorský, M. Pouzar, Food Chem. 98 (2006) 171–178.
[6] A. Ryan, ICP-AES Instruments at Work, Varian Australlia Pty. Ltd, Mullgrave, Victoria, Australia, 1997.
[7] N.S. Mokgalaka, R.I. McCrindle, B.M. Botha, J. Anal. At. Spectrom. 19 (2004) 1375–1378.
[8] G.A. Zachariadis, C.E. Michos, J. Pharm. Biomed. Anal. 43 (2007) 951–958.
[9] T. Mochizuki, A. Sakashita, H. Iwata, Y. Ishibashi, N. Gunji, Fresen. J. Anal. Chem. 339 (1991) 889–894.
[10] G.A. Zachariadis, A.F. Olympiou, J. Pharm. Biomed. Anal. 47 (2008) 541–546.
[11] A.N. Anthemidis, V.G. Pliatsika, J. Anal. At. Spectrom. 20 (2005) 1280–1286.
[12] P. Goodall, M.E. Foulkes, L. Ebdon, Spectrochim. Acta Pt. B: At. Spectrosc. 48 (1993) 1563–1577.
[13] T. Cernohorský, A. Krejcová, M. Pouzar, L. Vavrusová, Food Chem. 106 (2008) 1246–1252.
[14] P.J. McKinstry, H.E. Indyk, N.D. Kim, Food Chem. 65 (1999) 245–252.
[15] G. Zachariadis, P. Sarafidou, Microchim. Acta 166 (2009) 77–81.
[16] J.A. Nóbrega, M.C. Santos, R.A. de Sousa, S. Cadore, R.M. Barnes, M. Tatro, Spectrochim. Acta Pt. B: At. Spectrosc. 61 (2006) 465–495.
[17] E.J. Daftsis, G.A. Zachariadis, Microchim. Acta 160 (2008) 405–411.
[18] I.B. Brenner, A. Zander, S. Kim, A. Henderson, Spectrosc. Eur. 7 (1995) 24–32.
[19] L. Halicz, I.B. Brenner, Spectroc. Acta Pt. B: At. Spectrosc. 42 (1987) 207–217.
[20] J. Pettersson, unpublished work.
[21] J.-M. Mermet, J. Anal. At. Spectrom. 13 (1998) 419–422.
[22] E.H.v. Veen, M.T.C.d. Loos-Vollebregt, J. Anal. At. Spectrom. 14 (1999) 831–838.
[23] J. Borkowska-Burnecka, A. Lesniewicz, W. Zyrnicki, Spectrochim. Acta Pt. B: At. Spectrosc. 61 (2006) 579–587.
[24] J.M. Cano, J.L. Todolí, L. Gras, V. Hernandis, J. Mora, J. Anal. At. Spectrom. 17 (2002) 57–63.
[25] C. Jin, Y. Li, Y.L. Li, Y. Zou, G.L. Zhang, M. Normura, G.Y. Zhu, Nucl. Instrum. Methods Phys. Res. Sect. B: Beam Interact. Mater. Atoms 266 (2008) 3607–3613.
[26] S. D'Ilio, N. Violante, M. Di Gregorio, O. Senofonte, F. Petrucci, Anal. Chim. Acta 579 (2006) 202–208.
[27] E. Barany, I.A. Bergdahl, A. Schütz, S. Skerfving, A. Oskarsson, J. Anal. At. Spectrom. 12 (1997) 1005–1009.
[28] Y. Abdelnour, J. Murphy, ICP-MS Application note number 28, Varian Inc.
[29] J.-P. Goullé, L. Mahieu, J. Castermant, N. Neveu, L. Bonneau, G. Lainé, D. Bouige, C. Lacroix, Forensic Sci. Int. 153 (2005) 39–44.
[30] M.D. Ioannidou, G.A. Zachariadis, A.N. Anthemidis, J.A. Stratis, Talanta 65 (2005) 92–97.
[31] I.B. Brenner, A. Zander, M. Cole, A. Wiseman, J. Anal. At. Spectrom. 12 (1997) 897–906.
[32] E. Paredes, S.E. Maestre, J.L. Todolí, Spectrochim. Acta Pt. B: At. Spectrosc. 61 (2006) 326–339.
[33] R. Rahil-Khazen, H. Henriksen, B.J. Bolann, R.J. Ulvik, Scand. J. Clin. Lab. Invest. 60 (2000) 677–686.
[34] A. Ryan, ICP-AES Instruments at Work, Varian Australlia Pty. Ltd., Mullgrave, Victoria, Australia, 1998.
[35] NIOSH, Method 8005 (1994).
[36] G.V. Iyengar, W.E. Kollmer, H.J.M. Bowen, The Elemental Composition of Human Tissue and Body Fluids: A Compilation of Values for Adults, Verlag Chemie, Weinheim, 1978.
[37] ICP Nebulizers, http://www.icpnebulizers.com/selection.html, 2008.
[38] Snyder et al., Report of the Task Group on Reference Man, ICRP No. 23, Pergamon Press Ltd, Oxford, England, 1981.

Talanta 80 (2010) 2076–2082

Contents lists available at ScienceDirect

Talanta

journal homepage: www.elsevier.com/locate/talanta

Headspace solid-phase microextraction of oil matrices heated at high temperature and phthalate esters determination by gas chromatography multistage mass spectrometry

J.J. Rios [a,*], A. Morales [a], G. Márquez-Ruiz [b]

[a] Food Characterization and Quality Department, Instituto de la Grasa (C.S.I.C.), Av. Padre García Tejero 4, 41012 Seville, Spain
[b] Science and Technology of Dairy Products Department, Instituto del Frio (C.S.I.C.), Jose Antonio Novais 10 28040 Madrid, Spain

ARTICLE INFO

Article history:
Received 7 July 2009
Received in revised form 22 October 2009
Accepted 3 November 2009
Available online 12 November 2009

Keywords:
Phthalates
Solid-phase microextraction
Gas chromatography ion trap–mass spectrometry
Oil matrices

ABSTRACT

A solvent-free analytical approach based on headspace solid-phase microextraction (SPME) of oil matrices heated at high temperatures coupled to gas chromatography with mass spectrometry detector (GC-ion trap) has been developed for the determination of phthalic acid esters (PAEs) in oil matrices without sample manipulation. For this study, three fibers, i.e., 85 μm-polyacrylate (PA), 50/30 μm-divinylbenzene–carboxen–polydimethylsiloxane (DVB/CAR/PDMS) and 100 μm-polydimethylsiloxane (PDMS) were tested. Variables affecting the SPME headspace composition such as incubation sample temperature, sample incubation time and fiber exposition time were optimized. The optimal values found were 250 °C for sample incubation temperature and 30 min for incubation and extraction time. PA fiber was not suitable for the lightest polar phthalates which showed poor extraction and repeatability values. PDMS fiber had very poor response for some of the heavier and non-polar phthalates, whereas DVB/CAR/PDMS fiber showed the best response and repeatability values for the majority of the phthalates studied. The main benefit of the analytical method proposed is the absence of sample manipulation and hence avoidance of possible contamination coming from glassware, environment, solvents and samples.

© 2009 Elsevier B.V. All rights reserved.

1. Introduction

Worldwide production of phthalic acid esters (PAEs) and their common application in different products of everyday use has resulted in their widespread presence in environment and foods. PAEs are used extensively as plasticizers in different materials, especially polivinyl chloride, polyvinyl acetate, polystyrene, polyamide and polyester materials. Bis-(2-ethylhexyl) phthalate (DEHP) and benzylbutylphthalate (BBP) are the most abundant phthalate esters due their wide use in many industrial sectors like cosmetics and paints. As plasticizers are not chemically bound to the polymer, migration of PAEs in significant amounts is possible.

Some research papers have been published recently about the impact of PAEs on wild animals and human beings [1,2]. It is suggested that increasing exposure to PAEs might be partially responsible for some diseases. Furthermore, it was found that PAEs might persist in human body tissues [2]. Since foods are the major source of exposure to PAEs, it is important to monitor their levels in foods to provide data for human exposure assessment. The US Environmental Protection Agency (EPA) and several other agencies classified the commonly occurring PAEs as priority pollutants. Due to such health implications, there is increasing demand for reliable analytical methods that allow their detection and quantification at very low levels in different environmental, biological and food matrices.

Several analytical methods have been developed for determining PAEs in food samples and fatty matrices [3,4], and recently an interesting application to olive oil has been published [5]. Either adsorption chromatography on Florisil or alumina [6,7] or codistillation of PAEs [8] is usually applied. Quantification of low levels using solid-phase extraction (SPE) with C18 [9], C8 [10], polystyrene [11] and multi-walled carbon monotubes to concentrate PAEs [12] has been also proposed prior to analysis by either liquid or gas chromatography. These options have been preferred to solvent extraction due to lower consumption of organic solvents.

Several studies applying direct SPME extraction of PAEs have been proposed. This procedure significantly reduces the risk of secondary contamination and substantially simplifies the overall analytical process. It has been already applied to the determination of phthalates in wine [13,14], cow milk [15], vegetable oil using solvent-based matrix modification [16], and plastic for foods [17].

Cross contamination from chemicals, materials and laboratory equipment are common problems in all PAEs analysis methods

* Corresponding author. Tel.: +34 95 4611550; fax: +34 95 4616790.
E-mail address: jrios@ig.csic.es (J.J. Rios).

0039-9140/$ – see front matter © 2009 Elsevier B.V. All rights reserved.
doi:10.1016/j.talanta.2009.11.008

[18]. For example, di(2-ethylhexyl) phthalate and dibutyl phthalate are usually detected in blank samples. In addition, the difficulty for separating co-extracts as lipids, pigments, etc., makes the determination of low levels of PAEs in food matrices very difficult.

The aim of this work was to develop an analytical procedure to detect and quantify the phthalate levels in oil matrices without sample manipulation and thus avoiding external contamination from air, solvents, labware, etc. The novelty of this method consists of adsorption by SPME of the headspace of the oil heated at high temperature (250 °C) in a sealed vial followed by subsequent analysis by gas chromatography ion trap MS–MS. For the first time, high temperature is here used for determination of phthalates in oil matrices.

2. Materials and methods

2.1. Reagents and materials

Virgin olive oil purchased locally was used as oil matrix for experiments. A standard mixture solution of phthalates (EPA 8061 Mix Analytes) and benzyl benzoate containing 1 mg mL^{-1} of each compound in 95:5 hexane:acetone (v/v) (Cromlab, Barcelona, Spain) was used for setting instrumental conditions and spiking the olive oil samples. The standard mixture solution contained 1 mg mL^{-1} of methyl phthalate (DMP), diethyl phthalate (DEP), benzylbenzoate as internal standard (IS), di-isobuthyl phthalate (DIBP), di-n-buthyl phthalate (DBP), bis-2-methoxyethyl phthalate (MEP), bis-1,2-(4methyl-2pentyl) phthalate (1,2MPP), bis-1,3(4methyl-2pentyl) phthalate (1,3MPP), bis-2ethoxyethyl phthalate (EEP), di-n-amyl phthalate (DAP), di-n-hexyl phthalate (DHP), benzyl buthyl phthalate (BBP), bis-2-buthoxyethyl phthalate (BBEP), dicyclohexyl phthalate (DCHP), bis 2-ethylhexyl phthalate (DEHP), di-n-octyl phthalate (DOP) and di-n-nonyl phthalate (DNP). Five spiked levels of 0.05, 0.1, 0.5, 1.0 and 2.0 mg kg^{-1} were prepared. Initial olive oil used for experiments and the solvents for preparing spiking solutions were tested previously to verify absence of phthalates.

Six samples of virgin olive oils, purchased locally, were stored at room temperature (23 ± 5 °C) for 12 months, either in glass bottles or in PET (polyethylene terephthalate) bottles. Duplicate samples were taken at 8, 10 and 12 months.

Special care was taken with glassware, vials, caps and septa before use. All materials were dried and kept at 200 °C until use. To avoid phthalate contamination, all glassware used was soaked in acetone for at least 30 min, then washed with acetone, rinsed with hexane, and dried at 200 °C for at least 4 h. All the solvents, chromatographic system, standards and spiked samples were subjected to similar extraction and analysis procedures. Blank extraction was routinely performed. Also, the chromatographic system was initially and regularly checked for absence of phthalates by running blank injections.

2.2. SPME fibers

SPME fibers were purchased from Supelco (Bellefonte, PA, USA). Three types of fiber coating were tested, i.e., 85 μm-polyacrylate (PA), 50/30 μm-divinylbenzene–carboxen–polydimethylsiloxane (DVB/CAR/PDMS) and 100 μm-polydimethylsiloxane (PDMS), previously conditioned in accordance with manufacturer's instructions. Fibers were thermally cleaned in the injection port before sampling. Each ten extractions, fibers were cleaned by immersion with vigorous shaking in a mixture of 20:70:10 water:acetonitrile:acetic acid (v/v/v) for 1 h, dried under nitrogen and conditioned at 260 °C for 30 min.

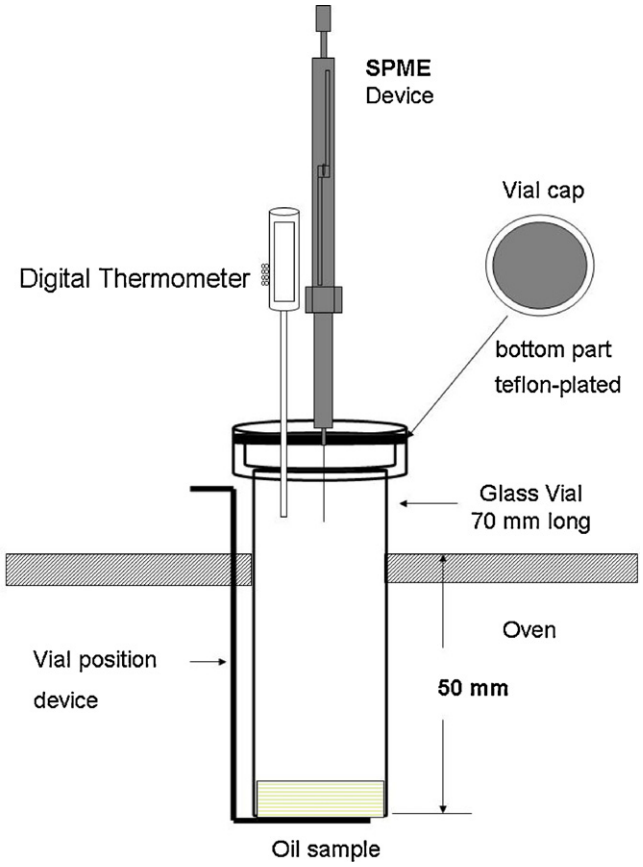


Fig. 1. Schematic representation of the extraction procedure.

2.3. SPME procedure

Samples of 1 g olive oil were weighed into glass vials (70 mm long and 22 mm diameter) and tightly capped. The bottom part of the caps was Teflon-plated to avoid plastic contact with headspace. Then, vials were heated at different temperatures (200–275 °C) and time periods (10–40 min) in order to promote release of the semivolatile compounds to headspace. Sampling was performed by exposing the SPME fiber to headspace for 30 min at the upper part of vial positioned outside the oven-heating zone (20 mm long), as shown in Fig. 1. After sample extraction, the SPME fiber was introduced into the GC injection port (260 °C) operating in splitless mode for 5 min. Samples were extracted only once from vial.

2.4. GC ion trap–MS analysis

The GC ion trap–MS experiments were performed using a Finnigan Trace-GC 2000 gas chromatograph coupled to a Polaris-Q Ion trap mass spectrometer (ThermoFinnigan, Austin, TX, USA) operating in fullscan and MS/MS mode. The column used was a Zebron ZB-5 ms (Phenomenex, Torrance, CA, USA) fused silica capillary column (30 m long × 0.25 mm i.d × 0.25 m film thickness). The GC conditions included helium as carrier gas at 1 mL min^{-1} in constant flow mode. The initial temperature of 70 °C was kept for 2 min, then raised to 200 °C at a rate of 6 °C min^{-1} and held for 5 min, then raised to 295 °C at a rate of 4° C min^{-1} and held for 8 min. Injector temperature was 260 °C and a 0.8 mm ID liner was used for SPME injection port.

The MS operating conditions were as follows: ion source and transfer line temperatures were 200 and 290 °C, respectively. The electron energy was 70 eV, resolution was unit and the emission current was 250 μA.

Table 1
Precursor and quantification ions for PAEs.

Peak no.	Analyte	Precursor MS^2	Q	CID	Quantification ion
1	DMP	163	0.45	2	133
2	DEP	149	0.45	2	121 + 93
3	IS	105	0.45	1	77
4	DIBP	149	0.45	2	121 + 93
5	DBP	149	0.45	2	121 + 93
6	MEP	149	0.45	2	121 + 93
7	1,2MPP	149	0.45	2	121 + 93
8	1,3MPP	149	0.45	2	121 + 93
9	EEP	149	0.45	2	121 + 93
10	DAP	149	0.45	2	121 + 93
11	DHP	149	0.45	2	121 + 93
12	BBP	149	0.45	2	121 + 93
13	BBEP	149	0.45	2	121 + 93
14	DCHP	149	0.45	2	121 + 93
15	DEHP	149	0.45	2	121 + 93
16	DOP	149	0.45	2	121 + 93
17	DNP	149	0.45	2	121 + 93

Abbreviations: DMP, Methyl phthalate; DEP, diethyl phthalate; IS, internal standard (benzylbenzoate); DIBP, di-isobuthyl phthalate; DBP, di-n-buthyl phthalate; MEP, bis-2-methoxyethyl phthalate; 1,2MPP, bis-1,2-(4methyl-2pentyl) phthalate; 1,3MPP, bis-1,3(4methyl-2pentyl) phthalate; EEP, bis-2ethoxyethyl phthalate; DAP, di-n-amyl phthalate; DHP, di-n-hexyl phthalate; BBP, benzyl buthyl phthalate; BBEP, bis-2-buthoxyethyl phthalate; DCHP, dicyclohexyl phthalate; DEHP, bis 2-ethylhexyl phthalate; DOP, di-n-octyl phthalate and DNP, di-n-nonyl phthalate.

The Xcalibur version 1.4 software was used for data acquisition and processing of the results.

3. Results and discussion

3.1. Mass spectrometry scanning method

Full scan and MS/MS (MS^2) were used alternately and consecutively for MS operations. The MS/MS method development was carried out in two steps. The first one was to set the retention time of the compounds of interest and to slice the chromatogram into 17 segments corresponding to specific PAEs and benzyl benzoate. First, the standard mixture (EPA 8061 Analytes) was injected in fullscan mode. Maximum excitation energy (Q) and CID excitation voltage were optimized for each individual standard compound and precursor ion in order to get the best isolation efficiencies and ensure maximum production or transmission of collision fragments.

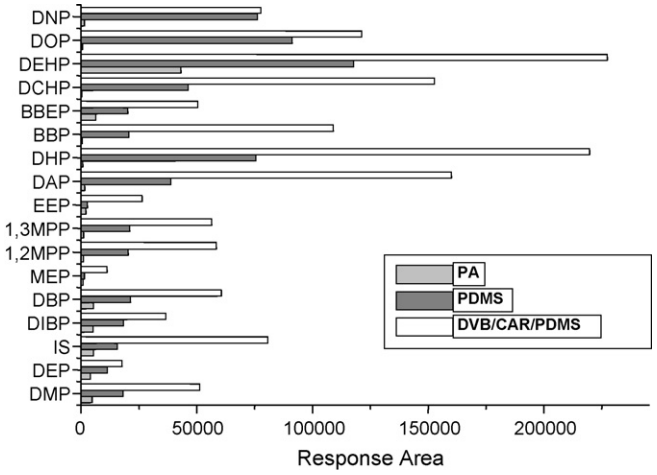


Fig. 2. Response areas obtained with the fibers tested. Means of five determinations. Coefficients of variation were lower than 10%. Abbreviations for fibers: PA, 85 μm-polyacrylate; PDMS, 100 μm-polydimethylsiloxane and DVB/CAR/PDMS, 50/30 μm-divinylbenzene–carboxen–polydimethylsiloxane. Abbreviations for phthalates: DMP, Dimethyl phthalate; DEP, diethyl phthalate; IS, internal standard (benzylbenzoate); DIBP, di-isobuthyl phthalate; DBP, di-n-buthyl phthalate; MEP, bis-2-methoxyethyl phthalate; 1,2MPP, bis-1,2-(4methyl-2pentyl) phthalate; 1,3MPP, bis-1,3(4methyl-2pentyl) phthalate; EEP, bis-2ethoxyethyl phthalate; DAP, di-n-amyl phthalate; DHP, di-n-hexyl phthalate; BBP, benzyl buthyl phthalate; BBEP, bis-2-buthoxyethyl phthalate; DCHP, dicyclohexyl phthalate; DEHP, bis 2-ethylhexyl phthalate; DOP, di-n-octyl phthalate and DNP, di-n-nonyl phthalate.

Each scan was subdivided into two events. The first one was performed in fullscan mode in the 50–600 amu scan range, and the second one in MS/MS mode with the precursor ion selected. The total scan time for each couple of segments was 0.38 s and the system performed 3 microscans per second. Table 1 shows precursor ions for each segment of MS/MS experiments and quantification ions for the PAEs studied.

Upon data acquisition, analysis of data was based on the following criteria: retention time for each peak should be within a 1% range, and integration of ion chromatograms was done with the Xcalibur Software using ICIS Peak Detection with ion ratio confirmation parameter, selecting each peak area for the base peak corresponding with the quantification ion selected. For all of PAEs, except DMP and internal standard, two ions were considered as

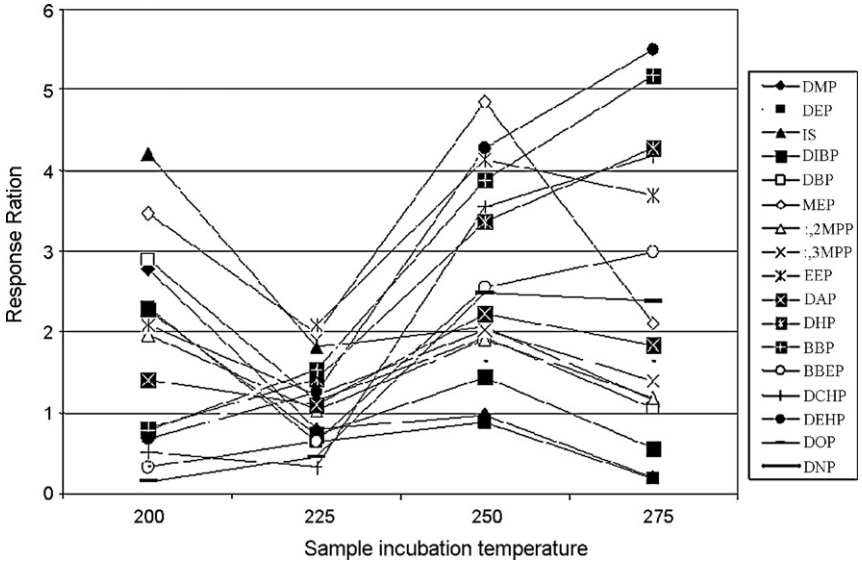


Fig. 3. Phthalate responses as a function of incubation temperature. Sample: EPA Mix 8061A standard mixture in olive oil (1 mg kg^{-1}).

quantification ions when relation of *m/z* 121 and *m/z* 93 was between 2.5 and 2.7 (±5%), as found for the standard compounds. For DMP and IS, single ions were selected for quantification due to their specificity.

3.2. Fiber and sample temperature optimization

Fiber type and sample temperature play an important role in the amounts of compounds absorbed and both have to be controlled separately. Three types of fiber coating were tested: PA, DVB/CAR/PDMS and PDMS fibers. PA and PDMS fibers, at headspace temperatures tested here, were not suitable for dimethyl and diethyl phthalates extraction and showed poor repeatability for the rest of PAEs studied (data not shown). As listed in Fig. 2, DVB/CAR/PDMS fiber showed the best response values for all of the phthalates studied from di-methyl phthalate (DMP) to di-nonyl phthalate (DNP).

Sample incubation temperature was tested between 200 and 275 °C since it was preliminarily observed that presence of the least volatile phthalates in headspace was reduced below 200 °C. Fig. 3 shows response ratios obtained between SPME of 1 g of olive oil spiked with 1 μg g^{-1} of each compound of the standard mixture (EPA 8061 Analytes) and direct liquid injection (in splitless mode) of 1 μL of standard solution (1 mg L^{-1}). The best results were obtained at 250 °C, with good SPME/direct liquid injection response ratio for all the compounds studied. This intermediate incubation temperature selected was a compromise between those most specifically suitable for compounds of lowest and highest volatility.

Vials were placed so as to leave their upper part (20 mm long) out of the heating system (Fig. 1). Thus, such upper parts of vials were not directly heated and temperature could be established between 80 and 115 °C to allow optimal response for all the PAEs tested. As headspace composition can vary depending on temperature, the SPME needle was punched through the cap and septum into the headspace and introduced at different depths (3.0, 2.0, 1.5 and 1.0 cm under cap bottom). Temperature was measured at the different depths using a digital microtermometer. For each point headspace temperature varied only less than ±3 °C during extraction time (30 min), as shown in Fig. 4. By using the internal standard, possible variations derived from lack of fiber thermostation or influence of glass surface characteristics [19] could be corrected.

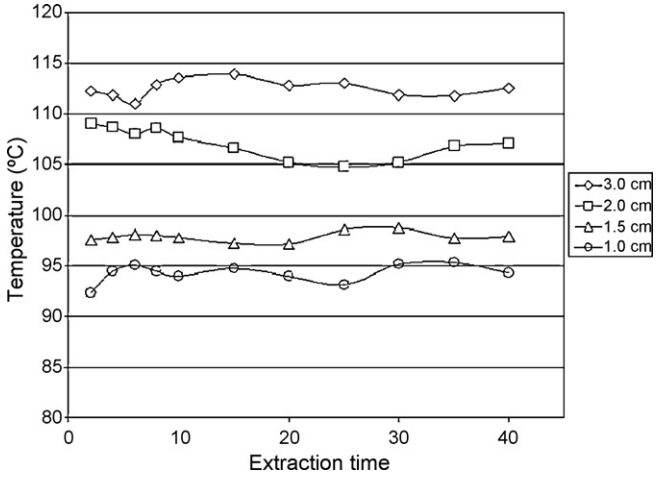


Fig. 4. Stability of headspace zone temperature during 40 min extraction period. Means of three analyses. Coefficients of variation were lower than 10%.

Fig. 5 shows response areas for phthalates absorbed from 1 g of oil sample containing 1 μg of each compound of the standard mixture (EPA 8061 Analytes) in function of the fiber position inside the headspace and the temperature on each position. The operating fiber position in the headspace selected was 1.0 cm under cap bottom, corresponding to 94 °C in headspace, according to the highest response areas obtained under such conditions.

Incubation time was studied from 10 to 40 min. Fig. 6 shows the results obtained, expressed as normalized response (% of each PAEs on total PAEs). Beyond 20 min of incubation time, this parameter was not critical, probably because the headspace equilibrium is reached relatively soon. However, it is important to stabilize the headspace zone temperature and that is why 30 min was selected as extraction time.

Fig. 7 shows the SPME–gas chromatogram ion trap MS/MS profile of an olive oil sample spiked with 1 μg g^{-1} of each compound of EPA 8061A Analytes compared with the profile corresponding to direct liquid injection of 1 μL of 1 mg L^{-1} EPA 8061A Analytes solution, in splitless mode. As can be observed, chromatograms were similar, which indicates that all phthalates were extracted without any distinctive suppression or promotion.

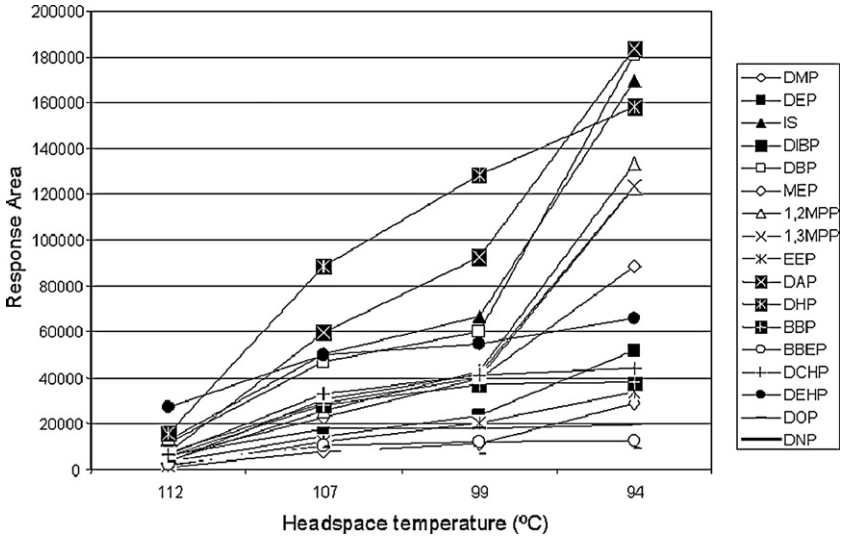


Fig. 5. Phthalate responses as a function of fiber sampling position (position 3, 2, 1.5 and 1 cm under the cup corresponds to 112, 107, 99 and 94 °C, respectively). Means of two analyses. Coefficients of variation were lower than 10%.

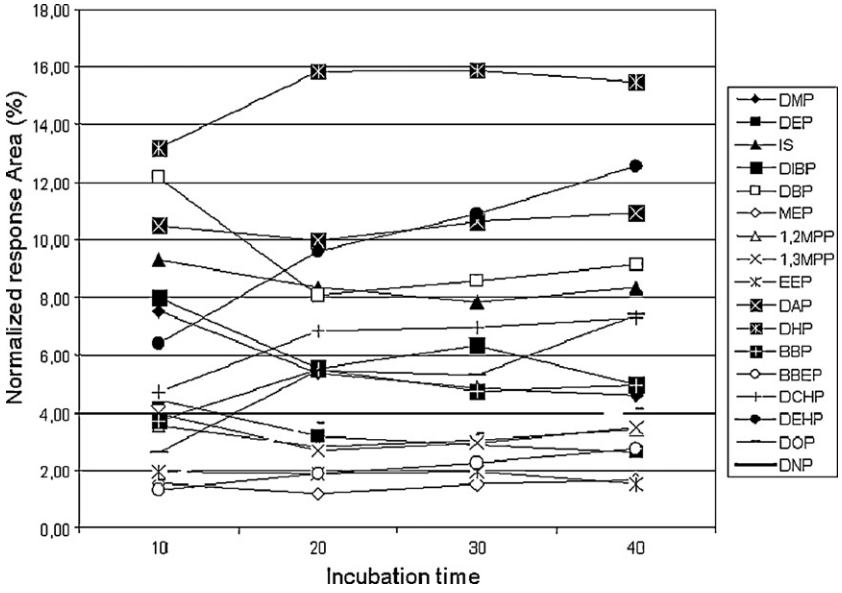


Fig. 6. Phthalate responses as a function of extraction time. Means of two analyses. Coefficients of variation were lower than 10%.

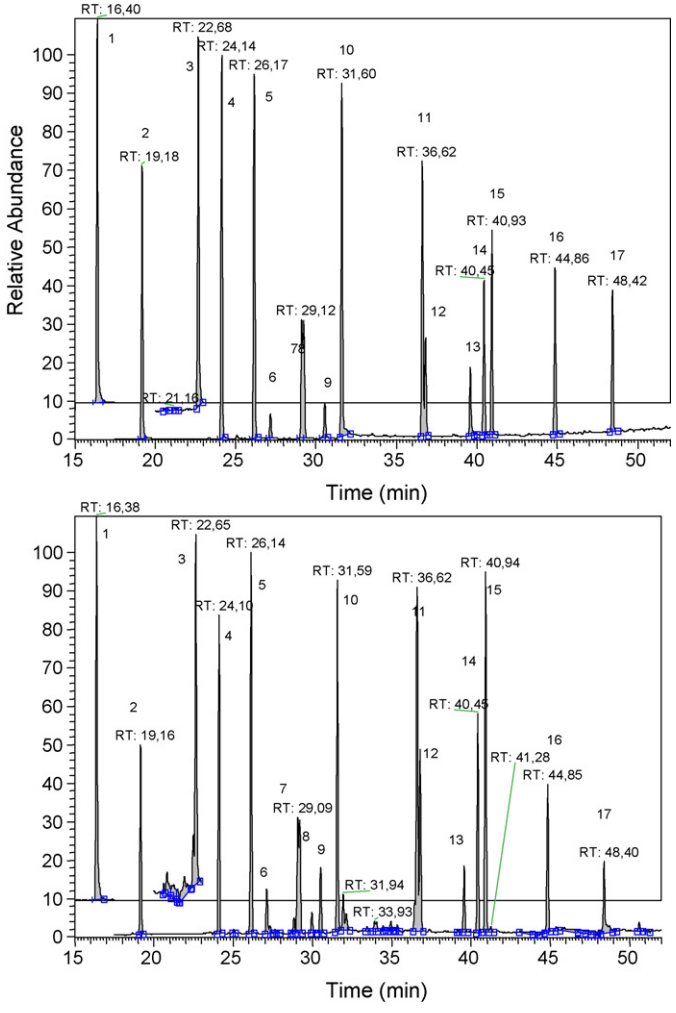


Fig. 7. Comparison of chromatograms obtained after: top, injection of 1 μL of phthalates standard solution (EPA 8061 standard mixture in acetonitrile, concentration 1 mg L^{-1}); bottom, HS-SPME of 1 g of olive oil (spiked with EPA 8061 standard mixture at the level of 1 μg g^{-1}). For peaks identification, see Table 1.

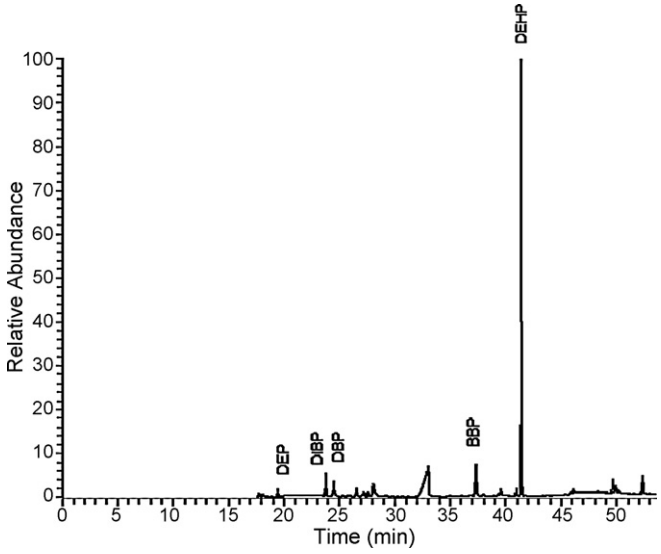


Fig. 8. Headspace GC-ion trap–MS/MS chromatogram of olive oil sample 1 (PET container) after applying the quantification layout.

Fig. 8 shows a representative example of the chromatographic profile obtained for a real sample by applying the method proposed. In this case, sample olive oil 1 (PET container), only DIBP, DBP, BBP and DEHP were detected in significant amounts.

3.3. Method performance

Repeatability of the SPME method was determined by five replicate analyses of olive oil spiked at levels of 0.1, 0.5 and 1.0 mg kg^{-1}. Linearity testing was carried out using olive oil spiked at levels of 0.05, 0.1, 0.5, 1.0 and 2.0 mg kg^{-1}. The resulting performance characteristics are summarized in Table 2.

Linearity of the analysis and extraction procedure of oil samples spiked with 0.05–2.0 mg kg^{-1} showed good correlation values for all of the compounds studied. The relative standard deviations (RSDs) for samples spiked with 0.1, 0.5 and 1.0 mg kg^{-1} were always below 20%. It is important to note that particularly low RSD, below 8.5%, were obtained for benzyl butyl phthalate (BBP)

Table 2
Resulting performance characteristics.

	Repeatability RSD (%), $n = 5$			Linearity R^2 (0.05–2 mg kg^{-1})	LOD[a] (mg kg^{-1})
	0.1 mg kg^{-1}	0.5 mg kg^{-1}	1.0 mg kg^{-1}		
DMP	17.3	18.7	14.1	0.989	0.04
DEP	11.6	13.1	10.6	0.995	0.04
IS	12.5	10.5	10.8	0.999	0.04
DIBP	18.2	16.7	17.4	0.988	0.03
DBP	8.5	10.5	4.7	0.998	0.03
MEP	16.3	14.8	13.0	0.997	0.03
1,2MPP	17.9	18.7	15.8	0.978	0.03
1,3MPP	18.6	14.1	18.0	0.988	0.03
EEP	12.1	14.5	10.9	0.992	0.03
DAP	17.8	16.7	14.6	0.986	0.04
DHP	8.0	8.1	5.3	0.987	0.04
BBP	7.6	7.7	6.1	0.983	0.03
BBEP	10.6	13.7	8.2	0.998	0.02
DCHP	8.3	8.1	7.3	0.975	0.02
DEHP	8.5	8.1	8.3	0.995	0.03
DOP	15.7	14.8	15.6	0.979	0.04
DNP	18.6	18.1	15.1	0.980	0.05

Abbreviations as in Table 1.
[a] Limit of detection.

Table 3
Contents of phthalates in stored olive oils.

Compound	Container PET			Container glass		
	Storage time (months)			Storage time (months)		
	8 Sample 1	10 Sample 2	12 Sample 3	8 Sample 4	10 Sample 5	12 Sample 6
DMP	–[a]	–	–	–	–	–
DEP	–	–	–	–	–	–
DIBP	120	119	216	–	–	–
DBP	97	111	175	–	–	–
BBP	173	207	211	87	110	112
DEHP	543	635	840	223	237	198
DOP	–	–	–	–	–	–
DNP	–	–	–	–	–	–

Abbreviation: PET, polyethylene terephthalate. Values in μg kg^{-1}. Mean of two determinations.
[a] Below LOD.

and bis(2-ethylhexyl) phthalate (DEHP), which are the most widely found PAEs. Relatively high RSDs for some of the PAEs were found, especially the most volatile ones. Such results could be expected under the conditions used, which favor overall extraction and absence of contaminants during the extraction process but may otherwise lead to overestimated values [18].

3.4. Determination of PAEs in olive oil samples

As an example of application of the method to real samples, three samples of olive oils packed in plastic (PET, polyethylene terephthalate) bottles and three of olive oils packed in glass containers were analyzed for PAEs. As only few of the phthalates studied in this work may really be encountered in edible oils, namely DBP, DEP, DIBP, DBP, BBP, DEHP, DOP and DNP only those, if detected, are shown in real sample results. Analyses were done in duplicate and, if any, levels in blank were substracted.

Samples kept in PET containers shown presence of DIBP, DBP, BBP and DEHP but in samples kept in glass containers only significative BBP and DEHP were detected in the samples analyzed as it is shown in Table 3.

4. Conclusions

The analytical method described in the present work is simple and highly selective for quantification of PAEs in oil matrices. As compared with the conventional clean-up process based on liquid–liquid extraction or solid-phase extraction, the present approach is faster and more economical. Furthermore, the main benefit of the method is the suppression of the main contamination sources, especially in relation to sample manipulation. Due to complexity of the headspace of heated oils, however, there are certain limitations as to fiber durability. Degradation of fibers gives rise to poor recovery of the least volatile PAEs, such as DNOP and DNP, thereby special care should be taken to control recovery values and reject fibers when necessary.

References

[1] N. Ghorpade, V. Metha, M. Khare, P. Sinkair, S. Krishnan, C.V. Rao, Ecotoxicol. Environ. Saf. 53 (2002) 255–258.
[2] X. Hu, B. Wen, X. Shan, J. Environ. Monit. 5 (2003) 649–653.
[3] C.S. Giam, M.K. Wong, J. Food Prot. 5 (1987) 769–782.
[4] B.D. Page, in: J.H. Hotchkiss (Ed.), Food Packaging Interation I, ACS Symposium Series No. 365, ACS, Washington, 1988, p. 118.
[5] B. Cavaliere, B. Macchione, G. Sindona, A. Tagarelli, J. Chromatogr. 1205 (2008) 137–143.
[6] T. Suzuki, K. Ishikawa, N. Sato, K.I. Sakai, JAOCS 62 (3) (1979) 689–694.
[7] A.A. Belisle, W.L. Reichel, J.W. Spann, Bull. Environ. Contam. Toxicol. 13 (1975) 129–132.
[8] A.D. Vethaak, G.B.J. Rijs, S.M. Schrap, H. Ruiter, A. Gerritsen, J. Lahr, Report no. 2002.001, Dutch National Institute of Inland Water Management and Waste Water Treatment, Lelystad, The Netherlands.
[9] I. Colon, D. Caro, C.J. Bourdony, O. Rosario, Environ. Health Perspect. 108 (2000) 895–900.
[10] B.D. Page, G.M. Lacroix, Food Addit. Contam. 12 (1995) 129–151.
[11] N. Casajuana, S. Lacorte, Chromatographia 57 (2003) 649–655.

[12] M.L. Davi, M. Liboni, M.G. Malfatto, Int. J. Environ. Anal. Chem. 74 (1999) 155–166.
[13] J.D. Carrillo, C. Salazar, C. Moreta, M.T. Tena, J. Chromatogr. A 1164 (2007) 248–261.
[14] J.D. Carrillo, M.P. Martinez, M.T. Tena, J. Chromatogr. A 1181 (2008) 125–130.
[15] Yong-Lai Feng, Jiping Zhu, Robert Sensenstein, Anal. Chim. Acta 538 (2005) 41–48.
[16] K. Holadova, G. Prokupkova, J. Hajslova, J. Poustka, Anal. Chim. Acta 582 (2007) 24–33.
[17] H.-Y. Shen, Talanta 66 (2005) 734–739.
[18] A. Fankhauser-Noti, K. Grob, Anal. Chim. Acta 582 (2007) 353–360.
[19] A. Fankhauser-Noti, K. Grob, Trends Food Sci Technol. 17 (2006) 105–112.

Talanta 80 (2010) 2083–2092

Contents lists available at ScienceDirect

Talanta

journal homepage: www.elsevier.com/locate/talanta

Simultaneous determination of carbonyl compounds and polycyclic aromatic hydrocarbons in atmospheric particulate matter by liquid chromatography–diode array detection–fluorescence detection

M.C. Prieto-Blanco[a], M. Piñeiro Iglesias[b], P. López-Mahía[a,b,*], S. Muniategui Lorenzo[a], D. Prada Rodríguez[a,b]

[a] Department of Analytical Chemistry, Faculty of Sciences, Campus A Zapateira, s/n., E-15071 A Coruña, Spain
[b] Institute of Environment, University of A Coruña, Pazo de Lóngora, Liáns-Oleiros, E-15179, Spain

ARTICLE INFO

Article history:
Received 27 July 2009
Received in revised form 23 October 2009
Accepted 3 November 2009
Available online 10 November 2009

Keywords:
Carbonyl compounds
Polycyclic aromatic hydrocarbons
HPLC–PDA–FL
Simultaneous analysis
PM_{10}
Water-soluble organic compounds (WSOC)

ABSTRACT

Simultaneous analysis of 24 carbonyl compounds (alkanals, unsaturated, dicarbonylic and aromatic aldehydes and ketones) derivatized with 2,4-dinitrophenylhydrazine and 16 polycyclic aromatic hydrocarbons (PAHs) using a photodiode-array (PDA) and a fluorescence (FL) detector in series is proposed.

The separation is carried out with a reversed-phase column and gradient elution using four solvents (acetonitrile, water, tetrahydrofuran and methanol) in less than 35 min. Several critical pairs of carbonyl compounds with 3 and 4 carbon atoms and different functional groups, isomers of tolualdehyde, aromatic and aliphatic aldehydes were conditional on the gradient elution. Common pre-treatment for two groups of compounds consists in a step of extraction and derivatization in aqueous medium and a further clean-up using a polymeric phase SPE and concentration in a mixture of dichloromethane:methanol. A pre-concentration factor of 50 was achieved by this procedure. Acetone and formaldehyde blanks were minimized and remain controlled with a specific cleaning of glass material and washing the SPE cartridge.

The limits of detection (LOD) ranged from 0.006 to 0.18 ng mL^{-1} for PAHs and from 2.4 to 10.1 ng mL^{-1} for carbonyl compounds and method precision was $\leq$15% for all analysed compounds. Recoveries were within the range of 95–104% for PAHs except for more volatile compounds (acenaphthene and fluorene) and within the range of 72–113% for carbonyl compounds. The method was applied in water-soluble fraction of PM_{10} (atmospheric particulate matter with an aerodynamic diameter less than 10 μm) and the spectral contrast technique was used in the identification of carbonyl compounds.

© 2009 Elsevier B.V. All rights reserved.

1. Introduction

Polycyclic aromatic hydrocarbons (PAHs) and carbonyl compounds (aldehydes and ketones) are two groups of ubiquitous pollutants in the environment. PAHs have carcinogenic and mutagenic activities [1,2] and they become more toxic as a result of nitration reactions (nitro-PAHs). Some carbonyl compounds (e.g., formaldehyde, acetaldehyde, acrolein, and methyl ethyl ketone) may even have adverse effects on human health [3].

PAHs are produced from incomplete combustion (automobile traffic, industrial plants, domestic use, cigarette smoke. . .) and lots of emission sources, such as road traffic emissions, that are also common sources for carbonyl compounds. In addition, the latter play an important role in secondary atmospheric reactions. They can be produced by addition of ozone to unsaturated hydrocarbons or photooxidation of hydrocarbons or volatile organic compounds with OH radicals. But carbonyl compounds may also be degraded by photochemical reactions [4].

The particulate matter is a complex atmospheric matrix which has an influence on the atmospheric chemistry and also an adverse health impact due to its ability to penetrate into the respiratory tracts and be absorbed by mucous membranes. Water-soluble fraction is a part of particulate matter which contains inorganic ions and water-soluble organic compounds (WSOC) such as carbonyl compounds. Water-soluble fraction has an influence on the cloud condensation nuclei activity, particulate matter size and toxicity. Consequently, water-soluble compounds act as surface-active reagents, increasing the solubility of toxic organic compounds such as PAHs [5].

High-performance liquid chromatography (HPLC) separation of PAHs may be carried out using normal or reversed-phase chromatography but a major number of applications use

* Corresponding author at: Department of Analytical Chemistry, Faculty of Sciences, Campus A Zapateira, s/n., E-15071 A Coruña, Spain. Tel.: +34 981 167000; fax: +34 981 167065.
E-mail address: purmahia@udc.es (P. López-Mahía).

0039-9140/$ – see front matter © 2009 Elsevier B.V. All rights reserved.
doi:10.1016/j.talanta.2009.11.009

reversed-phase with fluorescence or UV detection. Although the separation of 16 Environmental Protection Agency (EPA) priority PAHs may be possible using an octadecylsilane stationary phase and a gradient elution, the best results for ring-isomeric pairs are obtained with a polymeric C_{18} column [1]. These special columns for PAHs separation are employed with a mobile phase containing mixtures of water/acetonitrile [6], water/methanol [7] or water/methanol/acetonitrile [8], at a programmed temperature of 30–40 °C [6]. In order to carry out an environmental analysis, fluorescence detection is most frequently chosen under programmed fluorescence conditions (excitation and emission wavelength pairs programme).

Chromatographic separation of carbonyl compounds, with prior derivatization to form the 2,4-dinitrophenylhydrazones derivatives, has been used for the last twenty years and nowadays it is applied in air monitoring programmes [9,10]. The separation is carried out on octadecylsilica column and binary mixture of water/acetonitrile or water/methanol. Aliphatic aldehydes (C_1–C_4) and aromatic aldehydes (benzaldehyde) have been separated with water/acetonitrile under isocratic conditions [11]. Binary gradients of water/acetonitrile [12] and water/methanol [13] have been used to separate unsaturated aliphatic, aromatic aldehydes, ketones and dicarbonyls compounds. A ternary gradient of water/acetonitrile/tetrahydrofuran has been effective in specific problems such as separation of carbonyl compounds with 3 carbon atoms: aliphatic, olefinic and ketone [14]. Dye and Oehme [15] have proposed another alternative using two columns in series and a ternary gradient of water/methanol/acetonitrile. Only one column and this ternary mixture have separated ketone, olefinic and aliphatic aldehydes in isocratic [16] and gradient conditions [4]. Quaternary gradients of water/acetonitrile/tetrahydrofuran/methanol may be recommended for mixtures of aliphatic, aromatic and unsaturated aldehydes, aliphatic and unsaturated ketones and dicarbonyl compounds [9]. The updating of this analytical method is focused on the study of interferences and isomers, the use of analytical column with smaller dimensions, mobile phase changes (nature and composition solvent) and a simultaneous analysis with other organic compounds.

Frequently, each group of organic compounds in atmospheric matrices is analysed by different analytical techniques after several pre-treatments of samples. Organic acids and aldehydes have been analysed separately in air using ionic chromatography and HPLC [4] or gas chromatography (GC) and HPLC [17], respectively. These two classes of compounds have been determined in rainwater using capillary electrophoresis (CE) and HPLC [18] or GC/MS and HPLC [19]. Therefore, in ambient air, carbonyl compounds have been analysed together with other groups of compounds such as alkanes using two GC methods [20] and volatile organic compounds (VOC) using HPLC and GC [21] respectively. Nevertheless, Komenda et al. [22] have quantified isoprene, methacrolein and methylvinylketone (degradation products of isoprene) using a common GC method. Simultaneous analysis of carboxylic acids and aldehydes has been achieved using GC–MS with two-step derivatization [23] for air samples and one step for atmospheric aerosol [24]. Moreover, HPLC after DNPH derivatization has been a suitable technique for the simultaneous analysis of these two groups in indoor air [25]. Two HPLC methods for determination of carbonyl compounds and PAHs in rainwater have been used [26]. Ho and Lee [2] analysed carbonyl compounds, PAHs and VOC using three methods (HPLC for carbonyl compounds and GC/MS for PAHs and VOC) in atmospheric samples.

Due to the nature and complexity of environmental matrices, the development of an analytical method ought to consider a multicomponent analysis (with the greatest number of pollutant classes) and a simultaneous extraction and determination of these pollutant classes, if possible, from sampling to measurement.

In this work, the aim pursuits the simultaneous determination of this two pollutant groups from pre-treatment (extraction, clean-up, derivatization, concentration) to chromatographic separation using two detectors in series (photodiode-array (PDA) detector for carbonyl compounds and fluorescence detector for PAHs). In this way, the sample manipulation is simplified, the time operation, solvents and chemicals employed are reduced and, consequently, the analysis expenses. In comparison to the determination of these pollutants using two methods, the method proposed improves the analysis throughput for a large number of analytes of two different classes.

In addition to the improvement in the methodological aspects of the PAH and carbonyl compounds determination, novelties in the environmental application are proposed since the method is applied to the water-soluble fraction of PM_{10} (atmospheric particulate matter with an aerodynamic diameter less than 10 μm). The determination of organic compounds present in particulate matter is frequently performed by extraction with relatively non-polar organic solvents. In this way, most polar and water-soluble compounds are not analysed and an important fraction of organic compounds cannot be characterized well enough. Information on their nature and amount in particulate matter could be useful to know their sources and to understand their formation process [27].

Carbonyl compounds have been mainly determined in air [3,4,9–12,15–17,20–22,25] but scarcely in particulate matter [14,24]. Kiss et al. analysed 15 carbonyl compounds derivatized with DNPH by HPLC but the extraction is performed with organic solvent [14]. Only Wang et al. have measured two dicarbonylic compounds by GC–MS in water-soluble fraction [24]. This fraction is more easily absorbed by the body and therefore, the toxicity of particulate matter is increased [5,28]. The identification of individual carbonyl compounds present in particulate matter and their concentration levels are incomplete in the literature. Their determination can provide information about their potential chemistry. The method proposed allowed the determination of 24 carbonyl compounds in water-soluble fraction.

Moreover, PAHs are slightly water-soluble compounds which could be present in water extracts although in smaller concentrations [27]. To our knowledge, there are no published methods which determine PAHs in water-soluble fraction of particulate matter although the analysis in organic fraction has been extensively studied [1–2,7,8]. Their determination in water-soluble fraction would be useful for their correlation with atmospheric aqueous matrices, or with other pollutants.

2. Experimental

2.1. Standards and reagents

Tetrahydrofuran, methanol and acetonitrile were of HPLC grade (Merck, Darmstadt, Germany; Romil, Cambridge, UK; and Panreac, Barcelona, Spain, respectively). Dichloromethane, super purity solvent, was purchased from Romil (Cambridge, UK) and perchloric acid 69–72% from J.T. Baker (Pillipsburg, USA). Ultra-pure water was obtained by water ultrafiltration with a Direct Q 5 system (Millipore, Bedford, UK). 2,4-Dinitrophenylhydrazine (DNPH) (50% in water) was obtained from Fluka (Steinheim, Germany).

Two derivatized carbonyl compounds mixtures in acetonitrile (DCC8315-1JM and DCC8315-2JM, ChemService (West Chester, USA) (100 μg mL^{-1} of each derivatized carbonyl) containing altogether 20 carbonyl compounds, as follows: formaldehyde, acetaldehyde, acetone, acrolein, propionaldehyde, butyraldehyde, crotonaldehyde, valeraldehyde, isovaleraldehyde, hexaldehyde,

heptaldehyde, octyl alcohol, nonanaldehyde, decyl aldehyde, cyclohexanone, benzaldehyde, 2,5-dimethylbenzaldehyde, *o*-tolualdehyde, *m*-tolualdehyde, *p*-tolualdehyde were used. Also 2-butanone-DNPH and methacrolein-DNPH (Supelco, Bellefonte, PA, USA) (350 μg mL^{-1} of each derivatized carbonyl) and glyoxal 40% in water Fluka, methylglioxal 40% in water Sigma (Steinheim, Germany).

SRM 1647d 'Priority PAHs pollutant in acetonitrile' (NIST, Gaithersburg, MD, USA), which contains 16 EPA PAHs: naphthalene, acenaphthene, fluorene, phenanthrene, anthracene, fluoranthene, pyrene, benzo[*a*]anthracene, chrysene, benzo[*b*]fluoranthene, benzo[*k*]fluoranthene, benzo[*a*]pyrene, dibenzo[*a*]anthracene, benzo[*g*,*h*,*i*]perylene, indeno[1,2,3-*cd*]pyrene, was used. Acenaphthylene was omitted since it is only weakly fluorescent.

Oasis® HLB 60 cartridges (200 mg, 6 mL) (Waters Corporation, Mildford, MA, USA) and Albert® no. 135 ashless filter paper were used for manual solid-phase extraction and for filtration of aqueous extract of atmospheric particulate matter, respectively.

2.2. Materials and instrumentation

A Waters chromatographic system (Waters, Milford, MA, USA) was composed by a 2690 Alliance™ Separations module, UV–visible diode array and fluorescence detector in series (Waters 996 PDA and Waters 474) and Millenium 32® software. The tested analytical column was C_{18} Symmetry® 3.5 μm particle size (150 mm × 3.0 mm ID) with a precolumn 3.5 μm (10 mm × 2.1 mm ID).

2.3. Cleaning of glass material

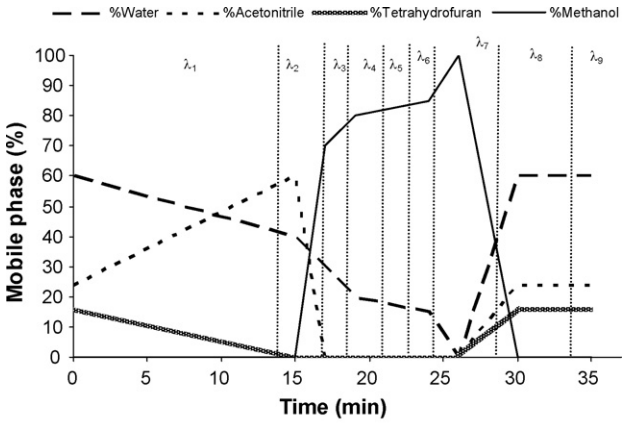
To achieve suitable procedure blanks, it is necessary to submit the glass material to an exhaustive cleaning process which starts with its immersion in an ultrasonic bath with an alkaline detergent (Derquim LA13, Panreac, Barcelona, Spain) during 1 h. After that, the different pieces of glass material were rinsed with fresh milli-Q water and again immersed in the ultrasonic bath filled with fresh milliQ-water during 15 min. This latter part of the process was repeated twice. Then, it is dried in an oven covered with aluminium foils and introduced in a muffle furnace at 350 °C during 12 h, or 500 °C during 6 h. The material is cooled down to 100 °C into muffle and keeps cooling down by gentle stream nitrogen. Finally, it is stored in sealed polyethylene bags.

2.4. Sampling and sample preparation

PM_{10} samples were collected over 24 h periods simultaneously from two sites by EN-12341 reference high volume sampler (Digitel) on 15 cm diameter QF20 Schleicher and Schuell quartz fibre filters. All filters were pre-backed at 400 °C overnight before use in order to remove organic compounds and they were stored in baked aluminium foil. Subsequently, sampling filters were conditioned at 20 ± 1 °C and 50 ± 5% relative humidity during 48 h according to the EN-12341 gravimetric determination of particulate matter. After that, the filters were stored at −18 °C until analysis. An eighth portion of PM_{10} samples were twice ultrasonically extracted with 10 mL milli-Q water at ambient temperature in 15 min.

2.5. Derivatization and pre-concentration SPE procedures

Briefly, 200 μL of DNPH in acetonitrile (7 mg mL^{-1}) and two drops of $HClO_4$ (2 M) were added to 25 mL of aqueous extract. Once derivatization reaction takes place at ambient temperature during 1 h, OASIS HLB cartridges 0.2 g are conditioned with 5 mL dichloromethane, 5 mL methanol and 5 mL milli-Q consecutively. Next, samples are loaded and cartridges are washed with 10 mL milli-Q water and 1.5 mL methanol. Compounds are eluted with 20 mL of dichloromethane/methanol (85:15). This eluate is concentrated to 0.2 mL and then to dryness under a gentle stream of nitrogen. Finally, the residue is solved in 0.5 mL acetonitrile previous chromatographic determination.



Program fluorescence detection

	λ_{Exc}/nm	λ_{Em}/nm		λ_{Exc}/nm	λ_{Em}/nm
λ_1	216	330	λ_6	272	390
λ_2	260	340	λ_7	276	406
λ_3	260	360	λ_8	286	410
λ_4	250	390	λ_9	300	500
λ_5	284	466			

Conditions UV-Vis detection

Range 210-600 nm

λ (quantitation)= 365 nm

Fig. 1. Elution gradient conditions, UV conditions and fluorescence programme of the method proposed.

2.6. Chromatographic conditions

The chromatographic conditions are shown in Fig. 1. Initially, the mobile phase flow was 0.5 mL min^{-1} at 0 min, increasing lineally at 0.55 mL min^{-1} in 15 min. This flow was maintained until minute 30 and decreased lineally to 0.5 mL min^{-1} at minute 35. Hydrazones of carbonyl compounds were detected in the wavelength interval 200–600 nm and quantified at 365 nm and a programme of nine excitation and emission wavelength was employed for PAHs [32]. The temperature of the pre-column and analytical column was maintained at 29 °C. The injection volume was 10 μL.

3. Results and discussion

3.1. Optimization of chromatographic separation

Firstly, separation of 24 carbonyl compounds: 11 aliphatic aldehydes C_1–C_{10} with an isomer of C_5 (isovaleraldehyde), 3 insaturated aldehydes (acrolein, C_3 and methacrolein, crotonaldehyde, C_4), 2 aliphatic ketones (acetone, 2-butanone) and 1 cyclic ketone (cyclohexanone), 5 aromatic aldehydes (benzaldehyde, 2,5-dimethylbenzaldehyde and *o*-,*m*-, *p*-tolualdehyde) and 2 dicarbonylic compounds (glyoxal and methylglioxal) is achieved. Next, PAHs separation is reviewed and adjusted with carbonyl conditions in order to achieve simultaneous analysis.

Last improvements in column technology allow working with columns of smaller dimensions and particle size. A review of some columns used in the literature for carbonyl compounds and PAHs is shown in Table 1. In this work, a column of octadecylsilica with dimensions of 3.5 μm particle size (150 mm × 3.0 mm ID) is chosen. These characteristics can provide a decrease of analysis time, a less solvent consumption and a sensitivity increase compared to a stan-

Table 1
Characteristics of some columns used for carbonyl compounds and PAHs in the literature (stationary phase of octadecylsilica for carbonyl compounds and special PAHs phase for PAHs).

Length × inner diameter × particle size (mm × mm × μm)	References	
	Carbonyl compounds	PAH
250 × 4.6 × 5	13, 16, 21	7, 8
250 × 3.0 × 5	12	
150 × 4.6 × 5	3	
150 × 4.0 × 3	17	
150 × 3.9 × 4	14	
150 × 2.1 × 5	31	
100 × 4.6 × 4		32
100 × 4.6 × 3	15	

dard column (250 mm, 5 μm). Three critical separations in tested compounds that limit gradient peak capacity are found.

One of the critical pairs which is tackled in the literature are the carbonyl compounds with three carbon atoms (an unsaturated aldehyde, acrolein and acetone). In environmental matrices, acrolein is determined at low concentration with high levels of acetone, which makes difficult the separation [15]. Acrolein and acetone have been separated using the binary mixture water/acetonitrile, gradient elution and two reversed-phase columns in series although they are not baseline separated [10]. The same as in C_4 series, whose separation of an unsaturated aldehyde, methacrolein and a ketone, 2-butanone is difficult [16].

In this work, acrolein and acetone were separated for binary mixtures of water/acetonitrile as 65/35, but with higher retention times and peak broadening. Neither binary mixtures of methanol/water in interval 65–85% nor isocratic ternary mixtures (methanol/water/acetonitrile) were effective for the separation of this critical pair. Ternary mixtures (water/acetonitrile/THF), which gave good results in literature [11], were tested using percentages of water among 50–65%. The introduction of a third solvent, as tetrahydrofuran, which has less polarity, produces a decrease on the retention time for all compounds related to binary mixtures. The effect of THF on system C_3 and C_4 was studied as the first step of the gradient, establishing a lineal relation between retention time and %THF (Fig. 2). For 60% water, 10% tetrahydrofuran was sufficient for the resolution of acetone-acrolein. Elution order of three carbonyl compounds was acetone, acrolein and propanal according to other authors that used this mixture [11]. Elution order to C_4 compounds was crotonaldehyde, 2-butanone, methacrolein and butanal. The separation close to the baseline of critical peak pair

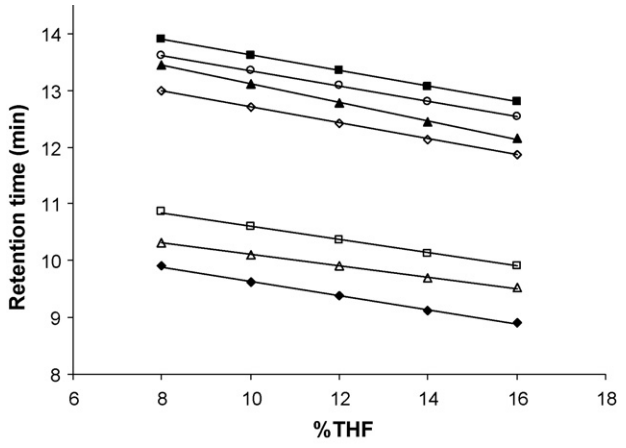


Fig. 2. Effect of tetrahydrofuran (THF) on the retention time of carbonyl compounds with three carbon atoms, system C_3 (♦ acetone, △ acrolein and □ propanal) and with four carbon atoms, system C_4 (◊ crotonaldehyde, ▲ 2-butanone, ○ methacrolein and ■ butanal).

(2-butanone and methacrolein) was reached using 16% tetrahydrofuran. The slope of the straight line is very similar for C_4 system except for 2-butanone which has a greater slope and therefore this fact makes selectivity possible with methacrolein. Concerning the system C_3, acetone also showed a higher slope in the studied interval. For the separation of C_4 compounds, 16%THF produces a worse selectivity between acrolein and propanal but a better selectivity between acrolein and acetone than 10%THF.

The separation of three isomers (*ortho*, *metha* and *para*) of tolualdehyde is another critical separation under a variety of tested conditions. In the literature, partial separation of three isomers is obtained or only one isomer (frequently *metha*-tolualdehyde) is determined. According to Kolliker et al. [12] the column had to contain high organic carbon content in order to obtain a separation with a valley of maximum 30–40%. In our case, the best conditions were achieved with binary mixtures water/acetonitrile using Symmetry column with a 19.5% of total carbon. For 45–50% percentages of acetonitrile, *ortho* and *metha* isomers have a resolution close to the baseline, and *metha* and *para*-tolualdehyde are separated partially. Higher values of acetonitrile make the separation worse. A first step of the gradient elution which starts with a ternary mixture (water/acetonitrile/tetrahydrofuran, 60/24/16) and finishes with a binary mixture (water/acetonitrile, 40/60) is a compromise between the elution of all compounds in a reasonable retention time and the partial separation of *metha* and *para* isomers.

Elution order of aromatic aldehydes was benzaldehyde after C_4 carbonyl compounds, tolualdehyde isomers after C_5 aldehydes, and 2,5-dimethylbenzaldehyde after hexaldehyde. These latter have revealed to be other critical pair of peaks. In the literature there are some separation systems that resolved satisfactorily two compounds with water/acetonitrile mixtures [10] and other authors have not obtained a baseline resolution [11]. A second step of the gradient elution includes 60% acetonitrile elutes hexaldehyde and 2,5-dimethylbenzaldehyde to higher retention times and broadening peaks. It was necessary a lineal increase of % acetonitrile but under these conditions the separation of these two compounds is partial (Fig. 3a). If the water/acetonitrile mixtures in the second step of the gradient elution are replaced by water/methanol (30/70), the separation of hexaldehyde and dimethylbenzaldehyde is total (Fig. 3b).

Other compounds such as glyoxal and methylglyoxal elute during the binary mixture of methanol with water, glyoxal between two isomers of pentanal, overlapping with one of them, isovaleraldehyde, and methylglioxal between tolualdehyde isomers and hexaldehyde. Moreover, in the separation proposed by Grosjean et al. [29], an overlapping between cyclohexanone and glyoxal occurred. In the proposed method, the cyclic ketone, cyclohexanone was eluted between benzaldehyde and C_5 compounds. Finally, the homologous series of semi-volatile C_7–C_{10} aldehydes elutes gradually according to the increasing values of alkyl chain length. Twenty-four carbonyl compounds are separated in less than 30 min analysis time.

Under conditions of separation for carbonyl compounds, the PAHs separation using fluorescence detection is reviewed. Using nine pairs of excitation and emission wavelengths and the same analytical column, the retention times of PAHs are found between 11 and 34 min. These retention times are within the interval of retention times of carbonyl compounds, making possible the simultaneous separation by dual detection (Fig. 4a).

Two compound pairs did not get separated: acenaphthene/fluorene and benzo[*a*]anthracene/chrysene. Fluorene and acenaphthene are separated with this column and binary mixtures water/acetonitrile (20/80) and water/methanol (25/75); however, these conditions are incompatible with the separation of carbonyl compounds of identical number (C_3 and C_4) carbon atom. A special stationary phase, containing a polymeric C_{18} or phenyl group

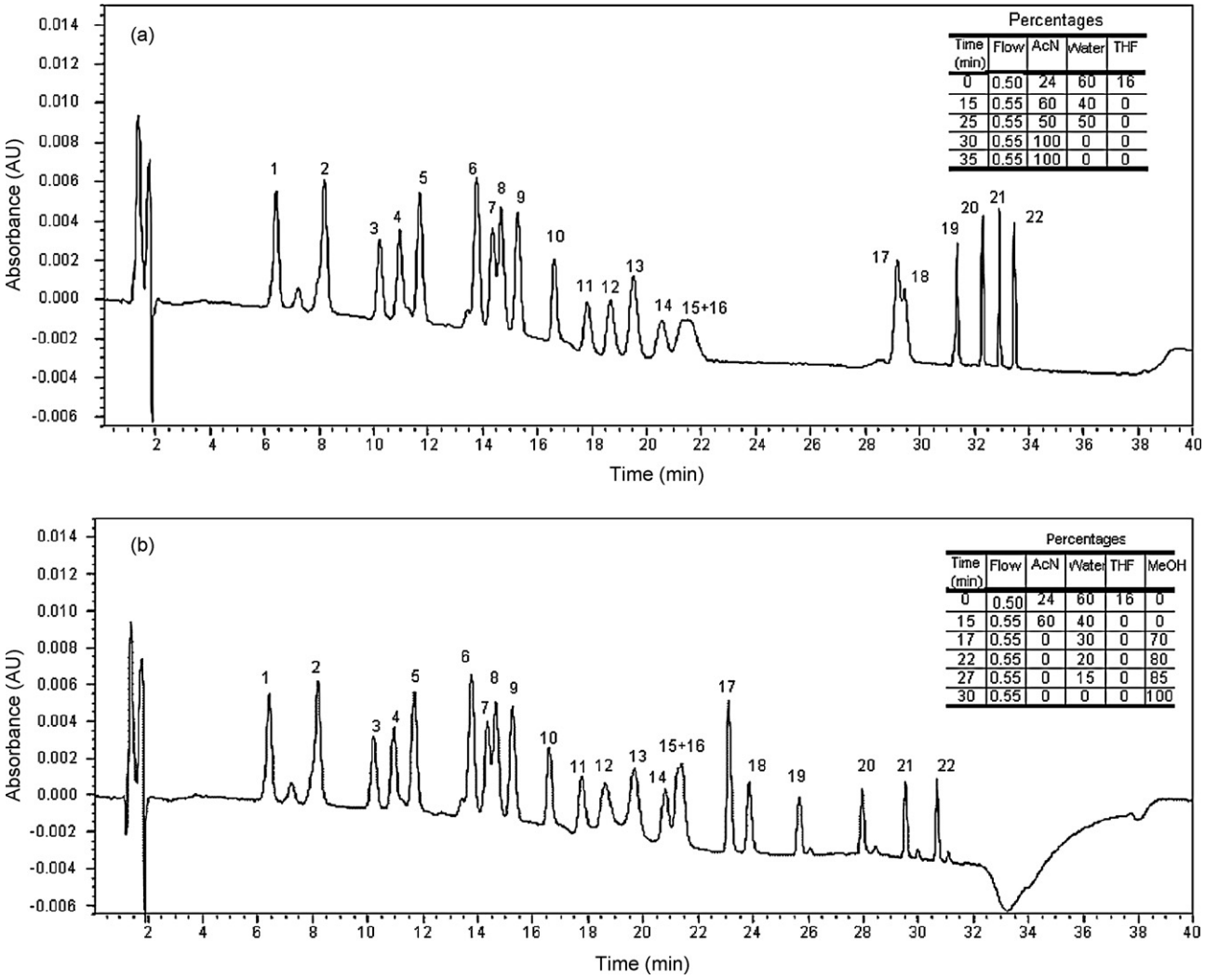


Fig. 3. Separation of critical pair hexaldehyde-dimethylbenzaldehyde with a ternary gradient (water/acetonitrile/THF) (a) and a quaternary gradient (water/acetonitrile/THF/methanol) (b). (1) Formaldehyde, (2) acetaldehyde, (3) acetone, (4) acrolein, (5) propionaldehyde, (6) crotonaldehyde, (7) 2-butanone, (8) methacrolein, (9) butyraldehyde, (10) benzaldehyde, (11) ciclohexanone, (12) isovaleraldehyde, (13) valeraldehyde, (14) o-tolualdehyde, (15 + 16) m + p-tolualdehyde, (17) hexaldehyde, (18) 2,5-dimethylbenzaldehyde, (19) heptaldehyde, (20) octyl aldehyde, (21) nonaldehyde, (22) decyladehyde. Concentration of hexaldehyde 304 ng mL^{-1} and 2,5-dimethylbenzaldehyde 185 ng mL^{-1}. The concentration of carbonyl compounds is in the range of 103–304 ng mL^{-1}.

[1], may be necessary for the other pair of 4 ring isomers. Also, the selectivity between benzo(g,h,i)perylene and indene(1,2,3-*cd*)pyrene is low because fluorescence conditions must be changed (Fig. 4b).

3.2. Pre-treatment (extraction, derivatization, clean-up and concentration)

Pre-treatment steps (extraction, derivatization, clean-up and concentration) to process atmospheric solid samples were studied. Filters of particulate material were extracted with 10 mL of water using ultrasound bath. A second extraction (10 mL of water) was necessary to achieve a recovery of 85% for PAHs since with one extraction only less than 50% of PAHs was extracted.

Extracted solid samples were derivatized with DNPH at ambient temperature during 1 h according to the procedure described in the literature, just as Tsai et al. [30] point out. Clean-up step is carried out by a SPE reversed-phase with a poly(divinylbenzene-co-N-vinylpyrrolidone copolymer and with characteristic lipophilic and hydrophilic which allow to retain polar and non-polar compounds. In our case, only one eluate containing two groups of pollutants is pursued. Acetonitrile (3–4 mL), used like elution solvent for Zwiener et al. [31], with this SPE phase, obtained good results in the case of C_1–C_5 carbonyl compounds and low recovery for aromatic carbonyl compounds and PAHs. Another solvent of great relative elution strength, tetrahydrofuran was suitable for carbonyl compounds but did not improve PAHs recovery. Dichloromethane is a solvent frequently used for extraction and [30] concentration of PAHs but incompatible with aqueous medium. In order to make compatible dichloromethane with aqueous medium, 1.5 mL of methanol is eluted before that the sample without carbonyl compound and PAHs are eluted. Methanol was also used to increase the polarity of the eluent in a mixture of dichloromethane and methanol (85:15). Finally, the eluate was evaporated easily due to the low boiling point of the mixture and re-dissolved in acetonitrile achieving a concentration factor of 50. Recoveries were greater than 90% for carbonyl compounds and PAHs except for the more volatile PAHs (naphthalene was lost and recovery of acenaphthene and fluorene was around 65%).

Nevertheless, this procedure of pre-concentration led to a high acetone blank and other interferences. In order to minimize blanks, washing was necessary to remove acid medium before elution to methanol. It was verified that pH of wash water arises around 3.

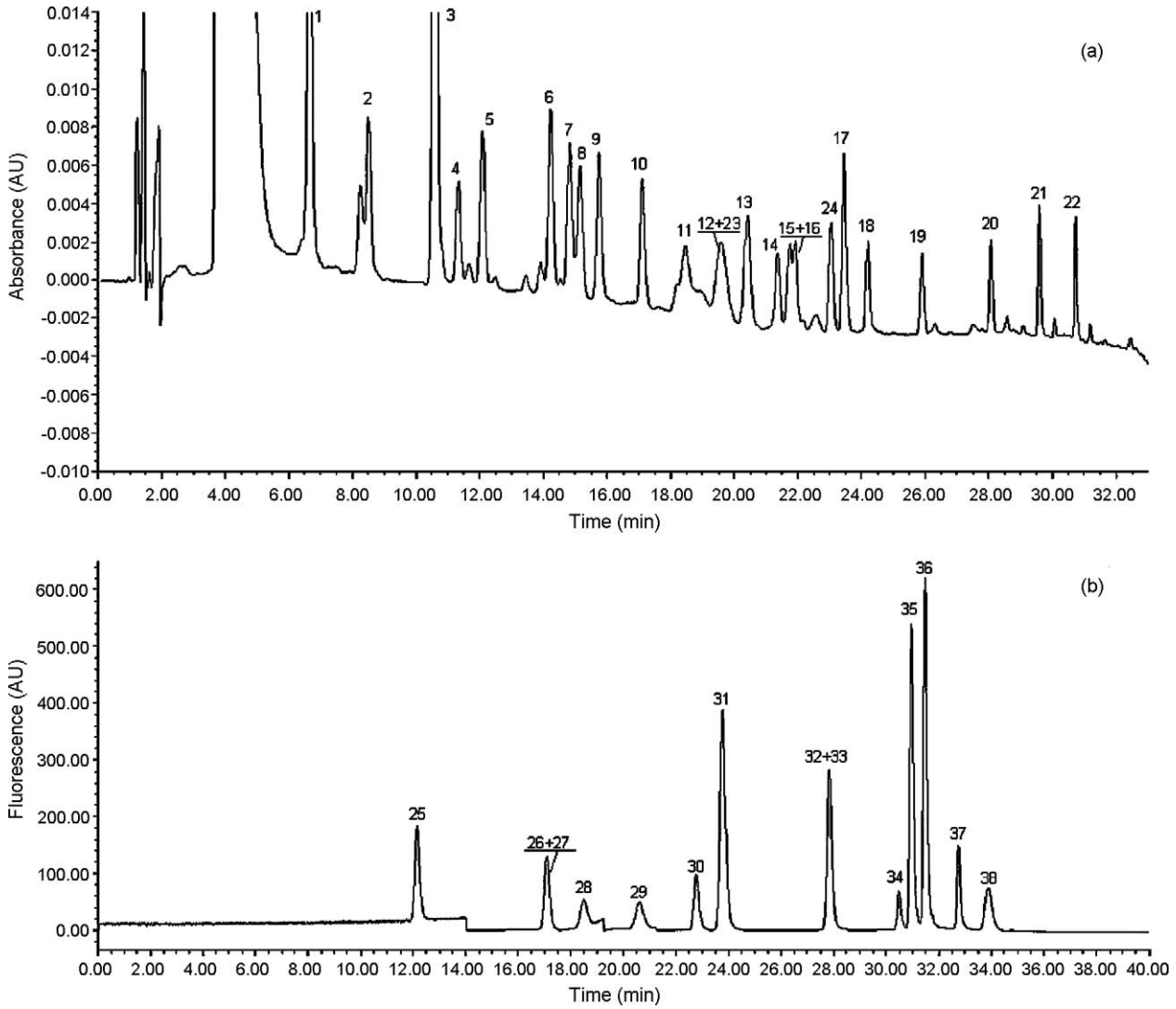


Fig. 4. Simultaneous separation of carbonyl compounds (a) and PAHs (b). (12 + 23) Isovaleraldehyde + glioxal, (24) methylglioxal, (25) naphthalene, (26 + 27) acenaphthene + fluorene, (28) phenanthrene, (29) anthracene, (30) fluoranthene, (31) pyrene, (32 + 33) benzo[*a*]anthracene + chrysene, (34) benzo[*b*]fluoranthene, (35) benzo[*k*]fluoranthene, (36) benzo[*a*]pyrene, (37) dibenzo[*a,h*]anthracene, (38) benzo[*g,h,i*]perylene. The concentration of PAHs is in the range of 5.9–191 ng mL^{-1}.

Thus, high blanks of acetone were minimized but a poor reproducibility to formaldehyde, acetone, benzaldehyde and nonanaldehyde in water blanks was observed. Several unidentified compounds with spectra similar to hydrazones and with retention times from volatile aldehydes to semivolatile aldehydes were also detected. The control of blanks and the reduction of background contamination was achieved by treatment of non-volumetric material (i.e., Pyrex glass tubes). This was heated in muffle furnace and cooled by a nitrogen stream. Glass Pyrex tubes with screw-top obtained the best results in all different materials tested for extraction. Also, 2,4-dinitrophenylhydrazine solution was prepared freshly prior to derivatization and acetone was not used like solvent in laboratory when the samples were processed. In this way, values around (6 ± 2) ng mL^{-1} of acetone, (9.5 ± 2.5) ng mL^{-1} of formaldehyde, (1.9 ± 0.7) ng mL^{-1} of benzaldehyde, (1.7 ± 0.5) ng mL^{-1} of nonanaldehyde, (0.5 ± 0.2) ng mL^{-1} of acetaldehyde for $n = 47$ were achieved.

3.3. Spectral validation

In this work, PDA has been employed to identify and classify hydrazone derivatives, to integrate with peak purity and detect interferences and to verify peak identification by comparing with a standard spectrum library.

All carbonyl compounds were identified initially by retention time and then by applying spectral contrast technique (incorporated in Millenium^{32} software), peak spectral homogeneity is confirmed. Finally, a spectral identification is carried out, contrasting the spectrum with a standard library.

A library was created with spectrums in wavelength interval of 210–600 nm at two different concentration levels of standards. One of them is close detection limit because the spectrum, at a low concentration, has a greater solvent contribution and noise and other level around 700 ng mL^{-1} derivative. Treatment of spectrum was carried out for standards and samples at a level concentration below 700 ng mL^{-1} of derivative by a mathematical process, Savitsky-Golay filters, that allow reducing spectrum noise [33]. In this way, the number of carbonyl compounds possible to identify by spectral contrast increased considerably (Fig. 5).

3.4. Performance of the analytical method

Calibration curves at five levels were prepared and each calibration level was injected twice. Good linearities with correlation

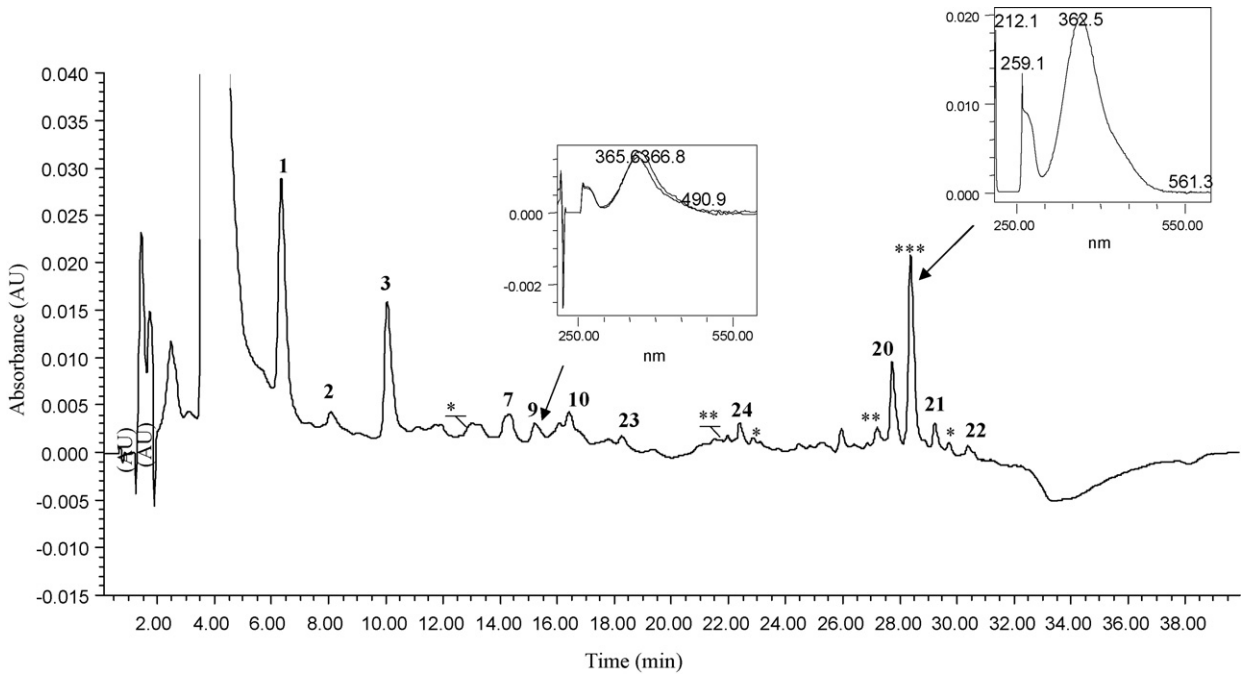


Fig. 5. Chromatogram of carbonyl compounds in PM_{10} sample at industrial site. Unidentified carbonyl compounds (*aromatic aldehydes/ketones, **aldehydes/ketones with conjugated double bounds, ***other aliphatic aldehydes/ketones).

coefficients (R^2) ranging from 0.9971 to 0.9999 for carbonyl compounds and from 0.9958 to 0.9987 were obtained. Table 2 summarizes concentration interval of calibration equations, precision, and detection and quantification limit [34]. Reproducibility was assessed on different days ($n = 10$) at a concentration in the range of 62–203 ng mL^{-1} for carbonyl compounds and 1.5–48 ng mL^{-1} for PAHs and relative standard deviation (%RSD) is reported in Table 2. Valeraldehyde isomers which elute on drift of gradient have had higher relative standard deviations.

Table 2
Analytical data obtained for the determination of PAHs and carbonyl compounds.

Compound	Concentration interval (ng mL^{-1})	LOD (ng mL^{-1})	LOQ (ng mL^{-1})	Precision inter-day (RSD%)
PAH				
Acenaphthene + Fluorene	9.6–191	0.4	1.3	6.1
Phenanthrene	1.3–25	0.18	0.6	14.9
Anthracene	0.3–6	0.04	0.13	15.0
Fluoranthene	2.9–57	0.4	1.3	3.5
Pyrene	0.16–64	0.03	0.09	2.5
Benzo[a] anthracene + Chrysene	0.14–58	0.04	0.12	4.0
Benzo[*b*] fluoranthene	0.6–32	0.099	0.33	5.8
Benzo[*k*] fluoranthene	0.09–36	0.009	0.03	3.8
Benzo[*a*] pyrene	0.7–37	0.04	0.12	2.7
Dibenzo[*a*,*h*] anthracene	0.5–27	0.006	0.02	3.4
Benzo[*g*,*h*,*i*] perylene	1.4–28	0.2	0.7	2.7
Carbonyl compounds				
Formaldehyde	10–893	2.5	8.4	5.2
Acetaldehyde	15–1317	3.3	11.1	3.0
Acetone	17–975	2.6	8.6	2.6
Acrolein	16–950	2.4	7.9	6.6
Propionaldehyde	17–1523	4.1	13.7	4.2
Crotonaldehyde	20–1750	2.9	9.6	2.4
2-Butanone	20–2000	4.4	14.7	3.2
Methacrolein	19–1933	2.6	8.7	4.6
Butyraldehyde	20–1787	4.0	13.2	3.1
Benzaldehyde	25–1483	6.1	20.1	5.5
Cyclohexanone	31–2204	7.6	25.3	10.0
Isovaleraldehyde	23–1294	5.9	19.8	9.9
Valeraldehyde	65–2022	10.1	33.6	9.4
o-Tolualdehyde	80–1600	7.3	22.1	12.8
Hexaldehyde	25–2230	3.5	11.9	2.3
2,5-Dimethylbenzaldehyde	30–1700	4.7	15.9	2.1
Heptaldehyde	27–2425	3.8	12.6	5.5
Octanaldehyde	29–2423	4.3	14.4	3.2
Nonanaldehyde	31–2557	4.3	14.3	3.1
Decanaldehyde	32–2900	4.6	15.5	2.3

Table 3
Analytical recoveries and standard deviation (%) from material particulate PM_{10} spiked with the analytes studied.

Compound	Concentration added (ng mL^{-1})	Recovery (%)	RSD (%), $n = 4$
PAH			
Acenaphthene + Fluorene	126	67	1.7
Phenanthrene	17.6	97	4.2
Anthracene	3.9	99	3.0
Fluoranthene	37.9	99	4.0
Pyrene	42.3	95	4.3
Benzo[*a*] anthracene + Chrysene	38.4	97	5.0
Benzo[*b*] fluoranthene	20.9	96	8.0
Benzo[*k*] fluoranthene	23.5	98	5.2
Benzo[*a*] pyrene	24.3	97	5.8
Dibenzo[*a*,*h*] anthracene	17.4	99	1.8
Benzo[*g*,*h*,*i*] perylene	18.3	104	8.2
Carbonyl compounds			
Formaldehyde	357	95	1.0
Acetaldehyde	148	102	8.4
Acetone	609	72	14
Acrolein	89	89	15
Propionaldehyde	183	111	6.4
Crotonaldehyde	210	101	2.1
2-Butanone	125	86	1.0
Metacrolein	121	113	4.4
Butyraldehyde	214	104	3.0
Benzaldehyde	139	110	13
Cyclohexanone	132	109	8.7
Isovaleraldehyde	809	97	0.4
Valeraldehyde	809	91	3.7
Hexaldehyde	268	93	3.7
2,5 Dimethylbenzaldehyde	161	94	6.3
Heptaldehyde	146	103	4.6
Octanaldehyde	157	91	0.9
Nonanaldehyde	166	91	2.9
Decanalaldehyde	174	101	3.4

Table 4
Concentrations of carbonyl compounds and PAHs (pg m^{-3}) in water-soluble fraction of particulate matter samples.

Compound	Rural site						Industrial site					
	January		February		March		January		February		March	
	Range	Mean	Range	Mean	Range	Mean	Range	Mean	Range	Mean	Range	Mean
Formaldehyde	4650–8663	6192	5364–13,319	7554	0–14,239	7359	5240–10,077	7345	0–10,414	4223	1604–5791	3176
Acetaldehyde	220–947	527	148–2953	1421	460–2953	1760	713–1541	1088	331–1748	951	850–2744	1651
Acetone	1339–3014	2301	15–4830	1805	0–3747	1493	1705–5602	2894	0–2539	1027	0–2407	896
Acrolein	ND	ND	ND	ND	0–810	202	ND	ND	ND	ND	ND	ND
Propionaldehyde	ND	ND	ND	ND	0–2150	744	ND	ND	ND	ND	ND	ND
Crotonaldehyde	542–1554	822	0–1042	705	163–1440	916	0–1791	945	0–2324	952	440–2586	1090
2-Butanone	573–1089	864	0–6825	2174	787–1982	1152	0–3793	1493	0–2178	1155	219–952	623
Methacrolein	ND	ND	ND	ND	ND	ND	ND	ND	ND	ND	ND	ND
Butyraldehyde	0–2136	695	0–3353	1333	880–3238	2284	430–1750	970	0–963	465	0–1744	759
Benzaldehyde	0–3630	1103	0–395	178	0–984	666	336–1817	728	0–1497	697	0–398	109
Cyclohexanone	ND	ND	ND	ND	ND	ND	ND	ND	ND	ND	ND	ND
Isovaleraldehyde	ND	ND	ND	ND	ND	ND	ND	ND	ND	ND	ND	ND
Valeraldehyde	ND	ND	ND	ND	ND	ND	ND	ND	ND	ND	ND	ND
o-Tolualdehyde	ND	ND	ND	ND	ND	ND	ND	ND	ND	ND	ND	ND
Hexaldehyde	0–263	66	0–980	245	1022–2598	1536	0–434	204	0–510	346	0–1190	597
2,5 Dimethylbenzaldehyde	ND	ND	ND	ND	ND	ND	ND	ND	ND	ND	ND	ND
Heptaldehyde	ND	ND	ND	ND	ND	ND	ND	ND	ND	ND	0–1573	393
Octanaldehyde	0–8223	2173	0–30,692	9736	0–8147	3002	0–10,821	4041	0–13,049	6254	0–1438	359
Nonanaldehyde	556–1942	1397	1619–4253	3053	1100–3971	2082	0–4467	2097	0–3337	1540	0–1427	357
Decanaldehyde	ND	ND	0–1642	411	0–618	154	0–490	122	0–885	221	ND	ND
Σ Carbonyl compounds		16,139		28,616		12,571		21,927		17,831		10,010
Acenaphthene + Fluorene	0–33	ND	0–12	3.0	ND	ND	ND	ND	0–59	23	0–83	21
Phenanthrene	0–4	23	0–192	72	22–243	88	9.3–96	43	0–727	272	23–403	141
Anthracene	18–75	46	7.4–31	18	0–46	19	3.9–35	18	12.1–182	96	5.0–59	24
Fluoranthene	11–64	37	50–279	124	20–282	116	0–305	119	40–2385	1085	10.4–1113	430
Pyrene	14–75	44	37–253	113	13–194	81	5.5–235	93	34–1892	804	14–681	293
Benzo[*a*]anthracene + chrysene	11–31	25	26–384	165	14–145	64	10.2–210	134	62–2493	1090	15–1351	432
Benzo[*b*]fluoranthene	11–32	21	15–273	92	10.3–72	43	0–215	103	22–1763	828	8.8–681	307
Benzo[*k*]fluoranthene	6.1–53	32	11–191	71	8.0–58	31	4–111	57	28–814	375	7.0–340	145
Benzo[*a*]pyrene	0–9.3	6	20–282	117	8.5–93	45	5.6–164	83	41–1218	554	6.9–493	185
Dibenzo[*a*,*h*]anthracene	24–96	61	0–21	10	0–11	8.2	0–16	10	9.4–80.6	42	0–37	18
Benzo[*g*,*h*,*i*]perylene	0.7–33	19	0–32	124	21–226	89	0–360	151	61–856	464	20–887	337
ΣPAH		293		909		584		811		5633		2333

ND = not detected.

Recoveries were determined by spiking portions of the filter from PM_{10} samples. The values obtained varied between 72 and 113% range for carbonyl compounds and higher than 95% (except acenaphthene and fluorene) for PAHs with relative standard deviations lower than 15 and 8% respectively (see Table 3).

3.5. Application to real samples

The method proposed was applied to samples of particulate matter of PM_{10} in order to analyse its water-soluble fraction. The samples were collected between January 2005 and March 2005 at two sites in A Coruña-Galicia (Northwestern Spain), with industrial and rural typologies. The results obtained for PAHs and carbonyl compounds are shown in Table 4. The level of concentration of PAHs was of pg m^{-3} excepting February 2005, when fluoranthene and chrysene/benzo[*a*]anthracene reached 1 ng m^{-3}. The total concentration of the PAHs at the industrial site was 4.9 times higher than at the rural site during the period studied. An increase in February for the two sites was observed, but this is more significant in the industrial site. High correlation coefficients among them in the range 0.87–0.99 were observed when the two sampling sites were accounted. Also, Alves et al. [35] obtained high correlations of PAHs but in organic fraction of PM_{10}. The comparison between water-extractable PAHs and organic solvent extractable PAHs according to their concentration level, individual compounds, and particulate size could be carried out in the next step of this study.

In the samples analysed, 10 carbonyl compounds (aliphatic, unsaturated and aromatic aldehydes and C_3–C_4 ketones), those which can be separated for the method proposed, were determined and other unidentified compounds with a spectrum similar to hydrazones were detected (Fig. 5). These unidentified compounds can be classified in different groups of carbonyl compounds (unsaturated with double or triple bonds, aromatic or aliphatic aldehydes or ketones), according to Potter and Karst [36], using ratios of areas peaks at two wavelength (300 and 360 nm). Although a LC–MS method could improve the identification and to confirm the structure of the carbonyl compounds found in water-soluble fraction; for the quantitative analysis, it would be necessary obtain standards of the identified carbonyl compounds.

The concentration of carbonyl compounds at ng m^{-3} levels was 100–1000 times higher in the case of PAHs. The total concentration is slightly higher in the rural site than in the industrial site. The concentrations of acetaldehyde, crotonaldehyde and decanaldehyde reached a higher value only in the industrial site. The main carbonyl compounds found were formaldehyde and octanaldeyde in both sampling sites. Due to the limited number of data, further studies are necessary for a more complete evaluation.

4. Conclusions

The method described showed the following advantages:

- The use of HPLC–PAD–FLD allowed to obtain two chromatograms, correspondent to each class of pollutants. DNPH-derivatized carbonyl compound can be detected only in UV region and PAHs are fluorescent but also exhibit UV absorption. Nevertheless, the latter do not interfere to UV wavelength and concentration used. Two different detection modes simplified the separation and reduced the analysis time since a smaller peak capacity is necessary.
- Spectral analysis of carbonyl compounds with diode-array detection was an adequate tool for verifying the identity of compounds and for detecting co-elutions. Its application to particulate material samples shows that a greater number of carbonyl compounds could be determined by the proposed method if other standard carbonyl compounds were available.
- The simultaneous pre-treatment prior to the chromatographic separation which involves sonication-assisted extraction, derivatization, clean-up and concentration reduced the analysis time and the sample manipulation with regard to the methods which carried out the pre-treatment separately. Therefore, good recoveries were obtained.
- Monodimensional chromatography was sufficient to separate the two kinds of organic compounds. In this way, the chromatographic system was simpler than if a bidimensional chromatography with two columns were used. However, it was necessary to study chromatographic behaviour of the two kinds of compounds to make compatible the chromatographic conditions required for each one of them.
- PAHs and carbonyl compounds were found in water-soluble fraction of PM_{10} at levels of pg m^{-3} and ng m^{-3} respectively. In future works, the application of the method to a greater number of samples will allow to establish the correlations between both kinds of organic compounds and their emission sources.

Acknowledgements

M.C. P.-B. is a Isidro Parga Pondal Fellowship, funded by the Xunta de Galicia, Spain. The authors are grateful to the Spanish Ministry of Education and Science for financial support (Project Ref. REN 2003-08603-C04-01).

References

[1] H.K. Lee, J. Chromatogr. 710 (1995) 79–92.
[2] K.F. Ho, S.C. Lee, Sci. Total Environ. 289 (2002) 145–158.
[3] S.S.H. Ho, H.Z. Yu, Environ. Sci. Technol. 38 (2004) 862–870.
[4] K. Granby, C.S. Christensen, C. Lohse, Atmos. Environ. 31 (1997) 1403–1415.
[5] G. Wang, H. Wang, Y. Yu, S. Gao, J. Feng, S. Gao, L. Wang, Atmos. Environ. 37 (2003) 2893–2902.
[6] E. Wauters, I. Lenelle, Fresenius Environ. Bull. 8 (1999) 629–637.
[7] Y. Liu, L. Zhu, X. Shen, Environ. Sci. Technol. 35 (2001) 840–844.
[8] J.L. Besombes, A. Maitre, O. Patissier, N. Marchand, N. Chevron, M. Stoklov, P. Masclet, Atmos. Environ. 35 (2001) 6093–6104.
[9] EMEP, Manual for Sampling and Chemical Analysis, Norwegian Institute for Air Research (EMEP/CCC-Report 1/95) Revision 1/2001.
[10] Compendium method TO-11A, Compendium of Methods for the Determination of Toxic Organic Compounds in Ambient Air, 2 ed., U.S. Environmental Protection Agency, 1999.
[11] E. Grosjean, D. Grosjean, M.P. Fraser, G.R. Cass, Environ. Sci. Technol. 30 (1996) 2687–2703.
[12] S. Kolliker, M. Oehme, C. Dye, Anal. Chem. 70 (1998) 1979–1985.
[13] U.S. Environmental Protection Agency, Environmental Monitoring Systems Laboratory, Method 554, EPA, Cincinnati, OH, USA, 1992.
[14] G. Kiss, B. Varga, Z. Varga Puchony, A. Gelencser, Z. Krivacsy, J. Hlavay, Talanta 48 (1999) 755–762.
[15] C. Dye, M. Oehme, J. High Res. Chromatogr. 15 (1992) 5–8.
[16] M. Possanzini, V. Di Palo, Chromatographia 40 (1995) 134–138.
[17] H. Satsumabayashi, H. Kurita, Y.S. Chang, G. Carmichael, H. Ueda, Atmos. Environ. 29 (1995) 255–266.
[18] R.M. Peña, S. García, C. Herrero, M. Losada, A. Vázquez, T. Lucas, Atmos. Environ. 36 (2002) 5277–5288.
[19] K. Kawamura, S. Steinberg, L. Ng, I.R. Kaplan, Atmos. Environ. 35 (2001) 3917–3926.
[20] L. Haszpra, I. Szilagyi, A. Demeter, T. Turanyi, T. Berces, Atmos. Environ. 25 (1991) 2103–2110.
[21] M.A. Cerqueira, C.A. Pio, P.A. Gomes, J.S. Matos, T.V. Nunes, Sci. Total Environ. 313 (2003) 49–60.
[22] M. Komenda, A. Schaub, R. Koppmann, J. Chromatogr. A 995 (2003) 185–201.
[23] J. Yu, R.C. Flagan, J.H. Seinfeld, Environ. Sci. Technol. 32 (1998) 2357–2370.
[24] G. Wang, S. Niu, C. Liu, L. Wang, Atmos. Environ. 36 (2002) 1941–1950.
[25] S. Uchiyama, E. Matsushima, S. Aoyagi, M. Ando, Anal. Chem. 76 (2004) 5849–5854.
[26] K. Levsen, S. Behnert, H. Winkeler, Fresenius' J. Anal. Chem. 340 (1991) 665–671.
[27] P. Saxena, L. Hildemann, J. Atmos. Chem. 24 (1996) 57–109.
[28] U.P. Kavanti, M.C. Schadweiler, A.D. Ledbetter, J.K. McGee, L. Walsh, P.S. Gilmour, J.W. Highfill, D. Davies, K.E. Pinkerton, J.H. Richards, K. Crissman, D. Andrewa, D.L. Costa, Environ. Health Perspect. 113 (2005) 1561–1568.
[29] E. Grosjean, D. Grosjean, E. Williams, Environ. Sci. Technol. 28 (1994) 186–196.

[30] C.F. Tsai, H.W. Shiau, S.C. Lee, S.S. Chou, J. Food Drug Anal. 11 (2003) 46–52.
[31] C. Zwiener, T. Glauner, F.H. Frimmel, Anal. Bioanal. Chem. 372 (2002) 615–621.
[32] M. Piñeiro-iglesias, M. Miñones-vázquez, E. Vázquez-Blanco, S. Muniategui-Lorenzo, P. López-Mahía, D. Prada-Rodríguez, Cromatographia 56 (2002) 483–488.
[33] A.A. Savitsky, M.J.E. Golay, Anal. Chem. 36 (1964) 1627.
[34] J.C. Miller, J.N. Miller, Statistics for Analytical Chemistry, Ellis Horwood Limited, Chischester, England, 1988, p. 115.
[35] C. Alves, C. Pio, A. Duarte, Atmos. Environ. 35 (2001) 5485–5496.
[36] W. Potter, U. Karst, Anal. Chem. 68 (1996) 3354–3358.

Talanta 80 (2010) 2093–2098

Contents lists available at ScienceDirect

Talanta

journal homepage: www.elsevier.com/locate/talanta

An rhodamine-based fluorescence probe for iron(III) ion determination in aqueous solution

Jie Mao [a,b,*], Qun He [b,**], Weisheng Liu [b]

[a] Department of Chemistry, Anhui Science and Technology University, Bengbu, Anhui 233100, PR China
[b] College of Chemistry and Chemical Engineering, Lanzhou University, Lanzhou 730000, PR China

ARTICLE INFO

Article history:
Received 17 December 2008
Received in revised form 31 October 2009
Accepted 3 November 2009
Available online 13 November 2009

Keywords:
Iron(III)
Probe
Fluorescence enhancement
Rhodamine

ABSTRACT

An "off–on" rhodamine-based fluorescence probe for the selective signaling of Fe(III) has been designed exploiting the guest-induced structure transform mechanism. This system shows a sharp Fe(III)-selective fluorescence enhancement response in 100% aqueous system under physiological pH value and possesses high selectivity against the background of environmentally and biologically relevant metal ions including Al(III), Cd(II), Fe(II), Co(II), Cu(II), Ni(II), Zn(II), Mg(II), Ba(II), Pb(II), Na(I), and K(I). Under optimum conditions, the fluorescence intensity enhancement of this system is linearly proportional to Fe(III) concentration from 6.0×10^{-8} to 7.2×10^{-6} mol L^{-1} with a detection limit of 1.4×10^{-8} mol L^{-1}.

© 2009 Elsevier B.V. All rights reserved.

1. Introduction

The development of fluorescent chemical devices is a promising field [1–3]. An important area within this field is the design of fluorescent probes for various metal ions [4–8]. Ions play a fundamental role in a wide range of chemical and biological processes, and numerous efforts have been made to the development of effective fluorescent probes. Sensors based on ion-induced changes in fluorescence appear to be particularly attractive due to their simplicity, high sensitivity and instantaneous response [1–8]. The trivalent form of iron is an essential element in man. It provides the oxygen-carrying capacity of heme and acts as a cofactor in many enzymatic reactions involved in the mitochondrial respiratory chain. On the other hand, iron deficiency chlorosis is a widespread agricultural problem that affects the development and decreases the yield of many susceptible crops growing on calcareous and alkaline soils [9]. Thus, there is an urgent need to develop chemical sensors that are capable of detecting the presence of iron ions in environmental and biological samples at physiological pH value. Considerable efforts have been devoted to developing fluorescent probes for various metal ions over the last few decades [10–13]. To date, some Fe(III)-selective fluorescent probes have been achieved [14–17], since paramagnetic Fe(III) is described as one of the most efficient fluorescence quenchers among the transition metal ions, the signal transduction occurrence via chelation enhanced fluorescence (CHEF) with these inherent quenching metal ions is a challenging task. The rhodamine framework is an ideal mode to construct CHEF OFF–ON fluorescent probes due to its particular structural property, i.e. it undergoes equilibrium between non-fluorescent spirocyclic ("off" signal) and strongly fluorescent ring-open ("on" signal) forms and the two forms always behave with completely different fluorescent properties [18]. Heretofore, some studies on rhodamine-based probes have been reported [13,19–24]. We synthesized a rhodamine-based probe (RC) able to recognize and determine Fe(III) at biological pH value in aqueous solution, depending on a fluorescence "off–on" mode.

Furthermore, the real samples contain lots of impurities, which influence the determination. Hence, an appropriate sample pretreatment method is necessary before the determination. Solid-phase extraction (SPE) techniques have recently been among the most popular separation methods for the enrichment of metal ions prior to their determination. The basic principle of SPE is the concentration and purification of analytes from solution by sorption on a solid sorbent [25]. This has several advantages over other techniques, namely conservation of species, good enrichment factors, and ease of automation [25,26]. Accordingly, the choice of the solid sorbent is the most crucial factor. According to previous research, activated carbon-bound ethylenediamin (AC-EDA) showed an excellent adsorption capacity toward Fe(III). And, the application of AC-EDA for the separation, preconcentration and

* Corresponding author at: Department of Chemistry, Anhui Science and Technology University, 222 Tianshui Road, Bengbu, Anhui 233100, PR China. Tel.: +86 550 6732036.
** Corresponding author. Tel.: +86 931 8912422.
E-mail addresses: maoj04@lzu.cn (J. Mao), hequn03@lzu.cn (Q. He).

0039-9140/$ – see front matter © 2009 Elsevier B.V. All rights reserved.
doi:10.1016/j.talanta.2009.11.013

elution of trace Fe(III) from real samples was performed with satisfactory results [27].

In this study, firstly, we applied AC-EDA to pretreat aqueous samples for the purification and Fe(III) enrichment. Secondly, based on the high selective response to Fe(III) of the fluorescent probe RC, a fluorescence method was establish to determine Fe(III) in aqueous solution with satisfactory result.

2. Experimental

2.1. Apparatus

Fluorescence spectra measurements were performed on an F-4500 spectrofluorimeter (Hitachi, Japan). The absorption spectra were observed by a UV-Cary100 spectrophotometer (Varian, Australia). Infrared spectra (4000–400 cm^{-1}) in KBr were recorded on a Nicolet NEXUS 670 FT-IR spectrometer, Nicolet (Madison, WI, USA). A VarioEL element analyzer (Elementar Analysensysteme, Hanau, Germany) was used for elemental analysis. An YL-110 peristaltic pump (General Research Institute for Non-ferrous Metals, Beijing, China) was used in the column process. A PTFE (polytetrafluoroethylene) column (50 mm × 9.0 mm i.d., Tianjin Jinteng Instrument Factory, Tianjin, China) was used. A pH-10C digital pH meter was utilized to measure the pH values of aqueous solutions. ^1H and ^{13}C NMR spectra were taken on a Varian mercury-300 spectrometer with TMS as an internal standard and $CDCl_3$ as solvent. HRMS were determined on a Bruker Daltonics APEXII 47e FT-ICR spectrometer.

2.2. Reagents and chemicals

All reagents were of analytical grade or the best grade commercially available, and were put into use without further purification. Activated carbon (AC, gas chromatographic grade, 40–60 mesh) (Tianjin Guangfu Fine Chemical Research Institute, Tianjin, China), ethylenediamine (EDA) (Dong Feng Biochemical Reagent Factory, Shanghai, China), Rhodamine 6G (Shanghai Chemical Reagent Company, Shanghai, China), diethylenetriamine (Tianjin The Second Reagent Factory, Tianjin, China), and *N*,*N*′-dicyclohexylcarbodiimide (DCC) (Sinopharm Chemical Reagent Co. Ltds., Shanghai, China) were used in this work. The solutions of metal ions were prepared from their nitrate salts (The First Reagent Factory, Shanghai, China). HEPES buffer solutions (0.2 mol L^{-1}, pH = 7.2) were prepared in water. Deionized water was used as solvents throughout.

2.3. Synthesis procedure

Activated carbon powder was first purified with 10% (v/v) hydrochloric acid solution for 24 h so as to remove the metal ions and other impurities sorbed on it. Then 10 g of purified activated carbon was suspended in 300 mL of 32.5% (v/v) nitric acid solution under stirring and heating for 5 h at 60 °C. The mixture was filtered and washed with deionized water to neutral and dried under vacuum at 80 °C for 8 h. The product was carboxylic derivative of activated carbon (AC-COOH).

For the synthesis of activated carbon-bound ethylenediamin (AC-EDA), a 5.0 g amount of AC-COOH was suspended in 150 mL of ethylenediamine under stirring and heating, then 5.0 g of *N*,*N*′-dicyclohexylcarbodiimide (DCC) was added into the suspension and refluxed at 120 °C for 48 h [28]. The product (AC-EDA) was filtered off, washed with ethanol and dried under vacuum at 80 °C for 8 h. The synthetic pathways of AC-EDA is illustrated in Fig. 1.

The modified activated carbon was confirmed by IR analysis. Comparison of the IR spectrum of AC-COOH with activated carbon, a new bang (1710.17 cm^{-1}) appeared in AC-COOH due to $\nu_{C=O}$ of the carboxylic acid group, which indicated the carboxylic derivative of activated carbon was prepared successfully. When AC-COOH was modified by EDA, several new peaks appeared in the spectrum. According to the literature [29,30], the new peaks can be assigned as follows: the peak at 1658.17 cm^{-1} is due to $\nu_{C=O}$, the peak at 1528.56 cm^{-1} is caused by ν_{C-N} and δ_{N-H}. The bands around 3379.73 cm^{-1} can be assigned to ν_{N-H}. Elemental analysis indicated 59.10% carbon, 7.818% nitrogen and 2.904% hydrogen in AC-EDA. It could be calculated that 1 g activated carbon contained 0.154 g EDA. Consequently, the above experimental results suggest that activated carbon is successfully modified by ethylenediamine.

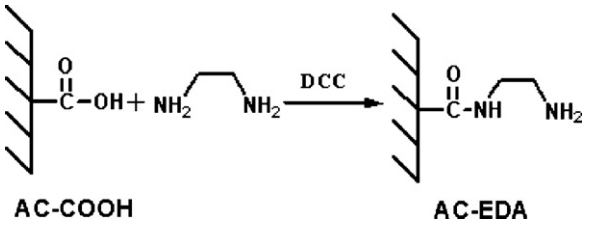


Fig. 1. synthetic pathways of AC-EDA.

The compound (RC) was prepared according to a minor modification of the literature procedure [21]. Rhodamine 6G (958 mg, 2 mmol) was dissolved in 20 mL of hot methanol, followed by the addition of diethylenetriamine (0.67 mL, 10 mmol). The reaction mixture was refluxed for 10 h till the fluorescence of the solution was disappeared. After cooling to the room temperature, the solvent was evaporated *in vacuo*. CH_2Cl_2 (100 mL) and water (200 mL) were added, and the organic layer was separated, washed twice with water and dried over anhydrous sodium sulfate. After filtration of sodium sulfate, the solvent was removed under reduced pressure. Then the resulting pink solid was purified by column chromatography (CH_2Cl_2:CH_3OH = 5:1, v/v) to give 148 mg of RC (pink solid) in 14.8% yield. ^1H NMR (300 MHz, $CDCl_3$): δ 7.90 (t, 1H), 7.43 (t, 2H), 7.01 (t, 1H), 6.32 (s, 2H), 6.22 (s, 2H), 3.52 (t, 2H), 3.20 (t, 4H), 2.54 (t, 2H), 2.31 (m, 4H), 1.85 (s, 6H), 1.36 (t, 6H) ppm; ^{13}C NMR (75 MHz, $CDCl_3$) δ 168.2, 153.3, 151.4, 147.1, 132.1, 130.7, 127.9, 127.7, 123.4, 122.3, 117.4, 105.6, 96.1, 64.7, 51.3, 47.3, 41.3, 39.9, 38.0, 16.4, 14.3 ppm; HRMS (ESI) *m*/*z* obsd 500.3025 ($[M+H]^+$ calcd 500.3020 for $C_{30}H_{37}N_5O_2$).

2.4. Sample pretreatment procedure

A total of 50 mg adsorbent AC-EDA was packed in the PTFE column (50 mm × 9.0 mm i.d.) plugged with a small portion of glass wool at both ends. Before use, HCl (0.5 mol L^{-1}) solution and doubly distilled deionized water were successively passed through the microcolumn in order to equilibrate, clean and neutralize it. Portions of aqueous standard or sample solutions containing metal ions were prepared. Each solution was passed through the column at a flow rate of 4.0 mL min^{-1} controlled by a peristaltic pump. Afterwards, the metal ions retained on column were eluted with a 3 mL of 0.5 mol L^{-1} HCl solution. The elution was collected for the fluorescence determination procedure.

2.5. Fluorescence determination procedure

The elution was adjust to pH 7.0 by NaOH solution and transferred into a 20.0 mL colorimetric tube. The solutions were added in the following order: 2.0 mL 0.2 mol L^{-1} HEPES buffer solutions (pH 7.2), 2.0 mL 1.0×10^{-4} mol L^{-1} RC solution. The mixture was diluted to 20.0 mL with water, and was allowed to stand for 5 min at 25 °C before a fluorescence measurement was made. The intensity of the fluorescence was measured at 552 nm (λ_{ex} = 500 nm) in a 1 cm quartz cell with a slit width of 5 nm for both excitation and emission.

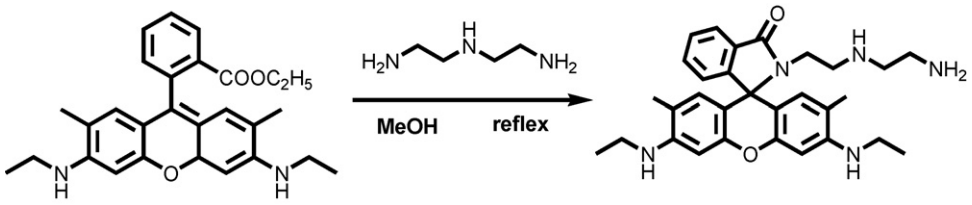


Fig. 2. Synthetic pathways of RC.

3. Results and discussion

3.1. Optical characteristics of the probe RC

As depicted in Fig. 2, compounds RC was facilely synthesized from the reaction of rhodamine 6G with triethylenetetriamine. Although RC is a derivative of rhodamine 6G, it form nearly colorless solutions in HEPES aqueous buffer solution (pH = 7.2), indicating that the spirocyclic forms exist predominantly. The characteristic peak near 64.7 ppm (9-carbon) in the ^{13}C NMR spectra of RC also supports this consideration [31].

When no metal ion was added to the solution of RC, almost no fluorescence signal in the range from 520 to 600 nm could be observed at pH 7.2 in water (Fig. 3 bottom line), whereas a significant enhancement of the characteristic fluorescence of rhodamine 6G emerged soon after Fe(III) was injected into the HEPES solution of RC. Besides, the fluorescence intensity at 552 nm enhanced as the Fe(III) concentration increased. Furthermore, the enhanced extents were in good proportion to the Fe(III) concentrations in a certain range, and other physiologically important cations, even if their concentrations were 50 times higher than that of Fe(III), and only Fe(III) ion can effectively enhance the fluorescence of RC. It was interesting that the enhanced extents of the fluorescence were in good proportion to the concentrations of Fe(III), indicating that an assay of Fe(III) in this way to be good practice. And, the distinct discrimination between Fe (III) and other ion made it possible for the RC to be used for the analysis of Fe (III) in the presence of other ions in aqueous system.

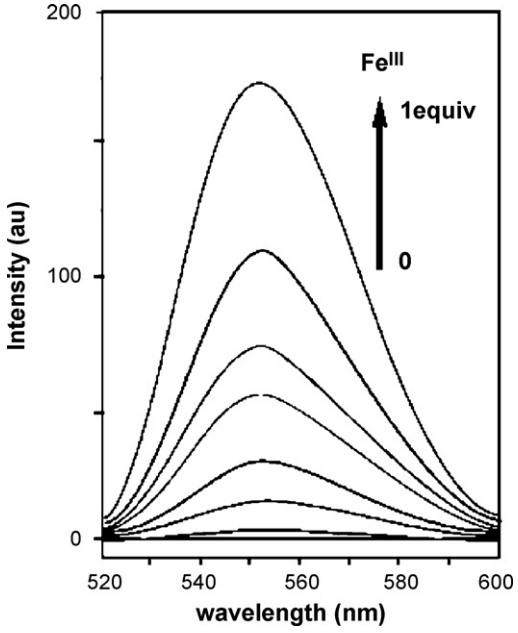


Fig. 3. Fluorescence spectra of RC (1.0×10^{-5} mol L^{-1}) with the addition of increasing concentrations of Fe(III) in HEPES buffer solution (pH = 7.2) with an excitation at 500 nm.

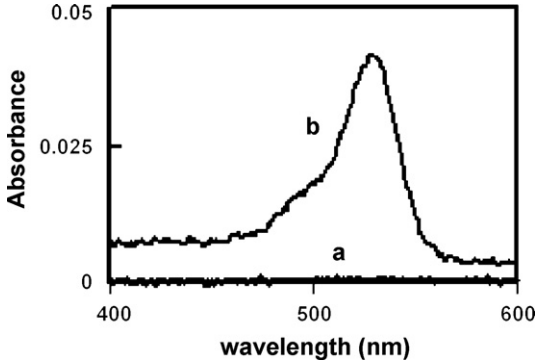


Fig. 4. Absorption spectra of RC (a) and RC with Fe(III) (b) [RC, 1.0×10^{-5} mol L^{-1}; Fe(III), 2.0×10^{-5} mol L^{-1}].

It is showed that RC had no rhodamine framework typical absorbance from 400 to 600 nm (Fig. 4a), which was in the visual range. For that reason, the aqueous solution of RC was colorless. However, with addition of Fe(III) the rhodamine typical absorbance at 527 nm appeared (Fig. 4b), which indicated rhodamine particular structure formed. Meanwhile, the job's plot indicated that a 1:2 stoichiometry for the binding mode of Fe(III) and RC (Fig. 5), and the binding constant was 6.43×10^3 mol^{-1}. It has been reported that many rhodamine derivatives are colorless and non-fluorescent substances due to their stable 'spirolactam form' [13,19,20]. In our study, RC is also colorless and non-fluorescent in aqueous solution for the same reason. If the 'spirolactam form' is opened, the fluorescence could be recovered due to substantially different spectral characteristics of spirocyclic and ring-open forms of rhodamine framework. The fluorescence spectra of RC in aqueous solution in the absence and presence of Fe(III) are shown in Fig. 3. It can be seen that RC displays almost no obvious spectral characteristics in either its absorbance or emission spectrum from 400 to 600 nm. However, a significant enhancement of fluorescence with an absorbance maximum at 527 nm and an emission maximum at 552 nm was observed when Fe(III) was added. We speculated that the spiro-

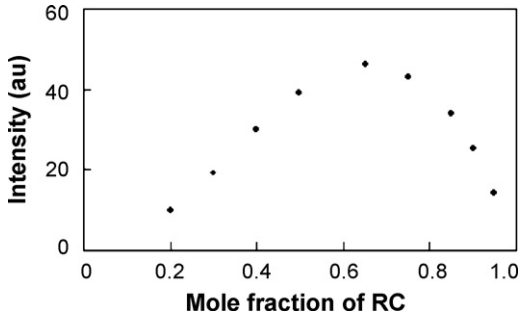


Fig. 5. Job's plot according to the method for continuous variations, indicating the 1:2 stoichiometry (Fe(III)/RC) [the total concentration of RC and Fe(III) is 2.0×10^{-5} mol L^{-1}].

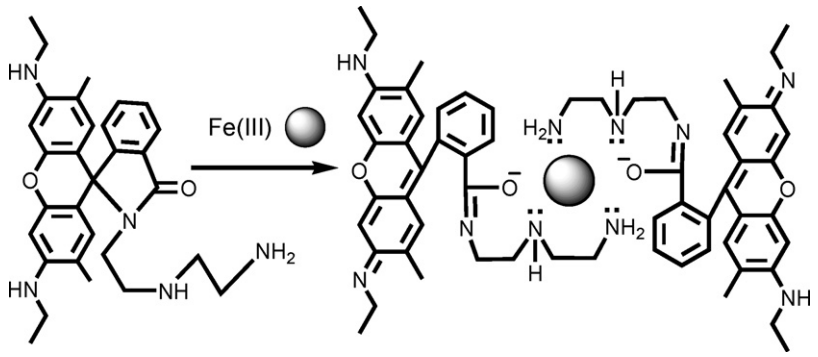


Fig. 6. Mechanism for the fluorescence enhancement of RC upon the addition of Fe(III).

lactam form was opened upon the addition of Fe(III) to RC, and a highly delocalized π-conjugated structure of RC was formed (Fig. 6) [13,19]. Thus, a significant enhancement of absorbance and fluorescence occurred. With this special coordinate mode, Fe(III) was able to enhance the fluorescence of RC, though the other ions failed, indicating the coordinate moiety of RC match perfect with Fe(III) instead of other ions.

3.2. Optimization of the analytical procedures

3.2.1. Effect of RC concentration

The concentration of RC influenced the Fe(III) determination. If the concentration of RC was too high, the sensitivity for the detection of Fe(III) would be decreased. On the contrary, the linear range would become narrow if the concentration was too low. For a balance between the sensitivity and the linear range, the optimum concentration of RC for the Fe(III) determination was 1.0×10^{-5} mol L^{-1}.

3.2.2. Effect of the pH

The effect of pH on the fluorescence intensity of RC in the system is shown in Fig. 7. It can be seen that the fluorescence kept constant tiny intensity between pH 5.5 and 8.5 in water. However, the fluorescence intensity increased sharply when pH value below 5.0 and became even more acidic. Finally, a physiological pH value 7.2 was chosen for the fluorescence intensity determination.

3.2.3. Effect of temperature

Under a temperature series, the fluorescence intensity of RC almost kept constant. For that reason, we could know that this system possessed stability to temperature for Fe(III) determination in aqueous solution. But considering the convenience and maneuverability, all the fluorescence measurements were conducted under 25 °C.

3.2.4. Effect of time

Under the optimum conditions, the effect of time on the Fe(III) determination was studied at room temperature. The fluorescence intensity changed soon after Fe(III) added into RC aqueous solution and remained stable from 1 min to 10 h. After all reagents had been added they were left standing for 5 min ahead of a measurement. In this study, 5 min was set as the standard for all fluorescence intensity measurements.

3.3. Tolerance of foreign substances

The effect of substances, including common metal ions was examined for interference. The results are summarized in Fig. 8 and Table 1. It is showed in Fig. 8 that other ions but Fe(III) failed to arouse fluorescence response of RC system. And, Table 1 shows that the influence of metal ions in biological systems, such as K^+, Ca^{2+}, Na^+, and Zn^{2+} though with much higher concentration compared with Fe(III), was tiny to the RC-Fe system. Consequently, it is clear that other ions' interference is slight to this system.

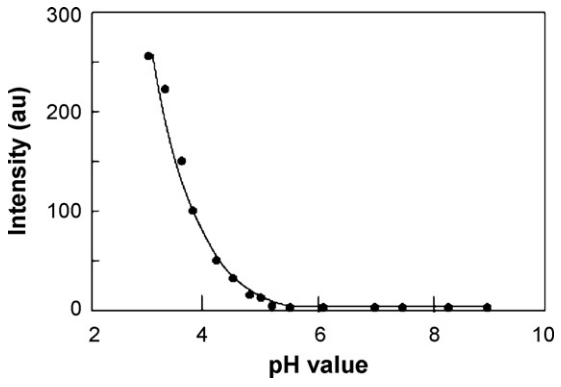


Fig. 7. Evaluation of the fluorescence intensity (at 552 nm) of RC (1.0×10^{-5} mol L^{-1}) under different pH values with an excitation at 500 nm.

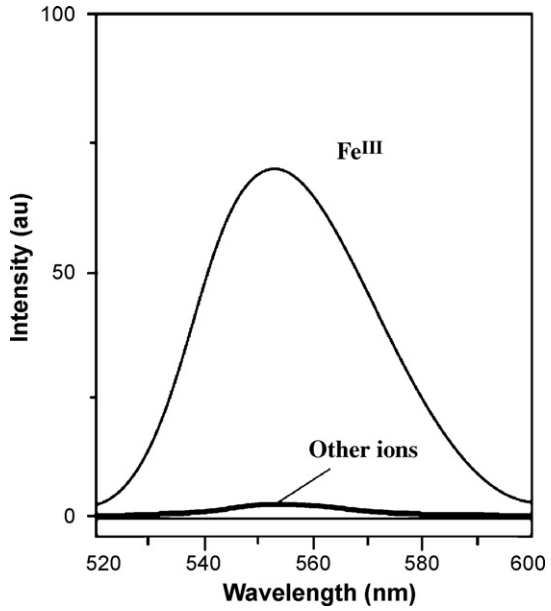


Fig. 8. Fluorescence spectra response of RC (1.0×10^{-5} mol L^{-1}) under the optimum conditions with different ions (4.0×10^{-6} mol L^{-1}) with an excitation at 500 nm. Other ions including K(I), Ca(II), Na(I), Mg(II), Zn(II), Pb(II), Co(II), Ba(II), Cu(II), Al(III), Cd(II), and Ni(II).

Table 1
Interference of potentially interfering ions.

Co-existing substance	Co-existing concentration ($\times 10^{-6}$ mol L^{-1})	Change in intensity of fluorescence (%)
K(I)	100	−1.95
Ca(II)	100	4.31
Na(I)	100	−0.40
Mg(II)	100	1.78
Zn(II)	100	−2.41
Pb(II)	100	−4.15
Co(II)	100	2.47
Ba(II)	100	−3.30
Cu(II)	50	3.63
Al(III)	50	4.32
Cd(II)	50	−2.1
Ni(II)	50	3.37
Fe(II)	50	4.83

Note: Determination conducted under the optimum conditions, samples contain 1.0×10^{-6} mol L^{-1} Fe(III) and other ions.

Table 2
Analytical parameters for the determination of Fe(III).

Sample	Linear range ($\times 10^{-8}$ mol L^{-1})	Linear regression equation (c, ng mL^{-1})	Detection limit (3σ, mol L^{-1})	Correlation coefficient
Fe(III)	6.0–720	$\Delta F = 1.67 \times 10^7 c + 3.25$	1.4×10^{-8}	0.998

Table 3
Results of the sample analysis.

Real samples	Fe(III) ($\times 10^{-8}$ mol L^{-1})				Recovery (%)
	Found[a]	Added[b]	Sum result[c] ($n = 5$)	Found[d]	
Tap		0	75.4	73.8	95–103
water	78.5	50.0	125.2		94–102
		100.0	170.9		95–104
Waste		0	187.3	181.4	94–105
water	189.3	200.0	384.4		95–106
		400.0	572.5		94–105

[a] Detected by ICP-AES method.
[b] Standard Fe(III) solution addition.
[c] Detected by the method of this paper.
[d] The result found by the method of this paper.

3.4. Analytical characteristics

Under the optimum conditions, the relationship between ΔF [the fluorescence intensity enhancement of RC upon the addition of varying concentrations of Fe(III)] and the concentration of Fe(III) was obtained. The analytical parameters are given in Table 2, which demonstrates a linear relationship between ΔF and the concentrations of Fe(III) over a wide range, and the limit of detection reaching the 1.4×10^{-8} mol L^{-1}.

3.5. Analytical applications

The present method was applied to determine real samples, tap water and industrial waster water (the samples were supplied by gansu center for disease prevention and control). Table 3 shows the analysis results which were very close to those detected by ICP-AES method, which were 78.5×10^{-8} and 189.3×10^{-8} mol L^{-1} in the determination of samples, respectively (the result was supplied by Analytical Chemistry Institute of Lanzhou University). Therefore, the present method could be applied for the analysis of Fe(III) in aqueous system.

4. Conclusions

In conclusion, we have developed a novel fluorescent probe RC for Fe(III) based on the enhancement of fluorescence intensity of RC after adding Fe(III). Under the optimum conditions, the relative fluorescence intensity increase was linearly proportional to the concentration of Fe(III) in a wide range, and the limit of detection was 14 nmol L^{-1}. The probe RC had remarkably high selectivity and sensitivity. Moreover, the analytical results of real samples were satisfactory. Fluorescence enhance mechanism is presumably due to the chelation of Fe(III) with the oxygen atoms of the amide groups of RC results in the formation of the open-ring form, which leads to the enhancement of fluorescence signals of RC.

Acknowledgements

This study was supported by the research fund of Anhui Science and Technology University and the NSFC (Grants 20431010, 20621091 and J0630962).

References

[1] J.P. Desvergne, A.W. Czarnik, Chemosensors of Ion and Molecule Recognition, Kluwer, Dordrecht, 1997, pp. 1–276.
[2] U.S. Spichiger-Keller, Chemical Sensors and Biosensors for Medical and Biological Applications, Wiley–VCH, Weinheim, Germany, 1998, pp. 1–413.
[3] D.A. Leigh, M.A.F. Morales, E.M. Perez, J.K.Y. Wong, C.G. Saiz, A.M.Z. Slawin, A.J. Carmichael, D.M. Haddleton, A.M. Brouwer, W.J. Buma, W.H. Wurpel, S. Leon, F. Zerbetto, Angew. Chem. Int. Ed. 44 (2005) 3062.
[4] A.P. de Silva, H.Q.N. Gunaratne, T. Gunnlaugsson, A.J.M. Huxley, C.P. McCoy, J.T. Rademacher, T.E. Rice, Chem. Rev. 97 (1997) 1515.
[5] B. Valeur, I. Leray, Coord. Chem. Rev. 205 (2000) 3.
[6] K. Rurack, Spectrochim. Acta 57A (2001) 2161.
[7] K. Rurack, U. Resch-Genger, Chem. Soc. Rev. (2002) 116.
[8] V. Amendola, L. Fabbrizzi, F. Forti, M. Licchelli, C. Mangano, P. Pallavicini, A. Poggi, D. Sacchi, A. Taglieti, Coord. Chem. Rev. 250 (2006) 273.
[9] Y. Chen, P. Barak, Adv. Agron. 35 (1982) 217.
[10] X.B. Zhang, J. Peng, C.L. He, G.L. Shen, R.Q. Yu, Anal. Chim. Acta 567 (2006) 189.

[11] J.S. Wu, P.F. Wang, X.H. Zhang, S.K. Wu, Spectrochim. Acta 65A (2006) 749.
[12] M.J.E. Resendiz, J.C. Noveron, H. Disteldorf, S. Fischer, P.J. Stang, Org. Lett. 6 (2004) 651.
[13] Y.K. Yang, K.J. Yook, J. Tae, J. Am. Chem. Soc. 127 (2005) 16760.
[14] L.J. Fan, E.J. Wayne, J. Am. Chem. Soc. 128 (2006) 6784.
[15] J.L. Bricks, A. Kovalchuk, C. Trieflinger, M. Nofz, M. Büschel, A.I. Tolmachev, J. Daub, K. Rurack, J. Am. Chem. Soc. 127 (2005) 13522.
[16] G.E. Tumambac, C.M. Rosencrance, C. Wolf, Tetrahedron 60 (2004) 11293.
[17] Y. Xiang, A. Tong, Org. Lett. 8 (2006) 1549.
[18] B. Valeur, Molecular Fluorescence: Principles and Applications, Wiley–VCH Verlag GmbH, New York, 2001, p. 273.
[19] J.Y. Kwon, Y.J. Jang, Y.J. Lee, K.M. Kim, M.S. Seo, W. Nam, J. Yoon, J. Am. Chem. Soc. 127 (2005) 10107.
[20] H. Zheng, Z.H. Qian, L. Xu, F.F. Yuan, L.D. Lan, J.G. Xu, Org. Lett. 8 (2006) 859.
[21] J.S. Wu, I.C. Hwang, K.S. Kim, J.S. Kim, Org. Lett. 9 (2007) 907.
[22] D. Wu, W. Huang, C. Duan, Z. Lin, Q. Meng, Inorg. Chem. 46 (2007) 1538.
[23] M.H. Lee, J.S. Wu, J.W. Lee, J.H. Jung, J.S. Kim, Org. Lett. 9 (2007) 2501.
[24] S.C. Burdette, S.J. Lippard, Inorg. Chem. 41 (2002) 6816.
[25] V. Camel, Spectrochim. Acta B 58 (2003) 1177.
[26] Y. Zhai, X. Chang, Y. Cui, N. Lian, S. Lai, H. Zhen, Q. He, Microchim. Acta 154 (2006) 253.
[27] Z. Li, X. Chang, X. Zou, X. Zhu, R. Nie, Z. Hu, R. Li, Anal. Chim. Acta 632 (2009) 272.
[28] G.J. Wang, J.L. Guo, Z.H. Qu, Fiber Reinf. Plast. Compos. 34 (2006) 8.
[29] H.T. Tang, Organic Compound Spectra Determination, Publishing House of Beijing University, Beijing, 1992, pp. 124–159.
[30] Q.N. Dong, IR Spectrum Method, Publishing House of the Chemical Industry, Beijing, 1979, pp. 104–168.
[31] U. Anthoni, C. Christophersen, P. Nielsen, A. Puschl, K. Schaumburg, Struct. Chem. 6 (1995) 161.

Talanta 80 (2010) 2099–2105

Contents lists available at ScienceDirect

Talanta

journal homepage: www.elsevier.com/locate/talanta

A novel molecularly imprinted solid-phase microextraction fiber coupled with high performance liquid chromatography for analysis of trace estrogens in fishery samples

Yuling Hu, Yangyang Wang, Xiaoguang Chen, Yufei Hu, Gongke Li*

School of Chemistry and Chemical Engineering, Sun Yat-sen University, 135 Xingang Xi Road, Guangzhou 510275, China

ARTICLE INFO

Article history:
Received 21 August 2009
Received in revised form 28 October 2009
Accepted 3 November 2009
Available online 13 November 2009

Keywords:
Molecularly imprinted
Solid-phase microextraction
Estrogens
Fishery sample

ABSTRACT

The combination of molecular imprinting and solid-phase microextraction (SPME) technique provides a powerful sample preparation tool in terms of selectivity, simplicity, and flexibility. This paper reports a novel molecularly imprinted polymer (MIP) coated SPME fiber with 17β-estradiol as template by improved multiple co-polymerization method. The obtained fiber exhibits excellent characteristics such as high porosity, good thermal and chemical stability. Extraction performance shows that the MIP-coated fiber has stronger affinity to the template molecule as compared with the commercial SPME fibers and the control polymer-coated fiber without addition of template. Owing to the shape and structural compatibility, the obtained fiber also demonstrated specific selectivity to the structural related compounds of 17β-estradiol, such as estriol, estrone and 17α-ethynylestradiol, and thus can be applied to simultaneous determination of these estrogens from complex samples coupled with high performance liquid chromatography. The variables that influence extraction were investigated. The MIP-coated fiber demonstrated its efficiency for extraction of estrogens in fishery samples. The detection limits were in the range of 0.98–2.39 μg L^{-1}, and the recoveries were 80.0–83.6% and 85.0–94.1% for fish and shrimp tissue samples, respectively.

© 2009 Elsevier B.V. All rights reserved.

1. Introduction

Estrogens are a group of strong endocrine-disrupting compounds that are of particular interest due to their high estrogenic activities. For example, 17β-estradiol, a natural steroid estrogen, has been shown to cause the feminization of male fish at much lower concentrations (pg mL^{-1}) in aquatic environment [1]. Over the last few decades, there has been a steady increase in estrogen consumption for human medicine and animal farming. The excretion into the environmental water may cause accumulation of the estrogens in fish bodies. In addition, illegal application of estrogens to promote growth rate of fishes or as repartitioning agents in fishery production became a main hazard to human health, because of their potential carcinogenic properties and other adverse effects. Therefore, a selective, accurate and sensitive analytical method for detecting estrogens in fishery samples is important for the investigation of potential use of estrogens in food-safety area.

Several methods for the determination of estrogens have been reported, including immunoassay [2], chemiluminescence [3], gas chromatography–mass spectrometry (GC–MS) [4,5], liquid chromatography (LC) with ultraviolet detection (UV) [6], fluorescence detection (FD) [7], and mass spectrometry (MS) [8–10]. Each method has its advantages and limitations in terms of sensitivity, selectivity and convenience of operation. Among these, chromatographic methods are the most widely used. However, their sensitivity and selectivity limit their direct use for determination of these contaminants at trace concentration with complex matrix. Therefore, a sample preparation step prior to chromatographic analysis is usually necessary.

Such sample preparation procedures as liquid–liquid extraction (LLE) [11] and solid-phase extraction (SPE) [12,13] have been usually applied for the determination of estrogens. However, these methods require large volumes of organic solvents or time-consuming operation. Recently, newly developed sample pretreatment method, including cloud point extraction [14], stir bar sorptive extraction (SBSE) [15,16], membrane extraction [17] and solid-phase microextraction (SPME) [18,19] have been reported for monitoring estrogens either in pharmaceutical formulation, in environment matrices or in biologic samples. Among these methods, SPME is advantageous due to its convenience, less consumption of solvent and easiness to couple with chromatographic instruments [20]. For the polar characteristics of the estrogenic compounds, recent developed novel SPME coatings for determination of estrogens were focused on the preparation of polar coatings

* Corresponding author. Tel.: +86 20 84110922; fax: +86 20 84112245.
E-mail address: cesgkl@mail.sysu.edu.cn (G. Li).

0039-9140/$ – see front matter © 2009 Elsevier B.V. All rights reserved.
doi:10.1016/j.talanta.2009.11.015

to improve the extraction capability, including both in-tube and fiber coatings [21,22]. However, those SPME coatings were mostly applied to environmental water samples which have relatively simple matrices. For analysis of those complex samples, such as biological samples, SPME coatings with higher selectivity are expected to develop in order to enrich the target molecules from these complex matrices.

Molecularly imprinted polymers (MIPs) are highly cross-linked and organized polymer aiming to mimic biological recognition. Removal of the template yields imprinted cavity capable of recognizing template molecule under appropriate conditions. The most common form of MIPs' application in sample pretreatment is solid-phase extraction (SPE) [23–25]. Recently, MIP was combined with simplicity and flexibility of SPME to develop novel recognition coatings in our and other laboratory, including using clenbuterol [26], prometryn [27,28], propazine [29], propranolol [30], diacetylmorphine [31], tetracycline [32] and propranolol [33] as template, respectively. The resulting MIP-SPME fiber showed specific selectivity towards the template molecules and their structural analogues in complex sample matrices such as food, soil and biological fluids. The preparation approaches were based on multiple co-polymerization method with repeated coating procedure on a silica fiber [26–28,32,33] or direct synthesis of MIP monoliths using silica capillaries as molds [29,31].

In this study, a novel MIP-coated SPME fiber with 17β-estradiol as template for selective extraction of estrogenic compounds in fishery samples was prepared by improved multiple co-polymerization method. Its characteristics, extraction capability and selectivity were investigated as compared with the commercial fiber and the non-imprinted polymer (NIP) coated SPME fiber. The MIP-coated SPME fiber has been coupled directly with HPLC for simultaneously multi-residue monitoring of four residual estrogens in fish and shrimp tissue samples.

2. Experimental

2.1. Instrumentation

A magnetic stirrer was obtained from Supelco (Bellefonte, PA, USA) for SPME procedure. A SPME–HPLC coupling device (Supelco, Bellefonte, PA, USA) was used for desorption. A XL-30 scanning electron microanalyzer (Philips, Eindhoven, The Netherlands) was employed to investigate the coating surface. A thermal gravity (TG) analyzer (Netzsch TG-209, Bavaria, Germany) was used to investigate the thermal stability of the coating.

The HPLC system assembled from Shimadzu LC-20A (Shimadzu, Japan) consists of a model LC 20AB pump and a model SPD-20A UV detector. A LC-solution workstation (Shimadzu, Japan) was utilized to control the system and also for data analysis.

2.2. Chemicals

Estrone, 17β-estradiol, estriol and 17α-ethynylestradiol with the purity >99% were purchased from Zizhu Tiangong Tech. (Beijing, China). Methacrylic acid (MAA), 4-vinylpyridine (4-VP) and azo(bis)-isobutyronitrile (AIBN) were obtained from Damao Reagent Plant (Tianjin, China). Trimethylolpropane trimethacrylate (TRIM) were purchased from Shenda Chemical Plant (Beijing, China). Acetonitrile and methanol of HPLC grade were purchased from Merck (Darmstadt, Germany). Water was doubly distilled. All other reagents were of analytical grade. All solutions used for HPLC were filtered through a nylon 0.45 μm filter before use. Fibers were kindly provided by FiberHome Telecommunication Technologies (Wuhan, China).

2.3. Preparation of molecularly imprinted polymer-coated silica fiber

The 17β-estradiol molecularly imprinted polymer-coated silica fiber was prepared by a modified procedure of our previous work [27,32]. Firstly, the silica fibers with diameter of 140 μm were etched with sodium hydroxide and then activated with hydrochloric acid. Prior to the coating procedure, the fibers were silylated for 1 h by immersing them into a 10% (v/v) 3-(methacryloxy) propyltrimethoxysilane solution in acetone at room temperature. Then the fibers were washed with methanol and dried with a stream of nitrogen. Pre-polymer solution for molecularly imprinted polymer (MIP) was prepared with 136.2 mg of 17β-estradiol and 0.34 mL MAA dissolved in 15.5 mL acetonitrile. This solution was incubated for 12 h at room temperature, and then 1.6 mL TRIM and 81.2 mg AIBN were added. Subsequently 1.5 mL of the mixture was transferred into a small glass tube and deoxygenized with a stream of nitrogen for 5 min. The silylated fiber was inserted in the tube and the whole reaction system was sealed immediately to perform the polymerization at 65 °C. When the polymerization solutions were transferred to semi-solid state about 2 h, the fiber was cautiously pulled out with a thin layer of MIP coating on the surface. The coating procedure was repeated for eight times. Subsequently the fiber was kept in nitrogen environment and heated at 150 °C for 3 h. In order to remove the template molecules, the fibers were soaked in 5 mL of 10% (v/v) acetic acid solution in methanol for 30 min. This procedure was performed repetitiously until 17β-estradiol could not be detected in the soaking solution. The NIP-coated silica fiber was prepared following the same procedure except for the addition of 17β-estradiol. The obtained coatings were kept for 1 cm long by scraping the unwanted coatings from the top. Then the uncoated end of fiber was adhered into the inner tube of the commercially SPME setup.

2.4. SPME procedure

In a typical assay, 4-mL estrogens standard solution in n-hexane was added into a 5-mL glass vial. An MIP-coated fiber was immersed into the solution to extract analytes for 40 min at stirring rate of 750 rpm. The six-way valve of the SPME–HPLC coupling device was switched to the LOAD position, and methanol, as the desorption solvent, was injected into the desorption chamber by syringe. The SPME fiber was then inserted into the chamber to desorb the analytes for 15 min. Subsequently, the six-way valve was switched to the INJECT position, all desorption solution was injected into the chromatographic system for analysis.

The commercial SPME fiber used for comparison study consists of the polydimethylsiloxane (PDMS), polydimethylsiloxane–divinylbenzene (PDMS/DVB) and Carbowax–Templated Resin (CW/TPR) fiber which were obtained from Supelco (Supelco, Bellefonte, PA, USA). The extraction was performed in 20 $\mu g\,L^{-1}$ of 17β-estradiol aqueous solution for 40 min at stirring rate of 750 rpm, and then desorbed by methanol for 15 min. The extraction ability of the NIP-coated fiber was compared with that of the MIP-coated fiber at the same extraction conditions.

2.5. Chromatographic conditions

A Diamonsil C18 (250 mm × 4.6 mm, 5 μm particle size, Dikma) column was used. The mobile phase consisted of acetonitrile and 0.12% acetate buffer. The acetonitrile composition was set at 25.5% initially and increased linearly from 15 min to 30 min till 45%. The mobile phase flow-rate through the column was 1.0 $mL\,min^{-1}$ at room temperature. UV wavelength was set at 225 nm. The injection volume was 20 μL.

2.6. Calibration and sample preparation

Calibration was made by the standard curve method. Stock solutions of estrogens were prepared at concentration of 1000 mg mL^{-1} in methanol. Diluting the stock solution serially with methanol yielded standard solutions. All solutions were sealed and refrigerated at 4 °C until use. Extraction of estrogens was performed by diluting standard solution with n-hexane to give the corresponding solution for calibrations, limits of detection (LODs) and linearity tests.

The fish and shrimp tissue samples were stored at −18 °C before analysis. The tissue samples were chopped and triturated in a blender. A portion of 5 g sample was mixed and homogenized with 100 μg L^{-1} estrogen standard solutions to obtain the spiked samples at the concentration of 0.010 μg g^{-1} of 17β-estradiol, estriol, and 0.020 μg g^{-1} of estrone, 17α-ethynylestradiol, respectively. Then 10 mL of acetonitrile was added in the samples, and the mixture was ultrasonicated for 30 min at room temperature. Then the sample was centrifuged at 3600 rpm for 15 min, and 4 mL of the supernatant was subjected to MIP-SPME procedure and HPLC analysis.

3. Results and discussions

3.1. Preparation and characterization of the MIP-coated fibers

The 17β-estradiol imprinted fiber coating was prepared by the multiple co-polymerization method according to our previous work [27,32] but with some modification. Usually, the silica fiber should be coated for several times to obtain the wanted film thickness. In our previous work, for the purpose of achieving higher cross-linked degree, the fiber was placed in tubes filled with N_2 and heated at 60 °C for 24 h after each coating procedure. In this work, the heating procedure between each coating was eliminated to reduce the preparation time. That is, the fiber was coated continuously for eight times. However, an additional heating step after accomplishment of the final coating under nitrogen at an elevated temperature at 150 °C for 3 h is essential to make the coating more robust. Therefore, the whole coating procedure for preparing a batch of fibers was accomplished within only 24 h. By comparison of the coating thickness, homogeneity and stability of the fiber prepared by two different coating methods, it was found that there was no obvious variation, but the preparation time was significantly reduced. Due to the multiple component structure of MIPs, any change in the nature and ratio of composition may change the mechanical and chemical characteristics of prepared fiber. Therefore, the optimization of experimental parameters such as functional monomer, polymerization solvent, time and temperature is indispensable. In view of the solubility for estrogens, acetone, chloroform, acetonitrile and toluene was selected as the possible polymerization solvent. A homogeneous surface was observed for MIP coating in each of these four solvents. Nevertheless, the thickest MIP film of 2.8 μm was obtained on naked fiber for a single coating procedure when acetonitrile was used as the polymerization solvent, and there was a good linearity between coating times and thickness of MIP coating. MAA and 4-VP were used for monomer optimization, and the coating with MAA as monomer had better homogeneity and morphological structure. TRIM, the most frequently used cross-linkers in the MIP preparation, were investigated with serial molar ratio of template: monomer: cross-linker from 1:8:10 to 1:8:40. The polymer became more and more dense and solid with the increase of cross-linker, which would make pulling out of fiber difficult. Finally, the molar ratio of 1:8:16 was selected owing to the best morphological coating with the large thickness of 3.2 μm obtained for a single coating. Under the optimized condition, the polymerization time was 2 h at 65 °C to obtain a semi-solid state of the polymer, and was shorter as compared to our previous study [32].

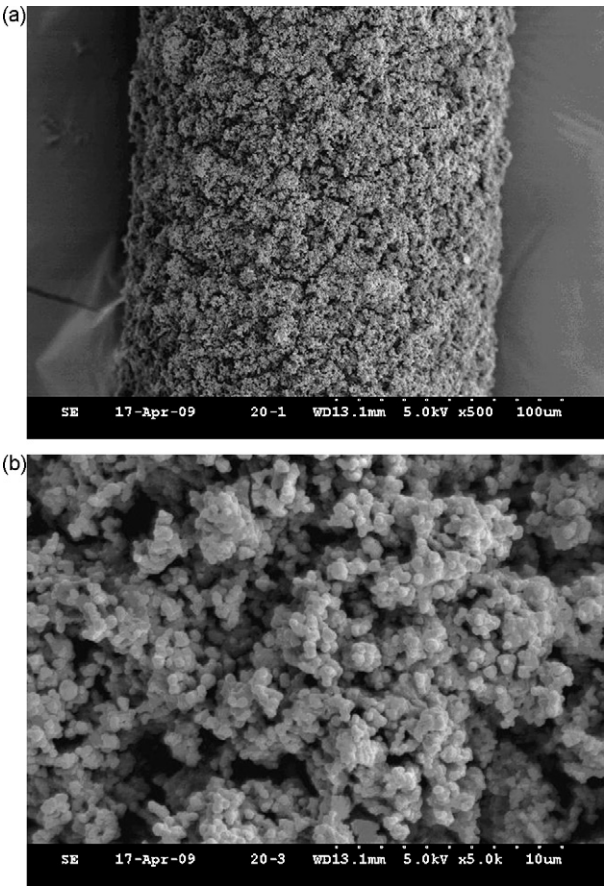


Fig. 1. The scanning electron micrographs images of the MIP-coated fiber under the magnifications of 500 (a) and 5000 (b).

The morphology and thickness of the coating was investigated by scanning electron micrograph after eight repeated polymerization, as illustrated in Fig. 1. The total diameter of the MIP-coated fiber is 160 μm from Fig. 1(a), therefore the absolute thickness of the MIP coating can be calculated by subtracting the diameter of the naked silica fiber, and is 20 μm. The relative standard deviation (RSD) for the thickness of a batch of different coatings is 6.5% (n = 7). Fig. 1(b) exhibits the morphological structure of the coating under the magnification of 5000. It can be seen that the MIP coating is composed of small and interconnected globules that form a porous structure. The morphology is benefit for increase of specific surface area, resulting in sufficient adsorption of solutes. The thermogravimetric analysis proved that the coating was stable within the temperature of 400 °C, and the solvent-resistance study showed a high chemical stability of the coating when immersed in conventional solvents, such as n-hexane, chloroform, toluene, methylene dichloride and acetonitrile.

3.2. Extraction ability

The extraction ability of the MIP-coated fiber was evaluated by comparison with that of the commercially available SPME fiber including PDMS, PDMS/DVB and CW/TPR fiber. Fig. 2 shows the extraction amounts of 17β-estradiol by the MIP fiber and three commercial SPME fibers at the initial concentration of 20.0 μg L^{-1}. The extraction procedure of the commercial SPME fiber was performed in aqueous solution owing to their distinct extraction mechanism from the MIP extraction procedure. The results reveal

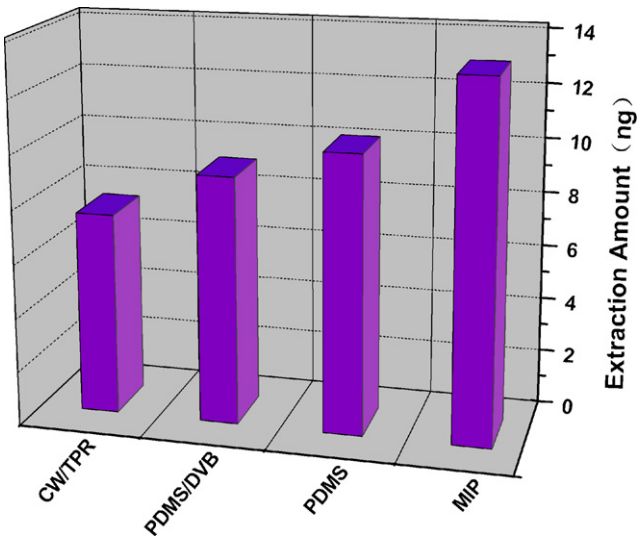


Fig. 2. The concentration of 17β-estradiol extracted on the prepared MIP-coated fiber with the initial concentration of 20 μg L^{-1} in n-hexane, and on the commercial PDMS, PDMS/DVB and CW/TPR fiber with the initial concentration of 20 μg L^{-1} in aqueous solution.

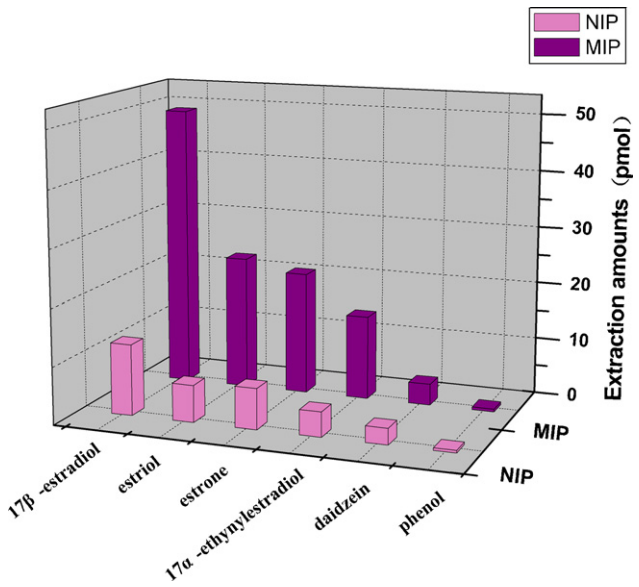


Fig. 4. Selectivity investigation of the MIP-coated fiber. SPME was performed in 4 mL of n-hexane standard solution containing 10 μg L^{-1} estrogens at room temperature for 40 min with desorption time of 15 min.

that the MIP-coated fiber possesses higher extraction ability than the three commercial SPME fiber investigated. It should be noted that the thickness of the MIP coating is much thinner as compared with that of the commercial fibers (100 μm for PDMS, 60 μm for PDMS/DVB, 50 μm for CW/TPR). Therefore, the extraction ability is even higher if the amounts of 17β-estradiol per extractant volume are considered. This high extraction ability is mainly owing to the specific adsorption of MIP to the template molecule and the hydrogen bonding interactions between the carboxylic groups in the MIP coating and hydroxyl groups in 17β-estradiol at corresponding positions.

The extraction ability of the MIP-coated fiber was further investigated by comparison with that of the NIP-coated fiber prepared in the same procedure except for the addition of the template molecule. Fig. 3 shows the binding amounts of the 17β-estradiol on the MIP- and NIP-coated fibers at different initial concentration of the template. It is clear that both the fibers show an increase in binding amounts as the initial concentration increases. However, the MIP-coated fiber generally binds more of the added 17β-estradiol

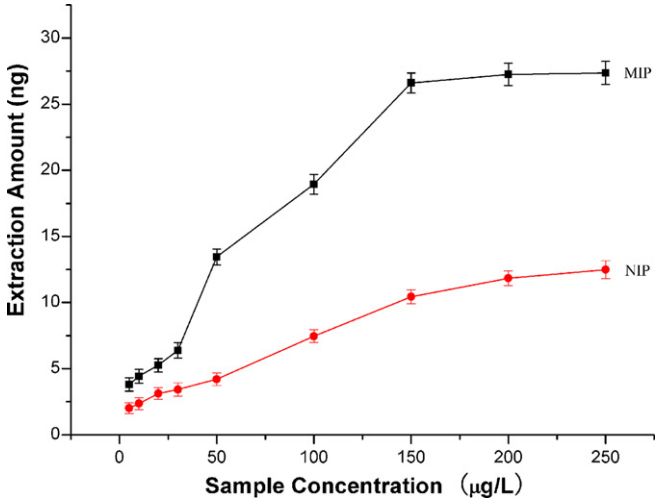


Fig. 3. The binding isotherms of 17β-estradiol on the MIP- and NIP-coated fibers. SPME was performed in 4 mL of n-hexane standard solution containing different concentration of 17β-estradiol at room temperature for 40 min.

than the corresponding NIP-coated fiber. This data is indicative of a true molecular imprinting effect being observed with the MIP-coated fiber.

3.3. Cross-selectivity

Successful imprinting cannot solely be evaluated on the ability of the MIP to rebind the template but also on its discrimination between analogue molecules. The selectivity test results among different compounds may also show some aspects of molecular recognition mechanisms. Therefore, the ability of the MIP-coated fiber to discriminate between other structural-related steroid compounds and reference compounds was investigated. The NIP-coated fiber was used for comparison. Fig. 4 shows the extraction amounts of 17β-estradiol, estriol, estrone, 17α-ethynylestradiol, daidzein and phenol with the MIP- or NIP-coated fiber. Their molecular structure is illustrated in Fig. 5. The results proved that the prepared MIP-coated fiber exhibited high selectivity for estrogenic compounds with the steroid structure, while other structurally unrelated compounds such as daidzein and phenol were poorly extracted. Moreover, 17β-estradiol exhibited the largest extraction amounts as compared with the other tested estrogens such as estriol, estrone and 17α-ethynylestradiol. However, NIP-coated fiber exhibited similar extraction ability towards these four estrogens. The minor extraction difference is approximately based on

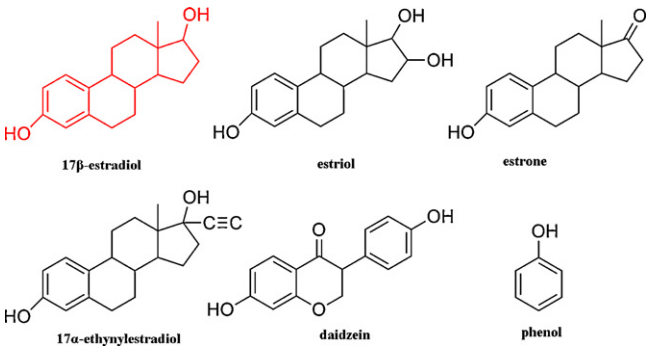


Fig. 5. The molecule structure of the compounds for selectivity investigation.

Table 1
Effect of solvent polarity on the extraction amounts of 17β-estradiol.

Extraction solvents	n-Hexane	Toluene	Methylene dichloride	Chloroform	Acetonitrile
Snyder polarity index [34]	0.06	2.4	3.4	4.4	6.2
Extraction amounts (ng)	19.829	0.992	0.222	0.106	0.085

their hydrophobic nature. For these reasons, it can be concluded that the selectivity of the prepared MIP fiber for estrogens was clearly induced during the imprinting process. This induction recognition ability is particularly noteworthy because the tested estrogenic compounds have only small structural differences. The structure of daidzein is similar to 17β-estradiol but lack of the steroid segment, which results in poor extraction. The obtained results show that the distance and angle of the hydroxyl groups is important for effective recognition of certain molecules with the 17β-estradiol imprinted fiber. On the other hand, the size and shape recognition by the imprinted polymer network possibly accounts for the poor extraction of phenol, which was almost not extracted by the MIP-coated fiber. The above results strongly support the conclusion that the obtained MIP-coated fibers are highly selective, and can be applied to enrichment of trace estrogenic compounds in complex samples.

3.4. Effective variables on the extraction performance

In SPME experiments, the extraction efficiency depends on the different variables such as time of extraction, stirring rate of the solution, the extraction and desorption solvent.

The solvent matrix of extraction usually plays the most important role on the extraction performance of the MIP-coated fiber. Consequently, the effect of solvents was investigated and illustrated in Table 1. Results show that the extraction amounts of 17β-estradiol have close relationship with the polarity of the solvent, increasing the solvent polarity leads to dramatic decrease of the extraction amounts of template. Best extraction capability was obtained with n-hexane as extraction solvent. This happens because n-hexane decreases to a minimum the non-specific hydrophobic interactions and creates the suitable environment for electrostatic interactions, which play a very important role in molecular recognition. The solute desorption is the reversed procedure of extraction, and was conveniently conducted with the commercial SPME–HPLC coupling device. The desorption solvent, in contrary to the extraction solvent, should effectively destroy the hydrogen interaction between the template solutes and the binding sites. Consequently, acetonitrile, methanol and their acetic acid mixtures were selected for investigating the effect of the desorption solvents (Fig. 6). Methanol and its mixture with acetic acids showed relative good desorption ability because these solvents could form hydrogen bonds with the binding sites, and finally methanol was chosen as desorption solvent.

The adsorption and desorption kinetics was investigated with 10.0 μg L^{-1} 17β-estradiol. As shown in Fig. 7, the extraction and desorption reach equilibrium at about 30 min and 10 min, respectively. This short equilibrium time was mainly ascribed to the thin thickness of the MIP coating. Highly porous structure of the MIP coating was another contributing factor, by which diffusion speed for the analytes into or out of the coating could be increased.

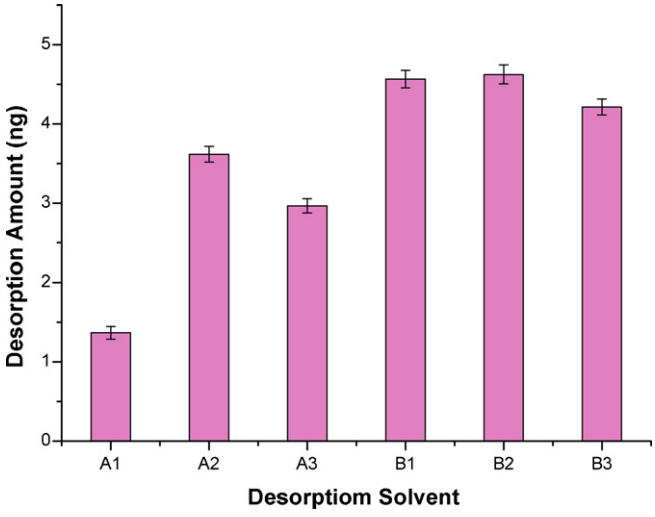


Fig. 6. Variations of 17β-estradiol amounts with the desorption solvents. SPME was performed in 4 mL of n-hexane standard solution containing 10 μg L^{-1} 17β-estradiol at room temperature for 40 min. A1, acetonitrile; A2, acetonitrile:0.12% acetic acid (45:55, v:v); A3, acetonitrile:acetic acid (99:1, v:v); B1, methanol; B2, methanol:0.12% acetic acid (45:55, v:v); B3, methanol:acetic acid (99:1, v:v).

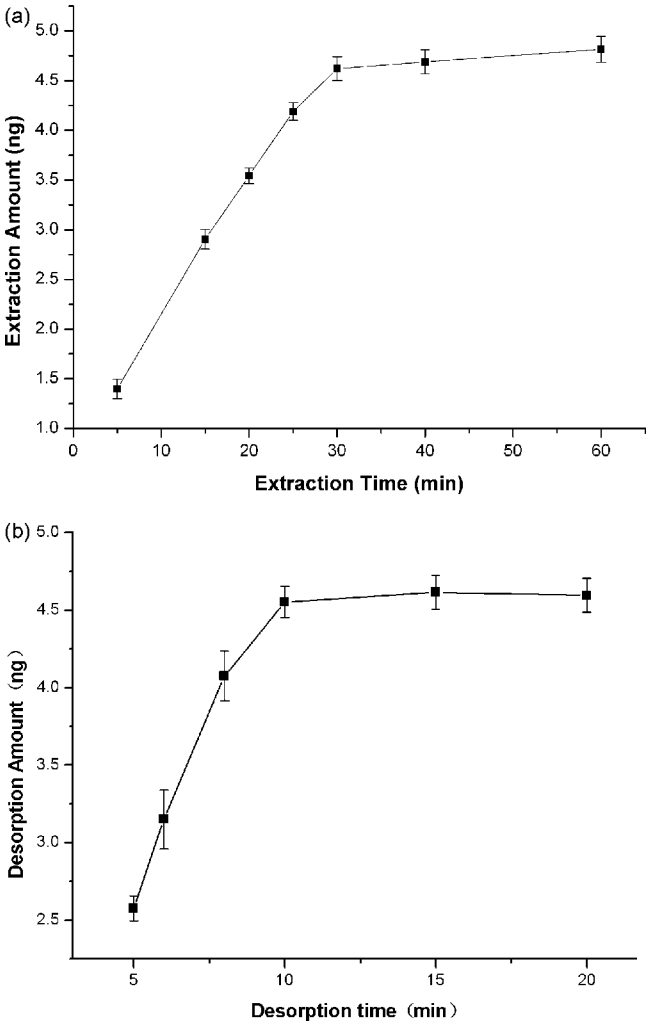


Fig. 7. Adsorption (a) and desorption (b) dynamics of the MIP-coated fiber for 10 μg L^{-1} 17β-estradiol.

Table 2
The linearity, precision and detection limit of the method.

Compounds	Calibration curve			Linear range ($\mu g\,L^{-1}$)	LOD ($\mu g\,L^{-1}$)	RSD[b] (%) ($n=6$)	
	Slope	Intercept	R^2			Intra-day	Inter-day
17β-Estradiol	3.15×10^2	11.6	0.9991	5.0–30.0	0.98	2.2	5.6
Estriol	1.48×10^2	16.9	0.9988	5.0–30.0	1.28	7.6	8.7
17α-Ethynylestradiol	1.40×10^2	15.6	0.9975	15.0–40.0	2.21	6.8	5.8
Estrone	3.27×10^2	39.2	0.9986	15.0–40.0	2.39	7.7	7.6

3.5. Method validation and comparison with other sample preparation techniques

The obtained MIP-coated fiber was coupled with HPLC and UV detection to establish a method for simultaneous determination of 17β-estradiol, estriol, estrone and 17α-ethynylestradiol under the optimized extraction conditions. The MIP-SPME procedure was performed in n-hexane for 40 min and then desorbed by methanol for 15 min. To validate the analytical methodology, the linearity, precision and detection limit of estrogens was investigated (Table 2). The MIP-SPME–HPLC procedure showed linear ranges of 5.0–30.0 $\mu g\,L^{-1}$ for 17β-estradiol and estriol, 15.0–40.0 $\mu g\,L^{-1}$ for estrone and 17α-ethynylestradiol. The square of correlation coefficients was above 0.9975. The linear range of the method is relatively short as compared with analytical methods based on conventional SPME technology. This can be ascribed to the limited interaction sites of the specific imprinted cavity on the MIP coating. For the conventional SPME coating, such as PDMS, the analytes absorb or adsorb on the coating by non-specific interaction, and the larger interaction sites result in a wider linear range. For calculation of the detection limits (LOD), we used three times standard deviations of calibration curves divided by their slopes. The LODs obtained for the studied estrogenic compounds are in the range 0.98–2.39 $\mu g\,L^{-1}$. These values are indicative of good performance of the prepared fiber. The precision of method for six replicate analyses of model solutions is also presented in Table 2 for a solution containing 10 $\mu g\,L^{-1}$ of each compound. The relative standard deviations for the compounds were below 10% for both inter- and intra-day precision study. The precision is acceptable by taking into account the low concentration levels of the analytes.

Some methods including cloud point extraction, stir bar sorptive extraction, SPE, and SPME coupled to HPLC with UV detection, diode array detection and fluorescence detection have been compared with the current method concerning the determination of estrogens, and are summarized in Table 3. The sensitivity of the proposed MIP-SPME–HPLC method was comparable with most of the other analytical methods. However, those sample preparation methods are usually not highly selective, and were applied to the water sample with relative simple matrix. For determination of estrogens in biological samples, interference could not be avoided for the reason of the complex sample matrix. Extraction methods based on MIP are very desirable for its high selectivity. As compared with the reported detection limits for 17β-estradiol with MIP-SPE–HPLC method [24], lower detection limits were obtained in the current study. In addition, the method based on MIP-SPME has the advantages of less solvent consumption, reduced operation procedure, and no requirement to add further purification procedure to remove co-extractant.

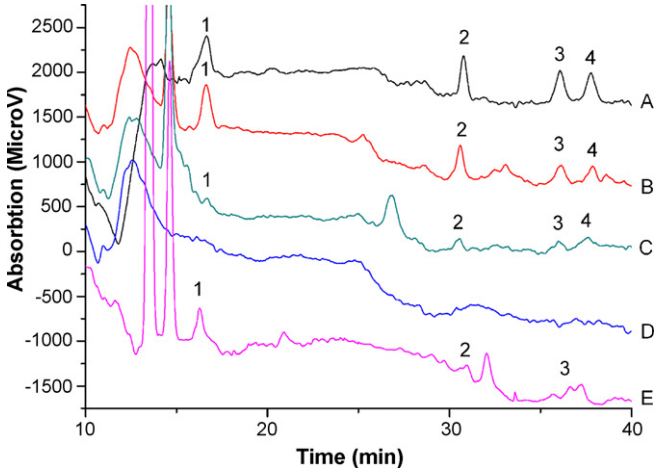


Fig. 8. Chromatograms of fish samples using MIP-SPME–HPLC method. (A) 500 $\mu g\,L^{-1}$ estrogens mixed standard solution; (B) fish samples spiked with 0.010 $\mu g\,g^{-1}$ estriol, 17β-estradiol, 0.020 $\mu g\,g^{-1}$ estrone and 17α-ethynylestradiol extracted by MIP-coated fiber; (C) fish samples spiked with 0.010 $\mu g\,g^{-1}$ estriol, 17β-estradiol, 0.020 $\mu g\,g^{-1}$ estrone and 17α-ethynylestradiol extracted by NIP-coated fiber; (D) blank samples extracted by MIP-coated fiber; (E) acetonitrile extracts of the spiked fish samples. Peaks: 1: estriol, 2: 17β-estradiol, 3: 17α-ethynylestradiol, and 4: estrone.

3.6. Sample analysis

The established MIP-SPME method was applied to analysis of trace amounts of estrogens in spiked fish and shrimp tissue samples. Firstly, acetonitrile which had good ability for precipitating protein, lower solubility of lipids than other solvents and could penetrate biological tissues after homogenization was selected to extract estrogens from fish and prawn samples with ultrasonication. After centrifugation, the supernatant was collected and directly subjected to a MIP-SPME procedure. Fig. 8 showed the chromatogram of the 500 $\mu g\,L^{-1}$ mixed standard estrogen solution (curve A), the blank fish sample by MIP-SPME (curve D), the spiked fish sample extracted by the MIP-SPME protocol (curve B), the NIP-SPME protocol (curve C) and direct injection of acetonitrile extracts (curve E). The results revealed that the chromatogram was complex for the acetonitrile extracts, showing large peaks at approximately 10 min, but was significantly cleaner after the MIP-SPME cleanup

Table 3
Comparison with other sample preparation methods for the determination of estrogens and analyzed by HPLC.

Extraction method	Analytical method	Sample type	LOD (μg/L)	Selective	References
Cloud point extraction	HPLC-UV	Waste water	0.23–5.0	No	[14]
Stir bar sorptive extraction	HPLC-DAD	River and lake water	0.04–0.11	No	[16]
Ultrasonic assisted extraction	HPLC-UV	Topic gel	10.3–19.8	No	[6]
SPME	HPLC-UV	River water	0.3–1.1	No	[35]
MIP-SPE	HPLC-FL	Fish and prawn	23.0	Yes	[24]
MIP-SPME	HPLC-UV	Fish and shrimp	0.98–2.39	Yes	This article

Table 4
Recoveries and RSD of the estrogens in the spiked fish and shrimp tissues ($n = 3$).

Compounds	Fish			Shrimp		
	Spiked ($\mu g\,g^{-1}$)	Recovery (%)	RSD (%)	Spiked ($\mu g\,g^{-1}$)	Recovery (%)	RSD (%)
Estriol	0.010	81.4	6.7	0.010	82.0	6.2
17β-Estradiol	0.010	83.6	5.1	0.010	85.1	5.7
Estrone	0.020	80.0	3.8	0.020	85.0	7.1
17α-Ethynylestradiol	0.020	81.9	8.0	0.020	94.0	8.3

protocol. Moreover, the sensitivities of four estrogens in the spiked samples were greatly enhanced with the MIP-SPME–HPLC analysis. The NIP-coated fiber possessed extraction capability much lower than that of the MIP-coated fiber for the four estrogens investigated. Owing to the specific recognition of the MIP-coated fiber to the structure-related estrogens, the method could be applied to selective and sensitive monitoring of trace estrogenic compounds in biological samples. As shown in Table 4, the recoveries for the spiked fish and shrimp samples were 80.0–83.6% and 85.0–94.1% with RSD from 3.8–8.0% and 5.7–8.3%, respectively. The MIP-coated SPME fiber was very stable, and can be repeatedly used for more than 100 times for standard solutions. For real sample analysis, the lifespan of the fiber was related with the degree of sample complexity, and an interval clean step by methanol and then heating at 120 °C would help regenerate the fibers. Owing to the selective characteristics of the MIP extracts, the proposed MIP-SPME–HPLC method is sufficiently accurate and precise for determination of estrogens in fishery tissue samples.

4. Conclusions

The novel SPME fiber based on MIP using 17β-estradiol as template was fabricated with an improved multiple co-polymerization method. The fabricated fibers were porous on surface, thermal and chemical stable, and can be directly coupled with chromatographic instruments. Under the optimized conditions the fabricated fiber showed better molecular recognition abilities for 17β-estradiol and the structure-related compounds, such as estriol, estrone and 17α-ethynylestradiol. Efficiency of the prepared fiber to extract and analyze these four estrogens has been investigated by implementation of SPME in fishery samples. The detection limits were in the range of 0.98–2.39 $\mu g\,L^{-1}$, and the recoveries were 80.0–83.6% and 85.0–94.1% for fish and shrimp tissue samples, respectively. The MIP-SPME–HPLC method was proved to be selective, sensitive, fast and convenient for determination of estrogens in complex samples.

Acknowledgements

The authors would like to thank the National Natural Science Foundation of China for financially supporting this research under grant number 20775095, 20705042 and 90817012, and by Key Program of Guangdong Provincial Natural Science Foundation of China under grant number 9251027501000004, respectively.

References

[1] P.D. Hansen, H. Dizer, B. Hock, A. Marx, J. Sherry, M. McMaster, C. Blaise, Trends Anal. Chem. 17 (1998) 448.
[2] T.B. Xin, S.X. Liang, X. Wang, H.F. Li, J.M. Lin, Anal. Chim. Acta 627 (2008) 277.
[3] L. Wang, P. Yang, Y.X. Li, C.Q. Zhu, Talanta 70 (2006) 219.
[4] Y. Hadef, J. Kaloustian, H. Portugal, A. Nicolay, J. Chromatogr. A 1190 (2008) 278.
[5] X.Y. Xiao, D.V. McCalley, J. McEvoy, J. Chromatogr. A 923 (2001) 195.
[6] L. Havlíková, L. Nováková, L. Matysová, J. Šícha, P. Solich, J. Chromatogr. A 1119 (2006) 216.
[7] A. Rachkova, S. McNiven, A. El'skaya, K. Yano, I. Karube, Anal. Chim. Acta 405 (2000) 23–29.
[8] J. Zweigenbaum, J. Henion, Anal. Chem. 72 (2000) 2446.
[9] A. Nieto, F. Borrull, E. Pocurull, R. Maria Marcé, J. Chromatogr. A 1213 (2008) 224.
[10] L. Sun, W. Yong, X.G. Chu, J.M. Lin, J. Chromatogr. A 1216 (2009) 5416.
[11] M.A. Soliman, J.A. Pedersen, I.H. Suffet, J. Chromatogr. A 1029 (2004) 223.
[12] A. García-Prieto, L. Lunar, S. Rubio, D. Pérez-Bendito, Analyst 131 (2006) 407.
[13] S. Wang, W. Huang, G.Z. Fang, J.X. He, Y. Zhang, Anal. Chim. Acta 606 (2008) 194.
[14] L. Wang, Y.Q. Cai, B. He, C.G. Yuan, D.Z. Shen, J. Shao, G.B. Jiang, Talanta 70 (2006) 47.
[15] M. Kawaguchi, Y. Ishii, N. Sakui, N. Okanouchi, R. Itoa, K. Inouea, K. Saito, H. Nakazawa, J. Chromatogr. A 1049 (2004) 1.
[16] Y.L. Hu, Y.J. Zheng, F. Zhu, G.K. Li, J. Chromatogr. A 1418 (2007) 16.
[17] S. Zorita, P. Hallgren, L. Mathiasson, J. Chromatogr. A 1192 (2008) 1.
[18] K. Mitani, M. Fujioka, H. Kataoka, J. Chromatogr. A 1081 (2005) 218.
[19] J. Carpinteiro, J.B. Quintana, I. Rodriguez, A.M. Carro, R.A. Lorenzo, R. Cela, J. Chromatogr. A 1056 (2004) 179.
[20] C.L. Arthur, J. Pawliszyn, Anal. Chem. 62 (1990) 2145.
[21] Y. Wen, B.S. Zhou, Y. Xu, S.W. Jin, Y.Q. Feng, J. Chromatogr. A 1133 (2006) 21.
[22] C. Basheer, S. Jegadesan, S. Valiyaveettil, H.K. Lee, J. Chromatogr. A 1087 (2005) 252.
[23] M.D. Celiz, D.S. Aga, L.A. Colón, Microchem. J. 92 (2009) 174.
[24] T.H. Jiang, L.X. Zhao, B.L. Chua, Q.Z. Feng, W. Yan, J.M. Lin, Talanta 78 (2009) 442.
[25] J.C. Bravo, R.M. Garcinuño, P. Fernández, J.S. Durand, Anal. Bioanal. Chem. 388 (2007) 1039.
[26] E.H.M. Koster, C. Crescenzi, W. den Hoedt, K. Ensing, G.J. de Jong, Anal. Chem. 73 (2001) 3140.
[27] X.G. Hu, Y.L. Hu, G.K. Li, J. Chromatogr. A 1147 (2007) 1.
[28] X.G. Hu, Y.L. Hu, G.K. Li, Anal. Lett. 40 (2007) 645.
[29] E. Turiel, J.L. Tadeo, A. Martin-Esteban, Anal. Chem. 79 (2007) 3099.
[30] W.M. Mullett, P. Martin, J. Pawliszyn, Anal. Chem. 73 (2001) 2383.
[31] D. Djozan, T. Baheri, J. Chromatogr. A 1166 (2007) 16.
[32] X.G. Hu, J.L. Pan, Y.L. Hu, Y. Huo, G.K. Li, J. Chromatogr. A 1188 (2008) 97.
[33] X.G. Hu, J.L. Pan, Y.L. Hu, G.K. Li, J. Chromatogr. A 1216 (2009) 190.
[34] L.R. Snyder, J. Chromatogr. 92 (1974) 223.
[35] A. Peñalver, E. Pocurull, F. Borrull, R.M. Marcé, J. Chromatogr. A 964 (2002) 153.

Talanta 80 (2010) 2106–2112

Contents lists available at ScienceDirect

Talanta

journal homepage: www.elsevier.com/locate/talanta

Evaluation of a new electrolytic cold vapor generation system for mercury determination by AFS

Wang-bing Zhang [a,*], Zhao-fei Su [a], Xiang-feng Chu [a], Xin-an Yang [b]

[a] Department of Applied Chemistry, Anhui University of Technology, Maanshan, Anhui 243002, PR China
[b] The Center of Lab, School of Chemical & Chemistry, Anhui University of Technology, Maanshan, Anhui 243002, PR China

ARTICLE INFO

Article history:
Received 15 September 2009
Received in revised form 24 October 2009
Accepted 3 November 2009
Available online 13 November 2009

Keywords:
Electrolytic cold vapor generation
Formic acid
Carrier gas
Traditional Chinese Medicines
Mercury

ABSTRACT

In this study we firstly report a new electrolytic cold vapor generation system for mercury determination on Pt/Ti cathode in the presence of organic acid catholyte. Comparing with the traditional inorganic acid, formic acid increased the signal intensity of Hg vapor from electrolytic generation on Pt cathode and reduced the impact of cathode erosion on the stability of signal intensity. Moreover, formic acid has better interference tolerance. The introduction location for carrier gas is probably the most important factor that influences the signal intensity of Hg from electrolytic vapor generation. The effects of the electrolytic conditions and interference ions on the ECVG have been studied. Under the optimized conditions, the detection limit (3σ) of Hg (II) in aqueous solutions is 1.4 ng L^{-1}; a relative standard deviation of 2.3% for 1 μg L^{-1} Hg was obtained. The accuracy of this method was verified by the determination of mercury in the certified reference materials. This system has been applied satisfactorily to the determination of Hg in Traditional Chinese Medicines samples.

© 2009 Elsevier B.V. All rights reserved.

1. Introduction

Traditional Chinese Medicines (TCMs) as natural medicinal materials have attracted much attention because of their outstanding therapeutic effects. One of the major problems in TCMs is the safety problem relating to the presence of high concentrations of toxic metals, including arsenic, mercury and lead [1,2] in some products. For instance, mercury could accumulate easily in the human bodies after long-term use of TCMs. Mercury accumulation induced an autoimmune ability in genetically susceptible mice, which characterized by lymphoproliferation, hypergammaglobulinemia and IgG antinucleolar antibodies [3]. Hence, there is a great demand for an accurate rapid analytical technique to monitor Hg in TCMs.

The most common procedure for the determination of mercury, namely chemical cold vapor generation (CVG) technique, involves the reduction of the analyte to its elemental form in an acidified solution; the reducing agent usually is $NaBH_4$ under ambient conditions [4–6]. The detection is normally carried out using inductively coupled plasma optical emission spectrometry (ICP-OES) [7], atomic absorption spectroscopy (AAS) [8] and special atomic fluorescence spectrometry (AFS) techniques [9]. Comparing with other technique, CVG technique has some merits such as high sensitivity, wide linear dynamic range, low noise level, fast analysis speed, ease of operation, and low cost. However, the drawbacks are also serious and remarkable. The $NaBH_4$ aqueous solution is expensive and unstable, the risk of contamination by reagents is high [10]. Therefore, it is necessary to develop a new method to reduce the use of chemical reagents.

Since 1990s a new sample introduction technique, electrochemical hydride generation (Ec-HG) for hydride forming-elements determinations, has drawn more and more attention. The analytes are reduced to vapors or hydrides on the surface of cathode in the electrolytic cell [11,12]. Most of the hydride forming elements was reported successfully by Ec-HG, such as As [13,14], Sb [15], Se [16,17], Ge [18,19], Bi [19], Sn [11,19] and Te [20], recently. In the past 19 years, the technique was also applied for analysis of water, medicines and biological samples [21]. Fundamental principles and the application of Ec-HG could be found in some review papers [22–23].

The electrolytic cold vapor generation (ECVG) for mercury determination has been reported by some groups. Červený et al. [24] developed a technique for determination of inorganic mercury in water samples by electrochemical mercury cold vapor generation and in situ trapping in a commercial graphite furnace covered with a gold foil. Pt and HCl were used as cathode and catholyte, respectively, and the LOD was 0.33 ng mL^{-1}. Arbab-Zavar et al. [25] described the ECVG technique for the determination of Hg, in which the batch mode electrolytic cell and a pre-activated graphite rod were used as generator and cathode, respectively, and the LOD was 2 ng mL^{-1}. Li and Wang [26] reported the detection of the mercury by AFS coupled with ECVG. The glassy carbon and H_2SO_4 were used

* Corresponding author. Tel.: +86 5552311807.
E-mail address: zhangwb@ahut.edu.cn (W.-b. Zhang).

0039-9140/$ – see front matter © 2009 Elsevier B.V. All rights reserved.
doi:10.1016/j.talanta.2009.11.016

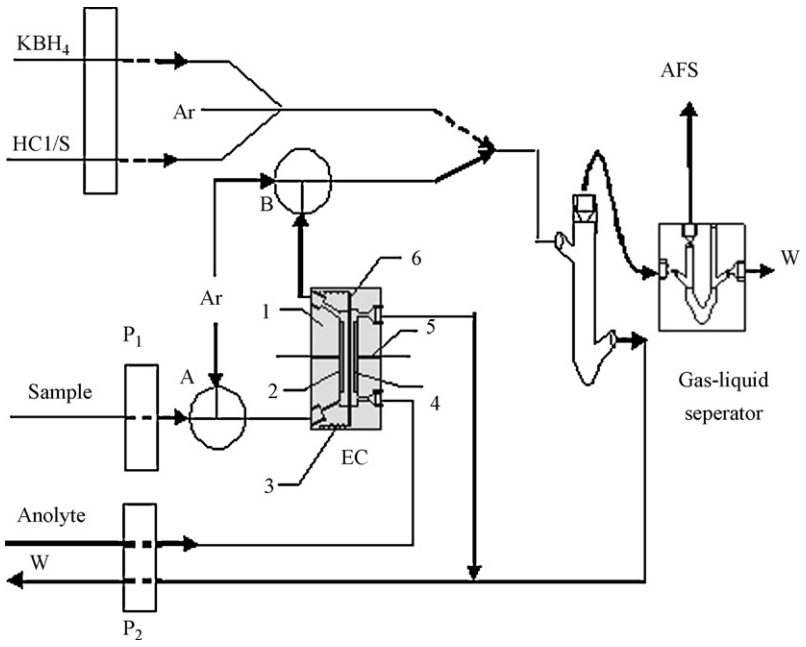


Fig. 1. Schematics of the Ec-HG system. A and B position of carrier gas imported, P: pump, EC: electrolytic cell, S: sample, W: waste, AFS: atomic fluorescence spectroscopy, 1: PTFE body, 2: Pt cathode, 3: sealing by screw thread, 4: Pt anode, 5: Pt wire, 6: ion-exchange membrane and gasket.

as cathode and catholyte, respectively, and the LOD was 1.2 ng L^{-1}. Comparing with CVG, however, the LOD of Hg by ECVG technology is poor.

The aim of this work is to develop a new ECVG system for the determination of Hg. The effects of catholytes and cathode on the signal intensity of Hg were evaluated and the reasons for the signal enhancement were also discussed. The influences of several factors on ECVG were investigated. The analytical figures of merit of the technique and its susceptibility to interferences were evaluated. The proposed method has been successfully applied to the determination of Hg in TCMs.

2. Experimental

2.1. Apparatus

A double-channel non-dispersive atomic fluorescence spectrometer (model AFS-230, Beijing Haiguang Instrument Co., Beijing, China) was employed throughout the experiment. A high-intensity mercury hollow cathode lamp (General Research Institute for Nonferrous Metals, Beijing, China) was used as the radiation source, which has advantages over electrode-less discharge lamps in both the stability and lifetime. A quartz tube (7 mm i.d. × 14 mm length) was used as the atomizer, into which the volatile species was carried by an argon flow. Two sequential gas–liquid separators were used for getting better hydrides transfer efficiency in our work, which depended on the gravity to separate the gas and liquid phases.

2.2. Vapor generation system

The electrolytic flow-through cell [21] was used to evaluate the ECVG of Hg. The polytetrafluoroethylene (PTFE) body of the cell consists of the cathodic and anodic compartments (both 55 mm × 11 mm × 2 mm, inner volumes of 1.2 mL). The cathode and the anode are embedded in them, separated by two slotted PTFE gaskets with an ion-exchange membrane (Huanyu Company of Beijing, Beijing, China) in between. The two compartments are held together with screw thread for easy dismounting the cell. A Pt foil anode was fixed on channel bottom of the anode cell. Some materials such as Pb foil, Ti foil, graphite and Pt foil were used as cathode and the surface area of the cathode was about 5 cm^2. Power supply for the electrolytic cell was DH1719A-3 constant current and constant voltage unit (Beijing Da Hua Wireless instrument Co, Beijing, China) working in the constant current mode.

A schematic of the ECVG–AFS system is shown in Fig. 1. The auto sampling device consisting of a peristaltic pump (IFIS-C, Xi'an Ruimai Electronic Technology Co., Ltd., Xi'an, China) was used to transport the samples. This system was controlled by a personal computer installed with lab-compiled software.

2.3. Chemical reagents

All reagents used in our experiment were of highest available purity, and of at least analytical grade. Doubly deionized water (DDW) was used throughout. The mercury standard solution was prepared by serial dilution of a 1000 mg L^{-1} mercury stock solution (Shanghai Institute of Measurement, Shanghai, China). The potassium tetrahydroborate (III) solution was prepared daily by dissolving the reagent in 0.5% (m/v) sodium hydroxide solution. High-purity HCOOH, HAc, HCOONa, NaAc, HCl, H_2SO_4 and HNO_3 were used to test the effects of the electrolytic solutions. Argon of 99.99% purity was used as the carrier gas (Nanjing special gases factory Co,. Ltd., Nanjing, China). All of the chemical reagents are buying from the Sinopharm Chemical Reagent Co. Ltd., except those indicated otherwise.

2.4. Analytic procedures

The analytical procedures of ECVG and CVG of Hg are schematically shown in Fig. 1. Firstly, the anolyte and catholyte/analyte were continuously pumped into the anode and cathode chambers of the cell, respectively. After the anode and cathode chambers were filled, changed the flow rate to 7.0 mL min^{-1} and started to electrolyze at current 1.4 A. The anolyte was reclaimed and recycled. At the same time, Hg vapor and hydrogen were generated on the cathode surface, and then the reaction products were mixed with Ar, delivered to a cross-tube. After gas–liquid separating, the gas containing Hg

Table 1
Operating parameters of the ECVG–AFS instrument.

Parameter	Setting
Atomic fluorescence spectrometry	
High voltage of PMT (V)	−300
Peak current of lamp (mA)	30
Atomizer height (mm)	8.0
Measurement mode	Standard curve
Read mode	Peak area
Read time (s)	10
Delay time (s)	1
Electrolytic cold vapor generation	
Cathode	Pt 5 cm^2
Catholyte ($mol\,L^{-1}$)	1.0 HCOOH
Anolyte ($mol\,L^{-1}$)	1.0 HCOOH
Electrolytic current (A)	1.4
Sample flow rate ($mL\,min^{-1}$)	7.0
Flow rate of carrier gas (Ar) ($mL\,min^{-1}$)	300
Flow rate of shield gas (Ar) ($mL\,min^{-1}$)	1000

vapor were directed to the atomizer and determined by AFS. The operating programs of the system are listed in Table 1, except those indicated otherwise. A complete cycle of the procedure lasts ca. 60 s.

As a reference method, CVG was used in our work. Here, 2% HCl and 0.5% $NaBH_4$ prepared within 0.5% NaOH were used as carrying solution and reductant. Sample flow rate was set to 7.0 $mL\,min^{-1}$.

2.5. Sample preparation

TCM samples and reference materials were weighed accurately and transferred into PTFE containers, respectively. Pre-digestion was performed by mixing 5 mL of ultra pure HNO_3 with the sample. The mixture was allowed to stand overnight. On the next day, the pre-digested samples were further digested in a microwave oven. The pressure of the oven was 15 MPa and the digestion time was 5 min. After cooling to ambient temperature, 1 mL H_2O_2 was added to the sample, which was then digested again at the pressure of 10 MPa for another 3 min to ensure complete dissolution. Finally, the samples were transferred into a 25 mL calibrated flask and made up to the volume with 1.0 $mol\,L^{-1}$ HCOOH.

3. Results and discussion

3.1. The effect of catholyte on the signal intensity of Hg

In general, catholyte can be divided into four types: acid (including inorganic acid and organic acid), alkali, salt and buffer solution. The inorganic acid catholyte is usually used; other catholytes have also been used under special circumstances, e.g. for improving the signal strength and stability [21]. The organic acid as reaction medium is usually used by other vapor generation techniques such as ultraviolet irradiation-VG (UV-VG) [27], solution cathode glow discharge (SCGD) [28] and ultrasound-assisted-VG (UA-VG) [29], however, its are not be used as catholyte in ECVG technique.

Firstly, we studied the effects of some organic acids and buffer solutions including HCOOH, HCOONa, HAc, NaAc, HCOOH–HCOONa buffer solution and HAc–NaAc buffer solution on the signal intensity of Hg by ECVG. Form Fig. 2 it was found that the signal intensities of Hg from ECVG within inorganic acid medium were 30–40% of that from CVG. The signal intensity of Hg from ECVG under HCOOH medium increased remarkably. The signal obtained by ECVG for 1.0 $mol\,L^{-1}$ HCOOH reached 75% of that by CVG for 1.0 $mol\,L^{-1}$ HCl under best conditions. Comparing with HCOOH, HAc caused fluorescence signal of Hg decrease about 30–40%. Moreover, the signal intensity of Hg in HCOOH–HCOONa and HAc–NaAc was about 80–90% of that in HCOOH medium.

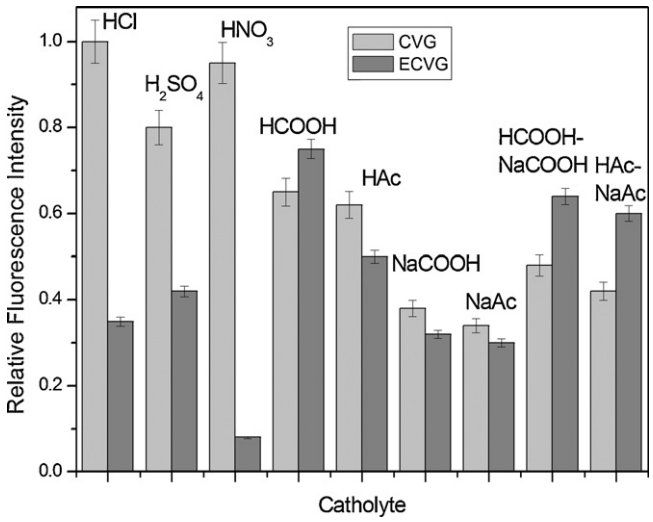


Fig. 2. The effects of the different catholyes on the fluorescence intensity of 1 $\mu g\,L^{-1}$ Hg. All of concentration of catholytes are 1 $mol\,L^{-1}$; Pt cathode. Catholyte flow rate of 7.0 $mL\,min^{-1}$; electrolytic current 1.4 A; 300 $mL\,min^{-1}$ Ar.

Comparing with inorganic acid medium, the major source of blank appears to arise from the use of the HCOOH catholyte. However, the signal intensities of Hg (II) in HCOOH by ECVG increased about 1–2 times. Moreover, the stability of signal intensity in HCOOH was better than that in inorganic acidic medium like H_2SO_4. The use of HCOOH is a good selection in view of the stability of signal intensity.

3.2. The effect of cathode on the signal intensity of Hg

The cathode material should have higher hydrides generating efficiency and good suppressing interference capability. It is generally believed that the efficiency of hydride forming by electrolysis depends primarily on the reducing ability of the cathode material under the operating conditions [22]. The higher the negative potential, the higher the reducing ability and the efficiency of hydride generation are, so lead and carbon cathode with high hydrogen over-voltage can bring higher hydride generating efficiency under the same conditions. However, the interference resulted from transition ions is an unavoidable problem. On the contrary, platinum is a good cathode material with suppressing interference capability and low hydride over-voltage, so it can only be applied to analyzing lower oxidation state of As, Sb and Se [23].

In present work, some materials including Pb, graphite, Pt and Ti were considered as cathode for Hg ECVG. The hydrogen over-voltage of Ti is higher than that of Pt, of course, lower than that of Pb and graphite under the same conditions.

Fig. 3 illustrates the effects of concentration of catholytes and cathode materials on signal intensity of Hg. Based on the above-mentioned reasons, the hydride generating efficiency and the signal intensity of Hg should change in this order: Pb > C > Ti > Pt. On the contrary, as shown in Fig. 3, the hydride generating efficiency and the signal intensity of Hg changed in the following sequence: Pb < C < Ti < Pt. Therefore, the electrolytic reduction mechanism of mercury may be different with those of other elements. At the same time, some authors thought that the graphite or glassy carbon was a good cathode material for Hg ECVG [25]; however, Ti and Pt were selected as cathode material for the Hg ECVG in our study based on the preliminary results obtained with this material, and the results were similar to those reported by Červený et al. [24].

Effects of HCOOH concentration on the signal response of Hg were examined as shown in Fig. 3. It was found that the intensity of Hg on Pt cathode remarkably increased with HCOOH concentration

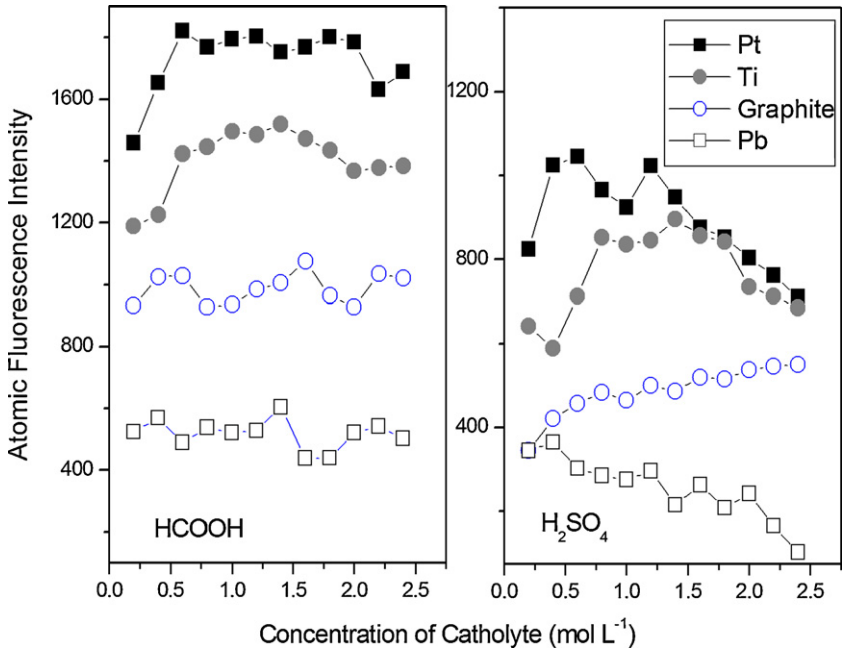


Fig. 3. The effects of the different cathodes and concentration of catholytes on the fluorescence intensity of 1 μg L^{-1} Hg. Catholyte flow rate of 7.0 mL min^{-1}; electrolytic current 1.4 A; 300 mL min^{-1} Ar.

increasing from 0.1 mol L^{-1} to 0.5 mol L^{-1}, and then leveled off, so 1.0 mol L^{-1} HCOOH was chosen as catholyte.

3.3. Interference study

Transition metals (Fe, Co, Cu and Ni) ions are easily reduced to their metallic states or colloidal forms by KBH_4 or $NaBH_4$, which scavenge or decompose the volatile analyte forms before the accomplishment of phase separation in CVG methods. In this study, the effects of these transition metal ions on the generation and determination of Hg were investigated. The effect is expressed as the recovery in the presence of interfering ions relative to the interference-free response. These metal ions concentration is about 100–1000 times Hg concentration in our choosing samples. Therefore, interference of these metal ions whose concentration was 500–20,000 times Hg concentration was investigated and the data were shown in Fig. 4.

Comparing with inorganic acid medium, the effect of transition metal ions on the signal intensity of Hg in HCOOH medium is slightly. On the Pt cathode, the Hg signal suppressions were observed to be 86% (Fe (III)), 76% (Co (II)), 63% (Ni (II)) and 37% (Cu (II)) when the 0.5 mol L^{-1} H_2SO_4 was used as catholyte, respectively, the Hg/metal weight ratios were 1:20,000 (20 mg L^{-1} metal ions). However, no significant interferences were observed in the presence of these transition metal ions (20 mg L^{-1}) for determination of Hg by the proposed method. Based on these results, the use of HCOOH is a good selection.

The effect of hydride-forming elements on the determination of 1 μg L^{-1} Hg (II) was also studied. The results were listed in Table 2. It was found that the hydride-forming elements, 0.5 mg L^{-1} Bi (III), Cd (II), Ge (IV), Pb (II), Se (IV), Sn (II), Zn (II) and As (III) had no significant influence on the measurement of 1 μg L^{-1} Hg (II). Moreover, large amounts of alkali and alkaline earth metal ions did not interfere with the determination. In addition, nitric acid and H_2O_2 are usually used in the digestion of sample. So the effect of nitrate ion and H_2O_2 were evaluated here for Hg determination. No interferences were observed in the presence of HNO_3 and H_2O_2 even the concentrations were 0.1 mol L^{-1}.

3.4. Effect of the carrier gas

Ar is usually used as carrier gas to transfer the product to detector. Traditionally, the introduction place of carrier gas is not taken into consideration because it does not influence the signal intensity of analytes. In our experiment, the effect of the introduction place of carrier gas on the signal intensity of Hg was studied. It was found that Hg response was low when Ar was introduced from sample outlet B (shown in Fig. 1); but a big signal intensity of Hg was detected by ECVG when the carrier gas was introduced from sample inlet A (shown in Fig. 1).

The reason for this phenomenon may be that the lifetime of Hg vapor is short and the vapor cannot transfer to the detector if the distance between the detector and introduction place; another possible cause is the deposition of the Hg vapor on the cathode surface and the walls of the transportation lines during the transferring process. When the 300 mL min^{-1} Ar was introduced from B point, in which the carrier gas did not go through the cathode compartment of the cell, the signal intensity of Hg

Table 2
Effect of coexisting ions on determination of Hg (1 μg L^{-1}).

Species	Concentration (mg L^{-1})	Concentration *M*/Hg	Signal change (%) ECVG
Ag (I)	0.1	100	−14
Ag (I)	0.5	500	−22
K (I)	10	10000	0
Na (I)	10	10000	0
Ca (II)	10	10000	0
Mg (II)	10	10000	−4
Mn (II)	5	5000	−5
Pb (II)	0.5	500	−10
Cd (II)	0.5	500	0
Sn (II)	0.5	500	−9
As (III)	0.5	500	+2
Sb (III)	0.5	500	+3
Bi (III)	0.5	500	0
Ge (IV)	0.5	500	−3
Zn (II)	0.5	500	+5

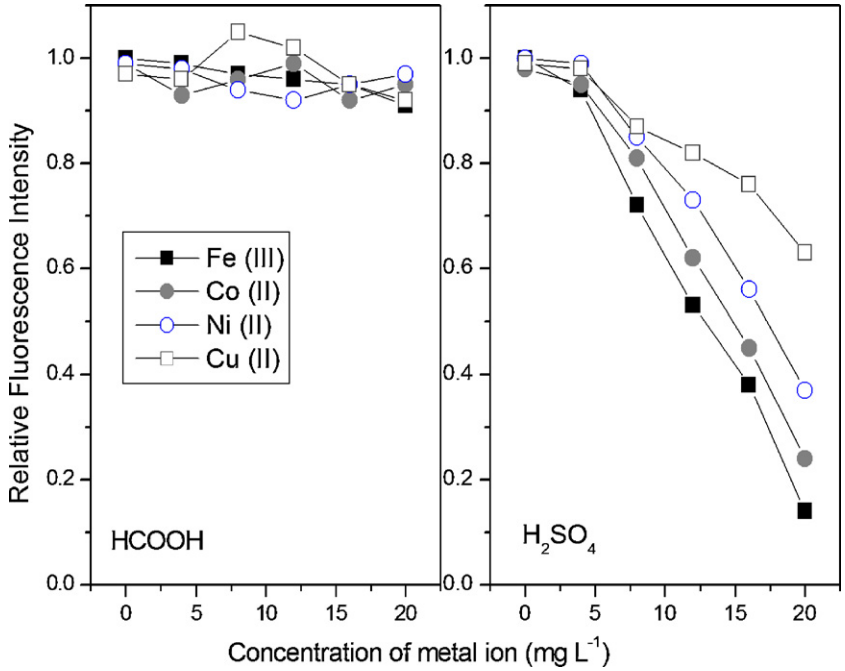


Fig. 4. Influence of the transition metal ions on the fluorescence intensity of 1 μg L^{-1} Hg involving HCOOH and H_2SO_4 catholyte. Pt cathode; catholyte concentration is 1 mol L^{-1}; catholyte flow rate of 7.0 mL min^{-1}; electrolytic current 1.4 A; 300 mL min^{-1} Ar.

was only about 5% that of CVG. When Ar entering the cathode cell (from A point) with a flow rate of 300 mL min^{-1}, the signal intensity of Hg increased remarkably and achieved about 75% that of CVG. These date suggest that the Hg vapor cannot be transported efficiently due to adsorption on the cathode surface of the cell. The result was similar to that reported by Ding and Sturgeon [14].

When the Ar flow rate increased continually, the signal intensity of Hg decreased remarkably, which is probably due to a significant dilution effect. Similar curves were also observed when graphite and Pb were used as cathode materials. Therefore, the Ar flow rate at 300 mL min^{-1} which was the smallest flow rate for our equipment was selected for the next experiments and the result was shown in Fig. 5.

3.5. Optimum conditions

It is well known that the rate of hydride formation is proportional to the electrolytic current. The dependence of fluorescence signals on Pt cathode was recorded for 1 μg L^{-1} Hg (II), at different electrolytic currents in the range of 0–1.6 A. The signal intensity increased proportionally with the electrolytic current from 0.0 to 1.2 A for 1 μg L^{-1} Hg solution, increased slightly in the range of 1.2–1.4 A, and then decreased after the current was higher than 1.4 A. Similar phenomena were observed when graphite and Pb were utilized as cathode materials. Based on these results, 1.4 A was selected as operating current.

The hydride generating efficiency is strongly affected by sample flow rate. The signal intensity of Hg (II) on Pt cathode increased remarkably along with sample flow rate varying from 1.5 to

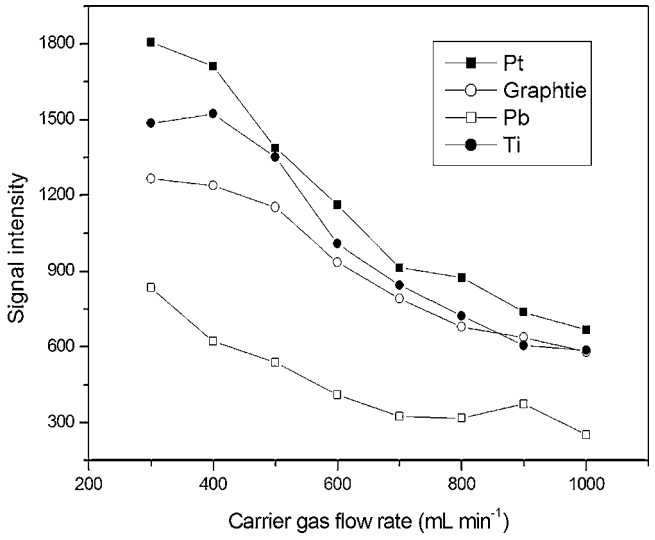


Fig. 5. The effects of the Ar flow rate on the fluorescence intensity of 1 μg L^{-1} Hg. Catholyte concentration is 1 mol L^{-1}; electrolytic current 1.4 A; 7.0 mL min^{-1} catholyte flow rate.

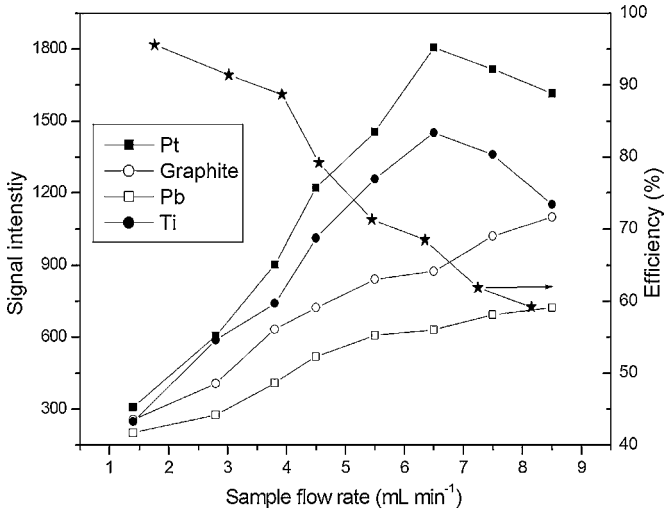


Fig. 6. The effects of the catholyte flow rate on the fluorescence intensity and hydride generation efficiency of 1 μg L^{-1} Hg. Catholyte concentration is 1 mol L^{-1}; electrolytic current 1.4 A; 300 mL min^{-1} Ar.

Table 3
Analytical parameters for Hg determination.

References	Analytical method	Cathode	Catholyte (mol L^{-1})	Limits of detection (ng L^{-1})	R.S.D. (%)
This work	ECVG–AFS	Pt	1.0 HCOOH	1.4	2.3
[24]	ECVG–AAS	Pt	1.0 H_2SO_4	7.6	3.5
[25]	ECVG–AAS	Graphite rode	0.1–1.0 H_2SO_4	2.0	2.5
[26]	ECVG–AFS	glassy carbon	0.5 H_2SO_4	1.2	1.8
[9]	CVG–AFS	–	–	8.5	4.6

Table 4
Analytical results of the determination of Hg in the certified reference material (CRM).

Sample	Certified value (μg g^{-1})	Found concentration (μg g^{-1})	Difference (%)
Tea leaf (GBW 07605)	0.013	0.014 ± 0.002	7.6
Rice (GBW 08508)	0.038 ± 0.006	0.037 ± 0.005	2.6
Peach leaves (GBW08501)	0.046 ± 0.006	0.044 ± 0.005	4.3

7.0 mL min^{-1}, then decreased slowly with further increase of the flow rate. At the same time, the hydride generating efficiency of Hg (II) on Pt cathode decreased from 98% to 57%. The decrease of the fluorescence intensity at low flow rate was caused by the slow mass transfer of the analyte to the cathode surface, while at high flow rate the reduction of the residence time of the analyte in the cathode chamber was responsible for the decrease of the signal intensity. Similar results were found when Ti, graphite and Pb were used as cathode materials. As a consequence, 7.0 mL min^{-1} sample flow rate was chosen in our work and the detailed data are plotted in Fig. 6.

3.6. Discuss on the reduction mechanism

On the cathode material, the reaction mechanism of electrochemical hydride generation could be divided into two types: the electrocatalytic mechanism (cathode with low hydrogen over-voltage) and the electrochemical mechanism [22]. For example, the low hydrogen over-voltage of Pt is affected by the large hydrogen adsorbing ability and by the high catalytic activity of these metals [11]. Moreover, Milss et al. [30] thought that neither formic acid nor formate ion is the reduced electroactive species. They claimed that the solution exited the following ionization equilibrium.

$$HCOOH + H_2O \rightarrow HCOO^- + H_3O^+ \quad (1)$$

H_3O^+ is reduced to hydrogen atoms and the nascent hydrogen is adsorbed on the cathode surface [22]. This reaction is characterized by the Volmer-reaction.

$$M + H_3O^+ + e^- \rightarrow M - H + H_2O^+ \quad (2)$$

In reaction (2), M means cathode surface. Hg ion may be reduced stepwise to produce Hg vapor by the adsorbed hydrogen atoms.

$$2M - H + Hg^{2+} + 2e^- \rightarrow M + M - Hg(\text{adsorbed}) + H_2 \quad (3)$$

$$M - Hg(\text{adsorbed}) \rightarrow M + Hg(\text{vapor}) \quad (4)$$

Milss et al. [30] thought that formic acid molecules served as a conveyor of protons to the electrode surface despite being electrochemically inactive towards reduction. The HCOOH maybe affects the hydrogen adsorbing ability and the catalytic activity of Pt, and then influences the rate of reaction (3).

Moreover, Denkhaus et al. [11] deemed that the whole process of the Ec-HG could be described as an electrodeposition step in which the electrodeposition yield was mainly controlled by the design of the electrolytic cell and the working medium. According to this opinion, HCOOH maybe affects the electrodeposition yield of Hg, and then influences the rate of Hg vapor formation.

Table 5
Analytical results of Hg in TCMs sample.

Sample	Found value (μg g^{-1})	R.S.D. (%)	Recovery (%)
Huang qi	0.070 ± 0.009	3.2	105
Dan shen	0.068 ± 0.010	2.0	103
Dang shen	0.023 ± 0.004	3.5	97
Shen sha shen	0.215 ± 0.036	2.9	96
Liu wei de huang wan	0.725 ± 0.077	4.5	106

3.7. Analytical figures of merit

Linear calibration graph is obtained in the range 0.05–5 μg L^{-1} with the linear regression equations: $I_F = -28.74 + 1821.26C_{Hg}$. C in the equation is the Hg concentration (μg L^{-1}). The regression coefficient R is 0.9973. Detection limits based on three times the standard deviation of the blank (3σ) was 1.4 ng L^{-1} for Hg. Under the optimum condition, the precisions (R.S.D.) for 11 replicate determinaitons of 1 μg L^{-1} Hg was 2.3%. The R.S.D.s obtained for the real TCM samples were 2.0–4.5%, the R.S.D.s were slightly higher than those for the peach leaves due to the highly heterogeneous nature of the TCMs. The contrasts between the principal analytical parameters in our experiment and those reported by several other authors are shown in Table 3.

In comparison to the traditional inorganic acid system, despite the LODs were comparable, the advantage of the proposed method is obviously. Firstly, the signal intensity increased 1–2 times. Secondly, the stability of signal intensity in HCOOH was better. Moreover, the interference from the transition ions was suppressed totally.

3.8. Analytical results of samples

The proposed method was successfully applied to the analysis of different types of certificated reference materials and TCM samples. The result showed a good agreement with the certified values and the results are listed in Tables 4 and 5, and their recoveries are satisfying.

The content of Hg in TCM samples is higher than in the leaf certificated reference materials because the measured TCM samples are the root of plant in which the Hg is usually accumulated in them. The content of Hg in TCM pills (Liu wei di huang wan) is very high due to the concentrating and the pollution in the production process.

4. Conclusion

The novel technique of electrochemical vapor generation of Hg was developed. The organic acid was firstly used as catholyte, the signal intensity of Hg by ECVG markedly increased in organic acid.

The proposed method is sensitive and suitable for the determination of inorganic Hg. Under optimum conditions, this method can totally replace the traditional CVG method in the determination of mercury. The detection limit (3σ) of Hg (II) in aqueous solutions is 1.4 ng L^{-1}. A relative standard deviation of 2.3% for 1 μg L^{-1} Hg was obtained.

HCOOH maybe affect the hydrogen adsorbing ability and the catalytic activity of Pt, comparing with inorganic acids, and then affects the electrodeposition yield of Hg. In the present study, the formic acid is able to restrain the interference from the transition ions. Moreover, the introduction location of carrier gas is found to be an important factor that influences the signal intensity of Hg by ECVG. The Hg vapor cannot be transported efficiently due to adsorption on the cathode surface of the cell.

References

[1] R.-J. Huang, Z.-X. Zhuang, Y. Tai, X.-R. Wang, F.S.C. Lee, Talanta 68 (2006) 728–734.
[2] K.A. Graeme, C.V. Pollack, J. Emerg. Med. 16 (1998) 45–56.
[3] K. Martinsson, L. Carlsson, S. Kleinau, P. Hultman, J. Autoimmun. 31 (2008) 22–29.
[4] D.P. Torres, M.A. Vieira, A.S. Ribeiro, A.J. Curtius, J. Anal. At. Spectrom. 20 (4) (2005) 289–294.
[5] E.V. Alonso, M.T.S. Cordero, A.G. de Torres, P.C. Rudner, J.M.C. Pavón, Talanta 77 (2008) 53–59.
[6] Y.-L. Zhang, S.B. Adeloju, Talanta 74 (2008) 951–957.
[7] E.J. dos Santos, A.B. Herrmann, M.A. Vieira, V.L.A. Frescura, A.J. Curtius, Spectrochim. Acta Part B 60 (2005) 659–665.
[8] G.P. Brandão, R.C. Campos, A.S. Luna, Spectrochim. Acta Part B 60 (2005) 625.
[9] Y.-G. Yin, J.-F. Liu, B. He, J.-B. Shi, G.-B. Jiang, J. Chromatogr. A 1181 (2008) 77–82.
[10] Y.-H. Lin, X.-R. Wang, D.-X. Yuan, P.-Y. Yang, B.-L. Huang, Z.-X. Zhuang, J. Anal. At. Spectrom. 7 (1992) 287–291.
[11] E. Denkhaus, F. Beck, P. Bueschler, R. Gerhard, A. Golloch, Fresenius J. Anal. Chem. 370 (2001) 735–743.
[12] W.-B. Zhang, W.-E. Gan, X.-Q. Lin, Anal. Chim. Acta 539 (2005) 335–340.
[13] F. Laborda, E. Bolea, J.R. Castillo, J. Anal. At. Spectrom. 15 (2000) 103–107.
[14] W.-W. Ding, R.E. Sturgeon, Spectrochim. Acta Part B 51 (1996) 1325–1334.
[15] W.-W. Ding, R.E. Sturgeon, J. Anal. At. Spectrom. 11 (1996) 225–230.
[16] S. Schermer, L. Jurica, J. Paumard, E. Beinrohr, F.-M. Matysik, J.A.C. Broekaert, Fresenius J. Anal. Chem. 371 (2001) 740–745.
[17] E. Bolea, F. Laborda, J.R. Castillo, R.E. Sturgeon, Spectrochim. Acta Part B 59 (2004) 505–513.
[18] W.-B. Zhang, W.-E. Gan, Q.-D. Su, X.-Q. Lin, Chinese J. Anal. Chem. 33 (2005) 1449–1451.
[19] N.H. Bing, Z. Stefanka, S.R. Mallada, Anal. Chim. Acta 479 (2003) 203–214.
[20] X.-J. Jiang, W.-E. Gan, S.-P. Han, Y.-Z. He, Spectrochim. Acta Part B 63 (2008) 710–713.
[21] W.-B. Zhang, X.-A. Yang, Anal. Chim. Acta 611 (2008) 127–133.
[22] E. Denkhaus, A. Golloch, X.-M. Guo, B.-L. Huang, J. Anal. At. Spectrom. 16 (2001) 870–878.
[23] F. Laborda, E. Bolea, J.R. Castillo, Anal. Bioanal. Chem. 388 (2007) 743–751.
[24] V. Červený, P. Rychlovský, J. Netolická, J. Šíma, Spectrochim. Acta Part B 62 (2007) 317–323.
[25] M.H. Arbab-Zavar, G.H. Rounaghi, M. Chamsaz, M. Masrournia, Anal. Sci. 19 (2003) 743–746.
[26] X. Li, Z.-H. Wang, Anal. Chim. Acta 588 (2007) 179–183.
[27] C.-B. Zheng, Y. Li, Y.-H. He, Q. Ma, X.-D. Hou, J. Anal. At. Spectrom. 20 (2005) 746–750.
[28] Z.-L. Zhu, G.C.-Y. Chan, S.J. Ray, X.-R. Zhang, G.M. Hieftje, Anal. Chem. 80 (2008) 7043–7050.
[29] S. Gil, I. Lavilla, C. Bendicho, Anal. Chem. 78 (2008) 6260–6264.
[30] M.H. Milss, An. Fletcher, G.E. Mcmanis, J. Electroanal. Chem. 163 (1984) 429–436.

Talanta 80 (2010) 2113–2119

Contents lists available at ScienceDirect

Talanta

journal homepage: www.elsevier.com/locate/talanta

Electrochemical biosensor based on nanogold-modified poly-eriochrome black T film for BCR/ABL fusion gene assay by using hairpin LNA probe

Liqing Lin[a], Jing Chen[a], Qihuang Lin[a], Wei Chen[a], Jinghua Chen[a], Hong Yao[a], Ailin Liu[a], Xinhua Lin[a,*], Yuanzhong Chen[b,**]

[a] Department of Pharmaceutical Analysis, Faculty of Pharmacy, Fujian Medical University, Fuzhou 350004, China
[b] Fujian Institute of Hematology, The Affiliated Union Hospital of Fujian Medical University, Fuzhou 350001, China

ARTICLE INFO

Article history:
Received 3 August 2009
Received in revised form 28 October 2009
Accepted 3 November 2009
Available online 13 November 2009

Keywords:
Electrochemical biosensor
NG/EBT film
BCR/ABL fusion gene
Locked nucleic acids

ABSTRACT

A novel electrochemical biosensor is described for detection of breakpoint cluster region gene and a cellular abl (BCR/ABL) fusion gene in chronic myelogenous leukemia (CML) by using thiolated-hairpin locked nucleic acids (LNA) as the capture probe. The hairpin LNA probe was immobilized on the nanogold (NG)/poly-eriochrome black T (EBT) film-modified glassy carbon electrode (GCE). The immobilized LNA probe could selectively hybridize with its target DNA on LNA/NG/EBT/GCE surface. The immobilization and hybridization of the LNA probe were characterized with cyclic voltammetry and electrochemical impedance spectroscopy. The hybridization of the immobilized LNA probe with the target DNA was detected by differential pulse voltammetry with the electroactive methylene blue as an indicator. The results indicated this new method has excellent specificity for single-base mismatch and complementary after hybridization, and a high sensitivity. This novel electrochemical biosensor has been used for assay of PCR real sample with satisfactory result.

© 2009 Published by Elsevier B.V.

1. Introduction

CML is a clonal myeloproliferative disorder, resulting from the neoplastic transformation of the primitive hemopoietic stem cell [1–3]. The chimeric oncogene breakpoint cluster region gene and a cellular abl gene (BCR/ABL) is the traditional gene existed in almost all cases of CML patients [4,5]. Thus, detection of BCR/ABL fusion gene will afford an early diagnosis and monitor of the disease. In recent years, there has been significant progress in developing nucleic acid hybridization biosensors for the rapid and accurate detections of specific gene sequence [6,7]. As with other types of biosensors, high selectivity is crucial for the success of hybridization biosensors [8]. The selectivity of nucleic acid hybridization assays depends primarily on the selection of the probe and then of the hybridization conditions. Thus, the design of the probe is the most important pre-analytical step. Recently, some reports described the synthesis and hybridization of a novel nucleotide termed LNA [9,10].

LNA is a nucleic acid analogue of RNA, in which the furanose ring of the ribose sugar is chemically locked by the introduction of a methylene linkage between 2′-oxygen and 4′-carbon. The covalent bridge effectively 'locks' the ribose in the N-type (3-endo) conformation that is dominant in A-form DNA and RNA. This conformation enhances base stacking and phosphate backbone pre-organization and results in improved affinity for complementary DNA or RNA sequences, with each LNA substitution increasing the melting temperatures (T_m) by as much as 3.0–9.6 °C [11,12]. LNA bases can be interspersed with DNA bases, allowing binding affinity to be tailored for individual applications. Due to the very high affinity of the LNA molecules, it demonstrates that LNA probes hybridize with very high affinity to perfectly complementary targets, and at the same time shows an extraordinary specificity to discriminate the targets that differ by a single-base.

Moreover, sensitive detection of specific gene sequence on the basis of the hybridization reaction is another key issue. Increasing the immobilization amount and controlling over the molecular orientation of probe oligonucleotides would improve the detection sensitivity [13,14]. In the DNA sequence detection, the nanogold not only can act as the immobilizing carrier to increase the immobilization amount of the DNA probe but also can serve as the signal particle to magnify the detection signal and lower the detection limit [15,16]. Therefore, in this article, we introduce a method of immobilizing the LNA probe with nanogold bound to the poly-EBT film on the GCE. Due to the rich electroactive center and three-dimensional available field potential, the polymerized film-modified electrode has stable performance with good infusible and insoluble capability. EBT has been used in the biological electro-

* Corresponding author. Tel.: +86 591 22862016; fax: +86 591 22862016.
** Corresponding author. Tel.: +86 591 83357896; fax: +86 591 83357896.
E-mail addresses: xinhua63@163.com (X. Lin), chenyz@pub3.fz.fj.cn (Y. Chen).

0039-9140/$ – see front matter © 2009 Published by Elsevier B.V.
doi:10.1016/j.talanta.2009.11.017

analysis [17]. Nanogold can integrate with the biological active components. LNA probe can form a powerful Au–S covalent bond with hydrosulfuryl and the excellent biocompatibility of nanogold with LNA. So a novel electrochemical DNA biosensor based on the NG/EBT/GCE was developed for recognition of target DNA by using hairpin LNA as the capture probe for hybridization with BCR/ABL fusion gene in CML.

2. Materials and methods

2.1. Reagents and apparatus

Methylene blue (MB) and $HAuCl_4{\cdot}4H_2O$ were purchased from Sigma (USA). Sodium dodecyl sulfate (SDS), sodium citrate and eriochrome black T (EBT) was purchased from Shanghai Chemical Reagents Company (China). The oligonucleotides were synthesized by Shanghai Shenggong Biotechnology Co. (Shanghai, China), and it has the following sequences:

Thiolated-hairpin LNA probe: 5′-SH-C**T**$^{\mathbf{L}}$G**C**$^{\mathbf{L}}$AG**A**$^{\mathbf{L}}$GT**T**$^{\mathbf{L}}$CA**A**$^{\mathbf{L}}$AA **G**$^{\mathbf{L}}$CC **C**$^{\mathbf{L}}$TT CGC AG-3′, (L: 2′-*O*,4′-*C*-methylene·(D-ribofuranosyl) nucleotides LNA. LNA probe is a DNA–LNA chimera, but for brevity it will be called LNA probe [18]. Bold letters represent LNA bases. Underlined letters are bases for stem). Complementary target: 5′-GAA GGG CTT TTG AAC TCT-3′, single-base mismatch: 5′-GAA GGG ATT TTG AAC TCT-3′, non-complementary: 5′-ACG TAA TCC CCA GCT CTC-3′.

The oligonucleotide stock solutions (100 μM) were prepared with 20 mM Tris–HCl, 10 mM $MgCl_2$, pH 8.0 and kept frozen. Real samples were kindly donated by Fujian Institute of Hematology, the Affiliated Union Hospital of Fujian Medical University. Millipore Milli-Q water was used in all experiments. Unless otherwise indicated, all reagents and solvents were purchased in their highest available purity and used without further purification.

A CHI 660C electrochemical analyzer (CH Instrument, USA), which was in connection with a GCE (3 mm diameter) as the working electrode, a Ag/AgCl reference electrode and a platinum wire auxiliary electrode, was used for the electrochemical measurement.

2.2. The preparation of surface of biosensor and its immobilization with LNA probe

The scheme for preparation of the electrochemical DNA biosensor is illustrated in Fig. 1. The surface modification of the GCE was performed by procedure reported in Ref. [17]. Before surface modification, the GCE was polished in sequential order with 1.0, 0.3 and 0.05 μm alumina (AlfaAesar, USA). The electrode was thoroughly washed with water, sonicated in ethanol, and finally dried thoroughly under N_2 flow. Then, GCE was polarized in 0.1 M H_2SO_4 by cyclic scanning between −0.40 and +1.50 V for 25 cycles and scanned in 0.1 M NaOH under the same conditions for 25 times to obtain the pretreated electrode. The poly-EBT was electropolymerized onto pretreated GCE in the presence of 0.1 M NaOH containing 0.5 mM EBT on the same conditions. The obtained electrode was donated as EBT/GCE. The EBT/GCE was immersed into 1% NG solution prepared by the citrate reduction of $HAuCl_4$ for 4 h [19,20]. NG was electro-deposited on the surface of EBT/GCE for 100 s at 0.15 V to prepare NG/EBT/GCE. Apparently a mount of nanogold provides an easier way to immobilize the probe LNA with thiol groups at the 5′ end [21].

Immobilization of the LNA probe on the NG/EBT/GCE surface is described as follows. 10 μl of 1.0 μM probe LNA was dropped on the surface of NG/EBT/GCE and air-dried to dryness. Then the electrode was washed with 0.1% SDS solution for 5 min to wash out the unimmobilized LNA probe. The probe modified electrode was donated as LNA/NG/EBT/GCE.

Table 1
Melting temperatures of the LNA and DNA capture probe against complementary and single-base-mismatched DNA targets.

Probe type	T_m (°C)		ΔT_m (°C)
	Complementary target	Single-base mismatch	
DNA	50.3	44.7	5.6
LNA	78.8	38.1	40.7

The hybridization was performed by pipetting 10 μl of different concentrations of complementary target (cDNA) onto the LNA/NG/EBT/GCE for 1 h at 60 °C. Thus, a double-stranded LNA-cDNA (dsDNA)/NG/EBT/GCE was obtained. The electrode surface was then washed with 0.1% SDS for 5 min to remove the unbound oligonucleotides. The same protocol as above-mentioned was applied to LNA/NG/EBT/GCE for hybridization with one-base mismatch and also with non-complementary sequences.

2.3. MB accumulation and voltammetric transduction

MB for DNA hybridization detection is illustrated in Fig. 1. MB was accumulated onto the surface of hybrid-modified NG/EBT/GCE by immersing the electrode into stirred 20 mM Tris–HCl (pH 7.0) containing 20.0 μM MB with 50 mM NaCl for 5 min without applying any potential. In the optimal condition, the concentration of MB was chosen as 20.0 μM and the accumulation time of MB was chosen as 5 min for optimum analytical performance. After accumulation of MB, the electrode was rinsed with 0.1 M PBS to remove the non-specific MB and subjected to electrochemical measurement.

3. Results and discussion

3.1. Spectrophotometric characterization of DNA and LNA probes

Melting temperature (T_m) is the temperature at which double-stranded DNA is changed (50%) to single-stranded DNA. The denaturation of double-stranded DNA can be conveniently monitored by the sharp increase in absorbance at 260 nm (the absorbance maximum for DNA) using the spectrophotometer UV–Vis Varian Cary 100 (Varian). T_m for the hybridization of LNA with their complemental DNA were examined to confirm their potential for selective recognition of complementary sequences. From Fig. 2 and Table 1, the T_m value of the LNA probe (78.8 °C) was greatly higher than that of its corresponding DNA probe (50.3 °C). Comparing with the analogous DNA–DNA hybrids, T_m value for LNA binding to DNA was increased 28.5 °C, which was equivalent to 4.1 °C per LNA compared to DNA duplexes [22,23]. T_m value for LNA binding to single-base mismatch was decreased to 38.1 °C. Therefore, the affinity and specificity of the LNA probes can be confirmed by measurement of duplex T_m.

Theoretically, the optimum hybridization temperature was about 20 °C lower than T_m. The T_m value of the LNA probe binding to complementary target was 78.8 °C, while for single-base mismatch was decreased to 38.1 °C, Therefore, the theoretical hybridization temperature was 58.8 and 18.1 °C for the complementary target and single-base mismatch, respectively. Accordingly, 60 °C was selected as hybridization temperature [10]. At this temperature, hybridization could be occurred only for the complementary target strand but not for the single-base mismatch. Therefore, the hybridization specificity was dramatically increased.

3.2. Covalent modification of GCE with EBT

The covalent modification of the GCE was performed by repeated cyclic voltammograms scanning over the range of −0.4

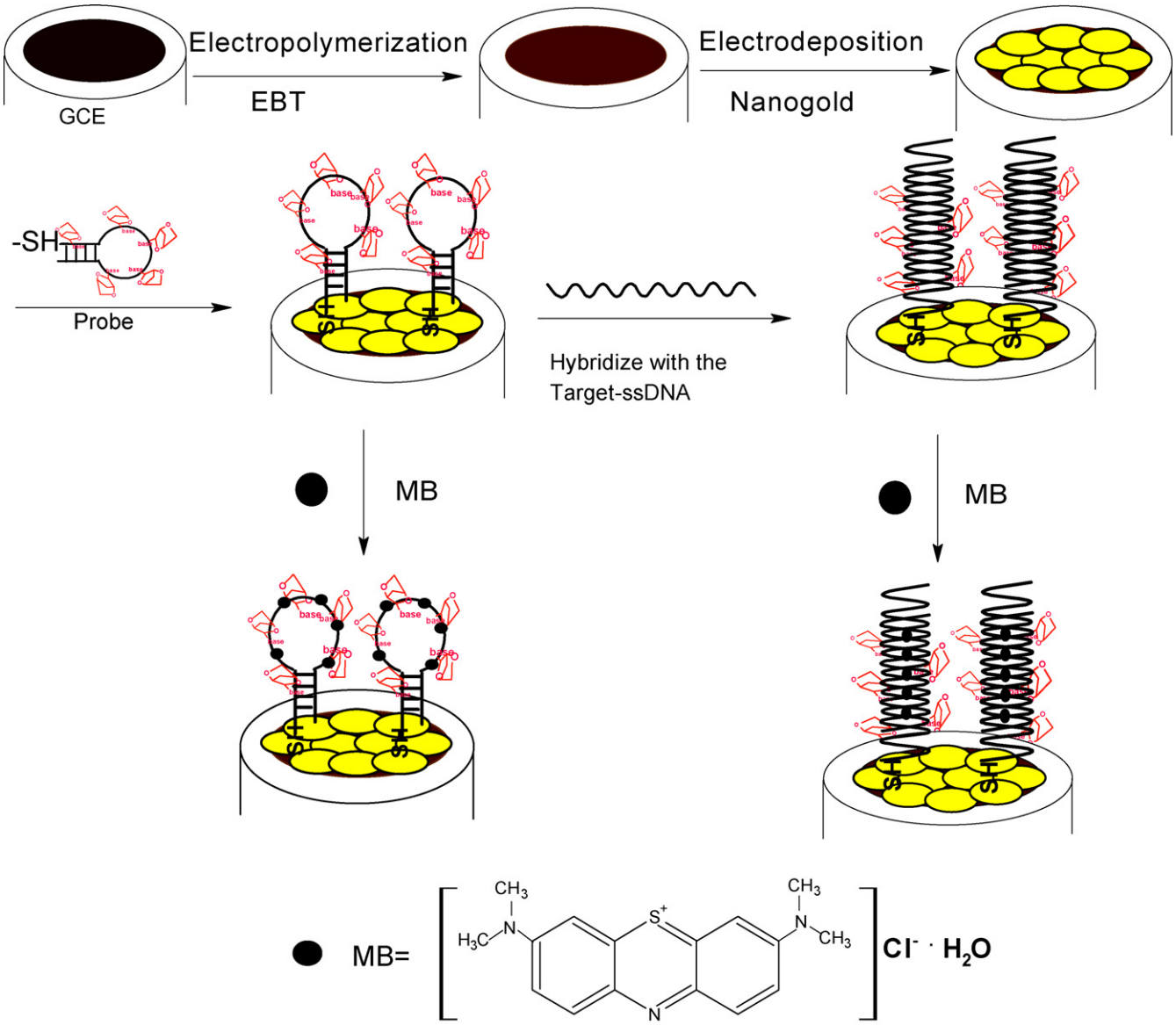


Fig. 1. Scheme of the procedure for the fabrication of DNA biosensor.

to 1.5 V at 100 mV/s for 25 cycles in 0.1 M NaOH containing 0.5 mM EBT. Typically, it was found that when cyclic time was increased, the peak currents gradually decreased. This phenomenon implies the formation of poly-EBT membrane on GCE [17]. The electrodeposited behavior of EBT at the GCE was similar to some reports referring to the electrochemical responses of a few azo compounds at solid electrode [24]. The reaction mechanism could be explained as follows: (1) EBT was first deposited at the surface of GCE and oxidized to form a benzoquinone diimine structure; (2) and then the benzoquinone diimine structure was reduced to EBT at the surface of GCE. The peak currents trended to be stable after 20 scans, which indicated that the GCE surface has been modified with a sulfonic-terminated monolayer to form the EBT/GCE.

3.3. *Electrochemical characterization of different modified electrodes*

Cyclic voltammograms (CV) of 10 mM $[Fe(CN)_6]^{3-/4-}$ redox couple in 0.1 M phosphate buffer solution at a bare GCE (a), EBT/GCE (b), NG/EBT/GCE (c), LNA/NG/EBT/GCE (d) and dsDNA/NG/EBT/GCE (e) were shown in Fig. 3A. Curve a shows that a symmetric, reversible

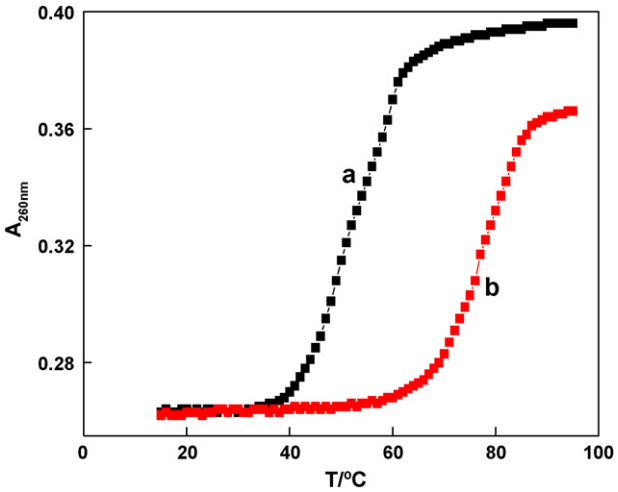


Fig. 2. Melting curves of DNA–DNA (a), LNA–DNA duplex (b).

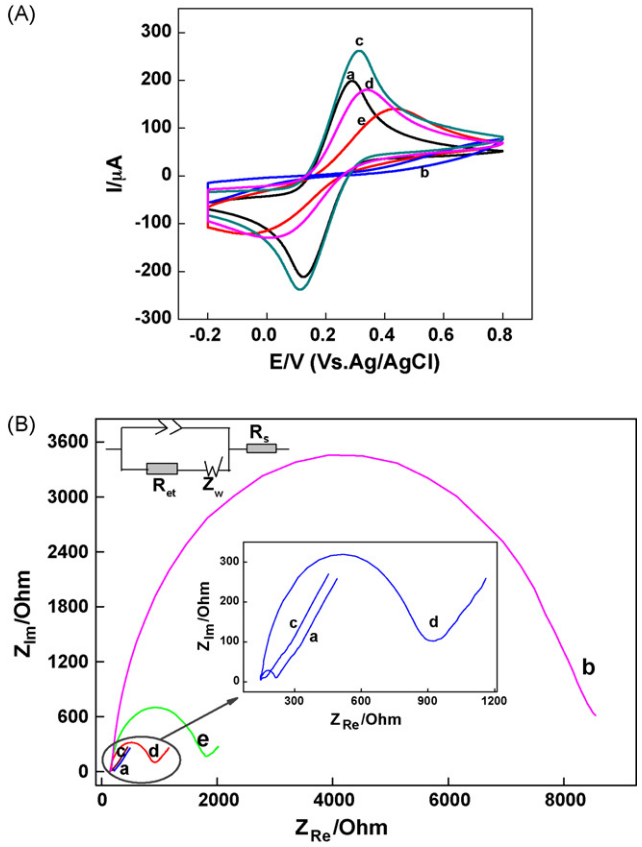


Fig. 3. (A) CV of 10 mM $[Fe(CN)6]^{3-/4-}$ for bare GCE (a), EBT/GCE(b), NG/EBT/GCE (c), LNA/NG/EBT/GCE (d) and dsDNA/NG/EBT/GCE (e). (B) Impedance plots on bare GCE (a), EBT/GCE (b), NG/EBT/GCE (c), LNA/NG/EBT/GCE (d) and dsDNA/NG/EBT/GCE (e) in 10 mM $[Fe(CN)6]^{3-/4-}$.

voltammogram was obtained for a bare GCE. Curve b clearly shows that the electron transfer of $[Fe(CN)_6]^{3-/4-}$ is completely blocked on the EBT/GCE. It can be explained by the electrostatic interactions between the modified surface and $[Fe(CN)_6]^{3-/4-}$. As it known, the pK_a value of R–SO_3H (R: alkyl or aryl groups) is usually between 3 and 4. When the solution pH was equal to 7, the –SO_3Na group of poly-(EBT) film could dissociate favorably into a negative charge group –SO_3^-. Thus, on the negatively charged EBT film, the electrostatic repulsion resists access of $[Fe(CN)_6]^{3-/4-}$ to the electrode surface and blocks its electron-transfer on the electrode surface. Curve c is the CV curve of the NG/EBT/GCE electrode in the same solution as above. The CV peak of curve c was much higher than that of curve b. This implies that NG had been successfully modified onto EBT film, resulting in the electrode having a larger electroactive surface and higher conductivity. When the LNA probe immobilized on the NG/EBT/GCE, compared with bare GCE and NG/EBT/GCE, the peak current decreased and the potential deviation increased (curve d). That is, the LNA probe had negative charge, so hampered $[Fe(CN)_6]^{3-/4-}$ to participate the electrode reaction. These results suggest that the NG/EBT/GCE surface is well covered with the LNA probe. After hybridization, there were more negative charges on the surface and the dsDNA modified layer became thicker. These two factors provide an effective barrier to electron-transfer of $[Fe(CN)_6]^{3-/4-}$ in solution (curve e).

Electrochemical impedance spectroscopy (EIS) can give information on the impedance changes of the electrode surface in the modification process. So EIS was also used to evaluate the interfacial electron-transfer efficiency at different stages of biosensor preparation [25]. Fig. 3B shows the typical EIS results of the bare GCE (a), EBT/GCE (b), NG/EBT/GCE (c), LNA/NG/EBT/GCE (d) and dsDNA/NG/EBT/GCE (e), respectively, which were obtained in a solution of 10 mM $[Fe(CN)_6]^{3-/4-}$ at a potential of 0.22 V (versus Ag/AgCl) in the frequency range of 0.1–10^5 Hz. The electron-transfer resistance (R_{et}) of the bare GCE was estimated to be 63 Ω (curve a). When a bare GCE was electropolymerized with EBT for 25 cyclic times, the electron transfer resistance increased significantly (R_{et} = 8386 Ω). The surface coverage (θ) of EBT film on a bare GCE can be calculated from the EIS in terms of the equation [26]

$$\theta = \frac{1 - R_{et}^{Bare}}{1 - R_{et}^{EBT}} \quad (1)$$

Using Eq. (1), the coverage was calculated to be 99.28%. When the gold nanoparticles was assembled on the EBT/GCE, the R_{et} value was found to be 16 Ω (curve c). As compared with curve a, the R_{et} value of the curve c reduced obviously. This might be due to the presence of nanoparticles playing an important role in accelerating the transfer of the electrons, thus decreasing the resistance of the NG/EBT/GCE to $[Fe(CN)_6]^{3-/4-}$. After the LNA probes were immobilized on the NG/EBT/GCE, its R_{et} value was 758 Ω (curve d), which was much larger than that of the curve c. The negatively charged phosphate backbone of the LNA probe prevented $[Fe(CN)_6]^{3-/4-}$ from reaching the electrode surface during the redox process, and therefore led to the obvious increase of R_{et} value. After hybridization, there were more negative charges on the surface and the DNA modified layer became thicker. These led to the further increase of R_{et} value. These results are in agreement with the CV data.

3.4. Hairpin LNA probe versus hairpin DNA probe

To clarify the role of the DNA sequence with locked nucleic acids modified probe (LNA probe), we tested the same sensing scheme immobilizing a DNA sequence that has no locked nucleic acids as probe (DNA probe) on the surface of NG/EBT/GCE. The experiment was performed with single-base mismatch sequences to investigate whether or not LNA probe improves the selectivity of the assay. Using DNA probe, the voltammetric signal obtained for single-base mismatch was found to be only about 1.42 times higher than the signal obtained for the same concentration of complementary target (see Fig. 4A). At the same time, the signal for the single-base mismatch was significantly increased when LNA was used as probe (see Fig. 4B). These data clearly show the high selectivity of LNA probe for the complementary target and single-base mismatch sequences compared with DNA probe. So in this study, we study the hybridization specificity by using LNA as the capture probe for detection of BCR/ABL fusion gene. The enhanced selectivity can be attributed to the LNA, LNA monomer contains a methylene bridge that connects the 2′-oxygen with the 4′-carbon of the ribose ring of RNA. This bridge results in a locked 3′-endo conformation, reducing the conformational flexibility of the ribose and increasing the degree of local organization of the phosphate backbone [27]. This entropic constraint leads to improving the binding to complementary RNA and DNA sequences.

3.5. The CV study of MB interacted with the LNA/NG/EBT/GCE along with change of scan rate

It had been reported that MB interacted in a different way with ssDNA and dsDNA [15,28]. So MB was used as an electrochemical indicator to study hybridization between LNA and target DNA. LNA modified NG/EBT/GCE electrode immersed in pH 7.0 Tris–HCl containing 20.0 μM MB and CV were collected with the scan rate of 50, 100, 200, 300, 400, 500, 600, 700 and 800 mV s^{-1}. As shown in Fig. 5A, a pair of evident oxidoreduction peak appeared, and the peak current increased along with the increasing of the scan rate. The plot of cathodic peak current (I) versus scan rate (v) is linear

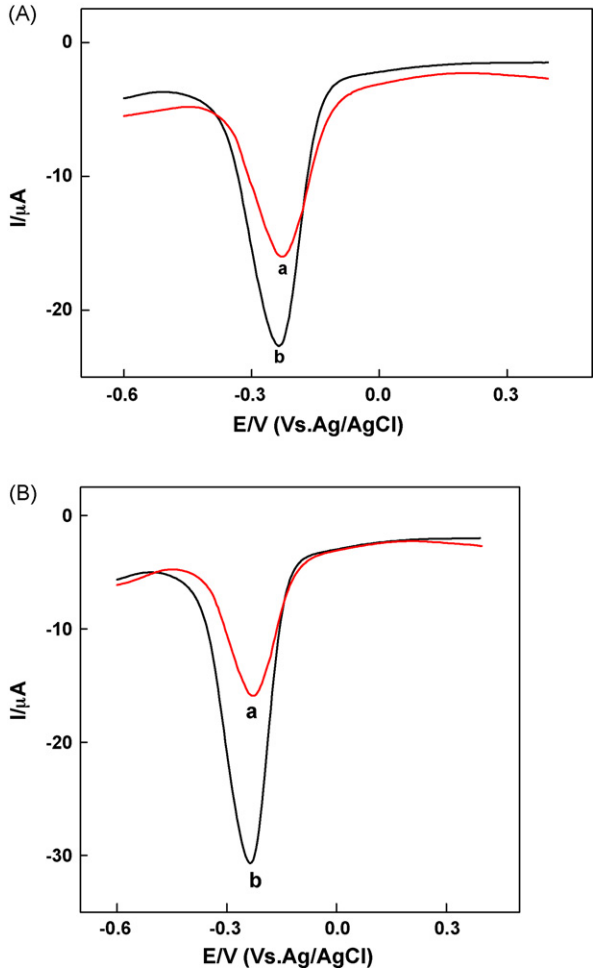


Fig. 4. (A) DPV of 20 μM MB at a DNA/NG/EBT/GCE hybridization with the complementary target (a) and single-base mismatch (b). (B) DPV of 20 μM MB at a LNA/NG/EBT/GCE hybridization with the complementary target (a) and single-base mismatch (b).

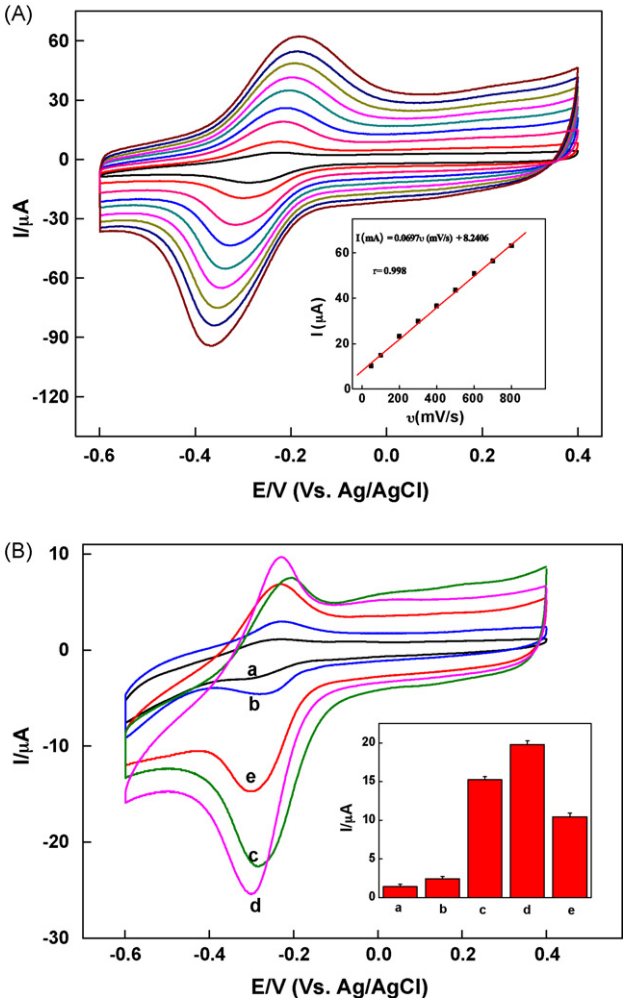


Fig. 5. (A) CV of 20 μM MB in 20 mM Tris–HCl buffer (pH 7.0) at the LNA probe modified NG/EBT/GCE surface with increasing scan rate from inner to outer: 50, 100, 200, 300, 400, 500, 600, 700, 800 mV s^{-1}. Inset shows plot of reduction peak current versus scan rate. (B) CV of 20 μM MB at the bare GCE (a), EBT/GCE (b), NG/EBT/GCE (c), LNA/NG/EBT/GCE (d) and dsDNA/NG/EBT/GCE (e). scan rate: 100 mV s^{-1}. Insert: corresponding histograms of the reduction peak currents.

(see Fig. 5A inset), indicating that MB was strongly bound to the LNA modified NG/EBT/GCE surface. Because MB could bind specifically to the LNA probe guanine bases [10,15]. The LNA probe was immobilized on the NG/EBT/GCE. So MB was strongly bound to the LNA modified NG/EBT/GCE surface.

3.6. Electrochemical behavior of MB on different electrodes

Fig. 5B shows the CV signals at different electrodes in 20 mM pH 7.0 Tris–HCl buffer solution containing 20.0 μM MB. It can be seen that a pair of weak redox peaks of MB was observed at the bare GCE (curve a) and EBT/GCE (curve b). For NG/EBT/GCE (curve c), the redox peak currents of MB were greatly enhanced. In addition, the immobilization of LNA probe on the NG/EBT/GCE modified electrode surface resulted in an increase in the peak currents of MB (curve d). It was attributed to nanogold thin film could provide a well platform for LNA probe immobilization and the electrostatic interaction between the negatively charged phosphate backbone of LNA and MB cation. At the same time, many more free guanine bases of LNA molecules were exposed out and had a strong affinity with MB, hence the greatest amount of MB accumulation occurs at this surface [29]. Therefore, the highest MB oxidoreduction signal was observed with LNA probe on NG/EBT/GCE. However, a significant decrease in the voltammetric peak current of MB was observed after complementary target sequence was allowed to hybridize with the LNA/NG/EBT/GCE (curve e). The decrease of current signal after hybridization was due to the inaccessibility of the guanine bases in dsDNA. This decrease is attributed to the steric inhibition of the reducible groups of MB packed between the bulky double helix of the hybrid. MB could bind specifically to the guanine bases and readily intercalate into dsDNA as well. Different binding modes of MB with LNA modified ssDNA and dsDNA resulted in variation in electrochemical responses.

3.7. Hybridization specificity of hairpin LNA probe

Hairpin LNA has high hybridization specificity because of its LNA and loop-stem structure [30], which can easily discriminate complementary oligonucleotide from single-base mismatch oligonucleotide. The selectivity of this assay was investigated by using the hairpin LNA as the capture probe to hybridize with various DNA sequences related to BCR/ABL fusion gene. Fig. 6A shows the differential pulse voltammetry (DPV) signal of MB at LNA/NG/EBT/GCE (d) and after hybridization with complementary target (a), single-base mismatch (b) and non-complementary (c). It is clear that curve d shows the highest peak current of MB on the LNA/NG/EBT/GCE, and after hybridization with complementary oligonucleotide, the peak current of MB is dramatically

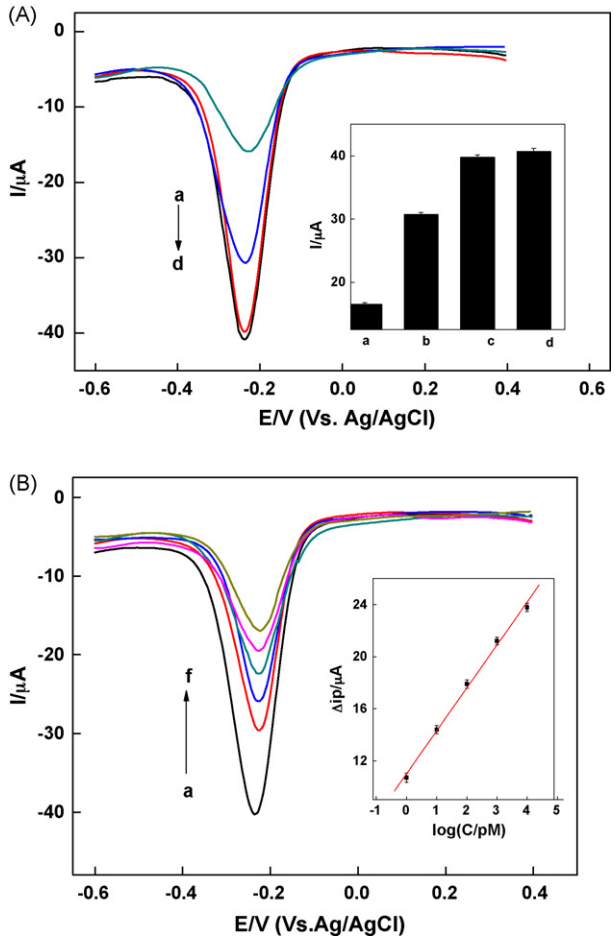


Fig. 6. (A) DPV of 20 μM MB at LNA/NG/EBT/GCE (d) and after hybridization with the complementary target (a), single-base mismatch (b) and non-complementary (c). Inset shows the bar graph of the peak current of MB when the LNA probe hybridized with different gene fragments. Error bars = ±relative standard deviation. (B) DPV of MB accumulated on the LNA after its hybridization with different concentration of the target sequence. Target concentration (*M*): (a) probe; (b) 1.0×10^{-12}; (c) 1.0×10^{-11}; (d) 1.0×10^{-10}; (e) 1.0×10^{-9}; (f) 1.0×10^{-8}. Inset shows the plot of the peak current of MB as a function of the target concentration. Error bars = ±relative standard deviation.

decreased (curve a). It can also easily discriminate the complementary oligonucleotide from single-base mismatch oligonucleotide. In the presence of oligonucleotide containing a single-base mismatch, significantly increased voltammetric signal can be observed (curve b), which indicates that the complete hybridization is not accomplished due to the base mismatch. So the hairpin LNA has high hybridization specificity for the complementary oligonucleotide and single-base mismatch oligonucleotide. In addition, as expected, no significant difference of peak current can be observed for the hairpin LNA probe and its hybridization with non-complementary (curve c), since no successful hybridization occurs due to the sequence mismatch between the hairpin LNA probe and non-complementary.

The sensitivity of this electrochemical biosensor for the target DNA was investigated by varying the target oligonucleotide concentration according to the procedure described in Section 2. The different current value obtained in the DPV response of MB after hybridization of LNA probe with target was recorded with three repetitive measurements. The current response decreased in proportion to the amount of the target sequence. The average current response shows excellent correlation with the amount of the complementary oligonucleotides in the range of 1.0×10^{-12}–1.0×10^{-8} M (Fig. 6B). The regression equation is

$$\Delta ip(\mu A) = 3.30(\log C/pM) + 11.0 \quad R = 0.9983$$

A detection limit of 1.0×10^{-13} M for the target DNA can be estimated using 3σ (where σ is the standard deviation of the blank solution, $n = 7$). The reproducibility of the biosensor for detection of 1.0×10^{-11} M target DNA is 7.35% ($n = 7$).

3.8. Detection of PCR products

This novel electrochemical biosensor based on the LNA probe on the NG/EBT/GCE has been used for assay of PCR product of real sample. When the hairpin LNA probe for BCR/ABL was immobilized and hybridized with real PCR samples in the hybridization step. The DPV signals of MB obtained from the LNA probe modified NG/EBT/GCE gave a mean average of 40.8 μA with a RSD of 5.12%. The DPV signals of MB obtained from the hybridization of the LNA probe with the positive and negative real samples gave mean average of 16.5 μA with RSD of 6.72% and 40.1 μA with RSD of 7.34%, respectively. The signal of MB for the LNA probe modified NG/EBT/GCE was much higher than that of LNA probe modified NG/EBT/GCE after hybridization with positive real sample. The decrease of DPV signals with positive real samples showed that the hybridization at the NG/EBT/GCE surface occurred and MB could not interact with the bound guanine base of the hybrid. The decrease in the reduction signal of MB was attributed to the steric inhibition of the reducible groups of MB because of the formation of hybrid at the NG/EBT/GCE surface. If the blood sample was negative, the negative real sample would not contain a target sequence complementary to the specific LNA probe. The hybridization between these negative real samples and the immobilized probe would not occur, so the signal of MB was higher than that of the positive real samples.

A gel electrophoresis method was performed. Fig. 7 shows the result of electrophoresis of PCR products. The PCR amplification products from a positive real sample (lane 3) show the light brands about 300 bp in the 1.5% agarose gel; however, the PCR amplification products from negative real sample (lane 2) do not present any brands in the gel. Thus, we can extrapolate that the primers have amplified specific band to discriminate the positive real sample

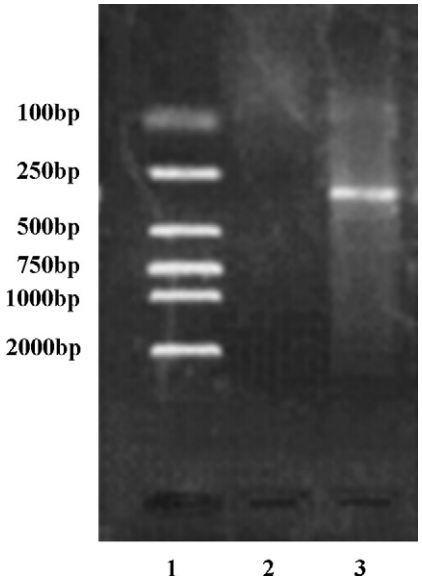


Fig. 7. Electrophoretogram of PCR amplified products. The lanes from left to right: lane 1: DL2000 DNA marker (the brands from up to down: 100 bp, 250 bp 500 bp, 750 bp, 1000 bp and 2000 bp); lane 2: negative real sample; lane 3: positive real sample.

from the negative real sample well. The results obtained from the gel electrophoresis are in good agreement with the ones obtained from the electrochemical DNA biosensor.

4. Conclusion

A novel electrochemical biosensor for detection of BCR/ABL fusion gene using hairpin LNA based on NG/EBT/GCE was fabricated. The hairpin LNA capture probe could selectively hybridize with its target DNA to form double-stranded DNA on NG/EBT/GCE surface. Since the quantities of LNA probe immobilized on the electrode surface can be greatly improved by nanogold-modified poly-EBT film approach. This novel DNA biosensor has higher sensitivity and better hybridization efficiency. The LNA probe was shown to be an effective biosensor for the detection of hybridization by using MB as the electrochemical indicator. This new method demonstrates its excellent specificity for single base mismatch and complementary after hybridization, and this method has been used for assay of PCR real sample with satisfactory result. The proposed method provided a simple, rapid tool for detection of DNA species in CML. It might have a promising future for investigation of DNA hybridization and solve the actual problem of the early diagnosis and prognosis monitor of CML and other diseases.

Acknowledgements

The authors gratefully acknowledge the financial support of the National Natural Science Foundation of China (20675015 and 20805006), the financial support of the National High Technology and Development of China (863 Project: 2006AA02Z4Z1 and 2008AA02Z433) and the Important Science and technology Foundation of Fujian Province (2008Y0045).

References

[1] P.J. Fialkow, S.M. Gartler, A. Yoshida, Proc. Natl. Acad. Sci. 58 (1967) 1468–1471.
[2] R.E. Champlin, D.W. Golde, Blood 65 (1985) 1039–1047.
[3] H.M. Kantarjian, A. Deisseroth, R. Kurzrock, Blood 82 (1993) 691–703.
[4] A. Butturini, B. Ralph, Leukemia Res. 20 (1996) 523–529.
[5] E.C. Jorge, T. Moshe, K. Hagop, Am. J. Med. 100 (1996) 555–570.
[6] Y. Zhang, N.F. Hu, Electrochem. Commun. 9 (2007) 35–41.
[7] H.L. Qi, X.X. Li, P. Chen, C.X. Zhang, Talanta 72 (2007) 1030–1035.
[8] J. Wang, Biosens. Bioelectron. 13 (1998) 757–762.
[9] S. Obika, D. Nanbu, Y. Hari, J. Andoh, K. Morio, T. Doi, T. Imanishi, Tetrahedron Lett. 39 (1998) 5401–5404.
[10] J.H. Chen, J. Zhang, K. Wang, X.H. Lin, L.Y. Huang, G.N. Chen, Anal. Chem. 80 (2008) 8028–8034.
[11] C.Y. James Yang, L. Wang, Y.R. Wu, Y.M. Kin, C.D. Medley, H. Lin, W.H. Tan, Nucleic Acids Res. 35 (2007) 4030–4041.
[12] J. Wengel, Acc. Chem. Res. 32 (1999) 301–310.
[13] R. Levicky, T.M. Herne, M.J. Tarlov, S.K. Satija, J. Am. Chem. Soc. 120 (1998) 9787–9792.
[14] T.A. Taton, C.A. Mirkin, R.L. Letsinger, Science 289 (2000) 1757–1760.
[15] N. Zhou, T. Yang, C. Jiang, M. Du, K. Jiao, Talanta 77 (2009) 1021–1026.
[16] H. Peng, L.J. Zhang, C. Soeller, J. Travas-Sejdic, Biomaterials 30 (2009) 2132–2148.
[17] H. Yao, Y.Y. Sun, X.H. Lin, Y.H. Tang, L.Y. Huang, Electrochim. Acta 52 (2007) 6165–6171.
[18] S. Fang, H.G. Lee, A.W. Wark, R.M. Corn, J. Am. Chem. Soc. 128 (2006) 14044–14046.
[19] J.J. Storhoff, R. Elghanian, R.C. Mucic, C.A. Mirkin, R.L. Letsinger, J. Am. Chem. Soc. 120 (1998) 1959–1964.
[20] M.H. Yang, J.H. Jiang, Y.S. Lu, Y. He, G.L. Shen, R.Q. Yu, Biomaterials 28 (2007) 3408–3417.
[21] B. Fang, S.F. Jiao, M.G. Li, Y. Qu, X.M. Jiang, Biosens. Bioelectron. 23 (2008) 1175–1179.
[22] Y. You, B.G. Moreira, M.A. Behlke, R. Owczarzy, Nucleic Acids Res. 34 (2006) e60.
[23] O. Richard, Biophys. Chem. 117 (2005) 207–215.
[24] A. Eriksson, L. Nyholm, Electrochim. Acta 44 (1999) 4029–4040.
[25] Z.S. Wu, F. Zheng, G.L. Shen, R.Q. Yu, Biomaterials 30 (2009) 2950–2955.
[26] C. Henke, C. Steinem, A. Janshoff, G. Steffan, H. Luftmann, M. Sieber, H.J. Galla, Anal. Chem. 68 (1996) 3158–3165.
[27] H. Kaur, A. Arora, J. Wengel, S. Maiti, Biochemistry 45 (2006) 7347–7355.
[28] F. Yan, A. Erdem, B. Meric, K. Kerman, M. Ozsoz, O.A. Sadik, Electrochem. Commun. 3 (2001) 224–227.
[29] N. Wei, J.H. Chen, J. Zhang, K. Wang, X.W. Xu, J.H. Lin, G.W. Li, X.H. Lin, Y.Z. Chen, Talanta 78 (2009) 1227–1234.
[30] R. Miranda-Castro, P. de-los-Santos-Alvarez, M.J. Lobo-Castanon, A.J. Miranda-Ordieres, P. Tunon-Blanco, Anal. Chem. 79 (2007) 4050–4055.

Talanta 80 (2010) 2120–2126

Contents lists available at ScienceDirect

Talanta

journal homepage: www.elsevier.com/locate/talanta

New method for speciation analysis of aluminium fluoride complexes by HPLC–FAAS hyphenated technique

M. Frankowski [a,b,*], A. Zioła-Frankowska [a], J. Siepak [a]

[a] Department of Water and Soil Analysis, Adam Mickiewicz University, Drzymały 24, 60-613 Poznań, Poland
[b] Department of Environmental Protection, Collegium Polonicum, Adam Mickiewicz University, Kościuszki 1, 69-100 Slubice, Poland

ARTICLE INFO

Article history:
Received 17 June 2009
Received in revised form 27 October 2009
Accepted 5 November 2009
Available online 13 November 2009

Keywords:
Speciation analysis
Aluminium
Aluminium fluoride complexes
HPLC
FAAS

ABSTRACT

Speciation analysis of aluminium in the presented system of HPLC–FAAS hyphenated technique lasts 4 min. Using the bifunctional column in model analysis and using the calculation methods for modelling using the Mineql program enabled the authors to presume that particular forms will be subjected to elution in the following order: (1) AlF_2^+ and AlF_4^-, (2) AlF^{2+} and AlF_3^0 and (3) Al^{3+}. Based on the obtained results for model solutions, the presented method enables the determination of aluminium fluoride complexes and Al^{3+} speciation form. The study compares the tendency of occurrence variability of aluminium fluoride complexes and Al^{3+} form, determined based on the results obtained using the HPLC–FAAS hyphenated technique with the trend defined based on the Mineql program calculation method. The method was successfully applied to soil samples.

© 2009 Elsevier B.V. All rights reserved.

1. Introduction

Characterised by high reactivity and amphoteric properties, aluminium in the natural environment shows strong tendency to create complex bonds, both with organic and inorganic ligands. Aluminium complexes with fluorides (AlF_2^+, AlF^{2+}, AlF_3^0, AlF_4^-, AlF_5^{2-}, AlF_6^{3-}) belong to the strongest ones and they significantly influence the increase in solubility of aluminium compounds. According to Martin [1], both elements show strong relationship to one another in forming stable complex compounds. The fraction of monomeric/labile inorganic aluminium responsible for toxic impact of aluminium on particular components of the natural environment consists of a free Al^{3+} ion, bonds of aluminium with fluorides, sulfates and hydroxy groups. Among these, Al^{3+}, $Al(OH)^{2+}$ and $Al(OH)_2^+$ are considered to be the most toxic aluminium forms. Aluminium and fluoride form soluble complexes, mainly AlF^{2+}, AlF_2^+, AlF_3^0, AlF_4^-, both in water and soil. They are less toxic than hydroxy forms and the Al^{3+} form. Stevens et al. [2] observed that the presence of aluminium fluoride complexes defined by the author as $AlF_x^{(3-x)}$ increases phytotoxicity of aluminium. Stevens's research showed that forms such as AlF^{2+} and AlF_2^+ are also toxic, but to a lesser extent than Al^{3+}, $Al(OH)^{2+}$ and $Al(OH)_2^+$ forms [2]. Based on his research, Martin [1] stated that the occurrence of fluorides will reduce the toxicity of Al^{3+} in relation to plants, fish and people. Similarly to Radić and Bralić [3], who relate the occurrence of fluoride and citrate ions in water to the decrease of aluminium toxicity in fish. However, according to Strunecká et al. [4], simultaneous activity of fluorides and aluminium both in water and the food chain, as well as their broad use in industry, medicine and agriculture, contributes to causing various diseases resulting in changes in metabolism, growing processes and homeostasis of living organisms. The negative influence of aluminium and fluorides, considering their ability to form AlF_x complexes, initiated research on the toxicity of these compounds, mainly at the intracellular level [5–8]. Strunecká and Potočka [4,9] showed that it is not only aluminium which is responsible for the Alzheimer disease etiology, which was confirmed in the studies by other authors [10–15]. Pathological changes in brain may also be caused by the aluminium fluoride complexes [9,16]. The increasing acidification of the natural environment and industrial development causes the increase of aluminium concentration in the environment. High aluminium concentration and low pH values are favourable conditions for forming soluble aluminium complexes, including aluminium fluoride complexes. For this reason, quantitative and qualitative determination of aluminium and the Al^{3+} form using speciation analysis is an important analytical task. The use of aluminium, including the aluminium fluoride complexes of chelating reagents [17–21] and ion-exchange resins [17,22–25] along with the following detection techniques: spectrophotometric and fluorometric in the aluminium determinations, does not enable the full separation of inorganic and organic forms of aluminium [26–29]. In order to determine stable AlF_x complexes, Bertsch and Anderson

* Corresponding author. Tel.: +48 61 829 3427; fax: +48 61 829 3448.
E-mail address: Marcin.Frankowski@amu.edu.pl (M. Frankowski).

0039-9140/$ – see front matter © 2009 Elsevier B.V. All rights reserved.
doi:10.1016/j.talanta.2009.11.018

used the HPLC technique (Dionex CS3 column) with UV detection along with the post-column reaction with Tiron (4,5-dihydroxy-m-benzene disulfonic acid). The determination conditions were used in the model solutions analysis in order to isolate Al^{3+} from fluoride, citrate and oxalate complexes. Forms AlF^{2+} and Al^{3+} were separated [30]. Willet used the CG2 guard column in his research along with post-column reagent PCV (Pyrocatechol Violet) and 1.10-phenanthroline, hydroxylamine. However, despite the quick separation, he did not obtain the full separation between the AlF^{2+} and AlF_2^+ forms [31]. Jones also used in his research the CG2 guard column, thermostated in 50 °C and fluorometric detection with post-column HQS (8-hydroxyquinoline-5-sulfonic acid) condensation in order to directly determine monomeric hydroxy aluminium forms [32]. Willet and Jones did not obtain the separation between the AlF^{2+} and AlF_2^+ forms, which were eluted close to the solvent front. Motellier and Pitsch used the cation CS2 analytical column with CG2 guard column and detection with post-column reaction with 3×10^{-4} M Tiron (4,5-dihdroxy-1,3 benzene disulfonic acid, di sodium salt monohydrate) in 3 M ammonium acetate. They did not get the full separation of AlF^{2+} and AlF_2^+ forms [33]. For speciating Al and its fluoro, oxalate and citrate complexes, Borrmann and Seubert used post-column reaction with Tiron (4,5-dihdroxy-1,3 benzene disulfonic acid, di sodium salt monohydrate) with UV detection and atomic spectrometry ICP-AES (for Al–citrate–oxalate complexes). Depending on the proportion of ligands in model solutions, in the case of Al–F complexes in the amount of 1:1 (Al:F), the obtained signals were related to the following forms: AlF_2^+, AlF^{2+} and Al^{3+} (for UV detection 310 nm following post-column reaction with Tiron) [34]. Previous solutions involved combining HPLC with ICP: mass spectrometry and atomic emission spectrometry (ICP-MS, ICP-AES) in the on-line [27,34–39] and off-line system [40,41] using the atomic absorption spectrometry with electrothermal atomisation as the detector in the off-line system [42,43]. Only the combination of HPLC with flame atomic absorption spectrometry (FAAS) detection enabled the full separation of aluminium fluoride complexes [44]. In the study by Zioła-Frankowska et al. [44], model analyses of synthetic solutions were presented and qualitative analysis of fully separated AlF_2^+, AlF^{2+} and Al^{3+} forms was performed. The use of HPLC and FAAS techniques brings along problems related to the quantitative analysis in order to perform speciation analysis of aluminium fluoride complex and the Al^{3+} form.

The main aims of this study were: (1) investigate qualitative and quantitative analysis of aluminium fluoride complexes and toxic form of aluminium Al^{3+}, (2) investigation of cation and anion forms of aluminium fluoride complexes in model system, (3) application of Mineql program to calculate and modelling occurrence of particular forms of aluminium, (4) evaluation and comparison between results obtained by calculated method with results of model solution from analytical system HPLC–FAAS, and (5) application of new system to speciation analysis of aluminium fluoride complexes and Al^{3+} in soil samples.

2. Materials and methods

2.1. Instrumentation

The chromatographic separation was performed by liquid chromatography system consisting of: Shimadzu solvent delivery module LC-10 ADVP liquid chromatograph (Shimadzu Corporation, Japan) and low pressure gradient flow control valve Shimadzu FCV-10 ALVP (Shimadzu Corporation, Japan), degasser DGU-20A5 (Shimadzu Corporation, Japan), column oven CTO-10ASvp (Shimadzu Corporation, Japan) with Rheodyne Model 7725i Injection Valve (Rheodyne LLC, USA) and with ion-exchange column—Dionex IonPac CS5A (analytical column, 250 mm, 4.0 mm i.d., particle size 9.0 μm, containing mixed anion and cation beds with sulfonic acid and alkanol quaternary ammonium functional groups) (Dionex, USA) and IonPac CG5A (guard column, 50 mm, 4 mm i.d., particle size 9.0 μm) (Dionex, USA). The chromatographic run was gradient at 2 ml min^{-1} with an injection volume of 500 μL. HPLC/IC system was controlled by CBM-20A (Shimadzu Corporation, Japan) communication bus module with LC Solution software. The gradient elution program is shown in Table 1.

Table 1
Gradient elution program with comments.

Time (min)	(A) H_2O	(B) NH_4Cl	Comment
0	100	0	Inject
1.00	100	0	Start linear gradient
1.30	0	100	Increase in eluent strength
1.30	0	100	Burner turn on
2.00	0	100	Return to initial conditions
2.01	100	0	Flame stabilization
2.30	100	0	Data collecting (value 0 on chromatograms)
4.00	100	0	Data collected (90 s)
4.00	100	0	Burner turn off

The species of aluminium were determined by the technique of atomic absorption spectrometry with acetylene–nitrous oxide flame atomisation (F-AAS) with the use of a SpectraAA 280FS spectrometer (Varian, Australia) with flame atomisation. Data capturing and peak analysis were performed with the use of Spectraa software ver. 5.1 pro (Varian, Australia). The analytical chromatographic column was directly connected to the nebulizer system simultaneously working type of atomic absorption spectrometer.

2.2. Reagents

All chemicals used were of high-purity grade. Deionised water from Milli-Q RG water unit (Millipore, France) was used for dilution of stock solutions as well as for any reagent preparation. All stock solutions of aluminium were obtained by dissolving standard solution 1000 mg L^{-1} from Merck (Darmstadt, Germany). Stock standard solutions of fluorine 1000 mg L^{-1} were prepared from Merck (Darmstadt, Germany). Working solutions were prepared daily just before measurements by appropriate dilution. The eluent used for gradient elution consisted of A: deionised water, B: ammonium chloride (1.8 M pH about 3). The eluent was made by dissolving a weighted portion of NH_4Cl (Merck, Darmstadt, Germany) in deionised water and finally diluted to 1000 ml by deionised water. The solution of NH_4Cl was acidified by 1 mM hydrochloric acid (Merck, Darmstadt, Germany) to pH about 3 in a volumetric flask. A series of standards mixtures of Al–F were prepared by the appropriate dilution of solutions containing aluminium and fluoride ions in various concentrations.

2.3. Modelling by Mineql 4.5+

The program for chemical modelling of the environment, Mineql 4.5+ (ERS, USA), was used to model and simulate the conditions in model solutions and in real samples. The program settings were as follows: for model solutions Al:F only the concentration of Al (1.85e-04, 9.27e-04, 1.85e-03, 2.78e-03 and 3.71e-03 M) and F (2.63e-04, 1.32e-03, 2.63e-03, 3.95e-03 and 5.26e-03 M) was taken into account, concentration of [H+] was 10^{-3}, temperature 25 °C, ionic strength correction was off.

3. Results and discussion

3.1. Results of model solution obtained by HPLC–FAAS hyphenated technique

Reaching the aims of the study involved preparing a series of model solutions with the concentration proportions Al:F in all possible combinations for Al (1.85e-04, 9.27e-04, 1.85e-03, 2.78e-03 and 3.71e-03 M) and F (2.63e-04, 1.32e-03, 2.63e-03, 3.95e-03 and 5.26e-03 M). The solutions analysis was performed in the system of HPLC–FAAS hyphenated technique. The speciation aluminium forms, separated in the chromatographic column, were directed to the flame atomic absorption nebulizer. Fig. 1 presents the obtained results in the form of overlapping chromatograms for a given stable concentration of aluminium and variable concentration of fluorides.

Based on the results obtained from the HPLC–FAAS system, the qualitative analysis is possible in the first place. On the other hand, the quantitative analysis is a more difficult task. The spectrometers and software available on the market produce certain limitations in terms of too short signal integration time, which is not long enough to perform a full analysis in the system using the said separation technique. The additional difficulty is the lack of possibility to calculate the surface area under particular analytical signals obtained under the peaks. The Spectraa (Varian, Australia) software was used in the research. The software enables obtaining the value repetitiveness and the continuity of signal counting, in spite of the short signal counting time: 30 s. The signal was received within 3× 30 s in one sequence (90 s). Based on the chromatograms obtained from the Spectraa software, absorbance values were counted manually every 0.5 s and recorded in a text file (*.txt). The text values were next deleted from the text file and moved to the Excel program, into the previously prepared columns with the values of time and absorbance respectively. The *.xls file prepared in this way for each signal separately was then imported to the Grapher program, where a typical linear diagram (time/absorbance) was drawn. Based on the diagram, using the calculate area function, the area under a peak was calculated. The surface area under particular signals was calculated for all model solutions and all data were collected for quantitative analysis. Qualitative analysis was initially based on literature data [33,37,44–50] and the property of the mixture components separation according to increasing charge of these forms. It was assumed that the first component (aluminium form) subject to elution was form AlF_2^+, then AlF^{2+} and finally Al^{3+}. The occurrence of a given form in the investigated model solutions at the constant aluminium concentration was dependent on the changing concentration of F^- ions. However, the research focused on the column type. The use of the bifunctional column poses a problem connected with the interpretation difficulties in relation to the obtained results in the case of aluminium fluoride complexes. In order to verify the speciation aluminium forms, which may be subject to elution (AlF_2^+, then AlF^{2+} and finally Al^{3+}), a simulation using the Mineql 4.5+ program was performed for the particular model solutions.

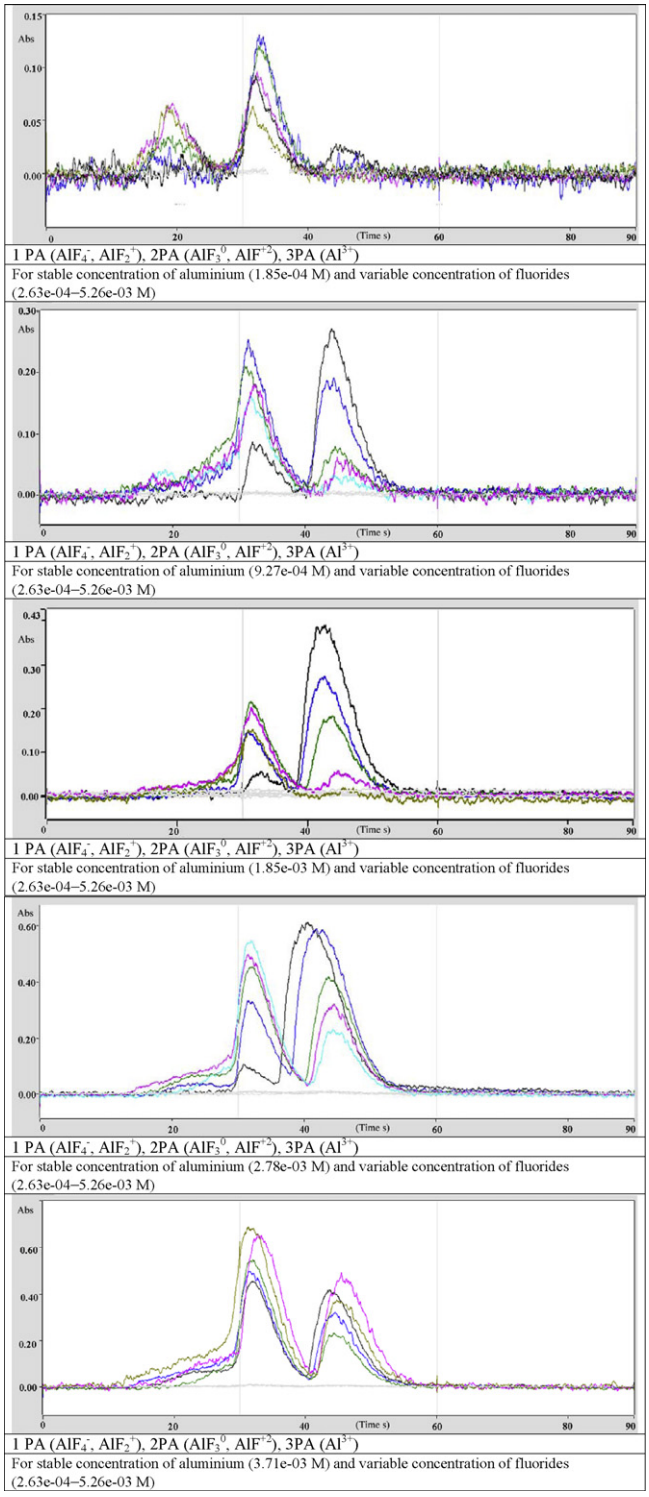


Fig. 1. Results in the form of overlapping chromatograms for a given stable concentration of aluminium and variable concentration of fluorides.

3.2. Results from Mineql+

The model analyses took into consideration both cation and anion forms of aluminium fluoride complexes: AlF_2^+, AlF^{2+}, AlF_3^0, AlF_4^-, and Al^{3+}. The obtained results were presented as the percentage participation of a given form [%], as a occurrence variability of these forms in relation to the variable concentration of aluminium and fluorides (Fig. 2).

Based on the obtained results it was observed that when the molar ratio Al/F is ≥0.7, three main forms of aluminium are formed: AlF_2^+ and AlF^{2+}, Al^{3+}. For the molar ratio Al/F = 0.01, these forms occur in the order according to the [%] concentration $AlF^{2+} > Al^{3+} > AlF_2^+$. On the other hand, for the concentration of Al/F = 0.003, Al^{3+} is the dominating form, and then $AlF^{2+} > AlF_2^+$. At the fluoride concentration higher than the aluminium concentration, AlF_3^0 forms and anion AlF_4^- form also begin to be formed. When the molar ratio Al/F = 0.035, AlF_3^0, AlF_4^- and AlF_2^+ forms are formed. The occurrence of these forms, when Al/F = 0.035, changes from $AlF_3^0 > AlF_4^- > AlF_2^+$ to $AlF_2^+ > (AlF^{2+}) > AlF_3^0 > AlF_4^-$

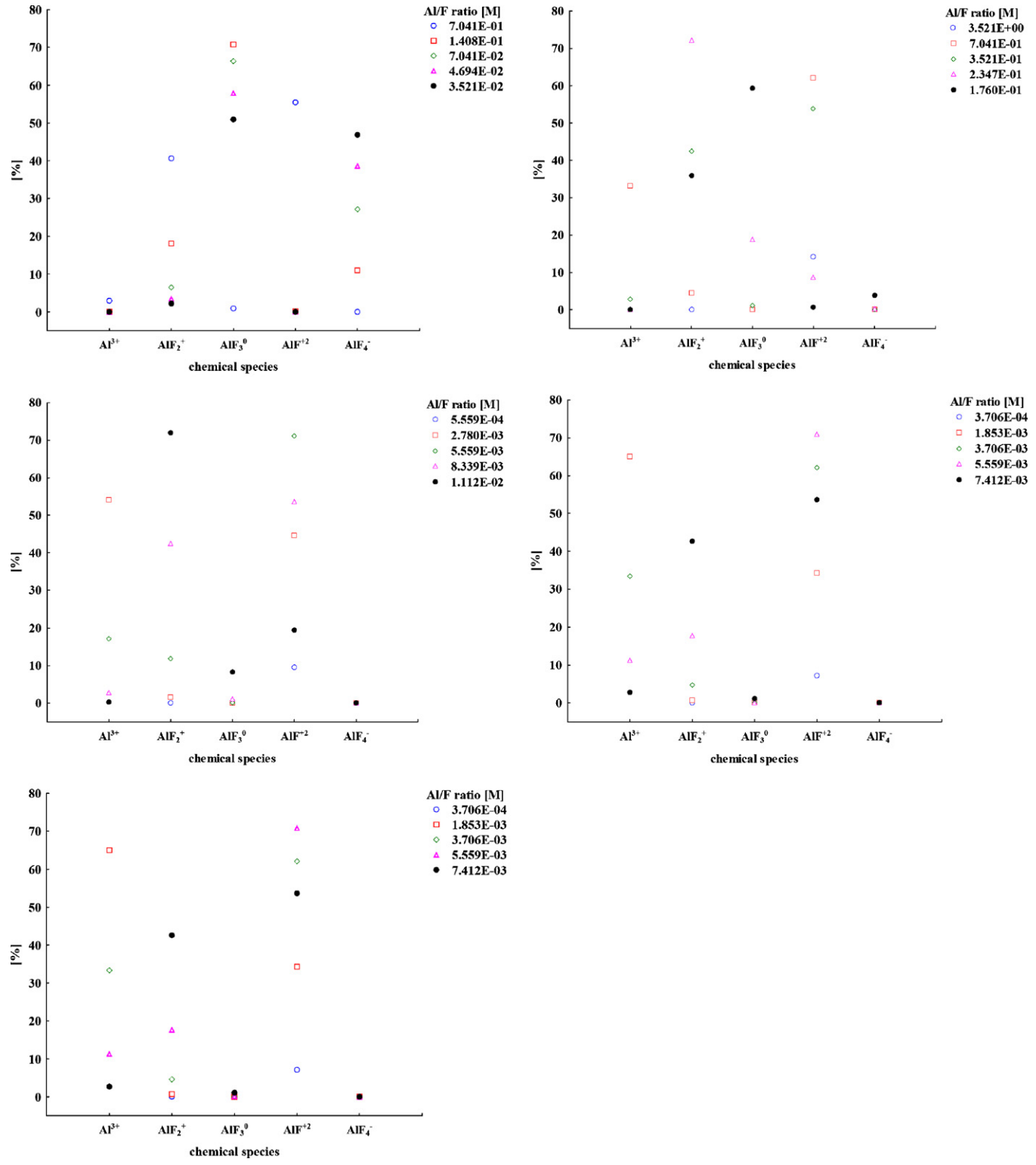


Fig. 2. Data obtained by Mineql program (all aluminium fluoride complexes and Al^{3+}).

when the proportion of molar ratio Al/F = 0.14. At the concentration value of Al/F = 0.14, strong formation of the AlF^{2+} form was observed. It should be underlined that in the case of bifunctional column one should expect such forms as: AlF_2^+, AlF^{2+}, AlF_3^0, AlF_4^-, Al^{3+}. The sequence of the particular signals was assumed based on the literature data and on the basis of the Mineql program calculations (Table 2).

Table 2
Proposed elution sequence forms: AlF_2^+, AlF^{2+}, AlF_3^0, AlF_4^-, Al^{3+}.

1PA—first signal AlF_2^+ and/or AlF_4^-	2PA—second signal AlF^{2+} and/or AlF_3^0	3PA—third signal Al^{3+}

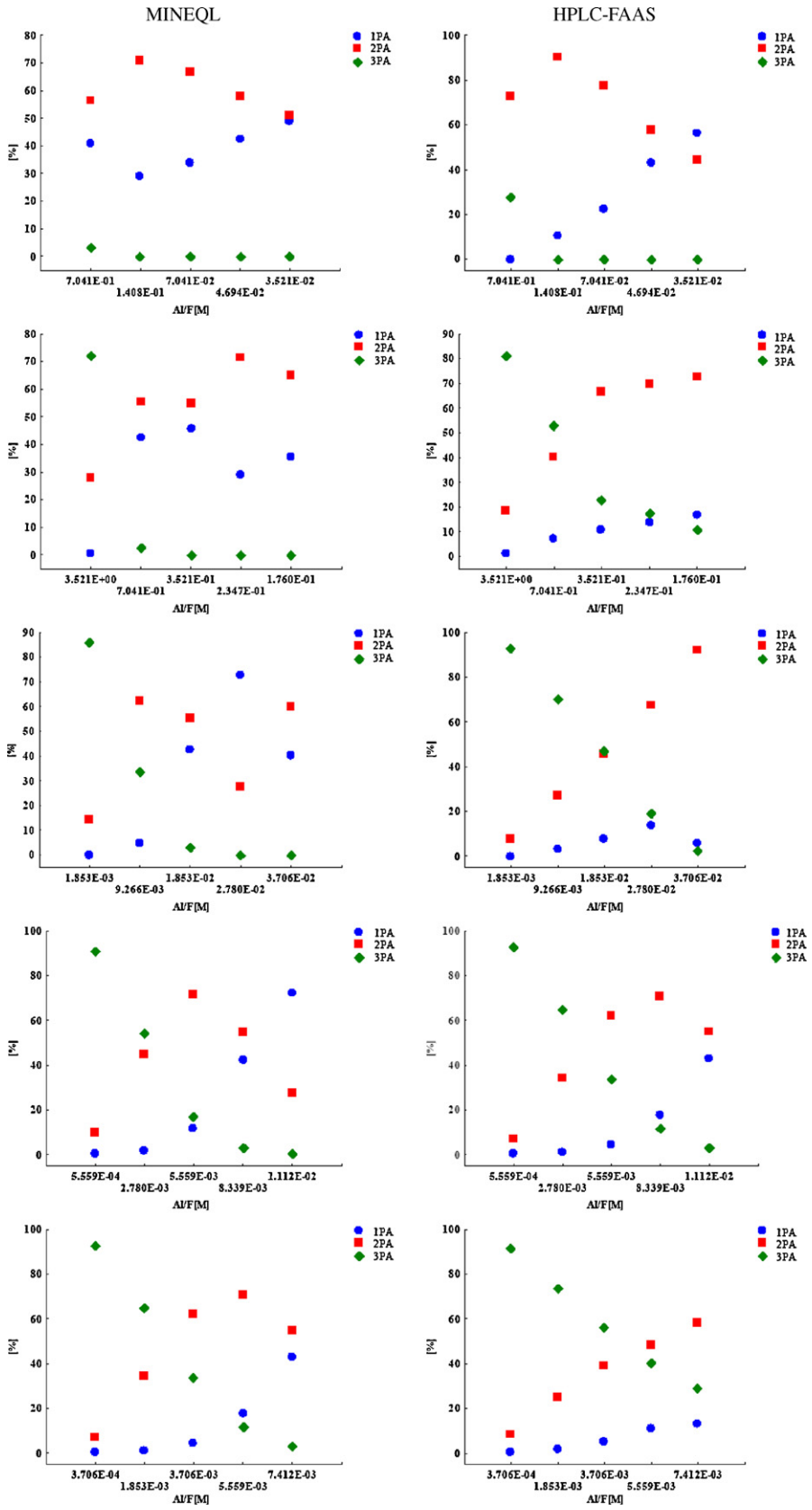


Fig. 3. Results obtained by Mineql program and by a new method of HPLC–FAAS hyphenated technique.

Then, in order to compare the results obtained from the Mineql program and the HPLC–FAAS system, the 1PA (AlF_2^+ and/or AlF_4^-), 2PA (AlF^{2+} and/or AlF_3^0), 3PA(Al^{3+}) forms were added respectively for better visualisation of the results (Fig. 3).

The results obtained for the model solutions in the HPLC–FAAS system and from the Mineql program calculations show significant similarity. For the diagrams (Mineql) with constant concentration of aluminium (1.85e-04 M) and variable concentration of fluorides (2.63e-04–5.26e-03 M), one can observe the participation shift towards the AlF^{2+} and/or AlF_3^0 (2PA) complex forms in relation to AlF_2^+ and/or AlF_4^- (1PA) at the decreasing fluoride concentration. On the other hand, together with the increasing concentration of fluorides, the balance shift towards the 1PA forms was observed. A similar tendency between the 1PA, 2PA and 3PA forms was observed for the HPLC–FAAS, 1.85e-04 M Al system results. It should be underlined that in the case of 1PA results for model solutions, % participation was much lower than for the Mineql results, and the 2PA and 3PA results stayed at the similar % level. The % increase to Al^{3+} of both 1PA and 2PA forms participation was observed, along with the increasing level of fluorides. In the case of the results obtained in model solutions, a similar tendency for 2PA forms was observed. A lower % participation for the 1PA form was recorded at a higher % participation of the Al^{3+} form. A growth tendency in 1PA of up to molar ratio 0.03 was observed at the aluminium concentration of 1.85e-03 M for the Mineql results. The similar tendency occurred in model solutions. In the case of 2PA this tendency is differential, in contrast with the HPLC–FAAS system results, where the proportional % increase was observed. Although the % participation of the Al^{3+} form in model solutions is higher, the 3PA in both cases show a similar tendency. In the solutions of aluminium concentration of 2.78e-03 and 3.71e-03 M, the distribution tendency of particular 1PA, 2PA, 3PA forms is similar. The differences between the Mineql and HPLC–FAAS results are related to the % participation, especially in the 1PA form (the values are lower) and 3PA (the values are higher). In the case of Al^{3+} form, the results obtained through the Mineql calculation method are lower in comparison with those obtained for model solutions, which in consequence explains the lower concentration of the AlF_2^+ and AlF_4^- forms. Moreover this difference can be connected with partly disintegrated during the chromatographic process [30,34–36].

3.3. Application to environmental samples

The environmental samples were taken in the area of Chemical Plants situated in Luboń (Poland). The soil samples of surface layer (0–1 m) were collected in two places located in the area of Chemical Plants (S1: N 521932.3 E 165344.6; S2: N 521932.7 E 165347.0). The samples lithology was medium sand. The research material was collected in polyethylene bags. Samples were dried at room temperature. The hygroscopic water and the substances dissolved in it were treated as an integral component of the sample. After drying a sample was passed through sieves with mesh sizes of 2.0, 1.0, 0.5, 0.25, 0.1, and 0.063 mm, according to the Polish Norms PN-ISO 565:2000 and PN-ISO 3310-1:2000, using a sieve shaker LAB-11-200/UP (EKO-LAB, Brzesko, Poland). Grain size fraction 0.125–0.25 mm was dominating and this fraction was used to prepare soil water extracts. In order to isolate the most environmentally available fraction, 5 g of a sample was collected and extracted in 50 ml of deionised water (1:10) for 1 h using a magnetic stirrer. The samples were then centrifugated (4000 rpm) for 15 min. The solution was decanted in 50 ml volumetric flasks. The pH H_2O determinations were performed in water extracts prepared for the HPLC–FAAS analysis using the ProfiLine Multi 197i (WTW, Germany) meter with Blueline pH electrode (Schott, UK). Furthermore, determinations of fluorides using an ion selective fluoride electrode (Orion, USA) were conducted. Aluminium water soluble

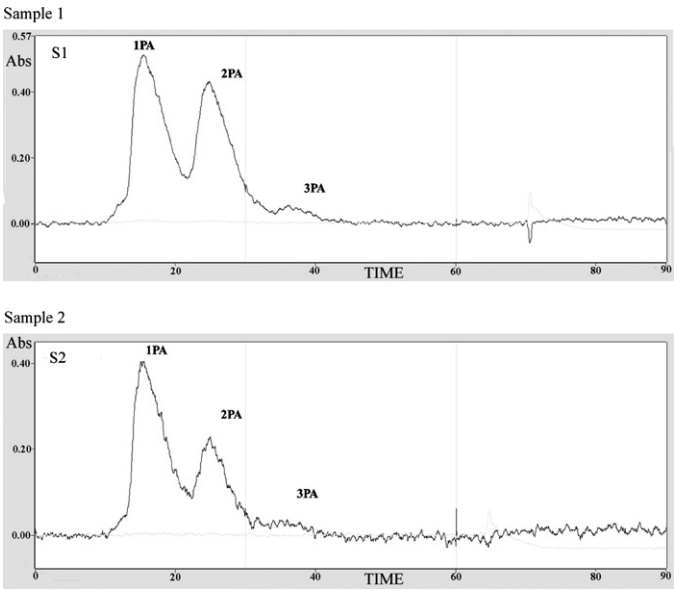


Fig. 4. Chromatograms obtained by HPLC–FAAS system in speciation analysis of aluminium in soil water extracts.

fraction determinations were performed directly in the solutions using the FAAS technique (Fig. 4).

Total concentration of aluminium and fluorides was: for S1 (Al = 458 mg kg^{-1} and F = 1325 mg kg^{-1}) for S2 (Al = 828 mg kg^{-1} and F = 2260 mg kg^{-1}). The reaction values were 3.81 and 4.08 respectively. Calculated values of aluminium fluoride complexes and Al^{3+} were compared between Mineql program and results obtained by HPLC–FAAS system. For S1 and S2 we obtained results for real samples S1: 231, 206, 20.9 and S2: 517, 258, 52.8 mg kg^{-1} for 1PA (AlF_2^+ and/or AlF_4^-), 2PA (AlF^{2+} and/or AlF_3^0) and 3PA (Al^{3+}) respectively. For results obtained by Mineql program S1: 334, 125, <0.05 and S2: 587, 241 and <0.05 mg kg^{-1} respectively.

4. Conclusions

The determination method of inorganic aluminium forms in the HPLC–FAAS hyphenated techniques system is a new solution in the analysis of this element. The use of the IonPac CS5A bifunctional column enabled the isolation of both anion and cation bonds this element forms with fluorides (AlF_2^+, AlF_4^-, AlF^{2+}, AlF_3^0), as well as the Al^{3+} form. Based on the modelling performed using the Mineql program, three groups of eluting components/forms were isolated in the following order: AlF_2^+ and AlF_4^-, AlF^{2+} and AlF_3^0, and Al^{3+}. It should be underlined that the method enables obtaining the most toxic aluminium form Al^{3+} as a single analytical signal. Moreover, the presented method enables both qualitative and quantitative determination of the Al^{3+} form and aluminium fluoride complexes (4 min). In addition, the analytical system in the presented method of aluminium determination operates in the on-line mode and it is not necessary to use derivatization reagents. The result analysis for model solutions along with the use of the supplementary tool (Mineql) to interpret the participation of the particular forms, showed the domination of the aluminium fluoride complexes in comparison to the Al^{3+} form, along with the increase in fluoride concentration. The participation of the Al^{3+} form was significantly reduced at the high concentrations of fluorides. It should be underlined that the analysis of the results obtained both from the Mineql program and the one performed for the model solutions using the HPLC–FAAS hyphenated technique, showed similarities in the occurrence variability tendency between the analysed aluminium forms. The quantitative analy-

sis of model solutions performed using both methods (HPLC–FAAS and Mineql), indicates higher concentration of the Al^{3+} form and lower concentration of AlF_2^+ and AlF_4^- forms. The suggested system of HPLC–FAAS hyphenated technique was successfully applied to speciation analysis of soil water extract.

Acknowledgement

The research was supported by the Polish Ministry of Science and Higher Education through research grants N 305 101235 and N 304 013 337.

References

[1] R.B. Martin, Coordin. Chem. Rev. 141 (1996) 23–32.
[2] D.P. Stevens, M.J. McLaughlin, A.M. Alston, Plant Soil 192 (1997) 81–93.
[3] N. Radić, M. Bralić, Sci. Total Environ. 172 (1995) 237–243.
[4] A. Strunecká, O. Struneckỳ, J. Potočka, Physiol. Res. 51 (2002) 557–564.
[5] M. Suwalsky, B. Norris, F. Villena, F. Cuevas, P. Sotomayor, P. Zatta, Food Chem. Toxicol. 42 (2004) 925–933.
[6] J.R. Dodam, N.C. Olson, J. Appl. Physiol. 78 (1995) 569–577.
[7] P.J. Morgan, M.H. Hastings, M. Thompson, P. Barrett, W. Lawson, G. Davidson, J. Mol. Endocrinol. 72 (1991) 134–144.
[8] A. Oguro, J. Cervenka, K. Horii, Pharmacol. Toxicol. 67 (1990) 411–414.
[9] A. Strunecká, J. Potocká, Fluoride 32 (1999) 230–242.
[10] B. Platt, A.J. Drysdale, C. Nday, E. Linstow Roloff, B.D. Drever, A. Salifoglou, Neurotoxicology 28 (2007) 576–586.
[11] G. Berthon, Coordin. Chem. Rev. 228 (2002) 319–341.
[12] J.R. McDermott, A.I. Smith, K. Iqbal, H.M. Wiśniewski, Neurology 29 (1979) 809–814.
[13] P. Zatta, R. Giordano, B. Corain, G.G. Bombi, Med. Hypotheses 26 (1988) 139–142.
[14] J. Patoka, M. Koupilová, J. Fusek, J. Homeostasis 37 (1996) 136–137.
[15] T.P. Flaten, Environ. Geochem. Health 12 (1990) 152–167.
[16] A. Strunecká, News Dementia 1 (1991) 2–3.
[17] C.T. Driscoll, Int. J. Environ. Anal. Chem. 16 (1984) 267–283.
[18] P. Matúš, J. Kubová, Anal. Chim. Acta 573 (2006) 474–481.
[19] E. Dixon, M. Gardner, Chem. Spec. Bioavalib. 10 (1998) 11–17.
[20] L. Xia, B. Hu, Z. Jiang, Y. Wu, L. Li, R.J. Chen, Anal. Atom. Spectrom. 20 (2005) 441–446.
[21] A.B. Tabrizi, Food Chem. 100 (2007) 1698–1703.
[22] G. Alberti, R. Biesuz, A. Profumo, M. Pesevento, J. Inorg. Biochem. 97 (2003) 79–88.
[23] S.B. Erdemoğlu, K. Pyrzyńska, S. Gücer, Anal. Chim. Acta 411 (2000) 81–89.
[24] T. Wickstrøm, N. Clarke, K. Derome, E. Røgeberg, J. Environ. Monitor. 2 (2000) 171–181.
[25] A. Ruszczyńska, K. Pyrzyńska, E. Bulska, Chem. Anal. (Warsaw) 49 (2004) 19–28.
[26] N. Clarke, L. Danielsson, A. Sparén, Pure Appl. Chem. 68 (1996) 1597–1638.
[27] J. Tria, E.C.V. Butler, P.R. Haddad, A.R. Bowie, Anal. Chim. Acta 588 (2007) 153–165.
[28] P.R. Bloom, S.M. Erich, in: G. Sposito (Ed.), The Environmental Chemistry of Aluminium, 2nd edn., Lewis Publishers, Boca Raton, FL, 1996, pp. 363–419.
[29] J. Ščančar, R. Milačič, Anal. Bioanal. Chem. 386 (2005) 999–1012.
[30] P.M. Bertsch, M.A. Anderson, Anal. Chem. 61 (1989) 535–539.
[31] I.R. Willet, Soil Sci. Am. J. 53 (1989) 1385–1391.
[32] P. Jones, Int. J. Environ. Anal. Chem. 44 (1991) 1–10.
[33] S. Motellier, H. Pitsch, J. Chromatogr. A 660 (1994) 211–217.
[34] G. Borrmann, A. Seubert, Anal. Chim. Acta 332 (1996) 233–239.
[35] O. Happel, A. Seubert, J. Chromatogr. A 1108 (2006) 68–75.
[36] G. Borrmann, A. Seubert, Anal. Chim. Acta 386 (1999) 77–88.
[37] M.M. Bayón, A.R. Garcia, J.I.G. Alonso, A. Sanz-Medel, Analyst 124 (1999) 27–31.
[38] A. Fairman, A. Sanz-Medel, P. Jones, E. Hywel, Analyst 123 (1998) 699.
[39] O. Happel, A. Seubert, J. Anal. Bioanal. Chem. 392 (2008) 1373–1381.
[40] B. Mitrović, R. Milačič, Sci. Total Environ. 258 (2000) 183–194.
[41] T. Bantan-Polak, B. Mitrović, R. Milačič, Anal. Chim. Acta 540 (2005) 83–89.
[42] B. Mitrović, R. Milačič, B. Pihlar, P. Simončić, Analusis 26 (1998) 381–388.
[43] T. Bantan-Polak, B. Mitrović, R. Milačič, Talanta 47 (1998) 929.
[44] A. Zioła-Frankowska, M. Frankowski, J. Siepak, Talanta 78 (2009) 623–630.
[45] O. Drábek, L. Boruvka, L. Mládková, M. Kocarek, J. Inorg. Biochem. 97 (2003) 8–15.
[46] O. Drábek, L. Mladkova, L. Boruvka, J. Száková, A. Nikodem, K. Nemecek, J. Inorg. Biochem. 99 (2005) 1788–1795.
[47] O. Drábek, L. Boruvka, L. Pavlu, A. Nikodem, I. Pírková, O. Vacek, J. Inorg. Biochem. 101 (2007) 1224–1233.
[48] R. Street, O. Drábek, J. Száková, L. Mládková, Food Chem. 104 (2007) 1662–1669.
[49] M.G. Whitten, G.S.P. Ritchie, I.R. Willet, J. Soil Sci. 43 (1992) 283–293.
[50] K. Tsunoda, T. Umemura, K. Ohshima, S. Lizawa, E. Yoshimura, K. Satake, Water Air Soil Pollut. 130 (2001) 1589–1594.

Talanta 80 (2010) 2127–2131

Contents lists available at ScienceDirect

Talanta

journal homepage: www.elsevier.com/locate/talanta

An on-line preconcentration/separation system for the determination of bismuth in environmental samples by FAAS

Serkan Şahan, Şerife Saçmacı*, Uğur Şahin, Ahmet Ülgen, Şenol Kartal

Erciyes University, Department of Chemistry, Faculty of Arts and Sciences, TR-38039, Kayseri, Turkey

ARTICLE INFO

Article history:
Received 22 June 2009
Received in revised form 29 October 2009
Accepted 5 November 2009
Available online 12 November 2009

Keywords:
Bismuth
On-line preconcentration
Lewatit TP-207

ABSTRACT

An on-line preconcentration procedure for the determination of bismuth by flame atomic absorption spectrometry (FAAS) has been described. Lewatit TP-207 chelating resin, including iminodiacetate group, packed in a minicolumn was used as adsorbent material. Bi(III) was sorbed on the chelating resin, from which it could be eluted with 3 mol L^{-1} HNO_3 and then introduced directly to the nebulizer-burner system of FAAS. Best preconcentration conditions were established by testing different resin quantities, acidity of sample, types of eluent, sample and eluent solution volumes, adsorption and elution flow rates, and effect of interfering ions. The detection limit of the method was 2.75 μg L^{-1} while the relative standard deviation was 3.0% for 0.4 μg mL^{-1} Bi(III) concentration. The developed method has been applied successfully to the determination of bismuth in pharmaceutical cream, standard reference materials and various natural water samples with satisfactory results.

© 2009 Elsevier B.V. All rights reserved.

1. Introduction

Determination of bismuth is important in environmental chemistry, cosmetic industry, medicine, semiconductors, alloys, metallurgical additives, recycling of uranium nuclear fuels and fabrication of catalysts. Since the use of bismuth and its compounds in different areas of life increased and this element started to be considered toxic for humans, animals and plants [1–3]. Although intestinal absorption of bismuth is limited in humans, because of its low solubility and its propensity to form insoluble oxychloride salts, some absorption must occur to produce measurable concentrations in body fluids and tissues [4]. As the use of bismuth in medicine increases, it has spread in the environment and the chance of exposure of organisms to bismuth has increased. A number of toxic effects in humans have been attributed to bismuth compounds [5–7]. Therefore, new methods are required for the low cost and rapid determination of Bi(III) in the pharmaceutical manufacture and quality control process. Cui et al. have proposed a new method for the determination of bismuth in pharmaceutical products using methyltriphenylphosphonium bromide as a molecular probe by resonance light scattering technique [8].

Several methods have been reported for the determination of Bi(III) in rock, water, alloy and biological samples. Some spectrophotometric methods have been applied for the determination of bismuth [9–11]. The extraction, in the presence of masking agents, with dithizone in chloroform or carbon tetrachloride is a selective spectrophotometric method for separating traces of bismuth [9]. 2,6-Dichloroarsenazo as chromogenic reagent has been used by Zhang et al. in the spectrophotometric determination of bismuth, in aqueous 0.6 mol L^{-1} $HClO_4$ solution, forming a deep blue complex with a maximum absorption at 631 nm [10]. Also, Hoshi et al. have used thiourea as a complexing agent in the spectrophotometric determination of bismuth after collection and elution of Bi(III) –thiourea complex on chitin [11]. Tzanavaras et al. reported a spectrophotometric method for the determination of bismuth in pharmaceutical products using sequential injection analysis [12]. Methylthymol blue (MTB) was used as a color forming reagent and the absorbance of the Bi(III)–MTB complex was monitored at 548 nm. On the other hand, hydride generation atomic absorption spectrometry (HG-AAS) [2,3,13], hydride generation inductively coupled plasma atomic emission spectrometry (HG-ICP-AES) [14], electrothermal vaporization ICP mass spectrometry (ETV-ICP-MS) [15], potentiometric stripping analysis (PSA) [16], anodic [17,18] and cathodic [19] stripping voltametry have also been applied in determination of bismuth in various samples. In another work made by Wang et al., the preconcentration and voltammetric behavior of Bi on a sodium humate modified carbon paste electrode were studied using cyclic voltammetry and differential pulse stripping voltammetry for the determination of bismuth in medicine for stomach [18].

Conventional off-line preconcentration procedures, although effective, are usually time consuming and tedious, require large quantities of sample and reagents, in consequence are vulnerable to contamination and analyte losses. Flow injection (FI) methods

* Corresponding author. Tel.: +90 352 4374937; fax: +90 352 4374933.
E-mail address: sacmaci@erciyes.edu.tr (Ş. Saçmacı).

0039-9140/$ – see front matter © 2009 Elsevier B.V. All rights reserved.
doi:10.1016/j.talanta.2009.11.019

provide an opportunity to avoid contamination and large reagent consumption by working with closed systems. In addition, on-line systems are excellent tools for solution management, allowing the easy implementation of different steps required for selectivity and/or sensitivity enhancement. On-line methods offer higher sample throughput and better precision and accuracy compared to off-line methods. In most on-line FAAS methods, the carrier and reagent solutions are continuously fed to the flow system, mixed on-line and passed through the microcolumns prior to detection [20,21].

In the present paper, we have evaluated a new on-line system with a home-made controller having five independent channels for preconcentration and determination of Bi(III) species. Because the studies made on determination of bismuth in various matrices are insufficient in the literature, especially using on-line systems with FAAS. For this purpose, Lewatit TP-207 resin was firstly used for the on-line determination of Bi(III) ions. According to our knowledge, an on-line preconcentration system (home-made) has not been used before in the determination of Bi(III) by FAAS.

2. Experimental

2.1. Instrument

A Perkin Elmer (Norwalk, CT, USA) model AAnalyst 800 flame atomic absorption spectrometer equipped with a deuterium background correction system and an air-acetylene burner was used for the determination of bismuth. The wavelength used for bismuth was 223.1 nm. Spectral bandwidth of 0.2 nm, acetylene flow rate of 1.4 L min^{-1}, and nebulizer flow rate of 10.0 mL min^{-1} were conventional working parameters. During the signal measurements, the integration time was 0.1 s.

The flow system comprises a peristaltic pump with variable speed (Watson-Marlow Inc., Wilmington, MA, USA), a multichannel peristaltic pump (Ismatec SA, Glattbrugg, Switzerland) furnished with silicone tubes to deliver all solutions, and two three-way valves (Cole-Parmer Inc. Co., IL, USA) to select solution ways. Peristaltic pumps (PP) and valves (V) were controlled by the five-channel controller and each channel can be set for 36 different timing periods with thumble switches. This unit was constructed in our instrumentation laboratory (at low cost). The flow system was made using fittings, unions and tees made of plastic and high density polyethylene (HDPE) materials. Lewatit TP-207, a weakly acidic, macroporous-type ion exchange resin with chelating iminodiacetate groups packed into a home-made minicolumn (glass, 3.5 cm length and 0.3 cm i.d.) was used for the on-line preconcentration of the bismuth(III) ions.

2.2. Reagents and standard solutions

All the chemicals were of analytical reagent grade and provided by Merck (Darmstadt, Germany). Deionized ultra pure water was used for the preparation of the solutions. 1000 μg mL^{-1} Bi(III) was prepared by dissolving 0.2321 g of $Bi(NO_3)_3{\cdot}5H_2O$ in a 100 mL volumetric flask using 3 mol L^{-1} HNO_3 to prevent hydrolysis of the Bi(III) ions. Dilute working solutions were prepared by appropriate dilutions of the stock solution of Bi(III) with 0.1 mol L^{-1} HNO_3 just before use [12,22]. Nitric acid was also used to adjust the acidity of the solutions and used as eluent throughout the experiments.

Lewatit TP-207 resin with iminodiacetate group was used (Fluka, Buchs, Switzerland) as the solid phase extractant. In order to remove organic and inorganic contaminants, the resin was washed with distilled water, 1 mol L^{-1} HNO_3 in acetone and distilled water, respectively. The glassware used was cleaned by soaking overnight in dilute HNO_3 (1:5, v/v), and then rinsed with distilled water several times.

2.3. Preparation of the minicolumn

The minicolumn was prepared by introducing 135 mg of the chelating resin, as a slurry of the polymer beads using a syringe. The ends of the column were fitted with glass wool to retain the packing material. Before use, ethanol, acetone, 5% (w/v) nitric acid solution and deionized water were passed through the column at a flow rate of 3.0 mL min^{-1} in order to clean it. The resin bed was approximately 3.5 cm length. The packed column was washed with blank solutions to condition the Lewatit TP-207 resin. After each elution, it was automatically pre-treated with deionized water and buffer solution, respectively.

2.4. On-line preconcentration system

The performance of the on-line preconcentration method was tested with model solutions before its application to the samples. The schematic diagram of the programmable on-line system was illustrated in Fig. 1. In the preconcentration step, PP1 and V1 are active while PP2 and V2 are inactive, and the sample and/or standard solutions acidified properly with 0.1 mol L^{-1} HNO_3 were continuously passed through the minicolumn (MC) for 3.4 min at a flow rate of 7 mL min^{-1}. The bismuth was retained on the minicolumn while the effluent was sent to waste. Afterwards, the minicolumn was washed with water in order to remove matrix ions from the resin. At this period, PP1 and V2 are active while PP2 and V1 are inactive. Finally, in the elution step; the eluent (E), 3 mol L^{-1} HNO_3, was aspirated by the PP2 at a flow rate of 7.2 mL min^{-1}. During the elution, PP1 is inactive. The released metal ions are directly

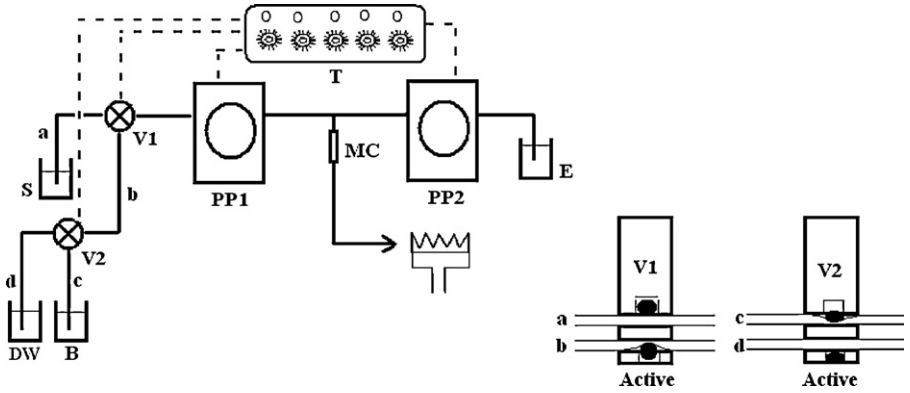


Fig. 1. Schematic diagram of on-line preconcentration system (V1: valve 1, V2: valve 2, PP: peristaltic pump, E: eluent, MC: minicolumn, T: timer, and a–d: solution ways; S: sample, B: buffer, and DW: deionized water).

transported into the nebulizer of the spectrometer. The signals were measured in the peak height mode (or maximum absorbance) using the instrument software. In the following step, the minicolumn was washed with water (PP1 and V2 are active, PP2 and V1 are inactive) to clean the resin. Afterwards, the buffer solution was pumped to the column to condition it before a new preconcentration cycle. During this period, PP1 was active while PP2, V1 and V2 were inactive. Calibration curve was linear for Bi(III) concentrations in the range of 0.1–1.0 μg mL^{-1}, with a correlation coefficient of 0.9996. Real sample solutions were similarly subjected to the on-line procencentration procedure as described above.

2.5. Application of the proposed method

The proposed method was successfully applied to the on-line determination of Bi(III) in tap water, waste water (Kayseri) and dam water samples (Seyhan Dam, Adana), which were collected in polyethylene bottles prewashed before. Tap water samples were taken from our research laboratory and analysed without pre-treatment. The other water samples were filtered through a cellulose membrane filter of 0.45 μm pore size (Millipore Co., MA, USA). 10 mL of concentrated HNO_3 (65%, w/w) and 5 mL of concentrated H_2O_2 (30%, w/w) were added to 100 mL of water samples and then evaporated near to dryness. The final volume was completed to 100 mL with 0.1 mol L^{-1} HNO_3 and the proposed procedure was applied to these sample solutions. Analyses for blank samples were carried out in the same way. Then the on-line preconcentration procedure given above was applied to the samples. The determination of Bi(III) ions in the final solutions was performed by FAAS.

The procedure was also applied for pharmaceutical cream samples. For this purpose, 10 mg of the samples were taken into 100 mL of beakers. The samples were dissolved with 5 mL of HNO_3 (65%, w/w) and evaporated near to dryness on a hot plate in hood. Then 2 mL of concentrated $HClO_4$ was added to the residue and the beakers were covered with glass watches. After the evaporation, the cooled residue was dissolved and made up to 100 mL with 0.1 mol L^{-1} HNO_3 solution. The proposed procedure given above was applied to these sample solutions. Blank analyses were carried out in the same way without the cream samples.

In order to ascertain the validation of the proposed procedure, the method was applied for the analysis of Bi(III) ions in two certified reference materials (TMDA-64 lake water and CWW TMD waste water). 100 mL portions of TMDA-64 lake water and CWW TMD waste water were previously treated with a mixture of 10 mL of HNO_3 (65%, w/w) and 5 mL of H_2O_2 (30%, w/w) and the procedures applied were similar to the preparation of water samples. Then the on-line preconcentration procedure was applied to the samples.

3. Results and discussion

The optimised chemical and hydrodynamic conditions in the flow system were determined by using a solution involving 0.5 μg mL^{-1} bismuth and the preconcentration procedure was applied to the aqueous sample solutions.

3.1. Effect of acidity on preconcentration

In order to evaluate the effect of acidity on the retention of the analyte ions, sample solutions were acidified from 0.025 to 0.5 mol L^{-1} with HNO_3, HCl and H_2SO_4, and processed according to the recommended procedure. The decrease in absorbance at acidity level lower than 0.01 mol L^{-1} HNO_3, is due to the hydrolysis of Bi(III) ions [7]. It is well known that, Bi(III) can only exist in very acidic media and it is hydrolyzed to $BiOH^{2+}$ or BiO^{+} at ≤0.1 mol L^{-1} acidic media. At these media, even insoluble compounds such as

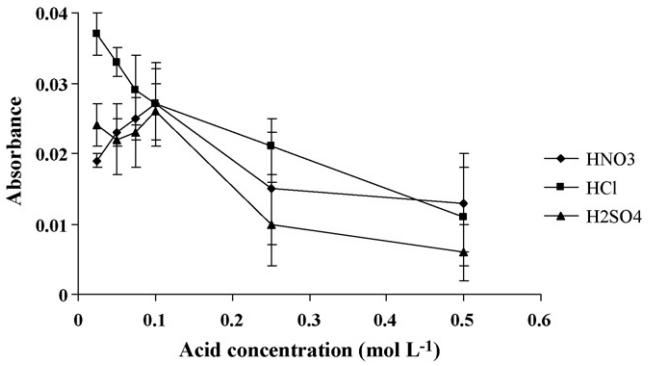


Fig. 2. Effect of acidity on the recovery of bismuth.

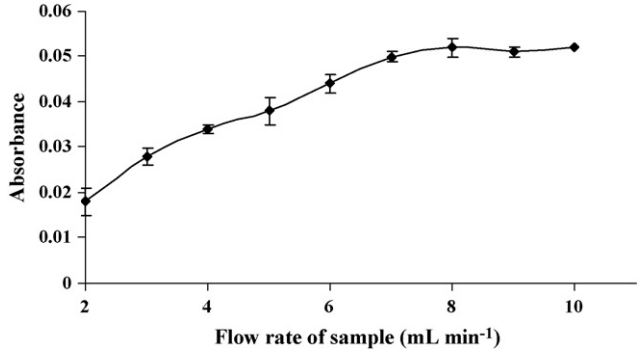


Fig. 3. Effect of sample flow rate on Bi(III) signals.

BiOCl or $BiONO_3$ could be formed [9]. These solutions were pumped through the minicolumn packed with the resin for a loading time of 3.4 min. Subsequently, the retained bismuth ions were eluted with 3.0 mol L^{-1} HNO_3 and then introduced to the nebulizer of FAAS. The corrected absorbances for bismuth as a function of the acidity are shown in Fig. 2. In the light of these results, the optimum acidity of the medium for the determination of Bi(III) was chosen 0.1 mol L^{-1} HNO_3 [7].

3.2. Flow rates of sample and elution solutions

The sample flow rate is an important parameter in on-line systems because it affects the retention of the cation on the minicolumn. At high flow rates of sample, metal ions could probably not equilibrate properly with the resin due to the increase in the velocity of the ions, which reduces the contact time between the two phases. In contrast, low flow rates decrease the sample throughput, resulting in long analysis times. For this reason, the effect of

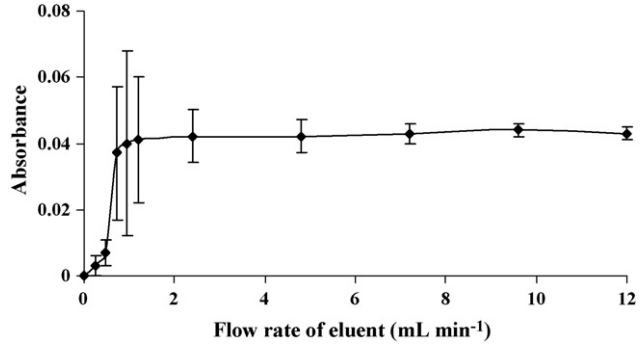


Fig. 4. Effect of eluent flow rate on Bi(III) signals.

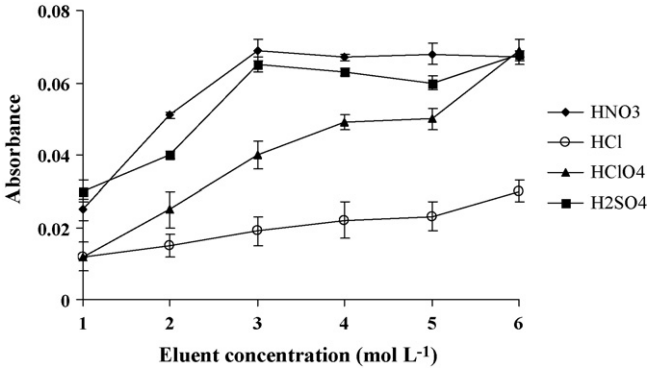


Fig. 5. Effect of eluent type and concentration on Bi(III) signals.

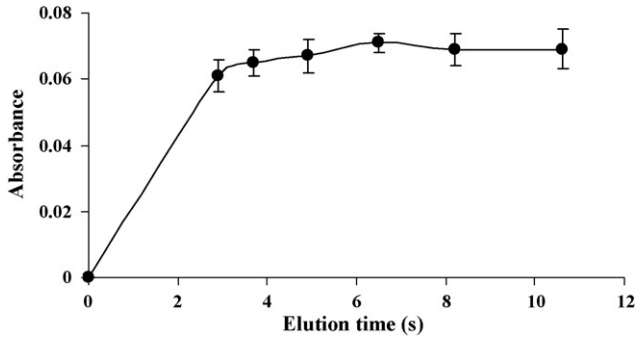


Fig. 6. Effect of elution time on Bi(III) signals.

sample flow rate on the sorption of bismuth was investigated. The results are illustrated in Fig. 3. The sample flow rate was nearly constant over 7 mL min^{-1}. Consequently, the optimum flow rate of sample was chosen to be 7 mL min^{-1} in subsequent experiments as a compromise between efficiency and stability.

The eluent flow rate is an important parameter for stripping the analytes off the column. In order to get an analytical signal as high as possible, the eluent flow rates were scanned. The scanning was carried out from 0.25 to 12 mL min^{-1}. The fluctuations of the analytical signal were too high at the eluent flow rates below the 5 mL min^{-1}, i.e., the repeatability decreased considerably resulting in broader and splitted peaks. This probably is due to an incompatibility between elution and nebulization flow rates, which causes significant dispersion when the eluent flow rate is smaller than the nebulizer flow rates. The optimum flow rate was selected to be 7.2 mL min^{-1}, corresponding to a certain rpm rate of the pump, for subsequent studies in order to match the elution and the nebulization flow rates. The results are shown in Fig. 4.

Table 1
Maximum tolerable quantities of foreign ions in the determination of 0.5 μg mL^{-1} Bi(III) using the on-line preconcentration system.

Ions	Added as	Tolerable concentration (mg L^{-1})	Recovery (%)
Na^+	$NaNO_3$	25,000	98 ± 1
K^+	KNO_3	7500	99 ± 2
Ca^{2+}	$Ca(NO_3)_2{\cdot}4H_2O$	4000	99 ± 2
Mg^{2+}	$Mg(NO_3)_2{\cdot}6H_2O$	5000	98 ± 1
Zn^{2+}	$Zn(NO_3)_2$	70	96 ± 1
Pb^{2+}	$Pb(NO_3)_2$	50	100 ± 2
Fe^{3+}	$Fe(NO_3)_3{\cdot}6H_2O$	50	101 ± 1
Cl^-	NaCl	1000	100 ± 1
SO_4^{2-}	Na_2SO_4	1500	101 ± 3
$H_2PO_4^-$	$NaH_2PO_4{\cdot}2H_2O$	1000	95 ± 1

Table 2
The determination of bismuth in the standard reference materials after the application of the presented procedure (N = 3).

Reference material	Certified value (μg mL^{-1})	Found (μg mL^{-1})	Recovery (%)
TMDA-64 (lake water)	0.142 ± 0.028	0.140 ± 0.005[a]	98.6 ± 1.0
CWW-TM-D (waste water)	Not certified	–	–
	0.5 added	0.510 ± 0.010	102.0 ± 1.0

[a] At 95% confidence level (mean ± $ts/\sqrt{N}$).

Table 3
The concentration of bismuth in the various samples (μg g^{-1}).

Sample	Bi content (μg g^{-1})	Found (μg g^{-1})	RSD (%)
Cream 1	265	210 ± 9[a]	4.2
Cream 2	106	120 ± 4	3.0

[a] At 95% confidence level (mean ± $ts/\sqrt{N}$).

3.3. Effects of eluent type and elution time

The desorption of the retained bismuth ions from the minicolumn was tested using HCl, HNO_3, H_2SO_4, and $HClO_4$ solutions. The results obtained are shown in Fig. 5, from which it is clear that 3 mol L^{-1} HNO_3 solution is the best eluent. Increasing of HNO_3 concentration from 3 to 6 mol L^{-1} did not give any improvement on the bismuth signals. Therefore, 3 mol L^{-1} HNO_3 was chosen as eluent for stripping off Bi(III) from the column in subsequent experiments.

The elution time is important for quantitative recovery of the analyte. For that reason, the effect of the elution time was studied. When the elution time is taken short, the elution volume will be small. In this case, the analytical signals will also be low due to the insufficient elution of the retained Bi(III) ions. The influence of this parameter on the analytical signals of bismuth is shown in Fig. 6. The optimum elution time for quantitative recovery of bismuth ions was 6.5 s at the optimum speed of the peristaltic pump.

3.4. Sorption capacity of the resin

The sorption capacity of the resin for the analyte ions was determined through the recommended procedure by equilibrating 135 mg of the resin with 0.1–20 μg mL^{-1} Bi(III) in 0.1 mol L^{-1} HNO_3 medium. The resin capacity was found to be 2.6 mg Bi(III) per gram resin.

3.5. Analytical figures of merit

The characteristic data for the performance of the on-line preconcentration system under the optimum conditions were studied. Linear regression equations were obtained for calibration curve, i.e.,

Table 4
Determination of Bi(III) in natural water and pharmaceutical cream samples (N = 3).

Sample	Added (μg mL^{-1})	Found (μg)	Recovery (%)
Tap water	–	–	–
	0.50	0.51 ± 0.02[a]	102 ± 2
Dam water	–	–	–
	0.50	0.49 ± 0.02	98 ± 2
Waste water	–	–	–
	0.50	0.48 ± 0.06	96 ± 1
Cream 1	–	0.42 ± 0.02	–
	0.50	0.93 ± 0.03	102 ± 2
Cream 2	–	0.96 ± 0.02	–
	0.50	1.45 ± 0.04	98 ± 4

[a] At 95% confidence level (mean ± $ts/\sqrt{N}$).

Table 5
Comparison of the characteristic data from the recent published articles.

Anaytes	Adsorbent or reagent	Technique	DL ($\mu g\,L^{-1}$)	RSD (%)	PF	Reference
Bi	Silica gel modified cyanex 3001	GFAAS	0.01	1.5	20	[2]
Bi	Amberlite IRA-410	FI- GFAAS	0.225	1.55–0.85	–	[4]
Bi, Cd	Chromosorb-107	GFAAS	0.8	2.0	10	[5]
Bi	XAD-2	Stripping voltametry	0.14	1.2	110	[6]
Bi	Activated carbon	UV–VIS	8×10^{-10} mol L^{-1}	2.2–3.1	250	[7]
Bi	Methylthymol Blue	UV–VIS	250	1.1	–	[12]
Bi	Lewatit TP-207	FI-FAAS	2.75	3.0	20	This work

$A = 0.00024 + 0.13 \times C$, where A is the absorbance and C is the Bi(III) concentration in the standard solution.

Enrichment factor was found to be 20. The detection limit as the concentration that gives a response equivalent to three times the standard deviation for the blank solutions ($n = 21$) was 2.75 $\mu g\,L^{-1}$. The precision (relative standard deviation, R.S.D.) was 3.0%, for the concentration of 0.4 $\mu g\,mL^{-1}$ Bi(III).

3.6. Effect of foreign ions

The effect of interferences on the determination of bismuth was investigated using the optimized on-line preconcentration system. Metal ions were added individually to model solutions containing 0.5 $\mu g\,mL^{-1}$ Bi(III) and then the proposed procedure was applied. The effect of each species was considered as interference when the analytical signal in the presence of the species resulted in an absorbance deviation of more than ±5%. The results are shown in Table 1. The results indicate that various substances commonly present in water and/or wastewater samples do not interfere in the analysis of bismuth(III) under the experimental conditions.

3.7. Accuracy of the method

The accuracy of the developed method was tested by measuring the bismuth content in the two certified reference materials (TMDA-64 lake water and CWW-TM-D waste water). The samples were digested using the procedure described in Section 2.5. The bismuth contents established with the present procedure agreed very well with the certified values (Table 2). The results indicate that the developed procedure can be applied to the determination of bismuth in the reference water samples being free from interference.

3.8. Application of the proposed procedure

The method was extended for the on-line determination of Bi(III) in various pharmaceutical cream samples. Preparation of the pharmaceutical cream samples to analysis was performed as described above in Section 2.5. The results are shown in Table 3.

The proposed method was applied to the analysis of various water samples, with satisfactory results for bismuth. The concentration of bismuth could not be determined due to its very low concentration. The recoveries for the additions of 0.5 $\mu g\,mL^{-1}$ Bi(III) varied from 96% to 102% (see Table 4). These results prove the validity of the proposed method. There was a good agreement between the added and the recovered amounts of the analyte.

4. Conclusions

An on-line preconcentration system using Lewatit MonoPlus TP-207 chelating resin has been successfully applied to the determination of bismuth by FAAS. Due to its high tolerance to interferences from the matrix, the proposed procedure has been demonstrated to be promising for trace bismuth analysis.

The relative standard deviation and preconcentration factor of the method were found satisfactory, i.e., 3% and 20, respectively. The elution was easily performed with 3 mol L^{-1} HNO_3. The method has a linear range from 0.1 to 1.0 $\mu g\,mL^{-1}$ Bi(III). Advantages of this method are: (a) low cost, (b) simplicity, (c) rapidity, (d) studying in acidic medium required for Bi(III) separation/preconcentration, and (e) all processes are made automatically by the system itself. The proposed method shows very good sensitivity and precision and some has good advantages over the other preconcentration methods reported in the literature. A comparison of the described method with the other preconcentration methods for bismuth is given in Table 5. As can be seen from the table, our results are comparable with the others. The developed method is probably one of the earlier works for the on-line determination of bismuth by FAAS.

References

[1] H. Matusiewicz, M. Krawczyk, Chem. Anal. (Warsaw) 52 (2007) 565.
[2] Y. Yamini, M. Chaloosi, H. Ebrahimzadeh, Talanta 56 (2002) 797.
[3] C.G. Magalhães, B.R. Nunes, M.B.O. Giacomelli, J.B.B. da Silva, J. Anal. Atom. Spectrom. 18 (2003) 787.
[4] P. Carrero, L. Gutiérrez, C. Rondón, J.L. Burguera, M. Burguera, Y.P. de Peña, Talanta 64 (2004) 1309.
[5] N. Tokman, S. Akman, Anal. Chim. Acta 519 (2004) 87.
[6] M.A. Taher, E. Rezaeipour, D. Afzali, Talanta 63 (2004) 797.
[7] T. Madrakian, A. Afkhami, A. Esmaeili, Talanta 60 (2003) 831.
[8] F. Cui, L. Wang, Y. Cui, J. Pharma. Biomed. Anal. 43 (2007) 1033.
[9] Z. Marczenko, Separation and Spectrophotometric Determination of Elements, Ellis Horwood, London, 1986.
[10] H.S. Zhang, J.A. Zhang, H. Wang, X.Y. Li, Anal. Chim. Acta 380 (1999) 101.
[11] S. Hoshi, N. Notoya, M. Uto, M. Matsubara, Anal. Sci. 7 (1991) 657.
[12] P.D. Tzanavaras, D.G. Themelis, A. Economou, Anal. Chim. Acta 505 (2004) 167.
[13] O. Acar, Z. Kılıç, A.R. Türker, Anal. Chim. Acta 382 (1999) 329.
[14] A. Marrow, G. Witshire, A. Huvsthous, Atom. Spectrosc. 18 (1997) 23.
[15] M.V. Hinds, D.C. Grégoire, E.A. Ozaki, J. Anal. Atom. Spectrom. 12 (1997) 131.
[16] P. Ostapczuk, Anal. Chim. Acta 273 (1993) 35.
[17] R.D. Ye, S.B. Khoo, Electroanalysis 9 (1997) 481.
[18] C.M. Wang, O.Y. Sun, H.L. Li, Electroanalysis 9 (1997) 645.
[19] T. Ferri, S. Paci, R. Morabito, An. Chim. (Rome) 86 (1996) 595.
[20] R.S. Praveen, G.R.K. Naidu, T. Prasada Rao, Anal. Chim. Acta 600 (2007) 205.
[21] S. Vicente, N. Maniasso, Z.F. Queiroz, E.A.G. Zagatto, Talanta 57 (2002) 475.
[22] D.G. Themelis, P.D. Tzanavaras, J.K. Papadimitriou, Analyst 126 (2001) 247.

Talanta 80 (2010) 2132–2140

Contents lists available at ScienceDirect

Talanta

journal homepage: www.elsevier.com/locate/talanta

Nitrite sensor based on multilayer film of Dawson-type tungstophosphate α-$K_7[H_4PW_{18}O_{62}]\cdot 18H_2O$ immobilized on glassy carbon

Malika Ammam[a,b,*], Bineta Keita[a], Louis Nadjo[a], Jan Fransaer[b]

[a] Laboratoire de Chimie Physique, UMR 8000, CNRS, Université Paris-Sud, Bâtiment 350, 91405 Orsay Cedex, France
[b] Department of Metallurgy and Materials Engineering (MTM), K.U. Leuven, Kasteelpark Arenberg 44, B-3001 Heverlee, Belgium

ARTICLE INFO

Article history:
Received 6 July 2009
Received in revised form 30 October 2009
Accepted 5 November 2009
Available online 13 November 2009

Keywords:
Nitrite sensor
Dawson-type tungstophosphate
α-$K_7[H_4PW_{18}O_{62}]\cdot 18H_2O$
Layer by layer assembly process

ABSTRACT

A nitrite sensor based on immobilized Dawson-type tungstophosphate α-$K_7[H_4PW_{18}O_{62}]\cdot 18H_2O$ (PW_{18}) in multilayers of charged polyelectrolyte poly(allylamine hydrochloride) (PAH) on a glassy carbon electrode is described. A nitrite sensor manufactured with 10 layers has a sensitivity of ~4 nA/μM nitrite, fast response time (<6 s), low detection limit (~0.1 μM), high selectivity towards endogenous interferences such as nitrate and molecular oxygen, a linear range from 0.1 μM to at least 20 mM nitrite and was stable for at least 2 months. In addition, such nitrite sensors can operate in a pH range from 1 to 9, and the sensitivity can be increased by increasing the number of layers at the expense of increasing the response time.

© 2009 Elsevier B.V. All rights reserved.

1. Introduction

Nitrite is a key species in the global nitrogen cycle. It is present in soils, waters, foods and physiological systems. Nitrite is used in meat curing [1–2] and as food preservative against poisoning by microorganisms such as clostridium botulinum [3]. Nitrites are known to react with amines forming nitrosamines, which are known to be carcinogenic [4–6]. Furthermore, when nitrite is present at high concentration in blood, they can react with the iron(III) of the hemoglobin, forming methemoglobin, which has no oxygen carrying ability; this medical condition is called methemoglobinemia or "blue baby syndrome" [7]. Therefore, nitrite with its potential toxicity has intrigued many specialists [8]. The environmental impact caused by the build-up of nitrite, due to the widespread use of fertilizers, and the problems caused by the contamination of water sources for human consumption are the driving force for research in this area [9]. Thus, the precise determination of nitrite is important for environmental reasons and for public health. Hence, many methods have been developed for nitrite determination including spectrophotometry [10], chromatography [11] and electrochemical methods [12–28]. Electrochemical detection methods are advantageous over the other methods in terms of cost and time.

Electrochemical determination of nitrite is reported in literature either by reduction or oxidation. An important point is that nitrite is electroactive at carbon electrodes. However, its reduction or oxidation requires undesirably high overvoltages [29–31]. Oxidative determination is preferable because reduction of nitrite is known to suffer from interferences such as reduction of nitrate and molecular oxygen [32]. In order to improve the sensitivity and the selectivity of the detection of nitrite, the operating potentials should be lowered and the oxidation or reduction currents should be increased. This can be achieved by modifying the surface of electrodes with suitable electrocatalysts.

Wells–Dawson heteropolytungstates belong to a class of polyoxometalates (POMs) which have been reported to show efficient electrocatalytic reduction toward nitrite, nitrate and molecular oxygen [33–35]. Some POMs, more particular α-$K_7[H_4PW_{18}O_{62}]\cdot 18H_2O$, have electrocatalytic properties toward nitrite without showing any catalytic activity toward nitrate [33,36]. In addition, our studies showed that α-$K_7[H_4PW_{18}O_{62}]\cdot 18H_2O$ has no catalytic activity towards molecular oxygen. This is important for the selective determination of nitrite because it eliminates the major interferences such as nitrate and molecular oxygen. For this reason, this complex was selected as a potential candidate for nitrite sensing. The complex was immobilized on the detector electrode using layer by layer (LBL) deposition. LBL deposition offers significant analytical advantages including good stability, reproducibility and ease of manufacturing [37–39]. Details relevant for the detection and electrocatalysis of nitrite have been reported using various types of POMs [40–43]. However, these studies did not focus on the use of POM modified electrodes for the accurate determination of nitrite.

* Corresponding author at: Department of Metallurgy and Materials Engineering (MTM), K.U. Leuven, Kasteelpark Arenberg 44, B-3001 Heverlee, Belgium.
Tel.: +32 16321260; fax: +32 16321991.
E-mail address: Malika.Ammam@mtm.kuleuven.be (M. Ammam).

0039-9140/$ – see front matter © 2009 Elsevier B.V. All rights reserved.
doi:10.1016/j.talanta.2009.11.020

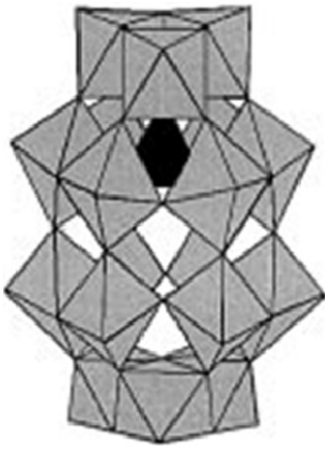


Fig. 1. Structure of the anion $[H_4PW_{18}O_{62}]^{7-}$.

The present work reports the development of an efficient and stable sensor for nitrite determination based on LBL immobilized α-$K_7[H_4PW_{18}O_{62}]\cdot 18H_2O$ (PW_{18}). The deposited films were investigated using cyclic voltammetry and amperometry. The electrochemical behavior of dissolved and immobilized PW_{18} was compared, the effect of the number of layers, scan rate, and pH were investigated. The electrocatalytic properties of the modified electrode toward nitrite reduction were demonstrated. The ability of the sensor for nitrite detection in real samples was examined by the amperometric determination of nitrite in tap water.

2. Experimental

2.1. Materials

Ultrapure milliQ water with a resistance of 18.2 MΩ cm was used for all the experiments. α-$K_7[H_4PW_{18}O_{62}]\cdot 18H_2O$ (PW_{18}) was synthesized and characterized following the procedure reported by Mbomekalle et al. [36]. The structure of the complex is shown in Fig. 1. Triton X-405, 3-aminopropyltriethoxysilane (ATS) 99%, poly(sodium 4-styrenesulfonate) (PSS) (MW 70,000), poly(allylamine hydrochloride) (PAH) (MW 15,000) were purchased from Aldrich. H_2SO_4, Li_2SO_4, LiCl, HCl, LiOH, CH_3COOLi, CH_3COOH, tris(hydroxylmethyl)aminomethane (trisH$^+$) analytical grade were purchased from Sigma–Aldrich or Acros Organic. Glassy carbon rod 3 mm in diameter was purchased from Alfa Aesar.

2.2. Methods and equipment

The electrochemical setup was an EG&G 273 potentiostat connected to a computer for data acquisition. The solutions were deaerated thoroughly for at least 30 min with pure argon and kept under a positive argon pressure during the experiments. A three compartment electrochemical cell was used. The side arms contained the saturated calomel reference electrode (SCE) and a platinum counter electrode with a surface area of approximately 1 cm^2. The reference and the counter electrodes were separated from the test solution by a fine and medium porosity ceramic, respectively. The working electrode which is also the nitrite sensor was a glassy carbon electrode (3 mm diameter, surface area ~7 mm^2). The glassy carbon rod was electrically connected to a copper wire with silver epoxy, encapsulated in epoxy resin and cured for 24 h. The surface of the glassy carbon electrode (GCE) was prepared by grinding with emery paper followed by polishing with 6, 3 and 1 μm diamond then abundantly rinsed with ultrapure water and dried.

2.3. Sensor preparation

The cleaned and well-dried GCE was first treated with pure ATS under nitrogen atmosphere for 10 min in a glove box, then removed and rinsed immediately with ultrapure water and dried under flowing nitrogen. It is observed that this treatment with ATS is important to increase the deposition rate of the POM. In other words, the electrodes prepared without ATS; by deposition of PAH as a first layer on the GCE electrode surface showed a very low deposition rate. The presence of the amine groups in ATS makes probably the electrode positively charged (see Fig. 2). The GCE/ATS was first immersed in acetate buffer solution pH 4 (1 M $CH_3COOLi + CH_3COOH$) containing 35 mg PSS/0.5 mL buffer (10^{-3} M) for 10 min. Thanks to the presence of sulfonate groups in PSS, this layer was found to be important for the deposition of a negative layer on which the PAH positively charged polyelectrolyte will deposit, and because of the presence of the aromatic rings in PSS, this may enhance the electron transfer between the immobilized PW_{18} and the carbon electrode. The GCE/ATS/PSS was rinsed with ultrapure water, dried under flowing nitrogen then immersed in a second acetate buffer solution pH 4 containing 10^{-3} M PAH (7.5 mg PAH in 0.5 mL buffer) for 10 min to provide a stable, positively charged surface to which the anion $[H_4PW_{18}O_{62}]^{7-}$ (PW_{18}) can be bound electrostatically. It was observed that addition of a small amount of Triton X-405 to the PAH solution ($\pm 10^{-5}$ M) increases the electrocatalytic activity of the film. This is perhaps due on the one hand to the presence of the aromatic ring in Triton X-405 which leads to a better electron transfer between the immobilized POM and the carbon electrode and, on the other hand, the long hydrocarbon chain of Triton X-405 may increase also the pore size of the deposited film, thus increasing the transport phenomena within the film. The GCE/ATS/PSS/PAH was immersed in 5×10^{-4} M PW_{18} in acetate buffer solution (pH 4) for 10 min. The electrode was then rinsed with ultrapure water and dried under a nitrogen stream. This procedure (POM/PAH) was repeated several times to permit the formation of multiple layers of POM on the GCE. The sensor was then stored under air at room temperature. Fig. 2 displays a schematic representation of the different layers of the PW_{18}/LBL film.

3. Results and discussion

3.1. Redox behavior of PW_{18}/LBL film

It has been reported that the complex PW_{18} is stable in the pH range of 0–4 [36]. We have observed that incorporation of this complex in LBL films increases the pH stability up to pH 12. In other words, no change in the shape of the cyclic voltammogram, current intensities or peak potentials of the PW_{18}/LBL film was observed when the modified electrode was tested at higher pH (pH > 4) and for long periods of time. This increase in the pH range stability of POMs encapsulated in LBL films has been reported elsewhere [44–45]. The encapsulation of the POM between two PAH layers prevents probably its decomposition at high pH, thus increasing its stability. Fig. 3 shows a comparison between the cyclic voltammogram of the dissolved and immobilized PW_{18} in LBL films of 2-POM layers (Fig. 3A) and 10-POM layers (Fig. 3B) in media of pH 1.2. In the domain of the explored potentials of Fig. 3A, the dissolved PW_{18} displays three merged quasireversible redox wave located respectively at $E_{pc} = -0.241$, -0.485 and -0.744 V vs. SCE. These redox waves correspond to the reduction of the tungsten centers within the POM. Immobilized in LBL film of 2-POM layers, PW_{18} displays a close similar electrochemical behavior for the two last redox waves. However, a slight decomposition in the redox process of the first wave can be observed, which disappears for LBL films with high number of layers as shown in

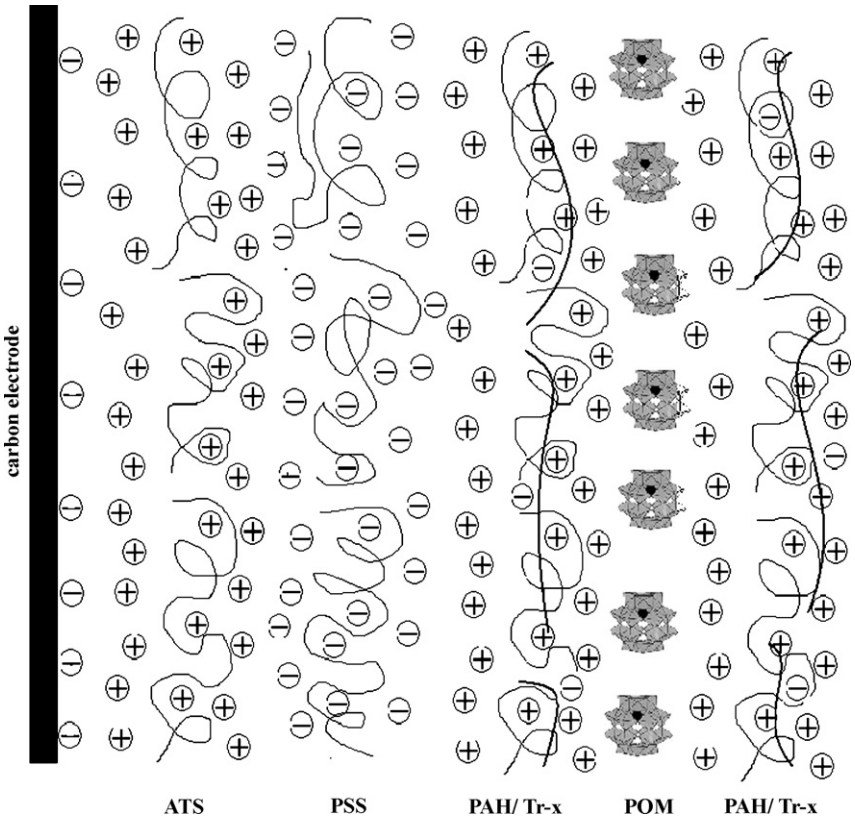


Fig. 2. Schematic cross-section of the POM/LBL film with one monolayer of PW_{18}. ATS: 3-aminotrimethoxysilane, PSS: poly(sodium 4-styrenesulfonate), PAH/Tr-x: poly(allylamine hydrochloride)/Triton X-405, POM: $[H_4PW_{18}O_{62}]^{7-}$.

Fig. 3B. It can be seen that the cathodic peak potentials of the dissolved and immobilized PW_{18} lie at the same potentials. This is related to the presence of a small amount of Triton X-405 in the film. In fact, the PW_{18}/LBL films prepared without Triton X-405 added to the PAH solution showed a shift of the cathodic peak potential to more negative values by about 8 mV. The presence of the aromatic ring in Triton X-405 probably leads to a better electron transfer between the immobilized PW_{18} and the carbon electrode, thus reducing the shift in potentials. According to Fig. 3B, immobilization of PW_{18} in LBL films of 10-POM layers, improves the reversibility of the redox process. The difference between the anodic and the cathodic peak potentials (ΔE_p) of the dissolved and immobilized PW_{18} reduces from 142 mV for dissolved to 41 mV for immobilized PW_{18}. For dissolved PW_{18}, it has been reported that the first redox wave is a two-electron transfer [36]. However, it is difficult to know the number of electrons transferred during the redox process of PW_{18} immobilized in LBL film. Controlled potential coulometry is not recommended for this kind of films because of the absence of an accurate concentration of the immobilized species. However, from the slight separation in the redox process of the first wave observed at low number of layers (Fig. 3A) and/or scan rates (2 mV/s) might indicate a two-electron process for the immobilized PW_{18}. As a matter of fact, it is observed that when PW_{18}/LBL film of 10-POM layers (Fig. 3B) was scanned at a low scan rate (e.g. 2 mV/s) a slight separation in the redox wave appears. It is believed that the merging of the redox waves observed at higher number of layers or scan rates is due to charge equilibrium within the film. In other words, when the deposited PW_{18}/LBL film is thin, the diffusion of ions through the film to insure charge neutrality is fast. However, when the film is thicker, the diffusion becomes slower. This also explains the effect of scan rate: at low scan rates, the electrochemical reduction of the immobilized PW_{18} will be slow and because the diffusion of the ions through the thicker film is slow, this will ensure adequate charge equilibrium.

The effect of the number of layers on the variation of the cyclic voltammogram on the first redox wave was investigated. As can be seen from Fig. 4A, the current response increases with number of the POM layers (curves from inside to outside: $n = 2, \ldots, 10$, respectively). In fact, the cathodic and anodic peak currents increase linearly with the number of layers (Fig. 4B). This demonstrates that equal amounts of PW_{18} are adsorbed in each layer, and implies that the thickness of the deposited film increases linearly with the number of layers.

Fig. 5A shows the variation of the cyclic voltammogram of the first redox wave of PW_{18}/LBL film of 10-POM layers with the scan rate (curves from inside to outside: $\nu = 10, \ldots, 100$ mV/s, respectively). The variation of the anodic and cathodic peak currents with scan rate is shown in Fig. 5B. It can be seen that the peak currents increase linearly with the scan rate up to 100 mV/s. This demonstrates that the redox process of the immobilized complex PW_{18} in LBL film are fast and not diffusion limited but surface-confined electron transfer processes [46,47]. Therefore, the surface coverage Γ of PW_{18} anions in the film can be estimated by Eq. (1), which is dealing with a reversible but nonideal redox process [48]:

$$\Gamma = \frac{I_p RT[4 - 2\delta\Gamma]}{n^2F^2\nu A} \cong \frac{4I_p RT}{n^2F^2\nu A} \quad (1)$$

where I_p is the peak current, δ is the interaction term, n is the number of electrons transferred per electroactive species, ν is the scan rate and A is the surface area of the electrode. Inspection of Eq. (1) and the plot of I_p vs. ν indicates that $2\delta\Gamma \ll 4$ [49]. The surface coverage of PW_{18} anions can be directly calculated from the peak current I_p because polyelectrolyte matrix is not electroactive. Based on the fact that the same amount of PW_{18} is deposited in each deposition cycle, as shown by cyclic voltammetry, the average surface con-

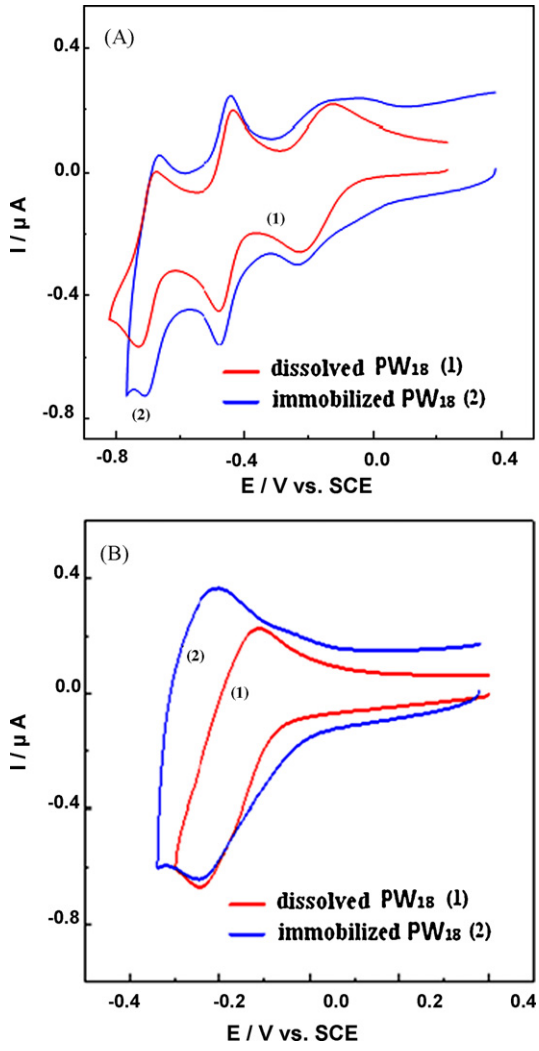


Fig. 3. Comparison between the cyclic voltammograms of dissolved (~10^{-4} M) and immobilized PW_{18}: (A) in the potential range of the three redox waves (LBL film of 2-POM layers) and (B) in the potential range of the first redox wave (LBL film of 10-POM layers). Electrolyte pH 1.2 (0.5 M $Li_2SO_4 + H_2SO_4$), scan rate 10 mV/s, reference electrode SCE.

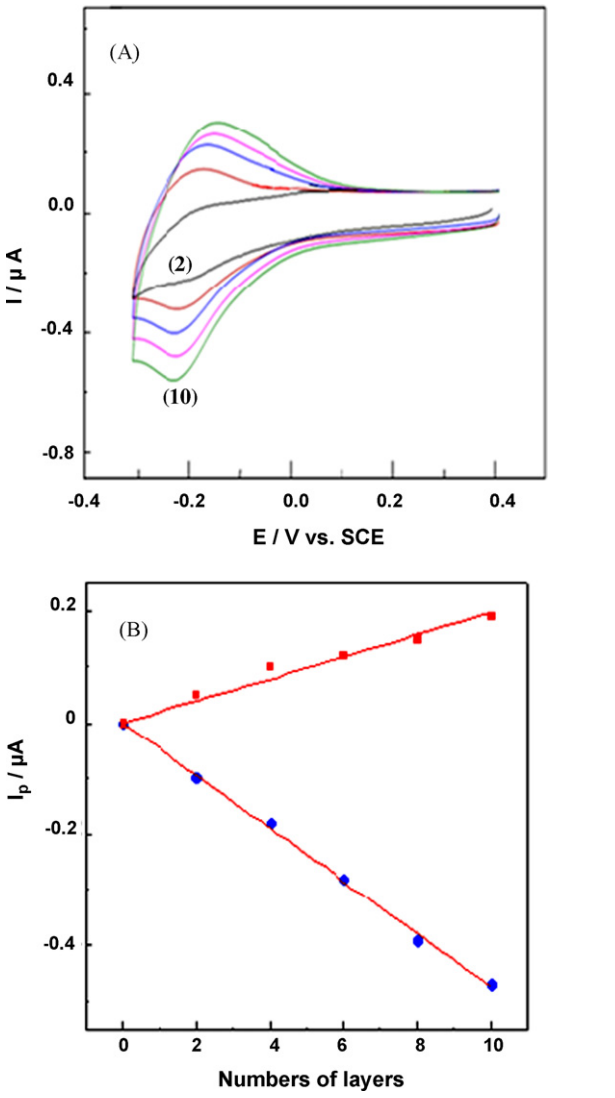


Fig. 4. (A) Variation of the cyclic voltammetry curve of PW_{18} with number of layers (2- to 10-POM layers). (B) Cathodic and anodic peak currents as a function of number of layers of PW_{18}/LBL film. Electrolyte pH 1.2 (0.5 M $Li_2SO_4 + H_2SO_4$), scan rate 10 mV/s, reference electrode SCE.

centration of PW_{18} anions per layer equals 2.95×10^{-11} mol cm^{-2} or 5.5 nm^2/PW_{18}. From structural X-ray analysis [50], the lateral dimensions of the cluster are 2.2 nm × 1.4 nm × 2.2 nm or a mean spherical diameter of 1.9 nm. Hence the projected surface area of PW_{18} is estimated to be 3.6 nm^2, which is close to the electrochemically determined surface coverage corresponding to a submonolayer.

The effect of pH on the redox behavior of immobilized PW_{18} was investigated for the LBL film of 10-POM layers. Fig. 6 illustrates the cyclic voltammograms of the immobilized PW_{18} at pH 1.2 and 4. A slight shift of the redox potentials to negative values is observed at higher pH. This is common in polyoxometallates, where the uptake of protons during reduction of the POM (PW_{18}) is to avoid charge concentration on the POM (accumulation of electrons) [51]. However, the shift in potentials due to variation of pH is surprisingly low. The cathodic peak potential shifts only by 70 mV for a pH variation of almost 3 units (or ~25 mV/pH unit). Similar behavior was reported for dissolved PW_{18} (in diffusion) and was explained by the low acidity of PW_{18} compared to other Wells–Dawson polyoxometallates [36]. Also, no significant separation in the redox wave was observed at pH 4 for the immobilized PW_{18}, while for the dissolved PW_{18}, the single two-electron wave splits into two one-electron waves [36]. This might be due to the microenvironment that the immobilized species experience inside the film [52] and especially as previously mentioned that the number of layers is also playing an important role in the merging in the redox wave. On the other hand, a decrease in the peak currents can be observed at pH 4 compared to pH 1.2, which can be explained by a slow penetration of protons to the surface of the electrode to maintain charge neutrality [53]. Finally, it is known for POMs that multiple electron uptake occurs generally through ECE, EEC and/or disproportion processes, in which the usual chemical steps are protonations [54]. The low dependence of the redox process of PW_{18}/LBL film (10-POM layers) towards the change in pH, may be explained through an EEC process as follows:

$$PW_{18}/LBL + 1e^- \Leftrightarrow PW_{18}^{\bullet -}/LBL \quad (2)$$

$$PW_{18}^{\bullet -}/LBL + 1e^- \Leftrightarrow PW_{18}^{2-}/LBL \quad (3)$$

$$PW_{18}^{2-}/LBL + 2H^+ \Leftrightarrow H_2PW_{18}/LBL \quad (4)$$

In summary, the observation of one merged redox wave for the first redox process and the apparition of the reduction process at less negative potentials are encouraging and constitute favorable conditions for electrocatalytic processes.

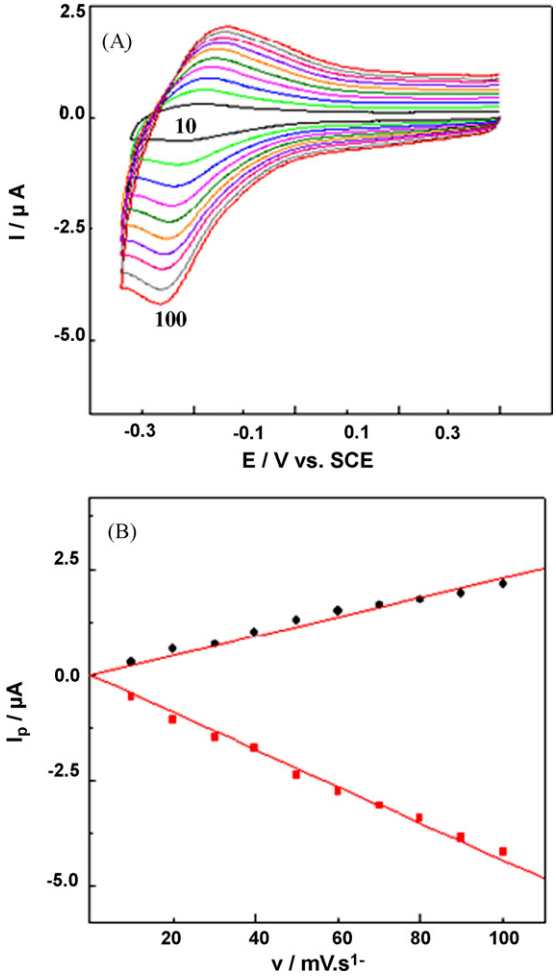


Fig. 5. (A) Variation of the cyclic voltammogram of PW_{18}/LBL film of 10-POM layers with scan rate. (B) Relationship between cathodic and anodic peak currents and scan rate. Electrolyte pH 1.2 (0.5 M $Li_2SO_4 + H_2SO_4$), reference electrode SCE.

3.2. Electrocatalytic reduction of nitrite by PW_{18}/LBL film

It has been reported that the PW_{18} complex catalyzes only the reduction of nitrite [36] and does not show catalytic activity toward the reduction of nitrate and, our experiments showed that this complex has no catalytic properties towards molecular oxygen,

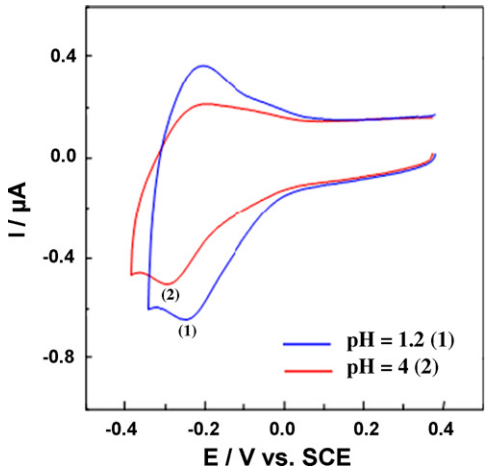


Fig. 6. Cyclic voltammograms of PW_{18}/LBL film of 10-POM layers at pH 1.2 and 4. Electrolytes: pH 1.2 (0.5 M $Li_2SO_4 + H_2SO_4$) and pH 4 (1 M $CH_3COOLi + CH_3COOH$), scan rate 10 mV/s, reference electrode SCE.

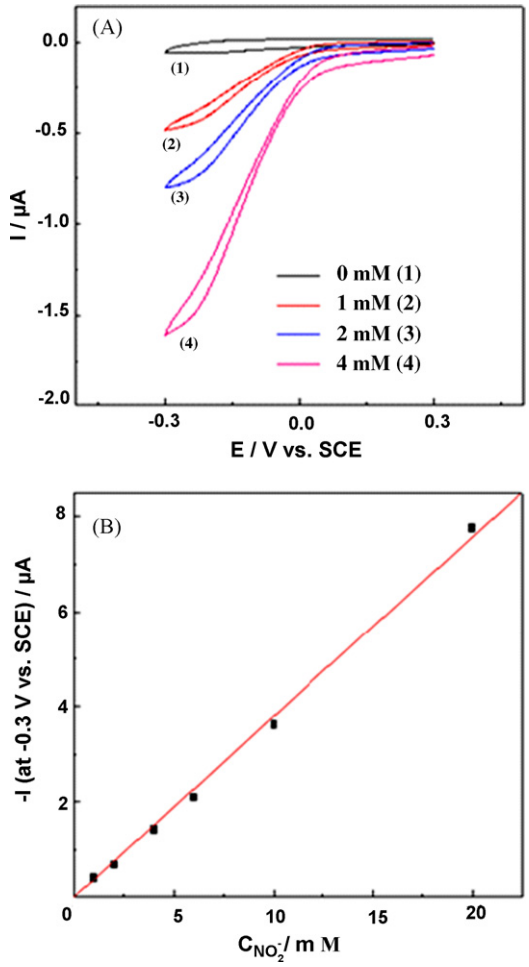


Fig. 7. (A) Cyclic voltammograms showing the catalytic activity of PW_{18}/LBL film (2-POM layers) at different nitrite concentrations. (B) Relationship between the catalytic current and nitrite concentrations at −0.3 V vs. SCE. Electrolyte pH 1.2 (0.5 M $Li_2SO_4 + H_2SO_4$), scan rate 2 mV/s, reference electrode SCE.

which are the two most important interferences for reduction-based nitrite sensors [32]. This is important for the selectivity of PW_{18}-based nitrite sensors. The behavior of the PW_{18}/LBL modified electrode towards the electrocatalytic reduction of nitrite was examined in detail. Fig. 7A shows the voltammetric behavior of PW_{18} immobilized in LBL film of 2-POM layers towards the reduction of nitrite at pH 1.2. At this pH, the active species could be HNO_2 and/or NO, as HNO_2 disproportionates in fairly acidic solution:

$$3HNO_2 \rightarrow HNO_3 + 2NO + H_2O \quad (5)$$

The rate of reaction (5) is known to be low. In the potential range of Fig. 7A, no direct reduction of nitrite on glassy carbon could be observed [34,55]. In addition, as can be seen from Fig. 8A, which compares the cyclic voltammetry curves of the GCE, GCE/ATS, GCE/ATS/PSS and GCE/ATS/PSS/PAH in presence of 4 mM nitrite, no catalytic activity of the LBL multilayer film without PW_{18} present towards nitrite can be observed. However, as can be seen from Fig. 7A, in presence of PW_{18} immobilized in the LBL film, the addition of nitrite (NO_2^-) leads to a large cathodic current enhancement that increases as the concentration of nitrite increases. In addition, no anodic trace was observed on potentials reversal, even for a small amount of nitrite. This implies that PW_{18} catalyzes the reduction of nitrite and the catalysis takes place during the reduction of the immobilized PW_{18}. Fig. 7B shows a linear relationship between the catalytic current taken at −0.3 V vs. SCE and the concentration of nitrite, which shows the efficiency of the PW_{18}/LBL film toward

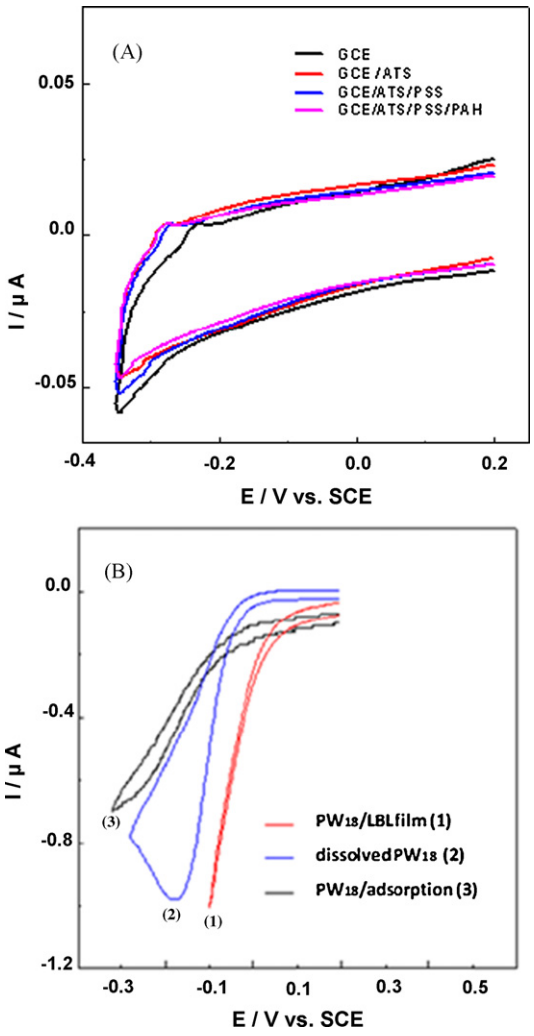


Fig. 8. Comparison between cyclic voltammograms of: (A) GCE, GCE/ATS, GCE/ATS/PSS and GCE/ATS/PSS/PAH in presence of 4 mM nitrite and (B) a PW_{18}/LBL film (2-POM layers), PW_{18} film prepared by simple adsorption and dissolved PW_{18} ($\sim 10^{-4}$ M) in the presence of 4 mM nitrite. Electrolyte pH 1.2 (0.5 M $Li_2SO_4 + H_2SO_4$), scan rate 2 mV/s, reference electrode SCE.

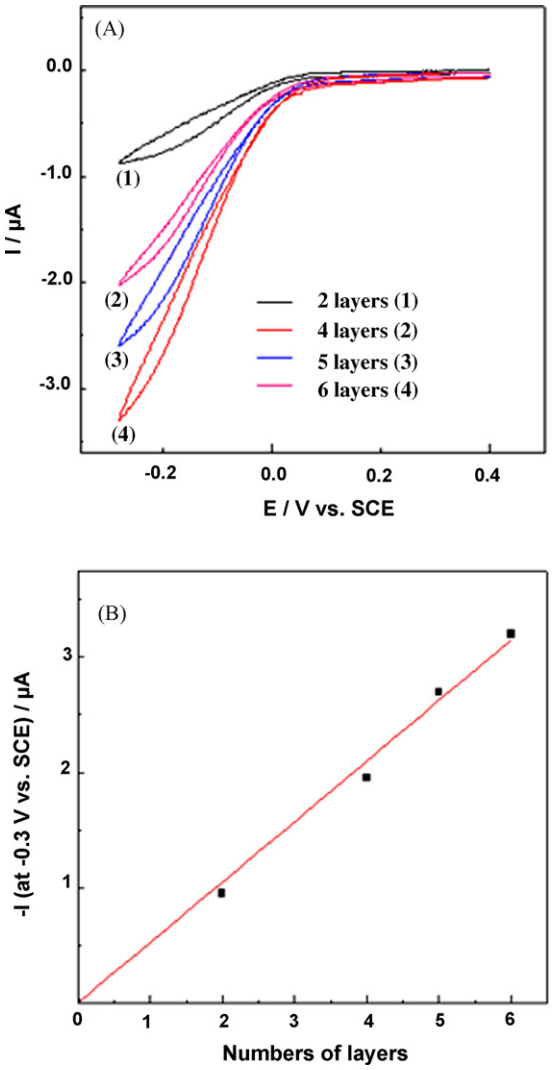


Fig. 9. (A) Variation of the catalytic current of a PW_{18}/LBL film towards 2 mM nitrite as a function of the number of POM layers. (B) Relationship between the catalytic current at −0.3 V vs. SCE and the number of layers. Electrolyte pH 1.2 (0.5 M $Li_2SO_4 + H_2SO_4$), scan rate 2 mV/s, reference electrode SCE.

the catalytic reduction of nitrite and the possibility of using the film for nitrite concentrations of at least up to 20 mM.

Fig. 8B compares the cyclic voltammograms in presence of 4 mM nitrite of PW_{18} immobilized in LBL film of 2-POM layers, PW_{18} adsorbed on the glassy carbon electrode without presence of the different polyelectrolyte layers and PW_{18} dissolved in solution. This figure shows that the catalytic reduction of nitrite is much more efficient for the PW_{18}/LBL film than the adsorbed or dissolved PW_{18}, and the reduction of nitrite starts ~100 mV earlier. The catalytic activity of the PW_{18}/LBL film for the reduction of nitrite might be related to the good three-dimensional distribution of PW_{18} in the LBL film and to the accessibility of nitrite to the immobilized complex. In addition, it is observed that the presence of a small amount of the surfactant Triton X-405 in PAH solution increases the catalytic activity and lowers the reduction potential. In fact, the electrodes prepared using the same procedure but without Triton X-405 showed less activity for the reduction of nitrite. The presence of Triton X-405 in the film probably increases the electron transfer between the immobilized POM and the electrode due to the presence of the aromatic ring and, the long hydrocarbon chain of the surfactant will also increase the pore size in the film, thus enhancing the accessibility of the immobilized PW_{18} for nitrite [56].

Fig. 9A shows the effect of the number of LBL layers on the electrocatalytic reduction of 2 mM nitrite. With increasing number of POM layers, the catalytic reduction of nitrite increases. For example, the electrocatalytic current observed with 6-POM layers is almost 3 times higher than the current observed with 2-POM layers. The relationship between the electrocatalytic current at −0.3 V vs. SCE and the number of POM layers is linear, as shown in Fig. 9B. This is understandable because equal amounts of PW_{18} are adsorbed in each layer.

Fig. 10 shows the variation of the cyclic voltammogram of PW_{18}/LBL film of 10-POM layers in presence of 2 mM nitrite as a function of pH. As the pH increases, the voltammograms shift to more negative potentials, indicating that the electrocatalytic activity decreases. The variation of the catalytic activity with pH indicates the involvement of protons in the catalyzed species and/or in its reduction products. Because the redox wave of the PW_{18}/LBL film shifts to negative potentials as the pH increases (Fig. 6), the catalytic reduction potentials displayed in Fig. 10 follow the same trend. In other words, with increasing pH, the electrocatalytic reduction of nitrite is carried out at more negative potentials, but because the shift of potential with pH is not significant (~25 mV/pH unit), it can be seen that even at higher pH the

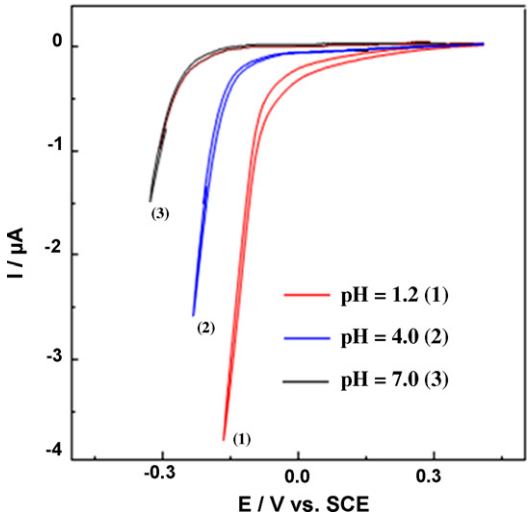


Fig. 10. Cyclic voltammograms of PW_{18}/LBL film (10-POM layers) in presence of 2 mM nitrite at three different pH. Electrolytes: pH 1.2 (0.5 M Li_2SO_4 + H_2SO_4), pH 4 (1 M CH_3COOLi + CH_3COOH), pH 7 (1 M LiCl + 0.2 M $trisH^+$), scan rate 2 mV/s, reference electrode SCE.

electrocatalysis of nitrite is carried out at relatively lower potentials, which is advantageous.

3.3. Analytical evaluation of the nitrite sensor

3.3.1. Amperometric detection of nitrite

For sensing purposes, amperometry is preferred over cyclic votammetry technique because it provides a fast evaluation of the sensor and attributes the main sensor characteristics such as sensitivity and response time. Amperometry was used to examine the characteristics of the nitrite sensor based on PW_{18}/LBL film of 10-POM layers deposited on glassy carbon. For that, the nitrite sensor and a reference SCE were immersed in 5 mL sulfate buffer solution pH 1.2. To permit a rapid diffusion of nitrite during its injection to reach the electrode and reduces, a small stirrer was added to the cell and the buffer solution was set under constant stirring during the experiments. The sensor electrode was polarization at −0.22 V and the curve current vs. time was recorded. After stabilization of the background current, successive injections of 20 µM nitrite were carried out. Fig. 11A shows the amperometric response. A current response of ~3.85 nA/µM nitrite is observed. In addition, after injection, the current reaches 95% of the final current within 6 s. As shown in Fig. 11B, the current increases linearly with increasing nitrite concentrations in the range from 20 to 220 µM. Our measurements showed that the linearity can be extended to at least 20 mM nitrite. The detection limit under these conditions was found to be around 0.1 µM (S/N = 3). However, these characteristics can be improved by increasing the number of layers. By increasing the number of layers (>10), the sensitivity and the detection limit will increase as shown previously in Fig. 9, at the expense of an increased response time.

3.3.2. Selectivity

In order to determine whether the nitrite sensor is affected by the presence of nitrate and molecular oxygen, 20 µM nitrate and 1 mL oxygen saturated solution (obtained by dissolution of pure oxygen in buffer solution for 30 min) were injected into 5 mL buffer solution at pH 1.2. Injection of 1 mL buffer solution saturated with oxygen, to 5 mL buffer solution approximately results in the normal

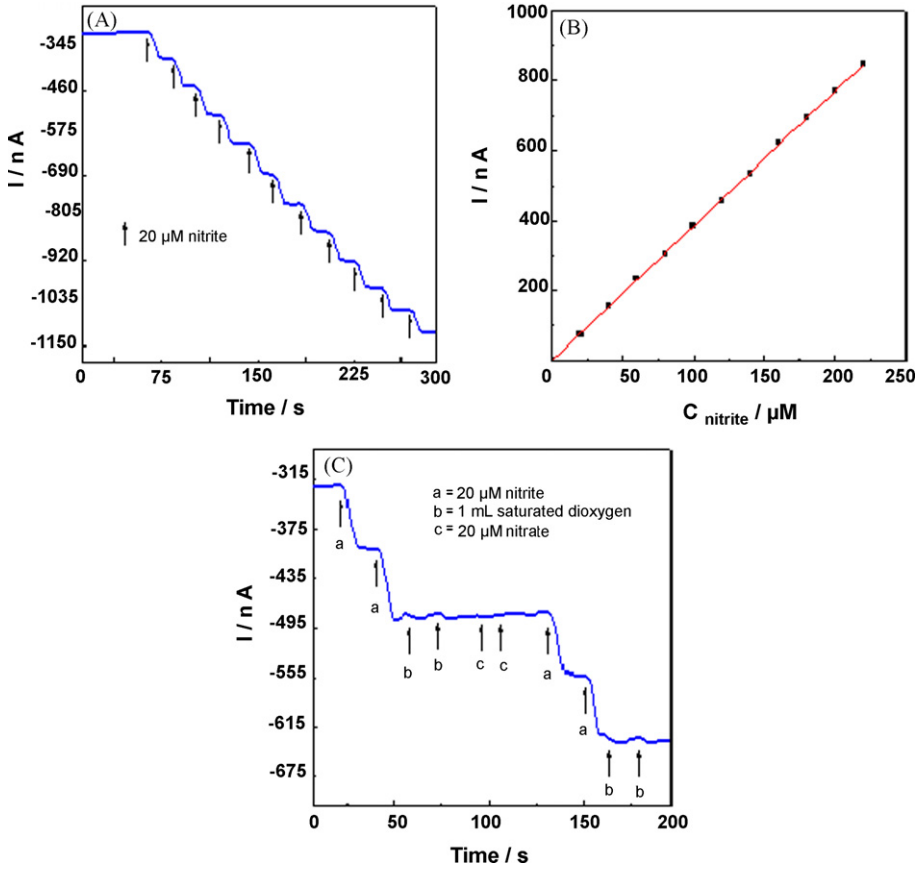


Fig. 11. (A) Amperometric response of nitrite sensor (PW_{18}/LBL film of 10-POM layers) to successive injections of 20 µM nitrite. (B) Relationship between the amperometric response and the concentration of nitrite injected. (C) Response to nitrite, molecular oxygen and nitrate (a = 20 µM nitrite, b = 1 mL saturated dioxygen and, c = 20 µM nitrate). Electrolyte pH 1.2 (0.5 M Li_2SO_4 + H_2SO_4), polarization set at −0.22 V, reference electrode SCE.

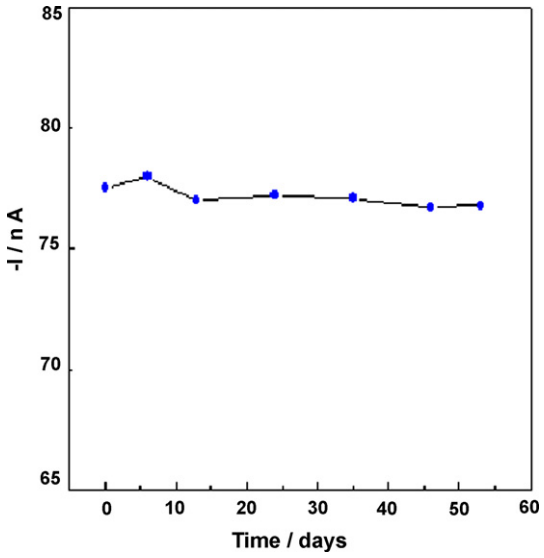


Fig. 12. Amperometric response of nitrite sensor (PW_{18}/LBL film of 10-POM layers) to injection of 20 μM nitrite over the course of 55 days. Sensor stored under air at ambient temperature. Electrolyte pH 1.2 (0.5 M $Li_2SO_4 + H_2SO_4$), polarization set at −0.22 V, reference electrode SCE.

oxygen concentration in the buffer solution. As shown in Fig. 11C, no significant increase in the amperometric response was observed. Hence, this proves that the nitrite sensor based on PW_{18}/LBL film is selective toward nitrate and molecular oxygen, the two most common interferences.

3.3.3. *Stability and reproducibility*

The stability of the nitrite sensor was investigated over a period of 55 days. The sensor was stored under air at room temperature and the current response to 20 μM nitrite injection in sulfate buffer solution pH 1.2 was checked at regular intervals. Fig. 12 shows the variation of the current to the nitrite injection. No significant change was observed within this period of time. The stability of this sensor can be attributed to the large amount of PW_{18} which is deposited on the surface of the electrode and the fact that the desorption of PW_{18} is strongly reduced by the electrostatic encapsulation inside the PAH/Triton X-405 layers (irreversible adsorption).

Table 1 illustrates the main characteristics of the nitrite sensor shown in Fig. 11.

3.3.4. *Determination of nitrite in real samples*

The nitrite sensor was tested by measuring the concentration of nitrite in drinking water. To increase the sensitivity, 20-POM layers were deposited using the LBL method. It was observed that the sensitivity of the sensor with 20-POM layers is almost double the sensitivity reported in Table 1. Under constant stirring, the nitrite sensor and a reference SCE were immersed in 2.5 mL sulfate buffer solution pH 1.2. The polarization was set at −0.22 V vs. SCE. After stabilization of the background current, injection of 500 μL of tap water was carried out, followed by successive injections of 1 μM commercial nitrite solution. The concentration of nitrite in tap water was calculated from the standard addition method (successive calibration points of 1 μM) and was found to be 0.66 ± 0.03 μM. The concentration of nitrite given by the water distribution company (Vlaamse Maatschappij voor Watervoorziening) is 0.6 μM. The accordance between the data indicates the reliability of the present sensor for nitrite determination in real samples.

Table 1
Characteristics of the PW_{18}/LBL film (10-POM layers) nitrite sensor shown in Fig. 11.

Area	∼7 mm^2
Sensitivity	3.85 ± 0.2 nA/μM nitrite
Detection limit	∼0.1 μM
Response time	<6 s
Linearity	From 0.1 μM to at least 20 mM nitrite
Response to O_2 and NO_3^-	None
Stability	At least 2 months

4. Conclusions

We have demonstrated the deposition of Dawson-type tungstophosphate α-$K_7[H_4PW_{18}O_{62}]\cdot 18H_2O$ using layer by layer assembly process. The modified electrode was characterized by cyclic voltammetry and amperometry. Compared to dissolved PW_{18}, the redox behavior of immobilized PW_{18}/LBL is more reversible. The peak currents of the deposited PW_{18}/LBL film increases linearly with the number of layers, which demonstrates that equal amounts of PW_{18} are adsorbed in each layer. The peak potential of the redox wave of the immobilized PW_{18} was found to be relatively insensitive to pH (shift of ∼25 mV/pH unit). In addition, no significant separation in the redox processes was observed at higher pH. Glassy carbon electrodes modified with PW_{18}/LBL films showed a high electrocatalytic activity towards reduction of nitrite. The activity increases linearly with nitrite concentrations and number of POM layers. Sensors based on such modified electrodes have a linear detection range from 0.1 μM to at least 20 mM nitrite, a variable sensitivity (∼4 nA/μM nitrite for 10-PW_{18}/LBL film), a low response from interferences such as nitrate and molecular oxygen, a fast response time (<6 s), can operate from pH 1 to 9, and are stable for at least 2 months, making them good candidates for nitrite determination.

Acknowledgements

The authors acknowledge the support of the National Science Foundation (Grant CHE-0236686), CNRS (UMR 8000), the University of Paris Sud XI (France) and the Belgian Federal Science Policy Office (BELSPO) through the IUAP project INANOMAT (contract P6/17). Dr. I-M Mbomekalle is gratefully acknowledged for assistance in synthesis.

References

[1] C.U. Carlsen, J.K.S. Moller, L.H. Skibsted, Coord. Chem. Rev. 249 (2005) 485–498.
[2] J.K.S. Moller, L.H. Skibsted, Chem. Rev. 102 (2002) 1167–1178.
[3] H. Yetim, A. Kayacier, Z. Kesmen, O. Sagdic, Meat Sci. 72 (2006) 206–210.
[4] W. Lijinsky, S.S. Epstein, Nature 225 (1970) 21–23.
[5] I.A. Wolf, A.E. Wasserman, Science 177 (1972) 15–19.
[6] K.K. Chio, K.W. Fung, Analyst 105 (1980) 241–248.
[7] V.Y. Titov, Y.M. Petrenko, Biochemistry 70 (2005) 473–483.
[8] C.S. Bruning-Fann, J.B. Kaneene, Vet. Hum. Toxicol. 35 (1993) 521–538.
[9] A. Aydin, O. Ercan, S. Tascioglu, Talanta 66 (2005) 1181–1186.
[10] G.M. Greenway, S.J. Haswell, P.H. Petsul, Anal. Chim. Acta 387 (1999) 1–10.
[11] M.I.H. Helaleh, T. Korenaga, J. Chromatogr. B 744 (2000) 433–437.
[12] W.J.R. Santos, A.L. Sousa, R.C.S. Luz, F.S. Damos, L.T. Kubota, A.A. Tanaka, S.M.C.N. Tanaka, Talanta 70 (2006) 588–594.
[13] J.E. Newbry, M.P.L. de Haddad, Analyst 110 (1985) 81–82.
[14] M. Trojanowiez, W. Matuszewski, B. Szostek, Anal. Chim. Acta 261 (1992) 391–398.
[15] Z.H. Wen, T.F. Kang, Talanta 62 (2004) 351–355.
[16] P. Tau, T. Nyokong, Electrochim. Acta 52 (2007) 4547–4553.
[17] J. Obirai, T. Nyokong, J. Electroanal. Chem. 573 (2004) 77–85.
[18] J. Davis, M.J. Moorcroft, S.J. Wilkins, R.G. Compton, M.F. Cardosi, Analyst 125 (2000) 737–742.
[19] F. Armijo, M.C. Goya, M. Reina, M.J. Canales, M.C. Arevalo, M.J. Aguirre, J. Mol. Catal. A: Chem. 268 (2007) 148–154.
[20] M.A. Kamyabi, F. Aghajanloo, J. Electroanal. Chem. 614 (2008) 157–165.
[21] A. Salimi, R. Hallaj, H. Mamkhezri, S.M.T. Hosaini, J. Electroanal. Chem. 619–620 (2008) 31–38.
[22] L.H. Chen, J.B. Zang, Y.H. Wang, L.Y. Bian, Electrochim. Acta 53 (2008) 3442–3445.
[23] A. Salimi, A. Noorbakhsh, M. Ghadermarzi, Sens. Actuators B 123 (2007) 530–537.

[24] X. Huang, Y. Li, Y. Chen, L. Wang, Sens. Actuators B 134 (2008) 780–786.
[25] O. Brylev, M. Sarrazin, L. Roué, D. Bélanger, Electrochim. Acta 52 (2007) 6237–6247.
[26] T.S. Liu, T.F. Kang, L.P. Lu, Y. Zhang, S.Y. Cheng, J. Electroanal. Chem. 632 (2009) 197–200.
[27] A. Salimi, H. Mamkhezri, S. Mohebbi, Electrochem. Commun. 8 (2006) 688–696.
[28] M.H. Pournaghi-Azar, H. Dastangoo, J. Electroanal. Chem. 567 (2004) 211–218.
[29] A.Y. Chamsi, A.G. Fogg, Analyst 113 (1988) 1723–1727.
[30] Z. Zhao, X. Cai, J. Electroanal. Chem. 252 (1988) 361–370.
[31] J.N. Barisci, G.G. Wallace, Anal. Lett. 24 (1991) 2059–2073.
[32] C.A. Caro, F. Bedioui, J.H. Zagal, Electrochim. Acta 47 (2002) 1489–1494.
[33] B. Keita, I.M. Mbomekalle, L. Nadjo, R. Cantant, Electrochem. Commun. 3 (2001) 267–273.
[34] A. Belhouari, B. Keita, L. Nadjo, R. Contant, New J. Chem. 22 (1998) 83–86.
[35] B. Keita, M. Benaissa, L. Nadjo, R. Cantant, Electrochem. Commun. 4 (2002) 663–668.
[36] I.M. Mbomekalle, B. Keita, Y.W. Lu, L. Nadjo, R. Cantant, N. Belai, M.T. Pope, Eur. J. Inorg. Chem. (2004) 276–285.
[37] G. Decher, J.D. Hong, Macromol. Chem. Macromol. Symp. 46 (1991) 321–327.
[38] S. Liu, D.G. Kurth, B. Bredenkotter, D. Volkmer, J. Am. Chem. Soc. 124 (2002) 12279–12287.
[39] A. Kuhn, N. Mano, C. Vidal, J. Electroanal. Chem. 462 (1999) 187–194.
[40] M. Huang, L. Bi, Y. Shen, B. Liu, S. Dong, J. Phys. Chem. B 108 (2004) 9780–9786; L. Bi, Y. Shen, J. Jiang, E. Wang, S. Dong, Anal. Chim. Acta 534 (2005) 343–351.
[41] K. Karnicha, M. Chojak, K. Miecznikowski, M. Skunik, B. Baranowski, A. Kolary, A. Piranski, B. Palys, L. Adamczyk, P.J. Kulesza, Bioelectrochemistry 66 (2005) 79–87.
[42] S. Zhai, S. Gong, J. Jiang, S. Dong, J. Li, Anal. Chim. Acta 486 (2003) 85–92.
[43] L. Chemg, J.A. Cox, Electrochem. Commun. 3 (2001) 285–289.
[44] S. Liu, D.G. Kurth, D. Volkmer, Chem. Commun. (2002) 976–977.
[45] M. Ammam, B. Keita, L. Nadjo, J. Fransaer, Sens. Actuators B 142 (2009) 347–354.
[46] K.B. Oldham, J. Electroanal. Chem. 121 (1981) 341–342.
[47] P. Daum, J.R. Lenhard, D. Rolisan, R.W. Murray, J. Am. Chem. Soc. 120 (1980) 4649–4653.
[48] A.P. Brown, F.C. Anson, Anal. Chem. 49 (1977) 1589–1595.
[49] D.F. Smith, K. Willman, K. Kuo, R.W. Murray, J. Electroanal. Chem. 95 (1979) 217–227.
[50] Y. Jeannin, J. Martin-Frere, Inorg. Chem. 18 (1979) 3010–3014.
[51] B. Keita, K. Essaadi, L. Nadjo, J. Electroanal. Chem. 259 (1989) 127–146.
[52] A. Mahmoud, B. Keita, L. Nadjo, O. Oung, R. Cantant, S. Brown, Y. De Kouchkovsky, J. Electroanal. Chem. 463 (1999) 129–145.
[53] C.M.A. Brett, A.M.O. Brett, Electrochemistry Principles, Methods and Applications, Oxford University Press, Oxford, 1993.
[54] B. Keita, L. Nadjo, Mater. Chem. Phys. 22 (1989) 77–103.
[55] B. Keita, E. Abdeljalil, L. Nadjo, R. Contant, R. Belghiche, Electrochem. Commun. 3 (2001) 56–62.
[56] S.D. Holmstrom, B. Karwowska, J.A. Cox, P.J. Kulesza, J. Electroanal. Chem. 456 (1998) 239.

Talanta 80 (2010) 2141–2148

Contents lists available at ScienceDirect

Talanta

journal homepage: www.elsevier.com/locate/talanta

NMR and chemometrics in tracing European olive oils: The case study of Ligurian samples

L. Mannina[a,b,*], F. Marini[c,**], M. Gobbino[b], A.P. Sobolev[b], D. Capitani[b]

[a] Department of STAAM, University of Molise, I-86100 Campobasso, Italy
[b] Institute of Chemical Methodologies, CNR, Magnetic Resonance Laboratory "Annalaura Segre", Research Area of Rome I, I-00015 Monterotondo Stazione, Rome, Italy
[c] Department of Chemistry, University Sapienza di Roma, I-00185 Rome, Italy

ARTICLE INFO

Article history:
Received 14 July 2009
Received in revised form 29 October 2009
Accepted 5 November 2009
Available online 13 November 2009

Keywords:
Olive oil
NMR
PLS-DA
SIMCA

ABSTRACT

An NMR and chemometric analytical approach to classify extra virgin olive oils according to their geographical origin was developed within the European TRACE project (FP6-2003-FOOD-2-A, contract number: 0060942). Olive oils (896 samples) of three consecutive harvesting years (2005, 2006, and 2007) coming from Mediterranean areas were analyzed by ^{1}H NMR spectroscopy. Olive oil samples from Liguria, an Italian region, were chosen as a case study and PLS-DA and SIMCA modeling analyses were used to build up statistical models both to discriminate between Ligurian and non-Ligurian olive oils and to define the Ligurian olive oil class to confirm the declared provenience.

© 2009 Elsevier B.V. All rights reserved.

1. Introduction

The development of accurate analytical fingerprinting methods for the authentication of olive oils and for the certification of the geographical origin is an actual issue and an important challenge also in view of the last EU Regulation 182/2009 [1] which requires mandatory labeling reporting the geographical origin of olive oils. In recent years many studies have been performed to characterize and classify olive oils using different techniques [2–6].

In our previous papers, it has been shown that high-field NMR spectroscopy together with a suitable statistical analysis allow extra virgin olive oils to be classified according to their geographical origin and cultivar [7–10]. However, up to now, the NMR methodology has been applied to compare olive oil samples coming prevalently from Italian geographical areas.

In this paper, the sampling was extended to 896 samples of three harvesting years (2005, 2006, and 2007) coming from different Mediterranean areas. The aim was to create, using ^{1}H high-field NMR data, statistical models able to trace olive oils according to the geographical origin. In particular, the Ligurian olive oils were chosen as study case and were analyzed together with olive oils coming from other Italian areas and from Spain, Greece, France and Turkey. The NMR results were processed using two different statistical pattern recognition techniques, i.e. PLS-DA and SIMCA chemometric techniques. PLS-DA and SIMCA techniques [11,12], being a discriminant technique and a class-modeling technique respectively, allow different information to be obtained [13,14]. Discriminant techniques such as PLS-DA [15,16] are focused on the differences between samples coming from different classes and operate by dividing the hyperspace of the variables in as many regions as the number of available categories, whereas class-modeling techniques such as SIMCA [17,18] are more focused on the similarities among samples of the same class than on the differences among the classes and act by defining the category space of one class at a time.

2. Materials and methods

2.1. Sampling

Olive oils (896) classified as PDO and/or extra virgin olive oil and produced in different Mediterranean areas during three consecutive harvesting years, namely, 2004/2005 (300 samples), 2005/2006 (351 samples) and 2006/2007 (245 samples), see Table 1, were collected and transported to a single laboratory (Joint Research Centre, Ispra, Italy) for subsampling and delivery to the Institute of Chemical Methodologies, CNR, Rome, Italy. Olive oils were stored at 4 °C between delivery and NMR measurements to avoid compositional changes.

* Corresponding author at: Department of STAAM, University of Molise, Via de Sanctis, I-86100 Campobasso, Italy. Tel.: +39 0874 404648; fax: +39 06 90672477.
** Corresponding author. Tel.: +39 06 49913856.
E-mail addresses: mannina@unimol.it (L. Mannina), fmmonet@hotmail.com (F. Marini).

0039-9140/$ – see front matter © 2009 Elsevier B.V. All rights reserved.
doi:10.1016/j.talanta.2009.11.021

Table 1
Olive oils analyzed within the TRACE project. The harvesting year, the country, the number of samples are reported. Ligurian olive oils used as case study are reported in *italic* character.

Harvesting year	Country	Number of samples
2004/2005	Italy	154
	Liguria	*62*
	Spain	38
	France	9
	Greece	23
	Turkey	14
2005/2006	Italy	172
	Liguria	*79*
	Spain	38
	Greece	10
	France	46
	Cyprus	6
2006/2007	Italy	116
	Liguria	*68*
	Spain	34
	Greece	7
	France	20

2.2. NMR measurements

Olive oil samples (20 μL) were dissolved in DMSO (20 μL) and $CDCl_3$ (700 μL) directly inside the 5 mm NMR tube. ^{1}H NMR analyses were performed on a Bruker AVANCE AQS600 instrument equipped with a 5 mm probe operating at the ^{1}H frequency of 600.13 MHz (B_0 = 14.3 T).

The ^{1}H NMR spectra were acquired at 300 K using the following experimental conditions: number of scans 1024; $\pi/2$ pulse ~8 μs; time domain (TD) 64 K data points; relaxation delay plus acquisition time 3.5 s; spectral width 18.5 ppm.^{1}H NMR spectra were obtained by the Fourier Transformation (FT) of the FID (Free Induction Decay) applying an exponential multiplication with a line-broadening factor of 0.3 Hz and a zero filling (size = 64 K) procedure. The resulting ^{1}H NMR spectra were phased manually. The error introduced in the quantitative analysis by phasing the spectra manually is <1%. Chemical shifts were reported with respect to the residual $CHCl_3$ signal set at 7.26 ppm. For ensuring a better quantitative comparability of the spectra, the baseline was corrected using a multiple point correction. In particular, the Cubic Spline Baseline Correction routine of the Bruker TOPSPIN software was used.

In order to perform the statistical analyses, the intensity, i.e. the maximum peak height, of 17 selected signals [10], see Fig. 1, was measured using an implemented semi-automatic peak-picking routine present in the Bruker TOPSPIN software [19]. The intensity of the selected signals was compared with the intensity of the resonance at 2.251 ppm, see in Fig. 1, due to α-methylene protons of all acyl chains, normalized to 1000.

To assess the repeatability of the method and to verify the applicability of the protocol, a few samples were analyzed five times. The obtained values show a very good repeatability (Relative Standard Deviation <2.5%) of the protocol for all signals.

2.3. Chemometric analysis

The intensity of 17 selected ^{1}H NMR resonances was processed using two different statistical pattern recognition techniques, i.e. PLS-DA as example of a discriminant technique and SIMCA, as example of a class-modeling approach [11].

2.3.1. Partial Least Squares-Discriminant Analysis (PLS-DA) [15,16]

Discriminant classification techniques can be viewed as aiming to find a relationship between a multivariate independent vector **X** and a qualitative vector of responses. Accordingly, if a suitably designed dummy response vector is introduced, traditional regression methods can be used also to tackle with classification problems. In particular, when dealing with a classification problem involving 2 classes, as in our case Liguria and non-Liguria, one can build a dummy binary-coded 1-dimensional response vector, so that, if a sample belongs to the class "Liguria", it will be coded as "1", while if it belongs to class "not Liguria", it will be coded as "0". Under this assumption, to compute a classification model corresponds to calculate the regression vector between the data matrix and the dummy vector of responses.

In order to compute a classification model, PLS-DA, as the name itself suggest, uses Partial Least Squares Regression [20], i.e. computes a bilinear decomposition of both X- and Y-spaces, under the assumption that a relationship between the two internal spaces exists. The result is a linear classifier that has proved to be statistically equivalent to Linear Discriminant Analysis [21], and that can be also applicable to all the cases when LDA cannot be (low number of samples to number of variables ratio and high collinearity among the variables) [16].

PLS-DA results are reported as score plots. Information about the variables most responsible for the observed classification was obtained by examining the VIP scores and the regression coefficients. The VIP score accounts for how much the single variable contributes to the bilinear model, and it is scaled in such a way that a value above 1 is considered to be significant.

Regression coefficients tell us which variables are most responsible of the separation between the categories: due to the coding used in this study, coefficients having a positive value will correspond to a variable being more concentrated in the samples from Liguria than in the others and *vice versa*.

2.3.2. Soft Independent Modeling of Class Analogies (SIMCA) [20,21]

In SIMCA, each class model is defined on the basis of a principal component model of opportune dimensionality. For instance, the model of class "Liguria" can be assumed to be described by an A principal components model, according to the equation:

$$\mathbf{X}_{Lig} = \mathbf{T}_A\mathbf{P}_A^T + \mathbf{E}$$

where $\mathbf{X}_{Lig}$ is the sub-matrix of the original data set obtained by selecting only the samples from Liguria, $\mathbf{T}_A$ and $\mathbf{P}_A$ are the matrices containing the first A scores and loading vectors, respectively, and $\mathbf{E}$ are the residuals [12]. Once the principal component model is computed, the class space is defined according to some statistically defined outlier detection criterion. In particular, the score matrix $\mathbf{T}_A$ and the residual matrix $\mathbf{E}$ are used to compute the probability distributions for the distances within the model space (T^2 statistics) and for the orthogonal distance to the model space (Q statistics), respectively. When a sample has a T^2 or a Q value exceeding a selected percentile of the corresponding distribution (usually 95%), the sample is considered to be an outlier for the category and rejected by the class model, otherwise, if the two values are lower than the thresholds, it is accepted and the sample is recognized as being part of the class.

As a consequence, SIMCA analysis provides two different figures of merit that are called sensitivity and specificity: sensitivity is the fraction of samples of the category, that we are modeling, accepted by the class model, whereas specificity is the fraction of samples from all the other categories rejected by the class model. The same figures of merit were also used as an optimality criterion to evaluate the best model complexity: indeed the principal components to be included in the SIMCA model of the class Liguria were chosen as those providing the highest value of the geometric mean between the sensitivity and the specificity, as evaluated by 10-fold

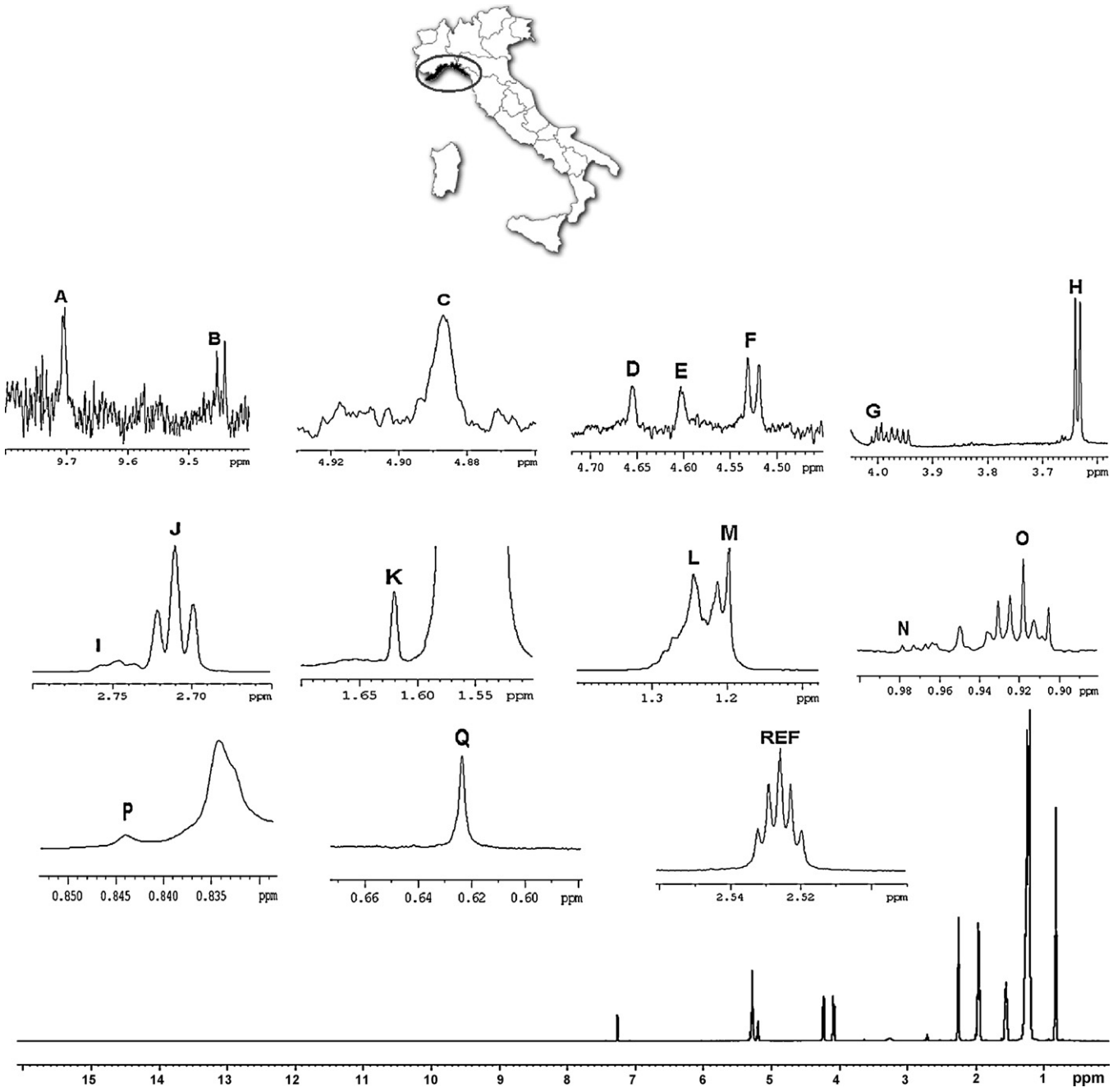


Fig. 1. 600.13 MHz ^{1}H NMR spectrum of an extra virgin olive oil. The selected NMR signals used in the statistical analysis are reported in expanded scale and labeled: A: hexanal (9.704 ppm); B: trans 2-hexenal (9.454 ppm); C: terpene 4 (4.885 ppm); D: terpene 3 (4.661 ppm); E: terpene 2 (4.609 ppm); F: terpene 1 (4.541 ppm); G: methylenic protons in α-glycerol moiety of *sn*-1,3 diglycerides (3.988 ppm); H: methylenic protons in α-glycerol moiety of *sn*-1,2 diglycerides (3.636 ppm); I: diallylic protons of linolenic fatty chains (2.746 ppm); J: diallylic protons of linoleic fatty chains (2.710 ppm); REF: reference peak due to methylenic protons bound to C2 normalized to 1000 (major peak at 2.251 ppm); K: squalene (1.620 ppm); L: methylenic protons of all unsaturated fatty chains (1.244 ppm); M: methylenic protons of palmitic and stearic fatty chains (1.197 ppm); N: wax (0.978 ppm); O: methyl of linolenic fatty chains (0.910 ppm); P: methyl of linoleic fatty chains (0.843 ppm); Q: methyl-18 of β-sitosterol (0.623 ppm). Map of Italy is also reported: Liguria region is evidenced by an ellipse.

cross-validation. Model space was built by taking into account both the distance to the model and the leverage.

3. Results and discussion

As the main objective of this work was to propose a methodology to confirm the geographical origin of olive oils, olive oils from a specific geographic area, Liguria region, see Fig. 1, were chosen as study case to develop and test the methodology. Ligurian olive oils have an important commercial value, being characterized by a mild taste in contrast to other famous Italian olive oils coming from Tuscany and Puglia, which tend to be fruity and strong. In Liguria, olive trees originate from typical cultivars such as Taggiasca and Lavagnina grown on barely accessible slopes terraced all the way down to the sea.

In order to perform this study, 896 olive oils samples, see in Table 1, were analyzed by ^{1}H NMR analysis following the protocol previously reported [10]. The intensity of 17 selected resonances sensitive to the geographical origin [10] was measured, see Fig. 1, and submitted to the chemometric analysis.

The intensities were gathered in a matrix having as many rows as the number of samples and as many columns as the number of variables. In particular, as the intensity of a relatively small number of NMR resonances was used as descriptor, the dataset contained 896 samples and 17 experimental indices.

Successively, since the goals were to discriminate between Ligurian samples and all the others and to characterize the Ligurian class, two pattern recognition methods were used, namely PLS-DA and SIMCA: while the former is a discriminant technique, the latter is an example of what are called class-modeling methods, i.e. those methods that, by focusing at one category at a time, are able to build up a model of each class separately and hence have been suggested to be more effective when in dealing with the problems of food traceability.

From the statistical viewpoint, the analysis was carried out in two stages: at first, a model including samples for all the three harvesting years was created, in order to account for as more sources of variability between the individuals as possible; then, in the following stage, three different models, one for each harvesting year, were built and validated on the samples from the two years left aside, in order to check how accurately models built on a single year could be able to recognize samples produced in different harvests and therefore to evaluate the year-to-year variability of the composition of the products.

3.1. Global model (all years)

In the first stage of our study, attention was focused on the possibility of building a model that could provide the best discrimination between the Ligurian samples and all the others. For this purpose, samples from all the available harvesting years had to be included in the set used for building the model (training set); in this way the maximum variability among the data could be represented. Samples used as training or test set were chosen randomly [2]. In order to have a balanced data set, the training set was built using 2/3 of all Ligurian samples (140) and comparable number of non-Ligurian samples (132). The test set used contains all the other samples not included in the training set: 624 samples (69 from Liguria and 555 from all the other regions). It has to be stressed that the samples included in the test set were not used at any stage of model building, so that they could be considered as really "unknown" to the models: indeed, whenever a choice had to be done to select the optimal model parameters, 10-fold cross-validation (on the training samples only) was used.

3.1.1. PLS-DA

At first modeling was performed using PLS-DA. The optimal model was selected based on the lowest non-error rate of cross-validation, as anticipated above, and it included 6 latent variables. A score plot of the projection of the training samples onto the first three PLS components is shown in Fig. 2. It evidences a good separation among the two classes. Indeed, a very good classification accuracy was obtained both in the training (89.3% for Ligurian, 87.1% for non-Ligurian) and the cross-validation (84.4% for Ligurian, 87.1% for non-Ligurian) phases. These data correspond to 15 and 18 Ligurian samples being misclassified in modeling and cross-validation, respectively. The results obtained for the model "Liguria" are shown in Table 2.

Information about the variables most responsible for the observed classification can be obtained by examining the VIP scores and the regression vector, both reported in Fig. 3. The VIP value, Fig. 3b, accounts for how much the single variable contributes to the bilinear model, and it is scaled in such a way that a value above 1 is considered to be significant: an inspection of Fig. 3b evidences that the variables that contribute the most to the projection are all the terpene peaks, the protons of *sn*-1,3 diglycerides and the diallylic protons of linolenic fatty chains.

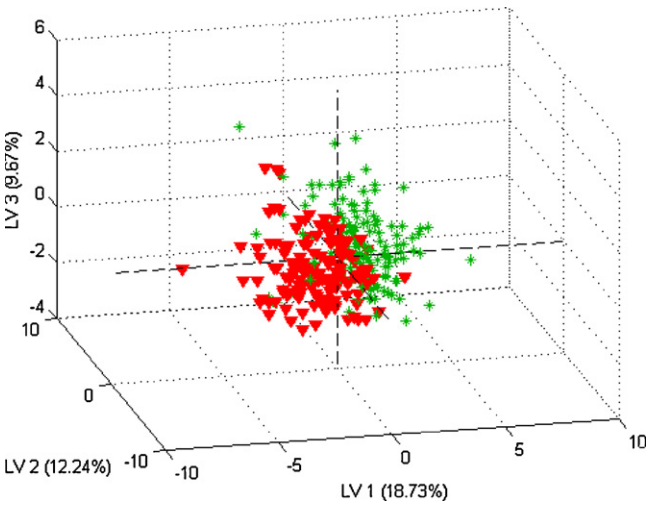


Fig. 2. A score plot of the projection of the training samples, relative to three harvesting years, onto the first three PLS component. ▼ = Ligurian olive oils, ✳ = non-Ligurian olive oils.

On the other hand, regression coefficients, Fig. 3a, tell us which variables are most responsible of the separation between the categories: due to the coding used in this study, coefficients having a positive value correspond to variables, and therefore to compounds, being more concentrated in Ligurian samples than in the others and *vice versa*. By looking at Fig. 3a, it is possible to observe that Ligurian samples have generally a higher terpene and hexanal content and a lower amount of saturated acids and β-sitosterol.

When this model was used to predict the test set samples, the resulting prediction accuracy was comparable to that evaluated in the modeling and the cross-validation phase. Indeed, 11 out of 69 (84.1% prediction accuracy) Ligurian and 79 out of 555 (85.8% prediction accuracy) non-Ligurian samples were misclassified.

3.1.2. SIMCA

The analysis on the dataset containing samples from all the three harvesting years was repeated using SIMCA. The main advantage of a class-modeling technique like SIMCA is that it is possible to build a model only for the category of interest and verify whether the samples are accepted by this category model or not. This is particularly effective in cases like the one we are studying where the discrimination is not among two well characterized classes, but between one class and all the others. A 10-fold cross-validation was used to select the optimal complexity of the model, which resulted to be 6 latent variables.

The optimal SIMCA model, reported in Fig. 4 in the form of a leverage *vs* orthogonal distance plot, resulted in a 84.3% sensitivity (118 out of 140 Ligurian samples accepted by the model) and in a 70.6% specificity (92 of the 132 samples from the other regions rejected by the model of Liguria). Similar results were obtained also in cross-validation (83.6% sensitivity and 72.0% specificity). The analysis of the modeling ability of the individual variables confirmed what already observed by PLS-DA, with terpenes and protons in glycerol moiety of *sn*-1,3 diglycerides being the indices contributing the most to the category model. All these results are shown in Table 2.

The model was also used to analyze the test set samples and, while a comparable specificity was obtained (70.6%), it showed a significantly higher sensitivity (92.8%, with 5 Ligurian samples only being refused by their own class model).

Table 2
Classification accuracy (PLS-DA), sensitivity and specificity (SIMCA) for the "Ligurian olive oil" model. All the values are given in %.

	Global model	2004/2005	2005/2006	2006/2007
PLS-DA				
Classification accuracy (modeling)	89.3%	88.7%	92.4%	86.8%
Classification accuracy (cross-validation)	84.4%	88.7%	91.1%	86.8%
Classification accuracy (test set)	84.1%	34.7%	79.2%	54.6%
SIMCA				
Sensitivity (model)	84.3%	96.8%	93.7%	94.0%
Specificity (model)	70.6%	87.0%	78.7%	78.5%
Sensitivity (cross-validation)	83.6%	82.3%	81.0%	85.1%
Specificity (cross-validation)	72.0%	89.1%	79.8%	80.8%
Sensitivity (test)	92.8%	0.0%	14.6%	41.5%
Specificity (test)	70.6%	100.0%	93.5%	90.2%

3.2. Year-to-year variability

The results obtained on the three years dataset were rather promising for the traceability of Ligurian olive oils. However, as evidenced especially by the values of the specificity in SIMCA, the built models were too prone to accept samples from other geographical regions as coming from Liguria. This result could be due to the fact that, in order to account for the various sources of variability, in particular the different year of harvesting, the class model had to be relatively large. To verify whether this assumption was correct and, anyway, to characterize in detail the year-to-year variability, in a second stage of our analysis a more thorough investigation of the year-to-year variability was carried out.

Operationally, this investigation was carried out by selecting the samples from a single year as training set and validating the obtained model on the samples from the remaining two years as external test set. As in the previous case, the analysis was done using both PLS-DA and SIMCA, the latter, due to its modeling properties, giving a more detailed result.

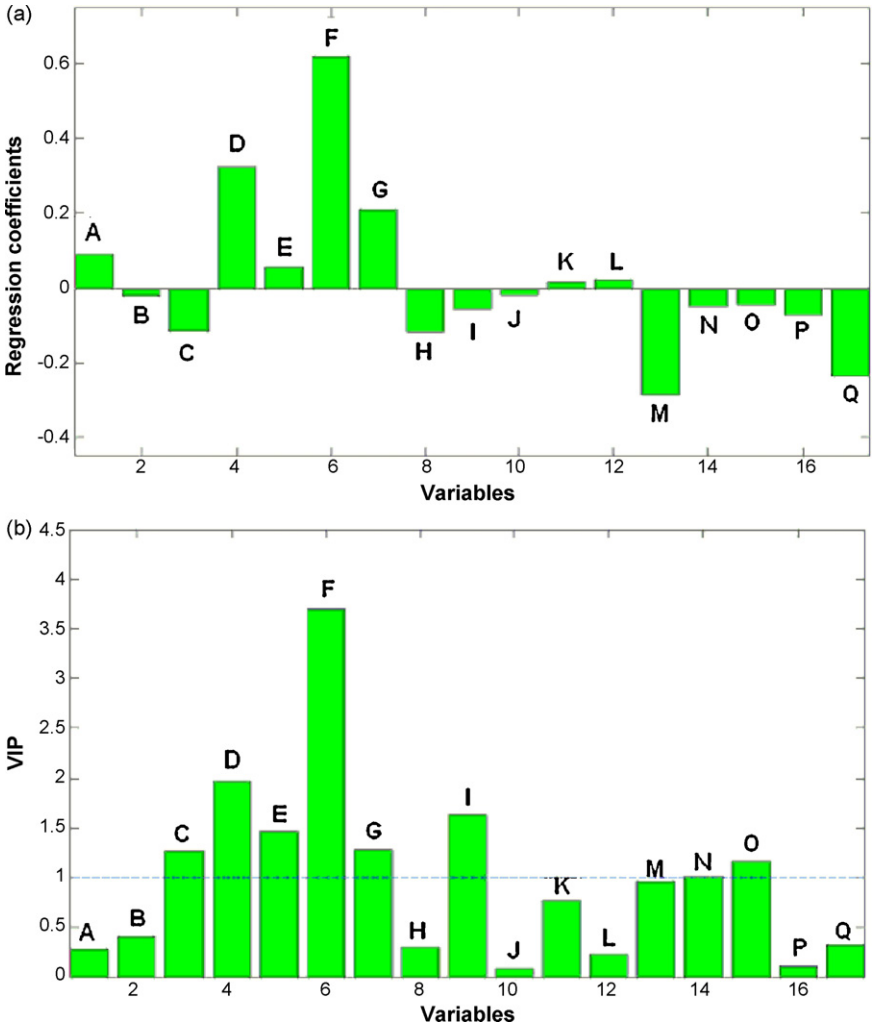


Fig. 3. The regression vector (a) and VIP scores (b) relative to three harvesting years samples. See Fig. 1 for the labeling.

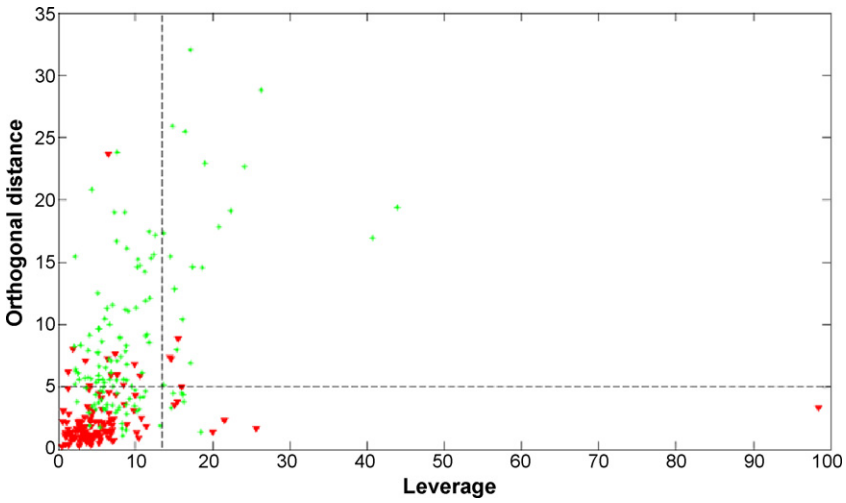


Fig. 4. SIMCA model relative to three harvesting years samples. ▼ = Ligurian olive oils, ✳ = non-Ligurian olive oils.

3.2.1. PLS-DA

PLS-DA analysis on the individual harvesting years was carried out at first by selecting as training set the data from 2004/2005 (62 Ligurian and 238 non-Ligurian) and validating the model built on the samples from the other two harvesting years (147 Ligurian and 449 non-Ligurian). As in the previous cases, 10-fold cross-validation was used to select the optimal complexity of the model, which resulted to be 4 latent variables. The classification ability of this model on the 2004/2005 samples, expressed as non-error rate, in modeling (88.7% for Liguria and 89.5% for the others) was similar to that in cross-validation (88.7% for Liguria and 89.1% for the others). However, when this model was used to predict the samples from the other harvesting years, left aside as our external validation set, the classification accuracy for the class Liguria was dramatically decreased. Indeed, non-error rates of 34.7% (Ligurian) and 98.9% (not-Ligurian) were obtained. The inspection of regression coefficients, see Fig. 5a, confirms that terpenes 1, 2 and 3 and saturated fatty chains have a significant discriminant power, terpenes being present in a higher concentration in Ligurian olive oils while saturated fatty chains in lower amount. With respect to the global model, a significant contribution of *trans*-hexenal, present in high concentration in Ligurian samples, is observable. The contribution of the variables to the model is reported as VIP scores in Fig. 5b. With respect to the global model, squalene becomes important for the model building whereas the *sn*-1,3 diglycerides do not contribute significantly to the model.

The same analysis was repeated using the 2005/2006 data (79 Ligurian and 272 non-Ligurian) as training set and leaving aside as external validation set the results of the analyses performed on the 2004/2005 and 2006/2007 samples (130 Ligurian and 415 non-Ligurian). The observed outcomes were similar to what already observed in the case of the 2004/2005 model. Indeed, the optimal model, which 10-fold cross-validation suggested to be the one including 4 latent variables, was able to provide very good classification both in modeling (92.4% Ligurian and 91.9% non-Ligurian) and in cross-validation (91.1% Ligurian and 91.2% non-Ligurian). Again, the inspection of regression coefficients, see Fig. 6a, confirms the importance of terpenes and saturated fatty chains in the olive oil discrimination. With respect to the model built on the 2004/2005 samples, some differences can be evidenced. Indeed, while in the 2004/2005 model *trans*-hexenal was important for the discrimination, in the 2005/2006 samples the *trans*-hexenal coefficient is almost zero while the hexanal coefficient is significant. On the other hand, some variables as *sn*-1,3 diglycerides, squalene, unsaturated fatty chains, wax, and linoleic fatty chains become positive and significant in the 2005/2006 model. As a consequence, when the model built on the 2005/2006 samples is used on the samples from the other two harvesting years, 79.2% and 80.0% non-error rates are obtained. In this case, the gap between the results on the training and on the validation set is smaller than for the 2004/2005 model, but is still relevant. With respect to the global model, VIP scores for 2005/2006 harvesting year, see Fig. 6b, suggest the importance of saturated fatty chains and wax in the model building whereas linolenic fatty chain does not contribute significantly to the model.

Lastly, a third model was built on the 2006/2007 samples (68 Ligurian and 177non-Ligurian) and validated on the samples from

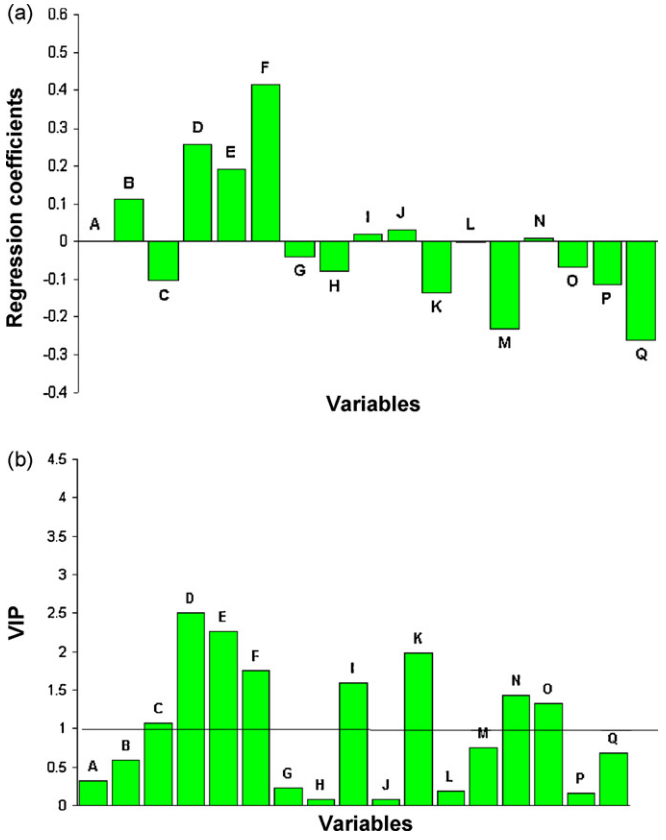


Fig. 5. The regression vector (a) and VIP scores (b) relative to the 2004/2005 harvesting year samples. See Fig. 1 for the labeling.

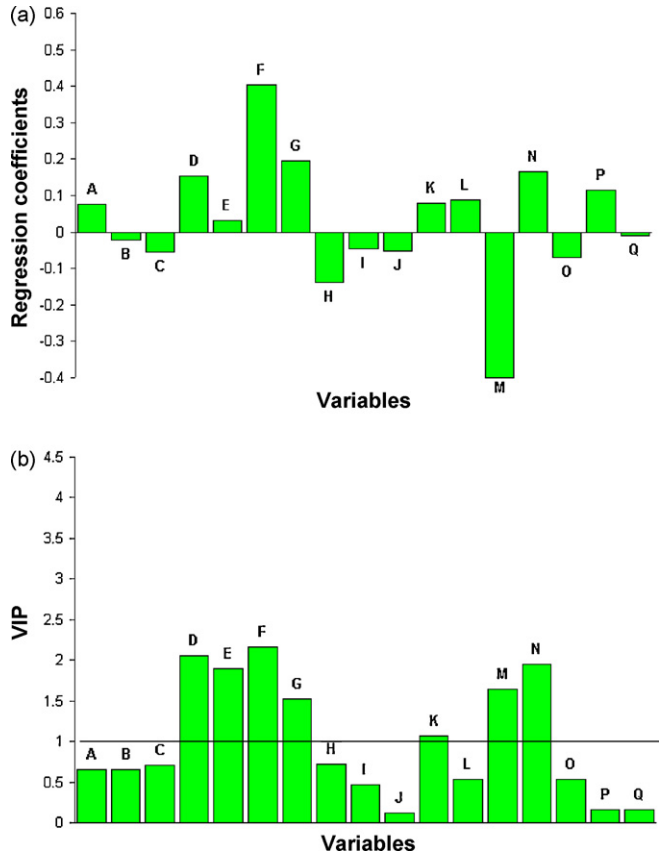


Fig. 6. The regression vector (a) and VIP scores (b) relative to the 2005/2006 harvesting year samples. See Fig. 1 for the labeling.

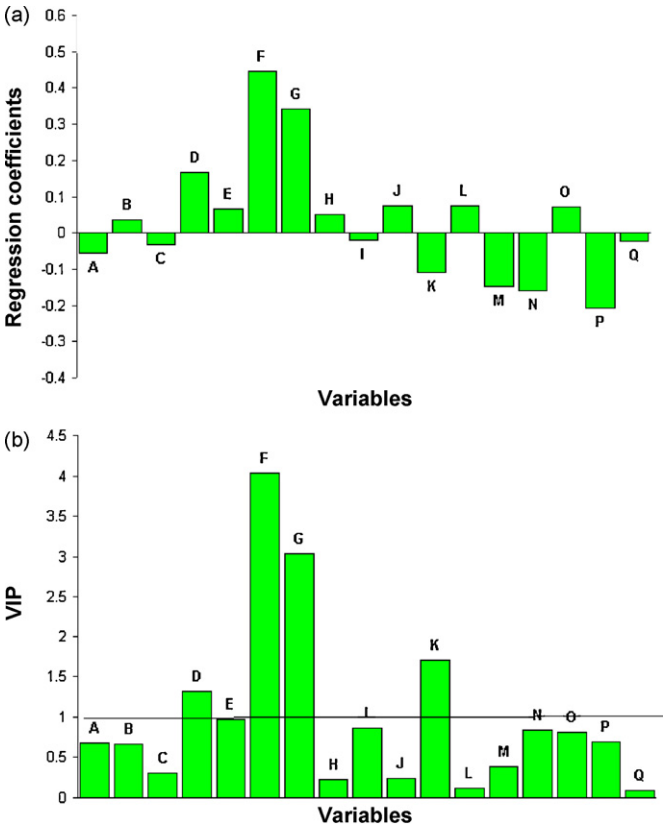


Fig. 7. The regression vector (a) and VIP scores (b) relative to the 2006/2007 harvesting year samples. See Fig. 1 for the labeling.

2004/2005 and 2005/2006 (141 samples from Liguria and 510 samples from the other regions). Three latent variables were selected on the basis of 10-fold cross-validation as the optimal complexity of the model, which provided, also in this case, a rather good and comparable non-error rate both in modeling (86.8% for Ligurian and 87.6% for the others) and cross-validation (86.8% for Ligurian and 86.4% for the others). Regression coefficients, see Fig. 7a, again confirm the importance of terpenes and saturated fatty chains in the discriminations. Ligurian samples of this harvesting year have a significantly lower amount of hexanal, squalene, saturated fatty chains, wax, and linoleic fatty chains. With respect to the global model, VIP scores, see Fig. 7b, suggest the importance of squalene in this model whereas linolenic fatty chain does not contribute significantly to the model.

When used for the prediction of the samples from the other two harvesting years, the 2006/2007 model showed a very poor classification ability in the case of the Ligurian samples (non-error rate was 54.6% for Liguria and 88.4% for the others).

All the results obtained for the model "Liguria" built in every single year are reported in Table 2.

3.2.2. SIMCA

The analysis of the year-to-year variability in the data and of the robustness of the pattern recognition models towards it was also carried out using SIMCA. As already described in the case of the global analysis, the use of SIMCA allows us to focus the attention on the category we want to trace, in particular the Ligurian samples, and build a model only of it. Accordingly, evaluation of the sensitivity and specificity of the optimized models provides a detailed information of whether the samples from other years are recognized by the category (or in other words "fall" within the category space) or not. As far as the 2004/2005 model is concerned, 9 principal components were selected on the basis of 10-fold cross-validation: this model showed a rather good sensitivity and specificity both in the modeling (96.8% sensitivity and 87.0% specificity) and in the cross-validation (82.3% sensitivity and 89.1% specificity) stages. However, this model was recognizing as outliers not only all the not-Liguria, but also all the Ligurian samples from the other two years (0% sensitivity and 100% specificity). Similar considerations, even if not as extreme as in this case, can be done for the 2005/2006 and 2006/2007 models.

The 2005/2006 model of Liguria (including 12 principal components) showed a rather good sensitivity and specificity for the samples of the same year (modeling: 93.7% sensitivity and 78.7% specificity; cross-validation: 81.0% sensitivity and 79.8% specificity) but a poor sensitivity for the Ligurian samples of the years 2004/2005 and 2006/2007 (14.6%). On the other hand, specificity with respect to non-Liguria samples of the other two harvesting years was rather high (93.5%).

Lastly, the model built on the 2006/2007 samples (9 principal components) resulted in 94.0% sensitivity and 78.5% specificity in modeling and in 85.1% sensitivity and 80.8% specificity in cross-validation, but in only 41.5% sensitivity and 90.2% specificity when it was applied to process the data of samples from 2005 and 2006. In all the examined cases, the analysis of the variables most contributing to the models confirmed the consideration already sketched when discussing the results of PLS-DA. The results obtained in modeling and in cross-validation for the model "Liguria" in every single year are reported in Table 2.

All the obtained results suggest some interesting general considerations. Olive oil as any natural "fruit juice" is a complex matrix

whose composition, quality etc depend on many different factors. Our study highlights two important aspects of Ligurian olive oils: Ligurian olive oils are always characterized by a high amount of terpenes and a low amount of saturated fatty chains. Although present in olive oils as minor components, terpenes, as volatile compounds, contribute to the sensory quality of olive oils and turned out to be important for the olive oil geographical characterization [7]. The high content of terpenes in Ligurian olive oils with respect to the other oils can be considered a "sensory marker" specific of these olive oils. On the other hand, the low amount of saturated fatty chains (probably due to the typical cultivar [8] present in this region and to the particular pedoclimatic conditions) is an important "quality marker" which makes these oils most suitable to particular diet regimes [22] among all others extra virgin olive oils. Saturated fatty acids are generally known as bad fats since they have the disadvantage of increasing the synthesis of cholesterol and promote cardiovascular problems.

The variability of some compounds in the three harvests can be due to different factors such as the different climatic conditions. The particularly hot summer in 2005 and 2006 years and/or the particularly rainy autumn in 2005 might be responsible for the observed variability.

Therefore, the NMR and chemometric approach extended to a relevant number of samples representative of the Mediterranean production has allowed not only to discriminate between Ligurian and not-Ligurian olive oils but also to define the Ligurian olive oil class which turned out to be characterized by specific sensory and quality markers. This methodology can give an important contribution in the actual debated problem of DPO characterization and confirmation.

Acknowledgement

This work was financially supported by EU TRACE project (FP6-2003-FOOD-2-A, contract number: 0060942: http://www.trace.eu.org/).

References

[1] European Communities, Commission Regulation (EC) No 182/2009 of 6 March 2009 amending Regulation (EC) No 1019/2002 on marketing standard for olive oil.
[2] T. Woodcock, G. Downey, C.P. O'Donnell, J. Agric. Food Chem. 56 (2008) 11520–11525.
[3] R. Boggia, P. Zunin, S. Lanteri, N. Rossi, F. Evangelisti, J. Agric. Food Chem. 50 (2002) 2444–2449.
[4] F. Balestrieri, R. Bucci, A.D. Magrì, A.L. Magrì, D. Marini, Chem. Int. Lab. Syst. 73 (2004) 85–93.
[5] G.J. Salter, M. Lazzari, L. Giansante, R. Goodacre, A. Jones, G. Surricchio, D.B. Kell, G. Bianchi, J. Anal. Appl. Pyrol. 41 (1997) 159–170.
[6] C. Armanino, R. Leardi, S. Lanteri, G. Modi, Chem. Int. Lab. Syst. 5 (1989) 343–350.
[7] L. Mannina, M. Patumi, N. Proietti, D. Bassi, A.L. Segre, J. Agric. Food Chem. 49 (2001) 2687–2696.
[8] L. Mannina, G. Dugo, F. Salvo, L. Cicero, G. Ansanelli, C. Calcagni, A.L. Segre, J. Agric. Food Chem. 51 (2003) 126–127.
[9] L. Mannina, M. Patumi, N. Proietti, A.L. Segre, Ital. J. Food Sci. 13 (2001) 53–63.
[10] M. D'Imperio, L. Mannina, D. Capitani, O. Bidet, E. Rossi, F.M. Bucarelli, G.B. Quaglia, A.L. Segre, Food Chem. 105 (2007) 1256–1267.
[11] B.G.M. Vandeginste, D.L. Massart, L.M.C. Buydens, S. De Jong, P.J. Lewi, J. Smeyers-Verbeke, Handbook of Chemometrics and Qualimetrics: Part B, Elsevier, Amsterdam, 1998, ISBN 0444828532, pp. 207–241.
[12] M. Forina, P. Olivieri, S. Lanteri, M. Casale, Chem. Int. Lab. Syst. 93 (2) (2008) 132–148.
[13] F. Marini, A.L. Magrì, R. Bucci, F. Balestrieri, D. Marini, Chem. Int. Lab. Syst. 80 (2006) 140–149.
[14] F. Marini, R. Bucci, A.L. Magrì, A.D. Magrì, Chem. Int. Lab. Syst. 84 (2006) 164–171.
[15] S. Wold, C. Albano, W.J. Dunn III, K. Esbensen, S. Hellberg, E. Johansson, M. Sjöström, in: H. Martens, H. Russwurm Jr. (Eds.), Food Research and Data Analysis, Elsevier Applied Science, Barking, 1983, ISBN 0853342067, pp. 147–188.
[16] M. Barker, W. Rayers, J. Chemometr. 17 (3) (2003) 166–173.
[17] S. Wold, Pattern Recognit. 8 (3) (1976) 127–139.
[18] S. Wold, M. Sjöström, in: B.R. Kowalski (Ed.), Chemometrics, Theory and Application, ACS Symposium Series No. 52, American Chemical Society, Washington, 1977, ISBN 0841203792, pp. 243–282.
[19] A.P. Sobolev, A.L. Segre, in: E. Brosio, S.G. Pandalai (Eds.), Basic NMR in Foods Characterization, Research Signpost, Kerala, India, 2009, ISBN 978-81-308-0303-6, pp. 63–78.
[20] S. Wold, H. Martens, H. Wold, in: A. Ruhe, B. Kagstrom (Eds.), Matrix Pencils: Proceedings of a Conference held at Pite Havsbad (Lecture Notes in Mathematics), Springer-Verlag, Heidelberg, 1983, ISBN 3540119833, pp. 286–293.
[21] R.A. Fisher, Ann. Eugen. 7 (1936) 179–188.
[22] J.J. Moreno, M.T. Mitjavila, J. Nutr. Biochem. 14 (4) (2003) 182–195.

Talanta 80 (2010) 2149–2156

Contents lists available at ScienceDirect

Talanta

journal homepage: www.elsevier.com/locate/talanta

Selective detection of dopamine in the presence of ascorbic acid using carbon nanotube modified screen-printed electrodes

Mónica Moreno[a,*], Alberto Sánchez Arribas[a], Esperanza Bermejo[a], Manuel Chicharro[a], Antonio Zapardiel[b], Marcela C. Rodríguez[c], Yamile Jalit[c], Gustavo A. Rivas[c]

[a] Dpto. Química Analítica y Análisis Instrumental, Universidad Autónoma de Madrid, C/Francisco Tomás y Valiente, 7, 28049 Madrid, Spain
[b] Dpto. Ciencias Analíticas, Universidad Nacional de Educación a Distancia, P° Senda del Rey, 9, 28040 Madrid, Spain
[c] INFIQC-Dpto. Físico Química, Facultad de Ciencias Químicas, Universidad Nacional de Córdoba, 5000 Córdoba, Argentina

ARTICLE INFO

Article history:
Received 16 July 2009
Received in revised form 29 October 2009
Accepted 5 November 2009
Available online 12 November 2009

Keywords:
Screen-printed electrode
Carbon nanotubes
Dopamine
Ascorbic acid

ABSTRACT

This work reports on the performance of carbon nanotube modified screen-printed electrodes (SPE-MWCNT) for the selective determination of dopamine (DA) in the presence of ascorbic acid (AA) by adsorptive stripping voltammetry (AdSV). Several operating conditions and parameters were examined including the electrochemical pre-treatment and the previous AA interaction and DA accumulation in the presence AA at physiological conditions. Under the chosen conditions, DA peak current of differential pulse voltammograms increases linearly with DA concentration in the range of 5.0×10^{-8} to 1.0×10^{-6} mol L^{-1} with a limit of detection of 1.5×10^{-8} mol L^{-1} in connection with 600 s accumulation time. The sensitivity obtained for DA was independent from the presence or absence of AA; therefore, the proposed method can be readily applied to detect DA in real samples. The proposed methodology was successfully used for the quantification of DA in urine samples.

© 2009 Elsevier B.V. All rights reserved.

1. Introduction

Dopamine (DA) is one of the most important and representative catecholamine which plays an important role in the function of the central nervous, renal, hormonal and cardiovascular systems. The determination of DA is a subject of great significance in the investigation of its physiological functions and the diagnosis of nervous diseases resulting from DA abnormal metabolism, such as epilepsy, Parkinsonism and senile dementia [1]. Since DA (and the like catecholamines) is an easily oxidizable compound, electrochemical methods based on its anodic oxidation are an ideal choice for its quantitative determination [2]. The electrochemical determination of dopamine allows reaching low detention limit but it is often complicated by many coexisting compounds. Among them, ascorbic acid (AA) is of particular importance because it accompanies dopamine in biological samples. Usually, the concentration of DA is 10^{-8} to 10^{-6} mol L^{-1} while AA is as high as 10^{-4} mol L^{-1} in these samples (in the extracellular fluid of the central nervous system) [3,4]. Furthermore, DA and AA are oxidized at nearly the same potential at almost all carbon-based or metal electrodes; hence an overlapping voltammetric response for the oxidation of a mixture of DA and AA is usually obtained. Moreover, the solid electrodes very often suffer from the fouling effect due to the accumulation of oxidized products on the electrode surface which results in rather poor selectivity and sensitivity [2].

Several examples are reported in the literature regarding on the detection of DA using chemically modified electrodes including electrochemically pre-treated electrodes [5], self-assembled monolayer modified electrodes [6,7], covalent modification [8–10], polymer film [11,12], composite electrodes [13–15], among other. The different properties of each type of electrode define its own associated advantages and limitations. The detection of DA in the presence of excess of AA is still a challenging task in electroanalytical research where both sensitivity and selectivity are equally important in the development of an appropriate sensor system. Screen-printing technique is a well-established and simple process for the mass production of single use electrodes and biosensors. These electroanalytical tools combine ease of use, portability and inexpensive manufacture procedure [16] with minimum analysis volume, low reagent and sample consumption or minor generation of contaminant residuals as well as their usefulness as disposable devices. Their inherent miniaturization promotes and facilitates the possibility of rapid in situ analysis even in a small scale environment. The incorporation of nanomaterials to these screen-printed devices is of great interest for the further development of electrochemical sensors. Among these materials, carbon nanotubes present a singular structure and dimensions together with unique electronic, chemical and mechanical properties [17,18].

* Corresponding author. Fax: +34 91 497 4931.
E-mail address: monica.moreno@uam.es (M. Moreno).

0039-9140/$ – see front matter © 2009 Elsevier B.V. All rights reserved.
doi:10.1016/j.talanta.2009.11.022

These remarkable features open new venues for the construction of sensors and the development of novel electrochemical bioassays [19–22]. As electrode material carbon nanotubes can facilitate electron transfer between the electroactive species and the electrode. In fact, different papers can be found in the literature where the enhancement of the rate constants for the electron transfer or electrocatalysis has been already demonstrated [23] and this was also observed when carbon nanotubes were employed in screen-printed electrodes [24]. The goal of the present paper is to investigate the voltammetric behavior of DA on screen-printed carbon nanotube electrode with the aim to propose a new methodology for its determination at low levels in the presence of ascorbic acid using a previous preconcentration step.

2. Experimental

2.1. Reagents

L-(+)-Ascorbic acid, $K_3Fe(CN)_6$ and $FeSO_4{\cdot}7H_2O$ were purchased from Panreac (Madrid, Spain) and 3-hydroxytyramine (dopamine) chloride, glucose, uric acid, 3,4 dihydroxyphenylacetic acid (dopac) and $Ru(NH_3)_6Cl_3$ were from Sigma (Madrid, Spain). All other chemicals were analytical grade and were used as received without further purification. Ultrapure water ($\rho > 18\,M\Omega\,cm$) from a Millipore-MilliQ system was used for preparing all solutions.

2.2. Apparatus and electrodes

The planar screen-printed electrode (DropSens, Oviedo, Spain) 3.4 cm × 1.0 cm × 0.05 cm (length × width × height) consists of three main parts which are a graphite counter electrode, a silver pseudo-reference electrode and a graphite working electrode, unmodified (SPE, ref. 110) or modified with multiwalled carbon nanotubes (10 nm diameter and 1–2 μm length) containing approximately 5% ratio of carboxylic groups (SPE-MWCNT, ref. 110CNT). The graphite working surface is 4 mm in diameter. Further details about them can be supplied from the following web site: www.dropsens.com.

Electrochemical measurements were performed by placing a 50 μL drop of the corresponding solution on the working area. Electrochemical measurements were conducted using a BAS 100B (BAS, West Lafayette, USA) electrochemical analyzer controlled by BAS W 2.3 software (BAS, West Lafayette, USA) through a Pentium IV PC computer or a μStat 100 potentiostat (DropSens, Oviedo, Spain) controlled by PSLite 1.6 software. A specific DropSens connector (ref. DSC) allowed the connection of the SPEs to the potentiostat. All experiments were carried out at room temperature (20–23 °C) using a new electrode for each assay.

2.3. Procedures

2.3.1. Electrode pre-treatment

The usual electrochemical pre-treatment of SPEs was carried out by applying +1.4 V for 300 s in 0.050 M phosphate buffer solution of pH 7.4.

2.3.2. Adsorptive stripping voltammetry

A 50 μL drop of 5.0×10^{-4} M AA in 0.050 M phosphate buffer (pH 7.4) was placed onto the working electrode area of a pre-treated SPE for 200 s, then rinsed with water and a volume of 50 μL of the given accumulation solution was placed for 10 min. Finally, after washing the electrode with water again, the differential pulse voltammetry (DPV) signal was recorded in fresh 0.050 M phosphate buffer (pH 7.4). The DPV parameters are the following: scan rate: 20 mV s^{-1}; pulse amplitude: 50 mV; sample width: 17 ms; pulse width: 50 ms; pulse period: 200 ms and quiet time: 2 s.

2.4. Sample preparation

Dopamine hydrochloride injection (CLORHIDRATO DOPAMINA GRIFOLS Amp. 200 mg/5 mL) was from GRIFOLS LABORATORY (Barcelona, Spain). Saline serum (Lactato de Ringer Hartmann Braun Sol. Iny) was from B. BRAUN MEDICAL, S.A. (Barcelona, Spain). Fresh urine samples from healthy donors were collected over a period of 24 h and they were acidified with HCl (to yield a final concentration of 1% of acid) and centrifuged to precipitate proteins. Then fractions of 10.0 mL of filtered urine were stored under refrigeration.

Dopamine hydrochloride injection samples were suitably diluted with 0.050 M phosphate buffer (pH 7.4) and doped with AA to obtain the desired concentration while saline serum was directly doped with AA and DA to obtain the desired concentrations. Urine samples were 10-fold diluted with 0.050 M phosphate buffer (pH 7.4) and spiked with DA and AA to obtain the desired concentrations.

3. Results and discussion

3.1. Electrode pre-treatment

Carbon electrodes are often preconditioned by electrochemical pre-treatments (EP) to enhance their electroactivity. The main effect of EP is the increase in the density of oxygenated groups on the electrode surface and the consequent improvement on the electron transfer [25,26]. In the case of SPE, the polymers present in the ink are responsible for slow charge transfer kinetics. Therefore, the activation of SPEs is often necessary for an optimum electrochemical performance *via* electrochemical pre-treatment [27].

To find an appropriate electrochemical pre-treatment for SPE and SPE-MWCNT, different electrolytes and conditions were studied using 1,4-benzoquinone in 0.050 M phosphate buffer solution of pH 7.4 as benchmark redox system. The electrochemical reduction of this marker in aqueous buffer to 1,4-hydroquinone is a well-known diffusion-controlled process involving 2 electrons and 2 protons [28].

Initially, the EP of SPE and SPE-MWCNT was carried out by applying anodic potentials ranging from +1.0 to +1.6 V in two different electrolyte solutions, 0.10 M H_2SO_4 and 0.050 M phosphate buffer solution of pH 7.4 for 60 s. The anodic-to-cathodic peak potential separation (ΔE_p), and the peak currents ratio (i_{pa}/i_{pc}) obtained from the cyclic voltammograms of 1,4-benzoquinone at untreated and pretreated SPE and SPE-MWCNT are summarized in Table 1. Regarding the untreated electrodes, the decrease in ΔE_p and the proximity of the obtained current ratio values to 1 at SPE-MWCNT, clearly demonstrate that the presence of MWCNTs at the SPE largely improved the electrochemical response of 1,4-benzoquinone. Considering pretreated electrodes, the EP mainly improves the electrochemical response of SPE. In general, as the EP applied potential increases, the reversibility of the redox couple improves at both electrodes, although in the case of SPE-MWCNT potentials as high as +1.6 V produce a negative effect on the response towards 1,4-benzoquinone. An EP is also necessary to eliminate small current contributions due to impurities present at SPE and SPE-MWCNT. Thus, a potential of +1.4 V was selected for further work.

The effect of the pre-treatment time at +1.4 V (0–300 s) in sulfuric acid and phosphate buffer solutions was also studied at SPE and SPE-MWCNT (not shown). As the pre-treatment time increased, up to 300 s, the reversibility of 1,4-benzoquinone improved. This EP time was also enough to eliminate the small contributions of fabrication impurities. A pre-treatment procedure consisting of

Table 1
Summary of cyclic voltammetry data for 5.0×10^{-4} M 1,4-benzoquinone before and after the pre-treatment[a].

Anodic potential (V)	SPE				SPE-MWCNT			
	0.10 M H_2SO_4		0.050 M phosphate buffer (pH = 7.4)		0.10 M H_2SO_4		0.050 M phosphate buffer (pH = 7.4)	
	ΔE_p (mV)	i_{pa}/i_{pc}	ΔE_p (mV)	i_{pa}/i_{pc}	ΔE_p (mV)	i_{pa}/i_{pc}	ΔE_p (mV)	i_{pa}/i_{pc}
Untreated	242	0.62	242	0.62	192	0.79	145	0.79
1.0	230	0.65	230	0.64	83	0.88	93	0.90
1.2	185	0.71	247	0.62	78	0.94	71	0.96
1.4	126	0.84	121	0.79	92	0.90	73	0.97
1.6	86	0.91	102	0.80	111	0.75	92	0.80

[a] Scan rate: 50 mV s^{-1}.

applying +1.4 V for 300 s in 0.050 M phosphate buffer solution of pH 7.4 was selected as the most advantageous and reproducible.

3.2. Electrochemical behavior of dopamine and ascorbic acid at SPE and SPE-MWCNT

Fig. 1 shows the cyclic voltammograms obtained for 1.0×10^{-3} M AA (A and D), 1.0×10^{-4} M DA (B and E) and a mixture of 1.0×10^{-3} M AA and 1.0×10^{-4} M DA (C and F) in 0.050 M phosphate buffer (pH 7.4) solution, on untreated SPE and SPE-MWCNT (a) and pre-treated ones (b). A decrease in the oxidation overvoltage for AA and a significant improvement in the reversibility for DA, compound that displays a quasi-reversible behavior at SPE (ΔE_p decreases 62 mV at SPE-MWCNT), was found at untreated SPE-MWCNT, demonstrating that the carbon nanotubes present at SPE-MWCNT make possible an important improvement in the voltammetric behavior of both compounds. At pre-treated SPE and SPE-MWCNT, the oxidation potential peak of AA shifts to more negative potentials at SPE and SPE-MWCNT (244 and 180 mV shifting, respectively); the ΔE_p for DA decreases (85 and 16 mV, respectively) while the anodic-to-cathodic peak currents ratio decreases from 2.5 to 2.3 at pre-treated SPE and from 3.1 to 1.7 at pre-treated SPE-MWCNT. Therefore, the EP improves the electrochemical response of AA and the reversibility of electron transfer processes for DA at both electrodes, although the most significant decrease in the oxidation overvoltages is obtained at pre-treated SPE. Nevertheless, as could be seen in panels C and F, these good features are not enough to allow the voltammetric quantification of a mixture of DA and AA, since unresolved signals were obtained either at untreated or pre-treated SPE and SPE-MWCNT. Indeed, DA oxidation signal was shifted to more positive potentials and overlapped with AA peak, probably as a consequence of crossing reactions of electrochemically generated DA oxidized forms with AA [2].

In order to evaluate the influence of adsorption processes on the electrochemical oxidation of AA and DA at pre-treated SPE and SPE-MWCNT, the effect of the scan rate on their voltammetric signals was studied from 5 to 200 mV s^{-1} (not shown). The anodic peak current, i_p, of AA (1.0×10^{-4} M) increased linearly with the square root of scan rate, $v^{1/2}$, at both electrodes (i_p (μA) = (0.26 ± 0.01) $v^{1/2}$ (mV s^{-1})$^{1/2}$, r = 0.990, n = 8 for SPE; i_p (μA) = (0.18 ± 0.01) $v^{1/2}$ (mV s^{-1})$^{1/2}$, r = 0.991, n = 7 for SPE-MWCNT), indicating that the AA electrode reaction is a diffusion-controlled process in both cases. On the other hand, the results obtained for DA (1.0×10^{-4} M) showed that, at variance with AA, the anodic (i_{pa}) and cathodic (i_{pc}) peak currents are proportional to the scan rate at SPE (i_{pa} (μA) = (0.073 ± 0.004) v (mV s^{-1}), r = 0.9997, n = 5; i_{pc} (μA) = (−0.047 ± 0.001) v (mV s^{-1}), r = −0.9997, n = 7) and at SPE-MWCNT (i_{pa} (μA) = (0.12 ± 0.01) v (mV s^{-1}), r = 0.997, n = 5; i_{pc} (μA) = (−0.073 ± 0.001) v (mV s^{-1}), r = −0.996, n = 7) suggesting that the electron transfer reaction is a surface (adsorption) controlled process [29].

For further demonstration, a preconcentration experiment was made by placing of AA (1.0×10^{-3} M) or DA (1.0×10^{-4} M) solutions on the working area of pre-treated SPE and SPE-MWCNT for 10 min and, after rising with water, recording the cyclic voltammogram in fresh buffer solution. No signal was obtained for AA, while DA peaks were clearly observed at SPE-MWCNT and weakly at SPE, pointing that DA is significantly adsorbed onto the surface of the SPE-MWCNT whereas AA was not.

3.3. Determination of DA in the presence of AA

The adsorption of DA at pre-treated SPE-MWCNT offers good possibilities for selective voltammetric detection of DA after a preconcentration in the presence of AA under physiological conditions.

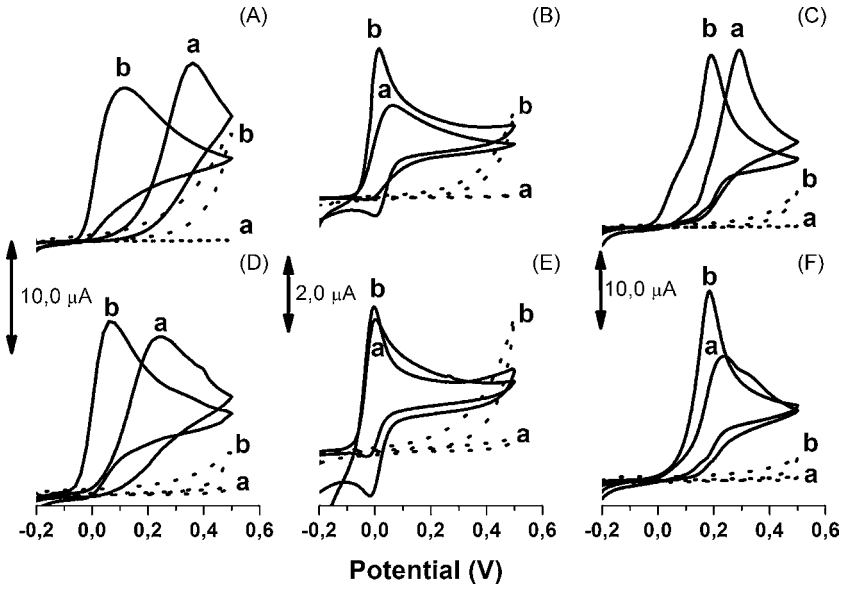


Fig. 1. Cyclic voltammograms for 1.0×10^{-3} M AA (A and D) and 1.0×10^{-4} M DA (B and E) and a mixture of both analytes in the same concentration as in individual solutions (C and F) in 0.050 M phosphate buffer (pH 7.4) solutions on SPE (A–C) and SPE-MWCNT (D–F) before (a) and after (b) the EP. The corresponding responses for the blank are also shown (dotted lines). Electrode pre-treatment: applying +1.4 V during 300 s in 0.050 M phosphate buffer (pH 7.4) solution. Scan rate: 25 mV s^{-1}.

In this sense, the selection of the experimental parameters was optimized for the development of a methodology employed differential pulse voltammetry (DPV), which allows the sensitive and selective determination of DA in the presence of a large excess of AA.

3.3.1. *Effect of AA on the voltammetric response of DA*

Fig. 2A displays differential pulse voltammograms obtained at pre-treated SPE-MWCNTs for 1.0×10^{-3} M AA, 1.0×10^{-5} M DA and a mixture of both analytes in the same concentration as in the individual solutions. The results are consistent with those obtained in the study by CV. The direct voltammetric determination of DA in the presence of AA is severely interfered due to the co-oxidation of ascorbic acid and an overlapping DPV response was obtained from a mixture of DA and AA. Furthermore, the results shown that the electrochemical process of DA is strongly influenced by the presence of AA (the oxidation peak of DA shifts to more positive potential), so different experiments were performed with the aim to acquire more insights about the influence of AA in the final DA electrochemical response. Fig. 2B displays a DPV obtained in 0.050 M phosphate buffer (pH 7.4) solution at a pre-treated SPE-MWCNT previously exposed for 5.0 min to 1.0×10^{-3} M AA and rinsed with ultrapure water (a). As expected, according to previous results, no oxidation current was obtained for AA after 5.0 min in the AA solution. Panel b shows a DPV obtained in 1.0×10^{-5} M DA solution at a pre-treated SPE-MWCNT previously exposed for 5.0 min to 1.0×10^{-3} M AA and rinsed with water, the DA oxidation peak shifts to more positive potentials (about 200 mV shifting) and the corresponding currents increases (2.0-fold) compared to DA signal obtained at an electrode previously exposed for 5.0 min to the phosphate buffer solution and rinsed with water (panel c). In this case, the oxidation peak potential and current for DA are the same as the ones obtained in the solution of DA (Fig. 2A). These results suggest that, although there is no electro-oxidation signal indicating the adsorption of AA, the interaction of AA with the electrode surface produces some modification that generates important changes in DA electrochemical process.

In order to take advantage of the improvement in DA sensitivity after AA exposure, the effect of the interaction time (from 0 to 10 min) of pre-treated SPE-MWCNT with 1.0×10^{-3} M AA on the differential pulse voltammetric peak of 1.0×10^{-5} M DA was evaluated and the corresponding results are shown in Fig. 3A. The peak current increases with the AA interaction time up to 150 s (2.0-fold) and then remains constant while the peak potential shifts to more positive potential up to 100 s (208 mV shifting). Hence, an interaction time of 200 s was selected for subsequent measurements.

The effect of AA concentration (from 5.0×10^{-6} to 1.0×10^{-3} M) on the differential pulse voltammetry peak of 1.0×10^{-5} M DA was also investigated. The experiments were carried out setting

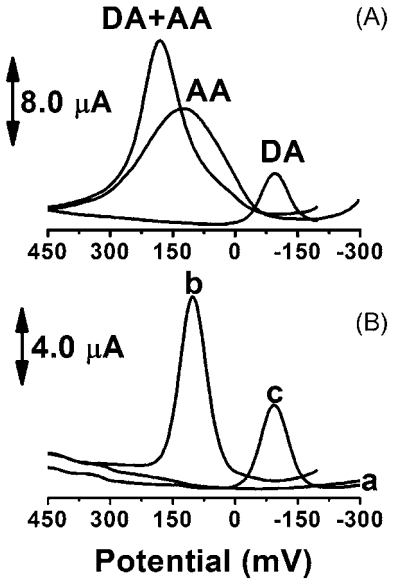


Fig. 2. DPV signals obtained in 0.050 M phosphate buffer (pH 7.4) with a pre-treated SPE-MWCNT. (A) Direct measurement of DA (1.0×10^{-5} M), AA (1.0×10^{-3} M) and a mixture of DA and AA (1.0×10^{-5} and 1.0×10^{-3} M, respectively). (B) DPV signals of blank phosphate buffer (a) and DA (1.0×10^{-5} M) (b and c) with prior exposition to 0.050 M phosphate buffer (pH 7.4) for 300 s at open circuit with (a and b) and without (c) AA (1.0×10^{-3} M). EP as in Fig. 1. DPV operational parameters: pulse amplitude: 50 mV; sample width: 17 ms; pulse width: 50 ms; pulse period: 200 ms; quiet time: 2 s; scan rate: 20 mV s^{-1}.

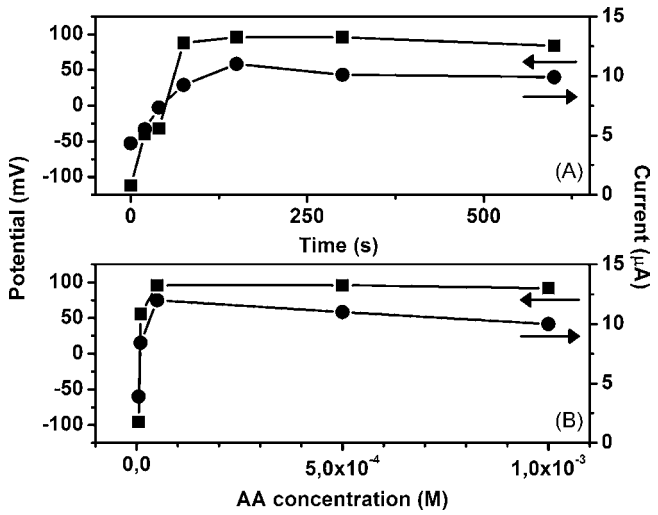


Fig. 3. Effect of AA on differential pulse voltammetry peak of DA (1.0×10^{-5} M) in 0.050 M phosphate buffer (pH 7.4). Effect of the interaction time (A): AA concentration: 1.0×10^{-3} M; effect of AA concentration (B): interaction time: 200 s. EP and DPV operational parameters as in Fig. 2.

an interaction time of 200 s. Fig. 3B shows that DA peak current increases with AA concentration up to 1.0×10^{-4} M, to remain constant thereafter. A similar trend was obtained for the peak potential which shifted to more positive values with AA concentration up to 1.0×10^{-4} M.

The results obtained suggest that no further improvement could be achieved in DA oxidation signal with larger AA concentration or longer interaction time. In view of these results and taking into account the concentration range of AA in biological samples, the selected conditions for AA interaction were 5.0×10^{-4} M AA in a 0.050 M phosphate buffer (pH 7.4) for 200 s. In this way, the DA voltammetric signal should be independent of the concentration of AA in the sample.

3.3.2. *Electrochemical characterization of the effect of AA interaction after EP*

As it was already mentioned in Section 3.1, during anodic EP several processes take place on SPE surface producing important changes, such as increase of surface active area, water oxidation to molecular oxygen (and other reactive species) [30,31] and formation of different carbon oxides [26]. When carbon nanotubes are present, EP could lead, in addition, to open their capped ends or side-walls, introducing in this way new edge plane like sites [31]. Usually, after these treatments the electrochemical performance of such electrodes is finally improved by introducing catalytic oxygenated groups and edge plane like sites within their graphene layers structure, that increase the electron transfer rate of many analytes [23,26].

Changes induced by an AA exposition on an anodized SPE-MWCNT surface could be related to its reducing properties towards carbon oxides and oxygenated species formed after EP. In order to evaluate such effect, CV of representative electrochemical benchmarks, namely hexaammineruthenium (III), hexacyanoferrate (III), iron (II), oxygen, AA and DA, were performed at untreated and pretreated SPE-MWCNT with and without AA interaction and the obtained results are summarized in Table 2.

The first tested probe was $Ru(NH_3)_6^{3+/2+}$ system, classified as an outer-sphere electrochemical process and typically unaffected by the chemical condition of the carbon electrode surface [26]. As expected, the observed electron transfer kinetics, expressed by the measured ΔE_p, was similar and relatively fast in all cases. The EP effect observed was just the increase of active surface, which was denoted by the peak current and capacitance (not shown) rise, and a slight increase in ΔE_p.

Concerning the electrochemical behavior of $Fe(CN)_6^{3-/4-}$ system, it has been reported that its electrochemistry is somehow surface dependant in several conditions [26,32]. The results obtained show that untreated SPEs display noticeable better reversibility than the treated ones, with larger ΔE_p after EP than after EP followed by AA interaction. This fact indicates that favorable electroactive sites for hexacyanoferrate were blocked after EP and part of them were recovered after AA treatment. Compton et al. have reported slower electron transfer kinetics for this electrochemical system when oxygenated species were generated in pyrolytic graphite and carbon nanotubes [32,33]. The suggested explanation was the formation of epoxy-like bridges between graphene layers in the edge plane of pyrolytic graphite which prevent the electron transfer in these sites. MWCNT employed in the SPE-MWCNT under study were functionalized with carboxylic groups by the manufacturer so these groups were present at untreated electrodes. Therefore, they did not affect the electron transfer rate as severely as EP did. It is very often assumed that EP of carbon electrodes only introduces new oxides (typically carboxylic, carbonyl and quinone groups) in their graphene planes structure but the generation of molecular oxygen and other reactive species at the edge plane like sites is usually ignored. Since most of these species were not removed from the electrode surface after EP, probably they could be adsorbed at edge plane sites and disturbing the electron transfer of redox systems such as hexacyanoferrate, especially sensitive to these sites. After AA treatment, these reactive oxygen species were reduced, liberating in this way the edge plane sites and subsequently increasing the observed hexacyanoferrate electron transfer. This rationale could also explain the slight increase on ΔE_p of hexaammineruthenium system after EP.

Next, attention was turned to $Fe^{2+/3+}$ system, whose electron transfer kinetics is well-known to be accelerated when carbonyl groups are present in the electrode surface [34]. Untreated SPE-MWCNT displayed large ΔE_p which indicated low density of carbonyl groups in MWCNT surface and poor catalytic activity of carboxylic substituents or edge plane like sites towards this system. As expected, EP largely improved the reversibility of the electrochemical system as a consequence of the introduction of new carbonyl groups. When SPE-MWCNTs were treated with AA after EP, measured ΔE_p was the same to the one obtained with SPE-MWCNT subjected only to EP. Thus, the generated carbonyl groups were not modified by AA and the same electron transfer kinetics was observed. These results reinforce the idea that AA interacts with other reactive substances or substituents distributed along MWCNT surface rather than with carboxylic, carbonyl or quinone ones.

The next electrochemical system studied was the molecular oxygen reduction which is favored when a high density of edge plane like sites is present at the electrode surface and it is also catalyzed by quinone groups [35,36]. The overpotential needed for oxygen reduction moderately decreases after EP while a larger decrease was observed after AA interaction. The peak currents were proportional to scan rate in all cases (not shown), indicating that this electrochemical process is adsorption-controlled. These results suggest again that after AA exposition, edge plane like sites are liberated, increasing the electron transfer rate and promoting the adsorption of oxygen. As a consequence of that, lower overpotentials and higher currents are obtained.

Similarly to oxygen reduction, AA oxidation is an example of inner-sphere electrochemical process [26] whose overpotential is typically decreased by the presence of edge plane like sites [37] as well as after EP [35,38]. As expected, EP of SPE-MWCNT produces a significant decrease of the overpotential and an important enhancement of the associated currents. The AA treatment only

Table 2
Summary of cyclic voltammetry data for different electrochemical benchmarks before and after the treatments[a].

Compound	Electrode treatment	Ep_a (mV)	Ep_c (mV)	ΔE_p (mV)	i_{pa} (μA)	i_{pc} (μA)	i_{pa}/i_{pc}
$Ru(NH_3)_6^{+3}$	Untreated	−194	−264	70	15.0	−19.9	0.75
	Pre-treated	−191	−271	80	13.4	−24.5	0.55
	Pre-treated + AA	−199	−276	77	12.2	−23.9	0.51
$K_3Fe(CN)_6$	Untreated	155	55	100	19.0	−19.2	0.99
	Pre-treated	188	35	153	15.1	−15.8	0.95
	Pre-treated + AA	184	60	124	17.5	−17.5	1.00
$FeSO_4{\cdot}7H_2O$	Untreated	591	68	523	13.6	−8.17	1.67
	Pre-treated	270	160	110	16.3	−21.5	0.76
	Pre-treated + AA	287	177	110	16.5	−22.7	0.73
AA	Untreated	358	–	–	21.8	–	–
	Pre-treated	205	–	–	19.0	–	–
	Pre-treated + AA	195	–	–	20.8	–	–
DA	Untreated	158	84	74	3.88	−1.72	2.26
	Pre-treated	147	100	47	9.36	−4.32	2.17
	Pre-treated + AA	150	110	40	10.4	−4.24	2.46
O_2	Untreated	–	−959	–	−43.6	–	–
	Pre-treated	–	−844	–	−53.1	–	–
	Pre-treated + AA	–	−495	–	−49.1	–	–

[a] Experimental conditions: 1.0×10^{-3} M $Ru(NH_3)_6^{+3}$ and 1.0×10^{-3} M $K_3Fe(CN)_6$ in KCl 0.1 M; 1.0×10^{-3} M $FeSO_4{\cdot}7H_2O$ in $HClO_4$ 0.1 M; 1.0×10^{-3} M AA and 1.0×10^{-4} M DA in 0.050 M phosphate buffer solution (pH 7.4). Scan rate: 50 mV s^{-1}. Results shown were obtained from the average at three measurements using different electrodes. Standard deviations of measured potentials were lower than 10 mV in all cases.

supposes a slight decrease in the observed peak potential indicating that the main improvement in the electron transfer kinetics was due to oxygenated groups generated after the EP. In all cases, this electrochemical process was diffusion-controlled as peak currents were proportional to the square root of scan rate. Since adsorption did not control this electrochemical process, the positive effect of AA treatment was lighter in this case.

Finally, the effect of EP and AA exposure on DA electrochemical oxidation was also studied. This process is known to be strongly affected by surface cleanliness, presence of oxygenated groups and presence of edge plane sites, since both electrocatalysis and adsorption play a key role in DA electrochemistry [39,40]. The results obtained were qualitatively equal to those described in the precedent section where EP promotes an enhancement in electron transfer kinetics as well as an electrocatalytic effect revealed by the increase of peak currents. The further improvement in ΔE_p and sensitivity after AA treatment should be ascribed to liberation of more edge plane sites for DA adsorption.

From the results exposed all along this section it could be concluded that the improvements achieved using the AA treatment after EP are related to the reduction and elimination of reactive species located preferentially at edge plane sites which decrease the electron transfer kinetics but also especially prevent the adsorption in these sites of electroactive targets as DA in our case. The result of such treatment is a noticeable improvement in the electron transfer process and an important favoring of adsorption-controlled processes.

3.3.3. *Adsorptive behaviour of Dopamine at pre-treated SPE-MWCNT*

Taking into account the capability of the pre-treated SPE-MWCNT for the selective adsorption of DA in the presence of AA, DA was determined by adsorptive stripping voltammetry (AdSV) in presence of a large excess of AA. The experiment was carried out as follows: a 5.0×10^{-4} M AA was placed onto the pre-treated electrode during 200 s, then it was rinsed with water and the given accumulation solution was placed on the electrode for 600 s at open circuit. Finally, after washing the electrode with water again, the DPV signal was recorded in a fresh phosphate buffer solution. Fig. 4 shows the voltammograms obtained employing different accumulation solutions: blank phosphate buffer (a), 5.0×10^{-4} M AA (b), 1.0×10^{-5} M DA (c) and a mixture of 5.0×10^{-4} M AA and 1.0×10^{-5} M DA (d). An oxidation peak around 120 mV was obtained only when DA was present in the accumulation solution, demonstrating that DA is selectively adsorbed on the electrode surface. These facts are consistent with the results obtained in the previous studies. The difference in the peak oxidation current for the neurotransmitter alone or in the presence of AA is 16% (16 μA *vs* 19 μA for DA and DA + AA, respectively). The same behavior was observed for an accumulation solution containing 10-fold lower DA concentration and the same AA excess.

The analytical features of DA detection using the proposed scheme were subsequently evaluated. Fig. 5A displays differential pulse voltammograms obtained from solutions containing DA in concentration between 5×10^{-8} and 1.0×10^{-6} M in the presence of 5.0×10^{-4} M AA and the resulting calibration plot (shown as inset). A linear dependence between DA concentration and stripping peak current was observed for the concentration range studied with a regression equation of i_p (μA) = (0.16 ± 0.04) + (3.01 ± 0.08) × 10^6 C (mol L^{-1}), $r = 0.993$, $n = 8$. The limit of detection was 1.5×10^{-8} M,

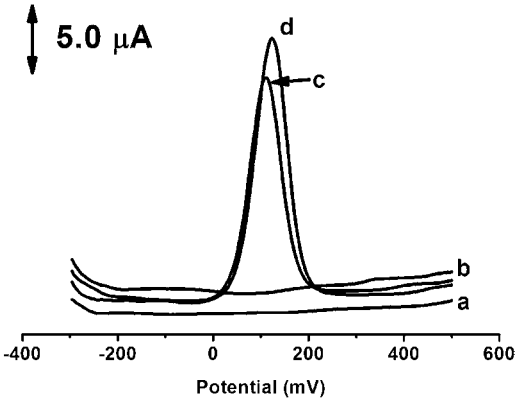


Fig. 4. AdSV obtained for different accumulation solutions: (a) blank 0.050 M phosphate buffer (pH 7.4); (b) 5.0×10^{-4} M AA; (c) 1.0×10^{-5} M DA and (d) mixture of 5.0×10^{-4} M AA and 1.0×10^{-5} M DA. Measuring procedure: (1) EP as in Fig. 2; (2) 50 μL drop of 5.0×10^{-4} M AA in 0.050 M phosphate buffer (pH 7.4) during 200 s; (3) 50 μL drop of accumulation solution during 600 s at open circuit; (4) DPV obtained in 0.050 M phosphate buffer (pH 7.4), operational parameters as in Fig. 2.

Table 3
Determination of dopamine in injections.

Sample no.	Content		Dopamine found ($\times 10^{-7}$ M)	Recovery (%)
	Dopamine ($\times 10^{-7}$ M)	Ascorbic acid ($\times 10^{-4}$ M)		
1	3.0	0	2.8	93
2	3.0	0	3.1	103
3	3.0	0	2.9	97
4	3.0	1.0	2.8	93
5	3.0	1.0	3.1	103
6	3.0	5.0	2.9	97
7	3.0	5.0	2.8	93

calculated using the $S/N = 3$ criterion, being S the sensitivity and N the standard deviation of 10 background signals. The reproducibility of the method was determined by performing 10 successive measurements of 1.0×10^{-6} M DA solutions in the presence of 5.0×10^{-4} M AA using different SPE-MWCNT. The relative standard deviation obtained was 5.6% ($n = 10$).

A closer approach to actual capabilities under physiological conditions was carried out using a synthetic serum as model matrix. Differential pulse voltammograms from samples with DA concentration between 5.0×10^{-8} and 1.0×10^{-6} M in the presence of 5.0×10^{-4} M AA in such saline serum (Na^+ 131, K^+ 5.4, Ca^{2+} 3.6, Cl^- 112, lactate 28 mEq L^{-1} with pH range 5.0–7.0) were obtained. As shown in Fig. 5B, the signal of DA was not affected by the presence of these ions and the sensitivity obtained working under these physiological conditions ($(3.2 \pm 0.2) \times 10^6$ (μA L mol^{-1})) was similar to that obtained measuring in phosphate buffer solution, indicating that the components of saline serum do not compromise the performance of the SPE and this methodology could be readily employed to DA analysis in serum samples. In addition the possible interference of coexisting 1.0×10^{-3} M glucose, 1.0×10^{-4} M uric acid or 5.0×10^{-5} M dopac was studied and variations on 1.0×10^{-6} M DA signal were similar to those observed for different SPE-MWCNT in the reproducibility study.

3.3.4. Analytical applications

The utility of the developed DA electrochemical detection scheme involving SPE-MWCNT was demonstrated in connection to the DA quantification in a pharmaceutical product (Dopamine chlorhydrate, 40 mg mL^{-1}) and in spiked samples of human urine.

Diluted samples of pharmaceutical product were determined using the proposed method in the presence or absence of different concentration of AA. Recovery results were obtained under these conditions by the standard addition method (three 2.0×10^{-7} M DA additions were made) and they are shown in Table 3. Recovery values close to 100% were obtained in all cases, demonstrating the ability of SPE-MWCNT for the selective determination of DA in real samples.

Fresh urine samples collected over a period of 24 h were treated as described in Section 2. Urine samples were 10-fold diluted with phosphate buffer (pH 7.4) and then spiked with increasing amounts of DA in the range of 1.0×10^{-7} to 2.0×10^{-6} M while keeping a constant AA concentration of 5.0×10^{-4} M. Fig. 6 shows the voltammograms obtained and the resulting calibration plot (shown as inset). Unspiked samples showed a weak DA response, insufficient for a suitable quantification. A linear dependence between DA concentration and stripping peak current was observed for spiked samples in the concentration range studied, with a regression equation of i_p (μA) = $(0.05 \pm 0.01) + (7.9 \pm 0.3) \times 10^5$ C (mol L^{-1}), $r = 0.9994$ $n = 4$. It could be noted that the sensitivity obtained in this matrix was lower than that achieved only in the presence of phosphate buffer, pointing that the proposed methodology is yet useful and applicable but the interference of urine components make mandatory the use of the standard

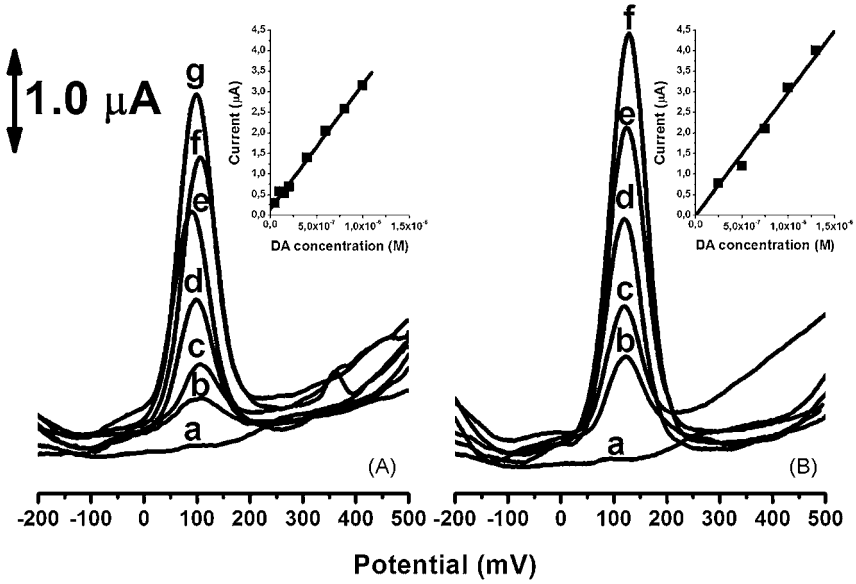


Fig. 5. Effect of DA concentration in the presence of AA 5.0×10^{-4} M upon the stripping voltammetric signal in 0.050 M phosphate buffer (pH 7.4) (A) and saline serum (B) at pre-treated SPE-MWCNT. Dopamine concentration: (A) (a) 0, (b) 5.0×10^{-8}, (c) 1.0×10^{-7}, (d) 4.0×10^{-7}, (e) 6.0×10^{-7}, (f) 8.0×10^{-7} and (g) 1.0×10^{-6} M; (B) (a) 0, (b) 2.5×10^{-7}, (c) 5.0×10^{-7}, (d) 7.5×10^{-7}, and (e) 1.0×10^{-6} and (f) 1.3×10^{-6} M. Measuring procedure as in Fig. 4.

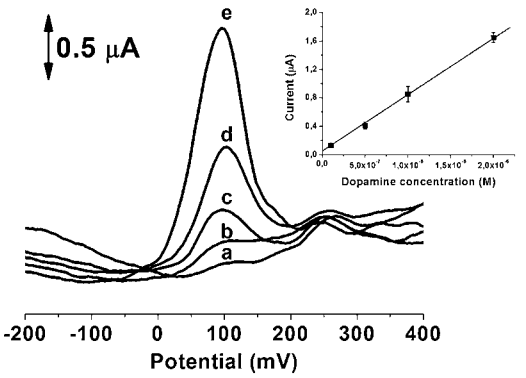


Fig. 6. Effect of DA concentration in the presence of AA 5.0×10^{-4} M upon the stripping voltammetric signal in urine sample at pre-treated SPE-MWCNT. Added DA concentration: (a) 0, (b) 1.0×10^{-7}, (c) 5.0×10^{-7}, (d) 1.0×10^{-6}, and (e) 2.0×10^{-6} M. Measuring procedure as in Fig. 4.

addition method for reliable DA quantification under these conditions.

4. Conclusion

The results presented in this work have demonstrated that the electrode pre-treatment and the presence of carbon nanotubes played a key role in the final electrochemical response of SPE-MWCNT. The proposed methodology have allowed the highly sensitive and selective DA quantification in the presence of large AA excess using low sample with little reagent consumption and simple sample treatment, showing potential application to DA determination in serum and urine. Therefore, the important advantages obtained when combining screen-printing devices with nanomaterials for one-shot electrochemical analysis, especially required for bionalytical applications, have been proved, opening the doors to the design of further bioanalytical devices.

Acknowledgement

Ministerio de Ciencia e Innovación (Grant CTQ2008-06489-C02-01-02) is gratefully acknowledged for funding this work.

References

[1] G. Zou, Basic Nerve Pharmacology, Science Press, Beijing, 1999, p. 203.
[2] A.R. Shah, P.R. Rishi, B. Yetunde, M. Yufeng, H. Huixin, Sensors 8 (2008) 8423–8452.
[3] A. Ciszewski, G. Milczarck, Anal. Chem. 71 (1999) 1055–1061.
[4] J. Zheng, X. Zhou, Bioelectrochemistry 70 (2007) 408–415.
[5] G. Haiying, X. Yi, P. Weilin, L. Gexi, C. Hong-Yuan, Microchim. Acta 146 (2004) 223–227.
[6] C.R. Raj, T. Okajima, T. Ohsaka, J. Electroanal. Chem. 543 (2003) 127–133.
[7] J.W. Kang, L. Zhuo, X.Q. Lu, X.Q. Wang, J. Solid State Electrochem. 9 (2005) 114–120.
[8] L. Zhang, X.Q. Lin, Fresenius, J. Anal. Chem. 370 (2001) 956–962.
[9] L. Zhang, Y.G. Sun, X.Q. Lin, Anal. Bioanal. Chem. 382 (2005) 1669–1677.
[10] L. Zhang, Y.G. Sun, X.Q. Lin, Analyst 126 (2001) 1760–1763.
[11] P.F. Huang, L. Wang, J.Y. Bai, H.J. Wang, Y.Q. Zhao, S.D. Fan, Microchim. Acta 157 (2007) 41–47.
[12] W. Chen, X.H. Lin, L.Y. Huang, H.B. Luo, Microchim. Acta 151 (2005) 101–107.
[13] C.Y. Liu, J.F. Hu, H.W. Tang, Electroanalysis 18 (2005) 479–485.
[14] H.S. Wang, T.H. Li, W.L. Jia, H.Y. Xu, Biosens. Bioelectron. 22 (2006) 664–669.
[15] Y.Z. Zhang, Y.J. Cai, S. Su, Anal. Biochem. 350 (2006) 285–291.
[16] K.C. Honeychurch, J.P. Hart, Trends Anal. Chem. 22 (2003) 456–469.
[17] M. Paradise, T. Goswami, Mater. Des. 28 (2007) 1477–1489.
[18] P.M. Ajayan, Chem. Rev. 99 (1999) 1787–1799.
[19] A. Merkoçi, M. Pumera, X. Llopis, B. Perez, M. Valle, S. Alegret, Trends Anal. Chem. 24 (2005) 826–838.
[20] M. Trojanowicz, Trends Anal. Chem. 25 (2006) 480–489.
[21] K. Balasubramanian, M. Burghard, Anal. Bioanal. Chem. 385 (2006) 452–468.
[22] M. Pumera, S. Sanchez, I. Ichinose, J. Tang, Sens. Actuators B 123 (2007) 1195–1205.
[23] C.E. Banks, R.G. Compton, Analyst 131 (2006) 15–21.
[24] P. Fanjul-Bolado, P. Queipo, P.J. Lamas-Ardisana, A. Costa-García, Talanta 74 (2007) 427–433.
[25] R.L. McCreery, in: A.J. Bard (Ed.), Electroanalytical Chemistry, Dekker, New York, 1991, pp. 221–374.
[26] R.L. McCreery, Chem. Rev. 108 (2008) 2646–2687.
[27] J. Wang, M. Pedrero, H. Sakslund, O. Hammerich, J. Pingarron, Analyst 121 (1996) 345–350.
[28] J. Zhang, S. Yao, L. Nie, W. Wei, Anal. Sci. 16 (2000) 87–91.
[29] A.J. Bard, R.L. Faulkner, Electrochemical Methods. Fundamentals and Applications, 2nd ed., Willey, New York, 2001.
[30] R. Larciprete, S. Gardonio, L. Petaccia, S. Lizzit, Carbon 47 (2009) 2579–2585.
[31] M. Pumera, T. Sasaki, H. Iwai, Chem. Asian J. 3 (2008) 2046–2055.
[32] X. Ji, C.E. Banks, A. Crossley, R.G. Compton, Chemphyschem 7 (2006) 1337–1344.
[33] A.F. Holloway, G.G. Wildgoose, R.G. Compton, L. Shao, M.H. Green, J. Solid State Electrochem. 12 (2008) 1337–1348.
[34] P. Chen, M.A. Fryling, R.L. McCreery, Anal. Chem. 67 (1995) 3115–3122.
[35] K. Gong, S. Chakrabarti, L. Dai, Angew. Chem. Int. Ed. 47 (2008) 5446–5450.
[36] G. Jürmann, K. Tammeveski, J. Electroanal. Chem. 597 (2006) 119–126.
[37] F. Wantz, C.E. Banks, R.G. Compton, Electroanalysis 17 (2005) 1529–1533.
[38] M. Musameh, N.S. Lawrence, J. Wang, Electrochem. Commun. 7 (2005) 14–18.
[39] S.H. DuVall, R.L. McCreery, J. Am. Chem. Soc. 122 (2000) 6759–6764.
[40] A.G. Crevillén, M. Pumera, M.C. González, A. Escarpa, Analyst 134 (2009) 657–662.

Talanta 80 (2010) 2157–2164

Contents lists available at ScienceDirect

Talanta

journal homepage: www.elsevier.com/locate/talanta

A novel low-cost and easy to develop functionalization platform. Case study: Aptamer-based detection of thrombin by surface plasmon resonance

Cristina Polonschii[a], Sorin David[a], Sara Tombelli[b], Marco Mascini[b], Mihaela Gheorghiu[a,*]

[a] International Centre of Biodynamics, Intrarea Portocalelor 1B, 060101 Bucharest, Romania
[b] Department of Chemistry, University of Florence, Via della Lastruccia 3, 50019 Sesto Fiorentino, Italy

ARTICLE INFO

Article history:
Received 4 August 2009
Received in revised form 27 October 2009
Accepted 5 November 2009
Available online 12 November 2009

Keywords:
Carboxylated cross-linked BSA film
Thrombin
Aptamer
Surface plasmon resonance
Spreeta

ABSTRACT

A novel low-cost platform to assess biomolecular interactions was investigated using surface plasmon resonance and an aptamer-based assay for thrombin detection. Gold SPR surface functionalized with a carboxylated cross-linked BSA film (cBSA) and commercially available carboxymethylated dextran chip (CM5) were used as immobilization platforms for the thrombin binding aptamer. The high end commercial instrument Biacore 3000 and a custom made FIA set-up involving TI Spreeta sensor (TSPR2K23) were used to assess different concentrations of thrombin within the range 0.1–150 nM both in buffer and in a complex matrix (plasma) using the obtained aptasensors. Based on data derived from both CM5 and cBSA platforms, the cBSA aptasensor exhibited good selectivity, stability and regeneration ability, both in buffer and in complex matrices (plasma), comparable with CM5.

© 2009 Elsevier B.V. All rights reserved.

1. Introduction

Bioaffinity-based methods of detection usually require immobilization of one interaction partner (ligand) to the biosensor surface. Typically the ligand can be a protein or a nucleic acid. As direct physical adsorption to surfaces induces denaturation of the proteins [1], an intermediate functionalization layer for protein immobilization is needed. Thus the protein ligand will not be in direct contact with the surface hence preserving its binding activity. Currently there are several functionalization protocols and commercially available platforms for biomolecules immobilization such as carboxymethylated dextran with various carboxymethylation levels, or self-assembled monolayer of thiols, proteins, etc. [2]. The commercial platforms are usually expensive, while less expensive custom preparation protocols may require several days. Moreover, the preparation requires thorough cleaning of the surface with strong oxidizing solutions that can damage the surface or, if the case, the plastic housing.

The aim of this study was to investigate the use of the carboxylated cross-linked bovine serum albumin (cBSA) film as a functionalization platform for immobilization of biomolecules and its feasibility for surface plasmon resonance assays for thrombin quantification in complex media. The cBSA film was selected due to its carboxyl groups which allow further immobilization of biomolecules via amino-coupling chemistry and its BSA background providing good blocking ability of the gold surface. As a reference we used the CM5 sensor (Biacore AB, now GE Healthcare), a carboxymethylated 3D dextran matrix, which is a general purpose chip for immobilization of a wide range of ligands, from small organic molecules to proteins, nucleic acids and carbohydrates. The cBSA and CM5 functionalization platforms immobilized with the thrombin binding aptamer were investigated comparatively in terms of thrombin detection using the Biacore 3000. Furthermore, the cBSA platform was also implemented on a low-cost, versatile Spreeta (Texas Instruments, USA) based SPR system for aptamer immobilization and thrombin detection in buffer and in plasma.

Thrombin and its specific aptamer were selected for this study not only because this bioaffinity pair is well studied, but also because thrombin detection and quantification in complex biological samples such as serum or plasma is clinically relevant and development of an easy to use and cost-effective measurement system is of great interest. Blood coagulation conventional assays are usually indirect because they measure the clotting fibrinogen, which also depends on other factors [3].

Thrombin (coagulation factor II) is a highly specific serine protease of trypsin-like specificity that converts soluble fibrinogen into insoluble strands of fibrin. This protein which plays an important role in thrombosis and hemostasis exhibits both enzymatic and

* Corresponding author. Tel.: +40 21 3104354; fax: +40 21 3104361.
E-mail address: mgheorghiu@biodyn.ro (M. Gheorghiu).

0039-9140/$ – see front matter © 2009 Elsevier B.V. All rights reserved.
doi:10.1016/j.talanta.2009.11.023

hormone-like properties that can be both pro- and anti-coagulant. Therefore, thrombin is a key element in various pathogenesis such as leukemia, arterial thrombosis, liver disease, etc. [4] and regulates numerous processes in inflammation and tissue repair at the vessel wall [5].

Thrombin also has hormone-like properties—it can regulate cell signaling by cleaving and activating receptors [6] and it binds with and activates blood cells (except erythrocytes), endothelial cells, fibroblasts, etc. [7].

Thrombin concentration in blood can vary significantly: under normal conditions thrombin is present in blood in its inactive form (prothrombin) and during the coagulation process can reach low micromolar concentrations. Low nanomolar levels of thrombin generated when hemostasis is initiated are also important to the entire process. Thrombin has also been detected at high picomolar range in blood of patients with coagulation abnormalities [8].

Aptamers are oligonucleic acid molecules that bind to a specific target molecule and are created by *in vitro* selection from a large random sequence pool by the SELEX (Systematic Evolution of Ligands by Exponential Enrichment) process. They are highly specific towards their molecular targets, which range from small inorganic and organic substances to proteins and even cells [4]. Although aptamers are equivalent to antibodies, they possess numerous advantages such as ease of synthesis, thermal stability and lack of immunogenicity. Also, they are designed *in vitro*, without the need for an animal host. Once selected, aptamers are readily produced with high reproducibility and purity by chemical synthesis. Moreover, an aptasensor can be used in a wide variety of sample matrixes, including non-physiological buffers and temperature conditions that would cause denaturation of typical antibodies [9].

For this study the DNA thrombin binding aptamer 15-mer 5′-GGTTGGTGTGGTTGG-3′ carrying a 20-mer poly thymine spacer was chosen because reported results indicated best performances in comparison with other available sequences. The spacer keeps the aptamer distant from the sensor surface, thus avoiding steric hindrance and allowing the proper conformation for molecular recognition [8].

The 15-mer thrombin binding aptamer was the first one selected *in vitro*, specific for a protein without nucleic acids-binding properties [10] and has a high specificity for the fibrinogen binding exosite of thrombin. This oligonucleotide is in equilibrium between a random and a folded state, equilibrium which is shifted towards the four-stranded structure by binding to thrombin. The thrombin aptamer undergoes a transition into a G-quadruplex structure upon binding thrombin [11] and restricts its activity [12]. The 15-mer thrombin binding aptamer is the most extensively investigated one although several other aptamers were also selected, including a 29-mer one specific to the heparin binding exosite of thrombin [13].

In bioaffinity assays, the aptamer immobilization to the surface is crucial. Thus, an ordered and oriented layer must be obtained to ensure the flexibility of the bioreceptor without altering the affinity for the target molecule.

Modifications induced at the biofunctionalized surface of transducers as result of specific interactions with target analytes are detected by various biosensing methods. In the present study we use surface plasmon resonance (SPR), an optical technique that enables real-time monitoring of changes in the refractive index of a thin film close to a surface (up to 150 nm distance from the surface) as a result of biomolecular interactions [14]. In the last years, SPR has matured into a powerful, well established, biosensing technique, providing real-time kinetic information on molecular binding and continuous process monitoring capabilities.

2. Experimental

2.1. Chemicals and reagents

Human α-thrombin, bovine serum albumin (BSA), streptavidin, avidin, human IgG, biotin, N-hydroxysuccinimide (NHS), 1-ethyl-3-(dimethylaminopropyl) carbodiimide (EDC) and ethanolamine were purchased from Sigma–Aldrich (Germany).

Human plasma (without fibrinogen) was provided by the National Institute of Transfusional Hematology "Prof. Dr. C.T. Nicolau" (Bucharest, Romania).

All the other reagents for buffers were purchased from Sigma, except for the Surfactant P20 which was provided by Biacore AB (Sweden).

The buffers used for the experiments are: phosphate buffer saline solution (PBS), pH 7.4 containing 137 mM NaCl, 10 mM phosphate, 2.7 mM KCl; streptavidin immobilization buffer, 10 mM acetate buffer pH 5; avidin immobilization buffer, 10 mM acetate buffer pH 4.5 containing 0.125 M NaCl; aptamer binding buffer, 300 mM NaCl, 20 mM Na_2HPO_4, 0.1 mM EDTA, pH 7.4 [8]; thrombin running buffer: 50 mM Tris–HCl, pH 7.4, 140 mM NaCl, 1 mM $MgCl_2$ [8]; streptavidin/avidin running buffer: HBS-EP buffer (10 mM HEPES pH 7.4, 150 mM NaCl, 3 mM EDTA, 0.005% Surfactant P20).

Succinic anhydride and sodium hypochlorite (NaOCl) were supplied by Acros Organics (Belgium).

The biotinylated 15-mer thrombin binding aptamer (TBA) with polyT(20) tail used in this study having the following sequence: 5′-biotin-TT TTT TTT TTT TTT TTT GGT TGG TGT GGT TGG-3′ was purchased from MWG Biotech.

Deionized water (Millipore) was used throughout the preparations. All chemical reagents were of analytical grade and were used without further purification.

2.2. Sensor chips

CM5 (Biacore AB, now GE Healthcare).

Plain gold unmounted chips (Ssense, The Netherlands).

2.3. Equipments

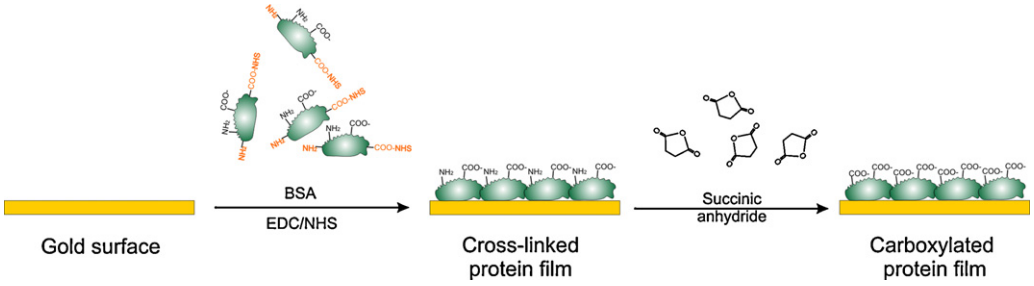
2.3.1. Biacore 3000

Comparative CM5 and cBSA measurements were performed using the Biacore 3000 instrument (Biacore AB, now GE Healthcare). The SPR signal provided by the instrument is a direct measure of the angle of minimum reflected intensity. The unit of SPR response (resonance unit, RU) is an arbitrary unit chosen so that 1 RU corresponds to a shift in angle of 10^{-4} degrees, which in turn correlates with a change in refractive index of about 10^{-6} [15].

2.3.2. Custom made cost-effective SPR system

A dual channel SPR system based on the Spreeta TSPR2K23 SPR sensor (Texas Instruments, TX, USA) has been developed within International Centre of Biodynamics, Bucharest, Romania.

A two channels polydimethylsiloxane (PDMS) flow cell is mounted on the Spreeta sensor and the liquid sample is delivered over the sensor surface by the automated fluidic system comprised of syringe pumps and valves actuated by computer. The flow channels are 8 mm long by 0.8 mm wide with a height of 150 μm. Each flow channel is connected to an independent flow circuit controlled by a syringe pump, allowing simultaneous, as well as independent analyses. The flow rate range is 40–1000 μl/min with increments of 1 μl/min. Sample injection is achieved using electrically actuated injection valves, one for each flow circuit. The sample loops of the injection valves are loaded with the desired sample through a selection valve. Sample loading, injection and washing protocols are preprogrammed and the user only selects the measurement



Scheme 1. Preparation of cross-linked protein film.

flow channel, the sample volume and flow rate for both buffer and sample. Data acquisition and processing is realized with a LabView controlled interface. The signal received from the SPR sensor is processed through various software routines to subtract background and reference data in order to obtain the SPR curve. The SPR minimum is calculated online by analysis of the SPR curve. This data is converted then to refractive index units, or response units using a calibration protocol. Both SPR data (as refractive index units or response units) as well as the SPR curve for each point can be saved for further analysis.

2.4. cBSA functionalization procedure

Before functionalization, the gold sensor surface was first cleaned with 5% NaOCl, thoroughly rinsed with deionized water, ethanol and another deionized water washing steps and finally dried under nitrogen stream.

As presented in Scheme 1, sensor functionalization involves a coupled set of processes:

(a) Formation of cross-linked BSA film: 20 μl of 0.4 M EDC were mixed with 20 μl of 0.1 M NHS and 50 μl of a freshly prepared solution of 5 mg/ml BSA in PBS pH 7.4 and allowed to incubate at room temperature for 5 min. On a horizontally aligned surface, 10 μl of the mixture were spread evenly to cover the whole sensor surface. Following a 15 min reaction time at room temperature, the sensor was rinsed with 20 mM HCl and deionized water and dried under nitrogen stream. The integrity of the film was checked using atomic force microscopy (data not shown) revealing a good sensor coverage.
(b) Adding carboxylic groups to the film. Freshly prepared succinic anhydride solution: 0.2 g succinic anhydride in 500 μl DMSO were thoroughly vortexed/sonicated until fully dissolved. 50 mM Na_2HPO_4 was added to make up to a final volume of 10 ml. The pH was adjusted to 6.5 using 5 M NaOH. The BSA coated plain gold sensors were incubated overnight at room temperature in the succinic anhydride solution [16].

2.5. Aptamer immobilization

The same protocols were used for the immobilization/binding of the biotinylated aptamer on both CM5 and cBSA chips.

Either streptavidin or avidin was first immobilized on the surface. The immobilization procedure was performed at a constant flow rate of 5 μl/min and at 25 °C. The surface was activated 7 min for streptavidin and 2 min for avidin using 1:1 volumetric mixtures of 50 mM NHS and 200 mM EDC, followed by a 20 min injection of 200 μg/ml streptavidin and 50 μg/ml avidin, respectively, and 7 min blocking with 1 M ethanolamine hydrochloride pH 8.5.

Before the immobilization, the biotinylated aptamer was heated at 90 °C for 1 min to unfold the DNA strand and then cooled in ice for 10 min in order to block the DNA in its unfolded structure [8]. The thermal treatment unfolds the DNA strand, making the biotin label at the 5′-end available for the interaction with streptavidin/avidin on the surface.

The thermally treated biotinylated aptamer (1 μM) was injected for 7 min, 5 μl/min over the chip surface.

A reference channel immobilized with streptavidin/avidin and blocked with biotin and BSA was used throughout the experiments.

3. Results and discussion

3.1. Biacore 3000 measurements

Several concentrations of thrombin in the physiologically relevant range (0.1–150 nM) in both buffer and in plasma were injected over the sensors surface. All injections were performed at a constant flow rate of 5 μl/min and at constant temperature, 25 °C, with an injection time of 20 min.

The two platforms, CM5 and cBSA, were analyzed using the Biacore 3000 considering: the immobilized TBA surface coverage, the response measured for the same concentration of thrombin, the non-specific response when injecting thrombin in plasma, the baseline evolution after injection–regeneration cycles, the derived average coefficient of variation (CV) and limit of detection (LOD).

3.1.1. Quality of the cBSA film

Before avidin/streptavidin immobilization and aptamer binding, the degree of carboxylation of the cBSA film was evaluated by assessing the charge pre-concentration effect [16]. At pH values above 3.5 the carboxylic groups of the functionalization layer are negatively charged and due to electrostatic attraction the positively charged ligands (in diluted solutions 10–50 μg/ml or less) will be concentrated on the surface. As this mechanism is suited for most proteins and several other biomolecules [17] it provides, with limited reagent consumption, a direct evaluation of the reactive sites on the surface.

The pre-concentration test was performed by injecting 50 μg/ml human IgG in 10 mM acetate buffer pH 5.5. The response was high (~5700 RU) indicating that the carboxylated surface was properly formed. A higher ionic strength buffer at neutral pH (HBS) was used as running buffer so that the non-covalently bound ligand was washed off the surface after injection. A short pulse (1 min) of 1 M ethanolamine hydrochloride pH 8.5 was used leading to removal of all the remaining traces of electrostatically bound ligand.

The same test was performed for a cross-linked BSA film which was not previously treated with succinic anhydride (ncBSA). The response was significantly lower (~2000 RU).

The non-specific binding of cBSA and ncBSA was compared with a bare gold surface. The non-specific binding of human IgG directly to the gold surface is not negligible: when 50 μg/ml antibody solution was injected over the bare gold sensor a response of ~3000 RU was recorded. Yet, for the bare gold sensor surface, in contrast with the cBSA and ncBSA surfaces, regeneration with a short pulse of

Table 1
Immobilization results for the CM5 and cBSA platforms.

Platform	Protein	Protein bound (RU)	TBA bound (RU)	Protein binding capacity (RU)	TBA binding stoichiometry	TBA surface coverage (ng/mm^2)	TBA surface coverage (molecules/cm^2)
CM5	Streptavidin	3850	1400	817.7	1.71	1.12	6.01E+12
	Avidin	5060	1370	846.9	1.62	1.09	5.89E+12
cBSA	Streptavidin	2760	800	586.2	1.36	0.64	3.44E+12
	Avidin	1600	415	267.8	1.55	0.33	1.78E+12

1 M ethanolamine hydrochloride pH 8.5 had little effect on the signal, suggesting that most of the protein remained bound non-specifically.

3.1.2. Immobilized TBA surface coverage

Since the SPR response is directly proportional to the mass concentration of material at the surface, assuming a 1:1 binding stoichiometry, the analyte binding capacity of a given surface is related to the amount of ligand immobilized as follows:

analyte binding capacity (RU) = analyte MW/ligand MW × *immobilized ligand (RU)* [17]. Thus the binding stoichiometry of the aptamer to the surface for CM5 and cBSA was calculated:

binding stoichiometry = analyte bound (RU)/analyte binding capacity (RU) for 1:1 stoichiometry.

The surface coverage of immobilized aptamer molecules for Biacore was estimated considering that 1000 RU = 0.8 ng/mm^2 [18].

TBA binding stoichiometry had similar values for CM5 and cBSA for both streptavidin (1.71 and 1.36, respectively), and avidin (1.62 and 1.55, respectively), yet TBA surface coverage for CM5 in comparison to cBSA, was from double, for streptavidin, to triple, for avidin (Table 1). These results are explained due to higher surface coverage of binding sites in the 3D carboxymethylated dextran matrix in respect to the "two-dimensional" cBSA.

When several cBSA aptasensors were immobilized with streptavidin/avidin, TBA binding stoichiometry was similar (1.44 and 1.36 for streptavidin, 1.55 and 1.43 for avidin,), showing a good reproducibility in surface functionalization.

3.1.3. Response measured for the same concentration of thrombin in different matrices

For cBSA immobilized with streptavidin and 0.4 ng/mm^2 TBA surface coverage, the response for 100 nM thrombin injection in buffer was 790 RU, 60% from the response generated with the same thrombin concentration on CM5 with streptavidin and almost a three times higher TBA surface coverage 1.12 ng/mm^2. When injecting 25 nM thrombin in plasma on the same cBSA-streptavidin platform (Fig. 1A), the response was 450 RU, 70% from the response measured for the same concentration on the analogous CM5-streptavidin platform.

Again the differences are to be explained due to higher surface coverage of binding sites in the carboxymethylated dextran matrix in respect to the cBSA.

While similar to the ones indicated by [19] based on a custom made set-up, the dissociation phase for both CM5 and cBSA platforms is faster when compared to the same type of experiments reported [20] on CM5 using the Biacore X instrument. This could be explained by the difference between the flow cell volume of Biacore X (0.06 μl) and of the Biacore 3000 (0.02 μl) used in our study: although the flow rate was the same (5 μl/min), larger wall velocities are effective in the Biacore 3000 set-up.

3.1.4. Non-specific response

As the platform is intended to assess target analytes in complex matrices, thrombin spiked plasma samples 1:400 diluted with running buffer have been analyzed to check for the non-specific adsorption of proteins (protein content ~0.2 mg/ml). Thrombin in plasma determines on the reference channel a non-specific binding signal for both CM5 and cBSA aptasensors. For CM5 the non-specific response was negligible for streptavidin and around 60 RU for avidin. For cBSA the non-specific response was around 30 RU for streptavidin and 100 RU for avidin. As expected, due to the lack of carbohydrate modification and near-neutral pI [21], streptavidin platforms show lower non-specific binding as compared to avidin ones, with good correlations between CM5 and cBSA.

While the non-specific signal is not negligible (~30 RU for cBSA with streptavidin chip), it is nevertheless one order of magnitude lower than the specific signal corresponding to 25 nM of thrombin (see Fig. 1A) and correlates well with the response of the CM5 chip, considered to posses a low non-specific binding potential.

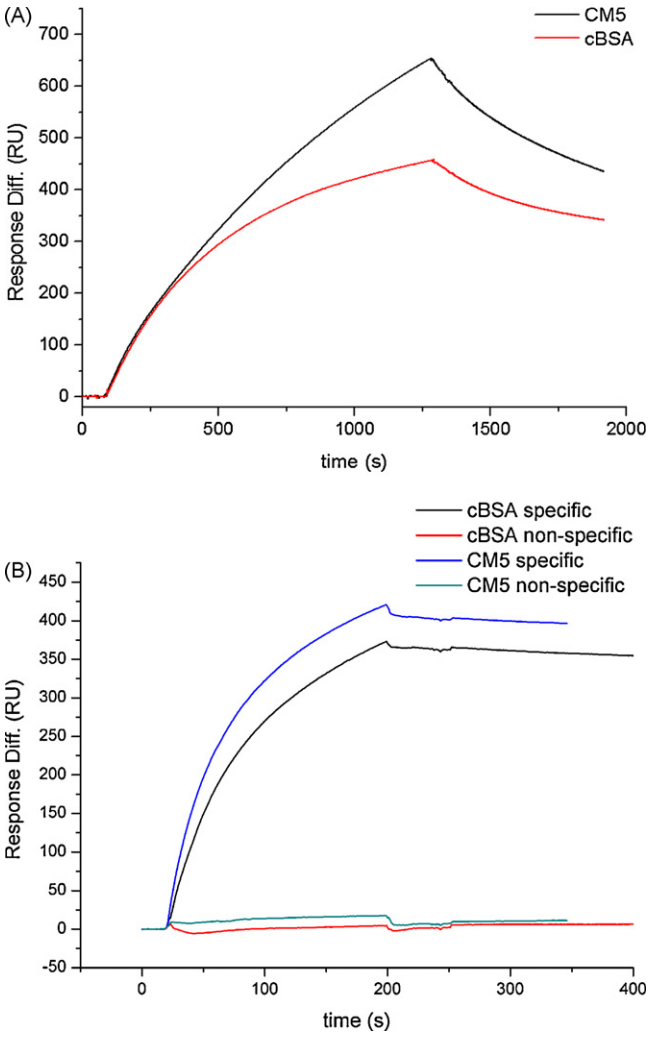


Fig. 1. (A) Injection of 25 nM thrombin in plasma on CM5 and cBSA immobilized with streptavidin. (B) Specific versus non-specific signals for cBSA and CM5 upon injection of 5 μg/ml human IgG.

Table 2
Non-specific response when injecting several proteins for cBSA and CM5 platforms.

Protein	Concentration	cBSA	CM5
		Non-specific response (RU)	
HIgG	5 μg/ml	6.5 ± 2.5	7.5 ± 2.5
BSA	1 mg/ml	20 ± 4	19 ± 4
Inactivated thrombin in diluted plasma	0.2 mg/ml	30 ± 2.5	Not tested

In order to investigate the nature of the higher non-specific binding response for the cBSA sensor, thrombin in plasma mixed with 150 nM TBA (called in the following "aptamer inactivated thrombin") was injected over the cBSA aptasensor. The specific and non-specific responses due to aptamer inactivated thrombin in plasma were the same and also similar with the non-specific response measured during regular thrombin in plasma injections, suggesting a significant effect of matrix components on the non-specific binding response.

Additional tests performed with BSA and antibody proteins (human IgG) confirmed a low non-specific binding for concentrations consistently higher than those of the target compound (Fig. 1B). A summary of the actual values related to different non-specific proteins in HBS running buffer is presented in Table 2.

3.1.5. Baseline evolution

Surface stability and efficiency of the regeneration protocol was evaluated by monitoring several injection–regeneration cycles.

For all surface types the regeneration was performed using a 1 min pulse of 50 mM NaOH, at a flow rate of 5 μl/min.

For thrombin in plasma injected on the CM5 and cBSA platforms, the baseline level after regeneration varied from one measurement cycle to another with a maximum standard deviation value of 5 RU and respectively 8 RU.

To check for the efficiency of regeneration and long term stability, we performed repeated cycles or injection–regeneration. For the CM5 aptasensor, at the end of 9 injection–regeneration cycles, the baseline decreased with 6 RU for the specific channel and with 1 RU for the reference channel for streptavidin (Fig. 2A), and with 30 RU for the specific and 10 RU for the reference channel for avidin (Fig. 2B). For the cBSA aptasensor, at the end of 9 injection–regeneration cycles, the baseline decreased with 10 RU for the specific channel and with 10 RU for the reference channel for streptavidin (Fig. 2C), and decreased with 22 RU for the specific and increased with 30 RU for the reference channel for avidin (Fig. 2D).

These results show a good efficiency of the regeneration protocol on both platforms and also a good stability of both platforms.

3.1.6. Calibration curves

Calibration curves consisting of relative response (recorded after 20 min of injection) versus concentration (for both cBSA and CM5) were fitted with a 4 parameters logistic equation (using BIAeval 4.1 software for Biacore measurements): $f(c) = R_{hi} - ((R_{hi} - R_{lo})/1 + (c/A_1)^{A_2})$, where $R_{hi} = f(c)$ when $c \to \infty$, $R_{lo} = f(c)$ when $c = 0$, A_1 is fitting constant 1 and A_2 is fitting constant 2.

In Figs. 3A and B the calibration curves for thrombin in plasma on CM5 aptasensor with avidin and streptavidin are presented, while Fig. 4A and B shows the cBSA aptasensor (with avidin and streptavidin) responses in respect to injections of thrombin in plasma.

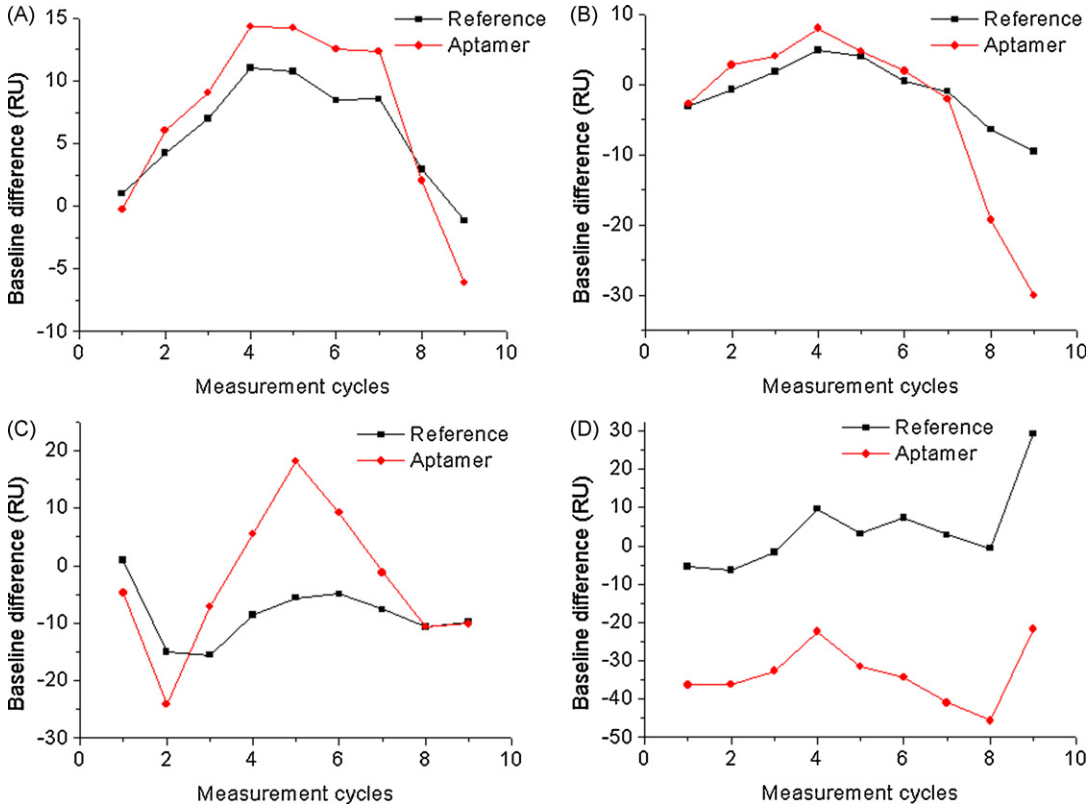


Fig. 2. Baseline variation for each injection–regeneration cycle against initial baseline at the beginning of the experiment for (A) CM5-streptavidin, (B) CM5-avidin, (C) cBSA-streptavidin, and (D) cBSA-avidin.

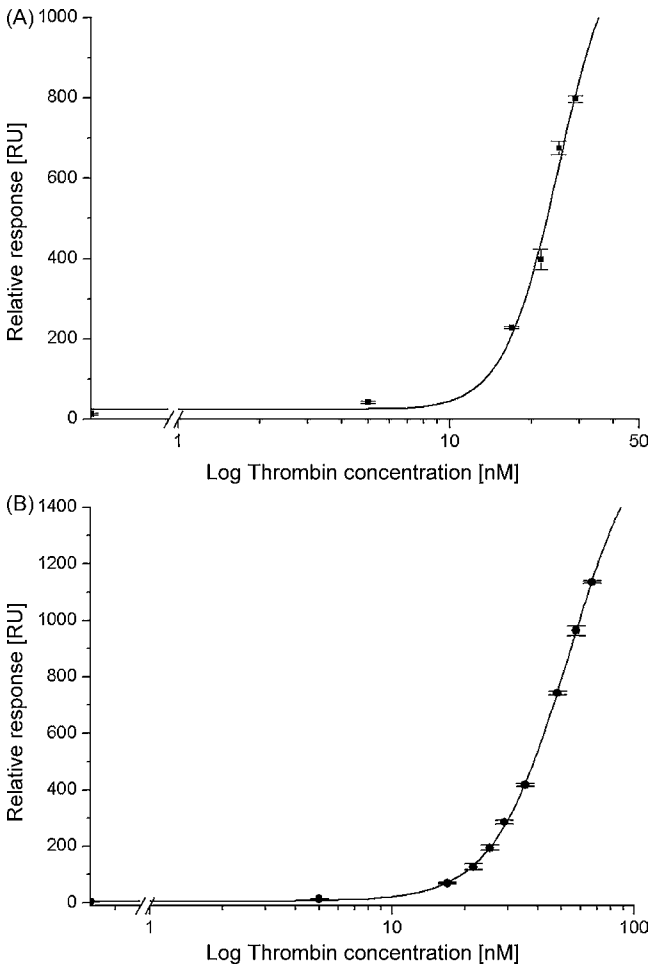


Fig. 3. (A) Calibration curve for thrombin in plasma on CM5 with streptavidin. (B) Calibration curve for thrombin in plasma on CM5 with avidin.

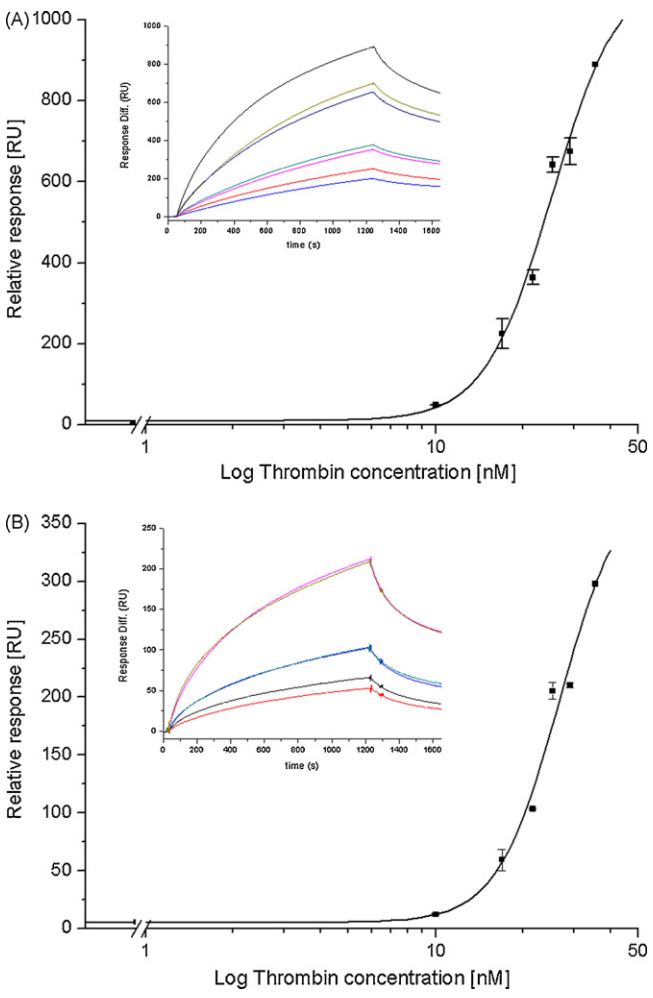


Fig. 4. (A) Calibration curve for thrombin in plasma on cBSA with streptavidin; in the inset, injection curves for different thrombin concentrations are included. (B) Calibration curve for thrombin in plasma on cBSA with avidin; in the inset, injection curves for different thrombin concentrations are included.

3.1.7. *Coefficient of variation and limit of detection*

The averaged coefficient of variation (CV) was calculated as the mean of all the coefficients of variation for all the concentrations considered. For CM5 (Biacore) the CV was 3.6% for streptavidin (data not shown) and 2.8% for avidin. For cBSA (Biacore) the CV was 5.8% for streptavidin and 5.15% for avidin.

The limit of detection (LOD) expressed as the concentration c_L is derived from the smallest measure, x_L, that can be detected with reasonable certainty for a given analytical procedure. The value of x_L is given by the equation $x_L = x_{bi} + ks_{bi}$, where x_{bi} is the mean of the blank measures, s_{bi} is the standard deviation of the blank measures, and k is a numerical factor chosen according to the confidence level desired [22].

LOD was calculated by the evaluation of the average response of the blank plus three times the standard deviation. For streptavidin, LOD for the CM5 platform (1.12 ng/mm^2 TBA surface coverage) was evaluated at 2.5 and 3 nM for cBSA (0.64 ng/mm^2 TBA surface coverage). In the case of avidin, LOD was 5 nM for CM5 (1.09 ng/mm^2 TBA surface coverage) and 5.5 nM for cBSA (0.33 ng/mm^2 TBA surface coverage), similar to the one previously reported for an aptamer-based SPR assay [19].

To increase the sensitivity of the platform, instead of binding of the aptamer directly on the gold surface of the SPR chip, an additional, intermediate layer has been considered providing: improved accessibility of the binding sites with likely better conformation of the recognition element, leading to increased binding potential and better blocking of the surface against non-specific binding.

Previous results [8] proved a 4-fold increase in the specific signal for the same concentration of target compound and aptamer for CM5 chip in comparison with bare gold. Upon optimal choice of the aptamer linker (20T) the sensitivity was further increased due to an 8-fold augmentation in the specific signal compared to bare gold.

Our present experimental data further support this improvement revealing an increased sensitivity when using streptavidin in comparison with avidin (due to the lack of carbohydrate modification and near-neutral pI of streptavidin). The surface coverage, though lower than for the 3D dextran matrix characteristic for CM5, is optimum for detection as revealed by the similar responses of cBSA-streptavidin and CM5 respectively. Notably, the surface blocking against non-specific binding is efficient (in complex matrix, the non-specific response was 6.5% of the specific response for cBSA and 1.5% for CM5).

3.2. *Custom made SPR system measurements*

Having in mind that an important goal of the study was to implement a cost-effective immobilization platform for the TBA on the Spreeta-based sensing system, avidin was chosen for immobilization on the cBSA sensor due to a better cost/performance ratio against streptavidin.

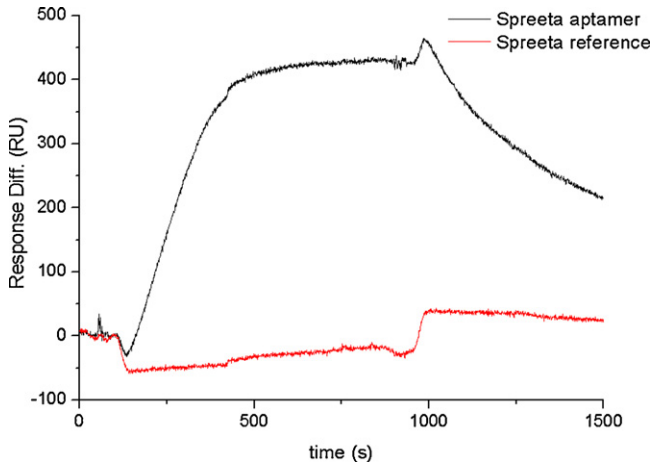


Fig. 5. 50 nM thrombin in buffer injection on cBSA aptasensor. Spreeta-based system measurement.

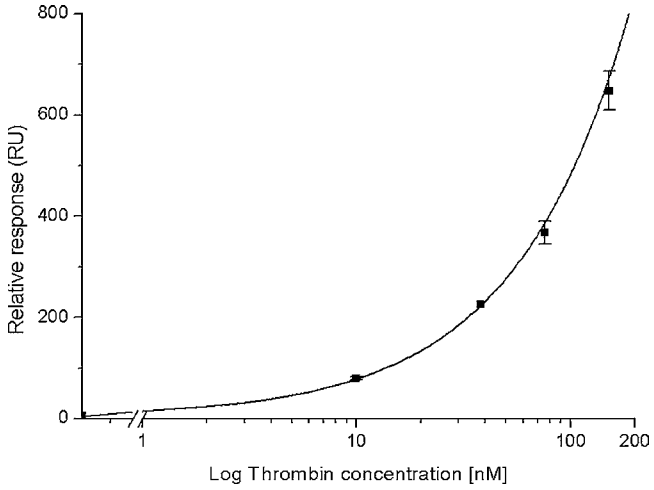


Fig. 7. Calibration curve for cBSA avidin platform measured on Spreeta sensor.

In order to maintain a similar concentration of the analyte over the surface as in the Biacore flow cell (2.4 mm × 0.5 mm × 0.02 mm), the flow rate was adjusted accordingly to our system's flow cell dimensions (0.8 mm × 8 mm × 0.15 mm).

The assay was performed using 50 μl/min flow rate and 16 min injection time (the maximum injection time for this flow rate due to sample loop volume). A typical thrombin in buffer injection on both specific and reference channel is presented in Fig. 5.

When injecting thrombin in plasma, the reference channel showed a small non-specific binding response, nevertheless, the baseline after regeneration returned to its initial value before injection (Fig. 6).

The calibration curve generated with thrombin in plasma using the same 4 parameters logistic equation is shown in Fig. 7: the signal increased with the increased concentration of the added analyte. The average coefficient of variation was 6% and a limit of detection of 10 nM was obtained for thrombin in plasma.

3.3. Further improvements

Even though the performances of the platforms are comparable to ones reported in literature [19], there are two aspects that are worth further investigating in order to improve the LOD. A recent study [23] showed that thrombin binding capacity increases as the linker length increases from 0 to 5 thymidine nucleotides and decreases as the number of thymidine residues increases to 20 (corresponding to the spacer used in our study). Furthermore, recent evidence pinpoint on the important role of cations present in solution on the G-quadruplex formation: this stabilizing conformation corresponding to aptamer–thrombin binding is not easily formed in the presence of Mg^{2+} and Ca^{2+} [24].

Thus using the optimum linker size and the optimum thrombin running buffer are possible ways to further increase the sensitivity of the assay.

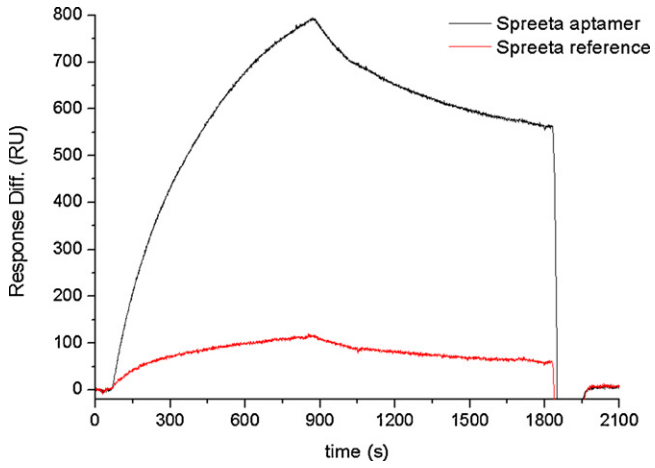


Fig. 6. 100 nM thrombin in plasma injection on a cBSA aptasensor on Spreeta-based system.

4. Conclusions

In this study a new bio-immobilization platform based on a carboxylated cross-linked BSA film was investigated and compared with the commercial available CM5 reference chip. We demonstrate that the cBSA platform is suitable for immobilization of bioaffinity compound and we tested it with streptavidin/avidin and a biotinylated aptamer. In comparison with the CM5 platform, cBSA exhibited similar sensitivity, considering the immobilized TBA surface coverage (LOD 2.5 nM for CM5-streptavidin with 1.12 ng/mm^2 and 3 nM for cBSA-streptavidin with 0.64 ng/mm^2), a similar coefficient of variation (3.6% for CM5 and 5% for cBSA) in detecting thrombin in the presence of other interfering proteins (plasma) and proved stable during numerous injection–regeneration cycles.

The low-cost cBSA aptasensor with avidin was successfully implemented on the cost-effective Spreeta-based SPR system (a LOD of 10 nM was obtained for thrombin in plasma and CV of 6%, similar to the one provided by the cBSA aptasensor measured with the Biacore) amenable for portable platforms development [25].

The cBSA platform exhibited good performance when used in complex media (plasma), the non-specific response being similar to the one obtained with the CM5 platform. This shows the potential of this immobilization platform as a low-cost analytical tool in conjunction with selected bioaffinity pairs for real samples (complex matrix) assessment.

The BSA functionalization procedure is a suitable alternative to self-assembled monolayers formation or carboxymethyldextran coatings, for most SPR chips, including the Spreeta sensor which, due to its plastic housing, can be easily altered by the organic solvents or strong oxidizing cleaning solutions (*e.g.* piranha solution).

Besides being a low-cost alternative to commercially available platforms, the cBSA film provides additional advantages: it is relatively easy to employ, the sensor surface does not require harsh washing methods and the procedure can be completed overnight, and is fully automatable. Moreover the cBSA chips can be stripped off and re-functionalized repeatedly without destroying the gold surface or other sensor components.

While current performances of the platforms are comparable to ones reported in literature, further optimizations are envisaged based on selection of appropriate linker size and thrombin running buffer as possible avenues to increase the sensitivity of the assay.

Acknowledgements

The study was supported by Romanian Grant 81028 PN-II BiosADN project and by EU NMP3-SL-2008-214107 Nanomagma project.

References

[1] S. Lofas, B. Johnsson, J. Chem. Soc. Commun. (1990) 1526–1528.
[2] R.B.M. Schasfoort, A.J. Tudos, Handbook of Surface Plasmon Resonance, Royal Society of Chemistry, Cambridge, 2008.
[3] H.C. Hemker, P. Giesen, R. AlDieri, V. Regnault, E. de Smed, R. Wagenvoord, T. Lecompte, S. Béguin, Pathophysiol. Haemos. Thromb. 32 (2002) 249–253.
[4] Z. Zhang, W. Yang, J. Wang, C. Yang, F. Yang, X. Yang, Talanta 78 (2009) 1240–1245.
[5] H. Inuyama, T. Saito, J. Takagi, Y.J. Saito, Cell. Physiol. 173 (1997) 406–414.
[6] K.K. Hansen, K. Oikonomopoulou, A. Baruch, R. Ramachandran, P. Beck, E.P. Diamandis, M.D. Hollenberg, Biol. Chem. 389 (2008) 971–982.
[7] S.M. Strukova, S.V. Khlgatyan, S.V. Zaitsev, Bull. Exp. Biol. Med. 112 (1991) 1438–1441.
[8] S. Centi, S. Tombelli, M. Minunni, M. Mascini, Anal. Chem. 79 (2007) 1466–1473.
[9] M. Mir, M. Vreeke, I. Katakis, Electrochem. Commun. 8 (2006) 505–511.
[10] L.C. Bock, L.C. Griffin, J.A. Latham, E.H. Vermaas, J.J. Toole, Nature 355 (1992) 564–566.
[11] M. Mascini, Aptamers in Bioanalysis, Wiley, New Jersey, 2009.
[12] T. Hermann, D.J. Patel, Science 287 (2000) 820.
[13] D.M. Tasset, M.F. Kubik, W.J. Steiner, Mol. Biol. 272 (1997) 688–698.
[14] S. David, M. Gheorghiu, C. Polonschii, E. Gheorghiu, IFMBE Proc. 17 (2007) 106–109.
[15] BIAapplications Handbook, 1998.
[16] TI Spreeta Application Brief 001, 2003.
[17] Biacore Sensor Surface Handbook, 2003.
[18] Biacore User Manual, 1999.
[19] V. Ostatná, H. Vaisocherová, J. Homola, T. Hianik, Anal. Bioanal. Chem. 391 (2008) 1861–1869.
[20] S. Centi, G. Messina, S. Tombelli, I. Palchetti, M. Mascini, Biosens. Bioelectron. 23 (2008) 1602–1609.
[21] R.J. McMahon, Avidin–Biotin Interactions: Methods and Applications, Springer-Verlag, New York, 2008.
[22] A.D. McNaught, A. Wilkinson, IUPAC. Compendium of Chemical Terminology, 2nd ed., Blackwell Scientific Publications, Oxford, 1997.
[23] S. Balamurugan, A. Obubuafo, R.L. McCarley, S.A. Soper, D.A. Spivak, Anal. Chem. 80 (24) (2008) 9630–9634.
[24] J.W. Shim, Q. Tan, L.-Q. Gu, Nucleic Acids Res. 37 (3) (2009) 972–982.
[25] T.M. Chinowsky, S.D. Soelberg, P. Baker, N.R. Swanson, P. Kauffman, A. Mactutis, M.S. Grow, R. Atmar, S.S. Yee, C.E. Furlong, Biosens. Bioelectron. 22 (2007) 2268–2275.

Talanta 80 (2010) 2165–2171

Contents lists available at ScienceDirect

Talanta

journal homepage: www.elsevier.com/locate/talanta

Detection of refined olive oil adulteration with refined hazelnut oil by employing NMR spectroscopy and multivariate statistical analysis

Alexia Agiomyrgianaki [a], Panos. V. Petrakis [b], Photis Dais [a,*]

[a] NMR Laboratory, Department of Chemistry, University of Crete, P.O. Box 2208, Voutes Campus, 710 03 Heraklion, Crete, Greece
[b] National Agricultural Research Foundation, Institute of Mediterranean Forest Research, Laboratory of Entomology, Terma Alkmanos, Ilissia, 115 28, Athens, Greece

ARTICLE INFO

Article history:
Received 3 November 2009
Accepted 5 November 2009
Available online 12 November 2009

Keywords:
NMR spectroscopy
Refined olive oil
Refined hazelnut oil
Adulteration
Canonical discriminant analysis
Classification binary tree

ABSTRACT

NMR spectroscopy was employed for the detection of adulteration of refined olive oil with refined hazelnut oil. Fatty acids and iodine number were determined by ^{1}H NMR, whereas ^{31}P NMR was used for the quantification of minor compounds including phenolic compounds, diacylglycerols, sterols, and free fatty acids (free acidity). Classification of the refined oils based on their fatty acids content and the concentration of their minor compounds was achieved by using the forward stepwise canonical discriminant analysis (CDA) and the classification binary trees (CBTs). Both methods provided good discrimination between the refined hazelnut and olive oils. Different admixtures of refined olive oils with refined hazelnut oils were prepared and analyzed by ^{1}H NMR and ^{31}P NMR spectroscopy. Subsequent application of CDA to the NMR data allowed the detection of the presence of refined hazelnut oils in refined olive oils at percentages higher than 5%. Application of the non-linear classification method of the binary trees offered better possibilities of measuring adulteration of the refined olive oils at a lower limit of detection than that obtained by the CDA method.

© 2009 Elsevier B.V. All rights reserved.

1. Introduction

Numerous attempts have been made in the past to detect virgin olive oil adulteration with seed oils and particularly with hazelnut oil [1–23]. Although no official analytical method has been adopted by the European Commission and other international institutions for the detection of hazelnut oil, several methods using chromatographic and spectroscopic techniques have been proposed to distinguish extra virgin or virgin olive oil from hazelnut oil. Several of these methodologies detect virgin olive oil adulteration with crude hazelnut oil on the basis of chemical compounds that are present in one oil but not in the other oil. For instance, filbertone, which was considered as a hazelnut oil marker [1], had been proposed to detect olive oil fraud [1–4], whereas other researchers suggested to determining chlorophylls [5], tocopherols [6], volatile compounds [7,8] and phenolic compounds [9,10]. Detection of virgin olive oil with refined hazelnut oil (RHzO) presents increasing difficulties because the filbertone marker and other minor components in hazelnut oil are removed upon refinement [3,4], and in addition the triacylglycerol profile of both oils is very similar. Chromatography has been employed to distinguish RHzO in virgin olive oil on the basis of triacylglycerol [11,12] and/or sterol [11–13] profiles. Several spectroscopic techniques in combination with multivariate statistical methods were successful in classifying edible oils and detect the presence of RHzO with little or great success [14–21]. The real problem, however, is the detection of RHzO in refined olive oil (ROO), since their minor components, and in particular their glyceridic composition, were considered to be very similar. Recent applications of FT MIR and FT-Raman and fluorescence spectroscopy [22,23] allowed detection of ROO adulteration with RHzO at concentrations >8%.

NMR spectroscopy is one of the most promising spectroscopic techniques for the analysis of complex systems, such as food matrices. It has been proven to be very successful in the analysis of olive oil and in combination with multivariate statistical methods was able to classify edible oils and detect olive oil adulteration with seed oils and olive oils of inferior quality [15,16,20,24–26]. It made possible the detection of the presence of refined hazelnut oil in virgin olive oil at concentrations 5–10% [14–16,20]. ^{1}H and ^{13}C NMR spectroscopy shows a number of advantages relative to other analytical techniques; it is fast (less than 5 min are required to record an one-dimensional ^{1}H NMR spectrum of an olive oil sample in chloroform-d); it needs no calibration with internal standards or separation of the various components prior to the analysis; it shows remarkable selectivity, inasmuch it identifies unknown compounds at a molecular level; it gives a wealth of information in a single experiment; it is quantitative with excellent repeatability and reproducibility. Disadvantages of NMR spectroscopy may be considered its low sensitivity compared with chromatographic

* Corresponding author. Tel.: +30 2810545037; fax: +30 2810545001.
E-mail addresses: pvpetrakis@fria.gr (Panos.V. Petrakis), dais@chemistry.uoc.gr (P. Dais).

0039-9140/$ – see front matter © 2009 Elsevier B.V. All rights reserved.
doi:10.1016/j.talanta.2009.11.024

and mass spectrometry techniques and the high cost of the analysis, since the NMR spectrometers are quite expensive. Nevertheless, sensitivity problems have been overcome lately by using strong magnetic fields produced by super-conductive selenoids and properly designed probes, especially cryogenic probes, whereas the screening of a large number of samples in a short period of time may compensate the high cost of the analysis. The same advantages shares the NMR spectroscopy of the phosphorus-31 nucleus, although derivatization with phosphorus reagent is needed prior to the analysis, since apart from phospholipids, compounds in olive oil do not contain phosphorus atoms in their molecules. This method is based on the replacement of the acidic hydrogens of the hydroxyl and carboxyl groups of olive oil constituents with the phosphorus reagent 2-chloro-4,4,5,5-tetramethyphospholane and the use of ^{31}P NMR spectroscopy to identify the phosphitylated compounds [27]. This facile magnetic resonance method supplements ^{1}H and ^{13}C NMR techniques, especially in cases where severe overlapped signals in ^{1}H NMR spectra or long relaxation times of the insensitive ^{13}C nuclei render the analysis a difficult task.

The aim of the present study was to assess the potential of ^{1}H and ^{31}P NMR spectroscopy to detect ROO adulteration with RHzO at low concentration. This goal will be achieved upon application to the NMR data two statistical methods, namely, forward stepwise canonical discriminant analysis (CDA) and classification binary trees (CBTs).

2. Experimental

2.1. Refined oils

A collection of 20 samples of refined olive oil were supplied by the olive oil company MINERVA (Athens, Greece). The refined oils were obtained upon refinement of lampante olive oils originated from various locations of Greece. Twenty commercial samples of RHzO were purchased from Henry Lamotte (Bremen, Germany). To detect ROO adulteration, admixtures were prepared by mixing different samples of ROO with different samples of RHzO. The percentage of RHzO in ROO of the adulterated refined olive oils (AOO) varied from 1% to 95% (1%, 2%, 3%, 4%, 5%, 7%, 10%, 12%, 15%, 17%, 20%, 25%, 30%, 50%, 60%, 70%, 80%, 90%, 95%: w/w), The ROO and RHzO samples were selected randomly for the formation of each one of the 19 admixtures. All oil samples and their admixtures were analyzed twice.

2.2. Reagents

Pinacol, triethylamine, phosphorus trichloride, protonated solvents (reagent or analytical grade), and deuterated solvents used in the present study were purchased from Sigma–Aldrich (Athens-Greece). The derivatizing phosphorous reagent 2-chloro-4,4,5,5-tetramethyldioxaphospholane used in ^{31}P NMR spectroscopy was synthesized from pinacol and phosphorus trichloride following the method described in the literature [28]. However, to increase the yield of the reaction, we utilized hexane solvent instead of benzene and pyridine instead of triethylamine suggested in the original method. This modification resulted in ~45% yield of the product against 19% obtained with the original method.

2.3. Extraction of minor polar components from refined oil

Phenolic compounds were extracted following the method developed by Montedoro et al. [29] using 35 g of olive oil and a mixture of methanol–water (80:20, v/v). The polyphenol extracts were used immediately for sample preparation and ^{31}P NMR measurements.

2.4. Sample preparation for ^{31}P NMR spectral analysis

A stock solution was prepared by dissolving 0.6 mg of chromium acetylacetonate, $Cr(acac)_3$ (0.165 μM) and 13.5 mg cyclohexanol (13.47 mM) in 10 ml of a mixture of pyridine and $CDCl_3$ solvents (1.6:1.0, volume ratio) and protected from moisture with 5A molecular sieves. Cyclohexanol was used as an internal standard for quantification purposes. 100–150 mg of each oil was placed in a 5 mm NMR tube. The required volumes of the stock solution (0.4 mL) and the reagent **1** (15 μL) were added. The reaction mixture was left to react for about 15 min at room temperature. Upon completion of the reaction, the solution was used to obtain the ^{31}P NMR spectra.

2.5. NMR experiments

All NMR experiments were conducted on a Bruker AMX500 spectrometer operating at 500.1 and 202.2 MHz for proton and phosphorus-31 nuclei, respectively, at 26 ± 1 °C.

One-dimensional ^{13}P NMR spectra were recorded by employing the inverse gated decoupling technique in order to suppress NOE effects. Typical spectral parameters for quantitative studies using reagent **1** were: 90° pulse width 12.5 μs, sweep width 55 kHz, relaxation delay 25 s, memory size 32 K. To ensure quantitative spectra, the magnitude of the relaxation delay adopted was more than five times the relaxation time (T_1 = 4.6 s) of the phosphitylated cyclohexanol; 32 transients were accumulated for each spectrum. For all FIDs, line broadening of 1 Hz was applied and drift correction was performed prior to Fourier transform. Polynomial fourth-order base-line correction was performed before integration.

One-dimensional high-resolution ^{1}H NMR spectra were acquired with the following acquisition parameters: time domain 32 K; 90° pulse width 9.3 μs; spectral width 12 ppm; relaxation delay 2 s. 16 scans and 8 dummy scans were accumulated. Baseline correction was performed carefully by applying a polynomial fourth-order function in order to achieve a quantitative evaluation of all signals of interest. The spectra were acquired without spinning the NMR tube in order to avoid artificial signals, such as spinning side bands of the first or higher order.

2.6. Statistical methods

Classification by stepwise forward CDA is used to achieve the most discriminative variables for the arrangement of samples in a space of reduced dimensionality in a way that maximizes the distances between the *a priori* formed groups and the independence of the axes of the configuration [30,31]. The *a priori* groups are ROO, RHzO, and the adulterated refined olive oils (AOO). The chemical compounds contributing most to the discrimination of preformed groups are shown by means of the *F-ratio* as a criterion for inclusion or removal of the compound in the forward stepwise CDA mode. *Wilks'* λ and the *F* approximation were used to check the significance and estimate the importance of each compound in CDA analysis. The significance of the representation of the original configuration of the samples by the newly formed discriminant axes was expressed by the last value of *Wilks'* λ. The performance of the method was measured by the percentage of total variance explained by all significant discriminant axes. In a sense, this is a measure of non-linearity and complex interrelations among variables, since CDA is a linear technique. The classificatory efficiency of CDA can be seen in the resulting classification tables which illustrate the group relations of the samples. The ability of the oil samples to be predicted by the rest is another property of CDA, although the percentage of the correctly classified oil samples is a property of the original data rather than an intrinsic feature

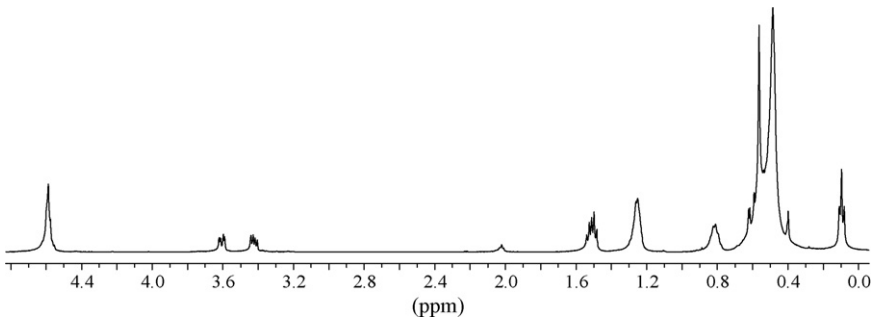


Fig. 1. 500 MHz ^{1}H NMR spectrum of a ROO sample, from which fatty acids and iodine value can be determined.

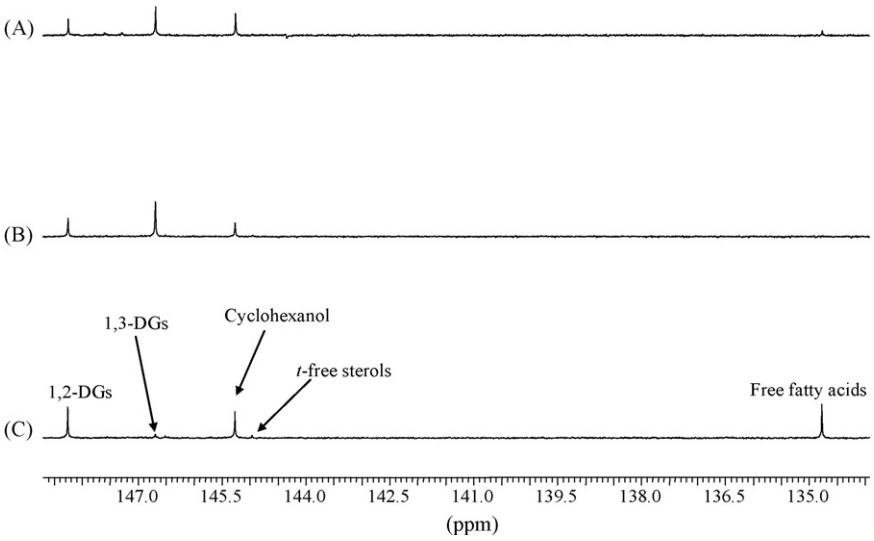


Fig. 2. 200.2 MHz ^{31}P NMR spectra of (A) RHzO, (B) ROO, and (C) virgin olive oil samples from which diacylglycerols, total free sterols and free acidity can be determined.

of the algorithm. Classification is achieved by means of the Mahalanobis distance of each oil sample from the group centroid in order to estimate the probability of misclassification for each one of the predefined groups. Oil samples, which were not engaged in the calculation of classification functions of CDA, are classified in the same way. This feature of CDA reveals its ability to classify oil samples with known compositional constitution, but unknown group affiliation [32]. In other words, CDA predicts class affiliation by using a linear combination of all compounds engaged in the construction of classification equations.

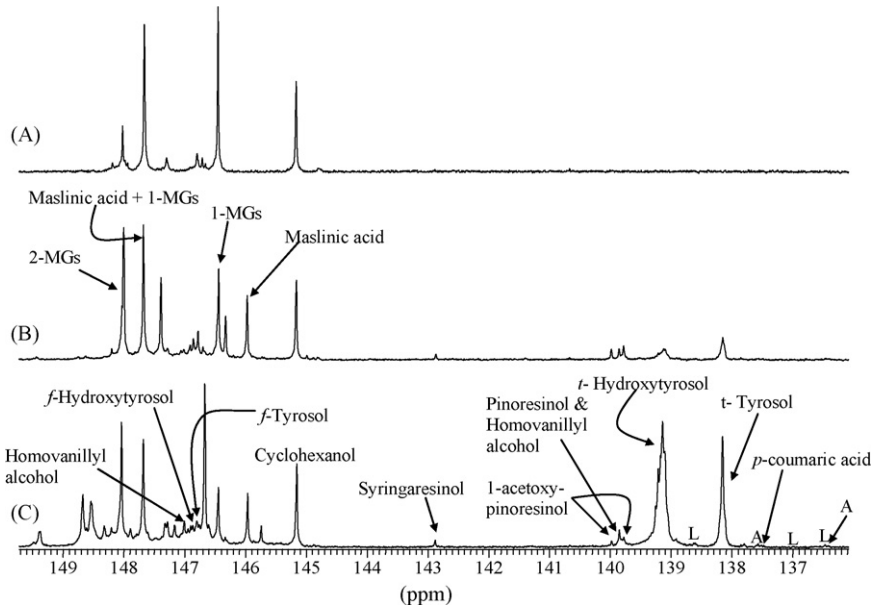


Fig. 3. 200.2 MHz ^{31}P NMR spectra of the polar fraction of (A) RHzO, (B) ROO, and (C) virgin olive oil samples from which phenolic compounds can be determined.

Table 1
Percentage content of the compounds in each group used in CDA and CBT analysis.

	Compound	RHzO		ROO		Adulterated oil samples (AOO)					
		Mean	Stdv	Mean	Stdv	*n1*		*n2*		*n3*	
						Mean	Stdv	Mean	Stdv	Mean	Stdv
1	Syringaresinol	0.00	0.00	0.16	0.23	0.12	0.04	0.05	0.06	0.04	0.06
2*	1-Acetoxypinoresinol#	0.00	0.00	0.51	0.71	0.11	0.05	0.10	0.09	0.01	0.01
3	*t*-Hydroxytyrosol#	0.00	0.00	9.33	25.14	0.00	0.00	0.00	0.00	0.00	0.00
4	*t*-Tyrosol	0.00	0.00	6.28	14.96	0.09	0.08	0.14	0.00	0.01	0.01
5	*p*-Coumaric acid	0.00	0.00	0.04	0.08	0.04	0.02	0.03	0.03	0.01	0.03
6	*f*-Tyrosol	0.00	0.00	0.89	1.87	0.60	0.72	0.42	0.31	0.15	0.21
7*	*f*-Hydroxytyrosol	0.00	0.00	0.03	0.10	0.00	0.00	0.00	0.00	0.00	0.00
8*	Homovanillyl alcohol	0.00	0.00	0.19	0.58	0.00	0.00	0.14	0.25	0.00	0.00
9*	Louteolin#	0.00	0.00	0.07	0.09	0.05	0.03	0.07	0.04	0.03	0.05
10	Apigenin#	0.00	0.00	0.05	0.06	0.04	0.04	0.04	0.02	0.03	0.04
11	Pinoresinol#	0.00	0.00	0.72	0.78	0.80	0.12	0.30	0.27	0.06	0.09
12	*t*-Phenols	0.00	0.00	18.28	41.71	1.85	0.88	1.30	0.33	0.34	0.44
13	1,2-DGs#	2.03	0.40	3.45	1.10	5.08	0.33	5.06	0.33	3.54	0.19
14*	1,3-DGs	0.81	0.22	1.73	0.35	2.37	0.15	2.39	0.15	1.67	0.14
15	*t*-DGs	2.85	0.61	5.18	1.40	7.45	0.48	7.45	0.46	5.21	0.32
16*	*D* (=1,2-DGs/*t*-DGs)	0.28	0.03	0.35	0.09	0.32	0.00	0.32	0.01	0.32	0.01
17*	Free acidity	0.07	0.05	0.09	0.19	0.02	0.01	0.07	0.04	0.11	0.03
18*	Sterols#	0.03	0.02	0.06	0.02	0.04	0.02	0.05	0.03	0.03	0.02
19	Linolenic acid#	0.09	0.06	0.31	0.11	0.37	0.06	0.35	0.06	0.19	0.07
20*	Linoleic acid	10.21	2.27	7.79	1.70	6.59	0.43	8.54	0.89	10.99	0.82
21*	Oleic acid	81.70	4.81	76.21	3.02	75.23	0.63	73.27	0.89	73.47	1.26
22	SFA	7.96	2.87	15.69	2.25	17.80	0.31	17.85	0.14	15.34	1.61
23*	IV#	88.23	1.68	79.66	2.24	77.42	0.77	80.02	0.51	84.50	1.82

f = stands for free, *t* = stands for total, DGs = diacylglycerols, *t*-DGs = total DGs, SFA = saturated fatty acids, IV = iodine value, stdv = stands for standard deviation.
* Index compounds that are important in CDA.
# Index compounds that are important in CBT.

In contrast to CDA, CBTs is a statistical method capable to handle non-linearity and any possible interactions of compositional parameters, in order to produce a set of simple rules in the form of inequalities, which identify existing samples and with this information find the group affiliation of any new sample [33]; the latter is essential in any adulteration detection system. The construction of a CBT comprises the split of the original set of samples into two parts on the basis of a criterion involving one or two compounds in an algebraic expression. All chemical compounds involved in the construction of a CBT comprise the best diagnostic variable set for the groups already defined prior to the analysis. The groups at the beginning of a CBT construction are RHzO, ROO, and *n1*, *n2*, *n3* groups of AOO with small (1–10%), medium (12–30%) and high (50–95%) RHzO content, respectively. The original AOO group is split into three subgroups because: (a) in this way the method is capable to reveal connections of the adulterated samples with the original groups of ROO and RHzO, and (b) this is the minimum number of groups that could manifest the "intermediacy principle", that is *n3* will be closer (clustered together) to RHzO, *n1* to ROO, while *n2* samples will be between them. It should be noted that CDA does not need this split because the final arrangement is expected to depict the picture of intermediacy [26]. The tree grows according to splits that produce maximally informative and 'pure', according to an impurity function. The reduction of error in the classification is monitored by means of a loss function. Several loss functions have been proposed [33]; in this study the splitting method has been made through the information theory compatible *Gini-Simpson* index in the form of "towing" a term coined by Breiman et al. [33] on the basis of the better reduction in error they achieved.

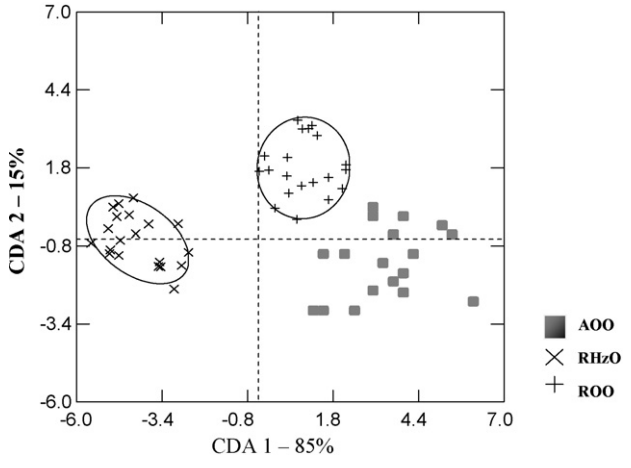


Fig. 4. CDA scattergram of refined olive oil (ROO) (+), refined hazelnut oil (RHzO) (×) samples, and adulterated ROO with RHzO. The latter admixtures denoted as AOO and shown as squares (■) were not taken into account in the construction of the scattergram. The two discriminant axes account for by all variation in the original data set (CDA 1 = 85% and CDA 2 = 15%). Ninety-five percent ellipses are drawn around the ROO and RHzO group centroids. Samples lying outside the group ellipses are correctly classified together with the AOO samples. The crosswire indicates the origin (0, 0) of the scattergram.

All statistical analyses used routines and packages in R system [34] and employed the packages "rpart" [35], and "vegan" [32]. Some algorithms and graphics were applied via SYSTAT (SYSTAT, 1999).

3. Results and discussion

3.1. Data analysis

Fig. 1 shows a typical ^{1}H NMR spectrum of a ROO sample from which the fatty acid profile and the iodine number can be calculated [16]. This spectrum shows similar characteristics with the proton spectra of RHzO samples (not shown), although it differs in certain signal intensities. Fig. 2 depicts the ^{31}P NMR spectra of the phosphitylated refined oils; diacylglycerols, free sterols, and free acidity can be determined from this spectrum [27]. The same figure shows the corresponding spectrum of a virgin olive oil sample. The

Table 2
Canonical discriminant functions of all important variables standardized by within their variances.

No	Chemical compound[a]	Important also in CBT[b]	Canonical function coefficient **1**	Canonical function coefficient **2**
1	1-Acetoxypinoresinol	E	0.654	0.749
2	*f*-Hydroxytyrosol		0.359	−0.597
3	Homovanillyl alcohol		−0.945	0.270
4	Louteolin	F	0.985	−0.247
5	1,2-DGs		1.076	−0.332
6	D (=1,2-DGs/*t*-DGs)		−0.601	0.408
7	Free acidity		1.195	−1.037
8	Sterols	D	0.191	0.494
9	Linoleic acid		−5.997	3.494
10	Oleic acid		−5.228	2.737
11	IV	A	4.094	−2.938

[a] See footnote in Table 1 for the meaning of symbols.
[b] Symbols at split in CBT (see Table 4).

higher acidity of the virgin olive oil sample as compared to those of ROO and RHzO is reflected on the much stronger signal of the free fatty acids at δ 134.8. Fig. 3 compares the ^{31}P NMR spectra of the polar part of the refined oils recorded after phosphitylation of the hydroxyl groups of their minor compounds. This methodology was used for the detection and quantification of polyphenols in olive oil [36]. Also, Fig. 3 illustrates the ^{31}P NMR spectrum of a virgin olive oil sample. The most characteristic feature of the ^{31}P NMR spectra in Fig. 3 is the complete absence of phenolic compounds in RHzO. Previous studies [37,38] have shown that refining process reduces significantly or even removes completely [39,40] the content of phenolic compounds of olive oil. The mean losses of total phenols of olive oil (virgin and lampante) amount to 75–85%, respectively. This is shown clearly upon comparison of the ^{31}P NMR spectra of a virgin olive oil sample and its refined counterpart (Fig. 3). Hazelnut oil, on the other hand, contains much smaller amounts of phenolic compounds than olive oil [41], and hence the polyphenol content is expected to be practically absent after refinement. The absence of phenolic compounds in RHzO serves as a means to differentiate between RHzO and ROO (see below).

Table 1 lists the mean values of phenolic compounds, fatty acids, diacylglycerols, free sterols, iodine values, and free acidity for both refined oils. The compositional parameters for each oil, including the adulterated oils, are provided as supporting material. The mean values in Table 1 shows that there are discernible differences in fatty acid profiles, especially for linolenic acid and saturated fatty acids. However, this interesting difference alone cannot detect the adulteration of ROO with RHzO at low percentage [41]. Both refined oils are characterized by a higher content of 1,3-DGs than 1,2-DGs, contrary with what is observed for the virgin olive oil samples. This is nicely reflected in Fig. 2 on the respective signal intensities between the refined oils and virgin olive oil. Refinement accelerates the isomerisation of 1,2-DGs to 1,3-DGs, which reaches rapidly its equilibrium state and the ratio *D* (=1,2-DGs/Total DGs) assumes its equilibrium value (∼0.33) [42]. These parameters may not be suitable to discriminate between the refined oils. However, measurable differences were observed in the mean values of free sterols and iodine values (Table 1). In particular, ROO samples are characterized by higher sterols content and lower iodine values than the corresponding values of the RHzO samples. The amounts of phenolic compounds as determined by NMR are within the range of phenolic content determined by HPLC [37,38].

3.2. Chemometric approach for the detection of adulteration of refined olive oil

The entire variation of compounds in the original data set within, ROO, RHzO, and AOO groups (Table 1) was fully explained by CDA (*Wilks'* $\lambda = 0.031$, $F_{approx} = 19.46$, $df_1 = 22$, $df_2 = 92$, $P < 10^{-4}$). The eigenvalues are $\lambda_1 = 10.35$, and $\lambda_2 = 1.82$ estimating the rate of the explained variation by the two discriminant axes, i.e. 85% and 15%, respectively. The discriminant scores of the oil samples can be seen in Fig. 4. Both axes have a chemical meaning since their canonical correlations with the original important compounds is high ($r_1 = 0.96$ and $r_2 = 0.80$). The important compounds are variously weighted on the two axes as shown by the standardized coefficients of the canonical functions in Table 2. Linoleic and oleic acids are highly weighted in the negative part of CDA-1 while the iodine value in the positive part. The same compounds are highly weighted with reversed signs on CDA-2. For the linoleic and oleic acids this pattern was expected since they are the products of the same biogenetic pathway [43]. The opposite sign of the iodine coefficients are explained on the basis of the chemical treatment of the oil for the production of ROO and RHzO. The dotted lines in Fig. 4 at the origin (0, 0) of the CDA diagram leave intact only the ROO group. RHzO and the adulterated samples are located at the two ends of CDA-1 but are cut by CDA-2. This indicates that no axis alone is enough to separate adulterated oils from the groups of RHzO and ROO. However, the classification efficacy of CDA is considered to be perfect as shown by the classification matrix in Table 3 (panel a). The percentage classification for the three groups of oils was 100%. The Jackknifed classification (cross-validation) in Table 3 (panel b) indicate that classification was correct for 95% of the samples, and only 5% of the adulterated olive samples cannot be predicted by the rest. Importantly, the adulterated oils are not found in the space between the two groups which comprise the source (RHzO) and the adulteration target (ROO) as a putative intermediate product of mixing [14,16]. The violation of the "intermediacy principle" can be explained on the basis of the non-biological chemical profile of ROO.

Classification of the NMR data into the 'leaves' of the binary trees is achieved by starting from an original configuration of five groups. The first two groups are the refined hazelnut oil (RHzO group) and the refined olive oil (ROO group) and in the next three groups are the

Table 3
Classification matrix of the CDA analysis of the NMR data in Table 1.

	Predicted group affiliation			
	RHzO	ROO	AOO	% correct classifications
[a] Actual groups of samples				
RHzO	19	0	0	100
ROO	0	20	0	100
AOO	0	0	20	100
Total classifications	19	20	20	100
[b] Actual groups of samples				
RHzO	17	0	2	89
ROO	0	20	0	100
AOO	1	0	19	95
Total classifications	18	20	21	95

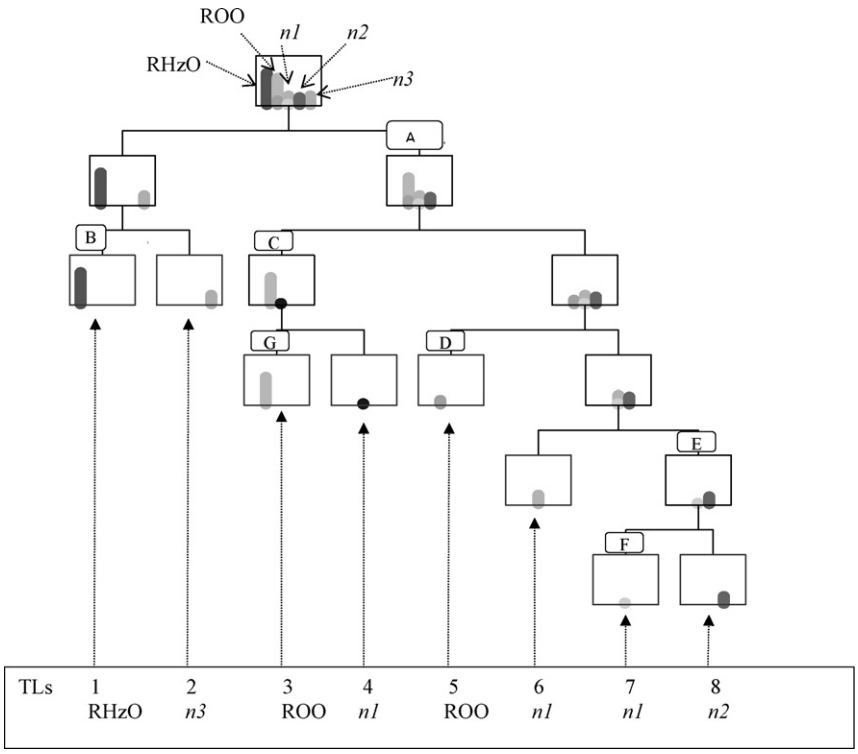


Fig. 5. CBT classification treegram (mobile) of all oil samples. The splitting criteria are those given in Table 4. The original groups are in the root node and in this order they are shown in the entire tree as circles stacked in proportion to the size of each group. The terminal leaves (TLs) at the bottom box correspond to a single group. Eight leaves – indicated by arrows – are required for a complete classification of the samples, since a specific group can form more than one TL.

adulteration levels—i.e. small (1–10%, *n1* group), medium (12–35%, *n2* group) (large 50–95%, *n3* group); ideally five site groups are produced. In the employed model the group identifier is the dependent variable, while the independent variables are the chemical compounds derived by NMR spectroscopy (Table 1). In the construction of the mobile (Fig. 5), the overall reduction in error was 100% and eight terminal leaves were found, each one corresponding to one group (Table 4). It is interesting to note that three compounds, namely *t*-hydroxytyrosol, pinoresinol, and louteolin occur twice in the splitting criteria. The growth of the tree shows that RHzO samples form the first terminal leaf (TL1) early in the process and in a second step the ROO group (TL3 & TL5) (Fig. 5). The adulterated oils spread at different terminal leaves on the basis of different compounds. On the basis of iodine value and pinoresinol (symbol A at split), oils of he *n3* group are clustered together with hazelnut oils but later they separate on the basis of 1,3-DGs and *t*-hydroxytyrosol (symbol B) (Fig. 5). The same pattern is presented with oils of the ROO group. However, here the oil samples at TL5 are separated from adulterated oil samples at another branch of the tree in accordance with the similarity of the refined hazelnut and olive oils in minor constituents. Overall the adulterated oil samples are distributed as follows: *n1* is found at TL4, TL6, and TL7; *n2* is found at TL8 while the group *n3* at TL2 as a result of the proximity to hazelnut oils. Eventually, all splitting criteria are used to separate the adulterated oils which form as many terminal leaves as their RHzO dictates. This means that *n1* is found at three terminal leaves while *n2* and *n3* at one leaf (Table 4 and Fig. 5).

With regard to the significant compounds, CDA uses a larger number of compounds (11 in Table 2) than CBT (9 compounds in seven linear combinations or splitting criteria in Table 4). The fatty acids oleic, linoleic and linolenic are of particular importance. With some exceptions, they were found to be significant in the geographical classification of Greek virgin olive oils either by CDA or CBT [31]. In this study, CDA estimates the first two acids as important while CBT the last one. It seems that the selection is justified in terms of the lipoxygenases pathway (LOX pathway) [43]. A classification method needs only one acid since both linoleic and linolenic acids are the substrates for LOX. In the same line of argumentation oleic is converted to linoleic acid in a bioreaction catalyzed by enzymes encoded by two widespread Fatty Acid Desaturases (FAD) genes. In CDA both oleic and linoleic are significant compounds (Table 2) and have very similar canonical correlations. The pure classification CBT technique does not need both acids. Instead, linoleic acid is enough for the entire classification to be described in CBT (Table 4). This is in agreement with the fact that the refinement process does not disturb the relative proportions of fatty acids.

Table 4
Significant compounds and linear combinations of two compounds expressed as improvement of CBT classification.

Symbol at split	Compounds[a]	Criterion	Fraction of predicted samples	Significance of compounds
A	IV-Pinoresinol	<83.24	0.367	0.367
B	1,3-DGs + *t*-hydroxytyrosol	<2.96	0.580	0.213
C	Louteolin-*t*-hydroxytyrosol	<0.03	0.738	0.158
D	Linoleic acid-Sterols	<0.15	0.822	0.084
E	Pinoresinol-1-acetoxypinoresinol	<0.59	0.918	0.096
F	Louteolin	<0.04	0.956	0.038
G	Apigenin	<0.19	1.000	0.044

[a] See footnote in Table 1 for the meaning of symbols.

For both methods, diacylglycerols appear to be significant compounds. 1,2-DGs is important for CDA, but with a different behavior of canonical coefficient than the ratio *D*. In CBT method 1,3-DGs are found significant. These compounds have lower variation within oil samples and vary substantially among the original groups. It is strange that *t*-DGs are not important in both methods presumably because of the similarity that exists in the lipid biosynthetic pathway that leads from diacylglycerols to triacylglycerols [44].

Phenols occur in ROO group though at reduced amounts in comparison to virgin olive oil but they are absent from RHzO as a result of chemical treatment of refinement, in spite the fact that phenols have been reported from hazel tree leaves and several species of hazel family (Angiospermae: Coryllaceae). Almost every split in the CBT tree (Fig. 5) contains one or two phenols. Exception is the split D which is the difference between linolenic acid and sterols. Amongst phenols, *t*-hydroxytyrosol, luteolin, and 1-acetoxypinoresinol are important in both CDA and CBT analyses, whereas homovanillic alcohol, apigenin and pinoresinol are important in CDA and CBT classification, respectively. Syringaresinol, *t*-tyrosol and *f*-tyrosol, *p*-coumaric acid and total phenols are not significant compounds. They have high standard deviation within groups (Table 1). Possibly, the large variation of these phenolic compounds amongst the various samples caused their exclusion from the important compound set in both classifications together with the fact that they are compounds of the same phenol biosynthetic path.

Phytosterols are also important compounds in both CDA and CBT analyses. In nature they are distributed to many species in small quantities less than 1% and usually much less. They are important nutrients for all eucaryotes; insects incapable in synthesizing them acquire the necessary amounts from endosymbiotic and in some case exobiotic bacteria from plant hosts, which supply sterols and in some cases vitamins. In CBT sterols appear in the splitting criterion that separates ROO oils from the adulterated ones in groups *n1* and *n2*.

4. Conclusions

^{1}H and ^{13}P NMR spectroscopy in conjunction with multivariate statistical analyses (CDA and CBTs) has been used with respect to its ability to discriminate between ROO and RHzO and to detect ROO fraud with RHzO. Overall, both statistical analyses showed perfect classification that is all oil samples were grouped correctly in the original group. Both analyses used different significant compounds, although in the same class and a more or less equal number of them. CBTs gave a more detailed and biologically sound hierarchical splitting while it started from more groups than CDA. This is the result of (a) non-predefined strategy, (b) its capability in treating non-linear and/or discontinuous data structures, and (c) its orientation towards hierarchical classification unlike CDA which keeps a balance between classification and ordination in a fixed number of groups [45]. RHzO was the source group of this adulteration and ROO was the group which was adulterated, and these groups cannot be altered in CDA. The reported CBTs classification is superior to other methods combining linear algorithms as principal components and simple non-linear techniques (e.g. artificial neural networks) that need a scarce knowledge of the engaged compounds and for this are unable to substantiate their biological basis.

Acknowledgments

We are indebted to the program Regional Pole of Innovation for Value Creation funded by the administration of the Region of Crete and the European Union.

References

[1] G.P. Blanch, M. Caja, M.L. Riuz del Castillo, J. Agric. Food Chem. 46 (1998) 5153–5157.
[2] M.T. Morales, G. Luna, R. Aparicio, Food Chem. 91 (2004) 293–301.
[3] G. Flores, M.L. del Castillo, M. Herraiz, G.P. Blanch, Food Chem. 97 (2006) 742–749.
[4] G. Flores, M.L. del Castillo, G.P. Blanch, M. Herraiz, Food Chem. 97 (2006) 336–342.
[5] A. Sayago, M.T. Morales, R. Aparicio, Eur. Food Res. Technol. 218 (2004) 480–483.
[6] C. Mariani, G. Bellan, G. Morchio, A. Pellegrino, Riv. Ital. Sostanze Grasse 76 (1999) 59–67.
[7] F. Peña, S. Cárdenas, M. Gallego, M. Velcárcel, J. Chromatogr. A 1074 (2005) 215–221.
[8] S. Milder-Szkudlarz, H.H. Jeleń, Food Chem. 110 (2008) 751–761.
[9] M.H. Gordon, C. Covell, N. Kirsch, J. Am. Oil. Chem. Soc. 78 (2001) 621–624.
[10] D. Zabaras, M.H. Gordon, Food Chem. 84 (2004) 475–483.
[11] S. Vichi, L. Pizzale, E. Toffano, R. Bartolomeazzi, L. Conte, J. AOAC Int. 84 (2001) 1534–1541.
[12] J. Parcerisa, I. Casals, J. Boatella, R. Codony, M. Rafecas, J. Chromatogr. A 881 (2000) 149–158.
[13] L. Cercasi, M.T. Rodriguez-Estrada, G. Lercker, J. Chromatogr. A 985 (2003) 211–220.
[14] C. Fauhl, F. Reniero, C. Guillou, Magn. Reson. Chem. 38 (2000) 436–443.
[15] L. Mannina, M. Patumi, P. Fiordiponti, M.C. Emanuele, A.L. Segre, Ital. J. Food Sci. 11 (1999) 139–149.
[16] G. Vigli, A. Philippidis, A. Spyros, P. Dais, J. Agric. Food Chem. 51 (2003) 5715–5722.
[17] D. Šmejkalova, A. Piccolo, Food Chem. 118 (2010) 153–158.
[18] B.F. Ozen, L.J. Mauer, J. Agric. Food Chem. 50 (2002) 3898–3901.
[19] E.C. Lòpez-Dìez, G. Bianchi, R. Goodacre, J. Agric. Food Chem. 51 (2003) 6145–6150.
[20] L. Diego, G. González, L. Mannina, M. D' Imperio, A.L. Segre, R. Aparicio, Eur. Food Res. Technol. 219 (2004) 545–548.
[21] M.J. Lerma-García, G. Ramis-Ramos, J.M. Herrero-Martínez, E.F. Simó-Alfonso, Food Chem. 118 (2010) 78–83.
[22] V. Baeten, J.A.F. Pierna, P. Dardienne, M. Meurens, D.L. García-González, R. Aparicio-Ruiz, J. Agric. Food Chem. 53 (2005) 6201–6206.
[23] A. Sayago, D.L. García-González, M.T. Morales, R. Aparicio, J. Agric. Food Chem. 55 (2007) 2068–2071.
[24] T. Mavromoustakos, M. Zervou, G. Bonas, A. Kolocouris, P. Petrakis, J. Am. Oil Chem. Soc. 77 (2000) 405–411.
[25] J. Vlahov, Magn. Reson. Chem. 35 (1997) S8–S12.
[26] G. Fragaki, A. Spyros, G. Siragakis, E. Salivaras, P. Dais, J. Agric. Food Chem. 53 (2005) 2810–2816.
[27] A. Spyros, P. Dais, J. Agric. Food Chem. 48 (2000) 802–805.
[28] A. Zwierzak, Can. J. Chem. 45 (1967) 2501–2512.
[29] G. Montedoro, M. Servili, M. Baldioli, R. Selvaggini, E. Miniati, J. Agric. Food Chem. 40 (1992) 1571–1576.
[30] R.A. Johnson, D.M. Wichern, Applied Multivariate Statistical Analysis, Prentice Hall, New Jersey, USA, 1998, p. 820.
[31] P.V. Petrakis, A. Agiomyrgianaki, S. Christophoridou, A. Spyros, P. Dais, J. Agric. Food Chem. 14 (2008) 3200–3207.
[32] J. Oksanen, R. Kindt, P. Legendre, R. O'Hara, G.L. Simpson, M.H.H. Stevens, H. Wagner, Vegan: Community Ecology Package, R package version 1.13-2. http://vegan.r-forge.r-project.org/ (accessed 17.05.2008).
[33] L. Breiman, J. Friedman, R. Olshen, C. Stone, Classification Regression Trees, Wadsworth, California, USA, 1984.
[34] R Development Core Team, R: A Language and Environment for Statistical Computing, R Foundation for Statistical Computing, Vienna, Austria, 2008.
[35] T.M. Therneau, B. Atkinson, rpart: Recursive Partitioning, R package version 3.1-41, R port by Brian Ripley, 2008.
[36] S. Christophoridou, P. Dais, J. Agric. Food Chem. 54 (2006) 656–664.
[37] R.W. Owen, W. Mier, A. Giacosa, W.E. Hull, B. Spiegelhalder, H. Bartsch, Food Chem. Toxicol. 38 (2000) 647–659.
[38] C. Nergíz, Int. J. Food Sci. Technol. 28 (1993) 461–464.
[39] N. Cortesi, A. Ponzizni, E. Fedeli, Riv. Ital. Sostanze Grasse 58 (1981) 108–114.
[40] A. García, M.V. Ruiz-Méndez, C. Romero, M. Brenes, J. Am. Oil Chem. Soc. 83 (2006) 159–164.
[41] S. Arranz, R. Cert, J. Perez-Jiménez, A. Cert, F. Saura-Calixto, Food Chem. 110 (2008) 985–990.
[42] A. Spyros, A. Philippidis, P. Dais, J. Agric. Food Chem. 52 (2004) 157–162.
[43] D.F. Hildebrand, Physiol. Plant 76 (1989) 249–253.
[44] R.E. Minto, B.J. Blacklock, Progr. Lipid Res. 47 (2008) 233–306.
[45] R.A. Pimentel, in: J.T. Sorensen, R. Foottit (Eds.), An Introduction to Ordination, Principal Component Analysis and Discriminant Analysis, Elsevier, Amsterdam, 1992, pp. 11–28.

Talanta 80 (2010) 2172–2176

Contents lists available at ScienceDirect

Talanta

journal homepage: www.elsevier.com/locate/talanta

Ultrasensitive Cu^{2+} sensing by near-infrared-emitting CdSeTe alloyed quantum dots

Guo-Xi Liang, Hong-Ying Liu, Jian-Rong Zhang, Jun-Jie Zhu*

Key Laboratory of Analytical Chemistry for Life Science (MOE), School of Chemistry and Chemical Engineering, Nanjing University, Nanjing 210093, China

ARTICLE INFO

Article history:
Received 3 August 2009
Received in revised form 4 November 2009
Accepted 6 November 2009
Available online 13 November 2009

Keywords:
Fluorescence
Near-infrared (NIR)
Alloyed quantum dots (AQdots)
Cu^{2+}

ABSTRACT

The near-infrared (NIR)-emitting CdSeTe alloyed quantum dots (AQdots) that capped with L-cysteine were applied for ultrasensitive Cu^{2+} sensing. The sensing approach was based on the fluorescence of the AQdots selectively quenched in the presence of Cu^{2+}. Experimental results showed a low interference response towards other metal ions. The possible quenching mechanism was discussed on the basis of the binding between L-cysteine and the metal ions. In addition, biomolecules have low effect on the fluorescence due to the minimized interferences in NIR region. The response of the NIR optical sensor was linearly proportional to the concentration of Cu^{2+} ranging from 2×10^{-8} to 2×10^{-6} mol L^{-1}. Furthermore, it has been successfully applied to the detection of Cu^{2+} in vegetable samples.

© 2009 Elsevier B.V. All rights reserved.

1. Introduction

In recent years, contamination by large amount of heavy metals poses a serious threat to human health and the environment [1,2]. Copper is one of the heavy metals and essential element for many living organisms, it becomes toxic at high concentrations [3]. Therefore, the design and development of selective as well as sensitive method for Cu^{2+} detection in environmental and biological samples is of great importance for analytical chemists. Many methods for the detection of Cu^{2+} have been developed such as atomic absorption spectroscopy [4,5], inductively coupled plasma mass spectroscopy [6,7], X-ray fluorescence [8]. These methods offer good limits of detection (LODs) and wide working concentration ranges. However, these methods may require the use of sophisticated and relatively costly apparatus, and are unsuitable for on-line or in-field monitoring [9].

Chemical sensors can overcome these disadvantages and become increasingly important for monitoring metal ion. Some sensors have been developed for the determination of Cu^{2+}. A variety of organic fluorophore-based sensors have been proposed to selectively respond to Cu^{2+} due to their relatively high sensitivity [10–13]. However, organic fluorophore often suffer from the disadvantages like narrow excitation bands, broad emission spectra and fast photobleaching. Recently developed quantum dots (Qdots) have substantial advantages over organic dyes, including excellent fluorescence properties, high photochemical stability and excellent resistant to chemical degradation [14–16]. Therefore, the Qdots-based sensors have great potential to overcome the problems encountered with existing organic fluorophore-based sensors.

Therefore, the synthesis and application of these Qdots are of great interest in the development of novel sensitive sensors. So far only a few studies on Qdots system for Cu^{2+} detection have been reported. Chen and Rosenzweig showed the first example of thioglycerol-coated CdS Qdots sensor for Cu^{2+} [17]. Later, the optical detection of Cu^{2+} with peptide-coated CdS Qdots [18], $Cd_{10}S_{16}$ molecular cluster [19], MPA-capped CdSe [20] or CdTe [21], ZnS Qdots [22] and CdSe/CdS Qdots [23] was also proposed. However, most of the existing Qdots-based sensors were emitting at wavelengths below 550 nm. In addition, selectivity, stability and limited applicability to real sample were still among the limitations for the Qdots-based sensors proposed [24]. Therefore, the stable Qdots with near-infrared (NIR)-emission between 650 and 900 nm are of particular interest for the detection because many molecules' autofluorescence and absorbance can be reduced to the minima in this region [16,25,26]. Up to now, the sensors based on NIR-emitting Qdots for metal ions detection are very rare.

In this study, the NIR-emitting CdSeTe AQdots were prepared in aqueous solution with L-cysteine as stabilizer, and then it was demonstrated as a selective fluorescent Cu^{2+} probe with low detection limit. Moreover, the proposed sensing system has been applied for the determination of Cu^{2+} in vegetable samples and the recovery test was satisfactory.

* Corresponding author. Tel.: +86 25 83594976; fax: +86 25 83594976.
E-mail address: jjzhu@nju.edu.cn (J.-J. Zhu).

0039-9140/$ – see front matter © 2009 Elsevier B.V. All rights reserved.
doi:10.1016/j.talanta.2009.11.025

2. Experimental

2.1. Apparatus

The fluorescence spectra of the Qdots samples were obtained with an Edinburgh FLS920P fluorescence spectrometer (Edinburgh Instruments Ltd., UK). The optical absorption spectra were measured using the Shimadzu 3600 UV–vis spectrometer (Shimadzu, Japan). The TEM images were acquired using a JEOL JEM-2100 (JEOL, Japan) transmission electron microscope operating at an acceleration voltage of 200 kV. The elemental analysis of Qdots was performed on VG PQExCell ICP-MS system.

2.2. Reagents

Selenium powder (Se, 99.5%, 200 mesh), tellurium powder (Te, 99.8%, 200 mesh) and mercaptopropionic acid (MPA, 99%) were purchased from Acros Organics (NJ, USA). L-Cysteine (98%) was purchased from Sigma–Aldrich. Cadmium chloride was purchased from Tingxin Chemical Reagent (Shanghai, China). Sodium borohydride was purchased from Tianjin Chemical Research Institute (Tianjin, China). The stock standard solutions (10 mmol L^{-1}) of Cu^{2+} were prepared by dissolving appropriate amounts of $Cu(NO_3)_2{\cdot}3H_2O$ in high purity water. Working solutions were prepared by appropriate dilutions of their stock solutions. All other reagents were of analytical grade and used without further purification. The ultrapure water with 18.2 MΩ cm^{-1} (Millipore Simplicity, USA) was used throughout the experiments.

2.3. Preparation of the AQdots

The L-cysteine-capped CdSeTe AQdots with NIR-emission were prepared through the incorporation of selenium ions into CdTe nanocrystals as reported in our previous method [27]. L-Cysteine as a sulfur amino acid was selected as capping agent for its good compatibility and the protection of Qdots-induced toxicity [28]. In the synthesis, all reactions were carried out in oxygen-free water under nitrogen. In brief, $CdCl_2$ (0.25 mmol) and L-cysteine (0.6 mmol) were dissolved in water (200 mL) and adjusted to pH 11.5 with 1 mol L^{-1} NaOH. The resulting transparent solution was deaerated by bubbling of nitrogen for 20 min and was heated to 95 °C. Under vigorous stirring, the freshly prepared 0.125 mmol of NaHTe and 0.04 mmol of NaHSe aqueous solutions were injected to the above solution. Afterward, the reaction mixture was further refluxed at 95 °C under a nitrogen atmosphere. The emission wavelength of the AQdots could be tuned by changing the refluxing time. Part of the refluxing solution was taken out at regular intervals for characterization. After 3 h, the CdSeTe AQdots with emission wavelength of 685 nm (CdSeTe685) was obtained.

2.4. Selectivity measurements

The following inorganic salts were used for the cation selectivity experiment: nickel acetate tetrahydrate, zinc acetate, barium chloride, calcium chloride, iron (III) chloride hexahydrate, iron (II) sulfate heptahydrate, sodium chloride, potassium chloride, lanthanum nitrate hexahydrate, aluminum nitrate, cobaltous sulfate, magnesium chloride, copper nitrate and lead nitrate. A 10 mmol L^{-1} salt stock solution was prepared with ultrapure water. Subsequently, the salt solutions were prepared by serial dilution with Tris–HCl solution (pH 7.4).

2.5. Procedure for spectrofluorometric detection of Cu^{2+}

Copper nitrate was used for the Cu^{2+} sensitivity studies. Various concentrations of Cu^{2+} were prepared using serial dilution of the copper nitrate stock solution to test the sensitivity limits of the AQdots. A known concentration of Cu^{2+} solution was added into the AQdots nanoparticle solution and mixed thoroughly for 10 min. The fluorescence intensity of the solution was recorded at 685 nm with the excitation wavelength of 300 nm. Both slit widths of excitation and emission were 2 nm.

2.6. Physical characterization of the fluorescence quenching

An amount of 5 μL of 1 mmol L^{-1} Cu^{2+} or Al^{3+} was added to 1 mL of 160 nmol L^{-1} CdSeTe685 AQdots solution. After incubation for 20 min, the suspended solutions of the nanoparticles were deposited onto copper grids with carbon support by slowly evaporating the solvent in air at room temperature. The high-resolution transmission electron microscopy (HR-TEM) images of Cu^{2+} and Al^{3+}-treated CdSeTe685 AQdots were acquired using a JEOL JEM-2100 (JEOL, Japan) transmission electron microscope.

2.7. Sample preparation

The vegetable samples of bean, cucumber and tomato were purchased from local market. And the accurately weighted samples were ground and then digested with 20 mL concentrated nitric acid on a gas burner until the solution became wet salt. Then, it was dissolved with 2 mol L^{-1} HNO_3 and heated until it was clear. Finally, the solution was diluted with water.

3. Results and discussion

3.1. Spectral characteristics of the AQdots

The ultrafiltration-purified L-cysteine-capped CdSeTe AQdots were well dispersed in PBS or Tris–HCl solution (10 mmol L^{-1}, pH 7.4). The absorption spectra and fluorescence spectra of the AQdots were obtained and shown in Fig. 1. The maximal fluorescence wavelength was 685 nm. It can be seen that the full width at half-maximum (FWHM) fluorescence intensity is about 60 nm and symmetric, showing that the CdSeTe AQdots were nearly of monodisperse and homogeneous. In addition, the fluorescence intensity of these AQdots was pH-dependent [29] as shown in Fig. 1B. The low fluorescence intensity in acidic medium is the result of dissociation of the nanoparticles due to protonation of the surface-binding thiolates [30]. With the increase of pH, the deprotonation of the thiol group in the L-cysteine molecule occurs. This deprotonation may strengthen the covalent bond between Cd and L-cysteine molecule, which leads to the fluorescence intensity increases with pH increasing. However, the fluorescence intensity was declined with the further increase of pH value.

3.2. Selective fluorescence quenching of the AQdots by Cu^{2+}

The experiment of selective fluorescence quenching was performed with the CdSeTe AQdots (160 nmol L^{-1}, λ_{max} = 685 nm). The purified AQdots solutions contained no free L-cysteine. The AQdots were dispersed in Tris–HCl buffer solution (10 mmol L^{-1}, pH 7.4) for its pH-dependent fluorescence intensity and then added to the same amount of metal cation solutions (1 μmol L^{-1}). The fluorescence intensity of these samples was measured and the results were shown in Fig. 2. It was found that the fluorescence intensity of AQdots has more sensitivity to Cu^{2+} than to Pb^{2+}, Fe^{2+} and no response to other cations such as K^+, Na^+, Mg^{2+}, Al^{3+}, Ca^{2+} and Zn^{2+}. In contrast, they demonstrated complete fluorescence quenching in the presence of Cu^{2+}. The quenching effect of Cu^{2+} on fluorescence emission of CdSeTe AQdots was found to be concentration dependent. Therefore, this selective response towards Cu^{2+} can be

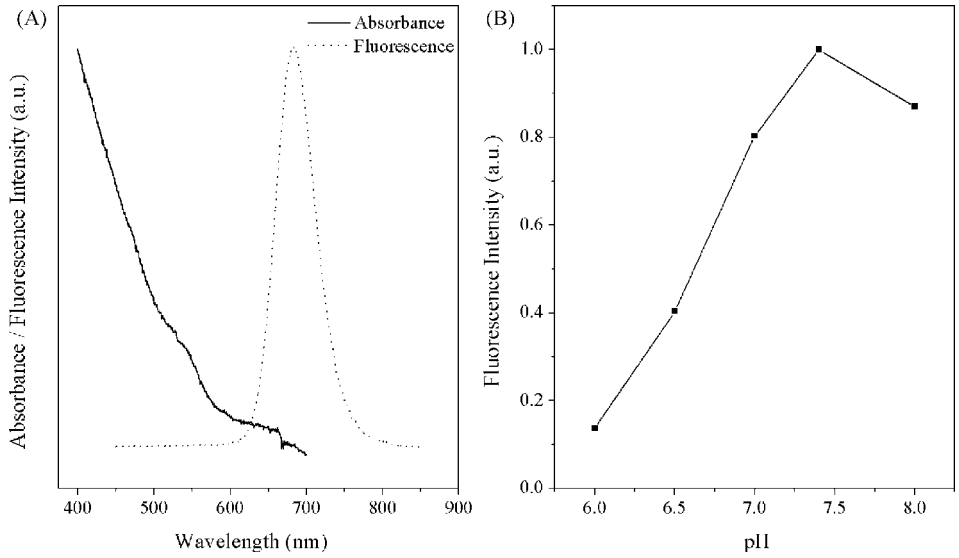


Fig. 1. (A) Absorption and fluorescence spectra of the L-cysteine-capped CdSeTe AQdots. (B) Fluorescence intensity of the CdSeTe AQdots (λ_{max} = 685 nm) in PBS buffer (10 mmol L^{-1}) at different pH values.

used for the development of a sensitive and selective sensor for Cu^{2+}.

3.3. Mechanism of the quenching effect by Cu^{2+}

L-Cysteine as a sulfur amino acid was an ideal capping agent for the CdSeTe AQdots synthesis. The cysteine capping layer was very important to improve water solubility and stability of the AQdots. Therefore, the metal–sulfide bond strength, which was characterized by their respective K_{sp} value, may be an important parameter for the fluorescence quenching effect. And the selective fluorescence quenching could be rationalized by the competitive cysteine binding between the AQdots and the metal ions present in the solution. The K_{sp} value of Cu–S (6.3×10^{-36}) is much lower than that of Cd–S (8.0×10^{-27}), Pb–S (8.0×10^{-28}), Zn–S (2.9×10^{-25}) and Fe(II)–S (6.3×10^{-18}) [31]. Therefore, we proposed that the cysteine capping layer was preferentially displaced from the surface of the CdSeTe AQdots upon the binding of Cu^{2+}. The displacement of cysteine capping consequently created imperfections on the AQdots surface, resulted in fluorescence quenching. In order to verify this hypothesis, the quenching effect of different metal ions on the fluorescence intensity of the MPA-capped CdTe Qdots (λ_{max} = 650 nm) was also investigated (Fig. 2). The MPA-capped CdTe Qdots were synthesized according to the reported methods [32]. It can be found that the quenching effect of the MPA-capped CdTe Qdots displays similar results with the L-cysteine-capped CdSeTe AQdots.

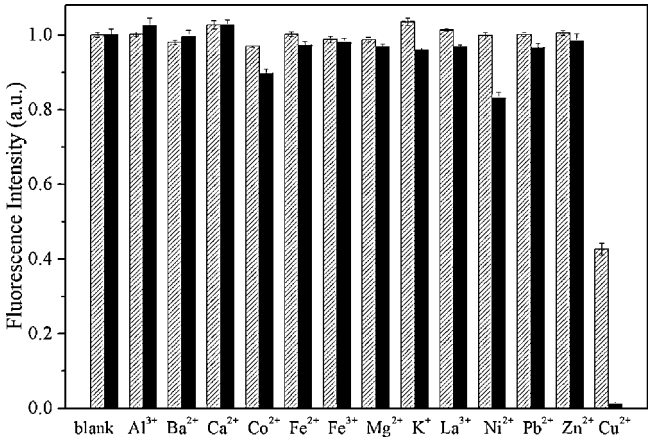


Fig. 2. The quenching effect of different ions on the fluorescence intensity of the MPA-capped CdTe Qdots (λ_{max} = 650 nm) (▨) and the L-cysteine-capped CdSeTe AQdots (λ_{max} = 685 nm) (■) in 10 mmol L^{-1} Tris–HCl buffer at pH 7.4. The excitation wavelength was 300 nm.

In addition, the fluorescence quenching experiments were conducted in the presence of free cysteine. The reduced fluorescence quenching in the presence of Cu^{2+} was observed in the CdSeTe AQdots solutions containing free cysteine. And similar reduced fluorescence quenching of the MPA-capped CdTe Qdots was observed in the presence of Cu^{2+} when the free MPA increased in the CdTe Qdots solution. This also suggested that the thiol capping agent of the Qdots was related to the fluorescence quenching effect. And the aggregation of the AQdots was also observed at high Cu^{2+} concentrations, leading to precipitation in the presence of 10 μmol L^{-1} Cu^{2+}. At high Cu^{2+} concentrations, loss of more cysteine would eventually cause the AQdots to aggregate and precipitate. The control experiment showed no aggregation of the AQdots in the same concentration of Al^{3+}. The low magnification TEM image (Fig. 3B and C) of CdSeTe confirmed the aggregation of the AQdots.

Based on the investigation, we concluded that the competitive binding of the cysteine with Cu^{2+} was the primary mechanism for the fluorescence quenching. The fluorescence intensity of CdSeTe AQdots was highly sensitive to their surface protection. Even the removal of a limited amount of surface-bound cysteine would lead to dramatic reduction in fluorescence intensity. Therefore, the lower detection limit and higher sensitivity were achieved with the lower concentration of cysteine-capped CdSeTe AQdots.

3.4. The detection of Cu^{2+}

The detection of Cu^{2+} is of particular interest due to copper importance in environment and living organisms. The CdSeTe AQdots displayed great fluorescence quenching at low concentration of Cu^{2+} compared to other metal ions. The fluorescence quenching was best described by the Stern–Volmer equation,

$$\frac{F^0}{F} = 1 + K_{SV}[Q],$$

where F and F^0 are the fluorescence intensity of the CdSeTe AQdots in the presence and absence of Cu^{2+} respectively, [Q] is the con-

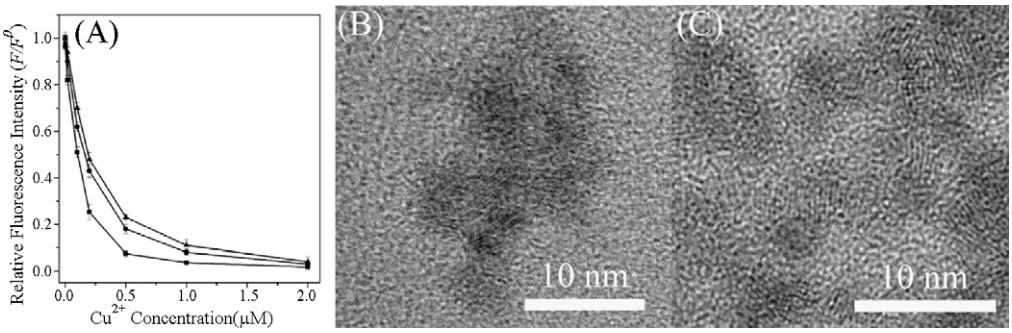


Fig. 3. (A) Fluorescence quenching by Cu^{2+} for 80 nmol L^{-1} of CdSeTe AQdots (λ_{max} = 685 nm) in the absence of free L-cysteine (■) and presence of 40 μmol L^{-1} (●) and 60 μmol L^{-1} (▲) of free L-cysteine, respectively. The excitation wavelength was 300 nm. (B) The TEM image of the CdSeTe AQdots (λ_{max} = 685 nm) in the presence of 5 μmol L^{-1} Cu^{2+}. (C) The TEM image of CdSeTe AQdots (λ_{max} = 685 nm) in the presence of 5 μmol L^{-1} Al^{3+}.

centration of the quencher (i.e., Cu^{2+}) and K_{SV} is the Stern–Volmer constant.

The influence of the concentration of L-cysteine-capped CdSeTe AQdots on fluorescence quenching by Cu^{2+} was studied. The strong fluorescence quenching was observed at low CdSeTe AQdots concentration in the presence of the same Cu^{2+} concentration as shown in Fig. 4A. Fig. 4B illustrated the high reproducibility of the CdSeTe AQdots response to Cu^{2+}. The linear relationship of the Stern–Volmer plot of F^0/F to Cu^{2+} concentration (Fig. 4C) was obtained. The linear relationship between $1/K_{SV}$ and CdSeTe AQdots concentration as shown in Fig. 4D, which suggested that the detection limit can be reduced with the decrease of AQdots concentration. Therefore, the CdSeTe AQdots concentration of 80 nmol L^{-1} was recommended. The calibration plot of F^0/F versus [Q] shows a good linear relationship (R^2 = 0.9976) for Cu^{2+} concentration in the range of 2×10^{-8} to 2×10^{-6} mol L^{-1} (Fig. 4C). The limit of detection was evaluated using $3\sigma/S$, and is found to be 7.1×10^{-9} mol L^{-1}, where σ is the standard deviation of the blank signal, and S is the slope of the linear calibration plot.

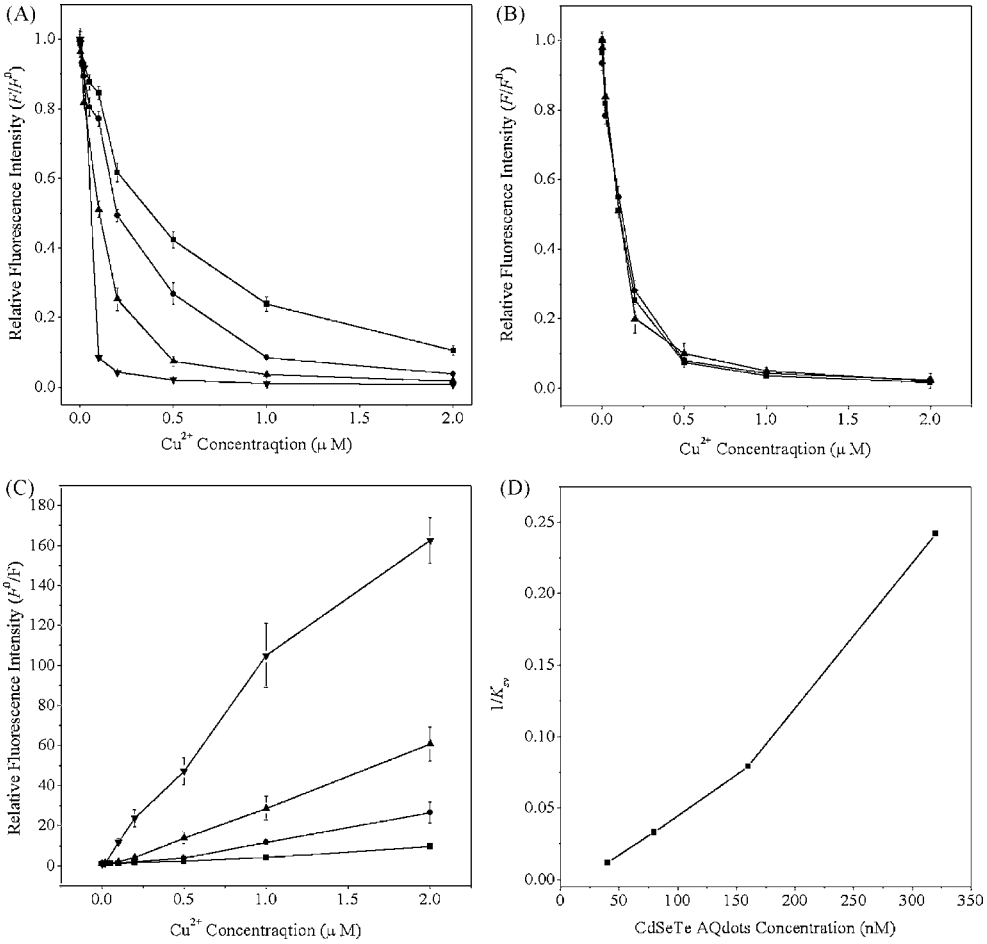


Fig. 4. (A) The quenching effect of Cu^{2+} concentration on the fluorescence intensity of 40 nmol L^{-1} (▼), 80 nmol L^{-1} (▲), 160 nmol L^{-1} (●) and 320 nmol L^{-1} (■) CdSeTe AQdots. (B) The reproducible determination of the fluorescence quenching effect of the 80 nmol L^{-1} CdSeTe AQdots. (C) Stern–Volmer plots of the different CdSeTe AQdots concentration. (D) Linear correlation of $1/K_{SV}$ values of the CdSeTe AQdots. The L-cysteine-capped CdSeTe AQdots (λ_{max} = 685 nm) was used. The excitation wavelength was 300 nm.

Table 1
Detection of Cu^{2+} in real samples.

Samples	Cu^{2+} concentration (mg/kg)				
	Proposed method	ICP-MS method	Added	Total	Recovery (%)
Bean	3.51	3.10	5	8.87	107.2
Cucumber	2.62	2.94	5	7.86	104.8
Tomato	1.96	1.65	5	7.44	109.6

3.5. Sample analysis

The proposed method has been applied to the analysis of vegetable samples including bean, cucumber and tomato. A control experiment was carried out using inductively coupled plasma-optical emission spectroscopy (ICP-OES) method. Table 1 gives the analysis results of Cu^{2+} in these vegetable samples. With standard addition method, the recoveries were found to be 104.8–109.6%. The analysis results agreed with those obtained with ICP-MS methods.

4. Conclusions

The near-infrared (NIR)-emitting L-cysteine-capped CdSeTe alloyed quantum dots (AQdots) have been demonstrated selective fluorescence quenching in the presence of Cu^{2+}. The selective quenching effect could be rationalized by the competitive cysteine capping layer binding between the CdSeTe AQdots and the metal ions present in the solution. Based on this finding, we proposed a novel NIR fluorescence sensor for sensitive Cu^{2+} detection in aqueous medium. The limit of detection (LOD) of this method is higher than that of the previous reported methods. Under the optimum conditions, the detection range of the proposed method was from 2×10^{-8} to 2×10^{-6} mol L^{-1} with the LOD of 7.1×10^{-9} mol L^{-1}. Furthermore, the practical utility of the CdSeTe AQdots sensor has been demonstrated by the determination of trace Cu^{2+} in vegetable samples, obtaining satisfactory results with the reference method. Our preliminary studies have demonstrated the potential of this method for practical applications.

Acknowledgements

We greatly appreciate the support of the National Natural Science Foundation of China for the Key program (20635020) and Creative Research Group (20821063). This work is also supported by National Basic Research Program of China (2006CB933201).

References

[1] M. Hola, J. Kalvoda, O. Babek, R. Brzobohaty, I. Holoubek, V. Kanicky, R. Skoda, Environ. Geol. 58 (2009) 141.
[2] A. Petroczi, D.P. Naughton, Food Chem. Toxicol. 47 (2009) 298.
[3] E. Merian, Metals and their Compounds in the Environment, VCH, Weinheim, 1991, pp. 893–898.
[4] H. Faghihian, A. Hajishabani, S. Dadfarnia, H. Zamani, Int. J. Environ. Anal. Chem. 89 (2009) 223.
[5] A.N. Anthemidis, K.G. Ioannou, Talanta 79 (2009) 86.
[6] D. Chen, B. Hu, C. Huang, Talanta 78 (2009) 491.
[7] D.K. Reddy, G. Anil, M.R.P. Reddy, K. Mukkanti, V. Balaram, T.G. Rao, Atom. Spectrosc. 48 (2009) 5016.
[8] M.P. Silva, A. Tomal, C.A. Perez, A. Ribeiro-Silva, M.E. Poletti, X-Ray Spectrom. 38 (2009) 103.
[9] X. Zhang, J. Peng, C. He, G. Shen, R. Yu, Anal. Chim. Acta 567 (2006) 189.
[10] I.S. Balogh, S. Ioseph, M. Ruschak, V. Andruch, Y. Bazel, Talanta 76 (2008) 115.
[11] K. Rurack, M. Kollmannsberger, U. Resch-Genger, J. Daub, J. Am. Chem. Soc. 122 (2000) 968.
[12] M. Royzen, Z. Dai, J.W. Canary, J. Am. Chem. Soc. 127 (2005) 1612.
[13] S. Khatua, S.H. Choi, J. Lee, J.O. Huh, Y. Do, D.G. Churchill, Inorg. Chem. 48 (2009) 1799.
[14] W.C.W. Chan, D.J. Maxwell, X. Gao, R.E. Bailey, M. Han, S. Nie, Curr. Opin. Biotechnol. 13 (2002) 40.
[15] E.R. Goldman, I.L. Medintz, H. Mattoussi, Anal. Bioanal. Chem. 384 (2006) 560.
[16] J.M. Klostranec, W.C.W. Chan, Adv. Mater. 18 (2006) 1953.
[17] Y. Chen, Z. Rosenzweig, Anal. Chem. 74 (2002) 5132.
[18] K.M. Gattas-Asfura, R.M. Leblanc, Chem. Commun. (2003) 2684.
[19] K. Konishi, T. Hiratani, Angew. Chem. Int. Ed. 45 (2006) 5191.
[20] M.T. Fernandez-Arguelles, W.J. Jin, J.M. Costa-Fernandez, R. Pereiro, A. Sanz-Medel, Anal. Chim. Acta 549 (2005) 20.
[21] C. Bo, Z. Ping, Anal. Bioanal. Chem. 381 (2005) 986.
[22] M. Koneswaran, R. Narayanaswamy, Sens. Actuators B 139 (2009) 104.
[23] Y. Zhang, H. Zhang, X. Guo, H. Wang, Microchem. J. 89 (2008) 142.
[24] J.M. Costa-Fernandez, Anal. Bioanal. Chem. 384 (2006) 37.
[25] J.V. Frangioni, Curr. Opin. Chem. Biol. 7 (2003) 626.
[26] Y. Xia, C. Zhu, Analyst 133 (2008) 928.
[27] G.X. Liang, M.M. Gu, J.R. Zhang, J.J. Zhu, Nanotechnology 20 (2009) 415103.
[28] P.J. Laura, S.M. Sandra, W.L. Laura, A.H. Jack, Toxicol. Sci. 75 (2003) 458.
[29] D.A. Skoog, F.J. Holler, T.A. Nieman, Principles of Instrumental Analysis, seventh ed., Saunders College, Philadelphia, 1998, pp. 601–608.
[30] M. Gao, S. Kirstein, H. Mohwald, A.L. Rogach, A. Kornowski, A. Eychmuller, H. Weller, J. Phys. Chem. B 102 (1998) 8360.
[31] R.L. David, Handbook of Chemistry and Physics, 78th edition, 1997–1998.
[32] H. Qian, J. Ren, Small 2 (2006) 747.

Talanta 80 (2010) 2177–2181

Contents lists available at ScienceDirect

Talanta

journal homepage: www.elsevier.com/locate/talanta

Direct electrochemistry and electrocatalysis of hemoglobin on gold nanoparticle decorated carbon ionic liquid electrode

Wei Sun*, Peng Qin, Ruijun Zhao, Kui Jiao

Key Laboratory of Eco-Chemical Engineering of Ministry of Education, College of Chemistry and Molecular Engineering, Qingdao University of Science and Technology, Qingdao 266042, People's Republic of China

ARTICLE INFO

Article history:
Received 3 September 2009
Received in revised form 5 November 2009
Accepted 6 November 2009
Available online 14 November 2009

Keywords:
Ionic liquid
Hemoglobin
Gold nanoparticle
Direct electrochemistry
Electrocatalysis

ABSTRACT

In this paper a carbon ionic liquid electrode (CILE) was fabricated by using ionic liquid 1-ethyl-3-methylimidazolium ethylsulfate ([EMIM]EtOSO$_3$) as modifier and further gold nanoparticles were in situ electrodeposited on the surface of CILE. The fabricated Au/CILE was used as a new platform for the immobilization of hemoglobin (Hb) with the help of a Nafion film. Electrochemical experimental results indicated that direct electron transfer of Hb was realized on the surface of Au/CILE with a pair of well-defined quasi-reversible redox peaks appeared. The formal peak potential ($E^{0\prime}$) was obtained as −0.210 V (*vs.* SCE) in pH 7.0 phosphate buffer solution (PBS), which was the characteristic of Hb heme Fe(III)/Fe(II) redox couple. The fabricated Nafion/Hb/Au/CILE showed excellent electrocatalytic activity to the reduction of trichloroacetic acid (TCA) and the reduction peak current was in proportional to TCA concentration in the range from 0.2 to 18.0 mmol/L with the detection limit as 0.16 mmol/L (S/N = 3). The proposed electrode showed good stability and reproducibility, and it had the potential application as a new third-generation electrochemical biosensor.

© 2009 Elsevier B.V. All rights reserved.

1. Introduction

Direct electrochemistry between metalloproteins with electrodes has aroused great interests in the preparation of the biosensor and bioreactor [1]. But the direct electron transfer on the bare working electrode is difficult to be realized due to the deep burying of the electroactive center or the partly denaturation of the redox protein. Many methods have been proposed for the construction of protein film electrodes to achieve the direct electron transfer process between proteins and the working electrode. For this purpose various supporting films including insoluble surfactants, biopolymers, polyelectrolytes and hybrid films are used [2–4]. The presence of film on the electrode surface can provide a biocompatible microenvironment for proteins to retain their nature structure and enhance the direct electron transfer rate between the electroactive center and the underlying electrode. In recent years there are increasing interests on the direct electrochemistry of redox protein with ionic liquids (ILs) interface. ILs are green solvent with many specific physicochemical properties such as high ionic conductivity, wide electrochemical window, good stability and excellent biocompatibility [5]. Wei and Ivaska had reviewed the recent progresses of ILs in the field of electrochemical sensor [6]. ILs can be used as not only the supporting electrolyte but also the modifier for the chemically modified electrodes [7,8]. Xiong et al. studied the direct electrochemistry of hemoglobin (Hb) and its electrocatalytic activity towards hydrogen peroxide on the modified electrode with 1-butyl-3-methylimidazolium tetrafluoroborate ([BMIM]BF$_4$) as the electrolyte [9]. Maleki and co-workers fabricated a high performance carbon ionic liquid electrode (CILE) with *n*-octylpyridinium hexafluorophosphate ([OP]PF$_6$) as binder [10,11]. Our group also applied CILE to the investigation of protein electrochemistry with different nanomaterials [12–14].

Gold nanoparticle has been widely used for the immobilization of proteins, which act as the good conductive mediator to facilitate the electron transfer rate [15]. Many reports indicate that the gold nanomaterials with different appearances can be used as the immobilization matrix to realize the direct electrochemistry of redox protein. Yang et al. investigated the direct electrochemistry of Hb on a gold nanowire array [16]. Zhang et al. combined gold nanoparticle with polyvinyl alcohol and 1-octyl-3-methylimidazolium hexafluorophosphate ([OMIM]PF$_6$) for the investigation on the electrochemical behaviors of Hb [17]. Hong and Dai constructed a novel amperometric biosensor for hydrogen peroxide and nitrite by immobilizing Hb on one-dimensional gold nanoparticle [18].

In this paper a gold nanoparticle decorated CILE was fabricated by in situ electrodeposition method. CILE has been elucidated with the advantages such as high conductivity, good stability and antifouling ability with a layer of IL also presented on the surface of CILE [5]. At the same time gold nanoparticles show good conductivity

* Corresponding author. Tel.: +86 532 4022681; fax: +86 532 4022681.
E-mail address: sunwei@qust.edu.cn (W. Sun).

0039-9140/$ – see front matter © 2009 Elsevier B.V. All rights reserved.
doi:10.1016/j.talanta.2009.11.026

and biocompatibility [19]. So a layer of gold nanoparticle was electrodeposited on the surface of CILE to get a novel platform for protein electrochemistry, which combined the advantages of CILE and gold nanoparticle. Then Hb was selected as the model redox protein and it was immobilized on the surface of Au/CILE with Nafion film. Nafion is a sulfonated tetrafluoroethylene based fluoropolymer–copolymer with many remarkable characteristics such as highly conductivity to cations, excellent film-forming ability, thermal and chemical stability as well as the selectively and highly permeable to water, which has been widely used in the fabrication of electrochemical biosensors [20]. The direct electrochemistry of Hb was further investigated carefully with a pair of well-defined redox peaks appeared on the cyclic voltammogram. The experimental results indicated that the direct electron transfer process was realized on the modified electrode, which proved the advantages of the prepared gold nanoparticle decorated electrode. The electrocatalytic ability of Hb on the modified electrode to the reduction of trichloroacetic acid (TCA) was further investigated.

2. Experimental

2.1. Reagents and apparatus

1-Ethyl-3-methylimidazolium ethylsulfate ([EMIM]$EtOSO_3$, Hangzhou Chemer Chemical Co. Ltd., China), bovine hemoglobin (Hb, MW 64500, Tianjin Chuanye Biochemical Co. Ltd., China), graphite powder (average particle size 30 μm, Shanghai Colloid Chemical Plant, China), chloroauric acid ($HAuCl_4$, Shanghai Chemical Plant, China) and trichloroacetic acid (TCA, Tianjin Kermel Chemical Reagent Co. Ltd., China) were used as received. 0.1 mol/L phosphate buffer solutions (PBS) were used as the supporting electrolyte. All the solutions were purged with highly purified nitrogen for 30 min and an inert nitrogen environment was maintained in the electrochemical cell during the electrodeposition and electrochemical measurements. Other chemicals used were of analytical reagent grade and the solutions were prepared with doubly distilled water.

A LK 2005 electrochemical workstation (Tianjing Lanlike Chemistry & Electron High Technology Co. Ltd., China) was employed for the electrodeposition and electrochemical measurements. Electrochemical impedance spectroscopy (EIS) was achieved on a CHI 750B electrochemical workstation (Shanghai CH Instruments, China). A traditional three-electrode system, which was consisted of a self-made Hb modified electrode as working electrode, a saturated calomel electrode (SCE) as reference electrode and a platinum wire as counter electrode, was used throughout. Scanning electron microscopy (SEM) was performed on a JSM-6700F scanning electron microscope (Japan Electron Company, Japan).

2.2. Electrode preparation

CILE was prepared according to the following procedure: 200 μL of [EMIM]$EtOSO_3$, 800 μL of liquid paraffin and 3.2 g of graphite powder were hand-mixed in an agate mortar and ground carefully. A portion of resulting homogeneous paste was packed firmly into a glass tube (Ø = 4 mm) and the electrical contact was established by a copper wire to the end of the paste in the inner hole of the tube.

Gold nanoparticle modified CILE (Au/CILE) was prepared based on a reported procedure [21]. In general gold nanoparticle was electrodeposited onto the newly prepared CILE with a solution of 5.0 mmol/L $HAuCl_4$ and 0.5 mol/L KNO_3 by controlled potential at −0.4 V for 300 s. The Au/CILE was rinsed with doubly distilled water and dried in air for further modification. Hb modified electrode was fabricated by casting 8.0 μL of 10.0 mg/mL Hb aqueous solution on the surface of Au/CILE and staying silent to allow the water evaporated gradually. Then 8.0 μL of 0.5% Nafion solution was cast on the electrode surface, which could form a stable film and fixed Hb on the surface of electrode tightly. During these procedures a small bottle was covered over the electrode so that the solvent could evaporate slowly to get a uniform film. The modified electrode was stored at 4 °C when not in use and denoted as Nafion/Hb/Au/CILE. Other modified electrodes were prepared by the similar procedure for the comparison.

3. Results and discussion

3.1. Characterization of gold nanoparticle modified carbon ionic liquid electrode

Fig. 1 showed the SEM images of different modified electrodes. On bare CPE (Fig. 1A) a layer of irregularly flasks of graphite powder was isolated. On the CILE (Fig. 1B) a more uniform surface was observed without the separated carbon layer. The results were in accordance with the previous reported results [12,13]. After electrodeposition of gold nanoparticle on the CILE surface, the interface appeared with highly regular and uniform (Fig. 1C). The average diameter of the formed gold nanoparticle was about 150 nm, indicating the successfully deposition of gold nanoparticle on the CILE. The resulted electrode was further used for the protein immobilization with an increased surface area and a three-dimensional structure.

Electrochemical behaviors of different modified electrodes in a 5.0 mmol/L $[Fe(CN)_6]^{3-/4-}$ and 0.1 mol/L KCl solution were investigated with the cyclic voltammetric results as shown in Fig. 2. A pair of quasi-reversible redox peaks was observed on the CPE (curve a), and the redox peak currents were much smaller than that of CILE (curve b). The result was attributed to the presence of the high conductive IL on the electrode surface. After the electrodeposition of gold nanoparticle on the surface of CILE (curve c), a remarkable enhance of redox peak currents occurred, indicating the high conductive metal of gold on the electrode surface. According to the Randles–Sevcik equation [22]: $I_{P,c} = (2.69 \times 10^5)n^{3/2}AD^{1/2}C^*v^{1/2}$, the effective surface area of different modified electrodes can be estimated. Where $I_{P,c}$ is the reduction peak current (A), n is the electron transfer number, A is the effective surface area (cm^2), D is the

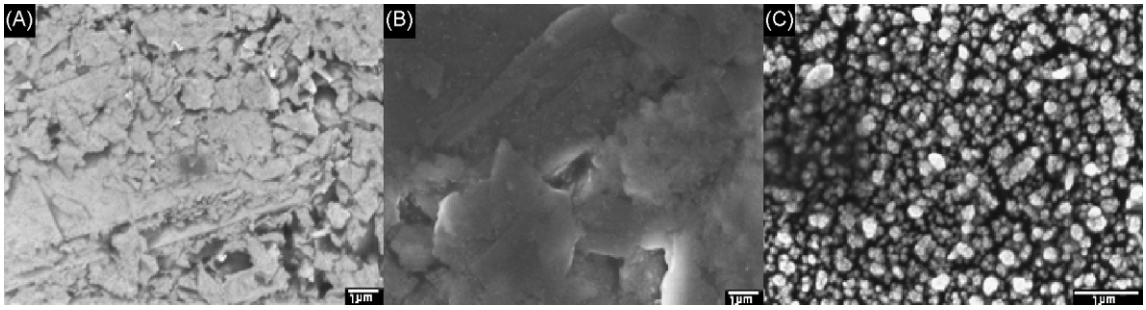


Fig. 1. SEM images of (A) CPE, (B) CILE and (C) Au/CILE.

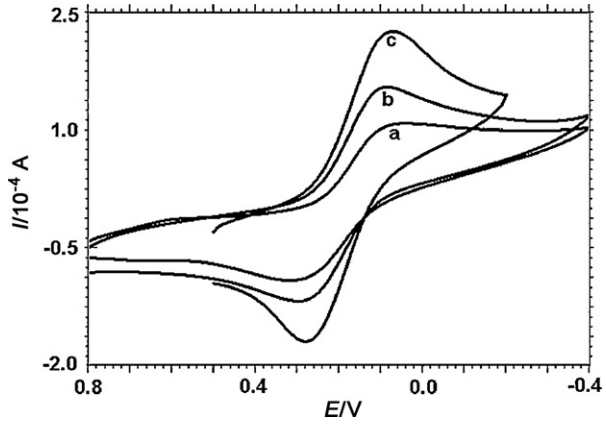


Fig. 2. Cyclic voltammograms of (a) CPE, (b) CILE and (c) Au/CILE in a 5.0 mmol/L $[Fe(CN)_6]^{3-/4-}$ and 0.1 mol/L KCl solution with the scan rate of 100 mV/s.

confusion coefficient of $K_3[Fe(CN)_6]$ in the solution (cm^2/s), C^* is the concentration of $K_3[Fe(CN)_6]$ (mol/cm^3) and v is the scan rate (V/s), Based on this method, the average effective surface area of CPE, CILE and Au/CILE were calculated as 0.109, 0.146 and 0.197 cm^2, respectively. So the effective surface area of Au/CILE was increased for 1.35 time than that of CILE, which was due to the presence of nanostructure gold particle on the electrode surface.

3.2. Electrochemical impedance spectroscopy of different electrodes

EIS is a commonly used method to probe the interface information of the impedance changes during the stepwise-assemble process of the surface modified electrode. In EIS the semicircular part at higher frequencies corresponds to the electron transfer limited process and the linear part at lower frequencies corresponds to the diffusion process. The value of electron transfer resistance (R_{et}) is estimated according to the diameter of the semicircle of the Nyquist plots at the high frequency region, which controls the electron transfer kinetics of redox probe at the electrode surface and reflects the interfacial electron transfer ability. The EIS results of different electrodes in a solution of 10.0 mmol/L $[Fe(CN)_6]^{3-/4-}$ and 0.1 mol/L KCl with the frequencies swept from 10^5 to 0.1 Hz were shown in Fig. 3. Here Z' and Z'' are the real variable and the negative value of the imaginary variable of impedance. Then the Randles circuit (inset) is further chosen to fit the impedance data obtained in the experiments. On the bare CILE a straight line appeared (curve a), which was due to the high ionic conductivity of ionic liquid present in the carbon paste electrode. On the Au/CILE, the R_{et} value was also close to zero (curve b), indicating that the high conductive gold nanoparticle present on the CILE facilitated the electron transfer. When Nafion was cast on the Au/CILE, the R_{et} value was estimated to be 480 Ω (curve c), which was due to the presence of Nafion film on the electrode surface hindered the electron transfer of $[Fe(CN)_6]^{3-/4-}$. After Hb was fixed in the Nafion film, the R_{et} value was further increased to 691 Ω (curve d), which indicated that Hb molecules were successfully immobilized on the surface of Nafion/Au/CILE and further hindered the electron transfer of electrochemical probe.

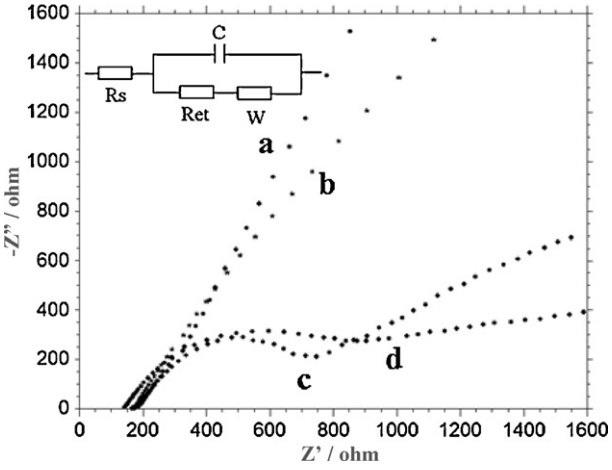


Fig. 3. Electrochemical impedance spectroscopy for (a) bare CILE, (b) Au/CILE, (c) Nafion/Au/CILE and (d) Nafion/Hb/Au/CILE in the solution of 10.0 mmol/L $[Fe(CN)_6]^{3-/4-}$ and 0.1 mol/L KCl with the frequencies swept from 10^5 to 0.1 Hz. Inset is the Randles circuit model for the modified electrodes in the cell.

3.3. Direct electrochemistry of Hb

Fig. 4A showed the cyclic voltammograms of different electrodes in 0.1 mol/L PBS at the scan rate (v) of 100 mV/s. No redox peak appeared on CILE (curve a) and Au/CILE (curve b) but with increased background current, which also proven the existence of gold nanoparticle on the CILE surface. While on Nafion/Hb/CILE (curve c) a pair of small redox peaks appeared, indicating that the direct electron transfer rate of Hb with CILE was very slow. While on the Nafion/Hb/Au/CILE (curve d) a remarkable enhanced electrochemical response was observed with a pair of well-defined

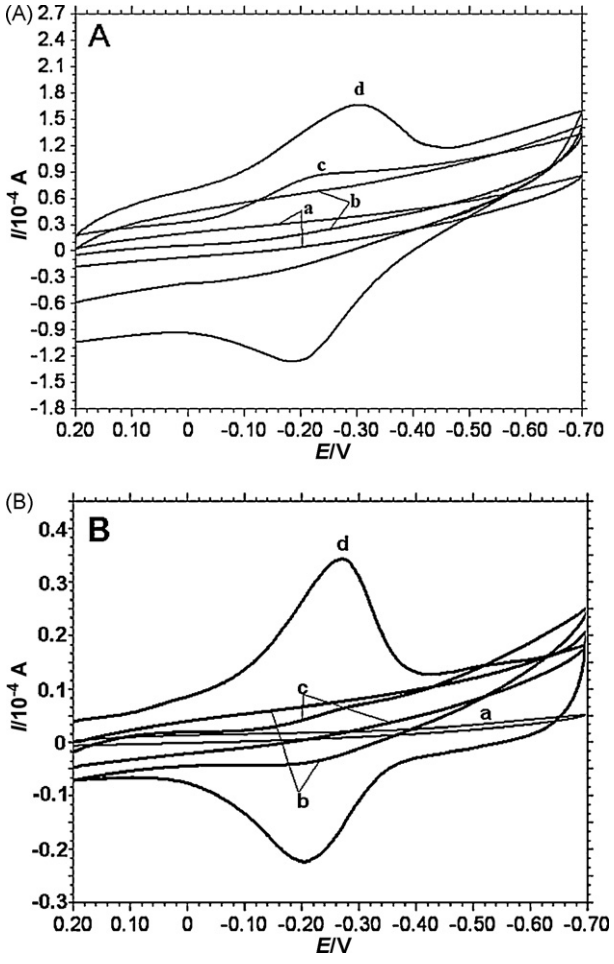


Fig. 4. (A) Cyclic voltammograms of (a) bare CILE, (b) Au/CILE, (c) Nafion/Hb/CILE and (d) Nafion/Hb/Au/CILE at the scan rate of 100 mV/s in pH 7.0 PBS. (B) Cyclic voltammograms of (a) bare CPE, (b) Au/CPE, (c) Nafion/Hb/CPE and (d) Nafion/Hb/Au/CPE at the scan rate of 100 mV/s in pH 7.0 PBS.

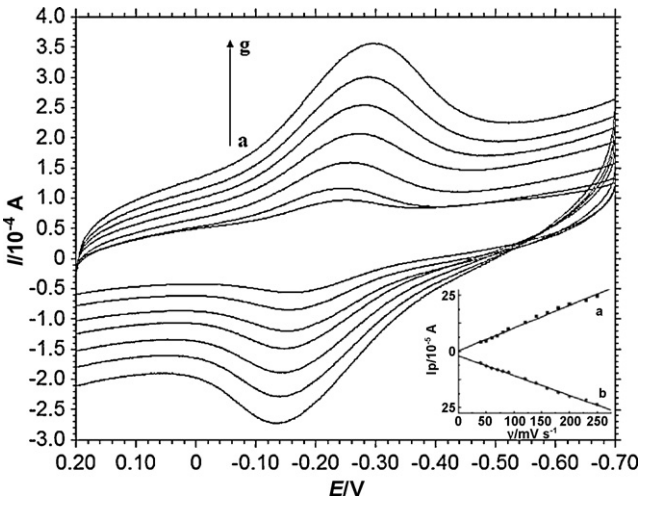


Fig. 5. Cyclic voltammograms of Nafion/Hb/Au/CILE in pH 7.0 PBS with the scan rates from a to g as 40, 60, 100, 120, 160, 200 and 250 mV/s, respectively. Inset: linear relationship of the cathodic (a) and anodic (b) peak current versus scan rate (v).

quasi-reversible redox peaks appeared. The results indicated that the presence of gold nanoparticle on the CILE surface greatly improved the direct electron transfer rate of Hb, which may be attributed to the high metal conductivity and three-dimensional structure of gold nanoparticle. The redox peak potentials were observed with the reduction potential (E_{pc}) as −0.257 V and the oxidation potential (E_{pa}) as −0.162 V. The formal peak potential [$E^{0\prime} = (E_{pc} + E_{pa})/2$] was estimated to be −0.210 V, which was the characteristic of the Hb heme Fe(III)/Fe(II) redox couple. The results showed that the Au/CILE interface was suitable for the electron transfer process between Hb and the electrode. For comparison the similar modified electrodes were prepared with carbon paste electrode (CPE) as the substrate electrode and the cyclic voltammograms were recorded at the same conditions. As shown in Fig. 4B no redox peaks appeared on the bare CPE, Au/CPE and Nafion/Hb/CPE (curve a–c) indicating no electrochemical reaction took place on the electrodes. On the Nafion/Hb/Au/CPE a pair of redox peak appeared with redox peak current much smaller than that of Nafion/Hb/Au/CILE. The results also indicated the superiority of CILE than CPE. CILE has been demonstrated to have the advantages of high conductivity, good stability and anti-fouling ability. On the surface of CILE a layer of IL was also present, which provided a specific interface for the electrodeposition of gold nanoparticle. So the electrochemical response of immobilized Hb was greatly improved with Au/CILE.

Cyclic voltammograms of Nafion/Hb/Au/CILE at different scan rates were recorded in the range from 40 to 250 mV/s with the results shown in Fig. 5. A pair of well-defined redox peaks appeared and the peak currents increased linearly with the scan rate, which indicated a typical surface-confined thin-layer electrochemical behavior [23]. Based on the following equation: $Q = nAF\Gamma^*$, the surface concentration of electroactive Hb (Γ^*) was calculated as 2.62×10^{-9} mol/cm^2, which accounted for 26.5% of the total amount of Hb cast on the electrode surface. The value was much higher than that of Hb monolayer (1.89×10^{-11} mol/cm^2) on the electrode surface [24], which indicated that several layers of Hb in the film took part in the electrode reaction. The reason can be attributed to the presence of Au nanoparticle on the surface of CILE provided a three-dimensional interface for Hb immobilization with the increased effective surface area. The redox peak potentials also exhibited linear relationship with the logarithm of the scan rate and two equations were calculated as $E_{pa}(V) = -0.034 \ln v - 0.346$ ($r = 0.980$) and $E_{pc}(V) = 0.015 \ln v - 0.114$ ($r = 0.968$). According to the Laviron's equation [23], the values of electron transfer coefficient (α) and electron transfer rate constant (k_s) were calculated as 0.573 and 0.412 s^{-1}, respectively.

3.4. Electrocatalytic reduction of trichloroacetic acid

TCA is an analogue of acetic acid in which the three hydrogen atoms of the methyl group have all been replaced by chlorine atoms. It is widely used in biochemistry for the precipitation of macromolecules, such as proteins, DNA and RNA, and cosmetic treatments, such as chemical peels and tattoo removal. It also is an environmental pollutant which can kill normal cells. For these reasons, the determination of TCA has received great attentions in recent years [25,26]. The electrocatalytic reduction of TCA on Nafion/Hb/Au/CILE was examined by cyclic voltammetry with the results as shown in Fig. 6. After the addition of TCA into the deoxygenated pH 7.0 PBS, an obvious reduction peak at −0.20 V appeared with the decrease of the corresponding oxidation peak current, which was a typical electrocatalytic reaction [13]. With the increase of TCA concentration in PBS a new reduction peak appeared at −0.42 V, which could be attributed to the formation of highly reduced form of Hb [27,28]. The catalytic peak current at −0.20 V had a good linear relationship with TCA concentration in the range from 0.2 to 18.0 mmol/L with the regression equation as $I_p(\mu A) = 0.533\,C\ (\text{mmol/L}) + 2.442$ ($r = 0.990$). The detection limit was calculated as 0.16 mmol/L based on the S/N = 3, which was lower than some previous reports [24,29]. When the TCA concentration was more than 20.0 mmol/L, the reduction peak current turned to level off, indicating a typical Michalies–Menten kinetic process. So the apparent Michalies–Menten constant (K_M^{app}) was estimated by using the electrochemical version of the Lineweaver–Burk equation [30]. By exploring the relationship of $1/I_{SS}$ versus $1/C_{TCA}$, the K_M^{app} value was calculated as 0.499 mmol/L, which was lower than some reported values [14,29]. A small K_M^{app} value suggests that the Hb on the modified electrode has higher affinity to the substrates, which can be attributed to the favorable microenvironment of Hb on the modified electrode.

3.5. Stability and repeatability of the modified electrode

The stability of the modified electrode was evaluated. After two-week storage at 4 °C, 97.3% of the initial current signal was obtained and 95.0% remained after four-week storage, indicating that the

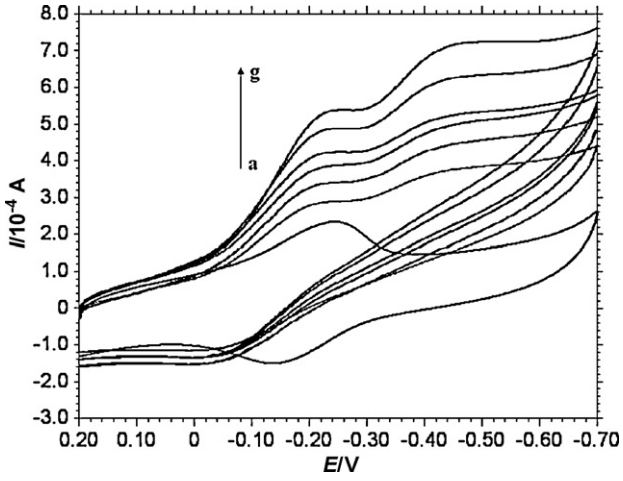


Fig. 6. Cyclic voltammograms obtained at a Nafion/Hb/Au/CILE in pH 7.0 PBS after the addition of 0, 2.0×10^{-3}, 5.0×10^{-3}, 8.0×10^{-3}, 1.0×10^{-2}, 1.4×10^{-2} and 1.8×10^{-2} mol/L TCA (a–g), respectively, at the scan rate of 100 mV/s.

prepared electrode had excellent long-term stability. To investigate the repeatability of the modified electrode, seven electrodes were made by the same procedure independently for the determination 1.0 mmol/L TCA and the relative standard deviation (RSD) value was got as 3.50%. While the RSD of 2.89% was estimated with one electrode for seven successive determinations of 1.0 mmol/L TCA, which indicated that the modified electrode had good reproducibility.

4. Conclusions

Gold nanoparticle was electrodeposited on the surface of CILE to get an effective supporting platform and Hb was immobilized on the electrode surface with Nafion film to get a Hb modified electrode. Due to the presence of gold nanoparticle direct electrochemistry of Hb was accelerated on the modified electrode and a pair of well-defined redox couples appeared with the formal peak potential ($E^{0\prime}$) as −0.210 V (*vs.* SCE). The results indicated the gold nanoparticle decorated carbon ionic liquid electrode provided an excellent interface to promote the direct electron transfer between Hb and the electrode. The Hb modified electrode showed good electrocatalytic activity to TCA with lower detection limit and wider dynamic range, which had the potential application as the third-generation electrochemical biosensor in the field of pathological research, environmental protection and quality control.

Acknowledgements

The authors appreciate the financial support of the National Natural Science Foundation of China (nos. 20635020, 20405008) and the Foundation of University Teacher International Training Project of Shandong Province.

References

[1] F.A. Armstrong, H.A.O. Hill, N.J. Walton, Acc. Chem. Res. 21 (1988) 407.
[2] P.M. Guto, J.F. Rusling, Electrochem. Commun. 8 (2006) 455.
[3] W. Sun, D.D. Wang, R.F. Gao, K. Jiao, Electrochem. Commun. 9 (2007) 1159.
[4] H. Zhang, N.F. Hu, Biosens. Bioelectron. 23 (2007) 393.
[5] N. Maleki, A. Safavi, F. Tajabadi, Anal. Chem. 78 (2006) 3820.
[6] D. Wei, A. Ivaska, Anal. Chim. Acta 607 (2008) 126.
[7] H.Y. Xiong, T. Chen, X.H. Zhang, S.F. Wang, Electrochem. Commun. 9 (2007) 2671.
[8] H. Liu, P.G. He, Z. Li, C. Sun, L. Shi, Y. Liu, G. Zhu, J. Li, Electrochem. Commun. 7 (2005) 1357.
[9] H. Xiong, T. Chen, X. Zhang, S. Wang, Electrochem. Commun. 9 (2007) 1648.
[10] A. Safavi, N. Maleki, F. Tajabadi, E. Farjami, Electrochem. Commun. 9 (2007) 1963.
[11] N. Maleki, A. Safavi, E. Farjami, E. Farjami, Anal. Chim. Acta 611 (2008) 151.
[12] W. Sun, X.Q. Li, Y. Wang, X. Li, C.Z. Zhao, K. Jiao, Bioelectrochemistry 75 (2009) 170.
[13] W. Sun, R.F. Gao, K. Jiao, J. Phys. Chem. B 111 (2007) 4560.
[14] W. Sun, D.D. Wang, G.C. Li, Z.Q. Zhai, R.J. Zhao, K. Jiao, Electrochim. Acta 53 (2008) 8217.
[15] C.X. Lei, S.Q. Hu, G.L. Shen, R.Q. Yu, Talanta 59 (2003) 981.
[16] M. Yang, F. Qu, Y. Li, Y. He, G. Shen, R. Yu, Biosens. Bioelectron. 23 (2007) 414.
[17] Y. Zhang, R. Yan, F. Zhao, B. Zeng, Colloid Surf. B 71 (2009) 288.
[18] J. Hong, Z. Dai, Sens. Actuators B 140 (2009) 222.
[19] J.F. Hicks, F.P. Zamborini, A.J. Osisek, R.W. Murray, J. Am. Chem. Soc. 123 (2001) 7048.
[20] K.A. Mauritz, R.B. Moore, Chem. Rev. 104 (2004) 4535.
[21] C.F. Ding, F. Zhao, R. Ren, J.M. Lin, Talanta 78 (2009) 1148.
[22] A.J. Bard, L.R. Faulkner, Electrochemical Methods, 2nd ed., Wiley, New York, 2001, p. 213.
[23] E. Laviron, J. Electroanal. Chem. 101 (1979) 19.
[24] S.F. Wang, T. Chen, Z.L. Zhang, X.C. Shen, Z.X. Lu, D.W. Pang, K. Wong, Langmuir 21 (2005) 9260.
[25] T.A. Piggot, R.W. Norris, Br. J. Plast. Surg. 41 (1988) 112.
[26] H.K. Bhat, M.F. Kanz, G.A. Campbell, G.A.S. Ansari, Fund. Appl. Toxicol. 17 (1991) 240.
[27] X. Ma, X.J. Liu, H. Xiao, G.X. Li, Biosens. Bioelectron. 20 (2005) 1836.
[28] A.E.F. Nassar, J.M. Bottitt, J.D. Stuart, J.F. Rusling, J. Am. Chem. Soc. 117 (1995) 10986.
[29] H.Y. Ma, N.F. Hu, J.F. Rusling, Langmuir 16 (2000) 4969.
[30] R.A. Kamin, G.S. Willson, Anal. Chem. 52 (1980) 1198.

Talanta 80 (2010) 2182–2186

Contents lists available at ScienceDirect

Talanta

journal homepage: www.elsevier.com/locate/talanta

Electrochemical determination of L-Tryptophan, L-Tyrosine and L-Cysteine using electrospun carbon nanofibers modified electrode

Xiaofeng Tang[a], Yang Liu[a], Haoqing Hou[b], Tianyan You[a,*]

[a] The State Key Laboratory of Electroanalytical Chemistry, Changchun Institute of Applied Chemistry, Chinese Academy of Sciences, Changchun 130022, PR China
[b] College of Chemistry and Chemical Engineering, Jiangxi Normal University, Jiangxi 330027, PR China

ARTICLE INFO

Article history:
Received 9 July 2009
Received in revised form 5 November 2009
Accepted 6 November 2009
Available online 13 November 2009

Keywords:
Carbon nanofibers
Modified electrode
Tryptophan
Tyrosine
Cysteine
Electrocatalytic oxidation

ABSTRACT

A novel and simple method for the direct and quantitative determination of L-tryptophan (Trp), L-tyrosine (Tyr) and L-cysteine (Cys) was proposed in this work. Carbon nanofibers (CNFs), made by electrospinning technique, were used to modify carbon paste electrode (CPE) without any treatment to study the electrochemical behaviors of the three amino acids using cyclic voltammetry (CV) and constant potential amperometric method. The results demonstrated that the CNFs modified carbon paste electrode (CNF-CPE) exhibited high electrocatalytic activity and good analytical performance towards the oxidation of the three amino acids. The linear ranges of Trp, Tyr and Cys were 0.1–119, 0.2–107 and 0.15–64 μM with correlation coefficients of 0.9994, 0.9985 and 0.9996, respectively. All the detection limits of the analytes were 0.1 μM (S/N = 3). In addition, the CNF-CPE displayed good reproducibility, high sensitivity and good selectivity towards the determination of the amino acids, making it suitable for the determination of Trp, Tyr and Cys in clinical and medicine.

© 2009 Elsevier B.V. All rights reserved.

1. Introduction

Some oxidizable amino acids such as L-tryptophane (Trp), L-tyrosine (Tyr) and L-cysteine (Cys) play important roles in many biochemical processes. Trp is an essential amino acid for human and herbivores as the precursor of hormones, neurotransmitters and other relevant biomolecules. The level of Trp in plasma is closely related with the extent of hepatic disease [1,2]. Tyr is the precursor of dopamine, thyroxin and neurotransmitters in mammalian central nervous systems [3]. The absence of Tyr could cause albinism and alkaptonuria, while a high Tyr concentration in culture medium results in increased sister chromatid exchange. Cys is another important amino acid owing to its crucial roles in biological systems, such as prospective radiation protector and cancer indicator [4]. Besides, it is widely used in the food industry as an antioxidant. Thus, simple and fast methods are needed to satisfy the great demand for the determination of Trp, Tyr and Cys in many fields such as food processing, biochemistry, pharmaceuticals and clinical analysis.

Various analytical methods have been applied to determine amino acids, such as high-performance liquid chromatography (HPLC) with fluorescence detection (FD), mass spectrum detection (MS) or ultraviolet detection (UV) [5–7], capillary electrophoresis (CE) with amperometric detection (AD) or laser induced fluorescence detection (FID) [8,9], gas chromatography (GC) with FID or MS [10,11] and ion exchange chromatography-FD [12]. In addition, spectroscopy [13,14] and electrochemical detection [15] were applied to determine amino acids. In recent years, electrochemical detection has gained considerable interest for electroactive compounds because of its simpleness, low-cost and sensitivity. Trp, Tyr and Cys are three oxidizable amino acids and have obvious electrochemical signals at various modified electrodes [16–19]. There are some reports [20–25] on the determination of these amino acids by electrochemical methods.

Carbon materials have been employed in electroanalytical investigations because of their chemical inertness, wide potential window and suitability for different types of analysis [26,27]. Because of their unique properties, carbon-based nanoscaled materials have been widely used for the preparation of modified electrodes including carbon nanotubes (CNTs) [28–30], fullerene-C_{60} [31] and carbon nanofibers (CNFs) [32–34]. As a new and interesting material member of carbon family, CNFs have attracted much attention due to their unique electronic properties and relatively high mechanical properties. Compared with CNTs, CNFs possess less order and more edge sites on the outer wall, which may lead to more facile electron transfer [28], along with better dispersion and wettability [35,36]. Because of their good electrochemical property and biocompability, CNFs have been used for designing electrochemical sensors and biosensors [32–34]. In our previous study, it had been revealed that CNFs displayed good

* Corresponding author. Tel.: +86 431 85262850.
E-mail address: youty@ciac.jl.cn (T. You).

0039-9140/$ – see front matter © 2009 Elsevier B.V. All rights reserved.
doi:10.1016/j.talanta.2009.11.027

catalysis towards the oxidation of dihydronicotinamide ademine dinucleotide and dopamine [37,38].

In this work, we synthesized CNFs by electrospinning and subsequent thermal treatment. Since electrospun CNFs provided with easy handling, large specific surface area and improved conductivity [37,39], an electrochemical sensor of Trp, Tyr and Cys was constructed by modifying carbon paste electrode (CPE) with the CNFs. Compared with the CNFs reported [32–34], the electrospun CNFs here were used without any treatment to ensure the property unchanged. The behaviors of Trp, Tyr and Cys were studied at CNF-CPE and the electrospun CNF showed high catalytic property towards the oxidation of the three amino acids. The results indicated that the electrospun CNFs could be a kind of good electrocatalytic nanomaterial for sensing amino acids.

2. Experimental

2.1. Apparatus

The scanning electron microscopy (SEM) experiments were made on a PHILIPSXL-30ESEM at an accelerating voltage of 20 kV. All the electrochemical measurements were performed using a CHI 832 electrochemical workstation (Shanghai, China) coupled with a conventional three-electrode cell. The three-electrode system consisted of the bare CPE or CNF-CPE working electrode, a platinum wire counter electrode and the Ag/AgCl (saturated KCl) reference electrode. The potentials in this paper are given against the Ag/AgCl. The cathodic current is assigned to be positive, and the anodic current is assigned to be negative.

2.2. Chemicals and reagents

Polyacrylonitrile (PAN), dimethylformamide (DMF), graphite powder (2 μm), L-tyrosine, L-cysteine and glutathione were purchased from Aldrich. Mineral oil, alanine, valine, leucine, isoleucine, serine, threonine, methionine, asparagines, glutamine, lysine, aspartic acid, arginine, phenylalanine, histidine, L-tryptophan, glucose, sodium citrate, oxalate and ascorbic acid (AA) were obtained from Beijing Chemical Co. (China). Dopamine hydrochloride (DA) and uric acid (UA) were purchased from Alfa Aesar. All other reagents were of analytical grade and were used without further purification. Phosphate buffer solution (PBS, 0.1 M, pH 7.0) was prepared by mixing 0.1 M Na_2HPO_4 and NaH_2PO_4. All solutions were prepared with doubly distilled water.

2.3. Synthesis of CNFs

The synthesis process of CNFs, as reported previously [37], is composed of two parts: first, PAN fibers were produced with PAN solution in DMF (8 wt.%) via an electrospinning technique; second, the CNFs were synthesized by stabilizing and carbonizing the PAN fibers. The electrospinning process was performed in the electric fields of the order of 100 kV m^{-1} obtained by applying a 30 kV voltage to a 30 cm gap between the spinneret and the collector. The stabilization and carbonization of PAN fibers were completed in a high temperature furnace by the following steps: (1) annealing in air for 3 h to oxidize PAN partially at 230 °C; (2) heating up to 300 °C at a rate of 5 °C min^{-1} and kept at this temperature in H_2 and Ar mixture (H_2/Ar = 1/3) for 2 h to stabilize the shape of the fibers; (3) heating up to 1100 °C in Ar at a rate of 5 °C min^{-1} to carbonize the fibers, staying at the highest temperature for 1 h, and then cooling down to room temperature in Ar.

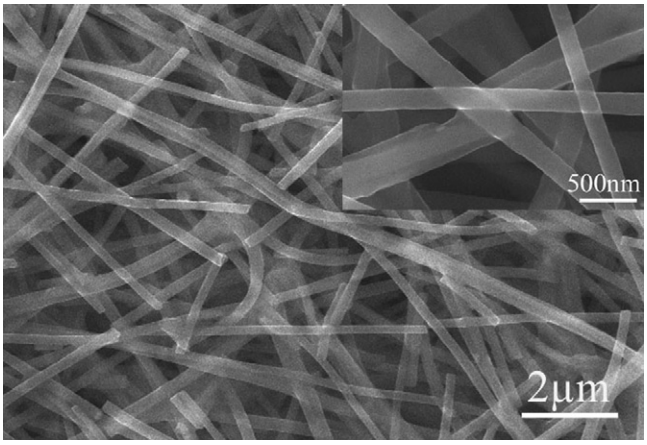


Fig. 1. SEM image of CNFs film. The inset is the SEM image of CNFs with high magnification.

2.4. Electrodes preparation and modification

The CPE was prepared via mixing graphite powder and mineral oil at the ratio of 70:30 (w/w) in a mortar followed by packing into a pipette tube (1 mm diameter; 1 cm depth) carefully. Electrical contact was established with a copper wire. And then the surface was smoothed against weighing paper and rinsed with double-distilled water. One milligram CNFs were dispersed in 1 mL water with vigorous agitation to form uniform suspension. At last, the CNF-CPE was obtained by casting 10 μL CNFs suspension, which had been proved to the optimum dosage, on the smoothed surface of the CPE followed by drying at room temperature in a desiccator.

3. Results and discussion

3.1. Characterization of CNF-CPE

The morphology of the as-prepared CNFs was investigated by SEM (Fig. 1). The inset is the SEM image of CNFs with high magnification. It can be observed that CNFs have a diameter of 200–400 nm with tens of micrometers in length. The CNFs show a uniform surface topography with cross and three-dimensional structure. This structure could significantly increase the effective electrode surface and facilitate the electron transfer.

To recognize the electrochemical properties of CNFs, cyclic voltammetries (CVs) of $K_3[Fe(CN)_6]/K_4[Fe(CN)_6]$ at CPE (curve a) and CNF-CPE (curve b) were investigated (Fig. 2). A pair of well-

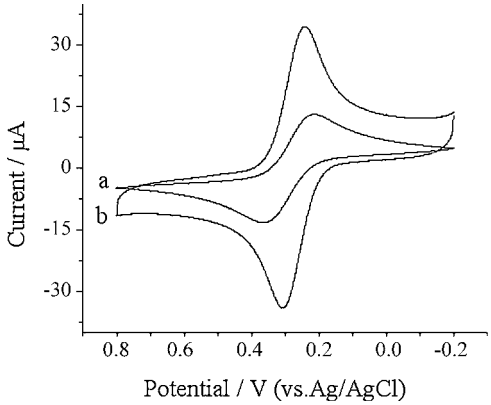


Fig. 2. CVs of 0.5 M KCl solution containing 5 mM $K_3[Fe(CN)_6]/K_4[Fe(CN)_6]$ at the CPE (a) and the CNF-CPE (b). Scan rate: 100 mV s^{-1}.

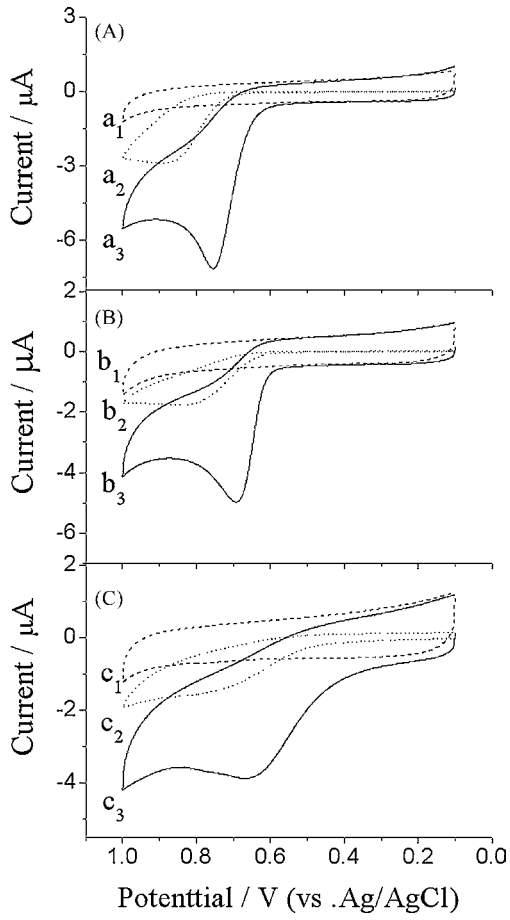


Fig. 3. CVs of CPE and CNF-CPE in the absence and presence of 1 mM Trp (A), Tyr (B) and Cys (C). The dash lines (– a_1, b_1, c_1) are CVs of CNF-CPE in PBS, the dot lines (... a_2, b_2, c_2) and the solid lines (▬ a_3, b_3, c_3) are CVs of CPE and CNF-CPE in PBS containing Trp, Tyr and Cys, respectively. Scan rate: 50 mV s^{-1}; Solution: 0.1 M PBS (pH 7.0).

defined redox peaks with peak-to-peak separation (ΔE_p) of 151 mV was observed at CPE (a), while the ΔE_p decreased to 64 mV at CNF-CPE (b). And the redox peak current at CNF-CPE was two times higher than that at CPE. Compared with that at the CPE, $[Fe(CN)_6]^{3-/4-}$ had better reversibility and much higher redox current at CNF-CPE, which indicated that CNF-CPE had the ability to accelerate electron transfer. Meanwhile, the influence of the dosage (2–16 μL) of CNFs suspension on the electrocatalytic capability was investigated in $K_3[Fe(CN)_6]/K_4[Fe(CN)_6]$ and KCl solution. The results showed the potential separation of the redox peak was affected little. The redox peak current of $[Fe(CN)_6]^{3-/4-}$ increased with the dosage of CNFs suspension increased from 2 to 10 μL. When the dosage of CNFs suspension exceeded 10 μL, the redox peak current decreased, which may be ascribed to the thick CNFs film. Furthermore, the CNFs film was easy to collapse when the dosage exceeded 14 μL, which confirmed 10 μL as the optimum dosage.

The effective surface area of CNF-CPE was estimated by CV using 5 mM $K_3[Fe(CN)_6]$ as a probe at various scan rates. The slope of the straight line ($r = 0.9990$) of I_{pc} vs.$\upsilon^{1/2}$ is 9.49×10^{-5} $As^{1/2}V^{-1/2}$. For a reversible process, $I_p = (2.69 \times 10^5)n^{2/3}$ $AD^{1/2}\upsilon^{1/2}C_0$. For 5 mM $K_3[Fe(CN)_6]$, $n = 1$, $D = 5.9 \times 10^{-5}$ cm s^{-2}, then the effective surface area of the CNF-CPE is calculated to be 1.57×10^{-2} cm^2, 4.7 times larger than that of the CPE which was estimated by the same method.

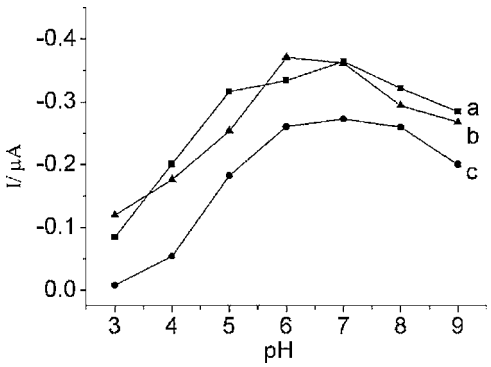


Fig. 4. Effect of pH on the oxidation current of 25 μM Trp (a), Cys (b) and Tyr (c) at CNF-CPE. The potentials were applied at 0.9, 0.8 and 0.75 V for Trp, Tyr and Cys, respectively.

3.2. Electrocatalytic oxidation of Trp, Tyr and Cys

Fig. 3 shows the CVs of CPE and CNF-CPE in 0.1 M PBS in the absence and presence of 1 mM Trp (A), Tyr (B) and Cys (C). It was found that each amino acid had only one oxidation peak in the cyclic voltammogram from 0.1 to 1.0 V at CPE or CNF-CPE, suggesting that the electrochemical processes of the amino acids were totally irreversible. The anodic peak currents responding to the oxidation of Trp, Tyr and Cys at CNF-CPE were two times higher than those obtained at CPE. Moreover, the oxidation peak potentials were 0.86, 0.8 and 0.75 V at the bare CPE, but they shifted to 0.75, 0.7 and 0.65 V at the CNF-CPE for Trp, Tyr and Cys, respectively. The results indicated that CNF-CPE could increase the peak currents and reduce the overpotentials, which proved that the CNFs film could efficiently catalyze the oxidation of these amino acids. The reasons should be attributed to the nanometer size, three-dimensional structure and more surface defects [32] of the material which bring in high surface area and large number of active sites.

3.3. Applied potentials and optimal pH for amperometric detection of Trp, Tyr and Cys

The effect of applied potentials on the amperometric responses of 25 μM Trp, Tyr and Cys at the CNF-CPE was investigated in range of 0.5–1.0 V with 0.05 V increments using constant potential amperometric method. The hydrodynamic voltammograms (not shown) showed that the response for Trp, Tyr and Cys reached peak values at 0.9, 0.8 and 0.75 V, respectively, which were chosen as the detection potentials.

The influence of the PBS pH value on the oxidation current of the three amino acids has also been studied at the optimum potentials as shown in Fig. 4. With increasing pH from 3.0 to 9.0, the oxidation current of Trp and Tyr increased from pH 3.0 to 7.0 and reached the maximum at pH 7.0, and then decreased with higher pH value. The oxidation current of Cys reached the maximum at pH 6.0 and then decreased a little at pH 7.0. Therefore, PBS at pH 7.0, which is close to the physiological level [3], was chosen for analytical experiments to obtain the maximum oxidation currents of the three amino acids.

3.4. Electrochemical determination of Trp, Tyr and Cys

The electrochemical determination of Trp, Tyr and Cys at the CNF-CPE has been studied at the optimum condition using constant potential amperometric method. Fig. 5 shows the current–time responses and the calibration curves (insets) for Trp (A), Tyr (B) and Cys (C), respectively. The results showed that the dynamic linear ranges of Trp, Tyr and Cys were 0.1–119, 0.2–107 and 0.15–64 μM with the correlation coefficients of 0.9994, 0.9985 and 0.9996,

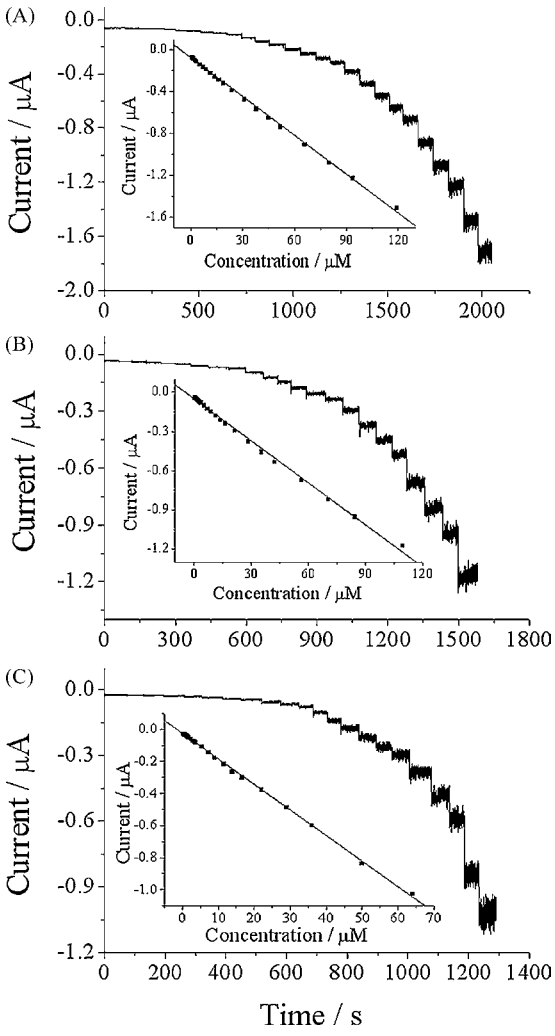


Fig. 5. Current–time responses of CNF-CPE upon successive addition of special concentration of Trp (A), Tyr (B) and Cys (C) to PBS under stirring. Insets are the calibration curves for these amino acids correspondingly. Solution: 0.1 M PBS (pH 7.0) under stirring. The potentials were applied at 0.9, 0.8 and 0.75 V for Trp, Tyr and Cys, respectively.

respectively. All the detection limits of the amino acids were 0.1 μM (S/N = 3) along with the sensitivities of 12.4 ± 0.09, 10.7 ± 0.1 and 15.9 ± 0.1 μA mM^{-1} for Trp, Tyr and Cys, respectively.

Table 1 compares the analytical performance of Trp, Tyr and Cys at the proposed CNF-CPE with that of other modified electrodes reported recently, especially those electrodes based on carbon materials. It can be seen that the detection limits of these amino acids at CNF-CPE, particularly Trp and Tyr, are among the lowest level. The linear ranges of CNF-CPE for Trp and Tyr are wider than the results reported previously and the linear range for Cys is wider than that obtained at boron-doped carbon nanotubes modified GCE [13], multi-wall carbon nanotubes (MWCNT) modified GCE [23] and screen-printed electrochemical sensor (SPES) [40]. The sensitivity of CNF-CPE is higher than that of MWCNT modified GCE [41], fluorosurfactant modified Au electrode [42], SPES [40] and SWCNT-arrayed modified Pt electrode [43]. The results above demonstrate that CNF-CPE has satisfactory analytical performance and it can be a feasible sensor for these amino acids.

3.5. Stability and reproducibility study

The stability of the modified electrode has been studied by investigating the amperometric responses of 5 μM Trp, Tyr and Cys at CNF-CPE and CPE for one hour. The results showed that the remained percentages of initial response for Trp, Tyr and Cys at CNF-CPE were 84, 86 and 70%, respectively, while those at CPE were 41, 39 and 15%, respectively, which demonstrated a good stability of the modified electrode.

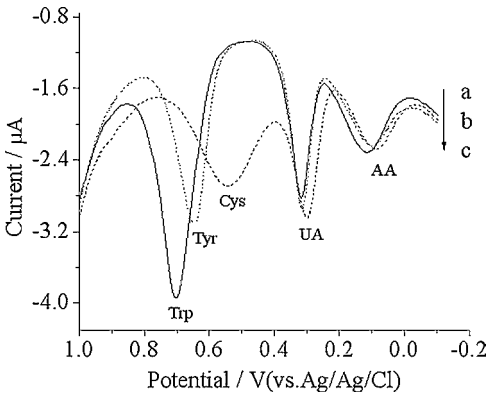


Fig. 6. DPVs of CNF-CPE in 0.1 M PBS (pH 7.0) containing 0.1 mM UA, 0.2 mM AA and 0.2 mM Trp (a), 1 mM Cys (b), 0.2 mM Tyr (c). DPV conditions: Scan rate, 6 mV s^{-1}; amplitude, 50 mV; pulse width, 100 ms; pulse period, 200 ms.

The reproducibility of CNF-CPE electrode was investigated by repetitive measurements (N = 6) of 25 μM Trp, Tyr and Cys, and the resulting relative standard deviation (RSD) was 1.0, 1.8 and 2.2%, respectively. It demonstrated that a freshly modified electrode surface could be obtained via electrochemical cleaning of the electrode, suggesting good ability of antifouling. Another extremely attractive feature of CNF-CPE is its excellent fabrication reproducibility. The result shows the response of 25 μM Tyr (a), Trp (b) and Cys (c) at seven different paralled CNF-CPEs with the RSD of 1.8, 2.2 and 1.6%, respectively. Therefore, the CNF-CPE has the advantage of good reproducibility.

3.6. Interference study

The possible interference for Trp, Tyr and Cys determination at CNF-CPE was investigated. Fourteen available amino acids (200 times content), including alanine, valine, leucine, isoleucine, serine, threonine, methionine, asparagines, glutamine, lysine, aspartic acid, arginine, phenylalanine and histidine, had no influence on the current response for 25 μM Trp, Tyr and Cys. Meanwhile, the CNFs showed an inhibiting effect on the oxidation of other electroactive species that are commonly present in biological fluids, such as glucose, sodium citrate and oxalate (200 times content). UA and AA as two kinds of important biological substances often coexist with Trp, Tyr and Cys in human fluid, food processing, pharmaceuticals and clinical analysis. Fig. 6 shows the differential pulse voltammetries (DPVs) of 0.2 mM Trp (a), 1 mM Cys (b) and 0.2 mM Tyr (c) at CNF-CPE when coexisting with 0.1 mM UA and 0.2 mM AA. The results indicated that UA and AA could be oxidized at the detached potentials of 0.3 and 0.1 V, far away from the oxidation potentials of the three amino acids at CNF-CPE. Therefore, the determination of the three amino acids had no interference from UA and AA. The interference of DA and glutathione has also been studied. The result showed that dopamine which could be oxidized at 0.1 V at CNF-CPE did not interfere with the determination of the three amino acids, while glutathione could be oxidized at 0.6 V which is close to the oxidation potential of Trp, Tyr and Cys at CNF-CPE. Thus glutathione could interfere with the detection. Furthermore, efficient simultaneous determination of these amino acids could be achieved at CNF-CPE in flow system when coupled to capillary electrophoresis (under study). The results above indicated the proposed method had good selectivity towards the determination of the amino acids.

Table 1
Comparison of the efficiency of some modified electrodes in the electrochemical determination of Trp, Tyr and Cys.

Method	Analyte	Detection limit (μM)	Linear range (μM)	Correlation coefficient	Sensitivity (μA mM^{-1})	References
4FEPE-CPE	Trp	0.56	0.85–63.4	0.9927	143.05	[2]
MWCNT-GCE	Tyr	0.4	2–500	0.9967	52	[3]
SWCNT-GCE	Tyr	0.09	5–20; 27–260	0.9952; 0.9998	45; 23	[17]
MWCNTs/4-ABSA-GCE	Tyr	0.08	0.1–1;1–50	0.9987; 0.9992	721; 202	[18]
OMC-GCE	Cys	0.002	18–2500	0.999	23.6	[22]
Fluorosurfactant-Au	Cys	0.3	To 200	0.997	4.6	[42]
BCNT-GCE	Cys	0.26 ± 0.01	0.78–20	0.998	0.25 ± 0.01	[44]
PbNP-CCE	Cys	0.46	1–67.2	0.9986	120	[20]
AMT-GCE	Cys	3.36	20–180	0.9895	–	[45]
Boron-doped diamond	Trp	10	20–1000	0.9990	21.1	[16]
	Tyr	1	100–700	0.9941	4.19	
Butyrylcholine-GCE	Trp	0.6	2–60	–	–	[41]
	Tyr	0.4	4–100	–	–	
Ag/Rutin-WGE	Trp	0.1	0.7–70	0.9920	–	[46]
	Tyr	0.07	0.3–10	0.9850	–	
SPES	Tyr	–	50–500	0.998	8.0 ± 0.013	[40]
	Cys	–	50–500	0.9985	2.9 ± 0.034	
SWCNT arrayed-Pt	Trp	0.1	To 100	0.9942	7	[43]
	Tyr	0.1	To 100	0.9996	8	
	Cys	0.01	To 100	0.9999	6	
MWCNT-GCE	Trp	0.2	0.55–150	>0.992	–	[23]
	Tyr	0.35	0.9–350	>0.992	–	
	Cys	0.7	1.5–250	>0.992	–	
CNF-CPE	Trp	0.1	0.1–118.5	0.9994	12.4 ± 0.09	This work
	Tyr	0.1	0.2–109	0.9985	10.7 ± 0.1	
	Cys	0.1	0.15–63.8	0.9996	15.9 ± 0.1	

4FEPE: 1-[4(ferrocenyl ethynyl) phenyl]-1-ethanone; 4-ABSA: 4-aminobenzeresulfonic acid; PbNP: lead nitroprusside; AMT: 5-amino-2-mercapto-1,3,4-thiadiazole.

4. Conclusions

The electrospun carbon nanofibers have excellent electrocatalytic activity towards Trp, Tyr and Cys. The CNF-CPE possesses many desirable properties including high sensitivity, low detection limit and satisfactory linear range which ensure trace amount determination of the three amino acids. Besides the good analytical performance, this proposed modified electrode has the advantages of good reproducibility, stability and selectivity. In addition, ease to construct, low cost and no treatment before use make it feasible to be applied in routine determination. The results indicated that the electrospun CNFs could be a kind of attractive and promising electrocatalytic nanomaterial for electrochemical sensing applications.

Acknowledgements

Special thanks to the financial support from the National Natural Sciences (20605020, 20875085) and Chinese Academy of Sciences (KJCX2-YW-H11).

References

[1] A. Agazzi, F. De Ponti, R. De Giorgio, S.M. Candura, L. Anselmi, E. Cervio, A. Di Nucci, M. Tonini, Digest. Liver Dis. 5 (2003) 590.
[2] J.B. Raoof, R. Ojani, K.M. Hassan, Electroanalysis 20 (2008) 1259.
[3] Q. Xu, S.F. Wang, Microchim. Acta 151 (2005) 47.
[4] Y.Z. Zhao, W.D. Zhang, H. Chen, Q.M. Luo, Sensor Actuator B 92 (2003) 279.
[5] D. Kutla'n, I. Molna'r-Perl, J. Chromatogr. A 987 (2003) 311.
[6] J. You, Y. Shan, L. Zhen, L. Zhang, Y. Zhang, Anal. Biochem. 313 (2003) 17.
[7] Y. Dale, V. Mackey, R. Mushi, A. Nyanda, M. Maleque, J. Ike, J. Chromatogr. B 788 (2003) 1.
[8] J. Wang, S. Mannino, C. Camera, M.P. Chatrathi, M. Scampicchio, J. Zima, J. Chromatogr. A 1091 (2005) 177.
[9] S. Zhao, Y. Song, Y. Liu, Talanta 67 (2005) 212.
[10] M.J. Nozal, J.L. Bernal, M.L. Toribio, J.C. Diego, A. Ruiz, J. Chromatogr. A 1047 (2004) 137.
[11] S.G. Villas-Bo^as, D.G. Delicado, M. Qkesson, J. Nielsen, Anal. Biochem. 322 (2003) 134.
[12] G. Ravindran, W.L. Bryden, Food Chem. 89 (2005) 309.
[13] A.L. Jenkins, R.A. Larsen, T.B. Williams, Spectrochim. Acta A 61 (2005) 1585.
[14] J.W. Costin, P.S. Francis, S.W. Lewis, Anal. Chim. Acta 480 (2003) 67.
[15] N.S. Lawrence, E.L. Beckett, J. Davis, R.G. Compton, Anal. Biochem. 303 (2002) 1.
[16] G.H. Zhao, Y. Qi, Y. Tian, Electroanalysis 18 (2006) 830.
[17] X.Z. Yu, Z.B. Mai, Y. Xiao, X.Y. Zou, Electroanalysis 20 (2008) 1246–1251.
[18] K.J. Huang, D.F. Luo, W.Z. Xie, Y.S. Yu, Colloid Surface B 61 (2008) 176.
[19] W.Y. Su, S.H. Cheng, Electrochem. Commun. 10 (2008) 899.
[20] H. Razmi, H. Heidari, Anal. Biochem. 388 (2009) 15.
[21] A. Abbaspour, A. Ghaffarinejad, Electrochimi. Acta 53 (2008) 6643.
[22] M. Zhou, J. Ding, L.P. Guo, Anal. Chem. 79 (2007) 5328.
[23] J.M. Xu, Y.P. Wang, Y.Z. Xian, L.T. Jin, K. Tanaka, Talanta 60 (2003) 1123.
[24] J.B. Raoof, R. Ojani, F. Chekin, J. Electroanal. Chem. 633 (2009) 187.
[25] M.M. Ardakani, A. Talebi, H. Naeimi, M.N. Barzoky, N. Taghavinia, J. Solid State Electrochem. 13 (2009) 1433.
[26] R.S. Robinson, K. Sternitzke, M.T. Mcdermott, R.L. Mccreery, J. Electrochem. Soc. 138 (1991) 2412.
[27] C.Y. Liu, A.J. Bard, F. Wudl, I. Weitz, J.R. Heath, Electrochem. Solid St. 2 (1999) 577.
[28] C.E. Banks, R.G. Compton, Analyst 130 (2005) 1232.
[29] C.E. Banks, R.R. Moore, T.J. Davies, R.G. Compton, Chem. Commun. 16 (2004) 1804.
[30] J. Wang, Electroanalysis 17 (2005) 7.
[31] R.N. Goyal, V.K. Gupta, N. Bachheti, R.A. Sharma, Electroanalysis 20 (2008) 757.
[32] V. Vamvakaki, K. Tsagaraki, N. Chaniotakis, Anal. Chem. 78 (2006) 5538.
[33] L. Wu, X.J. Zhang, H.X. Ju, Biosens. Bioelectron. 23 (2007) 479.
[34] X.B. Lu, J.H. Zhou, W. Lu, Q. Liu, J.T. Li, Biosens. Bioelectron. 23 (2008) 1236.
[35] M.L. Weeks, T. Rahman, P.D. Frymier, S.K. Islam, T.E. McKnight, Sensor Actuator B 133 (2008) 53.
[36] P. Werner, R. Verdejo, F. Wöllecke, V. Altstädt, J.K.W. Sandler, M.S.P. Shaffer, Adv. Mater 17 (2005) 2864.
[37] Y. Liu, H.Q. Hou, T.Y. You, Electroanalysis 20 (2008) 1708.
[38] Y. Liu, J.S. Huang, H.Q. Hou, T.Y. You, Electrochem. Commun. 10 (2008) 1431.
[39] C. Kim, K.S. Yanga, Appl. Phys. Lett. 83 (2003) 1216.
[40] M. Vasjari, A. Merkoci, J.P. Hart, S. Alegret, Microchim Acta 150 (2005) 233.
[41] G.P. Jin, X.Q. Lin, Electrochem. Commun. 6 (2004) 454.
[42] Z.F. Chen, H.Z. Zheng, C. Lu, Y.B. Zu, Langmuir 23 (2007) 10816.
[43] J. Okuno, K. Maehashi, Electrochem. Commun. 9 (2007) 13.
[44] C.Y. Deng, J.H. Chen, X.L. Chen, M.D. Wang, Z. Nie, Electrochim. Acta 54 (2009) 3298.
[45] P. Kalimuthu, S.A. John, Electrochem. Commun. 11 (2009) 367.
[46] G.P. Jin, X. Peng, Q.Z. Chen, Electroanalysis 20 (2008) 907.

Talanta 80 (2010) 2187–2190

Contents lists available at ScienceDirect

Talanta

journal homepage: www.elsevier.com/locate/talanta

Short communication

Simultaneous determination of Fe, P, Ca, Mg, Zn, and Cu in whole blood by two-jet plasma atomic emission spectrometry

Natalia P. Zaksas[a,*], Vladimir A. Gerasimov[a], Georgy A. Nevinsky[b]

[a] Nikolaev Institute of Inorganic Chemistry, Siberian Division, Russian Academy of Sciences, Pr. Akademika Lavrent'eva 3, Novosibirsk 630090, Russia
[b] Institute of Chemical Biology and Fundamental Medicine, Siberian Division, Russian Academy of Sciences, Pr. Akademika Lavrent'eva 8, Novosibirsk 630090, Russia

ARTICLE INFO

Article history:
Received 14 June 2009
Received in revised form 19 October 2009
Accepted 23 October 2009
Available online 29 October 2009

Keywords:
Two-jet plasma
Whole blood
Essential elements
Direct analysis
Sample carbonization
Graphite powder

ABSTRACT

Availability of many biological samples in ample quantity for biomedical investigations sometimes is very restricted. Therefore, there is the need for the simple techniques allowing the analysis of small amount samples. In the present work the two-jet plasma atomic emission spectrometry techniques for the determination of Fe, P, Ca, Mg, Zn, and Cu in whole blood are proposed. The first technique is developed for direct analysis of freeze-dried blood. The sample preparation consisted in a dilution of blood powder (particle size 20 μm or less) with a spectroscopic buffer (graphite powder containing 15 wt.% NaCl). For the analysis of liquid whole blood, previous carbonization (not ashing) of blood evaporated on graphite powder was applied. Calibration samples based on graphite powder containing 15 wt.% NaCl were used. The validation of the techniques was confirmed by the use of different sample preparation procedures (wet acid digestion and dry carbonization), the analysis of IAEA A-13 reference material (freeze-dried bovine whole blood), and the comparison of the results obtained by the proposed technique with the results of the stripping voltammetry technique. Just 20–50 μL of whole blood is quite enough for all determinations. The proposed techniques were successfully applied for the simultaneous determination of Fe, P, Ca, Mg, Zn, and Cu in whole blood of living experimental rats and mice and human blood.
© 2009 Elsevier B.V. All rights reserved.

1. Introduction

Metals play important roles in many normal physiological and pathologic processes in all biological systems. They participate in nutrient and gas transport, thermoregulation, pH maintenance, etc. Several recent reviews cover biological role of Ca and Mg in many cell functions such as energy metabolism, synthesis and function of proteins, cytoskeleton activation [1,2]; Al, Zn, Cu, and Fe in Parkinson's disease [3]; Cu in hepatic and neuronal functions, Cu transporters and Cu chaperone proteins [4], Zn in the homeostasis of the human organism [5] and in maternal and child mental health [6]; Fe in health and pathogenesis [7]. The participation of P in many important biochemical reactions is also described [8]. The emerging research field of "metallomics" is aimed at the understanding of the molecular mechanisms of metal-dependent life processes [9]. Therefore, reliable determination of the above elements in whole blood is an important analytical task.

The majority of the techniques described in the literature such as inductively coupled plasma (ICP) atomic emission spectrometry (AES) [10], ICP mass spectrometry (ICP-MS) [11–13], and total reflection X-ray fluorescence [14,15] apply wet acid digestion of blood to decompose the organic matrix. For direct determination of single elements in whole blood, electrothermal atomization atomic absorption spectrometry has found an application [16,17]. Direct multielement analysis of blood was performed using ICP-MS [12,18,19]. Sample dilution and additional reagents (EDTA, ammonia, and Triton X-100) were used in order to prevent blood clotting and to lyse the blood cells. The multielement techniques described usually require about 1 mL of blood, which is not always convenient in experiments with living small animals.

For analysis of small amount samples, two-jet plasma (TJP)-AES presented in this work is very suitable. A TJP is a direct current (dc) plasma. Nowadays, dc plasmas have been almost universally replaced by an ICP, an excellent source of excitation for analysis of solutions. In contrast to an ICP and dc plasmas described [20,21], a TJP is high-powered source (10–15 kW), which is successfully used for direct analysis of powdered samples. It was invented in the Kyrgyzstan Institute of Physics in the mid-1970s and has been applied for direct analysis of geological and mineral samples for over 20 years [22,23]. A complete evaporation of thermo stable materials is achieved in the analytical region after the confluence of the plasma jets when the sample passes through a high-temperature region of the jet confluence. To obtain detection limits at the level of 0.01–1 $\mu g\,g^{-1}$, a 150–300-mg sample has to be introduced into the plasma.

* Corresponding author. Tel.: +7 383 3306965; fax: +7 383 3309489.
E-mail address: zak@che.nsk.su (N.P. Zaksas).

0039-9140/$ – see front matter © 2009 Elsevier B.V. All rights reserved.
doi:10.1016/j.talanta.2009.10.046

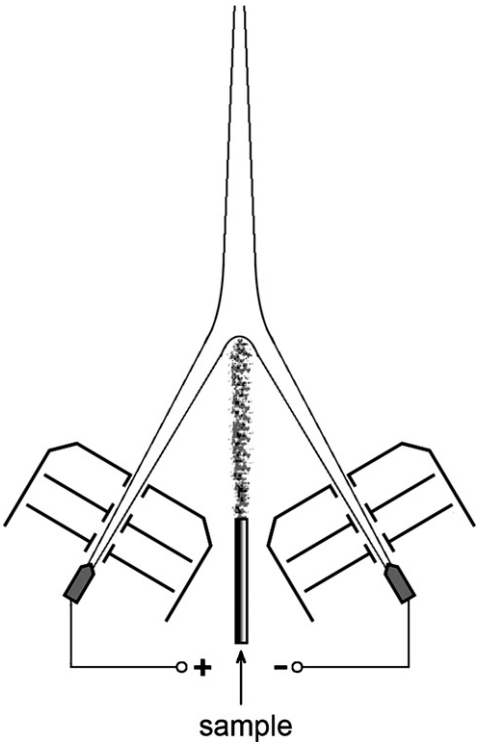


Fig. 1. Plasma burners.

In the recent papers we showed the capability of a TJP for direct multielement analysis of dry powdered biological samples including plants, bovine liver [24] and bone [25]. The use of the region before the confluence of plasma jets provided an opportunity of analysis of small samples.

The purpose of the present work was to develop the TJP-AES technique for the determination of the main essential elements (Fe, P, Ca, Mg, Zn, and Cu) in whole blood. One of the requirements to the technique was its applicability to analysis of small samples, which is important in experiments with living experimental animals (such as mice or rats).

2. Experimental

2.1. Instrumentation

2.1.1. Plasmatron

A two-jet high power plasmatron (10–15 kW) described in Ref. [26] was used. Argon plasma jets are generated in plasma burners. Every burner consists of a non-consumable tungsten electrode (anode or cathode) and three copper diaphragms (diameter ~50 mm) cooled by water. A scheme of the plasma burners is shown in Fig. 1. The experimental conditions are presented in Table 1.

2.1.2. Optical and registration system

A diffraction spectrograph with a 600 lines mm^{-1} grating covering the spectral range of 200–410 nm was used. The analytical region was focused on the slit of the spectrograph using an F–150 lens (1:1 image).

The spectra were registered using a multielement analyzer of emission spectra (MAES) produced by «VMK Optoelektronika» (Russia) [27]. The MAES system includes eight arrays, each containing 2580 photodiodes of 12.5 × 1000 μm.

The MAES is supplied with ATOM software for spectral data processing: measurement of analytical signals with background correction, construction of calibration curves, calculation of element concentrations and statistical treatment of the results. A more detailed description of the optical and registration system is given in Ref. [25].

Table 1
Working conditions of the two-jet plasma.

Parameter	Value
Current strength	80–85 A
Plasma gas	4 L min^{-1}
Carrier gas	0.7 L min^{-1}
Angle between jets	60°
Analytical region	4–5 mm lower than the point of the confluence

2.1.3. Sample introduction

A 20-mg powdered sample was placed into a Plexiglas beaker, which was inserted in a powder-introduction device where a high-frequency spark is generated between the circular and central zirconium electrodes over the surface of the powder. Blast waves from the spark agitate the powder and produce an aerosol, which is transported into plasma with a carrier gas for 6 s. A scheme of the sample introduction system was presented in Ref. [25]. The spark frequency can be varied in the range of 0.1–4 kHz. We have found that the introduction of organic biological matrices required the spark frequency not to exceed 1 kHz because the spark affected the organic matrix promoting sample melting and particle coagulation and/or partial decomposition. This resulted in both a decrease in the analytical signal and significant data scattering. For the analysis of blood, we used the frequency of 0.5 kHz.

2.2. Sample preparation and materials

For direct analysis of freeze-dried blood, a 10-mg sample ground in a Plexiglas mortar for 5 min was diluted stepwise with a spectroscopic buffer (graphite powder containing 15 wt.% NaCl) in the ratios of 1:9 and 1:99. If diluted samples were left for several hours or more, they had to be dried at 80 °C for 1 h under an IR-lamp before the analysis.

For analysis of liquid whole blood, 50 μL of blood was evaporated on 40 mg of graphite powder placed in a previously weighed quartz cup under an IR-lamp. The remainder was put into a quartz electric resistance furnace at room temperature, heated up to 400 °C and kept for 15 min at that temperature. The carbonized sample was mixed with graphite powder containing 30 wt.% NaCl in the ratio of 1:1 and ground in a Plexiglas mortar for 2–3 min. 10 mg of a diluted sample was additionally mixed with the buffer in the ratio of 1:9.

High-purity graphite powder and NaCl produced domestically were used.

2.3. Calibration samples

Calibration samples based on graphite powder containing 15 wt.% NaCl with impurity concentration range of 0.01–100 μg g^{-1} were used to construct calibration curves (lgI–lgC). These samples were prepared from Russian State reference material of graphite powder with different compositions of impurities (GSO 7751-2000, GSO 4519-89/4523-89; Ural State Technical University) by dilution of those with graphite powder containing 30 wt.% NaCl in the ratio of 1:1 in a clean room designed for manipulation with high-purity samples. The calibration samples are stable for at least a year.

3. Results and discussion

3.1. Analysis of freeze-dried blood

In contrast to quickly coagulating liquid blood, freeze-dried blood can be kept for a long time under normal conditions

Table 2
Concentration of elements in the freeze-dried blood samples ($\mu g\,g^{-1}$).

Analytical line	Human blood			Rat blood		
	Direct analysis	Carbonizing	Autoclave digestion	Direct analysis	Carbonizing	Autoclave digestion
Fe I 296.67	2300 ± 200[a]	2200 ± 160	2200 ± 200	2600 ± 200	2400 ± 170	2500 ± 200
P I 214.91	1700 ± 130	1600 ± 120	1500 ± 110	1400 ± 200	1400 ± 100	1300 ± 150
Ca II 317.93	320 ± 20	340 ± 30	300 ± 20	240 ± 30	250 ± 20	280 ± 30
Mg I 277.98	130 ± 15	150 ± 20	130 ± 10	120 ± 15	140 ± 15	150 ± 20
Zn I 213.86	28 ± 1.6	26 ± 1.4	29 ± 1.7	29 ± 2.0	32 ± 1.5	32 ± 1.4
Cu I 324.75	6.6 ± 0.5	6.2 ± 0.4	5.8 ± 0.4	3.6 ± 0.3	3.5 ± 0.3	3.3 ± 0.2

[a] 95% confidence interval, $n = 4$.

and is often used in continuous biomedical experiments. Usually 200–250 mg of dry powder is obtained from 1 mL of human whole blood.

We applied the same approach to the analysis of freeze-dried blood as in the case of the analysis of bovine liver [24]. The sample preparation procedure consisted in a 10-fold dilution of the dry powdered sample with a spectroscopic buffer (graphite powder containing 15 wt.% NaCl). Calibration samples based on graphite powder containing 15 wt.% NaCl and experimental conditions chosen for multielement analysis of graphite powder were used [28].

In order to confirm the capability of a TJP for direct analysis of freeze-dried blood, the analysis results obtained after different sample preparation procedures were compared. We used autoclave wet acid digestion in a mixture of nitric acid and hydrogen peroxide and dry carbonization of the samples. For direct analysis, 10- and 100-fold dilutions of freeze-dried blood with the spectroscopic buffer were used. A 100-fold dilution was applied for Fe and P determination because of the signal saturation. A mild carbonization procedure (400 °C, 15 min) was used instead of ashing to prevent the loss of elements. The results of the analysis of rat and human blood are presented in Table 2. The results of the direct analysis were in good agreement with the results obtained after wet acid digestion and carbonization of the samples.

For the reliable direct analysis, the particle size had to be 20 μm or less, otherwise, decreased concentrations of elements were obtained. Particles of this size were easily prepared by grinding freeze-dried blood in a Plexiglas mortar.

The proposed direct technique was additionally validated by the analysis of IAEA A-13 reference material (freeze-dried bovine whole blood). The results of the analysis are presented in Table 3.

Thereby, we have shown that TJP-AES can be used for direct determination of Fe, P, Ca, Mg, Zn, and Cu in freeze-dried blood. The relative standard deviation was in the 5–15% range. The detection limits of elements in blood powder and liquid whole blood calculated assuming that 250 mg of powder can be obtained from 1 mL of blood are given in Table 4. As evident from Tables 2 and 3, the limits are one to two orders of magnitude lower than the concentrations in the real samples. This allowed us to use less materials and a 20-fold dilution when a small amount sample was available. 5 mg of blood powder (approximately 20–25 μL liquid blood) was quite enough to obtain the result as a mean value from four replicates.

Table 3
The analysis results of IAEA A-13 freeze-dried bovine blood.

Element	Found ($\mu g\,g^{-1}$)	Target range ($\mu g\,g^{-1}$)
Fe	2300 ± 150[a]	2200–2500
P	950 ± 90	690–1120
Ca	290 ± 40	226–332
Mg	110 ± 10	81–139
Zn	12.6 ± 0.8	12–14
Cu	4.1 ± 0.2	3.7–4.8

[a] 95% confidence interval, $n = 4$.

Table 4
Detection limits of elements in blood.

Element	Freeze-dried blood ($\mu g\,g^{-1}$)	Liquid whole blood ($mg\,L^{-1}$)
Fe I 296.67	6.0	1.5
P I 214.91	30	7.5
Ca II 317.93	4.0	1.0
Mg I 277.98	5.0	1.2
Zn I 213.86	2.0	0.50
Cu I 324.75	0.2	0.05

Table 5
Concentrations of elements in human whole blood ($mg\,L^{-1}$).

Element	Sample					
	1	2	3	4	5	6
Fe	320	610	530	520	490	520
P	260	375	480	280	350	350
Ca	82	84	81	70	110	92
Mg	34	38	46	35	35	33
Zn	5.0	9.0	5.5	5.8	7.2	6.7
Cu	1.4	1.1	1.1	0.74	0.78	1.0

3.2. Analysis of liquid whole blood

Evaporation of blood aliquots on graphite powder under an IR-lamp produced glassy and hard to grind remainder. Therefore, we had to use a carbonization procedure. The remainder was converted to fine-dispersed powder after heating at 400 °C followed by grinding. The results of the analysis of human whole blood are presented in Table 5. They generally conform to the literature data. The relative standard deviation was in the 3–10% range.

The Cu and Zn determination was also validated using an independent method. The results of the determination of Cu ($0.65 \pm 0.06\,mg\,L^{-1}$) and Zn ($11.2 \pm 1.2\,mg\,L^{-1}$) obtained by the proposed technique were in good agreement with those obtained by the direct stripping voltammetry technique (Cu $0.71 \pm 0.02\,mg\,L^{-1}$ and Zn $10.5 \pm 0.7\,mg\,L^{-1}$).

4. Conclusions

The TJP-AES techniques for the determination of Fe, P, Ca, Mg, Zn, and Cu in freeze-dried and liquid whole blood were presented. The techniques allowed the use of a simple sample preparation procedure and calibration samples based on graphite powder. We used no reagents aside from a spectroscopic buffer. The techniques required only 20–50 μL of blood, which is important in biomedical experiments with living small animals.

References

[1] F.I. Wolf, A.R. Cittadini, J.A. Maier, Cancer Treat. Rev. 35 (2009) 378–382.
[2] M.D. Bootman, C. Fearnley, I. Smyrnias, F. MacDonald, H.L. Roderick, J. Cell Sci. 122 (2009) 2337–2350.
[3] D. Drago, S. Bolognin, P. Zatta, Curr. Alzheimer Res. 5 (2008) 500–507.

[4] S. Krupanidhi, A. Sreekumar, C.B. Sanjeevi, Indian J. Med. Res. 128 (2008) 448–461.
[5] K. Szentmihályi, P. Vinkler, J. Fodor, J. Balla, B. Lakatos, Orv. Hetil. 150 (2009) 681–687.
[6] A.M. DiGirolamo, M. Ramirez-Zea, Am. J. Clin. Nutr. 89 (2009) 940S–945S.
[7] H. Kobayashi, Y. Yamada, S. Kanayama, N. Furukawa, T. Noguchi, S. Haruta, S. Yoshida, M. Sakata, T. Sado, H. Oi, Gynecol. Endocrinol. 25 (2009) 39–52.
[8] M.A. Crook, Nutrition 25 (2009) 368–369.
[9] S. Mounicou, J. Szpunar, R. Lobinski, Chem. Soc. Rev. 38 (2009) 1119–1138.
[10] C. Prohaska, K. Pomazal, I. Steffan, Fresenius J. Anal. Chem. 367 (2000) 479–484.
[11] I. Rodushkin, F. Ödman, S. Branth, Fresenius J. Anal. Chem. 364 (1999) 338–346.
[12] I. Rodushkin, F. Ödman, R. Olofsson, M.D. Axelsson, J. Anal. At. Spectrom. 15 (2000) 937–944.
[13] J. Begerow, M. Turfeld, L. Dunemann, J. Anal. At. Spectrom. 12 (1997) 1095–1098.
[14] T. Martinez, J. Lartigue, P. Avila-Perez, G. Zarazua, M. Navarrete, S. Tejeda, A. Ramirez, J. Radioanal. Nucl. Chem. 259 (2004) 511–514.
[15] A. Kakuschke, S. Griesel, S. Fonfara, T. Rosenberger, A. Prange, Biol. Trace Elem. Res. 127 (2009) 28–36.
[16] C.H. Stephan, M. Fournier, P. Brousseau, S. Sauvé, Chem. Central J. 2 (2008) 14–21.
[17] S. Xiao-quan, J. Egila, D. Littlejohn, J.M. Ottaway, J. Anal. At. Spectrom. 2 (1987) 299–303.
[18] W.J. McShane, R.S. Pappas, V. Wilson-McElprang, D. Paschal, Spectrochim. Acta, Part B 63 (2008) 638–644.
[19] E. Barany, I.A. Bergdahl, A. Schütz, S. Skerfving, A. Oskarsson, J. Anal. At. Spectrom. 12 (1997) 1005–1009.
[20] P. Schramel, Spectrochim. Acta, Part B 43 (1988) 881–896.
[21] G.A. Meyer, Spectrochim. Acta, Part B 42 (1987) 333–339.
[22] I.G. Yudelevich, A.S. Cherevko, Chem. Anal. (Warsaw, Pol.) 35 (1990) 295–309.
[23] I.G. Yudelevich, A.S. Cherevko, V.S. Engelsht, V.V. Pikalov, A.P. Tagiltsev, Z.Z. Zheenbaev, Spectrochim. Acta, Part B 39 (1984) 777–785.
[24] N.P. Zaksas, T.T. Sultangazieva, T.M. Korda, J. Anal. Chem. 61 (2006) 582–587.
[25] N.P. Zaksas, T.T. Sultangazieva, V.A. Gerasimov, Anal. Bioanal. Chem. 391 (2008) 687–693.
[26] Z.Z. Zheenbaev, V.S. Engelsht, Dvukhstruinyi plazmatron (Two-jet plasmatron), Ilim, Frunze, 1983.
[27] V.A. Labusov, V.I. Popov, A.V. Bekhterev, A.N. Putmakov, A.C. Pak, Anal. Control. 9 (2005) 104–109.
[28] N.P. Zaksas, I.R. Shelpakova, V.A. Gerasimov, J. Anal. Chem. 59 (2004) 222–228.

Talanta 80 (2010) 2191–2195

Contents lists available at ScienceDirect

Talanta

journal homepage: www.elsevier.com/locate/talanta

Short communication

Determination of *Citrus aurantium* protoalkaloids using HPLC with acidic potassium permanganate chemiluminescence detection

Dane W. Percy[a,1], Jacqui L. Adcock[a], Xavier A. Conlan[b], Neil W. Barnett[a], Michelle E. Gange[a], Laura K. Noonan[a], Luke C. Henderson[a], Paul S. Francis[a,b,*]

[a] School of Life and Environmental Sciences, Deakin University, Geelong, Victoria 3217, Australia
[b] Institute for Technology Research and Innovation, Deakin University, Geelong, Victoria 3217, Australia

ARTICLE INFO

Article history:
Received 17 September 2009
Received in revised form 20 October 2009
Accepted 23 October 2009
Available online 31 October 2009

Keywords:
High performance liquid chromatography
Chemiluminescence detection
Monolithic column chromatography
Acidic potassium permanganate
Phenethylamine alkaloids

ABSTRACT

Acidic potassium permanganate chemiluminescence was explored as a sensitive and selective mode of detection for phenolic phenethylamines (adrenergic amines) in consumer products containing *Citrus aurantium* extracts. Nine commercially available weight-loss products were analysed using rapid reversed-phase chromatography with a monolithic column (separation time of 4 min). The results were in good agreement with package labelling, with some notable exceptions. The products contained a wide concentration range of synephrine and total adrenergic amines, and the difference in consumer intake was even greater when the manufacturers' recommended daily consumption was considered. The quantity of the extract, often specified on the packaging as equivalent grams of dry *C. aurantium* fruit, was a poor indicator of the concentration of the active ingredients. Methionine, a thioether amino acid contained in some weight-loss products, was identified as a potential interferent for this mode of detection.

© 2009 Elsevier B.V. All rights reserved.

1. Introduction

The U.S. Food and Drug Administration's ban of ephedrine (Fig. 1) and related *Ephedra* protoalkaloids as ingredients in weight-loss products, due to a long association with strokes, heart attacks, and other adverse health effects, has led to a dramatic increase in the use of *Citrus aurantium* (Seville orange; Bitter orange) [1]. Extracts from the unripe fruit or peel of *C. aurantium* are rich in synephrine (oxedrine), and contain several other phenolic phenethylamines, including octopamine, tyramine, *N*-methyltyramine and hordenine (Fig. 1), that each posses adrenergic activity. There is a long history of *C. aurantium* consumption in herbal medicine, but its contemporary use may involve much higher daily intakes. Ingredients of weight-loss products can include highly concentrated extracts (up to 95% synephrine), pure individual adrenergic amines (octopamine, tyramine and/or hordenine), and herbs that contain high levels of caffeine. Concern has been expressed about the safety of these products [2].

As described in a recent review by Pellati and Benvenuti [3], many chromatographic and electrophoretic methods for the determination of synephrine (and to a lesser extent, octopamine and tyramine) have emerged, but relatively few have included quantitation of the five adrenergic amines detected in *C. aurantium* extracts. However, when examined, *N*-methyltyramine has been found at much higher concentrations than octopamine, tyramine or hordenine [4,5]. Previous chromatographic procedures have involved reversed-phase and ion-pairing separations using C_{18} columns with UV-absorbance [6–8] or fluorescence [9] detection; or separation on pentafluorophenylpropyl columns using mobile phases containing high levels of organic solvent, with UV-absorbance [4], mass spectrometric [10] or tandem mass spectrometric [5] detection.

Flow-injection analysis procedures for the determination of synephrine based on its enhancing effect on the chemiluminescent reactions of luminol with hexacyanoferrate(III) [11], and cerium(IV) with rhodamine B [12] have been reported, but these procedures are not sufficiently selective towards the target analyte in the presence of other phenolic compounds [13]. Acidic potassium permanganate can also be used for sensitive chemiluminescence detection of phenolic compounds [14,15] and has been coupled to chromatographic separations for the determination of *Papaver somniferum* (opium poppy) alkaloids in process liquors [16,17], neurotransmitter metabolites in urine [18], and synephrine in plant extracts and dietary supplements [19]. The key advantages of this mode of detection, compared to UV-absorbance and fluorescence, include the relatively high sensitivity and greater selectivity, which reduces the number of interfering compounds

* Corresponding author at: School of Life and Environmental Sciences, Deakin University, Geelong, Victoria 3217, Australia. Tel.: +61 3 5227 1294; fax: +61 3 5227 1040.
E-mail address: psf@deakin.edu.au (P.S. Francis).
[1] Present address: Mars Petcare Australia, Wodonga, Victoria 3690, Australia.

0039-9140/$ – see front matter © 2009 Elsevier B.V. All rights reserved.
doi:10.1016/j.talanta.2009.10.052

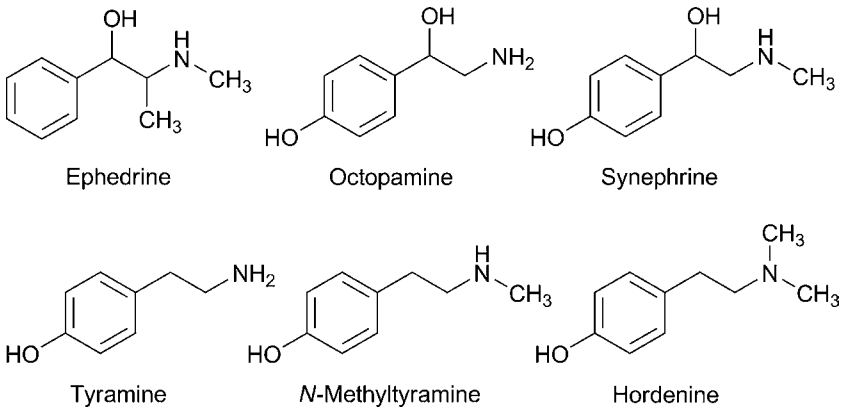


Fig. 1. Ephedrine (found in *Ephedra* species) and five phenolic phenethylamines found in *Citrus aurantium*.

that must be separated from the target analytes. However, the relationship between analyte structure and chemiluminescence intensity is yet to be fully elucidated [14]. Further investigation of potential interferences in complex sample matrices such as biological fluids and plant extracts is required to realise the full potential of chemiluminescence detection. In this study, we utilise monolithic column chromatography to explore acidic potassium permanganate chemiluminescence detection of the five bioactive phenethylamines found in weight-loss products containing *C. aurantium*.

2. Materials and methods

2.1. FIA and HPLC conditions

The flow-injection analysis (FIA) instrumentation was configured as previously described [19]. Each standard solution (70 μL) was injected into a water carrier stream that merged with the acidic potassium permanganate reagent stream at a T-fitting prior to entering a coiled transparent flow-cell, positioned against a photomultiplier tube within a light-tight housing. The solution flow rate was 3 mL/min per line. In the HPLC experiments, the column eluate (instead of the FIA carrier stream) was merged with the acidic potassium permanganate reagent stream within the chemiluminescence detector. The adrenergic amines were separated using a monolithic column (Chromolith SpeedROD RP-18e, 50 mm × 4.6 mm i.d., with 5 mm × 4.6 mm i.d. guard) under isocratic conditions (5 min: 98% deionised water adjusted to pH 2.15 with trifluoroacetic acid; 2% methanol). The column was flushed after each run, by increasing the methanol to 80% over 1 min and maintaining that concentration for 12 min, and was then re-equilibrated at the separation conditions. The flow-rate through the column was 1 mL/min and the injection volume was 10 μL.

2.2. Other instrumentation

^{1}H NMR was performed with a JEOL EX 270 MHz FT-NMR spectrometer, with samples dissolved in $CDCl_3$. Peaks were recorded as: chemical shift δ (ppm) (integral, multiplicity (s = singlet, d = doublet, m = multiplet), coupling constant J (Hz), assignment). Melting point was obtained using a heated block (SMP3, Stuart Scientific, UK). A 6210 MSDTOF mass spectrometer (Agilent Technologies, Australia) was used with the following conditions: drying gas: nitrogen (7 mL/min, 350 °C); nebuliser gas: nitrogen (16 psi); capillary voltage: 4.0 kV; vaporizer temperature: 350 °C; cone voltage: 60 V.

2.3. Reagents, standards and samples

The chemiluminescence reagent contained 1×10^{-3} M potassium permanganate (Chem-Supply, Australia) and 1% (w/v) sodium polyphosphate (Sigma–Aldrich, Australia) in deionised water and was adjusted to pH 2.5 with sulfuric acid (Merck, Australia). Synephrine, octopamine and tyramine were purchased from Sigma–Aldrich. Hordenine was synthesised using a modified Eschweiler Clark *N*-methylation reaction [20]: tyramine (1.01 g, 7.4 mmol) in methanol (50 mL) and formaldehyde (36% solution; 5.45 mL) was heated to reflux for 90 min, then cooled and stirred overnight. Sodium borohydride (1 g, 26.4 mmol) was added slowly over 30 min and stirred for a further 90 min. The solvent was removed *in vacuo*. The solid was then dissolved in water (50 mL) and extracted with chloroform (4 × 40 mL). The organic extracts were combined and dried with anhydrous sodium sulfate, filtered, and the solvent was removed. The crude product was recrystallised with 1:1 ethyl acetate:petroleum spirits to afford hordenine (615.8 mg, 51% yield; m.p. 117.3–118.1 °C, Lit. 117–118 °C [21]; MS: m/z 166.12559 $[M+H]^+$, calc. 166.12264. ^{1}H NMR (270 MHz, $CDCl_3$): δ 2.30 (6H, s, $N(CH_3)_2$), 2.55 (2H, m, $ArCH_2CH_2N$), 2.69 (2H, m, $ArCH_2CH_2N$), 6.62 (2H, d, J = 8.40, Ar), 6.99 (2H, d, J = 8.40, Ar). *N*-Methyltyramine was supplied by CSIRO Animal Health Laboratories, Australia.

The weight-loss products were supplied by or purchased from manufacturers in the USA and Australia. Tablets were ground with mortar and pestle. The powders from capsules were removed from their outer coating. A previous comparison of the effect of various solvents on the extraction of *C. aurantium* protoalkaloids from dietary supplements (using sonication or stirring with a magnetic bar) [4] revealed that water is more efficient than 0.1 M HCl, methanol or a mixture of 37% HCl and methanol (0.8:99.2, v/v). In a related study [9] it was shown that aqueous HCl (0.37% mass fraction) extracted greater quantities of the amines than methanol or acidified methanol (using sonication), but neutral aqueous solutions were not examined. In this study, samples were dissolved in a known volume of water (50–250 mL) by stirring for 45 min with a magnetic stir bar. The sample solutions were diluted with deionised water (if required) and filtered with Acrodisc PSF syringe filters (Pall Australia).

3. Results and discussion

3.1. Method development

N-Methyltyramine had not previously been detected with acidic potassium permanganate, and therefore the reaction was initially

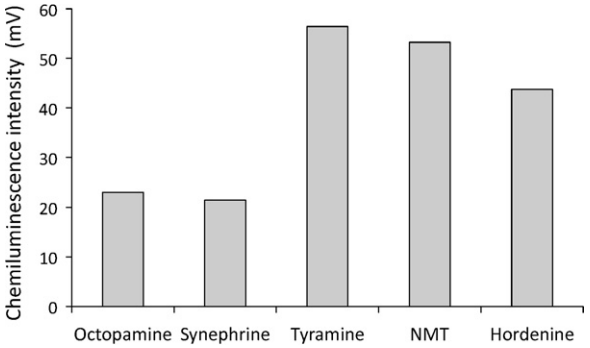


Fig. 2. Relative chemiluminescence intensity of *Citrus aurantium* protoalkaloids (1×10^{-5} M) with the acidic potassium permanganate reagent using flow-injection analysis methodology. NMT = *N*-methyltyramine.

examined in aqueous solution using FIA. The chemiluminescence intensity for this analyte was similar to that of tyramine and hordenine (Fig. 2). Phenolic compounds generally produce light with acidic potassium permanganate, but little is known of the relationship between chemical structure and emission intensity [14]. For this class of compound, it is clear that the presence of a hydroxyl group on the benzylic carbon (*i.e.* in octopamine and synephrine) and greater methyl substitution on the amine both have a detrimental effect on chemiluminescence intensity. The limit of detection (3σ) for *N*-methyltyramine was 4×10^{-9} M, which was similar to that of the other adrenergic amines (between 1×10^{-9} and 1×10^{-8} M [19]).

A HPLC solvent mixture of 98% water adjusted to pH 2.15 with trifluoroacetic acid and 2% methanol provided baseline resolution of the five adrenergic amines. Retention times for octopamine, synephrine, tyramine, *N*-methyltyramine and hordenine were 1.25, 1.56, 2.61, 3.18 and 3.66 min. Without methanol in the column eluent, greater resolution was obtained, but more time was required for both separation and re-equilibration from the elevated levels of methanol that were used to flush less polar sample components from the column. Linear calibrations were obtained using nine standard mixtures of the adrenergic amines over the range 1×10^{-5} to 1×10^{-3} M, but for the lower order of magnitude, greater accuracy was obtained by calculating the line-of-best-fit using standards from that region only. Precision was established using five replicate injections of a mid-range standard mixture (1×10^{-4} M). The relative standard deviations were 0.32%, 0.51%, 0.45%, 0.50% and 0.55% for retention time, and 2.9%, 2.4%, 3.5%, 4.1% and 4.0% for peak area, of octopamine, synephrine, tyramine, *N*-methyltyramine and hordenine, respectively.

3.2. Adrenergic amines in weight-loss products

Nine commercially available weight-loss products containing *C. aurantium* protoalkaloids were analysed. The products contained a wide range of other ingredients (including extracts from *Camellia sinesis* (green tea), *Paullinia cupana* (guarana), *Salix alba* (white willow), *Garcinia quaesita* (brindleberry), *Capsicum frutescens* (cayenne), *Zingiber officinale* (ginger), *Coleus forskohlii* and *Evodia rutaecarpa*, and pure compounds such as caffeine, tyrosine, carnitine, phenylalanine, evodiamine, theobromine, rutaecarpine, hydroxycitric acid, chromium picolinate).

Products 1 and 2 contained pure octopamine, tyramine and hordenine as ingredients. Synephrine was included as the hydrochloride salt or standardised herbal extract (95% synephrine). The measured values using the monolithic column separation with chemiluminescence detection were in reasonable agreement with the stated values (Table 1), with the exception that no tyramine was found (above the limit of detection) in product 2, which was claimed to contain 37.5 mg of tyramine per tablet. When consuming these products within the dosage range recommended by the manufacturers, daily intake of synephrine and total adrenergic amines would be 55–164 and 255–766 mg, respectively. Based on the specified values, daily intake of caffeine from these products would be 200–600 mg.

Products 3–9 contained *C. aurantium* extracts (in three cases the extract was standardised with regard to synephrine content). The quantity of the extract (per tablet/capsule) in each of these products was given in terms of equivalent dried fruit. However, this was not a good indicator of the level of active ingredients; the mass percentage of synephrine in the specified equivalent dry fruit was found to range between 0.06% and 0.46% (with an average of 0.29%), which is similar to the range reported by Avula et al. for 13 dried samples of *C. aurantium* fruits (0.04–0.41% with an average of 0.17%) [6]. For example, it was claimed that both products 8 and 9 contained an extract that was equivalent to 6000 mg of dry fruit per tablet, but the synephrine content was found to be over eight times higher in product 8 than in product 9. Unlike many of the other products, the synephrine content in these two was specified, but the content of product 9 was found to be lower than the specified value (Table 1). Lower concentrations of other adrenergic amines were detected and in agreement with several previous studies [6,8], tyramine and *N*-methyltyramine were the most prominent. Minor interferences from other ingredients prevented accurate quantification of the target analytes at below 0.5 mg per tablet/capsule. The daily intake of synephrine using products 3–9 under the manufacturers' recommended dosage would be 3–57 mg, which is lower than (but overlaps with) the range for products 1 and 2. The total adrenergic amine intake for products 3–9 was approximately 3–70 mg, which was far lower than that of the products containing individual *C. aurantium* protoalkaloids as ingredients. It should be noted that the original labelling of product 6 (which had been covered by modified directions) suggested a daily dosage of up to 6 capsules, giving a synephrine intake of over 300 mg.

3.3. Potential interferences

As described above, there are a wide range of products on the market that contain *C. aurantium* extracts and/or individual adrenergic amines, combined with many other ingredients (including other plant extracts). A close inspection of the peak shapes and retention times is warranted for new samples. We analysed four weight-loss products that did not specify *C. aurantium* extracts as ingredients (samples 10–13) and in two cases we observed a large chemiluminescence peak with a retention time similar to that for synephrine (see sample 12 in Fig. 3), but an equivalent peak was not observed in the chromatogram when UV-absorbance detection was used. To identify the compound responsible for this relatively large chemiluminescence response, the separation was coupled with mass spectrometric detection (positive ion), which showed mass peaks at *m*/*z* 150, 204, 299 and 407 for that retention time. The peak at *m*/*z* 150 was similar to a characteristic fragment peak $[M-OH]^+$ for synephrine, but the mass difference exceeded 200 ppm and the pseudo-molecular ion $[M+H]^+$ at *m*/*z* 168 for synephrine was not observed. An inspection of the specified sample ingredients indicated that *N*-acetylcarnitine ($[M+H]^+$ *m*/*z* 150) and methionine ($[M+H]^+$ *m*/*z* 204) may produce these mass peaks, which was confirmed by comparing the mass spectrum of respective standards. The peaks at *m*/*z* 299 and 407 were assigned as the $[2M+H]^+$ dimers.

Although *N*-acetylcarnitine and methionine both co-eluted with synephrine, only methionine (a thioether (R–S–R′)) was found to produce a signal with acidic potassium permanganate. Thiol compounds (R–S–H), such as cysteine, glutathione and captopril, have previously been found to produce a significant amount of

Table 1
Content, recommended daily dose and consumption of *Citrus aurantium* protoalkaloids in weight-loss products.

	Quantity per tablet or capsule[a] (mg)					Equiv. dry fruit[b] (mg)	Syn. in dry fruit (%)	Recommended daily dose[b]	Daily consumption[c] (mg)	
	Oct.	Syn.	Tyr.	Met.	Hor.				Syn.	Adrenergic amines
1	59.9 (50)	55.3 (50)	56.1 (50)		57.4 (50)			2 caps.	111 (100)	457 (400)
2	75.2 (75)	27.4 (25)	< 0.5 (37.5)		25.0 (25)			2–3 × 1–2 caps.	55–164 (50–150)	255–766 (325–975)
3		7.9				2,500	0.32	3 × 1 tabl.	24	24
4		9.5	1.7	0.5		5,000	0.19	1–3 × 1–2 tabl.	10–57	12–70
5		5.8 (5)				1,250	0.46	1–3 × 1–2 caps.	6–35 (5–30)	6–35
6	0.5	52.8		2.5		14,200	0.37	1 caps. [2 × 3][d]	53 [316][d]	56 [335][d]
7		6.2	0.9	1.3		3,000	0.21	1–3 × 2–3 tabl.	12–56	17–76
8		26.8 (28.8)	2.7	0.9		6,000	0.45	1 tabl.	27 (29)	30
9		3.3 (7)				6,000	0.06 (0.12)	1–3 × 1 caps.	3–10 (7–21)	3–10

[a] Specified values shown in parentheses. Quantities below 0.5 mg not shown.
[b] Specified.
[c] Values calculated from specified values shown in parentheses.
[d] Original product labelling suggested an intake of 2 × 3 capsules.

light with this reagent [22–25] (although in those studies, quinine and formaldehyde were used as enhancers rather than sodium polyphosphate). Lebedev and Tsibanova noted that the oxidation of methionine with permanganate produced light [26], but under conditions similar to those used in this study the response for methionine was far lower than that of the indolic amino acid tryptophan and the phenolic amino acid tyrosine [27], which is similar in structure to tyramine. Nevertheless, the quantity of methionine in the two weight-loss products (333 mg per tablet and 880 mg per serve (~3 g of powder)) was very high compared to the amount of synephrine in the products discussed in Section 3.2 (3.3–55.3 mg per tablet/capsule).

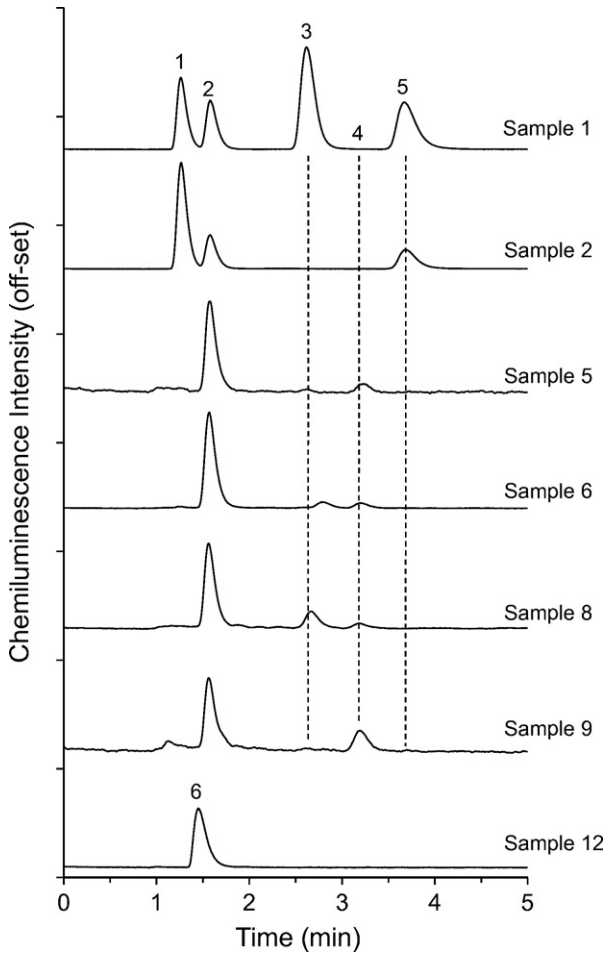


Fig. 3. Chromatograms for the determination of adrenergic amines in weight-loss products using HPLC with monolithic column (C_{18}) separation and acidic potassium permanganate chemiluminescence detection. Peaks: (1) octopamine, (2) synephrine, (3) tyramine, (4) *N*-methyltyramine, (5) hordenine, and (6) methionine. Sample 12 is discussed in Section 3.3.

4. Concluding remarks

Detection based on acidic potassium permanganate chemiluminescence offers greater selectivity for phenolic analytes than UV-absorbance, and products containing large quantities of adrenergic amines can be analysed with a rapid reversed-phase chromatographic separation coupled with chemiluminescence detection. An examination of commercially available weight-loss products showed reasonable agreement between measured quantities and package labelling (with some notable exceptions), and a very wide range of synephrine and total adrenergic amines per tablet, which was accentuated when suggested daily consumption of the products was considered.

In general, no other major peaks were observed in the same region of the chromatogram, but minor interferences from other herbal ingredients prevented accurate quantification of very low concentrations of the target analytes. Under these conditions, methionine eluted at a similar time to synephrine and when present at relatively high concentrations, produced a significant emission. Methionine is used as an ingredient in some weight-loss products, but was not included in any of the tested products that contained *C. aurantium* extracts.

To address these aspects and establish the full potential of acidic potassium permanganate for the detection of phenolic protoalkaloids in plant extracts and consumer products, we are currently exploring this mode of detection in conjunction with recent advances in the separation of *C. aurantium* samples described by Roman et al. (ion-pairing) [7] and Pellati and Benvenuti (pentafluorophenylpropyl columns) [4].

Acknowledgements

The authors thank Deakin University for funding, Dr. Steve Colgate (CSIRO) for donating the *N*-methyltyramine, and Gail Dyson (Deakin University) for assistance with the NMR characterisation of hordenine.

References

[1] A. Fugh-Berman, A. Myers, Exp. Biol. Med. 229 (2004) 698.
[2] D.M. Marcus, A.P. Grollman, Science 301 (2003) 1669.
[3] F. Pellati, S. Benvenuti, J. Chromatogr. A 1161 (2007) 71.
[4] F. Pellati, S. Benvenuti, J. Chromatogr. A 1165 (2007) 58.

[5] B.C. Nelson, K. Putzbach, K.E. Sharpless, L.C. Sander, J. Agric. Food Chem. 55 (2007) 9769.
[6] B. Avula, S.K. Upparapalli, A. Navarrete, I.A. Khan, J. AOAC Int. 88 (2005) 1593.
[7] M.C. Roman, J.M. Betz, J. Hildreth, J. AOAC Int. 90 (2007) 68.
[8] R.L. Evans, P.H. Siitonen, J. Chromatogr. Sci. 46 (2008) 61.
[9] K. Putzbach, C.A. Rimmer, K.E. Sharpless, L.C. Sander, J. Chromatogr. A 1156 (2007) 304.
[10] K. Putzbach, C.A. Rimmer, K.E. Sharpless, S.A. Wise, L.C. Sander, Anal. Bioanal. Chem. 389 (2007) 197.
[11] Q. Li, C. Huang, Y. Huang, Luminescence 21 (2006) 43.
[12] R. Wang, L. Wan, Q. Li, X. Liu, Y. Huang, Luminescence 22 (2007) 140.
[13] P.S. Francis, A.J. Brown, S.A. Bellomarino, A.M. Taylor, T. Slezak, N.W. Barnett, Luminescence 24 (2009) 90.
[14] J.L. Adcock, P.S. Francis, N.W. Barnett, Anal. Chim. Acta 601 (2007) 36.
[15] P.S. Francis, J.L. Adcock, J.W. Costin, S.D. Purcell, F.M. Pfeffer, N.W. Barnett, J. Pharm. Biomed. Anal. 48 (2008) 508.
[16] J.W. Costin, S.W. Lewis, S.D. Purcell, L.R. Waddell, P.S. Francis, N.W. Barnett, Anal. Chim. Acta 597 (2007) 19.
[17] J.L. Adcock, P.S. Francis, K.M. Agg, G.D. Marshall, N.W. Barnett, Anal. Chim. Acta 600 (2007) 136.
[18] J.L. Adcock, N.W. Barnett, J.W. Costin, P.S. Francis, S.W. Lewis, Talanta 67 (2005) 585.
[19] T. Slezak, P.S. Francis, N. Anastos, N.W. Barnett, Anal. Chim. Acta 593 (2007) 98.
[20] B.L. Sondengam, J.H. Hemo, G. Charles, Tetrahedron Lett. (1973) 261.
[21] M.J. O'Neil, P.A. Heckelman, C.B. Koch, K.J. Roman (Eds.), The Merck Index, 14th ed., Merck, Whitehouse Station, NJ, USA, 2006.
[22] J.A. Murillo Pulgarín, L.F. García Bermejo, P. Fernández López, Anal. Chim. Acta 546 (2005) 60.
[23] Y. Li, A. Zhang, J. Du, J. Lu, Anal. Lett. 36 (2003) 871.
[24] J.L. Adcock, P.S. Francis, N.W. Barnett, J. Fluoresc. 19 (2009) 867.
[25] J.L. Adcock, P.S. Francis, N.W. Barnett, Anal. Chim. Acta 652 (2009) 303.
[26] V.S. Lebedev, I.V. Tsibanova, Russ. J. Phys. Chem. 51 (1977) 819 (Engl. Transl.).
[27] J.W. Costin, P.S. Francis, S.W. Lewis, Anal. Chim. Acta 480 (2003) 67.

Talanta 80 (2010) 2196–2198

Contents lists available at ScienceDirect

Talanta

journal homepage: www.elsevier.com/locate/talanta

Short communication

Estimation of antioxidant capacity against peroxynitrite and hypochlorite with fluorescein

Agnieszka Robaszkiewicz [a,*], Grzegorz Bartosz [a,b]

[a] Department of Molecular Biophysics, University of Łódź, Banacha 12/16, 90-237 Łódź, Poland
[b] Department of Biochemistry and Cell Biology, University of Rzeszów, St. Pigonia 6, 35-959 Rzeszów, Poland

ARTICLE INFO

Article history:
Received 20 August 2009
Received in revised form 26 October 2009
Accepted 3 November 2009
Available online 10 November 2009

Keywords:
Antioxidant capacity
Hypochlotite
Peroxynitrite
Peroxyl radical

ABSTRACT

Peroxynitrite and hypochlorite are oxidants relevant in many pathological situations. We propose a simple spectrofluorometric assay to determine antioxidant capacity against hypochlorite and peroxynitrite based on protection against fluorescein bleaching. The assay can be performed on a microplate and requires minute amounts of material. Standard antioxidants show different reactivities for both oxidants. Antioxidant capacity of fruit bodies of edible mushrooms, tea, coffee and wine estimated as exemplary biological material point to considerable differences in the scavenging capacity of various biological material against hypochlorite, peroxynitrite and peroxyl radicals.

© 2009 Elsevier B.V. All rights reserved.

1. Introduction

The "Total antioxidant capacity" (TAC) assays have been widely used in various fields of research including analysis of food and beverages, analysis of plant material and analysis of body fluids, especially in pathologies. These assays quantify the resultant antioxidant activity of all molecules present in the biological material studied. Various assays of TAC rely either on inhibition of oxidation of an indicator by a chosen oxidant or on reduction of oxidized forms of appropriate indicators [1–3]. The choice of oxidants is an important issue in TAC assays. Assays based on the scavenging of the hydroxyl radical [4,5] have been criticized as this radical is very reactive, with respect not only to typical antioxidants but to virtually any organic compound. Most frequently, peroxyl radicals generated by thermolysis of an azo initiator AAPH are applied as a model oxidant due to the convenience of this system. There are, however, also other pathophysiologically relevant oxidants which are not disposed of by enzymatic means, so the total scavenging capacity of a biological material with respect to these species is of particular importance, viz. peroxynitrite and hypochlorite. Although assays for the capacity to scavenge oxyradicals have been proposed (e.g. ORAC assay, Oxygen Radical Antioxidant Capacity; TOSCA, Total Oxyradical Scavenging Capacity Assay) [2,6] a simple, cheap, high-throughput assay for the ability to scavenge hypochlorite and peroxynitrite is lacking. The most frequently and commonly applied kinetic ORAC assay, based on the calculation of the area under the curve of fluorescence and time (or lag time) of incubation is useless in case of fast reactive oxidants like hypochlorite and, especially, peroxynitrite. The commercially available OXY-Adsorbent Test which measures the antioxidant capacity of the sample against hypochlorite on the basis of the excess of oxidant after reaction is not applicable for peroxynitrite. Here, we propose a simple, competitive, end-point (instead of kinetic) assay for evaluation of the antioxidant capacity of biological fluids against hypochlorite and peroxynitrite based on the same assumption as the widely used $ORAC_{FL}$ assay—bleaching of fluorescein [7]. Both oxidants tested react rapidly with fluorescein what makes our end-point assay even simpler and much quicker.

2. Materials and methods

All reagents were from Sigma/Aldrich (Poznań, Poland). Peroxynitrite was synthesized from sodium azide and ozone according to the method of Pryor et al. [8] with small modifications [9].

Fluorescein (to obtain 2 μM final) in 100 mM phosphate buffer, pH 7.4, was mixed in the presence or absence of antioxidants (ascorbate, Trolox, uric acid, glutathione or bovine serum albumin; BSA) with 100 μM HOCl or $ONOO^-$ or 10 mM AAPH to the final volume of 100 μl on 96-well plate. Peroxynitrite and hypochlorite were added on a shaker. The immediate mixing of the sample with the oxidant added is critical for the reproducibility of the assay, especially in the case of peroxynitrite. The half-life of peroxynitrite at neutral pH is of an order of a second so it is important that, when added, the oxidant is distributed immediately in the whole reaction volume,

* Corresponding author. Tel.: +48 42 6354476; fax: +48 42 6354476.
E-mail address: agnieszka.robaszkiewicz@gmail.com (A. Robaszkiewicz).

0039-9140/$ – see front matter © 2009 Elsevier B.V. All rights reserved.
doi:10.1016/j.talanta.2009.11.004

in order to get reproducible results (otherwise part of the oxidant decomposes before reaching the substrate and the extent of fluorescein bleaching and its protection shows high variability). The way of addition must be reproducible between all samples compared. In our experience, the optimal procedure is to add peroxynitrite while keeping the microplate on a shaker, and use the same shaking conditions for the whole assay. After incubation at room temperature for 15 min the fluorescence of the samples containing HOCl and $ONOO^-$ was measured (excitation: 485 nm, emission: 538 nm). For comparison, we estimated the peroxyl radical scavenging capacity in our system using AAPH: samples were incubated with 10 mM AAPH at 37 °C in the dark for 1 h and fluorescence was read immediately after the end of incubation (excitation: 485 nm, emission: 538 nm). For each antioxidant the experiment was conducted in six independent repeats. The IC_{50} value was determined as the concentration of an antioxidant that provides 50% inhibition of fluorescein oxidation.

The fruiting bodies of edible mushrooms *Boletus edulis* and *Cantharellus cibarius* were collected in 2008 in Bory Tucholskie (a big forest area in the Northern part of Poland), cleaned and air-dried. Before extraction the dry fruiting bodies were cleaned carefully under running water to remove residual contamination and dried again. 1 g of dry caps of Boletus edulis and whole body of *Cantharellus cibarius* were ground into powder, then 15 ml of boiling hot water was added and all together was rubbed for the next 5 min and stirred at room temperature for 15 min. Then the mixture was centrifuged at 3000 × *g* at room temperature for 20 min. The supernatants were portioned and kept frozen at −23 °C until analysis. Individual bags of commercial teas: green PackerBest, red Dilmah Raspberry and black Lipton Imperial Earl Grey) were extracted in 50 ml of boiling water for 15 min. Similarly, 0.5 g of soluble coffee (Tchibo Family) was dissolved in 50 ml of boiling water. Cervantez De Alcardete Don Quijote semidry red wine (Spain) was used. The extracts were appropriately diluted (20–200 times) before the assay and various amounts of the diluted extracts (1–50 μl) were added to the microplate wells keeping the final volume of the reaction constant (200 μl).

Summary of the proposed procedure: Prepare 10 μM fluorescein in 100 mM phosphate buffer, pH 7.4 so to obtain final concentration of 2 μM in wells of a microplate, taking into account the volumes of additives. Measure decrease in fluorescence at the excitation/emission wavelengths of 485 nm and 538 nm, respectively, after addition of antioxidants (100 μM hypochlorite and 100 μM peroxynitrite, final). Calibrate the method using ascorbate in the concentration range from 10 to 100 μM to determine IC_{50} for ascorbate (IC_{50Asc}). Measure % inhibition of fluorescein bleaching by appropriately diluted fluids/extracts (1–50 μl in a total volume of 100 μl) and find the volume IV_{50} (corresponding to IC_{50}). Calculate the antioxidant capacity of the material analysed as equivalent concentration of ascorbic acid using the calibration curve according to the equation: AC [μM] = IC_{50Asc} [μM] × (dilution of the sample) × 100 [μl]/IV_{50} [μl].

3. Results and discussion

Fluorescein is bleached not only by hydroxyl or peroxyl radicals but also by peroxynitrite and hypochlorite. In all cases, the bleaching can be prevented by antioxidants so the degree of protection may be a measure of the antioxidant activity of a sample [10–12]. In kinetic assays, the area under curve of fluorescence intensity versus time or lag time of the oxidation are usually taken as a measure of oxidation of the probe and of its protection. In our approach the final fluorescence after completion of fast reaction with hypochlorite or peroxynitrite (or fixed time of reaction with AAPH) is used instead. Concentration of the oxidant must be chosen so to provide significant but not complete fluorescein bleaching. In our system addition of 100 μM hypochlorite and peroxynitrite to 2 μM fluorescein solution resulted in rapid drop of fluorescence (61.4 ± 7.3% fluorescein oxidation by hypochlorite, 78.7 ± 8.5% by peroxynitrite). After 1 h incubation with 10 mM AAPH the percent of fluorescein oxidized was about 51.5 ± 5.6%.

The protective action of antioxidants was expressed as per cent inhibition of the oxidation of detectors. From such plots, antioxidant or extract concentrations giving 50% protection against the fluorescein bleaching (i.e. reducing the fluorescence drop between the control and oxidant-treated samples by 50%) were read (IC_{50}).

Standard antioxidants and albumin showed different efficiency in the protection against fluorescein bleaching. In the case of HOCl, the sequence of IC_{50} values (reflecting the decreasing efficiency of protection) was: BSA (59 ± 11 nM) ≪ (glutathione (29.5 ± 0.6 μM) < urate (36.0 ± 1.9 μM) < ascorbate (67.5 ± 5.7 μM) < Trolox (72.7 ± 5.0 μM). For peroxynitrite, the sequence was: BSA (0.20 ± 0.05 μM) < urate (14.6 ± 6.8 μM) < glutathione (19.9 ± 4.9 μM) ≈ Trolox (21.6 ± 1.7 μM) < ascorbate (24.1 ± 3.3 μM). In the case of AAPH, the sequence of IC_{50} values was as follows: BSA (0.21 ± 0.06 μM < Trolox (43.1 ± 15.0 μM) ≈ urate (43.9 ± 2.1 μM) < ascorbate (69.0 ± 1.3 μM) < glutathione (105.2 ± 11.3 μM). A similar sequence of the scavenging ability of standard antioxidants against peroxyl radicals was found in the paper of Winston and co-workers [6]. Additionally, we determined the inter- and intra-day variability of this assay for ascorbate: for hypochlorite inter- and intra-day standard deviation was found to be 4.1 and 5.7 μM, respectively, while for peroxynitrite 2.1 and 3.3 μM and for AAPH 0.9 and 1.3 μM. Thus, we presented the IC_{50} values with intra-day standard deviation.

The high antioxidant activity of bovine serum albumin in the test of fluorescein bleaching is rather unusual, is not observed in other tests of antioxidant activity [13] and can be explained by the binding of fluorescein to this protein [14,15]. Binding by albumin seems to be the main factor in the protection of fluorescein against oxidants, rather than purely competitive scavenging of oxidants by the protein molecule and therefore represents a methodological artifact. Therefore, the fluorescein-based TAC assays should rather not be used for assays of albumin-containing fluids like blood plasma (though may be quite useful for deproteinized plasma). Indeed, TAC values obtained for blood plasma with $ORAC_{FL}$, based on fluorescein bleaching, are much higher than those obtained by the ORAC method based on phycoerythrin [7]. We did not find such an effect with other proteins. However, it cannot be excluded that some proteins having affinity for hydrophobic ligands could also bind the dye. Binding of fluorescein by BSA induces loss of fluorescence of the dye; in a case when such an effect is observed by addition of a sample in the absence of an oxidant, the presence of a binding protein could be expected and should be checked.

As Trolox appeared to be the weakest hypochlorite scavenger, we propose to use ascorbate as a standard and express the scavenging capacities in ascorbate equivalents.

Therefore, we used material of plant origin to test the assay for hypochlorite and peroxynitrite scavenging capacities. Results of analysis of mushroom fruiting bodies, tea, coffee and wine point to different scavenging capacities for these oxidants, generally lower for hypochlorite than for peroxynitrite, and lower than that found for the scavenging of peroxyl radicals (Table 1). Interestingly, there are considerable differences between various materials studied. Instant coffee showed an especially high ratio of the peroxynitrite to hypochlorite scavenging capacity while the fruiting body of Cantharellus showed a higher hypochlorite than peroxynitrite scavenging capacity, in contrast to Boletus.

In summary, we propose a simple and rapid spectrofluorometric test for estimation of the peroxynitrite and hypochlorite scavenging capacity of biological materials including food products, requiring very small amounts of material.

Table 1
Scavenging capacities of exemplary food products for hypochlorite, peroxynitrite and AAPH-derived peroxyl radicals (in ascorbate equivalents per liter). Mean ± SD, $n = 4$.

Material	Hypochlorite	Peroxynitrite	AAPH	Unit
Boletus edulis	47.8 ± 5.0	61.9 ± 1.1	382 ± 10	mmol/l
Cantharellus cibarius	10.5 ± 0.2	6.96 ± 1.14	251 ± 3	mmol/l
Red wine	491 ± 8	99.4 ± 6.1	573 ± 62	mmol/l
Green tea	57.6 ± 3.1	294 ± 14	728 ± 41	mmol/l
Black tea	48.1 ± 9.4	166 ± 34	367 ± 45	mmol/l
Red tea	14.0 ± 0.4	29.9 ± 3.4	695 ± 107	mmol/l
Coffee	14.9 ± 0.4	135 ± 2	219 ± 1	mmol/l

References

[1] G. Bartosz, Adv. Clin. Chem. 37 (2003) 219–292.
[2] L.M. Magalhães, M.A. Segundo, S. Reis, J.L. Lima, Anal. Chim. Acta 613 (2008) 1–19.
[3] R.L. Prior, G. Cao, Free Radic. Biol. Med. 27 (1999) 1173–1181.
[4] B. Ou, M. Hampsch-Woodill, J. Flanagan, E.K. Deemer, R.L. Prior, D. Huang, J. Agric. Food Chem. 50 (2002) 2772–2777.
[5] O. Erel, Clin. Biochem. 37 (2004) 112–119.
[6] G.W. Winston, F. Regoli, A.J.J. Dugas, J.H. Fong, K.A. Blanchard, Free Radic. Biol. Med. 24 (1998) 480–493.
[7] B. Ou, M. Hampsch-Woodill, R.L. Prior, J. Agric. Food Chem. 49 (2001) 4619–4626.
[8] W.A. Pryor, R. Cueto, X. Jin, W.H. Koppenol, M. Ngu-Schwemlein, G. Squadrido, P.L. Uppu, R.M. Uppu, Free Radic. Biol. Med. 18 (1995) 75–83.
[9] M. Soszynski, G. Bartosz, Biochim. Biophys. Acta 1291 (1996) 107–114.
[10] R.L. Prior, H. Hoang, L. Gu, X. Wu, M. Bacchiocca, L. Howard, M. Hampsch-Woodill, D. Huang, B. Ou, R. Jacob, J. Agric. Food Chem. 51 (2003) 3273–3279.
[11] A. Dávalos, C. Gómez-Cordovés, B. Bartolomé, J. Agric. Food Chem. 52 (2004) 48–54.
[12] C. Lucas-Abellán, M.T. Mercader-Ros, M.P. Zafrilla, M.I. Fortea, J.A. Gabaldón, E. Núnez-Delicado, J. Agric. Food Chem. 56 (2008) 2254–2259.
[13] A. Robaszkiewicz, G. Bartosz, Biochem. Biophys. Res. Commun. (2009).
[14] N. Barberoa, E. Barnib, C. Barolob, P. Quagliotto, G. Viscardi, L. Napionea, S. Pavana, F. Bussolinoa, Dyes Pigments 80 (2009) 307–313.
[15] S. Nagataki, I. Matsunaga, Invest. Ophthalmol. Vis. Sci. 26 (1985) 1175–1178.

Talanta 80 (2010) 2199–2200

Contents lists available at ScienceDirect

Talanta

journal homepage: www.elsevier.com/locate/talanta

Obituary

George-Emil Baiulescu, Professor, Mentor and Friend, 1931–2009



This year, June 9, 2009, the School of Analytical Chemistry from Romania lost the most important professor, the chief of this School, Professor George-Emil Baiulescu. He was born on August 4, 1931 in a famous family from Braşov, his grandfather being the first Romanian Lord Mayor. All his life he tried to improve the quality of Analytical Chemistry from Romania.

Professor George-Emil Baiulescu obtained his B.Sc. in 1954 from the Faculty of Chemistry, University of Bucharest and between 1954 and 1958 he was researcher at the Centre of Chemical Researches (Department of Inorganic Chemistry) of the Romanian Academy of Science. He took his Ph.D. in 1960 and D.Sc. in 1970, and in 1971 he obtained the authorization for directing Ph.D. students and 36 persons obtained this title under his supervision. He worked from 1958 at the Faculty of Chemistry as assistant, lecturer, reader and professor, and in 1961, together with Professor Grigore Popa, founded the Department of Analytical Chemistry in the Faculty of Chemistry at the University of Bucharest.

His scientific activity is evidenced by more than 200 scientific papers in prestigious journals, such as Analytical Chemistry, Trends in Analytical Chemistry, Analytica Chimica Acta, Analytical Letters, Analyst, Critical Reviews in Analytical Chemistry, Mikrochimica Acta, and Talanta. For more than 30 years Professor Baiulescu was a member in the editorial board of Analytical Letters journal. His research fields were: organic reagents, separation methods, ion selective electrodes, atomic absorption and emission spectrometry, molecular emission spectrometry, chromatographic techniques, sampling, and environmental analysis. One of the most important fields in which he published a lot of papers was ion selective electrodes, for cations and pharmaceutical compounds.

He worked for more than 40 years in environmental pollution, air and water, and seven Ph.D. thesis were granted for research in this field. His environmental researches were directed to the determination of gases, such as sulfur dioxide, and the reactions of sulfur oxide in the atmosphere; of carbon monoxide and nitrogen dioxide; of cations from mineral waters, river and sea waters; and also organic polutants from different type of samples.

His conclusion about all his activity is "No analysis is better than the sample itself". Professor Baiulescu published four books in foreign publishing houses: *Stationary Phases in Gas Chromatography* with V.A. Ilie as co-author (in 1975, published by Pergamon Press, Oxford), *Applications of Ion Selective Membrane Electrodes in Organic Analysis* with V.V. Coşofreţ, in 1977 published at Ellis Horwood, translated in 1980, also in Russian, Mir, Moscow), *Education and Teaching in Analytical Chemistry* together with C. Pătroescu and R.A. Chalmers (in 1982 published at Ellis Horwood, Chichester and translated in China, 1993), and *Sampling* (1991) together with P. Dumitrescu and P. Gh. Zugrăvescu (published at Ellis Horwood, Chichester and translated in China, 1996) and one chapter in *Gold Mining: Formation and Resource Estimation, Economics and Environmental Impact,* "The Influence of Gold Mining Industry on the Pollution of Roşia Montana District", together with A.I. Stoica and R.M. Florea in Nova Publishers House, 2009. In Romanian publishing houses, Professor Baiulescu published in 1974 together with T. Năşcuţiu, *Physical Methods of Trace Analysis*, in Editura Tehnică, Bucharest and *Environmental Analytical Chemistry. Concepts*, Ars Docendi, together with A.I. Stoica and C.H. Lochmüller.

One of his most important activities was the foundation of the Romanian Society of Analytical Chemistry (SCAR) in 1990. He put

0039-9140/$ – see front matter
doi:10.1016/j.talanta.2009.10.001

all his soul and energy in organizing national and international conferences. Therefore, in 1992 at Cluj-Napoca, he organized the first Conference on Analytical Chemistry from Romania with international participation, after the Romanian Revolution in December 1989. Before December 1989, the National Council of Engineers and Technicians organized International Conferences at Mamaia (1969) and at Braşov (1971). After these Conferences, the leadership from the communist period did not allow any International Conferences. Before December 1989 only National Conferences were organized, the last one being at Brăila (1989).

Nowadays, every year the National Conferences on Analytical Chemistry and every 2 years (1994—Constanţa, 1996—Craiova, 1998—Piatra Neamţ, 2000—Braşov, 2002—Timişoara, 2004—Braşov) the International Conferences on Analytical Chemistry were organized. In 2000, at Braşov the "1st Romanian International Conference on Analytical Chemistry" in cooperation with the Division of Analytical Chemistry was organized.

The Romanian Society of Analytical Chemistry organizes conferences every last Wednesday of the month, where are presented scientific papers regarding mainly analytical research and history, but also there are invited prestigious people from different fields, like Teodor Negoiţă, the first Romanian explorer of the North Pole and Constantin Lăcătuşu, the first Romanian who climbed Mt. Everest.

He considered that the best way to learn something is to be in direct contact with specialists and for this reason he participated at a lot of conferences, with plenary and keynote lecures, and oral and poster presentations. Professor Baiulescu participated at most of the Euroanalysis Conferences, Budapest—1975, Helsinki—1981, Cracow—1984, Paris—1987, Vienna—1990, Edinburgh—1993, Bologna—1996, where he presented a keynote entitled Sampling, Basel—1998, Lisbon—2000, Dortmund—2002, Salamanca—2004 and Antwerp—2007. He was invited as plenary lecturer at Sassari, Italy (1976), Zaragoza, Spain (1983), Chiba, Japan (1991), Gdansk, Poland (1986, 1990, 1997, 1998 and 2001), Changchun, China (1994), Mansoura (1997) and Cairo (1998), Egypt. He presented a plenary lecture at the meeting of the Chemical Society, England, 1980, the theme of this lecture was to evidence the importance of method–instrument, man–instrument and method–man–instrument correlations.

One of the passions of George was to climb mountains, and his favorite mountain was Piatra Craiului, where he marked some mountain ways. All he made in his life was done with enthusiasm and energy, and he had capacity to send these to all his coworkers. George-Emil Baiulescu was a great personality, a mentor for all his Ph.D. students and not only for them.

The most important conclusion that characterizes Professor Baiulescu is "The age of each person is the age of his soul". He will be a model for me and I hope that he will be proud about all I will do in my life.

Anca-Iulia Stoica
Deparment of Analytical Chemistry,
Faculty of Chemistry, University of Bucarest,
030018 Bucharest-3, Romania
E-mail address: anca_stoica2003@yahoo.com

Available online 29 October 2009

Talanta

The International Journal of Pure and Applied Analytical Chemistry

Aims & Scope

Talanta provides a forum for the publication of original research papers, preliminary communications, and critical reviews in all branches of pure and applied analytical chemistry. Papers are evaluated based on established guidelines, including the fundamental nature of the study, scientific novelty, substantial improvement or advantage over existing technology or methods, and demonstrated analytical applicability. Original research papers on fundamental studies, and novel sensor and instrumentation development, are especially encouraged. Novel or improved applications in areas such as clinical and biological chemistry, environmental analysis, geochemistry, and materials science and engineering are welcome.

Analytical performance of methods should be determined, including interference and matrix effects, and methods should be validated by comparison with a standard method, or analysis of a certified reference material. The developed method should especially comprise information on selectivity, sensitivity, detection limits, accuracy, and reliability. However, applying official validation or robustness studies to a routine method or technique does not necessarily constitute novelty. Proper statistical treatment of the data should be provided. Relevant literature should be cited, including related publications by the authors, and authors should discuss how their proposed methodology compares with previously reported methods.

Since classical spectrophotometric measurements and applications (including derivative spectrophometry), fluorimetry, solvent extraction, titrimetry, chemometrics, etc. are well established and are considered routine analytical methods, studies in such areas should demonstrate a unique and substantial advantage over presently known systems. New reagents or systems should demonstrate clear advantage, and their presentation should be comprehensive rather than generating a series of similar papers for several analytes or similar reagents. Modifications of reagents should demonstrate significant improvements. Obvious application of known chemistries or methods to established instrumental techniques are discouraged.

Application of established analytical approaches to relatively simple matrices having no major interferences, such as pharmaceutical preparations, are discouraged unless considerable improvements over other methods in the literature are demonstrated. Papers dealing with analytical data such as stability constants, pK_a values, etc. should be submitted to more specific journals, unless novel analytical methodology is demonstrated, or important analytical data are provided which could be useful in the development of analytical procedures.

Editors-in-Chief

Professor G.D. Christian, University of Washington, Department of Chemistry, 36 Bagely Hall, P.O. Box 351700, Seattle,WA 98195-1700, U.S.A.

Professor J.-M. Kauffmann, Université Libre de Bruxelles, Institut de Pharmacie, Campus de la Plaine, C.P. 205/6, Boulevard du Triomphe, B-1050 Bruxelles, Belgium

Associate Editors

Professor J.-H. Wang, Research Center for Analytical Sciences, Northeastern University, Box 332, Shenyang 110004, China

Professor J.L. Burguera, Los Andes University, IVAIQUIM, Faculty of Sciences, P.O. Box 542, 5101-A Mérida, Venezuela.

Assistant Editors

Dr R.E. Synovec, Department of Chemistry, University of Washington, Box 351700, Seattle, WA 98195-1700, U.S.A.

Professor J.-C. Vire, Université Libre de Bruxelles, Institut de Pharmacie, Campus de la Plaine, C.P. 205/6, Boulevard du Triomphe, B-1050 Bruxelles, Belgium

Talanta

R. Apak (Istanbul, Turkey)
E. Bakker (Auburn, AL, U.S.A.)
D. Barceló (Barcelona, Spain)
B. Birch (Luton, UK)
K. S. Booksh (Tempe, AZ, U.S.A.)
J.-L. Capelo-Martinez (Caparica, Portugal)
Z. Cai (Kowloon, Hong Kong)
O. Chailapakul (Thailand)
S. Cosnier (Grenoble, France)
D. Diamond (Dublin, Ireland)
W. Frenzel (Berlin, Germany)
A.G. Gonzales (Seville, Spain)
P. de B. Harrington (OH, U.S.A.)
A. Ho (Hsin-chu, Taiwan)
P. Hubert (Liège, Belgium)
J. Kalivas (Pocatella, ID, U.S.A.)
B. Karlberg (Stockholm, Sweden)
A.A. Karyakin (Moscow, Russia)
J.-M. Lin (Beijing, China)
Y. Lin (Richland, WA, U.S.A.)
M.D. Luque de Caastro (Cordoba, Spain)
I.D. McKelvie (Victoria, Australia)
S. Motomizu (Okayama, Japan)
J.-M. Pingarron (Madrid, Spain)
E. Pretsch (Zürich, Switzerland)
W. Schuhmann (Bochum, Germany)
M. Shamsipur (Kermanshah, Iran)
M. Silva (Porto Alegre, Brazil)
P. Solich (Hradec Králové, Czech Republic)
K. Suzuki (Yokohama, Japan)
D.G. Themelis (Thessaloniki, Greece)
D.L. Tsalev (Sofia, Bulgaria)
B. Walzcak (Katowice, Poland)
J. Wang (Tempe, AZ, U.S.A.)
J.D. Winefordner (Gainesville, U.S.A)
Xiu-Ping Yan (Tianjin, China)
E.A.G. Zagatto (Piracicaba, SP, Brazil)
X. Zhang (Beijing, China)

Copyright © 2009 Elsevier B.V. All rights reserved

Contents lists available at ScienceDirect

Talanta

journal homepage: www.elsevier.com/locate/talanta

Calendar of forthcoming meetings

25–30 April 2010
Pattaya, Thailand
ICFIA 16
16th International Conference on Flow Injection Analysis, including Related Techniques
http://www.science.cmu.ac.th/icfia2010/

26–28 May 2010
Glasgow, UK
Biosensors 2010: The Eleventh World Congress on Biosensors. URL: http://www.biosensors-congress.elsevier.com

1–4 June 2010
Ghent, Belgium
Sixth International Symposium on Hormone and Veterinary Drug Residue Analysis
E-Mail: vdra@ugent.be
URL: www.vdra.ugent.be

May 30 – June 4, 2010
Riva del Garda, Italy
34th International Symposium on Capillary Chromatography and 7th GCxGC Symposium
Chairman: Prof. Dr. P. Sandra
E-mail: riva2010@richrom.com
URL : www.richrom.com

12–15 September 2010
Stockholm, Sweden
13th Symposium on Preparative and Industrial Chromatography and Allied Techniques
URL: www.spica2010.se/

20–23 September 2010
Antwerp, Belgium
Drug Analysis. URL: www.druganalysis.org

17–21 October 2010
Raleigh, NC
FACSS 2010
URL: http://facss.org

18–21 October 2010
Antwerp, Belgium
12th International Conference on Chemometrics in Analytical Chemistry (CAC 2010)
URL: http://www.ua.ac.be/main.aspx?c=.CAC2010&n=78007

8–10 December 2010
Nagoya, Japan
International Conference on Polymer Analysis and Characterization & 15th Symposium on Polymer Analysis in Japan.
Contact: ohtani.hajime@nitech.ac.jp

doi:10.1016/S0039-9140(10)00074-3